IFMBE Proceedings

Lim · Goh (Eds.)

Volume 23

ICBME 2008 – 13th International Conference on Biomedical Engineering

3 – 6 December 2008, Singapore



Springer

IFMBE Proceedings Volume 23/1

Series Editors: R. Magjarevic and J. H. Nagel

The International Federation for Medical and Biological Engineering, IFMBE, is a federation of national and transnational organizations representing internationally the interests of medical and biological engineering and sciences. The IFMBE is a non-profit organization fostering the creation, dissemination and application of medical and biological engineering knowledge and the management of technology for improved health and quality of life. Its activities include participation in the formulation of public policy and the dissemination of information through publications and forums. Within the field of medical, clinical, and biological engineering, IFMBE's aims are to encourage research and the application of knowledge, and to disseminate information and promote collaboration. The objectives of the IFMBE are scientific, technological, literary, and educational.

The IFMBE is a WHO accredited NGO covering the full range of biomedical and clinical engineering, healthcare, healthcare technology and management. It is representing through its 58 member societies some 120.000 professionals involved in the various issues of improved health and health care delivery.

IFMBE Officers
President: Makoto Kikuchi, Vice-President: Herbert Voigt, Former-President: Joachim H. Nagel
Treasurer: Shankar M. Krishnan, Secretary-General: Ratko Magjarevic
http://www.ifmbe.org

Previous Editions:

IFMBE Proceedings ICBME 2008, "13th International Conference on Biomedical Engineering"
Vol. 23, 2008, Singapore, CD

IFMBE Proceedings ECIFMBE 2008 "4th European Conference of the International Federation for Medical and Biological Engineering", Vol. 22, 2008, Antwerp, Belgium, CD

IFMBE Proceedings BIOMED 2008 "4th Kuala Lumpur International Conference on Biomedical Engineering",
Vol. 21, 2008, Kuala Lumpur, Malaysia, CD

IFMBE Proceedings NBC 2008 "14th Nordic-Baltic Conference on Biomedical Engineering and Medical Physics",
Vol. 20, 2008, Riga, Latvia, CD

IFMBE Proceedings APCMBE 2008 "7th Asian-Pacific Conference on Medical and Biological Engineering",
Vol. 19, 2008, Beijing, China, CD

IFMBE Proceedings CLAIB 2007 "IV Latin American Congress on Biomedical Engineering 2007, Bioengineering Solution for Latin America Health", Vol. 18, 2007, Margarita Island, Venezuela, CD

IFMBE Proceedings ICEBI 2007 "13th International Conference on Electrical Bioimpedance and the 8th Conference on Electrical Impedance Tomography", Vol. 17, 2007, Graz, Austria, CD

IFMBE Proceedings MEDICON 2007 "11th Mediterranean Conference on Medical and Biological Engineering and Computing 2007", Vol. 16, 2007, Ljubljana, Slovenia, CD

IFMBE Proceedings BIOMED 2006 "Kuala Lumpur International Conference on Biomedical Engineering",
Vol. 15, 2004, Kuala Lumpur, Malaysia, CD

IFMBE Proceedings WC 2006 "World Congress on Medical Physics and Biomedical Engineering",
Vol. 14, 2006, Seoul, Korea, DVD

IFMBE Proceedings BSN 2007 "4th International Workshop on Wearable and Implantable Body Sensor Networks",
Vol. 13, 2006, Aachen, Germany

IFMBE Proceedings ICBMEC 2005 "The 12th International Conference on Biomedical Engineering",
Vol. 12, 2005, Singapore, CD

IFMBE Proceedings EMBEC'05 "3rd European Medical & Biological Engineering Conference, IFMBE European Conference on Biomedical Engineering", Vol. 11, 2005, Prague, Czech Republic, CD

IFMBE Proceedings ICCE 2005 "The 7th International Conference on Cellular Engineering",
Vol. 10, 2005, Seoul, Korea, CD

IFMBE Proceedings NBC 2005 "13th Nordic Baltic Conference on Biomedical Engineering and Medical Physics",
Vol. 9, 2005, Umeå, Sweden

IFMBE Proceedings APCMBE 2005 "6th Asian-Pacific Conference on Medical and Biological Engineering",
Vol. 8, 2005, Tsukuba, Japan, CD

IFMBE Proceedings BIOMED 2004 "Kuala Lumpur International Conference on Biomedical Engineering",
Vol. 7, 2004, Kuala Lumpur, Malaysia

IFMBE Proceedings MEDICON and HEALTH TELEMATICS 2004 "X Mediterranean Conference on Medical and Biological Engineering", Vol. 6, 2004, Ischia, Italy, CD

IFMBE Proceedings Vol. 23/1
Chwee Teck Lim · James C.H. Goh (Eds.)

13th International Conference on Biomedical Engineering

ICBME 2008
3–6 December 2008
Singapore

Springer

IFMBE Proceedings Volume 23/2

Series Editors: R. Magjarevic and J. H. Nagel

The International Federation for Medical and Biological Engineering, IFMBE, is a federation of national and transnational organizations representing internationally the interests of medical and biological engineering and sciences. The IFMBE is a non-profit organization fostering the creation, dissemination and application of medical and biological engineering knowledge and the management of technology for improved health and quality of life. Its activities include participation in the formulation of public policy and the dissemination of information through publications and forums. Within the field of medical, clinical, and biological engineering, IFMBE's aims are to encourage research and the application of knowledge, and to disseminate information and promote collaboration. The objectives of the IFMBE are scientific, technological, literary, and educational.

The IFMBE is a WHO accredited NGO covering the full range of biomedical and clinical engineering, healthcare, healthcare technology and management. It is representing through its 58 member societies some 120.000 professionals involved in the various issues of improved health and health care delivery.

IFMBE Officers
President: Makoto Kikuchi, Vice-President: Herbert Voigt, Former-President: Joachim H. Nagel
Treasurer: Shankar M. Krishnan, Secretary-General: Ratko Magjarevic
http://www.ifmbe.org

Previous Editions:

IFMBE Proceedings ICBME 2008, "13th International Conference on Biomedical Engineering"
Vol. 23, 2008, Singapore, CD

IFMBE Proceedings ECIFMBE 2008 "4th European Conference of the International Federation for Medical and Biological Engineering", Vol. 22, 2008, Antwerp, Belgium, CD

IFMBE Proceedings BIOMED 2008 "4th Kuala Lumpur International Conference on Biomedical Engineering",
Vol. 21, 2008, Kuala Lumpur, Malaysia, CD

IFMBE Proceedings NBC 2008 "14th Nordic-Baltic Conference on Biomedical Engineering and Medical Physics",
Vol. 20, 2008, Riga, Latvia, CD

IFMBE Proceedings APCMBE 2008 "7th Asian-Pacific Conference on Medical and Biological Engineering",
Vol. 19, 2008, Beijing, China, CD

IFMBE Proceedings CLAIB 2007 "IV Latin American Congress on Biomedical Engineering 2007, Bioengineering Solution for Latin America Health", Vol. 18, 2007, Margarita Island, Venezuela, CD

IFMBE Proceedings ICEBI 2007 "13th International Conference on Electrical Bioimpedance and the 8th Conference on Electrical Impedance Tomography", Vol. 17, 2007, Graz, Austria, CD

IFMBE Proceedings MEDICON 2007 "11th Mediterranean Conference on Medical and Biological Engineering and Computing 2007", Vol. 16, 2007, Ljubljana, Slovenia, CD

IFMBE Proceedings BIOMED 2006 "Kuala Lumpur International Conference on Biomedical Engineering",
Vol. 15, 2004, Kuala Lumpur, Malaysia, CD

IFMBE Proceedings WC 2006 "World Congress on Medical Physics and Biomedical Engineering",
Vol. 14, 2006, Seoul, Korea, DVD

IFMBE Proceedings BSN 2007 "4th International Workshop on Wearable and Implantable Body Sensor Networks",
Vol. 13, 2006, Aachen, Germany

IFMBE Proceedings ICBMEC 2005 "The 12th International Conference on Biomedical Engineering",
Vol. 12, 2005, Singapore, CD

IFMBE Proceedings EMBEC'05 "3rd European Medical & Biological Engineering Conference, IFMBE European Conference on Biomedical Engineering", Vol. 11, 2005, Prague, Czech Republic, CD

IFMBE Proceedings ICCE 2005 "The 7th International Conference on Cellular Engineering",
Vol. 10, 2005, Seoul, Korea, CD

IFMBE Proceedings NBC 2005 "13th Nordic Baltic Conference on Biomedical Engineering and Medical Physics",
Vol. 9, 2005, Umeå, Sweden

IFMBE Proceedings APCMBE 2005 "6th Asian-Pacific Conference on Medical and Biological Engineering",
Vol. 8, 2005, Tsukuba, Japan, CD

IFMBE Proceedings BIOMED 2004 "Kuala Lumpur International Conference on Biomedical Engineering",
Vol. 7, 2004, Kuala Lumpur, Malaysia

IFMBE Proceedings MEDICON and HEALTH TELEMATICS 2004 "X Mediterranean Conference on Medical and Biological Engineering", Vol. 6, 2004, Ischia, Italy, CD

IFMBE Proceedings Vol. 23/2
Chwee Teck Lim · James C.H. Goh (Eds.)

13th International Conference on Biomedical Engineering

ICBME 2008
3–6 December 2008
Singapore

Springer

IFMBE Proceedings Volume 23/3

Series Editors: R. Magjarevic and J. H. Nagel

The International Federation for Medical and Biological Engineering, IFMBE, is a federation of national and transnational organizations representing internationally the interests of medical and biological engineering and sciences. The IFMBE is a non-profit organization fostering the creation, dissemination and application of medical and biological engineering knowledge and the management of technology for improved health and quality of life. Its activities include participation in the formulation of public policy and the dissemination of information through publications and forums. Within the field of medical, clinical, and biological engineering, IFMBE's aims are to encourage research and the application of knowledge, and to disseminate information and promote collaboration. The objectives of the IFMBE are scientific, technological, literary, and educational.

The IFMBE is a WHO accredited NGO covering the full range of biomedical and clinical engineering, healthcare, healthcare technology and management. It is representing through its 58 member societies some 120.000 professionals involved in the various issues of improved health and health care delivery.

IFMBE Officers
President: Makoto Kikuchi, Vice-President: Herbert Voigt, Former-President: Joachim H. Nagel
Treasurer: Shankar M. Krishnan, Secretary-General: Ratko Magjarevic
http://www.ifmbe.org

Previous Editions:

IFMBE Proceedings ICBME 2008, "13th International Conference on Biomedical Engineering"
Vol. 23, 2008, Singapore, CD

IFMBE Proceedings ECIFMBE 2008 "4th European Conference of the International Federation for Medical and Biological Engineering", Vol. 22, 2008, Antwerp, Belgium, CD

IFMBE Proceedings BIOMED 2008 "4th Kuala Lumpur International Conference on Biomedical Engineering",
Vol. 21, 2008, Kuala Lumpur, Malaysia, CD

IFMBE Proceedings NBC 2008 "14th Nordic-Baltic Conference on Biomedical Engineering and Medical Physics",
Vol. 20, 2008, Riga, Latvia, CD

IFMBE Proceedings APCMBE 2008 "7th Asian-Pacific Conference on Medical and Biological Engineering",
Vol. 19, 2008, Beijing, China, CD

IFMBE Proceedings CLAIB 2007 "IV Latin American Congress on Biomedical Engineering 2007, Bioengineering Solution for Latin America Health", Vol. 18, 2007, Margarita Island, Venezuela, CD

IFMBE Proceedings ICEBI 2007 "13th International Conference on Electrical Bioimpedance and the 8th Conference on Electrical Impedance Tomography", Vol. 17, 2007, Graz, Austria, CD

IFMBE Proceedings MEDICON 2007 "11th Mediterranean Conference on Medical and Biological Engineering and Computing 2007", Vol. 16, 2007, Ljubljana, Slovenia, CD

IFMBE Proceedings BIOMED 2006 "Kuala Lumpur International Conference on Biomedical Engineering",
Vol. 15, 2004, Kuala Lumpur, Malaysia, CD

IFMBE Proceedings WC 2006 "World Congress on Medical Physics and Biomedical Engineering",
Vol. 14, 2006, Seoul, Korea, DVD

IFMBE Proceedings BSN 2007 "4th International Workshop on Wearable and Implantable Body Sensor Networks",
Vol. 13, 2006, Aachen, Germany

IFMBE Proceedings ICBMEC 2005 "The 12th International Conference on Biomedical Engineering",
Vol. 12, 2005, Singapore, CD

IFMBE Proceedings EMBEC'05 "3rd European Medical & Biological Engineering Conference, IFMBE European Conference on Biomedical Engineering", Vol. 11, 2005, Prague, Czech Republic, CD

IFMBE Proceedings ICCE 2005 "The 7th International Conference on Cellular Engineering",
Vol. 10, 2005, Seoul, Korea, CD

IFMBE Proceedings NBC 2005 "13th Nordic Baltic Conference on Biomedical Engineering and Medical Physics",
Vol. 9, 2005, Umeå, Sweden

IFMBE Proceedings APCMBE 2005 "6th Asian-Pacific Conference on Medical and Biological Engineering",
Vol. 8, 2005, Tsukuba, Japan, CD

IFMBE Proceedings BIOMED 2004 "Kuala Lumpur International Conference on Biomedical Engineering",
Vol. 7, 2004, Kuala Lumpur, Malaysia

IFMBE Proceedings MEDICON and HEALTH TELEMATICS 2004 "X Mediterranean Conference on Medical and Biological Engineering", Vol. 6, 2004, Ischia, Italy, CD

IFMBE Proceedings Vol. 23/3
Chwee Teck Lim · James C.H. Goh (Eds.)

13th International Conference on Biomedical Engineering

ICBME 2008
3–6 December 2008
Singapore

Springer

Editor

Chwee Teck LIM
Division of Bioengineering &
Department of Mechanical Engineering
Faculty of Engineering
National University of Singapore
7 Engineering Drive
1 Block E3A #04-15
Singapore (117574)
Email: ctlim@nus.edu.sg

James C.H. GOH
Department of Orthopaedic Surgery,
YLL School of Medicine & Division of Bioengineering,
Faculty of Engineering & NUS Tissue Engineering
Program, Life Sciences Institute
Level 4, DSO (Kent Ridge) Building
27 Medical Drive
Singapore 117510
Email: dosgohj@nus.edu.sg

ISSN 1680-0737
ISBN-13 978-3-540-92840-9 e-ISBN-13 978-3-540-92841-6

DOI 10.1007/978-3-540-92841-6

Library of Congress Control Number: 2008944088

© International Federation of Medical and Biological Engineering 2009

This work is subject to copyright. All rights are reserved, whether the whole or part of the material is concerned, specifically the rights of translation, reprinting, reuse of illustrations, recitation, broadcasting, reproduction on microfilm or in any other way, and storage in data banks. Duplication of this publication or parts thereof is permitted only under the provisions of the German Copyright Law of September 9, 1965, in its current version, and permissions for use must always be obtained from Springer. Violations are liable to prosecution under the German Copyright Law.

The use of general descriptive names, registered names, trademarks, etc. in this publication does not imply, even in the absence of a specific statement, that such names are exempt from the relevant protective laws and regulations and therefore free for general use.

The IFMBE Proceedings is an Offical Publication of the International Federation for Medical and Biological Engineering (IFMBE)

Typesetting: Data supplied by the authors
Production: le-tex publishing services oHG, Leipzig
Cover design: deblik, Berlin

Printed on acid-free paper

9 8 7 6 5 4 3 2 1

springer.com

About IFMBE

The International Federation for Medical and Biological Engineering (IFMBE) was established in 1959 to provide medical and biological engineering with a vehicle for international collaboration in research and practice of the profession. The Federation has a long history of encouraging and promoting international cooperation and collaboration in the use of science and engineering for improving health and quality of life.

The IFMBE is an organization with membership of national and transnational societies and an International Academy. At present there are 52 national members and 5 transnational members representing a total membership in excess of 120 000 worldwide. An observer category is provided to groups or organizations considering formal affiliation. Personal membership is possible for individuals living in countries without a member society The International Academy includes individuals who have been recognized by the IFMBE for their outstanding contributions to biomedical engineering.

Objectives

The objectives of the International Federation for Medical and Biological Engineering are scientific, technological, literary, and educational. Within the field of medical, clinical and biological engineering it's aims are to encourage research and the application of knowledge, and to disseminate information and promote collaboration.

In pursuit of these aims the Federation engages in the following activities: sponsorship of national and international meetings, publication of official journals, cooperation with other societies and organizations, appointment of commissions on special problems, awarding of prizes and distinctions, establishment of professional standards and ethics within the field, as well as other activities which in the opinion of the General Assembly or the Administrative Council would further the cause of medical, clinical or biological engineering. It promotes the formation of regional, national, international or specialized societies, groups or boards, the coordination of bibliographic or informational services and the improvement of standards in terminology, equipment, methods and safety practices, and the delivery of health care.

The Federation works to promote improved communication and understanding in the world community of engineering, medicine and biology.

Activities

Publications of IFMBE include: the journal *Medical and Biological Engineering and Computing*, the electronic magazine *IFMBE News*, and the Book Series on Biomedical Engineering. In cooperation with its international and regional conferences, IFMBE also publishes the IFMBE Proceedings Series. All publications of the IFMBE are published by Springer Verlag. The Federation has two divisions: Clinical Engineering and Health Care Technology Assessment.

Every three years the IFMBE holds a World Congress on Medical Physics and Biomedical Engineering, organized in cooperation with the IOMP and the IUPESM. In addition, annual, milestone and regional conferences are organized in different regions of the world, such as Asia Pacific, Europe, the Nordic-Baltic and Mediterranean regions, Africa and Latin America.

The administrative council of the IFMBE meets once a year and is the steering body for the IFMBE: The council is subject to the rulings of the General Assembly, which meets every three years.

Information on the activities of the IFMBE can be found on the web site at: http://www.ifmbe.org.

Foreword

On behalf of the organizing committee of the 13th International Conference on Biomedical Engineering, I extend our warmest welcome to you. This series of conference began in 1983 and is jointly organized by the YLL School of Medicine and Faculty of Engineering of the National University of Singapore and the Biomedical Engineering Society (Singapore).

First of all, I want to thank Mr Lim Chuan Poh, Chairman A*STAR who kindly agreed to be our Guest of Honour to give the Opening Address amidst his busy schedule. I am delighted to report that the 13th ICBME has more than 600 participants from 40 countries. We have received very high quality papers and inevitably we had to turndown some papers. We have invited very prominent speakers and each one is an authority in their field of expertise. I am grateful to each one of them for setting aside their valuable time to participate in this conference.

For the first time, the Biomedical Engineering Society (USA) will be sponsoring two symposia, ie "Drug Delivery Systems" and "Systems Biology and Computational Bioengineering". I am thankful to Prof Tom Skalak for his leadership in this initiative. I would also like to acknowledge the contribution of Prof Takami Yamaguchi for organizing the NUS-Tohoku's Global COE workshop within this conference. Thanks also to Prof Fritz Bodem for organizing the symposium, "Space Flight Bioengineering". This year's conference proceedings will be published by Springer as an IFMBE Proceedings Series.

Finally, the success of this conference lies not only in the quality of papers presented but also to a large extent upon the dedicated team efforts of the many volunteers, in particular members of the Organizing Committee and International Advisory Committee. Their dedicated contribution, diligence and encouragement have been exemplary. I would also like to thank the staff at Integrated Meetings Specialist, who have given their best to ensure the smooth running of the conference. Last but not least, I would like to acknowledge with sincere thanks to our sponsors, supporters and exhibitors.

To all our delegates, I hope the 13th ICBME 2008 will be memorable not only from the scientific perspective but in the joy of meeting old friends and making new ones. Do take time to experience Singapore, especially during this year-end festivity.

Best wishes

Prof James Goh
Chairman
13th ICBME Organising Committee

Conference details

Committees
Organising Committee

Conference Advisors
Yong Tien Chew
Eng Hin Lee

Chair
James Goh

Co-Chair
Siew Lok Toh

Secretary
Peter Lee

Asst Secretary
Sangho Kim

Treasurer
Martin Buist

Program
Chwee Teck Lim

Exhibition & Sponsorship
Michael Raghunath

Publicity
Peck Ha Khoo-Tan

Members
Johnny Chee
Chuh Khiun Chong
Chu Sing, Daniel Lim
Mei Kay Lee
Stephen Low
Teddy Ong
Fook Rhu Ong
Subbaraman Ravichandran

International Advisory Committee

An Kai Nan, Mayo Clinic College of Medicine
Leendert Blankevoort, Orthopaedic Research Center
Friedrich Bodem, Mainz University
Cheng Cheng Kung, National Yang Ming University
Cheng Dong, Penn State University
Shu Chien, Univeristy of California, San Diego
Barthes-Biesel Dominique, University of Technology of Compiegne
David Elad, Tel Aviv University
Fan Yu-Bo, Beihang University
Peter J. Hunter, University of Auckland
Walter Herzog, University of Calgary
Fumihiko Kajiya, Okayama University
Roger Kamm, Massachusetts Institute of Technology
Makoto Kikuchi, National Defense Medical College
Kim Sun I, Hanyang University
Chandran Krishnan B, University of Iowa
Kam Leong, Duke University
Lin Feng-Huei, National Taiwan University
Lin Kang Pin, Chung Yuan Christian University
Marc Madou, University of California Urvine
Banchong Mahaisavariya, Mahidol University
Karol Miller, University of Western Australia
Bruce Milthorpe, University of New South Wales
Yannis F. Misirlis, University of Patras
Joachim Nagel, University of Stuttgart
Mark Pearcy, Queensland University of Technology
Robert O. Ritchie, University of California, Berkeley
Savio L. Y. Woo, University of Pittsburg
Takami Yamaguchi, Tohoku University
Ajit P. Yoganathan, Georgia Institute of Technology & Emory University
Zhang Yuan-ting, City University of Hong Kong

Acknowledgments



History of ICBME

In 1983, a number of academics from the Faculty of Medicine and Faculty of Engineering at the National University of Singapore (NUS) organized a Symposium on Biomedical Engineering (chaired by N Krishnamurthy). It was held on NUS Kent Ridge Campus. The scientific meeting attracted great interest from members of both faculties. It also facilitated cross faculty research collaboration. The 2nd Symposium (chaired by J Goh) was held in 1985 at the Sepoy Lines Campus of the Faculty of Medicine with the aim to strengthen collaboration between the two faculties. The keynote speaker was Dr GK Rose, Oswestry, UK. In 1986, the 3rd Symposium (chaired by K Bose & N Krishnamurthy) was organized to promote the theme of "Biomedical Engineering: An Interdisciplinary Approach", it attracted regional participation. The keynote speaker was Prof JP Paul, Strathclyde, UK. It was highly successful and as such motivated the creation of the International Conference on Biomedical Engineering (ICBME). In order to maintain historical continuity, the ICBME series began in 1987 with the 4th ICBME. From 1997 onwards, the ICBME series was jointly organized by Faculty of Engineering & YLL School of Medicine, NUS and the Biomedical Engineering Society (Singapore). The following table shows the growth of the ICBME series over the years:

	Year	Chairs & Co-Chairs	Invited Speakers	Oral Papers	Poster Papers	Total
4th ICBME	1987	AC Liew, K Bose	8	29	10	47
5th ICBME	1988	K Bose, K Ong	7	67	18	92
6th ICBME	1990	YT Chew, K Bose	10	132	34	176
7th ICBME	1992	K Bose, YT Chew	19	140	37	196
8th ICBME	1994	YT Chew, K Bose	25	137	20	182
9th ICBME	1997	K Bose, YT Chew	39	178	23	240
10th ICBME	2000	SH Teoh, EH Lee	34	208	60	302
11th ICBME	2002	J Goh, SL Toh	44	261	150	455
12th ICBME	2005	SL Toh, J Goh	23	370	123	516
13th ICBME	2008	J Goh, SL Toh	36	340	299	675

ICBME 2008
Young Investigator Award Winners

YIA (1st Prize)
A Biofunctional Fibrous Scaffold for the Encapsulation of Human Mesenchymal Stem Cells and its Effects on Stem Cell Differentiation
S. Z. Yow [1], C. H. Quek [2], E. K. F. Yim [1], K. W. Leong [2,3], C. T. Lim [1]
1. National University of Singapore, Singapore
2. Duke University, North Carolina, USA
3. Duke-NUS Graduate Medical School, Singapore

YIA (2nd Prize)
Multi-Physical Simulation of Left-ventricular Blood Flow Based On Patient-specific MRI Data
S. B. S. Krittian, S. Höttges, T. Schenkel, H. Oertel
University of Karlsruhe, Germany

YIA (3rd Prize)
Landing Impact Loads Predispose Osteocartilage to Degeneration
C. H. Yeow [1], S. T. Lau [1], P. V. S. Lee [1,2,3], J . C. H. Goh [1]
1. National University of Singapore, Singapore
2. Defence Medical and Environmental Research Institute, Singapore
3. University of Melbourne, Australia

YIA (Merit)
Investigating Combinatorial Drug Effects on Adhesion and Suspension Cell Types Using a Microfluidic-Based Sensor System
S. Arora [1], C. S. Lim [1], M. Kakran [1], J. Y. A. Foo [1,2], M. K. Sakharkar [1], P. Dixit [1,3], J. Miao [1]
1. Nanyang Technological University, Singapore
2. Singapore General Hospital, Singapore
3. Georgia Institute of Technology, Atlanta, USA

YIA (Merit)
Synergic Combination of Collagen Matrix with Knitted Silk Scaffold Regenerated Ligament with More Native Microstructure in Rabbit Model
X. Chen, Z. Yin, Y.-Y. Qi, L.-L. Wang, H.-W. Ouyang
Zhejiang University, China

YIA (Merit)
Overcoming Multidrug Resistance of Breast Cancer Cells by the Micellar Drug Carriers of mPEG-PCL-graft-cellulose
Y.-T. Chen [1], C.-H. Chen [1], M.-F. Hsieh [1], A. S. Chan [1], I. Liau [2], W.-Y. Tai [2]
1. Chung Yuan Christian University, Taiwan
2. National Chiao Tung University, Taiwan

YIA (Merit)
Three-dimensional Simulation of Blood Flow in Malaria Infection
Y. Imai [1], H. Kondo [1], T. Ishikawa [1], C. T. Lim [2], K. Tsubota [3], T. Yamaguchi [1]
1. Tohoku University, Sendai, Japan
2. National University of Singapore, Singapore
3. Chiba University, Chiba, Japan

ICBME 2008
Outstanding Paper Award Winners

Oral Category

Assessment of the Peripheral Performance and Cortical Effects of SHADE, an Active Device Promoting Ankle Dorsiflexion
S. Pittaccio [1], S. Viscuso [1], F. Tecchio [2], F. Zappasodi [2], M. Rossini [3], L. Magoni [3], S. Pirovano [3]
1. Unità staccata di Lecco, Italy
2. Unità MEG, Ospedale Fatebenefratelli, Italy
3. Centro di Riabilitazione Villa Beretta, Costamasnaga, Italy

Amino Acid Coupled Liposomes for the Effective Management of Parkinsonism
P. Khare, S. K. Jain
Dr H S Gour Vishwavidyalaya, Sagar, MP, India

Transcutaneous Energy Transfer System for Powering Implantable Biomedical Devices
T. Dissanayake [1], D. Budgett [1,2], A. P. Hu [1], S. Malpas [1,2], L. Bennet [1]
1. University of Auckland, New Zealand
2. Telemetry Research, Auckland, New Zealand

Multi-Wavelength Diffuse Reflectance Plots for Mapping Various Chromophores in Human Skin for Non-Invasive Diagnosis
S. Prince, S. Malarvizhi
SRM University, Chennai, India.

Application of the Home Telecare System in the Treatment of Diabetic Foot Syndrome
P. Ladyzynski [1], J. M. Wojcicki [1], P. Foltynski [1], G. Rosinski [2], J. Krzymien [2]
1. Polish Academy of Sciences, Warsaw, Poland
2. Medical University of Warsaw, Warsaw, Poland

Nano-Patterned Poly-ε-caprolactone with Controlled Release of Retinoic Acid and Nerve Growth Factor for Neuronal Regeneration
K. K. Teo, E. K. F. Yim
National University of Singapore, Singapore

Organic Phase Coating of Polymers onto Agarose Microcapsules for Encapsulation of Biomolecules with High Efficiency
J. Bai [1], W. C. Mak [2], X. Y. Chang [1], D. Trau [1]
1. National University of Singapore, Singapore
2. Hong Kong University of Science and Technology, China

Patch-Clamping in Droplet Arrays: Single Cell Positioning via Dielectrophoresis
J. Reboud [1], M. Q. Luong [1,2], C. Rosales [3],L. Yobas [1]
1. Institute of Microelectronics, Singapore
2. National University of Singapore, Singapore
3. Institute of High Performance Computing, Singapore

Statistical Variations of Ultrasound Backscattering From the Blood under Steady Flow
C.-C Huang [1], Y.-H. Lin [2], S.-H Wang [2]
1. Fu Jen Catholic University, Taiwan
2. Chung Yuan Christian University, Taiwan

Postural Sway of the Elderly Males and Females during Quiet Standing and Squat-and-Stand Movement
G. Eom [1], J.-W. Kim [1], B.-K. Park [2], J.-H. Hong [2], S.-C. Chung [1], B.-S. Lee [1], G. Tack [1], Y. Kim [1]
1. Konkuk University, Choongju, Korea
2. Korea University, Seoul, Korea

Computational Simulation of Three-dimensional Tumor Geometry during Radiotherapy
S. Takao, S. Tadano, H. Taguchi, H. Shirato
Hokkaido University, Sapporo, Japan

Flow Imaging and Validation of MR Fluid Motion Tracking
K. K. L. Wong [1,2], R. M. Kelso [1], S. G. Worthley [2], P. Sanders [2], J. Mazumdar [1], D. Abbott [1]
1. University of Adelaide, Australia
2. Royal Adelaide Hospital, Adelaide, Australia

Successful Reproduction of In-Vivo Fracture of an Endovascular Stent in Superficial Femoral Artery Utilizing a Novel Multi-loading Durability Test System
K. Iwasaki, S. Tsubouchi, Y. Hama, M. Umezu
Waseda University, Tokyo, Japan

Fusion Performance of a Bioresorbable Cage Used In Porcine Model of Anterior Lumbar Interbody Fusion
A. S. Abbah [1], C. X. F. Lam [1], K. Yang [1], J. C. H. Goh [1], D. W. Hutmacher [2], H. K. Wong [1]
1. National University of Singapore, Singapore
2. Queensland University of Technology, Australia

A Low-Noise CMOS Receiver Frontend for NMR-based Surgical Guidance
J. Anders [1], S. Reymond [1], G. Boero [1], K. Scheffler [2]
1. Ecole Polytechnique Fédérale de Lausanne, Switzerland
2. University of Basel, Basel, Switzerland

Pseudoelastic alloy devices for spastic elbow relaxation
S. Viscuso [1], S. Pittaccio [1], M. Caimmi [2], G. Gasperini [2], S. Pirovano [2], S. Besseghini [1], F. Molteni [2]
1. Unità staccata di Lecco, Lecco, Italy
2. Centro di Riabilitazione Villa Beretta, Costamasnaga, Italy

Small-world Network for Investigating Functional Connectivity in Bipolar Disorder: A Functional Magnetic Images (fMRI) Study
S. Teng [1,2], P. S. Wang [1,2,3], Y. L. Liao [4], T. C. Yeh [1,2], T. P. Su [1,2], J. C. Hsieh [1,2], Y. T. Wu [1,2]
1. National Yang-Ming University, Taiwan
2. Taipei Veterans General Hospital, Taiwan
3. Taipei Municipal Gan-Dau Hospital, Taiwan
4. National Cheng Kung University, Taiwan

Finite Element Modeling Of Uncemented Implants: Challenges in the Representation of the Press-fit Condition
S. E. Clift
University of Bath, UK

Poster Category

Optimization and Characterization of Sodium MRI Using 8-channel 23Na and 2-channel 1H RX/TX Coil
J. R. James [1,2], C. Lin [1], H. Stark [3], B. M. Dale [4], N. Bansal [1,2]
1. Indiana University School of Medicine, Indianapolis, USA
2. Purdue University, West Lafayette, USA
3. Stark Contrast, MRI Coils Research, Erlangen, Germany
4. Siemens Medical Solutions, Cary, NC, USA

A Test for the Assessment of Reaction Time for Narcotic Rehabilitation Patients
S. G. Patil, T. J. Gale, C. R. Clive
University Of Tasmania, Hobart, Australia

Development of Noninvasive Thrombus Detection System with Near-Infrared Laser and Photomultiplier for Artificial Hearts
S. Tsujimura [1], H. Koguchi [1], T. Yamane [2], T. Tsutsui [3], Y. Sankai [1]
1. University of Tsukuba, Tsukuba, Japan
2. National Institute of Advanced Industrial Science and Technology, Tsukuba, Japan
3. Institute of Clinical Medicine, University of Tsukuba, Tsukuba, Japan

Magnetic field transducers based on the phase characteristics of GMI sensors and aimed at biomedical applications
E. Costa Silva, L. A. P. Gusmao, C. R. Hall Barbosa, E. Costa Monteiro
Pontifícia Universidade Católica do Rio de Janeiro, Brazil

Windowed Nonlinear Energy Operator-based First-arrival Pulse Detection for Ultrasound Transmission Computed Tomography
S. H. Kim [1], C. H. Kim [2], E. Savastyuk [2], T. Kochiev [2], H.-S. Kim [2], T.-S. Kim [1]
1. Kyung Hee University, Korea
2. Samsung Electro-Mechanics Co. LTD., Korea

Microfabrication of High-density Microelectrode Arrays for in vitro Applications
L. Rousseau [1,2], G. Lissorgues [1,2], F. Verjus [3], B. Yvert [4]
1. ESIEE, France
2. ESYCOM, Université Paris-EST, Marne-La-Vallée, France
3. NXP Caen, Talence, France

Packaging Fluorescent Proteins into HK97 Capsids of Different Maturation Intermediates: A Novel Nano-Particle Biotechnological Application
R. Huang[1,2], K. Lee [2], R. Duda [3], R. Khayat [2], J. Johnson [1,2]
1. University of California, USA
2. The Scripps Research Institute, USA
3. University of Pittsburgh, USA

Design and Implementation of Web-Based Healthcare Management System for Home Healthcare
S. Tsujimura, N. Shiraishi, A. Saito, H. Koba, S. Oshima, T. Sato, F. Ichihashi, Y. Sankai
University of Tsukuba, Tsukuba, Japan

Sensitivity Analysis in Sensor HomeCare Implementation
M. Penhaker [1], R. Bridzik [2], V. Novak [2], M. Cerny [1], M. Rosulek [1]
1. Technical University of Ostrava, Czech Republic
2. University Hospital Ostrava, Czech Republic

Fabrication of Three-Dimensional Tissues with Perfused Microchannels
K. Sakaguchi [1], T. Shimizu [2], K. Iwasaki [1], M. Yamato [2], M. Umezu [1], T. Okano [2]
1. Waseda University, Tokyo, Japan
2. Tokyo Women's Medical University, Twins, Tokyo, Japan

A Serum Free Medium that Conserves The Chondrogenic Phenotype of In Vitro Expanded Chondrocytes
S. T. B. Ho [1], Z. Yang [1], H. P. J. Hu [1], K. W. S. Oh [2], B. H. A. Choo [2], E. H. Lee [1]
1. National University of Singapore, Singapore
2. Bioprocessing Technology Institute, Singapore

Estimating Mechanical Properties of Skin using a Structurally-Based Model
J. W. Y. Jor, M. P. Nash, R. M. F. Nielsen, P. J. Hunter
University of Auckland, New Zealand

The Motility of Normal and Cancer Cells in Response to the Combined Influence of Substrate Rigidity and Anisotropic Nanostructure
T. Tzvetkova-Chevolleau, A. Stephanou, D. Fuard, J. Ohayon, P. Schiavone, P. Tracqui
Centre National de la Recherche Scientifique, France

Accurate Estimation of In Vivo Knee Kinematics from Skin Marker Coordinates with the Global Optimization Method
T.-W Lu, T.-Y. Tsai
National Taiwan University, Taiwan

A Brain-oriented Compartmental Model of Glucose-Insulin-Glucagon Regulatory System
G.-H. Lu, H. Kimura
Institute of Physical and Chemical Research, Nagoya, Japan

Mechanical Loading Response of Human Trabecular Bone Cores
M. Kratz, P. Hans, J. David
Universitat Marburg, Germany

Content

Track 1:
Bioinformatics; Biomedical Imaging; Biomedical instrumentation; Biosignal Processing; Digital Medicine; Neural Systems Engineering

Electroencephalograph Signal Analysis During Ujjayi pranayama 1
Prof. S.T. Patil and Dr. D.S. Bormane

A Study of Stochastic Resonance as a Mathematical Model of Electrogastrography during Sitting Position 5
Y. Matsuura, H. Takada and K. Yokoyama

Possibility of MEG as an Early Diagnosis Tool for Alzheimer's Disease: A Study of Event Related Field in Missing Stimulus Paradigm 9
N. Hatsusaka, M. Higuchi and H. Kado

New Architecture For NN Based Image Compression For Optimized Power, Area And Speed 13
K. Venkata ramanaiah, Cyril Prasanna raj and Dr. K. Lal kishore

A Statistical Model to Estimate Flow Mediated Dilation Using Recorded Finger Photoplethysmogram 18
R. Jaafar, E. Zahedi, M.A. Mohd Ali

Automatic Extraction of Blood Vessels, Bifurcations and End Points in the Retinal Vascular Tree 22
Edoardo Ardizzone, Roberto Pirrone, Orazio Gambino and Francesco Scaturro

Recent Developments in Optimizing Optical Tools for Air Bubble Detection in Medical Devices Used in Fluid Transport 27
S. Ravichandran, R. Shanthini, R.R. Nur Naadhirah, W. Yikai, J. Deviga, M. Prema and L. Clinton

General Purpose Adaptive Biosignal Acquisition System Combining FPGA and FPAA 31
Pedro Antonio Mou, Chang Hao Chen, Sio Hang Pun, Peng Un Mak and Mang I. Vai

Segmentation of Brain MRI and Comparison Using Different Approaches of 2D Seed Growing 35
K.J. Shanthi, M. Sasi Kumar and C. Kesavdas

SQUID Biomagnetometer Systems for Non-invasive Investigation of Spinal Cord Dysfunction 39
Y. Adachi, J. Kawai, M. Miyamoto, G. Uehara, S. Kawabata, M. Tomori, S. Ishii and T. Sato

Human Cardio-Respiro Abnormality Alert System using RFID and GPS - (H-CRAAS) 43
Ahamed Mohideen, Balanagarajan

Automatic Sleep Stage Determination by Conditional Probability: Optimized Expert Knowledge-based Multi-Valued Decision Making 47
Bei Wang, Takenao Sugi, Fusae Kawana, Xingyu Wang and Masatoshi Nakamuara

A Study on the Relation between Stability of EEG and Respiration 51
Young-Sear Kim, Se-Kee Kil, Heung-Ho Choi, Young-Bae Park, Tai-Sung Hur, Hong-Ki Min

The Feature-Based Microscopic Image Segmentation for Thyroid Tissue 55
Y.T. Chen, M.W. Lee, C.J. Hou, S.J. Chen, Y.C. Tsai and T.H. Hsu

Heart Disease Classification Using Discrete Wavelet Transform Coefficients of Isolated Beats 60
G.M. Patil, Dr. K. Subba Rao, K. Satyanarayana

Non-invasive Techniques for Assessing the Endothelial Dysfunction: Ultrasound Versus Photoplethysmography 65
M. Zaheditochai, R. Jaafar, E. Zahedi

High Performance EEG Analysis for Brain Interface **69**
Dr. D.S. Bormane, Prof. S.T. Patil, Dr. D.T. Ingole, Dr. Alka Mahajan

Denoising of Transient Visual Evoked Potential using Wavelets **73**
R. Sivakumar

A Systematic Approach to Understanding Bacterial Responses to Oxygen Using Taverna and Webservices **77**
S. Maleki-Dizaji, M. Rolfe, P. Fisher, M. Holcombe

Permeability of an In Vitro Model of Blood Brain Barrier (BBB) **81**
Rashid Amin, Temiz A. Artmann, Gerhard Artmann, Philip Lazarovici, Peter I. Lelkes

Decision Making Algorithm through LVQ Neural Network for ECG Arrhythmias **85**
Ms. T. Padma, Dr. Madhavi Latha, Mr. K. Jayakumar

A Low-Noise CMOS Receiver Frontend for NMR-based Surgical Guidance **89**
J. Anders, S. Reymond, G. Boero and K. Scheffler

Automated Fluorescence as a System to Assist the Diagnosis of Retinal Blood Vessel Leakage **94**
Vanya Vabrina Valindria, Tati L.R. Mengko, Iwan Sovani

A New Method of Extraction of FECG from Abdominal Signal **98**
D.V. Prasad, R. Swarnalatha

Analysis of EGG Signals for Digestive System Disorders Using Neural Networks **101**
G. Gopu, Dr. R. Neelaveni and Dr. K. Porkumaran

A Reliable Measurement to Assess Atherosclerosis of Differential Arterial Systems **105**
Hsien-Tsai Wu, Cyuan-Cin Liu, Po-Chun Hsu, Huo-Ying Chang and An-Bang Liu

An Automated Segmentation Algorithm for Medical Images **109**
C.S. Leo, C.C. Tchoyoson Lim, V. Suneetha

Quantitative Assessment of Movement Disorders in Clinical Practice **112**
Á. Jobbágy, I. Valálik

Design and Intra-operative Studies of an Economic Versatile Portable Biopotential Recorder **116**
V. Sajith, A. Sukeshkumar, Keshav Mohan

Comparison of Various Imaging Modes for Photoacoustic Tomography **121**
Chi Zhang and Yuanyuan Wang

Ultrasonographic Segmentation of Cervical Lymph Nodes Based on Graph Cut with Elliptical Shape Prior **125**
J.H. Zhang, Y.Y. Wang and C. Zhang

Computerized Assessment of Excessive Femoral and Tibial Torsional Deformation by 3D Anatomical Landmarks Referencing **129**
K. Subburaj, B. Ravi and M.G. Agarwal

Modeling the Microstructure of Neonatal EEG Sleep Stages by Temporal Profiles **133**
V. Krajča, S. Petránek, J. Mohylová, K. Paul, V. Gerlaand L. Lhotská

Optimization and Characterization of Sodium MRI Using 8-channel ^{23}Na and 2-channel ^{1}H RX/TX Coil **138**
J.R. James, C. Lin, H. Stark, B.M. Dale, N. Bansal

Non-invasive Controlled Radiofrequency Hyperthermia Using an MR Scanner and a Paramagnetic Thulium Complex **142**
J.R. James, V.C. Soon, S.M. Topper, Y. Gao, N. Bansal

Automatic Processing of EEG-EOG-EMG Artifacts in Sleep Stage Classification **146**
S. Devuyst, T. Dutoit, T. Ravet, P. Stenuit, M. Kerkhofs, E. Stanus

Medical Image Registration Using Mutual Information Similarity Measure **151**
Mohamed E. Khalifa, Haitham M. Elmessiry, Khaled M. ElBahnasy, Hassan M.M. Ramadan

A Feasibility Study of Commercially Available Audio Transducers in ABR Studies **156**
A. De Silva, M. Schier

Simultaneous Measurement of PPG and Functional MRI **161**
S.C. Chung, M.H. Choi, S.J. Lee, J.H. Jun, G.M. Eom, B. Lee and G.R. Tack

A Study on the Cerebral Lateralization Index using Intensity of BOLD Signal of functional Magnetic Resonance Imaging **165**
M.H. Choi, S.J. Lee, G.R. Tack, G.M. Eom, J.H. Jun, B. Lee and S.C. Chung

A Comparison of Two Synchronization Measures for Neural Data **169**
H. Perko, M. Hartmann and T. Kluge

Protein Classification Using Decision Trees With Bottom-up Classification Approach **174**
Bojan Pepik, Slobodan Kalajdziski, Danco Davcev, Member IEEE

Extracting Speech Signals using Independent Component Analysis **179**
Charles T.M. Choi and Yi-Hsuan Lee

Age-Related Changes in Specific Harmonic Indices of Pressure Pulse Waveform **183**
Sheng-Hung Wang, Tse-Lin Hsu, Ming-Yie Jan, Yuh-Ying Lin Wang and Wei-Kung Wang

Processing of NMR Slices for Preparation of Multi-dimensional Model **186**
J. Mikulka, E. Gescheidtova and K. Bartusek

Application of Advanced Methods of NMR Image Segmentation for Monitoring the Development of Growing Cultures **190**
J. Mikulka, E. Gescheidtova and K. Bartusek

High-accuracy Myocardial Detection by Combining Level Set Method and 3D NURBS Approximation **194**
T. Fukami, H. Sato, J. Wu, Thet-Thet-Lwin, T. Yuasa, H. Hontani, T. Takeda and T. Akatsuka

Design of a Wireless Intraocular Pressure Monitoring System for a Glaucoma Drainage Implant **198**
T. Kakaday, M. Plunkett, S. McInnes, J.S. Jimmy Li, N.H. Voelcker and J.E. Craig

Integrating FCM and Level Sets for Liver Tumor Segmentation **202**
Bing Nan Li, Chee Kong Chui, S.H. Ong and Stephen Chang

A Research-Centric Server for Medical Image Processing, Statistical Analysis and Modeling **206**
Kuang Boon Beh, Bing Nan Li, J. Zhang, C.H. Yan, S. Chang, R.Q. Yu, S.H. Ong, Chee Kong Chui

An Intelligent Implantable Wireless Shunting System for Hydrocephalus Patients **210**
A. Alkharabsheh, L. Momani, N. Al-Zu'bi and W. Al-Nuaimy

Intelligent Diagnosis of Liver Diseases from Ultrasonic Liver Images: Neural Network Approach **215**
P.T. Karule, S.V. Dudul

A Developed Zeeman Model for HRV Signal Generation in Different Stages of Sleep **219**
Saeedeh Lotfi Mohammad Abad, Nader Jafarnia Dabanloo, Seyed Behnamedin Jameie, Khosro Sadeghniiat.

Two wavelengths Hematocrit Monitoring by Light Transmittance Method **223**
Phimon Phonphruksa and Supan Tungjitkusolmun

Rhythm of the Electromyogram of External Urethral Sphincter during Micturition in Rats **227**
Yen-Ching Chang

Higher Order Spectra based Support Vector Machine for Arrhythmia Classification **231**
K.C. Chua, V. Chandran, U.R. Acharya and C.M. Lim

Transcutaneous Energy Transfer System for Powering Implantable Biomedical Devices **235**
T. Dissanayake, D. Budgett, A.P. Hu, S. Malpas and L. Bennet

A Complexity Measure Based on Modified Zero-Crossing Rate Function for Biomedical Signal Processing **240**
M. Phothisonothai and M. Nakagawa

The Automatic Sleep Stage Diagnosis Method by using SOM **245**
Takamasa Shimada, Kazuhiro Tamura, Tadanori Fukami, Yoichi Saito

A Development of the EEG Telemetry System under Exercising **249**
Noriyuki Dobashi, Kazushige Magatani

Evaluation of Photic Stimulus Response Based on Comparison with the Normal Database in EEG Routine Examination **253**
T. Fukami, F. Ishikawa, T. Shimada, B. Ishikawa and Y. Saito

A Speech Processor for Cochlear Implant using a Simple Dual Path Nonlinear Model of Basilar Membrane **257**
K.H. Kim, S.J. Choi, J.H. Kim

Mechanical and Biological Characterization of Pressureless Sintered Hydroxapatite-Polyetheretherketone Biocomposite **261**
Chang Hengky, Bastari Kelsen, Saraswati, Philip Cheang

Computerized Cephalometric Line Tracing Technique on X-ray Images **265**
C. Sinthanayothin

Brain Activation in Response to Disgustful Face Images with Different Backgrounds **270**
Takamasa Shimada, Hideto Ono, Tadanori Fukami, Yoichi Saito

Automatic Segmentation of Blood Vessels in Colour Retinal Images using Spatial Gabor Filter and Multiscale Analysis **274**
P.C. Siddalingaswamy, K. Gopalakrishna Prabhu

Automated Detection of Optic Disc and Exudates in Retinal Images **277**
P.C. Siddalingaswamy, K. Gopalakrishna Prabhu

Qualitative Studies on the Development of Ultraviolet Sterilization System for Biological Applications **280**
Then Tze Kang, S. Ravichandran, Siti Faradina Bte Isa, Nina Karmiza Bte Kamarozaman, Senthil Kumar

From e-health to Personalised Medicine **284**
N. Pangher

Quantitative Biological Models as Dynamic, User-Generated Online Content **287**
J.R. Lawson, C.M. Lloyd, T. Yu and P.F. Nielsen

Development of Soft Tissue Stiffness Measuring Device for Minimally Invasive Surgery by using Sensing Cum Actuating Method **291**
M.-S. Ju, H.-M. Vong, C.-C.K. Lin and S.-F. Ling

A Novel Method to Describe and Share Complex Mathematical Models of Cellular Physiology **296**
D.P. Nickerson and M.L. Buist

New Paradigm in Journal Reference Management **299**
Casey K. Chan, Yean C. Lee and Victor Lin

Incremental Learning Method for Biological Signal Identification **302**
Tadahiro Oyama, Stephen Karungaru, Satoru Tsuge, Yasue Mitsukura and Minoru Fukumi

Metal Artifact Removal on Dental CT Scanned Images by Using Multi-Layer Entropic Thresholding and Label Filtering Techniques for 3-D Visualization of CT Images **306**
K. Koonsanit, T. Chanwimaluang, D. Gansawat, S. Sotthivirat, W. Narkbuakaew, W. Areeprayolkij, P. Yampri and W. Sinthupinyo

A Vocoder for a Novel Cochlear Implant Stimulating Strategy Based on Virtual Channel Technology 310
Charles T.M. Choi, C.H. Hsu, W.Y. Tsai and Yi Hsuan Lee

Towards a 3D Real Time Renal Calculi Tracking for Extracorporeal Shock Wave Lithotripsy 314
I. Manousakas, J.J. Li

A Novel Multivariate Analysis Method for Bio-Signal Processing 318
H.H. Lin, S.H. Change, Y.J. Chiou, J.H. Lin, T.C. Hsiao

Multi-Wavelength Diffuse Reflectance Plots for Mapping Various Chromophores in Human Skin for Non-Invasive Diagnosis 323
Shanthi Prince and S. Malarvizhi

Diagnosis of Diabetic Retinopathy through Slit Lamp Images 327
J. David, A. Sukesh Kumar and V.V. Vineeth

Tracing of Central Serous Retinopathy from Retinal Fundus Images 331
J. David, A. Sukesh Kumar and V. Viji

A Confidence Measure for Real-time Eye Movement Detection in Video-oculography 335
S.M.H. Jansen, H. Kingma and R.L.M. Peeters

Development of Active Guide-wire for Cardiac Catheterization by Using Ionic Polymer-Metal Composites 340
B.K. Fang, M.S. Ju and C.C.K. Lin

Design and Development of an Interactive Proteomic Website 344
K. Xin Hui, C. Zheng Wei, Sze Siu Kwan and R. Raja

A New Interaction Modality for the Visualization of 3D Models of Human Organ 348
L.T. De Paolis, M. Pulimeno and G. Aloisio

Performance Analysis of Support Vector Machine (SVM) for Optimization of Fuzzy Based Epilepsy Risk Level Classifications from EEG Signal Parameters 351
R. Harikumar, A. Keerthi Vasan, M. Logesh Kumar

A Feasibility Study for the Cancer Therapy Using Cold Plasma 355
D. Kim, B. Gweon, D.B. Kim, W. Choe and J.H. Shin

Equation Chapter 1 Section 1Space State Approach to Study the Effect of Sodium over Cytosolic Calcium Profile 358
Shivendra Tewari and K.R. Pardasani

Preliminary Study of Mapping Brain ATP and Brain pH Using Multivoxel ^{31}P MR Spectroscopy 362
Ren-Hua Wu, Wei-Wen Liu, Yao-Wen Chen, Hui Wang, Zhi-Wei Shen, Karel terBrugge, David J. Mikulis

Brain-Computer Interfaces for Virtual Environment Control 366
G. Edlinger, G. Krausz, C. Groenegress, C. Holzner, C. Guger, M. Slater

FPGA Implementation of Fuzzy (PD&PID) Controller for Insulin Pumps in Diabetes 370
V.K. Sudhaman, R. HariKumar

Position Reconstruction of Awake Rodents by Evaluating Neural Spike Information from Place Cells in the Hippocampus 374
G. Edlinger, G. Krausz, S. Schaffelhofer, C. Guger, J. Brotons-Mas, M. Sanchez-Vives

Heart Rate Variability Response to Stressful Event in Healthy Subjects 378
Chih-Yuan Chuang, Wei-Ru Han and Shuenn-Tsong Young

Automatic Quantitative Analysis of Myocardial Perfusion MRI 381
C. Li and Y. Sun

Visualization of Articular Cartilage Using Magnetic Resonance Imaging Data 386
C.L. Poh and K. Sheah

A Chaotic Detection Method for Steady-State Visual Evoked Potentials **390**
X.Q. Li and Z.D. Deng

Speckle Reduction of Echocardiograms via Wavelet Shrinkage of Ultrasonic RF Signals **395**
K. Nakayama, W. Ohyama, T. Wakabayashi, F. Kimura, S. Tsuruoka and K. Sekioka

Advanced Pre-Surgery Planning by Animated Biomodels in Virtual Reality **399**
T. Mallepree, D. Bergers

Computerized Handwriting Analysis in Children with/without Motor Incoordination **402**
S.H. Chang and N.Y. Yu

The Development of Computer-assisted Assessment in Chinese Handwriting Performance **406**
N.Y. Yu and S.H. Chang

Novel Tools for Quantification of Brain Responses to Music Stimuli **411**
O. Sourina, V.V. Kulish and A. Sourin

An Autocorrection Algorithm for Detection of Misaligned Fingerprints **415**
Sai Krishna Alahari, Abhiram Pothuganti, Eshwar Chandra Vidya Sagar, Venkata Ravi kumar Garnepudi and Ram Prakash Mahidhara

A Low Power Wireless Downlink Transceiver for Implantable Glucose Sensing Biosystems **418**
D.W.Y. Chung, A.C.B. Albason, A.S.L. Lou and A.A.S. Hu

Advances in Automatic Sleep Analysis **422**
B. Ahmed and R. Tafreshi

Early Cancer Diagnosis by Image Processing Sensors Measuring the Conductive or Radiative Heat **427**
G. Gavriloaia, A.M. Ghemigian and A.E. Hurduc

Analysis of Saccadic Eye Movements of Epileptic Patients using Indigenously Designed and Developed Saccadic Diagnostic System **431**
M. Vidapanakanti, Dr. S. Kakarla, S. Katukojwalaand Dr. M.U.R. Naidu

System Design of Ultrasonic Image-guided Focused Ultrasound for Blood Brain Barrier disruption **435**
W.C. Huang, X.Y. Wu, H.L. Liu

A Precise Deconvolution Procedure for Deriving a Fluorescence Decay Waveform of a Biomedical Sample **439**
H. Shibata, M. Ohyanagi and T. Iwata

Laser Speckle Contrast Analysis Using Adaptive Window **444**
H.-Y. Jin, N.V. Thakor, H.-C. Shin

Neural Decoding of Single and Multi-finger Movements Based on ML **448**
H.-C. Shin, M. Schieber and N. Thakor

Maximum Likelihood Method for Finger Motion Recognition from sEMG Signals **452**
Kyoung-Jin Yu, Kab-Mun Cha and Hyun-Chool Shin

Cardiorespiratory Coordination in Rats is Influenced by Autonomic Blockade **456**
M.M. Kabir, M.I. Beig, E. Nalivaiko, D. Abbott and M. Baumert

Influence of White Matter Anisotropy on the Effects of Transcranial Direct Current Stimulation: A Finite Element Study **460**
W.H. Lee, H.S. Seo, S.H. Kim, M.H. Cho, S.Y. Lee and T.-S. Kim

Real-time Detection of Nimodipine Effect on Ischemia Model **465**
G.J. Lee, S.K. Choi, Y.H. Eo, J.E. Lim, J.H. Park, J.H. Han, B.S. Oh and H.K. Park

Windowed Nonlinear Energy Operator-based First-arrival Pulse Detection for Ultrasound Transmission Computed Tomography **468**
S.H. Kim, C.H. Kim, E. Savastyuk, T. Kochiev, H.-S. Kim and T.-S. Kim

Digital Dental Model Analysis **472**
Wisarut Bholsithi, Chanjira Sinthanayothin

Cervical Cell Classification using Fourier Transform **476**
Thanatip Chankong, Nipon Theera-Umpon, Sansanee Auephanwiriyakul

An Oscillometry-Based Approach for Measuring Blood Flow of Brachial Arteries **481**
S.-H. Liu, J.-J. Wang and K.-S. Huang

Fuzzy C-Means Clustering for Myocardial Ischemia Identification with Pulse Waveform Analysis **485**
Shing-Hong Liu, Kang-Ming Chang and Chu-Chang Tyan

Study of the Effect of Short-Time Cold Stress on Heart Rate Variability **490**
J.-J. Wang and C.-C. Chen

A Reflection-Type Pulse Oximeter Using Four Wavelengths Equipped with a Gain-Enhanced Gated-Avalanche-Photodiode **493**
T. Miyata, T. Iwata and T. Araki

Estimation of Central Aortic Blood Pressure using a Noninvasive Automatic Blood Pressure Monitor **497**
Yuan-Ta Shih, Yi-Jung Sun, Chen-Huan Chen, Hao-min Cheng and Hu Wei-Chih

Design of a PDA-based Asthma Peak Flow Monitor System **501**
C.-M. Wu and C.-W. Su

Development of the Tongue Diagnosis System by Using Surface Coating Mirror **505**
Y.J. Jeon, K.H. Kim, H.H. Ryu, J. Lee, S.W. Lee and J.Y. Kim

Design a Moving Artifacts Detection System for a Radial Pulse Wave Analyzer **508**
J. Lee, Y.J. Woo, Y.J. Jeon, Y.J. Lee and J.Y. Kim

A Real-time Interactive Editor for 3D Image Registration **511**
T. McPhail and J. Warren

A Novel Headset with a Transmissive PPG Sensor for Heart Rate Measurement **519**
Kunsoo Shin, Younho Kim, Sanggon Bae, Kunkook Park, Sookwan Kim

Improvement on Signal Strength Detection of Radio Imaging Method for Biomedical Application **523**
I. Hieda and K.C. Nam

Feature Extraction Methods for Tongue Diagnostic System **527**
K.H. Kim, J.-H. Do, Y.J. Jeon, J.-Y. Kim

Mechanical-Scanned Low-Frequency (28-kHz) Ultrasound to Induce localized Blood-Brain Barrier Disruption **532**
C.Y. Ting, C.H. Pan and H.L. Liu

Feasibility Study of Using Ultrasound Stimulation to Enhancing Blood-Brain Barrier Disruption in a Brain Tumor Model **536**
C.H. Pan, C.Y. Ting, C.Y. Huang, P.Y. Chen, K.C. Wei, and H.L. Liu

On Calculating the Time-Varying Elastance Curve of a Radial Artery Using a Miniature Vibration Method **540**
S. Chang, J.-J. Wang, H.-M. Su, C.-P. Liu

A Wide Current Range Readout Circuit with Potentiostat for Amperometric Chemical Sensors **543**
W.Y. Chung, S.C. Cheng, C.C. Chuang, F.R.G. Cruz

Multiple Low-Pressure Sonications to Improve Safety of Focused-Ultrasound Induced Blood-Brain Barrier Disruption: In a 1.5-MHz Transducer Setup **547**
P.H. Hsu, J.J. Wang, K.J. Lin, J.C. Chen and H.L. Liu

Phase Synchronization Index of Vestibular System Activity in Schizophrenia **551**
S. Haghgooie, B.J. Lithgow, C. Gurvich, and J. Kulkarni

Constrained Spatiotemporal ICA and Its Application for fMRI Data Analysis **555**
Tahir Rasheed, Young-Koo Lee, and Tae-Seong Kim

ARGALI : An Automatic Cup-to-Disc Ratio Measurement System for Glaucoma Analysis Using Level-set Image Processing **559**
J. Liu, D.W.K. Wong, J.H. Lim, H. Li, N.M. Tan, Z. Zhang, T.Y. Wong, R. Lavanya

Validation of an In Vivo Model for Monitoring Trabecular Bone Quality Changes Using Micro CT, Archimedes-based Volume Fraction Measurement and Serial Milling **563**
B.H. Kam, M.J. Voor, S. Yang, R. Burden, Jr. and S. Waddell

A Force Sensor System for Evaluation of Behavioural Recovery after Spinal Cord Injury in Rats **566**
Y.C. Wei, M.W. Chang, S.Y. Hou, M.S. Young

Flow Imaging and Validation of MR Fluid Motion Tracking **569**
K.K.L. Wong, R.M. Kelso, S.G. Worthley, P. Sanders, J. Mazumdar and D. Abbott

High Frequency Electromagnetic Thermotherapy for Cancer Treatment **574**
Sheng-Chieh Huang, Chih-Hao Huang, Xi-Zhang Lin, Gwo-Bin Lee

Real-Time Electrocardiogram Waveform Classification Using Self-Organization Neural Network **578**
C.C. Chiu, C.L. Hsu, B.Y. Liau and C.Y. Lan

The Design of Oximeter in Sleep Monitoring **582**
C.H. Lu, J.H. Lin, S.T. Tang, Z.X. You and C.C. Tai

Integration of Image Processing from the Insight Toolkit (ITK) and the Visualization Toolkit (VTK) in Java Language for Medical Imaging Applications **586**
D. Gansawat, W. Jirattiticharoen, S. Sotthivirat, K. Koonsanit, W. Narkbuakaew, P. Yampri and W. Sinthupinyo

ECG Feature Extraction by Multi Resolution Wavelet Analysis based Selective Coefficient Method **590**
Saurabh Pal and Madhuchhanda Mitra

Microarray Image Denoising using Spatial Filtering and Wavelet Transformation **594**
A. Mastrogianni, E. Dermatas and A. Bezerianos

Investigation of a Classification about Time Series Signal Using SOM **598**
Y. Nitta, M. Akutagawa, T. Emoto, T. Okahisa, H. Miyamoto, Y. Ohnishi, M. Nishimura, S. Nakane, R. Kaji, Y. Kinouchi

PCG Spectral Pattern Classification: Approach to Cardiac Energy Signature Identification **602**
Abbas K. Abbas, Rasha Bassam

Characteristic of AEP and SEP for Localization of Evoked Potential by Recalling **606**
K. Mukai, Y. Kaji, F. Shichijou, M. Akutagawa, Y. Kinouchi and H. Nagashino

Automatic Detection of Left and Right Eye in Retinal Fundus Images **610**
N.M. Tan, J. Liu, D.W.K. Wong, J.H. Lim, H. Li, S.B. Patil, W. Yu, T.Y. Wong

Visualizing Occlusal Contact Points Using Laser Surface Dental Scans **615**
L.T. Hiew, S.H. Ong and K.W.C. Foong

Modeling Deep Brain Stimulation **619**
Charles T.M. Choi and Yen-Ting Lee

Implementation of Trajectory Analysis System for Metabolic Syndrome Detection **622**
Hsien-Tsai Wu, Di-Song Yzng, Huo-Ying Chang, An-Bang Liu, Hui-Ming Chung, Ming-Chien Liu and Lee-Kang Wong

Diagnosis of Hearing Disorders and Screening using Artificial Neural Networks based on Distortion Product Otoacoustic Emissions **626**
V.P. Jyothiraj and A. Sukesh Kumar

Detection of Significant Biclusters in Gene Expression Data using Reactive Greedy Randomized Adaptive Search Algorithm 631
Smitha Dharan and Achuthsankar S. Nair

Development of Noninvasive Thrombus Detection System with Near-Infrared Laser and Photomultiplier for Artificial Hearts 635
S. Tsujimura, H. Koguchi, T. Yamane, T. Tsutsui and Y. Sankai

Using Saliency Features for Graphcut Segmentation of Perfusion Kidney Images 639
Dwarikanath Mahapatra and Ying Sun

Low Power Electrocardiogram QRS Detection in Real-Time 643
E. Zoghlami Ayari, R. Tielert and N. Wehn

Analytical Decision Making from Clinical Data- Diagnosis and Classification of Epilepsy Risk Levels from EEG Signals-A Case Study 647
V.K. Sudhaman, Dr. (Mrs.) R. Sukanesh, R. HariKumar

Magnetic field transducers based on the phase characteristics of GMI sensors and aimed at biomedical applications 652
E. Costa Silva, L.A.P. Gusmão, C.R. Hall Barbosa, E. Costa Monteiro

Effects of Task Difficulty and Training of Visuospatial Working Memory Task on Brain Activity 657
Takayasu Ando, Keiko Momose, Keita Tanaka, Keiichi Saito

Retrieval of MR Kidney Images by Incorporating Shape Information in Histogram of Low Level Features 661
D. Mahapatra, S. Roy and Y. Sun

Performance Comparison of Bone Segmentation on Dental CT Images 665
P. Yampri, S. Sotthivirat, D. Gansawat, K. Koonsanit, W. Narkbuakaew, W. Areeprayolkij, W. Sinthupinyo

Multi Scale Assessment of Bone Architecture and Quality from CT Images 669
T. Kalpalatha Reddy, Dr. N. Kumaravel

An Evolutionary Heuristic Approach for Functional Modules Identification from Composite Biological Data 673
I.A. Maraziotis, A. Dragomir and A. Bezerianos

An Empirical Approach for Objective Pain Measurement using Dermal and Cardiac Parameters 678
Shankar K., Dr. Subbiah Bharathi V., Jackson Daniel

A Diagnosis Support System for Finger Tapping Movements Using Magnetic Sensors and Probabilistic Neural Networks 682
K. Shima, T. Tsuji, A. Kandori, M. Yokoe and S. Sakoda

Increasing User Functionality of an Auditory P3 Brain-Computer Interface for Functional Electrical Stimulation Application 687
A.S.J Bentley, C.M. Andrew and L.R. John

An Electroencephalogram Signal based Triggering Circuit for controlling Hand Grasp in Neuroprosthetics 691
G. Karthikeyan, Debdoot Sheet and M. Manjunatha

A Novel Channel Selection Method Based on Partial KL Information Measure for EMG-based Motion Classification 694
T. Shibanoki, K. Shima, T. Tsuji, A. Otsuka and T. Chin

A Mobile Phone for People Suffering From The Locked In Syndrome 699
D. Thiagarajan, Anupama.V. Iyengar

Generating Different Views of Clinical Guidelines Using Ontology Based Semantic Annotation 701
Rajendra Singh Sisodia, Puranjoy Bhattacharya and V. Pallavi

A High-Voltage Discharging System for Extracorporeal Shock-Wave Therapy **706**
I. Manousakas, S.M. Liang, L.R. Wan

Development of the Robot Arm Control System Using Forearm SEMG **710**
Yusuke Wakita, Noboru Takizawa, Kentaro Nagataand Kazushige Magatani

Tissue Classification from Brain Perfusion MR Images Using Expectation-Maximization Algorithm Initialized by Hierarchical Clustering on Whitened Data **714**
Y.T. Wu, Y.C. Chou, C.F. Lu, S.R. Huang and W.Y. Guo

Enhancement of Signal-to-noise Ratio of Peroneal Nerve Somatosensory Evoked Potential Using Independent Component Analysis and Time-Frequency Template **718**
C.I. Hung, Y.R. Yang, R.Y. Wang, W.L. Chou, J.C. Hsieh and Y.T. Wu

Multi-tissue Classification of Diffusion-Weighted Brain Images in Multiple System Atrophy Using Expectation Maximization Algorithm Initialized by Hierarchical Clustering **722**
C.F. Lu, P.S. Wang, B.W. Soong, Y.C. Chou, H.C. Li, Y.T. Wu

Small-world Network for Investigating Functional Connectivity in Bipolar Disorder: A Functional Magnetic Images (fMRI) Study **726**
S. Teng, P.S. Wang, Y.L. Liao, T.-C. Yeh, T.-P. Su, J.C. Hsieh, Y.T. Wu

Fractal Dimension Analysis for Quantifying Brain Atrophy of Multiple System Atrophy of the Cerebellar Type (MSA-C) **730**
Z.Y. Wang, B.W. Soong, P.S. Wang, C.W. Jao, K.K. Shyu, Y.T. Wu

A Novel Method in Detecting CCA Lumen Diameter and IMT in Dynamic B-mode Sonography **734**
D.C. Cheng, Q. Pu, A. Schmidt-Trucksaess, C.H. Liu

Acoustic Imaging of Heart Using Microphone Arrays **738**
H. Kajbaf and H. Ghassemian

Statistical Variations of Ultrasound Backscattering From the Blood under Steady Flow **742**
Chih-Chung Huang, Yi-Hsun Lin, and Shyh-Hau Wang

Employing Microbubbles and High-Frequency Time-Resolved Scanning Acoustic Microscopy for Molecular Imaging **746**
P. Anastasiadis, A.L. Klibanov, C. Layman, W. Bost, P.V. Zinin, R.M. Lemor and J.S. Allen

Application of Fluorescently Labeled Lectins for the Visualization of Biofilms of Pseudomonas Aeruginosa by High-Frequency Time-Resolved Scanning Acoustic Microscopy **750**
P. Anastasiadis, K. Mojica, C. Layman, M.L. Matter, J. Henneman, C. Barnes and J.S. Allen

A Comparative Study for Disease Identification from Heart Auscultation using FFT, Cepstrum and DCT Correlation Coefficients **754**
Swanirbhar Majumder, Saurabh Pal and Pranab Kishore Dutta

Multi Resolution Analysis of Pediatric ECG Signal **758**
Srinivas Kachibhotla, Shamla Mathur

3D CT Craniometric Study of Thai Skulls Revelance to Sex Determination Using ogistic Regression Analysis **761**
S. Rooppakhun, S. Piyasin and K. Sitthiseripratip

Analysis of Quantified Indices of EMG for Evaluation of Parkinson's Disease **765**
B. Sepehri, A. Esteki, G.A. Shahidi and M. Moinodin

A Test for the Assessment of Reaction Time for Narcotic Rehabilitation Patients **769**
S.G. Patil, T.J. Gale and C.R. Clive

Track 2:
Biosensors, Biochips & BioMEMs; Nanobiotechnology

Microdevice for Trapping Circulating Tumor Cells for Cancer Diagnostics **774**
S.J. Tan, L. Yobas, G.Y.H Lee, C.N. Ong and C.T. Lim

In-situ Optical Oxygen Sensing for Bio-artificial Liver Bioreactors **778**
V. Nock, R.J. Blaikie and T. David

Quantitative and Indirect Qualitative Analysis Approach for Nanodiamond Using SEM Images and Raman Response **782**
Niranjana S., B.S. Satyanarayana, U.C. Niranjan and Shounak De

Non-invasive Acquisition of Blood Pulse Using Magnetic Disturbance Technique **786**
Chee Teck Phua, Gaëlle Lissorgues, Bruno Mercier

Microfabrication of high-density microelectrode arrays for in vitro applications **790**
Lionel Rousseau, Gaëlle Lissorgues, Fabrice Verjus, Blaise Yvert

A MEMS-based Impedance Pump Based on a Magnetic Diaphragm **794**
C.Y. Lee, Z.H. Chen, C.Y. Wen, L.M. Fu, H.T. Chang, R.H. Ma

Sample Concentration and Auto-location With Radiate Microstructure Chip for Peptide Analysis by MALDI-MS **799**
Shun-Yuan Chen, Chih-Sheng Yu, Jun-Sheng Wang, Chih-Cheng Huang, Yi-Chiuen Hu

The Synthesis of Iron Oxide Nanoparticles via Seed-Mediated Process and its Cytotoxicity Studies **802**
J.-H. Huang, H.J. Parab, R.S. Liu, T.-C. Lai, M. Hsiao, C.H. Chen, D.-P. Tsai and Y.-K. Hwu

Characterization of Functional Nanomaterials in Cosmetics and its Cytotoxic Effects **806**
J.-H. Huang, H.J. Parab, R.S. Liu, T.-C. Lai, M. Hsiao, C.H. Chen and Y.K. Hwu

Design and Analysis of MEMS based Cantilever Sensor for the Detection of Cardiac Markers in Acute Myocardial Infarction **810**
Sree Vidhya& Lazar Mathew

Integrating Micro Array Probes with Amplifier on Flexible Substrate **813**
J.M. Lin, P.W.Lin and L.C. Pan

Investigating Combinatorial Drug Effects on Adhesion and Suspension Cell Types Using a Microfluidic-Based Sensor System **817**
S. Arora, C.S. Lim, M. Kakran, J.Y.A. Foo, M.K. Sakharkar, P. Dixit, and J. Miao

Organic Phase Coating of Polymers onto Agarose Microcapsules for Encapsulation of Biomolecules with High Efficiency **821**
J. Bai, W.C. Mak, X.Y. Chang and D. Trau

LED Based Sensor System for Non-Invasive Measurement of the Hemoglobin Concentration in Human Blood **825**
U. Timm, E. Lewis, D. McGrath, J. Kraitl and H. Ewald

Amperometric Hydrogen Peroxide Sensors with Multivalent Metal Oxide-Modified Electrodes for Biomedical Analysis **829**
Tesfaye Waryo, Petr Kotzian, Sabina Begić, Petra Bradizlova, Negussie Beyene, Priscilla Baker, Boitumelo Kgarebe, Emir Turkušić, Emmanuel Iwuoha, Karel Vytřas and Kurt Kalcher

Patch-Clamping in Droplet Arrays: Single Cell Positioning via Dielectrophoresis **834**
J. Reboud, M.Q. Luong, C. Rosales and L. Yobas

Label-free Detection of Proteins with Surface-functionalized Silicon Nanowires **838**
R.E. Chee, J.H. Chua, A. Agarwal, S.M. Wong, G.J. Zhang

Bead-based DNA Microarray Fabricated on Porous Polymer Films **842**
J.T. Cheng, J. Li, N.G. Chen, P. Gopalakrishnakone and Y. Zhang

Monolithic CMOS Current-Mode Instrumentation Amplifiers for ECG Signals **846**
S.P. Almazan, L.I. Alunan, F.R. Gomez, J.M. Jarillas, M.T. Gusad and M. Rosales

Cells Separation by Traveling Wave Dielectrophoretic Microfluidic Devices **851**
T. Maturos, K. Jaruwongrangsee, A. Sappat, T. Lomas, A. Wisitsora-at, P. Wanichapichart and A. Tuantranont

A Novel pH Sensor Based on the Swelling of A Hydrogel Membrane **855**
K.F. Chou, Y.C. Lin, H.Y. Chen, S.Y. Huang and Z.Y. Lin

Simulation and Experimental Study of Electrowetting on Dielectric (EWOD) Device for a Droplet Based Polymerase Chain Reaction System **859**
K. Ugsornrat, T. Maturus, A. Jomphoak, T. Pogfai, N.V. Afzulpurkar, A. Wisitsoraat, A. Tuantranont

A Label-Free Impedimetric Immunosensor Based On Humidity Sensing Properties of Barium Strontium Titanate **863**
M. Rasouli, O.K. Tan, L.L. Sun, B.W. Mao and L.H. Gan

Physical Way to Enhance the Quantum Yield and Analyze the Photostability of Fluorescent Gold Clusters **867**
D.F. Juan, C.A.J. Lin, T.Y. Yang, C.J. Ke, S.T. Lin, J.Y. Chen and W.H. Chang

Biocompatibility Study of Gold Nanoparticles to Human Cells **870**
J.H. Fan, W.I. Hung, W.T. Li, J.M. Yeh

Gold Nanorods Modified with Chitosan As Photothermal Agents **874**
Chia-Wei Chang, Chung-Hao Wang and Ching-An Peng

QDs Capped with Enterovirus As Imaging Probes for Drug Screening **878**
Chung-Hao Wang, Ching-An Peng

Elucidation of Driving Force of Neutrophile in Liquid by Cytokine Concentration Gradient **882**
M. Tamagawa and K. Matsumura

Development of a Biochip Using Antibody-covered Gold Nano-particles to Detect Antibiotics Resistance of Specific Bacteria **884**
Jung-Tang Huang, Meng-Ting Chang, Guo-Chen Wang, Hua-Wei Yu and Jeen Lin

Photothermal Ablation of Stem-Cell Like Glioblastoma Using Carbon Nanotubes Functionalized with Anti-CD133 ..... **888**
Chung-Hao Wang, Yao-Jhang Huang and Ching-An Peng

A Design of Smart Dust to Study the Hippocampus **892**
Anupama V. Iyengar, D. Thiagarajan

Determination of Affinity Constant from Microfluidic Binding Assay **894**
D. Tan, P. Roy

Nucleic Acid Sample Preparation from Dengue Virus Using a Chip-Based RNA Extractor in a Self-Contained Microsystem **898**
L. Zhang, Siti R.M. Rafei, L. Xie, Michelle B.-R. Chew, C.S. Premchandra, H.M. Ji, Y. Chen, L. Yobas, R. Rajoo, K.L. Ong, Rosemary Tan, Kelly S.H. Lau, Vincent T.K. Chow, C.K. Heng and K.-H. Teo

In-Vitro Transportation of Drug Molecule by Actin Myosin Motor System **902**
Harsimran Kaur, Suresh Kumar, Inderpreet Kaur, Kashmir Singh and Lalit M. Bharadwaj

Track 3:
Clinical Engineering; Telemedicine & Healthcare; Computer-Assisted Surgery; Medical Robotics; Rehabilitation Engineering & Assistive Technology

Tumour Knee Replacement Planning in a 3D Graphics System **906**
K. Subburaj, B. Ravi and M.G. Agarwal

Color Medical Image Vector Quantization Coding Using K-Means: Retinal Image **911**
Agung W. Setiawan, Andriyan B. Suksmono and Tati R. Mengko

Development of the ECG Detector by Easy Contact for Helping Efficient Rescue Operation **915**
Takahiro Asaoka and Kazushige Magatani

A Navigation System for the Visually Impaired Using Colored Guide Line and RFID Tags **919**
Tatsuya Seto, Yuriko Shiidu, Kenji Yanashima and Kazushige Magatani

A Development of the Equipment Control System Using SEMG **923**
Noboru Takizawa, Yusuke Wakita, Kentaro Nagata, Kazushige Magatani

The Analysis of a Simultaneous Measured Forearm's EMG and f-MRI **927**
Tsubasa Sasaki, Kentaro Nagata, Masato Maeno and Kazushige Magatani

Development of A Device to Detect SPO_2 which is Installed on a Rescue Robot **931**
Yoshiaki Kanaeda, Takahiro Asaoka and Kazushige Magatani

A Estimation Method for Muscular Strength During Recognition of Hand Motion **935**
Takemi Nakano, Kentaro Nagata, Masahumi Yamada and Kazusige Magatani

The Navigation System for the Visually Impaired Using GPS **938**
Tomoyuki Kanno, Kenji Yanashima and Kazushige Magatani

Investigation of Similarities among Human Joints through the Coding System of Human Joint Properties—Part 1 ..... **942**
S.C. Chen, S.T. Hsu, C.L. Liu and C.H. Yu

Investigation of Similarities among Human Joints through the Coding System of Human Joint Properties—Part 2 ..... **946**
S.C. Chen, S.T. Hsu, C.L. Liu and C.H. Yu

Circadian Rhythm Monitoring in HomeCare Systems **950**
M. Cerny, M. Penhaker

Effects of Muscle Vibration on Independent Finger Movements **954**
B.-S. Yang and S.-J. Chen

Modelling Orthodontal Braces for Non-invasive Delivery of Anaesthetics in Dentistry **957**
S. Ravichandran

Assessment of the Peripheral Performance and Cortical Effects of SHADE, an Active Device Promoting Ankle Dorsiflexion **961**
S. Pittaccio, S. Viscuso, F. Tecchio, F. Zappasodi, M. Rossini, L. Magoni, S. Pirovano, S. Besseghini and F. Molteni

A Behavior Mining Method by Visual Features and Activity Sequences in Institution-based Care **966**
J.H. Huang, C.C. Hsia and C.C. Chuang

Chronic Disease Recurrence Prediction Model for Diabetes Mellitus Patients' Long-Term Caring **970**
Chia-Ming Tung, Yu-Hsien Chiu, Chi-Chun Shia

The Study of Correlation between Foot-pressure Distribution and Scoliosis **974**
J.H. Park, S.C. Noh, H.S. Jang, W.J. Yu, M.K. Park and H.H. Choi

Sensitivity Analysis in Sensor HomeCare Implementation **979**
M. Penhaker, R. Bridzik, V. Novak, M. Cerny, M. Rosulek

Fall Detection Unit for Elderly **984**
Arun Kumar, Fazlur Rahman, Tracey Lee

Reduction of Body Sway Can Be Evaluated By Sparse Density during Exposure to Movies on Liquid Crystal Displays **987**
H. Takada, K. Fujikake, M. Omori, S. Hasegawa, T. Watanabe and M. Miyao

Effects of Phototherapy to Shangyingxiang Xue on Patients with Allergic Rhinitis **992**
K.-H. Hu, D.-N. Yan, W.-T. Li

The Study of Neural Correlates on Body Ownership Modulated By the Sense of Agency Using Virtual Reality **996**
W.H. Lee, J.H. Ku, H.R. Lee, K.W. Han, J.S. Park, J.J. Kim, I.Y. Kim and S.I. Kim

Diagnosis and Management of Diabetes Mellitus through a Knowledge-Based System **1000**
Morium Akter, Mohammad Shorif Uddin and Aminul Haque

Modeling and Mechanical Design of a MRI-Guided Robot for Neurosurgery **1004**
Z.D. Hong, C. Yun and L. Zhao

The Study for Multiple Security Mechanism in Healthcare Information System for Elders **1009**
C.Y. Huang and J.L. Su

Individual Movement Trajectories in Smart Homes **1014**
M. Chan, S. Bonhomme, D. Estève, E. Campo

MR Image Reconstruction for Positioning Verification with a Virtual Simulation System for Radiation Therapy **1019**
C.F. Jiang, C.H. Huang, T.S. Su

Experimental setup of hemilarynx model for microlaryngeal surgery applications **1024**
J.Q. Choo, D.P.C. Lau, C.K. Chui, T. Yang, S.H. Teoh

Virtual Total Knee Replacement System Based on VTK **1028**
Hui Ding, Tianzhu Liang, Guangzhi Wang, Wenbo Liu

Motor Learning of Normal Subjects Exercised with a Shoulder-Elbow Rehabilitation Robot **1032**
H.H. Lin, M.S. Ju, C.C.K. Lin, Y.N. Sun and S.M. Chen

Using Virtual Markers to Explore Kinematics of Articular Bearing Surfaces of Knee Joints **1037**
Guangzhi Wang, Zhonglin Zhu, Hui Ding, Xiao Dang, Jing Tang and Yixin Zhou

Simultaneous Recording of Physiological Parameters in Video-EEG Laboratory in Clinical and Research Settings **1042**
R. Bridzik, V. Novák, M. Penhaker

Preliminary Modeling for Intra-Body Communication **1044**
Y.M. Gao, S.H. Pun, P.U. Mak, M. Du and M.I. Vai

Application of the Home Telecare System in the Treatment of Diabetic Foot Syndrome **1049**
P. Ladyzynski, J.M. Wojcicki, P. Foltynski, G. Rosinski, J. Krzymien, B. Mrozikiewicz-Rakowska, K. Migalska-Musial and W. Karnafel

In-vitro Evaluation Method to Measure the Radial Force of Various Stents **1053**
Y. Okamoto, T. Tanaka, H. Kobashi, K. Iwasaki, M. Umezu

Motivating Children with Attention Deficiency Disorder Using Certain Behavior Modification Strategies **1057**
Huang Qunfang Jacklyn, S. Ravichandran

Development of a Walking Robot for Testing Ankle Foot Orthosis- Robot Validation Test **1061**
H.J. Lai, C.H. Yu, W.C. Chen, T.W. Chang, K.J. Lin, C.K. Cheng

Regeneration of Speech in Voice-Loss Patients **1065**
H.R. Sharifzadeh, I.V. McLoughlin and F. Ahmadi

Human Gait Analysis using Wearable Sensors of Acceleration and Angular Velocity **1069**
R. Takeda, S. Tadano, M. Todoh and S. Yoshinari

Deformable Model for Serial Ultrasound Images Segmentation: Application to Computer Assisted Hip Athroplasty **1073**
A. Alfiansyah, K.H. Ng and R. Lamsudin

Bone Segmentation Based On Local Structure Descriptor Driven Active Contour **1077**
A. Alfiansyah, K.H. Ng and R. Lamsudin

An Acoustically-Analytic Approach to Behavioral Patterns for Monitoring Living Activities **1082**
Kuang-Che Liu, Gwo-Lang Yan, Yu-Hsien Chiu, Ming-Shih Tsai, Kao-Chi Chung

Implementation of Smart Medical Home Gateway System for Chronic Patients **1086**
Chun Yu, Jhih-Jyun Yang, Tzu-Chien Hsiao, Pei-Ling Liu, Kai-Ping Yao, Chii-Wann Lin

A Comparative Study of Fuzzy PID Control Algorithm for Position Control Performance Enhancement in a Real-time OS Based Laparoscopic Surgery Robot **1090**
S.J. Song, J.W. Park, J.W. Shin, D.H. Lee, J. Choi and K. Sun

Investigation of the Effect of Acoustic Pressure and Sonication Duration on Focused-Ultrasound Induced Blood-Brain Barrier Disruption **1094**
P.C. Chu, M.C. Hsiao, Y.H. Yang, J.C. Chen, H.L. Liu

Design and Implementation of Web-Based Healthcare Management System for Home Healthcare **1098**
S. Tsujimura, N. Shiraishi, A. Saito, H. Koba, S. Oshima, T. Sato, F. Ichihashi and Y. Sankai

Quantitative Assessment of Left Ventricular Myocardial Motion Using Shape–Constraint Elastic Link Model **1102**
Y. Maeda, W. Ohyama, H. Kawanaka, S. Tsuruoka, T. Shinogi, T. Wakabayashi and K. Sekioka

Assessment of Foot Drop Surgery in Leprosy Subjects Using Frequency Domain Analysis of Foot Pressure Distribution Images **1107**
Bhavesh Parmar

The Development of New Function for ICU/CCU Remote Patient Monitoring System Using a 3G Mobile Phone and Evaluations of the System **1112**
Akinobu Kumabe, Pu Zhang, Yuichi Kogure, Masatake Akutagawa, Yohsuke Kinouchi, Qinyu Zhang

Development of Heart Rate Monitoring for Mobile Telemedicine using Smartphone **1116**
Hun Shim, Jung Hoon Lee, Sung Oh Hwang, Hyung Ro Yoon, Young Ro Yoon

Cognitive Effect of Music for Joggers Using EEG **1120**
J. Srinivasan, K.M. Ashwin Kumar and V. Balasubramanian

System for Conformity Assessment of Electrocardiographs **1124**
M.C. Silva, L.A.P. Gusmão, C.R. Hall Barbosa and E. Costa Monteiro

The Development and Strength Reinforcement of Rapid Prototyping Prosthetic Socket Coated with a Resin Layer for Transtibial Amputee **1128**
C.T. Lu, L.H. Hsu, G.F. Huang, C.W. Lai, H.K. Peng, T.Y. Hong

A New Phototherapy Apparatus Designed for the Curing of Neonatal Jaundice **1132**
C.B. Tzeng, T.S. Wey, M.S. Young

Study to Promote the Treatment Efficiency for Neonatal Jaundice by Simulation **1136**
Alberto E. Chaves Barrantes, C.B. Tzeng and T.S. Wey

Low Back Pain Evaluation for Cyclist using sEMG: A Comparative Study between Bicyclist and Aerobic Cyclist **1140**
J. Srinivasan and V. Balasubramanian

3D Surface Modeling and Clipping of Large Volumetric Data Using Visualization Toolkit Library **1144**
W. Narkbuakaew, S. Sotthivirat, D. Gansawat, P. Yampri, K. Koonsanit, W. Areeprayolkij and W. Sinthupinyo

The Effects of Passive Warm-Up With Ultrasound in Exercise Performance and Muscle Damage **1149**
Fu-Shiu Hsieh, Yi-Pin Wang, T.-W. Lu, Ai-Ting Wang, Chien-Che Huang, Cheng-Che Hsieh

Capacitive Interfaces for Navigation of Electric Powered Wheelchairs **1153**
K. Kaneswaran and K. Arshak

Health Care and Medical Implanted Communications Service **1158**
K. Yekeh Yazdandoost and R. Kohno

MultiAgent System for a Medical Application over Web Technology: A Working Experience **1162**
A. Aguilera, E. Herrera and A. Subero

Collaborative Radiological Diagnosis over the Internet **1166**
A. Aguilera, M. Barmaksoz, M. Ordoñez and A. Subero

HandFlex **1171**
J. Selva Raj, Cyntalia Cipto, Ng Qian Ya, Leow Shi Jie, Isaac Lim Zi Ping and Muhamad Ryan b Mohamad Zah

Treatment Response Monitoring and Prognosis Establishment through an Intelligent Information System **1175**
C. Plaisanu, C. Stefan

A Surgical Training Simulator for Quantitative Assessment of the Anastomotic Technique of Coronary Artery Bypass Grafting **1179**
Y. Park, M. Shinke, N. Kanemitsu, T. Yagi, T. Azuma, Y. Shiraishi, R. Kormos and M. Umezu

Development of Evaluation Test Method for the Possibility of Central Venous Catheter Perforation Caused by the Insertion Angle of a Guidewire and a Dilator **1183**
M. Uematsu, M. Arita, K. Iwasaki, T. Tanaka, T. Ohta, M. Umezu and T. Tsuchiya

The Assessment Of Severely Disabled People To Verify Their Competence To Drive A Motor Vehicle With Evidence Based Protocols **1187**
Peter J. Roake

Track 4:
Artificial Organs; Biomaterials; Controlled Drug Delivery; Tissue Engineering & Regenerative Medicine

Viscoelastic Properties of Elastomers for Small Joint Replacements **1191**
A. Mahomed, D.W.L. Hukins, S.N. Kukureka and D.E.T. Shepherd

Synergic Combination of Collagen Matrix with Knitted Silk Scaffold Regenerated Ligament with More Native Microstructure in Rabbit Model **1195**
Xiao Chen, Zi Yin, Yi-Ying Qi, Lin-Lin Wang, Hong-Wei Ouyang

Preparation, Bioactivity and Antibacterial Effect of Bioactive Glass/Chitosan Biocomposites **1199**
Hanan H. Beherei, Khaled R. Mohamed, Amr I. Mahmoud

Biocompatibility of Metal Sintered Materials in Dependence on Multi-Material Graded Structure **1204**
M. Lodererova, J. Rybnicek, J. Steidl, J. Richter, K. Boivie, R. Karlsen, O. Åsebø

PHBV Microspheres as Tissue Engineering Scaffold for Neurons **1208**
W.H. Chen, B.L. Tang and Y.W. Tong

Fabrication of Three-Dimensional Tissues with Perfused Microchannels **1213**
Katsuhisa Sakaguchi, Tatsuya Shimizu, Kiyotaka Iwasaki, Masayuki Yamato, Mitsuo Umezu, Teruo Okano

The Effects of Pulse Inductively Coupled Plasma on the Properties of Gelatin **1217**
I. Prasertsung, S. Kanokpanont, R. Mongkolnavin and S. Damrongsakkul

Dosimetry of ^{32}P Radiocolloid for Radiotherapy of Brain Cyst **1220**
M. Sadeghi, E. Karimi

Overcoming Multidrug Resistance of Breast Cancer Cells by the Micellar Drug Carriers of mPEG-PCL-graft-cellulose **1224**
Yung-Tsung Chen, Chao-Hsuan Chen, Ming-Fa Hsieh, Ann Shireen Chan, Ian Liau, Wan-Yu Tai

Individual 3D Replacements of Skeletal Defects **1228**
R. Jirman, Z. Horak, J. Mazanek and J. Reznicek

Brain Gate as an Assistive and Solution Providing Technology for Disabled People **1232**
Prof. Shailaja Arjun Patil

Compressive Fatigue and Thermal Compressive Fatigue of Hybrid Resin Base Dental Composites **1236**
M. Javaheri, S.M. Seifi, J. Aghazadeh Mohandesi, F. Shafie

Development of Amphotericin B Loaded PLGA Nanoparticles for Effective Treatment of Visceral Leishmaniasis **1241**
M. Nahar, D. Mishra, V. Dubey, N.K. Jain

Swelling, Dissolution and Disintegration of HPMC in Aqueous Media **1244**
S.C. Joshi and B. Chen

A Comparative Study of Articular Chondrocytes Metabolism on a Biodegradable Polyesterurethane Scaffold and Alginate in Different Oxygen Tension and pH **1248**
S. Karbasi

Effect of Cryopreservation on the Biomechanical Properties of the Intervertebral Discs **1252**
S.K.L. Lam, S.C.W. Chan, V.Y.L. Leung, W.W. Lu, K.M.C. Cheung and K.D.K. Luk

A Serum Free Medium that Conserves The Chondrogenic Phenotype of In Vitro Expanded Chondrocytes **1255**
Saey Tuan Barnabas Ho, Zheng Yang, Hoi Po James Hui, Kah Weng Steve Oh, Boon Hwa Andre Choo and Eng Hin Lee

High Aspect Ratio Fatty Acid Functionalized Strontium Hydroxyapatite Nanorod and PMMA Bone Cement Filler **1258**
W.M. Lam, C.T. Wong, T. Wang, Z.Y. Li, H.B. Pan, W.K. Chan, C. Yang, K.D.K. Luk, M.K. Fong, W.W. Lu

The HIV Dynamics is a Single Input System **1263**
M.J. Mhawej, C.H. Moog and F. Biafore

Evaluation of Collagen-hydroxyapatite Scaffold for Bone Tissue Engineering **1267**
Sangeeta Dey, S. Pal

Effect of Sintering Temperature on Mechanical Properties and Microstructure of Sheep-bone Derived Hydroxyapatite (SHA) **1271**
U. Karacayli, O. Gunduz, S. Salman, L.S. Ozyegin, S. Agathopoulos, and F.N. Oktar

Flow Induced Turbulent Stress Accumulation in Differently Designed Contemporary Bi-leaflet Mitral valves: Dynamic PIV Study **1275**
T. Akutsu, and X.D. Cao

A Biofunctional Fibrous Scaffold for the Encapsulation of Human Mesenchymal Stem Cells and its Effects on Stem Cell Differentiation **1279**
S.Z. Yow, C.H. Quek, E.K.F. Yim, K.W. Leong, C.T. Lim

Potential And Properties Of Plant Proteins For Tissue Engineering Applications 1282
Narendra Reddy and Yiqi Yang

Comparison the Effects of BMP-4 and BMP-7 on Articular Cartilage Repair with Bone Marrow Mesenchymal Stem Cells 1285
Yang Zi Jiang, Yi Ying Qi, Xiao Hui Zou, Lin-Lin Wang, Hong-Wei Ouyang

Local Delivery of Autologous Platelet in Collagen Matrix Synergistically Stimulated In-situ Articular Cartilage Repair..... 1289
Yi Ying Qi, Hong Xin Cai, Xiao Chen, Lin Lin Wang,Yang Zi Jiang, Nguyen Thi Minh Hieu, Hong Wei Ouyang

Bioactive Coating on Newly Developed Composite Hip Prosthesis..... 1293
S. Bag & S. Pal

Development and Validation of a Reverse Phase Liquid Chromatographic Method for Quantitative Estimation of Telmisartan in Human Plasma..... 1297
V. Kabra, V. Agrahari, P. Trivedi

Response of Bone Marrow-derived Stem Cells (MSCs) on Gelatin/Chitosan and Gelatin/Chitooligosaccharide films..... 1301
J. Ratanavaraporn, S. Kanokpanont, Y. Tabata and S. Damrongsakkul

Manufacturing Porous BCP Body by Negative Polymer Replica as a Bone Tissue Engineering Scaffold..... 1305
R. Tolouei, A. Behnamghader, S.K. Sadrnezhaad, M. Daliri

Synthesis and Characterizations of Hydroxyapatite-Poly(ether ether ketone) Nanocomposite: Acellular Simulated Body Fluid Conditioned Study 1309
Sumit Pramanik and Kamal K. Kar

Microspheres of Poly (lactide-co-glycolide acid) (PLGA) for Agaricus Bisporus Lectin Drug Delivery..... 1313
Shuang Zhao, Hexiang Wang, Yen Wah Tong

Hard Tissue Formation by Bone Marrow Stem Cells in Sponge Scaffold with Dextran Coating..... 1316
M. Yoshikawa, Y. Shimomura, N. Tsuji, H. Hayashi, H. Ohgushi

Inactivation of Problematic Micro-organisms in Collagen Based Media by Pulsed Electric Field Treatment (PEF)..... 1320
S. Griffiths, S.J. MacGregor, J.G. Anderson, M. Maclean, J.D.S. Gaylor and M.H. Grant

Development, Optimization and Characterization of Nanoparticle Drug Delivery System of Cisplatin..... 1325
V. Agrahari, V. Kabra, P. Trivedi

Physics underling Topobiology: Space-time Structure underlying the Morphogenetic Process 1329
K. Naitoh

The Properties of Hexagonal ZnO Sensing Thin Film Grown by DC Sputtering on (100) Silicon Substrate..... 1333
Chih Chin Yang, Hung Yu Yang, Je Wei Lee and Shu Wei Chang

Multi-objective Optimization of Cancer Immuno-Chemotherapy..... 1337
K. Lakshmi Kiran, D. Jayachandran and S. Lakshminarayanan

Dip Coating Assisted Polylactic Acid Deposition on Steel Surface: Film Thickness Affected by Drag Force and Gravity..... 1341
P.L. Lin, T.L. Su, H.W. Fang, J.S. Chang, W.C. Chang

Some Properties of a Polymeric Surfactant Derived from Alginate 1344
R. Kukhetpitakwong, C. Hahnvajanawong, D. Preechagoon and W. Khunkitti

Nano-Patterned Poly-ε-caprolactone with Controlled Release of Retinoic Acid and Nerve Growth Factor for Neuronal Regeneration 1348
K.K. Teo, Evelyn K.F. Yim

Exposure of 3T3 mouse Fibroblasts and Collagen to High Intensity Blue Light **1352**
S. Smith, M. Maclean, S.J. MacGregor, J.G. Anderson and M.H. Grant

Preparation of sericin film with different polymers **1356**
Kamol Maikrang, M. Sc., Pornanong Aramwit, Pharm.D., Ph.D.

Fabrication and Bio-active Evolution of Mesoporous SiO_2-CaO-P_2O_5 Sol-gel Glasses **1359**
L.C. Chiu, P.S. Lu, I.L. Chang, L.F. Huang, C.J. Shih

The Influences of the Heat-Treated Temperature on Mesoporous Bioactive Gel Glasses Scaffold in the CaO - SiO_2 - P_2O_5 System **1362**
P.S. Lu, L.C. Chiou, I.L. Chang, C.J. Shih, L.F. Huang

Influence of Surfactant Concentration on Mesoporous Bioactive Glass Scaffolds with Superior in Vitro Bone-Forming Bioactivities **1366**
L.F. Huang, P.S. Lu, L.C. Chiou, I.L. Chang, C.J. Shih

Human Embryonic Stem Cell-derived Mesenchymal Stem Cells and BMP7 Promote Cartilage Repair **1369**
Lin Lin Wang, Yi Ying Qi, Yang Zi Jiang, Xiao Chen, Xing Hui Song, Xiao Hui Zou, Hong Wei Ouyang

Novel Composite Membrane Guides Cortical Bone Regeneration **1373**
You Zhi Cai, Yi Ying Qi, Hong Xin Cai, Xiao Hui Zou, Lin Lin Wang, Hong Wei Ouyang

Morphology and In Vitro Biocompatibility of Hydroxyapatite-Conjugated Gelatin/Thai Silk Fibroin Scaffolds **1377**
S. Tritanipakul, S. Kanokpanont, D.L. Kaplan and S. Damrongsakkul

Development of a Silk-Chitosan Blend Scaffold for Bone Tissue Engineering **1381**
K.S. Ng, X.R. Wong, J.C.H. Goh and S.L. Toh

Effects Of Plasma Treatment On Wounds **1385**
R.S. Tipa, E. Stoffels

Effects of the Electrical Field on the 3T3 Cells **1389**
E. Stoffels, R.S. Tipa, J.W. Bree

^{99m}Tc(I)-tricarbonyl Labeled Histidine-tagged Annexin V for Apoptosis Imaging **1393**
Y.L. Chen, C.C. Wu, Y.C. Lin, Y.H. Pan, T.W. Lee and J.M. Lo

Cell Orientation Affects Human Tendon Stem Cells Differentiation **1397**
Zi Yin, T.M. Hieu Nguyen, Xiao Chen, Hong-Wei Ouyang

Synthesis and Characterization of TiO_2+HA Coatings on Ti-6Al-4V Substrates by Nd-YAG Laser Cladding **1401**
C.S. Chien, C.L. Chiao, T.F. Hong, T.J. Han, T.Y. Kuo

Computational Fluid Dynamics Investigation of the Effect of the Fluid-Induced Shear Stress on Hepatocyte Sandwich Perfusion Culture **1405**
H.L. Leo, L. Xia, S.S. Ng, H.J. Poh, S.F. Zhang, T.M. Cheng, G.F. Xiao, X.Y. Tuo, H. Yu

Preliminary Study on Interactive Control for the Artificial Myocardium by Shape Memory Alloy Fibre **1409**
R. Sakata, Y. Shiraishi, Y. Sato, Y. Saijo, T. Yambe, Y. Luo, D. Jung, A. Baba, M. Yoshizawa, A. Tanaka, T.K. Sugai, F. Sato, M. Umezu, S. Nitta, T. Fujimoto, D. Homma

Synthesis, Surface Characterization and In Vitro Blood Compatibility Studies of the Self-assembled Monolayers (SAMs) Containing Lipid-like Phosphorylethanolamine Terminal Group **1413**
Y.T. Sun, C.Y. Yu and J.C. Lin

Surface Characterization and In-vitro Blood Compatibility Study of the Mixed Self-assembled Monolayers **1418**
C.H. Shen and J.C. Lin

Microscale Visualization of Erythrocyte Deformation by Colliding with a Rigid Surface Using a High-Speed Impinging Jet **1422**
S. Wakasa, T. Yagi, Y. Akimoto, N. Tokunaga, K. Iwasaki and M. Umezu

Development of an Implantable Observation System for Angiogenesis 1426
Y. Inoue, H. Nakagawa, I Saito, T. Isoyama, H. Miura, A. Kouno, T. Ono, S.S. Yamaguchi, W. Shi, A. Kishi, K. Imachi and Y. Abe

New challenge for studying flow-induced blood damage: macroscale modeling and microscale verification..... 1430
T. Yagi, S. Wakasa, N. Tokunaga, Y. Akimoto, T. Akutsu, K. Iwasaki, M. Umezu

Pollen Shape Particles for Pulmonary Drug Delivery: In Vitro Study of Flow and Deposition Properties 1434
Meer Saiful Hassan and Raymond Lau

Effect of Tephrosia Purpurea Pers on Gentamicin Model of Acute Renal Failure 1438
Avijeet Jain, A.K. Singhai

Successful Reproduction of In-Vivo Fracture of an Endovascular Stent in Superficial Femoral Artery Utilizing a Novel Multi-loading Durability Test System 1443
K. Iwasaki, S. Tsubouchi, Y. Hama, M. Umezu

Star-Shaped Porphyrin-polylactide Formed Nanoparticles for Chemo-Photodynamic Dual Therapies 1447
P.S. Lai

Enhanced Cytotoxicity of Doxorubicin by Micellar Photosensitizer-mediated Photochemical Internalization in Drug-resistant MCF-7 Cells 1451
C.Y. Hsu, P.S. Lai, C.L. Pai, M.J. Shieh, N. Nishiyama and K. Kataoka

Amino Acid Coupled Liposomes for the Effective Management of Parkinsonism 1455
P. Khare and S.K. Jain

Corrosion Resistance of Electrolytic Nano-Scale ZrO_2 Film on NiTi Orthodontic Wires in Artificial Saliva 1459
C.C. Chang and S.K. Yen

Stability of Polymeric Hollow Fibers Used in Hemodialysis 1462
M.E. Aksoy, M. Usta and A.H. Ucisik

Estimation of Blood Glucose Level by Sixth order Polynomial 1466
S. Shanthi, Dr. D. Kumar

Dirty Surface – Cleaner Cells? Some Observations with a Bio-Assembled Extracellular Matrix 1469
F.C. Loe, Y. Peng, A. Blocki, A. Thomson, R.R. Lareu, M. Raghunath

Quantitative Immunocytochemistry (QICC)-Based Approach for Antifibrotic Drug Testing in vitro 1473
Wang Zhibo, Tan Khim Nyang and Raghunath Michael

Fusion Performance of a Bioresorbable Cage Used In Porcine Model of Anterior Lumbar Interbody Fusion 1476
A.S. Abbah, C.X.F. Lam, K. Yang, J.C.H. Goh, D.W. Hutmacher, H.K. Wong

Composite PLDLLA/TCP Scaffolds for Bone Engineering: Mechanical and In Vitro Evaluations..... 1480
C.X.F. Lam, R. Olkowski, W. Swieszkowski, K.C. Tan, I. Gibson, D.W. Hutmacher

Effects of Biaxial Mechanical Strain on Esophageal Smooth Muscle Cells..... 1484
W.F. Ong, A.C. Ritchie and K.S. Chian

Characterization of Electrospun Substrates for Ligament Regeneration using Bone Marrow Stromal Cells..... 1488
T.K.H. Teh, J.C.H. Goh, S.L. Toh

Cytotoxicity and Cell Adhesion of PLLA/keratin Composite Fibrous Membranes 1492
Lin Li, Yi Li, Jiashen Li, Arthur F.T. Mak, Frank Ko and Ling Qin

Tissue Transglutaminase as a Biological Tissue Glue 1496
P.P. Panengad, D.I. Zeugolis and M. Raghunath

The Scar-in-a-Jar: Studying Antifibrotic Lead Compounds from the Epigenetic to the Extracellular Level in One Well..... 1499
Z.C.C. Chen, Y. Peng and M. Raghunath

Engineering and Optimization of Peptide-targeted Nanoparticles for DNA and RNA Delivery to Cancer Cells 1503
Ming Wang, Fumitaka Takeshita, Takahiro Ochiya, Andrew D. Miller and Maya Thanou

BMSC Sheets for Ligament Tissue Engineering 1508
E.Y.S. See, S.L. Toh and J.C.H. Goh

In Vivo Study of ACL Regeneration Using Silk Scaffolds In a Pig Model 1512
Haifeng Liu, Hongbin Fan, Siew Lok Toh, James C.H. Goh

Establishing a Coculture System for Ligament-Bone Interface Tissue Engineering 1515
P.F. He, S. Sahoo, J.C. Goh, S.L. Toh

Effect of Atherosclerotic Plaque on Drug Delivery from Drug-eluting Stent 1519
J. Ferdous and C.K. Chong

Perfusion Bioreactors Improve Oxygen Transport and Cell Distribution in Esophageal Smooth Muscle Construct 1523
W.Y. Chan and C.K. Chong

Track 5:
Biomechanics; Cardiovascular Bioengineering; Cellular & Molecular Engineering; Cell & Molecular Mechanics; Computational Bioengineering; Orthopaedics, Prosthetics & Orthotics; Physiological System Modeling

Determination of Material Properties of Cellular Structures Using Time Series of Microscopic Images and Numerical Model of Cell Mechanics 1527
E. Gladilin, M. Schulz, C. Kappel and R. Eils

Analysis of a Biological Reaction of Circulatory System during the Cold Pressure Test – Consideration Based on One-Dimensional Numerical Simulation – 1531
T. Kitawaki, H. Oka, S. Kusachi and R. Himeno

Identification of the Changes in Extent of Loading the TM Joint on the Other Side Owing to the Implantation of Total Joint Replacement 1535
Z. Horak, T. Bouda, R. Jirman, J. Mazanek and J. Reznicek

Effects of Stent Design Parameters on the Aortic Endothelium 1539
Gideon Praveen Kumar & Lazar Mathew

Multi-Physical Simulation of Left-ventricular Blood Flow Based On Patient-specific MRI Data 1542
S.B.S. Krittian, S. Höttges, T. Schenkel and H. Oertel

Spinal Fusion Cage Design 1546
F. Jabbary Aslani, D.W.L. Hukins and D.E.T. Shepherd

Comparison of Micron and Nano Particle Deposition Patterns in a Realistic Human Nasal Cavity 1550
K. Inthavong, S.M. Wang, J. Wen, J.Y. Tu, C.L. Xue

Comparative Study of the Effects of Acute Asthma in Relation to a Recovered Airway Tree on Airflow Patterns 1555
K. Inthavong, Y. Ye, S. Ding, J.Y. Tu

Computational Analysis of Stress Concentration and Wear for Tibial Insert of PS Type Knee Prosthesis under Deep Flexion Motion 1559
M. Todo, Y. Takahashi and R. Nagamine

Push-Pull Effect Simulation by the LBNP Device 1564
J. Hanousek, P. Dosel, J. Petricek and L. Cettl

An Investigation on the Effect of Low Intensity Pulsed Ultrasound on Mechanical Properties of Rabbit Perforated Tibia Bone **1569**
B. Yasrebi and S. Khorramymehr

Influence of Cyclic Change of Distal Resistance on Flow and Deformation in Arterial Stenosis Model **1572**
J. Jie, S. Kobayashi, H. Morikawa, D. Tang, D.N. Ku

Kinematics analysis of a 3-DOF micromanipulator for Micro-Nano Surgery **1576**
Fatemeh Mohandesi, M.H. Korayem

Stress and Reliability Analyses of the Hip Joint Endoprosthesis Ceramic Head with Macro and Micro Shape Deviations **1580**
V. Fuis, P. Janicek and L. Houfek

Pseudoelastic alloy devices for spastic elbow relaxation **1584**
S. Viscuso, S. Pittaccio, M. Caimmi, G. Gasperini, S. Pirovano, S. Besseghini and F. Molteni

Musculoskeletal Analysis of Spine with Kyphosis Due to Compression Fracture of an Osteoporotic Vertebra **1588**
J. Sakamoto, Y. Nakada, H. Murakami, N. Kawahara, J. Oda, K. Tomita and H. Higaki

The Biomechanical Analysis of the Coil Stent and Mesh Stent Expansion in the Angioplasty **1592**
S.I. Chen, C.H. Tsai, J.S. Liu, H.C. Kan, C.M. Yao, L.C. Lee, R.J. Shih, C.Y. Shen1

Effect of Airway Opening Pressure Distribution on Gas Exchange in Inflating Lung **1595**
T.K. Roy, MD PhD

Artificial High – Flexion Knee Customized for Eastern Lifestyle **1597**
S. Sivarasu and L. Mathew

Biomedical Engineering Analysis of the Rupture Risk of Cerebral Aneurysms: Flow Comparison of Three Small Pre-ruptured Versus Six Large Unruptured Cases **1600**
A. Kamoda, T. Yagi, A. Sato, Y. Qian, K. Iwasaki, M. Umezu, T. Akutsu, H. Takao, Y. Murayama

Metrology Applications in Body-Segment Coordinate Systems **1604**
G.A. Turley and M.A. Williams

Finite Element Modeling Of Uncemented Implants: Challenges in the Representation of the Press-fit Condition **1608**
S.E. Clift

Effect of Prosthesis Stiffness and Implant Length on the Stress State in Mandibular Bone with Dental Implants **1611**
M. Todo, K. Irie, Y. Matsushita and K. Koyano

Rheumatoid Arthritis T-lymphocytes "Immature" Phenotype and Attempt of its Correction in Co-culture with Human Thymic Epithelial Cells **1615**
M.V. Goloviznin, N.S. Lakhonina, N.I. Sharova, V.T. Timofeev, R.I. Stryuk, Yu.R. Buldakova

Axial and Angled Pullout Strength of Bone Screws in Normal and Osteoporotic Bone Material **1619**
P.S.D. Patel, D.E.T. Shepherd and D.W.L. Hukins

Experimental Characterization of Pressure Wave Generation and Propagation in Biological Tissues **1623**
M. Benoit, J.H. Giovanola, K. Agbeviade and M. Donnet

Finite Element Analysis into the Foot – Footwear Interaction Using EVA Footwear Foams **1627**
Mohammad Reza Shariatmadari

Age Effects On The Tensile And Stress Relaxation Properties Of Mouse Tail Tendons **1631**
Jolene Liu, Siaw Meng Chou, Kheng Lim Goh

Do trabeculae of femoral head represent a structural optimum? **1636**
H.A. Kim, G.J. Howard, J.L. Cunningham

Gender and Arthroplasty Type Affect Prevalence of Moderate-Severe Pain Post Total Hip Arthroplasty..... 1640
J.A. Singh, S.E. Gabriel and D. Lewallen

Quantification of Polymer Depletion Induced Red Blood Cell Adhesion to Artificial Surfaces..... 1644
Z.W. Zhang and B. Neu

An Investigation on the Effect of Low Intensity Pulsed Ultrasound on Mechanical Properties of Rabbit Perforated Tibia Bone..... 1648
B. Yasrebi and S. Khorramymehr

Integrative Model of Physiological Functions and Its Application to Systems Medicine in Intensive Care Unit 1651
Lu Gaohua and Hidenori Kimura

A Brain-oriented Compartmental Model of Glucose-Insulin-Glucagon Regulatory System 1655
Lu Gaohua and Hidenori Kimura

Linkage of Diisopropylfluorophosphate Exposure and Effects in Rats Using a Physiologically Based Pharmacokinetic and Pharmacodynamic Model..... 1659
K.Y. Seng, S. Teo, K. Chen and K.C. Tan

Blood Flow Rate Measurement Using Intravascular Heat-Exchange Catheter..... 1663
Seng Sing Tan and Chin Tiong Ng

Mechanical and Electromyographic Response to Stimulated Contractions in Paralyzed Tibialis Anterior Post Fatiguing Stimulations 1667
N.Y. Yu and S.H. Chang

Modelling The Transport Of Momentum And Oxygen In An Aerial-Disk Driven Bioreactor Used For Animal Tissue Or Cell Culture..... 1672
K.Y.S. Liow, G.A. Thouas, B.T. Tan, M.C. Thompson and K. Hourigan

Investigation of Hemodynamic Changes in Abdominal Aortic Aneurysms Treated with Fenestrated Endovascular Grafts..... 1676
Zhonghua Sun, Thanapong Chaichana, Yvonne B. Allen, Manas Sangworasil, Supan Tungjitkusolmun, David E. Hartley and Michael M.D. Lawrence-Brown

Bone Morphogenetic Protein-2 and Hyaluronic Acid on Hydroxyapatite-coated Porous Titanium to Repair the Defect of Rabbit's Distal Femu 1680
P. Lei, M. Zhao, L.F. Hui, W.M. Xi

Landing Impact Loads Predispose Osteocartilage To Degeneration 1684
C.H. Yeow, S.T. Lau, Peter V.S. Lee, James C.H. Goh

Drug Addiction as a Non-monotonic Process: a Multiscale Computational Model..... 1688
Y.Z. Levy, D. Levy, J.S. Meyer and H.T. Siegelmann

Adroit Limbs..... 1692
Pradeep Manohar and S. Keerthi Vasan

A Mathematical Model to Study the Regulation of Active Stress Production in GI Smooth Muscle..... 1696
Viveka Gajendiran and Martin L. Buist

Design of Customized Full Contact Shoulder Prosthesis using CT-data & FEA..... 1700
D. Sengupta, U.B. Ghosh and S. Pal

An Interface System to Aid the Design of Rapid Prototyping Prosthetic Socket Coated with a Resin Layer for Transtibial Amputee..... 1704
C.W. Lai, L.H. Hsu, G.F. Huang and S.H. Liu

Correlation of Electrical Impedance with Mechanical Properties in Models of Tissue Mimicking Phantoms..... 1708
Kamalanand Krishnamurthy, B.T.N. Sridhar, P.M. Rajeshwari and Ramakrishnan Swaminathan

Biomechanical Analysis of Influence of Spinal Fixation on Intervertebral Joint Force by Using Musculoskeletal Model **1712**
H. Fukui, J. Sakamoto, H. Murakami, N. Kawahara, J. Oda, K. Tomita and H. Higaki

Preventing Anterior Cruciate Ligament Failure During Impact Compression by Restraining Anterior Tibial Translation or Axial Tibial Rotation **1716**
C.H. Yeow, R.S. Khan, Peter V.S. Lee, James C.H. Goh

The Analysis and Measurement of Interface Pressures between Stump and Rapid Prototyping Prosthetic Socket Coated With a Resin Layer for Transtibial Amputee **1720**
H.K. Peng, L.H. Hsu, G.F. Huang and D.Y. Hong

Analysis of Influence Location of Intervertebral Implant on the Lower Cervical Spine Loading and Stability **1724**
L. Jirkova, Z. Horak

Computational Fluid Analysis of Blood Flow Characteristics in Abdominal Aortic Aneurysms Treated with Suprarenal Endovascular Grafts **1728**
Zhonghua Sun, Thanapong Chaichana, Manas Sangworasil and Supan Tungjitkusolmun

Measuring the 3D-Position of Cementless Hip Implants using Pre- and Postoperative CT Images **1733**
G. Yamako, T. Hiura, K. Nakata, G. Omori, Y. Dohmae, M. Oda, T. Hara

Simulation of Tissue-Engineering Cell Cultures Using a Hybrid Model Combining a Differential Nutrient Equation and Cellular Automata **1737**
Tze-Hung Lin and C.A. Chung

Upconversion Nanoparticles for Imaging Cells **1741**
N. Sounderya, Y. Zhang

Simulation of Cell Growth and Diffusion in Tissue Engineering Scaffolds **1745**
Szu-Ying Ho, Ming-Han Yu and C.A. Chung

Simulation of the Haptotactic Effect on Chondrocytes in the Boyden Chamber Assay **1749**
Chih-Yuan Chen and C.A. Chung

Analyzing the Sub-indices of Hysteresis Loops of Torque-Displacement in PD's **1753**
B. Sepehri, A. Esteki and M. Moinodin

Relative Roles of Cortical and Trabecular Thinning in Reducing Osteoporotic Vertebral Body Stiffness: A Modeling Study **1757**
K. McDonald, P. Little, M. Pearcy, C. Adam

Musculo-tendon Parameters Estimation by Ultrasonography for Modeling of Human Motor System **1761**
L. Lan, L.H. Jin, K.Y. Zhu and C.Y. Wen

Mechanical Vibration Applied in the Absence of Weight Bearing Suggest Improved Fragile Bone **1766**
J. Matsuda, K. Kurata, T. Hara, H. Higaki

A Biomechanical Investigation of Anterior Vertebral Stapling **1769**
M.P. Shillington, C.J. Adam, R.D. Labrom and G.N. Askin

Measurement of Cell Detaching force on Substrates with Different Rigidity by Atomic Force Microscopy **1773**
D.K. Chang, Y.W. Chiou, M.J. Tang and M.L. Yeh

Estimation of Body Segment Parameters Using Dual Energy Absorptiometry and 3-D Exterior Geometry **1777**
M.K. Lee, M. Koh, A.C. Fang, S.N. Le and G. Balasekaran

A New Intraoperative Measurement System for Rotational Motion Properties of the Spine **1781**
K. Kitahara, K. Oribe, K. Hasegawa, T. Hara

Binding of Atherosclerotic Plaque Targeting Nanoparticles to the Activated Endothelial Cells under Static and Flow Condition **1785**
K. Rhee, K.S. Park and G. Khang

Computational Modeling of the Micropipette Aspiration of Malaria Infected Erythrocytes **1788**
G.Y. Jiao, K.S.W. Tan, C.H. Sow, Ming Dao, Subra Suresh, C.T. Lim

Examination of the Microrheology of Intervertebral Disc by Nanoindentation **1792**
J. Lukes, T. Mares, J. Nemecek and S. Otahal

Effects of Floor Material Change on Gait Stability **1797**
B.-S. Yang and H.-Y. Hu

Onto-biology: Inevitability of Five Bases and Twenty Amino-acids **1801**
K. Naitoh

An Improved Methodology for Measuring Facet Contact Forces in the Lumbar Spine **1805**
A.K. Ramruttun, H.K. Wong, J.C.H. Goh, J.N. Ruiz

Multi-scale Models of Gastrointestinal Electrophysiology **1809**
M.L. Buist, A. Corrias and Y.C. Poh

Postural Sway of the Elderly Males and Females during Quiet Standing and Squat-and-Stand Movement **1814**
Gwnagmoon Eom, Jiwon Kim, Byungkyu Park, Jeonghwa Hong, Soonchul Chung, Bongsoo Lee, Gyerae Tack, Yohan Kim

Investigation of Plantar Barefoot Pressure and Soft-tissue Internal Stress: A Three-Dimensional Finite Element Analysis **1817**
Wen-Ming Chen, Peter Vee-Sin Lee, Sung-Jae Lee and Taeyong Lee

The Influence of Load Placement on Postural Sway Parameters **1821**
D. Rugelj and F. Sevšek

Shape Analysis of Postural Sway Area **1825**
F. Sevšek

Concurrent Simulation of Morphogenetic Movements in Drosophila Embryo **1829**
R. Allena, A.-S. Mouronval, E. Farge and D. Aubry

Application of Atomic Force Microscopy to Investigate Axonal Growth of PC-12 Neuron-like Cells **1833**
M.-S. Ju, H.-M. Lan, C.-C.K. Lin

Effect of Irregularities of Graft Inner Wall at the Anastomosis of a Coronary Artery Bypass Graft **1838**
F. Kabinejadian, L.P. Chua, D.N. Ghista and Y.S. Tan

Mechanical Aspects in the Cells Detachment **1842**
M. Buonsanti, M. Cacciola, G. Megali, F.C. Morabito, D. Pellicanò, A. Pontari and M. Versaci

Time Series Prediction of Gene Expression in the SOS DNA Repair Network of Escherichia coli Bacterium Using Neuro-Fuzzy Networks **1846**
R. Manshaei, P. Sobhe Bidari, J. Alirezaie, M.A. Malboobi

Predictability of Blood Glucose in Surgical ICU Patients in Singapore **1850**
V. Lakshmi, P. Loganathan, G.P. Rangaiah, F.G. Chen and S. Lakshminarayanan

Method of Numerical Analysis of Similarity and Differences of Face Shape of Twins **1854**
M. Rychlik, W. Stankiewicz and M. Morzynski

Birds' Flap Frequency Measure Based on Automatic Detection and Tracking in Captured Videos **1858**
Xiao-yan Zhang, Xiao-juan Wu, Xin Zhou, Xiao-gang Wang, Yuan-yuan Zhang

Effects of Upper-Limb Posture on Endpoint Stiffness during Force Targeting Tasks **1862**
Pei-Rong Wang, Ju-Ying Chang and Kao-Chi Chung

Complex Anatomies in Medical Rapid Prototyping **1866**
T. Mallepree, D. Bergers

Early Changes Induced by Low Intensity Ultrasound in Human Hepatocarcinoma Cells **1870**
Y. Feng, M.X. Wan

Visual and Force Feedback-enabled Docking for Rational Drug Design **1874**
O. Sourina, J. Torres and J. Wang

A Coupled Soft Tissue Continuum-Transient Blood flow Model to Investigate the Circulation in Deep Veins of the Calf under Compression **1878**
K. Mithraratne, T. Lavrijsen and P.J. Hunter

Finite Element Analysis of Articular Cartilage Model Considering the Configuration and Biphasic Property of the Tissue **1883**
N. Hosoda, N. Sakai, Y. Sawae and T. Murakami

Principal Component Analysis of Lifting Kinematics and Kinetics in Pregnant Subjects **1888**
T.C. Nguyen, K.J. Reynolds

Evaluation of Anterior Tibial Translation and Muscle Activity during "Front Bridge" Quadriceps Muscle Exercise **1892**
M. Sato, S. Inoue, M. Koyanagi, M. Yoshida, N. Nakae, T. Sakai, K. Hidaka and K. Nakata

Coupled Autoregulation Models **1896**
T. David, S. Alzaidi, R. Chatelin and H. Farr

Measurement of Changes in Mechanical and Viscoelastic Properties of Cancer-induced Rat Tibia by using Nanoindentation **1900**
K.P. Wong, Y.J. Kim and T. Lee

Surface Conduction Analysis of EMG Signal from Forearm Muscles **1904**
Y. Nakajima, S. Yoshinari and S. Tadano

A Distributed Revision Control System for Collaborative Development of Quantitative Biological Models **1908**
T. Yu, J.R. Lawson and R.D. Britten

Symmetrical Leg Behavior during Stair Descent in Able-bodied Subjects **1912**
H. Hobara, Y. Kobayashi, K. Naito and K. Nakazawa

Variable Interaction Structure Based Machine Learning Technique for Cancer Tumor Classification **1915**
Melissa A. Setiawan, Rao Raghuraj and S. Lakshminarayanan

Assessing the Susceptibility to Local Buckling at the Femoral Neck Cortex to Age-Related Bone Loss **1918**
He Xi, B.W. Schafer, W.P. Segars, F. Eckstein, V. Kuhn, T.J. Beck, T. Lee

Revealing Spleen Ad4BP/SF1 Knockout Mouse by BAC-Ad4BP-tTAZ Transgene **1920**
Fatchiyah, M. Zubair, K.I. Morohashi

The impact of enzymatic treatments on red blood cell adhesion to the endothelium in plasma like suspensions **1924**
Y. Yang, L.T. Heng and B. Neu

Comparison of Motion Analysis and Energy Expenditures between Treadmill and Overground Walking **1928**
R.H. Sohn, S.H. Hwang, Y.H. Kim

Simultaneous Strain Measurements of Rotator Cuff Tendons at Varying Arm Positions and The Effect of Supraspinatus Tear: A Cadaveric Study **1931**
J.M. Sheng, S.M. Chou, S.H. Tan, D.T.T. Lie, K.S.A. Yew

Tensile Stress Regulation of NGF and NT3 in Human Dermal Fibroblast **1935**
Mina Kim, J.W. Hong, Minsoo Nho, Yong Joo Na and J.H. Shin

Influence of Component Injury on Dynamic Characteristics on the Spine Using Finite Element Method 1938
J.Z. Li, Serena H.N. Tan, C.H. Cheong, E.C. Teo, L.X. Guo, K.Y. Seng

Local Dynamic Recruitment of Endothelial PECAM-1 to Transmigrating Monocytes 1941
N. Kataoka, K. Hashimoto, E. Nakamura, K. Hagihara, K. Tsujioka, F. Kajiya

A Theoretical Model to Mechanochemical Damage in the Endothelial Cells 1945
M. Buonsanti, M. Cuzzola, A. Pontari, G. Irrera, M.C. Cannatà, R. Piro, P. Iacopino

Effects Of Mechanical Stimulus On Cells Via Multi-Cellular Indentation Device 1949
Sunhee Kim, Jaeyoung Yun and Jennifer H. Shin

The Effect of Tumor-Induced Bone Remodeling and Efficacy of Anti-Resorptive and Chemotherapeutic Treatments in Metastatic Bone Loss 1952
X. Wang, L.S. Fong, X. Chen, X. Yang, P. Maruthappan, Y.J. Kim, T. Lee

Mathematical Modeling of Temperature Distribution on Skin Surface and Inside Biological Tissue with Different Heating 1957
P.R. Sharma, Sazid Ali and V.K. Katiyar

Net Center of Pressure Analysis during Gait Initiation in Patient with Hemiplegia 1962
S.H. Hwang, S.W. Park, H.S. Choi and Y.H. Kim

AFM Study of the Cytoskeletal Structures of Malaria Infected Erythrocytes 1965
H. Shi, A. Li, J. Yin, K.S.W. Tan and C.T. Lim

Adaptive System Identification and Modeling of Respiratory Acoustics 1969
Abbas K. Abbas, Rasha Bassam

Correlation between Lyapunov Exponent and the Movement of Center of Mass during Treadmill Walking 1974
J.H. Park and K. Son

The Development of an EMG-based Upper Extremity Rehabilitation Training System for Hemiplegic Patients 1977
J.S. Son, J.Y. Kim, S.J. Hwang and Youngho Kim

Fabrication of Adhesive Protein Micropatterns In Application of Studying Cell Surface Interactions 1980
Ji Sheng Kiew, Xiaodi Sui, Yeh-Shiu Chu, Jean Paul Thiery and Isabel Rodriguez

Modeling of the human cardiovascular system with its application to the study of the effects of variations in the circle of Willis on cerebral hemodynamics 1984
Fuyou Liang, Shu Takagi and Hao Liu

Low-intensity Ultrasound Induces a Transient Increase in Intracellular Calcium and Enhancement of Nitric Oxide Production in Bovine Aortic Endothelial Cells 1989
S. Konno, N. Sakamoto, Y. Saijo, T. Yambe, M. Sato and S. Nitta

Evaluation of Compliance of Poly (vinyl alcohol) Hydrogel for Development of Arterial Biomodeling 1993
H. Kosukegawa, K. Mamada, K. Kuroki, L. Liu, K. Inoue, T. Hayase and M. Ohta

People Recognition by Kinematics and Kinetics of Gait 1996
Yu-Chih Lin, Bing-Shiang Yang and Yi-Ting Yang

Site-Dependence of Mechanosensitivity in Isolated Osteocytes 2000
Y. Aonuma, T. Adachi, M. Tanaka, M. Hojo, T. Takano-Yamamoto and H. Kamioka

Development of Experimental Devices for Testing of the Biomechanical Systems 2005
L. Houfek, Z. Florian, T. Březina, M. Houfek, T. Návrat, V. Fuis, P. Houška

Stability of Treadmill Walking Related with the Movement of Center of Mass 2009
S.H. Kim, J.H. Park, K. Son

Stress Analyses of the Hip Joint Endoprosthesis Ceramic Head with Different Shapes of the Cone Opening 2012
V. Fuis and J. Varga

Measurement of Lumbar Lordosis using Fluoroscopic Images and Reflective Markers 2016
S.H. Hwang, Y.E. Kim and Y.H. Kim

Patient-Specific Simulation of the Proximal Femur's Mechanical Response Validated by Experimental Observations 2019
Zohar Yosibash and Nir Trabelsi

Design of Prosthetic Skins with Humanlike Softness 2023
J.J. Cabibihan

Effect of Data Selection on the Loss of Balance in the Seated Position 2027
K.H. Kim, K. Son, J.H. Park

The Effect of Elastic Moduli of Restorative Materials on the Stress of Non-Carious Cervical Lesion 2030
W. Kwon, K.H. Kim, K. Son and J.K. Park

Effect of Heat Denaturation of Collagen Matrix on Bone Strength 2034
M. Todoh, S. Tadano and Y. Imari

Non-linear Image-Based Regression of Body Segment Parameters 2038
S.N. Le, M.K. Lee and A.C. Fang

A Motion-based System to Evaluate Infant Movements Using Real-time Video Analysis 2043
Yuko Osawa, Keisuke Shima, Nan Bu, Tokuo Tsuji, Toshio Tsuji, Idaku Ishii, Hiroshi Matsuda, Kensuke Orito, Tomoaki Ikeda and Shunichi Noda

Cardiorespiratory Response Model for Pain and Stress Detection during Endoscopic Sinus Surgery under Local Anesthesia 2048
K. Sakai and T. Matsui

A Study on Correlation between BMI and Oriental Medical Pulse Diagnosis Using Ultrasonic Wave 2052
Y.J. Lee, J. Lee, H.J. Lee, J.Y. Kim

Investigating the Biomechanical Characteristics of Transtibal Stumps with Diabetes Mellitus 2056
C.L. Wu, C.C. Lin, K.J. Wang and C.H. Chang

A New Approach to Evaluation of Reactive Hyperemia Based on Strain-gauge Plethysmography Measurements and Viscoelastic Indices 2059
Abdugheni Kutluk, Takahiro Minari, Kenji Shiba, Toshio Tsuji, Ryuji Nakamura, Noboru Saeki, Masashi Kawamoto, Hidemitsu Miyahara, Yukihito Higashi, Masao Yoshizumi

Electromyography Analysis of Grand Battement in Chinese Dance 2064
Ai-Ting Wang, Yi-Pin Wang, T.-W. Lu, Chien-Che Huang, Cheng-Che Hsieh, Kuo-Wei Tseng, Chih-Chung Hu

Landing Patterns in Subjects with Recurrent Lateral Ankle Sprains 2068
Kuo-Wei Tseng, Yi-Pin Wang, T.-W. Lu, Ai-Ting Wang, Chih-Chung Hu

The Influence of Low Level Near-infrared Irradiation on Rat Bone Marrow Mesenchymal Stem Cells 2072
T.-Y. Hsu, W.-T. Li

Implementation of Fibronectin Patterning with a Raman Spectroscopy Microprobe for Focal Adhesions Studies in Cells 2076
B. Codan, T. Gaiotto, R. Di Niro, R. Marzari and V. Sergo

Parametric Model of Human Cerebral Aneurysms 2079
Hasballah Zakaria and Tati L.R. Mengko

Computational Simulation of Three-dimensional Tumor Geometry during Radiotherapy **2083**
S. Takao, S. Tadano, H. Taguchi and H. Shirato

Finite Element Modeling of Thoracolumnar Spine for Investigation of TB in Spine **2088**
D. Davidson Jebaseelan, C. Jebaraj, S. Rajasekaran

Contact Characteristics during Different High Flexion Activities of the Knee **2092**
Jing-Sheng Li, Kun-Jhih Lin, Wen-Chuan Chen, Hung-Wen Wei, Cheng-Kung Cheng

Thumb Motion and Typing Forces during Text Messaging on a Mobile Phone **2095**
F.R. Ong

Oxygen Transport Analysis in Cortical Bone Trough Microstructural Porous Canal Network **2099**
T. Komeda, T. Matsumoto, H. Naito and M. Tanaka

Identification of Microstructural Mechanical Parameters of Articular Cartilage **2102**
T. Osawa, T. Matsumoto, H. Naito and M. Tanaka

Computer Simulation of Trabecular Remodeling Considering Strain-Dependent Osteosyte Apoptosis and Targeted Remodeling **2104**
J.Y. Kwon, K. Otani, H. Naito, T. Matsumoto, M. Tanaka

Fibroblasts Proliferation Dependence on the Insonation of Pulsed Ultrasounds of Various Frequencies **2106**
C.Y. Chiu, S.H. Chen, C.C. Huang, S.H. Wang

Acromio-humeral Interval during Elevation when Supraspinatus is Deficient **2110**
Dr. B.P. Pereira, Dr. B.S. Rajaratnam, M.G. Cheok, H.J.A. Kua, Md. D. Nur Amalina, H.X.S. Liew, S.W. Goh

Can Stretching Exercises Reduce Your Risks of Experiencing Low Back Pain? **2114**
Dr. B.S. Rajaratnam, C.M. Lam, H.H.S. Seah, W.S. Chee, Y.S.E. Leung, Y.J.L. Ong, Y.Y. Kok

Streaming Potential of Bovine Spinal Cord under Visco-elastic Deformation **2118**
K. Fujisaki, S. Tadano, M. Todoh, M. Katoh, R. Satoh

Probing the Elasticity of Breast Cancer Cells Using AFM **2122**
Q.S. Li, G.Y.H. Lee, C.N. Ong and C.T. Lim

Correlation between Balance Ability and Linear Motion Perception **2126**
Y. Yi and S. Park

Heart Rate Variability in Intrauterine Growth Retarded Infants and Normal Infants with Smoking and Non-smoking Parents, Using Time and Frequency Domain Methods **2130**
V.A. Cripps, T. Biala, F.S. Schlindwein and M. Wailoo

Biomechanics of a Suspension of Micro-Organisms **2134**
Takuji Ishikawa

Development of a Navigation System Included Correction Method of Anatomical Deformation for Aortic Surgery **2139**
Kodai Matsukawa, Miyuki Uematsu, Yoshitaka Nakano, Ryuhei Utsunomiya, Shigeyuki Aomi, Hiroshi Iimura, Ryoichi Nakamura, Yoshihiro Muragaki, Hiroshi Iseki, Mitsuo Umezu

Bioengineering Advances and Cutting-edge Technology **2143**
M. Umezu

Effect of PLGA Nano-Fiber/Film Composite on HUVECs for Vascular Graft Scaffold **2147**
H.J. Seo, S.M. Yu, S.H. Lee, J.B. Choi, J.-C. Park and J.K. Kim

Muscle and Joint Biomechanics in the Osteoarthritic Knee **2151**
W. Herzog

Bioengineering Education

Multidisciplinary Education of Biomedical Engineers **2155**
M. Penhaker, R. Bridzik, V. Novak, M. Cerny and J. Cernohorsky

Development and Measurement of High-precision Surface Body Electrocardiograph **2159**
S. Inui, Y. Toyosu, M. Akutagawa, H. Toyosu, M. Nomura, H. Satake, T. Kawabe, J. Kawabe, Y. Toyosu, Y. Kinouchi

Biomedical Engineering Education Prospects in India **2164**
Kanika Singh

Measurement of Heart Functionality and Aging with Body Surface Electrocardiograph **2167**
Y. Toyosu, S. Inui, M. Akutagawa, H. Toyosu, M. Nomura, H. Satake, T. Kawabe, J. Kawabe, Y. Toyosu, Y. Kinouchi

Harnessing Web 2.0 for Collaborative Learning **2171**
Casey K. Chan, Yean C. Lee and Victor Lin

Special Symposium – Tohoku University

Electrochemical In-Situ Micropatterning of Cells and Polymers **2173**
M. Nishizawa, H. Kaji, S. Sekine

Estimation of E_{max} of Assisted Hearts using Single Beat Estimation Method **2177**
T.K. Sugai, A. Tanaka, M. Yoshizawa, Y. Shiraishi, S. Nitta, T. Yambe and A. Baba

Molecular PET Imaging of Acetylcholine Esterase, Histamine H1 Receptor and Amyloid Deposits in Alzheimer Disease **2181**
N. Okamura, K. Yanai

Shear-Stress-Mediated Endothelial Signaling and Vascular Homeostasis **2184**
Joji Ando and Kimiko Yamamoto

Numerical Evaluation of MR-Measurement-Integrated Simulation of Unsteady Hemodynamics in a Cerebral Aneurysm **2188**
K. Funamoto, Y. Suzuki, T. Hayase, T. Kosugi and H. Isoda

Specificity of Traction Forces to Extracellular Matrix in Smooth Muscle Cells **2192**
T. Ohashi, H. Ichihara, N. Sakamoto and M. Sato

Cochlear Nucleus Stimulation by Means of the Multi-channel Surface Microelectrodes **2194**
Kiyoshi Oda, Tetsuaki Kawase, Daisuke Yamauchi, Hiroshi Hidaka and Toshimitsu Kobayashi

Effects of Mechanical Stimulation on the Mechanical Properties and Calcification Process of Immature Chick Bone Tissue in Culture **2197**
T. Matsumoto, K. Ichikawa, M. Nakagaki and K. Nagayama

Regional Brain Activity and Performance During Car-Driving Under Side Effects of Psychoactive Drugs **2201**
Manabu Tashiro, MD. Mehedi Masud, Myeonggi Jeong, Yumiko Sakurada, Hideki Mochizuki, Etsuo Horikawa, Motohisa Kato, Masahiro Maruyama, Nobuyuki Okamura, Shoichi Watanuki, Hiroyuki Arai, Masatoshi Itoh, and Kazuhiko Yanai

Evaluation of Exercise-Induced Organ Energy Metabolism Using Two Analytical Approaches: A PET Study **2204**
Mehedi Masud, Toshihiko Fujimoto, Masayasu Miyake, Shoichi Watanuki, Masatoshi Itoh, Manabu Tashiro

Strain Imaging of Arterial Wall with Reduction of Effects of Variation in Center Frequency of Ultrasonic RF Echo **2207**
Hideyuki Hasegawa and Hiroshi Kanai

In Situ Analysis of DNA Repair Processes of Tumor Suppressor BRCA1 ..... **2211**
Leizhen Wei and Natsuko Chiba

Evaluating Spinal Vessels and the Artery of Adamkiewicz Using 3-Dimensional Imaging **2215**
Kei Takase, Sayaka Yoshida and Shoki Takahashi

Development of a Haptic Sensor System for Monitoring Human Skin Conditions **2219**
D. Tsuchimi, T. Okuyama and M. Tanaka

Fabrication of Transparent Arteriole Membrane Models **2223**
Takuma Nakano, Keisuke Yoshida, Seiichi Ikeda, Hiroyuki Oura, Toshio Fukuda, Takehisa Matsuda, Makoto Negoro and Fumihito Arai

Normal Brain Aging and its Risk Factors – Analysis of Brain Magnetic Resonance Image (MRI) Database of Healthy Japanese Subjects **2228**
H. Fukuda, Y. Taki, K. Sato, S. Kinomura, R. Goteau, R. Kawashima

Motion Control of Walking Assist Robot System Based on Human Model **2232**
Yasuhisa Hirata, Shinji Komatsuda, Takuya Iwano and Kazuhiro Kosuge

Effects of Mutations in Unique Amino Acids of Prestin on Its Characteristics **2237**
S. Kumano, K. Iida, M. Murakoshi, K. Tsumoto, K. Ikeda, I. Kumagai, T. Kobayashi, H. Wada

The Feature of the Interstitial Nano Drug Delivery System with Fluorescent Nanocrystals of Different Sizes in the Human Tumor Xenograft in Mice **2241**
M. Kawai, M. Takeda and N. Ohuchi

Three-dimensional Simulation of Blood Flow in Malaria Infection **2244**
Y. Imai, H. Kondo, T. Ishikawa, C.T. Lim, K. Tsubota and T. Yamaguchi

Development of a Commercial Positron Emission Mammography (PEM) **2248**
Masayasu Miyake, Seiichi Yamamoto, Masatoshi Itoh, Kazuaki Kumagai, Takehisa Sasaki, Targino Rodrigues dos Santos, Manabu Tashiro and Mamoru Baba

Radiological Anatomy of the Right Adrenal Vein: Preliminary Experience with Multi-detector Row Computed Tomography **2250**
T. Matsuura, K. Takase and S. Takahashi

Atrial Vortex Measurement by Magnetic Resonance Imaging **2254**
M. Shibata, T. Yambe, Y. Kanke and T. Hayase

Fabrication of Multichannel Neural Microelectrodes with Microfluidic Channels Based on Wafer Bonding Technology **2258**
R. Kobayashi, S. Kanno, T. Fukushima, T. Tanaka and M. Koyanagi

Influence of Fluid Shear Stress on Matrix Metalloproteinase Production in Endothelial Cells **2262**
N. Sakamoto, T. Ohashi and M. Sato

Development of Brain-Computer Interface (BCI) System for Bridging Brain and Computer **2264**
S. Kanoh, K. Miyamoto and T. Yoshinobu

First Trial of the Chronic Animal Examination of the Artificial Myocardial Function **2268**
Y. Shiraishi, T. Yambe, Y. Saijo, K. Matsue, M. Shibata, H. Liu, T. Sugai, A. Tanaka, S. Konno, H. Song, A. Baba, K. Imachi, M. Yoshizawa, S. Nitta, H. Sasada, K. Tabayashi, R. Sakata, Y. Sato, M. Umezu, D. Homma

Bio-imaging by functional nano-particles of nano to macro scale **2272**
M. Takeda, H. Tada, M. Kawai, Y. Sakurai, H. Higuchi, K. Gonda, T. Ishida and N. Ohuchi

Author Index **2275**

Subject Index **2289**

Electroencephalograph Signal Analysis During Ujjayi pranayama

Prof. S.T. Patil[1] and Dr. D.S. Bormane[2]

[1]Computer Dept. B.V.U. College of Engineering, Pune, India. Stpatil77@gmail.com
[2]Principal, Rajarshi Shahu Engineering college, Pune, India. bdattatraya@yahoo.com

Abstract — **Ujjai pranayama is one part of the Pranayama, as traditionally conceived, involves much more than merely breathing for relaxation. Ujjai pranayama is a term with a wide range of meanings. "The regulation of the incoming and outgoing flow of breath with retention.". Ujjai pranayama also denotes cosmic power. Because of this connection between breath and consciousness. Pranayama has devised ujjai pranayama to stabilize energy and consciousness.**

A wavelet transformation is applied to electroencephalograph (EEG) records from persons under ujjai pranayama. Correlation dimension, largest lyapunov exponent, approximate entropy and coherence values are analyzed. This model & software is used to keep track on the improvement of the persons mind, aging, balance, flexibility, personnel values, mental values, social values, love, sex, knowledge, weight reduction and body fitness.

Keywords — **Ujjai pranayama, approximate entropy, EEG, coherence, largest lyapunov exponent, correlation dimension, wavelets.**

I. Introduction

A. Ujjai pranayama

The word ujjai pranayama means stretch, extension, expansion, length, breadth, regulation, prolongation, restraint and control to create energy, when the self-energizing force embraces the body, fast inhalation and fast exhalation, followed by inhaling through right nostril and performing kumbhaka with bandhas and exhaling through left nostril. Patanjali has said that one develops concentration and clarity of thought by practicing ujjai pranayama. It helps in increasing the mental and physical powers of endurance. It is the path to deeper relaxation and meditation and is a scientific method of controlling breath. It provides complete relaxation to the nervous system. It provides relief from pain caused by the compression of nerve ending. It helps in increasing oxygen supply to the brain which in turn helps controlling the mind.

B. Electroencephalography

The brain generates rhythmical potentials, which originate in the individual neurons of the brain. Electroencephalograph (EEG) is a representation of the electrical activity of the brain.

Numerous attempts have been made to define a reliable spike detection mechanism. However, all of them have faced the lack of a specific characterization of the events to detect. One of the best known descriptions for an interictal "spike" is offered by Chatrian et al. [1]: " transient, clearly distinguished from background activity, with pointed peak at conventional paper speeds and a duration from 20 to 70 msec". This description, however, is not specific enough to be implemented into a detection algorithm that will isolate the spikes from all the other normal or artifactual components of an EEG record. Some approaches have concentrated in measuring the "sharpness" of the EEG signal, which can be expected to soar in the "pointy peak" of a spike. Walter [2] attempted the detection of spikes through analog computation of the second time derivative (sharpness) of the EEG signals. Smith [3] attempted a similar form of detection on the digitized EEG signal. His method, however required a minimum duration of the sharp transient to qualify it as a spike. Although these methods involve the duration of the transient in a secondary way, they fundamentally consider "sharpness" as a point property, dependent only on the very immediate context of the time of analysis. More recently, an approach has been proposed in which the temporal sharpness is measured in different "spans of observation", involving different amounts of temporal context. True spikes will have significant sharpness at all of these different "spans". The promise shown by that approach has encouraged us to use a wavelet transformation to evaluate the sharpness of EEG signals at different levels of temporal resolution.

C. Data Collection

Medic-aid systems, Chandigarh (India), machine was used to aquire 32-channel eeg signal with the international 10-20 electrode coupling. The sampling frequency of the device is 256 Hz with 12-bit resolution and stored on hard disc. 32 channel EEG data was recorded simultaneously for both referential and bipolar montages. Recordings are made before, meanwhile and after the person is doing ujjai pranayama, and also we have kept track on recording the EEG data after one, two and three months of the same

Chwee Teck Lim, James C.H. Goh (Eds.): ICBME 2008, Proceedings 23, pp. 1–4, 2009
www.springerlink.com

persons doing ujjai pranayama. Such 10 persons data is collected for analysis.

II. Parameters

The present work pertains to the analysis of the EEG signal using various characteristic measures like Correlation Dimension(CD), Largest Lyapunov Exponent(LLE), Hurst exponent(HE) & Approximate Entropy(AE).

A. Correlation Dimension

The dimension of a graph can give much more information about the nature of the signal

Grassberger & Procaccia Algorithm is used

$$C(r) = \frac{2}{N(N-1)}) \sum_{i=1+w}^{N} \theta(r - / x_i - x_j /)$$

N-no. of data points θ -Heaviside function
r- radial distance w-Tac x j step away from x i

B. Approximate Enropy

amount of disorder in the system. Amount of information stored in a more general probability distribution. Steyn-Ross algorithm is used

$$AE(m,r,l) = \frac{1}{L-m} \sum_{i=1}^{L-m} Log^{m+1} C_i(r) - \frac{1}{L-(m+1)} Log^{m} C_i(r)$$

Where m= Pattern Length = 2
r = noise threshold = 15%
L= Time interval between two datasets.
Ci (r) = correlation integral

C. Largest Lyapunov Exponent

It is rate at which the trajectories of a signal separate one from other.

Wolf algorithm is used to calculate Largest Lyapunov Exponent

$$\delta Z(t) = e\lambda t / \delta z_0 /$$

δz0=Initial seperation
λ= λ1, λ2, λ3,…….. λn Phase spaces

D. Hurst Exponent

Evaluates presence or absence of long range dependence and it degree. Hurst algorithm is used

$$H = Log(\frac{R}{S}) / LogT$$

R/S - Rescaled Range,
T- Duration of sample of data

III. Results

Artifactual currents may cause linear drift to occur at some electrodes. To detect such drifts, we designed a function that fits the data to a straight line and marks the trial for rejection if the slope exceeds a given threshold. The slope is expressed in microvolt over the whole epoch (50, for instance, would correspond to an epoch in which the straight-line fit value might be 0 μv at the beginning of the trial and 50 μ v at the end). The minimal fit between the EEG data and a line of minimal slope is determined using a standard R-square measure.

We usually apply the measures described above to the activations of the independent components of the data. As independent components tend to concentrate artifacts, we have found that bad epochs can be more easily detected using independent component activities. The functions described above work exactly the same when applied to data components as when they are applied to the raw channel data.

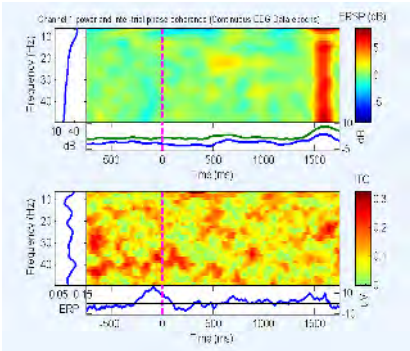


Fig.1: time frequency components

It is more interesting to look at time-frequency decompositions of component activations than of separate channel activities, since independent components may directly index the activity of one brain EEG source, whereas channel activities sum potentials volume-conducted from different parts of the brain. to visualize only frequencies up

to 30 Hz. decompositions using FFTs allow computation of lower frequencies than wavelets, since they compute as low as one cycle per window, whereas the wavelet method uses a fixed number of cycles (default 3) for each frequency.

The following time window appears IN Fig.1. The ITC image (lower panel) shows strong synchronization between the component activity and stimulus appearance, first near 15 Hz then near 4 Hz. The ERSP image (upper panel) shows that the 15-Hz phase-locking is followed by a 15-Hz power increase, and that the 4-Hz phase-locking event is accompanied by, but outlasts, a 4-Hz power increase.

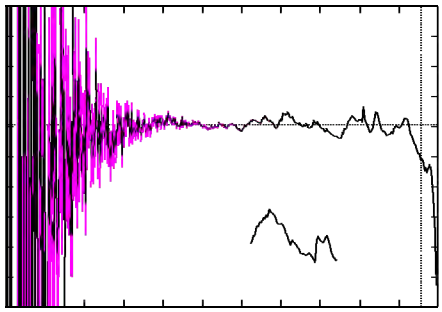


Fig.2: correlation dimension

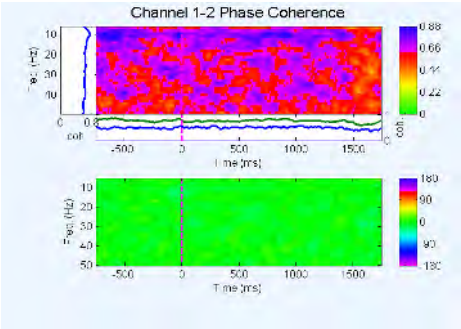


Fig.3: cross-coherence

To determine the degree of synchronization between the activations of two components, we may plot their event-related cross-coherence as shown in fig.3. (a concept first demonstrated for EEG analysis by Rappelsberger). Even though independent components are (maximally) independent over the whole time range of the training data, they may become transiently (partially) synchronized in specific frequency bands. In the cross window below, the two components become synchronized (top panel) around 11.5Hz (click on the image to zoom in). The upper panel shows the coherence magnitude (between 0 and 1, 1 representing two perfectly synchronized signals). The lower panel indicates the phase difference between the two signals at time/frequency points where cross-coherence magnitude (in the top panel) is significant. In this example, the two components are synchronized with a phase offset of about -120 degrees (this phase difference can also be plotted as latency delay in ms, using the minimum-phase assumption.

Channel statistics may help determine whether to remove a channel or not. To compute and plot one channel statistical characteristics.

Some estimated variables of the statistics are printed as text in the lower panel to facilitate graphical analysis and interpretation. These variables are the signal mean, standard deviation, skewness, and kurtosis (technically called the 4 first cumulants of the distribution) as well as the median. The last text output displays the Kolmogorov-Smirnov test result (estimating whether the data distribution is Gaussian or not) at a significance level of p=0.05.

The upper right panel shows the empirical quantile-quantile plot (QQ-plot). Plotted are the quantiles of the data versus the quantiles of a Standard Normal (i.e., Gaussian) distribution. The QQ-plot visually helps to determine whether the data sample is drawn from a Normal distribution. If the data samples do come from a Normal distribution (same shape), even if the distribution is shifted and re-scaled from the standard normal distribution (different location and scale parameters), the plot is linear.

IV. Conclusion

From this model & software we conclude that,

- The EEG signal after ujjai pranayama becomes less complex.
- Corretion dimension, Largest lyapunov exponent, Approximate entropy & Hurst exponent decreases.
- Less parallel functional activity of the brain
- predictability of the EEG signal increases.

V. Discussion

During the ujjai pranayama Meditation technique individuals often report the subjective experience of Transcendental Consciousness or pure consciousness, the state of least excitation of consciousness. This study found that many experiences of pure consciousness were associated with periods of natural respiratory suspension, and that during these respiratory suspension periods individuals displayed higher mean EEG coherence over all frequencies and brain areas, in contrast to control periods where subjects voluntarily held their breath. Results are 98 % true when discussed with doctors.

BIOGRAPHIES

Prof. S.T. Patil- Completed B.E. Electronics from Marathwada University, Aurangabad in 1988. M.Tech. Computer from Vishveshwaraya Technological University, Belgum in July 2003. Persuing Ph.D. Computer from Bharati Vidyapeeth Deemed University, Pune. Having 19 years of experience in teaching as a lecturer, Training & Placement Officer, Head of the department & Assistant Professor. Presently working as an Assistant Professor in computer engineering & Information Technology department in Bharati Vidyapeeth Deemed University, College of Engineering, Pune (India). Presented 14 papers in national & international conferences.

Dr. D.S. Bormane- Completed B.E. Electronics from Marathwada University, Aurangabad in 1987. M.E. Electronics from Shivaji University, Kolhapur. Ph.D. computer from Ramanand Tirth University, Nanded. Having 20 years of experience in teaching as a Lecturer, Assistant Professor, Professor, and Head Of Department. Currently working as a Principal in Rajrshi Shahu College of Engineering, Pune (India). Published 24 papers at national & international conferences and journals.

REFERENCES

[1] Prof. S. T. Patil & Dr. D. S. Bormane, “EEG Analysis Using FFT” (BVCON-March 2005, Sangli)

[2] Prof. S. T. Patil & Dr. D. S. Bormane, “ “Broadband Multi-carrier based air interface” (BVCON-March 2005, Sangli)

[3] Prof. S. T. Patil “ “Network security against cyber attacks” (BVCON- March 2005, sangli)

[4] Prof. S. T. Patil & Dr. D. S. Bormane, “ “Dynamic EEG Analysis Using Multi-resolution Time & frequency” (BIOCON- September, 2005, Pune)

[5] Prof. S. T. Patil & Dr. D. S. Bormane, “Fast Changing Dynamic & High non-stationary EEG signal Analysis Using Multi-resolution Time & frequency. In January 2006 at Government college of Engineering, Aurangabad.

[6] Prof. S. T. Patil “Wi-Fi” in February 2006 at Sanghavi college of Engineering, Mumbai.

[7] Prof. S. T. Patil & Dr. D. S. Bormane, “EEG Analysis during Ujjai pranayama, April 2006, JNEC, Aurangabad.

[8] Prof. S. T. Patil “Clustering Technology, April 2006, Bharati Vidyapeeth College of Engineering, New Delhi.

[9] Prof. S. T. Patil “Distributed Storage Management, July 2006, College of Engineering, Kopargaon.

[10] Prof. S. T. Patil & Dr. D. S. Bormane, “EEG Analysis during Kapalbhati, August 2006, ICEMCC – PESIT International conference, Bangalore.

[11] Prof. S. T. Patil & Dr. D. S. Bormane, “EEG Analysis during Bramari using wavelet, selected in CIT, International conference, Bhubaneshwar, December 2006.

[12] Prof. S. T. Patil & Dr. D. S. Bormane, “EEG Analysis during Ujjai pranayama using wavelet, selected in CODEC, International conference, Culcutta, December 2006.

[13] Prof. S. T. Patil & Dr. D. S. Bormane, “EEG Analysis during Ujjai pranayama using wavelet, ADCOM, NIT, Suratkal, International conference, Mangalore, December 2006.

[14] Prof. S. T. Patil “Enhanced adaptive mesh generation for image representation, NCDC-06, national conference, Pune, September 2006.

[15] Prof. S. T. Patil “Enhanced adaptive mesh generation for image representation, ETA-2006, National conference, Rajkot, October 2006.

[16] Prof. S. T. Patil & Dr. D. S. Bormane, “EEG Analysis during Kapalbhati, December 2006, BIOTECH-06, International conference, Nagpur.

[17] Chatrian et al., "A glossary of terms most commonly used by clinical electroencephalographers", Electroenceph.and Clin. Neurophysiol., 1994, 37:538-548.

[18] D. Walter et al., "Semiautomatic quantification of sharpness of EEG phenomena". IEEE Trans. on Biomedical Engineering, 3, Vol. BME-20, pp. 53-54.

[19] J. Smith, "Automatic Analysis and detection of EEG Spikes", IEEE Trans. on Biomedical Engineering, 1999, Vol. BME-21, pp. 1-7.

[20] Barreto et al., "Intraoperative Focus Localization System based Spatio-Temporal ECoG Analysis", Proc. XV Annual Intl. Conf. of the IEEE Engineering in Medicine and Biology Society, October, 2003.

[21] Lin-Sen Pon, “Interictal Spike Analysis Using Stochstic Point Process”,Proceedings of the International conference, IEEE – 2003.

[22] Susumo Date, “A Grid Application For An Evaluation Of Brain Function Using ICA” Proceedings of the International conference, IEEE - 2002.

A Study of Stochastic Resonance as a Mathematical Model of Electrogastrography during Sitting Position

Y. Matsuura[1,2], H. Takada[3] and K. Yokoyama[1]

[1] Graduate School of Natural Science, Nagoya City University, Nagoya, Japan
[2] JSPS Research Fellow, Tokyo, Japan
[3] Department of Radiology, Gifu University of Medical Science, Seki, Japan
[4] Graduate School of Design and Architecture, Nagoya City University, Nagoya, Japan

Abstract — **Electrogastrography (EGG) is an abdominal surface measurement of the electrical activity of the stomach. It is very important clinically to record and analyze multichannel EGGs, which provide more information on the propagation and co-ordination of gastric contractions. This study measured the gastrointestinal motility with an aim to obtain a mathematical model of EGG and to speculate factors to describe the diseases resulting from constipation and erosive gastritis. The waveform of the electric potential in the Cajal cells is similar to the graphs of numerical solutions to the van der Pol equation. Hence, we added the van der Pol equation to a periodic function and random white noises, which represented the intestinal motility and other biosignals, respectively. We rewrote the stochastic differential equations (SDEs) into difference equa-tions, and the numerical solutions to the SDEs were obtained by the Runge–Kutta–Gill formula as the numerical calculus, where we set the time step and initial values to be 0.05 and (0, 0.5), respectively. Pseudorandom numbers were substituted in the white noise terms. In this study, the pseudorandom num-bers were generated by the Mersenne Twister method. These numerical calculations were divided into 12000 time steps. The numerical solutions and EGG were extracted after every 20 steps. The EGG and numerical solutions were compared and evaluated by the Lyapunov exponent and translation error. The EGG was well described by the stochastic resonance in the SDEs.**

Keywords — **Electrogastrography (EGG), numerical analysis, Stochastic Resonance**

I. Introduction

It is known that attractors can be reconstructed by dynamical equation systems (DESs) such as the Duffing equation, Henon map, and Lorenz differential equation. It is very interesting to note that the structure of an attractor is also derived from time series data in a phase space.

The DESs were obtained as mathematical models that regenerated time series data. Anomalous signals are introduced by nonstationary processes, for instance, the degeneration of singular points in the potential function involved in the DESs; their degree of freedom increases or stochastic factors are added to them. The visible determinism in the latter case would be different from that in the case where random variables do not exist.

It is well known that the empirical threshold translation error of 0.5 is used to classify mathematical models as being either deterministic or stochastic generators [1]; however, the estimated translation error is generally not the same as that in the case of smaller signal-to-noise (S/N) ratios. Takada (2008) [2] quoted an example of analyzing numerical solutions to the nonlinear stochastic differential equations (SDEs):

$$\dot{x} = y - agradf\ (x) + \mu w_1(t)\,, \tag{1.1}$$

$$\dot{y} = -x + \mu w_2(t)\ , \tag{1.2}$$

$$s.t.\quad f(x) = \frac{1}{12}x^4 - \frac{b}{2}x^2 \tag{2}$$

where $w_1(t)$ and $w_2(t)$ were independent white noise terms $(\mu = 0,1,\cdots,20)$. By enhancing μ in eq.(1), we can obtain numerical solutions for smaller S/N ratios.

Percutaneous electrogastrography (EGG) is a simple method to examine gastrointestinal activity without constraint. EGG is a term generally applied to the measurement of human gastric electrical activity. In 1921, Walter C. Alvarez reported performing EGG for the first time in humans [3]. In EGG, the electrical activity of the stomach is recorded by placing the electrodes on the surface of the abdominal wall [4]. In the stomach, a pacemaker on the side of the greater curvature generates electrical activity at a rate of 3 cycles per minute (3 cpm); the electrical signal is then transferred to the pyloric side [5]–[7]. Previously, it was difficult to measure this electrical activity because the EGG signal was composed of low-frequency components and high-frequency noise caused by the electrical activity of the diaphragm and heart. However, the accuracy of EGG measurements has improved recently, and gastroenteric motility can be evaluated by spectrum analysis of the EGG signals [8]–[9].

Many previous studies on EGG have been reported, and most of these studies pertain to the clinical setting [10], e.g.,

Chwee Teck Lim, James C.H. Goh (Eds.): ICBME 2008, Proceedings 23, pp. 5–8, 2009
www.springerlink.com

evaluation of the effects of hormones and drugs on EGG and the relationship between EGG and kinesia. EGG has been used to study the effects of warm compresses (for the improvement of constipation) on gastrointestinal activity [11], the usefulness of warm compresses in the epigastric region for the improvement of constipation [12], and characterization of intestinal activity in patients with chronic constipation[13].

Gastric electrical potential is generated by interstitial cells of Cajal (ICCs) [14]. ICCs are pacemaker cells that spontaneously depolarize and repolarize at a rate of 3 cpm. They demonstrate low-amplitude, rhythmic, and circular contractions only if the electrical potential is over a threshold.

Human gastric pacemaker potential migrates around the stomach very quickly and moves distally through the antrum in approximately 20 seconds, resulting in the normal gastric electrical frequency of 3 cpm. This moving electrical wavefront is recorded in EGG, in which the gastric myoelectrical activity is recorded using electrodes placed on the surface of the epigastrium. However, electrogastrogram also contains other biological signals, for instance, electrical activity of the heart, intestinal movements, and myenteric potential oscillations in general.

In the present study, the gastrointestinal motility was measured with an aim to obtain a mathematical model of EGG and to speculate factors to describe the diseases resulting from constipation and erosive gastritis.

II. Methods

A. Mathematical Model and the Numerical Simulations

As a mathematical model of the EGG during sitting position, we propose the following SDEs in which the periodic function is added to Eq.(1.1).

$$\dot{x} = y - \lambda\, gradf\,(x) + s(t) + \mu w_1(t) \tag{3.1}$$

$$\dot{y} = -x + \mu w_2(t) \tag{3.2}$$

The function $s(t)$ and the white noise $w_i(t)$ represent intestinal movements and other biosignals, for instance, myenteric potential oscillations that are weak and random, respectively $(i = 1,2)$.

In most cases, there is an optimum for noise amplitude, which has motivated the name stochastic resonance (SR) for this rather counterintuitive phenomenon. In other words, the SR occurs when the S/N ratio (SNR) of a nonlinear system is maximized for a moderate value of noise intensity [15]. In this study, we numerically solve eq.(3) and verify the SR in the SDEs . We also investigate the effect of the SR and evaluate the SDEs as a mathematical model of the EGG.

B. Physiological Procedure

The subjects were 14 healthy people (7 M & 7 F) aged 21–25 years. Sufficient explanation of the experiment was provided to all subjects, and a written consent was obtained from them.

EGGs were obtained for 30 min in the sitting position at 1 kHz by using an A/D converter (AD16-16U (PCI) EH; CONTEC, Japan). EGGs were amplified using a bioamplifier (MT11; NEC Medical, Japan) and recorded using a tape recorder (PC216Ax; Sony Precision Technology, Japan).

To remove the noise from the time series of EGG data obtained at 1 kHz, resampling was performed at 0.5 Hz. For analysis, we then obtained a resampled time series as follows;

$$x_i = \frac{1}{2000}\sum_{j=0}^{1999} y(2000\,i + j) \quad (i = 0,1, \cdots ,1799)$$

In this experiment, 9 disposable electrodes (Blue Sensor; Medicotest Co. Ltd., Ølstykke, Denmark) were affixed on ch1–ch8 and e, as shown in Fig. 1. The electrode affixed on e was a reference electrode. Prior to the application of electrodes, the skin resistance was sufficiently reduced using SkinPure (Nihon Kohden Inc., Tokyo, Japan). Several methods have been proposed for analyzing the EGG data. The EGG data obtained at ch5, which is the position closest to the pacemaker of gastrointestinal motility, were analyzed in this study.

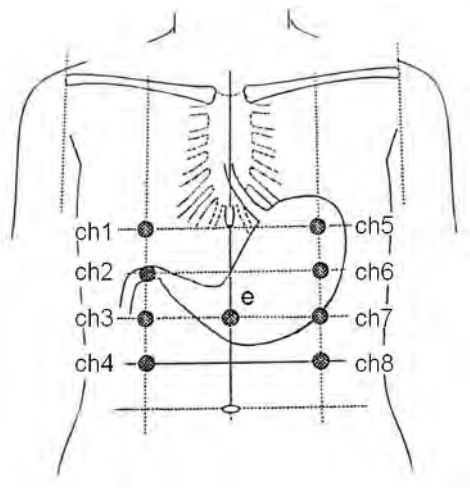


Fig. 1 Positions of electrode

C. Calculation Procedure

1. We rewrote eq.(3) as difference equations and obtained numerical solutions to them by the Runge–Kutta–Gill formula as the numerical calculus; the initial values were (0, 0.5). Pseudorandom numbers were substituted for . The pseudorandom numbers used here were generated using the Mersenne Twister [16]. These numerical calculations were performed in N = 12000 time steps. The unit of the time step is 0.05.
2. Values in the numerical solutions were recorded every 40 time step, which is related to a signal sampling rate of 0.5 Hz.
3. The autocorrelation function was calculated for each component of the numerical solution.

III. Results and Discussion

In the 12000 time steps, there was no exception wherein the numerical solutions did not diverge. For $\mu = 0,1,\cdots,20$, the value of τ derived from the first component of the numerical solution was not different from that derived from the second component.

With regard to eq.(3), the SR occurred under the condition of an appropriate coefficient μ. Some biosystems are based on the nonlinear phenomenon of SR, in which the detection of small afferent signals can be enhanced by the addition of an appropriate amount of noise [15]. Furthermore, this mechanism would facilitate behavioral, perceptive, and autonomic responses in animals and humans, for instance, information transfer in crayfish mechanoreceptors [17], tactile sensation in rats [18], availability of electrosensory information for prey capture [19], human hearing [20], vibrotactile sensitivity in the elderly[21], and spatial vision of amblyopes [22]. Here, we examined whether the SR generated by eq.(3) can describe the EGG time series (Fig.4).

A cross-correlation coefficient $\hat{\rho}_{zs}$ between observed signal $x(t)$ and the periodic function $s(t)$ was calculated as a substitute for the SNR in previous studies in which the occurrence of the SR was investigated. Fig. 2 shows $\hat{\rho}_{xs}$ between the numerical solutions and the periodic function in eq.(3.1). The cross-correlation coefficient was maximized for a moderate value of noise intensity $\mu = 12$ (Fig. 2). Thus, the SR could be generated by eq.(3) with $\mu = 12$, which is regarded as a mathematical model of the EGG in this study. We then compared this numerical solution with the EGG data (Fig. 3). Temporal variations in the numerical solutions were similar to those in the EGG data (Fig.4).

Numerical solutions involved in the SR highly correlated with the periodic function $s(t)$, which represented intestinal movements (6 cpm). Gastric electrical activity in a healthy person might synchronize with the intestinal one.

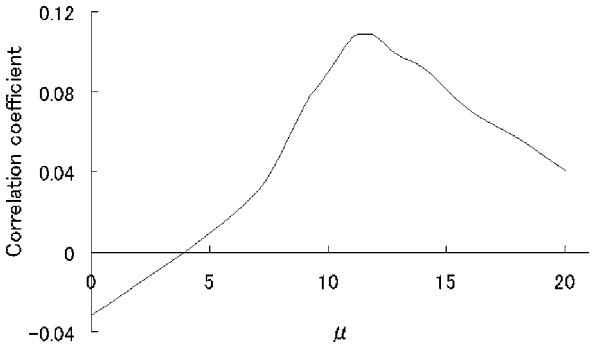


Fig. 2 The autocorrelation function for each component of the numerical solution

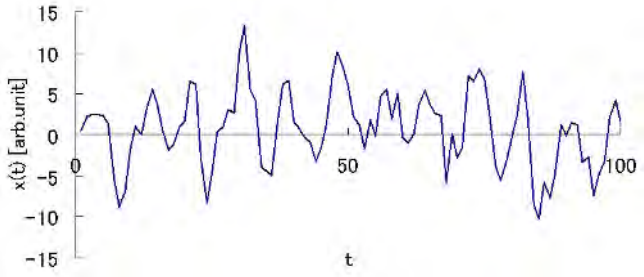


Fig. 3 An example of numerical solutions. $(\mu = 12)$

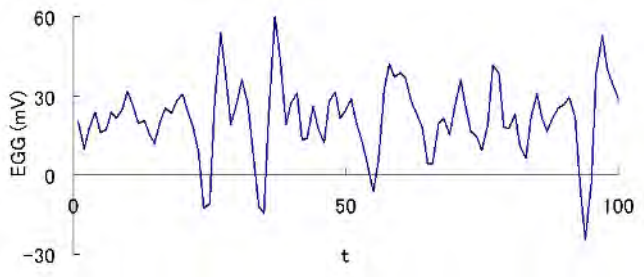


Fig. 4 A typical EGG time series. (Sampling frequency is 0.5 Hz.)

In the next step, we would quantitatively evaluate the affinity by using translation errors [23] and Lyapunov exponents [24]-[26] in embedding space. Translation error (E_{trans}) measures the smoothness of flow in an attractor, which is assumed to generate the time-series data. In general, the threshold of the translation error for classifying the time-series data as deterministic or stochastic is 0.5, which

is half of the translation error resulting from a random walk. The chaos processes are sensitively dependent on initial conditions and can be quantified using the Lyapunov exponent [26]. If the Lyapunov exponent has a positive value, the dynamics are regarded as a chaos process.

Acknowledgment

This work was supported in part by the JSPS Research Fellowships for Young Scientists, 07842, 2006.

References

1. Matsumoto T, Tokunaga R, Miyano T, Tokuda I (2002) Chaos and time series prediction, Tokyo, Baihukan, 49–64. (in Japanese)
2. Takada H (2008) Effect on S/N ratio on translation error estimated by double-wayland algorithm, Bulletin of gifu university of medical science, 2, 135-140
3. Alvarez W C (1922) The electrogastrogram and what is shows, J Am Med Assoc, 78, 1116–1118.
4. Hongo M, Okuno H (1992) Evaluation of the function of gastric motility, J. Smooth Muscle Res., 28, 192–195 (in Japanese).
5. Couturier D, Roze C, Paolaggi J, Debray C (1972) Electrical activity of the normal human stomach. A comparative study of recordings obtained from the serosal and mucosal sides, Dig. Dis. Sci., 17, 969–976.
6. Hinder R A, Kelly K A (1977) Human gastric pacesetter potentials. Site of origin, spread, and response to gastric transection and proximal gastric vagotomy, Amer. J. Surg., 133, 29–33.
7. Kwong N K, Brown B H, Whittaker G E, Duthie H L (1970) Electrical activity of the gastric antrum in man, Br. J. Surg., 57, 913–916.
8. Van Der Schee E J, Smout A J P M, Grashuis J L (1982) Application of running spectrum analysis to electrogastrographic signals recorded from dog and man, in Motility of the digestive tract, ed. M. Wienbeck, Raven Press, New York.
9. Van Der Schee E J, Grashuis J L (1987) Running spectrum analysis as an aid in the representation and interpretation of electrogastrographic signals, Med. Biol. Eng. & Comput., 25, 57–62.
10. Chen J D, Mccakkum R W (1993) Clinical applications of electrogastrography, Am. J. Gastroenterol, 88, 1324–1336.
11. Nagai M,,Wada M, Kobayashi Y, Togawa S (2003) Effects of lumbar skin warming on gastric motility and blood pressure in humans, Jpn. J. of Physiol., 53, 45–51.
12. Kawachi N, Iwase S, Takada H, Michigami D, Watanabe Y, Mae N (2002) Effect of wet hot packs applied to the epigastrium on electrogastrogram in constipated young women, Autonomic Nervous System, 39, 433–-437. (in Japanese)
13. Matsuura Y, Iwase S, Takada H, Watanabe Y, Miyashita E (2003) Effect of three days of consecutive hot wet pack application to the epigastrium on electrogastrography in constipated young women, Autonomic Nervous System, 40, 406–411. (in Japanese)
14. Cajal S R (1911) Historogie du systeme nerveux de l' homme et des vertebres. 2:942, Maloine, Paris.
15. Benzi R, Sutera A, Vulpiani A(1981) The mechanism of stochastic resonance. Journal of Physics. A14. L453-L457
16. Matsumoto M, Nishimura T: Mersenne Twister: A 623-dimensionally equidistributed uniform pseudorandom number generator, ACM Transaction Modeling and Computer Simulation, 8(1), 3-30, 1998
17. Douglass J K, Wilkens L, Pantazelou E, Moss F (1993) Noise enhancement of information transfer in crayfish mechanoreceptors by stochastic resonance. Nature. 365. pp. 337-340.
18. Collins J J, Imhoff T T, Grigg P (1996) Noise enhanced tactile sensation. Nature. 383. pp. 770.
19. Russell E V, Israeloff N E(2000) Direct observation of molecular cooperativity near the glass transition. Nature. 408. pp.695-698.
20. Zeng F G, Fu Q J, Morse R (2000) Human hearing enhanced by noise. Brain Res. 869. pp. 251-255.
21. Liu W, Lipsitz L A, M Montero-Odasso J Bean, Kerrigan D C, Collins J J (2002) Noise-enhanced vibrotactile sensitivity in older adults, patients with stroke, and patients with diabetic neuropathy. Arch Phys Med Rehabil. 83. pp. 171-176.
22. Levi D M, Klein S A (2003) Noise provides some new signals about the spatial vision of amblyopes. J Neurosci. 23. pp. 2522-2526.
23. Wayland R, Bromley D, Pickett D, Passamante A (1993) Recognizing determinism in a time series, Phys. Rev. Lett, 70, 580–582.
24. Lyapunov A M (1892) The general problem of the stability of motion, Comm. Soc. Math. Kharkow (in Russian) (reprinted in English, Lyapunov A M (1992) The general problem of the stability of motion. International Journal of Control, 55(3), 531-534)
25. Sato S, Sano M, Sawada Y (1987) Practical methods of measuring the generalized dimension and the largest Lyapunov exponent in high dimensional chaotic systems, Prog. Theor. Phys., 77, 1–5.
26. Rosenstein M T, Collins J J, De Luca C J (1993) a practical method for calculating largest Lyapunov exponents from small data sets, Physica. D., 65, 117–134.

Author: MATSUURA Yasuyuki
Institute: Graduate School of Natural Sciences, Nagoya City University and JSPS Research Fellow
Street: 1 Yamanohata, Mizuho-cho, Mizuho-ku
City: Nagoya
Country: Japan
Email: y.matsuura@nsc.nagoya-cu.ac.jp

Possibility of MEG as an Early Diagnosis Tool for Alzheimer's Disease: A Study of Event Related Field in Missing Stimulus Paradigm

N. Hatsusaka, M. Higuchi and H. Kado

Applied Electronics Laboratory, Kanazawa Institute of Technology, Kanazawa, Japan

Abstract — **We are investigating a diagnosis to find Alzheimer's disease (AD), which is a kind of dementia and one of the most prominent neurodegenerative disorders, using a magnetoencephalography (MEG). MEG is one of non-invasive technique to investigate the brain function by using an array of superconducting quantum interference device (SQUID) sensors arranged around the head. In this study, we observed the event-related field in 'missing stimulus' paradigm. The subjects were presented short beep tones with a certain interval. Some tones were omitted randomly from the sequence and this omission was called 'tone-omitted event'. We focused on the specific magnetic field component induced by the tone-omitted event. 32 patients with early AD and 32 age-matched controls were examined by 160-ch whole-head MEG system. The MEG signals related to the tone-omitted events were collected from each subject. The amplitude of the averaged waveform in the AD group was significantly smaller than that in the control group. This result suggests that MEG is useful for AD diagnosis.**

Keywords — **MEG, Alzheimer's disease, auditory stimulus, Event Related Field, missing stimulus paradigm**

I. Introduction

Magnetoencephalography (MEG) is one of the non-invasive methods to investigate the neural activity in the brain, based on biomagnetism measurement. MEG can detect magnetic field generated by electronic neural activity of the brain. The neural activity is inducing by post synaptic activity in the cortex. The intensity of the magnetic field elicited from the brain is several femto or pico tesla. Such small magnetic field can be detected only by superconducting quantum interference device (SQUID) sensors. A recent whole-head MEG system is equipped with a head-shaped array of more than one hundred SQUID sensors.

There are several brain imaging techniques to measure the brain function other than MEG system. Positron emission topography (PET) and single-photon emission computed tomography (SPECT) observe the brain function by using radioactive isotope doped in the subject's body. Functional MRI observes the brain function using a strong magnetic field. These systems measure the chemical changes by metabolic activity of nerves. MEG and electroencephalography (EEG) can directly observe the neural electronic activity. The EEG has the lower spatial resolution than the MEG because the electric potential distribution on the scalp is influenced by the difference of the conductivity among the tissues, such as skull and scalp etc. On the other hand, the magnetic field distribution is not distorted because the permeability of the body tissues is constant and is the almost same as the space permeability. MEG has higher temporal and/or higher spatial resolution than other techniques.

Alzheimer's disease (AD) is one of the most severe neurodegenerative disorders. AD diagnosis is mostly based on clinical features, and difficult to find this disease in early stages. MEG is expected to be an early diagnosis tool for cerebrodegenerative disorder. We are developing diagnostic protocols to find out the early stage of AD using MEG system.

II. Missing stimulus paradigm

Intensity of MEG signals responding to single stimulus is usually too small and submerged in noise. Therefore, the stimulus is repeatedly given to the subject and every MEG signal evoked by the stimulus is averaged to improve the signal to noise (S/N) ratio. For example, in the case of typical auditory evoked magnetic field measurement a tone must be repeated more than one hundred times. It takes several minutes to acquire the signals with the good S/N ratio.

It is often difficult for AD patients to control their concentration of attention to the stimulus during the MEG measurement. The missing stimulus paradigm is a kind of passive attention tasks, in which subjects don't need to pay attention to stimuli. The subjects were presented short beep tones with a certain interval. Some tones were omitted randomly from the sequence and omissions were called 'tone-omitted event'. In EEG study with the missing tone stimulus paradigm, it was reported that the specific response with about 200 ms in latency, called N200, was evoked by the tone-omitted event [1][2]. The N200 response is one of the event-related potential (ERP). It is considered as the components related to the stimulus discrimination and is used in cognitive function [3]. The missing tone stimulus paradigm is expected to be useful for diagnosis of the dementia because the subject has only to receive the tone sequence with the omission passively.

Chwee Teck Lim, James C.H. Goh (Eds.): ICBME 2008, Proceedings 23, pp. 9–12, 2009
www.springerlink.com

In this study, we measured event related magnetic field (ERF) which is the magnetic counterpart of ERP in the missing tone stimulus paradigm. AD patients and age-matched controls (NC) were examined. We compare the results of both group and discuss the possibility of MEG as an early diagnosis tool.

III. Materials and Methods

A. MEG measurement

MEG measurement was performed in a magnetically shielded room using a 160-ch whole-head type MEG system developed at Kanazawa Institute of Technology shown in Figure 1. The MEG signals were processed by an on-line band pass filter of 0.1-200 Hz and digitally sampled at 1000 Hz. Subjects lay down on a bed and closed their eyes during the measurement. Auditory stimuli were delivered to the left ear of the subjects through an air tube.

B. Subjects

32 patients with early AD [mean age, 70.8±9.2(SD); 19 male, 13 female] and 32 NC subjects [mean age, 71.4± 4.7(SD); 13 male, 19 female] participated in this study. AD patients were recruited and were ascertained clinical diagnosis of AD by the neurologists at Kanazawa University Hospital. Demographic clinical and neuropsychological data on subjects are shown in Table I. All subjects were checked by Mini Mental State Examination (MMSE). In addition, AD subjects were examined by Clinical Dementia Rating (CDR) scale.

C. Stimulus

We presented a sequence of 1000 Hz short beep tones (50 ms width, 80 dB) at fixed temporal intervals (800 ms inter-stimulus-interval). Some tones were omitted randomly with a probability of 15 % from the sequence. Time sequence of missing stimulus paradigm and MEG recording are illustrated in fig.2. One stimulus sequence was 3 minutes-long and about 30 stimuli were omitted. The stimulus sequence is repeated twice. We didn't tell to the subjects that there would be the omit events in the stimulus sequence. The subjects were told not to mentally count the number of the tones.

The MEG data for 2000 ms around the tone-omitted event were extracted. Each extracted data from a subject was averaged to improve the S/N ratio.

Table 1 Demographic clinical and neuropsychological data of AD and NC

Group	AD group mean±S.D.(range)	NC group mean±S.D.(range)
Number of subjects	32	32
Age	70.8±9.2 (54-86)	71.4±4.7 (64-83)
Sex (males/females)	19/13	13/19
MMSE	21.72±3.95 (14-30)*	28.56±1.72 (24-30)
CDR	0.96±0.26 (0.5-2)	-

Mean value ± S.D. and range in neuropsychological data for each group. MMSE, Mini Mental State Examination; CDR, Clinical Dementia Rating; *, P<0.001



Fig. 1 160-channel whole-head MEG system.

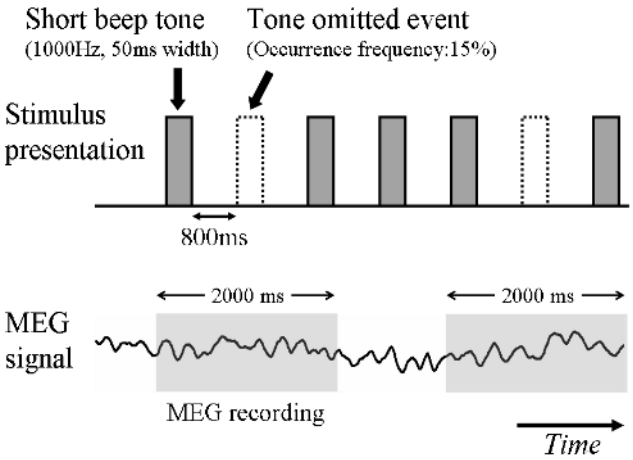


Fig. 2 Time sequence of the missing stimulus paradigm and MEG signal.

IV. Results

After the MEG measurement, we investigated whether the subjects noticed the omission of the some tones in the stimulus sequence. As a result, it was found that 15 NC subjects noticed the omitted events. 17 NC subjects and all AD patients did not notice the omission. We analyzed only

the right hemisphere which is dominant hemisphere to left ear stimulation.

Fig.3(a) shows an example of the averaged MEG signals including the most prominent response from a NC subject. There are three obvious peaks, A, B, and C, in the averaged MEG signal. The peak A and C correspond the typical auditory response to tone stimuli called N100m. The isofield contour map corresponding to the peak A is shown in Fig.3(b). The magnetic field pattern at the peak A was observed over the superior temporal area and its source was estimated at primary auditory cortex. The peak B was found at about 200 ms after the omitted event. This is considered as the magnetic counter part of the N200 response to the tone omitted event. In this paper, we call it N200m response. The isofield contour map corresponding to the N200m response is shown in Fig.3(c). The magnetic field pattern of the N200m response was similar to that of the N100m response. The source location of the N200m response was also close to that of the N100m response.

We estimated group mean waveforms of the averaged MEG signals separately between AD group and NC group as shown in Fig.4. The N200m response and N100m response were prominently observed in the NC group. On the other hand, the N200m response was not clear in the AD group. The amplitude of the signals corresponding to N200m response in the AD group was significantly smaller than that in the NC group ($p < 0.02$, paired t-test).

We separated the NC subjects into two groups. One is the group of the subjects who noticed the tone omission (omission-conscious group). The subjects in the other group didn't notice the omission (omission-unconscious group). We estimated group mean waveforms around the N200m response for the AD group, the NC omission-conscious group, and the NC omission-unconscious group separately as shown in Fig.5. We didn't obtain significant difference of the amplitude of the N200m response peak between the omission-unconscious group and omission-conscious group by paired t-test. This means the N200m response is found from the NC subject independently of consciousness of the tone omission.

On the other hand, all AD patients didn't notice the tone omission. The amplitude of the MEG signal corresponding to the N200m response from the AD group was significantly smaller than that from the NC omission-unconscious group ($p < 0.05$, paired t-test).

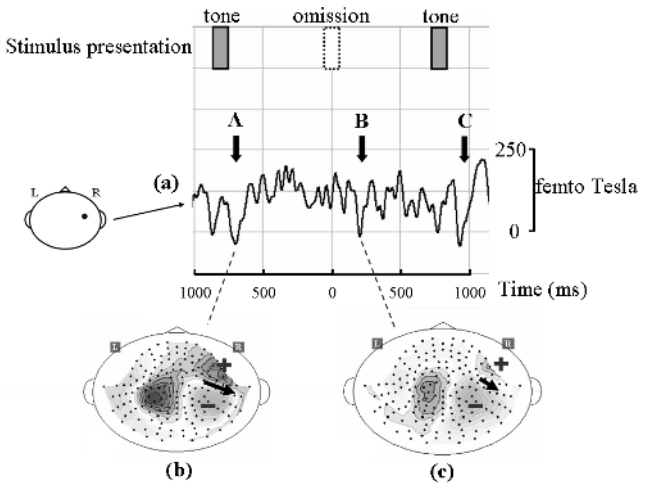


Fig. 3 The averaged MEG signals including the most prominent response from a NC subject.

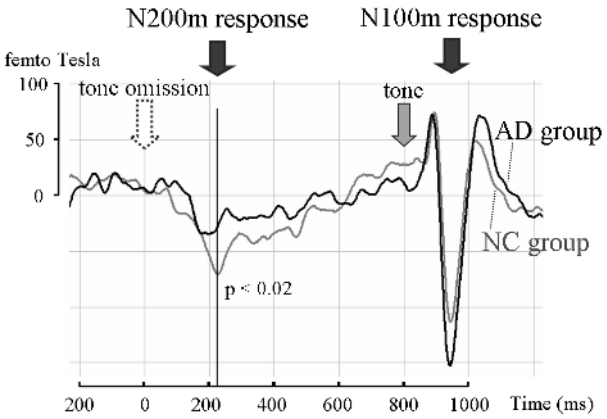


Fig. 4 The group mean waveforms of AD group and NC group.

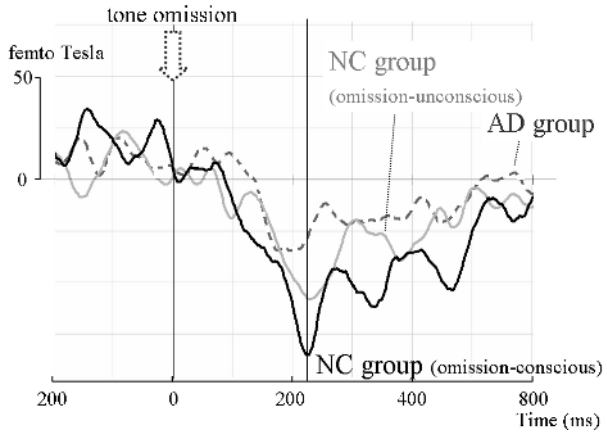


Fig. 5 The group mean waveforms of NC omission-conscious / unconscious group and AD group.

V. Discussion

We could detect the N200m response evoked by the tone omitted event in the NC group. This response was observed

regardless of consciousness of the stimulus in the NC group. However, it was not found in the AD group. This indicates that the absence of the N200m response to the tone omission would be an index of the early stage of AD.

There is a well-known event related potential called mismatch negativity (MMN) in EEG study. It is related to the 'deviant' in the stimulus sequence and is detected even if subjects didn't pay attention to the stimuli. To obtain auditory MMN, a passive oddball paradigm should be applied. In this paradigm, some tones in a stimulus sequence replaced to deviant tones with a certain probability. The subject is given the stimulus sequence with an instruction to ignore the tones. The specific negative component at about 200 ms only after the deviant stimulus is found. This component is called MMN.

The magnetic counterpart of auditory MMN is also detected using MEG with the passive oddball paradigm. It is called mismatch field or MMNm. Pekkonen et al. reported that the auditory MMNm would also be an index of the early stage of AD using the passive oddball paradigm. It is also useful examination for AD patients because the concentration of the attention to the stimulus during the MEG measurement is not necessary as well as the missing stimulus paradigm.

The response to the deviant tone in the passive oddball paradigm is mixture of the N100m response to the tone itself and the MMNm component. Therefore, the extra treatment is always necessary to extract the MMNm component from the obtained MEG response. The MMNm is usually extracted by the subtraction of the MEG response to the standard stimulus from that to the deviant.

In contrast to the MMNm test, the N200m response to the missing tone can be obtained without such an extraction process because the N100m response is not included in the response to the missing tone event.

We compared only amplitude of ERFs between AD subjects and NC subjects in this study. However, the amplitude of MEG signals is affected by the head size and relative position between the head and the sensor array. We are considering two parameters, the ratio between the N200m response and the N100m response and the correlation between magnetic field patterns. To use these parameters, the variable magnetic intensity among the subjects is normalized.

VI. Conclusion

We evaluated the specific MEG component in the missing stimulus paradigm. We could find the significant difference of the amplitude the MEG signals related to the omitted event between AD patients and NC subjects. The method using MEG proposed in this paper can be easily applied to any human subjects. It indicated that the absence of the response to the omitted tone event would be a good index for diagnosis of the early stage of AD.

Acknowledgment

This study was conducted collaboration from the Dept of Neurology of Aging, Kanazawa University Graduate School of Medical Science. This work was supported by CLUSTER project, MEXT, Japan. We thank Dr. Yoshiaki Adachi of Kanazawa Institute of Technology for fruitful discussion and technical advice.

References

1. Hirata K, Yabe H (2003) Electrophysiologic test of event-related N200. Nihon Rinshow 61 (9): 416-421 (in Japanese)
2. H C Hughes, T M Darcey, H I Barkan et al (2001) Response of Human Auditory Association Cortex to the Omission of an Expected Acoustic Event. NeuroImage Vol. 13, pp1073–1089
3. Niwa S, Tsuru N (1997) Event Related Potential. ShinkouIgaku, pp51-64, (in Japanease)
4. Pekkonen E, Huotilainen M, Virtanen J, Naatanen R (1996) Alzheimer's disease affects parallel processing between the auditory cortices. Neuroreport , May 31:7 (8), pp1365-1368

Author: Natsuko Hatsusaka
Institute: Kanazawa Institute of Technology
Street: 3 Amaike
City: Kanazawa
Country: Japan
Email: natsuko@neptune.kanazawa-it.ac.jp

New Architecture For NN Based Image Compression For Optimized Power, Area And Speed

K. Venkata ramanaiah[1], Cyril Prasanna raj[2] and Dr. K. Lal kishore[3]

[1]Principal, Malineni Lakshmaiah Institu of Engineeering andTechnology, Nellore, Andhra Pradesh India.
[2]Program Manger M.S. Ramaiah School of Advanced Studies Bangallore, Karnataka, India
[3]Rector, JNTU Kukatpally Hyderabad Andhra Pradesh, India

Abstract — **The aim of this paper is to investigate new neural network algorithms, architectures and models which are inspired by the image processing capability of the visual system in the human brain, and subsequently to apply these models to medical imaging(MI) applications. Realizing the neural network architecture on FPGA that supports parallelism and reconfigurability. A sincere attempt is taken up to implement the complex and massive parallel architecture on FPGA optimising speed, area, and power with out compromising on image quality and SNR that is a very important criteria for medical image compression. Multi layered neural network (NN) architecture is proposed for compression of high-resolution image, the architecture is implemented on FPGA as it supports reconfigurability. The architecture considered has N-M-N (64-4-64) multi-layered NN structure, which achieves compression ratio of (CR) 93.75. Compression ratio is reconfigurable with change in M. The architecture is generalized and can achieve compression ratios from 2 to 99, which is reconfigurable. Performance of any neural network architecture for compression depends on training; this architecture considers general back propagation training. The training is performed offline, with known set of image samples consisting most of the properties of any standard image. The Mean Square Error (MSE) computed during every iteration of training is scaled and fed back into the network to update the weight matrix at specific points, this reduces the training time. As the weight matrix occupies more space for storage, the redundancies in the weight matrix are exploited and a storage space is created with minimum memory requirement on FPGA. Compression ratios obtained demonstrate performance superiority of the network as compared with JPEG compression standard. Inserting noise on the compressed sets of data, tests the network performance. The hardware complexity, area requirement, speed is compared and discussed; there is a saving of 22% of space on FPGA, with 40% increase in speed, and reducing the power by 12%. The major advantage of this architecture is its reconfigurability on the architecture size that achieves different compression ratios.**

Keywords — **FPGA, Neural Networks, ANN, Matlab, VHDL, Canonic Signed Digit (CSD), Multipliers.**

I. Introduction

"A picture is worth a thousand words." This axiom expresses the essential difference between our ability to perceive linguistic information and visual information. Image that conveys more information than any other data requires huge storage unit and bandwidth for transmission. There is lot of challenges to realize image compression on either hardware or software. Whenever there are challenges there are opportunities.

Recently, there has been an increased interest in the investigation of parallel information processing systems [1]. These so called "artificial neural networks," or simply "neural networks" are networks of simple computational units operating in a parallel and highly interconnected fashion. A neural network can be defined as a "massively parallel distributed processor that has a natural propensity for storing experiential knowledge and making it available for use" [1].

Neural network based image compression techniques mainly involves selection of the network, selection of suitable training technique, selection of suitable training samples, training of the network and calculation of weights, freezing the weight matrix with bias and using the trained network for compression and decompression. In this work the NN architecture with N-M-N (64-4-64) is selected, which can achieve compression ratios from 2 to 99, back-propagation technique algorithm is used for accurate training but this consumes time, appropriate data sets have been selected for accurate computation of weight matrix that can compress any image having the common features.

Section II discusses the back-propagation technique for training the neural network for image compression. Section III discusses the design and Section IV discusses the results and V conclusion.

II. Neural network training

The neural network architecture selected in this work comprises of 64 input forming the input layer which is fed to the hidden layer of size 4x1, the outputs of the output layer is further fed to the output layer of size 64 to get back the original matrix. Back-propagation is one of the neural network training which are directly applied to image compression coding [2,3,4]. The neural network structure

Chwee Teck Lim, James C.H. Goh (Eds.): ICBME 2008, Proceedings 23, pp. 13–17, 2009
www.springerlink.com

can be illustrated as in Figure.1. The input layer and output layer are fully connected to the hidden layer. Compression is achieved by designing the value of *K*, the number of neurons at the hidden layer, less than that of neurons at both input and the output layers. The input image is split up into blocks or vectors of 8 X 8, 4 X 4 or 16 X 16 pixels. In accordance with the neural network structure shown in Fig.1, the operation of a linear network can be described as follows:

$$h_j = \sum_{i=1}^{N} w_{ji} X_i, 1 \le j \le K \qquad (2.1)$$

For encoding and

$$\overline{X_i} = \sum_{j=1}^{K} w'_{ij} h_j, 1 \le i \le N \qquad (2.2)$$

For decoding where $xi \in [0, 1]$ denotes the normalized pixel values for grey scale images with grey levels [0, 255] [2,5,6].

In this work the image samples have been appropriately selected to achieve accuracy in the image compression and decompression. The image data sets should consist some of the properties like edges, diagonals, curves, random variations and discontinuities. Figures,3,4, and 5 shows the kind of image samples selected for training the network.

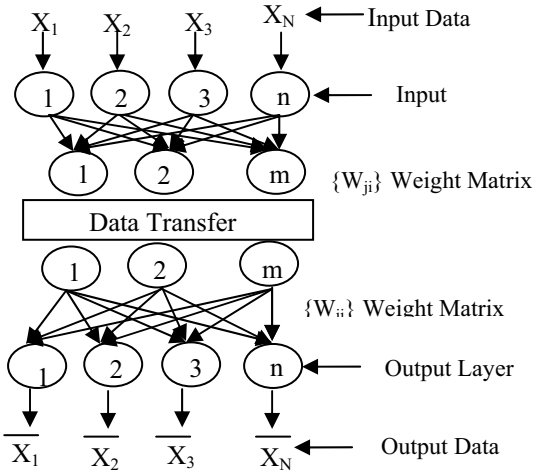


Fig.1 Simple Compression Model

III. Design

Table 1 shows the compression ratios with the network sizes. The training is accomplished on the network with maximum nets. This helps in varying the dimension, which can be reconfigured as per the requirements. Cottrell et al [6] has used a two layered neural network model with neurons in the second layer (output layer) more than the neurons in the first layer as shown in figure 1.

The input image of size N×N is regrouped in to smaller blocks of 4×4. Each 4×4 block is further converted to 16×1 linear matrix, and rearranged in to a linear set of 16×M matrix. The input matrix of size 16×1 is transformed to 4×1 by the first layer. The 4×1 matrix is further decompressed to 16×1 by the output layer bellow equation explains the process of compression.

Table 1. Network Size and Compression Ratios

Network size	Size of hidden layer	Compression ratio
64-64-64	64	0%
64-32-64	32	50%
64-16-64	16	75%
64-08-64	08	87.5%
64-04-64	04	93.75%
64-01-64	01	98.5%

[4×16] [16×1] = [4×1]
[W_f] [I] = [C]

W_f is the weight matrix on the input, I is the input matrix, C is the compressed output of the first layer. C matrix is fed to output layer to get back the original matrix.

$$[16\times4]\,[4\times1] = [16\times1]$$

$$[Ws]\,[C] = [D]$$

For the input to be equal to the target i.e. I=D, the weight matrix W_f and Ws is to be identified, which is achieved by the setting W_f and W_s to initial values and updating the values of W_f and W_s based on error between D and the actual target [T=I]. This processing of updating the weights to get minimum error in the output is training. The following are the complexities in training and hardware implementation:

1) To update the entire 128 weight matrix requires more time the updation time increases with increase in number of iterations.
2) Most of the weights are found to be redundant; even then they are stored separately in a memory.
3) The weights are in the range of ± 1.2, hence there is a need for accurate binary representation.
4) Compression depends upon number of neurons considered in the first layer.
5) There is a need for generalization of the network so that it can compress and decompress any set of image data.

The proposed work addresses these issues. The architecture is realized on FPGA. The results obtained are compared with the architecture reported in the literature.

Proposed Work

The Neural Network architecture of size 64-4-64 a two-layered network is considered. The input weight matrix which is of size [4×64] and output weight matrix of size [64×4] is initialized to an arbitrary value. To generalize the network for compression and decompression of any image, 20 sets of image samples are considered having all the properties of an image such as vertical lines, horizontal lines, diagonals, curves, edges, plain surfaces and sharp edges. The network is trained using these data sets, so that the weight matrix obtained can work with any unknown image having the basic qualities of the image. Keeping track of the way in which the weight matrix is being updated the algorithm developed for training is modified so that the weight gets updated only at required positions, which reduces the total time required for training. As the training is done offline using MATLAB simulator, the total time in training with the proposed work is compared in table 2. The time is reduced as the weights are not updated at every node, but is updated only at specific points based on the previous history of the network. This is shown in figure2.

Table2. Column3 depicts the total CPU time taken for training based on modified algorithm. Column 4 in table2 depicts the difference between the actual weights and the weights calculated using the proposed method.

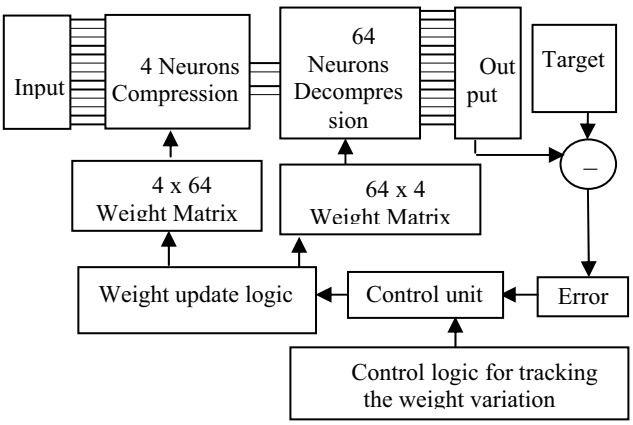


Fig. 2 Proposed model for updating the weights at specific location



Fig. 3 Medical Image (MRI Scan)

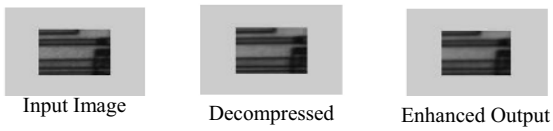


Fig. 4 Real World Pictures (Gunshot)

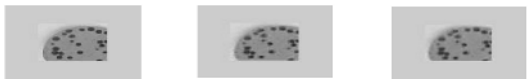


Fig. 5 Electronic Image (Circuit)

The MATLAB results after training and simulation it was found that even in the presence of noise the output layer was able to generate the original data. This is one of the major advantages of using NN techniques for compression. Enhancing further the decompressed data can eliminate the noise obtained at the receiver.

The accuracy of the receiver in reproducing the original image increases with increase in training sets and number of iteration. In this work the training is carried out until the error is reduced to 0.001. The weights calculated in the proposed method have the valves ranging from ±1.2. In order to represent the weight using binary number system, canonic signed digit number system is used which can represent the numbers ranging from ± 4/3. The advantage of this number system is such that it reduces the number of operations required in implementing the product of two matrices.

Table 2 CPU time for weight calculations/training

Images	Normal CPU time	Proposed CPU time	Error in weight matrix between general-proposed architecture
Test1	346 units	186 units	± 0.02
Test2	524 units	254 units	± 0.18
Test3	686 units	320 units	± 0.01
Test4	496 units	210 units	± 0.11
Test5	128 units	90 units	± 0.06

Simulation Results

Simulation waveforms obtained from for the CSD Multiplier done using Xilinx ISE and ModelSim, it is shown in figure 6 for 40 x 0.6.

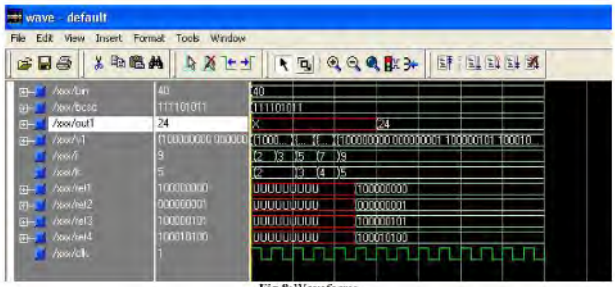


Fig. 6 CSD multiplier waveforms using ModelSim

Storage space requirement

The weight matrix on the input side consists of 4×64 and the output side consists of 64×4, there are totally 128 weight elements. Each weight is represented using 10-bit BCSD number system; this consumes a space of 1280bits. The weight matrix observed which is shown table4, explains the redundancy in the weights. It also demonstrates the range of the weight matrix, hence very much suitable for CSD representation.

Table 3. Weight Matrix 4x16 – only few columns are shown
net_s.IW (1,1) ans =

Columns 1 through 4			
0.6669	0.4804	0.1364	-0.1068
0.4005	0.2488	-0.0575	-0.3003
1.2619	1.0753	0.6092	0.2117
0.0247	0.0989	0.1955	0.2619
Columns 5 through 8			
0.4566	0.3721	0.2078	0.1188
-0.0236	- 0.0930	-0.1883	-0.2194
0.6837	0.6759	0.5840	0.5328
0.0023	0.0105	0.0342	0.0546

The results obtained have been compared with its MATLAB counterpart. It is found that both the results almost match. This RTL code is synthesized using Xilinx ISE targeting Spartan III 400K gate device.

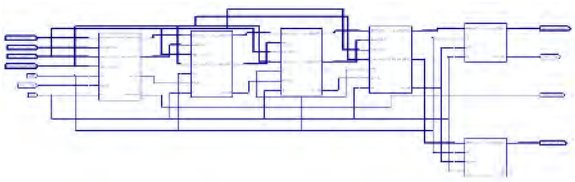


Fig. 7 Synthesized RTL using Xilinx ISE on Spartan III 400K gate device

IV. Hardware analysis and results

After the implementation of the above said CSD multiplier based NN architecture for image compression with modified weight storage matrix on FPGA we obtain the following results. Time taken, power consumed and hardware utilization by one multiplier to produce output is 13ns, 25mW, and 20%.

Table 4. Summary of the hardware implementation results

Gate count		Power	Max Frequency
Modified	General		
80K out of 400K (20% of the entire gate count available)	102K out of 400K gates (26% of the entire gate count available)	25mW (Leakage and switching power) reduced by 12% as when compared to the general architecture	13ns (76 MHz) increased by 40% as when compared to the general architecture

The number of I/O cells including the input, compressed data, output and control pins is reduced to 78; this can be reduced further if we increase the compression ratio. Figure 8 show the comparison of the area, timing and power report for different network size taken in table 1. The timing, area and power get optimized with higher compression ratio, however affecting the quality of the image.

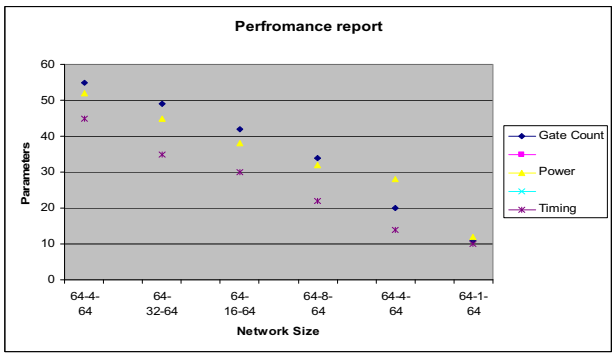


Fig. 8 Comparison of area, time and power.

V. Conclusion

The results obtained and discussed in this work clearly demonstrates the superiority of NN based techniques for medical image compression. With NN techniques being adopted SNR is within the expected limits and is better than classical techniques. SNR is remaining constant with increases in compression ratio. This demonstrates the effectiveness of NN based techniques proposed in this paper

for medical image compression. Different compression ratios can be achieved by only changing the hidden layer size. This is achieved by selecting the appropriate weights required at the input layer and out put layer. FPGA implementation of the proposed work optimizing speed, area, and power is discussed. This can be further optimized when implemented on ASIC, which looses the property of reconfigurability. Proper selection of training data sets with number of training iterations introduces redundancy in the weight matrix which can be exploited to reduce the storage space and hence optimized area. Selection of image sets for training imposes a limitation on the performance; different medical images have multiple properties that cannot be captured with unique weight matrix. This networks performance is found efficient for only a set class of medical images.

REFERENCES

1. S. Haykin, Neural Networks: A Comprehensive Foundation. New York, NY: Macmillan, 1994.
2. S.Carrato, Neural networks for image compression, Neural Networks: Adv. and Appl. 2 ed., Gelenbe Pub, North-Holland, Amsterdam, 1992, pp. 177-198.
3. R.D. Dony, S. Haykin, Neural network approaches to image compression, Proc. IEEE 83 (2) (February 1995) 288-303.
4. A. Namphol, S. Chin, M. Arozullah, Image compression with a hierarchical neural network IEEE Trans. Aerospace Electronic Systems 32 (1) (January 1996) 326-337
5. Benbenisti et al., New simple three-layer neural network for image compression, Opt. Eng. 36 (1997) 1814-1817
6. G.W. Cottrell, P. Munro, D. Zipser, Learning internal representations from grey-scale images: an example of extensional programming, in: Proc. 9th Annual Cognitive Science Society Conf., Seattle, WA, 1987, pp. 461-473.
7. M. Rabbani and R. Joshi, "An overview of the JPEG 2000 still image compression standard, "Signal Processing: Image Communication, Vol. 17, Elsevier Science B.V., 2002, pp. 3-48,.
8. J.Robinson and V. Kecman, "Combining Support Vector Machine Learning With the Discrete Cosine Transform in Image Compression," IEEE Transactions on Neural Networks, Vol. 14, No. 4,IEEE, July 2003, pp.950-958,.
9. Ivan Vilvovic, “An experience in Image compression using neural networks’, 48th International Symposium ELMAR-2006, June 2006, Zadar, Croatia.
10. K.Venkata Ramanaiah, K.Lal Kishore and P.Gopal Reddy “Power Efficient Multilayer Neural Network for Image Compression”, Information Technology Journal 6(8): 1252–1257, 2007 ISSN 1812–5638 @ 2007 Asian Network for Scientific Information.

Address of the corresponding author:

Author: K.VENKATA RAMANAIAH,
Institute: Malineni Lakshmaiah institute of engineering & technology
Street: Near Ramanna Palem
City: Nellore , Andhra Pradesh
Country: India -524366
Email: ramanaiahkota@yahoo.com

A Statistical Model to Estimate Flow Mediated Dilation Using Recorded Finger Photoplethysmogram

R. Jaafar[1], E. Zahedi[2], M.A. Mohd Ali[3]

[1] Medical Engineering Section, University Kuala Lumpur - British Malaysian Institute, Gombak, Selangor, Malaysia
[2] School of Electrical Engineering, SHARIF University of Technology, PO Box 11365-9363, Tehran, IRAN
[3] Department of Electrical, Electronic & Systems Engineering, Universiti Kebangsaan Malaysia, Bangi, Selangor, Malaysia

Abstract — **Noninvasive measurement of brachial artery (BA) flow mediated dilation (FMD), commonly measured by high resolution ultrasonography, has provided a non-invasive means for the evaluation of endothelial function. Recently, another technique based on finger photopletysmogram (PPG) analysis has been proposed by the authors. In this paper, simultaneous measurement of BA FMD and PPG signals data from 86 human subjects (43 healthy and 43 risk) is analyzed and a statistical model is proposed to estimate the BA FMD based on PPG signals, the BA diameter at baseline as well as other demographics factors such as age and gender. Linear regression by multivariate analysis was conducted to obtain the variables that were significantly related to BA FMD. The mean of absolute error for the model was 0.16 ± 0.12 and the estimated data (via PPG) is correlated to the measured one (via ultrasound) with a correlation factor R = 0.725. As a confirmation, it was found that the estimated FMD for the risk group (22.3 ± 3.4 %) was significantly lower than that of the healthy group (25.9 ± 3.5 %), $p < 0.01$, whereas a similar trend was observed from the measured data: risk group (22.3 ± 5.2 %) versus healthy group (26.1 ± 7.8 %), $p < 0.001$. The model can estimate peak BA (ultrasound) FMD from the information of the baseline BA diameter and peak PPG AC, allowing for an alternative means of evaluating the endothelial function.**

Keywords — **Endothelial function, flow mediated dilation, photoplethysmography**

I. Introduction

Endothelial function (EF) – a phenomenon known as the ability of the vascular endothelium to vasodilate [1] in response to physiologic and pharmacologic vasodilators [2], is commonly measured non-invasively through high resolution ultrasound measurement of the brachial artery (BA) before and after flow mediated dilation (FMD) stimulation by temporary cuff occlusion at the BA. Due to the main drawbacks of the technique which include the requirement of skilled operators to handle the ultrasound system and measure in real-time the BA diameter, and extended cuff occlusion time (up to 5 minutes) to stimulate for FMD response, we have proposed the evaluation of EF by analysis of the finger photoplethysmogram (PPG).

Parallel data acquisition of peak BA FMD and peak PPG pulse amplitude (AC) responses were conducted to validate the efficacy of the newly proposed method. We have demonstrated that the analysis of pulse amplitude changes of the finger PPG induced by BA FMD is capable of detecting the FMD response in the peripheral circulation in a similar manner to the conducting artery [3]. In this paper, using the available data of BA FMD and PPG AC gathered from the previous study, we examined a statistical modeling using linear multiple regression.

Data of 43 healthy subjects (free from any cardiovascular disease (CVD) risk factor) and 43 risk subjects (possessing at least one CVD risk factor) were included in the analysis of the statistical model. The healthy and risk groups comprised of males and females subjects of age matched. The main objective of the statistical modeling is to predict the individual subject's BA FMD response by using the subject's clinical parameters and the recorded PPG AC data.

II. Methods

A. Fundamentals of linear multiple regression

In a linear bivariate system, when two variables are correlated, then knowing one variable will allow one to predict the other variable by prediction through the linear regression equation. The stronger the correlation, the closer the variable will fall to the regression line and therefore the more accurate the prediction. Linear multiple regression is simply the extension of the linear bivariate principle, where one can predict a variable on the basis of several other variables. Having more than one independent variables is more rational and useful when predicting biological process as it is more likely to be influenced by some combination of several factors. Using the multiple linear regression one can test theories (or models) precisely which set of independent variables is influencing the dependent variable of the investigated system. The linear multiple regression can be represented as the following relationship:

$$Y_i = \beta_0 + \beta_1 X_{1i} + \beta_2 X_{2i} + \ldots + \beta_k X_{ki} + \varepsilon_i \quad (1)$$

Chwee Teck Lim, James C.H. Goh (Eds.): ICBME 2008, Proceedings 23, pp. 18–21, 2009
www.springerlink.com

where Y_i is the dependent variable
$X_{1,2,...ki}$ are the independent variables
β_0 is the y-intercept
$\beta_{1,2,...k}$ are the slopes between $X_{1,2,...ki}$ and Y_i
ε_i is random error

Modeling by linear regression requires one to make a few assumptions regarding the predicted (dependent) variables and the model errors. The predicted variable is assumed to be linearly distributed and can be tested using the Kolmogorov Smirnov (K-S) test for normality. The errors for the model are assumed to be independent and the probability distribution of the error is normal with constant variance and zero mean.

In order to achieve the main objectives to predict the BA FMD response by the use of recorded peak PPG AC data, the following processes have been involved throughout the course of statistical modeling:

- study the associations between outcomes and predictors
- investigate the behaviour of model residues and multicolinearity of the predictors
- obtain a mathematical equations that represent the linear model
- predict cases using the regression model
- evaluate model performance

B. Statistical modeling using SPSS

In SPSS, the independent variables are identified as the predictor variables while the dependent variable is identified as the criterion variable. Multiple regression requires a large number of observations. The number of cases (participants) must substantially exceed the number of predictor variables used in the regression. The absolute minimum is five times as many participants as predictor variables [4]. A more acceptable ratio is 10:1, but some people argue that this should be as high as 40:1 for some statistical selection methods [4].

In the statistical methods, the order in which the predictor variables are entered into (or taken out of) the model is determined according to the strength of their correlation with the criterion variable. Several versions of statistical methods include Enter, Forward, Backward and Stepwise selection [4]. The Enter method is the direct method where variables entered are evaluated in the model. In Forward selection, SPSS enters the variables into the model one at a time in an order determined by the strength of their correlation with the criterion variable. The effect of adding each is assessed as it is entered, and variables that do not significantly add to the success of the model are excluded. In Backward selection, SPSS enters all the predictor variables into the model. The weakest predictor variable is then removed and the regression re-calculated. If this significantly weakens the model then the predictor variable is re-entered - otherwise it is deleted. This procedure is then repeated until only useful predictor variables remain in the model. The Stepwise method is the most sophisticated of these statistical methods where each variable is entered in sequence and its value assessed. If adding the variable contributes to the model then it is retained, but all other variables in the model are then re-tested to see if they are still contributing to the success of the model. If they no longer contribute significantly they are removed. Figure 1 shows the snapshot of SPSS screen window for linear regression analysis.

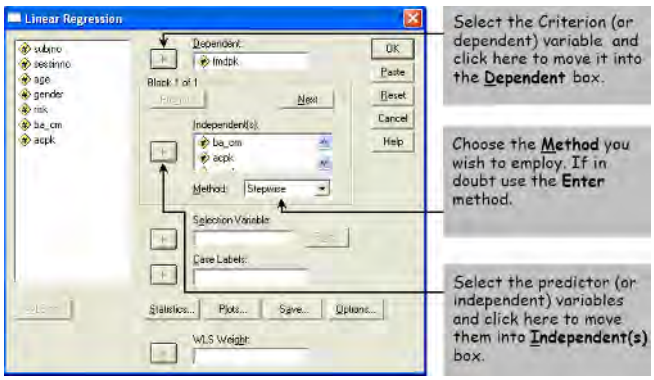


Fig. 1 Linear regression using SPSS

C. Model parameters

Beta (β): The β value is a measure of how strongly each predictor variable influences the criterion variable. It is also a measure of the correlation between the observed value and the predicted value of the criterion variable.

R Square (R^2): It is the square of the measure of correlation that indicates the proportion of the variance in the criterion variable which is accounted for by the model.

Adjusted R Square: It is the value calculated which takes into account the number of variables in the model and the number of observations (participants) the model is based on.

Multicolinearity: It is the correlations between pairs of variables which represent the measure of combined effects.

D. Model validation

Evaluation of the linear multiple regression model can be done by variation measure, residual analysis, parameter significance and test for multicollinearity. The indication of multicollinearity is correlations of pairs of X variables are more than correlations with Y variable. The remedy to this

problem is eliminating one correlated X variable from the model [5].

III. Results and discussion

Eighty six subjects (43 healthy and 43 risk) were included in the statistical model. The selected healthy and risk subjects have similar group mean age (42.7 ± 8.9 versus 46.5 ± 10.7, p = 0.077). All test variables (age, BA diameter, peak FMD and peak PPG AC) for the sample population were normally distributed. The first step to linear regression analysis was to obtain the information regarding the correlation between two variables. This was done by tabulating the Pearson correlation coefficients of pairs of variables. The variables that are significantly correlated will be entered into an initial model.

Since each of the variables included in the correlation test is correlated to some extent to another variable, the age, gender, risk, BA diameter, and peak PPG AC have been entered as the independent variables that were expected to influence the dependent variable of peak FMD. Results of the initial model coefficients computed using the enter method in SPSS were found non-significant ($p > 0.05$ in all situations) for age, gender and risk for CVD. However, the coefficients for BA diameter and peak PPG AC were significant coefficients ($p < 0.05$). Therefore, the age, gender and risk for CVD were removed from the model and the coefficients of the new model are shown in Table 1. In this model, only baseline BA diameter and peak PPG AC are the independent predictors for estimating the peak FMD.

All coefficients remain significant after the removal of the three variables in the initial model. Model residues (Table 2), which are the differences between observed value and the predicted value, for the new model have no outliers (minimum and maximum > ± 3), are independent (Durbin-Watson estimate ranges between 0 and 4.0 in Table 3) and are normally distributed [5]. There was no multicollinearity between BA diameter and peak PPG AC that is indicated by high tolerance, which gives the strength of the linear relationship among the independent variables [5]. Therefore, this model can be accepted and considered as the final model. The coefficients (B) from the final model coefficients represent the values of β_0, β_1 and β_2 of the generalized linear multiple regression as represented by equation 1. The final model can be represented as:

$$\text{peak FMD} = 35.72 - 4.71 \times \text{BA diameter} + 0.03 \times \text{peak PPG AC} \quad (2)$$

The adjusted R square (Table 3) indicates that 44.4 % of the BA diameter and peak PPG AC data are taken together to influence the dependent peak FMD data in the model. The estimated model output were then computed and compared to the measured data. The correlation between model output (estimated using equation 2) and measured data as well as the mean of the absolute error, which is the absolute difference between measured and estimated data, were evaluated to provide information regarding the model performance and the group statistics (Table 4).

Table 1 Model[a] coefficients

	Unstd. Coeff.		Std. Coeff.			
	B	Std. Error	Beta	t	Sig.	Tolerance
Constant	35.72	3.99	Nil	8.95	< 0.001	
BA diameter	-4.71	1.02	-0.43	-4.63	< 0.001	0.761
peak PPG AC	0.03	0.01	0.35	3.82	< 0.001	0.761

[a] Dependent variable: peak FMD. Predictors: Constant, BA diameter, peak PPG AC

Table 2 Residual statistics

	Minimum	Maximum	Mean	SD	N
Predicted Value	15.47	34.40	24.34	4.62	86
Residual	-11.67	11.45	0.00	5.03	86
Std. Predicted Value	-1.92	2.18	0.00	1.00	86
Std. Residual	-2.29	2.25	0.00	0.99	86

Table 3 Model summary

R	R Square	Adjusted R Square	Std. Error of the Estimate	Durbin-Watson
0.676	0.457	0.444	5.093	1.630

Table 4 Group statistics for the final model

	Healthy group			Risk group			*t*-test
	N	Mean	SD	N	Mean	SD	p value
Measured peak FMD	43	26.4	7.67	43	22.3	5.19	0.005
Estimated peak FMD	43	26.6	4.29	43	22.4	4.21	< 0.001
Model error	43	0.16	0.115	43	0.17	0.120	0.728*

* Not significant

The estimated FMD for the healthy group (26.4 ± 7.67 %) was significantly higher than that of the risk group (22.3 ± 5.19 %), p = 0.005; similar trend as observed from the measured data, risk group (22.4 ± 4.21 %) versus healthy group (26.1 ± 7.8 %), $p < 0.001$. There was no difference between the two groups in terms of the absolute model error (0.16 ± 0.115 versus 0.17 ± 0.120), p = 0.768. Thus, the model absolute error can be represented as the total mean

error of 0.16 ± 0.117. The model output (estimated peak FMD) is correlated with the measured peak FMD for the sample population (R = 0.725) (Fig. 2). The receiver operating characteristics (ROC) for the estimated model output and measured data is shown in Fig. 3. Obviously, the model has better performance as the total area under the ROC for the model is larger than that of the measured data.

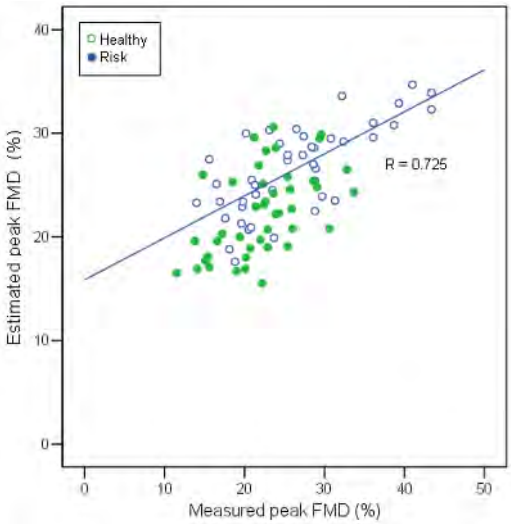


Fig. 2 Regression of the estimated and measured data

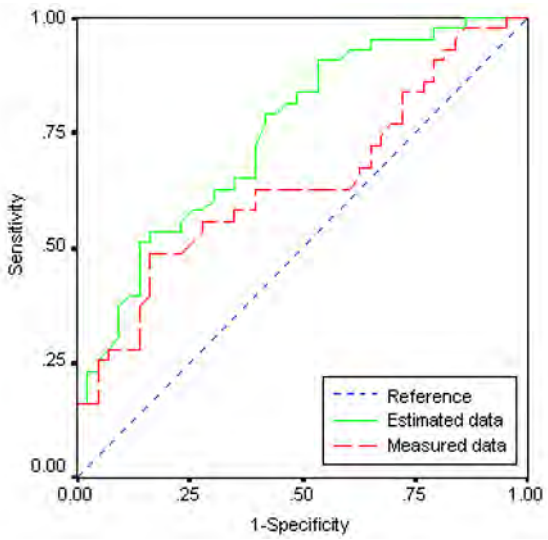


Fig. 3 ROC curve for the model (estimated) output and measured data

IV. Conclusions

In this paper, we demonstrated an exercise of statistical modeling. The results show that a statistical model by linear multiple regression can predict (by calculation) the peak BA FMD. The model uses the information of baseline BA diameter and peak PPG AC for a person to calculate for an estimated peak FMD for the person. The model provides means of estimating the peak BA FMD allowing for an alternative technique of evaluating the endothelial function.

Acknowledgment

This work has been supported by the Science Fund grant (01-01-02-SF0227) from the Ministry of Science, Technology and Innovation, Malaysia. We would like to thank Noraidatulakma Abdullah for her graceful involvement in the statistical data analysis.

References

1. Vanhoutte P M (1989) Endothelium and control of vascular function: State of the art lecture. *Hypertension* 13: 658-667
2. Abularrage C J, Sidawy A N, Aidinian G, et al. (2005) Evaluation of macrocirculatory endothelium-dependent and endothelium independent vasoreactivity in vascular disease. Perspectives in Vascular Surgery Endovascular Therapy 3: 45-53
3. Zahedi E, Jaafar R, Mohd Ali M A, et al. (2008) Finger photoplethysmogram pulse amplitude changes induced by flow mediated dilation. Physiological Measurement 29: 625-637
4. Brace N., Kemp R, Snelgar R (2006) SPSS for Psychologists. Psychology Press, London
5. Chan Y H (2004). Biostatistics 201: Linear Regression Analysis. Singapore Medical Journal 45(2): 55-61

Author: Rosmina Jaafar
Institute: University Kuala Lumpur-British Malaysian Institute
Street: Jalan Sg Pusu, Gombak,
City: Selangor
Country: Malaysia
Email: rosmina@bmi.unikl.edu.my

Automatic Extraction of Blood Vessels, Bifurcations and End Points in the Retinal Vascular Tree

Edoardo Ardizzone, Roberto Pirrone, Orazio Gambino and Francesco Scaturro

Università degli Studi di Palermo
Dipartimento di Ingegneria Informatica
Building 6-3rd floor – 90128 Palermo (Italy)

Abstract — **In this paper we present an effective algorithm for automated extraction of the vascular tree in retinal images, including bifurcations, crossovers and end-points detection. Correct identification of these features in the ocular fundus helps the diagnosis of important systematic diseases, such as diabetes and hypertension. The pre-processing consists in artefacts removal based on anisotropic diffusion filter. Then a matched filter is applied to enhance blood vessels. The filter uses a full adaptive kernel because each vessel has a proper orientation and thickness. The kernel of the filter needs to be rotated for all possible directions. As a consequence, a suitable kernel has been designed to match this requirement. The maximum filter response is retained for each pixel and the contrast is increased again to make easier the next step. A threshold operator is applied to obtain a binary image of the vascular tree. Finally, a length filter produces a clean and complete vascular tree structure by removing isolated pixels, using the concept of connected pixels labelling. Once the binary image of vascular tree is obtained, we detect vascular bifurcations, crossovers and end points using a cross correlation based method. We measured the algorithm performance evaluating the area under the ROC curve computed comparing the number of blood vessels recognized using our approach with those labelled manually in the dataset provided by the Drive database. This curve is used also for threshold tuning.**

Keywords — **Anisotropic Diffusion, Matched Filter, Retinal Vessels, ROC curve.**

I. Introduction

The retinal image is easily acquirable with a medical device called fundus camera, consisting in a powerful digital camera with a dedicated optics [1].

The two main anatomical structures of the retinal image involved in the diagnostic process are the blood vessels and the optic disc. In particular, the vascular tree is a very important structure because the analysis of the vascular intersections allows discovering lesions of the retina and performing clinical studies [2]. We propose a vessel extraction method that has been tested on the fundus images provided by the DRIVE database [6][4]. It contains 20 test images where three observers performed manual extraction of the retinal vessels along with the corresponding ROIs to distinguish the foreground from the background. In [10] the vessel extraction is performed using an adaptive threshold followed by a multi-scale analytical scheme based on Gabor filters and scale multiplication. The method described in [11] makes use of a tracking technique and a classification phase based on fuzzy c-mean for vessel cross-section identification. Moreover, a greedy algorithm is used to delete false vessels. A final step is devoted to detect bifurcations and crossing points. In [12] the optic nerve and the macula are detected using images acquired with digital red-free fundus photography. After the vascular tree extraction, spatial features like average thickness, and average orientation of the vessels are measured. Our method starts removing artefacts using the anisotropic diffusion filter. Then a suitable matched filter kernel has been developed that is used with a contrast stretching operator to put in evidence the vessels with respect to the background. A threshold is used to obtain a binary image of the vasculature. The threshold has been experimentally tuned using the ROC curve, which describes the efficiency of the vessels classification with respect to the reference one provided by the Drive dataset. The last step is the use of a length filter to erase little and isolated. End-, bifurcation-, and crossover- points are detected like in [8]. In the rest of the paper the processing steps are detailed and the performance evaluation set-up is described. Finally some conclusions are drawn.

II. Blood vessels extraction

A. Artifacts removal

The retinal image is corrupted by strong intensity variations. A circle-shaped luminance peak can be seen in the region of the optical nerve, the fovea region exhibits intensity attenuation, because it is a depression on the retinal surface, and a diffuse shading artifact afflicts all the eye fundus. Before applying any segmentation task, an intensity compensation phase must be performed. Being the retinal image a RGB one, we consider the G channel of the RGB triad as the intensity image component (see fig.1-a). The most common way to suppress intensity variations consists in the application of the homomorphic filter, but it generates a halo artifact on the

Chwee Teck Lim, James C.H. Goh (Eds.): ICBME 2008, Proceedings 23, pp. 22–26, 2009
www.springerlink.com

boundary between the retina and the background (see fig.1-b). The filter must take into account a suitable Region Of Interest (ROI) to select the retina, thus avoiding this undesirable phenomenon. The G channel image is filtered using an anisotropic diffusion filter [13] and it is tuned in correspondence of the region selected by the ROI. The ROI is created as a binary image where the region surrounded by the boundary of the retina is filled with 1s (see fig.1-c). The boundary is extracted using a Canny edge detector. The resulting image (see fig. 1-d) is obtained using the following formula:

$$R(i,j) = \frac{G(i,j)}{G_f(i,j)}$$

Where $G_f(i,j)$ is the filtered versions of the original image $G(i,j)$. We wanted low-pass behavior for the anisotropic diffusion filter D, so adopted the Gaussian-like diffusion function instead of the Lorentzian-like one:

$$D(\nabla G) = e^{\frac{|\nabla G|^2}{k^2}}$$

Being an edge-preserving filter aimed to noise removal, the value of the parameter k must be enough high to warrant the low-pass behavior and it has to be selected as a function of the retinal intensity gradient ∇G in correspondence of the ROI. The parameter k is chosen as follows:

$$k = \alpha \cdot std(\nabla G)$$

α =5 and 50 iterations have been used for all the dataset. The intensities of the resulting image $R(i,j)$ have been normalized to the interval [0,1] to be independent by the input dynamics. A side effect of the adopted filtering is a contrast decreasing, so a contrast stretching is performed, as shown in fig.1-e. The target dynamics to be obtained by the stretching operator has been selected as follows:

$$[\mu - \beta \cdot \sigma, \mu + \sigma]$$

where μ and σ are the mean and the standard deviation, respectively. To avoid residual halo phenomenon, the output dynamics has been limited to 60% of the available one, and the input interval is unbalanced by the β coefficient, as it can be seen above. The value of β has been set to 1.5 for all the dataset. A final noise removal step based on anisotropic filter is performed, obtaining the image in fig.1-f. We determined experimentally the parameters for this task: k=0.3 and 3 iterations.

B. Matched Filter

The matched filter is a spatial filter whose kernel is the template of the vessel cross section. The kernel can be rotated so that it imitates the vessel displacement; it is convolved with the image to enhance the blood vessels. A suitable definition of the kernel is fundamental to obtain good performance. We used a kernel defined as follows:

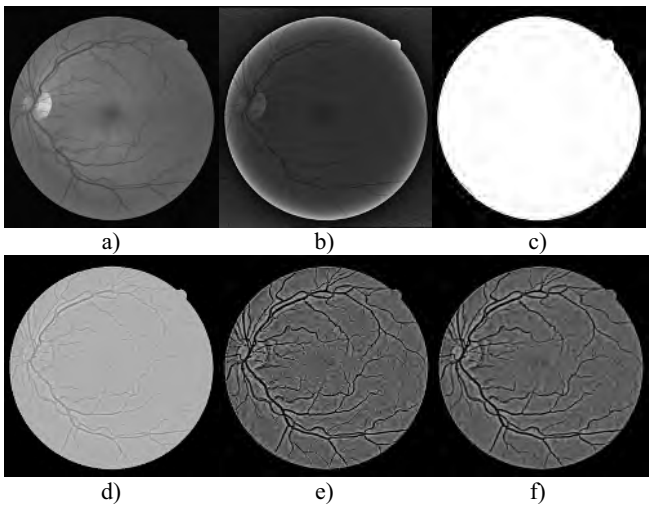


Fig. 1 a) Green channel of the RGB original image; b) the image in a) filtered with a standard homomorphic filter; c) the ROI; d) filtered image $R(i,j)$ using anisotropic diffusion; e) applying contrast stretching to the image in d); f) noise removal.

$$x_\theta = x\cos(\theta) + y\sin(\theta)$$

$$y_\theta = -x\sin(\theta) + y\cos(\theta)$$

$$f_1(x_\theta, y_\theta) = 0.5 - \frac{1}{1 + \left(\sqrt{\left(\frac{x_\theta}{\sigma_x}\right)^2 + \left(\frac{y_\theta}{\sigma_y}\right)^2}\right)^{esp}}$$

$$f_2(x_\theta, y_\theta) = -0.5 \cdot \frac{1}{1 + \left(\sqrt{\left(\frac{x_\theta}{k_1 \cdot \sigma_x}\right)^2 + \left(\frac{y_\theta}{k_2 \cdot \sigma_y}\right)^2}\right)^{esp}}$$

$$f(x_\theta, y_\theta) = f_1(x_\theta, y_\theta) \cdot f_2(x_\theta, y_\theta)$$

Here θ is the rotation angle, σ_x and σ_y control the length along the main directions, *esp* determines the roundness of the inverted Gaussian, k_1 and k_2 control lateral elongation along both x and y, and we subtract the mean value of f to keep them positive. We obtain 12 kernels varying θ [2]. The best results have been obtained using a 15x15 pixels wide kernel and the following parameters: σ_x = 100, σ_y = 0.18, *esp* = 2, $k_1 = k_2 = 3$ (see fig.2). Like in [8], a contrast stretching is performed on the Matched Filter Response (MFR) in the range $[\bar{x} - \sigma,\ \bar{x} + 2\sigma]$ where $\bar{x}$ is the mean value of the dynamics, and σ is the standard deviation.

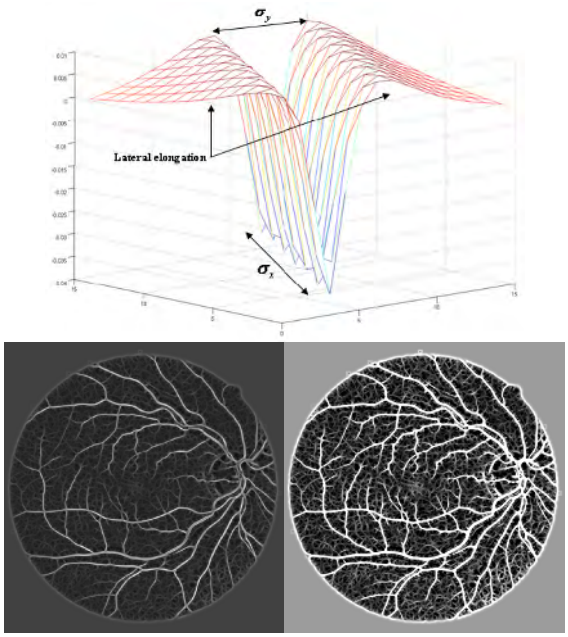


Fig. 2 UP: The kernel used for the Matching filter; DOWN: The Matched filter result (left) and contrast stretching application (right).

C. Threshold operator

A sliding threshold operator has been applied to the MFR image to obtain a binary image, which allows detecting blood vessels as connected components. The threshold value has been tuned comparing our result with the corresponding segmented image in the dataset. A ROC curve (Receiver Operating Characteristic) [7] has been drawn that is a Sensitivity vs. (1-Specificity) diagram while moving the threshold. These quantities are defined as follows:

$$Sens = \frac{TP}{TP + FN} \; ; \; Spec = \frac{TN}{FP + TN}$$

True positives (TP) are the recognized vessels, true negatives (TN) are non-vessel objects, and false positives (FP) are binary objects considered erroneously as vessels. Finally, we considered the background component in both images as the false negative (FN). The threshold value is selected in correspondence of the closest point to the unitary value of sensitivity and (1-specificity) (see fig. 4).

D. Small objects removal

The length filter cleans the image obtained applying the threshold operator by deleting little and isolated objects. Each object is labeled using the 8-connected component criterion and its area is measured. The object whose area is less than a threshold is cancelled. We fixed this value to 150 pixels.

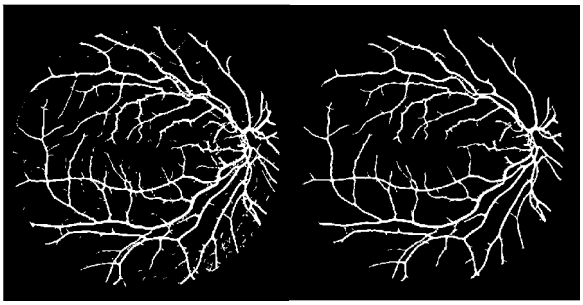


Fig. 3 Binary image obtained using the threshold (left), and small object removal (right).

III. Performance Evaluation

The efficiency analysis can be performed measuring the ROC curve area [7]. A ROC curve has been obtained for each test image in Drive database increasing the threshold values of the threshold. The mean sensitivity-specificity values have been used to draw the ROC curve in fig.4. The area under the ROC curve with our method is 0.953. Table 1 shows a comparison among different methods in literature (see [9] for a review) and our approach.

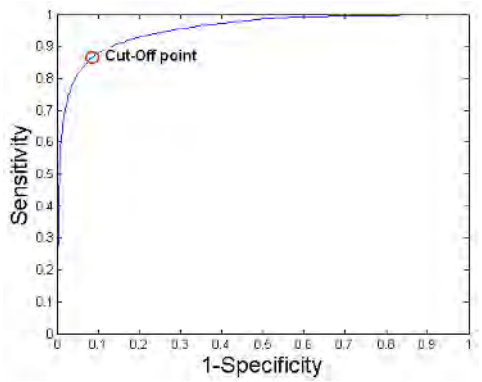


Fig. 4 ROC curve mean(sensitivity) vs. 1-mean(specificity) computed on the test images of DRIVE. The red circle indicates the best Cut-Off point used to select the threshold value.

Tab. 1

Detection method	Az
Matched filter; Chauduri et al. [14]	0.91
Adaptive local thresholding; Jiang and al. [3]	0.93
Ridge-baed segmentation; Staal et al. [4]	0.95
Single-scale Gabor filters; Rangayyan et al. [5]	0.95
Our Method	0.953
Multiscale Gabor filters; Oloumi at al. [9]	0.96

IV. Feature points detection

End-points, bifurcations, and crossover points are detected like in [8]. Briefly, the morphological skeleton filter is applied on the binary image of the vascular tree and dedicated kernels are convolved with the resulting image to detect the feature points (see fig. 5 and fig. 6).

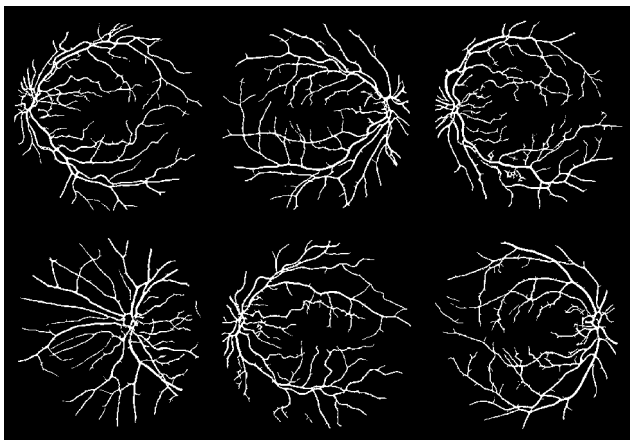


Fig. 5 Some examples of vascular trees extracted by the algorithm.

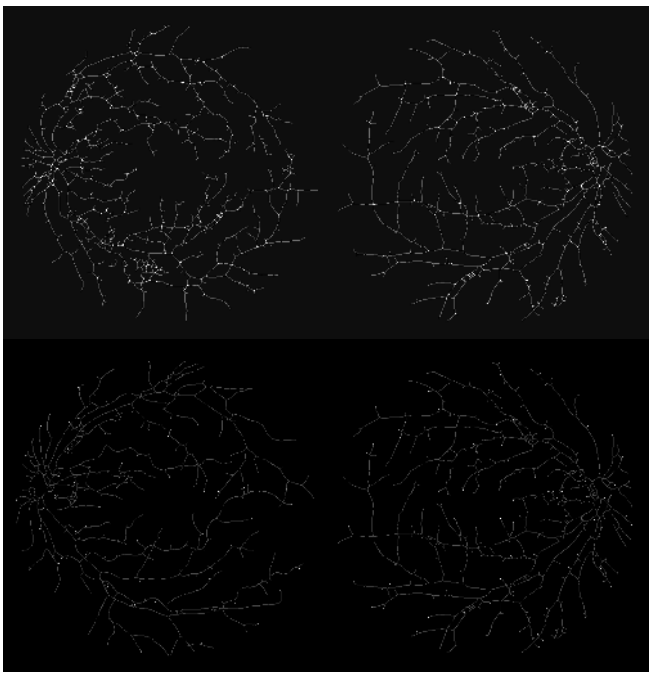


Fig. 6 Feature points detected on the trees depicted in fig. 5.

V. Conclusions and future work

A method for vessels extraction on retinal images has been presented. The performance is comparable with the most recent methods presented in literature, as shown in tab.1. The pre-processing plays a fundamental role so that better artifacts removal techniques and local filters must be developed to increase the contrast between vessels and background. In this way the Matched filter will be able to enhance the vessels in a better way.

References

1. Patton N, Aslam TM, MacGillivray T, Dearye IJ, Dhillon B, Eikelboom RH, Yogesan K, and Constable IJ. Retinal image analysis: Concepts, applications and potential. Progress in Retinal and Eye Research, 25:99–127, 2006.
2. Thitiporn Chanwimaluang, Guoliang Fan. An Efficient Blood Vessel Detection Algorithm for Retinal Images using Local Entropy Thresholding, in Proc. of the 2003 IEEE International Symposium on Circuits and Systems, Bangkok, Thailand, May 25-28, 2003.
3. Jiang X and Mojon D. Adaptive local thresholding by verification-based multithreshold probing with application to vessel detection in retinal images. IEEE Transactions on Pattern Analysis and Machine Intelligence, 25(1):131–137, 2003.
4. Staal J, Abramoff MD, Niemeijer M, Viergever MA, and van Ginneken B. Ridge-based vessel segmentation in color images of the retina. IEEE Transactions on Medical Imaging, 23(4):501–509, 2004.
5. Rangayyan RM, Oloumi Faraz, Oloumi Foad, Eshghzadeh-Zanjani P, and Ayres FJ. Detection of blood vessels in the retina using Gabor filters. In Proceedings of the 20th Canadian Conference on Electrical and Computer Engineering (CCECE 2007), page in press, Vancouver, BC, Canada, 22-26 April 2007. IEEE.
6. DRIVE: Digital Retinal Images for Vessel Extraction, http://www.isi.uu.nl/Research/Databases/DRIVE/, accessed on October 5, 2006
7. Metz CE. Basic principles of ROC analysis. Seminars in Nuclear Medicine, VIII(4):283–298, 1978.
8. E. Ardizzone, R. Pirrone, O. Gambino and S. Radosta. Blood Vessels and Feature Points Detection on Retinal Images. 30th Annual International IEEE EMBS Conference Vancouver, British Columbia, Canada, August 20-24, 2008
9. Faraz Oloumi, Rangaraj M. Rangayyan_, Foad Oloumi, Peyman Eshghzadeh-Zanjani, and F´abio J. Ayres. Detection of Blood Vessels in Fundus Images of the Retina using Gabor Wavelets. 29th Annual International Conference of the IEEE EMBS Cité Internationale, Lyon, France, August 23-26, 2007
10. Qin Li, Lei Zhang, David Zhang, Hong Kong A New Approach to Automated Retinal Vessel Segmentation Using Multiscale Analysis 18th International Conference on Pattern Recognition (ICPR'06) Volume 4 pp. 77-80
11. E. Grisan, A. Pesce, A. Giani, M. Forachhia, A. Ruggeri A new tracking system for the robust extraction of retinal vessel structure (2004) Proc. 26th Annual International Conference of IEEE-EMBS, pp. 1620-1623, IEEE, New York.

12. Kenneth W. Tobin, Edward Chaum, V. Priya Govindasamy and Thomas P. Karnowski, Detection of Anatomic Structures in Human Retinal Imagery. IEEE Trans. On Med. Imaging, vol 26, no.12, December 2007
13. P. Perona and J. Malik, Scale-Space and Edge Detection Using Anisotropic Diffusion, IEEE Transactions on Pattern Analysis and Machine Intelligence, 12(7):629-639, July 1990
14. Chaudhuri S, Chatterjee S, Katz N, Nelson M, and Goldbaum M. Detection of blood vessels in retinal images using two-dimensional matched filters. IEEE Transactions on Medical Imaging, 8:263–269,1989.

Recent Developments in Optimizing Optical Tools for Air Bubble Detection in Medical Devices Used in Fluid Transport

S. Ravichandran[1], R. Shanthini[2], R.R. Nur Naadhirah[2], W. Yikai[2], J. Deviga[2], M. Prema[2] and L. Clinton[2]

[1] Faculty, Temasek Engineering School, Temasek Polytechnic, Singapore
[2] Student, Temasek Engineering School, Temasek Polytechnic, Singapore

Abstract — **Modelling techniques for optimizing bubble detection tools in the infrared band used in conjunction with a drug transport mechanism for the transport of intravenous fluids in clinical practice have been evaluated qualitatively using simulation techniques. Sensors which are used in signal processing often have limitation when they are made to work in noisy environment. Noise in the working environment can be from various sources such as from power line, high frequency RF fields and background luminance. In case of certain optical sensors, coupling schemes and the interference from devices which are in close proximity to the sensors can also contribute to significant noise. Qualitative studies on the effect of background luminance noise have provided a good understanding on the degree of susceptibility of the optoelectronic receiver for various luminance noises resulting in interferences in the output of a tool developed for the detection of air bubbles in fluid pathways called the "Optical Bubble Detection Tool". Experience gained from the earlier studies has provided the required knowledge for developing a design which is less susceptible to external disturbances. The dynamic excitation method for the "Optical Bubble Detection Tool" was introduced by modifying the electronic interface of the earlier "Optical Bubble Detection Tool". This was easily achieved by understanding the requirements of the pulsed current for energizing the transmitter of the "Optical Bubble Detection Tool". As the frequency of excitation and the intensity of the emitted infrared are factors which decide the resolution and sensitivity of the "Optical Bubble Detection Tool", it was optimized for several operating environments which are under the influence of other external radiations in the visible range and non-visible range.**

Keywords — **Bubble detection tool, Background luminance noise, Optical sensors**

I. Introduction

The rate of infusion in intravenous fluid delivery depends on the selected drug, dosage and the pathological condition of the subject receiving infusion. It is important that any drug transported into the body through the venous circulation should be free from air bubbles as accidental induction of air bubble in the vascular system can cause serious complications and is sometimes fatal [1].

Air bubble detection in a drug transport system is an important safety parameter and there are a few ways of detecting air bubble in the tubing of the drug transport system. Our studies were focused on two popular tools namely the "Ultrasound Bubble Detection Tool" and the "Optical Bubble Detection Tool". As the coupling factor between transducer and the tubing are very critical in the "Ultrasound Bubble Detection Tool", it demands specific tubing and interfaces for reliable detection. This problem related to coupling factor is however not a serious issue with the "Optical Bubble Detection Tool" designed for detecting air bubble in the drug transport system.

Studies on the development of the "Optical Bubble Detection Tool" were conducted with matched emitters and receivers working in the infrared band and we optimized the receiver and the transmitter based on the optical band suitable for intravenous drug delivery applications [1].

Sensors used in signal processing often have limitations when they are made to work in noisy environment. Noise in the working environment can be from various sources such as from power line, high frequency RF fields, background luminance in case of certain optical sensors, coupling schemes and the interference from electro mechanical devices which are in close proximity to the sensors. Noise components associated with the electronic detector circuit and system electronics have been discussed in detail by several authors [2, 3] and these are mostly Johnson noise, Flicker noise and Short noise. Most of the problems related to electrical noise and RF interference can be overcome by using suitable signal conditioners and the proper shielding techniques. However, noise problems associated with the optical devices due to background luminance and other optical interference cannot be easily handled by simple electronic signal conditioning tools and thus necessitates alternative techniques to overcome the limitations [1]. Based on our experimental study, we have modeled the "Optical Bubble Detection Tool" to improve its performance in real time applications. We have carefully analyzed the factors which are critical in operating the "Optical Bubble Detection Tool" in a given Infra Red (IR) band based on a simulation study and have also assessed the performance of the tool under various conditions [4].

Chwee Teck Lim, James C.H. Goh (Eds.): ICBME 2008, Proceedings 23, pp. 27–30, 2009
www.springerlink.com

II. Materials and methods

Before evaluating the modeling techniques for this system, it is important to have some idea on the system architecture and the various modules it contains for meeting the requirements of the system as a whole.

The system architecture contains modules such as the optoelectronic module, microcontroller module, and the electromechanical module and these modules are all integrated in such a way that it is possible for the user to configure a model specific application protocol in drug delivery. Each module is further discussed in detail in this paper.

III. Modeling protocols

The conventional excitation mode, incorporating static excitation, is the most common mode of excitation seen in the earlier systems. A steady source of light in the infrared or near infrared range is generated with the help of constant current source generated from the common power supply. The steady beam of light after passing through the fluid transport tubing is translated as voltage variations reflecting the optical density of the medium transported. The advantages of the conventional excitation mode are that it is easy to tune the system for the required range of excitation for capturing the signals corresponding to a specific optical density and it is quite convenient to optimize the wavelength for a given optical pathway for the detection of the air bubble in the fluid transport tubing [5].

Though this excitation mode can easily be configured for the detection of the air bubble, it has many disadvantages in real time applications. The disadvantage of this excitation mode is that this mode is usually more susceptible to the ambient noise signal present around the source and the receiver. Thus, this system necessitates a very reliable optical shielding around the optical pathway to prevent interference from external luminance, which is present in any clinical setup. Qualitative studies on the effect of background luminance noise have provided a good understanding on the degree of susceptibility of the optoelectronic receiver for various luminance noises resulting in interferences in the output of the "Optical Bubble Detection Tool". The performance of the "Optical Bubble Detection Tool" for various operating conditions related to the external environment and the flow pattern has shown that there is no major deviation in the linearity of the system related to flow in the static excitation mode. However, in this mode, the "Optical Bubble Detection Tool" was found to be highly susceptible to the ambient noise created by the surrounding background luminance. A simplified scheme of the system is as shown in Fig. 1.

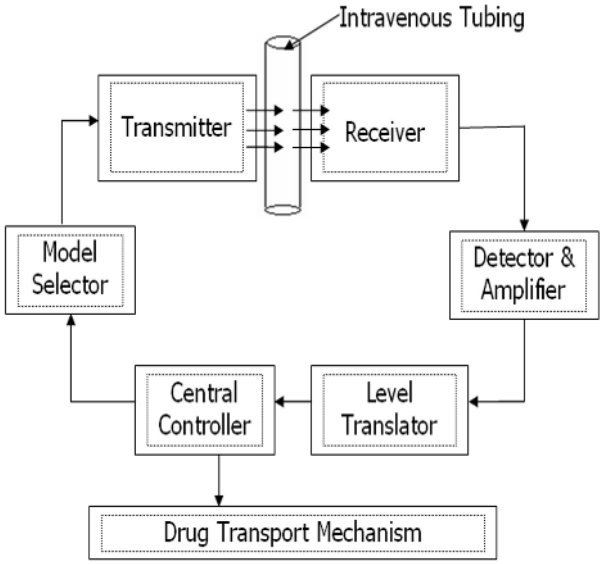


Fig. 1 Scheme for modelling "Optical Bubble Detection Tool" designed for Drug Transport System.

Studies conducted on the performance of the optoelectronic interface under various conditions have provided valuable data related to static excitation techniques.

Table 1 Result for Static Excitation Mode

Test Condition	Output in the Presence of Ambient Noise	
Air bubble present	Heavily Shielded Sensor	Unshielded Sensor
	Logic 1 (2.7V).	Logic 1 (2.7V).
Air bubble absent	Logic 0 (>0.6V).	Logic 1 (2.7V).

The limitations of the "static excitation" method have provided the basis for implementing "dynamic excitation" methods for using the "Optical Bubble Detection Tool". This has been further improved by the modeling techniques investigated during the development of the "Optical Bubble Detection Tool" in the drug transport system.

A. Dynamic Excitation Mode

In general, parameters such as optical wavelength, modulation frequency and receivers' capture threshold are critical in deciding the overall efficiency of the bubble detection system.

The dynamic excitation mode can be achieved in several ways and the most efficient way is to customize the parameters for a specific task related to the detection of bubble in the presence of common external interference in the given clinical setup. The dynamic excitation method for the "Op-

tical Bubble Detection Tool" was first introduced by modifying the electronic interface of the existing "Optical Bubble Detection Tool". This was easily achieved by providing pulsed current for energizing the transmitter of the "Optical Bubble Detection Tool". As the frequency of excitation and the intensity of the emitted infrared are factors which decide the resolution and sensitivity of the "Optical Bubble Detection Tool", it is to be optimized for an operating environment which is under the influence of other external radiations in the visible range and non-visible range. The microcontroller module, which is the heart of the central controller, is fully supported by essential interfaces such as system console and LCD display for setting the rate of infusion of the intravenous fluid and also for selecting an appropriate model for "Optical Bubble Detection Tool" [5].

Table 2 Results for Dynamic Excitation Mode

Test Condition	Output in the Presence of Ambient Noise	
Air bubble present	Heavily Shielded Sensor	Unshielded Sensor
	Logic 1 (2.7V).	Logic 1 (2.7V).
Air bubble absent	Logic 0 (>0.6V).	Logic 0 (>0.6V).

It can be seen that the results obtained using the dynamic excitation mode are more promising in the absence of air bubble, especially in situations where the output is to be realized in the presence of ambient noise with not fully shielded optical sensors.

IV. Operating principles

Flow of fluids in the drug transport mechanisms for therapeutic applications is assisted by the electromechanical module. The electromechanical module provides controlled peristalsis of the intravenous fluid through the transport tubing in a pre-programmed fashion and this is made possible by using the system console. The system console is user friendly and helps the user to set the parameters for treatment.

The "Optical Bubble Detection Tool" interfacing the central controller is at the entry point of the fluid transport mechanism and monitors for any air bubbles in the contents transported in the tubing.

A. Microcontroller Module

The basic program flow chart of the microcontroller architecture is shown in Fig. 2.

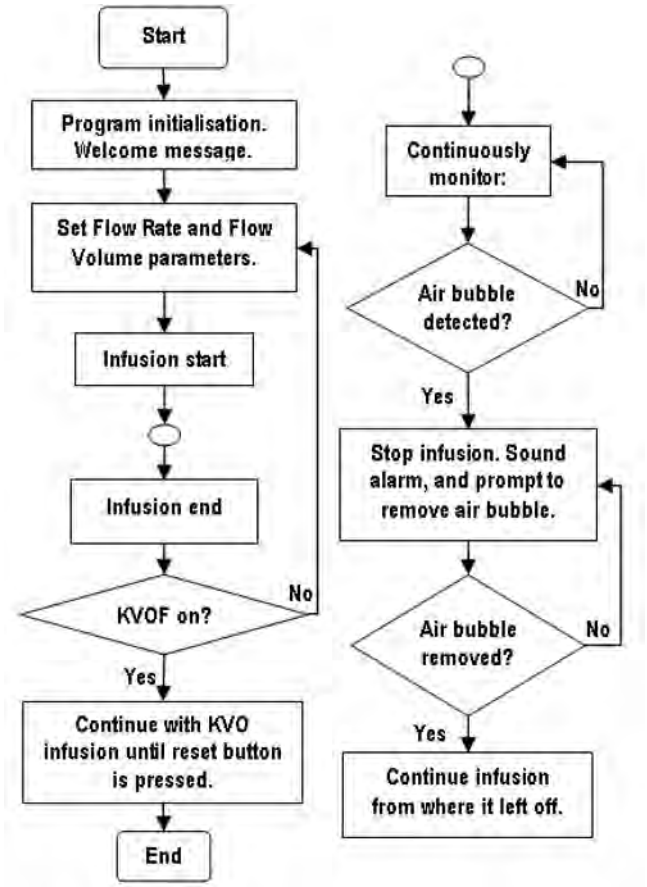


Fig. 2 Flowchart of the microcontroller module.

Intravenous fluid delivery mechanism is precisely controlled with the help of a microcontroller which has interfaces such as those linked to optical bubble detection system, system console for setting parameters, LCD display for displaying parameters and electromechanical module consisting of the linear peristalsis mechanism for regulating the fluid flow rate.

The ports of the microcontroller interfacing the system console allows the user to enter data related to flow volume and flow rate, and also to activate the "keep vein open function (KVOF)" if required.

B. System operations

After running the initialization routine, the microcontroller displays a welcome message on the LCD display of the system and prompts the user to set in parameters related to Flow Rate and Flow Volume. These parameters are entered using the system console.

Once the infusion process is activated, the process goes on and will end once the set amount of fluid is delivered at the pre-programmed rate. At the end of the fluid delivery it is possible to activate another function called the KVOF, which will ensure that the fluid pathway inside the intravenous needle will not get occluded due to the presence of venous blood flow.

If by accident, an air bubble should be present in the intravenous fluid infused, the "Optical Bubble Detection System" will detect the bubble and would activate an alarm for the user to remove the bubble before it could be infused into the venous system.

V. Preliminary studies

A. Reliability studies of flow rate and volume

The Linear Peristalsis Driver has been tested in real-time. We have tested the reliability of the device after setting a given Flow Rate and Flow Volume by running the system with the standard infusion package consisting of the infusion bag and intravenous tubing containing the drip chamber. By validating the settings for repeated trials for various settings, of flow rates and flow volumes, the reliability of the system was established under conditions existing in clinical setup.

B. Reliability studies on bubble detection

The sensitivity of the "Optical Bubble Detection Tool" was also checked under various conditions to record the immunity offered by the bubble detection circuitry in the presence of several luminance backgrounds. The luminance backgrounds were simulated to record the output of the "Optical Bubble Detection Tool" based on qualitative assessment.

VI. Results

In our studies we have modeled the "Optical Bubble Detection Tool" with the help of the central controller for dynamic excitation mode and we have found pulsed frequencies from 2 kHz to 10 kHz suitable in designing an application specific model for a given working environment. It was also possible to optimize the intensity of excitation based on the selected model working under a given situation.

VII. Conclusion

Studies carried out with the "Optical Bubble Detection Tool" in clinical practice has clearly indicated that the dynamic excitation mode modeled with the help of the central controller is more promising in providing reliable data in a noisy clinical environment. The electromechanical module of the system was found reliable in providing linear peristalsis of fluid over a long duration during preliminary studies.

References

1. Muhammad Bukhari Bin Amiruddin, S.Ravichandran, Teo Xu Lian Eunice, Low Wei Song Klement, Tho Wee Liang, Lim Yu Sheng Edward and Oon Siew Kuan, *"Studies on modelling techniques for optimizing optical bubble detection tools (OBDT) in drug delivery"*, Proceedings of the 12th International Conference on Biomedical Engineering (ICBME)December 2005, Singapore.
2. Watts, R.*, "Infrared Technology Fundamentals and System Applications: Short Course",* Environmental Research Institute of Michigan, June 1990.
3. Holst, G., "*Electro-Optical Imaging System Performance",* Orlando, FL: JCD Publishing, 1995, 146.
4. Ronald G. Driggers, Paul Cox, Timothy Edwards (1999): *"Introduction to Infrared and Electro- Optical Systems",* (Artech House INC.Norwood, MA 02062), 132-134
5. S. Ravichandran[1], R. Shanthini[2], R. R. Nur Naadhirah[2], W. Yikai[2], J. Deviga[2], M. Prema[2] and L. Clinton[2] *"Modelling and Control of Intravenous Drug Delivery System Aided by Optical Bubble Detection Tools"*, i-CREATe 2008 conference from 13 to 15 May 2008, Bangkok, Thailand.

Author: S.Ravichandran
Institute: Temasek Polytechnic
Street: 21 Tampines Ave 1
City: Singapore 529757
Country: Singapore
Emails: subbaram@tp.edu.sg, dr.sun.moon@gmail.com

General Purpose Adaptive Biosignal Acquisition System Combining FPGA and FPAA

Pedro Antonio Mou, Chang Hao Chen, Sio Hang Pun, Peng Un Mak and Mang I. Vai

Department of Electrical and Electronics Engineering, Faculty of Science and Technology, University of Macau, Macau SAR, China

Abstract — **This paper introduces a general purpose intelligent adaptive biosignal acquisition system both using Field Programmable Gate Array (FPGA) and Field Programmable Analog Array (FPAA). The design system inherits the powerful properties from the above devices to provide a stable and adaptive platform for processing various biosignals like ECG, EMG and EEG, etc. This system implementation solves the complexity in biosignal samples acquisition in home healthcare and stability in long term monitoring. It can be dynamically reconfigured and adapt to acquire different biosignals without changing any hardware. This system provides a simplified testing platform allowing different algorithms for processing real time biosignals embedded into it. In additions, the RS232 serial data port (or USB) can implement a connection with personal computer to ease and speed up the acquiring of biosignal samples or test results for further analysis. Alternatively, the system is also designed for outputting acquired and/or processed biosignals to PDA/PC at real time for visual inspection of results.**

Keywords — **adaptive, biosignal, acquisition, FPAA, FPGA**

I. Introduction

According to the World Health Organization (WHO), the percentage of death and disability caused by chronic diseases (including cardiovascular diseases) will soar from 43% in 2002 to 76% in 2020 [1]. WHO and governments in the world foresee this great demand for medical services and recognize the importance to reduce the rapidly growing pressure on limited medical resources. In addition, the growing concerns of people on self healthiness also speed up the pressure on medical resources and demand for home healthcare system.

Home healthcare system and telemedicine is one of the effective methods to assist in reducing the pressure on public medical resources by distributing health-caring and monitoring to patients' home or other remote locations. The cost in money and time can be controlled at a lower level (which could be very high in rural areas or developing countries) while providing more conveniences to patients in reading self-healthiness, and moreover, feasible to have functions for long term health status logging which is very rare but useful in today's medical system for treatment and prevention of diseases (including chronic diseases).

The emergence and rapid development of home healthcare system makes affordable and portable home healthcare devices available to patients. But on the other hand, these existing or proposed systems are usually signals dependant (for example, ECG only) like [2], [3]. One important reason or the difficulty for these systems to extend the usage to a wider range of biosignals is the fundamental differences between various common biosignals. Different biosignals require frontends with different characteristics (amplification, bandwidth, etc) for acquisition, and of which is an essential procedure before any processing or analysis. This difference restricted the possibility of having a single general purpose system which is efficient and capable of acquiring different biosignals at the same time with higher flexibility, lower cost and smaller in size for non-clinical medical usage.

In this paper, a novel concept is proposed to build a general purpose adaptive biosignal acquisition system combining Field Programmable Gate Array (FPGA) and Field Programmable Analogue Array (FPAA) to act as an intelligent and re-configurable general frontend for various biosignals including electrocardiogram (ECG), electromyography (EMG), electroencephalography (EEG), etc. This adaptive frontend can provide a simplified platform for integrating different algorithms for processing different biosignals at real time in home healthcare.

II. System architecture

In designing the acquisition system, characteristics and inherent properties of several hardware are studied and analyzed. To support a re-configurable environment and opportunity for converting to SOC in future, FPGA is chosen to be responsible for the digital part and FPAA for the analog part, with an ADC between them.

A. Field Programmable Gate Array (FPGA)

Field Programmable Gate Array, or FPGA, is a kind of semiconductor device with programmable and re-configurable logic blocks and interconnects which can build up digital components like basic logic gates (AND, OR, etc), make up more complex functions such as decoders or other mathematical functions. Because of this freely re-configura-

The work presented in this paper is supported by The Science and Technology Development Fund of Macau under grant 014/2007/A1 and by the Research Committee of the University of Macau under Grants RG051/05-06S/VMI/FST, RG061/06-07S/VMI/FST, and RG075/07-08S/VMI/FST.

Chwee Teck Lim, James C.H. Goh (Eds.): ICBME 2008, Proceedings 23, pp. 31–34, 2009
www.springerlink.com

ble characteristic, it can be programmed to process different functions in parallel and independently, using different sections in one FPGA. For example, the control of biosignal acquisitions can work independently with an ECG QRS detection algorithm and sending acquired data to a host computer without affecting each other. In our system, FPGA acts as the main controller to manage different components and I/Os between them.

B. Field Programmable Analogue Array (FPAA)

Field Programmable Analogue Array, or FPAA, is an analog counterpart device to FPGA but it contains configurable analog blocks instead of logic blocks which can be programmed and used to implement analog signal processing functions like amplifications, differentiation, integration, subtraction, addition, multiplication, log, exponential and configured to build up operational amplifiers and filters. The feasibility and performance in processing biosignals using FPAA is studied and tested in [34] with acceptable results. In the proposed system, FPAA acts as a general frontend to be dynamically programmed by the FPGA.

C. Biosignals Acquisition

The characteristics between different bioelectric signals vary a lot [5]. As illustrated in Fig. 1, the frequency range for electrocardiogram (ECG) is between 0.05-100Hz with a dynamic range of 1-10mV. For surface electromyography (surface EMG), the frequency range becomes 2-500Hz with a 50μV-5mV dynamic range. While for electroencephalogram (EEG), the dynamic range becomes 2μV -0.1mV although the frequency range is 0.5-100Hz which is similar to other signals. Comparing only these three commonly discussed biosignals, the great variance in the dynamic range among different biosignals induced the design challenge of a general frontend for multiple biosignals acquisition.

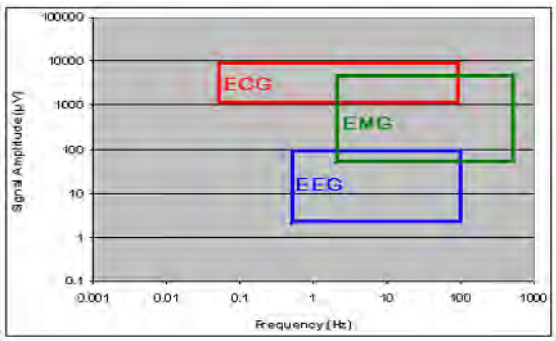


Fig. 1 – Signal Amplitude (μV) against Frequency (Hz) of different biosignals ECG, EMG and EEG

D. General Purpose Adaptive Biosignal Acquisition System

In order to achieve and build a general frontend for the acquisition of multiple biosignals, FPGA and FPAA are combined to be used in the proposed system.

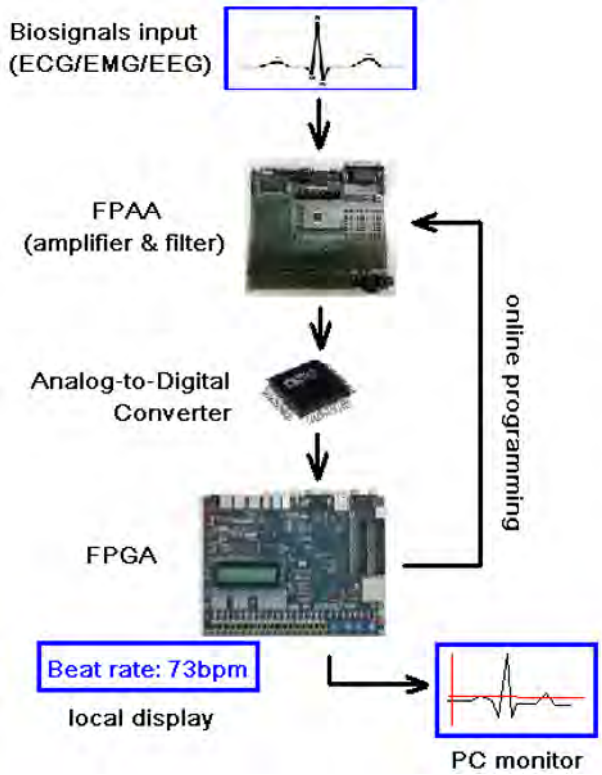


Fig. 2 – Architecture overview of acquisition system

In this adaptive acquisition system as illustrated in Fig. 2, biosignals input is amplified and filtered by the FPAA, digitized through the Analog-to-Digital Converter (ADC) and fed into the FPGA. FPAA is under the control of FPGA and the inherent re-configurable property of FPAA allows its amplification and filter to be dynamically re-configured through a serial interface. Appropriately selected parameters for the amplifiers and filters are programmed into the FPAA in order to retrieve a less tainted biosignal from the noisy human-body. This allows the acquisition frontend to adapt different biosignals to a common and an acceptable input range of the ADC before they can be processed in digital within the FPGA. In this way, signals will always be within the operating input range of the ADC.

Acquired samples of signal can be transferred to the PDA/PC for post-processing and displaying in real-time, and on the other hand, the FPGA provides a platform for embedding different signal processing algorithms to manipulate the

acquired data. It allows a single or multiple algorithms to be embedded for processing biosignals in parallel and independently. Local display is used as an indicator for verification of the results of the processed biosignals.

III. Implementation

In building the adaptive acquisition system, we used a DE2 FPGA evaluation board from Altera, an AN231 FPAA board from Anadigm and a 24-bit ADC AD7764 from Analog Device. Standard VHDL is also chosen as the programming language to implement the initial framework of the whole system because it leaves the opportunity for migrating the whole system to a System-On-Chip (SOC) in the future. The 24-bit ADC employed in this system is mainly for improving the dynamic range of the system to cope with any unexpected input. It also has an adjustable sampling rate for controlling power consumption (slower is lower). As this system mainly targets at non-clinical medical device for home healthcare or portable device, a low cost FPGA and FPAA with VHDL combination was chosen. This combination can provide the system with numerous advantages including but not limited to higher flexibility, lower power consumption, smaller in size.

In implementing the re-configurable frontend, configuration data of the FPAA for acquiring different biosignals are stored inside the FPGA non-volatile memory preventing data lost when power lost. Configuration code is loaded into the FPAA according to the input biosignals. The system allows user to easily switch the frontend between an ECG, an EMG or even an EEG configuration in real-time. Once the FPAA is configured correctly, the FPGA can start acquiring the signal samples through the ADC.

Through this dynamic programmable frontend and the freely programmable property of FPGA, the area inside FPGA is able to be designed into two separate sections. The first part is for configuring FPAA and acquiring samples from ADC, while the other part is reserved for embedding different signal processing algorithms and acting as the backend system for analyzing real-time data, which can miniaturize the system.

Transmission of acquired samples to personal computers (PC) using RS232 (or USB in the future) is considered in the design for extended usage which requires higher computational power for complicated algorithms that does not migrate-able to FPGA.

IV. Results

A general purpose adaptive biosignals acquisition system has been built for evaluation in this paper. For each biosignal (ECG, EMG, EEG), a separate configuration is designed to be programmed into the adaptive FPAA frontend which is stored inside the FPGA. The 24-bit ADC is configured to work at a sampling rate around 507Hz which is limited by the combination of DE2 onboard 27MHz clock generator and the decimation rate of AD7764. Although this is not a preferred sampling rate, this is enough for our experiment on verifying the system functionality.

In the experiment, an ECG patient simulator PS-420 from Metron is used instead of a human subject to provide raw ECG signal. An EEG simulator EEGSIM from Glass Technologies has also be used to acquire raw EEG signal, while the EMG signal is acquired from a human subject. A simple PC program is written to receive and display the acquired samples from FPGA through RS232 in real-time as shown in Fig. 3 for visual inspection. A simple algorithm [6] is also tuned and migrated into the FPGA with Standard VHDL for verification of the real-time signal processing capability with embedded algorithms. This algorithm can perform QRS detection and calculate the beat rate of the ECG signal. The local display on the FPGA evaluation board is used as an output displaying the beat rate in beat per minute (BPM). Algorithms for processing EMG and EEG are not implemented and the acquiring of these signals is only verified by real-time output of acquired data.

From Fig. 3, an ECG signal can be acquired using the system with clear characteristics and the embedded algorithms can successfully retrieve the heart beat rate. Comparing acquired EEG signal between Fig. 4 and Fig. 5, the EEG signal, which is acquired using our acquisition system, shown in Fig. 5 is similar to the signal from the EEG simulator captured using ADI PowerLab shown in Fig. 4.

After evaluative testing of the system, it is possible to achieve an adaptive frontend with acceptable performance using existing devices. The acquired samples of signal are similar to the input signal with amplification which is possible for post-processing, even for the microvolt-level signals. The combination of FPGA and FPAA is also proved to be able to cooperate with embedded algorithms to retrieve useful information from the input biosignals, for example, showing the correct beat rate of the input ECG.

The final resources usage of the FPGA is around 10% of "Logic Elements" for the system without counting the embedded algorithms in the post-processing part. The addition of a simple QRS detection algorithm (migrated to FPGA using standard VHDL) consumed a total of over 50% of "Logic Elements". This is considered as a weakness or disadvantage because this means that signal processing algorithms need effort to be tuned and optimized when migrating to work in FPGA using standard VHDL.

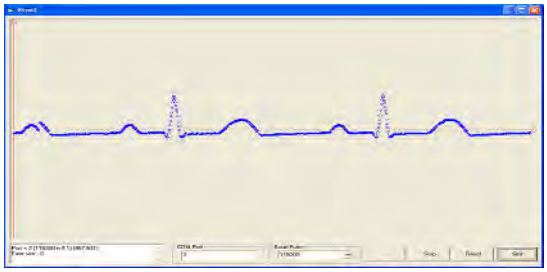


Fig. 3 – Simple program to receive and display the acquired samples in real-time for quick visual inspection (ECG)

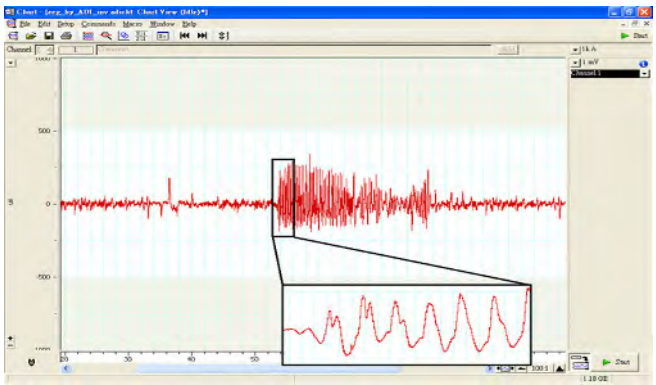


Fig. 4 –EEG signal from EEGSIMcaptured using ADI PowerLab

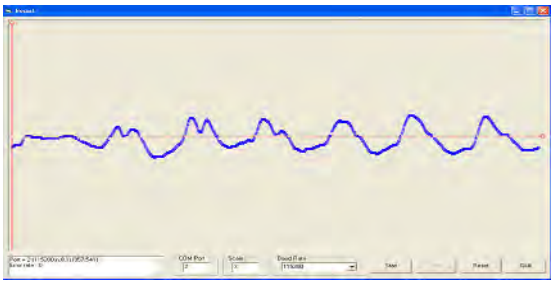


Fig. 5 – Simple program to receive and display the acquired samples in real-time for quick visual inspection (EEG)

V. Conclusions

A general purpose adaptive biosignals acquisition system is proposed and built for evaluation. The results from the evaluative testing are presented as a proof of concept in combining existing devices like FPGA and FPAA to form a simple and single platform at low cost for evaluating biosignal processing algorithms embedded into FPGA using multiple real-time biosignals. On the other hand, this can also be used as the essential part in building non-clinical medical devices for home healthcare or portable device with its inherent characteristics of low power and small in size, like a long term ECG monitoring device.

In designing the system, transformation of system from existing hardware to SOC is also considered, and therefore, standard VHDL language is chosen to provide maximum flexibility in the future. On the other hand, the difficulties and effort in migrating algorithms into the system for post-processing still needs to be analyzed and "automatic FPAA configurations selection" is considered as one of the useful feature in the current status.

Acknowledgment

I would here like to express my gratitude to all those who gave me the possibility to complete this paper. I want to specially thank you my supervisors, the department of Electrical and Electronics Engineering of the University of Macau and The Science and Technology Development Fund of Macau.

References

1. World Health Organization (WHO) at http://www.who.int/topics/chronic_diseases/en/
2. Ying-Chien Wei, Yu-Hao Lee, Ming-Shing Young (2008) A Portable ECG Signal Monitor and Analyzer, ICBBE 2008, The 2nd International Conference on Bioinformatics and Biomedical Engineering, 2008, pp 1336-1338
3. Borromeo S., Rodriguez-Sanchez C., Machado F., Hernandez-Tamames J.A., de la Prieta R., (2007) A Reconfigurable, Wearable, Wireless ECG System, EMBS 2007, 29th Annual International Conference of the IEEE Engineering in Medicine and Biology Society, 2007, pp 1659-1662
4. Chan U.F., Chan W.W., Sio Hang Pun, Mang I Vai, Peng Un Mak, (2007) Flexible Implementation of Front-End Bioelectric Signal Amplifier using FPAA for Telemedicine System, EMBS 2007, 29th Annual International Conference of the IEEE Engineering in Medicine and Biology Society, pp 3721–3724
5. Joseph D. Bronzino (1995) The Biomedical Engineering Handbook. CRC Press, IEEE Press, pp 808
6. Pan, Jiapu, Tompkins Willis J. (1985) A Real-Time QRS Detection Algorithm, IEEE Transactions on Biomedical Engineering, Volume BME-32 Issue 3 March 1985, pp 230 - 236

Author: Pedro Antonio MOU
Institute: Department of Electrical and Electronics Engineering, University of Macau, Macau SAR, China
Street: University of Macau, Av. Padre Tomas Pereira, Taipa, Macau SAR, China
City: Macau SAR
Country: China
Email: pedro@eee.umac.mo

Segmentation of Brain MRI and Comparison Using Different Approaches of 2D Seed Growing

K.J. Shanthi[1], M. Sasi Kumar[2] and C. Kesavdas[3]

[1] SCT College of Engg., Department of Electronics & Comm. Engg., Assistant Prof., Trivandrum, India
[2] Marian College of Engg. Department of Electronics & Comm.Engg., Prof., Trivandrum, India
[3]SCT Institute of Medical Sciences & Tech., Radiology Department, Associate Prof., Trivandrum, India

Abstract — **Automatic segmentation of human brain from MRI scan slices without human intervention is the objective of this paper. The DICOM images are used for segmentation. The Segmentation is the process of extraction of the White matter (WM), Gray matter (GM) and Cerebrospinal Fluid (CSF) from the MRI pictures. Volumetric calculations are carried out on the segmented cortical tissues. The accuracy in determining the volume depends on the correctness of the segmentation algorithm. Two different methods of seed growing are proposed in this paper.**

Keywords — **kull Stripping, Segmentation, Seed growing, White matter, Gray matter.**

I. Introduction

Segmentation in image processing has wide range of applications. Segmentation in medical imaging in general has wide applications. The imaging modalities such as CT and MRI along with image processing has revolutionized the diagnosis and treatment scenario. In brain MRI, segmentation is helpful in determining the volume of different brain tissues such as White Matter(WM), Gray Matter(GM) and Cerebrospinal Fluid(CSF). The volumetric changes in these brain tissues help in the study of neural disorders like Multiple Sclerosis, Alzheimer's disease, epilepsy etc. Brain MRI segmentation also helps in detection of tumours [4]. Many research papers are published in this area. Automatic segmentation also helps in guiding neurosurgery.

We have presented two different methods for segmentation based on region growing and presented a comparison of these two methods in this paper.

We have organized the remainder of this paper into the following sections. 2. Segmentation and the relative work in the area. 3. Overview 4. Method 1 Region growing based on seed value and connectivity. 5. Method 2. Region growing based only on seed value 6. Experimental Results 7. Comparison and conclusion

II. Segmentation

Segmentation or classification of data is defined as extracting homogeneous data from a wider set of data. Pixels with similar intensity or texture belong to the same group. Classification is based on looking for such similar properties in an image. There are numerous segmentation techniques available which are applied to medical imaging. Region growing is an important technique used for segmentation. One of the first region growing technique is the seed growing. Seed growing is done by choosing some pixels as seed points. The input seed points can be chosen based on a particular threshold value. Spatial information could also be specified along with the threshold gray value for choosing the seed pixel. Region of interest (ROI) can be grown from the seed and extracted. The result of segmentation depends on the correctness of the seed values chosen. Segmentation techniques based on seed growing can be fully automatic or semi automatic needing intervention. In some cases only the result need to be confirmed through the operator. Computer vision helps in saving much of the time. Manual segmentation will need hours together for segmenting a single image.

A lot of work has been done in the area of MR images segmentation. [2] uses edge based techniques combined with spatial intensity. Many image models are used for classifying such as Hidden markov model which uses random field model [5]. Many works are published using classification algorithms based on Fuzzy classification methods such as Fuzzy K means and FCM algorithms [7,8,9,10]. Fuzziness in classification helps to classify data better compared to hard clustering. Neural network and neuro fuzzy algorithms are also applied [11]. [3] uses the geometric snake model to extract the boundary and combines that along with the fuzzy clustering. The latest development in MR image segmentation [13] which uses propagation of charge fluid model through the contours of the imaging data. This method requires no prior knowledge of the anatomic structure for the segmentation.

Chwee Teck Lim, James C.H. Goh (Eds.): ICBME 2008, Proceedings 23, pp. 35–38, 2009
www.springerlink.com

III. Overview

Fig.1. Shows the different stages which gives the overview of the system developed in both the methods.

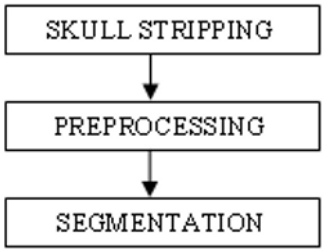


Fig. 1 System Overview

A. Skull Stripping

Volumetric analysis of brain requires segmenting the cortical tissues from the non cortical tissues. Removing these non cortical tissues is termed as skull stripping.

Surrounding extra cortical tissues such as fat, skin, eye ball are removed and separated from the brain tissues. Skull stripping classifies the image into two classes, brain and non brain tissues. Skull stripping forms the first processing step in the segmentation of brain tissues. The skull removed MRI pictures are used for further classification of the brain tissues into White matter, Gray matter and Cerebrospinal fluid.

The T1 weighted axial MR images has a distinct dark ring surrounding the brain tissues. We have exploited this spatial property and performed skull stripping.

Result of skull stripping is shown in Fig.2. Fig 2(a) is the original MR image and Fig 2(b) shows the skull stripped image.

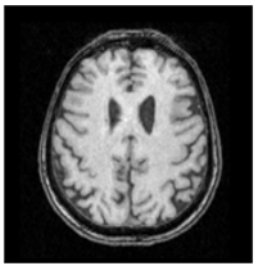


Fig. 2(a) Original image

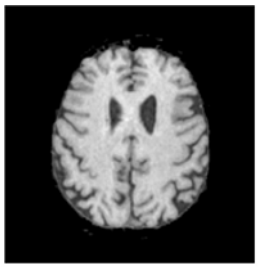


Fig. 2(b) Skull Stripped

B. Preprocessing

The MR images show variations and noise due to the inhomogeneity of the RF coils. Various filter transformations developed to enhance the MR brain images so far are discussed in [1]. We have used a median filter of mask size 3 X 3 which retains the information of the edges and at the same time avoids blurring.

C. Segmentation of Brain Tissues

After skull stripping and filtering the next step is to segment the brain into its constituent tissues such as White Matter (WM), Gray Matter(GM) and Cerebro Spinal fluid(CSF). We have developed two different methods based on the two dimensional seed growing. Both the methods proposed here are fully automatic.

IV. Method 1 based on seed value and connectivity

We have used the a priori information from the DICOM images regarding the intensity values of the different tissues represented in the DICOM images. The maximum intensity in the image correspond to the pixels representing WM in the skull stripped image. GM pixels are represented by intensity values lesser than WM. CSF pixels are represented by the lowest intensity values. These values from the histogram decide the threshold values in selecting the seed values. These ideas remained the same in both the methods developed.

A. Algorithm for Segmenting White Matter

- The algorithm begins by choosing the pixels automatically rather than manually.
- We computed the regional maxima from the histogram of the skull stripped image to get the seed value of the WM.
- The pixels within a range of small deviation to this seed value were grown through consecutive iterations.
- The number of iterations depend on the size of the image. The iterations have to be exhaustive such that all the pixels were checked.
- To make the algorithm more stable we checked along with the seed value the connectivity. The four neighbourhood connectivity ensures that the region is well connected. The connectivity test can be extended to eight point connectivity.
- An image corresponding to the mask of the WM was grown through iterations satisfying both the input criterion of seed value with a minimum deviation and four connectivity.
- The white matter was extracted from the skull stripped image using the WM mask and image arithmetic.

B. Segmenting gray matter

Study of the DICOM images show that the pixel values with a smaller offset to the white matter represents the gray matter. The algorithm for segmenting the gray matte is the same as in the previous step but for the seed point pixel value. Following the same procedure we segment the gray matter.

C. Segmenting Cerebrospinal fluid

After removing the white matter and the gray matter from the skull stripped image we are left with third constituent of the cortical tissue the cerebrospinal fluid. This is extracted using simple image arithmetic from the skull stripped image after removing WM and GM.

The segmented tissues using this method are shown in Fig. 3 (a) to 3(c).

V. Method 2 based on seed value

The second method we have developed is based only on the intensity value. It checks the pixels only for the intensity and neighbourhood connectivity is not a criterion for seed growing.

- The algorithm begins from the maximum intensity value. This is taken as the seed point for the white matter region. All the pixels with this value are added to grow the white matter region.
- In the next iteration the intensity value is decremented by one and the new pixels are added to the white matter region.
- Simultaneously the gray matter region is grown starting from the lower intensity and incrementing the intensity by one.
- This process is continued through the iterations.
- After every iteration an index is measured, we called it as the segmentation index.
- Segmentation index = (Total count till last iteration-Count in the present iteration) / Total count
- As the region grows the index value changes.
- With decrease in the index values, we test for common pixels between the two regions.
- The iterations are terminated if common pixels are found.

VI. Experimental results

We used the T1 weighted axial view MR brain images. The algorithm was implemented using MATLAB. The template image used was one the mid slices of the MRI slice no.44.



Results using Method 1. Fig. 3(a) Segmented White matter, Fig. 3(b) Segmented Gray matter



Fig. 3(c) Segmented CSF of MRI slice No.44



Results using Method 2. Fig. 4(a) White matter, Fig. 4(b) Gray matter

VII. Comparison and conclusion

Segmentation using both the methods yield the same result. The first method as it considers the neighbourhood connectivity takes excessively larger computation time for one single slice. The connectivity can also be tested across the 3 D images. The second method is faster as it picks all similar pixels simultaneously. The number of iterations change from one image to another. This method also ensures that all the pixels are properly classified and every pixel belong to one and only one class. In both the methods we have taken the seed values from the histogram and they

are totally automatic. For region growing we have allowed offsets in the seed values , this will take into account the variations of the intensity value within the same class due to the inhomogeneity of the RF coils of the MRI scanner. Table 1 shows the comparison of the iterations for an image of size 512*512.

Table 1. Comparison of Methods

Method	Method 1	Method 2
No. of iterations	512*512	Maximum 20 -25
Common count	180 (Slice. No.44)	Zero

ACKNOWLEDGEMENT

The authors acknowledge the financial support rendered by the Technical Education Quality Improvement Programme , Govt. of India and the authors would like to thank the following for their valuable contribution to the work: Vipin and Priyadarshan.

REFERENCES

1. 1 H M Zadeh, Joe P Windham, Donald J Peck and Andrew E Yagle "A Comparative Analysis of Several Transformations for Enhancement and Segmentation Magnetic Resonance Images" Medical Imaging Imaging IEEE Tansactions 0-7803-1487-5/94 IEEE 1994.
2. James L. Lee and Jefrey J. Rodriguez "Edge Based Segmentation of 3D magnetic Resonance Images" 0-8186-6950-0194 © 1994 IEEE
3. Jasjit S. Suri "Two-Dimensional Fast Magnetic Resonance Brain Segmentation" IEEE Engg .in Medicine and Biology July/August 2001 0739-5175/01/$10.00©2001IEEE
4. Nathan Moon, Elizabeth B, "Model Based Brain and Tumour Segmentation" IEEE 2002.
5. Y. Zhang, M. Brady, and S. Smith, "Segmentation of brain MR images through a hidden Markov random field model and the expectation-maximization algorithm," IEEE Transactions on Medical Imaging, vol. 20, pp. 45-57, 2001.
6. R. Kyle Justice and Ernest M. Stokely " 3 D Segmentation of MR Brain Images Using Seeded Region Growing" Annual International Conference of the IEEE Engineering in Medicine and Biology Society, Amsterdam 1996
7. R J Almeida and JMC Sousa : Comparison of fuzzy clustering algorithms for classification. International symposium on evolving fuzzy systems September 2006
8. Ahmed MN , Yamany SM, Mohamed N, Farag AA .Moriarty T . A modified fuzzy C means algorithm for bias field estimation and segmentation of MRI data . IEEE Transactions on Medical Imaging 2002
9. Cybele Ciofolo, Christian Barillot, Pierre Hellier, "Combining Fuzzy Logic and Level Set Methods for 3D MRI Brain Segmentation." 0-7803-8388-5/04 2004 IEEE
10. Y Zhou, Hong Chen, QZhu," The Researchof classification algorithm based on Fuzzy clustering "
11. Mohamed N. Ahmed and Aly A. Farag "Two-Stage Neural Network For Volume Segmentation of Medical Images" 0-7803-4122-8/97 1997 IEEE
12. Ting Song1, Elsa D. Angelini2, Brett D. Mensh3, Andrew Laine1 "Comparison Study of Clinical 3D MRI Brain Segmentation Evaluation" Proceedings of the 26th Annual International Conference of the IEEE EMBS San Francisco, CA, USA • September 1-5, 2004
13. Herng-Hua Chang*, Daniel J. Valentino, Gary R. Duckwiler, and Arthur W. Toga "Segmentation of Brain MR Images Using a Charged Fluid Model" IEEE Transactions in Bio Medical Engg. VOL. 54, NO. 10, OCTOBER 2007

Author: Shanthi K J
Institute: Sree Chitra Thirunal College of Engg.
Street: Pappanamcode
City: Trivandrum
Country: India
Email Shanti_kj@yahoo.co.in

SQUID Biomagnetometer Systems for Non-invasive Investigation of Spinal Cord Dysfunction

Y. Adachi[1], J. Kawai[1], M. Miyamoto[1], G. Uehara[1], S. Kawabata[2], M. Tomori[2], S. Ishii[2] and T. Sato[3]

[1] Applied Electronics Laboratory, Kanazawa Institute of Technology, Kanazawa, Japan
[2] Section of Orthopaedic and Spinal Surgery, Tokyo Medical and Dental University, Tokyo, Japan
[3] Department of System Design and Engineering, Tokyo Metropolitan University, Tokyo, Japan

Abstract — **We are investigating an application of the biomagnetic measurement to non-invasive diagnosis of spinal cord function. Two multichannel superconducting quantum interference device (SQUID) biomagnetometer systems for the measurement of the evoked magnetic field from spinal cords were developed as hospital-use apparatuses. One is optimized for sitting subjects. Another is for supine subjects. Both systems are equipped with an array of vector SQUID gradiometers. The conduction velocity, which is one of the significant information for the functional diagnosis of the spinal cord, was non-invasively estimated by the magnetic measurement.**

Keywords — **Biomagnetism, SQUID, biomagnetometer, medical device, non-invasive diagnosis, spinal cord.**

I. Introduction

Biomagnetic measurement is a method to investigate the behavior of nerve system, muscles, or other live organs by observation of magnetic field generated by their activity. The intensity of the magnetic field elicited from the body is quite small, which is several femto or pico tesla. Only SQUID (superconducting quantum interference device) based magnetometers can detect such weak magnetic field. One of the large applications of SQUID biomagnetic measurement is MEG (magnetoencephalography)[1,2]. The MEG is an apparatus to detect the magnetic field from the brain nerve activity by a sensor array with more than one hundred SQUID sensors arranged around the head. It can non-invasively provide the information of brain nerve activity at high temporal and spatial resolution, and is already used in many hospitals and brain research institutes.

In the field of the orthopaedic surgery and neurology, there is a strong demand for the non-invasive diagnosis of the spinal cord dysfunction. The conventional lesion localization of the spinal cord disease relies on image findings from MRIs or X-ray CTs in addition to clinical symptoms, physical findings and neurological findings. However, the doctors were often dissatisfied with false-positive findings because the abnormal findings on the image are not always symptom-related. Therefore, evaluation of spinal cord function based on electrophysiological examination is also necessary for the accurate diagnosis of spinal cord disease.

We are investigating the SQUID biomagnetic measurement systems as a non-invasive functional diagnosis tool for spinal cord[3–5]. In this paper, the multichannel SQUID measurement systems recently developed for the application in hospitals and preliminary examination with the systems are described.

II. Instrumentation

A. System Configuration

We focused on the cervical spinal cord evoked magnetic field (SCEF) measurement because spinal cord disease mainly occurs at the cervix. Two cervical SCEF measurement systems were developed. One was optimized for sitting subjects. The other was for supine subjects. The system for sitting subjects needs comparatively small footprint. Space-saving is a large advantage upon installation of the system to common hospitals. On the other hand, the supine mode system can be applied to patients, even if they have severe spinal cord disease, and provide larger observation area than the sitting mode system.

Fig. 1 shows the configuration of the system for supine subjects. Basically, both systems have the same configuration. An X-ray imaging apparatus was integrated to the

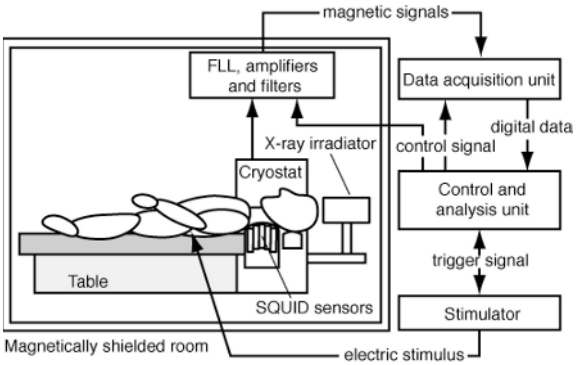


Fig. 1 Configuration of the supine mode system.

Chwee Teck Lim, James C.H. Goh (Eds.): ICBME 2008, Proceedings 23, pp. 39–42, 2009
www.springerlink.com

SQUID system to acquire anatomical structure images at the cervix. The two most distinctive components of the systems are the sensor arrays of vector SQUID gradiometers and the uniquely shaped cryostats, which are described in detail in this section.

B. Sensor array

The sensor arrays were composed of vector SQUID gradiometers[6] shown in Fig. 2(a). The vector SQUID gradiometer detects three orthogonal components of the magnetic field at one time thanks to the combination of three gradiometric pickup coils as shown in Fig. 2(b). Fig. 2(c) shows the sensor array of the sitting mode system. It has 5 × 5 matrix-like arrangement for the observation area of 80 mm × 90 mm. The sensor array arrangement and the observation area of the supine mode system are 8 × 5 and 140 mm × 90 mm, respectively. The sensors are positioned along the cylindrical surface to fit to the posterior of the cervix. All SQUID sensors are driven by flux locked loop (FLL) circuits for the linearization of the output and the improvement of dynamic range[7]. The resulting sensitivity and typical noise level in the white noise region are about 1–1.5 nT/V and 2.3 fT/Hz$^{1/2}$, respectively.

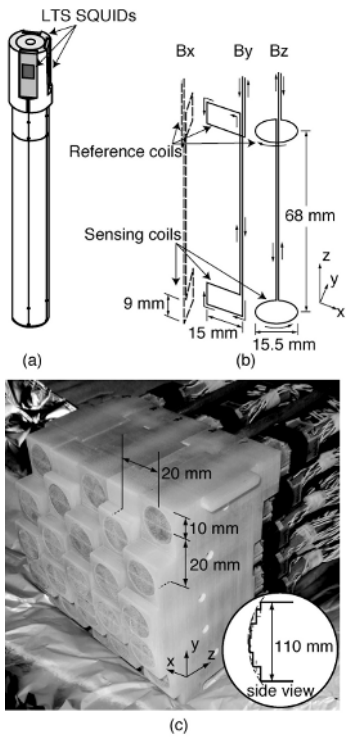


Fig. 2 Vector SQUID sensor array. (a) Conceptual drawing of a vector SQUID gradiometer. (b) Structure of pickup coils (c) Appearance of the sensor array of the sitting mode system.

C. Cryostat

The cryostat is a double-layered vessel with a vacuum thermal insulating layer to hold the SQUID sensors in liquid helium and to keep them in a superconducting state. The cryostats and their inner parts are made of glass fiber reinforced plastic to avoid interference from magnetic materials.

Fig. 3 shows the inner structure and the appearance of the cryostats. The cryostats of both sitting mode and supine mode have the same uniquely designed structure. They have a cylindrical main body to reserve liquid helium and a protrusion from its side surface. The sensor array of the sitting mode system is installed in the protrusion oriented in the horizontal direction. The sensor array of the supine mode system is also installed in the protrusion but is oriented in the vertically upward direction. In both systems, the surface that is in contact with the subject's cervix has a cylindrical curve, as does the front of the sensor array. The cool-to-warm separation of this surface is less than 7 mm. The cryostats are supported by the non-magnetic gantries and made tiltable so that the relative position between the sensor array and the cervix would readily be adjusted. The capacity of cryostats of

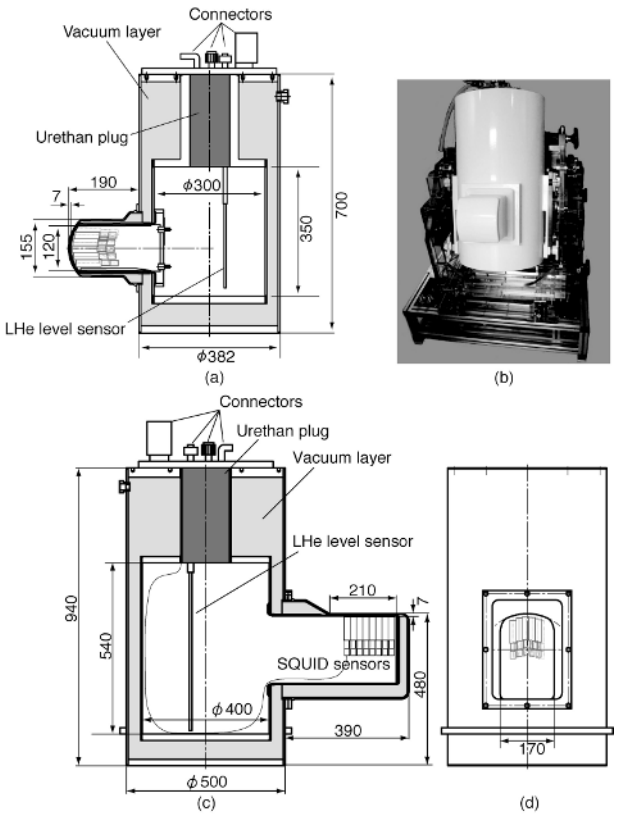


Fig. 3 (a) Inner structure and (b) appearance of the cryostat of the sitting mode system. (c) Inner structure and (d) front view of the cryostat of the supine mode system.

the sitting and the supine mode systems are about 25 liters and 70 liters, respectively. The intervals of the liquid helium refill are 84 hours and 120 hours, respectively.

III. SCEF MEASUREMENT

A. Material and method

For performance verification of the systems, preliminary cervical SCEF measurement of normal subjects was executed in a magnetically shielded room. Three volunteer male subjects, TS, MT, and KK at the ages of 23–30 were examined with the sitting mode system. The subject TS was also examined in the supine mode. All subjects didn't have dysfunction at the cervix.

In the sitting mode measurement, the subjects sat on a chair in the reclining position with the posterior of the cervix tightly fitted to the protrusion of the cryostat as shown in Fig. 4(a). In the supine mode measurement, the subject lay on a bed in the supine position with the cervix and the head running off the edge of the bed. The cervix was in close contact with the upper surface of the protrusion of the cryostat as shown in Fig. 1 and Fig. 4(b).

Fig. 4(c) and (d) are lateral X-ray images showing the relative positions between the cervical spine and the sensor array and the orientation of the coordinate system. The median line of the subject's body was roughly positioned at the center of the observation area in each measurement.



Fig. 4 SCEF measurement (a) in the sitting mode and (b) in the supine mode. Lateral X-ray image (c) in the sitting mode and (d) in the supine mode.

Electric stimulation was given to the median nerve at the left wrist with skin surface electrodes. The stimuli were repetitive square pulse current whose intensity and duration were 6–8 mA and 0.3 ms, respectively. The repetition rate was 17 Hz or 8 Hz.

Signals from all SQUID sensors were filtered with band pass filters of 100–5000 Hz before digital data acquisition. The sampling rate of the data acquisition was 40 kHz. The stimulus was repeated 4000 times and all responses were averaged for the improvement of the S/N ratio. After the data acquisition, a digital low pass filter of 1290 Hz was applied to the averaged data.

B. Result and discussion

The SCEF signals were successfully detected from every subject and the pattern transition of the SCEF distribution over the cervix was clearly observed about 10 ms after the stimulation. The SCEF pattern transition of every subject had the same tendency. Fig. 5(a) and (b) show the transition of the SCEF distribution from the subject TS acquired by the sitting mode system and the supine mode system, respectively. The maps represent views from the posterior of the subject. Upper and lower sides correspond to the cranial and caudal directions, respectively. The arrow maps show the orientation and intensity of the SCEF components tangential to the body surface. The contour maps represent the distribution of the radial component.

In both Fig. 5(a) and (b), a large outward component was found in the left side of the observation area in the early stage of the SCEF transition. After that, the zero field line of the radial component took on the anti-clockwise rotation. The tangential component was also turning as well as the radial component. This rotation was in good agreement with a result of a preceding study[8]. In the right side of the observation area, the progression of an inward component along the *y*-axis from the lower side to the upper side, which was parallel to the spinal cord, was clearly found. The inward component was followed by an outward component. This was interpreted that a quadrupole distribution, which is the specific magnetic distribution pattern corresponding to the axonal action potential[9], was partially observed. The whole of the behavior of the inward and outward extrema was observed in Fig. 5(b) while some part of the extrema was missing in Fig. 5(a). Thus, the wide observation area of the supine mode system is effective to survey the complicated pattern transition of cervical SCEF induced by the brachial nerve stimulation.

The conduction velocity, which is significant to functional diagnosis of the spinal cord, was estimated from the movement of the extrema to be about 60–90 m/s. This value was within the normal physiological range.

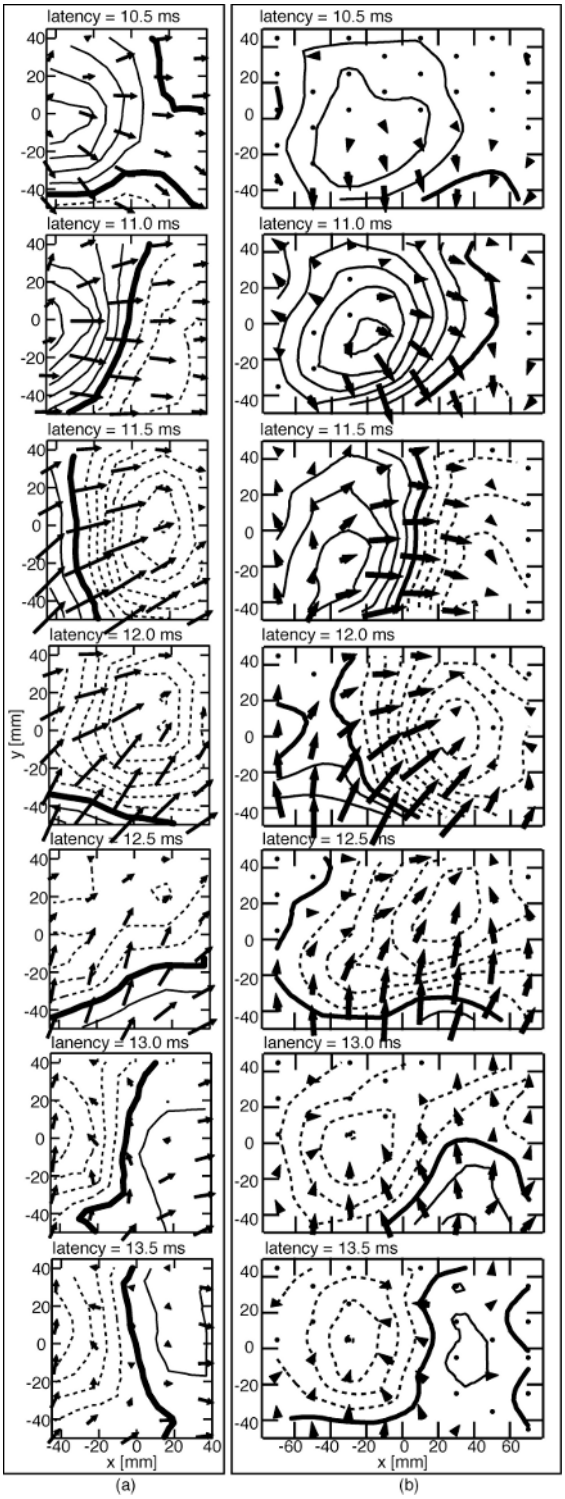


Fig. 5 Transition of the SCEF distribution between 10 ms and 13.5 ms in latency (a) in the sitting mode and (b) in the supine mode. Plain, dotted, and bold lines in the contour maps represent outward, inward, and zero magnetic fields, respectively. The interval between contour lines is 5 fT.

IV. Conclusion

Two SQUID spinal cord evoked field measurement systems, sitting mode and supine mode, were developed in the scope of the application at hospitals. The systems are equipped with an array of vector SQUID gradiometers and a uniquely shaped cryostat optimized for sitting or supine subjects. Using the developed systems, the SCEF signals were successfully detected and their specific pattern transitions were observed. The supine mode system had a wider observation area and was more suitable for the acquisition of the complicated SCEF distribution that induced especially by the brachial peripheral nerve stimulation.

The signal propagation along the spinal cord was found and its velocity was non-invasively estimated. This indicates that the SCEF measurement will be a powerful tool for the non-invasive diagnosis of the spinal cord dysfunction.

Acknowledgment

This work is partly supported by CLUSTER project, MEXT, Japan.

References

1. Hämäläinen M, Hari R, Ilmoniemi RJ et al. (1993) Magneto-encephalography – theory, instrumentation, and application to noninvasive studies of the working human brain. Reviews of modern physics 65:413–498
2. Kado H, Higuchi M, Shimogawara et al. (1999) Magneto-encephalogram system developed at KIT. IEEE Trans Applied Supercond 9:4057–4062
3. Kawabata S, Komori H, Mochida K, Ohkubo H, Shinomiya K (2003) Visualization of conductive spinal cord activity using a biomagnetometer. Spine 27:475–479
4. Adachi Y, Kawai J, Miyamoto M, Kawabata S, et al. (2005) A 30-channel SQUID vector biomagnetometer system optimized for reclining subjects. IEEE Trans Applied Supercond 15:672–675
5. Tomizawa S, Kawabata S, Komori H, Hoshino Fukuoka Y, Shinomiya K (2008) Evaluation of segmental spinal cord evoked magnetic fields after sciatic nerve stimulation. Clin Neurophys 119:1111–1118
6. Adachi Y, Kawai J, Uehara G, Kawabata S et al. (2003) Three dimensionally configured SQUID vector gradiometers for bio-magnetic measurement. Supercond Sci Technol 16:1442–1446
7. Drung D, Cantor R, Peters M, Scheer H.J, Koch H (1990) Low-noise high-speed dc superconducting quantum interference device magnetometer with simplified feedback electronics. Appl Phys Lett 57: 406–408
8. Marckert B.M, Burghoff M, Hiss L-H, Nordahn M et al. (2001) Magnetoneurography of evoked compound action currents in human cervical nerve roots. Clin. Neurophys. 112:330–335
9. Hashimoto I, Mashiko T, Mizuta T, et al. (1994) Visualization of a moving quadrupole with magnetic measurements of peripheral nerve action fields, Electroencephalograph. Clin. Neurophysiol. 93:459–467

Human Cardio-Respiro Abnormality Alert System using RFID and GPS - (H-CRAAS)

Ahamed Mohideen, Balanagarajan

Syed Ammal Engineering College, Anna University, Ramanathapuram, India

Abstract — **The most crucial minute in a human's life is the minute in which he oscillates between life and death. These deaths caused due to the failure of heart and respiratory mechanisms because of lack of medical assistance in time are increasing. This paper tries to give an insight of a technology about a whole new wireless and RFID (Radio Frequency Identification) enabled frontier in which victim's actual location is integral for providing a valuable medical service.**

This paper will be demonstrating for the first time ever the usage of wireless telecommunications systems and miniature sensor devices like RFID passive tags, which are smaller than a grain of rice and equipped with a tiny antenna which will capture and wirelessly transmit a person's vital body-function data, such as pulse/respiration rate or body temperature, to an integrated ground station. In addition, the antenna in the ground station will also receive information regarding the location of the individual from the GPS (Global Positioning satellite) System. Both sets of data of medical information and location will then be wirelessly transmitted to the ground station and made available to save lives by remotely monitoring the medical conditions of at-risk patients and providing emergency rescue units with the person's exact location.

It gives a predicted general model for Heart and respiration abnormality alert system. It discusses in detail the various stages involved in tracking the exact location of the Victim using this technology.

Keywords — **RFID tags, RFID reader, GPS, H-CRAAS.**

I. Introduction

InformID is an out of sight, out of mind medical technology that can save lives. This device consists of two parts. The first is a small tag shown in Fig-1 that is easily concealed on an individual and carries crucial medical information. The second is a reading device that, in the case of an emergency, a paramedic or doctor could use in a hands free way to access this important information. This protected medical information would then allow doctors and paramedics to quickly and easily diagnose and identify medical conditions and emergencies on a patient to patient basis. InformID is a truly unique medical system because it is powerless and wire free!

I.A. Overview: Medical applications for RFID are quickly becoming accepted as a safe and effective means in which to track patients in hospitals and to easily keep track of pets and children. Once this technology gains mass appeal, what other potential venues are available for using such a cheap, simple and effective identification technology.

Such technology has yet to be used effectively as preventative measures for medical complications of an average live at home individual. Many devices have come and gone that claim to help or aid the elderly in medical situations, but are deplorable in concept and highly ineffective at both preventing and solving medical crisis's in a time effective manner.

To better understand the intention of this project and the underlying problem, below is a sample scenario that I feel is worth potentially solving with the current state of RFID technology.

"An individual at their personal residence needs medical assistance and dials 9-1-1 but does not remain conscious for long. As paramedics arrive on scene, they are faced with many questions. Who is the individual in need of assistance and what is the nature of their problem? Does the medical emergency require medical assistance elsewhere or immediate resuscitation on the scene? What are the victim's vital signs? Is there an important medicinal history that could be vital to solving the medical problem?"

The above situation is quite often the brunt of any paramedics work during an average day. The time taken to answer those questions can ultimately determine the victims' chances of survival. It is my goal to aid a paramedic's deci-

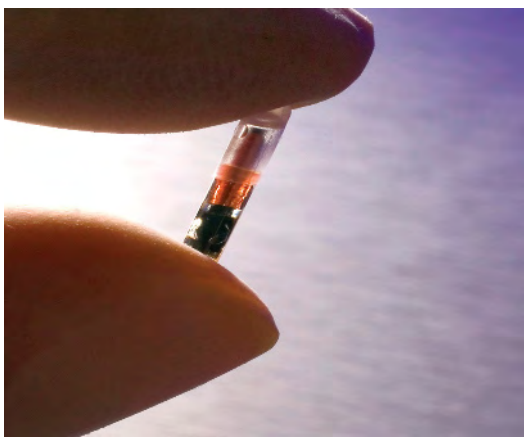


Fig 1- Grain sized RFID tag

Chwee Teck Lim, James C.H. Goh (Eds.): ICBME 2008, Proceedings 23, pp. 43–46, 2009
www.springerlink.com

sion-making process by potentially answering some of these questions using RFID technology. The key to potentially uncovering a viable solution to the problem lies mainly with the transparency of the technology involved, and a system that is totally passive that can be referenced only if the paramedic has the time or needs the information

Table 1 Different class of RFID

RFID tag class	Definition	Programming
Class0	Read only passive tags	Programmed by the manufacturer
Class1	"Write-once, Read-many" passive tags	Programmed by the customer cannot be reprogrammed
Class2	Rewritable passive tags	Reprogrammable
Class3	Semi passive tags	Reprogrammable
Class4	Active tags	Reprogrammable
Class5	Readers	Reprogrammable

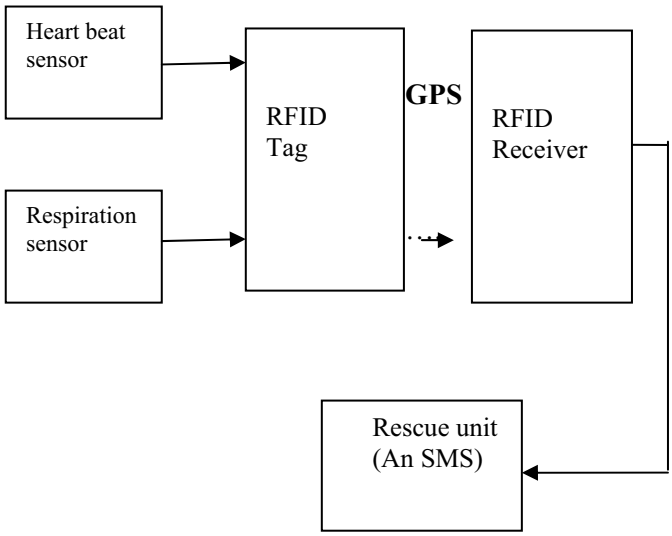


Fig 2- Block description of H-CRAAS

Radio Frequency Identification (RFID) is a system of transmitting a unique encrypted number wirelessly between a tag and a transponder (reader). The number is 96 bits long and has enough unique combinations to potentially label every atom in the universe. RFID is both interesting and unique for a variety of reasons. The system of reading embedded tags does not need line of site transmission like a barcode reader. Instead, multiple tags may be read simultaneously just by being within a few feet of them. RFID tags are unique in that they come in two flavors, passive and active. A battery of some sort, allowing the tag to be read at long ranges, usually powers active tags. A passive tag, much like the one used in my proposed system, does not require a power source at all! Instead, the range in which the tag can be read is very limited (sometimes less than six inches). RFID is safe and effective for maintaining privacy. Each tag is encrypted to allow a specific reader or set of readers to access their information

II. Methodology

II.A. Sensors: By Using separate sensors the heartbeat and respiration rate is monitored continuously. The outputs of the sensors are then given to the separate port in the RFID tag in the digitized form.

II.B. RFID tag: The RFID tag is working with the principle of Code Division Multiple Access (CDMA). Since RFID is a multiport tag, the two-sensor output is given separately. The RFID tag then analyzes the 8-bit digital inputs. If any one of the codes exceeds the predefined value then the corresponding code is encoded as a 4-bit code and it is transmitted to the RFID receiver. Passive e RFID systems that we used typically couple the transmitter to the receiver depending on whether the tags are operating in the near or far field of the reader, respectively.

II.C. Global positioning system (GPS): This technology is mainly used to collect the details of the victim's exact area of location, so that it is easy for the rescue unit to reach the victim with required medical assistance.

II.D. RFID receiver: With the information of the location of the victim under crucial condition the reader make an alert to the rescue unit. So that it is possible for them to reach the victim soon.

II. E. Rescue unit: Soon after the alert from the reader near by the rescue unit should reach the location as soon as possible.

III. Experimental results

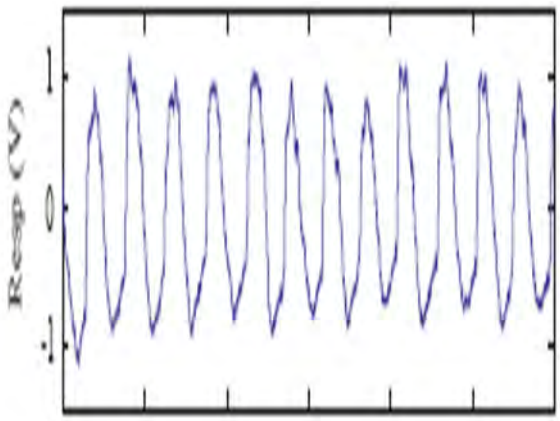


Fig 3- Output of normal respiration rate

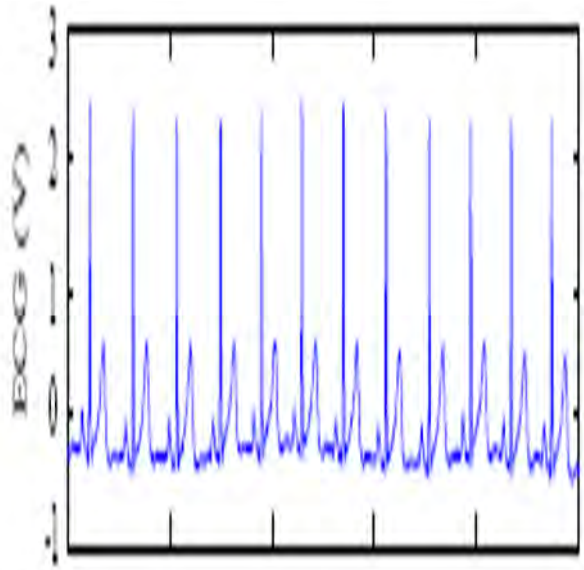


Fig 4- Output of normal heart beat rate

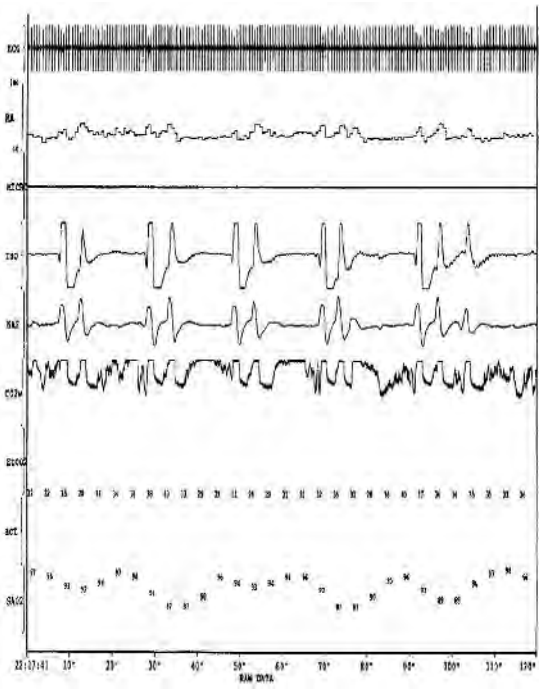


Fig 5- Output of abnormal heartbeat and respiration rate

IV. Conclusion

This new technology will open up a new era in the field of Biomedical Engineering. This paper aimed to provide an alert and there by providing required medical assistance to the victim. We have achieved this through the technology RFID and GPS. This technology would probably become cheaper in the future. In the near future we hope this new technology would probably reduce the deaths due to heart and respiratory abnormalities.

V. Acknowledgement

First of all our sincere gratitude goes to Almighty, because “without him we are nothing”, next our unfined thanks goes to our lovable parents because they are the backbone of all our endeavours. And our heartfelt thanks goes to our Correspondent, Principal, Vice Principal, HOD, and all other staff members who supported us in all possible ways to complete our paper. Finally we would like to thank our friends for their thankless encouragement and dedicated support.

Reference

[1] Nan Bu, Naohiro Ueno and Osamu Fukuda,"Monitoring of Respiration and Heartbeat during Sleep using a Flexible Piezoelectric Film Sensor and Empirical Mode Decomposition"

[2] "AMON: A Wearable Multiparameter Medical Monitoring and Alert System", Urs Anliker*, Student Member, IEEE*, Jamie A. Ward*, Student Member, IEEE*, Paul Lukowicz*, Member, IEEE*,Gerhard Tröster*, Senior Member, IEEE*, François Dolveck, Michel Baer, Fatou Keita, Eran B. Schenker,Fabrizio Catarsi*, Associate Member, IEEE*, Luca Coluccini, Andrea Belardinelli, Dror Shklarski, Menachem Alon,Etienne Hirt*, Member, IEEE*, Rolf Schmid, and Milica Vuskovic

[3] Mann, "Wearable computing as means for personal empowerment,"in *Proc. Int. Conf. on Wearable Computing (ICWC)*, Fairfax, VA, May 1998

[4] .Starner, "The challenges of wearable computing: Part 1," *IEEE Micro*,vol. 21, pp. 44–52, July 2001.

[5] A. Belardinelli, G. Palagi, R. Bedini, A. Ripoli, V. Macellari, and D. Franchi, "Advanced technology for personal biomedical signal logging and monitoring," in *Proc. 20th Annu. Int. Conf. IEEE Engineering Medicine and Biology Society*, vol. 3, 1998, pp. 1295–1298.

[6] E. Jovanov, T. Martin, and D. Raskovic, "Issues in wearable computing for medical monitoring applications: A case study of a wearable ecg monitoring device," in *4th Int. Symp. Wearable Computers (ISWC)*, Oct. 2000, pp. 43–49.

[7] E. Jovanov, P. Gelabert, B. Wheelock, R. Adhami, and P. Smith, "Real time portable heart monitoring using lowpower dsp," in *Int. Conf. Signal Processing Applications and Technology (ICSPAT)*, Dallas, TX, Oct. 2000.

[8] E. Jovanov, D. Raskovic, J. Price, A. Moore, J. Chapman, and A. Krish- Namurthy, "Patient monitoring using personal area networks of wireless intelligent sensors," *Biomed. Sci. Instrum.*, vol. 37, pp. 373–378, 2001.

[9] S. Pavlopoulos, E. Kyriacou, A. Berler, S. Dembeyiotis, and D. Koutsouris, "A novel emergency telemedicine system based on wireless communication technology–AMBULANCE," *IEEE Trans. Inform. Technol. Biomed.*, vol. 2, pp. 261–267, Dec. 1998.

[10] S. L. Toral, J. M. Quero, M. E. Pérez, and L. G. Franquelo, "A microprocessor based system for ecg telemedicine and telecare," in *2001 IEEE Int. Symp. Circuits and Systems*, vol. IV, 2001, pp. 526–529.

[11] F. Wang, M. Tanaka, and S. Chonan, "Development of a PVDF piezopolymer sensor for unconstrained in-sleep cardio respiratory monitoring", *J. Intell. Mater. Syst. Struct.*, vol. 14, 2003, pp. 185-190.

[12] N. Ueno, M. Akiyama, K. Ikeda, and H. Takeyama, "A foil type pressure sensor using nitelide aluminum thin film", *Trans. of SICE*, vol. 38, 2002, pp. 427-432. (in Japanese)

[13] Y. Mendelson and B. D. Ochs, "Noninvasive pulse oximetry utilizing skin reflectance photoplethysmography," *IEEE Trans. Biomed. Eng.*, vol. 35, pp. 798–805, Oct. 1988.

Author: A. Ahamed Mohideen,
Institute: Syed Ammal Engineering College
Street: Dr.E.M.Abdullah campus,
City: Ramanathapuram,
Country: India
Email: meam@india.com

Author: M. Balanagarajan,
Institute: Syed Ammal Engineering College
Street: Dr.E.M.Abdullah campus,
City: Ramanathapuram,
Country: India
Email: meam@india.com

Automatic Sleep Stage Determination by Conditional Probability: Optimized Expert Knowledge-based Multi-Valued Decision Making

Bei Wang[1,4], Takenao Sugi[2], Fusae Kawana[3], Xingyu Wang[4] and Masatoshi Nakamuara[1]

[1] Department of Advanced Systems Control Engineering, Saga University, Saga, Japan
[2] Department of Electrical and Electronic Engineering, Saga University, Saga, Japan
[3] Department of Clinical Physiology, Toranomon Hospital, Tokyo, Japan
[4] Department of Automation, East China University of Science and Technology, Shanghai, China

Abstract — **The aim of this study is to develop a knowledge-based automatic sleep stage determination system which can be optimized for different cases of sleep data at hospitals. The main methodology of multi-valued decision making includes two modules. One is a learning process of expert knowledge database construction. Visual inspection by a qualified clinician is utilized to obtain the probability density functions of parameters for sleep stages. Parameter selection is introduced to find out optimal parameters for variable sleep data. Another is automatic sleep stage determination process. The decision making of sleep stage is made based on conditional probability. The result showed close agreement comparing with the visual inspection. The developed system is flexible to learn from any clinician. It can meet the customized requirements in hospitals and institutions.**

Keywords — **Automatic sleep stage determination, Expert knowledge database, Multi-valued decision making, Parameter selection, Conditional probability.**

I. Introduction

There are two sleep states: rapid eye movement (REM) sleep and non rapid eye movement (NREM) sleep. The NREM sleep consists of stage 1 (S1), stage 2 (S2), stage 3 (S3) and stage 4 (S4). Another stage of awake is often included, during which a person falls asleep. The most well-known criteria for sleep stage scoring were published by Rechtschaffen and Kales (R&K criteria) in 1968 [1]. Currently, sleep stage scoring has been widely used for evaluating the condition of sleep and diagnosing the sleep related disorders in hospitals and institutions.

Automatic sleep stage determination can free the clinicians from the heavy task of visual inspection on sleep stages. The rule-based waveform detection methods, according to R&K criteria, can be found in many studies. The waveform detection method was firstly applied by Smith et al. [2], [3]. Waveform and phasic event detection of rule-based and case-based hybrid reasoning method was proposed in [4]. An expert system based on characteristic waveforms and background EEG activity by using a decision tree was described in [5]. The limitations of R&K criteria have been noticed [6]. The insufficiency is that it only provides typical characteristic waveforms of healthy and normal persons for staging.

Although various methodologies have been developed, effective technique is still needed for clinical application. Sleep data is inevitably being affected by various artifacts [7]. Individual differences are also commonly existed even under the same recording condition. For the patients with sleep-related disorders, their sleep data has particular characteristics. The recorded sleep data containing complex and stochastic factors will increase the difficulties for the computerized sleep stage determination techniques to be applied for clinical practice.

In this study, sleep stage determination is considered as a multi-valued decision making problem in the field of clinics. The main methodology, proposed in our previous study, has been proved to be successful for sleep stage determination [8], [9]. The aim of this study is to develop a flexible technique adapting to different cases of sleep data, which can meet the customized requirements in hospitals and institutions. Visual inspection by a qualified clinician is utilized to obtain the probability density function of parameters during the learning process of expert knowledge database construction. A process of parameter selection is introduced in order to make our algorithm flexible. Automatic sleep stage determination is manipulated based on conditional probability.

II. Methods

A. Data acquisition

The sleep data investigated in this study was recorded in the Department of Clinical Physiology, Toranomon Hospital, at Tokyo, Japan. Four subjects, aged 49-61 years old, were participated. These patients had breathing disorder during sleep (Sleep Apnea Syndrome). Their overnight sleeping data were recorded after the treatment of Continuous Positive Airway Pressure (CPAP) based on the polysomnographic (PSG) measurement. The PSG measurement used in Toranomon Hospital included four EEG (electroencephalogram) recordings, two EOG recordings and one

Chwee Teck Lim, James C.H. Goh (Eds.): ICBME 2008, Proceedings 23, pp. 47–50, 2009
www.springerlink.com

EMG (electromyogram) recording. EEGs were recorded on central lobes and occipital lobes with reference to opposite earlobe electrode (C3/A2, C4/A1, O1/A2 and O2/A1) according to the International 10-20 System [10]. EOGs were derived on Left Outer Canthus and Right Outer Canthus with reference to earlobe electrode A1 (LOC/A1 and ROC/A1). EMG was obtained from muscle areas on and beneath chin and termed as chin-EMG. Initially, EEGs and EOGs were recorded under a sampling rate of 100 Hz, with a high frequency cutoff of 35 Hz and a time constant of 0.3s. Chin-EMG was recorded under a sampling rate of 200 Hz, with a high frequency cutoff of 70 Hz and a low frequency cutoff of 10 Hz.

B. Visual inspection

A qualified clinician F.K. in Toranomon hospital scored sleep stages on the overnight sleep recording of subjects. In total, seven types of stages were inspected. In the stage of the awake, predominant rhythmic alpha activity (8-13 Hz) can be observed in EEGs (O1/A2, O2/A1) when the subject is relaxed with the eyes closed. This rhythmic EEG pattern significantly attenuates with attention level, as well as when the eyes are open. The awaking EOG consists of rapid eye movements and eye blinks when the eyes are open, while few or no eye movements when the eyes closed. The clinician determined the awake with eyes open (O(W)) or awake with eyes closed (C(W)) according to the alpha activity (8-13 Hz) in O1/A2 and O2/A1 channels as well as the existence of eye movements in EOG channels. The REM sleep was scored by the episodic REMs and low voltage EMG. The NREM sleep was categorized into S1, S2, S3 and S4 stages. S1 was scored with low voltage slow wave activity of 2-7 Hz. S2 was scored by the existence of sleep spindle or K-complex. Usually, S3 is defined when 20% to 50% of slow wave activity (0.5-2 Hz) presented in an epoch, whereas more than 50% for S4 according to R&K criteria. For elder persons, S3 and S4 of deep sleep may not be obviously determined. The clinician inspected S3 and S4 based on a relatively different presence of slow wave activity (0.5-2 Hz) within an epoch.

C. Multi-valued decision making

1) Expert knowledge database construction

The overnight sleep recording from subjects were divided into consecutive 30s epochs for training purpose. Each epoch was subdivided into 5s segments. A set of characteristic parameters, extracted from the periodogram of EEGs, EOGs and EMG, were calculated for each segment. There are three types of parameters: ratio, amplitude and amount. Totally, 20 parameters were calculated. The parameters of consisting segments were taken average to derive the parameter value of one epoch.

The epochs were classified into sleep stage groups according to the visual inspection by clinician. The histogram for each parametric variable was created for each sleep stage. The probability density function (*pdf*) was approximately evaluated using histogram with Cauchy distribution. The *pdf* of parameter y in stage ζ is mathematically expressed by

$$f(y \mid \zeta) = \frac{b}{\pi((y-a)^2 + b^2)}, \tag{1}$$

where a is the location and b is the scale of Cauchy distribution. a is determined by media and b is determined by quartile [11].

The distance of the *pdfs* between stage i and stage j was calculated by

$$d(i, j) = \left| a_i - a_j \right|. \tag{2}$$

The larger distance indicates smaller overlap between the *pdfs*. It is measured by

$$d(i, j) > \max\{3b_i, 3b_j\}. \tag{3}$$

When the distance is larger than three times of the deviations of the probability density functions of both stages, the parameter is selected.

2) Automatic sleep stage determination

The overnight sleep recordings of subjects were divided into the same length of epochs and segments as the training data. The values of selected parameters were calculated for each segment.

Initially, predicted probability of first segment $P_{1|0}$ for various sleep stages shared the probability equally with a value of $1/n$. n is the number of the types of sleep stages.

The joint probability of the parameters for current segment k was calculated by

$$f(y_k \mid \zeta^i) = \prod_{l=1}^{m} f(y_k^l \mid \zeta^i), \tag{4}$$

where $y_k = \{y_k^1, y_k^2, \cdots, y_k^m\}$ is a parameter vector, and ζ^i denotes the sleep stage. In Eq.4, parameters in y_k were assumed to be independent with each other.

Conditional probability of segment k was calculated based on the Bayesian rule,

$$P_{k|k}(\zeta^i) = \frac{f(y_k \mid \zeta^i) P_{k|k-1}(\zeta^i)}{\sum_{j=1}^{n} f(y_k \mid \zeta^j) P_{k|k-1}(\zeta^j)}, \tag{5}$$

where $P_{k|k-1}(\zeta^i)$ is the predicted probability of current segment.

The sleep stage ζ^* was determined by choosing the maximum value among the conditional probabilities corresponding to various sleep stages as

$$\zeta^* : \max(P_{k|k}(\zeta^i)) \cdot \tag{6}$$

The predicted probability $P_{k+1|k}(\zeta^i)$ of next segment *k+1* was given by

$$P_{k+1|k}(\zeta^i) = \sum_{j=1}^{n} t_{ij} P_{k|k}(\zeta^j), \tag{7}$$

where t_{ij} denotes the probability of transition from stage *i* to stage *j*.

III. Result

A. Probability density function

The overnight sleep recordings of two subjects were utilized as the training data for expert knowledge database construction. The *pdfs* of the selected parameters are illustrated in Fig. 1. In the ratio of *ω1* (0.5-2 Hz) in EEGs, S3 and S4 of deep sleep had lager location values separated from other stages. S3 and S4 were slightly separated from each other among the training subjects of elder persons. The amplitude of *ω2* (2-7 Hz) in EEGs, REM and light sleep (S1, S2) showed relatively large location values comparing with others. The ratio of *ω3* (8-13 Hz) in EEGs can be the evidence for C(W). The amplitude of *ω4* (25-35 Hz) in EEGs indicated that stage awake of O(W) and C(W) were separated from other stages. The amount of *ω5* (2-10 Hz) in EOGs, S2 showed larger location value comparing with other stages. In the amount of *ω6* (25-100 Hz) in EMG, REM had the smaller location value comparing with other sleep stages. The combination of those selected parameters was utilized for manipulating the automatic sleep stage determination.

B. Sleep stage determination

The overnight sleep recordings of another two subjects were analyzed, which were different from the training data. The result of automatic sleep stage determination was evaluated comparing with the visual inspection. The recognition of sleep stage was appreciably satisfied. The average accuracy of two test subjects showed that stage awake was 85.8%, stage REM was 76.2%, light sleep (S1 and S2) was 80.6% and deep sleep (S3 and S4) was 95.7%.

IV. Discussion

A. Expert knowledge database

Rule-based method, which had been designed based on R&K criteria, can be found in many studies of computerized sleep stage scoring. The R&K criteria provide rules for sleep stage scoring with typical and normal waveforms of healthy persons. Additionally the conventional rule-based

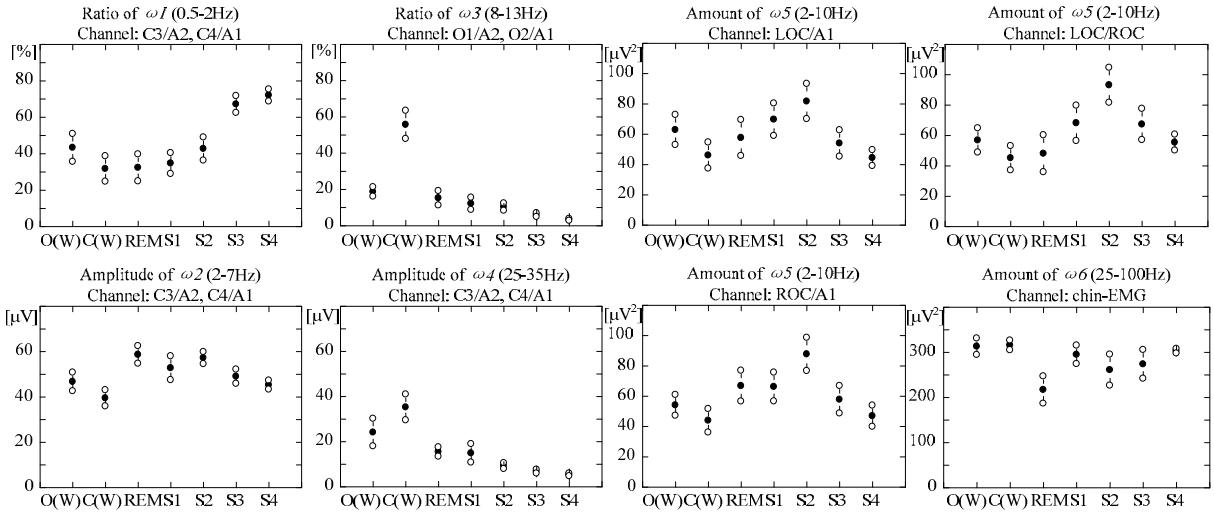


Fig. 1 Probability density functions of Cauchy distribution for the selected parameters corresponding to each sleep stage. The horizontal axis indicates the types of stages. The vertical axis is the value of parameters. "●" denotes the location of Cauchy distribution. "○" denotes the scale of Cauchy distribution.

methods did not consider the artifacts and surrounding circumstance in clinical practice. However, sleep data is inevitably affected by internal and external influences. The influences are complex and variable. Using R&K criteria only, those rule-based methods may be successful for the sleep data under ideal recording condition of healthy persons, but not for the sleep data under usual recording condition of patients at hospitals.

Unlike the rule-based method, our method is expert knowledge-based. The visual inspection by a qualified clinician takes an important role during the learning process of expert knowledge database construction. The clinician made visual inspection not only referring to R&K criteria, but also considering the artifacts and surrounding circumstance in the hospital. The visual inspection by a qualified clinician, thus, can be reliable to construct the knowledge database of probability density functions of parameters and manipulate the automatic sleep stage determination.

B. Parameter selection

Parameter selection was one component included in our learning process of expert knowledge database construction. The principle of parameter selection is to decrease the positive error and negative error of sleep stage determination. In our study, one parameter is not expected to distinguish all the sleep stages from each other. The *pdfs* of some stages may be overlapped. If the *pdf* of the stage is separated from others, this parameter can be selected. The next parameter would be selected if it can distinguish the stages in the overlapped part of previous parameters. A distance of three times of the deviation, which covers 99% of the *pdf*, is adopted for measurement. The combination of the selected parameters is optimized for manipulating the automatic sleep stage determination algorithm.

C. Clinical significance

In this study, the patients were from Toranomon hospital. Toranomon hospital is named for the diagnosing and treatment of Sleep Apnea Syndrome. A qualified clinician F.K. from Toranomon hospital made visual inspection on sleep stages. According to the visual inspection, expert knowledge database was constructed. The result of automatic sleep stage determination showed close agreement comparing with the visual inspection. Our system can satisfy the sleep stage scoring requirement in Toranomon hospital. In addition, our method is flexible to learn from any clinicians. Accordingly, the developed automatic sleep stage determination system can be optimized to meet the requirements in different hospitals and institutions.

V. Conclusion

An expert knowledge-based method for sleep stage determination was presented. The process of parameter selection enhanced the flexibility of the algorithm. The developed automatic sleep stage determination system can be optimized for clinical practice.

Acknowledgment

This study is partly supported by Nation Nature Science Foundation of China (NSFC) 60543005 and 60674089, and Shanghai Leading Academic Discipline Project B504.

References

1. Rechtschaffen A, Kales A A. (1968) Manual of standardized terminology, techniques and scoring system for sleep stages of human subject. UCLS Brain Information Service/Brain Research Institute, Los Angeles
2. Smith J R, Karakan I (1971) EEG sleep stage scoring by an automatic hybrid system. Electroencephalogr Clin Neurophysiol 31(3):231-237
3. Smith J R, Karakan I, Yang M (1978) Automated analysis of the human sleep EEG, waking and sleeping. Electroencephalogr Clin Neurophysiol 2:75-82
4. Park H J, Oh J S, Jeong D U, Park K S (2000) Automated sleep stage scoring using hybrid rule and case based reasoning. Comput Biomed Res 33(5):330-349
5. Anderer P et al. (2005) An E-health solution for automatic sleep classification according to Rechtschaffen and Kales: validation study of the Somnolyzer 24 x 7 utilizing the Siesta database. .Neuropsychobiology 51(3):115-133
6. Himanen S L, Hasan J (2000) Limitations of Rechtschaffen and Kales. Sleep Med Rev 4(2):149-167
7. Anderer P, Roberts S, Schlogl A et al. (1999) Artifact processing in computerized analysis of sleep EEG - a review. Neuropsychobiology 40(3):150-157
8. Nakamura M, Sugi T (2001) Multi-valued decision making for transitional stochastic event: determination of sleep stages through EEG record, ICASE Transactions on Control, Automation and Systems Engineering 3(2):1-5
9. Wang B, Sugi T, Kawana F, Wang X, Nakamura M (2008) Multi-Valued Decision Making of Sleep Stages Determination Based on Expert Knowledg, Proc International conference on Instrumentation, Control, and Information Technology, Chofu, Japan, 2008, pp 3194-3197
10. Jasper H H (1958) Ten-twenty electrode system of the international federation, Electroencephalogr Clin Neurophysiol 10:371-375
11. Spiegel M R (1992) Theory and Problems of Probability and Statistics. McGraw-Hill, New York.

Author: Bei Wang
Institute: Department of Advanced Systems Control Engineering, Saga University
Street: Honjoh machi 1
City: Saga 840-8502
Country: Japan
Email: wangbeish@gmail.com

A Study on the Relation between Stability of EEG and Respiration

Young-Sear Kim[1], Se-Kee Kil[2], Heung-Ho Choi[3], Young-Bae Park[4], Tai-Sung Hur[5], Hong-Ki Min[1]

[1] Dept. of Information & Telecom. Engineering, Univ. of Incheon, Korea
[2] Dept. of Electronic Engineering, Inha Univ., Korea
[3] Dept. of Biomedical Engineering, Inje Univ., Korea
[4] School of Oriental Medicine, Kyunghee Univ., Korea
[5] Dept. of Computing & Information System, Inha Technical College, Korea
hkmin@incheon.ac.kr
82-32-770-8284

Abstract — **In this paper, we analyzed the relation between Respiration and EEG. For this, we acquired the EEG signal, ECG signal and respiration signal synchronously with keep time. And we defined SSR and Macrate which represent beat rate of heart per single unit of respiration and relational ratio of alpha wave and beta wave in EEG respectively. The reason why we defined SSR and Macrate is to compare and analyze two signals quantitatively. From the examination result about 10 reagents, we verified our proposal.**

Keywords — **EEG, SSR, MACRATE, RESPIRATION**

I. Introduction

Traditionally, it is said that alpha wave is strongly appeared when the person is in stable state [1]. And in oriental medicine, it is said that long-length respiration is close to more stable state than short-length respiration [2].

Then in this paper, we tried to analyze the relationship between EEG and respiration from the viewpoint of stable state. But in that case, there is no outstanding method to compare the degree of stability between EEG and respiration quantitatively.

Because of this, we defined SSR and Macrate which mean respectively relational ratio of stable state in EEG and relational heartbeat count per one period of respiration. To find out SSR and Macrate from the biomedical signals, it is essential to extract alpha and beta wave of EEG and feature points of ECG and respiration signal.

Wavelet transform is widely used in the field of signal processing, compression and decompression, neural network and etc. Comparing with Fourier transform, it has strong advantage that don't lose information of time location when the data transformation from spatial domain to frequency domain [3]. It could be significant thing to notice the occurring points of particular event during the processing data in frequency domain. Then wavelet transform could be proper method in case of this paper which aims at pursuit of variation of EEG spectrum with flow of time.

Using wavelet transform, in this paper, we decomposed the EEG signal to various signals which has different frequency bandwidth such as alpha wave and beta wave. And we estimated the power spectrum of EEG, alpha wave and beta wave to calculate the SSR.

In case of Macrate, respiration count and heartbeat count from ECG are essential for calculation. We used zero-crossing method to extract respiration count per minute and used wavelet based algorithm [4] to extract heartbeat count per minute.

II. Definition of Macrate and SSR

We defined SSR(Stable State Ratio) as following equation (1). Alpha wave is said that it is strongly extracted when the state is stable and beta wave is strong when the state is active. But everybody has his own amount of alpha wave then it cannot explain accurate degree of stable state of EEG. And then we used relative ratio of stable state and active state of EEG.

$$SSR = \frac{power\ spectrum\ of\ alpha\ wave}{power\ spectrum\ of\ beta\ wave} \quad (1)$$

We assumed the most stable state period as the period which one unit length of respiration is most long in the whole data of 20 minute respiration data. The Macrate is defined as following equation 2.

$$Macrate = \frac{beat\ count\ \ per\ \ minute}{respiration\ count\ \ per\ \ minute} \quad (2)$$

Chwee Teck Lim, James C.H. Goh (Eds.): ICBME 2008, Proceedings 23, pp. 51–54, 2009
www.springerlink.com

III. Feature Point Extraction and Relational Analysis

To compute SSR, extraction of alpha wave and beta wave from EEG and estimation of power spectrum are necessary. EEG data used in this paper is the data from the frontal lobe (the sixth channel) among the data of eight channel EEG data. And its sampling frequency is 256 Hz. Then the valid range of frequency are 0 ~ 128Hz according to the Nyquist sampling principle. Following table 1 shows the seven level decomposition results of EEG data using wavelet transform

Table 1: Frequency band of EEG signal according to the decomposition level.

Level	A	Frequency	D	Frequency
1	cA_1	0 Hz ~ 64 Hz	cD_1	64 Hz ~ 128 Hz
2	cA_2	0 Hz ~ 32 Hz	cD_2	32 Hz ~ 64 Hz
3	cA_3	0 Hz ~ 16 Hz	cD_3	16 Hz ~ 32 Hz
4	cA_4	0 Hz ~ 8 Hz	cD_4	8 Hz ~ 16 Hz
5	cA_5	0 Hz ~ 4 Hz	cD_5	4 Hz ~ 8 Hz
6	cA_6	0 Hz ~ 2 Hz	cD_6	2 Hz ~ 4 Hz
7	cA_7	0 Hz ~ 1 Hz	cD_7	1 Hz ~ 2 Hz

Generally, according to frequency, brain wave pattern is classified to alpha wave correspond to 8~12Hz, beta wave correspond to 13~35Hz , theta wave correspond to 4~7 Hz, delta wave correspond to 0.3~3.5 Hz and etc. Alpha wave is the signal which is outstanding pattern among the various brain wave patterns and it is generally appeared when the eyes is closed, the stable state mentally and silence circumstances from the frontal lobe or occipital region of head [1].

As shown in the above table 1, the frequency band of alpha wave is belonged in the component cD_4. To decompose that component again using wavelet, cD_4A_1(8 ~ 12 Hz) and cD_4D_1(12 ~ 16 Hz) is appeared. Because frequency band of alpha wave is about 8 ~ 12Hz, we choose the cD_4A_1 component as alpha wave and cD_3 component as beta wave.

With extracted alpha and beta wave, we estimated the power spectrum of wave to find out SSR which represents the degree of stability quantitatively. There are generally three kinds of method in power spectral analyzing method such as correlation function method (Blackman-Tukey), FFT method and linear prediction model method. Among these, B-T method and FFT method are generally used and linear prediction model is used when the data length of acquisition is very short relatively [5]. So we used FFT method in this paper, it is because the length of EEG signal was sufficiently long as its length was 20 minutes.

Next, to get the Macrate, extraction of heartbeat from ECG and respiration count per minute is necessary. At first, to recognize QRS complex of ECG and to achieve heartbeat count per minute, we used wavelet method [6]. At second, to recognize period of respiration, we used zero crossing method

Relational analysis is the method which is used to find out the linear relationship between two different variables. And generally relational coefficient as seen as following equation (3) is used.

$$r = \frac{S_{XY}}{\sqrt{S_{XX}}\sqrt{S_{YY}}}, \qquad -1 \le r \le 1 \tag{3}$$

In this paper, we aimed to find out the quantitative relation between EEG and respiration at the viewpoint of stable state. Then, with accomplished SSR and Macrate, we did relational analysis.

IV. Results

The data used in this paper was EEG signal, ECG signal and respiration signal which were synchronized with time accurately from 10 persons for 20 minutes respectively. The following figure 1 shows acquired EEG signal and extracted alpha & beta signal by wavelet method. And the following figure 2 shows moving spectral result of alpha wave spectrum over EEG signal spectrum, beta wave spectrum over EEG signal spectrum and alpha wave spectrum over beta wave spectrum for 20 minutes. In the figure 3, horizontal axis means time and vertical axis rate of each spectrum.

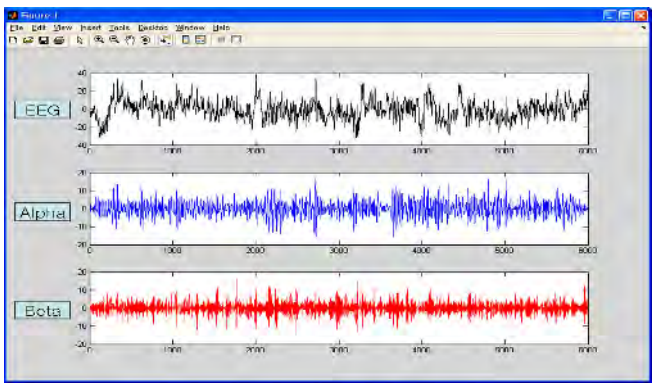


Figure 1: Extraction of alpha wave and beta wave.

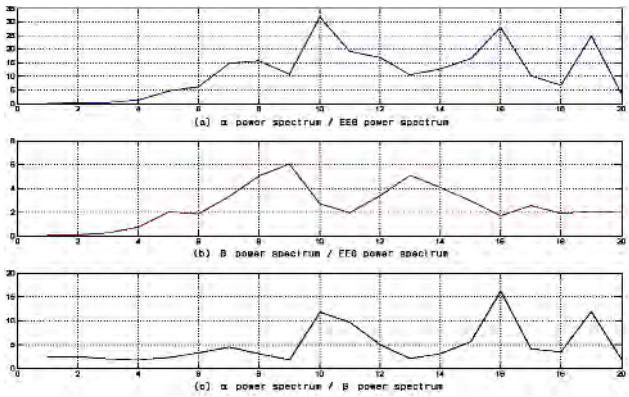


Figure 2: The result of power spectrum of EEG.

The following figure 3 shows SSR in most high Macrate in the whole respiration signal. In the figure 3, upside figure is SSR and downside figure is Macrate. And these two signals are synchronized with accurate time.

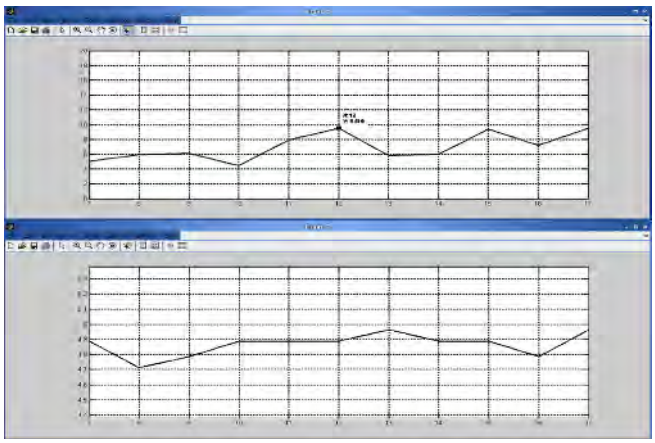


Figure 3: The SSR and Macrate.

The following table 2 is result of relational analysis about SSR and Macrate about a reagent. And figure 4 is the scatter plot of table 2. Relational analysis in this paper was performed by SPSS software version 12K.

Table 2: The result of relational analysis between SSR and Macrate

		SSR	Macrate
SSR	r	1	.431
	P-value		.000
	N	114	114
Macrate	r	.431	1
	P-value	.000	
	N	114	114

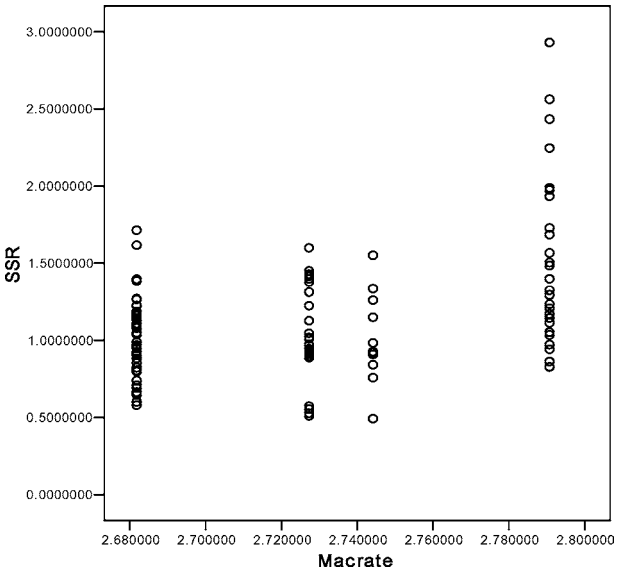


Figure 4: Scatter plot of result which is shown in table 2.
It can see that SSR is more growing in high Macrate.

The following table 3 is the result of all 20 reagents. As shown in table, SSR and Macrate have relation from 20.5% to 43.1%

Table 3: The result of relational analysis about 10 reagents

Reagent	Result	Reagent	Result
1	0.247	6	0.268
2	0.239	7	0.380
3	0.220	8	0.431
4	0.356	9	0.292
5	0.205	10	0.237
Average		0.290	

V. Conclusion

In this paper, we analyze the relationship between SSR and Macrate in order to find out quantitative relation between EEG and respiration at the viewpoint of stable state. To accomplish this aim, we extracted the feature points of bio-signals such as EEG, ECG and respiration signal from 10 reagents. And we defined and calculate the SSR and Macrate as a quantitative index of stable state. And last, from the relational analysis, we could come to conclusion that EEG and respiration have relation each other. Future work contains more plenty of experiment and etc.

REFERENCES

1. J. J. Carr, “Introduction to Biomedical Equipment Technology,” Prentice Hall Press, pp 369-394, 1998
2. B.K.Lee ,”Diagnostics in oriental medicine,” the schools of oriental medicine of Kyung Hee University, 1985.
3. Akram, Aldroubi & Michael Unser, "Wavelet in Medicine and Biology," CRC Press, 1996
4. S. K. Kil, “Concurrent recognition of ECG and human pulse using wavelet transform”, Journal of KIEE, Vol 55D, No. 7, pp. 75-81, 2006
5. N. H. Kim, “A Study on the Estimation of Power Spectrum of the Heart Rate using Autoregressive Model,” the thesis of degree of Ph.D, Inha Univ., 2001

The Feature-Based Microscopic Image Segmentation for Thyroid Tissue

Y.T. Chen[1], M.W. Lee[1], C.J. Hou[1], S.J. Chen[2], Y.C. Tsai[1] and T.H. Hsu[1]

[1] Institute of Electrical Engineering, Southern Taiwan University, Tainan, Taiwan
[2] Department of Radiology, Buddhist Dalin Tzu Chi General Hospital, Chia-Yi, Taiwan

Abstract — **Thyroid diseases are prevalent among endocrine diseases. The microscopic image of thyroid tissue is the necessary and important material for investigating thyroid functional mechanism and diseases. A computerized system has been developed in this study to characterize the textured image features of the microscopic image in typical thyroid tissues, and then the compositions in the heterogeneous thyroid tissue image were classified and quantified. Seven image features were implemented to characterize the histological structure representation for tissue types including blood cells, colloid, fibrosis tissue, follicular cell. The statistical discriminant analysis was implemented for classification to determine which features discriminate between two or more occurring classes (types of tissues). The microscopic image was divided to be contiguous grid images. The image features of each grid image were evaluated. Multiple discriminant analysis was used to classify each grid image into the appropriated tissue type and Markov random fields were then employed to modify the results. 100 random selected clinical image samples were employed in the training and testing procedures for the evaluation of system performance. The results show that accuracy of the system is about 96%.**

Keywords — **Image segmentation, Markov random fields, Thyroid nodule, Feature classification**

I. Introduction

Thyroid diseases including nodules, goiters, adenomas, even carcinomas, and other related diseases are prevalent among endocrine diseases [1,2]. A thyroid nodule is the common initial manifestation of most thyroid tumors. There are many methods in clinical examination for thyroid diseases. Observation and examination of histological tissue images can help in understanding the cause and pathogenesis of the thyroid diseases. The benignancy or malignancy of thyroid nodules and tumors can be discriminated by microscopic observation on image features of tissue.

From the viewpoint of morphological architectures in histopathology, many specific image features are important indexes and references for thyroid diseases [3]. The functional unit of the main endocrine system in the thyroid is the follicle, a closed spheroid structure lined by a single layer of epithelial cells. It is filled with colloid. With the onset of nodular goiter, the number of follicles is increased and the epithelial cells are enlarged and columnar. The follicle is a colloid-rich area. Epithelial cells lining the follicles are flat and most of the follicles are distended with colloid. Fig. 1 (a) shows the typical image of nodular goiter. Fig.1 (b) shows the architectural characteristics of papillae in papillary carcinoma. The cells are arranged around well-developed papillae. The stroma is represented by loose connective tissue. Fig. 1(c) shows the microscopic image of follicular adenoma. These types of tumors exhibit morphological evidence of follicular cell differentiation. A detail of the adenoma depicted in Fig.1(c) shows a regular microfollicular and solid architectural pattern with little cytological atypia. Medullary carcinoma usually has clear microscopic evidence of infiltration into the surrounding thyroid parenchyma. Blood vessel invasion is common, and involvement of lymph vessels and regional lymph nodes are also frequently found.

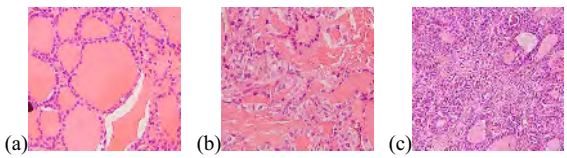


Fig. 1 Typical tissue microscope image of thyroid disease (H&E staining, 200X) (a) Thyroid nodular goiter (b) Papillary carcinoma (c) Follicular adenoma

Because of the histological complexity and diversity, the image examination and related clinical practices are redundant and time-consuming. Furthermore, the quality of clinical reading heavily depends on the experiences of clinical practicer. Therefore, a computerized system has been developed in this study to characterize the textured image features of the microscopic image in typical thyroid tissues, and then the compositions in the heterogeneous thyroid tissue image are classified and quantified. The image features and morphological differentiation of follicles within the thyroid are the determined characteristics for various diseases. With advancements of methodologies in digital image processing, digital images can assist in deducing meaningful revelations from implicit details. Armed with the image characteristics of thyroid tissue, the theorems and technologies of digital image processing and

Chwee Teck Lim, James C.H. Goh (Eds.): ICBME 2008, Proceedings 23, pp. 55–59, 2009
www.springerlink.com

feature classification can be implemented for thyroid tissue microscopic image feature characterizing and quantifying.

In this paper, methodologies using image and texture analysis techniques regarding characterizations and quantifications of typical microscopic images of follicles, colloid, blood cells, stroma are proposed. The results of identical tissue segmentation from heterogeneous images by implementing the statistics-based image segmentation with MRF modification technique are presented as well.

II. Materials and Methods

A. Image Acquisition

Slices of histopathological thyroid tissue were made through routine paraffin embedding and hematoxylin-eosin (H&E) staining. The digitized tissue images were obtained from microscope (Nikon 80i) at magnification of 100x using a DSLR camera (Nikon D80). The image resolution was set as 3872×2592 pixels and 24 bits per pixel. The aperture and shutter of camera was kept consistent between samples.

B. Statistical image Features analysis and tissue characterization

Seven image features including pixel-level features and high-order texture features were used in the study to evaluate the image characteristics of five typical histological thyroid tissues. The statistical pixel-level features include *mean of Brightness*, *Standard Deviation of Brightness*(SDB), *mean of Hue*, *Entropy*, and *Energy* of the selected image areas. These features provide quantitative information about the pixels within a segmented region [4]. *Hurst* value derived from fractal analysis reveals the roughness of the selected image areas. The high-order texture features are *Regularity* of *statistical feature matrix*(SFM). The statistical stepwise selection was implemented to exclude insignificant features. Then multiple discriminant analysis was used for the classification of features. Our previous study for tissue classification with these image and texture features has been proposed in [5].

C. Markov Random Fields

Markov random fields (MRF) theory is a stochastic model-based approach for texture analysis. The image and texture features are considered in the random status. For every latticed image, with the neighborhood system and the property of joint condition probability density, the texture data can be fitted with defined stochastic models and the one which gives the best approximation to the data can be determined. The approach are widely used for image recovery and denoising.[6-9]

Based on the concept of MRF, the states of the sites in the system have to be limited. After evaluating the conditional probabilities between neighber sites, the probabilities would be applied to determine the state of the site. With finite states space, the transition probability distribution can be represented by a matrix, called the transition probability matrix(TPM). The TPM with sites in n states takes the following basic form

$$P = \lfloor p_{ij} \rfloor \quad 0 \le i, j \le n \text{ , and} \tag{1}$$

$$p_{ij} \ge 0, \quad \sum_{j=0}^{\infty} p_{ij} = 1 \quad \text{for any } i \text{ .} \tag{2}$$

- Neighborhood System and Clique

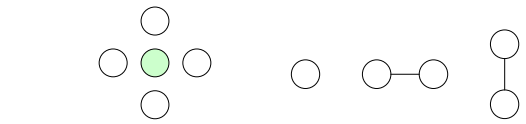
Let $S = \{s_{11}, s_{12}, ..., s_{ij}, ..., s_{nn}\}$ be a set of sites (grid images in this study). A set $NSS \equiv \{NSS_{s_{ij}}\}_{s_{ij} \in S}$ is called a neighborhood site set on the set of sites S if

$$s_{ij} \notin NSS_{s_{ij}} \tag{3}$$

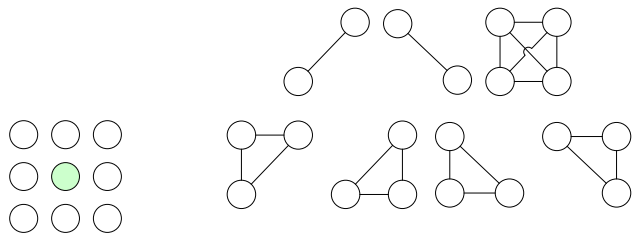
and

$$s_{ij} \in NSS_{s_{ml}} \Leftrightarrow s_{ml} \in NSS_{s_{ij}} \text{ .} \tag{4}$$

The size of *NSS* is determined by the geometrical configuration. A subset $c \subseteq S$ is a clique if every pair of distant sites in c is neighbors. C denotes the set of c. Fig. 1 shows two kinds of neighborhood system in different order with cliques.



(a) First order



(b) Second order

Fig. 1 neighborhood system and cliques

- Gibbs Distributions

Let $\Lambda = \{1,2,3,...,L-1\}$ denote the common state space, where L is the number of the state. In this study, Λ labels the classified type of tissue. Therefore, all of the sites in the MRF must belong to Λ.

Let $\Omega = \{\omega = (\omega_{s_1},...,\omega_{s_N}) : \omega_{s_i} \in \Lambda, 1 \le i \le N\}$ be the set o all possible configurations. X is an MRF with respect to *NSS* if

$$P(X = \omega) > 0 \quad \text{for all } \omega \in \Omega ; \tag{6}$$

$$\begin{aligned} &P(X_s = x_s \mid X_r = x_r, r \neq s) \\ &= P(X_s = x_s \mid X_r = x_r, r \in NSS) \end{aligned} \tag{7}$$

The probability distribution $P(X = \omega)$ in Eq(6) is uniquely determined by these conditional probabilities. Gibbs distribution and Hammersley-Clifford theorem were proposed to characterize the probability distribution [8]. The Gibbs distribution has a probability measure π on Ω with the following equation:

$$p(X = \omega) = \frac{1}{Z} e^{-U(\omega)}, \tag{8}$$

where Z is the normalizing constant represented by:

$$Z = \sum_{\omega \in \Omega} e^{-U(\omega)}, \tag{9}$$

and

$$U(\omega) = \sum_{c \in C} V_c(\omega). \tag{10}$$

The function $U(\cdot)$ is called the energy function, and $V_c(\cdot)$ is called a potential function determined from the relational entries of TPM depending on the values ω_s of ω for which $s \in C$.

D. System Operation

The aforementioned theories were implemented in this system to train the ability for recognition and improve the performance of the system for the tissue classification in heterogeneous tissue microscopic image. Fig. 2 shows the schematic flowchart of the proposed system. The image samples were divided to be contiguous grid images. Two phases, the training phase and recognition phase, were then established in the procedures and they are described in the following paragraphs.

- Training phase

Two steps were included in this phase. One step was performed to evaluate the feature weightings for applying the discriminant classification rules. The tissue type of every grid image was manually assigned. These aforementioned statistical texture features were then calculated. Finally, discriminant analysis was implemented to evaluate the feature weightings of discriminant classification rules for types of tissue including blood cells, colloid, fibrosis tissue, and follicular cell.

The following training step is performed to estimate the transition probability matrix for MRF-based class modification. The images in the database for training were extracted and latticed. All of the grid image were roughly classified by applying the discriminant analysis. The misclassified grid images were manually corrected. Finally, the MRF algorithm was implemented to the grid images to establish the TPM.

- Recognition phase

For every grid image of latticed microscopic image, the aforementioned image and texture features were implemented to characterize the histological structure representation for tissue types. These image and texture feature were implemented to evaluate the characteristics of textures. Using the feature weightings, the statistical discriminant analysis was implemented for classification to determine tissue type of grid image. MRF using established TPM were then employed to modify the results of the misclassified grid images.

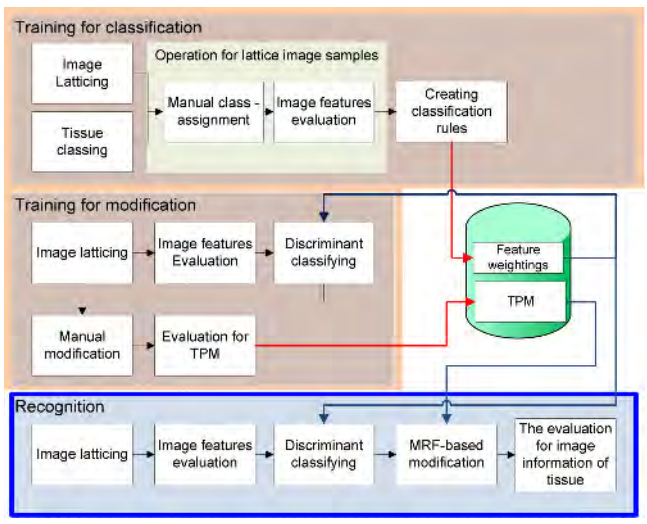
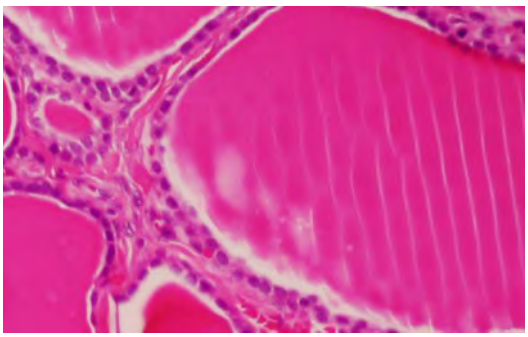


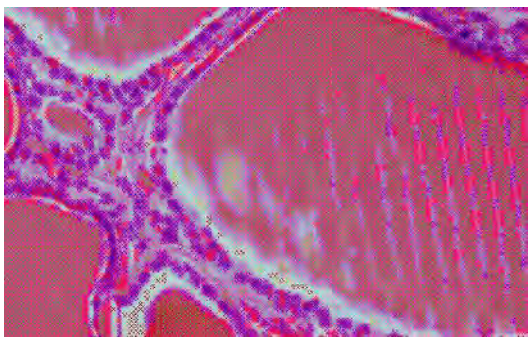
Fig. 2 Schematic flowchart of this proposed system

III. Results and discussion

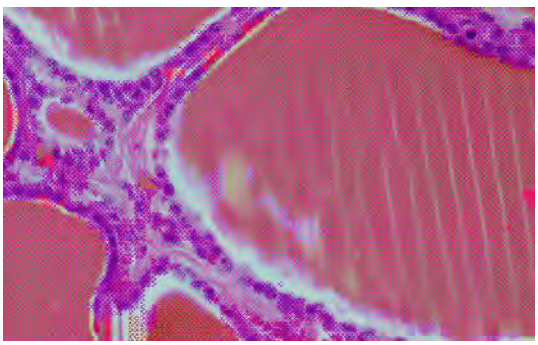
Fig. 3 shows an example of image segmentation by using this proposed system. This image in (a) mainly contains two types of tissue: follicular cells and colloid blocks. Because of the problem of tissue samples making and preserving, some empty areas and fissures appear between normal tissues. Fig. 3(b) shows the result of image classification applying discriminant analysis. Some grid images were misclassified as blood cells (red blocks). As shown in (c), after the process of MRF-based modifications, most of the misclassified grids were corrected.



(a) Original image with follicular cells and colloid



(b) The results of classification after discriminant analysis



(c)The results of modification after using MRF

Fig. 3 The examples for microscopic image segmentation with heterogeneous tissues

Sensitivity, specificity, and accuracy of four approaches with different combinatorial methods were evaluated. These methods used in this four approaches were: 1) the discriminant analysis (DA), 2) the discriminant analysis with empirical rules (DA+ER), 3) discriminant analysis with empirical rules and MRF-based modification (DA+ER+MRF), and 4) discriminant analysis and MRF-based modification (DA+MRF). The empirical rules were determined from the statistical distribution of the image features of tissue classes. The images of every kind of tissue were selected by our clinical fellow.

100 random selected clinical image samples were employed in the training and testing procedures for the evaluation of system performance. 50 images are used for training and the others are used for testing. The performance evaluations of the proposed methodologies are listed in Table 1. The results show the two approaches using MRF have higher sensitivity and specificity. The approach of DA+MRF has the highest performance with accuracy about 96%.

Table 1 Performance Measure of the proposed methods

	DA	DA+ER	DA+ER +MRF	DA+MRF
Sensitivity	0.576	0.561	0.655	0.793
Specificity	0.919	0.917	0.951	0.977
Accuracy	0.897	0.896	0.936	0.966

IV. Conclusions

In this paper, the microscopic images of thyroid heterogeneous tissues were characterized and classified by combinatorial approaches applying image features classification, statistical discriminant analysis and MRF based class modification. The results show the algorithm has good performance and high capability for classification of pathological tissues of thyroid nodule. We hope that the information provided from these succeeding studies will have a reliable means for the related clinical analysis of thyroid diseases.

Acknowledgment

This work was supported in part by the National Science Council, ROC, under the Grant# NSC 96-2221-E-218 -053

References

[1] Harburger JI (1989) Diagnostic Methods in Clinical Thyroidology, Springer-verlag, NY
[2] Wynford-Thomas D, Williams ED (1989) Thyroid Tumours: Molecular Basis of Pathogenesis, Churchill Livingstone, London
[3] Ljungburg O (1992) Biopsy pathology of the thyroid and parathyroid. Chapman & Hall Medical, London
[4] Dhawan AP (2003) Medical Image Analysis, Wiley-IEEE Press, NJ
[5] Chen YT, Hou CJ, Lee MW, Chen SJ, Tsai YC, Hsu TH (2008) The image feature analysis for microscopic thyroid tissue classification. 30th Annual International Conference of the IEEE EMBS, Vancouver, Canada, 2008, pp.4059-4062
[6] Geman S, Geman D (1994) Stochastic relaxation, Gibbs distributions, and the Bayesian restoration of images. IEEE Trans Pattern Anal Mach Intell PAMI-6(6):721-741
[7] Cai J, Liu ZQ (2002) Pattern recognition using Markov random field models. Pattern Recognit 35:725-733
[8] Szirányi T, Zerubis J, Czúni L, Geldreich D, Kato Z (2000) Image segmentation using Markov random field model in fully parallel cellular network architectures. Real-Time Imaging 6:195-211
[9] Wilson R, Li CT (2002) A class of discrete multi-resolution random fields and its application to image segmentation. IEEE Trans Pattern Anal Mach Intell 25(1):42-56

Author: Yen-Ting Chen
Institute: Department of Electrical Engineering, Southern Taiwan University
Street: No.1, Nan-Tai St.
City: Yung-Kung City, Tainan County
Country: Taiwan
Email: ytchen@mial.stut.edu.tw

Heart Disease Classification Using Discrete Wavelet Transform Coefficients of Isolated Beats

G.M. Patil[1], Dr. K. Subba Rao[2], K. Satyanarayana[3]

[1]Dept. of I.T., P.D.A. College of Engineering, Gulbarga-585 102 (Karnataka) INDIA
[2]Dept. of E&CE, UCE, Osmania University, Hyderabad-500 007 (A.P.) INDIA
[3]Dept. of BME, UCE, Osmania University, Hyderabad-500 007 (A.P.) INDIA

Abstract — **In this work the authors have developed and evaluated a new approach for the feature analysis of normal and abnormal beats of electrocardiogram (ECG) based on the discrete-wavelet-transform (DWT) coefficients using Daubechies wavelets. In the first step the real ECG signals were collected from the normal and abnormal subjects. DWT coefficients of each data window were calculated in the Matlab 7.4.0 environment using Daubechies wavelets of order 5 to a scale level of 11. The detail information of levels 1 and 2 was discarded, as the frequencies covered by these levels were higher than frequency content of the ECG. Thus for a scale level 11 decomposition, coefficients associated with approximation level 11 and details level 3 to 11 were retained for further processing. The recorded ECG was classified in to normal sinus rhythm (NSR) and three different disease conditions, namely: atrial fibrillation (AF), acute myocardial infarction (AMI) and myocardial ischaemia based on the discrete wavelet transform coefficients of isolated beats from the multi-beat ECG information.**

Keywords — **ECG, Discrete-wavelet-transform (DWT), atrial fibrillation (AF), acute myocardial infarction (AMI), myocardial ischaemia.**

I. Background

Cardiac arrhythmias can be catastrophic and life threatening. Special kind of arrhythmia: atrial fibrillation (AF) has its special pattern on the shape of ECG; it perturbs the electrocardiogram and in the same time complicates automatic detection of other kinds of arrhythmia [1]. The problem has been described as a challenge by both Computers in Cardiology and PhysioNet. Permanent and paroxysmal AF is a risk factor for the occurrence and the recurrence of stroke, which can occur as its first manifestation. However, its automatic identification is still unsatisfactory [2]. Atrial fibrillation (AF) is an arrhythmia associated with the asynchronous contraction of the atrial muscle fibres. It is the most prevalent cardiac arrhythmia in the western world, and is associated with significant morbidity. Heart diseases, in particular acute myocardial infarction (AMI), are the primary arrhythmic events in the majority of patients who present with sudden cardiac death [3]. Myocardial ischaemia is yet another cardiac disorder which needs urgent medical attention. The single most common cause of death in Western culture is ischaemic heart disease, which results from insufficient coronary blood supply [4]. Approximately 35 percent of all human beings who suffer from cardiac disorders in the United Sates die of congestive heart failure, the most common cause of which is progressive coronary ischaemia [5].

II. Introduction

Cardiac arrhythmias detection is important because they determine the emergency conditions (risk of life). Heart abnormalities are not identifiable in the electrocardiogram (ECG) recorded from the surface of the chest at the very early stage. They become visible in the ECG after the disease is in place. If certain heart diseases are not diagnosed, evaluated and treated at the early stage, such a condition may lead to the risk of sudden cardiac death. Since heart diseases can be treated, early recognition is important.

In particular, AF beat, AMI and myocardial ischaemia indicate susceptibility to life-threatening conditions. Moreover, the probability of recovery is often greatest with proper treatment during the first hour of a cardiac disturbance [6]. Measurements of the width or duration of waves in the ECG widely used to define abnormal functioning of the heart [7], to detect myocardial damage and to stratify patients at risk of cardiac arrhythmias is not only time consuming and slow but also inadequate. We therefore need a faster and accurate method of cardiac analysis using wavelet coefficients. In this study, a new wavelet-based technique has been proposed for the identification, classification and analysis of arrhythmic ECG signals.

In the recent times the wavelet transform has emerged as a powerful time–frequency signal analysis tool widely used for the interrogation of nonstationary signals. Its application to biomedical signal processing has been at the forefront of these developments where it has been found particularly useful in the study of these, often problematic, signals: none

Chwee Teck Lim, James C.H. Goh (Eds.): ICBME 2008, Proceedings 23, pp. 60–64, 2009
www.springerlink.com

more so than the ECG. The method is particularly useful for the analysis of transients, aperiodicity and other non-stationary signal features where, through the interrogation of the transform coefficients, subtle changes in signal morphology may be highlighted over the scales of interest. The method proposed by the authors makes use of the isolated beats from real ECG records by importing the ECG data files into Matlab 7.4.0 environment.

III. Methods

The authors collected the ECG records from 233 subjects and examined with the help of an expert cardiologist and are used throughout this study. The control data of 120 records comprising 80 normals (NOR) and 40 abnormals (ABN) with arrhythmias were sorted and analyzed using Daubechies wavelet transform. Then a validation group of 70 subjects' ECG records known as the *test data* were studied using these criteria. Out of the 70 records 40 taken from normal persons and 30 with pathological heart beats were analyzed which allowed the authors to establish the specific cardiac cycle characteristics to differentiate the healthy sinus rhythm from the abnormal cardiac functioning using wavelet analysis.

The ECG data files are converted to text (.txt) files and later to Mat (.mat) files. The Mat files were imported in to Matlab workspace and with the help of the code written in Matlab version 7.4.0 the decomposition of coefficients were computed.

This method decomposes the ECG originally into 5 transformed signals at 11 different scales and makes use of scales 3 to 11 of the wavelet transform. In this method only scales 3 to 11 are used to characterize the ECG signal as these prove to give optimum results. A derived criterion is applied on a combination of such scales to determine the abnormal cardiac waves, in addition to the specific level of coefficients as discussed hereafter.

For this study, the Daubechies wavelet family was retained that represented the most commonly used family of orthogonal wavelets for detecting ECG events. The member of the corresponding family, DB5, to use was then picked out: on the one hand by relying on a thorough investigation of related literature. And on the other, by analyzing the results of the applications. The complete separation of relevant waves from the ECG signals prior to interpretation is still an open problem because of the noisy nature of the input data.

A. Experimental setup and data acquisition

The battery operated, portable and cost effective ECG acquisition system has been designed and developed as a separate part of this project [8]. The module, developed and implemented is used for ECG recording. The ECG is amplified, filtered (0.5 -120 Hz) and converted into digital form before being processed. The signal is sampled at 2 kHz. A digital signal processing system, PC with Matlab 7.4.0 was placed for data acquisition, processing and storage. The 30 seconds of signals comprising 36 cycles for a normal heart rate of 72 beats per minute were recorded and stored for analysis.

Authors have used discrete wavelet transform (DWT) for data processing to extract classifier features' decomposition coefficients allowing authors to differentiate the heart diseases from the sinus rhythm (SR).

B. Selection of the wavelet functions

There is no absolute rule to determine the most adequate analyzing wavelets; the choice must always be specific to the application as well as to the analysis requirements. The efficiency in extracting a given signal based on wavelet decomposition depends greatly on the choice of the wavelet function and on the number of decomposition scales [9]. In this study, a straightforward approach for wavelet selection was based on: 1) Literature where wavelets have already been used for ECG processing. 2) Suitability of a particular member of the family of wavelets for the analysis of specific cardiac abnormality signals. The Daubechies wavelets DB5 have shown to be very adequate for the present analysis, based on the similarity between ECG samples and the selected member of the considered family. These two approaches resulted in an optimal group of results. Table 1 shows the ECG waves, their morphology and the suggested diseases.

Table 1 ECG waves, morphology and the suggested diseases

Wave	Morphology	Disease
P wave	Absent	Atrial fibrillation
S-T segment	Eleveted	Acute myocardial infarction
S-T segment	Depressed	Myocardial ischaemia
T wave	Too tall	Acute myocardial infarction
T wave	Inverted	Myocardial ischaemia

IV. Results and validation

The authors used their own ECG database to carry out tests on the method used, which is aimed at helping doctors analyze patient records. Finally real ECG records were used to determine the DWT coefficients. The method proposed by the authors makes use of the isolated beats from real ECG records. The sample numbers of onset of P wave and

offset of T wave were provided in the Matlab code for single cycle extraction and each ECG cycle both normal and abnormal was viewed before the corresponding mat file being used for computation of DWT coefficients. The DWT coefficient values corresponding to P and T waves and S-T segment appearing with certain morphologies are analyzed and classified. The efficiency of algorithm performance of the presented method was tested on the *control data* group and over the validation database namely *test data* group. Wavelet decomposition coefficients computed for *quite representative signals* were classified and tabulated for analysis. Real ECG signals recorded on healthy and pathological persons provided a very interesting aspect for the heart beats evaluation, given that the total ECG vector was viewed in the Matlab 7.4.0 environment and the positions of the arrhythmias in the signal were known *a priori* and hence could be isolated and compared to the result of the normal cycle extraction. The decomposition coefficients cd3 to cd11 of a normal sinus beat; the intervals and amplitudes defined by its features being within the normal limits are tabulated for the analysis.

Single cycles of normal cardiac cycles are shown in figures 1 and 2. The corresponding decomposition coefficients cd3 to cd11 are shown in table 2 for subject 1 and cycle 1.

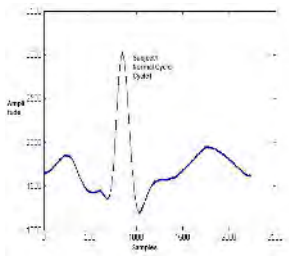


Figure 1 Normal cardiac cycle

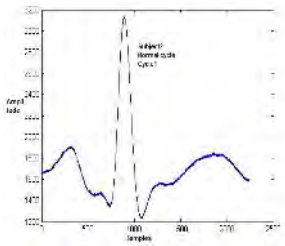


Figure 2 Normal cardiac cycle

Table 2 Detail coefficients cd3-cd11

Sub No	Cd11	Cd10	Cd9	Cd8
Sub1c1	-30.5687	-5.2672	-1.085	-0.7601
Cd7	Cd6	Cd5	Cd4	Cd3
-0.4279	-0.1813	-0.0518	-0.5416	-0.0335

All the coefficients cd3 to cd11 are found to be negative for the normal cardiac cycle.

The single cardiac cycles with P wave absent indicating atrial fibrillation are shown in figures 3 and 4.

The corresponding detail coefficients cd8 to cd11 pertaining to the low frequencies of P wave for cycles one each of subjects 1 and 2 are shown in table 3. The positive value of cd11 indicates the abnormal (P wave absent)

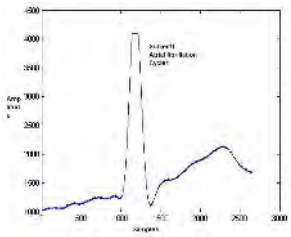


Figure 3 Atrial fibrillation

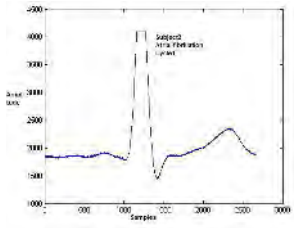


Figure 4 Atrial fibrillation

Table 3 Detail coefficients cd8-cd11

Sub No	Cd11	Cd10	Cd9	Cd8
Sub1c1	10.120	-12.948	-1.2119	-0.6643
Sub2c1	12.938	-6.9889	-0.0571	-0.0877

condition. The negative values of cd8 to cd10 and cd10 being the most significant one as examined by the authors represent presence of normal T wave.

S-T segment elevation merges with upstroke of the T wave and makes it too tall both being suggestive of acute myocardial infarction as shown in figures 5 and 6. The corresponding detail coefficients cd8 to cd11 are shown in table 4. In this particular abnormality it is again seen that the coefficients cd8 to cd11 are negative indicating the presence of normal P wave and too tall T wave. The authors used a derived criterion of combination of scales' coefficients is applied and determined that cd10 (11) is positive viz. 1353.417, 1404.941 for subjects 1 and 2 respectively.

Also S-T segment depression overlaps with the upward deflection of the T wave tending it to be inverted, which suggests myocardial ischaemia are shown in figures 7 and 8.

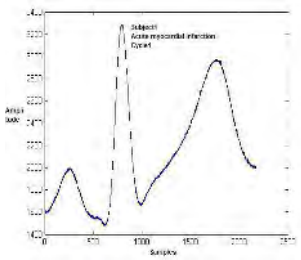


Figure 5 Acute myo cardial infarction

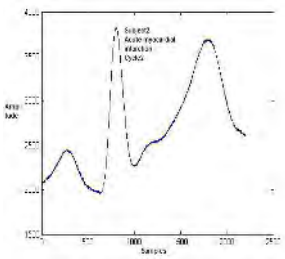


Figure 6 Acute myo cardial infarction

Table 4 Detail coefficients cd8-cd11

Sub No	Cd11	Cd10	Cd9	Cd8
Sub1c1	-50.254	-10.701	-1.5729	-1.4563
Sub2c1	-54.196	-14.072	-2.4537	-1.5028

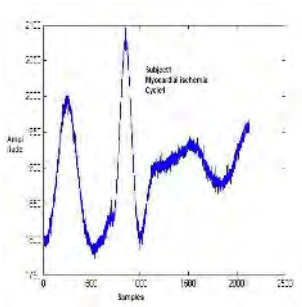


Figure 7 Myocardial ischaemia

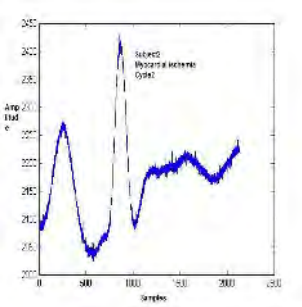


Figure 8 Myocardial ischaemia

The corresponding detail coefficients cd8 to cd11 pertaining to the low frequencies of T wave for cycles one each of subjects 1 and 2 are shown in the table 5. The negative value of cd11 indicates the presence of normal P wave. The coefficients cd8 to cd10 being positive represent the abnormal (inverted) T wave. Scales 8, 9 and 10 were found to characterize the ECG signals well enough for the detection T wave whereas scale 11 was used for the detection of the P wave.

Table 5 Detail coefficients cd8-cd11

Sub No	Cd11	Cd10	Cd9	Cd8
Sub1c1	-14.392	1.0497	0.0689	0.0742
Sub2c1	-12.257	1.6625	0.1379	0.1069

The classification of recorded ECG into normal cycles and diseases such as atrial fibrillation, acute myocardial infarction and myocardial ischaemia based on DWT coefficients is summarized in table 6.

Table 6 Classification of NSR and cardiac diseases based on DWT coefficients

	Cd8-Cd10	Cd11	Cd10 (11)
Normal *	Negative	Negative	Negative
AF	Negative	Positive	--------
AMI	Negative	Negative	Positive
Myocardial Ischemia	Positive	Negative	--------

* For normal ECG cycles all DWT coefficients including cd3-cd7 (table 2) are found to be negative.

V. Discussion and Concluding Remarks

The wavelet transform has emerged over recent years as a key time–frequency analysis and coding tool for the ECG. The wavelet transform allows a powerful analysis of non-stationary signals, making it ideally suited for the high-resolution interrogation of the ECG over a wide range of applications. It provides the basis of powerful methodologies for partitioning pertinent signal components, which serve as a basis for potent diagnostic strategies.

Much work has been conducted over recent years into AF, AMI and myocardial ischaemia centered on attempts to understand the pathophysiological processes occurring in sudden cardiac death, predicting the efficacy of therapy, and guiding the use of alternative or adjunct therapies to improve resuscitation outcomes. The authors have achieved 99.1% sensitivity for discriminating, AF episodes, AMI and myocardial ischaemia beats. The final structure for the proposed Matlab code is short and computationally very efficient and easily lends itself to real-time implementation. In conclusion, it has been shown that the wavelet transform is a flexible time–frequency decomposition tool that can form the basis of useful signal analysis and coding strategies. It is envisaged that the future will see further application of the wavelet transform to the ECG as the emerging technologies based on them are honed for practical purpose.

Detecting and separating P wave, T waves and S-T segment can be a difficult task. This technique provided a basis for distinguishing healthy patients from those presenting with atrial fibrillation, acute myocardial infarction and myocardial ischaemia. The study of the changes in DWT coefficients on a beat-by-beat basis provided important information about the state of heart mechanisms in both physiological and pathological conditions. The authors found that wavelet analysis was superior to time domain analysis for identifying patients at increased risk of clinical deterioration. The approaches shown here have proved to yield results of comparative significance with other current methods and will continue to be improved.

Acknowledgements

The author is highly indebted to Sri. Basavaraj S.Bhimalli, President H.K.E. Society, Gulbarga, for all the encouragement and support. The author is highly thankful to Dr. S.S.Chetty, Administrative officer, H.K.E. Society, Gulbarga, for the inspiration. The author is thankful to Dr. L.S. Birader, Principal, P.D.A. College of Engineering, Gulbarga, for the help. The author is profusely thankful to Dr. R.B. Patil, Professor,M. R. Medical College, Gulbarga, for the expert opinions. I thank Sri. Rupam Das for all the help. The author wishes to thank Sri. Dharmaraj M. for providing the technical help.

REFERENCES

1. R. Magjarevic and J. H. Nagel, Atrial fibrillation recognizing using wavelet transform and artificial neural network, *World Congress on Medical Physics and Biomedical Engineering* 2006, Imaging the Future Medicine, 978-83, August 27 – September 1, 2006 COEX Seoul, Korea.
2. Watson J.N., Addison P.S., Clegg G.R., et. al., Wavelet Transform-based Prediction of the Likelihood of Successful Defibrillation for Patients Exhibiting Ventricular Fibrillation, *Measurement Science and Technology*, 2005, Vol.16, L1-L6.
3. G.M. Patil, K. Subba Rao, K. Satyanarayana, Characterization of ECG using Multilevel Discrete Wavelet Decomposition, *National Symposium on Instrumentation*, NSI-32, Tiruchengode, Tamil Nadu, India, 24-26 Oct. 2007.
4. Erçelebi E, Electrocardiogram signals de-noising using lifting-based discrete wavelet transform, *Computers in Biology and Medicine*, 34(6)**:** 479-93, 2004.
5. M. Boutaa, F. Bereksi-Reguig, S. M. A. Debbal, ECG signal processing using multiresolution analysis, *Journal of Medical Engineering & Technology,* 6, 543-548, 2008.
6. G.M. Patil, K. Subba Rao, K. Satyanarayana, Emergency Healthcare and Follow-Up Telemedicine System for Rural Areas Based on LabVIEW, *World Scientific J. of Biomedical Engineering Applications, Basis and Communications* (in press).
7. G.M. Patil, K. Subba Rao, K. Satyanarayana, Analysis of the variability of waveform intervals in the ECG for detection of arrhythmia, *Interenational Conference on Information Processing*, ICIP 2007, Bangalore, India, 10-12 Aug 2007.
8. G.M. Patil, K. Subba Rao, K. Satyanarayana, Embedded microcontroller based digital telemonitoring system for ECG, *J. Instrum. Soc. India*, 37(2), pp. 134-149, June 2007.
9. Tewfik AH, Sinha D, Jorgensen P, On the optimal choice of a wavelet for signal representation, *IEEE Transactions on Information Theory*, 38(2)**,** 747-765, 1992.

Address of corresponding author :
Author : Prof. G. M. Patil
Institute: Head (I.T.), P. D. A. College of Engineering
City: GULBARGA – 585 102 (Karnataka State)
Country: INDIA
Email: gurulingappampatil@yahoo.com

Non-invasive Techniques for Assessing the Endothelial Dysfunction: Ultrasound Versus Photoplethysmography

M. Zaheditochai[1], R. Jaafar[1], E. Zahedi[2]

[1] Dept. of Electrical, Electronic & System Engineering, Universiti Kebangsaan Malaysia, Bangi, Selangor, Malaysia
[2] Medical Engineering Section, University Kuala Lumpur - British Malaysian Institute, Gombak, Selangor, Malaysia
[3] School of Electrical Engineering, SHARIF University of Technology, PO Box 11365-9363, Tehran, IRAN

Abstract — **Endothelial dysfunction, which can be non-invasively assessed by flow mediated vasodilation (FMD), predicts an increased rate of adverse cardiovascular events. The endothelial dysfunction is considered as a leading cause of development and progression of the atherosclerotic process. The main aim of this study is to review different non-invasive methods to assess the endothelial dysfunction and to propose enhancements to a new method based on photoplethysmography (PPG). First, non-invasive techniques developed for the evaluation of peripheral endothelial function (including the Doppler ultrasound (US)) will be reviewed. Although non-invasive, US -based techniques present a few disadvantages. To remedy to the above disadvantages, another technique based on pulse wave analysis is introduced. Although amplitude-based features from the photoplethysmogram has produced encouraging results, there are cases where the complete equivalence with US-FMD based on ultrasound measurement cannot be established. Therefore more elaborated features combined with data processing techniques are proposed which seem promising enough for the PPG-based technique to be used as a replacement method for US-FMD measurement. The ultimate aim is to assess the endothelial function and the presence of significant atherosclerotic events leading to peripheral vascular disease using a practical, simple, low-cost, non-operator dependent and alternative non-invasive technique in a clinical setting.**

Keywords — **Endothelial function, Flow mediated vasodilation, Photoplethysmography.**

I. Introduction

Endothelial cells play a critical role to control the vascular function. They are multifunctional cells which regulate vascular tone, smooth muscle cell growth, passage of molecules across their cell membranes, immune response, platelet activity and fibrinolytic system [1,2]. They are located in vascular wall which is consisted of 3 layers; intima that is the closest to the blood lumen, media is in the middle and adventitia which is the exterior ones. The endothelium is a thin layer of cells which are placed in the interior surface of intima. The strategic location of the endothelium allows it to sense changes in hemodynamic forces by membrane receptor mechanisms and respond to physical and chemical stimulus which provokes the endothelium to release nitric oxide (NO) with subsequent vasodilation [1,2,3].

Endothelial dysfunction (ED) is implicated in the pathogenesis and clinical course of the majority of cardiovascular diseases. It is thought to be an important factor in the development of atherosclerosis, hypertension, and heart failure and is strongly correlated with all the major risk factors for cardiovascular disease (CVD). ED by definition is any kind of alteration in the physiology of the endothelium which produces a decompensation (failure of compensation in cardiac) in its regulatory functions which represents a systemic disorder that affects the vasculature [4].

Many blood vessels respond to an increase in flow, or more precisely shear stress, by dilating. This phenomenon is designated as flow mediated vasodilation (FMD) where vascular dilation occurs in response to agents which stimulate the secretion of nitric oxide. FMD appears to be mediated primarily by the action of endothelium derived nitric oxide (NO) on vascular smooth muscle. Generation of NO is dependent on the activation of the enzyme endothelial Nitric Oxide Synthase (eNOS). Inhibition of this enzyme abolishes FMD in arteries. In recent years, various non-invasive techniques have been developed for the evaluation of coronary and peripheral endothelial function. Doppler ultrasonography is one of the non-invasive techniques which is based on detecting alterations in arterial vasoreactivity under different physiological and pharmacological stimuli [4].

II. Non-invasive techniques

A. FMD Ultrasound

Flow-mediated vasodilation is an endothelium-dependent process that reflects the relaxation of the artery when it is faced with increased flow following shear stress which is raised during post-occlusive reactive hyperemia.

In this technique the ultrasound system (US) must be equipped with two-dimensional (2D) imaging, color and spectral Doppler, an internal electrocardiogram (ECG) monitor and a high-frequency vascular linear array transducer with a minimum frequency of 7 MHz. Timing of each

Chwee Teck Lim, James C.H. Goh (Eds.): ICBME 2008, Proceedings 23, pp. 65–68, 2009
www.springerlink.com

image frame with respect to the cardiac cycle is via simultaneous ECG recording on the US video monitor. Flow stimulus in the brachial artery (BA) is produced by a blood pressure (BP) cuff which is placed above the antecubital fossa. The arterial 5-min occlusion is created by cuff inflation to suprasystolic pressure (typically 50 mmHg above the systolic pressure). Both BA diameter and ECG should be measured simultaneous during image acquisition to define when the artery is the largest. Based on the cardiac cycle, the diameter of the BA should be measured in the beginning of the R-wave which identifies the start of the systole. In this phase vessel expands to accommodate the increase in pressure and volume generated by left ventricular contraction.

Although this technique is non-invasive, it has some disadvantages. Firstly, this technique is subject to variations due to the subjectivity of the operator performing the experiment and requires a skilled operator. Secondly, accurate analysis of BA reactivity is highly dependent on the quality of US images and it is sensitive to the US probe location. Thirdly it is to say that arteries smaller than 2.5 mm in diameter are difficult to measure and vasodilation is generally less difficult to perceive in vessels larger than 5.0 mm in diameter. Blockage of blood supply to the BA for a relatively long period of time (up to 5 minutes) is another issue. The blockage duration has to last enough to ensure that the dilation reaches few millimeters for the imaging system to be able to detect it; otherwise image artifacts will prevent the investigation from having a clear view of the amount of dilation. This is why the main focus of this study is introducing the next method which is considered in previous research and promotes it to get the comparable results [5]. Another limitation of US-FMD is that due to the size of the equipment, the patient needs to be physically transferred to the laboratory where the test could be performed.

B. FMD Photoplethysmography

Photoplethysmography (PPG) is a non-invasive technique that measures relative blood volume changes through optical method. By this it is possible to measure the pulsation of the blood. During systole that the artery's diameter increases, the amount of transmitted light drops due to hemoglobin absorption and it goes into reverse during diastole. So there is a pulsatile signal which varies in time with the heart beat that is including both low (DC) and high frequency (AC) component. This means that the pulsatile signal is superimposed on a DC level which is related to respiration, sympathetic nervous system activity and thermoregulation. Whereas, the high frequency component is due to cardiac synchronous changes with each heart beat in skin micro-vascular blood volume [9]. As plethysmographic signal carries very rich information about cardiovascular regulation, it seems to be justified the use of advanced signal analysis techniques for the study of plethysmographic signals.

There are several studies based on pulse wave analysis to consider the properties of arteries as well as studying large-artery damage which is the common cause of mortality and in industrialized countries. They showed significant correlations between PWV (Pulse Wave Velocity) and cardiovascular risk factors, such as hypertension, high cholesterol level, diabetes and smoking [6]. Pulse wave analysis is a well recognized way to evaluate aortic stiffness and, consequently, could be useful to evaluate the vascular effects of aging, hypertension, and atherosclerosis [7,8]. Moreover, the multi-site PPG concept has considerable clinical potential. Some of these studies are based on disease diagnostic in the lower limbs by investigating the clinical value of objective PPG pulse measurements collected simultaneously from the right and left great toes [9]. The previous study [5] which would be improved here was conducted to investigate if there is any relationship between US measurement and finger PPG pulse amplitude (AC) change in response to FMD of the corresponding BA.

C. Simultaneous exams of PPG and Ultrasound

The ultrasound data were gathered by the help of a high resolution ultrasound system (US) with a 7.5 MHz linear array transducer. The subjects were asked to abstain from food, alcohol and caffeine for at least 8 hours prior to the experiment. The US images were captured while subjects were in supine position at rest and the transducer was placed at few centimeters above the elbow on the right arm. The arterial occlusion was created by cuff inflation 50 mmHg above systolic BP for 4 minutes. The baseline diameter was obtained from the average of 3 measurements before introduction of blockage. Shear stress that caused endothelium-dependent dilation would be made by releasing the cuff suddenly. BA diameter was measured from the longitudinal image of the artery using wall tracking technique, manually at intervals of approximately 30 seconds for approximately 5 minutes following the release of blood flow blockage. Beside US equipment, two PPG systems consisting of the sensors, software and hardware were used to record PPG signals from the right and left index fingers respectively.

By comprising diameter changes in two methods of PPG and US, we can see that AC of the PPG signal is similar to the US-FMD. However, this similarity is not observed for all subjects, probably for the following reasons:

1- The US-FMD dilation is not properly measured. It should be emphasized that the artery is being imaged with a high-resolution scanner but the viewing angle and position of the imaging probe held by the operator play an important role in correct evaluation of the dilation.

2- Currently, the measurement is done manually whereas images taken during the US-FMD experiment are examined one by one and the diameter is measured by positioning the cursor at chosen landmarks. It has been widely reported in the literature that this might be one of the main sources for errors.
3- The AC of the PPG is not sufficient to explain the FMD response alone. This is why we propose to complement this value by other demographic parameters.

In this study both ultrasound FMD and PPG FMD techniques were analyzed simultaneously. Furthermore, we focus on the role of clinical risk factors for cardiovascular diseases (CVD) in PPG FMD responses.

III. Results of PPG and Ultrasound Cross Study

Eighty one subjects aged 21 to 76 years were included in this study. The subjects were divided into three groups: Group 1 comprises healthy individuals (25 subjects), Group 2 comprises individuals having any one risk factor (31 subjects) and Group 3 comprises individuals having more than one risk factor (25 subjects).

Healthy subjects are free from any major CVD risk factors. The risk factors include obesity which is assessed by BMI (Body Mass Index), diabetes which is assessed by HbA1c and glucose level, hypertension which is assessed by systolic blood pressure and diastolic blood pressure and hypercholesterolemia which is assessed by LDL (low-density lipoprotein cholesterol) and total cholesterol in this study. To have a clear comparison graph of all risk factors, they were normalized in each group between 0 and 1. By this it means that for each risk factor the minimum value refers to 0 and maximum value refers to 1. The border line of each risk factor is identified in Table 1.

In signal processing, the amplitude of the PPG signal (AC value) was extracted from the left and right index fingers, before blockage (Figure 1) and after release (Figure 2).

Table 1 Risk factors

Risk factors	Border line	Normalized value	Min value	Max value
Systolic BP	>140 mmHg	0.57	100mmHg	170 mmHg
Diastolic BP	>90 mmHg	0.63	51 mmHg	112 mmHg
Glucose level	>6 mmol/L	0.17	4.1 mmol/L	15.2 mmol/L
HbA1c	>6.5 %	0.25	4.5 %	12.5 %
Total Cholesterol	>5.2 mmol/L	0.57	2 mmol/L	7.59 mmol/L
LDL	>3 mmol/L	0.42	1.2 mmol/L	5.47 mmol/L
BMI	>30	0.49>30	18.98	0.73 41.15

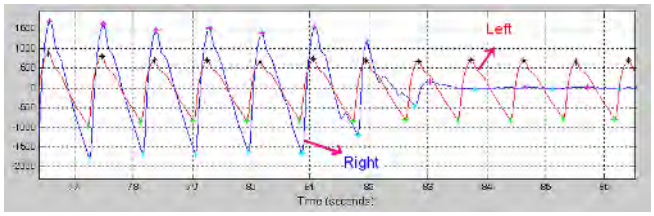


Fig. 1 PPG signals of the left and right arm before blockage

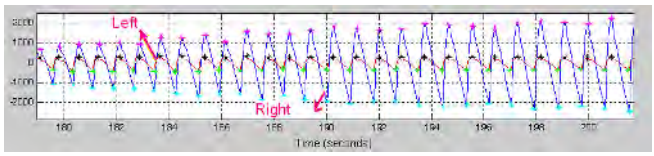


Fig. 2 PPG signals of the left and right arm after release blockage

The PPG signal of the left arm remains the same before blockage and after release and can be used as the baseline values. On the other hand, the amplitude of PPG signal of right arm decreases to zero during occlusion and increases after release.

Both PPG and ultrasound signals are normalized in amplitude between 0 and 1 and are shown along with the clinical data. In both PPG and ultrasound exam, all subjects show reactions to BA occlusion. Examples of the responses from each group are shown in Figure 3, 4 and 5, respectively. The dotted line shows the ultrasound response and the continuous line shows the PPG response. The clinical data refers to BMI, systolic BP, diastolic BP, heart rate, glucose level, HbA1c, total cholesterol, HDL, LDL, triglyceride, age and gender (female = 1, male = 0) from left to right. The risk is shown by the marker on top of identified risk factor. In 70 % of subjects who are in the first group (healthy) and second group (having only one risk factor),

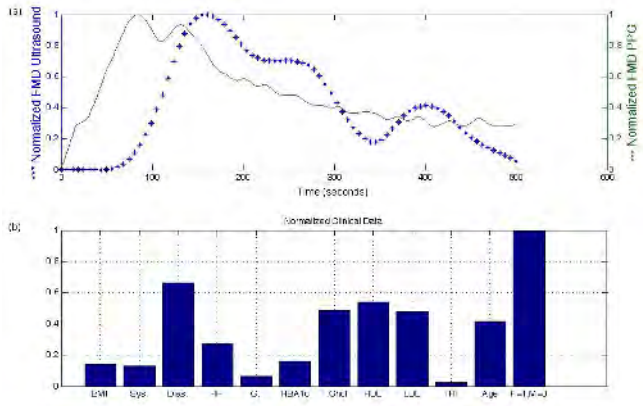


Fig. 3 Normalized (a) PPG and ultrasound responses and (b) clinical data (healthy subject)

both responses follow each other (Figure 3 and 4). In Figure 4 the risk factor refers to hypercholesterolemia (high in total cholesterol and LDL). In the third group which included subjects having more than one risk factor, PPG and ultrasound responses follow each other only in 50 % of the subjects (Figure 5). In this group the risk factors refer to hypercholesterolemia and diabetes.

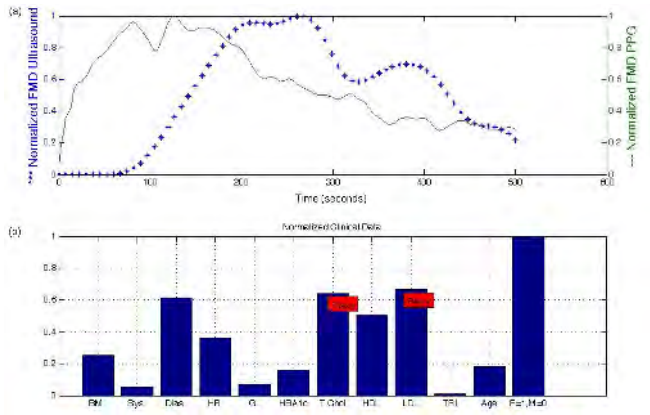


Fig. 4 Normalized (a) PPG and ultrasound responses and (b) clinical data (subject with only one risk factor)

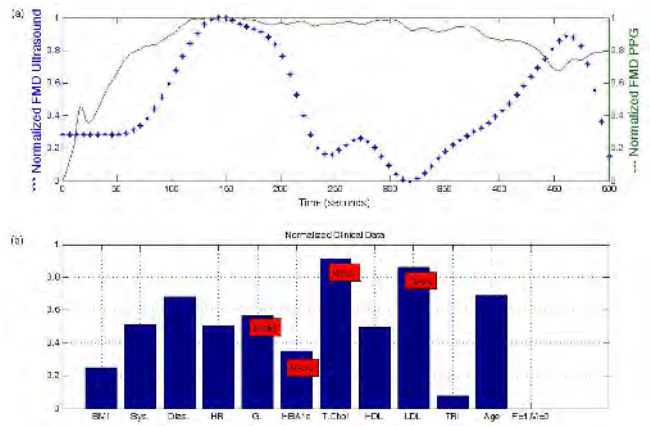


Fig. 5 Normalized (a) PPG and ultrasound responses and (b) clinical data (subject with more than one risk factor)

IV. Conclusions

In summary the results of this study show that PPG FMD and ultrasound FMD responses are similar in most of the healthy subjects as well as among those having just one risk factor. However, it is hard to say that with the increase in number of risk factors, the PPG and ultrasound responses can follow each other. This finding could explain the reason for non-similarity observed in some of the subjects in the earlier study.

Acknowledgment

This work has been supported by the Science Fund grant (01-01-02-SF0227) from the Ministry of Science, Technology and Innovation, Malaysia. It is also supported by the Technical BME Laboratory from Sharif University of Technology, Iran.

References

1- J.A. Vita, J.F. Keaney (2002) Endothelial Function A Barometer for Cardiovascular Risk?, American Heart Association, Inc. 106:640-642
2- M.E. Widlansky, N. Gokce, J.F. Keaney, J.A. Vita (2003) The Clinical Implications of Endothelial Dysfunction, Journal of the American College of Cardiology, Vol. 42, No. 7
3- Corretti M C, Anderson T J, Benjamin E J, Celermajer D, Charbonneau F, Creager M A, Deanfield J, Drexler H, Gerhard- Herman M and Herrington D (2002) Guidelines for the ultrasound assessment of endothelial-dependent flow-mediated vasodilation of the brachial artery - a report of the international brachial artery reactivity task force, J. Am. Coll. Cardiol. 39 257-65
4- J.P. Tomas, J.L. Moya, R. Campuzano, V. Barrios, A. Megras, S. Ruiz, P. Catalan, M.A. Recarte, A. Murielb (2004) Noninvasive Assessment of the Effect of Atorvastatin on Coronary Microvasculature and Endothelial Function in Patients With Dyslipidemia, Rev Esp Cardiol ;57(10):909-15
5- E. Zahedi, R. Jaafar, M.A. Mohd Ali, A.L. Mohamed, O. Maskon (2008),Finger photoplethysmogram pulse amplitude changes induced by flow mediated dilation, *Physiological Measurement*, Vol. 29(5), pp 625-637.
6- L. A. Bortolotto, J. Blacher, T. Kondo, K. Takazawa, M.E. Safar (2000), Assessment of Vascular Aging and Atherosclerosis in Hypertensive Subjects: Second Derivative of Photoplethysmogram Versus Pulse Wave Velocity, American Journal of Hypertension, Ltd. AJH 13:165–171
7- S.R. Alty, N. Angarita-Jaimes, S.C. Millasseau, P.J. Chowienczyk (2006), Predicting Arterial Stiffness from the Digital Volume Pulse Waveform, IEEE
8- R. Asmar (2007) Effects of pharmacological intervention on arterial stiffness using pulse wave velocity measurement, Journal of the American Society of Hypertension 1(2) 104–112
9- J. Allen, C. P Oates, T. A. Lees, A. Murray (2005) Photoplethysmography detection of lower limb peripheral arterial occlusive disease: a comparison of pulse timing, amplitude and shapen characteristics, Physiol. Meas. 26, 811–821

Author: Mojgan Zaheditochai
Institute: Dept. of Electrical, Electronic & System Engineering, Universiti Kebangsaan Malaysia
Street: 43600 UKM Bangi, Selangor
City: Kuala Lumpur
Country: Malaysia
Email: mojganzahedi@yahoo.com

High Performance EEG Analysis for Brain Interface

Dr. D.S. Bormane[1], Prof. S.T. Patil[2], Dr. D.T. Ingole[3], Dr. Alka Mahajan[4]

[1]Rajarshi Shahu college of Engineering, Pune, India, bdattatraya@gmail.com
[2]B.V.U. College of Engineering, Pune, India, stpatil@bvucoep.edu.in
[3]Ram Meghe Institute of technology and Research, Badnera, principal@coebadnera.com
[4]Aurora Technological Institute, Hydrabad, alkamahajan@gmail.com

Abstract — **A successful brain interface (BI) system enables individuals with severe motor disabilities to control objects in their environment (such as a light switch, neural prosthesis or computer) by using only their brain signals. Such a system measures specific features of a person's brain signal that relate to his or her intent to affect control, then translates them into control signals that are used to control a device. Recently, successful applications of the discrete wavelet transform have been reported in brain interface (BI) systems with one or two EEG channels. For a multi-channel BI system, however, the high dimensionality of the generated wavelet features space poses a challenging problem. In this paper, a feature selection method that effectively reduces the dimensionality of the feature space of a multi-channel, self-paced BI system is proposed. The proposed method uses a two-stage feature selection scheme to select the most suitable movement-related potential features from the feature space. The first stage employs mutual information to filter out the least discriminant features, resulting in a reduced feature space. Then a genetic algorithm is applied to the reduced feature space to further reduce its dimensionality and select the best set of features. An offline analysis of the EEG signals (18 bipolar EEG channels) of four able-bodied subjects showed that the proposed method acquires low false positive rates at a reasonably high true positive rate. The results also show that features selected from different channels varied considerably from one subject to another. The proposed hybrid method effectively reduces the high dimensionality of the feature space. The variability in features among subjects indicates that a user-customized BI system needs to be developed for individual users.**

Keywords — **EEG, Multiresolution Wavelet, Fuzzy C-means, Brain, BCI, Ensemble classifier**

I. Introduction

The brain generates rhythmical potentials, which originate in the individual neurons of the brain. Electroencephalograph (EEG) is a representation of the electrical activity of the brain. Numerous attempts have been made to define a reliable spike detection mechanism. However, all of them have faced the lack of a specific characterization of the events to detect. One of the best known descriptions for an interictal "spike" is offered by Chatrian et al. [1]: " transient, clearly distinguished from background activity, with pointed peak at conventional paper speeds and a duration from 20 to 70 msec". This description, however, is not specific enough to be implemented into a detection algorithm that will isolate the spikes from all the other normal or artifactual components of an EEG record. Some approaches have concentrated in measuring the "sharpness" of the EEG signal, which can be expected to soar in the "pointy peak" of a spike. Walter [2] attempted the detection of spikes through analog computation of the second time derivative (sharpness) of the EEG signals. Smith [3] attempted a similar form of detection on the digitized EEG signal. His method, however required a minimum duration of the sharp transient to qualify it as a spike. Although these methods involve the duration of the transient in a secondary way, they fundamentally consider "sharpness" as a point property, dependent only on the very immediate context of the time of analysis. More recently, an approach has been proposed in which the temporal sharpness is measured in different "spans of observation", involving different amounts of temporal context. True spikes will have significant sharpness at all of these different "spans". The promise shown by that approach has encouraged us to use a wavelet transformation to evaluate the sharpness of EEG signals at different levels of temporal resolution.

Bio kit datascope machine is used to aquire 32-channel eeg signal with the international 10-20 electrode coupling. The sampling frequency of the device is 256 Hz with 12-bit resolution and stored on hard disc. 32 channel EEG data was recorded simultaneously for both referential and bipolar montages. Recordings are made before, meanwhile and after the person is doing anulom vilom, and also we have kept track on recording the EEG data after one, two and three months of the same persons doing anulom vilom. Such 10 persons data is collected for analysis.

II. Problem formulation

Visual analysis and diagnosis of EEG signal using time domain analysis is very time consuming & tedious task it may vary from person to person. Frequency domain analysis also have limitations like more samples to be analyzed for

Chwee Teck Lim, James C.H. Goh (Eds.): ICBME 2008, Proceedings 23, pp. 69–72, 2009
www.springerlink.com

getting accurate results, More memory space required for storage of data, More processing time, More filter length, Non-linear phase, Lack of artifact removal, baseline rejection, lack of data epochs rejection, visualization of Data info, event fields and event values. In Greedy method decomposition problems. In Orthogonal matching complex computations.

EEG has several limitations, most important is its poor spatial resolution. EEG is most sensitive to a particular set of post-synaptic potentials: those which are generated in superficial layers of the cortex, on the crests of gyri directly abutting the skull and radial to the skull. Dendrites which are deeper in the cortex, inside sulci, are in midline or deep structures or produce currents which are tangential to the skull have far less contribution to the EEG signal. The meninges, cerebrospinal fluid and skull "smear" the EEG signal, obscuring its intracranial source. It is mathematically impossible to reconstruct a unique intercranial current source for a given EEG signal. This is referred to as the inverse problem.

III. Problem Solution

Bio-kit data acquisition system, Mumbai (India), is used to acquire 32-channel EEG signal with the international 10-20 electrode coupling. The sampling frequency of the device is 256 Hz with 12-bit resolution and stored on hard disc of a computer. To study the effect of a long term (six months or greater) practice of different techniques of ujyai, resting state and before examination on

the EEG signals of young to middle aged Males and Females. 32-channel EEG data was recorded simultaneously for both referential and bipolar montages. The Electrical waveforms were obtained for all the subjects under different groups mentioned above.The research work in this thesis proposes analysis of four different types of wavelets, including the Daubechies wavelets with 4 (Db4) and 8 (Db8) vanishing moments, symlets with 5 vanishing moments (Sym5), and the quadratic B-spline wavelets (Qbs). The quadratic B-spline wavelet was chosen due to its reported suitability in analyzing ERP data in several studies. Db4 and Db8 were chosen for their simplicity and general purpose applicability in a variety of time-frequency representation, whereas Sym5 was chosen due to its similarity to Daubechies wavelets with additional near symmetry property. Different mother wavelets have been employed in analysis of the signals; performances of six frequency bands (0–1Hz, 1–2 Hz, 2–4Hz, 4–8 Hz, 8–16 Hz and 0–4 Hz) have been individually analyzed, The proposed pearl ensemble based decision is designed, implemented and compared to a multilayer perceptron and AdaBoost classifier based decision; and most importantly, the earliest possible diagnosis of the alzeimer's disease is targeted. Some expected, and some interesting outcomes were observed, with respect to each parameter analyzed. To exploit the information on the time frequency structure using different Wavelet transforms like Daubechies (Db4 and Db8), sym5 and the quadratic B-spline wavelets (Qbs). along with The proposed pearl ensemble based decision is designed, implemented and compared to a multilayer perceptron and AdaBoost classifier based decision during meditation. To estimate deterministic chaos like correlation dimension, largest lyapunov exponent, approximate entropy and hurst exponent of 207 persons (subjects) before attending written examination state, normal resting state and during meditation state.

Figure: 1. shows the result of the classification of one experimental subject. Here the optimal number of clusters is 3. I have normalized every feature vector into 0 to 1.

From the figure above we could obtain that alpha increased in the middle interval and decreased in the late interval of ujyai. After ujyai, the appearance of cluster #3 (centered on Cz) increased.

As EEG is normally characterized by its frequency, the EEG patterns are conveniently classified into four frequency ranges: the delta (0-4Hz), theta (4-8 Hz), alpha (8-13 Hz), and beta (13-25 Hz). The meditationEEGsignals, although composed of these standard rhythmic patterns, are found to orchestrate

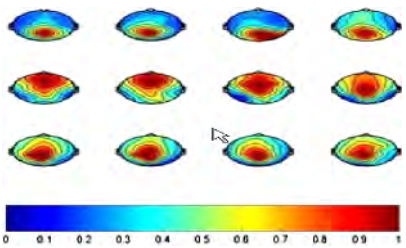


Fig:1. Three clusters

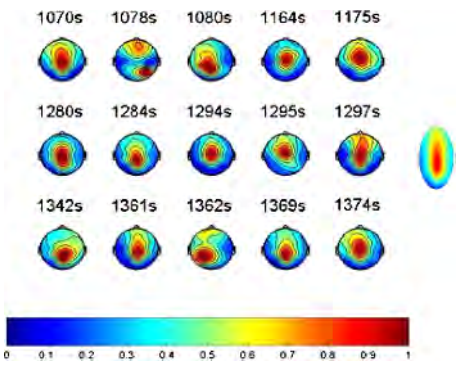


Fig:2. Selected samples and the centre of cluster # 1.

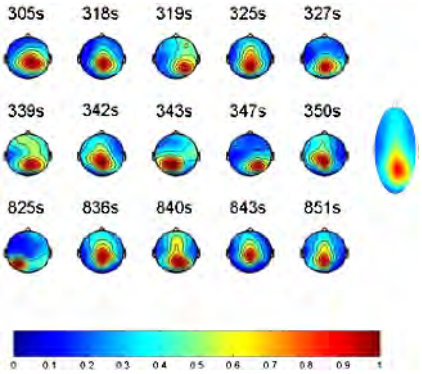


Fig:5. Selected samples and the centre of cluster #2.

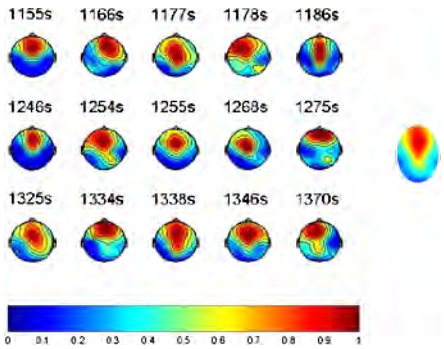


Fig:6. Selected samples and the centre of cluster #3.

symphonies of certain tempos. After systematic study by applying the FCM-merging strategies to a number of meditation EEG data sets, results of clustering indicate that rhythmic patterns reflecting various meditationstates normally involve five patterns:

IV. Conclusion

During the Meditationtechnique individuals often report the subjective experience of Transcendental Consciousness or pure consciousness, the state of least excitation of consciousness. This study found that many experiences of pure consciousness were associated with periods of natural respiratory suspension, and that during these respiratory suspension periods individuals displayed higher mean EEG coherence over all frequencies and brain areas, in contrast to control periods where subjects voluntarily held their breath. Results are 98 % true when discussed with experts and doctors.

In this study we developed a scheme to investigate the spatial distribution of alpha power, and we adopted this procedure to analysis this characteristics of meditators and normal subjects. The results show that alpha waves in the central and frontal regions appear more frequently in the experimental group.From the previous study, the enhancement of frontal alpha during meditationmay be related to the activation of the Anterior Cingulate Cortex (ACC) and medial Prefrontal Cortex (mPFC). The ACC has outflow to the autonomic, viscermotor and endocrine systems. Previous findings suggested that during meditation some changes of autonomic patterns and hormone are related to the ACC. Furthermore, the ACC and mPFC are considered to modulate internal emotional responses by controlling the neural activities of limbic system, that is, they may function via diffusing alpha waves. Besides, the trends of non-alpha are different in two groups. In control group the alpha wave was getting less during relaxation, and in the post-session it returned to the level which is the same in the pre-session. The reason of this trend may be drowsiness. Multiresolution M-Band wavelet (proposed) is most effective for EEG analysis in terms of high degree of accuracy with low computational load. This thesis reports a novel idea of understanding various meditationscenarios via EEG interpretation. Experimental subjects narration further corroborates, from the macroscopic viewpoint, the results of EEG interpretation obtained by the FCM-merging strategies. The FCM clustering method automatically identifies the significant features to be used as the meditationEEG interpreting protocol. The results show that the state of mind of a human body becomes more stable with ujyai, whereas the tense conditions affect inversely causing disturbance in the mind.

Biographies

Prof. S.T. Patil- Completed B.E. Electronics from Marathwada University, Aurangabad in 1988. M.Tech. Computer from Vishveshwaraya Technological University, Belgum in July 2003. Persuing Ph.D. Computer from Bharati Vidyapeeth Deemed University, Pune. Having 19 years of experience in teaching as a lecturer, Training & Placement Officer, Head of the department & Assistant Professor. Presently working as an Assistant Professor in computer engineering & Information Technology department in Bharati Vidyapeeth Deemed University, College of Engineering, Pune (India). Presented 14 papers in national & international conferences.

Dr. D.S. Bormane- Completed B.E. Electronics from Marathwada University, Aurangabad in 1987. M.E. Electronics from Shivaji University, Kolhapur. Ph.D. computer from Ramanand Tirth University, Nanded. Having 20 years of experience in teaching as a Lecturer, Assistant Professor, Professor, and Head Of Department.

Currently working as a Principal in Rajrshi Shahu College of Engineering, Pune (India). Published 24 papers at national & international conferences and journals.

REFERENCES

[1] Daubechies, Ingred. Ten Lectures on Wavelets SIAM (Society for Industrial and Applied Mathematics), Philadelphia, Pennsylvania, 1992.

[2] S. Mallat, "A Theory for Multiresolution Signal Decomposition: The Wavelet Representation", IEEE Trans. on Pattern Analysis and Machine Intelligence, vol. 14, pp710-732, July 1992.

[3] Chatrian et al., "A glossary of terms most commonly used by clinical electroencephalographers", Electroenceph.and Clin. Neurophysiol., 1994, 37:538-548.

[4] D. Walter et al., "Semiautomatic quantification of sharpness of EEG phenomena". IEEE Trans. on Biomedical Engineering, 3, Vol. BME-20, pp. 53-54.

[5] J. Smith, "Automatic Analysis and detection of EEG Spikes", IEEE Trans. on Biomedical Engineering, 1999, Vol. BME-21, pp. 1-7.

[6] Barreto et al., "Intraoperative Focus Localization System based Spatio-Temporal ECoG Analysis", Proc. XV Annual Intl. Conf. of the IEEE Engineering in Medicine and Biology Society, October, 2003.

[7] Lin-Sen Pon, “Interictal Spike Analysis Using Stochstic Point Process”,Proceedings of the International conference, IEEE – 2003.

[8] Susumo Date, “A Grid Application For An Evaluation Of Brain Function Using ICA” Proceedings of the International conference, IEEE - 2002 .

[9] Ta-Hasin Li, “Detection of Cognitive Binding During Ambiguous Figure”, Proceedings of the International conference, IEEE – 2000.

[10] Alison A. Dingle, Tichard D. Jones and others "A multistage system to detect epileptiform activity in the EEG" IEEE transaction on biomedical engineering, vol.40, no.12, December 2003.

Denoising of Transient Visual Evoked Potential using Wavelets

R. Sivakumar

ECE Department, RMK Engineering College, Kavaraipettai, Tamilnadu, India

Abstract — **Transient Visual Evoked Potential (TVEP) is an important diagnostic test for specific ophthalmological and neurological disorders. The clinical use of VEP is based on the amplitudes and the latencies of the N75, P100, and N145 peaks. The amplitude and latencies of these peaks are measured directly from the signal. Quantification of these latency changes can contribute to the detection of possible abnormalities. We have applied the wavelet denoising method to 100 numbers of pre-recorded signals using all the available wavelets in MATLAB signal processing toolbox. From the results it is clear that the positive peak is clearer in the denoised version of the signal using the wavelets Sym5 and Bior3.5. As opposed to the previous studies however our study clearly shows that the output using the former wavelet effectively brings out the P100 when compared to the latter. The first negative peak N75 is clear in the denoised version of the signal using the wavelets Bior5.5 Bior6.8 and coif4. The second negative peak N145 is clear using all the above wavelets. All the three peaks are fairly clear in the denoised output using the wavelet sym7.**

Keywords — **Transient Visual Evoked Potential, Latency, denoising, wavelets, MATLAB.**

I. Introduction

Evoked Potentials (EPs) are the alterations of the ongoing EEG due to stimulation. They are time locked to the stimulus and they have a characteristic pattern of response that is more or less reproducible under similar experimental conditions. In order to study the response of the brain to different tasks, sequence of stimuli can be arranged according to well defined paradigms. This allows the study of different sensitive functions, states etc., thus making the EPs an invaluable tool in neurophysiology. Transient Visual Evoked Potential (TVEP) is an import diagnostic test for specific ophthalmologic and neurological disorders. The clinical use of VEP is based on the amplitudes and the latencies of the N75, P100, and N145 peaks. Quantification of these latency changes can contribute to the detection of possible abnormalities [1-3].

Due to the low amplitudes of EPs in comparison with the ongoing EEG, they are hardly seen in the original EEG signal and therefore several trials are averaged in order to enhance the evoked responses. Since EPs are timed licked to the stimulus their contribution will add and while ongoing EEG will cancel. However, when averaging information related with variations between the single trials is lost. This information could be relevant in order to study behavioral and functional processes. Moreover, in many cases a compromise must be made when deciding on the number of trials in an experiment. If we take a large number of trials we optimize the EP/EEG ratio but if the number of trial is too large, then we could deal with effects such as tiredness, which eventually corrupts the average results. This problem can be partially solved by taking sub-ensemble averages. However, in many cases the success of such procedure is limited, especially when not many trials can be obtained or when characteristics of the EPs change from trial to trial.

Several methods have been proposed in order to filter averaged EPs. The successes of such methods world imply the need of less number of trials and would eventually allow the extraction of single trial EPs from the background EEG. Although averaging has been used since the middle of 1950's, up to now none of these attempts has been successful in obtaining single trial EPs, at least in a level that they could be applied to different types of EPs and that they could be implemented in clinical settings.

Most of these approaches involves Wiener filtering (or a minimum mean square error filter based on auto-and cross-correlations) and have the common drawback of considering the signal as a stationary process. Since EPs are transient responses related with specific time and frequency locations, such time-invariant approaches are not likely to give optimal results. Using the wavelet formalism can solve these limitations, as well as the ones related with time-invariant methods [4-6].

The wavelet transform is a time-frequency representation proposed first in, that has an optimal resolution both in the time and frequency domains and has been successfully applied to the study of EEG-EP signals. The objective of the present study is to follow an idea originally proposed and to present a very straight forward method based on the wavelet transform to obtain the evoked responses at the single trial level. The key point in the denoising of Eps is how to select in the wavelet domain the activity representing the signal (the EPs) and then eliminate the one related with noise (the background EEG [7-10].

In fact, the main difference between our implementation and previous related approaches is in the way that the wavelet coefficients are selected. Briefly, such choice should consider latency variations between the single trial responses and it should not introduce spurious effects in the time range where the EPs are expected to occur. In this

Chwee Teck Lim, James C.H. Goh (Eds.): ICBME 2008, Proceedings 23, pp. 73–76, 2009
www.springerlink.com

respect, the denoising implementation we propose will allow the study of variability between single trials, information that could have high physiological relevance.

II. Material and methods

Experiments were carried with subjects in the Neurology Department of the leading Medical Institute. TVEP was performed in a specially equipped electro diagnostic procedure room (darkened, sound attenuated room). Initially, the patient was made to sit comfortably approximately 1m away from the pattern-shift screen. Subjects were placed in front of a black and white checkerboard pattern displayed on a video monitor. The checks alternate black/white at a rate of approximately twice per sound. Every time the pattern alternates, the patient's visual system generates on electrical response that was detected and was recorded by surface electrodes, which were placed on the scalp overlaying the occipital and parietal regions with reference electrodes in the ear. The patient was asked to focus his gaze onto the center of the screen. Each eye was tested separately (monocular testing). Scalp recordings were obtained from the left occipital (O1) electrode (near to the location of the visual primary sensory area) with linked earlobes reference. Sampling rate was 250 Hz and after band pass filtering in the range 0.1-70 Hz, 2 s of data (256 data pre-and post-stimulations) were saved on a hard disk (Figure 1).

The average TVEP is decomposed by using the wavelet multi resolution decomposition. The wavelet coefficients are not correlated with the average VEP are identified and set to zero. The inverses transform is applied to recover the denoised signal. The same procedure is extended to all single trials. The denoising method was applied to a number of pre-recorded signals using all the available wavelets to analyze the peaks (N75, P100 and N145).

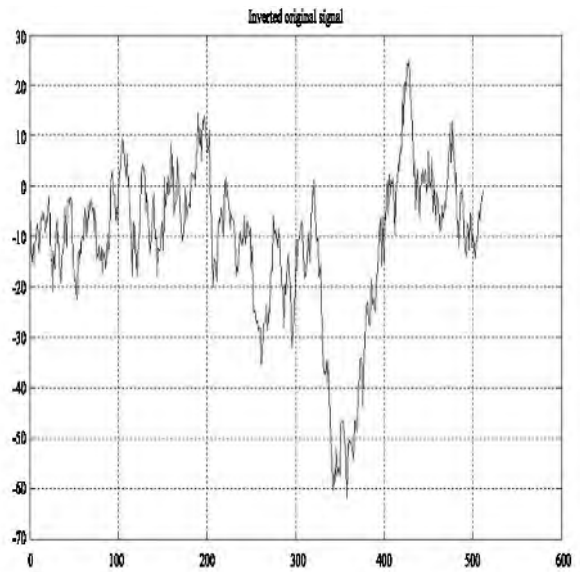


Figure 1 Single Trial TVEP

III. Results and discussion

The results show that the positive peak P100 is clearer in the denoised version of the signal using the wavelets Sym5 and Bior3.5 (Figure 2). The first negative peak N75 is clearer in the denoised version of the signal using the wavelets Bior5.5, Bior6.8 and coif4. The second negative peak N145 is clear in all the wavelets. All the peaks were clear in the denoised output using the wavelet sym7. This would greatly help the medical practitioners.

In fact, there are many different functions suitable as wavelets, each one having different characteristics that are more or less appropriate depending on the application. Irrespective of the mathematical properties of the wavelet of choose, a basic requirement is that it looks similar the patterns we want to localize in the signal. This allows a good localization of the structures of interest in the wavelet domain and moreover, it minimizes spurious effects in the reconstruction of the signal via the inverse wavelet transform. For this, the previous analysis have been done by choosing quadratic bioorthogonal B-splines as mother functions doe to their similarity with the evoked response [7-9]. B-splines are piecewise polynomials that form a base in L2. Bur our analysis shows that the there is more wavelets that can be used which similar to TVEPs.

We presented a method for extracting TVEPs from the background EEG. It is not limited to the study of TVEP/EEG and similar implementation can be used for recognizing transients even in signal with low signal to noise ratio. The denoising of EPs allowed the study of the variability between the single responses, information that could have a high physiological relevance in the study of different brain functions, states etc., It could be used to eliminate artifacts that do not appear in the same time frequency ranges of the relevant evoked responses. Our results proved that the method proposed in this paper gives better averaged EPs due to the high time-frequency resolution of the wavelet transform, this being hard to achieve with conventional Fourier filters. Moreover, since trials with good evoked responses can be easily identified, These advantages could significantly reduce the minimum number of trials necessary in a recording session, something of high importance for avoiding behavioral changes during the recording (e.g., effects of tiredness) of even more interesting, for obtaining EPs under strongly varying conditions, as with children, or patients with attention problems.

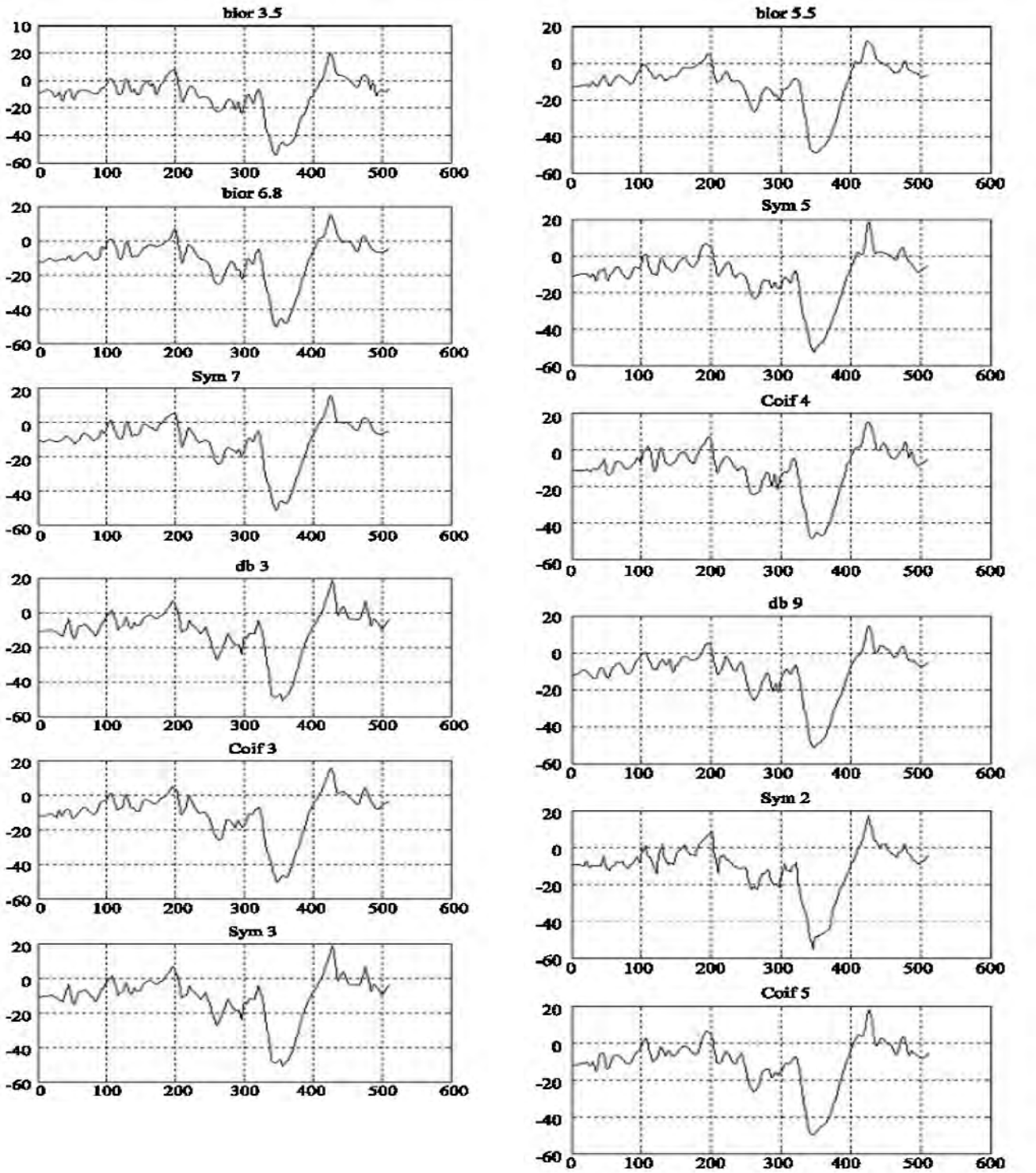


Figure 2 – denoised tvep

REFERENCES

1. Nuwer (1998) Fundamentals of evoked potentials and common clinical applications today. Electroencephalography and Clin. Neurophysiol., 106: 142-148.
2. Kalith J, Misra U.K (1999) Clin. Neurophysiol. Churchill Livingstone Pvt Ltd, New Delhi, India.
3. Nogawa T, Katayama K. Okuda H. Uchida M (1991) Changes in the latency of the maximum positive peak of visual evoked potential during anesthesia. Nippon Geka Hoken., 60: 143-153.
4. Burrus C.S. Gopinath R.A. Guo H (1998) Introduction to wavelets and wavelet transforms a primer. Prentice Hall, NJ, USA.
5. Kaiser G, (1994) A Friendly Guide to Wavelets. Birkhauser,Boston.
6. Raghuveer M.R, Ajit S.B (1998) Wavelet Transforms. Introduction to theory and Applications, Addision Wesley Longman, Inc.
7. Quiroga Q, Garcia H (2003) Single-trial event-related potentials with Wavelet Denoising. Clin. Neurophysiol., 114: 376-390.
8. Quiroga Q, Sakowicz O, Basar E, Schurmann M (2001) Wavelet Transform in the analysis of the frequency composition of evoked potentials. Brain Res. Protocols 8: 16-24.
9. Quiroga Q.R (2000) Obtaining single stimulus evoked potentials with Wavelet Denoising. Physica D, 145: 278-292.
10. Dvorak I, Holden A.V (1991) Editors Mathematical Approaches to Brain Functioning diagnostics. Proceedings in Nonlinear Science. Manchester University Press.

Author: Dr.R.Sivakumar
Institute: RMK Engineering College
Street: Kavaraipettai
City: Tamilnadu
Country: India
Email: gauthamsivakumar@yahoo.coin

A Systematic Approach to Understanding Bacterial Responses to Oxygen Using Taverna and Webservices

S. Maleki-Dizaji[1], M. Rolfe[3], P. Fisher[2], M. Holcombe[1]

[1] The University of Sheffield, Computer Science, Sheffield, United Kingdom
[2] The University of Manchester, Computer Science, Manchester, United Kingdom
[3] The University of Sheffield, Department of Molecular Biology and Biotechnology, Sheffield, United Kingdom

Abstract — ***Escherichia coli* is a versatile organism that can grow at a wide range of oxygen levels; although heavily studied, no comprehensive knowledge of physiological changes at different oxygen levels is known. Transcriptomic studies have previously examined gene regulation in *E. coli* grown at different oxygen levels, and during transitions such as from an anaerobic to aerobic environment, but have tended to analyse data in a user intensive manner to identify regulons, pathways and relevant literature. This study looks at gene regulation during an aerobic to anaerobic transition, which has not previously been investigated. We propose a data-driven methodology that identifies the known pathways and regulons present in a set of differentially expressed genes from a transcriptomic study; these pathways are subsequently used to obtain a corpus of published abstracts (from the PubMed database) relating to each biological pathway**

Keywords — ***E. coli*, Microarray, Taverna, Workflows, Web Services**

I. Introduction

Escherichia coli has been a model system for understanding metabolic and bio-energetic principles for over 80 years and has generated numerous paradigms in molecular biology, biochemistry and physiology [1]. *E. coli* is also widely used for industrial production of proteins and speciality chemicals of therapeutic and commercial interest. A deeper understanding of oxygen metabolism could improve industrial high cell-density fermentations and process scale-up. Knowledge of oxygen-regulation of gene expression is important in other bacteria during pathogenesis where oxygen acts an important signal during infection [2] and thus this project may underpin better antimicrobial strategies and the search for new therapeutics. However, current approaches have generally been increasingly reductionist, not holistic. Too little is known of how molecular modules are organised in time and space, and how control of respiratory metabolism is achieved in the face of changing environmental pressures. Therefore, a new systems-level approach is needed, which integrates data from all spatial and temporal domains. Many transcriptomic studies using microarrays have analysed data in a user-intensive manner to identify regulons, pathways and relevant literature. Here, a two-colour cDNA microarray dataset comprising a time-course experiment of *Escherichia coli* cells during an aerobic to anaerobic environment is used to demonstrate a data-driven methodology that identifies known pathways from a set of differentially expressed genes. These pathways are subsequently used to obtain a corpus of published abstracts (from the PubMed database) relating to each biological pathway identified. In this research Taverna and Web Services were used to achieve the goal.

II. Taverna and web services

Web services provide programmatic access to data resources in a language-independent manner. This means that they can be successfully connected into data analysis pipelines or workflows (Figure 1). These workflows enable us to process a far greater volume of information in a systematic manner. Unlike that of the manual analysis, which is severely limited by human resources, we are only limited by the processing speed, storage space, and memory of the computer executing these workflows. Still the major problems with current bioinformatics investigations remain; which are the lack of recording experimental methods, including software applications used, the parameters used, and the use of hyperlinks in web pages. The use of workflows limits issues surrounding the manual analysis of data, i.e. the bias introduced by researchers when conducting manual analyses of microarray data. Processing data through workflows also increases the productivity of the researchers involved in the investigations, allowing for more time to be spent on investigating the true nature of the detailed information returned from the workflows. For the purpose of implementing this systematic pathway-driven approach, we have chosen to use the Taverna workbench[3,4]. The Taverna Workbench allows bioinformaticians to construct complex data analysis pipelines from components (or web services) located on both remote and local machines. These pipelines, or workflows, are then able to be executed over a set of unique data values, producing results which can be visualised within the Taverna workbench itself. Advantages of the Taverna workflow work-

Chwee Teck Lim, James C.H. Goh (Eds.): ICBME 2008, Proceedings 23, pp. 77–80, 2009
www.springerlink.com

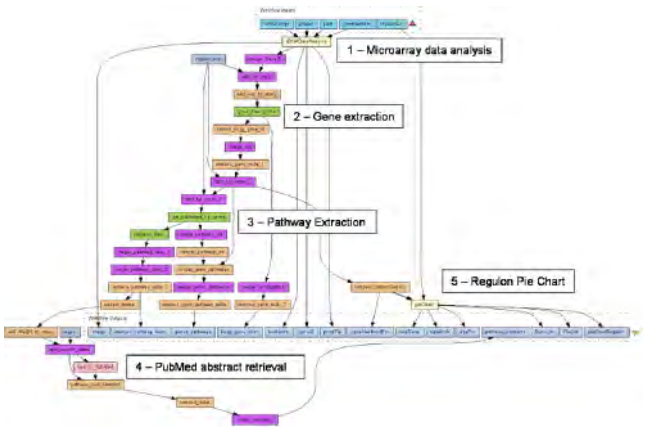


Figure 1 – Workflow Diagram

bench include, repeatable, re-useable the and limiting user bias by removing intermediate manual data analysis. Greater volume of data can be processed in a reduced time period We propose a data-driven methodology that identifies the known pathways from a set of differentially expressed genes from a microarray study (Figure 1). This workflow consists of three parts: microarray data analysis; pathways extraction; and PubMed abstract retrieval. This methodology is implemented systematically through the use of web services and workflows.

A. Microarray Data Analysis

Despite advances in microarray technology that have led to increased reproducibility and substantial reductions in cost, the successful application of this technology is still elusive for many laboratories. The analysis of transcriptome data in particular presents a challenging bottleneck for many biomedical researchers. These researchers may not possess the necessary computational or statistical knowledge to address all aspects of a typical analysis methodology; indeed, this is something which can be time consuming and expensive, even for experienced service providers with many users. Currently available transcriptome analysis tools include both commercial software (GeneSpring [5], ArrayAssist [6]) and non-commercial software (Bioconductor [7]).

The open source Bioconductor package [7] is one of the most widely used suites of tools used by biostatisticians and bioinformaticians in transcriptomics studies. Although both highly powerful and flexible, users of Bioconductor face a steep learning curve, which requires users to learn the *R* statistical scripting language as well as the details of the Bioconductor libraries.

The high overheads in using these tools provide a number of disadvantages for the less experienced user such as, requirement for expensive bioinformatics support, considerable effort in training, less than efficient utilisation of data, difficulty in maintaining consistent standards methodologies, even within the same facility, Difficult integration of additional analysis software and resources and limited reusability of methods and analysis frameworks.

The aim of this work was to limit these issues. Users will, therefore, be able to focus on advanced data analysis and interpretational tasks, rather than common repetitive tasks. We have observed that there is a core of microarray analysis tasks common to many microarray projects. Additionally, we have identified a need for microarray analysis software to support these tasks that has minimal training costs for inexperienced users, and can increase the efficiency of experienced users.

Microarray Data Analysis part provides support to construct a full data analysis workflow, including loading, normalisation, T-test and filtering of microarray data. In addition to returning normalised data, it produces a range of diagnostic plots of array data, including histograms, box plots and principal components analysis plots using R and Bioconductor.

B. Pathway extraction

This part of the workflow searches for genes found to be differentially expressed in the microarray data, selected based on a given p-value from the Microarray Data Analysis part. Gene identifiers from this part were subsequently cross-referenced with KEGG gene identifiers, which allowed KEGG gene descriptions and KEGG pathway descriptions to be returned from the KEGG database.

C. PubMed abstract retrieval

In this part, the workflow takes in a list of KEGG pathway descriptions. The workflow then extracts the biological pathway process from the KEGG formatted pathway descriptions output. A search is then conducted over the PubMed database (using the eFetch web service) to identify up to 500 abstracts related to the chosen biological pathway. At this stage, a MeSH tag is assigned to the search term, in order to reduce the number of false positive results returned from this initial search. All identified PubMed identifiers (PMID) are then passed to the eSearch function and searched for in PubMed. Those abstracts found are then returned to the user along with the initial query string – in this case, the pathway [3].

D. Pie chart

At present, results from transcriptional profiling experiments (lists of significantly regulated genes) have largely been interpreted manually, or using gene analysis software

(i.e. GeneSpring, GenoWiz) that can provide links to databases that define pathways, functional categories and gene ontologies. Many databases, such as EcoCyc [8] and RegulonDB [9], contain information on transcriptional regulators and regulons (genes known to be regulated by a particular transcription factor), and automatic interpretation of a transcriptional profiling dataset using these databases is still in its infancy. When applied to the results of a transcriptional profiling experiment, this may confirm the importance of a regulator that is already known, or suggest a role for a previously unknown regulator, which may be investigated further. The pie chart shown indicates the number of genes in a dataset that are regulated by a known transcriptional regulator, or by combination of regulators, and can suggest previously unknown regulatory interactions. The information for each regulon comes from files that are created manually from the EcoCyc database.

III. Case study: escherichia coli

Escherichia coli is a model laboratory organism that has been investigated for many years due to its rapid growth rate, simple growth requirements, tractable genetics and metabolic potential [10]. Many aspects of *E. coli* are well characterised, particularly with regards to the most familiar strain K-12, with a sequenced genome[11], widespread knowledge of gene regulation (Regulon DB; [9] and well documented metabolic pathways (EcoCyc; [8]). Indeed, it has been said that more is known about *E. coli* than about any other organism [1] and for these reasons *E. coli* stands out as a desirable organism on which to work (Mori, 2004).

A. Growth conditions

Escherichia coli K-12 strain MG1655 was grown to a steady-state in a Labfors-3 Bioreactor; Infors HT; Bottmingen, Switzerland) under the following conditions (vessel volume 2 L; culture volume 1 L; Evans medium pH 6.9 [12]; stirring 400 rpm; dilution rate 0.2 h^{-1}). To create an aerobic culture 1 L min^{-1} air was sparged through the chemostat, whilst for anaerobic conditions 1 L min^{-1} 5 % CO_2 95 % N_2 ($^{v}/_{v}$) was passed through the chemostat. For steady-state to be reached, continuous flow was allowed for at least 5 vessel volumes (25 hours) before cultures were used. Gas transitions were carried out on steady-state cultures by switching gas supply as required.

B. Isolation of RNA

A steady-state chemostat culture was prepared and samples were removed from the chemostat for RNA extraction just prior to the gas transition and 2, 5, 10, 15 and 20 minutes after the transition. Samples were taken by direct elution of 2 ml culture into 4 ml RNAprotect (Qiagen; Crawley, UK) and using RNeasy RNA extraction kit (Qiagen Crawley, UK) following the manufacturers instructions. RNA was quantified spectrophotometrically at 260 nm.

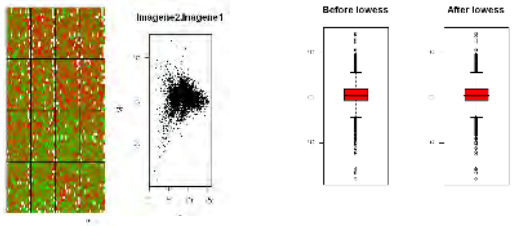
C. Transcriptional Profiling

16 µg RNA for each time point was labelled with Cyanine3-dCTP (Perkin-Elmer; Waltham, USA) using Superscript III reverse transcriptase (Invitrogen; Paisley, UK). Manufacturers instructions were followed for a 30 µl reaction volume, using 5 µg random hexamers (Invitrogen; Paisley, UK) with the exception that 3 nmoles Cyanine3-dCTP and 6 nmoles of unlabelled dCTP was used. Each Cyanine3-labelled cDNA sample was hybridised against 2 µg of Cyanine5-labelled K-12 genomic DNA produced as described by Eriksson[13]. Hybridisation took place to Ocimum OciChip K-12 V2 microarrays (Ocimum; Hyderabad, India) at 42 °C overnight and washed according to the manufacturers instructions. Slides were scanned on an Affymetrix 428 microarray scanner at the highest PMT voltage possible that didn't give excessive saturation of microarray spots. For each time point, two biological replicates and two technical replicates were carried out.

IV. Results

To analyze the transcriptional dataset, the proposed workflow was applied; this workflow can accept raw transcriptional data files and ultimately generates outputs of differentially regulated genes, relevant metabolic pathways and transcriptional regulators, and even potentially relevant published material. This has many advantages compared to standard transcript profiling analyses. From a user aspect, it will be quicker than the time-consuming analysis that currently occurs, and ensures that the same stringency and statistical methods are used in all analyses, and hence should make analyses more user-independent. It can also remove any possibility that users can subconsciously 'manipulate' the data. In order to run the work flow following parameters have been set: NormalizationMethod = rma, Statistical testMethod = limma, p-value = 0.05, foldChange = 1, geneNumber = 100.

The workflow results directly progress from a microarray file to outputs in the form of plots or text files in the case published abstracts from the PubMed database (Figure 2). Tables displaying the processed data can also be visualised From the outputs, the relevance of the transcriptional regulators FNR, ArcA, PdhR were immediately noticeable.



(a) (b) (c)

Gene.ID	logFC	AveExpr	t-value	P.Value	adj.P.Val	B
ybfD	-6.4251	12.53531	-20.9753	8.60E-20	1.59E-16	34.97318
emrY	-6.34166	9.717566	-22.7469	8.21E-21	3.78E-17	37.19892
bglG	-5.74389	11.21273	-20.1239	2.83E-19	1.84E-16	33.83456
b0309	-5.53166	11.29123	-18.5888	2.72E-18	3.62E-16	31.65645
hemA	-5.52479	11.21758	-18.469	3.27E-18	3.62E-16	31.47933
ydcC	-5.48627	12.03441	-19.6757	5.40E-19	1.91E-16	33.21571
ykgH	-5.44609	11.20526	-17.5063	1.48E-17	5.91E-16	30.01513
melB	-5.3852	11.64157	-19.8371	4.27E-19	1.84E-16	33.44017
insB_2	-5.3752	13.0089	-20.8395	1.04E-19	1.59E-16	34.79474

(d)

Query >> Two-component system AND "Metabolic Networks and Pathways"[MeSH Terms] AND "Escherichia coli"
•17616594 2007 AtoC has a dual function as both an antizyme, the posttranslational inhibitor .....
•16962353 2006 Escherichia coli has several elaborate sensing mechanisms for response to the availability of oxygen and the

(e)



(f)

Figure 2 – Workflow outputs: The workflow produced several at the end of each stage. These show (left-right, top-bottom): (a) raw data image; (b) plotting a MA plot after normalization; (c) box-plotting the summary data pre and post normalisation; (d) filtered and sorted list of differentially expressed genes. (e) tiltle list of relevant paper from; (f) regulon pie chart of Fnr and Arc;

V. Discussion

This workflow has successfully been used to interrogate a transcriptomic dataset and identify regulators and pathways of relevance. This has been demonstrated using experimental conditions in which the major regulators are known; however, the study of less characterised experiments the resulting outputs may have exciting and unanticipated results. From a knowledge point-of-view, an investigators experience is usually over a limited research theme; hence only regulators and pathways already well known to a researcher tend to be examined in detail. This workflow allows easy interrogation of a dataset to identify the role of potentially every known *E. coli* transcriptional regulator or metabolic pathway. This can suggest relevant transcriptional networks and unexpected aspects of physiology that would otherwise have been missed by conventional analysis methods.

Acknowledgment

We thank SUMO team for very useful discussions and SysMO and BBSRC for finical support.

References

1. Neidhardt, F. C. (Ed. in Chief), R. Curtiss III, J. L. Ingraham, E. C. C. Lin, K. B. Low, B. Magasanik, W. S. Reznikoff, M. Riley, M. Schaechter, and H. E. Umbarger (eds). (1996). ***Escherichia coli* and *Salmonella:* Cellular and Molecular Biology**. American Society for Microbiology. 2 vols. 2898 pages.
2. Rychlik, I. & Barrow, P.A. (2005) *Salmonella* stress management and its relevance to behaviour during intestinal colonisation and infection *FEMS Microbiology reviews* **29** (5) 1021-1040.
3. Fisher, P., Hedeler, C., Wolstencroft, K., Hulme, H., Noyes, H., Kemp, S., Stevens, R., Brass, A. A systematic strategy for large-scale analysis of genotype-phenotype correlations: identification of candidate genes involved in African Trypanosomiasis *Nucleic Acids Research* 2007 35(16): 5625-5633
4. Taverna [http://taverna.sourceforge.net]
5. **GenesSpring** [http://www.chem.agilent.com]
6. **ArrayAssist** [http://www.stratagene.com]
7. **Bioconductor** [http://www.bioconductor.org]
8. Keseler, I.M., Collado-Vides, J., Gama-Castro, S., Ingraham, J., Paley, S., Paulsen, I.T., Peralta-Gil, M. and Karp, P.D. (2005) EcoCyc: a comprehensive database resource for *Escherichia coli*. Nucleic Acids Research **33** D334-D337.
9. Gama-Castro, S., Jiménez-Jacinto, V., Peralta-Gil, M., Santos-Zavaleta, A., Peñaloza-Spinola, M.I., Contreras-Moreira, B., Segura-Salazar, J., Muñiz-Rascado, L., Martínez-Flores, I., Salgado, H., Bonavides-Martínez, C., Abreu-Goodger, C., Rodríguez-Penagos, C., Miranda-Ríos, J., Morett, E., Merino, E., Huerta, A.M., Treviño-Quintanilla, L. and Collado-Vides, J. (2008) RegulonDB (version 6.0): gene regulation model of *Escherichia coli* K-12 beyond transcription, active (experimental) annotated promoters and Textpresso navigation. *Nucleic Acids Research*. 36 D120-D124
10. Hobman, J.L., Penn, C.W. and Pallen, M.J. (2007) Laboratory strains of *Escherichia coli*: model citizens or deceitful delinquents growing old disgracefully? *Molecular Microbiology* **64** (4) 881-885.
11. Blattner, F.R., Plunkett, G., Bloch, C.A., Perna, N.T., Burland, V., Riley, M., Collado-Vides, J., Glasner, J.D., Rode, C.K., Mayhew, G.F., Gregor, J., Davis, N.W., Kirkpatrick, H.A., Goeden, M.A., Rose, D.J., Mau, B. and Shao, Y. (1997) The complete genome sequence of *Escherichia coli* K-12 *Science* **277**(5331) 1453-1474.
12. Evans, C.G.T., Herbert, D. and Tempest, D.W. (1970) The continuous culture of microorganisms. 2. Construction of a chemostat. In: Norris JR, Ribbons DW (eds) Methods in microbiology, vol 2. Academic Press, London New York, pp 277–327.
13. Eriksson, S., Lucchini, S., Thompson, A., Rhen, M. and Hinton, J.C. (2003) Unravelling the biology of macrophage infection by gene expression profiling of intracellular Salmonella enterica. *Molecular Microbiology* **47** (1) 103-118.

Permeability of an In Vitro Model of Blood Brain Barrier (BBB)

Rashid Amin[1,2,3], Temiz A. Artmann[1], Gerhard Artmann[1], Philip Lazarovici[3,4], Peter I. Lelkes[3]

[1]Aachen University of Applied Sciences, Germany,
[123]COMSATS Institute of Information Technology, Lahore, Pakistan,
[3]Drexel University, Philadelphia, USA,
[4]The Hebrew University, Israel

Abstract — **The blood brain barrier (BBB) is an anatomical structure composed of endothelial cells, basement membrane and glia; preventing drugs and chemicals from entering the brain. Our aim is to engineer an *in vitro* BBB model in order to facilitate neurological drug development that will ultimately benefit patients. Tissue engineering approaches are useful for the generation of an *in vitro* BBB model. Our experimental approach is to mimic the anatomical structure of the BBB on polyester terphthalate (PET) cell culture inserts. Endothelial cells derived from brain capillaries, different peripheral blood vessels and epithelial cells (MDCK) were cultured on the apical side of the filter. Different concentrations of thrombin were applied on compact monolayer of MDCK. Physiological functions of this BBB model was evaluated by measuring the transendothelial resistance (TEER) using an EndOhm™ electrode. The epithelial cytoskeletal organization was observed by staining with BBZ-phalloidin. Epithelial monolayer formation and later distortion by thrombin was confirmed by fluorescence microscopy. Measurements of the TEER generated values up to 2020 ohm/cm^2. A dose response of thrombin was observed, showing the permeability changes in the epithelial cells (MDCK). A relationship between permeability values TEER and cytoskeletal organization was observed.**

Keywords — **Blood Brain Barrier; Permeability; MDCK;Epithelial cell; Thrombin;Transendothelial Electrical Resistance; TEER; Thrombin receptors on MDCK**

I. Introduction

The presence of a barrier separating blood from brain and vice versa was described for the first time more than 100 years ago by Paul Ehrlich (1885) and confirmed later by Edwin Goldman (1909). Both researches showed that trypan-blue, an albumin-binding dye, following intravenous injection dispersed in whole body except the brain. On the other hand, direct subarachnoidal injection selectively stained only the brain. Neurological disorders include a large variety of brain diseases which may be treated with drugs. Unfortunately, the many drugs do not cross the Blood Brain Barrier (BBB). To evaluate pharmacokinetic properties of neurological drugs mainly animal studies are performed, which render the development of drugs a long high cost process. Therefore, there is a need to develop an *in vitro* BBB model to measure permeability of novel drugs which are under research and development. The aim of our research was to develop and characterize a new in vitro model involving endothelial and epithelial cells (MDCK). A novel approach was adopted to study the effects of thrombin on the permeability of a monolayer on transwel cell culture insert. Later, the results obtained from TEER measurements and changes in cytoskeleton were observed.

II. Materials and Methods

The cells and equipments used in our experiments are as under in Table 1 and Table 2.

Table 1, Cells

Cells	
BBMCEC	Bovine Brain Microvascular Capillary Endothelial Cells
MCEC	Microvascular Capillary Endothelial Cells
HAEC	Human Aortic Endothelial Cells
RAOEC	Rat Aortic Endothelial Cells
MDCK	Madin- Darby Canine Kidney (Epithelial Cells)

Table 2, Equipments

Equipment	Application	Manufacturers
Cell culture Inserts	Cell culture & permeability measurement	BD
Endohm™ Chambers	TEER Measurement	WPI
EVOM	TEER Measurement	WPI
CytoFluor ^{R} Series 4000	Fluorescence Plate reader	Biosystems
LSM 510 Microscope	Imaging	Zeiss
Permeability Analyzer	Permeability measurement	Cellular Engineering Lab. Fh.Aachen

A. In Vitro BBB Model

Minimal Essential medium (MEM) high glucose (4.5 mg/ml) medium (ATTC); 10% fetal calf serum (FCS) or Fetal Bovine Serum; 1% penicillin and streptomycin was

Chwee Teck Lim, James C.H. Goh (Eds.): ICBME 2008, Proceedings 23, pp. 81–84, 2009
www.springerlink.com

used to culture MDCK cells, 80,000 cells/cm^2 on transwell cell culture inserts. Ready to use phosphate buffered saline (PBS) and sterile 0.25% trypsin solution with 1:2000 ethylene-diamino-tetra-acetate (EDTA) was used to detach the cells from the surface of the flask., Transepithelial transport [6] was measured by Transepithelial Electrical Resistance, TEER [1] to calculate any increase or decrease in permeability of our model. MDCK cells need minimum ingredients to produce a high) TEER.

B. Phalloidin & BBZ Staining

Phalloidin / BBZ Stains were used to Stain Actin Filaments and Nuclei of cells. A cocktail of the stain was made by mixing 0.1 % triton –x in PBS, 2.5 µg /ml BBZ (2.5 µl from stock) and 1 µg/ml Phalloidin (1 µl/ml from stock). The samples were fixed with 10% formalin at RT for 30 minutes and then were washed for 2 – 3 minutes with PBS. Phalloidin/BBZ cocktail was applied for 20 minutes at room temperature and again the samples were washed 3*3 minutes with PBS and the images were observed under fluorescence Microscope.

C. Statistical Analysis

Statistical analysis were chosen as non parametric tests because the group size was n=9. Kruskal-Wallis- Test and Mann-Whitney-U tests were applied. The difference between the groups was accepted as significant when $p<0.05$.

D. TEER for different cell lines

Different endothelial cells and epithelial cell (MDCK) was seeded on the inserts and TEER was measured at different time intervals. TEER value in plotted against time.

In above experiment it was seen that the MDCK cells are able to produce a higher TEER value as compare to other cells. The epithelial cells producing tight junction proteins were purified to get cells producing tight junction proteins, thus producing a higher TEER value.

Again in the series of getting a high value of TEER; experiments were performed and we were able to get a higher value of TEER with MDCK cells. The Cells need minimum essential medium and it was observed that cell do not like frequent changes of medium.

Table 3

	BBMCEC	STDEV	MCEC	STDEV	RBMCEC	STDEV	MDCK	STDEV
48 HOUR	1.50	0.416	15.78	0.594	8.22	0.548	15.61	4.018
72 HOUR	2.67	0.383	14.67	0.924	10.83	1.0290	63.61	30.140

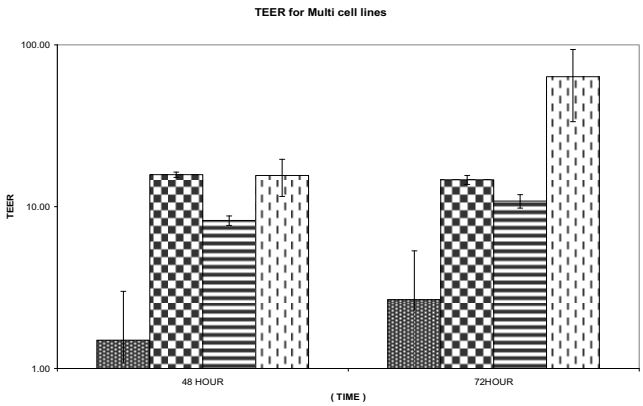


Fig.1 TEER for Multi cell Line

Table 4 TEER for Different Cell Lines

	BBMCEC	STDEV	MCEC	STDEV	RAOEC	STDEV
48 HOUR	10.111	0.850	0.722	0.000	2.722	0.000
72 HOUR	1.556	0.485	1 9.333	0.758	2.000	0.428
96 HOUR	1.389	0.323	24.167	0.686	1.722	0.548

Table 5 TEER for Different Cell Lines

HAEC		MDCK		MDCK-1	
5.167	0.511	423.500	39.329	423.278	31.118
5.167	0.802	500.222	56.122	339.667	34.488
7.222	0.669	259.333	14.292	233.944	6.306

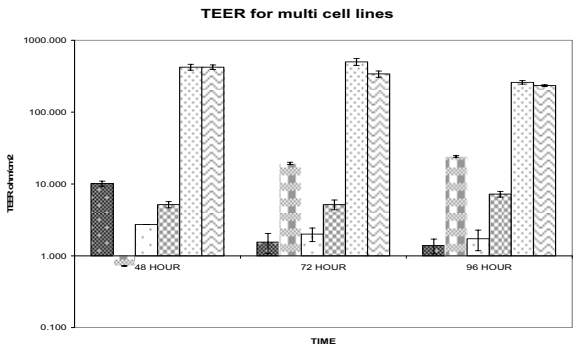


Fig. 2

E. Thrombin Concentrations

Thrombin is known to have receptors for epithelial cells [5]. It has cellular effects by Protease Activating Receptors (PARS) [2, 3]. We used thrombin to increase the paracellular permeability. The higher concentrations of thrombin used were 5 U/ml, 3 U/ml and 1 U/ml and the lower doses

were 0.01 u/ml, 0.001 u/ml, 0.0001 u/ml, 0.03 u/ml, 0.003 u/ml, 0.0003 u/ml.

III. Results

A. Thrombin dose Response on MDCK monolayer

The cells were treated with thrombin and then the culture medium was replaced with normal MEM media (serum added) and recovery of the cells was observed after four hours of serum MEM media addition. MDCK cell monolayer was stained with BBZ & Phalloidin staining technique and microscopic images were taken

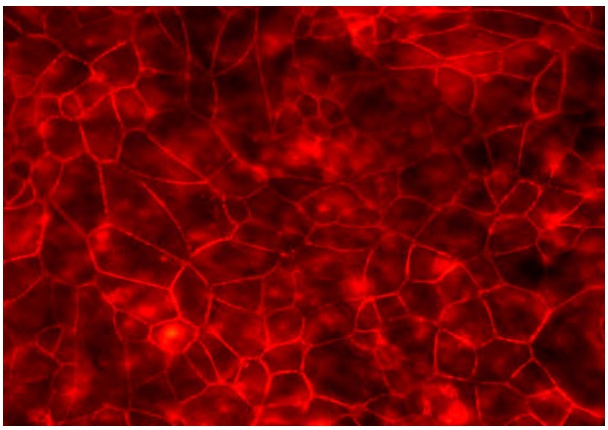


Fig. 3 MDCK Monolayer

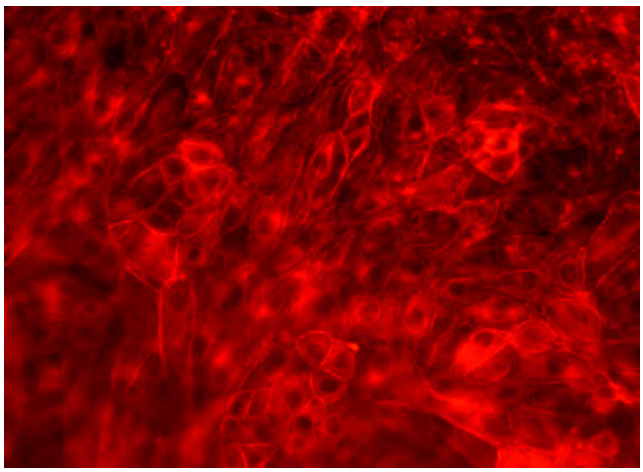


Fig. 4 MDCK Monolayer after thrombin treatment

The Serumless MEM medium was replaced with normal MEM medium and the MDCK cells showed a remarkable recovery towards their normal cytoskeleton structure

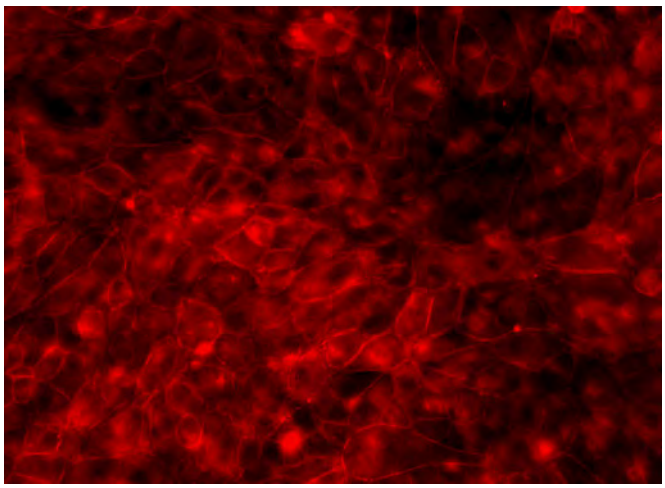


Fig. 5 MDCK Cells showing Recovery

MDCK Cells exposed to different thrombin concentrations and TEER was plotted against different thrombin concentrations. It was observed that we were able to get maximum increase in permeability at a lower concentration of thrombin i.e. 0.003 U/ml.

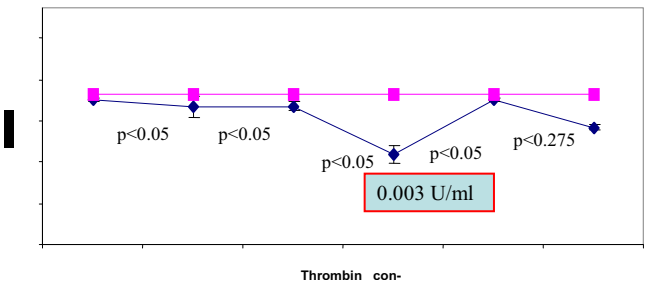


Fig. 6 n=9: Data as given average

All the thrombin groups were significantly different compared to control (p<0,05)

IV. Discussion

In vitro Blood Brain Model was made using different endothelial cells. And it was tried to obtain TEER of physiological level. But endothelial cells were not able to produce a high TEER value.

Efforts were made to increase the TEER of endothelial cells by using different growth factors (vNGF, mNGF, forskolin). Although we found some positive effects of vNGF but we were not able to increase TEER considerably. But with MDCK we obtained a good value of TEER. Because

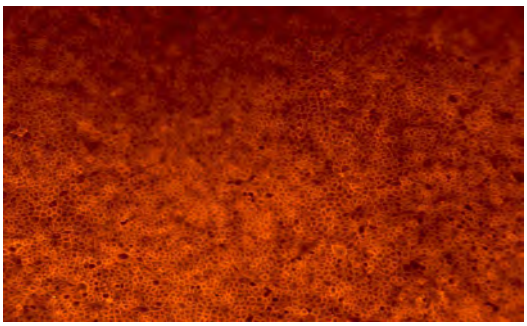


Fig. 7 MDCK compact monolayer

MDCK cells produce tight junction proteins and making a very nice and compact monolayer.

Epithelial cells are also used for i*n vitro* BBB modeling [4] because of their ability to produce a very tight monolayer by making tight junctions With MDCK cellular model a good TEER value of 2020 ohm/cm^2 was obtained. Studies have shown that endothelial cells and epithelial cells have receptors for thrombin [8]. The novel approach for thrombin effects on the permeability of epithelial cells (MDCK) was adopted and the effects of different concentrations of thrombin were seen. Thrombin concentrations from 5 U/ml, 3 U/ml and 1 U/ml were tried but we were not able to obtain good results. But it was observed that at lower concentrations the effect of thrombin is more as compare to higher concentration. Later very low concentrations of thrombin were used and dose response of thrombin was observed.

Six different concentrations of thrombin (0.01 u/ml, 0.001 u/ml, 0.0001 u/ml, 0.03 u/ml, 0.003 u/ml, 0.0003 u/ml) were used. It was observed that 0.003 u/ml showed maximum decrease in TEER or increase in permeability. From images we observed contraction of actin filaments and disruption of cytoskeleton caused a rapid decrease in TEER. Figure 3 & 7 show us a normal compact MDCK monolayer. In figure 4 we can see a very clear contraction and disorder of actin filaments; giving space ions to cross and causing a decrease in TEER. In figure 5 cells moving towards recovery can be seen after adding serum and inactivating thrombin (four hours). That shows us that thrombin is causing contraction in actin filaments, causing immediate decrease in TEER; showing increase in the permeability.

V. Conclusions

Endothelial cells were not able to make tight junctions and producing a high TEER value and thus were not used for our *in vitro* BBB cell culture model and permeability measurement. Epithelial cells (MDCK) were able to produce a higher TEER value because of tight junctions. Epithelial cells (MDCK) have thrombin receptors and thrombin can cause a rapid increase in the permeability.

Acknowledgment

I am thankful to all laboratory members and seniors involve in my work and their sincere support and guidance.

References

1. Bauer, R., Lauer, R., Linz, B., Pittner, F., Peschek, G., Ecker, G.F., Friedl, P., Noe, C.R., 2002. An in vitro model for blood brain barrier permeation. Sci. Pharm. 70, 317–324.
2. Chambers RC, Leoni P, Blanc-Brude OP, Wembridge DE, Laurent GJ.Thrombin Is a Potent Inducer of Connective Tissue Growth Factor Production via Proteolytic Activation of Protease-activated Receptor-1*J. Biol. Chem., Vol. 275, Issue 45, 35584-35591 PMID: 10952976
3. Chambers RC, Leoni P, Blanc-Brude OP, Wembridge DE, Laurent GJ.Thrombin Is a Potent Inducer of Connective Tissue Growth Factor Production via Proteolytic Activation of Protease-activated Receptor-1* J. Biol. Chem., Vol. 275, Issue 45, 35584-35591 PMID: 10952976
4. Elena v. Bhatrakova, Donald W. Miller, Shu Li, Valery Yu Alakhov, Alexender v. Kabanov, and William F.Elmquist. Pluronic P85 Enhances the delivery of digoxin to Brain: In vitro and in vivo studies. J.pharmacol EXP Ther. 2001 Feb;296(2):551-557
5. Hayashi S, Takeuchi K, Suzuki S, Tsunoda T, Tanaka C, Majima Y: Effect of Thrombin on Permeability of Human Epithelial Cell Monolayers. *Pharmacology 2006;76:46-52 (DOI: 10.1159/000089718)*
6. Misfeldt, D. S., Hamamoto, S. T., and Pitelka, D. R. (1976). Transepithelial transport in cell culture. Proc Natl Acad Sci U S A *73*, 1212-1216
7. Malik, A. B., and J. W. Fenton II. Thrombin-mediated increase in vascular endothelial permeability. *Semin. Thromb. Hemost.* 18: 193-199, 1992
8. Rondeau E, He CJ, Zacharias U, Sraer JD. Thrombin stimulation of Renal Cells. Semin Thromb Hemost. 1996;22(2):135-138 PMID 8807709

Decision Making Algorithm through LVQ Neural Network for ECG Arrhythmias

Ms. T. Padma[1], Dr. Madhavi Latha[2], Mr. K. Jayakumar[1]

[1]GRIET/BME, JNTU, Hyderabad, India
[2]JNTUCE/ECE, JNTU, Hyderabad, India

Abstract — **In this paper, learning vector quantization artificial neural network method was used for designing decision support system for Electrocardiogram (ECG) analysis. Four types of ECG patterns were chosen from the data obtained from ECG simulator device to be recognized, including Bradycardia, tachycardia, monomorphic preventricular contraction, myocardial infraction R-R interval, QRS complex duration, ST-segment slope change features were performed as the characteristic representation of the original ECG signals to be fed into the neural network models. LVQ network was trained and tested for ECG pattern recognition and the experimental results, performance graphs are plotted for varying number of samples. The LVQ network exhibited the best performance and reached an overall accuracy of 95.5% when. trained with 200 samples with learning rate at 0.9.**

Keywords — **ECG, Arrhythmia, LVQ Neural Network, Euclidean distance, Supervised learning.**

I. Introduction

Artificial neural networks can classify the data based on the features extracted from the biomedical signals. In this paper an attempt is made to design a decision support system for ECG analysis using Learning Vector Quantization (LVQ) neural network [4]. Five important features are extracted from the ECG [5] signal and are fed to the LVQ algorithm, which is implemented in MATLAB software [1].

II. Motivation

A typical ECG [9] waveform contains P wave, QRS complex and T wave in each heart beat Fig. 1 recognizing an ECG [6] pattern is essentially the process of extracting and classifying ECG feature parameters, which may be obtained either from the time domain or transform domain. The features being frequently used for ECG analysis in time domain include the wave shape, amplitude, duration, areas, and R-R intervals.

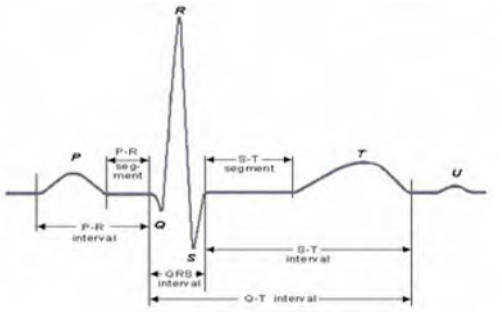


Fig. 1 Typical ECG waveform

The basic problem of automatic ECG analysis occurs from the non-linearity in ECG signals and the large variation in ECG morphologies [10], [11] of different patients. And in most cases, ECG signals are contaminated by background noises, such as electrode motion artifact and electromyogram - induced noise, which also add to the difficulty of automatic ECG pattern recognition.

III. Implementation

Various methods for pattern recognition, artificial neural network models have been successfully applied to the problem of ECG [8] classification. Artificial neural network is characterized by its nonlinearity and robustness, which confirms its efficiency on dealing with non-linear problems and good tolerance in the presence of noise and disturbance.

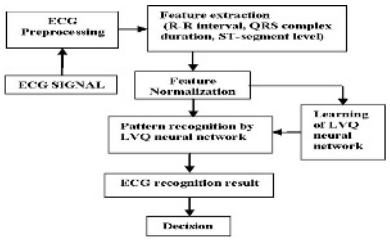


Fig. 2 Block diagram for Decision support system

Compared with the traditional clustering methods, the artificial neural network models have good adaptive ability to environmental changes and new patterns, and the

Chwee Teck Lim, James C.H. Goh (Eds.): ICBME 2008, Proceedings 23, pp. 85–88, 2009
www.springerlink.com

recognition speed of neural network is fast, owing to its parallel processing capability. The objective of our work is to design a decision supporting system for ECG analysis using Learning vector quantization neural network.

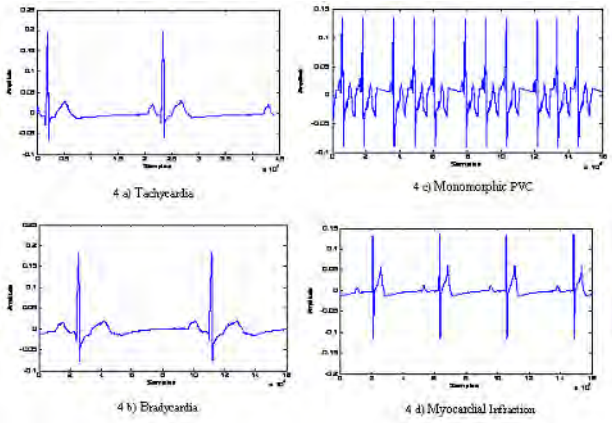


Fig. 3 different types of ECG Arrhythmias

IV. ECG Acquisition

Data acquisition is the sampling of real world to generate data that can be manipulated by a computer. Data acquisition typically involves acquisition of signals and processing the signals to obtain the desired information. The components of data acquisition system include appropriate sensors that convert any measured parameter to an electrical signal, which is acquired by data acquisition hardware. The signals like ECG, EMG EEG etc. are the analog signals, which are subjected to digitize before sending them to a computer. Analog to digital conversion of the data can be done using a data acquisition card or a sound card, where they have inbuilt A/D converters.

The vital parameter ECG is generated using a 12 lead ECG simulator [7]. The analog output from the simulator is sent to sound card extension slot of the computer through a wire. A/D converter present in the sound card converts it into digital signal which is read by the system bus as shown in fig.3. The obtained digital data is used for further analysis and classification.

V. Feature extraction

The task envisaged for signal processing is mainly the estimation of clinically important features from the ECG constituents, which, in turn will enable ECG waveform interpretation. The patterns that must be recognized in the ECG waveform like complexes, Inter wave segments Cardiac intervals,

In most cases of pattern recognition, feature extraction is needed to generate an adequately accurate representation of the original signals with lower dimension, which turns to form the input vector space. The ECG patterns to be recognized exhibit dissimilarity both in heartbeat timing and ECG morphology, so the following features were chosen like QRS complex duration, R-R interval, R-wave amplitude, ST segment slope change

VI. Learning vector quantization

Kohenen network has shown that it is possible to fine tune the class boundaries of a self organizing mapping (SOM) in a "supervised" way and has developed several methods for doing this. They are all variations of learning vector quantization. Vector quantization is a standard statistical clustering technique, which seeks to divide the input space into areas that are assigned as "code book" vectors. In LVQ network, target values are available for the input training pattern and the learning is supervised. In training process, the output units are positioned to approximate the decision surfaces. After training, an LVQ [2] net classifies an input vector by assigning it to the same class as the output unit that has its weight vector (reference or codebook vector) closest to the input vector.

In order to understand the LVQ techniques it should be borne in mind that the closest weight vector W_i to a pattern x may be associated with a node j that has the wrong class label for x. This follows because the initial node labels are based only on their most frequent class use and are therefore not always reliable. The procedure for updating W_j is given by,

$$\Delta W_j = \alpha(x - W_j) \quad \text{:if X is classified correctly}$$
$$= \alpha(x - W_{j)} \quad \text{:if X is classified incorrectly.}$$

The negative sign in the misclassification makes the weight vector move away from the cluster containing x, which on average, tends to make weights vectors move away from class boundaries.

A. ARCHITECTURE

The architecture is similar to the architecture of a Kohenen self organizing neural out without a topological structure assumed for the output units. In LVQ net, each

output unit has a known class, since it uses supervised learning, thus differing from Kohenen's SOM, which uses unsupervised learning. This is a competitive net where the output is known; hence it is a supervised learning network.

Take first 'm' training vectors and use them as weight vectors, the remaining vectors are used for training.

1. Initialize the reference vectors randomly and assign the initial weights and class randomly.
2. K-means clustering method can be adapted.

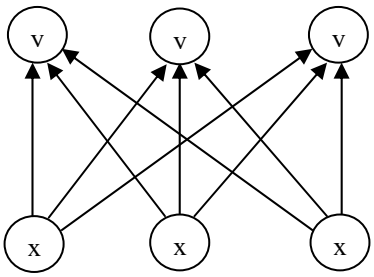


Fig. 4 Learning vector quantization neural net.

B. TRAINING DATA SET

The ECG data used to perform pattern recognition were taken from the ECG simulator database, which contains 200 recordings of two channel ambulatory ECG signals. Each record was annotated by cardiologists and the annotations were provided along with the ECG data. In this study, only one channel of ECG signals derived from modified-lead II was used. We chose four types of ECG patterns from the database, which are respectively annotated as the Premature Ventricular Contraction (PVC), Tachycardia, Bradycardia and Myocardial Infarction.

C. TRAINING ALGORITHM

The algorithm for the LVQ net is to find the output unit that has a matching pattern with the input vector. At the end of the process, if x and w belong to the same class, weights are moved toward the new input vector and if they belong to a different class, the weights are moved away from the input vector. In this case also similar to Kohenen self organizing feature map, the winner unit is identified. The winner unit index is compared with the target, and based upon its comparison result; the weight updating is performed as shown in the given algorithm [12] below. The iterations are further continued by reducing the learning rate.

The algorithm is as follows:

Step1: Initialize weight (reference) vectors.
Initialize learning rate.
Step2: While stopping is false, do step 3-7.
Step3: For each training input vector x, do steps 4-5.
Step4: Compute J using squared Euclidean distance.

$$D(j) = \sum (W_{ij} - x_i)^2$$

Find *j* when *D (j)* is minimum.

Step5: Update W_j as follows:

If $t = c_j$ then

$$W_{j(new)} = W_{j(old)} + \alpha[x - W_{j(old)}]$$

If $t \neq c_j$ then

$$W_{j(new)} = W_{j(old)} - \alpha[x - W_{j(old()}]$$

Step6: Reduce the learning rate.
Step7: Test for the stopping condition.

The condition may be fixed number of iterations or the learning rate reaching a sufficiently small value.

D. EXPERIMENTATION

An ECG signal with abnormal high heart rate is generated using a simulator, which signal is preprocessed and five features like R-R interval, QRS duration, Heart rate, ST slope change, R-amplitude are extracted from it. These features are fed to a Learning vector quantization neural network algorithm as shown above. Here the weight vectors are initialized as

Initial weight matrix

0.5100	1.2400	0.8100	0.8100
80.0000	80.0000	100.0000	76.0000
120.0000	48.0000	68.0000	68.0000
-0.0000	-0.0000	-0.0000	-0.0000

The stopping condition given here is the number of epochs equals to 100. After 100 epochs the weight updating process stops and the resultant model is used for further classification

Weights after 100 epochs

0.5362	1.6310	0.8169	0.8352
83.6009	84.8964	106.483	82.8675
118.641	36.9193	68.7839	67.7639
-0.0000	-0.0000	-0.0000	-0.0000

The neural network model thus developed is trained with 200 ECG signals to increase the efficiency of the network.

Then it is fed with the new ECG signal features, from the simulator, to classify into different classes. In our case four classes are considered like Tachycardia, Bradycardia, pre mature ventricular contraction and myocardial infarction. Any new signal fed to this model gets classified into one of these classes.

VII. Results

The result of the given signal is shown in a prompt dialog box which is created as a part of the program. This dialog box gives us the all values of the signal along with the distance calculated and prediction obtained. Next two figures shown are the results obtained for the sample signal taken.

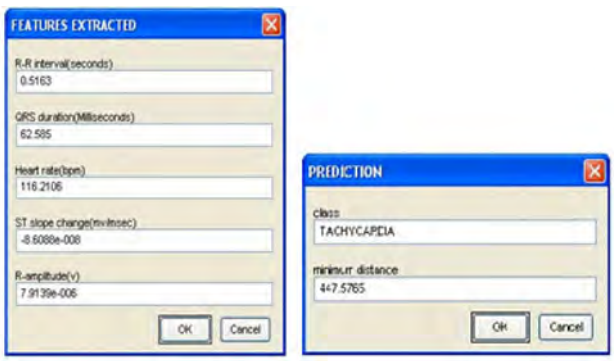


Fig. 5 dialogue box for feature extraction and prediction

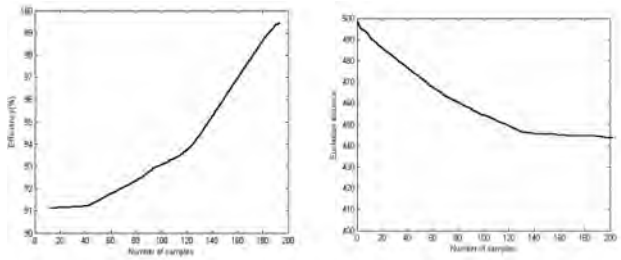


Fig. 6 trained data for Euclidean distance and efficiency

VIII. Conclusion

The decision support system is designed and that decides the subject based on only one parameter, ECG. The number of classes into which the signal is classified is constrained to four. It was observed that the efficiency of LVQ neural network for classifying the given input ECG signal increases as the number training samples increases and the Euclidean distance from class centre decreases. The changes in learning rate effects the classification efficiency. The classification efficiency increases as the learning rate is increased (from 0.1 to 0.9). As an extension to this work other biomedical signals like Respiratory signal, lab reports, Spo2 etc can also be used for the classification. The number of classes can also be extended.

References

1. Pan, J. and Tompkins, W. J. 1985 A real time QRS detection algorithm, IEEE trans. Biomed. Eng. BME – 32 pp230 – 36.
2. Rosaria Silipo and Carlo Marchesi, "Artificial neural networks for automatic ECG analysis", IEEE Transactions on Signal Processing, Vol.46.No.5, May 1998.
3. Bronzino J. D., The Biomedical Engineering Hand book, Volume I, CRC Press LLC 2000
4. Sivanandam, S. N., Sumathi, S. and Deepa, S. N. "Introduction to Neural Networks using - MATLAB 6.0, learning vector quantization, pp237 – 239, 2006, Tata McGraw-Hill.
5. Tompkins, W. J. Bio-Medical Digital signal processing, *ECG* QRS Detection, pp236 - 263. Prentice Hall India.
6. Kandhapur, R. S. Biomedical Engineering Hand book, Tata McGraw-Hill, pp 154-166
7. Patrons ES-401 ECG simulator user guide.
8. Medline plus Medical Encyclopedia: A service of US National Library of Medicine, www.nlm.nih.gov/medlineplus/ency/
9. Physiobank physiologic signal archives for Biomedical research, www.physionet.org/physiobank
10. Arrhythmia: a problem with your heart beat, www.familydoctor.org/x1943.xml
11. Prediction of Ventricular Tachyarrhythmia in Electrocardiograph, www.szabist.edu.pk/ncet2004/Docs/Session%20V%20Paper%20No%201(P%2082-87).PDF
12. Supervised classification of ECG Using Neural Networks, www.univtlemcen.dz/manifest/CISTEMA2003/cistema2003/articles/Articles%20-%20 GBM/GBM8.pdf

Author: T. Padma
Institute: Gokaraju Rangaraju Institute of Engg. and Tech.
Street: Bachupally
City: Hyderabad
Country: India
Email: tatipartipadma@gmail.com

Author: Dr. M. Madhavi Latha
Institute: J.N.T.U. College of Engineering
Street: Kukatpally
City: Hyderabad
Country: India
Email:

Author: K. Jayakumar
Institute: Gokaraju Rangaraju Institute of Engg. and Tech.
Street: Bachupally
City: Hyderabad
Country: India
Email: jaykumar70@yahoo.com

A Low-Noise CMOS Receiver Frontend for NMR-based Surgical Guidance

J. Anders[1], S. Reymond[1], G. Boero[1] and K. Scheffler[2]

[1] Ecole Polytechnique Fédérale de Lausanne (EPFL), Lausanne, Switzerland
[2] University of Basel, University Hospital, Basel, Switzerland

Abstract — **In this paper a novel architecture for an integrated NMR receiver front-end for surgical guidance applications is described. While the chip consumes only 9 mA supply current from a 3.3 V power supply it has a measured input referred noise density of 0.7 nV/√Hz. The receiver consists of the reception coil, an on-chip tuning capacitor an LNA and a 50 Ω output buffer. The system is designedfor operation in a B_0-field of 1.5 T corresponding to a frequency of 63MHz. It is implemented in a 0.35 µm CMOS high voltage process and occupies a chip area of 500 µm × 760 µm.**

Keywords — **CMOS, NMR, MRI, Surgical Guidance**

I. Introduction

Interventional radiology (IR) is used to perform minimally invasive procedures using image guidance. These procedures can be either for diagnostic purpose (e.g. angiogram) or for treatment purpose (e.g. angioplasty). IR is usually performed by inserting small needles or catheters into the human body and guiding their way using radiological methods such as X-ray, computed tomography, ultrasound or magnetic resonance imaging (MRI) to provide roadmaps for the Interventional Radiologist. In this paper, a chip is presented that will facilitate the monitoring of surgical equipment such as scalpels, scissors or tweezers using MRI-based tracking.

The paper is organized as follows. In section II.A a brief review of the physics behind nuclear magnetic resonance (NMR) – the phenomenon underlying MRI – will be given: section II.B explains how NMR can be used for surgical guidance. Having presented the necessary application background, section III will then introduce the circuit details of the receiver along with the simulated results: section IV presents the measured performance of the receiver, and section V presents our concluding remarks.

II. Working principle

A. Nuclear Magnetic Resonance

The physical mechanism underlying MRI is nuclear magnetic resonance (NMR). NMR exploits the fact that nuclei possessing an odd number of protons or neutrons have an intrinsic magnetic moment. In an external static magnetic field (B_0-field), the spins precess at the Larmor-frequency, ν_0, given by

$$\nu_0 = \frac{\gamma B_0}{2\pi}, \tag{1}$$

where γ is the gyromagnetic ratio of the nucleus, around this field. The net magnetization however is aligned with the B_0-field. If one now applies an RF-magnetic field (B_1-field) with a frequency close to ν_0 (resonance condition) and linearly polarized in a direction perpendicular to the B_0-field for a time τ, the net magnetization will be rotated around the axis of the B_1-field by a certain angle θ according to

$$\theta = \gamma B_1 \tau_1 \tag{2}$$

The NMR receiver then detects the component of the net magnetization in the plane perpendicular to the B_0-field as an induced voltage in the reception coil.

B. Surgical Guidance

The chip can be attached to any surgical instrument that would not interfere with the MRI image. By monitoring the frequency of the induced voltage in the reception coil and knowing the gradients in the static B_0-field during the image sequences, one can easily calculate back the position of the chip and thereby the position of the instrument to which it is attached to visualize it on the MRI image.

III. Circuit description

A. Coil Optimization

Given a reasonable size for an implantable device (here we fix the outer coil diameter to be 500 µm) the procedure below allows us to determine the coil that gives the best signal to noise ratio (SNR) at the LNA output. If we choose a particular metal layer and fix the spacing between two adjacent windings (here 3 µm) by the minimum design rule, the only two free parameters are the number of turns, N, and the inner radius, r_{in}. The SNR to optimize is considered at the output of the equivalent resonant circuit shown in Fig.(1):

Chwee Teck Lim, James C.H. Goh (Eds.): ICBME 2008, Proceedings 23, pp. 89–93, 2009
www.springerlink.com

$$\sqrt{SNR} = \frac{V_{ind}\left(Q + R_v / \left(R + 2R_v\right)\right)}{\sqrt{4kT\left(\left(R + 2R_v\right)\left(1 + Q^2\right) + R_{in}\right)}} \quad (3)$$

where V_{ind} is the NMR voltage induced across the coil, R is the coil resistance, $Q = \left(\omega L\right)/\left(R + 2R_v\right)$ is the circuit quality factor, L is the coil self inductance [2], R_v is the metal leads and vias resistance and R_{in} is the LNA input referred noise resistance obtained from Spectre simulations. This expression is valid when C is tuned so that the coil circuit is resonant.

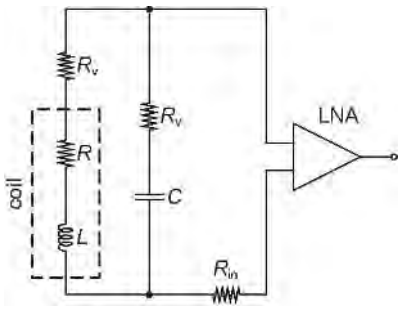


Fig. 1 Equivalent circuit for coil optimization

To calculate the induced voltage, we use the reciprocity principle [4]:

$$V_{ind} = \omega M \int B_{z,u} dv, \quad (4)$$

where M is the sample magnetization, which is assumed to be homogeneous over the sample volume V and $B_{z,u}$ is the perpendicular magnetic field produced by a unitary current circulating in the coil. The integration is performed over a volume that we model as a cylinder. Fig.(2) shows the SNR levels as a function of the two free parameters for the situation corresponding to the fixed parameters shown in Tab.1.

Table 1 Coil optimization parameters

Parameter	Value
Optimization Frequency	63 MHz
R_{in}	16 Ω
R_v	1Ω
Sample material	H_2O
Sample size	250 µm (diameter) × 250 µm
Coil-sample distance	10

The SNR maximum occurs at 16 turns and r_{in} = 75 µm, but if we impose an additional constraint, namely that the self resonating frequency remains well above the excitation frequency (here we chose f_{self} larger than 1 GHz), then too large winding numbers are prohibited. The chosen tradeoff coil is represented by the red dot in Fig.(2), it corresponds to N = 13 and r_{in} = 70 µm. Note that for very low N, the LNA produces the majority of the noise, resulting in poor SNR. At larger N, both the induced voltage and the coil resistance scale with N, which produces the relatively weak N dependence of the SNR. The upper right corner of Fig.(2) corresponds to narrow highly resistive coils.

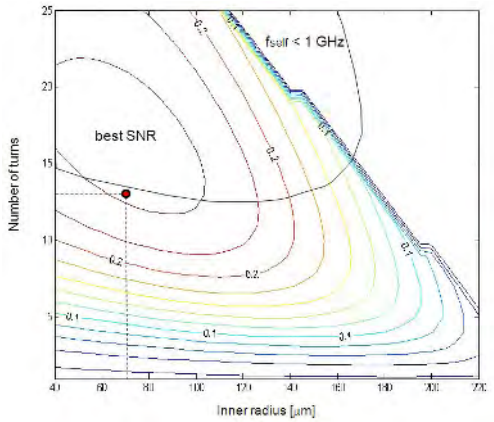


Fig. 2 Contour plot of coil optimization

B. LNA Design

The core of the LNA is a differential voltage amplifier consisting of input pairs M_{n1}-M_{n2} and M_{p1}-M_{p2} in parallel, cascoding devices Mn3-M_{n4} and load devices M_{p3} and M_{p4}. The parallel combination of the NMOS and the PMOS input pair effectively increases the transconductance for a given bias current and thus minimizes the input referred noise and maximizes the voltage gain [1], [2]. The differential topology is beneficial for on-chip signal processing. Unfortunately, conventional MRI receivers do not support differential signaling. Therefore, to be compatible with these systems, a differential-to-single-ended conversion had to be performed on chip. The most natural way to perform this conversion is a current-mirror load as it can be found in many Op-Amp circuits. However, in contrast to the Op-Amp case, where the external feedback defines the output DC voltage, in the design at hand this simple solution is not applicable for the following reason: no shunt-peaking can be applied because the tight area requirements prohibit the use of an additional inductor which would anyway have a very poor quality factor at the operating frequency of 63 MHz. Therefore, the amplifier has to provide the desired gain over the full bandwidth from DC up to the operating frequency. Because such a large bandwidth is hardly achievable in a 0.35 µm CMOS process, an open-loop archi-

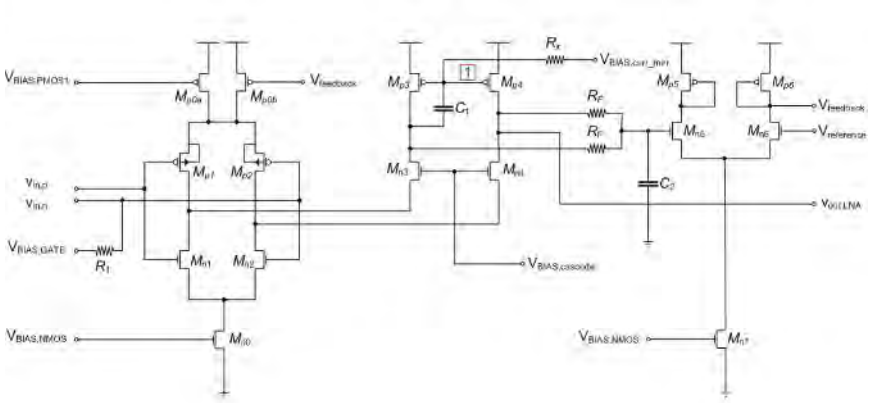


Fig. 3 LNA schematic

tecture had to be used. To still be able to set the DC output voltage of the current mirror in a way that is robust against process variations and mismatch in the input pairs, the AC behavior of the load has been separated from its DC performance in the following fashion. For DC signals, the capacitor C_1 can be viewed as an open-circuit and the voltage at the gates of transistors M_{p3} and M_{p4} is set by the biasing voltage $V_{bias,curr_mirr}$; that is M_{p3} and M_{p4} effectively present a current source load. To set the DC voltages at their drains, a common-mode-feedback (CMFB) network consisting of sensing resistors R_2 and R_3, differential pair M_{n5}-M_{n6} and diode connected loads M_{p5}-M_{p6} has been added. The CMFB is closed through transistor M_{p0b}. By means of this feedback, the output common mode voltage is compared to the reference voltage, $V_{reference}$, and adjusted appropriately. Of course, the CMFB has to be disabled for signals around the operation frequency of 63 MHz where the current mirror operation is needed to perform the differential-to-single-ended conversion. To achieve this, the values of capacitors C_1 and C_2 had to be carefully chosen. Capacitor C_2 defines the bandwidth of the CMFB and should be as large as possible because it should only set the DC operation point of the load and not affect the circuit's AC behavior. Thus, it will be treated as a short circuit in the following AC analysis. Capacitor C_1 on the other hand must perform the current mirroring at the operation frequency and thus C_1, and R_X, should be large enough to place the corresponding zero at a sufficiently low frequency. For a quantitative analysis we will now take a closer look at the transfer function $A_{diff}(s)$ from the input, $v_{in,p}$-$v_{in,n}$, to the output $v_{out,LNA}$. Neglecting the output load capacitance, the transfer function can be approximated by

$$A_{diff}(s) = g_{m,in}R_F \frac{\left(1+\frac{s}{s_{z1}}\right)\left(1+\frac{s}{s_{z2}}\right)}{\left(1+\frac{s}{s_{p1}}\right)\left(1+\frac{s}{s_{p2}}\right)}, \tag{5}$$

where

$$s_{z1} = -\frac{1}{2C_1 g_{m,p3} R_F R_X},\ s_{z2} = -\frac{2g_{m,p3}}{C_X},$$
$$s_{p1} = -\frac{1}{C_1 g_{m,p3} R_F R_X} = 2s_{z1},\ s_{p2} = -\frac{g_{m,p3}}{C_X} = \frac{1}{2}s_{z2}, \tag{6}$$

where $g_{m,in}$ is the total differential input capacitance, i.e. $g_{m,in}=g_{m,n1}+g_{m,p1}$, and C_x is the total capacitance from node 1 to ground. In the design at hand, R_x and C_1 were chosen to place the first zero, s_{z1}, around 10 MHz, which does not degrade the AC performance, i.e. the gain in the frequency region of interest is given by $2g_{m,in}R_F$, and still leads to reasonable device sizes for R_x and C_1.

The total input referred noise is dominated by the input differential pairs and it suffices to model the noise as an input referred voltage source because induced gate noise can be neglected for the given values of coil resistance [8], rendering the input transistor's drain noise the main overall noise contributor. With these assumptions, the total input referred voltage noise density can be expressed as

$$V_{noise}(f) = \sqrt{2\frac{4kT\left(\gamma_n g_{m,n} + \gamma_p g_{m,p}\right)}{\left(g_{m,n}+g_{m,p}\right)^2} + 4kTR_{G,tot}} \tag{7}$$

where γ_n and γ_p are booth equal to 2/3 for transistors in saturation and strong inversion, $g_{m,n}$ and $g_{m,p}$ are the differential transconductance of the NMOS and PMOS differential pair and $R_{G,tot}$ is the total gate resistance of the input transistors. Clearly, to avoid a degradation of the noise performance by the gate resistance it has to be a lot smaller than the coil resistance amplified by the coils Q-factor. This was achieved by careful layout of the input differential pairs. These were laid out as common centroids were each half transistor was first divided in six diffusion areas and then fingered.

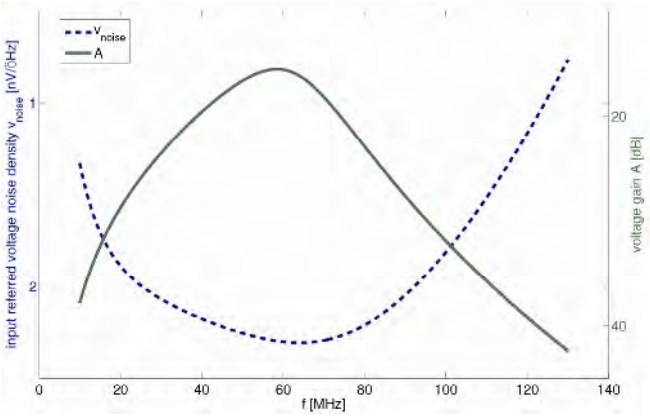


Fig. 4 Simulated LNA input noise and gain (extracted view)

The simulated (extracted view) LNA noise and gain performance are shown in Fig.(4).

IV. Measurement Results

The LNA performance has been verified using an NMR experiment with cis-PolyIsoprene as a sample. The corresponding free induction decay (FID) and spectrum are shown in Fig.(6) and Fig.(7). Knowing the sample dimensions and the reception coil properties it is possible to calculate the induced voltage in the coil with the aid of Eq.(4). Then, knowing the amplification of the rest of the receiver chain, one can deduce the LNA gain with an uncertainty of less than 2 dB. Once the gain has been calculated, the input referred noise was calculated from the measured output referred noise density and the gain value. The obtained values are listed in Tab. 2 together with the corresponding values from extracted view simulations. One clearly sees the good agreement between measurement and simulation.

Table 2 Performance Summary

	Measured	Extracted Sim
Voltage gain [dB]	43±1	44
Input referred noise [nV/√Hz]	0.7	0.7

V. Conclusion

A receiver front-end for NMR-based surgical guidance in 0.35 µm CMOS has been designed. The performance was evaluated using real NMR experiments and it proves to be at least an order of magnitude better in terms of sensitivity than the state of the art [9]. In the future, the receiver will be extended by co-integrating the mixer, as well as the local oscillator and a low-frequency gain stage chip on chip.

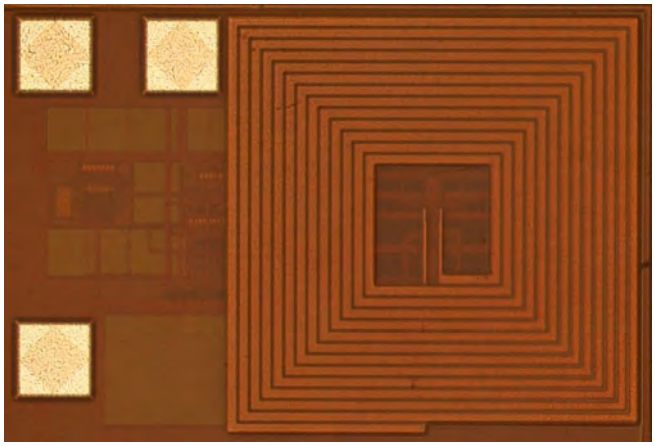


Fig. 5 Chip microphotograph

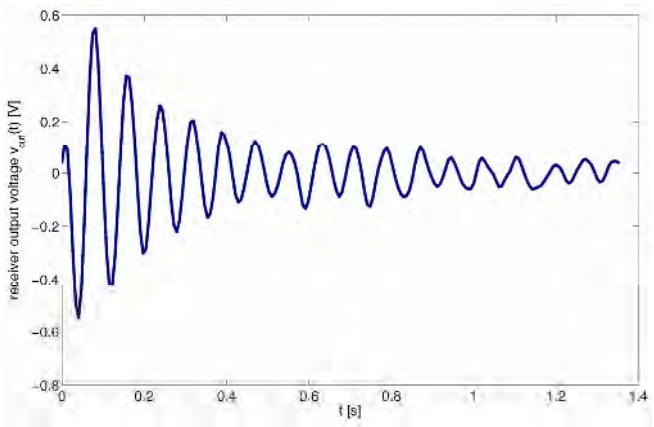


Fig. 6 Measured FID

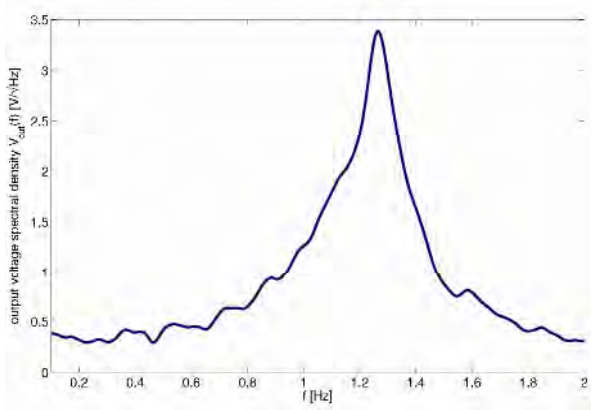


Fig. 7 Measured Spectrum

REFERENCES

1. A.N. Karanicolas (1996) A 2.7-V 900-MHz CMOS LNA and mixer, JSSC, Vol.31, No.12
2. S.S. Mohan et al. (1999) Simple and Accurate Expressions for Planar Spiral Inductances. JSSC,Vol.34, No.10
3. G. Boero et al. (2001) Fully integrated probe for proton NMR magnetometry. Rev. Sci. Instrum. 72, 2764
4. D.I. Hoult (2000) The principle of Reciprocity in Signal Strength Calculations – A Mathematical Guide, Concepts in Magnetic Resonance, Vol.12,No.4,p173-187
5. P.R. Gray, P.J. Hurst, S.H. Lewis and R.G. Meyer (2001) Analysis and Design of Analog Integrated Circuits, Fourth Edition, John Wiley & Sons, Inc.
6. F. Gatta et al. (2001) A 2-dB Noise Figure 900-MHz Differential CMOS LNA, JSSC, Vol.36,No.10
7. T. Cherifi et al. (2005) A CMOS Microcoil-Associated Preamplifier for NMR Spectroscopy, TCAS-I, Vol.52,No.12
8. C. Enz (2008) Advanced Analog and RF IC Design II, Lecture Notes
9. Y. Liu et al. (2008) CMOS Mini Nuclear Magnetic Resonance System and its Applications for Biomedical Sensing, ISSCC Difgest of Technical Papers

Automated Fluorescence as a System to Assist the Diagnosis of Retinal Blood Vessel Leakage

Vanya Vabrina Valindria[1], Tati L.R. Mengko[1], Iwan Sovani[2]

[1] Institut Teknologi Bandung(ITB), Imaging and Image Processing Group (I2PRG), Bandung, Indonesia
[2] Cicendo Eye Hospital, Bandung, Indonesia

Abstract — **Leakage in retinal blood vessel may cause retinal edema which is a sign of diabetic retinopathy. Diabetic retinopathy is a severe and widely spread eye disease which can be regarded as manifestation of diabetes on the retina. So far the most effective diagnosis for this eye disease is early detection through FFA (Fluorescence Fundus Angiography) regular screening that can lead to successful laser treatments in preventing visual loss. FFA is a fundus photography technique which captures the flow/circulation of contrast agent (fluorescence) in retinal blood vessel. The problem arises since the fluorescence is a costly contrast agent and has some side effects to the patients. Some patients felt nauseous and lose their consciousness when the substance was injected to their body. To lower the risks of such screening, the Automated Fluorescence (AF) system is developed to detect the presence of leakage in retinal images obtained from fundus camera, without contrast agent injection (non-invasive).**

An alternative method for automated detection of the vasculature in retinal images is introduced, which includes Gabor wavelet 2-D, scale addition, and Butterworth high-pass filtering. The experimental results demonstrate the accuracy of the algorithms in detecting both large and small vessels and the efficiency in reducing noise. Method for detection of retinal leakage consists of ANN (Artificial Neural Network), CLAHE (Contrast-Limited Adaptive Histogram Equalization), and morphological operation. The leakage feature in Gabor wavelet image is recognized by the trained ANN system, and this image is combined with CLAHE image in order to give a better detection result. Output images that have been tested by ophthalmologists, give 92% satisfaction in blood vessel detection and 75% correspondence with reference images in leakage detection.

Keywords — **leakage, retina, diabetic retinopathy, Gabor, Artificial Neural Network.**

I. Introduction

Image processing holds an important aspect in medical field, especially in assisting diagnosis. Diagnosis is one of the medical procedures to recognize the pathology of the patient. Fundus image shows the map of the retina, such as optic disk, macula area, fovea, and blood vessels. In several cases, the information of retinal vasculature and leakage area are needed to be enhanced. The FFA(*Fundus Fluorescence Angiography*) technique can give a detail information about circulation in the retina. Contrast agent (fluorescence) is injected to vena and it will flow to the blood vessels inside the patient body. This contrast agent makes the obtained images appear more detail and can be used for diagnosis. But, the problem arises since the fluorescence has some side effects to patients. Some patients feel nauseous and lose their consciousness when the subtance is injected to their body. Moreover, fluorescence is a costly contrast agent.

The solution to solve those problems is to develop an image processing technique which can give an image with leakage area similiar to the FFA image, without contrast agent injection to the patient. Without image processing, the information needed for diagnosis cannot be appeared clearly in fundus image.

In previous work [13], blood vessels and leakage area in retina images were enhanced by *matched filter* and ANN. This system failed to detect small blood vessels, presented noise on the retinal image background, and showed only 50% correspondence with reference images in leakage detection.

In this paper, the AF system is proposed to diagnose blood vessels leakage in diabetic retinopathy patients. The purposes of this paper are to find the appropriate methods to give an image with clear leakage area and to improve the previous system. With this AF system, doctors can approximate the location of blood vessels leakage in retinal image to do the LASER therapy and patients will feel more comfortable with the diagnosis.

II. Materials and Methods

A. Pre-processing of blood vessel detection

Input image from fundus camera – shown in Fig.1 is processed in pre-processing 1. In order to obtain the blood vessel information, three channels (RGB) of the images need to be extracted. The green channel was selected since it is more contrast in blood vessels than in the other channels. An obstacle for identification of retinal blood vessels is the wide variability in the colour of fundus from different

Chwee Teck Lim, James C.H. Goh (Eds.): ICBME 2008, Proceedings 23, pp. 94–97, 2009
www.springerlink.com

patients. We apply a colour normalization method to make the images invariant with respect to the background pigmentation variation between individuals. The colour normalization was performed using histogram specification [18]. Then, we invert the normalized green channel of the image, so that the vessels appear brighter than the background (see Fig.1).

B. Pre-processing of leakage detection

1. Pre-processing of ANN process

Input images for ANN training are green channel extracted image and its Gabor wavelet image. These images have the feature information needed for blood vessel leakage detection

2. Pre-processing of optic disk detection

Based on our observation, the optic disk is brighter and easier to be segmented in blue channel image. After extracting the blue channel from the input image, we normalize it with the reference image used in the previous step.

C. Main processing of blood vessel detection

One of the retinopathy diabetic symptoms is neovascularization – which can be recognized by abnormal vasculature structure of small blood vessels. It is much more difficult to detect small blood vessels due to their low contrast and tortuos patterns in the images.

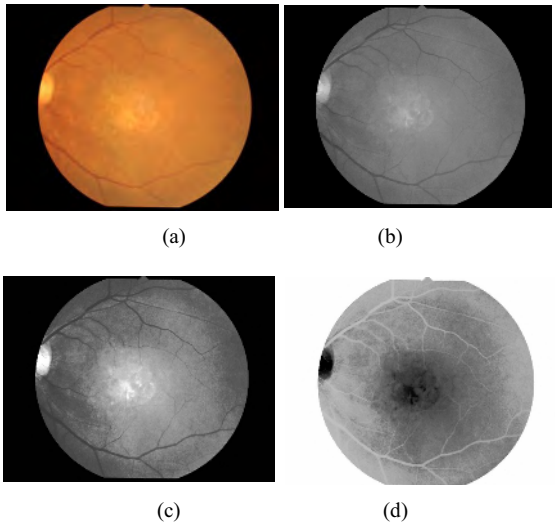
1. Blood vessel detection using Gabor wavelet 2-D

Gabor function here serves as the basis function (mother wavelet) in wavelet transform. The mother wavelet and its Fourier transform are well localized in time and frequency domain. This condition implied that the wavelet transformation is effective for singularity detection, such as blood vessels. The continous Gabor wavelet transform is defined as :

$$T(s,\tau_x,\tau_y) = \iint f(x,y)\psi^*_{s,\tau_x,\tau_y}(x,y)dxdy \qquad (1)$$

where *f(x,y)* is the input image, τ_x and τ_y are the translation parameters, *s* denotes the scaling parameter and ψ^* denotes the complex conjugate of ψ. Another benefit of Gabor filter is the availability of phase or orientation angle at each pixel, that may provides the largest magnitude response [16]. Then, the Gabor wavelet transform is computed for orientation θ, from 0 up to 170 degrees at step 10 degrees.

To meet the criterion for wavelet basis function, Gabor function must be arisen by translation and scaling. The centre coordinates of a pattern in multi-resolution analysis should contain *s*.



(a) (b) (c) (d)

Fig.1 Images in pre-processing 1. (a) Color input image. (b) Green channel image. (c) Normalization. (d) Inverted normalized image

Ignoring translation to multi-resolution analysis; we modified the equation to:

$$x' = \frac{x\cos\theta + y\sin\theta}{s}, y' = \frac{-x\sin\theta + y\cos\theta}{s} \qquad (2)$$

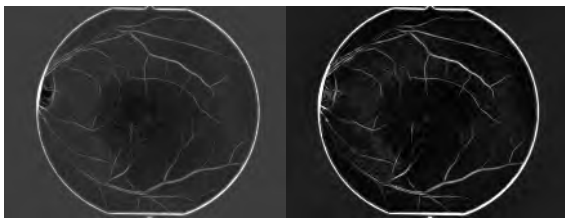
Gabor function consists of two parts, the complex exponential function and the Gaussian function. Therefore, the Gabor wavelet function in this paper is defined as:

$$\psi_G(x,y) = \frac{1}{2\pi s\sigma_x\sigma_y}\exp\left[-\frac{1}{2}\left(\frac{x^2}{\sigma_x^2}+\frac{y^2}{\sigma_y^2}\right)\right]\exp(jf_0y) \qquad (3)$$

In [14], frequency $f_o = 3$ is chosen for y-axis and $f_o = 0$ for x – axis. We set the σ_y parameter to 1, making the pattern characteristic to be strongly detected. In order to to make a sharper detection, [16] the value of σ_x should be adapted to the scale, with respect to the thickness of the detected blood vessels. The Gaussian amplitude is one half of its maximum at $x = s/2$ and $y = 0$. Thus, the parameter σ_x can be set as $s/2\sqrt{(2 \ln 2)}$.

We apply the Fourier transform to the conjugated basis function ψ_G^*. Then, 2-D Gabor wavelet transform is implemented as the inner product of an image and ψ_G^* in frequency domain:

$$T(s) = f(\omega_1,\omega_2).\psi^*_{G_s}(\omega_1,\omega_2) \qquad (4)$$



(a) (b)

Fig.2 Images in main processing of blood vessels detection. (a) Gabor wavelet 2-D image. (b) Enhancement result

For each scale, we compute the maximum response of its transform result. Some advantages of multi-resolution analysis are noise reduction and line filter response enhancement. In line detection, the parameter *s* must be carefully selected to capture the information of lines with different widths. After multi-resolution filtering using Gabor, we do the scale addition between the filter responses at two adjacent scales [17].

2. Enhancement

To produce a sharper detection in both large and small blood vessels; a high-pass filtering is applied to the image, as shown in Fig.2 (b). We use second order Butterworth high-pass filter with cut-off frequency 1, 8.

D. Main processing of leakage detection

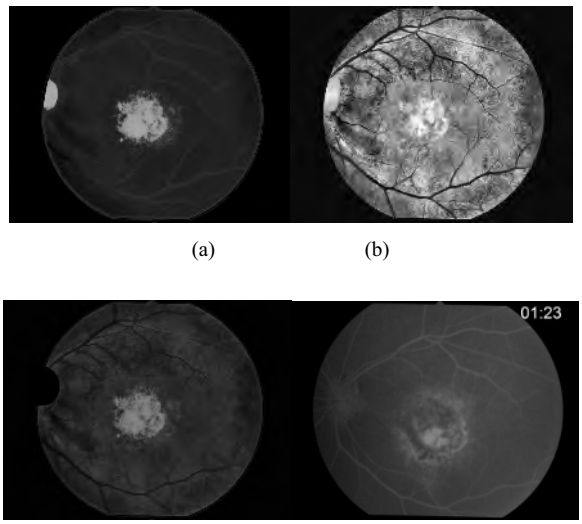
Generally, the retinal blood vessel leakage in fundus image is characterized by smoother texture and brighter intensity than the background. In a non-diffuse leakage, both the leakage source and edema area can be detected. On the other hand, in diffuse leakage, only edema area which can be detected due to many leakage sources in the blood vessels.

1. Artificial Neural Network (ANN)

In ANN training stage, we use backpropagation algorithm to train the ANN. To compose the feature vectors, two input images used in this stage consist of Gabor wavelet image and normalized green channel of fundus image. Meanwhile, the target image used here is FFA image.

By implementing the designed ANN to this system, we can obtain an output image with the detected retinal leakage area. In ANN main processing stage, we use feed-forward algorithm. Input images in this process are Gabor wavelet image and normalized green channel of fundus image. Applying those images to ANN system, it results in an output image with strong leakage area detection, as shown in Fig.3 (a).

The design of network in training and main processing consists of three layers; one input layer, one hidden layer and one output layer. Input layer has two input nodes, hidden layer has three nodes and output layer has one node.



(a) (b)

(c) (d)

Fig.3 Images in main processing of leakage detection. (a) ANN image. (b) CLAHE image. (c) Segmented optic disk. (d) Output image. (e) FFA image as a reference image

2. Contrast enhancement using CLAHE

CLAHE image gives a more detail blood vessels structure and accurate leakage area. Next, the CLAHE image is combined with the image obtained from ANN process. Using this combination, over-exposure in optic disk area can be reduced and leakage area in those two images is strengthened. To minimize wrong leakage detection, blood vessel appears darker than the leakage area (see Fig.3 (b)).

3. Optic disk detection

We use morphological operation to detect the optic disk in retina image. After we threshold the image to get the raw segmentation of optic disk area, the label is dilated and segmented. For each segmented area, we compute its circularity.

Then, we subtract the combined CLAHE and ANN image with the segmented optic disk. The aim of this subtraction is to discard the bright area in retina image except the leakage or edema, so that wrong detection can be minimized. Output image of this system in Fig.3(c) gives a high correspondence of leakage area with the reference image (FFA) in Fig.3(d).

III. Results

Experiments have been carried out on 64 images from our database. The database consists of two different sizes of images: 42 images of 1600x1216 pixels size and 22 images of 2588x1958 pixels size. Those images were sorted by

ophthalmologists to represent various conditions in retinal leakage. The performances are evaluated by four ophthalmologists from Cicendo Eye Hospital.

1. Blood vessel detection

Based on the ophthalmologists' visual observations, the detection of blood vessels gives a subjective satisfaction of 92%. Thus, the detection provides an optimal result in both sizes of images which can be used for diagnosis.

False detection occurs in some images for pathologies, such as exudates or abnormal retinal layer. The previous work [13] shows some difficulties in small blood vessel detection and noise reduction. Our approach separates the images of leakage area detection and blood vessel detection, ignoring any pathology in blood vessel detection.

2. Leakage detection

Output images and FFA reference images are labeled with five-part circle mark on the macula area. Both images are compared to see their correspondence of retinal leakage area. The results indicate that our approach is able to achieve 75% accuracy in retinal leakage detection.

However, the limitation of this detection is that it cannot distinguish leakage source from macula edema. Using Gabor wavelet in this AF system, leakage can be detected with stronger boundary and brighther area. This result shows that texture is an important feature in leakage detection.

IV. Conclusions

The results obtained indicate that AF system could assist in the detection and diagnosis of retinal blood vessel leakage in retinopathy diabetic without injecting the contrast agent to patients. Moreover, methods as above could give more accurate boundary in leakage area detection and better results in detecting both small and large vessels.

AF system gives a detail and accurate blood vessel detection in pathological retina images. This paper demonstrates the advantages of Gabor 2-D wavelet in detecting the thin blood vessels and capturing the texture information of leakage in images of retina.

Although strong boundary of leakage in macula area is presented, visual observation shows some difficulties of the method that must be solved by future work. Future work aims at analyzing the edema area accurately and classifying the edema from leakage source.

References

1. Jain K. Anil (1989) Fundamentals of Digital Image Processing. Prentice Hall, Singapore
2. Gonzalez C. Rafael and Richard E. Woods (2002) Digital Image Processing. Prentice Hall, New Jersey
3. S. Fadlisyah (2007) Computer Vision dan Pengolahan Citra. Penerbit ANDI, Yogyakarta
4. Sid-Ahmed, A. A (1995) Image Processing, Theory, Algorithms, &. Architectures. McGraw-Hill, New York
5. B. James, C. Chew, dan A. Bron (2006) Lecture Notes : Oftamologi. Erlangga Medical Series, Jakarta
6. D.G. Vaughan. T. Asbury, dan P. Riordan – Eva (1996) Oftamologi Umum. Penerbit Widya Medika, Jakarta
7. Kulkarni D. Arun (1994) Artificial Neural Network for Image Understanding. VNR Computer Library, New York
8. S. Kusumadewi (2004) Mengembangkan Jaringan Saraf Tiruan Menggunakan MATLAB dan Excel Link. Penerbit Graha Ilmu, Jakarta
9. A. Hermawan (2006) Jaringan Saraf Tiruan : Teori dan Aplikasi. Penerbit Andi, Yogyakarta
10. S.E. Mulyana (2005) Pengolahan Digital Image dengan Photoshop CS2. Penerbit Andi, Yogyakarta
11. D. Puspitaningrum (2006) Pengantar Jaringan Saraf Tiruan, Penerbit Andi, Yogyakarta
12. R.A. Simandjuntak (2005) Laporan Tugas Akhir: Segmentasi Mikroaneurisma dari Citra Retina Digital untuk Membantu Diagnosis Awal Retinopati Diabetes. Institut Teknologi Bandung, Bandung
13. M. Yaphary (2007) Laporan Tugas Akhir: Autofluorescence Angiography Sebagai Sistem Bantu Diagnosis Kebocoran Pembuluh Darah Tahap Awal pada Citra Retina Menggunakan Algoritma Matched Filter dan Jaringan Saraf Tiruan. Institut Teknologi Bandung, Bandung
14. Jo˜ao V. B. Soares, Jorge J. G. Leandro, Roberto M. Cesar-Jr. (2006) Retinal Vessel Segmentation Using the 2-D Gabor Wavelet and Supervised Classification. IEEE Transaction on Medical Imaging, September vol. 25
15. Qin Li, Jane You, Lei Zhang, and David Zhang (2006) A New Approach to Automated Retinal Vessel Segmentation Using Multiscale Analysis, The 18th International Conference on Pattern Recognition (ICPR'06)
16. R.M Rangayyan, F. Olomi, dan F.J. Ayres (2007) Detection of Blood Vessels in the Retina Using Gabor, CCECE vol.22, Canadian Conference on Electrical and Computer Engineering, Canada, 2007, pp.717 – 720
17. P. Bhattacharya, Qin Li dan Lei Zhang (2006) Automated Retinal vessel Segmentation Using Multiscale Analysis and Adaptive Thresholding**,** IEEE Southwest Symposium on Image Analysis and Interpretation, pp.139 – 143
18. Osareh (2004) Automated Identification of Diabetic Retinal Exudates and the Optic Disc. University of Bristol, England.

Author: Vanya Vabrina Valindria
Institute: Institut Teknologi Bandung
Street: JL. Tebet Timur 3A / 6
City: Jakarta
Country: Indonesia
Email: vanya2v@gmail.com

A New Method of Extraction of FECG from Abdominal Signal

D.V. Prasad[1], R. Swarnalatha[2]

[1]Department of Electronics & Instrumentation Engineering, BITS, PILANI, Dubai
[2]Department of Electronics & Instrumentation Engineering, BITS, PILANI, Dubai

Abstract — **This paper presents a method for extracting fetal ECG (FECG) from composite abdominal signal Adaptive filtering techniques along with denoising techniques were used to extract fECG. The results were validated using real signals. The signals are recorded at the thoracic and abdominal areas of the mother. The thoracic signal is purely that of mother (mECG) while the abdominal signal contains both mothers and fetus ECG signals (mECG + fECG). The results clearly show the effectiveness of the method in extracting fECG from very low maternal to fetal signal noise ratio.**

Keywords — **fECG, mECG, TECG**

I. Introduction

The fetal electrocardiogram (FECG) is the electrical activity of the fetal heart. It contains information on the health status of the fetus and therefore, an early diagnosis of any cardiac defects before delivery [1]. Non invasive techniques of fetal monitoring are Doppler ultrasound, fetal electrocardiography and fetal magneto cardiography. Among these methods the most commonly used is Doppler ultrasound because it is simple to use and cheap. However this method produces an averaged heart rate and therefore cannot give beat to beat variability. Fetal electrocardiogram offers the advantage of monitoring beat to beat variability. The disadvantage of fetal electrocardiogram is its reliability [2]. There are many technical problems with non invasive extraction of fECG. The fECG signal is corrupted by different sources of interferences such as maternal EMG, 50 Hz power line interference and base line wander. The low amplitude of the signals, the different types of noise and overlapping frequencies of mother and fetal ECG make the extraction of fECG a difficult task [3].

The fetal heart rate variations during pregnancy and labour have been used as an indirect indicator of fetal distress. Observation over longer periods may yield more information about the status of the fetus. The detection of fetal QRS complex on surface records is very difficult task which is mainly due to overlapping of mothers ECG. The mECG and fECG are partly uncorrelated. Also the mECG signal is very much stronger than the fECG signal embedded in it.

The noise in which fECG is embedded is also stronger depending on the gestation age. In this paper an improved method of extracting the P QRS T waves of the fetal ECG from composite abdominal signal is proposed. The proposed method uses cancellation of mothers ECG and denoising methods to improve the extracted signal quality. Real abdominal signals were used to test the algorithm.

II. Method

The block diagram of the proposed algorithm is shown in Fig 1.

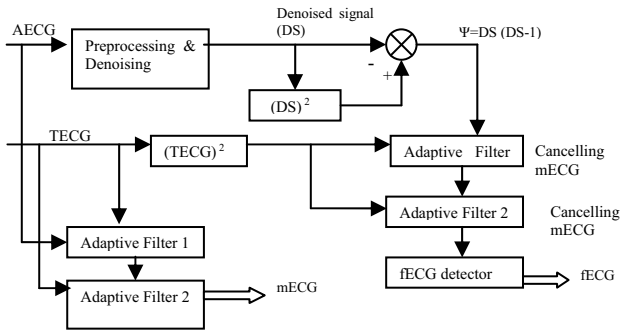


Fig 1 Block Diagram of the proposed algorithm

The proposed method detects fetal QRS wave from the preprocessing of abdominal ECG (AECG) and subsequent cancellation of maternal ECG in the abdominal ECG. The thoracic signal (TECG) which is mECG is used to cancel mECG and the fetal ECG detector extracts the fECG.

Preprocessing

The preprocessing consists of the following steps [4].(a) Read the abdominal ECG (b) Separate the high resolution components and low resolution components (c) Compensate for the phase (d) Derive the noise component (e) Separate the noise from the original signal (f) Reconstruct the signal back (g) Repeat the construction process iteratively.

Chwee Teck Lim, James C.H. Goh (Eds.): ICBME 2008, Proceedings 23, pp. 98–100, 2009
www.springerlink.com

Fetal QRS Detection

Fetal ECG detection was done by improving SNR of fetal QRS complex to the other components of the signal using a nonlinear operator. This reduces the maternal P and T waves. The operator is defined as follows.

$$\Psi = DS\ (DS\text{-}1)$$

where DS is the preprocessed and denoised signal obtained from the original abdominal ECG. Fig 2 (a) shows the abdominal signal to be analyzed and the maternal ECG recorded from thoracic region is shown in Fig 3(a). Fetal ECG can be extracted by direct application of BSS [5]. However such methods fail to give precise extraction. In order to reduce the mothers ECG effects on extraction, mECG was eliminated by using two stage adaptive filtering. The reference signal taken is shown in Fig 3(b) which is the squared signal of the thoracic signal corresponding to mECG Fig 3(a).The advantage of this method is that the reference signal need not closely mimic the signal to be cancelled. If such a reference signal could be generated, than this method can be applied where only the mothers ECG is available. The adaptive filter adopted behaves as an exponential averager, storing in the coefficients of the filter an averaged alias of the signal [6]. The output of the adaptive filter 1 is again adaptive filtered with $(TECG)^2$ to obtain the signal shown in Fig 3(d). The resultant signal depends on the value for the constant of adaptation. The output 3(d) is applied to fECG detector and extracted fECG and mECG are shown in Fig 4(b) and 4(c).

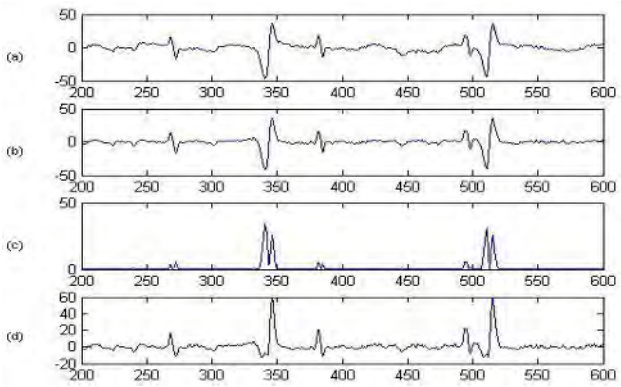


Fig 2. (a)Original abdominal ECG (b) Preprocessed signal (c) Square of preprocessed signal (d) Signal after adding b and c

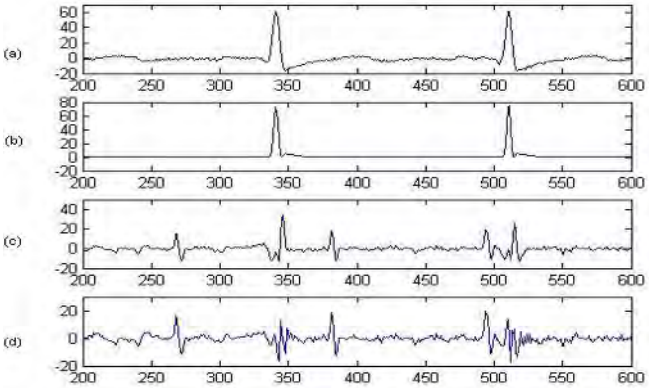


Fig 3. (a) Thoracic ECG (b) square of Thoracic ECG (c) Output of Adaptive filter 1 (d) Output of Adaptive filter 2

III. Results

The proposed algorithm was assessed by using real composite signal comprising of mECG and fECG. The noise is to due to mother's electromyogram activity. The performance of the method is seen from the extracted waveforms centering on R wave peak. The P and T waves can also be seen. Fig 4 gives the extracted fECG and mECG. Fig 5 shows the power spectrum of the original signal and the extracted fECG and mECG. The results show that the P, R and T waves are clearly visible in the extracted signals.

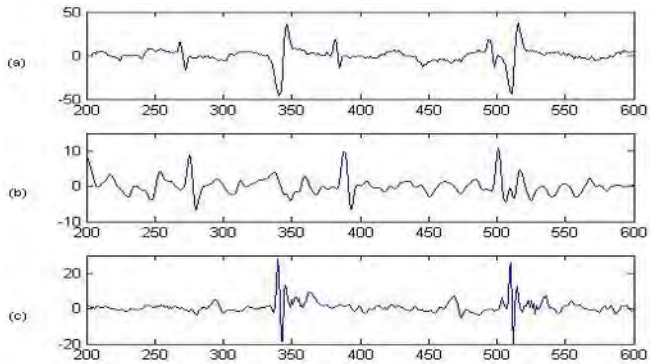


Fig 4. (a) Original abdominal ECG (b) Extracted fECG (c) Extracted mECG

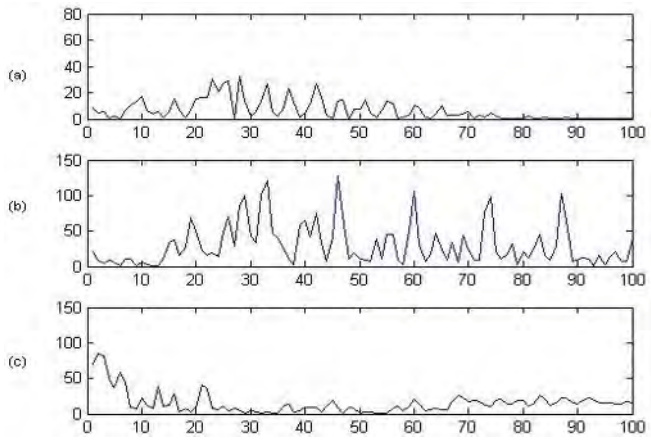


Fig 5. Power spectrum of (a) Original Abdominal ECG
(b) Extracted fECG (c) Extracted mECG

IV. Conclusions

The limitations of conventional methods led to the design of this extraction system which uses conventional system to improve the estimate the fetal ECG and maternal ECG. A two stage adaptive filter system is shown to retrieve fetal ECG from actual patients maternal ECG. It is not easy to see how well the fECG extraction is achieved by looking at a large number of samples. Thus a frame of 400 samples is taken to illustrate the effectiveness of the algorithm. In this frame there are both overlapping and non overlapping between maternal and the fetal components in the abdominal signal. This is a significant challenge to the extraction algorithm. The results show that the algorithm was able to successfully extract the fECG signal. It can be noted the visual quality of the extracted fECG is comparable to other methods. The advantage of this method is that the reference signal need not closely mimic the signal to be cancelled.

Acknowledgement

The authors would like to thank Prof. M. Ramachandran, Director, BITS, Pilani-Dubai for his constant encouragement and support.

References

1. J R Mazzeo, " Non Invasive fetal Electrocardiography", Med Prog technogy, 1994,20
2. Fukushima T, Flores CA, Hon EH, Davidson EC Jr, "Limitations of autocorrelation in fetal heart monitoring, Am J Obstet Gynecol,1985, 153(6),685-92
3. B A Goddard, " A Clinical fetal electrocardiograph", Med Biol Eng, vol 4 pp 159-167, Mar 1966
4. D V Prasad, R Swarnalatha, " A New Method to Detect Subtle Changes in ECG", WACBE World congress on Bioengineering, 2007, Bangkok, Thailand.
5. L De Lathauwer, B De Moor and J Vanderwalle, " Fetal Electrocardiogram extraction by blind source subspace separation, IEEE Trans Biomed Eng, vol 47, No 5 pp 567-572, May 2000
6. Laguna P, Jane R, Meste O et al, " Adaptive filter for event related bioelectric signals using an impulse correlated reference input: comparison with signal averaging techniques", IEEE Trans Biomed Eng, 92, 39(10):1032-44

The address of the corresponding author:

Author: Dr D V Prasad
Institute: BITS, Pilani-Dubai
Street: Dubai International Academic City
City: Dubai
Country: UAE
Email: prasad@bitsdubai.com

Analysis of EGG Signals for Digestive System Disorders Using Neural Networks

G. Gopu[1], Dr. R. Neelaveni[2] and Dr. K. Porkumaran[3]

[1] Research Scholar, Dept. of EEE. PSG College of Technology, Coimbatore- 04, India
[2] Assistant Professor, Dept. of EEE. PSG College of Technology, Coimbatore- 04, India
[3] Professor & Head, Dept. of BME, Sri Ramakrishna Engineering College, Coimbatore-22,India

Abstract — **A novel approach is proposed to analyze the digestive system disorders using the developed Electrogastrogram [EGG] setup. Current days the role of Endoscopy is more for the investigation of digestive system disorders, which is very tedious, expensive and invasive. EGG is a non-invasive, cheap and painless study. EGG is considered as a preliminary investigation before the Endoscopy procedure. Based on the finding from the EGG, if it is uncomplicated Gastric diseases, Benign (non cancer) we can start the treatment solely on EGG report alone. Only in case of suspected Malignancy (cancer) and complicated benign disorders we can go for Endoscopy procedure. The biosignal are recorded from the patients and normal individual cutaneously from the stomach includes the various stages such as amplification, filtering, pulse width modulation and demodulation. The EGG data are acquired using DSO or Data scope software and the same is analyzed using Matlab's neural network toolbox. The Adaptive Resonance Theory (ART1) and Learning vector Quantization (LVQ) networks are used as a Neural Network classifiers to classify the digestive system disorders. The proposed method is used to investigate the digestive system disorders such us ulcer, dyspepsia, etc.The investigation is carried out with 180 human being includes inpatient, outpatient of gastroenterology department and normal individual and normal individual. As a result of this investigation the EGG values for ulcer patient is between 4-4.5 cpm (cycle per minute), dyspepsia patient is between 1-2.5 cpm and for normal individual is between 3-3.5 cpm.The proposed new method results in greater accuracy comparable with other conventional methods to provide fair amount of accuracy.**

Keywords — **Electrogastrogram, Adaptive Resonance Theory, Learning vector Quantization, ulcer, dyspepsia.**

I. Introduction

A non-invasive, painless study is used to measure the gastric electrical activity of a stomach [1, 2] cutaneously is called Electrogastrogram [EGG]. EGG includes two components such as spikes and slow waves in the gastric myoelectrical activity of the stomach. The contraction of a stomach muscle produces a spike, where as slow wave activity controls the propagation and maximum frequency of the gastric electrical activity. In human 3 cycles per minute (cpm) is a normal frequency of the gastric slow wave.

The abnormality in the gastric slow wave frequency is known as gastric dysrhythmia which includes bradygastria (the frequency of the slow wave less than 2 cpm), tachygastria (the frequency of the slow wave greater than 4 cpm) and arrhythmia (no specific cyclic rhythm). Gastric dysrhythmia observed with the patients having gastric motility disorders and gastrointestinal symptoms namely nausea, dyspepsia, vomiting, abdominal pain, stomach ulcer, etc,[9].

EGG recorded in the patient with two conditions namely preprandial conditions (before food) and postprandial condition (after food) [13, 14]. The abnormality is found from the no raise in power and change in the frequency of the EGG signal obtained from the postprandial condition.

This paper deals with the classification of the EGG signals of the patients with the normal individual using the neural approach with a ART1 and LVQ networks. The EGG can be considered as an experimental procedure since its exact role in the diagnosis of digestive disorders of the stomach has not been defined yet.

II. Electrogastrogram

An EGG is similar to an electrocardiogram of the heart. It is a recording of the electrical signals that travel through the muscles of the stomach and control the muscle's contraction. EGG used when there is a suspicion that the muscles of the stomach or the nerves controlling the muscles are not working normally.

EGG done by placing the electrode cutaneously over the stomach and the electrical signals coming from the stomach's muscles are sensed by the electrode and recorded on a computer for analysis by lying patient quietly.

In normal individuals the EGG is a regular electrical rhythm generated by the muscles of the stomach and the power (voltage) of the electrical current increases after the meal. In patients with abnormalities of the muscles or nerves of the stomach, the rhythm often is irregular or there is no post-meal increase in electric power. EGG will not have any side effects and it is painless study.

Chwee Teck Lim, James C.H. Goh (Eds.): ICBME 2008, Proceedings 23, pp. 101–104, 2009
www.springerlink.com

III. EGG RECORDING SETUP

The Ag/Agcl electrodes are used as a sensor for recording EGG [4, 3, 5]. The electrodes are used to tap the electrical signals directly surface of the stomach. The electrical signals generated are usually of very low amplitude ranging from 0.01 to 0.5 mV.This is given as an input to an instrumentation amplifier which has a variable gain of 1000 to 10,000. The amplified signals under goes filtering section which includes high pass filter, low pass filter and notch filter to obtain the frequency response from 0.015 Hz to 0.5 Hz for Lower Cutoff frequency and 0.1 Hz to 2 Hz for upper cutoff frequency. The Mode Switch is used for selecting a calibration Mode and EGG measuring Mode. If the calibration mode is selected the clock pulse generated from square wave oscillator is obtained to confirm that the setup is in good condition for recording EGG. Now EGG Mode is selected for recording with in the frequency response range from 0.5 Hz to 0.1 Hz. The required amplified EGG signal is viewed via Digital Storage Oscilloscope or data scope for analysis purposes as shown in Figure 1 below.

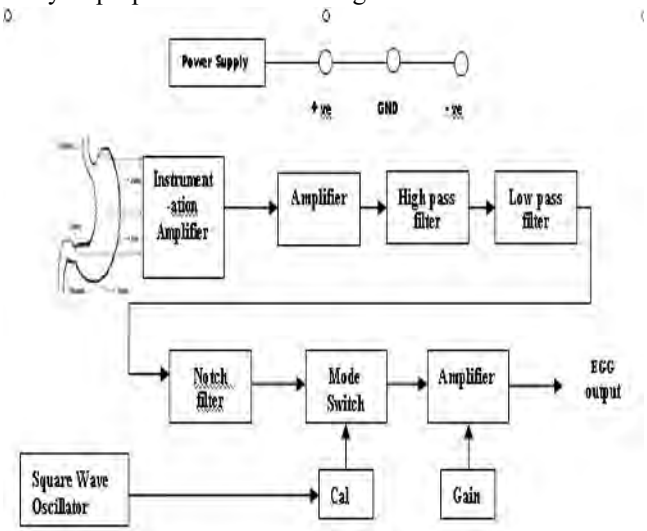


Fig. 1 General block diagram for recording EGG

IV. EGG ELECTRODES POSITIONING

The electrical signals are generally produced in the mid-corpus of the stomach where the electrical activity takes place. The positioning of the Ag/ Agcl electrodes for tapping of these signals is as shown Figure 2. Two electrodes A and B are placed in the fundus and the mid corpus of the stomach. The third electrode C is placed as ground at the end of the stomach region for patient safety [4].

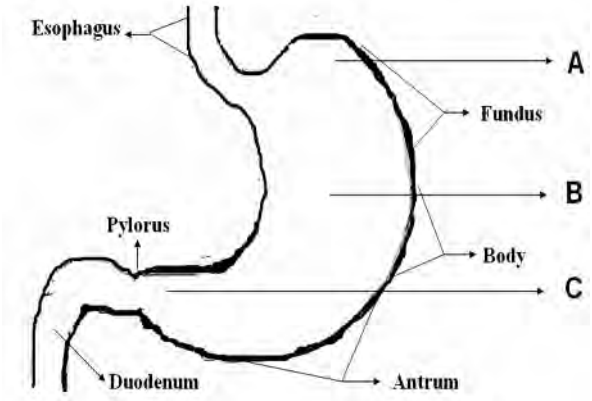


Fig. 2 Electrode Positioning for Recording EGG

V. MATERIALS AND METHODS

The patients who are consecutively attending a hospital outpatient's gastroenterology clinic for digestive system disorder were studied. The patients included 80 with Dyspepsia, 45 with Nausea, and 55 with Stomach ulcer. A gastrointestinal symptom profile was recorded on all patients immediately before the EGG [10, 12]. This profile detailed the presence or absence of the following dyspeptic symptoms in their previous history: Dyspepsia, Stomach ulcer, Nausea, vomiting and abdominal pain. The EGG was performed on the patient both preprandial condition and postprandial condition. All medication with the potential affect to gastric function was discontinued for more than 48 hours before the recording. Patients were studied in a semi recline position and requested to avoid any major movements. The skin was lightly abraded with gauze before placement of adhesive gel EGG electrodes. Two bipolar skin electrodes were placed on the abdomen, one on the fundus and the other on the mid-corpus. A reference electrode was placed on the right side of the abdomen. Visual inspection of the waveform detected any obvious major movement artifacts. These were defined as abnormally large positive or negative peaks in the tracing and were detected from the analysis. The EGG data was observed by the DSO or the Data Scope set up running on a personal computer. The EGG frequency, amplitude are recorded and its respective values are stored for further analysis of the same to investigate the digestive system disorders as shown in Figure 3

The EGG analysis is based on the frequency and amplitude of the signals. For the periods before and after the test meal, the frequency and amplitude values are observed. Normal electrical activity was defined as a frequency between 2-4 cycles per minute [6, 7]. Activity of 0-2 cycles per minute was termed bradygastria, and 4-9 cycles per minute as tachygastria. The percentage of normal electrical

activity, bradygastria, and tachygastria were calculated both before and after the test meal. The amplitude of the dominant frequency was measured both before and after the test meal. The electrical frequency is stable and does not change significantly after a standard test meal.

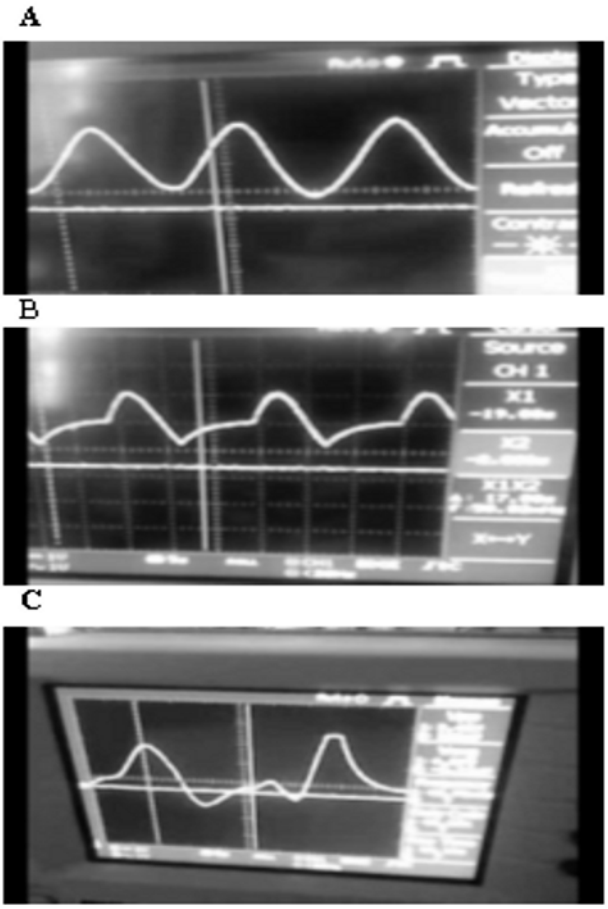


Fig. 3 EGG Signals recorded with DSO: A- for Normal Individuals, B-for Dyspepsia Patient and C- for Ulcer patient

VI. Algorithm

1. Lightly abrade the skin with abrasive pads, and put a spot of gel on the electrode contact area.
2. Two electrodes are placed on the Fundus and the mid-corpus and a reference electrode is placed on the right side of the abdomen.
3. The output of the electrodes is given to the Instrumentation amplifier.
4. The amplified output signal is filtered using high pass filter, low pass filter and notch filter.
5. The setup is calibrated with a clock pulse from square wave generator then it is changed to EGG measuring mode.
6. The EGG signal is obtained for a minute from DSO and its corresponding data are stored for analysis by neural network tool.
7. This data is displayed on the DSO or PC using data scope software and the data's are recorded for preprandial and postprandial conditions.
8. The recorded data are classified with two types Neural Network classifiers namely ART1 and LVQ Neural Network Classifiers.
9. As a result of classification the LVQ Classification rate is more than the ART1
10. The threshold for Classification of various disorders was fixed based on the observations and in consultation with the physician and the same was trained with Neural Networks tools.

VII. Neural networks classifier

The recognizer recognizes only whether the signal is known or unknown i.e., whether it is already in database or not. The purpose of using classifiers [11] is to find the actual identity of the digestive system disorders such us dyspepsia and ulcer. In this paper, Adaptive Resonance Theory (ART1) Network and Learning Vector Quantization (LVQ) Network are used as classifiers.

ART1 is designed for clustering binary vectors using unsupervised learning. This network is designed to control the degree of similarity of patterns placed on the same cluster. The network produces the clusters by itself if such clusters are identified in the input data, and stores the clustering information about patterns or features without prior information about the possible number and type of clusters.

LVQ is defined for adaptive pattern classification. The class information is used to fine-tune the code vector so as to improve the quality of the classifier decision regions. It is assumed that a set of training pattern with known classifications is provided along with an initial distribution of reference vectors. Learning vector Quantization (LVQ) [8] is a method for training competitive layers in a supervised manner. A competitive layer automatically learns to classify input vectors. If two input vectors are very similar, the competitive layer probably will put them in the same class. There is no mechanism in a strictly competitive layer design to say whether or not any two input vectors are in the same class or different classes.

VIII. Results and discussion

The effectiveness of the proposed methodology is illustrated in the Table. 1. From the table the classification rate of digestive system disorders with LVQ Neural Network classifier is more precise than ART1 Neural Networks Classifier. This result is obtained with 180 human beings data.

Digestive System Disorder's EGG with its frequency	Neural Network Classifier				Classification Rate in %	
	ART1(Adaptive Resonance Theory)		LVQ (Learning Vector Quantization)		ART1	LVQ
	Total Samples	Correctly Classified	Total Samples	Correctly Classified		
Normal Individual (3-3.5) cpm	30	25	30	29	83.33	96.66
Dyspepsia (1-2.5) cpm	70	60	70	69	85.71	98.57
Ulcer (4-4.5) cpm	80	67	80	78	83.75	97.50

Table 1 Comparison of LVQ and ART1 Classification

IX. Conclusions

In this paper a simplified novel approach is proposed for the recording of gastro electrical activity of the stomach. The EGG setup is used to record the activity of patients suffering from digestive disorders like Dyspepsia, Stomach ulcer , Nausea and Cyclic vomiting syndrome. About more than 180 patients were tested using this setup and the results are classified with Neural Network classifier namely ART1 and LVQ. The classification rate is found to be high in LVQ when compare to ART1 for the disorders Dyspepsia and ulcer. In future, the data can be analyzed with wavelet tool to perform further analysis which may improve the accuracy of diagnosis and also increase the scope.

Acknowledgment

The authors acknowledge their indebtedness to the following medical experts Dr L Venkatakrishnan, M.D., D.M., D.N.B., Head of Gastroenterology Dept., Dr.J. Krishnaveni, M.D., D.N.B., Gastroenterologist from PSG Hospitals, Coimbatore and Dr M G Shekar, M.S., D.N.B., M.R.C.S., Laparoscopic surgeon Stanley Medical College and Hospital, Chennai for their support and for permitting us to use the facilities at the hospitals for live testing of the recording setup and sharing valuable patient database with us.

References

1. W.C.Alvarez. (1922) The Electrogastrogram and what it shows. *JAMA* 1922, vol 78, pp.1116–1118.
2. A.J.P.M. Smout, E.J. Van Der Schee, J.L.Grashuis, (1980) What is measured in electrogastrography?. *Digestive Diseases and Sciences* 1980, pp.253.
3. T.L.Abell, J.R.Malagelada (1988) Electrogastrography: Current assessment and future perspectives. *Digestive Diseases and Sciences* 1988, vol 33, pp.982–992.
4. J. Chen, R.W. McCallum (1991) Electrogastrography: measurement, analysis and prospective applications. *Medical &Biological Engineering & Computing* 1991, vol 29, pp.339–350.
5. G.Riezzo, F.Pezzolla,J. Thouvenot , et al (1992) Reproducibility of cutaneous recordings of electrogasography in the fasting state in man. *Pathology Biology 1992*, vol 40, pp.889–894.
6. J. Chen, R.W. McCallum (1992) Gastric slow wave abnormalities in patients with gastroparesis. *Am J Gastroenterology* 1992, vol 87, pp.477-482.
7. M.P. Mintchev, Y.J. Kingma, K.L. Bowes (1993) Accuracy of coutaneous recordings of gastric electrical activity. *Gastroenterology* 1993, vol 104, pp.1273–1280.
8. Li Min Fu (1994) Neural Networks in Computer Intelligence, McGraw-Hill Inc., Singapore, 1994
9. Zhishun Wang, Zhenya He, J.D.Z.Chen. (1999) Filters Banks and Neural Network based Feature Extraction and Automatic Classification of Electrogastrogram. Annals of Biomedical Engineering 1999,vol. 27, pp 88-95.
10. A.Leahy, K.Besherdas, C.Clayman, I.Mason, O.Epstein. (1999) Abnormalities of the electrogastrogram in functional dyspepsia". *American Journal of Gastroenterology* 1999, vol 94(4), pp.1023–1028.
11. Xiao-Hua Liu, Zhe-zho yu, et.al (2003) Face Recognition Using Adaptive Resonance Theory, Proc. Of the Second International Conference on Machine Learning and Cybernetics, Xi-an, pp. 3 167-3171, 2-5 November 2003
12. DZ Chen, Zhiyue Lin. (2006) Electrogastrogram-Encyclopedia of Medical Devices and Instrumentation. Second Edition, edited by John G. Webster, *John Wiley & Sons*, Inc.2006.
13. G.Gopu, R.Neelaveni, K.Porkumaran. (2008) Investigation of Digestive System Disorders using Electrogastrogram. Proceeding International conference on Computer and Communication Engineering (ICCCE '08), Vol.2, pp.201-205, 13-15 May 2008, Kuala Lumpur, MALAYSIA.
14. G.Gopu, R.Neelaveni, K.Porkumaran. (2008) Acquisition and Analysis of Electrogastrogram for Human Stomach Disorders. Proceeding International conference on Recent Trends in Computational Science (ICRTCS'08), Vol.1,pp.162-169, 11-13 June 2008, Ernakulam, Kerala, INDIA

Author: G Gopu
Institute: Sri Ramakrishna Engineering College
Street: NGGO colony Post, Vattamalaipalayam
City: Coimbatore
Country: INDIA
Email: gopugovindasamy@gmail.com

A Reliable Measurement to Assess Atherosclerosis of Differential Arterial Systems

Hsien-Tsai Wu[1], Cyuan-Cin Liu[2], Po-Chun Hsu[2], Huo-Ying Chang[1] and An-Bang Liu[1,3]

[1] Dept. of Electrical Engineering, National Dong Hwa University
No. 1, Sec. 2, Da Hsueh Rd., Shou-Feng, Hualien, Taiwan 974
[2] The Institute of Electronics Engineering, National Dong Hwa University
No. 1, Sec. 2, Da Hsueh Rd., Shou-Feng, Hualien, Taiwan 974
[3] Department of Neurology, Tzu-Chi General Hospital
707, Sec. 3, Chung-Yang Rd.,Hualien, Taiwan 970

Abstract — **There are several assessments used to measure pulse wave velocity. We have ever designed an instrument to measure brachial-femoral pulse wave velocity by photoplethysmograpy with infrared sensors. This method is reliable and correlate with another instrument recorded with tonometry. Our method demonstrates the difference of velocity between brachial and femoral arteries. On some occasions, the measurement gets a false-negative result when the examinee has similar atherosclerotic changes of both brachial and femoral arteries. Therefore, we design a measurement to assess pulse wave velocities by the time difference between R wave of ECG and initiation point of the pulse wave. The infra-red sensors can be placed on the eardrops, fingertips or toes then measure pulse wave velocities in different arterial systems including carotid artery, brachial artery and femoral artery directly. These measurements also reflect atherosclerotic changes of aortic arch and descending aorta respectively. Although atherosclerosis is a systemic disorder, patients sometimes get various involvements in different regions of the arterial tree. In this study, 33 healthy adults (25 males and 8 females) are enrolled. They received measurement of pulse wave velocity by our new method and brachial-femoral pulse wave velocity. There is the statistically significant correlation between this new method and brachial-femoral pulse wave velocity ($r=0.453$, $p<0.01$). In the mean time, the new assessment shows the pulse wave velocities are different in carotid, brachial and femoral arterial system. The ratio of the speeds is 1:2:3, which relates to diameters of these vessels inversely. This finding is fit the continuity equation, Q=AV, in hydraulics.**

Herein, we demonstrate a new method, which can be used to measure pulse wave velocity in different arterial systems. This method is reliable and reproducible. In addition to be applied in assessment of aortic stiffness, it can also be used to evaluate atherosclerosis of different arterial systems.

Keywords — **PWV, ECG, cardiovascular diseases**

I. Introduction

Myocardial infarction, stroke, hypertension, etc. are common modern diseases that are related to arterial stiffness, and there is no apparent symptom in the early stage of formation of arterial stiffness. Therefore, to develop a proper and validate method for assessing the stiffness of arteries can reduce prevent further damage to personal heath or eventually lead to cardiovascular diseases [1].

There are two categories for assessing arterial stiffness: invasive [2] and non-invasive [1][3]. Invasive method has the advantage of directly observe or contact with the blood vessels which brings high accuracy of evaluating the health of arteries, but this is also its weakness since it needs to inject medicine into the blood vessels or even operation needed, which may cause unknown risks to the testing subjects, and these inconveniences make invasive technique not suitable for daily homecare environment. Hospitals are now leant toward non-invasive method of arterial stiffness assessment, and one of most commonly used instrument is Pulse Wave Velocity by Applanation Tonometry (PWV-AT) [1]. PWV-AT utilizes pressure sensor to extract the pulse waveforms from carotid and femoral arteries, it combines electrocardiogram (ECG) for reference point, the time difference among the reference point, femoral and carotid arteries is used for calculating pulse wave velocity (PWV) [4]-[6]. PWV is considered to be the golden standard for evaluating the stiffness of arteries, but using PWV-AT is very time consuming (more than 1 hrs) and specially trained operators are needed for the assessment.

To make non-invasive arterial stiffness assessment more suitable and convenience for homecare, a hand-foot PWV instrument (PWV-DVP) [3]was introduced in previous study, and its correlation with traditional PWV-AT is high ($r=0.678$) [3]. However, in hand-foot PWV system testing subject still needs to be in supine position and take off his or her shoes off, we had modified out instrument further to bring greater ease for user, the hand-ear PWV instrument (PWV-DVPE) [7] was developed, it gathers pulse waveforms from hand and ear in sitting position and it is accurate as former systems ($r=0.702$) [7].

Although both PWV-DVP and PWV-DVPE were proven to have the capability to assess the stiffness of arteries, as PWV-AT, both utilize two pulse waveforms from two different sites of body for PWV calculation, this may cause difficulty to differentiate which site is stiff, and some stud-

Chwee Teck Lim, James C.H. Goh (Eds.): ICBME 2008, Proceedings 23, pp. 105–108, 2009
www.springerlink.com

ies [8] had indicated that if both sites are affected by arterial stiffness then the PWV value measured would be close to healthy blood vessel's PWV value. This study proposes a new method which utilizes ECG combined with hand, foot and ear pulse waveforms (ECG_H-PWV, ECG_F-PWV and ECG_E-PWV). Again, to be more suitable for homecare, we use Lead-II ECG to make it more convenient for users, make them easier to monitor their personal health. 33 health subjects were tested in this study, they had received tests of 3 different pulse waveforms combined with ECG and were able to show statistical significance and responded well to risk factor- age.

II. PWV-DVP & PWV-DVPE

Previously, PWV-DVP [3] places the sensor on the subject's finger and toe for measuring, therefore the subject needs to take off the socks and rests in supine position; PWV-DVPE [7] showed that it can improve the disadvantage of PWV-DVP which requires taking off socks and resting in supine position by measuring subject's pulse waveforms of ear and finger with sitting position. Before measuring with PWV-DVP and PWV-DVPE, measuring tape is used to measure the subject's length, which are the distance from the sternal notch to the left index finger (l_1), the distance from the sternal notch to the left second toe (l_2) and the distance from the sternal notch to the left ear lobe (l_3) (Fig. 1), then calculate $\Delta l_1=l_2-l_1$, $\Delta l_2=l_1-l_3$ and use following PWV formula:

$$PWV = \Delta l_i / \Delta t_i \ , i = 1,2 \qquad (1)$$

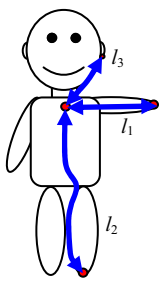


Fig. 1 Measured Distance

In PWV-DVP and PWV-DVPE calculation, the Δl_i is the difference of the distance among the measuring places, it may cause a problem where the error of the measurement occurs. For example, PWV-DVP requires to measure difference of the distance of the sternal notch to the finger and the toe before measuring hand-foot PWV. If both subject's vessel of the hand and foot become stiff, then difference of the transmitting time of the two pulse waves is Δt, and PWV-DVP=$\Delta l_1/\Delta t$. If only subject's vessel of the hand had become stiff, then the pulse wave velocity of the finger become fast, but if the vessel of the foot didn't become stiff, then the pulse wave velocity of the toe would not be fast, so it makes the difference of the transmitting time of two pulse wave (Δt') becomes bigger, shown in the Fig. 2. Because Δt' >Δt, PWV-DVP' is smaller than PWV-DVP, this would lead the subject to misunderstand this PWV value is an indication of healthy arteries. In similar, if the subject's vessels of the hand and foot both become stiff, then the pulse waves of the finger and toe become fast, and the difference of the transmitting time of two pulse waves does not become smaller, it may also cause the PWV-DVP value to be normal and the subject dose not assess the level of arterial stiffness accurately.

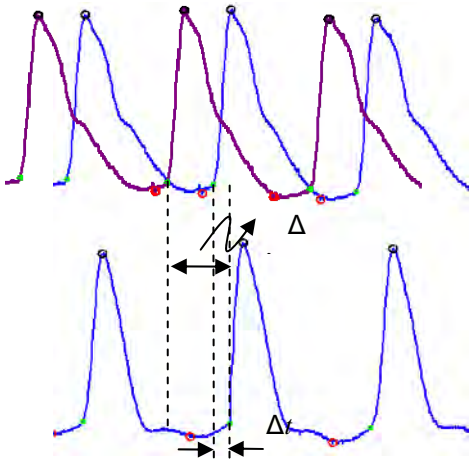


Fig. 2 The part vessel of the hand become stiffness, the difference of the transmitting time increase result from the pulse wave of inside vessel become fast (Δt'>Δt)

III. METHOD

In this experiment, we did not eliminate any subject. The study group comprised 33 healthy subjects (25 male/ 8 female), the mean age of these subjects was 25 (aged 19 to 47), none of the subjects had any cardiovascular diseases history. Table 1 described the characteristics of the study population.

Blood pressure was measured with the subjects in sitting position after 5 minutes, in a quiet, temperature-controlled environment set at 24°C. Then we measure subject's distance from the sternal notch to the left index finger (l_1), left second toe (l_2), and left ear lobe (l_3); moreover, we placed the ECG (Lead-II) sensors on the subject's right wrist (negative), left ankle (positive), and right ankle (ground). Before

Table 1 The characteristics of the study population

	Male (n=25)	Female (n=8)
Age, yr	26.2±5.8	22.1±2.2
Body Height, cm	171.8±4.6	158.1±6
Body Weight, kg	68.16±10.8	52±10.8
Body Mass Index (BMI), kg/m^2	23.1±3.5	20.7±3.5
Heart Rate, bpm	79.4±11.7	92.2±12.3
Systolic Blood Pressure (SBP), mmHg	115±11	115.9±15.5
Diastolic Blood Pressure (DBP), mmHg	69.9±7.9	72.9±9

measuring PWV, let the subject rest in the supine position (4 min), then obtained and stored the ECG-Finger pulse wave, ECG-Toe pulse wave, and ECG-Ear pulse wave at the same time. Afterward system could automatically calculate ECG_H-PWV, ECG_F-PWV, and ECG_E-PWV. Overall we recorded 20 times data and average as one time result. The ECG_H-PWV, ECG_F-PWV, and ECG_E-PWV formulas are as following:

$$ECG_H-PWV = l_1 / \Delta t_3 \quad (2)$$

$$ECG_F-PWV = l_2 / \Delta t_4 \quad (3)$$

$$ECG_E-PWV = l_3 / \Delta t_5 \quad (4)$$

In the formulas, Δt_3, Δt_4, and Δt_5 are the R wave of ECG to pacemaker of the finger, the toe, and the ear pulse wave, respectively. Fig. 3 shown the difference time of the R wave of ECG to the finger's pacemaker, Δt_4 and Δt_5 are similar.

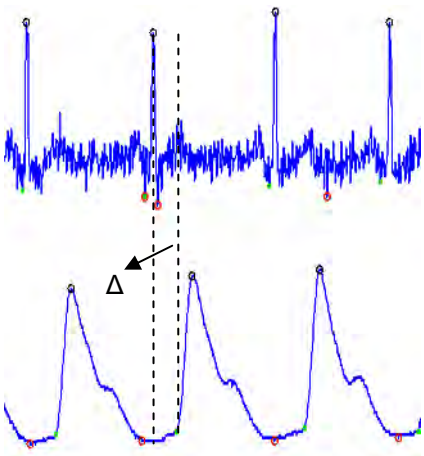


Fig. 3 The difference time of ECG R wave to finger's pacemaker

IV. Results

As Table 2 shown, this study measured five types of PWV for 33 healthy subjects, and ECG matched the value which the finger, the toe and the ear pulse wave could observe the minimum value that happened to ECG_E-PWV and could not over 2 m/s, and the maximum value was ECG_F-PWV. As Table 3 shown, these three methods were relative to each other in statistical significance. As Fig. 4 shown, ECG_F-PWV and PWV-DVP had statistical significance, but PWV-DVP and PWV-DVPE did not (r=-0.41, p=0.819)

Table 2 The characteristics of the study population

	Male	Female	All Subjects
ECG_H-PWV, m/s	4.6±0.5	4.3±0.4	4.5±0.5
ECG_F-PWV, m/s	6.1±0.5	5.5±0.6	6±0.6
ECG_E-PWV, m/s	1.4±0.1	1.3±0.1	1.4±0.1

Table 3 Statistical analysis of the ECG_H-PWV, ECG_F-PWV and ECG_E-PWV

	ECG_H-PWV	ECG_F-PWV	ECG_E-PWV
ECG_H-PWV		r=0.698, p<0.01	r=0.470, p<0.01
ECG_F-PWV	r=0.698, p<0.01		r=0.443, p<0.01
ECG_E-PWV	r=0.470, p<0.01	r=0.443, p<0.01	

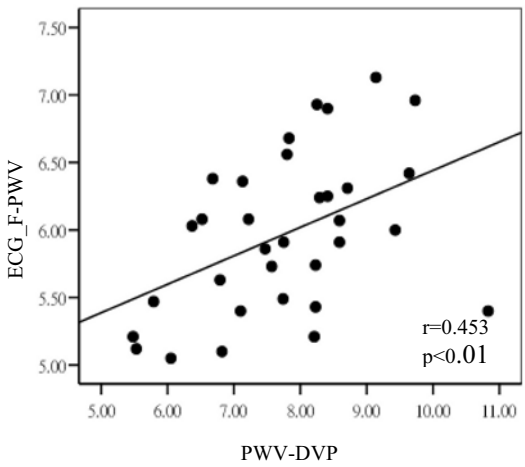


Fig. 4 The linear regression analysis of ECG_F-PWV and PWV-DVP

As Table 4 shown, age was risk factor of cardiovascular diseases for ECG_H-PWV, ECG_F-PWV and ECG_E-PWV(r=0.386, p<0.05, r=0.362, p<0.05 and r=0.457, p<0.01), and SBP only had statistical significance with

ECG_E-PWV(r=0.467, p<0.01), but height and weight had statistical significance with ECG_F-PWV(r=0.491, p<0.01, r=0.429, p<0.05).

Table 4 Relations of ECG_H-PWV, ECG_F-PWV and ECG_E-PWV with risk factor

	ECG_H-PWV	ECG_F-PWV	ECG_E-PWV
Age	r=0.386(p<0.05)	r=0.362(p<0.05)	r=0.457(p<0.01)
Height	r=0.217(p=0.225)	r=0.491(p<0.01)	r=0.307(p=0.083)
Weight	r=0.118(p=0.514)	r=0.429(p<0.05)	r=0.290(p=0.102)
SBP	r=0.236(p=0.186)	r=0.305(p=0.084)	r=0.467(p<0.01)

V. Discussion

This study mainly goal is to measure PWV by Lead-II ECG to collocate each part pulse wave, to decrease the error caused by difference of the distance of varied sites in previously measured PWV-DVP and PWV-DVPE. The proposed system can assess the level of the arterial stiffness accurately.

In this experiment, 33 subjects are measured ECG_ H-PWV, ECG_F-PWV, and ECG_E-PWV, all the ECG_F-PWV value have the highest PWV and the ECG_E-PWV value are the lowest. Because the blood circulation system is a closed system, the blood flow volume in each minute is constant; therefore, the blood flow velocity is related to vessel cross-sectional area. The blood flow velocity is inversely proportional with vessel cross-sectional area. Therefore if the blood vessel cross-sectional area is smaller, the blood flow velocity becomes faster. Because the aorta cross-sectional area is bigger than arteriole, and the ECG_F-PWV value is the highest and the ECG_E-PWV value is the lower. Therefore the experimental result conforms to the blood hydromechanics principle.

The measurement of pulse wave velocity has been proven to be a reliable and noninvasive method to evaluate the progression of atherosclerosis. We design a novel multichannel instrument to measure pulse wave velocities in different arterial systems. The method can measure pulse wave velocity directly by using time difference between R wave of ECG and initiation point of pulse wave recorded in eardrops, fingertips and toes. The first one assesses atherosclerotic changes in ascending aorta, common carotid and external carotid artery. The second one evaluates stiffness in the aortic arch and brachial artery. The last one represents atherosclerotic changes in the aortic arch, descending aorta, femoral and tibial arteries. The instrument with easy performance can be applied in patients with atherosclerosis involving different arterial systems.

Acknowledgment

This study was supported by Grant NSC 96-2221-E-259-006 from the National Science Council.

References

1. Wei-Chuan Tsai, Ju-Yi Chen, Ming-Chen Wang, Hsien-Tsai Wu, Chih-Kai Chi, Yung-Kung Chen, Jyh-Hong Chen, and Li-Jen Lin, “Association of Risk Factors With Increased Pulse Wave Velocity Detected by a Novel Method Using Dual-Channel Photoplethys- mography”, AJH, 8, pp.1118-1122, 2005.
2. PATRICK J. SCANLON, MD, FACC, Co-Chair and DAVID P. FAXON, MD, FACC, Co-Chair, “ACC/AHA Guidelines for Coronary Angiography”, Journal of American College of Cardio- logy, 33, pp.1756-1824, 1999.
3. Yung-Kang Chen, Hsien-Tsai Wu, Chih-Kai Chi,Wei-Chuan Tsai, Ju-Yi Chen, and Ming-ChunWang, ”A New Dual Channel Pulse Wave-Velocity Measurement System”, Fourth IEEESymposium on Bio-Informatics and Bio-Engineering, Taichung, Taiwan, pp.17-21, 2004.
4. Hallock P., “Arterial elasticity in man in relation to age as evaluated by the pulse wave velocity method”, Arch Inter Med, 54, pp.770-798, 1934.
5. Haynes F., Ellis L.B., and Weiss S., “Pulse wave velocity and arterial elasticity in arterial hypertension, Arteriosclerosis and related conditions”, Am Heart J, 11, pp.385-401, 1936.
6. Pierre Boutouyrie, Anne Isabelle Tropeano, Roland Asmer, Isabelle Gautier, Athanase Benetos, Patrick Lacolley, “Stephane laurent aortic stiffness is an independent predictor of primary coronary events in hypertensive patients”, A Longitudinal Study Hypertension, 39, pp.10-15, 2002.
7. Hsien-Tsai Wu, Cheng-Tso Yao, Tsang-Chin Wu and An-Bang Liu, “Development of Easy Operating Arterial Stiffness Assessment Instrument for Homecare”, Proceedings of the 29th Annual International Conference of the IEEE Engineering in Medicine and Biology Society, Lyon, France, pp5868-5871, August 23-26, 2007.
8. Tomoyuki Yambe, Makoto Yoshizawa, Yoshifumi Saijo, Tasuku Yamaguchi, Muneichi Shibata, Satoshi Konno, Shinichi Nitta, Tashashi Kuwayama, “Brachio-ankle pulse wave velocity and cardio-ankle vascular index (CAVI)”, Biomedicine & Pharmacotherapy, 58, pp.S95-S98, 2004.

An Automated Segmentation Algorithm for Medical Images

C.S. Leo[1], C.C. Tchoyoson Lim[2], V. Suneetha[1]

[1] School of Engineering, Nanyang Polytechnic, Singapore
[2] Department of Neuro-radiology, National Neuroscience Institute, Singapore

Abstract — **The goal of image segmentation is to identify and differentiate one object or region from another. The problems associated with image segmentation or groupings have always been a challenge to the image processing community especially in the case of medical imaging where segmentation can play a key role to 3D model re-construction for medical diagnosis and planning. Though it can be said that there is no 'one-size-fits-all' algorithm available and that manual segmentation remains the best available technique, current on-going works have focused on hastening the computational intensive process and to achieve a high level of accuracy with as little human intervention as possible. This is especially true when fast segmentation is required for tomography images such as MRI or CT images.**

In this paper, we present an automated segmentation algorithm that utilizes an integrated hybrid method based on intensity, region growing and edge related techniques. The algorithm checks for connectivity and continuity to ensure that the segmented region is of one enclosed entity. Results have shown the algorithm to be fairly accurate and it is able to detect irregular shapes. The algorithm is also implementable on a Single Instruction Multiple Data (SIMD) or on multiple SIMD cards. The automated hybrid segmentation method can be robust, fairly accurate and simple to implement.

Keywords — **Segmentation, Intensity, Pixels, Image-Processing, MRI**

I. Introduction

Segmentation has always remained as an important and challenging part of image processing as wide-ranging practical medical applications can often be derived from it. Some of these applications can range from simple analysis as in the case of anatomical structure, size measurement to a more sophisticated task such as Computer-aided surgery and tissue engineering applications. In many of these cases, accuracy and speed is of paramount importance. It is therefore not surprising that many researchers have attempted to research and develop new and creative methods to segment regions [1]; the most difficult task being the segmenting of soft tissue as in the case of brain tumor or liver tissues. In MRI, bone structures are always easy to detect as they appear as the brightest region in an image. However, this is not necessary so for soft tissues.

In this paper, we will present an automated segmentation algorithm that utilizes an integrated hybrid of techniques that is based on intensity, region growing and edge-based. The algorithm checks for connectivity and continuity to ensure that the segmented region is of one enclosed entity.

II. Current segmentation methods

Many current segmentation techniques use the gray scale histogram such as thresh-holding; spatial and intensity technique (e.g. Region Growing) or others using fuzzy set theoretic approaches. Active contours or 'snakes'' can be used to segment objects automatically. In this method, the basic idea is to shape and reshape a curve, or curves subject given the constraints from the input data. The curve would eventually evolve until its boundary segments the object of interest. This framework has been used successfully by Kass et al. [2] to extract boundaries and edges. However, one problem with this approach is that the topology of the region to be segmented must be known in advance. During evolution, curves may change connectivity and split.

Noise has also been a source of concern in segmentation. As some techniques may not be very effective for noisy images, works have been done using the Markov Random Field model [3] which is robust to noise, but is computationally intensive. To speed-up in the computational performance, parallelizing the processes were used. Neural network architectures can help to get the output in real time because of their parallel processing ability, have also been used for segmentation [4] and they work fine even when the noise level is very high.

III. Integrated hybrid method

Our integrated hybrid method is a series of 3-stage processing integrated together to achieve the goal of segmentation. The 3 stages include Region-Growing, Flood-and-Fill followed by Edge Detection algorithm in that order.

As in the case of traditional region growing algorithm, the process begins with the selection of a seed pixel. The pixel selected must be a point within the region to be

Chwee Teck Lim, James C.H. Goh (Eds.): ICBME 2008, Proceedings 23, pp. 109–111, 2009
www.springerlink.com

segmented as its position shall be used as the starting point; and its intensity as the initial input for computing the reference value, μ. The computation of the reference value is the mean of the surrounding 3x3 pixels intensity values. Convoluting in a clockwise manner, the algorithm proceeds to check adjacent pixels surrounding the starting point. A pixel is considered accepted as part of the region only if it is within the threshold limit, β, from the reference value. (A good estimate of the threshold limit is about 15 percent of the reference value). Also, at least one of the adjacent pixels must have been identified as part of the region. The adjacent pixels can be the pixel beneath or the left adjacent pixel. The purpose of checking adjoining pixels is to ensure that there is continuity. In this way, there will not be any stand-alone pixels present.

$$|f(x_n,y_n) - \mu| \leq \beta \qquad (1)$$

where: β : Threshold value.

For each new layer, a new reference value has to be computed. This subsequent reference value will be the average of all the accepted pixel intensities of the previous layer. The process repeats layer after layer until it encompasses the whole region. For each pixel that has its intensity falls within the selected range, a flag or marker is used to keep track. This marker acts as an indicator to highlight that it is part of the accepted region and will be used in the next stage of the algorithm.

In image processing, noise has always been a source of concern as it can increase complexity and affects the segmentation computation. After the first stage (region growing) where noise can be an issue, the subsequent 2 stages computation is independent of any noise. Using an outer boundary that enclosed the region entirely, we work towards the previously segmented region by using the 'flood and fill' concept The idea is to draw a boundary stretching beyond the intended region and then 'flood and fill' the region outside. It is done by using each pixel along the boundary to check for pixels in respective north, south, east and west directions until it touches the first marked pixel along the row or column (See Figure 1).

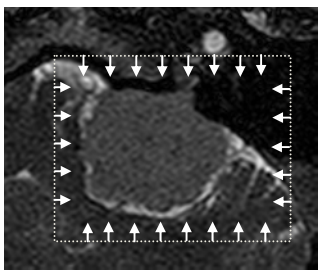


Fig 1: Filling of region starting from boundary

As the 'flood and fill' computation does not require any pixel intensity comparison, any noise within the region does not complicate the processing. The task is to create a mask (i.e. another set of array) of the entire region by setting it to either 255 (white) or 0 (black). The default is white unless the filling process overrides it to black (See Figure 2).

0	0	255	0	0
0	0	255	0	0
0	255	255	255	255
0	255	255	255	255
255	255	255	0	0
0	255	255	255	0
0	0	255	255	0
0	255	255	255	0

Fig 2: Filling of mask with zeros

In the final step of the method, edge detection is used to obtain the outline of the bounded region. With the mask obtained previously, image gradient can then be easily computed. The computation of the image gradient computation, G(x,y), is as follows:

$$G(x,y) = \sqrt{\left(\frac{\partial(f(x,y))}{\partial x}\right)^2 + \left(\frac{\partial(f(x,y))}{\partial y}\right)^2} \qquad (2)$$

Effectively what this mean is that for every pixel in the mask, subtract the right adjacent pixel value with the left adjacent pixel and squared it. This computation is repeated vertically with pixels above and beneath it. Gradient is obtained by taking only the positive root of the square root of the sum of these two values. The result will be an outline surrounding the segmented region.

IV. Results

The result has so far been encouraging and the algorithm has been tested extensively and found to be feasible. The advantage of this algorithm is that in all cases, a continuous outline of the segmented region with no broken lines is always obtained (See Figure 3a and 3b). This is because, the outline is computed using gradient of only a black and white mask. Noise within the segment region is eliminated as the 'flood and fill' stage fills the region from an enclosed boundary outside the segmented region towards the

segmented region and hence noise within the region does not constitute a hindrance to the computation. The result of the segmentation shows that it is able to enclose very irregular shapes as the topology of the region is not an important factor. Also, throughout the process, the algorithm works mainly on pixel intensity, hence coding can be simple and does not require sophisticated formulas. It is also foreseeable that parallel processing especially using the Single Instruction Multiple Data (SIMD) or Hybrid System [5] is also possible in this case.

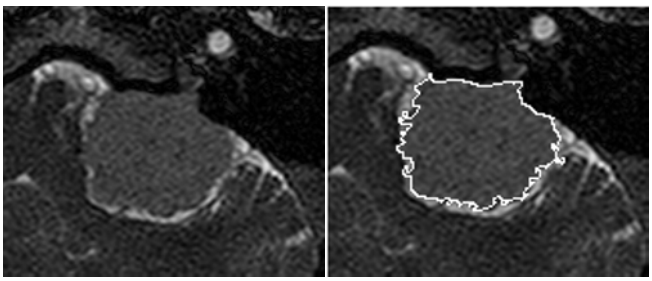


Fig 3a: Original MRI image showing the tumor

Fig 3b: Segmented tumor region

V. Conclusion

In this paper, we have presented an automated segmentation algorithm that utilizes an integrated hybrid method. It is a series of 3-stage processing combined together to achieve the goal of segmentation.. The algorithm checks for connectivity and continuity to ensure that the segmented region is of one enclosed entity. Results have shown the algorithm to be fairly accurate and it is able to detect irregular shapes**.** The method can be robust, simple to implement and also possible to be implemented using parallel processing.

References

1. Dzung L. Pham, Chenyang Xu, and Jerry L. Prince (2000) Current Methods in Medical Image Segmentation, Annual Review of Biomedical Engineering 2:315-337
2. M Kass, A. Witkin and D. Terzopoulos (1987) Snakes: Active Contour Models. In First International Conference on Computer Vision, pp 259-268
3. T. Sziranyi1, J. Zerubia et. al. (2000) Image Segmentation Using Markov Random Field Model in Fully Parallel Cellular Network Architectures. J. of Real-Time Imaging 6:195-211 DOI:10.1006/rtim.1998.0159
4. J.C.L Chow, P.C.W Fung,Y.H. Zhang, J. P. Kerr, E. B. Bartlett (1995) Medical Image Processing Utilizing Neural Networks Trained On A Massively Parallel Computer. J. of Computers in Biology and Medicine, Volume 25, Number 4, pp 393-403(11)
5. C. S. Leo, H. Schröder, G. Leedham (2002) Hybrid System, A New Low Cost Parallel Cluster. High Performance Computing Symposium (HPCS), pp 28 – 34

Quantitative Assessment of Movement Disorders in Clinical Practice

Á. Jobbágy[1], I. Valálik[2]

[1] Budapest University of Technology and Economics/Dept. Measurement and Information Systems, Budapest, Hungary
[2] St. John's Hospital/Dept. Neurosurgery, Budapest, Hungary

Abstract — **Assessment of tremor and dystonia is crucial to characterize their patients' clinical state. Three different devices have been used: (1) PAM, a passive marker based motion analyzer, (2) a digitizing tablet with spiral drawing test, and (3) a 3D accelerometer. PAM fits excellently to testing different kinds of human movements by detecting the displacement. Even the involuntary movements of different regions on the face can be quantitatively assessed. Seventeen disk shaped adhesive markers were attached to the face of two patients with Meige syndrome, presenting blepharospasm and oromandibular dystonia. 20-s recordings were taken with PAM, an inexpensive and clinically easily applicable motion analyzer. The evaluation of the recordings before, and after surgery showed significant reduction of the intensity and rate of uncontrolled movements while the difference between the movement of the left and right cheeks diminished substantially. The paper gives the marker pattern used as well as the evaluation method. Tracking a spiral with a pen on a digitizing tablet is challenging for patients with movement disorders affecting their upper limbs. 68 patients with neural diseases were tested, altogether 544 recordings were made and evaluated. Typical trajectories are shown together with the evaluation. Tremor is present even in healthy subjects. A 3D accelerometer based, clinically applicable tool has been developed. 60-s recordings were taken from ten healthy subjects. Persons held the device in their hand while their wrist was supported. The time-frequency diagrams of the recordings show patient specific characteristics. Based on recordings taken at rest the actual stress level can be estimated. Though not measured generally, this is an important parameter during many clinical tests, especially during blood pressure measurement.**

Keywords — **movement disorders, quantitative assessment, tremor, dystonia.**

I. Introduction

There are a lot of difficulties in quantifying human movement disorders like tremor and dystonia. We have been searching for simple, clinically applicable and highly informative methods for assessment. Three devices have been used. PAM, a passive marker based motion analyzer [1], a digitizing tablet and a 3D accelerometer.

There are no widely used standard tests with a big enough measurement data set. The tests we suggest need to be completed by a great number of patients as well as age-matched control subjects. The measured data are expected to provide the necessary feedback to specify a clinically applicable test procedure.

II. Passive marker based motion analyzer

Passive marker based motion analysis fits well to testing human movements. The markers are lightweight, and they can easily be attached to any anatomical landmark point of the body surface.

General purpose motion analyzers [2] are not optimal for routine clinical assessment of movement disorders. These devices are expensive and require technically skilled operators. If the distance between the marker trajectories and the camera lens is fixed, a two dimensional view is enough to assess the movement. Such an analyzer has been developed at Budapest University of Technology and Economics. The analyzer, PAM (see Figure 1.), is inexpensive, its operator interface is simple. PAM is especially suitable for testing the finger-tapping movement [3].

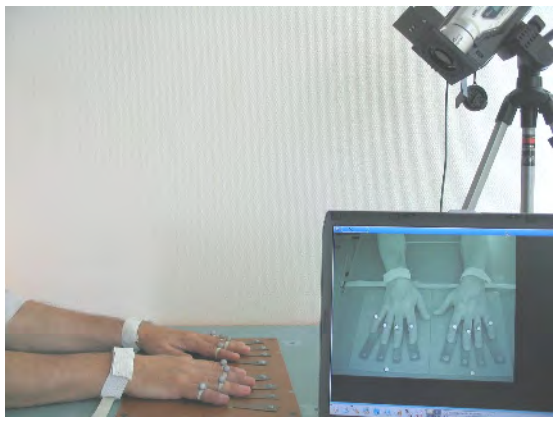


Fig. 1. PAM used for testing the finger-tapping movement.

A challenging task is to measure the actual state of patients with the Meige syndrome [4]. It is difficult to quantify the muscle contractions on the face where the application of electromyography (EMG) is not well tolerated by patients and the number of electrodes is limited. During PAM recording of blepharospasm and oromandibular dystonia seventeen 5-mm diameter markers were attached to the face of

Chwee Teck Lim, James C.H. Goh (Eds.): ICBME 2008, Proceedings 23, pp. 112–115, 2009
www.springerlink.com

the patients, see Figure 2. The subjects were asked to sit still for 20 s. Based on the trajectories, the total displacement was determined for each anatomical landmark point where markers were attached to.

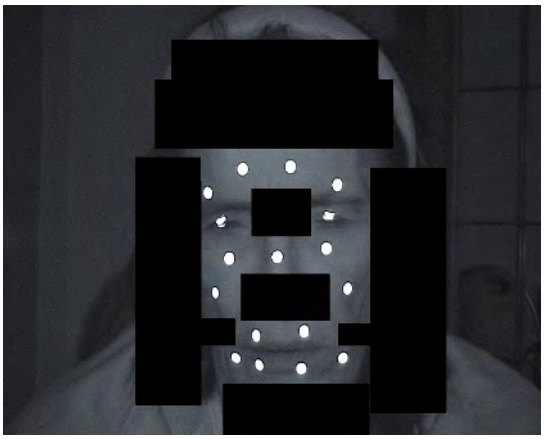


Fig. 2. Marker pattern used in testing patients with Meige syndrome.

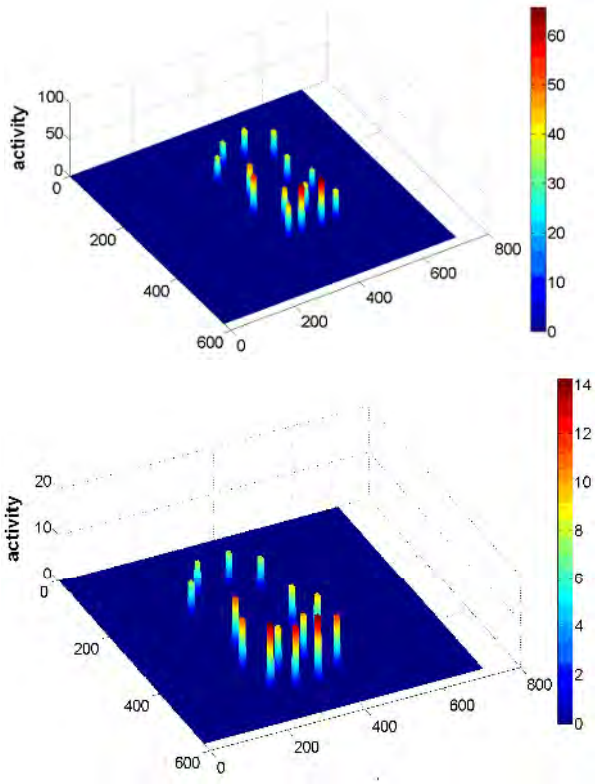


Fig. 3. Activity of marked points on the face, before (top) and after (bottom) operation for patient M1. Notice the different scaling.

Figure 3. and 4. show the results of a patient before (top) and after (bottom) surgical procedure, namely ventro-posteo-lateral pallidotomy on the left side of the brain. The change in the activity of marked points (Figure 3.) and in the relative activity of four sections of the face (Figure 4.) show impressive improvement after surgery. The activity dropped to approximately one fourth, and the two cheeks' behavior became rather symmetrical.

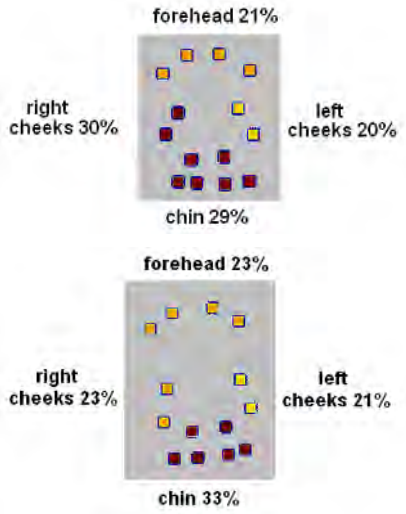


Fig. 4. Activity of four sections of the face before (top) and after (bottom) operation for patient M1.

Blepharospasm and oromandibular dystonia is well characterized by the displacement vector set of all markers at a given moment, see Figure 5.

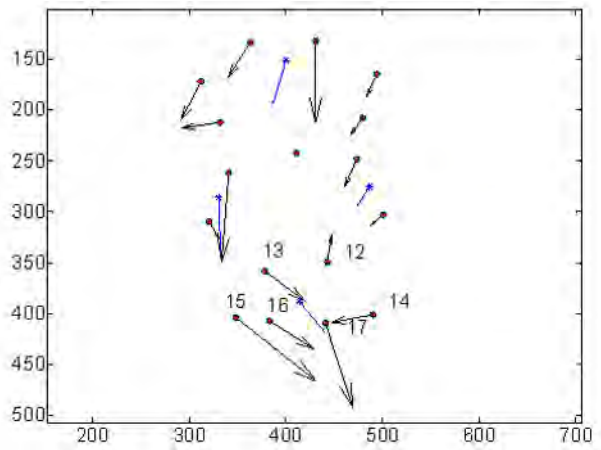


Fig. 5. Displacement vectors of markers on a frame.

This made possible the filtering out of head movement which was further aided by a marker attached to the bridge of the nose. Figure 5. reflects movement of sections of the face on a still image. While the head moves downwards and to the right, some markers move from right to left and marker 12 on the chin moves upwards. The resulting vectors of the markers on every section of the face are also shown. The directions of the resulting vectors are different.

Passive marker based motion analysis can give an objective measure of the blepharospasm and oromandibular dystonia that is hardly possible based on human observation. ***The result of the measurement facilitates the decision whether or not neurosurgical operation is needed.*** The procedure is also appropriate for grading the efficacy of both drug therapy and surgical intervention.

III. Digitizing tablet

A spiral is drawn on the tablet that has to be followed by the patient using the related pen. The reference spiral and the trajectory drawn by a Parkinsonian patient are shown in Figure 6. The trajectory was analyzed using software developed in MATLAB. High-pass filtering makes possible the analysis of kinetic hand tremor.

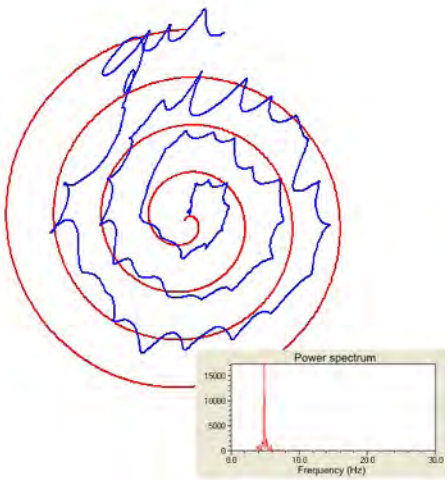


Fig. 6. Reference spiral, trajectory of tracking and the power spectrum of a Parkinsonian subject

On the other hand different movement disorders, like dystonia (see Figure 7.), myoclonus or bradykinesia can be recognized and analyzed during different treatment algorithms. Based on initial displacement dataset, along with both time and frequency domain analysis a quantitative mistracking assessment scoring can be developed for clinical use.

Up to now the spiral test was performed in the St. John's Hospital by 68 patients. Altogether 544 recordings were made and evaluated. The results help the neurologist in differential diagnosis of different tremor types and in deciding on the proper treatment. In case of insufficient drug effect the method has been used by neurosurgeon to make proper indication for surgery in order to control the tremor and to select the targeted brain area for intervention.

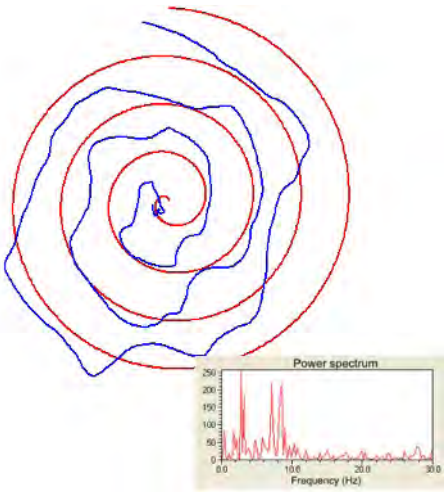


Fig. 7. Reference spiral, trajectory of tracking, and the power spectrum of a patient with left hand dystonia

IV. Three dimensional accelerometer

A battery operated, wireless 3D accelerometer was developed at Budapest University of Technology and Economics. The size of the device is 61 x 30 x 15 mm. The

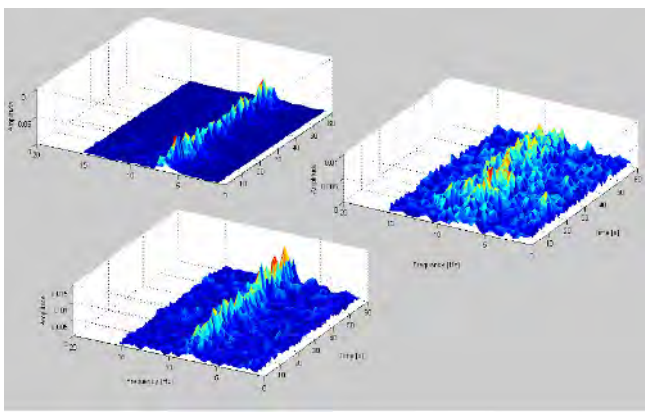


Fig. 8. Hand tremor of three subjects without known neural disease.

actual position of the device – and thus the hand that holds it – cannot be determined, tremor assessment is based on the acceleration data set. The main advantage of this method is that the recording can be done in different conditions, even out of laboratory. Figure 8. shows the result of three subjects without known neural disease. The frequency spectra over time are rather different for the three subjects. The spectra – and their later changes – give valuable information about possible tremor foci.

V. Conclusions

Many diseases influence the movement coordination of patients. Objective assessment of movement disorders greatly helps neurologists and neurosurgeons to make differential diagnosis as well as track the progress of the disease or beneficial effect after surgery. Preferred devices are easy in handling and suitable for clinical application after short training of the operator.

Acknowledgment

This study was supported by OTKA (Hungarian National Research Fund) project *Objective assessment of movement disorders* (T 049357, 2005 - 2008).

References

1. Jobbagy A, Hamar G: PAM: Passive Marker-based Analyzer to Test Patients with Neural Diseases. Proc. of 26th Annual Conference of IEEE EMBS, 1-5 Sept. 2004, San Francisco, CA USA, pp. 4751-4754.
2. http://isbweb.org/~byp/Motion_Capture_Analysis.html
3. Jobbágy Á, Harcos P, Karoly R, Fazekas G: Analysis of the Finger-Tapping Test. Journal of Neuroscience Methods, January 30, 2005. Vol 141/1, pp. 29-39
4. Tolosa E, Marti MJ. Blepharospasm-oromandibular dystonia syndrome (Meige's syndrome): clinical aspects. In: Jankovic J, Tolosa E, editors. Advances in Neurology. Vol. 19. Facial dyskinesias. New York: Raven Press; 1988. p 73–84

Author: Ákos Jobbágy
Institute: Budapest University of Technology and Economics
Street: Magyar Tudósok krt. 2.
City: Budapest
Country: Hungary
Email: jobbagy@mit.bme.hu

Design and Intra-operative Studies of an Economic Versatile Portable Biopotential Recorder

V. Sajith[1], A. Sukeshkumar[2], Keshav Mohan[1]

[1] College of Engineering Trivandrum, Department of Electronics and Communication, Thiruvananthapuram, India.
[2] College of Engineering Trivandrum, Department of Electronics and Communication, Thiruvananthapuram, India.

Abstract — **An economic, versatile, compact and portable biopotential amplifier [Electroneurograph] has been designed and implemented intra operatively. The most significant features of the instrument are variable cutoff for the low pass filter, variable gain, attenuation and optical isolation for the output. A fourth order low pass filter with bessel characteristic was designed using active filters. An attenuator is provided in between the gain stage and optical isolator such that the signals during supramaximal stimulations are attenuated. In this versatile bio-potential recorder, one of the outputs of the amplifier is isolated optically using IC MOC 3020 such that patient safely is ensured. The output portion of the instrumentation amplifier which is named head stage is designed separately and the inputs from the electrodes are given to the head stage by means of shielded coaxial cable. Also the whole bio-potential amplifier is properly shielded and grounded to minimize the noise effect. Offset control is provided for base line shift. The stimulating and recording electrodes were placed in appropriate positions and evoked responses were recorded. Conduction velocity was calculated by measuring the latency of waveform by stimulating at two different points along the nerve. Nerve conduction studies have been undertaken on leprosy patients who had undergone median and ulnar nerve corrective surgery and the result presented.**

Keywords — **Electroneurograph, Biopotential amplifier, Conduction velocity, Nerve action potential, Supramaximal stimulation.**

I. Introduction

Neurological examination of peripheral nerve function refers to nerve conduction study which is based on evoked potentials. Evoked potentials are obtained when electric pulses are passed through excitable tissues like nerves and muscles. With this method it is easy to conduct study of neurological examinations like conduction velocity measurements and location of nerve lesion. The present paper deals with conduction velocity measurements in patients suffering from leprosy using a stimulator and a bio-potential recorder to find the most proximal site of conduction failure which helps the surgeon to perform the corrective surgery [1]. Leprosy is not known to present without neural involvement. The most commonly affected nerves are those of the extremities, in particular the ulnar, the median, lateral popliteal, posterior tibial nerves and their branches. Leprosy invariably results in enlargement of peripheral nerves. Due to the thickening of the multi layered perineurium, its normal properties like semi permeability and elasticity are adversely affected which in turn would block the transmission of impulses.

Leprosy is characterized by involvement of the cutaneous sensory nerves and superficial nerve trunks. The phrenic nerve which is a deeply situated motor nerve is accessible for electro diagnostic studies. The nerve conduction time (NCT), amplitude and duration of compound muscle action potential (CMAP) were recorded. For comparison with peripheral nerves, the motor and sensory conduction of the median nerve was studied [2]. Selected leprosy patients were studied for sensory nerve action potential (SNAP) and motor nerve action potential (MNAP). 55 peripheral nerves were involved in the patients. Ulnar nerve was the commonest by median and posterior tibial nerves. Motor conduction and sensory conduction studies have demonstrated that marked slowing of conduction may occur in affected nerves and changes in latency and amplitude were observed [3][4]. Supramaximal stimuli were used for most of the recordings. Here studies have been done on both clinically affected and clinically unaffected nerves of patients with Leprosy.The forgoing observation promted our team to focus attention in the design and implementation of a low cost, portable, versatile biopotential recorder.

II. Methodology

In order to study the function of neurons it is necessary to stimulate the nerve and study the action potentials generated by it, which can be accomplished by electrical stimulation which is easily controllable. It can be either constant voltage or constant current. It actually involves passing an appropriate electric current through a region of tissue and there by causing the neurons in the area to be depolarized. The nerve stimulation techniques are performed with a variable stimulus generator. The stimulus frequency, stimulus intensity and stimulus duration must be known, adjustable and have an ON / OFF control. In Leprosy patients, for recording the mixed motor and sensory nerve action potential, the stimu-

Chwee Teck Lim, James C.H. Goh (Eds.): ICBME 2008, Proceedings 23, pp. 116–120, 2009
www.springerlink.com

lus given was a rectangular pulse of 50 μ S or 100 μ S duration or a capacitive discharge waveform of the same duration. The standard stimulus is a rectangular wave pulse of current passing between the cathode and the anode. The cathode is always placed closer to the recording electrodes than the anode, because the cathode activates by depolarizing and the anode may block conduction in some axons by hyperpolarization. Standard nerve conduction studies use a supramaximal stimulus, selected to be one third greater than that required to obtain a response of maximal amplitude. A stimulus of 25 mA, 100 V and 0.1 m S duration is usually adequate. However, for abnormal nerves, the stimulus may need to be as high as 75 mA, 300 V and 0.5 m S in duration [5].The electrode positions for the recordings and responses of the ulnar nerve and median nerve are shown in fig.3 and fig. 4 respectively.

III. Biopotential recorder

There are some recent progress in the development of amplifiers and other signal acquisition and signal conditioning systems for biopotential recording [6]. A typical design of the various stages of a biopotential amplifier is formed by preamplifier or instrumentation amplifier, low pass filter, 50Hz notch filter[7] [8]. The developed biopotential recorder consists of a head stage which is a combination of a two stage instrumentation amplifier and a high pass filter followed by difference amplifier, offset control, low pass filter, gain stage, attenuator and isolator. CMRR should be above 90 dB and the sensitivity should be around 10 μ V. The DC power is given by a rechargeable battery. Protection circuits are also used to protect the head stage from high voltage hazards. The block diagram of the recorder is shown in fig.1

A. Instrumentation Amplifier (Head Stage)

For recording biopotential signals from the body, the first and most crucial stage of the instrument is the instrumentation amplifier which consists of the head stage and difference amplifier. The evoked potentials picked up by Ag/AgCl concave disc electrodes are fed to the stage, designed using quad operational amplifier TL 084. A two stage instrumentation amplifier is designed with a gain of 3000 to get an output voltage of 6V for an input of 2 mV. A capacitor is connected in series with R1 of the instrumentation amplifier which acts as a high pass filter, whose cutoff frequency is fixed at 100 Hz to reduce the 50 Hz mains interference. A cutoff of 100 Hz is selected because the signal of interest for our study lies between 150 Hz to

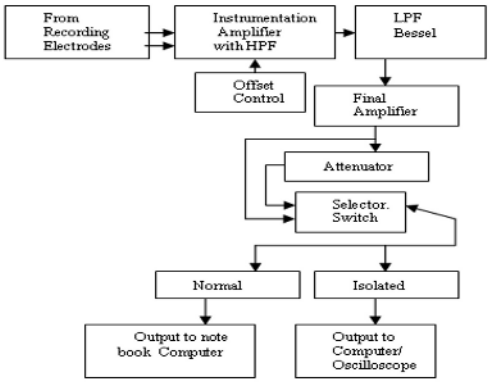


Fig. 1 Block Diagram of Biopotential Recorder

2KHz. Since the circuit provides a CMRR of 97 dB, the recording performance of the amplifier is adequate.

The head stage consisting of two gain stages along with high pass filter is enclosed in a shielded metal cabin and kept close to the recording electrodes to eliminate noise pick up [9]. The transfer characteristics of the instrumentation amplifier along with the high pass filter is

$$Vo/\ Vi = [\ 1+(R_1C + 2\ R_2\ C)s] / (1+ R_1Cs) \qquad (1)$$

Where Vi and Vo are the input and output voltage of the amplifier. R_2 is the feedback resistance and R_1 and C are connected in series between the output of the operational amplifier. The CMMR vs. frequency of the instrumentation amplifier is shown in fig. (2) a.

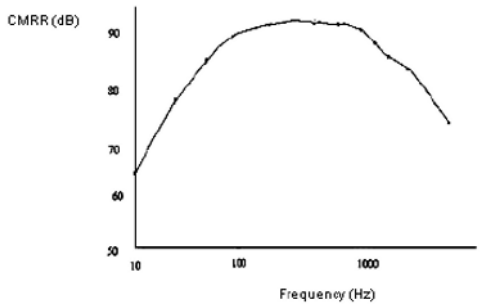


Fig. (2) a CMRR vs. freq. of instrumentation Amplifier

B. Low pass filter

For better cutoff, a fourth order low pass filter with bessel characteristics is designed with variable cutoff at 2 KHz and 3 KHz using active filters. The bessel filter has the most damped characteristics and are used where flat low frequency and good transient responses are needed [10].

In the case of linear response, the out put will simply be a delayed version of the input but in the non linear case the

output will exhibit significant ringing. It turns out that the steeper the cutoff characteristics in the transition band, the higher the amount of ringing [11] . The frequency response of the bessel filter is shown in the fig. 2(b).

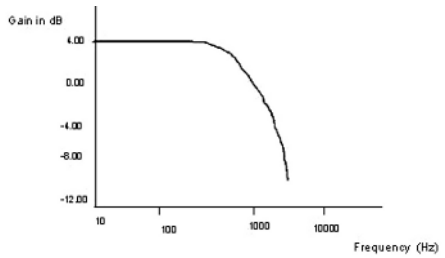


Fig. (2) b. Frequency response of Bessel filter

C. Final Amplifier

A non inverting amplifier with selective gain of 1, 2, 5 and 10 are provided for final amplification. This is implemented by using low noise quad operational amplifier TL 084. The output of the amplifier is coupled through a 0.1 μ F capacitance to eliminate DC offset in the amplified signal. An offset control is provided for adjusting the DC shift occurring at the output of the amplifier.

D. Attenuator and Isolator

An attenuator is provided in between the gain stage and the optical isolator. This is provided to attenuate the signals during supramaximal stimulation, other wise the signal gets saturated. For connecting the high voltage display devices one of the amplifier outputs is isolated optically using IC MOC 3020.

IV. Recording

Electroneurography is the recording and study of action potential propagation along peripheral nerves. The nerve conduction studies helps to distinguish between axonal degeneration, segmental demyelination and abnormal nerve function. For nerve conduction studies the parameters of the evoked responses required are the amplitude, latency and area of the responses recorded. By using the newly developed electroneurograph, electrophysiological studies have been conducted on leprosy patient. The above studies have been done on mainly the ulnar nerve and median nerve since these nerves are the most accessible ones. The method adopted for the measurement of conduction velocity is by stimulating at two different points along the nerve and measuring the latency for each electrical response recorded from the muscle. For each stimulation the time between the start of the stimulus and the onset of the response is measured which is termed as the 'Latency'. The length of the nerve segment is then obtained by measuring on the surface of the skin the distance between the cathodes when placed for each stimulation. The conduction velocity is obtained by dividing the nerve length between the two stimulation points by difference in Latency which is expressed in meter per second [12]. The recording setup is shown in fig. 3.

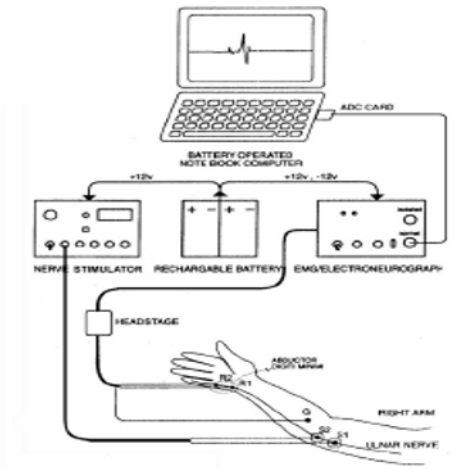
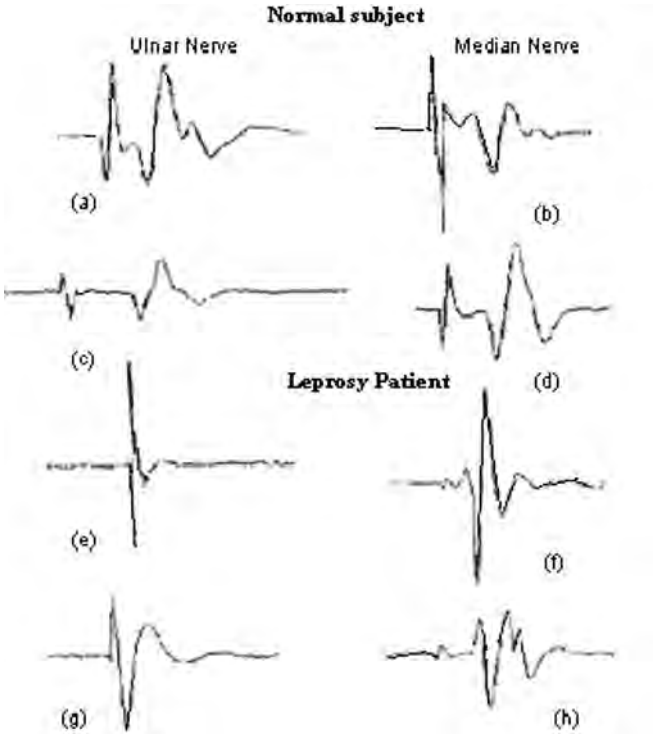


Fig. 3 Recording setup of Nerve action Potential

The conduction velocity of both ulnar and median nerves from elbow to wrist of both arms was calculated. From the recordings it is observed that the ulnar nerve is not functional in both arms where as the median nerve appears to have retained function. The recorded waveform of the ulnar and median nerve of leprosy patient compared with normal patient is shown in fig. 4. The conduction velocity of the median nerve from elbow to wrist was calculated for both arms. In the right median nerve, a conduction velocity of 59.72 m/s and in the left median nerve, a conduction velocity of 57.5 m/s was measured as shown in Table 1. Comparing the conduction velocity of the median nerve from the normal subjects, it was observed that the median nerves of both arms were functioning normally. However, latency at wrist (6.6 ms) was found to be larger than compared with the latency of the normal subjects which was around 3.1 ms.

Some conduction delay is observed between the wrist and thumb indicating nerve compression or nerve damage. A prolonged latency is found in this case which could be due to carpal tunnel syndrome.



(a), (b), (e), (f) – Simulation at wrist
(c), (d), (g), (h) -- Simulation at elbow

Fig (4). The recorded waveform of the ulnar and median nerve of leprosy patient compared with normal subject.

Table 1. Conduction velocity of median nerve

Hand	Nerve	Latency at wrist in sec	Latency at elbow in sec	Difference in latencies (▲L)	Difference in mtrs (▲L)	velocity in m/s
Right	Ulnar	.....	.....	.....	.....	.....
	Median	0.0066	0.0102	0.0036	0.215	59.72
Left	Ulnar	.....	.....	.....	.....	.....
	Median	0.0059	0.0099	0.0040	0.23	57.5

V. Results and conclusion

In the recordings, the 50Hz interference was negligible because of the HPF and the base line was seen to be almost a straight line. As the noise level is less than 5 μ V, the recordings were adequately sensitive [13]. From the recordings of the leprosy patients, the conclusions are,

1. The median nerve appears normal between the elbow and wrist but some conduction delay or blockage between the wrist and abductor pollicis brevis. So the conduction delay could be due to carpal tunnel syndrom. 2. The ulnar nerve is unstimulatable in both arms. 3. The abductor digiti minimi muscle of both arms is not responding to voluntary command.

VI. Conclusion

This method can be used to perform conduction studies on normal volunteers and also subjects with clinical conditions with maximum patient safety. It can also be used in remote areas where there is no electric power. This instrument helps the doctors to locate the exact position of the nerve lesion or nerve damage in the case of peripheral neuropathy and to do corrective surgery. The results of conduction velocity studies from presently available literature are comparable with those of our studies indicates not only the proper functioning of the electroneurograph but also the appropriateness of methodology of our study.

Acknowledgment

I take this opportunity to acknowledge generous support extended by the Principal, College of Engineering Trivandrum, and my colleagues there.

References

1. Dyck, P.J., Thomas, P.K., Lambert, E. L., Bunge, R., (1984) "Peripheral Neuropathy", W.B.Sanderscompany, Vol.11, pp.1975-1978.
2. Dhand, V. K., Bhusgab Kumar, Dhand, R., Chopra, J. S., Kaur, S. (1988) "Phrenic nerve conduction in leprosy", International journal of lep rosy, vol.56, pp.389 – 392.
3. Husain, S., Malaviya, G. N., (2007) "Early nerve damage in leprosy: An electro physiological study of ulnar and median nerves in patients with and without clinical neural defects", Neurol India, 55:pp. 22 – 26.
4. Varghese, M., Ithimani, M., Sathyanarayan, K. R., Mathai, E., Phakthavizian, C., (1970), "A study of conduction velocity of ulnar and median nerves in leprosy", International journal of leprosy, vol. 38, pp.271-272.
5. Aminoff, M. J., (1992) "Electro diagnosis in clinical neurology", Churchill Livingstone Inc., 3rd edition, pp. 249 – 326.
6. Taylor, J., Masanotti, D., Seetohul, V., Hao, S., (2006) "Some recent developments in the design of biopotential amplifier for ENG recording system", IEEE. Asia Pacific Conference on Circuits and Systems, Dec.4 - 7, pp.486 – 89.
7. Webster, J. G., (1998), Medical Instrumentation Application and Design, John Wiley & Sons, Inc., 3rd edition, N.Y., U.S.A.
8. Spinelli, E. M., Pallas-Areny, R., Mayosky, M. A., (2003), "AC-Coupled Front- End for biopotential measurements", IEEE. Trans. Biomed. Eng., Vol. 50, no.3, pp. 391-395.
9. Harrison, R. R.,(2007), "A versatile integrated circuit for the acquisition of biopotential", IEEE, Custom Integrated Circuit Conference.
10. Rutkowski, G.B.,(1993), Operational amplifiers: Integrated and hybrid circuits. A wiley interscience publications, pp. 1-14.

11. Franco, S.,(1988), Design with operational amplifiers and analog integrated circuits. Mc Graw Hill, New York, pp. 151-153.
12. Webster, J. G., (1974), "Encyclopedia of medical devices and instrumentation", Wiley Inter science publication, vol. 2, pp.1120-1126.
13. Badillo, L., Ponomaryob, V., Ramos, E., Igartua, L., (2003), "A Low noise multi channel amplifier for portable EEG biomedical application", Engineering in medicine and biology society, proceedings of the 25th annual Internal Conference of the IEEE. ,vol. 4, Sept.17 – 21, pp.3309 – 3312.

Author: V. Sajith
Institute: College of Engineering Trivandrum.
Street: Sreekaryam.
City: Trivandrum
Email: sajithvijayaraghavan@hotmail.com

Comparison of Various Imaging Modes for Photoacoustic Tomography

Chi Zhang and Yuanyuan Wang

Department of Electronic Engineering, Fudan University, Shanghai 200433, China

Abstract — **Photoacoustic tomography (PAT) has shown great potential in many medical applications. According to the geometry of electromagnetic irradiation and acoustic signal detection, PAT can be categorized into three imaging modes, the forward mode, the backward mode and the sideward mode. To deeply understand their theorems and suitable applications, simulation studies are carried out to compare the precision and noise robustness of reconstructions of these modes. The absorbed energy density of the irradiated tissue is modeled by the Monte Carlo method. Then generated photoacoustic signals are simulated by the finite-difference time-domain method. Four representative algorithms are employed to reconstruct the image from simulated signals. It is found that in the sideward mode, the reconstructed image around the center of the scanning circle has better precision and stronger robustness to noise compared with the marginal region. In both forward and backward modes, the region relatively close to transducers can be reconstructed more clearly, but is more sensitive to noises. The sideward mode has better precision but slower reconstruction speed compared with forward and backward modes. Moreover, the choice of the time-domain or frequency-domain reconstruction algorithm is shown to have an impact on the noise pattern of the reconstructed image. Therefore, the sideward mode PAT is suitable for the precise imaging of protuberant human tissues, and the optimum imaging region (OIR) is around the center of the scanning circle. The forward/backward mode PAT is suitable for the fast imaging of plane human parts, and the OIR is at an appropriate distance from the scanning line.**

Keywords — **Photoacoustic tomography, imaging mode, comparison.**

I. Introduction

Photoacoustic tomography (PAT), emerging as a new technique of noninvasive medical imaging, combines the optical contrast and ultrasonic resolution, and has demonstrated great potential in many important medical applications including breast tumor detection and brain functional imaging [1-3].

In PAT, a short-pulsed laser or microwave is used to irradiate the biological tissue, which results in generation of acoustic waves due to thermoelastic expansion. The acoustic wave, called photoacoustic wave, is then detected by the ultrasonic transducer and utilized to reconstruct the absorbed energy density of the tissue. According to the geometry of electromagnetic irradiation and photoacoustic signal acquisition, PAT can be categorized into three imaging modes [4], the forward mode [5], the backward mode [6] and the sideward mode [7]. In the forward mode the ultrasonic transducer and radiation source are on opposite sides of the object, while in the backward mode they are on the same side. In the sideward mode, the ultrasonic transducer is perpendicular to the direction of electromagnetic irradiation. These three modes hold different mechanisms, therefore being suitable for different applications.

In this paper, the principles of these three modes are theoretically analyzed. Simulation studies are conducted to corroborate the analysis. The generation and propagation of photoacoustic signal are simulated by the combination of Monte Carlo (MC) model [8-9] and finite-difference time-domain (FDTD) method [10, 4]. The image reconstruction is fulfilled by four representative algorithms [11-14]. It is found that these modes vary in precision and noise sensitivity and have diverse optimum imaging regions (OIR).

II. Methods

A. Three modes

The medical applications of these three modes depend largely on their physical configurations. The backward mode may be the most convenient one to be carried out. Since the irradiation source and ultrasonic transducer are on the same side, these two parts can be integrated into one device, working like the transducer in B-mode ultrasound imaging. So the backward mode can be applied to the detection of most human parts. The forward mode, with the irradiation source and ultrasonic transducer on opposite sides, is not suitable for the imaging of thick tissues. This is because the laser attenuates very quickly in biological tissues. As a result, the detected photoacoustic signal of thick tissue on the opposite side of irradiation source is much weaker than that detected on the same side. In both the backward and forward modes, the ultrasonic transducer array is usually employed for the fast imaging. The sideward mode is the only one in which the transducer can scan around (normally in the circular geometry) biological tissues to acquire photoacoustic signals. In fact, although time consuming, the circular scanning is often used in PAT due to the high imaging resolution. However, limited by its physical configura-

Chwee Teck Lim, James C.H. Goh (Eds.): ICBME 2008, Proceedings 23, pp. 121–124, 2009
www.springerlink.com

tion, this mode can only be conveniently applied to the imaging of protuberant human parts.

Simulation studies are carried out to compare the precision and noise robustness of reconstructions of these three modes. The simulation is conducted in the 2-D case to reduce the computational complexity, but the conclusion can be easily extended to the 3-D case. The simulation process is described in following sections.

B. Monte Carlo model

In PAT, the biological tissue is first irradiated by a short-pulsed laser. The basic equation of PAT is given by [11]

$$\nabla^2 p(\mathbf{r},t) - \frac{1}{c^2}\frac{\partial^2 p(\mathbf{r},t)}{\partial t^2} = -\frac{\beta}{C_p} A(\mathbf{r}) \cdot \frac{\partial I(t)}{\partial t} \qquad (1)$$

where **r** is the spatial position, t is the time, $I(t)$ is the laser pulse function, $A(\mathbf{r})$ is the absorbed energy density, $p(\mathbf{r}, t)$ is the acoustic pressure, β is the coefficient of volumetric thermal expansion, c is the acoustic speed and C_p is the specific heat. Here the MC model, a gold standard technique in the simulation of biomedical optics, is utilized to simulate the light propagation and $A(\mathbf{r})$.

The MC model treats light as photons and ignores wave features. The light propagation is modeled by photon movements. The step length of the photon movement between sites of the photon-tissue interaction (scattering) is given by probability distributions, and the refraction and reflection occurring at the interface of different mediums are calculated by Snell's law and Fresnel's formulas. By simulating the movements of a large amount of photons, this model can precisely simulate the light propagation and optical absorption in tissues. But at the same time, this statistical model is computationally inefficient.

The MC model used here is similar to that described in [9], which can be referred to by readers for more details.

C. Finite-difference time-domain method

Given that $A(\mathbf{r})$ is calculated by the MC model, the generated photoacoustic signal p, as shown in (1), can be simulated by the FDTD method, which has been widely used in the simulation of acoustic waves and electromagnetic waves. In the FDTD method, parameters in (1) are discretized so that (1) can be expressed as difference equations. Then p can be calculated by the numerical method.

The excitation pulse I is very short, so extremely dense meshes are required in the FDTD method. However, in most practical applications, the used ultrasonic transducer is with the center frequency at the order of MHz. Therefore, there is no need to model frequencies higher than the bandwidth of the detector. Accordingly, a useful improvement is to rewrite (1) as [10]

$$\nabla^2 (p * h) - \frac{1}{c^2}\frac{\partial^2 (p * h)}{\partial t^2} = -\frac{\beta}{C_p} A \cdot \frac{\partial (I * h)}{\partial t} \qquad (2)$$

where h is the impulse response of the ultrasonic transducer and * represents the convolution. Obviously the detected photoacoustic signal is $p * h$ and is generated by the source $I * h$ as shown by (2). Since high frequency components of I are filtered by h, better precision can be achieved even using relatively sparse meshes in the FDTD simulation.

The specific steps of the FDTD method can be found in [15] and will not be introduced here on account of space limitation.

D. Four reconstruction algorithms

Detected by the ultrasonic transducer, the photoacoustic signal can be used to reconstruct the inner image of the tissue. Since the performance of reconstruction algorithm is important to the image quality, here four representative and commonly used algorithms are chosen for the image reconstruction.

The scanning geometries of these three modes play a critical role in the choice of reconstruction algorithms. Therefore, in the sideward mode the spherical time-domain reconstruction (STDR) algorithm [11] and the deconvolution reconstruction (DR) algorithm [12] are chosen; the former is a time-domain method and the latter is a frequency-domain method. In both backward and forward modes, the planar time-domain reconstruction (PTDR) algorithm [13] and the Fourier-based projection (FP) algorithm [14] are applied; the former is a time-domain method and the latter is a frequency-domain method. Algorithms in different domains are used for each mode in order to reduce the effect of algorithm's performance and focus on the characteristic of different modes.

E. Parameters

The optical absorption distribution of the simulated tissue is shown in Fig. 1. The image size is 18 mm×18 mm. It can be seen that nine objects are imbedded in the background of turbid medium.

In the forward mode, the laser source irradiates homogeneously from the left side, and the ultrasonic transducer scans along a line on the right side (6.3 mm from the centre of Fig. 1, 120 positions with the interval of 0.12 mm). In the backward mode, the laser source still irradiates from the left side, and the ultrasonic transducer scans along a line on the left side (6.3 mm from the centre of Fig. 1, 120 positions

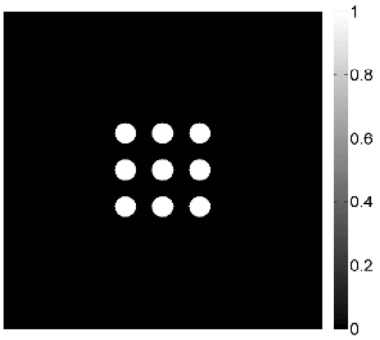


Fig. 1 The optical absorption distribution of the simulated tissue.

with the interval of 0.12 mm). In the sideward mode, the laser source irradiates from the outside perpendicular to the image plane, and the ultrasonic transducer scans along a circle (with the radius of 9 mm, 240 positions).

Parameters of the MC model are set as follows: the index of refraction is 1.33, the scattering coefficient is 15 cm^{-1}, the absorption coefficient of objects is 4 cm^{-1}, the absorption coefficient of the background is 0.05 cm^{-1} and the anisotropy factor is 0.9.

Parameters of the FDTD method are set as follows: the acoustic speed is 1500 m/s, the space interval of the mesh is 0.03 mm and the time interval is 5 ns.

III. Results and discussions

Figure 2 shows the reconstructed images (from noisy signals with the signal-to-noise ratio of 7 dB). The three columns from left to right correspond to the results of forward, backward and sideward modes, respectively. The two rows from top to bottom correspond to the results of time-domain and frequency-domain algorithms, respectively.

In both the forward and backward modes, it can be found that the objects relatively close to the transducer are reconstructed more clearly. This is because the transducer only scans along a line with a finite length, causing the image reconstruction to be a limited-view problem [12, 16]. Since close objects have a larger view than distant ones, they can be reconstructed more clearly. At the same time, the near region is more sensitive to noises when reconstructed using time-domain algorithms, because in the reconstruction the signal, including noise, is divided by the distance. The noise effect is averaged at various distances when using frequency-domain algorithms. Additionally, considering the performance limitation of the transducer's near field region, the OIR of forward/backward mode PAT should be at an appropriate distance from the scanning line.

In the sideward mode the objects are reconstructed with good precision, clearer than those in forward and backward

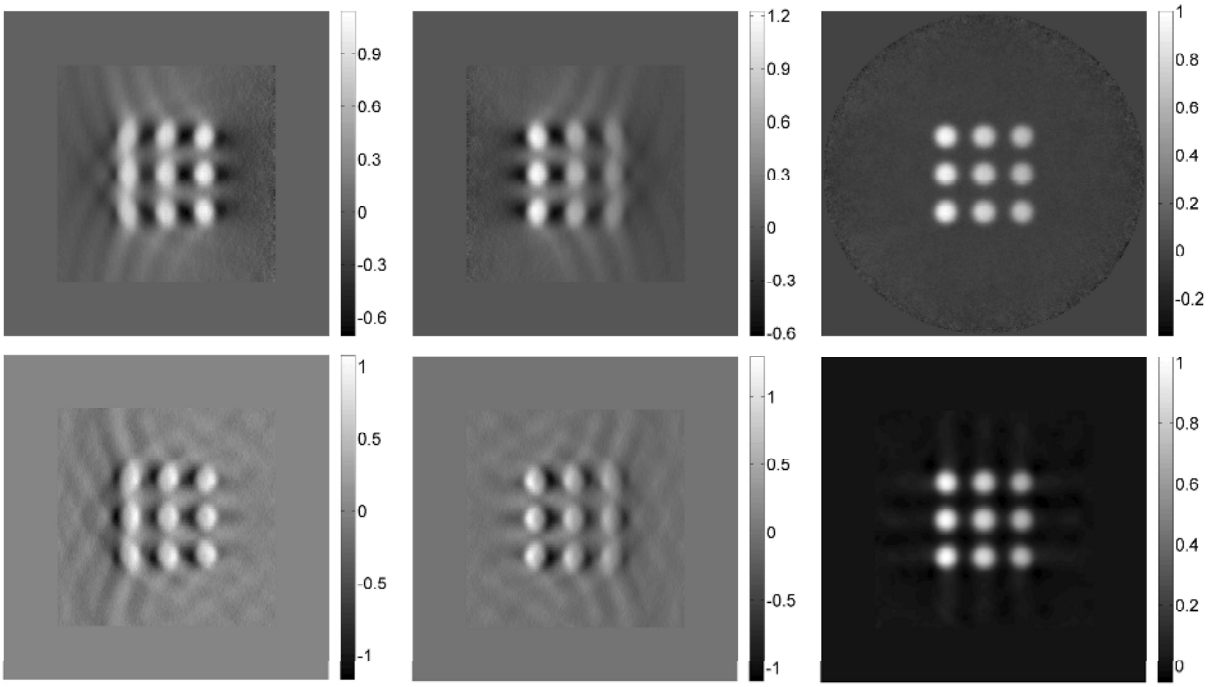


Fig. 2 Reconstructed images of the tissue (as shown in Fig. 1). The three columns from left to right correspond to the results of forward, backward and sideward modes, respectively. The two rows from top to bottom correspond to the results of time-domain and frequency-domain algorithms, respectively.

modes, because here the image reconstruction is a full-view problem. It can be seen that the region relatively close to the scanning circle is more sensitive to noises when reconstructed by the time-domain algorithm. This effect results from the same reason as discussed in forward and backward modes. Also, similar to forward and backward modes, the frequency-domain algorithm could homogenize the noise effect. In short, obviously, the OIR of the sideward mode PAT is around the center of the scanning circle.

IV. Conclusions

Three modes of PAT—forward mode, backward mode and sideward mode—are described and analyzed in this paper. Simulation studies are carried out, in which the light propagation and optical absorption are simulated by the MC model, and the generated photoacoustic signal is simulated by the FDTD method. Four representative algorithms, two time-domain ones and two frequency-domain ones, are utilized for the image reconstruction.

In the forward mode and backward mode PAT, the region relatively close to transducers can be reconstructed more clearly, but is more sensitive to noises. Meanwhile, the fast or even real-time imaging is possible by using the transducer array. So the forward/backward mode is suitable for the fast imaging of plane human parts, and the OIR is at an appropriate distance from the scanning line.

In the sideward mode PAT, the reconstructed image around the center of the scanning circle has good precision and strong robustness to noise, generally better than forward and backward modes. But this mode can only be conveniently applied to the imaging of protuberant tissues, limited by its physical configuration, and is slow due to the circular scanning. Therefore, the sideward mode is suitable for the precise imaging of protuberant human parts, and the OIR is around the center of the scanning circle.

Acknowledgment

This work was supported by the National Basic Research Program of China (No. 2006CB705707) and Shanghai Leading Academic Discipline Project (No. B112).

References

1. Xu M, Wang L V (2006) Photoacoustic imaging in biomedicine. Rev Sci Instrum 77: 041101–1–22
2. Guo B, Li J, Zmuda H et al (2007) Multifrequency microwave-induced thermal acoustic imaging for breast cancer detection. IEEE Trans Ultrason Ferroelectr Freq Control 54: 2000–2010
3. Wang X, Pang Y, Ku G et al (2003) Noninvasive laser-induced photoacoustic tomography for structural and functional in vivo imaging of the brain. Nat Biotechnol 7: 803–806
4. Huang D, Liao C, Wei C et al (2005) Simulations of optoacoustic wave propagation in light-absorbing media using a finite-difference time-domain method. J Acoust Soc Am 117: 2795–2801
5. Kostli K P, Beard P C (2003) Two-dimensional photoacoustic imaging by use of Fourier-transform image reconstruction and a detector with an anisotropic response. Appl Opt 42: 1899–1908
6. Niederhauser J J, Jaeger M, Lemor R et al (2005) Combined ultrasound and optoacoustic system for real-time high-contrast vascular imaging in vivo. IEEE Trans Med Imaging 24: 436–440
7. Kruger R A, Liu P, Fang Y et al (1995) Photoacoustic ultrasound (PAUS)-reconstruction tomography. Med Phys 22: 1605–1609
8. Patrikeev I, Petrov Y Y, Petrova I Y et al (2007) Monte Carlo modeling of optoacoustic signals from human internal jugular veins. Appl Opt 46: 4820–4827
9. Wang L, Jacques S L, Zheng L (1995) MCML–Monte Carlo modeling of light transport in multi-layered tissues. Comput Method Program Biomed 47: 131–146
10. Zhang C, Wang Y (2008) A reconstruction algorithm for thermoacoustic tomography with compensation for acoustic speed heterogeneity. Phys Med Biol 53: 4971–4982
11. Xu M, Wang L V (2002) Time-domain reconstruction for thermoacoustic tomography in a spherical geometry. IEEE Trans Med Imaging 21: 814–822
12. Zhang C, Wang Y (2008) Deconvolution reconstruction of full-view and limited-view photoacoustic tomography: a simulation study. J Opt Soc Am A 25: 2436-2443
13. Xu M, Xu Y, Wang L V (2003) Time-domain reconstruction algorithms and numerical simulations for thermoacoustic tomography in various geometries. IEEE Trans Biomed Eng 50: 1086–1099
14. Kostli K P, Frenz M, Bebie H et al (2001) Temporal backward projection of optoacoustic pressure transients using Fourier transform methods. Phys Med Biol 46: 1863–1872
15. Kunz K S, Luebbers R J (1993) The finite difference time domain method for electromagnetics. CRC Press
16. Xu Y, Wang L V (2004) Reconstructions in limited-view thermoacoustic tomography. Med Phys 31: 724–733

Author: Yuanyuan Wang
Institute: Department of Electronic Engineering, Fudan University
Street: No.220 Handan Road
City: Shanghai
Country: China
Email: yywang@fudan.edu.cn

Ultrasonographic Segmentation of Cervical Lymph Nodes Based on Graph Cut with Elliptical Shape Prior

J.H. Zhang[1], Y.Y. Wang[2] and C. Zhang[2]

[1] Department of Electronic Engineering, Yunnan University, Kunming, China
[2] Department of Electronic Engineering, Fudan University, Shanghai, China

Abstract — **A modified graph cut algorithm was proposed under the elliptical shape constraint to segment ultrasonograms of cervical lymph nodes. Since cervical lymph nodes were usually oval-shaped, the prior of the elliptical shape information, which was expressed as a distance function, was used to constrain the cut cost of the graph cut algorithm. The initially segmented contour was fitted by an ellipse to get the constraint. Then the segmentation was obtained by minimizing the cut cost function constrained by the elliptical prior. The procedure was iterated until the tolerance of convergence was met. Under the same user inputs, the algorithm successfully segmented nodes on low contrast sonograms whereas the traditional graph cut approach failed. For 30 ultrasonograms, the distance between contours manually delineated by the radiologist and those segmented by the proposed algorithm was far less than the distance resulted from the traditional graph cut algorithm. Both the qualitative and the quantitative evaluation of segmentation results indicate that utilizing the elliptical shape prior can significantly improve the graph cut algorithm for segmenting cervical nodes on sonograms.**

Keywords — **Graph cut, elliptical shape prior, cervical lymph node, ultrasonogram.**

I. Introduction

Lymph node is one of the important organs, acting as the immunologic filter in the body. The abnormity of lymph nodes often denotes pathological changes within their attributive areas. Therefore, the evaluation of lymph nodes is meaningful for the disease diagnosis. Since cervical lymph nodes are prone regions of the lymphadenopathy, they are especially important in the clinical examination. Among all kinds of imaging modalities, the ultrasound is the preferred technique for the evaluation of cervical lymph nodes, due to its good attributes of non-invasion, absence of radiation, real time, low cost, and convenience. However, ultrasonic images often exhibit the poor quality with speckle noises and low contrast, which results in difficulties in image processing procedures, especially in the image segmentation. Most fully automatic segmentation techniques are slow, and cannot satisfy the accuracy requirement for the clinic practice, while interactive segmentation methods have the advantage of the reliability under users' control.

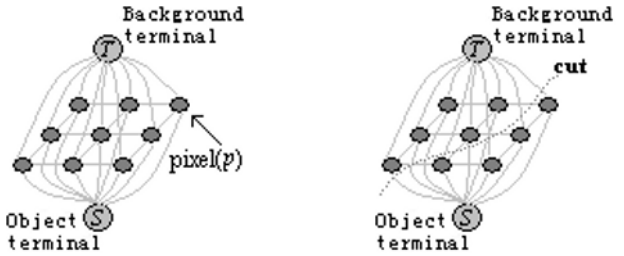
The graph cut developed by Boykov *et al.* [1] is an interactive image segmentation method based on the energy minimization, which finds the globally optimal segmentation under hard constraints from users and soft constraints including both the boundary and region information. However, even with a significant amount of user inputs, the performance of the traditional graph cut approach is not satisfactory to segment cervical lymph nodes on sonograms. Many segmentation methods [2-4] have taken advantage of the shape information to improve the performance. Especially, Freedman *et al*. [3] improved the graph cut method by using the level-set template to add shape constraints. In their method, a particular fixed template should be known and transformed to get the appropriate shape prior. Since cervical lymph nodes are usually oval-shaped, we incorporated the elliptical shape prior, which was adaptively obtained from the initial segmentation, into the graph cut approach to get better segmentation results. It should be noted that Slabaugh *et al.* [4] also proposed to use the elliptical shape prior to improve the graph cut segmentation, where the ellipse constraint was incorporated into the graph cut in a different way from our method. They also obtained improvement for lymph nodes segmentation in MR images that had the higher quality than ultrasonograms.

II. Materials and methods

A. Graph cut

In this section, we review the graph cut algorithm [1] for the interactive segmentation. To segment a given image, an undirected graph $G = <V, E>$ is created. The graph is composed of a set of vertices V and a set of undirected edges E that connect vertices, as shown in Fig.1(a). Vertices include all pixels P in the image and two special terminals (S and T) which respectively correspond to the object (O) and background (B) labels assigned to pixels by a user. Therefore, $V = P \bigcup \{S,T\}$. Each pixel $p \in P$ has two terminal edges connecting it to terminals, S and T, i.e., $\{p, S\}$ and $\{p, T\}$. Each pair of neighboring pixels is connected by the neighborhood edge N. Therefore, $E = N \bigcup \{\{p,S\},\{p,T\}\}$.

Chwee Teck Lim, James C.H. Goh (Eds.): ICBME 2008, Proceedings 23, pp. 125–128, 2009
www.springerlink.com



(a) (b)

Fig. 1 A graph and its minimum cost cut: (a) a graph for a 3×3 image; (b) minimum cost cut

As illustrated in Fig. 1(b), a cut partitions vertices into two sets separating two terminals. Accordingly, the image is segmented into the object (A_p = 1, A_p, the attribute of the pixel p), and the background (A_p = 0). The cost of the cut is the sum of all costs of edges that are severed by the cut. Typically, the cost of the neighborhood edge is defined by

$$w(p,q)=\exp\left[-\frac{(I_p-I_q)^2}{2\sigma^2}\right]\frac{1}{dist(p,q)} \qquad \{p,q\}\in N, A_p\neq A_q \tag{1}$$

where I_p and I_q are intensities of pixels p and q respectively; dist(p, q) is the Euclidean distance between two pixels; and σ is an empirical value, used as the threshold for the difference between two pixels. It can be seen that if two pixels are significantly different ($|I_p - I_q| > \sigma$), the cost is low. However, this function penalizes those cuts between pixels with similar intensities.

On the other hand, according to labels (O and B) assigned by users, costs for terminal edges are respectively defined as

$$w(p,S)=\begin{cases} K & p\in \mathrm{O} \\ 0 & p\in \mathrm{B} \\ -\ln \Pr(I_p/\mathrm{B}) & \text{else} \end{cases} \tag{2}$$

$$w(p,T)=\begin{cases} 0 & p\in \mathrm{O} \\ K & p\in \mathrm{B} \\ -\ln \Pr(I_p/\mathrm{O}) & \text{else} \end{cases} \tag{3}$$

where $K = 1 + \max_{p\in P} \sum_{q:\{p,q\}\in N} w(p,q)$, and Pr($I_p$/O) and Pr($I_p$/B) are histograms of the object and background intensity distributions, respectively derived from labels. Therefore, user inputs provide hard constraints for the segmentation.

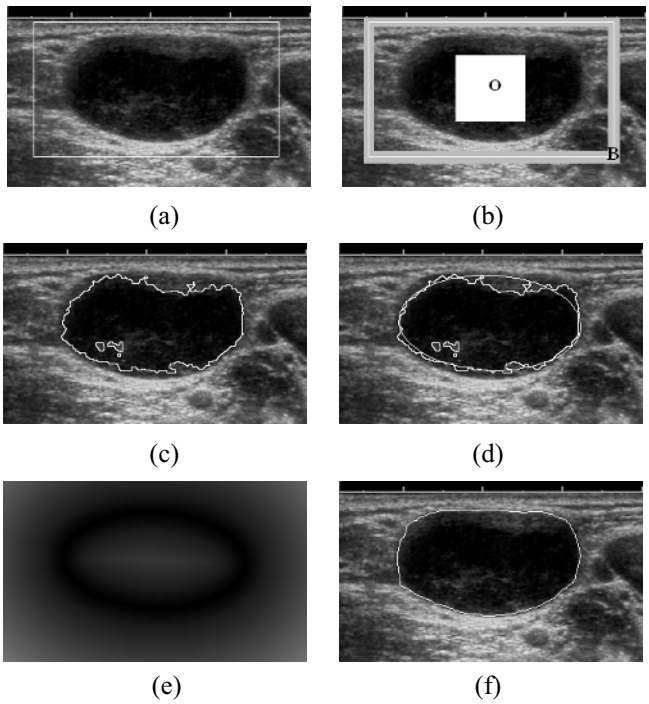
The boundary between the object and the background is obtained by finding the cost cut on the graph G, which minimizes the energy function:

$$E=\lambda\sum_{p\in P}[w(p,S)+w(p,T)]+\sum_{p\in P,\{p,q\}\in N} w(p,q) \tag{4}$$

where the first term is usually called the region term, the second one is the boundary term, and λ is the weight factor between two terms. In such way, the segmentation is performed under hard constraints from users, and soft constraints incorporating both the boundary and region information.

B. Improved graph cut with elliptical shape prior

Even though the graph cut algorithm has many successful applications [1, 5], it shows limitations to segment cervical nodes on ultrasonograms. Due to the poor quality of ultrasonic images with speckle noises and low contrast, a large amount of user inputs are needed to obtain an accurate boundary. Since the shape of the cervical node is usually oval, the elliptical shape constraint is incorporated into the graph cut to reduce the sensitivity to speckle noises and to avoid the leak in weak boundaries. The proposed algorithm is illustrated in Fig. 2.



(a) (b) (c) (d) (e) (f)

Fig. 2 Improved graph cut segmentation: (a) ROI selected by a user; (b) "O" and "B" labels created by the computer; (c) initial contour obtained by the traditional graph cut; (d) ellipse fitted to the initial contour; (e) distance function of the ellipse; (f) final segmented contour

In the graph cut method [1], background and object labels should be assigned by a user. To compare the improved graph cut with the traditional one under the same user inputs, the user is required to select the region of interest (ROI) with a rectangle, as shown in Fig. 2(a). In Fig.2(b), pixels in the central square of the ROI are assigned as "object" seeds, where the width of the square is just half of the width of the ROI. Pixels in the surrounding region of the ROI are assigned as "background" seeds of ten pixels wide. Fig. 2(c) shows the boundary obtained by the traditional graph cut. The result is not satisfactory. In the following, the elliptical shape constraint is combined with the graph cut to iteratively improve segmentation results.

Firstly, as shown in Fig. 2(d), we fitted an ellipse to the previously obtained boundary using the algorithm described in [6]. Secondly, we generated a distance function $D(p)$ between the pixel p and the nearest point on the ellipse [7], as illustrated in Fig. 2(e). The zero distance corresponds to points on the ellipse. Thirdly, the energy function was modified by incorporating the distance function to realize the elliptical shape constraint:

$$E = (1-\mu)\left\{\lambda\sum_{p\in P}[w(p,S)+w(p,T)]+\sum_{p\in P,\{p,q\}\in N}w(p,q)\right\} + \mu\sum_{p\in P,\{p,q\}\in N}D\left(\frac{p+q}{2}\right) \quad (5)$$

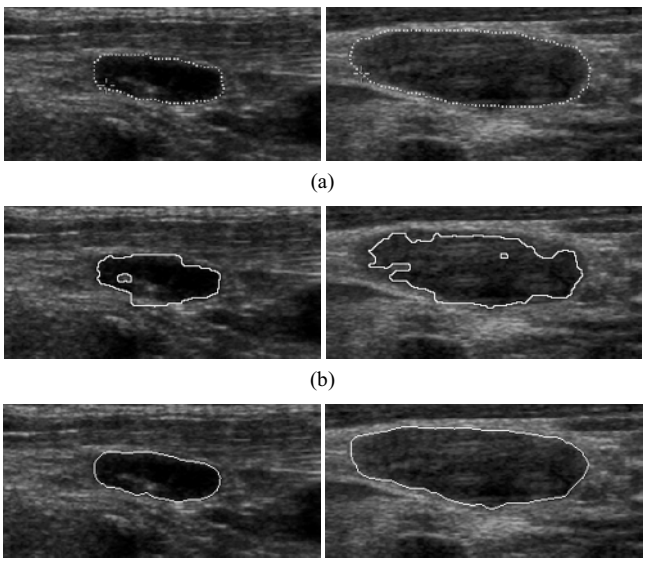
where $\mu \in [0, 1]$ is a weighting factor. Therefore, under the same region and boundary conditions, the cost of a cut near the ellipse will be smaller than that further from the ellipse. Lastly, the new energy function is minimized to obtain the new segmentation. These steps are iterated until the convergence. The convergence is achieved when either the number of iteration is reached or the difference between the current and previous results is smaller than a preset tolerance. The final segmented contour is shown in Fig. 2(f).

The segmented contour will be more like an ellipse when the value of μ is large. In this study, we took $\mu = 0.5$ for the segmentation of cervical nodes on ultrasonograms. For the segmentation of higher quality images, a smaller value of μ should be taken to reduce elliptical constraints. The value of σ was set as the average of difference values between two neighboring pixels in a given image. As for the parameter λ, it was demonstrated in the traditional graph cut that segmentation leak may take place in weak edges when the region term in Eq. (4) is missing, i.e. $\lambda = 0$. If $\lambda \neq 0$, results are almost the same for a large range of λ (λ = 7-43). Therefore, we assigned $\lambda = 10$ in this study.

III. Experimental results and discussions

A total of 30 sonograms of cervical nodes were used in this study. Images were obtained by a Sequoia 512 ultrasound system with a high-frequency transducer of 8-14MHz in Huashan Hospital of Fudan University, Shanghai, China. Images were segmented by the traditional graph cut approach and the proposed method. As an example, segmentation results of two nodes were presented in Fig. 3. The manual segmentation by a radiologist was presented in Fig. 3(a); the segmentation by the traditional graph cut was shown in Fig. 3(b); and the segmentation by the proposed method was shown in Fig. 3(c). User inputs were the same for two graph cut based methods, i.e., a rectangle selected by a user.

It was shown that the segmentation of the traditional graph cut could not satisfy the accuracy for the subsequent image processing. More labels must be added to improve segmentation results. Under the same user inputs, the proposed algorithm successfully segmented contours of nodes.



(a) (b) (c)

Fig. 3 Segmentation comparison for cervical nodes on sonograms: (a) segmentation by a radiologist; (b) segmentation by the traditional graph cut; (c) segmentation by the proposed algorithm

On the other hand, to quantitatively evaluate these methods, distances between contours manually delineated by the radiologist and those segmented by the computer was calculated. Two distance measures, the average minimum Euclidean distance (AMINDIST) [8] and the Hausdorff distance [9], were considered in this study. For two contours $A = \{a_1,...,a_m\}$ and $B = \{b_1,...,b_n\}$, the $AMINDIST(A,B)$

measures the average distance, while the Hausdorff distance $H(A, B)$ measures the maximum distance between two contours. They are respectively defined as

$$AMINDIST(A,B) = \frac{\sum_{i=1}^{m} MINDIST(a_i, B)}{2m} + \frac{\sum_{j=1}^{n} MINDIST(b_j, A)}{2n} \quad (6)$$

and

$$H(A,B) = \max\{\max_{i\in\{1,\ldots,m\}}\{MINDIST(a_i,B)\}, \max_{j\in\{1,\ldots,n\}}\{MINDIST(b_j,A)\}\} \quad (7)$$

where $MINDIST(x,B)$ is the minimum Euclidean distance between the point x to the contour B, i.e.,

$$MINDIST(x,B) = \min_{i\in\{1,\ldots n\}} \| x - b_i \| \quad (8)$$

For 30 sonograms studied, means of two distances resulted from the traditional graph cut, and the proposed algorithm were listed in Table 1. Results show that under the same user inputs, the proposed method is superior to the traditional graph cut.

Table 1 Comparison of segmentation results for 30 ultrasonograms

	AMINDIST (pixels)	Hausdorff (pixels)
Traditional graph cut	13.9	27.6
Improved graph cut	4.6	10.4

IV. Conclusions

An improved algorithm has been proposed to segment cervical nodes on ultrasonograms. The method takes advantage of the elliptical shape information of cervical nodes to improve the graph cut method. Both the qualitative and the quantitative evaluation of segmentation results indicate that the incorporation of the elliptical shape prior into the graph cut can significantly improve the graph cut segmentation results of cervical nodes on sonograms. The method has a potential to segment other objects with the elliptical shape, such as for the cell or the face detection.

Besides the elliptical shape prior, the investigation of other shape information in the graph cut algorithm for wider applications is one of our future research directions.

Acknowledgments

This work was supported by the National Basic Research Program of China (2006CB705707), Natural Science Foundation of China (No.30570488), Science Foundation of Education Department of Yunnan, China (No. 6Y0042D).

References

1. Boykov Y, Jolly M (2001) Interactive graph cuts for optimal boundary & region segmentation of objects in N-D images, ICCV Proc., Vancouver, BC, Canada, 2001, pp105-112
2. Arias P, Pini A, Sanguinetti G et al. (2007) Ultrasound image segmentation with shape priors: application to automatic cattle rib-eye are estimation. IEEE Trans. on Image Processing 16: 1637-1645
3. Freedman D, Zhang T (2005) Interactive graph cut based segmentation with shape priors, IEEE Computer Society Conference on Computer Vision and Pattern Recognition, San Diego, CA, USA, 2005, pp 755-762
4. Slabaugh G, Unal G (2005) Graph cut segmentation using an elliptical shape prior, IEEE International Conference on Image Processing, Genoa, Italy, 2005, pp1222-1225
5. Funka-Lea G, Boykov, Florin C et al. (2006) Automatic heart isolation for CT coronary visualization using graph-cuts, 3rd IEEE International Symposium on Biomedical Imaging, Arlington, VA, USA, 2006, pp 614-617
6. Fitzgibbon A, Pilu M, Fisher R (1999) Direct least square fitting of ellipses. IEEE Transactions on Pattern Analysis and Machine Intelligence 21: 476-480
7. Cohen L, Cohen I (1993) Finite-element methods for active contour models and balloons for 2-D and 3-D images. IEEE Transactions on Pattern Analysis and Machine Intelligence 15: 1131-1147
8. Sahiner B, Petrick N, Chan H et al. (2001) Computer-aided characterization of mammographic masses: accuracy of mass segmentation and its effects on characterization. IEEE Transactions on Medical Imaging, 20: 1275-1284
9. Huttenlocher D, Klanderman G, Rucklidge W (1993) Comparing images using the Hausdorff distance. IEEE Transactions on Pattern Analysis and Machine Intelligence 15: 850-86

Author: Yuanyuan Wang
Institute: Department of Electronic Engineering
Street: Handan Road
City: Shanghai
Country: China
Email: yywang@fudan.edu.cn

Computerized Assessment of Excessive Femoral and Tibial Torsional Deformation by 3D Anatomical Landmarks Referencing

K. Subburaj[1], B. Ravi[1] and M.G. Agarwal[2]

[1] OrthoCAD Network Research Centre, Indian Institute of Technology Bombay, Mumbai, India
[2] Department of Surgical Oncology, Tata Memorial Hospital, Mumbai, India

Abstract — **Bone torsional deformity is excessive anatomical or axial twist of proximal portion with respect to distal. Accurate, simple, and quick measurement of torsional deformities at preoperative stage is clinically important for decision making in prosthesis design and surgery planning. Commonly used 2D methods for assessing excessive torsion use radiographic images or a set of slices of CT/MR images. The slices representing reference axes of distal and proximal portion are superimposed; the angle between the axes provides a measure of torsion. Representing 3D anatomical landmarks and reference axes in a 2D transverse slice or projected radiographic image leads to inaccurate and inconsistent values. Owing to the complex 3D shape of bones (ex. femur and tibia), there is a need for 3D model based assessment methods with little or no human intervention. Excessive torsion in the tibia and femur affects the procedure of total knee replacement. We present an automated methodology for assessing excessive torsional deformation of femur and tibia bone based on 3D anatomical landmarks based referencing. Reconstructed 3D bone model from a set of CT scan images using tissue segmentation and surface fitting is used in this methodology. Anatomical landmarks on femur and tibia bone are automatically identified based their shape and predefined landmarks spatial adjacency matrix. The identified 3D anatomical landmarks and computed functional and reference axes (femur: neck axis, condylar axis, and long axis; tibia: tibial plateau axis, long axis, and malleolus axis) are used for measuring torsional deformation, using 3D shape reasoning algorithms. The methodology has been implemented in a software program and tested on five sets of CT scan images of lower limb. The computerized methodology is found to be fast and efficient, with reproducible results.**

Keywords — **anatomical landmarks, femoral torsion, tibial torsion, torsional deformities, virtual surgery planning**

I. Introduction

Anatomically deformed femur and tibia (secondary to trauma, congenital defects, prior surgery, etc) give significant challenges to orthopaedic surgeons [1]. This also changes the loading pattern [2] owing to the altered functional axes and distorted anatomic landmarks. Bone torsional deformity can be defined as the excessive anatomical or axial twist of proximal portion with respect to distal one. In case of femur (F), it is a projected angle of femur neck axis and femur condylar line on a plane, which is perpendicular to the longitudinal axis of the bone. This is measured as femoral anteversion or retroversion according to nature of the twist. In tibial bone, tibial torsion is measured as twist of the tibial plateau axis with respect to distal tibia malleolus line.

Torsional deformation has been studied, both in vivo and in dry bone, using a variety of techniques by various researchers. This leads to a wide range of reported femoral and tibial torsion values. The most accurate technique of assessment is by measuring the angle formed by the pins inserted in bone to represent the axes required to measure. However, this method cannot be used in vivo. The next best methods are based on diagnostic medical images, which give a good representation of the underlying anatomy [3]. In image based (2D) studies, various sources of images are used such as x-ray [4], ultrasonic [5], CT [6,7,3], and MRI [8]. In 3D studies, Kim et al [7] studied the femoral anteversion on a set of dry bones using CT data. The fundamental axes (neck axis, long axis, and condylar line) are estimated semi-automatically from the extracted edge coordinates. Liu et al [9] used interactively located landmarks on a digitized model for tibial torsion assessment.

In summary, estimating deformities is important in anatomical understanding for performing virtual surgery planning. 2D methods of measuring torsion using images suffer from inherited issues in various stages, such as (i) orientation of patient (ii) inexact abduction, flexion, and rotation of hip while scanning, (iii) selecting reliable 3D anatomical landmarks, and (iv) choosing best slice representing reference axis. It is difficult to estimate and represent complex 3D reference axes in a x-ray image or CT slice. There is a poor consensus concerning the optimal techniques for their clinical assessment [10]. Researchers have used varieties of axes and reference landmarks in measuring torsion with no established standard in defining them. None of the available methods are suitable for automatic assessment of anatomical deformations. Owing to the complex 3D shape of bones, there is a need for a 3D assessment method, which is simple, reliable, robust, and suitable for use in busy clinical environment.

Chwee Teck Lim, James C.H. Goh (Eds.): ICBME 2008, Proceedings 23, pp. 129–132, 2009
www.springerlink.com

II. Materials and methods

A. Computerized Methodology

Our objective is to accurately measure the torsional deformation of long bones of the lower limb. Each step of the proposed methodology is as follows:

*Algorithm: A*ssessment of torsional deformities
Input: A set of CT scan images of the lower limb
Output: Torsional deformation of the long bones

Procedure:
Step 1: Reconstruct 3D bone models from CT images
Step 2: Identify the required anatomical landmarks
Step 3: Compute medial axis of the long bones
Step 4: Segment the medial axis for computing axes
Step 5: Compute reference axes from the landmarks
Step 6: Measure torsional deformation by reference axes

The reference axes and centers which are needed to assess the torsional deformation are given in table 1.

Table 1 Reference axes

Axis	Terms	Axis	Terms
FNA	Femoral Neck Axis	TML	Tibial Malleolus Line
CL_F	Condylar Line of Femur	CL_T	Condylar Line of Tibia
LA_F	Longitudinal Axis of Femur	LA_F	Longitudinal Axis of Tibia

B. Reference Axes

Anatomical Landmarks: The required anatomical landmarks (Fig. 1) in computing reference axes include, on femur bone: medial and lateral epicondyles (ME and LE), most distal point of each (medial and lateral) condyle (MC and LC), and greater and lesser tronchater (GT and LT); on tibia bone: medial and lateral intercondylar tubercles (spines) (MT and LT), most medial and lateral points of tibial plateau (MP and LP), and medial and lateral malleolus (MM and LM). Anatomical landmarks are localized and identified based on their intrinsic geometric characteristics and spatial-adjacency (Fig. 4). It employs curvature derivatives (curvature gradient, peaks, ridges, pits, and ravines), as well as topology (relative position) of identified landmark regions [12].

Centre of the Femur Head (C_{FH}): The femur head is approximated into sphere from a set of profiles of the cortical bone extracted from CT images. These edge profiles are approximated to circular shape before used as a reference for fitting the sphere. Centre of sphere referred as the centre femur head.

Condylar Lines: Condylar line of the femur (CL_F) is defined as a connecting line between MC and LC landmarks. Condylar line of the tibia (CL_T) is defined as a line connecting MP and LP landmarks on the tibial plateau.

Malleolus Line (TML): A line connecting medial malleoli (MM) on tibia and lateral malleoli (LM) on fibula.

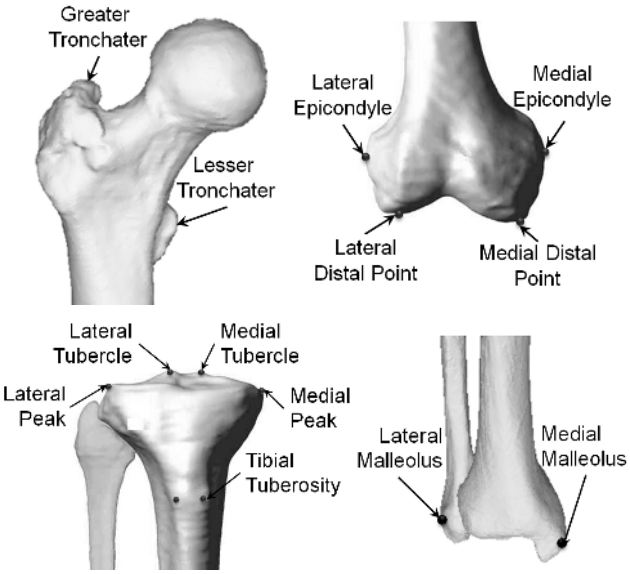


Fig. 1 Required anatomical landmarks on (a) proximal femur, (b) distal femur, (c) proximal tibia, and (d) distal tibia

Longitudinal or Anatomical Axis: This axis passes through the middle of the bone structure rather than connecting only end points. To compute LA_F, we used medial axis [12] of middle long portion (5/8) of the femur. The steps are

Step 1: Orient and divide the femur model into sections
Step 3: Compute medial axis for each section
Step 4: Collect the medial points of the long section
Step 5: Fit a best curve for localizing the axis

The same procedure is applied for computing longitudinal axis of tibia (LA_T) also.

Femoral Neck Axis: Medial axis of the top division (1/4) of the femur is used to establish the femoral neck axis (FNA). This is carried out by identifying a junction in medial axis.

C. Measurement of Torsional Deformation

Femoral Torsion: Three reference axes (FNA, CL_F, and LA_F) are required in computing femoral torsion. Due to the complex orientation, FNA and CL_F are projected on a plane perpendicular to the LA_F. The angle formed between these projected lines measured as femoral torsional angle (Fig. 2).

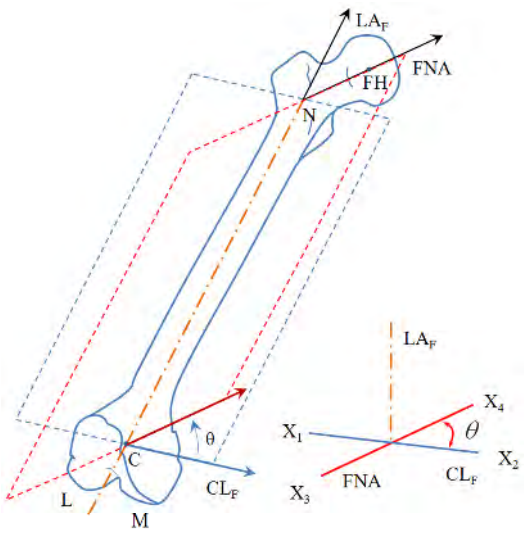


Fig. 2 Method of measuring femoral torsion

Tibial Torsion: Three reference axes (CL_T, TML and LA_T) are required in computing tibial torsion. TML and CL_T are projected on a plane perpendicular to the LA_T. The angle formed between these projected lines is measured as tibial torsional angle (Fig. 3).

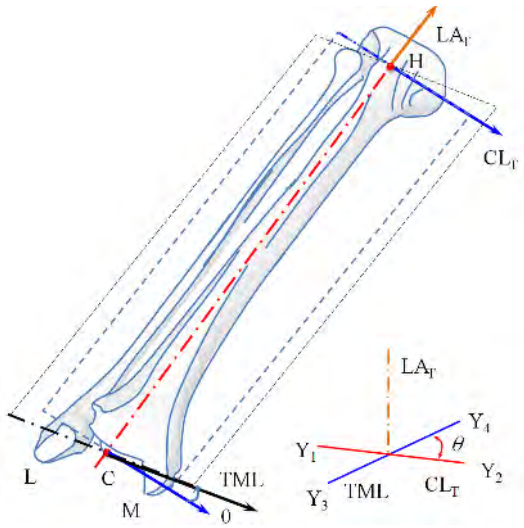


Fig. 3 Method of measuring tibial torsion

III. Implementation and Results

The results are presented here for a knee reconstructed from a set of 496 CT scan image slices (pixel size was 0.782 mm and slice thickness was 2 mm). The CT images were imported in DICOM format, followed by filtering and bony tissue segmentation; the 3D bone surface model is reconstructed in a lab-built 3D reconstruction software program. The reconstructed model's accuracy range with respect to the original model was 0.65 to1.95 mm [11]

Anatomical landmarks are identified on this triangulated surface model before dividing it for medial axis computation. Both landmarks (Fig. 4) and medial axis (Fig. 5) are used in establishing reference axes as explained in section II-B. Since the identified landmarks are on bone rather on body surface, errors caused by skin movement and patient's position during data acquisition are minimized. Each anatomical landmarks is referred in terms of the relative coordinates with respect to the coordinate system established for the corresponding bone. The anatomical landmarks are identified with the accuracy range of 2 to 6 mm [12].

Once the reference axes are established, measurement of torsional deformation is carried out as per the methods de-

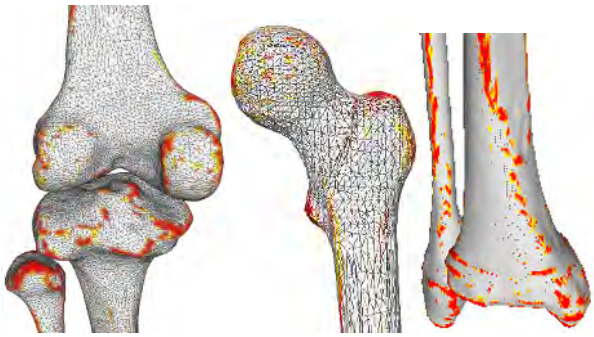


Fig. 4 Identified anatomical landmarks of femur and tibia bone

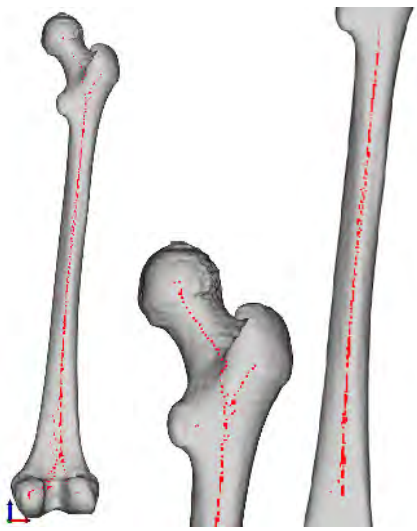


Fig. 5 Medial axis for reference axis (a) complete model, (b) for determining femur neck axis, and (c) for longitudinal axis of the femur

scribed in section II-C. Figure 6a and 6b show the measurement of the femoral and tibial torsion with reference axes and landmarks respectively. The measured femoral torsion was 12.8^0 (anteversion) and tibial torsion was 22.12^0.

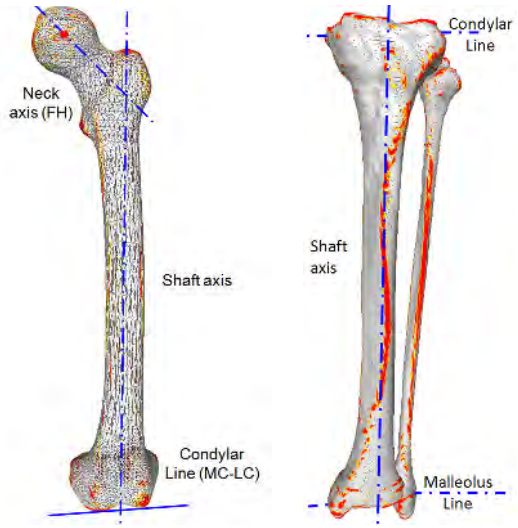


Fig. 6 Measurement of femoral and tibial torsion

Three sets of CT scan images were used in verifying the effectiveness of the proposed methodology. The measured femoral and torsional deformation angle are verified with respect to the angle obtained by manually placed reference axes on the same 3D reconstructed bone models. The deviation observed in femoral torsion was 1.98^0 to 3.13^0 and in tibial torsion was 2.12^0 to 2.89^0. Even though the sample lot is low in numbers to establish the relations, the results and accuracy obtained establish the superiority of the 3D based approach.

IV. Conclusions

This article presents a new methodology for assessing torsional deformities of long bones (femur and tibia) of the lower limb. The method ensures repeatability by the characterized anatomical landmarks (bone) and established reference axes (medial axis and landmarks referencing). The method offers automated, fast, and non-invasive measurement of torsional deformation. It works well where non-imaging methods (laser scanning and palpation) do not work; when anatomical landmarks are on bone rather on body surface. For example on obese patients, the required anatomical landmarks on legs are often not distinguishable from the surrounding subcutaneous fat.

Further work includes verification of reproducibility and accuracy with more data. We plan to use the measured deformation values in virtual surgery planning of total knee replacement and implant fixation analysis.

Acknowledgment

This work is a part of an ongoing project in OrthoCAD Network Research Centre at IIT Bombay in collaboration with Non-Ferrous Materials Technology Development Centre, Hyderabad and Tata Memorial Hospital, Mumbai, supported by the Office of the Principal Scientific Adviser to the Government of India, New Delhi.

References

1. Lackman RD, Torbert JT et al (2008) Inaccuracies in the assessment of femoral anteversion in proximal femoral replacement prostheses. J Arthroplasty 23:97-101
2. Schwartz M, Lakin G (2003) The effect of tibial torsion on the dynamic function of the soleus during gait. Gait & Posture 17:113-118
3. Bouchard R, Meeder PJ et al (2004) Evaluation of tibial torsion-comparison of clinical methods and CT. Rofo 176:1278-1284
4. Brunner R, Baumann JU (1998) Three-dimensional analysis of the skeleton of the lower extremities with 3D-precision radiography. Arch Orthop Trauma Surg 117:351-356
5. Butler-Manuel P, Guy R et al (1992) Measurement of tibial torsion-a technique applicable to ultrasound and CT. Br J Radiol 65:119-126
6. Murphy SB, Simon SR, Kijewski PK et al (1987) Femoral anteversion. J Bone Joint Surg Am 69:1169-76
7. Kim JS, Park TS et al (2000) Measurement of femoral neck anteversion in 3D. 3D modeling method. Med Biol Eng Comput 38:610-616
8. Schneider B, Laubenberger J et al (1997) Measurement of femoral anteversion and tibial torsion by MRI. Br J Radiol 70:575-579
9. Liu X, Kim W, Drerup B et al (2005) Tibial torsion measurement by surface curvature. Clin Biomech 20:443-450
10. Davids JR, Davis RB (2007) Tibial torsion: significance and measurement. Gait & Posture 26:169-171
11. Subburaj K, Ravi B (2007) High resolution medical models and geometric reasoning starting from CT/MR images. Proc. IEEE Int Conf CAD Comput Graph, Beijing, China, 2007, 441-444.
12. Subburaj K, Ravi B, Agarwal MG (2008) Shape reasoning for identifying anatomical landmarks. Comput Aided Des Appl 5:153-160
13. Cornea ND, Silver D, Min P (2007) Curve-Skeleton Properties, Applications, and Algorithms. IEEE Trans Visualization Comput Graphics 13:530-548

Corresponding author:

Author: Dr. Bhallamudi Ravi
Institute: Indian Institute of Technology Bombay
Street: Powai
City: Mumbai
Country: India
Email: b.ravi@iitb.ac.in

Modeling the Microstructure of Neonatal EEG Sleep Stages by Temporal Profiles

V. Krajča[1], S. Petránek[1], J. Mohylová[2], K. Paul[3], V. Gerla[4] and L. Lhotská[4]

[1] Department of Neurology, Faculty Hospital Na Bulovce, Prague, Czech Republic
[2] VŠB-Technical University, Ostrava, Czech Republic
[3] Institute for Care of Mother and Child, Prague, Czech Republic
[4] Czech Technical University in Prague, Czech Republic

Abstract — **The electroencephalogram (EEG) and neonatal sleep analysis provide sensitive markers of brain maturation and developmental changes in term and preterm newborns. A new method for automatic sleep stages indication was developed. The procedure is based on processing of time profiles using adaptive segmentation and subsequent classification of extracted signal graphoelements. The time profiles, functions of the class membership in the course of time, reflect the dynamic EEG structure and may be used for indication of changes in the neonatal sleep. The method is able to detect the sleep stage changes even in preterm infants´ EEG.**

Keywords — **EEG, neonates, adaptive segmentation, profiles.**

I. Introduction

One of the most important indicators to study the maturation of the child brain is the electroencephalogram (EEG). Visual analysis of the EEG activity in newborns is a difficult and tedious task; a quantitative method of objective analysis is needed.

The critical evaluation of recent techniques of automated sleep analyses in neonatal neurointensive care units can be found in [1]. One of the first approaches to formalize the visual EEG analysis was a structural analysis of the EEG segments by hierarchical modeling of the EEG [2]. The pioneering work in the field of adaptive segmentation was done by Bodenstein and Praetorius [3]. For the segment boundary detection, the difference measure computed from fixed and moving windows was estimated. This prevents the multichannel adaptive segmentation from working independently in each channel. Barlow [4] was the first who applied the structural time profiles for description of tracé alternant and REM sleep patterns in the neonatal sleep EEG. The profiles were computed from one EEG channel and spectral and statistical parameters were computed from the segments without further analysis of the dynamic structure of the profile.

We have developed a new method for automatic sleep stages detection in neonatal EEG based on time profiles processing and modeling the sleep EEG microstructure using adaptive segmentation and cluster analysis. We have applied it to fullterm neonatal EEG [5], and tested it also on modeling the EEG of preterm infants. It is based on processing and smoothing of the temporal profiles. The purpose of the present study was to show, that the method is sufficiently sensitive to detect the sleep stages both in the EEG of the preterm and fullterm infants. The detection curve specification is based on adaptive segmentation, feature extraction and subsequent classification by cluster analysis. The resulting structural time profiles (temporal profiles) are further processed to reveal the sleep stages in preterm infant EEG. In fullterm EEG, sleep stages are reflected in compressed voltage graphs of the raw EEG, where the increased voltage during quiet sleep (QS) and decreased voltage during active sleep (AS) manifests itself in compressed time scale of 1-2 hours. This signal structure is not apparent in preterm neonates in postconception age (PCA) of 38 weeks and less and in the cases of abnormal recordings. So it is more suitable to use more advanced methods for hidden EEG structure disclosing. The automatic sleep stage detection is very desirable for functional brain maturation study in neonates, where sleep stages are determined by an expert visually. Further on, for objective quantitative analysis of the maturation of the child brain, we need the precise signal statistics [6]. Adaptive segmentation can contribute to this purpose by finding the instants of burst/interburst events and changes of signal stationarity. Both aforementioned tasks can be made by structural analysis of the EEG time profiles. The structural time profiles analysis can provide a unified approach both to the sleep state change detection and feature extraction and signal statistics computing. In some cases the method can reveal the hidden structure of the neonatal sleep EEG, which was not apparent in compressed time scale and therefore was very difficult to detect automatically. The alternative approach using both EEG and polygraphic channels is discussed in [7].

II. Material

Three groups of healthy sleeping newborns of different age (total 40 infants) were recorded in standard conditions

Chwee Teck Lim, James C.H. Goh (Eds.): ICBME 2008, Proceedings 23, pp. 133–137, 2009
www.springerlink.com

with reference montage (linked ears) for 90-120 minutes. The postconceptial age (PCA) was 31-40 weeks. An experienced physician evaluated the records. He marked the periods of quiet sleep (QS) and active sleep (AS) by flags during visual inspection of the EEG recordings. The polygraphic channels were not used for the automatic analysis. The antialiasing bandpass filter (0.4 – 50 Hz) was used for signal conditioning. The typical periods of quiet and active sleep were marked by flags. Polygraphic channels were recorded, but not used in the signal analysis. The bipolar montage was used to eliminate the moving artefacts. The sampling frequency was 256 Hz for newer recordings and 128 Hz for the older ones.

III. Methods

The procedure is based on processing of time profiles computed by adaptive segmentation and subsequent feature extraction and classification of signal graphoelements

Adaptive segmentation: The used adaptive segmentation method is based on two connected windows that are sliding along the signal. The change of stationarity is indicated by local maxima of their difference measure (the difference of the mean amplitude and the mean frequency in the window). The threshold limits the small random fluctuations of the measure. This approach makes the multichannel adaptive segmentation working independently and simultaneously in all channels possible [8]. The algorithm divides the EEG signal into piece-wise stationary segments of variable length depending on the change of stationarity of the signal. The feature extraction from such relatively homogeneous epochs is more effective than from the fixed epochs. This holds especially true when analyzing such highly variable pattern as tracé alternant. The example of multichannel adaptive segmentation of the signal recorded during quiet and active sleep is shown in Figure 1.

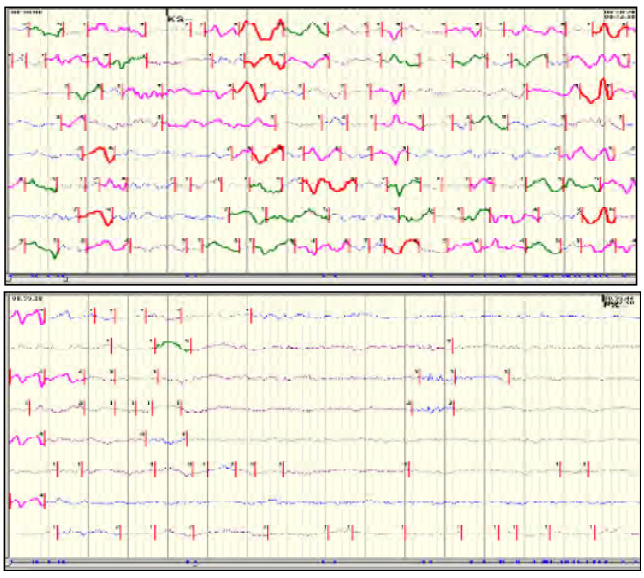


Fig. 1. Multichannel adaptive segmentation and classification. Quiet sleep (above), active sleep (below). Numbers indicate the segment labels - the class's membership. Vertical lines designate the segment boundaries.

Feature extraction: The EEG segments detected by adaptive segmentation were described by ten features: the amplitude variance, power in the frequency bands delta, theta, and alpha, mean frequency, first and second derivative of the signal [8].

Classification: The EEG segments characterized by the above features were classified into several classes by cluster analysis (k-means algorithm [9]). The classes were ordered by increasing value of amplitude. The example of classification of quiet and active sleep segments is shown in Fig. 1. The segments are designated by relevant class number and identified by different color directly in the real EEG recordings.

Multichannel temporal profiles:

The temporal profiles are the functions of the class membership in the course of time in relevant channels. They reflect the dynamic microstructure and the trends in EEG recordings; they represent a compressed schematic plot of the EEG signal (see Fig. 2). If computed from several channel derivations, they reflect also the topography of the EEG, and possible asymmetry [6]. In our case the 8 channel recording was used.

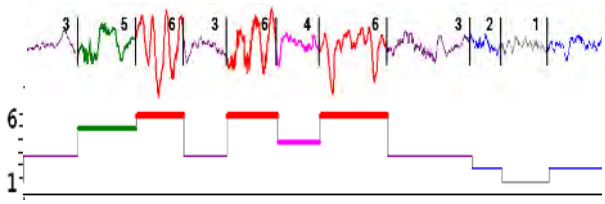


Fig. 2. The temporal profile – the class membership in the course of time (below). The corresponding EEG with segment membership identified by a color is above. The numbers denote the classes, vertical lines are the segment boundaries estimated by adaptive segmentation.

Algorithm: The processing of time profiles consists of the following steps (Fig. 3):

1. Multichannel time profiles were created by adaptive segmentation and cluster analysis.
2. Profiles were divided by vertical raster of the width WL_{Bin}.

3. The class membership was averaged in all channels into one curve. The moving average is computed in the window of length WL_{Mean}.
4. WL_{Mean} is subtracted from the averaged class membership and it is squared (variance of the class membership)
5. The resulting curve is smoothed by another MA (moving average) filter of the length WL_{Smooth}.
6. The sleep stage change is signaled by threshold crossing.

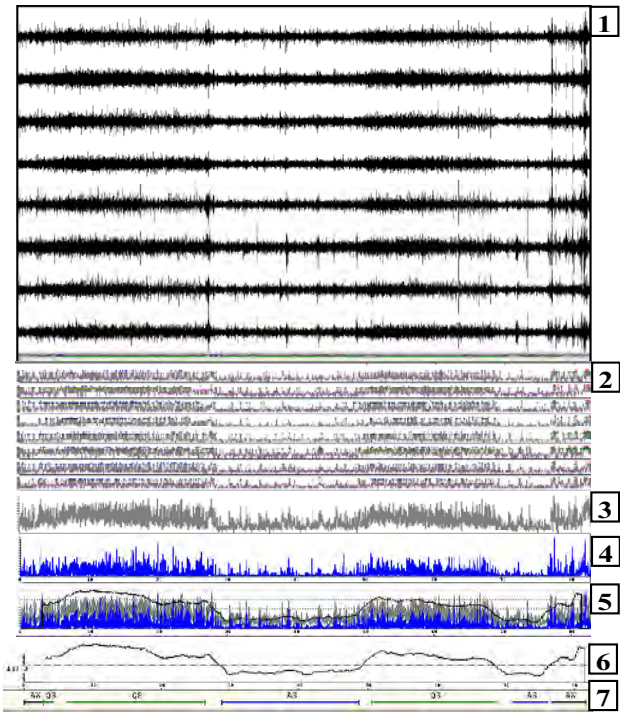


Fig. 3. The temporal profile computing and processing. 1-comprimed original EEG (80 min), 8 channels. 2-temporal profiles. 3-average of 8 profiles. 4-profiles variance (subtraction of the mean and squaring). 5-variance smoothing (solid black line). 6-sleep stages detection by threshold crossing. 7-visual evaluation by a physician (AW-awake, QS-quiet sleep, AS-active sleep). Full term neonate of 40 weeks PCA.

The length of MA filters was found experimentally. They differ for preterm and full term neonates (Tab.1).

Nevertheless, as soon as they were set (one set of values for one group with the same age, the other for the group of a different age), the parameters remain the same for each group (age must be known in advance). Another parameter which contributed to the detection curve smoothing was the width of the raster used for summing and averaging the class membership for each channel (WL_{Bin}). Its value was constant for all age groups.

Tab. 1. The parameter settings (window lengths) used for detection curve smoothing and the delay in transition resolution for step-like changes of the sleep stage for sampling frequency 256 Hz.

PCA (weeks)	31-38	>40
WL_{Mean}	80	5
WL_{Mean}	400	240
WL_{Bin}	100	100
Delay [sec]	156	93

IV. Results

The following picture shows the results of application of the described methods to neonatal EEG record. Above is the compressed EEG signal (80 min); below are the temporal profiles, under them are the curves corresponding to the steps 1-5 from Fig. 3. At the bottom is the final detection curve.

Artefacts cause the problems in the automatic EEG analysis. We show a simple method for artefact detection and elimination. The moving artefacts are classified into classes with highest value of amplitude feature. If we cut off the last classes exhibiting the highest amplitude values in temporal profile, and if we process the profiles without such grapholeements, the artefacts are eliminated and the quality of detection curve is improved. An example is shown in Fig. 4. In the original EEG there are amplitude artefacts in the

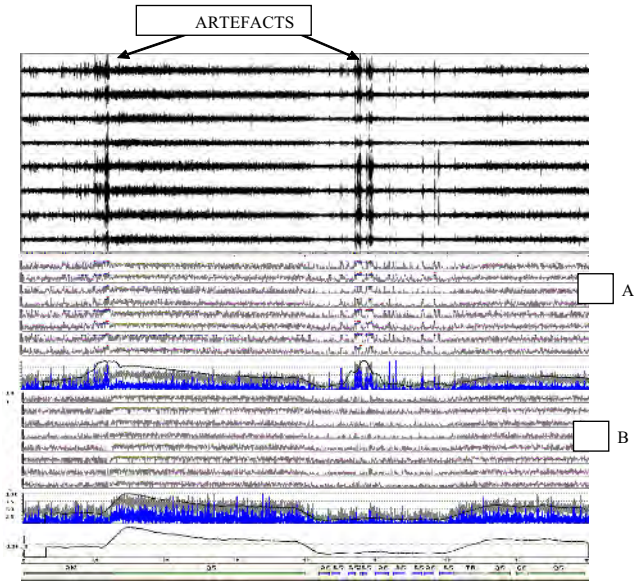


Fig. 4. Elimination of the artefacts by cutting the number of classes in the profile. The last three classes of total 14 containing artefacts were eliminated. They are not present in relevant profiles (B). A-original profiles, 14 classes. B-artefacts elimination, only 10 classes processed.

upper part of the picture. Below (4A) is the temporal profile with uncorrected class membership (14 classes). The artefacts signaled the false detection curve increase. If we use only the parts of the profile with the class membership less than 11, the noisy part of the profile (with the highest class membership containing artefacts) is eliminated (4B).

The results of computerized analysis compared with the visual evaluation are presented in Tab. 2. In most cases there was a good agreement. In some individual cases, the above mentioned artefact correction must be used. Two records of 32 postconception age neonates exhibit no visible changes in the detection curve.

Tab. 2. The three groups of neonates and the agreement with the visual evaluation. In the table the numbers of cases are presented.

PCA (weeks)	31-33	36-38	>40	Total / %
Number of records	10	13	17	40 [100,0%]
Agreement with expert	8	13	12	33 [82,5%]
Correction of artefacts	0	0	5	5 [12,5%]
Not possible to evaluate	2	0	0	2 [5,0%]

V. Discussion

Adaptive segmentation parameters

In all analyzed graphs the same adaptive segmentation parameters were used (window length 256 samples, segmentation threshold 0.5, and minimum length of segments 128 samples).

Optimal number of classes

The optimal number of classes was estimated with Bezdek´s criterium of validity for fuzzy c-means algorithm [10]. The optimal values were in the range of 12-18 classes both for term and preterm newborns.

Parameters for profiles processing

The only optional parameters for temporal profiles were the window lengths for detection curve creating and smoothing. The parameters were kept fixed during all experiments. It was very interesting (and it corresponds to our knowledge of the brain maturation), that we have to use two different sets of parameters for fullterm and preterm neonates. As soon as we selected the parameters, their values were kept constant within both groups.

The resolution of stages

The transition from one sleep stage to another is continuous, it does not occur abruptly. There is a question with what delay we are able to detect the step like changes in the detection curve. It depends on the width of relevant windows and it can be expressed as Delay = WL_{Bin}*WL_{Smooth}. Tab. 1 shows the values for the sampling frequency 256 Hz. The delay affects the initial part of the detection curve processing, and also the transition from one stage to another (Fig. 5).

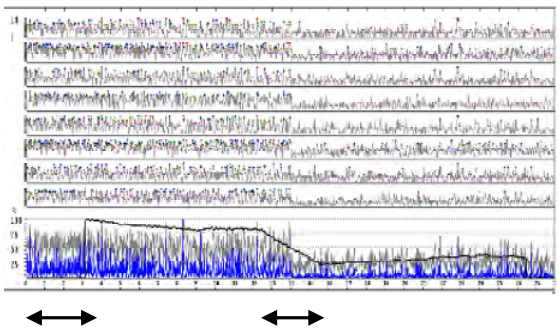


Fig. 5. The delays in stages resolution in the beginning of the signal and during the step-like change of sleep stage. 28 min, delay is 3 minutes (sampling frequency 128 Hz), window lengths are WL_{Bin} 100 samples and WL_{Smooth} is 240 samples.

VI. Conclusions

The examples proved a good ability of proposed methodology to model the sleep microstructure for groups of children of a different age ranging from 31 to 40 weeks of PCA, even for the cases, where the sleep transition was not evident in the original EEG records. The best results were observed for the newborns of 36-38 weeks of PCA. The older children (40 weeks) exhibited the structure of EEG stages too, but because of their activity, the EEG was more contaminated by movement artefacts. Nevertheless, the QS could be detected very reliably and also the transitions from QS to AS and vice versa were clearly visible. The age of children (the brain maturation) was reflected in values of parameters necessary for successful distinction of the sleep stages in the detection curve: there were two stable sets of parameters, one set for fullterms and another set for preterms. If the EEG analysis did not prove to be distinctive with the use of relevant parameter set, the consultation with the physician disclosed, that the EEG graph of the neonate was visually described as immature. The part of the methodology is also the extraction of quantitative parameters (segment boundaries detected by adaptive segmentation, features describing each segment) which reflect the differences between quiet and active sleep and related neonatal brain maturation.

Acknowledgment

This work was supported by grants IGA 1A8600-4, and AV 1ET101210512

REFERENCES

1. Scher M. S., (2004): 'Automated EEG-sleep analyses and neonatal neurointensive care', Sleep Medicine, 5, pp. 533-540
2. Jansen B.H., Hasman A., Lenten R., Pikaar R. (1980): Automatic sleep staging by means of profiles. In Lindberg D.A.B, Kaihara S., eds., MEDINFO 80, Amsterdam: North-Holland, 385-9
3. Bodenstein G., Praetorius H.M.: Feature extraction from the Electroencephalogram by adaptive segmentation, Proc. of the IEEE, vol. 65, no.5, (1977) 642-652.
4. Barlow, J.S."Computer characterization of trace´ alternant and REM patterns in the neonatal EEG by adaptive segmentation - an exploratory study", Electroenceph Clin. Neurophysiol. 60, pp.163–73, 1985.
5. Krajca, V., Petranek, S., Paul, K., Matousek, M., Mohylova, J., and Lhotska L. Automatic Detection of Sleep Stages in Neonatal EEG Using the Structural Time Profiles , in EMBC05, Proceedings of the 27th Annual International Conference of the IEEE-EMBS, September 1-4, Shanghai, China
6. Paul K., Krajča V., Roth Z., Melichar J., Petránek S. Quantitative topographic differentiation of the neonatal EEG. Clinical Neurophysiology 117, (2006) 2050-2058.
7. Gerla, V., Paul, K., Lhotska, L., and Krajca, V. Multivariate Analysis of the Full-Term Neonatal Polygraphic Data, IEEE Trans. Inf. Tech in Biomed., 2008 (in press)
8. Krajca V., Petranek S., Pataková I, and Varri A. (1991): 'Automatic identification of significant graphoelements in multi-channel EEG recordings by adaptive segmentation and fuzzy clustering', Int. J. Biomed. Comput. 28, pp.71-89,
9. Anderberg M.R. (1974): 'Cluster Analysis for Applications'. Academic Press, New York.
10. Bezdek J.C.: Pattern Recognition with Fuzzy Objective Functions Algorithms. New York, Plenum Press (1981)

Author: Vladimír Krajča
Institute: Faculty Hospital Na Bulovce
Street: Budínova 2
City: Prague 6
Country: Czech Republic
Email: krajcav@fnb.cz

Optimization and Characterization of Sodium MRI Using 8-channel ^{23}Na and 2-channel ^{1}H RX/TX Coil

J.R. James[1,2], C. Lin[1], H. Stark[3], B.M. Dale[4], N. Bansal[1,2]

[1]Department of Radiology, Indiana University School of Medicine, Indianapolis, IN, USA
[2]School of Health Sciences, Purdue University, West Lafayette, IN, USA
[3]Stark Contrast, MRI Coils Research, Erlangen, Germany
[4]Siemens Medical Solutions, Cary, NC, USA

Abstract — **The initial results of *in vivo* ^{23}Na magnetic resonance imaging (MRI) of the human torso at 3-Tesla using an 8-channel dual tuned ^{23}Na and ^{1}H transmit/receive coil for various body applications are presented. We are able to obtain ^{23}Na images of the human torso with 0.3 cm spatial resolution and ~ 20 SNR in ~15 min. These images were acquired with imaging parameters optimized under specific absorption rate limit for human scans. Because a trans-membrane sodium gradient is critical for cell survival, the ability to perform ^{23}Na MRI of the torso in clinical settings would be useful to non-invasively detect and diagnose a number of diseases of the liver, gallbladder, pancreas, kidney, spleen and other body organs.**

Keywords — **sodium, MRI, in vivo, SAR**

I. Introduction

Non-invasive sodium (^{23}Na) MRI has the ability to advance MR imaging beyond the routinely used proton (^{1}H) MRI because it can provide profound information about tissue physiology and metabolism at the cellular level. The motivation of ^{23}Na MRI is based on the fact that in certain diseased state, there is an increase in tissue [Na^+] due to interstitial and/or cytotoxic edema. Interstitial edema is caused by inflammation and vascular changes, and results in increased relative extracellular space where the Na^+ concentration is ~10 times higher than the intracellular concentration. Cytotoxic edema is caused by plasma membrane disruption and improper functioning of the Na^+-K^+ pump, and results in increased intracellular [Na^+]. The impact of ^{23}Na MRI has been overshadowed by existing technical difficulties when performing ^{23}Na MR scans. These difficulties arise from the inherent biological and MR properties of the ^{23}Na nucleus. Tissue ^{23}Na MR signal is ~10^{-4}-times weaker than the water signal because of its lower tissue concentration and MR receptivity compared to ^{1}H. In addition, ^{23}Na has very short transverse relaxation time (T_2: ~10 ms) which results in significant signal loss from excitation to imaging data acquisition. These properties of ^{23}Na translate to long image data acquisition times, limited spatial resolution and low signal-to-noise ratio (SNR).

Some of the areas that could be improved upon for obtaining better quality ^{23}Na MRI include: 1) increased main magnetic field strength 2) efficient RF coil design, and 3) pulse sequence and imaging protocol optimization. Our goal in this work was to enhance the quality of ^{23}Na MRI of the human torso using a 3-Tesla Siemens MR scanner and an 8-channel phase-arrayed dual tuned ^{23}Na and ^{1}H transmit (Tx)/receive (Rx) coil. A gradient-echo imaging sequence, commonly available on all clinical scanners, was optimized for the best possible combination of SNR, spatial resolution, and scan time without exceeding the US Food and Drug Administration (FDA) recommended specific absorption rate (SAR).

II. Methods

A. Coil design

The dual tuned ^{23}Na/^{1}H coil design for developing ^{23}Na imaging on Siemens 3T TIM Trio scanner was adapted from Lanz *et al*. [1]. The coil array consisted of two identical top and bottom plates (30 x 30 cm^2) as shown in Figure 1. The top plate was slightly curved to fit the curvature of the human torso. Each plate consisted of one ^{23}Na Tx loop and four ^{23}Na Rx elements that covered a field-of-view (FOV) of 20 x 24 cm^2. The two large Tx loops provided a relatively homogenous radio-frequency (RF) excitation and deep penetration, and the eight Rx elements provided a high filling-factor and SNR. Each coil plate also consisted a ^{1}H

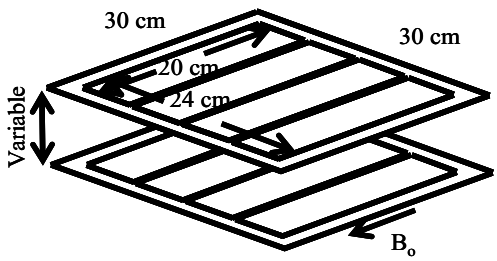


Fig. 1: Design of a dual tuned 8-channel ^{23}Na and ^{1}H Torso Coil.

Chwee Teck Lim, James C.H. Goh (Eds.): ICBME 2008, Proceedings 23, pp. 138–141, 2009
www.springerlink.com

Tx/Rx loop arranged around the ^{23}Na Rx arrays for ^{1}H MRI for co-registration purposes without having to use the inbuilt body coil. The flexibility to use the inbuilt body coil, when the 8-channel dual tuned ^{23}Na/^{1}H coil is plugged-in, was made possible by cable traps and detuning units. A number of low noise pre-amplifiers were also incorporated to reduce noise in the image.

Two sets of polyethylene tubes (Φ = 6 mm) filled with 150 mM NaCl were placed around the top and bottom ^{23}Na Rx elements covering 20 x 24 cm^2. These tubes served as fiduciary markers for co- registration purposes, signal intensity normalization and RF inhomogeneity correction.

B. Pulse sequence optimization

A 10 L plastic carboy filled with 50 mM sodium chloride (NaCl) was used for pulse sequence development and protocol optimization. A modified 3D gradient-echo sequence was used for acquiring trans-axial ^{23}Na images with the 8-channel dual tuned ^{23}Na/^{1}H coil. A very short echo time (TE) was used to minimize signal loss due to transverse relaxation. The short TE was achieved by using asymmetric echoes combined with volumetric interpolation. The minimum allowed receiver bandwidth (BW) was used to reduce the noise level. RF transmitter was calibrated by measuring ^{23}Na signal intensity as a function of transmitter voltage and a flip angle that matched the Ernst angle condition was used for achieving maximum SNR. Use of a short repetition time (TR) allowed collection of large number of signal averages over a reasonable time period. Elliptical acquisition was applied to further improve the SNR and to maintain the spatial resolution while reducing imaging time.

The 10 L phantom was imaged using both the 8-channel dual tuned ^{23}Na/^{1}H coil and the scanner's in-built body coil for SNR comparisons in the ^{1}H images. Trans-axial ^{1}H images were acquired using Half Fourier Acquisition Single Shot Turbo Spin Echo (HASTE) sequence with clinically approved and optimized parameters. The center of the slices for both ^{23}Na and ^{1}H images were matched for co-registration and further quantification.

Shimming of the magnet was done using the water ^{1}H signal prior to acquiring any MR images. An automatic 3D field map technique and manual shimming was employed to achieve the minimum full width half maximum (FWHM) for signal in frequency domain over the entire volume to improve SNR.

C. Specific Absorption Rate (SAR) evaluation of the coil for patient safety

SAR for the 8-channel dual tuned ^{23}Na/^{1}H coil was characterized using the FDA recognized 'Calorimetric Method' described in the National Electrical Manufacturers Association (NEMA) Standards [2]. The SAR measurements were performed at both ^{23}Na and ^{1}H frequencies using the optimized pulse sequence and imaging parameters as to be used for *in vivo* human imaging. The same phantom was used as used for pulse sequence optimization. 50 mM NaCl in the filling solution yielded a coil loading equivalent to that of a human. The phantom also contained 0.5 mM Omniscan Gadodiamide *(Nycomed Inc, Princeton, NJ)* to shorten the ^{1}H relaxation times. The phantom was wrapped in two layers of plastic sheet to avoid heat loss. A Digi-sense standard temperature controller with Type-T high temperature thermocouple probe *(Barnant Co., Barrinton, IL)* was used to measure the temperature of the phantom filler material. Accuracy of this temperature measuring device was 0.1 ˚C over -200 to 400 ˚C.

The phantom was equilibrated with the surrounding temperatures in the magnet bore for at least 2 hrs with fan in the scanner turned on. The initial temperature of the phantom (T_i) was noted using the temperature sensor. The phantom was then placed at the iso-center of the magnet for scanning. ^{23}Na and ^{1}H MRI sequences were run repeatedly for ~ 1 hr each to achieve a significant increase in temperature. The final temperature (T_f) of the phantom was noted after completing each of the ^{23}Na and ^{1}H scans. The energy, E (in joules), absorbed by the phantom of mass, M (in kilograms), and specific heat, c (in joules/ kg °C), was calculated using the equation: $E = M \times c \times (T_f - T_i)$. The average power, P (in watts), during the total scan time, τ (in seconds) was calculated using the equation: $P = E/\tau$. The SAR was calculated using the equation: SAR = P /M.

D. Feasibility studies for in vivo imaging

In vivo 3D ^{23}Na images of healthy volunteers were acquired using the 8-channel dual tuned ^{23}Na/^{1}H coil after obtaining informed consent. The subjects were positioned supine on the bottom plate of the coil with liver positioned in the centre of the coil. The curved top plate was placed at the top of the torso and aligned with the bottom plate using laser markers. No respiratory or cardiac gating was used.

3D trans-axial ^{23}Na images were acquired with the following optimized parameters: pulse sequence: FLASH, TR = 12 ms, TE = 2.81 ms, number of transits = 128, BW = 130 Hz/px, flip angle = 50°, data matrix = 128 ×128, FOV = 40 × 40 cm^2, number of slices = 12, slice thickness = 20 mm. Total imaging time was 14.15 min.

3D multi-slice ^{1}H images were acquired using the dual tuned ^{23}Na/^{1}H coil without moving the patient for anatomical comparison. The following imaging parameters were used: pulse sequence: HASTE, TR = 1000 ms, TE =

105 ms, number of transits = 1, slice orientation =trans-axial, data matrix = 512 × 512, FOV = 40 × 40 cm^2, number of slices = 24, slice thickness = 8 mm, and slice gap = 2 mm. Total imaging time was 1.25 min.

SNR for all images was estimated by dividing the average signal in a given region of interest (ROI) with the standard deviation of the background noise.

III. Results

^{1}H MR images of the 10 L NaCl phantom collected using the HASTE imaging sequence with the 8-channel $^{23}Na/^{1}H$ coil and the in-built body ^{1}H coil are compared in Figure 2. The 8-channel dual-tuned $^{23}Na/^{1}H$ coil gave approximately two times better average SNR than the in-built body coil. The 8-channel $^{23}Na/^{1}H$ coil also provided better shimming compared to the body coil with both automatic 3D phase mapping technique and manual adjustments of shim currents. ^{23}Na images of the same phantom collected using the 8-channel $^{23}Na/^{1}H$ coil with 3D FLASH imaging sequence and the optimized imaging parameters had an average SNR of ~20.

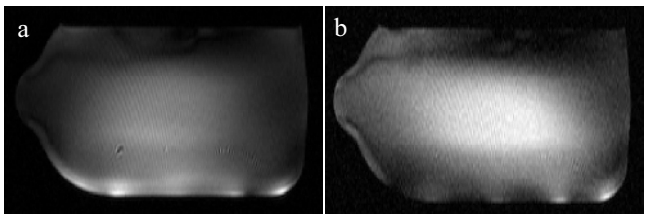


Fig. 2: Proton images of 10 L NaCl phantom acquired with (a) dual tuned 8-channel $^{23}Na/^{1}H$ coil and (b) in-built body coil for SNR comparisons

SAR measurements using the FDA recognized NEMA Standards "Calorimetric Method" showed that the 8-channel $^{23}Na/^{1}H$ coil produced a temperature increase of 1.1 °C during ^{23}Na MRI and 1.0 °C during ^{1}H MRI over one hour. These temperature changes correspond to an SAR of 1.1 W/kg at ^{23}Na frequency and 1.2 W/kg at ^{1}H frequency. The accuracy of the thermocouple used for measuring the phantom temperature was ±0.1°C. This accuracy introduced approximately 10% error in the SAR measurements. These experimentally determined SAR values are approximately one-fourth of the maximum safe SAR of 4 W/kg recommended by FDA for torso and head MRI.

The feasibility of acquiring ^{23}Na images of the human torso with the 8-channel $^{23}Na/^{1}H$ coil is shown in Figure 3. A series of representative trans-axial ^{23}Na and the corresponding ^{1}H images of the torso are shown in the figure. The left and right ventricles and the septum of the heart can be seen in the first slice of the ^{23}Na images. The ventricles appear hyper-intense in ^{23}Na MRI due to high $[Na^+]$ in the blood. The liver can be seen in slices 2-5 with relatively homogeneous signal intensity. The gallbladder is seen as a hyper-intense feature between the liver lobes in slices 5 and 6. The kidneys in the last three slices appear hyper-intense because of high $[Na^+]$ in the medulla. The vertebral canal and spine also show hyper-intense signal in all the slices due to high $[Na^+]$ in the cerebral spinal fluid. The in-plane resolution of the ^{23}Na images was 3.1 × 3.1 mm^2 and the average SNR in the image was ~ 20. The corresponding ^{1}H images collected for anatomical comparison had a resolution of 0.08 x 0.08 cm^2.

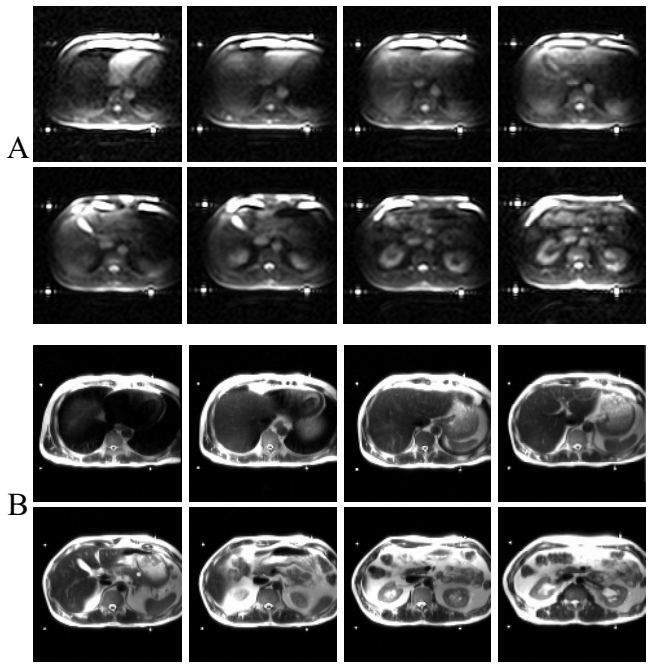


Fig. 3: Selected trans-axial ^{23}Na images (A) and the corresponding ^{1}H image (B) of a healthy volunteer acquired on the 3-T system using the 8-channel dual tuned $^{23}Na/^{1}H$ coil.

IV. Discussion

The ability to obtain *in vivo* ^{23}Na images of the torso at 3T using the 8-channel $^{23}Na/^{1}H$ coil appear very promising. These images were acquired in >15 minutes, a time period acceptable for clinical imaging. The images had reasonably good resolution and SNR considering that the ^{23}Na signal in tissue is ~10^{-4}-times weaker than the water ^{1}H signal. 3D imaging of the whole volume was employed for better coverage and for shorter imaging time since it aided in

reducing the TE considerably by allowing the use of a non-selective RF excitation pulse. The various changes made to the pulse sequence included the use of an asymmetric k-space sampling combined with volumetric interpolation, use of minimum allowed receiver BW, a flip angle that matched the Ernst angle condition and a short TR with large number of signal averages. The optimizations were done to the modified 3D GE pulse sequence to obtain ^{23}Na images with a maximum SNR.

For *in vivo* human imaging, the FDA recommends that the SAR should not exceed 8 W/kg in any gram of tissue (head or torso) and 4 W/kg averaged over the whole body. SAR is directly related to the square of RF amplitude (B_1). B_1 is inversely proportional to the gyro-magnetic ratio of the concerned nuclei. Therefore a ^{23}Na pulse would require four times more RF power than a ^{1}H nucleus. But SAR is also directly proportional to the square of frequency (ω^2). Due to a lower ω for ^{23}Na than ^{1}H, the SAR values computed for ^{23}Na and ^{1}H are almost identical [3]. The results of our SAR measurements show that the SAR values for ^{23}Na and ^{1}H MRI were 1.1 ± 1 and 1.2 ± 1 Watts/kg, respectively. These values are approximately one-fourth of the maximum safe SAR of 4 W/kg recommended by FDA. The heat deposition is expected to be less than 1.1-1.2 W/kg during *in vivo* ^{23}Na MRI experiments because of heat dissipation by blood flow and perfusion.

Though the efficient coil design with eight receive-elements allowed us to image a large torso region in all directions with optimum SNR, a significant B_1 inhomogeneity artifact was present in the images because the sensitivity of a coil decreases as a function of distance from the coil elements. There was an exponential drop in the signal intensity towards the centre of the image which made the central liver region appear darker (Figure 3). We plan to overcome this problem by applying RF field inhomogeneity corrections using fiduciary markers and a reference placed near the torso.

There are numerous possible applications of *in vivo* ^{23}Na MRI in the abdominal region. ^{23}Na MRI could be useful for detecting and assessing ischemic damage which results in an increase in intracellular [Na^+] [4]. It could aid in the diagnosis of hepatitis and cirrhosis which produce changes in intracellular [Na^+] and extracellular matrix structure [5]. ^{23}Na MRI may also prove useful for distinguishing between benign and malignant tumor since rapidly proliferating tumor cells are shown to have a high intracellular [Na^+] [6]. This technique could also be used for monitoring response to cancer therapy. ^{23}Na MRI is expected to be useful for the diagnosis of many acute and chronic renal diseases because the kidneys play a key role in maintaining the sodium homeostasis of the body. Thus, the feasibility of high-quality ^{23}Na MRI demonstrated here encourages us to develop ^{23}Na MRI for a wide range of clinical applications.

V. Conclusions

With 8-channel ^{23}Na/^{1}H coil and optimized imaging parameters, ^{23}Na MR images can be acquired with an in-plane spatial resolution of 0.3 cm and an SNR of ~20 within 15 min at 3T without exceeding the SAR limit for human imaging. The obtained ^{23}Na images allow clear delineation between different abdominal organs and their sub-regions. It is likely that this technique can yield useful information to study normal and abnormal physiology because of the great physiological significance of trans-membrane sodium gradient. The future area of development of ^{23}Na MRI would be focused on evaluating the use of the technique for disease diagnosis and monitoring therapy response.

References

1. Lanz T., Mayer .M., Roboson M.D., Neubauer S., Ruff J., Weisser A, (2007) *An 8-channel ^{23}Na Heart Array for Application at 3 T.* Proceedings in International Society of Magnetic Resonance Medicine.
2. Characterization of the Specific Absorption Rate for Magnetic Resonance Imaging systems at *http://www.nema.org/stds/ms8.cfm.* (1997), National Electrical Manufacturers Association, NEMA Standards Publication.
3. Perman, W.H., et al., (1986) Methodology of in vivo human sodium MR imaging at 1.5 T. Radiology,. 160(3): p. 811-20.
4. Babsky, A.M., et al., (2008) Evaluation of extra- and intracellular apparent diffusion coefficient of sodium in rat skeletal muscle: effects of prolonged ischemia. Magn Reson Med, 59(3): p. 485-91.
5. Hopewell, P.N., Bansal N., (2008) Noninvasive Evaluation of Nonalcoholic Fatty Liver Disease (NAFLD) Using ^{1}H and ^{23}Na Magnetic Resonance Imaging and Spectroscopy in a Rat Model. Proceedings in International Society of Magnetic Resonance Medicine.
6. Nagy, I..Z., et al., (1981) Intracellular Na+:K+ ratios in human cancer cells as revealed by energy dispersive x-ray microanalysis. J Cell Biol, 90(3): p. 769-77.

Non-invasive Controlled Radiofrequency Hyperthermia Using an MR Scanner and a Paramagnetic Thulium Complex

J.R. James[1,2], V.C. Soon[1], S.M. Topper[1], Y. Gao[1], N. Bansal[1,2]

[1]Department of Radiology, Indiana University School of Medicine, Indianapolis, Indiana, USA
[2]School of Health Sciences, Purdue University, West Lafayette, Indiana, USA

Abstract — **An MR technique has been developed to administer controlled radiofrequency (RF) hyperthermia (HT) to treat sc-implanted tumors using an MR scanner and its components. The method uses the ^{1}H chemical shift of TmDOTA^{-} to monitor tumor temeprature non-invasively. The desired HT temeprature is achieved and maintained using a feedback loop mechanism that uses a proportional-derivative (PD) controller. The RF HT techqinue has been able to heat the tumor from 33 to 45 ˚C in ~ 10 min and was able to mainatain the tumor temeprature within ±0.2 °C of the target temperature. Simultaneous monitoring of the metabolic changes with RF HT using multinuclear MRS techniques showed a significant increase in the $[Na_i]^+$ as measured by TQF ^{23}Na MRS and a significant decrease in cellular bio-energetics and pH as measured by ^{31}P MRS.**

Keywords — **RF hyperthermia, MRI, sodium, pH, cellular energy**

I. Introduction

Radiofrequency (RF) hyperthermia (HT) in combination with radiotherapy or chemotherapy has been proved to be useful for treating some human cancers. In HT therapy, the temperature of a tumor is raised by few degrees (~ 42 - 45 ˚C) above the normal body temperature. HT can cause changes in cellular membrane permeability and ion exchange processes that could play a key role in cellular damage and death [1,2]. A magnetic resonance (MR) spectrometer that is equipped with RF system to excite spins enables an in-magnet HT application with simultaneous non-invasive temperature monitoring and control. Combining RF HT with multinuclear MR measurements enables investigation of metabolic and physiological effects of HT treatment on tumors.

Our goal in this work were: a) to develop a robust non-invasive method for delivering in-magnet controlled RF HT to subcutaneously- (sc-) implanted tumors using the same RF volume coil as used for MR data collection, and incorporate this RF HT technique with ^{23}Na and ^{31}P MR spectroscopy (MRS) data collection and b) to apply the developed controlled HT technique to monitor the effects of HT on total and intracellular Na^+ measured by single-quantum (SQ) and multiple-quantum-filtered (MQF) ^{23}Na MRS, and cellular energy status (ATP/P_i), and intra- and extra-cellular pH, (pH_i and pH_e, respectively) by ^{31}P MRS in sc-implanted 9L-glioma in rats.

II. Methods

A. In-magnet controlled RF HT during ^{23}Na and ^{31}P MRS

All MR experiments were performed on a Varian 9.4-T, 31 cm diameter horizontal bore scanner. A 20 mm diameter slotted tube resonator dual tuned to 400 MHz for ^{1}H, and either 106 MHz for ^{23}Na or 163 MHz for ^{31}P was used for MR data collection and heating. Initial development and testing was performed on a 2 ml bottle containing 2 mM TmDOTA^{-}, 10 mM sodium phosphate and 0.9% NaCl in 6% agarose gel. The temperature of the sample was derived from the ^{1}H chemical shift of TmDOTA^{-}. RF heating was irradiated at 400 MHz during ^{23}Na or ^{31}P MRS data collection. The phantom was initially heated at different constant RF power levels to obtain open loop temperature curves. These curves were used to model in-magnet RF heating in a simulation program designed to evaluate the optimum values for the proportional (K_p), integral (K_i) and derivative (K_d) constants for the proportional-intigral-derivative PID controller. The simulation program was developed in Simulink, Matlab 7.0 *(Math Works, MA)*. As shown in Fig 1 the program used a feedback loop mechanism to adjust the RF power, *u(t)*, based on the error between the target temperature and the current sample temperature, *e(t)*, using the following equation:

$$u(t+1) = u(t) + K_p e(t) + K_d \frac{de(t)}{dt} + K_i \int e(t)dt \qquad (1)$$

The following criteria were used for choosing the optimal values for K_p, K_i and K_d: (a) a rise time of >10-15 min to reach the target temperature, (b) a maximum overshoot of 0.5 °C, and (c) a maximum settling time of 5 min after achieving the target temperature.

After optimizing the PID controller with computer simulations, the controller was implemented on the Varian MR scanner and tested using the same phantom and dual tuned volume coil as used for the open loop curves. ^{1}H and

Chwee Teck Lim, James C.H. Goh (Eds.): ICBME 2008, Proceedings 23, pp. 142–145, 2009
www.springerlink.com

^{23}Na or ^{31}P spectra were continuously collected during the heating experiment. The RF power was set to a maximum of 33 watts and modulated between 0 to 4095 DAC (digital-to-analog) units. The PID controller constants were set to the optimal values as determined from simulation results.

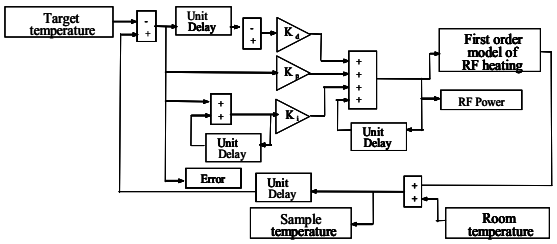


Fig 1 Block diagram of a PID controller for maintaining tumor temperature during RF HT

B. Controlled Hyperthermia with MR Thermometry and Metabolic Measurements

The above in-magnet controlled RF HT technique combined with ^{23}Na and ^{31}P MRS data collection was applied to investigate the effects of HT (45° for 30 min) on [Na_t^+] and [Na_i^+], cellular energy status (ATP/P_i), pH_i and pH_e in sc-implanted 9L tumors before, during and after HT treatment.

9L glioma cells (4 x 10^6) were subcutaneously implanted and grown in Fisher rats that were 6 weeks of age (70-135 g). The tumors were grown to ~2 cc before they were used for MR experiments. A nephrectomy was performed to avoid renal clearance of $TmDOTA^-$ during imaging experiments. A jugular vein was cannulated through a midline neck incision to inject 3-4 ml of 100 mM $TmDOTA^-$ prior to the MR experiments. A rectal fiber-optic probe (FOP) was inserted to monitor core body temperature. The rat was positioned on the cradle and the tumor was placed inside the 20 mm diameter slotted tube resonator through a copper tape placed above the coil to avoid contamination from muscles around the tumor. A pneumatic pillow sensor *(SA Instruments Inc., NY)* was placed under the animal for monitoring respiration during the MR experiments. The whole set up with the cradle was then positioned inside the horizontal bore magnet. The animal core body temperature was maintained at ~35 °C by blowing warm air with a commercial hair dryer into the magnet bore.

The protocols for ^{23}Na and ^{31}P MR data collection during in-magnet controlled RF HT experiments are shown in Fig 2. After baseline data collection, the RF power was turned on at 400 MHz during ^{23}Na or ^{31}P data collection. The target temperature was set to 45 °C and the PID controller was set to the optimal values determined from computer simulations. The RF heating was turned off after 30 min of HT and the tumor temperature was allowed to return to the baseline temperature. The heating and cooling rate constants were estimated using exponential fitting equations using PSI Plot *(Poly Software International, UT)*. The thermal dose at 43 ˚C *(tdm_{43})* in degree-minutes (°C min) was calculated from the time interval, Δt, initial temperature, T_0, and the average temperature, T_{av}, during Δt [3].

a. Effect of HT on SQ and MQF ^{23}Na MRS

A 1 ml vial containing 500 mM NaCl and 2.5 mM $TmDOTP^{5-}$ in 10 % agarose gel was placed inside the dual tuned ^{1}H/^{23}Na coil and used as a SQ and TQF ^{23}Na signal reference. $TmDOTP^{5-}$ was used to shift the reference ^{23}Na signal away from the tumor signal and agarose was used to generate a TQF ^{23}Na signal from the reference. ^{23}Na MRS data were collected at 106 MHz using a 170 μs excitation pulse followed by an acquisition of 1,000 data points over a spectral width of 5 kHz. The data collection time for a SQ ^{23}Na spectrum was 13 sec and that for a TQF ^{23}Na spectrum was 1 min and 24 sec.

^{23}Na SQ and TQF spectra were transferred to and processed with NMR Utility Transform Software (*NUTS-Acorn NMR, CA*). ^{23}Na free-induction decays (FIDs) were

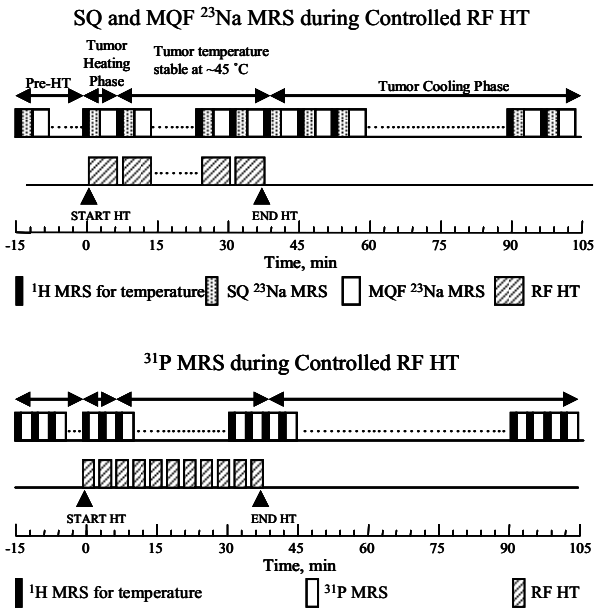


Fig 2 Experimental protocols for SQ and MQF ^{23}Na (top) and ^{31}P (bottom) MRS data collection during controlled RF HT

baseline corrected and multiplied by a single exponential corresponding to 10 Hz line broadening and Fourier transformed. The signal intensities in ^{23}Na SQ and TQF tumor and reference peaks were determined by integration.

b. Effect of HT on pH_i, pH_e and cellular energy status

^{31}P MRS experiments were performed on separate group of rats. Effects of HT on pH_i, pH_e and cellular energy status (ATP/P_i) in 9L-glioma were examined before, during, and after HT treatment.

The animals were prepared for ^{31}P MRS experiments in a similar manner as described previously except a solution containing 75 mM 3-aminopropylphosphonate (3-APP) and 100 mM $TmDOTA^-$ was infused through the jugular vein. ^{31}P signal from 3-APP was used for monitoring the pH_e. A 1 ml vial containing 100 mM methyl-phosphonic acid (MPA) was placed inside the dual tuned $^1H/^{31}P$ coil and used as a ^{31}P signal reference. The protocol for ^{31}P MRS data collection during controlled RF HT and temperature monitoring was similar to that used for ^{23}Na experiments as shown in Fig 2. ^{31}P MRS data was collected at 165 MHz using a 100 μs excitation pulse followed by an acquisition of 4,000 data points over a spectral width of 20 kHz. The total data collection time for each ^{31}P spectrum was 1 min and 11 s.

After data acquisition, four sets of ^{31}P spectra were added together to obtain a better SNR and quantification. ^{31}P FIDs were baseline corrected and multiplied by a single exponential corresponding to 25 Hz line broadening and Fourier transformed. The various signal intensities from the corresponding peaks on ^{31}P spectra were determined by integration. pH_i was estimated using the chemical shift of P_i signal referenced to α-ATP signal [4]. pH_e was calculated from the shift of 3-APP signal referenced to α-ATP.

III. Results

The PID based temperature controller simulation yielded optimal values K_p = 1000, K_d = 1000, and K_i = 0. The controlled RF HT technique was able to heat the phantom from 30 to 45 °C in ~10 min and maintain the phantom temperature at 45.0 ± 0.1 °C for over 60 minutes.

The feasibility of controlling and maintaining the temperature in sc-implanted tumors using the PID controller is shown in Fig 3. The tumor temperature was raised from 33.7 to 45.0 °C in about 10-15 minutes. After the target temperature was achieved, the RF heating power was adjusted automatically as per Eq. 1 to maintain the tumor temperature at 45.0 °C. The RF power varied between 4095 and 2717 DAC units during heating. The rise time for heating the tumor was slightly longer than that for the phantom due to heat dissipation by blood. In spite of this, the PID controller was able to maintain the tumor temperature at 44.9° ± 0.2 °C. After 30 minutes of HT, the RF power was turned off and the tumor returned to its baseline temperature (33.4 °C) in ~ 1 hr. The average cooling rate constant was estimated to be 16.9 ± 3.4 min. The tumor tdm_{43} was estimated to be 57 ± 2 min. The rectal temperature was 35 ± 1 °C throughout the experiment including during the HT treatment.

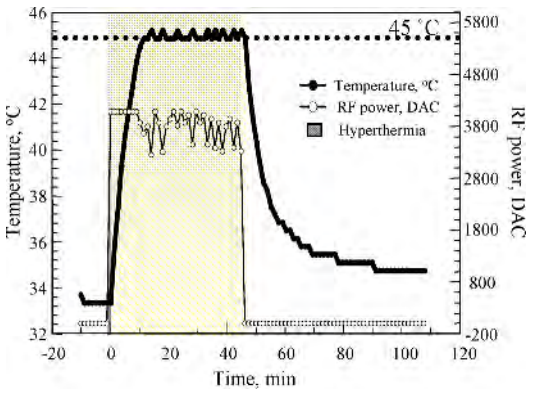


Fig 3 Changes in heating RF power level and tumor temperatures during controlled HT with the PID controller

Relative changes in SQ and TQF ^{23}Na signal intensity averaged for all the tumors (n = 5) are shown in Fig 4A. Controlled RF HT produced a gradual increase in both SQ and TQF ^{23}Na SI. There was a 30-40 % increase in TQF ^{23}Na SI compared to only a 12% increase in SQ ^{23}Na SI. TQF ^{23}Na SI continued to increase even after the heating was stopped and tumor temperature returned to the baseline value.

Effects of HT in pH_i and pH_e, and relative ATP/P_i from ^{31}P spectra averaged for all the tumors are shown in Fig 4B and C respectively. Prior to HT, the tumor pH_i and pH_e were 7.08 ± 0.10 and 6.89 ± 0.05, respectively. This trans-membrane pH gradient in the tumor is opposite to that seen in normal tissues which have a pH_i of 7.1 and a pH_e of 7.3-7.4. As the tumor temperature increased with the onset of HT, pH_i decreased by ~0.2 units ($p \leq 0.05$) but then returned back to the normal value within 15 minutes during HT. pH_i remained at the baseline value during the remaining experimental period including the post HT period. pH_e decreased by ~0.15 units ($p \leq 0.05$) with onset of HT, but 10-12 min after the decrease in pH_i. pH_e remained decreased during the HT period but gradually returned back to the baseline value (6.9 ± 0.1) when the

heating was turned off. ATP/P_i decreased by 40% ($p \leq 0.05$) during HT and remained depressed after HT.

IV. Discussion

We have been able to develop an in-magnet controlled RF HT technique using the following features: 1) RF HT was delivered using the same RF coil and MR system hardware as used for exciting the nuclear spins. 2) The tumor temperature was monitored from the ^{1}H chemical shifts of $TmDOTA^-$, which are 50-100 times more sensitive to temperature than water ^{1}H signal. 3) The tumor temperature was maintained within ±0.2 °C of the target temperature with an integrated PD controller based RF heating technique 4) ^{23}Na MRS or ^{31}P MRS data were collected consecutively with ^{1}H MRS data collection during controlled RF HT for monitoring the metabolic and physiological effects of the treatment. Among all the NMR parameters that were simultaneously monitored with RF HT in the sc-implanted tumors, Na_i^+ signal intensity and cellular bioenergetics were the most sensitive to temperature. The dramatic increase in TQF ^{23}Na SI suggests that HT causes an increase in [Na_i^+]. The initial increase in [Na_i^+] during HT may be a metabolic response to heating. This increase may result from 1) a decrease in the activity of Na^+/K^+-ATPase due to reduced cellular ATP levels or 2) an increase in the activity of Na^+/H^+ antiporter which helps maintain pH_i. The continued late increase in [Na_i^+] after HT may result from cellular membrane damage leading to potential cell death.

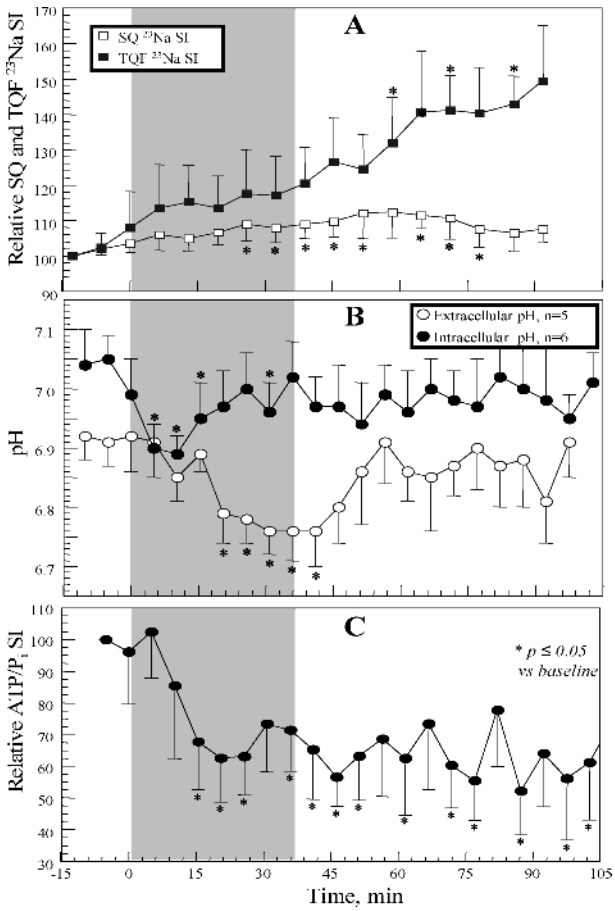


Fig 4 Effekts of HT on A) Na_i^+ as measured from SQ and Na_i^+ as measured from TQF ^{23}Na signal intensity, B) pH_i and pH_e and C) ATP/P_i measured from ^{31}P MRS

Decrease in the ATP/P_i suggests a compromised cellular energy metabolism which could reduce the activity of Na^+/K^+-ATPase and lead to an increase in [Na_i^+]. The decrease in pH_i can also increase the activity of Na^+/H^+ antiporter to maintain cellular pH homeostasis. This explains the initial drop in pH_i followed by its recovery during HT and a consecutive decrease in pH_e. In summary, the data presented show that HT causes a marked increase in [Na_i^+] in sc-implanted 9L glioma due to both a decrease in cellular energy status and increased acid production.

V. Conclusions

The above presented PD based RF HT technique, using an MR scanner for both RF HT application and MR data acquisition provides a robust non-invasive method for delivering controlled RF HT to sc-implanted tumors in-magnet using the same RF volume coil as used for MR data collection. Simultaneous measurements of sodium and cellular energetics during HT treatment show that ^{23}Na and ^{31}P will prove very useful for monitoring therapy responses during HT treatment. The *in vivo* tumor data presented show that HT causes a dramatic increase in [Na_i^+] due to significant decreases in cellular ATP and pH.

References

1. Amorino GP, Fox MH. Heat-induced changes in intracellular sodium and membrane potential: lack of a role in cell killing and thermotolerance. Radiat Res 1996;146(3):283-292.
2. Babsky A, Hekmatyar SK, Wehrli S, Nelson D, Bansal N. Hyperthermia-induced changes in intracellular sodium, pH and bioenergetic status in perfused RIF-1 tumor cells determined by 23Na and 31P magnetic resonance spectroscopy. Int J Hyperthermia 2005;21(2):141-158.
3. Sapareto SA, Dewey WC. Thermal dose determination in cancer therapy. Int J Radiat Oncol Biol Phys 1984;10(6):787-800.
4. Kost GJ. pH standardization for phosphorus-31 magnetic resonance heart spectroscopy at different temperatures. Magn Reson Med 1990;14(3):496-506.

Automatic Processing of EEG-EOG-EMG Artifacts in Sleep Stage Classification

S. Devuyst[1], T. Dutoit[1], T. Ravet[1], P. Stenuit[2], M. Kerkhofs[2], E. Stanus[3]

[1] Faculté Polytechnique de Mons, TCTS Lab, Avenue Copernic, 1, B-7000 Mons, Belgium, Stephanie.devuyst@fpms.ac.be
[2] Sleep Laboratory CHU Vésale, Montigny-le-Tilleul, Belgium
[3] Tivoli hospital , La Louvière, Belgium

Abstract — **In this paper, we present a series of algorithms for dealing with artifacts in electroencephalograms (EEG), electrooculograms (EOG) and electromyograms (EMG). The aim is to apply artifact correction whenever possible in order to lose a minimum of data, and to identify the remaining artifacts so as not take them into account during the sleep stage classification. Nine procedures were implemented to minimize cardiac interference and slow ondulations, and to detect muscle artifacts, failing electrode, 50/60Hz main interference, saturations, highlights abrupt transitions, EOG interferences and artifacts in EOG. Detection methods were developed in the time domain as well as in the frequency domain, using adjustable parameters. A database of 20 excerpts of polysomnographic sleep recordings scored in artifacts by an expert was available for developing (excerpts 1 to 10) and testing (excerpts 11 to 20) the automatic artifact detection algorithms. We obtained a global agreement rate of 96.06%, with sensitivity and specificity of 83.67% and 96.47% respectively.**

Keywords — **Artifacts processing, EEG, EOG, EMG, ECG.**

I. Introduction

While trying to automatically classify sleep stages, one is generally faced with the problem of artifacts. Indeed, artifacts contained in the analyzed polysomnographic signals introduce spurious components during features extraction, which lead to incorrect interpretation of the results [1]. Dealing with artifacts is therefore mandatory before any other classification operation.

In the literature, three main approaches have been proposed to detect and correct them. The first approach is based on autoregressive modeling [2, 3, 4] and is used for two purposes: (i) estimating the recorded EEG and identifies transient events like muscle or movement artifacts by locating the abrupt variations of the parameters; (ii) removing artifact from the EEG by estimating the parameters of the mathematical model that describe the recorded EEG as an overlap of the real EEG and the artifact interference.

The second approach uses standard voltage thresholds (overflow check) [4-5]. While these thresholds can sometimes be fixed (e.g 50µV), it is univocally accepted that using values related to the energy distribution of the signal in the frequency or time domain is preferable since voltage levels can strongly vary between subjects and recordings.

Finally, some authors investigated the use of independent component analysis (ICA) to remove the artifacts [6-7]. Unfortunately, their methods often required many EEG channels and implied to visually select the origin of the interference among estimated sources.

In the present study, we introduce algorithms for processing artifacts on EEG, EOG and EMG which are suitable for automatic sleep stages classification. The strategy is to imitate human behavior by locating the short duration artifacts so as to ignore them during the feature extraction stage of sleep stage classification.

However, cardiac interferences and slow undulations (e.g caused by breath interferences or by sweat) could not be processed using this strategy because these artifacts can last several hours. This is why we also developed two artifact correction algorithms in order to minimize the loss of data.

Nine procedures were finally implemented to remove cardiac interference and slow ondulations, and to detect muscle artifacts, failing electrode, 50/60Hz main interference, saturations, highlights abrupt transitions, EOG interferences and artifacts in EOG.

The performances of the algorithms were evaluated on a database of 20 polysomnographic sleep recordings scored in artifacts by an expert.

II. Materials and methods

A. Data

Data used in this study were recorded at the Sleep Laboratory of the André Vésale hospital (Montigny-le-Tilleul, Belgium). They are composed of 20 excerpts of 15 minutes-long polysomnographic (PSG) sleep recordings carried out during the night. The recordings were taken from 20 patients (15 males and 5 females aged between 31 and 73) with different pathologies (dysomnia, restless legs syndrome, insomnia, apnoea/hypopnoea syndrome). The sampling rates were 50, 100 and 200Hz. The 20 excerpts were visually examined by an expert to identify the various artifacts. Then they were separated into two groups for devel-

Chwee Teck Lim, James C.H. Goh (Eds.): ICBME 2008, Proceedings 23, pp. 146–150, 2009
www.springerlink.com

oping (excerpts 1 to 10) and testing (excerpts 11 to 20) the automatic artifact detection algorithms.

B. Artifacts detection/correction processes

Two procedures were developed to minimize cardiac interference and slow ondulations (*P1-P2*) and seven other procedures were implemented to indentify the remaining short artifacts (*P3-P9*). These detection algorithms operate on fixed length epochs (1.25 second by default). They are mainly binary: if any of the parameters exceeds the corresponding threshold, the epoch is marked as an artifact. As the signal energy distribution in the frequency or time domain varies strongly between subjects, we have chosen thresholds relative to the statistical properties of the considered signal. For example:

$$threshold = mean(EEG) + k * std(EEG)$$

where k is a factor of proportionality and *std* is the standard deviation.

The various procedures are the following (for more details, see *http://tcts.fpms.ac.be/publications/techreports/DEA_sd.pdf*):

P1. Cardiac interference detection and correction on EEG (Atf_cardE) and on EOG (Atf_cardO). The basis of the method for removing cardiac interference was presented in [8]. It is based on a modification of the independent component analysis algorithm which gives promising results while only using a single-channel EEG (or EOG) and the ECG.

P2. Slow ondulations detection and correction on EEG (Atf_ondE) and on EOG (Atf_ondO). Slow ondulation artifacts are generally due to breathing or sweating. Their frequencies are lower than those of the slowest waves of the sleep (rhythm delta). Therefore, their extraction can be realized by a simple filtering, with cut-off frequency adjusted to the smallest frequency of the delta band.

P3. Saturations detection on EEG (Atf_satE), on EOG (Atf_satO) and on EMG (Atf_satM). The basic idea of this procedure is to locate epochs where the EEG signal remains at its maximal value of saturation during a sufficient time.

P4. Unusual increase of EEG detection (Atf_highE). These artifacts can for example be caused by EOG interferences. If the amplitude of the EEG signal exceeds a first threshold for any of the epochs, the onset and the offset of the artifact are researched. These are defined as the instant after which the amplitude of the EEG becomes lower than a second threshold (lower than the first threshold). Then the corresponding epochs are marked as artifact epochs.

*P5. Failing electrode detection on EEG (Atf_noE) and on EOG (Atf_noO).*This procedure locates the relatively constant amplitude (near to zero) of the signals EEG or EOG. Such artifacts are sometimes obtained at the end of the nights when the electrodes are disconnected.

P6. Highlights abrupt transitions detection on EEG (Atf_transE). Highlights abrupt transitions such as spikes are identified by locating slopes above some threshold. Let

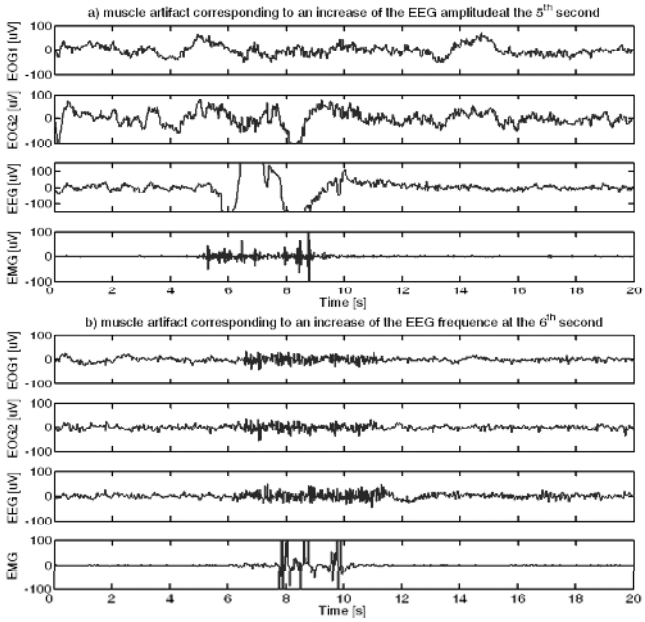


Fig. 1 Examples of muscle or movement artifacts

us note that epileptic spikes are not actually artifacts (since they have no artificial origin), but they can nonetheless obstruct the sleep stage classification. This is why we identified them as the artifacts.

P7. 50/60Hz mains interferences detection on EEG (Atf_50E). This interference network can easily be detected given the evident peak which takes place around 50Hz (or 60Hz) on the Fourier transform.

P8. Muscle or movement artifacts detection on EEG (Atf_mvtE). This algorithm detects temporary increase of muscular tone accompanied by disturbances on the EEG. These disturbances are of two types: they can be either a voltage increase as illustrated on Fig 1a. , or a change of rhythm of the EEG activity such as illustrated on Fig 1b.

P9. Detection of artifacts in EOG constituted of in-phase movements (Atf_phaseO). As the ocular movements are binocular and synchronous, the EOG recordings should appear in opposition of phase while placing electrodes on the lateral canthi and by using the same reference on the mastoid. The ocular artifacts are therefore easily identifiable since they correspond to in-phase movements of the EOG.

III. Results

A. Content of the artifact database

On the basis of the artifact scoring carried out by the expert, we first examined the content of the database in terms of short duration artifacts (Table 1).

Table 1 content of the artifact database based on the visual artifact scoring

Code	Type	Number of seconds	%
P3-a	Saturations of EEG (Atf_satE)	0	0
P3-b	Saturations of EOG (Atf_satO)	0	0
P3-c	Saturations of EMG (Atf_satM)	0	0
P4	Unusual increases of EEG (Atf_highE)	639,180	3,551
P5-a	Failing electrode on EEG (Atf_noE)	118,610	0,659
P5-b	Failing electrode on EOG (Atf_noO)	118,520	0,658
P6	Highlights abrupt transitions of EEG (Atf_transE)	46,790	0,260
P7	50/60Hz on EEG (Atf_50E)	23,980	0,133
P8	Muscle or movement artifacts on EEG (Atf_mvtE)	494,600	2,748
P9	artifacts in EOG (Atf_phaseO)	566,270	3,146
O-a	Other artifacts on EEG	129,73	0,72
O-b	Other artifacts on EOG	6,190	0,034
	All short artifacts on EEG	1014,930	5,639
	All short artifacts on EOG	690,980	3,839
	All short artifacts on EMG	0,000	0,000

The difference between the total duration of all short artifacts on EEG and the sum of durations of each type of artifact on this signal (P3-a+P4+P5a+P6+P7+P8) is due to the presence of multiple artifacts in some epochs.

As it can be seen, 5.64% of the total EEG recorded time contains artifacts. Among those, most frequent artifacts are "unusual increase of EEG" followed by "artifacts in EOG" and then "Muscle or movement artifacts".

No "saturation" artifact was found in the database. We therefore used other polysomnographic signals to tune the parameters of this procedure. These signals were not scored by the expert but simply examined visually by the authors.

B. Results of the minimization procedures

The ECG artifact removal procedure was previously tested on 10 excerpts of polysomnographic sleep recordings containing ECG artifacts and other typical artifacts [8]. It was shown that it is robust to various waveforms of cardiac interference and to the presence of other artifacts. Two hundred successive interference peaks of each of these excerpts were visually examined to compute the number of corrected peaks. We found a correction rate of 91.1%.

The removal of slow ondulations artifacts was only checked visually by the expert. It seems that the artifact can be well corrected without distorting the EEG, as it can be seen in Fig 2.

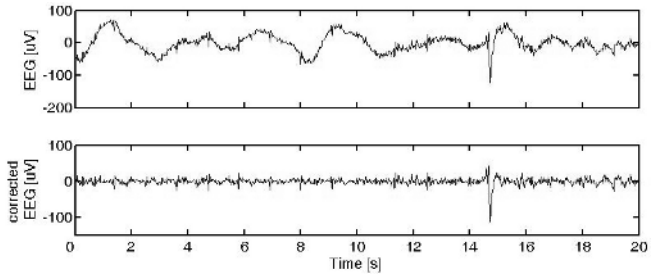


Fig. 2 Removal of slow ondulations artifacts on EEG

C. Results of the detection procedures

Concerning the short duration artifacts, the concordance between the expert scoring and the automatic detection procedures with the default thresholds, was examined as follows: 1) a true positive (TP) was counted when an artifact was automatically detected in an epoch also marked as an artifact by the expert, 2) a false positive (FP) when an artifact was automatically detected in an epoch classed as non-artifact by the expert, 3) a true negative (TN) when no artifact was detected neither automatically nor visually by the expert, 4) a false negative (FN) when no artifact was automatically detected in an epoch marked as artifact by the expert.

Then we computed the *agreement rate= (TP+TN)/(TP+TN+FP+FN)*, the *sensitivity=TP/(TP+FN)* and the *specificity=TN/(TN+FP)*.

The results obtained for each detection procedure on the central EEG are exposed in Fig 3, as well as the global results of the detection of any artifacts on this EEG. The results corresponding to the EOGs and the EMG are shown on Fig 4. If an artifact is not present (according to the expert) in the training database, the sensitivity figure has no sense. That is why we indicated it by an asterisk (*).

As it can be seen, the procedures corresponding to the more frequent artifacts (i.e. unusual increase of EEG, artifacts in phase on EOG and Muscle artifacts) are unfortunately those which have the lowest sensitivities. However, as a whole, the results show an acceptable agreement between our package of software and the human scoring with agreement rates of 92.18%, 95.98% and 100% respectively on the EEG, EOG and EMG. Without making distinction between the various signals, these results correspond to a

global agreement rate of 96.06%, a global sensitivity of 83.67% and a global specificity of 96.47%.

Finally, by varying the length of the analysis epoch from 1.25s to 1s, we observed that it introduced only little changes in the expert/software concordance (agreement rate = 96.46%, sensitivity = 82.33% and specificity =96.90%).

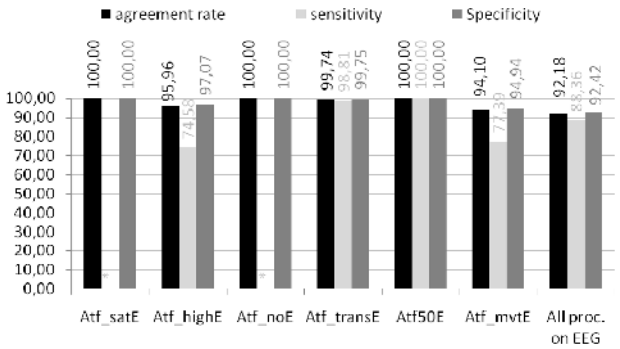


Fig. 3 Results of the detection procedure on the central EEG

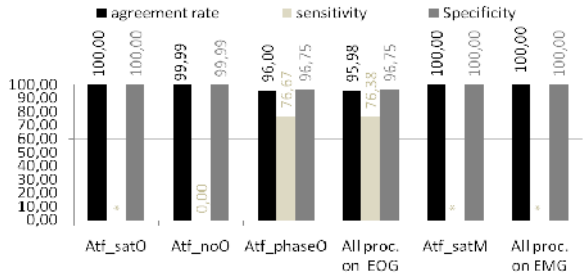


Fig. 4 Results of the detection procedure on the EEGs and on the EMG

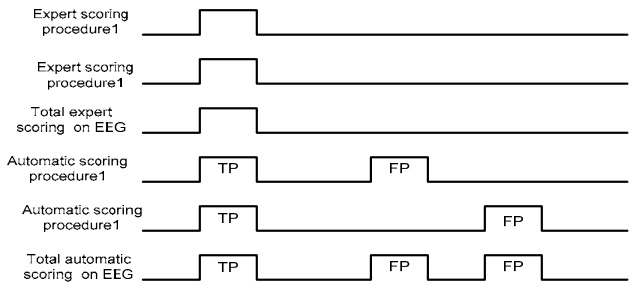


Fig. 5 Illustrative example of detection process

IV. Discussion

By looking at the Fig 3, one could be surprised of obtaining a total rate of agreement on the EEG of only 92.18% whereas each separate procedure has a higher agreement rate. Actually, this is due to the fact that false positives (FP) introduced by the various algorithms are not always located at the same place, while true positives (TP) are sometimes detected at the same epochs (fig 5). There is thus an increase in FP (proportionally to the number of TP) in the global detection on EEG. This explains why the total agreement rate is lower, while sensitivity is slightly modified and sensitivity is not affected. Fortunately, the number of epochs classified as non-artifact remains sufficient for feature extraction and sleep stage classification.

V. Conclusions

In conclusion, our findings showed that the proposed artifact minimization procedures and detection algorithms (although rather simple since they are mainly binary) are reliable in a context of classification in sleep stage classification. Indeed they give promising and repeatable results (agreement rate = 96.06%, sensitivity = 83.67% and specificity =96.47%) without requiring any human intervention.

The approach has however some limitations: (i) it is running on epochs of fixed length rather than locating the actual onset and offset of the artifacts. However using fixed length epochs dramatically simplifies the algorithm and the remaining part of signal is generally sufficient for the sleep stage classification. (ii) Although the parameters are calculated according to the statistical properties of the signal, their values (once determined) remain unchanged for all the duration of the recording. This can be can be inappropriate in sleep recording with fluctuation of tonicity level. The use of adaptive threshold rather than absolute threshold could then be investigated in future works.

Acknowledgment

This work was partly supported by the Région Wallonne (Belgium) and the DYSCO Interuniversity Attraction Poles.

References

1. Anderer P. et al. (1999), Artifact Processing in Computerized Analysis of sleep EEG - A Review, Neuropsychobiology 40: 150-157
2. Schlögl A. et al (1999), Artefact detection in sleep EEG by the use of Kalman filtering, EMBEC'99 Proc, Medical & Biological Engineering & Computing, Supplement 2, November 4-7 1999, Vienna, Austria, pp 1648-1649.
3. Van den Berg-Lenssen MM et al. (1989), Correction of ocular artifacts in EEGs using an autoregressive model to describe the EEG - a pilot study, Electroencephalogr Clin Neurophysiol, 73:72-83
4. Durka, P.J. et al. (2003), A simple system for detection of EEG artifacts in polysomnographic recordings, IEEE Transactions on Biomedical Engineering, Volume 50, Issue 4:526 – 528

5. Moretti D.V. et al. (2003), Computerized processing of EEG-EOG-EMG artefacts for multicentric studies in EEG oscillations and event-related potential, international journal of psychophysiology, vol. 47, no3, pp. 199-216
6. Iriarte J., Urrestarazu E., Valencia M. (2003), Independent component analysis as a tool to eliminate artifacts in EEG: a quantitative study, Journal of Clinical Neurophysiology, 20(4): 249–257.
7. Delorme A. et al (2007), Enhanced detection of artifacts in EEG data using higher-order statistics and independent component analysis, NeuroImage Volume 34, Issue 4, pp 1443-1449
8. S. Devuyst et al.(2008), Removal of ECG Artifacts from EEG using a Modified Independent Component Analysis Approach, EMBC Proc, 30th Annual International Conference of the IEEE Engineering in Medicine and Biology Society, Vancouver, Aug 20-24 2008, SaET1.1, pp 5204-5207

Medical Image Registration Using Mutual Information Similarity Measure

Mohamed E. Khalifa[1], Haitham M. Elmessiry[2], Khaled M. ElBahnasy[3], Hassan M.M. Ramadan[4]

[1] Dean of Faculty of Computer and Information Sciences, Ain Shams University,Cairo,Egypt
[2] Assistant Professor in Computer Science Department Ain Shams University,Cairo,Egypt
[3] Assistant Professor in Information System Department Ain Shams University,Cairo,Egypt
[4] TA, Faculty of Computer and Information Sciences, Minia University ,Egypt
hassan_eldosokey@yahoo.com

Abstract — **Nowadays Medical Imaging has an increasing need in patient treatment ,not only it aids physicians in determining the correct diagnosis but also it reduces overall cost and speedup treatment plans .Medical Image Registration is a vital medical imaging application it aligns one image to another ,to obtain a registered image has the information content of both images .**

Our paper purpose is to provide a literature of Medical image registration methods based on Mutual Information, showing implementation techniques ,challenges ,and optimization approaches ,Mutual Information have been shown to be accurate and robust similarity measure at registering images specially for multimodal images taken from different imaging devices and/or modalities .

Keywords — **Image Registration, Image fusion, Mutual Information**

I. Introduction

Image Registration is the process of determining the optimal spatial transformation that brings at least two images into alignment with each other [1], Often in image processing, images must be spatially aligned in order to perform quantitative analyses of the images .Image registration applications grows daily ,it is used in computer vision, pattern recognition, target identification, remote sensing, and medicine (the focus of the current research).

*Transformation or warping function***:** This is the function used to warp the sensed image to take the geometry of the reference image. ***T (x A) = x B*** .

In choosing the transformation function ,and registration method or similarity metric ,we shall consider set of image characteristics such as [2] :

- Dimensionality 2D/3D .
- Transformation Domain (Global Vs Local).
- Transformation Type(Rigid-Affine-Curved-Projective).
- Subject of registration (Head-Knee-Heart-etc.).
- Image Modality(CT ,MR ,PET ,etc.).
- Extrinsic Vs Intrinsic features, in Extrinsic methods other objects are added to image to detect features like(using frames on patient brain),while Intrinsic methods extract and operates on image features like (edges, curves , Intensity values).

Fully automated algorithms based on Intensity similarity measures have been shown to be accurate and robust at registering images compared to feature based methods, Registration process works to find the optimal spatial and intensity transformations function so that the images are matched using a similarity measure between both images.

The choice of an image similarity measure depends on the nature of the images to be registered. Common examples of image similarity measures include Cross-Correlation, Mutual Information, Mean-square difference and Ratio Image Uniformity. Mutual Information and its variant, Normalized Mutual Information, are the most popular image similarity measures for registration of multimodality images. Cross correlation, Mean-square difference and Ratio Image Uniformity are commonly used for registration of images of the same modality.

Collignon [3],and Viola [4] proposed A widely used Intensity based similarity measure which is Mutual Information (MI). Registration based on mutual information is robust and data independent and could be used for a large class of mono-modality and multimodality images. This method requires estimating joint histogram of the two images. As a result, it requires an extremely high computation time. This is its main drawback ,another implementation challenges are local extrema ,and image noise which may a rise because of interpolation during registration process.

This paper illustrates Mutual Information based registration approach ,Section II, demonstrates methodology of Mutual Information technique(MI) ,concept ,properties ,and framework ,Section III discuss implementation issues and suggested optimization techniques, Section IV compares between some MI registration, finally our conclusion .

Chwee Teck Lim, James C.H. Goh (Eds.): ICBME 2008, Proceedings 23, pp. 151–155, 2009
www.springerlink.com

II. METHOD

A. Mutual Information image based Registration

Mutual information (MI) is usually used to measure the statistical dependence between two random variables, or the amount of information that one variable contains about the other. The method applies mutual information to measure the information redundancy between the intensities of corresponding Intensity in both images, which is assumed to be maximal if the images are geometrically aligned.

There exist many important technical issues to be solved about the method such as how to compute MI more accurately and how to obtain the maximization of MI. There are some implementation issues, for example, sub sampling, interpolation, outlier strategy. The combination of these computation techniques and searching strategy leads to a fast and accurate multi-modality image registration.

B. Entropy and Mutual Information

Let: X be a random variable (R.V) , P(X) be the probability distribution of X , p(x) be the probability density of X. Then The entropy of X, H(X) is defined by:

$$H(X) = -E_X[\ \log(P(X))\ ] \quad (1)$$

The joint entropy is a statistics that summarizes the degree of dependence of a RV X on an other RV Y. It is defined by:

$$H(X,Y) = -E_X\ [E_Y\ [\ \log(P(X,Y))\ ]\ ] \quad (2)$$

Entropy is a measure of randomness. The more random a variable is, the more entropy it will have.

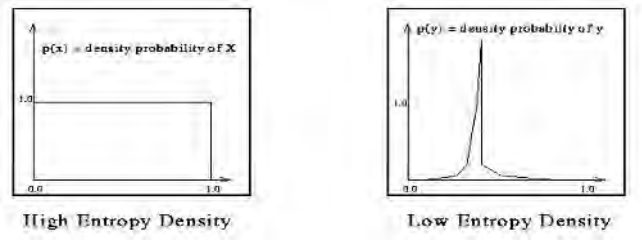


Fig.1 relation between Entropy ,and probability

The conditional entropy is a statistics that summarizes the randomness of Y given knowledge of X. It is defined by:

$$H(Y|X) = -E_X\ [E_Y\ [\ \log(P(Y|X))\ ]\ ] \quad (3)$$

Two random variables are considered to be independent if:

$$H(X,Y) = H(X) + H(Y) \quad (4)$$

The Mutual Information, MI, between two random variables X and Y is given by: [5]

$$MI(X,Y) = H(Y) - H(Y|X) = H(X) + H(Y) - H(X,Y) \quad (5)$$

Maximizing the mutual information is equivalent to minimizing the joint entropy . Advantage in using mutual information over joint entropy is it includes the individual input's entropy Works better than simply joint entropy in regions of image background (low contrast) .

C. Some Properties of Mutual Information[6]

- Mutual Information is symmetric: $I(X,Y) = I(Y,X)$ (6)
- $I(X,X) = H(X)$ (7)
- $I(X,Y) <= H(X)$, $I(X,Y) <= H(Y)$ (8)
  information each image contains about the other can not be greater than the information they contain about themselves.
- $I(X,Y) >= 0$ Cannot increase uncertainty in X by knowing Y ,If X,Y are independent then $I(X,Y)=0$ (9)

D. Normalized Mutual Information as a similarity measure

Mutual information depends on the overlapping region between registered images ,that a small overlapping area reduces the number of samples, which affects the probability distribution estimation. Image Registration can be seen as an optimization problem to find a cost function and then use an optimization method to get its minimum. Normalized mutual information is less sensitive to changes in overlapping region ,Its calculation is based on the joint histogram of the fixed and transformed moving images[7].

$$NMI(X,Y) = (H(X) + H(Y))\ /\ H(X,Y)\ . \quad (10)$$

Normalized measure proved better results for rigid registration of MR-CT and MR-PET images.

E. Mutual Information Registration framework

Image registration is performed on two or more images, The source or reference image is the image to which all the others will be registered., while The remaining images are referred to as target images. Registration problem is to find the optimal spatial and intensity transformations function so that the images are matched .

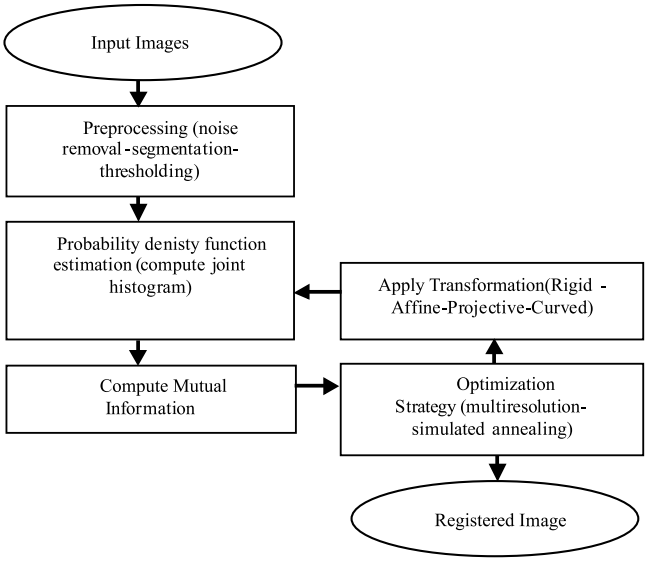


Fig.2 Mutual Information Registration Framework

III. Discussion

Mutual Information based registration use image gray values to create joint histogram between source and target images based on image nature we shall compromise between choosing suitable method to create joint histogram, generally mutual information proposed approaches may be classified into three approaches which are Probability Density Estimation ,Interpolation ,and Optimization approaches.

Probability Density Estimation

Computes the joint histogram h(X,Y) of images .Each entry is the number of times an intensity X in one image corresponds to an intensity Y in the other image, The discrete joint histogram does not allow the cost function to be explicitly differentiated, so it can only use non-gradient based optimization methods, such as Powell's method, to seek the minimum .a parzen-window based method is proposed to estimate the continuous joint histogram in order to make it possible to derive [7] . The distribution is approximated by a weighted sum of sample points Sx and Sy ,The weighting is a Gaussian window Interpolation.

$$P(x, y, Sx, Sy) = \frac{1}{N}\sum_{S} W(Dist(x, y; Sx, Sy)) \quad (11)$$

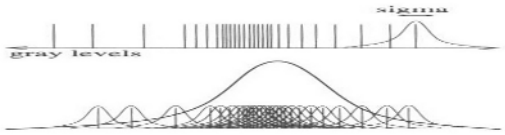


Fig.3 Parzen Window sub sampling

Interpolation

Interpolation is used to estimate gray values of one of the images at positions other than the grid points. grid lines for 2D images may be aligned along that dimension under certain geometric transformations. Therefore, fewer interpolations are needed to estimate the joint histogram of these two images than in the case that none of the grid planes are aligned. It is dependent on the image transformation. One of challenges is local extrema it impedes the registration optimization process. More importantly, they rule out registration accuracy.

Optimization

Generally Registration using mutual information is considered maximization problem ,Genetic algorithm(GA)is not suitable in our case because it does not avoid local maxima which may occur in Mutual information registration .

Current methods of multimodal image registration usually seek to maximize the similarity measure of mutual information (MI) between two images over their region of overlap Registration is achieved by adjustment of the relative position and orientation until the mutual information between the images is maximized .Additionally ,stochastic approximation may be used The main disadvantage of Mutual information is that it is known to be highly non-convex as a result a local maxima may occur .

Registration by maximization of mutual information

In it we seek an estimate of the transformation T that registers the reference image *u* and test image *v* by maximizing their mutual information.

$$T = \arg\max I(u(x), v(T(x))) \quad (12)$$

For optimization, a multi-resolution approach based on the Gaussian Pyramid representation may be used .Rough estimates of T can be found using down sampled images and treated as starting values for optimization at higher resolutions. Then the fine-tuning of the solution can be derived at the original image resolution [8].

local region-of-interest image registration

Mutual information-based methods may be used to improve local region-of-interest (ROI)image registration ,in some cases a diagnostician is more concerned with registration over specific (ROI). A main challenge when using small regions have limited statistics and thus poor estimates of entropies.

Maximization of Gradient Code of Mutual Information

Use pixel gradient information rather than pixel intensity, and simulated annealing to reduce next search space, combined with hill climbing method [9] .

Expectation Maximization Algorithm[10]

Solves registration of partial or missing data, by applying simultaneous segmentation and registration. is used to resolve this circular estimator, and proceeds as follows:

- E-step: compute the weights w (with an initial estimate of from the solution of smoothing
- M-step: estimate the model parameters, (rotation-translation).
- Repeat steps 1 and 2 until the difference between successive estimates of is below a specified threshold.
- The E-step is the segmentation stage, where pixels that do not have a corresponding match between source, and target images have a close to zero weight These pixels are given less consideration in the M-step which estimates the registration parameters. The EM algorithm allows for simultaneous segmentation and registration, and hence allows us to contend with missing data .

IV. Results

We applied Mutual Information based Registration using different techniques and applied it on different cases taken from different modalities , representing different objects of body ,the following table shows the error ,and time obtained for each case ,our results showed that Mutual information had proved better accuracy .

Mutual Information requires iterative technique ,and may have more than one iteration ,one of the disadvantages is local maxima which may occur in interpolation for example in second case had taken longer time and gave lower accuracy compared to Expectation maximization algorithm , optimization techniques applied to mutual information differ focused on increasing registration accuracy ,reduce time via sampling for example ,and try to avoid local maxima, one of the remarked causes of local maxima is noise ,and image has low resolution ,which tried to be solved in some techniques like Expectation Maximization algorithm to smooth intensity ,and segment regions of missing data or noise resident in images before applying registration phase .

Table 1 Experimental Results

Item	Mutual Information	Interpo-lation	Expectation maximiza-tion
1-Modality: CT -Head			
Time (min):	15	35	20
RMSE :	0.71025	0.809	0.096034
2-Modality: MR- Head			
Time(min) :	18	30	15
RMSE :	0.334	0.2159	0.134622
3-Modality:CT-MR Head			
Time :	32	30	28
RMSE	0.5433	0.2445	0.0585085
4.Modality: CT- Knee			
Time :	35	23	27
RMSE :	0.730155	0.002	0.0373583
5.Modality: MR -Brain			
Time :	14	12	28
RMSE :	0.818602	0.1816	0.169452
6.Modality: CT -Heart			
Time :	25	27	10
RMSE	0.776717	0.194	0.163478
7.Modality: MR -:Knee			
Time :	8	10	6
RMSE	0.745903	0.00529	0.068

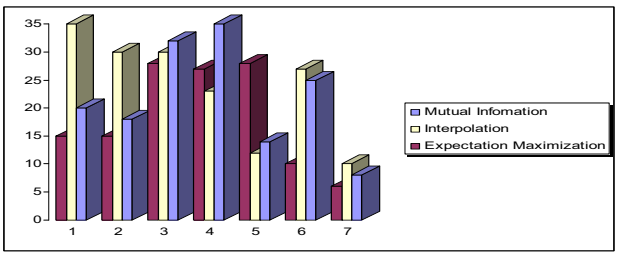


Fig.4 Comparison between time of 7 cases using Standard Mutual Information(MI), and using MI with Interpolation, and finally Information Expectation Maximization

V. Conclusion

Intensity based methods using mutual information as a similarity measure are robust accurate ,and invariant. Theoretically, these are the most flexible of registration methods, since they unlike all other methods do not start with reducing the grey valued image to relatively sparse extracted information, but use all of the available information throughout the registration process .An

increasing clinical call for accurate and retrospective registration, along with the development of ever-faster computers with large internal memories, have enabled full-image-content methods to be used in clinical practice.

VI. References

1. Dana Paquin (2007)Hybrid multiscale landmark and deformable image registration, Mathematical BIOSCIENCES Journal, Volume 4, Number 4, October 2007, pp. 711-737.
2. J.B.Antonie Manitz ,Erik H.W. Meijering ,and Max A.Viergever (1998)General multimodal elastic registration based on mutual information, SPIE. v3338. 144-154
3. A.Collignon ,D.Vandermeulen ,and P.Suetens,G.Marchal (1995) Automated multimodality image registration based on information theory. Computational Imaging and Vision ,3:263-274.
4. P.Viola (1995) Alignment by Maximization of Mutual Information.. PhD Thesis ,M.I.T.
5. Zhiyong Gao ,Bin Gu ,and Jiarui Lin (2008) Monomodal image registration using mutual information based methods, Image and Vision Computing, Volume 26, Issue 2, Pages 164-173 .
6. Frederik Maes ,Andr´e Collignon ,and Dirk Vandermeulen, Guy Marchal, and Paul Suetens (1997) Multimodality Image Registration by Maximization of Mutual Information, IEEE TRANSACTIONS ON MEDICAL IMAGING, VOL. 16, NO. 2,,.
7. XU Rui, CHEN Yen-Wei, TANG Song-Yuan, Shigehiro Morikawa,and Yoshimasa Kurumi (2008), Parzen-Window Based Normalized Mutual Information for Medical Image RegistrationIEICE Transactions on Information and Systems, Vol. E91-D, No. 1, pp. 132-144.
8. Xuesong Lu ,Su Zhang, He Su ,and Yazhu Chen (2008) Mutual information-based multimodal image registration using a novel joint histogram estimation .Computerized Medical Imaging and Graphics, Volume 32, Issue 3, April 2008, Pages 202-209.
9. XIAOXIANG WANG ,and JIE TIAN (2005) Image Registration based on Maximization Of Gradient Code Mutual Information, Image Analysis and Stereology , Slovenia, 24:1-7.
10. Senthil Periaswamy , and Hany Farid (2005) Medical Image Registration with Partial Data, Siemens Medical Solutions USA, Inc., Malvern, PA 19355, USA.

A Feasibility Study of Commercially Available Audio Transducers in ABR Studies

A. De Silva, M. Schier

Sensory Neuroscience Laboratory, Faculty of Life & Social Sciences, Swinburne University of Technology, Melbourne, Australia

Abstract — **Among numerous sources of electrical interference, stimulus artifact produced by the audio transducer (typically headphones or earphones) affects the features of an auditory Brainstem Response (ABR). At high stimulus intensities, artifacts may create a serious problem because they extend into the time frame of the ABR. The stimulus artifact depends upon the type of transducer and the electrode arrangements used. At present, expensive and complex methods are being employed to eliminate this problem.**

This paper presents data recorded from a phantom head and human participants with two of the most common electrode arrangements to investigate the artifacts produced by different audio transducers. Additionally, the quality of the ABR produced by each transducer was studied through absolute latencies of wave I, II, III and V. Several commercially available audio transducers were tested, including supra-aural, circum-aural, ear-bud and in-ear transducer types with moving coil (dynamic) technology. For the point of comparison, standard TDH-49 and TDH-39 headphones for ABR studies were also used.

Our results indicate that in general, the artifact present in commercially available audio transducers is of a similar level to that with the standard headphones. The quality of the ABRs produced using these audio transducers at a high intensity level were found to be normal. However, with some responses, small aberrations were noticed. We thus describe a method to benchmark new audio devices before using them in practice.

Keywords — **Auditory brainstem response (ABR), audio transducer, stimulus artifact, phantom.**

I. Introduction

The Auditory Brainstem Response (ABR) consists of a series of potentials recorded from the human scalp generated by the brainstem in response to a brief auditory stimulation. This signal is used to assess the conduction through the auditory pathway to midbrain. Among different stimulus methods, the 'click' stimulus is widely used because of its broad frequency spectrum. The high frequencies affect the basal end of the cochlea and the low frequencies affect the apical end of the cochlea. Thus 'click' stimuli' provide ample information to the clinician to assess the functionality of the auditory pathway of a patient [1].

The normal ABR recording window is 15 ms with 10% of it dedicated to pre-stimulus time to record spontaneous electroencephalographic (EEG) activity. The amplitude of ABR potentials are in the range of tenths of a microvolt, and thus susceptible to electrical noise from other physiological signals and from external devices. To avoid contamination, care should be taken with the recording environment and with the equipment used. They should produce minimal noise to avoid interference with the ABR signal.

The major source of external noise at the point of stimulation is from the audio transducer which will result in a 'stimulus artifact'. Stimulus artifact is generated when the electromagnetic field produced by the audio transducer interacts with the electrodes placed on the scalp. The electrode and instrumentation which are fine tuned to pickup small ABRs could easily record this noise and suppress early components of the ABR.

In common clinical ABR measurements, headphones (that fit over the head) are used as the audio transducer, although in 1994 earphones (that fit into the ear) have been tested as a stimulation device by Yoshiko [2].

To minimize the impact of the stimulus artifact, two frequently applied methods are:

1. The use of mu-metal shielded headphones
2. The use of audio couplers, to create a distance between the head phone and the scalp electrodes [3]

Due to the cost and complexity of these methods, it is worthwhile to examine cheaper and less complicated audio transducers that will produce minimal stimulus artifacts with little or no impact on the ABR.

This paper compares results from several types of audio transducers to determine their suitability for use in ABR studies as substitutes for the more expensive and complicated transducers.

The testing includes two stages involving a phantom scalp on a realistic shaped head; and then using human participants. These two stages included two different electrode arrangements to find out the minimum impact of the magnetic field created.

II. Methods and equipment

A. Selection of audio transducers

Eight audio transducers of moving coil technology were tested in this study. Their specifications are summarised in

Chwee Teck Lim, James C.H. Goh (Eds.): ICBME 2008, Proceedings 23, pp. 156–160, 2009
www.springerlink.com

Table 1. As the TDH-49 and TDH-39 headphones are commonly used in ABR recordings, they were considered as the standard for comparison purposes.

Table 1 Description of the audio transducers used

Model	Type	Description
TDH-49p	Supra-aural Headphones	Telephonics ™ (Audiometer)
TDH-39	Supra-aural Headphones	Telephonics™ Voyager 522
Qantas™	Earphones	Comfort kit (Entertainment)
Panasonic™	Earphones	RQ-E27V (Entertainment)
Nokia™	Earphones	5200 (Communication)
1.2M (in-ear)	In-ear	Capdase™ (Entertainment)
Altronics™	Circum-aural Headset	C 9073 (Professional pilot)
Philips™	Circum-aural Headphone	SB347 (Entertainment)

An average of published ABR absolute wave latencies at similar experimental conditions in Table 2 were used to compare results presented in this study.

Table 2 Published data for absolute latencies of ABR wave I, II, III and V

Source	Audio transducer	Wave I		Wave II		Wave III		Wave V	
		$\bar{x}$	SD	$\bar{x}$	SD	$\bar{x}$	SD	$\bar{x}$	SD
[4]	TDH-49	1.62	0.12	N/A		3.76	0.14	5.74	0.20
[4]	TDH-39	1.61	0.13	N/A		3.78	0.17	5.76	0.21
[5]	TDH-39	1.54	0.08	2.67	0.13	3.73	0.10	5.52	0.15
[6]	TDH-39	1.87	0.18	2.88	0.20	3.83	0.20	5.82	0.25
[7]	ER-3A	1.54	0.10	N/A		3.70	0.15	5.60	0.19

B. Experimental Design

The two approaches to measure the effect of stimulus artifact from audio transducers were carried out using:

1. A phantom head
2. Human participants

The phantom head was used to examine the actual stimulus artifact produced without the complication of any physiological potential or current sources. Then the same audio transducers were tested on human participants to analyse the total effect.

The amount of noise generated depends upon the position of electrodes with reference to the orientation of this potential. Therefore two electrode arrangements were tested for each audio transducer. One with non-inverting at the vertex (C_z), inverting at right earlobe (A_2), and ground at forehead (F_{pz}); the other with the inverting at right mastoid (M_2).

Four healthy human participants (two male and two female) were involved in this study with an age range of 24 – 26 years. The participants gave their written informed consent in accordance with University Human Experimentation Ethics requirements.

C. Equipment

A polystyrene phantom head was used with dimensions similar to an average human head. Electrodes were placed on this phantom scalp at the locations described in the previous section.

Simulating the inter-electrode impedances was the aim of constructing a conductive phantom scalp. A series combination of resistors and capacitors was used in between electrodes on the phantom scalp [8]. All the impedances were measured using GW Digital LCR meter at 100 Hz.

A gel-injected disk electrode was used at C_z and 3M® disposable electrodes were used at A_2, M_2 and F_{pz}. All these had silver chloride surfaces. PowerLab™ amplifiers and Chart-5 by ADInstruments™ was used to record data. Custom written Matlab® scripts were used for offline analysis.

D. Technical conditions

A rarefaction 'click stimulus' was used with a 0.1 ms pulse width (negative polarity) at a repetition frequency of 21.1 Hz. This rate was used to match the standard experimental protocol and to produce comparable data with Table 2 [3, 4].

ABRs were sampled at a frequency of 40 kHz with a band-pass filter of 10-5000 Hz. An intensity of 80 dB SPL was maintained for each audio transducer output, by adjusting the amplitude of the stimulus, regardless of the impedance of the audio transducer used.

E. Analysis methods

The human and phantom data were analysed according to the following criteria:

1. Comparison of the stimulus artifact end time (SAET) of each audio transducer with respect to measured ABR wave I. This will determine the extent of effect of stimulus artifact on ABR waves.
2. Comparison of absolute latency of waves I, II, III and V with published data to determine the quality of ABRs.
3. Comparison of the earlobe and mastoid electrode arrangements for SAET and ABR wave latencies to determine electrode arrangement with minimum impact.

III. Results

Impedance measurements obtained using the phantom and human scalp are tabulated in Table 3. This clearly indicates that the model used reflects the actual scalp conductive properties, thus data obtained from the phantom are comparable to human scalp data.

Table 3 Inter-electrode impedance measurements (at 100 Hz)

	Resistance (kΩ)	Capacitance (μF)	n
Phantom	3.1	3	16
Human scalp	3.0 ± 1.4	2.3 ± 0.9	32

Fig. 1 shows the ABRs obtained by a randomly selected participant using each audio transducer listed in Table 1. The bar under each recording shows the SAET. The SAET was determined by waiting until the value of the signal returned to within 1 standard deviation of the pre-stimulus baseline.

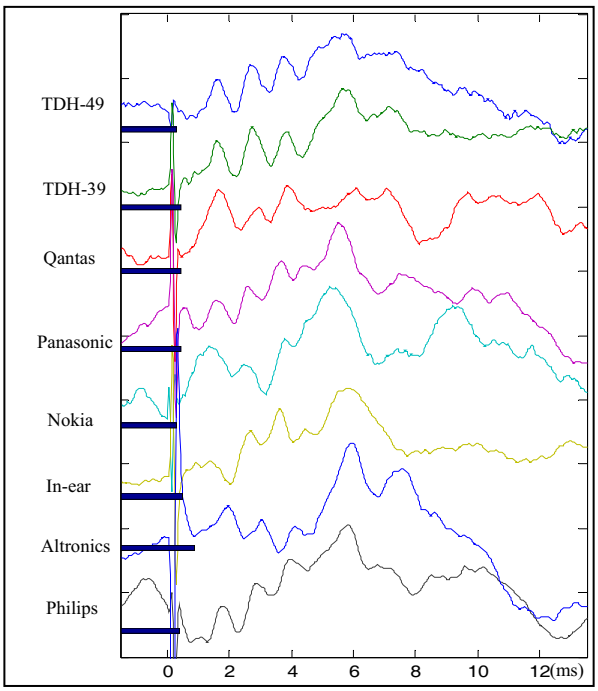


Fig. 1 ABRs of a selected participant using 8 different audio transducers (vertical axis) with the earlobe electrode arrangement. Each ABR shown is an average of 1024 epochs. The stimulus artifact is at t=0. The horizontal bars show the SAET for each audio transducer.

Fig. 2 illustrates the SAET obtained using the phantom and the participants with inverting electrode at earlobe. These values are categorized according to the audio transducer used on the vertical axis.

Fig. 3 shows the mean and the standard deviation of the absolute latencies of ABR waves I, II, III and V obtained from 4 participants, with inverting electrode at earlobe. The width of shaded vertical bars indicates the ranges in which each wave should occur. These ranges were determined using published data in Table 2.

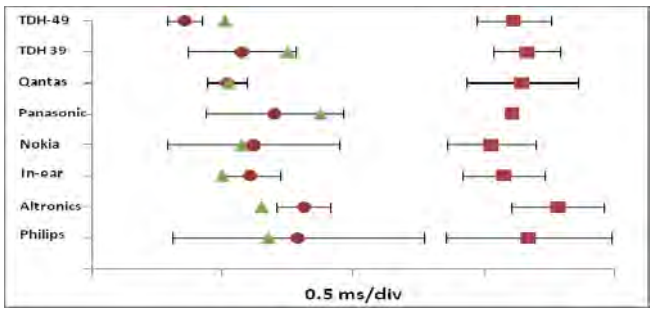


Fig. 2 SAET from the human scalp and the phantom with the ABR wave I from different audio transducers. Horizontal error bars show the standard deviation of SAET and wave I of human scalp. Earlobe electrode arrangement. All human data include an average of 4 participants.

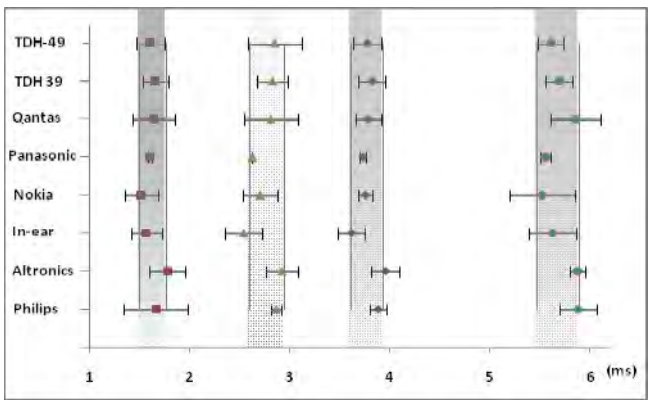


Fig. 3 Average absolute latency of wave I, II, III and V from 4 participants. Standard deviation is in horizontal error bars. Vertical grey bars represent the average range of published data for ABR waves at earlobe.

IV. Discussion

A. Separation of the stimulus artifact from ABR wave I

Due to the close proximity, prolonged stimulus artifacts can distort characteristics of the ABR wave I. Therefore the separation between stimulus artifact and onset of wave I is critical in choosing audio transducers.

Separation values in Table 4 are the time gaps between the highest of either phantom or average of human SAET and the onset of ABR wave I variation (using Fig. 2).

According to Table 4, all the introduced audio transducers are well above the standard TDH-39 except Philips transducer at the earlobe electrode arrangement. Qantas provides the best separation and Philips with a low 0.56 ms.

Table 4 Separation between the stimulus artifact and the ABR wave I

Audio transducer	Earlobe (ms)	Mastoid (ms)
TDH-49p	0.96	0.84
TDH-39	0.78	0.94
Qantas	0.91	0.86
Panasonic	0.71	0.60
Nokia	0.74	0.86
1.2M (in-ear)	0.81	0.68
Altronics	0.79	0.94
Philips	0.56	0.56

At the mastoid electrode arrangement, except for Panasonic, 1.2M (in-ear) and Philips transducers, the others are comparable with standard transducers.

As a whole, all separation values are acceptable as illustrated in Fig. 1, although, better clarity could be obtained by using different transducers at different electrode arrangements. Given the high variation in SAET of the Nokia and Philips devices, we would not recommend their usage for ABR recordings.

B. Quality of the ABR produced

The absolute latencies of ABR waves show little variation, and have almost constant values for a person at a specific sound intensity [1]. Therefore the quality of the ABR produced by each audio transducer could be determined by comparing absolute latencies of wave I, II, III and V with published data (Table 2) with similar sound intensities.

As shown in Fig. 3 the recorded latencies of all waves by the TDH-49 and TDH-39 (gold standard) transducers fall well within the expected range of values. Therefore, we conclude that the remaining values of the other transducers are valid.

Referring to Fig. 3, all the average values fall within published data ranges with little variations. A pattern to notice here is ABR waves always appear later for the Altronics (suggesting a time delay) and earlier for the 1.2M (in-ear) (suggesting an earlier arrival of sound at the eardrum due to proximity), but not enough to warrant latency correction.

With the mastoid electrode arrangement, measurement of standard latencies occurred for both Qantas and Panasonic earphones, but the Nokia produced wave II and III with a large variability in latency. The 1.2M (in-ear), Altronics and Philips produced similar results to the earlobe electrode arrangement.

In terms of quality of ABR wave latencies, both earlobe and mastoid electrode arrangements provided good results from all the introduced audio transducers, except the Nokia earphone at mastoid.

V. Conclusions

We conclude that, it is feasible to use most of the commercially available audio devices in ABR studies, but we recommend that a comparison of the new audio transducer with the gold standards should be carried out in the user's laboratory.

From the results of this study, we cannot recommend Philips headphones or Nokia earphones.

The other factor of consideration is that of sound intensity. In this study, the sound intensity used (80 dB SPL) is appropriate for diagnosis of neural disorders where a fully featured ABR is required. But, in the case of hearing screening, the participant should undergo recordings at different sound intensity levels. This may create further aberrations to the ABR wave form. Thus we recommend that those sound levels be analysed in this type use.

Acknowledgment

The authors thank the volunteers who participated for ABR recordings and Chris Anthony for technical assistance.

References

1. Misra U K,Kakita J (1999) Clinical Neurophysiology. B.I. Churchill Livingstone, New Delhi
2. Yoshiko K,Fujita Y (1994) Auditory brainstem responses by click stimuli via an earphone--comparison with a headphone. Rinsho byori. The Japanese journal of clinical pathology 42(12): 1287-1293
3. Hall J W (1992) Handbook of Auditory Evoked Responses. Allyn and Bacon, Massachusetts
4. Van Campen L E, et al. (1992) Comparison of Etymotic insert and TDH supra-aural earphones in auditory brainstem response measurement. Journal of the American Academy of Audiology 3(5): 315-323
5. Antonelli A R, Bellotto R, and Grandori F (1987) Audiologic diagnosis of central versus eighth nerve and cochlear auditory impairment. Audiology 26(4): 209-226
6. Rowe III M J (1978) Normal variability of the brain-stem auditory evoked response in young and old adult subjects. Electroencephalography and Clinical Neurophysiology 44(4): 459-470

7. Schwartz D M, Pratt Jr R E, and Schwartz J A (1989) Auditory brain stem responses in preterm infants: Evidence of peripheral maturity. Ear and Hearing 10(1): 14-22
8. Wood A W, Hamblin D L, and Croft R J (2003) The use of a 'phantom scalp' to assess the possible direct pickup of mobile phone handset emissions by electroencephalogram electrode leads. Medical and Biological Engineering and Computing 41(4): 470-472

Author: Anjula De Silva
Institute: Swinburne University of Technology
Street: Burwood Road
City: Melbourne
Country: Australia
Email: adesilva@swin.edu.au

Simultaneous Measurement of PPG and Functional MRI

S.C. Chung*, M.H. Choi, S.J. Lee, J.H. Jun, G.M. Eom, B. Lee and G.R. Tack

Department of Biomedical Engineering, Research Institute of Biomedical Engineering,
College of Biomedical & Health Sciences, Konkuk University, Chungju, South Korea,

Abstract — **The purpose of the current study was to develop a magnetic resonance (MR)-compatible photoplethysmograph (PPG) system which could measure the raw PPG signal during MR image acquisition. The system consisted of an optic sensor which measured the optic signal, an optic cable which transmitted a near-infrared optic signal, a signal amplifier, and a filter for noise removal. To minimize interactive noise, only the optic cable and the optic sensor module were located inside the MR room; the signal amplifier and filter were located outside the MR room. The experiment verified that a reliable PPG signal can be obtained without deteriorating the MR image. Especially, it was possible to get a reliable PPG signal while acquiring MR images with EPI method which has been used for functional magnetic resonance imaging (fMRI) study. This system can simultaneously measure the response of the central nervous system using fMRI and that of the peripheral nervous system using the PPG.**

Keywords — **Photoplethysmograph, Magnetic resonance image, Optic sensor and cable**

I. Introduction

Compared with other physiological signals and imaging modalities, magnetic resonance (MR) imaging has outstanding spatial resolution, but has a shortcoming with respect to temporal resolution. Physiological signals, such as the electroencephalogram (EEG), the electrocardiogram (ECG), the galvanic skin response (GSR), the skin conductance response (SCR), and the photoplethysmograph (PPG), have excellent temporal resolution, but poor spatial resolution. To simultaneously achieve excellent temporal and spatial information, a number of studies regarding MR image acquisition with physiological signals are underway.

Recently, a reliable EEG signal measurement technique with MR acquisition has been introduced. During MR image acquisition, the main magnetic field, the gradient magnetic field, and the radio frequency (RF) pulse induce considerable noise on the EEG signal. To minimize induced noise, a carbon electrode was used instead of a Ag/AgCl electrode, and the electromagnetic field behind the leads was offset by twisting the leads. A study on induced noise removal by post-signal processing was carried out [1], and a real time noise removal algorithm was created [2]. A surface coil was used to minimize the effects of the RF pulse [3]. As the MR environment can affect physiological signals, physiological signal measuring instruments can distort MR images. To minimize the distortion of MR images, the length of the transmitter was minimized, the measuring instrument was shielded, and the use of metallic materials was minimized [4,5]. Based on these techniques, it was possible to perform functional magnetic resonance imaging (fMRI) and receive an EEG signal simultaneously. Through the use of this technique, it was possible to examine the mechanism by which the central nervous system (CNS) satisfies temporal and spatial resolution at the same time, and studies have been initiated which attempt to clarify the mutual relationship [6,7,8].

Studies are in progress which examine the mechanism whereby the CNS and the peripheral nervous system (PNS) simultaneously satisfy temporal and spatial resolution using fMRI and ECG, respectively, but are still in the beginning stages [9,10]. Investigations on the mutual relationships between the SCR, the GSR signal, and fMRI have been partially studied, but are insufficient to clearly examine both central and peripheral [11,12]. Thus, it is necessary to examine such mechanisms utilized by the CNS and PNS and to study the mutual relationships through the simultaneous measurement of fMRI and physiological signals.

The PPG signal can yield the information regarding the autonomic nerves among the peripheral nerves [13,14]. To minimize the interactive effects with MR, MR-compatible PPG or pulse oximeter system which uses fiber optic sensor and cable is commercially available [15,16,17]. However those systems are mainly used for patient monitoring and provide only numerical values of blood oxygen saturation and heart rate.

This study tried to develop the system that extracts raw PPG signal with fMRI under MR environment. In so doing, we sought to develop a technique which reliably and simultaneously measured the central and peripheral signals.

II. Methods

As shown in Fig. 1, this system consisted of an optic cable and an optic sensor module which were located inside the MR room, and a signal amplifier and filter which were located outside the MR room. The optic cable consisted of

Chwee Teck Lim, James C.H. Goh (Eds.): ICBME 2008, Proceedings 23, pp. 161–164, 2009
www.springerlink.com

36 optic fibers, 1 mm in diameter, and divided into 18 fibers each, which sent and received the optic signal. After binding a bundle that combined each of the 18 optic fibers, the optic sensor module was built for measuring the PPG signal using a reflectance method with the sensor in contact with the skin. During measurement, the movement-induced noise was minimized by a band-type housing of contact between the optic sensor and the skin.

The light transmitter, which utilized an infrared (IR) LED, receiver, and amplifier, receives reflected light signal from the skin, and the filter was located outside the MR room. The IR LED in the transmitter used a 650 nm wavelength signal. The phototransistor was a signal receiver that used a non-inverting amplifier. To achieve optimal gain by preventing clipping phenomena, the amplification ratio could be varied up to 1,000 times. A 4th order low-pass filter was used for high frequency noise removal and base line drift was removed by a high-pass filter. This provided the possibility of measuring a main frequency range of 0.5-20Hz for the PPG signal. When the amplifier was located near the operating room, there was considerable electric noise. Thus, the hum was removed by the notch filter.

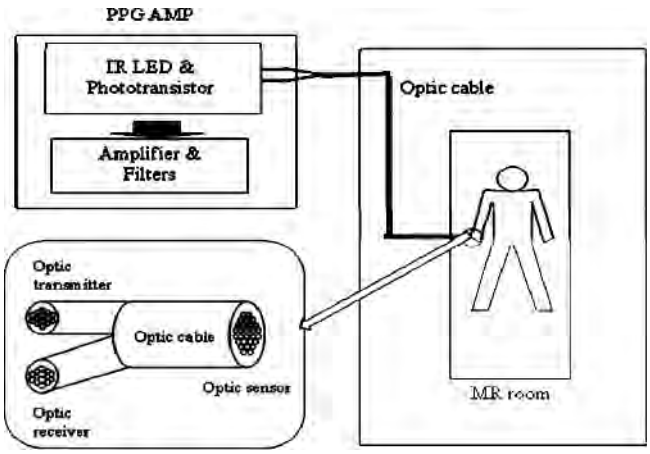


Fig. 1 Structure of a MR-compatible PPG system

The effect of the MR environment on the PPG signal was investigated by performing human subject experiments while measuring the PPG signal and MR image simultaneously. Images were acquired using a 3.0 Tesla MR system (Magnum 3.0, Medinus Inc., Korea) system with the fast spin echo (FSE) method and the following imaging parameters: TR/TE, 4400/96ms; field of view, 240mm; matrix size, 256×256; slice thickness, 3mm; and number of slices, 19. The PPG signal was also measured while acquiring images with the echo planar imaging (EPI) method which has been used for fMRI study using the following imaging parameters: TR/TE, 3000/96ms; field of view, 240mm; matrix size, 64×64; slice thickness, 3mm; and number of slices, 9. The PPG signal, at 300 samples/sec, was measured using a data acquisition board (DAQpad-6015, National Instruments, USA). The PPG signal was displayed, saved, and retrieved by using Labview (version 7.1) and Matlab (version 6.5) software.

III. Results

Two types of MR images were acquired by measuring the PPG signal with human subjects (Fig. 2). Figure 3 illustrates the measured PPG signal while performing MR image acquisition with the EPI method, which showed a slight noise, but a reliable signal.

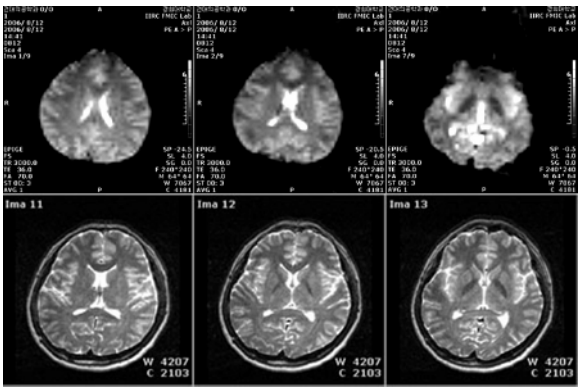


Fig. 2 MR images of the subject (upper, EPI sequence; lower, FSE sequence)

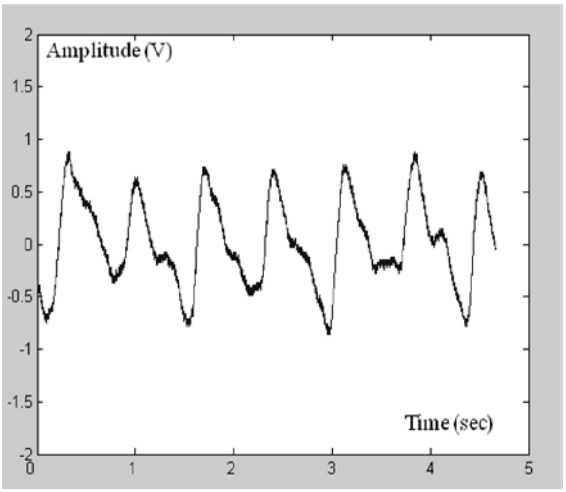


Fig. 3 Measured PPG signal during MR image acquisition with the EPI method

IV. Discussion

To prevent mutual interference between MR image acquisition and physiological signal measurement, sensors, cables, and amplifiers should not have an effect on MR images. Further, the main magnetic field, gradient magnet field, and RF pulse should not have an effect on physiological signals. Therefore, in the current study a MR-compatible PPG system was developed using an optic cable and an optic sensor to minimize the mutual interference between the MR image and the raw PPG signal [15,16,17].

When the physiological signal measuring instrument (i.e., the amplifier) was located inside the MR room, metallic material in the instrument had an effect on the MR image. A digital device, such as a microprocessor, induced RF noise, and induced noise had an effect on the MR image. Since the magnetic field and RF pulse of the MR system can cause a noise on the physiological signal measurement system, the instrument requires perfect shielding. To minimize the mutual interference effect in this study, the measuring instrument was located outside the MR room and only the optic cable and the optic sensor were located inside the MR room.

In general, the PPG amplifier used a 560-940nm wavelength IR LED, and the wavelength and intensity were selected for the specific application [18]. This study used a 650nm IR LED, which incurred the least amount of light loss by considering the distance between a subject in bed inside the MR room and the instrument outside the MR room. When a single optic fiber is used to transmit an optic signal, it is possible to cause a motion artifact on the PPG signal which is sensitive to movement. The amplitude and quality of the optic signal is increased by increasing the number of optic fibers [18]. Therefore, an optic cable with a maximum of 36 optic fibers was used in the current study by considering a penetrating hole across the MR room.

The results showed that the optic cable and the optic sensor did not have an effect on the MR image, but the measured PPG signal showed a slight noise. There is a possibility that MR environment such as strong magnetic field might induce the physiological changes of the subject and the signal might be slightly distorted, but there was not any published result about this problem. Therefore it could be concluded that the signal distortion was due to the complex effects of static magnet field, gradient magnetic field, and RF pulse. It will be necessary in future investigations to remove this induced noise.

The findings of this experiment verified that a reliable raw PPG signal could be obtained without deteriorating the MR image. Especially, it was possible to get a reliable PPG signal while acquiring MR images with EPI method which has been used for fMRI study. This system can simultaneously measure the response of the central nervous system using fMRI and that of the peripheral nervous system using the PPG.

Acknowledgements

"This work was supported by the Korea Research Foundation Grant funded by the Korean Government (Ministry of Education, Science and Technology)" (The Regional Research Universities Program/Chungbuk BIT Research-Oriented University Consortium).

References

1. Goldman RI, Stern JM, Engel J et al. (2000) Acquiring simultaneous EEG and functional MRI. Clin Neurophysiol 111: 1974-1980
2. Garreffa G, Carni M, Gualniera G et al. (2003) Real-time MR artifacts filtering during continuous EEG/fMRI acquisition. Mag Reson Imaging 21: 1175-1189
3. Van Audekerke J, Peerters R, Verhoye M et al. (2000) Special designed RF-antenna with integrated non-invasive carbon electrodes for simultaneous magnetic resonance imaging and electroencephalography acquisition at 7T. Mag Reson Imaging 18: 887-891
4. Obler R, Köstler H, Weber BP et al. (1999) Safe electrical stimulation of the cochlear nerve at the promontory during functional magnetic resonance imaging. Mag Reson Med 42: 371-378
5. Liu JZ, Dai TH, Elster TH et al. (2000) Simultaneous measurement of human joint force, surface electromyograms, and functional MRI-measures brain activation. J Neurosci Meth 101: 49-57
6. Laufts H, Kleinschmidt A, Beyerle A et al. (2003) EEG-correlated fMRI of human alpha activity. NeuroImage 19: 1463-1476
7. Mirsattari SM, Lee DH, Jones D et al. (2004) MRI compatible EEG electrode system for routine use in the epilepsy monitoring unit and intensive care unit. Clin Neurophysiol 115: 2175-2180
8. Sammer G, Blecker C, Gebhardt H et al. (2005) Acquisition of typical EEG waveforms during fMRI: SSVEP, LRP, and frontal theta. NeuroImage 24: 1012-1024
9. Abi-Abdallah D, Chauvet E, Bouchet-Fakri L et al. (2006) Reference signal extraction from corrupted ECG using wavelet decomposition for MRI sequence triggering: application to small animals. BioMed Eng OnLine 5:11, doi:10.1186/1475-925X-5-11
10. Chung SC, Yi JH, Tack GR et al. (2006) Development of an MR-compatible ECG amplifier. Key Eng Mater 321-323: 1032-1035
11. Williams LM, Phillips ML, Brammer MJ et al. (2001) Arousal dissociates amygdala and hippocampal fear responses: Evidence form simultaneous fMRI and skin conductance recording. NeuroImage 14: 1070-1079
12. Nagai Y, Critchley HD, Featherstone E et al. (2004) Brain activity relating to the contingent negative variation: An fMRI investigation. NeuroImage 21: 1232-1241
13. Demmel R, Ridt F, Olbrich R (2000) Autonomic reactivity to mental stressors after single administration of lorazepam in male alcoholics and healthy controls. Alcohol Alcoholism 35(6): 617-627
14. Lundström JN, Olsson MJ (2005) Subthreshold amounts of social odorant affect mood, but not behavior, in heterosexual women when tested by a male, but not a female, experimenter. Biol Psychol 70: 197-204

15. Von Smekal A, Seelos KC, Küper CR et al. (1995) Patient monitoring and safety during MRI examinations. Euro Radiol 5: 302-305
16. Gehealthcare at http://www.gehealthcare.com/accessories/2006%20A&S%20DI%20Catalog.pdf
17. Nonin at http://www.nonin.com/documents/8600%20Series%20Brochure.pdf
18. Ugnell H, Öberg PÅ (1995) The time-variable photo-plethysmographic signal: Dependence of the heart synchronous signal on wavelength and sample volume. Med Eng Phys 17(8): 571-57

*Corresponding author

Author: Soon-Cheol Chung
Institute: Department of Biomedical Engineering, Research Institute of Biomedical Engineering, College of Biomedical & Health Science, Konkuk University
City: Chungju, Chungbuk
Country: South Korea
Email: scchung@kku.ac.kr

A Study on the Cerebral Lateralization Index using Intensity of BOLD Signal of functional Magnetic Resonance Imaging

M.H. Choi, S.J. Lee, G.R. Tack, G.M. Eom, J.H. Jun, B. Lee and S.C. Chung*

Department of Biomedical Engineering, Research Institute of Biomedical Engineering,
College of Biomedical & Health Sciences, Konkuk University, Chungju, South Korea,

Abstract — **This study proposes a new cerebral lateralization index on the basis of neural activation intensity. Eight right-handed male college students (mean age 23.5 years) and ten right-handed male college students (the mean age - 25.1 years) participated in this study of visuospatial and verbal tasks, respectively. Functional brain images were taken from 3T MRI using the single-shot EPI method. A cerebral lateralization index based on neural activation area (i.e. number of activated voxels) and another based on neural activation intensity (i.e. intensity of BOLD) were calculated for both cognition tasks. The result of calculating a cerebral lateralization index based on neural activation area suggested that the right hemisphere is dominant during visuospatial tasks and the left hemisphere is dominant during verbal tasks. When a cerebral lateralization index was computed on the basis of the neural activation intensity, it was shown that the area of cerebral lateralization closely related to visuospatial tasks is the superior parietal lobe, and the area of cerebral lateralization closely related to verbal tasks is the inferior and middle frontal lobes. Since the proposed method can determine the dominance of the cerebrum by each area, it can be helpful to determine cerebral lateralization accurately and easily.**

Keywords — **Cerebral lateralization, BOLD, fMRI**

I. Introduction

There have been two major methods used to study the change in brain activation during cognitive tasks with the functional magnetic resonance imaging (fMRI). The first method measures the number of activated voxels based on blood oxygen level dependent (BOLD) signal and the other measures the neural activation intensity of activated voxels [1,2]. The former, which has been widely used, easily identifies the activated brain areas by using subtraction method designed to measure the number of activated voxels in response to cognitive activity. The latter measures the neural activation intensity of activated voxels, which is based on the assumption that an increase in the intensity reflects an increase in brain activation. This is because there is positive relationship between the intensity of BOLD signal and the magnitude of brain activation [2].

Generally, cerebral lateralization is calculated by the lateralization index (LI), which is based on neural activation area [3]. Calculation of LI is by the equation (LV-RV)/(LV+RV), where LV and RV are the number of activated voxels of the left and right hemisphere, respectively. When LI is positive, the left hemisphere is dominant, and when LI is negative, the right hemisphere is dominant. This method can determine which hemisphere is dominant, but it was difficult to calculate the regional LI of the cerebrum. For example, during visuospatial cognition tasks, neural activation occurs at proximal regions, including the cerebellum, the occipital lobe, and the parietal lobe. Since activated voxels are clustered, it is difficult to distinguish individual regions and difficult to calculate a regional LI [1].

This study tries to avoid the drawbacks of the existing cerebral LI calculation method, and proposes a new cerebral LI calculation method that uses the signal intensity of activated voxels (neural activation intensity) to calculate a regional LI.

II. Methods

Eight right-handed male college students (mean age, 23.5 years) and ten right-handed male college students (mean age, 25.1 years) participated in this fMRI study of visuospatial and verbal tasks, respectively. All subjects signed informed participation consent forms. All examinations were performed under the regulations of our Institutional Review Committee.

A total of 20 items for the visuospatial cognition task were selected from Korean versions of an intelligence test, an aptitude test, and a general aptitude battery (GATB) [4,5,6]. The selected items consisted of (1) selecting a figure that has the exact shape of a given diagram from among four examples and (2) finding the next one in a series of diagrams. A verbal cognition task (consisting of verbal analogy and antonym tasks) was developed. A total of 28 items were selected from Korean versions of an intelligence test and the GATB [4,6]. The verbal analogy testing required the subject to select one of a group of words with the same meaning as a given word. The verbal antonym testing required the subject to select a word that had a different meaning from among four words.

Chwee Teck Lim, James C.H. Goh (Eds.): ICBME 2008, Proceedings 23, pp. 165–168, 2009
www.springerlink.com

The experiment consisted of four blocks (8 min.); each block (2 min.) had both control (1 min.) and cognitive (1 min.) items. The control and cognitive tasks were presented using SuperLab 1.07 (Cedrus Co.). Items were projected onto a screen and subjects were instructed to provide the correct answers. In response to control tasks, subjects were instructed to press a button corresponding to the number (1, 2, 3, or 4) projected onto the screen. In the cognition task, subjects were asked to press a button to correctly identify the number of an item projected on the screen (visuospatial task, 5 trials per block; verbal task, 7 trials per block).

Imaging was conducted on a 3.0T ISOL Technology FORTE (ISOL Technology, Korea) equipped with whole-body gradients and a quadrature head coil. Single-shot echoplanar fMRI scans were acquired in 35 continuous slices, parallel with the AC-PC line. The parameters for fMRI included the following: the repetition time (TR) and echo time and (TE) were 3000 ms and 35 ms, respectively; flip angle, 60º; field of view, 240 mm; matrix size, 64 × 64; slice thickness, 4 mm; and in-plane resolution, 3.75 mm. T1-weighted anatomic images were obtained with a 3-D FLAIR sequence (TR, 280 ms; TE, 14 ms; flip angle, 60º; FOV, 240 mm; matrix size, 256 × 256; slice thickness, 4 mm).

The fMRI data were analyzed with SPM99 (Wellcome Department of Cognitive Neurology, London, UK). All functional images were realigned to the image taken proximate to the anatomical study by using affine transformation routines built into SPM99. The realigned scans were coregistered to the participant's anatomical images obtained within each session, and normalized to SPM99's template image that uses the space defined by the Montreal Neurologic Institute (MNI). Motion correction was done using Sinc interpolation. Time series data were filtered with a 240 s high-pass filter, to remove artifacts due to cardiorespiratory and other cyclical influences. The functional map was smoothed with a 7 mm isotropic Gaussian kernel prior to statistical analysis. Statistical analysis was done individually, and then as a group using the general linear model and the theory of Gaussian random fields implemented in SPM99. Using the subtraction procedure (cognition tasks – control tasks), activated areas in the brain during cognitive tasks were color-coded by *t*-score.

The cerebral lateralization index (LI) is calculated from the number of activated voxels by equation (1):

$$LI = (LV - RV) / (LV + RV) \quad (1)$$

where LV and RV are the number of activated voxels of the left and right hemisphere, respectively. By using small volume correction (SVC) among SPM methods, the number of activated voxels of each hemisphere is measured after assigning regions of the left and the right hemisphere.

On the basis of regional activated voxel intensity, the lateralization index using intensity (LII) is calculated by equation (2):

$$LII = (LI - RI) / (LI + RI) \times 100 \quad (2)$$

where LI and RI are the average intensity of activated voxels of the left and right regions, respectively. To observe the average intensity of BOLD signal at each activated region, the 5×5×5 region around the voxel that has the highest t-score (selection criteria) was selected.

For visuospatial tasks, three regions were selected as follows: the middle frontal lobe (MF), the superior parietal lobe (SP) and the occipital lobe (O). For verbal tasks, four regions were selected as follows: the middle frontal lobe (MF), the inferior frontal lobe (IF), the superior parietal lobe (SP) and the occipital lobe (O).

III. Results

Significant activation was observed in the cerebellum, occipital lobe, parietal lobe, and frontal lobe during the visuospatial tasks. Significant activation was observed in the cerebellum, occipital lobe, parietal lobe, temporal lobe, and frontal lobe during the verbal tasks.

The activated voxels are divided into the left and right hemisphere during visuospatial and verbal cognition tasks, the cerebral lateralization index (LI) based on equation (1) is calculated. During visuospatial tasks, the number of activated voxels of the right hemisphere showed significant increase compared with that of the left hemisphere (t = –9.057, df = 7, p = .001), and LI was negative, which means that the right hemisphere was dominant. During verbal tasks, the number of activated voxels of the left hemisphere showed significant increase compared with that of the right hemisphere (t = 6.498, df = 9, p = .001), and LI was positive, which means that the left hemisphere was dominant.

The lateralization index using intensity (LII) was calculated by equation (2) based on the intensity of activated voxels. Tables 1 and 2 show the intensity of activated voxels and LII of visuospatial and verbal tasks, respectively. As shown in Table 1, during visuospatial tasks, LII of all three regions was negative and the right region was dominant. But only at superior parietal lobes (SP) did the voxel signal intensity of the right region show a significant increase compared with that of the left region (t = –2.345, df = 7, p = .05). As shown in Table 2, during verbal tasks, LII of three regions, except the occipital lobe (O), were positive and the left region was dominant. But only at the middle frontal lobe (MF) (t = 4.559, df = 7, p = .003) and inferior frontal lobe (IF) (t = 4.689, df = 7, p = .002), did the voxel signal intensity of the left region show a significant increase com

Table 1. Average intensity of activated voxels and lateralization index using intensity (LII) at the middle frontal lobe (MF), superior parietal lobe (SP), and occipital lobe (O) in visuospatial tasks. The Talairach coordinates of the center voxel in each region are given

Subjects	Left			Right			LII		
	MF (-46,18,24)	SP (-24,68,56)	O (-28,-94,6)	MF (46,18,24)	SP (24,-68,56)	O (32,-94,8)	MF	SP	O
#1	100.85	100.78	100.51	100.99	101.04	100.58	-0.07	-0.13	-0.04
#2	101.09	100.61	100.62	101.65	100.69	101.25	-0.28	-0.04	-0.31
#3	100.60	100.31	100.70	100.33	100.73	101.07	0.14	-0.21	-0.18
#4	100.73	100.57	100.59	100.75	101.11	101.41	-0.01	-0.27	-0.41
#5	99.93	100.44	100.68	100.40	100.61	100.71	-0.23	-0.09	-0.01
#6	101.12	100.46	100.85	100.20	100.68	100.78	0.46	-0.11	0.04
#7	100.16	101.05	100.84	100.59	100.72	101.08	-0.21	0.16	-0.12
#8	100.18	100.48	100.69	99.89	100.93	100.55	0.15	-0.22	0.07
Mean ±SD	100.58 ±0.44	100.59 ±0.23	100.69 ±0.12	100.60 ±0.54	100.81 ±0.19	100.93 ±0.32	-0.01 ±0.20	-0.11 ±0.10	-0.12 ±0.20

Table 2. Average intensity of activated voxels and lateralization index using intensity (LII) at the superior parietal lobe (SP), occipital lobe (O), middle frontal lobe (MF), and inferior frontal lobe (IF) in verbal task. The Talairach coordinates of the center voxel in each region are given

Subjects	Left				Right				LII			
	SP (-28,72,58)	O (-30,86,18)	MF (-46,14,26)	IF (-32,30,-10)	SP (28,-72,58)	O (30,-86,-18)	MF (46,14,26)	IF (32,30,-10)	SP	O	MF	IF
#1	101.69	100.91	100.86	100.88	101.11	101.56	100.81	100.50	0.29	-0.32	0.02	0.19
#2	100.50	100.30	100.76	100.36	100.00	100.26	99.96	100.01	0.25	0.02	0.40	0.17
#3	100.81	99.83	100.64	100.64	-	100.12	99.97	100.15	-	-0.15	0.33	0.24
#4	100.92	100.53	100.97	100.42	99.89	99.93	100.34	99.88	0.52	0.30	0.31	0.27
#5	100.20	100.11	100.28	-	-	-	-	-	-	-	-	-
#6	101.06	100.91	100.84	100.67	-	100.09	100.37	100.37	-	0.41	0.23	0.15
#7	101.06	99.91	100.99	100.46	-	100.82	100.01	100.19	-	-0.45	0.49	0.13
#8	-	100.10	101.86	100.40	-	101.19	100.30	100.37	-	-0.54	0.77	0.01
#9	100.22	99.94	101.50	-	100.47	100.12	99.93	-	-0.12	-0.09	0.78	-
#10	101.00	99.57	100.95	100.61	100.45	100.21	-	99.74	0.27	-0.32	-	0.43
Mean ±SD	100.82 ±0.47	100.21 ±0.45	100.96 ±0.44	100.56 ±0.17	100.38 ±0.48	100.48 ±0.57	100.21 ±0.30	100.15 ±0.26	0.24 ±0.23	-0.13 ±0.32	0.42 ±0.26	0.20 ±0.12

pared with that of the right region. There is no activation for some subjects at selected regions; we did not include the calculation of LII in those cases, as shown in Table 2.

IV. Discussion

During visuospatial tasks, cerebellum, occipital lobe, parietal lobe, and frontal lobe are activated and it is well-known that especially the parietal lobe plays an important role [1,7]. For studies of verbal reasoning, verbal concept, and internal verbal generation, it is reported that cerebellum and occipital lobe and the inferior frontal lobe including Broca, parietal and temporal lobes, including Wernicke, play important roles in verbal cognition [8,9]. The activated cerebral regions during the cognition tasks of this study agree with previous results.

The number of activated voxels (activated area) has been used reliably to determine the dominant hemisphere during diverse cognition tasks. On the basis of these results for

cerebral lateralization, it is concluded that the right hemisphere is dominant for visuospatial tasks and the left hemisphere is dominant for verbal tasks, and these results agree with those of previous studies. However, there is a lack of information concerning in which region of the cerebrum this dominance occurs. Especially during the visuospatial tasks, since the cerebellum, the occipital lobe, and the parietal lobe regions are clustered, it is difficult to distinguish individual regions and it is difficult to calculate the regional LI.

This study showed that the new LII; which is based on the intensity of the activated voxels, can be used to overcome these limitations. On the basis of the LII calculation of the middle frontal lobe (MF), the superior parietal lobe (SP) and the occipital lobe (O) during visuospatial tasks, it can be concluded that all three regions showed negative values, which means that the right region is dominant, but there was statistical significance only at the superior parietal lobe (SP). This is convincing evidence that the superior parietal lobe is closely related with cerebral lateralization of visuospatial cognition. On the basis of the LII calculation of the middle frontal lobe (MF), the inferior frontal lobe (IF), the superior parietal lobe (SP) and the occipital lobe (O) during verbal tasks, it can be concluded that three regions, except the occipital lobe (O), were positive, which means that the left region is dominant. There was statistical significance only at the middle frontal lobe (MF) and the inferior frontal lobe (IF). This suggests strongly that the cerebral lateralization region for verbal tasks is the inferior frontal lobe, including the Broca region, and the middle frontal lobe is closely related with cerebral lateralization of verbal cognition tasks.

The BOLD signal intensity of specific regions in fMRI can be an index for the neuronal activation level. It is well known that the absolute magnitude of the change in MR signal (BOLD) has a nearly arbitrary relationship to the magnitude of brain activation [1,2]. Therefore, it is possible to calculate the amount of left and right neuronal activation using the magnitude of BOLD signals, and to calculate a regional LI from these values. Since the proposed LII was used to calculate the regional cerebral LI exactly and easily, this method could be used to help to understand human brain function.

Acknowledgements

This work was supported by the Korea Research Foundation Grant funded by the Korean Government (KRF-2008-314-D00532).

References

1. Chung SC, Sohn JH, Lee B et al. (2007) A comparison of the mean signal change method and the voxel count method to evaluate the sensitivity of individual variability in visuospatial performance. Neurosci Lett 418:138-142
2. Logothetis NK (1998) The neural basis of the blood-oxygen-level-dependent functional magnetic resonance imaging signal. Philos T Roy Soc B 29:1003-1037
3. Springer SP, Deutsch G (1998) Left Brain, Right Brain (5th ed.,) W.H.Freeman, New York
4. Lee SR (1982) Intelligence test 151-Ga Type (High school students ~ adults) Jungangjucksung Press, Seoul
5. Lee SR, Kim KR (1985) Aptitude test 251-Ga (High school students ~ adults) Jungangjucksung Press, Seoul
6. Park SB (1985) GATB (General Aptitude Test Battery): Academic, job aptitude test type II (for students of middle schools, high schools and universities, and general public) Jungangjucksung Press, Seoul
7. Fink GR, Marshall JC, Weiss PH et al. (2001) The neural basis of vertical and horizontal line bisection judgments: An fMRI study of normal volunteers. NeuroImage 14:59-67
8. Jessen F, Erb M, Klose U et al. (1999) Activation of human language processing brain regions after the presentation of random letter strings demonstrated with event-related functional magnetic resonance imaging. Neurosci Lett 270:13-16
9. Sekiyama K, Kanno I, Miura S et al. (2003) Auditory-visual speech perception examined by fMRI and PET. Neurosci Res 47:277-278

* Corresponding author
Author: Soon-Cheol Chung
Institute: Department of Biomedical Engineering, Research Institute of Biomedical Engineering, College of Biomedical & Health Science, Konkuk University
City: Chungju, Chungbuk
Country: South Korea
Email: scchung@kku.ac.kr

A Comparison of Two Synchronization Measures for Neural Data

H. Perko, M. Hartmann and T. Kluge

Austrian Research Centers GmbH, Neuroinformatics, Vienna, Austria

Abstract — **In this paper we analyze the capability of two different signal synchronization measures to detect synchronized periodic signal components. We compare the periodic synchronization index (PSI), which was first introduced for the detection of epileptic seizures in EEG signals, with the widely known phase locking value (PLV). The PSI automatically detects the dominant periodic signal components utilizing Fourier series expansions and measures the synchronization between equivalent components in two signals. The PLV averages the difference between the analytic phases of two signals. Applying these two measures to synthetic data and EEG recordings we found clear advantages of the PSI over the PLV. Experiments with synthetic data and high signal to noise ratio (SNR) revealed no significant difference between the PSI and the PLV in their ability to detect small frequency deviations. However, in the presence of noise the detection performance of the PLV drops significantly. In particular, we found that the PLV relies on an SNR of nearly 3dB. In contrast, the performance with the PSI remained almost unchanged for SNR down to -4dB. This noise robustness of the PSI is due to the incorporation of harmonic oscillations resulting in an improved estimation of periodic signal components. When applied to the detection of early seizure phenomena in EEG data we found that the increase of the PSI at seizure onset is more pronounced and the variance of the measure during pre-ictal time periods is lower than for the PLV.**

Keywords — **signal synchronization, periodic synchronization index, phase locking value**

I. Introduction

Many studies in the field of neuroscience, epilepsy research and brain computer interfaces investigate changes in neural synchronization utilizing scalp EEG signals [1-4]. The majority of methods to measure neural synchronization are based on spectral representations as Fourier, Hilbert or Wavelet transform which are then used to derive synchronization measures as coherence or phase coupling. From a mathematical point of view these approaches are quite similar [5]. In practise however, the performance of a specific synchronization measure relies on the quality of the spectral representation and on the susceptibility to contaminating noise [6, 7]. In this paper we analyze the capability of two different signal synchronization measures to detect synchronized periodic signals contaminated by additive noise. In particular, we compare the periodic synchronization index (PSI), which we introduced for the detection of epileptic seizures in EEG signals [8, 9], with the widely known phase locking value (PLV) [10-13]. The PSI automatically detects the dominant periodic signal components utilizing Fourier series expansions and measures the synchronization between equivalent components in two signals. The PLV averages the difference between the analytic phases of two signals. Applying these two measures to synthetic data and EEG recordings, we found clear advantages of the PSI over the PLV. Experiments with synthetic data revealed a higher noise robustness of the PSI. When applied to the detection of early seizure phenomena in EEG data we found that the increase of the PSI at seizure onset is more pronounced and the variance of the measure during pre-ictal time periods is lower than for the PLV.

II. Method

To derive the PSI, we consider the signals $y_k[n]$ with channel index k and time index n. Our approach is based on the model that these signals are composed of periodic components $x_k[n]$ disturbed by additive noise $z_k[n]$, i.e. $y_k[n] = x_k[n] + z_k[n]$. The periodic components $x_k[n]$ with fundamental frequencies θ_k can be represented in terms of a Fourier series given by

$$x_k[n] = \sum_{m=1}^{M} \left(c_k[m]\, e^{j2\pi\theta_k mn} + c_k^*[m]\, e^{-j2\pi\theta_k mn} \right).$$

Our signal model is thus based on the assumption that there are periodic components hidden in additive noise. Since the periodic components are unknown, we have to estimate them from the observed signal $y_k[n]$. With the Fourier series representation, this is equivalent to an estimation of the fundamental frequencies θ_k and coefficients $c_k[m]$. To estimate these parameters we introduce the Fourier series

$$x_{k,\theta}[n] = \sum_{m=1}^{M} \left(c_{k,\theta}[m]\, e^{j2\pi\theta mn} + c_{k,\theta}^*[m]\, e^{-j2\pi\theta mn} \right),$$

Chwee Teck Lim, James C.H. Goh (Eds.): ICBME 2008, Proceedings 23, pp. 169–173, 2009
www.springerlink.com

with a variable fundamental frequency θ and coefficients given by

$$c_{k,\theta}[m] = \sum_n y_k[n]\ e^{-j2\pi\theta mn}.$$

Using the coefficient vectors

$$\mathbf{c}_{k,\theta} = \left(c_{k,\theta}[1],...,c_{k,\theta}[M]\right)^T,$$

we define estimates for the fundamental frequencies as

$$\hat{\theta}_k = \arg\max_\theta \left\|\mathbf{c}_{k,\theta}\right\|.$$

With $\hat{\theta}_k$ a reasonable estimate of the Fourier coefficients is given by $c_k[m] \approx c_{k,\hat{\theta}_k}[m]$. The PSI is now[1]

$$S_{k,l} = \frac{\left|\left\langle \mathbf{c}_{k,\hat{\theta}_k}, \mathbf{c}_{l,\hat{\theta}_k} \right\rangle\right|}{\left\|\mathbf{c}_{k,\hat{\theta}_k}\right\| \ \left\|\mathbf{c}_{l,\hat{\theta}_k}\right\|}.$$

Note that both coefficient vectors ($\mathbf{c}_{k,\theta}$ and $\mathbf{c}_{l,\theta}$) are taken at the fundamental frequency $\hat{\theta}_k$ which maximizes $\left\|\mathbf{c}_{k,\theta}\right\|$ and is independent of l. Hence, the dominant periodic signal component of $x_k[n]$ is identified and the normalized inner product is taken at the corresponding fundamental frequency. Furthermore, note that $\arccos\left(S_{k,l}\right)$ can be interpreted as angle between the two coefficient vectors taken at $\hat{\theta}_k$. The PSI equals unity for two signals that are equal up to a constant factor and zero for signals with orthogonal coefficient vectors. In order to avoid numerical problems when the coefficients $\mathbf{c}_{l,\theta}$ are small for the fundamental frequency $\hat{\theta}_k$ we introduced the following regularization

$$\tilde{S}_{k,l} = (1+\alpha)\ \frac{\left|\left\langle \mathbf{c}_{k,\hat{\theta}_k}, \mathbf{c}_{l,\hat{\theta}_k} \right\rangle\right|}{\left\|\mathbf{c}_{k,\hat{\theta}_k}\right\| \ \left\|\mathbf{c}_{l,\hat{\theta}_k} + \alpha\ \mathbf{c}_{k,\hat{\theta}_k}\right\|},$$

[1] The inner product $\left\langle \mathbf{a}, \mathbf{b} \right\rangle$ is given by $\sum_{m=1}^{M} a_m b_m^*$ and the norm $\left\|\mathbf{a}\right\|$ is given by $\sqrt{\left\langle \mathbf{a}, \mathbf{a} \right\rangle}$.

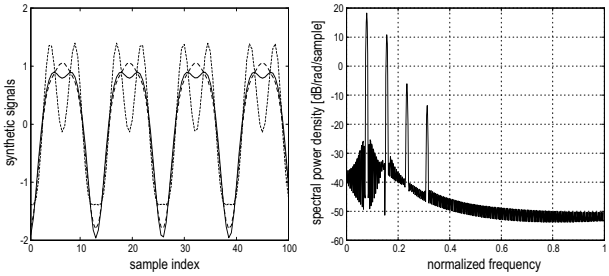


Fig. 1: Three realizations of synthetic signals and an example power spectrum consisting of a dominant fundamental component and three.

with a regularization factor α close to zero. Using that regularization, we still get $\tilde{S}_{k,l} = 1$ for $\mathbf{c}_{k,\theta} = \mathbf{c}_{l,\theta}$ and $\tilde{S}_{k,l} = 0$ for orthogonal coefficient vectors.

In this paper we compare the PSI to the widely known PLV. The PLV is based on the complex valued analytic signal [14] $a_k[n]$ associated to $x_k[n]$ and is defined as

$$P_{k,l} = \frac{1}{N}\left|\sum_n \frac{a_k[n]\ a_l^*[n]}{\left|a_k[n]\right|\ \left|a_l[n]\right|}\right|.$$

It measures the degree of similarity of the angles belonging to the analytic signals $a_k[n]$ and $a_l[n]$. It is easy to show, that for pure sinusoidal signals the PSI is equal to the PLV.

III. Results

A. Synthetic Signals

We analyzed our measure using synthetic signals with a duration of 12s and a sampling frequency of 256Hz. For the generation of these signals we use sinusoidals and applied a nonlinear transformation to yield

$$y_k[n] = \sum_{m=1}^{M} b_k[m]\ \sin^m\left(2\pi\theta_k n\right) + z_k[n].$$

The coefficients $b_k[m]$ where chosen as zero mean Gaussian random numbers and restricted to $\left|b_k[1]\right| > \left|b_k[m]\right|$ for $m > 1$. Three realizations of $x_k[n]$ and one example power spectrum are shown in Fig. 1. For this example, we used $M = 4$, hence the power spectrum shown in the right part consists of a dominant fundamental component and three harmonics.

In a first experiment we analyzed the capability of the PSI and the PLV to detect small frequency deviations in noiseless signals. For this reason, we generated two signals $y_1[n]$ and $y_2[n]$ without noise ($z_1[n] = z_2[n] = 0$). The fundamental frequency of $y_1[n]$ was fixed to 10Hz whereas that of $y_2[n]$ varied between 10Hz and 11Hz. The resulting PSI (dark gray curve) and PLV (light gray curve) for this experiment are shown in the upper left part of Fig. 2. Both measures start to decrease for very small frequency deviations and are close to zero for deviations of approximately 0.04Hz. The periodic peaks seen for increased frequency deviations in both PSI and PLV are due to suboptimal estimation of signal spectra coming from the use of time-limited signals. We found that the maximum PSI and PLV values for frequency deviations above 0.04Hz are below 0.18 and a reasonable detection of frequency shifts in noiseless signals can be done with both measures.

In our next experiment, we analyzed the robustness of the PSI and the PLV in the presence of noise. First, we measured the PSI and the PLV of signals $y_1[n]$ and $y_2[n]$ consisting of identical periodic components disturbed by additive white Gaussian noise. The mean values obtained from 2000 realizations for a SNR of -2dB are depicted in the upper right part of Fig. 2. It can be seen that the PSI value for zero frequency deviation is decreased to 0.85 while the corresponding PLV value dropped to 0.25. Hence, the PLV for two non-synchronized signals with small freqeuncy deviations is identical to the PLV of two synchronized signals in the presence of noise. The PSI also decreases in the presence of noise but the drop is much less pronounced than for the PLV such that a non-synchronized signal can be easily separated from a synchronized signal in the presence of noise. To further analyze the noise robustness of the PSI and the PLV we tried to detect the synchronized periodic components using a fix threshold of 0.5. This threshold value would be appropriate for the noiseless case (cf. left part of Fig. 2). Furthermore, it would be an intuitive value in the usual situations where no information on the SNR is available. The false negative rate for this experiment calculated from 2000 realizations is shown in the lower left of Fig. 2. For the PSI (dark gray curve) an SNR of approximately -4dB was sufficient to achieve a false negative rate of zero. In contrast, an SNR of nearly 3dB was needed for the PLV (light gray curve). Similar results where obtained for a wide range of thresholds.

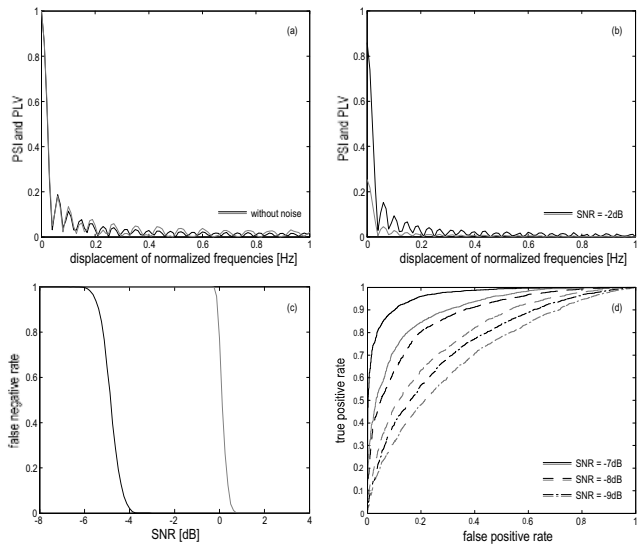


Fig. 2: Mean PSI (dark gray curve) and PLV (light gray curve) values for frequency shifted signal pairs without (a) and with noise (b). False negative rate for the detection of synchronized noisy signals obtained with the PSI and the PLV (c). ROC for the detection of synchronized signal pairs (d).

In a third experiment, we analyze the capability of the PSI and the PLV to distinguish between signal pairs without deviation of fundamental frequencies and signal pairs with a frequency shift of 1Hz, both in the presence of noise. In contrast to our previous experiment, we varied the detection threshold to capture the best possible detection performance for a given SNR. The receiver operating characteristic[2] (ROC) for this experiment is depicted in the lower right part of Fig. 2. The dark gray curves show the ROC obtained with the PSI and the light gray curves represent the ROC obtained with the PLV for SNR of -9dB, -8dB and -7dB. Each curve was derived from 2000 signal realizations. For any false negative fraction between 0 and 1, the PSI led to a higher true positive fraction compared to the PLV. Note that although the PSI outperformed the PLV, reasonable detection accuracy for low SNR could be reached with both measures. This accuracy however relies on the choice of a detection threshold appropriate for a certain SNR. Unfortunately, the SNR of a real life signal is rarely known and difficult to estimate.

B. Brain Signals

Fig. 3 compares the PSI and the PLV calculated from EEG data obtained from a patient with temporal lobe epilepsy. We used 15 minutes of data recorded from electrodes according to the international 10–20 system. A vertical dashed line marks the onset of the epileptic

[2]The ROC shows the fraction of true positives vs. the fraction of false positives as the detection threshold varies.

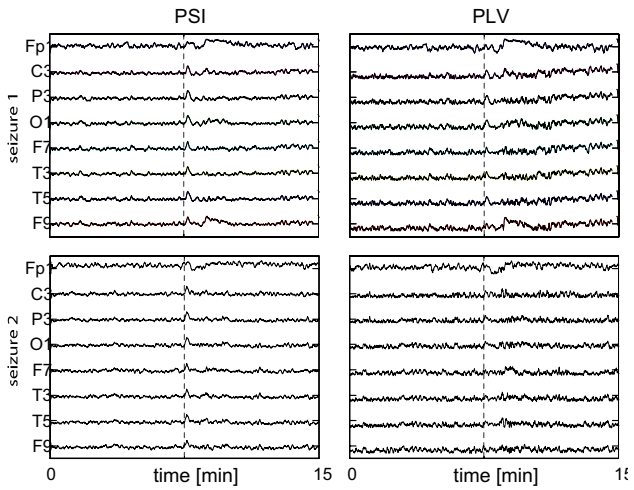


Fig. 3: PSI and PLV of electrode F3 vs. all other electrodes of the left hemisphere for two seizures. Results for seizure one are shown in the upper part and results for seizure 2 are shown in the lower part.

seizures. The upper plots and the lower plots of the figure correspond to two different seizures, respectively. The PSI and the PLV are shown for electrodes in the left hemisphere relative to electrode F3. The left hemisphere includes the seizure onset and propagation zone for this patient. For the calculation of PSI we optimized the number of harmonics experimentally. It turned out, that the optimal number of harmonics is three (used for results in Fig. 3) and that it can be chosen from three to five without large loss of performance. The example of Fig. 3 clearly shows that the PSI rises with approximately the same latency to the seizure onset as the PLV but the early signs of the upcoming seizure are much clearer. This is particularly pronounced in the second seizure shown in the lower part of Fig. 3. Whereas the PSI shows a unique peak in many channels, only small or no increases are seen for the PLV for this seizure. In addition to this well pronounced peak at seizure onset, the PSI shows a smaller variance during the inter-ictal period. This is especially important for automatic seizure detection that needs to distinguish the ictal from the inter-ictal period.

IV. Conclusions

In this paper we compared the capability of the PSI and the PLV to detect synchronized periodic signal components disturbed by different levels of additive noise. Our experiments with noiseless synthetic data revealed that both measures are sensitive to these components. In the presence of noise, the performance obtained with the PSI remained almost unchanged for an SNR down to -2dB and a reasonable detection is still possible with an SNR of -4dB. In contrast to the PSI, the detection performance drops significantly for noisy data when applying the PLV. In particular, we found that the PLV relies on an SNR of nearly 3dB. When applied to the detection of early seizure phenomena in EEG data we found that the increase of the PSI at seizure onset is more pronounced and the variance of the measure during pre-ictal time periods is lower than for the PLV.

Aknowlegdement

We are grateful to K. Schindler (Department of Neurology, Inselspital, Bern University Hospital, and University of Bern, Switzerland) for providing the EEG-data and his medical advice.

References

1. J. P. Lachaux, E. Rodriguez, J. Martinerie, and F. J. Varela, "Measuring phase synchrony in brain signals." *Hum Brain Mapp*, Vol. 8 (4), pp. 194-208, 1999
2. M. Le Van Quyen, J. Foucher, J. Lachaux, E. Rodriguez, A. Lutz, J. Martinerie and FJ. Varela, "Comparison of Hilbert transform and wavelet methods for the analysis of neuronal synchrony", *J Neurosci Methods*, Vol. 111 (2), pp. 83-98, 2001
3. M. Chávez, M. Le Van Quyen, V. Navarro, M. Baulac, and J. Martinierie, "Spatio-temporal dynamics prior to neocortical seizures: Amplitude versus phase couplings", *IEEE Transactions on Biomedical Engineering*, Vol. 50 (5), pp. 571–583, 2003
4. E. Gysels and P. Celka, "Phase Synchronization for the Recognition of Mental Tasks in a Brain-Computer Interface", *IEEE Transactions on Neural Systems and Rehabilitation Engineering,* Vol. 12 (4), pp. 406-415, 2004
5. A. Bruns, "Fourier-, Hilbert- and wavelet-based signal analysis: are they really different approaches?", *J Neurosci Methods*, Vol. 137 (2), pp. 321-332, 2004
6. R. Quian Quiroga, A. Kraskov, T. Kreuz, and P. Grassberger, "Performance of different synchronization measures in real data: a case study on electroencephalographic signals", *Phys Rev E,* Vol. 65, 041903, 2002
7. E. Gysels, M. Le Van Quyen, J. Martinerie, P. Boon, K. Vonck, I. Lemahieu and R. Van De Walle, "Long-term evaluation of synchronization between scalp EEG signals in partial epilepsy," *Proceedings of the 9th International Conference on Neural Information Processing,* Vol.3, pp. 1495-1498, 2002
8. H. Perko, C. Baumgartner, and T. Kluge, "Epileptic Seizure Detection Utilizing a Novel Feature Sensitive to Synchronization and Energy", *Epilepsia,* Vol. 48 (6), pp. 190-191, 2007
9. H. Perko, M. Hartmann, K. Schindler and T. Kluge, "A novel synchronization measure for epileptic seizure detection based on Fourier series expansions", Proceedings of the 4th European Conference of the IFMBE , in press
10. P. Tass, M. G. Rosenblum, J. Weule, J. Kurths, A. Pikovsky, J. Volkmann, A. Schnitzler, and H. J. Freund, "Detection of n:m phase locking from noisy data: Application to magnetoencephalography", *Physical Review Letters*, Vol. 81, pp. 3291-3294, 1998

11. M. Chavez, M. Besserve, C. Adam, and J. Martinerie, "Towards a proper estimation of phase synchronization from time series", *J Neurosci Methods*, Vol. 154, pp. 149-160, 2006
12. P. Celka, "Statistical Analysis of the Phase-Locking Value", *IEEE Signal Proc. Letters*, Vol. 14 (9), pp. 577-580, 2007
13. F. Mormann, K. Lehnertz, P. David, and C. E. Elger, "Mean phase coherence as a measure for phase synchronization and its application to the EEG of epilepsy patients"*, Physica D: Nonlinear Phenomena*, Vol. 144 (3), pp. 358-369, 2000
14. A. V. Oppenheim and A. S. Willsky, "Signals and Systems", *Prentice-Hall Inc.*, New Jersey, USA, 1996

Protein Classification Using Decision Trees With Bottom-up Classification Approach

Bojan Pepik, Slobodan Kalajdziski, Danco Davcev, Member IEEE

[1] Ss. Cyril and Methodius University,
Faculty of Electrical Engineering and Information Technologies,
Skopje, Republic of Macedonia

Abstract — **The classification of protein structures is essential for their function determination in bioinformatics. In this work, we use PDB files to extract descriptors based on structural characteristics of the protein, enriched with the biological features of the primary and secondary structure elements. Then we apply C4.5 algorithm and 10-fold-cross-validation decision trees to select the most appropriate descriptor features for protein classification based on the SCOP hierarchy. Empirical tests are provided for the usefulness and contribution of the different protein descriptor features to the decision tree classification precision. We propose a novel approach by transforming the hierarchical SCOP classification problem into a bottom - up classification flow. The results show that this approach provides much higher performances (it is much faster) than other algorithms with comparable accuracy: about 80% accuracy for DOMAIN recognition and 84% for SUPERFAMILY recognition.**

Keywords — **Protein Classification, SCOP, Decision Trees, C4.5**

I. Introduction

Proteins play vital structural and functional role in every living cell in the living organisms. The knowledge of the protein function is of great significance in many biochemical researches, especially in those researches that are trying to develop drugs for diseases. Nowadays there are very strong indications which confirm that protein function is strongly influenced by its structure. Therefore, it is reasonable to believe that proteins with a similar structure might have a similar function [1].

The classification of proteins based on their structure can play an important role in the deduction or discovery of protein structure and therefore, function prediction. Many classification schemes have been developed in order to describe the different kinds of similarity between proteins. Among the other classification schemes, SCOP (Structural Classification of Proteins) [2] has been accepted as the most relevant and the most reliable classification hierarchy [3]. This is due to the fact that SCOP strictly builds its classification decisions based on visual observations made by experts in the area. Also SCOP builds its classification hierarchy in such manner that brings to front the structural and functional relationships between protein structures. Although SCOP is highly reliable and precise system, it has one negative drawback. Namely, due to its manual classification methods, the dynamic of classification of new proteins in SCOP can't follow the dynamic of discovering novel protein structures (32.000 proteins classified in SCOP vs. 51.000 protein entries in PDB till 2008). This clearly brings to front the necessity of a system which will classify proteins in a precise and reliable manner as SCOP does, but in an automated fashion. Automated classification schemes have the advantage that the view of the protein universe can be updated frequently to include newly-discovered protein structures in a timely manner.

Some structure alignment methods are used in automating the classification process. These methods, like CE [5], DALI [7], MAMMOTH [6] etc. are used to detect and highlight distant homology relations between protein structures. In general these methods are very precise and efficient and they have high degree of successful mapping of existing structures in new proteins. Having in mind that structure alignment methods are quite cost expensive, the speed of classification with these methods is always questioned. For example CE takes 209 days [5] to classify 11000 novel protein structures. The classification approach used in our work took 5 hours in order to classify 9994 proteins.

There are numerous research approaches that combine sequence and structure alignment of the proteins. SCOPmap [8] is a system that uses a pipelined architecture for the classification. SCOPmap uses four sequence alignment methods: BLAST, PSI-BLAST, RPS-BLAST and COMPASS [10] and two structure alignment methods: VAST and DaliLite [9]. This pipelined approach brings to front high complexity of the classification process. FastSCOP [9] is another, more efficient system than SCOPmap which is based on 3D-BLAST [11] and MAMMOTH. 3D-BLAST is structure alignment method that is used as a preprocessing filter for MAMMOTH and it produces the top 10 scores. Afterwards, these top 10 results are used by MAMMOTH in order to find the most similar protein structure with the query structure. Although fastSCOP possesses

Chwee Teck Lim, James C.H. Goh (Eds.): ICBME 2008, Proceedings 23, pp. 174–178, 2009
www.springerlink.com

high precision, the used combination of methods eventually in future will produce increasing classification complexity.

Instead of using the alignment methods, in some researches the classification based on the mapping of the protein structure in the descriptor spaces can be found. In [13] protein descriptor is formed by first producing distance matrix. The distance matrix is treated as image and local distance histograms are computed thus giving local protein features. Additionally the descriptor has global protein features. The whole descriptor dimension is 33, consisted from 24 local features and 9 global features. This protein descriptor afterwards is used for protein classification into the SCOP hierarchy based on the E-predict algorithm [13]. In [1] protein descriptor is generated solely from the protein sequence information in order to avoid complex structure comparison. The protein descriptor gives information for the number of different amino acids, the hydrophobicity, the polarity, the Van der Waals volume, the polarizability and for the secondary structures in the protein structure. With this protein descriptor, proteins are classified hierarchically into the SCOP hierarchy with Naive Bayes and boosted C4.5 methods [1]. The results from approaches described in [1] [13] will be compared with the results obtained from our work.

In this work, we propose novel classification logic that is based on generated protein descriptors in combination with C4.5 decision tree classification algorithm. As a classification scheme, the SCOP classification hierarchy is used. The classification flow is based on a bottom-up classification according to the SCOP hierarchy. The implemented classification logic is original and new due to the fact that according to the related work there were no protein classification approaches which use similar classification architecture. The implemented system introduces tremendous speed up compared with the structure alignment algorithms. It is ~816 times faster than CE [5] and ~68 times faster than MAMMOTH [9]. It is less correct than fastSCOP which has accuracy of 98% for the SUPERFAMILY level compared with our 84%. However, our algorithm is ~70 times faster.

In section 2 we present the system architecture and the used research methods. Section 3 presents the experimental results, while the section 4 concludes the paper.

II. System Architecture and Research Methods

The system has three main features. First, the system is based, and it uses the SCOP classification scheme. Second, it uses 3D protein descriptor [13] which transforms the protein tertiary structure into N-dimensional feature vector, and additionally gives some other protein structural features. And finally, as a classification algorithm decision trees trained with C4.5 are used.

This classification logic is based on the fact that the SCOP classification hierarchy is tree–like hierarchy, providing only one parent node for every child node in the hierarchy. According to this fact, if we know the DOMAIN of the protein, then we know the upper SCOP levels (the whole hierarchy) for that protein. Basically this classification flow is by all means very much similar to the classical top – down approach, except that the starting point is changed. Instead of starting the classification from the root, it is started from the leafs.

Chronologically the system is consisted of two phases: training phase and testing or classification phase. The training or offline data flow takes into consideration the knowledge given in the SCOP hierarchical database to build predicative classification flow for each SCOP hierarchy level. The training procedure can be divided in two general processes. The first one is the descriptor extraction (shown on figure 1) and data set generation process. Descriptors consisting of 450 features (416 of them describe the protein's geometry, while 34 of them give information for the primary and secondary protein structure) are generated for each protein forming a training set for the C4.5 decision tree algorithm. This descriptor relies on the geometric 3D structure of the proteins. After triangulation, normalization and voxelization of the 3D protein structures, the Spherical Trace Transform is applied to them to produce geometry - based descriptors, which are completely rotation invariant.

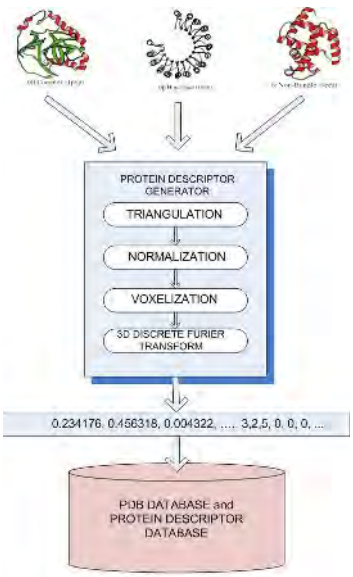


Fig. 1 Protein descriptor generation process

The second process is the process of forming and training of the decision trees for the bottom-up classifier. Decision trees are built for each level of the SCOP hierarchy, providing separate trees for classification in CLASS, FOLD, SUPERFAMILY, FAMILY and DOMAIN. In order to satisfy the bottom-up classification logic, additional level-specific decision trees for determination of DOMAIN are built. In this way, there are CLASS specific, FOLD specific, SUPERFAMILY specific and FAMILY specific decision trees for determination of DOMAIN. Also, additional decision trees are built for determination of one-level up SCOP levels (CLASS specific decision trees for FOLD determination etc.). These decision trees are afterwards used in the classification process of novel proteins.

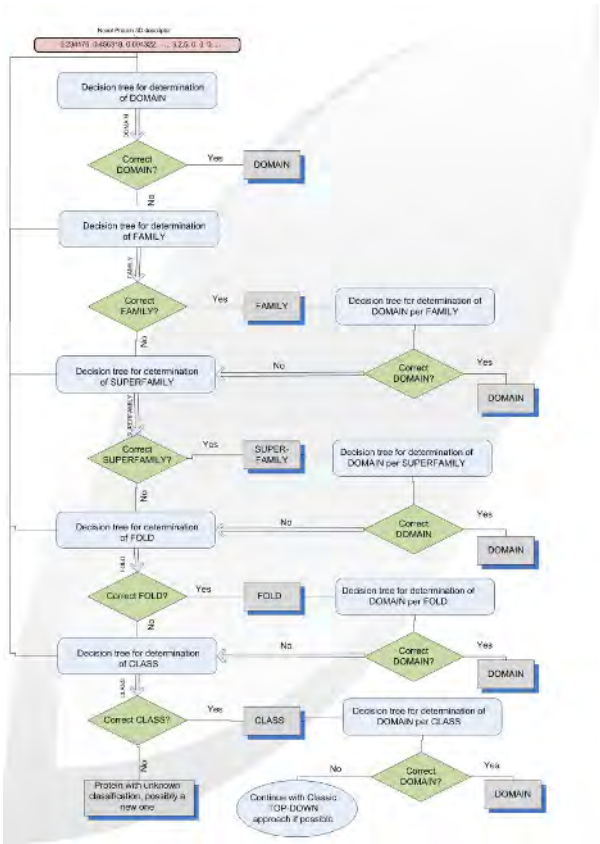


Fig. 2 Bottom-up classification approach

The classification or online data flow takes the unknown protein structure as query through the classification flow to generate new knowledge. The classification phase of new protein structures is shown on figure 2. As can be seen from the figure 2, new protein structure is preceded to the decision tree for determination of DOMAIN. If the protein is classified into the correct DOMAIN, then the classification process stops because we know the whole classification hierarchy of this protein, otherwise the protein is being proceeded to the classifier into the higher level of the hierarchy, in this case the decision tree for determination of FAMILY. If the classified FAMILY is correct, than the rest of the levels of the hierarchy for the protein are known, except the DOMAIN remains unknown. Therefore, the new protein is being preceded to the decision tree for determination of DOMAIN, trained only with instances from the predicted FAMILY. If the classified FAMILY is mistaken, the classifier continues one level up into the hierarchy, in this case it continues with predicting the SUPERFAMILY level of the new protein. This step is also the next step if the FAMILY specific decision tree mistakes the protein DOMAIN. Otherwise the classification is finished.

The process of protein classification continues with the backward recursion explained in the previous paragraph until it reaches the top level of the hierarchy, the CLASS. If there is no success in recognizing the correct protein DOMAIN, then the protein is announced as a protein with unknown SCOP classification, possibly a new one SCOP hierarchy.

III. Implementation, Experiments and Evaluation Results

The main GUI and the system logic were made with C#.NET. For implementation of the C4.5 algorithm, the WEKA API was used. The protein descriptor generation was made with C++. The SCOP hierarchy from the last two versions SCOP1.71 and SCOP 1.73 was downloaded and integrated into Oracle 10g database. The experiments were obtained on an Intel Core 2 machine with 2.2GHz and 2GB of RAM.

In the training phase, 73642 out of 75930 classified proteins from SCOP v1.71 were used for training the decision trees. Instead of having one decision tree for each level of the SCOP hierarchy, ensemble of decision trees is used for each level of the SCOP hierarchy. The idea for ensemble of trees came as a result of the huge memory requirements of the approach with one tree per level. The number of trees per ensemble in one level and number of output classes per tree in each level is presented in Table 1.

In the test phase proteins from the latest version of SCOP at the moment, SCOP v1.73, were taken. The test set consisted of 9994 proteins. We use only one condition for choosing these proteins. They have to belong to DOMAIN's which exist in the previous version of SCOP, SCOP v1.71, and the proteins from SCOP v1.71 which are classified in these DOMAIN's have to be classified into the same DOMAIN's in the SCOP v1.73.

Table 1. Number of trees per ensemble in one level and number of output classes per tree in each l

Level	Classes per tree	Num of trees per level
CLASS	11	1
FOLD	256	5
SUPERFAM	169	12
FAMILY	341	11
DOMAIN	659	14

Table 2. Results of the classification with the bottom-up approach

Level	Correct Classif.	Incorr. Classif.	Accuracy
CLASS	8817	1117	88,223%
FOLD	8460	1534	84,651%
SUPFAM	8364	1630	83,690%
FAMILY	8066	1928	80,708%
DOMAIN	7934	2060	79,388%

The classification results are shown in Table 2. The classification time was 6 hours, approximately. For example it is ~816 times faster than CE [5] and ~68 times faster than MAMMOTH [9]. As can be seen from the obtained results, the precision of the classification is satisfying. In [13] the precision is approximately 72% for 100% recall for protein DOMAIN prediction and 79,77% for 90% recall of the test set for DOMAIN prediction. In our work, the last percentage is 79,3876%. In [1] the best classification accuracy for protein CLASS recognition is 84% with boosted C4.5 classifier, and in our approach this percentage is 88,223%. When it comes to protein FOLD recognition in [13] the precision is 92% for SCOP v1.69 when E-predict is used as a classification algorithm. When NN (Nearest Neighbors) is used then the precision is ~92% when 1-NN is used, 91% when 3-NN and 5-NN are used as classifiers. If C4.5 decision tree is used as classifier the precision for FOLD prediction in [13] is 82%. The precision in our system is 84,651% for the FOLD level. There is no prediction of SUPERFAMILY, FAMILY and CLASS in [13] and SUPERFAMILY, FAMILY and DOMAIN in [1]. From this point of view our system has comparable accuracy and produces classification results for the whole SCOP hierarchy. However, fastSCOP [9] predicts the protein SUPERFAMILY with 98% accuracy compared with 84% accuracy in our work. On the other hand, our approach classifies proteins nearly ~70 times faster then fastSCOP thus providing much higher efficiency.

IV. Conclusion

The objective of this paper was to make empirical tests of the usefulness and the contribution of the different protein features to the decision tree classification precision and the usefulness of the bottom-up classification approach. It is evident that this approach which uses protein descriptor and decision tree algorithm for classification introduces high level of efficiency which can be concluded from the time taken to classify a protein and the percent of correctly classified proteins. The provided comparison with some other relevant works proves the satisfying results obtained with this work.

For the time being, our system can recognize the existing DOMAIN features in a novel protein but it cannot tell us if the novel protein belongs to new, yet no existing category. In future, there will be attempts to solve the problems explained here.

References

[1] Marsolo K., Parthasarathy S., Ding C., (2005) "A Multi-Level Approach to SCOP Fold Recognition", IEEE Symposium on Bioinformatics and Bioengineering, pp. 57 – 64.

[2] Murzin A. G., Brenner S. E., Hubbard T., and Chothia C., (1995) "Scop: a structural classification of proteins database for the investigation of sequences and structures", Journal of Molecular Biology, vol. 247, pp. 536–540.

[3] Camoğlu O, Can T, Singh AK, Wang YF., (2005) "Decision tree based information integration for automated protein classification.", J Bioinform Comput Biol. Jun;3(3), pp. 717-724.

[4] Abola, E.E., Bernstein, F.C., Bryant, S.H., Koetzle, T.F. & Weng, J. (1987) "*Protein Data Bank. In rystallographic Databases — Information Content, Software Systems, Scientific Application"*. (Allen,H.,Bergerhoff, G. & Sievers, R., eds), pp. 107–132.

[5] Shindyalov H. N. and Bourne P. E., (1998) "Protein structure alignment by incremental combinatorial extension (ce) of the optimal path", *Protein Eng., vol. 9* , pp. 739–747.

[6] Ortiz A. R., Strauss C. E., and Olmea O., (2002) "Mammoth (matching molecular models obtained from theory): An automated method for model comparison", *Protein Science, vol. 11*, pp. 2606–2621.

[7] Holm L. and Sander C., (1993) "Protein structure comparison by alignment of distance matrices", *Journal of Molecular Biology, vol. 233*, pp. 123–138.

[8] Cheek S, Qi Y, Krishna SS, Kinch LN, Grishin NV. (2004) "SCOPmap: Automated assignment of protein structures to evolutionary superfamilies", BMC Bioinformatics; 5:197.

[9] Tung C.H., Yang J.M., (2007) "fastSCOP: a fast web server for recognizing protein structural domains and SCOP superfamilies", Nucleic Acids Res. July; pp. W438–W443.

[10] Holm L, Sander C, (1995) "Dali: a network tool for protein structure comparison", *Trends Biochem Sci*, 20: pp. 478-480.

[11] Sadreyev R, Grishin N, (2003) "COMPASS: a tool for comparison of multiple protein alignments with assessment of statistical significance", *J Mol Biol*, 326: pp. 317-336.

[12] Yang,J.M. and Tung,C.H., (2006) "Protein structure database search and evolutionary classification", Nucleic Acids Res., 34, pp. 3646–3659.

[13] Kalajdziski S., Mirceva G., Trivodaliev K., Davcev D., (2007) "Protein Classification by Matching 3D Structures.", IEEE Xplore, pp. 147-152.

[14] Chi P.H., (2007) "Efficient protein tertiary structure retrievals and classifications using content based comparison algorithms", – Phd thesis, University of Missouri-Columbia

Extracting Speech Signals using Independent Component Analysis

Charles T.M. Choi[1] and Yi-Hsuan Lee[2]

[1] Department of Computer Science and Institute of Biomedical Engineering, National Chiao Tung University, Taiwan
ctchoi@cs.nctu.edu.tw
[2] Department of Computer and Information Science, National Taichung University, Taiwan
yslee@mail.ntcu.edu.tw

Abstract — **Independent component analysis (ICA) is the dominant method to resolve blind source separation (BSS) problem. In this article we conducted experiments to evaluate the separation performance of ICA for acoustic signals. Experiments results show that if we can find appropriate placement of microphones, applying ICA to hearing prostheses as pre-processing can help the wearer hear more clear sounds.**

Keywords — **Independent Component Analysis (ICA), Acoustic Signals Separation, Hearing Prostheses.**

I. Introduction

With the influence of disease, tumor, exposure to noise, and aging process, many adults and children suffer from hearing loss [1]. These people usually require a hearing-aid, and some of them even wear a cochlear implant. These hearing prostheses both use microphones to record and amplify sounds, so environmental noise is one of the main reasons which will lower their performance [2-4]. The addition of adaptive filters typically can improve this situation [5-6]. However, for environmental noise whose spectrum overlaps the desired signal, it cannot be suppressed simply by a filter. Therefore, how to extract the desired components from mixed signals is an important issue in hearing applications, which refers to the *blind source separation* (*BSS*) problem [7-8].

BSS is an approach taken to estimate source signals from only observed mixed signals without a priori information about source signals and mixing environment [7-8]. *Independent component analysis* (*ICA*) is the dominant method for performing BSS. ICA is originally developed to deal with problems that are closely related to the *cocktail-party problem* as shown in Figure 1 [9]. Consider a cocktail party where many people are talking at the same time. If a microphone is present then its output is a mixture of voices. When given such a mixture, ICA looks for hidden statistically independent and non-gaussian components. ICA has wide range of applicability, such as biomedical signals analysis, speech signals separation, telecommunications, and finial data analysis [8, 10-12]. In this article we first describe the formal ICA definition and the usage for separating acoustic signals. Then, we conduct experiments in a soundproof room to evaluate the separation performance of ICA.



Fig. 1 Illustration of cocktail-party problem

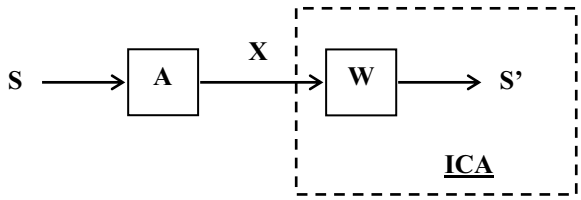


Fig. 2 Illustration of ICA formulation

II. Formal ICA Definition [7-8, 10, 12]

Given a set of observed signals $\mathbf{X} = (x_1, x_2, \ldots, x_m)^T$, which is a m-dimensional random variables. Assume that they are mixtures generated by linear combination of independent components $\mathbf{X} = \mathbf{AS}$, where $\mathbf{S} = (s_1, s_2, \ldots, s_n)^T$ is a set of source signals and $\mathbf{A}$ is a $m \times n$ mixing matrix. Both matrix $\mathbf{A}$ and signal set $\mathbf{S}$ are unknown. ICA is aimed to estimate $\mathbf{S}$ and $\mathbf{A}$, and obtains an $n \times m$ de-mixing matrix $\mathbf{W}$ where $\mathbf{S} \approx \mathbf{S'} = \mathbf{WX}$. Figure 2 illustrates the ICA formulation. It should be noted that sources are assumed be statistically independent and non-gaussian in ICA. In general the best de-mixing matrix $\mathbf{W}$ cannot be found, and ICA will make source components as independent as possible.

Chwee Teck Lim, James C.H. Goh (Eds.): ICBME 2008, Proceedings 23, pp. 179–182, 2009
www.springerlink.com

III. ICA FOR ACOUSTIC SIGNALS SEPARATION

Conventional ICA is originally developed for the cocktail-party problem, but it is actually not well suit for separating mixed acoustic signals. One major problem is that conventional ICA assumes sources are linear mixing. However, in the real case sounds recorded by microphones are convolutive signals, because the mixing environment is noisy and reverberant. Thus, the observed signals **X** should be redefined as $\mathbf{X}(t) = \mathbf{A}(t)\mathbf{S}(t) = \sum_{k=-\infty}^{k=\infty} a(k)s(t-k)$, where t is the time index. It also make BSS problem of acoustic signals become to solve the de-convolution problem. Methods based on ICA for convolutive signals can perform in time-domain or frequency-domain [13]. Time-domain ICA is computational intensive due to computing many convolutions, such as [11-12, 14]. Frequency-domain ICA, such as [2-3, 9, 15], usually applies windowed Fourier transform to transfer mixed signals to frequency-domain, and does separation in each frequency bin individually. It may be more time efficient, but the derived permutation and scaling problems must be well resolved. In our experiment we select three ICA for comparison, two belong to time-domain and one is frequency-domain. Besides, although using ICA can separate mixed signals to original sources, the amplitude of separated signals may not equal to corresponding sources. If we want to apply ICA to real hearing prostheses, these separated signals must be scaled appropriately, in order to meet the volume of original sources.

In addition, noted that using ICA we need at least two recorded signals. Because the velocity of acoustic signals transferred in the air is really slow, there must be time-delay differences between different microphones from the same sources. Conventional ICA assumes sources are mixed instantaneously. That is, when the sampling rate or the distance between microphones is increasing, the *spatial aliasing effect* may degrade the separating performance. Intuitively that putting microphones near to each other can prevent the spatial aliasing effect. However, ICA requires more distinct mixed signals to get better separating results, which leads to put microphones apart. In our experiment we will compare the separating performance for different placements and distances between microphones.

IV. EXPERIMENTAL RESULTS

Figure 3 shows our experimental allocation in a soundproof room. Two sources, one speech and one noise, are produced by two loudspeakers. Two microphones are used to record mixing sounds, and then ICA is applied to separate the speech signal. In order to deal with the spatial aliasing effect, we add an artificial pulse into the speech source. This pulse will be visible in two recorded signals but at different timestamps. We then shift one recorded signals to make pulses align with the same timestamps, which will satisfy the assumption of ICA. Three ICA methods including FastICA, InfomaxICA, and Murata et al. [15] are applied for signals separation. FastICA and InfomaxICA belong to time-domain, and Murata et al. [15] is a frequency-domain ICA. Separated signals are scaled to have the same *average RMS* (*root-mean-square*) values as mixing sounds. As for the measurement we calculate the *improved segmental signal-to-noise ratio* (*SNR*), which equals the difference between segmental SNR of signals before and after separating. Larger segmental SNR indicates the separated speech signal is clearer.

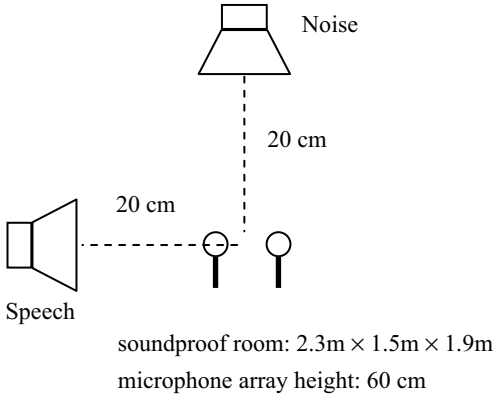


Fig. 3 The experimental allocation in the soundproof room

Three experiments are conducted in this article: the distance between microphones, the SNR between sources, and the placement of loudspeakers. According to Table 1, the improved segmental SNR is basically increasing when the distance between microphones increases. This result is predictable due to the principle of ICA, which requires more distinct mixed signals to get better separating performance. When we various the input SNR of sources, we will find that the segmental SNR is apparently improved only if the input SNR is non-positive. This is because speech signal has already quite clear in the mixed signals if the input SNR ≥ 5, the potential improvement can be achieved using ICA will be limited. About the third experiments, we place loudspeakers at different angles as shown in Figure 4. Results of this experiment are irregular, but in most cases the improved segmental SNR becomes larger when two loudspeakers are put opposite, such as 135°, 180°, or 225°. This situation is similar to that of in the first experiment. When two sources are produced farther from each other, two mi-

Table 1 Experimental results of various distances of microphones (Input SNR is 0, loudspeakers are placed in 90°)

	FastICA				InfomaxICA				Murata et al. [15]			
	aircon	traffic	party1	party2	aircon	traffic	party1	party2	aircon	traffic	party1	party2
1 cm	0.74	0.86	0.32	0.28	0.62	0.76	0.1	0.19	1.41	0	5.24	4.54
3 cm	4.05	1.73	0.45	1.61	0.07	3.64	-1.51	2.82	1.39	5.83	1.99	7.63
5 cm	2.86	0.9	0.23	1.63	6.69	9.39	3.78	8.64	7.61	11.19	4.09	14.76
7 cm	3.53	7.38	1.44	0.21	8.11	10.9	10.14	10.74	10.46	10.03	11.35	12.07
9 cm	6.14	6.31	9.85	1.95	5.52	6.39	11.07	6.96	6.47	6.52	8.23	10.83

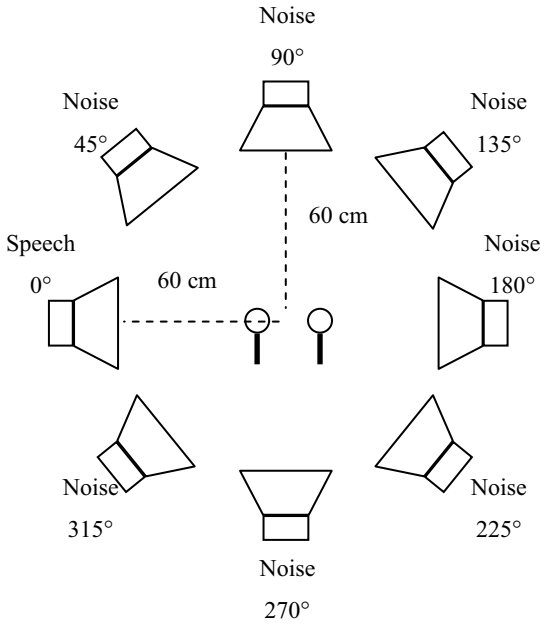


Fig. 4 The placement of loudspeakers at different angles

crophones will record more distinct mixed signals, which benefit ICA doing separation.

Comparing separating performances achieved by three ICA methods, we find that InfomaxICA performs inferior to other two methods. In addition, after applying ICA we almost obtain positive improved segmental SNR values, which indicate the volume of noise is definitely suppressed in the separated speech signals. Therefore, we believe applying ICA to real hearing prostheses will help the wearer hear more clear sounds.

V. Conclusions

In this paper we conducted experiments to evaluate the separation performance of ICA. Experimental results show that although using ICA cannot perfectly extract the speech signal, the volume of noise is definitely suppressed. Factors such as input SNR and placements of microphones and sources also affect the separating performance of ICA. We expect that after finding an appropriate placement of hardware, ICA will be a useful technique to be used in real hearing prostheses.

Acknowledgment

This research was supported in part by National Science Council research grant: NSC95-2221-E-009-366-MY3.

References

1. Loizon P.C. (1998) Mimicking the Human Ear. IEEE Signal Processing Magazine. vol. 15, issue 5, pp. 101-130
2. Mori Y, Takatani T., Saruwatari H. et al. (2007) High-presence Hearing-aid System using DSP-based Real- time Blind Source Separation Module, IEEE International Conference on Acoustics, Speech and Signal Processing Proc. vol. 4, Apr. 2007, pp. IV/609-IV/612
3. Mori Y., Takatani T., Saruwatari H. et al. (2006) Two-stage Blind Separation of Moving Sound Sources with Pocket-size Real-time DSP Module, EU-SIPCO2006 Proc. 2006
4. Chen Y.M. (2004) Extracting Speech from Background Noise by Independent Component Analysis – Potential Application for Hearing Aids. Master Thesis, National Yang-Ming University
5. Benesty J., Makino S., Chen J. (2005) Speech Enhancement. Springer-Verlag Berlin Heidelberg
6. Cohen I., Berdugo B. (2001) Speech Enhancement for Non-Stationary Noise Environments. Signal Processing. vol. 81, issue 11, pp. 2403-2418
7. Hyvarinen A., Karhunen J., Oja E. (2001) Independent Component Analysis. Wiley InterScience

8. Cichocki A., Amari S.I. (2002) Adaptive Blind Signal and Image Processing: Learning Algorithms and Applications. Wiley Inter-Science
9. Prasad R. (2005) Fixed-Point ICA based Speech Signal Separation and Enhancement with Generalized Gaussian Model. PhD Thesis, Nara Institute of Science and Technology
10. Stone J.V. (2002) Independent Component Analysis: An Introduction. Trends in Cognitive Sciences. vol. 6, no. 2, pp. 59-64
11. Lee T.W., Girolami M., Sejnowski T.J. (1999) Independent Component Analysis using an Extended Infomax Algorithm for Mixed Subgaussian and Supergaussian Sources. Neural Computation. vol. 11, pp. 417-441
12. Hyvarinen A., Oja E. (2000) Independent Component Analysis: Algorithms and Applications. Neural Networks. vol. 13, pp. 411-430
13. Pedersen M.S., Larsen J., Kjems U. et al. (2007) A Survey of Convolutive Blind Source Separation Methods. Springer Handbook on Speech Processing and Speech Communication
14. Bell A.J., Sejnowski T.J. (1995) An Information-Maximization Approach to Blind Separation and Blind Deconvolution. Neural Computation, vol. 7, pp. 1129-1159
15. Murata N., Ikeda S., Ziehe A. (2001) An Approach to Blind Source Separation Based on Temporal Structure of Speech Signals. Neurocomputing. vol. 41, pp. 1-24

Age-Related Changes in Specific Harmonic Indices of Pressure Pulse Waveform

Sheng-Hung Wang[1], Tse-Lin Hsu[2], Ming-Yie Jan[2], Yuh-Ying Lin Wang[3] and Wei-Kung Wang[1,2]

[1]Department of Electrical Engineering, National Taiwan University, Taiwan
[2]Institute of Physics, Academia Sinica, Taiwan
[3]Department of Physics, National Taiwan Normal University, Taiwan

Abstract — **The central elastic arteries and the peripheral muscular arteries are different in their responses to aging. Aorta stiffens in much larger extent with age than peripheral arteries do. Peripheral blood pressure indices such as pulse pressure (PP) or augmentation index (AI) were preferred as surrogates in assessing arterial stiffness for clinical convenience. AI and PP both increase progressively with age.**

In this study, we present a harmonic based pulse waveform analysis method which may give similar result about central pressure as augmentation index. This method avoids the extra but necessary manipulations such as flow measuring, 4th derivative of pressure wave in determining the inflection point, the second systolic peak for augmentation index calculating, all these manipulations can introduce error. The non-invasive peripheral pulse waveforms copied from published reports for several ageing studies were analyzed. The mean pulse height *A0* and the harmonic proportion of the 1st harmonic *C1* increased but the harmonic proportion of the 3rd harmonic *C3* and the harmonic proportion of the 4th harmonic *C4* decreased with ageing. Aging had no significant effect on the harmonic proportion of the 2nd harmonic *C2*. Among all these harmonic indices, *A0*, the mean pulse pressure increased dramatically since the 6th decade.

These results suggest that A0 is related to aorta stiffen or PP sensitive. The gradual increasing of C1 and gradual decreasing of C3 and C4 by ageing suggest that C1, C3 and C4 could be similar to AI; it corresponds to the pressure pulse waveform affected from ageing.

The harmonic indices could be clinically useful in non-invasive cardio risk assessing for the elderly patients.

Keywords — **Ageing, Augmentation Index, Harmonic Analysis, Blood Pressure Pulse Waveform, Biosignal Processing**

I. Introduction

With the advancement of health care the average age of death is increased every year. The issue of gerontology is more and more important with the ageing population. It has been noted that aorta stiffens in much larger extent with age than peripheral arteries [1] [2]. It is convenient to assess arterial stiffness in clinic by peripheral blood pressure indices such as pulse pressure (PP) or augmentation index (AI) which both increase progressively with age [3].

However to calculate AI value needs to measure pressure and flow velocity at the same time [4] or 4th derivative of the measured pressure wave [5] [6] to determine the second systolic peak or the inflection point. The previous method needs extra flow measuring; and the latter one may give erroneous results sometimes [7] [8].

In this study, we analyze the pulse waveform from the published report of ageing effect. The pulse waveform was described by the harmonic proportions together with the mean pulse height where the harmonic proportions equal the amplitude of each harmonic divided by mean pulse height [9] [10]. The change of harmonics with ageing is expected.

II. Method

A. The data source

The data source is scanned from the report of Kelly et al. 1989 as shown in figure 1 [5]. Radial pulse waveforms were collected from 420 normal subjects who were 2-91 years old (207 men and 213 women) of whom 82 were smokers. Each pulse waveform is average of 40-70 individual pulse. Amplitude is showed in uncalibrated voltage (mV) units which can be translated into pressure unit (mm Hg) from the Millar preamplifier box as 1 mV to 1 mm Hg.

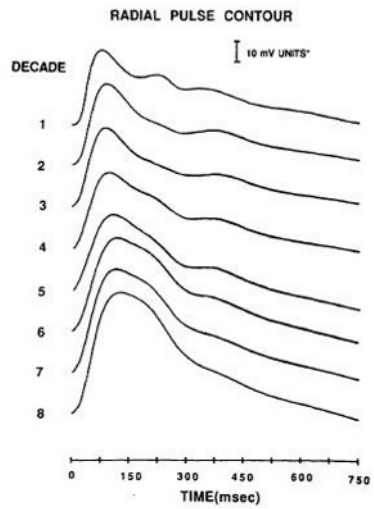


Fig. 1 Pulse waveform of 1 to 8 decades from 420 subjects

Chwee Teck Lim, James C.H. Goh (Eds.): ICBME 2008, Proceedings 23, pp. 183–185, 2009
www.springerlink.com

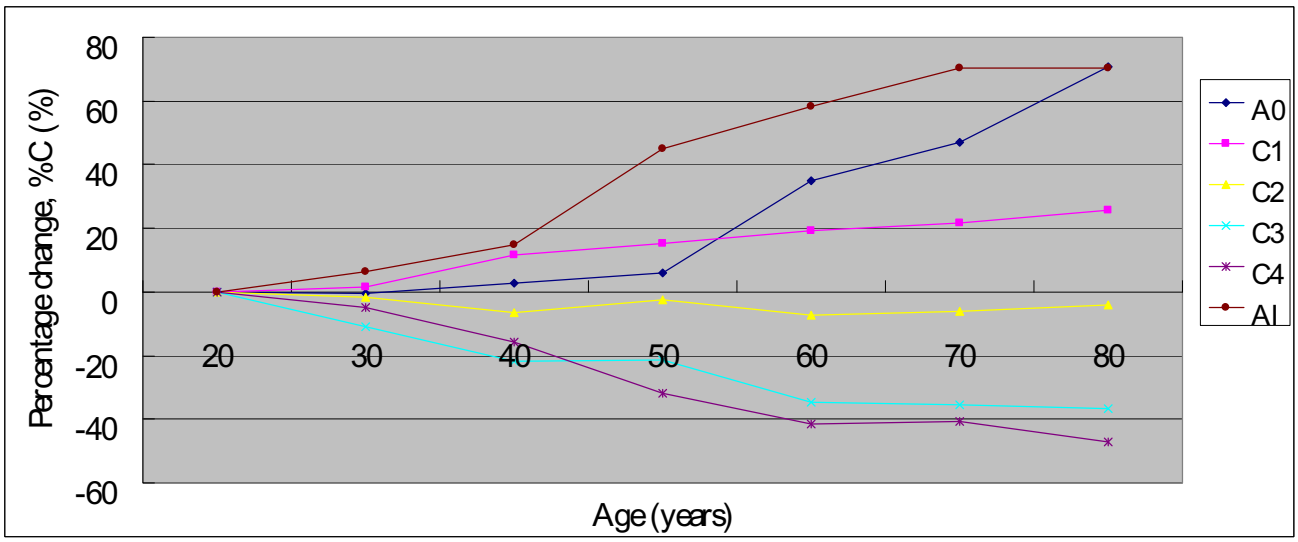


Fig. 2 Percent changes of pressure pulse harmonic proportions and AI with ageing

B. Digitalization and Analysis

Each pulse is scanned form the data source and is digitalized into 1068 points on the same time interval by the program "MATLAB". The digitalized pulse waveform was adjusted with the slope to make the start and the end point at the same height. The adjusted data are Fourier transformed into frequency domain. In this study, we only focused on the change in the first four harmonics and compute the harmonic proportion *Cn* as a pattern instead of the amplitude *An* of the nth harmonic. *Cn* was defined as *Cn = An/A0*, where *A0* is the mean value of pulse pressure.

The pulse waveform of the 2nd decade of age was used as control. The other ages such as 3rd, 4th, 5^{rh}, 6th, 7th and 8th decade were presented as the percentage changes $\%C^{Cn}$ in the harmonic proportion of the n^{th} harmonic between the spectrums of each decade of age and control,

$$(\%C^{Cn}) = 100 \times \frac{Cn,test - Cn,cont}{Cn,cont}, \qquad (1)$$

where Cn,cont is the harmonic proportion of the nth harmonic of the control, Cn,test is the harmonic proportion of the nth harmonic of the testing pulse waveform under aging.

The percent change $\%C^{A0}$ of the mean pulse pressure was presented as

$$(\%C^{A0}) = 100 \times \frac{A0,test - A0,cont}{A0,cont}, \qquad (2)$$

where A0,cont is the mean pulse pressure of the control, A0,test is the mean pulse pressure of the testing pulse wave form under aging.

The percent change $\%C^{AI}$ of the augmentation index was presented as

$$(\%C^{AI}) = 100 \times \frac{AI,test - AI,cont}{AI,cont}, \qquad (3)$$

where AI,cont is the augmentation index of the control, AI,test is the augmentation index of the testing pulse waveform under aging which was intercepted from the data source directly.

III. Result

The calculated data of the 2nd decade of age as the control is showed on table 1. The testing data is based on the control.

Figure 2 is the result of the testing harmonic proportion of 3rd to 8th decade of age which is compared with that of the control. The mean pulse pressure *A0* and the harmonic proportion of the 1st harmonic *C1* increased with ageing. The harmonic proportion of the 3rd harmonic *C3* and the

Table 1 data of 2nd decade of age (the control)

A0 (mm Hg)	C1	C2	C3	C4	AI (%)
14.3	77.8	52.1	38.1	21.5	3

Table 2 Averaged percent changes of %C and AI on 3rd- 4th, 5rh- 6th and 7th -8th decade

Age (yr)	% C^{A0} (%)	%C^{C1} (%)	%C^{C2} (%)	%C^{C3} (%)	%C^{C4} (%)	%C^{AI} (%)
30-40	1.25	6.46	-4.02	-16.5	-12.3	10.5
50-60	20.5	17.1	-4.80	-28.1	-47.7	51.7
70-80	58.9	23.7	-5.12	-36.1	-46.8	70.3

harmonic proportion of the 4th harmonic *C4* decreased but no significant change on the harmonic proportion of the 2nd harmonic *C2* with ageing. Among all these harmonic indices *A0* increased conspicuously at the 6th decade.

Table 2 averaged the percent change of AI, *A0* and harmonic proportions of harmonic 1 to 4 into three age groups. Averaged *A0* on age group between the 7th to 8th decades is about 2.8 times of the value on age group between the 5th and 6th decades. But the percent changes of C1, C2, C3, C4 and AI on age group between the 7th to 8th decades are only 1 to 1.4 times of the value on age range between the 5th and 6th decades. Averaged *A0* on age group between the 5th to 6th decades is about 16 times of the value on age group between the 3rd and 4th decades. But the percent changes of C1, C2, C3, C4 and AI on age group between the 5td to 6th decades are only 1 to 4 times of the value on age group between the 3rd and 4th decades.

IV. Discussion

From the results of this study, the mean pulse pressure, A0, is changed noticeably with ageing. Ageing could cause the increase of aorta stiffen and the pulse pressure. A0 may be an index that related to aorta stiffen or PP sensitive. The gradual increasing of C1 and gradual decreasing of C3 and C4 by ageing suggest that C1, C3 and C4 could be similar to AI which corresponds to the pressure pulse waveform affected from ageing. These harmonic indexes all have high correlation coefficient to augmentation index (C1: R=0.96; C3: R=-0.93; C4: R=-0.92) but use an easier algorithm. Only we need to do is to get the pulse waveform from the subject non-invasively and use Fourier transform for these pulse waveform. This analysis leaves out the measurement of blood flow and avoids the errors caused by the determination of the shoulder of pressure pulse. We could easily estimate the change of pulse waveform by harmonic analysis method. The harmonic indices could be clinically useful in not only geriatric hypertension research but also cardiovascular drugs development.

V. Conclusions

In this study we present an assessment of the change on the pulse waveform by harmonic analysis method. The harmonic index provides the similar result as augmentation index without the measurement of blood flow. The harmonic indices could be clinically useful in non-invasive cardio risk assessing for the elderly patients.

References

1. Liang YL, Teede H, Kotsopoulos D et al (1998) Non-invasive measurements of arterial structure and function, repeatability, interrelationships and trial sample size. Clinical Science 95: 669-679.
2. Sonesson B, Hansen F, Stale H, et al (1993). Compliance and diameter in the human abdominal aorta-the influence of age and sex. European Journal of Vascular Surgery 7: 690-697.
3. Nichols WW and O'Rourke MF. (2005) McDonald's blood flow in arteries: Theoretic, experimental and clinical principles. 5th ed. Edward Arnold, London.
4. Nichols WW, Edwards DG. (2001) Arterial elastance and wave reflection augmentation of systolic blood pressure: deleterious effects and implications for therapy. J Cardiovasc Pharmacol Ther 6(1):5-21.
5. Kelly RP, Hayward CS, Avolio A et al. (1989) Noninvasive determination of age-related changes in the human arterial pulse. Circulation; 80: 1652-1659
6. Takazawa K, Tanaka N, Takeda K, Kurosu F, Ibukiyama C. (1995) Underestimation of vasodilator effects of nitroglycerin by upper limb blood pressure. Hypertension 26:520-523.
7. Gatzka C D, Cameron J D, Dart A M, et al. (2001) Correction of carotid augmentation index for heart rate in elderly essential hypertensives. Am J Hypertens, 14(4) : 573-577.
8. Söderström S, Nyberg G, O'Rourke MF, Sellgren J, Pontén J. (2002) Can a clinically useful aortic pressure wave be derived from a radial pressure wave? Br J Anaesth 88(4):481-488.
9. Yuh Ying L. Wang, S.l. Chang, Y.E. Wu, T.L. Hsu and W.K. Wang, (1991) The missing Phenomenon in Hemodynamics. Circulation Research 69:246-249
10. T.L. Hsu, P.T. Chao, H. Hsiu, W.K. Wang, S.P. Li and Y.Y. Lin Wang (2005) Organ-specific ligation-induced changes in harmonic components of the pulse spectrum and regional vasoconstrictor selectivity in Wistar rats. Exp Physiol 91.1:163-170

Address of the corresponding author:

Author: Sheng-Hung Wang
Institute: Department of Electrical Engineering, National Taiwan University
Street: No. 1, Sec. 4, Roosevelt Road
City: Taipei
Country: Taiwan
Email: raxwang@yahoo.com.tw

Processing of NMR Slices for Preparation of Multi-dimensional Model

J. Mikulka[1], E. Gescheidtova[1] and K. Bartusek[2]

[1] Brno University of Technology, Dept. of Theoretical and Experimental Electrical Engineering, Kolejni 4, 612 00 Brno, Czech Republic
[2] Institute of Scientific Instruments, Academy of Sciences of the Czech Republic, Kralovopolska 147, 612 64 Brno, Czech Republic

Abstract — **The paper describes the pre-processing and subsequent segmentation of NMR images of the human head in the region of temporomandibular joint in several slices. Image obtained by means of the tomograph used are of very low resolution and contrast, and their processing may prove to be difficult. A suitable algorithm was found, which consists in pre-processing the image by a smoothing filter, sharpening, and the four-phase level set segmentation. This method segments the image on the basis of the intensity of regions and is thus suitable for processing the above-mentioned NMR images, in which there are no sharp edges. The method also has some filtering capability. It is described by partial differential equations that have been transformed into corresponding difference equations, which are solved numerically. In the next stage, segmented slices of temporomandibular joint will be used to create a multidimensional model. A spatial model gives a better idea of the situation, structure and properties of tissues in the scanned part of patient's body. Multidimensional modeling mainly represents a change in describing input NMR data. The segmented regions need to be transformed from discrete to vector description i. e. the outer geometry of objects needs to be described mathematically.**

Keywords — **NMR imaging, image segmentation**

I. Introduction

NMR images serve the purpose of following the development and quantitative measurement of tissues. Segmentation can be applied to images and subsequent evaluation of the parameters of individual regions such as circuit, area or volume in case images from several slices are available. The present paper is concerned with the segmentation of images of the human head in the temporomandibular joint region. Available were 12 slices of the human head, with 2 test images being chosen for the experiment with the selected segmentation method. Image segmentation in several slices can be used for subsequently constructing a multidimensional model of the selected part of image.

Processing the NMR images obtained is difficult since they are of low resolution (the human head in the image is 256x256 pixels) and not very high contrast. The images need to be processed properly and then segmented by an appropriate method [1]. Fig. 1 gives an example of such an NMR test image and a detail of the temporomandibular joint that has been segmented.

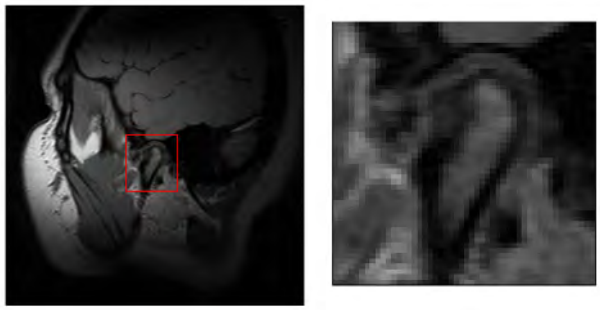


Fig. 1 NMR image of human head, slice with visible temporomandibular joint

The goal of segmentation is to find the temporomandibular joint in the NMR images. Prior to the segmentation itself, the image was focused and then smoothed with a simple averaging mask. The method chosen for segmentation was the four-phase level set method, which searches for regions of similar intensity in the image. This approach is of much advantage in NMR images since there are no sharp transitions here between the regions sought. The result of segmentation is an image with four levels of brightness, which correspond to the mean intensity value of the regions of original image. The segmented image can be further processed. The regions can be measured at random and a quantitative description can be obtained or the individual slices can be used to construct a multidimensional model of the selected part of image.

II. Multiphase level set segmentation

The multiphase level set for image segmentation is a generalization of an active contour model without edges based on 2-phase segmentation developed by T. Chan and L. Vese [2]. It is based on minimizing the energy given by energy functional:

$$F_n(\mathbf{c},\mathbf{\Phi}) = \sum_{1\le I\le n=2^m} \int_\Omega \left(u_0(x,y)-c_I\right)^2 \chi_I \mathrm{d}x\mathrm{d}y + \sum_{1\le i\le m} \nu \int_\Omega \left|\nabla H(\Phi_i)\right|, \quad (1)$$

Chwee Teck Lim, James C.H. Goh (Eds.): ICBME 2008, Proceedings 23, pp. 186–189, 2009
www.springerlink.com

where n is the number of phases (different intensity recognition), m is number of level set functions, u_0 is the observed image as intensity function of x and y, $\mathbf{c}$ is a constant vector of averages, where $c_I = mean(u_0)$ in the class I, χ_I is a characteristic function associated with phase Ω_i, $\nu > 0$ is a fixed parameter to weight the different term (length functional) in the energy, H is the Heaviside function $H(z)$, equal to 1 if $z \geq 0$ and to 0 if $z < 0$. $\mathbf{\Phi}$ is a vector of level set functions.

The boundary of region is given by the zero level set of a scalar Lipschitz continuous function Φ (called level set function). A typical example of level set function is given by the signed distance function to the curve of boundary. In figures 2 and 3 we can see the principle of region classification by the Heaviside function. There are two initial level set functions, Φ_1 and Φ_2, and their zero levels (boundaries of regions). Clearly, we will need only the $\log_2 n$ level set functions for the recognition of n segments with complex topologies.

In our case for $n = 4$ (and therefore $m = 2$) we obtain the 4-phase energy given by:

$$\begin{aligned} F_4(\mathbf{c},\mathbf{\Phi}) = & \int_\Omega (u_0 - c_{11})^2 H(\Phi_1) H(\Phi_2)\,dxdy \\ & + \int_\Omega (u_0 - c_{10})^2 H(\Phi_1)(1 - H(\Phi_2))\,dxdy \\ & + \int_\Omega (u_0 - c_{01})^2 (1 - H(\Phi_1)) H(\Phi_2)\,dxdy \\ & + \int_\Omega (u_0 - c_{00})^2 (1 - H(\Phi_1))(1 - H(\Phi_2))\,dxdy \\ & + \nu \int_\Omega |\nabla H(\Phi_1)| + \nu \int_\Omega |\nabla H(\Phi_2)|, \end{aligned} \tag{2}$$

where $\mathbf{c} = (c_{11}, c_{10}, c_{01}, c_{00})$ is a constant vector and $\mathbf{\Phi} = (\Phi_1, \Phi_2)$.

We can express the output image function u as:

$$\begin{aligned} u = & c_{11} H(\Phi_1) H(\Phi_2) + c_{10} H(\Phi_1)(1 - H(\Phi_2)) \\ & + c_{01}(1 - H(\Phi_1)) H(\Phi_2) \\ & + c_{00}(1 - H(\Phi_1))(1 - H(\Phi_2)). \end{aligned} \tag{3}$$

By minimizing the energy functional (2) with respect to $\mathbf{c}$ and $\mathbf{\Phi}$ we obtain the Euler-Lagrange equations:

$$\begin{aligned} \frac{\partial \Phi_1}{\partial t} = & \delta_\varepsilon(\Phi_1)\left\{\nu \operatorname{div}\left(\frac{\nabla \Phi_1}{|\nabla \Phi_1|}\right)\right. \\ & - \left[\left((u_0 - c_{11})^2 - (u_0 - c_{01})^2\right) H(\Phi_2)\right. \\ & \left.\left. + \left((u_0 - c_{10})^2 - (u_0 - c_{00})^2\right)(1 - H(\Phi_2))\right]\right\}, \end{aligned} \tag{4}$$

$$\begin{aligned} \frac{\partial \Phi_2}{\partial t} = & \delta_\varepsilon(\Phi_2)\left\{\nu \operatorname{div}\left(\frac{\nabla \Phi_2}{|\nabla \Phi_2|}\right)\right. \\ & - \left[\left((u_0 - c_{11})^2 - (u_0 - c_{10})^2\right) H(\Phi_1)\right. \\ & \left.\left. + \left((u_0 - c_{01})^2 - (u_0 - c_{00})^2\right)(1 - H(\Phi_1))\right]\right\}, \end{aligned} \tag{5}$$

where t is a artificial time, δ_ε is the Dirac function (derivation of Heaviside function). By applying the finite differences scheme we will give the numerical approximations of Euler-Lagrange equations for iterative process implementation.

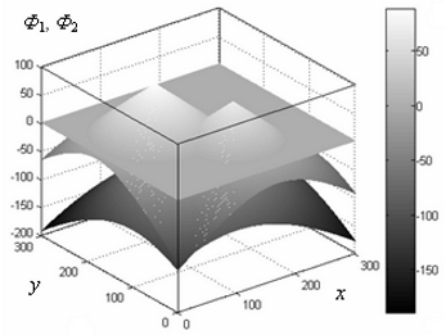


Fig. 2 Two initial level set functions and zero level

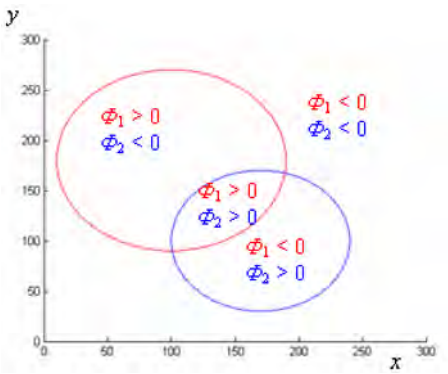


Fig. 3 Zero-cross levels and regions classification by level set functions signs

III. Implementation

In view of the image properties, the segmentation can be performed after an appropriate pre-processing. The first to be performed was convolution, with subsequent sharpening mask to enhance the contrast:

$$H = \frac{1}{(\alpha+1)}\begin{bmatrix} -\alpha & \alpha-1 & -\alpha \\ \alpha-1 & \alpha+5 & \alpha-1 \\ -\alpha & \alpha-1 & -\alpha \end{bmatrix}, \quad (6)$$

where the coefficient α determines the form of the Laplace filter used; the suitable value 0.001 was established experimentally.

The next step consists in smoothing the focused image. For this purpose, the simplest 3rd - order averaging mask was used:

$$H = \frac{1}{9}\begin{bmatrix} 1 & 1 & 1 \\ 1 & 1 & 1 \\ 1 & 1 & 1 \end{bmatrix}. \quad (7)$$

The pre-processed image was further subjected to the above-mentioned four-phase level set segmentation. Partial differential equations were transformed into corresponding difference equations, which are solved in iterations. The number of iterations was controlled by following the derivatives of energy function, which via successive segmentation of regions with similar intensities converged to zero.

IV. Experimental results

The result of segmentation is shown on the example of two NMR images in Figs. 4 and 5. These are two slices of the human head in the region of temporomandibular joint. At the top of the figures we can see a slice of the original image and the result of the segmentation of pre-processed image with the contours of segmented regions marked out. In the bottom of the figures the segmented image by four-phase segmentation is given. The intensity of each region is given by the mean intensity value of individual pixels in the respective region of the original image.

Table 1 Parameters of segmentation with Celeron 1.4 GHz, 768 MB RAM and Windows XP, Matlab 7.0.1

Image	Number of iterations	Duration [s]
A	14	Bold
B	12	Regular

V. 3D modeling

The aim of the next work is creation of 3D model of tissue from segmented 2D slices. This process consists of three steps [3]:

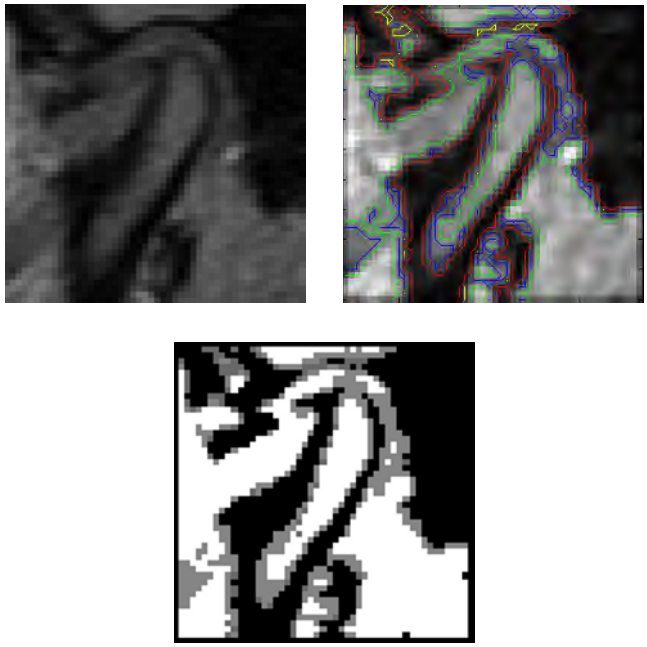


Fig. 4 Image A segmentation

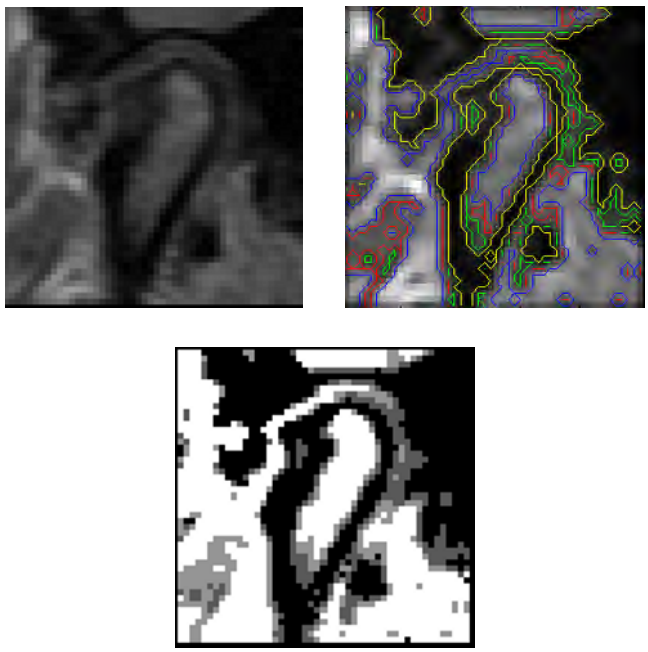


Fig. 5 Image B segmentation

1. Change of the data description – from discrete to vectorial description by the most used “Marching cubes” method for fully automated creation of geometrical models

2. Smoothing – e.g. by Laplace operator, because the changing of description cause that the geometrical model is stratified
3. Decimation – elimination of small triangles with maximal geometry preservation for surface simplification.

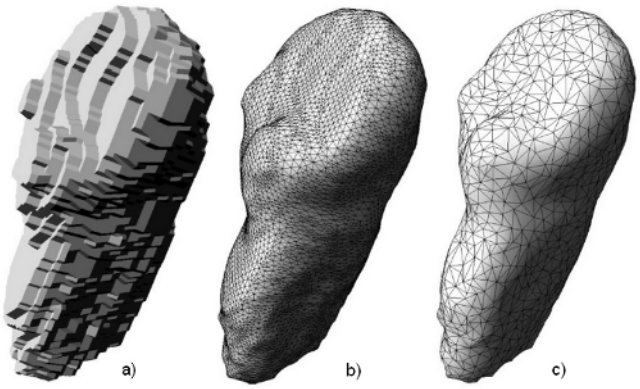


Fig. 6 Process of 3D creation (tooth), a) example of "Marching cubes" model, b) smoothed model, c) decimated model [3]

VI. Conclusions

The paper describes the application of a modern segmentation method with a suitable combination of pre-processing of NMR image of the human head. The images used are of low contrast and low resolution. The region of temporomandibular joint that was the subject of segmentation is of a mere 60 x 60 pixels, which makes precise processing difficult.

The output of the algorithm used is an image made up of regions with four levels of gray. These levels correspond to the mean values of pixel intensities of the original image. Segmenting the temporomandibular joint in several slices by the above-given method can be used, for example, to construct a three-dimensional model. Using the multiphase segmentation method, a more precise model can be obtained because by means of several levels of two-dimensional slice the resultant model can be approximated with greater precision.

Acknowledgment

This work was supported within the framework of the research plan MSM 0021630513 and project of the Grant Agency of the Czech Republic 102/07/1086 and GA102/07/0389.

References

1. Aubert G, Kornprobst P (2006) Mathematical problems in image processing. Springer, New York
2. Vese L, Chan F (2002) A multiphase level set framework for image segmentation using the Mumford and Shah model. International Journal of Computer Vision 50(3) 271-293 at www.math.ucla.edu/~lvese/PAPERS/IJCV2002.pdf
3. Krsek P (2005) Problematika 3D modelovani tkani z medicinskych obrazovych dat. Neurologie v praxi 6(3) 149-153

Author: Jan Mikulka
Institute: Brno University of Technology, Dept. of Theoretical and Experimental Electrical Engineering
Street: Kolejni 4
City: Brno
Country: Czech Republic
Email: xmikul16@stud.feec.vutbr.cz

Application of Advanced Methods of NMR Image Segmentation for Monitoring the Development of Growing Cultures

J. Mikulka[1], E. Gescheidtova[1] and K. Bartusek[2]

[1] Brno University of Technology, Dept. of Theoretical and Experimental Electrical Engineering, Kolejni 4, 612 00 Brno, Czech Republic
[2] Institute of Scientific Instruments, Academy of Sciences of the Czech Republic, Kralovopolska 147, 612 64 Brno, Czech Republic

Abstract — **The paper describes the pre-processing and subsequent segmentation of NMR images of growing tissue cultures. Images obtained by the NMR technique give three separately growing cultures. The aim of the work was to follow the speed of their development. Images obtained by means of the NMR device used are of very low resolution and contrast and there are no sharp edges between regions. Processing such images may prove to be quite difficult. A suitable algorithm was found, which consists of the pre-processing of the image and subsequent multiphase level set segmentation. The proposed method segments the image based on the intensity of the regions sought, and is suitable for working with NMR images in which there are no sharp edges. The method is described by partial differential equations that were transformed into corresponding difference equations solved numerically. Processing the detected images and measuring the sequence of NMR data give a graph of the growth development of the tissue cultures examined in comparison with manual measurement of their content.**

Keywords — **NMR imaging, image segmentation.**

I. Introduction

MRI is useful to obtain the number of hydrogen nuclei in biology tissue or to follow growing of cultures. There was provided examination by MR techniques [1] for rate of growth considering, rising of percentage of protons and cluster's shape of somatic germ. These measurements were part of research for hypothesis verification about increase percentage of water in process of tissue culture growth in case of cadmium contamination. In this case we put into tomograph operating area the measured tissue, choose the right slicing plane and measure MR image in this plane. The image is weighted by spin density and pixel intensity is equal to number of proton nucleus in chosen slice. MR image is a map of protons distribution in measured cluster of growing tissue culture [2].

The same technique was used for growth characterizing of early spruce germs contaminated by lead and zinc. There was computed intensity integral characterizing the number of protons in growing cluster and there were specified the changes of this value during the growth from MR images.

For measurement was used the spin-echo method because in contrast to gradient-echo technique the influence of the base magnetic field non-homogeneity is eliminated and images have better signal to noise ratio. The signal to noise ratio depends on the chosen width of slice. With thinner slices is the number of nucleus which generates signal smaller and the signal to noise ratio decreases. However the minimum width of slice is useful for tissue cultures imaging. The optimum width 2 mm was found. We must choose a size of image with a view to size of the tissue clusters and to size of operating probe. To improve the signal to noise ration we can repeat the measurement and average the results but it is more time-consuming. It is impossible to repeat the measurements quickly with regard to time of relaxation of water ($T_1 \approx 2$ s, $T_2 \approx 80$ ms). It is appropriate to choose the repetition cycle equal to spin-grid time of relaxation $T_R \approx T_1$. In our case for size of image 256x256 pixels is measurement time 256 x T_R.

There was placed small flask filed by deionized water for tomograph parameters instability suppression during long-term measurement. Obtained intensities of each image were scaling according to intensity of water in the flask (fig. 1).

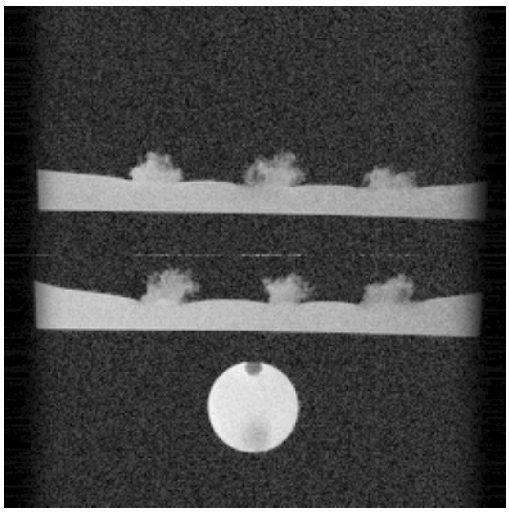


Fig. 1 Example of obtained image with 6 clusters and small flask filed by water for checking and scaling the image, at the top are the clusters contaminated by Zn, at the bottom are the clusters contaminated by Pb

Chwee Teck Lim, James C.H. Goh (Eds.): ICBME 2008, Proceedings 23, pp. 190–193, 2009
www.springerlink.com

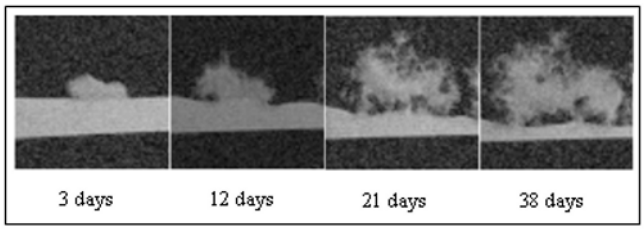


Fig. 2 Example of one cluster growth which is contaminated by lead 1000 mg/l

For described experiments was used MR tomograph with horizontal magnet (magnetic field 4.7 T) and operating area with diameter of 120 mm. Active shield gradient coils generate the maximal gradient field 180 mT/m.

At the first the data were processed in MAREVISI software where was achieved the manual computation of cluster surface from diffusion image and intensity integral of clusters from images weighted by spin density. Further the images weighted by spin density were filtered by wavelet transformation and segmented by region level set method. From segmented clusters was computed their surface and intensity integral too. Both methods were compared.

II. Measurement methods

The integral of image data could be established by two approaches. The first of them is sum of intensities in chosen part of image containing contaminated clusters divided by count of pixels

$$I_i = \frac{x_{\max} y_{\max}}{M.N} \sum_{1}^{M} \sum_{1}^{N} s_i \,, \tag{1}$$

where I_i is intensity integral, $x_{\max}$ a $y_{\max}$ are maximum dimensions of image in axis x and y.

The second approach utilizes properties of Fourier transformation and relation between MR image and interferential image which consist of obtained complex data. This relation could be described by following equation [3]:

$$s_i\left(k_x, k_y\right) = \int_{-\infty}^{\infty} \int_{-\infty}^{\infty} \rho_i\left(x, y\right).\mathrm{e}^{-2\pi\left(k_x x + k_y y\right)} \mathrm{d}x\mathrm{d}y, \tag{2}$$

where k_x and k_y are axis in measured interferential image called spatial frequency, $\rho_i(x,y)$ is distribution of spin density in MR image. For $k_x = k_y = 0$ we obtain:

$$s_i\left(0,0\right) = \int_{-\infty}^{\infty} \int_{-\infty}^{\infty} \rho\left(x, y\right) \mathrm{d}x\mathrm{d}y = I_i \,. \tag{3}$$

Number of the protons nucleus in measured sample is proportional to integral I_i which is equal to intensity of interferential image in zero point, i.e. for $k_x = k_y = 0$. Integral of MR image after DFT could be computed by this equation:

$$I_i = \frac{x_{\max} y_{\max}}{M.N} s_i\left(0,0\right). \tag{4}$$

The results of both methods are identical and the error is less than 1%. This approach is useful in case measurement of one tissue cluster.

For the results verification were the images filtered by means of wavelet transformation and consequently segmented by four-phase level set method. In fig. 3 is shown the example of processed image by described approach. The surface and intensity integral is then computed only from bounded clusters and due to the result is not devaluated by noise around clusters. The results are compared in the next chapter.

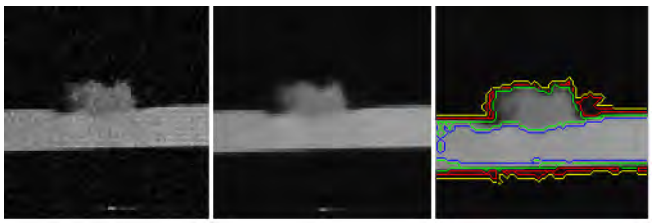


Fig. 3 Example of the image processing, on the left is the original image, in the middle is the wavelet transform filtered image and on the right is the segmented cluster by four-phase level set segmentation (green curve)

III. Results

Relation between intensity of cluster (thereby relative number of protons) and time of growth is for various Zn and Pb contaminations shown in fig. 4 and fig. 5. Clearly, the proton concentration in cluster of tissue culture grows all the time independently on tissue culture growth capability. The capability of growth dramatically decreases after 14 – 20 days to minimum. Relation between number of protons in tissue culture with contamination Zn or Pb and level of concentration by this element is shown in fig. 6 and fig. 7. We can find a concentration in which the percentage of protons is the highest all the time of growing. With zinc contamination is the optimal concentration 250 mg/l and for lead is the concentration 50 mg/l. In diffusion images are the clusters more precisely bounded and the evaluation of cluster surface is more accurately. It does not reflect a concentration of proton nucleus and the results are different from intensity integral measurement. The cluster's surfaces were evaluated from images weighted by spin density by wavelet filtration method and consequential region four-phase level set segmentation.

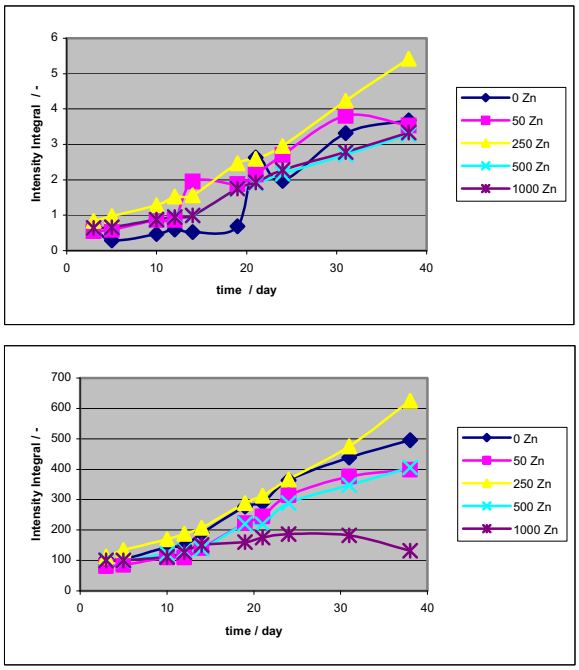


Fig. 4 Measurement of intensity integral of clusters in the time for various Zn concentrations, on the top is the result of the manual method, on the bottom is the result of the segmented image processing

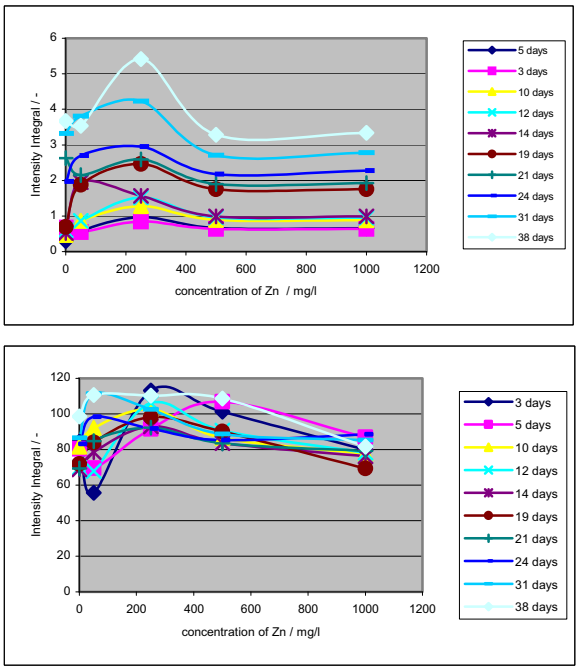


Fig. 6 Measurement of intensity integral of clusters for various Zn concentrations, on the top is the result of the manual method, on the bottom is the result of the segmented image processing

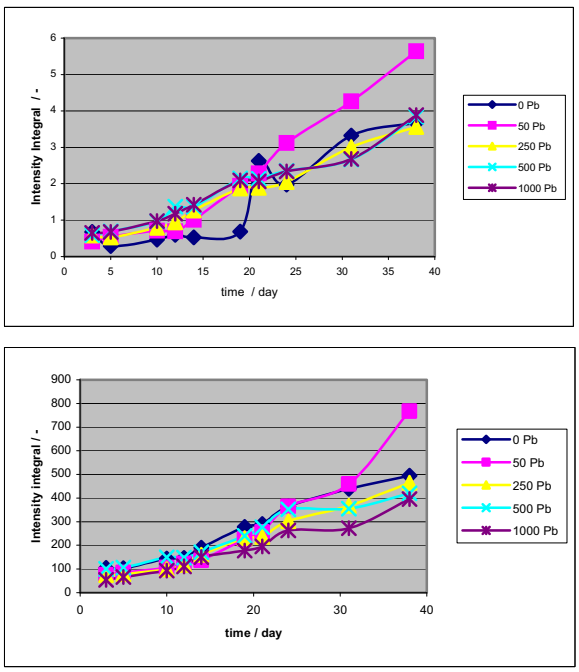


Fig. 5 Measurement of intensity integral of clusters in the time for various Pb concentrations, on the top is the result of the manual method, on the bottom is the result of the segmented image processing

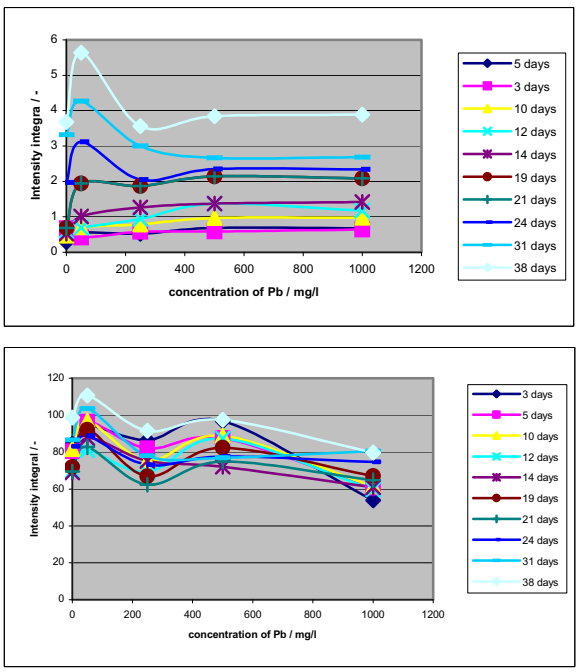


Fig. 7 Measurement of intensity integral of clusters for various Pb concentrations, on the top is the result of the manual method, on the bottom is the result of the segmented image processing

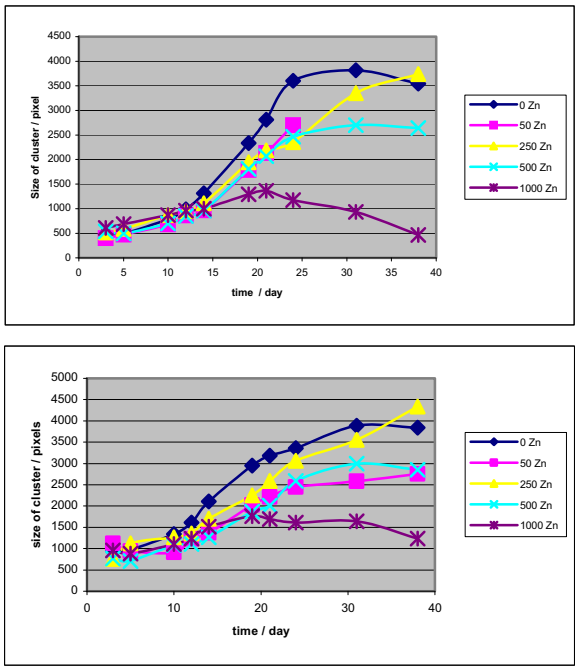


Fig. 8 Measurement of cluster size for various Zn concentrations, on the top is the result of the manual method, on the bottom is the result of the segmented image processing

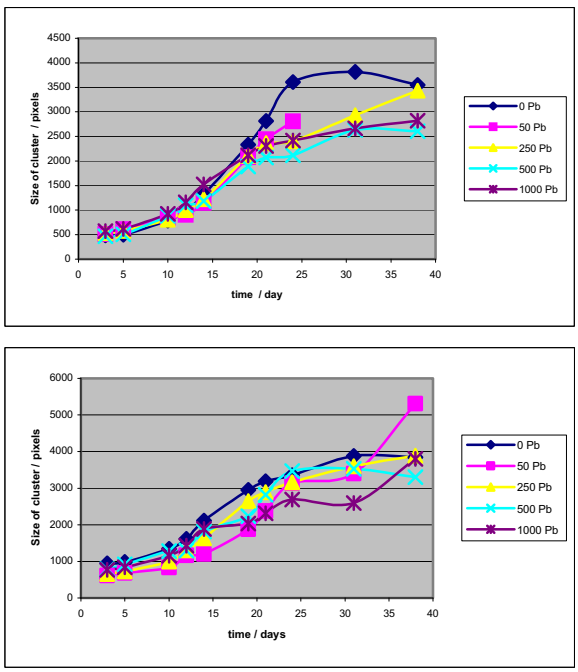


Fig. 9 Measurement of cluster size for various Pb concentrations, on the top is the result of the manual method, on the bottom is the result of the segmented image processing

IV. Conclusions

The MRI technique is useful for observing of the growth of the spruce germs and for verification of the hypothesis of increasing amount of water in the growing tissue cultures with various metal contaminations thereby their faster elutriation. The basic measurements and data processing by two different methods were taken. The aim of this work was the surface and the intensity integral measurement in time. Firstly the data were manually processed in the MAREVISI software by measuring of the cluster's surface in the diffusion images and then by the measuring of the intensity integral in the images weighted by the spin density. Further the images weighted by the spin density were processed by the wavelet transformation and segmented by the four-phase level set method and both monitored values were obtained in the Matlab. Both methods gives similar results thereby the measurement was verified.

Acknowledgment

This work was supported within the framework of the research plan MSM 0021630513 and project of the Grant Agency of the Czech Republic GA102/07/0389.

References

1. Supalkova, et al. Multi-instrumental Investigation of Affecting of Early Somatic Embryos of Spruce by Cadmium(II) and Lead(II) Ions. *Sensors* 2007, *7,* 743-759
2. Callaghan, P.T., Principles of Nuclear Magnetic Resonance Microscopy, Clarendon Press, Oxford, 1991
3. Liang, Z.P., Lauterbur, P. Principles of Magnetic Resonance Imaging, IEEE Press, New York, 1999
4. Vese L, Chan F (2002) A multiphase level set framework for image segmentation using the Mumford and Shah model. International Journal of Computer Vision 50(3) 271-293 at www.math.ucla.edu/~lvese/PAPERS/IJCV2002.pdf

Author: Jan Mikulka
Institute: Brno University of Technology, Dept. of Theoretical and Experimental Electrical Engineering
Street: Kolejni 4
City: Brno
Country: Czech Republic
Email: xmikul16@stud.feec.vutbr.cz

High-accuracy Myocardial Detection by Combining Level Set Method and 3D NURBS Approximation

T. Fukami[1], H. Sato[1], J. Wu[2], Thet-Thet-Lwin[2], T. Yuasa[1], H. Hontani[3], T. Takeda[2] and T. Akatsuka[1]

[1] Yamagata University, Department of Bio-System Engineering, Yonezawa, Japan
2 University of Tsukuba, Graduate School of Comprehensive Human Sciences, Tsukuba, Japan
3 Nagoya Institute of Technology, Department of Computer Science and Engineering, Nagoya, Japan

Abstract — **Accurate detection of myocardium is much important in diagnosis of heart diseases. In this study, we proposed the myocardial detection method by combining level set method in 2D image and 3D NURBS approximation. We first extracted epi- and endocardial walls by level set method in 2D image. Calculation cost was reduced by the processing on the slice. In this extraction, we used a near-circular shape of left ventricle and set the initial circle in the myocardial region surrounding the endocardium. We then approximated these extracted walls with 3D NURBS (Non-uniformed rational B-spline) model. Here, we used third-order B-spline basis function. In our study, we applied the method to MRI T1-weighted heart images of 10 subjects (5 normal subjects and 5 patients with apical hypertrophic cardiomyopathy). The pixel size was 1.62 ×1.62 mm, and the slice interval and the number of slices were 6.62 mm and 18, respectively. Evaluation of our method was done by comparing with manual detection by two cardiologists. As a result, the accuracy of endocardial detection was about the same as or less than the difference between cardiologists. While on the other hand, that of epicardial detection was larger than the difference between cardiologists. We inferred that epicaridial contour is clearer than endocardial one. Average of detection error by the method combining level set method and NURBS approximation (endocardium: 2.58 mm / epicardium: 2.71 mm) was smaller or almost same as only level set method (2.77 mm / 2.51 mm). However, as for variance of the error, combining method (0.58 mm / 0.59 mm) was smaller than only level set method (1.07 mm / 1.06 mm). These results show that NURBS approximation suppressed the variation of the detection accuracy.**

Keywords — **level set method, NURBS approximation, myocardial wall thickness.**

I. Introduction

In recent years, cardiac disease has become one of the most common causes of death. Therefore, quantitative evaluation of myocardial function is much important in diagnosis including disease prevention. We have already proposed the method to extract the left ventricle (LV) of apical hypertrophic cardiomyopathy and made wall thickness map from cardiac magnetic resonance imaging (MRI)[1]. However, in the method, we used the slice-based method and linear approximation between slices for obtaining myocardial volume. In this study, we extended the method by introducing the NURBS (Non-uniformed rational B-spline) model considering 3-D shape.

Some reports applying the NURBS model to heart images can be found. Segars et al.[2] developed realistic heart phantom which is patient-based and flexible geometry-based phantom to create a realistic whole body model. Then they make polygon surfaces fit the points extracted from the surfaces of heart structures for each time frame and smoothed. 4-D NURBS surfaces were fit through these surfaces. Same research group Tsui[3] also investigated the effects of upward creep and respiratory motion in myocardial SPECT by using NURBS modeling the above phantom. Tustison et al. [4] used NURBS for biventricular deformation estimated from tagged cardiac MRI based on four model types with Cartesian or Non-Cartesian NURBS assigned by cylindrical or prolate spheroidal parameter.

Lee et al.[5] developed hybrid male and female newborn phantoms to take advantages of both stylized and voxel phantoms. NURBS surfaces was adopted to replace limited mathematical surface equations of stylized phantoms, and the voxel phantom was utilized as its realistic anatomical framework. In the method we have already proposed, it has a problem that the error due to local misdetected contours gives the nonsmooth map of final result. In this study, to suppress local misdetection on slice level, we introduced NURBS model reflecting 3-D structral myocardial shape to the previous method.

II. Methods

In this study, MRI images were acquired using a Philips GyroscanNT. T1 images (256 × 256 pixels) at LV end-diastolic were obtained under synchronization with the electrocardiogram at echo time 40 ms to cover the whole heart region. The pixel size of the images was 1.62 × 1.62 mm2 and the slice thickness was 5 mm. The slice interval and the number of slices were 6.62 mm and 18, respectively. Short axial slices were acquired through the heart,

Chwee Teck Lim, James C.H. Goh (Eds.): ICBME 2008, Proceedings 23, pp. 194–197, 2009
www.springerlink.com

perpendicular to the line connecting the cardiac apex and base.

We first detected the contours of endcardium and epicardium on the axial slice by level set method. And then, we constructed 3-D curved-surfaces on each myocardium by NURBS approximation. By applying NURBS, the misdetection by the level-set method in slice-based processing can be absorbed. We subsequently described about cardiac wall detection, NURBS fitting and image registration in detail. We finally show the constructing the bull's eys map for easy visual understanding.

A. Cardiac Wall Detection

The level set function we used is the model introduced by Malladi et al.[6] that considers curvature. We chose this model because it is considered that myocardial walls have smooth contours. In MRI images, we manually set the initial circle of the level set in the myocardial region to obtain the endocardial and epicardial walls because the LV has a near-circular shape in the MRI short-axis cardiac images. We then applied the level set method to contour detection.

Application and an example of an extracted result by this processing are shown in Fig. 1.

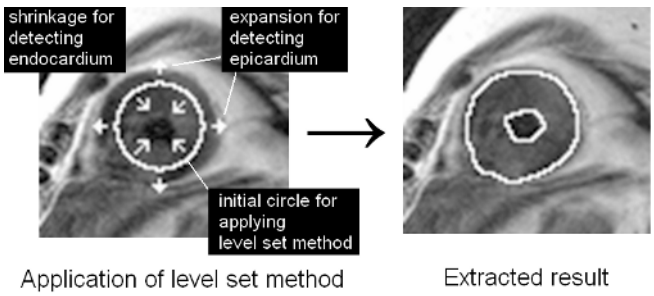


Fig. 1 Extraction of myocardial walls by level set method

We implemented 2-D image processing because we can stably extract myocardial contours. Namely, we can determine the number of times to update the level set function, after-mentioned, on every slice even if there are variations in image contrast between slices. This method uses a dynamic contour model that iteratively deforms the contour, beginning from the initial contour, to increase the gradient of the pixel values. The surface is presented as an equipollent level of the function $\phi^t(x,y)$. Zero crossover points form the contour by updating $\phi^t(x,y)$. The equation is described as follows, when the boundary surface at the time $t+\delta t$ is defined as $\phi^{t+\delta t}(x,y)$.

$$\phi^{t+\delta t}(x,y) = \phi^t(x,y) - \delta t(1-\varepsilon\kappa)V(x,y)\nabla\phi^t(x,y) \tag{1}$$

Here, δt and κ are the time interval and curvature, respectively. We set ε at 0.5.

$$\varepsilon = \nabla\cdot\frac{\nabla\phi}{|\nabla\phi|} = \frac{\phi_{xx}\phi_y^2 - 2\phi_y\phi_x\phi_{xy} + \phi_{yy}\phi_x^2}{(\phi_x^2+\phi_y^2)^{3/2}} \tag{2}$$

The function $V(x,y)$ in the right-hand side of (1) is the function that adjusts the growth of the border surface. In this study, we used the velocity function:

$$V(x,y) = -\frac{1}{1+\nabla(G_\sigma * I(x,y))} \tag{3}$$

, where $I(x,y)$ are pixel values at arbitrary coordinates (x, y) and G_σ is the Gaussian smoothing filter whose standard deviation is σ. Here, we give the following equation as the initial function $\phi_0(x,y)$:

$$\begin{cases} \phi_0(x,y) = (x-x_0)^2 + (y-y_0)^2 - r_0^2 \\ \qquad\qquad \text{(for endocardium detection)} \\ \phi_0(x,y) = -(x-x_0)^2 - (y-y_0)^2 + r_0^2 \\ \qquad\qquad \text{(for epicardium detection)} \end{cases} \tag{4}$$

Updating in Eq.(1) was stopped when the variation of summation of $\phi(x,y)$ in an enclosed region by the border was at the minimum.

NURBS Fitting

3-D NURBS surface of degree p in the u direction and degree q in the v direction is defined as a piecewise ratio of B-spline polynomials by the folloing equation. In this study, we set both parameters p and q at 3.

NURBS function, $S(u,v)$, can be described with next equation.

$$\begin{aligned} S(u,v) &\equiv (x(u,v), y(u,v), z(u,v)) \\ &= \frac{\sum_{i=0}^{n}\sum_{j=0}^{m} N_{i,p}(u)N_{j,q}(v)\omega_{ij}P_{ij}}{\sum_{i=0}^{n}\sum_{j=0}^{m} N_{i,p}(u)N_{j,q}(v)\omega_{ij}} \\ &\qquad (0\le u\le 1,\ 0\le v\le 1) \end{aligned} \tag{5}$$

P_{ij} represent the control points defining the surface, ω_{ij} are weights determining a point's influence on the shape of the surface, and $N_{ip}(u)$ and $N_{iq}(v)$ are the nonrational B-spline basis functions defined on the knot vectors.

$$U = [\underbrace{0,\ldots,0}_{p+1}, u_{p+1}\cdots u_n, \underbrace{1,\cdots,1}_{p+1}]$$
$$V = [\underbrace{0,\ldots,0}_{q+1}, u_{q+1}\cdots u_m, \underbrace{1,\cdots,1}_{q+1}] \quad (6)$$

B-spline basis functions are calculated using the Cox-deBoor reccurence relation described in following equations.

$$N_{i,0}(t) = \begin{cases} 1 & (t_i \le t < t_{i+1}) \\ 0 & (t < t_i, t_{i+1} \le t) \end{cases}$$
$$N_{i,m} = \frac{t - t_i}{t_{i+m} - t_i} N_{i,m-1} + \frac{t_{i+m+1} - t}{t_{i+m+1} - t_{i+1}} N_{i+1,m-1} \quad (7)$$

In this study, we acquired points on the myocardial contour by searching radially from the center which is the intersection of LV-long axis and each short-axis slice. We then calculated control points, P_{ij}, from the points on the myocardial contour. NURBS surface was obtained by using control points in Eq.(5). We showed the example of 3-D NURBS surface constructed from the MRI myocardial contours obtained in cardiac wall detection in Fig. 2. This figure was drawn by using the software, Real INTAGE (KGT Inc.).

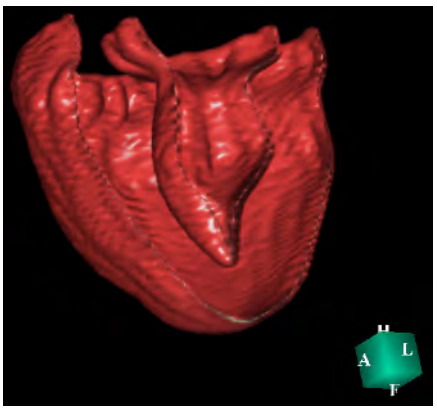


Fig. 2 Application the NURBS model to endocardium and epicardium detected from MRI images

B. Calculation of wall thickness

We will describe about the method to calculate blood flow volume per unit LV myocardial volume and the method for constructing bull's map. We calculated myocardial volume by using wall thickness. It is defined by the distance between the points of endocardium, $P_{end}(u,v)$, and epicardium, $P_{epi}(u,v)$, whose u and v are same in

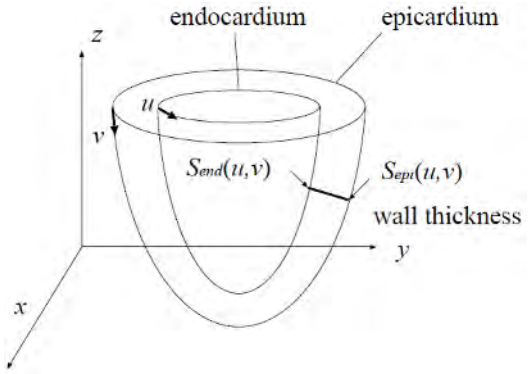


Fig. 3 Definition of myocardial wall thickness

MRI images as shown in Fig. 3. This wall thickness, $W(u,v)$, is described by following equation.

$$V(u,v) = \left\| P_{end}(u,v) - P_{epi}(u,v) \right\| \quad (8)$$

III. Results and Discussions

We applied our method to 5 normal cases and 5 APH cases.

In this study, we show the average map of 5 normal cases in Fig. 4 and 5. Figure 4 is the bull's eye map based on wall thickness extracted by level set method. And Fig. 5 is the map extracted by both level set method and NURBS approximation. We compared the detected myocardial walls with the results manually-extraction by two cardiologists to examine the performance of NURBS approximation. Here, NURBS surface was resliced at the original short-axis slices.

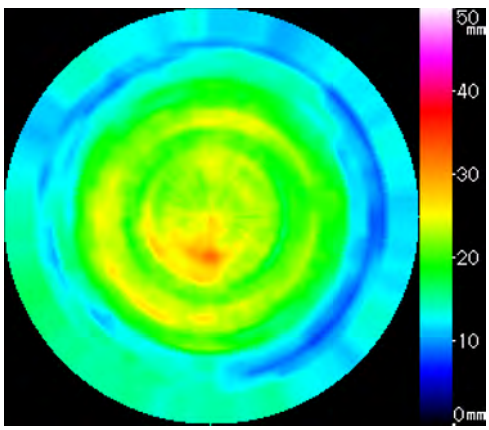


Fig. 4 Bull's eye map based on wall thickness extracted by level set method

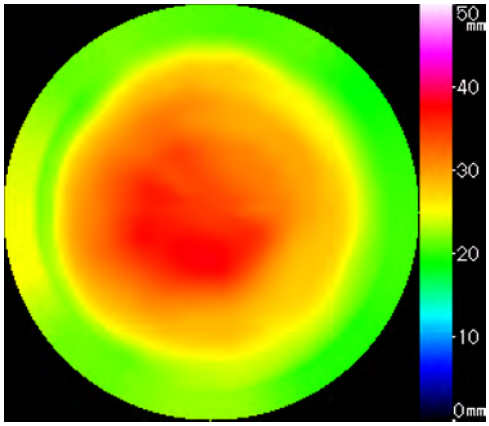


Fig. 5 Bull's eye map based on wall thickness extracted by both level set method and NURBS approximation.

In Fig.4 shows some striping because 3D myocardial shape is not considered. 3D NURBS approximation eliminates these striping. In Table.1, we can see that standard deviation of error decreases by adding NURBS approximation into level set method. These results show that NURBS approximation suppressed the variation of the detection on the slice level. Our method shows relatively good performance for endocardium detection. While on the other hand, that of epicardium detection was larger than the difference between cardiologists, namely the method is inferior in epicardium detection.

Table. 1 Detection error of myocardial wall

	endocardium (mm)	epicardium (mm)
Level set method (LSM)	2.51 ± 1.06	2.77 ± 1.07
Combined method (LSM + NURBS)	2.71 ± 0.59	2.58 ± 0.58
the difference of two cardiologists	3.44 ± 1.57	2.00 ± 0.71

IV. Conclusions

In this study, we proposed the method combining level set method and NURBS approximation for myocardial detection and calculation of wall thickness.

We first extracted epi- and endocardial walls by level set method in 2D image. Calculation cost was reduced by the processing on the slice. In this extraction, we used a near-circular shape of left ventricle and set the initial circle in the myocardial region surrounding the endocardium. We then approximated these extracted walls with 3D NURBS (Non-uniformed rational B-spline) model. In our study, we applied the method to MRI T1-weighted heart images of 10 subjects (5 normal subjects and 5 patients with apical hypertrophic cardiomyopathy). Evaluation of our method was done by comparing with manual detection by two cardiologists. As a result, the accuracy of endocardial detection was about the same as or less than the difference between cardiologists. While on the other hand, that of epicardial detection was larger than the difference between cardiologists. Bull's eye maps of wall thickness also show that NURBS approximation suppressed the variation of the detection.

References

1. Fukami T, Sato H, Wu J et al. (2007) Quantitative evaluation of myocardial function by a volume-normalized map generated from relative blood flow, Phys. Med. Biol., 52: 4311-4330. doi: 10.1088/0031-9155/52/14/019
2. Segars W P, Lalush D S, Tsui B M W, (1999) A realistic spline-based dynamic heart phantom, IEEE Trans. on Nucl. Sci., 46, 503-506.
3. Tsui B M W, Segars W P, Lalush D S, (2000) Effects of upward creep and respiratory motion in myocardial SPECT, IEEE Trans. on Nucl. Sci., 47, 1192-1195.
4. Tustison N J, Abendschein D, Amini A A, (2004) Biventricular myocardial kinematics based on tagged MRI from anatomical NURBS models, Proc. of the 2004 IEEE Computer Society Conference on Computer Vision and Pattern Recognition (CVPR 2004), 2, 514-519.
5. Lee C, Lodwick D, Hasenauer D, et al., (2007) Hybrid computational phantoms of the male and female newborn patient: NURBS-based whole-body models, Phys. Med. Biol., 52, 3309-3333.
6. Malladi R, Sethian J A, Vemuri B C, (1994) Evolutionary fronts for topology-independent shape modeling and recovery, Proc. of Third European Conference on Computer Vision, 800,3-13.

Author: Tadanori FUKAMI
Institute: Yamagata University
Street: Jonan 4-3-16
City: Yonezawa
Country: Japan
Email: fukami@yz.yamagata-u.ac.jp

Design of a Wireless Intraocular Pressure Monitoring System for a Glaucoma Drainage Implant

T. Kakaday[1], M. Plunkett[2], S. McInnes[3], J.S. Jimmy Li[1], N.H. Voelcker[3] and J.E. Craig[4]

[1] School of Computer Science, Engineering and Mathematics, Flinders University, Adelaide, Australia
[2] Ellex Medical Lasers R & D, 82 Gilbert Street, Adelaide, Australia
[3] School of Chemistry, Physics and Earth Sciences, Flinders University, Adelaide, Australia
[4] Department of Ophthalmology, Flinders Medical Centre, Adelaide, Australia

Abstract — **Glaucoma is a common cause of blindness. Wireless, continuous monitoring of intraocular pressure (IOP) is an important, unsolved goal in managing glaucoma. An IOP monitoring system incorporated into a glaucoma drainage implant (GDI) overcomes the design complexity with incorporating a similar system in a more confined space within the eye. The device consists of a micro-electro-mechanical systems (MEMS) based capacitive pressure sensor combined with an inductor printed directly onto a polyimide printed circuit board (PCB). The device is designed to be placed onto the external plate of a therapeutic GDI. The resonance frequency changes as a function of IOP and is tracked remotely using a spectrum analyzer. A theoretical model for the reader antenna was developed to enable maximal inductive coupling with the IOP sensor implant, including modeling of high frequency effects. Pressure chamber tests indicate that the device has adequate sensitivity in the IOP range with excellent reproducibility over time. Additionally, we show that sensor sensitivity does not change significantly after encapsulation with polydimethylsiloxane (PDMS) to protect the device from the aqueous environment. *In vitro* experiments showed that the signal measured wirelessly through sheep corneal tissue was adequate indicating potential for using the system in human subjects.**

Keywords — **Glaucoma, intraocular pressure, glaucoma drainage implant, micro-electro-mechanical systems (MEMS), and capacitive pressure sensor**

I. Introduction

The most commonly used technique, and current gold standard for intraocular pressure (IOP) measurement is applanation tonometry. In addition to requiring topical anesthetic and a skilled operator, a major disadvantage of applanation tonometry is that it is influenced by many variables, thereby providing only a surrogate measure of true IOP. Additionally, diurnal measurements are difficult to obtain, particularly overnight.

Remote continuous monitoring of IOP has long been desired by clinicians and the development of such technology has the prospect of revolutionizing glaucoma care. Several groups have described an active remote measuring device that can be incorporated into the haptic region of an intraocular lens (IOL). [1-3] IOL's are universally used to replace the natural lens in cataract surgery and are in direct contact with the aqueous humor inside the anterior chamber, thus providing an accurate measurement of IOP. However, the IOL has size and weight constraints requiring the implant to be miniaturized and therefore requiring on-chip circuitry to process signals (i.e. active telemetry). Whilst active devices are accurate and sensitive, their complexity and manufacturing price are potentially major obstacles to a wide spread use.

In another approach, Leonardi et al [4] described an indirect method in which a micro strain gauge is embedded into a soft contact lens that allows measurement of changes in corneal curvature which correlates with IOP. However, the correlation between corneal curvature and IOP is not universally accepted.

A glaucoma drainage implant (GDI) is a device implanted to enable lowering of IOP in severe glaucoma cases. The explant plate of a GDI which is implanted under the conjunctiva is directly connected to the anterior chamber of the eye via a tube. The plate provides a larger surface area compared to an IOL allowing greater flexibility in design. A passive telemetry approach is suitable in such a case. This reduces the fabrication complexity making the device low cost and simple to fabricate. In addition, there are no active parts in the system making it desirable for implantation.

A feasibility study (beyond the scope of this paper) was done to verify that the explant plate of a GDI is a suitable location to incorporate an IOP measuring system. In this paper an IOP monitoring device is designed and implemented onto the explant plate of a Molteno GDI. In addition, an optimal design for the reader antenna to maximize coupling between itself and the sensor implant is proposed. This paper focuses on the Molteno GDI, however this method can be adapted to other GDI's available on the market.

Chwee Teck Lim, James C.H. Goh (Eds.): ICBME 2008, Proceedings 23, pp. 198–201, 2009
www.springerlink.com

II. Materials and Methods

A. Sensor implant

The sensor implant is designed to be placed onto the explant plate of the Molteno GDI (Molteno Ophthalmic Limited - New Zealand) as shown in Figure 1.



Figure 1: The IOP sensor implant placed on the explant plate of a Molteno GDI.

The IOP sensor implant consists of a MEMS capacitive pressure sensor (Microfab Bremen – Germany) and planar inductor printed directly onto a flexible, biocompatible polyimide printed circuit board (PCB) (Entech Electronics – Australia) to complete the parallel resonant circuit.

The planar sensor inductor and capacitive pressure sensor were both characterized using the Vector Impedance Meter (VIM) (Model 4815A Hewlett Packard). The sensor implant was encapsulated with biomaterial polydimethylsiloxane (PDMS) to protect against aqueous environment. All PDMS coatings were prepared from a Sylgard® Brand 184 Silicone Elastomere Kit.

B. Wireless communication

The wireless communication between the sensor implant and external reader antenna is an important determinant in implantable systems. When the sensor implant is brought near the vicinity of the external reader antenna a portion of the RF energy is absorbed by the sensor implant, creating a 'dip' in the signal as observed on the spectrum analyzer. The greater 'dip' signifies a greater coupling between the reader antenna and sensor implant.

The sensor implant is placed inside a pressure chamber connected to an inflation cuff at one end and a sphygmomanometer at the other. The sensor implant is separated from the reader antenna by a 4 mm thick non-conducting PDMS layer. The pressure was varied in the desired IOP range (5-50 mmHg) using the inflation cuff and the shift in the resonance peak was recorded. Experiments were repeated using explanted sheep scleral and corneal tissue to determine if wireless communication was possible through biological tissue.

C. Reader antenna design

Reader antenna design involves maximizing its read range by optimizing its coupling with the sensor implant. The coupling coefficient k is given by the following expression.[5 6]

$$k = \frac{M}{\sqrt{L_1 L_2}}$$

Where, M is the mutual inductance, L_1 and L_2 are the inductance of sensor and reader inductor coils respectively. In order to obtain the best system characteristics, the value of k should be designed for unity.

The inductances L_1 and L_2 can be directly determined from the VIM and M is calculated by the solution provided by Zierhofer et al. [7]. In order to determine the optimal reader antenna size for a specified read range the M between the two spiral coil geometries given by the expression below needs to maximized.[8]

$$M = \frac{\mu_o \pi N_1 N_2 (ab)^2}{2\left(a^2 + r^2\right)^{3/2}} \quad (2)$$

Where a, b are the radius of the reader and sensor coils respectively. N_1, N_2 the number of turns in reader and sensor coil respectively, 'r' is the distance between the two coils. The above equation can be reduced to

$$a = \sqrt{2}r \quad (3)$$

To validate the described model by experimentation, four planar inductors of different size, inductance and number of turns were printed directly onto a PCB. Their properties are listed in Table 1. The experimental setup consists of a LC

Table 1 Antenna coil properties

	Coil A	Coil B	Coil C	Coil D
Number of turns	18	15	7	15
Inductance (μH)	2.14	4.45	2.5	1.75
Self Resonating Frequency (MHz)	63	49	73	102
Diameter (mm)	9.4	32.51	32.5	16.76

resonant circuit comprising of a planar sensor inductor (L) and a 22 pF chip capacitor (C) mounted onto a vernier calipers separated from the reader antenna. The reader antenna is connected to a spectrum analyzer. To determine the maximum read range, the distance between the reader antenna and LC resonant circuit was increased until no further 'dip' in the signal was observed. The above experiment is then repeated using the sensor implant in place of the LC resonant circuit.

III. Results and discussion

A. Sensitivity of the sensor implant in the IOP range

VIM results showed the quality factor (Q) of the capacitive pressure sensor to be quite low at the resonant frequency of the sensor implant (8.71 @ 38.61 MHz) as compared to the maximum Q of 57.29 @ 10MHz.

Pressure chamber tests were repeated randomly (50 iterations) over a period of one week, the results are shown in Figure 2. The current resolution of the sensor implant in the IOP range is 10 mmHg. The resolution of the current system is limited by the sensitivity and Q of the MEMS capacitive sensor.

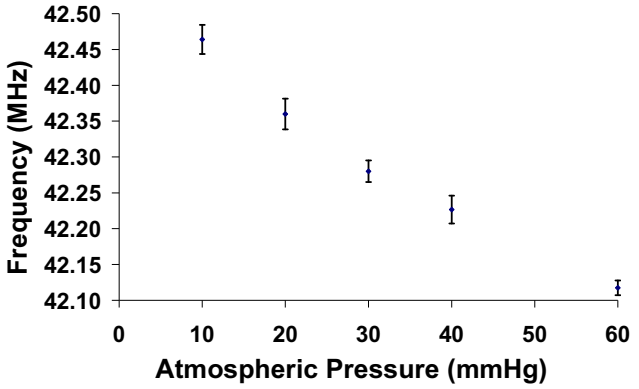


Figure 2: The resonance frequency response of the IOP sensor implant. The error bars indicate the standard deviation.

In vitro experiments were carried out by substituting the PDMS barrier with explanted sheep corneal and scleral tissue in aqueous environment. The results showed that the signal measured was adequate, indicating potential for using such a system in human subjects.

B. Reader antenna performance

Experimental results showing coupling between the reader antenna and LC resonant circuit represented by the 'dip' height are presented in Figure 3. The theoretical coupling coefficient k between the reader antenna and sensor implant is shown in Figure 4. The theoretical model closely follows the trend from the experimental results (Figure 3).

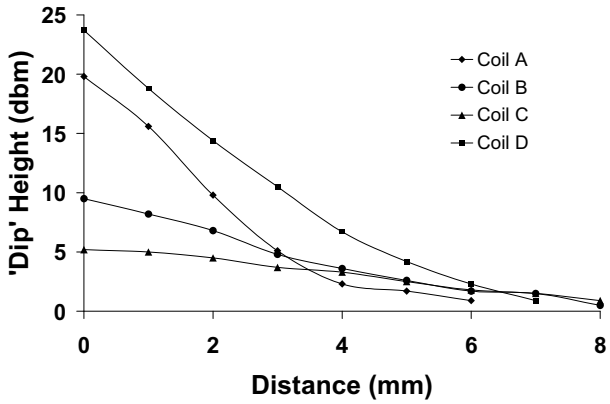


Figure 3: Experimental evaluation of reader coil geometries at varying distances from the LC resonant circuit. The better coupling results in a greater 'dip' height which decreases with increasing distance from the LC resonating circuit.

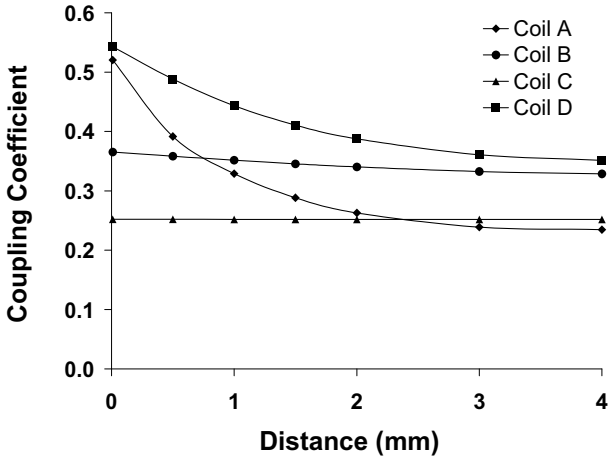


Figure 4: Theoretical coupling coefficients of reader coils at varying distances from the IOP sensor implant calculated from (3).

A summary of results showing the performance of each reader coil with the LC resonant circuit and sensor implant are presented in Table 2. The maximum read range between the reader antenna and sensor implant is greatly attenuated due to its low Q as compared to a high Q LC resonant circuit. The effect of self resonating frequency (SRF) on the reader coil performance is evident when coupled with the sensor implant. The SRF is the frequency beyond which the inductor starts to behave as a capacitor. Although coil B gives a maximum read range of 10 mm with the LC reso-

Table 2: Summary of results

	Coil A	Coil B	Coil C	Coil D
Theoretical read range (mm) (3)	4	10	10	6
Experimental range - LC circuit (mm)	6	8	8	7
Experimental range – sensor implant (mm)	3	0	0	4

nant circuit it produces zero 'dip' when coupled with the sensor implant. This is due to a) low Q of the sensor implant, b) the SRF of coil B is in close proximity to the resonant frequency of the sensor implant.

Coil D gave the maximum read range of 4 mm with the sensor implant. This result is anticipated due to a number of reasons a) its SRF is at least twice the resonant frequency of the sensor implant b) the number of turns are maximized to increase mutual inductance, which is directly proportional to k, c) coil D is larger than the sensor implant allowing for lateral and angular misalignments.

C. Encapsulation of sensor with PDMS

The results from encapsulating the capacitive pressure sensor with biomaterial PDMS as obtained from the VIM show that the sensitivity of the sensor does not change significantly upon encapsulation. The minor offset due to the influence of the silicone coating can be compensated by calibration of each sensor after encapsulation. The average sensitivity of the sensor in the IOP range determined over several repeated measurements was determined to be 1.167x10-3 pF/mmHg.

IV. Conclusion

An IOP sensor implant comprising of a MEMS based capacitive pressure sensor and planar inductor was designed to be incorporated into the explant plate of a Molteno GDI. The IOP sensor implant has been shown to have reasonable resolution (10 mmHg) in the IOP range such a resolution can be able to differentiate between normal and high IOP. In addition, the sensor implant showed excellent repeatability over time. Better resolution of small differences in IOP will be desirable in future iterations. In addition, sensor sensitivity was not significantly affected by encapsulation with PDMS bio-coating.

The reader antenna is designed to maximize its coupling with the sensor implant. Theoretical models are proposed to predict the coupling of the reader antenna coils with a resonant circuit of interest including its optimal size for a specified read range. We found the theoretical predictions closely followed experimental results. Signals from the sensor implant were measured though 4 mm thick PDMS bio-material and though explanted sheep scleral and corneal tissue indicating high potential for using the system in human subjects.

The IOP monitoring system incorporated into a GDI overcomes the design complexity and associated costs of incorporating such a system in an IOL. Such a device will open new perspectives, not only in the management of glaucoma, but also in basic research for mechanisms of glaucoma.

References

1. Walter P, Schnakenberg U, Vom Bogel G*, et al.* Development of a Completely Encapsulated Intraocular Pressure Sensor [Original Paper]. *Ophthalmic Research* 2000;**32**:278-84.
2. Schnakenberg. U, Walter. P, Bogel. Gv*, et al.* Initial investigations on systems for measuring intraocular pressure. *Sensors and Actuators* 2000;**85**:287-91.
3. Eggers T, Draeger J, Hille K*, et al.* Wireless Intra-Ocular Pressure Monitoring System Integrated into an Artificial Lens. *1st Annual International IEEE-EMBS Special Topic Conference on Microtechnologies in Medicine & Biology.* Lyon, France 2000.
4. Leonardi M, Leunberger P, Bertrand D, Bertsch A, Renaud P. First Steps toward Non-invasive Intraocular Pressure Monitoring with a Sensing Contact Lens. *Investigative Ophthalmology & Visual Science* 2004;**45**:3113-7.
5. Ong KG, Grimes CA, Robbins CL, Singh RS. Design and application of a wireless, passive, resonant-circuit environmental monitoring sensor. *Sensors and Actuators* 2001;**A 93**:33-43.
6. Akar O, Akin T, Najafi K. A wireless batch sealed absolute capacitive pressure sensor. *Sensors and Actuators* 2001;**A95**:29-38.
7. Zierhofer C, M., Hochmair E, S. Geometric Approach for Coupling Enhancement of Magnetically Coupled Coils. *IEEE transactions on Biomedical Engineering.* 1996;**43**:708-14.
8. Reinhold. C, Scholz. P, John. W, Hilleringmann. U. Efficient Antenna Design of Inductive Coupled RFID-Systems with High Power Demand. *Journal of Communications* 2007;**2**:14-23.

Author: Tarun Kakaday
Institute: Flinders University of South Australia
Street: Sturt Road, Bedford Park
City: ADELAIDE - 5042
Country: AUSTRALIA

Integrating FCM and Level Sets for Liver Tumor Segmentation

Bing Nan Li[1], Chee Kong Chui[2], S.H. Ong[3,4] and Stephen Chang[5]

[1]Graduate Programme in Bioengineering, National University of Singapore, Medical Drive 28, Singapore
[2]Department of Mechanical Engineering, National University of Singapore, Engineering Drive 1, Singapore
[3]Department of Electrical and Computer Engineering, National University of Singapore, Engineering Drive 3, Singapore
[4]Division of Bioengineering, National University of Singapore, Engineering Drive 1, Singapore
[5]Department of Surgery, National University Hospital, Kent Ridge Wing 2, Singapore

Abstract — **Liver and liver tumor segmentations are very important for a contemporary planning system of liver surgery. However, both liver and liver tumor segmentations are a grand challenge in clinics. In this paper, we proposed an integrated paradigm with fuzzy c-means (FCM) and level set method for computerized liver tumor segmentation. An innovation in this paper is to interface the initial segmentations from FCM and the fine delineation with level set method by morphological operations. The results in real medical images confirm the effectiveness of such integrated paradigm for liver tumor segmentation.**

Keywords — **liver tumor segmentation, fuzzy c-means, level set methods, medical image processing**

I. Introduction

Information and computer technologies exhibit great impact on liver tumor treatment. For instance, by them, the physicians are now possible to inspect liver components and plan liver surgery in an augmented reality. To this goal, one of essential steps is to capture the profile of internal components of human body and reconstruct them accurately. Medical imaging modalities, including computed tomography (CT) and magnetic resonance imaging (MRI), are among the most popular ones in this field. Take the CT for example. Their results have been applied to computerized planning system of liver tumor treatment in various publications [1-2].

In conventional planning systems of liver surgery, the physicians have to inspect a series of CT images and analyze liver components by hand. Obviously, it is not an easy job. Segmentation is a field of technology oriented to computerized distinguishing of anatomical structure and tissue types in medical images. It leads to the useful information like spatial distributions as well as pathological regions of physiological organs in medical image. Thus, for a contemporary planning system, one of essential components is for accurate liver segmentation, in particular hepatic vessels and liver tumors.

The underlying object of image segmentation is to separate the regions of interest from their background and from other components. A typical paradigm of image segmentation can be achieved by either allocating the homogeneous pixels or identifying the boundaries among different image regions [3]. The former often takes advantage of pixel intensities directly, while the latter depends on intensity gradients. Other than intensity information, it is possible to segment image by utilizing model templates and evolving them to matching the interested objects. In addition, various soft computing methods have been applied to image segmentation too. However, it is noteworthy that, till now, there is yet no universal method for image segmentation. The specific application and the available resources usually determine the individual method's strengths and weaknesses.

Among the state-of-the-art methods, active contours or deformable models are among the most popular ones for image segmentation. The idea behind them is quite straightforward. The user specifies an initial guess, and then let the contour or the model evolve by itself. If the initial model is parametrically expressed, it operates as snakes [3]. In contrast, the level set methods do not follow the parametric model, and hereby own better adaptability. But the level set methods, without the parametric form, often suffer from a few refractory problems, for example, boundary leakage and excessive computation [4]. Thus a good initialization is very important in level set methods for image segmentation.

In reference [5], the authors utilized a fast marching approach to propagate the initial seed point outwards, and followed by a level set method to fine tune the results. In this paper, we proposed to initialize the level set evolution by the segmentations from fuzzy c-means (FCM), which has gained esteem in medical image segmentation. In other words, an integrated technique was presented in this paper for liver tumor segmentation from CT scans. The first part is based on the unsupervised clustering by FCM, whose results are then selected out for a series of morphological operations. The final part is by an enhanced level set method for fine delineation of liver tumors.

Chwee Teck Lim, James C.H. Goh (Eds.): ICBME 2008, Proceedings 23, pp. 202–205, 2009
www.springerlink.com

II. Initial segmentation by FCM

Segmentation is a classical topic in the field of medical image processing and analysis. Suppose a medical image as u_0: $\Omega \to R^2$. Image segmentation is to find out the optimal subset u_i: Ω_i so that $\Omega = \bigcup \Omega_i$ and u_i has a nearly-constant property within each Ω_i. It is hereby possible to segment a medical image based on its pixel intensities or variational boundaries. For the latter case, image segmentation may be formulated as $\Omega = \bigcup \Omega_i \bigcup \Gamma_j$, where Γ_j is the boundary separating Ω_i. However, due to the intrinsic noises and discontinuities, neither of them is universally robust [7]. As a consequence, an integrated technique was proposed in this paper to utilize FCM, based on image intensity information, for initial segmentation and the level set method for object refinement by the variation information of image boundaries.

FCM has been widely utilized for medical image segmentation. In essence, it originates from the classical *k*-means algorithm. However, in the *k*-means algorithm, every image pixel is limited to one and only one of *k* clusters, which is not true in medical image segmentation. Generally speaking, each pixel in a medical image should be attributed to the superimposition of different human organs. In other words, it is usually not appropriate to assign an image pixel to a specific organ or organ component only. In stead, FCM utilizes a membership function μ_{ij} to indicate the belongingness of the *j*th object to the *i*th cluster. Its results are hereby more justifiable in medicine.

The objective function of FCM is:

$$J = \sum_{j=1}^{N}\sum_{i=1}^{c} \mu_{ij}^{m} \left\| x_j - v_i \right\|^2 \tag{1}$$

where μ_{ij} represents the membership of pixel x_j in the *i*th cluster, v_i is the *i*th cluster center, and m (m>1) is a constant controlling the fuzziness of the resulting segmentation. The membership functions are subject to the constraints $\sum_{i=1}^{c} \mu_{ij} = 1$, $0 \le \mu_{ij} \le 1$ and $\sum_{j=1}^{N} \mu_{ij} > 0$. In accordance with the following (2)-(3), the membership functions μ_{ij} and the centroids v_i are updated iteration by iteration respectively:

$$\mu_{ij} = \frac{\left\| x_j - v_i \right\|^{-2/(m-1)}}{\sum_{k=1}^{c} \left\| x_j - v_k \right\|^{-2/(m-1)}} \tag{2}$$

$$v_i = \frac{\sum_{j=1}^{N} \mu_{ij}^{m} x_j}{\sum_{j=1}^{N} \mu_{ij}^{m}} \tag{3}$$

The system is optimized when the pixels close to their cluster's centroid are assigned high membership values, and low membership values are assigned to the pixels far away from that centroid.

The performance of FCM for medical image segmentation relies on the prefixed cluster number and the initial clusters substantially. It has been found in our practice that the random initialization was not robust enough for liver tumor segmentation in CT scans. Other investigators ever successfully carried out the optimal initialization by histogram analysis for brain segmentation in MRI [7]. But it is found that there is merely tiny but variable discrepancy between the liver's and liver tumors' histogram in CT images. In our experiment, we experientially designated the initial cluster centroids by averaging the histogram of the CT image.

III. Tumor delineation by level set methods

The level set method, proposed by Osher and Sethian, is a versatile tool for tracing the interfaces that may separate an image Ω into different parts. The main idea behind it is to characterize the interface function $\Gamma(t)$ by a Lipschitz function Φ:

$$\begin{cases} \phi(t,x,y) > 0 & (x,y)\ is\ inside\ \Gamma(t) \\ \phi(t,x,y) = 0 & (x,y)\ is\ at\ \Gamma(t) \\ \phi(t,x,y) < 0 & (x,y)\ is\ outside\ \Gamma(t) \end{cases} \tag{4}$$

In other words, the interface $\Gamma(t)$ is implicitly solved as the zero-level curve of the function $\Phi(t, x, y)$ at time t. In general, $\Gamma(t)$ evolves in accordance with the following nonlinear partial differential equation (PDE):

$$\begin{aligned} &\frac{\partial \phi}{\partial t} + F \cdot \left| \nabla \phi \right| = 0 \\ &\phi(0,x,y) = \phi_0(x,y) \end{aligned} \tag{5}$$

where F is a velocity field normal to the curve $\Gamma(t)$, and the set $\{(x, y)|\ (\Phi_0(x, y))=0\}$ is the initial contour. A few limitations have been recognized in standard level set methods too. The first of all, the evolution of level set functions has to be reinitialized periodically in order to guarantee the solutions' stability and usability. Otherwise, it often confronts with the threats of boundary leakage. On the other hand, standard level set methods are carried out on the entire image domain. Nevertheless, in terms of image segmentation, merely the zero-level level set is interested eventually. In other words, it is meaningful if the computation is limited within a narrow band near the zero level.

In this paper, we follow the approach proposed in reference [6] for a distance preserving level set evolution. In the first side, the authors revised the level set model as:

$$\frac{\partial \phi}{\partial t} = \mu[\nabla \phi - div(\frac{\nabla \phi}{|\nabla \phi|})] + \lambda \cdot \delta(\phi) \cdot div(g \frac{\nabla \phi}{|\nabla \phi|}) + v \cdot g \cdot \delta(\phi) \quad (6)$$

where μ>0 is the weight of the internal energy term, which controls the smoothness of level set curve; λ>0 and v are constants controlling external contraction; g is the edge indicator function as in (11) ; δ is the univariate Dirac function. In practice, δ is regularized as:

$$\delta_\varepsilon(x) = \begin{cases} 0 & |x| > \varepsilon \\ \dfrac{1+\cos(\pi \cdot x / \varepsilon)}{2} & |x| \le \varepsilon \end{cases} \quad (7)$$

The distance preserving level set model eliminates the iterative reinitialization in standard level set method. Another benefit of such model is allowing a more general initialization but not the signed distance function. The authors proposed an efficient bi-value region-based initialization. Given an arbitrary region Ω_0 in an image, the initial level sets may be simply defined as:

$$\phi_0(x,y) = \begin{cases} -c & (x,y)\ is\ inside\ \Omega_0 \\ c & Otherwise \end{cases} \quad (8)$$

where c should be a constant larger than ε in (7). The initial region Ω_0 may come from manual region of interest or computer algorithms, for example, thresholding, region growing, and so on.

IV. Interfacing by Morphological Operations

It is desired in this paper to combine the advantages of fuzzy clustering and level set method for image segmentation. On one hand, each cluster by FCM, theoretically speaking, represents a significant object in that image. On the other hand, the different initialization strategies do impose effects on the final performance of level set segmentation. Intuitively, the initial segmentation by FCM may serve as the initial guess for level set evolution.

However, it is noteworthy that, unlike the original medical image, whose pixels are color intensities, the clusters by FCM are a series of membership functions to their centroids. The process of converting them to a grayscale image will amplify noise effects, and thus will not be suitable to initiate level set evolution directly. Meanwhile, as FCM pays most attention on intensity information only, the results inevitably suffer from image noise and background inhomogeneity. In other words, the initial segmentation by FCM is discrete and diverse, which is a great challenge to the following level set evolution. In this paper, we suggested to process the initial FCM segmentations by morphological operations, which involve a few simple graphic instructions only.

In essence, a morphological operation modifies an image based on the predefined rules and templates. The state of any image pixel is determined by its template-defined neighborhood. In general, morphological operations run very fast because they merely involve simple computation. For instance, the template is often defined as a matrix with elements 0 and 1. The template shape such as disk or diamond is approximated by the elements 1. In terms of morphological operations, merely max and min are utilized to expand or shrink the regions in the image. Take image shrinkage for example. The value of each pixel is the minimum among that pixel and its neighboring pixels.

The underlying object of morphological operations here is to filter out the objects in FCM clusters due to noises but preserve the genuine image components. In our practice, it is observed that most of noises are discrete and diverse. So morphological operations should firstly shrink and remove the small objects in FCM segmentation, and then expand and recover the interested objects. In this paper, it is desired to detect and delineate liver tumors in CT scans. Although liver tumors are amorphous, they are nearly round in most cases. So a disk-like template was empirically defined in our experiments.

Three real liver CT images, all of which were deemed with tumors, were randomly selected out for tumor detection and delineation. The first two images in Fig. 1 were from the Department of Surgery, National University Hospital, Singapore. The others were adopted from the 3D Liver Tumor Segmentation Challenge 2008 [8]. It is evidenced in Fig. 1 that the results by FCM may reflect the rough locations and extents of liver tumors in an unsupervised manner. Nevertheless, with the increasing of noises and artifacts, the initial segmentation by FCM turns to misleading gradually, as shown in Fig. 1(a).

Fig. 1(b) illustrates the effects of morphological operations on liver tumor delineation. It is initialized by FCM segmentation and finalized by level set evolution. No matter by visual inspection or numerical comparison, the latter results are obviously more robust and credible.

V. Conclusions

In this paper, we presented an integrated system for computerized liver tumor segmentation. In the first part, the method of FCM was adopted for initial segmentation and liver tumor detection; the second part was based on mor

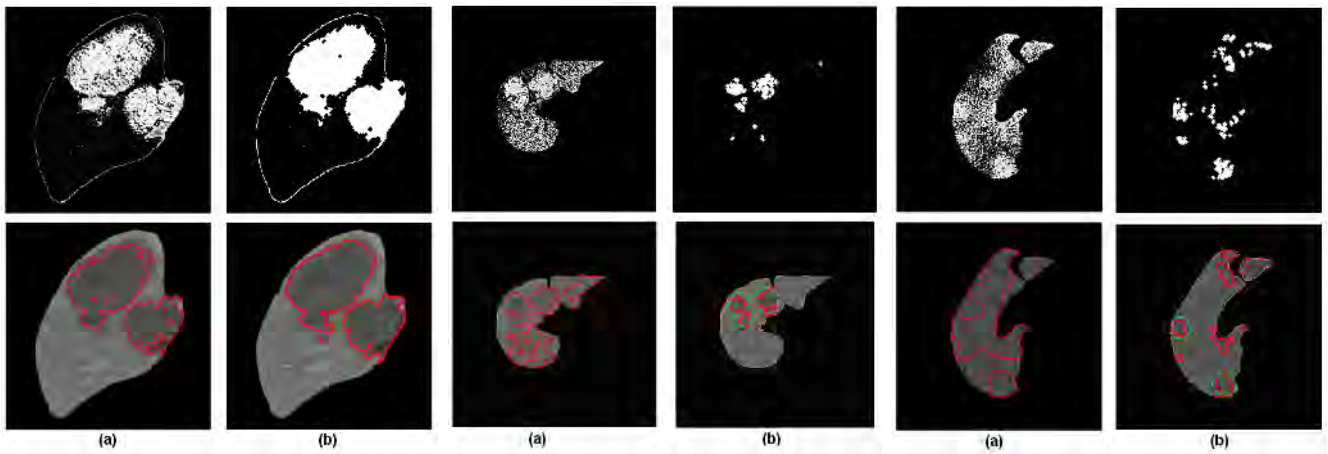


Fig. 1 Interfacing FCM and level sets by morphological operations
(Red line: computerized delineation by level set evolution; Green dash line: manual delineation from reference [14])

phological operations for segmentation refinement; the final part was a level set method for fine delineation of liver tumors. In the experiments by various methods, it was observed that the performance of thresholding and the method proposed in this paper was better than that of others. However, it is eventually difficult to find out a set of effective thresholds due to the intensity variety of liver tumors. In contrast, FCM separates different objects in an unsupervised manner. Thus it is able to detect liver tumors regardless of intensity variety.

As aforementioned, the results of liver tumor segmentation are oriented to an integrated surgical planning system for liver tumor treatment by radio-frequency (RF) ablation. Their accuracy and reliability are of vital importance: if false positive, it incurs the risk of impairing good hepatic tissues; if false negative, it will confront with the risk of leaving liver tumors without treatment. So, up to now, it is yet unlikely that a fully automated method or system is reliable enough for surgical planning system for liver tumor treatment. Instead of attending a fully automated segmentation method, our methods and systems are essentially in a semi-automated manner.

In summary, the complexity of liver tumor segmentation is far more challenging than expected. As illustrated in our experiments, neither intensities nor morphological features are robust enough for computerized segmentation and recognition. In addition, our current work merely focused on the segmentation of tumors from the liver. But how to segment the liver out from abdominal CT scans is a problem with equivalent difficulty (www.sliver07.org). In a word, there are many steps before we are able to set up a high-fidelity model for surgical planning of liver tumor ablation.

Acknowledgment

This research is supported by a grant from National University of Singapore (R-265-000-270-112 and R-265-000-270-133).

References

1. Glombitza G, Lamade W, Demiris AM et al (1999) Virtual planning of liver resections: image processing, visualization and volumetric evaluation. International Journal of Medical Informatics 53: 225-237
2. Meinzer HP, Thorn M, Cardenas CE (2002) Computerized planning of liver surgery – an overview. Computers and Graphics 26: 569-576
3. Bankman IN (2000) Handbook of Medical Imaging: Processing and Analysis. Academic Press, San Diego
4. Suri J, Liu L, Singh S et al (2002) Shape recovery algorithms using level sets in 2-D/3-D medical imagery: a state-of-the-art review. IEEE Transactions on Information Technology in Biomedicine 6(1): 8-28
5. Malladi R, Sethian JA, Vemuri B (1995) Shape modeling with front propagation: a level set approach. IEEE Transactions on Pattern Analysis and Machine Intelligence 17(2): 158-175
6. Li CM, Xu CY, Gui CF et al (2005) Level set evolution without re-initialization: a new variational formulation. IEEE CVPR 2005 Proc. vol. 1, pp. 430-436
7. Pham DL, Xu C, Prince JL (2000) Current Methods in Medical Image Segmentation. Annual Review of Biomedical Engineering 2: 315-337
8. 3D Liver Tumor Segmentation Competition 2008 at http://lts08.bigr.nl/

Author: Bing Nan LI
Institute: Graduate Programme in Bioengineering, National University of Singapore
Street: Medicine Drive 28
City: Kent Ridge 117456
Country: Singapore
Email: bingnan@nus.edu.sg

A Research-Centric Server for Medical Image Processing, Statistical Analysis and Modeling

Kuang Boon Beh[1], Bing Nan Li[2], J. Zhang[1], C.H. Yan[1], S. Chang[4], R.Q. Yu[4], S.H. Ong[1], Chee Kong Chui[3]

[1] Department of Electrical and Computer Engineering, National University of Singapore, Engineering Drive 3, Singapore
[2] Graduate Programme in Bioengineering, National University of Singapore, Medical Drive, Singapore
[3] Department of Mechanical Engineering, National University of Singapore, Engineering Drive 1, Singapore
[4] Department of Surgery, National University Hospital, Kent Ridge Wing 2, Singapore

Abstract — **Dealing with large numbers of image data is considered as a compulsory routine for medical imaging researchers. With the growing number of medical image data, the effective management and interactive processing of imaging data become essential necessity. The scenario poses a challenge to researcher community on how to construct effective data management and processing systems, in order to promote collaboration, maintain data integrity and circumvent resource redundancy. In this paper, we present a Medical Image Computing Toolbox (MICT) for Matlab® as a extension to Picture Archive and Communication System (PACS). MICT is oriented to providing interactive images processing and archiving service to medical researchers. In a nutshell, MICT is desired to be a cost effective and enriched collaboration solution for medical image sharing, processing and analysis in research communities.**

Keywords — **Medical Image Computing, Picture Archive and Communication System (PACS), Computed Tomography (CT)**

I. Introduction

With the growing number of medical image data, the effective management of imaging data becomes more and more important. This scenario poses many challenges to medical image researchers. It is in some sense an answer to the popularity of Picture Archive and Communication Systems (PACS) [1-3]. Moreover, there are more and more open-source PACS and simple extensions for image processing [4-5]. All of them evidence the essential needs of researchers to have an effective image management system. Such kind of systems should be able to provide integration, archiving, distribution and presentation of medical images.

As a matter of fact, there have been several long-standing PACS and DICOM toolboxes. Most of them are open source and freely downloadable. Some merely fulfill the basic functionality [1-2], some are powerful enough with PACS image management and DICOM image viewer [3-5], and some have their source codes of them opened for academic research [6-7]. However, all of them have limited capability for effective image processing and analysis only.

The presented medical image computing toolbox (MICT) for Matlab® in this paper originates from our earlier works, Virtual Spinal Workstation (VSW), for managing and processing over 8,000 computed tomography (CT) images. In essence, VSW is a program developed for studying spine diseases, including spine segmentation and virtualization. MICT is a progressing project aimed to not only manage large volumes of image data but also have competence to process and analyze them. Its underlying goal is to provide a cost effective, collaboration enriched, research-centric medical image management and processing toolbox for academic researchers.

The rest of this paper is organized as follows. Section II provides the overall infrastructure of MICT, design considerations and implementation details. We give an exemplified application of MICT for medical image studies in Section III. The final parts, Section IV and V, cover discussions and concluding remarks on system performance, future works and possible improvement.

II. Infrastructure and design Considerations

Currently MICT has three component modules, namely: (1) An image pre-processing module for extraction, conversion and classification of DICOM images based on their meta information. (2) Several image processing modules include image viewer, annotation tools and segmentation tools. (3) A database module is in charge of image archiving, process enquiry and data retrieval. All of them are programmed, compiled and running in Matlab®. In addition, their infrastructures have been shown in Fig. 1 with a color of deep blue. Three blocks colored in olive green belong to a PACS system. Finally, the block colored in light blue refers to the communication layer that mediates communication between MICT and the PACS system.

Chwee Teck Lim, James C.H. Goh (Eds.): ICBME 2008, Proceedings 23, pp. 206–209, 2009
www.springerlink.com

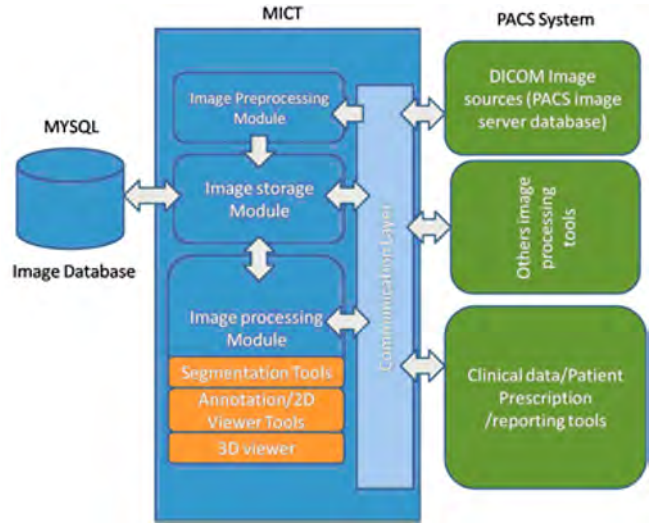


Fig.1. Overall architecture of MICT consisting of three different modules: 1) image pre-processing module; 2) image archiving module; and 3) image processing module.

A. Image Preprocessing Module

This module is in charge of carrying out image preprocessing before an image is archived into the database. It consists of classification, extraction and conversion of DICOM CT or MRI images. The component of classification is on the top of whole process. It scans DICOM meta information, which is abided together with the images, to classify and categorize CT or MRI images. Our module fully utilizes the DICOM tools available at Matlab® to acquire DICOM meta information. After that, the component of classification fetches all relevant images together, for example, from a same patient, due to a same scan. Furthermore, the preprocessing module continues to group all images with similar physician studies into a same group of each patient in sequence.

B. Image Processing Module

The image processing module includes image viewer, annotation tool, segmentation tool, and volume virtualization. It acts as an extension module or application where its application tools provide image processing functionality to academic researchers. All of them are developed with Matlab® and fully utilized the image processing and statistical toolboxes of Matlab®. To minimize user intervention, the image processing module is integrated and resided in the graphic user interface (GUI) layer of database management.

The annotation tool utilizes GUI drawing toolkit to place an annotation mask on top of an image. Conventional annotation masks have been implemented till now, for example, circle, rectangle, text and freehand drawing. In addition, the annotation may be interactively modified and saved as regions of interest (ROI) into image database. Such interactive annotation is necessary for computerized medical image segmentation, annotation and classification. Anyway, accurate annotation by hands is time-consuming and error-prone, while computerized processing is not robust and reliable yet. As a matter of fact, a common computer-aided medical image processing procedure may be described as follows: one or more researchers are required to provide the representative images as training set for computer programs. Thus they have to annotate and edit ROI carefully. During performance evaluation, the researchers may monitor the results of computer programs and modify them manually. The enhanced results may serve as the new training set to improve computer programs. Fig. 2 shows the integrative GUI including data management, image viewer, and interactive annotation tools.

Currently, MICT have been equipped with two automatic segmentation tools, that is, a tool for spinal cord segmentation and the other for active contour segmentation. The tool for spinal cord segmentation in this paper is a knowledge-based program [8]. It utilizes a few clinical knowledge and experience to allocate spine cord. For instance, the spinal cord resides inside the spinal column and above lamina, which has relatively high density compared with other tissues. After potential spinal cord location being indentified, a region growing method is applied to find spinal cord boundary.

C. Database Management Module

Database management module is in charge of data storage, processes enquiry and image retrieval in a text-based manner. In essence, this module includes two parts: 1) a relational database which controls, organizes, stores and retrieves various images and associated meta information; 2) an interface between that database and Matlab® modules. Our current design is built on MySQL® database management system. MySQL® provides open source interfaces and supports Open Database Connectivity (ODBC). In our current system, MySQL® acts as an agent to manage image data and various relevant information. The contents are reachable via standard SQL statement. At present, there are four major tables, named in accordance with their usage: patient ID; DICOM meta information; image data table; processed image data Table.

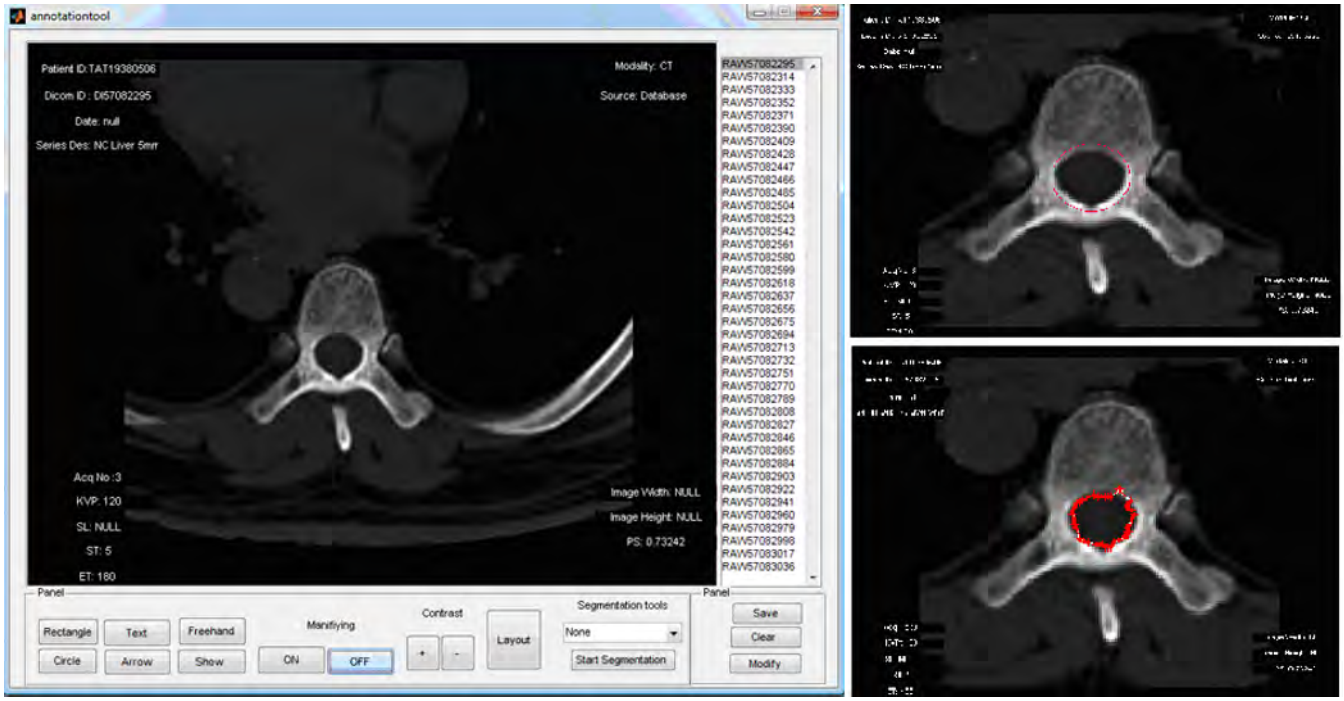


Fig.2. The integrative GUI allows image management, interactive annotation and modification.

III. Example Application: Interactive Image Processing, Analysis and Management

MICT leads itself to various academic researches and applications. The potential applications include image analysis workstation, machine learning and training workstation, image-based teaching and performance evaluation tools. To demonstrate the competence of MICT, we present our experience in this section of using it in the previously-reported VSW project. The first phase is medical imaging. In the second phase, the researchers need to annotate those collected medical images, where an interactive GUI is often of great help. The third phase is computerized analysis. In the fourth phase, the researchers check the performance of computer programs. In VSW project, we successfully dealt with a dataset of 8,000 CT images from 100 patients or so. The overall process is illustrated in Fig. 3.

All of three modules of MICT were used in that project, including CT image archiving, interactive image segmentation and text-based image management.

1) Image preprocessing module: It was used to get representative dataset. The module read DICOM meta information and classified CT images. The meta information was identified as the key reference to categorize types of spine column and segments (Fig.4).

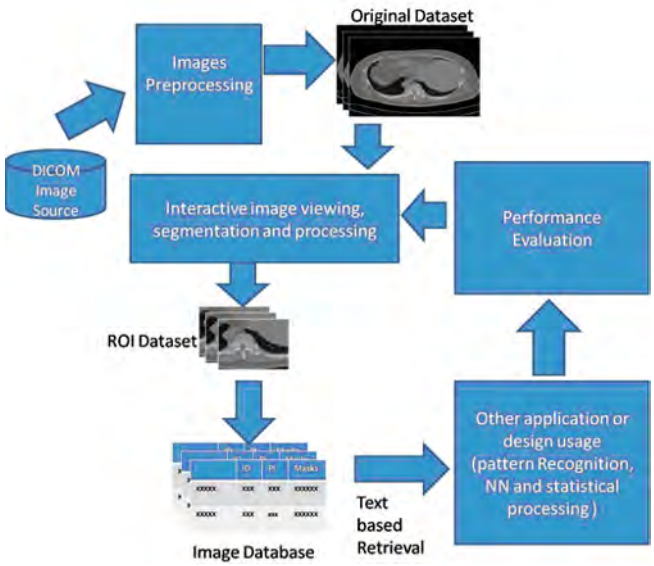


Fig.3. Overall process flow of MICT Example application that promotes interactive image processing and data management.

2) Image processing module: It was used for segmentation and performance evaluation. This module provided the interactive GUI to ease segmentation. A scalable rectan-

gle was used to manually define the ROI. The segmentation algorithms were then used to refine those ROI. During performance evaluation, the interactive annotation tool was applied to further refine those ROI. It was helpful to collect robust and reliable medical image segmentation.

3) Data management module: It was used to collaborate to manage both original and analytical results. The relational database and the text-based retrieve made image and result management particularly easy. Such kind of open infrastructure caters to the needs of academic researchers.

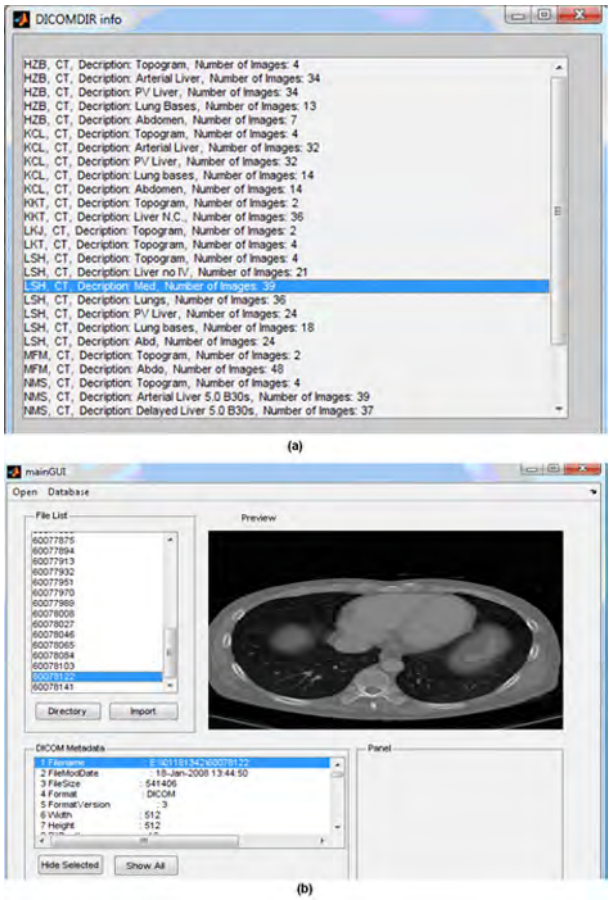


Fig.4. Image pre-processing module is designed able to read DICOM header information and conduct image classification.

IV. DISCUSSION AND CONCLUSION

In previous section, we demonstrated that how MICT provide a cost effective and enriched collaboration solution for image management, processing and analysis. In particular, MICT has been used in VSW project and successfully archived and processed over 8000 CT scans so far. MICT made it easy to process and analyze those medical images. Its interactive annotation module allowed the researchers to focus on their core studies.

MICT is written, compiled and running in Matlab®. It makes full use of the built-in toolkits such as image processing, database, statistics, GUI and other toolkit libraries. All of them guarantee the compatibility of MICT. Furthermore, it is also friendly to the third-party modules written in Matlab®.

MICT is a progressing project. There are still many points to be improved. Some of them are:

1) Cross platform deployment: The demonstrated MICT is just a prototype. It currently runs in Matlab® only. But we desire to make it a cross platform component-based toolbox, for example, supporting various PACS systems. In addition, it should be friendly to third-party components. As a consequence, we will evolve MICT to Java®.
2) Content-based image retrieval: It is desired to provide the language-like environment for image archiving and management. Currently, MICT runs in a content-based manner. It is still far away from language-like archiving and management.
3) Intelligent analysis module: The ability of performing intelligent analysis, such as statistical analysis and data mining, would be interesting to most academic researchers. A GUI for intelligent image analysis will be developed in future works.

ACKNOWLEDGMENT

This research is supported by a grant from National University of Singapore (R-265-000-270-112 and R-265-000-270-133).

REFERENCES

1. Muto K, Emoto Y, Katohji T, Nageshima H, Iwata A, and Koga S (2000) PC-based web-oriented DICOM server. Proceedings of Radiological Society of North America (RSNA), Chicago, IL.
2. Rainbow Fish Software at http://www.pacsone.net/index.htm
3. Herck M and Zjip L (2005) Conquest DICOM software website at http://www.xs4all.nl/~ingenium/dicom.html
4. Mini Web PACS at http://miniwebpacs.sourceforge.net/
5. My Free PACS at http://pacsoft.com/
6. Bui AAT, Morioka C, Dionisio JDN, Johnson DB, Sinha U, Ardekani S, Taira RK, Aberle DR, Suzie ES, and Kangarloo H (2007) Open-Source PACS: An extensible infrastructure for medical image management. IEEE Transactions on Information Technology in Biomedicine 11(1): 94-109.
7. DIOWave Visual Storage at http://diowave-vs.sourceforge.net
8. Archip N, Erard PJ, Michael EP, Haefliger JM, and Germond JF (2002) A knowledge-based approach to automatic detection of the spinal cord in CT images. IEEE Transactions on Medical Imaging 21(12): 1504-1516.

An Intelligent Implantable Wireless Shunting System for Hydrocephalus Patients

A. Alkharabsheh, L. Momani, N. Al-Zu'bi and W. Al-Nuaimy

Department of Electrical Engineering and Electronics, University of Liverpool, Liverpool, UK

Abstract — **Hydrocephalus is a neurological disorder whereby the cerebro-spinal fluid surrounding the brain is improperly drained, causing severe pain and swelling of the head. Existing treatments rely on passive implantable shunts with differential pressure valves; these have many limitations, and life-threatening complications often arise. In addition, the inability of such devices to autonomously and spontaneously adapt to the needs of the patients results in frequent hospital visits and shunt revisions.**

This paper proposes replacing the passive valve with a mechatronic valve and an intelligent microcontroller that wirelessly communicates with a hand-held device that would have a GUI and an RF interface to communicate with the patient and the implantable shunt respectively. This would deliver a personalised treatment that would aim to eventually reduce or eliminate the shunt dependence. This system would also enable a physician to monitor and modify the treatment parameters wirelessly, thus reducing, if not eliminating, the need for shunt revision operations.

To manage the shunt, four methods were investigated, simulated and compared. As a result a method was selected based on performance. This method involves an implantable pressure sensor and intelligent software, which will cooperate in monitoring and determining vital parameters that will help in determining a decision regarding the optimal valve schedule. The decision will be either modifying the schedule or contacting the external device for consultation.

Initial results are presented, demonstrating different valve regulation scenarios and the wireless interaction between the external and implanted sub-systems. Also presented are important parameters from the ICP data that would help in optimising system resources. To conclude, an intelligent shunting system is seen as the future in hydrocephalus treatment, potentially reducing significantly hospitalisation periods and shunt revisions. Furthermore, a new technique was investigated that would help to circumvent the problem of updating software using read-only memories.

Keywords — **Hydrocephalus, shunt, mechatronic valve, wireless programming.**

I. Introduction

A. Hydrocephalus

Hydrocephalus comes from the Greek word 'hydro' meaning water and 'cephalie', meaning brain. Human brains constantly produce and absorb about a pint of CSF every day. The brain keeps a delicate balance between the amounts of CSF it produces and the amount that is absorbed. Hydrocephalus is a result of disruption in this balance and this is caused by the inability of CSF to drain away into the bloodstream. The number of people who develop hydrocephalus or who are currently living with it is difficult to establish since there are no national registry or database of people with the condition. However, experts estimate that hydrocephalus affects approximately 1 in every 500 children [1].

Since the 1960s the usual treatment for hydrocephalus is to insert a shunting device in the patient's CSF system [2]. Shunting controls the pressure by draining excess CSF from the ventricle of the brain to other areas of the body, so preventing the condition from becoming worse. A shunt is simply a device which diverts the accumulated CSF around the obstructed pathways and returns it to the bloodstream. It consists of a flexible tube with a valve to control the rate of drainage and prevent back-flow.

The valves used are typically mechanical, opening when the differential pressures across the valves exceed some predetermined threshold. This passive operation causes many problems such as overdraining and underdraining. Overdraining occurs when the shunt allows CSF to drain from the ventricles more quickly than it is produced. This Overdraining can cause the ventricles to collapse, tearing blood vessels and causing headache, hemorrhage (subdural hematoma), or slit-like ventricles (slit ventricle syndrome). Underdraining occurs when CSF is not removed quickly enough and the symptoms of hydrocephalus recur. These problems may have dramatic effects on the patients such as brain damage.

Also, current shunts cannot handle real-time patient discomfort and emergency situations, thus satisfying less than 50% of patients [3]. In addition, some complications can lead to other problems, the most common being shunt blockage, as a result the patient's life and cognitive faculties are placed at risk. There hasn't been a significant improvement in the level of blockages in recent years. The rate of shunt blockages is highest in the first year after insertion, when it can be in the order of 20-30% - decreasing to approximately 5% per year [4]. Currently, shunt blockage cannot be detected without invasively revising the shunt. Whilst symptoms and additional investigations such as CT scan, plain X-rays and a shunt tap may be decisive, a definitive diagnosis is sometimes only possible through surgery

Chwee Teck Lim, James C.H. Goh (Eds.): ICBME 2008, Proceedings 23, pp. 210–214, 2009
www.springerlink.com

[5]. Furthermore, shunts are subject to other problems that sometimes require them to be revised, such as cracked and disconnected catheters. The longer the shunt system is in place, the more prone it is to some form of structural degradation [6].

All these problems and more urged the need for a shunt that responds to the dynamic needs of the patients and at the same time that can achieve a gradual weaning of the patient off the shunt, wherever possible. A further need is for the shunt to be able to carry out a self-diagnostic test, monitoring of all implantable components, detecting shunt malfunctions such as shunt blockage and disconnected catheters in an autonomous way. In order to develop such a shunt, a mechatronic valve which is electrically controlled by software, and that communicates wirelessly with the physician, is needed

B. Proposed Intelligent Shunting

In this paper we present an intelligent implantable wireless shunting system for hydrocephalus patients with features that help in reducing or eliminating the problems with current shunts. This shunting system would consist of hard and soft components. The overall system is shown in Figure 1. The implanted hardware components would mainly consist of a microcontroller, electronic valve [7], ICP sensor and transceiver. This implantable shunting system would wirelessly communicate with a hand-held Windows Mobile-based device operated by the patient, or on the patient's behalf by a clinician or guardian. This device would have a graphical user interface and an RF interface to communicate

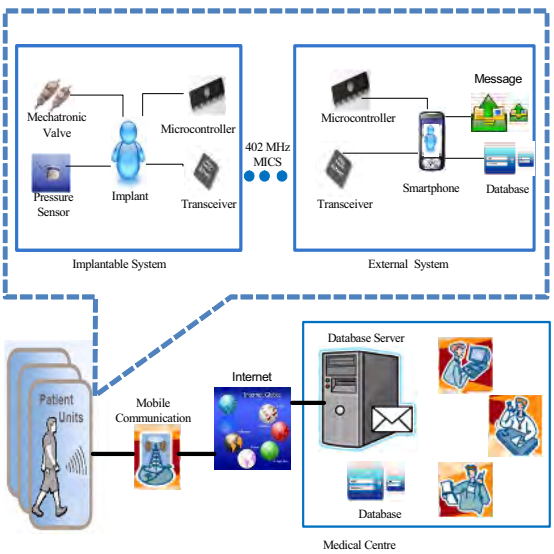


Fig. 1: Overall shunting system.

with the user and the implantable wireless e-shunt respectively.

The main tasks of the implantable embedded software are summarised below. One of the tasks would involve receiving ICP data from the sensor, analysing it and regulating the valve accordingly.

Another task would be wirelessly receiving modifications from the physician through the external patient device. Such modification might be ICP management parameters such as pressure threshold, valve schedule, etc. On the other hand, the implantable shunting system would send a report either on regular basis or upon request to the physician through the external device. Such reports would consist of information that is useful in understanding this particular patient case , thus might help in achieving shunt weaning on the long run, and in understanding of hydrocephalus which help other hydrocephalus patients. The implantable embedded code would handle self testing of the implanted shunt components such as the valve, ICP sensor, microcontroller and transceiver. This task is would be mainly detecting any shunt malfunctions such as valve blockage or disconnected catheters, that would use to verify the shunt is not blockage and fully functional. One of the important tasks that make this proposed system unique is dealing with the emergency case. In an emergency situation, the implantable shunting system would receive requests either from patient or physician through the external patient device to open/close valve or collect ICP readings instantaneously. As the result of monitoring the shunt components, the implantable system might request help when facing problem in meaning valve open, whereas ICP still high which is mean ICP not responding to the opening and closing of the valve due to valve malfunction.

II. Materials and Method

Two sources for ICP data were used to test the design of shunting software. One is a real data collected at 125Hz sampling rate [8]. The other source is a model of the simulated ICP data for hydrocephalus patients. To reach the optimal design of the implanted embedded software, four scenarios of designing the implantable code have been investigated and simulated.

A. Fixed-Time Schedule Scenario

In this scenario, the implanted shunt system would consist of a mechatronic valve, a microcontroller and an RF transceiver. The valve would permit fluid flow only based on a fixed time schedule i.e. would open at specific times for certain periods irrespective of ICP. The implanted valve

manager would be changed remotely by a physician, who determines at what time during the day or night the shunt is opened or closed.

The problem of such scenario is a mismatch between what is required and what is delivered. This mismatch would cause serious drawbacks e.g. overflow, underflow. In addition, it cannot handle real-time patient satisfaction and emergency situations e.g. headache, sneezing because the dynamic nature of ICP for the same patient. This scenario has been simulated and tested using real ICP data. Figure 2 illustrates the problems of using such approach i.e. overdraining and underdraining.

B. Fixe-Time Schedule Scenario with Pressure Sensor

This scenario differs from the previous one is utilising implanted pressure sensor. The sensor would be used to collect ICP data, and then these readings would be sent wirelessly via the RF transceiver to the external patient device. This data would help the physician modify the fixed time schedule in order to be more suitable for the patient. The new fixed schedule is uploaded remotely to the implanted shunting system.

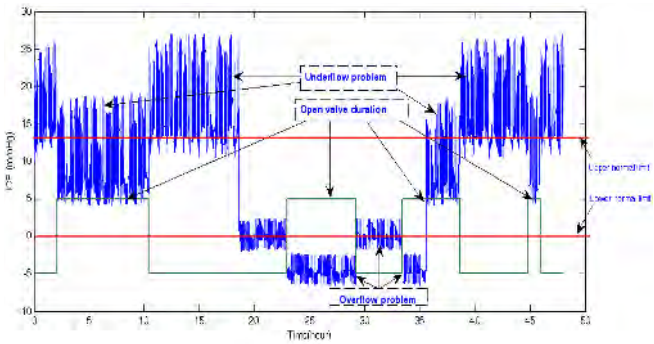


Fig. 2: Fixed schedule problems.

C. Closed Loop Scenario

A close loop shunt would consist of a mechatronic valve, microcontroller and pressure sensor. In this scenario the valve would be instantaneously managed (opened or closed) according to the measured ICP. Where the collected ICP would be analysed by the implantable software on the microcontroller to decide whether it is an appropriate time to open or close the valve. Many but not all problems can be solved by using such scenario e.g. overflow, underflow. Figure 3 illustrates the resulted ICP waveform for closed loop shunting system. Thus the collected ICP would be utilised only within implanted shunting system. Such data would not reach the physician since there is no mean for sending it outside the patient's body.

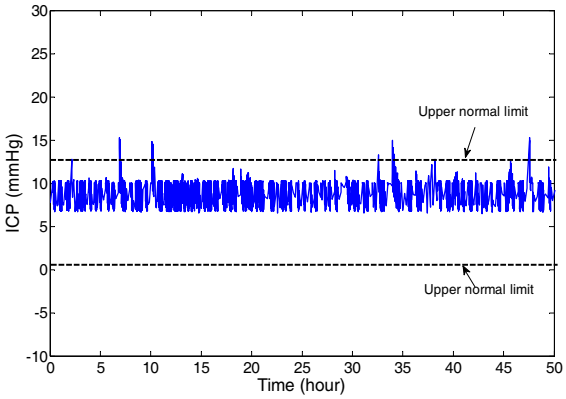


Fig. 3: The resulted ICP waveform for closed loop shunting.

D. Dynamic Shunting System Scenario

In this scenario, the implanted shunt system includes the mechatronic valve, microcontroller, RF transceiver, ICP sensor and smart software. As a result of investigated the previous scenarios, their drawbacks would be eliminated if the shunting system perform the following tasks.

1. ICP analysis: the ICP readings would be analysed to figure out some important parameters such as ICP waveform components. These parameters would be useful in autonomously modifying the valve schedule internally.
2. Self testing: this task involves testing all implanted shunt components for example, ICP readings collected when valve is open would be analysed and parameters are calculated to help in detecting shunt malfunction such as shunt blockage or disconnected catheter. Also this task would work on checking the capacity of the implanted battery and the functioning of ICP sensor.
3. Emergency call: this task is responsible for all emergency cases that might be happen during shunt operation. For example, it would send a signal to inform the external device when shunt malfunctions is detected. On the other hand, it will handle any emergency signals received from the physician through the external device to open/close the valve or to request ICP readings.
4. Updating task: the implantable ICP sensor and the smart software would cooperate in monitoring and determining vital parameters that would help in modifying and optimising the valve schedule.
5. Report generating: this task involves generating ICP information report consisting of ICP waveform components, valve status, real ICP readings and their corre-

sponding time, mean ICP and self shunt testing result. This report would be stored in implanted memory and a copy of this report would be sent remotely to the physician through the external device regularly or upon request. Thus, such report would be useful tool for the physician to decide any modification on the valve schedule. Also, it would be helpful in understanding hydrocephalus in general.

6. ICP compression: a peak detection algorithm has been designed and tested to overcome the problem of the implantable memory size limitation. By this algorithm, only the peaks (upper, lower) of the ICP waveform would store. Where it was noticed that the output waveform of such algorithm give a good estimation of the original waveform.
7. Wireless updating: an algorithm was designed and tested to enable the physician through the external device wirelessly modifying different implanted parameters such as valve schedule, ICP threshold value. Such algorithm rarely mention in literatures especially for implanted microcontroller. A self learning packet technique has been used in this algorithm to access the implanted memory address of each parameter needed to modify. This packet made up of packet length, patient identification, packet identification and the modified parameters value with their addresses, shown in Figure 4(b).
8. The power consumption algorithm has been designed and tested to minimise power consumption needed for the implanted shunt. A sleeping mode for the implantable microcontroller and RF transceiver is used to reduce the power needed for these components more than 90%. A wake up signal from physician through external device would be used to wake up these components when it is needed.

Most of these tasks are built using assembly and C language. MSP430 development kits shown in Figure 4(a) used to test these tasks. A packet format shown in Figure 4(b) manipulated between two kits through transceivers.

III. Result and discussion

The results of simulating a fixed-time schedule are presented in Figure 2. It can be noticed that mismatch between what is required and what is delivered by such shunt. The simulation results of closed loop shunting system shown in Figure 3 illustrates the efficacy of the closed loop shunt in keeping the ICP within the normal range. On the other hand, other current shunt problems such as difficulty of shunt malfunction detection, is not solved in closed loop shunt.

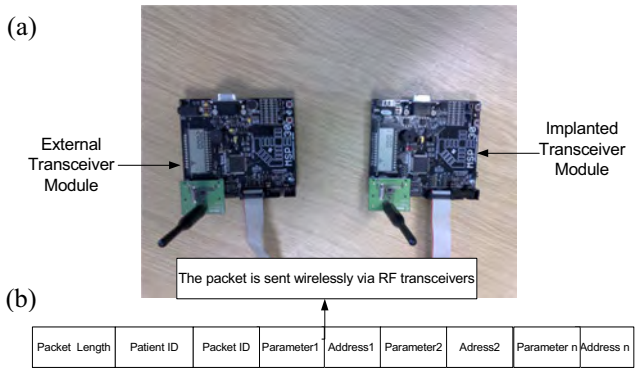


Fig. 4: Hardware and software tools for software testing. (a) MSP430 microcontrollers with RF transceivers, (b) packet format.

These problems could be solved by using a dynamic shunting system having a degree of "intelligence". One of the most difficult challenges of using an implantable microcontroller in medical applications is how to access, modify and replace the implanted program. An updating algorithm is used to remotely modify some parameters which are embedded into the microcontroller via RF transceivers. A peak detection algorithm of ICP waveform is utilised by which the size of ICP data is reduced by 93%, thus overcoming the implantable memory size limitation.

IV. Conclusion

An innovative, intelligent implantable wireless shunting system was introduced in this paper for the treatment of hydrocephalus. We attempted to replace the passive mechanical shunt with a dynamic shunt that maximizes the potential quality of life for each patient, reduces hospitalisation periods and shunt revisions. Furthermore, a new technique was investigated that would help to circumvent the problem of updating software remotely through RF transceiver.

Acknowledgement

The authors' thanks to Connor Mallucci and Mohammed Al-Jumaily for their fruitful inputs.

References

1. Hydrocephalus at http://www.medicinnet.com
2. Aschoff A, Kremer B, Hashemi B (1999) The scientific history of hydrocephalus and its treatment Neurosurg Rev 22:67–93

3. Momani L, Alkharabsheh A, Al-Nuaimy W (2008) Design of an intelligent and personalised shunting system for hydrocephalus, IEEE EMBC Personalized Healthcare through Technology, Vancouver, Canada.
4. Association for spina bifida hydrocephalus at http://www.yourvoice-youth.com
5. Watkins L, Hayward R, Andar U, Harkness W (1994) The diagnosis of blocked cerebrospinal fluid shunts: a prospective study of referral to a paediatric neurosurgical unit, Child's Nerv Syst 10:87-90
6. Shunt malfunctions and problems at http://www.noahslifewithhydroce- phalus.com
7. Miethke C (2006) A programmable electronical switch for the treatment of hydrocephalus. In XX Biennial Congress of the European Society for Paediatric Neurosurgery, Martinique, France
8. Biomedical signal processing laboratory/ Portland State University at http://bsp.pdx.edu

Author: Abdel Rahman Alkharabsheh
Institute: Department of Electrical Engineering and Electronics, University of Liverpool.
Street: Brownlow Hill
City: Liverpool L693GJ
Country: UK
Email: a.kharabsheh@liv.ac.uk

Intelligent Diagnosis of Liver Diseases from Ultrasonic Liver Images: Neural Network Approach

P.T. Karule[1], S.V. Dudul[2]

[1]Department of Electronics and Communication Engineering, YCCE, Nagpur, INDIA
[2]Department of P.G.Studies in Applied Electronics, SGB Amravati University, INDIA

Abstract — **The main objective of this study is to develop an optimal neural network based DSS, which is aimed at precise and reliable diagnosis of chronic active hepatitis (CAH) and cirrhosis (CRH). Multilayer perceptron (MLP) neural network is designed scrupulously for classification of these diseases. The neural network is trained by eight quantified texture features, which were extracted from five different region of interests (ROIs) uniformly distributed in each B-mode ultrasonic image of normal liver (NL), CAH and CRH. The proposed MLP NN classifier is the most efficient learning machine that is able to classify all three cases of diffused liver with average classification accuracy of 96.55%; 6 cases of cirrhosis out of 7 (6/7), all 7 cases of chronic active hepatitis (7/7) and all 15 cases of normal liver (15/15). The advantage of proposed MLP NN based Decision Support System (DSS) is its hardware compactness and computational simplicity.**

Keywords — **Chronic Active Hepatitis, Cirrhosis, Liver diseases, Decision Support System, Multi Layer Perceptron, Ultrasound imaging**

I. Introduction

Medical diagnosis is quite difficult and complex visual task, which is mostly done reliably only by expert doctors. An important application of artificial neural network is medical diagnosis. Chronic infection with hepatitis virus (HV) has been a major health problem and is associated with over 10,000 deaths a year in the United States [1]. In the early stages, HV tends to be asymptomatic and can be detected only through screening. Ultrasonography is a widely used medical imaging technique. It is the safest method used for imaging of human organs or their functions. The attenuation of sound wave or difference in acoustic impedance in the organ yield complicated texture on the ultrasound B-mode images. For the diagnosis of diffuse liver diseases ultrasonography is commonly used, but visual criteria provide low diagnostic accuracy, and it depends on the ability radiologist. To solve the problem, tissue characterization with ultrasound has become important topic of research. For quantitative image analysis many feature parameters have been proposed and used in developing automatic diagnosis system [2]-[4]. The several quantitative features are used in diagnosis by ultrasonography. K. Ogawa [5, 7] developed a classification method which used an artificial neural network to diagnose diffuse liver diseases. Another work [6]-[13] presents the classifier for diagnosis of normal liver (NL), chronic active hepatitis (CAH) and cirrhosis (CRH) more accurately.

Quantitative tissue characterization technique (QTCT) is gaining more acceptance and appreciation from the ultrasound diagnosis community. It has the potential to significantly assist radiologists to use this system for second opinion . The grey scale ultrasound images provide significant contribution to the diagnosis of liver diseases, however at the resolution it is difficult to diagnose active hepatitis and cirrhosis from normal liver [10, 11]. A pattern recognition system can be considered in two stages, the first stage is feature extraction and the second is classification [12].

This paper presents new optimal designed MLPNN based decision support system for diagnosis of diffused liver diseases from the ultrasound images.

II. Material and methods

A. Data acquisition

Ultrasound images used in our research were obtained on Sony (US) model ALOKA-SSD-4000 ultrasonic machine with a 2-5 MHz multi frequency convex abdominal transducer. All images were of 640 × 480 pixels with 8-bit depth. Ultrasound images for different liver cases taken from patients with known histology and accurately diagnosed by expert radiologist from Midas Institute of Gastroenterology, Nagpur, INDIA. Three set of images have been taken: normal liver, chronic active hepatitis and cirrhosis with 22, 10 and 10 images respectively.

System outline: Fig. 1 shows the overall sketch of the proposed system; our approach is divided in three parts. First step is selection of region of interest (ROI). Second step is texture feature extraction from ROI and create a database. Third step is use neural network for classification of these images in one of the categories i.e. normal liver, chronic active hepatitis and cirrhosis

Chwee Teck Lim, James C.H. Goh (Eds.): ICBME 2008, Proceedings 23, pp. 215–218, 2009
www.springerlink.com

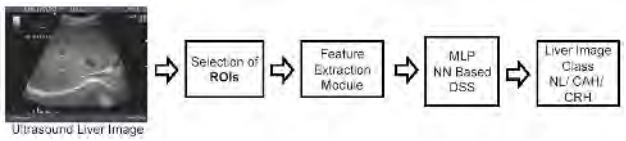


Fig. 1 Overall scheme for classification of liver image

Defining the region of interest (ROI): Selection of ROI is one of the first and the most important step in the process. In order to accurately identify and quantify regions, they should be as free as possible from the effect of the imaging system. For example their depth and location in the beam should be such that the effects of the side lobes and the beam diffraction, acoustic shadowing be a minimum. The important thing in selecting ROI position is not to include major vascular structures in the ROI. In the system we freely choose any of five regions of interest (ROIs) from the given liver image. The four ROIs were located to overlap half of each ROI with the"Center ROI". Fig. 2 shows the location of five ROIs. Each ROI is 32 x 32 pixels about 1 x 1 cm^2 in size.

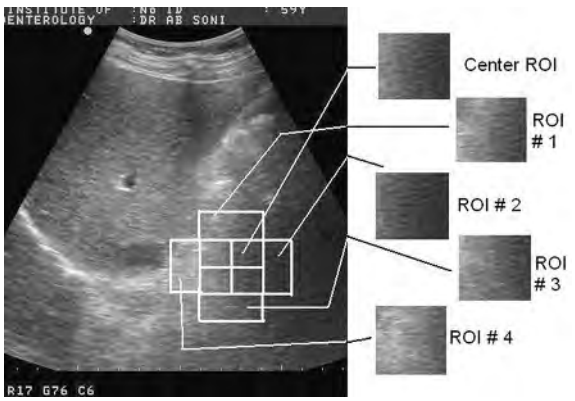


Fig. 2 Location of five ROIs of 32 x 32 pixels

Texture analysis of liver: Texture contains important information, which is used by human for the interpretation and the analysis of many types of images. Texture refers to the spatial interrelationship and arrangements of the basic elements of an image. The Grey Level Difference Method (GLDM) is very powerful for statistical texture description in medical imaging.

The texture features are extracted within the 32 x 32 pixels ROIs selected in the liver region by the method introduced by Haralick et al. [9]. The following parameters were calculated from the ROI: variance (V), coefficient of variation (CV), annular Fourier power spectrum (AFP) and longitudinal Fourier power spectrum (LFP). These parameters have been used in the diagnostic system [7] for chronic hepatitis with an artificial neural network. K. Ogawa et al.[5] also added three more parameters for the diagnosis of CAH and Cirrhosis: variation of the mean (VM) and the parameters ASM and CON derived from a co-occurrence matrix. VM was calculated from five ROIs, that is, the "center ROI" and the other four ROIs generated by this system around the "center ROI". The parameters ASM and CON were calculated from only the "center ROI".

The following are definitions of the parameters, where N (=32) is the size of the ROIs and *f(i,j)* is the density of a pixel in an ROI and $\hat{f}(I,J)$ is the Fourier power spectrum of *f(i,j).*We have selected one more parameter entropy (ent), calculated from the gray level co-occurrence matrix.

1) Variance (V):

$$V = \frac{1}{N^2}\sum_{i=1}^{N}\sum_{i=1}^{N}(f(i,j)-m)^2, \tag{1}$$

Where

$$m = \frac{1}{N^2}\sum_{i=1}^{N}\sum_{i=1}^{N}f(i,j), \tag{2}$$

2) Coefficient of variation:

$$CV = \frac{\sqrt{V}}{m} \tag{3}$$

3) Annular Fourier Power Spectrum (AFP):

$$AFP = \sum_{R=2}^{4}\left(\sum_{R^2\le I^2+J^2<(R+1)^2}\left(\frac{\hat{f}(I,J)}{R}\right)\right), \tag{4}$$

Where $R = \sqrt{I^2+J^2}$

4) Longitudinal Fourier Power Spectrum (LFP):

$$LPF = \sum_{J=3}^{5}\sum_{I=1}^{N}\hat{f}(I,J) \tag{5}$$

5) Variation of mean (VM)

$$VM = \frac{1}{5}\sum_{k=1}^{5}(m_k - m_0)^2, \tag{6}$$

Where m_k is the mean value of k-th AOI and

$$m_0 = \frac{1}{5}\sum_{j=1}^{5}m_j \tag{7}$$

6) Angular Second Moment (ASM):

These parameters are extracted form gray level co-occurrence matrix (GLCM) obtained from selected ROI. This was on the estimation of the second order joint conditional probability of one gray level a to another gray level b with inter-sample distance d and the given direction by angle θ. Gray level co-occurrence matrix (GLCM) is a repeated spatial pattern. This is obtained by computation of a number of co-occurrence matrices, which essentially measure the number of times a pair of pixels at some defined separation have a given pair of intensities. The normal

GLCM is given as C (a, b; d, θ). For calculating ASM from GLCM C (a, b; 1, 0º) we have:

$$C(a,b;1,0^0)=\frac{1}{T(1,0^0)}cardinaly\begin{Bmatrix}[(k,l),(m,n)]\\ \in AOI:|k-m|=1,\\ l=n,\\ f(k,i)=a,\\ f(m,n)=b\end{Bmatrix} \quad (8)$$

$$ASM=\sum_{a=0}^{M-1}\sum_{b=0}^{M-1}C(a,b;1,0^0)^2 \quad (9)$$

7) Contrast (con):

$$con=\sum_{a=0}^{M-1}\sum_{b=0}^{M-1}(a-b)^2C(a,b;1,90^0) \quad (10)$$

8) Entropy (ent):

$$ent=-\sum_{a,b\in G}c(a,b)*\log[c(a,b)] \quad (11)$$

The eight features mentioned above are extracted from five ROIs of each image. The descriptive statistics of eight extracted features are shown in Table 1. These texture features are used by neural network as input parameters for classification.

Table 1 Descriptive statistics of features of ultrasonic images

Sr. No.	Features	Minimum	Maximum	Mean	Std. deviation
1	V	0.002	0.030	0.006	0.005
2	CV	0.110	1.265	0.271	0.240
3	VM	0.003	0.329	0.083	0.071
4	LFP	0.000	0.239	0.037	0.047
5	AFP	0.000	0.151	0.039	0.037
6	ASM	0.167	6.382	1.613	2.313
7	con	0.098	0.559	0.252	0.098
8	ent	0.148	6.969	1.958	2.386

B. Design of MLP NN classifier

Artificial neural network (ANN), which has been successfully applied in many fields on medical imaging [29, 32], is easy for less experienced doctors to make a correct diagnosis by generalizing new inspections from past experience. We construct a fully connected neural network as shown in Fig. 3, which is a conventional three-layer feed-forward neural network with 8 input units, 3 hidden units and 3 output units. The network is trained by using the well known backpropagation (BP) algorithm [31]. After establishing the relationship function between the inputs and outputs, we can apply the ANN to the doctors' practical routine inspection to test the generation ability of ANN.

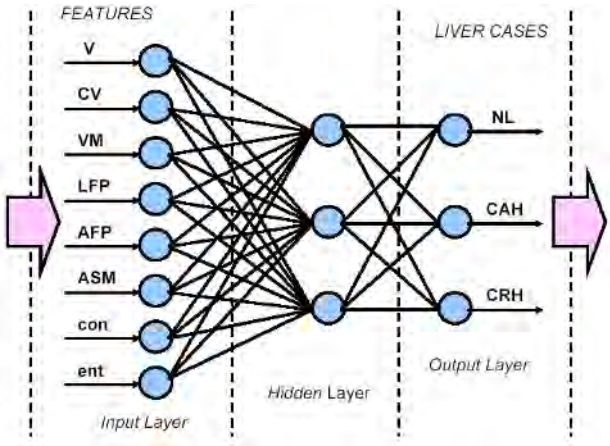


Fig. 3 MLP NN model for Classification

Table 2 Optimal Parameters of MLP NN DSS

S.N.	Parameter	Hidden Layer#1	Output Layer
1	Processing Elements	3	3
2	Transfer Function	Linear Tanh	Linear Tanh
3	Learning rule	DeltaBarDelta	DeltaBarDelta

Table 2 indicates optimal parameters used for MLP NN based DSS.

Performance measure: The learning and generalization ability of the estimated neural network based decision support system is assessed on the basis of certain performance measures such as MSE and confusion matrix [31]. Nevertheless, for DSS the confusion matrix is the most crucial parameter.

MSE (Mean Square Error): The MSE is defined by Eq. (12) as follows:

$$MSE=\frac{\sum_{j=0}^{P}\sum_{i=0}^{N}\left(d_{ij}-y_{ij}\right)^2}{N.P} \quad (12)$$

where P = number of output neurons, N = number of exemplars in the dataset, y_{ij} = network output for exemplar i at neuron j, d_{ij} = desired output for exemplar i at neuron j.

C. Data partitioning

These 42 sets of 8 features each are then used as inputs to the neural networks for the classification of liver disease. Different spit-ratios are used for training-testing exemplars. The percentage of exemplars used for training the NN was varied from 10% to 90% with corresponding 90% to 10% variation in exemplars used for testing. It is observed that with only first 30 % samples (1:13) used for training and the next 70 % samples (14:42) for testing, the classifier is seen to deliver optimal performance with respect to the MSE and classification accu-

racy. This also confirms the remarkable learning ability of the MLP NN as a classifier comprising of the lone hidden layer. The following Table 3 highlights the data partition schemes employed in order to design a classifier.

Table 3 No. of exemplars in training and testing data set

Sr. No.	Data Sets	No. Of Exemplars	Cirrhosis	Chronic Active	Normal
1	Training Set (30%)	13 (1:13)	3	3	7
2	Testing Set (70%)	29 (14:42)	7	7	15

The confusion matrix MLP NN based classifier for the testing data set with 70% samples is shown in Table 4. The average classification accuracy achieved is 96.55%.

Table 4 Confusion matrix for MLP NN based DSS

Output / Desired	Cirrhosis	Chronic Active	Normal
Cirrhosis	6	0	0
Chronic Active	1	7	0
Normal	0	0	15
Classification accuracy	85.71%	100%	100%

Table 5 displays the important performance measures of MLP NN classifier MSE and Classification accuracy.

Table 5 Performance measures of MLP NN based DSS

Performance Parameter	Cirrhosis	Chronic Active	Normal
MSE	0.03450	0.04942	0.01580
Classification accuracy	85.71%	100%	100%

III. Conclusions

After rigorous and careful experimentation optimal model of MLP was selected. MLP NN with 8 input PEs, one hidden layer with 3 PEs, and an output layer with 3 output PEs. The results on testing data set show that MLP NN classifier is able to classify the three cases of diffused liver diseases with average accuracy of 96.55%. In testing phase, 85.71% (6/7) cirrhosis, 100% (7/7) chronic active hepatitis and 100% (15/15) cases of normal liver were classified correctly.

The results also indicate that proposed MLP NN based classifier can provide a valuable ‘‘second opinion’’ tool for the radiologists in the diagnosis of liver diseases from ultrasound images, thus improving the diagnosis accuracy, and reducing the needed validation time.

Acknowledgment

The author would like to thank the doctors of Midas Institute of Gastroenterology, Nagpur, INDIA, for providing the ultrasound images of diffused liver of patients admitted at their hospital for our study.

References

1. Pratt Daniel and Kalpan Marshall, Evaluation of abnormal liver enzyme results in asymptomatic patients, New England Journal of Medicine, Vol. 347 (17), April 2000, 1266-1271
2. Abou zaid Sayed Abou zaid and Mohamed Waleed Fakhr, Automatic Diagnosis of Liver Diseases from Ultrasound Images, IEEE *Transactions on Medical Imaging (2006) 313-319.*
3. Y-N Sun and M-H Horng, Ultrasonic image analysis for Liver Diagnosis, *Proceeding of IEEE Engineering in Medicine and Biology (Nov 1996) 93-101*
4. A. Takaishi, K. Ogawa, and N. &a, “Pattern recognition of diffuse liver diseases by neural networks in ultrasonography,” in Proc. of the IEICE (The Institute of Electronics, Information and Communication Engineers) Spring conference 1992 (March), p.6-202.
5. K. Ogawa and M. Fukushima, Computer-aided Diagnostic System for Diffuse Liver Diseases with Ultrasonography by Neural Networks, IEEE *Transactions on Nuclear Science (vol.45-6, 1998) 3069-3074.*
6. Y.M. Kadah, Statistical and neural classifiers for ultrasound tissue characterization, in Proc. A NNIE-93, Artificial Neural Networks in Engineering, Roolla, MO, 1993.
7. K. Ogawa, N. Hisa, and A. Takaishi, “A study for quantitative evaluation of hepatic parenchymal diseases using neural networks in B-mode ultrasonography,” Med Imag Technol, vol.11, pp.72-79, 1993.
8. M. Fukushima and K. Ogawa, Quantitative Tissue Characterization of Diffuse Liver Diseases from Ultrasound Images by Neural Network, IEEE *Transactions on Medical Imaging, (vo1. 5, 1998) 1233-1236.*
9. R.M.Haralick, K. Shanmugam, J.Din, Texture features for image classification, IEEE *Transactions on System, Man and Cybernetics (Vol. SMC-3, 1973) 610-621.*
10. Elif Derya Übeylı and İnan Güler, Feature extraction from Doppler ultrasound signals for automated diagnostic systems, *Computers in Biology and Medicine* (*Volume 35, Issue 9*, *November 2005) 735-764.*
11. Stavroula G. Mougiakakou and Ioannis K. Valavanis, Differential diagnosis of CT focal liver lesions using texture features, feature selection and ensemble driven classifiers, Artificial Intelligence in Medicine (Volume 41, Issue 1, September 2007) 25-37.
12. Elif Derya Übeylı and İnan Güler, Improving medical diagnostic accuracy of ultrasound Doppler signals by combining neural network models, Computers in Biology and Medicine (Volume 35, 2005) 533-554
13. Y.M. Kadah, A.A. Farag, M. Zurada, A. M. Badawi, and A.M. Youssef, Classification algorithms for quantitative tissue characterization of diffuse liver diseases from ultrasound images, IEEE Transactions on Medical Imaging (col. 15, no. 4, 1996) 466-477.

Author: Pradeep T. Karule
Institute: Yeshwantrao Chavan College of Engineering
Street: Wanadondri, Hingna Road
City: Nagpur – 441 110
Country: INDIA
Email: ptkarule@rediffmail.com

A Developed Zeeman Model for HRV Signal Generation in Different Stages of Sleep

Saeedeh Lotfi Mohammad Abad[1], Nader Jafarnia Dabanloo[2], Seyed Behnamedin Jameie[3], Khosro Sadeghniiat[4]

[1, 2] Department of Biomedical Engineering Science & Research Branch, Islamic Azad University, Tehran, Iran
Email:s_lt80@yahoo.com, n_jafarnia@yahoo.com
[3] Neuroscience Lab, CMRC/IUMS, Tehran, Iran
Email:behjam@yahoo.com
[4]Tehran University of Medical Sciences, Tehran, Iran
Email: khosro sadeghniiat @ tums.ac.ir

Abstract — **Heart Rate Variability (HRV) is a sophisticated measure of an important and fundamental aspect of an individual's physiology. Heart rate variability (HRV) measurement is an important tool in cardiac diagnosis that can provide clinicians and researchers with a 24-hour noninvasive measure of autonomic nervous system activity. Heart Rate Variability is analyzed in two ways, either over time (Time Domain) or in terms of the frequency of changes in heart rate (Frequency Domain). Preliminarily studying on the different effects of sleep on HRV signal can be useful for finding out the function of autonomic nervous system (ANS) on heart rate. In this paper, we consider a HRV signal for one normal person in different sleep stages: stage1, stage2, stage3 and REM. Therefore, we use FFT on HRV signal and show differences in various stages. In addition, we evaluate these differences in quantitative and qualitative. This model can be used as a basic one for developing models to generate artificial HRV signal.**

Keywords — **autonomic nervous system, HRV, sleep, stage, signals.**

I. INTRODUCTIONT

The electrocardiogram (ECG) signal is one of the most obvious effects of the human heart operation. The oscillation between systole and diastole states of the heart is reflected in the heart rate (HR). The surface ECG is the recorded potential difference between two electrodes placed on the surface of the skin at pre-defined points. The largest amplitude of a single cycle of the normal ECG is referred to as the R-wave manifesting the depolarization process of the ventricle. The time between successive R-waves is referred to as an RR-interval, and an RR tachogram is then a series of RR-intervals. The development of a dynamical model for the generation of ECG signals with appropriate HRV spectra is a subject that has been widely investigated. Such a model will provide a useful tool to analyse the effects of various physiological conditions on the profiles of the ECG. The model-generated ECG signals with various characteristics can also be used as signal sources for the assessment of diagnostic ECG signal processing devices. Now, in co strutting a comprehensive model for generating ECG signals there are two steps. Step one is producing the artificial RR-tachogram with HRV spectrum similar to experimental data—the RR-tachogram shows where the R-waves of the ECG are actually placed. And step two is constructing the actual shape of the ECG. Using Gaussian functions method for generating ECG model can be also considered too [8].

Here, we develop a new model based on modifying the original Zeeman model to produce the RR-tachogram signal, which now incorporates the effects of sympathetic and parasympathetic activities to generate the appropriate significant peaks in the power spectrum of the HRV. By using a neural network approach based upon a modified McSharry model, the actual shape of the ECG in a single cycle can be successfully re-produced by using our model generated power spectrum of RR time intervals.

II. ECG AND HRV MORPHOLOGY

In any heart operation there are a number of important events. The successive atrial depolarization/repolarization and ventricular depolarization/repolarization occurs with every heartbeat. These are associated with the peaks and valleys of the ECG signal, which are traditionally labeled P, Q, R, S, and T (see Fig. 1). The P-wave is caused by depolarization of the atrium prior to atrial contraction. The QRS-complex is caused by ventricular depolarization prior to ventricular contraction. The largest amplitude signal (i.e. R-wave) is located here. The T-wave is caused by ventricular repolarization which lets the heart be prepared for the next cycle. Atrial repolarization occurs within ventricular depolarization, but its waveform is masked by the large amplitude QRS-complex. The HR, which is the inverse of the RR-interval, directly affects the blood

Chwee Teck Lim, James C.H. Goh (Eds.): ICBME 2008, Proceedings 23, pp. 219–222, 2009
www.springerlink.com

pressure. The autonomic nerve system (ANS) is responsible for short-term regulation of the blood pressure. The ANS is a part of the central nervous system (CNS). The ANS uses two subsystems—the sympathetic and parasympathetic systems. The HR may be increased by sympathetic activity or decreased by parasympathetic (vagal) activity. The balance between the effects of the sympathetic and parasympathetic systems is referred to as the sympathovagal balance and is believed to be reflected in the beat-to beat changes of the cardiac cycle (McSharry et al., 2002). Spectral analysis of HRV is a useful method to investigate the effects of sympathetic and parasympathetic activities on heart rate (HR). The afferent nerves provide the feedback information to the CNS. The sympathetic system is active during stressful conditions, which can increase the HR up to 180 beats per minute (bpm). When sympathetic activity increases after a latent period of up to 5 s, a linearly dependent increment in HR begins and reaches its steady state after about 30 s. This affects the low frequency (LF) component (0.04–0.15 Hz) in the power spectrum of the HRV, and slightly alters the high frequency (HF) component (0.15–0.4 Hz). The parasympathetic activity can decrease the HR down to 60bpm.

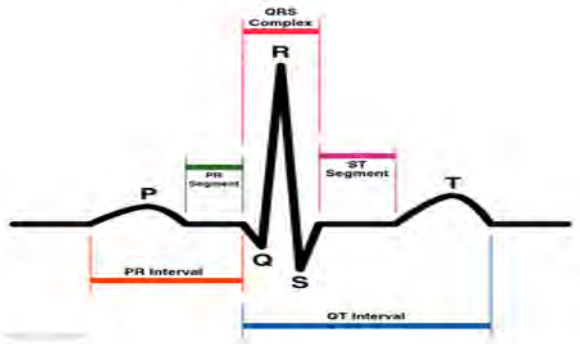


Fig. 1. A single cycle of a typical ECG signal with the important points labeled—i.e. P, Q, R, S and T.

The parasympathetic system is active during rest conditions. There is a linear relationship between decreasing the HR and the parasympathetic activity level, without any considerable latency. This affects only the HF in the power spectrum of the HRV. The power in the HF section of the power spectrum can be considered as a measure for parasympathetic activity. Now our proposed model will artificially produce a typical power spectrum as shown in Fig. 2, but for different sicknesses the model also has the capability to alter both the magnitudes, and central frequencies, of the peaks of the power spectrum to reflect different illnesses.

III. Sleep

Sleep is a dynamic state of consciousness characterized by rapid variations in the activity of the autonomic nervous system. The understanding of autonomic activity during sleep is based on observations of the heart rate and blood pressure variability. However, conflicting results exist about the neural mechanisms responsible for heart rate variability (HRV) during sleep. Zemaityte and colleagues [1] found that the heart rate decreased and the respiratory sinus a rhythmia increased during sleep. On the other hand, two other studies [2, 3] revealed high sympathetic activity during deep sleep. Thus the complete understanding of the autonomic activity during sleep is still elusive. Moreover, there are five different sleep stages and the HRV varies differently with these stages of sleep [4]. The comparison of HRV during different sleep stages is outside the scope of this paper. The causes of heart rate variability have been widely researched because of its ability to predict heart attack and survivability after an attack. The power spectral density (PSD) of the heart rate has been found to vary with the rate of respiration, changes in the blood pressure, as well psychosocial conditions such as anxiety and stress [5, 6]. All these phenomena are in turn related to the activity of the autonomic nervous system. The objective of this project was to understand how sleep affects the body in terms of what is already understood about the heart rate PSD. Also there are some disorders in sleep cycle which don't remove, they can be sign of some diseases such as angry, lack of confuses, etc. some of disorders which we can point to is on the stage of going to sleep and the second is the last of sleep. So if they don't cure, they can make some serious problems.

IV. Methods

In this paper we use developed zeeman model for generating HRV signal in different stages of sleep. As we want to point to the model, see [7]

$$\begin{aligned} \varepsilon \dot{x} &= -(x^3 + ax + b), \\ \delta \dot{a} &= -2x - 2a, \\ \delta \dot{b} &= -a - 1. \end{aligned} \tag{1}$$

where x (which can be negative) is related to the length of the heart muscle fiber, e is a positive scalar, b is a parameter representing an electrochemical control, and parameter a is related to the tension in the muscle fiber.

It is easy to see that the frequency of the oscillation in this model now depends upon the value of δ.

Now we consider the chronoscopic modulations of HR by relating the parameter δ to the four states of sympathetic and parasympathetic activity levels, e.g., s1, s2, p1 and p2. For simplicity, we assume that the states of sympathetic and parasympathetic activities are sinusoidal and can be modeled by the equations given below [7]:

$$\begin{aligned} \ddot{s}_1 &= -\omega_1^2 s_1, \\ \ddot{s}_2 &= -\omega_2^2 s_2, \\ \ddot{p}_1 &= -\omega_3^2 p_1, \\ \ddot{p}_2 &= -\omega_4^2 p_2. \end{aligned} \tag{2}$$

Now we can relate the parameter δ to the states of sympathetic and parasympathetic activity by the following equations[7]:

$$\begin{aligned} s_1 &= c_1 \sin(\omega_1 t + \theta_1) + A_1 \\ s_2 &= c_2 \sin(\omega_2 t + \theta_2) + A_2 \\ p_1 &= c_3 \sin(\omega_3 t + \theta_3) + A_3 \\ p_2 &= c_4 \sin(\omega_4 t + \theta_4) + A_4 \end{aligned} \tag{3}$$

$$\begin{aligned} q_1 &= s_1 + s_2 \\ q_2 &= p_1 + p_2 \end{aligned}$$

$$\begin{aligned} Q &= q_1 - q_2 \\ \delta &= 1/h(Q) \end{aligned}$$

The parameter δ determines the HR, and the function h and the coupling factors (c1, c2, c3 and c4) determine how the sympathetic and parasympathetic activities alter the HR.
Although the function h (q) (in (3)) is nonlinear, it can be approximated with either piecewise linear modules (as we will do in this paper) or with a neural network (currently research in progress by the authors). Finally, the parameters $\omega_1, \omega_2, \omega_3$ and ω_4 are the angular frequencies for the sinusoidal variations of the sympathetic and parasympathetic.
It is important to pay attention that we get a PSG test from one healthy person which dos not have any problems in sleep and cardiac cycle. In our test, we can get stage 1, 2, 3 and REM from the sample.
By considering these parameters in different stages of sleep we can see some various changes on them. We can see the parameters which are specify for sleep stages, these results are in table 1.

Table1- Coupling parameter in different stages

	stage 1	Stage 2	Stage 3	Stage R
C_1	0.001	0.001	0.1	1
C_2	1	1	1	1
C_3	0.4	0.4	0.4	0.01
C_4	0.25	0.3	0.7	1.2
A_1	0.3	0.3	0.4	0.5
A_2	0.75	0.75	0.8	0.9
A_3	0.1	0.1	0.1	0.01
A_4	0.8	0.8	1	1.5

V. Conclusion

As regards heart operation, it is well-known (see Braunwald et al., 2004) that HRV is used to evaluate vagal and sympathetic influences on the sinus node and to identify patients at risk for a cardiovascular event or death. So the major contribution of this study is to present an improved model that is able to produce a more comprehensive simulation of a realistic ECG than is observed in practice. So, based upon the original Zeeman model of 1972a, we have proposed a new model to generate the heart-rate time-series in different stages of sleep. In this model, considering the effects of sympathetic and parasympathetic activities on the VLF, LF and HF components in the HRV power spectrum. We can show all differences in four stages as a PSD in one shape. (See Fig2)
The model presented here has some important advantages over existing models. Compared to the original Zeeman model, model has the improved ability to generate signals that better resemble those recorded in practice. And importantly, is its ability to show various changes in stages. Also we can use this model in the pacemakers which will use in future. In addition we can use it for controlling in artificial gate of heart.

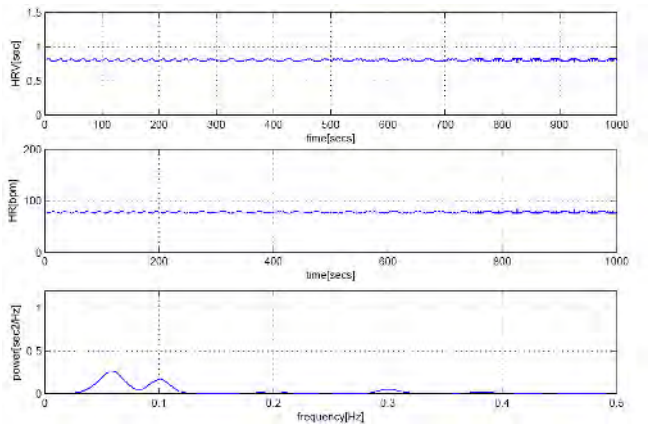


Fig2-HRV, HR, PSD of combined stage1, 2, 3 & REM of sleep

REFERENCES

1. de Boer, R.W., Karmaker, J.M., Strackee, J., 1987. Hemodynamic fluctuations and baroreflex sensitivity in humans: a beat-to-beat model. Am. J. Physiol. 253, 680–689.
2. Braunwald, E., Zipes, D.P., Libby, P., Bonow, R., 2004. Heart Disease: a Textbook of Cardiovascular Medicine. W.B. Saunders Company.
3. Brennan, M., Palaniswami, M., Kamen, P.W., 1998. A new cardiac nervous system model for heart rate variability analysis. Proceedings of the 20th Annual International Conference of IEEE Engineering in Medicine and Biology Society 20, 340–352.
4. Jafarnia-Dabanloo, N., McLernon, D.C., Ayatollahi, A., Johari-Majd, V., 2004. A nonlinear model using neural networks for generating electrocardiogram signals. Proceedings of the IEE MEDSIP Conference, Malta, 41–45.
5. Jones, D.S., Sleeman, B.D., 2003. Differential Equations and Mathemat cal Biology. Chapman & Hall, London.
6. Lavie, P., 1996. The Enchanted World of Sleep. Yale University Press, New Haven.
7. N.Jafarnia-Dabanlooa,D.C.McLernona,,H. Zhangb, A. Ayatollah, V. Johari-Majdd. A modified Zeeman model for producing HRV signals and its application to ECG signal generation Journal of Theoretical Biology 244 (2007) 180–189
8. S Parvaneh, M Pashna, 2007. Electrocardiogram Synthesis Using a Gaussian Combination Model (GCM), Computers in Cardiology 2007; 34:621−624.
9. Malik, M., Camm, A.J., 1995. Heart Rate Variability. Futura Publication Comp., New York.
10. McSharry, P.E., Clifford, G., Tarassenko, L., Smith, L.A., 2002. Method for generating an artificial RR tachogram of a typical healthy human over 24-hours. Proc. Compute. Cardiol. 29, 225–228.
11. McSharry, P.E., Clifford, G., Tarassenko, L., Smith, L.A., 2003. A dynamical model for generating synthetic electrocardiogram signals. IEEE Trans. Biomed. Eng. 50 (3), 289–294.
12. Park, J., Sandberg, J.W., 1991. Universal approximation using radial basis functions network. Neural Compute. 3, 246–257.
13. Suckley, R., Biktashev, V.N., 2003. Comparison of asymptotic of heart and nerve excitability. Phys. Rev. E 68.
14. Tu Pierre, N.V., 1994. Dynamical Systems—an Introduction with Applications in Economics and Biology, 2e. Springer, Berlin.
15. Zeeman, E.C., 1972a. Differential Equations for the Heartbeat and Nerve Impulse. Mathematics Institute, University of Warwick, Coventry, UK.
16. Zeeman, E.C., 1972b. Differential equations for the heartbeat and nerve impulse. In: Waddington, C.H. (Ed.), Towards a Theoretical Biology, vol. 4. Edinburgh University Press.
17. Zeeman, E.C., 1977. Catastrophe Theory. Selected Papers 1972–1977. Addison-Wesley, Reading, MA.
18. Zhang, H., Holden, A.V., Boyett, M.R., 2001. Modeling the effect of beta-adrenergic stimulation on rabbit senatorial node. J. Physiology. 533, 38–39.
19. Zhang, H., Holden, A.V., Noble, D., Boyett, M.R., 2002. Analysis of the chronoscopic effect of acetylcholine on sinoatrial node. J. Cardiovascular. Electrophysiology. 13, 465–474.

Two wavelengths Hematocrit Monitoring by Light Transmittance Method

Phimon Phonphruksa[1] and Supan Tungjitkusolmun[2]

[1] Department of Electronics, King Mongkut's Institute of Technology Ladkrabang Chumphon Campus 17/1 Moo 6 Tambon Chumkho, Pathiu, Chumphon, Thailand, 86160 Email: kpphimon@kmitl.ac.th
[2] Department of Electronics, Faculty of Engineering, King Mongkut's Institute of Technology Ladkrabang Chalongkrung Road, Ladkrabang, Bangkok, Thailand, 10520

Abstract — **Methods for measuring the hematocrit level of whole blood includes measuring transmittance light at multiple wavelengths within the visible and infrared spectrum, calculating light transmittance at each of the multiple wavelengths, performing a comparison in a change in light transmittance between the multiple wavelengths, and comparison to total hematocrit value. A system for measuring total hematocrit of whole blood may include discrete LEDs for light source in the range of 430 nm to 950 nm, one photo detector, data processing circuitry, and/or a display unit. We constructed a simplified system and probe, design with LEDs and a photodiode was placed at the other side of the finger, we compare the results of the system with hematocrit levels measured by centrifuge that using blood sample drawn from 120 patients. From our analysis, the wavelengths between 700 nm to 950 nm are insensitivity to hematocrit levels, and between 470 nm to 610 nm are sensitivity to hematocrit levels. The potential optimal wavelengths for light transmittance hematocrit measuring system are in the range of 700 nm-900 nm and 470 nm-610 nm. Then, we used two potential optimal LEDs wavelengths at 585 nm and 875nm for linear algorithm to design of the noninvasive hematocrit measuring system, from the acquired information the system able to predict the hematocrit value to obtained 90% of the 120 data is given an error less than 25%.**

Keywords — **light, Transmittance, Hematocrit**

I. Introduction

Blood hematocrit refers to the packed red blood cell (RCB) volume of the whole blood sample. Blood is made up of [1] red and white blood cells and plasma. Hematocrit can be measured by various methods, but the blood drawn from a finger stick is often used for hematocrit testing. The blood fills a small tube, which is then spun in a small centrifuge. As the tube spins, is the red blood cell go to the bottom of the tube, the white blood cells cover the red in a thin layer, and the liquid plasma rises to the top. The spin tube is examined for the line that divides the red cell column is measured as a percent of the total blood column. The higher column of red cells the higher of hematocrit level. With regard to the determination of the hematocrit via optical means, it is well known that the transmission of the light through red blood cells is complicated by scattering components from plasma. The scattering from plasma vary from person to person. There by complicating the determination of hematocrit, but some wavelength possible for optical hematocrit [2-5] monitoring. The optical method is advantage the traditional for faster, real time and no finger stick similarly pulse oximeter [6-9]. The most method collected the blood sample and used spectro-photometer for optical blood constitutes transmittance spectrum. The large and heavy of spectrophotometer and puncture to drawn blood sample is disadvantage method to use direct with patients. In this present study we constructed the simplified system to measure the transmittance spectra across the finger. The LEDs was used as the light source and a photo diode was place another side to detect the light intensity. The information from this study is base to consideration the optimal wavelength for real-time optical hematocrit monitoring.

II. Detailed description of the investigate

The methods provide an optical and probe to determining the transmittance spectra from finger. The 25 LEDs used as the light source in difference wavelength in the range of 430 nm to 950 nm and a photo diode was placed at the other side of the finger. Figure (1) the experiment system and probe. The photo diode was placed other side for visible light and infrared detection. Figure (2) the hematocrit at 0% and 100% oxygen saturation. Figure (3) a given of light transmitted through a finger proportional to the intensity. The transmittance (T) and absorbance (A) from Beer's law able write to equation (1) and equation (2).

$$T = \frac{I}{Io} = e^{-\varepsilon(\lambda)cd} \tag{1}$$

$$A = 2 - \log(\%T) \tag{2}$$

Where I_0 is the intensity of the incident light, I is the intensity of transmittance light, d is the optical path length, c is the concentration of the substance and ε (λ) is the extinction coefficient at a given wavelength.

Chwee Teck Lim, James C.H. Goh (Eds.): ICBME 2008, Proceedings 23, pp. 223–226, 2009
www.springerlink.com

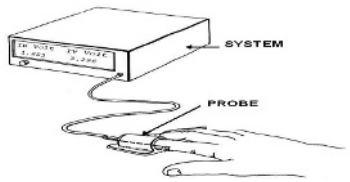


Fig. 1 The experiment system and probe

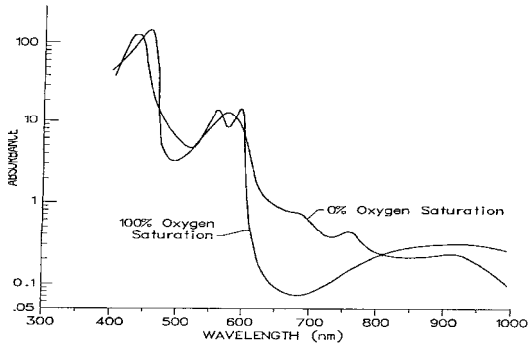


Fig. 2 Hematocrit at oxygen saturation 0%, 100%

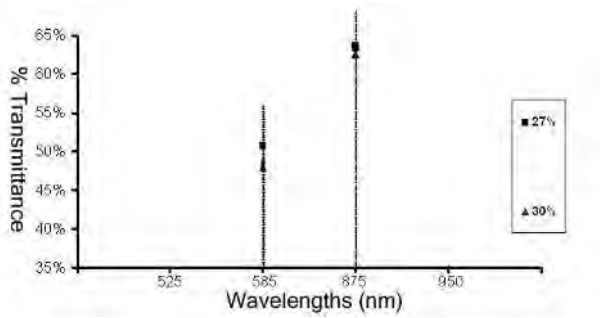


Fig. 3 Light Transmittance at hematocrit 27% and 30%

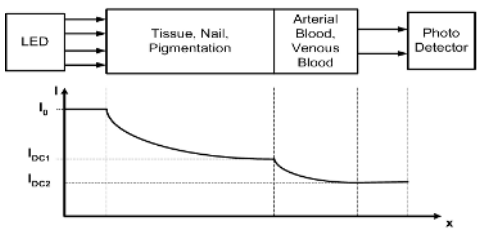


Fig. 4 Distance and Light travel passes the finger

A. Noise reduction

The reduce method for thermal noise and ambient light or any other common mode noise. Fig (4) shown when LED turn on the measures of light transmittance of finger plus thermal noise plus ambient light. After that, when LED turns off there is no measure of transmittivity or reflected light from the finger. But, thermal noise and ambient light still exist and may be measured during LED turn off. The result of signal when LED turn off may then be subtracted from the result of signal when LED turn on to reduce effect of thermal noise and ambient light and other common mode noise that may be interfere with the measurement.

$$I_{LEDon} = Ifinger + Iambient + Ithermal + Iother$$
$$I_{LEDoff} = Iambient + Ithermal + Iother$$
$$I_{finger} = I_{LEDon} - I_{LEDoff}$$

Fig. 4 Noise reduction of Light Transmittance passed the finger

From fig (4) after reduce thermal noise and ambient light and any noise may be interfere during measurement, to calculates the result of light transmittance from the corrected LEDs turn on signal passed the finger equation (1) can be normalize percentage of light as follows to equation (3).

$$T_{(\lambda)\%} = \frac{I_{finger}}{I_{reference}} \qquad (3)$$

$T_{(\lambda)\%}$ is the percentage of light transmittance passed the finger after normalize, I_{finger} is the light transmittance from light source (LED) passed the finger to photo diode when the finger tip in the probe (I), $I_{reference}$ is the light transmittance from LED to photo diode in the probe without the finger tip that mean 100% of light transmittance (I_0).

B. Hematocrit monitoring equations

From [10] wavelength in the range of 470 nm to 610 nm are sensitivity to hematocrit level and wavelength in the range of 700 nm to 900 nm are insensitivity to hematocrit level. From fig (2) we chose two wavelengths are insensitivity to Oxygen saturation at 585 nm and 875 nm that are potential to calculate the hematocrit value. Fig (3) graphs from 22 patients' (Men 10, hematocrit 27% = 5, hematocrit 30 % = 5 and Women 12 hematocrit 27% = 6, hematocrit 30 % = 6) data collected of light transmittance at the finger tip from our system and compare to hematocrit value with blood drawn and centrifugation method. From fig (3) shown the wavelength 585 nm is sensitivity to hematocrit level and wavelength 875 nm is insensitivity to hematocrit level. From Fig (4) light transmittance at the finger from LED to photo diode can be writing to equation (4) and equation (5). We normalize the light transmittance to equation (6) and equation (7). Equation (8), Equation (9) showed the extinction coefficient of oxyhemoglobin and deoxyhemoglobin are equal at wavelengths 585 nm and 875

nm and able write to new constant K. Equation (10) H_{bO} is the oxyhemoglobin, H_b is the Deoxyhemoglobin, the total hemoglobin (tHb) of whole bloods that summation of H_{bO} and H_b is Hematocrit (Hct). Apply Equation (9) and Equation (10), summation H_{bO} and H_b with new constant K to Equation (11). Equation (12) to eliminate exponential term by applies natural logarithm. Equation (13) finds the difference intensity of light transmittance wavelengths is sensitivity and insensitivity to hematocrit value. Equation (14) showed the algorithm to measure the hematocrit value by light transmittance from two wavelengths method that the difference intensity of light transmittance at two wavelengths divides by constant K.

Equation (4) shown light transmittance at 585 nm is sensitivity to hematocrit level.

$$I_{585} = I_0 e^{-(aHbO + bHb + RBC + Plasma + Nail + Tissue + Pigmentation)} \quad (4)$$

Equation (5) shown light transmittance at 875 nm is insensitivity to hematocrtit level

$$I_{875} = I_0 e^{-(RBC + Plasma + Nail + Tissue + Pigmentation)} \quad (5)$$

Equation (6) normalizes the light transmittance by device with $I_{reference}$ (I_0) for sensitivity to hematocrit wavelengths.

$$T_{585} = \frac{I}{I_0} = e^{-(aHbO + bHb + RBC + Plasma + Nail + Tissue + Pigmentation)} \quad (6)$$

Equation (7) normalizes the light transmittance by device with $I_{reference}$ (I_0) for insensitivity to hematocrit wavelengths.

$$T_{875} = \frac{I}{I_0} = e^{-(RBC + Plasma + Nail + Tissue + Pigmentation)} \quad (7)$$

Equation (8) finds the difference of light transmittance at wavelength at 585 nm and 875 nm

$$T_{585} - T_{875} = e^{-(aH_{bO} + bH_b)} \quad (8)$$

Equation (9) extinction coefficient of oxyhemoglobin and deoxyhemoglobin very small, estimate equal to new constant K.

$$a = b = K \quad (9)$$

Equation (10) summation of total hemoglobin (H_{bO} and H_b) is hematocrit.

$$H_{bO} + H_b = Hct \quad (10)$$

Equation (11) applies with equation (9) and equation (10).

$$T_{585} - T_{875} = e^{-K(Hct)} \quad (11)$$

Equation (12) takes logarithm to eliminate exponential term.

$$KHct = \ln(T_{585}) - \ln(T_{875}) \quad (12)$$

Equation (13) finds the difference of light transmittance at two wavelengths (585 nm and 875 nm).

$$\Delta T = \ln(T_{585}) - \ln(T_{875}) \quad (13)$$

Equation (14) the hematocrit value is the difference of light transmittance at two wavelengths divides by the constant K.

$$Hct = \frac{\Delta T}{K} \quad (14)$$

Equation (15) the relationship between Hct and tHb is as follows.

$$tHb(\frac{g}{dL}) = 0.33 \times Hct(\%) \quad (15)$$

Figure (5) shown the system process of the light transmittance by two wavelengths method after press start the machine will collected the important data and to

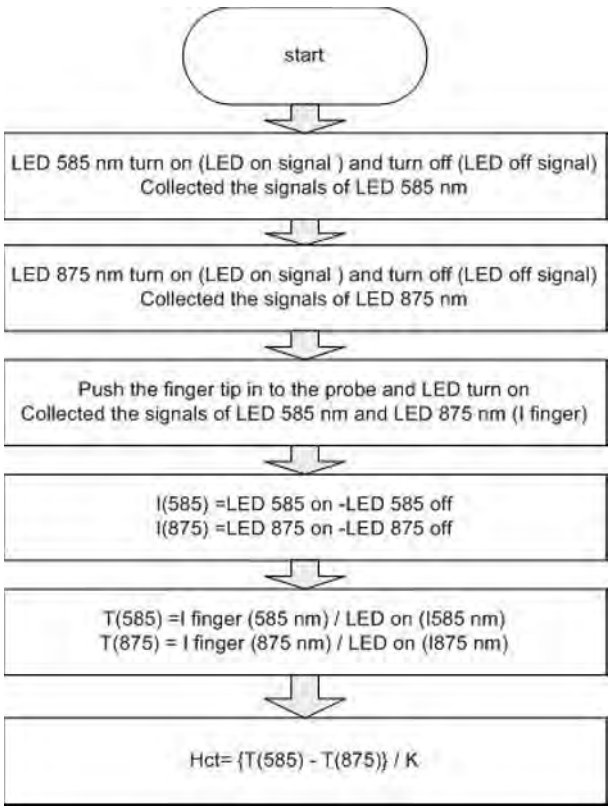


Fig. 5 The process flowchart of the system

eliminate noise (Fig 4) and follow by equation (3) to calculate the correct light intensity and finally to predicted the hematocrit value by equation (14)

C. Trial 1

This experiment used the hematocrit values measured by IEC Micro-MB centrifuge (International Equipment Company, measure the hematocrit value by blood drawn and centrifugation, compare with two wavelengths light transmittance method (Equation (14). We collected the hematocrit value with 60 patients (men); by the experiment we can find the constant K (0.0047) with equation (16).

$$K = \frac{\Delta T}{Hct} \tag{16}$$

After that we apply the constant K to equation (14), Table 1 shown the result and error from trial 1.

D. Trial 2

We collected the hematocrit value by blood drawn and centrifugation method and our system (equation 14) again with 60 patients (women), result of trial 2 shown in table 1.

Table 1 centrifugation Hematocrit value and Transmittance method.

No.	Measured (%)	Trial 1	Error (%)	Trial 2	Error (%)
1	22	28.032	12.1	24.688	5.8
2	23	28.807	11.2	33.152	0.3
3	26	30.908	8.6	26.662	1.3
4	27	27.719	1.3	29.476	4.4
5	28	32.596	7.6	30.270	3.9
6	29	32.721	6.0	30.247	2.1
7	30	30.083	0.1	34.40	6.8
8	31	30.42	-0.9	31.495	0.8
9	32	36.634	6.8	34.944	4.4
10	33	31.633	-2.1	32.221	-1.2
11	34	34.909	1.3	37.282	4.6
12	35	34.259	-1.1	34.491	-0.7
13	36	32.633	-4.9	35.852	-0.2
14	37	32.758	-6.1	45.518	10.3
15	38	32.508	-7.8	37.599	-0.5
16	39	34.584	-6.0	33.061	-8.2
17	40	34.734	-7.0	39.074	-1.2
18	43	42.636	-0.4	41.298	-2.0

III. Conclusions

The system and probe in this experiment as shown in Fig (1) and the process flowchart in Fig (5) can be obtained the optical transmittance by two wavelengths method, when chose the wavelengths 585 nm is sensitivity to hematocrit level and 875 nm is insensitivity to hematocrit level and both wavelengths are insensitivity to oxygen saturation in the linear equation (14) when used the average K (0.0047) value by blood sample drawn from the finger and centrifugation method to measure the hematocrit level from 120 patients. The table 1 and Fig (6) to compare of the hematocrit value reference from centrifugation and light transmittance by two wave lengths method can be predicted the hematocrit value to obtained 90% of the data is given an error less than 25%.

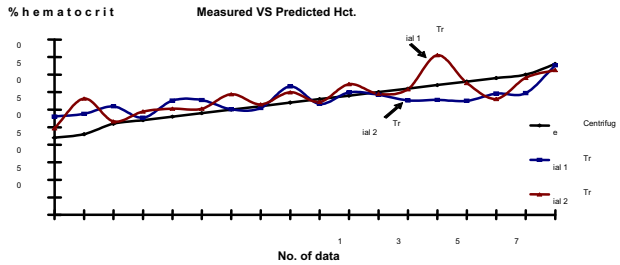


Fig. 6 Centrifugation and light transmittance method

Acknowledgment

The authors would like to thank the Department of Orthopedics Ramathibodi Hospital for providing the measured hematocrit value by centrifuge and patients for optical transmittance information.

References

1. Wintrobe M.M. “Clinical Hematology” 5th edition, Lea & Febiger, Philadelphia, 1961.
2. Yitzhak Mendelson “Pulse oximeter and method of operation” US. Patent No.2002/0042558, Apr.11, 2002.
3. Eric Kinast “Pulse Oximeter” US. Patent No.5995858,Nov.30, 1999.
4. Teiji Ukawa, Kazumasa Ito, Tadashi Nakayama “Pulse Oximeter” US. Patent No. 5355882, Oct.18, 1994.
5. Luis Oppenheimer “Spectrophotometrice Blood Analysis” US. Patent No.5331958, Jul.26, 1994.
6. Kouhei Kabuki, Yoshisada Ebata, Tadashi Suzuki, Atsushi Hiyama “Spectrophotometer” US.Patent No. 2002/ 0050560, May. 2, 2002.
7. Wylie I. Lee, Jason E. Alderete, William V. Fower “Optical Measurement of blood Hematocrit incorporating a self calibration Algorithm” US. Patent No. 6064474 May. 16, 2000.
8. Michael J. Higgins, Huntington Beach ,“Continuous Spectroscopic Measurement of total Hemoglobin” US7319894, Jan. 15, 2008.
9. Takuo Aoyagi, Masayoshi Fuse, Michio Kanemoto, Cheng Tai Xia “ Aparatus for Measuring Hemoglobin” US. Patent No. 57200284, Feb.24, 1998.
10. Phimon Phonphruksa and Supan Tungjitkusolmun, “A Photo-plethysmographic Method For real time Hematocrit Monitoring”, International Congress on Biological and Medical Engineering (ICBME), Singapore, 2002.

Rhythm of the Electromyogram of External Urethral Sphincter during Micturition in Rats

Yen-Ching Chang

Department of Applied Information Sciences, Chung Shan Medical University, Taichung, Taiwan, ROC

Abstract — **Either Fractional Brownian motion (FBM) or fractional Gaussian noise (FGN), depending on characteristic of real signal, usually provides a useful model to describe biomedical signals. Its discrete counterpart of the FBM or FGN, referred to as the discrete-time FBM (DFBM) or discrete-time FGN (DFGN), is used to analyze them in practical applications. This class of signals possesses long-term correlation and 1/*f*-type spectral behavior. In general, these signals appear to be irregular property in macroscopic view. However, in physiological signals they maybe exist certain regularity or rhythm in microscopic view in order to achieve the purpose of synergia. To find out these phenomena, the wavelet transform is invoked to decompose these signals and extract possible hidden characteristics. In this study, we first calculate fractal dimension of the electromyogram (EMG) of external urethral sphincter (EUS) to determine where the voiding phase is. Then sample a piece of signal during voiding phase to further investigate regularity or rhythm. Results indicate that certain regularity or rhythm indeed exists in irregular appearance.**

Keywords — **Discrete-Time fractional Brownian motion, discrete-time fractional Gaussian noise, wavelet transform, electromyogram, rhythm.**

I. Introduction

Many physiological signals can be modeled as either DFBM or DFGN [1], [2]. These two models are easily described by one parameter, called Hurst parameter (*H*), which has finite interval $(0,1)$. Hurst parameter is related to fractal dimension by $D=2-H$, which is a useful tool for the systems that demonstrate long-term correlations and 1/*f*-type spectral behavior. When the Hurst parameter estimated, its corresponding fractal dimension can be obtained. Among estimators for estimating Hurst parameter, maximum likelihood estimator (MLE) [1] is optimal. However, its computational complexity is high and difficult to execution. In particular, the problem is more apparent as the length of dataset is large. For this reason, we use an approximate MLE [3] to estimate Hurst parameter. This method is relatively quick and has acceptable accuracy.

Time-frequency analysis [4] is a frequently used tool in biomedical field. When describing periodic signals, Fourier transform is widely used. This method can capture periodic characteristic. In order to grasp irregularity of signals, a full-time interval is divided into a number of small, equal-time intervals. These intervals then are individually analyzed using the Fourier transform. The approach provides extra time information except frequency. It is well-known as the short-time Fourier transform (STFT). However, there is still a problem with this method. The time interval cannot be adjusted. If high frequencies exist, they cannot be discovered when time interval is short. In this situation, wavelets [5], [6] are invoked to improve this problem. It can keep track of time and frequency information very well. Moreover, wavelets can detect hidden information and extract important features. This function is a very useful tool for biomedical signals.

Physiological signals generally come from a very complex system. Signals generated from this system are usually irregular and fluctuating over time. However, some regular features maybe exist behind these phenomena. These regular components may facilitate tissues or organs effectively to implement functions themselves. Without their assistance, their responsibility may not complete and even failure. In order to investigate whether rhythm exists in physiological system, the EMG of EUS in female Wistar rats are invoked. The waveform of EMG exhibiting statistical self-similarity can be modeled as DFGN. Its accumulative signal can be viewed as DFBM. The fractal dimension of signal will assist us to judge when voiding phases happen during micturition. Wavelet transform will help us further analyze these phenomena and detect hidden information. Rhythm generally happens at low frequency band. Besides, an average power is also invoked to identify the difference during micturition.

II. Materials and Methods

The experiments were carried out on female Wistar rats anesthetized with urethane [7]. The EMG of EUS and cystometrogram (CMG) of bladder with an infusion rate of

Chwee Teck Lim, James C.H. Goh (Eds.): ICBME 2008, Proceedings 23, pp. 227–230, 2009
www.springerlink.com

0.123 ml/min using saline solutions were recorded simultaneously at two different temperatures: room and cold temperature (6-8^{o} C). In this work, only the EMG of EUS is adopted for identifying muscular responses at two temperatures. The sampling rate was 500 points/s (time resolution as 0.002 s).

The time series of EMG are analyzed as follows. The processing window size was N=1024 points (2.048 s, frequency resolution as 0.4883 Hz). The total window size were 8192 points (16.384 s) for room temperature and 16384 points (32.768 s) for cold temperature. The first 1024 points was collected as the first window. Shifted by 64 points to the right, the second window was obtained and analyzed. These steps were repeated until the last window was gathered. The total windows were 113 for room temperature and 241 for cold temperature. For each window, fractal dimension, average power, power spectral density (PSD) via the fast Fourier transform (FFT) was executed. Although, the FFT is not suitable for estimating the PSD of DFGN, which possesses long-term correlation and 1/f-type spectral behavior, but appropriate for identifying the frequencies with periodic signals. In general, rhythm happens at low frequencies. In order to avert the interference of high frequency components and capture hidden information, the signals analyzed were decomposed into 3 levels via wavelet transform using Daubechies-2 filter coefficients [6]. Afterwards, we reconstructed signal from its corresponding approximated signal at each level. The original signal was labeled as Level 0, and reconstructed signal as Level j $(1 \le j \le 3)$ for other level. Each signal was calculated the PSD via the FFT. Their time-frequency diagrams were displayed to illustrate signal's phenomena during micturition. For the purpose of clearness, unimportant frequencies, where the PSDs were lower than 1 for room temperature and 0.35 for cold one, were suppressed.

III. Results

The results at two temperatures show that the collected signals roughly are classified as three possible outcomes as illustrated in Figures 1-3.

Figure 1 shows that the time interval (about 6-12 s) with fractal dimension below 1.5 can be suggested as voiding phase. It is reasonable because the fractal dimension between 1 and 1.5 indicates positive correlation on signal, while the one between 1.5 and 2 indicates negative correlation on signal. When voiding, coordination is important for animals. The activity of time series during voiding is obvious, but the time interval between filling and voiding phase is not apparent. The same is for the time interval between voiding

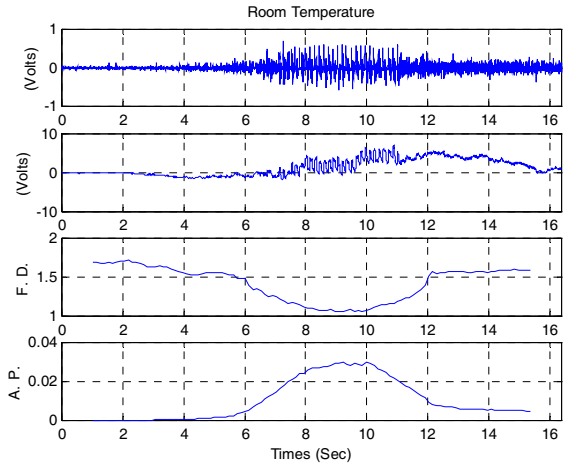


Fig. 1 From top to bottom: Original signal, accumulative signal, fractal dimension (F. D.), and average power (A. P.) at room temperature.

and next filling phase. On the other hand, average power also says that voiding phase needs more power to facilitate emptying. The average power is at least 0.01 during voiding. It is reasonable that the power needed after voiding is larger than filling phase. The extra power can be viewed as recovery or transient power. Moreover, certain rhythm exists at accumulative signal during voiding. It will be discovered via the FFT as illustrated in this section.

Figures 2 and 3 are both coming from cold temperature. In Figure 2, the voiding phase is not easy to discover from time series, whereas accumulative signal is easier than original one. According to the same line, the time interval with fractal dimension below 1.5 can be suggested as voiding phase. When the figure is zoomed in, the time series also roughly

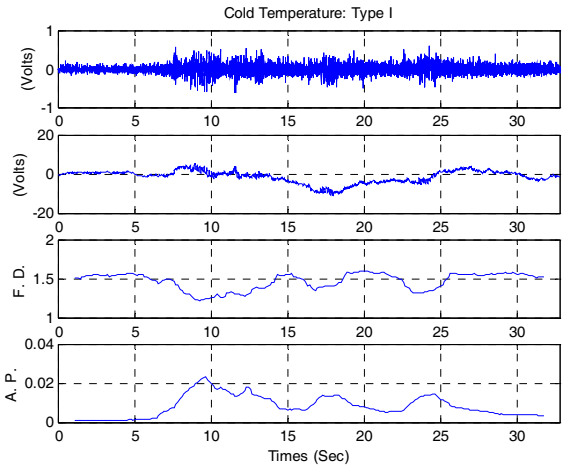


Fig. 2 From top to bottom: Original signal with Type I, accumulative signal, fractal dimension (F. D.), and average power (A. P.) at cold temperature.

displays certain rhythm, but cannot be decided without other indicator. Here fractal dimension helps us to explain importance of coordination among muscles. Likewise, average power during voiding is at least larger than 0.01. Here average power is a good auxiliary tool.

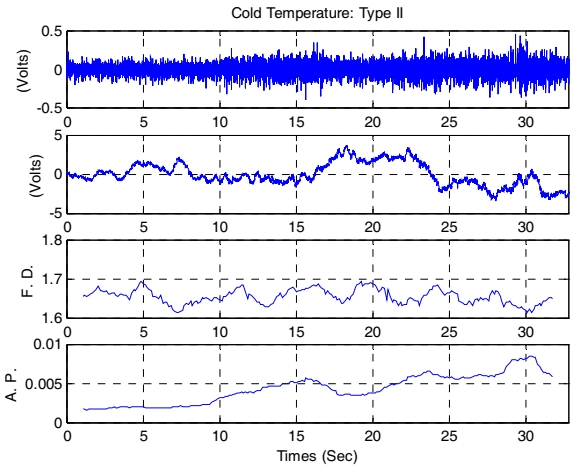


Fig. 3 From top to bottom: Original signal with Type II, accumulative signal, fractal dimension (F. D.), and average power (A. P.) at cold temperature.

In Figure 3, all fractal dimensions are larger than 1.5 and average power is lower than 0.01. We cannot discover any voiding response from the EMG of EUS. This phenomenon can be explained as incontinence. That is to say, cold-water stimulation can destroy coordination among muscles. It is interesting that signal with Type I still preserves intermittent voiding phases, but signal with Type II not. It can be explained that the rats of Type I possess robust physiological mechanism to self-organize, which can resist larger external stimulation. However, the rats of Type II lack of the ability to self-organization, because they have ordinary mechanism, not robust one.

From time series of Figures 1 and 2, it is implied that certain rhythm exists. In order to detect it, we resort to the FFT. The results show that rhythm indeed exists during voiding only if the physiological function of EUS is not damaged completely. Figures 4-6 illustrate the phenomena as follows:

Figure 4 shows that the main frequency is 6.8359 Hz and happens between 8.192 and 10.752 s. The second one is 6.3477 Hz and happens at two time intervals: 7.936-8.704 s and 10.24-11.008 s. In general, the signals on both sides of main frequency include other non-rhythmic signals, which must affect the estimate of PSD. Therefore, the main frequency can be viewed as the one of real rhythm. Rhythm will help the process during micturition.

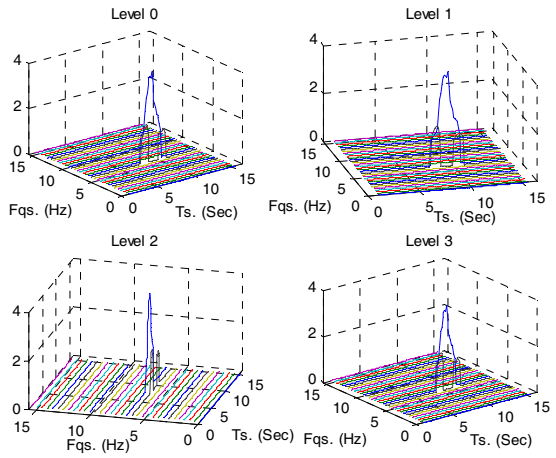


Fig. 4 From top to bottom and left to right: Original signal, reconstructed signal via Level 1, reconstructed signal via Level 2, and reconstructed signal via Level 3 at room temperature.

It is observed from Figure 5 that there exist five frequencies with PSD larger than 0.35. They are 5.8594 (third), 6.3477 (main frequency), 6.8359 (second), 7.3242 (fourth) and 7.8125 (fifth) Hz. The main frequency happens at two time intervals: 8.576-10.88 s and 23.296-24.576 s. The second one happens at two time intervals: 8.32-8.96 s and 10.624-11.008 s. The third one happens at 9.728-10.368 and 17.536-17.92 s. The fourth one happens between 11.776 and 12.672 s. The fifth one happens at 11.136 s. As mentioned before, the signals on both sides of main frequency are affected by other non-rhythmic signals. These rhythmic regions suggest us where voiding phases occur.

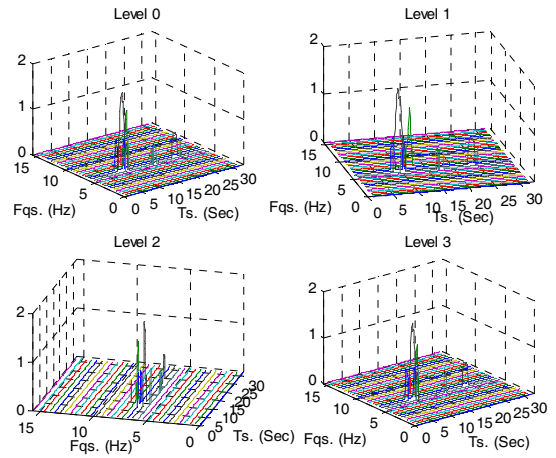


Fig. 5 From top to bottom and left to right: Original signal with Type I, reconstructed signal via Level 1, reconstructed signal via Level 2, and reconstructed signal via Level 3 at cold temperature.

In addition, the value also tells us that the main frequency at cold temperature is slight lower one-step frequency resolution than one at room temperature. These five obvious frequencies suggest us that rhythm still exists even though under cold-water stimulation for robust rats.

Figure 6 shows that no rhythm happens in signal with Type II at cold temperature. This suggests that physiological function with this type of rats is worse than one with Type I.

For revealing the rhythm on signal, one time interval with rhythm is extracted from full-time interval under room temperature. This interval of signal first is processed via wavelet transform and reconstructed them using approximated signal. Then it is processed via the FFT. The result shows in Figure 7. It is obvious from this figure that rhythm occurs during voiding phase and its main frequency is 6.8359 Hz.

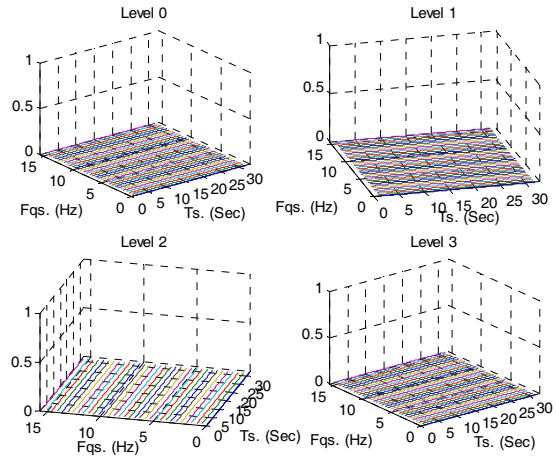


Fig. 6 From top to bottom and left to right: Original signal with Type II, reconstructed signal via Level 1, reconstructed signal via Level 2, and reconstructed signal via Level 3 at cold temperature.

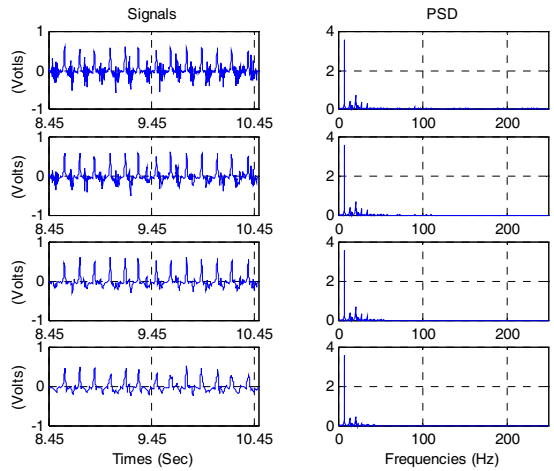


Fig. 7 From top to bottom and left to right: Original signal, its corresponding PSD, reconstructed signal via Level 1, its corresponding PSD, reconstructed signal via Level 2, its corresponding PSD, and reconstructed signal via Level 3, its corresponding PSD at one time interval at room temperature.

IV. Conclusion

Micturition is abnormal when muscles or nerves problem may be present and interfere with the ability of bladder to hold or release urine normally. In this study, it is suggested that nerves are numbed at cold-water stimulation more or less according to animal's physiological condition. Numbed nerves will result in coordination problem among muscles. Healthy animal should at least have one voiding phase and only one at best. Under cold-water stimulation, animal with robust mechanism exist many voiding phases, but rhythm still exist to facilitate micturition. Nevertheless, animal with bad function will result in incontinence. Results show that rhythm plays an important role during micturition. It facilitates the bladder to empty. In addition, hybrid methods usually provide some meaningful explanations.

Acknowledgment

This work was partially supported under the Grant number NSC 97-2914-I-040-008-A1 and Chung Shan Medical University.

References

Lundahl T, Ohley J, Kay SM, and Siffert R (1986) Fractional Brownian motion: A maximum likelihood estimator and its application to image texture. IEEE Transactions on Medical Imaging MI-5:152-161.

Chang S, Mao ST, Hu SJ, Lin WC, and Cheng CL (2000) Studies of detrusor-sphincter synergia and dyssynergia during micturition in rats via fractional Brownian motion. IEEE Transactions on Biomedical Engineering 47:1066-1073.

Chang YC and Chang S (2002) A fast estimation algorithm on the Hurst parameter of discrete-time fractional Brownian motion. IEEE Transactions on Signal Processing 50:554-559.

Akay M (1996) Detection and estimation methods for biomedical signals. Academic Press, New York.

Daubechies I (1992) Ten lectures on wavelets. SIAM, Philadelphia, PA.

Boggess A and Narcowich FJ (2001) A first Course in wavelets with Fourier analysis. Prentice Hall, New Jersey.

Chang S, Mao ST, Kuo TP, Hu SJ, Lin WC, and Cheng CL (1999) Fractal geometry in urodynamics of lower urinary tract. Chinese Journal of Physiology 42:25-31.

Higher Order Spectra based Support Vector Machine for Arrhythmia Classification

K.C. Chua[1], V. Chandran[2], U.R. Acharya[1] and C.M. Lim[1]

[1] Division of Electronics and Computer Engineering, Ngee Ann Polytechnic, Singapore.
[2] Faculty of Built Environment and Engineering, Queensland University of Technology, Brisbane, Australia.

Abstract — **Heart rate variability (HRV) refers to the regulation of the sinoatrial node, the natural pacemaker of the heart by the sympathetic and parasympathetic branches of the autonomic nervous system. HRV analysis is an important tool to observe the heart's ability to respond to normal regulatory impulses that affect its rhythm. Like many bio-signals, HRV signals are non-linear in nature. Higher order spectral analysis (HOS) is known to be a good tool for the analysis of non-linear systems and provides good noise immunity. A computer-based arrhythmia detection system of cardiac states is very useful in diagnostics and disease management. In this work, we studied the identification of the HRV signals using features derived from HOS. These features were fed to the support vector machine (SVM) for classification. Our proposed system can classify the normal and other four classes of arrhythmia with an average accuracy of more than 85%.**

Keywords — **HOS, heart rate, bispectrum, SVM, classifier**

I. Introduction

Electrocardiogram (ECG), a time varying signal that concerns the electrical manifestation of the heart muscle activity is an important tool in diagnosing the condition of the heart [1]. Heart rate variability, which is the changes of beat rate of heart over time, reflects the autonomic control of the cardiovascular system [2]. It is a simple, noninvasive technique which provides an indicator of the dynamic interaction and balance between the sympathetic nervous system and the parasympathetic nervous system. These signals are not linear in nature and hence, analysis using nonlinear methods can unveil the hidden information in the signal. A detailed review of HRV analysis that includes both linear and non-linear approaches is discussed [3].

An automated method for classification of cardiac abnormalities is proposed based on higher order spectra analysis of HRV. Higher order spectra (HOS) are spectral representations of moments and cumulants and can be defined for deterministic signals and random processes. They have been used to detect deviations from Gaussianity and identify non-linear systems [4].

II. Materials and Methodology

ECG data for the analysis was obtained from Kasturba Medical Hospital, Manipal, India arrhythmia database. Prior to recording, the ECG signals were processed to remove noise due to power line interference, respiration, muscle tremors, spikes etc. The R peaks of ECG were detected using Tompkins's algorithm [5]. The ECG signal is used to classify cardiac arrhythmias into 5 classes, namely, *normal sinus rhythm (NSR*), *premature ventricular contraction (PVC)*, *complete heart block (CHB)*, *type III-sick sinus syndrome (SSS-III)* and *complete heart failure (CHF)*. The number of dataset chosen for each of the five classes is given in Table 1. Each dataset consists of around 10,000 samples and the sampling frequency of the data is 320 Hz. The interval between two successive QRS complexes is defined as the RR interval ($t_{r\text{-}r}$ seconds) and the heart rate (beats per minute) is given as:

$$HR=60/t_{r\text{-}r} \quad (1)$$

Table 1 Number of Datasets in each class.

Cardiac Class	No. of Datasets
NSR	183
PVC	37
CHB	42
SSS-III	43
CHF	25

III. HOS and its features

The HRV signal is analyzed using different higher order spectra (also known as polyspectra) that are spectral representations of higher order moments or cumulants of a signal. In particular, this paper studies features related to the third order statistics of the signal, namely the bispectrum. The Bispectrum is the Fourier Transform of the third order correlation of the signal and is given by

$$B(f_1,f_2) = E[X(f_1)X(f_2)X^*(f_1+f_2)] \quad (2)$$

Chwee Teck Lim, James C.H. Goh (Eds.): ICBME 2008, Proceedings 23, pp. 231–234, 2009
www.springerlink.com

Where X(f) is the Fourier transform of the signal x(nT) and E[.] stands for the expectation operation. In practice, the expectation operation is replaced by an estimate that is an average over an ensemble of realizations of a random signal. For deterministic signals, the relationship holds without an expectation operation with the third order correlation being a time-average. For deterministic sampled signals, X(f) is the discrete-time Fourier transform and in practice is computed as the discrete Fourier transform (DFT) at frequency samples using the FFT algorithm. The frequency f may be normalized by the Nyquist frequency to be between 0 and 1.

In our earlier study, we proposed the general patterns for different classes of arrhythmia. Bispectral entropies [6] were derived to characterize the regularity or irregularity of the HRV from bispectrum plots. The formulae for these bispectral entropies are as follows:

Normalized Bispectral Entropy (BE 1):

$$P_1 = -\sum_n p_n \log p_n \tag{3}$$

where $p_n = \dfrac{|B(f_1,f_2)|}{\sum_\Omega |B(f_1,f_2)|}$, Ω = the region as in figure 1.

Normalized Bispectral Squared Entropy (BE 2):

$$P_2 = -\sum_n q_n \log q_n \tag{4}$$

where $p_n = \dfrac{|B(f_1,f_2)|^2}{\sum_\Omega |B(f_1,f_2)|^2}$, Ω = the region as in figure 1.

The normalization in the equations above ensures that entropy is calculated for a parameter that lies between 0 and 1 (as required of a probability) and hence the entropies (P_1 and P_2) computed are also between 0 and 1.

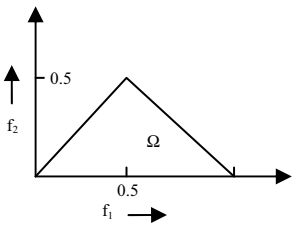


Figure 1 Non-redundant region of computation of the bispectrum for real signals. Features are calculated from this region. Frequencies are shown normalized by the Nyquist frequency.

In this study we also make use of features related to moments [7] and the weighted centre of bispectrum (WCOB) [8] to characterize these plots. The features related the moments of the plot are:

The sum of logarithmic amplitudes of the bispectrum:

$$H_1 = \sum_\Omega \log\left(\left|B\left(f_1,f_2\right)\right|\right) \tag{5}$$

The sum of logarit hmic amplitudes of diagonal elements in the bispectrum:

$$H_2 = \sum_\Omega \log\left(\left|B\left(f_k,f_k\right)\right|\right) \tag{6}$$

The first-order spectral moment of amplitudes of diagonal elements in the bispectrum:

$$H_3 = \sum_{k=1}^{N} k \log\left(\left|B\left(f_k,f_k\right)\right|\right) \tag{7}$$

These features (H_1-H_3) were used by Zhou et al [7] to classify mental tasks from EEG signals.

The definition of WCOB [8] is given by:

$$f_{1m} = \frac{\sum_\Omega iB(i,j)}{\sum_\Omega B(i,j)} \qquad f_{2m} = \frac{\sum_\Omega jB(i,j)}{\sum_\Omega B(i,j)} \tag{8}$$

where i, j are the frequency bin index in the non-redundant region.

Blocks of 1024 samples, corresponding to 256 seconds at the re-sampled rate of 4 samples/sec were used for computing the bispectrum. These blocks were taken from each HRV data record with an overlap of 512 point (i.e 50%).

IV. Support Vector Machine (SVM) Classifier

In this study a kernel-based classifier is adopted for classification of the cardiac abnormalities. Herein, the attribute vector is mapped to some new space. Despite the fact that classification is accomplished in a higher dimension space, any dot product between vectors involved in the optimization process can be implicitly computed in the low dimensional space [9].

For a training set of instance-label pairs $\left(x_i, y_i\right)$, $i = 0,...,l$ where $x_i \in R^n$ and $y_i = \{-1, 1\}$. If $\phi(.)$ is a non-linear operator mapping the attribute vector x to a higher dimensional space, the optimization problem for the new points $\phi(x)$ becomes

$$\min_{w,b,\xi} \quad \frac{1}{2} w^T w + C \sum_{i=1}^{l} \xi_i \quad \text{subject to the constraints}$$

$$y_i \left(w^T \varphi(x_i) + b \right) \geq 1 - \xi_i, \qquad \xi_i \geq 0 \tag{9}$$

where C>0 is the penalty parameter for the error term and ξ_i are a set of slack variables that are introduced when the training data is not completely separable by a hyper plane . The SVM finds a linear separating hyper plane with the maximal margin in this higher dimensional space. As in the linear case, the mapping appears in terms of the kernel function $K(x_i, x_j) = \phi(x_i)^T \phi(x_j)$. Despite the fact there are several kernels, typical choice for kernels are radial basis functions. The RBF kernel non-linearly maps samples into a higher dimensional space. There are several methods that can be used to extend a binary class SVM to multi-class SVM. In this work, we used the One against all method SVM to classify the five classes of HRV data [10].

V. Test vector generation

In order to measure and validate the performance of a classifier, there should be a sufficiently large set of the test data. When only a small database is available, different combinations of training and test sets can be used to generate more trials. In our experiment, we choose approximately two third of the data from each class of HRV signals for training and one third for testing. This experiment was repeated five times by choosing different combinations of training data and test data. Combinations of training and test data were randomly chosen. In each of these experiments, a new SVM model was generated and the test data sets did not overlap with the training data sets.

VI. Result

Table 2 shows the range of values for all the seven features for the five classes. The ANOVA test result of these HOS features are of very low p-value (i.e. p-value < 0.001).

For normal cases, heart rate varied continuously between 60bpm-80 bpm. The bispectrum entropies (P_1 and P_2) appear to be high due to higher variation in the heart rate. The mean value of P_1 is 0.719 while that of P_2 is 0.43. The mean values of moments H_1, H_2, H_3 are 2.81e5, 1.29e3 and 1.42e5 respectively. The WCOB mean values for f_{1m}, f_{2m} are 60 and 22.32 respectively. It may be that these values are related to the rate of breathing and its harmonics. And there may be a modulating effect on the heart rate variability due to the breathing pattern.

During PVC, there will be ectopic beats in the normal ECG signals. The mean entropies (P_1 and P_2) indicated in the Table 2 are correspondingly higher than the normal case due to higher variation. The mean values of moments H_1, H_2, H_3 are 2.81e5, 1.29e3 and 1.42e5 respectively. The WCOB mean values for f_{1m}, f_{2m} are 126.7 and 56.35 respectively.

Table 2 Results of ANOVA on various bispectral features. Entries in the columns correspond to mean and standard deviation. (all these features are of p-value < 0.001)

Features	Normal	PVC	CHB	SSS	CHF
P_1	0.719 ±0.086	0.824 ±0.063	0.710 ±0.022	0.780 ±0.091	0.605 ±0.129
P_2	0.430 ±0.146	0.542 ±0.181	0.428 ±0.150	0.420 ±0.255	0.187 ±0.140
H_1	2.81e5 ±5.82e4	3.64e5 ±4.55e4	1.79e5 ±4.23e4	4.64e5 ±3.40e4	2.02e5 ±5.43e4
H_2	1.29e3 ±2.31e2	1.60e3 ±1.74e2	8.94e2 ±1.66e2	1.98e3 ±1.22e2	9.74e2 ±2.18e2
H_3	1.42e5 ±3.04e4	1.90e5 ±2.39e4	8.94e4 ±2.15e4	2.38e5 ±1.87e4	1.02e5 ±2.89e4
f_{1m}	60.00 ±61.90	126.70 ±43.10	41.95 ±10.90	62.85 ±36.80	33.71 ±25.5
f_{2m}	22.32 ±31.40	56.35 ±36.80	12.91 ±4.28	31.05 ±23.2	10.50 ±9.89

Table 3 Percentage of classification accuracy for five different classes of arrhythmia with a SVM classifier.

Class	**NSR**	**PVC**	**CHB**	**SSS**	**CHF**	**Average**
Accuracy	87.93	74.00	80.00	98.46	88.57	85.79

In the case of CHB, the Atrio-ventricular node is unable to send electrical signals rhythmically to the ventricles and as a result the heart rate remains low. The bispectrum entropies (P_1 and P_2) indicated in the Table 2 are lower as compared to the normal subject due to the reduced beat to beat variation. The mean values of moments H_1, H_2, H_3 are 1.79e5, 8.94e2 and 8.94e4 respectively. The WCOB mean values for f_{1m}, f_{2m} are 41.95 and 12.91 respectively.

In SSS – III, there is a continuous variation of heart rate between bradycardia and tachycardia. The bispectrum entropies (P_1 and P_2) indicated in the Table 2 are comparable with the normal case due to the higher variation in the beat to beat. The mean values of moments H_1, H_2, H_3 are 4.64e5, 1.93e3, 2.38e5 and 8.94e4 respectively. The WCOB mean values for f_{1m}, f_{2m} are 62.85 and 31.05 respectively.

During CHF, the heart is unable to pump the blood (supply enough oxygen) to the different parts of the body. The mean bispectrum entropies (P_1 and P_2) are lower than the normal case due to the reduced beat to beat variation. The mean values of moments H_1, H_2, H_3 are 2.02e5, 9.74e2,

1.02e5 and 8.94e4 respectively. The WCOB mean values for f_{1m}, f_{2m} are 33.71 and 10.50 respectively.

Table 4 Result of Sensitivity (SENS) and Specificity (SPEC) for the SVM classifier. Entries to the left are the numbers of True negatives (TN) , False negatives (FN), True positive (TP) and False positives (FP).

TN	FN	TP	FP	SPEC	SENS
255	21	189	35	87.93%	90.00%

The result of classification efficiency is shown in Table 3. Our results show that, our proposed method can classify the unknown cardiac class with an efficiency of about 85%, sensitivity and specificity of 90% and 87.93% respectively (Table 4).

VII. Discussion

Different non-linear methods have been used to classify the cardiac classes using the heart rate signals [11-14]. In all these studies, different non-linear parameters namely correlation dimension, Lyapunov exponent, approximate entropy, fractal dimension, Hurst exponent and detrended fluctuation analysis have been used to identify the unknown class of the disease.

In this work, we have applied HOS as a non-linear tool to analyze cardiac signals. We have used the SVM and bispectral features to diagnose the different cardiac arrhythmia. Table 3 and 4 shows promising results of the application of HOS features for cardiac signals classification.

One of the major challenges in non-linear biosignal processing is the presence of intra-class variation. Another challenge is that there are overlaps among the derived features for various arrhythmias. Hence in our present work, we have used two bispectrum entropies and three features related to the moments and two weighted centre of bispectrum as descriptors to differentiate different arrhythmia. These features were then fed to the SVM classifier for automated classification. We achieve about 85% of classification accuracy with the current set of features. The accuracy may be further increased by extracting better features and taking more diverse training data.

VIII. Conclusion

The HRV signal can be used as reliable indicator of the cardiac diseases. In this work, we have extracted different HOS features from heart rate signals for automated classification. We have evaluated the effectiveness of different bispectrum entropies, moments and weighted centre of bispectrum as features for the classification of various cardiac abnormalities. Our proposed system utilizes combination of the different features with a SVM classifier and is able to identify the unknown cardiac class with a sensitivity and specificity of 90% and 87.9% respectively. The accuracy of our proposed system can be further increased by increasing the size of the training set, rigorous training, and better features.

References

1. M. Sokolow, M. B. Mclhoy, M. D. Chiethin, "Clinical Cardiology", Vlange Medical Book, 1990.
2. Kamath MV, Ghista DN, Fallen EL, Fitchett D, Miller D, McKelvie R, “Heart rate variability power spectrogram as a potential noninvasive signature of cardiac regulatory system response, mechanisms, and disorders,” Heart Vessels, 3, 1987, 33–41.
3. U. R. Acharya, K. P. Joseph, N. Kannathal, C. M. Lim, J. S. Suri, "Heart rate variability: A review", *Med Biol Comp Eng*., 88, pp. 2297, 2006.
4. Nikias CL, Petropulu AP, Higher –order spectra analysis: A nonlinear signal processing framework. Englewood Cliffs, HJ, PTR Prentice Hall; 1993.
5. Pan Jiapu, Tompkins WJ, “Real Time QRS Detector algorithm”, IEEE Transactions on Biomedical Engineering 32(3), pp. 230-236, March 1985.
6. Chua KC, Chandran V, Acharya UR, Lim CM, “Cardiac State Diagnosis Using Higher Order Spectra of Heart Rate Variability”, Journal of Medical & Engineering Technology, 32(2), 2008, 145-155.
7. Zhuo SM, Gan JQ, Sepulveda F, “Classifying mental tasks based on features of higher-order statistics from EEG signals in brain–computer interface”, Information Sciences, 178(6), 2008, pp 1629-1640.
8. Zhang J, Zheng C, Jiang D, Xie A., ”Bispectrum analysis of focal ischemic cerebral EEG signal”, In: Proceedings of the 20th annual international conference of the IEEE engineering in medicine and biology society, 20, 1998, pp 2023–2026.
9. Vapnik, V., “Statistical Learning Theory”, New York: Willey, 1998.
10. Lingras P, Butz C, “Rough set based 1-v-1 and 1-v-r approaches to support vector machine multi-classification”, Information Sciences, 177(18), 2007, pp 3782-3798.
11. Acharya UR, Jasjit Suri, Jos A. E. Spaan, Krishnan SM, “Advances in Cardiac Signal Processing”, Springer Verlang GmbH Berlin Heidelberg, March, 2007.
12. Radhakrishna RKA, Yergani VK, Dutt ND, Vedavathy TS, “ Characterizing Chaos in heart rate variability time series of panic disorder patients”, Proceedings of ICBME, Biovision 2001, Bangalore , India, 2001,pp 163-167.
13. Mohamed IO, Ahmed H, Abou-Zied, Abou-Bakr M, Youssef, Yasser MK, “Study of features on nonlinear dynamical modeling in ECG arrhythmia detection and classification”, IEEE transactions on Biomedical Engineering, 49(7), 2002, pp733-736.
14. Kannathal N, Lim CM, Acharya UR, Sadasivan PK, “Cardiac state diagnosis using adaptive neuro-fuzzy technique”, Med. Eng Phys., 28(8), 2006, pp 809-815.

The address of the corresponding author:
Author: Chua Kuang Chua
Institute: ECE Division, Ngee Ann Polytechnic
Street: 535 Clementi Road
Country: Singapore
Email: ckc@np.edu.sg

Transcutaneous Energy Transfer System for Powering Implantable Biomedical Devices

T. Dissanayake[1], D. Budgett[1, 2], A.P. Hu[3], S. Malpas[2,4] and L. Bennet[4]

[1] Auckland Bioengineering Institute, University of Auckland, Auckland, New Zealand
[2] Telemetry Research, Auckland, New Zealand
[3]Department of Electrical and Computer Engineering, University of Auckland, Auckland, New Zealand
[4]Department of Physiology, University of Auckland, Auckland, New Zealand

Abstract — **Time varying magnetic fields can be used to transfer power across the skin to drive implantable biomedical devices without the use of percutaneous wires. However the coupling between the external and internal coils will vary according to orientation and posture. Other potential sources of power delivery variations arise from changes in circuit parameters and loading conditions. To maintain correct device function, the power delivered must be regulated to deal with these variations. This paper presents a TET system with a closed loop frequency based power regulation method to deliver the right amount of power to the load under variable coupling conditions. The system is capable of regulating power for axially aligned separations of up to 10mm and lateral displacements of up to 20mm when delivering 10W of power. The TET system was implanted in a sheep and the temperature of implanted components is less than 38.4 degrees over a 24 hour period.**

Keywords — **Magnetic field, coupling, Transcutaneous Energy Transfer (TET)**

I. Introduction

High power implantable biomedical devices such as cardiac assist devices and artificial heart pumps require electrical energy for operation. Presently this energy is provided by percutaneous leads from the implant to an external power supply [1]. This method of power delivery has the potential risk of infection associated with wires piercing through the skin. Transcutaneous Energy Transfer (TET) enables power transfer across the skin without direct electrical connectivity. This is implemented through a transcutaneous transformer where the primary and the secondary coils of the transformer are separated by the patient's skin providing two electrically isolated systems. A TET system is illustrated in figure 1. The electromagnetic field produced by the primary coil penetrates the skin and produces an induced voltage in the secondary coil which is then rectified to power the biomedical device.

Compared to percutaneous wires, TET systems become more complex to operate under variable coupling conditions as it result in a variation in power transfer [2]. One source of variation in coupling is due to posture changes of the patient causing variation in the alignment between the primary and the secondary coils. The typical separations between the internal and external coils are in the range of 10-20mm. If insufficient power is delivered to the load then the implanted device will not operate properly. If excessive power is delivered, then it must be dissipated as heat with the potential for causing tissue damage. Therefore it is important to deliver the right amount of power matching the load demand.

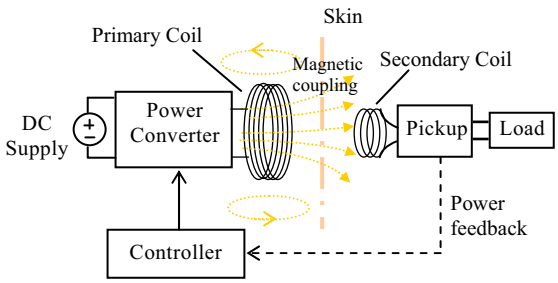


Fig. 1 Block diagram of a TET system

Power can be regulated either in the external or the implanted system. However, regulation in the implanted system results in dissipation of heat in the implanted circuitry [3]. Furthermore, it also increases the size and weight of the implanted circuitry therefore power regulation in the external system is preferred over the implanted system. There are two main methods of regulating power in TET systems, magnitude and frequency control methods. In the case of magnitude control, input voltage to the primary power converter is varied in order to vary the power delivered to the load. This method of control is very common in TET systems however it does not take into account the miss-match of the resonant frequency of the secondary resonant tank and the operating frequency of the external power converter. This miss-match in frequency reduces the power transferred to the load, consequently, a larger input voltage is required which results in a reduction in the overall power efficiency of the system. Frequency control involves varying the operating frequency of the primary power converter to vary the

Chwee Teck Lim, James C.H. Goh (Eds.): ICBME 2008, Proceedings 23, pp. 235–239, 2009
www.springerlink.com

power delivered to the load. Depending on the actual power requirement of the pickup load, the operating frequency of the primary power converter is varied so the secondary prick-up is either tuned/detuned, thus the effective power delivered to the implantable load is regulated [4]. The system discussed in this paper uses frequency control to control power delivery to the load, and a Radio Frequency (RF) link is used to provide wireless feedback from the implanted circuit to the external frequency controller.

II. System Arcitechture

The TET system is designed to deliver power in the range of 5W to 25W. Figure 2 illustrates the architecture of the overall system. A DC voltage is supplied to the system with an external battery pack. A current fed push pull resonant converter is used to generate a high frequency sinusoidal current across the primary coil. The magnetic coupling between the primary and the secondary systems produces a sinusoidal voltage in the secondary coil which is rectified by the power conditioning circuit in the pickup to provide a stable DC output to the implanted load. As shown in figure 2, a DC inductor is added to the secondary pick up following the rectifier bridge in order to maximize the power transfer to the load. The DC inductor aids to sustain a continuous current flow in the pick up [5].

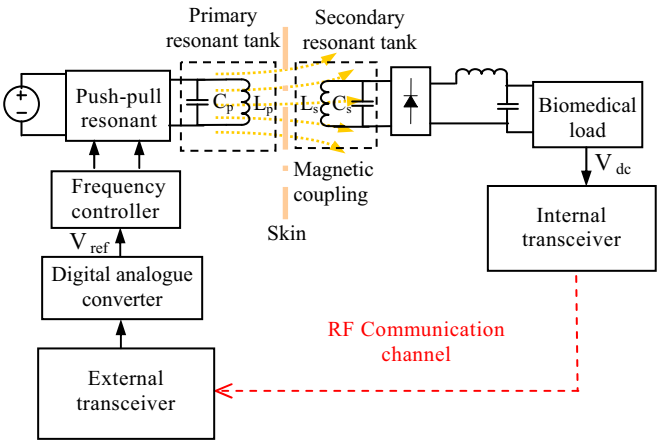


Fig. 2 System architecture

Two nRF24E1 Nordic transceivers are used for data communication. The DC output voltage of the pickup is detected and transmitted to the external transceiver. The external transceiver processes the data and adjusts the duty cycle of the output PWM signal in order to vary the reference voltage (V_{ref}) of the frequency control circuitry. The PWM signal is passed through a Digital to Analogue Converter (DAC), in order to obtain a variable reference voltage. This variable reference voltage is then used to vary the frequency of the primary resonant converter which in turn varies the power delivered to the implantable system. The response time of the system is approximately 360ms.

A. Frequency controller

The frequency controller employs a switched capacitor control method described in [7]. The controller varies the overall resonant frequency of the primary resonant tank in order to tune/detune to the secondary resonant frequency. The frequency of the primary circuit is adjusted by varying the effective capacitance of the primary resonant tank. This is illustrated in figure 3.

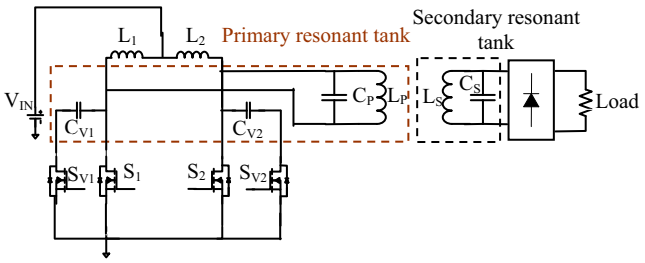


Fig. 3 System based of primary frequency control [4]

Inductor L_P, capacitor C_P and switching capacitors C_{V1} and C_{V2} form the resonant tank. The main switches S1 and S2 are switched on and off alternatively for half of each resonant period and changing the duty cycle of the detuning switch S_{V1} and S_{V2} varies the effective capacitances of C_{V1} and C_{V2} by changing the average charging or discharging period. This in turn will vary the operating frequency of the primary converter. Each C_{V1} and C_{V2} is involved in the resonance for half of each resonant period. The variation in reference voltage (V_{ref}) obtained from the DAC is used to vary the switching period of these capacitors. This method of frequency control maintains the zero voltage switching condition of the converter while managing the operating frequency. This helps to minimize the high frequency harmonics and power losses in the system. As shown in figure 3 the pickup circuitry is tuned to a fixed frequency using the constant parameters L_S and C_S. The operating frequency of the overall system is dependent on the primary resonant tank which can be varied by changing the equivalent resonant capacitance [6], therefore the tuning condition of the power pickup can be controlled.

III. Experimental Method

A prototype TET system was built and tested in a sheep. The internal coil and the resonant capacitor were Parylene coated and encapsulated with medical grade silicon to provide a biocompatible cover. The total weight of the implanted equipment was less than 100g. As illustrated by the cross sectional view in figure 4, thermistors were attached to the primary and the secondary coils to measure the temperature rise caused by the system in the surrounding tissue.

- Thermistor 1: Placed on top of primary
- Thermistor 2: Placed under the skin
- Thermistor 3: Placed on the muscle side
- Thermistor 4: 1cm from the secondary coil
- Thermistor 5: 2cm from the secondary coil
- Thermistor 6: Near the subcutaneous tissue near the exit of the wound.

Prior to experimentation, the thermistors were calibrated against a high precision FLUKE 16 Multimeter temperature sensor and a precision infrared thermometer.

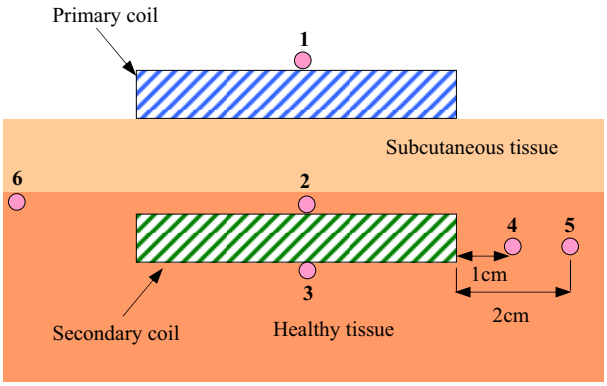


Fig. 4 The placement of the temperature sensors

Prior to the surgery all implantable components were sterilized using methanol gas. The sheep was put under isoflurane anesthesia and the right dorsal chest of the sheep was shaved. Iodine and disinfectant was applied over the skin to sterilize the area of surgery. Using aseptic techniques a 5 cm incision was made through the skin on the dorsal chest. A tunnel was created under the skin approximately 20 cm long and a terminal pocket created. The secondary coil and the thermistors were placed within this pocket. The thickness of the skin at this site was approximately 10mm. The secondary coil was then sutured in place and the power lead from the coil and leads of the thermistors were tunneled back to the incision site and exteriorised through the wound. The wound was stitched and Marcain was injected to the area of the wound. Iconic powder was also put on the site of the wound to reduce infection. Following the surgery the sheep transferred to a crate where it was kept over a three week period. The primary coil was placed directly above the secondary coil and held on the sheep using three loosely tied strings. A PowerLab ML820 data acquisition unit and Labchart software (ADInstruments, Sydney Australia) was used for continuous monitoring of the temperature, the output power to the load and the variation in input current of the system during power regulation. The data acquisition was carried out at a frequency of 10 samples per second.

IV. Experimental Results

Experimental results were obtained for delivering 10W of power to the load when the system was implanted in sheep. Figure 5 illustrates the closed loop controlled power delivered to the load over a period of 24 hours. The input voltage to the system was 23.5V. The controller is able to control the power to the load for axially aligned separations and lateral displacements between 10mm to 20mm. Beyond this range the coupling is too low for the controller to provide sufficient compensation, and delivered power will drop below the 10W set point. Evidence of inadequate coupling can be seen at intervals in Figure 5.Variation in input current reflects the controller working to compensate for changes in coupling using frequency variation between 163 kHz (fully detuned) and 173 kHz (fully tuned). When the coupling between the coils is good, the primary resonant tank is fully detuned in order to reduce the power transferred to the secondary. When the coils are experiencing poor coupling, the primary resonant tank is fully tuned to increase the power transfer between the coils.

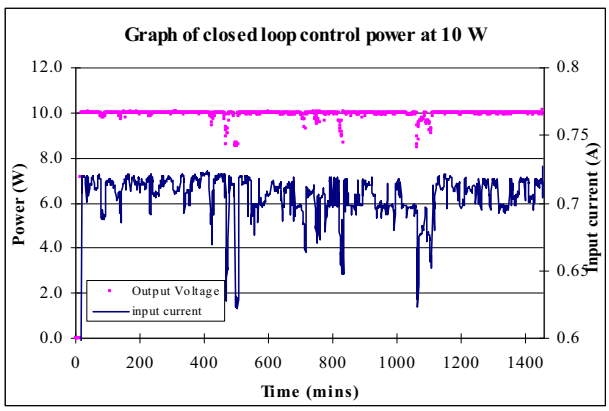


Fig. 5 Regulated power to the load and the input current to the system

Figure 6 shows the temperature recorded from the six thermistors. It takes approximately 20 minutes for the tem-

perature to reach a steady state after turn-on. The maximum temperature was observed in the thermistor placed under the secondary coil on the muscle side. The maximum temperature observed in this thermistor over the 24 hour period was 38.1^0C. The maximum temperature rise observed was 3.8^0C in the thermistor placed under the skin. The large variation in the primary coil temperature is due to the changes in current through the coil from the frequency control mechanism. When the system is in the fully tuned condition, the current in the primary coil is at a maximum to compensate for the poor coupling. The temperature rise in the thermistors 1cm and 2cm from the secondary coil is well below 2^0C.

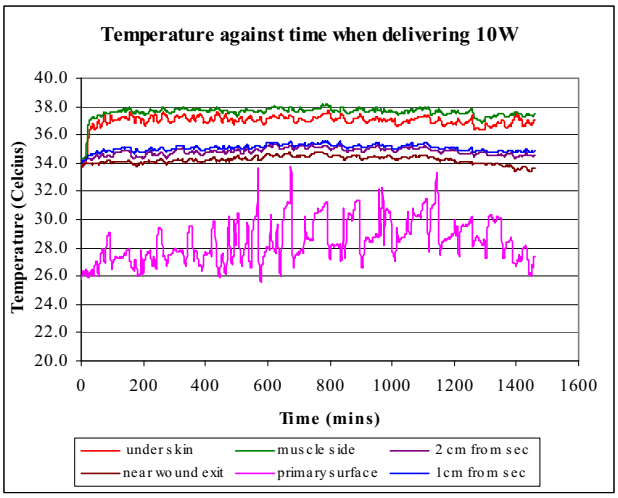


Fig. 6 Temperature profile of the thermistors

V. Discussion

Although the system performs well at delivering 10W over a 24 hour period, there are short intervals when this power level was not delivered. These intervals correspond to times when the coupling is too low for the controller to compensate. A variety of approaches can be taken to solve this problem. The first is to tighten the coupling limitations to prevent coupling deteriorating to beyond the equivalent limit of 20mm of axial separation. The second approach is to allow occasional power drops on the basis that an internal battery could cover these intervals, (patient alarms would activate if the problem persists). The third approach is to increase the controller tolerance to low coupling. The ability to tolerate misalignments of the frequency controlled system is mainly determined by the systems quality factor (Q value), which is defined by:

$$Q = \frac{R}{\omega L} \quad (1)$$

Where R is the load resistance, ω (2πf) is the system angular operating frequency, and L is the secondary coil inductance. A larger Q will enable the system to be more tolerant. This benefit is traded off against the need for a more sensitive and faster feedback response from the control system.

VI. Conclusions

We have successfully implemented a system that is capable of continuously delivering power to a load in a sheep. The results have been presented for delivering 10W of power to the load with closed loop frequency control technique for a period of 24 hours. The external coil was loosely secured to lie over the region of the internal coil and subjected to alignment variations from a non-compliant subject. The maximum temperature observed in this system is 38.1^0C on the thermistor placed on the muscle side under the primary coil. The maximum temperature rise was 3.8^0C on the thermistor placed under the skin.

References

1. Carmelo A. Milano, A.J.L., Laura J. Blue, Peter K. Smith, Adrian F. Hernadez, Paul B. Rosenberg, and Joseph G. Rogers, *Implantable Left Ventricular Assist Devices: New Hope for Patients with End stage Heart Faliure.* North Carolina medical journal, 2006. **67**(2): p. 110-115.
2. C. C. Tsai, B.S.C.a.C.M.T. Design of Wireless Transcutaneous Energy Transmission System for Totally Artificial Hearts. in IEEE APPCAS. 2000. Tianjin, China.
3. Guoxing Wang, W.L., Rizwan Bashirullah, Mohanasankar Sivaprakasam, Gurhan A. Kendir, Ying Ji, Mark S. Humayun and James D.Weiland. A closed loop transcutaneous power transfer system for implantable devices with enhanced stability. in IEEE circuits and systems. 2004.
4. Ping Si, P.A.H., J. W. Hsu, M. Chiang, Y. Wang, Simon Malpas, David Budgett Wireless power supply for implantable biomedical device based on primary input voltage reglation. 2nd IEEE conference on Industrial Electronics and Applications, 2007.
5. Ping Si, A.P.H., Designing the DC inductance for ICPT Power pickups. 2005.
6. Ping Si, A.P.H., Simon Malpas, David Budgett, A frequency control method for regulating wireless power to implantable devices. IEEE ICIEA conference, Harbin, China, 2007.

Author: Thushari Dissanayake
Institute: Auckland Bioengineering Institute
Street: 70, Symonds Street
City: Auckland
Country: New Zealand
Email: t.dissanayake@auckland.ac.nz

Author: David Bugett
Institute: Auckland Bioengineering Institute
Street: 70, Symonds Street
City: Auckland
Country: New Zealand
Email: d.budgett@auckland.ac.nz

Author: Patrick Hu
Institute: University of Auckland
Street: 38, Princess Street
City: Auckland
Country: New Zealand
Email: a.hu@auckland.ac.nz

A Complexity Measure Based on Modified Zero-Crossing Rate Function for Biomedical Signal Processing

M. Phothisonothai[1] and M. Nakagawa[2]

[1] Department of Electrical Engineering, Burapha University, 169 Bangsaen, Chonburi 20131 Thailand
[2] Department of Electrical Engineering, Nagaoka University of Technology, 1603-1 Kamitomioka, Nagaoka-shi 940-2188 Japan
E-mail: [1] montrip@buu.ac.th, [2] masanaka@vos.nagaokaut.ac.jp
Tel.: +66-38-102-222 ext 3380, Fax: +66-38-745-806

Abstract — **A complexity measure is a mathematical tool for analyzing time-series data in many research fields. Various measures of complexity were developed to compare time series and distinguish whether input time-series data are regular, chaotic, and random behavior. This paper proposes a simple technique to measure fractal dimension (FD) values on the basis of zero-crossing function with detrending technique or is called modified zero-crossing rate (MZCR) function. The conventional method, namely, Higuchi's method has been selected to compare output accuracies. We used the functional Brownian motion (fBm) signal which can easily change its FD for assessing performances of the proposed method. During experiment, we tested the MZCR-based method to determine the FD values of the EEG signal of motor movements. The obtained results show that the complexity of fBm signal is measured in the form of a negative slope of log-log plot. The Hurst exponent and the FD values can be measured effectively.**

Keywords — **Complexity, fractal dimension, biomedical signal, modified zero-crossing rate, MZCR, Hurst exponent**

I. Introduction

Time-series data formed by sampling method based on the suitable rate of frequency. It can be measured as the complexity in order to show whether the data are regular, chaotic, or random behavior. Basically, we can measure irregularity of time-series data in terms of quantity's complexity. Especially, in the field of biomedical signal analysis, complexity of heartbeat signal (electrocardiogram; ECG) and brain signal (electroencephalogram; EEG) can be able to distinguish emotion, imagination, movement, and can be used for medical diagnosis purposes [1].

To determine the quantity's complexity, fractal dimension (FD) value is a one of indicative parameters which most widely used. Moreover, the FD value has been proved to be effective parameter in characterizing such biomedical signals. Fractal geometry is a mathematical tool for dealing with complex systems. A method of estimating FD has been widely used to describe objects in space, since it has been found useful for the analysis of biological data [2][3].

For related works, classical methods such as moment statistics and regression analysis, properties such as the Kolmogorov-Sinai entropy [4], the apparent entropy [5], and the existing methods in estimating FD value have been proposed to deal with the problem of pattern analysis of waveforms. The FD may convey information on spatial extent and self similarity and self affinity [6]. Unfortunately, although precise methods to determine the FD have already been proposed, their usefulness is severely limited since they are computer intensive and their evaluation is time consuming [7]. Recently, the FD is relatively intensive to data scaling and shows a strong correlation with the human movement of EEG data [8]. The time series with fractal nature are to be describable by the functions of fractional Brownian motion (fBm), for which the FD can easily be set. Waveform FD values indicate the complexity of a pattern or the quantity of information embodied in a waveform pattern in terms of morphology, spectra, and variance.

In this paper, we propose algorithm in which the FD value is on the basis of zero-crossing function with detrending technique or is called modified zero-crossing rate (MZCR) function. The proposed MZCR function is a simple technique in estimating FD and presents the fast computation time.

II. Method

A. Basic concept

On the assumption of a high value of the complexity of time-series data can be easily found by obtaining the high rate of zero-crossing point. It means that we can directly compute the complexity of time-series data on the basis of the zero-crossing rate function. Based on the general relationship of power law, during the locally computation period of input data, Δx, and time period, Δt, which can be defined by

$$f_z(\Delta x) \propto \Delta t^{\mu} \tag{1}$$

where $f_z(\cdot)$ is the MZCR function, μ is a scaling parameter.

Chwee Teck Lim, James C.H. Goh (Eds.): ICBME 2008, Proceedings 23, pp. 240–243, 2009
www.springerlink.com

B. MZCR function

The input time-series data are formed in the length of 2^n-point. To determine FD value by means of proposed method, there are three main steps of processing as follows:

Step 1: Zero-mean data by subtracted the mean value of locally sampled period from each value:

$$\hat{x}_n = x_n - \bar{x} \tag{2}$$

Step 2: Bride detrending by subtracted the regression line from each value. The zero-mean data, $\hat{x}_n$, is then locally detrended by subtracting the theoretical values, y_d, given by the regression:

$$\hat{y}_n = \hat{x}_n - y_d \tag{3}$$

Step 3: Zero-crossing rate (ZCR) determination, after that data were detrended we will use the zero-crossing rate function to determine the ZCR value which is defined by:

$$z_n = \frac{1}{L}\sum_{n=0}^{L-1} \Phi(\hat{y}_n \hat{y}_{n-1}) \tag{4}$$

where

$$\Phi(A) = \begin{cases} 1 & \text{if } A < 0 \\ 0 & \text{otherwise} \end{cases}$$

Finally, we can determine the scaling parameter by taking logarithmic function on both sides of Eq. (1). This computation is repeated over all possible interval lengths (in practice, we suggest minimum length 2^4-point and maximum length is 2^{n-1}-point.)

III. Assessment Conditions

A. Fractional Brownian motion (fBm)

Due to the fractional Brownian motions (fBms) take an important place among self-similar processes, fBms are selected to be input signal for assessing performance of the proposed method. The fBms are the only self-similar Gaussian processes with stationary increments, and they provide interesting models of self-similar processes [9]. General model of the fBm signal can be written as the following fractional differential equation [10] :

$$\frac{d^{H+1/2} B_H(t)}{dt^{H+1/2}} \propto w(t) \tag{5}$$

Where $w(t)$ is a white Gaussian function. The typical examples of two fBm signals of parameters H = 0.2 and H = 0.8 length 1,024 points generated by wavelet-based synthesis of Abry and Sellan's algorithm [11] are shown as Fig. 1. The Hurst exponent in the process, H, is related to the fractal dimension D:

$$H = E + 1 - D \tag{6}$$

where E is the Euclidean dimension (E = 0 for a point, 1 for a line, 2 for a surface). In this case, therefore, for one-dimensional signals:

$$H = 2 - D \tag{7}$$

B. Classical method

Since many methods were developed to determine FD value on time and frequency domains [7], we will select the method; namely, Higuchi's method [12] for comparison in this study because it has been proved to use in many research fields include in the biomedical engineering.

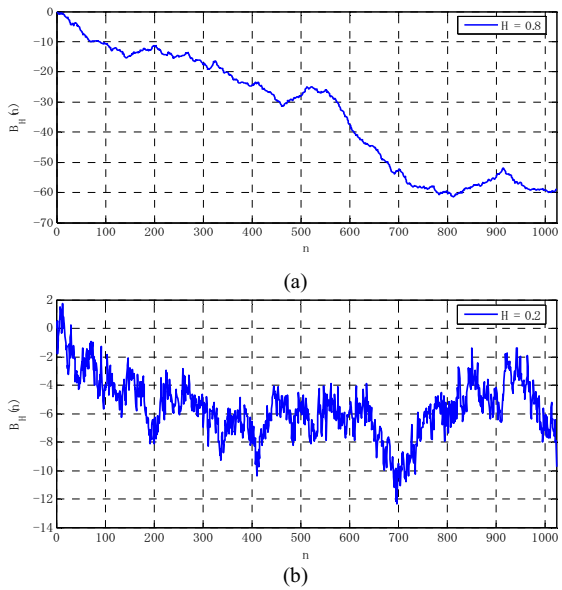


Fig. 1. Two fBm signals generated by different Hurst exponent values. (a) Parameter H=0.8. (b) Parameter H=0.2.

IV. Experiments

The fBm is also referred to as 1/*f*-like profile, since it can be generated from Gaussian random variables and its fractal dimension can easily be set. Therefore, fBm is used to be input signal for assessing in this experiment. Based on the

assumption of the given concept in the Eq. (1), we found that the estimation of H for one-dimensional data is in a negative form of a scaling parameter which can be expressed as the following definition:

$$H \approx -\mu \tag{8}$$

or,

$$\mu \equiv D - 2 \tag{9}$$

For all $n = 2^4, 2^5, \ldots, \log_2 L - 1$, where L is the total length of fBm. In Fig. 2 shows a log-log plot of MZCR function the H is a slope of regression line (dash line). During experiment, we fix step of H changing by 0.01 ranged from 0 to 1 with randomly repeat of five times for each step. Then, the mean-squared error (MSE) of the theoretical and estimated values, $\hat{D}$, can be computed by:

$$MSE = \sum \left(D - \hat{D}\right)^2 \tag{10}$$

MSE value will be used for showing output performance of our proposed method with the classical one. The comparison results and the results of different H (at the length of 1,024 points) are shown as Table 1 and 2, respectively. Table 1 also shows the average computation time which the methods were performed on a laptop CPU 1.66 GHz Pentium with memory of 1 GB.

Table 1 Comparison results of average MSE and computation time.

fBm Length	MSE [1×10^{-4}]		Computation time [ms]	
	MZCR	Higuchi	MZCR	Higuchi
2^8	2.82	3.17	33.4	54.0
2^9	2.54	3.38	48.2	61.8
2^{10}	1.71	1.92	91.2	94.3

Table 2 Estimating results of Hurst exponent (fBm length of 1,024 points.)

H	MZCR	Higuchi
0.1	0.1196	0.1567
0.3	0.2995	0.3079
0.5	0.5058	0.5057
0.7	0.7013	0.6811
0.9	0.9177	0.9199

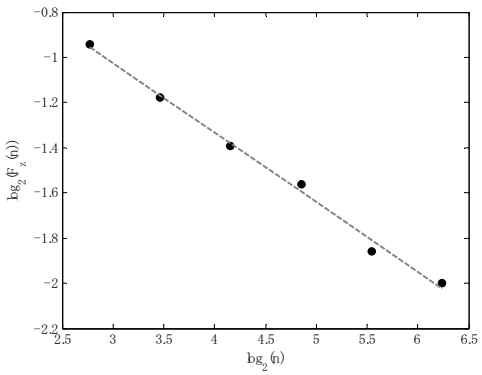


Fig. 2. Log-log plot of MZCR method for evaluating FD.

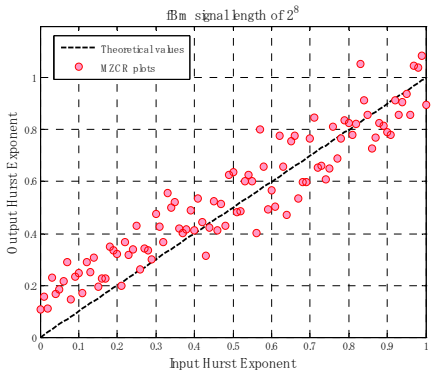


Fig. 3. Estimated Hurst exponent based on MZCR function (input fBm length of 256 points).

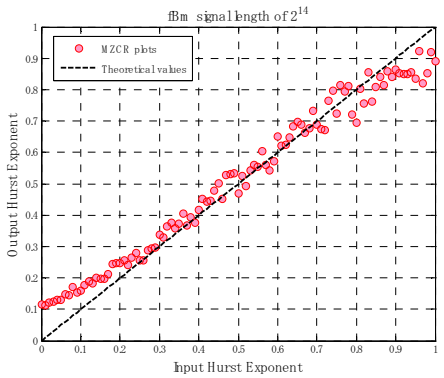


Fig. 4. Estimated Hurst exponent based on MZCR function (input fBm length of 1,024 points).

V. Discussions

The proposed MZCR function is the method to change the crossing lines over zero point. Fig. 5 shows a key process of the regression lines in determining ZCR values of

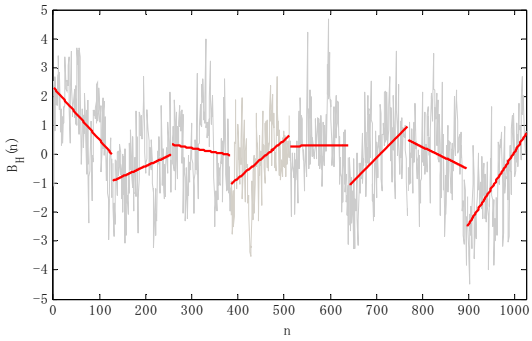


Fig. 5. Regression lines of detrending process in the length of 128 points.

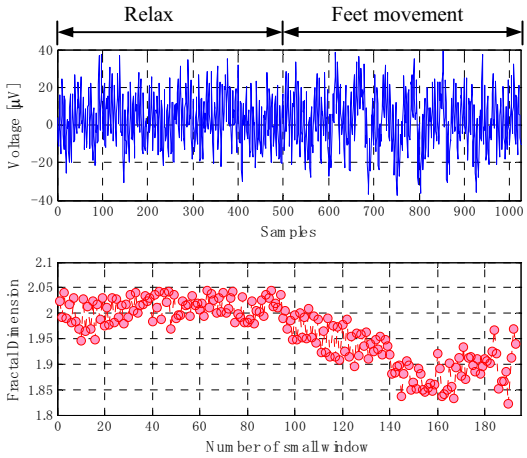


Fig. 6. Raw EEG data of feet movement and its FD waveform.

locally segmented data. If we do process the input data directly without bridge detrending the ZRC function does not play an important role, the results become out of accurate range. Based on the obtained results, we found that the Higuchi's method is more suited than our proposed method in case the length of data greater than 2^{12}-point. However, in practice, biomedical signal is mostly addressed with short-time analyzing, i.e., electroencephalogram (EEG) data were used as features [3][13]. The MZCR function presents the computation time faster than conventional method when the length of input time series less than 2^9 (512 points). To prove the assumption of the estimation method on the basis of MZCR function can be used effectively, the complexity of EEG data of feet movement was analyzed by using the MZCR function shown in Fig. 6. The electrodes were placed according to the 10-20 international system. FD values of recorded EEG data at C3 position were computed based on windowing size 256 points with the moving interval 4 points. The trajectory waveform of FD shows that the complexity during feet movement period less than relaxing period.

VI. Conclusions

In this paper, the complexity measure based on MZCR function is proposed. The proposed method estimates Hurst exponent in a negative slope of log-log plot, and the calculating procedure has three main steps. It is a simple technique for measuring complexity of time-series data in terms of fractal dimension value. The main challenge in estimating fractal dimension of time-series data is that the method can be employed accurately in a short-time analysis, and easy to implement. The proposed method in this paper can considerably be a one choice for such purpose.

Acknowledgment

This research was partially supported by the grant-in-aid for scientific research from the Faculty of Engineering, Burapha University, Chonburi, Thailand. The author gratefully acknowledges Prof. M. Nakagawa for his valuable comments and the equipments for recording EEG data.

References

[1] Yuan Y, Li Y, Mandic DP, "Comparison analysis of embedding dimension between normal and epileptic EEG time series," *J. Physiol. Sci.*, vol.59, pp 239-247, 2008, DOI:10.2170/physiolsci.RP004708.

[2] Lutzenberger W, Preissl H, and Pulvermuller F, "Fractal dimension of electroencephalographic time series and underlying brain processes," Biological Cybernetics, vol.73, pp 477–482, 1995.

[3] Bashashati A, Ward RK, Birch GE, Hashemi MR, and Khalizadeh MA, "Fractal dimension-based EEG biofeedback system," IEEE Int. Conf. EMBS'03, pp 2220–2223, Sep. 2003.

[4] Grassberger P and Procaccia I, "Estimation of the Kolmogorov entropy from a chaotic signal," Phys. Rev. A, vol. 28, pp 2591-2593, 1983.

[5] Pincus SM, Gladstone LM, and Ehrenkranz RA, "A regularity statistic for medical data analysis," J. Clin. Monit. Comp., vol. 7, pp 335-345, 1991 DOI: 10.1007/BF01619355.

[6] Nakagawa M, (1995) Chaos and fractals in engineering, pp.41–53, World-Scinecetific, Singapore.

[7] Phothisonothai M and Nakagawa M, "Fractal-based EEG data analysis of body parts movement imagery tasks", J. Physiol. Sci., vol.57, no.4, pp 217–226, Aug. 2007 DOI:10.2170/physiolsci.RP006307.

[8] Phothisonothai M and Nakagawa M, "EEG-based classification of motor imagery tasks using fractal dimension and neural network for brain-computer interface," IEICE Trans. Info. & Syst., vol.E91-D, no.1, pp 44-53, January 2008 DOI:10.1093/ietisy/e91-d.1.1.

[9] Bardet JM, "Statistical study of the wavelet analysis of fractional Brownian motion," IEEE Trans. Info. Theo., vol. 48, no. 4, April 2002, pp 991–999.

[10] Mandelbrot BB and Van Ness JW, "Fractional Brownian motions, fractional noises and applications," SIAM Rev., vol.10, pp 422-437, 1968.

[11] Abry P and Sellan F, "The wavelet-based synthesis for the fractional Brownian motion proposed by F. Sellan and Y. Meyer: Remarks and fast implementation," Appl. and Comp. Harmonic Anal., vol. 3, no. 4, 1996, pp 377–383.

[12] Higuchi T, "Approach to an irregular time series on the basis of the fractal theory," Physica D, vol.31, pp 277–83, 1988.

[13] Phothisonothai M and Nakagawa M, "EEG signal classification method based on fractal features and neural network," *IEEE Int. Conf. EBMS'08*, British Columbia, Canada, Aug. 2008, pp 3880–3883.

The Automatic Sleep Stage Diagnosis Method by using SOM

Takamasa Shimada[1], Kazuhiro Tamura[1], Tadanori Fukami[2], Yoichi Saito[3]

[1] School of Information Environment, Tokyo Denki University, Japan
[2] Faculty of Engineering, Yamagata University, Japan
[3] Research Institute for EEG Analysis, Japan

Abstract — **In psychiatry, the sleep stage is one of the most important evidence for diagnosing mental disease. However, when doctor diagnose the sleep stage, much labor and skill are required, and a quantitative and objective method is required for more accurate diagnosis. For this reason, an automatic diagnosis system must be developed. In this paper, we propose an automatic sleep stage diagnosis method by using Self-Organizing Maps (SOM). Neighborhood learning of SOM makes input data which has similar feature output closely. This function is effective to understandable classifying of complex input data automatically. We didn't only applied SOM to EEG of normal subjects but also applied to EEG of subjects suffer from disease. The spectrum of characteristic waves in EEG of disease subjects is often different from it of normal subjects. So, it is difficult to classify EEG of disease subjects with the rule for normal subjects. On the other hand, SOM classifies the EEG with features which data include. And rules for classification are made automatically. So, even the EEG of disease subjects is able to be classified automatically. In our experiment, first, the features included in EEG were extracted and learned by the Elman-type feedback SOM on competitive layer. The EEG data were preprocessed and the spectrums at sixteen bands were calculated. Second, the spectrum data were inputted to the Elman-type feedback SOM and data were classified on competitive layer. Third, the data were diagnosed by doctor and the sleep stages were labeled. The data of stage wake were input to the learned Elman-type feedback SOM, and the neuron which fires mostly was decided. This neuron is called wake winner neuron (WWN). Finally, data for testing were inputted to the learned Elman-type feedback SOM and corresponding sleep stage was diagnosed by the distance from WWN to Best Matching Unit. Experimental results indicated that the proposed method is able to achieve sleep stage diagnosis along with doctor's diagnosis.**

Keywords — **EEG, Self-Organizing Maps, sleep stage.**

I. Introduction

In psychiatry, sleep staging is one of the most important means for diagnosis. The sleep staging of EEG, however, is liable to be subjective since it depends on the doctor's skill and requires much labor. An automatic diagnosis system must therefore be developed to reduce doctor's labor and realize quantitative diagnosis of sleep EEG.

For sleep staging by EEG analysis, it is especially important to detect the characteristic waves from EEG. Most conventional methods of diagnosing the sleep stage, however, use long-term spectrum analysis [1][2]. However, the spectrum of characteristic waves in EEG of disease subjects is often different from it of normal subjects. So, it is difficult to classify EEG of disease subjects with the rule for normal subjects. Moreover some methods are based on a kind of template matching. This also makes it difficult to cope with the large variation of EEG. So, the method of detecting the characteristic waves in EEG which is required in clinic must therefore be able to cope with fluctuations of pattern of frequency between individuals.

Recently, neural networks have been applied to various kinds of problems in many fields due to their ability to analyze complicated systems without accurate modeling in advance [3]. Especially, Self-Organizing Maps (SOM) has an ability of making classification rule automatically and classifying the data without teaching. Neighborhood learning of SOM makes input data, which has similar feature, output closely. This function is effective to understandable automatic classification of complex input data.

An Elman-type feedback SOM is a same type neural network as SOM. It has not only a function of SOM, but also a function of coping with temporal signal processing. For accurate sleep stage diagnosis, considering contextual information is important.

In this paper, we propose a new sleep stage diagnosing method using an Elman-type feedback SOM [4]. It is expected that the function of automatic making of classification rule is effective to classifying complex signal from human body and that even the EEG with disease subjects is able to be classified automatically.

II. Method

A. Self-Organizing Maps

The Self-Organizing Maps (SOM) is one of Neural Networks which was developed by T. Kohonen. SOM doesn't need to be taught by operator when it learn classification rule.

Chwee Teck Lim, James C.H. Goh (Eds.): ICBME 2008, Proceedings 23, pp. 245–248, 2009
www.springerlink.com

SOM consists of two layers, input layer and competitive layer. Input data are inputted to input layer of SOM. And the neuron which fires mostly on competitive layer (winner neuron) is decided. The weights of winner neuron and neighborhoods of it are increased. This learning process is repeated. Generally, if input data has more complex feature, the learning process is repeated more. This neighborhood learning of SOM makes input data, which has similar feature, output closely. This function is effective to understandable automatic classification of complex input data.

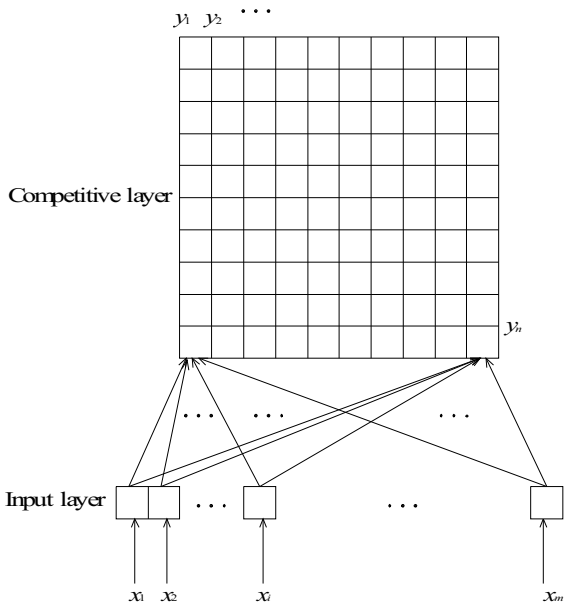


Fig. 1 SOM architecture.

B. An Elman-type feedback SOM

For achieving more accurate sleep stage diagnosis, considering contextual information is important. In clinical medicine, doctor uses the information of context for sleep stage diagnosis, because the state of short term EEG data often fluctuates from general EEG pattern of sleep stage in which subject is. So, the diagnosed sleep stage with short term EEG is improved by considering contextual information. In our experiment, an Elman-type feedback SOM was used for coping with contextual information.

An Elman-type feedback SOM is a model which has a feedback loop from competitive layer to input layer. There are context units at the middle of feedback loop. The number of context units is same with it of units of competitive layer and they are one-to-one correspondence. Each context unit always maintains a copy of the previous values of the corresponding unit in competitive layer. Thus the network can maintain a sort of previous state.

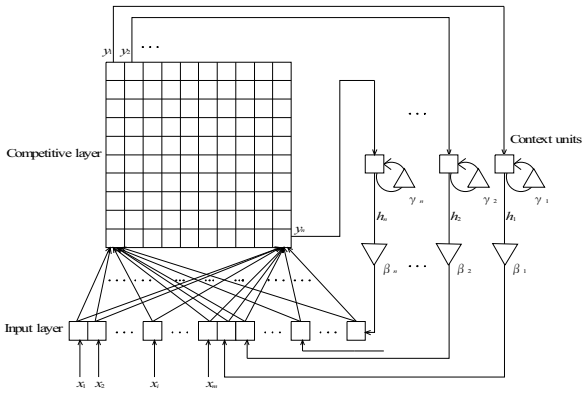


Fig. 2 Elman-type feedback SOM architecture. This architecture recognizes the contextual information of EEG.

C. Learning process

The training or testing data is generated as follows. First, the EEG data is sampled (at the rate of 200Hz) with a 2.56sec (512-point) hamming window. Its logarithmic power spectrum coefficients are calculated by FFT. In our experiment, the powers at 16 power bands were used for input data as shown in table 1.These 16 power bands were decided by considering the important spectrum range which are often used in clinical medicine for diagnosing sleep stages. Each power band of 16 power bands is corresponding to important spectrum range for diagnosing sleep stages as shown in Table 1. Generally, most of power spectrum of sleep EEG is included in this spectrum range (from zero to 100.0Hz).

Table 1 16 power bands corresponding to important spectrum range for diagnosing sleep stages

Name of bands	Spectrum range[Hz]
delta 0	0 - 1.17
delta 1	1.17 - 2.34
delta 2-3	2.34 - 4.30
theta 1	4.30 - 6.25
theta 2	6.25 - 8.20
alpha s	8.20 - 9.38
Alpha m	9.38 - 11.33
alpha f = omega 1	11.33 - 13.28
omega 2	13.28 - 15.23
beta 11	15.23 - 17.19
beta 12	17.19 - 19.14
beta 2	19.14 - 23.05
beta 3	23.05 - 26.95
gamma 1	26.95 - 39.45
gamma 2	39.45 - 60.16
gamma 3	60.16 - 100.0

These spectrum data were inputted to input layer of Elman-type feedback SOM. The clustering map was made on competitive layer automatically. The EEG data which have similar feature are classified closely on competitive layer by neighborhood learning of SOM.

The learning data were diagnosed by doctor and the sleep stages were labeled. The data of stage wake were inputted to the learned Elman-type feedback SOM, and the neuron which fires mostly was decided. This neuron is called wake winner neuron (WWN).

D. Testing process

Data for testing were inputted to the learned Elman-type feedback SOM, and the unit which fires mostly in competitive layer (BMU: Best Matching Unit) was searched.

The corresponding sleep stage to input data was diagnosed by the distance from WWN to BMU.

E. subjects

The number of subjects is four. And symptom of each subject is as described in Table 2. Twos of subjects are healthy and the others are suffering from disease.

Table 2 symptom of each subject

Subject	symptom
A	Healthy male, aged 16.
B	Healthy female, aged 39.
C	Epileptic mental disorder, female, aged 55. Power band of characteristic waves in EEG shift lower band
D	Epileptic mental disorder, female, aged 32.

III. Results

The test data of subjects A, B, C and D were applied to learned Elman-type feedback SOM, and results of diagnosis were decided by the distance from WWN to BMU. Results were acquired at each time and plotted them on the graphs. Figs 3, 4, 5 and 6 show the results of data of subjects A, B, C and D, respectively.

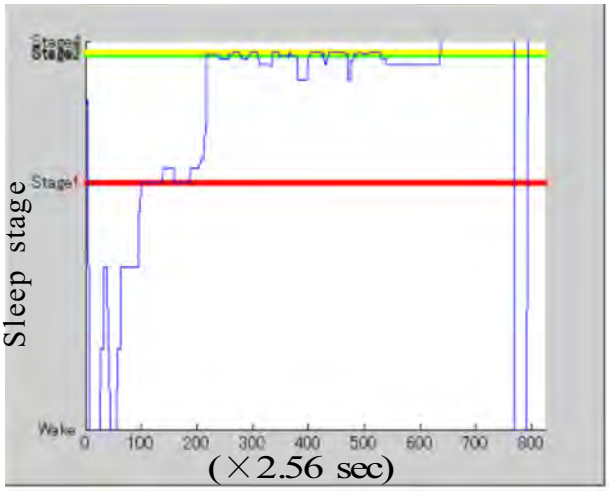


Fig. 3 The result of sleep stage diagnosis of data of subject A with Elman-type feedback SOM.

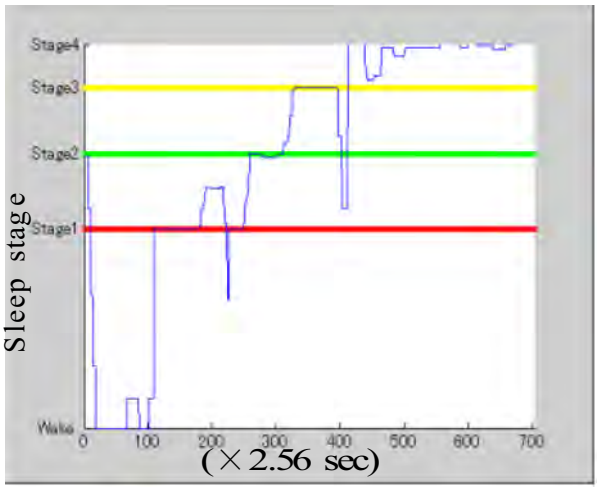


Fig. 4 The result of sleep stage diagnosis of data of subject B with Elman-type feedback SOM.

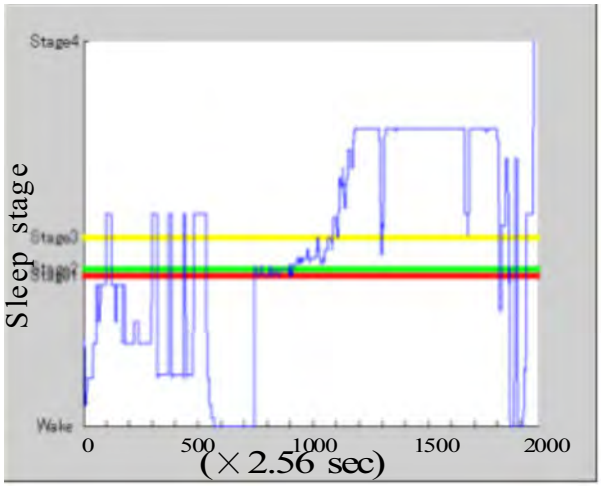


Fig. 5 The result of sleep stage diagnosis of data of subject C with Elman-type feedback SOM.

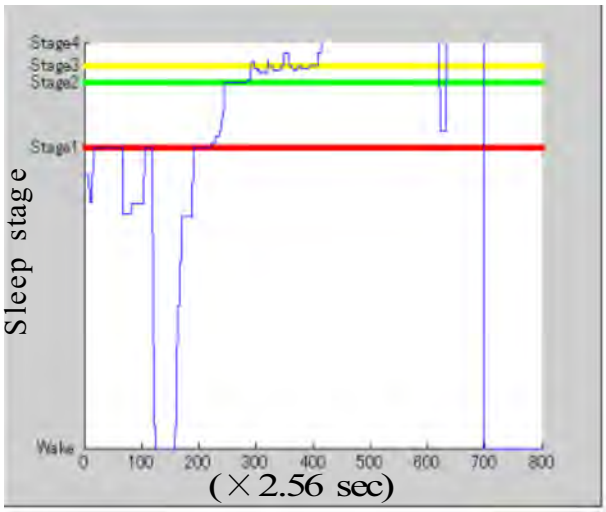


Fig. 6 The result of sleep stage diagnosis of data of subject D with Elman-type feedback SOM.

IV. Discussions

The correct rates of diagnosis were calculated by Equation (1).

$$\text{Correct rate} = \frac{\text{The number of correctly diagnosed period}}{\text{The total number of periods}} \times 100[\%] \quad (1)$$

Table 3 shows the correct rate of diagnosis with Elman-type feedback SOM.

Table 3 the correct rate of diagnosis with Elman-type feedback SOM

Subject	Correct rate[%]
A	70
B	89
C	81
D	85

The average correct rate of diagnosis with conventional SOM is 34.5%. On the other hand, the average correct rate of diagnosis with Elman-type feedback SOM is 81.3%. This result shows that the more accurate sleep stage diagnosis is achieved by considering contextual information with Elman-type feedback SOM.

Though the power bands of characteristic waves of subject C are different from that of normal subject, the high correct rate was achieved. This fact shows that Elman-type feedback SOM can cope with abnormal EEG of disease subjects with the function of automatic making of classification rules.

V. Conclusion

In this paper, we propose an automatic sleep stage diagnosis method by using Elman-type feedback SOM.

The data of four subjects including disease subjects whose power bands of characteristic waves are different from normal subjects were applied, and sleep stage were diagnosed.

Experimental results indicated that the proposed method is able to achieve sleep stage diagnosis along with doctor's diagnosis.

References

1. Jose C. Principe and Jack R. Smith (1986) SAMICOS-A Sleep Analyzing Microcomputer System, IEEE Trans. Biomed. Eng., vol. BME-33, pp. 935-941.
2. Jose C. Principe, Sunit K. Gala and Tae G. Chang (1989) Sleep Staging Automaton Based on the Theory of Evidence, IEEE Trans. Biomed. Eng., vol. 36, pp. 503-509.
3. Richard P. Lippmann (1987) An Introduction to Computing with Neural Nets, IEEE ASSP Mag., pp.4-22, apr.
4. Elman, J. L. (1990) Finding structure in time, Cognitive Science, vol. 14, 1990, pp. 179-211.

Author: Takamasa Shimada
Institute: School of Information Environment, Tokyo Denki University
Street: 2-1200 Muzai Gakuendai
City: Inzai City, Chiba Prefecture
Country: Japan
Email: shimada@sie.dendai.ac.jp

A Development of the EEG Telemetry System under Exercising

Noriyuki Dobashi[1], Kazushige Magatani[1]

[1] Department of Electrical and Electronic Engineering TOKAI University, Japan

Abstract — **Our purpose of the research is a development of the detecting method of EEG under exercising. Usually, measuring EEG is done in the quiet state. In case of the measuring EEG under exercising, a movement of the body causes vibration of electrodes and artifact for the EEG. Therefore, detection of the EEG under exercising is said to be difficult. So, we developed the measuring method of EEG under exercising by using our designed algorithm.**

In our previous system, measured signals were amplified by a system amplifier that was equipped with subject's body. And output of a system amplifier is connected to a personal computer with wire. In this condition, a subject could not move freely. In order to improve this problem, we developed telemetry system. In this system, we can obtain output from a system amplifier by wireless. So in our new system, a subject can move his/her body freely under measuring EEG.

Keywords — **Electroencephalogram (EEG), Acceleration censer, telemetry system**

I. Introduction

The mental state of a human under playing a game is one of important factors which decide a result of the game. We can assess the state of the athlete by bio-signals (e.g. heart rate, EMG, etc.). However, these signals can only express physical condition and cannot express mental condition. It is well known that EEG expresses mental condition. For example, human emotional factor can be estimated from frequency analysis of EEG. If a measuring EEG under exercising is possible, we can assess the mental condition of an athlete and the results of this assessment will be useful for mental training. Therefore, our objective of this study is a development of the remote sensing method of EEG under exercising. The relationship between frequency band of EEG and mental condition are shown the following.

δ- rhythm … Band:0.5~3[Hz]
→ Under unconsciousness and a deep sleep.
θ- rhythm … Band:4~7[Hz]
→ Shallow sleep and a relaxed state.
α- rhythm … Band:8~13[Hz]
→ While being devoted to meditation and concentration something, when mentally stable.
β- rhythm … Band:14~30[Hz]
→ Worries and strain and working promptly.

It is said that measuring EEG under exercising is difficult because of motion artifact. Actually, movement of the body causes vibration of EEG electrodes and, this vibration causes artifact for EEG. However, there is a close correlation between this artifact and acceleration of a subject's head, and no correlation between artifact and EEG. From these facts, we will be able to reduce artifact using adaptive filtering or ICA (Independent Component Analysis). Our developing system consists of the EEG and acceleration measuring system and the noise reduction system. One channel EEG signal and acceleration of subject's head are measured simultaneously, and these are frequency division multiplexed. Multiplexed signal is transmitted as radio frequency using frequency modulation in the EEG and acceleration measuring system. Received signal is de-multiplexed and digital filtered in order to obtain noise free EEG data in the noise reduction system. In this paper, we will talk about this system.

II. Methodology

II-I System hardware

Fig.1 shows a block diagram of our measurement system. Our system consists of an EEG amplifier, an acceleration sensor, a 16bit analog to digital converter and a personal computer. Our EEG amplifier is made of operational amplifier mainly. EEG amplifier amplifies The EEG about 2,000 times, and this signal is converted to the digital value after high pass (0.5Hz) and low pass (40Hz) filtered. Electrodes for EEG measurement are set on left earlobe (common), frontal pole (positive), vertex (negative). And EEG was measured under this bipolar condition. The position of EEG electrodes is shown in Fig.2. An acceleration sensor senses the head movement that will cause artifact of EEG. This acceleration output is amplified and high pass (0.5Hz) filtered and then converted to the digital value for the personal computer. This acceleration data is used for the reference signal of artifact, and a personal computer discriminates between EEG and noise from measured EEG data with artifact by using algorithm that we designed. Fig.3 shows the EEG amplifier of the system. Fig.4 shows an acceleration sensor unit (star precision ACB302). As mentioned earlier, our new system uses wireless system to transmit EEG and acceleration signals. Fig.5 shows a block

Chwee Teck Lim, James C.H. Goh (Eds.): ICBME 2008, Proceedings 23, pp. 249–252, 2009
www.springerlink.com

diagram of our telemetry system. A surrounded area by dotted line in Fig.1 is the telemetry unit of our system. The details of this unit are shown in Fig.5. Wired connection between amplifiers that is equipped with subject's body and a personal computer disturbs the free exercise of the object. Therefore, amplified EEG data and acceleration data are transmitted to a personal computer by using telemetry system. So in our system, a subject can exercise freely.

Frequency modulation technique is used for the telemetry system, because this modulation has low noise characteristics. A carrier frequency of this telemeter is set about 80MHz. So, we can use a FM receiver on market as a receiver of our telemeter. This telemeter can transmit one signal. However, two kinds of signal (EEG and acceleration of head) are necessary in our system. So, the frequency division multiplexing technique is used to combine these signals in our system. As shown in Fig.5, EEG and acceleration data are frequency modulated by using 5kHz and 1kHz carrier frequency respectively. After frequency modulation, two modulated signals are combined to one signal by summing amplifier. This multiplexed signal is transmitted as 80MHz radio signal. A FM transmitter on market is used in this part. A FM receiver on market receives this signal. As shown in Fig.5, output of a FM receiver is frequency divided by filters and then separated signals are frequency demodulated and low pass filtered. And then EEG and acceleration data are obtained as transmitted data. Fig.6 shows the frequency division multiplexing system. Fig.6(a) is a multiplexing unit and Fig.6(b) is a de-multiplexing unit.

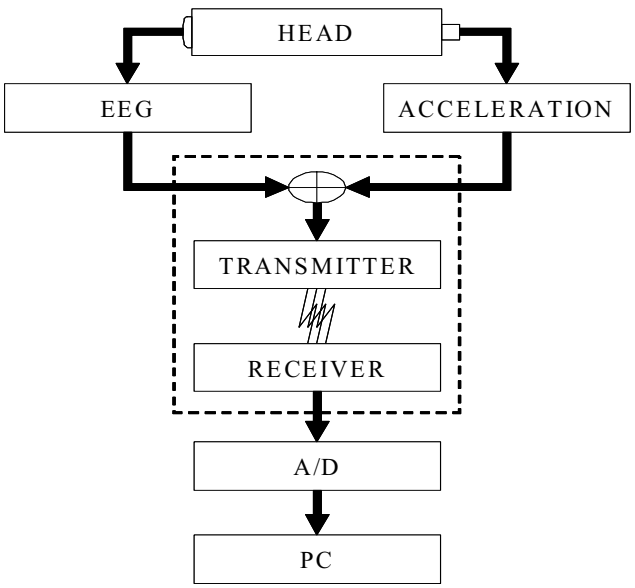


Fig.1 A block diagram of our measurement system.

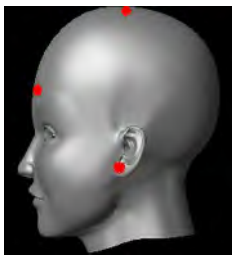


Fig.2 Three position of the EEG electrodes.

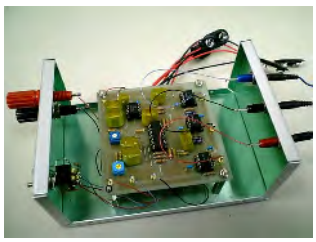


Fig.3 EEG amplifier.

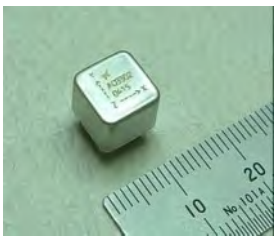


Fig.4 ACB302.

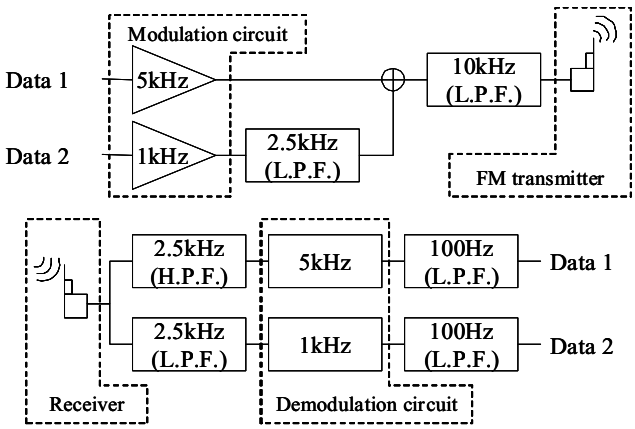
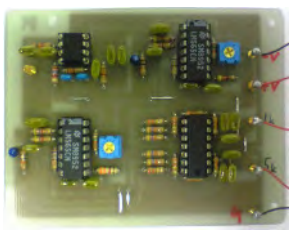


Fig.5 A block diagram of our telemetring.



Fig.6 a) Modulation circuit.



b) Demodulation circuit.

II-II System software

We analyze digitized EEG and acceleration data of the head in a computer, and perform the noise removal. The most of noises of EEG under exercising are confirmed that

it is an acceleration origin of the head. We can reduce the noise of the acceleration origin using Adjustment Noise canceller as a digital filter.

Adjustment Noise canceller

The method of the adjustment noise cancellation is used for the noise removal, and this algorithm was developed by us. This method removes the noise element from the signal that contains the noise, and is one of the basic filters in the signal conditioning that takes out only the interested signal. In this theory, the noise source is assumed X(t), and the signal that we want to know is assumed S(t). We suppose that S(t) and X(t) have no correlation. Where, we define D(t) that is the liner summation of S(t) and X(t). Therefore, D(t) is expressed the following equation.

$$D(t)=aS(t)+bX(t)$$

And we suppose that D(t) and X(t) are observable. In our system, we have to discriminate between S(t)(real EEG signal under exercising) and X(t)(artifact) from D(t)(EEG with artifact). In our system, in order to obtain a coefficient "b", the variable "b' " is changed it's value step by step, and the correlation coefficient between D(t) and b'X(t) is calculated for each "b' ". From this procedure, we can obtain the "b' " that bring the highest value of correlation coefficient between D(t) and b'X(t). We regard this "b' " as the coefficient "b". And then interested signal S(t) is obtained. Fig.7 shows a principle of the adjustment noise cancellation.

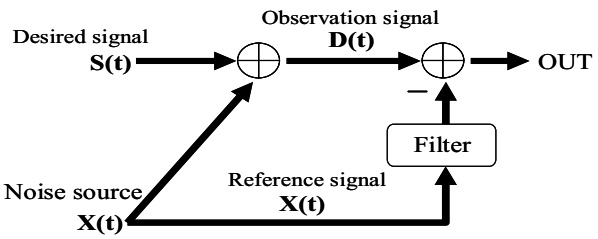


Fig.7 A principle of the adjustment noise cancellation.

III. Experiment

First, we measured the EEG at rest in this time. Second, we simulated the telemetry system with modulate and demodulate circuit of the Fig.6 a) and b). Electrodes for EEG measurement are set on left auricular (common), midline frontal (Fz), vertex (Cz). And EEG was measured under this bipolar condition.

IV. Results

Fig.8 shows an example of the EEG data that was measured under resting and their power spectrum. Fig.9(a) shows the EEG data with noise and Fig.9(b) shows the noise reduced EEG data by using adjustment noise canceller. Fig.9(c) also shows the power spectrum of noise reduced EEG data. As shown in Fig.8(b) and Fig.9(c), we can see that our developed noise canceller worked very well.

Simulated results of the telemetry system are shown in fig.10 and Fig.11. Fig.10 shows input data of multiplexing unit. Both Fig.10(a) and (b) are sinusoidal wave and these frequency are 10Hz and 40Hz respectively. Sinusoidal wave of 40Hz is inputted as “Data 1”and 10Hz is inputted as “Data 2” in Fig.5. Fig.11 shows the de-multiplexed data. Fig.11(a) is de-multiplexed “Data 2” and (b) is “Data 1”. As shown in these results, noise free de-multiplexed data were obtained. And we think that the developed data multiplexing unit worked perfect.

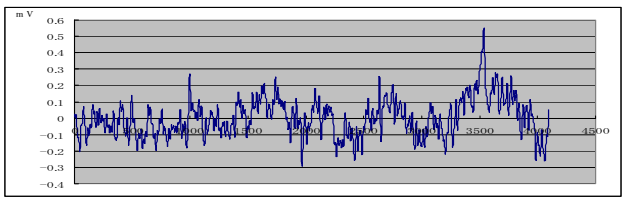


Fig.8 a) The EEG at rest of the time domain.

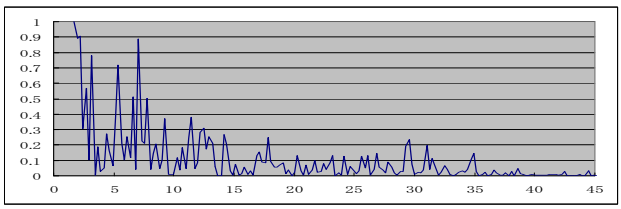


Fig.8 b) The EEG at rest of the FFT.

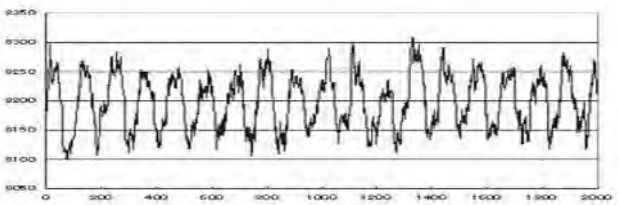


Fig.9 a) The EEG data with noise.

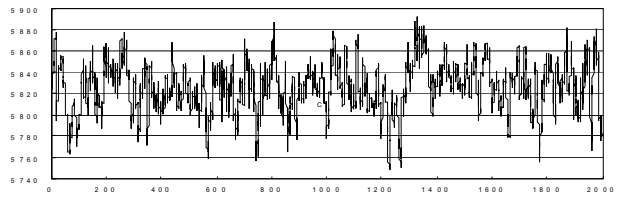


Fig.9 b) The noise reduced EEG data by using adjustment noise canceller.

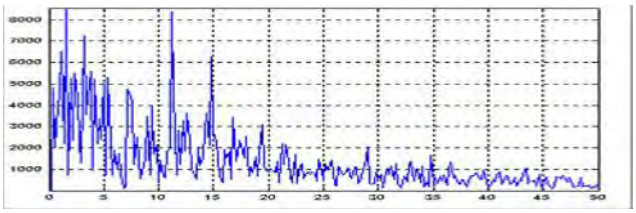


Fig.9 c) The power spectrum of noise reduced EEG data.

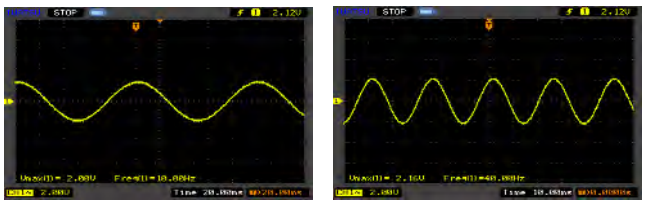


Fig.10 a) The wave pattern is input of the modulate circuit of 1 kHz (left). b) The wave pattern is input of the modulate circuit of 5 kHz (right).

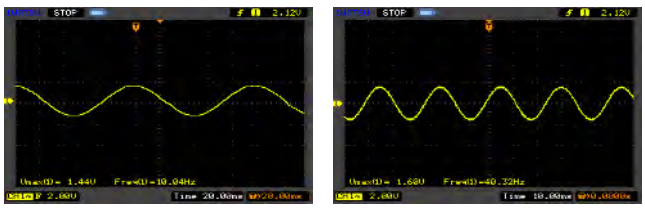


Fig.11 a) The wave pattern is the output of the demodulate circuit of 1 kHz (left). b) The wave pattern is the output of the demodulate circuit of 5 kHz (right).

V. Conclusions

In this paper, we talked about our EEG artifact reduction system and telemetry system. From experimental results, we can see that our artifact reduction system is able to reduce noise that includes measured EEG. And developed data multiplexing and de-multiplexing system worked perfect. Therefore, we concluded that if this system is completed, our EEG measurement system will be a valuable one for athletes.

References

1. Junya TANAKA, Mitsuhiro KIMURA, Naoya HOSAKA, Hiroyuki SAWAJI, Kenichi SAKAKURA, Kazushige MAGATANI ”Development of the EEG measurement technique under exercising” proceeding of the International Federation for Medical & Biological Engineering VoL.12(2005)
2. Naoya HOSAKA Junya TANAKA, Akira KOYAMA, Kazushige MAGATANI “The EEG measurement technique under exercising”

Author: Noriyuki DOBASHI
Institute: TOKAI University
Street: 1117 Kitakaname Kanagawa
City: Hiratsuka
Country: Japan
Email: dobatarian@yahoo.co.jp

Evaluation of Photic Stimulus Response Based on Comparison with the Normal Database in EEG Routine Examination

T. Fukami[1], F. Ishikawa[2], T. Shimada[3], B. Ishikawa[2] and Y. Saito[4]

[1] Yamagata University, Department of Bio-system Engineering, Yonezawa, Japan
[2] Hotokukai Utsunomiya Hospital, Utsunomiya, Japan
[3] Tokyo Denki University, Inzai, Japan
[4] The Institute for EEG Analysis, Tokyo, Japan

Abstract — **The aim of our research is the evaluation of the photic driving response, a routine EEG examination for diagnosis. It is well-known the EEG responds not only to the fundamental frequency but also to all sub and higher harmonics of a stimulus. In this study, we propose a method for detecting and evaluating responses in screening data for individuals. This method consists of two comparisons based on statistical tests. One is an intraindividual comparison of the amplitudes between the EEG at rest and the photic stimulation (PS) response reflecting enhancement and suppression by PS, and the other is a comparison between data from an individual and a distribution of normals in the normal database. These tests were evaluated using the Z-value based on the Mann-Whitney U-test. The experiment was conducted using PS frequencies of 3, 6, 7, 10, 14 and 18Hz. We used the measured data at electrode O1 where PS appears the greatest. We measured EEGs from 130 normal subjects and 30 patients with any of schizophrenia, dementia and epilepsy. Normal data were divided into two groups, the first consisting of 100 data for database construction and the second of 30 data for test data. We evaluated amplitudes at a subharmonic frequency, the fundamental frequency, the second harmonic frequency, higher order harmonic frequencies less than 40Hz, and the alpha peak frequency. From the results of the comparison of patients and the normal database, frequencies with Z-values smaller than those of the normal database could be recognized. At the alpha peak frequency, patient data have higher Z-values than does the normal database though there were no significant differences for the subharmonics. Moreover, in the patient data, both the enhancement of harmonic components including the fundamental wave by PS and suppression of the alpha component were weak.**

Keywords — **electroencephalography(EEG), photic driving response, alpha suppression, Mann-Whitney U-test.**

I. Introduction

Photic stimulation (PS) is a commonly used stimulation in electroencephalogram (EEG) routine examinations. The PS response consists of the elicited rhythmic activity. Generally, three types of driving components are measured when PS is given to a human and they are diagnostically helpful. One is the fundamental driving for which the frequency is equivalent to the stimulus frequency (f_0), and the others are the harmonic driving and subharmonic driving for which the frequencies are nf_0 and $f_0/n\,(n \geq 2)$, respectively.

The effect of intermittent PS on the human EEG was first studied by Adrian and Matthews [1]. Numerous reports on human measurements were then presented. However, there have not been so many reports relating to an analyzing method for quantitative evaluation. Fukushima applied EEG-interval-spectrum-analysis to photic driving responses [2]. Drake et al introduced the quantitative measure of frequency times the duration of the driving response [3].

Regarding the analysis of clinical data, some researchers reported the relationship between normals and patients with a specific disease. Kikuchi et al analyzed EEG signals using the absolute power of harmonic responses to PS [4]. Jin et al compared PS responses between schizophrenics and normals[5]. However, the results in these studies were obtained by a statistical comparison between two groups such as a normal group and patient group. A comparison between groups is useless for diagnosis using data for individuals during screening. An analysis method using data for individuals aimed at diagnosis support has never been reported.

Therefore, in this study, we propose a method for evaluating data for individuals quantitatively.

II. Methods

EEG signals were recorded during a state of relaxed wakefulness with closed eyes. A multichannel EEG signal was acquired using a Nihon Koden polygraph (EEG-1100) with a 0.3s time constant, 60Hz high cut filter and 97.5nV quantization level. EEG signals were measured at 19 electrodes according to the International 10/20 system. Here, monopolar derivation with bilateral references to the corresponding earlobes was used.

The measurement of the photic driving response and a flowchart of our analysis are shown in Fig. 1. A cycle without PS (at rest) for 10s then with PS for 10s was re-

Chwee Teck Lim, James C.H. Goh (Eds.): ICBME 2008, Proceedings 23, pp. 253–256, 2009
www.springerlink.com

peated. The frequency of PS was varied in the order of 3, 6, 7, 10, 14 and 18Hz. The EEG signals were digitized at a sampling frequency of 200Hz. Photic pulse characteristics were as follows. The brightness of the flash stimulus was 30,000 cd/m^2, the light intensity was 4.0 lx/s, the pulse width was 2 ms, and the equipment was placed 30cm in front of the subjects. All data on subjects and patients in this paper were taken at Utsunomiya Hospital after informed consent.

Our method consists of two kinds of comparisons for evaluation of the PS response. One is a comparison of responses at rest and during PS as shown in Fig.1, and the other is a comparison of data for individuals (screening data) and a distribution of normals. The former comparison implies an index reflecting the enhancement or suppression by PS in intraindividual data and the latter comparison implies an index reflecting the position of the individual's data in the distribution of normal data.

In this study, we measured PS responses from 130 normal subjects (18-40 years old, ave.=23.8, s.d.=4.38) and 30 patients (36-89 years old, ave.=67.7, s.d.=12.8). Patients have a disease of any of schizophrenia, dementia and epilepsy. Normal data were divided into two groups; 100 data (18-40 years old, ave.=23.8, s.d.=4.89) for database construction and 30 data (20-27 years old, ave.=23.6, s.d.=1.97) for test data.

We first explain the former comparison shown in Fig.1.The EEG measurements at rest and with PS are repeated every 10 seconds alternately. In each period, the first 2s of data were discarded to avoid the effect of the orienting response and off-response due to the stimuli immediately. We need to construct a distribution consisting of plural samples when we perform a statistical test. In this study, a window having 100 sample points (0.5s) was slid from 2s after the onset of the cycle. The frequency analysis described below was performed in 16 sections for each cycle.

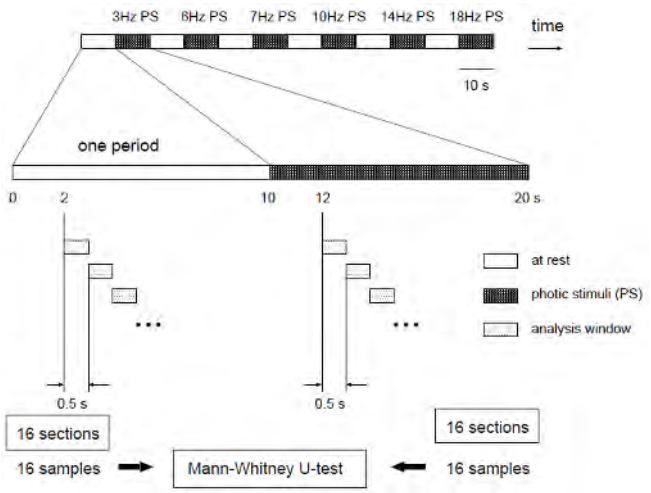


Fig.1 Analysis of EEG data

Generally, discrete Fourier transform (DFT) make it possible to calculate only the frequency components at integer multiples of the fundamental frequency, 2Hz in this study.

However, we need to estimate other frequency components which can not be calculated by limitation of DFT. We therefore used the method based on trapezoidal integral approximation of continuous Fourier transform. In this study, we performed the above calculation after elimination of bias (0Hz) component by subtraction of average in the analysis window. We then obtained the amplitude spectrum from 0 to 40Hz with 0.5Hz intervals by the following equation. This frequency analysis based on the Fourier transform was performed in 16 sections at rest and in 16 sections during PS. Amplitudes at these frequencies in each cycle were collected as a distribution of 16 samples.

The after-mentioned Mann-Whitney U-test was executed for the distributions before and during PS (16 vs. 16 samples) and the Z-value for each analysis frequency and each PS frequency was then calculated.

In the latter comparison, based on the Z-value for before and during PS response acquired in the former comparison, we introduced the rank among normal distributions in a database as the index. This index was expressed as a percentile rank such that a higher Z-value has a smaller rank.

In this study, we used the Mann-Whitney U-test, which is known as a statistical test for comparing non-parametric distributions, because we do not know if these distributions are necessarily specific distributions such as Gaussian or gamma distributions. This test is based on the Wilcoxon rank-sum test and a non-parametric test for assessing whether two sample sets of observations come from the same distribution. It is executed under the null hypothesis of samples from the same general population. We defined the rank-sum of two groups composed of amplitudes at rest and during PS after arranging data with higher rank (small ordinal number) for larger amplitude. We then executed the U-test.

General U-test prevents the Z-value from being less than zero. In our method, when the Z-value is negative, there is suppression due to PS, and when the Z-value is positive, there is enhancement due to PS. A zero Z-value indicates no change due to PS. In this study, we defined the thresholds for the judgment of significance as $|Z| = 1.96$ and 2.81. The thresholds correspond to $p<0.05$ and $p<0.005$. Under the condition of $|Z|>1.96$ or $|Z|>2.81$, we recognize a significant difference between the two distributions by judging that the null hypothesis is rejected. We finally show the results of applying this method to amplitudes at a subharmonic frequency (f/2), harmonic frequencies (2f, 3f, 4f, 5f) less than

40Hz and the alpha peak frequency (alpha peak) where the PS frequency (f) is the fundamental frequency. In this study, we used the measured data at electrode O1 where PS appears the greatest.

Judgment is performed by classifying the maximal Z-value mentioned above as one of five levels as follows. Five notations ((++),(+),N.S.,(-),(--)) are assigned depending on the Z-value. The notations "(++)" and "(--)" designate the cases satisfying $|Z|>2.81$ corresponding to $p<0.005$ and there being a very significant difference between the two amplitude distributions.The notations "(+)" and "(-)" indicate the cases satisfying $|Z|>1.96$ corresponding to $p<0.05$ and there being a significant difference between the two distributions. When $|Z|<1.96$, the notation N.S. indicates there is no significant difference between the distributions.

III. Results and Discussions

We evaluated amplitudes at a subharmonic frequency ($f_0/2$), the fundamental frequency (f_0), the second harmonic frequency ($2f_0$), higher order harmonic frequencies less than 40Hz, and the alpha peak frequency in this study.

We show the results for normal and patient groups, with 30 data used for each. In Table 1, we summarize the results for all combinations of PS frequency and analysis frequency based on the judgement corresponding to the averaged Z-value of 30 data. In this report, intraindividual evaluation is expressed in the row labeled "at rest vs. during PS" using the five levels in the U-test for subharmonics, the fundamental wave and harmonics less than 40Hz. For the alpha peak frequency, the frequency with maximal amplitude before PS was adopted.

Regarding the normal database comparison, evaluation of each subject data is difficult, so we showed the U-test results between 30 normals/patients and database (30 normal test data (patient data) vs. DB). This processing was performed by the U-test between two Z-value distributions, which is 30 samples vs. 100 samples for the normal database, and then classified the results into the five levels. For all PS frequencies, results for 30 normals and 30 patients are test are shown in Tables 1 and 2, respectively.

In the intraindividual test, a significant difference between at rest (before PS) and during PS can be recognized in the case that the PS frequency is greater than 6Hz. The significance is greater for high order harmonics more so than for the third harmonic in the case that the PS frequency is less than 7Hz. For PS with a frequency greater than 14Hz, a significant difference is seen for all harmonic frequencies, including the fundamental frequency, and Z-value is larger than that for a PS frequency less than 7Hz. There is no apparent difference for subharmonic and alpha peak frequencies.

Analysis results for data of the 30 patients are tabulated in Table 2. We can find significant differences were detected in similar cases to those of the normal test. However, enhancement by PS is smaller than that for the normal test.

In the comparison of the normal test and database data, there are no difference at all fundamental and harmonic frequencies for all PS frequencies. This result is appropriate because both test data and database data consist of normal subjects' data.

From the results of the comparison of patients and the normal database, frequencies with Z-values smaller than those of the normal database can be recognized. At the alpha peak frequency, patient data have higher Z-values

Table 1 Results obtained from average of 30 normal test data

PS 3Hz	$f/2$	f	$2f$	$3f$	$4f$	$5f$	α peak
At Rest vs. during PS	N.S.	N.S.	N.S.	N.S	N.S.	N.S.	N.S.
30 normal test data vs. DB	N.S.	N.S.	N.S.	N.S.	N.S	N.S.	N.S.
PS 6Hz	$f/2$	f	$2f$	$3f$	$4f$	$5f$	α peak
At Rest vs. during PS	N.S.	(+)	N.S.	(+)	(+)	(+)	N.S.
30 normal test data vs. DB	N.S.	N.S.	N.S.	N.S.	N.S	N.S.	N.S.
PS 7Hz	$f/2$	f	$2f$	$3f$	$4f$	$5f$	α peak
At Rest vs. during PS	N.S.	N.S.	N.S.	(+)	(+)	(+)	N.S.
30 normal test data vs. DB	N.S.	N.S.	N.S.	N.S.	N.S	N.S.	N.S.
PS 10Hz	$f/2$	f	$2f$	$3f$	$4f$	$5f$	α peak
At Rest vs. during PS	N.S.	N.S.	(++)	(++)	(+)		N.S.
30 normal test data vs. DB	N.S.	N.S.	N.S.	N.S.	N.S		N.S.
PS 14Hz	$f/2$	f	$2f$	$3f$	$4f$	$5f$	α peak
At Rest vs. during PS	N.S.	(++)	(++)				N.S.
30 normal test data vs. DB	N.S.	N.S.	N.S.				N.S.
PS 18Hz	$f/2$	f	$2f$	$3f$	$4f$	$5f$	α peak
At Rest vs. during PS	N.S.	(++)	(++)				N.S.
30 normal test data vs. DB	N.S.	N.S.	N.S.				N.S.

Table 2 Results obtained from average of 30 patients data

PS 3Hz	$f/2$	f	$2f$	$3f$	$4f$	$5f$	α peak
At Rest vs. during PS	N.S.	N.S.	N.S.	N.S	N.S.	N.S.	N.S.
30 patients data vs. DB	N.S.	N.S.	N.S.	(+)	(+)	N.S.	(++)
PS 6Hz	$f/2$	f	$2f$	$3f$	$4f$	$5f$	α peak
At Rest vs. during PS	N.S.	N.S.	N.S.	N.S.	N.S.	N.S.	N.S.
30 patients data vs. DB	N.S.	(– –)	N.S.	(–)	(–)	N.S.	N.S.
PS 7Hz	$f/2$	f	$2f$	$3f$	$4f$	$5f$	α peak
At Rest vs. during PS	N.S.	N.S.	(+)	(+)	N.S.	N.S.	N.S.
30 patients data vs. DB	N.S.	N.S.	N.S.	N.S.	(–)	(–)	(++)
PS 10Hz	$f/2$	f	$2f$	$3f$	$4f$	$5f$	α peak
At Rest vs. during PS	N.S.	N.S.	(+)	(+)	N.S.		N.S.
30 patients data vs. DB	N.S.	N.S.	(–)	(–)	(–)		(++)
PS 14Hz	$f/2$	f	$2f$	$3f$	$4f$	$5f$	α peak
At Rest vs. during PS	N.S.	(+)	(+)				N.S.
30 patients data vs. DB	N.S.	(–)	(–)				(++)
PS 18Hz	$f/2$	f	$2f$	$3f$	$4f$	$5f$	α peak
At Rest vs. during PS	N.S.	N.S.	N.S.				N.S.
30 patients data vs. DB	N.S.	(–)	(–)				(++)

than does the normal database though there are no significant differences for the subharmonics. This means the amplitude at the alpha peak frequency is never enhanced more than the amplitude for the normal database is. It may be more accurate to say that the degree of alpha suppression by PS in patients is small compared with the normal database than to say there is enhancement by PS. These results indicate that both the enhancement of harmonic components including the fundamental wave by PS and suppression of the alpha component are weak.

IV. Conclusions

In this study, we proposed a method for the quantitative evaluation of the photic driving response for individual data.This method consists of two statistical processes. One is an evaluation of the enhancement or suppression by PS. The other is an evaluation of the position of the individual data in the distribution of normals. We calculated Z-values using the Mann-Whitney U-test, which is a statistical test for comparing nonparametric distributions. The experiment was conducted using PS frequencies of 3, 6, 7, 10, 14 and 18Hz. A subharmonic frequency, fundamental frequency, and higher harmonic frequencies less than 40Hz were categorized according to the above five levels. We constructed a normal database of 100 normal subjects' data.

We then applied this method to the data of 30 normals and 30 patients and presented the results in this study. For patients, Z-values at fundamental and harmonic frequencies are larger than those for normals and the degree of alpha suppression is smaller than that for normals.

We suggest that these insensitivities are new potential criteria for discriminating between normals and psychiatric and neurologic patients.

In future research, we plan to apply our method to many kinds of diseases.

References

1. Adrian E D (1934) The Berger rhythm: Potential changes from the occipital lobes in man., Brain, 57: 355-385.
2. Fukushima T (1975) Application of EEG-interval-spectrum-analysis (EISA) to the study of photic driving responses. A preliminary report. Arch. Psychiatr. Nervenkr., 220: 99-105.
3. Drake M E Jr, Shy K E, Liss L (1989) Quantitation of photic driving in dementia with normal EEG. Clin. Electroencephalogr. 20: 153-155.
4. Kikuchi M, Wada Y, Koshino Y (2002) Differences in EEG harmonic driving responses to photic stimulation between normal aging and Alzheimer's disease. Clin. Electroencephalogr., 33: 86-92.
5. Jin Y, Castellanos A, Solis E R, Potkin S G (2000) EEG resonant responses in schizophrenia: a photic driving study with improved harmonic resolution. Schizophr. Res., 44: 213-220.

Author: Tadanori FUKAMI
Institute: Yamagata University
Street: Jonan 4-3-16
City: Yonezawa
Country: Japan
Email: fukami@yz.yamagata-u.ac.jp

A Speech Processor for Cochlear Implant using a Simple Dual Path Nonlinear Model of Basilar Membrane

K.H. Kim[1], S.J. Choi[1], J.H. Kim[2]

[1] Yonsei University/Biomedical Engineering, Wonju, South Korea
[2] Nurobiosys, Co., Seoul, South Korea

Abstract — **We present a novel speech processing strategy for cochlear implant (CI) based on active nonlinear characteristics of biological cochlea that contribute to hearing under noisy conditions. A simple dual path nonlinear model (SDPN) was developed to utilize the advantage of level-dependent frequency response characteristics in robust formant representation. The model was motivated from the function of basilar membrane so that level-dependent frequency response can be reproduced. Compared to dual resonance nonlinear model (DRNL) which has been proposed as an active nonlinear model of basilar membrane, the proposed model is much simpler and thus better suited to be incorporated in CI speech processor. We developed a CI speech processing strategy based on the SDPN for frequency decomposition and an adaptive envelope detector. It was verified from spectral analysis that the formants of speech is robustly represented after the frequency decomposition by the array of SDPN, compared to a linear bandpass filter array of conventional strategies. From acoustic simulation and hearing experiments on normal subjects, it was verified that the proposed strategy yielded enhanced syllable recognition under speech-shaped noise than the conventional strategy.**

Keywords — **Cochlear implant, speech processor, basilar membrane, adaptive frequency response, simple dual path nonlinear model (SDPN)**

I. Introduction

Cochlear implants (CIs) have been successfully used for the restoration of hearing function due to profound sensorineural hearing loss, by direct stimulation of spiral ganglions using electrical pulses generated by processing of incoming speech. In spite of great progress during more than two decades, there remain a lot of things to be done in order to achieve successful restoration of hearing under noisy environment, melody recognition, and the reduction of cognitive loads of the patients [1].

Several methods can be utilized for the improvement of CI. Among them, the development of novel speech processing strategy is very effective in that it does not require the change of current hardwares and can be adopted in already implanted devices by modification of embedded program. Speech processing strategy here means an algorithm used to generate electrical stimulation pulses based on the processing of incoming speech waveforms. More accurate imitation of normal auditory function is one of the most promising approaches among several directions in speech processing strategy development [1], [2]. It has been suggested that speech perception performance can be considerably improved by adopting an active nonlinear model of basilar membrane in cochlea, which is called dual resonance nonlinear (DRNL) model [2].

Spectral peaks of speech waveforms, which are called formants, are very important cues for speech perception. It is known that the information on formant frequencies are encoded in the population responses of the auditory nerve [3]. The improved speech perception enabled by active nonlinear model is due to robust representation of formants under noisy environments. We also have recently presented a detailed performance analysis of the DRNL-based CI speech processing strategy, focusing on the formant representation characteristics and enhanced vowel perception [2].

We propose a new active nonlinear model of frequency response of the basilar membrane, called simple dual path nonlinear (SDPN) model. The SDPN model was motivated from further simplification of the DRNL model, with the purpose of developing a CI speech processing strategy. Many building blocks and parameters of the DRNL model were not necessary to implement the level-dependent frequency response of the biological cochlea, because they were adopted for the detailed replication of experimental results. The proposed SDPN is much simpler than the DRNL, yet it can provide the level-dependent frequency response, which is beneficial for real-time processing with lower power consumption.

We developed a CI speech processing strategy based on the SDPN for frequency decomposition. It was verified from spectral analysis that the formants of speech is robustly represented after the frequency decomposition by the array of SDPN, compared to the linear bandpass filter array of conventional strategies. From acoustic simulation and hearing experiments on normal subjects, the proposed strategy was shown to provide enhanced syllable identification performance under speech-shaped noise, much better than the conventional strategy using fixed linear bandpass filter array and envelope detector.

Chwee Teck Lim, James C.H. Goh (Eds.): ICBME 2008, Proceedings 23, pp. 257–260, 2009
www.springerlink.com

II. Materials and Mehtods

A. Proposed speech processing strategy

Fig. 1 (a) shows the general structure of the speech processor for a CI. Incoming speech is decomposed into multiple frequency bands (stage 2 of Fig. 1 (a)), and then, relative strength of each subband is obtained from an envelope detector (stage 3) to be used to modulate the amplitudes of stimulus pulses after logarithmic compression. Most modern CI devices utilize this structure [4]. In the strategy proposed in this paper, each channel of the speech processor is made of an active nonlinear filter model of basilar membrane with variable response characteristic, instead a fixed linear bandpass filter employed in conventional CIs. The variable response characteristic originates from the input-dependent tuning property of basilar membrane resulting from active motility of outer hair cell (OHC), and this active nonlinear response property is known to contribute to robust representation of speech cues under noise [5].

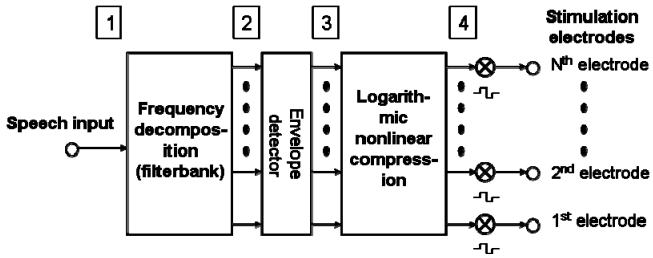


Fig. 1 General structure of the CI speech processing strategies.

Fig. 2 (a) illustrates a dual resonance nonlinear (DRNL) model, which was proposed as a numerical model of the basilar membrane response characteristic [6]. In the DRNL model, the output of each cochlear partition is represented as a summation of the outputs from a linear and a nonlinear pathway. The effective center frequencies of the linear and nonlinear pathways are slightly different. The DRNL model can replicate the frequency response of biological cochlea in that the level-dependent tuning and level-dependent gain properties could be successfully reproduced [6]. Because our aim here is only to utilize the advantages of the active nonlinear response and it is not necessary to replicate the biological cochlea in detail, we propose a new simplified model, which we call simplified dual path nonlinear (SDPN) model. The block diagram of the SDPN model is shown in Fig. 2 (b). While developing the SDPN model, we did not try to reproduce numerical details obtained from neurophysiological experiments. It was motivated by the purpose of implementing the level-dependent frequency response characteristics of biological cochlea.

As in the DRNL model, the incoming speech is given to two pathways. The linear pathway consists of a linear gain (fixed to 6 here) and a broad bandpass filter, which is called tail filter. The nonlinear pathway is made of a sharper bandpass filter, which is called tip filter, and a compressive nonlinearity that is employed to mimic the saturation property of the OHC. The nonlinearity is expressed as;

$$y = 2\arctan(15x) \quad (1)$$

Both the tail and tip filters are made of Butterworth bandpass filters (tail filter: 2nd order, tip filter: 4th order). The bandwidth of the tail filter is set to be three-times larger than that of the tip filter. In order to realize the variable response property, relative contribution of each pathway is controlled according to the input level (root-mean-square value) by the nonlinearity. The overall output from one channel of the frequency decomposition block is obtained by summing outputs from the two pathways. As we will show later in Results (Fig. 3), we can enable variable frequency response characteristics of biological cochlea with much lower computation cost than the DRNL model.

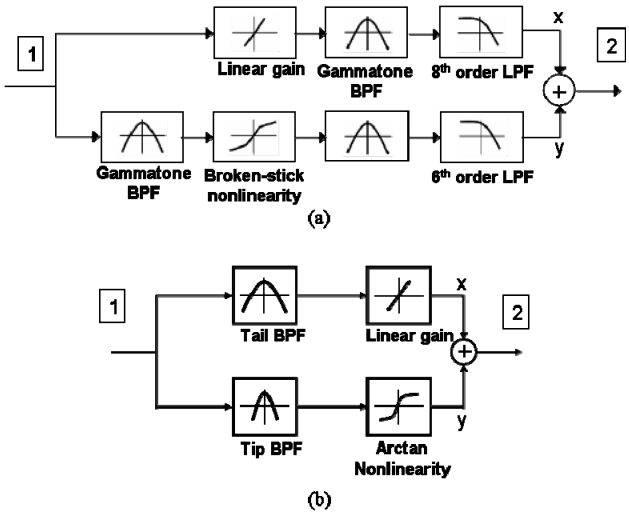


Fig. 2 (a) Block diagram of the DRNL model. (b) Block diagram of the proposed SDPN model.

B. Acoustic simulation

Acoustic simulation can provide an objective quantification of potential performance of a specific processing strategy and a reference to clinical tests, and thus it has been utilized for many studies on the development of novel speech processing strategies. The center frequencies of the channels were chosen according to the method of Loizou et al. [7], since this enables systematic computation of the filter bandwidths, and is used in current CI devices.

The method of acoustic simulation of conventional strategy was similar to that of Dorman et al [8]. After applying a linear bandpass filter array for frequency decomposition, an envelope detector consisting of a full-wave rectifier and a 4th order Butterworth lowpass filter (cutoff frequency: 400 Hz) was applied. The detected envelopes were used to modulate the sinusoids with frequencies same as the center frequencies listed in Table I. Finally, the amplitude-modulated sinusoids from all the channels were summed.

C. Hearing experiment

Ten normal-hearing subjects volunteered to participate in the hearing experiment (ages: 25.8 ± 4.08 years; six men, four women). The experiments were performed under two noise conditions: without any noise (i.e., SNR of ∞ dB) and with speech-shaped noise (SSN) of 2 dB signal-to-noise ratio (SNR). The number of channels was varied to 4, 8, and 12 channels.

Syllable identification tests were performed using multiple-choice tasks. Consonant-vowel-consonant-consonant (CVCV) disyllables were constructed mainly for the vowel perception performance test. Each speech token was fixed to the form of /sVda/, i.e., only the first vowel was changed while the others were fixed to /s/, /d/, and /a/. The first vowel was selected from /a/, /ə/, /o/, /u/, /i/, and /e/. Vowel-consonant-vowel (VCV) type monosyllables were also constructed. The vowels at the beginning and end were the same and fixed to /a/. The consonants between vowels were selected from /g/, /b/, /m/, /n/, /s/, and /j/.

The acoustic waveforms of speech tokens were generated by 16-bit mono analog-to-digital conversion at sampling rate of 22.050 kHz and stored as .wav files. The stored files were played by clicking icons displayed in a graphic user interface prepared for the experimental run. The speech tokens were presented binaurally using a headphone (Sennheiser HD25SP1) and a 16-bit sound card (SoundMAXTM integrated digital audio soundcard). A 5-min training session was given before the main experiment. If the subjects requested, the waveforms were played once more. After hearing each speech token, the subjects were requested to choose the presented syllable among six given examples as correctly as possible, and the percentage of correct answers was scored.

III. Result

A. Variable frequency response of the SDPN model

Fig. 3 shows the variable frequency response of the proposed SDPN model with 1500 Hz center frequency. When the input amplitude was low (35 dB sound pressure level (SPL)), the contribution of nonlinear pathway was relatively large so that overall response showed a sharp frequency selectivity determined by the tip filter. Peak gain was 9.44, and the full width at half maximum (FWHM) was 140.27 Hz. As the amplitude increases (85 dB SPL), the contribution of linear pathway became dominant, and thus, overall frequency response became broader (FWHM= 424.08 Hz). Meanwhile, the overall gain decreased due to the compressive nonlinearity (peak gain= 4.26). Hence we could achieve the goal of replicating the level-dependent frequency response characteristics of biological cochlea qualitatively. Compared to the DRNL model, the proposed simplified structure could be executed very quickly. For example, in order to process 1 s speech, the CPU time was 0.054 ± 0.012 s for the SDPN model while it took 1.33 ± 0.034 s for the DRNL (Average from 40 trials, Matlab implementation, 3.0 GHz Pentium 4 processor, 2 GB RAM). I.e., the processing time for the proposed model was only about 1/24.6 of the DRNL model.

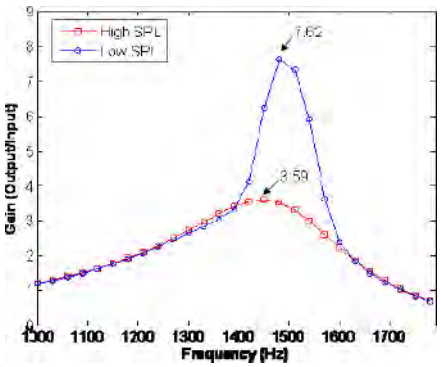


Fig. 3 Variable frequency response of the proposed SDPN model

B. Acoustic simulation and hearing experiment

The results of hearing experiments are shown in Fig. 7. The percentages of correct answers were plotted as functions of the number of channels for 4, 8, and 12 channels. For quiet conditions, the proposed strategy was better than the conventional strategy for all channel conditions. The superiority was statistically significant for 8 and 12 channel conditions (t-test, $p<0.05$ (uncorrected) for 4 channels, and $p<0.01$ for 8 and 12 channels). Under SSN of 2 dB SNR, the proposed strategy provided considerably better syllable identification for all channel conditions (t-test, $p<0.05$ (uncorrected) for 4 and 8 channels, and $p=0.06$ for 12 channels).

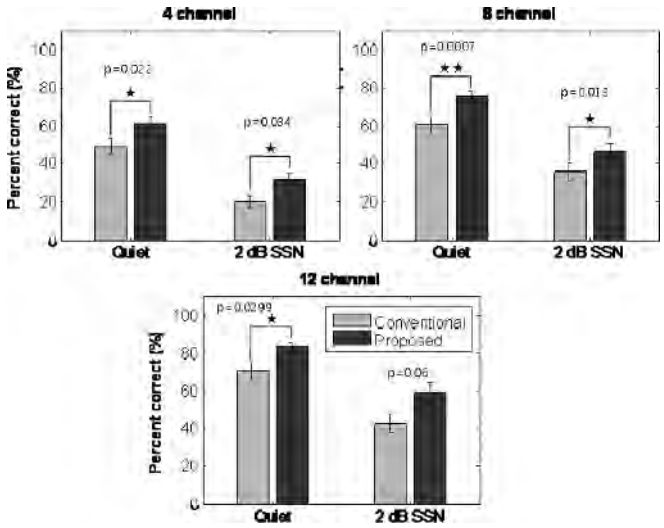


Fig. 4 Results of syllable identification tests

IV. Conclusions

In this paper, we proposed a simple active nonlinear model of biological cochlea and developed a novel speech processing strategy for CIs based on it. We showed that it is very useful for the robust representation of spectral cues to utilize the variable frequency response property originating from the function of biological cochlea.

Some previous experimental studies reported that the active, variable frequency response property of basilar membrane contributes significantly to the robust representation of formant information under noisy environments, and several numerical models were suggested to reproduce this property [5], [9]. For example, Deng and Geisler [5] proposed a nonlinear differential equation model with a variable damping term to simulate level-dependent compression effect, and successfully reconstructed the response characteristics of the biological cochlea that are beneficial for robust spectral cue representation under noise. This implies that the speech perception of CI recipients can be improved by adopting the active nonlinear response property, as was demonstrated by enhanced performances of the CI speech processors based on the DRNL model [2].

Although the DRNL model is one of the most efficient models considering computational costs, its purpose is to replicate detailed experimental results and many parameters are included so that it may still not be adequate for CI speech processor. Instead we proposed a simplified model for implementing variable frequency response. The proposed SDPN model consists of dual pathways just as the DRNL model, however, we did not make any attempt to reproduce experimental results quantitatively. Its advantage as a building block of the CI was verified by acoustic simulation and hearing experiment on normal subjects. Based on this result, we assume that the detailed imitation of the frequency response characteristics of the human cochlea is not essential for the purpose of the improvement of the CI speech perception performance, although it was suggested to use the DRNL model with parameters fitted to human basilar membrane [10]. Further verification is required to confirm this assumption.

In our SDPN model, the bandpass filters in linear and nonlinear pathways were implemented using Butterworth filter, which possesses maximally-flat frequency response. Thus, it may be possible to alleviate the 'picket fence effect' [10], i.e. the decrease of frequency response at the position of the boundaries between nearby channels, resulting from the sharp frequency response of the gamma-tone filter used in the DRNL model.

Acknowledgment

This study was supported by the Korea Science and Engineering Foundation through the Nano Bioelectronics and Systems Research Center (NBS-ERC) of Seoul National University under grant R11-2000-075-01005-0.

References

1. Wilson S, Lawson T et al (2003) Cochlear implants: some likely next steps. Annu Rev Biomed Eng 5:207-249
2. Kim. K, Choi S et al. (2008) An improved speech processing strategy for cochlear implants based on an active nonlinear filterbank model of the biological cochlea. IEEE Trans Biomed Eng *in press*
3. Young D, Sachs B (1979) Representation of steady-state vowels in the temporal aspects of the discharge patterns of populations of auditory-nerve fibers. J Acoust Soc Am 66:1381-1403
4. Wilson B, Finley C (1991) Improved speech recognition with cochlear implants. Nature 352:236-238
5. Deng L, Geisler D (1987) A composite auditory model for processing speech sounds. J Acoust Soc Am 82:2001-2012
6. Meddis R, O'Mard P et al. (2001) A computational algorithm for computing nonlinear auditory frequency selectivity. J Acoust Soc Am 109:2852-2861
7. Loizou C, Dorman M et al. (1999) On the number of channels needed to understand speech. J Acoust Soc Am 106:2097-2103
8. Dorman F, Loizou C et al. (1997) Speech intelligibility as a function of the number of channels of stimulation for signal processors using sine-wave and noise-band outputs. J Acoust Soc Am 102:2403-2411
9. Robert A, Eriksson L (1999) A composite model of the auditory periphery for simulating responses to complex sounds. J Acoust Soc Am 106:1852-1864
10. Wilson S, Schatzer R et al. (2006) Possibilities for a closer mimicking of normal auditory functions with cochlear implants, Cochlear Implants, 2nd Ed., edited by SB Waltzman and JT Roland, New York, USA, 2006, pp 48-56

Mechanical and Biological Characterization of Pressureless Sintered Hydroxapatite-Polyetheretherketone Biocomposite

Chang Hengky[1], Bastari Kelsen[2], Saraswati[2], Philip Cheang[2]

[1] Nanyang Polytechnic, School of Engineering (Manufacturing), Biomedical Engineering Group , Singapore
[2] Nanyang Technological University, School of Chemical and Biomedical Engineering, Singapore

Abstract — **Bioactive particulate reinforced polymer composite comprising synthetic Hydroxyapatite (HA) and Polyetheretherketone (PEEK) has been fabricated by injection molding for load-bearing applications in these past few years. The limited degree of customization of injection molding process and the high cost of the mold fabrication and processing cost lead to the fabrication of HA-PEEK composites by pressureless sintering method. The aim of the project is prepared a HA-PEEK composite block from HA-PEEK powder blends using simple detachable cubic stainless steel mold in the furnace with specific temperature and duration. The resultant HA-PEEK composite block will be machine with CAD machining system to produce desired final shape and size of the implant device.**

The microstructural observations by scanning electron microscopy (SEM), mechanical testing and biological testing of the composites were performed. The averaged tensile and compressive strengths were around 15 MPa and 55 MPa respectively. On the other hand, biological tests showed very positive results which verified bioactivity, biocompatibility and non-toxicity of the composite with the formation of biological apatite layer deposited on the surface of the materials which is critical to establishing bonding between living tissue and biomaterials, without forming the fibrous tissue among them. These results suggested that pressureless sintered HA-PEEK biocomposites have the potential to replace injection molded composites in the load-bearing applications.

Keywords — **Hydroxyapatite; Polyetheretherketone; Biocomposites, Presureless Sintering, Biocompatibility.**

I. Introduction

In recent years, the fabrication of bioactive particulate reinforced polymer composites for orthopaedic implants has been receiving considerable attention from biomedical sector [[i]]. One of them is Hydroxyapatite-Polyetheretherketone (HA-PEEK) biocomposite that has been produced by injection molding in the past few years [1,2,3,4]. Injection molding process however has a few drawbacks. The mold and the machineries used in this process are very expensive, especially for highly specialised and customised implant products such as jaw bones implant, pelvic bone implant and augmentation implant. The other disadvantage of this method is that when the product's design changes, the mold also need to be changed. In other words, this method is not customizable and flexible. To overcome those problems, this research attempts to synthesize a general HA-PEEK biocomposite block using pressureless sintering method and followed by CNC machining for producing a desirable shape and size of implant. This method is considerably cheaper and more customizable than injection molding.

The concept of bioactive particulate reinforced polymer composite as bone analogue was introduced in the early 1980s by Bonfield et al [2]. Natural HA reinforced collagen found in the human bone is simulated by using synthetic HA reinforced polymer matrix. There are many bioactive HA-polymer composites which were developed using polymer matrices. And among the numerous choice of polymer matrices that have been widely promoted, PEEK and its composites have been highlighted as having the potential for such application.

In this study, the main objective is to produce HA-PEEK biocomposite using pressureless sintering method with equally good mechanical and biological properties as those obtained from injection molding and will be investigated on their mechanical and biological properties.

II. Experimental techniques

2.1 Chemicals and Materials

The Hydroxyapatite feedstock slurry suspension was synthesized by direct precipitation method using calcium hydroxide and orthophosporic acid (85%) as the starting materials and spray dried to obtain spherical HA powder [5]. The PEEK polymer used was PEEK™ (150XF) from Victrex plc.

2.2 Processing of HA-PEEK composite block

The HA powder was mixed with PEEK powder with certain composition to form biocomposite block by pressureless sintering method. As majority part of the project is fine tuning the process, the composition was limited to only 10 vol% HA. They were mixed together using horizontal ball mill to produce a homogeneous mixture of HA and PEEK in

Chwee Teck Lim, James C.H. Goh (Eds.): ICBME 2008, Proceedings 23, pp. 261–264, 2009
www.springerlink.com

the duration of 8 hours. After milling process was finished, the powder mixture was placed in the stainless steel mold with dimension of 10 cm x 10 cm x 10 cm and then compacted by a manual hydraulic pressing machine with an applied load of 10 tons or equivalent to pressure of 10 MPa.

During sintering process, good control over heating rate, time, and temperature is required for reproducible results. Therefore in this study, those 3 parameters were varied to find the best fabricated biocomposite block. There are 7 samples obtained from the sintering process with different parameter values, shown in Table 1. They would be then compared to each other through Scanning Electron Microscopy observation, mechanical and biological testing.

Table 1 Different parameters used for the samples

Sample	Holding Temperature (ºC)	Holding Time (hours)	Heating Rate (ºC/min)
S1	300	5	1
S2	300	10	1
S3	350	10	1
S4	325	10	1
S5	325	15	1
S6	325	15	0.5
S7	325	15	0.1

2.3 Microstructural Observation using SEM

JEOL JSM-6700F SEM was used to analyze and observe the microstructure and surface morphology of the samples after sintering showing how well the encapsulation of the PEEK polymer to HA is and how even the distribution of the 2 components is. The sample needed to be trimmed first into an appropriate size of around 7 mm x 7 mm using cutting machines. The samples were coated with platinum for conduction path before SEM observation.

2.4 Mechanical Test

There are 2 types of mechanical tests that were done in this experiment; tensile test and compression test. The testing was carried out using Instron® 5582 at room temperature in accordance to ASTM638 for tensile testing and ASTM D695 for compression testing.

2.5 Biological Test

There are 2 biological tests conducted in this experiment: Simulated Body Fluid test and Cell Seeding test. All of these tests want to prove whether the biocomposite blocks produced earlier are bioactive, biocompatible and non-toxic to the human body.

2.5.1 Simulated Body Fluid (SBF) Test

Simulated Body Fluid is an acellular solution that has inorganic ion concentrations similar to those of human extracellular fluid or blood plasma, which can stimulate the formation of apatite layer on bioactive materials *in vitro* [6]. The ion concentrations of SBF in comparison with human blood plasma are given on Table 2.

Table 2 Comparison between ion concentrations of SBF and human blood plasma [6]

Ion	Concentration (mmol/litre)	
	Simulated body fluid (SBF)	Human blood plasma
Na^+	142.0	142.0
K^+	5.0	5.0
Mg^{2+}	1.5	1.5
Ca^{2+}	2.5	2.5
Cl^-	147.8	103.0
HCO_3^-	4.2	27.0
HPO_4^{2-}	1.0	1.0
SO_4^{2-}	0.5	0.5

The trimmed and polished biocomposite specimens obtained from the sintering process were immersed in 30 ml of SBF in the centrifuge tube for 0, 1, 4, 7, 14, 28 days at 37ºC where the temperature was maintained using a water bath. Upon removal from SBF, the specimens were dried in fume hood and were ready to be observed under SEM whether they have an apatite layer on their surface which indicates their potential for bonding with bone [7].

2.5.2 Cell Seeding

The trimmed and sterilized samples were put in the 6-well plate then 2 ml solution of cell and medium was poured onto the samples. They were then incubated for 24 hours at 37 ºC incubator to allow the cells to attach on the samples' surfaces. Samples were fixed before the cell morphology on the material could be observed using SEM.

III. Results and Discussions

3.1 Microstructural Observation

From Figure 1, it can be seen that surfaces of S1 and S2 which was sintered at 300ºC are not smooth and solid even though they are actually cut surfaces. The morphology of the powders still can be seen clearly suggesting that the samples had not been sintered well. However, there are some molten polymers that encapsulate some area of the HA powders.

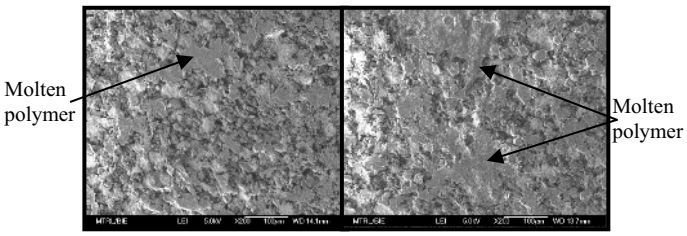


Figure 1 Comparison between cut surfaces of (a) S1 and (b) S2

Further observation of Figure 1 showed that the molten polymers, which look like some sort of layer, exist more in S2. This could be explained by the fact that holding time of S2 was longer than S1 which could give more time for the polymer to melt and encapsulate the HA powders.

From Figure 2 it clearly shows that S3 and S4 with holding temperature of 350ºC and 325ºC respectively have a very well-sintered surface which is smooth (not powdery) and solid if compared to S2 in Figure 1(b).

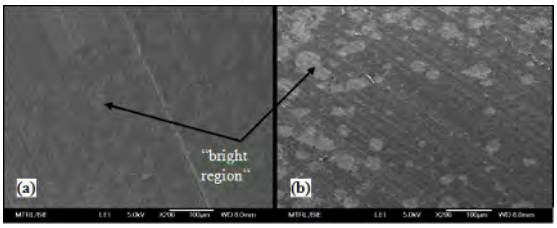


Figure 2 Comparison between cut surfaces of (a) S3 and (b) S4

Additionally from Figure 2, it also can be seen that specimen for S3, shows that the encapsulation of HA by the polymer is better than in S4. This can be observed from the obvious "bright region" on the surface of S4 while they are not clearly seen in S3. The bright region is the region of HA powder, while the dark region surrounding it is the PEEK polymer.

Therefore in conclusion, the higher the holding temperature of the process is, the better the encapsulation of HA by the PEEK polymer, resulting in better sintering.

3.2 Mechanical Test Results

Mechanical testing was only done to those samples which were well-sintered (S4 to S7).

3.2.1 Tensile Test Results

Each sample had 3 specimens tested using the machine, and the values obtained by the 3 specimens were averaged and shown in the chart Figure 3.

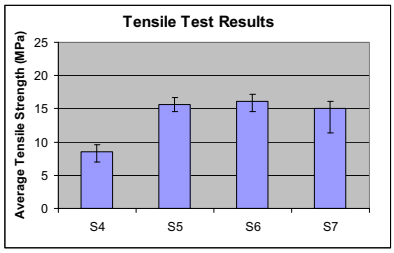


Figure 3 Chart of tensile test results of sample S4 to S7

From the tensile test results chart, it can be seen that only S4 has a lower tensile strength from the rest of the samples. The difference between S4 and the other 3 samples' parameters is the holding time. S4 was sintered at duration of 10 hours while the others 15 hours. Therefore, it can be concluded that holding time can determine the tensile strength of the composite. The longer the duration of the sintering could make a higher tensile strength. From the previous work done on mechanical properties of injection molded HA-PEEK biocomposite, tensile strength of 10 vol% HA – 90 vol% PEEK was 83.3 MPa which was within the cortical bone range of 50-150 MPa [i]. And taking 15 MPa as the average tensile strength value of pressureless sintered 10 vol% HA–90 vol% PEEK biocomposite block, the result is still way below the expected value.

3.2.2 Compression Test Results

From the chart in figure 4, it can be seen that all of the 4 samples have quite similar average values, around 55 MPa.

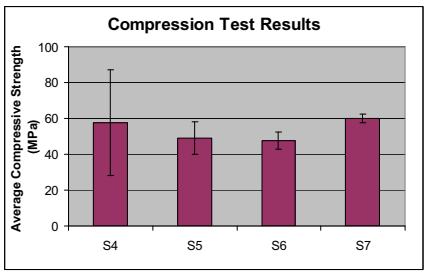


Figure 4 Chart of compression test results of sample S4 to S7

From the previous work done on injection molded HA-PEEK biocomposite, compressive strength of 10 vol% HA – 90 vol% PEEK was 125 ± 3.5 MPa which was in the lower limit of cortical bone (i.e. 106-215 MPa) [i]. And in this case taking 55 MPa as the average compressive strength value of pressureless sintered biocomposite block, the result is also still way below the expected value.

From the same previous work done, it is known that injection molding was using a pressure higher than 10 MPa

(injection pressure: 14MPa, follow-up pressure: 8-12 MPa) and this could be the reason. In addition, by only using a pressure of 10 MPa, the density achieved by the compaction process was far below the theoretical value. The theoretical value of the composite is 1.464 g/cm^3 while the density obtained after compaction is 0.67 g/cm^3 which is only 45.53% from the theoretical value.

3.3 Biological Test Results

Similar to mechanical test, biological tests were done only to those samples which were well-sintered (S4 to S7), which is Simulated Body Fluid (SBF) test and Cell Seeding test.

3.3.1 SBF test results

It is commonly believed that when artificial bioactive materials are implanted in the body, there will be spontaneously formation of biological apatite layer deposited on the surface of the materials which is critical to establishing bonding between living tissue and biomaterials, without forming the fibrous tissue among them [7].

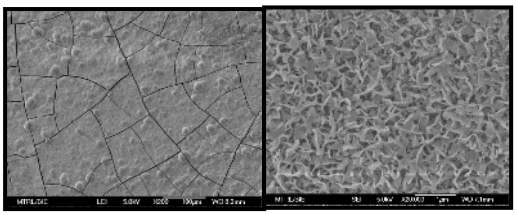


Figure 5 SEM results of SBF test for S4 with (a) magnification of 200 after 14 days upon immersion in SBF and (b) high magnification of S4 surface of the precipitated apatite layer after 28 days immersion in SBF

Figure 5 shows a layer formed in the surface of S4 upon immersion in SBF fluid after 14 days. This layer is an apatite layer which is actually precipitated crystals that had been confirmed as apatite through phase and composition analysis done in earlier report [7].

3.3.2 Cell Seeding Test Results

Bone is a connective tissue that contains different bone cells. And osteoblast, which was used in this experiment, is one type of bone cells (bone-forming cell). Hence, detection of these bone cells getting attached and becoming confluent on a material is one in-vitro technique to show the biocompability of the material [9].

Figure 6 shows the attachment of the osteoblast on top of control sample of S4 surface with their 'arm-like' structures. These results conclude that the biocomposite samples are biocompatible to the human body.

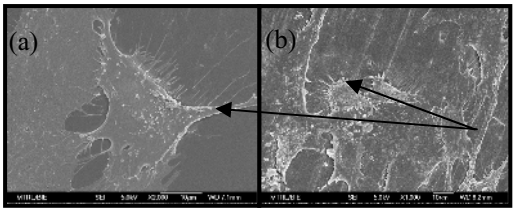


Figure 6 SEM micrograph of cell seeding control (a) and sample S4 (b)

IV. Conclusions

From the results obtained in this study, it can be said that pressureless sintering has the potential to replace injection molding in order to reduce cost, increase flexibility and yet still achieve similar results.

Mechanical test of the biocomposite obtained from the pressureless sintering were evidently below expectation. It was perhaps caused by several limitations inherent to the equipments used in the experiment. However the biological tests were extremely positive which verified that pressureless sintered HA-PEEK biocomposite blocks with composition of 10 vol% of HA were actually bioactive, biocompatible and non-toxic to the human body.

V. References

[1] Abu Bakar MS, Cheang P, Khor KA, 'Mechanical properties of injection molded hydroxyapatite-polyetheretherketone biocomposites', Composite Science and Technology 2003; 63: 421-425.

[2] Abu Bakar MS, Cheng MHW, Tang SM, Yu SC, Liao K, Tan CT, Khor KA, Cheang P, 'Tensile properties, tension-tension fatigue and biological response of polyetheretherketone- hydroxyapatite composites for load-bearing orthopedic implants', Biomaterials 2003; 24: 2245-2250.

[3] Tang SM, Cheang P, Abu Bakar MS, Khor KA, Liao K, 'Tension-tension fatigue behaviour of hydroxyapatite reinforced polyetheretherketone composites', International Journal of fatigue 2004; 26: 49-57

[4] Abu Bakar MS, Cheang P, Khor KA, 'Tensile properties and microstructural analysis of spheroidized hydroxyapatite-poly (etheretherketone) biocomposites', Material Science and engineering 2003; A345: 55-63

[5] Cheang P, Khor KA, 'Addressing processing problems associated with plasma spraying of hydroxiapatite coatings', Biomaterials 1996; 17: 537-44

[6] Ohtsuki, Chikara. "How to prepare the simulated body fluid (SBF) and its related solutions." Nagoya University. 05 March 2008.

[7] Yu SC, Prakash KH, Kumar R, Cheang P, Khor KA, 'In vitro apatite formation and its growth kinetics on hydroxyapatite/polyetheretherketone biocomposites', Biomaterials 2005; 26: 2343-2352.

[8] Suh PG. "Cytotoxicity Test Result." Department of Life Science. Pohang University of Science and Technology (Korea). 10 March 2008.

[9] Chen TY. 'Rapid Prototyping of Hydroxyapatite - PEEK biocomposite for clinical orthopaedics implant.' Final Year Project Report. 2004. Nanyang Technological University School of Material Engineering, Singapore.

Computerized Cephalometric Line Tracing Technique on X-ray Images

C. Sinthanayothin

National Electronics and Computer Technology Center, National Science and Technology Development Agency, Pathumthani, Thailand

Abstract — **Cephalometric radiography analysis is an important diagnostic tool in orthodontics and cranio-maxillofacial surgery. Conventionally, cephalometric variables are measured manually on X-ray film. The clinician need to trace all the lines to show skull, teeth and jaw structures by themselves, which is inconvenient and time consuming. 2D cephalometric analysis can analyze in both lateral and frontal (PA) x-ray images. Therefore, this paper presents the method on producing the digital cephalometric tracing lines on x-ray images. The cephalometric tracing lines can lead to the measurement of the skull both in lateral and PA views in both bones and soft tissue sections and also can lead to the diagnostic of abnormalities of skull, face and teeth as well. Especially, PA view can use for analysis on symmetry of the skull. The computerized cephalometric lines tracing method combines with 4 steps. Firstly, the x-ray images are processed via adaptive, local, contrast enhancement. Secondly, the landmarks are defined by the dentists on both lateral and PA x-ray images. Next the cephalometric tracing lines are automatic generated by using the deformable template registration and cubic spline fitting techniques. Finally, the tracing lines are smoothed by put all lines into bitmap data which an interpolation technique is applied when the tracing lines are zooming. In this study, 10 laterals and 10 PA x-ray images are tested by this technique and the result shows very well drawing comparing to the manual method. Also the tracing lines are satisfied by the clinicians as a smoothed lines and curves. The cephalometric tracing lines will aid the future orthodontic and orthognathic analysis, diagnostic and planning in the next step.**

Keywords — **Cephalometric Line Tracing, Lateral, PA**

I. Introduction

Cephalometric analysis has been applied as tools in orthodontic diagnoses as well as cranio-maxillofacial surgery. The measurement of skull, jaw and soft tissue is simply called Cephalometric analysis where "cephalo" means head and "metric" comes from measurement. The cephalometric measurement in x-ray film can be done by locating the standard landmarks which is world wide well know for many years and continue developing for diagnostic for more than 50 abnormalities. Two-dimensional cephalometric measurements from lateral and/or frontal cephalograms were widely studied for diagnostic of abnormalities of skull bone and tissue and could be a tool that leads to an appropriated treatment planning by clinician. Currently, dentists perform orthodontic planning by initially taking the X-ray pictures of lateral and PA and then drawing the structure of surface, jaws, and teeth. At the same time the distance and angles are measured and calculated by using the stationary which taking a large amount of work and time. However, the software for cephalometric analysis are available such as OrisCeph Rx3 [1], OnyxCeph [2], Dolphine [3], Quick Ceph [4], Dr.Ceph (FYI) [5] and etc. [6-8]. Also group of researcher in Thailand have developed the software for cephalometric analysis called CephSmile [9] as well. Also many researchers are developed an automatic drawing of the cephalometric line tracing such as the review work by Leonardi [10] that the systems described in the literature are not accurate enough to allow their use for clinical purposes as errors in landmark detection were greater than those expected with manual tracing. Therefore, this paper proposes the technique on producing the digital cephalometric tracing lines on x-ray images. The method combines with 4 steps. First, contrast the x-ray images by local contrast enhancement technique. Second, define the landmarks by the dentists. Next draw the cephalometric line tracing which can be done by using the deformable template and cubic spline fitting. Finally, the tracing lines are smoothed. The cephalometric tracing lines can be use for both orthodontic and orthognathic planning in the next step.

II. Methodology

The method on producing the digital cephalometric tracing lines on x-ray images can lead to the measurement of the skull both in lateral and PA views in both bones and soft tissue sections and also can lead to the diagnostic of abnormalities of skull, face and teeth as well. Especially, PA view can use for analysis on symmetry of the skull. The method combines with 4 steps are as follow:

A. Radiographic Image Enhancement using "Local Contrast Enhancement" technique.

Most of x-ray images in this work are loss of detail and create of artifacts especially the digital image that taken from the x-ray film that placed on the view box or scanned as can be seen in figure 1. Therefore x-ray image is necessary pre-processed in order to perform the clearer image,

Chwee Teck Lim, James C.H. Goh (Eds.): ICBME 2008, Proceedings 23, pp. 265–269, 2009
www.springerlink.com



Fig 1: Original x-ray images of PA and Lateral views.



Fig 2: X-ray images with local contrast enhancement.

which the local contrast enhancement technique has been applied in this paper [11]. For the local contrast enhancement technique, let the intensity, *f*, of the picture elements (pixels) of an $N \times N$ digital image be indexed by (i,j) $1 \le i, j \le N$. Consider a subimage of size $M \times M$ centered on (i, j), in this paper $M=49$. Denote the mean and standard deviation of the intensity within W by $\langle f \rangle_W$ and $\sigma_W(f)$ respectively. The objectivity for this method is to define a point transformation dependent on W such that the distribution is localized around the mean of the intensity and covers the entire intensity range. The implicit assumption is that W is large enough to contain a statistically representative distribution of the local variation of grey levels, yet small enough to be unaffected by the gradual change of contrast between the centre and the periphery of the x-ray image. The adaptive contrast enhancement transformation is defined by

$$f(i,j) \to g(i,j) = 255 \frac{[\psi_w(f) - \psi_w(f_{\min})]}{[\psi_w(f_{\max}) - \psi_w(f_{\min})]} \quad (1)$$

Where the sigmoidal function was

$$\psi_w(f) = \left[1 + \exp\left[\frac{< f >_w - f}{\sigma_w}\right]\right]^{-1} \quad (2)$$

While f_{max} and f_{min} are the maximum and minimum values of intensity within the whole image with

$$< f >_{W(i,j)} = \frac{1}{M^2} \sum_{(k,l) \in W(i,j)} f(k,l) \quad (3)$$

$$\sigma_W^2(f) = \frac{1}{M^2} \sum_{(k,l) \in (i,j)} \left(f(k,l) - < f >_w\right)^2 \quad (4)$$

The result of local contrast enhancement technique can be seen in figure 2.

B. Cephalometric Landmarks on Lateral and PA Views.

The method in this paper could be able to draw the cephalometric line tracing of skull and face in both bones and soft surface sections on both lateral and PA images by using the landmarks defined by the dentists. Therefore, the landmarks need to be located by the clinician following the guideline in a step by step, 79 reference points for lateral view and 57 reference points for PA view as shown in figure 3. Some landmarks can be generated automatically or the ruler can appeared as a guideline for locating the reference point. The program also provides tools that allow users to mark the correct points with ease as well.

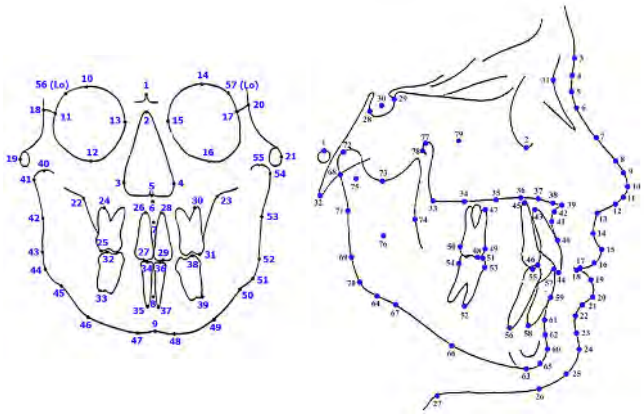


Fig 3: Reference points: 57 points for PA and 79 points for Lateral View.

C. Cephalometric Line Tracing on Lateral and PA Views

In this paper, there are 2 methods for cephalometric line tracing on lateral and PA views. Firstly, cephalometric line tracing using deformable template is described. Secondly, the cephalometric line tracing using cubic spline technique is explained. One technique will be applied at a time depends on the characteristic of the reference points.

C.1Cephalometric Line Tracing using Deformable Template

Cephalometric line tracing using deformable template can be applied when the tracing line has a unique shape such as tooth, circle and etc. This specific shape line can be matched with a few reference points. Therefore, the template of specific shape must be prepared as can be seen in figure 4.

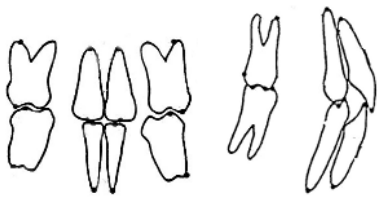


Fig 4: Templates with difference shapes.

Once the templates have been prepared, then the template is fitted to a few reference points. In this paper shows the example of tooth template matching with 2 reference points on x-ray image as shown in figure 5. The template matching can be done by determine the vector of two reference points on template and x-ray image respectively. Then the angle between two vectors has been calculated using dot product for template rotation. Next the distance of each vector indicates the size of template on x-ray image. Last the middle of the vector on x-ray image indicates the position that the template needs to be translated.

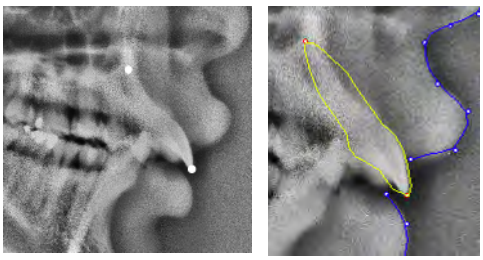


Fig 5: Tooth template matching with 2 reference points on x-ray image.

Equation 5, 6 and 7 shows the translation, rotation and scaling matrixes of template's coordinates on x-ray image.

$$\begin{bmatrix} x' \\ y' \end{bmatrix} = \begin{bmatrix} x \\ y \end{bmatrix} + \begin{bmatrix} d_x \\ d_y \end{bmatrix} \tag{5}$$

$$\begin{bmatrix} x' \\ y' \end{bmatrix} = \begin{bmatrix} \cos\theta & -\sin\theta \\ \sin\theta & \cos\theta \end{bmatrix} \begin{bmatrix} x \\ y \end{bmatrix} \tag{6}$$

$$\begin{bmatrix} x' \\ y' \end{bmatrix} = \begin{bmatrix} s_x & 0 \\ 0 & s_y \end{bmatrix} \begin{bmatrix} x \\ y \end{bmatrix} \tag{7}$$

C.2 Cephalometric Line Tracing using Cubic Spline

Cubic spline technique is used for drawing curve along the reference points. The spline is obtained by calculating the second derivatives of the interpolating function at the tabulated points based on the formulation given in "Numerical Recipes in C". [12] One dimensional cubic spline fitting can be explained as in Eq. (8) – Eq.(13). With this method, a series of unique cubic polynomials is fitted between each of the data points with the condition that the curve obtained be continuous and appears smooth. This spline consists of weights attached to a flat surface at the points to be connected. A flexible line is then bent across each of these weights, resulting in a smooth curve.

$$G(x) = \begin{cases} g_1(x) & \text{if} \quad x_1 \le x < x_2 \\ g_2(x) & \text{if} \quad x_2 \le x < x_3 \\ \vdots & \\ g_{n-1}(x) & \text{if} \quad x_{n-1} \le x < x_n \end{cases} \tag{8}$$

Where g_i is a 3rd degree polynomial defined by

$$g_i(x) = a_i(x - x_i)^3 + b_i(x - x_i)^2 + c_i(x - x_i) + d_i \tag{9}$$

for $i = 1, 2, \ldots, n\text{-}1$.

Since the piecewise function $G(x)$ will interpolate all of the data points, we can conclude that

$$G(x_i) = y_i \tag{10}$$

for $i = 1, 2, \ldots, n\text{-}1$. Since $x_i \in [x_i, x_{i+1}]$, $y_i = g_i(x_i)$

The coefficients a_i, b_i, c_i, and d_i in (9) are determined from the first and second derivatives of the n-1 equations of $g_i(x)$. The routine must ensure that $g_i(x), g_i'(x)$ and $g_i''(x)$ are equal at the interior node points for adjacent segments. Substituting a variable S_i for the $g_i''(x_i)$ and y_i for $s_i(x_i)$ will reduce the number of equations and simplify the tasks.

Given the spacing between successive data points is

$$h_i = x_i - x_{i-1} \tag{11}$$

Finally, the variables a_i, b_i, c_i and d_i in (9), or termed the weights of each n-1 equations, will be

$$\begin{aligned} a_i &= \frac{S_{i+1} - S_i}{6h} \\ b_i &= \frac{S_i}{2} \\ c_i &= \frac{y_{i+1} - y_i}{h} - \left(\frac{S_{i+1} + 2S_i}{6}\right)h \\ d_i &= y_i \end{aligned} \tag{12}$$

When substituting these weights in (9), its 1st and 2nd derivatives, and including the condition of natural spline where 2nd derivative is equal to zero at the endpoints ($S_1 = Sn = 0$), the system can be determined in matrix equation as follows

$$\begin{bmatrix} 4 & 1 & 0 & \cdots & 0 & 0 & 0 \\ 1 & 4 & 1 & \cdots & 0 & 0 & 0 \\ 0 & 1 & 4 & \cdots & 0 & 0 & 0 \\ \vdots & \vdots & \vdots & \ddots & \vdots & \vdots & \vdots \\ 0 & 0 & 0 & \cdots & 4 & 1 & 0 \\ 0 & 0 & 0 & \cdots & 1 & 4 & 1 \\ 0 & 0 & 0 & \cdots & 0 & 1 & 4 \end{bmatrix} \begin{bmatrix} S_2 \\ S_3 \\ S_4 \\ \vdots \\ S_{n-3} \\ S_{n-2} \\ S_{n-1} \end{bmatrix} = \frac{6}{h^2} \begin{bmatrix} y_1 - 2y_2 + y_3 \\ y_2 - 2y_3 + y_4 \\ y_3 - 2y_4 + y_5 \\ \vdots \\ y_{n-4} - 2y_{n-3} + y_{n-2} \\ y_{n-3} - 2y_{n-2} + y_{n-1} \\ y_{n-2} - 2y_{n-1} + y_n \end{bmatrix} \quad (13)$$

Therefore, Eq. (13)[13] is used to find the interpolation values in all dimensions. In this paper, a data point is equivalent to the number of reference points. The result of fitting the cephalometric line with cubic-spline interpolation can be seen as in figure 6.

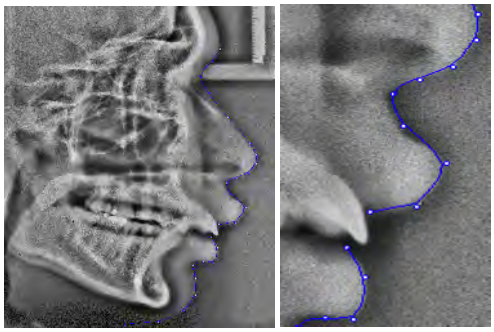
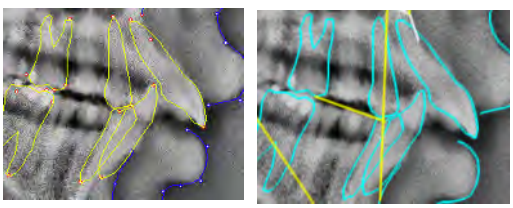


Fig 6: Tracing cephalometric line with cubic spline.

D. Cephalometric Line Smoothening

Cephalometric tracing lines are automatic generated by using the deformable template registration and cubic spline fitting techniques as mention above. However, the lines are not smooth when zoom into specific area as can be seen in figure 7(A). Therefore cephalometric line smoothening technique has been proposed by transform the window/canvas coordinates of the tracing lines into bitmap coordinates. Then the program will draw lines on bitmap instead of canvas and apply image interpolation when the user zooms into the specific area of x-ray image. The result of cephalometric line smoothening technique shows as figure 7(B) which the user zooms into the specific area.

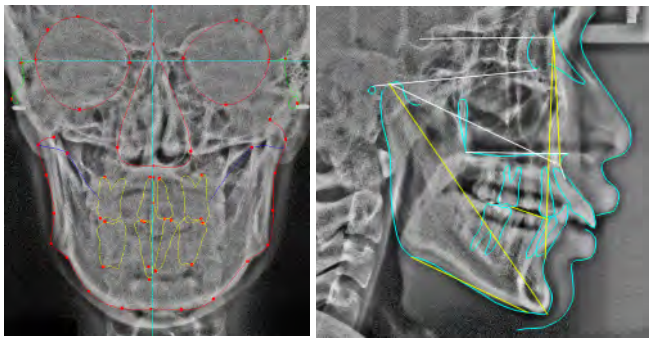


(A) On Canvas (B) On bitmap plus interpolation

Fig 7: Cephalometric lines.

III. Result

The result of cephalometric line tracing on both PA and Lateral x-ray images can be displayed as figure 8(A) and 8(B) respectively. This method has been tested on 10 PA and 10 Lateral x-ray images and found that cephalometric lines showed the similar result depends on the coordinate of reference points.



(A) PA View (B) Lateral View

Fig 8: Cephalometric line tracing result.

IV. Conclusion

The result of the computerized cephalometric line tracing technique on x-ray images is reasonable and acceptable by collaboration clinicians. Since the tracing lines from computerized are similar to a hand drawing but more convenient and less time consuming. Therefore, this method can perform automatic drawing of the significant traces of face, skull, and teeth by using the reference points. The cephalometric analysis with different types of analysis, such as Mahidol Analysis, Down Analysis, Steiner Analysis, Tweed Analysis, Jaraback Analysis, Harvold Analysis, Rickette Analysis, and McNamara Analysis can be performed in the near future in order to show the structural problems on skulls, face, and teeth.

Acknowledgment

This project is a part of CephSmile V.2.0. Thanks to National Electronics and Computer Technology center (NECTEC) for grant supporting. Special thanks to the orthodontics team from Mahidol University for their advices.

References

1. OrisCeph Rx3, Ref: http://www.orisline.com/en/orisceph/pricelist.aspx
2. OnyxCeph, by OnyxCeph Inc. Ref: http://www.onyx-ceph.de/i_functionality.html

3. Dolphin Imaging 10, by Dolphin Imaging System Inc.
Ref: http://www.dolphinimaging.com/new_site/imaging10.html
4. QuickCeph 2000, by QuickCeph System Inc,
Ref: http://www.quickceph.com/qc2000_index.html
5. Dr.Ceph (FYI),
Ref: http://www.fyitek.com/software/comparison.shtml
6. Dental Software VWorks, CyberMed,
Ref: http://www.cybermed.co.kr/e_pro_dental_vworks.html
7. Dental Software VCeph, by CyberMed,
Ref: http://www.cybermed.co.kr/e_pro_dental_vceph.html
8. Cephalometric AtoZ v8.0E
Ref: http://www.yasunaga.co.jp/CephaloM1.html
9. CephSmile Ref:
www.typo3hub.com/chanjira/CephSmileV2/cephsmileV2Eng.html
10. Leonardi R, Giordano D, Maiorana F, Spampinatod C. Automatic Cephalometric Analysis. The Angle Orthodontist: Vol. 78, No. 1, pp. 145–151.
11. Sinthanayothin C , Boyce JF, Cook HL, Williamson TH. Automated localisation of the optic disc, fovea, and retinal blood vessels from digital colour fundus images. British Journal Ophthalmology (BJO) 1999;83:902-910.
12. Press W.H.. et. al., “Cubic Spline Interpolation, Numerical Recipes in C: The Art of Scientific Computing”, Cambridge, UK: Cambridge University Press, (1988).
13. McKinley S, Levine M. Cubic Spline Interpolation. Ref: http://online.redwoods.cc.ca.us/instruct/darnold/laproj/Fall98/SkyMeg/proj.pdf

Author: Chanjira Sinthanayothin
Institute: National Electronics and Computer Technology Center
Street: 112 Thailand Science Park, Phahonyothin Rd.
City: Pathumthani
Country: Thailand
Email: chanjira.sinthanayothin@nectec.or.th

Brain Activation in Response to Disgustful Face Images with Different Backgrounds

Takamasa Shimada[1], Hideto Ono[1], Tadanori Fukami[2], Yoichi Saito[3]

[1] School of Information Environment, Tokyo Denki University, Japan
[2] Faculty of Engineering, Yamagata University, Japan
[3] Research Institute for EEG Analysis, Japan

Abstract — **Previous studies have demonstrated that the stimulus of a fearful and disgustful face images lead to activation of neural responses in the medial temporal lobe. In particular, it was reported that seeing disgustful face image activated the insula area of brain. In these studies, no background images were used with facial stimuli. However, normal day-to-day images always have a background. Moreover, background images are considered important in art forms (painting, photography, and movies, etc.) for eliciting effective expressions. We assessed the effect of background images on brain activation by using functional magnetic resonance imaging (fMRI). During fMRI scanning, face images with background images were presented repeatedly to 8 healthy right-handed males. Facial stimuli comprised 5 photographs of a disgustful face selected from the Paul Ekman's database (Ekman and Friesen 1976). The background images comprised 2 photographs—one is worms and the other is a flower garden. It is thought that disgustful face images coincide with worms background image on the point of impression. After scanning, the subjects rated the impression created by the images on the Plutchik scale. Significant effects of the image of the disgustful face against the worms background minus that against the flower garden were assessed using a t-test and displayed as statistical parametric maps (SPMs) using SPM2 software. The results demonstrated activation of the right insula, and the image of the disgustful face against the worms background created a more disgustful impression than that against the flower garden. Therefore, the image of the face and the background together create the overall impression. The difference in the activation of the insula is possibly induced by the creation of this overall impression. This demonstrates the importance of background images in forming an impression of face images.**

Keywords — **Face image, background image, functional magnetic resonance imaging.**

I. Introduction

In recent years, many studies have been conducted in an attempt to clarify the neural systems involved in emotional perception. Previous studies have demonstrated that the stimulus of a fearful and disgustful face images lead to activation of neural responses in the medial temporal lobe. Previous studies have suggested the involvement of the limbic system in emotional perception. The relationship between emotional perception and the hippocampus was shown by Papez et al. [1]. In particular, it was reported that seeing disgustful face image activated the insula area of brain.

One of the concepts of emotion, called Plutchik's psychoevolutionary theory of basic emotions, was suggested by Plutchik et al. [2]. These postulated basic emotions are acceptance, anger, anticipation, disgust, joy, fear, sadness, and surprise.

In many art forms (painting, photography, movies, etc.), background images are thought to be very important for enhancing the effect of the subject.

In most of the recent studies on anthropomorphic user interfaces [3][4], only a face image is used and background images are either not used or are considered unimportant. However, in daily conversations with individuals, the absence of a background is unnatural. It is expected that adding a background to face images will be useful in producing emotional effects. However, the mechanism through which background images affect face images has not been cleared. In addition, there are few studies on brain functions in the field of computer interface technology.

An objective evaluation method is important for evaluating the effect of background images on humans. In particular, clarifying the relation between background images and the activation of the brain is thought to be a key for such an objective estimation. However, the mechanism by which information related to background images is processed in the brain has not been investigated.

In this research, we attempted to elucidate this mechanism by using an fMRI scanner to detect brain activation induced by images that include not only a face image but also background images. In our research, the subjects were shown face images with background images. We focused on the brain activation and impression change induced by the different combinations of facial expressions and background images, which were further analyzed. Two background images were used for the experiment. One image induced the same type of emotional effect as the face images, whereas the other image induced a different type of emotional effect from the face images. The effect on brain acti-

Chwee Teck Lim, James C.H. Goh (Eds.): ICBME 2008, Proceedings 23, pp. 270–273, 2009
www.springerlink.com

vation was analyzed by means of the fMRI scanner. This experiment analyzed the relation between emotions and brain activation induced by images. Moreover, the effect induced only by background images was also analyzed by means of a questionnaire and the fMRI scanner.

II. Method

A. Experimental paradigm

The face images used in our experiment expressed disgust. The five face images used were selected from Paul Ekman's database (Ekman & Friesen, 1976). These images comprise two male and three female images.

The face image was superimposed on the background image. Two types of background images were used—one depicted worms; the other, a flower garden.

We selected two background images to investigate whether the emotional effect of the face images with one background is consistent with that elicited by the face images with another background.

Figs. 1 and 2 are samples of the face image with a background image of worms and a flower garden, respectively. It is believed that face images expressing disgust correspond to a background depicting worms; however, face images expressing disgust are in contradiction with a background depicting a flower garden.

In this experiment, we focused only on the changes in brain activity resulting from disgust; subsequently, we focused on changes in the insula areas, which are associated with the emotion of disgust.

During the fMRI scanning, the subjects, who were asked to wear earplugs, lay on the bed of the fMRI scanner. The total scanning time was 5 min per subject, and the scanning was carried out in blocks of 10 s wherein a face image along with the background image of either worms or a flower garden was repeatedly presented to the subject. The face presentation block was preceded and followed by a 10s block of a crosshair cursor, as seen in Fig. 3. During the 10-s face block, the stimulus of one face image (with a background image) of either a male or female was presented 5 times (stimulus duration, 200 ms; interstimulus interval, 1800 ms) because repeated stimulation is assumed to enhance corresponding cortical activation [5][6].

The combination of the face and background images was randomly selected for every 10s face block; however, the number of images with the worms and flower garden backgrounds was counterbalanced. In addition, the number of face images of a particular person with both the backgrounds was counterbalanced.

B. Questionnaire

In order to assess the difference in the psychological effects caused by different background images, the subjects were required to rate their impressions by using a questionnaire based on Plutchik's eight basic emotional categories. The subjects were required to rate the intensity of their impression of each category of emotion on a scale of 0 to 6 (seven levels). A rating of 0 implied that the subject did not feel anything for that particular category, and a rating of 6 implied that the subject experienced that emotion very strongly (maximum intensity). The subjects answered the questionnaire immediately after the fMRI scanning.



Fig. 1 Sample of a face image expressing disgust with the background image of worms



Fig. 2 Sample of a face image expressing disgust with the background image of flower garden

C. Subjects

The subjects were 8 healthy right-handed male adults (mean age is 21.8 years, standard deviation is 0.97). All the subjects provided written informed consent for participation in the experiment. In all the paradigms, the subjects, who

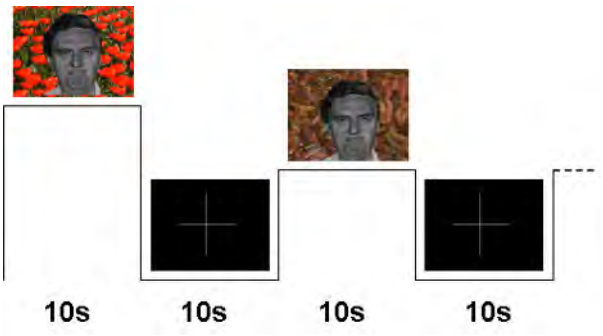


Fig. 3 Schematic diagram of the experimental paradigm

were monitored through a window, were forbidden to move, except when the task required them to do so.

D. Image Acquisition and Analysis

In this experiment, gradient-echo echo-planar magnetic resonance (MR) images were developed using a 1.5 Tesla Hitach Stratis II System at the Applied Superconductivity Research Laboratory, Tokyo Denki University, Chiba, Japan. T2*-weighted time-series images depicting the blood oxygenation level-dependent (BOLD) contrast were developed using a gradient-echo echo-planar imaging (EPI) sequence (TR, 4,600 ms; TE, 74.2 ms; inter-TR time, 400 ms; total scanning time, 5.00 min; flip angle, 90°; field of view (FOV), 22.5 cm × 22.5 cm; slice thickness, 4.0 mm; slice gap, 1.0 mm; voxel, 3.52 × 3.52 × 5 mm). In all, 28 axial contiguous slices covering the entire brain were collected.

The developed data were analyzed using the statistical parametric mapping (SPM) technique (using SPM2 from the Wellcome Department of Cognitive Neurology, London, UK) implemented in Matlab (Mathworks Inc., Sherborn, MA, USA). The analysis involved the following steps: correction for head movements between the scans, realignment of the functional images acquired from each subject to the first image using rigid body transformation. A mean image was created using the realigned volumes. The high-resolution, T1-weighted anatomical images were coregistered to this mean (T2*) image to ensure that the functional and anatomical images were spatially aligned. The anatomical images were then normalized into the standard space [7] by matching them to a standardized Montreal Neurological Institute (MNI) template (Montreal Neurological Institute, Quebec, Canada), using both linear and nonlinear 3D transformation [8][9]. The transformation parameters determined here were also applied to the functional images. Finally, these normalized images were smoothed with a 12 mm (full width at half maximum) isotropic Gaussian kernel to accommodate intersubject differences in anatomy and to permit the application of Gaussian random field theory to provide corrected statistical inference [8][9]. The SPMs {Z} for the contrasts were generated and thresholded at a voxel-wise P value of 0.01.

III. Results

The differences in the activation between the conditions of viewing face images expressing disgust with the background image of either worms or a flower garden (disgustful face images with the worms background minus those with the flower garden background) were analyzed. The results are shown in Fig. 4. The difference in activation was detected in the insula of the right hemisphere of the brain.

The results of questionnaire shown that the intensity of the impression was stronger for the basic emotional categories of disgust when the worms background was used than when the flower garden background was used.

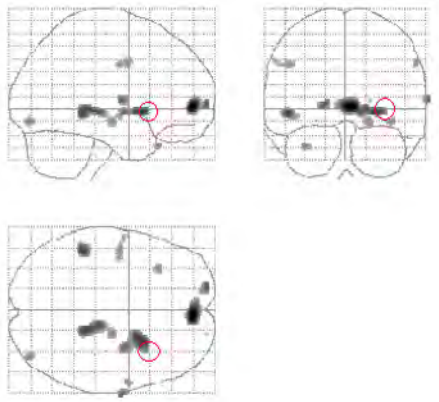


Fig. 4 Results of the difference in activity between the case of the disgustful face images with the worms background and that of the disgust images with the flower garden background (worms minus flower garden)

IV. Discussion

In our research, we attempted to reveal the effect of combining the background image with disgustful face images. As a result, stronger activity was detected in the insula area when the worms background image was used than when the flower garden background image was used.

The area in which activation was detected coincide with the areas in which activation was observed in a previous study in which subjects were shown disgustful faces.

The results of the questionnaire revealed that the subjects formed a stronger impression of disgust when they saw disgustful face images with the worms background than when they saw disgust images with the background image

of a flower garden. This reveals that the impression of disgust was enhanced by using the image with a worms background because this image corresponds with the image of a disgustful face.

In the abovementioned experiment, the background images comprised images of worms and a flower garden. Even if these images are shown to the subject without the face image, it is believed that the images will have their own emotional effects on humans. The average results of the ratings for the images with the backgrounds of worms and a flower garden indicate that the impression of disgust is stronger when the worms background is used than when the background with a flower garden is used. This may imply that the difference in the activation of the brain between the condition in which face images with the worms background are presented and that in which face images with the background of a flower garden are presented is caused merely by adding the activation in the case of the background image to that in the case of the disgustful face image.

We investigated this point by performing an additional experiment. In this experiment, the paradigm was the same but the face image was removed.

The results are shown in Fig. 5. In this experiment, the difference in activation was not detected in the insula area. This experiment showed that the background image had little effect on activity in the insula, although it considerably influenced the activation resulting from the stimuli of disgustful face images.

V. Conclusions

We investigated the effect of combining disgustful face images and background images to study the activation of the brain by using fMRI.

As a result, stronger activation was detected in the insula area when the worms background image was used than when the background image of a flower garden was used. It is believed that this difference in brain activity relates to the degree of disgust impression induced by the images. The results of the questionnaire revealed that the impression of disgust induced by the disgustful face image with the worms background image was stronger than that induced by the disgustful face image with the background of a flower garden.

In addition, the effect of the background image was investigated qualitatively. The difference in activation in the insula area was compared; no difference in activation was detected in the insula area. An image of worms creates an impression of disgust but may not involve biological processing.

Further, these results reveal that although the background image has little effect in activating the insula area, it considerably influences the activation resulting from the stimuli of the disgustful face images. These results indicate the probability of their application to the objective estimation of the emotional effect that the images have.

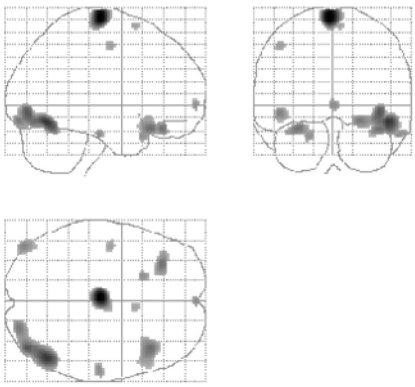


Fig. 5 The results of the difference in activation between the cases of the two background images (worms minus the flower garden)

References

1. J. W., Papez (1937) A proposed mechanism of emotion, Arch Neurol Psychiatry, Vol. 79, pp. 217–224.
2. R., Plutchik (1962) Emotion: A Psychoevolutionary Synthesis, Haper and Row.
3. H., Dohi & M. A., Ishizuka (1996) Visual software Agent: An Internet-Based Interface Agent with Rocking Realistic Face and Speech Dialog Function, AAAI technical report “Internet-Based Information Systems”, No. WS-96-06, pp. 35–40.
4. P., Murano (2003) Anthropomorphic Vs Non-Anthropomorphic Software Interface Feedback for Online Factual Delivery, Seventh International Conference on Information Visualization (IV'03), pp. 138.
5. E. K., Miller, L., Li, & R., Desimone (1991) A neural mechanism for working and recognition memory in inferior temporal cortex, Science, Vol. 254, pp. 1377–1379.
6. C. L., Wiggs & A., Martin (1998) Properties and mechanisms of perceptual priming; Curr Opin Neurobiol, Vol. 8, pp. 227–233.
7. J., Thalairach & P., Tournoux (1988) Co-Planar Stereotactic Atlas of the Human Brain, Thieme, Stuttgart.
8. K., Friston, J., Ashburner, J., Poline, C., Frith, J., Heather, & R., Frackowiak (1995) Spatial registration and normalization of images, Hum Brain Mapp, Vol. 2, pp. 165–189.
9. K., Friston, A., Holmes, K., Worsley, J., Poline, C., Frith, & R., Frackowiak (1995) Statistical parametric maps in functional imaging: A general approach, Hum Brain Mapp, Vol. 5, pp. 189–201.

Author: Takamasa Shimada
Institute: School of Information Environment, Tokyo Denki University
Street: 2-1200 Muzai Gakuendai
City: Inzai City, Chiba Prefecture
Country: Japan
Email: shimada@sie.dendai.ac.jp

Automatic Segmentation of Blood Vessels in Colour Retinal Images using Spatial Gabor Filter and Multiscale Analysis

P.C. Siddalingaswamy[1], K. Gopalakrishna Prabhu[2]

[1] Department of Computer Science & Engineering, Manipal Institute of Technology, Manipal, India
[2] Department of Biomedical Engineering, Manipal Institute of Technology, Manipal, India

Abstract — **Retinal blood vessels are significant anatomical structures in ophthalmic images. Automatic segmentation of blood vessels is one of the important steps in computer aided diagnosis system for the detection of diseases such as Diabetic Retinopathy that affect human retina. We propose a method for the segmentation of retinal blood vessels using Spatial Gabor filters as they can be tuned to the specific frequency and orientation. A new parameter is defined to facilitate filtering at different scales to detect the vessels of varying thicknesses. The method is tested on forty colour retinal images of DRIVE (Digital Retinal Images for Vessel Extraction) database with manual segmentations as ground truth. An overall accuracy of 84.22% is achieved for segmentation of retinal blood vessels.**

Keywords — **Colour Retinal Image, Vessel Segmentation, Gabor filter, Diabetic Retinopathy.**

I. Introduction

Diabetic retinopathy is a disorder of the retinal vasculature that eventually develops to some degree in nearly all patients with long-standing diabetes mellitus [1]. It is estimated that by the year 2010 the world diabetic population will be doubled, reaching an estimated 221 million [2]. The timely diagnosis and referral for management of diabetic retinopathy can prevent 98% of severe visual loss. Colour retinal images are widely used for detection and diagnosis of Diabetic retinopathy. In computer assisted diagnosis the automatic segmentation of the vasculature in retinal images helps in characterizing the detected lesions and in identifying false positives [3]. The performance of automatic detection of pathologies like microaneurysms and hemorrhages may be improved if regions containing vasculature can be excluded from the analysis. Another important application of automatic retinal vessel segmentation is in the registration of retinal images of the same patient taken at different times [4]. The registered images are useful in monitoring the progression of certain diseases.

In the literature [5] it is reported that many retinal vascular segmentation techniques utilize the information such as contrast that exists between the retinal blood vessel and surrounding background and all vessels are connected and originates from the same point that is the optic disc. Four techniques used for vessel detection are classified as filter based methods, tracking of vessels, classifiers based methods and morphological methods. In filter based methods the cross-sectional gray-level profile of a typical retinal vessel matches the Gaussian shape and the vasculature is piecewise linear and may be represented by a series of connected line segments [6]. These methods employ a two-dimensional linear structural element that has a Gaussian cross-profile section, rotated into different angles to identify the cross-profile of the blood vessel. Tracking methods [7] [8] use a model to track the vessels starting at given points and individual segments are identified using a search procedure which keeps track of the center of the vessel and makes some decisions about the future path of the vessel based on certain vessel properties. Classifier-based methods use a two-step approach [9]. They start with a segmentation step often by employing one of the mentioned matched filter-based methods and next the regions are classified according to many features. In the next step neural networks classifier is constructed using selected features by the sequential forward selection method with the training data to detect vessel pixels. Morphological image processing exploits features of the vasculature shape that are known a priori, such as it being piecewise linear and connected. The use of mathematical morphology for segmentation of blood vessels is explained in [10] [11]. These approaches works well on normal retinal images with uniform contrast but suffers in the presence of noise due to pathologies within the retina of eye.

In our work the vessel segmentation is performed using Gabor filter. Gabor filters have been widely applied to image processing and computer vision application problems such as face recognition and texture segmentation, strokes in character recognition and roads in satellite image analysis [12][13]. A few papers have already reported work on segmentation of vessels using Gabor filters [14] [15]. But still there is a scope of improvement as they fail to detect vessels of different widths. Also detection process becomes much more complicated when lesions and other pathological changes affect the retinal images. We focus to develop a much robust and fast method of retinal blood vessel segmentation using Gabor filter and introduce new parameter

Chwee Teck Lim, James C.H. Goh (Eds.): ICBME 2008, Proceedings 23, pp. 274–276, 2009
www.springerlink.com

for designing filter of different scales that facilitates the detection of vessels of varying width.

II. Segmentation of blood vessels

The detection of blood vessels is an important step in automated retinal image processing system as the colour of hemorrhages and microaneurysms is similar to the colour of blood vessels and appear darker than the background. The blood vessels appear most contrasted in the green channel of the RGB colour space because of that only the green component is retained for the segmentation of vessels using Gabor filter. Figure 1 shows digital colour fundus image and green channel image.



Fig. 1 Digital colour Retinal image and its green channel image

A. Spatial Gabor filter

The 2D Gabor filters are a set of orientation and frequency sensitive band pass filters which have the optimal localization in both the frequency and space domains. Thus they are suitable for extracting orientation dependent frequency contents of the patterns [13]. The spatial Gabor filter kernels are sinusoids modulated by a Gaussian window, the real part of which is expressed by

$$g(x,y)=\exp\left[-\frac{1}{2}\left(\frac{x_p^2}{\sigma_x^2}+\frac{y_p^2}{\sigma_y^2}\right)\right]\cos(2\pi fx) \quad (1)$$

Where,

$$x_p = x\cos\theta + y\sin\theta$$

$$y_p = -x\sin\theta + y\cos\theta$$

θ : Orientation of the filter, an angle of zero gives a filter that responds to vertical features.

f : Central frequency of pass band.

σ_x : Standard deviation of Gaussian in x direction along the filter that determines the bandwidth of the filter.

σ_y : Standard deviation of Gaussian across the filter that control the orientation selectivity of the filter.

The parameters are to be derived by taking into account the size of the lines or curvilinear structures to be detected. To produce a single peak response on the center of a line of width t, the gabor filter kernel is rotated in different orientations with the parameters set as follows

$f = 1/t$,

$\sigma_x = t*k_x$, k_x is scale factor relative to σ_x

$\sigma_y = 0.5\sigma_x$,

k_x is required so that the shapes of the filters are invariant to the scale. The widths of the vessels are found to lie within a range of 2-14 pixels (40-200 μm). Thus for the values of k_x = 0.4 and t = 11, Figure 2 shows the Gabor filter spatial frequency responses at different orientations (60^0,120^0 and 180^0) on the retinal image in Figure 1.

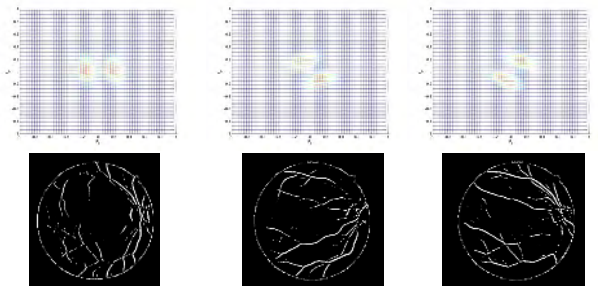


Fig. 2 Orientation of Gabor filter at 180^0, 60^0 and 120^0 (first row) applied to retinal image and corresponding response output (second row)

B. Blood vessel segmentation

Only six Gabor filter banks with different orientations (0 to 180 with interval of thirty degrees) are used to convolve with the image for fast extraction of vessels. The magnitude of each response is retained and combined to generate the result image. Figure 3 show the result of vessel segmentation using Gabor filter. Parameter are set to t=11 in Figure 3(c) and t=12 in Figure 3(d). It can be seen that at t=11 along with the thick vessels the thin vessels are also detected with true positive rate of 0.8347 and false positive rate of 0.21. With t=12 the true positive rate comes down to 0.7258, it can be seen in the Figure 3(d) that only thick vessels are segmented.

III. Experiment results

The image data required for the research work is obtained from publicly available DRIVE (Digital Retinal Im-

ages for Vessel Extraction) database and also from the Department of Ophthalmology, KMC, Manipal using Sony FF450IR digital fundus camera and stored in 24-bit colour compressed JPEG format with 768×576 pixel resolution.

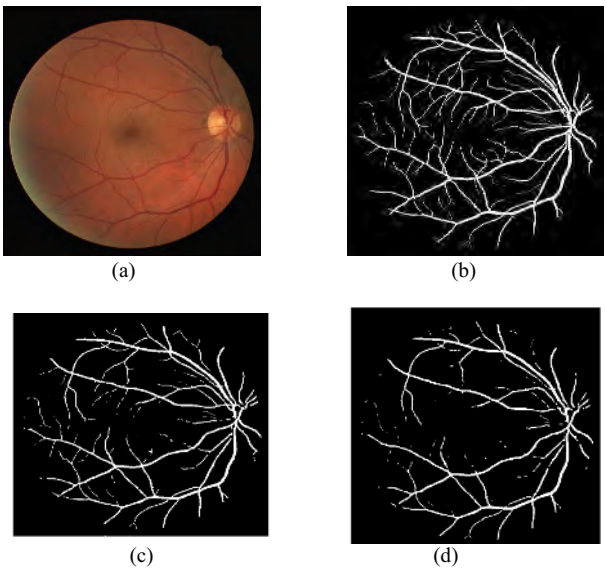


Fig. 3 Segmentation of blood vessels. (a) 19_test colour image from DRIVE database; (b) Manual segmentation of vessel; (c) Segmentation with t=11; (d) Segmentation with t=12.

It is reported in the literature that matched filter method of extraction provides an accuracy of 91% on drive database. We have implemented the matched filter for comparison with our method and found that the accuracy depends on threshold selected and applied to the filtered image the same is not the case with Gabor filter. It is also found that the matched filter method works well on normal retinal images but it suffers when an image with pathologies is considered. The proposed method is capable of segmenting retinal blood vessels of varying thickness. We tested our method on DRIVE database and obtained an accuracy of 84.22%.

IV. Conclusions

In this paper, we presented a method to detect vessels of varying thickness using Gabor filters of different scales and orientation and found that it provide better way of extracting vessels in retinal images. We also tested the method on retinal images containing lesions and varying local contrast and it gives a reasonable good result. It is hoped that automated segmentation of vessel technique can detect the signs of diabetic retinopathy in the early stage, monitor the progression of disease, minimize the examination time and assist the ophthalmologist for a better treatment plan.

References

1. Emily Y Chew, “Diabetic Retinopathy”, American academy of ophthalmology – Retina panel, Preferred practice patterns, 2003.
2. Lalit Verma Gunjan Prakash and Hem K. Tewari, “Bulletin of the World Health Organization”, vol.80, no.5, Genebra 2002.
3. Thomas Walter, Jean-Claude Klein, Pascale Massin, and Ali Erginay, “A contribution of Image Processing to the Diagnosis of Diabetic Retinopathy—Detection of Exudates in Color Fundus Images of the Human Retina”, IEEE Trans. Medical. Imaging, vol. 21, no. 10, October 2002.
4. Laliberté .F, Gagnon .L, and Sheng .Y, “Registration and fusion of retinal images: An Evaluation study”, IEEE Trans. Medical. Imaging, vol. 22, pp. 661–673, May 2003.
5. Hoover, A., Kouznetsoza, V., Goldbaum, M., “Locating blood vessels in retinal images by piecewise threshold probing of a matched filter response”, IEEE Transactions on Medical Imaging, vol. 19, pp. 203–210, 2000.
6. S. Chaudhuri, S. Chatterjee, N. Katz, M. Nelson, and M. Goldbaum, “Detection of blood vessels in retinal images using two-dimensional matched filters,” IEEE Transactions on Medical Imaging, vol. 8, no. 3, pp. 263–269, 1989.
7. Di Wu, Ming Zhang, Jyh-Charn Liu, and Wendall Bauman,” On the adaptive detection of blood vessels in retinal images”, IEEE Transactions on Biomedical Engineering, vol. 53, no. 2, February 2006.
8. A. Pinz, S. Bernogger, P. Datlinger, and A. Kruger, “Mapping the human retina”, IEEE Transactions on Medical imaging, vol. 17, no. 4, August 1998.
9. C. Sinthanayothin, J. F. Boyce, H. L. Cook, and T. H.Williamson, “Automated location of the optic disc, fovea, and retinal blood vessels from digital color fundus images,” British Journal of Ophthalmology, vol. 83, no. 8, pp. 902–910, 1999.
10. F. Zana and J. Klein., “Segmentation of vessel-like patterns using mathematical morphology and curvature evaluation”, IEEE Transactions on Image Processing, vol. 10, pp.1010–1019, 2001.
11. P. C. Siddalingaswamy, G. K. Prabhu and Mithun Desai, “Feature extraction of retinal image”, E Proc. Of the National Conference for PG and Research scholars, NMAMIT, Nitte, April 2006.
12. T.S. Lee, “Image representation using 2D Gabor wavelets”, IEEE Transactions of Pattern Analysis and Machine Intelligence, vol. 18, pp. 959-971,October 1996.
13. J.Chen, Y.Sato, and S.Tamura, “Orientation space filtering for multiple orientation line segmentation”, IEEE Transactions of Pattern Analysis and Machine Intelligence, vol.22, May 2000, pp.417-429.
14. Ming Zhang, Di Wu, and Jyh-Charn Liu, “On the small vessel detection in high resolution retinal images”, Proceedings of the 2005 IEEE Engineering in Medicine and Biology, Shanghai, China, September 2005.
15. Rangaraj M. Rangayyan, Faraz Oloumi, Foad Oloumi, Peyman Eshghzadeh-Zanjani, and F´abio J. Ayres, “Detection of blood vessels in the retina using gabor filters”, Canadian Conference on Electrical and Computer Engineering, April 2007.

Corresponding author

Author: P. C. Siddalingaswamy
Institute: Manipal Institute of Technology
City: Manipal
Country: India
Email: Pcs.swamy@manipal.edu

Automated Detection of Optic Disc and Exudates in Retinal Images

P.C. Siddalingaswamy[1], K. Gopalakrishna Prabhu[2]

[1] Department of Computer Science & Engineering, Manipal Institute of Technology, Manipal, India
[2] Department of Biomedical Engineering, Manipal Institute of Technology, Manipal, India

Abstract — **Digital colour retinal images are used by the ophthalmologists for the detection of many eye related diseases such as Diabetic retinopathy. These images are generated in large number during the mass screening of the disease and may result in biased observation due to fatigue. Automated retinal image processing system could save workload of the ophthalmologists and also assist them to extract the normal and abnormal structures in retinal images and help in grading the severity of the disease. In this paper we present a method for automatic detection of optic disc followed by classification of hard exudates pixels in retinal image. Optic disc localization is achieved by iterative threshold method to identify initial set of candidate regions followed by connected component analysis to locate the actual optic disc. Exudates are detected using k means clustering algorithm. The algorithm is evaluated against a carefully selected database of 100 color retinal images at different stages of diabetic retinopathy. The methods achieve a sensitivity of 92% for the optic disc and 86% for the detection of exudates.**

Keywords — **Diabetic retinopathy, Optic disc, Exudates, clustering.**

I. Introduction

Diabetic retinopathy causes changes in the retina, which is the most important tissue of the eye [1]. There are different kinds of abnormal lesions caused by diabetic retinopathy in a diabetic's eye such as microaneurysm, hard exudates, soft exudates and hemorrhages that affect the normal vision. The timely diagnosis and referral for management of diabetic retinopathy can prevent 98% of severe visual loss. Mass screening of Diabetic retinopathy is conducted for the early detection of this disease, wherein the retinal images are captured using standard digital colour fundus camera resulting in large number of retinal images that need to be examined by ophthalmologists. Automating the preliminary detection of the disease during mass screening can reduce the workload of the ophthalmologists. This approach involves digital fundus image analysis by computer for an immediate classification of retinopathy without the need for specialist opinions. In computer assisted diagnosis automatic detection of normal features in the fundus images like blood vessels, optic disc and fovea helps in characterizing the detected lesions and in identifying false positives.

Optic disc and hard exudates are the brightest features in the colour retinal image. It is found that the optic disc is the brightest part in the normal fundus image that can be seen as a pale, round or vertically slightly oval disc. It is the entrance region of blood vessels and optic nerves to the retina and its detection is essential since it often works as a landmark and reference for the other features in the fundus image and in correct classification of exudates [2]. The optic disc was located by the largest region that consists of pixels with the highest gray levels in [3]. The area with the highest intensity variation of adjacent pixels was identified as optic disc in [4]. Even the geometrical relationship between optic disc and blood vessels was utilized in the identification of optic disc [4]. In [5] region growing algorithm was used for detecting hard exudates. They report 80.21% sensitivity and 70.66% specificity for detecting overall retinopathy. In [6] red free fundus images are divided into sub-blocks and use artificial neural networks for classifying the sub blocks as having exudates or not. They report 88.4% sensitivity and 83.5% specificity for detecting retinopathy as a whole and 93.1% sensitivity and 93.1% specificity for hard exudates.

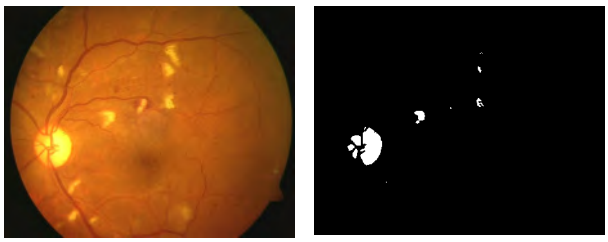
In this paper we propose detection of optic disc by detected using iterative threshold method followed by correctly identifying optic disc out of many candidate regions. Exudates are detected using k means clustering algorithm to classify exudate and non exudate pixels.

II. Methods

A. Optic Disc detection

In retinal images it has been observed that the green component of the RGB colour space contains the maximum data that can be used for efficient thresholding of the optic disc. The optic disc is observed to be brighter than other features in the normal retina. Optimal thresholding is applied to segment the brightest areas in the image. It is a method based on approximation of the histogram of an image using a weighted sum of two or more probability densities with normal distribution. The threshold is set as the closest gray level corresponding to the minimum probability between the maximum of two or more normal distribution. It is observed that it resulted in maximization of

Chwee Teck Lim, James C.H. Goh (Eds.): ICBME 2008, Proceedings 23, pp. 277–279, 2009
www.springerlink.com



(a) (b)

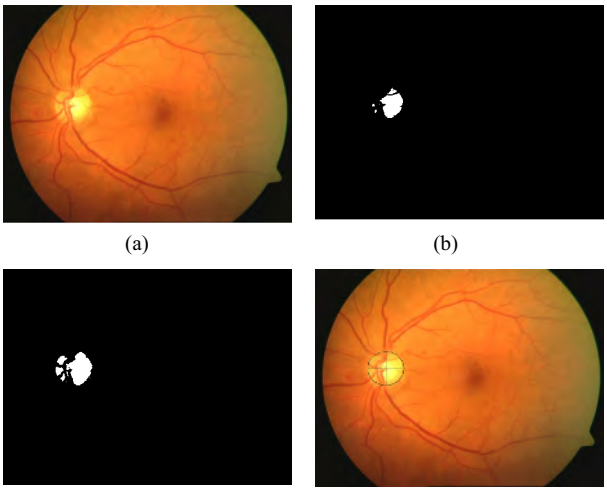
Fig. 1 Result of optimal thresholding. (a) Colour retinal image affected with diabetic retinopathy. (b) Distributed bright connected components in the threshold image.

gray level variance between object and background. The result of optimal thresholding is as shown in the Figure 1.

A data structure is used to find the total number of connected components in the threshold image. The component having the maximum number of pixels is assumed to be having the Optic cup part of the optic disc and it is considered to be the primary region of interest. The mean of this region is computed in terms of x and y coordinates. The maximum length of optic disc can be 100 pixels, only the components whose mean coordinates are within 50 to 60 pixels distance from the mean coordinates of the largest component are considered to be parts of the optic disc. The extent of the Optic disc in horizontal and vertical directions is computed by finding the overall minimum and maximum x and y coordinates among all the components that are considered as a part of optic disc. If this region is greater than 80 pixels in width and 90 pixels in height, an ellipse is drawn using the x and y coordinates so obtained. Otherwise the threshold is decremented by one and applied to the initial image. But this time the threshold is applied only in the vicinity of the mean x and y coordinates computed earlier so as to avoid misclassifying large exudates as a part of the optic disc. The above process is repeated until an optimum size of the optic disc has been obtained. The Figure 2 shows the result of optic disc segmentation.

B. Hard Exudates detection

Hard exudates are considered to be bright intensity regions in the retinal images. It is found from the literature that the green layer contains the most information on the brightness and structure of exudates. The image is smoothed and elimination of Also fundus images are characterized by uneven illumination that is, the center region of a fundus image is usually highly illuminated while the illumination decreases closer to the edge of the fundus. In other words, objects of the fundus (lesions and blood vessels) are differently illuminated in different locations of the image due to the non-uniform illumination. Median filter is applied to the



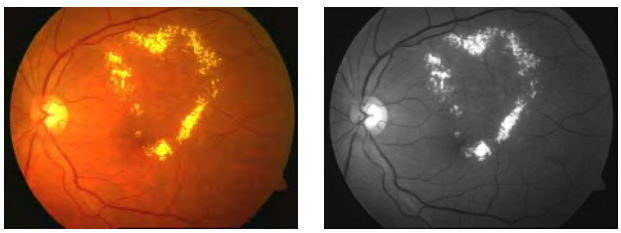
(a) (b)

(c) (d)

Fig. 2 Detection of optic disc (a) Colour retinal image (b) - (c) optic disc detection phase (e) Detected optic disc marked by ellipse

retinal image and the filtered image is subtracted from original green channel image to eliminate intensity variation. Figure 3 shows intensity image in which lesion areas are properly highlighted. The darker background features and brighter lesion features can be clearly seen.

Fig. 3 Digital colour retinal image and Image after illumination correction



K means clustering technique have been used to automatically determine clusters without prior thresholds. The set of data within the cluster are more similar to each other the data from other clusters in the specific features. Each cluster has its own cluster center in the feature space. An important measurement of similarity for data is distance between cluster centers and between points inside one cluster. Here the distance measure is the difference in the intensity values between two pixels in the intensity difference image. Since we are interested in exudates and non exudates regions the number of clusters will be two. Exudates cluster will be located in the higher intensity range and background cluster in the lower intensity range. The maximum and minimum intensity levels in the intensity difference image calculated are termed as *min* and *max* respectively and

forms initial cluster centers. Intensity difference is taken as distance measure and it is used to find distance between pixels and initial cluster centers resulting in two clusters and the cluster centers are updated. The process is repeated iteratively there is not much variation in the values of cluster centers. Figure 4 shows the result of application of k means clustering method to the intensity image in Figure 3.



Fig. 4 Detected exudates

III. Results

The image data required for the research work is obtained from the "Lasers and Diagnostics", Department of Ophthalmology, Kasturba Medical College, Manipal. The colour fundus images are of dimension 768×576 pixels captured from Sony FF450IR digital fundus camera. Each fundus image comprises of a red, green, and blue grayscale image combined to form a three dimensional color image. The green plane was used in the algorithms due to the greater distribution of intensity through the image. The algorithm is evaluated against a carefully selected database of 100 color retinal images at different stages of diabetic retinopathy. Optic disc is located with the sensitivity of 92%. It failed in eight of the testing images, because of presence of large area of lesions around the optic disk. For the detection of hard exudates the optic disc is masked to avoid misclassification. The proposed clustering method detected the hard exudates with 86% sensitivity.

IV. Conclusion

The algorithms for the automatic and robust extraction of features in color retinal images were developed in this paper. Optimal iterative threshold method followed by connected component analysis is proposed to identify the optic disc. Clustering method was used for identifying hard exudates in a digital colour retinal image. The algorithm performed better on variety of input retinal images, which show the relative simplicity and robustness of the proposed algorithm. This is a first step toward the development of automated retinal analysis system and it is hoped that a fully automated system can detect the signs of diabetic retinopathy in the early stage, monitor the progression of disease, minimize the examination time and assist the ophthalmologist for a better treatment plan.

Acknowledgment

The authors would like to express their gratitude to the Department of Ophthalmology, Kasturba Medical College, Manipal for providing the necessary images and clinical details needed for the research work.

References

1. Emily Y Chew, "Diabetic Retinopathy", American academy of ophthalmology – Retina panel, Preferred practice patterns, 2003.
2. Huiqi Li and Opas Chutatape, "Automated Feature Extraction in Color Retinal Images by a Model Based Approach", IEEE Trans. Biomedical Engineering, vol. 51, no. 2, February 2004.
3. Z. Liu, O. Chutatape, and S. M. Krishnan, "Automatic image analysis of fundus photograph", Proc. 19th Annu. Int. Conf. IEEE Engineering in Medicine and Biology Society, vol. 2, pp. 524–525, 1997.
4. C. Sinthanayothin, J. F. Boyce, H. L. Cook, and T. H.Williamson, "Automated location of the optic disc, fovea, and retinal blood vessels from digital color fundus images," British Journal of Ophthalmology, vol. 83, no. 8, pp. 902–910, 1999.
5. M. Foracchia, E. Grisan, and A. Ruggeri, " Detection of Optic Disc in Retinal Images by Means of a Geometrical Model of Vessel Structure", IEEE Trans. Medical imaging, vol. 23, no. 10, October 2004.
6. G. Gardner, D. Keating, T.H. Williamson, and A. T. Elliot, "Automatic Detection of diabetic retinopathy using an Artificial neural network: a screening tool", British Journal of Ophthalmology, vol. 80, pp. 940–944, 1996.

Corresponding author

Author: P. C. Siddalingaswamy
Institute: Manipal Institute of Technology
City: Manipal
Country: India
Email: Pcs.swamy@manipal.edu

Qualitative Studies on the Development of Ultraviolet Sterilization System for Biological Applications

Then Tze Kang[1], S. Ravichandran[2], Siti Faradina Bte Isa[1],
Nina Karmiza Bte Kamarozaman[1], Senthil Kumar[3]

[1] Student, Temasek Engineering School, Temasek Polytechnic, Singapore
[2] Faculty, Temasek Engineering School, Temasek Polytechnic, Singapore
[3] Student, Nanyang Technological University, Singapore

Abstract — **Ultraviolet rays have been widely used in providing antimicrobial environment in hospitals and also in certain sterilization procedures related to water treatment. The scope of the paper is to investigate the design of an ultraviolet sterilization unit developed to work in conjunction with a fluid dispenser for dispensing fluids in measured quantities periodically. Common problems associated with contamination of fluids in these dispensers have been carefully investigated to qualitatively document the requirements of the system. The most important part of this study has been focused on the qualitative assessment of the antimicrobial effects at various parts of the dispenser and also the variations of the antimicrobial effects at various depths of the fluid contained in the dispenser. We have designed a protocol to study the efficiency of the system and in order to have a real picture of the antimicrobial effects of ultraviolet radiation at various depths. To implement this protocol, we have designed an implantable array which is capable of containing microorganisms in sealed Petri dishes to be immersed in the fluid contained in the dispenser. Studies on the microbial growth conducted periodically under the influence of ultraviolet radiation of a known intensity provide a qualitative picture on the antimicrobial effects of ultraviolet rays at various depths. Thus it is possible to qualitatively analyze each sample for documenting antimicrobial effect. This study provides a good understanding on the intensity of the ultraviolet radiation required for providing a perfect antimicrobial environment and also other factors that are critical in the design of the system as a whole for dispensing fluids in biological applications.**

Keywords — **Ultraviolet rays, Antimicrobial effects, Fluid dispenser, Biological applications, Sterilization procedures**

I. Introduction

Purification and sterilization of water is considered important for all biological applications. Some of the conventional methods referred in practice are as briefly discussed [1]. Filtration of the water is considered very important before any sterilization procedures and a wide variety of filters are available for filtration of water. Filters remove sand, clay and other matter as well as organisms by means of a small pore size.

Filtration and sterilization is achieved by passing water usually through iodine exchange resins. In this method, when negatively charged contaminants contact the iodine resin, iodine is instantly released and kills the microorganisms without large quantities of iodine being in the solution. Boiling water is considered the most reliable and often the cheapest. Ideally, boiling the water for 5 minutes is considered safe in killing the microorganisms [2]. Alternatively, sterilization using chlorine and silver-based tablets can destroy most bacteria's when used correctly, but these are less effective for viruses and cysts.

In recent years, the ultraviolet (UV) sterilization is gaining popularity as a reliable sterilization method and is environmental-friendly too [1]. UV disinfection technology is of growing interest in the water industry since it was demonstrated that UV radiation is very effective against certain pathogenic micro-organisms of importance for the safety of drinking water [3]. In most of the sterilization equipments, the light source is a low-pressure mercury lamp emitting UV in the wavelength of 253.7 nm and this source is referred to as UVC [4]. Ultraviolet rays have been a known mutagen at the cellular level and it is used in a variety of applications, such as food, air and water purification.

II. Ultraviolet rays in sterilization

A. Germicidal Mechanisms of Ultraviolet Rays

The germicidal mechanism of UVC light has the ability to alter deoxyribonucleic acid (DNA) code, which, in turn, disrupts an organism's ability to replicate [5]. Absorption of UV energy by nuclei in DNA is primary lethal mechanism for the destruction of microorganisms. The antimicrobial effect is dependent on both the time of exposure and the intensity of the UVC ray. However, the UVC sterilization will not be effective if the bacterial or mold spores are hidden or not in the direct path of the rays. Organisms that are large enough to be seen are usually too resistant to be killed by practical UVC exposure. The radiation dose of UVC energy is measured in microwatts per centimeter square

Chwee Teck Lim, James C.H. Goh (Eds.): ICBME 2008, Proceedings 23, pp. 280–283, 2009
www.springerlink.com

(μW/cm²). With the known wavelength of 253.7nm, it has been found that intensities from 2500 μW/cm to 26,400μW/cm² are effective against various bacterial organisms. For mold spores, intensities ranging from 11,000μW/cm² to 220,000μW/cm² are effective. Though most of common viruses, such as influenza, poliovirus and viruses of infectious hepatitis, are susceptible to intensities less than 10,000μW/cm², some of the viruses such as tobacco mosaic virus seen in plants are susceptible to UVC rays at very high intensity (440,000μW/cm²) [6].

B. Sterilization in Hospitals and Clinics

UVC rays are very widely used in sterilization procedures in hospital and clinics. UVC light (100-280 nm) has been reported to be very effective in decontamination of hospital-related surfaces, such as unpainted/painted aluminum (bed railings), stainless steel (operating tables), and scrubs (laboratory coats) [7]. It has been reported that UVC lighting is an alternative to laminar airflow in the operating room and that it may be an effective way for lowering the number of environmental bacteria. It is also believed that this method can possibly lower the infection rates by killing the bacteria in the environment rather than simply reducing the number at the operative site [8]. As infections represent a major problem in dialysis treatment, dialyzing rooms need be kept antibacterial to the extent possible. It has been reported that 15-watt UVC lamps installed for every 13.5m² on the ceiling for the purpose of the room disinfection used for 16 hours nightly after working hours provide an antimicrobial environment even in areas which were not directly exposed to the UVC radiations [9].

C. Sterilization in Water Purification System

Transmission of pathogens through drinking water is a well-known problem, which affects highly industrialized countries and also countries with low hygienic standards. Chlorination of drinking water was introduced to the water supply in the beginning of the 19th century in order to stop the spreading of pathogens. Disinfection of drinking water with chlorine has undoubtedly contributed to the reduction of typhoid fever mortality in many countries. Despite the worldwide use of chlorine for disinfection of drinking water, other safe methods of disinfection had gained popularity [10]. Ultraviolet disinfection technology is of growing interest in the water industry ever since it was found very effective against common pathogenic micro-organisms in water [3]. Ultraviolet disinfection systems are commonly incorporated into drinking water production facilities because of their broad-spectrum antimicrobial capabilities, and the minimal disinfection by-product formation that generally accompanies their use [11].

D. Ultraviolet Sterilization for Clinical Applications

Filtered water free from microorganisms and chemicals disinfectants is an absolute requirement for the preparation of solutions for certain biological applications in medicine. The process of reverse osmosis is an invaluable technology to provide filtered water free from pathogens. Since water filtered through the process of reverse osmosis is free from chemical disinfectants, it serves as the ideal solvent for the preparation of biochemical solutions used in biological applications. This paper will discuss briefly the various parts of the ultraviolet sterilization system developed for providing the solvent required for preparation of biochemical solutions used in biological applications.

III. Architecture of the System

The architecture of the system essentially consist of ultraviolet radiation chamber, fluid dispensing chamber, embedded adjustable profile, fluid inlet and outlet system and a microcontroller module. The block diagram of the architecture is shown below.

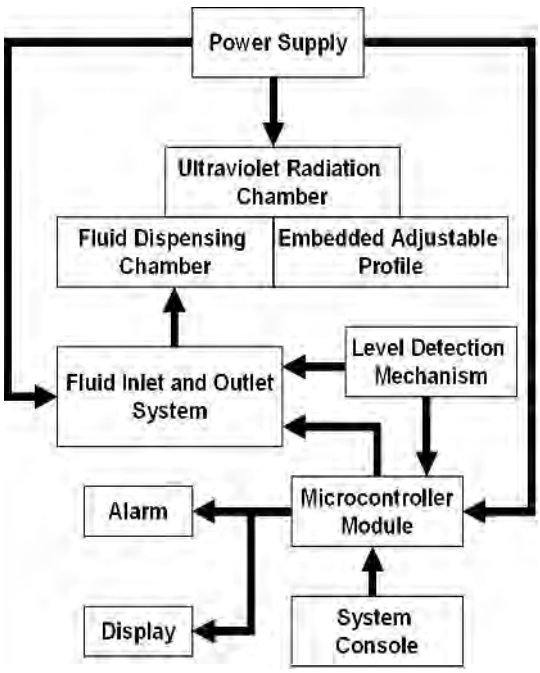


Fig. 1 Block Diagram of the Architecture

A. Ultraviolet Radiation Chamber

In order to provide an antimicrobial environment in the chamber, an ultraviolet radiation chamber was built. The ultraviolet radiation chamber has two ultraviolet lamps installed to provide maximal sterilization throughout the whole fluid dispensing chamber. The ultraviolet radiation module used in our system is shown in Fig. 2.

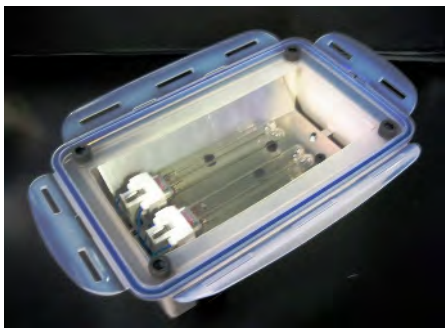


Fig. 2 Ultraviolet Radiation Module

B. Fluid Dispensing Chamber

The material used for building the chamber has to be a medically approved material for biological applications. Medical grade stainless steel and food-grade polyethylene often meet the requirements. In our preliminary studies, we have made use of food-grade polyethylene to build the fluid dispensing chamber. This chamber has been designed to hold the measured volume of fluid stored for dispensing which is eventually used to prepare biochemical solution for the biological applications.

C. Embedded Adjustable Profile

Qualitative studies had been made using the embedded adjustable profile capable of holding the sealed Petri dishes at various positions in the fluid dispensing chamber.



Fig. 3 Adjustable Profile in Chamber

This adjustable profile had been indigenously fabricated in such a way that it could be well accommodated within the chamber. The embedded adjustable profile along with the fluid dispensing chamber is shown in Fig. 3.

D. Fluid Inlet and Outlet System

The system is installed with two solenoid pinch valves that controlled the filling and dispensing of the fluid into and also out of the fluid dispensing chamber. Volume of the fluid is measured precisely by the level detection mechanism. A microcontroller module interfaces a level detection module to control the fluid inlet and outlet system.

E. Microcontroller Module

The architecture is built around PIC18F4520 microcontroller containing five ports. The ports are configured to support some of the modules such as display interface, keyboard interface, activation of the pinch valves and the level detection mechanism. The implementation of the microcontroller allows integration of the different modules of the system.

IV. Qualitative Studies on Ultraviolet Irradiation

The object of this study is to qualitatively evaluate the antimicrobial effects of the UV radiation. In order to assess the effects, we have constructed the adjustable profile capable of holding the sealed Petri dishes at various positions in the fluid dispensing chamber. The sealed Petri dishes within the chamber contain the required environment for bacterial growth. In our studies, we have used Lysogeny broth (LB) agar for the bacteria to multiply and we have conducted studies using this medium extensively. With the help of this set-up, it was possible to conduct studies on the bacterial colonies after exposure to UV radiations at various positions inside the fluid dispensing chamber. Studies were conducted for various exposure durations to assess the antimicrobial effects of UV radiations on the bacterial colonies positioned at various levels of the fluid dispensing chamber.

V. Results and Discussion

Preliminary studies of ultraviolet radiations had clearly demonstrated the effects of ultraviolet on the bacterial colonies at various depths within the fluid dispensing chamber. These studies have provided a clear picture on the effects of the ultraviolet rays of a known intensity and its capability to provide an antimicrobial environment deep inside the fluid

dispensing chamber. Fig. 4 shows the growth of the bacterial without ultraviolet radiation in an incubator retained as a control for our studies. Fig. 5 shows the absence of bacterial growth in the agar medium after exposure. The Petri dish was maintained within the fluid dispensing chamber at level two, which is approximately the middle portion of the chamber. Fig. 6 shows the absence of bacterial growth in the agar medium after exposure. The Petri dish was maintained within the fluid dispensing chamber at level three, which is approximately the bottom portion of the chamber.



Fig. 4 Control Petri Dish

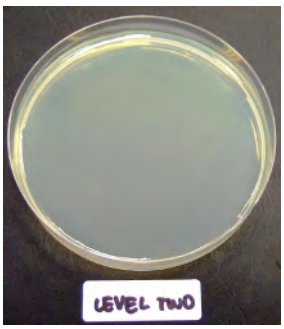


Fig. 5 Petri Dish at Level Two

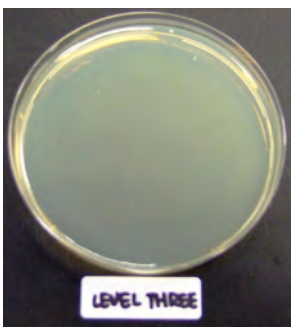


Fig. 6 Petri Dish at Level Three

VI. Conclusion

Preliminary studies conducted on the newly developed Ultraviolet Sterilization System have demonstrated the antimicrobial effects of the ultraviolet radiations as seen in Fig. 5 and Fig. 6. Theses studies were conducted with E.Coli bacterial strains to qualitatively document the antimicrobial effects of UVC at various depths. This system was built indigenously for providing a measured quantity of solvent for the preparation of biochemical solution for certain biological applications.

References

1. Yagi, N. Mori, M. Hamamoto, A. Nakano, M. Akutagawa, M. Tachibana, S. Takahashi, A. Ikehara, T. Kinouchi, Y. (2007) Sterilization Using 365nm UV-LED, Proceeding of 29th Annual International Conference of IEEE/EMBS, 2007, pp 5841-5844 DOI 10.1109/IEMBS.2007.4353676
2. Anthony T.Spinks, R.H. Dunstan, T. Harrison, P. Coombes, G. Kuczera (2006) Thermal inactivation of water-borne pathogenic and indicator bacteria at sub-boiling temperatures. DOI 10.1016/j.watres.2006.01.032
3. W.A.M. Hijnen, E.F. Beerendonk, G.J. Medema (2005) Inactivation credit of UV radiation for viruses, bacteria and protozoan (oo) cysts in water: A review. DOI 10.1016/j.watres.2005.10.030
4. Mirei Mori, Akiko Hamamoto, Akira Takahashi, Masayuki Nakano, Noriko Wakikawa, Satoko Tachibana, Toshitaka Ikehara, Yutaka Nakaya, Masatake Akutagawa, Yohsuke Kinouchi (2007) Development of a new water sterilization device with a 365 nm UV-LED. DOI 10.1007/s11517-007-0263-1
5. Janoschek, r., G. C. Moulin (1994) Ultraviolet Disinfection on Biotechnology: Myth vs. Practice. BioPharm (Jan./Feb.), pp24-31
6. Anne F. Booth (1999) Sterilization of Medical Devices. Interpharm Press, Inc, Buffalo Grove, IL60089, USA
7. Rastogi VK, Wallace L, Smith LS. (2007) Disinfection of Acinetobacter baumannii-contaminated surfaces relevant to medical treatment facilities with ultraviolet C light. Mil Med. 2007 Nov; 172(11):1166-9. PMID: 18062390
8. Merrill A. Ritter, Emily M. Olberding, Robert A. Malinzak (2007) Ultraviolet Lighting during Orthopaedic Surgery and the Rate of Infection. The Journal of Bone and Joint Surgery (American). 2007; 89:1935-1940. DOI 10.2106/JBJS.F.01037

Inamoto H, Ino Y, Jinnouchi M, Sata K, Wada T, Inamoto N, Osawa A (1979) Dialyzing room disinfection with ultra-violet irradiation. J Dial. 1979; 3(2-3):191-205. PMID: 41859

10. D. Schoenen (2002) Role of disinfection in suppressing the spread of pathogens with drinking water: possibilities and limitations. DOI 10.1016/S0043-1354(02)00076-3
11. Isaac W. Waita, Cliff T. Johnstonb, Ernest R. Blatchley IIIc (2007) The influence of oxidation-reduction potential and water treatment processes on quartz lamp sleeve fouling in ultraviolet disinfection reactors. DOI 10.1016/j.watres.2007.02.057

Authors: Then Tze Kang[1], S.Ravichandran[2]
Institute: Temasek Polytechnic
Street: 21 Tampines Ave 1
City: Singapore
Country: Singapore
Emails: blue_taurus5@hotmail.com, subbaram@tp.edu.sg, dr.sun.moon@gmail.com

From e-health to Personalised Medicine

N. Pangher

ITALTBS SpA, Trieste,Italy

Abstract — **The research agenda of the TBS group is aiming at offering a complete solution for the management of molecular medicine in the standard care environment. The impact of the different –omics (genomics, proteomics, metabolomics,….) is already representing a very important part of the research effort in medicine and is expected to modify dramatically the model of delivery of healthcare service. The TBS group is facing this challenge through a R&D effort in order to transform its Clinical Information System into a complete suite for the management of clinical research and care pathways, supporting a completely personalised approach. The IT suite allows research to integrate the Electronic Clinical Records with data from technologies such as DNA and protein microarrays, data from diagnostic and molecular imaging, and workflow management solution. In this paper we will discuss the results from the participation to different European and national research projects, sharing this development aim. We provided the IT integration suite for projects for the identification of therapy-relevant mutations of tumor suppressor genes in colon cancer (MATCH EU project), for the genetic base for the impact of metabolic diseases on cardiovascular risk (MULTIKNOWLEDGE EU project) and for the identification of biomarkers for Parkinson disease (SYMPAR project in Italy).**

Keywords — **Bioinformatics, e-health, personalized medicine, Electronic Medical Records, health risk profiles.**

I. Introduction

The mantra in healthcare services in the past years has been quality through formalization and standardization of processes. Accreditation, Evidence Based Medicine, Best practices, Risk management: processes are described, guidelines established, outcomes defined as targets. The quality revolution has become the daily bread for most industrial sectors: we expect fully functional products wherever we obtain them and services that are effective independent of the particular person involved. At the same level we pretend from our healthcare provider to deliver the best possible service independent of the location and the professional that are treating us: the great effort towards a standardization of the quality of healthcare is not yet completed, but we are facing a changing scenario. The impact of molecular medicine is going to impact dramatically on the service delivery models: personalization of treatment will have a strong scientific background. Treatment will be based on our molecular make up: genomics, transcriptomics, proteomics, metabolomics will become the tools of the day. Advanced diagnostic will result not only in a more tailored treatment, but will allow the identification of risk profiles that will be essential to design improved prevention protocols, aiming at remaining healthy and not only cure or manage diseases. The personalization of the treatment process will also be based on the availability of new tissues and organs that will be obtained through the most advanced applications of tissue engineering: regenerative medicine, based on extensive exploitation of stem cells, will allow the repair and substitution of defective organs. But again the compatibility of the new tissues and organs will have to be tailored to the characteristics of the single human being, Engineered stem cells will be used to set up tissue banks: the patient himself will be one of the sources of these new tissues.

While we have still not achieved the target of the standardization of healthcare services, a discontinuity in the complexity of healthcare is appearing: good quality healthcare will require a very personalized approach, starting from diagnostic systems based on "-omics" analysis and molecular imaging through targeted drugs, new compatible tissues and organs, gene therapy and drug delivery solutions. Prevention will be based not only on more general rules, but will also depend on our actual predisposition to diseases.

This trend is impacting the development of IT solutions for the healthcare sector: workflow systems allowing supporting healthcare processes are not widely available and suddenly IT systems will have to abandon a "few sizes fit all" approach to present solutions systems that will allow the setting up of prevention , treatment and disease management processes ecompassing all kind of environments, data sources and knowledge basis. IT solution will have to allow continuity of prevention and care, collecting data from different sources ranging from home-based monitors to sequencing technologies to PET scanners. Treatment options should range from diet and exercise prescriptions to the design of viral vectors for gene therapies to the production of stem cells for organ replacement.

Chwee Teck Lim, James C.H. Goh (Eds.): ICBME 2008, Proceedings 23, pp. 284–286, 2009
www.springerlink.com

II. Research strategy

A. The Match Project

The MATCH project entitled the development of an automatic diagnosis system that aimed to support treatment of colon cancer diseases by discovering mutations that occurs to tumour suppressor genes (TSGs) and contributes to the development of cancerous tumours. The colon cancer automated diagnosis system is a computer based platform that addresses doctors, biologists, cancer researchers and pharmaceutical companies. The project goal was to perform medical integration between medicine and molecular biology by developing a framework where colon cancer diseases will be efficiently handled. Through this integration real time conclusion can be drawn for early diagnosis and more effective colon cancer treatment. The constitution of the system is based on a) colon cancer clinical data and b) biological information that will be derived by data mining techniques from genomic and proteomic sources.

B. The Multiknowledge Project

MULTI-KNOWLEDGE starts from the data processing needs of a network of Medical Research Centres, in Europe and USA, Partners in the Project and co-operating in researches related to the link between metabolic diseases and cardiovascular risks. These needs are mostly related to the integration of three main sources of information: clinical data (EHR), patient-specific genomic and proteomic data (in particular data produced through Micro-arrays technology), and demographic data.

MULTI-KNOWLEDGE has created an intelligent workflow environment for multi-national multiprofessional research consortia aiming at cooperatively mining, modelling, visualizing biomedical data under a single common perspective.

This will allow retrieval and analysis of millions of data through bio-informatics tools, with the intent of improving medical knowledge discovery and understanding through integration of biomedical information.

Critical and difficult issues addressed are the management of data that are heterogeneous in nature (continuous and categorical, with different order of magnitude, different degree of precision, etc.), origin (statistical programs, manual introduction from an operator, etc.), and coming from different data achieving environments (from the clinical setting to the molecular biology lab). The MULTI-KNOWLEDGE architecture and set of tools have been tested for the development of a structured system to integrate data in a single informative system committed to cardiovascular risk assessment. Therefore this project will also contribute to establish guidelines and operating procedures to manage and combine data coming from protein arrays and make them easily available for the imputation of study algorithms.

C. The Sympar Project

The target of the project is to develop an informatic system for research in the biomarkers and treatment of Parkinson's Disease (PD), the second most common progressive neurodegenerative disorder in western countries.

We are testing how an integrated IT solution can support researchers in identifying molecular biomarkers of the disease. These biomarkers will be used for early diagnosis in pre-symptomatic individuals and to follow at the molecular level the response to old and new therapies.

Our IT solution is based on the following elements:

1) A data repository where all data relevant to patient health are stored. Data will consist on routine medical records, brain-imaging data, filmed records of behavioural assessments, gene expression profiles from peripheral tissue.
2) A workflow engine: medical and research procedures should be standardized. The IT system should support users in collecting medical data and in following laboratory protocols. The system should help the user both in identifying and classifying patients, and in activating medical and research procedures.
3) An access to the external knowledge base: a unique interface to access literature, external scientific databases, specialised healthcare resources.

III. The toolbox

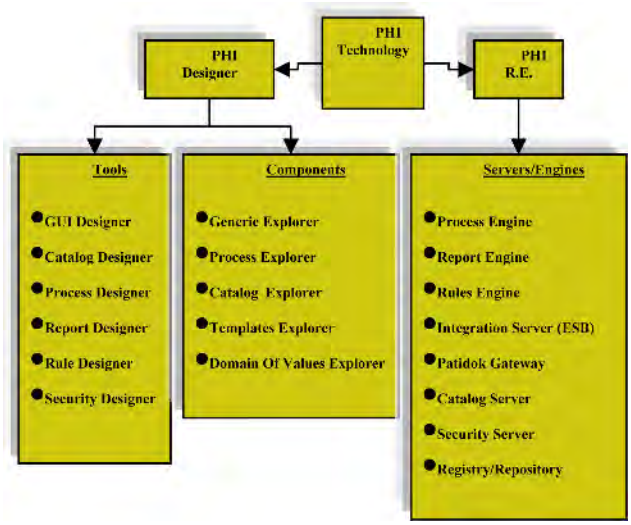
During the development of these different solutions,, we have identified the need to set up a unique toolbox to develop IT solutions addressing the needs of biomedical research and healthcare services tackling the issues of a the need of integrating different knowledge sources, biomedical instruments and personalised treatment options. We have realised this toolbox baptized PHI technology.

PHI Technology is divided in two separate parts called PHI Designer and PHI Runtime Environment (PHI RE). The PHI Designer is used to generate healthcare applications named PHI Solutions, deployed and executed upon the PHI RE runtime environment.

PHI Designer and PHI RE share a common Reference Information Model (PHI RIM), fully extensible and customizable, derived from the international standard HL7 RIM (www.hl7.org). PHI RIM stores the metadata catalog, de-

scribing objects' attributes, services, events, vocabularies and ontologies. Applications, named "solutions", are designed and executed upon the RIM.

The physical database (PHI RIM DB) is invisible to designers and applications; its conceptual and physical model is derived from the RIM, that makes it an open database, based on the most popular international healthcare standard. Its mixture of Entity-Relationship and Entity-Attribute-Value physical structures makes it extremely flexible and performing.



The PHI Designer is intended to assist you with developing easy to use and intuitive reusable applications for your daily work with information. Finally, the PHI Technology provides you with a runtime environment independent from underlying operating systems, named PHI RE, based on J2EE (Java 2 Enterprise Edition) and open standards, where you can deploy your applications once you have designed them with the PHI Designer. Servers and Engines can be seen as being nearly synonyms.

The main purpose of the PHI RE is to enable the applications exchange and reusability among partners and customers, making it as easy as a plug-and-play setup.

PHI RE is mainly composed by Servers and Engines, which are, finally, J2EE components developed in JBoss SEAM framework, which are deployed in JBOSS Application Server.

Both PHI Designer and PHI RE are reliable and scalable: you can install the whole PHI Technology either on a personal computer or in a network of distributed servers, in single node configuration as well as in a cluster configuration for high availability.

IV. Conclusions

The need of IT solutions for the management of biomedical research and personalized medicine tretments will be a major issue: these tools will b enecessary to navigate in the sea of informationa dn find the correct personalize route.

corresponding author:

Author: Nicola Pangher
Institute: ITALTBS SpA
Street: Padriciano 99
City: Trieste
Country: Italy
Email: pangher@italtbs.com

Quantitative Biological Models as Dynamic, User-Generated Online Content

J.R. Lawson, C.M. Lloyd, T. Yu and P.F. Nielsen

Auckland Bioengineering Institute, The University of Auckland, Auckland, New Zealand

Abstract — **Quantitative models of biological systems are dynamic entities, with modelers continually tweaking parameters and equations as new data becomes available. This dynamic quality is not well represented in the current framework of peer-reviewed publications, as modelers are required to take a 'one-dimensional snapshot' of their model in a particular state of development.**

The CellML team is developing new software for the CellML Model Repository that treats models as dynamic code, by providing server-side storage of models within a version control system, rather than as static entities within a relational database. Version control systems are designed to allow a community to collaborate on the same code in parallel and to provide comprehensive revision histories for every file within the repository.

Because CellML 1.1 espouses a modular architecture for model description, it is possible to create a library of modular components corresponding to particular biological processes or entities, which can then be combined to create more complex models. For this to be possible, each component needs to be annotated with a set of metadata that describes its provenance, a detailed revision history and semantic information from ontologies. A high level of collaboration is also essential to leverage domain-specific knowledge about the components of a large model from a number of researchers.

By treating quantitative biological models as dynamic, user-generated content, and providing facilities for the expert modeling community to participate in the creation and curation of a free, open-access model repository, the the next-generation CellML Model Repository will provide a powerful tool for collaboration and will revolutionise the way cellular models are developed, used, reused and integrated into larger systems.

Keywords — **databases, e-science, CellML, quantitative modeling**

I. Introduction

Quantitative models of biological systems are dynamic entities, with modelers continually tweaking parameters and equations as new data becomes available. This dynamic quality is not well represented in the current framework of peer-reviewed publications, as modelers are required to take a 'one-dimensional snapshot' of their model in a particular state of development.

The glut of data about biological systems can present a challenge to the ability of individual researchers or groups to manage and utilize their knowledge of these systems. One solution to this challenge is to encode this information into structured systems of knowledge, and the resulting models are rapidly becoming integral to many fields of biology. The sheer volume and rate of production of new data is stressing the traditional scientific publication process because it cannot keep up [1], and because the print medium is simply not appropriate in many cases. The internet must be leveraged to disseminate data as it is collected and incorporated into models, and to facilitate the mass collaborative initiatives required to merge these models into ever larger, more complex systems.

II. Limitations of the Conventional Scientific Publishing System

The ability of researchers to describe a quantitative biological model within a conventional printed academic publication is limited. As these models become more complex and detailed, this limitation has begun to hamper the ability of other researchers to work with these models. At best, this issue limits the critical second stage of peer-review: reproduction of experiments described in publications by the scientific community. If a model cannot be easily reproduced because it is inadequately described in the literature, not only is its validity questioned, but a barrier is created to the construction of complex models of biological systems, which are commonly built by combining smaller models. The greater levels of transparency required by this field of research will be difficult to provide by merely extending print-based the publication model. At present, publications that discuss quantitative models take can take one of several forms:

- Model equations and parameters are often interspersed throughout the paper, with salient discussions on each. This format can be frustrating to researchers attempting to reproduce a model, as the primary emphasis is often on the commentary describing why particular values were chosen or how equations were derived, rather than providing a complete description. Furthermore, descriptions of these models are frequently missing important parameters and initial conditions.
- Supplemental datasheets published with the article define the model by listing equations and parameters. This information provides a more concise, and often

Chwee Teck Lim, James C.H. Goh (Eds.): ICBME 2008, Proceedings 23, pp. 287–290, 2009
www.springerlink.com

more complete, description of the model, although typographical errors still present a persistent barrier to model reproduction.

- Alternatively, the predictions and outputs of a model are simply discussed, without any real attention to how the model is constructed. These articles tend to be reviews or short format publications in journals such as *Science.* This approach is sometimes extended by providing links to the author's website, which either elaborates in the form of a listing of equations and parameters, or provides a download of the original model code. Providing 'external supplemental data' can be useful, but again, typographical errors can be an issue. This can be quite effective, although the fact that the model is not officially part of the publication, and thus not subject to the same oversight and peer review, gives no guarantee that the available model is the identical to the one used to produce the outputs shown and discussed in the publication. Making model code available in a widely accepted and utilised language such as MATLAB is helpful, but more often the model code is only available in obscure formats specific to small, in-house software packages developed by the authors or their colleagues.
- Some publishing groups, such as PLoS, Nature and BMC are actively moving towards requiring model authors to deposit a copy of their model in an open-access, recognised, online repository, in the same manner that most journals now require authors to deposit novel DNA sequence information or protein structures in a database (such as GenBank [2] or PDB [3], respectively) as a prerequisite to publication. This is an ideal solution to removing the barriers to transparency and reproduction presented above, but it involves a significant shift in the scientific publishing paradigm that has existed to date.

III. Storing models in online version control systems

CellML [4] is an XML-based format designed to allow description of quantitative models based on ordinary differential equations and systems of differential algebraic equations and to facilitate wide dissemination and reuse of these models. The CellML Model Repository [5] is an online resource that provides free, open access to CellML models. Currently Physiome Model Repository (PMR) software underlying this repository allows limited interaction with the models it stores; they can be associated with documentation and metadata and or organized thin a primitive versioning system.

The CellML team is developing new software (PMR2) for the CellML Model Repository that dispenses with the concept of quantitative biological models as static snapshots of knowledge and treats them as dynamic, software-like entities by providing server-side storage of models within a Mercurial, distributed version control system (DVCS). DVCS are designed to allow a community to collaborate on the same code in parallel and to provide comprehensive revision histories for every file within the repository. This concept of model development is drawn from the open source software development. Programmers are able to build large systems by drawing on libraries of pre-existing code, and online communities such as Sourceforge form around these efforts to discuss implementation.

Comprehensive revision histories which define provenance and the rationale of each and every addition to and modification of a piece of code are fundamental to any open source initiative because information about who did what and when provides the foundation for collaboration. PMR2 can support the signing of changesets with cryptographic signatures using the GPG plugin provided by Mercurial, ensuring the integrity of the information within and proper attribution to the author who signed the changeset. Changing the data without breaking the checksum and signature is extremely difficult without the original signature key that was used to sign the model.

Storing models within a DVCS allows collaborative software development methods to be used in model construction: rollbacks, branching, merging of branches and parallel revisions to the same code are all possible. Powerful access control systems can also be implemented to allow modelers to control who is able to see and interact with their work.

The PMR2 software and associated systems for online publishing are described in detail by Yu et al. [6]

IV. Modularity and model reuse

Complex systems in engineering are almost always constructed as hierarchical systems of modular components [7]. Such modularity can be seen in human engineered systems but also in biology [8]. Models should be designed with reuse in mind and implemented in formats which facilitate their combination into the kinds of hierarchical systems familiar to engineers.

Such methodology leverages ‘black-box’ abstraction and allows for separation of concerns. For example, a disparate group of researchers may be collaborating on the construction of a system: one may be responsible for organizing the top level hierarchy, while others may be responsible for lower level subcomponents or hierarchies. If the compo-

nents of the system are constructed in a sufficiently modular fashion, the researcher organizing the hierarchy needs to know very little about how they actually work – only their input and output. Terkildsen et al. [9] demonstrate this in a recent article discussing their use of the CellML standard to integrate multiple models, [10,11,12] each describing discrete but interrelated systems within a rat cardiac myocyte; the result was a model of excitation-contraction coupling. Similarly, descriptions of systems involving multiple cell types can be created from pre-existing models. Sachse et al. [13] recently used a model of the interaction between cardiac myocytes and fibroblasts as a platform to develop and number of novel hypotheses about the role of fibroblasts in cellular electric coupling within the heart. The model of the cardiac myocyte used in this work was a curated, (but unpublished through official channels,) form of the influential Pandit 2001 model [10], downloaded from the CellML Model Repository.

Because CellML 1.1 espouses a modular architecture for model description, it is possible to create a library of modular components corresponding to particular biological processes or entities, which can then be combined to create more complex models [14]. For this to be possible, each component needs to be annotated with a set of metadata that describes its provenance, a detailed revision history and semantic information from ontologies. A high level of collaboration is also essential to leverage domain-specific knowledge about the components of a large model from a number of researchers.

The CellML project seeks to provide the tools and infrastructure for both creating these libraries of components and disseminating them over the internet. PMR2 will provide a framework for users to reuse, review and modify pre-existing components, create new components, to collaborate securely and privately with any number of other users and to rapidly share and their work public. Methods for composing models from such libraries of components and practical applications of such have been described in the literature [15] and best practice approaches are beginning to be developed [16]. Further, the requirement within the synthetic biology community for a library of 'virtual parts' representing Standard Biological Parts [17], or 'Biobricks' which can be slotted together and simulated for rapid prototyping has been voiced repeatedly [18].

Implementing models as dynamic, online content opens up possibilities for programmatic interaction and processing, which represents a considerable development in the field of computational biology. The BioCoDa [19] project is working to create libraries of CellML models of biochemical reactions which source parameter values from databases that hold kinetic parameters. This will allow these models to dynamically update themselves as new information becomes available in the database. Description Logics [20] can be used to define rules to impose constraints on models to assure their biological validity. Assertions may be made about how particular processes act or how entities are related in a biological system; if a model violates these assertions it can be denoted as biologically invalid. In concert with comprehensive ontologies describing biological systems, these rules can also be used to automate the model building process. A modeler might define what parts of a system he wants to represent and where to draw the information from. This model could then be simulated and the results checked against databases containing wetlab experimental data about how the system should behave. Key to these possibilities is the digital representation and hyperaccessible nature of CellML models.

V. The Role of Online Communities

The possibilities presented by internet-based scientific collaboration do not end at simply building models: linking elements of models to online content through metadata promises to do for descriptions of biological systems what hyperlinking has done for basic text. For example, curation is essential to the integrity of any large repository of information. This is currently done primarily by small groups of highly skilled experts, but the job of curating every single entry in a repository or database is beginning to overwhelm curators of large datasets. This suggests a new job for current curation experts as 'meta-curators,' checking the validity of curation done by the community. A number of recent initiatives, such as the WikiPathways [21] and GeneWiki [22] projects, are taking such an approach to the challenging of organizing large datasets. Academic analysis has revealed that the community-sourced 'anyone-can-edit' Wikipedia online encyclopedia is in fact as trustworthy as Encyclopedia Brittannica; the Wikipedia system also involves a small group of 'Wikipedians' who take an active role in cleaning up and standardizing public contributions [23]. While the formal scientific review and publication process will likely remain in place for some time to come, many elements of peer review are amenable to online fora. Additionally, annotation with quality community-generated commentary and analysis can add significant value to a piece of research.

VI. Conclusions

The rise of 21st century communications technologies is profoundly affecting the way the science of quantitative computational biology is practiced through digitization,

decentralization and democratization. By treating quantitative biological models as dynamic, user-generated content, and providing facilities for the expert modeling community to participate in the creation and curation of a free, open-access model repository, the next-generation CellML Model Repository will provide a powerful tool for collaboration and will revolutionize the way cellular models are developed, used, reused and integrated into larger systems.

Acknowledgment

The authors would like to acknowledge the Wellcome Trust, the Maurice Wilkins Centre for Molecular Biodiscovery and the IUPS Physiome Project.

References

1. Butler, D "Science in the web age: joint efforts" Nature. 2005 Dec 1;438(7068):548-9.
2. Berman HM, Westbrook J, Feng Z, Gilliland G, Bhat TN, Weissig H, Shindyalov IN, Bourne PE "The Protein Data Bank." Nucleic Acids Res, 2000, 28 pp. 235-242
3. Benson DA, Karsch-Mizrachi I, Lipman DJ, Ostell J, Wheeler DL "Genbank" Nucleic Acids Res. 35 Database issue:D21-D25, January 1, 2007
4. Lloyd CM, Halstead MD, Nielsen PF. "CellML: its future, present and past." Prog Biophys Mol Biol. 2004 Jun-Jul;85(2-3):433-50.
5. Lloyd CM, Lawson JR, Hunter PJ, Nielsen PF "The CellML Model Repository" Bioinformatics. 2008 Sep 15;24(18):2122-3. Epub 2008 Jul 25
6. Yu T, Lawson JR, Britten R "A distributed revision control system for collaborative development of quantitative biological models" Proc. ICBME2008 [in print]
7. Grau BC, Horrocks I, Kazakov Y, Sattler U "A logical framework for modularity of ontologies" Proc. IJCAI, 2007
8. Kitano H "Systems biology: a brief overview" Science. 2002 Mar 1;295(5560):1662-4.
9. Terkildsen JR, Niederer S, Crampin EJ, Hunter P, Smith NP "Using Physiome standards to couple cellular functions for rat cardiac excitation-contraction" 2008, Experimental Physiology , 93, 919-929.
10. Pandit SV, Clark RB, Giles WR, Demir SS "A Mathematical Model of Action Potential Heterogeneity in Adult Rat Left Ventricular Myocytes" 2001, Biophysical Journal , 81, 3029-3051.
11. Hinch R, Greenstein JR, Tanskanen AJ, Xu L, Winslow RL "A Simplified Local Control Model of Calcium-Induced Calcium Release in Cardiac Ventricular Myocytes" 2004 Biophysical Journal Volume 87 pp.3723-3736
12. Niederer SA, Hunter PJ, Smith NP. "A quantitative analysis of cardiac myocyte relaxation: a simulation study." Biophys J. 2006 Mar 1;90(5):1697-722.
13. Sachse FB, Moreno AP, Abildskov JA. "Electrophysiological modeling of fibroblasts and their interaction with myocytes."Ann Biomed Eng. 2008 Jan;36(1):41-56. Epub 2007 Nov 13.
14. Wilmalaratne S, Auckland Bioengineering Institute, The University of Auckland - personal communication
15. Nickerson D, Buist M. "Practical application of CellML 1.1: The integration of new mechanisms into a human ventricular myocyte model." Prog Biophys Mol Biol. 2008 Sep;98(1):38-51.
16. Cooling MT, Hunter P, Crampin EJ. "Modelling biological modularity with CellML." IET Syst Biol. 2008 Mar;2(2):73-9.
17. Endy D "Foundations for engineering biology" Nature. 2005 Nov 24;438(7067):449-53
18. Cai Y, Hartnett B, Gustafsson C, Peccoud J. "A syntactic model to design and verify synthetic genetic constructs derived from standard biological parts." Bioinformatics. 2007 Oct 15;23(20):2760-7
19. Beard DA et al. "CellML Metadata: standards, tools and repositories" *Phil. Trans. R. Soc. B* [in print]
20. Baader F, Calvanese D, McGuinness DL, Nardi D, Patel-Scneider PF "The Description Logic Handbook - Theory, Implementation and Applications" 2007 - Cambridge University Press New York, NY, USA
21. Pico AR, Kelder T, van Iersel MP, Hanspers K, Conklin BR, Evelo C. "WikiPathways: pathway editing for the people." PLoS Biol. 2008 Jul 22;6(7):e184.
22. Hoffman R "A wiki for the life sciences where authorship matters" Nat Genet. 2008 Sep;40(9):1047-51.
23. Giles J "Internet encyclopaedias go head to head" Nature. 2005 Dec 15;438(7070):900-1.

Author: James R. Lawson
Institute: Auckland Bioengineering Institute
Street: 70 Symonds Street
City: Auckland
Country: New Zealand
Email: j.lawson@auckland.ac.nz

Development of Soft Tissue Stiffness Measuring Device for Minimally Invasive Surgery by using Sensing Cum Actuating Method

M.-S. Ju[1], H.-M. Vong[1], C.-C.K. Lin[2] and S.-F. Ling[3]

[1] Dept. of Mechanical Engineering, National Cheng Kung University, Taiwan
[2]Dept. of Neurology, Medical Center, National Cheng Kung University, Taiwan
[3]School of Mechanical & Aerospace Engineering, Nanyang Technological University, Singapore

Abstract — **Surgeon's perception of palpation is limited in a minimally invasive surgery so devices for *in situ* quantification of soft tissue stiffness are necessary. A PZT-driven miniaturized cantilever served as actuator and sensor simultaneously was developed. By using the sensing cum actuating method, the mechanical impedance functions of soft tissues can be measured. Bioviscoelastic materials silicone rubber and dissected porcine livers under room temperature or in frozen state were utilized to test the performance of the device. The frozen porcine liver was employed to simulate liver cirrhosis. The results showed that the dissipative modulus around the resonant frequency might be utilized to quantify the stiffness of the cancerous and normal liver structure. The application of the device to robot-assisted surgery was discussed.**

Keywords — **Soft tissue stiffness, sensing-cum-actuating, minimally invasive surgery, mechanical impedance, electrical impedance.**

I. Introduction

Minimally invasive surgery (**MIS**), also known as endoscopic surgery, is a new and popular surgical operation. Surgical equipments such as endoscope, grasper and blade can be inserted through small incisions rather than making a large incision to provide access to the operation site. Distinct advantages of this technique are: reduction of trauma, milder inflammation, reduced postoperative pain and fast recovery. However, reduced dexterity, restricted field of vision and lack of tactile feedback are main drawbacks of MIS. Liver cirrhosis is one of the most deadly diseases in Taiwan. Surgeons usually rely on palpation to assess the boundary of abnormality of liver tissues during surgery. However, this information is no longer available in MIS. It is believed that in-situ estimation of soft tissue's mechanical property may improve quality of MIS such as image-guided laparoscopic liver operation.

Recently, new techniques and instruments have been appeared for *in-vivo* determination of tissue properties. Dynamic testing methods such as indentation probes [1], compression techniques [2], rotary shear applicators [3] or aspiration [4] have been developed. However, all these methods need at least an actuator and a sensor to measure the dynamic response, i.e. applying force or torque and measuring displacement or velocity of the tissue simultaneously. The requirement makes the miniaturization of theses testing systems a challenge technical problem. Recently, Ling et al. [5] propose a new dynamic testing method- sensing cum actuating(SCA) in which the mechanical impedance of soft viscoelastic materials can be measured by detecting input electrical current and voltage of an activated electro-mechanical actuator without employing any traditional force and displacement sensors.

The goals of this study were three-folds: First was to develop a PZT-based miniaturized stiffness measuring device based on SCA method. Second was to test the system on biomaterials and in vitro tests of porcine livers. Third was to develop a method for quantify stiffness of liver from their electrical and mechanical impedances. Feasibility of the method for MIS of liver will be discussed.

II. Methods

Fig. 1 shows the PZT-based soft tissue measurement system designed in this work. The outer diameter of the pen holder was 10mm and the PZT- coated cantilever and the ring base were machined from a brass cylinder to avoid the fracture at the root of the cantilever. Dimension of the brass cantilever was 6.5mm × 2.0mm × 0.1mm and 5.0mm × 2.0mm × 0.2mm for the PZT. The height of stinger was 3mm to prevent direct contact between cantilever surface and specimen.

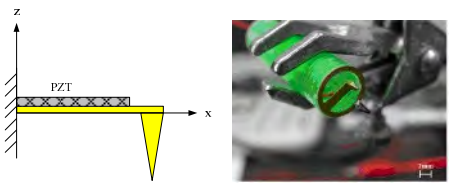


Fig.1 Schematic diagram of the PZT-coated cantilever (left) and the assembly of the pen-like soft tissue measurement device (right)

Chwee Teck Lim, James C.H. Goh (Eds.): ICBME 2008, Proceedings 23, pp. 291–295, 2009
www.springerlink.com

The experimental setup shown in Fig. 2 consisted of a function generator to provide swept sinusoidal signals to the power amplifier to drive the PZT and a current amplifier to measure the potential induced from the direct piezoelectric effect. The potential, E, and current, I, were acquired simultaneously into the PC and real-time fast Fourier transforms were performed and the electrical impedance, $Z_e(\omega)=E(j\omega)/I(j\omega)$, $j=\sqrt{-1}$ was computed.

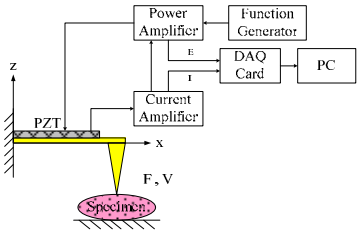


Fig. 2 Experimental setup of the soft tissue stiffness measurement system

From the two-port model (Fig. 3) of the system relationship between the input port (electrical) variables and the output port (mechanical) variables was given by:

$$\begin{bmatrix} E(j\omega) \\ I(j\omega) \end{bmatrix} = \begin{bmatrix} t_{11}(j\omega) & t_{12}(j\omega) \\ t_{21}(j\omega) & t_{22}(j\omega) \end{bmatrix} \begin{bmatrix} F(j\omega) \\ V(j\omega) \end{bmatrix} \tag{1}$$

where t_{ij}, i,j = 1, 2 were elements of the transduction matrix, $\mathbf{T}(j\omega)$, of the system and $F(j\omega)$ and $V(j\omega)$ were Fourier transform of the force and velocity at the output port. If $\mathbf{T}(j\omega)$ and $Z_e(j\omega)$ were known, the mechanical impedance, defined as $Z_m(j\omega)=F(j\omega)/V(j\omega)$ of the biological specimen at the contact point could be computed as

$$Z_m(j\omega) = \frac{F}{V} = \frac{t_{22}Z_e - t_{12}}{t_{11} - t_{21}Z_e} \tag{2}$$

To determine elements of the matrix **T** one could mechanically constrain the output port of the device to obtain the first column or free it to obtain the second column. The other approach was to add different masses on the stinger and solve a linear algebraic equation. In this study, due to the miniaturization, it was difficult to calibrate the transduction matrix experimentally. An alternative method suggested in [6] was employed in which finite element simulations were adopted. After the transduction matrix was calibrated, the mechanical impedance, Z_m, could be estimated. If no internal energy was generated or dissipated in the system the determinant of the matrix **T** should be unity.

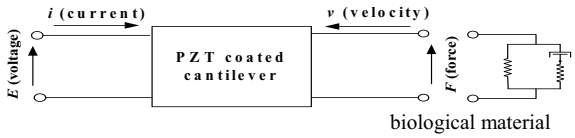


Fig. 3 Two-port model of the sensing-cum-actuating measurement system

All the finite element analyses were performed by using software package ANSYS. First, modal analysis of the PZT-coated cantilever was performed and next harmonic analyses of the PZT-coated cantilever were conducted to obtain the frequency response of the system. For simplification, the stinger was modeled as an equivalent rectangle mass. Element Solid 5 was used to model the PZT layer and element Solid 45 for modeling the brass cantilever and adhesive layer (Loctite-3880). The material properties of the probe can be found in [8]. Fig. 4 showed the finite element mesh of the composite cantilever beam. After a convergent test, the element size was set to 0.13mm and the output port was located at 6mm from the clamped end. Two simulations were performed to obtain the transduction matrix. In the first case, a spring with a spring constant of 1,000 N/m was connected to the stinger and the frequency response functions E_1, I_1, F_1, V_1, were computed from the harmonic analysis. In the second case, the spring constant was changed to 5,000 N/m and the corresponding frequency response functions were: E_2, I_2, F_2, V_2. The transduction matrix T can then be calculated by:

$$\mathbf{T} = \begin{bmatrix} \dfrac{E_1V_2 - E_2V_1}{F_1V_2 - F_2V_1} & \dfrac{E_1F_2 - E_2F_1}{F_2V_1 - F_1V_2} \\ \dfrac{I_1V_2 - I_2V_1}{F_1V_2 - F_2V_1} & \dfrac{I_1F_2 - I_2F_1}{F_2V_1 - F_1V_2} \end{bmatrix} \tag{3}$$

In the experiments, four specimens were utilized to evaluate the applicability of the soft tissue stiffness measurement system. There were two silicon gels (SC-725, PDMS) and two biological soft tissues (fresh and frozen porcine liver unfrozen for 20 minutes at room temperature) To simulate the application of the stiffness measurement system in robotic assisted surgery or traditional surgery, the porcine liver was measured by either holding the device by hand or by clamped on a fixture. The driving signal for PZT was swept sinusoidal with frequency ranged from 10Hz to 3.0 kHz and amplitude of 40 Volts. The initial indentation depth was set at 1 mm. Each sample was tested for five trials and the mean electrical impedances are computed. Then the mechanical impedance was computed by using the transduction matrix obtained from the aforementioned FEM simulations. The frozen porcine liver was employed to simulate cirrhotic liver tissyes.

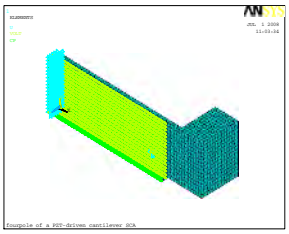


Fig. 4 Finite element model of the PZT-coated cantilever

III. Results

The measured electrical impedances of the four specimens, from fixture clamped test, were compared in Fig. 5. Within 10 Hz to 2 kHz (not shown), the difference between specimens was insignificant but around 2,250 Hz, except PDMS, there were resonant frequencies (valley) for SC-725, normal liver and frozen liver. PDMS was so stiff that no resonant frequency can be found. There was a local maximum higher than the resonant frequency. The difference between the local maximum and the resonant was defined as the peak-to-peak value of electrical impedance. The mean peak-to-peak values of SC-725, normal liver and frozen liver were: 0.478×10^4, 1.391×10^4 and 0.132×10^4 Ω respectively. The peak-to-peak value increased with the compliance of specimens.

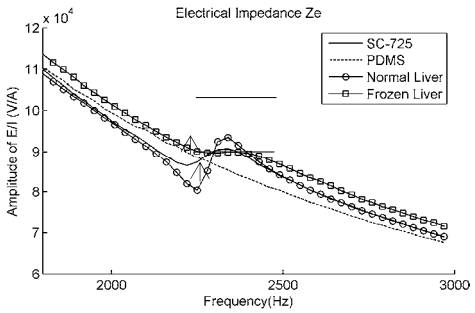


Fig. 5 Comparison of specimen electrical impedances, resonant frequency of each sample indicated by arrow and peak-to-peak value of normal liver is defined

In Fig. 6 the effects of holding the device on electrical impedance were compared. The peak-to-peak values of the hand-held tested samples were less than those of the clamped tested samples. For the normal porcine liver, the reduction of peak-to-peak value was about 74.2% by hand-held test.

In Fig. 7, the measured electrical impedance of the device was compared with the impedance computed from finite element simulations. The peak-to-peak value of the

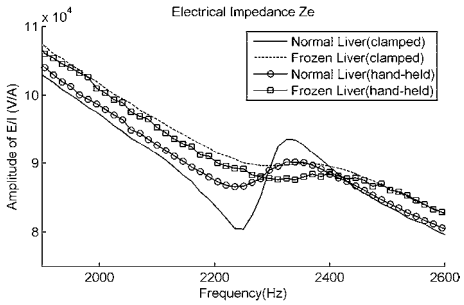


Fig. 6 Effects of holding the stiffness device on measured electrical impedance

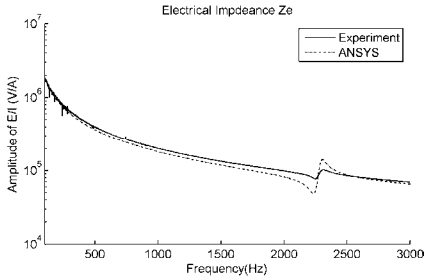


Fig. 7 Comparison of measured and simulated electrical impedance when tip was fixed

measured electrical impedance was less than that of the simulated and the resonant frequency of the simulated electrical impedance was lower than that of the measured electrical impedance.

In Fig. 8 the mechanical impedances of the porcine livers under different testing conditions were compared. In general, the magnitude decreased with the frequency from 1400 Hz to 2200Hz and it increased with the frequency for frequency higher than 2400 Hz. Similar to the electrical impedance, the peak-to-peak value around the resonant frequency for the liver under room temperature can be read from the figure as: 0.07145 Ns/m for the clamped test and 0.037 Ns/m for the hand-held test. For the frozen liver, it was

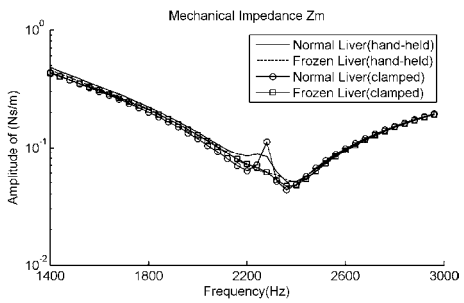


Fig. 8 Mechanical impedances of normal liver and frozen liver under different holding conditions

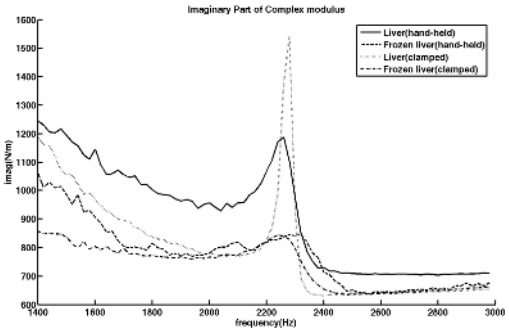


Fig. 9 The imaginary part of the complex modulus of stiffness of the porcine livers tested under different conditions

difficult to define the peak-to-peak values for both test conditions.

Fig. 9 showed the imaginary modulus of the liver samples under room temperature had a peaks around the resonant frequency for both handheld and clamped tests.

IV. Discussion

From the electrical impedance results, one may observe that the samples can be qualitatively separated into two groups: the soft materials (porcine liver at room temperature and SC-725) and the stiff materials (frozen porcine liver and PDMS).

In a previous work, we found that the apparent Young's moduli of the specimens were ordered as: liver < SC-725 < frozen liver < PDMS. The peak-to-peak values of the electrical impedance of the liver and SC-725 seemed to be inversely proportional to the apparent Young's modulus. For PDMS there is no peak-to-peak value. This may due to the stiffness of PDMS was higher than the mini cantilever and around the resonant frequency the beam deflection was small and the current induced by direct piezoelectric effect was small. On the other hand, the fresh porcine liver (at room temperature) and the silicone rubber SC-725 were less stiff than the mini cantilever so at the resonant frequency the beam deflection was large so did the current and thus the impedance decreases for same input voltage.

In this work, the finite-element method was employed to compute the transduction matrix. However, there were errors between the computed electrical impedance and the measured one. The error might come from the uncertainty in modeling the adhesive layer and the damping model of the mini cantilever. Further improvement on structural damping of the beam model might reduce the amplitude error. Unlike the experimental approach, the determinant of the transduction matrix was very close to one.

Unlike the electrical impedances, the mechanical impedances of the porcine liver specimens had a minimum around 2,500 Hz. Physically it means that, at this frequency, the same amplitude of sinusoidal force could result in higher amplitude of sinusoidal velocity signal. The peak-to-peak value of the liver tested under clamped test was larger than that of the hand-held test. The difference might be that the initial depth of hand-held test was higher than that of the clamped test (1 mm). It is well known that soft tissue like liver has a stress-strain curve consisted of three regions: toe, linear and nonlinear. The apparent Young's modulus at the toe region is much less than that of the linear region. It is very easy for the hand-held test to enter into the linear region and yield higher stiffness.

From the complex modulus of stiffness ($F(j\omega)/X(j\omega)$) of the porcine livers, one may observe that the real part or the storage modulus decreases with the frequency monotonically although, around 2,250 Hz small variations can be observed for liver tested at room temperature. However, significant variations of the imaginary part or the dissipation modulus can be found around the same frequency. It reveals that the porcine livers at room temperature had a higher damping or more like fluid than the frozen liver. The imaginary modulus at resonant frequency might be used as quantitative index for assessing the stiffness of cancerous liver tissue.

In this work, through the in vitro experiments the performance of the soft tissue stiffness measurement has been tested. The next stage is to design a system suitable for *in vivo* experiments by considering the control of initial indentation and the sterilization of the probe and the integration with robotic assisted surgery.

V. Conclusions

In this work, the sensing-cum-actuating method was adopted to develop a PZT-based soft tissue stiffness measurement system. In vitro tests on porcine livers revealed that the dissipative modulus computed from the mechanical impedance could quantify the stiffness of normal and pathological tissues.

Acknowledgement

Research supported partially by a grant from ROC National Science Council under contract NSC 95-2221-E-006 -009 -MY3.

REFERENCES

1. Mark P, Salisbury J(2001) In Vivo Data Acquisition Instrument for Solid Organ Mechanical Property Measurement. Proc 4th Intl Conf on Medical Image Computing and Computer-Assisted Intervention.
2. Narayanan N, Bonakdar A, et al.(2006) Design and analysis of a micromachined piezoelectric sensor for measuring the viscoelastic properties of tissues in minimally invasive surgery. Smart Mater & Struct 15:1684-1690.
3. Valtorta D, Mazza E(2005) Dynamic measurement of soft tissue viscoelastic properties with a torsional resonator device. Medical Image Analysis 9:481-490.
4. Kauer M, Vuskovic V et al.(2002) Inverse finite element characterization of soft tissues. Medical Image Analysis 6:275-287.
5. Ling S, Xie Y(2001) Detecting mechanical impedance of structures using the sensing capability of a piezoceramic inertial actuator. Sensors and Actuators A Physical 93:243-249.
6. Ling S, Wang D, Lu B(2005) Dynamics of a PZT-coated cantilever utilized as a transducer for simultaneous sensing and actuating. Smart Materials and Structures 14:1127-1132.
7. Fung Y(1993) Biomechanics Mechanical Properties of Living Tissues. 2nd ed New York Springer-Verlag.
8. Vong A (2008) Development of Soft Tissue Stiffness Measuring Device for Minimally Invasive Surgery by using Sensing Cum Actuating Method. MS Thesis Dept of Natl Cheng Kung Univ Tainan Taiwan.

Corresponding: Ming-Shaung Ju
Dept. of Mechanical Eng,
National Cheng Kung Univ.,
1 University Rd.,
Tainan,
Taiwan 701.
e-mail: msju@mail.ncku.edu.tw

A Novel Method to Describe and Share Complex Mathematical Models of Cellular Physiology

D.P. Nickerson and M.L. Buist

Division of Bioengineering, National University of Singapore, Singapore

Abstract — **With improved experimental techniques and computational power we have seen an explosion in the complexity of mathematical models of cellular physiology. Modern lumped parameter models integrating cellular electrophysiology, mechanics, and mitochondrial energetics can easily consist of many tens of coupled differential equations requiring hundreds of parameters. The reward of this increase in complexity is improved biophysical realism and an increase in the predictive qualities of the models. One of the most significant challenges with such models is being able to completely describe the model in such a manner that the authors can share the model with collaborators and, potentially, the scientific community at large.**

In this work we have developed methods and tools for the specification of the complete description of mathematical models of cellular physiology using established community standards combined with some emerging and proposed standards. We term the complete description of the cellular model a 'reference description'. Such a description includes everything from the mathematical equations, parameter definitions, numerical simulations, graphical outputs, and post-processing of simulation outputs. All of these are grouped into a hierarchy of tasks which define the overall reference description structure and provide the documentation glue to enable the presentation of a complete story of the model development and application.

Our reference description framework is based primarily on the CellML project, using annotated CellML models as the basis of the model description. Being based on CellML allows the underlying mathematical model to be shared with the community using standard CellML tools, and allows tools capable of interpreting the annotations to present the complete reference description in various manners.

Keywords — **CellML, mathematical model description, Physiome Project, electrophysiology, bioinformatics.**

I. Introduction

We have witnessed a dramatic increase in the complexity of mathematical models of cellular physiology in recent years. Due to an increased availability of experimental data and computational power, model authors are now able to create biophysically based models of cellular physiology incorporating finer and finer details. Recent models contain multiple compartments and the transportation kinetics between them, as well as combining several different aspects of cellular function into single models. The Cortassa *et al.* [1] model, for example, includes cellular electrophysiology, calcium dynamics, mechanical behavior, and mitochondrial bioenergetics, defined using fifty differential equations and more than 100 supporting algebraic expressions (c.f., the four differential equations in the classic Hodgkin and Huxley [2] model).

When dealing with such complicated mathematical models, it becomes very difficult to share the model with collaborators or the scientific community at large. Traditional peer reviewed journal articles restrict how much detail can be presented and require the translation of the model implementation into a format suitable for the particular journal. Such translation is an error prone process leaving much room for typographical mistakes when translating complex models. To address this deficiency, standard model encoding formats have been applied to the sharing and archiving of mathematical models of cellular physiology. The most notable standards being SBML [3, 4, http://sbml.org/] and CellML [5, 6, http://www.cellml.org/].

Both SBML and CellML address similar requirements for a machine readable and software independent model encoding format, but they each approach the issue from a quite different perspective. SBML developments have traditionally focused on representing models of biochemical pathways, whereas CellML has placed emphasis on representing related mathematical equations. These different approaches has resulted in two quite different model encoding standards, although there is some degree of compatibility between them – the mathematics can be translated from one to the other, but the biological concepts represented by a model may not be so easily translated in an automated fashion.

Using these model encoding standards, it is possible to define mathematical models of cellular physiology in a machine readable and software agnostic format. Models encoded in these standard formats can then be exchanged between scientists with confidence. The only potential loss of information in such an exchange is the "correctness" with which the tools used by each scientist interpret the model encoding [for a discussion of this problem, see 7]. While these standards provide for the specification of the mathematical models, further information is required in order to completely define the application of mathematical models

Chwee Teck Lim, James C.H. Goh (Eds.): ICBME 2008, Proceedings 23, pp. 296–298, 2009
www.springerlink.com

in various scenarios. It is this additional information that is the subject of this manuscript.

II. Methods

In this work, we utilize CellML for encoding mathematical models. The discussion below applies equally as well to SBML. Metadata is used to provide additional, context dependent data about the mathematical model. In CellML the data represented are the definition of the mathematical equations. This work also falls under the IUPS Physiome Project (http://www.physiomeproject.org/) and as such it is desirable that this work should be able to extend to types of mathematical models and spatial scales other than those discussed below.

A. CellML

CellML is an XML-based model encoding standard that utilizes MathML (http://www.w3.org/Math/) to define mathematical equations and custom XML elements to define the variables used in the equations. CellML includes capabilities to define abstract hierarchies of mathematical components which can be connected together to form larger models of complete systems. These components can be defined locally within a model or imported from external models. Given the generic nature of CellML, it is applicable to a wide range of mathematical models covering the full spectrum of computational physiology [8–12].

The CellML project provides a freely accessible model repository (http://www.cellml.org/models/) as a valuable community resource [13]. With over 350 models in the repository, this provides an excellent demonstration of the range of models capable of being described using CellML. There are also several tools now available capable of utilizing CellML [for a recent review, see 14].

B. CellML Metadata

The CellML community is currently developing several metadata standards that greatly enhance model descriptions. The CellML Metadata specification (http://www.cellml.org/specifications/metadata/) provides a standard framework for the annotation of mathematical models with common data. This includes annotations such as model authorship, modification history, literature citations, biological constituents, human readable descriptions, *etc*. Such metadata provides the core description of the model allowing biological significance to be inferred.

The CellML Simulation Metadata specification (http://www.cellml.org/specifications/metadata/simulations/) aims to provide a standard framework for the description of specific numerical simulations. This provides for the instantiation of mathematical models into specific computational simulations. CellML Graphing Metadata (http://www.cellml.org/specifications/metadata/graphs/) defines a framework for the specification of particular observations to be extracted from simulation results. Graphing metadata also provides a mechanism for the association of external data with specific simulation observations. External data may consist of the experimental data from which the model was derived or the data used to validate the model. For the case of validating simulation tools rather than the mathematical models, the external data could be curated simulation output against which simulation tools can be tested. This therefore provides a quantitative validation of new simulation tools as opposed to the largely qualitative validation currently used [7].

All three of these metadata specifications leverage upon the Resource Description Framework (RDF, http://www.w3.org/RDF/) in their specification, providing a powerful technology for the annotation of models with no specific requirements on the serialized format of the model encoding. This therefore makes it straightforward to annotate models serialized in XML documents stored on the local computer, models stored remotely on the Internet as XML documents, or even models stored in remote databases.

C. Reference Descriptions of Cellular Physiology Models

We have previously described an approach to annotating mathematical models of cellular physiology using the metadata standards described above [15, 16]. This approach makes extensive use of graphing and simulation metadata in order to completely define simulation observations in terms of the mathematical models, their parameterization, and the numerical methods used in performing the computational simulations.

We envision these simulation observations forming the basis of journal articles submitted for peer review, allowing the articles to focus on the novel developments or observations being presented rather than devoting much of the article content to a description of the mathematical model. From the model reference description, web-friendly presentations can be generated, as illustrated in Nickerson *et al*. [15, http://www.bioeng.nus.edu.sg/compbiolab/p2/], which provide a complete description of the mathematical models and all associated annotations. Such presentations of the models allow for significantly more detail to be provided in regard to the development and implementation of the models. In addition, as they are generated directly from the model implementation, there is no longer the possibility of

translation errors when translating model implementations into journal articles.

III. Discussion

Annotated mathematical model descriptions using the community standards being developed by the CellML project provide the technology for completely describing the development of mathematical models. Supporting data, such as literature citations or experimental observations, can easily be incorporated into such model descriptions to substantiate modeling assumptions and justify parameter choices. Model authors using this framework are able to provide human-friendly presentations of model reference descriptions as supplements to peer reviewed journal articles. Providing such supplements as part of a curated web repository provides assurance to the scientific community that the reference description will be available as well as some degree of support in terms of the validity of the model encoding. This leaves the journal article able to focus on the novel aspects of the model development and outcomes rather than needing to devote a large portion of each article to basic model development and validation.

Work is currently underway to develop interactive presentations of the model reference descriptions to ensure relevant information is readily available to the various user communities. Such presentation environments must be sufficiently flexible to accommodate the different types of "views" users may desire from the underlying reference description. For example, following the presentation mode developed in Nickerson *et al*. [15] we are developing a more mathematically oriented view as well as a biologically focused view.

Acknowledgment

A*STAR BMRC Grant #05/1/21/19/383.

References

1. Sonia Cortassa, Miguel A Aon, Brian O'Rourke, Robert Jacques, Hsiang-Jer Tseng, Eduardo Marban, and Raimond L Winslow. A computational model integrating electrophysiology, contraction, and mitochondrial bioenergetics in the ventricular myocyte. Biophys J, 91(4): 1564–1589, Aug 2006. doi: 10.1529/biophysj.105.076174.
2. A L Hodgkin and A F Huxley. A quantitative description of membrane current and its application to conductance and excitation in nerve. J. Physiol., 117(4):500–544, August 1952.
3. A Finney and M Hucka. Systems biology markup language: Level 2 and beyond. Biochem. Soc. Trans., 31(Pt 6):1472–1473, 2003. URL http://www.biochemsoctrans.org/bst/031/bst0311472.htm.
4. M. Hucka, A. Finney, H. M. Sauro, H. Bolouri, J. C. Doyle, H. Kitano, A. P. Arkin, B. J. Bornstein, D. Bray, A. Cornish-Bowden, A. A. Cuellar, S. Dronov, E. D. Gilles, M. Ginkel, V. Gor, I. I. Goryanin, W. J. Hedley, T. C. Hodgman, J-H. Hofmeyr, P. J. Hunter, N. S. Juty, J. L. Kasberger, A. Kremling, U. Kummer, N. Le Nov`ere, L. M. Loew, D. Lucio, P. Mendes, E. Minch, E. D. Mjolsness, Y. Nakayama, M. R. Nelson, P. F. Nielsen, T. Sakurada, J. C. Schaff, B. E. Shapiro, T. S. Shimizu, H. D. Spence, J. Stelling, K. Takahashi, M. Tomita, J. Wagner, J. Wang, and SBML Forum. The systems biology markup language (SBML): a medium for representation and exchange of biochemical network models. Bioinformatics, 19(4):524–531, Mar 2003. doi: 10.1093/bioinformatics/btg015.
5. A A Cuellar, C M Lloyd, P F Nielson, M D B Halstead, D P Bullivant, D P Nickerson, and P J Hunter. An overview of CellML 1.1, a biological model description language. Simulation, 79(12):740–747, 2003. doi: 10.1177/0037549703040939.
6. D. P. Nickerson and P. J. Hunter. The Noble cardiac ventricular electrophysiology models in CellML. Prog Biophys Mol Biol, 90(1-3): 346–359, 2006. doi: 10.1016/j.pbiomolbio.2005.05.007.
7. Frank T Bergmann and Herbert M Sauro. Comparing simulation results of SBML capable simulators. Bioinformatics, 24(17):1963–1965, Sep 2008. doi: 10.1093/bioinformatics/btn319.
8. D P Nickerson, M P Nash, P F Nielsen, N P Smith, and P J Hunter. Computational multiscale modeling in the IUPS Physiome Project: modeling cardiac electromechanics. IBM J. Res. & Dev., 50(6):617–630, 2006. doi: 10.1147/rd.506.0617.
9. A. Corrias and M. L. Buist. A quantitative model of gastric smooth muscle cellular activation. Ann Biomed Eng, 35(9):1595–1607, September 2007. doi: 10.1007/s10439-007-9324-8.
10. H. Schmid, M. P. Nash, A. A. Young, O. R¨ohrle, and P. J. Hunter. A computationally efficient optimization kernel for material parameter estimation procedures. J Biomech Eng, 129(2):279–283, Apr 2007. doi: 10.1115/1.2540860.
11. M. T. Cooling, P. Hunter, and E. J. Crampin. Modelling biological modularity with CellML. IET Syst Biol, 2(2):73–79, Mar 2008. doi: 10.1049/iet-syb:20070020.
12. Alberto Corrias and Martin L Buist. Quantitative cellular description of gastric slow wave activity. Am J Physiol Gastrointest Liver Physiol, 294(4):G989–G995, Apr 2008. doi: 10.1152/ajpgi.00528.2007.
13. Catherine M Lloyd, James R Lawson, Peter J Hunter, and Poul F Nielsen. The CellML model repository. Bioinformatics, 24(18):2122–2123, Jul 2008. doi: 10.1093/bioinformatics/btn390.
14. Alan Garny, David P Nickerson, Jonathan Cooper, Rodrigo Weber dos Santos, Andrew K Miller, Steve McKeever, Poul M F Nielsen, and Peter J Hunter. CellML and associated tools and techniques. Philos Transact A Math Phys Eng Sci, 366(1878):3017–3043, Sep 2008. doi: 10.1098/rsta.2008.0094.
15. David P Nickerson, Alberto Corrias, and Martin L Buist. Reference descriptions of cellular electrophysiology models. Bioinformatics, 24 (8):1112–1114, Apr 2008. doi: 10.1093/bioinformatics/btn080.
16. David Nickerson and Martin Buist. Practical application of CellML 1.1: The integration of new mechanisms into a human ventricular myocyte model. Prog Biophys Mol Biol, 98:38–51, Jun 2008. doi: 10.1016/j.pbiomolbio.2008.05.006.

David Nickerson
National University of Singapore
7 Engineering Drive 1, Block E3A #04-15
Singapore 117574
biendp@nus.edu.sg

New Paradigm in Journal Reference Management

Casey K. Chan[1,2], Yean C. Lee[3] and Victor Lin[4]

[1] Division of Bioengineering, National University of Singapore, Singapore
[2] Department of Orthopaedic Surgery, National University of Singapore, Singapore
[3] Department of Biological Sciences, National University of Singapore, Singapore
[4] WizPatent Pte Ltd, Singapore

Abstract — **The activity of generating bibliographic data and the storage of the article (PDF) are usually separate activities. Desktop journal reference management software have been developed to manage bibliographic data but the PDF files are usually managed separately or added on later as a special feature. Based on a strategy used in tagging of MP3 files, a web based application in which the bibliographic data is embedded to the PDF has been developed. Such a paradigm shift allows highly efficient web applications to be developed for management of citations, bibliographic data and documents.**

Keywords — **reference, management, bibliographic, data, software**

I. Introduction

Life science research has undergone rapid expansion in both scope and depth in the recent years. The phenomenal growth is reflected by the exponential increase in the number of citations indexed by Medline in the last ten years. Shown in Fig. 1 is the citation collection in Medline on February 21, 2008, grouped according to publishing years of indexed citations [1]. As shown in the graph, there has been an exponential growth in the number of life science journal articles published from 2000 to 2006.

Rapid growth in life science research is only possible if the information on the field is readily accessible. Realizing the importance of open access information, the US government has required publications originated from research funded by National Institute of Health to be made publically available [2]. Shortly after the introduction of the bill, the European Commission poposed a similar recommendation which enable public access of publications that arise from EC funded research [3].

Traditionally, citations for peer-reviewed publications are managed as a list independent from the corresponding collection of electronic articles (mostly as PDF) [4]. In this new era of research where information can be freely accessed, the old way of managing references and full text articles as separate objects need to be reconsidered. In this article, we will introduce a new paradigm of managing the bibliographic data together with the corresponding electronic article (PDF) as a single object. This new approach allows for more versatile management of academic papers and increases the efficiency of research collaboration.

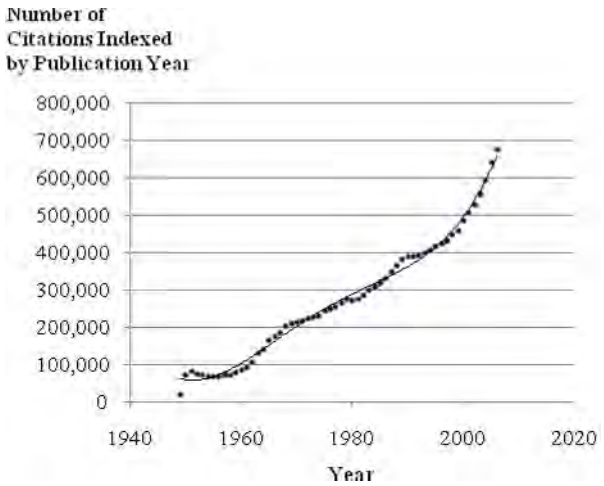


Fig. 1 Citations available in Medline as of February 21, 2008, sorted according to years the original articles were published. Data for citations published in year 2007 is incomplete and hence omitted.

II. Old paradigm

A. Embedded Metadata

In 2004, James Howison and Abby Goodrum from Syracuse University demonstrated the importance of metadata for effective management of music files [4]. Metadata refers to machine-readable information which describes content of a file, in a way labels describe contents of can foods. Examples of music metadata include song title, artist, and genre. Metadata facilitates management of music files by allowing users to sort and group the files according to various fields without having to run the files.

Music metadata can be directly stored in music files. The advantage of embedding metadata to a file is that whenever the file is moved or transferred, its metadata goes along with the file. According to Howison and Goodrum, it is the tight coupling of music metadata to music files which makes management of the files "the best personal informa-

Chwee Teck Lim, James C.H. Goh (Eds.): ICBME 2008, Proceedings 23, pp. 299–301, 2009
www.springerlink.com

tion management experience available to individuals today [4]".

B. Metadata in Academic Papers

Bibliographic data is basically metadata for academic papers which is used to identify specific publications. References cited in academic papers allow authors to substantiate their arguments and enable readers to access sources of information.

Contrary to music files, bibliographic data is not usually embedded onto PDF of academic papers; it is separately obtained from a database and managed independent of PDF. The consequence is evident: a PDF cannot be identified without firstly opening the file. This makes management of PDF troublesome.

One can use file names to identify a PDF but file names alone do not usually provide sufficient information for the file because of the limitation in number of characters a file name can hold. Furthermore, publishers usually name their PDF in a way nonsensical to readers which makes identification of the file even more difficult.

The process of reference management involves collecting references from multiple sources, obtain the PDFs from publishers, organize the references and cite relevant ones while writing papers.

After obtaining a list of references from multiple sources (often from references found in research papers), a researcher will need to download PDF from journal database. Usually, researchers use Digital Object Identifier (DOI) to retrieve PDF. DOI is a link which points a reference to its publisher's website. The PDF is saved on local drive but because bibliographic data is not embedded in PDF, the PDF cannot be easily tracked. For some, it might be easier to download the same article again using DOI [4]. As convenient as it might be, DOI is not a replacement of actual PDF for a variety of reasons. Firstly, the publishers' website that DOI links to always require users to login. Secondly, collaborators will need to repeat the same process of downloading the PDF which makes the process inefficient, given that the effort done by other collaborators is lost.

Reference managers help to ease the problem to some extent. Although reference management can be done manually but for a more organized approach, researchers use reference managers such as Endnote, Refworks, and WizFolio. Reference managers contain tools for researchers to collect references, obtain PDFs, organize and insert citations into documents. Reference managers can be broadly classified into two major groups according to the way they are accessed: desktop and web-based reference managers.

Most desktop reference managers link references and PDF stored on hard drive via shortcuts. Whenever PDF is moved or transferred, bibliographic data is not transferred together. The recipient will need to repeat the process of searching for bibliographic data; all the effort done by previous users is lost. On the other hand, most web-based reference managers do not allow users to upload PDF and hence do not assist in management of the documents.

III. New paradigm

Since bibliographic data is an integral for PDF management, we propose that the two should be managed as one object using soft embedment.

Soft embedment refers to embedment of metadata to a file using a file wrapper. As opposed to hard embedment (as in music files), the wrapper is not physically tied to PDF but is linked to PDF via software pointers.

In order for soft embedment to work, there must be a new platform which redefines the linkage between PDF and references. The new platform links both PDF and bibliographic data together. Whenever an item is moved or transferred, both PDF and corresponding bibliographic data are moved together as one item. The power of internet which connects users together can be harnessed and the independence of the web from users' operating system can be leveraged to bring management of references and files to a whole new level.

By applying concepts in the new paradigm, we have developed a web based application [5] that allows users to store both the bibliographic data and PDFs together as single object. Whenever an item is shared, both metadata and PDF can be shared together. By allowing sharing of both bibliographic data and PDF as a single entity we believe research efficiency is improved because effort done by previous collaborators is shared.

IV. Conclusion

Bibliographic data and PDFs for journal articles have long been managed as separate entities. Because of this practice, scattered PDFs are impossible to identify unless one opens the files. Management of PDFs is therefore convoluted especially when sharing is concerned. Although PDFs allow embedment of some bibliographic data, its current file system severely limits the amount of bibliographic data that can be stored in the file. It is proposed that soft-embedment can be used to embed bibliographic data onto PDF. This allows for more efficient and manipulation of journal reference articles.

REFERENCES

1. MEDLINE® Citation Counts by Year of Publication at http://www.nlm.nih.gov/bsd/medline_cit_counts_yr_pub.html.
2. Revised Policy on Enhancing Public Access to Archived Publications Resulting from NIH-Funded Research at http://grants.nih.gov/grants/guide/notice-files/NOT-OD-08-033.html.
3. Study on the Economic and Technical Evolution of the Scientific Publication Markets in Europe. p. 69.
4. Howison Jand Goodrum A (2004) Why can't I manage academic papers like MP3s? The evolution and intent of Metadata standards. Colleges, Code and Copyright, 2004, Adelphi, Association of College & Research Libraries.
5. WizFolio Homepage at http://www.wizfolio.com/

Author: Casey K. Chan
Institute: National University of Singapore
Street: Lower Kent Ridge Road
City:
Country: Singapore
Email: doschanc@nus.edu.sg

Author: Yean Chert Lee
Institute: National University of Singapore
Street: Lower Kent Ridge Road
City:
Country: Singapore
Email: yeanchert@nus.edu.sg

Author: Victor Lin
Institute: WizPatent Pte Ltd
Street: Pandan Loop
City:
Country: Singapore
Email: victor@wizpatent.com

Incremental Learning Method for Biological Signal Identification

Tadahiro Oyama[1], Stephen Karungaru[2], Satoru Tsuge[2], Yasue Mitsukura[3] and Minoru Fukumi[2]

[1] Systems Innovation Engineering, The University of Tokushima, Tokushima, Japan
[2] Institute of Technology and Science, The University of Tokushima, Tokushima, Japan
[3]Graduate School of Bio-Application & Systems Engineering, Tokyo University of Agriculture and Technology, Tokyo, Japan

Abstract — **There is electromyogram(EMG) as one of biological signals generated along with motions of the human body. This EMG has information corresponding to condition of power, tenderness of motions and motion level. Therefore, it is thought that it is useful biological information for analyzing person's motions. Recently, researches on this EMG have been actively done. For instance, it is used as a control signal of electrical arms, because EMG can be gathered from the remaining muscle about upper-extremity amputee. In addition, the pointing device that uses EMG has been developed. In general, EMG is measured from a part with comparatively big muscular fibers such as arms and shoulders. There is a problem that placing and removing the electrode is inconvenient when EMG is measured by placing the electrode in the arm and the shoulder. Therefore, if we can recognize wrist motions using EMG which is measured from the wrist, the range of application will extend furthermore. Currently, we have constructed a wrist motion recognition system which recognizes the wrist motion of 7 types as an object by using the technique named Simple-FLDA as a feature extraction technique. However, motions with low recognition accuracy were observed, and it was found that the difference of the recognition accuracy is significant at each motion and subject. Because EMG is highly individual and its repeatability is low. Therefore, it is necessary to deal with these problems. In this paper, we try the construction of a system that can learn by giving incremental data to achieve an online tuning. The improvement of the algorithm of Simple-FLDA that incremental learning becomes possible was tried as a technique for the construction of online tuning system. As a recognition experimental result, we can confirm the rising of the recognition accuracy by incremental learning.**

Keywords — **EMG, incremental learning, Simple-FLDA, Incremental Simple-FLDA**

I. Introduction

There is ElectroMyoGram(EMG) as one of biological signals generated along with motions of the human body. This EMG has information corresponding to condition of power, tenderness of motions and motion level. Therefore, it is thought that it is useful biological information for analyzing person's motions. However, there is a problem where the individual variation of EMG is large and its repeatability is low [1].

Recently, researches on this EMG have been actively done. For instance, it is used as a control signal of electrical arms, because EMG can be gathered from the remaining muscle about upper-extremity amputee [2,3]. In addition, the pointing device that uses EMG was developed [4]. In general, EMG is measured from a part with comparatively big muscular fibers such as arms and shoulders. There is a problem that placing and removing the electrode is inconvenient when EMG is measured by placing the electrode in the arm and the shoulder. Therefore, if we can recognize wrist motions using EMG which is measured from the wrist, the range of application will extend furthermore.

In this research, we aim toward the development of a device of wristwatch type that consolidates operation interface of various equipments. In particular, as an early stage, we propose a wrist motion recognition system which recognizes the wrist motions of 7 types as an object by using the technique named Simple-FLDA as a feature extraction technique [5,6,7]. Simple-FLDA is an approximation algorithm that calculates eigenvectors sequentially by an easy iterative calculation without the use of matrix calculation in the linear discriminant analysis. The verification experiments are carried out using this system. As a result, motions with low recognition accuracy were observed, and it was found that the difference of the recognition accuracy is significant at each motion and subject. As these reasons, we think that the difference between individual EMGs is related. To achieve the construction of the system that has the high general versatility, it is necessary that the system adapt to users.

In this paper, we try the construction of a system that can learn by giving incremental data to achieve an online tuning. The improvement of the algorithm of Simple-FLDA was tried as a technique for the construction of online tuning system. This improved algorithm that is called Incremental Simple-FLDA can perform an incremental learning by updating eigenvectors.

The rest of this paper is organized as follows. We describe a constructed system configuration and techniques used in this system in section 2. Section 3 explains about experimental details, experimental result, and discussion. Finally we conclude this paper with comments and remarks on future work in section 4.

Chwee Teck Lim, James C.H. Goh (Eds.): ICBME 2008, Proceedings 23, pp. 302–305, 2009
www.springerlink.com

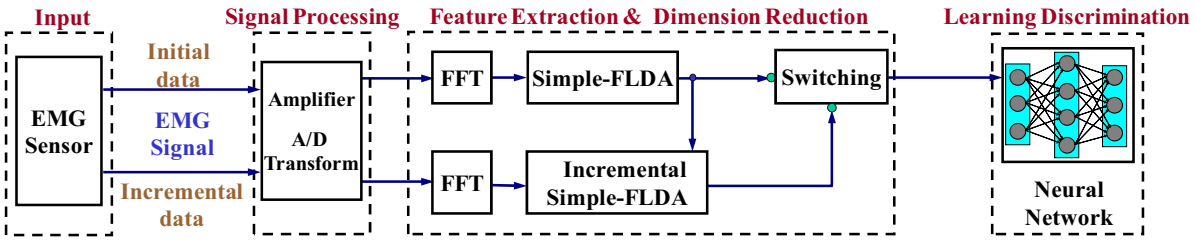


Fig.1 : Configuration of EMG recognition system

II. Icremental learning system

A. System configuration

The construction of an EMG pattern recognition system that we propose in this paper is shown in Fig1. The system consists of an input part, a signal processing part, a feature extraction & dimension reduction part, and a learning discrimination part.

In the input part, EMG is measured form the wrist by the electrode in four poles. In this paper, we use the surface electrode in consideration of practical application. Furthermore, because its treatment is easy, a dry-type electrode is adopted though surface electrodes are divided into the wet-type (used electrolysis cream) and dry-type (non-used electrolysis cream). The electrode is attached from the aspect of convenience in the wrist though it is necessary to place in flexor carpi radialis muscle and flexor carpi ulnaris muscle that can strongly measure EMG in high accuracy. The motions of the wrist at this time are set in seven states of the neutral, up, down, right, left, inside and outside as shown in Fig. 2, and measured in each state. In general, it was reported that from a few Hz to 2 kHz frequency of the EMG were important [9]. In this research, we have extracted the signal between 70Hz and 2 kHz from the measured EMG to avoid the influence of the commercial frequency noise (70Hz) in the signal processing part. Then, the extracted signal is converted to the digital signal by the A/D conversion. Next, we execute the fast Fourier transform(FFT) to the signal in the feature extraction & the dimension reduction part. Moreover, the eigenvectors are obtained using Simple-FLDA to spectra made by FFT. At the same time, the reduction in the dimension is carried out by doing this processing. Finally, wrist motions are discriminated using the eigenvectors by a classifier such as a neural network(NN) in the learning discrimination part.

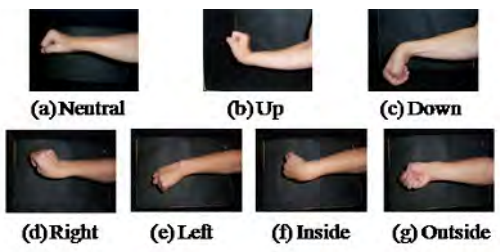


Fig.2 : Wrist motion patterns

When an incremental data was input, the eigenvectors are updated by using Incremental Simple-FLDA. Similarly, NN recognizes motions by using the updated eigenvectors. Thus, this system is expected to adjust to an individual by the influence of the incremental data. Therefore, feature extraction and dimension reduction is performed by using Simple-FLDA when the input EMG is the initial data. When the input EMG is the incremental data, the eigenvector that the influence of incremental data was considered is updated by using Incremental Simple-FLDA. Furthermore, the weights of NN are updated by using the updated eigenvectors at the same time. Next, we explain techniques named Simple-FLDA and Incremental Simple-FLDA.

B. Simple-FLDA

The fisher linear discriminant analysis is one of techniques of discriminant analysis. This technique can find eigenvectors that achieve maximization of variance between classes and minimization of variance in each class at the same time. However, matrix calculation cost becomes huge and a calculation time becomes very long. Simple-FLDA (Simple Fisher Linear Discriminant Analysis) is an algorithm from which eigenvectors are found without using matrix calculation, and by using the repetition calculation of an approximation algorithm. The Simple-FLDA is an approximated algorithm that achieves maximization of the variance between classes and minimization of the variance in each class at the same time. First, the maximization of the variance between classes as a description of this algorithm is described. First of all, a set of vectors to use is defined as follows.

$$V = \{v_1, v_2, \cdots v_m\} \quad (1)$$

The mean value of all data is assumed to be zero. The mean vector $\bar{h}_j$ of the data of each class is calculated. The following calculations are carried out by using this $\bar{h}_j$.

$$y_n = (\alpha_n^k)^T h_j \tag{2}$$

$$f(y_n, h_j) = \begin{cases} h_j & if \quad y_n \geq 0 \\ -h_j & otherwise \end{cases} \tag{3}$$

where α_n^k is an approximated vector of the *n*-th eigenvector, and *k* shows an index of repetition of the calculation. The threshold function (3) is summed using every mean vector. It can converge to the eigenvector that maximizes the variance between classes by these formulas. eq. (2) can be replaced by another form. Next, we describe the algorithm of the minimization of variance in each class. The vector x_j s have zero mean in the class. The positional relation between data x_j and an arbitrary vector assumed to be α_n^k is considered. The direction where x_j is projected and vector length is minimized is the orthogonal direction to x_j. Therefore, direction b_j where the direction component of x_j was removed from α_n^k can be expressed by the following eq. (4).

$$b_j = a_n^k - (\hat{x}_j \cdot a_n^k)\hat{x}_j \tag{4}$$

$$\hat{x} = \frac{x_j}{\|x_j\|} \tag{5}$$

This is the same as Schmidt orthogonalization procedure. An actual quantity is obtained by normalization of the vector length of b_j as follows.

$$f_i(b_j, x_j) = \frac{\|x_j\|}{\|b_j\|} b_j \tag{6}$$

The averaging is carried out by using all input vectors in each class during the repetition calculation. In other words, the influence of a component that the norm of a vector is large in this eq. (6) is significant. Therefore, it is hoped that it converges to a direction to minimize the variance in each class. The repetition calculation is shown by the following formulas.

$$f_n^k = \sum_{i=1}^{c} N_i f(y_n, h_i) + \sum_{i=1}^{c} \sum_{j=1}^{N_i} f_i(b_j, x_j) \tag{7}$$

$$a_n^{k+1} = \frac{f_n^k}{\|f_n^k\|} \tag{8}$$

where *c* is the number of classes and N_i shows the number of data in class *i*. N_i in the first term is used for equalizing the number of data in both terms. Thus, an arbitrary vector is converged to the eigenvector by achieving maximization of the variance between classes and minimization of the variance in each class at the same time.

C. Incremental Simple-FLDA

Incremental Simple-FLDA enables to update the eigenvector obtained by Simple-FLDA according to incremental data. First of all, incremental data is defined as v_{m+1} and the last mean value is assumed to be $\bar{v}$. Furthermore, the mean vector of the data of each class is shown $\bar{h}_j$ and *m* is the number of all data until last time. The calculation shown in eq. (9) is executed, a new mean $\bar{v}'$ is found.

$$\bar{v}' = \frac{1}{m+1}(m\bar{v} + v_{m+1}) \tag{9}$$

Next, new class mean vector $\bar{h}_j'$ is calculated in eq. (10)

$$h_j' = \frac{1}{M+1}(Mh_j + (v_{m+1} - \bar{v}')) \tag{10}$$

where *M* is the number of data in each class. The mean vector of the class $\bar{h}_j'$ where v_{m+1} belongs is updated. Next, we introduce the following threshold functions as well as the case of Simple-FLDA.

$$y_n = (\alpha_n)^T h_j' \tag{11}$$

$$f(y_n, h_j') = \begin{cases} h_j' & if \quad y_n \geq 0 \\ -h_j' & otherwise \end{cases} \tag{12}$$

where α_n shows a *n*-th eigenvector calculated last time. Moreover, we carry out the orthogonalization by using as well as the case of Simple-FLDA and the new orthogonal vector b_j' is obtained.

$$b_j' = a_n - (\hat{x}_j' \cdot a_n)\hat{x}_j' \tag{13}$$

$$\hat{x}' = \frac{x_j'}{\|x_j'\|} \tag{14}$$

where x_j' have zero mean in the class where v_{m+1} belongs. The normalization of b_j' is done in eq. (15)

$$f_i(b_j', x_j') = \frac{\|x_j'\|}{\|b_j'\|} b_j' \tag{15}$$

The new eigenvector α_n' is obtained by using $f(y_n, \bar{h}_j')$ and $f_i(b_j', x_j')$ in the following eq. (16)

$$\alpha_n' = \frac{1}{m+1}\left(\frac{f(y_n, h_j') + f_i(b_j', x_j')}{\|f(y_n, h_j') + f_i(b_j', x_j')\|}\right) + \frac{m}{m+1}\alpha_n \tag{16}$$

Finally, the previous eigenvector α_n' is removed from the new data and the mean vector in each class by using Gram-Schmidt orthogonalization. The eigenvector is sequentially updated by repeating these calculations.

III. Incremental learning experiment

A. Experimental details

In this section, incremental learning experiments are conducted by using the EMG recognition system to verify the effectiveness of incremental learning. This system obtains the eigenvectors using Simple-FLDA in the initial state and

using Incremental Simple-FLDA in the incremental learning. In this experiment, EMG that is measured different person is used as the initial data and the incremental data. Because, it is necessary that the system adapts to user by using user's incremental data. Thus, EMG of subject A(male: 30 years old) and subject B(male: 22 years old) are used as initial data and incremental data, respectively. Moreover, we use EMG of subject B as the evaluation data. Therefore, it is expected that the recognition accuracy in the initial state is extremely low. This system can increase the recognition accuracy using incremental data.

As a comparison experiment, we tried the incremental learning experiment by using the eigenvectors that are not updated with the incremental data, which means eigenvectors in the initial state. The number of initial data, incremental data, and evaluation data are 70(7 classes x 10 trials) in each.

B. Experimental result

The incremental learning experimental result is shown in Fig.3. The horizontal axis is the number of incremental data, and the vertical axis is recognition accuracy. In the graph, the lines labeled "Inc. SFLDA" and "Non Inc. SFLDA" are ones obtained by the Incremental Simple-FLDA and the method that the eigenvectors are not updated, respectively.

The recognition accuracy in the initial state is about 41%. In previous study, when the initial learning and the evaluation are performed using same person's data, the recognition accuracy is obtained about 90%. Therefore, this result is extremely low. This is because the initial leaning data and evaluation data are different person's ones. In the incremental learning, the recognition accuracy increases gradually according to the number of incremental data in each case. However, the recognition accuracy is obtained by using the Incremental Simple-FLDA is higher than the case when the eigenvector is not updated. As a result, the Incremental Simple-FLDA is effective in incremental learning in EMG recognition. However, more high recognition accuracy is required to use in actual environment. Thus, it is necessary to improve further this system.

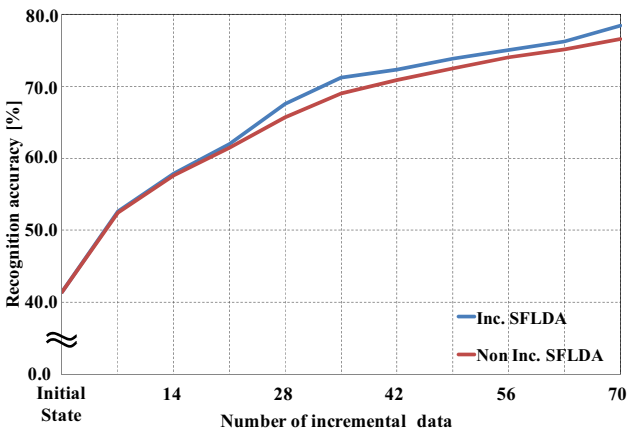


Fig.3 : Recognition accuracy in the incremental learning experiment

IV. Conclusions

In this paper, we constructed the online tuning system that built incremental learning function into the wrist motion recognition system that used wrist EMG. As the method, we proposed Incremental Simple-FLDA that gave the incremental learning function to the algorithm of Simple-FLDA. The construction of the online tuning system was tried by doing incremental learning with this algorithm. Moreover, the recognition experiment was carried out with this system. As a result, we can confirm the effectiveness of proposed system. However, further improvement is necessary to develop the various equipments using this system. In the future, we aim at the completion of the system.

References

1. Japanese Automatic Recognition System Society, "Biometrics that Understands from this", Ohm Company, 2001, in Japanese
2. D.Nishikawa, W.Yu, H.Yokoi, Y.Kakazu, "On-Line Learning Method for EMG Prosthetic Hand Controlling", IEICE Trans. D-II, Vol.J82, No.9, pp.1510-1519, 1999, in Japanese
3. O.Fukuda, N.Bu, T.Tsuji, "Control of an Externally Powered Prosthetic Forearm Using Raw-EMG Signals", T.SICE, Vol.40, No.11, pp. 1124-1131, Nov. 2004, in Japanese
4. O.Fukuda, J.Arita, T.Tsuji, "An EMG-Controlled Omnidirectional Pointing Device", IEICE Trans. J87- D-II, No.10, pp.1996-2003, Oct.2004, in Japanese
5. T.Oyama, Y.Matsumura, S.Karungaru, M.Fukumi, "Feature Generation Method by Geometrical Interpretation of Fisher Linear Discriminant Analysis", Trans. of IEEJ, Vol.127-C, No.6
6. T.Oyama, Y.Matsumura, S.Karungaru, Y.Mitsukura, M.Fukumi, "Construction of Wrist Motion recognition System", Proc. of 2006 RISP InternationalWorkshop on Nonlinear Circuits and Signal Processing, pp.385-388, Hawaii, March 2006
7. T.Oyama, Y.Matsumura, S.Karungaru, Y.Mitsukura, M.Fukumi, "Recognition of Wrist Motion Pattern by EMG", Proc. of SICE-ICCAS'2006, pp.599-603, Busan, Korea, Oct. 2006
8. Y. Ishioka, "Standard and Application of Stomatognathic Function Analysis", dental Diamond Company, pp.260-273, 1991, in Japanese
9. Shingo Kuroiwa, Satoru Tsuge, Hironori Tani, Xiaoying Tai, Masami Shishibori and Kenji Kita, "Dimensionality reduction of vector space model based on Simple PCA", Proc. Knowledge-Based Intelligent Information Engineering Systems & Allied Technologies (KES), Vol.2, pp.362-366, Osaka, Sep. 2001

Metal Artifact Removal on Dental CT Scanned Images by Using Multi-Layer Entropic Thresholding and Label Filtering Techniques for 3-D Visualization of CT Images

K. Koonsanit, T. Chanwimaluang, D. Gansawat, S. Sotthivirat,
W. Narkbuakaew, W. Areeprayolkij, P. Yampri and W. Sinthupinyo

National Electronics and Computer Technology Center, Pathumthani, Thailand

Abstract — **Metal artifact is a significant problem in computed tomography (CT). Degradation of the quality of an image is a direct consequence of the metal artifacts in the image data. A number of papers and articles have been published regarding the subjects. However, none of the approach can be employed to incorporate in commercial CT scanners. Besides, all of the methods, to the best of our knowledge, are performed in the reconstruction process which means the CT images are created at the same time as the metal artifact removal process. In this research, we assume that the CT images with metal artifacts are given and we have no control over the reconstruction approach.**

Hence, we propose a new method to automatically remove metal artifacts in dental CT images in the post-processing steps. The proposed technique consists of two main steps. First, the local entropy thresholding scheme is employed to automatically segment out the dental region in a CT image. Then, the Label filtering technique is used to remove isolated pixels, which are the metal artifacts, by using the concept of connected pixel labeling.

The algorithm has been tested on thirty sets of the dental CT scanned images. The experimental results are compared with hand-labeled dental images and are evaluated in terms of accuracy, sensitivity and specificity. The numerical results showing sensitivity, specificity, and accuracy are 87.89%, 99.54%, and 99.21% respectively. The experiments demonstrate the robustness and effectiveness of the proposed algorithm. The algorithm provides promising performance in detecting and removing metal artifacts from dental CT images. Therefore, automatic artifact removal can greatly help with the 3-D Visualization of CT images.

Keywords — **Artifact Removal, CT scanned image, Dentistry, Entropic Thresholding, Label Filtering**

I. Introduction

At present, computed tomography streak artifacts caused by metallic objects remain a challenge for the automatic processing of image data. A three-dimensional assessment of the bone architecture needs to be available for the planning of surgical placement of dental implants. Therefore, automatic artifact removal can greatly help with the 3-D object reconstruction process as shown in Fig.1.

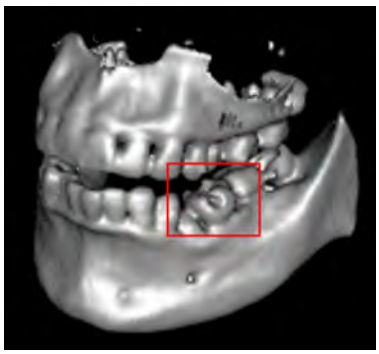


Fig.1. 3-D Visualization of CT Images

II. The Proposed Algorithm

Dental CT is a three-dimensional (3-D) scan from a large set of 2-D X-ray images which can be used for dental and maxillofacial applications. A 3-D object is generated from a series of 2-D images by selecting regions of interest. Then only regions of interest are used to generate a 3-D shape. In our case, dental bones, possessing brighter gray-scale intensities compared to other tissues, are our regions of interest. A user or dentist has to select an appropriate threshold to segment out the dental bones. Therefore, automatic threshold selection can greatly help with the 3-D object reconstruction process.

In this paper, we propose a new method for automatic segmentation, which is based on entropic thresholding scheme. While a traditional co-occurrence matrix specifies only the transition within an image on horizontal and vertical directions, in this work we embrace the transition of the gray-scale value between the current layer and its prior layer as well as the current layer and its next layer into our co-occurrence matrix. The proposed method can be used to automatically select an appropriate threshold range in dental CT images as shown in Fig.2.

The proposed technique consists of two main steps. First, the local entropy thresholding scheme is employed to automatically segment out the dental region in a CT image. Then, the Label filtering technique is used to remove iso-

Chwee Teck Lim, James C.H. Goh (Eds.): ICBME 2008, Proceedings 23, pp. 306–309, 2009
www.springerlink.com

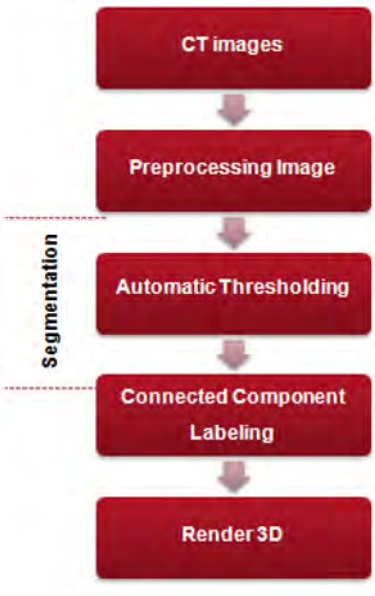


Fig.2. Metal Artifact Removal Algorithm on Dental CT Scanned Image

lated pixels, which are the metal artifacts, by using the concept of connected pixel labeling.

A. Entropy Thresholding

Our test data are the dental CT (Computed Tomography) scan images which consist of different cross-section images as shown in Fig.3.and Fig.4.

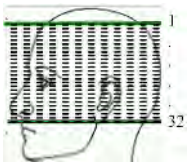


Fig.3. Position of CT slices from top to bottom

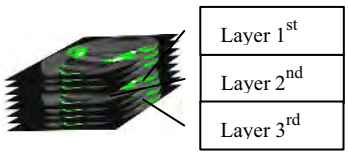


Fig.4. Examples from layer number

Because image pixel intensities are not independent of each other, an entropic-based thresholding technique is employed. Specifically, we implement a Multi-layer Entropy method which can preserve the structure details of an image. Our definition of a co-occurrence matrix is based on the idea that the neighboring layers should affect the threshold value. Hence, we define a new definition for a co-occurrence matrix by including the transition of the gray-scale value between the current layer and its prior layer as well as the current layer and its next layer into our co-occurrence matrix illustrated in Fig 6.

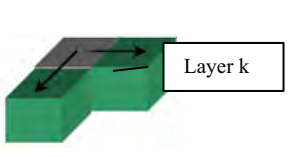


Fig.5. right and bottom of pixel in a co-occurrence matrix

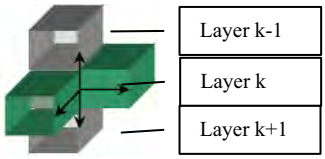


Fig.6. the prior and the next layers in a co-occurrence matrix

Let **F** be the set of images. Each image has dimension of P×Q. Let t_{ij} be an element in a co-occurrence matrix depending upon the ways in which the gray level i follows gray level j

$$t_{ij} = \sum_{x=1}^{P} \sum_{y=1}^{Q} \delta \begin{cases} (F_k(x,y) = i) \text{ and } (F_k(x,y+1) = j) & \text{or} \\ (F_k(x,y) = i) \text{ and } (F_k(x+1,y) = j) & \text{or} \\ (F_k(x,y) = i) \text{ and } (F_{k-1}(x,y) = j) & \text{or} \\ (F_k(x,y) = i) \text{ and } (F_{k+1}(x,y) = j) & \end{cases}$$

Where $\delta = 1$

$$, \delta = 0 \quad otherwise. \tag{1}$$

where F_k denotes the k[th] slice in the image set, **F**

The total number of occurrences, t_{ij}, divided by the total number of pixels, P×Q, defines a joint probability, p_{ij}, which can be written as

$$p_{ij} = \frac{t_{ij}}{\sum_i \sum_j t_{ij}} \tag{2}$$

If $s, 0 \le s \le L-1$ is a threshold. Then s can partition the co-occurrence matrix into 4 quadrants, namely A, B, C, and D shown in Fig.7.

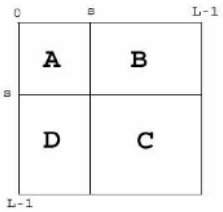


Fig.7. an example of blocking of co-occurrence matrix

Let us define the following quantities:

$$P_A = \sum_{i=0}^{s} \sum_{j=0}^{s} p_{ij} \quad , \quad P_{ij}^{A} = \frac{t_{ij}}{\sum_{i=0}^{s} \sum_{j=0}^{s} t_{ij}} \tag{3}$$

for $0 \le i \le s, 0 \le j \le s$

$$P_C = \sum_{i=s+1}^{L-1}\sum_{j=s+1}^{L-1} p_{ij}, \qquad P_{ij}^{C} = \frac{t_{ij}}{\sum_{i=s+1}^{L-1}\sum_{j=s+1}^{L-1} t_{ij}} \quad \text{for } s+1 \le i \le L-1, s+1 \le j \le L-1 \tag{4}$$

$$H_A^{(2)}(s) = -\frac{1}{2}\sum_{i=0}^{s}\sum_{j=0}^{s} P_{ij}^{A} \log_2 P_{ij}^{A} \tag{5}$$

$$H_C^{(2)}(s) = -\frac{1}{2}\sum_{i=s+1}^{L-1}\sum_{j=s+1}^{L-1} P_{ij}^{C} \log_2 P_{ij}^{C} \tag{6}$$

Where $H_A^{(2)}(s)$ *and* $H_C^{(2)}(s)$ represent the local entropy of the background and foreground respectively. Since two of the quadrants shown in Fig.5, B and D, contain information about edges and noise alone, they are ignored in the calculation. Because the quadrants, which contain the object and the background, A and C, are considered to be independent distributions, the probability values in each case must be normalized in order for each of the quadrants to have a total probability equal 1. The gray level corresponding to the maximum of $H_A^{(2)}(s) + H_C^{(2)}(s)$ give the optimal threshold for object-background classification.

$$S_{opt} = \arg\max_{s}\left[H_A^{(2)}(s) + H_C^{(2)}(s)\right] \tag{7}$$

For the given original image shown in Fig. 8. The result after Multi-layer entropy thresholding shows in Fig. 10. For comparison purpose, the local entropic result is illustrated in Fig.9 where the metal artifacts have been segmented out in the amount greater than those in Fig. 9.

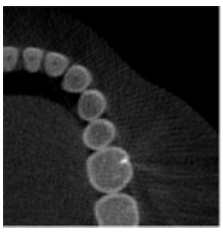


Fig.8. original Image



Fig.9. Resulted image after Local Entropic Thresholding

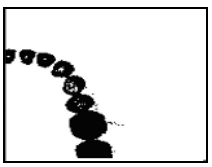


Fig.10. Resulted image after the integration of the prior-layer and the next-layer relationship

B. Connected Component Labeling

Connected component labeling or labeling filtering is used to remove some misclassified pixels in image as shown in Fig. 10. Label filtering is used to remove isolated pixels by using the concept of connected pixels labeling. The Label filtering tries to isolate the individual objects by using the eight-connected neighborhood. The result after label filtering shows in Fig. 11.



Fig.11. Resulted image after connected component labeling

III. Experiment and Results

On Pentium 4, CPU 2.0 GHz, using MATLAB version R2006b, the computational time of the whole algorithm takes approximately a few minutes for each sets of the dental CT scanned images. We used the thirty sets of the dental CT scanned images. The dental images and dental ground truth data are obtained from the National Metal and Materials Technology Center (MTEC), Advanced Dental Technology Center (ADTEC) and hand-labeled.

The performance of the metal artifact removal algorithm is conventionally measured using accuracy sensitivity and specificity. The definitions of the three indices are follows:

Table 1 Calculations of Accuracy

	Reference Test Results		
		+	-
New Test Results	+	TP	FP
	-	FN	TN

$$Sensitivity = \frac{TP}{TP + FN} \tag{8}$$

$$Specificity = \frac{TN}{TN + FP} \tag{9}$$

$$Accuracy = \frac{TP + TN}{TP + FP + TN + FN} \tag{10}$$

where TP=number of true positive specimens
FP=number of false positive specimens

FN=number of false negative specimens
TN=number of true negative specimens

The algorithm has been tested on thirty sets of the dental CT scanned images. The experimental results are compared with hand-labeled dental images and are evaluated in terms of accuracy, sensitivity and specificity. The numerical results showing sensitivity, specificity, and accuracy are 87.89%, 99.54%, and 99.21% respectively, and show on Table 2. The experiments demonstrate the robustness and effectiveness of the proposed algorithm. The algorithm provides promising performance in detecting and removing metal artifacts from dental CT images.

Table 2 Comparison of purposed Metal Artifact Removal Algorithm and hand-labeled techniques

index	Comparison of purposed Metal Artifact Removal Algorithm and hand-labeled techniques		
	Sensitivity (%)	Specificity (%)	Accuracy (%)
Dataset 1	96.1512	94.4695	94.5731
Dataset 2	74.7131	99.9919	99.7589
Dataset 3	85.4737	99.9958	99.5002
Dataset 4	92.3677	99.9097	99.7638
Dataset 5	89.7465	99.9962	99.8632
Dataset 6	90.0708	99.8815	99.6517
Dataset 7	91.9688	99.7759	99.4221
Dataset 8	93.9094	99.9029	99.6731
Dataset 9	95.1024	99.1150	98.8994
Dataset 10	88.4291	99.9244	99.6448
Dataset 11	85.6647	99.9912	99.7158
Dataset 12	96.8132	99.9382	99.7784
Dataset 13	97.2216	99.3522	99.1856
Dataset 14	93.6635	99.9935	99.7231
Dataset 15	94.084	99.9987	99.8632
Dataset 16	27.1539	99.994	98.9462
Dataset 17	94.0643	99.9676	99.7727
Dataset 18	87.8229	99.9762	99.8913
Dataset 19	93.916	95.3802	95.3385
Dataset 20	94.877	99.8086	99.6062
Dataset 21	94.4785	99.9705	99.8431
Dataset 22	91.2738	99.9967	99.9515
Dataset 23	93.7396	99.7321	99.4825
Dataset 24	94.4697	99.9915	99.7633
Dataset 25	77.4510	99.9964	99.9880
Dataset 26	83.4507	99.9971	99.9799
Dataset 27	75.4415	99.9345	99.7870
Dataset 28	93.0513	99.9672	99.8325
Dataset 29	77.2059	99.9983	99.9906
Dataset 30	92.8948	99.4268	99.2183
MINIMUM	27.1539	94.4695	94.5731
MAXIMUN	97.2216	99.9987	99.9906
AVERAGE	87.88902	99.54581	99.21792

The result after final step which is 3-D object reconstruction process is shown in Fig.12.

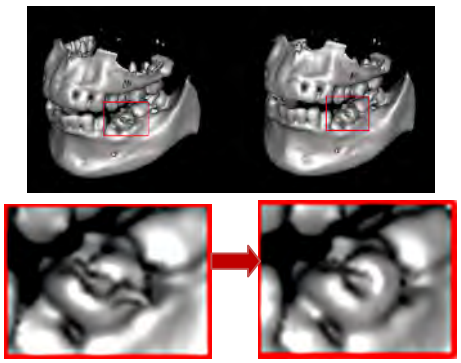


Fig.12. 3D rendering after Metal Artifact Removal

IV. Conclusions

Multi-layer Entropic Thresholding and Label Filtering Technique methods for metal artifact removal on dental CT scanned image are presented in this paper. We define a new definition for a co-occurrence matrix which can both preserve the structure within an image and at the same time can present the connection between adjacent images. The approach can be applied to automatically indicate an appropriate thresholding range in dental CT images. The algorithm provides promising performance in detecting and removing metal artifacts from dental CT images. Therefore, automatic artifact removal can greatly help with the 3-D Visualization of CT images.

Acknowledgment

The authors would like to thank MTEC and ADTEC for providing CT data.

References

1. N. R. Pal and S. K. Pal, "Entropic thresholding," Signal processing, vol. 16, pp. 97-108, 1989.
2. T. Chanwimaluang and Guoliang Fan, "An efficient algorithm for extraction of anatomical structures in retinal images," ICIP 2003 Proceedings, Sept 4-17, 2003.
3. K. Koonsanit, T. Chanwimaluang, C.Watcharopas, "Automatic segmentation of dental CT using entropic threshold," Proceedings of the 1st International Bone and Dental Technology Symposium 2007, November 12-13, 2007.

A Vocoder for a Novel Cochlear Implant Stimulating Strategy Based on Virtual Channel Technology

Charles T.M. Choi[1*], C.H. Hsu[1], W.Y. Tsai[1] and Yi Hsuan Lee[2]

[1] Department of Computer Science and Institute of Biomedical Engineering, National Chiao-Tung University, Taiwan R.O.C.
[2] Department of Computer and Information Science, National Taichung University, Taiwan R.O.C.
[*] c.t.choi@ieee.org

Abstract — **Cochlear implant provides opportunity for profoundly hearing impairment patient to have a chance to hear sound again. However, the limited number of electrodes is in sufficient to provide enough hearing resolution for hearing impaired people, especially for application in tonal language and music. Virtual channel technology opens up the possibility to increase the hearing resolution under the limited electrodes available and improve and quality for tonal language and music. In this paper, vocoder implementation of a new speech strategy based on virtual channel technology is used to study the improvement. The test result shows improved understanding and quality with virtual channels over the traditional strategies, ex. CIS, especially for mandarin and music.**

Keywords — **Cochlear Implant, Current Steering, Virtual Channel, Vocoder, Speech Strategy.**

I. Introduction

Cochlear implant (CI) helps people with profoundly hearing impairment to recover partial hearing through electrical stimulating the hearing nerves. The mechanism is to pick up sound by a microphone and a speech processor turns the input sound to frequency representations fit to the tonotopic organization of human cochlea and generates electrical current to implanted electrode array to stimulate the corresponding hearing nerves [1], [2]. Current available commercial CI devices provide 12~24 electrodes but the limited number of electrodes cannot fully cover the whole auditory nerve fibers and are not sufficient for satisfactory stimulation quality.

Current steering is designed to improve the stimulation resolution without increasing the originally implanted electrode count. By controlling the input currents of adjacent electrodes in a suitable manner simultaneously, intermediate channels, virtual channels, between the electrodes can be generated [3], [4]. This can increase the perceptual channels over the limited electrodes and improve the listening quality, especially for tonal language and music. To benefit from the virtual channels, new speech strategies are required to exploit this effect.

In this paper, new speech strategy based on virtual channel technology is designed and a vocoder is developed to realize the new strategy to study the improvement of performance.

II. Methods

A. Spectrum representations in CI

To give an impression how a CI user may perceive the sound, a spectrum comparison in Fig. 1 shows the difference between original signal and the stimulation channels in CI. Because of the tonotopic organization of human cochlea, the locations along the basilar membrane represent the corresponding frequencies. In Fig. 1, the upper one is an example spectrum of the original signal and the lower two are the stimulation channels in CI. The bottom squares represent the electrodes in an electrode array and eight electrodes are present in this example.

It can be observed that in most commercial CI devices, the limited number of electrodes does not allow for satisfactory tracing of spectrum variation, resulting in inconsistent perception and thus compromised understanding. Virtual channels allow intermediate channels between adjacent electrodes can be generated, the stimulation channels similar to the original signal which can provide better stimulation results for CI users and better hearing quality. This can be compared by the peak positions from the figure (arrows)

B. New speech strategy and vocoder

In this study, we proposed a new speech strategy based on virtual channel technology for better efficacy. To assess the performance, an adapted vocoder is developed using National Instrument LABVIEW programming environment [7]. Fig. 2 provides the block diagram of the vocoder, including new speech strategy and the sound synthesis. In the simulation, digitized sound data stored in disk is used as input directly. Two main paths in the new strategy are processed according to the input sound data. Spectrum processing analyzes the spectrum information by using FFT and then selects the peak signal between adjacent electrodes. This will be used to locate the virtual channels. Magnitude

Chwee Teck Lim, James C.H. Goh (Eds.): ICBME 2008, Proceedings 23, pp. 310–313, 2009
www.springerlink.com

processing analyzes the magnitude of the spectral band between adjacent electrodes and then nonlinear maps to the CI user's dynamic range. This will be used to set the magnitude of the virtual channels stimulation.

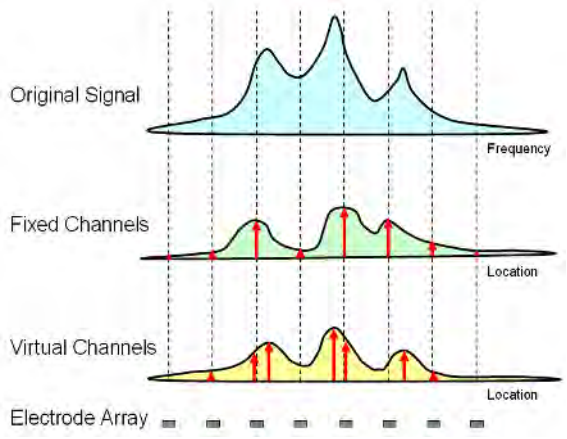


Fig.1 Spectrum comparison between original signal and the CI channels. The arrows represent the stimulation channels by the electrodes.

After processed by the new speech strategy, noise and pure tonal carrier are used to synthesize the sound to emulate the hearing of CI users [8].A band pass filter (BPF) control module is used to control the bandwidth of synthesis BPF. By adjusting the bandwidth of synthesis BPF, The current spread from the electrodes or virtual channels can be represented. This makes the outputs from the vocoder closer to the hearing of CI users.

C. Test materials

To assess the performance of the new speech strategy, Mandarin and music were selected in this study. For Mandarin source, a phrase including four different tone words is used : "ton(/) shi(\) ten(-)ya(/)". For music source, a clip of music played by a violin is used. All test materials are sampled at 16kHz and the signal bandwidth is 8kHz according to Nyquist-Shannon sampling theorem which covers the typical hearing frequen cy range of CI users.

The configuration of HiFocus electrode array from Advanced Bionics Corporation [9] was used in this experiment. There are 16 electrodes, representing 16 fixed channels generated by traditional strategy and 15 virtual channels between 15 electrode pairs. The mapping between frequencies and the corresponding electrodes are listed in Table 1 [10].

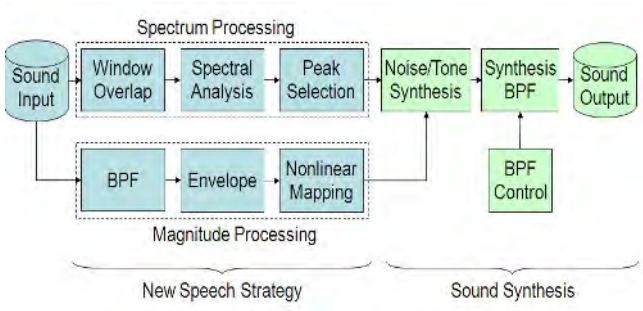


Fig. 2 Block diagram of the vocoder, including new speech strategy and sound synthesis.

Table 1 Mapping between frequencies and corresponding electrodes

Electrode ID	1	2	3	4
Frequency (Hz)	333	455	540	642
Electrode ID	5	6	7	8
Frequency (Hz)	762	906	1076	1278
Electrode ID	9	10	11	12
Frequency (Hz)	1518	1803	2142	2544
Electrode ID	13	14	15	16
Frequency (Hz)	3022	3590	4264	6665

III. Results

Fig. 3 shows the waveform and spectrum of the test Mandarin phrase."ton(/) shi(\) ten(-) ya(/)". A typical Chinese word is usually composed of consonant, vowel and

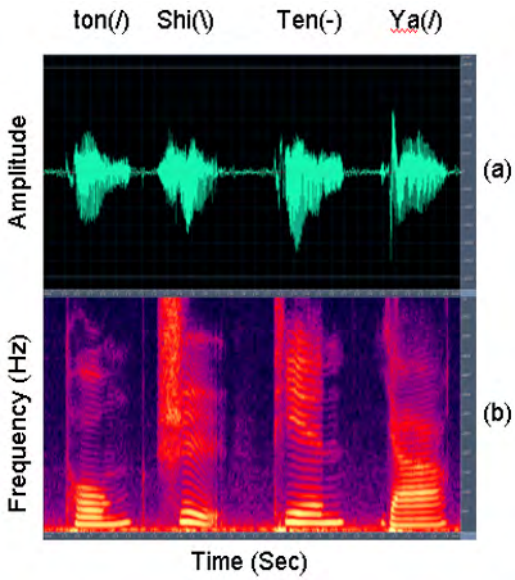


Fig. 3 The original test Mandarin phrase sample: ton(/) shi(\) ten(-) ya(/). (a) Speech waveform. (b) Corresponding spectrum.

tonal information. In the spectrum representation (Fig. 3b), it is observed clearly that the four words comprise the consonant and vowel while the second word is more obvious. The tones are different between words. The rising tone of the first word is associated with a rising frequency while the falling tone of the second word is associated with a falling frequency and so on. This tonal information is important to the understanding of Mandarin and any other tonal language, such like Cantonese. So how to maintain the tonal information for CI users using tonal language is crucial.

Fig. 4 shows the spectral comparison of the synthesized sounds by using traditional fixed channel strategy and new strategy based on virtual channel. As Fig. 1 show, the spectrum is composed of fixed frequency components as the electrode located for the fixed channel strategy (Fig. 4a). The tonal information is lost and sounded like flat tone for all words. This makes the understanding more difficult.

Observing the spectrum of the tonal synthesized sound (Fig. 4b), the frequency variation between adjacent electrodes, the stimulation sites can be adjusted and the frequency perceived will follow accordingly. In the perceptual test, the signal from the virtual channel strategy sounded much clearer and more natural than the traditional approach. Fig. 4c shows the spectrum using noise synthesis. By controlling the bandwidth of synthesis BPF, the synthesized sound can be made easier to understand. Since tonal carrier is a very narrow band noise signal, the spectral spread of tonal synthesis is narrower and more concentrated than that of noise synthesis and can be observed by comparing Fig. 4b and 4c, especially in the high frequency region.

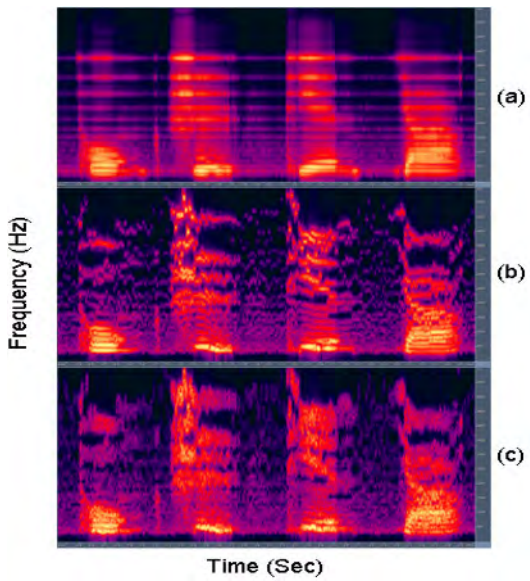


Fig. 4 Spectral comparison of the synthesized sounds. (a) Spectrum of the tonal synthesized sound using traditional fixed channel speech strategy. (b) Spectrum of the tonal synthesized sound using new speech strategy. (c) Spectrum of the noisy synthesized sound using new speech strategy.

IV. Discussion

Traditional fixed channel strategy performs well for non-tonal language now, however the fixed approach of stimulation cannot trace the frequency variation for tonal language. The proposed new speech strategy preserves the main spectral information since the main peaks of the spectrum between each electrode pairs are selected for stimulation and adopts the virtual channel technology to trace the frequency variation. So the simulation result reveals that the new speech strategy is superior to the traditional strategy. In addition to the preservation of tonal information, the consonant also sounded more natural than traditional approach. Since the consonant is a noise like signal, the peaks are also distributed randomly. Using the virtual channel technology, the signal spectrum can be represented easily and therefore sounds more natural. The simulation result shows that the new strategy also performs better than the traditional approach.

V. Conclusions

This paper presented a new speech strategy based on virtual channel technology to improve the understanding of tonal language. The acoustic simulation showed that it is superior to the traditional strategy. For the music listening, the new strategy also performed better but there is still room for improvement.

The vocoder implementation can help to develop a new strategy without involving CI users which can simplify the development effort and reduce the development time. The new CI strategy can therefore be improved based on the result of the vocoder simulation. Systematic perceptual experiment will be performed to validate the new speech strategy in the future.

Acknowledgment

This research was supported in part by National Health Research Institute (NHRI-EX97-9735EI) and National Science Council, R.O.C. (NSC95-2221-E-009-366-MY3)

REFERENCES

1. Spelman F (1999) The past, present, and future of cochlear prostheses. IEEE Eng Med Biol 18(3):27-33
2. Loizou P (1998) Mimicking the human ear. IEEE Signal Process Mag 15(5):101-130
3. Advanced Bionics Corporation (2005) Increasing spectral channels through current steering in HiResolution bionics ear users
4. Firszt, Koch JB, Downing DB et al (2007) Current steering creates additional pitch percepts in adult cochlear implant recipients. Otol and Neurotol 28:629-636
5. Peddigari V, Kehtarnavaz N, Loizou P et al (2007) Real-time LABVIEW implementation of cochlear implant signal processing on PDA platforms. Proc. IEEE intern. Conf. Signal, Acoust. Speech Proc. II, Honolulu, USA, 2007, pp 357-360
6. Advanced Bionics Corporation (2005) HiRes90K: surgeon's manual for the HiFocus Helix and HiFocus 1j electrodes
7. Advanced Bionics Corporation (2006) SoundWave professional suit: device fitting manual, software version 1.4
8. Choi CTM, Hsu CH (2007) Models of virtual channels based on various electrode shape. Proc. 6th APSCI, Sydney, Australia, 20
9. Sit JJ, Simonson AM, Oxenham AJ et al (2007) A low-power asynchronous interleaved sampling algorithm for cochlear implants that encodes envelope and phase information. IEEE Trans Biomed Eng 54(1):138-149

Author: Charles T. M. Choi
Institute: Department of Computer Science and Institute of Biomedical Engineering, National Chiao-Tung University
Street: 1001, Ta Hsueh Road
City: Hsinchu 300
Country: Taiwan, R.O.C.
Email: c.t.choi@ieee.org

Towards a 3D Real Time Renal Calculi Tracking for Extracorporeal Shock Wave Lithotripsy

I. Manousakas, J.J. Li

Department of Biomedical Engineering, I-Shou University, Kaohsiung County, Taiwan

Abstract — **Extracorporeal shock wave lithotripsy can fragment renal stones so that they can pass out during urination. Breathing can induce motion of the kidneys which results in reduced efficiency of the treatment. This study attempts to evaluate if a three dimensional method of stone tracking could be possible with existing hardware and software components. A gelatin phantom was imaged with ultrasound to create a three dimensional volume image. Subsequently, two dimensional images acquired in parallel and perpendicular directions to the scans that produced the volume image were registered within the image volume. It is shown that data reduction methods and optimized software can achieve processing times suitable for real time processing.**

Keywords — **ESWL, renal stone, image analysis.**

I. Introduction

Extracorporeal shock wave lithotripsy (ESWL) is the preferred method of treatment for renal calculi. It is a non invasive treatment and has been already in routine clinical practice for many years. During treatment, the stone formation is commutated to small fragments by exposing the stone to focused shock waves. The fragments, if they are of small size, can spontaneously pass out during urination. The most common practice is that the stone is localized using fluoroscopy. The focal area of the shock wave generator is positioned in such way that it will coincide with the stone location. It is usually a painful procedure and has complications such as hematuria and injuries at other healthy tissues near the treated area. Renal function may be reduced and most of it is recovered after a period of time. Internal injuries are caused because of reasons such as focus area that is larger than the size of the stone, breathing induced motion of the organs in the abdomen including the kidneys, involuntary movements of the patient, non-accurate localization, overtreatment and so on. Moreover, fluoroscopy with its radiation nature is not the ideal choice for localization purposes and ultrasound is now available for the majority of the commercial systems. Nevertheless, it is seldom used because requires more training for the technicians and doctors and also more time during treatment for the stone localization.

During the recent years, methods for automatic renal stone tracking have been proposed based in ultrasound imaging 1-3. These methods use stone positioning information from the images to reposition the shock wave focal area in real time. The benefits of such tracking methods are such as: smaller stone fragments, reduced treatment time, reduced injuries to healthy tissues, reduced pain and less radiation exposure for the patient. The efficiency that could be achieved is commented by other independent researchers 4.

The main reasons why these treatment methods are not yet accepted and widely used today are that the methods are difficult to use and there are possibilities of erroneous tracking of other structures that may look like stones to the system's image analysis software. These problems mostly arise from the nature of the two dimensional ultrasound imaging that is used with these systems. For a perfect stone tracking the stone should be visible in the image at all times. This could only be achieved if the imaging plane is perfectly aligned with the stone motion. Repositioning the patient on the system may improve the alignment but this needs some time and the cumbersome procedure may have to be repeated through a treatment. As somebody could imagine, such treatments are not welcome by doctors or patients. Moreover, if the alignment is poor and the stone gets out of the imaging plane, the software has difficulty in deciding whether to track something else or stop and wait for the stone to reappear at a close position.

While three dimensional ultrasound imaging systems could certainly solve the above mentioned problems, are of high cost and not supported by any software system for stone tracking. In the research presented here, a method that uses pseudo three dimensional imaging is used in conjunction with classical two dimensional imaging. This method, although in an initial state, shows the potential of a three dimensional method. A study with a phantom shows that real time processing with current computer technology is possible.

II. Materials and methods

The method presented here uses a three dimensional image composed from individually acquired slices. This image volume acts as a reference for registration of subsequently

Chwee Teck Lim, James C.H. Goh (Eds.): ICBME 2008, Proceedings 23, pp. 314–317, 2009
www.springerlink.com

acquired images. The study was performed using a simplified gelatin phantom.

A. Phantom Model

A simplified kidney stone phantom was used in this study for collection of ultrasound images. The phantom was structured as a kidney with a clearly visible stone formation in the calyx and was constructed with widely available materials for a single use. The kidney tissue was mimicked using material used for gelatin based desserts. Various other materials, like agar, could have been used but with no difference to the results. Since these materials are usually looking transparent in the ultrasound images, scattering materials are usually added, such as graphite powder. A more easy to prepare method that we have been using for some time is the addition of a small portion of common wheat flour that is firstly diluted with cold water and then added to the hot gelatin solution as the last preparation step before pouring into a mold. As could be expected a more irregular grain is produced in the image that could be claimed to be more realistic for a tissue mimicking phantom. The exact proportions of the added materials and water are not critical to this study and could be altered to produce phantoms of various sound impedances, if that was necessary. The stone model was mimicked with a small irregular natural stone positioned within a small balloon full of water. This balloon was first fixed at a position within the mold and then the gelatin was poured around. The phantom was used after refrigeration for one day which reduces the air bubbles that may present during manufacturing.

B. Ultrasound Imaging

The constructed phantom was placed inside a water tank lined with materials to reduce reflections. A commercial ultrasound imaging system was used for this study (Sonos 500, Hewlett Packard). Ultrasound imaging was performed for the constructed phantom at 2.5 MHz and at the maximum depth of 12 cm. The ultrasound probe was mounted on a XYZ positioning system and a small front part of the probe was immersed in the water. A drawing of the experiment's configuration is shown in Fig. 1. The whole phantom volume was imaged using two different probe directions. The space between successive slices was 1 mm. In a clinical case, a free hand three dimensional ultrasound imaging of the kidney could be acquired within a short time period during hold breath.

During a treatment, the morphology of the kidney in the image is not expected to be strongly altered and therefore this image volume could be used as a reference. Within this volume the position of the stone under treatment should be identified by a system user. A subsequently acquired two dimensional image of the same area could be registered to this volume.

C. Image Analysis

Software was written in both Matlab® (ver. 2007a, The MathWorks, Inc, USA) and Visual C++® (Visual studio 2005, Microsoft, USA) for performance comparison. The software was used on a Windows XP® based PC with an Intel Pentium D® 930 CPU at 3GHz having 4Gbytes of memory. The Intel's Integrated Performance Primitives software library (ver. 5.3, Intel, USA) was used to increase performance of the C++ program.

In a basic three dimensional stone tracking method, the task would be to follow an already identified target through time and space. The available processing time for a realistic tracking system could be equal or less to the frame rate of the ultrasound system. Often this is about 15 frames per second, allowing about 66 ms for image analysis and the necessary motion of the system until the next image becomes available.

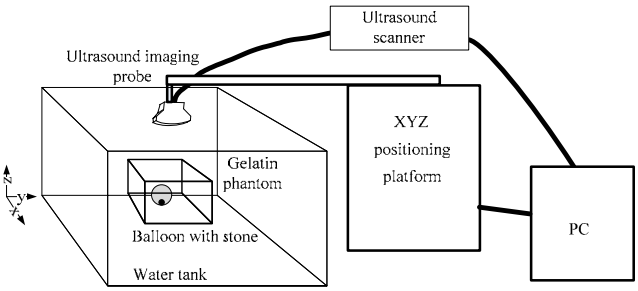


Fig. 1 Drawing of the configuration for the phantom experiments.

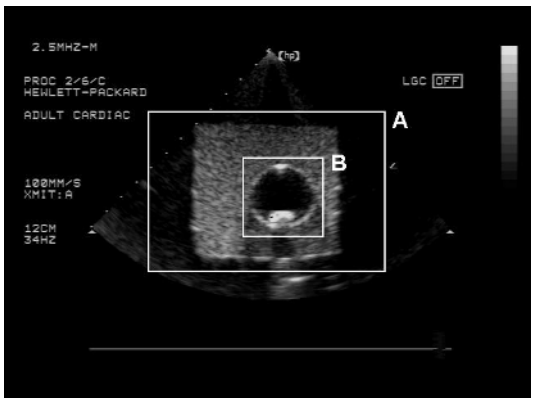


Fig. 2 Ultrasound image of the phantom. The region marked A depicts the 3D ROI for the registration and the region B depicts the 2D template size.

The proposed approach relates the tracking performance to the software's ability to register the most recent acquired two dimensional image to the three dimensional image that was initially acquired. The difference between the displacement of the stone position in the 3D and 2D images and the current position of the system represents the required motion for the systems shock wave focal area positioning motors.

D. Algorithm

Image registration was performed between each of the 2D images and each of the individual slices inside the acquired three dimensional volumes. Normalized correlation coefficients were computed for the image registration 5. The images were acquired as 640x480 pixel images, see Fig. 2. Each time, a template region from the two dimensional image of size 100x100 pixels (2D template) was related to regions of interest (3D ROIs) of size 290x200 pixels on each slice in the three dimensional volume image. Tests were also performed with the same images after been resized to a 1:3 and 1:5 ratio. When the images had different resolutions, the data were interpolated to produce more slices and result in a volume with the same resolution in all axes. The relative position of the 3D ROIs and the 2D templates are shown in Fig. 3. In the first case the 2D templates were extracted from the volume image, so they are at the same direction. In the second case, the 3D ROIs and the 2D templates were acquired in a perpendicular to the volume scans direction. The number of 3D ROIs images and 2D templates used in the parallel scans case were 42 and 20 respectively and for the perpendicular scans case 45 and 20 respectively. The sizes of the 3D ROIs and the 2D templates were selected so that to contain the whole balloon area.

III. Results

In Fig. 4 the results from the registration are shown. Each line in the graphs show the values achieved when a specific 2D template is compared with all the 3D ROIs. The normalized correlation coefficient is in the range between zero and one. The ideal experiment in the parallel scans case, Fig. 4(a), shows that there is always a distinct peak of maximum height. When we perform resizing (1:5), distinct peaks still exist but with lower values. In the perpendicular scans case were the acquisition directions differ, the peaks are lower and when also using resizing, the peaks are even lower.

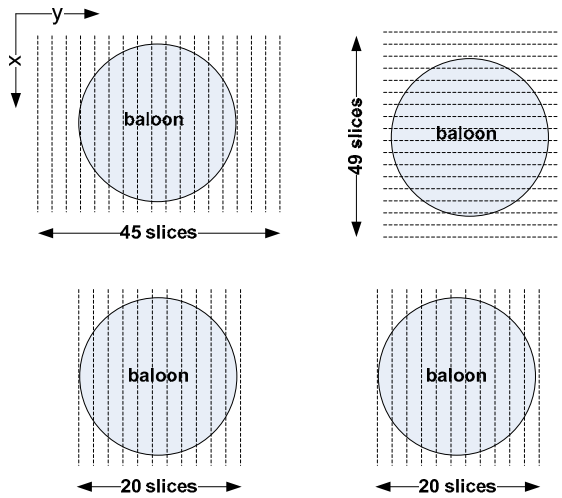


Fig. 3 The relative direction between the 3D ROIs (top row) and the 2D templates (bottom row) for the parallel scans case (left column) and the perpendicular scans case (right column). The dashed lines depict the direction that the scans cut the balloon.

The processing times for the experiments in (ms) are shown in Table I. These times represent the time needed for a single 2D template to a 3D ROI registration.

IV. Discussion

The results shown in Fig. 4 show that registration of the phantom images is ideal when the direction of both the 3D ROI and the 2D template are the same and the images are practically the same. Furthermore, stronger values are achieved when the images are of the original size. The lines in the graphs also show that there are two distinct peaks within an area of higher values. The higher value areas depict the balloon area where higher similarity exists as compared to the further away area. As the balloon with the stone was constructed as a very symmetrical structure, two peaks appear in the graphs representing positions with similar appearance on the left and on the right of the stone. In a real case, tracking would be sufficient when the shock waves' focal area is positioned so that intersects with the calyx. Therefore, small errors could be of small importance. The relative directions of the 2D templates and the 3D ROIs may reduce the correlation coefficient but do not affect drastically the registration results. In a clinical case, it is more likely that all the 2D and 3D scans would be parallel. Even so, reasons such as movement of the patient or fan shape 3D image acquisition are expected to cause reduction of the correlation coefficient.

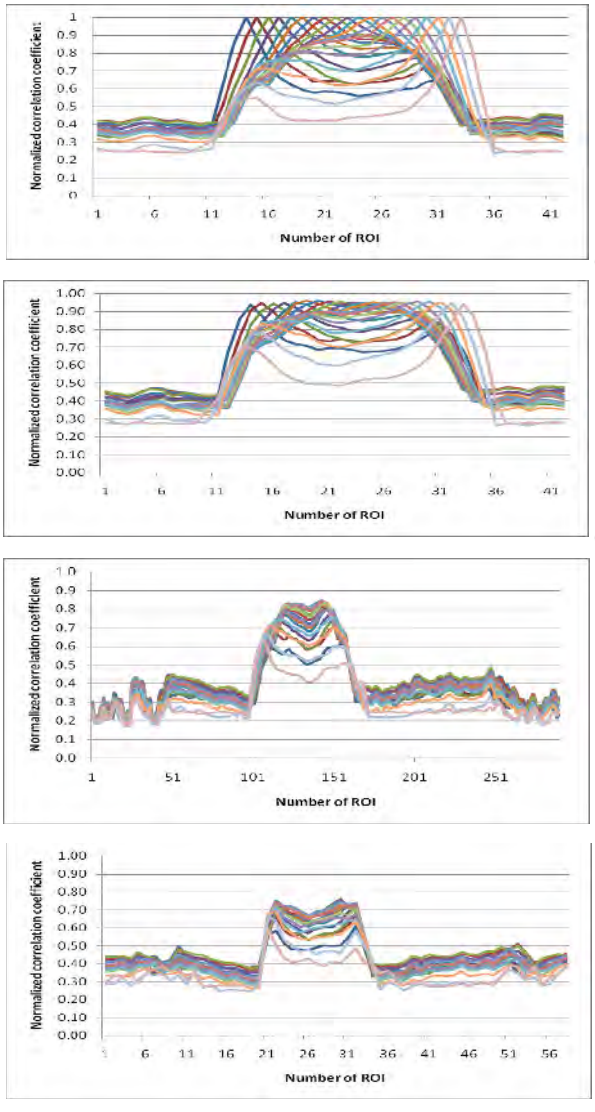


Fig. 4 Crosscorelation figures for (a) parallel scans case with original size, (b) parallel scans case with resize 1:5, (c) perpendicular scans case with original size, (d) perpendicular scans case with resize 1:5.

The time needed for processing shows that processing is time consuming with non specific software like Matlab®. This software is often used for prototyping but for a real time application is not recommended. Some difference in processing time is noticed between the parallel and perpendicular scans cases due to the different data sizes. Nevertheless, the shortest time achieved for a single slice to slice registration using the original sized data was 9.7 ms and is also very long for a real time application. Reduction of the dataset using resizing or skipping individual slices, or any other appropriate method, is highly recommended. As an example, a 1:5 resizing of the data and registration between a whole 42 slices volume would require 42 times 0.28ms which is about 12 ms. Such processing time is within the time available for a real time stone tracking. Further in-vitro and in-vivo studies are necessary to verify the applicability of the method in clinical conditions.

V. Conclusion

Using a simplified kidney stone phantom we have shown that three dimensional stone tracking could be achieved using a normalized correlation coefficient method. The time required for the proposed method is within the range of real time processing.

Table 1 Single registration processing time (ms)

Resize ratio	1:1	1:3	1:5
Parallel scans case using Matlab®	230	15.9	5.9
Perpendicular scans case using Matlab®	120	12.6	5.2
Parallel scans case using the Intel® library	9.7	0.65	0.28

Acknowledgment

This research was partially supported by I-Shou University research grand ISU97-01-17

References

1. Orkisz M, Farchtchian T, Saighi D et al. (1998) Image based renal stone tracking to improve efficacy in extracorporeal lithotripsy. J Urol 160: 1237-1240
2. Chang C C, Manousakas I, Pu Y R et al. (2002) In vitro study of ultrasound based real-time tracking for renal stones in shock wave lithotripsy: Part II--a simulated animal experiment. J Urol 167:2594-2597
3. Chang C C, Liang S M, Pu Y R (2001) In vitro study of ultrasound based real-time tracking of renal stones for shock wave lithotripsy: part 1. J Urol 166:28-32
4. Cleveland R O, Anglade R, Babayan R K (2004) Effect of stone motion on in vitro comminution efficiency of Storz Modulith SLX. J Endourol 18:629-633
5. Gonzalez R C, Woods R E (1992) Digital Image Processing (third edition). Reading, Massachusetts: Addison-Wesley.

Author: Ioannis Manousakas
Institute: Dep of Biomedical Engineering
Street: No.1, Sec. 1, Syuecheng Rd., Dashu Township
City: Kaohsiung County 840
Country: Taiwan
Email: i.manousakas@ieee.org

A Novel Multivariate Analysis Method for Bio-Signal Processing

H.H. Lin[1], S.H. Change[1], Y.J. Chiou[1], J.H. Lin[2], T.C. Hsiao[1]

[1] Institute of Computer Science/Institute of Biomedical Engineering, National Chiao Tung University, Taiwan
[2] Department of Electronic Engineering, Kun Shan University, Taiwan

Abstract — **Often, multivariate analysis is wildly used to process "signal information", which includes spectrum analysis, bio-signal processing and etc. In general, Least Squares (LS) and PLS fall into overfitting problem with ill-posed condition, which means the future selections make the training data have better adaptability, but the quality of the prediction would be poor, compared with the testing data. However, the goal of these models is to have consistent prediction between testing and training data. Therefore, in this study, we present a novel MVA model, Partial Regularized Least Squares, which applies regularization algorithm (entropy regularization), to Partial Least Square (PLS) method to cope with the problem mentioned above.**

In this paper, we briefly introduce the conventional methods and also clearly define the model, PRLS. Then, the new approach is applied to several real world cases and the outcomes demonstrate that while calibrating data with noises, PRLS shows better noise reduction performance and lower time complexity than cross-validation (CV) technique and original PLS method which indicates that PRLS is capable of processing "Bio-signal". Finally, in the future we expect utilizing another two regularization techniques instead of the one in the paper to identify the performance differentiations.

Keywords — **Multivariate Analysis, Partial Regularize Least Squares, Noise reduction-**

I. Introduction

Multivariate analysis technique is of great importance in signal processing field, such as application in spectrum analysis [1], bio-signal and image processing [2,3]and pattern reorganization [4]. Typically, MVA can be classified into two categories: regression analysis and iterative method. In regression analysis, Least Square (LS) and Partial Least Square (PLS) are the most commonly used method. Also, the iterative method, which is well known as artificial neural network (ANN), uses Multilayer perceptron [5] as its main model. Although, both regression and iterative methods have their unique properties and are suitable for different applications, some researches in the past have demonstrated that integrating these two techniques shows significant impact on the analyzing data and verify with real case data [7, 8].

Chen (1991) presented by using the regression strategy, orthogonal least squares (OLS), to construct a ANN, radial basis function network (RBFN) [9]. Moreover, Hsiao (1998) suggested that PLS can be implemented in multilayer architecture as back-propagation (BP) network [10]. However, LS criterion in certain condition is prone to overfitting. If data are highly noisy, results may still fit into noise. Regularization is one of the techniques to overcoming the overfitting problem. Chen (1996) applied regularization techniques to his algorithm, which is regularized orthogonal least squares learning algorithm for radial basis function networks (ROLS based on RBFN) [11], and the prediction results demonstrate better generalization performance than the original non-regularized method. Therefore, follow the concept of ROLS based on RBFN, we develop a novel calibration model called Partial Regularized Least Square (PRLS) to overcome the overfitting problem that Hisoa's algorithm encountered.

II. Methods and materials

Before specifying the PRLS algorithm, we briefly describe the basic principle of PLS and its implementation in ANN architecture.

PLS regression is a widely used multivariate analysis method and is particularly useful when we need to predict a set of dependent variables from a large set of independent variables. The independent variable matrix X_{msn} and dependent variable matrix Y_{nxl} can be both decomposed into a matrix with corresponding weight matrix:

$$\begin{aligned}\mathbf{X}_{nxm} &= \mathbf{X}^{(1)} + \mathbf{X}^{(2)} + \ldots + \mathbf{X}^{(a)} + E \\ &= \hat{u}_1 \hat{p}_1^{\mathrm{T}} + \hat{u}_2 \hat{p}_2^{\mathrm{T}} + \ldots \hat{u}_a \hat{p}_a^{\mathrm{T}} + E \\ &= \mathbf{U}_{nxa}\mathbf{P}_{axm}^{\mathrm{T}}\end{aligned} \quad (1)$$

$$\begin{aligned}\mathbf{Y}_{nx1} &= \mathbf{Y}^{(1)} + \mathbf{Y}^{(2)} + \ldots + \mathbf{Y}^{(a)} + F \\ &= \hat{v}_1 \hat{q}_1 + \hat{v}_2 \hat{q}_2 + \ldots + \hat{v}_a \hat{q}_a + F \\ &= \mathbf{V}_{nxa}\mathbf{Q}_{ax1}\end{aligned} \quad (2)$$

- *Partial Least Squares (PLS)*

Fig. 1 shows the schema of PLS algorithm.

By performing the algorithm in Fig. 1, $||E_{nxm}||$ and $||F_{nxl}||$ are minimized regressively and when number of iterations

Chwee Teck Lim, James C.H. Goh (Eds.): ICBME 2008, Proceedings 23, pp. 318–322, 2009
www.springerlink.com

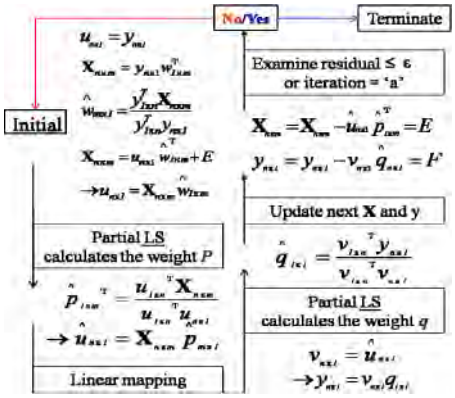


Fig. 1 PLS algorithm

equals to a certain value "a" or the "examine residual" is less or equal than a certain value ε, the process terminates. The best generalized result would be found out.

Fig. 2 illustrates the implementation of PLS in multi-layer architecture as BP network. Hsiao's contribution is to provide possible findings for the constituents within the convergent weight matrix and is a more effective method for the necessary number of hidden nodes in BP.

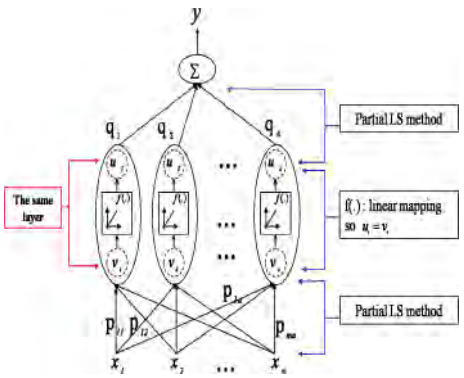


Fig. 2 Three layer PLS architecture

- *Regularization*

Generally, regularization is used to prevent overfitting and to minimize the error function of residual. Essentially it involves adding some multiple of a positive definite matrix to an ill-conditioned matrix so that the sum is no longer ill-conditioned and is equivalent to simple weight-decay in gradient descent methods. The symbols, A[u] > 0 and B[u] > 0, are two positive functions of u, so that u can be determined by either minimizing A[u] or B[u]. To summarized, regularization uses Lagrange Multipliers combines with quadratic constraint to minimize the weighted sum A[u] + λB[u] and lead to a adequate solution for u.

- *Partial Regularized Least Squares (PRLS)*

In general PLS calibration only minimizes the residual ||Enxm|| and ||Fnxl|| during the processing of decomposing independent and dependent matrices. In ideal situation, the calibration will approximate the desired output minimum. In most cases, undesired information always hide behind the real world data which we called "nosie" will interfere the prediction. However, in some circumstances, PLS calibration may suffer from overfitting problem by the undesired noises within the data. As mentioned earlier, to prevent overfitting, we introduce regularization, entropy regularization, concept into PLS and rewrite the error criterion of PLS as:

$$E_e = E_D + \lambda E_{\tilde{R}} = E^T E + \lambda q^T q, \lambda \geq 0 \quad (3)$$

(Where q is weighting vector which inferences the output directly)

Fig. 3 demonstrates the schema of PRLS algorithm.

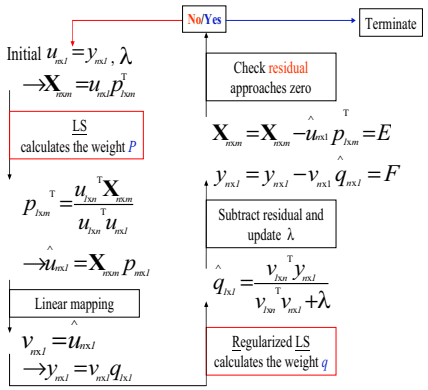


Fig. 3 PRLS algorithm flow chart

In Fig. 3, we can see that PLS are used in two different phases, however, only the later one, which calculates the weight q, influences the output directly. Hence, we only apply regularization into the second PLS phases.

Apart from integrating regularization into the original PLS, we also adjust the three-layer PLS architecture with regularization method (Fig. 4).

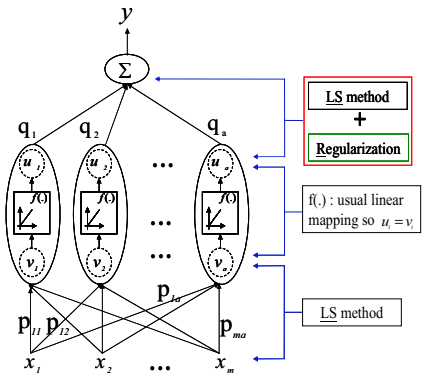


Fig. 4 PRLS three layer calibration system

III. Results

In the previous work, the PRLS algorithm has been proved have better performance than PLS with the simulation data - sigmoid and polynomial function and imitative spectrum data under SCSP (self calibration and self prediction) and CV (cross-validation). In this study, we apply PRLS method to the real data, sound and blood glucose to illustrate the performance of PRLS.

- **Sound file - Power-station ambience**

In the experiments, ex-99 data are used to predict the 100 data in the sound data - power-station-ambience. Followings are the results of the experiment.

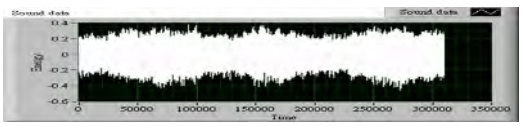


Fig.5-1 Power station ambience source data

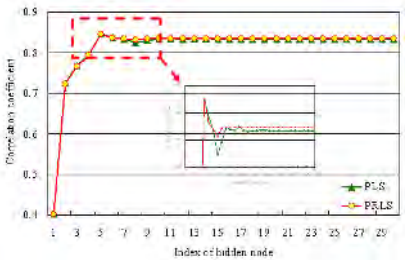


Fig.5-2 Correlation coefficient as a function of index of hidden node under SCSP

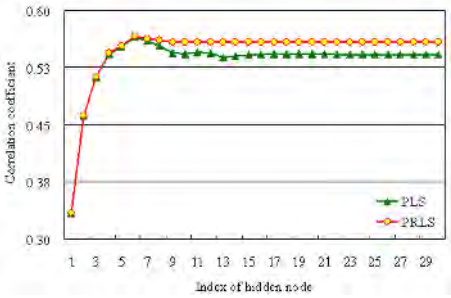


Fig.5-3 Correlation coefficient as a function of index of hidden node under CV

Table 1 Optimal CV results for power station ambience prediction data

	PLS	PRLS
Correlation coefficient	0.5646	0.5658
RMSE	0.0415	0.0411
Adequate iteration	6	6

- **Blood glucose data**

Diabetes mellitus is one of the most common diseases in the present day, we can analysis the blood glucose data and further control when the density is irregular. In the experiment, we select 37 data sets to evidence our purpose. Fig.6-1 shows blood glucose data with noise. Fig6-2 – Fig.6-7are the results of calibration under SCSP and CV.

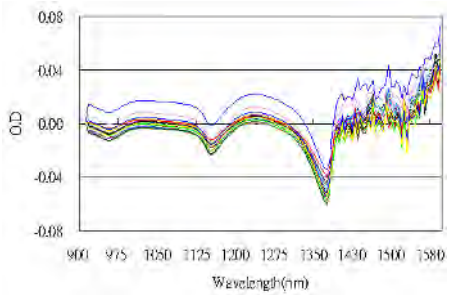


Fig.6-1 Blood glucose data with noise

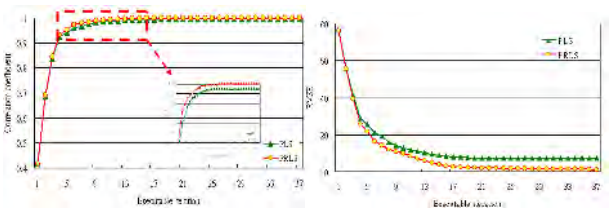


Fig.6-2 Correlation coefficient as a function of executable iteration under SCSP. Fig. 6-3 RMSE as a function of executable iteration under SCSP

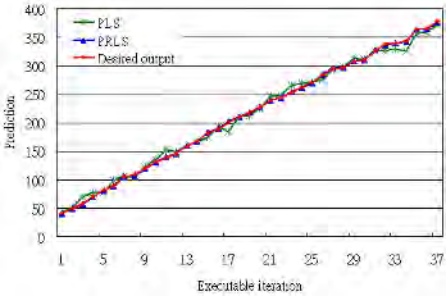


Fig.6-4 Network mapping constructed by PRLS and PLS algorithm under SCSP

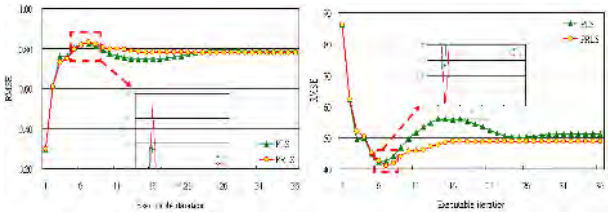


Fig.6-5 Correlation coefficient as a function of executable iteration under CV. Fig. 6-6 RMSE as a function of executable iteration under CV

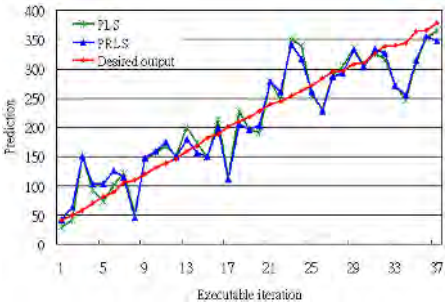


Fig. 6-7 Network mapping constructed by PRLS and PLS algorithm under CV

Table 2 Optimal CV results for blood glucose data

	PLS	PRLS
Correlation coefficient	0.8240	0.8320
RMSE	42.280	40.993
Adequate iteration	6	7

IV. Discussion

Table 3 is drawn from the results of our experiments. It is hoped that the prediction results are in high correlation coefficient, small RMSE and consumes little computation which means, the height of correlation coefficient always keeps high, slope of RMSE is not abrupt and the time complexity could be as low as possible. From the table, it clearly shows that PRLS has better performance than other methods.

Table 3 Compilation of real experimental results

Condition / Criterion	SCP		CV	
	PLS	PRLS	PLS	PRLS
Correlation Coefficient				
RMSE				
Time complexity	O(n)		$O(n^2)$	

V. Conclusions

In this study, we accomplish integrating regularization method, entropy regularization, into PLS algorithm called PRLS as a brand new MVA technique. PRLS illustrates better calibration result than the original method.

Despites manipulating PRLS with simulation data, PRLS method is successfully applied to real world problems – sound and blood glucose in this study. PRLS illustrates better calibration results both in performance and time complexity than the original method when calibrating data with large undesired noise. The result demonstrates that PRLS is suitable for analyzing bio-signal, which particularly has a lot of noise within the raw data.

Furthermore, we would like to extend our work by using another two regularization techniques (gradient based regularization and square-error based regularization) to enhance multivariate analysis technique.

Acknowledgment

The authors would like to thanks the National Science Council, ROC Taiwan, for financially supporting this study (NSC 94-2213-E-214-042 and NSC 97-222-E-009-121).

References

1. Bhandare P, Mendelson Y, Peura RA, Janatsch G, Kruse-Jarres JD, Marbach R, Heise HM (1993) Multivariate determination of glucose in whole blood using partial least-squares and artificial neural networks based on mid-infrared spectroscopy. Appl Spectrosc 47:1214-1221
2. Möcks J, Verleger R (1991) Multivariate methods in biosignal analysis: application of principal component analysis to event-related. Techniques in the behavioral and neural sciences 5:399-458

3. Castellanos G, Delgado E, Daza G, Sanchez LG, Suarez JF (2006) Feature selection in pathology detection using hybrid multidimensional analysis. Annual International Conference of the IEEE EMBS, New York, USA, 2006
4. Huang KY (2003) Neural networks and pattern recognition, Wei-Keg Book Co. Ltd., ROC, Taiwan
5. Oja E (1982) A simplified neuron model as a principal component analyzer. J Math Biol 15:267-273
6. Harald M, Tormod N (1996) Multivariate calibration, John Wiley & Sons, Great Britain
7. Wang CY, Tsai T, Chen HM, Chen CT, Chiang CP (2003) PLS-ANN based classification model for oral submucous fibrosis and oral carcinogenesis. Laser Surg Med 32:318-326
8. Chu CC, Hsiao TC, Wang CY, Lin JK, Chiang HH (2006) Comparison of the performances of linear multivariate analysis method for normal and dyplasia tissues differentiation using autofluorescence spectroscopic. IEEE T Bio-Men Eng 53:2265-2273
9. Hsiao TC, Lin CW, Tseng MT, Chiang HH (1998) The implementation of partial least squares with artificial neural network architecture. IEEE-EMBS'98, Honk Kong, China, 1998
10. Chen S, Cowan CFN, Grant PM (1991) Orthogonal least squares learning algorithm for radial basis function networks. IEEE T Neural Network 2:302-309
11. Chen S, Chng ES, Alkadhimi K (1996) Regularized orthogonal least squares algorithm for constructing radial basis function networks. Int J Control 64:829-837
12. Hsiao TC, Lin CW, Chiang HH (2003) Partial least squares algorithm for weights initialization of the back-propagation network. Neurocomputing, 50:237-247

Multi-Wavelength Diffuse Reflectance Plots for Mapping Various Chromophores in Human Skin for Non-Invasive Diagnosis

Shanthi Prince and S. Malarvizhi

[1] Department of Electronics and Communication Engineering, SRM University,
SRM Nagar -603203, Tamil Nadu, Chennai, India.

Abstract — **Optical techniques have the potential for performing in vivo diagnosis on tissue. Spectral characteristics of the components provide useful information to identify the components, because different chromophores have different spectroscopic responses to electromagnetic waves of a certain energy band.**

The basis for this mapping method arise from the differences in the spectra obtained from the normal and diseased tissue owing to the multiple physiological changes associated with increased vasculature, cellularity, oxygen consumption and edema in tumour. Different skin and sub-surface tissues have distinct or unique reflectance pattern which help us differentiate normal and cancerous tissues.

An optical fibre spectrometer is set up for this purpose, which is safe, portable and very affordable relative to other techniques. The method involves exposure of skin surface to white light produced by an incandescent source. These back scattered photons emerging from various layers of tissue are detected by spectrometer resulting in tissue surface emission profile.

For the present study, three different skin diseases - warts, moles and vitiligo are chosen. The spectral data from the scan is presented as a multi-wavelength plot. Further, ratio analysis is carried out in which, the relative spectral intensity changes are quantified and the spectral shape changes are enhanced and more easily visualized on the spectral curves, thus assisting in differentiating the part which is affected by disease visually.

The unique information obtained from the multi-wavelength reflectance plots makes it suitable for a variety of clinical applications, such as therapeutic monitoring, lesion characterization and risk assessment.

Keywords — **Multi-wavelength, diffuse reflectance, chromophores, ratio-analysis, non-invasive.**

I. Introduction

Advances in the understanding of light transport through turbid media during the 1990s led to the development of technologies based on diffuse optical spectroscopy and diffuse optical imaging [1] [2]. There has recently been significant interest in developing optical spectroscopy as a tool to augment the current protocols for cancer diagnosis [3], as it has the capability to probe changes in the biochemical composition of tissue that accompany disease progression. A non-invasive tool for skin disease diagnosis would be a useful clinical adjunct. The purpose of this study is to determine whether visible/near-infrared spectroscopy can be used to non-invasively characterize skin diseases.

Many benign skin diseases resemble malignancies upon visual examination. As a consequence, histopathological analysis of skin biopsies remains the standard for confirmation of a diagnosis. Visible/near-infrared (IR) spectroscopy may be that tool which could be utilized for characterization of skin diseases prior to biopsy.

A variety of materials in skin, absorbs mid-IR light (>2500 nm), thus providing an insight into skin biochemistry. But, if the sample thickness is greater than 10-15μm, mid-IR light is completely absorbed. Therefore, the diagnostic potential of mid-IR spectroscopy in-vivo is limited, In contrast, near-IR light is scattered to a much greater extent than it is absorbed, making tissues relatively transparent to near-IR light, thus allowing the examination of much larger volumes of tissue [4] and the potential for in-vivo studies.

The near-IR region is often sub-divided into the short (680-1100 nm) and long (1100-2500 nm) near-IR wavelengths, based upon the technology required to analyze light in these wavelength regions. At shorter near-IR wavelengths, oxy- and deoxyhemoglobin, myoglobin and cytochromes dominate the spectra, and their absorptions are indicative of regional blood flow and oxygen consumption.

The purpose of this study is to determine whether the information obtained from visible/near-IR spectroscopy for a variety of skin diseases will enable us to characterize the tissues based on chromophore mapping and be used as a diagnostic tool.

II. Materials and Methods

Optical spectrum from the tissue yield diagnostic information based on the biochemical composition and structure of the tissue. Different skin and sub-surface tissues have distinct or unique reflectance pattern which help us differentiate normal and cancerous tissues [5].

Chwee Teck Lim, James C.H. Goh (Eds.): ICBME 2008, Proceedings 23, pp. 323–326, 2009
www.springerlink.com

Light reflected from a surface consists of specularly reflected and diffusely reflected components. The intensity of the specular component is largely determined by the surface properties of the sample and is generally not of analytical utility. The intensity of the diffuse component, which includes the contributions from the absorbance of light by the specimen and the scattering of light by the specimen and the substrate, can be used to determine the concentration of the indicator species [6].

The schematic diagram of the visible/near-infrared (IR) spectroscopy system is shown in Fig.1. It consists of Tungsten Halogen Light Source (LS-1) which is a versatile white-light source optimized for the VIS-NIR (360-2500nm) and the spectrometer (USB4000) [7]. The spectrometer consists of 3648 element detector with shutter, high speed electronics and interface capabilities. The USB4000 is responsive from 360-1100nm.

Acquisition of visible/near-IR data is straightforward. White light from a tungsten halogen lamp is brought to the skin via a reflectance probe (R400). The reflectance probe consists of bundle of seven optical fibers. Six illumination fibers and one read fiber – each of which is 400µm in diameter. The fiber ends are coupled in such a manner that the 6-fiber leg (the illumination leg) is connected to the light source and the single fiber leg is connected to the spectrometer. The light penetrates the skin, and water, hemoglobin species, cytochromes, lipids and proteins absorb this light at specific frequencies. The remaining light is scattered by the skin, with some light being scattered back to the fiber optic probe. The light is collected by the probe and transmitted back to the spectrometer for analysis.

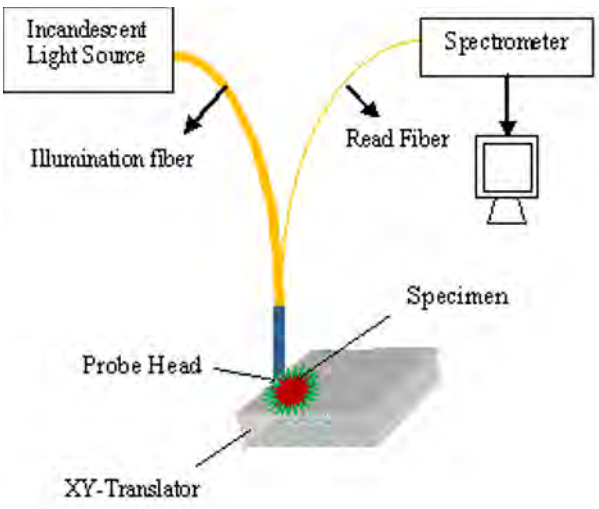


Fig.1 The schematic diagram of Visible/near-infrared (IR) spectroscopy system based on diffused reflectance

III. Aquisition of spectra and analysis

For the present study, three different skin diseases - warts, moles and vitiligo are chosen. Warts are small skin growths caused by viral infections. There over 100 types of human papilloma virus (HPV). Some warts share characteristics with other skin disorders such as molluscum contagiosum (a different type of viral skin infection), seborrhoeic keratosis (benign skin tumor) and squamous cell carcinoma (skin cancer). It is important to distinguish and diagnose.

Mole (nevus) is a pigmented spot on the outer layer of the skin epidermis. Most moles are benign, but typical moles (dysplastic nevi) may develop into malignant melanoma, a potentially fatal form of skin cancer. Congenital nevi are more likely to become cancerous.

Vitiligo is a zero melanin skin condition . The characteristics of this disease are the acquired sudden loss of the inherited skin color. The loss of the skin color yields white patches of various sizes, which can be localized anywhere on the body. However, not all white skin patches are vitiligo. There are other conditions and diseases that are associated with white skin called leucoderma. Clearly, it seems mandatory to make the correct diagnose.

Malignant Melanoma (MM) is another skin cancer which can be very dangerous if not recognized early. These tumors can develop in existing moles but they can also arise totally new as pigmented as well as non-pigmented tumors. Early recognition and excision are important for the outcome. The observation that melanoma is more frequent in patients with vitiligo originates from a study which included 623 Caucasian patients with melanoma of the Oncology Clinic at the Department of Dermatology at the University of Hamburg/Germany [8]. Some individuals with melanoma develop patches of white skin in the vicinity of their melanoma or after their tumor had been excised. In this context it seems important that these white patches are not vitiligo. This skin shows a very different molecular biology and biochemistry compared to true vitiligo [9].

Each reflectance spectrum is acquired by an Ocean Optics USB4000 spectrometer with a spectral resolution of 3.7nm. Spectra are acquired and recorded in the360 -1100 nm ranges using the system described in the previous section.

Firstly, white light is directed into a portion of the skin afflicted with the skin disease, the diffusely reflected light is collected, thereby producing a condition spectrum. Next, the same light is directed into a control skin portion of the patient which is not afflicted with the skin disease. A spectrum is taken of an unaffected skin portion as a control from each patient.

Prior to obtaining the readings, the subject's skin and the end of the probe are cleansed with 70% alcohol. The fiber optic probe is then positioned 1.0 mm from the measure-

ment site and data acquired. A plot of the amount of light backscattered at each wavelength (the spectrum) is computed. Measurements are rapid, non-destructive and non-invasive

The ratio technique is used to aid spectra interpretation. In the ratio analysis technique, the lesional spectra are divided by the corresponding spectra of the normal neighboring skin. In this way, the relative spectral intensity changes are quantified and the spectral shape changes are enhanced and more easily visualized on the spectral curves. As a consequence, these differences can be used to identify or diagnose a skin disease by comparing the visible/near-IR spectrum of a control region to a spectrum taken of the region of interest.

For the present study, spectrum is obtained from wart, mole and vitiligo skin. Also, for each case a control spectrum is obtained. The control spectrum and the disease spectrum is compared at wavelengths corresponding to visible/ near-IR absorption by oxyhemoglobin, deoxyhemoglobin, water, proteins, lipids or combinations thereof.

IV. Results and Discussion

As mentioned above, three different skin abnormalities are studied viz. wart, mole and vitiligo regions. Fig. 2 shows the plot of the original reflectance spectra of wart and the control skin along with the reflectance ratio between the wart region and the normal skin. The wart region shows very low reflectance but the shapes of the two curves are visually same.

By obtaining the ratio spectrum we observe that there is a valley around 610nm which is unique to wart and which cannot be discerned by only looking at the original spectrum. The values of the ratio plot are higher in the lower and higher wavelengths, except for the visible region.

Fig. 3 shows the spectra of mole and the control skin along with the reflectance ratio plot. Except for a slight decrease in the reflected intensity for the mole region nothing specific can be obtained from the original spectra.

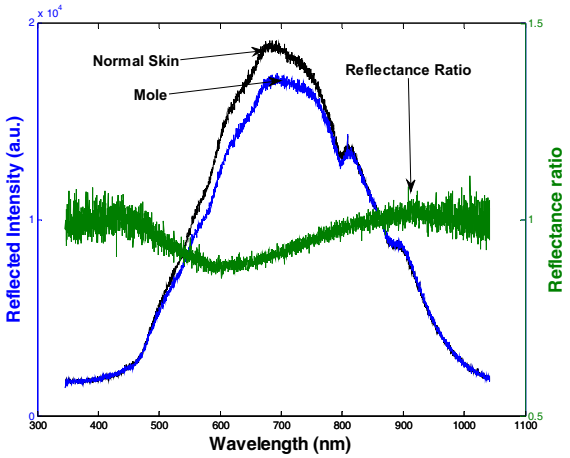


Fig.3 Reflected Intensity and Reflectance ratio spectra for the mole and the normal skin

By observing the reflectance ratio plot we find a valley at around 580nm which is specific to that particular mole type. The ratio value is more or less equa1 to 1, indicating that there is a close resemblance of mole to the control spectra.

Fig. 4 shows the reflectance spectra of vitiligo and the control skin. The absolute value of the ratio spectrum is larger than 1, indicating that the reflected intensity for a

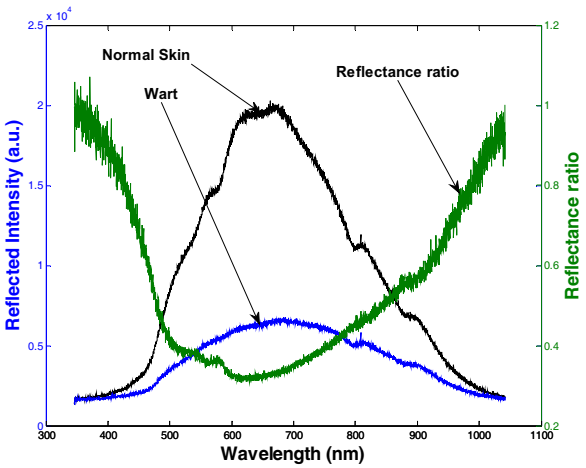


Fig.2 Reflected Intensity and Reflectance ratio spectra for the wart and the normal skin

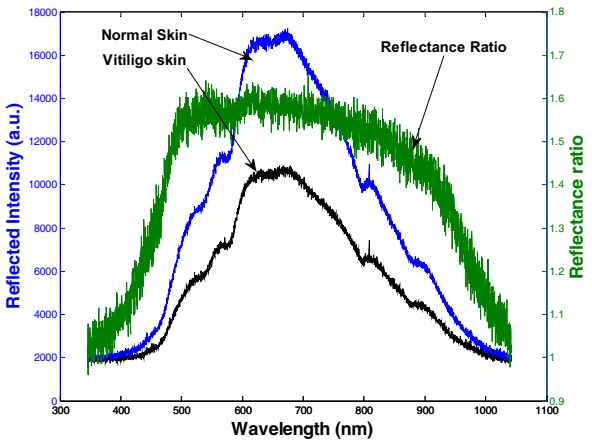


Fig.4 Reflected Intensity and Reflectance ratio spectra for the vitiligo and the normal skin

vitiligo skin is higher than that for the normal skin. Since vitiligo corresponds to region of zero-melanin skin it has little absorption and hence maximum reflectance. The ratios with values less than 1 indicate that the lesional reflectance is lower than the surrounding normal skin. The numerical ratio values quantify this difference as a function of wavelength.

Fig.5 shows the three dimensional multi-wavelength reflectance plots along the region of wart. As seen in the Fig. 2 the intensity is much lower when compared to the neighboring control skin. This plot along with the reflectance ratio plots will aid in the visible-NIR spectroscopy to be used as a diagnostic tool for detecting various skin pathologies.

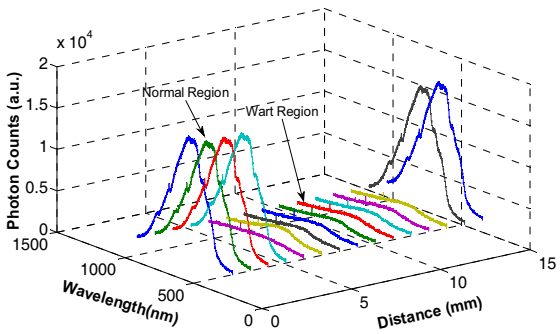


Fig.5 Multi-wavelength reflectance plot along the wart region

The visible/near-IR spectra of different skins presented here exhibit strong absorption bands from water and a number of weak, but consistent, absorption bands arising from oxy- and deoxy- hemoglobin, lipids and proteins. However, visual examination of spectra did not show distinct differences in these spectral features that could be used to distinguish between spectra of skin diseases and healthy skin.

V. Conclusions

The spectrum depends on the depth and the type of chromophore contained in the inclusion. An increase in the concentration of a given molecule may produce different contrast, independently of the depth, depending on the characteristics of the skin layer where this change occurs.

Each peak in the spectrum can be assigned to a specific compound found in the skin. Visually, strong absorption bands arising from OH groups of water dominate the spectrum. However, much information is present in the weaker spectral features. For instance, the relatively strong absorption feature at 550 nm arises from hemoglobin species and provides information relating to the oxygenation status of tissues. Further information on tissue oxygenation can be obtained from analysis of a weak absorption feature at 760 nm, arising from deoxyhemoglobin.

Information on tissue architecture/optical properties can be obtained from the spectra. Changes in tissue architecture/optical properties may affect the basic nature of the interaction of light with the tissue. For example, changes in the character of the epidermis (i.e. dehydration) may result in more scattering of light from the surface, reducing penetration of light into the skin in a wavelength dependant manner. Also, different tumor densities may result in more scattering of light from the surface. Such phenomena would be manifest in spectra as changes in the slope of the spectral curves, especially in the 400-780 nm regions.

Acknowledgment

This research work is being funded and supported by All India Council for Technical Education (AICTE), Government of India, New Delhi under the scheme of Career Award for Young Teacher (CAYT).

References

1. N. Shah, A.E. Cerussi, D. Jakubowski, D. Hsiang, J. Butler and B.J. Tromberg (2003-04) The role of diffuse optical spectroscopy in the clinical management of breast cancer Disease Markers 19:95-105
2. Scott. C. Bruce, et al (2006) Functional near Infrared spectroscopy IEEE Eng in Med. and Biol. Magazine 54-62
3. R. Manoharan, K. Shafer, L. Perelman, J. Wu, K. Chem, G. Deinum, M. Fitzmaurice, J. Myles, J. Crowe, R.R. Dasari, M.S. Feld (1998) Raman Spectroscopy and Fluorescence Photon Migration for Breast Cancer Diagnosis and Imaging Photochem. Photobiol 67:15-22
4. Shanthi Prince and S. Malarvizhi (2007) Monte Carlo Simulation of NIR Diffuse Reflectance in the normal and diseased human breast tissues Biofactors Vol. 30, No.4:255-263
5. Welch, A., v. Gemert, M. (1995) Optical-thermal response of laser-irradiated tissue- Lasers, photonics and electro-optics , Plenum Press, New York, USA, 19-20
6. Tuan Vo-Dinh (2003) Biomedical Photonics Handbook, CRC Press
7. Ocean Optics at http://www.oceanoptics.com/products
8. Schallreuter KU, Levenig C, Berger J. Vitiligo and cutaneous melanoma. Dermatologica(1991) 183: 239– 245
9. Hasse, S., Kothari, S., Rokos, H., Kauser, S., Schurer, N. Y., Schallreuter, K. (2005) In vivo and in vitro evidence for autocrine DCoH/HNF-1[alpha] transcription of albumin in the human epidermis Experimental Dermatology 14(3):182-187

Diagnosis of Diabetic Retinopathy through Slit Lamp Images

J. David[1], A. Sukesh Kumar[2] and V.V. Vineeth[1]

[1] College of Engineering, Trivandrum, India
[2] College of Engineering, Trivandrum, India

Abstract — **A new system is developed for the diagnosis of diabetic retinopathy. It is developed with the help of slit lamp biomicroscopic retinal images. The results are compared with digital fundus image using image processing techniques. The slit lamp, offering users both space savings and cost advantages. By using slit lamp biomicroscopic equipment with an ordinary camera, users can reduce the cost more than 30 times compared to digital fundus camera. The fundus examination was performed on human volunteers with a hand held contact or non-contact lens (90D).The lens providing an extremely wide field of view and better image resolution. The slit lamp equipment is used to examine, treat (with a laser), and photograph (with a camera) of the retina. A digital camera is permitted to capture the image and store this image by using slit lamp, each photograph have small potion of the entire retinal image. The individual slit lamp biomicroscopic fundus images are aligned and blended with block matching algorithm to develop an entire retinal image same as the fundus camera image and detect optic disk, blood vessel ratio from the images. This image can be used for the diagnosis of diabetic retinopathy.**

Keywords — **Block matching algorithm, Sum of squared difference, Diabetic retinopathy, Optic disk, Blood vessel ratio.**

I. Introduction

The retina is a light sensitive tissue at the back of the eye. When light enters the eye, the retina changes the light into nerve signals. The retina then sends these signals along the optic nerve to the brain. Without retina eye cannot communicate with the brain, making vision impossible.

Fundus cameras provide wide field, high quality images of posterior segment structures including the optic disc macula and blood vessels [1]. However, the slit lamp biomicroscope, the workhorse for ophthalmic diagnosis and treatment is easy and it is now often equipped with camera attachments to permit image capture for documentation, storage, and transmission. In many cases, image quality may be low, in part attributable to a narrow field of view and specular reflections arising from the cornea, sclera, and hand held lens.The cost of fundus camera is very high compared to slit lamp camera and this is the motivation of this work. Digital retinal cameras are now being used in a variety of conditions to obtain images of the retina to detect diseases such as; glaucoma, diabetic retinopathy, hypertensive retinopathy and age related macular degeneration.

The main parts for the slit lamp images consist of slit lamp equipment, digital camera and 90D lens, without using 90D lens we can capture only the front portion of the eye [2]. The slit lamp images from the slit lamp camera is combined by using Block Matching Algorithm with a typical criteria used is Sum of Squared Difference (SSD) in terms of cross correlation operations [3]. Diabetic retinopathy is the leading cause of blindness in the Western working age population. Screening for retinopathy in known diabetics can save eyesight but involves manual procedures which involve expense and time [4].In this work, detect the arteries to vein ratio of main blood vessels from the fundus image and the combined slit lamp image then compare the values between these two images. The diabetic level, both for these two set of images are determined and compared with clinical data.

II. Proposed system

The fundus photographs were taken with a fundus camera during mass screening. These photographs were then scanned by a flat-bed scanner and saved as a 24-bit true color JPG file of 512x512 pixels. The slit lamp images of the same person is taken with a slit lamp camera and saved as a JPG file of size 512x512 pixels. The basic block diagram to describe the methodology is shown in Fig (1).

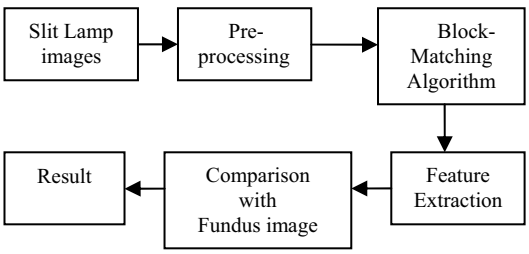


Fig (1) Block diagram of methodology

A. Slit Lamp Image

The slit lamp biomicroscopic images are small portions of the entire retinal fundus image; this is shown below in Fig (2).

Chwee Teck Lim, James C.H. Goh (Eds.): ICBME 2008, Proceedings 23, pp. 327–330, 2009
www.springerlink.com

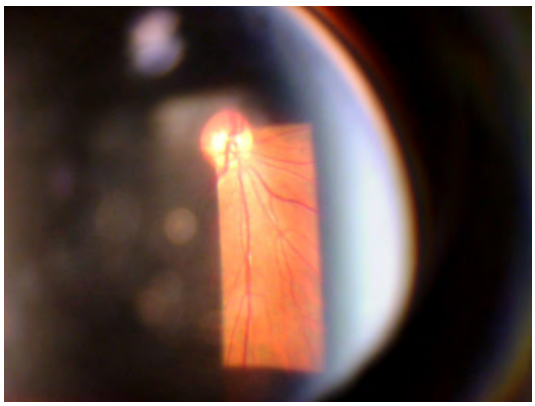


Fig (2) Slit Lamp Biomicroscopic image

B. Pre-processing

Pre-processing of the slit lamp image is done to improve the visual quality and reducing the amount of noise appearing in the image. RGB color coordinate is not required for this purpose; color system of the original image was converted to RGB components. Applied histogram equalization [5] to B component only and combined to three color coordinate, which is converted to grayscale image. The resultant image is shown below in Fig (3),

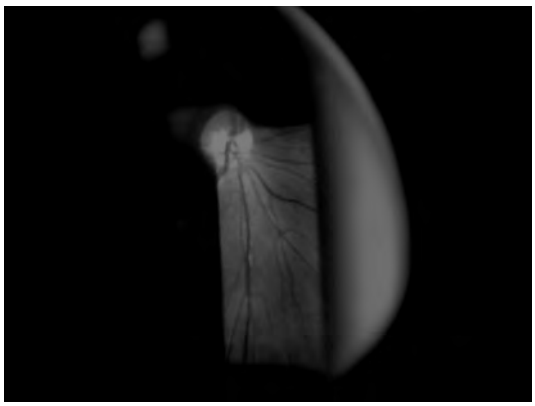


Fig (3) Pre-processed image

C. Block Matching Algorithm

In this paper, The block based method is to determine the position of a given block *g* from the current block *f*. Let *g(k,l)* denotes the luminance value of the block *g* of size (a x b) at the point *(k,l)* and *f(k,l)* denotes the luminance value of the current block *f* of size (c x d) at the point *(k,l)*.

The common used optimal block based algorithm is the Full Search Block Matching Algorithm (FS) which compares the current block *f* to all of the candidate blocks , and selects the motion vector corresponding to the candidate block, which yields the best criterion function value [6]. In this paper, we compare only the boundaries of current block *f* to the boundaries of the candidate blocks to optimizing the algorithm. Typical criteria used is the sum of squared differences (SSD),

$$SSD(x,y)=\sum_{l=0}^{n-1}\sum_{k=0}^{m-1}(f(k+x,l+y)-g(k,l))^2 \quad (1)$$

The motion vector (mv_x , mv_y) is measured from the position of the minimum in (1). The original fundus image from digital fundus camera and the resultant combined slit lamp fundus image are shown in Fig (4) and (5).

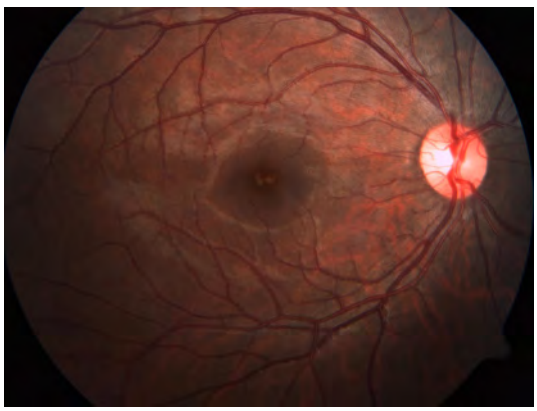


Fig (4) Original Fundus image

The combined slit lamp image is shown below,



Fig (5) Combined slit lamp image

D. Optic Disk Detection

Optic disk is the brightest part in the normal fundus image, which can be seen as a pale, round or vertically oval disk. It is the entrance region of blood vessels and optic nerves of the retina. The optic disk was identified by the area with the highest variation in intensity of adjacent pixels. First convert the color image into gray level image; enhance this image by using histogram equalization, then apply morphological closing followed by opening to suppress most of the vasculature information [7]. The structuring element is a disc lager than the largest vessel cross-section. Finally we got a bright area as plausible optic disk candidate. This is shown in Fig (6).



Fig (6) Optic Disk

E. Ratio of blood vessel width

Blood vessels appear as networks of either deep or orange-red filaments that originate with in the optic disk and are progressively diminishing width. Information about blood vessels in retinal images can be used in grading disease severity.

The normal ratio of the diameter of the main venule to the main arteriole in the retinal vascular system is about 3:2. This value is standardized by ophthalmologists all over the world [8]. In a diseased retina, one that is affected by diabetic, ratio of the diameter of the main venule to the main arteriole increases above 1.5 and can go up to 2. Due to blockages in the vessels and change in the blood sugar levels caused by diabetes, there will be a change in the diameters of the blood vessels. The diameter of arteries will decrease and that of veins increases. By detecting this change in the blood vessel diameter ratio increase, it can diagnose diabetic as early as possible [9].

Ratio of blood vessel width is estimated using concentric circle method. The centre of the optic disk is found by binary matrix calculations [10]. The next step is to find the ratio of the widths of the blood vessels. The centre of the optical disk is used to draw concentric circles of uniformly increasing radius. Traveling along the circles, the sudden intensity changes are noted, which are used to identify the width of the veins and arteries.

F. Comparison with fundus image

Image data base consist of 11 images from both digital fundus camera and slit lamp camera of diabetic retinopathy with clinical details. All images are classified in to four categories like normal, mild, moderate and severe. The comparison between fundus image and slit lamp image is shown in Table 1.

- Error Calculation

Calculating the error between fundus image and slit lamp image by using equation (2) given below,

$$\text{Error in \%} = \frac{|A-B|}{A} \times 100 \qquad (2)$$

Where A is the blood vessel ratio of fundus image and B is the blood vessel ratio of slit lamp image

Table: 1. Comparison between fundus image and slit lamp image.

No.	Blood vessel ratio (fundus image) (A)	Diabetic Stage of fundus image	Blood vessel ratio (slit lamp image) (B)	Diabetic Stage of slit lamp image	Error (%)
1	1.6667	moderate	1.7333	moderate	4.00
2	1.4981	normal	1.5618	mild	4.25
3	1.4688	normal	1.5321	mild	4.30
4	1.9704	severe	2.0461	severe	3.84
5	1.6144	moderate	1.6819	moderate	4.18
6	1.7934	moderate	1.8648	moderate	3.98
7	2.0680	severe	2.1441	severe	3.68
8	1.5685	mild	1.6345	moderate	4.21
9	1.5695	mild	1.6357	moderate	4.22
10	1.9264	severe	2.0008	severe	3.86
11	1.4684	normal	1.5316	mild	4.30

III. Conclusions

On the basis of slit lamp image information, can combine the slit lamp images and detect diabetic retinopathy. The error between slit lamp image and fundus image is small in terms of blood vessel ratio, hence in the detection of diabetics, the results are matched with clinical data. Although the

present work is focused on diabetic retinopathy in terms of blood vessel ratio, it is extensible to the detection of diseases based on retinal condition.

Acknowledgment

The authors would like to thank Dr. K. Mahadevan, Department of ophthalmology, Regional Institute of ophthalmology, Thiruvananthapuram for valuable suggestions. We also grateful to chakrabarti eye hospital, Thiruvananthapuram for providing images and clinical details.

References

1. David. J, Deepa A. K., January (2006) " Diagnosis of Diabetic Retinopathy and Diabetes using Retinal Image Analysis" Proceedings of National Conference on Emerging Trends in Computer Science and Engineering, K. S. Rangasamy College of Technology, Tiruchangode, India, PP 306-311.
2. Madjarov BD, Berger JW, (2000) Automated, real-time extraction of fundus images from slit lamp fundus biomicroscope video image sequences. Br J Ophthalmol*,* 84:645–7.
3. Y.C Lin and S.C Tai, may (1997) " Fast full-search block matching algorithm for motion-compensated video compression", IEEE transactions on communication vol. 45, no. 5,pp. 527-531.
4. D. Klein, B. E Klein, S. E Mos et al, (1986) "The Wisconsin epidemiologic study of diabetic retinopathy VII. Diabetic nonproliferative retinal lesions", Br. J Ophthalmology, vol 94.
5. K. Rapantzikos, M. Zervakis,(2003) " Detection and segmentation of drusen deposits on human retina: Potential in the diagnosis of age-related macular degeneration", Medical Image Analysis Elsevier Science PP 95-108.
6. Fedwa Essannouni, Rachid Oulad Haj Thami, Ahmed Salam, march (2006) " An efficient fast full search block matching algorithm using FFT algorithms " , IJCSNS International Journal of Computer Science and Network Security, vol. 6 No. 3B.
7. David. J, Sukesh Kumar. A, Rekha Krishnan, May (2008) "Neural Network Based Retinal Image Analysis Diagnosis", Proceedings of 2008 Congress on Image and Signal Processing, IEEE Computer Society, Sanya, China, PP 49-53, 27-30.
8. C. Sinthanayothin, J. Boyce, H.Cook, and T. Williamson, August (1999) "Automated localization of optic disc, fovea and retinal blood vessels from digital color fundus images", Br.J Ophthalmology, vol. 83.
9. Xuemin Wang, Hongbao Cao, Jie Zhang, (2005)"Analysis of Retinal Images Associated with Hypertensionand Diabetes", IEEE 27th Annual International Conference of the Engineering in Medicine and Biology Society, pp. 6407- 6410.
10. Kavitha, D. Shenbaga Devi, S, (2005)" Automatic Detection of optic disc and exudates in retinal Images", Proceedings of International Conference on Intelligent Sensing and Information Processing, pp. 501- 506.

Author: J. David
Institute: College of Engineering, Trivandrum
Street: Sreekariyam
City: Trivandrum
Country: India
Email: daviddavisdale@yahoo.com

Tracing of Central Serous Retinopathy from Retinal Fundus Images

J. David[1], A. Sukesh Kumar[2] and V. Viji[1]

[1] College of Engineering, Trivandrum, India
[2] College of Engineering, Trivandrum, India

Abstract — **The Fundus images of retina of human eye can provide valuable information about human health. In this respect, one can systematically assess digital retinal photographs, to predict various diseases. This eliminates the need for manual assessment of ophthalmic images in diagnostic practices. This work studies how the changes in the retina caused by Central Serous Retinopathy (CSR) can be detected from color fundus images using image-processing techniques. Localization of the leakage area is usually accomplished by Fluorescein angiography. The proposed work is motivated by severe discomfort occurring to certain patients by the injection of fluorescein dye and also the increase in occurrence of CSR now days. This paper presents a novel segmentation algorithm for automatic detection of leakage site in color fundus images of retina. Wavelet transform method is used for denoising in the preprocessing stage. Contrast Enhancement method is employed for non-uniform illumination compensation and enhancement. The work determines CSR by the localization of leakage pinpoint in terms of pixel co-ordinates and calculates the area of the leakage site from normal color fundus images itself.**

Keywords — **Central Serous Retinopathy, Fundus Imaging, Wavelet Analysis, Watershed Algorithm, Neural Network Classification.**

I. Introduction

Central serous Retinopathy (CSR) [1] is a serous macular detachment that usually affects young people and it leads to visual prognosis in most patients. It may also develop as a chronic or progressive disease with widespread decompensation of the Retinal Pigment Epithelium (RPE) and severe vision loss. Localization of the leakage site is crucial in the treatment of CSR. It is usually accomplished by Fluorescein angiography (FA). Despite the widespread acceptance of FA, its application has been restricted because of the possibility of severe complication and the discomfort to patients, as well as the time needed to perform the test. A normal fundoscopy of the eye also reveals the features of CSR. However, the images obtained through the normal fundoscopy are not as specific as Angiogram and they cannot be used as an efficient method for the analysis of CSR. A computer assisted diagnosis system can effectively employ Image Processing techniques to detect specifically the leakage area of CSR without taking the angiogram of the patient. The major structures of the retina such as Optic disk and Macula are detected during the work using Image Processing Techniques. This work describes image analysis methods for the automatic recognition of leakage area from color fundus image. A comparative study of the Angiogram and the color fundus images is done. The error between the coordinates of detected leakage point from color fundus and the angiogram leakage point is calculated. From the set of parameters, the images are distributed into two different groups, mild and severe. Neural network is used effectively in data classification.

II. Proposed System

The fundus photographs were taken with a fundus camera. The angiogram images of the patients are also taken by the injection of the fluorescein dye. These photographs were then scanned by a flatbed scanner and saved as a 24-bit true color JPG file of 576x768 pixels. Both the images of the same patient are taken and collected as a database for the comparison purpose. The block diagram of the proposed system is shown in figure (1). The image files are analyzed using the algorithms described in the following section: 1. Detection of optic disc 2. Detection of Fovea. 3. Detection of leakage site and the corresponding pixel co-ordinates. 3. Calculation of area of the leakage site. 4. Classification of images using Neural Network.

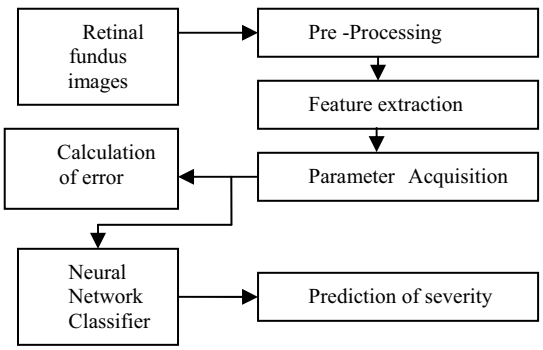


Fig (1) Block diagram of the proposed system

Chwee Teck Lim, James C.H. Goh (Eds.): ICBME 2008, Proceedings 23, pp. 331–334, 2009
www.springerlink.com

III. Pre-processing

A. Method

Pre-processing is used to improve the visual quality of the fundus image and it helps in color normalization [2]. It helps in highlighting the features that are used in image segmentation. Two typical techniques used are filtering and contrast enhancing. Filtering is used for enhancing the quality of images. It helps in sharpening blurry images. Images having low contrast can result from inadequate illumination, wrong lens aperture. Contrast enhancement increases the dynamic range of an image. For the image, local contrast enhancement [3] gave a superior result compared to contrast stretching transformation and histogram equalization. The results are shown in Fig (2) a. and b.

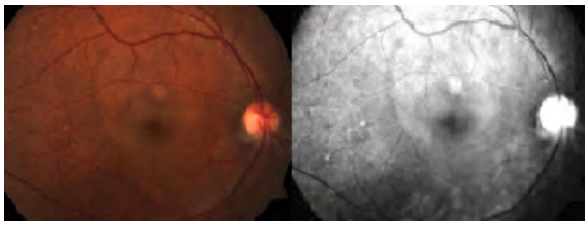


Fig (2) a. Original image Fig (2) b. Contrast Enhanced image

B. De-Noising.

De-Noising is done by wavelet analysis using wavelet toolbox, as shown in Fig (3). The advanced stationary wavelet analysis [4] is employed. The basic idea is to average many slightly different discrete wavelet analyses.

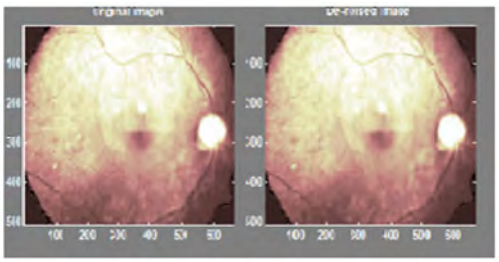


Fig (3) Denoising using wavelet analysis.

IV. Detection of optic disc

Optic disk is the entrance region of blood vessels and optic nerves to the retina and it often works as a landmark and reference for other features in the retinal fundus image [5]. Its detection is the first step in understanding fundus images. It determines approximately the localization of the macula, which is of great importance, as leakage area is more prominent there.

An area threshold is used to localize the optic disc. A best fitting circle is drawn for determining the boundary. The centre point and hence the diameter of the optic disk (ODD) is thus defined. The Optic disk detection is significant for the work because the centre point of the Optic disk is taken as the reference point for locating pixel co-ordinates of the leakage point. The result is shown in Fig (4).

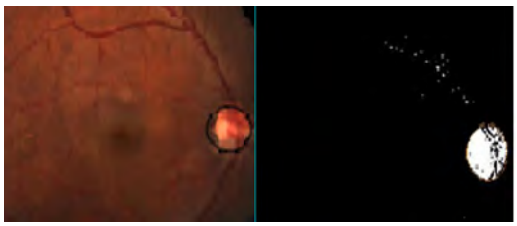


Fig (4) Optic Disc located

V. Detection of fovea

The macula is localized by finding the darkest pixel in the coarse resolution image following a geometric criterion.

The gradient is calculated and certain morphological operations are done to recognize the fovea, as shown in Fig (5). The candidate region of fovea is defined as an area of circle, which forms 2ODD [6], shown in Fig (6). Location of fovea is significant because, for the classification scheme, the distance of the leakage point co-ordinates from the fovea is to be measured as it determines whether Laser Photocoagulation is necessary for the patient or not.

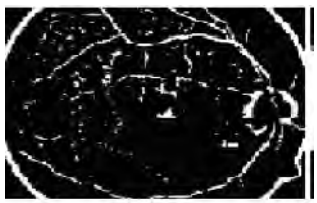


Fig (5) Gradient calculated and fovea recognized



Fig (6) Fovea located

VI. Detection of leakage area.

It is the green channel that the leakage area appears more contrasted. We first identify the candidate regions; these are regions that mostly contain the leakage area. Then morphological techniques [7] are applied in order to find the exact contours.

A. The Segmentation Paradigm

The information on objects of interest are extracted from the images. Image Segmentation [8] plays a crucial role in medical imaging by facilitating the delineation of regions of interest. Watershed transform [9] is the technique employed for the purpose. The principle of the watershed technique is to transform the gradient of a gray level image in a topographic surface. A watershed is obtained which is the boundary between the two minima influence zone. The real image is often noisy and leads to over-segmentation. So in order to avoid that, the advanced Gradient and Marker Controlled algorithm is employed. The watershed transform gives good segmentation results if topographical relief and markers are suitably chosen for different type of images. [10] The minima and maxima of a function are calculated by SKIZ algorithm [11].

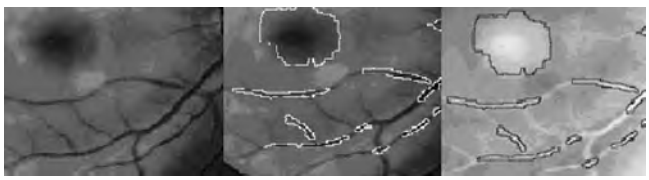


Fig (7) a. Original image Fig (7) b. Watershed of the image. Fig (7) c. Ridgelines

VII. Parameter acquisition

A. Area of the Leakage site

As the disease progresses, the area of the leakage site increases. It indicates the severity of the disease, as increase in leakage area means the RPE leak is more prominent. Leakage area is estimated by taking the ratio of No. of pixels in the leakage site to that of total pixels in the image.

B. Measurement of the distance of leakage site from fovea

The leakage point is defined by the particular pixel coordinate of the region. The co-ordinate distance is measured with respect to centre of OD and fovea [12]. If the RPE leak region is less than $1/4^{th}$ of ODD distance from fovea, the disease is mild and can wait for 4 months without any treatment. If it is greater than $1/4^{th}$ of ODD, then Laser Photocoagulation is needed.

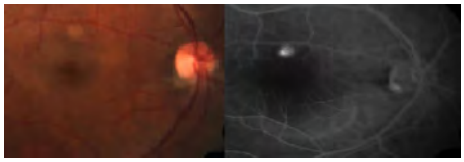


Fig (8) a. Color fundus image Fig (8) b. Angiogram image

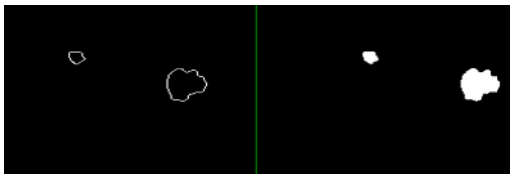


Fig (9) Leakage point detected from color fundus image.

Image database consists of 20 images. For each image, area of leakage site and the distance from fovea are measured.

Table 1 shows the pixel co-ordinates with respect to optic disk from both color fundus images and angiogram images. The pixel co-ordinates represent the leakage pinpoint. The distance of the leakage co-ordinate from the reference point. i.e., from the centre of optic disk is also calculated.

Error percentage of Coordinates is measured by least square method.

Table 1. Calculation of error between leakage point pixel co-ordinates of color fundus image and Angiogram images

Co-ordinates Angio	Co-ordinates Fundus	Error %	Dist: From Ref: Angio(*X*)	Dist from Ref: Fundus(*Y*)	Error %
178,145	174,151	2.81	132	128	3.03
123,136	126,132	2.23	128	131	2.34
145,128	140,136	3.20	146	140	4.05
192,162	187,166	1.68	198	202	2.02
135,122	141,124	2.90	127	131	3.14
232,179	239,177	2.58	211	206	2.36
188,203	184,211	3.02	192	187	2.67
211,192	215,199	1.19	213	217	1.84
122,149	117,155	2.90	142	137	2.54
176,141	168,143	1.53	159	163	2.01
201,176	207,179	2.11	213	219	2.36
122,177	118,169	1.16	129	131	1.53
190,211	185,201	3.03	208	213	3.21
151,193	162,189	2.61	165	159	2.41
212,221	207,229	1.22	213	209	1.74
144,187	133,185	1.17	152	147	1.19
253,232	246,220	1.90	261	258	2.04
136,198	127,186	3.01	159	165	3.77
165,211	152,216	2.26	206	199	2.92
137,181	129,192	2.06	187	183	2.13

$$\text{Error percentage of distance} = \frac{|X - Y|}{X} \times 100\ \% \qquad (1)$$

where X and Y are distance from reference point to leakage site for angiogram and fundus images respectively.

VIII. Neural network classifier

In this work, Back Propagation Network [13] is used for the classification scheme. The network is used to classify the images according to various disease conditions. All the images are distributed into two categories as severe and mild according to the parameter values. Table 2 shows the distribution of the parameters with CSR conditions.

Table 2. Classification of images based on disease conditions.

No.	Area of Leakage site(A)	OD diameter (D)	Distance from Fovea(d)	Stages Of Disease
1	0.0361	84	76.94	mild
2	0.0362	89	51.00	mild
3	0.0678	82	29.21	severe
4	0.0523	91	46.52	severe
5	0.0852	79	23.01	severe
6	0.0961	89	56.12	severe
7	0.0361	78	21.82	mild
8	0.0511	93	98.31	mild
9	0.1321	86	32.63	mild
10	0.0932	84	19.82	severe
11	0.0756	82	78.52	severe
12	0.0462	83	63.52	mild
13	0.0382	87	21.63	mild
14	0.0621	83	19.86	severe
15	0.0500	77	21.36	mild
16	0.0112	93	82.37	mild
17	0.0718	92	63.00	severe
18	0.0819	84	49.58	severe
19	0.0911	82	23.12	severe
20	0.1667	85	73.06	mild

IX. Conclusion

In this paper, an image-processing technique is proposed, which can play a major role in the diagnosis of CSR. A comparative analysis of the detected leakage area from Color Fundus images and Angiogram images is done. The accuracy is determined by the calculated error percentage between the two, and it is found that the error is small.

Acknowledgment

Authors would like to thank Dr. K. Mahadevan, Regional Institute of Ophthalmology, Thiruvananthapuram and Chaithanya eye Research Centre, Thiruvananthapuram for providing database of Retina images and Clinical details.

References

1. Bennett. (1995) G. Central Serous Retinopathy, Br .J. Ophtalmol,; 39:605-618.
2. RekhaKrishnan, David J, Dr. A. Sukeshkumar, (2008) Neural Network based retinal image analysis. Proceedings of 2008 congress on image and signal processing,IEEE Computer Society, China, pp-49-53
3. Chanjira Sinthanajyothin, (1999) Image Analysis for Automated Diagnosis of Diabetic Retinopathy. Thesis submitted, Doctor of Philosophy, University of London.
4. Donoho, D.L. (1995), "De-Noising by soft-thresholding," IEEE Trans. on Inf. Theory, vol. 41, 3, pp. 613-627.
5. Emmanuele Trucco and Pawan. J. Kamath , (2004) Locating the Optic Disc in retinal images via plausible detection and constraint satisfaction,0-7803-8554-3/04 IEEE, International Conference on Image Processing(ICIP).
6. L. Gagnon, M.lalonde. (2001) Procedure to detect anatomical structures in optical fundus images. Proceedings on Conference on medical Imaging (SPIE#4322) P-1218-1225.
7. Thomas Walter, Jean –Claude Klien, (2002) A Contribution of Image Processing to the diagnosis of Diabetic Retinopathy-Detection of exudates in Color Fundus image of the human Retina. IEEE transactions on medical imaging Vol 21 No.10, PP-1236-1244,
8. Gonzalez, Rafel.C. Woods, Steven. Digital Image processing using Mat lab, L, Pearson Education.
9. Gang Luo, Opas Chutatape, (2001) Abnormality Detection in Automated Screening of Diabetic Retinopathy. IEEE pp-132-137.
10. J. Roerdink and Meijster (2001) “The Watershed Transform”. Definitions algorithms and parallelization strategies. Fundamenta Informaticae, 41, pp 187-228, IOS Press.
11. Sequeira RE, Preteux FJ. (1997) Discrete Voroni Diagrams and SKIZ Operator- A Dynamic Algorithm. IEEE Transactions on pattern Analysis and machine Intelligence, vol 19 pp 1165-1170.
12. J Korean(2005) Comparison of Results of Electroretinogram, Fluorescein Angiogram and Color Vision Tests in Acute Central Serous Chorioretinopathy. Ophthalmol Soc Jan; 46(1):71-77.
13. Simon Haykin, (2001). Neural networks –A comprehensive foundation, Pearson Education Asia.

Author: J. David
Institute: College of Engineering, Trivandrum
Street: Sreekaryam
City: Trivandrum
Country: India
Email: daviddavisdale@yahoo.com

A Confidence Measure for Real-time Eye Movement Detection in Video-oculography

S.M.H. Jansen[1], H. Kingma[2] and R.L.M. Peeters[1]

[1] Department of Mathematics, MICC, Maastricht University, The Netherlands
[2] Division of Balance Disorders, Department of ENT, University Hospital Maastricht, The Netherlands

Abstract — **Video-oculography (VOG) is a frequently used clinical technique to detect eye movements. In this research, head mounted small video-cameras and IR-illumination are employed to image the eye. The need for algorithms to extract the eye movements automatically from the video recordings is high. Many algorithms have been developed. However, to our knowledge, none of the current algorithms, is in all cases accurate and provides an indication when detection fails. While many doctors draw their conclusions based on occasional erroneous measurement outcomes too, this can result in a wrong diagnosis. This research presents the design and implementation of a robust, real-time and high-precision eye movement detection algorithm for VOG. But most importantly, for this algorithm a confidence measure is introduced to express the quality of a measurement and to indicate when detection fails. This confidence measure allows doctors in a clinical setting to see if the outcome of a measurement is reliable.**

Keywords — **Eye movement detection, video-oculography, confidence measure, pupil detection, reliability**

I. Introduction

Medical studies of eye movement are important in the area of balance disorders and dizziness. For example, studying nystagmus (rapid, involuntary motion of the eyeball) frequently allows localization of pathology in the CNS. Nystagmus can occur with and without visual fixation. Therefore, detection of nystagmus or eye movements in general, is required in the dark and in the light.

Various methods have been developed to examine human gaze direction or to detect eye movement. However, the remaining problems in these methods are simplicity of measurement, detection accuracy and the patient's comfort. E.g., electro-oculography (EOG) [1] is affected by environmental electrical noise and drift. In the corneal reflection method [2], the accuracy is strongly affected by head movement. The main drawback of the scleral search coil technique [3], is the need for a patient to wear a relatively large contact lens, causing irritation to the eye and limiting the examination time to a maximum of about 30 minutes.

In the nineties, clinical Video Eye Trackers (c-VET) were developed. The c-Vet can be described as a goggle with infrared illumination, where small cameras have been attached to the goggle. With this construction it is possible to record a series of images (movie) while the relative position of the head and the camera remain constant. The need for algorithms to extract the eye movements automatically from the video recordings is high. However, this is not an easy task as IR-illumination results in a relatively poor image contrast. Furthermore, a part of the pupil can be covered by the eyelid, by eyelashes or reflections. Also the pupil continuously changes in size and shape. Another design issue is that the algorithm has to perform in real-time, because direct feedback with the patient is desirable.

Many algorithms have been developed, some with analytical methods and others with neural networks. However, to our knowledge, none of the current algorithms is in all cases accurate and provides an indication when detection fails. While many doctors draw their conclusions based on occasional erroneous measurement outcomes too, this can result in a wrong diagnosis.

This research presents the design and implementation of a real-time high-precision eye movement detection algorithm for VOG in combination with a confidence measure to express the reliability of the detection. By this, clinical application will gain substantial reliability.

II. Algorithm design

While the pupil is much darker than the rest of the eye, it can be detected 'easily', and is therefore a perfect marker to determine the eye movement. Because the shape and the size of the pupil vary continuously, it is necessary to determine one point in the pupil that is constant on the same position of the eye ball: the center of the pupil.

Before starting with complex time consuming calculations to find the exact center of the pupil, it is suitable to design a quick and less time consuming algorithm to approximate the location of the center of the pupil and to determine a region of interest (ROI). Consequently, applying complex calculations in the ROI is less time consuming than applying the same calculations in the original image.

Chwee Teck Lim, James C.H. Goh (Eds.): ICBME 2008, Proceedings 23, pp. 335–339, 2009
www.springerlink.com

A. Rough localization of the pupil center

By taking horizontal lines through an image recording by the c-VET, see Figure 1, a corresponding gray value pattern can be obtained. All points with a gray value lower than a certain threshold are considered to be part of the pupil.

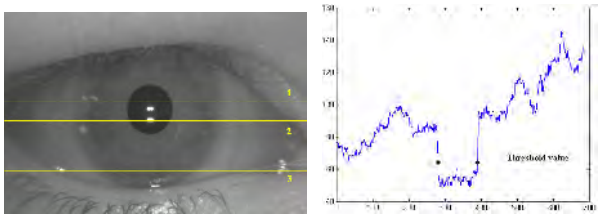


Fig. 1 Horizontal line through the pupil with corresponding RGB pattern

This threshold value is for each recording different, mainly caused by different positioning of the c-Vet. Setting this threshold by hand before every recording is time-consuming and error-sensitive. Therefore, a method was developed to determine the threshold automatically. An RGB histogram of the first image (Figure 2) is made. The small peak on the left side represents the RGB values of the pupil. By performing a local minimum search after this peak, the threshold is determined.

To approximate the center of the pupil, the method of Teiwes [4] is used. Teiwes method determines circles through points on the edge of the pupil. The left and right borders of the pupil are detected by comparing the gray value of points on horizontal lines in the image with the threshold. The center of the pupil is calculated by using the points on the left and right border of two horizontal lines, see Figure 3.

By taking the median of the outcomes for 50 randomly chosen combinations of two horizontal lines through the pupil, the center of the pupil is determined.

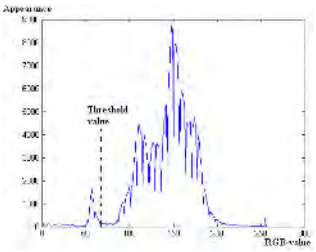


Fig. 2 Using a histogram of the RGB-values to find the threshold value

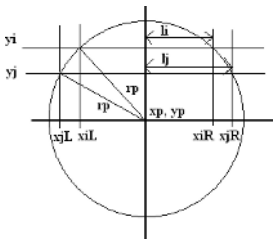


Fig. 3 Approximation of the pupil center by Teiwes method

B. Determining a region of interest

With the approximation of the pupil center point, one is able to place a window around this point, see Figure 4.

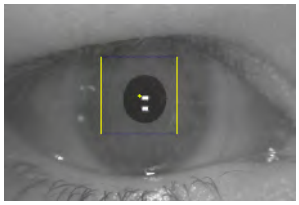


Fig. 4 A window is placed around the approximated pupil center

The window size is chosen in such a way that, in all practical situations, the pupil will fit in the window. Taking the resolution of the images into account, this led to a window size of 210x210 pixels, the ROI, which is much smaller than the original image (680x460).

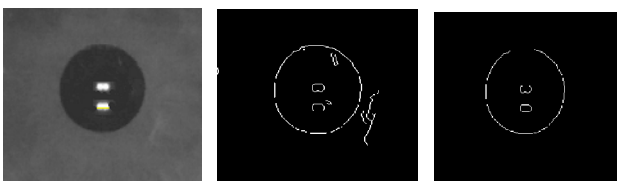
C. Edge detection

Within this ROI, an edge detection algorithm is applied. After several analyses on a dataset with artificially created pupil images, the Canny Edge Detector [5] is decided to be the most suitable edge detector for this situation.

To avoid the selection of noise, detection with a high threshold is applied. Also the 8-directional connection method is used to further delete noise, see Figure 5.

Unfortunately, a high threshold makes that a part of the pupil edge remains undetected. In Section II D it is discussed how to reconstruct the boundary of the pupil.

Even when edge detection with a high threshold is applied, the white reflections caused by the IR-light source are



(a) **(b)** **(c)**

Fig. 5 At the region of interest, displayed in (a), edge detection is applied with a low threshold in (b) and with a high threshold in (c)

still selected as edges. However, they can be filtered out with a simple analytical method. As can be seen in Figure 2, the small peak on the right represents the RGB-values of the reflections. If one or more adjacent pixels have such a high RGB-value, the edge point is deleted.

During the experiments, patients will lose their concentration and eyelids and lashes will cover a part of the pupil. This disturbs the edge detection process, see Figure 6.

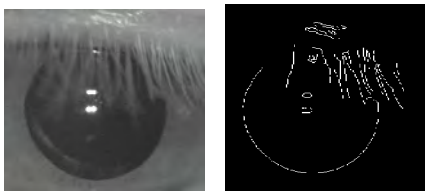


Fig. 6 Eyelashes disturb the process of edge detection

Kong and Zhang proposed an accurate method for eyelash detection [6]. In this method, as implemented, edge detection is applied to detect separable eyelashes, and intensity variances are used to recognize multiple eyelashes.

D. Reconstruction of the pupil shape

With the set of edge points found by the algorithm, it is possible to reconstruct the complete edge of the pupil by applying a stable direct least squares ellipse fit [7]. In Figure 7, an example of ellipse fitting is given.

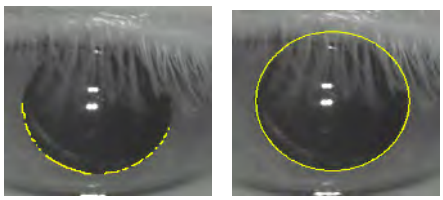


Fig. 7 Reconstruction of the pupil shape with least squares ellipse fitting

E. Feasibility check

When only a few edge points are detected and those edge points lie on one side of the pupil, it can happen that the algorithm returns an inadequate ellipse fit, see Figure 8.
A method was developed to detect those wrong ellipses. In an experimental set up, the relation between the shape and angle of the pupil and ellipse fit of two successive frames was studied. From the experiments it followed that an ellipse is generally accurately computed correct if:

- The rotation angle of the ellipse differs no more than 6.88 degrees from the previous ellipse.

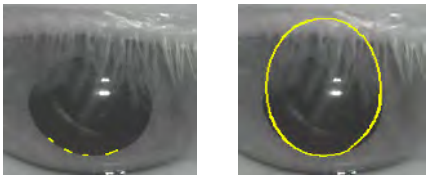


Fig. 8 Ellipse fit can fail when there are not enough edge points or the distribution of the edge points on the pupil border is not suitable

- The ratio of the two axis lengths of the ellipse differs no more than 0.1 from the ratio for the previous ellipse.

If one or both conditions are not met, a minimization procedure is started to compute an ellipse that fits the conditions and minimizes the average distance from the ellipse to the edge points. Note that this process will only work, if the data of the previous ellipse is correct. Therefore, it is necessary that, in the beginning of the measurement, the eyes of a patient are wide open. If the algorithm detects at least 10 stable pupils in a row, this procedure is started.

III. Confidence measure

Many authors, e.g. [8, 9], have described an algorithm to find the pupil center in images. However, to our knowledge, none of these authors paid attention to the reliability of the outcome of such a measurement. In many cases, the average error of the algorithm was given, but none of the authors gave information about what happens in situations when the measurement is wrong. In some situations it is impossible, even for humans, to detect the exact pupil center. In other situations the detection process is hampered by many eyelashes and it is not unlikely that the algorithm makes an error in the exact location of the pupil center. In those situations, doctors would like to know that the measurement has failed. This will help to prevent them to draw conclusions based on an erroneous measurement.

The proposed algorithm, described in the previous section is designed in such a way that it will be possible to design a confidence measure which makes use of data from the pupil detection algorithm. Some aspects of the algorithm contain information on the likelihood that pupil detection will fail.

First, the quality of the image is assessed by determining the number of pixels that contain noise, as found by the edge detection algorithm. Second, the number of pixels with eyelashes that have been filtered out are used. More eyelashes will decrease the reliability of the measurement. A third aspect concerns the number of detected edge points. More such points increase the confidence of the measurement. Another feature is the distribution of the edge points on the pupil boundary. It is better that a few edge points are

located on all sides of the pupil border than many edge points all on one side of the pupil. Therefore, the size of the largest gap between the edge points is used for the confidence measure. The last information that is derived from the algorithm concerns consistency. If the ellipse fit does not differ much from the previous ellipse, it is considered more reliable. Summarizing, the design of the confidence measure takes the following features into account.

- Number of pixels in ROI containing noise
- Number of pixels in ROI containing eyelashes
- Number of edge points that is found
- Largest gap between edge points
- Difference in angle with the previous ellipse fit
- Difference in axis ratio with the previous ellipse fit

To express the relation of these features with the outcome and accuracy of a measurement, certain weights have to be assigned to each feature. In this research it was chosen to train a neural network to assess these weights.

IV. Experimental results

A. Test environment

To design the confidence measure and to validate the algorithm, a dataset of 50.000 images was created. This dataset exists of 25.000 images where the pupil center can be easily detected by humans (part A) and 25.000 images where it is harder or (almost) impossible to locate the exact pupil center by visualization (part B). In all images, the location of the (expected) pupil center was annotated by human experts. Also the Helmholtz coordinates of the pupil center in the images are determined using the scleral search coil technique simultaneously with the c-Vet recordings. Patients with conjugate eye movements of the left and right eye wore a contact lens in one eye during the experiments. The recording of the eye without the contact lens was used for the dataset. Patients were tested on saccadic and persuit eye movements and the head impulse test was performed.

B. Performance of the algorithm

To express the quality of the algorithm, the pupil centers found by the algorithm are compared with the experts annotated pupil centers and with the outcome of the scleral search coil technique. In Figure 9, the performance of the algorithm on images of part A and B are shown.

The average error in the detected pupil location in the images in part A is 1.7 pixels, with a maximum error of 14 pixels. The average error in the images of part B is 3.3 pixels with a maximum of 22 pixels.

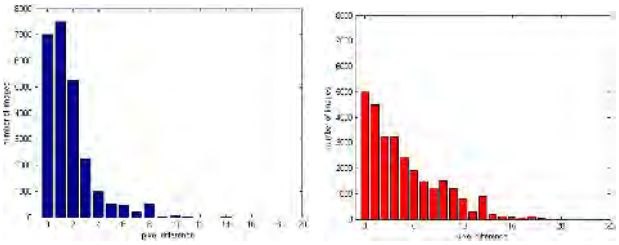


Fig. 9 Performance of the algorithm on part A and part B of the dataset

C. Performance of the confidence measure

For the confidence measure, a neural network was trained with 6 input parameters, as described in Section III, and 1 output parameter, the error of the pupil center. The idea is that the neural network predicts the accuracy of the pupil center algorithm. The result of the neural network was validated with a test set, see Table 1.

Table 1 Result of confidence measure in relation with real error (in %).

Conf. measure / Real error	0	1	2	3	4	5	6	7	8	9	10	10+
0	58.1	24.1	13.8	7.1	6.8	6.8	6.4	4.4	2.6	1.4	2.7	4.1
1	24.5	48.7	23.2	9.2	12.7	13.5	2.4	4.7	0.1	0.7	3.0	0.6
2	16.0	15.8	24.9	29.4	11.9	12.4	4.5	5.9	0.0	0.2	2.1	0.1
3	1.3	10.8	24.3	33.4	20.0	8.9	3.0	6.3	3.1	0.5	2.9	0.4
4	0.0	0.4	11.6	19.0	40.5	11.2	2.6	8.6	14.5	0.6	3.4	0.7
5	0.1	0.2	2.1	1.6	5.7	22.7	3.7	17.6	20.0	0.3	2.7	2.4
6	0.0	0.0	0.1	0.3	2.2	18.6	22.5	14.5	16.2	0.2	2.8	3.2
7	0.0	0.0	0.0	0.0	0.1	4.5	15.1	21.8	12.5	2.4	11.0	10.4
8	0.0	0.0	0.0	0.0	0.1	0.9	19.3	11.4	23.8	29.3	24.6	11.5
9	0.0	0.0	0.0	0.0	0.0	0.5	18.4	4.6	0.8	35.6	19.3	17.4
10	0.0	0.0	0.0	0.0	0.0	0.0	1.7	0.2	0.1	24.5	18.8	20.6
10+	0.0	0.0	0.0	0.0	0.0	0.0	0.4	0.0	0.3	4.3	6.7	28.6

V. Conclusions

Tests have shown that the algorithm of this paper can find the pupil center in images that are not extremely hampered by eyelashes and eyelids with a high accuracy. On images where the pupil is covered by many eyelashes, a pupil center is found with lower accuracy. When the accuracy can not be guaranteed, this is well expressed by the confidence measure. If the confidence measure expresses a high accuracy, a doctor can rely on the measurement. Otherwise, he needs to be on his guard.

References

1. Barber H, Stockwell C (1980) Manual of Electronystagmography. The C.V. Mosby Company, 2nd edition
2. Carpenter R (1988) Movement of the eyes. Pion Limited, 2nd edition

3. Robinson D (1963) A method of measuring eye movement using scleral search coil in a magnetic field. IEEE Trans Biomed Electr, 10:137-145
4. Teiwes W (1991) Video-Okulographie. PhD-thesis, Berlin, 74-85
5. Canny J (1986) A Computational Approach To Edge Detection. IEEE Trans. Pattern Analysis and Machine Intelligence, 8:679-714
6. Kong W, Zhang D (2003) Detecting eyelash and reflections for accurate iris segmentation. Int. J. Pattern Recognition Artif. Intell. 17 (6) 1025-1034
7. Fitzgibbon A, Pilu A, Fisher R (1996) Direct least-square fitting of Ellipses. International Conference on Pattern Recognition, Vienna
8. Kim S et al. (2005) A Fast Center of Pupil Detection Algorithm for VOG-Based Eye Movement Tracking. Conf Proc IEEE Eng Med Biol Soc. 3:3188-91
9. Cho J. et al. (2004) A pupil center detection algorithms for partially-covered eye image. Conf Proc. IEEE Tencon, 183- 186 Vol. 1

Development of Active Guide-wire for Cardiac Catheterization by Using Ionic Polymer-Metal Composites

B.K. Fang[1], M.S. Ju[2] and C.C.K. Lin[3]

[1, 2] Dept. of Mech. Engineering, National Cheng Kung University, Tainan 701, Taiwan
[3] Dept. of Neurology, National Cheng Kung University Hospital, Tainan 701, Taiwan

Abstract — **Due to the inconvenience in passing bifurcated blood vessels via changing curvature of guide-wires during surgery, active catheter or guide-wire systems are developed recently. For lightweight and large bending deformation, the ionic polymer metal composites (IPMCs) have been employed in many biomedical applications. For controlling an IPMC-based active cardiac guide-wire system, the goal of this research is to develop methods that can actuate an IPMC and detect its deformation without extra sensors. The method is to parallel a reference IPMC with an actuated IPMC. Then a mixed driving signal that consisted of high and low frequencies was applied to drive the IPMCs. The low frequency signal makes the IPMC to deform and change its surface electrical resistance, while the high frequency signal retains the deformation information. By utilizing a lock-in amplifier to demodulate the high frequency signal, the deformation can be measured. When low frequency actuation signal is absent, the sensing signal follows the deformation well. However, when sinusoidal or square wave actuation signals of frequency 0.1Hz was applied transient error appeared. The error may due to the mismatch of electric resistances and capacitances between the actuation and reference IPMCs. However, when the frequency of actuating signal was reduced to 0.01Hz, the transient error disappeared. For practical applications like catheter guide wire, a low frequency actuation signal induces a large deformation so the method might be feasible for simultaneously sensing and actuating an IPMC.**

Keywords — **Ionic polymer-metal composites (IPMC), actuator, active catheter, control, guide wire.**

I. Introduction

For diagnosing or treating coronary heart diseases, cardiac catheterization is a common procedure (Fig. 1). To improve the inconvenience in changing guide-wires during surgery to pass bifurcated blood vessels, there have been many studies on active catheter or guide-wire systems, which can tune the tip-curvature of guide-wire or catheter in real-time [1-4].

Due to lightweight, large bending deformation, biocompatibility and low power consumption, ionic polymer metal composites (IPMCs) have high potential for many biomedical applications. The IPMC is a proton exchange membrane (PEM) plated with platinum or gold on both surfaces and typically working in a hydrated condition. When a electric potential is applied on the electrode pair, the hydrophilic cations within the IPMC migrate to the cathode of potential and make an unsymmetrical swelling of PEM. Then the IPMC bends toward the anode. In the reverse way, bending of the IPMC also induces a transient electric potential which can be utilized as a sensing signal. Therefore, the characteristics of IPMC are similar to piezoelectric materials which can be served as an actuator and a sensor [5-7].

In general, an actuated IPMC has nonlinear and time-variant behaviors, e.g. hysteresis and back relaxation, which deteriorate precision of the control system. To solve these problems, using feedback control schemes are common strategies [8, 9]. For position or force controls, the feedback signals are mostly measured by using bulky sensors, e.g. laser displacement sensor, CCD camera and load cell. For this reason, the applications of feedback control are restrictive for bulky size of system. Therefore integrating a sensory function into the actuated IPMC without using extra sensors is an important subject in this area.

In this research, the ultimate goal is to develop an IPMC-based active cardiac guide wire system (Fig. 1). In previous work, a position feedback control scheme was applied to actuate an IPMC [10]. For implementing the control scheme to our application, the next objective is to combine position sensing method with the actuation of IPMC.

The goal of this study is to develop a sensor-free system to measure the tip position and to actuate the IPMC simultaneously.

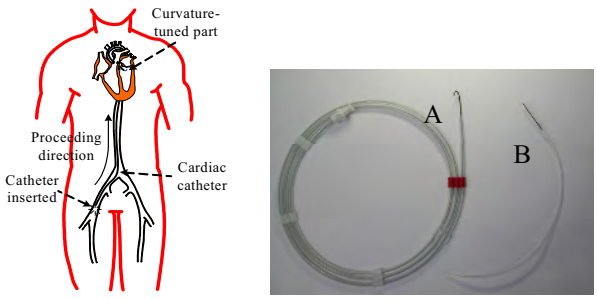


Fig. 1 Sketch of cardiac catheterization with active guide-wire. A-traditional guide-wire, B-IPMC based active guide wire

Chwee Teck Lim, James C.H. Goh (Eds.): ICBME 2008, Proceedings 23, pp. 340–343, 2009
www.springerlink.com

II. METHODS

Depending on its size, the bandwidth of an IPMC is generally lower than several hundred Hzs, so a driving voltage of several thousand Hzs does not actuate an IPMC [10, 11]. In this study, a driving signal, V_{dm}, that consisted of a low frequency (0.01~10Hz) actuating signal, V_{act}, and a high frequency (5kHz) carrier signal, V_{car}, was used to actuate the IPMC and to measure the deformation, simultaneously(Eq. 1). In Eq. (1), v_{act}, v_{car} are amplitudes, and ω_{act}, ω_{car} are frequencies. With V_{dm}, the deformation of the IPMC follows the waveform of V_{act}, and V_{car} carries the deformation signal due to the changes of surface resistances.

$$V_{dm} = V_{act} + V_{car} = v_{act}\sin(\omega_{act}t) + v_{car}\sin(\omega_{car}t) \quad (1)$$

To eliminate the noise from environments, a fixed reference IPMC connected parallel with the actuated IPMC was employed (Fig. 2). The equivalent circuit shown in Fig. 3 is similar to a Wheatstone bridge circuit, in which V_{a1} and V_{a2} are voltage signals, R_a, R_b, R_{am}, and R_{bm} are electrical resistances, C_p and C_{pm} are capacitances. The sensing signal $V_{aa}(t)$ from the connected IPMCs can be written as

$$V_{aa}(t) = V_{a1} - V_{a2} = \left(\frac{R_b + 1/C_p s}{R_a + R_b + 1/C_p s} - \frac{R_{bm} + 1/C_{pm} s}{R_{am} + R_{bm} + 1/C_{pm} s} \right) V_{dm} \quad (2)$$

Because V_{act} in V_{dm} could be treated as a low frequency noise in $V_{aa}(t)$, the high frequency band signals in V_{a1} and V_{a2} are first separated by using a high-pass filter. Eq. (2) can then be further simplified as:

$$V_{aa}'(t) = \left(\frac{R_b}{(R_a + R_b)} - \frac{R_{bm}}{(R_{am} + R_{bm})} \right) \left(v_{car}\sin(\omega_{car}t) \right) \quad (3)$$

Furthermore, multiply Eq. (3) by $v_c\sin(\omega_c t)$ and expend yield:

$$V_{aa}''(t) = \left(v_{car}\sin(\omega_{car}t) \right) V_{aa}'(t)$$
$$= \frac{v_{car}^2}{2} \left(\frac{R_b}{(R_a + R_b)} - \frac{R_{bm}}{(R_{am} + R_{bm})} \right) \left(1 - \cos(2\omega_{car}t) \right) \quad (4)$$

The high frequency band $\cos(2\omega_c t)$ in $V_{aa}''(t)$ can be eliminated by using a low-pass filter to yield the demodulated sensing signal $V_{sen}(t)$. $V_{sen}(t)$ is related to the amplitude of carrier signal and electrode resistances by:

$$V_{sen}(t) = \frac{v_{car}^2}{2} \left(\frac{R_b}{(R_a + R_b)} - \frac{R_{bm}}{(R_{am} + R_{bm})} \right) \quad (5)$$

The surface resistances of the actuated IPMC, after deformation, can be written as:

$$\begin{cases} R_a = R_{a0} + \Delta R_a \\ R_b = R_{b0} + \Delta R_b \end{cases} \quad (6)$$

where R_{a0}, R_{b0} are initial resistance of the IPMC, and ΔR_a, ΔR_b are changes of resistances due to deformation. R_{a0}, R_{b0}, R_{am}, R_{bm} are equal to a constant R_i. Substitute Eq. (6) into Eq. (5) and simplify it to yield:

$$V_{sen}(t) \approx \frac{v_{car}^2}{8} \frac{\Delta R_b - \Delta R_a}{R_i} \quad (7)$$

where ΔR_a, ΔR_b are assumed much smaller than R_i. Eq. (7) showed that $V_{sen}(t)$ is proportional to the difference between variations of resistance at the compression and tension surface of the ated IPMC.

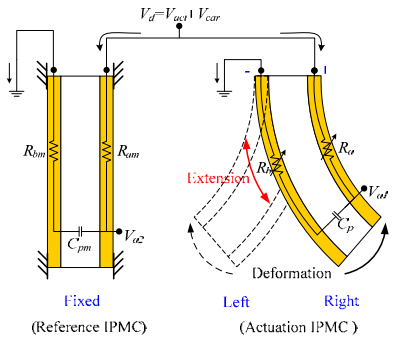


Fig. 2 Parallel connection between the reference and the actuated IPMC

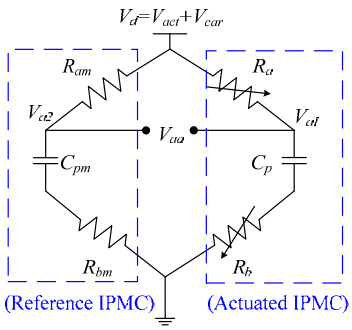


Fig. 3 Equivalent circuit of reference IPMC paralleled with reference IPMC

Two encapsulated IPMCs and an experimental setup were implemented to verify the feasibility of the proposed method. Dimension of the two IPMCs are 30mm in length, 5mm in width, 0.2mm in thickness (Fig. 4). The values of electrical resistances are close to 10Ω, and the values of

capacitances are 1.8mF. The sensing method was realized by using an analog circuit (Fig. 5). In the experimental setup a laser displacement sensor is utilized to detect the deformation of the actuated IPMC at the end, and an electromagnetic shaker controlled by the displacement feedback is used to deform the IPMC for actuation-free tests (Fig. 6).

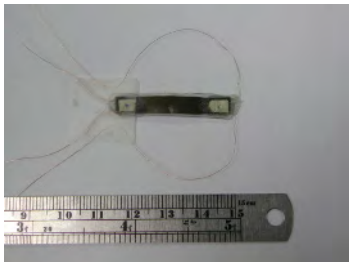


Fig. 4 Sample of IPMC manufactured in this study

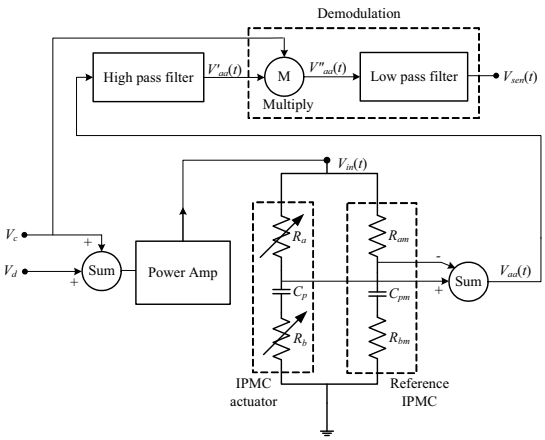


Fig. 5 Diagram of the sensing circuit

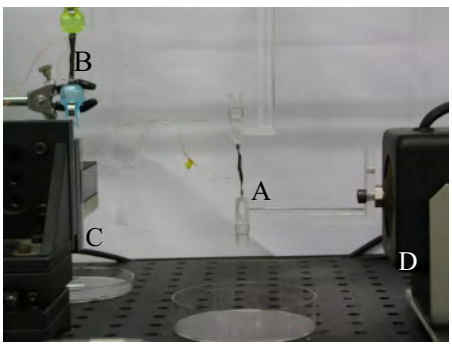


Fig. 6 Experimental setup. A-actuated IPMC, B-reference IPMC, C-Laser displacement sensor, D-electromagnetic shaker

III. Results and Discussions

Typical testing results are depicted in Fig. 7. A tip displacement of amplitude 2mm deformed by the shaker induced a sensing signal of amplitude 5mV even though the waveforms are slightly different. A 4th-order polynomial was fitted to the relationship between sensing signals and deformations (Fig. 8). From the results, sensing deformation of IPMC with the method proposed in this study was achieved successfully.

However, while applying a 0.1Hz low frequency actuating signal into the driving signal and restricting the displacement of the actuated IPMC, the sensing signal was coupled with noise that increased with the amplitude of actuating signal (Fig. 9). This may due to the electric resistances and capacitances of the reference and actuated IPMCs are not equal exactly, so the transient error was exhibited to the sensing signal. Comparing results of actuating signals with frequencies of 0.1Hz and 0.01Hz, the noise for the 0.01Hz actuation is much smaller than that of the 0.1Hz (Fig. 10). It indicates that deformation of actuated IPMC can be measured by current method if the actuating frequency is lower than 0.01Hz.

For an actuated IPMC, the longer DC actuating time induces the larger deformation [12]. So the sensing approach proposed in this study might be feasible for an IPMC despite the limitation of low actuating frequency.

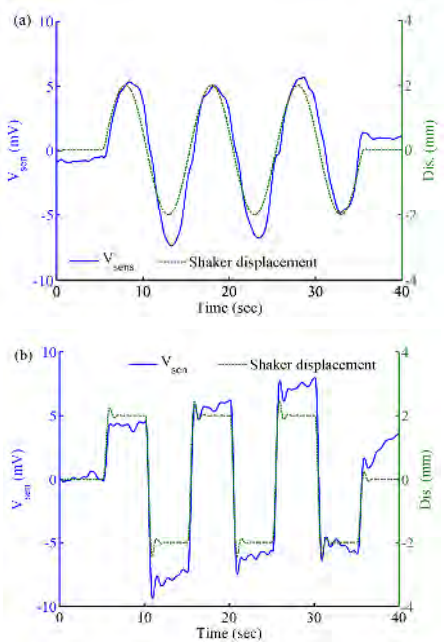


Fig. 7 Sensing signals in response to deformation induced by the shaker, sinusoidal (a) and square wave (b)

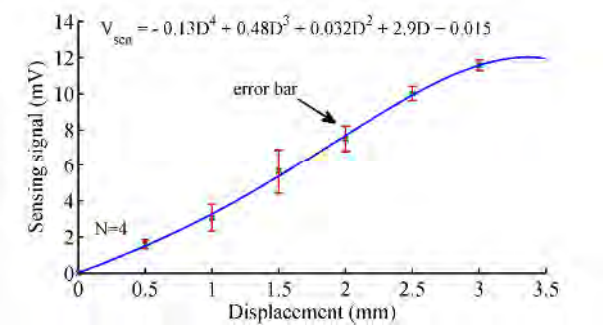


Fig. 8 Relationship between deformation and sensing signal

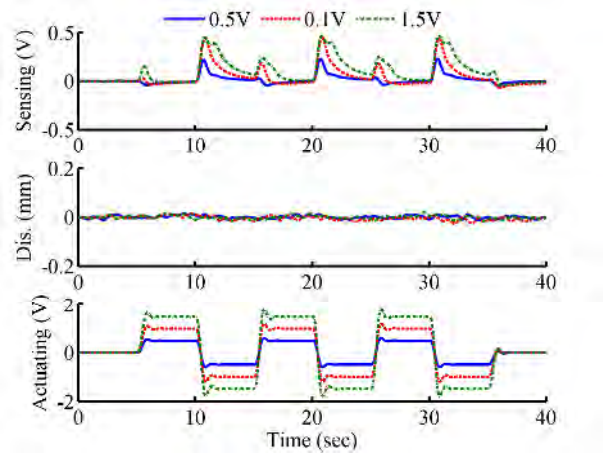


Fig. 9 Sensing signals in response to 0.1Hz square-wave actuating signals of different amplitudes

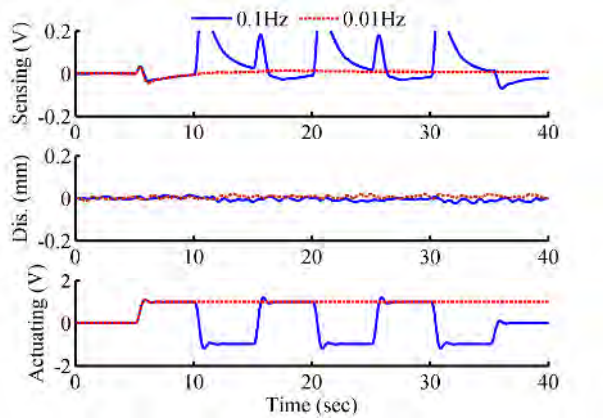


Fig. 10 Comparison between low (0.01Hz) and high (0.1Hz) frequency actuating results

IV. Conclusions

A method of sensing deformation and actuating of IPMC simultaneously was developed and tested. The results revealed that the method can be applied for IPMC at low frequency of 0.01Hz. For further development, the degree of deformation of IPMC is much concerned than the frequency of manipulation. The developed method might be feasible for a large deformed IPMC induced by DC actuating signal.

Acknowledgment

This work is supported by a grant from ROC National Science Council. The contract number is NSC-95-2221-E-006-009-MY3.

References

1. Mineta T, Mitsui T, Watanabe Y et al. (2002) An active guide wire with shape memory alloy bending actuator fabricated by room temperature process. Sens Actuator A-Phys 97-98 : 632-637
2. Ishiyama K, Sendoh M, Arai KI (2002) Smart actuator with magnetoelastic strain sensor. J Magn Magn Mater 242: 41-46 Part 1
3. Haga Y, Muyari Y, Mineta T et al. (2005) Small diameter hydraulic active bending catheter using laser processed super elastic alloy and silicone rubber tube, 3rd IEEE/EMBS Special Topic Conference, Microtechnology in Medicine and Biology, Oahu, HI, pp 245-248.
4. Guo SX, Nakamura T, Fukuda T (1996) Micro active guide wire using ICPF actuator-characteristic evaluation, electrical model and operability evaluation, IEEE IECON 22nd International Conference, pp.1312-1317.
5. Shahinpoor M, Kim KJ (2001) Ionic polymer-metal composites: I. Fundamentals. Smart Mater Struct 10:819-833
6. Bonomo C, Fortuna L, Giannone P et al. (2005) A method to characterize the deformation of an IPMC sensing membrane. Sens Actuators A: Phys 123-24:146-154
7. Biddiss E, Chau T (2006) Electroactive polymeric sensors in hand prostheses: Bending response of an ionic polymer metal composite. Med Eng Phys 28(6):568-578
8. Lavu BC, Schoen MP, Mahajan A (2005) Adaptive intelligent control of ionic polymer-metal composites. Smart Mater Struct 14(4):466-474
9. Arena P, Bonomo C, Fortuna L et al. (2006) Design and control of an IPMC wormlike robot. IEEE Trans Syst Man Cybern Part B-Cybern 36(5):1044-1052
10. Fang BK, Ju MS, Lin CCK (2007) A new approach to develop ionic polymer-metal composites (IPMC) actuator: Fabrication and control for active catheter systems. Sens Actuators A: Phys 137(2):321-329
11. Paquette JW, Kim KJ (2004) Ionomeric electroactive polymer artificial muscle for naval applications. IEEE J Ocean Eng 29(3):729-737
12. Pandita SD, Lim HT, Yoo YT et al. (2006) The actuation performance of ionic polymer metal composites with mixtures of ethylene glycol and hydrophobic ionic liquids as an inner solvent. J Korean Phys Soc 49(3):1046-1051

Design and Development of an Interactive Proteomic Website

*K. Xin Hui[1], C. Zheng Wei[2], Sze Siu Kwan[3] and R. Raja[4]

[1,2&4] Biomedical Informatics Engineering, Temasek Polytechnic, Singapore
[3] Asst. Professor, SCBS, Nanyang Technological University, Singapore.

Abstract — **The interactive proteomic core facility website was done with Apache, PHP & MySQL. This website aims to allow researchers to submit information about their samples via a webpage and at the same time, provides clear and accurate cost of the experiment. This would minimize information mix up and provides a platform for them to manage their expenses better. The server program would process the information sent and return a generated code about their sample. The end results would be stored into our database and our servers would email users to download the results from our servers. Users would have to register first before they could start using our services and a tutorial (FAQ) is provided to facilitate the users. This website would increase the efficiency of work done, reducing the trouble on both sides. User now can submit entry anytime at anywhere and the staff can manage the submission better from the lab. The staff will also gain a much more manageable system for them to trace or perform any calculation. Errors like missing forms; unreadable handwriting and etc will be reduced to the minimum.**

Keywords — **Proteomics, information processing, database.**

I. Introduction

Proteomic is a study of protein's structures and function. As we know protein is essential for all living organisms because they are the main component of the physiological metabolic pathway of cells. [1] Protein is a very complex structure form by many peptides or amino acids, thus identifying them are not an easy task.

At Nanyang Technology University (NTU)'s proteomics facility, they are equipped with a high-tech proteomic facility mass spectrometry lab which can carry out protein test like "Protein Identification", "Mass Weight determination" and "Chromatography-mass Spectrometry (LC-MS)". With these services protein can be easily analysis in the lab with some specialist machines.

Most proteomic researcher does not have these equipments to carry test on their own. So they have to send all samples to the proteomic facility. A better platform is needed to interact between researcher and service provider, hence an interactive proteomic website needed to be create to handle sending and receiving data or information.

II. Flow Chart

Module [2]-[18]	Principle
PHP	- Open Source - Used to write our webpage and to create website functions such as login and user profile update - Highly flexible: able to use together with JavaScript, HTML & any database systems - Widely supported by many online communities and reference materials
MySQL	- Open Source - Database for our system - Used to store information and to be used with the website
Apache Server	- Open Source - The program makes the system into a website server - Highly customizable: able to configure to suit the website's demand - Widely used; internet companies such as Google & Yahoo! uses Apache
MySQL Navicat Lite 8.0	- Free to use - Used to edit, create and maintain MySQL database - Able to remote connect via Server's IP address - Fast & easy to use
Adobe Dreamweaver CS3	- To create websites - Easier to develop websites with Dreamweaver as there are many inbuilt functions - Able to view our websites as we create it - Also enable us to connect to the database
Macromedia Fireworks 8	- Used hand in hand with Flash 8 - To create images for the website and also for the flash animations - To edit some of the image background to transparent in order to prevent white background to overlap other words or images.
Macromedia Flash 8	- To create flash web links - Makes the website more colorful with nicer looking buttons

Chwee Teck Lim, James C.H. Goh (Eds.): ICBME 2008, Proceedings 23, pp. 344–347, 2009
www.springerlink.com

Work Flow

The work flow for the development of this website project can be grouped into seven stages.

First Stage: Defining the Concept

At this stage the project is defined. The project scope is discussed and it is designed with the needs and demands of the end users in mind

Second Stage: Initialization

The initialization stage begins by deciding on the technology used. Firstly, a research was done on the available options. This includes researching on the software used to code the website and the type of programming language used. It was decided on PHP, MySQL and Apache because it was cheaper and widely supported. The necessary software was then installed.

Third Stage: Design

At this stage, the layout for the website was decided. Essential functions for this website were also decided at this stage. It is important to decide on those that are relevant, suitable and practical so as to suit the demands and the ease of use.

Fourth Stage: Development & Debugging

At this stage, we begin the coding of the website. Developing under local host, it was to minimize the number of error and bugs that are persistent on the system before posting on the server. Common bugs and errors that were usually spotted were incomplete database queries and white space. As the project continues, there were changes made to the design. Certain planned functions were either removed or improved on.

Fifth Stage: Finalizing the Concept

The prototype was shown. During this stage, a third party's point of view is essential to this project, due to the fact that they are the target users. Their comments and ideas are incorporated into making this website better.

Sixth Stage: Development & Debugging (live)

This is a repeat of the fourth stage. On the other hand, at this stage, it is tested first on local host and then tested on the live server.

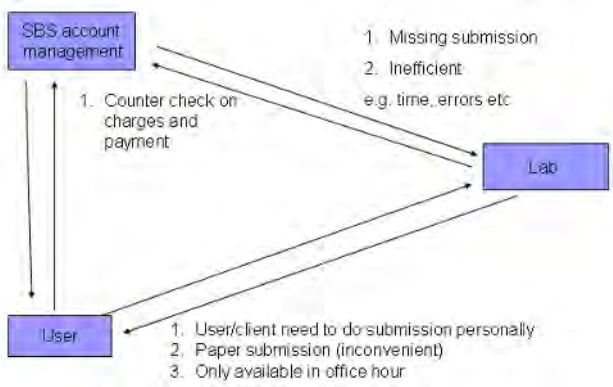
Final Stage: Launch

The completed programme is launched to the server.

III. Results

In the diagram on the right show the old system that is practice by the proteomic facility lab. There are many inconvenient causes by this system.

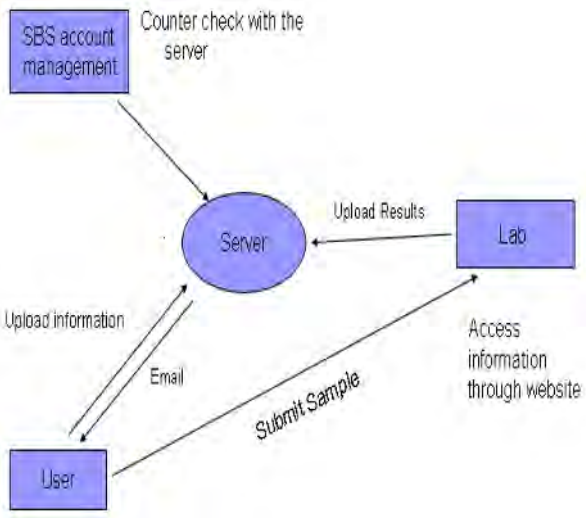
With this system, the three parties which are the lab, the SBS account management and user (researcher) need to meet up personally with each other in order to get the work-done.



With this system, error and problem usually occur as stated in the diagram for all three parties.

With this new interactive proteomic website is setup (server) shown in the diagram on the right, we can solve the above problem and simplify the procedure of the whole process.

The website (server) acts as a main brain of the system. All the information is send directly to the server with is 24/7 operated. System is automated which help to cut down time and cost needed compare to the old system.



Features

Admin

Admin home page which includes

- Search for sample using the search bar
- Sign up new admin
- View incomplete submission/filter completed submission
- View mass weight/protein id/user's detail with more information
- Update payment



Admin can

- Upload results to the web for the user to download
- Sent email to notify user

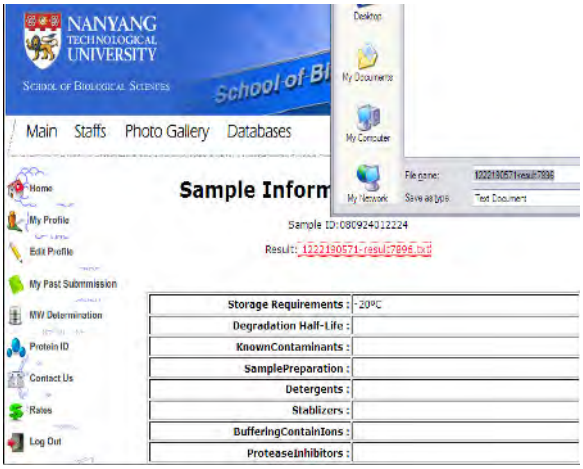
User can

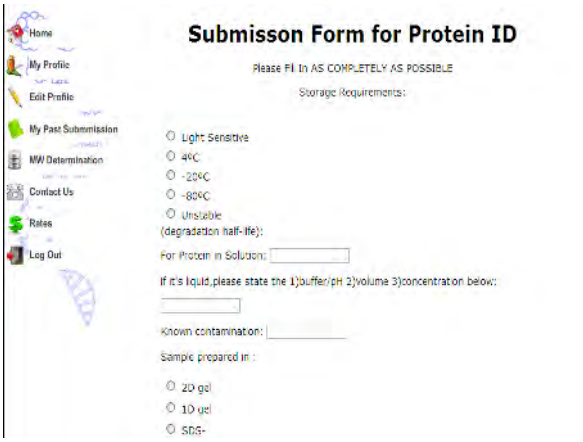
- Download the result after they login their account



User

Submission and calculation

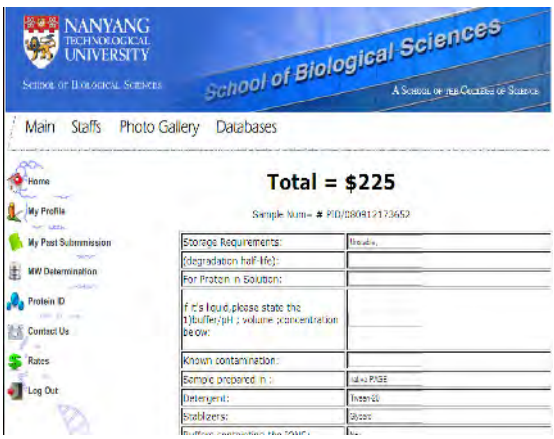




User can

Submit their sample information form (mass weight/ protein id)

- Cost calculation of the service will be done
- Detail will be show for and edit before confirmation



Records

User can view

- Sample reference no.
- Status (Complete/Incomplete)
- Cost
- Payment (Paid/Pending)
- Full detail by clicking "View"

User also can

Update file (image or text) by clicking "Update File"

IV. Discussion & Conclusion

Minimize human related errors

- Computerized forms removes unreadable handwriting
- Inbuilt program prevents important fields from not filling up
- Makes data analyzing faster and efficient as there's little need to call back to double confirm

Saves cost

- The manpower in the lab can be redeployed to other areas, reducing unused manpower

Convenient

- Reduces the number of unnecessary trips down to the lab. Example: a researcher would have to make multiple trips if he could not submit his form as the staff is missing or he would have to make a advance appointment to arrange a time to come down to the lab.
- Reduce the demand of sending emails or making phone calls to arrange appointments or sample pick up
- Digitalized database of received forms makes it possible to make back up and to change address of business easily

Acknowledgment

We acknowledge with thanks the management of NTU & Temasek Polytechnic for the opportunity provided to create, design and develop an interactive proteomic website for mass spectrophotometric analysis.

References

1 Naramore, E (2004). Beginning PHP5, Apache, and MySQL Web Development, Apress,
2 Valade, J (2005). PHP & MySQL Everyday Apps for Dummies, Wiley Publishing.
3 Babin, L(2005), PHP 5 Recipes: A Problem-Solution Approach, Apress.
4 Williams, HE, and Lane, D (2004). Web Database Applications with PHP and MySQL, 2nd Edition, O'Reilly Media, Inc.,
5 Finkelstein, E, and Leete, G. (2005) Macromedia Flash 8 for Dummies, Wiley Publishing.
6 Bride, Mac, Teach Yourself Flash 8, Teach Yourself
7 Darie, C, and Bucica, M(2004). Beginning PHP 5 and MySQL e-Commerce: from Novice to Professional, Apress.
8 Kent, A, Powers, D, and Andrew, R (2004) PHP Web Development with Macromedia Dreamweaver MX 2004, Apress.
9 Gilmore, W.J (2008). Beginning PHP and MySQL 5: from Novice to Professional, 3rd Edition, Apress.
10 Bardzell, J(2005). Macromedia Dreamweaver 8 with ASP, Cold Fusion and PHP, Macromedia Press.
11 Cogswell, J (2003). Apache, MySQL and PHP Web Development All-in-one Desk Reference for Dummies, Wiley Publishing, 2003
12 Davis, M E and Phillips, J A (2006). Learning PHP and MySQL, O'Reilly Media, Inc.
13 Harris, A. (2004), PHP5/MySQL Programming for the Absolute Beginner, 1st Edition, Course Technology PTR.
14 Hughes, S. and Zmievski, A (2000). PHP Developer's Cookbook, 1st Edition, SAMS.
15 Sklar, D and Trachtenberg, A (2002). PHP Cookbook, O'Reilly Media, Inc.
16 Converse, T., Park, J. and Morgan, C (2004). PHP5 and MySQL Bible, Wiley Publishing.
17 "PHP Tutorial" http://w3schools.com/php/default.asp (25 April 2008 –1 September 2008)
18 Proteomics – Wikipedia http://en.wikipedia.org/wiki/Proteomics (9 August 2008)

Author: Dr. R. Raja
Institute: Temasek Polytechnic
Street: Tampines Avenue 1
City: Tampines
Country: Singapore 529757
Email: raja@tp.edu.sg

A New Interaction Modality for the Visualization of 3D Models of Human Organ

L.T. De Paolis[1,3], M. Pulimeno[2] and G. Aloisio[1,3]

[1] Department of Innovation Engineering, Salento University, Lecce, Italy
[2] ISUFI, Salento University, Lecce, Italy
[3] SPACI Consortium, Italy

Abstract — **The developed system is the first prototype of a virtual interface designed to avoid contact with the computer so that the surgeon is able to visualize models of the patient's organs more effectively during surgical procedure. In particular, the surgeon will be able to rotate, to translate and to zoom in on 3D models of the patient's organs simply by moving his finger in free space; in addition, it is possible to choose to visualize all of the organs or only some of them. All of the interactions with the models happen in real-time using the virtual interface which appears as a touch-screen suspended in free space in a position chosen by the user when the application is started up. Finger movements are detected by means of an optical tracking system and are used to simulate touch with the interface and to interact by pressing the buttons present on the virtual screen.**

Keywords — **User Interface, Image Processing, Tracking System.**

I. Introduction

The visualization of 3D models of the patient's body emerges as a priority in surgery both in pre-operative planning and during surgical procedures.

Current input devices tether the user to the system by restrictive cabling or gloves.

The use of a computer in the operating room requires the introduction of new modalities of interaction designed in order to replace the standard ones and to enable a non-contact doctor-computer interaction.

Gesture tracking systems provide a natural and intuitive means of interacting with the environment in an equipment-free and non-intrusive manner. Greater flexibility of action is provided since no wired components or markers need to be introduced into the system.

In this work we present a new interface, based on the use of an optical tracking system, which interprets the user's gestures in real-time for the navigation and manipulation of 3D models of the human body.

The tracked movements of the finger provide a more natural and less-restrictive way of manipulating 3D models created using patient's medical images.

Various gesture-based interfaces have been developed; some of these are used in medical applications.

Grätzel et al. [1] presented a non-contact mouse for surgeon-computer interaction in order to replace standard computer mouse functions with hand gestures.

Wachs et al. [2] presented "Gestix", a vision-based hand gesture capture and recognition system for navigation and manipulation of images in an electronic medical record database.

GoMonkey [3] is an interactive, real time gesture-based control system for projected output that combines conventional PC hardware with a pair of stereo tracking cameras, gesture recognition software and customized content management system.

O'Hagan and Zelinsky [4] presented a prototype interface based on tracking system where a finger is used as a pointing and selection device. The focus of the discussion is how the system can be made to perform robustly in real-time.

O'Hagan et al. [5] implemented a gesture interface for navigation and object manipulation in the virtual environment.

II. Technologies used

In the developed system we have utilized OpenSceneGraph for the construction of the graphic environment and 3D Slicer for building the 3D models starting from the real patient's medical images.

OpenSceneGraph [6] is an open source high performance 3D graphics toolkit used by application developers in fields such as visual simulation, computer games, virtual reality, scientific visualization and modeling. The toolkit is a C++ library and is available on multiple platforms including Windows, Linux, IRIX and Solaris.

3D Slicer [7] is a multi-platform open-source software package for visualization and image analysis, aimed at computer scientists and clinical researchers.

The platform provides functionality for segmentation, registration and three-dimensional visualization of multi-modal image data, as well as advanced image analysis algo-

Chwee Teck Lim, James C.H. Goh (Eds.): ICBME 2008, Proceedings 23, pp. 348–350, 2009
www.springerlink.com

rithms for diffusion tensor imaging, functional magnetic resonance imaging and image-guided therapy.

Standard image file formats are supported, and the application integrates interface capabilities with biomedical research software and image informatics frameworks.

The optical tracking system used in this application is the Polaris Vicra of the NDI. The Polaris Vicra [8] is an optical system that tracks both active and passive markers and provides precise, real-time spatial measurements of the location and orientation of an object or tool within a defined coordinate system.

The system tracks wired active tools with infra-red light-emitting diodes and wireless passive tools with passive reflective spheres. With passive and active markers, the position sensor receives light from marker reflections and marker emissions, respectively.

The Polaris Vicra uses a position sensor to detect infra-red-emitting or retro-reflective markers affixed to a tool or object; based on the information received from the markers, the position sensor is able to determine position and orientation of tools within a specific measurement volume.

The system is able to track up to 6 tools (maximum 1 active wireless) with a maximum of 32 passive markers in view and the maximum update rate is 20 Hz.

The systems can be used in a variety of surgical applications, delivering accurate, flexible, and reliable measurement solutions that are easily customized for specific applications.

III. The Developed Application

The developed system is the first prototype of a virtual interface designed to avoid contact with the computer so that the surgeon can visualize models of the patient's organs more effectively during the surgical procedure.

A 3D model of the abdominal area, reconstructed from CT images, is shown in Figure 1 using the user interface of the 3D Slicer software.

In order to build the 3D model from the CT images some segmentation and classification algorithms were utilized.

The Fast Marching algorithm was used for the image segmentation; some fiducial points were chosen in the interest area and used in the growing phase.

After a first semi-automatic segmentation, a manual segmentation was carried out.

All of the interactions with the models happen in real-time using the virtual interface which appears as a touch-screen suspended in free space in a position chosen by the user when the application is started up.

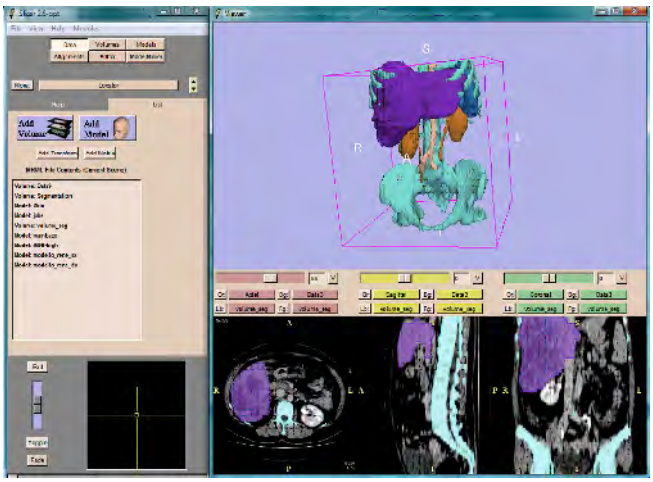


Fig. 1 User interface of 3D Slicer with the reconstructed model

Finger movements are detected by means of an optical tracking system (the Polaris Vicra) and are used to simulate touch with the interface where some buttons are located.

The interaction with the virtual screen happens by pressing these buttons, which make it possible to visualize the different organs present in the built 3D model (buttons on the right) and to choose the possible operations allowed on the selected model (buttons on the left).

For this reason, when using this graphical interface, the surgeon is able to rotate, to translate and to zoom in on the 3D models of the patient's organs simply by moving his finger in free space; in addition, he can select the visualization of all of the organs or only some of them.

In figure 2 the interaction with the user interface by means of the tracking system is shown.

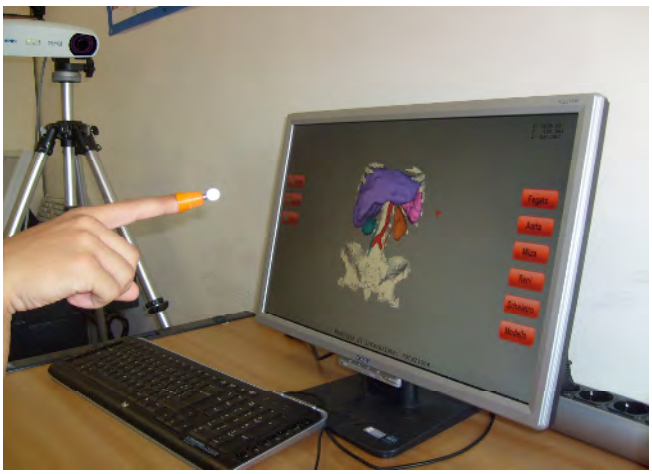


Fig. 2 The interaction with the virtual user interface

IV. Conclusions and future work

The described application is the first prototype of a virtual interface which provides a very simple form of interaction for navigation and manipulation of 3D virtual models of the human body.

The virtual interface created provides an interaction modality with models of the human body, a modality which is similar to the traditional one which uses a touch screen, but in this interface there is no contact with the screen and the user's finger moves through open space.

By means of an optical tracking system, the position of the finger tip, where an IR reflector is located, is detected and utilized first to define the four vertexes of the virtual interface and then to manage the interaction with this.

The optical tracker is already in use in computer aided systems and, for this reason, the developed interface can easily be integrated in the operation room.

Taking into account a possible use of the optical tracker in the operating room during surgical procedures, the problem of possible undesired interferences due to the detection of false markers (phantom markers) will be evaluated.

The introduction of other functionalities of interaction with the models is in progress, after further investigation and consideration of surgeons' requirements.

References

1. Grätzel C, Fong T, Grange S, Baur C (2004) A non-contact mouse for surgeon-computer interaction. Technology and Health Care Journal, IOS Press, Vol. 12, No. 3
2. Wachs J P, Stern H I, Edan Y, Gillam M, Handler J, Feied C, Smith M (2008) A Gesture-based Tool for Sterile Browsing of Radiology Images. The Journal of the American Medical Informatics Association, vol. 15, Issue 3
3. GoMonkey at http://www.gomonkey.at
4. O'Hagan R, Zelinsky A (1997) Finger Track - A Robust and Real-Time Gesture Interface. Lecture Notes In Computer Science; vol. 1342, pp 475 - 484
5. O'Hagan R, Zelinsky A, Rougeaux S (2002) Visual gesture interfaces for virtual environments. Interacting with Computers, vol. 14, pp 231-250
6. OpenSceneGraph at http://www.openscenegraph.org
7. 3D Slicer at http://www.slicer.org
8. NDI Polaris Vicra at http://www.ndigital.com

Performance Analysis of Support Vector Machine (SVM) for Optimization of Fuzzy Based Epilepsy Risk Level Classifications from EEG Signal Parameters

R. Harikumar[1], A. Keerthi Vasan[2], M. Logesh Kumar[3]

[1]Professor, Bannari Amman Institute of Technology, Sathyamangalam, India
[2,3]U.G students, ECE, Bannari Amman Institute of Technology, Sathyamangalam, India

Abstract — **In this paper, we investigate the optimization of fuzzy outputs in the classification of epilepsy risk levels from EEG (Electroencephalogram) signals. The fuzzy techniques are applied as a first level classifier to classify the risk levels of epilepsy based on extracted parameters which include parameters like energy, variance, peaks, sharp spike waves, duration, events and covariance from the EEG signals of the patient. Support Vector Machine (SVM) may be identified as a post classifier on the classified data to obtain the optimized risk level that characterizes the patient's epilepsy risk level. Epileptic seizures result from a sudden electrical disturbance to the brain. Approximately one in every 100 persons will experience a seizure at some time in their life. Some times seizures may go unnoticed, depending on their presentation which may be confused with other events, such as a stroke, which can also cause falls or migraines. Unfortunately, the occurrence of an epileptic seizure seems unpredictable and its process is very little understood The Performance Index (PI) and Quality Value (QV) are calculated for the above methods. A group of twenty patients with known epilepsy findings are used in this study. High PI such as 98.5% was obtained at QV's of 22.94, for SVM optimization when compared to the value of 40% and 6.25 through fuzzy techniques respectively. We find that the SVM Method out performs Fuzzy Techniques in optimizing the epilepsy risk levels. In India number of persons are suffering from Epilepsy are increasing every year. The complexity involved in the diagnosis and therapy is to be cost effective in nature. This paper is intended to synthesis a cost effective SVM mechanism to classify the epilepsy risk level of patients.**

Keywords — **Epilepsy, EEG signals, fuzzy techniques, performance Index, Quality Value.**

I. Introduction

Support Vector Machine (SVM) is an important machine learning technique which involves creating a function from a set of labeled trained data. People attacked by epilepsy [2] are unnoticed and this leads to other events such as a stroke, which also causes falls or migraines. In India number of persons suffering from epilepsy is increasing per year. The complexity involved in the diagnosis and therapy is to be cost effective in nature. Airports, amusement parks, and shopping malls are just a few of the places where computers are used to diagnosis a person's Epilepsy risk levels if a life threatening condition occurs. In some situation there is not always a trained doctor's and neuro scientists on hand. This project work is intended to synthesis a cost effective SVM mechanism to classify the epilepsy risk level of the patients and to mimic a doctor's and neuro scientist's diagnosis.

The EEG (Electroencephalogram) signals of 20 patients are collected from Sri Ramakrishna Hospitals at Coimbatore and their risk level of epilepsy is identified after converting the EEG signals to code patterns by fuzzy systems. This type of classification helped doctor's and neuro surgeons in giving appropriate therapeutic measures to the patients. This paper helps to save a patient's life when a life threatening condition occurs. This scientific paper is carried in order to save a patient's life and also to create public awareness among people about the risk ness of epilepsy.

II. Methodology

Support Vector Machine (SVM) is used for pattern classification and non linear regression like multilayer perceptrons and Radial Basis Function networks. SVM is now regarded as important example of 'Kernel Methods'. The main idea of SVM is to construct a hyper plane as the decision surface in such a way that the margin of separation between positive and negative examples is minimized. The SVM is an approximate implementation of method of structural minimization. In SVM we investigate the optimization of fuzzy outputs in the classification of Epilepsy Risk Levels from EEG (Electroencephalogram) signals. The fuzzy techniques are applied as a first level classifier to classify the risk levels of epilepsy based on extracted parameters like energy, variance, peaks, sharp and spike waves, duration, events and covariance from the EEG signals of the patient.

The block diagram of epilepsy classifier is shown in figure1. This is accomplished as:

1. Fuzzy classification for epilepsy risk level at each channel from EEG signals and its parameters.
2. Each channel results are optimized, since they are at different risk levels.

Chwee Teck Lim, James C.H. Goh (Eds.): ICBME 2008, Proceedings 23, pp. 351–354, 2009
www.springerlink.com

3. Performance of fuzzy classification before and after the SVM optimization methods is analyzed.

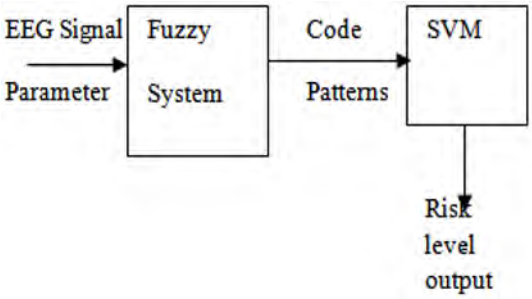


Fig 1 SVM- Fuzzy Classification System

The following tasks are carried out to classify the risk levels by SVM which are,

1. First a simplest case is analyzed with hyper plane as decision function with the known linear data.
2. A non linear classification is done for the codes obtained from a particular patient by using quadratic discrimination.
3. Then the k-means [8][5] clustering is performed for large data with different sets of clusters with centroid for each.
4. The centroid obtained is mapped by the kernel function for obtaining a proper shape.
5. A linear separation is obtained by using SVM with kernel and k-means clustering

In fuzzy techniques [3] more suboptimal solutions are arrived. These solutions are to be optimized to arrive a better solution for identifying patient's epilepsy risk level. . Due to the low value of performance index (40%), quality value (6.25) it is necessary to optimize the output of the fuzzy systems. Hence we are moving to SVM classification which gives a performance index of 98% and a quality value of 22.94. For optimization of fuzzy outputs the Support Vector Machine (SVM) method is identified.

The following solutions constrain steps are followed:

Step 1: The linearization and convergence is done using Quadratic Optimization [7][4]. The primal minimization problem is transformed into its dual optimization problem of maximizing the dual lagrangian L_D with respect to α_i:

$$\text{Max } L_D = \sum_{i=1}^{l} \alpha_i - \frac{1}{2} \sum_{i=1}^{l} \sum_{j=1}^{l} \alpha_i \alpha_j y_i y_j (X_i \cdot X_j) \quad (1)$$

Subject to

$$\sum_{i=1}^{l} \alpha_i y_i = 0 \quad (2)$$

$$\alpha i \geq 0 \; \forall \; i = 1, ..., l \quad (3)$$

Step 2: The optimal separating hyper plane is constructed by solving the quadratic programming problem defined by (1)-(3). In this solution, those points have non-zero Lagrangian multipliers ($\alpha_i > 0$) are termed support vectors.

Step 3: Support vectors lie closest to the decision boundary. Consequently, the optimal hyper plane is only determined by the support vectors in the training data.

Step 4: The k-means [8][5] clustering is done for the given set of data. The k-means function will form a group of clusters according to the condition given in step2 and step3. Suppose for a group of 3 clusters, k-means function will randomly choose 3 centre points from the given set. Each centre point will acquire the values that are present around them.

Step 5: Now there will be six centre points three from each epochs and then the SVM training process is done by the Kernel methods. Thus, only the kernel function is used in the training algorithm, and one does not need to know the explicit form of ∅. Some of the commonly used kernel [10] functions are:

Polynomial function: $K(X, Y) = (X^T Y - 1)^d$

Radial Basis Function: $k(xi, xj) = \exp\left\{ \frac{-|xi - xj|^2}{(2 \cdot \sigma)^2} \right\}$

Sigmoid function: $K(X, Y) = \tanh(kX^T Y - \theta)$

III. Radial Basis Function Kernel

The hyper plane and support vectors are used to separate linearly separable and non-linearly separable data. In this project we used, Radial Basis Kernel function (RBF) [4] for this non-linear classification. RBF is a curve fitting approximation in higher dimensional space. According to this learning it is equivalent to finding a surface in multi dimensional space that provides a best fit by utilizing the training data and generalization is equivalent to use of this multidimensional surface to interpolate the test data. It draws up on a traditional strict interpolation in multidimensional space. Thus RBF provides a set of the testing data which acts as a "basis" for input patterns when expanded into hidden space. From the set of RBF testing values the Mean Square Error (MSE) and Average MSE is performed and error values are calculated. The tool used in this study is mat lab v7.2.

An important factor for the choice of a classification method for a given problem is the available a-priori knowledge. During the last few years support vector machines

(SVM) have shown to be widely applicable and successful particular in cases where a-priori knowledge consists of labeled learning data. If more knowledge is available, it is reasonable to incorporate and model this knowledge within the classification results or to require less training data. Therefore, much active research is dealing with adapting the general SVM methodology to cases where additional a-priori knowledge is available. We have focused on the common case where variability of data can be modeled by transformations which leave the class membership unchanged. If these transformations can be modeled by mathematical groups of transformations one can incorporate this knowledge independently of the classifier during the feature extraction stage by group integration, normalization etc. this leads to variant features, on which any classification algorithm can be applied.

It is noted that one of main assumptions of SVM is that all samples in the training set are independent and identically distributed (i.i.d), however, in many practical engineering applications, the obtained training data is often contaminated by noise. Further, some samples in the training data set are misplaced on the wrong side by accident. These known as outliers. In this case, the standard SVM training algorithm will make decision boundary deviate severely from the optimal hyper plane, such that, the SVM is very sensitive to noise, and especially those outliers that are close to decision boundary. This makes the standard SVM no longer sparse, that is, the number of support vectors increases significantly due to outliers. In this project, we present a general method that follows the main idea of SVM using adaptive margin for each data point to formulate the minimization problem, which uses the RBF kernel trick. It is noted that the classification functions obtained by minimizing MSE are not sensitive to outliers in the training set. The reason that classical MSE is immune to outliers is that it is an average algorithm. A particular sample in the training set only contributes little to the final result. The effect of outliers can be eliminated by taking average on samples. That is why the average technique is a simple yet effective tool to tackle outliers.

In order to avoid outliers we utilized the RBF kernel functions and also decision functions for determining the margin of each classes. Since we are analyzing twenty epilepsy patients through leave one out methods and ten fold cross validation. Based on the MSE value and Average MSE values of SVM models the classifications of epilepsy risk levels are validated. The following fig 2 depicts the training and testing MSE of SVM models. The out liers problem is solved through Average MSE method which is shown in figure 3

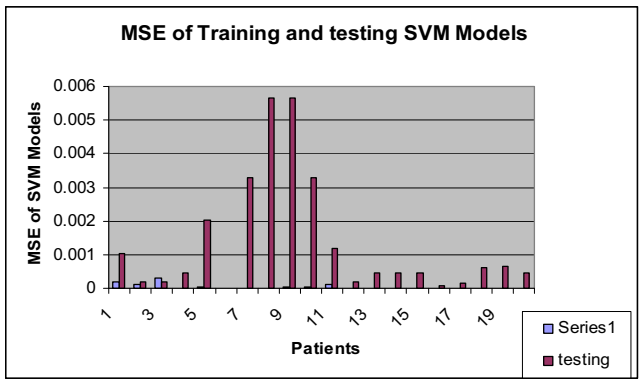


Fig 2 MSE of Training and Testing of SVM Models

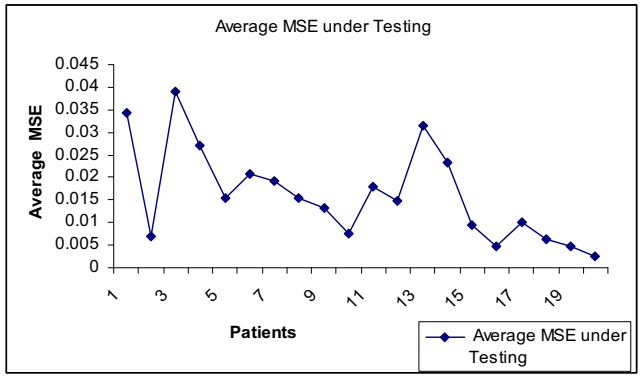


Fig 3 Average MSE under Testing of SVM Models

IV. Test Results

In SVM the performance classification is about 97.39% which is very high when compared with Fuzzy logic which is 50% only. The sensitivity and selectivity of SVM is also more when compared to the latter. The missed classification

Table 1: Comparison Results of Classifiers Taken As Average of All Ten Patients

Parameters	Fuzzy Techniques Without Optimization	Optimization With SVM Technique
Perfect Classification (%)	50	97.39
Missed Classification (%)	20	1.458
Performance Index (%)	40	97.07
Sensitivity	83.33	98.59
Specificity	71.42	98.52
Quality Value	6.25	22.94

of SVM is 1.458% but it is about 20% in Fuzzy Network and the value of PI in SVM is 97.07 and 40 in Fuzzy.

V. Conclusion

This Project investigates the performance of SVM in optimizing the epilepsy risk level of epileptic patients from EEG signals. The parameters derived from the EEG signal are stored as data sets. Then the fuzzy technique is used to obtain the risk level from each epoch at every EEG channel. The objective was to classify perfect risk levels with high rate of classification, a short delay from onset, and a low false alarm rate. Though it is impossible to obtain a perfect performance in all these conditions, some compromises have been made. As a high false alarm rate ruins the effectiveness of the system, a low false-alarm rate is most important. SVM optimization techniques are used to optimize the risk level by incorporating the above goals. The classification rate of epilepsy risk level of above 98% is possible in our method. The missed classification is almost 1.458 for a short delay of 2.031 seconds. The number of cases from the present twenty patients has to be increased for better testing of the system. From this method we can infer the occurrence of High-risk level frequency and the possible medication to the patients. Also optimizing each region's data separately can solve the focal epilepsy problem. The future research is in the direction of a comparison of SVM between heuristic MLP and Elman neural network optimization models.

Acknowledgement

The authors wish to express their sincere appreciation to the Management Principal of Bannari Amman Institute of Technology, Sathyamangalam for their support. We wish to express our sincere thanks to Dr.Asokan, Neurologist, Sri Ramakrishna Hospitals, Coimbatore for providing us EEG signals of the patient.

References

1. Pamela McCauley-Bell and Adedeji B.Badiru, Fuzzy Modeling and Analytic Hierarchy Processing to Quantify Risk levels Associated with Occupational Injuries- Part I: The Development of Fuzzy-Linguistic Risk Levels, IEEE Transaction on Fuzzy Systems, 1996,4 (2): 124-31.
2. R.HARIKUMAR AND, B.SABARISH NARAYANAN Fuzzy Techniques for Classification of Epilepsy risk level from EEG Signals, Proceedings of IEEE Tencon – 2003, 14-17 October 2003,Bangalore, India, 209-213.
3. R.Harikumar and B.Sabarish Narayanan, Fuzzy Techniques for Classification of Epilepsy risk level from
4. S.Haykin, Neural networks a Comprehensive Foundation, Prentice-Hall Inc. 2nd Ed. 1999.
5. Mu-chun Su, Chien –Hsing Chou, A modified version of the k-means clustering algorithm with a distance based on cluster symmetry, IEEE Transactions on Pattern Analysis and Machine Intelligence June 2001, 23 (6): 674-680.
6. Qing song, Wenjie Hu, and Wenfang Xie, Robust Support Vector Machine With Bullet Hole Image Classification, IEEE Transaction on SMC Part C, 2002,32 (4):440-448.
7. Sathish Kumar-Neural Networks, A Classroom Approach, McGraw-Hill New York, 2004.
8. Richard O. Duda, David G. Stroke, Peter E. Hart-Pattern Classification, second edition, A Wiley-Interscience Publication, John Wiley and Sons, Inc, 2003.
9. Jehan Zeb Shah, Naomie bt Salim- Neural Networks and Support Vector Machines Based Bio-Activity Classification, Proceedings of the 1st Conference on Natural Resources Engineering & Technology 2006, 24-25th July 2006: Putra Jaya, Malaysia, 484-491.
10. V.Vapnik, Statistical Learning Theory, Wiely Chichester, GB,1998.
11. Joel.J etal, Detection of seizure precursors from depth EEG using a sign periodogram transform, IEEE Transactions on Bio Medical Engineering, April 2004,51 (4):449-458.
12. Celement.C etal, A Comparison of Algorithms for Detection of Spikes in the Electroencephalogram,IEEE Transaction on Bio Medical Engineering, April 2003, 50 (4): 521-26.

A Feasibility Study for the Cancer Therapy Using Cold Plasma

D. Kim[1], B. Gweon[2], D.B. Kim[2], W. Choe[2] and J.H. Shin[1]

[1] Division of Mechanical Engineering, Aerospace and Systems Engineering, Korea Advanced Institute of Science and Technology(KAIST), Daejeon, Republic of Korea
[2] Department of Physics, KAIST, Daejeon, Republic of Korea

Abstract — **Cold plasma generated at the atmospheric pressure has been applied to disinfect microorganisms such as bacteria and yeast cells in biomedical research. Especially, due to its low temperature condition, the heat-sensitive medical device can be easily sterilized by the cold plasma treatment. In recent years, the effects of plasma on mammalian cells have arisen as a new issue. Generally, plasma is known to induce intensity dependent necrotic cell death. In this research, we investigate the feasibility of cold plasma treatment for cancer therapy by conducting comparative study of plasma effects on normal and cancer cells. We select THLE-2 (human liver normal cell) and SK-Hep1 (human liver metathetic cancer cell) as our target cells. Two types of cells have different onset plasma conditions for the necrosis, which may be explained by difference in electrical properties of these two cell types. Based on this work, a feasibility of the novel selective cancer therapy is tested.**

Keywords — **Cold plasma, Cancer therapy, Biomedical engineering**

I. Introduction

Plasma is generated by ionizing the neutral gas molecules, resulting in the mixture of energetic particles, including electrons and ions. Generally, the low pressure plasma is well characterized over many years and applied particularly in semiconductor industry applications. In recent years, new technique has been developed to generate plasma at the atmospheric pressure. The temperature of the nonthermal atmospheric plasmas, so called the cold plasmas, is at the minimum around the room temperature. When the substrate is treated by the cold plasma, it induces chemical reactions due to the active radicals even at the low temperature. Also, the vacuum system is not required in the cold plasma, making it possible to be used in many applications, for examples, plasma waterproofing of textiles [1].

In biomedical engineering, cold plasma is used to sterilize medical equipments, especially heat-sensitive devices [2, 3]. Membranes of bacteria and yeast cells are broken by radicals mechanically and chemically. In addition, in a few years, the plasma effects on mammalian cells have been studied [4, 5]. In this research, we investigate the difference in plasma effects on the human liver normal and cancer cells. This study could evaluate the feasibility for the cancer therapy using cold plasma.

II. Materials and Matheds

A. Target cells and sample preparation

We select THLE-2 (human liver normal cell) and SK-Hep1 (human liver metathetic cancer cell) cell lines as the target cells. THLE-2 cells are cultured in the complete media (BEGM + 1% antibiotics + 10% Fetal Bovine Serum (FBS)). SK-Hep1 cells are also cultured the recommended complete media (DMEM + 1% antibiotics + 10% FBS). Cells are seeded on the slide glasses to prepare the experiment. After culturing two types of cells at the same coverage, the cells are rinsed twice by Phosphate Buffered Saline (DPBS) solution for the sample preparation.

B. Experimental setup

We use jet type plasma device which consists of a single pin electrode of 360 μm in radius as shown in Fig. 1. Helium (99.99% purity) gas flows at 2 lpm through the 3 mm diameter pyrex tube. When 50 kHz AC voltage (950 ~ 1200 V) is applied to the pin electrode, the plasma is generated by the electric discharge. The sample is placed on the substrate about 15 mm below the device and treated by the plasma at a certain applied voltage and exposure time.

C. Experimental procedure and imaging

The intensity of the generated plasma depends on the distance (d) between the pin electrode and the slide glass, gas flow rate (r), the applied voltage (V) and frequency (f), and liquid thickness on the sample (l). To prevent cells from being dehydrated, we add DPBS solution on the slide glass to 0.15 mm thickness (l). We set the parameters same during the plasma experiment except the applied voltage: f = 50 kHz, r = 2 lpm, d = 15 mm, l = 0.15 mm, and V = 950 ~ 1200 V. After loading a sample on the center of the substrate, we have plasma treatment on cells and the exposure time ranges 30 ~ 120 sec.

Chwee Teck Lim, James C.H. Goh (Eds.): ICBME 2008, Proceedings 23, pp. 355–357, 2009
www.springerlink.com

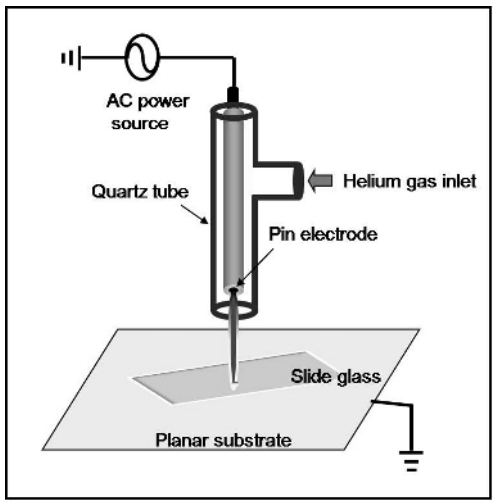


Fig. 1 Schematic drawling of pin-type plasma jet device

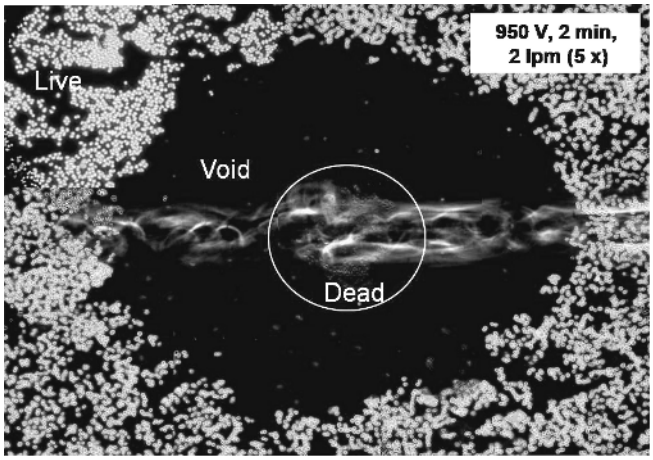


Fig. 2 A microscopic image of plasma-treated SK-Hep1 cells at V= 950 V, t = 120 sec and r = 2 lpm. Green and red dots are live and dead cells, respectively

The plasma treated sample is stained with the dye (ethidium homodimer 5 ul + calcine 2.5 ul + DPBS 5 ml for the live/dead assay. In imaging processes, the live and dead cells are stained in green and red colors, respectively.

III. Results

A. Characteristics of the plasma treated cells

At short exposure times and low applied voltages, both types of cells, THLE-2 and SK-Hep1 are live and their morphologies are unchanged, compared to the control cells. Over the onset plasma condition of necrosis, however, we observe the plasma treated area. The typical plasma treated area shows two different circular zone, void and dead zone, as shown in Fig. 2. In the dead zone, the necrotic cell death occurs while there are no cells in the donut-like void zone. The cells seem to be detached or lysed in the void zone. We find out the higher the applied voltage is, the larger the plasma treated zone is. Considering that the diameter of the plasma jet gets longer as the applied voltage increases, this result is given from the change of plasma beam diameter. Also, higher intensity of plasma in large voltage conditions gives more influence to the cells.

B. Differences in plasma effects on both types of cells

After we perform experiments for THLE-2 and SK-Hep1 cells with the same plasma condition, which is described in the section 2, except fixing t = 120 sec, we compare sample viabilities of both cells. The sample viability is defined by N/N_0 times 100 %, where N is the number of surviving samples and N_0 is the number of total samples. THLE-2 has the sample viability over 60 % in all of plasma conditions. While, the sample viability of SK-Hep1 is much lower than that of THLE-2. It is below 50 % over V = 950 V. At the highest voltage of 1200 V, SK-Hep1 samples completely have necrosis. Therefore the necrosis-onset voltage of SK-Hep1 is lower than that of THLE-2.

C. Differences in electrical properties of both types of cells

We measure the total capacitance of the system, including air, DPBS solution, cells and slide glass. We find that the capacitance of THLE-2 system is higher than that of SK-Hep1 system, suggesting that SK-Hep1 cells could be more conductive in electricity.

IV. Disccusions

In the necrotic sample, we observe the phase separation into void and dead zones. We propose that this feature results from the spatial characteristics of the pin-type plasma device. Generally, pin-type plasma has Gaussian distribution in the plasma density, which is maximum at the center of plasma [6]. Thus, at the center of the plasma treated region, necrosis could occur due to the strong intensity of plasma. Cell detachment could occur around the boundary region, resulting in a void.

On the other hand, we see that the sharp boundary line between non-plasma-treated and plasma-treated regions. This result implies that we can have plasma treatment on cells with a high-precision. This high-precision removal of cancer cells could be applied to the direct cancer therapy

without excessive damage of surrounding normal cells in biomedical application.

Even at the same plasma condition, samples have a distribution in both of survival and necrosis. This could result from the fluctuation of cell coverage. Basically, plasma effects on cells could rely on the cell coverage. Because cells are dielectric materials, the difference in cell coverage could give rise to the difference in the plasma condition. We maintain the same coverage of THLE-2 and SK-Hep1 cells. However, there could be a fluctuation in the cell coverage. To estimate this effect, we can study the dependence of plasma effects on cell coverage.

In the results of capacitance measurement, SK-Hep1 cells could be more conductive in electricity than THLE-2 cells. The higher conductivity of a sample is, the stronger intensity of plasma is. Thus, even at the same plasma condition, the generated plasma in SK-Hep1 system is stronger than that in THLE-2 system. This result could give rise to the difference in the onset voltages of necrosis between normal and cancer cells. Using this difference in plasma effects on THLE-2 and SK-Hep1 cells, we may apply this device to a novel cancer therapy, which kills cancer cells selectively without damages of normal cells.

V. Conculsions

We perform a comparative study of plasma effects on human liver normal and cancer cells for the feasibility of cancer therapy using cold plasma. In necrotic plasma conditions, the local area of cells can be treated by plasma with a high-precision. On the other hand, the total capacitance of normal cell system is larger than that of cancer cell system. This difference in electrical properties of cells could result in the difference in onset voltages of necrosis between normal and cancer cells. Based on the results of this research, we may provide a novel method of cancer treatment to biomedical field.

References

1. Radetic M, Jocic D, Jovancic P, Trajkovic R, Petrovic Z Lj (2000) The Effect of Low-Temperature Plasma Pretreatment on Wool Printing. Textile Chem. Col. 32: 55-60
2. Kieft I E, Laan E P v d, Stoffels E (2004) Electrical and optical characterization of the plasma needle. New J. Phys. 6: 149
3. Moisan M, Barbeau J, Moreau S, Pelletier J, Tabrizian M, Yahia LH (2001) Low-temperature sterilization using gas plasma: A review of the experiments and an analysis of the inactivation mechanisms. Int. J. Pharm. 226: 1-21
4. Kieft I E, Darios D, Roks A J M, Stoffels E (2005) Plasma treatment of mammalian vascular cells: A quantitative description. IEEE Trans. Plasma Sci. 33: 771-775
5. Stoffels E, Kieft I E, Sladek R E J (2003) Superficial treatment of mammalian cells using plasma needle. J. Phys. D: Apple. Phys. 36: 2098-2913
6. Radu I, Bartnikas R, Wertheimer M R (2003) Dielectric barrier discharges in helium at atmospheric pressure: experiments and model in the needle-plane geometry. J. Phys. D: Apple. Phys. 36: 1284-1291

Author: Jennifer H. Shin
Institute: Korea Advanced Institute of Science and Technology
Street: Gusung-dong, Yusung-gu 373-1
City: Daejeon
Country: Republic of Korea
Email: j_shin@kaist.ac.kr

Space State Approach to Study the Effect of Sodium over Cytosolic Calcium Profile

Shivendra Tewari and K.R. Pardasani

Department of Mathematics, M.A.N.I.T., Bhopal, INDIA

Abstract — **Calcium is known to play an important role in signal transduction, synaptic plasticity, gene expression, muscle contraction etc. A number of researchers have studied Cytosolic calcium diffusion but none have studied the effect of sodium over Cytosolic calcium profile. Here in this paper we have developed a mathematical model which incorporates all the important parameters like permeability coefficient, calcium flux, sodium flux, external sodium, external calcium etc. Thus we can study dynamically changing calcium with respect to dynamically changing sodium. Further, we have used Space State approach for the simulation of the proposed model which is a novel technique in itself developed in the later part of the twentieth century.**

Keywords — **Cytosolic calcium, permeability coefficient, sodium flux, calcium flux.**

I. Introduction

Intracellular calcium is known to regulate a number of processes [1]. One of the most important process is the process of signal transduction. Calcium acts as a switch in the process of signal transduction while converting electrical signal into a chemical signal. Calcium helps in the mechanism of exocytosis by combining with synaptotagmin to release neurotransmitters [2]. There are a number of parameters that affect its mobility and concentration like channels, pumps, leaks etc. Further, Reuter and Seitz found that calcium extrusion in heart muscles is caused by the electrochemical sodium gradient across the plasma membrane. Blaustein also observed that the sodium gradient across the plasma membrane influences the intracellular calcium concentration in a large variety of cells via a counter transport of Na^+ for Ca^{2+}. The dependence of Na^+ – Ca^{2+} electrochemical gradient has been studied by Sheu and Fozzard for sheep ventricular muscle and Purkinje strands. Thus, there is enough evidence that Na^+ is an important parameter to be considered when modeling cytosolic [Ca^{2+}] concentration. Matsuoka *et al.* also found that Na^+ – Ca^{2+} is the major mechanism by which cytoplasmic Ca^{2+} is extruded from cardiac myocytes [3, 4, 5, 6]. The mathematical models proposed so far have not incorporated the effect of Na^+ in their models [1, 7, 8]. Thus in this model we have incorporated the effect of dynamically changing Na^+ over dynamically changing Ca^{2+}. In this mathematical model we have incorporated Ca^{2+} influx, Na^+ influx, Na^+ / Ca^{2+} exchange pump. Since we have used Space State approach [9] to simulate the given model, we needed to linearise the given model. The results showed the effect of Na^+ / Ca^{2+} exchange over intracellular Ca^{2+} and intracellular Na^+.

II. The Mathematical Model

The mathematical model consists of a Ca^{2+} flux, Na^+ flux and a Na^+ / Ca^{2+} exchange pump. The influx of Ca^{2+} and Na^+ currents is modeled using the famous *Goldman-Hodgkin-Katz* (GHK) current equation [10] while the third parameter Na^+ / Ca^{2+} exchange pump is modeled using the free energy principle [11]. We have assumed a cytosol of radius 5 μm and thickness 7 nm. The proposed mathematical model can be framed using the following system of ordinary differential equations:

$$\frac{d[Ca^{2+}]}{dt} = -\sigma_{Ca} - \sigma_{NCX}$$
$$\frac{d[Na^{+}]}{dt} = -\sigma_{Na} - \overline{\sigma}_{NCX} \tag{1}$$

Along with the initial conditions,

$$[Ca^{2+}] = 0.1\mu M$$
$$[Na^{+}] = 12mM$$

A. Ca^{2+} and Na^+ currents

The influx of Ca^{2+} and Na^+ is modeled using the GHK equation:

$$I_S = \frac{P_S z_S^2 (\frac{V_m F^2}{RT})([S]_i - [S]_o exp(-\frac{(z_S V_m F)}{RT}))}{(1 - exp(-\frac{z_S V_m F}{RT}))} \tag{2}$$

here, 'S' is any ion in this case Ca^{2+} or Na^+. All the parameters have their usual meanings and have values as stated in Table 1. The value of permeability constant of Ca^{2+} and Na^+ is determined from the fact that conductance or permeability is equal to $\frac{D}{L}$ where D is the diffusion coeffi-

Chwee Teck Lim, James C.H. Goh (Eds.): ICBME 2008, Proceedings 23, pp. 358–361, 2009
www.springerlink.com

cient and L is the thickness of the membrane [10]. The diffusion coefficients were taken as from Stryer *et al.* [12] and membrane thickness is taken to be 7 nm [10]. Further, the inward current was taken to be negative and is converted into Molar / second using the faradays constant and using the fact that 1 L = 10^{15} μm^3 before being substituted in equation (1).

$$\sigma_{Ca} = \frac{-I_{Ca}}{z_{Ca}FV}$$

where, all the parameters have their usual meanings and V is the volume of the cytosol. Similarly, we can calculate the net flux of Na^+ ions from the Na^+ channel.

B. Na^+ / Ca^{2+} exchange

The Na^+ / Ca^{2+} exchange pump is known as the most important mechanism of Ca^{2+} extrusion [6]. This exchange is modeled by equating the electrochemical gradient of both the ions,

$$\Delta_{Ca} = RT\log(\frac{Ca_i}{Ca_o}) + z_{Ca}FV_m \tag{3}$$

Similarly, we can frame for electrochemical gradient of Na^+ (Δ_{Na}). The pump is assumed to be electrogenic in nature as one Ca^{2+} leaves the cytosol for intake of three Na^+ ions. Thus,

$$\Delta_{Ca} = 3\Delta_{Na} \tag{4}$$

Using equation 4 and solving we can obtain the required relation for Na^+ / Ca^{2+} exchange, given in the following equation:

$$\sigma_{NCX} = Ca_o(\frac{Na_i}{Na_o})^3 \exp(\frac{FV_m}{RT})$$
$$\bar{\sigma}_{NCX} = Na_o(\frac{Ca_i}{Ca_o})^{1/3} \exp(-\frac{FV_m}{RT}) \tag{5}$$

Before solving equation (1) by Space State technique the equations were linearised. For our convenience we write 'u' in lieu of Ca^{2+} and 'v' in lieu of Na^+. Further, the equations were transformed into matrix equations after using a number of transformations:

$$\frac{du}{dt} = au - b - a'v$$
$$\frac{dv}{dt} = cv - d + c'u \tag{6}$$

where, $a = \dfrac{2P_{Ca}FV_m \exp(\frac{2FV_m}{RT})}{RT(1-\exp(\frac{2FV_m}{RT})}$

$$b = \frac{2P_{Ca}FV_m u_{out}}{RT(1-\exp(\frac{2FV_m}{RT}))}, a' = \frac{u_{out}}{v_{out}}\exp(\frac{FV_m}{RT})$$
$$c = \frac{P_{Na}FV_m \exp(\frac{FV_m}{RT})}{(1-\exp(\frac{FV_m}{RT}))}, d = \frac{P_{Na}FV_m v_{out}}{(1-\exp(\frac{FV_m}{RT}))}$$
$$c' = \frac{v_{out}}{u_{out}}\exp(-\frac{FV_m}{RT})$$

Using another transformation of

$$\bar{u} = u\exp(\frac{2FV_m}{RT}) - u_{out}$$
$$\bar{v} = v\exp(\frac{FV_m}{RT}) - v_{out} \tag{7}$$

Using equation (7) in equations (6) it is reduced to

$$\frac{d}{dt}\begin{bmatrix}\bar{u}\\ \bar{v}\end{bmatrix} = \begin{bmatrix} -\frac{u_{out}}{v_{out}}\exp(2\varepsilon) & \frac{2P_{Ca}\exp(2\varepsilon)}{1-\exp(2\varepsilon)} \\ \frac{P_{Na}\varepsilon\exp(\varepsilon)}{1-\exp(\varepsilon)} & -\frac{v_{out}}{u_{out}}\exp(-2\varepsilon)\end{bmatrix}\begin{bmatrix}\bar{u}\\ \bar{v}\end{bmatrix} - \begin{bmatrix} u_{out} \\ -v_{out}/\exp(2\varepsilon)\end{bmatrix} \tag{8}$$

here, ε is a dimensionless quantity equal to FV_m/RT. If we use matrix notations and use another transformation then equation (8) can be reduced to the form which is readily solvable by the method of Space State,

$$\frac{dY}{dt} = AY \tag{9}$$

where,

$$Y = AX + C, X = \begin{bmatrix}\bar{u}\\ \bar{v}\end{bmatrix}, C = \begin{bmatrix} u_{out} \\ -v_{out}/\exp(2\varepsilon)\end{bmatrix},$$
$$A = \begin{bmatrix} -\frac{u_{out}}{v_{out}}\exp(2\varepsilon) & \frac{2P_{Ca}\exp(2\varepsilon)}{1-\exp(2\varepsilon)} \\ \frac{P_{Na}\varepsilon\exp(\varepsilon)}{1-\exp(\varepsilon)} & -\frac{v_{out}}{u_{out}}\exp(-2\varepsilon)\end{bmatrix}$$

with initial conditions,

$$Y(0) = \begin{bmatrix} 0.002 \\ 74.361 \end{bmatrix} \quad (10)$$

Solving equation (9 – 10) with help of space state technique and using inverse transformations, we have,

$$u(t) = 256.41(0.002 - 0.00005(-37.18 - 37.31(Sinh(kt)$$
$$+74.36(Cosh(kt) - 0.012(Sinh(kt)))) + 0.012(-0.002($$
$$-0.002 - 0.004(Sinh(kt)) + 0.002(Cosh(kt)$$
$$+0.0002(Sinh(kt)))))$$
$$v(t) = 16(0.145 - 0.0002(-37.18 - 37.31(Sinh(kt)))$$
$$+74.36(Cosh(kt) - 0.0118(Sinh(kt))))$$
$$-18589.7(-0.002 - 0.004(Sinh(kt))$$
$$+0.002(Cosh(kt) + 0.0002(Sinh(kt)))))$$

here, k is the eigen value of matrix A which has two values:

$$k_1 = -1.00579$$
$$k_2 = 0.99253$$

That is $k_1 \approx k_2 \approx k \approx 1$

III. Results and Discussion

This section comprises of the results and conclusion obtained from our methodology and hypothesis. The parameters used for simulation are as stated in Table 1

Table 1 Values of the parameters used

Parameter	Symbol	Value
Faraday's Constant	F	96487 Coulombs / moles
Membrane Potential	V_m	-70 mV
Real Gas Constant	R	8.314 J per Kelvin mole
Temperature	T	293 K
External Calcium Concentration	u_{out}	2 mM
External Sodium Concentration	v_{out}	145 mM
Ca^{2+} diffusion coefficient	D_{Ca}	250 μm^2/second
Na^+ diffusion coefficient	D_{Na}	480 μm^2/second
Membrane thickness	L	7 nm
Ca^{2+} permeability	P_{Ca}	3.3 x 10^{-2}metre / second
Na^+ permeability	P_{Na}	6.4 x 10^{-2}metre / second

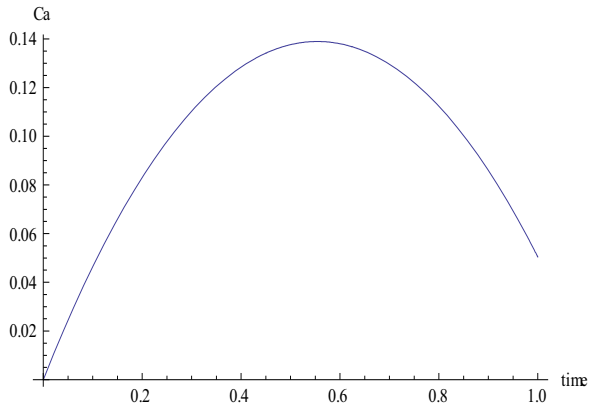


Fig. 1shows the plot of Ca^{2+} against time

In figure 1, the impact of Na^+ / Ca^{2+} exchange is shown on the temporal scale. Ca^{2+} is shown on the mM scale and time is shown on the second scale. It is evident from the figure when Ca^{2+} concentration rises above a certain level it triggers Na^+ / Ca^{2+} exchange protein and initializes the extrusion of Ca^{2+} for intake of Na^+ ions. As soon as, Na^+ / Ca^{2+} exchange is triggered the rising of Ca^{2+} stops and it starts decaying.

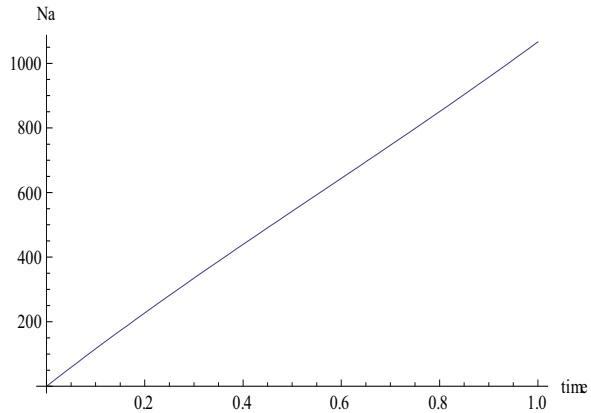


Fig. 2 shows the plot of Na^+ against time

In figure 2, the increasing Na^+ is plotted against time. Intracellular Na^+ is in the units of mM and time is on the scale of seconds. Since, there is no parameter in equation 1 to regulate intracellular concentration, therefore, Na^+ concentration goes on increasing. But that is not the case in reality as there is a Na^+ / K^+ ATPase which extrudes excess Na^+ from inside the cytosol [13]. Further, the Na^+ / Ca^{2+} exchange functions both ways when the Ca^{2+} is high it exchanges intracellular Ca^{2+} for extracellular Na^+ and when Na^+ is high it exchanges intracellular Na^+ for extracellular

Ca^{2+} [14]. The numerical results and graphs are obtained using Mathematica 6.0.

Since the model proposed needed to be a linear one we have to drop the non-linear terms and hence the Na^{+} concentration is not decreasing. On the other hand, this paper helps us to observe the apparent effect of Na^{+} / Ca^{2+} exchange over intracellular Ca^{2+} concentration while keeping the model a simple one. Further, the use of space state technique simplifies the solution and gives an analytic solution. In a similar manner, we can incorporate more parameters in this model to have a more realistic model which can be used either for simulation of cytosolic diffusion or excitation contraction coupling problem.

Acknowledgment

The authors are highly grateful to Department of Biotechnology, New Delhi, India for providing support in the form of Bioinformatics Infrastructure Facility for carrying out this work.

References

1. Rüdiger, S., Shuai, J. W., Huisinga, W., Nagaiah, C., Warnecke, G., Parker, I. & Falcke, M. (2007) Hybrid Stochastic and Deterministic Simulations of Calcium Blips, Biophysical J., 93, 1847-1857
2. Brose, N., Petrenko, A. G., Sudhof, T. C., & Jahn, R. (1992) Synaptotagmin: a calcium sensor on the synaptic vesicle surface. Science, 256, 1021-1025
3. Reuter, H. & Seitz, N. (1968) The dependence of calcium efflux from cardiac muscle on temperature and external ion composition. J. Physiol., 195, 451-470
4. Blaustein, M. P. & Hodgkin, A. L., (1969) The effect of cyanide on the efflux of calcium from squid axons. J. Physiol., 200, 497-527
5. Sheu, S. S., & Fozzard, H. A. (1982) Transmembrane Na+ and Ca2+ Electrochemical Gradients in Cardiac Muscle and Their Relationship to Force Development, J. Physiol., 80, 325 – 351
6. Fujioka, Y., Hiroe, K. & Matsuoka, S. (2000) Regulation kinetics of Na+-Ca2+ exchange current in guinea-pig ventricular myocytes, J. Physiol., 529, 611-623
7. Smith, G.D. (1996) Analytical Steady-State Solution to the rapid buffering approximation near an open Ca2+ channel. Biophys. J., 71, 3064-3072
8. Smith, G.D., Dai, L., Miura, Robert M. & Sherman, A. (2000) Asymptotic Analysis of buffered Ca2+ diffusion near a point source. SIAM J. of Applied of Math, 61, 1816-1838
9. Ogatta K. (1967) State Space Analysis of Control Systems. Prenice-Hall, INC., Englewood Cliffs, N.J.
10. Neher, E. (1986) Concentration profiles of intracellular Ca2+ in the presence of diffusible chelator. Exp. Brain Res. Ser., 14, 80-96
11. Nelson D.L., Cox M.M. (2001) Lehninger Principles of Biochemistry
12. Keener J., Sneyd J. (1998) Mathematical Physiology Springer. New york
13. Allbritton, N.L., Meyer, T., & Stryer, L. (1992) Range of messenger action of calcium ion and inositol 1,4,5-trisphosphate. Science, 258, 1812–1815
14. Clarke R. J., Kane D. J., Apell H.J., Roudna M., Bamberg E. (1998) Kinetics of Na+ -Dependent Conformational Changes of Rabbit Kidney Na+, K+ ATPase. Biophys. J., 75:1340-1353
15. Barry W.H., Bridge J.H. (1993) Intracellular calcium homeostasis in cardiac myocytes. J. of American Heart Association 87:1806-1815

Author: Dr. K.R. Pardasani
Institute: Department of Mathematics
Street: Maulana Azad National Institute of Technology
City: Bhopal
Country: INDIA
Email: kamalrajp@hotmail.com

Preliminary Study of Mapping Brain ATP and Brain pH Using Multivoxel ^{31}P MR Spectroscopy

Ren-Hua Wu[1,3], Wei-Wen Liu[1], Yao-Wen Chen[1], Hui Wang[2,3], Zhi-Wei Shen[1], Karel terBrugge[3], David J. Mikulis[3]

[1]Department of Medical Imaging, Shantou University Medical College, Shantou, China
[2]School of Biomedical Science and Medical Engineering, Southeast University, Nanjing, China
[3]Department of Medical Imaging, University of Toronto, Toronto, Canada

Abstract — **Magnetic resonance (MR) spectroscopy is a valuable method for the noninvasive investigation of metabolic processes. Although brain ATP studies can be found in multi-voxel ^{31}P MR spectroscopy, previous studies of intracellular brain pH was conducted in single-voxel ^{31}P MR spectroscopy. The purpose of this study was to explore the feasibility of mapping brain ATP and brain pH by using multivoxel ^{31}P MR spectroscopy. Phantom studies were carried out by using a GE 3T scanner firstly. Many available sequences were tested using phantom and the 2D PRESSCSI sequence was selected because of better signal to noise ratio. TR was 1000 msec and TE 144 msec with 128 scan averages. The acquisition matrix was 16 x 16 phase encodings over a 24-cm FOV. Slice thickness was 10 mm. Then a healthy volunteer from MR research team was studied. Data were processed offline using the SAGE/IDL software. Baseline and phase corrections were performed. Multivoxel spectra and brain ATP map were analyzed. Brain pH values were calculated from the difference in chemical shifts between inorganic phosphate (Pi) and phosphocreatine (PCr) resonances. Color scaling map was generated using MatLab software. Multivoxel ^{31}P spectra were obtained for phantom and the healthy volunteer. PCr map was obtained in phantom. At this moment, peaks of PCr were not homogeneous in phantom studies. There was noise for multivoxel ^{31}P spectra in volunteer study. Phosphomonoester (PME) peak, P*i* peak, phosphodiester (PDE) peak, PCr peak, γATP peak, αATP peak, and βATP peak can be identified. Preliminary brain ATP map and brain pH map were generated in the volunteer. It is feasible to map brain ATP and brain pH using multivoxel ^{31}P MR spectroscopy. However, endeavors should be made to improve quality of multivoxel ^{31}P MR spectroscopy.**

Keywords — **MR spectroscopy, brain pH mapping, brain ATP mapping**

I. Introduction

Magnetic resonance (MR) spectroscopy is a valuable method for the noninvasive investigation of metabolic processes. Many fundamental physiological, biochemical and metabolic events in human body can be evaluated by using MR spectroscopy. Single voxel MR spectroscopy has been an important tool to investigate metabolites in the regions of brain, prostate, muscle, etc. However, the drawback of single voxel technique is obvious in terms of anatomical coverage and small structure, compared with multivoxel MR spectroscopy. Multivoxel MR spectroscopy is a welcome change over previous single voxel method [1-5].

Brain energy metabolism can be assessed by using ^{31}P MRS to measure changes in the intracellular pH and relative concentrations of adenosinetriphosphate (ATP), phosphocreatine (PCr), and inorganic phosphate (P*i*) [6]. Intracellular pH values can be calculated from the difference in chemical shifts between P*i* and PCr resonances [7-11]. Mitochondrial activities can be evidenced by measuring ATP peaks. Brain pH study will be beneficial for diagnosis and treatment of many diseases, such as brain tumor, brain infarction, neurodegenerative diseases, and so on. Although brain ATP studies can be found in multi-voxel ^{31}P MR spectroscopy, previous studies of intracellular brain pH was conducted in single-voxel ^{31}P MR spectroscopy.

To our knowledge, mapping brain pH using multivoxel ^{31}P MR spectroscopy has not been published. The hypothesis of this study was that if multivoxel ^{31}P MR spectroscopy could be used to measure brain metabolites directly, we should be able to generate brain pH map indirectly. In order to enhance visual observation, brain pH map could be enhanced by color scaling. Therefore, the purpose of this study was to explore the feasibility of mapping brain ATP and brain pH by using multivoxel ^{31}P MR spectroscopy. We report our preliminary results in a sense of encouraging our future endeavors.

II. Materials and Methods

Phantom studies were carried out at first in this study. Phantom was a sphere filled with physiological metabolites of brain, including phosphocreatine (GE Braino). Then a healthy volunteer from MR research team was studied. All procedures were approved by the research committee at the Toronto Western Hospital. The studies were performed on a 3-T GE scanner (General Electric Medical Systems, Milwaukee, WI). The scout images were obtained with a gradient echo sequence. Many available sequences were tested using

Chwee Teck Lim, James C.H. Goh (Eds.): ICBME 2008, Proceedings 23, pp. 362–365, 2009
www.springerlink.com

phantom. The 2D PRESSCSI sequence is the best sequence for multivoxel ^{31}P MR spectroscopy concerning signal to noise ratio. The 2D PRESSCSI sequence was utilized for both ^{1}H scans with a standard head coil and ^{31}P scans with a GE service coil. TR was 1000 msec and TE 144 msec with 128 scan averages. A single PRESS volume of interest was prescribed graphically. The acquisition matrix was 16 x 16 phase encodings over a 24-cm FOV. Slice thickness was 10 mm. Before ^{31}P scan, a ^{1}H MRS pre-scan was performed to obtain shimming values. The ^{1}H pre-scan was performed using first and automatic shimming. Shimming values of ^{1}H MRS scan in x, y, z directions were copied to ^{31}P MRS scans. The standard head coil was unplugged when ^{31}P scan was performed.

Data were processed offline using the SAGE/IDL software. Baseline and phase corrections were performed. Multivoxel spectra, phantom PCr map, and brain ATP map were generated using SAGE/IDL software.

Because of noise spectra in the volunteer, brain pH values were roughly calculated from the difference in chemical shifts between P*i* and PCr resonances using the following standard formula [7-10]:

$$\mathrm{pH} = 6.77 + \log\{(A - 3.29)/(5.68 - A)\} \quad (1)$$

where A = chemical shift difference in parts per million between P*i* and PCr. Color scaling map was generated using MatLab software.

III. Results

Multivoxel ^{31}P spectra were obtained for phantom and the healthy volunteer. However, the peaks of PCr were heterogeneous in phantom study (Figure 1). From the data of this scan, a corresponding PCr map could be generated by SAGE/IDL software (Figure 2).

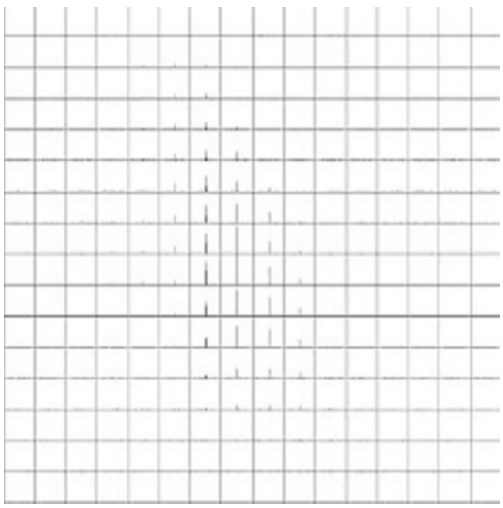


Fig. 1. Multivoxel ^{31}P MR spectroscopy of phantom obtained by the 2D PRESSCSI sequence. The heterogeneous PCr peaks were observed.

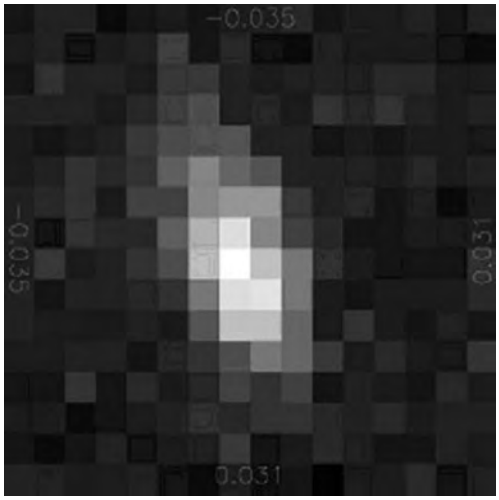


Fig. 2. PCr map generated by the data of Figure 1.

At this moment, there was noise for multivoxel ^{31}P spectra in volunteer study. A cumulated spectra from the multivoxel ^{31}P MR spectroscopy is shown in Figure 3. Roughly, phosphomonoester (PME) peak, inorganic phosphate (P*i*) peak, phosphodiester (PDE) peak, phosphocreatine (PCr) peak, γATP peak, αATP peak, and βATP peak could be identified. The individual spectra were with similar quality. From the data of same scan, corresponding metabolite maps could be generated by SAGE/IDL software. Figure 4 shows a brain γATP map as an example.

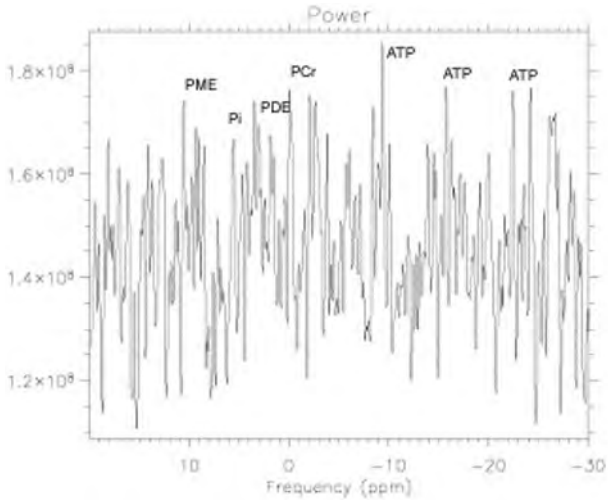


Fig. 3. Cumulated spectra of multivoxel ^{31}P MR spectroscopy in vivo. Although there was too much noise, brain metabolites could be identified.

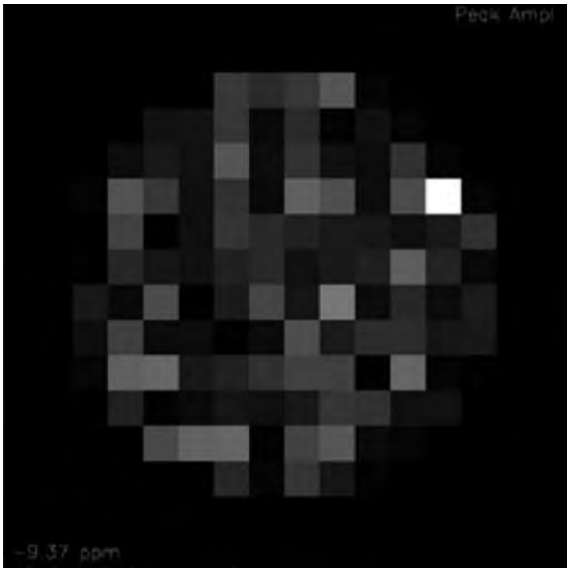


Fig. 4. γATP map generated by SAGE/IDL software from same data of Figure 3.

Figure 5 shows the results of rough brain pH calculation based on multivoxel ^{31}P data of the volunteer scan. The lowest value was 7.01 and the highest value was 7.24. From the values of Figure 5, a color scaling map was generated using MatLab software (Figure 6). Red color represents higher pH value and blue color represents lower pH value. Although the brain pH map might be just preliminary, we did obtain the brain pH map.

na	na	na	na	na	na	na	na	na	na	na	na	na	na	na	na
na	na	na	na	na	na	na	na	na	na	na	na	na	na	na	na
na	na	na	na	na	na	na	7.12	7.22	7.09	na	na	na	na	na	na
na	na	na	na	7.15	7.09	7.14	7.18	7.16	7.13	7.14	7.16	na	na	na	na
na	na	na	7.17	7.16	7.12	7.11	7.19	7.17	7.11	7.07	7.12	7.15	na	na	na
na	na	na	7.16	7.11	7.14	7.07	7.16	7.18	7.03	7.11	7.18	7.20	na	na	na
na	na	7.19	7.22	7.09	7.06	7.11	7.18	7.16	7.12	7.12	7.08	7.19	7.21	na	na
na	na	7.21	7.16	7.11	7.05	7.13	7.09	7.17	7.01	7.04	7.16	7.14	7.23	na	na
na	na	7.18	7.18	7.20	7.02	7.12	7.22	7.23	7.08	7.14	7.16	7.09	7.19	na	na
na	na	7.23	7.09	7.08	7.02	7.14	7.24	7.20	7.10	7.14	7.11	7.08	7.16	na	na
na	na	na	7.23	7.13	7.14	7.04	7.21	7.20	7.01	7.04	7.10	7.22	na	na	na
na	na	na	7.18	7.15	7.07	7.06	7.23	7.22	7.09	7.11	7.20	7.20	na	na	na
na	na	na	na	7.12	7.09	7.03	7.19	7.22	7.06	7.12	7.21	na	na	na	na
na	na	na	na	na	na	na	7.19	7.19	7.13	na	na	na	na	na	na
na	na	na	na	na	na	na	na	na	na	na	na	na	na	na	na
na	na	na	na	na	na	na	na	na	na	na	na	na	na	na	na

Fig. 5. Brain pH values calculated using formula (1).

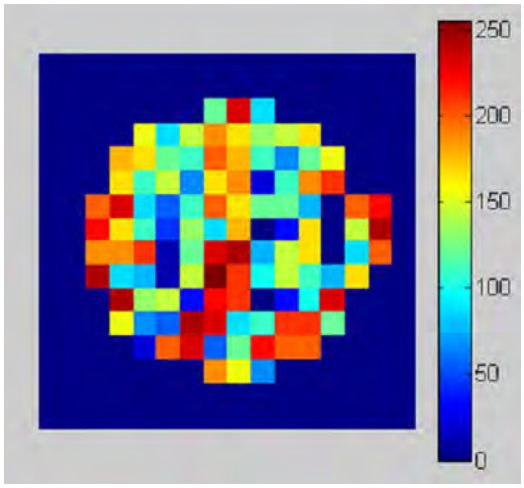


Fig. 6. Color scaling map based on the values of Figure 5.

IV. Discussion

What multivoxel ^{31}P MR spectroscopy measures at this time is limited in quality, but it does provide a window to noninvasively measure small structure of brain tissue. The advantage of using multivoxel ^{31}P MR spectroscopy over single voxel arises from its capability of offering metabolite information in spacing distribution, and continuous spectra to be obtained from tissue in real-time. By generating color map using multivoxel ^{31}P MR spectroscopy, evaluation of physiological or pathological information becomes much easy. Mapping brain metabolites has received increasing interest and could be utilized in other organs and tissue of human body [12-14].

Although our results of generating brain ATP map and brain pH map are preliminary, bright future could be expected in terms of technique improving. At this moment, MR hardware and software are not perfect so that our brain ATP map and brain pH map might just be at their earliest stage. But we did obtain our preliminary maps based on previous outcomes. What we should endeavor in the future is finding better hardware and software to improve homogeneity of magnetic filed and perfect shimming for multivoxel ^{31}P MR spectroscopy. More sensitive detection techniques and better post-processing should also be taken into account. As long as source signals of multivoxel ^{31}P MR spectroscopy are accurate, the corresponding maps are just visual enhancement. We are confident of that brain ATP map and brain pH map will be feasible in the near future. Accurate metabolite information for small region of organ tissue will be available for studies of gene expression, identifying progenitor cells, early detection of various diseases, differential diagnosis of diseases, etc [15-17].

V. Conclusions

This study was conducted to prove the possibility of mapping brain ATP and brain pH by using multivoxel ^{31}P MR spectroscopy. We report our preliminary results in a sense of encouraging our future endeavors.

Acknowledgment

This work was supported in part by the National Natural Science Foundation of China (30570480) and Guangdong Natural Science Foundation (8151503102000032). This work was mainly done in the University of Toronto, Canada. We thank MR staffs in the Toronto Western Hospital, University of Toronto, Canada.

References

[1] Wu RH, Mikulis DJ, Ducreux D, et al. (2003) Evaluation of chemical shift imaging using a two-dimensional PRESSCSI sequence: work in progress. 25th Annual international conference of the IEEE Engineering in Medicine and Biology Proceedings, Cancun, Mexico, 2003, pp. 505-508

[2] Keshavan MS, Stanley JA, Montrose DM, et al. (2003) Prefrontal membrane phospholipid metabolism of child and adolescent offspring at risk for schizophrenia or schizoaffective disorder: an in vivo ^{31}P MRS study. Mol Psychiatry 8:316-323

[3] Stanley JA, Kipp H, Greisenegger E, et al. (2006) Regionally specific alterations in membrane phospholipids in children with ADHD: An in vivo 31P spectroscopy study. Psychiatry Res 148:217-221

[4] Kemp GJ, Meyerspeer M, Moser E (2007) Absolute quantification of phosphorus metabolite concentrations in human muscle in vivo by ^{31}P MRS: a quantitative review. NMR Biomed 20:555–565.

[5] Mairiang E, Hanpanich P, Sriboonlue P (2004) In vivo ^{31}P-MRS assessment of muscle-pH, cytolsolic-[Mg2_] and phosphorylation potential after supplementing hypokaliuric renal stone patients with potassium and magnesium salts. Magnetic Resonance Imaging 22:715–719.

[6] Wu RH, Poublanc J, Mandell D, et al. (2007) Evidence of brain mitochondrial activities after oxygen inhalation by ^{31}P magnetic resonance spectroscopy at 3T. Conf Proc IEEE Eng Med Biol Soc, 2007, pp. 2899-2902.

[7] Patel N, Forton DM, Coutts GA, et al. (2000) Intracellular pH measurements of the whole head and the basal ganglia in chronic liver disease: A phosphorus-31 MR spectroscopy study. Metab Brain Dis 15:223–240.

[8] Petroff OAC and Prichard JW (1983) Cerebral pH by NMR. Lancet ii(8341):105–106.

[9] Taylor-Robinson SD and Marcus CD (1996) Tissue behaviour measurements using phosphorus-31 NMR. In (Grant DM, Harris RK, ed.), Encyclopedia of Nuclear Magnetic Resonance. Wiley, Chichester, UK, pp. 4765–4771.

[10] Hamilton G, Mathur R, Allsop JM, et al. (2003) Changes in Brain Intracellular pH and Membrane Phospholipids on Oxygen Therapy in Hypoxic Patients with Chronic Obstructive Pulmonary Disease. Metabolic Brain Disease 18:95-109.

[11] Brindle KM, Rajagopalan B, Williams DS, et al. (1988) 31P NMR measurements of myocardial pH in vivo. Biochem Biophys Res Commun, 151:70-77.

[12] Mannix ET, Boska MD, Galassetti P, et al. (1995) Modulation of ATP production by oxygen in obstructive lung disease as assessed by 31P-MRS. J Appl Physiol 78:2218-2227.

[13] Kutsuzawa T, Shioya S, Kurita D, et al. (2001) Effects of age on muscle energy metabolism and oxygenation in the forearm muscles. Med Sci Sports Exerc 33:901-906.

[14] Haseler LJ, Lin AP, and Richardson RS (2004) Skeletal muscle oxidative metabolism in sedentary humans: 31P-MRS assessment of O2 supply and demand limitations. J Appl Physiol 97:1077–1081.

[15] Brindle K (2008) New approaches for imaging tumour responses to treatment. Nat Rev Cancer 8:94-107.

[16] Cunningham CH, Chen AP, Albers MJ, et al. (2007) Double spin-echo sequence for rapid spectroscopic imaging of hyperpolarized 13C. J Magn Reson 187:357-362.

[17] Drummond A, Macdonald J, Dumas J, et al. (2004) Development of a system for simultaneous 31P NMR and optical transmembrane potential measurement in rabbit hearts. Conf Proc IEEE Eng Med Biol Soc, 3:2102-2104.

Corresponding authors:

Author:	Mikulis DJ	Wu RH
Institute:	University of Toronto	Shantou University
Street:	399 Bathurst Street	22 Xinling Road
City:	Toronto	Shantou
Country:	Canada	China
Email:	mikulis@uhnres.utoronto.ca	rhwu@stu.edu.cn

Brain-Computer Interfaces for Virtual Environment Control

G. Edlinger[1], G. Krausz[1], C. Groenegress[2], C. Holzner[1], C. Guger[1], M. Slater[2]

[1]g.tec medical engineering, Guger Technologies OEG, Herbersteinstrasse 60, 8020 Graz, Austria,
edlinger@gtec.at
[2] Centre de Realitat Virtual (CRV), Universitat Politècnica de Catalunya, Barcelona, Spain

Abstract — **A brain-computer interface (BCI) is a new communication channel between the human brain and a digital computer. Furthermore a BCI enables communication without using any muscle activity for a subject. The ambitious goal of a BCI is finally the restoration of movements, communication and environmental control for handicapped people. However, in more recent research also BCI control in combination with Virtual Environments (VE) gains more and more interest. Within this study we present experiments combining BCI systems and control VE for navigation and control purposes just by thoughts. A comparison of the applicability and reliability of different BCI types based on event related potentials (P300 approach) will be presented.**

BCI experiments for navigation in VR were conducted so far with (i) synchronous BCI and (ii) asynchronous BCI systems. A synchronous BCI analyzes the EEG patterns in a predefined time window and has 2-3 degrees of freedom. A asynchronous BCI analyzes the EEG signal continuously and if a specific event is detected then a control signal is generated. This study is focused on a BCI system that can be realized for Virtual Reality (VR) control with a high degree of freedom and high information transfer rate. Therefore a P300 based human computer interface has been developed in a VR implementation of a smart home for controlling. the environment (television, music, telephone calls) and navigation control in the house.

Results show that the new P300 based BCI system allows a very reliable control of the VR system. Of special importance is the possibility to select very rapidly the specific command out of many different choices. This eliminates the usage of decision trees as previously done with BCI systems.

Keywords — **Brain-Computer Interface, P300, evoked potential, Virtual Environment**

I. Introduction

An EEG based Brain-Computer Interface (BCI) measures and analyzes the electrical brain activity (EEG) in order to control external devices. A BCI can be seen as novel and additional communication channel for humans. In contrast to other communication channels a BCI does not need using any muscle activity from the subject. BCIs are based on slow cortical potentials [1], EEG oscillations in the alpha and beta band [2, 3, 4], the P300 response [5] or steady-state visual evoked potentials (SSVEP) [6]. BCI systems are used mainly for moving a cursor on a computer screen, controlling external devices or for spelling purposes [2, 3, 5].

BCI systems based on slow cortical potentials or oscillatory EEG components with 1-5 degrees of freedom were realized up to now. However, high information transfer rates were reached based on 2 degrees of freedom as otherwise the accuracy of the BCI systems dropped down. SSVEP based systems allow selecting up to 12 different targets and are limited by the number of distinct frequency responses that can be analyzed in the EEG. P300 response based BCIs typically used a matrix of 36 characters for spelling applications [5]. The underlying phenomenon of a P300 speller is the P300 component of the EEG which is induced if an unlikely event occurs. The subject has the task to concentrate himself on a specific letter he wants to select [5, 7, 8]. When the character flashes on, a P300 is induced and the maximum in the EEG amplitude is reached typically 300 ms after the flash onset. Several repetitions are needed to perform EEG data averaging for increase the signal to noise ratio and accuracy of the system. The P300 signal response is more pronounced in the single character speller than in the row/column speller and therefore easier to detect [7, 8].

II. Methods

Three subjects participated in the experiments. EEG from 8 electrode positions located over the parietal and occipital areas was measured. The sampling frequency was set to 256 Hz and EEG was digitally bandpass filtered between 0.1 to 30 Hz. Then a hardware interrupt driven device driver was used to read the biosignal data with a buffersize of 1 (time interval ~ 4ms) into Simulink which runs under the MATLAB environment [4]. Within Simulink the signal processing and feature extraction (see [5] for details) and the paradigm presentations are performed. The paradigm module controls the flashing sequence of the symbols. In this work, a smart home VR realization should be controlled with the BCI. Therefore the subjects were trained firstly in spelling characters and numbers based on their P300 EEG response. Therefore, the characters of the English alphabet (A, B,…Z) and Arabic numbers (1, 2,…9) were arranged in

Chwee Teck Lim, James C.H. Goh (Eds.): ICBME 2008, Proceedings 23, pp. 366–369, 2009
www.springerlink.com

a 6 x 6 matrix on a computer screen. Then the characters were highlighted in a random order and the subject had the task to concentrate on the specific character he/she wanted to spell. All experiments were undertaken in 2 modi: (i) the row/column speller – all items of one row or column are highlighted at the same time, (ii) the single character speller – only one character is highlighted. For the single character speller each character was highlighted 15 times. For the row/column speller each row and each column was also highlighted 15 times. This results in a speed up of 3 for the row/column speller. Another important parameter in the P300 experiment is the flash time (character is highlighted) and the dark time (time between 2 highlights). Both times should be as short as possible to reach a high communication speed, but must be long enough so that the subject can react on the flash and that the single P300 responses are not overlapping.

At the beginning of the experiment the BCI system was trained based on the P300 response of 42 characters of each subject with 15 flashes per character (about 40 minutes training time). All 3 subjects needed between 3 and 10 flashes (mean 5.2) per character to reach an accuracy of 95 % for the single character speller and between 4 and 11 flashes (mean 5.4) for the Row/Column speller. This resulted in a maximum information transfer rate of 84 bits/s for the single character speller and 65 bits/s for the row column speller. Figure 1 yields the a typical P300 response to the target letters.

Then the P300 based BCI system was connected to a Virtual Reality (VR) system. A virtual 3D representation of a smart home with different control elements was developed as shown in Figure 2.



Figure 2: Virtual representation of a smart home

In the experiment it should be possible for a subject to switch on and off the light, to open and close the doors and windows, to control the TV set, to use the phone, to play music, to operate a video camera at the entrance, to walk around in the house and to move him/herself to a specific location in the smart home. Therefore special control masks for the BCI system were developed containing all the different necessary commands. In total 7 control masks were created: a light mask, a music mask, a phone mask, a temperature mask, a TV mask (see Figure 3), a move mask and a go to mask (see Figure 4).

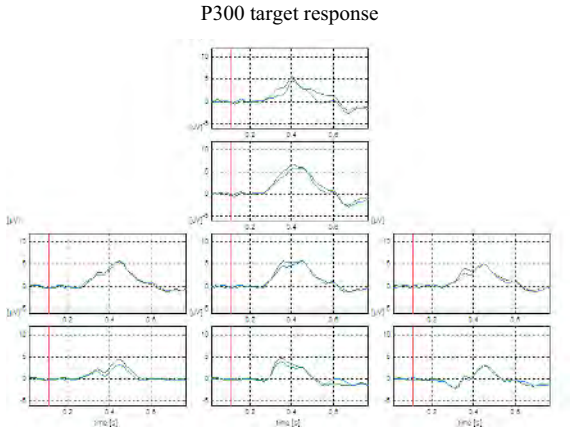


Figure 1: Typical averaged P300 responses for a single character flasher. The graphs represent the P300 responses from electrode positions Fz, Cz, P3, Pz, P4, Fp1, Oz and Fp2 (from upper left to lower right). The red vertical bar represents the occurrence of the target letter. Amplitudes on the y-axis are given in [µV] and the x-axis represents the time from 100 ms before target occurrence to 700ms after target occurrence.

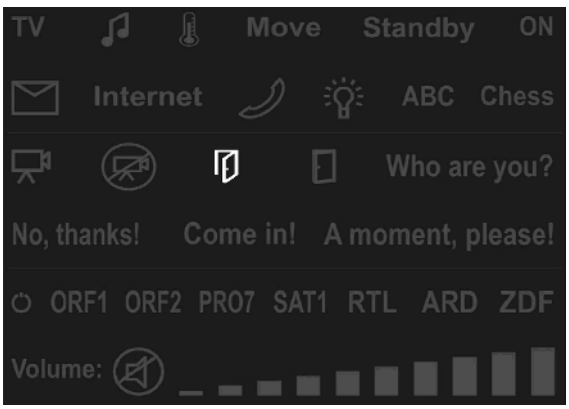


Figure 3: Control mask with the main menu in the first 2 rows, the icons for the camera, door control and questions in the 3rd and 4th row and the TV control in the last 2 rows.

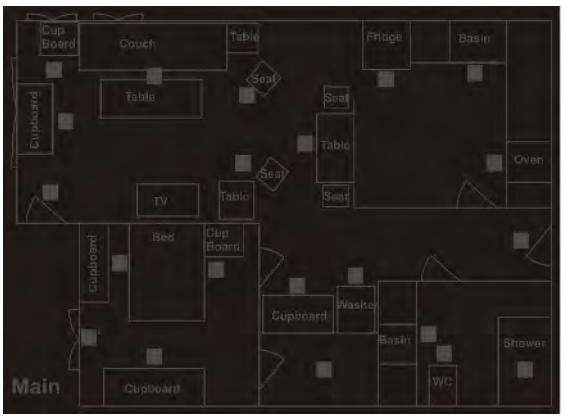


Figure 4: Control mask for going to a specific position in the smart home (bird view).

III. Results

Table 1 shows the results of the 3 subjects for the 3 parts of the experiment and for the 7 control masks. Interestingly, the light, the phone and the temperature mask were controlled by 100 % accuracy. The Go to mask was controlled with 94.4 % accuracy. The worst results were achieved for the TV mask with only 83.3 % accuracy.

Table 2 shows the number of symbols for each mask and the resulting probability that a specific symbol flashes up. If more symbols are displayed on one mask then the probability of occurrence is smaller and this results in a higher P300 response which should be easier to detect. The flashes column shows the total number of flashes per mask until a decision is made. The translation time per character that is longer if more symbols are on the mask.

Table 1. Accuracy of the BCI system for each part and control mask of the experiment for all subjects.

Mask	Part1	Part2	Part3	Total
Light	100%	100%	100%	100%
Music	-	89,63%	-	89,63%
Phone	-	100%	-	100%
Temperature	100%	-	-	100%
TV	83,3%	-	-	83,3%
Move	88,87%	-	93,3%	91,1%
Go to	100%	-	88,87%	94,43%

Table 2. Number of symbols, occurrence probability per symbol, number of flashes per mask (e.g. 25 x 15 = 375) and conversion time per character for each mask.

Mask	Symbols	Probability [%]	Flashes	Time per character [s]
Light	25	4	375	33,75
Music	50	2	750	67,50
Phone	30	3.3	450	40,50
Temperature	38	2.6	570	51,30
TV	40	2.5	600	54,00
Move	13	7.7	195	17,55
Go to	22	4.5	330	29,70

IV. Discussion & conclusion

The P300 based BCI system was successfully used to control a smart home environment with accuracy between 83 and 100 % depending on the mask type. The difference in accuracy can be explained by the arrangement of the icons.

However, the experiment yielded 2 important new facts: (i) instead of displaying characters and numbers to the subject also different icons can be used, (ii) the BCI system must not be trained on each individual character. The BCI system was trained with EEG data of the spelling experiment and the subject specific information was used also for the smart home control. This allows using icons for many different tasks without prior time consuming and boring training of the subject on each individual icon. This reduces the training time in contrast to other BCI implementations were hours or even weeks of training are needed [1, 2, 3]. This reduction in training time might be important for locked-in and ALS patients who have problems with the concentration over longer time periods. The P300 concept works also better if more items are presented in the control mask as the P300 response is more pronounced if the likelihood that the target character is highlighted drops down [4]. This results of course in a lower information transfer rate, but enables to control almost any device with such a BCI system. Especially applications which require reliable decisions are highly supported. Therefore the P300 based BCI system enables an optimal way for the smart home control. The virtual smart home acts in such experiments as a testing installation for real smart homes. Also wheelchair control, which many authors identify as their target application, can be realized with this type of BCI system in a goal oriented way. In a goal oriented BCI approach it is then not necessary e.g. to move a robotic hand by thinking about hand or foot movements and controlling right, left, up, down commands. Humans just think “I want to grasp the glass” and the real command is initiated by this type of BCI implementation.

A P300 based BCI system is optimally suited to control smart home applications with high accuracy and high reliability. Such a system can serve as a easy reconfigurable and therefore cheap testing environment for real smart homes for handicapped people.

Acknowledgement

The work was funded by the EU project PRESENCCIA.

REFERENCES

1. N. Birbaumer, N. Ghanayim, T. Hinterberger, I. Iversen, B. Kotchoubey, A. Kübler, J. Perelmouter, E. Taub, and H. Flor (1999) A spelling device for the paralysed, Nature, vol. 398, pp. 297- 298
2. C. Guger, A. Schlögl, C. Neuper, D. Walterspacher, T. Strein, and G. Pfurtscheller (2001) Rapid prototyping of an EEG-based brain-computer interface (BCI), IEEE Trans. Rehab. Engng., vol. 9 (1), pp. 49-58
3. T.M. Vaughan, J.R. Wolpaw, and E. Donchin (1996), EEG-based communication: Prospects and problems, IEEE Trans. Rehab. Engng., vol. 4, pp. 425-430
4. G. Edlinger, C. Guger, Laboratory PC and Mobile Pocket PC Brain-Computer Interface Architectures (2006), Engineering in Medicine and Biology Society, 2005. IEEE-EMBS 2005. 27th Annual International Conference, 5347 - 5350
5. D. Krusienski, E. Sellers, F. Cabestaing, S. Bayoudh, D. McFarland, T. Vaughan, J. Wolpaw (2006) A comparison of classification techniques for the P300 Speller, Journal of Neural Engineering, vol. 6, pp. 299 – 305.
6. G.R. McMillan and G.L. Calhoun et al. (1995) Direct brain interface utilizing self-regulation of steady-state visual evoke response in Proceedings of RESNA, June 9-14, pp.693-695.
7. G. Cuntai, M. Thulasidas, and W. Jiankang (2004). High performance P300 speller for brain-computer interface, Biomedical Circuits and Systems, IEEE International Workshop on, S3/5/INV - S3/13-16.
8. M. Thulasidas, G. Cuntai, and W. Jiankang (2006), Robust classification of EEG signal for brain-computer interface. IEEE Trans Neural Syst Rehabil Eng., 14(1): p. 24-29.
9. Zhang H, Guan C, Wang C (2006). A Statistical Model of Brain Signals with Application to Brain-Computer Interface. Proceedings of the 2005 IEEE on Engineering in Medicine and Biology 27th Annual Conferenc:5388 - 5391

FPGA Implementation of Fuzzy (PD&PID) Controller for Insulin Pumps in Diabetes

V.K. Sudhaman[1], R. HariKumar[2]

[1] U.G Student, ECE, Bannari Amman Institute of Technology, Sathyamangalam, India
[2] Professor, ECE, Bannari Amman Institute of Technology, Sathyamangalam, India

Abstract — **This paper emphasizes on a FPGA Implementation of Fuzzy PD&PID Controller in biomedical application. A novel approach aims to identify and design a simple robust Fuzzy PD&PID Controller system with minimum number of fuzzy rules for the diabetic patients as a single injection process through the blood glucose level from Photo plethysmogram is discussed. VLSI system is simulated and analyzed then FPGA system is synthesized and implemented using VHDL.A simulation of VLSI design of the above automatic controller is analyzed. In this process insulin is administrated through an infusion pump as a single injection. The pump is controlled by the automatic control Fuzzy PD Controller which is more efficient compared to the conventional PD Controller.**

Keywords — **blood glucose level, Photo plethysmogram, FPGA, Fuzzy PD&PID Controller.**

I. Introduction

The motto of this paper is to identify a proper methodology for the infusion process of insulin to diabetic patients using an automated Fuzzy logic controller. FPGA Implementation of the above automatic controller is analyzed by using VHDL. In this process insulin is administrated through an infusion pump as a single injection. The pump is controlled by the automatic control Fuzzy PD& PID Controller which is more efficient compared to the conventional PD&PID Controller. In case of non- linear inputs, Fuzzy PD &PID Controller performs better compared to the conventional controller.

The task organization for obtaining FPGA Implementation of Fuzzy PD&PID Controller is as follows:

1. Measurement of Blood glucose level using Photo plethysmography method which is explained in ref [6],[8]
2. Design of Fuzzy PD controller (2x1) based on error and error rate as inputs and output signal to control the movement of infusion pump.
3. Performance study of conventional PD&PID controller with Fuzzy PD&PID controller.
4. VLSI Design and Simulation of Fuzzy PD &PID Controller are analyzed.
5. FPGA Implementation of Fuzzy PD&PID Controller is analyzed.

The FPGA architecture is designed such that its very simple and occupies less memory ,so that our system can also be adaptable in low level FPGA's.

II. Materials and Methodology

A logical system, which is much closer to the spirit of human thinking and natural language than the traditional logic system is called a Fuzzy logic. Here the Fuzzy Controller is considered as new approchement between the conventional mathematical control and human like decision making. The Fuzzy controller has to be provided with a predefined range of control parameters or sense of fields. The determination of these sets is normally carried out by initially providing the system with a set of data manually fed by the operator. The Fuzzy system can be further enhanced by the adaptive control where the time constant and gain are varied to self tune the controller at various operating point.

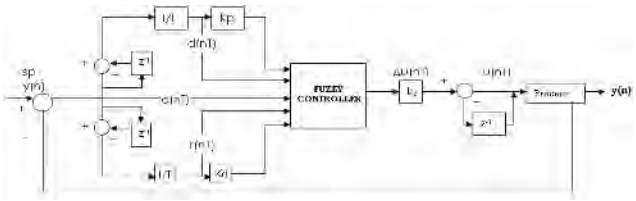


Fig.1 Fuzzy PD controller system

The Figure 1 depicts the Fuzzy PD Controller with Y(nT) is the output of photoglucometer (Photo plethysmography) which is compared with set point (sp), the error and rate of error are calculated and they are given as an input to the Fuzzy inference system which consists of fuzzifier, rule base and defuzzification, which produces the control input Δu(nT). The input u (nT) of the plant is calculated which act as the position control of an insulin pump. Photo-glucometer is an instrument that uses IR radiation (850 nm) from a source, a sensor, amplifier and an output display unit to give the blood sugar of a diabetic patient. The IR radiation when incident on the skin a part of it is transmitted reflected and absorbed by the skin. The transmitted ray is sensed by the sensor and the output of sensor is applied and it is displayed.

Chwee Teck Lim, James C.H. Goh (Eds.): ICBME 2008, Proceedings 23, pp. 370–373, 2009
www.springerlink.com

III. Analysis of fuzzy PD controller

Fuzzy logic control technique has found many successful industrial applications and demonstrated significant performance improvements. In standard procedure the design consist of three main parts Fuzzification, Fuzzy logic rule base, and Defuzzification[1].

A. Mathematical analysis

Ackerman et al (1965) used a two compartment model to represent the dynamics of glucose and insulin concentration in the blood system. The blood Glucose dynamics of an individual can be written as

$$\dot{x_1} = -m_1 x_1 - m_2 x_2 + p(t) \quad (1)$$

$$\dot{x_2} = -m_3 x_2 + m_4 x_1 + u(t) \quad (2)$$

where $\dot{x_1}$ represents blood glucose level deviations, $\dot{x_2}$ denotes the net blood glycemic harmonic level, p(t) represents the input rate of infusion of glucose, u(t) denotes the input rates of infusion of insulin and m_1,m_2,and m_3 and m_4 are parameters. The photo glucometer output levels are shown in table1.

Table 1 Photo Glucometer Output Levels

Sl No.	Blood Glucose Level (mg/dl)	Photo Glucometer Output (V)	Control levels
1.	50	8	Lower point
2.	100	9	Set point
3.	200	10	Upper point

For severe diabetes we shall take m4 to have the value of Zero. We are considering a group of diabetics with no insulin secretion whose blood glucose level is 200 mg/dl while fasting. Based on the observation we derived the following insulin injection needed for the group in a single injection process in the time duration of 30 min. The above case needs 2950 micro units/ml insulin at a single stroke of injection.

B. Design of Fuzzy PD controller

The conventional continuous time PD control law is described by

$$u(t) = k_p^c e(t) + k_d^c e(t) \quad (3)$$

Where k and k are the proportionality derivative gains of the controller and e(t) is the error signal defined by

$$e(t) = sp(t) - y(t) \quad (4)$$

Sp (t) is the set point and y (t) is the system output

In fuzzification step we employ two inputs ,the error signal e(nT) ,and the rate of change of error signal r(nT), with only one control output u(nT). Both the error and the rate have two membership values, positive and negative while the output has three; positive, negative and zero. Based on the membership functions, the fuzzy control rules that we used are the following

Fr1: IF error = ep AND rate = rp THEN output = oz
Fr2: IF error = ep AND rate = rn THEN output =op
Fr3: IF error = en AND rate = rp THEN output =on
Fr4: IF error = ep AND rate = rn THEN output = oz

Here the output is the fuzzy control action Δu (nT), ep means error positive and oz means output zero etc., In the defuzzification center of mass formula is employed

$$\Delta u(nT) = \frac{rp \times oz + rn \times op + en \times on + en \times oz}{rp + rn + en + en} \quad (13)$$

We use op = 2; on = -3; z=0

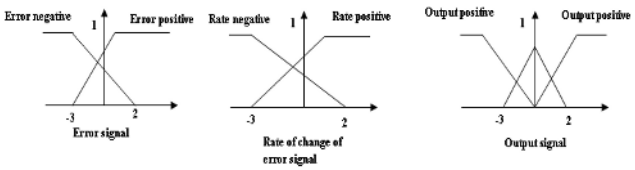


Fig.2 The membership function of e (nT), r (nT) and u (nT)

C. Design of Fuzzy PID controller

The Fuzzy PID controller is designed similar to that of PD controller and it has seven fuzzy control rules.

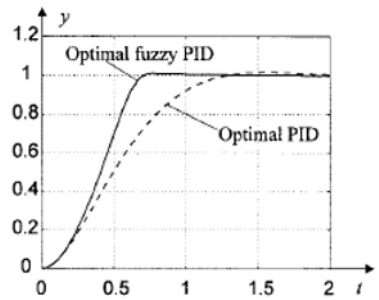


Fig.3 Step responses of optimal PID and optimal fuzzy PID controller

The simulation results of the design shows that the Fuzzy PID controller performs better than conventional PID controller.

IV. VLSI DESIGN OF FUZZY PROCESSOR

VLSI architecture is designed to implement the fuzzy based controller for insulin pumps in diabetic neuropathy patients. This implementation aims at improvement of speed and efficiency of the system. This can be done by incorporating parallel computing system to the architecture. In the design of Fuzzy PD&PID controller there are two inputs, the error signal, error rate and the output is the control signal for the insulin pump. The design we decided to develop was that of a low cost, high performance fuzzy processor with 5 inputs and a single control output.

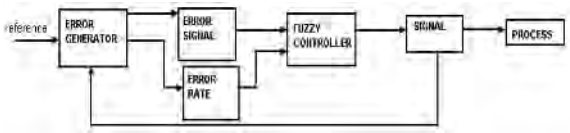


Fig.4: VLSI architecture of fuzzy controller

As shown in the block diagram the controller has an error generator, fuzzy controller, output control signal and the process of infusion being carried on by the insulin pump in a single injection process. In this work the fuzzy architecture is implemented and simulated using VHDL which is IEEE standard language for both simulation and synthesis. VLSI system is incorporated using VHDL Design unit called PROCESS. Atypical test bench is created using VHDL by which simulation of online testing is carried out.

V. FPGA IMPLEMENTATION OF FUZZY CONTROLLERS

Field Programmable Gate Arrays (FPGAs) represent reconfigurable computing technology, they are processors which can be programmed with a design, and then reprogrammed (or reconfigured) with virtually limitless designs as the designer's needs change.FPGA Generic Design Flow has three steps. They are Design Entry, Implementation, and Design verification. Design Entry is created by design files using a schematic editor or hardware description language. Design Implementation on FPGA has partition, place, and route to create bit-stream file. Design verification by using simulator to check function, other software determines max clock frequency.

In this paper the Xilinx Spartan-3 family of FPGA is used. Xilinx Spartan-3 features are low cost, high performance logic solution for high-volume, consumer-oriented applications. Table.2 & 3 shows the for the Device utilization summary for output membership function of Fuzzy PD & PID controllers synthesis process respectively. It shows

Table 2 Device Utilization Summary for Fuzzy PD controller output

Device Utilization Summary		
Logic Utilization	**Used**	**Available**
Number of Slice Latches	2	3,840
Number of 4 input LUTs	125	3,840
Logic Distribution		
Number of occupied Slices	66	1,920
Number of Slices containing only related logic	66	66
Number of Slices containing unrelated logic	0	66
Total Number of 4 input LUTs	125	3,840
Number of bonded IOBs	22	173
IOB Latches	2	
Number of MULT18X18s	4	12
Total equivalent gate count for design	17,016	
Additional JTAG gate count for IOBs	1,056	

Table 3 Device Utilization Summary for Fuzzy PID controller output

Device Utilization Summary		
Logic Utilization	**Used**	**Available**
Number of Slice Latches	202	7,168
Number of 4 input LUTs	593	7,168
Logic Distribution		
Number of occupied Slices	376	3,584
Number of Slices containing only related logic	376	185
Number of Slices containing unrelated logic	0	185
Total Number of 4 input LUTs	593	7,168
Number of bonded IOBs	43	97
IOB Latches	26	
Number of MULT18X18s	8	16
Number of GCLKs	2	8
Total equivalent gate count for design	38,165	
Additional JTAG gate count for IOBs	2,064	

that only less part of the resources are utilized for the FPGA synthesis process.

Densities up to 74,880 logic cells, Select IO™ signaling Up to 784 I/O pins, 622 Mb/s data transfer rate per I/O, 18 single-ended signal standards, Eight differential I/O standards including LVDS, RSDS. Logic resources are abundant logic cells with shift register capability. Wide, fast multiplexers, Fast look-ahead carry logic, Dedicated 18 x 18 multipliers, JTAG logic compatible with IEEE 1149.1/1532,

Select RAM™ hierarchical memory, Up to 1,872 Kbits of total block RAM, Up to 520 Kbits of total distributed RAM, Digital Clock Manager (up to four DCMs), Clock skew elimination, Frequency synthesis, High resolution phase shifting, Eight global clock lines and abundant routing. By using the RTL schematic internal components also can be analyzed.

VI. Results and discussion

The Implementation result shows that the Fuzzy PD controller has Minimum input arrival time before clock is 2.951 ns; Maximum output required time after clock is 7.078ns. The Fuzzy PID controller has Minimum period is 5.512ns (Maximum Frequency: 181.429MHz), Minimum input arrival time before clock is 6.657ns, Maximum output required time after clock is 6.141ns.The FPGA system is very simple in architecture and higher in performance with less power dissipation.FPGA Fuzzy control system, which is capable of processing under different input conditions.

The architecture is simulated with various values of error and error rate values. The initial conditions for the overall control systems have the following natural values. For the fuzzy control action $\Delta U(0) = 0$; for the system output y (0) =0and for the original error and rate signals e(0)=r (the set point) and r(0)=r respectively. For our diabetic pump which is a second order system [4], the transfer function is $H(S) = \frac{1}{s^2 + s + 1}$. we remark that the Fuzzy PD controller designed above has a self-timing control capability i.e., when the tracking error e(nT) keeps increasing, the term d(nT)=[e(nT)+e(nT-T)]/T becomes larger. In this case the fuzzy control action $\Delta u(nT)$ also keeps increasingly accordingly, which will continuously reduce the tracking error. Under the steady-state condition $|d(nT)| = 0$, we found that the control performance of the Fuzzy PD controller in VLSI Simulation is also as good as, if not better than the conventional controller.

VII. Conclusion

This paper discusses about the treatment of diabetic neuropathic patients using an automated Fuzzy PD&PID Controller system by FPGA. This system is designed by VLSI System and Implemented using FPGA technology. The control system consists of photoglucometer and an insulin pump. The simulation results have shown that this PD Controller overrides the conventional controller in handling non-linear inputs. In this paper it is assumed that the patient is continuously attached to the infusion pump and the blood glucose level is monitored at regular intervals. The VHDL code is implemented in FPGA and tested for its performance.

Acknowledgement

The author wish to express their sincere thanks to the Management, Principal and IEEE Student Branch Counselor of Bannari Amman Institute of Technology, Sathy for providing the necessary facilities for the completion of this paper. This paper is supported by the grants of IEEE Student Enterprise Award, 2007-2008.

References

1. Harikumar R and Selvan.S. Fuzzy controller for insulin pumps in diabetes. Proceedings of International Conference on Bio medical Engineering, Anna University, Chennai, India. pp 73-76, Jan.24-26, 2001.
2. Paramasivam K and R Harikumar and R Sundararajan, Simulation of VLSI design using Parallel Architecture For Epilepsy risk level diagnosis in diabetic neuropathy. IETE Journal of Research Vol50, no.4,pp 297-304, August 2004.
3. Giuseppe Ascia, Vincenzo Catania, and Marco Russo, VLSI Hardware Architecture for complex Fuzzy systems. IEEE Transaction on fuzzy systems, vol 7,No.5,pp 521-539,October 1999
4. Baogang Hu, George K.I. Mann, and Raymond G.Gosine, New Methodology for Analytical and Optimal design of fuzzy PID Controllers. IEEE Transactions on fuzzy systems,vol 7,No.5,October 1999
5. K.H.Kienitz and T.Yoneyama. A Robust Controller for Insulin pumps based on H-infinity Theory. IEEE Trans on BME, Vol 40, No: 11 pp 1133-1137, Nov 1993.
6. C.C.Lim and K.L.Teo. Optimal Insulin Infusion Control via a Mathematical Blood Glicoregulator Model with Fuzzy Parameters. Cybernatics and Systems: Vol 22, Pp 1-16, 1991.
7. B.Hu, G.K.I.Mann and R.G.Gosine. New Methodology for Analytical and Optimal Design of Fuzzy PID Controllers. IEEE Trans On Fuzzy Systems, Vol 7, No: 5 Pp 512-539, Oct1999.
8. C.-L.Chen and F.-C.Kuo. Design and analysis of a fuzzy logic controller. Int.J. Syst. Sci., vol.26, pp.1223-1248, 1995.
9. C.C.Lee, .Fuzzy logic in control systems: Fuzzy logic controller- part 1 and part 2 . IEEE Trans. Syst., Man, Cybern. Vol. 20 pp.404-435, 1990.
10. J. Rose, R. J. Francis, D. Lewis and P. Chow. Architecture of field-programmable gate arrays: The effects of logic block functionality on area efficiency. IEEE J. of Solid-State Circ., vol. 25, no. 5, pp. 1217-1225, Oct. 1990.
11. J. Di Giacomo. Design methodology in VLSI Handbook, J. Di Giacomo, Ed., New York: McGraw-Hill, pp. 1.3-1.9, 1989.
12. A. E. Gamal, et al. An architecture for electrically configurable gate arrays . IEEE J. of Solid-state Circ., vol. 24, no. 2, pp. 394-398, Apr.1989.
13. Xilinx- FPGA Reference Manual, 2006.

Position Reconstruction of Awake Rodents by Evaluating Neural Spike Information from Place Cells in the Hippocampus

G. Edlinger[1], G. Krausz[1], S. Schaffelhofer[1,2], C. Guger[1], J. Brotons-Mas[3], M. Sanchez-Vives[3,4]

[1]g.tec medical engineering GmbH, Graz, Austria
[2]University of Applied Sciences Upper Austria, Linz, Austria
[3]Instituto de Neurociencias de Alicante, Universidad Miguel Hernandez-CSIC, Alicante, Spain;
[4]ICREA – Institut d'Investigacios Biomediques August Pi i Sunyer, Barcelona, Spain

Abstract — **Place cells are located in the hippocampus of the brain and play an important role for spatial navigation. In this study neural spike activity of freely moving rats along with the position of the rats was acquired. The study was performed to investigate if position reconstruction is possible if the rat is freely moving in open arenas of different sizes based on neural recordings from CA1 and subiculum regions.**

The neural spike activity was measured using tetrodes from 6 chronically implanted rats in CA1 and subiculum regions. The position of the rats was monitored using a video tracking system .In the encoding step spike activity features of the place cells and position information from the rats were used to train a computer system. In the decoding step, the position was estimated from the neural spiking activity. Different reconstruction methods were implemented: (i) Bayesian 1-step and (ii) Bayesian 2-step. The results show, that the reconstruction methods are able to determine the position of the rat in 2-dimensional open space from cell activity measured in the CA1 and subiculum regions. Better accuracies were achieved for CA1 regions because the firing fields show more localized spots. Higher accuracies are achieved with a higher number of place cells and higher firing rates.

Keywords — **place cells, hippocampus, online position reconstruction, Bayesian 2-step method**

I. Introduction

Cells with spatially modulated firing rates have been found in almost all areas of the hippocampus and in some surrounding areas. Such place cells (PC) encode an internal representation of an animal's position in its environment. The background firing rate of a PC is very low (0.1 Hz), but when an animal enters the receptive field of the neuron, its firing rate rapidly increases (up to ~ 5- 15 Hz) [1,2]. The location inducing the increased cell activity is called the firing field (FF) or place field (PF) of the particular neuron. However, also other sensory cues can influence place cell activity, but visual and motion-related cues are the most relevant [3].

Recently place cells were also used to reconstruct the foraging path of rats by investigating the firing field patterns [1, 5]. In an encoding stage the place cell spiking activity together with video tracking information is used to train a computer system on the data. In a decoding stage only the spike activity is used to reconstruct the path of the animal. In this study it was of interest to test if position reconstruction is also possible in open environments in contrast to the linear arenas used in previous studies [5]. The reconstruction was tested in square arenas with different side length (0,5m, 0,7m, 0,1m, 1m) and a square arena with a smaller square barrier inside (outer square: 1m x 1m, inner square: 0,6 x 0,6m). Two different algorithms based on Bayesian methods were implemented after a Template matching approach was ruled out for reconstruction.

II. Material and methods

A. Neural spike and video data acquisition

Action potential data were measured from 6 rats from CA1 or subiculum by the Instituto de Neurociencias de Alicante (Universidad Miguel Hernández-CSIC, UMH), Institute of Cognitive Neuroscience (University College London, UCL) and Center for Neural Systems, Memory and Aging (University of Arizona, UA). The rats were connected to the recording system via a head stage pre-amplifier. From 1 to 8 tetrodes were used for the recordings. Each data channel was amplified up to 40,000 times and a sampling frequency of 48,000 Hz was used. For tracking purpose small infrared light-emitting diodes were attached to the rat's head and a video camera system was mounted above the experimental arena. The number of recorded cells, the recording region and the arena sizes and shapes are shown in Table 1. The sampling frequency for the position-tracking signal was 50 Hz (*UMH, UA*) and 46.875 Hz (*UCL*).

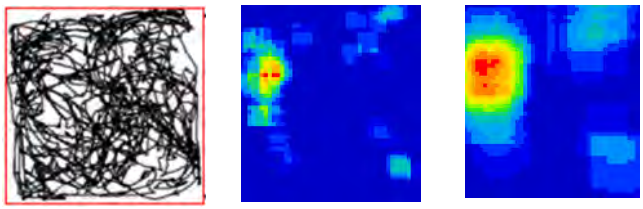
Table 1: Recording information of the 6 rats.

Rat #	1	2	3	4	5	6
No. of cells	5	26	9	6	4	11
Hippocampal region	CA1	CA1	CA1	CA1	Subiculum	Subiculum
Test field side length [m]	0,7	0,8	0,5	1	1	1
Test field shape						

Chwee Teck Lim, James C.H. Goh (Eds.): ICBME 2008, Proceedings 23, pp. 374–377, 2009
www.springerlink.com

B. Dwell Time and Firing Rate

In the first step the recorded spike activity was used as input for the cluster cutting. The cluster cutting was performed manually to separate neuronal activity picked up by the electrodes into single cell activity. In a second step firing rate maps were created. Therefore the arena was divided into small subsets of space and class labels were assigned to these subsets (pixels). Then the firing rate for each pixel was calculated by counting the number of spikes in each class. The test fields were divided into 64x64 classes, leading to an edge length for each class of 1.09 cm (rat 1), 1.25 cm (rat 2), 0.78 cm (rat 3) and 1.56 cm (rats 4, 5, 6). Figure 1A shows the movement trajectory of a rat obtained from the video tracking system for one full experiment with one rat.



A B C

Figure 1: A: arena divided into 64 fields, the cells are firing with a specific rate at each position. B: movement trajectories of the rat recorded with the video tracking system seen from top. C, D: firing maps of 1 neuron with different smoothing factors (5x5 and 10x10 Kernel).

The average firing rate of a cell *i* for each position $\boldsymbol{x}$ is described by the firing rate distribution, i.e. a vector of firing rates per cell *i*: $f(x) = (f_1(x), f_2(x), ..., f_N(x))$. In the training step, the firing rate maps *f(x)* are calculated for the whole population of *N* recorded cells and for every single position $\boldsymbol{x}$. The average firing rates are calculated from the total number of spikes collected for a cell while the rat was at position *S(x),* divided by the total amount of time the rat spent there *V(x).*

$$f(x) = \frac{S(x)}{V(x) \cdot \Delta t} \tag{1}$$

Δt is the time interval of the position tracking system.

The firing rate distribution is independent of how often the rat populates a certain position, it rather describes the tendency of a cell to fire at a given position $\boldsymbol{x}$ as shown in Figure 1B for one neuron.

C. Position reconstruction algorithms

First firing rates of all cells within a sliding time window are compared with the firing rate vectors of each class that were setup in the training phase. Depending on the algorithm, a matching class number is returned which identifies the reconstructed position. To calculate the reconstruction error, the reconstructed position can be compared to the position known from the position tracking data. Then the time window is moved to the next reconstruction position.

For position reconstruction the two algorithms were implemented that were already tested in linear arenas: (i) Bayesian 1-step and (ii) Bayesian 2-step with continuity constraint. For the analysis all datasets were divided into three equally long parts. Training was performed on two thirds of the recordings; the other third was used for the testing and reconstruction.

Bayesian method (1-step)

When the rat moves to specific positions then certain spike trains are produced as response to the sensory stimuli The probability of observing a number of spikes $n = (n_1, n_2, ..., n_N)$ given the stimulus $\boldsymbol{x}$ is $P(n \mid x)$. The probability of a stimulus (rat at position $\boldsymbol{x}$) to occur is defined as $P(x)$. The joint distribution

$$P(n, x) = P(n \mid x) \cdot P(x) \tag{2}$$

measures the likelihood of observing both a stimulus $\boldsymbol{x}$ and a spike train n.

For the reconstruction, the observation of a number of spikes n found in the measured data occur with a probability of $P(n)$. The likelihood of observing both stimulus and spikes is finally given by [5]

$$P(x \mid n) = C(\tau, n) \cdot P(x) \cdot \left(\prod_{i=1}^{N} f_i(x)^{n_i} \right) \cdot \exp\left(-\tau \cdot \sum_{i=1}^{N} f_i(x) \right) \tag{3}$$

Were $C(\tau, n)$ is a normalization factor and τ is the length of the time window. In this study the normalization factor $C(\tau, n)$ was set to 1.

The most probable position will be regarded as the animal's position:

$$\hat{x}_{Bayes,1-step} = \arg\max_{x} P(x \mid n) \tag{4}$$

Bayesian method with continuity constraint (2-step)

A continuity constraint can improve the accuracy of reconstruction. Sudden jumps in the reconstruction are observed by the low instantaneous firing rates of the recorded place cells. If not enough cells are firing then there is a lack of information. However the firing information is needed for the position reconstruction. The continuity constraint incorporates the reconstructed position from the preceding

time step as well as the current speed information. Based on the 1-step Bayesian method the reconstructed position at the preceding time step $t-1$ is also used to calculate the reconstructed position at time *t:*

$$P(x_t \mid n_t, x_{t-1}) = k \cdot P(x_t \mid n_t) \cdot P(x_{t-1} \mid x_t) \quad (5)$$

For more on this approach and details see [5].

III. Results

Figure 2 shows the reconstruction results computed with the Bayesian 2-Step algorithm of rat 3. Data from seconds 160 to 480 were used to train the algorithm and the interval 0 to 160 was used to test the method. The figure shows that the reconstructed path follows the real path very well in many data points of the recording. The mean reconstruction error of rat 3 was 9.5 cm. Figure 2 shows clearly erratic jumps of the reconstructed path in both x- and y-coordinates. If the reconstruction is only performed for time intervals where a minimum number of spikes (4 spikes in reconstruction window) are present the accuracy is increased as shown by the grey thin line in Figure 2B. In this case the mean error is 8 cm. Interesting is the erratic jump around second 51 were the running speed (Figure 2C) was almost 0.

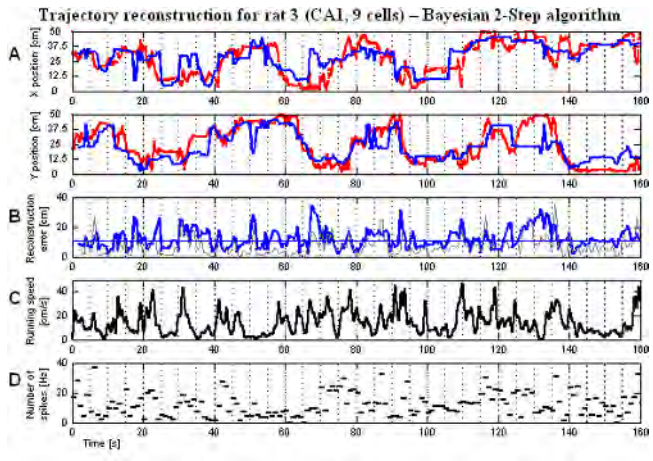


Figure 2: Reconstruction results for rat 3. A: Real (red) and reconstructed x- and y-positions. B: Reconstruction error (thick line), reconstruction error weighted by the instant place cell firing rate (thin line) and median error of the whole recording (horizontal line). C: Running speed. D: Firing rate of all neurons.

The two reconstruction algorithms were tested on all 6 rats by using a 3 x 3 fold cross-validation technique. Additionally, the Bayesian 2-step algorithm was trained and tested on 100 % of the data to test the theoretically achievable accuracy. In Figure 3 one example of CA1 cells and one example for subiculum cells are shown. Rat 3 reached a minimum error of 9.4 cm for a reconstruction window of 4 seconds using CA1 neurons. Rat 6 reached 26 cm with subicular units. For all rats the Bayesian 2-step (100 % training) version performed obviously best.

The horizontal dotted line at 5cm in each graph displays the intrinsic tracking error, which is defined as the average uncertainty in position tracking, due to the size of the diode (LED) arrays, the distance of the diodes above the rat's head and variations in posture [6].

IV. Discussion

The reconstruction algorithms for neural spike trains were implemented and applied to hippocampal place cell activity. The goal was to reconstruct the position of the rats just by investigating the spike activity as accurate as possible and therefore to minimize the reconstruction error. The best performance was found for the Bayesian 2-Step algorithm. The reason is that the algorithm considers also the previous position of the rat and does not allow large jumps from one reconstruction point to the next one. The Bayesian 1-Step algorithm performed less accurate but it is very interesting to see the results because it is only based on the current reconstruction window.

Despite subicular units tend to be more stable than CA1 cells, the results show that position reconstruction is more accurate with CA1 units. However, it is also interesting that subicular units contain enough information for the reconstruction. This can also be seen from the place field density plots, where the place fields of subicular units are much more blurred than place fields of CA1 units. Distinct place fields in combination with a high number of cells guarantee good reconstruction results. But it must be noted that only 2 data-sets from the subiculum and 4 data-sets from CA1 regions were investigated. The investigation of more data-sets is necessary to proof that.

Theoretically the reconstruction error is inversely proportional to the square root of the number of cells. This has been confirmed by the data analysis of all 6 rats as well as in other publications [5,7]. Interesting is that for 3 rats (1, 2, 3) the reconstruction error was below 20 cm with less than 10 place cells. Wilson [7] reported an error of 33 cm with 10 cells and Zhang [5] of 25 or 11 cm for 10 cells. This shows that with even a few cells the reconstruction can already be performed. But important is to consider the different arena sizes.

Erratic jumps occur also when the animal stops running. This has two reasons: (i) the firing rate is modulated by speed and therefore lower and (ii) the animal received food

rewards to move around in the arena and therefore the eating can produce artifacts in the neural data recorded. Zhang also suggests biological reasons for the erratic jumps like the rat is looking around or planning the next move. As already mentioned in the results section, minimizing the reconstruction to points where the firing rate is above a certain threshold only punctually yields to better reconstruction results. It does not reduce the overall error rate, because the positions that have not been reconstructed have to be interpolated. This estimation leads to reconstruction errors for the interpolated positions again, and increases the error rate.

Next steps in this research will include the investigation of grid cells as well as the realization of real-time reconstruction hardware and software setup.

Acknowledgement

This work was supported by the EU-IST project Presenccia.

References

1. O'Mara S. M. (1995). Spatially selective firing properties of hippocampal formation neurons in rodents and primates. Progress in Neurobiology Vol. 45, 253-274
2. Anderson M. I. and O'Mara S. M., (2003) Analysis of recordings of single-unit firing and population activity in the dorsal subiculum of unrestrained, freely moving rats. *The Journal of Neurophysiology* Vol. 90 No. 2, 655-665
3. Poucet B., Lenck-Santini P. P., Paz-Villagrán V. and Save E. (2003) Place cells, neocortex and spatial navigation: a short review. *J Physiol Paris* Vol. 97 Issues 4-6, 537-546
4. Brown E. N., Frank L. M., Tang D., Quirk M. C. and Wilson M. A. (1998) A Statistical Paradigm for Neural Spike Train Decoding Applied to Position Prediction from Ensemble Firing Patterns of Rat Hippocampal Place Cells. *The Journal of Neuroscience* Vol. 18(18), 7411-7425
5. Zhang K., Ginzburg I., McNaughton B. L. and Sejnowski T. J. (1998) Interpreting Neuronal Population Activity by Reconstruction: Unified Framework With Application to Hippocampal Place Cells. *The Journal of Neurophysiology* Vol. 79, No. 2, 1017-1044
6. Skaggs W. E., McNaughton B. L., Wilson M. A. and Barnes C. A. (1996) Theta Phase Precession in Hippocampal Neuronal Populations and the Compression of Temporal Sequences. *Hippocampus* Vol. 6(2), 149-172
7. Wilson M. A. and McNaughton B. L. (1993) Dynamics of the Hippocampal Ensemble Code for Space. *Science* Vol. 261 (5124), 1055-1058.

Heart Rate Variability Response to Stressful Event in Healthy Subjects

Chih-Yuan Chuang, Wei-Ru Han and Shuenn-Tsong Young

Institute of Biomedical Engineering, National Yang-Ming University, Taipei, Taiwan

Abstract — **The purpose of this study was to investigate the autonomic nervous system function in healthy subject under stress event by analyzing heart rate variability (HRV). The participants were eight graduate students exposed to a cognitive stress task involving preparation for an oral presentation. Measurements of subjective tension, muscle bound level and electrocardiograms of 5 minutes were obtained at 30 minutes before oral presentation as pretest and at 30 minutes after oral presentation as posttest. R-R intervals of electrocardiogram were calculated, and the R-R intervals' tracks were analyzed using power spectral analysis to quantify the frequency domain properties of HRV. The results showed that subjective tension, muscle bound level and heart rate were significantly higher in pretest and normalized high frequency power of HRV was significantly lower in pretest, compared with posttest. These findings suggest that stress event will reduce cardiovascular parasympathetic nervous responsiveness and increase sympathetic nervous responsiveness and subjective tension. The normalized high frequency power of HRV can response the affective state under stress event. This psychophysiology measurement will be used for detect human affective state and stress management.**

Keywords — **Autonomic nervous system, Heart rate variability, Stress, Tension**

I. Introduction

Mental stress can cause psychosomatic and other types of disease. Quantitative evaluation of stress is very important for disease prevention and treatment.

Heart rate variability (HRV) is the variation in the time interval between heartbeats, from beat to beat. It is controlled by autonomic nervous system including the sympathetic nervous system (SNS) and the parasympathetic nervous system (PNS). Generally, the SNS activity increases heart rate and the PNS activity decreases heart rate [1]. Frequency-domain analysis of HRV can obtain the HRV spectrum which is a noninvasive tool for the evaluation of autonomic regulation of the heart. HRV spectrum can be categorized into high-frequency (HF 0.15-0.40Hz) and low-frequency (LF 0.04-0.15Hz) components. The HF component is equivalent to the respiratory sinus arrhythmia (RSA) and is generally assumed to represent parasympathetic control of heart. The LF component is jointly contributed by both sympathetic and parasympathetic nerves. The ratio LF/HF is considered to reflect sympathetic modulation.

A reduction of HRV has been associated with several cardiologic diseases, especially lethal arrhythmic complications after an acute myocardial infarction [2]. Therefore, HRV is often used as a predictor of disease risk [3]. A reduced HRV is also associated with psychosocial factors such as stress, anxiety, and panic disorder [4]. It is suggested as a good tool to estimate the strength of psychological effects [5].

Previous studies reported that the HF component of HRV significantly increased during relaxation training, and the cardiac parasympathetic tone also increased associating with relaxation response [6].

The purpose of this study was to investigate the autonomic nervous system function and subjective tension in healthy subject under stress event. We hypothesized those participants who are exposed to a cognitive stress task will demonstrate significant higher tension, higher muscle-bound level and lower arousal of parasympathetic nervous system compared to finish stress task.

II. Methods

A. Experimental Protocol

The participants were recruited from Institute of Biomedical Engineering, Nation Yang Ming University. Total of 8 healthy graduate students, aged 22-32 without symptoms or histories of cardiovascular or other diseases were recruited in this study. The participants were exposed to a cognitive stress task involving preparation for one-hour oral presentation. The presentations were related to participants' research topics.

Measurement of subjective tension, muscle-bound level and electrocardiogram (ECG) of 5 minutes were obtained at 30 minutes before oral presentation as pretest and at 30 minutes after oral presentation as posttest (Fig. 1). Instantaneous ECG recordings were taken for 5 min while each subject sat quietly and breathed normally.

ECG recordings were obtained by Biopac ECG-100C, digitalized using a 14-bit analog-to-digital converter (NI USB-6009, National Instruments) with a sampling rate of 1024 Hz, and stored on a personal computer for off-line analysis.

Chwee Teck Lim, James C.H. Goh (Eds.): ICBME 2008, Proceedings 23, pp. 378–380, 2009
www.springerlink.com

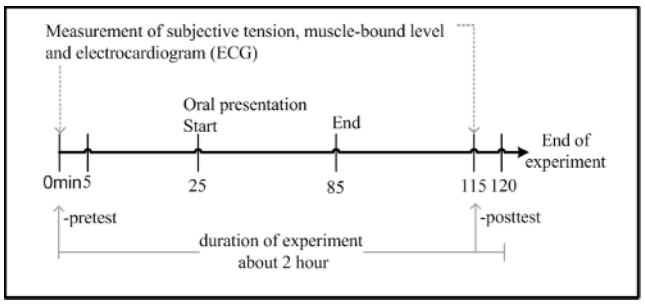


Fig. 1 Experiment procedure

Participants also rated their subjective tension and muscle-bound level on five-point scales which ranged from "very little"(1) to "very much"(5).

B. Data Analysis

The HRV analysis of ECG signals was performed with a standard procedure [3]. The R point of each valid QRS complex was defined as the time point of each heart beat, and the interval between two R points (R-R interval) was calaculated. Frequency-domain analysis of HRV was also performed using the nonparametric method of Fourier transform. For the ECG of 5 minutes, the R-R intervals were linearly interpolated to produce a continuous track by 3Hz resample rate, and the track was analyzed by Fourier transform with a hamming window to have the power sectrum of HRV. The HRV power spectrum was subsequently quantified into various frequency-domain indices as total power, LF (0.04-0.15 Hz) and HF (0.15-0.40 Hz) power, LF and HF in normalized units (LF%, HF %), and ratio of LF to HF (LF/HF).

Statistical data analysis was performed using software SPSS 15.0. Data were expressed as mean and standard error (SE). Comparisons of the HRV indices and subjective tension between pretest and posttest were performed with the Mann-Whitney U-test. Significant levels were assumed at $p<0.05$.

III. Results

The study data consisted of 8 male healthy graduate students. Each participant was evaluated within two times.

Quantitative measurements of HRV indices from the the 8 pariticipants showed that the pretest had significantly lower %HF power of HRV and significantly higher heart rate compared with the posttest ($P<0.05$)(Table 1). However, mean HF, LF, %LF power, total power and L/H ratio were no significant differ between pretest and posttest.

Table 1 Heart Rate and Heart Rate Variability indices

	Pretest (M±SE)	Posttest (M±SE)	p value
HR	96.38±6.49	80.96±5.04	0.011
HF(ms2)	267.62±154.73	215.04±69.69	0.483
LF(ms2)	874.15±296.56	649.18±239.30	0.262
%HF	20.51±4.45	31.34±6.66	0.035
%LF	84.40±4.10	73.15±7.0	0.068
LF/HF	6.21±1.70	4.37±1.51	0.262
TP	2589.96±1534.29	1307.83±350.46	0.888

Values are presented as means ± SE; HR: heart rate, LF: low-frequency power, HF: high-frequency power, LF/HF: ratio of LF to HF, and LF%: normalized LF in normalized units (nu) of heart rate variability; P values: vs. pretest by Mann-Whitney U-test.

The assessments of subjective tension were changed in the levels on the five-point scales (Table 2). The mean value of tension and muscle-bound level in pretest were significant higher than those in posttest ($p<0.05$).

Table 2 Subject assessment of tension, muscle-bound

	Pretest (M±SE)	Posttest (M±SE)	p *value*
Tension level	3.87±0.64	1.62±0.74	0.009
Muscle bound level	2.62±0.74	1.5±0.75	0.024

Values are presented as means ± SE; P values: vs. pretest by Mann-Whitney U-test.

IV. Discussion

In the present study, we reliably described the measurable changes in subjective tension in response to the preparation for an oral presentation. The tension and muscle-bound level were significant higher at preparation time compared with those at time after finishing the oral presentation.

The high frequency component of the HRV has been reported to reflect the activity of vagal parasympathetic nerve, and the LF/HF ratio to reflect the activity of sympathetic nervous system [7]. Mental stress will change the balance of the activities between sympathetic and parasympathetic nervous system. The present study found the LF and LF/HF

ratio were higher during pretest compared with posttest. Low frequency component reflected the activities of sympathetic nervous system, preparation for an oral presentation task might activate sympathetic nervous system. On the other hand, the preparation for an oral presentation task caused significant increase of heart rate and decrease of normalized high frequency power of HRV. These results regarding HRV support the findings of previous studies [8]. The high frequency component of HRV was reduced during stress tasks. Therefore, these results suggest that the mental stress task can decrease the parasympathetic nervous activity and the %HF power may be sensitive to stress elicitation and reduction.

In conclusion, the %HF power of HRV can response the affective state under stress event. This psychophysiology measurement will be used for detect human affective state and stress management.

REFERENCES

1. Sherwood L (2006): Human physiology : from cells to systems 6th ed ed: Belmont, CA : Thomson.
2. Terathongkum S, Pickler RH (2004): Relationships among heart rate variability, hypertension, and relaxation techniques. J Vasc Nurs 22:78-82; quiz 83-74.
3. (1996): Heart rate variability: standards of measurement, physiological interpretation and clinical use. Task Force of the European Society of Cardiology and the North American Society of Pacing and Electrophysiology. Circulation 93:1043-1065.
4. Vrijkotte TG, van Doornen LJ, de Geus EJ (2000): Effects of work stress on ambulatory blood pressure, heart rate, and heart rate variability. Hypertension 35:880-886.
5. Roscoe AH (1992): Assessing pilot workload. Why measure heart rate, HRV and respiration? Biol Psychol 34:259-287.
6. Sakakibara M, Takeuchi S, Hayano J (1994): Effect of relaxation training on cardiac parasympathetic tone. Psychophysiology 31:223-228.
7. Kuo TB, Lin T, Yang CC, Li CL, Chen CF, Chou P (1999): Effect of aging on gender differences in neural control of heart rate. Am J Physiol 277:H2233-2239.
8. Hughes JW, Stoney CM (2000): Depressed mood is related to high-frequency heart rate variability during stressors. Psychosom Med 62:796-803.

Author: Chih-Yuan Chuang
Institute: Institute of Biomedical Engineering, National Yang-Ming University
Street: No. 155, 2 Sec., Li-Nung St., Shih-pai
City: Taipei
Country: Taiwan
Email: edwin@bme.ym.edu.tw

Automatic Quantitative Analysis of Myocardial Perfusion MRI

C. Li and Y. Sun

Department of Electrical & Computer Engineering, National University of Singapore, Singapore

Abstract — **In this paper, we propose an automatic analysis method to facilitate the quantitative evaluation of myocardial perfusion MR images. We first extract the perfusion parameters from the intensity-time curve and combine them in a color image, in which myocardial ischemia is relatively easy to detect. Then we use the appropriate parameter maps to segment the myocardium by evolving level set functions. The experimental results show that the proposed method succeeds in extracting parameters and segmenting the myocardium.**

Keywords — **myocardial perfusion MRI, parameter map, level set, image segmentation, temporal information**

I. Introduction

Segmentation is an important step in MR image analysis. Due to the low contrast and complicated background in myocardial perfusion MR images, most of the popular segmentation techniques based on single frames either are not robust enough or require manual initialization.

Several methods incorporating temporal information into myocardium segmentation have been proposed. Stegmann et al. proposed a motion-compensation method using active appearance model with cluster analysis [1]. This method is learning-based and requires training sets provided by medical doctors. Spreeuwers et al. proposed a boundary correction method using perfusion information, assuming that a rough segmentation has been provided [2]. In [3], Adluru et al. use the temporal variance image to locate the heart, select reference frame, and initialize the segmentation. They then independently obtain the myocardium masks in several frames adjacent to the reference frame and threshold the sum of these masks to generate the myocardium boundary. Although better than using one frame for segmentation, this method relies too much on the image quality of the chosen frames. Recently, Schöllhuber classifies the myocardium and the background according to the intensity-time curve and then converts the segmentation problem into a shortest path problem [4]. Because the classifier does not consider any spatial information, the myocardial boundaries are often not smooth and hence need refinement.

Here we propose a method that first extracts the perfusion parameters and then automatically segments the myocardium using the parameter maps. The final results can be shown in a color image that combines the extracted perfusion parameters as well as the myocardium mask.

The rest of this paper is organized as follows: In section II, we introduce the temporal characteristics of myocardial perfusion MRI. Our method for parameter extraction is described in section III. Section IV presents the experimental results, and we conclude the paper with section V.

II. Background

First-pass myocardial perfusion MR images are scanned immediately after the injection of a contrast agent. Fig.1 displays four representative frames of a typical first-pass myocardial perfusion sequence, while Fig.2 plots the intensity-time curves of pixels from different tissues. As can be seen, the intensity of the right ventricle (RV) increases due to the wash-in of the contrast agent, followed by the left ventricle (LV), and then the myocardium. In contrast, the intensity-time curve of the background is like noise during the entire perfusion period.

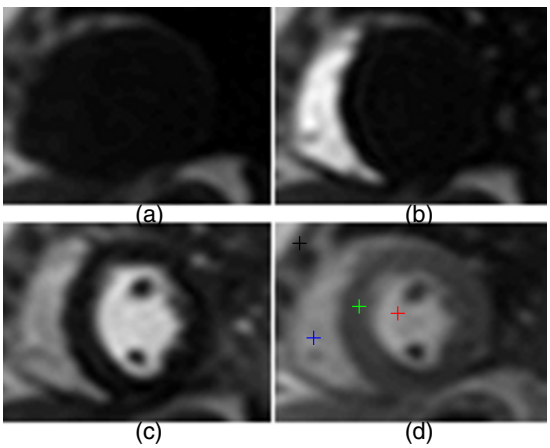


Fig. 1 Myocardial perfusion MR images: (a) the 5th frame, (b) the 15th frame, (c) the 20th frame, (d) the 40th frame

The intensities of pixels from the same tissue usually vary in a similar way, i.e., they follow the same intensity-time curve model. Such a model can be characterized by several perfusion parameters such as *maximum upslope*, *peak*, and *absolute time to peak* (refer to III-*B* for defini-

Chwee Teck Lim, James C.H. Goh (Eds.): ICBME 2008, Proceedings 23, pp. 381–385, 2009
www.springerlink.com

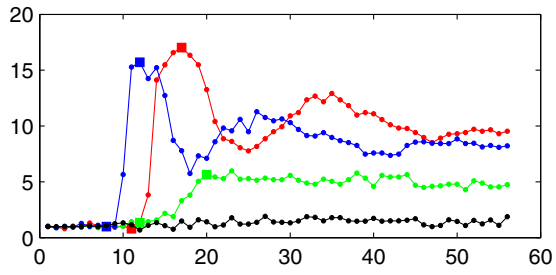


Fig. 2 Intensity-time curves of RV (blue), LV (red), myocardium (green), and background (black). The positions of these pixels are shown in Fig. 1 in corresponding colors

tions), etc. It is reasonable to use these distinctive parameters for myocardium segmentation.

III. Methodolagy

Our method consists of three steps. First, an image registration algorithm is used to compensate for patient motion. Second, we calculate perfusion parameters including *maximum upslope*, *peak*, and *absolute time to peak,* based on the intensity-time curve of each pixel; a combination of these parameters is displayed in a color parameter map for visualization. Finally, automatic detection of the myocardial boundaries is achieved by applying a region based level set method with shape priors using appropriate parameter maps.

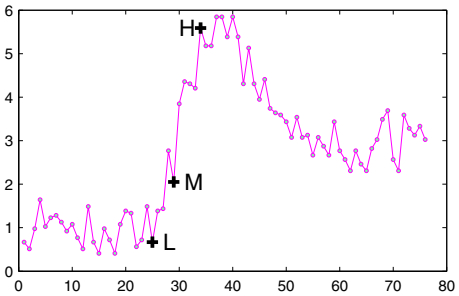


Fig. 3 Intensity-time curve of a myocardium pixel

A. Registration

Before applying registration, a reference frame is automatically selected and the LV mask is detected. To achieve this, we first find a range of frames with good contrast by assessing temporal intensity variation. For each selected frame, a binary image is obtained by thresholding. Then we remove small connected components, and look among remaining components for the one being least eccentric, most circular, and most convex. The winner corresponds to the LV mask, and its frame number is the reference frame number. We then apply a rigid registration algorithm to register the time series to the reference frame [5].

B. Parameter extraction

Fig.3 shows the intensity-time curve of a myocardium pixel. When calculating the *maximum upslope*, *absolute time to peak*, and *peak*, it is crucial to determine the start instant and the end instant of the wash-in phase. Due to the image noise and the limitations of motion compensation, the local gradient during the wash-in phase is not always positive, and the intensity at the end of the wash-in phase is not always the global maximum. These issues make the parameter extraction step more challenging.

For each intensity-time curve, we first normalize it with respect to the average intensity of the first four frames. Then we generate a smooth curve by applying a moving average filter in the time domain. After that, we estimate the center M and the average local gradient Δh of the wash-in phase, using the smoothed curve.

Let L and H denote frame indices of the start and the end of the wash-in phase, respectively. Let N denote the total number of frames, and let $I(n)$ denote the pixel intensity in the n^{th} frame. Then H is defined as the smallest frame number n that satisfies the following conditions.

$$\begin{cases} M < n < N-2 \\ I(n) > I(n+1) \\ I(k) < I(n) + (k-n) \times \Delta h,\ k = n+2, n+3, \ldots, N \end{cases} \quad (1)$$

Similarly, L is defined as the largest frame number n that satisfies:

$$\begin{cases} 2 < n < M \\ I(n) < I(n-1) \\ I(k) > I(n) - (n-k) \times \Delta h,\ k = 1,2,\ldots,n-2 \end{cases} \quad (2)$$

Next we use a small window sliding from L to H to calculate the local upslope, and select the maximum of them to be the *maximum upslope*; the *peak* is calculated by $I(H) - I(L)$; and the *absolute time to peak* is given by H.

By using each parameter as one color channel, an RGB color map is generated. All the parameters are normalized for better contrast. To prevent the background from dominating the normalization, in the final results, we only show the parameter map of the myocardium for visualization.

C. Myocardium segmentation

To segment the myocardium of the LV, we need to detect two boundaries: the endocardial boundary between the myocardium and the LV blood pool, and the epicardial boundary between the myocardium and the background. In our method, we first segment the endocardium and then segment the epicardium based on the segmentation results of the endocardium.

As shown in Fig.2, the intensity of the LV blood pool increases faster than that of the myocardium during the wash-in of the contrast agent. In addition, the *maximum upslope* is less sensitive to the choices of L and H than the other two parameters. Therefore, we use the *maximum upslope* map (see Fig.5 (a)) to segment the endocardium.

The epicardium is more difficult to segment than the endocardium due to the complicated background. In the *maximum upslope* map shown in Fig.5 (a), the RV is brighter than the myocardium while many other areas of the background are darker than the myocardium. This makes it hard to estimate the intensity distribution model of pixels outside the epicardium. The *peak* map also has similar problem since the *peak* of the RV is larger than that of the myocardium (see Fig.2). As shown in Fig.5 (b), the intensities of the RV and the background are similar in the *absolute time to peak* map. Therefore, we chose to use the *absolute time to peak* map for epicardium segmentation.

The energy functional is defined as:

$$E = \lambda_1 E_{region} + \lambda_2 E_{shape} + \lambda_3 E_{length} + \lambda_4 E_{penalizing}, \quad (3)$$

where λ_1, λ_2, λ_3, and λ_4 are constant parameters balancing different energy terms.

Assuming that the intensities of the background and the foreground follow Gaussian distributions, we use the stochastic region model [6] for E_{region}. In each iteration, we fix the contour and estimate the Gaussian intensity models for the inside and outside of the contour, respectively, as $M_i\left(\overline{I_i}, \sigma_i\right)$ and $M_o\left(\overline{I_o}, \sigma_o\right)$. The region term is given by

$$E_{region} = \iint_{in(c)} \left(-\ln M_i\right) dxdy + \iint_{out(c)} \left(-\ln M_o\right) dxdy .$$

Based on the assumption that the shape of myocardium is close to an ellipse, we use the shape prior term E_{shape} to incorporate such prior knowledge [6, 7], and define the shape energy term as

$$E_{shape} = \iint D^p \delta_x \left|\nabla \phi(x, y)\right| dxdy ,$$

where D is the normalized distance to the estimated ellipse.

When estimating the ellipse, we first generate the convex hull of the contour, and then calculate the distance d of each point on the contour to the convex hull. According to this distance, we assign a weight of $w = \exp\left(-d^2/2\right)$ to each point, such that the points close to the papillary muscles contribute less in estimating the ellipse. Finally we estimate the ellipse using weighted least square fitting [8].

Fig.4 shows the estimated ellipse and the force vectors at five contour points for endocardium segmentation. In order to keep the LV cavity pixels inside the evolving contour, we set $D=0$ for pixels outside the estimated ellipse. As a result, the black arrows in Fig. 4 will not take effect.

For endocardium segmentation, we set $p=4$ for less penalty on the pixels near the estimated ellipse, thus maintaining the shape of the LV. For epicardium segmentation, we set $p=2$, and penalize both sides of the estimated ellipse to make the boundary resemble an ellipse.

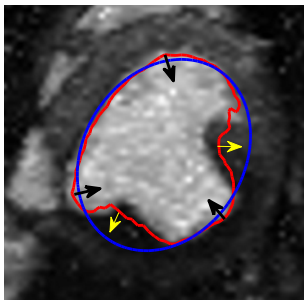


Fig. 4 Ellipse fitting: The red curve is the current contour; the blue curve is the estimated ellipse; and the arrows indicate the force vectors resulting from the shape term at five selected points on the contour

E_{length} in (3) controls the smoothness of the contour:

$$E_{length} = \iint \delta_x \left|\nabla \phi(x, y)\right| dxdy .$$

The penalizing term $E_{penalizing}$ in (3) helps avoid re-initialization [9] and is defined as

$$E_{penalizing} = \iint \frac{1}{2}\left(\left|\nabla \phi\right| - 1\right)^2 dxdy .$$

We use the LV mask in III-*A* as the initial contour for endocardium segmentation. After the energy functional converges, we expand the resulting endocardial contour outwards by 5 pixels to obtain the initial contour for epicardium segmentation.

IV. Results

We tested the proposed method on two animal data sets and four patient data sets. The automatic quantitative analysis tool succeeds in generating the parameter maps and automatically segmenting the myocardium.

Fig.5 (a)-(c) show the *maximum upslope* map, the *absolute time to peak* map, and the segmentation results of one animal data set. As shown, although the myocardial boundaries, especially the epicardial boundary, are not clear in the reference frame, these two boundaries are easy to detect in the *maximum upslope* map and the *absolute time to peak* map, respectively. Segmentation results of one animal data set and 3 patient data sets are shown in Fig.6, demonstrating the effectiveness and accuracy of the proposed method.

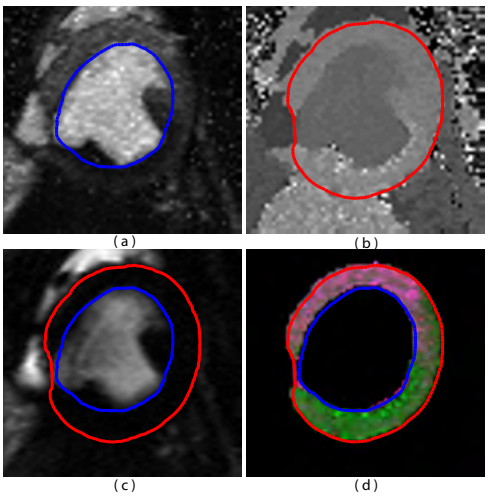


Fig. 5 Segmentation results and parameter maps: (a) the *maximum upslope* map, (b) the *absolute time to peak* map, (c) the reference frame with segmentation results overlaid, and (d) the final color parameter map

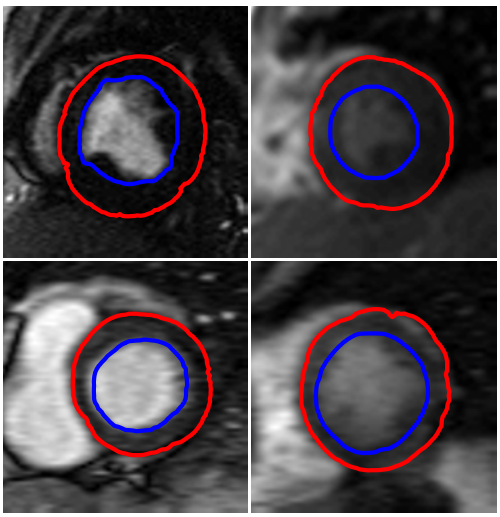


Fig. 6 Segmentation results of one animal and three patient data sets

Ischemic myocardium usually demonstrates delayed wash-in and lack of increase in intensity, which results in larger *absolute time to peak* and smaller *maximum upslope*. Fig.5 (d) shows the color parameter map of an animal data set, in which a bright green area in the LV free wall indicates a myocardial perfusion defect (ischemia).

V. Conclusions

In this paper, we presented an automatic quantitative analysis tool for first-pass myocardial perfusion MRI. By combining distinct perfusion parameters including *maximum upslope, peak* and *absolute time to peak* that are extracted from the intensity-time curves, in a single color map, the ischemic tissues can be easily identified. By using the appropriate corresponding parameter map for segmenting the endo and epicardium, the myocardial boundaries can be detected using a level set based method with an elliptical shape prior. Our experimental results with real patient data sets show that the proposed method can successfully generate parameter maps and segment the myocardium.

Acknowledgment

The authors would like to thank Stefan Schoenberg from the Institute of Clinical Radiology, Klinikum Grosshadern, Munich, Germany, for providing the datasets. This work was supported by NUS grant R-263-000-470-112.

References

1. Stegmann MB, Larsson HBW (2003) Motion-Compensation of cardiac perfusion MRI using a statistical texture ensemble. FIMH 2003, pp 151-161
2. Spreeuwers LJ et al. (2002) Automatic correction of myocardial boundaries in MR cardio perfusion analysis. CARS 2002, pp 902-907
3. Adluru G, et al. (2006) Automatic segmentation of cardiac short axis slices in perfusion. ISBI 2006, Virginia, 2006, pp 133-136
4. Schöllhuber A (2008) Fully automatic segmentation of the myocardium in cardiac perfusion MRI. CESCG 2008 (available at http://www.cescg.org/CESCG-2008/papers/VRVis-Schoellhuber-Andreas.pdf).
5. Sun Y, Jolly MP, Moura JMF (2004) Contrast-invariant registration of cardiac and renal MR perfusion images. MICCAI Proc. vol 3216, France, 2004. pp 903-910
6. Pluempitiwiriyawej C, Moura JMF et al. (2005) STACS: new active contour scheme for cardiac MR image segmentation. IEEE Trans. Medical Imaging. vol 24, no. 5, 2005, pp 593-603

7. Chen T et al. (2008) Semiautomated segmentation of myocardial contours for fast strain analysis in cine displacement-encoded MRI. IEEE Trans. Medical Imaging. vol 27, no. 8, 2008, pp 1084-1094
8. Fitzgibbon A et.al. (1999) Direct least square fitting of ellipses. IEEE Trans. Patt. Analy. and Mach. Intell. vol 21, no. 5, 1999, pp 476-480
9. Li CM, Xu CY et al. (2005) Level set evolution without re-initialization: A new variational formulation. CVPR. vol 1, San Diego, 2005, pp 430-436

Author: Li Chao
Institute: Department of Electrical & Computer Engineering,
Street: National University of Singapore
City: Singapore
Country: Singapore
Email: chaoli@nus.edu.sg

Visualization of Articular Cartilage Using Magnetic Resonance Imaging Data

C.L. Poh[1] and K. Sheah[2]

[1] Nanyang Technological University/Division of Bioengineering, Singapore
[2] Singapore General Hospital/Department of Diagnostic Radiology, Singapore

Abstract — **Osteoarthritis (OA) is a common disease, with the majority of people over 65 showing radiographic evidence of the disease. To carry out effective diagnosis and treatment, it is necessary to understand the progression of cartilage loss and to study the effectiveness of therapeutic interventions. Hence, it is important to have accurate and fast diagnosis of the disease. Magnetic Resonance Imaging (MRI) is the most widely used non-invasive tool to assess intra articular soft tissues, and cartilage in particular. MRI allows detailed, multi-planar analysis of the joint anatomy, as well as cartilage and underlying bone, with the ability to view articular surfaces at any angle. In addition to anatomical information, MR $T_{1\rho}/T_2$ mapping are potentially useful parameters in detecting early biochemical and biophysical changes in the articular cartilage. However, the presence of both anatomical and $T_{1\rho}/T_2$ mapping data results in a large amount of multi-dimensional dataset. Consequently, clinicians have to study more data, which is a time consuming process. New visualization techniques are required to aid clinicians to visualize the large amount of data. In this paper, we present a visualization interface to study articular cartilage using MR data. This interface allows studying of OA using both anatomical images and T_2 mapping data. The interface includes semi-automatic segmentation of cartilage using localized thresholding; and visualization of the averaged T_2 mapping data at various regions of the cartilage in 2D/3D using a radii search method. Our results suggest that the visualization technique allows clinicians to study both anatomical images and T_2 mapping data in a more efficient manner.**

Keywords — **Magnetic Resonance Imaging, Visualization, Osetoarthritis**

I. Introduction

Many adults suffer from Osteoarthritis (OA), with the majority of people over 65 showing radiographic evidence of the disease [1]. To carry out effective diagnosis and treatment, it is necessary to understand the progression of cartilage loss and to study the effectiveness of therapeutic interventions. Hence, it is important to have accurate and fast diagnosis of OA. In this context, the use of Magnetic Resonance Imaging (MRI) has gained significant support. MRI allows detailed, multi-planar analysis of the joint anatomy, as well as cartilage and underlying bone status, with the ability to view articular surfaces at any angle. MRI is becoming the recognized imaging method for accurate visualization of cartilage morphology and thickness depiction.

Early detection of cartilage disorder is important to predict the progression of OA, and to determine the appropriate timing for treatment. MR images have been used to provide high-resolution anatomical information to detect degenerated cartilage [2]. However, using MR anatomical images alone is unlikely to show early degeneration of cartilage [3]. In addition to anatomical information, $T_{1\rho}/T_2$ mapping are potential parameters in detecting early biochemical and biophysical changes in the articular cartilage [4-6]. $T_{1\rho}/T_2$ mapping could provide the functional information of the articular cartilage. Loss of proteoglycans in the extracellular matrix (ECM) is an initiating event in early OA [4-5]. Previous studies indicate that T_2 of articular cartilage is only sensitive to the collagen content in the ECM and T_2 is less sensitive to loss of proteoglycans [4-5]. On the other hand, $T_{1\rho}$ relaxation time is sensitive to changes in the proteoglycans content of cartilage and $T_{1\rho}$ decreases linearly with changes in the proteoglycans content of cartilage [4]. T_2 mapping has been shown to have the potential in detecting localized degeneration of cartilage [6]. It has been shown that aging is associated with an asymptomatic increase in T_2 of the transitional zone of articular cartilage [6].

The presence of both anatomical and $T_{1\rho}/T_2$ mapping data results in large amount of multi-dimensional dataset. Consequently, clinicians have to study more data to make a diagnosis, which increases the time needed. Hence, new visualization techniques are required to aid clinicians to study the large amount of data.

In this paper we present a visualization interface to study articular cartilage using MR data. This interface allows studying of the OA disease using both anatomical images and T_2 mapping data. The interface developed in this paper includes (i) semi-automatic segmentation of cartilage using localized thresholding, and (ii) visualization of the averaged T_2 mapping data at various regions of the cartilage in 2D/3D using a radii search method. To demonstrate the interface, 3T MR knee datasets (i.e. T_2 weighted images and T_2 mapping data) of patients with varying degree of OA were studied.

Chwee Teck Lim, James C.H. Goh (Eds.): ICBME 2008, Proceedings 23, pp. 386–389, 2009
www.springerlink.com

II. Methods

Fig. 1 shows the schema of the software interface. Referring to the figure, both anatomical and functional images are read by the program. Once all the images are input into the program, the user will first perform segmentation. This can be carried out manually or semi-automatically. For manual segmentation, the user will click a number of points along the boundary of the cartilage. The points will then be connected using a B-Spline function to form the boundary of the cartilage. For semi-automatic segmentation, the user will define a Region of Interest (RoI) to first localize the cartilage. A semi-automatic segmentation program [7] is then used to delineate the cartilage using the anatomical images. The semi-automatic segmentation program uses a radii search technique which based on a threshold method to identify the boundaries of the cartilage. Using the cartilage delineated by the segmentation program, an image mask is produced. The mask is used to delineate the T_2 mapping data of cartilage. The T_2 mapping data of the cartilage is color coded to show the variation of the T_2 values.

It is important to visualize the T_2 values so that the clinician can easily identify abnormality. It has been shown that the T_2 values vary along the cartilage in the direction from the subcondral bone towards the surface of the cartilage [6]. T_2 values at the surface of the cartilage tend to be higher than the T_2 values at the interface of the cartilage and subcondral bone [6].

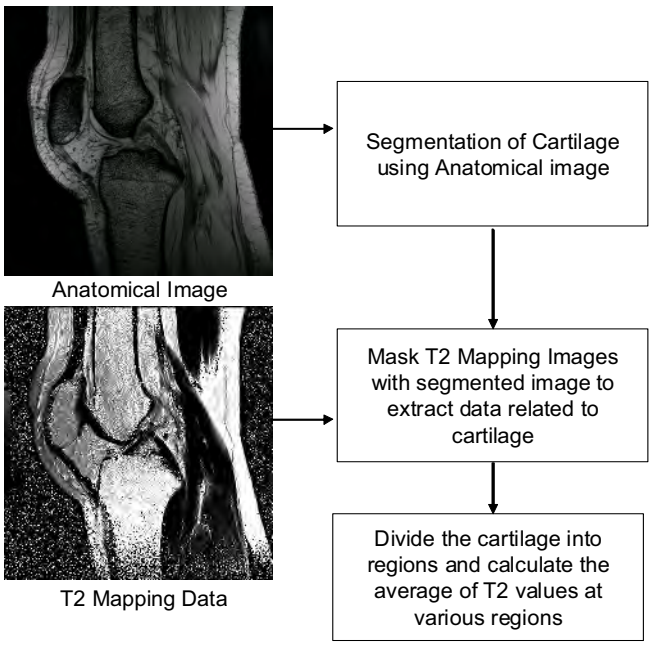


Fig. 1. Schema of the visualization software interface.

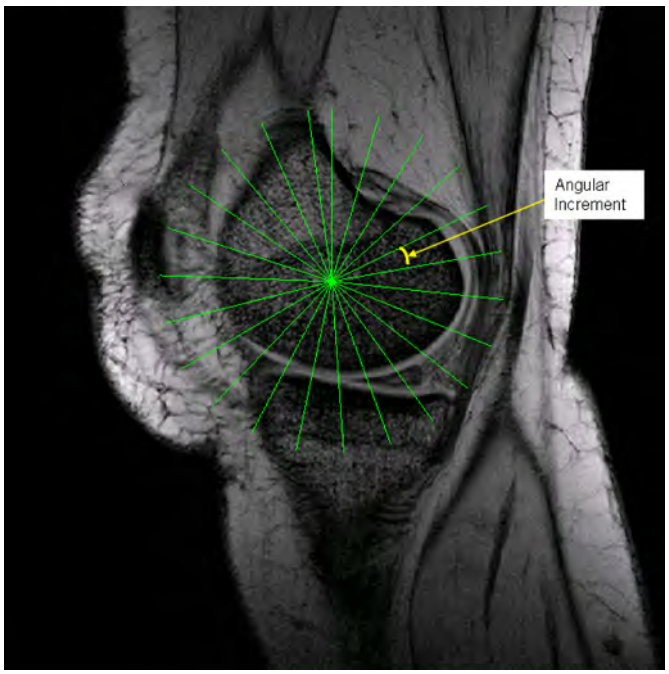


Fig. 2. Dividing cartilage into different regions.

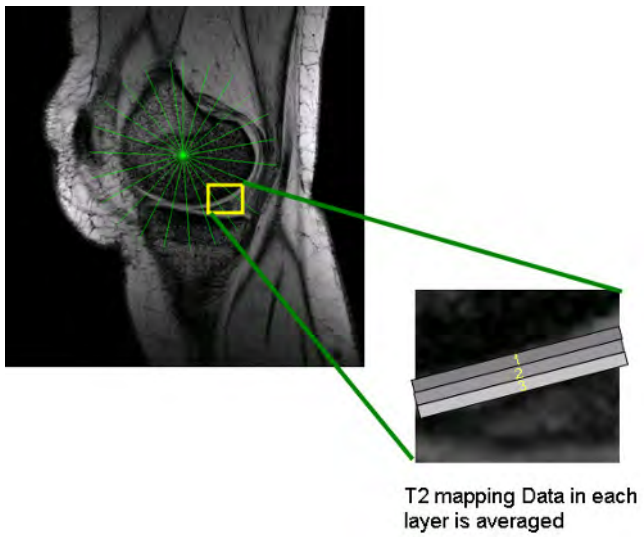
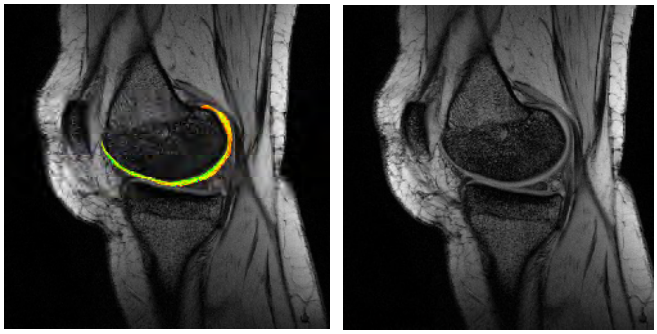


Fig. 3. Dividing each cartilage region into 3 layers.

Average $T_{1\rho}$ and T_2 values can be quantified from several pixels of the selected Regions of interest or from every pixel of different layers. In our approach, the cartilage is first divided into regions based on a radii division (refer to Fig. 2). Based on pre-defined angular increment, the regions are



(a) (b)

Fig. 4. (a) Color coded T2 mapping data of the femoral cartilage overlapped with the corresponding anatomical image. (b) Using the Toggling function, the T2 mapping data can be removed so that the structural details of the cartilage can be studied.

divided. The value of the angular increment will determine the number of regions that will be obtained (i.e. a small angular increment will divide the cartilage into more regions). Once the cartilage is divided into regions, the cartilage within each region is divided into 3 layers (see Fig. 3). Dividing cartilage into superficial, mid and deeper layers is required due to topographic variation in cartilage orientation. In particular, the superficial layer of cartilage has been shown to be easily separable from the underlying cartilage [8]. Cartilage repair techniques vary according to the width and depth of cartilage defect seen on arthroscopy. Hence, this technique allows surveillance and follow-up of cartilage defects and repair over time. The average of the T_2 values in each layer at different sampling points is calculated and plotted in a 2D/3D contour plot.

In this technique, we assume that the thickness of different cartilage layers is uniform, while it is known that the laminar architecture of cartilage varies depending on the type and location of the joint. However, the parameter being measured is the rate of change of cartilage T_2 properties over time. Hence, a consistently reproducible and robust method of cartilage segmentation is clinically adequate. Depiction of microscopic transition points between the cartilage layers is currently beyond the resolution of clinical scanners (given limitations of imaging time).

A. Toggling

Toggling of images is considered by radiologists as an important functionality when viewing both anatomical and functional images. Consequently, a toggling function is developed. The anatomical images are used as the base and the color coded $T_{1\rho}/T_2$ images are overlay onto the anatomical images. Only the regions of the cartilage of the $T_{1\rho}/T_2$ images that have been segmented are overlay onto the corresponding anatomical images. This toggling function is controlled using a radio button.

III. Results

To demonstrate the interface, two sets of MR images are used. Each set of MR data comprises anatomical and T_2 mapping data. One set of the data is a normal knee whereas the other set of data is a knee showing thinning cartilage. The interface developed was used to visualize the two sets of MR data.

Fig. 4 shows an example result of the toggling between the anatomical image and T_2 mapping data. Using the interface, it is possible to view both anatomical and T_2 mapping data interactively. This function was performed by clicking a radio button. As a result, it is possible to view the details of the cartilage and surrounding tissues using the high resolution anatomical image and studying the functional information of the cartilage using the T_2 data, as opposed to viewing two images (anatomical and T_2 mapping) separately.

Fig. 5 shows an example plot of the calculated T_2 mapping values from one image slice of a normal knee and a knee with thinning articular cartilage. Referring to the figure, the contour shows the variation in the T_2 values at different regions of the cartilage. The vertical axis of the plot is the three different layers of the cartilage (from the subcondral bone to the surface of the cartilage) and the horizontal axis is the different regions along the cartilage. The plots show that the overall T_2 values of the knee with thinning cartilage are larger as compared to the T_2 values of the normal knee. The plots also show that the thinning cartilage has more variation in the T_2 data. The 3D contour plot enables the user to visualize the change in the T_2 values. Using the 3D contour plot, the user is able to rotate and to enlarge the plot while studying the data. These plots were generated automatically once the segmentation was performed. The trend of the cartilage T_2 values were visualized in the plots.

IV. Discussions

Using the visualization interface, it is possible to visualize both anatomical and functional images in a more efficient manner. The interface enables the clinician to delineate the cartilage and focus on the study of the T_2 values of the cartilage. The segmentation method allows faster segmentation of the cartilage to be carried out interactively. This enables more images to be studied in a shorter time. The plotting of T_2 values using the contour plot enables the clinician to study the change in T_2 values throughout the whole cartilage.

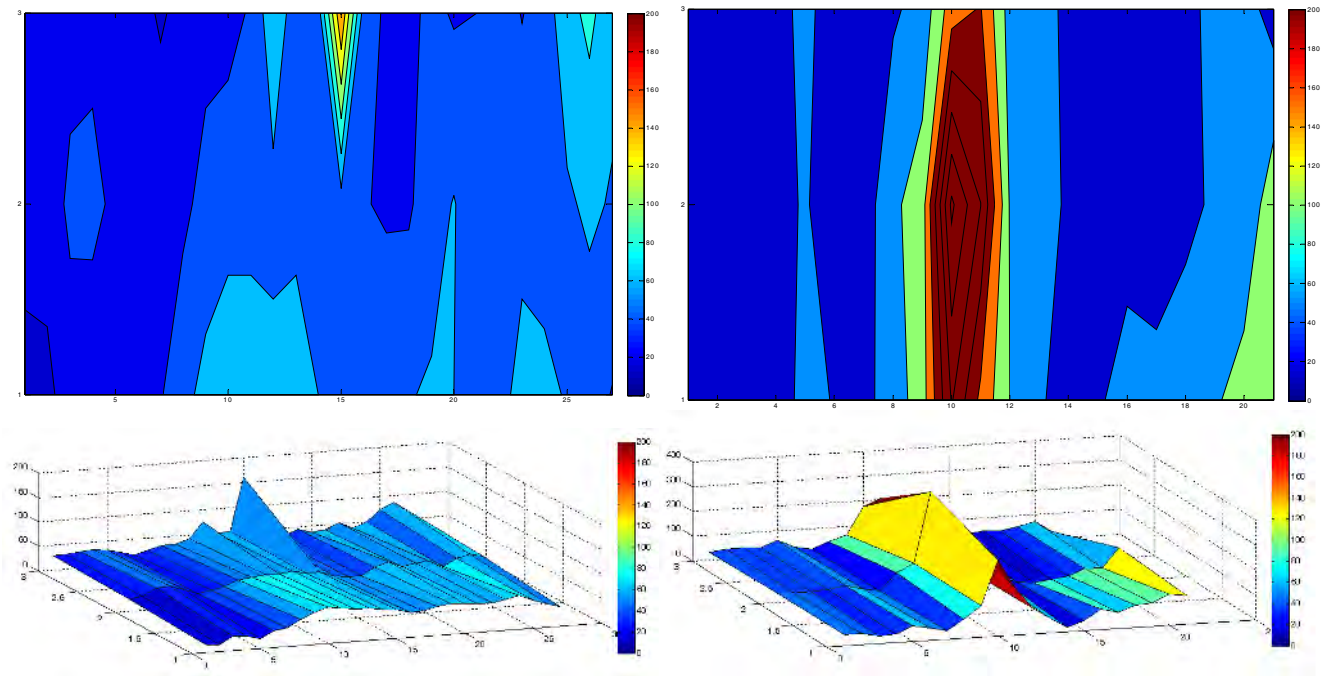


Fig. 5. Contour plots of T_2 mapping data for one image slice of cartilage. (i) Left - from a normal knee. (ii) Right – from a knee showing thinning cartilage.

Combining the anatomical and functional information may enhance our ability to detect early cartilage degeneration, and to distinguish between different stages of degeneration. Future work includes using the interface to perform longitudinal clinical studies of the T_2 and $T_{1\rho}$ mapping to further understand the characteristics of the changes in T_2 and $T_{1\rho}$ at the different stages of OA.

Acknowledgment

The authors would like to acknowledge the financial support from NTU Start-Up Grant.

References

1. Arden N and Nevitt MC (2006) Osteoarthritis: Epidemiology. Best Practice & Research Clinical Rheumatology 20(1):3-25.
2. Cashman PMM, Kitney RI, Gariba MA, and Carter ME (2002). Automated techniques for visualization and mapping of articular cartilage in MR images of the osteoarthritic knee: a base technique for the assessment of microdamage and submicro damage. IEEE Transactions on Nanobioscience, 1:42-51.
3. De Smet AA, Monu JU, Fisher DR, Keene JS, Graf BK (1992). Signs of patellar chondromalacia on sagittal T2 weighted magnetic resonance imaging. Skeletal Radiology 21(2):103-5.
4. Regatte RR, Akella SVS, Lonner JH, Kneeland JB, and Reddy R (2006). T1ρ Relaxation mapping in Human Osteoarthritis (OA) Cartilage: Comparison of T1ρ with T2. J.Magn. Reson. Imaging 23:547-553.
5. Li X, Ma CB, Link TM, Castillo DD et al. (2007) In vivo T1ρ and T2 mapping of articular cartilage in osteoarthritis of the knee using 3 T MRI. Osteoarthritis and Cartilage , Volume 15 , Issue 7 , Pages 789 - 797
6. Mosher TJ, Dardzinski BJ, Smith MB (2000). Human articular cartilage: influence of aging and early symptomatic degeneration on the spatial variation of T2-prelimenary findings at 3T. Radiology 214(1):259-66
7. Poh CL and Kitney RI (2005). Viewing Interfaces for Segmentation and Measurement Results. Proceedings of the 2005 IEEE Engineering in Medicine and Biology 27th Annual Conference, Shanghai, China, pp. 5132 – 5135, 2005.
8. Teshima R, Otsuka T, Takasu N, Yamagata N, and Yamamoto K. Structure of the most superficial layer of articular cartilage. Journal of Bone and Joint Surgery - British 77-B(3):460-464.

Chueh-Loo Poh
Nanyang Technological University
School of Chemical and Biomedical Engineering
Singapore
clpoh@ntu.edu.sg

A Chaotic Detection Method for Steady-State Visual Evoked Potentials

X.Q. Li and Z.D. Deng*

State Key Laboratory of Intelligent Technology and Systems
Tsinghua National Laboratory for Information Science and Technology
Department of Computer Science, Tsinghua University, Beijing 100084, China

Abstract — **This paper investigates the application of chaotic detection theory to brain-computer interfaces (BCI) technology. We present a chaotic oscillator array (COA)-based method using the steady-state visual evoked potential (SSVEP) paradigm. The presented chaotic oscillator array model is used for electroencephalogram (EEG) signal feature extraction, which works based on the phase transition characteristics of the chaotic oscillator. The dynamic characteristics of Duffing system and the corresponding bifurcation process are discussed in detail. We define a quantitative measure to characterize the response in dynamic behaviors of COA considering the trajectory divergence degree in phase space. The learning vector quantization networks (LVQ) is viewed as classification model in our method. Different response patterns of COA can be clustered and mapped with predefined BCI commands through a well-trained LVQ model. The experimental results show the feasibility of the proposed method.**

Keywords — **Chaotic detection, Learning Vector Quantization Networks (LVQ), Brain-computer interface (BCI), electroencephalogram (EEG).**

I. Introduction

Brain-computer interface (BCI) is the system that uses brain activity to control external devices such as robots, computers, switches, wheelchairs, or neuroprosthetic extensions [1]. It provides a new approach to restoring communication and control to people with severe motor disorders. In recent years, BCI researches based on noninvasive scalp electrencephalography (EEG) have become an active research area. Event-related potentials, mu and beta rhythms, event-related synchronization and desynchronization, slow cortical potentials, and visual evoked potentials (VEPs) are commonly used signals in EEG-based BCIs [2]. Among which, the VEP-based BCI has the advantages of requiring less training and having less influence from individual difference and is receiving increasing research interest.

The spectrum method is extensively adopted in SSVEP-based BCI research and it obtains remarkable achievement [1-3]. However, the uncertainty principle in signal processing field places intrinsic limitation in further improvement of information transfer rate (ITR) through spectrum method. To be more concrete, the frequency resolution of a time domain limited signal can only reach the level of the reciprocal of the length of the signal segment. That is to say the high frequency resolution and short signal length can't be realized simultaneously. Because of this, a tradeoff must be taken between response speed and the number of selections in a single trial. This problem emerges as one of the obstacles hindering further improvement of the ITR of current SSVEP-based BCIs.

Chaotic detection theory is a newly developed method for weak signal detection [4]. It detects the changes of a weak signal by identifying the transformation of the phase state of chaotic oscillator from chaotic to large-scale periodic when the weak external signal is applied [5]. In this paper, we present a new framework for SSVEP-based BCI research based on chaotic detection. The proposed method can reach a much more high frequency resolution with required time resolution than traditional spectrum method, and thus provides a promising solution for designing a new SSVEP-base BCI system of high ITR.

The rest of this paper is organized as follows. First, the Duffing chaotic oscillator is introduced and the fundamental principle of chaotic detection is discussed. Then in section III, a chaotic oscillators array (COA) model is constructed for EEG feature extraction and the quantitative term of TDI for measuring the response in dynamic behavior of COA is given. Also a LVQ model is introduced and employed as classifier. Furthermore, the experimental results are given in section 4. Finally, we draw conclusions.

II. Fundamental principle

Chaos describes the complex behaviors of a nonlinear deterministic systems abound in our life. Chaotic oscillator acts as a chaotic attractor and has the characteristic of the sensitivity of to its parameters. Based on this property, chaotic oscillator detection has developed to a useful weak signal detection theory and been extensively studied in the past few years [4-6].

The Duffing equation is one of the classic non-linear system and is chosen for modeling chaotic oscillator in our study, which can be formulated as,

Chwee Teck Lim, James C.H. Goh (Eds.): ICBME 2008, Proceedings 23, pp. 390–394, 2009
www.springerlink.com

$$\frac{1}{\omega^2}\ddot{x}_\tau(\tau)+\frac{f}{\omega}\dot{x}_\tau(\tau)-x_\tau(\tau)+x^3{}_\tau(\tau)=\gamma\cos(\omega\tau) \quad (1)$$

where $\gamma\cos(\omega t)$ denotes the periodic driving force, f the damping ratio, and $-x+x^3$ the nonlinear recovery force.

The state equations are given by

$$\begin{aligned}\dot{x}&=\omega y\\ \dot{y}&=\omega[-fy+x-x^3+\gamma\cos(\omega\tau)]\end{aligned} \quad (2)$$

To study the dynamic behaviors of (2), we fix $f=0.5$ and let γ increase gradually starting from 0. As γ is small, for example, $\gamma=0.25$, the phase trajectories form an attractor in the meaning of Poincaré map. They perform periodic oscillation around one of the two focus points. When γ increases above a certain threshold γ_b, periodic-doubling bifurcations appear and the system gets into chaotic state. This transition happens rapidly and the system will continues to keep chaotic state within a large scope of γ until reach another threshold γ_c. Here a very short intermittent chaotic state happens and then the system goes fast into the large-scale periodic state. The thresholds γ_b and γ_c can be determined using the Melnikov method in combination with tests [7].

To detect weak signals buried in noise, we introduce the mixed signal *Input* to chaos oscillator as illustrated in (3),

$$\begin{aligned}\dot{x}&=\omega_0 y\\ \dot{y}&=\omega_0[-fy+x-x^3+\gamma_c\cos(\omega_0\tau)+Input]\end{aligned} \quad (3)$$

where

$$\begin{aligned}Input&=s(\tau)+N(\tau)\\ &=a\cos((\omega_0+\Delta\omega)\tau+\varphi)+N(\tau)\end{aligned}$$

ω_0 is the driving frequency (or reference frequency). $\Delta\omega$ the frequency difference. φ the primary phase difference. $N(\tau)$ the noise.

Now we can see that the total periodic force of the Duffing oscillator is

$$\begin{aligned}A(\tau)&=\gamma_c\cos(\omega_0\tau)+a\cos((\omega_0+\Delta\omega)\tau+\varphi)\\ &=\gamma(\tau)\cos(\omega_0\tau+\theta(\tau))\end{aligned}$$

where

$$\gamma(\tau)=\sqrt{\gamma_c{}^2+2\gamma_c a\cos(\Delta\omega\tau+\varphi)+a^2} \quad (4)$$

$$\theta(\tau)=\arctan\frac{a\sin(\Delta\omega\tau+\varphi)}{\gamma_c+a\cos(\Delta\omega\tau+\varphi)} \quad (5)$$

From (4) we can see that if $\Delta\omega=0$,i.e. $\omega=\omega_0$, only the phase difference can affect the system state. If $\pi-\arccos(a/2\gamma_c)\le\varphi\le\pi+\arccos(a/2\gamma_c)$, $\gamma\le\gamma_c$, the system remains in chaotic motion. Otherwise the state of chaotic oscillator will be changed into periodic state.

If $\Delta\omega$ exits, $\gamma(\tau)$ will be periodically less than or more than the critical value γ_c within the scope between γ_c-a and γ_c+a, the cycle time T_Δ is $2\pi/\Delta\omega$. As $\gamma(\tau)$ approaches γ_c-a, the oscillator is in chaotic motion. The system changes to periodic state as $\gamma(\tau)$ approaches γ_c+a. This is why the intermittent chaotic phenomenon takes place [8]. It has been pointed out in [5] that when $|\Delta\omega/\omega_0|\le 0.03$, the regular intermittent chaos state can be easily identified and the theoretical value of $T_\Delta(2\pi/\Delta\omega)$ accurately coincides with the experimental results. Otherwise the regular intermittent chaos is difficult to maintain and the state of chaotic oscillator remains in chaos state.

From the analysis above, we can see that a single Duffing oscillator is only sensitive to signals, the frequency of which is very close to the oscillator's driving frequency. In another word, a specific oscillator is only responsible for detection of a very narrow frequency extent. The immunity of chaotic oscillator to other components, including noise and frequency components with frequency difference $|\Delta\omega/\omega_0|>0.03$, has been testified in [4].

III. Method

A. Feature Extractions

In this study, a chaotic oscillators array (COA) based EEG feature extraction model is proposed. It works based on a chaotic oscillators array composed of R chaotic oscillators. The driving frequencies of each member are tuned corresponding to the frequencies of each stimulus in the SSVEP experimental environment. When the subject is asked to gaze at one of the flash stimuli encoding a specific command, a trigger is given and the recorded sampling EEG signals by scalp electrodes are provided with the chaotic oscillators array and feed into all the R chaotic oscillators in parallel.

As can be seen from (4) and (5), if $\Delta\omega = 0$, the phase difference plays an important role in the system state. Only when φ fall into an appropriate range of $\varphi < \pi - \arccos(a/2\gamma_c)$ or $\varphi > \pi + \arccos(a/2\gamma_c)$, the expected phase transition can be guaranteed. So in our COA-based feature extraction method, the phase difference is fixed at $\varphi = 0$ by a proper phase shift $\Delta\varphi$ at the start of feeding of EEG signal. Now (4) is changed to $\gamma(\tau) = \sqrt{\gamma_c^2 + 2\gamma_c a\cos(\Delta\omega\tau) + a^2}$, and each chaotic oscillator in COA will response to a narrow band of frequencies centered in it's driving frequency.

According to the basic principle of an SSVEP-based BCI, large areas of the visual cortex are allocated to process the center of our visual field, so the amplitude of SSVEP increases enormously as the stimulus is moved closer to the central visual field. Different SSVEP can be produced by directly looking at one of a number of frequency coded stimuli [2].

When a stimulus target is selected by subject through changing his/her gaze direction, the SSVEP of the related frequency is induced and the corresponding member of COA will be activated once the condition $\gamma \le \gamma_c$ is satisfied. This motivates the phase state of this chaotic oscillator to be transformed from the chaotic state to the large-scale periodic state while the other members of COA remain in chaotic state. Thus the user intent can be identified.

All BCI research programs share the same goal of rapid and accurate communication. Unfortunately, a limitation in frequency resolution handicaps the further improvement of ITR through traditional spectrum method. For instance, if the frequency band of 1~10Hz is used and the sliding window is 2s, the frequency resolution can reach 0.5Hz using the short-time Fourier transform analysis method, and thus only 20 frequencies can be used to configure the flash buttons in SSVEP-based BCI research.

In this COA-based feature extraction method, the driving frequencies of the member of the chaotic oscillator array can be arranged based on the frequency selectivity condition of $|\Delta\omega/\omega_0| \le 0.03$ as discussed above. For a working frequency band of 1~10Hz, an equal-ratio array can be used for driving frequencies arrangement. i.e.

$$\omega_1 = 1, \omega_2 = 1.06, \cdots, \omega_k = 1.06\omega_{k-1}, \cdots, \omega_K = 10.286$$
$$(K = 41)$$

Up to 41 frequencies can be used in the COA-based method to configure the splash stimuli given the sliding window length of 2s. Thus more selections can be provided by the COA-based feature extraction method than traditional spectrum method with the same time resolution.

B. Trajectory Divergence Degree Measure

In our SSVEP-based BCI scheme, the responses in phase state of each member of COA are characterized through a quantitative measure to produce a feature vector for further classification. In this section, we define a descriptive term named trajectory divergence index (TDI) to characterize, in phase map, the dynamic behavior of the chaotic oscillator. It calculates the average distance of initially adjacent trajectories after certain steps of evolvement.

Let $Y_i = (y_i(1), \cdots y_i(m)) \in R^m, (i = 1, 2, \cdots, N)$ be the points in m-dimension phase space and the trajectory of the chaotic oscillator is formed by joining the points $\{Y_1, Y_2, \cdots, Y_N\}$ up continuously. For each point Y_i, we can find its nearest neighbor $Y_{\hat{i}}$ as follows,

$$\hat{i} = \{j \mid \min_j \|Y_i - Y_j\|, |i - j| > P, j \in (1, 2, \cdots, N)\}$$

where $\|Y_i - Y_j\| = \sum_{k=1}^{m} |y_i(k) - y_j(k)|$ and P is used to eliminate the false nearest neighbor that located continuously in the same trajectory segment. The calculation of P is the same as the average period in the estimating of Lyapunov index [9].

Then the trajectory divergence index of the dynamic behavior of a chaotic oscillator in certain phase state can be calculated as

$$TDI = \frac{1}{N}\sum_{i=1}^{N} \ln(\|Y_{i+d} - Y_{\hat{i}+d}\|) \quad (6)$$

where d is the discrete time step after which the divergence of trajectories is measured. It can be determined through a cross-validation process.

C. LVQ Classification

The Learning Vector Quantization Networks (LVQ) is a supervised neural network model based on competitive learning using winner-take-all Hebbian approach [10]. For our R-dimension chaotic oscillator array, which comprises R individual chaotic oscillators with different driving frequencies, a LVQ neural network is constructed with R neurons in each of its three layers. A set of training pairs $\{x^\mu, y^\mu\}$ are used to train the parameters of LVQ model,

where $x^{\mu} = (x_1^{\mu}, x_2^{\mu}, \cdots, x_R^{\mu})$, x_i^{μ} is the trajectory divergence index (TDI) of the ith member of COA when the EEG signal from the μth trial in SSVEP experiment is applied. The target output vector y^{μ} is constructed beforehand with a specific configuration of one 1 and $R-1$ 0s to represent uniquely the μth stimulus or alternatively the μth BCI command.

In the evaluating stage, when a new pattern of COA response, coded using the trajectory divergence index (TDI), is presented to the well trained LVQ model, the classification process is performed by detecting regularities and correlations between input and training patterns, and a proper output vector is given out.

IV. Experimental results

The experiments were carried out using EEG data of three different subjects provided by the Department of Biomedical Engineering in Tsinghua University [2]. The subjects are referred to as s1, s2, and s3 in the following text.

Three virtual buttons flashed at different repetition rates (11Hz, 12Hz, 13Hz), composing a frequency-coded stimulator. The subjects were asked to gaze at the target attentively, ignoring the other buttons in the operation. The attention duration of a single trial was asked to keep for no less than 2s. A COA model with three chaotic oscillators was constructed for this experiment and the driving frequencies of each member were set according to the flashing frequencies of the three stimuli.

According to the feature extraction algorithm described in section III, whenever a trial was taken the EEG signal recorded was applied to each member of the chaotic oscillator array in parallel. The responses in dynamic behavior of the COA were measured using the quantitative measure of the trajectory divergence index. The feature vectors were produced and classified by the LVQ model. The experimental results are listed in Table 1.

Table 1 Extracted feature vectors and classification results

Subject	Task	Feature Vector			Classification results
s1	1	-0.19882	0.87386	0.83011	1
	2	0.16304	-0.91172	-0.21528	2
	3	1.1536	0.87043	-1.3062	3
s2	1	-1.034	0.92112	-0.055455	1
	2	0.88419	-0.60986	0.27625	2
	3	1.0849	1.3031	-0.32175	3
s3	1	-1.245	-0.20017	-0.27617	1
	2	0.50466	0.98019	1.7361	1
	3	0.36226	1.1399	-0.95068	3

We can see from the experimental results above that the presented feature extraction and classification method can correctly recognize the gaze target of the subject except for task 2 of subject s3.

V. Conclusion

In this paper, we propose a chaotic detection method for EEG feature extraction in BCI research. The theoretical basis is discussed and the COA-based BCI scheme including feature extraction, quantification and classification is presented. The advantages of the chaotic detection based BCI method in frequency resolution make it a promising solution for SSVEP-based BCI research. The experimental results using real EEG signal show the feasibility of the proposed method.

Acknowledgment

This work is supported in part by the National Science Foundation of China (NSFC) under Grant Nos. 60621062 and 60775040.

References

1. Martinez P., Bakardjian H. and Cichocki A. (2007) Fully-online, multi-command brain computer interface with visual neurofeedback using SSVEP paradigm. J. Comp. Intell. Neurosci., online article ID 94561
2. Wang Y. J., Wang R. P., Gao X. R., Hong B., and Gao S. K. (2006) A practical VEP-based brain-computer Interface. IEEE Trans. Neural Syst. Rehabil. Eng. 14:234-239
3. Trejo L. J., Rosipal R., and Matthews B. (2006) Brain-computer interfaces for 1-D and 2-D cursor control: designs using volitional control of the EEG spectrum or SSVEP. IEEE Trans. Neural Syst. Rehabil. Eng. 14(2): 225-229
4. Wang G. Y., Chen D. J., Lin J. Y., and Chen X. (1999) The application of chaotic oscillators to weak signal detection. IEEE Trans. Ind. Electron. 46:440-444
5. Li C. S., Qu L. S. (2007) Applications of chaotic oscillator in machinery fault diagnosis. Mech. Syst. Signal Process. 21:257-269
6. Birx D. L., Pipenberg S. J. (1992) Chaotic oscillators and complex mapping feed forward networks (CMFFNS) for signal detection in noisy environments. Proceeding of the IEEE International Joint Conference on Neural Network (IJCNN) 2:881–888
7. Liu Z. (1994) Perturbation Criteria for Chaos, Shanghai Scientific and Technology Education Publishing House, Shanghai, China
8. P1att N., Spiege1 E. A., Tresser C. (1993) On-off intermittency: a mechanism for bursting. Phys. Rev. Lett. 70(3):279-282

9. Rosenstein M. T., Collins J. J., Deluca C. J. (1993) A practical method for calculating largest lyapunov exponents from small data sets. Physica D 65:117-134.
10. Somervuo P., Kohonen T (1999). Self-organizing maps and learning vector quantization for feature sequences. Neur. Process. Lett. 10(2):51-159

Author: Zhidong Deng
Institute: Tsinghua University
Street: Tsinghua Yuan
City: Beijing
Country: China
Email: michael@tsinghua.edu.cn

Speckle Reduction of Echocardiograms via Wavelet Shrinkage of Ultrasonic RF Signals

K. Nakayama, W. Ohyama, T. Wakabayashi, F. Kimura, S. Tsuruoka[1] and K. Sekioka[2]

[1] Graduate School of Engineering, Mie University, Tsu, Japan
[2] Sekioka Clinic, Minami–Ise, Japan

Abstract — **We propose a new speckle reduction algorithm for clinical echocardiograms. The proposed method employs Wavelet Shrinkage to reduce the noise on an ultrasonic signal. In the wavelet shrinkage, at first, original ultrasonic signal is decomposed into wavelet coefficients by multiresolution decomposition using orthogonal wavelet. A threshold of which objective is suppression of noise component is estimated on the resultant complex wavelet coefficient. Wavelet coefficients corresponding to noise are eliminated by soft–thresholding. The noise reduction by the wavelet shrinkage can remove specific frequency components. In this study, we employed the RI-Spline wavelet that was proposed as a shift-invariant mother wavelet. We conducted experiments using clinical ultrasonic signals to evaluate the noise reduction performance of the proposed method. Ten clinical subjects were used in the experiments. The experimental results show that the algorithm provides superior performance on speckle and noise reduction compared to that of existing speckle reduction method.**

Keywords — **Echocardiogram, Ultrasound, Wavelet Shrinkage, Speckle Reduction.**

I. Introduction

An echocardiograph has built its strong position in today's diagnosis of the cardiovascular system as an indispensable imaging device. Its frequently usage is a result from its multifold advantages in cardiovascular performance assessment. Using an echocardiograph provides us noninvasive, low–cost, portable and real–time assessments of heart.

However, echocardiograms contain certain amount of speckles and noise due to the inherent property of ultrasound. These speckles and noise not only degrade the image quality of echocardiograms but make clinical diagnosis based on echocardiography difficult. To obtain enough quality of images, doctors or ultrasonologists should adjust several parameters like dynamic range or time gain compensation using a control panel of ultrasonic equipment. Though speckles and random noise appearing in the heart chamber can be removed by eliminating small amplitude using the reject–level control, the homogeneous influence of the reject–level control to the all ultrasonic signal also removes meaning appearance in myocardium. To improve clinical diagnosis, automatic reducing speckles and enhancing image quality are required.

Several methods intending to improve image quality of echocardiograms have been proposed. Zong *et.al* [1] proposed an algorithm for speckle reduction and contrast enhancement of echocardiograms. They applied a multi-scale wavelet shrinkage to eliminate noise and employed a nonlinear processing of feature energy to enhance contrast of images. Yue *et.al* [2] proposed a multiscale wavelet diffusion method for speckle suppression and edge enhancement. These methods subjected two–dimensional echocardiograms acquired using a ultrasonic diagnosis equipment. This means that these methods behave as a post–process which follows image generation process in an echocardiograph so that they oversimplify the images.

In contrast to these two–dimensional echocardiogram based methods, we propose a new noise reduction method subjecting the radio–frequency (RF) signal of ultrasound. The method employs Discrete Wavelet Transform (DWT) where the Real–Imaginary Spline Wavelet (RI–Spline wavelet)[3] is used as a mother wavelet. For noise reduction, Wavelet Shrinkage [4] is widely used by its simple usage. However, since the ordinary DWT has a problem of which the translation invariance is lacking, artifacts is generated. The RI–Spline wavelet has been developed to overcome this problem of DWT.

The paper is organized as follows. In section II, the proposed speckle reduction method is described. In this section, we explain how the method suppresses the speckle in ultrasonic RF signals. Availability of the proposed noise reduction method is observed and evaluated in section III. And finally, we conclude the paper in section IV.

II. Speckle Reduction of Echocardiogram

In this section, we explain our proposed noise reduction method employing the DWT with RI–Spline wavelet on the ultrasonic RF signals.

Chwee Teck Lim, James C.H. Goh (Eds.): ICBME 2008, Proceedings 23, pp. 395–398, 2009
www.springerlink.com

A. Ultrasonic Data Acquisition

Fig.1 illustrates the system used for ultrasonic RF data acquisition. An ultrasonic transducer placed on the chest transmits pulsed ultrasonic toward the heart, and receives the backscattered ultrasonic. The transducer coverts the received ultrasound to electric signal $y(t)$.

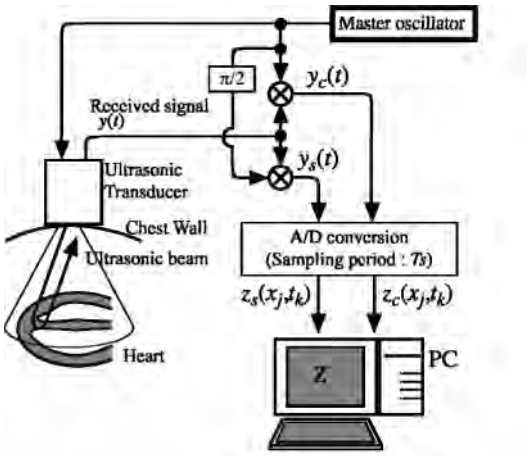


Fig. 1 Data acquisition system

The electric signal $y(t)$ is quadrature demodulated and-then A/D conveted to be imported to PC as discrete ultrasonic signal $\boldsymbol{Z} = \{\boldsymbol{z}(n,m)\}$. The ultrasonic signal $\boldsymbol{z}(n,m)$ is expressed as follows,

$$\boldsymbol{z}(n,m) = z_s(n,m) + jz_c(n,m) \tag{1}$$

where z_s and z_c denote the sine and cosine components obtained by the orthogonal demodulation. n and m denote the radial and angular indices of the B–scan sector image samples, respectively. The location of the sampling point indicated by (n,m) is defined as,

$x_n = nc_0T_s,$

$$\psi_m = m\Delta\psi, \tag{2}$$

where x_n and ψ_m denote the distance and angle from ultrasonic transducer. The constant C_0 is sound velocity in human body, i.e. 1530 [m/s]. T_s and $\Delta\psi$ are sampling period and angle interval, respectively.

Fig.2 illustrates an example of acquired ultrasonic data and an ultrasonic B–scan image generated from the ultrasonic data. In the figure, the signals located on the lower part exhibit original ultrasonic signal $\boldsymbol{Z}$ on the scan–lines A and B, which are displayed by the white lines in the image.

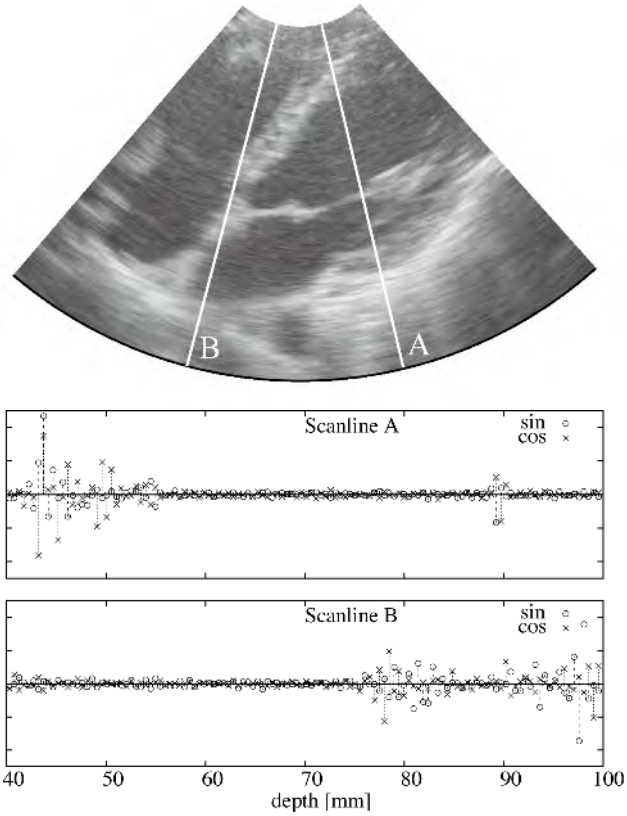


Fig. 2 Example of acquired ultrasonic data (lower) and ultrasonic image generated from the data (upper)

B. Noise Reduction by Wavelet Shrinkage

The noise reduction process in the proposed method consists of three main stages. In the first stage, the original ultrasonic signal is decomposed into complex wavelet coefficients by Complex Multi–Resolution Analysis (CMRA) with RI–Spline wavelet. In the next stage, Soft–Thresholding is applied on the wavelet coefficients to eliminate the noise components. And finally, de–noised ultrasonic signal is synthesized from the wavelet coefficients after Soft–Thresholding. Using the CMRA, a wavelet coefficient is expressed as a pair of coefficient. The each of them is corresponding to the real and imaginary parts of synthetic wavelet:

$$d^r_{k,l}\psi^r_{k,l}(t) + d^i_{k,l}\psi^i_{k,l}(t) \tag{3}$$

This equation denotes the synthetic wavelet on the level k and shift l.

To accomplish the wavelet shrinkage using such complex coefficients, we should calculated the norm $n_{k,l}$ of the synthetic wavelet by follows:

$$n_{k,l} = \sqrt{\left(d^r_{k,l}\right)^2 + \left(d^i_{k,l}\right)^2}\,, \tag{4}$$

Where $d^r_{k,l}$ and $d^i_{k,l}$ denote the real and imaginary part of wavelet coefficient. The threshold for noise reduction is estimated on the level–1 (highest–frequency) wavelet coefficients. The noise magnitude in the signal is estimated using the following:

$$\delta = \frac{Median\left(\left|n_{-1,l} - Median\left(n_{-1,l}\right)\right|\right)}{0.6745}, \tag{5}$$

where, Median(nl) denote the median of $\left\{n_l \mid l = 1,2,3,\ldots,\frac{L}{2}\right\}$. Using estimated noise magnitude, we obtain the threshold,

$$\lambda = \delta\sqrt{2\ln L} \tag{6}$$

where L denotes the number of sampling point on one scan–line.

Obtained threshold is applied in the soft thresholding process following the CMRA. The soft thresholding process is defined as:

$$\dot{n}_l = \begin{cases} n_l - \lambda, & n_l \geq \lambda \\ 0, & n_l < \lambda \end{cases} \tag{7}$$

Prior to the reconstruction process, we should transform $\dot{n}_l$ to wavelet coefficients using:

$$\dot{d}^r_{k,l} = \frac{\dot{n}_{k,l}}{n_{k,l}} d^r_{k,l}$$
$$\dot{d}^i_{k,l} = \frac{\dot{n}_{k,l}}{n_{k,l}} d^i_{k,l} \tag{8}$$

III. Experiments and results

To demonstrate and evaluate the noise reduction performance of the proposed method, we conducted an experiment using clinical ultrasonic data. The set of test ultrasonic data were acquired using an ultrasonic diagnose system (Hitachi–Medical EUB–6500). One ultrasonic data is corresponding to one systolic and diastolic sequence of echocardiogram. Ten data sets were subjected to the experiment.

Fig.3 exhibits three examples of experimental result. The upper three images are ultrasonic images generated from original ultrasonic data. These examples contain a certain amount of speckle in both cavity and myocardium regions. The lower three are ultrasonic images generated with the proposed noise reduction. One can see that the speckles in cavity and myocardium regions are reduced and the contrast of images are enhanced.

Table 1 Image quality measure obtained in the evaluation experiment using different noise reduction method

	Original	with noise reduction
SNR	4.22	5.11

To quantify the effectiveness of noise reduction, we conducted the following evaluation process. We evaluate the image quality using the following signal to noise ratio.

$$\mathrm{SNR} = \frac{\left|\bar{f}_m - \bar{f}_c\right|}{\sigma_B} \tag{9}$$

where, $\bar{f}_m$ and $\bar{f}_c$ denote the mean pixel value in the regions corresponding to myocardium and cavity, respectively. σ_B denotes the standard deviation of pixel value in the generated ultrasonic image calculated by:

$$\sigma_B = \sqrt{\frac{\omega_c\sigma_c^2 + \omega_m\sigma_m^2}{\omega_c + \omega_m}} \tag{10}$$

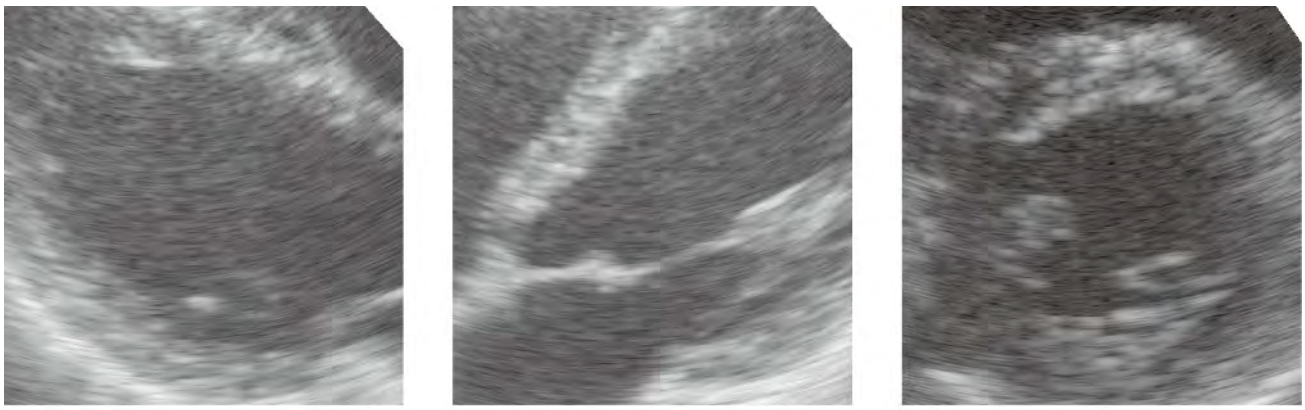
where, σ_c and σ_m denote the standard deviation of pixel value in the myocardium and cavity regions, and ω_m and ω_c denote the area (number of pixel) of myocardium and cavity, respectively. The myocardium and cavity regions are extracted manually on the generated ultrasonic images.

The evaluation experiment subjected ten ultrasonic images generated with and without the proposed noise reduction method. Table.1 shows the comparison between two methods. One can see that the SNR is improved by the proposed noise reduction method.

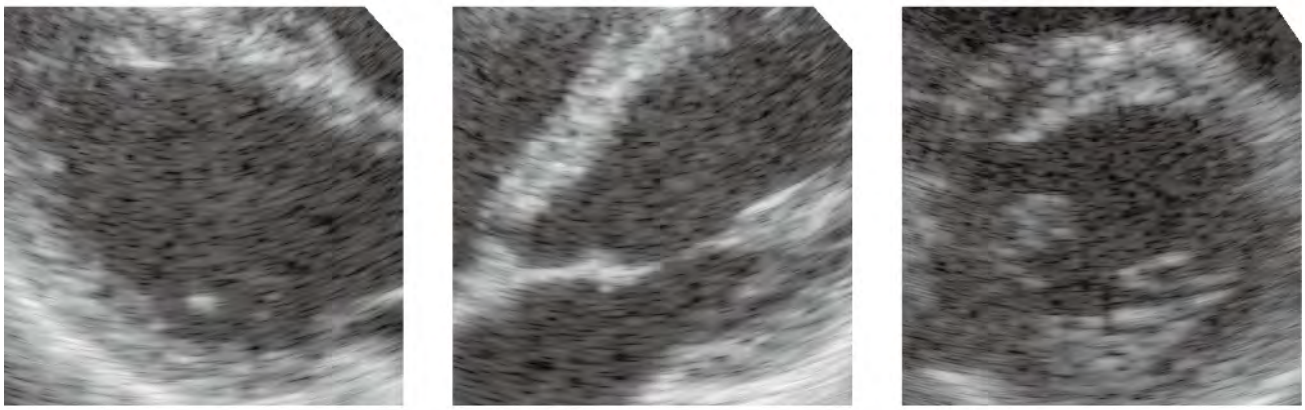
IV. Conclusions

We proposed a new noise reduction method for echocardiograms. The proposed method employs the wavelet shrinkage which using the RI–Spline wavelet as the analyzing wavelet.

The future research topics include (1) detailed comparisons among the proposed method and other noise reduction method for image quality, and (2) improvement of processing speed.



(a) Ultrasonic images generated from ordinary ultrasonic signal



(b) Ultrasonic images generated from ultrasonic signal with noise reduction

Fig. 3 Visual comparison of noise reduction performance

References

[1] Xuli Zong, Andrew F. Laine, and Edward A. Geiser. Speckle reduction and contrast enhancement of echocardiograms via multiscale nonlinear processing. *IEEE Transactions of Medical Imaging*, 17(4):532–540, August 1998.

[2] Yong Yue, Mihai M. Croitoru, akhil Bidani, Joseph B. Zwischenberger, and Jr John W. Clark. Nonlinear multiscale wavelet diffusion for speckle suppression and edge enhancement in ultrasound images. *IEEE Transactions of Medical Imaging*, 25(3):297–311, March 2006.

[3] Zhong Zhang, Hiroshi Tada, Satoshi Horihata, and Tetsuo Miyake. Nonstationary signal analysis using the ri–spline wavelet. *Integrated Computer–Aided Engineering*, 13:149–161, 2006.

[4] D.L. Donoho. De–noising by soft–threholding. *IEEE Transactions of Infomation Theory*, 41:613–627, 1995

Advanced Pre-Surgery Planning by Animated Biomodels in Virtual Reality

T. Mallepree, D. Bergers

University of Duisburg-Essen, IPE-PP, Duisburg, Germany

Abstract — **Complex anatomies like the human nose are more difficult to understand from conventional two-dimensional anatomy images than from interactive virtual three-dimensional models of the individual human anatomy. The objective of the present study was to establish a procedure necessary to develop an animated three-dimensional virtual reality model of a complex anatomy like the human nose from high-resolution computerized-tomography scans. With high-resolution scans, accurate 3D reconstruction of the human nose was possible. A reconstructed triangulated .VRML model was separated in sagittal and coronal direction in order to realize a component based animation that provides navigation through the virtual environment. For a virtual reality representation a passive stereoscopic visualization system was used. Accurate three-dimensional virtual reality models of the human nose and its structures can enhance our understanding of anatomy and physiology of this complex part of the body. Thus, it supports accurate and faster surgical intervention planning.**

Keywords — **Pre-Surgery Planning, Biomodels, Virtual Reality**

I. Introduction

The success of a surgery can depend on a reliable pre-surgical plan. To elaborate a surgical plan for each individual patient, surgeons need revealing image information. Especially, complex anatomies are difficult to understand by two-dimensional (2D) gray-value images.

Currently, tomographic slice images are used for the presentation of medical image data. Standardized static three-dimensional (3D) visualizations are provided as surgical planning support [1,2,3,4]. However, there are major limitations: (a) The difficulty to recognize exact spatial relations between two or more objects and (b) the occlusion of relevant objects or parts thereof. Especially in minimally invasive surgery, the surgeon is confronted with difficult conditions during the surgical procedure. In contrast to common surgery, a direct insight to the specific area of interest is missing.

These drawbacks can be compensated by interactive 3D virtual reality (VR) visualizations. Nevertheless, navigating in 3D environments is time consuming and the viewer can lose sight of important objects or lose orientation [5]. Some of those disadvantages of both static visualizations and interactive environments can be avoided by using animations which effectively provide information in a limited and pre-defined time span.

We developed a process for generating animations in VR of complex anatomies for surgical intervention planning. A novel procedure was applied in order to support surgeons especially in minimally invasive surgery in gaining insight in the present situation. Finally, the process of surgical intervention planning could be accelerated in terms of setting-up a faster diagnosis and treatment plan.

II. Methods

High-resolution scans were used for an accurate 3D reconstruction of an exemplary nose model. The parameters were as follows: the image matrix was set to 512x512 pixels, the slice thickness was set to 1 mm and the slice increment to 0,5 mm. The scanned images were imported as .DICOM files into the 3D reconstruction software Mimics (Materialise's Interactive Medical Image Control System, Materialise NV, Leuven) (Fig. 1). The model was segmented by selecting different densities (Hounsfield Units) as threshold for extracting the model. Air appeared with a mean intensity of approximately -1024 Hounsfield units (HU), most tissue of the cavity was in the range of 20 HU to 130 HU, while cartilage and bone structures were much more dense (well above 800 HU). That operation was followed by the connected component analysis of region growing. The reconstructed model and its components (nasal conchae, nasal septum) were separated in sagittal and coronal direction in order to realize a component based animation. The triangulated mesh was enhanced by triangle reduction and smoothing in order to improve the surface quality and to reduce the file size. Then, the optimized model was imported as .VRML (Virtual Reality Modeling Language) file to CosmoWorlds (Silicon Graphics Inc.). After the setting of actors and frames, the software interpolated the frames in between. After setting the sequence, the animation had been defined directly by creating a JavaScript (Fig. 1). A script node was defined by at least one *EventIn* and one *EventOut* field. A necessary *TouchSensor* is linked by *Route* to *Script* (*EventIn*). Finally, that script is integrated by the use of an *URL* in order to control the .VRML file.

Chwee Teck Lim, James C.H. Goh (Eds.): ICBME 2008, Proceedings 23, pp. 399–401, 2009
www.springerlink.com

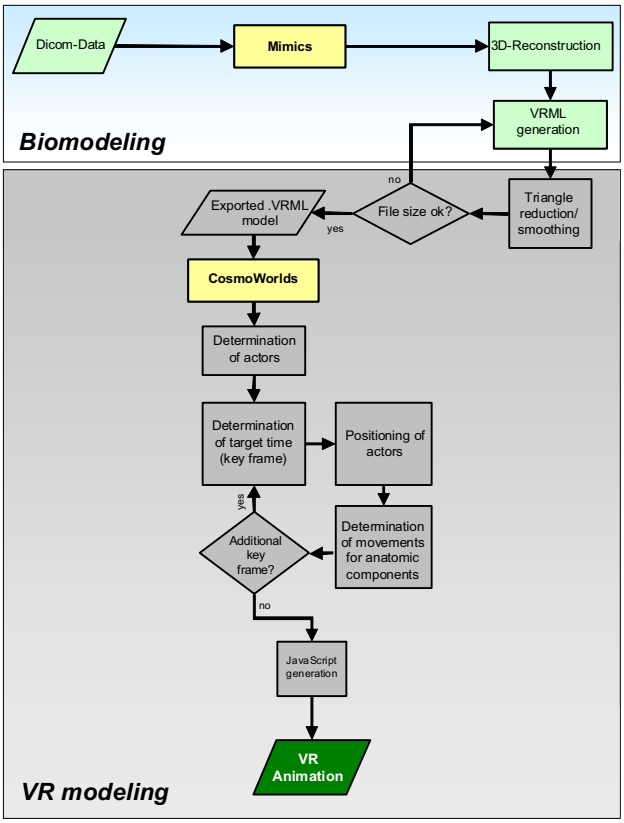


Fig. 1 VR animation process

The defined .VRML model was visualized in stereovision using the VR visualization software VRED (VREC GmbH, Darmstadt). Stereovision glasses were used to display the model in 3D.

III. Results

The generated nose model consisted of 59.000 triangles and its file size was defined to 2.400 Kbyte. The animation procedure generated, allowed interacting and exploring the 3D model from any geographical position. The representation of the applied procedure is depicted in Figure 2. It was possible to convert 2D image slices into a component based 3D animation in VR.

Table 1: Animation sequence

Sequence	Components	Plane
1	Complete nose	Coronal
2	Setum nasi (Sn)	Sagittal
3	Meatus nasi: inferior (Mni), medius (Mnm)	Coronal
4	Nasal cavitiy, nasal conchae	Sagittal

Components difficult to visualize as the nasi septum (Sn), concha inferior (Ci), concha media (Cm), concha superior (Cs), meatus nasi inferior (Mni), and meatus nasi medius (Mnm) had been displayed in animated sequence (Table 1).

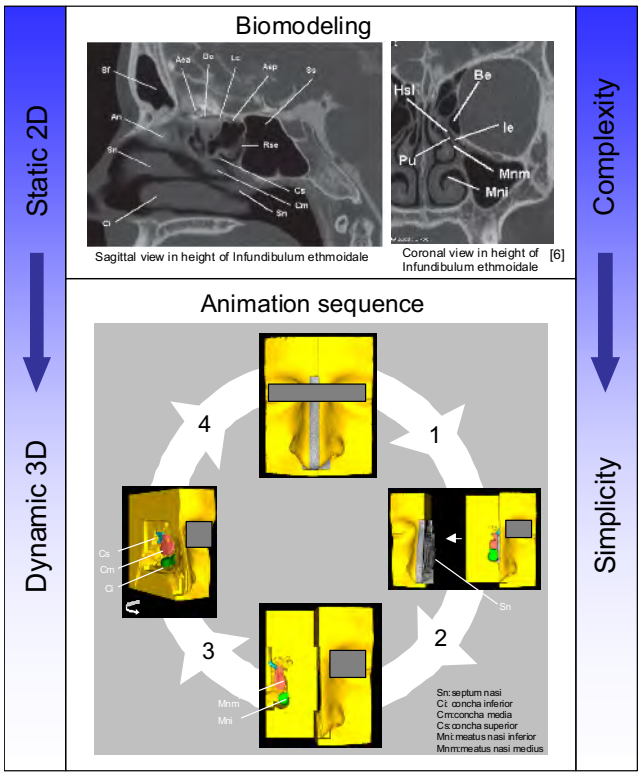


Fig. 2 Animated components

First, the animation procedure provided a coronal view on the nasal conchae. After the inspection of the nasal conchae and nasi septum, a sagittal view was given secondly to explore the nasal conchae in length. The user was enabled to change the given direction of view any time during the animation to start an individual exploration interactively.

IV. Conclusions

A procedure for creating animations of complex 3D biomodels like the human nose is shown. The complexity of 2D images is reduced by dynamic 3D animated component based parts of the human nose.

The current study aims to establish a process that can be used for the generation of animated anatomical models in order to provide surgeons with best possible image information for pre-surgery planning. Moreover, the introduced

procedure enables surgeons to communicate with each other even if they are located at different sites. That is possible both by analyzing the provided .VRML file in a standard internet browser that includes a .VRML plug-in.

An additional field of use can be seen in both medical teaching and patient information. Students would be enabled to examine complex anatomical structures interactively. They are guided by the animation to get to know specific sections difficult to find. Surgeons are enabled to communicate with patients especially in situations where deceases and treatments are difficult to explain by 2D gray-value images only. Pre-operative and post-operative situations can be discussed easily.

Overall, due to Hu [2] 3D visualizations play a significant role in planning surgeries reducing planning time as distinctive advantage over two-dimensional images by about 30 %. With the shown excerpt of our work, we are able to show that the procedure has the potential to be used as both a virtual planning and research instrument to reduce the time for understanding the morphology and physiology of complex parts of the body.

This is the first demonstration of a procedure for processing animated 3D VR models of the human nose within biomedical engineering.

References

1. Gering, D., Nabavi, A., Kikinis, R., Hata, N., and O´Donell, L. (2001). An Integrated Visualization System for Surgical Planning and Guidance Using Image Fusion and an Open MR. J. Magn. Reson. Imaging. 13:967–975
2. Hu, Y. (2005) The Role of Three-Dimensional Visualization in Surgical Planning of Treating Lung Cancer. Proc. 2005 IEEE Eng. in Medicine and Biology 27th Ann. Conf. Shanghai. 646-649
3. Lee, T., Lin, CH., and Lin, HY. (2001). Computer-Aided Prototype System for Nose Surgery. IEEE T. Inf. Technol. Biomed., 5:271-278
4. Vartanian, A., Holcomb, J., Ai, Z. et al. (2004) The Virtual Nose. Arch Facial Plast Surg. 6:328-333
5. Bade, R., Ritter, F., Preim, B. (2005) Usability Comparison of Mouse-Based Interaction Techniques for Predictable 3d Rotation. In: Smart Graphics. 138-150
6. Hofmann, E. (2005) Anatomy of Nose and Paranasal Sinuses in Sagittal Computed Tomography Anatomie der Nase und der Nasennebenhöhlen im sagittalen Computer-tomogramm. Klin Neurodiol 15:258-64

Author: Mallepree, T., Bergers, D.
Institute: University of Duisburg-Essen, IPE-PP
Street: Lotharstr. 1
City: Duisburg
Country: Germany
Email: timon.mallepree@uni-due.de

Computerized Handwriting Analysis in Children with/without Motor Incoordination

S.H. Chang[1] and N.Y. Yu[2]

[1] Department of Occupational Therapy, I-Shou University, Kaohsiung County, Taiwan
[2] Department of Physical Therapy, I-Shou University, Kaohsiung County, Taiwan

Abstract — **We used computerized kinematic and kinetic analyses to determine the mechanism of handwriting deficit in children with developmental coordination disorder (DCD).**

Totally, 72 children (33 DCD and 39 non-DCD) with handwriting deficit and 22 children without handwriting deficit (normal control) were recruited. The speed that subjects learned to write an unfamiliar character (i.e., the speed of execution) was used to assess motor learning of handwriting. Three simple and 3 complex Chinese characters were written, and the changes in the velocity and pressure for corresponding strokes were observed.

In children with DCD, handwriting execution was markedly slower. They were able to speed up stroke movement to maintain stability (phasic strategy) in the writing of simple characters but not complex characters, and failed to use more pressure on the writing surface (tonic strategy) to stabilize movement.

In conclusion, the parameters in this study are linked to underlying perceptual-motor functions and can be used to characterize handwriting problems arising from motor incoordination.

Keywords — **motor learning, handwriting, developmental coordination disorder, kinematic analysis s.**

I. Introduction

In fine motor control of handwriting movement, the coordination of muscle movements and the regulation of pen speed and force are the key components of legible writing. In 1994, Marquardt et al. developed a computer controlled handwriting evaluation tool [1]. The procedure records the handwriting of the subject on a digital tablet, especially loops like ℓℓℓℓℓℓ. The movement is traced automatically and divided into segments corresponding to individual strokes. These strokes can be used as diagnostic measures of motor control.

Normal handwriting movement does not require continuous modification of motor output or use visual or kinesthetic feedback from the hand. This kind of movement is achieved using open-loop control. Learning to write a new letter uses closed-loop feedback control and requires a lot of practice [2]. In their study, normal adults were recruited to write two similar but unfamiliar letters 60 times. They used the number of acceleration peaks of every stroke segment to estimate the degree of movement automation.

To characterize fine motor skills in DCD, Smits-Engelsman et al. (2001) asked children to draw the flower-trail-drawing item of the Movement Assessment Battery for Children (M-ABC) test and found that serious handwriting problems are associated with fine motor deficits. They suggested that handwriting to children with motor deficits is a kind of stress that may enhance neuromotor noise—the noise being the result of random muscle fiber recruitment. Children can speed up stroke movement (phasic movement), or hold the pen more tightly (tonic movement) to provide stability, thereby filtering the neuromotor noise [3]. However, it is not known whether DCD children respond similarly, how phasic and tonic movements reduce enhanced noise, and whether simple and complex tasks differ? Most of the current studies on handwriting use the Western alphabet. Since Chinese and Western alphabets differ in form and since there are cultural differences, studies using the Western alphabet may not necessarily have implications for Chinese children with DCD.

Furthermore, there is still no published article on the mechanism of handwriting deficit in DCD involving computerized evaluation and use of Chinese characters. In this study, children with handwriting problems (with or without DCD) were compared to children without handwriting problems. Computerized handwriting movement analysis was utilized to analyze the motor and control sequence used in writing Chinese characters.

II. Methods

A. Subject Recruitment

From five public elementary schools, 1258 children in grade 1 or 2 were screened by the Beery-Buktenica Developmental Test of Visual-Motor Integration (VMI) (Beery, Buktenica, & Beery, 2004). A score lower than the mean minus 1.5 times standard deviation was the criterion for inclusion. School teachers who administered the Chinese Handwriting Evaluation Questionnaire (CHEQ) (Chang & Yu, 2005) selected 75 children with handwriting deficits and these were recruited into this study as the experimental

Chwee Teck Lim, James C.H. Goh (Eds.): ICBME 2008, Proceedings 23, pp. 402–405, 2009
www.springerlink.com

group. In addition, 22 non-DCD children without a handwriting deficit were randomly recruited from the same pool as the experimental group.

B. Research Design

For measuring the motor learning of a handwriting task, we tested the proficiency of children to render an unfamiliar character with two rectangular angled strokes. To assess motor control during handwriting, we tested the ability of children to copy 3 simple and 3 complex Chinese characters. Differences in stroke velocity and pen-tip pressure for the same strokes were compared among the three groups.

C. Measures Used to Verify Motor Incoordination

DCD was diagnosed on the basis of results from the M-ABC test and Developmental Coordination Disorder Questionnaire (DCDQ) (Henderson & Sugden, 1992; Wilson, Kaplan, Crawford, Campbell, & Dewey, 2000). The DCDQ is a 17-item parent self-report questionnaire, which assists clinicians to identify children with motor problems. The total DCDQ score is the sum of the scores for each item. On the basis of the above selection criteria, DCD was diagnosed in 33 children and non-DCD in 39. Three children without either diagnosis were excluded.

D. Measuring Instruments

The handwriting tasks were performed on A4 size paper affixed to the surface of a 2-D digitizing tablet (444.0 x 435.5 x 37.0 mm, Wacom, Intuos 2, Japan) using a wireless electronic ball-point pen with pressure sensitive tip. The digitizer tablet also samples the axial pen force, with a maximum frequency of 200 Hz, a resolution of 2540 lines per inch, and a temporal accuracy of 1 ms.

E. Handwriting Tasks

(1). Test for Automated Handwriting

An A4-sized blank paper was placed on the digitizing tablet. The content of the page was arranged in 5 rows and 8 columns (40 grid cells), each cell being 18*18 mm. The subjects were instructed to write two rectangular characters (「 and 」) in the cells. The subjects were told that they could write at their own speed. They were required to write the character 40 times.

(2). Measuring the Control of Handwriting Movement

The content of the page was arranged in 6 rows and 6 columns (36 grid cells), each cell being 18*18 mm. The children were instructed to write three simple characters: "三" (san; composed of three horizontal strokes), "川" (chuan; composed of three vertical strokes), and "八" (ba; two slant strokes) and three complex characters "書" (shu; mostly horizontal strokes), "刪" (shan; mostly vertical strokes), and "參" (tsan; mostly slant strokes). All strokes of simple characters were compared with the 6 horizontal, 6 vertical, and 5 slant strokes of the respective complex characters.

G. Data Processing and Analysis

The data was processed and analyzed using a self-programmed MATLAB routine (The MathWorks, v 6.5, Natwick, MA, USA). The first (velocity) and second derivatives (acceleration) of each stroke were calculated (Marquardt and Mai, 1994). In the first experiment, the number of acceleration peaks per stroke movement was counted. In the second experiment, the mean stroke velocity and pen tip pressure of every stroke were measured. The following are the derived parameters processed from the registered coordinates and pen tip pressure.

1. Number of Corrective Movements (COMs): The number of vertical (or horizontal) acceleration peaks for every vertical (or horizontal) stroke was determined as an approximation of the number of corrective movements. It represents the level of automation. The number of COMs decreases as movement becomes automatic; otherwise movement is still deliberate. When movement is fully automated, the ideal number of COMs is 2 per vertical or horizontal stroke. Decrease in the number of COMs indicates a switch from closed feedback control to open loop control.
2. Inflection Point: To characterize the automation process, a hyperbolic tangent equation, generally used for the description of empirical data with a sigmoid-like distribution, was adopted to describe the change in the number of COMs:

$$Y = a \times \tanh(b \times n - c) + d \cdots\cdots \quad (1)$$

3. where Y is the number of COMs and n is the number of practice attempts. The coefficients a, b, c, and d are estimated by using a least-squares error method. The inflection point was obtained from c/b. It is the number of practice attempts required for the number of COMs to decrease to 50% of their initial value. It represents the speed needed to reach automation in handwriting.

Statistical Analysis

SPSS for Windows/PC (10.0) was used for the statistical analyses. In the handwriting automation experiments, the

DCD group was compared to the non-DCD group and children in the two experimental groups were compared to children in the control group. More than two comparisons were needed. For reducing the accumulation of type I error, one-way analysis of variance (ANOVA) was used to compare the differences among the three groups. The significance level was set at α=0.05. Significant ANOVA results were followed by Tukey's post hoc comparisons. In the comparison between simple and complex character tests, a two-way repeated measure ANOVA with Tukey's post hoc analysis was employed. The significance level was also set at α=0.05.

III. Results

A. Differences in Learning between the Control and Experimental Groups

An abrupt drop in the COM number to the inflection point indicated automated movement was achieved. Figure 1 shows the learning curve of a child in the DCD group tasked with writing the target letter. The inflection point indicates that automation was achieved after about 16 letters. The graph of the measured COM numbers is circles connected by dotted lines. The solid line is the fitted sigmoid curve. Figure 2 shows the learning curve of a child in the non-DCD group tasked with writing the target letter. Automation was observed after about 6 letters.

Table 1 lists the mean numbers of practice attempts (±SD) needed to learn to write the test letter automatically. The group factor was found to have a significant effect on the number of practice attempts needed to achieve automation ($F_{2,91}$=15.52, p<0.001). The result of *post-hoc* tests showed that the difference in this mean number between the DCD and non-DCD groups and between the DCD and control groups reached statistical significance. The difference between the non-DCD and control group was insignificant.

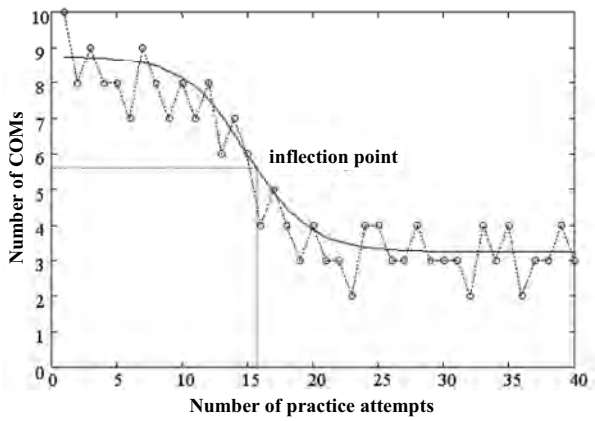


Figure 1: The learning curve of a DCD child in writing the target letter.

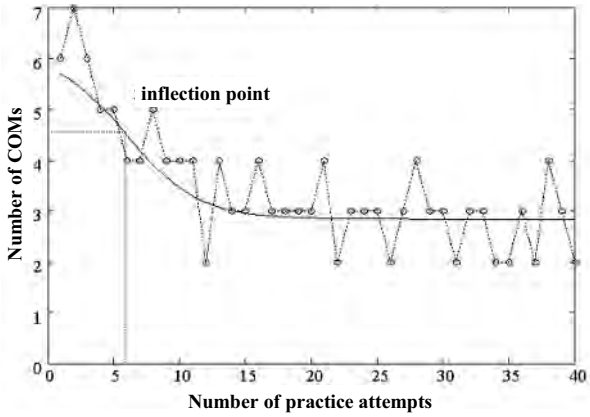


Figure 2: The learning curve of a non-DCD child in writing the target letter.

Table 1: Average number of practice attempts needed to achieve automation

Items \ Groups	DCD	n-DCD	Comparison
No of letters to automation	14.6 (7.9)	7.6 (5.1)	6.2 (5.2)

B. Movement Control in Handwriting

To assess the ability to control stroke movements, velocity changes occurring during the tasks of writing simple and complex characters were compared. Table 2 shows the mean and standard deviations of stroke velocity for the three groups. The repeated measures ANOVA showed that the mean stroke velocity significantly differed between the simple and complex character writing tasks. The velocity was much slower in writing a complex character than a simple character ($F_{1,91}$=129.81, p<0.001). The differences

Table 2: The mean and standard deviation of stroke velocity in writing simple and complex characters

Items \ Groups	DCD n=33	n-DCD n=39	Control n=22
Velocity in the simple task	5.90 (1.68)	5.58 (1.41)	4.85 (0.98)
Velocity in the complex task	4.07 (1.10)	4.34 (1.28)	4.79 (0.98)
Mean velocity	4.98 (1.64)	4.96 (1.40)	4.82 (1.00)

1. unit: cm/s

among the three groups were also significant ($F_{2,91}$=5.22, p=0.007). Furthermore, the two factors interacted, i.e., different groups exhibited different changes in stroke velocity ($F_{2,91}$=15.40, p<0.001). There were differences in stroke velocity among the three groups as well as a difference in the stroke velocity between writing simple and complex characters. The result of *post hoc* showed that, in the simple character test, the stroke velocity was higher in the DCD group than the non-DCD and control groups, but in the complex character test, it was much lower in the DCD group than the non-DCD and control groups.

IV. Discussion & conclusions

This study found that children with DCD needed to practice more to reduce the number of acceleration peaks needed to produce a single stroke. Learning to write a new letter automatically was much slower in DCD children than average children. Most previous studies also found children with DCD experience difficulty in achieving automation of motor skills. Motor learning was also found to be slower in DCD children than normally developed children [4]. The difficulties in motor learning are directly reflected by the problem of learning to write a new letter. Much more practice seems to be necessary for learning the letter.

In studying the learning of handwriting, Kharraz-Tavakol et al. (2000) found that mean corrective movements were reduced 34.5% after 30 practice attempts [2]. We found that a typical child achieves automation after only 6 attempts. On average, children with DCD needed to write the character more than 17 times to reach automation. Automation was defined in this study by a 50% reduction in the number of COMs. The children in our study were faster than those in the study of Kharraz-Tavakol et al. In comparing the target letters used in the two studies, ours was simpler than theirs "ل". There were only two turning points (changes in direction of movement) to complete the task of our study, while at least 4 turning points (changes in movement direction) were required to complete their task, i.e., "ل." In addition, Mergl et al. (1999) found that learning to write rectangular strokes automatically is faster than learning to make curvalinear strokes. Kharraz-Tavakol et al. (2000) found that motor planning subroutines for similar strokes can be practiced and used interchangeably. The two strokes used in the task of this study are geospatially similar, though rotated 90 degrees; therefore, motor planning subroutines can be used interchangeably, which might account for the faster learning in the setting of this study [2].

Smits-Engelsman et al. (2001) speculated that poor handwriting is part of a wider neuromotor condition characterized by faster and cruder movements, lack of inhibition of co-movements, and poor coordination of fine motor skills [3]. As expected, the DCD children in our study used a faster stroke velocity to write simple characters than did control children. However, there was no between-group difference in the stroke velocity used to write complex characters. Moreover, we also found the stroke speed of children with DCD was slowed as compared with control children by writing complex characters. The complexity of complex characters (i.e., involving strokes of many different lengths, directions, and turning points) may account for this slowing. Learning of complex procedures requires closed-loop control with more visual feedback to adjust the procedure. Most children with DCD have impaired visual feedback control and integration of the visual and motor systems [5]. When visual feedback is limited, the number of times the model characters are looked at increases, and so stroke velocity is significantly reduced.

Acknowledgment

The authors would like to thank the National Science Council of the Republic of China for supporting this work financially under contract nos. NSC-92-2614-B-214-001- and NSC-93-2614-B-214-001-.

References

1. Marquardt C, Mai, N (1994) A computational procedure for movement analysis in handwriting. J of Neuroscience Methods 52: 39-45.
2. Kharraz-Tavakol OD, Eggert T, Mai N, Straube A (2000) Learning to write letters: transfer in automated movements indicates modularity of motor programs in human subjects. Neuroscience Letters, 282: 33-6.
3. Smits-Engelsman BCM, Niemeijer AS, van Galen GP (2001). Fine motor deficiencies in children diagnosed as DCD based on poor grapho-motor ability. Human Movement Science, 20: 161-182.
4. Wilson PH, Maruff P, Ives S, Currie J (2001) Abnormalities of motor and praxis imagery in children with DCD. Human Movement Science, 20: 135-159.
5. Wilson PH, McKenzie BE (1998) Information processing deficits associated with developmental coordination disorder: a meta-analysis of research findings. Journal of Child Psychology and Psychiatry, 39: 829-840.

Author: Nan-Ying Yu
Institute: I-Shou University
Street: No 8, Yi-Da Rd, Jiau-Shu Village, Yan-Chao Township
City: Kaohsiung County
Country: Taiwan, ROC
Email: ying@mail.isu.edu.tw

The Development of Computer-assisted Assessment in Chinese Handwriting Performance

N.Y. Yu[1] and S.H. Chang[2]

[1] Department of Physical Therapy, I-Shou University, Kaohsiung County, Taiwan
[2] Department of Occupational Therapy, I-Shou University, Kaohsiung County, Taiwan

Abstract — **This study investigated the utility of assessment for Chinese handwriting performance. In an attempt to computerize the existing Tseng Handwriting Problem Checklist (THPC), this study employed MATLAB to develop a set of computer programs entitled Chinese Handwriting Assessment Program (CHAP) to be used for the evaluation of handwriting performance.**

Through a template-matching approach, the program processed each character by using size adjustable standard models to calculate the 2-dimensional cross correlation coefficient of the template and its superimposed handwritten character. With the help of image processing, it could measure the size control, spacing, alignment, and the average resemblance between standard models and handwritten characters.

The results of CHAP's test-retest reliability showed that high correlation coefficients (from 0.809 to 0.939) all reached statistical significance. The results of correlation analyses between each CHAP and THPC item reached statistical significance. As these two assessment items for handwriting performance are required for objectivity and quantification, further development of CHAP is necessary.

Keywords — **Elementary education, evaluation methodologies, handwriting, computer application, image processing.**

I. Introduction

Children often have difficulties producing legible output both at the speed required to keep up in class or in the amount essential to complete their school work. Generally speaking, poor spacing between consecutive characters, deficient character formation, missing or extra strokes in a character, reversals, sloppiness, and slow writing speed are the problems most often encountered in children as they learn to write [1].

A sophisticated evaluation system should provide not only a score or list, but also an analysis of the problems found in a child's handwriting. Assessment of handwriting legibility involves a subjective examination of characters, numbers or sentences. However, the factors that contribute to legible handwriting are multi-factorial and complex. The test-retest reliability of these methods is still questionable [2][3].

Chinese characters are usually composed of more than two components and constructed primarily by pictographic component. Each component of a character is arranged within a square frame. Writing a Chinese character is similar to delineating an image. It requires harmonic, symmetry, and equilibrium structures for the completion of a character. More attention is necessary to assess neatness, proper stroke placement and alignment.

For a standardized Chinese handwriting performance assessment, Tseng has developed a set of items entitled the Tseng Handwriting Problem Checklist (THPC) used for the evaluation of handwriting in schoolchildren. She has studied the factorial validity of THPC and found that it an effective tool to assess a child's handwriting from 6 dimensions [1]. Chang has used THPC as the assessment tool for handwriting performance to explore the correlation between the latter and perception performance. Although the inter-rater reliability of the THPC reached up to r=0.96 (p=.0001), the advance training of the examiners required considerable time and effort [4].

In recent years, many researchers have used computer technology to analyze the relationship between handwriting and fine motor control while attempting to employ handwriting performance as an indicator for the evaluation of neural motor control [5][6]. Since the spatial layout of a Chinese character is square in nature, the application of image processing techniques may make standardized Chinese handwriting assessment possible. This study used the THPC and other handwriting evaluation tests to develop a new assessment of the neatness and legibility of handwriting for diagnostic purposes. Drawing from the related literature reviews it was determined that letter formation, spacing, size, alignment, and slant are the aspects most frequently adopted as criteria for evaluating the legibility of handwriting [7][8]. Thus, this research aimed to develop a set of computerized evaluations that involved assessments of spatial arrangement, character size control, neatness and legibility of handwriting scripts.

II. Methods

A. The development of the Chinese Handwriting Assessment Program (CHAP)

Since a handwriting performance evaluation requires models as standard for assessment, we first created the stan-

Chwee Teck Lim, James C.H. Goh (Eds.): ICBME 2008, Proceedings 23, pp. 406–410, 2009
www.springerlink.com

dard model in Kai-Shu font and saved it into a 1-bit image. Kai-Shu, known as standard regular, is the newest of the Chinese calligraphy styles. The test sheet written by the participants was scanned (Scanmaker E6, Microtek) with a 100 dpi and saved by 1-bit image.

The main function of the CHAP is to quantify the resemblance between pencil written and standard characters, to scale the character size and to measure spatial arrangement through an image processing algorithm. The program was written by MATLAB language (The MathWorks, v 6.5, MA). The program first loaded the handwritten samples and graphic files of standard models into the computer memory. Compared with the standard models, the pencil written characters revealed thinner strokes. The first step in image processing was to dilate each stroke in the image four times with a 3*3 matrix operator and then overlap five images (including the original image) into one image [9]. The step could thicken the strokes and produce the effect of gradient.

CHAP takes a template matching approach. This approach to identifying a character within an image cross correlates the image with a size adjustable template. The template is itself an image of a standard character. Where the template and the handwritten character being sought are similar, the cross correlation will be high. In the image identification process, the template may need to be scaled at each position to measure the size of the handwritten character. As shown on Figure 1, the template is centered at every pixel in the image and the cross correlation calculated. This forms a 2D array of correlation coefficients.

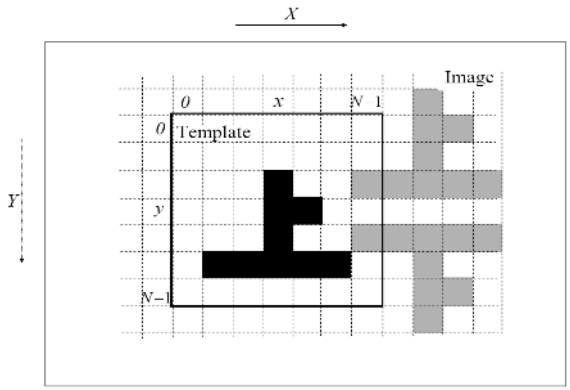


Figure 1. Template matching approach for localizing the handwritten characters. Black: Character in template. Gray: Handwritten character in image.

The form of the un-normalized correlation coefficient at position (X, Y) on the image is given by $r[X][Y] = \sum_{y=-N/2}^{y<N/2} \sum_{x=-N/2}^{x<N/2} \left(template[x+N/2][y+N/2] - \overline{template} \right) \left(image[X+x][Y+y] - \overline{image} \right)$ where $\overline{template}$ is the mean of the templates pixels and $\overline{image}$ is the mean of the image pixels under (covered by) the template.

The peaks in this cross correlation "surface" are the positions of the best matches in the image of the template. Using the above processes, we could identify the accurate coordinate position of each handwritten character. The correlation coefficient referred to the resemblance between handwritten and standard character. Subsequent to the identification of the position of each character, the spatial arrangement of characters could be quantified. Assume the coordinate positions of two characters next to each other were (*Xi, Yi*) and (X_{i+1}, Y_{i+1}). The distance between the two characters (inter-character distance) is $\sqrt{(X_{i+1} - X_i)^2 + (Y_{j+1} - Y_j)^2}$. For measuring the alignment control, the difference between X_i and the X coordinate value of each vertical middle line is the horizontal distance between the center of each character and the middle line. The shorter the distance was, the better the control of the linear alignment of handwritten characters.

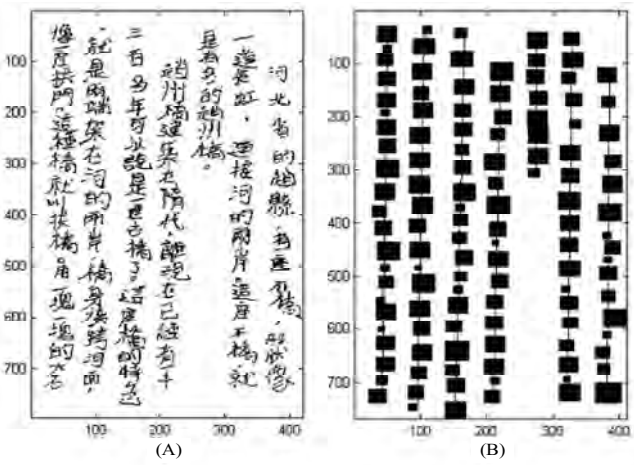
The image processing program could calculate the number of characters written or skipped by the participants, the average/standard deviation of inter-character distance (for spacing control), the average/standard deviation of distance deviated from the mid-line (for alignment control), the average/standard deviation of resemblance with a standard model (for legibility), and the average/standard deviation of character size (for size control). Character sizes were divided into 34 levels ranging from 6*6, 8*8 ...to 72*72 (unit: pixel). Using millimeters as the unit, character sizes ranged from 1.52*1.52, 2.03*2.03 ...to 18.29*18.29 (unit: mm).

B. Reliability of Chinese handwriting assessment program (CHAP)

1. Participants: 20 fourth grade students (10 males and 10 females) were recruited to participate in the experiment.
2. Process: The participants were asked to copy a text selected for this research. The text included four paragraphs. Both the first two and last two paragraphs were printed on two separate papers as two handwriting samples. To counterbalance the arrangement, they were randomly assigned to write any one of the handwriting samples first. Hence, there was no fixed copy order.
3. Statistical analysis: SPSS for Windows/PC (SPSS Inc., Ver 10.0) was used for the statistical analyses. The first two and last two paragraphs were allocated into two groups of samples and respectively evaluated by CHAP. Pearson's correlation analysis was conducted to explore the reliability of this assessment program.

C. Comparison between CHAP and THPC

1. Participants: 66 third grade elementary schoolchildren (34 boys and 32 girls) were recruited into this study.
2. Experimental Procedures: The participating subjects copied the text on the test sheet in the regulated 10 minutes and were told to write in their most natural manner instead of at their fastest speed. The test sheet made in advance was not drawn with checks and lines. Instead, they were drawn with dotted lines of 1.4 cm width as the base for the students.
3. Assessment Tools: The tests for assessing the children's handwriting performance in this research included: a subjective handwriting performance assessment - THPC and computerized assessment program - CHAP.
   (1) Tseng Handwriting Problem Checklist (THPC)
   For the evaluation of Chinese handwriting performance, THPC includes 24 items for the assessment of legibility and handwriting behavior. The first through twelfth items assess handwriting legibility; the thirteenth through the twenty-fourth items involve the observation of handwriting behavior. This research only adopted scores from the first through twelfth items. Scoring was based on the frequency of mistakes. These twelve items included 6 categories of measurement for handwriting performance evaluation (interval, space relation, character size, form, reverse character and strokes).
   (2) Chinese Handwriting Assessment Program (CHAP)
   For this research, four parameters were computed by CHAP for the evaluation of handwriting performance. (1) The standard deviation of character size was utilized for assessing *the control of character size*. (2) The standard deviation of inter-character distance and (3) the average distance deviated from the mid-line were calculated to measure *the control of inter-character space and the straight line alignment*. (4) The average resemblance with the standard model was the indicator for neat and legible handwriting.
4. Validity Tests: Pearson's correlation analyses were conducted for the four parameters of the computer assessment with the corresponding items in THPC. Thus, based on the results of THPC, the significance of CHAP can be evaluated and validated.



◇Total characters written (including punctuation marks)	108	◇Total skipped characters	5
◇Average inter-character space (mm)	9.57	◇SD of inter-character space*	2.08
◇Average deviated distance from mid-line (Unit: mm)*	0.70	◇SD of deviated distance from mid-line	0.55
◇Average resemblance with standard model (0-1)*	0.551	◇SD of resemblance with standard model	0.09
◇Average character size (1-34)	18.90	◇SD of character size*	4.96

(C)

Figure 2. An example of results reported by CHAP. (A) Handwritten script by participant (B) Black boxes show the location and size of all characters (C) Data layout of the processing results.

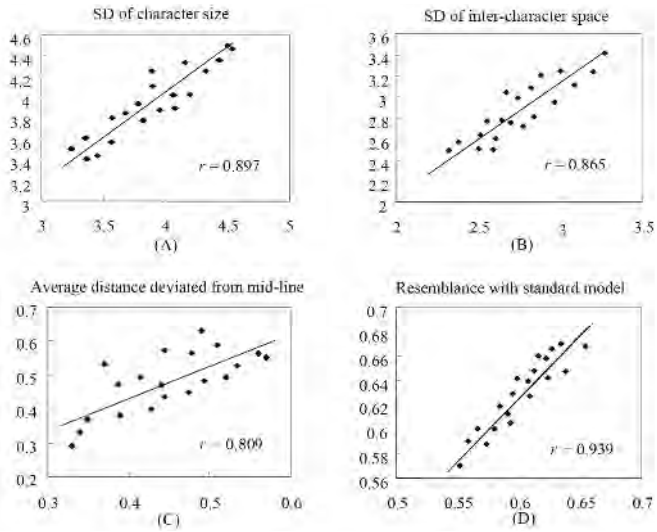


Figure 3. The correlation analyses for the test-retest reliability of CHAP. X- and Y-axes are the results of the first and the last two paragraphs of the same participants.

III. Results

A. Assessment Results and the Reliability of CHAP

Figure 2 is a demonstrative report of a CHAP assessment. It shows the handwritten scripts and the positioning process for quantitative assessment. Figure 3 is the CHAP assessment results for ten fourth grade students. The horizontal coordinate was the assessment result of the first two paragraphs of text and the vertical coordinate was that of the

last two paragraphs. It depicted four results of the correlation analyses: (a) the average inter-character space, (b) the average deviation from the mid-line, (c) the standard deviation of character size, and (d) the resemblance with the standard model. The result showed that correlation coefficients ranged from 0.809 to 0.939 and the *p* values were all less than 0.001, which reached statistical significance.

B. Comparison between THPC and CHAP

According to the results of statistical analysis, viewed from the perspective of CHAP, the correlation between CHAP and the corresponding items of THPC all reached statistical significance ($p < 0.001$). Putting the SD of character size ($r = -0.51$) aside, a strong strength of correlations between CHAP and the corresponding items of THPC was found (r=-0.77 in average distance deviated from the mid-line; r=-0.78 in SD of inter-character distance; r=0.82 in the resemblance with the standard model). An explanation for the negative correlation coefficients is that CHAP observed the deviated distance of the characters from the mid-line and the variance of inter-character distance, whereas in THPC, the neater the spatial arrangement, the higher the assessment scores. As for control of character size, positive results lead to higher evaluation scores in THPC. Thus, it also showed negative correlation.

IV. Discussions and conclusions

The results of this research showed that the CHAP could accurately identify the positions of characters and measure the size of each. Subsequent to the positioning of each character, their spatial arrangement can be successfully parameterized. Based on a set of objective standards, this study was a novel attempt to objectively assess handwriting performance with the help of computer technology. While the traditional evaluation of handwriting neatness and legibility is also based on a set of criteria, it depends on strenuous visual inspection and subjective judgment. Another achievement of CHAP was that it could assess the resemblance to each character to evaluate the neatness and legibility of handwriting. In the past, teachers only scored a student's tasks using their own judgment. When the development and implementation of related techniques mature, the computer is very likely to replace subjective assessments so as to make the assessment of neatness and legibility automatic and more objective.

The further implications of this study include the assessment of perceptual motor functions in children of developmental age. A child with a handwriting problem may have underlying developmental dysfunctions. In addition to academic performance, the measurement of size control and spatial arrangement in CHAP could be associated with the fine motor skills of children. For future studies, CHAP could be utilized for the off-line measurement of neuromotor control in children of developmental age or subjects with neuromuscular conditions. In addition, the approach proposed in this study might be applied to the evaluation of a machine method of coding a subjective rating scheme.

The correlation analyses between THPC and CHAP, among all items, only the one of THPC did not show strong correlation with the corresponding items in CHAP. As mentioned, THPC could complement an examination for the accuracy of handwriting scripts. However, with more objective or quantitative items, the CHAP appeared to be more suitable for an assessment of spatial arrangement.

This study revealed that the combination of CHAP and THPC may be complementary. The integration of CHAP and THPC can be applied to the study of handwriting problems and its remediation in children with special needs or low academic achievement. If the computer techniques and AI of the future reached a more mature level, children's handwriting tasks could be assessed in a more automatic method which could be as objective, rapid and accurate as a present-day computer scoring answer sheet system.

Acknowledgment

The authors would like to thank the National Science Council of the Republic of China for financially supporting this work under contract nos NSC-92-2614-B-214-001.

References

1. Tseng MH (1993) Factorial validity of the Tseng Handwriting Problem Checklist. Journal of the Occupational Therapy Association of the Republic of China, 11: 13-26.
2. Feder KP, Majnemer A, Bourbonnais D, Blayney M, Morin I (2007) Handwriting performance on the ETCH-M of students in a grade one regular education program. Physical & Occupational Therapy in Pediatrics, 27: 43-62.
3. Stefansson T, Karlsdottir R (2003) Formative evaluation of handwriting quality. Perceptual & Motor Skills, 97: 1231-1264.
4. Chang SH (1997) Relationships between handwriting and perceptual performance in third-grade Chinese Children. Unpublished master's thesis. University of Southern California, Los Angeles.
5. Smits-Engelsman BC, Swinnen SP, Duysens J (2004) Are graphomotor tasks affected by working in the contralateral hemispace in 6- to 10-year-old children? Motor Control, 8: 521-33.
6. Rosenblum S, Dvorkin AY, Weiss PL (2006) Automatic segmentation as a tool for examining the handwriting process of children with dysgraphic and proficient handwriting. Human Movement Science, 25: 608-21.

7. Ziviani J, Elkins J (1984) An evaluation of handwriting performance. Educational Review, 36: 249-261.
8. Phelps I, Stemple L, Speck G (1985) The children's handwriting scale: A new diagnostic scale. Journal of Educational Research, 79: 46-50.
9. Gonzalez RC, Woods RE (2002) Digital Image Processing. (2nd ed.) (pp. 75-142). New Jersey: Prentice Hall.

Corresponding Author: Shao-Hsia Chang
Institute: I-Shou University
Street: No 8, Yi-Da Rd, Jiau-Shu Village, Yan-Chao Township
City: Kaohsiung County
Country: Taiwan, ROC
Email: stacey12@mail.isu.edu.tw

Novel Tools for Quantification of Brain Responses to Music Stimuli

O. Sourina[1], V.V. Kulish [2] and A. Sourin[3]

[1] Nanyang Technological University/School of Electrical and Electronic Engineering, Singapore
[2] Nanyang Technological University/School of Mechanical and Aerospace Engineering, Singapore
[3] Nanyang Technological University/School of Computer Engineering, Singapore

Abstract — **Therapeutic effect of music is known for long time. Music therapy can be used to improve the current patient's state or even prevent some deceases of psychosomatic origin. For decades, the basic research methods of music psychology mainly relied on survey with questionnaire or on observations of subjects. Investigating the effect of music through electroencephalograms (EEG) could be more precise and objective. In this paper, we describe fractal dimension model for quantification of brain responses to external stimuli. Human EEG evoked by music stimuli are analysed with the developed software. The proposed technique of processing EEG is based on the Rényi entropy – the concept of generalized entropy of a given probability distribution. It allows defining generalized fractal dimension of EEG. The experiments involved ten subjects, both male and female twenty years old university students. The EEGs were processed by the fractal dimension analysis tools. Analysis of fractal dimension values demonstrates that the method can be used to quantitatively distinguish between different states of the brain. Correlation between music, and subject's emotion and concentration was studied. Few hypotheses were validated.**

Keywords — **EEG, music therapy, brain response quantification, fractal dimension, emotions.**

I. Introduction

For decades, the basic research methods of music psychology is no different from other disciplines in social science domain, mainly relying on survey with questionnaire and attaining results through statistical approach, or otherwise through the observation of subjects. Investigating the effect of music through EEG was still new to the research community until recent times. Now, combination of the accomplishment of past study of music psychology with EEG-based research is already bearing fruit, as therapeutic effect of music is now widely recognized and music is used for treatment of neural abnormality or mental disorder. Modeling of brain activity with EEG signals is more precise and objective than survey, because the subject being surveyed might not be fully aware of his/her psychological and emotional status when answering questions. On the other hand, EEG signals would not be altered by the subject's own judgment. Therefore this approach would be more used in the coming years.

EEG signals are the records of electrical potential produced by the brain along with its activities. Quantification of responses of human brain to various external stimuli is a research area that can help to solve a mystery of the human brain. Researchers attempt to create tools and models to study and describe the behaviors and nature of EEG signal. The current methodology is to analyze real-time EEG readings in frequency domain. But there is a new trend for EEG signal processing as moving from linear Fast Fourier Transform (FFT) to non-linear Fractal Time Series analysis to study dynamic nature of EEG signals. The analysis of EEG data in fractal dimension domain is based on its geometric pattern, rather than frequency content.

In our works [1-3], we proposed to process EEG signals using fractal dimension model and implemented novel algorithm to process EEG signals evoked by odor stimuli. We studied brain responses to six basic olfactory stimuli given to the subjects in our experiments.

In this paper, we describe results of experiments with music used as external stimuli. The psychological effect of music measured in terms of EEG responses is studied. In this paper, we describe fractal dimension analysis model and apply it to analyze EEG evoked by music stimuli. We extend fractal dimension model with dynamic component and develop a novel algorithm and software system. The fractal dimension changing over time is visualized dynamically on the chosen EEG channels. The experiments are conducted with music used as the external stimulus, and the EEG response of the subjects, university students, are recorded and subjected to fractal dimension analysis. The analysis results are plotted graphically for intuitive investigation and visualized dynamically with the developed visualization software. Few hypotheses were validated.

In Section II, an introduction to fractal dimension analysis is given. Section III describes the experiment setting and analyzes experiments results. Section IV summarizes the outcomes of the project and provides recommendations for the future development.

Chwee Teck Lim, James C.H. Goh (Eds.): ICBME 2008, Proceedings 23, pp. 411–414, 2009
www.springerlink.com

II. Fractal analysis model description

Fractal dimension analysis can be generally applied to non-linear systems. It basically tells how many points lie in the set and how scattered they are or how "strange" is a geometric structure [4].

A common practice to distinguish among possible classes of time series is to determine their so-called correlation dimension. The correlation dimension, however, belongs to an infinite family of fractal dimensions [5]. Hence, there is a hope that the use of the whole family of fractal dimensions may prove to be advantageous in comparison with using only some of these dimensions.

The concept of generalized entropy of a probability distribution was introduced by Alfred Rényi [6]. Based on the moments of order q of the probability p_i, Rényi obtained the following expression for entropy

$$S_q = \frac{1}{q-1}\log\sum_{i=1}^{N} p_i^q \tag{1}$$

where q is not necessarily an integer and log denotes $\log_2$. Note that for $q \to 1$, Eq. (1) yields the well-known entropy of a discrete probability distribution [7]

$$S_1 = -\sum_{i=1}^{N} p_i \log p_i \tag{2}$$

The probability distribution of a given time series can be recovered by the following procedure. The total range of the signal is divided into N bins such that

$$N = \frac{V_{\max} - V_{\min}}{\delta V} \tag{3}$$

where $V_{\max}$ and $V_{\min}$ are the maximum and the minimum values of the signal achieved in the course of measurements, respectively; δV represents the sensitivity (uncertainty) of the measuring device. The probability that the signal falls into the ith bin of size δV is computed as

$$p_i = \lim_{N\to\infty} \frac{N_i}{N} \tag{4}$$

where N_i equals the number of times the signal falls into the ith bin. Alternatively, in the case of a time series, the same probability can be found from the ergodic theorem, that is

$$p_i = \lim_{T\to\infty} \frac{t_i}{T} \tag{5}$$

where t_i is the time spent by the signal in the ith bin during the total time span of measurements T.

Further, the generalized fractal dimensions of a given time series with the known probability distribution are defined as

$$D_q = \lim_{\delta V\to 0} \frac{1}{q-1} \frac{\log\sum_{i=1}^{N} p_i^q}{\log \delta V} \tag{6}$$

where the parameter q ranges from $-\infty$ to $+\infty$. Note that for a self-similar fractal time series with equal probabilities $p_i = 1/N$, the definition Eq. (6) gives $D_q = D_0$ for all values of q [8]. Note also that for a constant signal, all probabilities except one become equal to zero, whereas the remaining probability value equals unity. Consequently, for a constant signal, $D_q = D_0 = 0$. The fractal dimension

$$D_0 = -\frac{\log N}{\log \delta V} \tag{7}$$

is nothing else but the Hausdorff-Besicovitch dimension [8].

The correlation dimension, mentioned previously, is the fractal dimension with q = 2.

As $q \to 1$, Eq. (6) yields the so-called information dimension

$$D_1 = \lim_{\delta V\to 0} \frac{-\sum_{i=1}^{N} p_i \log p_i}{\log(1/\delta V)} \tag{8}$$

where the numerator is Shannon's entropy given by Eq. (2).

Note also that

$$D_\infty = \lim_{\delta V\to 0} \frac{\log p_{\max}}{\log \delta V} \tag{9}$$

and

$$D_{-\infty} = \lim_{\delta V\to 0} \frac{\log p_{\min}}{\log \delta V} \tag{10}$$

such that $D_{-\infty} \geq D_{\infty}$. In general, if a < b, $D_a \geq D_b$, such that D_q is a monotone non-increasing function of q [7]. For a given time series ("signal"), the function D_q, corresponding to the probability distribution of this signal, is called the fractal spectrum. Such a name is well-justified, because the fractal spectrum provides information about both frequencies and amplitudes of the signal.

This definition of fractal dimension covers a very large family corresponding to different q values. When $q = 0$, it is the Hausdorff-Besicovitch Dimension. When $q = 1$, it is so-called the information dimension; the entropy will become Shannon's entropy. The correlation dimension is the fractal dimension with $q = 2$.

As EEG signals are not stationary traces, but a dynamic and time varying measure, it is necessary to reveal the history of fractal dimension in time. Hence an algorithm is implemented to calculate a time-series dynamic fractal dimension data.

Thus, the introduction of fractal dimension analysis is to change the way of EEG signal analysis from frequency perspective to geometric or pattern-based perspective. The described equation for general fractal dimension model is for a sample set of fixed number of data entities *N,* or can be otherwise called a static model. But in real application, the samples set size would be accumulating all the time to accommodate incoming data. Therefore, we proposed and implemented novel algorithm to handle sample set of growing size or in this sense a dynamic one.

III. Experiments and Results

As human brain is processing in a tremendous speed, the real time EEG signal should be sampled in a reasonably high sampling frequency. In our project, the equipment used for EEG signal recording, called MINDSET24, records 256 EEG samples per second for every single channel. There are 24 channels in total covering the entire skeleton sculp.

We proposed and conducted experiments using different music stimuli. We had series of experiments spiritual (religious), hard rock music, classical music, and hip-hop music. The questionnaire was used to record emotional state of subjects to discover correlation between fractal dimension values and mental state induced by music.

The results of experiments were processed with the implemented dynamic fractal dimension algorithm and were visualized as graph changing over time/frequency. Fractal dimension changing over time can be also visualized with the developed Brain Visualization system. In Fig. 1, fractal dimension values are represented by changing in heights "sticks" showing which channels are active and how active they are during listening music. The subjects investigated in our experiments were the university students, both males and females 22-25 years old.

The results processing confirmed our hypothesis that it is possible to recognize happiness and sadness emotions by computing fractal dimension values. By processing the EEG during experiments it was also proved that fractal dimension model can be used to differ between concentration/relaxation states of the mind.

Hard Rock music showed the biggest fractal dimension values for all subjects throughout the whole experiment. It was also supported by the interview conducted during the experiment that such song gives the most disturbing effect.

The subjects were required to answer the survey questionnaires before and after the experiments.

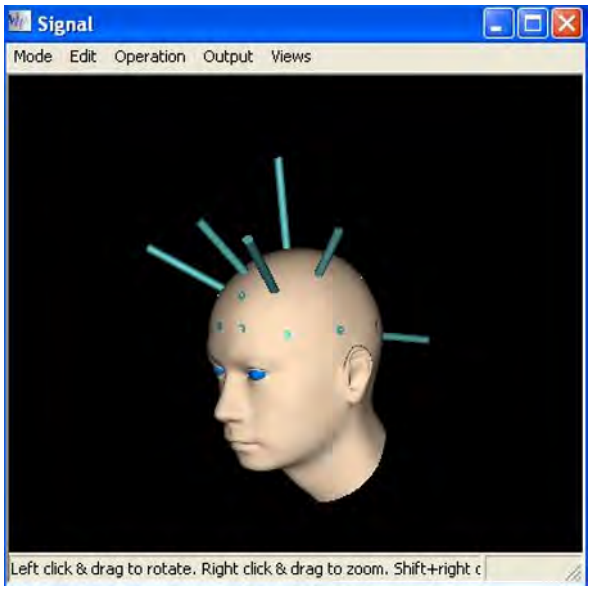


Fig. 1 Visualization of fractal dimension in 6 active channels with VisuBrain

The following questions were asked:

- Do you have any musical background?
- What genre of music do you like to listen?
- What emotion does the music evoke?
- Have you heard the song before?

The subjects were given the memory tests during experiments to assess their level of concentration when they were listening different types of music. The following observations were drawn after processing the results. Subjects generally performed better in the memory test while listening to the songs which induce feeling of happiness. Subjects

have the lowest score when they are listening to songs which they find disturbing or irritating. Jazz song was the most disturbing to the subjects, followed by hard rock song, except for one subject who named hard rock music as favorite. All the subjects indicated that classical songs make them feel happy and comfortable. Music which evoked positive emotions such as happiness, acceptance and pleasantly surprise resulted in subjects scoring better for the memory test. Music which brings negative emotions such as anger and distress generally resulted in the subjects performing their worst in the memory test.

After processing both EEG and survey questionnaires the following hypotheses have been confirmed:

- The subjects' concentration levels will show significant differences among different genres of songs.
- The subjects' EEG responses do not depend on gender of subjects.
- The subjects' EEG responses depend on music familiarity.
- Music which evokes positive emotions will results in better concentration as compared to music evoking negative emotions.
- The subjects' levels of concentration depend on their preferred genre of music.
- The subjects' EEG responses depend on music background of subjects. Subjects that took music clases have higher fractal dimension values in all experiments.

The following hypotheses have not been confirmed:

- Music which brings relaxation will result in the highest level of concentration.
- The subjects perform better on memory test while listening to any music.

Some other hypotheses were inconclusive.

IV. Conclusions

Music stimulus could be used for subject's concentration and to put subjects into different emotional states. In our experiments, the highest level of concentration was evoked by music that evokes positive emotions. Since concentration is relative to emotions, it is therefore reasonable to say that a person's emotional state can influence a person's level of concentration.

In our experiments, it was confirmed that it is possible recognize happiness and sadness emotions by computing fractal dimension values that could be used in development of music therapy applications. We believe that fractal dimension model can be used for quantification of brain responses to develop personally adaptive music therapy program. Further research and experiments should be carried out. The more conclusive results could be achieved in the case of more careful choice of subjects, regarding their musical affinities and cultural background.

This field of research is still relatively new, and there is still much to be done to improve on emotions quantification models and algorithms. The list of basic emotions to be studied should be extended as well.

References

1. Kulish V, Sourin A, Sourina O (2005) Human electroencephalograms seen as fractal time series: mathematical analysis and visualization. Computers in Biology and Medicine 36:3, 291-302
2. Kulish V, Sourin A, Sourina O (2006) Analysis and visualization of human electroencephalograms seen as fractal time series. Journal of Mechanics in Medicine & Biology 26:2, 175-188
3. Kulish V, Sourin A, Sourina O (2007) Fractal spectra and visualization of the brain activity evoked by olfactory stimuli, Proc. of the 9th Asian Symposium on Visualization Hong Kong, 4-9 June, pp.37-1 - 37-8
4. Moon F C (1992) Chaotic and fractal dynamics: an introduction for applied scientists and engineers. John Wiley & Sons
5. Hentschel H G E., Procaccia I (1983) The infinite number of generalized dimensions of fractals and strange attractors, Physica, 8D, 435-444
6. Rényi A (1955) On a new axiomatic theory of probability, Acta Mathematica Hungarica, 6, 285-335
7. Shannon C E (1998) The mathematical theory of communication. University of Illinois Press
8. Schroeder M R (1991) Fractals, chaos, power laws. W. H. Freeman & Co

Author: Olga Sourina
Institute: Nanyang Technological University
Street: 50 Nanyang Crescent
City: Singapore
Country: Singapore
Email: eosourina@ntu.edu.sg

An Autocorrection Algorithm for Detection of Misaligned Fingerprints

Sai Krishna Alahari[1], Abhiram Pothuganti[2], Eshwar Chandra Vidya Sagar[3], Venkata Ravi kumar Garnepudi[4] and Ram Prakash Mahidhara[5]

[1] B.V.Raju Institute of Technology, Hyderabad, India
[2] B.V.Raju Institute of Technology, Hyderabad, India
[3] B.V.Raju Institute of Technology, Hyderabad, India
[4] B.V.Raju Institute of Technology, Hyderabad, India
[5] B.V.Raju Institute of Technology, Hyderabad, India

Abstract — **Biometric security systems are becoming more and more predominant these days and are rapidly replacing every other security sytem.Also,these are getting involved in and out of our daily life. In this scenario, these systems are expected to be highly intelligent and sophisticated in nature. Even small errors or mistakes may post huge security threats. This paper addresses the basic problem encountered by fingerprint recognition systems. The problem of inaccuracy caused due to improper placement of the finger on the scanner either intentionally or accidentally is dealt with using this algorithm. The algorithm is developed using the basic concepts of radon transform on the MATLAB platform. A misaligned fingerprint (image) in query is compared with the fingerprints (images) in the database by applying radon transform to correct the angle to match the fingerprints. Different images were tested using this algorithm and satisfactory results have been obtained in most of the cases. Experimental evaluation demonstrates an efficient performance of the proposed algorithm.**

Keywords — **Fingerprints, radon transform, misaligned, matching.**

I. Introduction

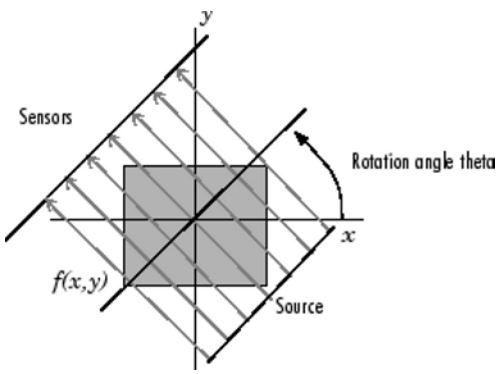
Biometrics can be defined as the study of methods for uniquely recognizing humans based upon one or more of their intrinsic physical(fingerprint, face recognition, iris, retina, palm-print, etc.) or behavioral traits.Biometric authentication has been receiving extensive attention over the past decade with increasing demands in automated and secure identification.

Fingerprint based biometric security systems are the oldest and widely used for authentication purposes because of their universality, uniqueness, performance and acceptability**.** A **fingerprint** is an impression of the friction ridges of all or any part of the finger. A friction ridge is a raised portion of the epidermis of the skin. These ridges are sometimes known as "dermal ridges" or "dermal papillae". The three basic patterns of fingerprint ridges are the arch, loop, and whorl. Traditional fingerprint recognition methods employ feature-based image matching, where minutiae [1] (i.e., ridge ending and ridge bifurcation) are extracted from the fingerprint image in the database and the input fingerprint image in query, followed by their pairings to recognize the valid fingerprint[2]. Even though fingerprint identification techniques are age old, there are still some problems associated with them.[3]

This paper is an attempt to address one such problem which is recognition of misaligned fingerprints using a new approach which makes use of the concepts of radon transforms and bilinear rotations.

II. Radon transform for fingerprints

Radon transform computes projections of an image matrix along specified directions. A projection of a two-dimensional function f(x,y) is a set of line integrals. The *radon* function available in MATLAB computes the line integrals from multiple sources along parallel paths, or beams, in a certain direction[4]. The beams are spaced 1 pixel unit apart. To represent an image, the radon function takes multiple, parallel-beam projections of the image from different angles by rotating the source around the center of the image. The following figure shows a single projection at a specified rotation angle.



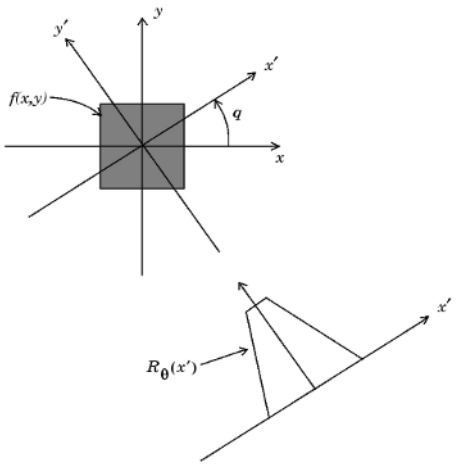
Chwee Teck Lim, James C.H. Goh (Eds.): ICBME 2008, Proceedings 23, pp. 415–417, 2009
www.springerlink.com

Projections can be computed along any angle. In general, the Radon transform of f(x,y) is the line integral of f parallel to the y′-axis:

$$R_\theta(x') = \int_{-\infty}^{\infty} f(x'\cos\theta - y'\sin\theta,\ x'\sin\theta + y'\cos\theta)\, dy'$$

$$\begin{bmatrix} x' \\ y' \end{bmatrix} = \begin{bmatrix} \cos\theta & \sin\theta \\ -\sin\theta & \cos\theta \end{bmatrix} \begin{bmatrix} x \\ y \end{bmatrix}$$

The following figure illustrates the geometry of the Radon transform.



III. Procedure of Implementation

A. Image Rotation

This concept is applied to the original fingerprint and also to the fingerprint in query. The radon projections for the prints are taken in step increases of one degree from 0 to 180 degrees. Here, the main aim is to find out whether the finger print in query is identical to the original fingerprint or not. The image in query is rotated using the *imrotate* command in MATLAB making use of bilinear interpolation[6]. After each rotation the procedure of applying radon transform is repeated.



a. Normal fingerprint

b. Misaligned fingerprint under query

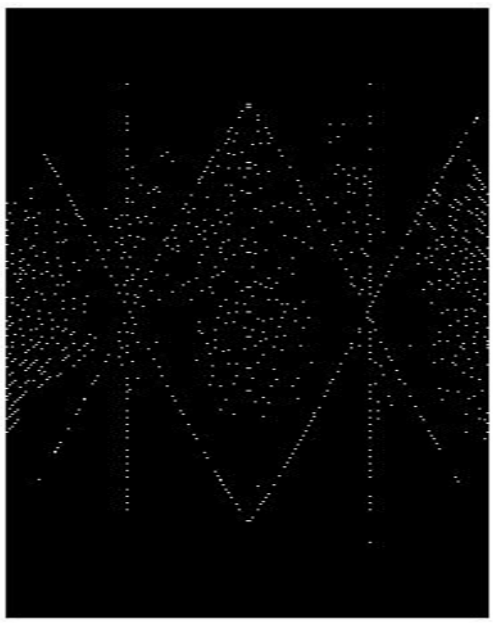
B. Computing the local maxima

As shown above the radon transform is applied on misaligned finger print. The radon coefficients are stored in a matrix. On this matrix we compute the extended-maxima transform, which is the regional maxima of the H-maxima transform. H is a nonnegative scalar.[7]

Regional maxima are connected components of pixels with the same intensity value t, whose external boundary pixels all have a value less than t. all this is implemented using the MATLAB function *imextendedmax (I,H).*

By default, *imextendedmax* in MATLAB uses 8-connected neighborhoods for 2-D images and 26-connected neighborhoods for 3-D images.

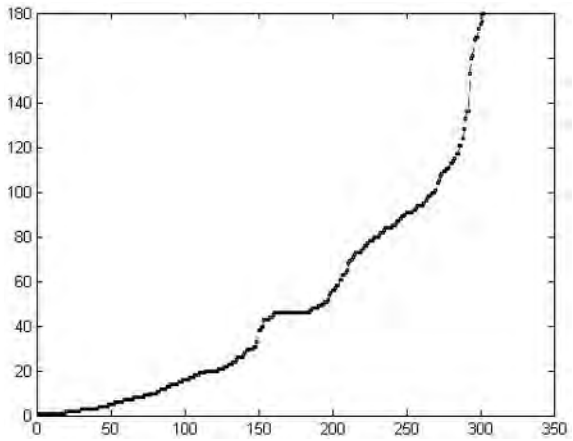
On applying this function to the misaligned fingerprint we get the following figure which is an implication of the local maxima points in the fingerprint.[8]



C. Calculating the angle of rotation

The rotation angle of the misaligned finger print, if it matches to that in the database is calculated[9]. This is implemented by taking all the angles of the local maxima points and sorting them in an array in the increasing order to find the smallest angle, which is the angle by which the

finger print is misaligned. We now plot this array to get the following graph which can also be used as a tool for matching the fingerprints.



Same finger prints results in similar graphs. Using the angle measured from this graph the image can be used for re-registration.

IV. Experimental results

The proposed algorithm has been tested with FVC 2000 2 A data base. This database consists of 100 different fingers, with 8 samples per finger, giving a total of 800 fingerprints. Substantial equal error rate(ERR) has been achieved .This algorithm worked well with both high resolution and low resolution images. The algorithm has been implemented in MATLAB v7.0 in a Intel dual core processor-2.99GHz,1gb RAM system and the time taken to achieve correct matching for one sample is around half minute. But still the algorithm is having good efficiency and reliability.

V. Conclusion

A novel technique to align and match two fingerprint images is proposed in this paper. The experiments presented in this paper demonstrate that this approach produces acceptable results even with low resolution images.Currently we are investigating the methods to reduce the time taken by the algorithm by minimizing the number of radon projections. This technique makes the biometric fingerprint detection system more intelligent and highly reliable. This algorithm finds its profound applications in the fields of forensic science, electronic voting machines and many more, where fool proof fingerprint recognition is required.

References

1. Maltoni, D., Maio, D., Jain, A. K., Prabhakar, S.: "Handbook of Fingerprint Recognition". Springer-Verlag New York (2003).
2. Crouzil,A., Massip-Pailhes, L., Castan, S.: "A New Correlation Criterion Based on Gradient Fields Similarity". Proc. 13th Int. Conf. on Pattern Recognition, (1996).632-636.
3. Anil Jain, Arm Ross, Salil Prabhakar. “Fingerprint matching using minutiae and texture features”. Image Processing, 2001 International Conference on, Volume Page(s):282 - 285 vol.3, 2001
4. Beylkin.G “Discrete radon transform" Acoustics, Speech and Signal Processing, IEEE Transactions on Volume 35, Issue 2, Feb 1987 Page(s): 162 – 172.
5. Maio, D., Maltoni D., Cappelli R., Wayman J.L., Jain, A.K. FVC2002: Second Fingerprint Verification Competition. Pattern Recognition, 2002. Proceedings. 16th International Conference on, Volume 3, Page(s):811 - 814 vol.3, 2002
6. Lin Hong; Yifei Wan; Jain, A.: "Fingerprint image enhancement: algorithm and performance evaluation". IEEE Transactions on Pattern Analysis and Machine Intelligence, Volume 20, Issue 8, (1998) 777 - 789.
7. Xiong Wu Xin Ye “Simulated performance of local maximum likelihood detection with interferences of unknown signature waveforms” Vehicular Technology Conference, 2003. VTC 2003-Fall.2003IEEE58th.
8. Piotr Porwik1 and Krzysztof Wrobel “The New Algorithm of Fingerprint Reference Point Location Based on Identification Masks” springer publications.
9. Sergios Theodoridis, Konstantinos Koutroumbas “MATLAB INTRODUCTION TO PATTERN RECOGNITION” Elsevier Publications.

Author1: SAIKRISHNA ALAHARI
Institute: B.V.RAJU INSTITUTE OF TECHNOLOGY
Street: MALKAJGIRI
City: HYDERABAD
Country: INDIA
Email: ALAHARI_SAIKRSH@YAHOO.COM

Author2 : ABHIRAM POTHUGANTI
Institute: B.V.RAJU INSTITUTE OF TECHNOLOGY
Street: NEW BOWWENPALLY
City: HYDERABAD
Country: INDIA
Email: ABHIRAM06@GMAIL.COM.

Author3: ESHWAR CHANDRA VIDYASAGAR
Institute: B.V.RAJU INSTITUTE OF TECHNOLOGY
Street: KUKATPALLY
City: HYDERABAD
Country: INDIA
Email: KESHWARCHANDRAVIDYASAGAR@GMAIL.COM

Author4: VENKATA RAVI KUMAR GARNEPUDI
Institute: B.V.RAJU INSTITUTE OF TECHNOLOGY
Street: KUKATPALLY
City: HYDERABAD
Country: INDIA
Email: GVRAVIKUMAR08@GMAIL.COM

Author5: RAM PRAKASH MAHIDHARA
Institute: B.V.RAJU INSTITUTE OF TECHNOLOGY
Street: MEHDIPATNAM
City: HYDERABAD
Country: INDIA
Email: RAZRRSHARP@ROCKETMAIL.COM

A Low Power Wireless Downlink Transceiver for Implantable Glucose Sensing Biosystems

D.W.Y. Chung[1], A.C.B. Albason[1], A.S.L. Lou[2] and A.A.S. Hu[3]

[1] Department of Electronic Engineering, Chung Yuan Christian University, Taiwan, R.O.C.
[2] Department of Biomedical Engineering, Chung Yuan Christian University, Taiwan, R.O.C.
[3] Pinestar Electronic Technology, Chung Yuan Christian University Innovation & Incubation Center, Taiwan, R.O.C.

Abstract — **A novel capacitor-less amplitude demodulation receiver architecture is used in the design of a downlink transceiver for a wireless implantable glucose sensing biosystem. The transceiver system is composed of a high efficiency class E power amplifier utilized as an external transmitter and an implantable data detection receiver, communicating through an inductive link. Amplitude shift keying digital scheme is used to externally modulate the 2 MHz carrier frequency at a data rate of 2 kbps. Transmitter spectral power was measured at 1.51 mW during transmission in air and data was successfully decoded at an effective distance of 3 cm between antennas. Implantable receiver off-chip antenna is implemented using a ferrite core, wire wound coil. A low power, low area consumption implantable receiver module is produced in the research with internal receiver core area measuring at 64.8µm by 55.9µm. Average power dissipation is 1.15 mW at a 3.3V single rail power supply, the lowest to date. Power consumption was measured at both 10 pF and 100 pF load capacitances. Implantable receiver chip was designed and implemented using a TSMC 0.35µm mixed-signal 2P4M 3.3V/5V standard CMOS process.**

Keywords — **Low power, downlink transceiver, implantable systems, glucose sensing, inductive link.**

I. Introduction

Research in micro-dose drug delivery systems and a substantial and increasing diabetic population are pushing the field of implantable electronic devices.

Diabetic patients usually monitor glucose levels by a painful finger pricking process to obtain blood samples. This inefficient and excruciating procedure, especially when administered to aged people and children, has led to developments of glucose sensors that are non invasive or implanted subcutaneously [1].

Several factors have to be considered when designing implantable sensing systems. An implanted system needs an efficient power amplifier to transmit commands to the implanted module. One also needs to consider that magnetic coupling could interfere with the biological signals. Carefully designing the signal acquisition circuitry with high signal to noise ratio is a necessity. Distance and data transmission rate are key factors that affect the entire system architecture.

II. Overall System Architecture

Fig.1 shows the downlink transceiver system, composed of an external transmitter subsystem and an internal data demodulator subsystem. This external module will give command, power and data to the implantable module. This internal unit will recover power, demodulate the data and give command to the internal MCU. The internal module will have an off-chip implantable ferrite core antenna. The internal device receives data through RF telemetry, achieved by the amplitude modulation of the carrier frequency. The telemetry link is a transformer like coupled pair of coils previously used in implantable devices [2] [3].

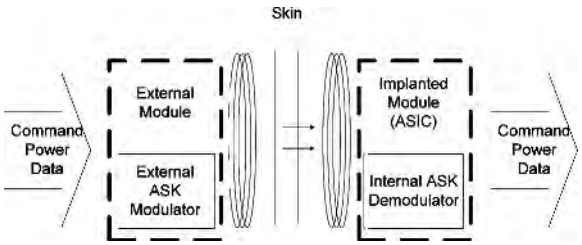


Fig. 1 Downlink transceiver system architecture displaying external and implantable subsystems.

III. Downlink Transceiver Prototype

The class E power amplifier was chosen as transmitter for its high efficiency and simplicity. The specific transmitter schematic used in this paper is shown in Fig. 2. Class E amplifiers, typically can operate at power losses at a factor of 2.3 times smaller compared to conventional class B or C at the same frequency and output power using the same transistor M1. This efficiency in the active device is necessary due to the very low coupling between transmitter and receiver coils with the implanted system receiving less than

Chwee Teck Lim, James C.H. Goh (Eds.): ICBME 2008, Proceedings 23, pp. 418–421, 2009
www.springerlink.com

1% of the average emitted RF power. Research showed that RF technology is practical for clinical applications [2][3][4].

Carrier generator was implemented using a 2MHz crystal oscillator circuit. The selection for the 2MHz carrier frequency allows enough power to be transmitted to the receiver without much tissue heating and RF absorption while permitting tolerable miniaturization. The choice of the frequency must consider the attenuation of magnetic field intensity in non magnetic materials such as air and the power absorption of biological tissue with magnetic fields inducing eddy currents. For coil based coupling technique, the received signal is proportional to the transmission frequency; although the power attenuation rate of lower frequencies is less than that of higher frequency EM waves. A lower carrier frequency can produce a slow and detrimental data transmission rate; however a higher frequency can cause excessive heating and damage body tissue. 2 MHz is between hundreds of kilohertz and few megahertz, the suggested range by researchers for implantable devices or bio microsystems [3] [4] [5].

ASK modulation was chosen because it uses the simplest modulation circuitry, therefore implementation complexity is minimized. Acceptable signal to noise ratio (SNR) and modulating index is achievable through proper design. With efficient design, the quality of digital data transmission will be more than sufficient in most applications [6].

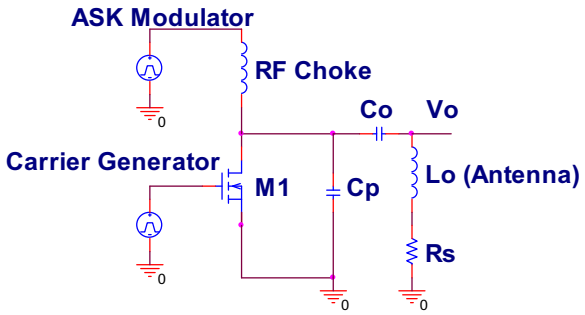


Fig. 2 External ASK modulator (transmitter) prototype schematic.

Fig. 3 shows the transmitter spectral power of 1.8 dBm or 1.51 mW measured at the 2 MHz center frequency. Using the Agilent 3585A Spectrum Analyzer up to a full range of 40 MHz, frequency harmonics were at least 20 dBm lower with respect to center frequency, guaranteeing transmission to be immune to harmonic distortions.

Fig. 4 shows the schematic of the ASK data demodulator circuit and is composed of three main blocks: the envelope detector, high pass filter and Schmitt trigger. The low pass filter (envelope detector) serves to extract the envelope from the 2 MHz carrier. Diode D1 is used to detect the peaks of the envelope while R1 and C1 determine the corner frequency of the detector. The high pass filter is a standard RC circuit composed of R2 and C2 and is necessary to remove the DC offset of the envelope and provide breakdown protection for the CMOS gate inputs of the Schmitt trigger [3].

Table 1 shows parameters for both external and implantable coil: LS–series inductance, LP–parallel inductance,

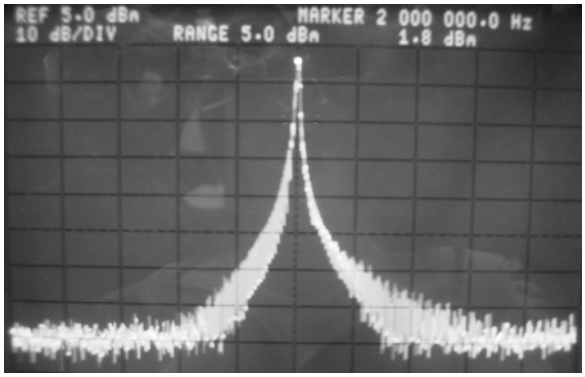


Fig. 3 External transmitter data modulated spectrum taken at 2 MHz center frequency.

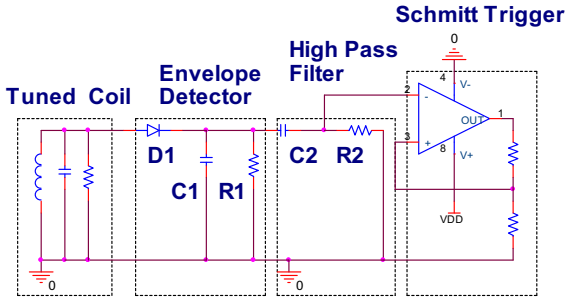


Fig. 4 Internal ASK demodulator (receiver) prototype schematic.

Table 1 Inductive Link Coil Parameters

Parameters	External Coil	Implantable Coil
L_S	43.905 µH	132 µH
L_P	43.95 µH	130.152 µH
C_S	-143.946 pF	-48.55 pF
C_P	-143.962 pF	-48.56 pF
R_S	1.75 Ω	14.2 Ω
R_P	180K Ω	193K Ω
Q	307	114.7
Length	4.5 cm	1.25 cm
Diameter	1.5 cm	0.4 cm
Core Type	Air	Ferrite
f_{CENTER}	2 MHz	2 MHz

CS–series capacitance, CP–parallel capacitance, RS–series resistance, RP–parallel resistance and Q–quality factor. These were measured using the 2-MHz model of Quadtech 7600 LCR meter. Successful data detection was seen at the receiver end of the downlink operation as proven in Fig. 5.

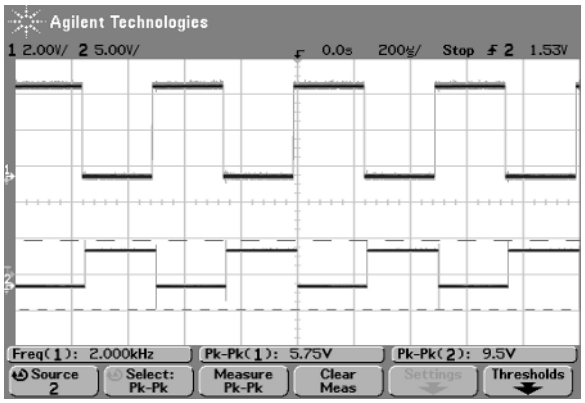


Fig. 5 Data modulating signal input to the class E transmitter (channel 1) and the data as decoded by the internal receiver (channel 2).

IV. Integrated Circuit Implementation

Previous implementations of the implantable receiver make use of passive components which resulted in large chip area consumption. For the integrated circuit implementation, the proposed architecture for the implantable receiver prototype was revised to allow for a smaller design. Actual voltage and noise levels were measured using the downlink transceiver prototype; MATLAB® was used to reconstruct the actual data measures. Ideal input levels were first created, and then a 6dB noise level was added, in accordance to the actual signal received. The reconstructed data was then written out as a SPICE file format VPWL function at a sampling rate of 8 MHz. This VPWL function was used as input stimulus to the transistor level post layout simulation using Hspice®, giving the internal receiver design a much more realistic stimulus than an ideal input [7].

A novel capacitor less internal receiver module in Fig. 6 was developed and largely referenced from [8]. This circuit features an input buffer stage, which effectively eliminates noise levels by forcefully pulling up logic 1 to VDD (3.3V) and logic 0 to GND (0V). Fig. 7 depicts the integrated circuit layout of the capacitor less internal receiver with dimensions of 64.8 µm by 55.9 µm.

The integrated circuit architecture of the internal data receiver is composed of an input buffer, envelope detector, Schmitt trigger and a load driver. Fig. 8 shows simulation results and the signal transformation waveforms as the input signal passes through each stage of data detection.

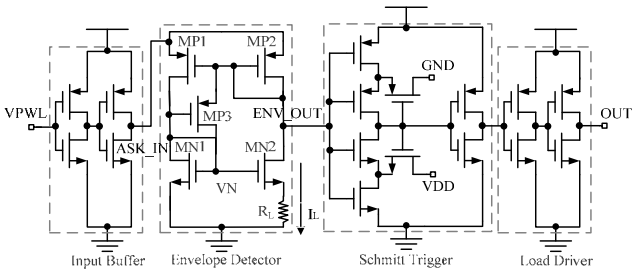


Fig. 6 Internal receiver integrated circuit design schematic.

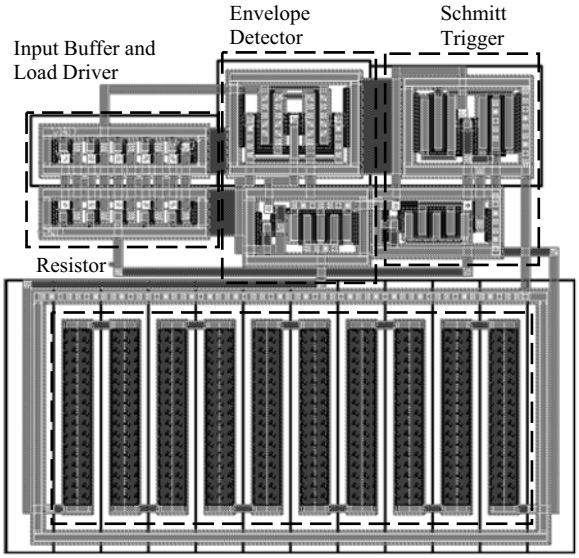


Fig. 7 Internal data receiver chip layout.

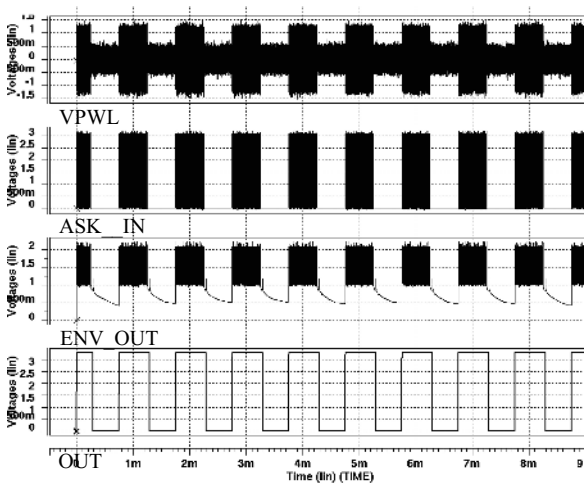


Fig. 8 Simulation results of the input signal as it passes through the different stages of demodulation.

The envelope detector not only extracts the ASK_IN signal envelope but the supply independent bias circuit also locks DC levels. Current through MP2 and MN1 are provided by MP3 upon start up. During envelope detection, PMOS MP3 effectively disappears as it only functions as a start up device. MP2 and MN1 are effectively modelled as diodes with their gates connected to the drain terminals.

The first cycle of envelope detection occurs when VN=ASK_IN-$V_{SD\ (MP1)}$. Initially VN<V_{TN}, so both MN1 and MN2 are cutoff, thus ENV_OUT is 0. As the ASK signal changes from logic "0" to logic "1" and when ASK_IN–ENV_OUT>V_{TP} and VN>V_{TN}, shifting all of MP1, MP2, MN1 and MN2 to saturation. This gives ENV_OUT=$V_{DS\ (MN2)}$ + $I_L \cdot R_L$. Where V_{TN} is the threshold voltage for NMOS, V_{TP} is for PMOS, VN is the gate voltage of both MN1 and MN2, I_L is the current passing through load resistor R_L and ENV_OUT is the output of the envelope detector.

As the ASK signal reverts back from logic high to logic low and if ASK_IN–ENV_OUT<V_{TP} and VN<V_{TN}, forcing MP1, MP2, MN1 and MN2 into cutoff. However ENV_OUT does not entirely go to zero as the Schmitt trigger input gates acts as loading capacitance to the envelope detector block. This gives a characteristic transient curve as the signal exponentially decays to 0V. The load driver, composed of cascaded inverters, serves to increase the signal driving capability of the circuit [8].

Table 2 Internal Receiver Specifications

Receiver Specifications	
Data Rate	2 Kbps
Input Frequency	2 MHz carrier
Input Voltage Level	Low Logic Level: 0.4V~0.6V High Logic Level: 1.1V~1.3V
Demodulator Output Logic Level	Low Logic Level: 0V High Logic Level: 3.3V
Power Supply	Single (3.3V)
Load Capacitance	10 pF, 100pF
Temperature	37
Power Consumption	1.15 mW

V. Results and conclusions

Successful data transmission and detection was exhibited at an effective air distance of 3cm between antenna cores. A discrete component prototype was used as a model for the integrated circuit design. This prototype uses an ASK modulated 2 MHz carrier frequency at a data rate of 2 Kbps. Class E transmitter spectral power was measured at 1.51 mW during transmission. After having measured the actual voltage received at the secondary coil, MATLAB® was used to digitally reconstruct the signal. This reconstructed voltage piece wise linear function was written into an Hspice® compatible file to serve as stimulus to the internal receiver integrated circuit design.

This research has addressed issues of designing biomedical circuits especially for implantable sensing systems. An internal receiver chip with average power consumption of 1.15 mW was developed. Such a low power consumption coupled with a small area, owing to the capacitor less design is ideal for implantable biochips. Furthermore, the design is not specific for glucose sensing, as it is well suited for other biochemical sensing or other implantable chip applications.

Acknowledgment

The authors deeply appreciated the technical support from the National Chip Implementation Center (CIC) and financial support from National Science Council of R.O.C. The funding is under the grant of NSC 96-2218-E-033-001.

References

1. Parramon JP (2001) Energy Management, Wireless and System Solutions for Highly Integrated Implantable Devices. Universitat Autonoma de Barcelona, Department d'Enginyeria Electronica.
2. Sokal NO (2001) Class-E RF Power Amplifiers.
3. Ziaie B, Nardin MD, Coghlan AR, Najafi K (1997) A Single-Channel Implantable Microstimulator for Functional Neuromuscular Stimulation. IEEE Transactions on Biomedical Engineering, Vol. 44, No. 10, October.
4. Lou AS, Chen HZ (2004) A Study of RF Power Attenuation in Biotissues. Journal of Medical and Biological Engineering, 24(3): 141-146
5. Liang CK, Chen JJ, Chung CL, Cheng CL, Wang CC (2005) An implantable bi-directional wireless transmission system for transcutaneous biological signal recording. Physiological Measurement 26 83-97.
6. Sawan M, Hu Y and Coulombe J (2005) Wireless Smart Implants Dedicated to Multichannel Monitoring and Microstimulation. IEEE Circuits and Systems Magazine, First Quarter.
7. Zhu Z (2004) RFID Analog Front End Design Tutorial (version 0.0). Auto-ID lab at University of Adelaide North Terrace Adelaide, SA 5005
8. Wang CC, Hsueh, YH, Chio UF, Hsiao YT (2004) A C-Less ASK Demodulator for Implantable Neural Interfacing Chips. IEEE International Symposium on Circuits and Systems 2004.

Author: Danny Wen-Yaw Chung
Institute: Department of Electronic Engineering,
Chung Yuan Christian University
Street: 200 Chung Pei Road
City: Chung Li City
Country: Taiwan, R.O.C.
Email: eldanny@cycu.edu.tw

Advances in Automatic Sleep Analysis

B. Ahmed and R. Tafreshi

Texas A&M University at Qatar, Doha, Qatar

Abstract — **In this paper we investigate the innovative spectral analysis techniques that have been used in sleep analysis with some success. A comparative analysis of these proposed classification techniques have been presented and the findings discussed. The paper identifies the problems faced in interpreting published results and performs an accurate comparison of different proposed systems. Future strategies to improve the performance of sleep analysis algorithms and novel signal processing tools suitable for sleep analysis are proposed.**

Keywords — **sleep, EEG, automatic sleep analysis, sleep classfication.**

I. Introduction

The electroencephalogram (EEG) is extensively used to study sleep and sleep-related disorders. Research conducted over the past few decades has led to several approaches that identify and classify the various stages of sleep. Polysomnography (PSG), which measures breathing efforts, blood oxygen levels, brain electrical activity (EEG), electrocardiogram (ECG), electrooculogram (EOG), and muscle activity (EMG), is now the main diagnostic tool in sleep medicine.

Normal healthy sleep is organized into sequences of stages that typically cycle every 60-90 min. The R&K sleep scoring rules, proposed by Rechtschaffen & Kales, divided sleep into two phases called rapid eye movement (REM) and non-rapid eye movement (NREM) sleep on the basis of pattern changes in the EEG, EOG, and EMG [1]. The American Academy of Sleep Medicine (AASM) in its recent revision, subdivided NREM sleep into three stages; referred to by N1 through N3 [2].

Sleep researchers have been hindered in understanding the relationship between sleep disorders and other physiological conditions due to the unavailability of an accurate and robust automatic sleep analyzer. Till now data collected from polysomnography is visually screened by a trained sleep technologist that is both time-consuming and expensive. The automatic sleep staging systems commercially available are not reliable, requiring manual validation. These systems are also unable to detect transient events occurring at the microlevel. Clinicians are thus hesitant to take advantage of computerized polysomnography, including the potential capability of these systems; preferring visual classification by a sleep technologist.

II. Automatic sleep staging

The key to any automated sleep monitoring system is the accurate detection of the sleep stages and the microstructure. Sleep staging is based on the idea that a pattern is assumed to exist for a time interval until a new pattern emerges indicating changes in state. Since there is in fact a continuum from light sleep to deep sleep, the artificial demarcation of sleep stages is a simplification implemented to standardize analysis across reviewers and laboratories. The exact time of change of state is highly subjective and leaves room for varying interpretations of transitional epochs by scorers. Studies have shown inter-scorer agreement ranging from 67% to 91% depending on different scoring epoch lengths and number of readers [3]. Most data on inter-scorer agreement are based on the study of normal subjects [4].

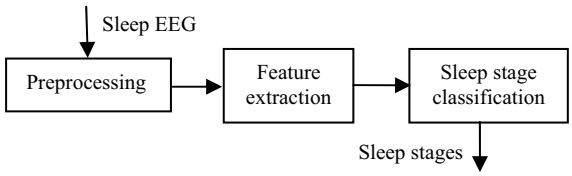


Fig. 1 : Block diagram of automatic sleep classifier

Automatic sleep analysis consists of a number of consecutive steps, as shown in Figure 1. Preprocessing reduces the vast amount of raw data to an amount which can be managed by statistical tools. It also removes artefacts in the EEG signal. Next features such as the amplitude or power of regular EEG waves (alpha, beta, theta and delta waves), in addition to specific patterns such as K-complexes and sleep spindles are extracted. Analysis is performed in short epochs, usually ranging from one to two seconds, to avoid loss of time resolution.

The final stage of the analysis is the combination of the extracted features and waveforms to a limited number of sleep stages. Rule-based logics are used to classify stages based upon features extracted from the EEG, which imitate visual inspection according to standards, such as the R&K and AASM rules. In systems used for clinical purposes the final results of the automatic sleep scoring have to come close to a visual AASM scoring. Most published studies on automatic sleep classifiers compare results from healthy subjects, with reliabilities between 70-90% [5].

Chwee Teck Lim, James C.H. Goh (Eds.): ICBME 2008, Proceedings 23, pp. 422–426, 2009
www.springerlink.com

Some characteristic waves in sleep EEG which provide clues to the sleep stages are short-term and appear sporadically in the background waves. A method to detect them must, therefore, be able to take a large view of the EEG and recognize these isolated characteristic waves. However, most conventional techniques for diagnosing the sleep stages are based on long term spectral analysis and consequently not suited for detecting such transient characteristic waves.

III. Signal processing tools used

During the last few decades, different EEG signal processing techniques have been applied to develop an automated sleep stage classification system. Because the EEG, like other biological signals, is highly non-stationary, there have been limits to the information that can be obtained from simple spectral estimation techniques like the fast Fourier transform (FFT), leading to the use of more complex time-frequency analysis techniques.

A. Feature Extraction

Innovative spectral analysis techniques are being applied to the sleep EEG for sleep staging with some success. Features such as the normalized amplitude of frequency bands [6, 7] features derived from the autoregression and linear predictor coefficients, harmonic parameters, parameters of Hjorth sub-band energies [8] have all been used to identify the stages in sleep EEG on an epoch to epoch basis. An advantage of frequency measures is that they are not affected by the age- and gender-dependent EEG changes. They thus provide a uniform feature that requires minimal tailoring to specific cases. However as the frequency bands used are generally fixed, they can lead to misleading results in epochs with activity due to more than one characteristic waves.

Due to the non-stationary nature of the EEG signal, decomposition using time frequency analysis has become popular in automatic sleep stage classification. The discrete wavelet transform, matching pursuit, Gabor transform and the wavelet transform modulus maxima have all been used to characterize the sleep stages [9, 10]. As the EEG signal stems from a highly non-linear system, non-linear dynamic methods such as chaos theory and multifractal analysis have been also applied to derive EEG features [11, 12]. As it is difficult to adapt these features, these techniques are not completely successful in epochs with ambiguous properties due to the presence of multiple superimposed waves.

The choice of features in most systems is generally made based on heuristic reasons. To compensate, most systems use multiple features; each targeting different characteristic waves present in the sleep EEG, e.g. alpha, beta, slow wave sleep, sleep spindles and K-complexes. There is no analysis which compares the performance of all these features to verify their actual effectiveness in sleep classification.

B. Classification

A significant amount of work has been done in developing sleep staging systems based on linear and nonlinear classifiers, specifically artificial neural network (ANN) classifiers and fuzzy logic. This is because they do not require any classification rules, or complex domain knowledge. Neural networks have a learning ability that enables them to form their own structure based on training instances. This allows them more flexibility with differences in experts or subjects.

The sleep staging process has been modeled with different types of ANNs; such as a finite state machine [13], hybrid neuro-fuzzy system [14, 15], and feed-forward multilayer neural network [16-18]. Decision tree learning [19] and support vector machines (SVM) [20] have also been utilized in sleep classification.

However systems based on ANNs have problems as the R&K scoring rules are mainly based on marking events such as sleep spindles, K-complexes, rapid eye movement and slow delta waves rather than background signal activities. If no marking events are found in the sleep epochs, then the R&K rules apply smoothing to these epochs. This reduces the performance of neural network based systems as they are not event driven detectors. This has led to systems using rule-based systems for event detection which are being supported with neural network based classifiers.

Most of the methods discussed try to mimic the R&K rules, but run into problems as they are unable to take advantage of the additional information that can be extracted using signal processing tools. Adaptive systems, introduced now, allow the classes to develop intrinsically, based on the patterns present in the signal. Most of these systems use clustering and other modeling techniques to differentiate the signal into distinct classes. Feature extraction is separated from clustering to improve efficiency, and can even be done while recording. This allows repeated applications of the clustering process without repeating the segmentation and feature extraction, thus reducing the computational load of the system.

Separation of the sleep classes has been performed using repeated k-means clustering on sleep-related features extracted from EEG segments [4, 12, 21, 22], principal component analysis to develop 2D density plots [23] and Hidden Markov Models (HMM) to model the sleep stages as a mixture of different processes [24].

Table 1 Comparison table of sleep staging methods with testing results

Authors	features	classfier	subjects	accuracy
Vivaldi (2006)	PCA of spectum of subbands	clustering	1 healthy	
Saastamoinen (2006)	amplitude spectrum of subbands	rule based	1 healthy & 1 sleep apnea	
Huuponen (2003)	amplitude spectrum of subbands	rule-based	15 healthy	
Agarwal (2001)	amplitude, dominant frequency, FEW, spindles, theta-slow-wave index	clustering	12 healthy subjects	76.80%
Chao (2006)	FEW, NLEO, wavelet coefficients	adaptive clustering	1 healthy	
Schwaibold (2001)	periodic activity, spindles, K-complexes	ANN	8 OSA patients	31.5%-87.4%
Van Hese (2001)	Hjorth & harmonic parameters, relative band energy	clustering	1 healthy	
Hanaoka (2002)	zero-crossing, wave period, amplitude, duration, transient events	decision tree learning		40%-91.8%
Estrada (2004)	autoregression coefficients, harmonic parameters, Itakura distance	rule based		
Flexer (2002)	reflection coefficients, stochastic complexity	HMM	20 healthy	68%-82%
McGrogan (2001)	reflection coefficients	ANN	9 healthy, 3 disturbed	72.2%, 96%
Li (2005)	parameters from wavelet coefficients	rule-based	1 subject	
Song (2007)	wavelet transform modulus maxima	rule based		55.4%-97.7%
Ma (2005)	wavelet transform modulus maxima		6 subjects	
Ma (2006)	zerocrossing, signal asymmetry	multifractal analysis	4 subjects	
Kaplan (2001)	segmentation	clustering		
Huang (2003)	Lempel-Ziv complexity measure	ANN	6 healthy	90.83%
Gudmundsson (2005)	Hjorth parameters, power spectrum, amplitude and frequency distribution	SVM, ANN		81%
Kim (2000)	Frequency, chaos measures	ANN		
Principe (1989)	frequency band, spindle, K-complex	fuzzy logic	5 healthy	84.74%
Park (2000)	frequency band, LPC coefficients	ANN & rule-based	2 healthy	62.6%-95.4%

The high degree of adaptability to individual subject behavior afforded by clustering systems is attractive; however it does not guarantee a classification in accordance with AASM rules. It is possible for clustering to not identify all the relevant patterns and also introduce irrelevant patterns.

It is difficult to compare the performance of different proposed systems due to the lack of standardized uniform assessment criteria or a gold standard. The results presented in literature are usually highly individualistic and subjective as seen in Table 1; hence the quoted level of agreement between automatic systems and manual scoring cannot be generalized. Furthermore, most of the systems are developed using limited subject data and are generally restricted to healthy subjects. This leaves the performance of these systems open to interpretation when used on patients suffering from a range of disorders.

IV. Limitations in current systems

In spite of the extensive research aimed at automating sleep analysis, no standardized sleep analysis system has emerged with widespread acceptance in clinical settings. The performance of these systems is limited in situations which cannot be described by existing scoring rules and those with no marking events.

The limitations of the R&K rules, which were initially intended for use only as a reference, are well documented [25]. These rules are based on empirical observations of only young normal subjects and neglect the less understood micro-structure of sleep. These rules are not reliable for a robust and accurate computer analysis. Very little work has been done on understanding how the sleep structure changes in the wide range of disorders suffered. These are partly due to the high degree of variability between different EEGs leaving much room for subjective interpretation. There is a need for techniques which adapt to differences in subjects' physiological measures. They must take into account the considerable variability of data, both intra and inter-individual, and the inherent stochastic nature of the EEG.

Due to the absence of a wide training dataset in which includes subjects suffering from a range of disorders, their performance is accurate only in a subset of people. These algorithms are limited in their adaptability due to strong

inter-patient variability, which occur specifically due to artifacts in patients of different pathological conditions.

There is also limited published information on their reliability, with most of the studies using data collected from healthy subjects. There is limited clinical validation of these systems, specifically on patients with different disorders. Proposed improved sleep scoring systems must perform more reliably than that achieved through visual classification based on the new AASM scoring rules [2, 26].

There are still many unanswered questions about the microstructure of sleep which must be answered before automatic scoring can be successful. Part of the problem is due to the rigid epoch size used [27]. Epochs during transition phases have characteristics of at least two stages. Adaptive segmentation could increase the temporal resolution where errors often occur and increase inter-rater and man/machine agreements. However as sleep EEG typically consists of a number of superimposed phenomena, it might be necessary to use two different simultaneous epoch lengths to analyze the micro- and macro-structure of the signal.

There is also concern that these systems have developed in the absence of any professionally endorsed and uniform standards [28]. The strong dependence of clinicians on scoring rules has forced developers to design systems following these rules. This has compromised the quality of these systems and limited the information that they can provide. There is a need for clinicians and engineers to join forces and develop joint guidelines and performance criteria for automated sleep analysis systems.

REFERENCES

[1] A. Rechtschaffen & A. Kales, "A manual of standardized terminology, techniques & scoring system for sleep stages of human subjects," US Dept of Health, NIH Publication 1968.

[2] M. H. Silber, S. Ancoili-Israel, M. H. Bonnet, S. Crockroverty, M. M. Grigg-Damberger, M. Hirshkowitz, S. Kapen, S. A. Keean, M. H. Kryger, T. Penzel, M. R. Pressman, & C. Iber, "The Visual Scoring of Sleep in Adults," Journal of Clinical Medicine, vol. 3, 2007.

[3] R. G. Norman, I. Pal, C. Stewart, J. A. Walsleben, & D. M. Rapoport, "Interobserver agreement among sleep scorers from different centers in a large dataset.," Sleep, vol. 23, pp. 901-8, 2000.

[4] R. Agarwal & J. Gotman, "Computer-Assisted Sleep Staging," IEEE Transactions on Biomedical Engineering, vol. 48, 2001.

[5] J. Caffarel, G. J. Gibson, J. P. Harrison, C. J. Griffiths, & M. J. Drinnam, "Comparison of Manual Sleep Staging with Automated Neural Network-based Analysis in Clinical Practice,," Medical Biological Engineering Computer, vol. 44, pp. 105-110, 2005.

[6] E. Huupponen, S. Himanen, J. Hasan, & A. Varri, "Sleep Depth Oscillations: An Aspect to Consider in Automatic Sleep Analysis, ," Journal of Medical Systems, vol. 27, pp. 337-345, August 2003.

[7] A. Saastamoinen, E. Huupponen, A. Varri, J. Hasan, & S. Himanen, "Computer Program for Automated Sleep Depth Estimation," Computer Methods & Programs in Biomedicine, vol. 82, pp. 58-66, 2006.

[8] E. Estrada, H. Nazeran, P. Nava, K. Behbehani, J. Burk, & E. Lucas, " EEG Feature Extraction for Classification of Sleep Stages," in 28th IEEE EMBS Int. Conf. San Francisco: IEEE, 2004, pp. 196-9.

[9] A. Takajyo, M. Katayama, K. Inoue, K. Kumamaru, & S. Matsuoka, "Time-frequency analysis of human sleep EEG," in SICE-ICASE International Joint Conference Korea, 2006, pp. 3303-7.

[10] C. F. Chao, J. A. Jiang, M. J. Chiu, & R. G. Lee, "Wavelet-Based Processing & Adaptive Fuzzy Clustering For Automated Long-Term Polysomnography Analysis," in ICASSP. vol. 2, 2006, pp. 1176-9.

[11] I. H. Song, Y. S. Ji, B. K. Cho, J. H. Ku, Y. J. Chee, J. S. Lee, S. M. Lee, I. Y. Kim, & S. I. Kim, "Multifractal Analysis of Sleep EEG Dynamics in Humans," in 3rd Int. IEEE EMBS Conference on Neural Engineering Hawaii, 2007, pp. 546-9.

[12] Q. Ma, X. Ning, J. Wang, & J. Li, "Sleep-stage Characterization by Nonlinear EEG Analysis Using Wavelet-based Multifractal Formalism," 27th IEEE EMBS Int. Conf. Shanghai: IEEE, 2005, pp. 4526-9.

[13] J. C. Principe, S. K. Gala, & T. G. Chang, "Sleep Staging Automaton Based on the Theory of Evidence," IEEE Trans.Biomedical Engineering, vol. 36, pp. 503-9, 1989.

[14] H. J. Park, K. S. Park, & D. U. Joeng, " Hybrid Neural-network & Rule-based Expert System for Automatic Sleep Stage Scoring," in 22nd IEEE EMBS Int. Conf.: IEEE, 2000, pp. 1316-9

[15] M. H. Schwaiblod, T. Penzel, J. Schohlin, & A. Bolz, "Combination of AI Components for Biosignal Processing Application to Sleep Stage Recognition," in 23rd IEEE EMBS Int. Conf. Istanbul: IEEE, 2001, pp. 1692-4.

[16] B. Y. Kim & K. S. Park, "Automatic Sleep Stage Scoring System Using Genetic Algorithms & Neural Network," in 22nd IEEE EMBS Int.Conf. Chicago, 2000, pp. 849-850.

[17] N. McGrogan, E. Braithwaite, & L. Tarassenko, "Biosleep: A Comprehensive Sleep Analysis System," in 23rd IEEE EMBS Int. Conf. Istanbul: IEEE, 2001, pp. 1608-11.

[18] L. Huang, Q. Sun, & J. Cheng, "Novel Method of Fast Automated Discrimination of Sleep Stages," in 25th IEEE EMBS Int. Conf. Cancun: IEEE, 2003, pp. 2273-6.

[19] M. Hanaoka, M. Kobayahsi, & H. Yamazuki, "Automatic sleep stage scoring based on waveform recognition method & decision-tree learning," Systems & Computers, vol. 33, pp. 1-13, 2002.

[20] S. Gudmundsson, T. P. Runarsson, & S. Sigurdsson, "Automatics Sleep Staging Using Support Vector Machines with Posterior Probability Estimates," in IEEE Int. Conf. CIMCA-IAWTIC: IEEE, 2005.

[21] P. V. Hese, W. Phillips, J. D. Konick, R. V. d. Walle, & L. Lemahieu, "Automatic detection of sleep stages using the EEG," in 23rd IEEE EMBS Int. Conf. Istanbul: IEEE, 2001, pp. 2216-2219.

[22] A. Kaplan, J. Roschke, B. Darkhovsky, & J. Fell, "Macrostructural EEG Characterization Based on Nonparametric Change Point Segmentation: Application to Sleep Analysis," J. Neuroscience Methods, vol. 106, pp. 81-90, 2001.

[23] E. A. Vivaldi & A. Bassi, "Frequency Domain Analysis of Sleep EEG for Visualization & Automated State Detection," in 28th IEEE EMBS Int. Conf. New York: IEEE, 2006, pp. 3740-3.

[24] A. Flexer, G. Gruber, & G. Dorffner, "Improvements on Continuous Unsupervised Sleep Stages," pp. 687-95, 2002.

[25] S. Himanen & J. Hasan, "Limitations of Rechtschaffen & Kales," Sleep Medicine Reviews, vol. 4, pp. 149-167, 2000.

[26] M. H. Bonnet, K. Doghramji, T. Roehrs, E. J. Stepanski, S. H. Sheldon, A. S. Walters, M. Wise, & A. L. C. Jr., "The Scoring of Arousal in Sleep: Reliability, Validity, & Alternatives," J. Clin. Sleep Medicine, vol. 3, 2007.

[27] J. Hasan, "Past & Future of Computer-Assisted Sleep Analysis & Drowsiness Assessment," J. Clin. Neurophys, v.13, p. 295-313, 1996.
[28] T. Penzel, M. Hirshkowitz, J. Harsh, R. D. Chervin, N. Butkov, M. Kyger, B. Malow, M. V. Vitiello, M. H. Silber, C. A. Kushida, & A. L. C. Jr, "Digital Analysis & Technical Specifications," J. Clin. Sleep Medicine, vol. 3, 2007.

Author: Beena Ahmed
Institute: Texas A&M University at Qatar
Street: PO. Box 23874
City: Doha
Country: Qatar
Email: beena.ahmed@qatar.tamu.edu

Early Cancer Diagnosis by Image Processing Sensors Measuring the Conductive or Radiative Heat

G. Gavriloaia[1], A.M. Ghemigian[2] and A.E. Hurduc[3]

[1]University of Pitesti/Electronic and Computing Department, Pitesti, Romania
[2]Endocronological Institute of Bucharest, Bucharest, Romania
[3] Oncological Institute of Bucharest, Bucharest, Romania

Abstract — **The heat is one of the most important parameters of living beings. The tissues heat, generated at normal or diseases states, is lost to environment through several mechanisms: radiation, conduction, convection, evaporation, etc. Skin temperature is not the same on the entire body and a thermal body signature can be got. The temperature of neoplasic tissue is different up to 1.5 ^{0}C than the healthy tissue as a result of the specific metabolic rate. The infrared camera images show the heat transferred by radiation very quickly. A lot of factors disturb the conversion temperature-pixel intensity. A very sensitive sensor, a video camera showing its spatial position and a special computer fusion program were used for early cancer diagnosis.**

By using the high resolution maps, the diagnosis for about 78.4% of patients with thyroid cancer, and more than 89.6% from patients with breast cancer were right.

Keywords — **Bioheat, thermal imaging, cancer, radiation or conductive heat**

I. Introduction

Humans and animals in general, are usually in a thermal steady state with respect to their surroundings. The heat is one of the most important parameters of living beings. All our common activities rely on energy cost. Sleeping, for instance, needs 35 cal/m2 hr, and running 600 cal/m2 hr [1]. Approximately 80% of these costs are given by waste heat. Thermal physiology describes all body functions related to thermal energy given to or removed from a living body. Therefore, the body needs a temperature regulation, which keeps the temperature on a constant level, about 37 ^{0}C. There is equilibrium between outside of body and skin temperature. The sympathetic nerve fibers are involved in temperature regulation, and this is the autonomic nerve system function, it is a non-voluntary control. As a result of different situations, the core temperature may be increase (hyperthermia) or decrease (hypothermia). The skin temperature and the core temperature determine the regulation process [2], [3]. The temperature distribution on the human skin gives a thermal image, a thermal pattern of the body, with highly symmetrically distributed related to a symmetry axis situated in the median plane of the human body. In many situations, this pattern is not symmetric and hyperthermic or hypothermic areas appear. There is a strong link between these thermographic changes and diseases. Hyperthermic or hypothermic skin areas may be caused by increased or decrease blood flow, tumors, inflammation process, etc. Tumor vascularity particularly played a fundamental role in promoting cancer growth, invasion, and metastasis [1], [4]. Solid tumors rely on blood vessels to obtain necessary nutrients and oxygen [5]. New vessels also offer path way for tumor expansion; therefore, increase the opportunity for tumor cells to enter the blood or lymph circulation. Rapid and noninvasive imaging techniques may be a better alternative for assessing tumor vascularity. In medical applications, infrared imaging can produce reliable and valid results and it is based on the physics of heat radiation or conduction and the physiology of thermoregulation of the human body.

The final aim of the research is to find some clues in order to get an early cancer diagnosis. As a result of angiogenesis process, the skin projection of the certain tumors modifies the local area temperature. The temperature can be measured by many means: contact thermocouples, non-contact infrared thermocouples, resistance temperature detectors, thermistors, liquid crystal sensors, and microbolometers. All of them have advantages and disadvantages concerning to this medical application. The thermistor sensor is the cheapest and IR camera with microbolometres is the most expensive sensor. The problem, we are looking for, is in what way the measurement results by the two sensors are the same. The heat, generated in the region of interest, is spreaded through several mechanisms: radiation, conduction, convection, evaporation, breathing, etc. The contact thermistor sensor uses the conduction component of this mechanism, and IR camera, radiation one. Some aspects have to be taking in consideration. The thermistor sensor measures the heat with an infinite range of wavelengths, from theoretical point of view, and IR camera on 8-14 microns only. Human skin temperature is the product of heat dissipated from the vessels and organs within the body, and the effect of the environmental factors on heat loss or gain. There are a number of further influences which are controllable, such as cosmetics, alcohol intake or smok-

Chwee Teck Lim, James C.H. Goh (Eds.): ICBME 2008, Proceedings 23, pp. 427–430, 2009
www.springerlink.com

ing. The radiated heat depends on a lot of parameters: skin emissivity, environment between cameras and the investigated area, other heat sources, etc. So, do the results reflect the same situation when the measurements are made by thermistor or IR camera?

II. Materials and Methods

The heat transfer by conduction from skin gives information more appropriate to reality and can be used to early cancer diagnosis, but up to now, only point temperature measurement has done. We used a very sensitive sensor, 0.04 ^{0}C temperature resolution, and a video camera showing the sensor spatial position. A special computer program was created for sensor and video camera data fusion. The investigated surface and a red circle showing the sensor position are displayed. When the successive temperatures values are appropriated, the circle becomes green. The temperature sensor is moved on the region of interest and a green patch appears. A computer program using the spatial adaptive spline functions assures 0.5 mm spatial resolution. The IR camera has about 1-3 mm spatial resolution and 0.1^{0}C as a temperature resolution of one microbolometer from the focal plane array.

From spectral point of view, the thermistor sensor covers almost entire frequencies range but IR camera 8-14 microns only. The amount of radiation energy E_o, emitted by a blackbody at an absolute temperature T, per unit time, per unit area of surface, per unit wavelength λ, is given by Planck's law, [6]:

$$E_\lambda = \varepsilon_\lambda E_{\lambda o} = \frac{\varepsilon_\lambda c_1}{\lambda^5\left[\exp\left(\frac{c_2}{\lambda T}\right)-1\right]} \tag{1}$$

where

$c_1 = 3.74310^8 \ \frac{watt\ \mu m}{m^2}$, $c_2 = 1.4387 \mu m K$, and ε_λ is the spectral hemispherical emittance [7]. On Fig. 1 is shown radiated energy for biomedical range, 32^{0}C – 40^{0}C. For entire temperature range, the blackbody emissive power is:

$$E_o = \int_0^\infty E_{\lambda o} d\lambda = \sigma T^4 \tag{2}$$

where $\sigma = 5.6710^{-8} \ \frac{watt}{m^2 K^4}$ Stefan-Boltzman constant.

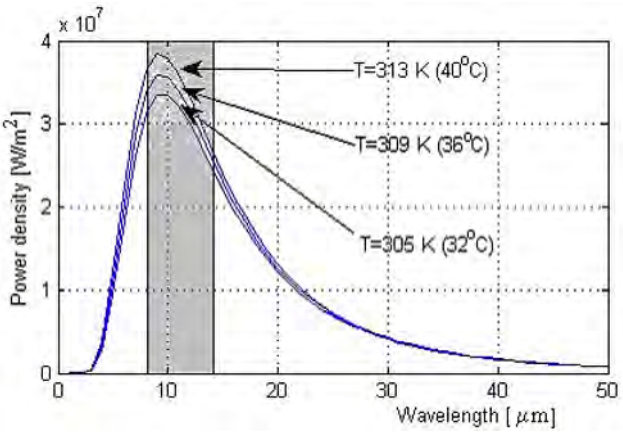


Fig. 1 The radiated energy versus medical temperature range

IR camera operates on a part of this spectrum, so we need to determine the fraction f_{12} of blackbody emissive power between two wavelengths by integration of Equation (1) and division by Equation (2):

$$f_{12} = \frac{\int_{\lambda_1}^{\lambda_2} \frac{c_1}{\lambda^5\left[\exp\left(\frac{c_2}{\lambda T}\right)-1\right]} d\lambda}{sT^4} \tag{3}$$

The fraction of blackbody emissive power on 8-14 microns band is about 6.5%, and this thing means the thermistor sensor gives more information about temperature. Its main disadvantage is concerning to large rise time, more than 2 s, but for our application it doesn't matter because the investigated skin area is at the steady state.

In this paper three sensors: video and IR cameras and a 2.5 mm diameter thermistor were used:.

The air temperature in the room used for thermal imaging was at about 22°C during the measurement process, [3], [8], [9]. The time required to achieve the adequate values from thermistor was 15 minutes.

III. Results

On the Fig. 2 an infrared image of a patient suffering of thyroid cancer is depicted. The abnormal thyroid aria, a rectangular one, is selected as region of interest, ROI. Most of the temperature pixels show values about 1.5 ^{0}C smaller than neighboring skin surfaces. The ROI temperature is measured by a microbolometer focal plane array. The microbolometers are very sensitive, but don't have the same characteristics. As a result, two adjacent microbolometers

give different results, about 0.1^0C, for two adjacent regions of the investigation object, and it is seen as a small noise. On the Fig. 3, the out signal of a horizontal line from the infrared camera is shown.

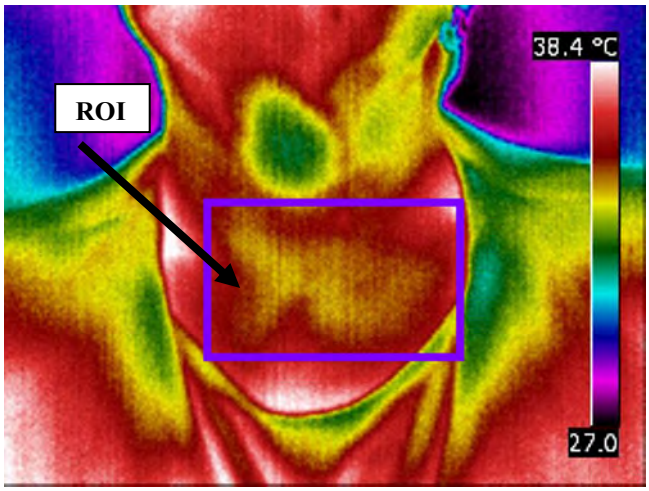


Fig. 2 IR image of a patient with cancer thyroid

In order to reduce this kind of noise a single sensor was used. The association between the sensor position on the patient skin and its temperature values is obtained by a data fusion computer program.

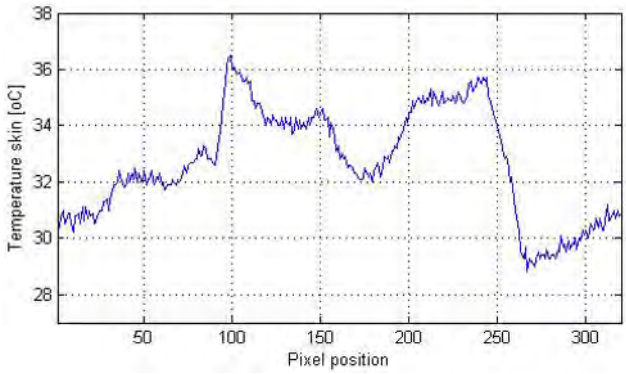


Fig. 3 The output signal from a micobolometer line of an IR camera

The temperature map of ROI, evaluated by the thermistor with 0.04^0C temperature resolution is shown on Fig. 4. Its spatial position was processed with a computer program using the spatial adaptive spline functions, assuring 0.5 mm as spatial resolution. The neoplasic tissue has a better contour.By looking on Fig. 5, a nonhomogenous thyroid aria can be seen. The 3D image shows many small warmer regions on The ROI, as a result nonuniform cell multiplications.

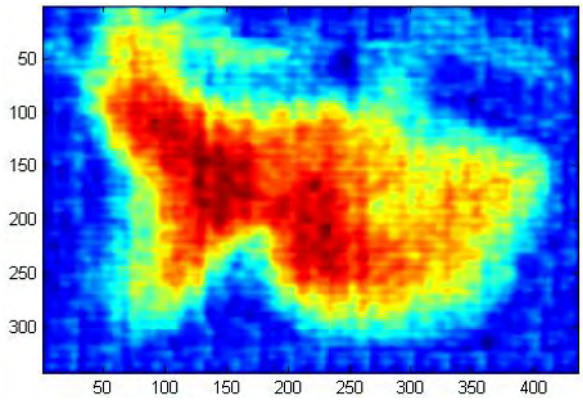


Fig. 4 The temperature map of ROI, the 2D case

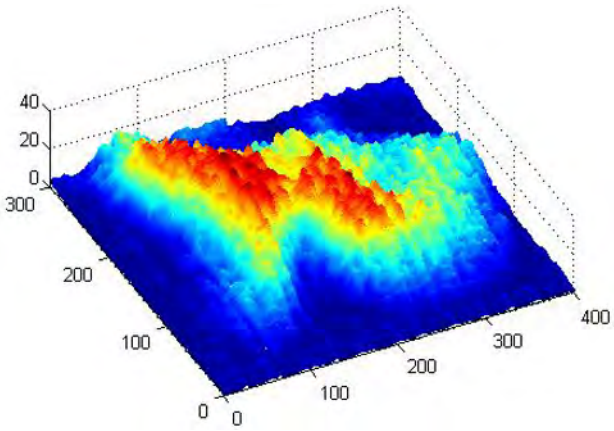


Fig. 5 The temperature map of ROI, the 3D case



Fig. 6 IR image of a patient with thyroid disorders but no cancer

The method was tested on patients with thyroid or breast cancer. On the maps of high resolution temperature, the ABCD (asymmetry, border, color, and differential structure)

method gives good results, [4]. On the Fig 3 and 4 the strong asymmetry and irregular border can be seen. Other patient, who suffers of thyroid disorders, but no cancer, the two lobes have a regular contour and the same shape.

A data base, containing 100 temperature maps for healthy people, was created before. As a result of direct comparison, the diagnoses were right for about 78.4% of patients with thyroid cancer and more than 89.6% from patients with breast cancer.

IV. Conclusions

A cheaper method for thyroid and breast cancer diagnosis was described. Rapid and noninvasive imaging techniques may be a better alternative for assessing the neoplasic tissue. The sensor, a quick thermistor, measures the radiative heat of the human skin and gives data for a map of ROI with high resolution temperatures. The map is generated by a computer program using data fusion and the spatial adaptive spline functions. The map of high resolution temperatures gives the possibility to do an early diagnosis by looking at the irregular shape of ROI and its structure. The results are pretty good and they can be improved in next future by the fractal analysis.

References

1. Webster Ed, (2001) Minimally Invasive Medical Technology Department of Biomedical Engineering, University of Wisconsin-Madison, USA
2. Kollorz E.N.K., Hahn D.A., Linke R, Goecke T.W., Hornegger J, Kuwert T (2008), Quantification of Thyroid Volume Using 3-D Ultrasound Imaging, Medical Imaging, IEEE Transactions on Volume 27, Issue 4, April 2008 pp.457 - 466 DOI 10.1109/TMI.2007.907328
3. Ambros R.A., Trost R.C., Campbell A.Y., Lambert W.C. (1988) Prognostic value of morphometry in papillary thyroid carcinoma Engineering in Medicine and Biology Society, 1988. Proceedings of the Annual International Conference of the IEEE 4-7 Nov 1988, pp. :299 - 300 vol.1 DOI 10.1109/IEMBS.1988.94527
4. Keramidas E, Iakovidis D, Maroulis D, Dimitropoulos N (2008) Thyroid Texture Representation via Noise Resistant Image Features Computer-Based Medical Systems, 2008. CBMS '08. 21st IEEE International Symposium on 17-19 June 2008 pp 560 – 565 DOI 10.1109/CBMS.2008.108
5. Helmy A., Holdmann M, Rizkalla M (2008) Application of Thermography for Non-Invasive Diagnosis of Thyroid Gland Disease Biomedical Engineering, IEEE Transactions on Volume 55, Issue 3, March 2008 pp 1168 – 1175 DOI 10.1109/TBME.2008.915731
6. Reston V,(1998) Breast Imaging Reporting and Data System (BI-RADSTM), 3rd ed. American College Radiology,.
7. Savelonas M, Maroulis D, Iakovidis D, Dimitropoulos N (2008)Computer-Aided Malignancy Risk Assessment of Nodules in Thyroid US Images Utilizing Boundary Descriptors, Informatics, 2008. PCI '08. Panhellenic Conferece on 28-30 Aug. 2008 pp 157 - 160 DOI 10.1109/PCI.2008.44
8. Sierra A, Echeverria A (2006) Evolutionary discriminant analysis Evolutionary Computation, IEEE Transactions on Volume 10, Issue 1, Feb. 2006 pp 81-92 DOI 10.1109/TEVC.2005.856069
9. Kneppo P, Tysler M, Rosik V, Zdinak J (2005) Modular Measuring System for Assessment of the Thyroid Gland Functional State Engineering in Medicine and Biology Society, 2005. IEEE-EMBS 2005. 27th Annual International Conference of the 2005 pp 6646 - 6649 DOI 10.1109/IEMBS.2005.1616026

Author: Gavriloaia Gheorghe
Institute: University of Pitesti
Street: Targul din Vale nr. 1
City: Pitesti
Country: Romania
Email: ggavriloaia@gmail.com

Analysis of Saccadic Eye Movements of Epileptic Patients using Indigenously Designed and Developed Saccadic Diagnostic System

M. Vidapanakanti[1], Dr. S. Kakarla[2], S. Katukojwala[3] and Dr. M.U.R. Naidu[4]

[1]Dept. of BME, University College of Engineering, Osmania University, Hyderabad, India
[2]Dept. of ECE, University College of Engineering, Osmania University, Hyderabad, India
[3]Dept. of BME, University College of Engineering, Osmania University, Hyderabad, India
[4]Clinical Pharmacology & Therapeutics, Nizam's Institute of Medical Sciences, Hyderabad, India

Abstract — **Aim: The study aimed to record and analyse saccadic eye movements of epileptic patients. The specific purpose was to determine and compare saccadic parameters of normal subjects with those of age-matched epileptic patients. The selected parameters were saccadic duration, latency, peak saccadic velocity and the main sequence relationship. Any possible relationship between these parameters and severity of epilepsy was also examined.**

Methodology: A microcontroller-based saccadic diagnostic system was indigenously designed and developed for the above purpose. It was used to elicit, record and analyse around 80 saccadic eye movement recordings from 53 normal subjects for a visual angle range of -60^0 to $+60^0$. These data have been analysed and the saccadic parameters were determined using MATLAB 2007. Saccadic detection was done using amplitude threshold and velocity threshold techniques and the results were compared. Saccadic eye movement data from 14 epileptics have been recorded. Saccadic parameters in respect of these data was calculated. Data collection from some more epileptics is under progress.

Salient results: The system was tested successfully on human subjects and its performance was found satisfactory as per the design requirements with a good feedback from the medical personnel who are presently using it.

Analysis of data collected revealed that the amplitude threshold technique was more efficient to detect a saccade in 97% determinations. The saccadic parameters and their relationships for normal subjects were found to be in good agreement with those reported in literature. The saccadic parameters showed a change in epileptics.

Conclusions and significance: Our saccadic diagnostic system could be of immense help to those working in the field of saccadic studies due to its simplicity, portability, ease of use and user-friendly features. Additional data to be collected from epileptics and similarly treated will provide concrete and meaningful information diagnosis.

Keywords — **Saccadic eye movements, saccadic stimulator, saccadic duration, skewness, peak saccadic velocity.**

I. Introduction

Measurement of eye movements plays a significant role in many areas of neurological and oculomotor research. There are different types of eye movements, namely, saccadic, smooth pursuit, vergence, and vestibulo ocular movements, associated with varying visual functions. Many techniques like electrooculography (EOG), photoelectric oculography have been developed over the past 30 years for tracking eye movements. These methods vary greatly in their resolution, range, and tolerance to head motion, ease of use, invasiveness, and cost [1]. Saccades are fast movements of the eyes, which are employed to position the images of objects of interest onto the fovea and have been studied. The motivation for using the Electrooculography (EOG) method in this study was to develop an unobtrusive, inexpensive and non-invasive way of recording saccadic eye movements with clinically acceptable accuracy.

Electrooculography is based on recording the potential between the cornea and the retina. This potential, in the range of 0.4 to 1.0mV is considered to be a result of a steady electrical dipole with a negative pole at the retina and a positive pole at the cornea. Surface recording electrodes are typically placed on the skin close to the eyes in horizontal and vertical planes to pick up the potential. The relationship between EOG output and horizontal angle of gaze is approximately linear for $\pm 30^0$ of eye movement. Through careful calibration, horizontal eye movements can be measured with a resolution of 1^0.

An attempt to quantitatively assess the saccadic movements of epileptics as compared with normal subjects is done in this study. The assessment is done in terms of the comparison of the saccadic parameters namely, saccadic duration, skewness, signal amplitude and peak saccadic velocity. Some changes in the saccadic parameters and their characteristics were observed in case of epileptic subjects.

II. Materials and Methods

The major subsystems of the saccadic diagnostic system [2] include the saccadic stimulator, EOG signal conditioner, RCM 3710-based data acquisition system and the Personal Computer-based analysis system as shown in figure 1.

Chwee Teck Lim, James C.H. Goh (Eds.): ICBME 2008, Proceedings 23, pp. 431–434, 2009
www.springerlink.com

Saccadic Stimulator

Each type of eye movement requires a specific stimulus [3]. A saccadic stimulator, designed and built around the microcontroller PIC 18F452, generates visual stimuli for triggering horizontal saccadic movements [4]. LEDs lit in various specific or random sequences from an array of LEDs stimulate eye movements of various angles.

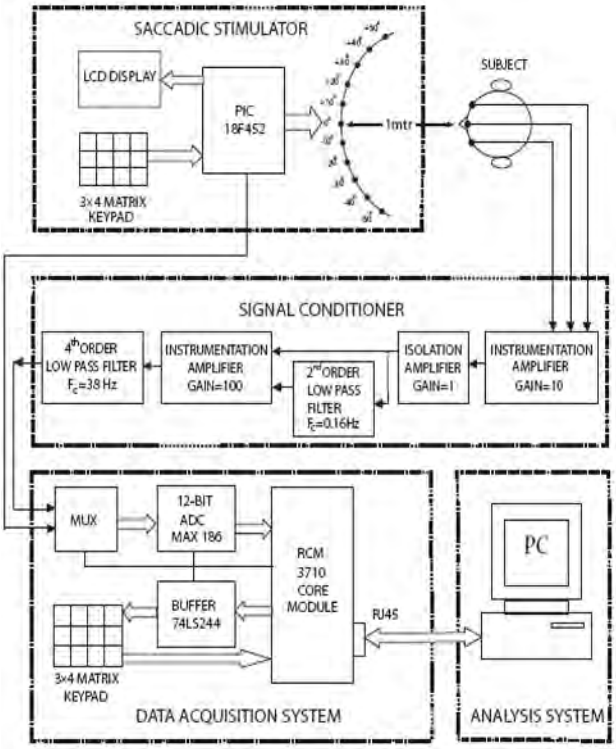


Fig. 1. Block diagram of the saccadic diagnostic system

Thirteen LEDs are mounted on a curvilinear wooden board of 1m radius subtending an angle of 120^0 at its centre. The array of lights is arranged in a horizontal plane covering a visual angle of $\pm 60^0$ in steps of $+10^0$. The distance between any two adjacent LEDs is about 17.5cm. Subject sits at a distance of 1m from the LED board. The stimulator consists of PIC 18F452 microcontroller, a 3X4 matrix keyboard and a 16X2 LCD module. PIC 18F452 controls the lighting sequence and duration of the LEDs through input/output ports configured as digital output lines, in accordance with the test selected by the user.

Signal Conditioner

The signal conditioner amplifies the EOG signal picked up by surface electrodes without significant distortion and is not affected by external noise/interference. The conventional EOG amplifiers suffer from DC drifts that result in amplifier saturation [5,6]. The designed system overcomes this problem by incorporating DC drift removal circuit. The other modules are Preamplifier, Isolation Amplifier, Voltage Amplifier and Low pass filter.

Preamplifier: The preamplifier is built around the instrumentation amplifier INA114 with high input impedance, good CMRR and excellent accuracy. This stage provides a gain of 10 and suitably raises the signal amplitude for isolation and subsequent analog processing.

Isolation amplifier: The electrical isolation of the subject is achieved by the isolation amplifier, ISO122 and a DC-DC converter combination to protect the subject from leakage currents.

DC drift removal circuit and Voltage amplifier: A second order low pass filter with a cut off frequency of 0.16 Hz is connected as shown in figure 1. The output of this filter consists of the low frequency DC drift components of the signal being amplified. It is continuously subtracted from the original signal using another instrumentation amplifier (INA114). This technique successfully eliminates the DC drift from the EOG signal. A gain of 100 is provided by this stage.

Low pass filter: The final stage of the signal conditioner is a fourth order Butterworth low pass filter with a cut off frequency of 38Hz. This filter minimizes out of band noise and reduces power line interference and unwanted EMG and EEG interference.

Data Acquisition System

The conditioned EOG signal from the signal conditioner and the sync signal from the saccadic stimulator are fed to the Rabbit core module through a multiplexer, which facilitates the channel selection. Analog signal from the selected channel is converted into digital form by an analog-to-digital converter MAX 186. The digital values are stored in the RAM of the core module. Acquisition parameters like sampling frequency, number of channels, input voltage range are set from the matrix keyboard. The program run by Rabbit core module is developed in Dynamic C. The data are subsequently transferred to the PC through LAN interface.

Experimental Procedure

EOG recordings from 53 normal and 14 epileptic subjects were collected at the department of Clinical Pharmacology & Therapeutics, Nizam's Institute of Medical Sciences, Hyderabad, India. All the subjects had normal or corrected-to-normal vision. Recordings were obtained in a

uniformly/adequately lit room in a noise-free environment with controlled temperature, to avoid distraction and increase the comfort level of the subject. Each subject was made to sit in a comfortable chair with height adjustment arrangement.

Two electrodes are placed on the left and right external canthi of the subject, to pick up the EOG signal. A ground electrode is placed on the middle of the forehead. A chin-rest is used to restrict the subject's head movement during recording. The height of the subject's chair was adjusted to ensure that the subject's eyes were in visual alignment with the stimulator. The subject was asked to look at the glowing LED, without moving the head. The saccadic stimulus pattern was then presented. When the subject looks at the glowing LEDs, EOG signal was acquired by the electrodes, processed in the signal conditioner and acquired by the data acquisition system. Then the digitized signal is further processed and the results are displayed on the PC.

III. Results and Discussions

The EOG data collected was first smoothened using the 3-point moving average technique. The saccades are then detected using the amplitude threshold technique, as this technique yielded better results compared to the velocity threshold technique. For the data collected from the normal and the epileptic subjects so far, the saccadic parameters namely, saccadic duration, skewness, signal amplitude and peak saccadic velocity were computed and compared.

Saccadic duration: Saccadic duration is the time taken to complete a saccade, that is, till the target is focused upon.

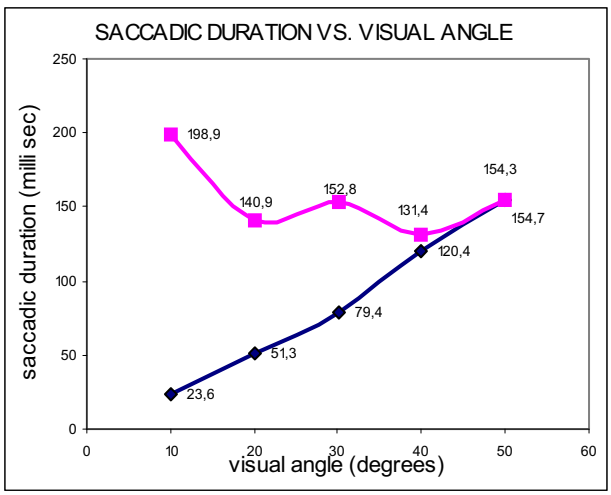


Fig. 2. Saccadic duration vs. visual angle for normal (lower graph) and epileptic (upper graph) subjects

As reported in literature [7], the saccadic duration for the normal subjects increased linearly with the visual angle (Figure 2, lower graph).

Skewness: Skewness, a measure of asymmetry of the saccadic profile, is taken as the ratio of the acceleration duration to the saccadic duration. Acceleration duration is the time lapse between the beginning of the saccade to the instant of peak velocity. The skewness values were quite different for normal and epileptic subjects as can be seen from Figure 3. The skewness showed a peak at a visual angle of 30^0 for the normal subjects (minimum 0.18 and maximum 0.85). But the variation for epileptic subjects was very less (minimum 0.27 and maximum 0.47).

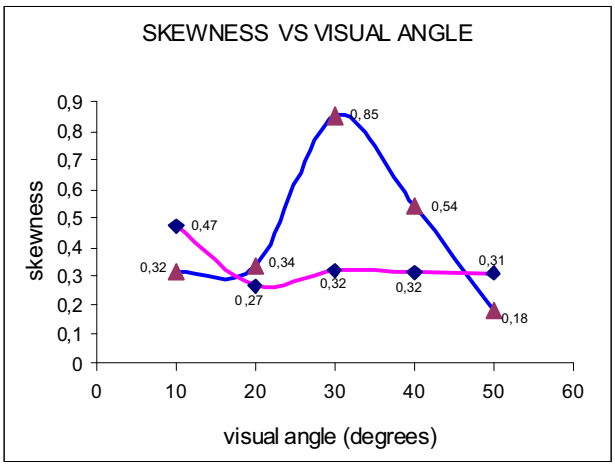


Fig. 3. Skewness vs. visual angle for normal (upper graph) and epileptic (lower graph) subjects

Signal amplitude: The signal amplitude is calculated as the difference between the amplitudes at the starting and the ending of the saccade. The mean of this parameter showed an almost linear increase with visual angle in both cases as can be seen from Table 1. The mean signal amplitude of epileptic subjects was observed to be higher than that of normal subjects.

Table 1 Mean signal amplitude of normal and epileptic subjects at various visual angles

S.No.	Visual angle	Mean signal amplitude (micro volts)	
		Normal subjects	Epileptic subjects
1	10	54.6	96.8
2	20	101.4	144.6
3	30	147.2	199.1
4	40	185.7	260.4
5	50	207.7	315.2

Peak saccadic velocity: The EOG data collected, which represents the eye position signal, is differentiated to yield saccadic velocity. Saccadic velocity is defined as the rate at which saccadic movement occurs.

For each visual angle, the mean peak velocity of each subject is determined from the velocity profile. The peak velocity at each visual angle is plotted as shown in Figure 4.

The peak velocity for normal and epileptic subjects showed a similar characteristic and it increased non-linearly with visual angle.

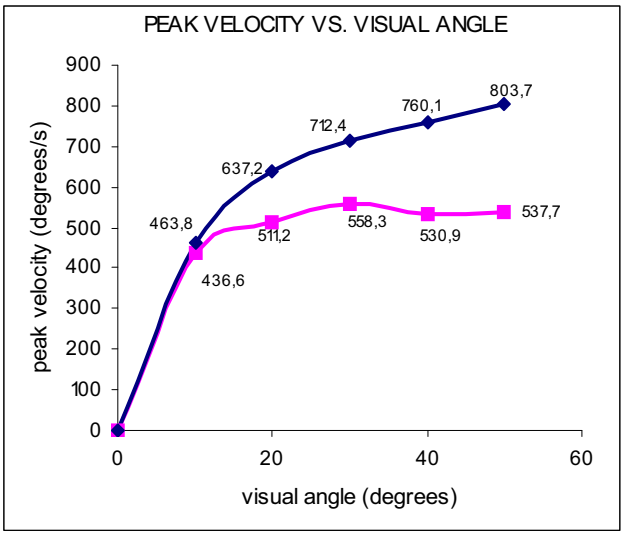


Fig. 4. Peak saccadic velocity vs. visual angle for normal (lower graph) and epileptic (upper graph) subjects

IV. Conclusions

A saccadic diagnostic system has been indigenously designed and developed for saccadic data acquisition and analysis. Its performance is found to be satisfactory and met the design specifications. The system is found to be reliable and user-friendly according to the feedback from the medical personnel. Saccadic parameters have been successfully extracted from the data collected from normal and epileptic subjects. The preliminary analysis showed that the saccadic parameters of normal and epileptic subjects are found to significantly different. More data from epileptic subjects is being collected to explore and possibly establish any relationship between the saccadic parameters and the severity of epilepsy.

Acknowledgements

The authors wish to thank the staff of the Department of Clinical Pharmacology and Therapeutics, Nizam's Institute of Medical Sciences, Hyderabad, who has helped in the EOG data collection.

References

1. Carrie A. Joyce, Irina F. Gorodnitsky, Jonathan W. King and Marta Kutas (2002) Tracking eye fixations with electroocular and electroencephalographic recordings, Psychophysiology, 607-618.
2. V.Malini, Dr.K.Subba Rao, K.Satyanarayana and Dr.M.U.R.Naidu (2007) Micro controller-Based Diagnostic System for Electrooculography, National Conference on Biomedical Engineering, Manipal, India, October 5-6, 2007.
3. Hugh O. Barber & Charles W. Stockwell (1980). Manual of Electronystagmography, The C.V.Mosby Company.
4. V.Malini, K.Satyanarayana, Dr.K.Subba Rao and Dr.M.U.R.Naidu (2007) Design and development of a saccadic stimulator using PIC 18F452 Microcontroller, IETE Zonal Seminar on Emerging and Converging Technologies, Visakhapatnam India, February 10-11, 2007.
5. Barry R. Greene, Stephen Meredith, Richard B. Reilly and Gary Donohoe (2004), A novel, portable eye tracking system for use in Schizophrenic Research, ISSC 2004, Belfast, June 30-July 2, 2004.
6. Shubhodeep Roy Choudhury, S.Venkataramanan, Harshal B. Nemade, J.S. Sahambi (2004) Design and Development of a Novel EOG Biopotential Amplifier, Journal of Bioelectromagnetism.
7. Joseph D. Bronzino (1995) The Handbook of Biomedical Engineering, CRC Press.

System Design of Ultrasonic Image-guided Focused Ultrasound for Blood Brain Barrier disruption

W.C. Huang[1,3], X.Y. Wu[2], H.L. Liu[1]

[1]Department of Electrical Engineering, Chang-Gung University, Taiwan
[2]Department of Medical Image and Radiological Sciences, Chang-Gung University, Taiwan
[3]Molecular Imaging Center and Department of Nuclear Medicine, Chang-Gung Memorial Hospital, Taiwan

Abstract — **The purpose of this study is to propose the ultrasonic-imaging guided focused ultrasound induced blood-brain barrier (BBB) disruption system design. This system comprises of a 270-kHz, 80-channel hemispherical ultrasound phased array, RF power amplifier, animal holder, and a clinical used ultrasound imager. Before animal treatment, we propose to use high-precision hydrophone and ultrasound imager coordinate transformation to achieve the alignment, focused ultrasound guidance, and treatment position targeting. During the treatment, Forty Sprague-Dawley rats were sonicated, and burst-mode ultrasonic energy was delivered in the presence of micro bubbles injected IV to disrupt the BBB. All Rats were skull-intact during the sonication, and different power output and duration durations were tested. Evans Blue dye was serves as an indicator to verify the BBB disruption in gross animal sectioning, and hematoxylin and eosin (H&E) staining was conducted for brain tissue damage analysis. Results showed that the designed hemispherical multiple channel phased array system under the ultrasonic imaging guidance can successfully disrupt BBB through intact skull at the targeting position. Safety parameter was characterized which ranges from 5 – 7.5 w of electrical power with the sonication duration of 30 – 180 s. The design provides the possibility toward using ultrasonic imaging to guide the focused ultrasound induced BBB disruption process for targeting drug delivery.**

Keywords — **Focused Ultrasound, Blood Brain Barrier, Burst mode, Delivery drug, Image-guided.**

I. Introduction

The blood brain barrier (BBB) structure serves as a natural protection in the brain from the invasion of virus attack or exogenous molecule entrance into parenchyma. However, the BBB is also regarded as a major challenge when intend-ing to deliver therapeutic agent into brain. At the neurosci-ence point of view, disrupting BBB can provide benefit on the application of brain drug delivery. Recently, it has been discovered that using focused ultrasound under the presence of ultrasound microbubbles can disrupt BBB. [1, 2]. More noticeably, since the ultrasonic energy can be tightly con-centrated, this approach enhances the BBB permeable re-gion locally. The BBB-permeable duration may retain sev-eral hours, which is sufficient for delivering molecules into parenchyma [ref].

Current ultrasound induced BBB disruption and brain drug delivered application relies on the guidance of magnetic-resonance imaging (MRI) [ref]. MRI guidance contains advantages including good anatomical image quality and the capability of utilizing MRI contrast agent to detect the BBB-disruptive region. However, there are also many challenges of this approach including the very-high complexity of the system integration between MRI and focused ultrasound apparatus, relatively high cost of MRI usage, and only semi-real-time when imaging the treatment process.

The purpose of this paper is to investigate the feasibility of using ultrasound to guide the focused ultrasound induced BBB disruption process. The potential of using ultrasonic imaging includes the (1) real-time imaging capability, (2) the lower-cost in imaging the treatment process, and (3) the its higher simplicity of integrating therapeutic and diagnostic ultrasound. The procedure of ultrasonic imaging guidance was proposed. A hemispherical ultrasound phased array was employed to generated concentrated energy. Animal experiments were conducted to in-vivo test the efficiency of the system, and the induced brain hemorrhage was also accessed and analyzed.

II. Methods

A. Focused Ultrasound transducer design

Figure 1 shows the design overview of the multiple-channel ultrasound phased array driving system. The hemispherical phased arrays were constructed in house. The phase array contained 80 round piezoelectric ceramic elements (center frequency = 270 kHz, -3 dB bandwidth =20 kHz; PZT-4, Huachen Inc., Chung-Li, Taiwan).Each element had a diameter and thickness of 25 and 7 mm respectively. The electric-to-acoustic efficiency of the PZT-4 element ranges from 15 to 20%, as measured by an acoustic power meter (Ohmic Instruments, Easton, Maryland,USA). The element was fixed in the hemispherical mold with an inner diameter of 250 mm and a curvature radius of 125

Chwee Teck Lim, James C.H. Goh (Eds.): ICBME 2008, Proceedings 23, pp. 435–438, 2009
www.springerlink.com

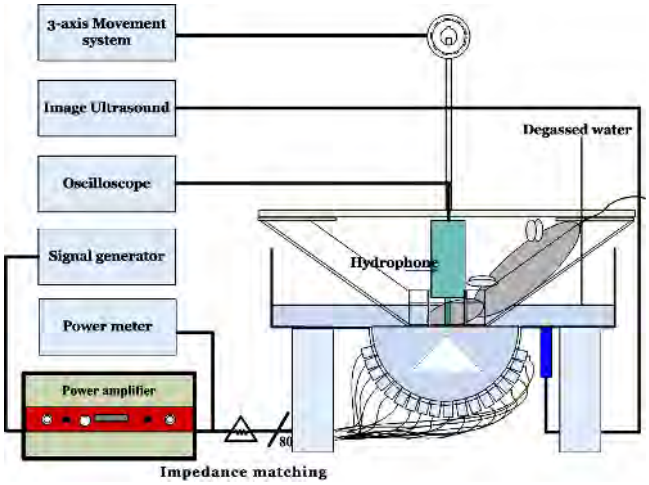


Fig. 1 Diagram showing the experimental setup

mm. Each element was equally spaced around the mold surface. All elements were sprayed with silicone-rubber and used with acrylic plastic housing.

B. Animal preparation

All animal procedures were approved by the institutional Animal Care and Use Committee of the Chang-Gung University. Adult male Sprague-Dawley rats were anesthetized by a mixture of ketamine and xylazine administered intravenously, and removed the animal skull area hair .An animal positioning device was designed for the *in-vivo* animal experiments. The hemispherical phased array was fixed at the bottom of a water tank filled with degassed water. A holder was designed to carry the animal with supine position, and this was moved by a three-axis precision-movement table (with a spatial resolution of 50μm).

C. Ultrasonic image guidance

A procedure of using diagnostic ultrasound to guide the treatment process was described below: (1) One needle hydrophone (Onda, Sunnyvalc, California,USA; calibration range: 50 kHz to 20MHz) was attached besides of the stereotactic animal holder (mounted on a 3-D high precision positioning stage) with the distance between animal brain and hydrophone been fixed and defined; (2) The peak pressure was searched by using the attached hydrophone. Once the peak pressure location been identified, the stage can easily move a definite distance to steer focal energy into animal brain; (3) One diagnostic ultrasound (Model T3000, Terason, MA, USA) was employed, and the imaging probe was mounted at the bottom of the water tank with the location also predefined; (4) The positioning table first move the animal to the top of the diagnostic imaging probe to acquire the image before the animal treatment; then move back the animal back to the focal spot and align the focal point to unilateral brain and then treated; (5) The positioning system then move the animal back to the top of the diagnostic probe and acquire the second image (i.e., imaging after treatment). Figure 2 shows the ultrasound imaging acquired during the process. Figure 2(a) shows the imaging acquired from step (3), and Fig. 2(b) and 2(c) shows the imaging acquired from step (5). In order to examine the procedure can acquire pre- and post-treatment imaging at the identical plane, two line markers were built (pointed in Fig. 2(b) by white arrows). The subtraction of pre- and post-treated brain in Fig. 2(d) shows that the line markers align well and whole process can guide precisely without position errors.

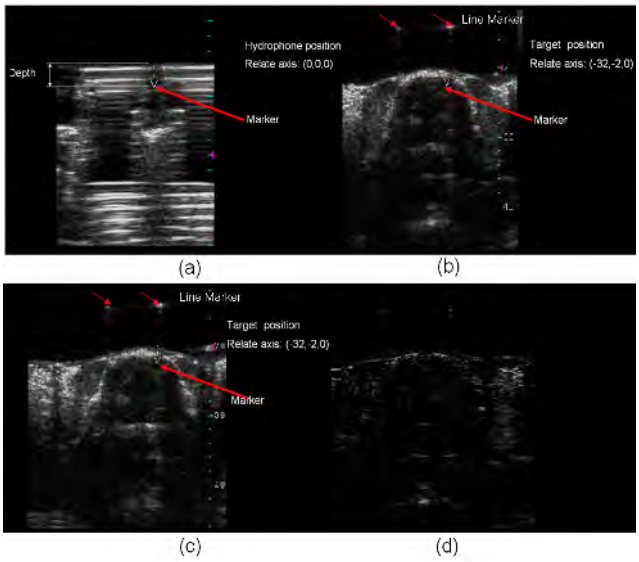


Fig. 2 Ultrasound image guided procedure; use marker and got the relation distance. (a) Needle hydrophone; (b) animal brain before treatment; (c) animal brain after treatment; (c) subtraction between before and after treatment

D. Parameter select

The animal brain was sonicated in the presence of an ultrasound microbubble-based contrast agent (SF_6 coated with mean diameters of 2-5 μm; SonoVue®, Bracco, Milan, Italy), which was injected intravenously prior to sonications. Each bolus injections contained the contrast agent at 2.5μl/kg for an individual sonication. Using the Burst-mode single output for sonication which with a burst length of 10 ms, a PRF of 1Hz. The delivered electrical powers ranged

from 2 to 90 W were tested, combined with the duration times from 30 to 180 s. TABLE I lists all parameters and the animal numbers been sonicated and examined.

Table 1 The number of animal experiments under different sonication parameters

		Electrical Power (W)									
		90	75	60	40	30	20	10	7.5	5	2
Duration (s)	180						1	1	1	3	3
	120	1	1	1	2	1	1	1	1	1	1
	60							1	3	14	1
	30	1	1		2	1	3	3	1	10	2

E. Histological and pathologic examinations

Evans blue was injected intravenously as a bolus immediately after sonication. According to the Evans blue dye the Brain sample BBB disruption area will be observed. All animals were sacrificed 2-3hours after sonication, and the brain sample were section with 10μm thickness. Representative sections were stained by hematoxylin and eosin (H&E) for cell damage, the system performers can be found.

The level of cell damage and hemorrhage were classified into four categories as Fig. 3. Level 0 was defined as a little necrosis phenomena. Level 1 was defined as some discontinuous form of bleeding phenomena. Level 2 was defined as some continuous form of bleeding phenomena. Level 3 was defined as some continuous bleeding and tissue injuring phenomena.

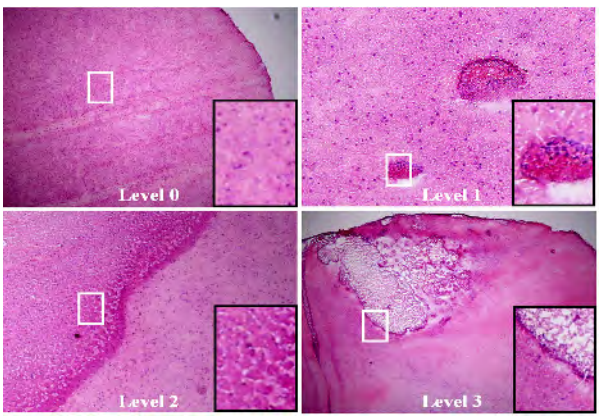


Fig. 3 Hematoxylin and eosin (H&E) cell damage level

III. Result

A. Focal ability of hemispherical phased array

The three-dimensional positioning system with the hydrophone was used to measure the hemispherical phase arrays transducer focusing. Figure 4 shows measured ultrasonic pressure distribution at the focal depth. The -3dB dimension of the pressure was estimated to be about 3 mm, demonstrated that the designed 80–channel hemispherical array contains excellent focusing ability and capable of delivering concentrated energy into animal brain.

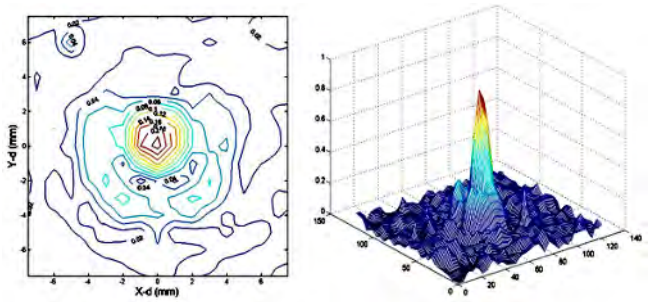


Fig. 4 Measured ultrasonic pressure distribution along the cross-sectional plane at the focal depth

B. In-vivo animal experiment

All animal was sacrificed and the BBB-disruption region was detected by the blue-stain in the brain tissues. Figure 5 shows different level of BBB disruption effect when different focused ultrasound powers were employed. When observing the power great then 5-W the BBB disruption was found. On the contrary, the hemorrhage was found when power output was greater then 10-W. This *in-vivo* animal experiment confirms the feasibility of using the design system to disrupt the BBB.

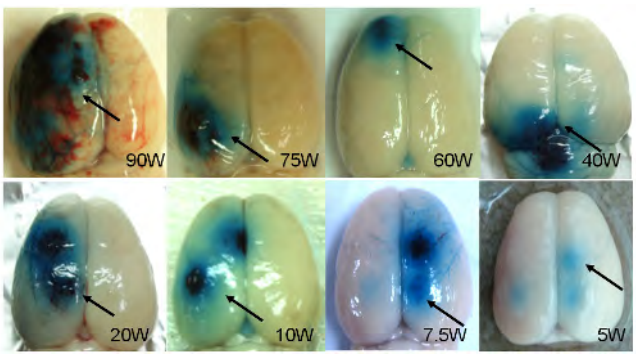


Fig. 5 Gross observation showing blue-dye deposition in animal brain under different acoustic parameters

Brian tissue damage was also examined. 2 W of power was found to be the lower threshold to produce BBB disruption. The power ranging from 2 – 7.5 W was considered to be safe since only a few of erythrocyte extravasations was detected (level 1). In the power range of 7.5 to 20 W, a few hemorrhagic damage can be found in brain tissues; For power larger than 20 W, Some tissue damage including tissue large scale hemorrhage and tissue necrosis were observed.

C. Conformal BBB disruption

Although the system feasibility parameter was found, sometimes the region of BBB disruption may not wide enough to cover the disease region. Figure 6 demonstrate one example showing the BBB-disruptive region can be well controlled and the affective region can be defined and constructed by multiple sonications.

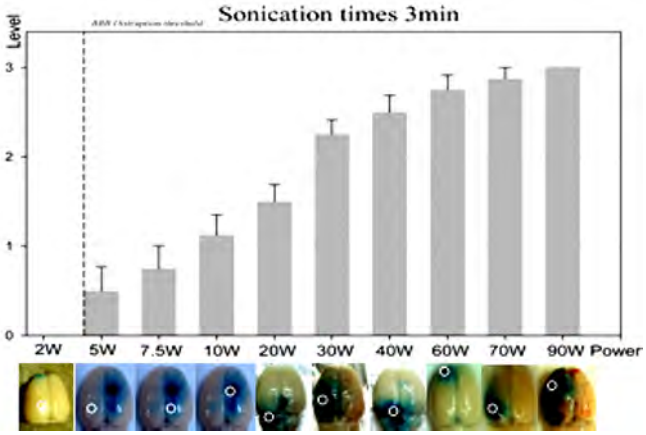


Fig. 5. Hemorrhage level occurred accompanying with sonication under different applied powers

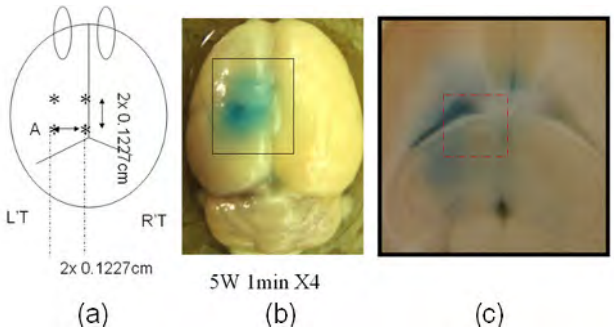


Fig. 7 BBB disruption to conform the designated regions. An example of using four sonication to confine a rectangular shape was shown. (a) Sonication plan; (b) Gross observation from brain surface; (c) gross observation 3 mm beneath brain surface. 5W of power were employed

IV. Conclusions

In this paper, we have proposed a successful integration to use diagnostic ultrasound imaging to guide the focused ultrasound induced BBB disruption procedure. The feasibility to use diagnostic ultrasound imaging to guide the brain drug delivery was confirmed. The system may be further improved to achieve the following aim points:

- Real-time monitor the focused-ultrasound induced BBB disruption process
- Design the phased array which confocal with he imaging probe to reduce the focal point identification process in each treatment.
- More comprehensive therapeutic transducer can be deigned such as increasing the element of the phased array for larger steering distance
- Increase the operating frequency of the imaging probe to gain the image resolution.

Acknowledgment

The project has been supported by the National Science Council (NSC-95-2221-E-182-034-MY3) and the Chang-Gung Memorial Hospital (CMRPD No. 34022, CMRPD No. 260041).

References

1. McDannold, N.J., N.I. Vykhodtseva, and K. Hynynen (2006) Microbubble contrast agent with focused ultrasound to create brain lesions at low power levels: MR imaging and histologic study in rabbits. Radiology, 2006. 241(1): pp. 95-106.
2. McDannold, N., N. Vykhodtseva, and K. Hynynen (2008) Blood-brain barrier disruption induced by focused ultrasound and circulating preformed microbubbles appears to be characterized by the mechanical index. Ultrasound Med Biol, 2008. 34(5): pp. 834-40.
3. Hynynen, K., et al (2001) Noninvasive MR imaging-guided focal opening of the blood-brain barrier in rabbits. Radiology, 2001. 220(3): pp. 640-6.
4. Kinoshita, M., et al (2006) Targeted delivery of antibodies through the blood-brain barrier by MRI-guided focused ultrasound. Biochem Biophys Res Commun, 2006. 340(4): pp. 1085-90.
5. McDannold, N., K. Hynynen, and F. Jolesz (2001) MRI monitoring of the thermal ablation of tissue: effects of long exposure times. J Magn Reson Imaging, 2001. 13(3): pp. 421-7.

Author: Wen-Cheng Huang
Institute: Chang Gung university
Street: 259 Wen-Hwa 1st Road, Kwei-Shan
City: Tao-Yuan
Country: Taiwan
Email: Wenchengenator@gmail.com

A Precise Deconvolution Procedure for Deriving a Fluorescence Decay Waveform of a Biomedical Sample

H. Shibata, M. Ohyanagi and T. Iwata

Graduate School of the University of Tokushima, Japan

Abstract — **We propose a simple and convenient method for measuring the wavelength dependency of the delay time of the response of a photomultiplier tube (PMT) by using a normal time-correlated single-photon-counting (TCSPC) instrument for use in a precise deconvolution procedure. In order to derive the delay time, we employed an algorithm that was used in a modified Gerchberg- Papoulis' band-extrapolation algorithm that we had already reported. Fundamental simulation results and basic experimental results are shown.**

Keywords — **fluorescence lifetime, time delay, photomultiplier tube, wavelength dependency, deconvolution.**

I. Introduction

In the field of biomedical engineering, to measure fluorescence decay waveforms or to obtain fluorescence lifetimes are important when shapes of fluorescence spectra for given two samples are similar with respect to each other. This is because the two samples might be distinguished qualitatively if there are differences in the values of fluorescence lifetimes. To obtain the value of the fluorescence lifetime itself is also important because it is one of the most fundamental material parameters to characterize the sample. However, to measure the fluorescence decay waveform becomes difficult when the value becomes small so as to be comparable with that of the pulse width of the excitation light.

In such a situation, the delay time of the response of a photomultiplier tube (PMT), depending on the kind of the material of the photocathode of the PMT and the applied voltage, should be a serious problem. This is because the peak wavelength of fluorescence emission is Stokes-shifted toward the longer wavelength in comparison with that of the excitation light and because the time delay of the response of the PMT depends on the wavelength [1-3]. The conventional deconvolution technique cannot be carried out precisely in the presence of the time delay.

In order to determine the wavelength dependency of the delay time of the response of the PMT and to obtain the accurate fluorescence lifetime values, we have to establish a precise deconvolution procedure. In the present article, we propose such a method, which is applicable to biomedical samples whose lifetimes are short as the same order as a pulse width of the excitation light. Our proposed method is based on an iterative Gerchberg-Papoulis algorithm that is usually used for a band-extrapolation procedure applicable for data obtained from a band-limited measurement system. This means that the normal time-correlated single-photon-counting (TCSPC) instrument in combination with a nanosecond-pulsewidth light source can be used without paying much attention.

We describe the principle of operation, how to determine various parameters, and show fundamental simulation and experimental results.

II. Principle of the Delay Time Estimation

We have already proposed a deconvolution procedure that is combined with a band-extrapolation technique to obtain a true fluorescence-decay waveform from a reference and a measured fluorescence-decay waveform that are both band-limited. To carry out the band-extrapolation procedure, we proposed two kinds of algorithms: (i) a method by use of an iterative Hilbert-transform technique in a frequency domain [4], and (ii) a method by use of the Gerchberg-Papoulis algorithm carried out in a frequency and a time domain alternatively [5]. We have confirmed that both algorithms are equivalent mathematically and that the convergence of the iteration becomes worse when there is a difference in time origins between the reference and the measured fluorescence-decay waveform. Without the difference, on the one hand, the fastest convergence to the true value is attained. By make use of this fact, we can estimate the time delay by introducing the time delay parameter t_d and by searching the t_d value that makes the convergence rate fastest.

As was described in the previous section, the peak wavelength of fluorescence is shifted toward the longer wavelength in comparison with that of the excitation light and the time delay of the response of the PMT depends on the wavelength. Then, we can estimate the wavelength dependency of the delay time of the response of a PMT as the following fashion: First we prepare several kinds of a narrow band-pass interference filters and a fluorescent sample whose emission spectrum is broad. And then we measure

Chwee Teck Lim, James C.H. Goh (Eds.): ICBME 2008, Proceedings 23, pp. 439–443, 2009
www.springerlink.com

the reference and the fluorescence decay waveform at each transmission wavelength of the interference filter. Finally, we apply the deconvolution procedure for the corresponding data. Because the procedure is based on the band-extrapolation algorithm, we can use band-limited measurement instrument for measuring the reference and the fluorescence-decay waveform. This means that the normal time-correlated single-photon-counting (TCSPC) instrument in combination with a nanosecond-pulsewidth light source can be employed without paying much attention.

III. Parameters for use in the proposed procedure

The proposed deconvolution procedure has the following parameters that influence the final result: t_d : the delay time to be estimated, τ : fluorescence lifetime of the sample, W: the full width at the half maximum (FWHM) of the excitation light pulse, f_c: a cut-off frequency that is used in the iteration algorithm for band-extrapolation, N: the number of the iteration. In order to confirm the precision and accuracy of the proposed procedure, we carried out three kinds of numerical simulations. We put the pulse shape of the excitation light as a Gaussian with W=1.0ns and the waveform of the fluorescence decay as a single exponential function with the number of a peak count 10000. We superimposed Poisson noise on the decay waveform and put t_d=100 ps, f_c=1.0 GHz, and N=10000.

Figure 1 shows the absolute value of the averaged estimation errors $|\Delta t_d|$ over the true delay-time t_d=100ps as a function of τ (black circle) and the corresponding standard deviation of the errors (white triangle), where the number of trials was 50. From this result, we found that $|\Delta t_d|/t_d \le 0.6$ % can be obtained for $0.5 \le \tau \le 3.0$ ns. For the large value of τ , the value of the standard deviation in estimation is increased. This is because the decay rate of the signal component in the frequency domain becomes fast at the cut-off frequency f_c, which brings about a worse condition in the band extrapolation procedure.

Figure 2 shows the $|\Delta t_d|$ as a function of W (black circle) and the corresponding standard deviation (white triangle) of the errors, where the number of trials was 50 again. From this result, we found that $|\Delta t_d|/t_d \le 0.5$ % can be obtained for $0.5 \le W \le 1.3$ ns. For the large value of W, the value of the standard deviation in estimation is increased. This is based on the same reason as that described in Fig.1.

Figure 3 a plot of the $|\Delta t_d|$ versus $\Delta\tau_{res}$, where we introduced $\Delta\tau_{res}$ to taking into account of the wavelength dependency of the shape of the instrumental response func-

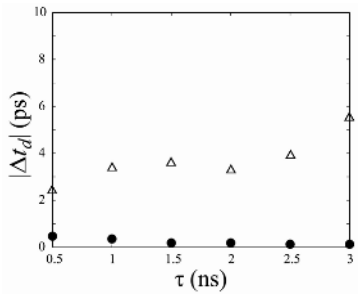


Fig. 1 $|\Delta t_d|$ as a function of τ (black circle) and its standard deviation (white triangle) in the estimation of the delay time t_d .

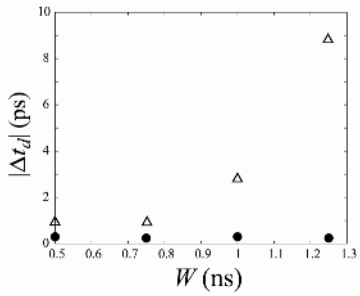


Fig. 2 $|\Delta t_d|$ as a function of W (black circle) and its standard deviation (white white triangle) in the estimation of the delay time t_d .

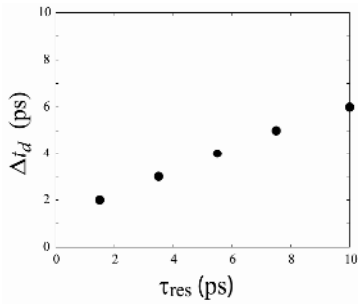


Fig. 3 A plot of $|\Delta t_d|$ versus $\Delta\tau_{res}$.

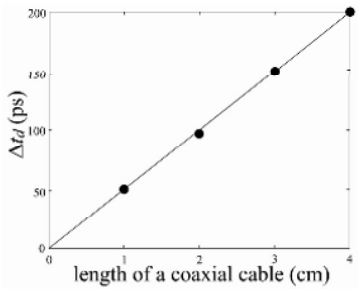


Fig. 4 A plot of Δt_d versus length of a coaxial cable.

tion of the measurement system representatively including that of the PMT. For such a purpose, we convolved the Gaussian function of W=1.0ns with a single exponential-decay function of a time constant $\Delta\tau_{res}$ as the excitation waveform. From this result, we can understand that $|\Delta t_d| \le 6\text{ps}$ when $\Delta\tau_{res} = 10\text{ps}$. The delay is introduced mainly by the numerical convolution procedure. The shape of the response function or the value of $\Delta\tau_{res}$ itself brings about less problem in estimating the value of t_d in a practical situation for the deconvolution procedure than the t_d does[7].

IV. Results and Discussion

A. Delay time estimation by use of a coaxial cable

In order to demonstrate that the proposed method works well in the real measurement system, we measured the delay time of a 50 Ω -coaxial cable (3C2V) by changing its physical length step by step. In the TCSPC instrument, we measured fluorescence decay curve of a business card at a wavelength 450 nm, whose fluorescence lifetime was around 0.9 ns. Then we varied the length of the coaxial cable relatively from 0 to 4.0 cm by 1.0 cm, which is used for connection between the PMT (1P28; applied voltage; -900V, Hamamatsu Photonics) and a high-speed pulse amplifier set before a time-to-amplitude converter (TAC). The measurement result is shown in Fig.4, which agrees well with the theoretical delay time of the coaxial cable 5 ps/mm.

B. Dependency of the delay time on the applied-voltage for the PMT

Next, we measured the dependency of the delay time on the applied voltage for the PMT. Using the TCSPC instrument, we measured fluorescence decay of the business card three times at a wavelength 450 nm as the manner in described in the previous section. Then the applied voltage for the PMT was varied from -800 V to -900 V by a step of 20 V. The result is shown in Fig.5. As is expected, the larger applied voltage results in the smaller delay time and the smaller variation in the estimation.

C. Wavelength dependency of the delay time of the response of the PMT

Next, we measured the wavelength dependency the delay time of the response of the PMT. Experimental setup is the same as above. For the selection of the wavelength, we used four interference filters in sequence: the center of transmission wavelength of which were 400 nm (VPF-25C-40-40000, Sigma Koki), 450, nm (VPF-25C-45-45000), 500 nm (VPF-25C-50-50000), and 550 nm (VPF-25C-50-55000). At each wavelength, seven measurements were carried out. The fluorescent sample used is the business card again, whose excitation spectrum and emission spectrum are shown in Fig.6, together with the normalized transmission spectra of the four interference filters. The applied voltage for the PMT (1P28) was fixed at -900V. From this result we can understand that the longer wavelength gives the longer delay time. The value of the delay time is around 20ps/50 nm at a wavelength between 400 and 450nm. Although literature values for proving correctness of our measurement have not been found, our measurement value seems reasonable by considering the type of the PMT, its applied voltage, and the literature values of other PMTs [1-3,6].

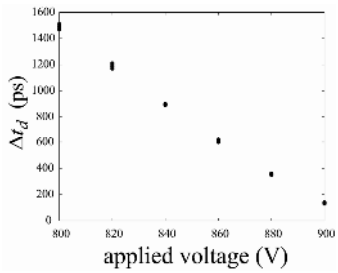


Fig. 5 Dependency of the delay time on the applied-voltage.

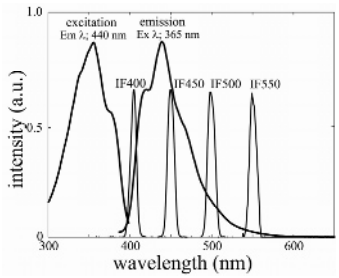


Fig. 6 Excitation and emission spectra of a business card used as a fluorescent sample and transmittance spectral profiles of four kinds of interference filters.

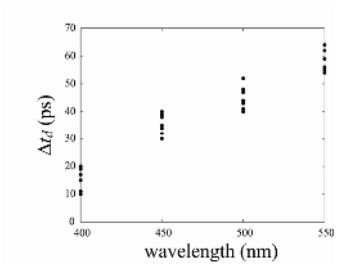


Fig. 7 Wavelength dependency of the delay time of the response of the PMT.

D. Deconvolution procedure by taking into consideration of the wavelength dependency of the time delay of the response of the PMT

In order to demonstrate the usefulness of the proposed procedure as a tool for deriving values of fluorescence lifetimes in analytical practice, we carried out numerical simulations in a comparative way with the normal curve-fitting method in a controllable condition. Figure 8(a) shows an artificial excitation profile: We assumed a Gaussian function with FWHM 0.5 ns, where data interval Δt and the number of total data point *NM* were 0.1 ns and 500, respectively. Figure 8(b) shows an assumed three-component exponential-fluorescence-decay waveform, where individual fluorescence lifetimes are τ_1 = 0.5 ns, τ_2 = 2.0 ns, and τ_3 = 6.0 ns with their amplitude ratios are $a_1 : a_2 : a_3$ = 12 : 4 : 1. Here, we put the delay time as t_d = 100.0 ps. Figure 8(c) shows a waveform obtained from a convolution integral of the waveform shown in Fig. 8(a) with that in 8(b), where a symbol ∗ stands for the convolution procedure. Figure 8(d) shows an instrumental function of the measurement system. We assumed it by a Gaussian function with FWHM 0.8 ns. Figure 8(e) shows a band-limited excitation profile, which is obtained from a convolution integral of Fig. 8(a) with 8(d). Then Poissonian noise was added on it. Figure 8(f) also shows a band-limited time-delayed fluorescence-decay-waveform with addition of Poissonian noise. For such simulated excitation and fluorescence-waveforms shown in Figs. 8(e) and 8(f), we tried to apply the normal Gauss-Newton curve-fitting method and the proposed deconvolution method separately.

For the fitting method, it is better to know the number of components *n* and the value of time delay t_d before procedure. When we set *n* and t_d as 3 and 100.0 ps, respectively, the estimated results were as follows: $\hat{\tau}_1$ = 0.51 ns, $\hat{\tau}_2$ = 2.01 ns, and $\hat{\tau}_3$ = 6.01 ns with their amplitude ratios $\hat{a}_1 : \hat{a}_2 : \hat{a}_3$ = 12.1 : 4. 0 : 1.0. Relative accuracy in estimating these parameter values over true ones was less than 2.0 %. Figure 8(g) shows the fitting result: A solid line shows the fitted curve and a dotted line shows the simulated waveform shown in Fig. 8(f). Figure 8(h) shows a plot of weighted residuals r_i of the fitted curve to the simulated one. From a test of goodness of fit, we found that the fitted curve could not be rejected with a significance level α = 0.05.

On the other hand, a solid line and a dashed line shown in Fig. 8(i) are the fluorescence decay waveform obtained from the proposed method and the true one shown in Fig. 8(b), respectively, where the derived delay time is $\hat{t}_d$ = 100.0 ps for σ = 1.0 GHz and *N* = 10000. The two curves are almost identical except small oscillating behavior on the tail. By applying the same curve fitting method for the derived fluorescence-decay waveform with considering the excitation profile as a delta function, we obtained the following estimates: $\hat{\tau}_1$ = 0.49 ns, $\hat{\tau}_2$ = 1.98 ns, and $\hat{\tau}_3$ = 5.95 ns with their amplitude ratios $\hat{a}_1 : \hat{a}_2 : \hat{a}_3$ = 11.8 : 4.0 : 1.0. The relative accuracy in estimating parameter values over the true ones was again less than 2.0 %. For an explicit comparison purpose, we show a convoluted waveform of the derived waveform with the excitation profile shown in Fig. 8(a) and the instrumental function shown in Fig. 8(d) by a solid line in Fig. 8(j). A dotted line in the same figure shows the simulated waveform shown in Fig. 8(f). Figure 8(k) shows a plot of weighted residuals. The proposed method gives an accurate decay waveform.

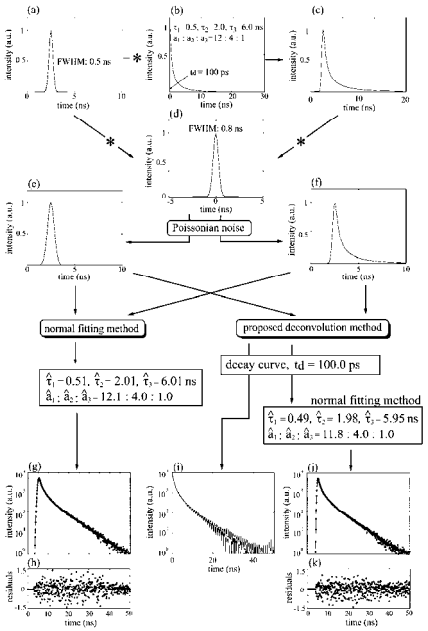


Fig. 8 Comparison of the proposed deconvolution method with the normal curve-fitting method. See text.

Although the proposed deconvolution procedure had the frequency-band-extrapolation stage, the relative accuracy in estimating the fluorescence lifetimes and amplitude ratios was almost the same as that of the normal fitting method. The fact that the normal fitting method worked quite well is quite reasonable in a sense because we knew the accurate mathematical model for the fitting in advance: the form of the mathematical function, the number of components, and the value of the delay time. In addition, the fitting procedure

works so as to cancel the waveform distortion due to band limitation, because both the excitation and the fluorescence waveform have distortion as the same manner at least mathematically. Although we can use the delay time as one of the estimating parameters in the fitting, to do so might be somewhat difficult in analytical practice. If we do not consider the delay time in the fitting, the residuals and uncertainty are increased. Also, if we do not know the number of components, the fitting procedure might be somewhat difficult. For a successful use of the fitting, determination of adequate initial values is important. On the other hand, the proposed method gave a fluorescence decay waveform directly with no information on such as the presence of the time delay and the number of components. In order to derive values of fluorescence lifetimes and amplitude ratios, however, we have to make an adequate mathematical model like the fitting method except the delay time. In this sense, the proposed method might be useful for making more precise model, especially when the fluorescence decay waveform is difficult to be expressed by a sum of exponential decay curves.

V. Conclusions

We have proposed a simple method for measuring the wavelength dependency of the delay time of the response of a photomultiplier tube (PMT) by using a normal time-correlated single-photon-counting (TCSPC) system for use in a precise deconvolution procedure. In order to derive the delay time, we employed an algorithm that was used in a modified Gerchberg-Papoulis' band-extrapolation algorithm that we had already reported. Fundamental simulation and basic experimental results were shown.

References

1. Wahl Ph, Auchet J C, ,Donzel B (1974) The wavelength dependence of the response of a pulse fluorometer using the single photoelectron counting method. Rev. Sci. Instrum 45: 28-32
2. Rayner D M, McKinnon A E, Szabo A G (1977) Correction of instrumental time response variation with wavelength in fluorescence lifetime determinations in the ultraviolet region. Rev. Sci. Instrum 48: 1050-1054
3. James D R, Demmer D R M, Verral R E et al. (1983) Excitation pulse-shape mimic technique for improving picoseconds-laser-excited time-correlated single-photon counting deconvolutions. Rev. Sci. Instrum 54: 1121-1130.
4. Iwata T, Shibata H, Araki T (2007) Extrapolation of band-limited frequency data using an iterative Hilbert-transform method and its application for Fourier-transform phase-modulation fluorometry. Meas Sci Technol 18: 288-294
5. Iwata T, Shibata H, Araki T (2008) A deconcolution procedure for determination of a fluorescence decay waveform applivcable to a band-limited measurement system that has a time delay. Meas Sci Technol 19: 015601
6. O'Connor D V, Phillips D (1984) Time-Correlated Single Photon Counting. Academic, London

Author: Tetsuo Iwata
Institute: Graduate School of the University of Tokushima
Street: 2-1, Minami-Jyosanjima,
City: Tokushima, 770-8516
Country: Japan
Email: iwata@me.tokushima-u.ac.jp

Laser Speckle Contrast Analysis Using Adaptive Window

H.-Y. Jin[1], N.V. Thakor[2], H.-C. Shin[1]

[1]Soongsil Univ., Seoul, Republic of Korea
[2]Johns Hopkins Univ., Baltimore, U.S.A.

Abstract — **This paper proposes a new image processing method for laser speckle, adaptive windowing laser speckle contrast analysis (aLASCA) that adaptively processes laser speckle images in the temporal and spatial direction. Conventional fixed window based LASCA has shortcoming in that it uses the same window size regardless of target areas. Inherently laser speckle contains undesired noise. Thus a large window is helpful for removing the noise but it results in low resolution of image. Otherwise a small window may detect small vascular but it has limits in noise removal. To overcome this trade-off, we newly introduce the concept of adaptive windowing to conventional laser speckle image analysis. We have compared conventional LASCA and its variants with the proposed method in terms of image quality and processing complexity**

Keywords — **Laser speckle contrast analysis(LASCA), adaptive window, Laser speckle, micro vessel.**

I. Introduction

The laser speckle technique has progressively become a emerging technique for real-time medical imaging [1]. A laser speckle is created when laser light illuminates an object, and the speckle contrast values are calculated from the time-varying statistics.

The laser speckle imaging (LSI) technique can detect vascular and blood flow changes in the underlying medium [2]. The detection of blood flow is an important in medical diagnosis. Using LSI, it is possible to observe of skin capillary flow and retinal flow in a noninvasive way. Also LSI is a relatively simple and inexpensive technique but it may support the investigation of complex interactions between neuronal activities and hemodynamic affairs [3].

Investigation of the spatiotemporal characteristics of blood flow is important in understanding the interest region of tissues. Various signal processing techniques for LSI exist but mostly they are based on laser speckle contrast analysis (LASCA). As variants, Spatial way[5], temporal way[6], spatial-temporal[7] and adaptive spatial mean filter[8] and temporal mean filter[2] have been studied to see micro vascular better.

Conventional fixed window based LASCA has shortcoming in that it uses the same window size regardless of target areas. Inherently LSI contains speckle noise. Thus a large window is helpful for removing the noise but it results in low resolution of image. Otherwise a small window may detect small vascular but it has limits in noise removal. To overcome this trade-off, we newly introduce the concept of adaptive windowing to conventional laser speckle image analysis. Adaptive windowing is applied to both spatial and temporal processing.

This paper is organized as follows. The experimental setup and techniques, laser speckle imaging of various LASCA and adaptive windowing LASCA are described in section II. In section III, the result images are presented Finally, section IV deals with the conclusion and observations.

II. Material and Method

A. Laser Speckle Imaging

A laser speckle is a random pattern that has a granular appearance produced by reflected light when a coherent laser illuminates an irregular course surface. Goodman [4] asserts that useful information can be attained by examining the statistical properties of laser speckle patterns defined after storing the granular image in a CCD camera.

Figure 1 shows the experimental setup used to obtain laser speckle images. When a He-Ne Laser (655nm) illumi-

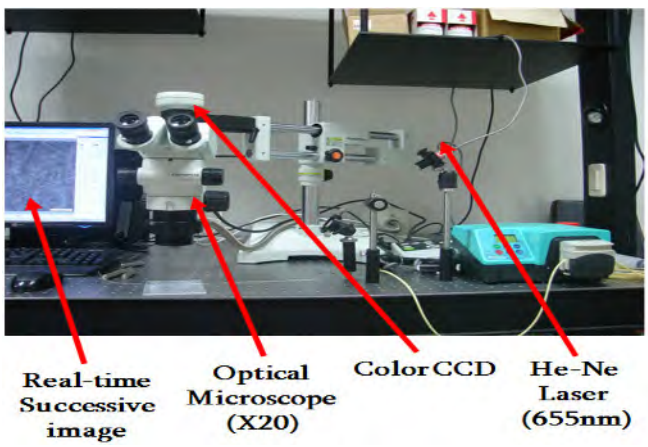


Fig. 1 Experimental setup

Chwee Teck Lim, James C.H. Goh (Eds.): ICBME 2008, Proceedings 23, pp. 444–447, 2009
www.springerlink.com

nates the target region, the light is reflected by the surface of the object, and a microscope then magnifies the image. Finally, CCD camera captures the image and the images are stored in the computer. In this experiment, the 384×364 pixel images were stored and Matlab was used for simulation.

B. Speckle Contrast , K

The definition of the speckle contrast is

$$K=\frac{\sigma_s}{\langle I\rangle} \tag{1}$$

where K is the speckle contrast, σ_s is the spatial standard deviation, and $<I>$ is the spatial mean intensity of a window of pixels. The range of the contrast K is $0\le K\le 1$. The contrast value is low when an object moves quickly, whereas the value is high when an object moves slowly.

Applying this definition, vascular and non-vascular areas can be distinguished since the contrast is low where blood flow occurs, whereas it is high when no blood flow occurs.

C. Conventional LASCA based Techniques

LASCA based techniques can be divided into three categories: spatial, temporal, and spatial-temporal.

Generally, spatial LASCA is known as LASCA [5].

In spatial LASCA, (1) a square-shaped fixed $M\times M$ window is used around target pixel to calculate the contrast in eq.(1).

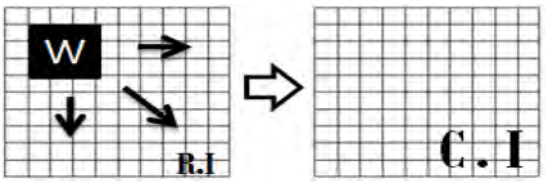


Fig. 2 LASCA operation

Figure.2 shows the spatial LASCA operation, where W is $M\times M$ window, R.I is the raw speckle image, and C.I is speckle contrast image. As the sliding window W is moving by one pixel, the contrast is calculated.

Figure.3 shows the temporal LASCA operation where n is the image frame number. Temporal LASCA can be defined according to equation (2) [6]

$$K_{tem}(i,j)=\sigma_{i,j,n}/<I_{i,j}>_n \tag{2}$$

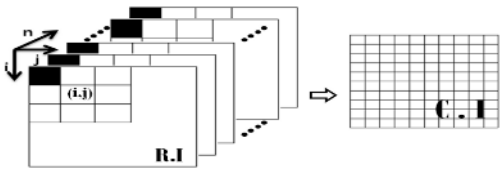


Fig. 3 Temporal LASCA operation

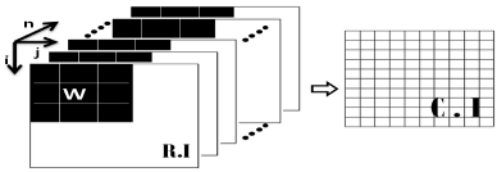


Fig. 4 mLSI operation

Figure.4 shows the mLSI operation which was proposed by H. Cheng [7]. In mLSI spatial and temporal LASCA are applied simultaneously and calculated by using eq.(3)

$$N_{mLSI}=[<I_{i,j}^2>_n-<I_{i,j}>_n^2]/<I_{i,j}>_n^2 \tag{3}$$

D. Proposed adaptive LASCA

The proposed method attempts to improve spatial and temporal resolution over the basic variable LASCA techniques. The key is that the window size for calculating speckle statistics adaptively changes.

The measure for applying variable-sized square windows is K, σ_K and σ_s where K is speckle contrast, σ_K is the variance of contrast, and σ_K is the variance of raw images.

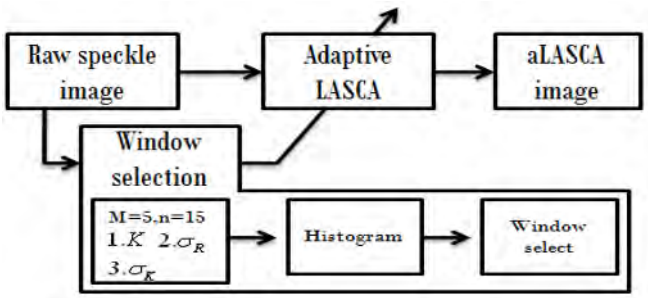


Fig. 5 Proposed aLASCA block diagram

Figure 5 is a block diagram of the proposed aLASCA. From the raw image, K, σ_K and σ_s are calculated using M=5, n=13. Then based on K, σ_K and σ_s, the adaptive

window M and the frame number n are determined by using Image Intensity Histogram. The window size and the frame number are adaptively changed among M = 3, 5, and 7, and n = 3, 5, 7, 9, 11, 13, and 15. aLASCA and $a_{temporal}$LASCA are obtained by applying the various M and n in each pixel to the raw speckle image. In this case, a_{spa}LASCA follows formula (1) and a_{tem}LASCA follows formula (2).

III. Results

A. Images using conventional LASCA techniques

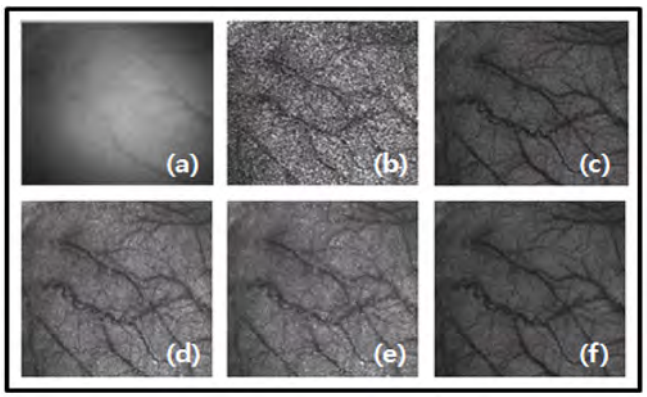


Fig. 6 Laser speckle images (a) the raw image, (b) the LASCA image, (c) the temporal LASCA image, (d) the mLSI image, (e) the sLASCA image, and (f) the tLASCA image

Figure 6 shows the conventional laser speckle images where M = 3 and n = 15 are applied to the 384×368 pixel raw image.

Every image has white spots, or speckle noise. Because many spots are concentrated in (d), (e), and (b), it is reasonable to assume that speckle noise occurred more frequently in spatial operation. Looking at (e) and (f), we can see that when the mean filter is used, noise is decreased. The image, however, is slightly blurred compared to (b) and (c). Moreover, noise is also decreased by using the temporal operation. Therefore, (f) is the best quality image in the sense of the noise reduction.

B. Adaptive LASCA

The most important part of LASCA imaging is to separate vascular areas from non-vascular areas. Adaptive LASCA increases resolution by applying small-sized windows to vascular areas and decreases error by using large-sized windows to non-vascular areas.

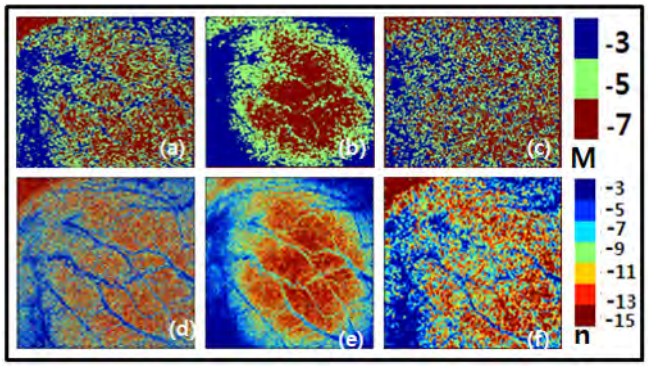


Fig. 7 Window distribution in spatial LASCA: (a) using Kspa (M = 5), (b) using variance of raw image (M = 5) (c) using variance of K (M = 5). Window distribution in temporal LASCA: (d) using Ktem (N = 15), (e) using variance of raw image (n=15), (f) using variance of K (M = 5).

Figure 7 shows the distribution of the adaptive windowing size. The vascular areas in (a) and (d) are the most remarkable in spatial and temporal processing, respectively. Thus, the window selection of adaptive LASCA follows the value of K.

Figure 8 shows adaptive LASCA images using window selection based on K. In (c), speckle noise with white spots is removed, although the occurrence of black spots is slightly increased in comparison to (a).

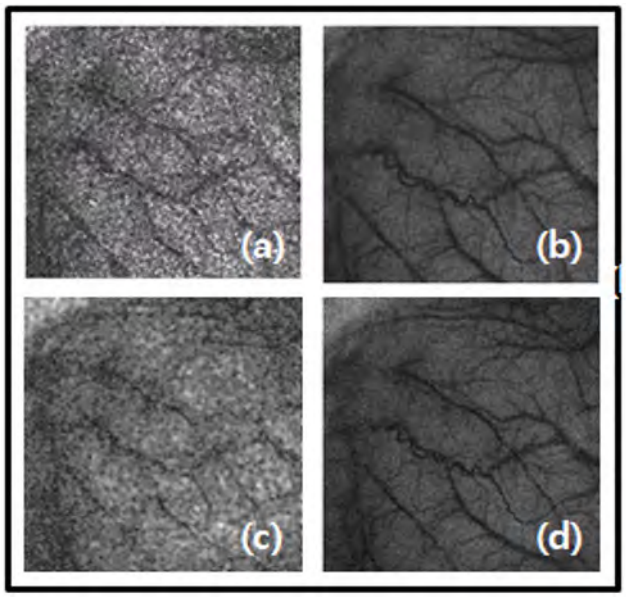


Fig. 8 Comparison of conventional and proposed methods (a) the LASCA image (b) the temporal LASCA image (c) the adaptive spatial LASCA image (d) the adaptive temporal LASCA image

A close examination of (d) reveals that the number of thinner vascular areas is less apparent than (b). However, there is little difference in quality between the two images.

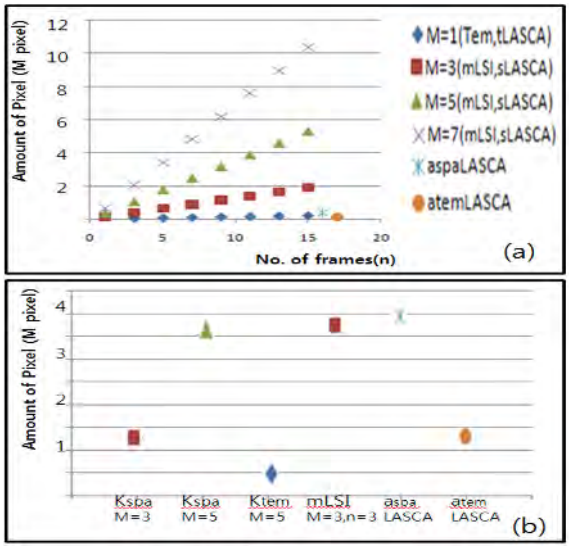


Fig. 9 Comparison of the computational cost (a) all of LASCA (b) LASCA similar to aLASCA

Figure 9 shows the comparison of the number of pixels involved in image processing. An examination of (a) reveals that mLSI uses a large amount of pixels so that the amount of computation is more than 10 times that of other procedures. Looking at (b), it can be recognized that a_{spa}LASCA is calculated with the similar or less amount of pixel to temporal LASCA (n = 3), spatial LASCA (M = 5), and mLSI (M = 5, n = 3).

a_{tem}LASCA has the same quantity of pixels as spatial LASCA (M = 3), and both procedures use the minimum number of pixels. By comparing Figure 6 (b) and Figure 8 (b), it can be seen that the quality of the image in Figure 8 (b) is better than the other with the same computation. Additionally, by comparing Figure 6 (c) and Figure 8 (b), it is apparent that the computation was reduced by 50% even though the image quality remained the same.

IV. Conclusions

We have proposed a new technique, spatial & temporal adaptive LASCA which uses the adaptive windowing size for calculating speckle statistics. We have compared conventional LASCA and its variants with the proposed aLASCA images through Matlab simulation. Based on the results, we expect that in a real-time LSI system, the adaptive LASCA technique will be advantageous.

Acknowledgment

The research was supported by the SEOUL R&BD NT070079 , Korea.

References

1. J. D. Briers (2001), Laser Doppler, speckle, and related techniques for blood perfusion mapping and imaging,, Physiological Meas., vol. 22, pp.35–66.
2. Thin M.Le (2007), New Insight into Image Processing of Cortical Blood Flow Monitors Using Laser speckle Imaging , IEEE TRANSACTION ON MEDICAL IMAGING, VOL.26, pp.833-842.
3. J.David Briers(1999), Capillary Blood Flow Monitoring Using Laser Speckle Contrast Analysis(LASCA) , Journal of Biomedical Optic 4(1), pp.164-175.
4. J.W. Goodman (1984), Statistical properties of laser speckle patterns," in Laser Speckle and Related Phenomena, J. C. Dainty, Ed. Berlin: Springer-erlag, pp. 9–75.
5. J.D.Briers and S.Webster (1996), Laser speckle contrast analysis (LASCA): A non-scanning, full-field technique for monitoring capillary blood flow, J.Biomed Otics,vol. 1, no.2 pp.174-179.
6. Nan Li (2006), Micro Vascular Imaging by Temporal Laser Speckle Contrast Analysis, Master thesis, Johns Hopkins Univ.
7. H.Cheng, Q. Luo, S.Zeng,S.Chen, J. Cen, and H. Gong, (2003), Modified Laser speckle imaging method with improved spatial resolution, J. Biomed. Optics, vol.8, no. 3, pp. 559-564.
8. A. K. Dunn, H. Bolay, M. A. Moskowitz, and D. A. Boas (2001), Dynamic imaging of cerebral blood flow using laser speckle," J.Cereb. Blood Flow Metabol., vol. 21, pp. 195–201.

Author: Ho-Young Jin
Institute: Soongsil Univ
Street: 511 Sangdo-dong,Dongjak-Gu
City: Seoul
Country: Rep. of Korea
Email: miyabbang@naver.com

Author: Nitish Thakor
Institute: Johns Hopkins Univ.
Street: 720 Rutland Ave.
City: Baltimore
Country: U.S.A.
Email: nitish@jhu.edu

Author: Hyun-Chul Shin
Institute: Soongsil Univ
Street: 511 Sangdo-dong,Dongjak-Gu
City: Seoul
Country: Rep. of Korea
Email: shinhc@ssu.ac.kr

Neural Decoding of Single and Multi-finger Movements Based on ML

H.-C. Shin[1], M. Schieber[2] and N. Thakor[3]

[1]Soongsil Univ./Dept. of Information and Communications, Rep. of Korea
[2]Univ. of Rochester/Dept. of Neuroscience, New York, U.S.A.
[3]Johns Hopkins Univ./Dept. of Biomedical Eng., Baltimore, U.S.A.

Abstract — **We present an optimal method for decoding the activity of primary motor cortex (M1) neurons in a non-human primate during finger movements. The method is based on the maximum likelihood (ML) inference. Each neuron's activation is first quantified by the change in firing rate before and after finger movement. We then estimate the probability density function of this activation given finger movement. Based on the ML criterion, we choose finger movements to maximize the likelihood. With as few as 20-25 randomly selected neurons, the proposed method decoded single finger movements with 99% accuracy. Since the training and decoding procedures in the proposed method are simple and computationally efficient, the method can be extended for real-time neuroprosthetic control of a dexterous hand.**

I. Introduction

Most neural systems incorporate large number of neurons to process sensory and motor information. The way the neural systems represent such information has been the subject of intense investigation. Understanding these neural population activities is very important for the development of neuroprosthetic control as well as for neural mechanisms [1][2]. For the neural control of external devices such as computer peripherals or prosthetic arms, we need to infer which movements are intended from neural population activities.

This is the so called *neural decoding* procedure. Although it has not been clearly explained how neuronal populations represent movements, it may be possible to infer which finger movements are active, assuming we have enough information on activities of neural populations. With the help of accurate decoding of movement, we should be able to generate a prosthetic movement or control signal. Many neural decoding methods have been developed and demonstrated in prosthetic control applications.

The population vector (PV) method was introduced in [3] where the population vector was obtained by combining weighted contributions from each neuron along its preferred direction. The PV method works well if the preferred directions are distributed uniformly in space [4]. Since this early work, many neural decoding algorithms have been developed. The simplest approach uses a linear estimator [5], which has been used effectively for real-time neural control of a 2D cursor in brain-computer interface research [6]. But this approach requires the use of data over a long time window [7]. One of the popular approach for neural decoding is to use artificial neural networks [8]-[9]. In addition Kalman filter based methods have been exploited for inferring hand position and velocity [7][10]. Recently probabilistic approaches such as maximum likelihood (ML) methods have provided promising results in decoding movements [11]-[13]. Moreover, in [14] the authors provide a neuron model that can realize the likelihood function for an optimal decoding of sensory information.

Here, we present a statistically optimal method, based on the ML inference, for decoding the activity of primary motor cortex (M1) neurons during single movements. Most conventional decoding schemes incorporate the absolute firing rate for quantifying neural activities and model it by a Poisson random process. For modeling of neuron discharge patterns, we quantified the activity of each neuron as the change in firing rate before and after finger movements. The mathematical modelling is done by using the Skellam distribution, which is the probability distribution of the difference of two random variables following Poisson distribution [15]. Then we inferred the finger movement for which the Skellam based likelihood function has a maximum. Based on ML criterion, we choose finger movements to maximize the likelihood. The investigations presented here involved experiments on primates performing 12 possible movement task involving flexion and extension of individual fingers. The methods and decoding accuracies are presented in the following sections. Data were collected from 115 task-related neurons in M1. Only with randomly selected $20-25$ neurons, the proposed method decoded single finger movements with 99% accuracy.

II. Maximum likelihood neural decoding of M1 neuronos

A. Data recording from m1 neurons

Most neural systems incorporate large number of neurons to process sensory and motor information. The way the neural systems represent such information has been the subject of intense investigation. Understanding these neural

Chwee Teck Lim, James C.H. Goh (Eds.): ICBME 2008, Proceedings 23, pp. 448–451, 2009
www.springerlink.com

population activities is very important for the development of neuroprosthetic control as well as for neural mechanisms [1][2]. A male rhesus monkey (Macaca mulatta) was trained to perform visually cued individuated finger movements. There are 12 different types of the movements: flexion and extension of the right five fingers and wrist. Sitting in a primate chair, the monkey placed the right hand in a pistol-grip manipulandum which separated each finger into a different slot. At the end of each slot, each fingertip lay between two micro-switches. By flexing or extending a digit a few millimeters, the monkey closed the ventral or dosal switches, respectively. This pistol grip manipulandum was mounted, in turn, on an axis permitting flexion and extension wrist movements.

The monkey viewed a display on which each digit (or wrist) was represented by a row of five light emitting diodes (LEDs). When the monkey flexed or extended a digit, a microswitch was closed and the LEDs provided the feedback. We abbreviate each instructed movement with the number of the instructed digit (1=thumb through 5=little finger, w=wrist), and the first letter of the instructed direction (f =flexion and e =extension). For example, '$4e$' indicates instructed extension of the ring finger.

Data were recorded from 115 task-related neurons in the $\mathrm{M}1$ neurons of the monkey. The monkey performed all \$12\$ possible movements involving flexion and extension of a single digit or of the wrist. The neurons were recorded for \$7\$ trials of each type of finger movement.

B. Maximum likelihood neural decoding

Here, we describe the modified ML based neural decoding method for individuated finger movements. Let $r_n(m)$ be the neural activity, i.e., firing rate, of neuron n for single finger movement m among 12 possible choices. We then define the neural activation related with the movement by

$$x_n(m) = r_n(m) - r_n(0) \tag{1}$$

where $r_n(0)$ is the baseline activity of neuron n before finger movement. Therefore, $x_n(m)$ represents the activity change in neuron $x_n(m)$ before and after the instructed finger movement m. Note that $x_n(m)$ may have a negative value, unlike $r_n(m)$. Experimentally we observed the neural activities of some neurons to decrease for certain finger movements.

Now given the observed neural activations $x_1, x_2, ..., x_N$, we want to infer which finger is intended to move. ML decoding estimates an unknown parameter, m, so that the probability function $\Pr(x_1, x_2, ..., x_N | m)$ is maximized, i.e.,

$$\hat{m} = \arg\max_m \Pr(x_1, x_2, ..., x_N | m) \tag{2}$$

where N is the total number of neurons used for ML decoding. Obviously the challenging task in ML decoding is to estimate the probability function. To do this we consider two probabilistic models: Skellam and Gaussian distributions.

Literature has shown that the Poisson process provides a useful approximation of stochastic neural firing rate, although this assumes no dependence at all on preceding events [2]. When the firing rate $r_n(m)$ follows the Poisson process, the probability, $f_n(k|m)$, that k spikes will be in the interval of Δt given m movement equals

$$f_n(k|m) = e^{-\mu_n(m)\Delta t} \cdot \frac{(\mu_n(m)\Delta t)^k}{k!} \tag{3}$$

where $\mu_n(m)$ is the ensemble mean of $r_n(m)$, i.e., $\mu_n(m) = E[r_n(m)]$. Also the probability of the baseline activity, $f_n(k|m=0)$ is represented by (3) if we replace $\mu_n(m)$ with the ensemble mean of $r_n(0)$, $\mu_n(0)$.

Since we are interested in the difference of two rates as in (1), we need to get the probability of $x_n(m)$. This can be modeled by the Skellam distribution, which is the probability distribution of the difference of two random variables following Poisson distribution [15]. The Skellam probability, $h_n(x_n|m)$ of $x_n(m)$ can be obtained by cross-correlating two Poisson distributions

$$\begin{aligned} h_n(x_n|m) &= \sum_{q=-\infty}^{\infty} f_n(x_n+q|m) f_n(q|m=0) \\ &= \alpha_n(m) \cdot \sum_{q=-\infty}^{\infty} \frac{(\mu_n(m)\Delta t)^{q+x_n} (\mu_n(0)\Delta t)^q}{q!(x+q)!} \end{aligned} \tag{4}$$

where $\alpha_n(m) = e^{-(\mu_n(m)+\mu_n(0))^{\Delta t}}$. The above formulae have assumed that any term with a negative factorial is set to zero. Using the *modified Bessel function of the first kind* $I_x(z)$, (4) reduces to

$$h_n(x_n|m) = \alpha_n(m)\left(\frac{\mu_n(m)}{\mu_n(0)}\right)^{x_n/2} \cdot I_x\left(2\sqrt{\mu_n(m)\mu_n(0)\Delta t^2}\right) \quad (5)$$

Now we have the probability distribution of each neuron's activation, $x_n(m)$ given a finger movement m:

$$\Pr(x_n|m) = h_n(x_n|m)$$

To obtain $\Pr(x_1, x_2, \ldots, x_N|m)$, we assume that x_i and x_j are independent as in [14]. Although it is possible that the firing response of neurons i and j may be interdependent and correlated kind of convey the same meaning, we use the independence assumption because the neurons in our study were randomly chosen from different electrode positions and trials. Assuming x_i and x_j are independent, we have

$$\Pr(x_1, x_2, \ldots, x_N|m) = \prod_{n=1}^{N} h_n(x_n|m) \quad (6)$$

and finally based on (2) the finger movement is estimated by

$$\hat{m} = \arg\max_m \prod_{n=1}^{N} h_n(x_n|m) \quad (7)$$

Note that the only variables required to solve (\ref{eq:m2}) are $\mu_n(m)$ and $\mu_n(0)$, which can be estimated from training data sets.

Another choice for modeling the probability distribution of the neural activations is Gaussian. This is motivated by the fact that the Skellam distribution is bell-shaped and has a similar shape as the Gaussian.

The Gaussian-based probability function for each neuron's activation is given by

$$\Pr(x_n|m) = \frac{1}{\sqrt{2\pi}\sigma_n(m)} e^{-\frac{(x_n-\mu_n(m))^2}{2\pi\sigma_n^2(m)}} \quad (8)$$

where $\mu_n(m) = E[x_n(m)]$ and $\sigma_n^2(m) = E\left[\left(x_n(m)-\mu_n(m)\right)^2\right]$. Thus to estimate an unknown finger movement, all that we need are $\mu_n(m)$ and $\sigma_n^2(m)$, which can also be estimated from training data sets.

III. Experimental Results

Fig.1 shows the performance of the proposed decoding method compared to the conventional population vector decoding approach. The performance of the ML decoding was evaluated by randomly choosing N neurons and this random selection was repeated \$40\$ times. Thus, the success rate in Fig.1 is calculated over 2880 movements for each N. As can be seen in Fig.1, the ML decoding with Skellam modelling performed best. With as few as 20-25 randomly selected neurons, it achieved greater than 99% decoding accuracy. The ML decoding performance with Gaussian modeling was comparable to but slightly poorer than Skellam as the number of neurons is greater for a given decoding accuracy. For comparison purposes, the performance of conventional population vector method was also plotted but the decoding accuracy was only 65-70% even with up to 100 neurons.

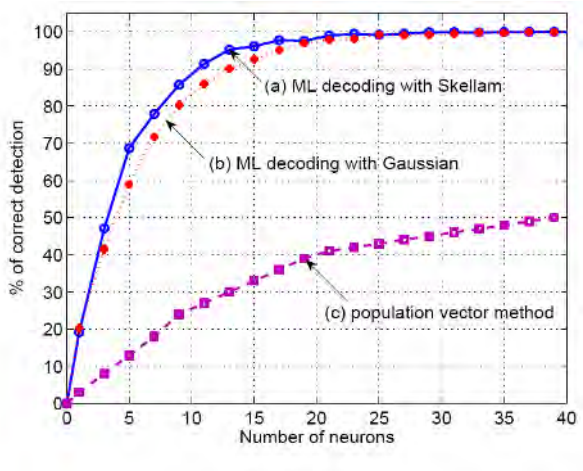


Fig. 1. Decoding accuracy

IV. Conclusions

We have described ML-based neural decoding results for single movements. The decoding was done by the newly introduced Skellam-based likelihood function model. Since the Skellam model considers neural activity both before and after finger movements, it can quantify task-related neural responses better than the conventional Poisson model, which considers the absolute firing rate itself.

Acknowledgements

This research is supported in part by funding from the Defense Advanced Research Project Agency contract "Revolutionizing Prosthetics 2009 program" and in part by the MKE(The Ministry of Knowledge Economy), Korea, under the ITRC(Information Technology Research Center) support program supervised by the IITA(Institute for Information Technology Advancement) IITA-2008-C1090-0803-0006.

References

1. P.Dayan and L.F.Abbott, Theoretical neuroscience: computational and mathematical modeling of neural systems, MIT Press, 2001.
2. F. Rieke, D. Warland, R. R. Steveninck, and W. Bialek, Spikes: exploring the neural code, MIT Press, 1999.
3. A. P. Georgopoulos, A. B. Schwartz, R. E. Kettner, “Neural population coding of movement direction,” Science, vol. 233, pp. 416-419, 1986.
4. B. A. Schwartz, “Cortical neural prosthetics,” Annu. Rev. Neurosci., vol. 27, pp. 487-507, 2004
5. A. Pouget, S. A. Fisher, T. J. Sejnowski, “Egocentric spatial representation in early vision,” J. Cognitive Neurosci., vol. 5, pp. 150-161, 1983.
6. M. D. Serruya, N. G. Hatsopoulos, L. Paninski, M. R. Fellow, and J. P. Donoghue, “Brain-machine interface: instant neural control of a movement signal,” Nature, vol. 416, pp. 141-142, 2002.
7. W. Wu, M. J. Black, Y. Gao, E. Bienestock, M. Serruya, A. Shaikhouni, J. P. Donoghue, “Neural decoding of cursor motion using a Kalman filter,” Advances in Neural Information Processing Systems 14, The MIT Press, 2002.
8. A. Pouget, K. Zhang, S. Denerve, P. E. Latham, “Statistically efficient estimation using population coding,” Neural Computation, vol. 10, pp. 373-410, 1998.
9. J. Wessberg, C. stambaugh, J. Kralik, P. Beck, M. Laubach, J. Chapin, J. Kim, S. Biggs, M. Srinivasan, M. Nicholelis, “Real-time prediction of hand trajectory by ensembles of cortical neurons in primates,” Nature, vol. 408, pp. 361-365, 2000.
10. L. Paninski, M. R. Fellows, N. G. Hatsopoulos, J. P. Donoghue, “Spatiotemporal tuning of motor cortical neurons for hand position and velocity,” J. of Neurophysiol., vol. 91, pp. 515-32, 2004.
11. C. Kemere, K. V. Shenoy, T. H. Meng, “Model-based neural decoding of reaching movements: a maximum likelihood approach,” IEEE Trans. Biomed. Eng., vol. 51, no. 6, pp. 925-932, June 2004.
12. K. V. Shenoy, et al., “Neural prosthetic control signals from plan activity” Neuroreport, vol. 14, no. 4, pp. 591-596, Mar. 2003.
13. M. Serruya, N. Hatsopoulos, M. R. Fellows, L. Paninski, J. Donoghue, “Robustness of neuroprosthetic decoding algorithms,” Biological Cybernetics, vol. 88, no. 3, pp. 219-228, Mar. 2003.
14. M. Jazayeri and J. A. Movshon, “Optimal representation of sensory information by neural populations,” Nature Neurosci., vol. 9, no. 5, pp. 690-696, May 2006.
15. J. G. Skellam, “The frequency distribution of the difference between two Poisson variables belonging to different populations,” J. the Royal Statistical Society: Series A, vol. 109, no. 3, pp. 296, 1946.

Author: Hyun-Chul Shin
Institute: Soongsil Univ
Street: 511 Sangdo-dong,Dongjak-Gu
City: Seoul
Country: Rep. of Korea
Email: shinhc@ssu.ac.kr

Author: M. Schieber
Institute: Univ. of Rochester
Street: 601 Elmwood Ave.
City: New York
Country: U.S.A.
Email: mhs@cvs.rochester.edu

Author: Nitish Thakor
Institute: Johns Hopkins Univ.
Street: 720 Rutland Ave.
City: Baltimore
Country: U.S.A.
Email: nitish@jhu.edu

Maximum Likelihood Method for Finger Motion Recognition from sEMG Signals

Kyoung-Jin Yu[1], Kab-Mun Cha[1] and Hyun-Chool Shin[1]

[1]Soongsil Univ., Seoul, Rep. of Korea

Abstract — **We provide a method could recognize finger flexing motions using a 4-channel surface EMG (electromyogram). Surface EMG is harmless to human body and easy to be acquired. But it could not be reflected activity of specific nerves or muscles as compared to the invasive EMG. Accordingly, it was so difficult to discriminate various motions using low number of electrodes. EMG data were obtained from 4 electrodes placed around the forearm. The motions we chosen are flexing of each 5 single fingers (thumb, index finger, middle finger, ring finger, and little fingers) and 3 hand motions like 'O.K. sign'. One object trained these motions enough and another one didn't. The proposed method uses the short-time entropy using windowing function as the criterion for detect activation moment of muscle. Overall information entropy was a measurement that could represent the pattern of muscle activity. Maximum likelihood estimation was used to determine motion models reconstructed with statistical properties of data. Results showed that this method could be useful for recognizing finger motions. The average accuracy was more than 95 %.**

Keywords — **surface EMG, finger flexing motion, pattern recognition, classification, neural signal processing**

I. Introduction

Surface EMG (sEMG) signal processing is commonly studied to control electronic devices for amputees. Pattern recognition is indispensable to this technology. As compared to the invasive type EMG that is suitable for checking each motor unit action potential (MUAP) on muscle fiber in small area, the non-invasive type sEMG is appropriate for recording muscle activity within a large skin area [1]. The main object of pattern recognition study has been the upper limb or hand, but each finger has also been studied recently. Many nerve tissues and muscles with individual functions are in the forearm; therefore, decoding an intentional motor command which is indirectly detected on the skin's surface is not simple. Many attempts to extract features and recognize patterns this way have been widely studied.

Englehart [2]-[3] used wavelet analysis and PCA analysis to classify two arm motions and two wrist motions. Later, Englehart used the absolute mean value, the zero crossing rate, and the wavelength to classify four arm and wrist motions. Momen [4] used RMS and FCMs to classify arm and wrist motions that had been selected by the subject. Hudgin [5] obtained an ensemble average of EMG signals, and used a neural network (NN) to classify four arm motions. Nishikawa [6] used the Gabor transform and absolute mean value to extract the feature and classify ten wrist and finger motions in real-time learning based on NN. Nagata [7] used absolute sum analysis, canonical component analysis, and minimum Euclidean distance to classify four wrist motions and five finger motions.

In this paper, we propose a new method to recognize the motion pattern of unknown sEMG signals. We obtained the sEMG signal when five fingers were flexed. To emphasize the uncertainty of bio-signal which likes the random variable, we figure out the information entropy by use of the probability of presence in the specified absolute sEMG range. With the collected entropies for training, we calculate approximate probability density functions using Gaussian distribution to improve the observed histogram of entropies.. Assuming statistical independence in each channel, we can find the likelihood functions of the each flexing motion then estimate motion which was really performed. We demonstrated a significant recognition accuracy by cross-validation.

II. sEMG recording

A signal acquisition device (Laxtha Inc. Poly-G-A), bipolar Ag-AgCl electrodes (Tyco Healthcare Ltd. Kendall ARBO H124SG), and snap electrodes (Laxtha Inc. SECS-4) were used. The EMG signal was observed at the sampling frequency of 256 Hz. This was 60 Hz and 120 Hz bandstop-filtered to reduce power line noise.

Two able-bodied subjects with no upper limb deficiencies participated in performing finger motions for this study. Subject A (a 23 year-old male) mastered the finger motions and learned about the acquisition system, but subject B (a 24 year-old male) practiced just fifteen minutes. Subjects were ordered to maintain normal speed and strength. However, they were not told specifically how to flex their fingers.

The sEMG signal was acquired with four channels on the left forearm (around the wrist) for three seconds. During the first 1.5 seconds, the subjects did not perform any motion — termed 'relaxation' — and waited for an acoustic alarm.

Chwee Teck Lim, James C.H. Goh (Eds.): ICBME 2008, Proceedings 23, pp. 452–455, 2009
www.springerlink.com

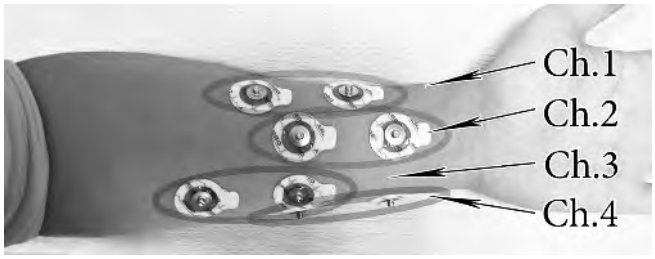


Fig. 1 Locating four channel electrodes for acquiring sEMG on the forearm

After 1.5 seconds, subject heard the alarm and then flexed a finger immediately. After 3 seconds, the sEMG signal recoding procedure ended. To avoid muscle fatigue and cramping, the subjects took a long rest between recording procedures.

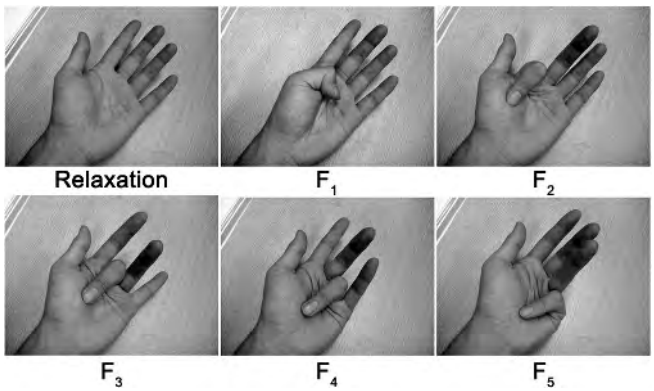


Fig. 2 Relaxation and each five-finger flexing motion (F_1—F_5)

III. Proposed Method

A. Preprocessing of sEMG signal

Let c and k be channel and motion indexes respectively. Here we consider 4 channels and 5 finger flexing motions. Then during F_k movement, the recorded raw sEMG from c^{th} channel can be denoted by $r_c^k[n]$ where n is a discrete time index.

Since the sEMG signal has both positive and negative levels, we take an absolute of $r_c^k[n]$

$$x_c^k[n] = \left| r_c^k[n] \right| , \tag{1}$$

i.e., Fig 3 shows the $r_2^3[n]$ and $x_2^3[n]$.

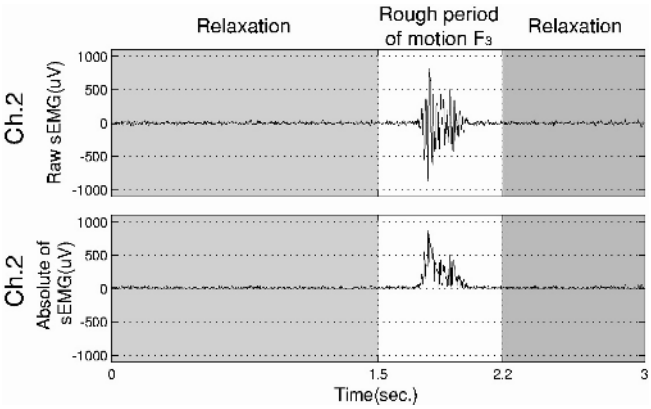


Fig. 3 Examples of raw sEMG signal and absolute of sEMG signal corresponding 2nd and 3rd channel during F_3 motion. The recorded samples that treated as signals are limited in 1.5~2.2 sec (brightened area).

B. Entropy based sEMG model

Entropy (information entropy, H) was used to present the characteristics of each EMG signal of finger flexing motions. Entropy is a sound measure that is able to reveal the uncertainty or variance of random variability as follows:

$$H(X) = -\sum_{m=1}^{M} p(x_m) \log_2 p(x_m) . \tag{2}$$

Here X represents discrete random variable, $p(x_m)$ means $\Pr(X = x_m)$ with $0 \le p(x_m) \le 1$ and $\sum_{m=1}^{M} p(x_m) = 1$.

The probability $p_c^k(m)$ is calculated by

$$p_c^k(m) \equiv \frac{\text{number of samples} \in I_m}{\text{number of total samples}} ,$$
$$I_m = \left\{ x_c^k[\cdot] \middle| \frac{x_{\max}(m-1)}{M} \le x_c^k[\cdot] < \frac{x_{\max} m}{M} \right\} , \tag{3}$$
$$m = 1, \ldots, M$$

where M determines the number of step. The parameter $x_{\max}$ is the maximum value that the signal acquisition device can represent; it is adjusted as follows: $x_{\max} = 1,050 \mu\text{V}$. However, this value can be modified to correspond to the subject's sEMG characteristics.

The information entropy of the sEMG signal $x_c^k[n]$ is

$$H_c^k = H\left(x_c^k[n]\right) = -\sum_{m=1}^{M} p_c^k(m) \log_2 p_c^k(m) . \tag{4}$$

Fig. 4 shows the histograms of H_c^k from 100 independent trials.

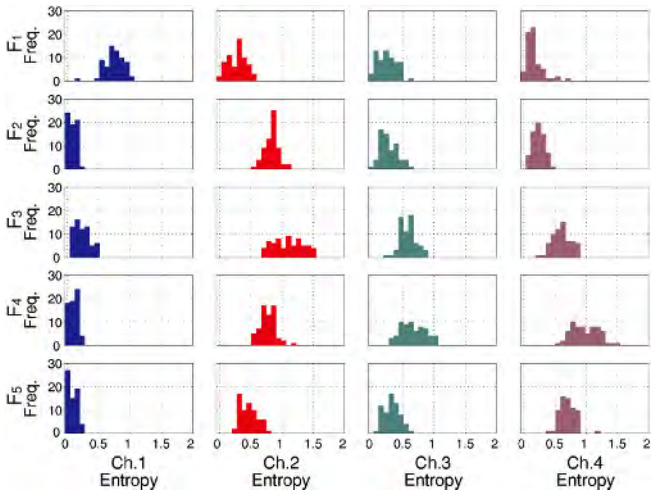


Fig. 4 Histograms of entropy of F_1 — F_5

With the training entropy data ${}^{l}H_c^k$ where $l = 1,..,L$, continuous function of t_c^k be:

$$f_{T_c^k}\left(t_c^k\right) = \frac{1}{\sqrt{2\pi\sigma^2}} \exp\left[-\frac{1}{2\sigma^2}\left(t_c^k - \mu\right)^2\right], \quad \mu = \frac{1}{L}\sum_{l=1}^{L} {}^{l}H_c^k, \ \sigma^2 = \frac{1}{L}\sum_{l=1}^{L}\left(\mu - {}^{l}H_c^k\right)^2. \tag{5}$$

Here $f_{T_c^k}\left(t_c^k\right)$ is the approximate probability density function derived from the mean and variance of ${}^{l}H_c^k$. This is shown in Fig. 5.

The joint density function of t_c^k (entropy) on each channel when motion k is performed is

$$f_{T_c^k}\left(t_c^k \middle| \omega_k\right) \tag{6}$$

where ω_k is class k. Equation (6) also could be a likelihood function of multivariate probability density function. Furthermore, assuming the statistical independence in each channel's sEMG signal, the likelihood function $L(k)$ as follows:

$$L(k) = f_{T^k}\left(t^k \middle| \omega_k\right) = \prod_{c=1}^{4} f_{T_c^k}\left(t_c^k \middle| \omega_k\right). \tag{7}$$

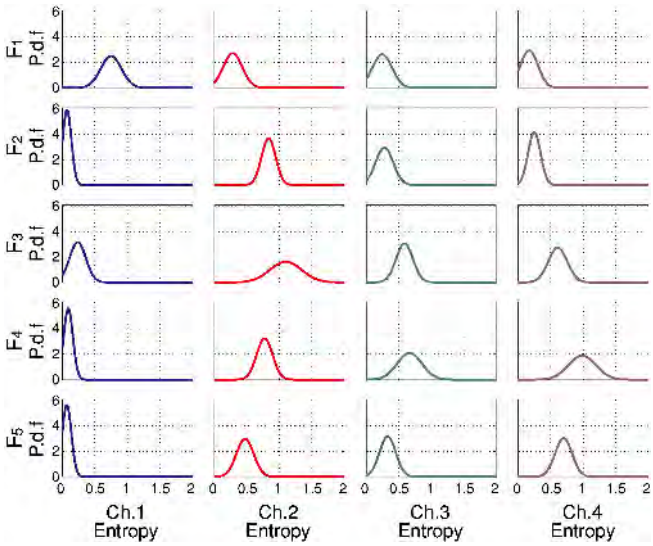


Fig. 5 Approximate probability density functions of F_1 — F_5

We find $\hat{k}$ which maximizes the logarithm for $L(k)$ as

$$\hat{k} = \arg\max_{k} \sum_{c=1}^{4} f_{T_c^k}\left(t_c^k \middle| \omega_k\right). \tag{8}$$

$\hat{k}$ means the estimated motion. Fig. 6 shows the likelihoods ($L(1)$ — $L(5)$) corresponding each motion.

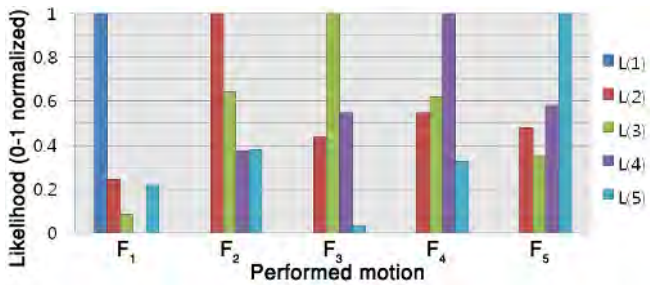


Fig. 6 Example of finding the maximum likelihood

IV. Experiments

A cross-validation was used to estimate the recognition rate. Alternating the ratio of the number of test data (J) and the number of total data, the range was about 0.02–0.95. Each experiment was done 100 times. All test data were excluded from the training data. Fig. 7 shows recognition accuracy when changing the ratio of the number of test data to the number of total data.

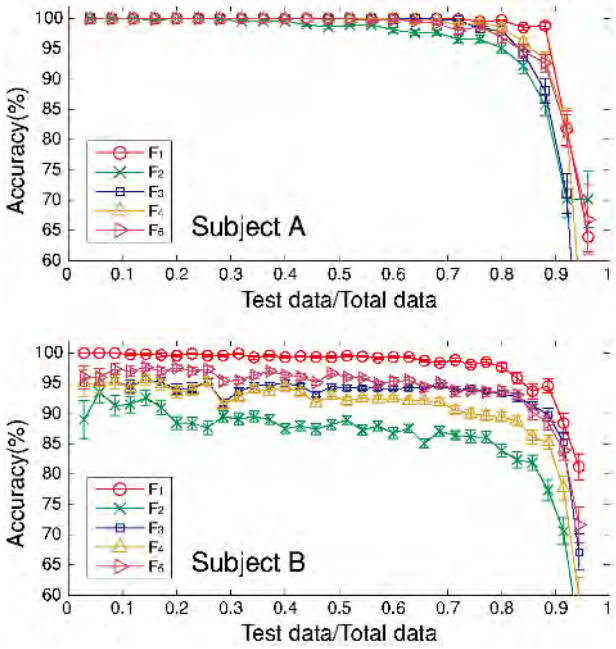


Fig. 7 Average recognition accuracy with gradual change of the ratio of training data to total data. (top: Subject A, bottom: Subject B)

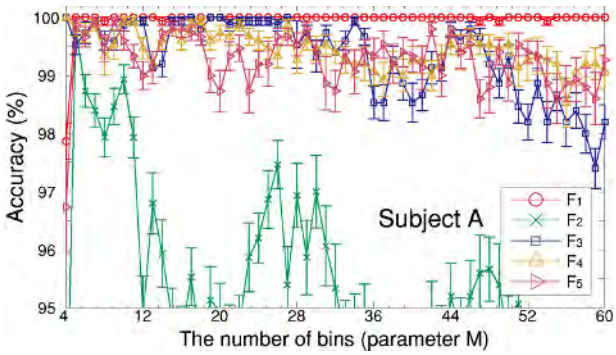


Fig. 8 Average recognition accuracy with gradual change of the number of bins in the range 4—60.(Subject A with total of 25 data)

The parameter M in equation (3) changes the entropy value H_c^k and also the accuracy of the proposed method. In the validation of data from subjects, the ratio of the number of test data to the number of total data was fixed at 0.4. As shown in Fig. 8, M was suitable in the 5–7 range.

V. Conclusions

We proposed a new method to classify finger flexing motions based on entropy and the maximum likelihood estimation method. The average recognition accuracy of subject A was 99.80%, and subject B's was 93.75%.

Acknowledgements

This research was supported by the MKE(The Ministry of Knowledge Economy), Korea, under the ITRC (Information Technology Research Center) support program supervised by the IITA(Institute for Information Technology Advancement) IITA-2008-C1090-0803-0006

References

1. Leif Sornmo, and Pablo Laguna (2005), Bioelectrical signal processing in cardiac and neurological applications. Elsevier academic press, Burlington.
2. Kevin Englehart, Bernard Hudgins, and Philip A. Parker (2001) A Wavelet-Based Continuous Classification for Multifucntion Myoelectric Control, IEEE Trans. on Biomedical Engineering, Vol. 48, No 3, March 2001.
3. Kevin Englehart, and Bernard Hudgins (2003), A robust, real-time control scheme for multifunction myoelectric control, IEEE Trans. on Biomedical engineering, Vol. 50, No. 7, July 2003
4. B. Hudgins, P. Parker, and R. Scott (1993), A new strategy for multifunction myoelectric control, IEEE Trans. on Biomedical Engineering., Vol. 40, No 1, pp. 82-94, Jan. 1993
5. Kaveh Momen, Sridhar Krishnan, and Tom Chau (2007), Real-Time Classification of Forearm Electromyographic signals Corresponding to User-Selected Intentional Movements for Multifunction Prosthesis Control, IEEE Trans. on Neural Systems and Rehabilitation Engineering, Vol. 15, No. 4, Dec. 2007
6. Daisuke Nishikawa, Wenwei Yu, Hiroshi yokoi, and Yukinori Kakazu,(1999), EMG Prosthetic Hand Controller Discriminating Ten Motions using Real-time Learning Method, Proc. vol.3, IEEE/RSJ Intl. Conf. on Intelligent Robots and Systems, Kyongju, South Korea, Oct. 1999, pp. 1592-1597
7. Kentaro Nagata, Keiichi Ando, Kazushige Magatani, and Masafumi Yamada (2007), Development of the hand motion recognition system based on surface EMG using suitable measurement channels for pattern recognition, Proc., the 29th Annual Intl. Conf. of the IEEE EMBS, Cité Internationale, Lyon, France, August 23-26, 2007

Author: Kyoung-Jin Yu
Institute: Soongsil Univ.
Street: 511 Sangdo-dong,Dongjak-Gu
City: Seoul
Country: Rep. of Korea
Email: fabric@gmail.com

Author: Kab-Mun Cha
Institute: Soongsil Univ.
Street: 511 Sangdo-dong,Dongjak-Gu
City: Seoul
Country: Rep. of Korea
Email: indie486@naver.com

Author: Hyun-Chool Shin
Institute: Soongsil Univ.
Street: 511 Sangdo-dong,Dongjak-Gu
City: Seoul
Country: Rep. of Korea
Email: shinhc@ssu.ac.kr

Cardiorespiratory Coordination in Rats is Influenced by Autonomic Blockade

M.M. Kabir[1], M.I. Beig[2], E. Nalivaiko[2], D. Abbott[1] and M. Baumert[1]

[1]School of Electrical and Electronic Engineering, University of Adelaide, Adelaide, SA 5005, Australia
[2]School of Biomedical Sciences, University of Newcastle, Callaghan, NSW 2308, Australia

Abstract — **Autonomic disturbance creates changes in the modulation of heart rate. In this study we analyzed the influence of sympathetic and vagal blockade on the interaction between cardiac and respiratory rhythms. In seven anaesthetized rats, electrocardiogram (ECG), and respiratory rate were recorded continuously before and after autonomic blockade with either methyl-scopolamine or atenolol. For the assessment of cardiorespiratory coordination, we analyzed the phase locking between heart rate, computed from the R-R intervals of body surface ECG, and respiratory rate, computed from impedance changes, using Hilbert transform. The procedure was carried out for different m:n coordination ratios where, m, is the number of heart beats and n, is the number of respiratory cycles. The changes in percentage of synchronization and duration of synchronized epochs before and after injection were assessed with one-way ANOVA. Sympathetic blockade with atenolol caused an increase (baseline: 0.49 ± 0.03s vs. blockade: 0.54 ± 0.06s) and vagal blockade with methyl-scopolamine caused a decrease (baseline: 0.49 ± 0.03s vs. blockade: 0.45 ± 0.08s) in the duration of synchronized epochs. Neither the overall percentage of synchronized epochs, (baseline: 10.76 ± 3.5% vs. blockade 9.44 ± 4.3%), nor the average locking ratio, 3:1, was significantly affected by autonomic blockade. In conclusion, the phase-locking between heart rhythm and respiration is modulated by both vagal and sympathetic efferences, in the opposite directions.**

Keywords — **sympathetic nervous system, vagal blockade, respiration, heart rate**

I. Introduction

The interaction between cardiac and respiratory oscillations can be studied through synchronization of these oscillators. Several studies have been undertaken on cardiorespiratory synchronization not only for subjects at rest [1,2,3], but also for subjects under the influence of anesthesia and drugs [4,5]. Synchronization is proven to be an intrinsic cardio-respiratory phenomenon and not just an artifact [6]. However, little is known about the physiological basis and the underlying mechanism responsible for the cardiorespiratory interaction.

The parasympathetic (vagal) system is known to have a great influence on heart rate [5] and heart rate variability [7], but its effect on cardiorespiratory coordination is yet to be revealed.

In this study we investigated the effect of sympathetic and vagal blockade on cardiorespiratory coordination in rats.

II. Methods

A. Animal preparation

Seven male Wistar Hooded rats, weighing 250-300 g (obtained from Flinders University, Bedford Park, South Australia), were used for this study. Experiments were conducted in accordance with the European Community Council Directive of 24 November 1986 (86/609/EEC), and were approved by the Flinders University Animal Welfare Committee. During the experiment, ECG, respiratory rate and blood pressure were recorded continuously before and after autonomic blockade with either methylscopolamine or atenolol. The signals were acquired using MacLab interface and Chart software (ADInstruments, Sydney, Australia).

B. Data analysis

Pre-processing: Custom made computer software developed under MATLAB® was used to extract the R-peaks from the recorded ECG signal using parabolic fitting. The RR intervals obtained from the time-points of the R-peaks were scanned for artifacts and, if necessary, manually edited. In order to obtain baseline values, we selected a 40 minute interval, starting 10 minutes prior to the blockade. For the analysis of synchronization during blockade, we selected 30 minute epochs each after vagal blockade with methyl-scopolamine and sympathetic nervous system blockade with atenolol, starting 5 minutes after the injection.

Respiration analysis: Respiratory signals consist of noisy, linear, nonlinear and non-stationary components. To extract the essential respiratory rhythm related components from the signal, we used empirical mode decomposition (EMD). EMD separates data into non-overlapping time-scale components. The multi-component signal is decomposed into a series of intrinsic mode functions (IMF) where each IMF represents a simple oscillatory mode embedded in the data [8]. The IMF that best matched the respiratory rhythm was selected for further analysis.

Chwee Teck Lim, James C.H. Goh (Eds.): ICBME 2008, Proceedings 23, pp. 456–459, 2009
www.springerlink.com

In order to determine the maximum and minimum points of each respiratory cycle, known as maxima and minima respectively, we calculated the derivative of the respiratory signal and considered those points that were equal to or very close to zero (window length: 0 - 0.2 mV). The average of the time series obtained from minima-to-minima intervals was used to calculate the average respiratory period.

Synchronization analysis: Synchronization between two periodic oscillators can be defined as the appearance of some relationship in the form of locking of their phases or adjustment of rhythms. We used Hilbert transform to calculate the phases of the cardiac and respiratory signals. If we denote the phase of heartbeat as Φ_c and respiratory signal as Φ_r and considering that the cardiovascular system completes m heartbeats in n respiratory cycles, then the condition for phase locking can be given as

$$\left|m\Phi_c - n\Phi_r\right| \le const \quad (1)$$

In other words, if the phase difference between the two oscillators was within a certain threshold value and remained stable for n respiratory cycles, the oscillators were considered synchronized. The cardiorespiratory synchrogram, CRS, provide a visual tool to detect synchronization. If t_k is the time of the kth R-peak, then the normalized relative phase of heart beat is

$$\Psi_n = \frac{1}{2\pi}\left(\phi(t_k) \bmod 2\pi m\right) \quad (2)$$

CRS is generated by plotting Ψ_n against t_k which, in case of m:n synchronization, results in m horizontal lines. In order to determine the values of m and n, we selected one value of n at a time and looked for coordinations at different values of m. The study was carried for the following m:n coordinations: n = 1: m = 2,…,7 and n = 2: m = 5,7,9,11,13. We used a threshold value of 0.035 for the phase difference as it was suggested by Cysarz et al. [9].

Statistical analysis: Statistical analysis was performed with GraphPad Prism® version 5.0. The differences before and after autonomic blockade were analyzed by one-way analysis of variance (ANOVA) for multiple measurements and Wilcoxon test for paired comparisons. Data are expressed as the mean±SD. For the analysis, $p < 0.05$ was considered statistically significant.

III. Results

A. Effect of autonomic blockade on heart rate

Methyl-scopolamine, which was used to block the parasympathetic nervous system, caused an increase in heart rate, while atenolol, used to block the sympathetic nervous system, caused a decrease in heart rate (Fig. 1). The differences were statistically significant, $p < 0.01$, and are summarized in Tab.1.

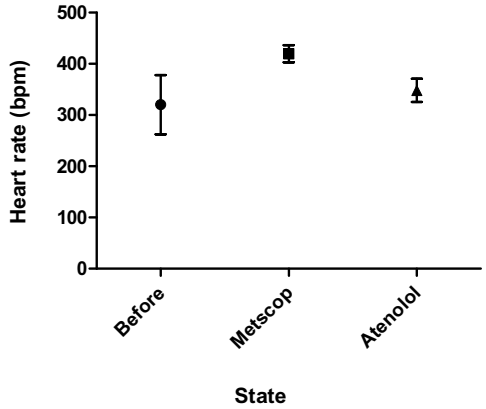


Fig. 1 Mean±SD of heart rate (beats per minute) obtained from seven rats prior and after injection of methyl-scopolamine (metscop) and atenolol

B. Effect of autonomic blockade on respiratory frequency

There was no significant effect (Fig. 2) of either atenolol or methyl-scopolamine on the respiratory frequency.

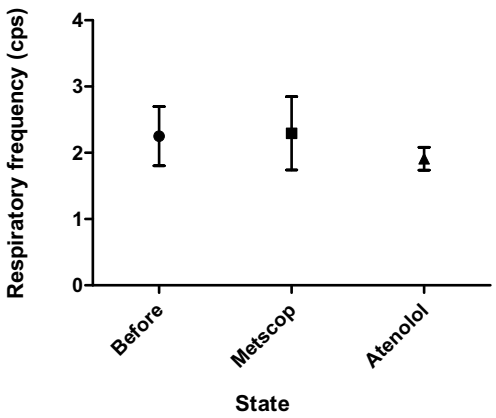


Fig. 2 Mean±SD of respiratory frequency (cycles per second) obtained from seven rats prior and after injection of methyl-scopolamine (metscop) and atenolol

C. Effect of autonomic blockade on average duration of synchronized epochs

The average duration of synchronized epochs was longer (Fig. 3) after injecting with atenolol (baseline: 0.49 ± 0.03s

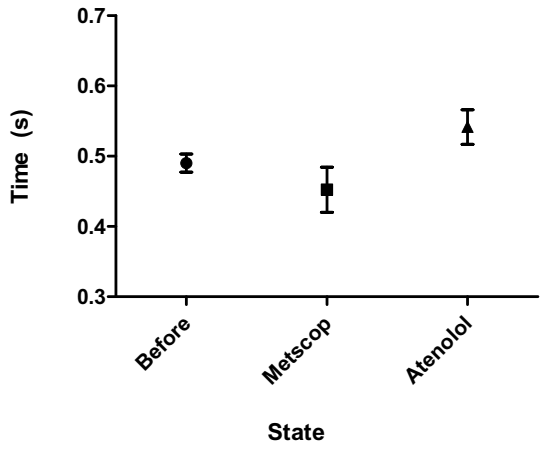


Fig. 3 Mean±SD of duration of synchronized epochs obtained from seven rats prior and after injection of methyl-scopolamine (metscop) and atenolol.

vs blockade: 0.54 ± 0.06s). On the other hand, injection of methylscopolamine caused a decrease in the average duration of synchronized epochs (baseline: 0.49 ± 0.03s vs blockade: 0.45 ± 0.08s). These effects were statistically significant.

D. Effect of autonomic blockade on percentage of synchronization

Vagal blockade caused a decrease while sympathetic blockade caused an increase in percentage of synchronization in six rats. In one rat, the percentage of synchronization was higher after vagal blockade. The results were not statistically significant. However, percentage of synchronization followed a similar trend (Fig. 4) after vagal blockade showing significant results in six rats.

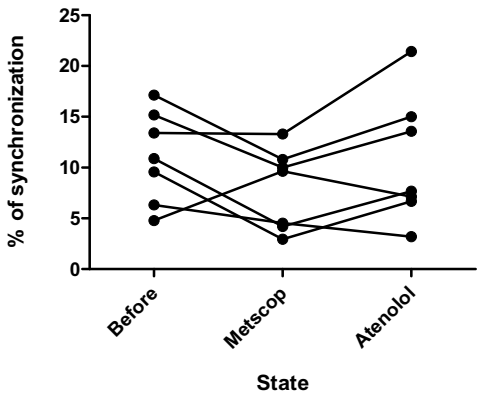


Fig. 4 Percentage of synchronization in seven rats prior and after injection of methyl-scopolamine (metscop) and atenolol.

Table 1 Total recording time (TRT), heart rate (HR), RR interval (RRint), respiratory frequency (RespFr), percentage of synchronization (PofSync) and duration of synchronized epochs (SyncDur) in seven rats represented as mean±SD as well as p-values of Wilcoxon test for paired comparisons

	Before	Metscop	Atenolol	p
TRT (min)	40.2 ± 4.5	30.5 ± 5.1	29.7 ± 4.3	-
HR (bpm)	320.1 ± 27.6	419.5 ± 16.9	347.9 ± 22.7	0.01
RRint (s)	0.18 ± 0.01	0.14 ± 0.01	0.17 ± 0.01	0.01
RespFr (cps)	2.25 ± 0.45	2.29 ± 0.56	1.91 ± 0.17	0.69
Pof Sync	11.04 ± 4.5	7.78 ± 4.1	10.81 ± 6.1	0.08
SyncDur (s)	0.49 ± 0.03	0.45 ± 0.08	0.54 ± 0.06	0.03

E. Effect of autonomic blockade on the average locking ratio

The cardiorespiratory coordination occurred for the phase-locking ratios of 2:1, 3:1, 4:1, 5:2 and 7:2. The 3:1 phase-locked state was frequently observed and was not significantly affected by autonomic blockade.

IV. Discussions

This is the first study to investigate the effect of autonomic blockade on cardiorespiratory coordination. Both sympathetic as well as vagal efferents affect cardiorespiratory coordination with opposite directions.

Our results show that autonomic blockade produces changes in heart rate. These findings are in accordance with the results reported earlier in the literature [5,7,10]. Contrary, no changes in the respiratory rate were observed. Consequently, heart rate rather than respiratory rate seems to be the predominant factor causing the phenomenon of phase locking between heart rate and respiration.

The reduction of cardiorespiratory coupling after vagal blockade is in line with the observation that vagal outflow to the sinus node of the heart is the predominant driver of respiratory sinus arrhythmia.

The increase of cardiorespiratory coordination after sympathetic blockade was unexpected. Possibly, sympathetic effects on heart rate disturb the respiratory sinus rhythm and a sympathetic blockade consequently increases the amount of observed phase locking between heart rate and respiration. Although the average duration of synchronized epochs and percentage of synchronization was found to increase with sympathetic blockade and decrease with vagal blockade, the change in percentage of synchronization did not

reach statistical significance. This is because one of the rats showed an opposite behavior compared to others, (see Fig. 4) whose results would otherwise considered being statistically significant.

V. Conclusions

Vagal and sympathetic blockade cause a respective decrease and increase in the duration of synchronized epochs and percentage of synchronization between heart rate and respiration in rats.

References

1. Schafer C, Rosenblum MG, Kurths J, Abel HH (1998) Heartbeat synchronized with ventilation. Nature 392:239-240
2. Schafer C, Rosenblum MG, Abel HH, Kurths J (1999) Synchronization in the human cardiorespiratory system. Physical Review E 60(1):857-870
3. Lotric MB, Stefanovska A (2000) Synchronization and modulation in the human cardiorespiratory system. Physica A 283(1):451-461
4. Stefanovska A, Haken H, McClintock PVE et al. (2000) Reversible transitions between synchronization states of the cardiorespiratory system. Physical Review Letters 85(22):4831-4834
5. Marano G, Grigioni M, Tiburzi F et al. (1996) Effects of isoflurane on cardiovascular system and sympathovagal balance in New Zealand white rabbits. J Cardiovascular Pharmacology 28(4):513-518
6. Toledo E, Akselrod S, Pinhas I, Aravot D (2002) Does synchronization reflect a true interaction in the cardiorespiratory system. Med Eng & Physics 24(1):45-52
7. Baumert M, Nalivaiko E, Abbott D (2007) Effects of vagal blockade on the complexity of heart rate variability in rats, IFMBE Proc. vol. 16, 11th Mediterranean Conference on Med. & Biomed. Eng. & Computing, Ljubljana, Slovenia, 2007, pp 26-29
8. Wu MC, Hu CK (2006) Empirical mode decomposition and synchrogram approach to cardiorespiratory synchronization. Physical Review E 73(051917):1-11
9. Cysarz D, Bettermann H, Lange S et al. (2004) A quantitative comparison of different methods to detect cardiorespiratory coordination during night-time sleep. Biomed. Eng. Online 3(1) DOI 10.1186/1475-925X-3-44
10. Beckers F, Verheyden B, Ramaekers D et al. (2006) Effects of autonomic blockade on non-linear cardiovascular variability indices in rats. Clinical and Experimental Pharmacology and Physiology 33:431-439

Author: Muammar Muhammad Kabir
Institute: School of Electrical and Electronic Engineering, The University of Adelaide
Street: North Terrace
City: Adelaide, SA 5005
Country: Australia
Email: mkabir@eleceng.adelaide.edu.au

Influence of White Matter Anisotropy on the Effects of Transcranial Direct Current Stimulation: A Finite Element Study

W.H. Lee[1], H.S. Seo[2], S.H. Kim[2], M.H. Cho[2], S.Y. Lee[2] and T.-S. Kim[2]

[1]Department of Biomedical Engineering, University of Minnesota, Minneapolis, MN, USA
[2]Department of Biomedical Engineering, Kyung Hee University, Yongin, Republic of Korea

Abstract — **Although the use of transcranial direct current stimulation (tDCS), a noninvasive brain stimulation technique, has become popular in cognitive neuroscience research and clinical applications, there still exists limited knowledge on how to optimally use tDCS for the brain stimulation. To understand the underlying principles and effects of tDCS, finite element analysis (FEA) has been successfully applied due to its truly volumetric analysis and capability of incorporating the anisotropic tissue property. However, there are still many factors to be considered in stimulation: the influence of the white matter (WM) anisotropy is one of them which has not been considered in tDCS. In this study, we have examined the influence of the WM anisotropic conductivities on tDCS via high-resolution FE head models of the whole head. The effects of the WM anisotropy has been assessed by comparing the current density maps computed from the anisotropic FE model against those of the isotropic model using the similarity measures. The results show that there are significant differences caused by the tissue anisotropy, indicating that the anisotropic electrical conductivity is one of the critical factors to be considered during tDCS for accurate and effective stimulation of the brain.**

Keywords — **Transcranial direct current stimulation, Finite element analysis, White matter anisotropic conductivity**

I. Introduction

Transcranial direct current stimulation (tDCS) is a noninvasive brain stimulation technique that applies weak current electrical currents (normally 1-2 mA) to the brain using surface electrodes placed on the scalp to modulate membrane polarization and firing rates of cortical neurons. tDCS does not affect resting nerve neurons to fire, but the spontaneous firing rate of neurons is rather modulated by acting at the level of the membrane potentials [1]. Nitsche and Paulus [2] have reported that tDCS of the human motor cortex results in cortical excitability changes due to the tDCS polarity: the excitability of the underlying neurons increases when anodal tDCS is induced, whereas cathodal stimulation decreases it. The electrical stimulation of the brain by means of tDCS has been utilized as a promising therapeutic tool for the treatment of depression, stroke, Parkinson's disease, and epilepsy [1], [3].

Although the use of tDCS has become popular in cognitive neuroscience research and clinical applications, there still exists limited knowledge on how to optimally utilize tDCS for the brain stimulation. To understand the underlying principles and effects of tDCS, finite element analysis (FEA) has been successfully applied due to its truly volumetric analysis and capability of incorporating anisotropic electrical properties. Previous studies have used a simplified FE model consisting of three concentric spheres [4] and rather realistic head models [5], [6]. However, there still many factors to be considered in the brain stimulation: the influence of the white matter (WM) anisotropy is one of them which has not been considered fully in tDCS. To our best knowledge, only a couple of studies have reported the influence of its effects on tDCS in 2-D [7] and 3-D [8].

In this work, we have examined the influence of the WM anisotropic conductivities on tDCS via our high-resolution FE head models of the whole head (referred to as *wMeshes*) suitable for modeling the WM anisotropic property [9]. The effects of the WM anisotropic electrical conductivity tensors have been assessed by comparing current density maps computed from the anisotropic wMesh head model against those of the isotropic model. The results describe that there are significant differences caused by the tissue anisotropy, indicating that the WM anisotropic conductivity is one of the critical factors to be considered during tDCS for more precise and accurate simulation of the brain.

II. Methods

A. High-resolution FE head modeling

To construct a high-resolution FE model of the entire head, we utilized our adaptive FE meshing technique that generates the DT-MRI WM anisotropy-adaptive FE meshes [9]. The steps of our wMesh generation are briefly described as follows: i) To generate MRI content-adaptive FE meshes (cMesh), adaptive node sampling is done from a set of T_1-weighted MRIs as described in [10]. ii) A map of fractional anisotropy (FA) as an anisotropy feature map is computed using the eigenvalues of the diffusion tensor (DT)

Chwee Teck Lim, James C.H. Goh (Eds.): ICBME 2008, Proceedings 23, pp. 460–464, 2009
www.springerlink.com

matrix derived from the measured DT-MRIs. iii) WM anisotropy-adaptive FE nodes in the WM tissues are extracted based on the spatial anisotropic density of the WM FA maps. iv) wMesh nodes are created by combining the cMesh nodes and WM nodes. v) wMeshes are generated using the Delaunay tessellation algorithm. The detailed methodology of generating wMesh is described in [9]. The wMesh models of the whole head is made up with 160,231 nodes and 1,009,447 tetrahedral elements with 1 mm^3 voxel resolution, consisting of five sub-regions including WM, gray matter, CSF, skull, and scalp.

B. Modeling tissue anisotropy conductivity

In the generation of the isotropic FE model, we used the isotropic electrical conductivity values according to each tissue type as follows: WM=0.14 S/m, gray matter=0.33, CSF=1.79, skull=0.0132, and scalp=0.33 [11], [12].

To generate the anisotropic wMesh model, we computed the anisotropic conductivity tensors in the WM regions with the anisotropy ratio of 1:10 as in [9]: We used the eigenvectors of the DTs from DT-MRIs [13] and eigenvalues from the volume constraint algorithm [11]. We incorporated the following anisotropic conductivities into the WM elements: WM=0.65 S/m (longitudinal) and 0.065 (transverse) based on the assumption that the conductivity value of the principal eigenvector is ten times larger than the values of the other two eigenvectors.

C. tDCS simulation

For the tDCS simulation, we used the three-electrode configuration [4] over the scalp to compute forward solutions. An anodal electrode was placed over the premotor cortex near Cz according to the electrode placement of the international 10/20 EEG system. We also set two cathodal electrodes over the mastoids bilaterally. The scalp electrodes were modeled as constant current electrodes where electrical current of +2 mA was injected through the anodal electrode and -1 mA for two cathodal electrodes. Then, the quasi-static Laplace equation was solved due to no internal sources as follows [3]:

$$\nabla \cdot (\sigma \nabla \Phi) = 0 \tag{1}$$

where Φ and σ represent the electrical potential and the electrical conductivity of the tissues respectively. The current density within the head, $\sigma\mathbf{E}$, was then calculated from the computed conductivity tensors and electrical fields, $\mathbf{E}$.

D. Numerical differences of the current densities: isotropic vs. anisotropic

To evaluate numerical differences of the current density maps from the isotropic and anisotropic head models, we used two similarity measures: linear correlation coefficient (CC) and residual errors (RE) [10]. We also examined the directions of current flows to visualize the effects of the WM anisotropic conductivities.

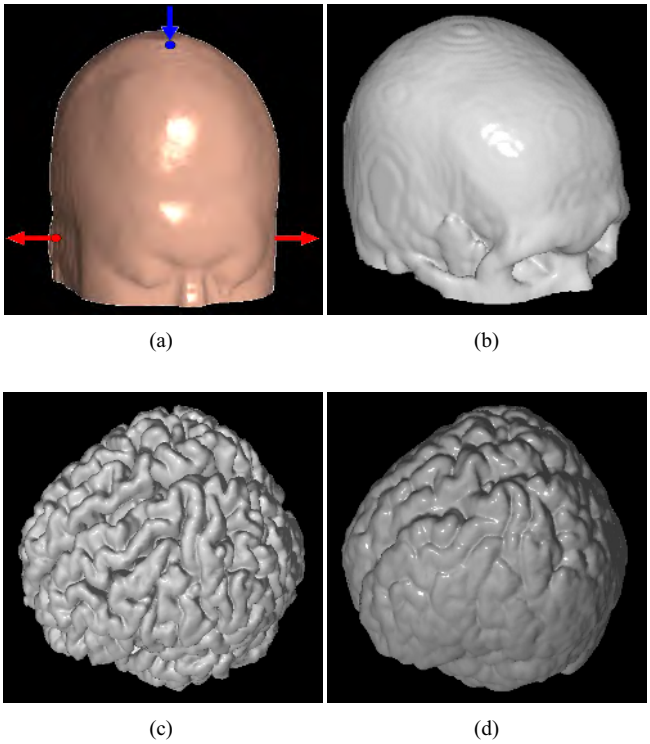
III. Results

Fig. 1 shows the results of 3-D surface rendered volumes according to each tissue type of the head segmented from the MRI data set. Fig. 1 (a) displays 3-D surface rendered scalp including the electrode montage for the computation of the current density. As can be seen in Fig. 1 (a), the blue and red arrows represent the anode and cathodes respectively. The 3-D outer skull, white matter, and gray matter volumes extracted are also visualized in Figs. 1 (b)-(d) respectively.

Fig. 2 displays a set of exemplary results of a transaxial DT-MRI from which anisotropic conductivity tensors are derived. A transaxial T_2-weighed MRI and corresponding FA map derived from the DT data are shown in Figs. 2 (a) and (b) respectively. As shown in Fig. 2 (b), the strong anisotropy is clearly observed in the corpus callosum and the pyramidal tracts. Fig. 2 (c) shows the color-coded FA. A region of interest (ROI), enclosing 30 x 30 pixels, is superimposed with a red box in Fig. 2 (c). In Fig. 2 (d), DT ellipsoids of the WM tissue overlaid on its corresponding T_1-weighed MRI are visualized. The directions of the principal tensor eigenvectors are shown according to the RGB sphere (i.e., red: mediolateral, green: anteroposterior, and blue: superoinferior direction).

Fig. 3 shows a set of results of the 3-D wMesh model covering the whole head through the five segmented subregions. The axial, sagittal, and coronal cutplanes of the wMesh head model are displayed in Figs. 3 (a)-(c) respectively. The anisotropy-adaptive meshes are clearly visible in the WM compartments. It is also seen that there are dense and adaptive meshes in the WM regions in accordance with the FA information of the WM tissues.

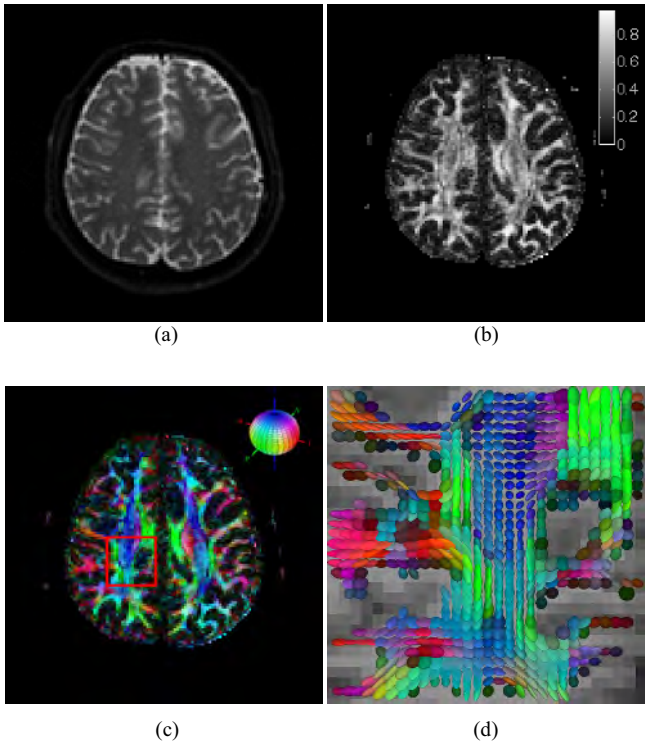
Fig. 4 shows an exemplary of the current density maps computed from the isotropic and anisotropic wMesh models due to the given three-electrode configuration shown in Fig. 1 (a). Figs. 4 (a) and (b) display the current density distributions in the coronal view from the isotropic and anisotropic wMesh models respectively. The resultant current densities were normalized by the maximum value of the current density for better visualization. We also set the color coding of



(a) (b)

(c) (d)

Fig. 1 Visualization of the 3-D rendered volumes: (a) scalp with electrode montages (arrows represent anode with 2 mA in blue and cathodes with -1 mA in red respectively), (b) outer skull, (c) white matter, and (d) gray matter



(a) (b)

(c) (d)

Fig. 2 (a) A transaxial T_2-weighed MR slice, (b) corresponding FA map derived from the DTs, (c) color-coded FA map according to the red-green-blue sphere (red: mediolateral, green: anteroposterior, and blue: superoinferior direction), and (d) color-coded white matter ellipsoids overlaid on the ROI T_1-weigted MRI.

the current density distributions from 0 to 0.01 A/m^2. As observed in Fig. 4, much of the current was shunted through the skull. We found that the largest current density magnitude near the electrodes.

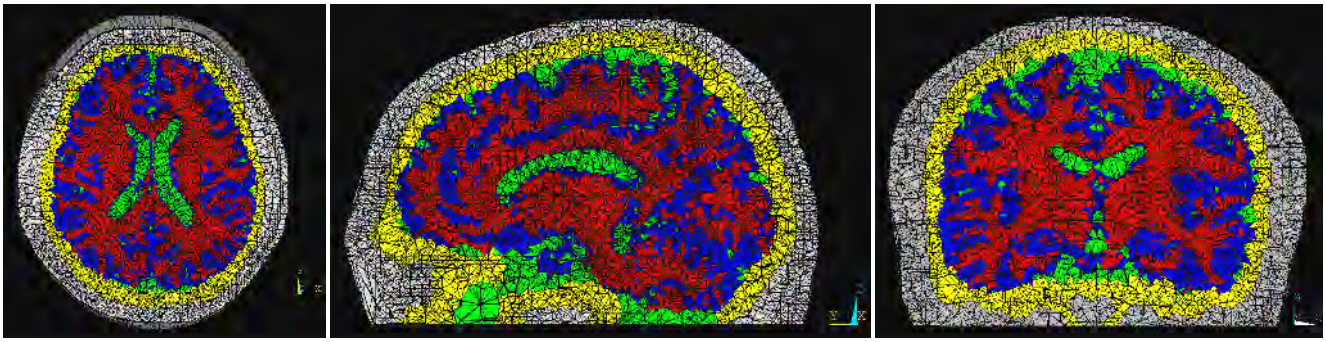
The effects of the skull and CSF compartments in current density distributions are also shown inside the brain due to its low and high electrical conductivity. The directions of the current flows are also plotted. In comparison to the isotropic model in Fig. 4 (a), the current vector lines in the anisotropic model in Fig. 4 (b) are relatively non-uniform and inhomogeneous due to the influences of the anisotropic conductivities according to the WM fiber directions. The results indicate that the WM anisotropic tensors strongly results in the errors of the current density magnitude and directions during tDCS. Note that the magnitudes of the current densities vary with the tissue electrical conductivities.

As mentioned above, we also assessed the numerical differences of the current density maps using CC and RE. The results produce CC=0.56/RE=0.53 (in WM), CC=0.94/RE=0.17 (in gray matter), and CC=0.99/RE=0.02 (skull), indicating that there are meaningful changes of the current densities between the isotropic and anisotropic head models.

IV. Disccusion and Conclusion

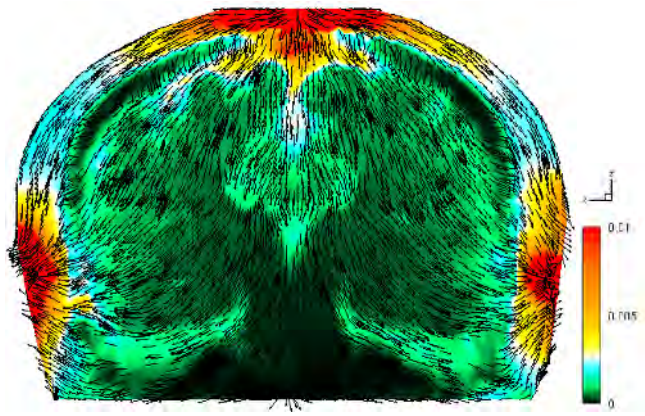
The goal of this work was to investigate the influence of the WM anisotropic conductivity on the effects of tDCS via high-resolution FE head models of the whole head. We have examined the effects of the WM anisotropy by comparing the computed current density maps from the anisotropic head model against those from the isotropic model. The results demonstrate that there are significant numerical differences in the current densities caused by the tissue anisotropy, indicating that the WM anisotropy produces significant variations of the current magnitudes and directions. Our study suggests that the inclusion of the WM anisotropic conductivity is one of the important factors to be considered for more precise analysis in the brain stimulation via tDCS.

There still remain several factors to be taken into account for more accurate brain stimulation via tDCS in this study. As for the electrodes, we modeled the electrodes as the point sources instead of pads available commercially. Modeling skull anisotropy should be considered, since the elec-

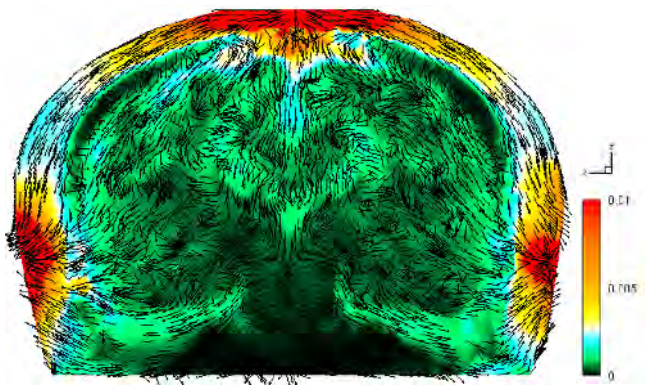


(a) (b) (c)

Fig. 3 Visualization of the 3-D wMesh head models with 160,231 nodes and 1,009,447 tetrahedral elements through the five sub-regions segmented: (a) an axial, (b) sagittal, and (c) coronal view (gray: scalp, yellow: skull, gray matter: blue, white matter: red, and green: CSF)



(a)



(b)

Fig. 4 Current density maps of the coronal cutplane computed from (a) the isotropic and (b) anisotropic wMesh head model with the WM anisotropic ratio of 1:10.

trical conductivities in the tangential directions are larger than those in the radial directions [8]. In deriving the WM anisotropic conductivity tensors, the eigenvalues could be derived from DT-MRIs directly as well [14]. The influences of the electrical anisotropy on the spatial focality and tissue safety via tDCS will be investigated using optimal electrode configurations. For the future works, we plan to involve the investigation of these factors for more precise analysis of tDCS.

Acknowledgment

This work was supported by a grant of Korea Health 21 R&D Project, Ministry of Health and Welfare, Republic of Korea (02-PJ3-PG6-EV07-0002). This study was also supported by the MKE (Ministry of Knowledge Economy), Korea, IITA (IITA 2008-(C1090-0801-0002)).

References

1. Sparing R, Mottaghy F M (2008) Noninvasive brain stimulation and transcranial magnetic or direct current stimulation: from insights into human memory to therapy of its dysfunction. Methods 44:329-337
2. Nitsche M A, Paulus W (2000) Excitability changes induced in the human motor cortex by weak trancranial direct current stimulation. J Physiol 527: 633-639
3. Wagner T, Valero-Cabre A, Rascual-Leone A (2007) Noninvasive human brain stimulation. Annu Rev Biomed Eng 9:19.1-19.39
4. Miranda P C, Lpomarev M, Hallett M (2006) Modeling the current distribution during transcranial direct current stimulation. Clin Neurophysiol 117:1623-1629
5. Im C H, Jung H H, Choi J D et al. (2008) Determination of optimal electrode positions for transcranial direct current stimulation. Phys Med Biol 53:N219-M225
6. Wagner T, Fregni F, Fecteat S et al. (2007) Transcranial direct current stimulation: a computer-based human model study NeuroImage 35:1113-1124

7. Holdefer R N, Sadleir R, Russell M J (2006) Predicted current densities in the brain during transcranial electrical stimulation. Clin Neurophysio 117:1388-97
8. Oostendorp T F, Hengeveld Y A, Wolters C H et al. (2008) Modeling transcranial DC stimulation Proc. IEEE EMBC, Vancouver, Canada, 2008, pp 4226-4229
9. Lee W H, Kim T S, Kim A T et al. (2008) Diffusion tensor MRI anisotropy content-adaptive finite element model generation for bioelectromagnetic imaging IEEE EMBC, Vancouver, Canada, 2008, pp 4003-4006
10. Lee W H, Kim T S, Cho M H et al. (2006) Methods and evaluations of MRI content-adaptive finite element mesh generation for bioelectromagnetic problems Phys Med Biol 51:6173-6186
11. Wolters C H, Anwander A, Tricoche X et al. (2006) Influence of tissue anisotropy on EEG/MEG field and return current computation in a realistic head model: a simulation and visualization study using high resolution finite element modeling NeuroImage 30:813-826
12. Kim S, Kim T S, Zhou Y et al. (2003) Influence of conductivity tensors on the scalp electrical potential: study with 2-D finite element models IEEE Trans Nucl Sci 50:133-138
13. Basser P J, Mattiello J, Bihan D L (1994) Diffusion tensor spectroscopy amd imaging Biophys J 66:259-267
14. Tuch D S, Wedeen V J, Dale A M et al. (2001) Conductivity tensor mapping of the human brain using diffusion tensor MRI Proc Natl Acad Sci USA 98:11697-11701

Address of the corresponding author:

Author: Tae-Seong, Kim
Institute: Kyung Hee University, Dept. of Biomedical Engineering
Street: 1 Seocheon-dong, Giheung-gu
City: Yongin-si
Country: Republic of Korea
Email: tsim@khu.ac.kr

Real-time Detection of Nimodipine Effect on Ischemia Model

G.J. Lee[1,2], S.K. Choi[3], Y.H. Eo[1,2], J.E. Lim[1,2], J.H. Park[1,2], J.H. Han[1,2], B.S. Oh[1,2,4] and H.K. Park[1,2,4]

[1]Dept. of Biomedical Engineering, School of Medicine, Kyung Hee University, Seoul, Korea
[2]Healthcare Industry Research Institute, Kyung Hee University, Seoul, Korea
[3]Dept. of Neurosurgery, Kyung Hee University Medical Center, Seoul, Korea
[4]Program of Medical Engineering, Kyung Hee University, Seoul, Korea

Abstract — **It is generally thought that neuronal damage by cerebral ischemia is associated with extracellular concentrations of the excitatory amino acids. L-glutamate over production initiated the neuronal cell death in ischemic condition. Real time quantitative measurement of glutamate would be applicable to evaluate brain injury during or after surgery, as well as to demonstrate immediate function by Nimodipine, which is one of L-type calcium channel blocker.**

For in-vivo glutamate measurement, the eleven vessel occlusion (11VO) was prepared by using rat model. Changes in cerebral blood flow were monitored by laser-Doppler flowmetry simultaneously with cortical glutamate level by amperometric biosensor. Ten minute ischemia was initiated by pulling the snares on the common carotid arteries (CCAs) and the external carotid arteries (ECAs) while Nimodipine was dripped on the vicinity of burr hole for CBF probe during ischemic period.

In comparison with the Nimodipine-treatment and non-treatment group, peak concentration and the area under the curve (AUC) of glutamate release showed statistically significant difference between two groups. It is considered that decreased glutamate level in Nimodipine treated group is attributed to the neuroprotective effect by Nimodipine.

Keywords — **Glutamate, Nimodipine, 11 vessel occlusion model, neuroprotective effect, real time monitoring**

I. Introduction

It was generally accepted that glutamate was the principal excitatory neurotransmitter in the brain, and its excessive release might play a key role in neuronal death associated with a wide range of neurological disorders.[1] Various studies demonstrated the mechanism of excitotoxic cellular injury from the pharmacological effect to block the cascading injury process.[2-5] Nimodipine was a well known neural protective drug which was applied for the ischemic vascular disease and the ischemia after subarachnoid hemorrhage.[6] Many researchers suggested that calcium channel blocker could facilitate vasodilatation on small arteriole.[7-10] And it was reported that the L-type voltage-gated calcium channels blocker such as Nimodipine prevented calcium influx which induced apoptosis.[11] On the other hand, J.W. Lazarewicz et al. reported that Nimodipine could protected directly neurons in the rabbit brain by intracellular calcium antagonism rather than by inhibition of calcium influx.[12] Although many researchers reported about the calcium channel blockade, the role of Nimodipine on the presynaptic glutamate release was not fully understood.[13-16] A better understanding of these excitotoxic processes requires accurate assessment of the time course of changes in extracellular glutamate levels.

In this paper, we hypothesized that the calcium channel blocker, Nimodipine, could reduce the glutamate release because the same type calcium channel existed in both side of pre- and post-synaptic membrane. Therefore we performed real time monitoring about glutamate release to validate the Nimodipine effect during ischemic period.

II. Materials & methods

A. 11 VO model preparation

Male Sprague-Dawley rats (250-350 g), which had been allowed food and water, were anesthetized with chloral hydrate (0.4 g/kg i.p.). During the entire preparation, the body temperature was maintained at 37.1 ± 0.10°C with Homeothermic Blanket Control Unit (Harvard apparatus, Holliston, MA). On supine position, after midline vertical incision from cricoids cartilage to sternal border with platysma incision, the common carotid artery was defined at the between the sternocleidomastoid muscle and sternohyoid muscle. The occipital artery, ascending pharyngeal artery and superior thyroid artery of external carotid artery were occluded with bipolar electrocautery. The pterygopalatine artery of the internal carotid artery was found at the just medial of the tympanic bulla and coagulated. Before the occlusion of the basilar artery, a tracheostomy was made at the level of the 3-4th tracheal ring level, then the silastic tube (inner diameter: 1.8-2.1mm) was inserted and tied up with 4-0 black silk. After the retraction of the trachea, esophagus and both lounges coli muscles, there was the clivus which was drilled out with 3mm diameter size. The basilar artery was selected at the mid pontine groove at the inferior level of anterior cerebellar artery after the dura incision and arachnoid dissection, and then the basilar artery

Chwee Teck Lim, James C.H. Goh (Eds.): ICBME 2008, Proceedings 23, pp. 465–467, 2009
www.springerlink.com

was coagulated permanently. We sealed the pore with bone wax to prevent the leakage of cerebrovascular fluid. At last, the carotid arteries were prepared for the ischemia induction. In order to safely expose the common carotid artery, model was prepared as followed. Carotid artery was dissected with caution not to injure vagus nerve and autonomic nervous chains. On ischemia induction, we had hanged the rubber ring on the common carotid artery and internal carotid artery at both sides, to make a flow down temporally, which enabled the vessel to restore the vascular patency upon the reperfusion.

B. Real time monitoring

Animals were placed in a stereotaxic head holder. The laser Doppler flow probe placed over the dura, was adjusted to avoid large blood vessels and record stable blood flows. EEG (electroencephalogram) electrodes were fixed bilaterally at the skull on the parietal cortex adjacent to the laser probe. Body temperature was maintained at 37.5±0.1°C by a rectal thermistor probe connected to a dual temperature controller, then coupled to the heating pad. The microdialysis electrode was purchased from Sycopel International Ltd. (Type: General 20-10-4-4, UK) The dialysis electrode was filled with phosphate buffer saline (PBS) to electropolymerize the O-phenylenediamine on the platinum electrode at 0.65V for 20min with Sycopel BD2000 potentiostat. And then fresh PBS containing glutamate oxidase was perfused in the dialysis electrode at a flow rate of 0.5μl/min. The dialysis electrode showed linear response in the concentration range of 50~450μM standard glutamate solution with a sensitivity of 0.22nA/μM. (R^2 coefficient of regression of 0.998) The Microdialysis electrode was inserted into motor cortex at coordinates A 1: L 4: V 4mm (from bregma and the dura) through a small incision in the dura.

Ten minute 11VO cerebral ischemia was initiated by pulling the snare on the common carotid arteries (CCAs) and external carotid arteries (ECAs). Snares were released and withdrawn after 10 min.

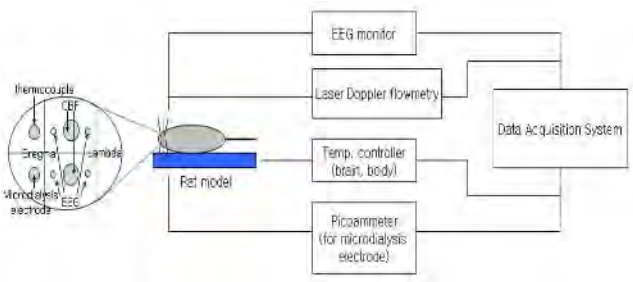


Fig. 1 The diagram of experimental setup for real-time glutamate monitoring system in 11 VO rat model. Zoomed image showed the coordinates for craniotomy

Nimodipine, which was diluted 20 times with normal saline, was dripped (0.025μg/100gm/min) on the vicinity of burr hole for CBF probe during ischemic period. The infusion syringe was protected from light source by thin aluminum foil.

III. Results & Discussion

The pattern of ischemia-evoked response in 11VO rat model was shown in Figure 2(a). As soon as the ischemia was induced, basic CBF declined rapidly to near zero levels, coincident with the development of a flat EEG. With a dialysis electrode, the elevation in glutamate release began approximately 100s after the onset of ischemia episode and continued to rise throughout the entire ischemic period. Then the glutamate level was rapidly declined to pre-ischemic levels during reperfusion. However, the elevation

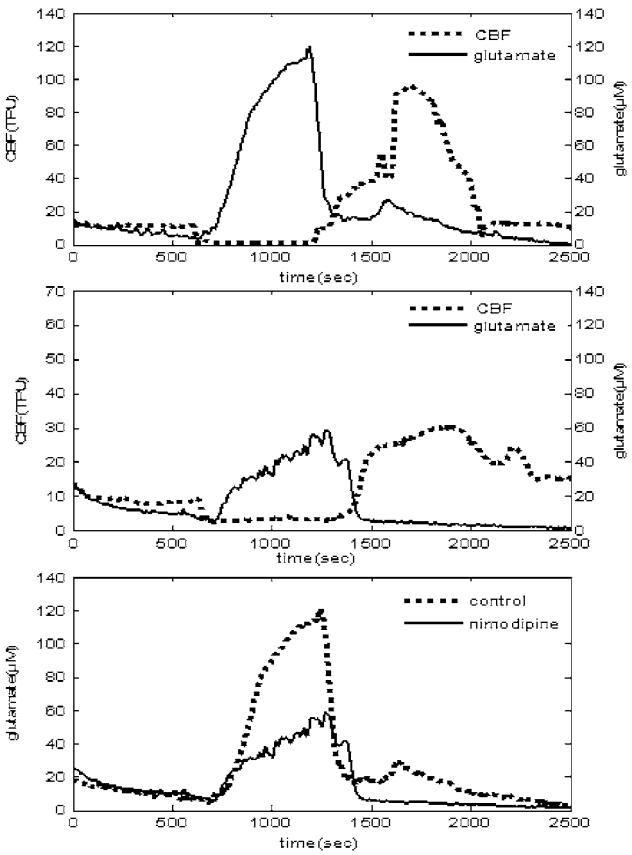


Fig. 2 (a) Real time measurement of glutamate and CBF on non-Nimodipine-treatment group (representative) (b) Real time measurement of glutamate and CBF in Nimodipine-treatment group (representative) (c) The comparison of glutamate dynamics between two groups

Table 1 Changes of glutamate concentration between non-treatment group and Nimodipine-treatment group in global ischemia induced by 11VO method

Changes of glutamate concentrations (n=4)	Control group (mean±S.E.M)	Nimodipine group (mean±S.E.M)	p-value
Maximum (in ischemic period)	129.67±3.64	70.77±0.85	p<0.001
Maximum (in reperfusion period)	136.75±2.02	81.3±3.11	p<0.001
Total amount	57657±3714	31154±1105	p<0.001

in glutamate release was suppressed in the Nimodipine-treatment group, as shown in Figure 2(b).

As shown in Table 1, the maximum change of glutamate concentration was 129.67± 3.64 μM in control group and 70.77± 0.85 μM (55%) in Nimodipine-treatment group during ischemic period. The maximum change of glutamate concentration was 136.75± 2.02 μM in control group and 81.3± 3.11 μM (59%) in Nimodipine-treatment group during reperfusion period. Total amount of glutamate release was 57657 ± 3714 in control group and 31151 ± 1105 (54%) in Nimodipine-treatment group.

IV. Conclusions

In this study, we examined the effects of Nimodipine on glutamate release in acute ischemic condition. In comparison with the Nimodipine-treatment and non-treatment group, peak concentration and the area under the curve (AUC) of glutamate release showed statistically significant difference between two groups. It was showed that the glutamate could be partially regulated by Nimodipine. (L-type calcium channel blocker), though glutamate release could not block completely. This fact indirectly supported that the exocytosis of glutamate was mediated by multiple types of calcium channels.[17]

It is considered that decreased glutamate level in Nimodipine treated group is attributed to the neuroprotective effect by Nimodipine. From this result, we demonstrated that Nimodipine could be applied to clinical condition in neurosurgical area which was performed the multiple clipping or carotid occlusion by continuous drug infusion during the ischemic period.

Acknowledgment

This study was supported by the research fund from Seoul R&BD program (grant # CR070054).

References

1. Zhao H. Asai S., Kohno T. and Ishikawa K (1998) Effects of brain temperature on CBF thresholds for extracellular glutamate release and reuptake in the striatum in a rat model of graded global ischemia. Neuroreport 9(14) 3183-3188
2. Alps BJ. (1992) Drugs acting on calcium channels: Potential treatment for ischaemic stroke. Brit J Clin Pharmaco 34 199
3. Miljanich GP, Ramachandran J. (1995) Antagonists of neuronal calcium channels: Structure, function, and therapeutic implications. Annu Rev PharmacolToxicol. 35 707-734
4. Morley P, Hogan MJ, Hakim AM. (1994) Calcium-mediated mechanisms of ischemic injury and protection. Brain Pathol. 4 37-47
5. Siesjo BK, Bengtsson F. (1989) Calcium fluxes, calcium antagonists, and calcium-related pathology in brain ischemia, hypoglycemia, and spreading depression: A unifying hypothesis. J Cerebr Blood F Met. 9 127-140
6. Gelmers HJ, Gorter K, de Weerdt CJ, Wiezer HJ. (2001) A controlled trial of nimodipine in acute ischemic stroke. New Engl J Med. 318 203-207
7. Welsch M, Nuglisch J, Krieglstein J. (1990) Neuroprotective effect of nimodipine is not mediated by increased cerebral blood flow after transient forebrain ischemia in rats. Stroke 21 105-107
8. Steen PA, Newberg LA, Milde JH, Michenfelder JD. (1983) Nimodipine improves cerebral blood flow and neurologic recovery after complete cerebral ischemia in the dog. J Cereb Blood F Metab. 3 38-43
9. Milde LN, Milde JH, Michenfelder JD. (1986) Delayed treatment with nimodipine improves cerebral blood flow after complete cerebral ischemia in the dog. J Cereb Blood F Metab. 6 332-337
10. Feinberg WM, Bruck DC. (1993) Effect of oral nimodipine on platelet function. Stroke 24 10-13
11. Bullock R, Zauner A, Woodward J, Young HF. (1995) Massive persistent release of excitatory amino acids following human occlusive stroke. Stroke 26 2187-2189
12. Lazarewicz JW, Pluta R, Puka M, Salinska E. (1990) Diverse mechanisms of neuronal protection by nimodipine in experimental rabbit brain ischemia. Stroke 21 108-110
13. Kulik A, Trapp S, Ballanyi K. (2000) Ischemia but not anoxia evokes vesicular and ca2+-independent glutamate release in the dorsal vagal complex in vitro. J Neurophysiol.83 2905-2915
14. Estevez AY, O'Regan MH, Song D, Phillis JW. (1999) Effects of anion channel blockers on hyposmotically induced amino acid release from the in vivo rat cerebral cortex. Neurochem Res. 24 447-452
15. Fujisawa A, Matsumoto M, Matsuyama T, Ueda H, Wanaka A, Yoneda S, Kimura K, Kamada T. (1986) The effect of the calcium antagonist nimodipine on the gerbil model of experimental cerebral ischemia. Stroke 17 748-752
16. Dirnagl U, Jacewicz M, Pulsinelli W. (1990) Nimodipine posttreatment does not increase blood flow in rats with focal cortical ischemia. Stroke 21 1357-1361
17. Terrian DM, Dorman RV, Gannon RL. (1990) Characterization of the presynaptic calcium channels involved in glutamate exocytosis from rat hippocampal mossy fiber synaptosomes. Neurosci Lett. 119 211-214

Author: Hun Kuk Park
Institute: Dept. of Biomedical Engineering, School of Medicine
Street: #1 Hoeki-dong, Dongdaemun-gu
City: Seoul
Country: Korea
Email: sigmoidus@khu.ac.kr

Windowed Nonlinear Energy Operator-based First-arrival Pulse Detection for Ultrasound Transmission Computed Tomography

S.H. Kim[1], C.H. Kim[2], E. Savastyuk[2], T. Kochiev[2], H.-S. Kim[2] and T.-S. Kim[1]

[1]Department of Biomedical Engineering, Kyung Hee University, Republic of Korea
[2]Samsung Electro-Mechanics Co. LTD., Korea

Abstract — **A windowed nonlinear energy operator (wNEO)-based algorithm is proposed to detect the first-arrival pulse of ultrasound transmission computed tomography (UTCT). In UTCT, the detection of first-arrival pulse is critical to derive imaging indices such as attenuation coefficients and time-of-flight (TOF). Currently, various algorithms utilizing a threshold, maximum, wavelet, etc. have been tested for the detection of the pulse, but each technique suffers from its own intrinsic limitations, failing in detecting the first-arrival pulse reliably. Especially the most widely used wavelet technique, which is also considered as the most effective technique to handle frequency-dependent attenuation, dispersion, and noise of ultrasound, often fails to detect the first-arrival pulse due to the inconsistency of ultrasound pulse shapes with respect to a best mother wavelet. Furthermore, the wavelet technique is impractical for real-time processing. In this work, we propose the use of wNEO for the first time to detect the first-arrival pulse and show its outperforming results in comparison to those conventional techniques through simulation and experimental data with a pair of 5MHz ultrasound transmit-receive transducers.**

Keywords — **Computed Tomography, NEO, Pulse Detection, Ultrasound Transmission**

I. Introduction

Ultrasound imaging system is an intensive research area due to its properties of non-ionizing radiation and abundant information contents. Typically, echo-mode imaging systems (EMIS) have been widely used as they provide images of internal tissues according to the differences in acoustic impedance. Recently, there is an increased activity in developing UTCT [1],[2], since it yields more accurate and quantitative information of objects. The main advantages of UTCT over the conventional EMIS are as following: (1) it provides more quantitative information of tissue characteristics [1]; (2) soft tissue differentiation is possible with the transmitted ultrasound [3]. One of the imaging complications in UTCT is the multi-path problem of the received pulses [1]: multiple pulses are received in one transducer. To mitigate this multi-path problem, it is critical to detect the first-arrival pulse (or we call it a 'snippet'). Also, in UTCT image indices such as the attenuation and TOF are typically derived from the snippet [1],[3].

In this paper, we propose the use of wNEO to detect the snippet for UTCT. Previously, NEO has been successfully applied for the detection of neural spikes [4] and QRS complexes [5]. In this work, we improve the conventional NEO via convolution with data specific windows to improve its performance. To assess the performance of wNEO, we have compared the technique against the various conventional pulse detection algorithms.

II. Methods

A. Conventional Pulse Detection Techniques

In this section, we describe the most commonly used methods for the detection of ultrasound pulses.

1) Three Times Noise Standard Deviation Method

The three times noise standard deviation (3xNSD) method is one of the threshold methods in which a snippet are detected through a threshold defined as three times standard deviation of noise. We have considered the first fifty samples of acquired signal as the noise for the calculation of noise standard deviation.

2) Maximum Peak Detection Method

The maximum peak detection method detects a snippet by picking up the maximum value of received ultrasonic pulses. After detecting the maximum peak value from a signal, a snippet is extracted with a fixed duration.

3) Wavelet-based Method

The wavelet-based method detects a best correlated position with a 'best mother wavelet.' The best mother wavelet is chosen by its similarity to the reference ultrasound signal which is obtained through water only signals.

Chwee Teck Lim, James C.H. Goh (Eds.): ICBME 2008, Proceedings 23, pp. 468–471, 2009
www.springerlink.com

4) Pan-Tompkins Algorithm

The Pan-Tompkins algorithm is a most widely used and powerful detection method for the QRS detection [6]. We adopt this technique for the snippet detection and extraction.

5) Nonlinear Energy Operator

Kaiser has defined a nonlinear energy operator for the continuous and discrete time in [7]. For the discrete time case, NEO is defined as,

$$\Psi_d[x[n]] = x^2[n] - x[n+1]x[n-1] \quad (1)$$

where $x[n]$ is the sample of signal representing the oscillation.

$x[n]$ can be expressed again as,

$$x[n] = A\cos(\Omega n + \phi) \quad (2)$$

where A is amplitude, Ω the angular frequency, and ϕ initial phase.

Using Eq. (2) as the input of NEO, the output is rewritten as,

$$\Psi_d[x[n]] \approx A^2 \sin^2(\Omega n) \approx A^2\Omega^2 . \quad (3)$$

The energy of a simple oscillation is proportional the multiplication of the square of the amplitude and the square of the frequency [7]. Hence, Eq. (3) means the energy of $x[n]$ and therefore NEO is called the energy operator. Eq. (3) can also show that NEO is suitable for the detection of a discontinuity part or transient term because the output of NEO is sensitive to instantaneous amplitude and frequency.

B. Windowed Nonlinear Energy Operator for Detection

wNEO is the convolution of NEO with a time-domain window to reduce negative values and remove noise term, which is expressed as,

$$\Psi_w[x[n]] = \Psi_d[x[n]] * w[n] \quad (4)$$

where $w[n]$ represents the window and $*$ represents a convolution operator. In addition, wNEO can serve as $E[\Psi_d[\bullet]]$ [4].

The window type and width are important factors to achieve sufficient reduction of noise without losing much of its time resolution. Consequently, the factors have to be taken into account depending on the state of systems. In this paper, the Bartlett window function is chosen, of which its width is 30 (i.e., 300ns) under our experimental setting.

C. Experimental Setup

An experimental setup is designed as shown in Fig. 1, in which an object (agar gel containing a glass bar), immersed in the water tank, is horizontally scanned with a pair of ultrasonic transducers in the transmission mode. One of the transducers is set up as a transmitter and the other as a receiver. The transducer consists of 128 elements with its crystal size of 2×2mm and the center frequency of 5MHz. The signal is sampled at 100MHz. In total of 250 transmitted ultrasound signals are obtained in each scan.

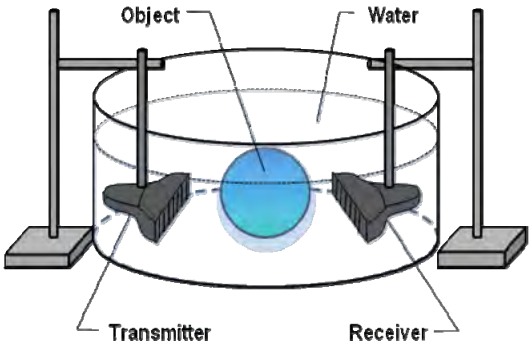


Fig. 1 Experimental Setup

III. Results and Discussion

For the validation of our proposed wNEO-based algorithm, we have manually examined every result derived from those algorithms. One set of result for detection accuracy and computation time is given in Table 1: (1) the detection accuracy of each technique is calculated by counting the correct results among 250 samples; (2) the computation time of individual method is the time to process all 250 signals.

Table 1 Detection Accuracy and Computation Time

Methods	Accuracy (%)	Computation Time (second)
3xNSD	91.6	0.16
Max Peak	80.4	0.23
Wavelet	89.4	4.82
Pan-Tompkins	93.6	1.02
NEO	92	0.18
wNEO	99.2	0.39

The 3xNSD technique achieves the best computation time and the reasonable level of accuracy rate among the applied techniques. Despite of the accuracy rate of 91.6%

comparable to the NEO result, the method however has a serious problem: it frequently detects noise as pulses in low SNR (see Fig. 2(a)).

The max peak detection algorithm shows the worst accuracy and high computation time. The method cannot detect the first-arrival pulse if the other pulses have a bigger maximum peak value than the first-arrival pulse (see Fig. 2(b)). In spite of its low accuracy, however, the detected pulse might reflect some frequency-dependent attenuation indices for UTCT, since most pulses detected by the maximum peak detection are usually located in the actual transmitted pulses. However, TOF cannot be correctly derived from this technique.

The wavelet-based technique results can be useful in the case that the waveforms are similar with a best mother wavelet but it often fails to detect a snippet due to the inconsistency of ultrasound pulse shapes caused by the nonlinear properties of ultrasound such as frequency-dependent attenuation and dispersion (see Fig. 2(c)). In addition, the wavelet-based method shows the longest computation time among those algorithms. As both of the accuracy rate and the computation time, the wavelet based method does not seem to be suitable for UTCT.

The Pan-Tompkins algorithm performs the second-highest accuracy rate whereas the computation time is the second-longest (see Fig. 2(d)). The computation time can be a disadvantage in our case because UTCT requires processing of huge amount of data.

The NEO-based method achieves reasonably high accuracy rate and the second-lowest computation time. NEO is capable of detecting the envelopes of signal based on energy [8], hence the envelope of ultrasonic waves can be emphasized because the ultrasonic waves have bigger energy than noise. However, through the term of multiplication sometimes it can also be sensitive to noise (see Fig. 2(e)). This disadvantage of NEO can be improved through the convolution with data specific windows.

Our proposed technique, wNEO which is an improved version of NEO, achieves the highest accuracy rate and the third-lowest computation time (see Fig. 2(f)). The convolution of NEO with data specific window achieves the decrease of noise sensitivity hence the accuracy rate improves. Although it also decreases the computation time a little, the technique can be applied in real-time.

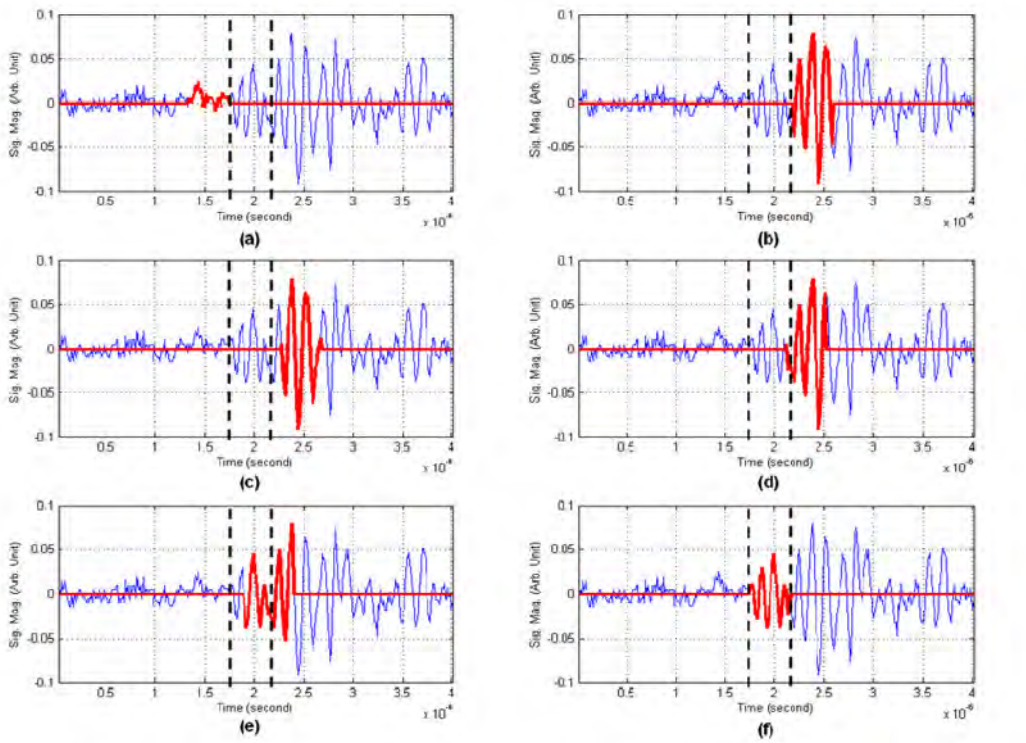


Fig. 2 A set of results for the first-arrival pulse detection using (a) 3xNSD, (b) maximum peak detection, (c) wavelet analysis, (d) Pan-Tompkins method, (e) NEO, and (f) wNEO. The true first-arrival pulse is indicated with the two dashed bars, the detected in red, and the original in blue.

IV. Conclusion

In this paper, we propose the wNEO-based first arrival time detection technique for UTCT. The technique achieves the best accuracy of detecting the first-arrival pulse and reasonable computation time for real-time processing of UTCT data.

Acknowledgement

This work was supported by Samsung Electro-Mechanics, Korea.

References

1. Vasilis Z. Marmarelis, Tae-Seong Kim, Ramez E. N. Shehada (2003) High Resolution Ultrasonic Transmission Tomography, Medical Imagign 2003, Ultrasonic Imaging and signal Processing, SPIE Proc., vol. 5035, pp 33-40
2. Cuiping Li, Neb Duric, Lianjie Huang (2008) Breast Imaging Using Transmission Ultrasound: Reconstructing Tissue Parameters of Sound Speed and Attenuation, 2008 International Conference on BioMedical Engineering and Informatics, pp 708-712
3. Jeong-Won Jeong, Tas-Seong Kim, Dae C. Shin, Synho Do, Manbir Singh, Vasilis Z. Marmarelis (2005) Soft Tissue Differentiation Using Multiband Signatures of High Resolution Ultrasonic Transmission Tomography, IEEE Transactions on Medical Imaging, vol. 24, no. 3, pp 399-408
4. Sudipta Mukhopadhyay, G. C. Ray (1998) A New Interpretation of Nonlinear Energy Operator and Its Efficacy in Spike Detection, IEEE Transactions on Biomedical Engineering, vol. 45, no. 2, pp 180-187
5. Zhang Aihua, Chai Long, Dong Hongsheng (2008) QRS Complex Detection of ECG Signal by Using Teager Energy Operator, ICBBE 2008, Bioinformatics and Biomedical Engineering, pp 2095-2098
6. Jiapu Pan, Willis J. Tompkins (1985) A Real-Time QRS Detection Algorithm, IEEE Transactions on Biomedical Eng., vol. BME-32, no. 3, pp 230-236
7. James F. Kaiser (1990) On a Simple Algorithm to Calculate the Energy of a Signal, IEEE Proc. Acoustic Speech and Signal Processing, Albuquerque, NM, pp381-384
8. Fabien Salzenstein, Paul C. Montgomery, Denis Montaner, Adbel-Ouahab Boudraa (2005) Teager-Kaiser Energy and Higher-Order Operators in White-Light Interference Microscopy for Surface Shape Measurement, EURASIP Journal on Applied Signal Proc. pp 2804-2815

Address of the corresponding author:

Author: Tae-Seong Kim
Institute: Department of Biomedical Engineering, Kyung Hee University
Street: Seocheon-Dong, Giheung-Gu
City: Yongin-Si
Country: Republic of Korea
Email: tskim@khu.ac.kr

Digital Dental Model Analysis

Wisarut Bholsithi[1], Chanjira Sinthanayothin[2]

[1]National Electronics and Computer Technology Center, National Science and Technology Center, Pathum Thani, Thailand
[2]National Electronics and Computer Technology Center, National Science and Technology Center, Pathum Thani, Thailand

Abstract—**This paper is to introduce dental model analysis software with facilitating functions to allow direct dental measurement along with simulation after dental alignment and extraction. Model analysis is one of the orthodontic analyses to assess dental alignment and dental space whether the teeth are at the appropriated positions and space for orthodontic treatment or dental extraction is in need. There are several model analysis researches done by local researchers done by tedious and time-consuming manual means while there are a few cases model analyses by using dental software but most using imported and expensive orthodontic software. There are very few local researches on the software to perform dental model analysis but none of them could perform direct dental measurement and dental simulation after dental alignment and extraction. This model analysis software could perform dental width and dental arches measurements which results have been applied for Bolton analysis, which calculate the dental ratios. User could perform dental model simulation after selecting individual teeth appeared on the dental simulation image. Further developments of this model analysis program will allow the measurement of dental curve widths and curve heights along with other measurements relating to dental model analyses.**

Keywords—**Dental Model Analysis, Bolton Analysis, Dental Widths, Dental Arches, Orthodontic Analyses.**

I. Introduction

Model analysis is a part of the orthodontic analyses to investigate the dental alignment if individual teeth are at proper alignment. There are several researches on dental model analyses by local Thai orthodontists including dental sizes [1], the predictions of dental curve widths and heights [2], the mandibular width comparisons before and after orthodontic treatments at the canine, the first premolar, and the first molar [3], average values of dental sizes from Thai people [4], relationships between the tooth sizes and dental curves for those Class I [5] as well as Class II patients [6], malocclusal analyses from dental models [7] and so on.

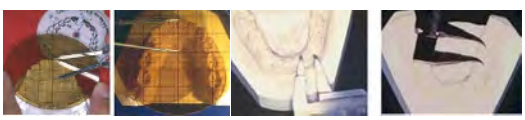


Fig. 1 Examples of Model Analyses by Manual Means [8] [9]

Fig.1 is showing dental width and dental curve analysis by manual that require dental width measurements by veneer [8] along with the dental curves by apply bronze wires [9], vulnerable to intrapersonal or interpersonal discrepancies and accuracy limit of measuring instruments.

There are software developments for dental model analysis to reduce analysis time, shorten the dental analysis procedure, and reduce the measurement discrepancies as orthodontic treatments became more popular. Cadant Ltd. has developed OrthoCAD for model analysis in 1999 [10] with patent approved in 2000 [11]. Geodigm Corp. has developed E-Models in 2001 with patent approved in 2003 [12]. For the case of 2D dental model analysis, Dolphin Imaging 10 from Dolphin Imaging Inc. invented a dental model analysis module with patent approved in 2007 [13].

There are a few local researches on model analysis software such as the 3D model analyzer by Eimtaveecharern in 2001[14] and 2D computerized orthodontic model analysis by Thongti-amporn in 2003 [15]. However neither of them fully met the orthodontists' requirements since [14] did not go into complicated model analysis as [15] while [15] used data from manual measurements instead of digital image measurements.

Therefore, this new research on dental model analysis software will have facilitated functions to cut down the procedure along with shortening the analysis time. Furthermore, the dental model analysis program has functions to simulate dental movement during orthodontic movement.

II. Linear and Angular Measurements

There are two major types of measurements for dental model analysis, linear measurements and angular measurements, which can be shown in details as follows:

A. Linear Measurements

Linear measurements could be divided into direct measurements and perpendicular measurements. Direct measurement is the linear measurement of distance between two points to be applied to for curve measurement shown in (1).

$$|ab| = \sum_{i=0}^{N-1} \sqrt{(x_{i+1} - x_i)^2 + (y_{i+1} - y_i)^2} \qquad (1)$$

Chwee Teck Lim, James C.H. Goh (Eds.): ICBME 2008, Proceedings 23, pp. 472–475, 2009
www.springerlink.com

Perpendicular measurement is the linear measurement of triangular height h to be calculated by applying Heron's Formula [16] shown in (2) with A as the distance opposite to a angle, B as the distance opposite to b angle and C as the distance opposite to c angle respectively.

$$h = (2/C) * \sqrt{S(S-A)(S-B)(S-C)}, S = (A+B+C)/2 \quad (2)$$

B. Angular Measurements

The angular measurement can be done by applying dot product on 2 vectors to calculate θ_{vec} as shown in (3) while the alternative is to measure θ_{Slope} as shown in (4).

$$\theta_{vec} = \cos^{-1}(|\vec{A} \bullet \vec{B}| / (|A||B|)) \quad (3)$$

$$\theta_{Slope} = \tan^{-1}((a_y - b_y)/(a_x - b_x)) \quad (4)$$

III. Dental Model Analysis

Dental model analysis is a part of orthodontic treatments to analyze dental model details including dental widths and curve lengths and assess if malocclusion exists along with the malocclusion severity by comparing results with the standard sets of measurements before deciding to either extract teeth to increase space or apply orthodontic treatments without extraction. This paper will mention only the analyses implemented in the model analysis software.

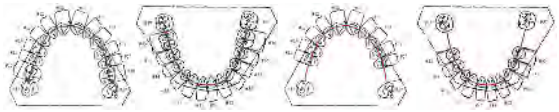
A. Bolton Analysis

Bolton analysis is the dental analysis to measure dental width of the individual teeth along with the comparisons between maxilla and mandibular sum of dental widths in percentage invented by Bolton in 1958 [17] for the following dental assessments:

1. When the dental ratios are not proportional with standard values, it would indicate where irregularity occurs
2. This analysis can be applied for orthodontic treatment and cephalometric analysis to indicate if orthodontists and craniofacial surgeons would either extract the teeth or perform cephalometric surgery along with dental stripes to correct dental positions and space.
3. This analysis can estimate overjet and overbite after orthodontic treatment.
4. Sum of 12 maxilla and 12 mandibular dental widths could be applied for malocclusion assessments.

Bolton ratios will be explained in details as follows:

1. Ratio of 12 teeth (B_1) is the ratio between the sum of 12 maxilla dental widths Mx_{12} from the first right molar (#16) to the first left molar (#26) shown in Fig. 2(A) and the sum of 12 mandibular dental widths Md_{12} from the first right molar (#46) to the first left molar (#36) shown in Fig. 2(B). If the first molars are missing, the end points would be at the last positions to measure the the second molar shown in Fig 2(C) for the maxilla and Fig 2(D) for mandibular and the ratio is shown in (5).



(A) (B) (C) (D)

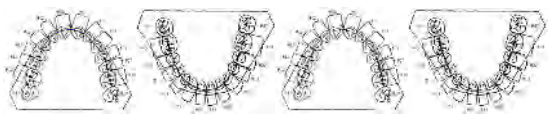
Fig. 2 Bolton Ratio of 12 Maxilla and 12 Mandibular Teeth

2. Ratio of 6 frontal teeth (B_2) is the ratio between the sum of 6 maxilla dental widths Mx_6 from the first right canine (#13) to the first left canine (#23) shown in Fig. 3(A) and the sum of 6 mandibular dental widths Md_6 from the first right canine (#13) to the first left canine (#23) shown in Fig. 3(B) from the first right to the first left canine shown in (6).
3. Ratio of 6 lateral teeth (B_3) is the ratio between the different sum of 12 teeth and 6 frontal teeth shown in Fig. 3(C) for maxilla and Fig. 3(D) for the mandibular and the ratio can be shown in (D) shown in (7).

$$B_1 = 100 Md_{12} / Mx_{12} \quad (5)$$

$$B_2 = 100 Md_6 / Mx_6 \quad (6)$$

$$B_3 = 100 Md_{6d} / Mx_{6d} = 100 \frac{Md_{12} - Md_6}{Mx_{12} - Mx_6} \quad (7)$$



(A) (B) (C) (D)

Fig. 3 Bolton Ratio of 6 Maxilla and 6 Mandibular Teeth

B. Arch Length Analysis or Space Analysis

Arch length analysis is to assess the arch length discrepancy (ALD) by measuring the arch length (AL) within mesial surface area from the front of the first left molar to the front of the right molar to calculate the space available by applying (2) as shown in Fig. 4. The arch lengths will be compared with the space requirement measure from the sum

of dental width from the second right premolar (#15) to the second left premolar (#25) for maxilla and #45 to #35 for mandibular since these teeth are movable by applying brackets and dental wires. If arch length discrepancy (ALD) is negative, it implies that the space requirement is more than the corresponding space available (AL) so tooth extraction is a necessary measure to ensure positive arch length discrepancy before further orthodontic treatment.

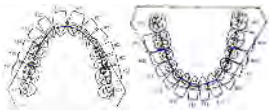
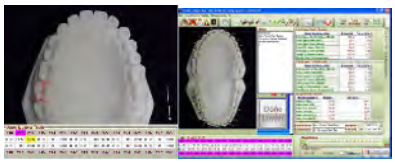


Fig. 4 Maxilla and Mandibular Arch Length

IV. Dental Model Analysis

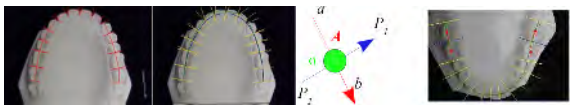


(A) (B)

Fig. 5 Tooth Size Measurement by Mouse

Dental model analysis has been developed by using Borland C++ Builder 6 as a compiler and VCL components from TMS Software to develop software for dental model analysis. After opening the dental model image, user can define the dental widths of the maxilla by mouse, which can be skipped clicking right mouse button for the section without tooth as shown in Fig. 5 (A). After drawing the maxilla arch, user can define mandibular tooth sizes and draw the mandibular arch by following the same procedure as maxilla cases. Dental width sums along with the space requirement accumulated and the results along with the user interface of the model analysis program shown in Fig. 5(B).

After finishing tooth width definition on the maxilla as shown in Fig 6(A), user can draw the line divided individual teeth and dental arches from the dental width positions along with the averaged corresponding position as shown in Fig. 6(B) by applying cubic spline interpolation [18] along with averaging to smooth the dental curves. The Drawing of segmentation line $\vec{P_1P_2}$ with the length of K perpendicular to vector from the middle of one dental width to the neighbor dental width and crossed at point O can be shown in Fig. 6(C) with the results shown in Fig. 6(D). Calculation for the perpendicular line position can be expressed as equations from (8) to (11).



(A) (B) (C) (D)

Fig. 6 Drawing Dental Arches and Segmentation lines

$$P_1 = (P_{1x}, P_{1y}) = (O_x + K_x, O_y - K_y) \quad (8)$$

$$P_2 = (P_{2x}, P_{2y}) = (O_x - K_x, O_y + K_y) \quad (9)$$

$$K_x = K(a_y - b_y) / \sqrt{(a_x - b_x)^2 + (a_y - b_y)^2} \quad (10)$$

$$K_y = K(a_x - b_x) / \sqrt{(a_x - b_x)^2 + (a_y - b_y)^2} \quad (11)$$

After finishing dental arch drawing, user could start dental segemntation by clicking four landmarks in clockwise or counter clockwise direction around each tooth to set up the dental boundary. After marking all 4 point, the cubic spline interpolation will be applied to draw the boundary section by section and the starting and ending point for cubic spline interpolation will be rotated to ensure a closed loop with suitable form along with segmented teeth shown in Fig. 7.

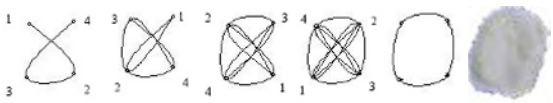
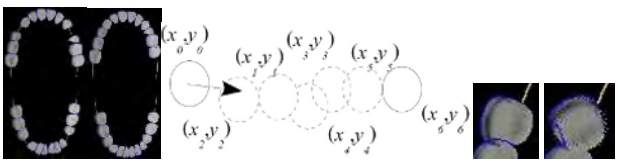


Fig. 7 Results after Drawing Dental Arches

After dental segmentation shown in Fig. 8 (A), user could simulate the dental movement by moving and rotating the individual teeth first and simulating the dental movement, according to (12) for translation with (x_0,y_0) for the starting position, (x_i,y_i) for the intermediate position, and (x_N,y_N) for the final position at step N. For the rotation case, the rotation angle θ will be according to (4) and the rotation mechanic will follow (13) with (x_0,y_0) as the starting position, (x_c,y_c) as rotation center. Results from translation movement can be expressed in Fig. 8(B) while the result from rotation can be seen in Fig. 8(C).



(A) (B) (C)

Fig. 8 Results before and after Dental Alignment along with translation and rotation of individual teeth

$$\begin{bmatrix} x_i \\ y_i \end{bmatrix} = \begin{bmatrix} x_0 \\ y_0 \end{bmatrix} + \left(\frac{i}{N}\right)\begin{bmatrix} x_N - x_0 \\ y_N - y_0 \end{bmatrix} \quad (12)$$

$$\begin{bmatrix} x_i \\ y_i \end{bmatrix} = \begin{bmatrix} x_c \\ y_c \end{bmatrix} + [x_c - x_0, y_c - y_0]\begin{bmatrix} \sin(i\theta / N) \\ \cos(i\theta / N) \end{bmatrix} \quad (13)$$

V. Results

During software development period, there are several problems to be listed along with the solutions as follows:

1. Slow processing for drawing dental arches that can be solved by the following measurements.
   a) Separated drawing function, cubic spline algorithm and data saving to reduce code redundancy.
   b) Dynamic arrays with proper memory managements to prevent memory leak.
   c) Appropriated logics for drawing functions.
2. Applying bilinear interpolation to calculate pixel colors to fill missing pixels of individual tooth during rotation.
3. Further dental segmentation improvements are to apply gradient vector flow along with edge detection to push the dental boundary to be exactly on the dental edges.
4. Designing user interface to meet requirements has to stick with the dental model analysis results used by orthodontists. However, additional model views are in need to obtain more dental model analysis data.

VI. Conclusions

This dental model analysis software could perform Bolton analysis and dental arch analysis along with simulation of orthodontic treatments. However, further development of model analysis software to obtain the data and analyses in frontal and lateral views of dental models to complete the dental model analysis procedures.

Acknowledgment

The proposal of this paper is to mention about a dental model analysis module to be integrated as a part of software modules in the CephSmile V2.0 project to create the cephalometric analysis software for orthodontists.

We would like to thank National Electronics and Computer Technology Center for providing the grant for this project and orthodontists from Orthodontic Department, Faculty of Dentistry, Mahidol University for providing the photographic data of dental model along with other information relating to dental model analysis.

We appreciated Mr. Phanaphon Panjamanee for the contributions on image segmentation to simulate orthodontic treatment along with the dental arch drawing.

References

1. Patanaporn V (1983) Tooth size analysis. Thesis (MDen) Graduate School Chulalongkorn U., Bangkok
2. Meesil C (1981) Prediction of arch width and arch height from sum of incisors. Thesis (MSc) Graduate School Chulalongkorn U., Bangkok
3. Nitasnoraset P (1990) Comparison of intercanine width, anterior arch width, posterior arch width, anterior arch height before and after orthodontic treatment. Thesis (MSc) Graduate School Chulalongkorn U., Bangkok
4. Tangmongkol F, Sakulbunchuen P (1992) Average maxilla molar sizes of Thai people. Dental Research Paper, Faculty of Dentistry Chulalongkorn U., Bangkok
5. Aukvongseree C (2005) The form of dental arch in angle's classification I in Thai. Thesis (MSc (Orthodontics)), Mahidol U., Bangkok
6. Aukvongseree C (2006) The form of dental arch in angle's classification II in Thai. Thesis (MSc (Orthodontics)), Mahidol U., Bangkok
7. Tiptawonnugul A (2004) Intermaxillary tooth size discrepancies among Class I, II, III occlusion in a group of Thai. Thesis (MSc (Orthodontics)), Mahidol U., Bangkok
8. Chiewcharat P Model Analysis at http://www.ortho.dent.chula.ac.th/Webbase/modelanalyse2.html
9. Chiewcharat P Dental Curve Analysis at http://www.ortho.dent.chula.ac.th/Webbase/dental%20archl.html
10. Peluso MJ, et. al.(2004) Digital models: An introduction. Seminars in Orthodontics, 10(3): 226-238, DOI:10.1053/j.sodo.2004.05.007
11. Kopelman A et. al. (2000) Method and system for acquiring three-dimensional teeth image. US Patent No. 6,099,314, August 8, 2000
12. Marshall MC et al. (2003) Mating parts scanning and registration methods. US Patent No. 6,579,095, June 17, 2003
13. Lai ML, and Tzou TZ (2007) Orthodontic systems with resilient appliances. US Patent 7,234,936, June 26, 2007
14. Eimtaveecharern S (2001) The development of model analyzer in orthodontics. Dissertations (MEng (Biomed)), Dept. of Biomed. Eng., Mahidol U., Bangkok
15. Thongti-amporn A (2003) Computerized orthodontic model analysis, Thesis (MSc (Orthodontic)), Chulalongkorn U., Bangkok
16. Heron's Formula at http://en.wikipedia.org/wiki/Heron's_formula
17. Bolton WA (1958) Disharmony in ToothSize and Its Relation to the Analysis and Treatment of Malocclusion. Ang. Orthod, 28(3):113-130
18. Press WH et. al. (2003) Numerical Recipes in C++: The Art of Scientific Computing (2nd edn). Cambridge University Press, London

Author: Wisarut Bholsithi
Institute: National Electronics and Computer Technology Center, National Science and Technology Center
Street: 112 Thailand Science Park, Phaholyothin Road
City: Pathum Thani
Country: Thailand
Email: wisarut.bholsithi@nectec.or.th

Cervical Cell Classification using Fourier Transform

Thanatip Chankong[1], Nipon Theera-Umpon[1,3], Sansanee Auephanwiriyakul[2,3]

[1]Department of Electrical Engineering, Faculty of Engineering, Chiang Mai University, Thailand
[2]Department of Computer Engineering, Faculty of Engineering, Chiang Mai University, Thailand
[3]Biomedical Engineering Center, Chiang Mai University, Thailand

Abstract — **A method of classifying the precancerous cells from Papanicolaou smear images is proposed in this paper. The proposed method utilizes a set of simple features extracted from the two-dimensional Fourier transform of the cell images in order to avoid the problem of cell and nucleus segmentation. The features used to discriminate between the normal and the abnormal cells are calculated based on the mean, variance, and entropy obtained from the frequency components along the circle of radius r centered at the center of the spectrum and the frequency components along the radial line having an angle θ.**

The classification results achieved by five classifiers are compared in order to evaluate the utilization of the selected features in normal and abnormal cell classification using four-fold cross validation. The classifiers used in this research include Bayesian classifier, linear discriminant analysis (LDA), K-nearest neighbor (KNN) algorithms, artificial neural network (ANN), and support vector machine (SVM). The classification rates obtained from these classifiers show promising performances. The result from the support vector machine provides the best accuracy and the lowest false rate. It achieves more than 92% correct classification rate on a set of 276 cervical single-cell images containing 138 normal cells and 138 abnormal cells.

Keywords — **Cervical cell, Fourier transform, Image classification, Frequency spectra, Feature extraction.**

I. Introduction

Cervical cancer is the most common cancer among women. This type of cancer, however, has good prognosis if it is detected and treated in the early stage. In Thailand, the National Cervical Cancer Prevention and Control Program suggests that women aged 35-60 years should perform the screening by Papanicolaou smear or the so-called Pap smear every 5 years [1]. The major problem of the screening program is the lack of an expert cytotechnologist and a large number of slides per day. For the past thirty years, many researches have focused on creating the automatic system for Pap smear screening in order to help solving these problems.

Several previous works have been focused on finding the effective features for the automated screening system. Most of the proposed techniques employed the features which depend on the accurate segmentation of cytoplasm and nucleus. In [2], a set of single cell images were segmented into nucleus and cytoplasm. The features were calculated from characteristics of nucleus and cytoplasm. The method in [3] proposed the feature sets based on the texture of nucleus only. One of the techniques for extracting features from a cervical cell is the Malignancy Associated Changes (MACs) measurements [4, 5]. MACs are the changes of DNA distribution in nuclei due to the effect of malignancy which can be observed from nucleus texture alteration. The image database used in these works was a taken in high resolution. It was also taken from slides that were stained by the Feulgen-Thionin technique since it provided strong nuclear-cytoplasmic contrast which is suitable for automated cell classification system. However, such high quality cell images are not commonly used in the cervical cancer screening program.

To avoid the problem of cell and nucleus segmentation, several attempts have been focused on Pap smear classification using the feature sets derived from frequency domain. The method for classifying cervical cells based on the optical power spectrum using analog system was proposed [6]. The idea of utilizing the features from frequency spectrum was investigated by using Discrete Fourier Transform implemented on digital computer [7-11]. The advantage of this approach is that the accurate segmentation of cell and its nucleus is not needed. However, it should be noted that this approach was applied to the single cell image captured in high resolution only.

This paper proposes a new method to classify the normal cervical cells and the abnormal cells (precancerous cells) by using a set of simple features extracted from the Fourier transform of the low resolution cell images. This allows us to avoid the cell segmentation process and a high resolution image acquisition system. The results of classification by several classifiers are compared in order to evaluate the ability of the extracted features used in classification of normal and abnormal cells.

This paper is organized as follows. Section II describes the data set and methods applied in this research including feature extraction and classifiers. The classification results are shown and discussed in section III. The conclusion is drawn in section IV.

Chwee Teck Lim, James C.H. Goh (Eds.): ICBME 2008, Proceedings 23, pp. 476–480, 2009
www.springerlink.com

II. Materials and Methods

A. Data Description

The images of cervical cell are obtained from [12]. The examples of the images in this data set are shown in Fig 1. There are 276 single cell images consisting of:

- 138 normal cell images with 63 superficial cells and 75 intermediate cells, and
- 138 abnormal cell images with various degrees of abnormality. The abnormal data consists of 34 light dysplastic cells, 34 moderate dysplastic cells, 35 severe dysplastic cells, and 35 carcinoma in situ (CIS) cells.

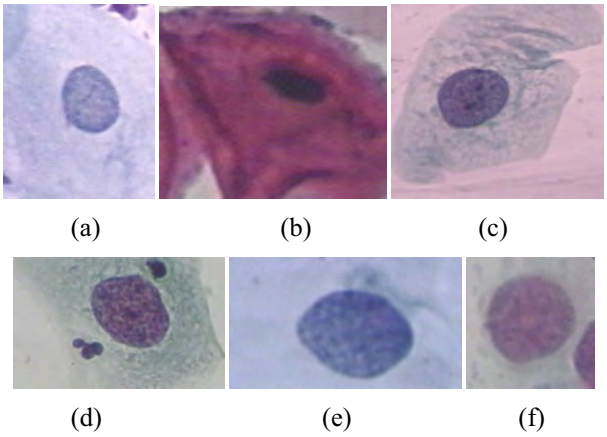


Fig. 1 Sample image of different cervical cell types (a) Normal intermediate cell, (b) Normal superficial cell, (c) Light dysplastic, (d) Moderate dysplastic, (e) Severe dysplastic, and (f) CIS

B. Fourier Transform-based Features

Each $M \times N$ cell image is transformed to the 2-D Fourier spectrum using the discrete Fourier transform defined by:

$$F(u,v) = \sum_{x=0}^{M-1}\sum_{y=0}^{N-1} f(x,y) e^{-j2\pi\left(\frac{ux}{M}+\frac{vy}{N}\right)} \quad (1)$$

for $u = 0,1,2,...,M-1$ and $v = 0,1,2,...,N-1$. The zero-frequency component is moved to the center of spectrum. Each component in the 2-D spectrum is transformed to the domain of polar coordinates, $F(r,\theta)$. This function is separated into two 1-D functions, i.e., the radial function $F(r)$, and the angular function $F(\theta)$. The radial function is defined as the frequency components along the circle of radius r centered at the center of the spectrum. The angular function is the frequency components along the radial line having an angle θ with respect to the u-axis. The radial and angular functions in frequency domain are illustrated in Fig 2.

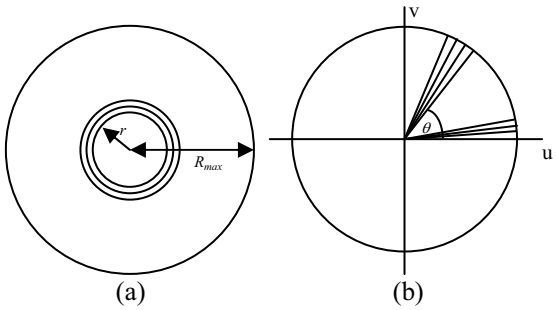


Fig. 2 Frequency spectrum in terms of (a) radial function, $F(r)$ and (b) angular function $F(\theta)$

The behavior of the frequency component at each pair of values of r and θ is represented by three statistical values, i.e., mean, variance, and entropy. The features used to discriminate between the normal and abnormal cells are calculated based on these values in the following equations:

Mean of $F(r)$ for any r :

$$\mu_r = \frac{1}{n_r}\sum_{i=1}^{n_r} F_i(r) \quad (2)$$

Variance of $F(r)$ for any r :

$$\sigma_r^2 = \frac{1}{n_r}\sum_{i=1}^{n_r}\left[F_i(r) - \mu(r)\right]^2 \quad (3)$$

Entropy of $F(r)$ for any r :

$$H_r = -\sum_{k=0}^{M-1} p_k(r)\cdot\log_2 p_k(r) \quad (4)$$

Mean of $F(\theta)$ for any θ :

$$\mu_\theta = \frac{1}{n_\theta}\sum_{j=1}^{n_\theta} F_j(\theta) \quad (5)$$

Variance of $F(\theta)$ for any θ :

$$\sigma_\theta^2 = \frac{1}{n_\theta}\sum_{j=1}^{n_\theta}\left[F_j(\theta) - \mu(\theta)\right]^2 \quad (6)$$

Entropy of $F(\theta)$ for any θ :

$$H_\theta = -\sum_{k=0}^{M-1} p_k(\theta)\cdot\log_2 p_k(\theta) \quad (7)$$

where n_r is the number of components in a circle of radius r. n_θ is the number of components along the radial line with angle θ. $p(r)$, $p(\theta)$ are the normalized histogram counts of the components of radius r and angle θ, respectively. M is the number of intensity levels in the frequency spectrum.

In total, 43 features are obtained by extracting the features in two ways: 1) calculating from the whole frequency spectrum and 2) calculating from subsections by dividing the spectrum into annular rings and radian wedges. The equations of each feature are defined below.

1. Features from whole frequency spectrum

Six features are extracted from the whole frequency spectrum in both radial and angular functions. The calculations are as follows:

Summation of mean of

$$F(r): f_1 = \sum_{r=1}^{R_{\max}} \mu_r \tag{8}$$

Average variance of

$$F(r): f_2 = \frac{1}{N_r} \sum_{r=1}^{R_{\max}} \sigma_r^2 \tag{9}$$

Average entropy of

$$F(r): f_3 = \frac{1}{N_r} \sum_{r=1}^{R_{\max}} H_r \tag{10}$$

Summation of mean of

$$F(\theta): f_4 = \sum_{\theta=0}^{2\pi} \mu_\theta \tag{11}$$

Average variance of

$$F(\theta): f_5 = \frac{1}{N_\theta} \sum_{\theta=0}^{2\pi} \sigma_\theta^2 \tag{12}$$

Average entropy of

$$F(\theta): f_6 = \frac{1}{N_\theta} \sum_{\theta=0}^{2\pi} H_\theta \tag{13}$$

where N_r is the total number of circles in the frequency image. N_θ is the total number of radial lines in the frequency image, and $R_{\max}$ is the maximum possible radius of a circle inscribed in the spectrum area.

2. Features from spectral subsections

In order to create spectral subsections, the frequency spectrum is divided in two manners, i.e., the annular ring and the radian wedge.

2.1 Annular ring subsection

Since the information of an image is mostly contained in a frequency component with small radius, the annular ring is then limited to the radius ranged from r=2 to 60% of $R_{\max}$. This area is divided into 5 annular rings with equal distance (Δr) between the adjacent rings.

A total of 25 features are obtained from the annular ring subsections. Each ring consists of 5 features as follows:

Summation of mean of the j^{th} ring:

$$f_7 = \sum_{r=r_j}^{r_j+\Delta r} \mu_r \tag{14}$$

Average variance of the j^{th} ring:

$$f_8 = \frac{1}{N_{rj}} \sum_{r=r_j}^{r_j+\Delta r} \sigma_r^2 \tag{15}$$

Average entropy of the j^{th} ring:,

$$f_9 = \frac{1}{N_{rj}} \sum_{r=r_j}^{r_j+\Delta r} H_r \tag{16}$$

Average variance of the product of the j^{th} ring:

$$f_{10} = \frac{1}{N_{rj}} \sum_{r=r_j}^{r_j+\Delta r} \sigma_{Fr}^2 \tag{17}$$

Average entropy of the product of the j^{th} ring:

$$f_{11} = \frac{1}{N_{rj}} \sum_{r=r_j}^{r_j+\Delta r} H_{Fr} \tag{18}$$

where N_{rj} is the total number of circles in the j^{th} ring. σ_{Fr}^2 is the variance of the function $r \cdot F(r)$. H_{Fr} is the entropy of the function $r \cdot F(r)$ and r_j is the inner radius of the j^{th} ring.

2.2 Radian wedge subsection:

The frequency spectrum between 0 and 180 degrees is divided into 4 equiangular $(\Delta\theta)$ subsections. Three features of each wedge-liked section are calculated by (19) to (21).

The calculation on these four subsections results in 12 wedge features.

Summation of mean of the k^{th} wedge:

$$f_{12} = \sum_{\theta=\theta_k}^{\theta_k+\Delta\theta} \mu_\theta \tag{19}$$

Average variance of the k^{th} wedge:

$$f_{13} = \frac{1}{N_{\theta k}} \sum_{\theta=\theta_k}^{\theta_k+\Delta\theta} \sigma_\theta^2 \tag{20}$$

Average entropy of the k^{th} wedge:

$$f_{14} = \frac{1}{N_{\theta k}} \sum_{\theta=\theta_k}^{\theta_k+\Delta\theta} H_\theta \tag{21}$$

where $N_{\theta k}$ is the total number of the radial lines in the k^{th} wedge, and θ_k is the left edge of the k^{th} wedge.

The total of 43 features values from radial and angular distributions are scaled to the range of [−1, 1] prior to the classification process.

C. Classification

Five classifiers including Bayesian classifier, linear discriminant analysis (LDA), K-nearest neighbor (KNN), artificial neural networks (ANN), and support vector machine (SVM), are investigated. The performance of 5 classifiers on discriminating the normal and abnormal cells is evaluated. In this research, 5 nearest neighbors are used for KNN. For ANN, we use three-layer backpropagation neural network which composed of 43 inputs in the input layer, 1 hidden layer with 20 neurons and 2 outputs in the output layers as suggested in [8]. For SVM, the exponential radial basis function (ERBF) kernel is chosen. After extensive trials, the best parameters for SVM in this research are the kernel spread parameter σ=0.8, the regularization parameter C=10^5, and ε = 0.1.

III. Experimental results and discussion

The classification results from each classifier are obtained using 4-fold cross validation. A total of 276 single cell images are separated into 2 groups, i.e., 68 images (one-fourth of the total images) are used as a test set. The rest of the images (208 images) are used as a training set. Due to space limitation, we cannot show all confusion matrices of the classifiers. The classification accuracy, the false positive and false negative rates are summarized in Table 1. The false positive rate (FP) is the proportion of normal cells (negative cases) that are incorrectly classified as abnormal cells (positive cases.) The false negative rate (FN) is the proportion of abnormal cells (positive cases) that are incorrectly classified as normal cells (negative cases.)

Considering the results in Table 1, the selected features provide good classification results even with a simple classifier such as Bayesian or LDA. The LDA give the lowest accuracy compared with other classifiers tested in this study. This may be because the data in this study is not linearly separable. KNN, ANN and SVM produce the classification rate higher than 90%. The best classification rate at 92.65% is obtained from SVM.

The false negative rate is important for cancer cell classification. If the abnormal cell is predicted as a normal cell, it will lead to undiagnosed abnormality which can progress to cancer. Even though the false negative rate of Bayesian is the lowest, the false positive rate is the highest. This could be because the Gaussian distribution of classes is not suitable for this dataset. Among all classifiers, SVM gives the optimum rates of both false positive and false negative of 7.35% for both parameters. SVM is the best classifier for this research.

Table 1 Classification results (%) from each classifier

	Classifier				
	Bayes	LDA	KNN	ANN	SVM
Accuracy	88.97	88.60	91.18	91.91	92.65
False positive	14.67	10.53	8.82	8.09	7.35
False negative	6.56	12.23	8.82	8.09	7.35

IV. Conclusion

This research proposed the method for classifying images of cervical cell by using a set of 43 simple features calculated from Fourier spectrum of the images. The images are classified into 2 classes, i.e., normal cervical cell and abnormal cells which are the cell that potentially progress to cancer. The classification rates obtained from 5 classifiers are quite good with the accuracy higher than 85%. The results show that Support Vector Machine provides the best result with 92.65% accurate and the false rates are 7.35% for both false positive and false negative. It is shown that the simple features from Fourier spectrum are usable in classification of the single cell image. For further development, the classification for non-isolated cells such as overlapping cells and cell cluster will be developed to avoid the cell isolation step.

REFERENCES

1. Linasmita V (2006) Cervical cancer screening in Thailand – 2006 FHI-satellite meeting on the prevention and early detection of cervical cancer in the Asia and the Pacific region, pp
2. Bazoon M, Stacey DA, Chen C, et al. (1994) A hierarchical artificial neural network system for the classification of cervical cells. IEEE World Congress on Computational Intelligence., 1994 IEEE International Conference on Neural Networks, pp 3525-3529 vol.3526
3. Walker RF, Jackway P, Lovell B, et al. (1994) Classification of Cervical Cell Nuclei using Morphological Segmentation and Textural Feature Extraction.Second Australian and New Zealand Conference on Intelligent Information Systems, pp 297-301
4. Kemp RA, MacAulay C, Garner D, et al. (1997) Detection of malignancy associated changes in cervical cell nuclei using feed-forward neural networks. Analytical Cellular Pathology 14:31-40
5. Hallinan JS (2005) Evolving neural networks for the classification of malignancy associated changes.Intelligent Data Engineering and Automated Learning - IDEAL 2005., pp
6. Pernick BJ, Kopp RE, Lisa J, et al. (1978) Screening of cervical cytological samples using coherent optical processing. Part 1 (ET). Appl. Opt. 17:21
7. McKenna SJ, Ricketts IW, Cairns AY, et al. (1992) Cascade-correlation neural networks for the classification of cervical cells. Neural Networks for Image Processing Applications, IEE Colloquium on, pp 5/1-5/4
8. Ricketts IW (1992) Cervical cell image inspection - a task for artificial neural networks. Network: Computation in Neural Systems 3:15 - 18
9. Ricketts IW, Banda-Gamboa H, Cairns AY, et al. (1992) Automatic classification of cervical cells-using the frequency domain. Applications of Image Processing in Mass Health Screening, IEE Colloquium on, pp 9/1-9/4
10. Ricketts IW, Banda-Gamboa H, Cairns AY, et al. (1992) Towards the automated prescreening of cervical smears.Applications of Image Processing in Mass Health Screening, IEE Colloquium on, pp 7/1-7/4
11. McKenna SJ, Ricketts IW, Cairns AY, et al. (1993) A comparison of neural network architectures for cervical cell classification.Third International Conference on Artificial Neural Networks, 1993, pp 105-109
12. The ERUDIT PapSmear tutorial at http://fuzzy.iau.dtu.dk/smear/

An Oscillometry-Based Approach for Measuring Blood Flow of Brachial Arteries

S.-H. Liu[1], J.-J. Wang[2] and K.-S. Huang[3]

[1]Department of Computer Science & Information Engineering, Chaoyang University of Technology, Taiwan
[2]Department of Biomedical Engineering, I-Shou University, Taiwan
[3]Hsinchu General Hospital, Department of Health, Executive Yuan, Taiwan

Abstract — **Although the oscillometric method has been widely used to measure arterial systolic and diastolic blood pressures, its potential for arterial blood flow measurement is still remained to be explored. Thus, the aim of the study was to noninvasively determine the arterial artery blood flow using an oscillometric blood flow measurement system. The system consisted of an elastic cuff, an air-pumping motor, a releaser valve, a pressure transducer, and an airflow meter. To build a nonlinear air cuff model, we detected the pumped airflow into the cuff and the cuff pressure using the airflow meter and pressure transducer during the inflation period, respectively. During the deflation period, only the pressure transducer was used to record the cuff pressure. Based on the air cuff model, the oscillometric blood flow waveform could be obtained by integrating the oscillometric pressure waveform. We compared the derived artery blood flow from the maximum amplitude of the oscillometric blood flow waveform with the Doppler-based blood flow calculated with diameters and blood velocities of the brachial arteries in 32 subjects undergoing diagnostic evaluation for peripheral arterial embolism. A linear regression coefficient of r = 0.72 was found between the oscillometry- and Doppler-based blood flow measurements for the 32 subjects. In conclusion, the oscillometric method can be applied to quantitatively measure the blood flow through a brachial artery.**

Keywords — **Oscillometry, Blood flow, Cuff mode, Doppler, Brachial artery.**

I. Introduction

The profile of the arterial blood flow is a potential marker of generalized arteriosclerotic disease. Several artery-related diseases, such as stenosis [1], aneurysm [2], atherosclerosis[3] and arterial stiffness[4], can be directly or indirectly diagnosed by measuring changes in the arterial blood flow. Therefore, the ability to measure the blood flow significantly helps medical physicians and researchers to understand not only the patency but also the hemodynamic characteristics of the artery of interest.

Several methods have been proposed for non-invasively assessing the forearm blood flow in normal, stress and diseased conditions. Doppler ultrasound can yield the maximum or average blood velocity in an artery of interest, and then the arterial blood flow can be obtained by multiplying the measured velocity by the cross-sectional area if the diameter of the artery is assumed to remain constant [5]. In the photoplethysmographic approach, the arterial blood flow is indirectly derived from the absorption of incident light by red blood cells and other constituents in an arterial vessel [6]. In electrical-impedance plethysmo-graphy, the blood flow is implicitly assessed by measuring changes in impedance for electrical current passing through the arterial lumen [7].

Oscillometry is most frequently used to measure the arterial blood pressure, but it can also quantify the blood flow in an artery of interest. This study investigated a proposed oscillometric flow measurement system for determining the brachial arterial blood flow.

II. Oscillometric flow measurement

A. System design

Fig. 1 shows a block diagram of our proposed oscillometric blood flow measurement system. The relationship between the cuff pressure and the cuff air volume (i.e. the cuff model) was constructed using a non-linear regression approach. During the deflation period, only the pressure

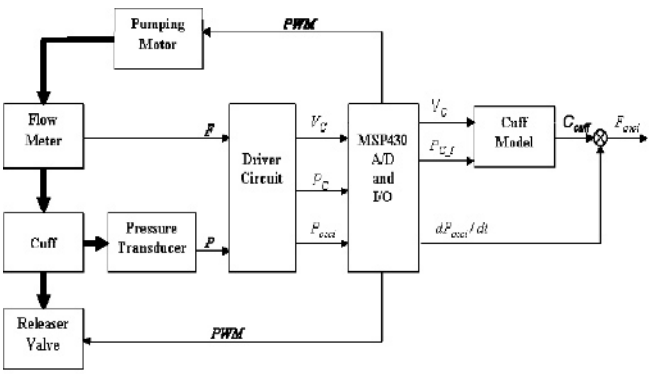


Fig. 1 Block diagram of the proposed measurement system. The thick arrows represent the air pathways and the thin arrows the electric current flow. F is the pumped flow, P_{C_I} is the cuff pressure during the inflation period, P_{osci} is the oscillometric pressure waveform during the deflation period, V_C is the cuff volume, C_{cuff} represents the slope of the cuff model, and F_{osci} is the oscillometric flow waveform.

Chwee Teck Lim, James C.H. Goh (Eds.): ICBME 2008, Proceedings 23, pp. 481–484, 2009
www.springerlink.com

transducer was used to record the cuff pressure, from which the oscillometric pressure waveform was extracted.

In the sensing module of Fig. 1, the cuff pressure is measured with a silicon-membrane pressure transducer (range: 3.45×10^4 N/m^2; SCX05DNC, SenSym). The output of the pressure transducer is calibrated using a mercury column sphygmomanometer. The oscillometric pressure waveform is obtained after band-pass filtering the analog cuff pressure signal from 0.1 to 3 Hz. The airflow meter (AWM3300, Honeywell) has a maximum operating range of 1000 sccm (ml min^{-1}). The cuff pressure, oscillometric pressure waveform and airflow signals are then digitized by a 12-bit A/D converter at a sampling rate of 250 Hz.

B. Brachial blood flow

The pumped airflow and cuff pressure were simultaneously recorded during the inflation period, with the airflow converted into the volume by integration:

$$V_c(t) = \frac{1}{60}\int_0^t F(s)ds\,, \tag{1}$$

where V_C is the cuff volume, F is the airflow and t is the time in seconds. It was assumed that initially the cuff was wrapped around the upper arm sufficiently tightly so that there was negligible residual air inside the cuff, with the cuff pressure being close to zero. This non-linear characteristic of the cuff model during the ascending pressure portion may be described by a hyperbolic function:

$$V_C = \frac{aP_{C_I}}{b + P_{C_I}} + cP_{C_I}\,, \tag{2}$$

where P_{C_I} is the air pressure inside the cuff during the inflation period, V_C is the volume of air pumped into the cuff, and a, b and c are constants. The slope of the cuff model is given by

$$C_{cuff}(P_{c_I}) = \frac{dV_c}{dP_{c_I}}. \tag{3}$$

During the deflation period, cuff pressures P_{C_D} and P_{osci} were respectively used as the input and output variables to describe the envelope of the oscillometric pressure waveform. According to the oscillometric pressure waveform, P_{osci} represents the change in the waveform superimposed on the cuff pressure since it resulted from the change in the arterial volume. Therefore, the change in the oscillometric volume (V_{osci}) embedded in the cuff volume can be calculated from C_{cuff} and P_{osci}:

$$dV_{osci}(P_{C_D}) = C_{cuff}(P_{C_D})dP_{osci}(P_{C_D})\,. \tag{4}$$

The change in the oscillometric volume is defined here as the instantaneous change in the vascular volume of the arterial segment of interest under the cuff. The oscillometric flow waveform is determined by differentiating the oscillometric volume waveform:

$$F_{osci}(t) = \frac{dV_{osci}(t)}{dt}. \tag{5}$$

III. Calibration and Experimental Material

A. System design

Eqs. (4) and (5) can be used to calculate the oscillometric flow from the oscillometric pressure. During the deflation period, an airflow pulse provided by a non-invasive blood pressure analyzer (CuffLink, DNI NEVADA) was used to simulate the arterial blood pulse. In the calibration process, the cuff was wrapped around a phantom and the pressure analyzer was connected to the cuff. We used an airflow meter (range: 100 sccm [ml min^{-1}]); AWM3100, Honeywell) to quantitatively record the airflow pulse generated by the pressure analyzer during the deflation period.

We compared the peak amplitudes of $F_{osci}(t)$ in the oscillometric flow waveform with those in the simulator-pumped pulse flow. Fig. 2 shows the estimated oscillometric volume and flow waveform obtained by using Eqs. (4) and (5). Because the pressure–volume relationship of the cuff model was almost linear at higher pressures (>60 mmHg), we only compared these data for these pressures. Fig. 3 compares the estimated peak F_{osci} values with the simulator-pumped pulse flows. The peak F_{osci} values were more precise at lower cuff pressures (r = 0.973) than at higher cuff pressures (r = 0.936).

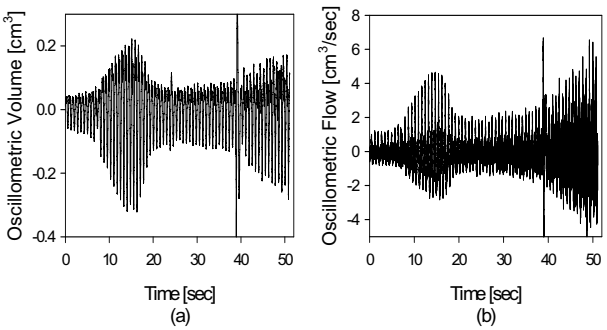


Fig. 2 The oscillometric flow was estimated by Eq. (4): (a) the oscillometric volume signal; (b) the oscillometric flow signal.

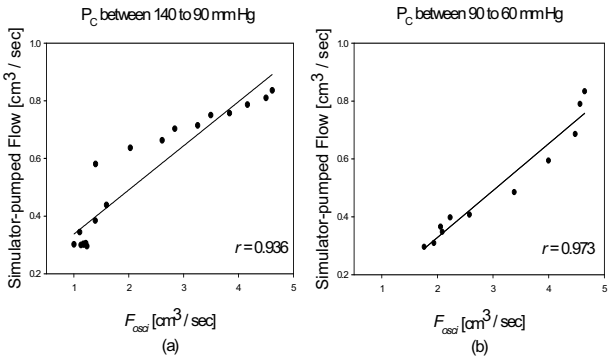


Fig. 3 The peak F_{osci} values compared with the simulator-pumped pulse flows. (a) The cuff pressure is limited above MAP; (b) The cuff pressure is limited below MAP.

B. Brachial blood flow

The experimental protocol was applied to 32 subjects (14 men and 18 women) aged 68 ± 15 years (mean ± SD; range: 19 to 93 years) undergoing diagnostic evaluations for peripheral arterial embolism. The brachial arterial blood pressure was measured with an electric sphygmomanometer (DINAMAP PROCARE 100, GE Medical Systems) in the left arm of each patient. Our designed instrument was used to measure the blood flow in the brachial artery. Thereafter, a duplex ultrasound scanner (7.5 MHz; M2410B, AGILENT, Hewlett Packard) was applied by a doctor to measure the pulse wave of peripheral vessels, and then to detect if an arterial or venous embolism was present and, if it was, to locate it. Finally, a duplex ultrasound scan was used to measure the arterial internal diameter and velocity of blood flow in the left brachial artery. The Doppler-based flow (F_{echo}) was then calculated by the multiplication of the arterial internal cross section and the maximum blood flow velocity.

IV. Results

Baseline hemodynamic data of the important variables for characterizing the patients are presented in Table 1, which indicates the wide range of arterial blood pressures. Since the amplitude of the oscillometric pressure waveform is maximal at the unloaded condition when the cuff pressure is equal to the mean arterial pressure, the maximum peak amplitude of the oscillometric flow waveform represented the optimal estimated blood flow $V_{p_}F_{osc}$. The proposed method was validated by comparing the oscillometry-based blood flow with the Doppler-based blood flow. The linear relation of the F_{echo} values with those of $V_{p_}F_{osci}$ is demonstrated in Fig. 4. The results indicated that for the peak value, the blood flow as measured using the oscillometry-based method was in reasonable agreement with the echocardiography-derived blood flow.

Table 1 Hemodynamic characteristics of the 32 patients in the study

Quantity	Value
Internal diameter of brachial artery (cm)	0.344 ± 0.079
Brachial blood flow velocity (cm s^{-1})	80.5 ± 21.7
Arterial compliance (10^{-3} cm^4 $dyne^{-1}$)	6.864 ± 2.645
MAP (mmHg)	92.3 ± 11.9
SBP (mmHg)	135.4 ± 23.6
DBP (mmHg)	67.5 ± 8.8

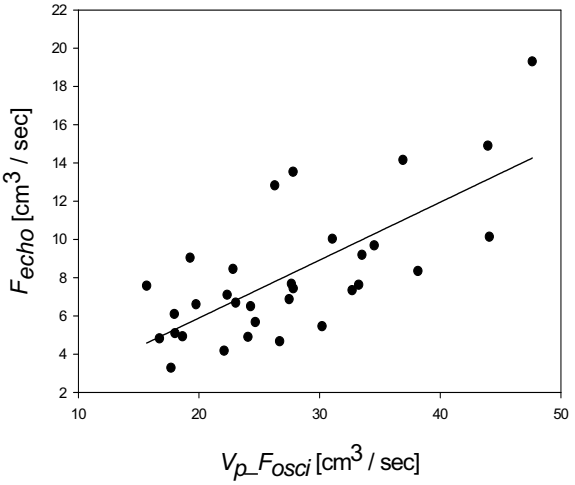


Fig. 4 Scatter plot of $V_{p_}F_{osci}$ vs. F_{echo}: n = 32, r = 0.72 (p < 0.0001), SEE = 2.52.

V. Discussion

Oscillometry has been extensively applied for assessments of systolic and diastolic pressures for many years [8], but few studies have used the method for blood flow measurements[9,10]. In the present study, an oscillometric blood flow measurement system was constructed for determining the brachial arterial blood flow. The system has been shown to be capable of detecting the pneumatic cuff pressure and volume simultaneously. Furthermore, the presence of moderate linear correlation coefficients between the oscillometry- and Doppler-based arterial blood flow measurements in the 32 subjects suggest that the oscillometry-based system can be dependably used to non-invasively determine the arterial blood flow. Thus, its ability to measure blood flow as demonstrated here might herald another use for automatic oscillometric blood pressure meters.

One of the important challenges in this study was deriving the pneumatic cuff model that mathematically describes the pneumatic cuff pressure–volume relationship. The model was established using real measurements of the cuff pressure and volume made by precise pressure sensors and flow meters. Furthermore, the non-linear relationship between the cuff pressure and cuff volume was found to be well fitted by a regression function (r = 0.999). Many biomechanical factors affect the systolic and diastolic characteristic ratios, and hence also oscillometric blood pressure measurements, such as the cuff elastance, mean arterial pressure, heart rate, pulse pressure, Young's modulus and arterial wall viscosity[11,12]. The cuff model was affected by the cuff elastance and Young's modulus of the tissue. The present and previous findings together suggest the need to consider more complicated systolic and diastolic characteristic ratios for oscillometric measurements according to the pneumatic cuff pressure–volume relationship.

Drzewiecki and co-workers have indicated that an occlusive arm cuff can be used as a volume sensor [9], suggesting that the blood flow can be obtained from the derivative of the cuff volume signal. Whitt and Drzewiecki used oscillometric data to non-invasively determine the flow from the derivative of the cuff pressure at a cuff pressure when the arterial compliance was nearly maximal[10]. According to these previous results, we performed oscillometry-based blood flow measurements after the cuff pressure–volume relationship was established during the inflation period.

VI. Conclusions

A measurement system has been successfully developed for detecting the brachial arterial blood flow using the oscillometric method. A mathematical model of the pneumatic cuff is established using data measured during the deflation period, which is then used to estimate the oscillometry-based arterial blood flow. The results showed a linear regression coefficient of r = 0.72 between the oscillometry- and Doppler-based brachial arterial blood flow measurements in 32 subjects, suggesting that the blood flow in the brachial artery can be quantitatively determined with the oscillometric technique once a satisfactory calibration procedure has been performed.

Acknowledgment

This work was supported by the National Science Council, Taiwan, under grant numbers NSC 96-2221-E-264-001-MY3 and NSC 95-2221-E-214-004-MY3.

References

1. Bluestein D, Niu L, Schoephoerster RT et al. (1997) Fluid mechanics of arterial stenosis: Relationship to the development of mural thrombus. Ann Biomed Eng 25:344–356
2. Swillens A, Lanoye L, De Backer J et al. (2008) Effect of an abdominal aortic aneurysm on wave reflection in the aorta. IEEE Trans Biomed Eng 55:1602–1611
3. Stary HC (1989) Evolution and progression of atherosclerotic lesions in coronary arteries in children and young adults. Arteriosclerosis 9:I19–I32
4. Liu SH, Wang JJ, Wen ZC (2007) Extraction of an arterial stiffness index from oscillometry. J Med Bio Eng 27:116–123
5. Simon AC, Laurent S, Levenson JA et al. (1983) Estimation of forearm arterial compliance in normal and hypertensive men from simultaneous pressure and flow measurements in the brachial artery using a pulsed Doppler device and a first-order arterial model during diastole. Cardiovasc Res 17:331–333
6. Jönsson B, Laurent C, Skau T et al. (2005) A new probe for ankle systolic pressure measurement using photoplethysmography (PPG). Ann Biomed Eng 33:232–239
7. Wang JJ, Wang PW, Liu CP et al. (2007) Evaluation of changes in cardiac output from the electrical impedance waveform in the forearm. Physiol Meas 28:989–999
8. Geddes LA, Voelz M, Combs C et al. (1983) Characterization of the oscillometric method for measuring indirect blood pressure. Ann Biomed Eng 10:271–280
9. Drzewiecki GM, Karam E, Bansal V et al. (1993) Mechanics of the occlusive arm cuff and its application as a volume sensor. IEEE Trans Biomed Eng 40:704–708
10. Whitt MD, Drzewiecki GM (1994) Non-invasive method for measuring flow from oscillometric data. IEEE Proc. Vol. 2, 16th Ann. Intern. Conf. of the Eng. Advances: New Opportunities for Biomed Eng, pp 946–947
11. Drzewiecki G, Hood R, Apple H (1994) Theory of the oscillometric maximum and the systolic and diastolic detection ratios. Ann Biomed Eng 22:88–96
12. Ursino M, Cristalli C (1996) A mathematical study of some biomechanical factors affecting the oscillometric blood pressure measurement. IEEE Trans Biomed Eng 43:761–778

The address of the corresponding author:

Author: Jia-Jung Wang
Institute: Department of Biomedical Engineering, I-Shou University
Street: No. 1, Sec. 1, Syuecheng Rd., Dashu Township
City: Kaohsiung County
Country: Taiwan
Email: wangjj@isu.edu.tw

Fuzzy C-Means Clustering for Myocardial Ischemia Identification with Pulse Waveform Analysis

Shing-Hong Liu[1], Kang-Ming Chang[2] and Chu-Chang Tyan[1]

[1] Department of Computer Science and Information Eneering, Chaoyang University of Technology, Taichung, Taiwan
[2] Department of Computer and Communication, Asia University, Taichung, Taiwan
[3] Division of Chinese Medicine, Buddhist Tzu Chi General Hospital, Sindian City, Taipei, Taiwan

Abstract — **The purpose of this study is to build an automatic disease classification system using pulse waveform analysis, based on a Fuzzy C-means clustering algorithm. A self designed three-axis mechanism was used to detect the optimal site to accurately measure the pressure pulse waveform (PPW). Considering the artery as a cylinder, the sensor should detect the PPW with the lowest possible distortion and hence an analysis of the vascular geometry and an arterial model were used to design a standard positioning procedure based on the arterial diameter changed waveform for the *X*- and *Z*-axes. A fuzzy C-means algorithm was used to identify myocardial ischemia symptoms in 35 elderly subjects with the PPW of the radial artery. Two type parameters are used to make the features, one is a harmonic value of Fourier transfer, and the other is a form factor value. A receiver operating characteristics curve is used to determine the optimal decision function. The harmonic feature vector (H_2, H_3, H_4) performed at the level of 69% for sensitivity and 100% for specificity while the form factor feature vector (LFF, RFF) performed at the level of 100% for sensitivity and 53% for specificity. A negative group was used to determine the tolerance of the FCM algorithm. The harmonic feature vector (H_2, H_3, H_4) had a better correct result, at 57%.**

Keywords — **Fuzzy C-means, Form Factor, Harmonic, Myocardial Ischemia, Pulse Waveform Analysis.**

I. Introduction

Myocardial ischemia occurs as a result of the heart muscle being deprived of oxygen and is accompanied by inadequate removal of metabolites because of reduced blood flow or perfusion. In the case of a slight attack, myocardial ischemia subjects may complain of chest pains. But, in a more serious condition, sudden death will occur. In the clinic the Duke treadmill exercise score, a composite of measures of functional capacity and stress-induced ischemia, has been shown to predict prognosis in coronary artery diseases [1]. It has been reported that exercise electrocardiogram examination reveals the presence of chest pain during exercise or exertion, with the accuracy of diagnosis reaching 90% [2]. But the treadmill exercise is a dangerous and hard exercise for the patients. The patients must run until their heart rate attains at least 85% to 90% of the maximum heart rate for 1 minute, or until fatigue develops. Therefore, how to easily examine myocardial ischemia is a challenging study.

O'Rourke *et al*, have shown that arterial sclerosis is caused by the fracture and fragmentation of the elastic lamellae with the diabetes [3]. Consequently, many studies have been developed to assess arterial stiffness as a means of predicting the cardiovascular risk to the patient. Most of these studies have focused on the analysis of the pulse pressure waveform (PPW) measured from the radial artery. This kind of method is known as pulse waveform analysis (PWA). Research into PWA of the radial artery was initiated by the invention of a pulse waveform scanner by Vierordt in 1855 [4], which have since proven to be a safe and effective diagnostic tool. In 1993, Wang *et al*, used a Fourier transform to study the PPW, which would be affected by mechanical resonance between the heart and other organs [5]. Form factor (FF) value is a time domain feature that comes from the ratio of the standard deviation of the derivative signal. The FF value has been used in biomedical signal analysis, such as EEG and ECG [6]. The FF value is very sensitive to noise, and is only suitable for narrow band signals, not for wide band signals, such as EMG. Because PPW is a narrow band signal, the FF value also could be used to describe the PPW's characteristic in time domain.

A hard k-means algorithm executes a sharp classification, in which each object is either assigned to a class, or not. The application of fuzzy sets in a classification function causes the class membership to become a relative one and an object can belong to several classes at the same time but with different degrees [7]. Therefore, a fuzzy C-means (FCM) algorithm which is an unsupervised clustering method has a better performance than the hard k-mean algorithm for identifying the medical problems. A receiver operating characteristics (ROC) curve is used to determine the optimal decision function which is based on the feature centers derived by FCM.

In our studies, the radial artery can be regarded as a three-dimensional cylinder, and locating the best measuring point requires three axes to be considered. In order to get a standard measurement, we had designed a three-axis

Chwee Teck Lim, James C.H. Goh (Eds.): ICBME 2008, Proceedings 23, pp. 485–489, 2009
www.springerlink.com

mechanism and a standard positioning procedure for detecting the optimal measurement site [8]. A modified sensor was designed to detect the arterial diameter changed waveform (ADCW) and PPW simultaneously. We analyzed the vascular geometry to estimate the optimal *X* position, and used an artery model to estimate the optimal *Z* position to get a standard PPW. In the PWA, the harmonic and FF values of the PPW being the frequency and time domain features were passed into the FCM algorithm to identify the myocardial ischemia symptoms that used the exercise electrocardiogram (ECG) as a reference. Furthermore, in order to test the clustering tolerance of FCM algorithm, a negative group was used whose treadmill ECG examination was normal.

II. Experimental materials and methods

A. Myocardial ischemia diagnosis

All subjects had to be free from any confounding factors such as infection of the respiratory tract, acute whole-body diseases, severe stenosis of the aorta, congestive uncontrolled heart failure, severely high blood pressure, chest pain under a resting condition, and severe arrhythmia. A standard diagnosis of myocardial ischemia was made based on a treadmill ECG showing horizontal or lower slope ST depression that followed the PPW measurement. Its lowest level had to reach the J point (the border between the QRS and ST phases), followed by a decrease of 0.1 mV every 80 msec. The treadmill ECG (SCHILLER STM-55, Polymed Chirurgical, Canada) measurements were made according to conventional methods at the hospital, in which the patient was allowed to run freely on the treadmill. The ECG monitoring device was attached to the patient to record the heartbeat. The speed and treadmill slope were increased every few minutes until any of the following four scenarios occurred: (1) patient could no longer continue running for any reason, (2) the heart rate reached a maximal value, (3) myocardial ischemia occurred, or (4) the ECG showed significant changes. Patients who showed scenario 1 were not included in the analysis. Scenario 2 was considered negative for ischemia if the ECG had not shown any significant change, while scenarios 3 and 4 were considered positive.

B. Features of PPW

The harmonic values of the PPW were obtained by Fourier transformation, as reported previously. The Fourier series is given by:

$$f(t) = H_0 + \sum_{k=1}^{N} H_k \cos(\frac{2\pi k}{T} t + \phi k), \tag{1}$$

where T is the beat time, H_0 is the mean value of the radial pulse, and the H_k values are the harmonic components of the PPW. The harmonic components were all normalized to H_1 before calculating differences.

The FF value of the PPW is as following:

$$FF = \frac{\sigma x \times \sigma x''}{(\sigma x')^2}, \tag{2}$$

where σx is the variance of the signal, $\sigma x'$ is the variance of the first derivative signal; $\sigma x''$ is the variance of the second derivative signal. The FF value of a sinusoidal wave is unity; other waveforms have FF values increasing with the extent of variations present in them.

C. Fuzzy C-Mean

In order to develop a diagnostic decision algorithm for myocardial ischemia, FCM is adopted. A feature vector belongs to a cluster to some degree that is specified by a membership matrix. The FCM function analyzes the PPW parameters and produces three outputs: (1) the membership matrix $\underline{\boldsymbol{U}}$, (2) the cluster centers $\{c_i, i=1, \ldots, K\}$, and (3) the PPW coding vector (row matrix) $\underline{\boldsymbol{S}}$. Four steps in the FCM function are depicted below. The cluster center $K=2$ in this paper.

Step 1: Initialize the membership matrix $\underline{\boldsymbol{U}}$ with random values between 0 and 1. The size of $\underline{\boldsymbol{U}}$ is $K \times L$, where K is number of clusters, and L is the length of input data. In this paper, L is the summation number of the positive group patients and the normal group. The element of membership matrix $\underline{\boldsymbol{U}}$, u_{ij}, is the probability that the jth feature vector belongs to the ith cluster ($1 \le i \le K$ and $0 \le j \le L-1$). Note that, for a given feature vector, summation of degrees of belongness equals unity. Elements of $\underline{\boldsymbol{U}}$ must satisfy the constraint below

$$\sum_{i=1}^{K} u_{ij} = 1, \quad 0 \le j \le L-1. \tag{3}$$

Step 2: Calculate fuzzy cluster centers for all K clusters according to

$$c_i = \frac{\sum_{j=0}^{L-1} v[j] \cdot u_{ij}}{\sum_{j=0}^{L-1} u_{ij}}, \quad 1 \le i \le K, \tag{4}$$

where $v[j]$ is the feature vector derived from normalized harmonic components and the FF values defined in Eq. (1) and (2)..

Step 3: Compute the cost function defined below

$$J(\underline{\boldsymbol{U}}, c_1, c_{2,\ldots,} c_K) = \sum_{i=1}^{K} J_i = \sum_{i=1}^{K} \sum_{j=0}^{L-1} u_{ij}^m D_{ij}^2, \tag{5}$$

where $D_{ij} = \|c_i - v[j]\|$ is the Euclidean distance between the *i*th cluster center and the *j*th feature vector. The weighting exponent, *m*, in Eq. (5) is selected to be *m*=2. The criterion requires *J* to be as small as possible. The iteration terminates if improvement of ***J*** over previous iteration is below a pre-specified threshold. Otherwise, the algorithm proceeds with next step to update the membership matrix $\underline{\boldsymbol{U}}$.

Step 4: Compute a new membership matrix $\underline{\boldsymbol{U}}$ whose element u_{ij} is adjusted by

$$u_{ij} = \frac{1}{\sum_{k=1}^{K} \left(\frac{D_{ij}}{D_{kj}} \right)^{2/m-1}}, \quad 1 \le i \le K, \quad 0 \le j \le L-1 \qquad (6)$$

According to the above equation, u_{ij} is inversely proportional to the squared distance from the feature $v[j]$ to the cluster center c_i.

The iteration process from *Step* 2 to *Step* 4 continues.

Four clustering results are determined: True Positive (*TP*), True Negative (*TN*), False Positive (*FP*) and False Negative (*FN*). A ROC curve is used to turn an optimal cluster performance which was defined by cluster specificity and sensitivity.

D. Experimental material

There were 16 patients in the positive group (11 male and 5 female, mean age 58.9 years with SD 11.6 years), 19 patients in normal group (9 male and 10 female, mean age 63.9 years with SD 13.7 years), 28 patients in negative group (18 male and 10 female, mean age 54.2 years with SD 9.1 years). The positive group is those who are judged as myocardial ischemia patients by treadmill ECG. The negative group is those who have the symptoms of myocardial ischemia but the treadmill ECG result shows no myocardial ischemia. The normal group is those who are healthy elders.

All the subjects were asked to stop smoking, stop alcohol intake, and avoid consuming stimulants (e.g., coffee and tea) and medications for at least 24 hours before participating in the experiments. They rested in a temperature-controlled room (at 22±1°C) for 30 minutes before the waveform examination was performed. During the waveform measurement, each subject was asked to sit on an adjustable-height chair. The subject's left or right hand was placed on a table at the same horizontal height as the heart with the palm pointing upwards and the wrist resting on a soft pillow. The radial artery PPW was measured at 10 mm proximal to the styloid process for both right and left hands. An exercise ECG was obtained immediately after PPW measurement.

III. Results

Traditional pulse signals contain one major peak and two following minor peaks within one period. The minor peaks of myocardial ischemia patients are more insignificant than those of a normal group. Figure 1 illustrates the typical PPW of myocardial ischemia patients (age 69 years, female) and normal subjects (age 56, female). Corresponding harmonics are also demonstrated in Fig. 2. From Fig. 2(a) we can see that the normal group has larger harmonic rhythms than positive group. Table 1 lists the harmonic features of left hand and the FF features of left and right hands for the positive groups and the normal group. Their corresponding t-test p values are also included. Therefore, the significant parameters ($p < 0.05$) were chosen as FCM clustering input features.

In the following step, Table 2 shows that the feature vectors are used as features in the FCM algorithm. After the FCM clustering steps for selected features, two cluster centers and two separate clustering groups are determined. The original decision function is determined by the perpendicular bisector on the cluster centers. One decision function

Table 1 List of harmonics and FF values of PPW.

	Positive Group Mean (STD) n=16	Normal Group Mean (STD) n=19	
H_2	0.567 (0.289)	0.227 (0.104)	0.002**
H_3	0.198 (0.184)	0.073(0.058)	0.024*
H_4	0.060 (0.065)	0.014 (0.013)	0.014*
H_5	0.023 (0.019)	0.013 (0.012)	0.065
H_6	0.017 (0.025)	0.017 (0.008)	0.196
H_7	0.007 (0.009)	0.004 (0.005)	0.209
H_8	0.006 (0.007)	0.004 (0.008)	0.586
H_9	0.002 (0.003)	0.001 (0.002)	0.374
LFF	14.0813 (3.7764)	19.8407 (7.4085)	0.0062**
RFF	13.3054 (4.0565)	18.2092 (7.1779)	0.0169*

*p<0.05; ** p<0.01.

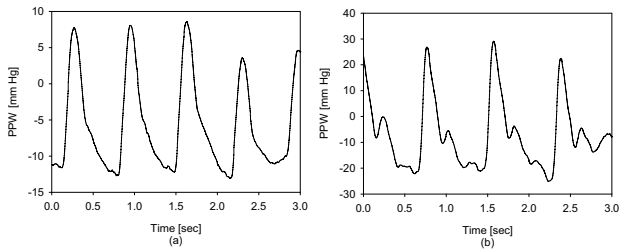


Fig 1. Typical pulses waveforms as measured at the optimal *X*- and *Z*-axis position: (a) positive group and (b) normal group.

Table 2 Clustering performances of various harmonics and FF features

	Sensitivity %	Specificity %
(H_2, H_3)	56	100
(H_2, H_4)	56	100
(H_3, H_4)	38	100
(H_2, H_3, H_4)	69	100
(H_2~H_9)	56	100
(LFF, RFF)	100	84
(LFF, H_2)	75	100
(LFF, H_2, H_4)	75	100

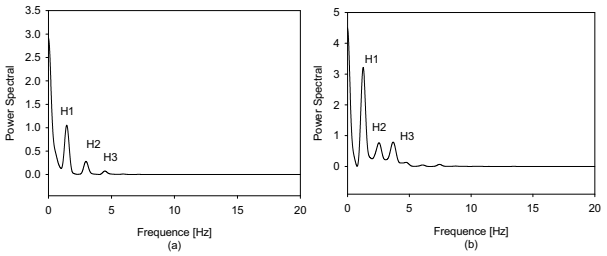


Fig 2. Frequency spectra of waveforms in Fig. 9: (a) positive group and (b) normal group. The harmonic peaks are denoted as H1, H2, and H3.

has corresponding sensitivity-specificity pairs for its clustering performances. Moving the original decision function with the same slope to get the other decision function, there are new clustering results and new sensitivity-specificity pairs. A ROC curve is then established by these sensitivity-specificity pairs of various decision functions. Figure 6 demonstrates three ROC curves from features with three input feature vectors, one is from (H_2, H_3, H_4), another is from (LFF, RFF), and the other is from (LFF, H2, H_4). The most optimal clustering performance is determined at the turnover of the ROC for different features, as shown in Table 2. The harmonic feature vector (H_2, H_3, H_4) has performances of 69% and 100% for sensitivity and specificity respectively, while the FF feature vector (LFF, RFF) has a performance of 100% for sensitivity and 53% for specificity. We also combined the harmonic and FF parameters as clustering features. We also combined with the harmonic and FF features as a feature vector to identify the myocardial ischemia. The two dimension feature vector (LFF, H_2) and three dimensions feature (LFF, H_2, H_4) all have 75% sensitivity and 100% specificity.

A negative group was used to understand the tolerance of the FCM algorithm. The PPW was analyzed to extract harmonic and FF parameters, and apply the corresponding decision function to the same feature distribution. We found that, using (H_2, H_3, H_4) features, there were 16 subjects classified in the normal group (57%). But when, using (LFF, RFF) as features, there were only 5 subjects classified in the normal group (18%). Using a mixed feature (LFF, H_2) there were 14 subjects classified in the normal group (50%).

IV. Discussions and conclusions

Spectrum feature, harmonic, and time-domain feature, FF, are used in this study. The harmonic value is a standard method for PWA analysis. Harmonic features had a sensitivity 69% and specificity 100% in this study. According to Wang [5], the second harmonic value and the forth harmonic value have corresponding physiological resonances with heart related diseases. This is the first time that the FF was applied in PWA. In Table 1, the FF features have lower p values between positive and normal subjects than harmonic features. The FF is a kind of time domain feature, and the two pulse's minor peaks of the PPW in the positive group are weaker than that of normal subjects. Therefore, the PPW variation of the positive group is lower, and results in a lower FF value than the normal group. The FF features have a sensitivity of 100% and a specificity of 53%, which is different from harmonic features, based clustering performance. The FF features demonstrate a better discrimination performance, but in different way.

A PWA based myocardial ischemia classification system was developed and tested. With the harmonic and FF features of PPW, higher identification specificity and sensitivity are achieved. The tolerance of the FCM algorithm is compared with the negative group. This system is non-invasive and is a standard measurement for the PPW. It is a good candidate for screening myocardial ischemia patients before further treadmill ECG examinations.

Acknowledgment

This project was supported by project numbers CCMP95-RD-016 and NSC 96-2221-E-264-001-MY3 form the National Science Council.

References

1. Mark B, Hlatky A et al (1987) Exercise treadmill score for predicting prognosis in coronary artery disease, *Ann. Intern. Med*., 106: 793-800.
2. O'Rourke A (2005) Should patients with type 2 diabetes asymptomatic for coronary artery disease undergo testing for myocardial ischemia?, *Nat Clin Pract Cardiovasc Med.*, 2:492-493.
3. Vierordt, K (1855) Die Lehre vom Arterienpuls in gesunden und kranken Zustanden, gegrundet auf eine neue Methode der bildlichen Darstellung des menschlichen Pulses, Braunshweig F Vieweg, 1855.
4. Chen C-Y, Wang W-K et al (1993) Spectral analysis of radial pulse in patients with acute uncomplicated myocardial infarction, *Jpn. Heart J.*, 34:37-49.

5. Rangayyan M (2002) *Biomedical Signal Analysis─A Case Study Approach*, Chap. 9, New York: Wiley-Interscience.
6. Berks G, Keyserlingk G et al (2000) Fuzzy clustering- a versatile mean to explore medical database, *ESIT, Aachen*, Germany, 2000.
7. Tyan C-C, Liu S-H et al (2008) A Novel Noninvasive Measurement Technique for Analyzing the Pressure Pulse Waveform of the Radial Artery, *IEEE. Trans. Biomed. Eng.,* 55:286-297.

Author: Shing-Hong Liu
Institute: Department of Computer Science and Information Eneering, Chaoyang University of Technology
Street: 168 Jifong E. Rd., Wufong Township, 41349
City: Taichung
Country: Taiwan
Email: shliu@cyut.edu.tw

Study of the Effect of Short-Time Cold Stress on Heart Rate Variability

J.-J. Wang[1] and C.-C. Chen[1]

[1] Department of Biomedical Engineering, I-Shou University, Kaohsiung, Taiwan

Abstract — **The present work focuses on whether the heart rate variability (HRV) evaluated during the cold stress is different from that in the control condition. In fifteen subjects (12M & 3F, aging 21~24 yrs), a five-minute ECG record was performed in the room temperature condition (27°C), and the other five-minute ECG record was then measured in the cold stress during which an ice bag was placed on the forehead. After the R-R intervals were extracted from these two 5-minute ECG recording signals, we analyzed them using the time- and frequency-domain techniques. The results showed a significant decrease in PNN50 defined as the count of two continuous R-R intervals larger than 50 ms divided by the total number (control 25.4±20.9 versus cold stress 19.8±18.3 %, $p < 0.05$). In addition, there was a significant difference in the power in the high frequency range of 0.15 ~ 0.4 Hz (control 14.63±7.38 versus cold stress 12.03±5.14 ms^2, $p < 0.05$). Thus, as the human body encounters a short-term cold stress exposure, only a 5-minute HRV analysis can also demonstrate a significant reduction in the parasympathetic nervous activity.**

Keywords — **Heart rate variability, Cold stress, R-R interval, Power spectral alysis.**

I. Introduction

Heart-rate variability (HRV) analysis has been extensively used as a tool to examine the underlying mechanisms involved in autonomic control of the heart [1-4]. The two common forms of HRV analysis are often designated as time- and frequency-domain measures.

Time-domain HRV indices are derived either directly from interbeat intervals or from differences between adjacent interbeat intervals in the RR interval time series [1,2]. Frequency-domain measures such as power spectral analysis mathematically decompose the RR interval time series into its component frequencies [3,5-8]. Traditionally, spectral analysis of the rhythmic fluctuations in the beat-to-beat time series has led to the identification of three fairly distinct peaks: the very low frequency spectral power (VLFP, < 0.04 Hz), the low frequency spectral power (LFP, 0.04~0.15 Hz) and the high frequency spectral power (HFP, 0.15~0.4 Hz) [2]. The VLFP in the HRV spectra has been associated with thermoregulation [9]. The LFP reflects sympathetic and parasympathetic influences on cardiac control via baroreceptor-mediated regulation of blood pressure [10,11]. The HFP is a function of respiratory modulation of vagal activity [11].

Several previous results have demonstrated that whole-body, limb or local-skin cold stress really affects human thermoregulation and autonomic control of cardiac rhythm [12-18]. Nevertheless, how the short-term forehead cold stress influences the time- and frequency-domain indices of HRV deserves more investigations. Thus, the purpose of the study aimed to observe the effect of five-minute forehead cold stress on conventional HRV measures in healthy adults.

II. Methods

A. Subjects and protocol

Fifteen healthy college volunteers (12M and 3F) with an age range from 21 to 24 years were recruited in the study. Each subject was asked to be in supine position during the measurement period, and one 5-minute Lead II ECG record was performed in a room temperature condition (about 27°C) and the other in cold stress. In the cold stress experiment, a plastic bag containing crushed ice and water (-3°~-4°C) was placed on the volunteer's forehead for 5 minutes. The analog ECG signals were measured with a HRV measurement device (BioEngineering Sense Tech corp., Taiwan) and then digitalized with a sampling rate of 1000 Hz (MP100-UIM100C, BIOPAC System). After the R-R intervals were extracted from those 5-minute ECG records, they were further analyzed using the time- and frequency-domain methods.

B. Time-domain analysis

Time-domain measures derived from each 5-minute RR intervals (NN intervals) and used for assessing HRV in the study mainly include mean, standard deviation (SD), RMSSD, NN50 and pNN50. RMSSD is defined as the square root of the mean squared differences of the successive 5-minute NN intervals, as follows:

$$RMSSD = \sqrt{\frac{\sum (RR_i - RR_{i-1})^2}{n-1}} \quad (1)$$

NN50 is determined from the number of interval differences of the successive 5-minute NN intervals greater than 50 ms, whereas pNN50 is defined as the proportion

Chwee Teck Lim, James C.H. Goh (Eds.): ICBME 2008, Proceedings 23, pp. 490–492, 2009
www.springerlink.com

derived by dividing NN50 by the total number of the 5-minute NN intervals [2].

C. Power spectral analysis

The 5-minute NN interval series was equal-spaced with a re-sampling rate of 4 Hz and a linear interpolation method was used to yield the new NN intervals, before the application of the fast Fourier transform to the new beat-to-beat interval time series. Several frequency bands of interest have been defined in the study, including the total power (< 0.4 Hz), the very low frequency spectral power (VLFP, < 0.04 Hz), the low frequency spectral power (LFP, 0.04~0.15 Hz) and the high frequency spectral power (HFP, 0.15~0.4 Hz) [2].

D. Statistical analysis

All continuous data are expressed as the mean value ± SD. Continuous time- and frequency-domain variables between the room temperature condition and the cold stress were compared using the paired *t* test. All results were analyzed using a two-sided significance level of 0.05. Data analyses were performed by using the statistical software SPSS 10.0 for Windows (SPSS Inc., Chicago, Illinois).

III. Results

Table 1 summaries the commonly used time-domain indices for assessing the RR interval variability. In the fifteen subjects, SD, NN50 and pNN50 were found to be significantly declined during the 5-minute cold stimulation than baseline (all $p<0.05$), with no significant difference in mean and RMSSD.

Table 2 lists the power spectral indices useful for assessing HRV. We found in the fifteen subjects that a significant decrement of VLFP, HFP and total power resulted from the 5-minute cold stress (all $p<0.05$), as compared with baseline, whereas no significant difference in LFP and LFP/LHP ratio was present.

Table 1 Comparison of various time-domain indices computed at room temperature and in cold stress (N=15)

Index	Room Temperature (27°C)	Cold stress (0°C)	p value
Mean (ms)	876±102	864±124	0.41
SD (ms)	61±19	48±11	<0.005
RMSSD (ms)	46.6±22.9	41.0±17.9	0.11
NN50 (count)	85±71	66±61	<0.05
pNN50 (%)	25.4±20.9	19.8±18.3	<0.05

Table 2 Comparison of various frequency-domain indices computed at room temperature and in cold stress (N=15)

Index	Room Temperature (27°C)	Cold stress (0°C)	p value
VLFP (ms^2)	109.7±13.2	105.9±15.2	<0.05
LFP (ms^2)	11.67±3.65	10.65±2.66	0.32
HFP (ms^2)	14.63±7.38	12.03±5.14	<0.05
Total power (ms^2)	135.8±19.0	128.5±20.2	<0.05
LFP/HFP	0.93±0.35	1.01±0.40	0.26

IV. Discussion

The current analysis of HRV shows that not only the traditional time-domain but also power spectral measures can be used to observe the RR interval variability before and during the forehead cold stress. Also, a 5-minute ECG record seems to be long enough for successfully assessing cold response.

The present results show that both the VLFP and HFP of HRV, but not both the LFP and LFP/LHP, become significantly smaller during the 5-minute forehead cold stress than at the room temperature in the fifteen healthy subjects. Mäkinen and coworkers have reported that acute whole-body cold exposure to a 10 °C environment increased total (36%), low (16%), and high frequency power (25%) and RMSSD (34%) [12]. Also, they have shown a cold-induced significant elevation in the HFP after cold acclimation, while other HRV parameters remained unchanged. Kinugasa and Hirayanagi have demonstrated that the HFP of HRV is significantly greater and the LFP/HFP ratio is significantly less at skin surface temperature of 18 °C than of 60 °C [19].

The heart rate fluctuation in response to the regional cold stress in the study is different from that in response to whole-body cold stress [12-16]. It is clear that at least, three factors including the localization, temperature and period of cold stress contribute to its effect on the HRV. This implies that more attention must be taken into account in comparing results from different cold stress conditions.

V. Conclusion

The analysis results indicate a significant reduction in the parasympathetic nervous activity in response to a 5-minute forehead cold stress. This suggests that it is appropriate for traditionally linear time-domain and power spectral measures to assess the short-term RR interval fluctuation caused by a regional cold stimulus.

REFERENCES

1. Stein PK, Kleiger RE (1999) Insights from the study of heart rate variability. Annu Rev Med 50:249-261
2. Task Force of the European Society of Cardiology and the North American Society of Pacing and Electrophysiology (1996) Heart rate variability: standards of measurement, physiological interpretation, and clinical use. Circulation 93:1043-1065
3. Pomeranz B, Macaulay RJB, Caudill MA et al. (1985) Assessment of autonomic function in humans by heart rate spectral analysis. Am J Physiol 248: H151–H153
4. Sztajzel J, Jung M, Bayes de Luna A (2008) Reproducibility and gender-related differences of heart rate variability during all-day activity in young men and women. Ann Noninvasive Electrocardiol 13:270-277
5. Pagani M, Lombardi F, Guzzetti S et al. (1986) Power spectral analysis of heart rate and arterial pressure variabilities as a marker of sympathovagal interaction in man and conscious dog. Circ Res 59:178–193
6. Akselrod S, Gordon D, Ubel FA et al (1981) Power spectrum analysis of heart rate fluctuation: a quantitative probe of beat-to-beat cardiovascular control. Science 213:220-222
7. Baselli G, Cerutti S, Civardi S, et al (1986) Spectral and cross-spectral analysis of heart rate and arterial blood pressure variability signals. Comput Biomed Res 19:520-534
8. Kimura Y, Okamura K, Watanabe T et al (1996) Power spectral analysis for autonomic influence in heart rate and blood pressure variability in fetal lambs. Am J Physiol 271:H1333–H1339
9. Kitney RI (1974) An analysis and simulation of the human thermoregulatory control system. Med Biological Eng 12:56-64
10. Pagani M, O. Rimoldi O and Malliani A (1992) Low-frequency components of cardiovascular variabilities asmarkers of sympathetic modulation, Trends Pharmacol Sci 13:50-54
11. Saul JP (1990) Beat-to-beat variations of heart rate reflect modulation of cardiac autonomic outflow. News Physiol Sci 5:32-37
12. Mäkinen TM, Mäntysaari M, Pääkkönen T et al. (2008) Autonomic nervous function during whole-body cold exposure before and after cold acclimation. Aviat Space Environ Med 79:875-882
13. Bortkiewicz A, Gadzicka E, Szymczak W et al. (2006) Physiological reaction to work in cold microclimate. Int J Occup Med Environ Health 19:123-131
14. Sevre K, Bendz B, Hankø E et al. (2001) Reduced autonomic activity during stepwise exposure to high altitude. Acta Physiol Scand 73:409-417
15. Farrace S, Ferrara M, De Angelis C et al. (2003) Reduced sympathetic outflow and adrenal secretory activity during a 40-day stay in the Antarctic. Int J Psychophysiol 49:17-27
16. Sollers JJ 3rd, Sanford TA, Nabors-Oberg R et al. (2002) Examining changes in HRV in response to varying ambient temperature. IEEE Eng Med Biol Mag 21:30-34
17. Yamazaki F, Sone R (2000) Modulation of arterial baroreflex control of heart rate by skin cooling and heating in humans. J Appl Physiol 88:393–400
18. Kelsey RM, Alpert BS, Patterson SM et al. (2000) Racial differences in hemodynamic responses to environmental thermal stress among adolescents. Circulation 101:2284-2289
19. Kinugasa H, Hirayanagi K (1999) Effects of skin surface cooling and heating on autonomic nervous activity and baroreflex sensitivity in humans. Exp Physiol 84:369-377

The address of the corresponding author:

Author: Jia-Jung Wang
Institute: Department of Biomedical Engineering, I-Shou University
Street: No. 1, Sec. 1, Syuecheng Rd., Dashu Township
City: Kaohsiung County
Country: Taiwan
Email: wangjj@isu.edu.tw

A Reflection-Type Pulse Oximeter Using Four Wavelengths Equipped with a Gain-Enhanced Gated-Avalanche-Photodiode

T. Miyata[1], T. Iwata[2] and T. Araki[3]

[1] Niihama National College of Technology, Ehime, Japan
[2] Graduate School of Advanced Technology and Science, The University of Tokushima, Tokushima, Japan
[3] Graduate School of Engineering Science, Osaka University, Osaka, Japan

Abstract — **We propose a reflection-type pulse oximeter, which employs four kinds of light-emitting diodes (LEDs) and a gated avalanche photodiode (APD) for monitoring four different wavelengths. Wavelengths of the LEDs are 635 nm, 760nm, 810nm and 945nm. The four LEDs are driven by a pulse mode in a sequence manner at a frequency *f* (=10 kHz). The APD is operated in a gated "gain-enhanced" mode at a frequency 4*f* (= 40 kHz) in synchronized with the operation of the LEDs. Superposition of a transistor-transistor-logic (TTL) gate pulse on a direct-current (dc) bias that is set so as not exceeding the breakdown voltage of the APD makes the APD work in a gain-enhanced operation mode. Output signal from the APD is fed into a four-channel boxcar integrator that works to subtract the background signal and to enhance the precision in the analysis. The propose scheme is useful for the reflection-type pulse oximeter thanks to the capability of detecting a weak signal against disturbance such as a large background (BG) light.**

Keywords — **Pulse oximeter, avalanche photodiode, LED, gate mode, boxcar integrator.**

I. Introduction

Many optical techniques have proposed to measure blood components with a noninvasive manner. Among them, a pulse oximeter is one of the most popular instruments to measure the arterial oxygen saturation (SpO_2). The pulse oximeter has two types: a transmission type and reflection type [1]. Comparing the two types, the reflection type seems more promising because any region on the skin surface can be measured. However, for the reflection type, the weak reflection signal obtained from the skin surface and the relatively large background (BG) light incident on the light detector preclude precise measurements. In our previous report, in order to overcome the problem, we have proposed the reflection-type pulse oximeter by using a gain-enhanced operation mode of a gated avalanche photodiode (APD) and the lock-in light detection scheme [2].

The conventional transmission-type pulse oximeter consists of two LEDs with different peak emission wavelengths, typically 660 nm and 940 nm. On the other hand, three wavelengths (805 nm, 660 nm, 940 nm) can be used to improve the accuracy of the analysis of SpO_2 [3, 4]. Using the reflection-type pulse oximeter, also three wavelengths are useful for that. However, best experimental results are limited finger [1, 2, 5]. For the practical use, it should be applied to other skin surface that cannot apply transmission-type pulse oximeter, for example, wrist [6], neck, face [7], head, and other areas [8].

In our experiments, the intensity of pulsation from the wrist was lower in comparison than those from forefinger under measuring with three wavelengths (635 nm, 810 nm, 945 nm). Especially, that intensity was less than 10% of that from forefinger when the wavelength was 635 nm. As a result, the weak pulsation signal caused error in the calculation of SpO_2.In order to compensation for that, we introduce an additional wavelength (760 nm) to the system.

In this report, we propose a new light detection scheme, whose four kinds of wavelengths (635 nm, 760 nm, 810 nm, 945 nm) and the gain-enhanced gated APD and boxcar signal processing unit are effective for the reflection-type pulse oximeter thanks to the capability of detecting the weak signal against disturbance such as a large BG light.

II. Gain enhanced operation of a gated APD

Fig. 1 shows a schematic diagram for the gated APD [9]. The APD is dc-biased by a supply voltage through a bias-tee circuit. We set the value of the dc bias voltage so as to be slightly below the breakdown voltage (Vb) of the APD, because which is how one usually uses the APD for the purpose of high sensitive detection in dc operation mode.

In the proposed gate mode, we superimpose a transistor-transistor-logic (TTL) gate pulse, whose pulse height is 5.0 V, on the dc bias voltage so as not to exceed the breakdown voltage, through a coupling capacitor in the bias-tee circuit. The bias-tee circuit works as a filter to preventing the TTL gate pulse flow against the dc power supply while to applying the dc bias current to the APD. At that time, the multiplication factor of the APD is increased markedly because the gate pulse overdrives the APD effectively. On the one hand, however, the dark noise of the APD is also increased to some extent. A key point of the gated APD is that the

Chwee Teck Lim, James C.H. Goh (Eds.): ICBME 2008, Proceedings 23, pp. 493–496, 2009
www.springerlink.com

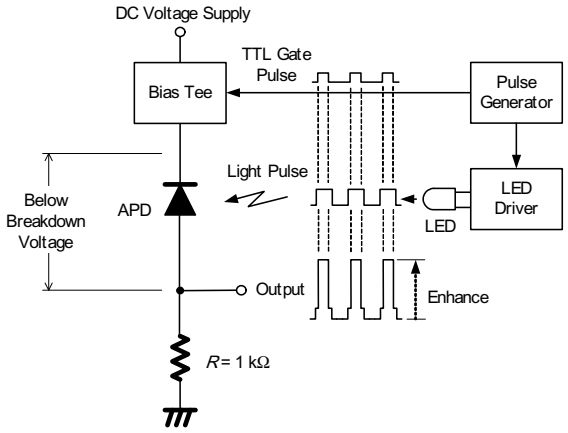


Fig. 1 A schematic diagram for explaining the gain-enhanced operation mode of the gated APD.

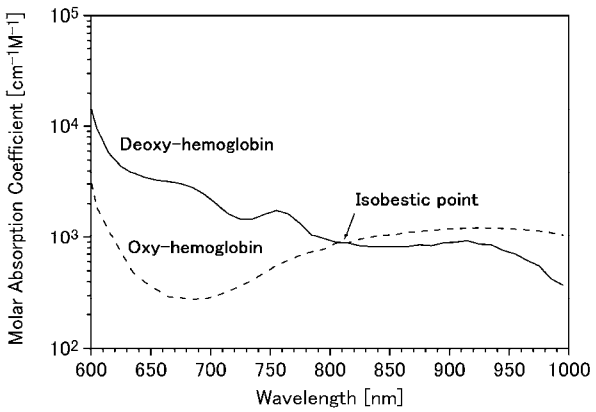


Fig. 2 Dependence of the molar absorption coefficient of oxy-hemoglobin and deoxy-hemoglobin on the wavelength [9].

over-all sensitivity for the signal light detection is enhanced in comparison with that of the conventional dc-biased APD, although depending on the incident light power and the value of the supply bias voltage. We operate the APD in an analogue mode for the purpose of detecting the weak signal light or picking up the weak signal superimposed on the large BG light. The attainable gain of the gated APD itself was enhanced about one hundred times in comparison with that of the conventional dc-biased APD.

III. Pulse Oximetry

For the calculation of the SpO_2, a ratio (ϕ) of two quotients, two ratios of alternative current (ac) amplitudes (I_{ac}) to dc ones (I_{dc}) of the photoplethysmographs (PPG) at the red (R) and the near-infrared (NIR) wavelengths, calculate according to the following the equation,

$$\phi(R/NIR) = \frac{I_{ac}(R)/I_{dc}(R)}{I_{ac}(NIR)/I_{dc}(NIR)}. \quad (1)$$

Then, the value of SpO_2 (S) is estimated by the following equation [3],

$$S = \frac{\phi E_{\mathrm{dNIR}} - E_{\mathrm{dR}}}{\phi(E_{\mathrm{dNIR}} - E_{\mathrm{oIR}}) + E_{\mathrm{oR}} - E_{\mathrm{dR}}}, \quad (2)$$

where E_o and E_d were molar absorption coefficients of oxy and de-oxy hemoglobin (see Fig. 2), respectively, and subscripts NIR and R indicate the near-infrared and red wavelengths, respectively.

Although previous equation (2) is useful for two wavelengths use, another formula considered the scattering light in the blood and tissue may have to be applied in the case of more than three wavelengths [4]. In either case, S is indicated by a function of ϕ,

$$S = f(\phi). \quad (3)$$

To verify the following combinations for SpO_2, for the calculation of the higher-accuracy ϕ, we propose the high sensitive detection scheme for weak pulsation from skin surface.

$$S_1 = f(\phi(^{635nm}/_{945nm}), \phi(^{810nm}/_{945nm})), \quad (4)$$

$$S_2 = f(\phi(^{760nm}/_{945nm}), \phi(^{810nm}/_{945nm})), \quad (5)$$

$$S_3 = f(\phi(^{635nm}/_{945nm}), \phi(^{760nm}/_{945nm}), \phi(^{810nm}/_{945nm})). \quad (6)$$

The $\phi(^{810\ \mathrm{nm}}/_{945\ \mathrm{nm}})$ is less affected by S, because of difference in the molar absorption coefficients between oxy and de-oxy hemoglobin is low (see Fig. 2).

IV. Experimental Setup

Fig. 3 shows a schematic block diagram of the reflection type pulse oximeter. For kind of wavelengths were used, a near-infrared light-emitting diode (LED, SLR938CV, λ = 945 nm, Sanyo), a red LED (GL5HD43, λ = 635 nm, Sharp), near-isobestic wavelength LED (L810-03AU, λ = 810 nm, epitex) and near-infrared LED (L760-03AU, λ = 760 nm, epitex), respectively. APD (S2382, Vb = 181 V, Hamamatsu Photonics Co.) was operated with the gain-

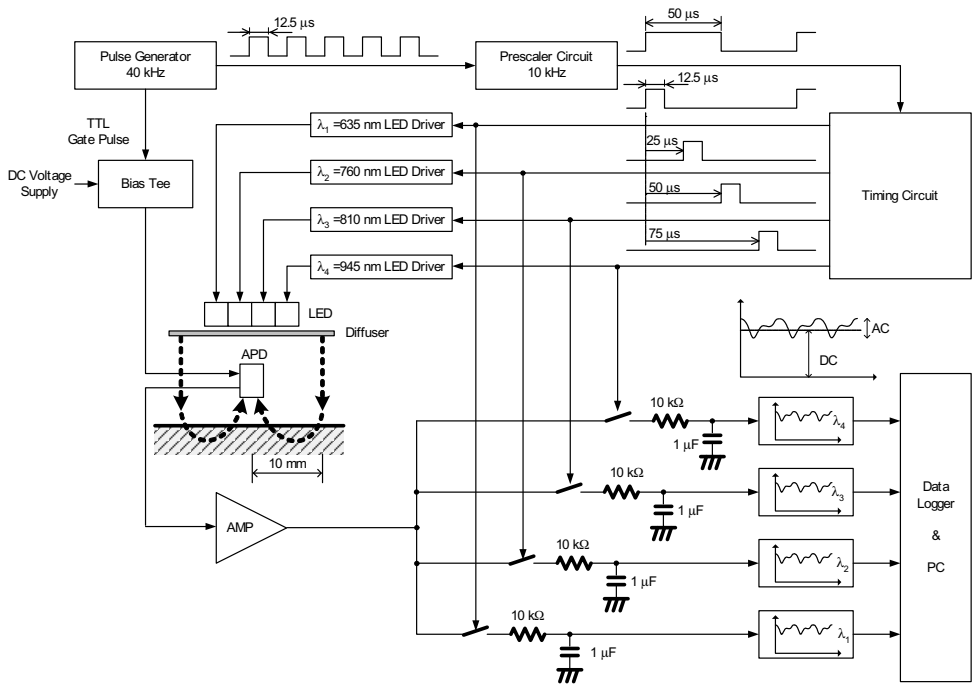


Fig. 3 Schematic block diagram of the reflection-type pulse oximeter.

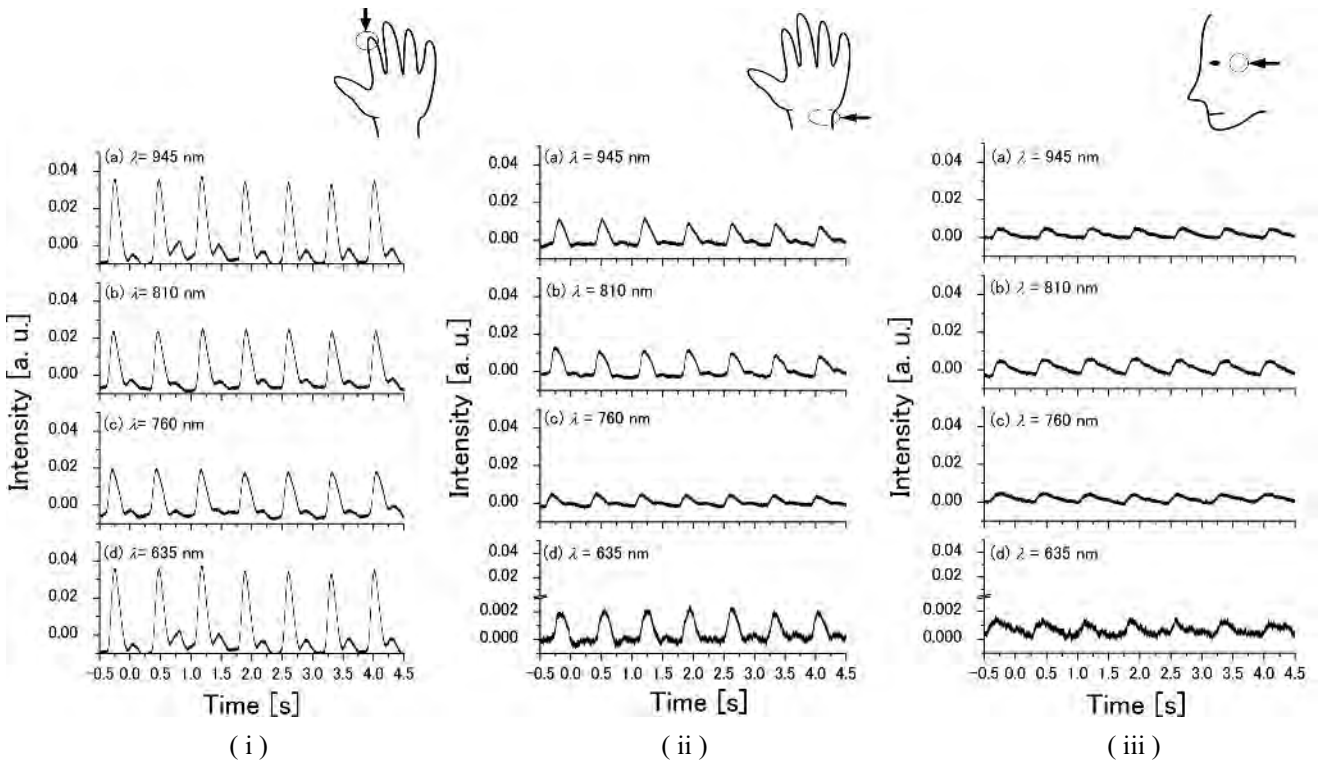


Fig. 4 Photoplethysmographs from skin surfaces at individual points: (i) from a forefinger, (ii) from a left wrist, and (iii) from a left temple area.

enhanced gate mode. A dc bias voltage was 173.4 V. Distance of between light source and APD were from 2.5 mm to 10 mm. The repetitive frequency and the duty ratio of emission from each LEDs were f =10 kHz and 0.125, respectively.

On the one hand, the gain-enhanced gate mode of operation for APD was attained by superposition of a transistor-transistor logic (TTL) pulse on the dc bias with not exceeding the breakdown voltage of the APD at a frequency $4f$ = 40 kHz.

Such four output signals obtained from the APD were fed into four gated integrators (R = 10 kΩ, C = 1 μF) separately whose reference timing of each LED. As the results, the photoplethysmographs for each wavelength can be obtained.

V. Results and discussion

Fig. 4 shows photoplethysmographs from skin surface: (i) from a left forefinger, (ii) from a left wrist, and (iii) from a left temple area. The signals are obtained by making local pressure with itself. These pulsation signals are weak signals embedded in the large dc reflection signals as BG signals. The intensity of the signals in each places, (ii) and (iii) when wavelength was 635 nm are 3 % and 1.7% as compared with that of forefinger as the case of (i). It is caused by the variation of optically penetration depth and pass depending on the pressure between the probe and the skin, the components under the skin, and so on. At that time, the intensity of the dc reflectance light is several thousand times as compared with those pulsations.

VI. Conclusions

We demonstrated that four kinds of LEDs (635 nm, 760nm, 810nm and 945nm), a gain-enhanced gated APD and boxcar integrator. The propose scheme is useful for the reflection-type pulse oximeter thanks to the capability of detecting a weak signal against disturbance such as a large background (BG) light. The system we have just posed has contributed to high accuracy of ϕ. The technique might be applicable to various wearable SpO_2 probe, for example, wristwatch type or glasses type.

References

1. Takatani S, Cheung P W, Ernst E A (1980) A Noninvasive Tissue Reflectance Oximeter. Annal. Biomed. Eng. 8: 1-15
2. Miyata T, Iwata T, Araki T (2005) A sensitive Reflection-type Pulse Oximeter Using a Gated Avalanche Photodiode. Trans. JSMBE 43: 724-729
3. Aoyagi T (1998) Pulse Oximeter. Jpn. J. Med. Instrum. 68: 315-319
4. Aoyagi T (1996) Theory and Improvement of Pulse Oximetry. Jpn. J. Med. Instrum. 66: 440-445
5. Yao J, Warren S (2004) A Novel Algorithm to Separate Motion Artifacts from Photoplethysmographic Signals Obtained with a Reflectance Pulse Oximeter. Proc. of the 26th Annual International Conference of the IEEE EMBS, San Francisco, CA, USA, 2004, pp 2153-2156
6. Humphreys K, Ward T (2007) Noncontact Simultaneous Dual Wavelength Photoplethysmography: A Further Step Toward Noncontact Pulse Oximetry. Rev. Sci. Instrum. 78: 044304
7. Matsushita K, Aoki K, Kakuta N, Yamada Y (2003) Fundamental Study of Reflection Pulse Oximetry. Opt. Rev. 10: 482-487
8. Kyriacou P A, Powell S, Langford R M, Jones D P (2002) Esophageal Pulse Oximetry Utilizing Reflectance Photoplethysmography. IEEE Trans. Biomed. Eng. 49: 1360-1368
9. Miyata T, Iwata T, Araki T (2005) Construction of a Pseudo-lock-in Light-detection System Using a Gain-enhanced Gated Silicon Avalanche Photodiode. Meas. Sci. Technol. 16: 2453-2458
10. Takatani S and Graham M D (1987) Theoretical Analysis of Diffuse Reflectance from a Two-layer Tissue Model. IEEE Trans. Biomed. Eng. 26: 656-664

Author: Tsuyoshi Miyata
Institute: Niihama National College of Technology
Street: 7-1 Yagumo-cho, Niihama
City: Ehime
Country: Japan
Email: miyata@mec.niihama-nct.ac.jp

Author: Tetsuo Iwata
Institute: Graduate School of Advanced Technology and Science, The University of Tokushima
Street: 2-1 Minamijyosanjima-cho
City: Tokushima
Country: Japan
Email: iwata@me.tokushima-u.ac.jp

Author: Tsutomu Araki
Institute: Graduate School of Engineering Science, Osaka University
Street: 1-3 Machikaneyama-cho, Toyonaka
City: Osaka
Country: Japan
Email: araki@me. es. osaka-u.ac.jp

Estimation of Central Aortic Blood Pressure using a Noninvasive Automatic Blood Pressure Monitor

Yuan-Ta Shih[1], Yi-Jung Sun[1], Chen-Huan Chen[2,3], Hao-min Cheng[2] and Hu Wei-Chih[1]

[1] Dept. of Biomedical Engineering, Chung Yuan Christian University, Chung-Li, Taiwan
[2] Dept. of Medical Research and Education, Taipei Veterans General Hospital, Taipei, Taiwan
[3]Dept. of Public Health, National Yang-Ming University, Taipei, Taiwan

Abstract — **Automatic blood pressure monitors are the most important healthcare products. The abnormal blood pressure values and waveform could indicate many cardiovascular diseases. The pressures measured using oscillometric method, which compared with invasive blood pressure devices, are often slight overestimation in SBP and underestimation in DBP.Recent studies indicated that the continuous pulse volume recording (PVR) could predict the central aortic blood pressure using a transfer function. Therefore, this study was implementing a novel device using the oscillometric method to predict the central aortic blood pressure to measure central blood pressure as well as the SBP, MBP and DBP automatically. The ensemble averaging 10 heart-beats of continuous PVR was used to extract the value of (cSBP), central SBP2 (cSBP2), central pulse pressure (cPP) and incisura point (inciP) for central blood pressure calculation. The method estimating the central blood pressure was correlated with the invasive measurement of pressure at aortic root at catheter Lab with high accuracy.**

I. Introduction

Automatic blood pressure monitors are the most important healthcare products. Most of them are using the oscillometric method with proprietary algorithms that is to determine the heart rate, systolic blood pressure, mean blood pressure and diastolic blood pressure. The cuff pressure (Bladder pressure) at the maximum of oscillometric amplitude determined by commercial automatic blood pressure monitors is the MBP. Pressures at the one half fold and 0.8-fold of the maximum oscillometric amplitude which before and after the MBP respectively are determined as the SBP and DBP generally [1]. The pressures measured using oscillometric method, which compared with invasive blood pressure devices, are often slight overestimation in SBP and underestimation in DBP.

Recently, many hypertension committees and cardiovascular associations agree that to estimate the central aortic blood pressure is the importance for preventing and diagnosing cardiac disease, such as hypertension, atherosclerosis. Central aortic blood pressures generally mean the systolic and diastolic pressure at the ascending aortic root. Systolic blood pressure represents the maximum force of the heart, and diastolic blood pressure means the pressure of heart against the pressure that generated by the impedance of circular system. So, it is important to estimate the central aortic blood pressure and pulse waveform accurately for evaluating the function of heart and diagnosing damage factors of cardiovascular diseases [2].

In the past, the evaluation of heart function was using invasive devices, such as Millar Catheter or Filled-Fluid. Invasive devices are more accurate than noninvasive blood pressure monitor and can acquire the pulse wave of blood pressure for estimating the cardiovascular functions. However, invasive devices may have disadvantages; 1) invasive devices may have risks of invading human body, 2) they must operate by an experienced expert, 3) cost expensive, 4) it is not suit for homecare utilization.

Many studies indicated that the continuous pulse volume recording (PVR) could have the ability to predict the central aortic blood pressure using a transfer function. In 1997, Todd J. Brinton et al. demonstrated that using the pattern recognition algorithm identifies characteristic phase changes directly from the continuous digital signals could have great potential clinical value to determine arterial pressure and vascular compliance [3]. Chen-Huan Chen et al. using mathematical transfer function from radial tonometry pressure estimated the central aortic pressure wave, and demonstrated that clinically acceptable prediction of central arterial pressure and the pressure waveform could be obtained by mathematic transfer function [4]. Further in 2006, James E. Sharman et al. presented that using generalized transfer function could noninvasively derive central blood pressure from radial pressure waveform even during exercise [5].

The aim of this study is to develop a novel automatic blood pressure monitor which can predict central blood pressure using transfer function. Furthermore, the data acquired from this novel blood pressure will be verified with invasive clinical data to prove the capability of the novel automatic blood pressure monitor.

Chwee Teck Lim, James C.H. Goh (Eds.): ICBME 2008, Proceedings 23, pp. 497–500, 2009
www.springerlink.com

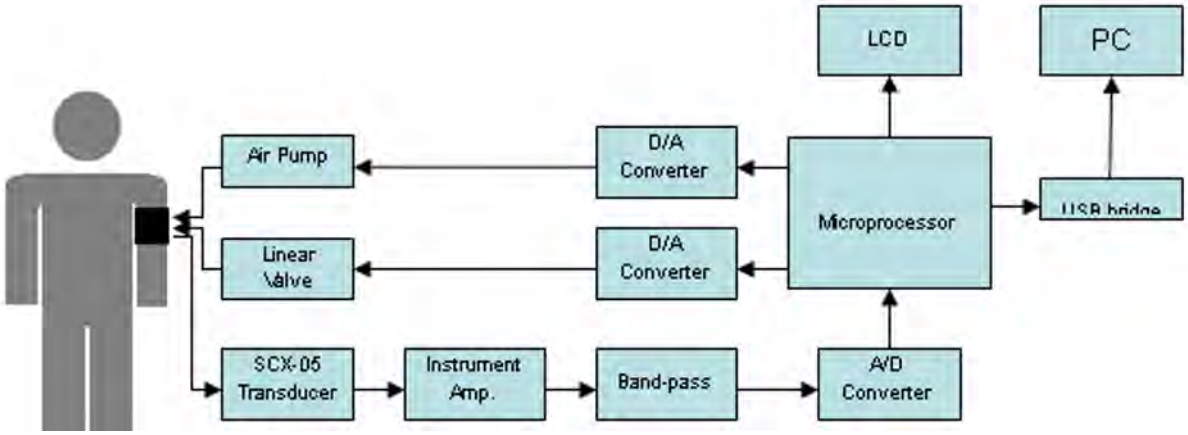


Fig.1 The block diagram of predictive central blood pressure monitor

II. Materials and Methods

A. Hardware System

In order to extract the specific blood pressure values, this study has developed a system and method with using microcontroller MSP430F149 (Texas Instruments). Several peripheral modules were used to acquire and store continuous PVR signal, such as pressure transducer for what, 12-bits analog to digital converter (ADC) for what, LCD module to present what, flash memory to store what, digital to analog converter (DAC) to do what and serial communication interface (USART) (Fig.1) for what.

This pressure transducer was using SCX-05 (HoneyWell) with a linear range of 0-300mmHg for acquiring the oscillometric signal of cuff pressure. The oscillometric waveform generated by the coupling of pressure changes in brachial artery to pressure changes in cuff. An instrumentational amplifier was seated behind the pressure transducer for reducing common mode signal and amplifying oscillometric signal. A band-pass filter was to mininimized the the effect of baseline shift. and the cutoff frequency was set at 0.5 to 30Hz. A 12-bit ADC which sampling rate of 120Hz was used to digitize the continuous pressure signal.

To accurate maintain the pressure in cuff, an air pump and an electrical controlled linear valve were used with the DAC module of MSP430F149 to adjust the inflating and deflating rate respectively. And, the LCD module will be presenting the real time oscillometric signal and displaying the SBP, DBP and heart rate that derived from oscillometric method. Assessment of the accuracy of this system was using the same data and the same algorithm at PC with the program written in C using Borland C++ Builder6, The data was transmitted to PC using USB to Serial Bridge Controller.

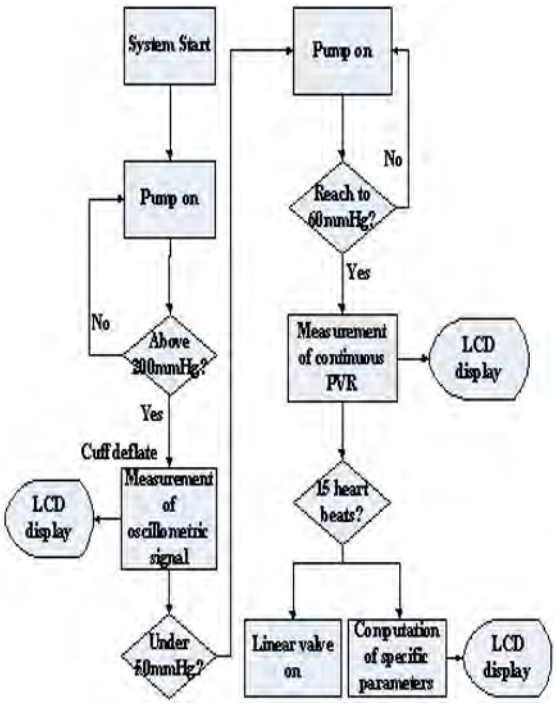


Fig.2 The procedure of measurement of central blood pressure

B. Measurement procedure

There were two steps in measurement procedure for acquire SBP, MBP, DBP and continuous PVR from oscillometric method (Fig.2):

- First step, using an air pump to inflat the cuff which was situated at the arm until the cuff pressure was above 200mmHg;, and the cuff pressure was remained for a few seconds to obtain a steady state. Then, the cuff was to deflat at a rate of 2-3mmHg per second. The

SBP, MBP and DBP were determined from the oscillation of cuff by using oscillometric method during the deflation state.



Fig.3 The prototype of central aortic blood pressure monitor

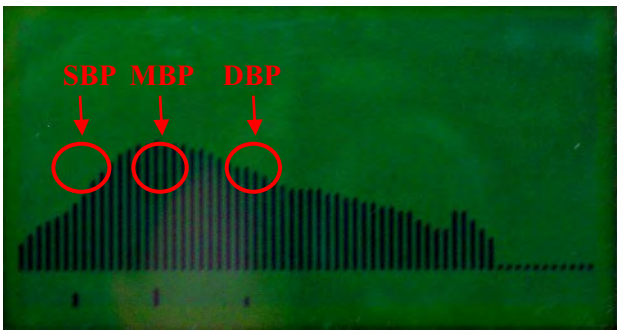


Fig.4 Amplitudes of oscillometric method. Red arrows indicated the amplitudes of SBP, MBP and DBP

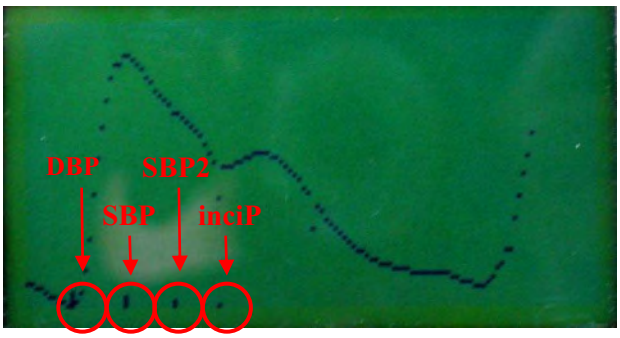


Fig.5 The ensemble averaging 10 heart-beats of continuous PVR waveform. Red arrows indicated the DBP, SBP, SBP2 and inciP of pressure waveform.

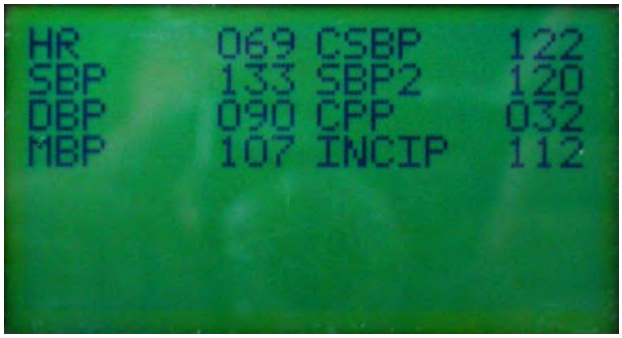


Fig.6 All parameters presented on the LCD module.

- Second step, after blood pressure values were determined. The air pump will be inflating the cuff pressure again and will be maintained the pressure at 60mmHg. The system waited for a steady state then acquired continuous PVR for 15 heart beats. After all acquisition was completed, the computation of specific parameters for pSBP, pSBP2, PP and pMBP were performed, and the LCD module will be presenting all the specific parameters and signal waveform as shown in Figure 5 and 6.

C. Algorithm

For assessing of central aortic blood pressure by oscillometric method, the continuous PVR signal must be normalized. In this study, the continuous PVR will be averaged using at least 10 selected heart beats for an average PVR signal. Specific parameters were derived from the average PVR dP/dt signal. All blood pressures could be determined by normalized PVR signal and calibrated with DBP and MBP from the oscillometric signal. Then, predictive central aortic blood pressures such as cSBP, cSBP2 and cPP could be derived by a transfer function which was developed previously by Dr. Chen and Dr. Cheng et al. in Taipei Veterans General Hospital in R.O.C.

III. Results and Discussions

In this study, the ability of this novel system can predict central aortic blood pressures by using oscillometric method using the acquired waveform and extracted data from noninvasive blood pressure device. The prototype of this new novel device in this study was shown in Figure 3.

After the procedure of first step described in previous section, the result of oscillometric amplitudes could show on LCD monitor, and specific parameter points indicated as SBP, MBP and DBP of oscillometric method (See Figure 4

for reference). The maximum amplitude (shown in Figure 4) indicated the oscillometric amplitude of MBP. The amplitude before the MBP and half fold of the maximum amplitude indicated the oscillometric amplitude of SBP. And, the amplitude after the MBP and 0.8-fold of the maximum amplitude indicated the oscillometric amplitude of DBP. The result of the ensemble averaging 10 heart-beats of continuous PVR waveform was shown in Figure 5. This waveform was used to extract the value of cSBP, cSBP2, cPP and inciP for central blood pressure calculation. The calculated result of all parameters could be presented on LCD module as shown in Figure 6.

IV. Conclusion

This development was based on the objective that was having hope of that people could use a blood pressure monitor at anytime to monitor their central aortic blood pressure, the cardiovascular diseases could be discovered in early stage.

The algorithm used to predict central aortic blood pressure is the computation result of the relationship between to area under PVR and the extracted parameters such as MBP and DBP. The transfer function is also including the ratio of the extracted value of cSBP, cSBP2, inciP and cPP. The result has been correlated to the invasive measurement at catheter Lab with high accuracy.

Furthermore, we will be proceeding in clinical validation to demonstrate the practicability of this novel automatic blood pressure monitor.

Acknowledgment

This study was supported by Nation Science Council (NSC 96-2314-B-010-035-MY3, NSC 95-2221-E-033-034-MY3), Taiwan.

References

1. L.A.Geddes, M.Voelz, C.Combs, D.Reiner, and C.F.Babbs, "CHARACTERIZATION OF THE OSCILLOMETRIC METHOD FOR MEASURING INDIRECT BLOOD PRESSURE," Annals of Biomedical Engineering, vol. 10, pp. 271-280, 1982.
2. Kozo Hirata, Masanobu Kawakami, and Michael F O'Rourke, "Pulse Wave Analysis and Pulse Wave Velocity - A Review of Blood Pressure Interpretation100 Years After Korotkov -," Circulation Journal, vol. 70, pp. 1231-1239, 2006.
3. Todd J.Brinton, Bruno Cotter, Mala T.Kailasam, David L.Brown, Shiu-Shin Chio, Daniel T.O'Connor, and Anthony N.DeMaria, "Development and Validation of a Noninvasive Method to Determine Arterial Pressure and Vascular Compliance," The American Journal of Cardiology, vol. 80, pp. 323-330, 1997.
4. Chen-Huan Chen, Erez Nevo, Barry Fetics, Peter H.Pak, Frank C.P.Yin, Lowell Maughan, and David A.Kass, "Estimation of central aortic pressure waveform by mathematical transfer function of radial tonometry pressure. Validation of generalized transfer function," Circulation, vol. 95, no. 7, pp. 1827-1836, 1997.
5. James E.Sharman, Richard Lim, Ahmad M.Qasem, Jeff S.Coombes, Malcolm I.Burgess, Jeff Franco, Paul Garrahy, Ian B.Wilkinson, and Thomas H.Marwick, "Validation of a Generalized Transfer Function to Noninvasively Derive Central Blood Pressure During Exercise," Hypertension, vol. 47, pp. 1203-1208, 2006.
6. Maynard R. III, "Noninvasive automatic determination of mean arterial pressure," Med. & Biol. Eng. &Comput., vol. 17, pp. 11-18, 1979.
7. Mateo A., James M.N., Tran T., Daniel T., Miles S.E., Brahm G., "An Automatic Beat Detection Algorithm for Pressure Signals," IEEE Trans. Bio. Eng., vol. 52, no. 10, 2005.
8. Kozo H., Masanobu K., Michael F.O., "Pulse Wave Analysis and Pulse Wave Velocity- A Review of Blood Pressure Interpretation 100 Years After Korotkov-," Circ. J., vol. 70, pp. 1231-1239, 2006.

Address for correspondence :
Wei-Chih Hu
Institute: Department of Biomedical Engineering,
Chung Yuan Christain University
Street: No. 200, Chung-Pei Rd., Chung-Li,
City: Taoyuan
Country: Taiwan, Republic of China
Email: weichih@cycu.edu.tw

Design of a PDA-based Asthma Peak Flow Monitor System

C.-M. Wu[1] and C.-W. Su[1]

[1] Department of Electrical Engineering, National Central University, Taiwan, Republic of China

Abstract — **Recent study indicates that one of the important reasons that asthmatic condition could not be effectively controlled is that patients could not comply with the prescription of physician. One possible reason for this is that the conventional approach for physician to monitor the symptoms of asthmatic patients is based on the daily peak expiratory flow records of the patient. Because of the chronic essence of asthma, a long-term patient monitoring would be the necessary step to control the asthmatic condition. However, the asthmatic patients often stop following the prescription of physician once their symptoms of asthma are largely improved. This often leads to deterioration of treatment efficacy or even the patient's death. The main purpose of this study is to design an asthmatic peak expiratory flow monitor that is based on a personal digital assistant (PDA) and internet communication. Such a system would improve not only the communication between the asthmatic patients and physician but also the symptom of asthmatic patients.**

The device developed in this study is based on a Windows CE-based PDA. The peak expiratory flows (PEF) of asthmatic patient are converted into analog signals via a pneumotachometer (ADInstruments Inc., Sydney, Australia). These analog signals are digitized by a microcontroller and transferred to PDA by a serial interface (RS-232). The PEF data of asthmatic patients can be either stored in the database of PDA or synchronized with the computer in the office of physician to update the data through the internet or wireless local area network (LAN). The physician can also use the software program developed from this study to send short message to patients. Therefore, communication between the patients and physician not only will not be limited by time and distance, but also can achieve the goal of monitoring and improvement of patients' symptoms.

Keywords — **asthma, PDA, peak expiratory flow (PEF), monitor, LAN.**

I. Introduction

According to the report of National Heart, Lung, and Blood Institute, USA [1], long-term control of asthmatic symptoms with objective home peak expiratory flow (PEF) monitoring and corresponding action on medication becomes widely introduced in asthma patient self-management. Recent study indicates that one of the important reasons that asthmatic condition could not be effectively controlled is that patients could not comply with the prescription of physician. One possible reason for this is that the conventional approach for physician to monitor the symptoms of asthmatic patients is based on the daily peak expiratory flow records of the patient. Because of the chronic essence of asthma, a long-term patient monitoring would be the necessary step to control the asthmatic condition. However, the asthmatic patients often stop following the prescription of physician once their symptoms of asthma are largely improved. This often leads to deterioration of treatment efficacy or even the patient's death. Therefore, issues of home asthma telemonitoring (HAT) [2] were concerned highly in the management of patients with asthma. There are various types of commercial peak flow meters [3][4], but none of them show long-term graphic PEF records as well as update the data through internet or wireless local area network between the asthmatic patients and physician. Therefore, The main purpose of this study is to design an asthmatic peak expiratory flow monitor that is based on a personal digital assistant (PDA) and internet communication. Such a system would improve not only the communication between the asthmatic patients and physician but also the symptom of asthmatic patients.

II. Methods

A. Configuration of the system

The device developed in this study is based on a Windows CE-based PDA. The peak expiratory flows (PEF) of asthmatic patient are converted into analog signals via a pneu-

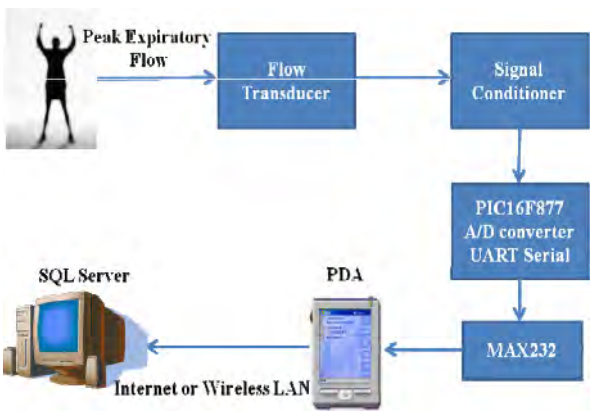


Fig. 1 Configuration of the system.

Chwee Teck Lim, James C.H. Goh (Eds.): ICBME 2008, Proceedings 23, pp. 501–504, 2009
www.springerlink.com

motachometer (ADInstruments Inc., Sydney, Australia). These analog signals are digitized by a microcontroller and transferred to PDA by a serial interface (RS-232). The PEF data of asthmatic patients can be either stored in the database of PDA or synchronized with the computer in the office of physician to update the data through the internet or wireless local area network (LAN). The configuration of the system is shown in Fig. 1.

B. Hardware Devices

The peak expiratory flow was measured with the respiratory flow head (MLT1000L) from ADInstruments Inc. (Sydney, Australia). The transduced signal was amplified and digitized by a microcontroller (PIC16F877, Microchip,Chandler AZ, USA) and transferred to PDA (iPAQ H3950, HP, Palo Alto CA, USA) by a serial interface (RS-232). Because we developed our own PEF data acquisition system, we have to verify the accuracy of the process. The output of signal conditioner for the flow transducer was verified with commercial Power Lab. system from ADInstruments Inc. The results of this verification are shown in Figs. 2 and 3.

In addition, the output of the A/D converter and RS232 connection was also verified with the interface provided by Microchip Inc. The results of this verification are shown in Figs. 4 and 5. The hardware device is shown in Fig. 6.

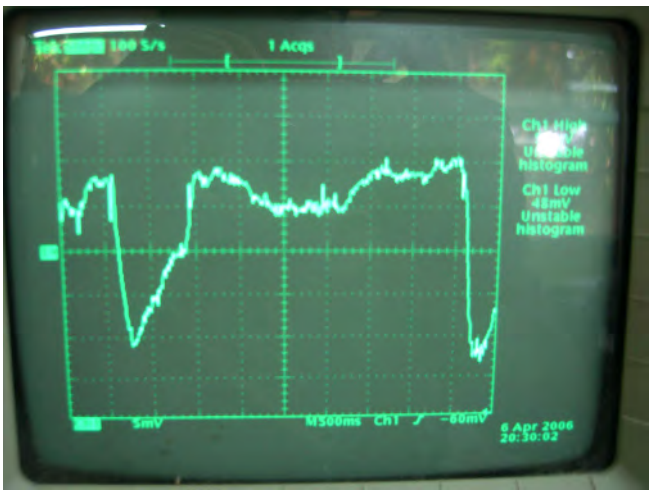


Fig. 2 Output of the signal conditioner on the oscilloscope.

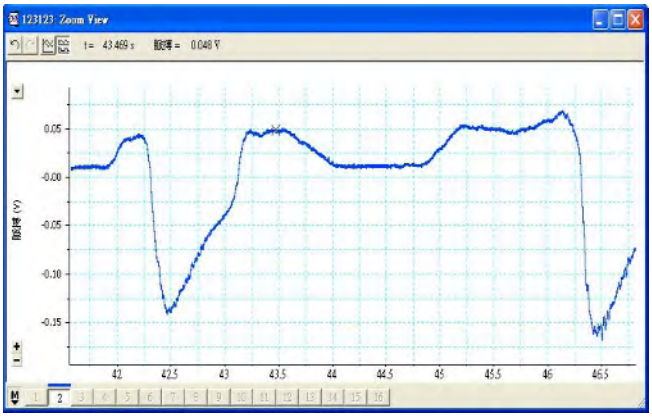


Fig 3. Output of the flow transducer from Power Lab system.

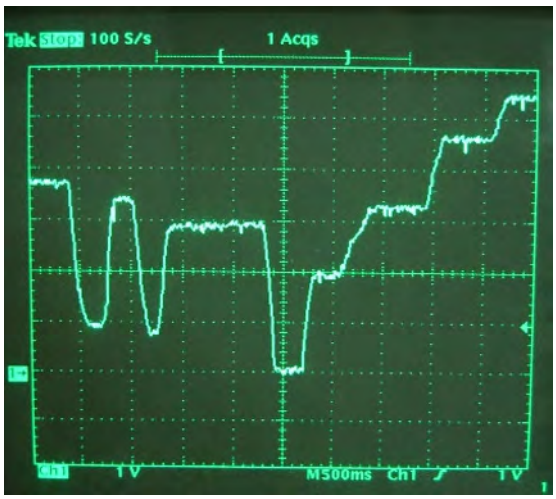


Fig. 4 Analog input signal for the microcontroller PIC16F877 shown on the oscilloscope.

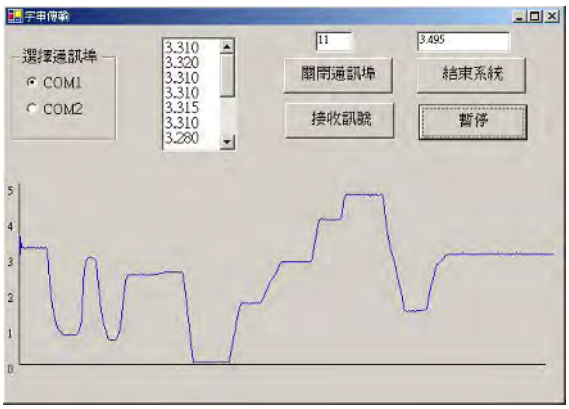


Fig. 5 Digitized signal transferred to the interface through RS232.

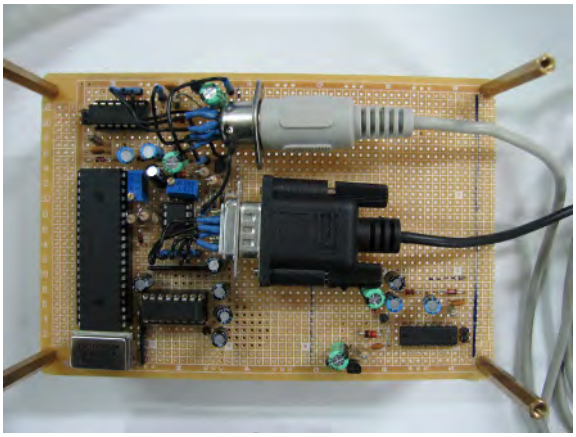


Fig. 6 Picture of the hardware device.

C. Software Development

The software developed in this study is based on a Windows CE-based PDA. The PEF data of asthmatic patients from the hardware device can be either stored in the database of PDA or synchronized with the computer in the office of physician to update the data through the internet or wireless local area network (LAN).

In order to protect the privacy of patient's medical record, the user account and password was designed to access the PEF monitor system through the PDA user interface. The database design on the PDA of patient and the computer in the physician office was based on Microsoft SQL CE 2.0 and Server 2000, respectively. Synchronization of data on both databases can be made by internet or wireless LAN (802.11b) connection through remote data access concept. Fig. 7 shows the user interface for this process.



(a) (b)

Fig. 7 (a) Receive patient medical record from remote physician office; (b) Transfer patient data to remote physician office.

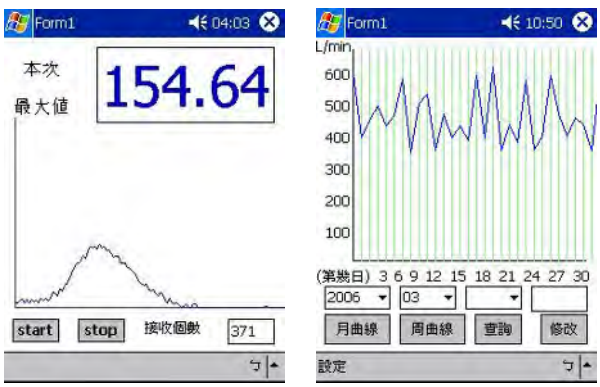
The physician can also use the software program developed from this study to send short message to patients. Fig. 8 shows the patient receive message from the physician and read the contents of the message.

The user interface could record and display the PEF of the patient and store the PEF value to the database of the PDA (Fig. 9(a)). In addition, the patient could also graphically display the long-term PEF data (Fig. 9(b)).



(a) (b)

Fig. 8 (a) Patient receives 5 messages from the physician; and (b) read the contents of message.



(a) (b)

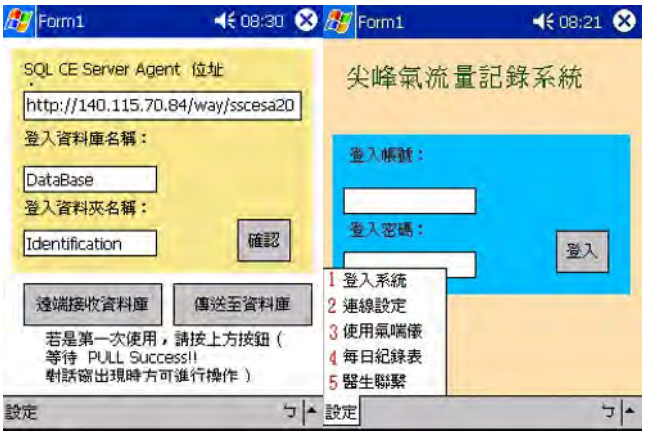
Fig. 9 (a) User interface to record the PEF; and (b) graphically display long-term PEF data.

III. Results

The final user interface on the PDA is shown in Fig. 10 (a). There are five functions developed for the user interface. The first function is to log-in the system with user name and password. The second function is to set up the internet or wireless LAN connection for patient and physician communication (Fig. 10(b)). The third function is to

measure the PEF. The fourth function is to store the measured PEF for the long-term display. The current version could show one month long PEF data. The final (fifth) function is to communicate with the physician.

Finally we verified the measured PEF of our monitor system with commercial Power Lab. system. During verification, the same flow transducer was used for both systems to measure PEF for one subject. Table 1 shows the measured PEF for both systems and the error between them. Fig. 11 depicts the prototype of our PEF monitor system



(a) (b)

Fig. 10 (a) Five functions of user interface; (b) the display of the second function.

Table 1 Comparison between measured PEF of PDA and Power Lab.

Measured voltage (V)	Measured PEF by PDA (L / min)	Measured PEF by Power Lab. (L / min)	Error (%)
1.31	198.97	209.35	5.96%
1.42	217.24	225.54	3.68%
1.75	263.05	272.8	3.57%
2.185	327.34	335.15	2.33%
2.355	354.03	359.46	1.51%
2.58	389.36	391.62	0.58%
2.61	394.07	395.92	0.47%
2.66	401.92	403.08	0.29%
2.715	410.55	410.96	0.1%
2.84	430.18	428.9	0.29%



Fig. 11 The protype PDA-based asthma PEF monitor system.

IV. Conclusions

An asthmatic peak expiratory flow monitor that is based on a personal digital assistant (PDA) and internet communication was developed. Such a system would improve not only the communication between the asthmatic patients and physician but also the symptom of asthmatic patients..

References

1. National Heart Lung and Blood Institute (1997) Expert Panel Report 2: Guidelines for the diagnosis and management of asthma. NIH Publication No.97-4051
2. Finkelstein J, Friedman RH (2000) Home asthma telemonitoring (HAT) system. Proc. IEEE 26th Annual Northeast on Bioengineering Conf., pp.103 – 104.
3. Kim, KA, Lee, JH et al (2003) Peak expiratory flow meter capable of spirometric test for asthma monitoring, IEEE EMBS Asian-Pacific Conference on Biomedical Engineering, pp.254 – 255.
4. Michael, G, Panagiotis, C (2004) Technological innovations in asthma patient monitoring and care, Expert Systems with Applications 27 pp.121–131

Development of the Tongue Diagnosis System by Using Surface Coating Mirror

Y.J. Jeon[1], K.H. Kim[1], H.H. Ryu[1], J. Lee[1], S.W. Lee[1] and J.Y. Kim[1]

[1] Department of Medical Research, Korea Institute of Oriental Medicine, Korea

Abstract — **Tongue diagnosis consists of many parameters, including shape, substance and coating of the tongue and so on, to examine health condition and the property of a disease. A new instrument is demand, however, to exclude the effect of various medical examination environments and clinician's subjective sense. In this study, to acquire a clear image of the whole tongue, 500 mega pixel CCD camera and 35mm lens were used and a right angle shape body with surface coating mirror for sufficient object distance. To reduce a specular reflection on the surface of the tongue due to saliva, the LED lighting with a diffusing acrylic was applied. Furthermore, to adjust light interference in the color of the tongue, color charts were inserted. In further study, we will develop the tongue diagnosis algorithm so that this system can be used widely in clinical and research fields**

Keywords — **Tongue diagnosis, Coating of the tongue, Substance of the tongue, Surface coating mirror.**

I. Introduction

The tongue diagnosis is a unique diagnostic method in the Oriental medicine that studies a tongue to understand the condition of health and disease characteristics in human body, and it is based on the shape, substance, coating and movement of the tongue, etc. The shape of tongue represents shape changes in the body of tongue such as width and fissure of tongue, teeth mark, etc. And the substance of the tongue indicates color and quality of tongue's body. The coating of the tongue is a substance covered on the tongue as mosses, and its width, color and distributed area reflect various conditions of the body [1].

The shape, substance, coating and movement of the tongue, etc which constitute the tongue diagnosis are studied generally depending on visual information. And since this information can be affected by environment of examination such as lightning or weather, etc and the subjective sense of the Oriental medical doctor, it is difficult to obtain the objective and reproducible results. The studies to obtain a consistent environment of the tongue diagnosis and objective results are in progress to develop and bring the tongue diagnosis to be scientific [2, 3].

In order to obtain accurate images, the methods to control lightning angle, luminance, a position of measurer, the environment of image acquisition, the method to adjust the iris, a shutter and exposure of camera, and the methods to detect the required area of the tongue for diagnosis from the acquired images have been studied [4].

The tongue diagnosis system, developed in this study, focused on providing clear images of the tongue through securing a proper photographing distance, the lightning part which can suppress the reflection by sputum in maximum, securing area up to the inner tongue and the face contact region considering a testee's convenience to objectify and quantify the tongue diagnosis system.

II. Method

A. Hardware

Securing the proper photograph distance becomes a critical element in order to photograph clear images of the tongue; however, since securing the photograph distance by arranging a camera and a subject linearly can lower the overall design aspect and utilization, in this study the photograph unit and subject are arranged to be right angle and the surface coating mirror is positioned at the right angle to photograph. Figure 1 shows a detach map of the body part of the tongue diagnosis system developed. The photo unit consists of 35mm lens (HF35SA, Fujinon) and the camera (GRAS-50S5, Grasshopper) that supports 5 million pixels, and to connect the photograph unit perpendicular to subject, the surface coating mirror is installed at the right angle. The lightning unit was produced with LED of high luminance, and a diffusion acrylic was used to suppress the light reflection maximally from the sputum on the tongue's surface caused by the direct ray of LED, and the polarization filter was added to lens. Also, to compensate difference in color by effect of lightning, the color chart was attached near to the face contact region. Considering convenience of a testee, the face contact region was designed to have the increased contact area to have a comfortable contact ergonomically, and it was developed to be capable of photographing up to the inner tongue. The body part of the tongue diagnosis system developed as the above is connected with the desk unit. And to enable a testee to stick out his tongue easily, the body part and desk unit are connected so that the body part forms angle of about 45 degree with the desk unit. Figure 2 shows the actual tongue diagnosis system that the body part and desk unit are connected.

Chwee Teck Lim, James C.H. Goh (Eds.): ICBME 2008, Proceedings 23, pp. 505–507, 2009
www.springerlink.com

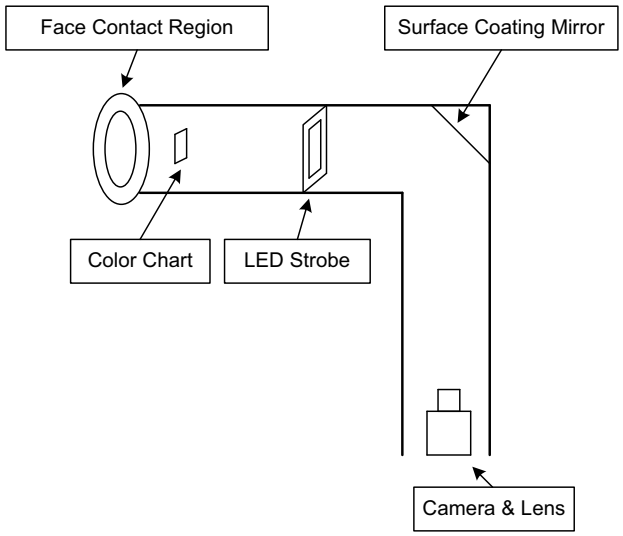


Fig. 1 The separation diagram of the body part of tongue diagnosis system



Fig. 2 The actual image of tongue diagnosis system

B. Software

The measurement program equipped with photographing and saving tongue's image and the database function of testee's information was produced with visual C. As shown in the block diagram(Fig. 3) with regard to the process of software driving, identifications and date of examination for a testee, opinions from the Oriental medical doctor, etc are inputted, and photograph is taken after qualifying whether the elements such as the position and size of the tongue's image of a testee are suitable for photographing. Figure 4 shows the actual image of the tongue taken with the measurement program. When photographing tongue is completed, the tongue area is automatically detected and when there is error in the detected area the detection area can be adjusted manually with the thick dot on the screen. And with the snake algorithm the curve between dots can be restructured [5].

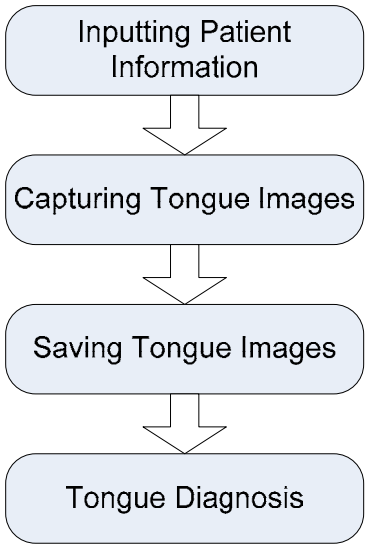


Fig. 3 The process of software driving

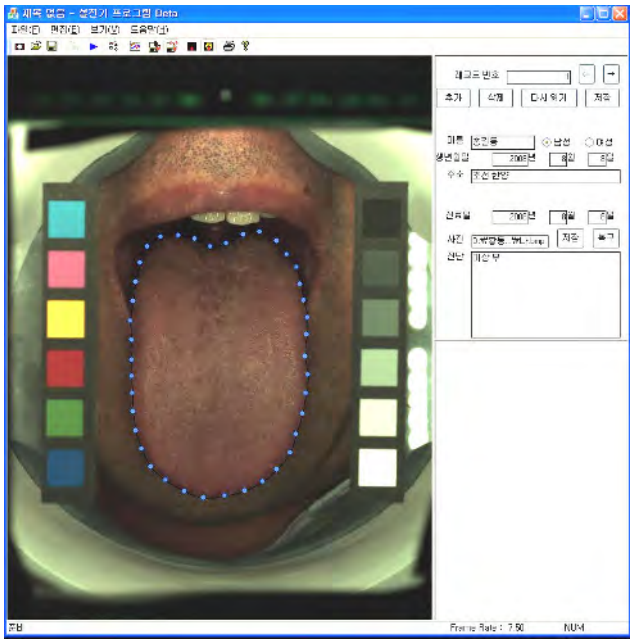


Fig. 4 The actual image of tongue taken with the measurement program

III. Conclusions

The tongue diagnosis system developed in this study allows securing sufficient photograph distance with the surface coating mirror in order to photograph clear images of the tongue. And the lightning unit was produced with the diffusion acrylic and polarization filter to suppress the reflection of light by sputum on the tongue's surface. Also, it allows photographing the color chart with the tongue in order to correct color affected by lightning and allows a testee to stick out his tongue easily by designing the face contact region.

Using this tongue diagnosis system, it was checked that the photographed images of the tongue could be classified as identical coating after photographing images of the tongue from the testee whose coating was clearly identified by the Oriental medical doctor as a yellow coating or a white coating on the tongue. In the future, advancement in accuracy of tongue area detection and adding the automatic algorithm of classifying coating and substance of the tongue to the tongue diagnosis system in this study are expected to contribute to the scientific tongue diagnosis.

Acknowledgment

This work has been supported in Development of Standard on Constitution Health Status.

References

1. Chuang C (2000) A novel approach based on computerized image analysis for traditional Chinese medical diagnosis of the tongue, Computer Methods and programs in Biomedicine 61:77-89
2. Bo P, David Z (2004) Computerized tongue diagnosis based on Bayesian networks. IEEE Transactions on Biomedical Engineering 51:1803-1810
3. Zhang H, Wang K, Zhang B, Smith J et al. (2005) Computer Aided Tongue Diagnosis System, Proceedings of the 2005 IEEE Eng. in Medicine and Biology, vol. 7, Shanghai, China, 2005, pp 6754-6757
4. Jia W, Yonghong, Z, Jing B (2005) Tongue area extraction in tongue diagnosis of traditional Chinese medicine, Eng. in Medicine and Biology 5:4955-4957
5. Michael K, Andrew W and Demetri T (1988) Snake: Active contour models, Int. J. Comput. Vision 1:321-331

Author: J.Y. Kim
Institute: Korea Institute of Oriental Medicine
Street: 461-24, Jeonmin-dong, Yuseong-gu
City: Daejeon
Country: Republic of Korea
Email: ssmed@kiom.re.kr

Design a Moving Artifacts Detection System for a Radial Pulse Wave Analyzer

J. Lee[1], Y.J. Woo[1], Y.J. Jeon[1], Y.J. Lee[1] and J.Y. Kim[1]

[1] Korea Institute of Oriental Medicine, Daejeon, Korea

Abstract — **Despite recent studies on development of pulse wave analyzers and needs for commercializing them, the reproducibility is one of the most controversial issues as ever. Because the pulse pressure value, which is one of the important parameters to evaluate reproducibility, is very vulnerable to moving artifacts, the reproducibility can not be obtained easily.**

In this paper, we designed a moving artifacts detection system for a radial pulse wave analyzer so that it can be robust to this kinds of artifacts by excluding the contaminated parts from the pulse wave signal to be analyzed. This moving artifacts detection system was designed to consist of a three-axis accelerometer, an electromyography amplifier and a two-axis tilt sensor.

To assess the suitability of the system, we examined the characteristics of each sensor's output signals with regard to the three motions such as extension, flexion and rotation. And, we also examined the each sensor's response to the high-frequency and low-frequency moving artifacts while the pulse wave signal was acquired from a pressure sensor for the pulse diagnosis. From these results, we could find that the response to subject's motions would be reflected in electromyography signal first, accelerometer signals and tilt sensor sequentially. And, the facts that a stable pulse wave can be acquired in two seconds after high frequency or low frequency motions ended were also found.

Consequently, based on these findings, we set up some rules on the moving artifacts detection and designed an algorithm which is fit for our moving artifacts detection system.

Keywords — **radial pulse waveform, moving artifacts, accelerometer, tilt sensor, EMG.**

I. Introduction

Non-invasive radial artery pulse waveform has been widely used since the radial tonometry is simple to perform and well tolerated. Indeed, in contrast to the carotid artery, the radial artery is well supported by bony tissue, making optimal applanation easier to achieve. It has been, however, known that the deformation of pulse shape can be caused readily by moving artifacts, changing measuring position and hold-down pressure [1].

The first solution to guarantee reproducible radial pulse waveform is to keep the hold-down pressure constant along with using the high fidelity pressure sensors. But even though a system meets these requirements, it has been found that, with an automated system, 63% of the measured data was useless without a proper measurement procedure [2]. And also it has been known that the pulse waveform is a low frequency signal with the maximum frequency of around 30 Hz, and it is very susceptible to the moving artifacts [3]. The traditional band pass filters cannot be used since the moving artifacts' and the pulse waveform signal are in the same frequency range, and an algorithm is used to remove the noise by estimating the base line with the reference of the beginning of systolic period in every beat, but still it is susceptible to the moving artifacts which are in higher frequency than the heart beating frequency of 1H-1.5 Hz [4].

Therefore the best method to get good signal quality would be to identify the source of the moving artifacts and eliminate the data taken from the corresponding period for the analysis as well as to keep the SOP(standard operating procedure) for minimizing the moving artifacts.

This paper presents a system to detect the moving artifacts with the electromyogram taken from antebrachium, the acceleration signal taken from the wrist, and the performance of the system was evaluated.

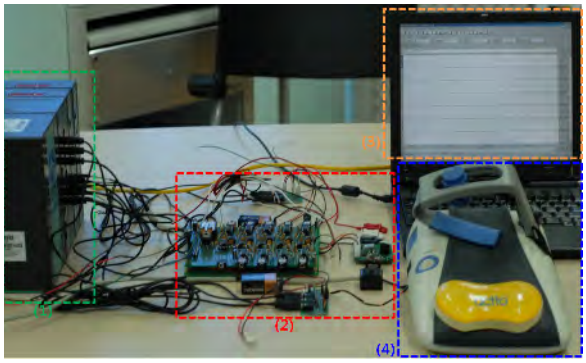
II. Method and Reseults

A. System configuration

During the radial pulse waveform measurement, the subjects should be asked to keep the same posture as much as possible, but the moving artifacts will always be generated by the human factors including measurement posture and physiological and mental status, and the equipment factors including the hold-down pressure control and the structures to support the arm.

To remove moving artifacts during the measurement with the pulse diagnosis system, in this paper, a system which consists of an accelerometer, a tilt sensor, and electromyography amplifier is proposed. The accelerometer used in the system is MMA7260Q (Freescale Semiconductor Inc, USA) with low power consumption and the measurement range was set to ±1.5g with the high sensitivity of 800mV/g. The 2-axis polymer based electrolyte tilt sensor, DX-045-90 (Advanced Orientation Systems Inc, USA) was used. Its measurement range is maximum ±90°, and the response time is lower than 20 msec. Biopotential amplifier module MP150(BIOPAC Systems Inc, USA) was used to acquire

Chwee Teck Lim, James C.H. Goh (Eds.): ICBME 2008, Proceedings 23, pp. 508–510, 2009
www.springerlink.com



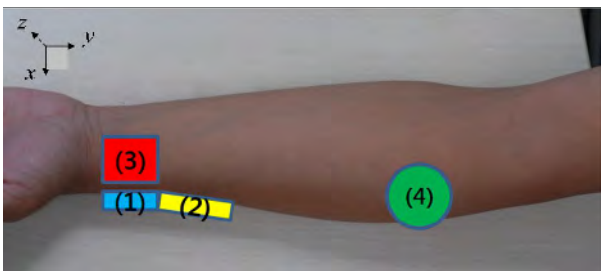
(1) Biopac (2) analog circuit (3) signal monitoring system (4) wrist holder

Fig. 1 Developed analog circuit and experimental setting

electromyogram signal which was amplified 1000 times. And the Pressure Sensor 1451(Measurement Specialties Inc, USA), which can measure the absolute pressure with superior linearity, was used to measure a pulse waveform. Biopac UIM module and MP150 module were used for the signal acquisition, and the total number of channels was seven, that is, three for the accelerometer, two for tilt sensor, one for electromyogram sensor, and one for the pulse waveform signal sensor. The developed analog circuit and experimental setting for moving artifact detection is shown in Fig. 1.

B. Experiments and results

With the proposed system for removing moving artifacts, the characteristics of the signals was observed for three movement patterns including extension, flexion, and rotation, and for low-frequency and high-frequency moving artifacts. The sensors attached near to the left hand of the subject are as shown in Fig. 2. The X axis of the accelerometer was attached to -y axis of the local coordinates, Y axis to -x, and Z axis to -z, and X axis of the tilt sensor was attached to z axis of the local coordinate, Y axis to x axis. The pulse waveform sensor was put to -z direction, and EMG electrode was attached near to the brachioradialis muscle.

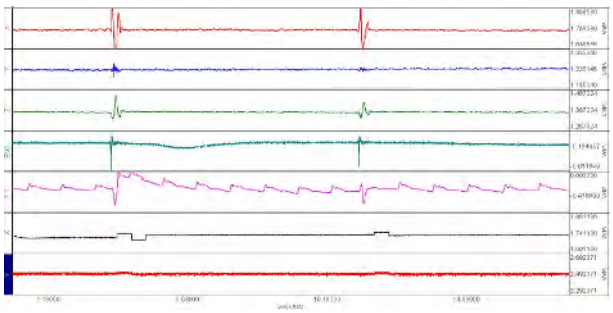


(1) accelerometer (2) tilt sensor (3) pressure sensor (4) EMG electrode

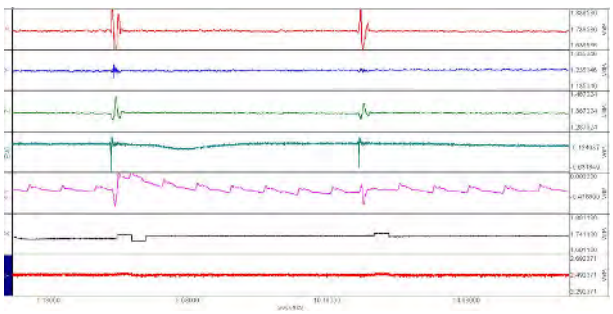
Fig. 2 Developed analog circuit and experimental setting

For the Z axis of the accelerometer, downward squared waveform was observed for the extension move, and relatively smaller upward squared waveform was observed for the flexion move since the wrist moving distance of flexion move was shorter than that of extension move. For the rotation move, prominent upward squared waveform was observed from both Y-axis and Z-axis. Electromyogram signal could be observed at the beginning of the all events, but it was hard to extract the differences among the different movement patterns, so it turned out to be not suitable for estimation of the movement. And, the tilt sensor required around 0.5 second of initial settling time, and there was a delay in the response time between the accelerometer signal and electromyogram.

The output signal characteristics for each sensor were observed when high-frequency and low-frequency moving artifacts were generated during the pulse diagnosis. In Fig. 3, an example of sensors' output signals is shown for high-frequency and low-frequency moving artifacts. The first panel is X axis signal of accelerometer, second panel is Y axis signal and third panel is Z axis signal of accelerometer. Electromyogram is shown in fourth panel and pulse pressure signal is shown in fifth panel. The sixth and seventh panel is for X axis and Y axis signal of tilt sensor respectively.



(a) high-frequency moving artifacts



(b) low-frequency moving artifacts

Fig. 3 An example of sensors' outputs for high-frequency and low-frequency moving artifacts

When a high-frequency moving artifacts was generated, with the electromyogram signal as a reference point, the noise in pulse pressure signal continued for around 0.2 seconds. And moving artifacts related response occurred in the electromyogram signal, the accelerometer signal and the tilt sensor signal sequentially. And also it was found that it took around 1.5 seconds to get the stabilized pulse waveform after moving artifacts response in the electromyogram signal ended. For low-frequency moving artifacts, the moving artifacts were detected first in the electromyogram signal, the accelerometer signal, and then tilt sensor signal. It took about 2 seconds to get the stable pulse waveform from the moment the muscle contraction stops.

From these results, it was confirmed that the suggested moving artifacts detection system comprising accelerometer, electromyogram, and tilt sensor could detect both low-frequency and high-frequency moving artifacts successfully.

C. Detection logic rules

The logic rules to detect the moving artifacts with suggested system comprising accelerometer, electromyogram amplifier, and tilt sensor based on the experimental results are summarized in Table 1. Every rule can be implemented by some simple equations – summation, square, differential and integration so that moving artifacts detection algorithm is expected to be embedded into the system easily.

Table 1 Summarized detection rules

# of rules	Description
1	It is considered that a moving artifact happens in the accelerometer only when a moving artifact is detected on at least one of X, Y, and Z axis signals.
2	It is considered that a moving artifact happens in electromyogram signal only when high impulse or muscle contraction is detected.
3	It is considered that a moving artifact happens in tilt sensor only when it is found on more than one of X and Y axis.
4	It is confirmed that a moving artifact occurs when moving artifacts happen in more than two sensors among the accelerometer, electromyogram, and tilt sensor.
5	The end point of the moving artifact for the total system is 2 seconds past the end of moving artifacts in electromyogram if the a moving artifact was found in electromyogram. If the moving artifact was not found in the electromyogram, then the end of the moving artifact in tilt sensor will be the end point of artifact of the system.

III. Conclusions

One of the most important parameters in radial pulse waveform is the magnitude of pulse pressure and it is very susceptible to the moving artifact. This paper presented a moving artifacts detection system configuration and an algorithm to detect moving artifacts.

The moving artifacts detection system comprises three-axis accelerometer, electromyogram, and two-axis tilt sensor. With the pulse waveform sensor placed on the pulse measurement position, the output signals' characteristics form each sensor by moving artifacts were reviewed. Based on these observations, the rules were set to detect the moving artifacts, and a detection algorithm was proposed. Applying the system to the pulse diagnosis system will improve the quality and reliability of the data, and it is expected to be possible to collect the data even in u-Healthcare environment where the system is greatly exposed to the moving artifacts like a wearable pulse diagnosis machine.

Acknowledgment

This work was supported by the Korea Ministry of Knowledge Economy (10028438).

References

1. Kelly R, Daley F, Avolio A, O'Rourke MF (1989) Arterial dilation and reduced wave reflection, Hypertension, 14:14-21
2. Jeon L, Yu-Jung L, Hae-Jung L, Eun-Ji C, Jong-Yeol K (2006) A Case Study of Six Sigma Project for Improving method of measuring pulse wave, Korean Journal of Oriental Medicine 12:2:85–92
3. Webster JG (1998) Medical Instrumentation: Application and Design, John Wiley & Sons Inc., 11-12
4. St-Amant Y, Rancourt D, Clancy EA (1998), Influence of Smoothing Window Length on Electromyogram Amplitude Estimates, IEEE Trans. Biomedical Engineering 45:6; 795-800

Author: Jong-Yeol Kim
Institute: Korean Institute of Oriental Medicine
Street: 483 Exporo Yuseong-gu
City: Daejeon
Country: Korea
Email: ssmed@kiom.re.kr

A Real-time Interactive Editor for 3D Image Registration

T. McPhail[1] and J. Warren[1]

[1] Rice University/Computer Science Department, Houston, TX, United States

Abstract — **Creating deformations between 3D volumes has received attention in areas such as animation, fluid dynamics, and medical imaging. Volume data often represents some anatomical structure or fluid which moves in a smooth, continuous manner. Particularly in the medical imaging community, there have been a number of attempts to automatically compute these smooth deformations between successive volume data sets, however due to the considerable amount of imaging artifacts, manual deformation methods are often required. There have been several human-assisted systems that facilitate manual deformation of volumetric data, however, they either do not facilitate real-time interaction from a user, or are too cumbersome for substantially large data sets. We present an interactive tool for creating and validating high-quality point-based and coordinate frame-based deformations. At its core, there is a visualization framework interactively renders deformed volumes and visually assesses the quality of deformations as volumes are manipulated.**

Keywords — **Volume Visualization, Deformation, Biomedical Imaging, Hardware Rendering.**

I. Introduction

Image deformation of volumetric data has many applications in medical imaging, image matching, fluid dynamics, and animation. Many standard approaches in these areas utilize automatic methods to generate deformations between sequences of images. However, automatically finding deformations for relatively noise-free images is an NP-complete problem [1, 2] because any algorithm can fall into local minima (see figure 1). The performance of such methods is worsened by the introduction of noisy images.

In radiation oncology, doctors are developing methods for determining the healthiness of human lungs from properties of the deformations between pairs of 3D computed tomography (CT) images. During the acquisition of these images, substantial imaging artifacts can be generated due to ct gating error [3] (see figure 3). Gating noise introduces features in one image that are not present in the next image, which makes automatic deformation an even harder problem.

In fields such as oncology, extremely high-quality deformations are needed, and ultimately assessed by humans for quality assurance. For this reason, we have chosen to create semi-automatic methods and tools to aid humans in generating and validating deformations. Ideally, we want to create an interactive environment that 1) interactively generates volume deformations and 2) gives real-time feedback for quality assurance.

A. Related Work

Substantial progress has been made in the area of volume visualization [4, 5, 6] However, the problem of integrating volume manipulation and visualization needs more attention. Systems for manipulating and visualizing volume data are either too cumbersome or non-intuitive for the user, and/or suffer from a lack of real-time interaction.

[7, 8] present techniques for generating volume deformations using skeletons and methods based on tradition skeletal animation. This work is intuitive for data which represent objects with rigid skeletal structure, but limits its effectiveness on a wider class of images. Both works do not have real-time capabilities. [8] shows results for near interactive performance, however, we desire a real-time solution.

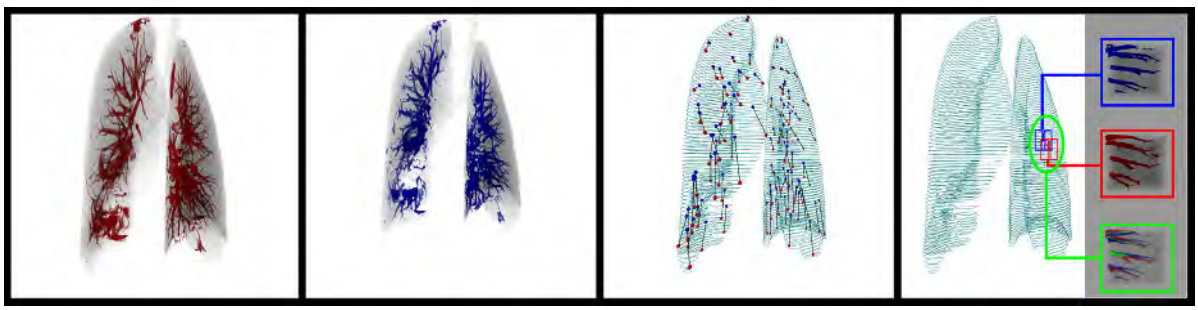


Fig. 1 Series of images from our application (left to right): Source Volume, Target Volume, Correspondences, and Comparisons of local volumes.

Chwee Teck Lim, James C.H. Goh (Eds.): ICBME 2008, Proceedings 23, pp. 511–518, 2009
www.springerlink.com

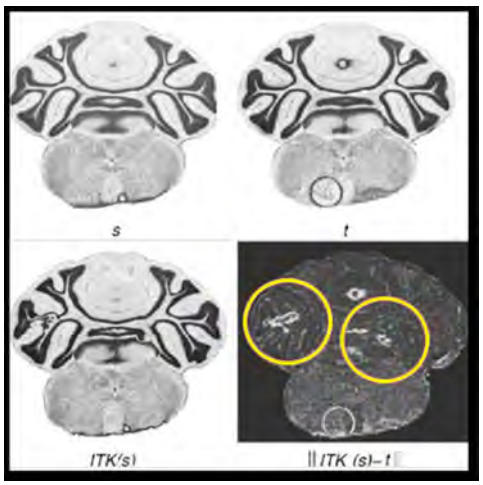


Fig. 2 Comparison of a source image, S, target image, T, the deformed image generated by ITK, and the difference between the deformed image and the target image.

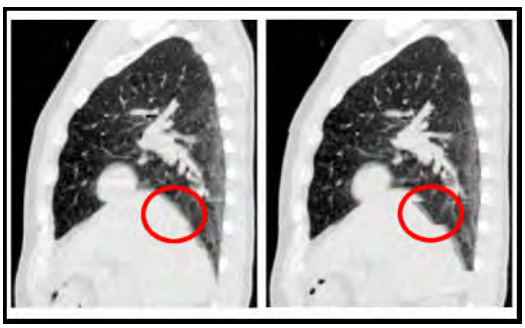


Fig. 3 Example of imaging artifacts due to gating error during the ct acquisition process.

[9, 10] have deformation frameworks that allow users to establish static correspondences between sets of landmarks for pairs of images, and induces deformations based on these correspondences. These environments have sub-real-time performance and use static landmark correspondences, not allowing users to manipulate these correspondences interactively. [11] provides one of the first true interactive volume deformation environments. The controlling handles for this tool are curved wires which limit its effectiveness much like [8]. Additionally, this environment only deforms a source image and does no comparison to a target image. It is also not clear if this method can generate the high-quality deformations needed for our purposes while maintaining interactive speeds.

B. Volume Deformation

Substantial work has also been done in the realm of volume deformation. Automatic deformation methods based on conservation of energy equations such as Optical Flow [12] and modified versions such as Compressible Combined Local Global registration [13] are extensively used in the medical fields. These methods are computationally intensive, having run-times on the order of hours depending on the size of deforming volume. Also, while these methods are theoretically sound, flow methods suffer from noise from real-world data which can yield unrealistic results (see figure 2).

Grid-based methods require the generation of a controlling grid which can be cumbersome to generate. For example, free-form deformations require an alignment of a lattice of control points with features in an image to generate C2 deformations using bivariate cubic splines. For 3D images, finite element methods require the generation of a tetrahedral mesh which can be time-intensive. This class of methods is typically not well-suited for fast interaction which is needed for the purposes of our framework.

Due to their performance and intuitive manipulation, we use several techniques that can be organized in a manner similar to Shepard interpolants (i.e. $f(v) = \sum \alpha_i w_i \cdot q_i$). Due to the methods' simple structure, the CPU can process these deformations in real-time for data with a reasonable set of control handles, p_i (e.g. $200 < |p_i| < 700$).

C. Contribution and Overview

We provide an intuitive environment for generating and validating 3D deformations between pairs of volume data images. In order to deform volumes, we provide two existing point-based methods and create a new frame-based method for generating deformations between pairs of subsequent images, S and T. To aid in user control, our system automatically finds a set of landmarks in S and their corresponding displacements and frames in T. Our main contribution is a rendering framework that facilitates interactive feature based deformations. At its core, we sample deformations on a uniform grid. This sampled deformation is stored as a RGB texture. We then use the synthesized texture to sample the respective volume data using conventional volume rendering techniques. This framework also provides real-time validation of the quality of the generated deformations.

The structure of the rest of the paper is as followed:

- Controlling and generating deformations (section 2 and 3)
- Volume rendering and our rendering framework (section 4)
- Implementation results and conclusion (sections 5 and 6)

II. Controlling Deformation

Our application provides a set of methods that generate deformations between pairs of input images. We first discuss generating control handles and establishing their correspondences between the two input images.

A. Handle Selection

Given a pair of 3D images, *S* and *T*, there are many techniques for producing deformations from *S* to *T*. A straightforward approach is to manually assign a displacement for each voxel in *S* (A displacement for a voxel *v* is the vector $d_v = f(v) - v$, where *f* is our deforming function). This approach is extremely accurate; however, manually producing displacements for each voxel in a 3D image is impractical for even moderate sized data. A more reasonable approach is to establish displacements for a subset of the voxels in *S* (300-500 voxels) and then create a mathematical function that blends these displacements to generate a deformation for all voxels in *S*. Even with this more tractable approach, the amount of work required can still be substantial. For this reason we have developed a computer-aided approach to select handles in a source image and setting the displacements of these handles in a target image.

We now consider the selection of handles that will control the deformation from a source image to a target image. We shall treat our source and target images as functions $S, T : \mathrm{N}^3 \mapsto \mathrm{N}$. Desirable control handles lie on features that are distinguishable in an image. These features lie on discontinuities, or edges of the images. To exploit this fact, we create $\widetilde{S} = \Omega * S$ and $\widetilde{T} = \Omega * T$ where $(*)$ is convolution and $\Omega : \mathrm{N}^3 \mapsto \mathrm{N}$ is a Sobel operator. We then generate $\hat{S} = | S - \widetilde{S} |$ and $\hat{S} = | S - \widetilde{S} |$ to enhance the edges of *S* and *T* respectively. From this enhanced image, we generate a set of control handles by repeatedly finding the brightest voxel in the image and blackening a ball of user-specified radius around the selected voxel. The resulting set of handles corresponds to the strongest features in the image.

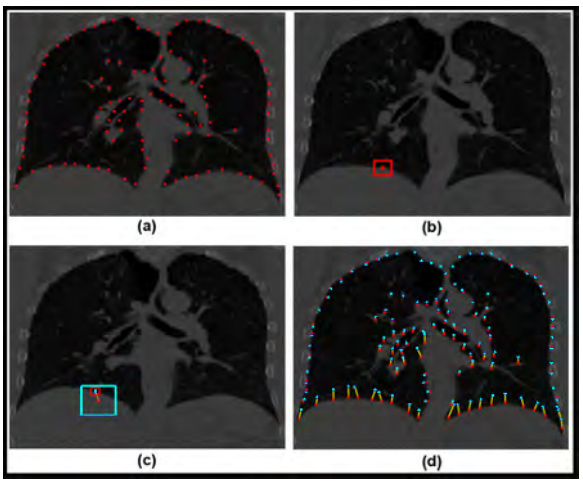


Fig. 4 Depiction of the automatic handle selection and correspondence process. (a)Source image with control handles. (b-c) Search for correspondence for a control handle, (d) Correspondences for all of the handles.

B. Handle Correspondences

We now wish to establish correspondences for our control handles between pairs of images. Using *S* and *T* as previously mentioned and given corresponding handles p_i and q_i, we generate 3D sub-windows, W_S and W_T centered about p_i and q_i respectively.

$$C[x,y,z] = \sum_i \sum_j \sum_k W_T[i,j,k] W_S[x+i-\alpha, y+j-\beta, z+k-\gamma] \tag{1}$$

The voxel location of the maximal value in *C* represents the best displacement so that W_S locally matches a window in *T* of the same size. However, there is no guarantee of a unique global maximum for *C*, so we create the function $\hat{C}$ that penalizes voxels that are far away from the control handle.

$$\hat{C}[x,y,z] = C[x,y,z] - \alpha \,|\, (x,y,z) = (p_{ix}, p_{iy}, p_{iz}) \,| \tag{2}$$

where (p_{ix}, p_{iy}, p_{iz}) is the location of the handle we are investigating. It should be noted that the size of W_T is substantially larger than that of W_S. This enables our editor to compare the local neighborhood of a handle in a source image, and find the best match within the target image. For more accurate correspondences, we iterate this process several times. During every successive iteration, each new target window W_T is centered at the corresponding match from the previous iteration. We also use the final correspondences to establish the best affine transformation centered at each control handle which is used by our frame-based deformation technique (the best affine transformation is explained in section 3).

III. Deformation Techniques

We now discuss building deformations using a set of controlling handles, either of the form of points or coordinate frames. We treat a 3D deformation as a function that maps points in a source volume to points in a target volume.

Imagine a set of control handles p_i associated with S that are moved to q_i associated with T. Now in order for a deformation function, f, to provide meaningful results there are several properties that the deformation must satisfy:

- Smoothness: f should smoothly deform the volume
- Identity: If $\forall_i p_i = q_i$, then $\forall_v v = f(v)$
- Interpolation or Approximation: Either $f(p_i) = q_i$ or $| f(p_i) - q_i | < \varepsilon$.

In order to generate real-time deformations, our framework assumes that the handles for the source image are fixed at the time the deformations are generated. We exploit this property and precompute information to facilitate real-time manipulation. If a user alters the source handles, the real-time deformation computation is halted due to the necessary precomputations (we quantify the performance delay in section 5). The intended use of our editor is to manipulate q_i in order to take advantage of the real-time capabilities of our deformation methods.

All of our techniques reduce the deformation of a voxel to the form: $f(v) = \sum \alpha_i q_i$. Here f is the deformation function, α_i are scalar coefficients, and q_i are the displaced handles in the target image. Expressing deformations as a weighted combination of the deformed control handles is the key feature that allows our application to compute deformations in real-time.

A. Thin Plate Splines

We move to the use of thin-plate splines to generate deformations from image S to T. We will proceed with a brief description of the theory behind thin-plate splines [14]. For a more in depth look into thin-plate splines, refer to [14]. A d-dimensional thin-plate spline is the fundamental solution to the biharmonic equation with the form

$$f(v) = U(r) = r^2 \ln r \tag{3}$$

where $v \in \Re^d$ and $r = | v |$. At the root of thin-plate spline theory is the physical notion of bending a thin sheet of metal represented by lofting $U(\{x, y\})$ over the xy-plane. Here the physical lifting is orthogonal to the plane. To apply thin plate splines to the problem of interpolating scattered control points, one treats the lifting of the plate as the actual displacements of the individual components of the control points. We now wish to generate a function $f(x, y, z)$, comprised of scaled translates of our thin-plate spline basis function $\hat{f}$, such that $f(x, y, z)$ minimizes the bending energy given by

$$\iiint_{\Re^3} f_{xx}^2 + f_{yy}^2 + f_{zz}^2 + 2(f_{xy}^2 + f_{xz}^2 + f_{yz}^2) dx\, dy\, | \tag{4}$$

The thin-plate algorithm reduces to a system of linear equations that are directly solved in [14]. We slightly reorganize the approach in [14] to generate a deformation of the form $f(v) = \sum \alpha_i q_i$.

B. Moving Least Squares Deformation

Next, we discuss generating a deformation from S to T using an affine moving least squares approach controlled by control points [15]. Now given a voxel v in S, we want to find the best affine transformation, A_v, which minimizes

$$\sum_i w_i \, | A_v(p_i) - q_i |^2 \tag{5}$$

Here, p_i and q_i are the control points in $\Re^3$ and w_i is either $w_{i_{\text{int}erp}} = \frac{1}{|p_i - v|^{2\alpha}}$ or $w_{i_{approx}} = \frac{1}{|p_i - v|^{2\alpha} + \varepsilon}$ where $\varepsilon > 0$.

With this approach our deformation function becomes $f(\{x, y, z\}) = A_v(\{x, y, z\})$. For brevity, we proceed to a closed form solution for this minimization problem. For a complete derivation of this method, refer to [15]. After manipulation, we can rewrite the minimization problem in equation 5 as

$$\sum_i w_i \, | \hat{p}_i M - \hat{q}_i |^2 \tag{6}$$

Here $p_* = \frac{\sum_i w_i p_i}{\sum_i w_i}$ and $q_* = \frac{\sum_i w_i q_i}{\sum_i w_i}$ are weighted centroids.

After using the classical normal equation solution to determine the minimizing M, we can rewrite our deformation function as $f_v(\{x, y, z\}) = \sum_j \alpha_j q_j$. Here α_j is determined by

$$\alpha_j = \Lambda_j + \frac{w_j (1 - \Lambda_j)}{\sum w_k k} \tag{7}$$

and Λ_j is a scalar that can be determined by

$$\Lambda_j = (x - p_*)(\sum_i \hat{p}_i^T w_i \hat{p}_i)^{-1} w_j \hat{p}_j^T \tag{8}$$

Observe that although the points q_i can change, the points p_i are fixed and allow Λ_j being precomputed. Thus, we can predetermine α_j reducing our deformation function f to a summation of scalar multiples of the points, q_i.

C. Frame-based Moving Least Squares Deformation

We now extend this moving least squares framework to generate deformations by manipulating coordinate frames as opposed to control points. Let the set of coordinate frames in our source image, $\{p_{ix}, p_{iy}, p_{iz}\}$ and their corresponding

matches in $\{q_{ix}, q_{iy}, q_{iz}\}$. Here, $\{p_{ix}, p_{iy}, p_{iz}\}$ and $\{q_{ix}, q_{iy}, q_{iz}\}$ are the local origins, x-vectors, and y-vectors for the respective coordinate frames. Now given a voxel v in our source image, we want to find the best affine transformation, A_v, which minimizes a modified version of equation 5

$$\sum_i w_i \mid A_v(p_i) - q_i \mid^2 + \beta(\mid p_{ix}M - q_{ix} \mid^2 + \mid p_{iy}M - q_{iy} \mid^2) \quad (9)$$

where β is a scalar which regulates the influence of the vector constraints in our new minimization problem. Note that $\beta = 0$ reduces our expression to equation 5.

As before, we define our deformation function $f_v(\{x,y,z\}) = \sum_j A_v(\{x,y,z\})$. Observe that after expanding the quadratic represented by equation 9, we have an expression that is quadratic in *T* and has no new terms involving *T*. This enables us to use the same solution for *T* in terms of M described in [15]. Substituting *T* in equation 9 allows the minimization problem to be expressed as

$$\sum_i w_i \mid \hat{p}_i M - \hat{q}_i \mid^2 + \beta(\mid p_{ix}M - q_{ix} \mid^2 + \mid p_{iy}M - q_{iy} \mid^2) \quad (10)$$

As in the previous moving least squares method, we use the normal equation solution to find the *M* that minimizes equation 10

$$M = \underbrace{(\sum_i \hat{p}_i^T w_i \hat{p}_i + \beta(\hat{p}_{ix}^T w_i \hat{p}_{ix} + \hat{p}_{iy}^T w_i \hat{p}_{iy})^{-1}}_{M_*}$$
$$\sum_j w_j (\hat{p}_j^T \hat{q}_j + \beta(\hat{p}_{jx}^T \hat{q}_{jx} + \hat{p}_{jy}^T \hat{q}_{jy}))$$

With our closed-form solution for *M*, we can now write a simple expression for our deformation function $f_v(\{x,y,z\})$.

$$f_v(\{x,y,z\}) = \sum_j \alpha_j q_j + \Lambda_{jx} q_{jx} + \Lambda_{jy} q_{jy} \quad (11)$$

where Λ_{jx} , Λ_{jy} and α_j are precomputed scalars determined by

$$\Lambda_j = (x - p_*) M_* \hat{p}_j^T$$
$$\Lambda_{jx} = \{1,0,0\} M_* \hat{p}_{jx}^T$$
$$\Lambda_{jy} = \{0,1,0\} M_* \hat{p}_{jy}^T$$
$$\alpha_j = \Lambda_j + \frac{w_j(1-\Lambda_j)}{\sum_k w_k}$$

Note the constant vectors, $\{1,0,0\}$ and $\{0,1,0\}$, which constrains our source handles to be axis aligned.

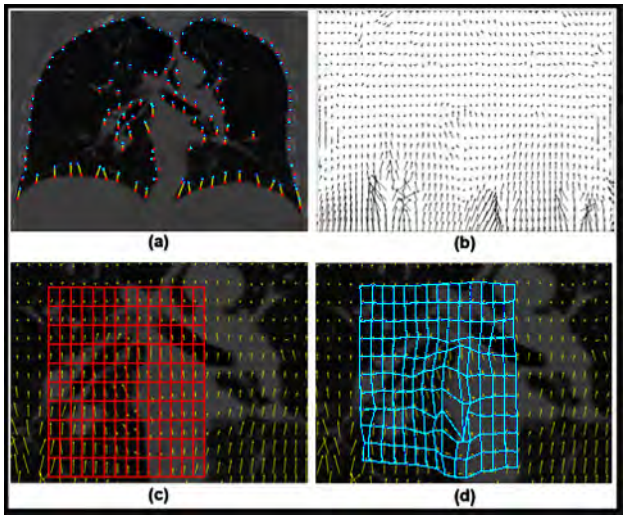


Fig. 5 2D depiction of viewing deformations using our framework. (a) Source image with control handles and displacements. (b) Deformation field from *S* to *T*. (c-d) Regular and deformed grid used to sample *S* and *T*.

IV. Visualization and Quality Validation

We will begin with an overview of volume rendering followed by our specific methodology for visualizing the source and target images. We then discuss the methodology of our rendering framework.

A. Volume Rendering

Volumes are typically viewed either by extracting isosurfaces in the form of surface meshes or by directly rendering the volume. Contouring algorithms such as marching cubes [16] or dual-contouring [17] are used to create surfaces from volume data; however, this approach is not well suited for viewing interior information. One of the more widespread class direct volume rendering methods is texture-based methods [4, 5, 6].

In texture-based methods, volume data is commonly represented as a regular grid of values that sample a function (e.g. a scalar field $\tilde{V}: \Re^3 \mapsto \Re$). This data is treated as a texture $\tilde{V}: [0,1]^3 \mapsto [0,1]$ and stored on a graphics card. With this texture information, the standard approach to visualizing the volume requires the generation of a dense sequence of planes parallel to the image plane and intersecting them with the unit cube $[0,1]^3$. The intersections are treated as polygons with the texture coordinates of each vertex being equal to its position (i.e. $tex(\{x,y,z\}) = \{x,y,z\}$). These polygons are processed by a simple vertex shader and the texels of these polygons are processed by a transfer function implemented on a pixel shader.

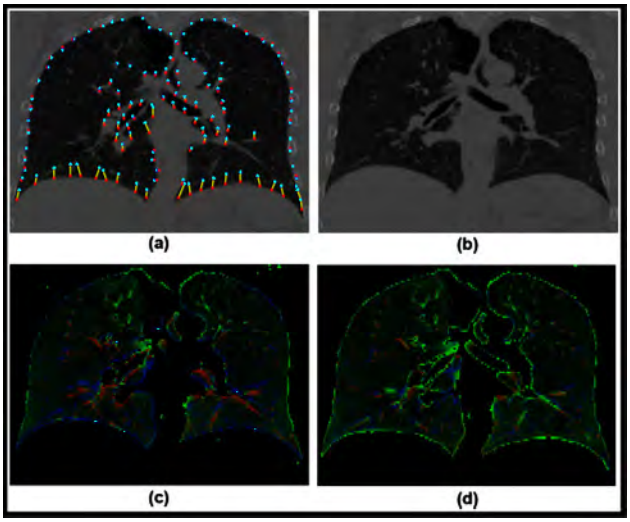


Fig. 6 2D depiction of the quality assessment feature of our application. (a)Source image with control handles and displacements. (b)Target image. (c)Comparison of *S* and *T*. (d) Comparison of *S* and $f^1(T)$ (Note the number of blue or red areas is lessened and major features are better matched than in (c).

Viewing deformed volumes imposes an additional challenge. With present hardware capabilities, real-time calculation of deformed volume sets is not feasible. However, using our feature-based techniques, interactively sampling the deformation on coarser grids is achievable.

B. Rendering Framework

We now discuss our methodologies for the rendering framework. In order to have an effective tool for validating and generating deformed images, a user should be able to:

- View subvolumes around corresponding control handle in order to asses the quality of the displacements (used for generating deformations).
- Visually determine the global quality of the deformed target volume (generated by our framework) with respect to the undeformed source volume.

We accomplish this by synthesizing a texture coordinate space on a uniform grid embedded in the unit cube. The sampled texture coordinates from the grid are encoded as a RGB texture and passed to the GPU. Using a sweeping algorithm (see [18]), we create a set of planes that intersect the cube from front to back. Next, the vertex shader generates texture coordinates equal to the vertex position of the rendered polygons (i.e. $tex(\{x,y,z\}) = \{x,y,z\}$). As the graphics card processes a polygon, the pixel shader fetches the synthesized texture coordinate that corresponds to the incoming fragment. Using this synthesized texture coordinate, the pixel shader then samples the data being visualized.

$$(u_S, v_S, w_S) = tex(\Omega_S, (x,y,z))$$
$$(u_T, v_T, w_T) = tex(\Omega_T, (x,y,z))$$
$$i_S = tex(S, (u_S, v_S, w_S))$$
$$i_T = tex(T, (u_T, v_T, w_T))$$

if $i_S \neq 0 \wedge i_T \neq 0$ *then*
$$\gamma = \min(i_S, i_T)$$
$$col.rgb = (i_S - \gamma, 2\gamma, i_T - \gamma)$$
$$col.a = (i_S + i_T - i_S \cdot i_T)$$
return $col \cdot \beta$
return (0, 0, 0, 0)

Fig. 7 Pseudocode for our quality assessment pixel shader.

C. Local Comparison of Correspondences

Now consider locally comparing the handle correspondences used in our deformation methods. Our goal is to overlay a sub-cube, $Cube_{source}$, of the source image centered at the source handle and a sub-cube, $Cube_{target}$, of the target image centered at the target handle. Assume the dimensions of $Cube_{source}$ and $Cube_{target}$ are identical. For each node in our uniform grid, we store a texture coordinate in our synthesized target image for $Cube_{target}$ (i.e. $tex(\{x,y,z\}) = A_v(\{x,y,z\})$). Here $A_v(\{x,y,z\})$ is a thin plate spline or best affine transformation for q_i as described in section 3. Afterwards, we perform a normal volume rendering pass for $Cube_{source}$ then using our generated target texture coordinate space, we visualize

$Cube_{target}$ as described in the previous paragraph. This overlays the two sub-cubes around the handles, p_i and q_i, in the same cube.

D. Viewing Deformations

Our last goal is to globally determine the quality of the deformed target image in real-time. In order to exactly view the entire deformed volume, our application would need to store and compute the sum of the scaled control handles for each voxel in the deformed image. Real-time performance for this approach is impractical, even for modestly size data sets. To compensate, we generate an approximation of the deformed image using the rendering framework mentioned earlier.

Data Set	Size	#of handles	Setup Times			Manipulation Times			
			MLS	MLS Frame	TP	MLS	MLS Frame	TP	Frame Rate
CT5	256x256x112	200	1.501	1.703	13.22	0.00062	0.00031	0.00031	69.1
Bunny	512x512x360	125	0.781	0.907	5.13	0.00078	0.00032	0.00032	68.5
Brain	256x256x109	216	1.36	1.563	15.50	0.00063	0.00047	0.00047	69.4
CT5	256x256x112	312	1.969	2.297	35.33	0.00063	0.00047	0.00047	68.9
bunny	512x512x360	343	2.172	2.516	44.11	0.00078	0.00047	0.00047	68.3

When comparing the quality of our deformation, note that producing the image $f(S)$ is not a surjective mapping from *S* to *T*. In light of this, we must compare our source image, *S*, with our deformed image $f^{-1}(T)$. We begin by altering the content of the previously mentioned synthesized target image. At each node in our uniform grid, we now store weights corresponding to each control handle. Now whenever a user moves a handle in the target image, we recompute a deformed texture coordinate for each node in our uniform grid. We then update the synthesized target image with these deformed coordinates and render both

volumes as mentioned in the local comparison section. This results in a trilinear approximation to $f^{-1}(T)$ (see Figure 1.2).

Due to the nature of the deformations, trilinear blending yields high-quality approximations when the grid is sampled to a reasonable resolution. In order to maintain real-time calculations with a dense set of sample points, we exploit the fact that $f(v) = \sum \alpha_i q_i$ to speed up the deformation calculation. Whenever a user selects a pair of handles (p_i, q_i) to alter, we store $\hat{f}(v) = \sum_{j \neq i} \alpha_i q_i$ for each sampled vertex. Storing $\hat{f}(v)$ enables our application to modify the synthesized target coordinate space with a simple multiplication and addition for each node in the grid. To further aid, in the time costs of our method, we only recompute the weights in the grid when the source handles are generated. The necessary precomputations of the weights are on the order of seconds for our provided methods (Results are given in the section 5).

E. Quality Assessment

Manually comparing two overlaid volumes can be a tedious process. In light of this, our framework gives aid in quality validation via a transfer function provided by one of the provided pixel shaders. Transfer functions are ran on fragments from the graphics card and return an rgba color tuple to be outputted for viewing. When assessing the quality of matching volumes, a transfer function should be:

- Symmetric (i.e. $h_{T\ to\ S}(\{x,y,z\}) = h_{S\ to\ T}(\{x,y,z\})$)
- Penalize for divergent values

We provide pseudocode for the transfer function used by our framework (see figure 1.4). As can be seen in line 9 of figure 1.4, the color returned by this function is green if there is a match and either red or blue if either the source or target image has greater intensity at the input location. This function also changes the opacity linearly in regards to the magnitude of the intensity difference between the two volumes at a given texel. The rightmost image in figure 4.2 gives a 3D example of this quality assessment.

V. RESULTS

We performed a series of performance tests to assess the performance of different components of our application. These results were taken on a PC with an Intel(R) Xeon 3.2GHz processor with 4GB RAM and a GeForce 8800 GTX graphics card. We used three test images: CT5 (a ct image of human lung), bunny (a ct ct image of the Stanford bunny), and brain (an mri image of a human brain). In all cases, the grid used to synthesize our textures had dimensions 32*x*32*x*32.

All timing results are measured in seconds except for the frame rate which is measured in frames/sec. From our results, the bottle-neck of our software application is processing the weights for our control handles for our different deformation methods. Of the three methods, our thin-plate spline implementations suffers from large setup times as the number of control handles increase. The other two deforming algorithms based on a moving least squares approach have reasonable setup costs. It should be noted that once the weight computation is complete, the time required to alter the deformations is negligible in comparison to the time needed to render a single volume image. For all of the frame rate measurements, the volume encompassed a 900*x*900 pixel^2 screen area.

VI. Conclusion and future results

We have provided an editor for deforming pairs of 3D images. Our editor automatically generates a set of controlling handles on features within a 3D source image. It determines correspondences for these handles in a subsequent target image. Our application then uses these correspondences to generate deformations via several handle-based methods. Further manipulation of these handles induces change in the generated deformation which is reflected in real-time.

The framework also provides visualization methods for real-time fidelity assessment of local handle correspondences and global deformation matching.

As far as limitations, our tool currently does not model non-smooth motion. For example, our editor could not create a deformation that captured the motion of a brick sliding across another brick. This limitation is due to the smoothness property of the deformations generated by this framework. One way to approach this problem in the future is to give the user the ability to paint, or segment, the various portions of the volumes and tag handles to only affect voxels of particular color. This painting feature would allow for discontinuities to exist on the boundaries of different segmented regions. We would also like to address fill-rate limitations of our rendering framework with new methodologies for empty-space culling. There are existing methods that address this problem [19]; however, these methods do not facilitate our visualization framework. We also want to synthesize finer texture coordinate images (i.e. 64^3vand 128^3 grids), however for moderate data, we would need to use improve the setup times for our deformation methods with parallel computing.

References

1. LEI H., GOVINDARAJU V.: Direct image matching by dynamic warping. cvprw 05 (2004), 76.
2. KEYSERS D., UNGER W.: Elastic image matching is np-complete, 2003.
3. SUI S., JUN D., FIVEASH J., PLAN B., SPENCER S., POPPLE R., PAREEK P., BONNER J.: Validation of target volume and position in respiratory gated ct planning and treatment. Medical Physics 30 (2003), 9.
4. WEILER M., WESTERMANN R., HANSEN C., ZIMMERMANN K., ERTL T.: Level-of-detail volume rendering via 3d textures. In VVS '00: Proceedings of the 2000 IEEE symposium on Volume visualization (New York, NY, USA, 2000), ACM, pp. 7.13.
5. REZK-SALAMA C., ENGEL K., BAUER M., GREINER G., ERTL T.: Interactive volume on standard pc graphics hardware using multitextures and multi-stage rasterization. In HWWS '00: Proceedings of the ACM SIGGRAPH/EUROGRAPHICS workshop on Graphics hardware (New York, NY, USA, 2000), ACM, pp. 109. 118.
6. LAMAR E., HAMANN B., JOY K. I.: Multiresolution techniques for interactive texture-based volume visualization. In VIS '99: Proceedings of the conference on Visualization '99 (Los Alamitos, CA, USA, 1999), IEEE Computer Society Press, pp. 355.361.
7. GAGVANI N., SILVER D.: Animating volumetric models. Graph. Models 63, 6 (2001), 443.458.
8. SINGH V., SILVER D., CORNEA N.: Real-time volume manipulation. In VG '03: Proceedings of the 2003 Eurographics/IEEE TVCG Workshop on Volume graphics (New York, NY, USA, 2003), ACM, pp. 45.51.
9. FANG S., SRINIVASAN R., RAGHAVAN R., RICHTSMEIER J. T.: Volume morphing and rendering: an integrated approach. Computer. Aided Geom. Des. 17, 1 (2000), 59.81.
10. HE T., WANG S., KAUFMAN A.: Wavelet-based volume morphing. pp. 85.92.
11. WALTON S., JONES M.: Interacting with volume data: Deformations using forward projection. medivis 0 (2007), 48.53.
12. HORN B. K., SCHUNCK B. G.: Determining Optical Flow. Tech. rep., Cambridge, MA, USA, 1980.
13. CASTILLO E., ZHANG Y., TAPIA R., GUERRERO T.: Compressible image registration for thoracic computer tomography images.
14. BOOKSTEIN F.: Principal warps: Thin-plate splines and the decomposition of deformations. IEEE Transactions on Pattern Analysis and Machine Intelligence 11, 6 (1989), 567.585.
15. SCHAEFER S., MCPHAIL T., WARREN J.: Image deformation using moving least squares. ACM Trans. Graph. 25, 3 (2006), 533.540.
16. LORENSEN W. E., CLINE H. E.: Marching cubes: A high resolution 3d surface construction algorithm. In Computer Graphics (Proceedings of SIGGRAPH 87) (July 1987), vol. 21, pp. 163.169.
17. JU T., LOSASSO F., SCHAEFER S., WARREN J.: Dual contouring of hermite data. In SIGGRAPH '02: Proceedings of the 29th annual conference on Computer graphics and interactive techniques (New York, NY, USA, 2002), ACM, pp. 339.346.
18. MCPHAIL T., FENG P., WARREN J.: Sweeping planes for volume rendering. To be published.
19. LI W., MUELLER K., KAUFMAN A.: Empty space skipping and occlusion clipping for texture-based volume rendering. In VIS '03: Proceedings of the 14th IEEE Visualization 2003 (VIS'03) (Washington, DC, USA, 2003), IEEE Computer Society, p. 42.

A Novel Headset with a Transmissive PPG Sensor for Heart Rate Measurement

Kunsoo Shin[1], Younho Kim[1], Sanggon Bae[1], Kunkook Park[1], Sookwan Kim[1]

[1] Bio & Health Group, Samsung Advanced Institute of Technology, P.O.Box 111, Suwon 440-600, Korea

Abstract — **In this paper, a headset with an ear-clip type, transmissive PPG (Photo-plethysmography) sensor is presented which allows a continuous and real-time monitoring of the heart rate (HR) whilst listening to music during daily activities. Also, the proposed headset is equipped with a tri-axial accelerometer, which enables the measurement of calorie consumption and step counting. During a variety of daily activities (e.g., walking, jogging, and sleeping etc.), a PPG may be contaminated with motion artifacts. To remove these motion artifacts, we designed an adaptive filter based on the accelerometer.**

To evaluate the accuracy of heart rate detection, for 13 subjects the HR from the headset was compared with that detected from the ECG simultaneously recorded with a conventional ECG recorder. As a result, the error rates of the headset are 0.6%, 1.7%, 0.7%, and 5.7% over rest, walking (3km/h), jogging (6 km/h), and running (9km/h), respectively.

From these results, it is likely that the proposed headset shows the performance good enough to be used in the continuous and real-time monitoring of the HR during daily activities. It is expected that the proposed headset is very efficient in the assessment of autonomic nervous activities under various physiological conditions, the exercise monitoring, and the evaluation of physical training performance.

Keywords — **Headset, PPG, Heart Rate measurement, Accelerometer, Adaptive filter**

I. Introduction

The skyrocketing healthcare cost in world-wide due to growth in aging population and chronic diseases will continue to put increased pressure on healthcare systems. In this respect, it is needed an innovative paradigm shift in healthcare system, i.e. connected healthcare, which is a cost effective, efficient and high quality healthcare delivery system. Unlike the conventional healthcare system, which has placed emphasis on a physician-operated and hospital centered "diagnosis and treatment" practice, connected healthcare will pursue a proactive, personalized, and preventive health management, such as the prevention and early detection of chronic diseases and the health promotion. This connected healthcare opens the opportunity to reduce healthcare cost and improve the quality of healthcare by avoiding unnecessary hospitalization and tests for the aged and chronically ill people. In connected healthcare, a core technology is one for continuous, real-time, and long-term monitoring of various vital signs, such as ECG, blood pressure, blood glucose level, respiration, heart rate, etc. It is well known that the heart rate is one of the most important vital signs reflecting the individual health status. That is, the heart rate has recently gained interesting interest in wellness applications, including the sport (providing criteria for an assessment of an athlete's performance and a monitoring of exercise load during exercise) and the fitness (providing a guide of a remedy for lifestyle modification). Also, heart rate variability (HRV) has become a popular noninvasive tool for assessing the influences of autonomous nervous system on cardiovascular control system, which enables us to assess a stress level or an emotional status.

In recent, those increase who listen to the music with MP3 player or cellular phone while taking workout. Thus far, a chest-strip type device has been extensively utilized as a device for continuously monitoring the HR during exercise, which allows a user to get the most out of our training by measuring performance, setting new goals and staying motivated [1]. Meanwhile, PPG devices have attracted significant attention in recent years due to their ease of being integrated into wearable accessories, i.e. a headset, a ring, and a wrist watch. The HR can be measured from PPG signal of which a pulsatile component reflects cardiac synchronous changes in the blood volume with each heart beat. In other words, as the heart pumps out the blood around the body, the volumetric changes of the blood vessels modify the absorption, reflection or scattering of the incident lights, such that the resultant reflective/transmittal lights indicate the timing of the cardiovascular events, such as heart rate.

In this paper, we implemented a wearable headset type of the heart rate monitoring device based on PPG sensing technology and investigated its feasibility as a wearable ambulatory device for continuously and on-line monitoring the heart rate.

II. Method

A. Practical Implementation

Sensor Architecture: Figure 1 illustrates a schematic diagram of the headset which consists of three parts: main body, sensing board, and sensor. The sensor part includes a LED (940 nm, Kodenshi), a Photodiode (Kodenshi) and a

Chwee Teck Lim, James C.H. Goh (Eds.): ICBME 2008, Proceedings 23, pp. 519–522, 2009
www.springerlink.com

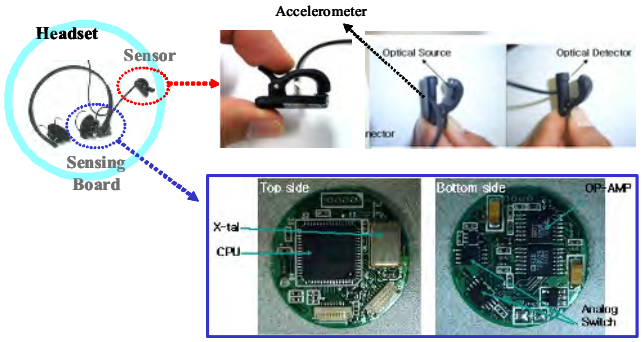


Fig. 1 A schematic diagram of the proposed headset.

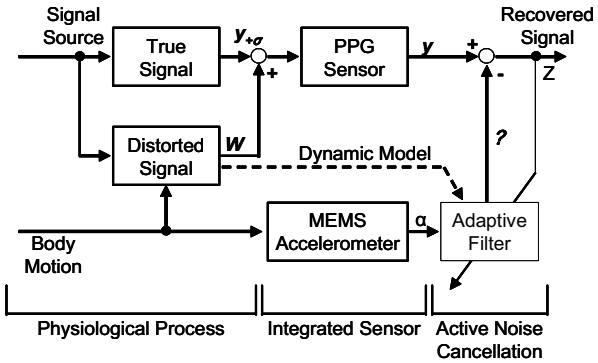


Fig. 3 The block diagram of the proposed ADF.

tri-axial accelerometer (±6g, Kionix). As shown in Fig. 1, by separating the sensor part from the main body, anyone can easily wear it, irrespective of an inter-individual difference in the ear anatomy. Also, the position of the optical sensor does not change significantly when the ear is accelerated because the inertia of the sensor part is very small.

As illustrated in Figure 2, the sensing board consists of a CPU (MSP430), 3 accelerometer inputs (Ax, Ay, Az), a LED driver, I-V converter, 2 sample-and-holder circuits (one is for the ambient light data, the other for the LED), a main amplifier, a high-pass filter (the cutoff frequency is 0.3 Hz), and a low-pass filter (the cutoff frequency is 7 Hz). The CPU controls the LED lighting sequence as well as data acquisition and processing process. The LED driver operates in a pulse mode with a duty cycle of approximately 1/10, i.e., turns the IR LED on and off. It allows to save the power and to remove the influence of ambient light noises. The photodiode current, which is proportional to the amount of light received, is converted into a voltage signal by the I-V converter. And then, the voltage signal is fed into two sample & holder circuits whose timings are synchronized with those when the LED turns on and off. The output signal from a sample-and-holder at the turn-on time of the LED represents ambient light signal. Thus, this ambient light noise can be cancelled by the ambient light removal circuit, in which it was subtracted from the signal at the turn-on time of the LED. After this phase, the continuous PPG signal is finally obtained by filtering with a low-pass filter the quantized signal from the ambient light removal circuit. And then, the resultant signal is fed to the A/D converter port (with 10-bits resolution) which converts it into digital format at the sampling frequency of 64 Hz.

Motion Artifacts cancellation: There is still important motion artifacts, in the PPG signal obtained through a chain of processes mentioned above. Several methods have been proposed to reduce the influence of motion artifacts on a PPG signal [2]. Recently, some studies have addressed that model based techniques showed good performance in optical measurements as compared with other techniques [3]. In this paper, the NLMS (Normalized Lease Mean Squares) method shown in Figure 3 is chosen for real-time processing and computability on mobile CPU. As shown in Figure 3, a reference signal of motion is needed for parametrically modeling the influence of motion artifacts on optical signals. The reference signal used in this model is also recorded with a tri-axial accelerometer. FIR filter parameters are estimated from the motion signals using the normalized least mean square, where the sampling frequency was 64 Hz

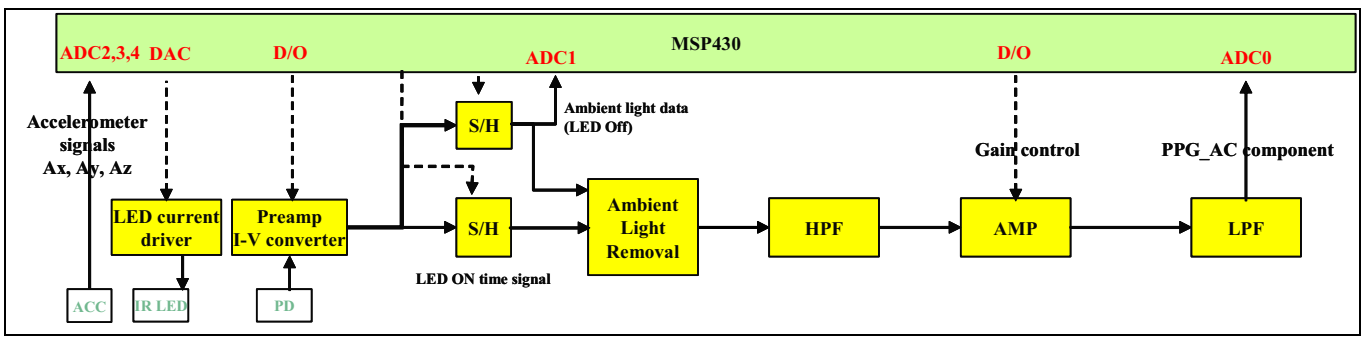


Fig. 2 Functional block diagram of the proposed headset.

and the order of the ADF (Adaptive Filter) was 32. This filtering method allows the efficient removal of only noise components due to movement.

However, the adaptive filtering showed undesirable performance in case the period of a PPG signal is identical to that of the reference signal, which may attribute to the unwanted filtering of the PPG signal with the adaptive filter. To circumvent this problem, an intelligent algorithm is proposed to decide whether or not the ADF will be applied to any segment of PPG signal. Let's define *R(n)* as follows:

$$R(n) = Y(n) / D(n)$$

where

Y(n): the 64-point moving average of the absolute of ADF' output

D(n): the 64-point moving average of the absolute of the PPG data

Then, the ADF will be applied to only segments with *R(n)* being more than a preset threshold (0.5). In the application of this algorithm, on the other hand, it was found that *R(n)* became very small even when the periods of the desired signal and noise signal are different, which results from large noise components relative to the desired PPG signal. To overcome this problem, another parameter (*NW*), called the norm of ADF's coefficients, is introduced, which is calculated as $\sqrt{w_1+w_2+\cdots+w_i}$. Similarly, the ADF filtering will be performed only when the *NW* is below the predetermined threshold.

B. Performance evaluation

Thirteen patients (11 males, 2 females) participated in this study who gave informed written consent after being fully aware of the study protocol and its purpose.

Figure 4 illustrates a typical experimental setup for the feasibility test of the proposed headset as a wearable HR monitoring device. The subjects are first asked to wear the headset and the MP3 player, which is equipped with an ECG measurement module and a BT wireless communication module. And then, they performed exercise test on a treadmill, during which the running speed was increased by 1km/h at an interval of 30 seconds. During each test stage, the PPG signal, 3 accelerometer signals (Ax, Ay, Az), and one-channel ECG signal were continuously recorded, and then transmitted to a host PC via the BT wireless communication module for off-line analysis. To evaluate the performance of the headset as a wearable HR monitor, the HR calculated from the ECG was compared with that obtained from the headset's PPG signal. To facilitate convenient comparison, the signal measured was classified into 4 categories, such as the rest, the walk (from 1km/h to 3km/h), the jogging (from 4km/h to 6km/h) and the run (from 7km/h to 9km/h).

III. Results and Discussion

Figure 5 showed a representative example of a PPG signal, an accelerometer signal (Ax), and an ECG signal recorded with our proposed system. The symbol 'red circle'

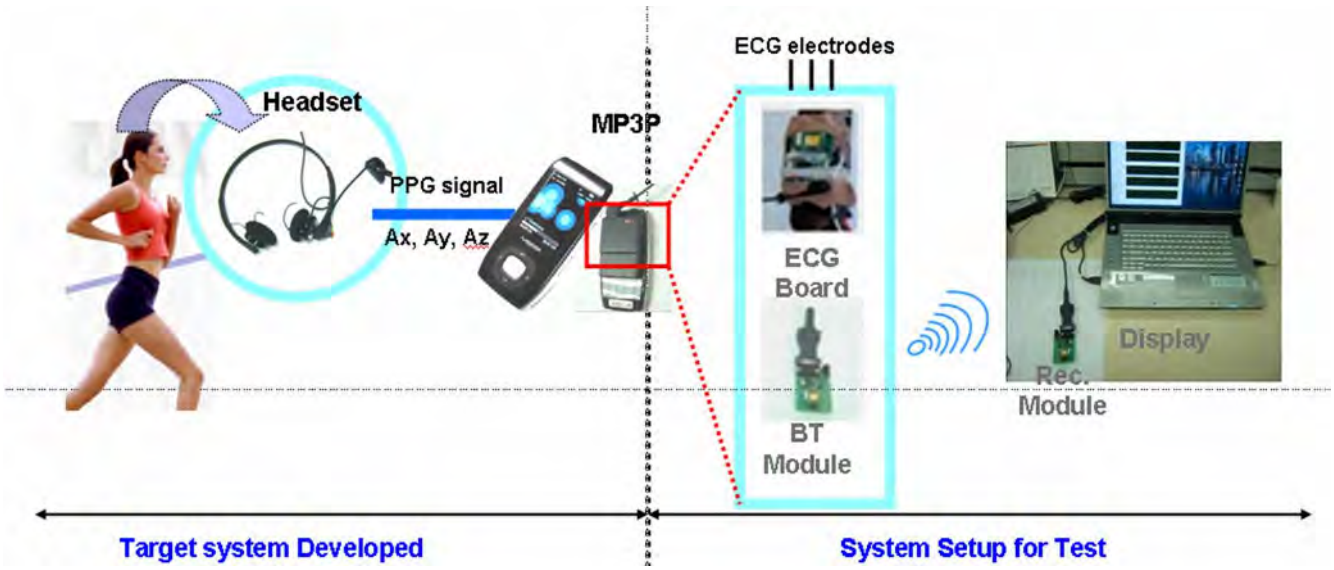


Fig. 4 A typical experimentaö setup of the proposed headset.

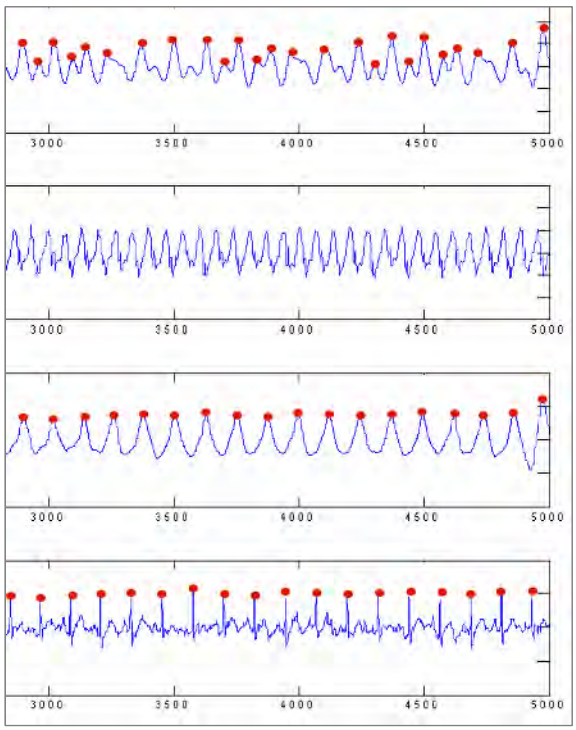


Fig. 5 A representative epochs of various signals recorded with the proposed system.

on traces (a), (c), and (d) in figure 5 represents the R-peak detected. The peak detection algorithm was implemented by a slight modification of an existing peak detection algorithm. In the preprocessed PPG signal (a), which is contaminated with motion artifacts of figure 5(b), the peak-detection algorithm led to erroneous HR measurement. As shown in Figure 5(c), where the motion artifacts were removed with the ADF, the peaks were accurately detected by it. As it were, those peaks accurately corresponded to those on ECG trace (Figure 5(d)).

Figure 6 depicted another example of various signals recorded with the proposed headset. From (c) in figure 6, it was observed that the output of the ADF was largely corrupted. It might attribute to the fact that the period of the PPG signal is identical to that of the reference signal.

To evaluate the accuracy of heart rate detection, for 13 subjects the HR from the headset was compared with that detected from the ECG simultaneously recorded with a conventional ECG recorder. As a result, the error rates of the headset are 0.6%, 1.7%, 0.7%, and 5.7% over rest, walking (3km/h), jogging (6 km/h), and running (9km/h), respectively.

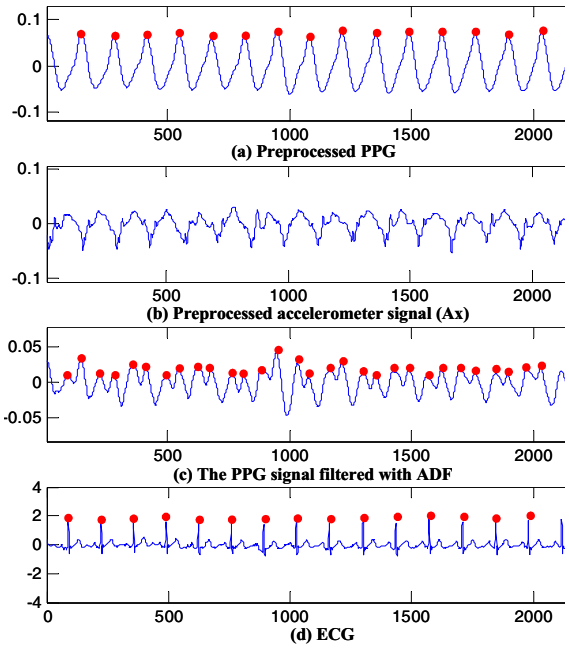


Fig. 6 A representative epochs of various signals recorded with the proposed system.

IV. Conclusions

This paper presented a novel, wearable heart activity monitor (WHAM) which allows the continuous and on-line monitoring of a user's HR. Our results indicated that the headset has enough potential for a wearable, ambulatory HR monitoring device. It is expected that the headset proposed is very efficient in the assessment of autonomic nervous activities under various physiological conditions, the exercise monitoring, and the evaluation of physical training performance

References

1. Training with Polar at http://www.polar.fi/en/training_with_polar
2. Lei Wang, Benny PL Lo, Guang-Zhong Yang (2007) Multichannel Reflective PPG Earpiece Sensor with Passive Motion Cancellation. IEEE Trans. on BME Vol. 1, No. 4: 235-241.
3. Philippe Renevey, Rolf Vetter, Jens Krauss, Patrick Celka, Roland Gentsch and Yves Depeursinge (2001) Wrist-located pulse detection using IR signals, activity and nonlinear artifact cancellation. Engineering in Medicine and Biology Society, 2001. Proceedings of the 23rd Annual International Conference of the IEEE Vol. 3: 3030-3034

Author: Kunsoo Shin
Institute: Bio & Health Group, Emerging Center, SAIT
Street: P.O.Box 111
City: Suwon 440-600
Country: Korea
Email: bosco.shin@samsung.com

Improvement on Signal Strength Detection of Radio Imaging Method for Biomedical Application

I. Hieda[1] and K.C. Nam[2]

[1] National Institute of Advanced Industrial Science and Technology (AIST), Tsukuba-city, Japan
[2] Korea Electrotechnology Research Institute (KERI), Ahnsan-city, Korea

Abstract — **The authors were applying Radio Imaging Method (RIM) to measurement of the living human body that was originally developed for geological measurement. Small antenna was used to measure electric field intensity changes effectively that was influenced by dielectric material, such as the living body. Experiments were performed with high frequency electric field, such as 50MHz. Water tank was used as phantom of human organ because permittivity of some human organ was as high as that of water. Some problems should be settled that related to the principle and technology. One of the drawbacks was insufficient change of signal strength. When a water tank of 6 x 8 x 25cm was used as a phantom of relatively large human organ, provided signal strength change was approximately 1dB. It only affected lower three bits of 12bit A/D converter instrumented for the experiment. To improve the total resolution, the measurements had been repeated ten to forty times, and the acquired data had been averaged. By improving accuracy of single measurement, the number of trials could be decreased and it was essential for practical systems. In this paper, a new measurement method was introduced. Two plate electrodes of transmission antenna were located side by side, and fed opposed phases to cancel electric field intensity at the receiving antenna that was located 30 cm from the transmission antenna. When dielectric material was located in the measurement field, it broke the balance of electric field, and signal strength change was detected. Because base signal intensity was virtually zero, better resolution was expected than the basic method. The method was tested both by simulation and by experiment. Advantages and disadvantages were discussed based on the results.**

Keywords — **Radio Imaging Method, electric field, biomedical measurement, FDTD, Python.**

I. Introduction

Medical equipment that uses electricity and magnetism, well represented by MRI, contributes to medical care and welfare of the human. On the other hand, high-level and large-scaled medical equipment is one of the factors to push up medical and welfare costs. It becomes financial burden of most of the developed countries. In addition, the developing countries have few benefits of these high-level devices. From the point of view, simple and easy equipment for medical care and health care is demanded. The authors are developing electromagnetic measurement method aimed at medical screenings and welfare applications shown in Figure 1 [1-4]. This is simple, safe and economical method.

Experiments were performed using electromagnetic waves in VHF band. Non-metallic (acrylic) water tank filled with water was measured by the method. The relative permittivity of water at room temperature and pressure was approximately 70 that was as high as some human organs, for example, muscles and internal organs because these tissues contained much moisture than other tissues. The tank filled with water was used as a phantom in the study to imitate portion of human body or some organs.

Early studies of the authors showed signal strength increased when the water moved closer to each of transmission or receiving antenna [1-3]. This suggests that the increments of signal strength were not caused by magnetism but by water permittivity influencing electric field intensity. In the recent paper, the fact was backed by experimental results where electric field antennas were used, and by numerical simulation [5] that was called the Finite-Difference Time-Domain (FDTD) Method [6].

One of the drawbacks of the developing method was insufficient level of signal strength changes. When a water tank of 6 x 8 x 25cm was used as a phantom of relatively large human organ, measured signal strength change was

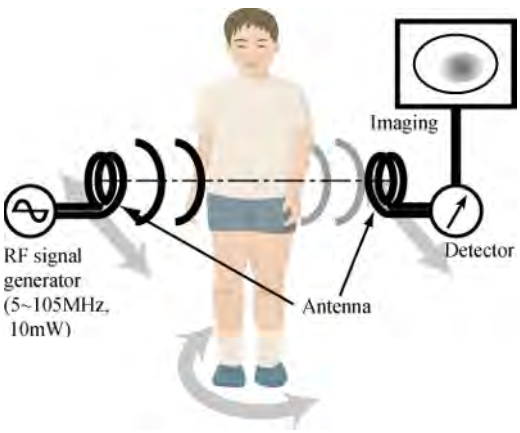


Fig. 1 Conceptual blockdiagram of Radio Imaging Method for medical application.

Chwee Teck Lim, James C.H. Goh (Eds.): ICBME 2008, Proceedings 23, pp. 523–526, 2009
www.springerlink.com

1dB. It was only acquired as a few effective bits of 12bit A/D converter instrumented for the experiment. At this level of changes, instability of the measurement system could not be ignored. To improve the total resolution, the measurements had been repeated ten to forty times, and the acquired data had been averaged. By improving accuracy of single measurement, the number of trials could be decreased and it was essential for practical systems.

In this paper, a new measurement method was introduced. Two plate electrodes of transmission antennas were placed side by side, and fed opposed phases to cancel electric field intensity at the receiving antenna. When dielectric material was located in the measurement field, it broke the balance of electric field, so that signal strength change was detected. Because base signal intensity was cancelled and it was virtually zero, better resolution was expected than the basic method that had certain level of base signal strength.

II. Methods

A. Experiments

Figure 2 showed overview of the experiments. Transmission and receiving antennas were located 300mm apart. Figure 3 showed two types of antennas. Type A was always used for receiving antenna. Type A and B were used for transmission antenna alternatively.

Two series of measurement were performed for the two types of transmission antenna, respectively. To obtain two-dimensional characteristics, a tall water tank whose dimension was 20 x 60 x 250 mm, shown in Figure 2, was used as phantom and it was moved on a 670 x 200 mm (650 x 140 mm movable area) horizontal plane laid between the antennas. The water tank was driven along paths in the Y-axis direction.

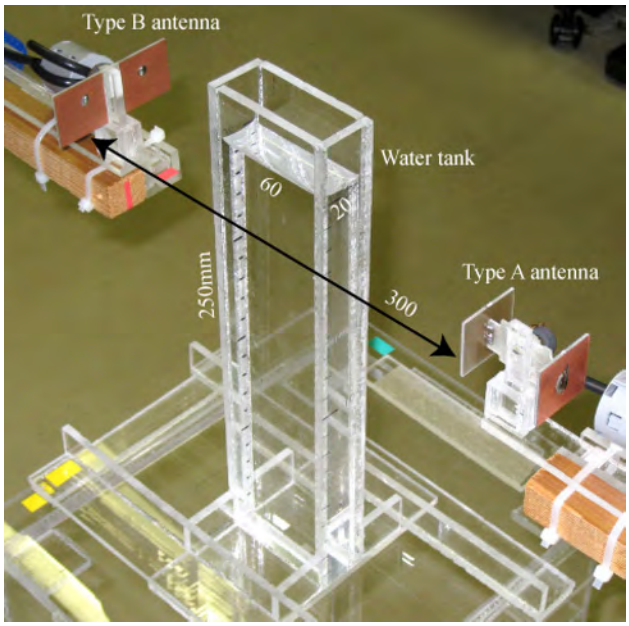


Fig. 2 Overview of the experiment.

Electric field intensity was measured as signal strength by a spectrum analyzer (Anritsu MS2621B) at every 1cm position of the water tank. It was measured forty times per position and the averages were calculated.

In the experiments, 10 mW of power at 50 MHz was fed from RF generator build in the spectrum analyzer to the transmission antenna. Because the antenna did not match the characteristic impedance of the coaxial cable, 50 ohm, the less power was actually transmitted.

B. FDTD Simulation

The Finite-Difference Time-Domain Method (FDTD) was employed to confirm the electromagnetic field changes [6]. The authors used Python script [7,8] that implemented the Uniaxial Perfectly Matched Layer (UPML) Method .for the boundary condition to prevent reflections [6, 7].

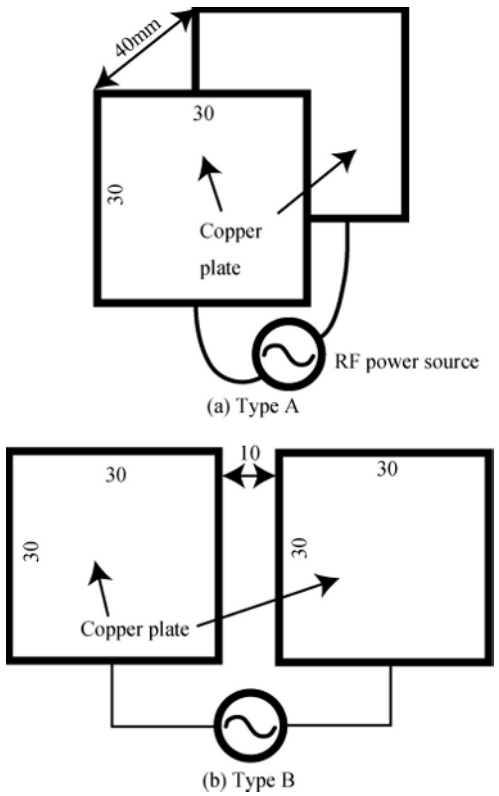


Fig. 3 Schematic diagram of two types of electric field dipole antennas.

The dimension of the simulation space was 860 x 560 x 560 mm and it was meshed in 86 x 56 x 56 square elements so that each square element had 10mm long sides. The simulated water tank had the same dimension as the experiment; however, it had no wall for simplification. The region occupied by the water tank had the relative permittivity of 70. The water tank was moved in the simulation space according to the experimental conditions and electric field intensity was calculated for each water tank position.

Another difference of the conditions between simulation and experiment was the thicknesses of antenna plates. Antennas used for the experiment were made of copper films on printed circuit board that was 0.035mm thick. For the simulation, electrodes were 10mm thick because of the square element dimension. The electric field dipole antenna mainly excited electric field between the two plates; therefore, notable effect caused by thickness of the plates was not expected.

III. Results and Discussion

Figures 4 and 5 showed results of the experiment and simulation, respectively. X- and Y-axes indicated water tank position. The lines where ***x=0*** and ***x=14*** were the water tank paths closest to the receiving and transmission antennas, respectively. In each figure, the upper figure (a) showed results where Type A antenna was used for the transmission antenna, and the lower figure (b) showed results where Type B antenna was used. Type A antenna was always used for the receiving antenna.

In Figure 4, forty measurements were averaged that were performed per water tank position. Z-axis indicated relative signal changes in percentage to base signal strength where no water tank was located in the measurement field.

The simulation results were also relative signal changes in percentage to the electric field intensity without water tank that was shown in Figure 5.

Generally, Figures 4(a) and 5(a) had common characteristics. When water tanks were located on the centerline

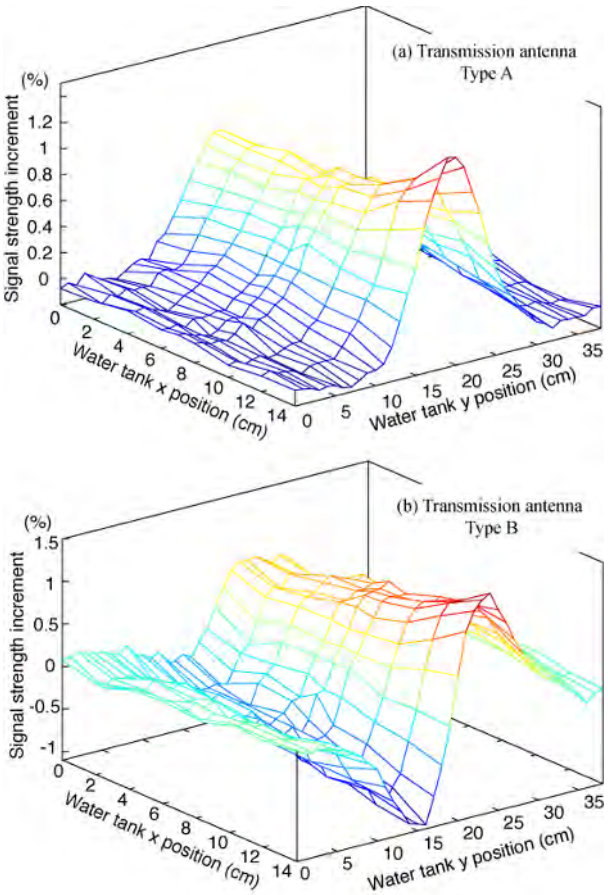


Fig. 4 Measured signal strength changes according to water tank location.

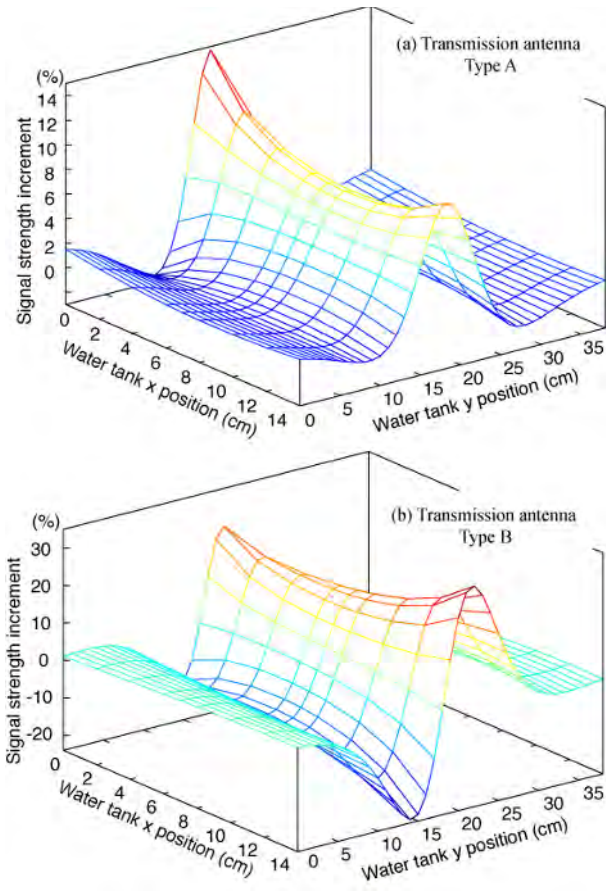


Fig. 5 Simulated signal strength changes according to water tank location.

between transmissions and receiving antennas (***y=18***), signal strength had peaks that formed ridges between the two antennas. The peaks were minimized where water tank was at the center of the centerline (***x=7***, ***y=18***). However, peak heights closest to the antennas didn't have common relative tendency in the two figures.

These qualitative characteristics corresponded to the results of experiments where electric field dipole antennas and loop antennas were used, and to the FDTD simulation that were reported in the authors' previous paper [5].

Figures 4(b) and 5(b), where Type B antenna was used for transmission antenna, corresponded to each other, too. Because two electrodes of Type B antenna were excited 180-degree different phase voltages and the distances from the two electrodes to the receiving antenna were the same, electric field intensity at the receiving antenna was expected to be cancelled when no water tank was located. If the water tank was on the centerline between transmission and receiving antennas (***y=18***), electric field intensity could be cancelled, too. However, Figure 4(b) showed the electric field intensity was not cancelled even if the water tank was centered. When water tank moved a few centimeters forward along Y-axis, the balance was broken more and signal strength increased. On the other hand, the signal strength had minimum points at few centimeters backward along Y-axis from the center. The balance was compensated by the water location.

Interestingly, Figure 5(b) had the same tendency as Figure 4(b). The simulation was expected to have null electric field intensity at receiving point. This result suggests the balance was delicate, and that possible rounding errors and anisotropy of the algorithm caused the unbalance.

The main purpose of the study was to confirm whether the new method provided more significant signal changes than the conventional method. In Figure 4, the maximum changes were 1.2% and 1.5% for (a) and (b), respectively. Because signal strength decreased 1.0% where ***y=15*** in Figure 4(b), total signal change for (b) was 2.5% that was twice as great as (a). However, the improvement was not sufficient to the number of decrease measurement trials.

The simulation results of the conventional method that used Type A antenna had signal changes of 10 to 14 % on the centerline as shown in Figure 5(a). The new method that used Type B antenna provided -20 to +30 % signal changes shown in Figure 5(b) that were significant enough for applications.

In the experiment, unexpected linkages might exist between transmission and receiving antennas that were not affected by water or dielectric materials, for example, magnetic linkage (mutual inductance), radiation from measurement device and coaxial cables. Those linkages pushed up the base signal strength and weakened relatively changes of electric field intensity that the authors were focusing on.

Figures 4(b) and 5(b) had wider waves of signal strength changes than Figures 4(a) and 5(a). This was a drawback of Type B antenna that provided less accuracy than Type A antenna. This was caused by the wider dimension of Type B antenna in the Y-axis direction.

IV. Conclusion

In this paper, a new method to improve signal strength changes was introduced, and results of experiment and simulation were reported and discussed. The improvement of the signal changes was indicated; however, more improvement was necessary for practical usages. The authors plan to upgrade the system to measure some portion of human body, and to develop pilot systems focusing on a certain application field.

References

1. Hieda I, Nam K C, Takahashi A (2004) Basic characteristics of the radio imaging method for biomedical applications, Med Eng & Phys 26:431-437
2. Hieda I (2004) Preliminary Study of 2D Image Construction by Radio Imaging Method (RIM) for Medical Application, Proc Intl Conf on Biomedical Eng, Kuala Lumpur, Malaysia, IFMBE ISSN 1680-0737, pp 91-94
3. Hieda I, Nam K C (2005) 2D Image Construction from Low Resolution Response of a New Non-invasive Measurement for Medical Application, ETRI Journal 27-4:385-393
4. Hieda I (2005) Application of Electromagnetic Biomedical Measurement System as an Ergonomic Sensor, Proc of ICBME 2005, Singapore, IFMBE ISSN 1727–1983, 3B2-01
5. Hieda I, Nam K C (2008) FDTD Simulation of Radio Imaging Method for Biomedical Application, Biomed 2008, IFMBE Proc, 21, pp. 566–569, Kuala Lumpur
6. Taflove A, Hagness S C (2000) Computational Electrodynamics: The Finite-Difference Time-Domain Method (2nd Ed), Artech House, Boston & London
7. Lytle R (2002) The Numeric Python EM project, IEEE Antennas and Propagation Magazine 44-6:146
8. Python Official Website at http://www.python.org/

Author: Ichiro Hieda
Institute: National Institute of Advanced Industrial Science and Technology (AIST)
Street: Tsukuba Central 6 1-1-1 Higashi
City: Tsukuba-city
Country: Japan
Email: i-hieda@aist.go.jp

Feature Extraction Methods for Tongue Diagnostic System

K.H. Kim, J.-H. Do, Y.J. Jeon, J.-Y. Kim

Korea Institute of Oriental Medicine, Korea

Abstract — **The status of a tongue is the important indicator to diagnose one's health like physiological and clinicopathological changes of inner parts of the body. The method of a tongue diagnosis is not only convenient but also non-invasive and widely used in Oriental medicine. However, a tongue diagnosis is affected by examination circumstances a lot like a light source, patient's posture, and doctor's condition. To develop an automatic tongue diagnosis system for an objective and standardized diagnosis, segmenting a tongue from a facial image and finding many features from the tongue surface are inevitable but difficult since the colors of a tongue, lips, and skin in a mouth are similar and the features have ambiguous boundaries on the tongue surface. The proposed method includes the segmentation of the tongue region to include detecting positions with a local minimum over shading from the structure of a tongue, correcting local minima or detecting edge with color difference and smoothing edges, the decomposition of the color components of the region into hue, saturation and brightness to result in segmenting the regions of tongue coatings and classify them, and the extraction of the red spots and the crack on the tongue surface by computing the distribution of color intensity in a window. Finally, the results show the segmented region to include effective information, excluding a non-tongue region, the accurate diagnosis of coatings and the spots of the tongue surface. It can be used to make a standardized diagnosis for a u-healthcare system.**

Keywords — **Diagnosis, tongue body, segmentation, feature extraction**

I. Introduction

A tongue is an organ that reflects physiological and clinicopathological condition of one's body. Each part of the tongue is related to corresponding internal organs. [1]

Especially, the visual information is used in tongue diagnosis. The color, the form, and the motion of a tongue, tongue substance, and tongue coating are main factors for the diagnosis. The geometrical shape also helps to diagnose one's health, whose method diagnoses the illness by observing the change of the tongue body such as thickness, size, cracks, and teeth-marks. The tongue coating, covered on a tongue like moss is the most important factor, depending on color, degree of wetness, thickness, form, and distributed range to determine a patient's disease and body condition. It is classified by its color – white, yellow, grayish, black, mixed color, and so on.

Even if a tongue diagnosis is convenient and non-invasive, it has the problem of objectification and standardization. The change of the inspection circumstance like a light source affects the result a lot. Moreover, since the diagnosis relies on doctor's experience and knowledge, it is hard to get a standardized result. Recently, many researches are being carried out to solve these problems. [2]-[4]

Since the properties of color and texture are different according to the light condition, it is difficult to divide the tongue area by using a general segmentation method and to decide the optimal parameters to include the entire area automatically. Moreover, since the area near a tongue includes lips and the oral cavity to have the similar color with it and the color and the texture on a tongue have little difference, it is hard to segment a tongue from the facial image with it and to classify tongue coatings, substance and spots. In this study, we put emphasis on the method to extract the tongue area and to classify the tongue coating automatically from the systematic point of view for a tongue diagnosis. A facial image with a tongue was obtained by using the digital tongue diagnosis system (DTDS). The segmentation method optimized on the digital tongue diagnosis to extract the area of the tongue from a facial image by using its feature and to classify the tongue coating by considering statistical color property was proposed. In addition, the primitive method to detect the spot on a tongue was proposed.

II. Proposed methods

A. Tongue diagnosis in Oriental medicine and digital tongue diagnosis system

The tongue diagnosis is the most necessary thing to be researched in order to quantize an OMD's diagnosis. The DTDS to quantize the condition of a tongue should extract a tongue region from a facial image with a tongue above all. Here, the region of a tongue body including tongue substance and coating should be segmented and then the coating and substance regions should be classified.

The system was designed to get a clear facial image using standardized light sources, a digital camera, and color correction. [5] The system was designed to make a darkroom efficiently wherein a face touches the contact surface of the system and uses the strobe light to have the color

Chwee Teck Lim, James C.H. Goh (Eds.): ICBME 2008, Proceedings 23, pp. 527–531, 2009
www.springerlink.com

temperature, 5500K, almost similar to sun light in order to standardize the light source.

B. How to acquire facial images

We put facial images including tongue bodies together using the DTDS. A graphic user interface (GUI) of the system shows the facial image in real time and the cross mark, which is at the center of the image, should be located on the part of the tongue when the image is captured. The captured image has the resolution of 1280×960 with RGB 24 bit-BMP format and then images were classified into 5 kinds of non-coated one, white-coated one, yellow-coated one, mixed-coated one with the white-coated and yellow-coated, and non-classified one by OMDs.

C. Segmentation of tongue body

The overall structure of the segmentation method for a tongue diagnosis is illustrated in Fig. 1. The preprocessing is the first step for the segmentation. Due to time consumption from the large-sized image, the down-sampling of the resolution into 533×400 is necessary. Then, edge enhancement [6] is carried out to make the discrimination of the edges larger through making the large value larger and the small value smaller at the edges, which is the last step of the preprocessing.

In segmenting the tongue body, over-segmentation is performed to make the image divided into smaller regions. The used over-segmentation method is the graph-based segmentation method [7]. Using the method, the majority of tongue region with its center area is segmented into one region, but the region can be subdivided due to the reflection and stain on the center area. In addition the region at the boundary regions and tongue coating regions due to different structural and color property is subdivided. In this case, the probability in a fixed area around the center point was measured and then the segmented region was found, namely the largest major region. If like (1) P_A, the probability of the segmented region of A in the fixed area is larger than P_B, that of the segmented region of B in the same area, the major segmented region is decided as A and all regions in the A region and in the fixed area are merged into A. Even if more than 3 regions exist in the fixed area, every region is merged into the region with the largest probability.

$$\left\{ I_{x,y} \in A \middle| P_B < P_A, I_{x,y} \in B \right\} \tag{1}$$

where $I_{x,y}$ means the pixel of (x, y). Also, all the other regions inside the major region are included in the major region.

In this case, since the change of color occurs from the cubic structure of a tongue near its boundary, some areas near its boundary isn't segmented into the tongue because of shading caused from the strobe light. Namely, the intensity is very low at the outer boundary, which is the minimum value near the boundary since the boundary is almost orthogonal to the direction of light incidence. The position of the local minimum is decided as the boundary of the tongue body, which is the step of local minimum detection. The minimum value crossing each side of the tongue in the X direction with a range is found and then using the result, the minimum value crossing the bottom of the tongue in the Y direction is found.

By the way, in the case that the boundary from a merged region is far away from the real boundary, a local minimum for the shading area can't be detected, resulting in the discontinuity of a boundary. To find a real boundary, the discontinuity point with large difference between the current and the next positions of points on edges should be found in each direction, and then the next point with a local minimum is detected at a new point moved to the progressing direction by one pixel from the current point, where the progressing direction is Y direction for left and right boundaries, or X direction for a bottom boundary. This procedure is performed for left, right, and bottom edges, respectively until the next point meets the point that was detected in the previous step, which is local minimum correction.

However, occasionally in the case of a flat tongue with small volume, the shading can't appear at the boundary. To meet the case, the color edge detection to find the position

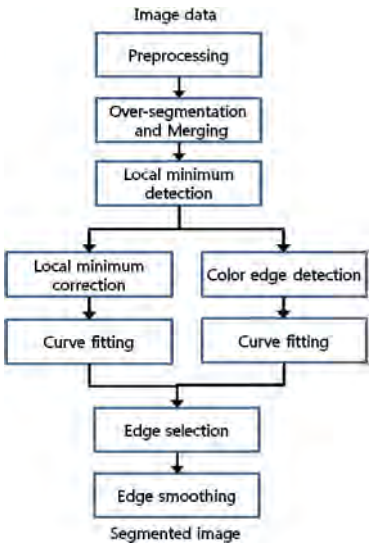


Fig. 1 The overall structure of segmentation for tongue body

that has the largest color-difference is performed from the position of the local minimum value minus a range to the position plus a range as the next step compatible with local minimum correction. In the step, the boundary where makes the difference, d of r (red intensity) largest is found since r is most used at the skin and the tongue, which makes discrimination between skin and a tongue easy.

After the compatible procedures of local minimum correction and color edge detection, curves are drawn in Catmul-Rom spline with sampled points of start, end and a few mid points, which are obtained from the consistent intervals of local minimum correction and color edge detection, respectively. The following procedure is required to select one among the compatible procedures: Firstly, the curve should be checked to have a convex shape due to the shape of a tongue. Secondly, the difference between the curves and the original points should be compared as the step of curve fitting. If the curve is convex, the step with less difference is chosen, which means that the points from the step have soft connection.

After these steps, edge smoothing makes edges smooth with a median filter as the final step. The median filter uses 5 neighboring points and keeps frequency response of edges, excluding its discontinuity.

D. Classification method of tongue coatings

The region of a tongue body consists of tongue substance and coating. The major colors of coating are white and yellow and that of substance is red. To classify white and yellow coating and substance, we select the 2nd order discriminant, assuming that the color distribution of coating and substance is Gaussian conditional density model, where the two dimensional domains are H and S since S is a degree of saturation of a white component, which decides white coating, and the yellow coating and the red-colored substance are classified by H.

Acquisition of the color table to classify tongue coating and substance has three steps as follows; in the first step, the transformation of RGB is performed to resolve color components into hue (H), saturation (S) and brightness (V). Highlights happen on the tongue due to reflection of a light source and since they are saturated, the values of RGB are 255, which are decided as invalid regions.

We use white-, yellow-, and no coated areas segmented by OMDs from 42 images, 8 images and 6 images diagnosed as white, yellow and no coating, respectively, where no coating means substance. In the second one, the distributions of H and S values for all the white-, yellow- and no coated areas are computed, respectively. Statistical data like each mean and covariance for each coating and substance is calculated. In the third one, after low distribution values less than 0.005% are eliminated to reduce noise parts, the values for the distributions are applied to the 2nd order discriminant. In the fourth one, the table for regions in H and S domains to classify coatings and substance are obtained with three 2nd order discriminants.

The coating and substance regions can be classified and segmented when an image is inputted to the table.

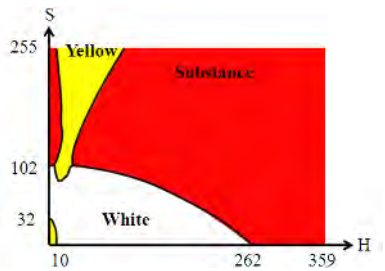


Fig. 2 Table to classify white and yellow coatings and substance

E. Detection of spots

In the previous procedure, the color component of the S domain is resolved. The spot is known as the exposure of tongue substance on the surface covered with coatings. In the first step, the average is measured in a rectangle window in the S domain. In the second one, the area over a threshold is searched since the S value of substance is higher than that of coating. In the third one, white 3×3 points are drawn around the area in order to visualize the spots.

III. Experimental Results

To find the main segmented region, 50×50 pixels were searched around the center, and the location of a local minimum was found in the pixel range of -40 to 40 from each boundary of a region merged from over-segmented regions.

Table 1 The range of color components to classify tongue coating and substance

Types		Mean		Covariance	
		H	S		
Coating	White	12.2	83.6	717.5	-4.7
				-4.7	130.7
	Yellow	18.8	108.8	37.8	55.6
				55.6	252.4
No coating		11.4	116.9	1648.8	-35.8
				-35.8	125.5

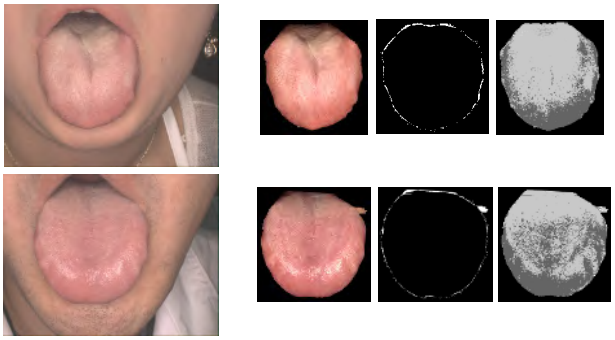


Fig. 3 Original, segmented images, the differences, white-coated images

The threshold to find discontinuous points was 10 pixels, that is, if the distance between the current and the next points at the edges is above 10 pixels, the next point is called the discontinuous point. The search range for local minimum correction or color edge detection narrowed down to -20~20 from the discontinuous point in the boundary processed by the local minimum detection, where color edge detection finds the location to represents the maximum difference of a red value.

For a classification table, we get the means and covariances like Table 1 for Gaussian conditional density models in the H and S domains to produce the 2nd order discriminants, to decide kinds of coatings and substance. Fig. 2 is the table to show the classification region of white and yellow coatings and substance.

Fig. 3 shows the facial images, the segmented results, the differences from reference images and the classified ones, where what a reference image is what an OMD extracted manually and prudently as a tongue body and the classified ones correspond to what were classified by OMDs. The white coated images were not used for obtaining the classification table. It is shown that almost all tongue regions that have different shapes and colors were well-segmented, not affected by either color or status of skin.

The difference rate of the area between a reference image and a segmented image was obtained like (2).

$$r_d = \left| \frac{A_{ref} - A_{seg}}{A_{ref}} \right| \times 100 \qquad (2)$$

where A_{ref} and A_{seg} are the areas of a reference image and a segmented image, respectively. The average difference rate of the selected 40 images was 5.5% and the difference happened at the boundary region slightly like Fig. 3.

Fig. 4 shows the spot detection from S domain image, where a threshold is 10 above the average in the window.

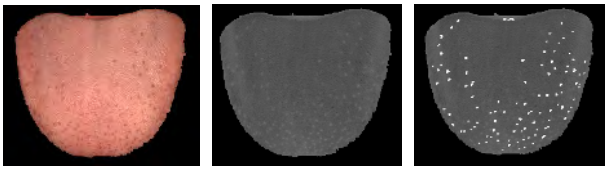


Fig. 4 A segmented, an S domain, and a spot-detected images

IV. Conclusions

In this study, the effective method to segment the tongue area and to classify tongue coatings and substance was proposed for an automatic tongue diagnosis. According to the structural and color properties of a tongue, its boundary were extracted, and using the statistical color property, the tongue substance and coatings were classified.

Preprocessing makes edges more distinct by using the distribution of intensity. After the preprocessing, graph-based over-segmentation with the fixed parameters, region merging, local minimum detection, edge correction to select local minimum correction or color edge detection and edge smoothing to segment the tongue body were performed. Then, the segmented tongue region was classified into kinds of coating and substance areas by resolving color components of HS. As a result, it was possible to segment a tongue body region that is difficult to distinguish from skin inside a mouth and lips. Also, the proposed method could segment the tongue body effectively in spite of the non-uniformity of color, which is caused from tongue coating and reflection of light. The 2nd order discriminants and the table were obtained from statistical data. The tongue body can be divided into white and yellow coatings and substance. Finally, spots could be detected from the difference of S.

Acknowledgment

This work has been supported in Development of Standard on Constitutional Health Status and partially in Development of Intelligent contents on Traditional Korean Medicine by the Korea Ministry of Knowledge Economy.

References

1. Chiu C-C (2000) A novel approach based on computerized image analysis for traditional Chinese medical diagnosis of the tongue. Computer Methods and Programs in Biomedicine 61:77-89
2. Yue X-Q, Liu Q (2004) Analysis of studies on pattern recognition of tongue image in traditional Chinese medicine by computer technology. J. Chin. Integr. Med. 2:326-329

3. Pang B, Zhang D (2004) Computerized tongue diagnosis based on bayesian networks. IEEE Trans. Biomedical Engineering 51:1803-1810
4. Zhang HZ et al. (2005) Computer aided tongue diagnosis system. Proc. the 2005 IEEE Engineering in Medicine and Biology 27th Annual Conference, Shanghai, China, pp. 6754-6757
5. J.G. Kim (2005) Development of Digital Tongue Inspection System. Kyunghee Univ., Suwon, Korea
6. Liu N, Yan H (1994) Colour image edge enhancement by two-channel process. Electronics Letters 30:939-940
7. Felzenszwalb PF (2004) Efficient graph-based image segmentation. International Journal of Computer Vision 59:167-181

Author: Keun Ho Kim
Institute: Korea Institute of Oriental Medicine
Street: 461-24 Jeonmin-dong Yuseong-gu
City: Daejeon
Country: South Korea
Email: rkim70@kiom.re.kr

Mechanical-Scanned Low-Frequency (28-kHz) Ultrasound to Induce localized Blood-Brain Barrier Disruption

C.Y. Ting[1], C.H. Pan[1] and H.L. Liu[2]

[1]Department of Medical Image and Radiological Sciences, Chang-Gung University, TAIWAN
[2]Department of Electrical Engineering, Chang-Gung University, TAIWAN

Abstract — **Recent technical advances showed that focused ultrasound can induce localized blood-brain barrier disruption, however, usually accompanied with the occurrence of hemorrhage. Low-frequency ultrasound has the nature of not been obstructed by skull and has been widely in the industrial applications, but yet have not been applied for biomedical purpose due to its difficulty in concentrating the ultrasonic energy. The purpose of this study is to first demonstrate the feasibility to employ mechanical-scanned low-frequency (28 kHz) ultrasound in localized BBB disruption, which is believed to be the lowest frequency been applied for this application. To examine this, SD rats were anesthesia IV, and ultrasound contrast agent was administered before ultrasound energy excitation to enhance the BBB disruption effect. Blue dye was also administered before animal sacrifice for gross observation of the affected region, and H&E as well as TUNEL staining were performed to evaluate the ultrasound induced brain tissue damage. Results confirmed that low-frequency can be mechanical-scanned for localized BBB-disruption.**

Keywords — **low-frequency ultrasound, blood-brain barrier(BBB), mechanical scan**

I. Introduction

Blood-brain barrier (BBB) plays an important role in brain. It not only transports nutrients into brain by diffusion, but also limits the passage of many native and exogenous molecules from the circulation into the brain parenchyma. But in some cases, including delivering of potent agents for therapy or neural imaging, BBB has to be disrupted manually to raise its feasibility. By the use of cavitation effect of ultrasound, drug can be directed locally into brain. [1]

Focused ultrasound has been shown to be able to induced localized BBB disruption. According to the literature, by applying the operating frequency ranging form 260 kHz to 3.5 MHz, the concentrated ultrasonic energy can be well generated. However, it was also shown that the frequency exceed 500 kHz can encounter noticeable phase aberration problem and distort the concentrated energy, thereby hamper the energy delivery into the brain [2,3,5]

Another potential issues is that, when intending to deliver drug through BBB in some disease brain trauma or acute stroke, the area need to be treated may be large, whereas limit the treatment efficiency by using the point-like energy to conform the large brain damage area.

The purpose of this study is to propose a new ultrasound BBB-disruption system which utilizes the 28-kHz as the operating frequency. The advantage of the proposed frequency is in two fold: (1) The effect of skull absorption of ultrasound energy is limited and can be almost ignored; (2) The ultrasound energy is non-focused, and can be deposited with a much larger area than operating frequency at this level; (3) The system is easier to be setup. In this report, we aim to examine the feasibility and efficiency of the proposed system on localized BBB disruption. Moreover, we also demonstrate the feasibility to apply the mechanical scanning to improve the capability of enhance the BBB disruption at deeper brain region.

II. Material and methods

A. Experimental setup

Figure 1 shows the experimental setup and the 28-kHz sonication system. One 28-kHz originally applied for industrial purpose machine was employed as the ultrasound energy generator. One single triggering circuit where the synchronized single provided from the functional generator (28-kHz sinusoidal wave was continues generated from the signal generator and gated by the designed circuit) was designed in order to control the sonication parameter including the pulse repetition frequency (PRF) and the burst length. The transducer was mounted on either a stainless-steel made fixed gantry or a in house acrylic -made rotating gentry to provide mechanical scanning. The geometrical center was tuned to align at the unilateral brain of the animal in case the ultrasound either fixed or mechanical-scanned energy can affect the unilateral brain of the animal. At the bottom of the water tank, a 5 cm × 5 cm window was made but sealed by a thin ultrasound-permeable membrane. The animal was carefully placed under the tank the its head was shaved and tightly attached beneath the membrane. Degassed was filled in the water tank to provide good ultrasound coupling to the animal.

Chwee Teck Lim, James C.H. Goh (Eds.): ICBME 2008, Proceedings 23, pp. 532–535, 2009
www.springerlink.com

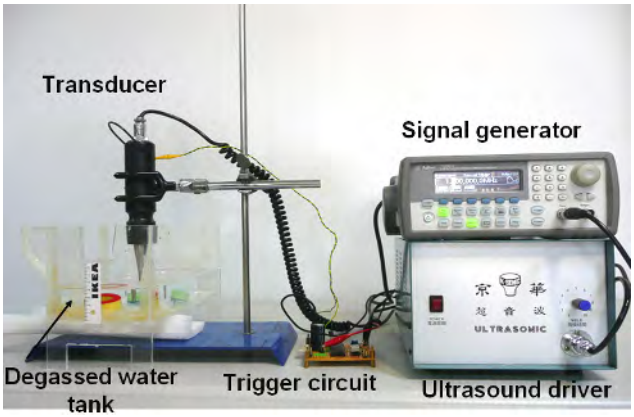


Fig. 1. Experimental setup.

B. Animal preparation

The experiments conducted in this study were approved by the Animal Committee of Chang Gung University and adhered to the experimental animal care guideline. Twenty-eight adult male Sprague-Dawley (SD) rats (each weights 300 ~ 400 g) were anesthesia I.P. by injecting chlorohydrate (30mg/kg). A PE-50 catheter was then inserted into the jugular vein for the following microbubble and blue dye injection. The head of the animal was placed in a plastic holder and set in the treatment position.

C. 28-kHz ultrasound sonications

After setting animal in this low-frequency ultrasound apparatus, Blue Dyes (Evans Blue, 4mg/100g) was injected I.V. to prove the presence of BBB disruption. Approximately 10 seconds before each sonication, ultrasound contrast agent (SonoVue, Bracco UK Ltd.) was poured into I.V. catheter to promote the cavitation effect. After all, the sonications were delivered. The acoustic power of this system is about 1~2W which was measured by ultrasound power meter (Easton®, Model-21601, OHMICO, USA). In order to find the electrical parameter to induce optimal BBB disruption, parameters including sonication time, burst length were tuned. The sonication time in our experiments were given ranging from 2 to 10 min. The burst length was given ranging from 10 to 50 ms under a pulse repetition frequency of 1 Hz.

In order to evaluate the effect of consecutive injection of the microbubble in the effectiveness of microbubble, we conduct ultrasound sonications either (1) by only injecting the microbubble before the sonication start or (2) consecutive microbubble injection for every two minutes.

Moreover, in order to evaluate the effectiveness of mechanical scanning for altering the BBB-disruption region, animal experiments by using fixed gentry or applying mechanical scanning were both attempted. For mechanical scanning, the ultrasonic wave can be steered to the target region and concentrate the energy at targeted locations.

D. Frozen Section and Staining

Evans blue was administered before animal sacrifice for gross observation of the affected region.3 to 4 hours later; animals were sacrificed, and were perfused with normal saline. After perfusion, brain tissue was frozen rapidly, and was embedded in OCT (Tissue-Tek, SAKURA, USA). The tissues were sectioned using a Microtome (Model 3050S, Leica, German). The brain sections were first judged with eyes (Observe whether the brain tissue was dyed by Evans Blue). Finally, the slices were preserved and stained with hematoxylin and eosin (H&E) to evaluate the ultrasound induced brain tissue damage [4].

E. Pathologic examinations

The level of cell damage and hemorrhage were classified into four categories as Fig. 2. Level 0 was defined as a little necrosis phenomena. Level 1 was defined as some discontinuous form of bleeding phenomena. Level 2 was defined as some continuous form of bleeding phenomena. Level 3 was defined as some continuous bleeding and tissue injuring phenomena.

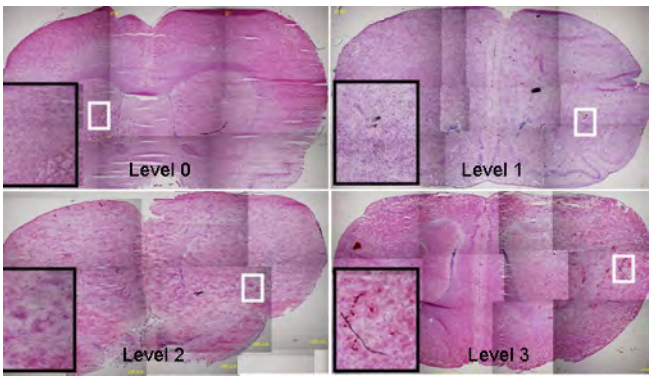


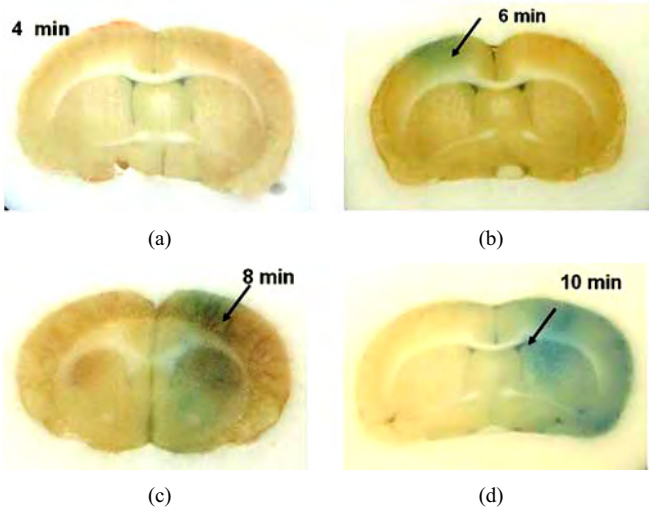
Fig. 2. HE staining sections. (a) Level 0; (b) level 1; (c) level 2; (d) level 3.

III. Results

A. Comparison between Sonication Time

Figure 3 are examples showing brain sections underwent low-frequency ultrasound exposure and the BBB-disruption effect when varying the sonication time ranging from 4 to 10 min.. BBB was intact when apply 4 min. sonication, whereas the BBB can be locally disrupted when increasing sonication

time to 6 min. The sonication time of 6 min. was regarded as the threshold and as a baseline to disrupt BBB in the following experiments.



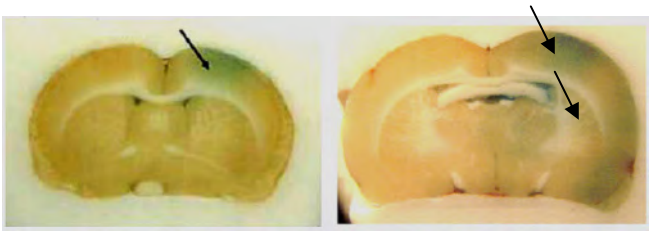
(a) (b)

(c) (d)

Fig. 3. BBB-disruptive section from the 28-kHz ultrasound sonication under different sonication times without applying mechanical scanning: (a) 4 min.; (b) 6 min.; (c) 8 min.; (d) 10 min.

B. Effect of different sonication burst lengths

Next, the effect of the applied burst length of ultrasound sonication was investigated. Figure 4 demonstrates the brain sections underwent different sonication burst length ranging from 10 to 100 ms. It can be found that, as the burst length increase, the BBB disruptive region was also increased. For the burst length of 10 ms, only a small range of BBB-disruption was found, but the BBB-disruptive region was apparently increased when increasing the burst length to 50 ms. When increasing the burst length up to 50 ms, not only the BBB-disruptive region was enlarged but the stained color was darker, showing that the concentration of the blue dye deposited at the sonication region was also increased.

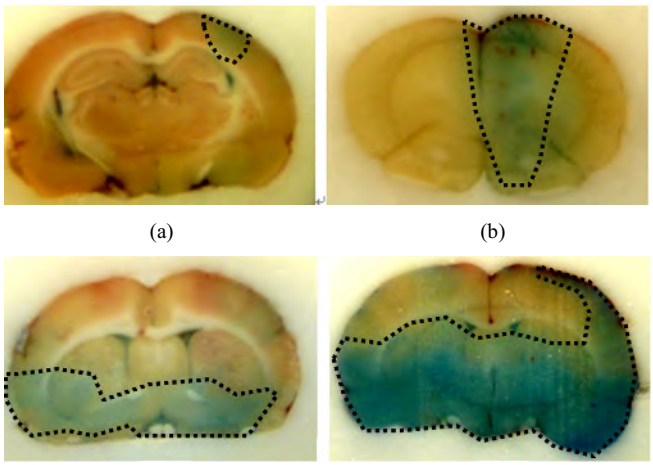


(a) (b)

Fig. 4. Brain sections showing the effect of varying burst length on BBB-disruption. Pulse repetition frequency and the exposure time were controlled to be 1 Hz and 6 min. respectively. (a) burst length = 10 ms; (b) burst length = 50 ms.

C. Effect of mechanical scanning

To increase the potentiality of this low-frequency ultrasound system, we try to focus the ultrasound in a manual way. Through the results of the experiment, we can find out while adopting the same time parameter. The upper and lower row of Fig. 5 demonstrates the difference between the BBB-opening region distribution between sonication without and with mechanical scanning. In transducer-fixed condition, as the burst length increases from 10 to 100 ms, it can be seen that the BBB-disruptive region extend its coverage from the brain surface. However, for mechanical-scanned condition, the BBB-disruptive region appears at deeper region.



(a) (b)

(c) (d)

Fig. 5. Effect of the application of mechanical-scanning on BBB-disruption. (a, b) Sonication with the transducer fixed, burst length = 10 and 100 ms respectively; (c, d) sonication accompanying with mechanical scan. Sonication duration of 6 min. were employed.

D. Histological examination

Figure 6 demonstrates the tissue damage level caused by 28-kHz ultrasound sonication under the sonication time ranging from 4 to 10 min. There was no BBB-disruption effect been observed when the sonication duration of 4 min. was employed. For sonication time equal or larger than 6 min., BBB-disruption can be induced but varies of tissue damage level was also accompanied. Only a few of erythrocyte extravasations was found in the 6 to 8min. case, therefore it was still considered to be a safe sonication parameter. When increasing the sonication time up to 10 min., local microhemorrhage was detected.

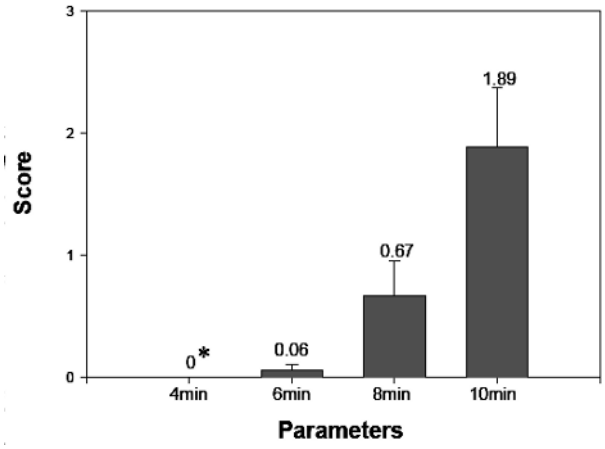


Fig. 6. Tissue damage level analyzed by histological examination at different sonication durations. The soncaiton time was varied from 4 to 10 min. "*" represents no BBB-disruption has been observed under gross observation.

IV. Conclusion

In this paper, we have demonstrated that the 28-kHz in conjunction with the mechanical scan can manipulate the BBB-disruptive region in the animal brain. In our knowledge, it is the first sonication system that employs non-focused ultrasound in this BBB-disruption, and so far the lowest frequency ever been investigated. The feasibility, safety, and efficiency have been confirmed. The designed system may have the potential to explore a wide application benefit from the portability and the improved effective area

Acknowledgment

The project has been supported by the National Science Council (NSC-95-2221-E-182-034-MY3) and the Chang-Gung Memorial Hospital (CMRPD No. 34022, CMRPD No. 260041).

References

1. Abbott NJ, Romero IA(1996), Transporting therapeutics across theblood-brain barrier, Mol Med Today 2:106–113
2. M. Kinoshita, N. McDannold (2005), Targeted delivery of antibodies through the blood-brain barrier by MRI-guided focused ultrasound, Biochemical and Biophysical Research Communications 340 1085-1090
3. S. Meairs, A. Alonso (2006), Ultrasound, microbubbles and the blood-brain barrier, Progress in Biophysics and Molecular Biology.
4. K. Hynynen, N. McDannold (2005), Local and reversible blood–brain barrier disruption by noninvasive focused ultrasound at frequencies suitable for trans-skull sonications, NeuroImage 24(2005) 12-20
5. K. Hynynen, N. McDannold (2003), The threshold for brain damage in rabbits induced by bursts of ultrasound in the presence of an ultrasound contrast agent (Optison), Ultrasound in Med. & Bio., Vol. 29, No. 3, pp. 473-481, 2003
6. N. Sheikov, N. McDannold (2004), Cellular mechanisms of the blood-brain barrier opening induced by ultrasound in presence of microbubbles, Ultrasound in Med. & Bio., Vol. 30, No. 7, pp. 979-989, 2004.
7. J. Sun, K. Hynynen (1999), The potential of transskull ultrasound therapy and surgery using the maximum available skull surface area, J. Acoust. Soc. Am. 105 (4) 2519-2527 April 1999
8. J. Sun, K. Hynynen (1998), Focusing of therapeutic ultrasound through a human skull:A numerical study, J. Acoust. Soc. Am. 104 (3) Pt. 11705-1715 September 1998
9. Po-Hung Hsu(2007), Feasibility of Enhancing Focal Blood-Brain Barrier Disruption by Using Focused Ultrasound with the Presence of SonoVue® in a Rat Model, ISTU
10. KULLERVO HYNYNEN(2006), Focal disruption of the blood–brain barrier due to 260-kHz ultrasound bursts: a method for molecular imaging and targeted drug delivery, J Neurosurg 105:445–454, 2006

Feasibility Study of Using Ultrasound Stimulation to Enhancing Blood-Brain Barrier Disruption in a Brain Tumor Model

C.H. Pan[1], C.Y. Ting[1], C.Y. Huang[2], P.Y. Chen[2], K.C. Wei[2], and H.L. Liu[3]

[1]Department of Medical Image and Radiological Sciences, Chang-Gung University, Taipei, Taiwan
[2]Department of Neural Surgery, Chang-Gung Memorial Hospital, Taipei, Taiwan
[3]Department of Electrical Engineering, Chang-Gung University, Taipei, Taiwan

Abstract — **The purpose of this study is to demonstrate the feasibility of using ultrasound induced BBB-disruption technology to enhance brain-permeable area in a brain tumor model for the enhancement of brain-tumor drug delivery. In our system setup, either 28-kHz non-focused ultrasound or 400-kHz focused ultrasound was used. To examine this, SD rats (n = 14) with C-6 Cell been intestinally implanted to regarded as brain-tumor model. The animals were treated 10 days after tumor implant. During the treatment, the animal were anesthesia I.P., and ultrasound contrast agent was administered I.V. before ultrasound energy excitation to enhance the BBB disruption effect. Blue dye was also administered before animal sacrifice for gross observation of the affected region, and H&E staining were performed to evaluate the ultrasound induced brain tissue damage. BBB-disruptive regions were compared between controlled and ultrasound-treated animals to see the enhancement of the ultrasound treatment. Results confirmed that ultrasound sonication either 28-kHz or 400-kHz sonication can enhance the BBB-disruption. The pressure threshold of BBB disruption has been confirmed to be 2.25 MPa and 1 MPa in 28 kHz and 400 kHz, respectively. In the 28-kHz sonication case, the BBB-disruptive region surrounding the tumor area can be increased up to 17 fold. Also, tumor-implant animals which underwent localized BBB disruption didn't affect the animal survival, which indicates the ultrasound-induced BBB disruption is secure. The ultrasound-induced BBB disruption may have the potential for brain tumor treatment in the sense of increase the vessel permeability surrounding the brain tumor to increase the local drug concentration near brain tumor.**

Keywords — **low-frequency ultrasound, blood-brain barrier, brain tumor, drug delivery**

I. Introduction

The blood-brain barrier (BBB) plays important roles in protecting the brain. It's not only allows the passage of substances essential to metabolic function by diffusion, but also restricts the passage of various chemical substances. However, we have to enhance the BBB permeability to assist the penetration through the tight junction for therapeutic purpose. Focused ultrasound surgery is an attractive method for performing tissue thermal ablation non-invasively and has become more popular recently. The ultrasound energy has the ability to sharply focused into soft tissues, then induce a localized temperature elevation with the range of 30-55˚C which resulted irreversible tissue necrosis at the target region while surrounding tissues intact. Moreover, acoustic cavitation, which acoustically induced activity of gas-filled cavities, is another mechanism of focused ultrasound to be applied clinically. It has been shown recently that focused ultrasound can also provide a safe operation to conduct temporal and reversible BBB opening in the presence of ultrasound contrast, leading to the potential to perform targeting delivery without intervening tissue damage for brain treatment [1],[2],[4],[8].

Brain tumors affect approximately 170,000 people annually in the United States and each year more than 13,000 of the population die from a primary malignant brain tumor. In USA, Brain tumors are the second leading cause of cancer-related death in children and men aged 20-39 years. Glioblastomas and astrocytomas that account for more than 40% of all central nervous system tumors are the most common brain tumors that affect adults between 45 and 60 years of age. The most common treatment for glioblastomas currently is surgery followed by radiation and chemotherapy. The procedures for initial treatment are beneficial, but tumor cells often don't remove completely. So the poor prognosis is resulting from high recurrent rate. Therefore, developing an adjuvant therapy is necessary. Moreover, many research shows that glioblastoma may not necessary to disrupt the BBB structure in its early developmental stage especially for the tumor peripheral, thus restrict the drug permeability in those tumor regions to reduce the treatment performance of the drugs.

In this paper, we intend to show the ultrasound induced BBB disruption at the tumor peripheral for the purpose of increasing the local drug concentration at tumor location. Two ultrasonic systems which can delivery either planar or focused wave were shown to both capable of inducing localized BBB disruption. Brain tumor animal models were employed in this study. *In-vivo* animal experiments were conduct and the brain tissues were examined histologically to confirm its feasibility and efficiency.

Chwee Teck Lim, James C.H. Goh (Eds.): ICBME 2008, Proceedings 23, pp. 536–539, 2009
www.springerlink.com

II. Material and Meyhod

A. Low-frequency ultrasound equipment

Figure 1(a) shows the experimental setup and the 28-kHz sonication system. One 28-kHz originally applied for industrial purpose machine was employed as the ultrasound energy generator. One single triggering circuit where the synchronized single provided from the functional generator (28-kHz sinusoidal wave was continues generated from the signal generator and gated by the designed circuit) was designed in order to control the sonication parameter including the pulse repetition frequency (PRF) and the burst length. The transducer was mounted on a stainless-steel made fixed gantry. The beam path of 28-kHz was positioned to align with the unilateral brain of the animal in case. At the bottom of the water tank, a 5 cm × 5 cm window was made but sealed by a thin ultrasound- permeable membrane. The animal was carefully placed under the tank with its head shaved and tightly attached beneath the membrane. Degassed was filled in the water tank to provide good ultrasound coupling to the animal.

B. High-frequency ultrasound equipment

The ultrasonic focal beam was generated by a 400 kHz focused ultrasound transducer (diameter = 60 mm, curvature radius = 80 mm) which put in an acrylic water tank with a three-axis positioning stage. An arbitrary-function generator was used to generate the driving signal that was fed to a radio-frequency power amplifier (100A250A, Amplifier Research, USA). In addition, using a power meter (Model 4421, Bird, USA) to monitor the energy of signal delivered to the transducer. The design of water tank was the same as low-frequency equipment. Its bottom had a square window sealed with a thin film to allow the ultrasound energy went through. The animal was placed under the water tank with its head tightly attached to the thin-film window. The setup of high-frequency equipment was showed in Figure 1(b).

C. Tumor model preparation

Adult male Sprague-Dawley rats (250 - 400g) were purchased from the National Laboratory Animal Breeding and Research Center (Nan-Kang, Taipei, Taiwan). Animals (each weighting from 250 to 400g) were anesthetized by Chlorohydrate (300 mg/kg, IP injection), then removed their uppermost cranial hair with an aid of clippers. After fixing rats on a stereotactic instrument, drill a hole on the skull at the site above striatum which was away from bregma 0.03 mm in axial, 0.32 mm in lateral, 0.56 mm in vertical direction, respectively. The cultured C-6 cell was implanted and

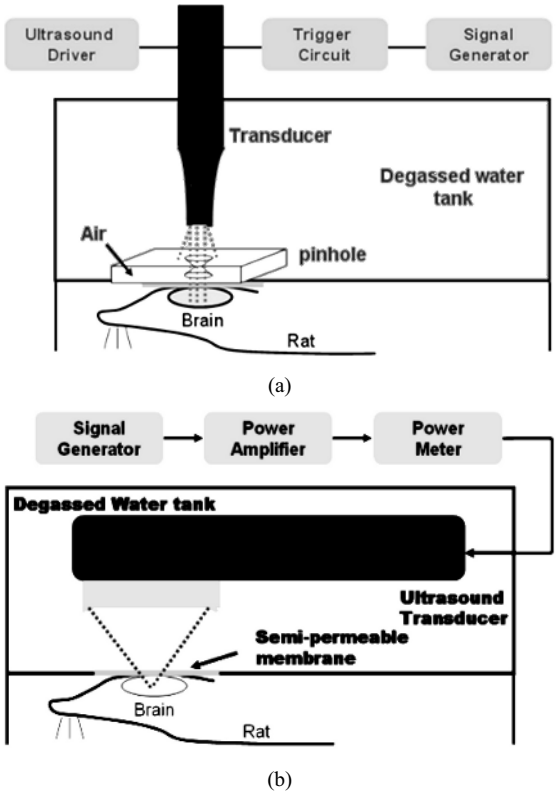


Fig. 1 The schematic diagram of the ultrasound sonication system. (a) low-frequency ultrasound equipment. (b) High-frequency ultrasound equipment.

bone wax was used to seal the hole. The implanted cell concentration was $1X10^5/\mu\iota$, and volume was $5\mu\iota$.

D. Cell culturing and preparation

C-6 Cells was necessary to be sub-cultured every 3-4 days and the following list the procedure. First, removed and discard the cultured medium (95%DMEM + 10%FBS+L-Glutamine). Washed cells by PBS and rocked it back and forth to remove all traces of fetal bovine serum. Added trypsin-EDTA to round up the cells from the bottom of the dish followed removed the wash solution. In a few minute, added growth medium to cell suspension. Collected the suspended cells in a centrifuge tube, and removed some dissociating agents by centrifugation with 1500 rpm, 5 minutes. Then, trypsin-containing medium were removed and replaced with fresh medium. The last step is to place the dish on a shelf in a 37°C, humidified CO_2 incubator.

E. Ultrasound sonications

The cultured cells were implanted into animal brain, and conducted the ultrasound experiments 10 days after. When

conducting experiments, animals were anesthetized and removed the hair of their neck. PE-50 catheter was placed in the jugular vein of animal for later contrast agent administration (SonoVue ®, Braco UK Ltd.). The sonication was conducted by either by low-frequency ultrasound (28-kHz) or high-frequency ultrasound (400 kHz). The measured delivered peak pressure in low frequency setup was 2.25MPa with the pulse-width, pulse-repetition frequency and sonication time were set to 10 ms, 1 Hz, and 6 min. respectively; For 400-kHz focused ultrasound, the measured delivered peak pressure was set to 1 MPa, and the pulse-width, pulse-repetition frequency and sonication time were set to 10 ms, 1 Hz, and 30s, respectively. For 400-kHz sonication, magnetic resonance imaging (MRI) were also conducted. 3-T MRI scanner (Trio with Tim, Siemens, Erlangen, Germany) were used after the animal experiments but the time points were controlled no longer than 30 min. MR contrast agent were injected (Magnevist®, Berlex Laboratories, Wayne, NJ) and T1-weighted imaging sequence were performed to detect the BBB-disruptive region. Evans blue was administered before animal sacrifice for gross observation of the affected region.3 to 4 hours later; animals were sacrificed, and were perfused with normal saline.

F. Pathologic examinations

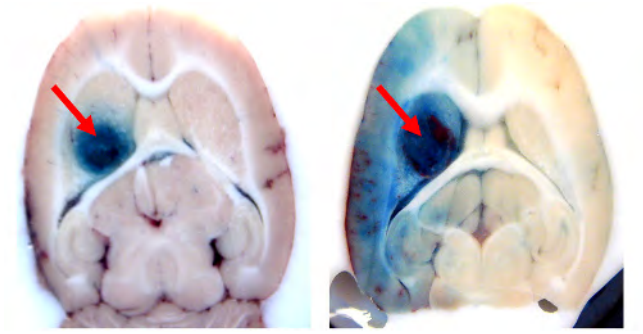
Blue-dye was IV injected into animals to confirm the BBB-disruption, and observed in the process of frozen tissue sectioning by using a Microtome (Model 3050S, Leica, German). The animals were sacrificed about 3-4 hours experiments. The brains were immediately removed and frozen in an OCT compound. (Tissue-Tek, SAKURA, USA).

III. Results

A. Local BBB disruption induced by low-frequency ultrasound

Figure 2 is a typical case showing the comparison of the blue-dye stained region between controlled and ultrasound-sonicated brain. In this comparison, 28-kHz ultrasound was delivered. For control, it can be observed that the implanted tumor can be stain due to the exogenous tissue existed in brain and the BBB structure was destroyed. After the animal brain been sonicated, a noticeable BBB disruptive region increase can be observed, showing that the focused ultrasound sonication can effectively induce a wide local BBB disruption to cover a target such as brain tumor.

Figure 3 analyzes the BBB-disruptive area of the above two groups, and their BBB-disruptive regions (in blue) were measured by using an in-house designed imaging processing tools established in Matlab. From the slice measurement, the measured area in controlled group were 0.598 mm^2 in average, but the sonicated brain appears to have an noticeable increase up to 11.01 mm^2. Compared with the BBB-disruptive region surrounding tumor area, the BBB disruption region induced by low-frequency ultrasound significantly increased up to 17 fold. This confirms the feasibility of using low frequency ultrasound to enhance BBB permeability in a tumor region.



(a) (b)

Fig. 2 The photograph of BBB disruption. (a) disrupted by tumor (b) use ultrasound induced BBB-disruption technology.

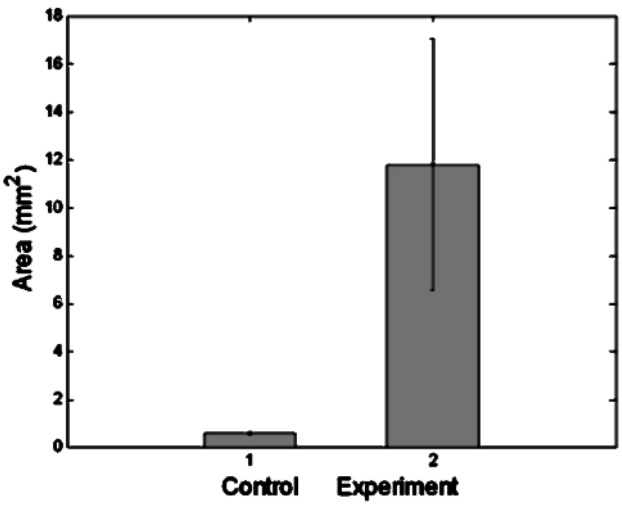
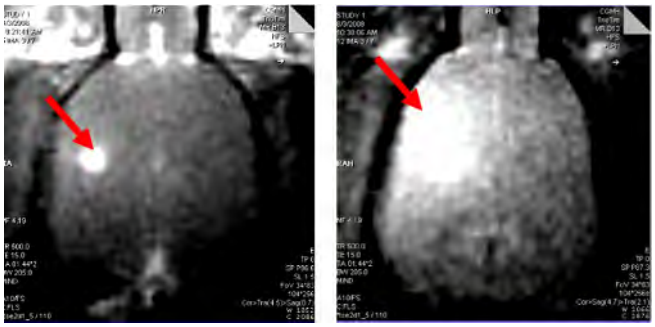


Fig. 3 The BBB-disruptive region of surrounding tumor area and induced by low-frequency ultrasound

B. Localized BBB disruption induced by high-frequency ultrasound

The following shows the feasibility of using focused ultrasound to enhance BBB disruption in the tumor model. Figure 4 shows a typical example to compare the controlled and sonicated brain under the contrast-enhanced T1-weithed MRI. BBB disruption is indicated by localized signal en-

hancement (arrows) due to higher concentration of MR contrast agent penetrated into the BBB-disruptive region. The BBB-disruptive area induced by the tumor and 400 kHz focused ultrasound are 0.06 mm^2 and 0.24 mm^2 respectively. The BBB disruption region induced by high-frequency ultrasound significantly increased up to 4 fold. This confirms the feasibility of using high frequency ultrasound to enhance BBB permeability in a tumor region.



(a) (b)

Fig. 4 Contrast-enhanced axial T1-weighted MR image of BBB-disruption (a) disrupted by tumor (b) disrupted by using ultrasound induced BBB-disruption technology.

C. Safety of ultrasound exposure

In order to confirm the safety of the ultrasound-induced BBB disruption, controlled and experimental animals were placed under observation and the body weights were measured up to 60 days. No specific difference of these two groups were found, and no abnormal behaviors were observed from the experimental group. The body weight of these two groups both shows to have steady increase, representing the tumor implant up to 60 days neither provide significantly health problem, and nor the animal been added the additional ultrasound treatment. The ultrasound sonication is confirmed to have no significant hazard for animals.

IV. Conclusions

Our study demonstrated that the feasibility to noninvasively enhance BBB disruption in brain-tumor model either low- or high-frequency ultrasound exposure. The potentiality of this approach was considered to be potential for brain tumor treatment in the sense of increasing the vessel permeability surrounding the brain tumor as well as to increase the local drug concentration surrounding the brain tumor. We also thought this technology may be benefit during chemotherapy especially for the condition when the high-toxicity drug were administered and the total drug amount may be able to reduce due to the help of increasing local drug deposition.

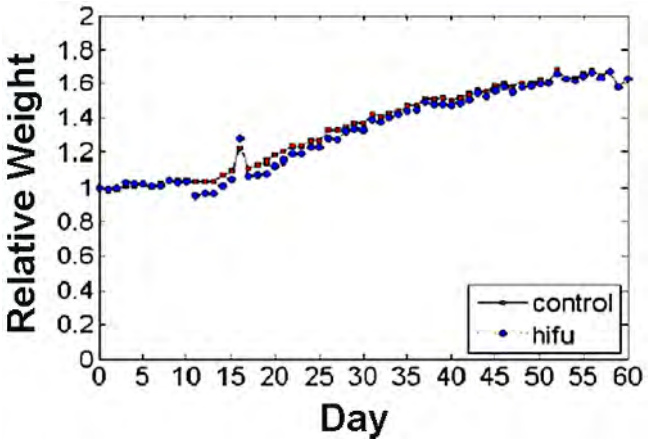


Fig. 5 Relative tumor-implanted animal weight between controlled and experiment groups.

Acknowledgment

The project has been supported by the National Science Council (NSC-95-2221-E-182-034-MY3) and the Chang-Gung Memorial Hospital (CMRPD No. 34022, CMRPD No. 260041).

References

1. Manabu Kinoshita, Nathan McDannold(2005),"Targeted delivery of antibodies through theblood-brain barrier by MRI-guided focused ultrasound", Biochemical and Biophysical Research Communications 340 (2006) 1085-1090
2. Stephen Meairs, Angelika Alonso, "Ultrasound, microbubbles and the blood-brain barrier", Progress in Biophysics and Molecular Biology
3. Kullervo Hynynen, Nathan McDannold(2005),"Local and reversible blood–brain barrier disruption by noninvasive focused ultrasound at frequencies suitable for trans-skull sonications", NeuroImage 24(2005) 12-20
4. Kullervo Hynynen, Nathan McDannold(2003),"The threshold for brain damage in rabbits induced by bursts of ultrasound in the presence of an ultrasound contrast agent (Optison)", Ultrasound in Med. & Bio.,Vol. 29, No. 3, pp. 473-481, 2003
5. Nickolai Sheikov, Nathan McDannold(2004), No. 7, pp. 979-989, 2004"Cellular mechanisms of the blood-brain barrier opening induced by ultrasound in presence of microbubbles", Ultrasound in Med. & Bio., Vol. 30,
6. Jie Sun, Kullervo Hynynen(1999),"The potential of transskull ultrasound therapy and surgery using the maximum available skull surface area", J. Acoust. Soc.Am. 105 (4) 2519-2527 April 1999
7. Jie Sun, Kullervo Hynynen(1998),"Focusing of therapeutic ultrasound through a human skull: A numerical study", J. Acoust. Soc. Am. 104 (3) Pt. 11705-1715 September 1998

On Calculating the Time-Varying Elastance Curve of a Radial Artery Using a Miniature Vibration Method

S. Chang[1], J.-J. Wang[1], H.-M. Su[1], C.-P. Liu[2]

[1] Department of Biomedical Engineering, I-Shou University, Taiwan
[2] Department of Internal Medicine, Kaohsiung Veterans General Hospital, Taiwan

Abstract — **We examined the time-varying elastance of the radial arterial wall using a minute vibration approach in fifteen volunteers. A sinusoidal displacement of 1.5~2.0 mm with a frequency range from 50 to 100 Hz was used to impose on the superficial radial artery. Meanwhile, a force sensor was used to pick up the contact force exerted by the radial arterial wall. The amplitude of the complex force was found to be negatively proportional to the squared angular frequency imposed on the radial artery. A linear regression line can be obtained using the different frequencies (x-axis) and their force responses (y-axis). The intercept of the regression line with the y-axis denotes the elastance and the slope the effective contact mass. Ten elastance values corresponding to 10 different timings in a cardiac cycle were used to construct a time-varying elastance curve. It was found that the elastance curve fundamentally follows the arterial pressure waveform. In conclusion, we have successfully calculated the arterial elastance values at various cardiac timings by applying the minute vibration method, and the pattern of the elastance curve bears a resemblance to a blood pressure waveform.**

Keywords — **Arterial stiffness, Minute vibration technique, Time-varying elastance, Arterial compliance**

I. Introduction

In addition to aging, several kinds of disease result in vascular hardening, such as the cerebral vessel disease [1], cardiovascular disease [2], diabetes mellitus [3] and renal disease [4]. Thus, it is important to perform an early detection of the arterial stiffness using a reliable method. To date, there have been different technologies for directly or indirectly assessing the arterial stiffness, including the ultrasound echo-tracking (Doppler)[5], analysis of pulse transit time[6], impedance plethysomgraphy [7], photoplethysmography [8], oscillometry [9], tonometry [10], and analysis of pressure waveform [11].

Up to now, there is no reliable way to evaluate the degree of the arterial stiffness (elastance) in the clinical setting. Thus, the purpose of this thesis is to develop a noninvasive apparatus for measuring the arterial wall properties by means of minute vibration technique, and to calculate the time-varying arterial elastance curve.

II. Materials and methods

A measurement system consisting mainly of a micro-vibration generator, a force-sensing device, an analog-to-digital and digital-to-analog converters, and a personal computer was constructed to calculate radial arterial time-varying elastance curve using the minute vibration method.

Characteristics of arterial wall were assumed to be governed by three components, including the inertia, viscosity, and elastance [12]. Furthermore, the force exerted by the inertia component was denoted by the product of mass (M) and acceleration (d^2x/dt^2), the force induced by the viscosity component was equal to the product of blood viscosity (η) and velocity (dx/dt), and the force generated by the elastance component was represented by the product of elastance (E) and displacement (x). According to the concept of force balance, an external force imposed on the arterial wall should equal to the sum of the forces from the three components [12], as follows:

$$F = M\frac{d^2x}{dt^2} + \eta\frac{dx}{dt} + Ex \tag{1}$$

The viscosity term is relatively very small, as compared with the other two force terms. After neglecting the viscosity term, we can obtain

$$F \approx M\frac{d^2x}{dt^2} + Ex \tag{2}$$

If a sinusoidal displacement is imposed on the arterial wall, then relation between the complex contact force and the angular frequency can be represented by

$$F(\omega) = (E - M\omega^2) + j(\eta\omega) \tag{3}$$

From Eq. (3), the real part of the complex contact force is inversely proportional to squared angular frequency (ω^2). Thus, if we make a plot using the real part of the contact force (vertical axis) with respect to ω^2 (horizontal axis). By exciting the arterial wall with a small and different-frequency sinusoidal displacement, a regression line can be obtained. Thus, the intercept of the vertical axis with the regression line corresponds to the wall elastance and the inverse of the slope of the regression line is equivalent to the effective mass of the arterial contact wall.

Chwee Teck Lim, James C.H. Goh (Eds.): ICBME 2008, Proceedings 23, pp. 540–542, 2009
www.springerlink.com

Eighteen healthy college volunteers (17M and 1F) were included in the study. In the beginning, we asked the volunteers to take a five-minute break to make their hemodynamic condition stable. In the baseline experiment, displacement excitation with different frequencies (40, 45, 50, 55, 60, 80 and 85 Hz) was imposed on the subject's radial artery, and the corresponding contact force signal was recorded. In the pressurized upper arm condition, an air cuff wrapped the upper arm was inflated up to diastolic pressure plus 10 mmHg. The pressurized cuff tended to considerably block the venous return but not the brachial arterial blood flow. This blockage experiment caused blood accumulation not only in the venous vessels but also in the radial artery in the lower arm. Similar to the baseline test, different frequencies were selected to excite the arterial wall, and the corresponding contact force signals were measured for later analysis.

To derive the arterial elastane curve, the elastance values corresponding to ten timing points in one cardiac cycle were calculated, respectively. For a specific timing point, the elastance value was determined to be the intercept of the vertical axis in the force versus ω^2 plot.

III. Result

Typical elastance values (=intercepts) corresponding to the ten timing points in one volunteer in baseline condition are listed in Table 1. It is interesting to note that the elastance value quickly increases in the initial timing points, but gradually decreases in the subsequent timing points. Meanwhile, the values of effective mass of the arterial contact wall, equivalent to the inverse of the slope, are found to be maintained for all the timing points. Fig. 1 shows two time-varying radial elastance curves calculated in the normal and pressurized conditions. Obviously, there is an upward shift in the elastance curve during the upper arm pressurized situation, as compared with that in the baseline condition. In addition, a moderate change in the waveform shape exists between these two radial arterial elastance curves.

Table 1 Representative values of arterial elastance (= intercept) corresponding to 10 different timings in a cardiac cycle in the subject no. 2 in baseline condition

Time (ms)	Intercept (10^6 dyne/cm)	Slope (ms*cm/10^6dyne)	r
0	1.335	-0.0313	0.976
50	1.526	-0.0360	0.974
100	1.577	-0.0393	0.975
200	1.494	-0.0367	0.979
300	1.430	-0.0346	0.973
400	1.434	-0.0350	0.974
500	1.389	-0.0335	0.976
600	1.360	-0.0319	0.973
700	1.348	-0.0321	0.977
800	1.330	-0.0312	0.977
Mean ± SD	1.422±0.086	-0.0342±0.003	0.975±0.002

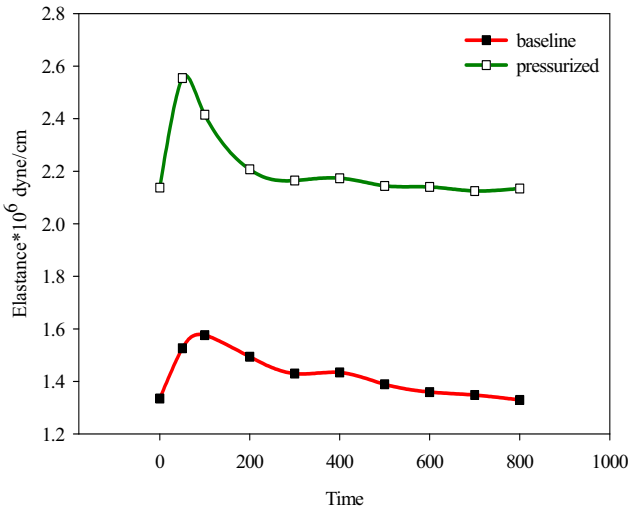


Fig. 1 Typical time-varying elastance curves calculated in baseline (upper) and in the upper arm-pressurized condition (lower)

As shown in Table 2, the dynamic range of the radial wall elastance was found between 0.883×10^6 and 3.778×10^6 dyne/cm, and the average of maximum elastance was $1.879\times10^6 \pm 0.854\times10^6$ dyne/cm in baseline conditions for the eighteen subjects. As an air cuff around one upper arm was pressurized to 10 mmHg over the subject's diastolic

Table 2 Comparison of maximum elastance values between the baseline and the pressurized condition

Subject No.	Baseline (10^6 dyne/cm)	Pressurized (10^6 dyne/cm)	Increase in Percentage (%)
1	0.883	1.422	61.0
2	1.592	2.571	61.5
3	1.633	2.048	25.4
4	2.927	1.819	-37.9
5	1.835	3.266	78.0
6	2.564	5.882	129.4
7	2.121	6.557	209.1
8	1.879	1.790	-4.7
9	1.024	2.387	133.1
10	3.778	6.381	68.9
11	1.376	1.693	23.0
12	1.380	1.922	39.3
13	1.187	1.592	34.1
14	1.243	3.188	156.5
15	3.720	5.554	49.3
16	1.367	1.463	7.0
17	1.935	2.304	19.1
18	1.379	2.467	78.9
Mean ± SD	1.879 ± 0.854	3.017 ± 1.779	62.8 ± 61.5

pressure, the dynamic radial wall elastance varied from 1.422×10^6 to 6.557×10^6 dyne/cm, and the average of maximum elastance became $3.017\times10^6 \pm 1.779\times10^6$ dyne/cm. In the pressurized situation, the average of maximum elastance was increased by 62.8%. But, two of the eighteen subjects showed a decrease in their maximum elastance with the pressurized cuff around the upper arm.

Whereas, in the other results of participants were corresponding with a Psychophysiology theory. It was found in the current result that the elastance curve varied synchronously with the radial blood pressure waveform. Therefore we can estimate the dynamic radial artery elastance with the response to changes in the radial artery.

IV. Discussion

Using the minute vibration method, we have successfully determined 10 values of the radial arterial elstance at 10 different timing points in one cardiac cycle. A full arterial elastance curve is then constructed on the basis of these 10 values. The present elastance, a local index of arterial stiffness, is totally different from that measured from an arterial segment [6-8] or the whole arterial system [13].

The radial artery of interest in the current study is assumed equivalent to a mechanical system, and the elastance is equal to a spring's constant. Although local, the arterial elastance determined by the vibration technique obviously represents an absolute rather than a relative value. Thus, one advantage of the study is capable of calculating a regional and absolute elastance value. Another advantage is the construction of an entire elastance curve over one cardiac cycle.

The drawbacks of the present study include high sensitivity of the measurement location, mechanical instability of the measurement system, and lack of a precise calibration method.

V. Conclusions

We have calculated the arterial elastance values at various cardiac timing points by applying the minute vibration method, and then constructed the whole time-varying arterial elastance curve in a cardiac cycle. It is found that basically the shape of the calculated elastance curve bears a resemblance to the arterial blood pressure waveform.

Acknowledgment

This work was supported by the National Science Council, Taiwan, under grant number NSC 95-2221-E-214-004-MY3.

References

1. Collins R, Armitage J, Parish S et al (2004) Effects of cholesterol-lowering with simvastatin on stroke and other major vascular events in 20536 people with cerebrovascular disease or other high-risk conditions. Lancet 363:757-767
2. Sato H, Haysashi J, Harashima K et al. (2005) A population-based study of arterial stiffness index in relation to cardiovascular risk factors. J Atheroscler Thromb 12:175-180
3. Woodman RJ, Watts GF (2003) Measurement and application of arterial stiffness in clinical research: focus on new methodologies and diabetes mellitus. Med Sci Monit 9: RA101-109
4. Pannier B, Guerin AP, Marchais SJ et al. (2005) Stiffness of capacitive and conduit arteries: Prognostic significance for end-stage renal disease patients. Hypertension 45:592-596
5. Long A, Rouet L, Bissery A et al. (2005) Compliance of abdominal aortic aneurysms evaluated by tissue Doppler imaging: correlation with aneurysm size. J Vasc Surg 42:18-26
6. Cruickshank K, Riste L, Anderson SG et al. (2002) Aortic pulse-wave velocity and its relationship to mortality in diabetes and glucose intolerance: an integrated index of vascular function? Circulation 106:2085-2090
7. Shimazu H, kawarada A, Ito H et al. (1989) Electric impedance cuff for the indirect measurement of blood pressure and volume elastic modulus in human limb and finger arteries. Med Bio Eng comput 27:477-483
8. Ando J, Kawarada A, Shibata M et al. (1991) Pressure-volume relationships of finger arteries in healthy subjects and patients with coronary atherosclerosis measured non-invasively by photoelectric plethysmography. Jpn Circ J 55:567-575
9. Ursino M, Cristalli C (1996) A mathematical study of some Biomechanical factors affecting the oscillometric lood pressure measurement. IEEE Trans Biomed Eng 43:761-778
10. Wang J-J, Liu S-H, Chern C-I et al. (2004) Development of an arterial applanation tonometer for detecting arterial blood pressure and volume. Biomed Eng: App Basis Commun 16:322-330
11. Jagomagi K, Raamat R, Talts J et al. (2005) Recording of dynamic arterial compliance changes during hand elevation. Clin Physiol Funct Imaging 25:350-356.
12. Shishido T, Sugimachi M, Kawaguchi O et al. (1998) A new method to measure regional myocardial time-varying elastance using minute vibration. Am J Physiol 274: H1404-H1415
13. aluska BA, Jeffriess L, Fathi RB et al. (2005) Pulse pressure vs. total arterial compliances as a marker of arterial health. Eur J Clin Invest 35:438-443

The address of the corresponding author:

Author: Jia-Jung Wang
Institute: Department of Biomedical Engineering, I-Shou University
Street: No. 1, Sec. 1, Syuecheng Rd., Dashu Township
City: Kaohsiung County
Country: Taiwan
Email: wangjj@isu.edu.tw

A Wide Current Range Readout Circuit with Potentiostat for Amperometric Chemical Sensors

W.Y. Chung[1], S.C. Cheng[1], C.C. Chuang[2], F.R.G. Cruz[1]

[1] Department of Electronic Engineering, Chung Yuan Christian University, Chung-Li City, Taiwan R.O.C.
[2] Department of Biomedical Engineering, Chung Yuan Christian University, Chung-Li City, Taiwan R.O.C.

Abstract — **This paper presents a novel readout circuit with potentiostat for amperometric chemical sensors that has wide output current range and has low power consumption, with its application towards the implantable glucose sensing system. This new design of electrochemical interface circuit operates in current-to-current transfer mode, has low input impedance characteristic and has stable loop gain unaffected by sensor resistance variation. Post layout simulations showed detection of redox current from 50 pA to 50 μA with power consumption from only 390 μW to 745 μW, while experimental verification using on-board prototype provided measurements from 10 nA to 50 μA, with 10 nA as the lowest capability of the semiconductor device analyzer used in the setup. This novel readout circuit was implemented using TSMC 0.35 μm mixed-signal 2P4M 3.3 V CMOS technology with a chip area of 0.1767 mm^2.**

Keywords — **Glucose, Potentiostat, Readout Circuit, Integrated Interface Circuit, Amperometric Chemical Sensor**

I. Introduction

Potentiostat is an electronic interface for amperometric chemical sensors that are capable of detecting many biologically and environmentally significant analytes [1]. Recent works describe this kind of potentiostat for biomedical application, particularly glucose measurement [2-3]. Typical implementation of amperometric chemical sensors uses three electrodes [1-6]; the working electrode (WE), reference electrode (RE), and auxiliary counter electrode (CE).

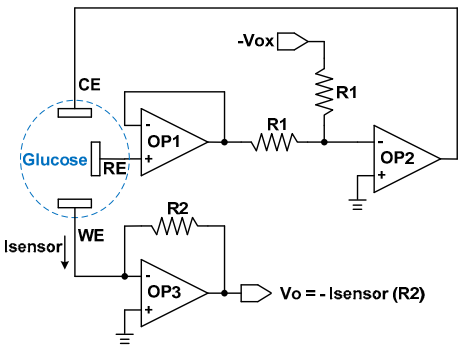


Fig. 1 The standard potentiostat

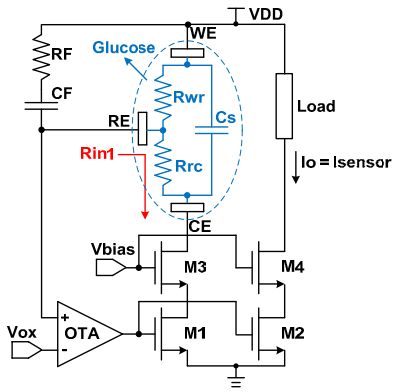


Fig. 2 Readout-1, the original low power potentiostat

The standard potentiostat for amperometric chemical sensors uses three operational amplifiers (OP), as shown in Fig. 1. When the applied reduction-oxidation (redox) potential (Vox) across the RE and WE equals the redox potential of the analyte, a redox current (Isensor) that is proportional to the concentration of the analyte is generated at WE. The Isensor is then transferred into an output voltage (Vo) using resistor R2. Accordingly, by using voltage as output, this circuit limits its output range based on the output swing of OP. Moreover, three OP consumes relatively high power.

With efforts toward miniature implantable glucose sensing systems [2-3], a low-power potentiostat for amperometric chemical sensors [2] is presented in Fig. 2. This circuit needs only one operational transconductance amplifier (OTA) and four MOS transistors. It detects Isensor and mirrors it as output current (Io). This potentiostat improves the output range by operating in current-to-current instead of traditional current-to-voltage transfer mode. However, even with compensation components (RF, CF), its output signal has unwanted oscillations especially when the sensor operates in very small current range.

This paper aims to provide a new design of readout circuit with potentiostat for amperometric chemical sensors that has wide current range including pico-ampere scale, has low power consumption, and has circuit stability not affected by sensor impedance. Availability of such potentiostat makes our research endeavors a step closer in realizing the implantable glucose sensing system.

Chwee Teck Lim, James C.H. Goh (Eds.): ICBME 2008, Proceedings 23, pp. 543–546, 2009
www.springerlink.com

II. Circuit Design

A. Basic concept of current-mode readout circuit

Electrochemical cells, such as glucose sensors, appear to readout circuit as a current source [3]. This is illustrated in Fig. 3. Therefore, a good readout circuit that operates in current-to-current transfer mode must have very low input impedance characteristic (Rin(readout)) so that it sensitively receives most of the generated sensor current (Isensor). Take also into account that the resistance of electrochemical cells (Rsensor) varies as the concentration of analyte changes [3]. Thus, a reliable readout circuit should be insensitive to the variation in sensor resistance.

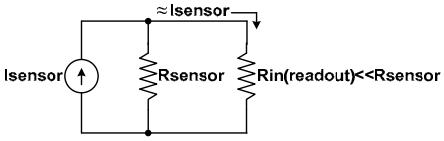


Fig. 3 Glucose sensor appears as current source to readout circuit

B. Readout-1, original low power potentiostat

The original low power potentiostat circuit is illustrated in Fig. 2 and is referred here onwards as Readout-1.

$$R_{in1} \cong g_{m3} \cdot r_{o3} \cdot r_{o1} \tag{1}$$

$$A_1\beta_1(s) \cong A_1(s) \cdot \frac{g_{m1}}{g_{m3}} \cdot R_{sensor} \tag{2}$$

The equivalent input resistance of Readout-1 (R_{in1}) is taken from the drain of NMOS M3 where the sensor is connected and is stated in equation (1). The output resistances (r_{o1}, r_{o3}) of cascode M1 and M3 transistors are inversely related with their drain currents. Consequently, when the sensor current which is also the drain currents of M1 and M3 goes low, the r_{o1} and r_{o3} increase and cause the R_{in1} to be extremely high. This high R_{in1} makes Readout-1 non-ideal as current-to-current readout circuit and insensitive to the sensor current.

Based on equation (2), the loop gain of Readout-1 ($A_1\beta_1(s)$) is directly affected by any change in the sensor resistance (R_{sensor}). This causes the poles of OTA and of sensor to move with R_{sensor} [2], then degrades phase margin, generates oscillations in the output, and becomes unstable.

C. Readout-2, proposed wide current range potentiostat

The proposed novel design of wide current range potentiostat is presented in Fig. 4 and is referred here onwards as Readout-2.

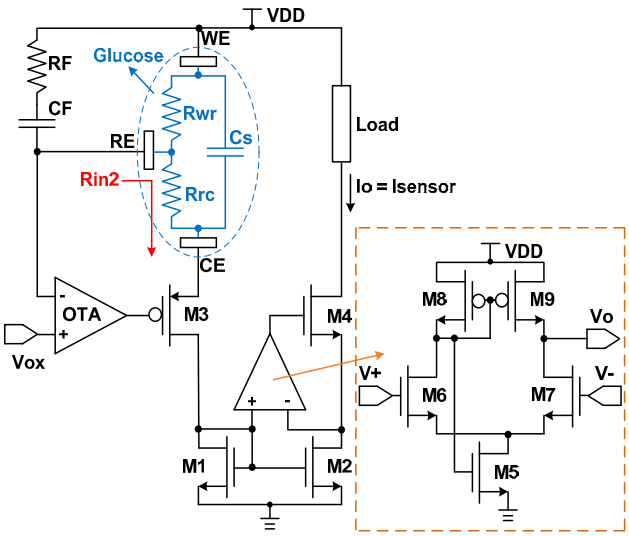


Fig. 4 Readout-2, the proposed wide current range potentiostat

The new readout adopts the structure of potentiostat in Fig. 2 so that it inherits the low power advantage. However, the important low input impedance characteristic is included in the circuit design so that it improves the current sensing range and enhances the stability.

$$R_{in2} \cong \frac{\frac{1}{g_{m1}} + r_{o3}}{1 + g_{m3} \cdot r_{o3}} \cong \frac{1}{g_{m3}} \tag{3}$$

$$A_2\beta_2(s) \cong A_2(s) \cdot \frac{R_{sensor}}{\frac{1}{g_{m3}} + R_{sensor}}, \frac{1}{g_{m3}} << R_{sensor} \tag{4}$$

To establish the low input resistance, the source terminal of MOS is chosen as input point. Then, to maintain the direction of current, the transistor M3 is changed into PMOS. Thus, the source terminal of PMOS M3 serves as input of Readout-2 and from it a very low input resistance (R_{in2}) is derived and is given in equation (3). The low R_{in2} guarantees that Readout-2 is suited for current-to-current transfer interface circuit and is sensitive even when the sensor current is in pico-ampere range.

The loop gain of Readout-2 ($A_2\beta_2(s)$) becomes stable and unaffected by R_{sensor} as specified in equation (4), especially when the input resistance of PMOS M3 ($1/g_{m3}$) is designed to be very small compared with R_{sensor}.

The transistors M1 and M2 serve as current mirror to transfer the sensor current (Isensor) into the output current (Io). The transistors M5 to M9 form the self-bias differential pair.

III. Results and Discussions

A. Set-up of circuit simulation

The post layout performances of Readout-1 and Readout-2 were simulated in HSPICE using the TSMC 0.35 μm mixed-signal 2P4M 3.3V CMOS models.

The amperometric chemical sensor was replaced with Rwr, Rrc and Cs model [2,6], as shown in Fig. 2 and Fig. 4, during circuit simulations.

The redox potential (Vox) was set to 0.4 V.

B. Improvement on feedback stability

Modifying the sensor resistance (Rwr) simulated the change of concentration of analyte. When the Rwr was set to 8 kΩ, 800 kΩ, 8 MΩ and 8 GΩ, that corresponded to generated sensor current of 50 μA, 0.5 μA, 50 nA and 50 pA respectively.

Fig. 5 shows the effect of Rwr variation to circuit loop gain (|L|). Readout-1 had loop gain (|L1|) that variably changes with Rwr while Readout-2 had loop gain (|L2|) that remains stable and unaffected by Rwr. This feature is evident at the lower frequencies.

In Fig. 6, Readout-2 exhibits a stable loop gain (|L|(max)) and a steady phase margin (PM) over the entire Rwr range unlike in the Readout-1. The Rwr used in this part was from 8 kΩ to 8 GΩ.

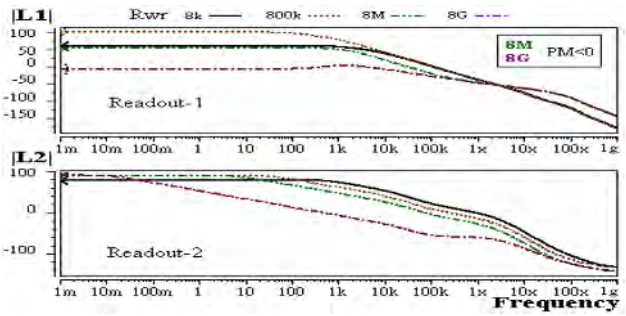


Fig. 5 Bode plot of loop gain |L| at various sensor resistance Rwr

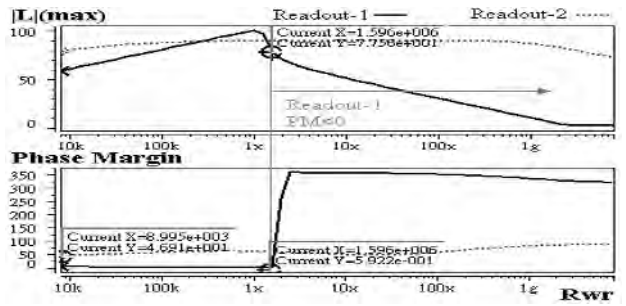


Fig. 6 Characteristics of loop gain |L| (max), phase margin against Rwr

C. Elimination of signal oscillations

The Readout-2 circuit was able to remove the unwanted oscillations in its output signal (Io2) because of improved feedback stability. On the other hand, Readout-1 took longer time to stabilize its output (Io1) as displayed in Fig. 7.

D. Widening of current sensing range

Fig. 8 and Fig. 9 show the agreement of simulation and experimental results regarding the current sensing range of Readout-2. Simulation used 3.3 V while experimental test used 5 V supply. Nevertheless, both results confirmed that Readout-2 can detect current down the nano-ampere range. Post-layout simulation results gave 50 pA to 50 μA range while experimental test provided 10 nA to 50 μA. The 10 nA is the lowest limit of the instrument used.

Fig. 8 also displays the linearity between the input sensor current (Isensor) and mirrored output current (Io) of Readout-2. There was a mismatch between the sensor current and output current. It was attributed to the load device that limited the drain source voltage of transistor M4. In experimental measurement in Fig. 9, when the Isensor was 25 μA, the Io was only 24.55 μA.

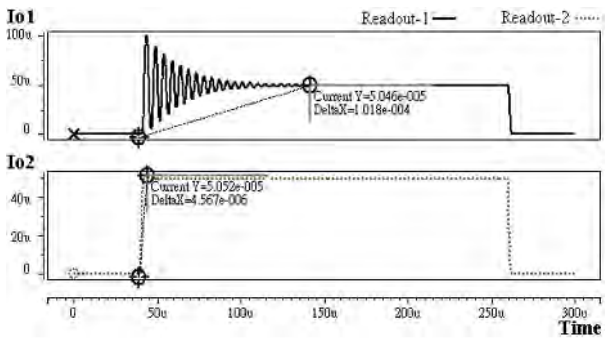


Fig. 7 Transient analysis showing signal oscillations

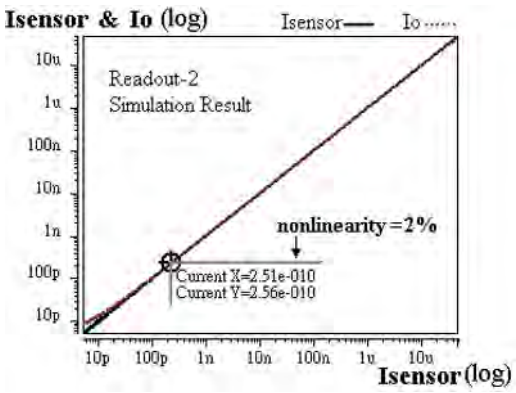


Fig. 8 Post-layout transfer characteristics of Readout-2

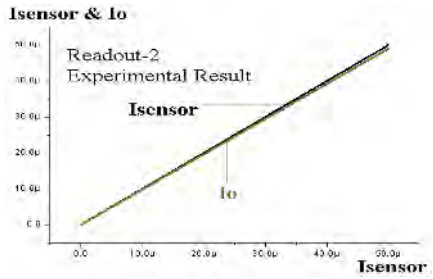


Fig. 9 Experimental transfer characteristics of Readout-2

E. Set-up of experimental test

An on-board module of Readout-2 was built to verify its design and performance. The OTA used the LMC6484AIN because of rail-to-rail output range, the MOS transistors employed the CD4007UBE chip, and the power was set to 5V. The Agilent B1500 Semiconductor Device Analyzer was used to source and sense current down the nano-ampere range, with 10 nA as its lowest limit.

F. Physical layout of the proposed readout circuit

Excluding the pads, the whole layout of Readout-2 circuit presented in Fig. 10 only occupied a chip area of 0.43835 mm by 0.403 mm or 0.1767 mm^2 using the TSMC 0.35 μm mixed-signal 2P4M 3.3 V CMOS technology.

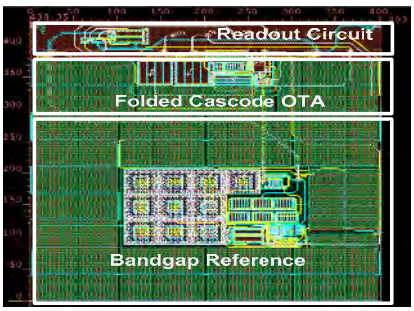


Fig. 10 Physical layout of Readout-2

IV. Conclusions

The proposed Readout-2 with potentiostat for amperometric chemical sensors is able to operate at a wider current range from 50 pA to 50 μA with power consumption from only 390 μW to 745 μW. Availability of this novel design allows us to move closer towards the realization of an implantable glucose sensing system. Table 1 summarizes the performances of Readout-2 as compared to Readout-1. Future work includes the improvement of current mirror to better match the sensor current to the output current.

Table 1 Comparison of original Readout-1 and proposed Readout-2

Characteristics	Readout-1	Readout-2
Sensing range	1 μA to 50 μA	50 pA to 50 μA
Power consumption (Isensor at 50 pA to 50 μA)	390 μW to 720 μW	390 μW to 745 μW
Input resistance (open loop)	924 MΩ	31.6 kΩ
Phase margin (worst case)	PM < 0 when Isensor at nA range	47° when Isensor = 50 μA
Loop gain affected by sensor resistance	Yes	No
Signal with oscillations	Yes	No
Settling time (at 1%)	101.8 μs	4.57 μs
Chip area	0.16 mm^2	0.176 mm^2

Acknowledgment

The authors deeply appreciate the National Science Council, Republic of China for research fund NSC 97-2221-E-033-054 and the National Chip Implementation Center, Taiwan for technical support and future chip fabrication.

References

1. Martin S M, Gebara F H, Strong T D, Brown R B (2004) A low-voltage chemical sensor interface for system-on-chip: the fully-differential potentiostat, ISCAS Proc. vol. 4, International Symposium on Circuits and Systems, Vancouver, Canada, 2004, pp 892–895
2. Chung W Y, Paglinawan A C, Wang Y H, Kuo T T (2007) A 600 μW readout circuit with potentiostat for amperometric chemical sensors and glucose meter applications, EDSSC Proc., IEEE Conference on Electron Devices and Solid-State Circuits, Tainan, Taiwan, 2007, pp 1087–1090
3. Beach R D, Conlan R W, Godwin M C, Moussy F (2005) Towards a miniature implantable in vivo telemetry monitoring system dynamically configurable as a potentiostat or galvanostat for two- and three-electrode biosensors. IEEE Transactions on Instrumentation and Measurement, vol. 54, issue 1, pp 61–72
4. Li H, Luo X, Liu C et al. (2004) Multi-channel electrochemical detection system based on LabVIEW, ICIA Proc., International Conference on Information Acquisition, Hefei, China, 2004, pp 224–227
5. Zhang J, Trombly N, Mason A (2004) A low noise readout circuit for integrated electrochemical biosensor arrays, ICSENS Proc. vol. 1, IEEE Conference on Sensors, Vienna, Austria, 2004, pp 36–39
6. Fidler J C, Penrose W R, Bobis J P (1992) A potentiostat based on a voltage-controlled current source for use with amperometric gas sensors. IEEE Transactions on Instrumentation and Measurement, vol. 4, issue 2, pp 308–310

Author: Wen-Yaw Chung
Institute: Department of Electronic Engineering, Chung Yuan Christian University
Street: 200 Chung-Pei Road
City: Chung-Li City
Country: Taiwan, R.O.C. 32023
Email: eldanny@cycu.edu.tw

Multiple Low-Pressure Sonications to Improve Safety of Focused-Ultrasound Induced Blood-Brain Barrier Disruption: In a 1.5-MHz Transducer Setup

P.H. Hsu[1], J.J. Wang[2], K.J. Lin[2,3], J.C. Chen[4] and H.L. Liu[1]

[1]Department of Electrical Engineering, Chang-Gung University, Taoyuan, Taiwan
[2]Department of Medical Image and Radiological Sciences, Chang-Gung University, Taoyuan, Taiwan
[3]Department of Nuclear Medicine and Molecular Imaging Center, Chang Gung Memorial Hospital, Linkou, Taiwan
[4]Graduate Institute of Basic Medical Science, Chang-Gung University, Taoyuan, Taiwan

Abstract — **Burst-mode driven high intensity focused ultrasound (HIFU) with the presence of ultrasound micro bubbles has been proven to be capable of locally and reversibly increasing the permeability of blood-brain barrier (BBB). However, the use of excessive acoustic pressure usually accompanied with intracerebral hemorrhage, which is considered a deterred side effect, especially when in applications such as drug delivery. The purpose of the current study is to provide a secure protocol using multiple low-pressure sonications, to disrupt localized BBB and preserve sonicated area without producing intracerebral hemorrhage.**

The brains of 10 Sprague-Dawley rats were subjected to 16 sonications, either unilaterally or bilaterally. A 1.5-MHz spherically curved 1-3 composite transducer was used to deliver the burst-mode ultrasonic focal energy into the rat brain after both craniotomy and micro bubble injection. Electric powers from 1 to 10 W were tested and sonication mode was adjusted from single high-pressure sonication (2.45 MPa, 30s ×1) to multiple shoots (1.1 MPa, 30s ×6). The path of sonication could be either a row or a triangle, which depends on the treatment plan. Pathologic examination includes hematoxylin and eosin (H&E) and immuno-histochemistry (IHC) staining. It was used to quantify the damage in accompany with BBB disruption which includes hemorrhage and tissue necrosis. MR imaging was employed to evaluate the BBB disruption and brain tissue hemorrhage *in vivo*. Pathological examinations showed that the average hemorrhage score decreased from 2.3+/- std (severe) to 0.3+/- std (slight) by using the proposed protocol. The finding was confirmed by *In vivo* MRI examinations. Compared with single high-pressure sonication, multiple low-pressure sonication effectively reduced the occurrence of hemorrhage noticed in T2*-weighted images. The efficiency of BBB-disruption increased as observed in contrast-enhanced T1 weighted Turbo-spin-echo sequence. The current study provides an improved sonication protocol which could temporally and locally disrupt the Blood-Brain-Barrier. It therefore demonstrated the possibility of safe drug delivery into restricted brain regions in the future applications.

Keywords — **Focused ultrasound, blood-brain barrier, hemorrhage**

I. Introduction

The blood-brain barrier (BBB) is a specialized structure of blood vessel walls that limits the free transportation and diffusion of molecules from the vasculature to the surrounding neurons. Many methods have been developed to enhance the BBB permeability to assist the penetration through the tight junction for therapeutic purpose, all of which, unfortunately, induce systemic BBB disruption and fail to deliver drug to a specific brain region.

High-intensity focused-ultrasound (HIFU) has been shown with the potential to increase BBB permeability [1, 2]. Hynynen et al showed that BBB can be selectively disrupted with a reduced ultrasound energy exposure[3], which minimized the parenchyma damage through the use of low-power burst mode HIFU sonications and under the presence of an ultrasound contrast agent [4]. However, hemorrhage still persists under the low power used and remains the major adverse effect. Intracerebral hemorrhage can be hazardous, especially in applications such as to deliver therapeutic molecules into brain. Therefore, the safety ultrasound exposure, which only disrupts BBB without any hemorrhage raised widespread interest.

The current study demonstrates a new strategy by using multiple burst sonications instead of high-pressure single-shot sonication to reduce the occurrence of hemorrhage. Animal experiments were conducted, and imaging modalities by both magnetic resonance imaging (MRI) and single-photon emission computed-tomography (SPECT) were employed. The extent of tissue damage was analyzed histologically.

II. Methods

A. Animal preparation

Adult male Sprague-Dawley rats (300–350 g) from the National Laboratory Animal Breeding and Research Center (Nan-Kang, Taipei, Taiwan) were used in the study. The

Chwee Teck Lim, James C.H. Goh (Eds.): ICBME 2008, Proceedings 23, pp. 547–550, 2009
www.springerlink.com

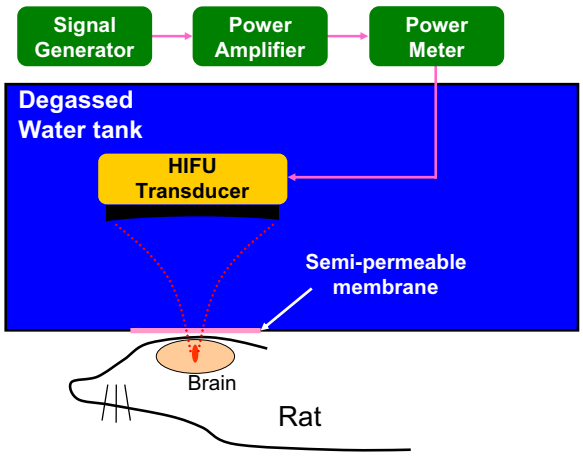


Fig. 1 Experiment setup.

experiments were approved by the Institutional Animal Care and Use Committee of Chang Gung University and adhered to the experimental animal care guideline.

Animals were anesthetized using chlorohydrate (300 mg/kg) through IP injection. Craniotomy was performed before the ultrasound sonication to reduce distortion of the ultrasound focal beam. A cranial window of approximately 7×7 mm^2 was opened with a high-speed drill and a PE-50 catheter was placed in the jugular vein. The skull defects were covered with saline-soaked gauze to prevent dehydration and infection during the process.

B. Ultrasound Sonication

Figure 1 shows the experiment setup. The ultrasonic focal beam was generated by a 1-3 Piezocomposite focused ultrasound transducer (Imasonics, France. Diameter = 60 mm, Curvature radius = 80 mm, Frequency = 1.5 MHz, electric-to-acoustic efficiency = 70%). An arbitary-function generator (33220A, Agilent, USA) was used to generate the driving signal that was fed to a radio-frequency power amplifier (100A250A, Amplifier Research, USA). The energy of signal delivered to the transducer was monitored by a power meter (Model 4421, Bird, USA). An acrylic water tank was used. A window of approximately 4×4 cm^2 was opened at its bottom, which was sealed with a thin film to allow the entry of ultrasound energy. The animal was placed directly under the water tank with its head tightly attached to the thin-film window. The animals were placed below the water tank as figure 1.

Micro-bubbles were injected during the HIFU treatment to enhance the efficiency of BBB opening. SonoVue® (Bracco, Milan, Italy. SF_6 coated with mean diameter = 2.0-5.0 μm) was injected through the catheter 10 seconds prior to the sonications. Each bolus injection contains 10 μl.

Two experiments were conducted in order to compare the sonication strategy. In the first experiment, the animal sonications were conducted with single-shot focused ultrasound. A relatively high pressure of 2.45 and 3.48 MPa were employed. The sonication was pulsed with a burst length of 10 ms and a repetition frequency of 1 Hz. The duration of each sonication was 30 seconds. In the second experiment, the animal sonications were conducted with six sonications with a small spacing (1 mm) between each targeting point. The peak pressure was 1.1 MPa, 2 and 3 times lower than the acoustic powers used in the first experiment.

C. Pathologic Examinations

Animals were sacrificed approximately 3-4 hours after HIFU sonication. The brains were immediately removed and frozen in an O.C.T. compound (Optimal Cutting Temperature compound, Tissue-Tek®, SAKURA, USA). The tissues were sectioned in Microtome (Model 3050S, Leica, German). The slices were preserved and stained with hematoxylin and eosin (H&E). The results were classified into 4 categories as described in figure 2, which depends on the level of hemorrhage and cell damage. The neuronal cell damage and hemorrhage were evaluated quantitatively by four different grades. The grade 0 was defined as neither tissue damages nor erythrocyte extravasations were observed after sonication. In grade 1, small extravagated erythrocytes were occasionally observed, but H&E staining showed neither neuronal loss nor cell structure changed. In grade 2, there is continuous and extensive hemorrhage, accompanied by neuronal loss, or apoptotic cell death. Grade 3 observed neuronal cell necrotic death, next to the findings in grade 2. It was the most severest damage in tissue.

D. Magnetic resonance imaging (MRI)

After ultrasound sonication, the animals were immediately scanned by MRI. All images were acquired on a 3-T scanner (Trio a Tim system, Magnetom, Siemens, Erlangen, Germany) using the standard wrist coil with an inner diameter of 13 cm. The animals were placed in an acrylic holder and then positioned in the center of the magnet. Images were acquired using a fully flow compensated T2*-weighted 3D Gradient Recalled Echo sequence and dynamic contrast-enhanced (DCE) T1-turbo-spin-echo sequence. An IV bolus (0.125 mmol/kg) of MRI contrast agent (Magnevist®, Berlex Laboratories, Wayne, NJ) was administered through the unilateral jugular vein during the dynamic acquisition of the T1-weighted images.

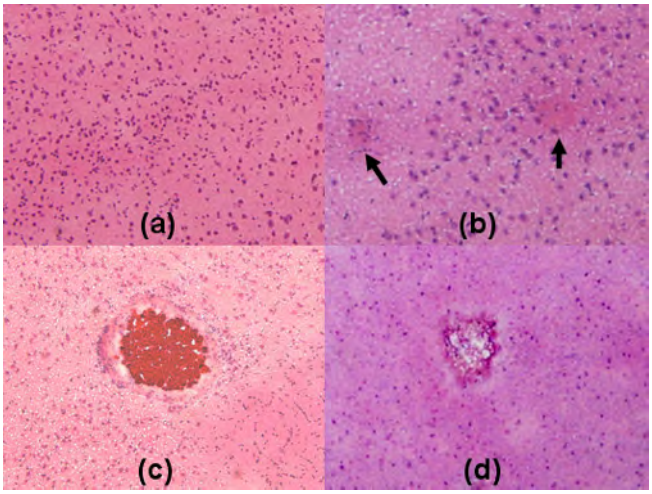


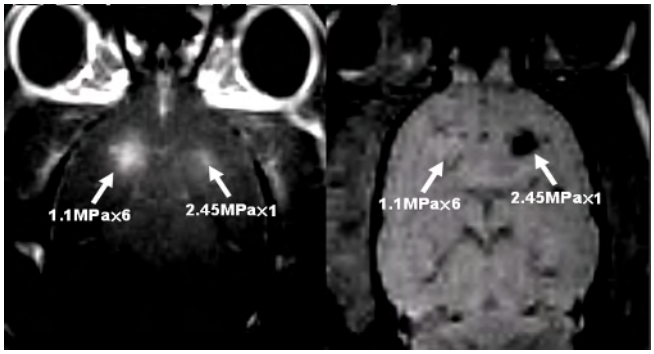
Fig. 2 Four categories of cell necrosis and damage induced by focused ultrasound. (a) level 0: neither tissue damages nor erythrocyte extravasations were observed. (b) level 1: small extravasated erythrocytes were occasionally observed, but H&E staining showed neither neuronal loss nor cell structure changed; (c) level 2: continuous and extensive hemorrhage, accompanied by neuronal loss, or apoptotic cell death; (d)level 3: the most severeest damage in tissue, neuronal cell necrotic death was observed besides findings in level 2.

E. Single-proton emission computed tomography (SPECT) imaging

SPECT imaging was acquired to evaluate the potential radiotracer leakage through the disrupted BBB. After HIFU sonication, isotope (^{99m}Tc-DTPA,5 mCi) was intravenously injected and SPECT images of the brain was acquired using a dedicated small animal SPECT/CT scanner (Nano-SPECT®, Bioscan Inc. Washington D.C., resolution = 1.4 mm, voltage = 140keV). Images were reconstructed by OSEM (Ordered Subsets-Expectation Maximization).

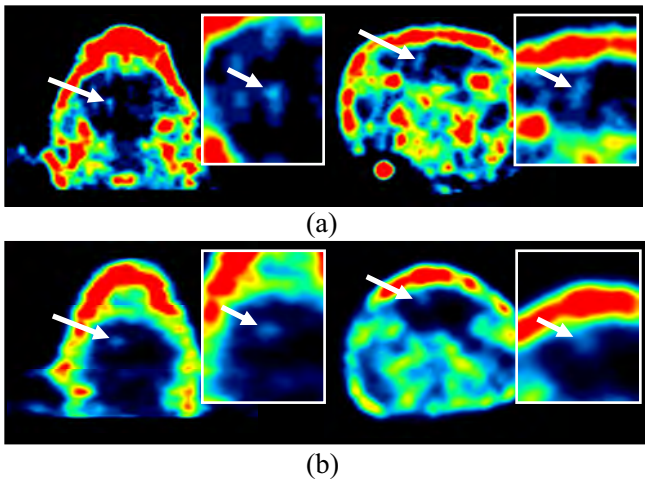
III. Results

The area of BBB opening and hemorrhage were confirmed by contrast-enhanced T1-weighted MRI. In normal case, MRI contrast agent cannot pass through the BBB into the brain tissue but it can be observed in image by MRI scanner once BBB been disrupted and the MRI contrast agent leak into brain parenchyma. Figure 3(a) shows that BBB can be disrupted in both power of sonication in the first experiment. The single sonication of 2.45 MPa was targeted at the right brain and the six sonications of 1.1 MPa at left brain. The signal changes by MRI contrast agent were better visualized in experiments of multiple sonications of lower-pressure shot. Figure 3(b) shows that a single 2.45 MPa sonication can cause severe intracerebral hemorrhage



(a) (b)

Fig. 3 MRI (a) contrast –enhanced T1-weighted image to identify the BBB-disruptive region and (b) MR-SWI to identify the intracerebral hemorrhage occurrence.



(a)

(b)

Fig. 4 SPECT images showing the ^{99m}Tc DTPA tracer leaked into parenchyma after sonication with the sonication parameter of (a) single-shot with pressure 2.45 MPa and (b) multi-shot with 1 MPa × 6 points. Left images show the coronal view and right ones show the transverse view of the animal brain.

rather than the multiple 1.1 MPa sonications. This finding indicated that the proposed strategy not only contributes to a higher BBB-disruption efficiency but also reduce or even remove the occurrence of intracerebral hemorrhage. Figure 4 showed one typical SPECT image, which indicated a radiotracer leakage into brain parenchyma through the disrupted BBB under single and multiple sonication protocols. The radio-tracer can be detected in the unilateral sonicated brain, which suggests that a successful BBB disruption by both sonication protocols. No direct imaging from SPECT can indicate the intracerebral hemorrhage such as MR-SWI (Maybe delete this, a negative comment). However, it was noticed that the radio-tracer distribution in the BBB-disruptive region, when using multiple low-pressure bursts,

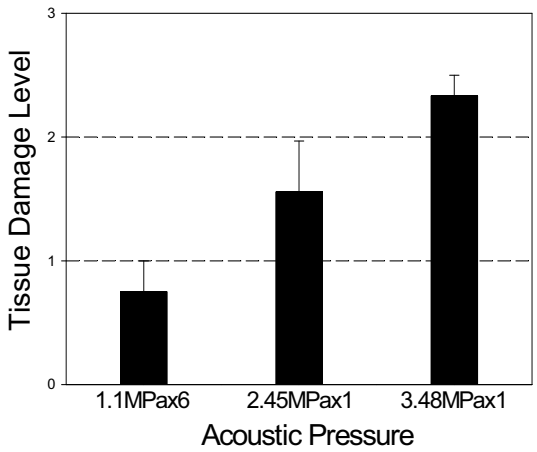


Fig. 5 Quantified grade of tissue damage from low pressure (1.1 MPa) to high pressure (3.48 MPa)

is more uniform when compared to that in single high-pressure burst protocol, which becomes apparent in the coronal view. A high radiation count spot was noticed, when compared to that in the surrounding BBB disruptive region, which suggest hemorrhage because of increased leakage by the radio-tracer.

The level of tissue damage is an issue of importance in HIFU experiment. Figure 5 showed the result from histology examination. The average hemorrhage score decreased from 2.33 +/- std (severe) to 0.75 +/- std (slight) by the proposed protocol. This suggests that the proposed strategy only produce mild erythrocyte extravasations, which can be considered as safe. In contrast, the single high-pressure burst creates BBB-disruption which was accompanied by severe intracerebral hemorrhage and was therefore hazardous.

IV. Conclusions

The current study confirmed that in the proposed strategy (please say explicitely what was proposed) the HIFU energy can lead to reduced level of hemorrhage and at the same time maintain the efficiency of BBB-disruption. Applications such as drug delivery into the brain can therefore be feasible because of increased safety measures.

Acknowledgment

The project has been supported by the National Science Council (NSC-95-2221-E-182-034-MY3) and the Chang-Gung Memorial Hospital (CMRPD No. 34022, CMRPD No. 260041).

References

1. Mesiwala, A.H., et al., (2002) High-intensity focused ultrasound selectively disrupts the blood-brain barrier in vivo. Ultrasound Med Biol, 2002. 28(3): pp. 389-400.
2. Sun, J. and K. Hynynen, (1999) The potential of transskull ultrasound therapy and surgery using the maximum available skull surface area. J Acoust Soc Am, 1999. 105(4): pp. 2519-27.
3. Hynynen, K., et al., (2005) Local and reversible blood-brain barrier disruption by noninvasive focused ultrasound at frequencies suitable for trans-skull sonications. Neuroimage, 2005. 24(1): pp. 12-20.
4. Hynynen, K., et al., (2003) The threshold for brain damage in rabbits induced by bursts of ultrasound in the presence of an ultrasound contrast agent (Optison). Ultrasound Med Biol, 2003. 29(3): pp. 473-81.

Phase Synchronization Index of Vestibular System Activity in Schizophrenia

S. Haghgooie[1], B.J. Lithgow[1], C. Gurvich[2], and J. Kulkarni[2]

[1] Diagnostic and Neurosignal Processing Group, Monash University, Melbourne, Australia
[2] Alfred Psychiatry Research Centre, The Alfred Hospital, Melbourne, Australia

Abstract — **Schizophrenia is a severe mental illness associated with multiple neuropathological and neurochemical abnormalities. The aim of this study is to examine if patients with schizophrenia exhibit any abnormality in the level of functional connectivity between the neuronal centers responsible for the processing of vestibular information in the left and right side of the head. Signals were recorded simultaneously in response to tilt stimuli by a special hydraulic chair via a pair of electrodes inserted in the left and right ear canals to rest on tympanic membrane. Using the complex Morlet wavelet transform, we compared instantaneous phase synchronization indices on a set of recordings collected from a group of control subjects (n=24) against schizophrenia group (n=11). Our results show differences between groups in the level and duration of synchrony mostly during dynamic rather than static phases of the tilts. Larger study sample is required to verify these findings.**

Keywords — **Schizophrenia, vestibular system, phase synchronization, complex Morlet wavelet**

I. Introduction

Schizophrenia is a serious mental disorder with annual incidence between 0.2 and 0.4 per 1000 and a lifetime risk of about 1%. Schizophrenia is the most disabling among the psychiatric disorders and is characterized by positive symptoms (e.g., delusions, hallucinations), negative symptoms (e.g., apathy, social withdrawal), disorganized symptoms (e.g. disorganized thought, communication, and behavior), and cognitive impairment (e.g., learning, memory, and executive functioning problems).

Schizophrenia is associated with several pathophysiological conditions that involve an extended network of brain structures including cortex, cerebellum, thalamus, hippocampus, and the basal ganglia. In terms of neurochemistry; converging evidence from different studies suggests several neurotransmitter systems are clearly involved. These include dopamine (DA), serotonin, gamma-amino butyric acid (GABA) and glutamate (Glu) systems [1].

The vestibular system is responsible for providing the sense of balance and the information on the motion and position of the head in space. The peripheral part of the vestibular system is located in the inner ear and consists of two sack-like otolith organs (OTO), the utricle and saccule, and three semicircular canals (SCC). The OTO detect linear acceleration and head position while SCC sense direction and speed of angular accelerations (e.g. onset of head rotations). Hair cells within the vestibular apparatus are responsible for generating receptor potentials.

Vestibular nerve fibers that innervate the hair cells project via the VIII cranial nerve to cerebellum and integrative centers in brainstem also known as vestibular nuclei (VN). The four nuclei of the VN are the lateral, the medial**,** the superior, and the inferior vestibular nucleus. There are reciprocal interconnections between the four VN. VN also communicate bilaterally through a commissural system that is predominantly inhibitory. Most of these connections are inhibitory GABA-ergic and provide pathways by which information from pairs of corresponding SCCs and OTOs can be compared. The posterior cerebellum has extensive inhibitory (GABA-ergic) and excitatory (Glu) reciprocal connections with the VN that are involved in regulatory mechanisms for the control of the eye movements, head movements, and posture [2]. Converging evidence from literature, e.g. abnormal posture and proprioception, impaired eye blink conditioning, and impaired adaptation of the vestibular-ocular reflex suggests that some of the symptoms of schizophrenia may be associated with cerebellar anomalies [3]. Recent literature has examined the close links between the vestibular system and emotion processing systems e.g. Parabrachial Nucleus (PBN) with some researchers suggesting a causal relationship [4].

The vestibular system can therefore be regarded as a potential window for exploring the brain function. Measuring the activity of the vestibular system can be providing a quantitative, indirect measure of activity in the brain regions and neural pathways that are frequently compromised in neuropsychiatric disease. Our studies have suggested that vestibular responses acquired by a new method named Electrovestibulography (EVestG) are different in schizophrenia as well as depression and Parkinson's disease.

Affected neurotransmitter pathways in schizophrenia, especially reciprocal pathways that link VN to cerebellum and PBN, may also compromise the VN bilateral commissural connections leading to a change in the index of connectivity between the left and right VN.

Phase synchronization in coupled chaotic systems was introduced by Rosenblum et al. [5]. In area of brain re-

Chwee Teck Lim, James C.H. Goh (Eds.): ICBME 2008, Proceedings 23, pp. 551–554, 2009
www.springerlink.com

search, patterns of synchronized oscillations have been studied for different frequency bands in EEG signals and it has been pointed out that they reflect various brain states and cognitive processes [6]. Using the same recording set up as EVestG, in order to measure the level of connectivity between the activity of the left and right VN, we have compared averaged dynamic phase synchronization as well as *coherence interval* patterns [7] in the recorded signal from a group of schizophrenia patients with respect to control subjects.

II. Methods

A. Subjects

35 subjects between 20 and 67 years of age, both male and female, took part in this study. 11 participants (7 males, 4 female) aged between 29 and 46 years (Mean= 37.2, SD=5.9 years) met DSM-IV diagnostic criteria for schizophrenia, with disease duration ranging from 15 to 28 years. Symptoms of psychopathology were assessed by a trained clinician using Positive and Negative syndrome Scale (PANSS), a 30-item, 7 point rating instrument. The mean total PANSS score was 53.5 (SD=16.8). A comparison group of 24 healthy, control subjects (12 males, 12 females) aged between 20 and 67 (Mean= 38.9, SD=15.4 years) without a history of neurological or psychiatric illness, also participated. All the participants were screened for cognitive decline using the Mini-Mental State Examination (MMSE). Average score was 29.6 (SD=.7) for control participants and 29.2 (SD=1.3) for schizophrenia group (maximum score of 30). Participants also self-rated their alertness using the Stanford sleepiness test, and all scored below 3 indicative of being alert at the time of testing. A standard hearing test was conducted on all participants to ensure they don't have hearing problems.

No participant demonstrated hearing or balance impairment. All experiments completed under Monash University Human Ethics approval number 2006/604MC.

B. Stimuli

The methodology used in this study is adopted form EVestG recording technique [8]. To avoid neck muscle artifact, the vestibular system was stimulated by passively tilting a participant, with eyes closed, who is seated in a special hydraulic and instrumented chair, housed in an electrically and acoustically shielded chamber. The chair was programmed to move in the defined plane until it made a 45 degrees angle with its original position within 3 seconds. Fig.1 shows the resulted s-shaped position and velocity profiles.

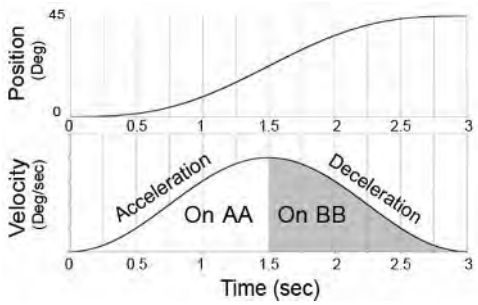


Fig. 1 Smooth position and velocity profiles of hydraulic chair motion. The first 1.5 seconds after onset of the motion is marked as OnAA that corresponds to acceleration. The chair decelerated during OnBB segment until reached steady state.

C. Procedure

A 60 second recording was conducted. The recorded signal was divided into different time segments to investigate dynamic and static phases (i.e. when the tilt chair is moving or when is stationary) for back tilt stimuli. Prior to the tilt (t=0-20 sec) the subject was seated in an upright neutral position to measure background neuronal activity (BG). The transient section of the recorded signal at the onset (On) of the tilt will help to determine the dynamic response (t=20-25 sec). This onset response is made up of an acceleration (OnAA) and deceleration (OnBB) phase and labeled at t=20-21.5 sec and t=21.5-23 sec respectively (see figure 1). The steady state (SS) region labeled at t=30-40 sec.

D. Electrophysiological recordings and Preprocessing

Signals were obtained via a pair of electrodes consist of a wick inserted into the left and right ear canals and positioned to rest on the tympanic membrane. This method of recording was previously used in EVestG and Electrocochleography [9]. Each electrode was referenced to the linked earlobe and signals were amplified using a CED1902 amplifier and digitized by CED1409 A/D converter. The sampling rate was initially 44.1 KHz that is suitable for EVestG analysis but later signals were down sampled to 3 KHz as we did not need very high frequency components for this study. The raw signals were screened in time and frequency domains for muscle and motion artifacts both visually and automatically to find and remove large artifacts. To remove low frequency noise due to the motion and power line artifact, signal was high pass filtered at 5 Hz and notch filtered at harmonics of 50Hz with 3db attenuation factor. Forward and reverse filtering with resultant zero phase shifts was employed in order to preserve the phase information of the signal.

E. Data analysis

Our data analysis method was centered on the dynamic phase synchronization index of the signals recorded from the electrodes in the left and right ear. Phase of the signals, were obtained using the complex Morlet wavelet defined as:

$$\psi(t) = \frac{1}{\sqrt{\pi f_b}} e^{2i\pi f_c t} e^{-\frac{x^2}{f_b}} \quad (1)$$

where f_c is the center frequency of the wavelet and f_b is the bandwidth parameter. For the signal $S(t)$ recorded from an electrode, wavelet coefficients at time t_0 and scale a are defined as:

$$W_S(t_0, a) = \frac{1}{a} \int_{-\infty}^{+\infty} S(t) \psi^*(\frac{t - t_0}{a}) dt \quad (2)$$

where the $\psi^*(\frac{t-t_0}{a})$ is the complex conjugate of the equation (1) above. In the current study, f_c is adjusted at each scale and f_b is set to one. The wavelet coefficients are a complex numbers and can be described as:

$W_S(t_0, a) = A(t_0, a) e^{i\varphi(t_0, a)}$, where $A(t_0, a)$ and $\varphi(t_0, a)$ are amplitude and phase at the moment t_0. The signals $S_r(t)$ and $S_l(t)$ are n:m synchronized if they meet the 'phase locking' condition suggested by Rosenblum et al.[5]:

$$\left|\varphi_{r,l}(t, a, n, m)\right| = \left|n\varphi_r(t, a) - m\varphi_l(t, a)\right| < const. \quad (3)$$

where m and n are integers. In current study, our aim is to study the signals recorded from the same physiological system, so we restricted ourselves to the case of 1:1 phase synchronization:

$$\varphi'_{r,l}(t, a) = \varphi_{r,l}(t, a, 1, 1) \quad (4)$$

When studying the synchronization in noisy dynamical systems we have to take a statistical point of view by analyzing the relative phase angles on the unit circle (i.e. [0, 2π] interval). In this sense, synchronization is understood by appearance of peaks in the relative phase difference histogram [10]. We employed the first Fourier mode of the distribution of relative phase differences to measured 1:1 phase synchronization, $R_{l,r}(t, a)$ [11]:

$$R_{l,r}(t, a) = \left\{ \left\{ \frac{1}{n+1} \sum_{k=-n/2}^{n/2} \sin[\varphi'_{r,l}(t + k\Delta t, a)] \right\}^2 + \cdots \right.$$

$$\left. \left\{ \frac{1}{n+1} \sum_{k=-n/2}^{n/2} \cos[\varphi'_{r,l}(t + k\Delta t, a)] \right\}^2 \right\}^{1/2} \quad (5)$$

Where Δt is the sampling interval (1/3000 Sec.) and n is the length of sliding window (n=300). It is evident that R is restricted to the interval [0,1] and reaches 1 if and only if the condition (3) is met whereas for unsynchronized time series, e.g. uniform distribution of phases, R=0.

III. Results

The recorded signal was wavelet transformed and the phase was calculated as a function of time and frequency. 33 different frequencies between 4 Hz and 100 Hz were analyzed by changing center frequency to desired frequency. The segments of signal during the back tilt stimuli that were analyzed for each subject named as BG, onAA, onBB, On, and SS. Phase synchronization index, R(t,a), was calculated at each frequency. Since we were interested to investigate the total duration of synchronized intervals in the dynamic segments (during or immediately after the tilt) with respect to the BG recording (with the subject seated in a neutral position), a threshold value was calculated based on the mean and standard deviation of each subject's BG segment R value.

During other segments, all the R values that were greater than the threshold were considered significant. The total duration of the significant intervals were computed and averaged across control and schizophrenia groups for each segment. Figure 2 shows the averaged values for synchronized events during On, OnAA, OnBB, and SS phases. There are differences, although not significant across all frequencies, between control and schizophrenia groups. The differences are higher in dynamic phases On, onBB, and onAA with respect to SS and it is appeared that in the frequency range of 6Hz-14Hz the differences are larger between groups. It is also evident that OnBB (deceleration phase) results are better differentiating the groups than OnAA.

Furthermore, the R values during OnAA (acceleration) and OnBB (deceleration) segments were averaged for the frequencies in the selected 6Hz-14Hz range that appeared to be more sensitive to different tilt segments. Figure 3 illustrates the smoothed average synchronization curves. OnBB segment shows better separation between the groups.

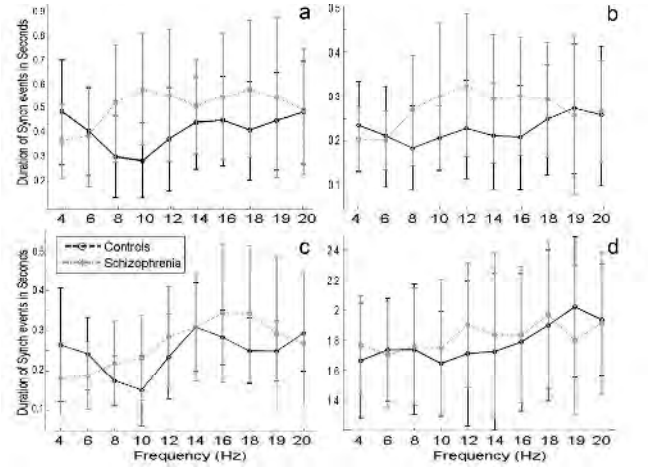


Fig. 2 Averaged duration of synchronization index above the threshold level (Sec.) versus different frequency bands. a) On, b) OnBB, c) onAA, and d) SS response. Error bars show standard deviation.

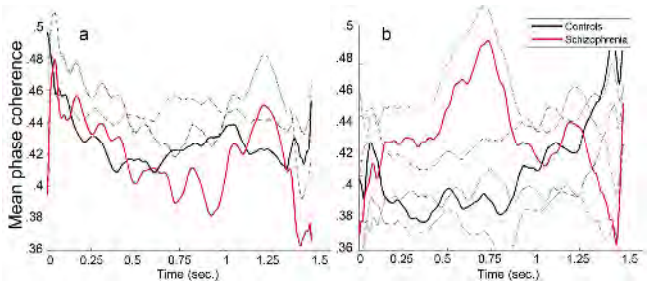


Fig. 3 Smoothed averaged synchronization curves in the frequency range 6Hz to 14Hz during a) OnAA and b) OnBB segments of the tilt. Dotted lines show the overlapping standard error bars.

IV. Conclusions

The results that we observed in the index of phase synchronization revealed some mild differences in the control and schizophrenia group however, differences were consistently higher in the 6Hz-14Hz range. It was also evident that dynamic phases of the tilt were more powerful in terms of separating controls and schizophrenics rather than the SS phase. It is also apparent from the graphs that schizophrenia subjects generally exhibit a slight hyper activity in the level of synchronization between the left and right VN. These evidences can be an indication of the compromised dynamic activity profile of vestibular system in schizophrenia.

The schizophrenia subjects were on different types of medication during the experiments and had different scores on the positive and negative symptoms scale, separation of the responses by the type of medication taken or grouping the patients into different categories of symptoms may improve the results.

Acknowledgment

Thanks to the ARC and Neural Diagnostics Pty. Ltd. for funding and supporting this research.

References

1. Abi-Dargham, A., *Do we still believe in the dopamine hypothesis? New data bring new evidence.* Int J Neuropsychopharmacol, 2004. 7 Suppl 1: p. S1-5.
2. Barmack, N.H., *Central vestibular system: vestibular nuclei and posterior cerebellum.* Brain Res Bull, 2003. 60(5-6): p. 511-41.
3. Picard, H., et al., *The Role of the Cerebellum in Schizophrenia: an Update of Clinical, Cognitive, and Functional Evidences.* Schizophrenia Bulletin, 2007.
4. Balaban, C.D. and J.F. Thayer, *Neurological bases for balance-anxiety links.* J Anxiety Disord, 2001. 15(1-2): p. 53-79.
5. Rosenblum, M.G., A.S. Pikovsky, and J. Kurths, *Phase Synchronization of Chaotic Oscillators.* Physical Review Letters, 1996. 76(11): p. 1804-1807.
6. Mima, T., et al., *Transient Interhemispheric Neuronal Synchrony Correlates with Object Recognition.* Journal of Neuroscience, 2001. 21(11): p. 3942.
7. van Leeuwen, C., *Task, Intention, Context, Globality, Ambiguity: More of the Same.* Ambiguity in Mind and Nature: Multistable Cognitive Phenomena, 1995: p. 85.
8. Lithgow, B.J., *A neural event process*. (WO 2006/024102, priority date 1st September 2004), (Inventor) Patent.
9. Ferraro, J.A., *Clinical Electrocochleography: Overview of Theories, Techniques and Applications*. 2000, Hearing and Speech Department, University of Kansas, Medical Center.
10. Tass, P., et al., *Detection of n: m Phase Locking from Noisy Data: Application to Magnetoencephalography.* Physical Review Letters, 1998. 81(15): p. 3291-3294.
11. Rosenblum, M.G. and A.S. Pikovsky, *Detecting direction of coupling in interacting oscillators.* Physical Review E, 2001. 64(4): p. 45202.

Author: Saman Haghgooie
Institute: Monash University
Street: Wellington Rd.
City: Clayton, VIC3800
Country: Australia
Email: Saman.Haghgooie@eng.monash.edu.au

Constrained Spatiotemporal ICA and Its Application for fMRI Data Analysis

Tahir Rasheed[1], Young-Koo Lee[1], and Tae-Seong Kim[2]

[1] Department of Computer Engineering, Kyung Hee University, Republic of Korea
[2] Department of Biomedical Engineering, Kyung Hee University, Republic of Korea

Abstract — **In general, Independent Component Analysis (ICA), a blind source separation technique, is used in either spatial or temporal domain. For spatiotemporal data, however, in which the statistical independence criteria of the underlying sources cannot be guaranteed, ICA does not perform well simultaneously in both domains. Thus, spatiotemporal ICA (stICA) has been proposed. However, these conventional ICAs in spatial, temporal, or spatiotemporal mode suffer from a problem of source ambiguity: each source must be identified by users. To extract only the desired sources, recently constrained ICA (cICA) has been proposed in which a priori information of the desired sources are used as constraints in either spatial or temporal domain. In this study, we propose constrained spatiotemporal ICA (constrained-stICA), as an extension of cICA, for better analysis of spatiotemporal data. The proposed algorithm tries to find the maximally independent, yet desired sources in both the spatial and temporal domains. The performance of the proposed algorithm is tested against the conventional ICAs using simulated data. Then, its application to the analysis of spatiotemporal fMRI data indicates improved data analysis against the conventional functional MRI data analysis via SPM.**

Keywords — **Spatiotemporal ICA, Constrained spatiotemporal ICA, Functional MRI**

I. Introduction

Independent component Analysis (ICA), a blind source separation (BSS) method based on higher order statistics, decomposes the linear memory-less mixed observations into their underlying independent sources and the corresponding mixing weights [1, 2]. There are two conventional modalities in which ICA can be used to decompose spatiotemporal data like image sequences into a set of images and a corresponding set of time sequences. Spatial ICA finds underlying independent spatial sources and their corresponding set of time weight sequences. Temporal ICA finds independent temporal sequences and their corresponding set of spatial weights.

With the success of ICA in medical signal processing there is a strong interest in ICA for the analysis of spatiotemporal data (e.g., functional MRI data). Functional MRI (fMRI) is a non-invasive imaging technique to study the spatiotemporal brain functions in both research and clinical areas [7]. In 1998, McKeown *et al.* [6] for the first time introduced ICA for fMRI data analysis, with the assumption that fMRI data is a mixture of spatially independent components. ICA is very successful in the identification of various source signals in fMRI [4] which are considered challenging for the second order techniques such as correlation and regression analysis. So far, most of the applications of ICA for fMRI are based on ICA using the spatial mode (Spatial ICA). However the choice of spatial or temporal ICA is controversial: Comparison and discussion on the underlying assumptions for the use of spatial and temporal ICA is given in [3]. For spatiotemporal data of fMRI, where the underlying sources are not really independent, spatial or temporal ICA tries to find a set of independent sources at the cost of their corresponding unconstrained set of temporal and spatial weights respectively.

Spatiotemporal ICA however, for image sequences data of fMRI where underlying independence assumption is not fulfilled, tries to create a balance by jointly optimizing the two sources [8]. For the high dimensional data, it gives large number of independent components making the subsequent analysis very complicated and subjective. In other words, there exists source ambiguity for ICAs in the conventional spatial, temporal, and spatiotemporal modes.

To find some specific source, constrained ICA (cICA) algorithm incorporates a priori information about the desired source [5]. This algorithm has been applied for fMRI data in [9] with either its spatial or temporal mode.

In this study, considering the nature of spatiotemporal fMRI data, we extend cICA into constrained spatiotemporal ICA (constrained stICA) that finds maximally independent, yet desired temporal and spatial sources. The performance of the algorithm against the conventional ICA is tested using the simulated data. Then it has been applied to fMRI data and its results are compared to those of the conventional fMRI data analysis tool, Statistical Parametric Mapping (SPM).

II. Independent component analysis

Independent component Analysis (ICA) assumes that a linear memory-less observation matrix $\mathbf{X} = (\mathbf{x}_1, ..., \mathbf{x}_n)^t$ can be decomposed into underlying set of independent sources $\mathbf{S} = (\mathbf{s}_1, ..., \mathbf{s}_n)^t$ such that,

Chwee Teck Lim, James C.H. Goh (Eds.): ICBME 2008, Proceedings 23, pp. 555–558, 2009
www.springerlink.com

$$\mathbf{X} = \mathbf{SA} \quad \text{or} \quad \hat{\mathbf{S}} = \mathbf{XW} \tag{1}$$

where $\mathbf{A}$ is the mixing matrix and $\mathbf{W}$ is the un-mixing matrix.

General implementations of ICA can be found in the literature [1, 2]. If the observation matrix contains image sequence, Equation 1 can be written as $\mathbf{X} = \mathbf{S\Lambda T^t}$ where $\mathbf{S} = (\mathbf{s_1}, ..., \mathbf{s_k})^\mathbf{t}$ represent the independent spatial sources, $\mathbf{T} = (\mathbf{t_1}, ..., \mathbf{t_k})^\mathbf{t}$ the corresponding independent time courses, and $\mathbf{\Lambda}$ the diagonal scaling parameters.

A. Spatial and Temporal ICA

The observation matrix $\mathbf{X}$ can be decomposed into $\mathbf{X} = \mathbf{UDV^t}$ using singular value decomposition (SVD) where $\mathbf{U}$ is an $m \times m$ Eigen image matrix, $\mathbf{V}$ a $n \times n$ matrix of corresponding Eigen sequences, and $\mathbf{D}$ a $m \times n$ diagonal matrix of singular values. By retaining the k singular value we can reduce the rank of the matrix.

$$\mathbf{X} \approx \hat{\mathbf{X}} = \hat{\mathbf{U}}\hat{\mathbf{D}}\hat{\mathbf{V}}. \tag{2}$$

Spatial ICA assumes that the $m \times k$ Eigen image matrix $\hat{\mathbf{U}}$ can be decomposed into the k spatially independent components $\mathbf{S} = (\mathbf{s_1}, ..., \mathbf{s_k})^\mathbf{t}$. The corresponding time courses can be obtained as follows.

$$\hat{\mathbf{X}} = \mathbf{SA_s}\hat{\mathbf{D}}\hat{\mathbf{V}}^\mathbf{t} \quad = \mathbf{ST_s} \tag{3}$$

where the rows of $\mathbf{T_s} = \mathbf{A_s}\hat{\mathbf{D}}\hat{\mathbf{V}}^\mathbf{t}$ contain corresponding time courses. On the other hand, temporal ICA assumes that $n \times k$ Eigen sequence matrix can be decomposed into the k independent temporal components $\mathbf{T} = (\mathbf{t_1}, ..., \mathbf{t_k})^\mathbf{t}$. The corresponding spatial modes can be obtained as follows.

$$\hat{\mathbf{X}} = \hat{\mathbf{U}}\hat{\mathbf{D}}\mathbf{A}^\mathbf{t}_\mathbf{t}\mathbf{T}^\mathbf{t} \quad = \mathbf{S_t}\mathbf{T}^\mathbf{t} \tag{4}$$

where each column of $\mathbf{S_t} = \hat{\mathbf{U}}\hat{\mathbf{D}}\mathbf{A}_\mathbf{t}^\mathbf{t}$ is the spatial mode.

B. Spatiotemporal ICA

The Spatiotemporal ICA (stICA) [8] is based on the assumption that sometimes underlying spatial and temporal sources are not completely independent. In these cases, spatial or temporal ICA will not produce good results in their corresponding temporal and spatial domains respectively. stICA treats the spatial and temporal domains equally by maximizing the following cost function

$$\mathrm{h_{st}}(W_s, \Lambda) = \alpha H(\mathbf{Y}_s) + (1-\alpha) H(\mathbf{Y}_t) \tag{5}$$

where W_s is the spatial un-mixing matrix, Λ scaling matrix, α the relative weighting factor, $H(\mathbf{Y}_t)$ the temporal entropy, $\mathbf{Y_t} = \sigma_t \mathbf{y}_t$ the cdfs of temporal signals, $\mathbf{y_t} = \hat{V}W_t$ extracted temporal signals, $H(\mathbf{Y}_s)$ the spatial entropy, $\mathbf{Y}_s = \sigma_s \mathbf{y}_s$ the cdfs of spatial signals, and $\mathbf{y}_s = \hat{U}W_s$ the extracted spatial signals.

C. Constrained ICA

When a priori information about the desired source is available, we can incorporate this information in the cICA algorithm [9]. These constraints (or references) guide the algorithm in the direction of only desired independent sources during the optimization process. If we let the reference be $\mathbf{r}(t) = (r_1(t), ..., r_k(t))^t$, the closeness constraint for single IC can be written as

$$\mathrm{g}(\mathbf{w}) = \varepsilon(\mathbf{w^t x}, r_i) - \xi \le 0 \tag{6}$$

where ε is some closeness measure. The closeness threshold parameter is denoted by ξ. This algorithm only extracts only the desired subset from the entire sources.

III. Constrained spatiotemporal ICA

In this algorithm, we exploit the salient features of SVD: (i) it decomposes the observed spatiotemporal data into a set of spatial and temporal modes, (ii) both the modes are orthonormal and (iii) the rank reduction can be done by selecting an appropriate number of k vectors. Based on the first property, corresponding underlying sources in the two domains can be found independently if some a priori information about them is available. The a priori information can be incorporated in the process of finding ICs using the cICA. Constrained stICA uses two cascaded cICA stages, one for each domain. A priori information available in either domain is fed to the first cICA stage along with the appropriate mode. The output will be the independent source in that domain plus the approximate information about the corresponding mode. This information along with the other mode is fed to next cICA stage that will give the independent source in that domain. The procedure is summarized in Table 1. The other properties of SVD can be exploited to simplify the cICA algorithm presented in [9]. Both the modes are orthonormal; we can remove the equality constraint from the constrained ICA algorithm. Also the input data is inherently white, which further simplifies the constrained ICA algorithm. With these modifications the constrained ICA algorithm will become:

$$\begin{aligned} &\textit{maximize}: \ J(y) \approx \rho[E\{G(y)\} - E\{G(v)\}]^2 \\ &\textit{Subject to}: g(\mathbf{w}) \le 0 \ \ or \ \ \hat{g}(\mathbf{w}) + b^2 \end{aligned} \tag{7}$$

where J*(y)* denotes the one-unit ICA contrast function introduced by [2], ρ a positive constant, v a zero mean, unit variance Gaussian variable. G(.) is a non-quadratic function as defined in [2], g(**w**) the closeness constraint mentioned in Equation 5, and b the slack variable. Equation 7 is a constrained optimization problem which can be solved through the use of an augmented Lagrangian function. Learning of the weights is achieved through a Newton like learning process.

$$\begin{aligned} C(\mathbf{w}, \mu) &= J(y) + \mu^t \hat{g}(\mathbf{w}) + \frac{1}{2} \| \hat{g}(\mathbf{w}) \|^2 \\ \mathbf{w}_{k+1} &= \mathbf{w}_k - \eta (C'')^{-1} C' \\ \mathbf{w} &\leftarrow \frac{\mathbf{w}}{|\mathbf{w}|} \end{aligned} \tag{8}$$

where C represents the new contrast function to be optimized.

Table 1. Constrained stICA Algorithm

Step 0: The observation matrix X contains the fMRI image sequence.
Step 1: Reduce the dimension of the observation matrix **X** using SVD. Find $\hat{\mathbf{U}}$ and $\hat{\mathbf{V}}$ according to equation 2.
Step 2: Generate reference signal from a priori information
Step 3: Zero mean and normalize the reference signal.
Step 4: Call the constrained ICA stage (equations 8) with $\hat{\mathbf{U}}$ or $\hat{\mathbf{V}}$ (depending upon the domain of reference used, spatial or temporal) and reference as the inputs. Upon convergence the output will be the independent source in the same domain as that of reference.
Step 5: To determine the corresponding independent source, find approximate of this source according to the following equation and used it as the reference for next stage. $\mathbf{r} = \hat{\mathbf{X}}((\hat{\mathbf{V}}\mathbf{w}_t)^t)^{-1}$, $\mathbf{r} = \hat{\mathbf{X}}(\mathbf{T}^t)^{-1}$ *or* $\mathbf{r} = \hat{\mathbf{X}}((\hat{\mathbf{U}}\mathbf{w}_s)^t)^{-1}$, $\mathbf{r} = \hat{\mathbf{X}}(\hat{\mathbf{S}}^t)^{-1}$ where $\mathbf{w}_t$ or $\mathbf{w}_s$ are the un-mixing vector found in step 4 and **T** or **S** is the independent source recovered at step 4.
Step 6: Zero mean and normalize the reference.
Step 7: Call the constrained ICA stage (equation 8) with $\hat{\mathbf{U}}$ or $\hat{\mathbf{V}}$ and reference from step 6 as the inputs. Upon convergence the output will be independent source corresponding to the independent source found in step 4.

IV. Results

The performance of the proposed constrained-stICA algorithm was tested using the simulated data set shown in Figure 1. As evident in the figure neither the temporal nor the spatial sources are independent. The results of spatial ICA and temporal ICA on the mixture of this simulated data set are shown in Figure 2 (only two output sources are shown). Both the spatial and temporal ICA tries to find independent sources at the cost of the sources in the corresponding domain, therefore sources in the corresponding domain get distorted. On the other hand constrained-stICA finds maximally independent sources in two stages with minimal inter domain affect. The results of constrained stICA are shown in Figure 3. It is evident from the Figure 3 that the results are superior to both the temporal and spatial ICA results.

For the fMRI data, a series of 60 FLASH images were acquired at twenty nine axial levels from four healthy persons. After several minutes of dark adaption, we asked each subject to open his eyes for 10 sec and then close for 10 sec

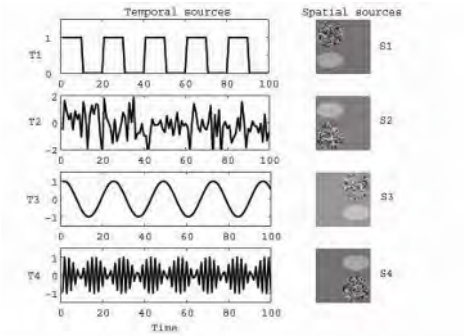
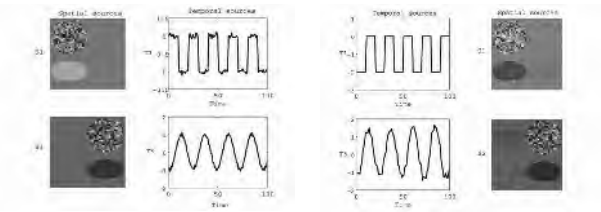


Fig. 1 Simulated temporal and spatial sources.



(a) (b)

Fig. 2 Sources recovered using (a) spatial and (b) temporal ICA and their corresponding sources

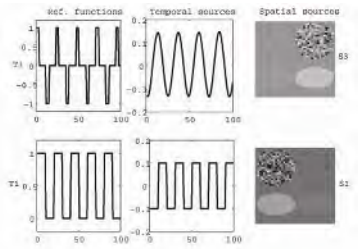


Fig. 3 Temporal (middle column) and spatial sources (right column) recovered with constrained stICA using different reference functions (left column)

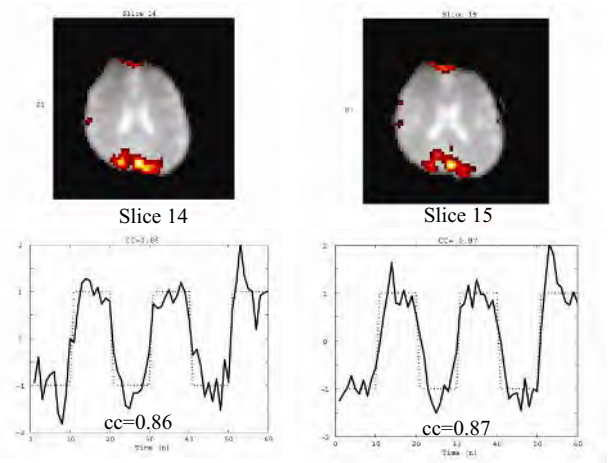


Fig. 4 Z-score maps of the spatial component and their corresponding time courses obtained with constrained-stICA

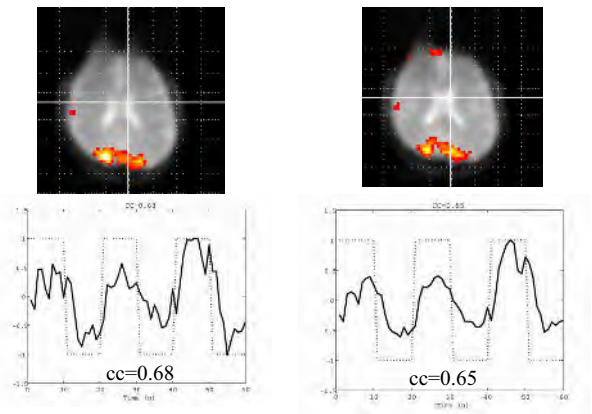


Fig. 5 Z-score maps of the spatial components and their corresponding time courses obtained with SPM

This cycle was repeated for 3 times. The collected data for each individual is normalized and realigned. The data from each individual was processed separately on a single volume basis. Each row of an observation matrix **X** contains an image. The ON-OFF stimulation is used as the initial reference. Independent spatial and temporal components are recovered according to the algorithm in Table 1. Once a component map is recovered, it is converted to the z-map [6] according to the Equation 9.

$$z_{ij} = \frac{s_{ij} - m_i}{\sigma_i} \geq threshold \tag{9}$$

where s_i is the component recovered, m_i the mean, and σ_i the standard deviation of the component.

The functional maps obtained from constrained-stICA are compared with those from SPM. The results for the slice 14 and 15 are presented in Figure 4 and Figure 5. The spatial ICs found by constrained-stICA indicate some frontal activities, missed by SPM,. Also, the recovered time courses have high correlation with the ON-OFF stimulation reference (cc = 0.86 ~ 0.87) compared to SPM (cc = 0.65 ~ 0.68) results. The results indicate that the proposed constrained stICA may be a more effective method for fMRI data analysis.

V. Conclusions

In this study a new algorithm, constrained-stICA is proposed. The method tries to find the desired independent spatial and temporal components by incorporating a priori information. The results of the proposed algorithm on the simulated data and fMRI data are presented.

Acknowledgment

This research was supported by the MKE (Ministry of Knowledge Economy), Korea, under the ITRC (Information Technology Research Center) support program supervised by the IITA (Institute of Information Technology Advancement) (IITA-2008-C1090-0801-0002).

References

1. Bell A J, Sejnowski T J (1995) An information-maximization approach to blind separation and blind deconvolution. Neural Computation 7:129–1159
2. Hyv¨arinen A, Oja E (1997) A fast fixed-point algorithm for independent component analysis. Neural Computation 9:483–492
3. Calhoun V D, Adali T, Pearlson G D, Pekar J J (2001) Spatial and temporal independent component analysis of functional MRI data containing a pair of task related waveforms. Human Brain Mapping 13:43–53
4. Jung T P, Makeig S, Westerfeld M, Townsend T, Courshesne E, Sejnowski T J (2001) Analysis and visualization of single-trial event-related potentials. Human Brain Mapping 14(3):166–185.
5. Rasheed R, Myung H In, Lee Y-K, Lee S Y, Lee S Y, Kim T-S (2006) Constrained ICA Based Ballistocardiogram and Electro-oculogram Artifacts Removal from Visual Evoked Potential EEG Signals Measured inside MRI: 1088-1097
6. McKeown M J, Makeig S, Brown G G, Jung T P, kindermann S S, Bell A J, Sejnowski T J (1998) Analysis of fMRI data by blind separation into independent spatial components. Human Brain Mapping 6:160–188
7. Pekar J J (2006) A brief introduction to functional MRI – history and today's developments. IEEE Engineering in Medicine and Biology Magazine 25(2):24–26
8. Stone J, Porrill J, Porter N, Hunkin N (2000). Spatiotemporal ICA of fMRI data. Computational Neuroscience Report, 202.
9. Lu W, Rajapakse J C (2005) Approach and application of constrained ICA. IEEE Transactions on Neural Networks 16(1):203–212

Address of the corresponding author:

Author: Tae-Seong, Kim
Institute: Kyung Hee University, Dept. of Biomedical Engineering
Street: 1 Seocheon-dong, Giheung-gu
City: Yongin-si
Country: Republic of Korea
Email: tsim@khu.ac.kr

ARGALI : An Automatic Cup-to-Disc Ratio Measurement System for Glaucoma Analysis Using Level-set Image Processing

J. Liu[1], D.W.K. Wong[1], J.H. Lim[1], H. Li[1], N.M. Tan[1], Z. Zhang[1], T.Y. Wong[2], R. Lavanya[2]

[1] Institute for Infocomm Research, A*STAR, Singapore
[2] Singapore Eye Research Institute, Singapore

Abstract — **Glaucoma is a leading cause of blindness worldwide, accounting for 12.3% of the permanently blind according to the World Heath Organization. The disease is particularly prevalent in Asia, with up to 50% of total glaucoma cases found in the region. Although glaucomatous damage is irreversible, studies have shown that early detection can be effective in slowing or halting glaucomatous atrophy. The ratio of the size of the optic cup to the optic disc, also known as the cup-to-disc ratio (CDR), is an important indicator for glaucoma assessment, since glaucomatous progression corresponds to increased excavation of the optic cup. In current clinical practice, the CDR is measured manually and can be subjective, limiting its use in screening for early detection. We describe the ARGALI system which automatically calculates the CDR from non-stereographic retinal fundus photographs, providing a fast, objective and consistent measurement. The ARGALI system consists of a series of steps. As the optic disc occupies only a small region of the entire retinal image, a region of interest is first extracted via pixel intensity analysis. Variational level-set algorithm is next used to segment the optic disc. Optic cup segmentation is more challenging due to the cup's interweavement with blood vessels and surrounding tissues. A multi-modal approach consisting of different methods is used extract the cup. To obtain a smoother contour, ellipse fitting is applied to the extracted cup and disc. A neural network has also been proposed to fuse the results obtained via the various modes. The ARGALI system was tested using images collected from patients at the Singapore Eye Research Institute and achieves an RMS error of 0.05 with a risk assessment accuracy of 95%. The results are promising for ARGALI to be developed into a low cost, objective and efficient screening system for automatic assessment glaucoma risk assessment.**

Keywords — **cup-to-disc ratio, level set, glaucoma**

I. Introduction

Glaucoma is a leading cause of blindness and is characterized by the progressive loss of axons in the optic nerve. From the World Health Organization's Global Data Bank on Blindness[1], glaucoma accounts for 5.1 million out of an estimated 38 million blind people, or about 13.4%, worldwide. It is expected that by 2010, there will as many 60 million glaucoma cases globally. Moreover, due to the close association of glaucoma with age, as the aging population rapidly increases, glaucoma morbidity will rise as well, resulting in increased health care costs and economic burden. In the Tanjong Pagar Study[2] conducted in 1996-97 in Singapore, the age-standardized prevalence of glaucoma was found to be 3.2% in the 40 years and older population. There is no cure for glaucoma, as damage to the ganglion cells is permanent and as yet is irrecoverable. However, with early detection, the advancement of glaucomatous optical neuropathy can be significantly slowed or even halted. Mass screening is thus critical to prevent the further development of glaucomatous damage in a person.

A classic feature of glaucoma is the specific abnormal appearance of the optic nerve head: cupping or excavation of the optic disc, with loss of the neuroretinal rim, typically seen as an enlargement of the optic disc cup to disc ratio (CDR). The cupping of optic nerve head corresponds to increased ganglion cell death, and thus the CDR can be used as a measured of the risk factor for glaucoma. However, a screening test for glaucoma with high accuracy has yet to be developed. In current clinical practice, the CDR is measured manually by an ophthalmologist and is subjective due to differences in intra-observer experiences and training. The reliance on manual efforts restricts the use of the CDR for deployment in mass screening.

Some efforts have been reported in the development of methods for the automatic segmentation of the optic cup and disc from retinal fundus images, with more reports [3,4] on the automatic segmentation of optic disc, but with fewer on [5,6] on optic cup detection due to the cup's interweavement with blood vessel and surrounding tissues. A model-based approach for automated feature extraction in fundus images was previously proposed by Li. H, et al [3]. Optic disc shape detection is done using a modified active shape model (ASM). A disc boundary detection rate of 94% was attained on 100 datasets collected by the authors. No cup and CDR calculation were done in this paper. Automatic segmentation of the papilla in a fundus image based on the C-V model and a shape restraint was proposed by Y. Tang etc [4]. Optic disk detection achieves 94% fully satisfactory image using a database containing 50 color fundus images, including 20 low contrast ones, but no Cup and CDR calculation were done in this paper. The development of a simple diagnostic method for glaucoma using ocular

Chwee Teck Lim, James C.H. Goh (Eds.): ICBME 2008, Proceedings 23, pp. 559–562, 2009
www.springerlink.com

fundus pictures was proposed by Naoto Inoue, etc [5], which describes using discriminatory analysis to decide thresholds, and subsequently utilizes these to segment the cup and disc. Although the Cup-to-Disc Ratio (CDR) was measured in this paper, no clear results are given and the image sets used for testing is not clearly described. A method to diagnose glaucoma via optic disk feature extraction via modified deformable model technique was proposed by Xu et al [6]. Disc and cup segmentation were conducted in the paper and the CDR was also calculated. The optic disc center is found by applying the Circular Hough Transformation, and subsequently the disc boundary detection is done through active shape model (ASM) by defining 72 points around the disc following which an energy expression was used to deform the contour.

The ARGALI (Automatic cup-to-disc Ratio measurement system for Glaucoma Analysis using Level-set Image processing) system is developed through inter-disciplinary collaborative efforts between clinician ophthalmologists and computer scientists. It aims to be a novel, state-of-the-art, diagnostic system for glaucoma screening. ARGALI also aims to compliment clinical practices and advance the latest intelligent medical image processing based glaucoma diagnosis algorithm using 2D retinal fundus images which can be obtained through the use of existing, commercially available, low-cost equipment.

In this paper, we present the ARGALI system and report on the experiments and results obtained. Section II provides a description of the various processes involved in ARGALI. Subsequently, in Section III, an experiment is run to determine the performance of ARGALI on a sample of retinal images obtained from the Singapore Eye Research Institute and the results of the experiment are presented. The final section presents the conclusions and future directions.

II. ARGALI

The ARGALI system as shown in Figure 1 is to be developed into a cost effective diagnosis system which will be of clinical significance for glaucoma screening, diagnosis and analysis. Through an innovative fusion of various image processing technologies and clinical experiences, ARGALI is able to automatically calculate the CDR from retinal photographs, providing a fast, objective and consistent measurement with potential for mass screening.

In order to calculate the CDR, the cup and disc boundaries are segmented in ARGALI. As shown in Figure 1, the variational level-set algorithm, which is based on global optimization concepts, is used to segment the disc boundary and extract the optic disc region from the retinal image. Segmentation of the optic cup is more challenging than the optic disc due to the optic cup's interweavement with blood vessel and surrounding tissues. An innovative technique to extract the cup is proposed, in which a multi-modal approach is employed. A color histogram analysis of the image is first carried out, and is subsequently followed by the application of level-set algorithms to segment the cup boundary. The segmented cup is then smoothened using ellipse fitting. Finally, adaptable neural networks are to be trained to fuse the cup-to-disc calculation results from the level-set algorithms as well as the results after different smoothing processes.

The complete process is capable of producing a CDR result in a few seconds which makes the system attractive for screening large numbers rapidly and efficiently. This learning mechanism integrates the knowledge embedded in the clinical practice and provides an optimal CDR for the glaucoma screening, diagnosis and analysis. The complete process can be divided into the following 6 steps. A more detailed description of the processes is described in [7].

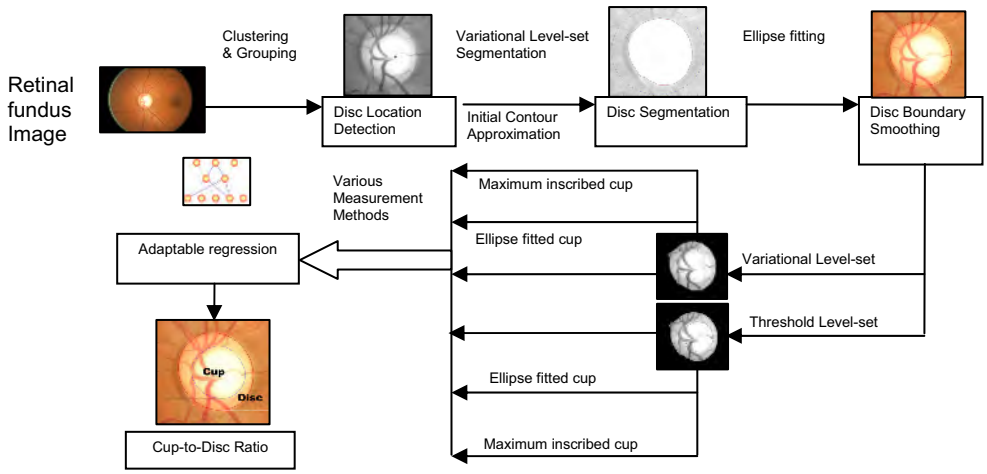


Figure 1.

A. Disc Segmentation

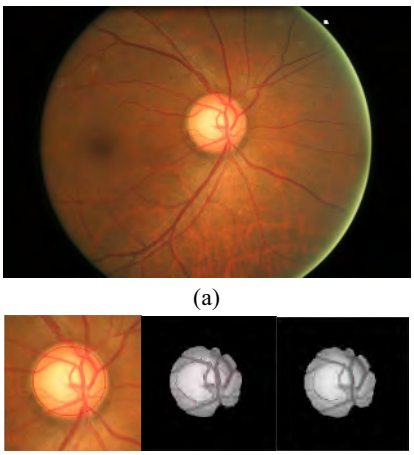
For a typical retinal fundus image obtained from the Singapore Eye Research Institute (SERI), the image resolution is approximately 3072 x 2048. However, the size of the optic disc, and cup, typically takes up less than 10% of the entire retinal image. Although the whole image can be analyzed to obtain the cup and the disc, region of interest (ROI) localization would help to significantly reduce the computational requirements and improve the accuracy of segmentation by focusing the efforts on an approximate region. Using the physiological characteristic of the optic disc being of a higher intensity than the surrounding retinal area, histogram-based analysis, whereby the pixels corresponding to the top 0.5% of the cumulative intensity distribution is pre-selected as preliminary feature points. Subsequently, the retinal image is subdivided into 64 regions, and an approximate ROI centre is selected based on the region containing the highest number of pre-selected pixels. Following this, the ROI is defined as a rectangle around the ROI centre with dimensions of twice the typical optic disc diameter, and is used as the initial boundary for the optic disc segmentation.

B. Disc segmentation

The variational level-set algorithm [8] is applied to the fundus image to detect the disc boundary using the optimal color channel as determined by the color histogram analysis and edge analysis in the ARGALI framework. Variational level-set is based on global processing concepts which analyze the entire image in order to find the globally optimum boundary for the disc. Unlike traditional level-set algorithms which need periodic re-initialization to avoid shocks during the level-set process, the variational formulation avoids this by introducing an energy term to keep the evolving level-set function close to a signed distance function, in this way avoiding errors in segmentation due to shocks and discontinuities from the re-initialization process.

C. Boundary smoothing of detected disc

Despite the use of a global optimization technique, the disc boundary detected by level-set in this step may not represent the actual shape of the disc, as the disc boundary can be affected by a remarkable number of blood vessels entering the disc. This can often result in sudden changes in curvature. To avoid this, ellipse fitting [9] is applied to reshape the obtained disc boundary. Ellipse fitting helps to smooth the sudden changes of curvature in the boundary caused by blood vessels and helps to find the ellipse with minimum error to fit the disc boundary.



(a) (b) (c) (d)

Figure 2. (a) Original fundus image, (b) Segmented disc boundary (red line), (c) segmented cup (red line) and (d) ellipse-fitted cup (red line)

D. Cup segmentation

Cup boundary segmentation is more challenging than disc segmentation due to the cup's much intensive interweavement with blood vessels and surrounding tissues. Furthermore, the transition between the cup and the rim is often not as prominent as that at the disc boundary. In this paper we make use of the threshold-initialized level-set function in ARGALI. In threshold-initialization-based level set, the green channel of the extracted optic disc is processed using histogram analysis to determine a threshold value which segments out the pixels corresponding to the top 1/3 of the grayscale intensity was used to define the initial contour in the ROI. Next, the level set formulation discussed earlier was employed to the initial contour to segment the optic cup. Previously, other methods were also compared with level-set for optic cup segmentation, and it was found that use of level-set method provides increased accuracy for cup segmentation [7]

E. Boundary smoothing of detected cup

After the threshold level-set algorithm is applied to obtain the cup boundary, an additional post-processing step using ellipse fitting is employed to eliminate some of the obtained cup boundary's sudden changes in curvature. Ellipse fitting is especially useful when portions of blood vessels in the neuro-retinal rim outside the cup are included within the detected boundary.

F. Learning Network-based Intelligent Fusion

An adaptable multi-layer neural network has also been proposed in the last stage of ARGALI. Using various meth-

ods for cup and disc segmentation, a neural network is to be trained using clinical data, with the clinical ground truth to be set as the target value. The inputs to the neural network correspond to the CDR results obtained from the different individual methods. By training the neural network to optimize the weights of the various inputs, the system hopes to integrate the individual results in an optimal way, integrating the knowledge embedded in the clinical practice to provide an optimal CDR value. This aspect of ARGALI is not explored in the scope of this paper but will be done so in future reports.

III. Experimental results

In our previously reported work [7], we tested some of the component algorithms on a sample of retinal images from normal patients. For this paper, we obtained a sample set of 23 retinal images of patients which have been verified as suffering from glaucoma from the Singapore Eye Research Institute to test the ARGALI system. For the ground truth, we make use of the clinician assessment of the CDR_{clinic}. The image set of 23 glaucoma patients was processed using ARGALI and the calculated CDR using ARGALI is defined as CDR_{clinic}. The results are presented in Figure 3(a). Based on these results, the correlation coefficient was calculated and found to be 0.89, indicating a close correlation between the ARGALI-obtained results and the clinical ground truth.

The error, defined as the difference between the calculated CDR and the clinical ground truth, $Error = CDR_{ARGALI} - CDR_{clinic}$ was also calculated and the results are plotted in Figure 3(b). It can be readily observed from the results in Figure 3(b) that the maximum error for the CDR results obtained by ARGALI is less than 0.1 CDR units, with the root mean square error calculated to be approximately 0.05. Furthermore, using a clinically-derived value of a CDR more than 0.65 to assess a patient as a possible glaucoma case, the ARGALI system was able to correctly identify 95% of the cases, or 21 out of 22. It was observed that one of the patients had been clinically diagnosed as having glaucoma although the clinical CDR is less than 0.65. Despite this, the ARGALI system was still able to determine the CDR relatively close to the clinical value for this patient (CDR_{clinic}=0.55; CDR_{ARGALI}=0.5687).

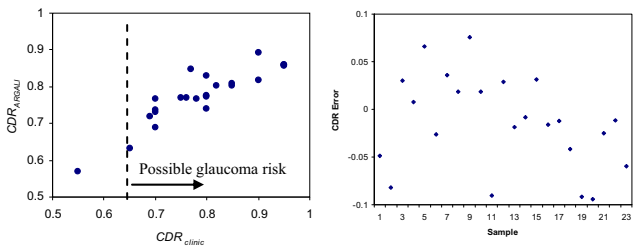


Figure 3. (a) Comparison between CDR_{clinic} and CDR_{clinic}. The correlation coefficient was calculated to be 0.89. Note the patient with a CDR less than 0.65 but still clinically diagnosed as having glaucoma. (b) Error between CDR_{clinic} and CDR_{clinic}. The maximum error is 0.1 CDR units and the RMS error was calculated to be 0.05.

IV. Conclusions

An innovative system integrating existing and new image processing technologies, intelligent fusion technology and clinical experiences is developed and proposed in the paper. The proposed ARGALI system automatically calculates the CDR from retinal photographs, and provides a fast, objective and consistent measurement with potential for screening. The technological novelty and promising experimental results demonstrate ARGALI's potential to be developed into a low cost and efficient glaucoma mass screening system. We will further enhance the performance of the system with more clinical input and validation, as well as to incorporate machine learning aspects into future.

References

1. World Health Organisation: Magnitude and Causes of Visual Impairment, http://www.who.int/mediacentre/factsheets/fs282/en/index.html, 2002
2. Foster P. J., Oen F. T. S., Machine D., Ng T.-P., Devereux J. G., Johnson G. J., Khaw P. T., and Seah S. K. L. (2000). The Prevalence of Glaucoma in Chinese Residents of Singapore: A Cross-Sectional Population Survey of the Tanjong Pagar District. Arch Ophthalmol, vol. 118, pp. 1105-1111, August 2000.
3. Li H., Chutatape O. (2003) A model-based approach for automated feature extraction in fundus images. In Proc. of the 9th IEEE International Conference on Computer Vision, Nice, France, 2003.
4. Tang Y., Li X., Freyberg A., Goch G. (2006) Automatic segmentation of the papilla in a fundus image based on the C-V model and a shape restraint. In Proc. of the 18th International Conference on Pattern Recognition, Hong Kong, 2006.
5. Inoue N., Yanashima K., Magatani K., Kurihara K. (2005) Development of a simple diagnostic method for the glaucoma using ocular fundus pictures. In Proc. of the 27th IEEE engineering in medicine and biology annual conference, Shanghai, China, 2005.
6. Xu J., Chutatape O., Sung E., Zheng C., Kuan P. C. T. (2007). Optic disk feature extraction via modified deformable model technique for glaucoma analysis. Pattern Recognition 40 2063-2076, 2007.
7. Li C., Xu, C., Gui C., Fox M. D. (2005) Level set evolution without re-initialization: a new variational formulation. In Proc. of the 2005 IEEE Computer Society Conference on Computer Vision and Pattern Recognition, San Diego, USA, 2005.
8. Liu J., Wong D.W.K., Lim J.H., Li H., Jia X., Yin F., Xiong W. (2008). Optic Cup and Disk Extraction from Retinal Fundus Images for Determination of Cup-to-Disc Ratio. IEEE Conference on Industrial Electronics and Applications. Singapore, 2008.
9. Fitzgibbon A., Pilu M., Fisher R. B.. Direct least-squares fitting of ellipses. IEEE Transactions on Pattern Analysis and Machine Intelligence, 21(5), 476--480, May 1999.

Validation of an In Vivo Model for Monitoring Trabecular Bone Quality Changes Using Micro CT, Archimedes-based Volume Fraction Measurement and Serial Milling

B.H. Kam[1], M.J. Voor[2], S. Yang[3], R. Burden, Jr.[2] and S. Waddell[2]

[1]School of Applied Science, Republic Polytechnic, Singapore, Singapore
[2]Department of Orthopedic Surgery, University of Louisville, Kentucky, USA
[3]Med Institute Inc, IN, USA

Abstract — **A combination of three techniques – high resolution computed tomography (micro CT) scanning, Archimedes-based volume fraction measurement and serial sectioning or milling – were used to determine the volume fraction as a measurement of trabecular bone quality changes in rabbit distal femur. The objective of this study was to develop the capabilities of micro CT scanning and micro CT image segmentation based on a slice-by-slice global thresholding technique to investigate trabecular microstructural changes in vivo and in vitro. These results were validated within the in vivo and invitro scans at the same time, and validated with the Archimedes-based volume fraction measurements and serial sectioning experiments. A total of six six-month-old New Zealand white rabbits were utilized in this study. The rabbits were scanned twice in vivo seven days a part and all of the left and right femurs (medial and lateral) were scanned in vitro. All micro CT images were obtained at 28 µm (in vivo) or 14 µm (in vitro) nominal resolutions. Specimens from six left and right rabbit distal femurs (medial and lateral) were also measured based on Archimedes' principle and serial milling. These findings have shown that the in vivo and in vitro micro CT scanning are consistently repeatable while the accuracy of the serial milling to Archimedes-based volume fractions and the in vitro micro CT scanning to Archimedes-based were within ± 2.5% estimation respectively.**

Keywords — **micro CT, Archimedes', serial-miling, volume-fraction, trabeculae**

I. Introduction

High resolution micro computed tomography (micro-CT) has been utilized in the study of detailed structure for cancellous bone [1, 2]. The objective of this study was to demonstrate the accurate high-resolution micro-CT images of 3-D trabecular architecture (in vivo and in vitro) to Archimedes' based and serial sectioning technique. A volume fraction comparison was made to ensure the in vivo and in vitro scanning produced accurate results.

II. Materials and Methods

Six New Zealand white rabbits weighing approximately 4 to 5 kg were utilised in this study. The rabbits were scanned twice in vivo seven days apart and all rabbits were then sacrificed and the femurs were scanned again in vitro. The size of the rabbit distal femur and its position of scanning made it possible to obtain 28 µm and 14 µm (nominal resolution) micro-CT (Model ACTIS 200/225 Ffi-HR CT/DR system, BIR Inc., Chicago, IL with built-in X-ray system FXE 225.20, Fein Focus U.S.A.) scans in vivo and in vitro, respectively. The machine is equipped with a 225 KV x-ray source with a focal spot size of 5 µm. In addition, an anesthesia machine (Landmark Model VSA-2100, Hallowell Modeal 2000) was added to the micro-CT scanner such that in vivo scanning could be performed with the animals sedated to minimize unwanted motion.

For the invivo scanning, the rabbit was sedated with a cone mask under anesthesia as shown in Figure 1. The rabbit was completely sedated within 10 and 15 minutes before placing it in an animal holder. The femurs were excised, made into bone cubes and scanned in vitro. The in vitro scan was carried out in a smaller specimen holder. The in vivo scans consisted of 214 slices while the in vitro scans consisted of 428 slices spanning a six-millimetre distance from above the condylar notch to the bottom of the



Fig. 1 A set up of an in vivo micro CT scanning.

Chwee Teck Lim, James C.H. Goh (Eds.): ICBME 2008, Proceedings 23, pp. 563–565, 2009
www.springerlink.com

medial condyle (region of interest). The in vivo and in vitro images were cropped and rotated for the purpose of image registration. The two sets of data were registered using a custom registration algorithm technique written in MATLAB 7 looking for maximum mutual information to allow direct comparison. The same region of interest from both data sets were extracted and globally threshold slice-by-slice based on Otsu's method of thresholding isolating the bone tissue from the less dense material in the images.

After in vitro scanning, the bone cubes were cleaned using tricholoroethylene in an ultrasonic agitation for an hour followed by rinsing with a waterpik system (model WP-60W) at a pressure control speed of 60psi using about 500ml of water on all sides of the cube. The cleaning process was repeated five times to ensure marrow removal without trabecular damage. Volume fraction measurement was made based on Archimedes' principle.

Then, the cleaned bone cubes were stained black at room temperature by immersion in a 10% (wt) silver nitrate solution, first for 30 minutes in an ultrasound chamber and then for 20 hours. The bone cubes were rinsed and water was drained out and placed into 100% ethanol where they were exposed to 365nm UV light for 120 minutes giving the bone a deep black matted non-reflective colour. The bone cubes were then embedded in a bone embedding media. The serial milling was performed on a custom-made micro milling machine – Ultra-High-Precision Micro Milling with a computer-numeric-controlled (CNC) milling station.

III. Results

The volume fraction measurement is made on left medial (LM), left lateral (LL), right medial (RM) and right lateral (RL) for six rabbits. The volume fraction for lateral condyles between in vivo scans seven days apart (0.401±0.015, 0.397±0.021), between in vitro micro CT (0.352±0.035) and Archimedes (0.365±0.031) and between in vitro micro CT (0.352±0.035) and serial milling (0.369±0.031) were not significantly different. The medial condyles were also not significantly different between in vivo scans seven days apart (0.513±0.010, 0.515±0.011), in vitro micro CT (0.454±0.049), Archimedes(0.460±0.060) and serial milling (0.467±0.050) and it is also illustrated in Figure 2.

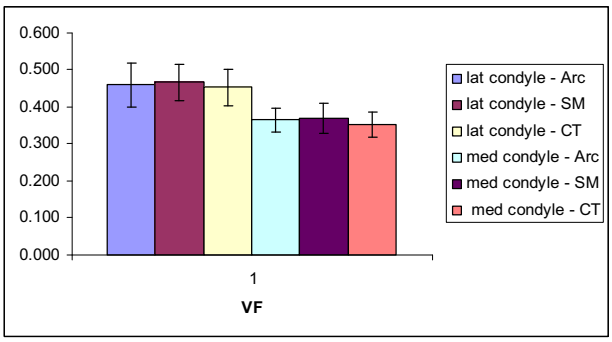


Fig. 2 Average values of volume fraction (VF) for lateral and medial among Archimedes (arc), serial milling (SM) and in vitro micro CT (CT) are shown with standard deviation (n = 11). The coefficient of variation in VF between Arc and SM ranged between 0.10% and 0.22%. The VF for lateral and medial condyles between CT and Arc and between CT and SM were not significantly different (p = 0.294, p = 0.649, p = 0.115, p = 0.118). The y-axis is unitless for VF.

IV. Discussions

Our studies have shown a consistency of in vivo to in vitro micro-CT scans within an acceptable accuracy of 1%. This shows that the micro CT scanning is consistently repeatable. The results between the in vitro micro CT and Archimedes-based volume fractions showed 2.5% underestimation and it is well within 4% [3]. Meanwhile, the results between the serial milling and Archimedes-based data showed 2.5% overestimation and it is well within 5% [4]. The accuracy of the in vitro micro-CT scan is also confirmed by the excellent agreement between our scan data and the Archimedes'-based and serial sectioning data as shown in Figure 3.

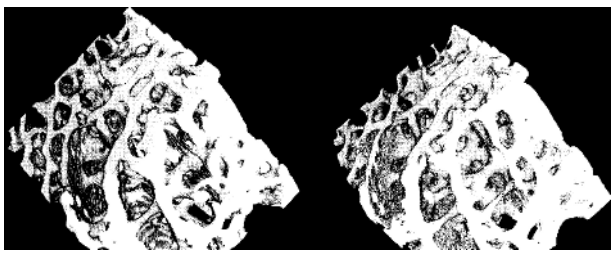


Fig. 3 Three dimensional image stacks of micro-CT (left) and serial sectioning (right)

V. Conclusions

The results in this study have demonstrated the reliability, sensitivity and consistency of in vivo and in vitro micro CT scanning. It indicates that the results of micro CT scanning are statistically comparable to those obtained from density measurement based on Archimedes' principles and serial milling experiments. With this validation, it proved the repeatability of the high resolution micro CT scanning can be used to investigate the trabecular micro structural changes within a living animal that is consistently achievable.

REFERENCES

1. Hildebrand T, Rüegsegger P: Quantification of Bone Micro-architecture with the Structure Model Index. Computational Methods Biomechanics Biomedical Engineering 1(1), 15-23, 1997.
2. Müller R, Van Campenhout H, Van Damme B, Van Der Perre G, Dequeker J, Hildebrand T, Rüegsegger P: Morphometric analysis of human bone biopsies; a quantitative structural comparison of histological sections and mico-computed tomography. Bone 23(1), 59-66, 1998.
3. Ding M, Odgaard A & Hvid I: Accuracy of cancellous bone volume fraction measured by micro-CT scanning. Journal of Biomechanics 32, 323-326.
4. Beck JD, Canfield BL, Haddock SM, Chen TJH, Kothari M & Keaveny TM: Three-dimensional imaging of trabecular bone using the computer numerically controlled milling technique. Bone 21(3), 281-287.

A Force Sensor System for Evaluation of Behavioural Recovery after Spinal Cord Injury in Rats

Y.C. Wei, M.W. Chang, S.Y. Hou, M.S. Young

Department of Electrical Engineering, National Cheng-Kung University, Tainan, Taiwan

Abstract — **In animal model, the feature of spinal cord injury is hindlimbs paralysis, muscle weakness, and a common complaint in humans, so the animal test is necessary for the neurology, pathophysiology study and development of drug therapies. Various methods had been developed and widely used to examine the motor function and behavioural recovery following the spinal cord injury of rats, most of these methods were observed by the observer, then converted the results into the score grade. This study is used to set up the measurement system, use the ground reaction force method to evaluate the hindlimb can support its weight or not and measure the ground reaction force of hindquarter. This system is microcontroller-based , can save the test data to the flash memory, and communication with the PC for save test data to disk and statistical analysis.**

Keywords — **spinal cord injury, behavioural recovery microcontroller-based**

I. Introduction

In the spinal cord injury (SCI), the behavioural response in animal models is relevant to the clinical signs of SCI in human patients. Therefore, it is necessary to have the tools to measure the behavioural function for evaluation the recovery following spinal cord injury in animal models.

According to the type of data collected, these measurement tools include: (1) endpoint measures, (2) kinematic measures, (3) kinetic measurements, (4) electrophysiological measurements [1,2,3], but most of these tools observed by observer. In order to eliminate the influenced by observer, this study is intend to design a quantitative and objective test system for evaluating behavioural recovery focus on hindlimbs and hindquarter of rats.

This system is made up of five force plate and each force plate use two strain gauge as force sensor, when the limbs of rat stand at correct force plate, user touch the any key on the PC, PC will record the test data to the disk for analysis. From the test data, we find the percentage of hindquarter force is decrement when the function of hindlimbs recovery gradually in rat.

II. Methods

A. System Design

This study is used to set up a microcontroller-based system for measure the ground reaction force of hindlimb and hindquarter after spinal cord injury in rats. The system consists of two major parts, one is the test apparatus and the other is control unit. Test apparatus is shown in Fig 1, and block diagram of the control unit is shown in Fig 2.

A general description of the system components and its operation follows.

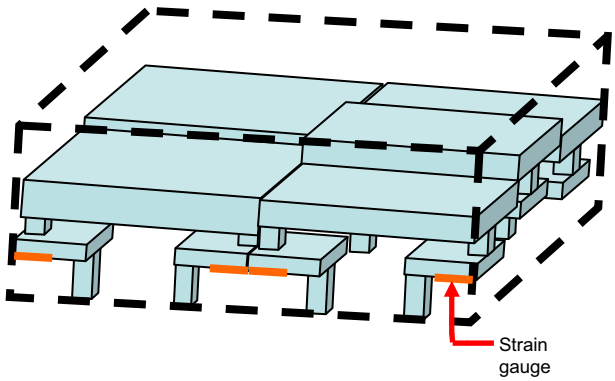


Fig 1. Apparatus of the inclined plane system

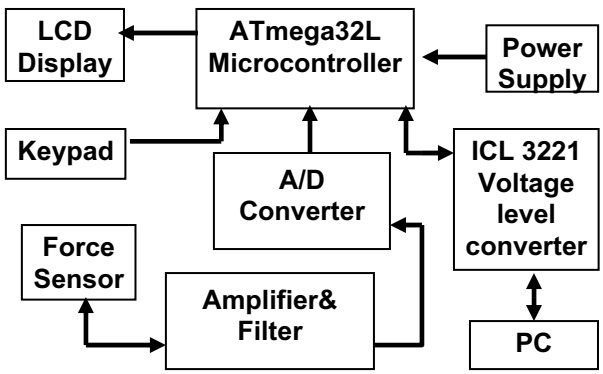


Fig 2. Block diagram of the control unit

Chwee Teck Lim, James C.H. Goh (Eds.): ICBME 2008, Proceedings 23, pp. 566–568, 2009
www.springerlink.com

1. Test apparatus

The test apparatus is 20cm*8cm*10cm (L*W*H) cuboid and made up of the black acrylic, five plate stick on the bottom to measure the vertical ground reaction force of the forelimbs, hindlimbs and hindquarter. Each force plate use the strain gauge stick on the acrylic, at the rear part the middle force plate is higher than the two sides force plate 0.5 cm. This arrange of force plate can detect the animal stance or not, and can measure the animal ground reaction force of the hindlimbs and hindquarter, when the animal squat.

2. Control unit

a. Hardware

a.1. AVR Microcontroller

The system is based on a ATmega32 microcontroller (ATMEL Corporation), it is a RISC architecture provides fast execution time. The ATmega32 includes four programmable ports, three external interrupt source, three timer/counter, one programmable serial USART, and 32K program memory size, 2K SRAM for data memory. The assignment of the various functions to the ports in theμC is shown in Table 1. The function of AVR microcontroller is read the keypad signal and start the A/D convert, then display the data to the LCD display and send data to PC.

Table 1. Assignment of port function in the μC

Port in microcontroller	Function
Port C	LCD data bus
Port A.0 – port A.1	Touch-button switch
PortA.5,6,7	LCD control bus
Port B.0,1	A/D chip selector
Port B.5,6,7	A/D interface bus
Port D.0,1	RS-232

a.2. Keypad

There are two push-button switch in the controller unit, when pushed by the user, the microcontroller start the A/D converter and display data on LCD display.

a.3. LCD Display

The LCD display is 2*20 characters and included backlight permits easy visualization of the display even in subdued light conditions. It's used to present the ground reaction force of limbs in rat .

a.4. RS-232 voltage lever converter

The input/output signals of the microcontroller are TTL levels. These are not compatible with the RS232 protocol, so need the RS-232 voltage level converter to change the TTL levels match the RS-232 protocol.

a.5. Force sensor

The force sensor is strain gauge, struck on the acrylic, so the rat stance on the acrylic, the strain gauge bended and change the output resister.

a.6. Amplifier and filter circuit

The strain gauge is connected to a bridge circuit, the bridge output is connected to the instrument amplifier and filter circuit. The circuit is used to amplify the force signal to the desired level and filter out the noise.

a.7. A/D converter

The A/D converter is 16 bits resolution and serial data out, used to change the analog signal (output signal of the amplifier and filter circuit) to the digital signal.

b. Software

The program on the AVR microcontroller was written by the C language and coding of the PC for data save and analysis was down in LabView.

B. Operation

When the measurement system is set up, verification is the first step, then take the rat into the acrylic box,and the hindlimbs on the two side force plate, the hindquarter on the middle force plate. If the system connect with PC through the RS-232, the force data can display on the display of the PC continuous, at the time the rat squat steady state, the user touch any key on the PC, the LabView program will save the data in the hard disk. If the system was controlled by the control unit only (No connect with the PC) , when the user press the key on the control unit, the only one test data will showed on the LCD display of the control unit.

III. Results

The prototype of this measurement system had finished, and is testing use the spinal cord injury rats. Fig 3 shows the results of the percentage of the hindquarter, and indicates the percentage of weight of hindquarter is decrement as the time increase. This is the preliminary results, right now, we do more test and verify this system can evaluate the behaviour recovery after spinal cord injury in rats.

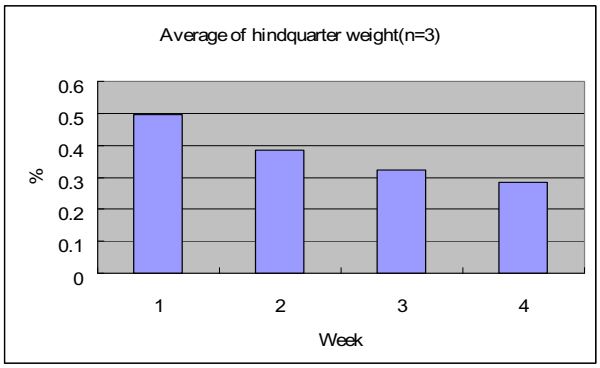


Fig 3. average percentage of hindquarter weight

REFERENCES

1. Metz G.A.S., Merkler D., Dietz V., Schwab M.E., Fouad K., (2000) Efficient testing of motor function in spinal cord inkured rats. Brain Res. 883 pp 165-177.
2. Muir G.D., Webb A.A. (2000) Assessment of behavioural recovery following spinal cord injury in rats. Eur J Neurosci 12 pp. 3079-3086.
3. Sedy J., Urdzikova L., Jendelova P., Sykova E., (2008) Methods for behavioural testing of spinal cord injured rats. Neurosci Biobehav R. 32 pp. 550-580
4. ATmega32 datasheet, ATMEL corporation.

Flow Imaging and Validation of MR Fluid Motion Tracking

K.K.L. Wong[1,3], R.M. Kelso[2], S.G. Worthley[3], P. Sanders[3], J. Mazumdar[1] and D. Abbott[1]

[1] Centre for Biomedical Engineering and School of Electrical and Electronic Engineering, University of Adelaide, SA 5005, Australia
[2] School of Mechanical Engineering, University of Adelaide, SA 5005, Australia
[3] Cardiovascular Research Centre and School of Medicine, Royal Adelaide Hospital and University of Adelaide, SA 5005, Australia

Abstract — **This paper presents flow results of a magnetic resonance imaging velocimetry system which relies on fluid motion estimation, and uses vorticity map differencing for calibrating its reliability. To validate this new concept, phase contrast magnetic resonance imaging on the right atrium of a healthy subject has been suggested. The study has demonstrated the state of change in blood flow patterns within a cardiac chamber using our implemented system and a well established flow imaging modality. Based on the gold standard imaging technique, flow fields can be used to establish a set of reference data to compare against magnetic resonance fluid motion tracking results. We conclude that our validated technique can be reliable enough for establishing a cardiac based velocimetry system.**

Keywords — **Phase contrast magnetic resonance imaging, Fluid motion tracking, Right atrium**

I. Introduction

Using a velocimetry framework that is different from velocity encoded medical imaging modalities, we implemented MR fluid motion tracking [1] which is based on motion estimation of blood signal shifts that appears as changes in intensity distribution over the entire registered signal image. The speed of the latter technique in terms of processing these images is dependent on the computational platform and the machine that runs it. A strong limitation, however, is the accuracy of the motion predication which is highly affected by the configuration of the algorithm as well as the clarity of signal contrast temporally. And it is the key purpose of this study to validate the output flow fields of MR fluid motion tracking against those produced by phase contrast magnetic resonance images.

For our implementation, we have developed a dual flow imaging and comparison system that enables processing of phase contrast data as well as MR fluid motion tracking of non-velocity encoded MR images. Since velocity flow field is limited in terms of flow analysis, vorticity measurement has been devised to present the strength of rotational blood in the heart chamber. In addition, we have described a concise flow visualisation system which encompasses flow imaging, flow vector presentation, and vorticity mapping, to analysis of vorticity pertaining to the imaged fluid.

Our article is organized as follows: Section II gives an overview of the system implementation for flow results comparison based on two imaging techniques. Section III provides the information on preparing a subject for MRI scanning and data analysis. The results of the two imaging modalities are displayed for selected time frames of a cardiac cycle in section IV. We give a discussion on the reliability of MR fluid motion tracking based on the flow results and in the last section, a conclusion of our implementations and findings.

II. Vorticity visualisation system implementation

A. MR Fluid Motion Tracking

A series of MR images are taken temporally as the fluid is in motion. The velocity of dynamic fluid can be quantified in real time by computing the shift of intensities within the quantised regions of every prior and post images numerically. A velocity flow field can be constructed using a graphical plot as such and other fluid dynamics properties can be derived from the velocity flow measurement. From the results, the characteristics of the fluid flow can be analysed using these properties.

Application of flow based on the use of motion estimation algorithm [2] allows us to produce flow vectors over the region of defined analysis. This technique makes use of images from two subsequent phases to predict flow field. Typically, cine MRI scanning results in a sequence of N phases. Post-processing of data from (N-1) pairs of images gives a series of vector fields for evaluation and analysis.

B. Phase Contrast MRI Velocimetry

Phase contrast MRI works on the concept that hydrogen nuclei from blood that has been exposed to magnetic fields accumulate a phase shift in spin that is proportional to blood velocity in x, y, and z directions [3,4] as shown in Fig. 1.

To quantify a velocity in one spatial dimension, at least two phase images has to be taken for subtraction of flow-induced phase shift from background phases caused by susceptibility-induced non-homogeneities and coil sensitivity changes [5]. Blood velocity can be aliased to an artifi-

Chwee Teck Lim, James C.H. Goh (Eds.): ICBME 2008, Proceedings 23, pp. 569–573, 2009
www.springerlink.com

cially low value if it exceeds the maximum velocity encoded (VENC) by flow sensitization gradients.

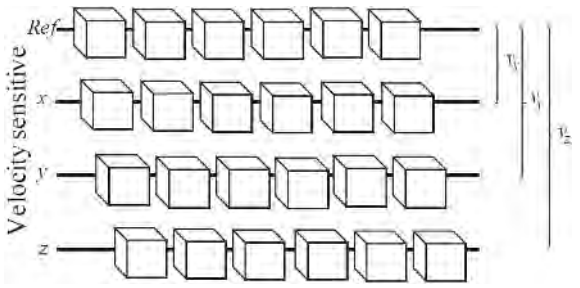


Fig. 1. Phase contrast MRI velocimetry. Velocities v_x, v_y and v_z can be calculated by subtraction of spin phase of measured volumes with that of the reference spaces *Ref*.

C. Visual tools for presentation of flow fields

The magnitude of vorticity ω (in units of s^{-1}) can be indicated by a colour contour map. Reconstruction of such a vorticity map as a colour image display can be achieved by representing vorticity using colours over a spatial grid. The presence of red pixels illustrates counter-clockwise swirling of blood while the blue ones correlate to clockwise swirl. Therefore, the colour and intensity of the image can give an indication of the magnitude of vorticity as well as the direction of rotation over a region.

D. Vorticity Field Differencing

Using Fig. 2, we demonstrate the systematic implementation of vorticity field differencing based on four stages.

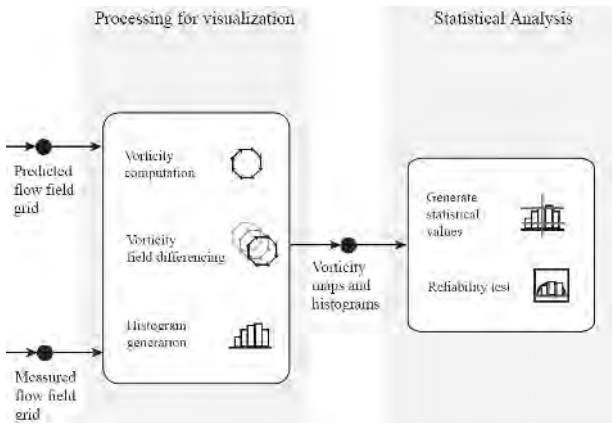


Fig. 2. Reliability test system for MR fluid motion tracking based on vorticity differencing. This system is specially constructed to calibrate the performance of MR fluid motion tracking against the well-established phase contrast MR image velocimetry system.

The first stage starts with scanning of a normal heart with steady-state free precession MR imaging and on a separate occasion, the same scanning using phase contrast MR imaging. During this pre-processing stage, blood motion information is encoded within images in a different manner. The cardiac MR images contain temporal positions of magnetic resonating blood, whereas the phase contrast images have local blood velocities encoded within them. In the visualisation processing stage, both field grids are further processed to give their respective vorticity field, which are then differenced.

III. Methodology

A. Subject for Case Study

In this study, we performed flow imaging on the right atrium of a 22 years old normal subject using phase contrast VENC flow imaging, and then using MR fluid motion tracking. The flow information from these two types of imaging can be used to explain the behaviour of vortices that develop in the right atrium of a heart.

B. Investigation Procedure

A scan is performed at the section of the heart where the atria are positioned. The scan section is taken at a location shown in Fig. 3 whereby the scan is perpendicular to an axis joining the top of the heart to the apex through the septum. Table I is created to configure the flow velocimetry system so that the tracking can be effected.

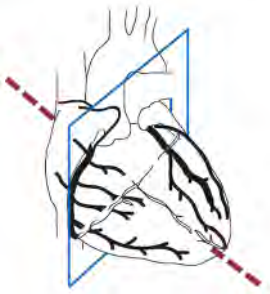


Fig. 3. MRI scan through heart of normal subject. The scanning of the heart is taken at short axis and through two chambers, namely the left and right atria. Therefore this sectional view pertains to the 2-chamber short axis scan.

C. MRI Scan Procedure

The velocity-encloded MR imaging was performed using a Siemens Avanto, 1.5 Tesla, model—syngo MRB15 scan-

ner with Numaris—4, Series No: 26406 software. Cine-MR imaging was performed using one slice in short axis views through the atria. All images were acquired with retrospective gating and 25 phases (from t=1 to 25) for a single slice.

D. Phase Contrast MRI Scan Procedure

For this purpose, velocity-encloded MR imaging was performed using a Siemens Sonata, 1.5 Tesla, model—syngo MR 2004A scanner with Numaris—4, Series No:

Table 1 MR imaging and vorticity measurement properties. The scan properties of standard True FISP and phase contrast MR imaging are presented here. The vorticity flow maps can be determined from them. These parameter values are used to calibrate these flow maps, as well as indicating the sampling vorticity mask size in metric units.

1 - TRUE FISP MRI SCAN		2 - PHASE CONTRAST MRI SCAN		
Symbol	Quantity	1	2	Units
p	Pixel spacing	1.67	1.54	mm/pixel
t_s	Trigger time interval	35.72	29.43	ms
s	Slice thickness	6	6	mm

VORTICITY MEASUREMENT PARAMETERS			
Symbol	Quantity	Value	Units
X	Image width	120	pixel
Y	Image height	150	pixel
W_v	Velocity interrogation window	3x3	pixel

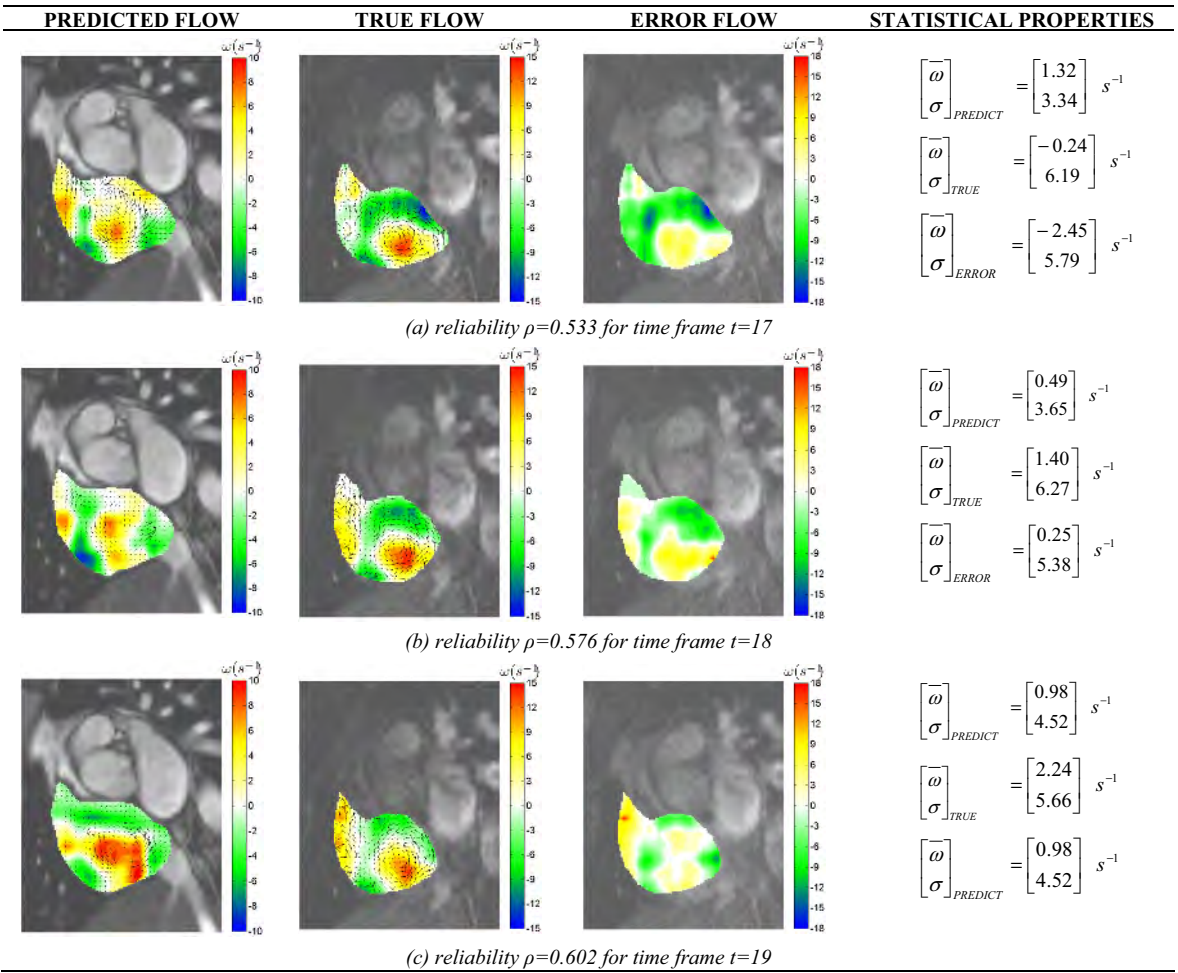


Fig. 4. *Vorticity differencing based on MR fluid motion field and phase contrast MR image field.* Predicted flow fields are verified against the measured ones based on phase contrast MRI velocimetry (taken as true data). Their vorticity map differences can be taken as the deviation of MR fluid motion field from the true flow field. We have performed flow field differencing using time frames t=[17,18,19] out of 25 frames in a cardiac cycle.

21609 software. Cine-MR imaging was performed using one slice in short axis views through the atria. All images were acquired with retrospective gating and 25 phases.

E. Parameters for Data Analysis

The histogram of a vorticity map with vorticity values in the range [0, *L*-1] is a discrete function $h(r_k) = n_k$, where r_k is the kth vorticity value and n_k is the number of pixels in the flow map having vorticity value r_k [6].

Statistical quantification of the blood vorticity map in the right atrium is performed by translating all the scalar values into histogram format. The size of right atrium is different for every phase. Normalization is performed by standardizing the total count of pixels within a segmented region of interest to create an equal integral area under the frequency plot of the flow map. The total counts correspond to the number of pixels representing the atrium per slice.

IV. Results

We varied this parameter from (3×3) to (33×33) pixels with increments of 2 pixels at each interval to chart the reliability of flow measurement using MR fluid motion tracking versus phase contrast MR imaging technique. From Table 1, the width of flow image is 120 pixels, and we have set the interrogation window to a 3 by 3 pixels frame. We observed vorticity flow maps pertaining to time frames t=[17,18,19] out of a maximum of 25 frames in a cardiac cycle for a series of sampling window sizes in Fig. 4.

V. Discussion

In this study using a normal atrium, we assume that the true-score variance σ_{TRUE}^2 is the equivalent of the vorticity variance based on a true map measured by phase contrast MRI. We note that the error variance with the expression σ_{ERROR}^2 is the variance of an error map which is produced by differencing the predicted and true vorticity maps. The reliability of flow field prediction using MR fluid motion tracking ρ is the ratio of true vorticity variance σ_{TRUE}^2 to total measured variance given by $(\sigma_{TRUE}^2 + \sigma_{ERROR}^2)$ [7]:

$$\rho = \sigma_{TRUE}^2 / (\sigma_{TRUE}^2 + \sigma_{ERROR}^2) \quad (1)$$

Implementing an appropriate sampling window size for vorticity measurement can bring the vorticity maps to be as close as possible to the physically measured one.

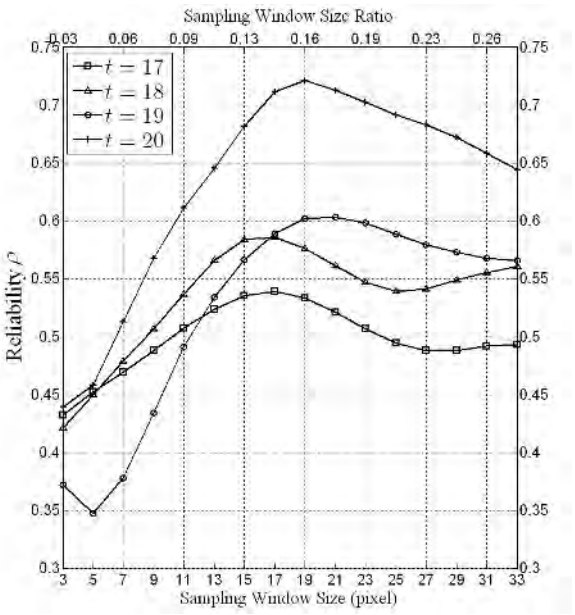


Fig. 5. Reliability study using predicted and true variance. Reliability for the predicted MR fluid motion field data ρ with respect to the phase contrast MRI data (taken as the true data) is computed. The variation of vorticity sampling window size can affect the reliability of computational measurement of the vorticity.

The graph of reliability measurement is shown in Fig. 5 for sampling window dimension of (3×3) to (33×33) pixels. The results are based on 4 cardiac time frames from t=17 to 20 to illustrate variation of measurement reliability.

VI. Conclusion

We have successfully studied one chamber at this stage. The framework developed in this work can be extended to assess flow in the other heart chambers or cardiovascular structures. This study has improved our understanding of blood motion within the heart chamber, which may have implications in the study of blood circulation efficiency.

Considering that the True FISP and phase contrast magnetic resonance imagings are performed on separate occasions with slight dissimilarities in planar imaging configuration, perfect alignments of the right atria region is difficult. Based on this discrepancy, we have to take into account additional error contributed by the imperfect comparison scheme. Therefore, the results suggest that MR fluid motion tracking is reliable enough for cardiac flow assessment.

REFERENCES

1. Wong KKL, Kuklik P, Worthley SG, Sanders P (2007) Flow analysis, International (PCT) Patent Application, PCT/AU/2007/000827
2. Bouguet JY (2000). Pyramidal implementation of the Lucas Kanade feature tracker, Technical report, OpenCV documentation, Micro-processor Research Labs, Intel Corp
3. Gatehouse PD, Keegan J, Crowe LA et al. (2005) Applications of phase-contrast flow and velocity imaging in cardiovascular MRI, Eur Radiol, 15:2172–2184
4. Yang GZ, Mohiaddin RH, Kilner PJ, Firmin DN (1998) Vortical flow feature recognition: A topological study of in-vivo flow patterns using MR velocity mapping, JCAT, 22:577–586
5. Baltes C, Kozerke S, Hansen MS et al. (2005) Accelerating cine phase-contrast flow measurements using k-t BLAST and k-t SENSE, *Magn Reson Med*, 54(6):1430–1438
6. Gonzalez RC, Woods RE (2002) Digital Image Processing, 2nd edition, Prentice-Hall, Inc., New Jersey, USA
7. Bohrnstedt G. (1983) Measurement, Handbook of Survey Research, (eds Rossi, P., Wright, K. & Anderson, A.), Academic Press, NY.

High Frequency Electromagnetic Thermotherapy for Cancer Treatment

Sheng-Chieh Huang[1], Chih-Hao Huang[2], Xi-Zhang Lin[2,3], Gwo-Bin Lee[1,3]

[1] Department of Engineering Science, Cheng Kung University, Tainan, Taiwan
[2] Department of Internal Medicine, Cheng Kung University, Tainan, Taiwan
[3] Institute of Nanotechnology and Microsystems Engineering, National Cheng Kung University, Tainan, Taiwan

Abstract — **Background/Aim: Electromagnetic thermotherapy is a new modality for cancer treatment. It applies a high-frequency electrical current to generate a magnetic field and heat up magnetic materials for treating targeted cancers. Using such system, we treat big tumors (more than 1.5 cm in diameter) in a colon cancer bearing murine model.**

Material and Methods: The high-frequency electromagnetic machine has an input of 220V-55A-60Hz. The output frequency and power are 40 kHz and 20 kW, respectively. The magnetic materials are fine needles made of stainless steel. We used agarose gel and porcine liver for thermo-dosimetry *in vitro* and *ex vivo*. During the experiments, IR camera was used to detect the temperature distributions. In an animal model, BALB/C mice were implanted with CT-26 colon cancer cells subcutaneously over their back. After the tumor size grew bigger than 15mm x 15mm, mice were divided into two groups randomly. Group I (n=8) were put in the magnetic field for twenty minutes as a control group. Group II (n=15) were inserted with fine needles into the tumor and magnetic field was used to treat the tumors for twenty minutes.

Results: From IR thermography, the needles in a matrix can achieve better temperature distributions in the targeted area than that from a needle alone. In the animal model, the survival rate achieved 90% in the treated group and no residual tumors over their back at the end of observation (60 days); while in the control group, the survival rate on the 45th day was 0%.

Conclusion: Our experiments showed that using high frequency electromagnetic thermotherapy is very effective to treat big tumors in the animal model, and our method has great potential for future clinical applications.

Keywords — **Thermotherapy, Superparamagnetic, Nanoparticles, Thermography, Matrix**

I. Introduction

Superparamagnetic nanoparticles can enhance localized temperature high enough to ablate focal lesions. Therefore, instead of using systemic hyperthermia, targeting hyperthermia using these superparamagnetic nanoparticles under a high-frequency magnetic field seems promising and warrants extensive investigation [1]. The nanoparticles are heated up by the hysteresis energy loss and eddy-current energy loss under an alternating magnetic field. By this means, magnetic nanoparticles can generate large amounts of heat to kill cancer cells [2]. However, It is very difficult to keep nanoparticles in situ after injection to the target; and they may disperse unevenly in big tumors. Therefore, we try to use magnetic needles as well as nanoparticles which are put in the matrix to make heat distributions better and treat bigger tumors (>15 mm, 1688mg).

II. Materials and Methods

A. Hardware

Machine for electromagnetic field generation: A lab-built instrument including a high-frequency induction machine, a set of coils to provide an alternate magnetic field (AMF) and a thermocouple to provide temperature monitoring was used for this study. Figure 1 is a schematic representation of our developed system.

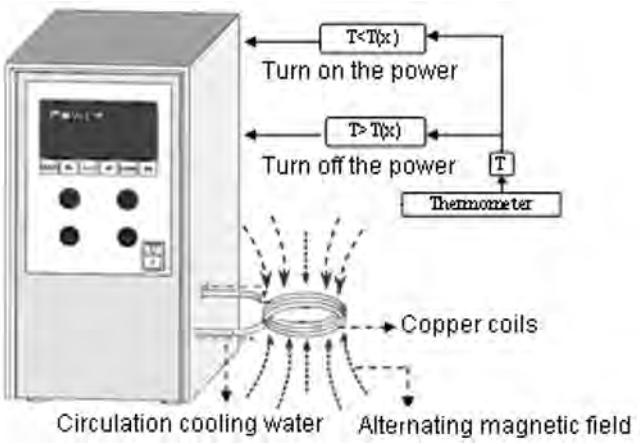


Fig. 1 Schematic representation of the proposed system, including a thermocouple, a lab-built, high-frequency induction machine, copper coils and a feedback temperature control system.

The dimensions of the machine are measured to be 35.5 cm in height and 19.5 cm in width, respectively. The depth of the machine is 42 cm. The diameter of the double coils is 7.5 cm. The operation frequency of the magnetic field is 62.1 kHz. The power consumption is estimated to be 2.2 kW.

Chwee Teck Lim, James C.H. Goh (Eds.): ICBME 2008, Proceedings 23, pp. 574–577, 2009
www.springerlink.com

Magnetic needles: We used a disposable fine needle (30 G). It is made of stainless steel.

Temperature feedback control system: For monitoring the temperature, a thermocouple which was carefully checked in the AMF to make sure magnetic inertia before employed in our system (R-type, InterTech Technology Inc., Taiwan), then was used to provide a feedback control signal for precise temperature control.

B. Experimental design

In vitro tests: To detect the temperature distribution of our design, needles were inserted to the agarose gel and porcine liver in the matrix. Then, the agarose gel and porcine liver were treated for twenty minutes in the AC magnetic field. After the treating, we used IR camera to detect the agarose gel and porcine liver.

Cancer animal experiments: BALB/c mice, about 6-7 weeks old, were inoculated with CT-26 cells, $1x10^6$, into their back subcutaneously. After two weeks, the tumor grew to about 15mm X 15mm in each mouse. Then, they were divided into control (N=8) and treatment group (N=15). We used 30 G disposable fine needle 1.5 cm to 2.0 cm inserting to the tumors in the matrix. Then, the tumors were treated for twenty minutes in the AC magnetic field and a feedback temperature control was used to keep the temperature between 50°C ~ 55°C. The tumors were treated repeatedly 1 to 2 times in two weeks.

III. Results

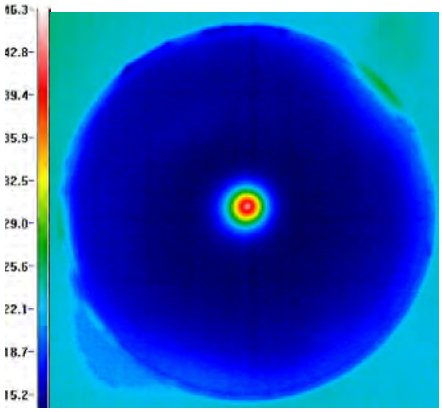
A. In vitro tests

The temperature distribution which was generated by inserting needles in the matrix to the agarose gel was found to perform better than that by inserting a single needle. The results are shown in Figure 2 and Figure 3. In Figure 2, the highest temperature in the center of the picture is 48.8°C and the area of the effective temperature (>42°C) is about $1cm^2$. In Figure 3, the highest temperature in the center of the picture is 58.3°C and the area of the effective temperature is measured to be about $16cm^2$.

The results for the porcine liver show the same trend with the agarose gel test. The results are shown in Figure 4 and Figure 5. In Figure 4, porcine liver is inserted with a single needle. The highest temperature in the center of the picture is measured to be 48.6°C and the area of the effective temperature is about $0.7cm^2$. Conversely, when the porcine liver is inserted with needles in the matrix, the temperature is raised up to 83.1°C, and the area of the effective temperature is about $14cm^2$. From these experimental results, it



(a)



(b)

Fig. 2 (a) Agarose gel with a single needle. (b) The IR image which shows the temperature distributions. The highest temperature is 48.8°C and the area of the effective temperature (>42°C) is about $1cm^2$

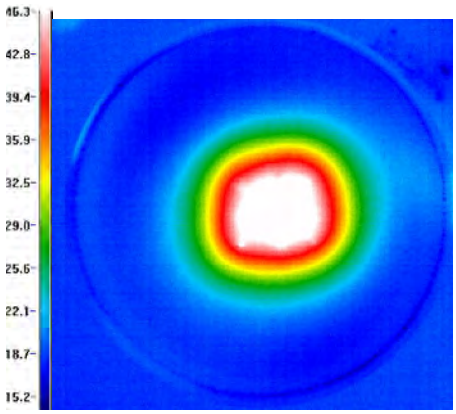
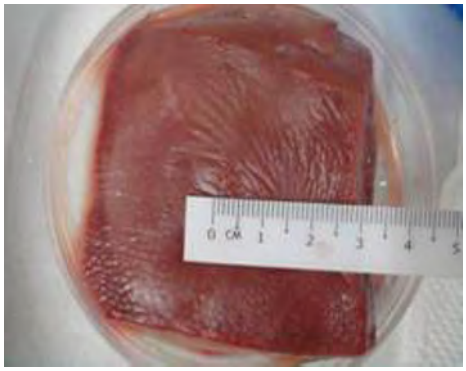
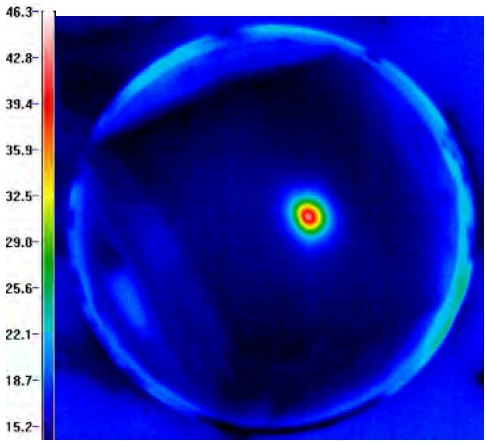


Fig. 3 The IR image which shows the temperature distribution for agarose gel with needles in a matrix. The highest temperature is 58.3°C and the area of the effective temperature is about 16 cm^2. Note that the temperature for the white area is higher than 46 °C



(a)



(b)

Fig. 4 (a) Porcine liver with a single needle. (b) The IR image which shows the temperature distribution. The highest temperature is 48.6°C and the white area temperature is up then 46 °C and the range is about 0.7 cm^2 .

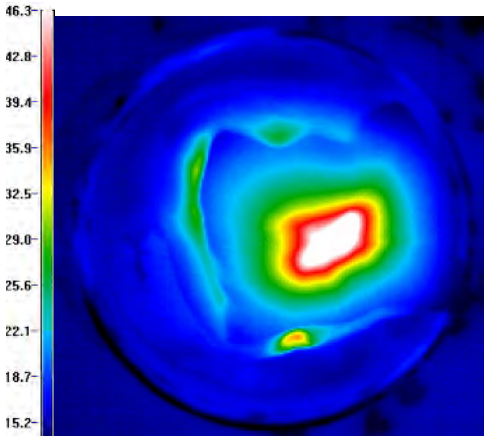
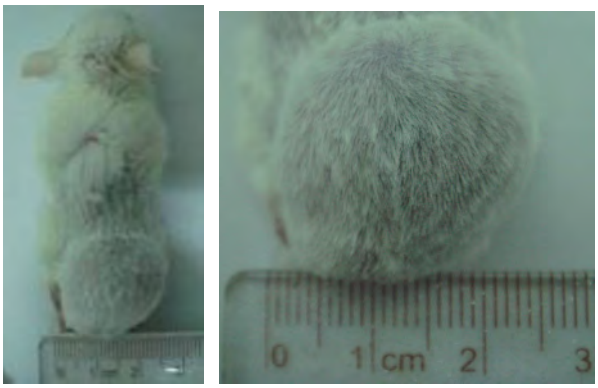


Fig. 5 The IR images for inserting needles in a matrix inside a porcine liver. The highest temperature is 83.1°C and the area of the effective temperature is about 14 cm^2. Note that the temperature of the white area is higher than 46 °C.

reveals that needles in the matrix are better than a single needle. For this reason, we use the needle matrix to treat the CT-26 tumors in the animal models.

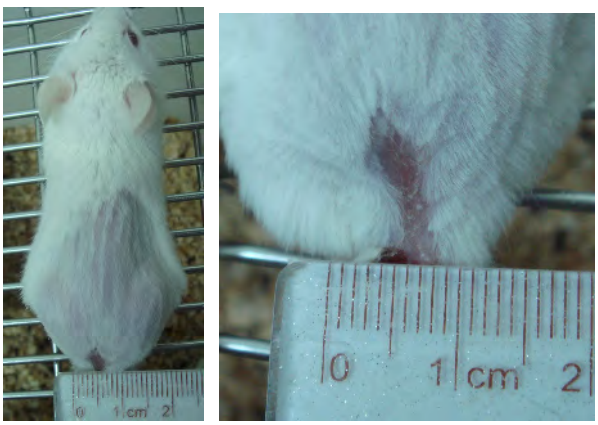
B. Animal experiments

The control group (n=8) mice with tumor died at 11th day. The mouse is shown in Figure 6. The tumor kept growing during the experiment. For the treatment group (n=15), complete regression of CT-26 tumors can be observed in the most of the animals, two of them were dead during the experiment. Figure 7 shows the tumor regression of the treatment group. Figure 8 shows the changes in tumor weight during the observation period. For the control group, the tumor weights increase steadily leading to death and the survival rate at 45th day was 0%. In this animal model, the survival rate achieved 90% in the treated group and no re-



(a) (b)

Fig. 6 Tumor keeps growing in the control group.
(a) Tumor bearing mice. (b) Close-up view of the tumor.



(a) (b)

Fig. 7 The tumor becomes necrotic and regressed in the treatment group.(a)The tumor is regressed. (b) Close-up view of the tumor.

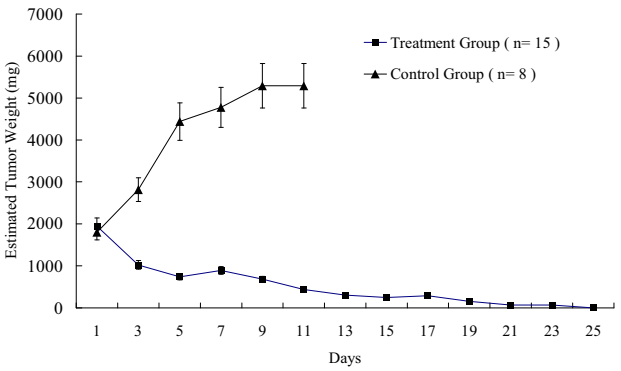


Fig. 8 Tumor growth curves of the cancer bearing mice.

sidual tumor over their back was observation at the end of observation. The comparison is statistically significant.

IV. Conclusions

Fine needles can improve the temperature distribution in the in-vitro tests for hyperthermia cancer therapy. Needles inserted into tumor in the matrix form can induce a localized high temperature in the animal model when placed in an alternating magnetic field. A new feedback temperature control system was successfully integrated into a high-frequency induction machine to create a safer treatment environment. Animal tests showed that focal cancer thermotherapy can eliminate tumors completely in three weeks. We anticipate that the developing system and technology will evolve into a new thermal therapeutic system that can be applied in clinical settings.

Acknowledgments

The study is supported by the National Science Council of Taiwan (NSC-94-2218-E-006-031 and NSC 96-2120-M-006-008). All authors have no potential conflicts of interest for this work.

References

1. Zee J. Heating the patient: a promising approach. Ann Oncol 13, 2002: 1173-1184.
2. Shinkai M, Ito A. Functional magnetic particles for medical application. Adv Biochem Eng Biotechnol 91, 2004:191-220.

Author: Sheng - Chieh Huang
Institute: National Cheng Kung University
Street: University Road
City: Tainan
Country: Taiwan
Email: xaviersty@hotmail.com

Real-Time Electrocardiogram Waveform Classification Using Self-Organization Neural Network

C.C. Chiu[1], C.L. Hsu[1], B.Y. Liau[2] and C.Y. Lan[3]

[1] Department of Automatic Control Engineering, Feng Chia University, Taichung, Taiwan, R.O.C.
[2]Department of Biomedical Engineering, Hung Kung University, Taiwan, R.O.C.
[3]Graduate Institute of Electrical and Communications Engineering, Feng Chia University, Taichung, Taiwan, R.O.C.

Abstract — **In this study, a self-organizing neural network system is presented to classify the real-time electrocardiogram (ECG) signal. This system can not only organize continuous analog waveforms but also output useful recognition codes. The system contains a pre-processor and a self-organizing neural network. By using the MIT-BIH electrocardiogram database, the proposed neural network system can be trained to create the waveforms of cardiac diseases and to recognize the ECG waveforms. Also, a novel R point detection method is presented. The exercise ECG signals including 3,614 R points are tested. The proposed R point detection result reaches sensitivity being 99.94%. The self-organizing neural network system was tested using the MIT-BIH ECG database. 18 data for each with five hours durations were segmented to many beat samples. 5 ECG models (without noise) were created. The results of normal and premature ventricular contraction (PVC) samples classifying using MIT-BIH Arrhythmia Database were obtained. We separated the samples into normal and abnormal signals by 15 trained normal models, then we classified the abnormal ones by 44 trained PVC models. The overall accuracy of the classification results is higher than 87%.**

Keywords — **Self-organization neural network, electrocardiogram, model classification, premature ventricular contraction**

I. Introduction

Heart is one of the most important organs in human body. It uses the blood to transport nutrient to each organ, and removes the useless product from human body to balance each elements. The heart is the main center of blood stream, and the electrocardiogram (ECG) is the best indication to observe the cardiac activity. The heart diseases along with different ages and habits are diverse, and the disease symptoms and the conditions are also different. Therefore, it is desirable to realize the human health conditions by reading the outcomes of ECG and find out the disease of either arrhythmia, myocardial infarction, or others.

It has been shown that 90 to 95 percents of patients with acute myocardial infarction have some associated cardiac arrhythmia. Two most common cardiac arrhythmias during an acute myocardial infarction are premature ventricular contractions and sinus tachycardia. The analysis of the electrocardiogram (ECG) signal is the most readily available method for diagnosing cardiac arrhythmias [1]. New techniques of arrhythmia detection using morphology of the waveform have shown promising results in correctly detecting fatal arrhythmias [2-3]. The purpose of this study is to present a self-organizing neural network system to classify the real-time electrocardiogram (ECG) signal. This system can not only organize continuous analog waveforms but also output useful recognition codes. The beat of ventricular premature contraction will be classified on the basis of beat morphology. In previous research, Chiu et al. has proposed an approach for arterial pressure pulse classification using self-organizing neural network [4], and successfully created the normal and abnormal arterial pressure pulse waveform and applied them to the autonomic nerve recognizing. They also had a collaborated project with Taiwan textile research institute (TTRI) to create the exercise ECG models by the similar self-organizing neural network. Based on self-organizing neural network application experiences, we further use the neural network to classify the ECG signal. Many normal and abnormal ECG models are trained and created. We can therefore classify the unknown ECG signal by these well-trained models.

II. Material and methods

A. ECG signal

In this research, the ECG signals from the MIT-BIH Normal Sinus Rhythm Database and the MIT-BIH Arrhythmia Database are adopted. We also acquired the ECG signals from exercise Lead II ECG provided by Taiwan Textile Research Institute. The exercise ECG data contain 3,614 heart beats.

B. Self-organizing neural network

The characteristics of neural network are quite useful. It is able to preserve the original knowledge and learn the new knowledge. However, most neural networks lack of this kind of characteristics, and cause these neural networks being inconvenient to use in practical applications.

Chwee Teck Lim, James C.H. Goh (Eds.): ICBME 2008, Proceedings 23, pp. 578–581, 2009
www.springerlink.com

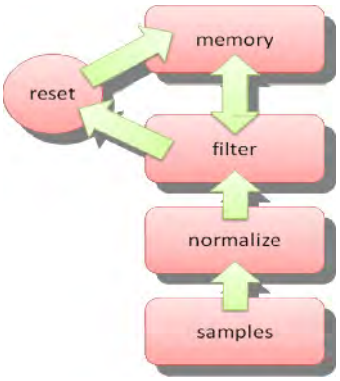


Fig. 1. Block diagram of modified ART neural network

The problem comes to the neural network that it wants to learn the new knowledge without harassing old memory. It is called the stability-plasticity question. In order to make the neural network flexible and being able to learn immediately, Grossberg et al. presented an adaptive resonance theory, ART [5][6][7]. In this research, we slightly modify the ART neural network to be used in classifying the ECG beat signals. The block diagram of underlying algorithm is shown in Fig. 1.

First, we normalize the input sample amplitude to ±1, and resample the input sample to 250 points. Then we process the sample by 1~40Hz band-pass filter. Finally, we calculate the correlation between sample and model in memory. The model is modified if the resulting correlation is higher than our preset threshold. On the other hand, if the resulting correlation is lower than the threshold, the neural network adds the sample into the memory to be a new model. The formula to calculate the correlation is shown as below.

$$R(X,Y)=\frac{\sum(X_i-X_{mean})(Y_i-Y_{mean})}{\sqrt{\sum(X_i-X_{mean})^2\sum(Y_i-Y_{mean})^2}} \tag{1}$$

Where $R(X, Y)$ is the calculated correlation between an incoming sample X and an existed model Y. X_i and Y_i are the i^{th} signal in the sample X and model Y, respectively. X_{mean} and Y_{mean} are the mean values of the sample X and model Y, respectively.

C. Sample definition

In this research, the input sample is defined as an R-R segment. We segment the signal from R point to next consecutive R point. We then resample all the R-R-segment samples to 250 point to make sure that the samples have the same fixed length. The sample definition of an R-R segment is shown in Fig. 2.

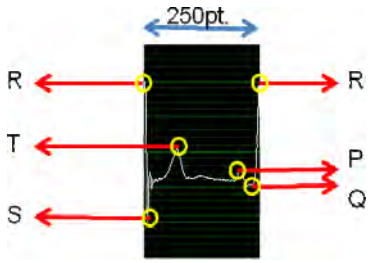


Fig. 2. A sample with a 250-point fixed length

D. A novel R point detection algorithm

According to the result of earlier research, the accuracy of classifying the lead II R point detection in rest position was over 90% using the "So and Chan" method [8]. However, the accuracy of classifying the exercise ECG became lower than 70% by using that method. Therefore, it is inevitable to design a novel detection method in order to segment the ECG signal accurately in real-time. Due to the ECG signal is a time series signal, we are able to make use of the previous QRS segment and predict the following ones. Our proposed novel R point detection algorithm is described as follows.

1. Initialization.

$X(n)$ is incoming ECG series, and the X_n is n^{th} point of the ECG series. R_i is the location index of the i^{th} R point. SR_i is the estimate length of i^{th} RR interval. RR_i is the actual length of i^{th} RR interval. c is the weighted constant. Assume that SR_1 is the scan rate, in our case is 250. At the very beginning 250 points, we can find the first QRS segment and R point location, say R_1, by the following equation.

$$R_1=\text{argmax}[X(n)],\quad 1\le n\le SR_1 \tag{2}$$

2. Iteration

The QRS segment usually appears to be close to periodicity, that is, (i+1th) R point should be located nearby the duration within the range of R_i+SR_i. The range to search the R point can therefore be set by the following equation.

$$\begin{aligned} &R_{i+1}=\text{argmax}[X(n)],\\ &R_i+SR_i-cSR_i\le n\le R_i+SR_i+cSR_i\\ &RR_i=R_i-R_{i-1} \end{aligned} \tag{3}$$

As one knows that the heart rate may fluctuate due to exercise or emotion, the estimate of RR interval, i.e., SR_{i+1}, should be adjusted based on the average value of previous k RR intervals. The following equation show how the SR_i is modified.

$$SR_{i+1}=\frac{RR_i+RR_{i-1}+\cdots+RR_{i-k+1}}{k} \tag{4}$$

3. Validation

The slope examination method similar to the one proposed by So and Chan [10] is applied to validate our proposed R point detection algorithm to avoid misjudging between R and T point. Let S_n be the n^{th} slope in the series $X(n)$. a is a weighted constant. S_n is defined as follows.

$$S_n = (X_{n-2} - X_{n-1}) + a(X_{n-1} - X_n) - a(X_n - X_{n+1}) - (X_{n+1} - X_{n+2}) \quad (5)$$

At most cases, the slope at R point is much higher than that at T point. Therefore, if the slope value detected is smaller that our preset threshold, then the weighted constant c in equation (3) should be adjusted to be smaller. Since the search range becomes smaller, the possibility to obtain R point wrongly will be reduced.

III. Results and Discussion

During the recording of a real-time ECG signal, the ECG signal usually contaminates with noise or motion artifact. The noise or artifact makes the detection accuracy of R points becomes lower without any manipulation.

Table 1. Comparison of sensitivities between "So and Chan" method and the novel R point detection algorithm

Method	true positives	false negatives	false positives	sensitivity
So and Chan	2759	1231	855	61.62%
Novel algorithm	3612	1	2	99.94%

Sensitivity = true positives / (true positives+ false negatives)

Table 1 shows the sensitivity of our proposed R point detection algorithm outperforms previous method in exercise Lead II ECG R-point detection. When detect the ECG signal, So and Chan method should set the detection threshold accurately. If the detection threshold can't change dynamically, the sensitivity using So and Chan method will get even lower. Our proposed R point detection algorithm can change the search range and location dynamically, so the performance of novel algorithm works much better in this study.

The results list in Table 2 are the classification results of signals in MIT-BIH Normal Sinus Rhythm Database using the self-organizing neural network.

Database: MIT-BIH Normal Sinus Rhythm Database
Number of records: 18
Testing signal channel: Signal 1 / 5Hr
Sampling rate: 128 samples/sec.
Filter: none
Training spent time: 560sec.
Classifying spent time: 10sec.

Table 2. Classification results of signals in MIT-BIH Normal Sinus Rhythm Database

Record No.	Samples	Model(s) with noise	Sample-Model ratio	Model(s) without noise
16265	27651	9	0.03%	5
16272	19289	267	1.38%	5
16273	25176	26	0.10%	1
16420	25919	53	0.20%	4
16483	27856	58	0.21%	5
16539	23618	70	0.30%	4
16773	22804	12	0.05%	4
16786	24022	10	0.04%	1
16795	25387	75	0.30%	13
17052	22352	110	0.49%	4
17453	26220	40	0.15%	4
18177	27745	72	0.26%	5
18184	25113	26	0.10%	4
19088	28691	28	0.10%	4
19090	23467	44	0.19%	2
19093	20939	9	0.04%	2
19140	26558	17	0.06%	3
19830	32568	58	0.18%	9
Average	25298.5	54.67	0.22%	4.38

The classification results shown in Table 2 indicate that the self-organizing neural network classifies the input samples into only a few output models. The sample-model ratios are almost lower than 1% of the total input samples. The results point out that the models can be created very effectively and concisely. One can also see from Table 2 that some signals have only one model left after certain noise models are removed from our classification results,. This result indicates that the sample model in the original signal can be very uniform or regular. In some case, signals contain a very low frequency drift. Due to the signal drifting, the correlations between the segmented samples become lower. Therefore, the neural network creates more models than the others recorded signals.

After using the neural network to classify the samples into models, we test the classification results and count the accuracy rate by the following steps. The testing block diagram is shown in Fig. 3.

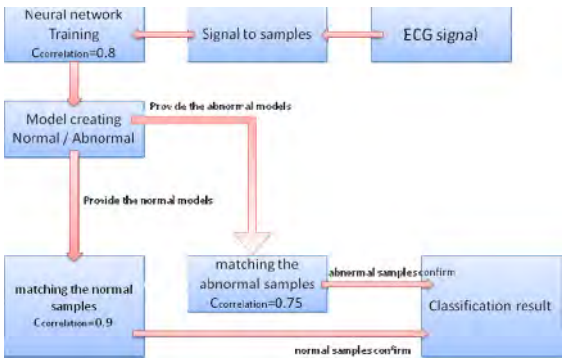


Fig. 3. Block diagram of testing processes

At our experiment, we obtain 15 normal models and 44 typical PVC models. The correlation threshold is set to be 0.9 to match the normal models with testing samples. We set the correction threshold to 0.75 to match the normal models with the remaining test samples. Then we can recognize the abnormal samples using lower correlation threshold with abnormal models, and filter out the samples can't be recognized.

Table 3 indicates the classification results of signals in MIT-BIH Arrhythmia Database. We select the database to be the testing objects because the PVC waveforms usually appear in arrhythmia ECG waveforms.

Database: MIT-BIH Arrhythmia Database
Testing object: Normal / PVC ECG
Testing signal channel: MLII / 5min. data

Table 3. Classification results of signals in MIT-BIH Arrhythmia Database

NO.	+PVC in record	+Normal in record	Normal	Abnormal	$ Correct classification%
105	12	405	391	21	94.48%
106	60	271	227	41	80.96%
114	13	261	249	15	94.89%
116	11	384	374	8	96.70%
119	80	246	243	79	98.77%
#200	126	305	183	118	69.83%
208	168	278	287	184	94.39%
210	30	413	367	33	88.93%
213	25	432	488	22	87.08%
215	33	534	503	34	94.35%
221	80	327	344	58	90.41%
#228	60	290	167	57	64.00%
233	139	371	267	144	78.62%

+record list:
http://www.physionet.org/physiobank/database/html/mitdbdir/records.htm
#noisy signal
$Correct classification% = (1-(failure classification number/ actual record number))x100%

The normal ECG samples in each record are almost the same. Therefore, we can easily identify the normal ECG samples by the normal models, and then we indentify the fewer remain samples by abnormal models. We can make the classification more efficient by increasing the correct classification rate. The table above shows that the correct classification rates in most cases are higher than 80%. And the average correct classification rate is over 87%. The self-organizing neural network system presented in this study can classify many samples into a few normal/abnormal models effectively and correctly.

IV. Conclusions

A self-organizing neural network system has been presented to classify the real-time ECG signal. The recognized results are useful to find out models of cardiac diseases. By using the signal data in MIT-BIH electrocardiogram database, the proposed neural network system can be trained to create the waveforms of cardiac diseases and to recognize the ECG waveforms. Also, a novel R point detection method has been presented. The proposed R point detection result reaches sensitivity of 99.94%. The results of normal and premature ventricular contraction (PVC) samples classifying with MIT-BIH Arrhythmia Database, we separated the samples into normal and abnormal signals by 15 trained normal models, then we classified the abnormal ones by 44 trained PVC models. The accuracy of the classification results is higher than 87%.

Acknowledgment

The authors would like to thank the National Science Council, Taiwan, R.O.C., for supporting this research under Contract No. NSC96-2628-E035-083-MY3.

References

1. Chiu, C.C., Lin, T.H., Liau, B.Y. (2005) Using correlation coefficient in ECG waceform for arrhythmia detection. Biomedical Engineering-Application, Basis & Communications, 17:147-152.
2. Kumar, V.K. (1988) A novel approach to pattern recognition in real-time arrhythmia detection. Proceedings of the Annual International Conference of the IEEE Engineering in Medicine and Biology Society, 1: 7-8.
3. Dickhaus H, Gittinger J, Maier C (1999) Classification of QRS morphology in Holter monitoring. Engineering in medicine and biology. Proceedings of the Annual International Conference of the IEEE Engineering in Medicine and Biology Society, 1: 270.
4. Chiu, C.C., Yeh, S.J., Chen, C.H. (2000) Self-organizing arterial pressure pulse classification using neural networks: theoretical considerations and clinical applicability. Computers in Biology and Medicine, 30:71-88.
5. Hush, D.R., Horne, B.G. (1993) *Pro*gress in supervised neural networks. IEEE Signal Processing Magazine, 10:8-39.
6. Carpenter, G.A., Grossberg, S. (1991) Pattern recognition by self-organizing neural networks. The MIT Press, Massachusetts, Cambridg, 397-424.
7. Carpenter, G.A, Grossberg, S. (1998) The ART of adaptive pattern recognition by a self-organizing neural network. IEEE Computer, 21:77-88.
8. So H.H., Chan K.L. (1997) Development of QRS detection method for real-time ambulatory cardiac monitor. Proceedings of the Annual International Conference of the IEEE Engineering in Medicine and Biology Society, 1: 289 -292.

Address of the corresponding author:

Author: Chuang-Chien Chiu
Institute: Department of Automatic Control Engineering, Feng Chia Unicversity
Street: 100, Wenhwa Rd.
City: Taichung
Country: Taiwan, R.O.C.
Email: chiuc@fcu.edu.tw

The Design of Oximeter in Sleep Monitoring

C.H. Lu[1], J.H. Lin[2], S.T. Tang[3], Z.X. You[2] and C.C. Tai[1]

[1] Department of Electrical Engineering, National Cheng Kung University, Tainan, Taiwan
[2] Department of Electronic Engineering, Kun Shan University, Tainan, Taiwan
[3] Department of Biomedical Engineering, Ming Chuan University, Taipei, Taiwan

Abstract — **One-third of the lifetime is spent asleep, and the quality of sleep significantly affects health and the quality of life. Many people are unaware that they snore during sleep, and also consider that snoring occurs when the body is too tired, whereas it is actually is an indicator of good health. There is accumulating evidence that snoring is indicative of sleep apnea syndrome, which can decrease blood oxygenation and induce hypertension, right ventricle failure, angina pectoris, and even sudden death. Given the importance of snoring and its relation to blood oxygenation, we built a small oximeter with low power consumption and based on optical penetration, with the acquired physiological data being transferred to a personal computer via a serial interface. In this system the computer measures physiological data of blood oxygen, heart rate, and heart rate variability using Poincaré plots. The stability of the oximeter results was determined using a standard biosignal simulator, with three subjects being monitored: those prone to snoring. This system is noninvasive, makes continuous measurements, and is highly portable, which make it a good choice for monitoring sleep in the home environment.**

Keywords — **Sleep apnea syndrome, oxygen saturation, sleep, snoring**

I. Introduction

Sleep is an important physiological function, with humans spending one-third of their lifetimes asleep, and the quality of sleep significantly affects the quality of life and health. Physiologically, snoring is cased by obstruction of the upper respiratory tract. Sleep apnea during snoring can be a temporary condition or lead to sleep apnea syndrome (SAS) [1–3].

Improvements in living standards, eating habits, and environmental pressures have increased the prevalence of people with chronic disease. However, obstruction of the upper respiratory tract is now experienced by 85–90% of people. Airway obstruction caused by apnea further reduces the oxygen saturation (SaO_2), interfering with sleep and increasing the risk of cardiovascular disease. Moreover, many traffic accidents are due to lethargy and inattention, conditions that are also associated with SAS.

The standard procedure for diagnosing SAS is quite complicated, with several physiological signals being monitored throughout the night, such as the electrooculogram, electroencephalogram, and electromyography, airflow in the mouth and nose cavity, and occurrence of snoring. This process has unfavorable characteristics, such as being cumbersome, costly, and wasteful of medical resources. However, improvements in biomedical photoelectric technology have led to the development of oximeters [4] for the noninvasive method of measuring SaO_2 using optical sensors, which provides convenience and safety advantages.

The aim of this study was to design a small, power-efficient, and inexpensive oximeter that was simple to use. The device used both red light (660 nm) and infrared light (940 nm) produced by two light-emitting diodes (LEDs) to illuminate the body. The reflection and transmission of light energy were determined from the detected light, from which the heart rate and SaO_2 were calculated. In order to reduce medical costs and enable continuous monitoring, the oximeter was linked with a personal computer to provide a system for the real-time analysis of heart-rate variability (HRV). The system can record SaO_2 and HRV changes during sleep, and provide long-term data of snoring for clinical trials.

II. Methods

Heme oxygen containing the hemoglobin share of the total volume is defined as the percentage of oxygen in the blood flow, referred to as SaO_2:

$$SaO_2 = \frac{\mathrm{HbO_2}}{\text{Total hemoglobin}} = \frac{[HbO_2]}{[HbO_2]+[Hb]} \times 100\% \quad (1)$$

where $[HbO_2]$ is the volume of oxygenated hemoglobin, and [Hb] is the volume of deoxygenated hemoglobin in the blood.

Lambert clarified the relationship between the degree and material thickness absorption of optical in 1760, and Beer proposed the relationship between the degree of optical absorption and absorption concentration in 1852. These two observation are combined into the Beer-Lambert law. We define the absorption and concentration along an optical path as exponential functions as follows:

$$I(\lambda) = I_o(\lambda) \times 10^{-\varepsilon \cdot c \cdot d} \quad (2)$$

Chwee Teck Lim, James C.H. Goh (Eds.): ICBME 2008, Proceedings 23, pp. 582–585, 2009
www.springerlink.com

where $I(\lambda)$ is the transmission optical intensity, $I_o(\lambda)$ is the incident optical intensity, ε is the absorption coefficient, c is the concentration, and d is the optical path length through the sample.

The absorption factor of a material is affected by the wavelength of the incident light and the temperature. A larger value indicates a higher absorption capacity, which results in measurements of higher sensitivity.

We define the optical density (O.D.) by taking the logarithm of both sides of Equation 2, which corresponds to the absorbance shown in Figure 1:

$$O.D. = \log\left(\frac{I_o(\lambda)}{I(\lambda)}\right) = \varepsilon \cdot c \cdot d = \mathrm{A} \tag{3}$$

where A is the absorbance.

When the optical wavelength and optical path length are fixed, there is a linear relationship between the optical intensity and the concentration of the sample. Therefore, in optical measurement applications, as long as the optical density has been measured with a known light absorption ε and optical path length d, can be obtained under test concentration c. However, the Beer-Lambert law applies only to the absorption of the solution without scattering.

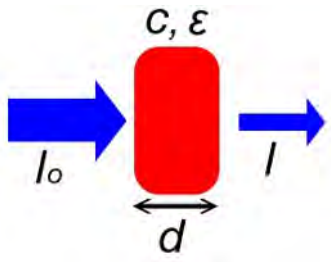


Fig.1 Optical pathway through the material.

Oxygenated and deoxygenated hemoglobin exhibit different absorption properties for different optical wavelengths. Therefore, our system applies light at two wavelengths to the test tissue (usually a finger) to detect changes in optical energy transmittance, and then calculate SaO_2. From results of near-infrared spectroscopy, we chose absorption points either side of 800 nm (i.e., 660 and 940 nm) for the optical source wavelength in a two-wavelength system. Note that these two wavelengths are often used by oximeters available in the marketplace.

We used the small-artery model of the human finger shown in Figure 2. The thickness of the small artery is D during vasoconstriction and $D+\Delta D$ during vasodilation, with change in thickness ΔD being due to stretching and relaxing of blood vessels during the pressure pulse. Assuming that the blood vessels contain only oxygenated and deoxygenated hemoglobin, the Beer-Lambert law can be used to determine the transmission of infrared (940 nm) and red (660 nm) light as follows:

$$I_{IR} = I_{(DC+AC)IR} = I_O \cdot 10^{-\left(\varepsilon_{IR}^{HbO_2} \cdot C_{HbO_2} + \varepsilon_{IR}^{HB} \cdot C_{Hb}\right)D} \cdot 10^{-\left(\varepsilon_{IR}^{HbO_2} \cdot C_{HbO_2} + \varepsilon_{IR}^{HB} \cdot C_{Hb}\right)\Delta D} \tag{4}$$

$$I_R = I_{(DC+AC)R} = I_O \cdot 10^{-\left(\varepsilon_R^{HbO_2} \cdot C_{HbO_2} + \varepsilon_R^{HB} \cdot C_{Hb}\right)D} \cdot 10^{-\left(\varepsilon_R^{HbO_2} \cdot C_{HbO_2} + \varepsilon_R^{HB} \cdot C_{Hb}\right)\Delta D} \tag{5}$$

where ε_{IR}^{Hb} and $\varepsilon_{IR}^{HbO_2}$ are the infrared optical absorption coefficients of Hb and HbO_2, respectively, and ε_R^{Hb} and $\varepsilon_R^{HbO_2}$ are the corresponding red optical absorption coefficients.

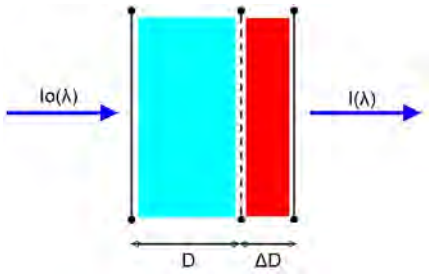


Fig.2 Small-artery model of the human finger.

To simplify the calculation of the SaO_2, we divide both sides of Equations 4 and 5 by $I_{DC(IR)}$ and $I_{DC(R)}$, which after rearranging yields the following definition of the absorbance ratio for red and infrared light:

$$ratio = \frac{R}{IR} = \frac{\log\left(\frac{I_{(DC+AC)R}}{I_{DC,R}}\right)}{\log\left(\frac{I_{(DC+AC)IR}}{I_{DC,IR}}\right)} = \frac{\varepsilon_R^{HbO_2} \cdot c_{HbO_2} + \varepsilon_R^{Hb} \cdot c_{Hb}}{\varepsilon_{IR}^{HbO_2} \cdot c_{HbO_2} + \varepsilon_{IR}^{Hb} \cdot c_{Hb}} \tag{6}$$

Merging Equations 1 and 6 yields the possible theoretical value of SaO_2:

$$SaO_2 = \frac{\varepsilon_{IR}^{Hb} \cdot \frac{R}{IR} - \varepsilon_R^{Hb}}{\left(\varepsilon_{IR}^{Hb} - \varepsilon_{IR}^{HbO_2}\right) \cdot \frac{R}{IR}\left(\varepsilon_R^{Hb} - \varepsilon_R^{HbO_2}\right)} \tag{7}$$

III. System Design

To implement a system using a small oximeter with low power consumption, we selected the MSP430FG439 microcontroller for signal processing. The system was designed to transfer data to a computer using a peripheral interface to allow physiological data analysis and recording. A block diagram of the hardware is shown in Figure 3.

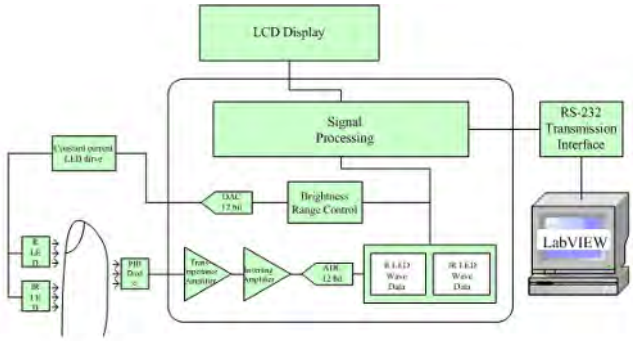


Fig.3 Hardware block diagram.

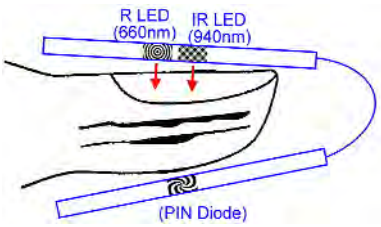


Fig.4 Optical sensor: orientation with finger.

The system's optical sensor uses an oxygen probe (S0010A, MED LINKET) of the optical transmission type, as shown in Figure 4. The optical detector is a light diode that converts light energy into a current signal.

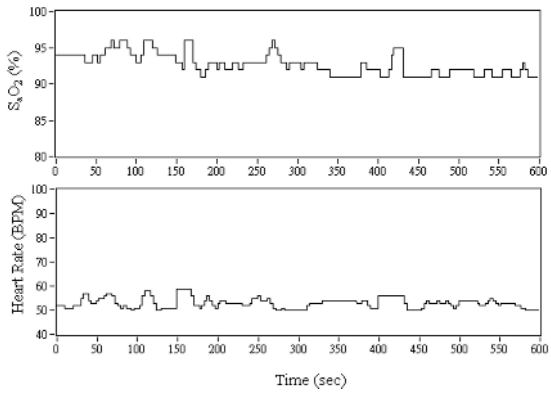
We adopted a time-division pulse modulation method for controlling the timing of the red and infrared LEDs. The MSP430FG439 microprocessor was used to alternately drive the red and infrared light sources and the optical detector. The sensitivity of the optical detector varies with the incident light, and hence the signals for the red and infrared light sources need to be adjusted to the same level.

The signal from the optical detector is sampled and processed by filtering and amplification by the internal operational amplifier in the microprocessor. The system converts the analog signals into digital signals for calculating the SaO_2 and the heart rate, which are finally displayed on an LCD with the data also being sent to a personal computer via a serial interface for recording and analysis using LabVIEW software (National Instruments) [5]. A patient simulator (PS97, BAPCO Instruments) is used to calibrate and verify the SaO_2 value before each sleep experiment.

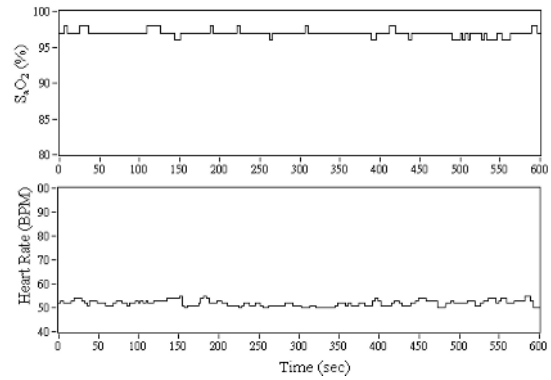
IV. Results

4.1 Preliminary experiments for monitoring snoring

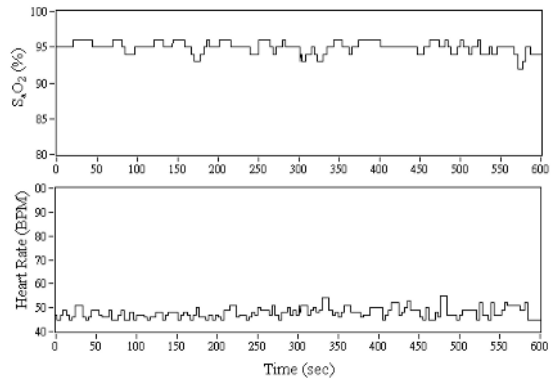
We explored the impact of snoring on SaO_2, heart rate, and HRV during sleep. Sleep snoring was monitored in three people prone to snoring (mean age=25 years, mean BMI=22.5 kg/m^2). To improve the consistency and objectivity of the experiments, the subjects were asked not to consume food that might affect the central nervous system (e.g., tea, coffee, and alcohol) for 8 hours before participating in the sleep experiment. Moreover, none of the subjects had recently taken any medications. In each experiment, a



(a)



(b)



(c)

Fig.5 Data recorded in three subjects (a, b, and c) in preliminary experiments for monitoring snoring.

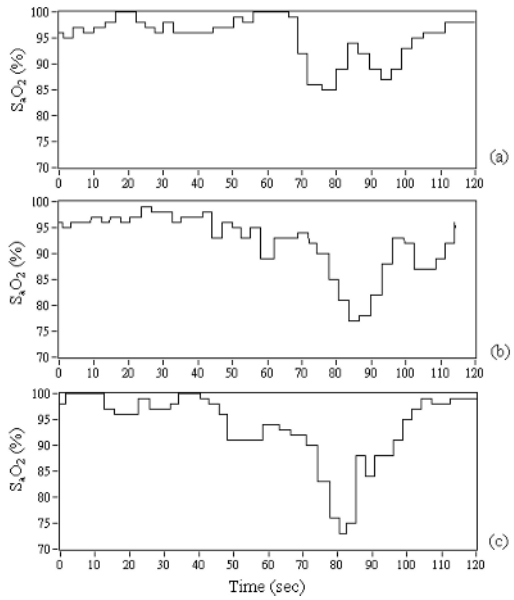


Fig.6 Data recorded in three subjects (a, b, and c) in breath-holding experiments.

staff member monitored the subject throughout the night and recorded significant data for 10 minutes when the subject was snoring. Figure 5 shows the data recorded from the three subjects.

4.2 Human breath-holding experiments

We verified the efficacy of the system in detecting oxygen deficits in the human body induced by breath holding. Changes in SaO_2 were measured using the following experiment (see Figure 6):

1. Seconds 1 to 10: normal breathing.
2. Seconds 10 to 70: stop breathing.
3. Beyond 70 seconds: restore breathing.

V. Discussion and conclusions

In order to explore the impact of sleep snoring on the heart rate and HRV, we have developed an oximeter that is small, portable, has a low power consumption, and can record long-term data. In breath-holding experiments, the device detected a downward trend in SaO_2 as the physiological response to oxygen deficit. In preliminary experiments for monitoring snoring during sleep, no peculiar changes were observed in the SaO_2, heart rate, and HRV in subjects prone to snoring, which indicates that sleep apnea does not necessarily occur during snoring. However, this negative result might be due to the inclusion of only a few patients with clinical sleep disorders.

The described system could be expanded to record snoring sounds, breathing rate, and other important parameters. We believe that this system is suitable for monitoring experiments associated with sleep snoring.

Acknowledgment

The authors thank the National Science Council (NSC 96-2622-E-168-030-CC3 and 96-2221-E-168-001-) in Taiwan for their support.

References

1. Haponik E.F., et al. (1983) Computerized tomography in obstructive sleep apnea. Correlation of airway size with physiology during sleep and wakefulness, American Review of Respiratory Disease, Vol. 127, pp. 221–226.
2. Suratt P.M., et al. (1983) Fluoroscopic and computed tomographic features of the pharyngeal airway in obstructive sleep apnea, American Review of Respiratory Disease, Vol. 127, pp. 487–492.
3. Schwab R.J., et al. (1993) Dynamic upper airway imaging during awake respiration in normal subjects and patients with sleep disordered breathing, American Review of Respiratory Disease, Vol. 148, pp. 1385–1400.
4. Yoshiya I., et al. (1980) Spectrophotometric monitoring of arterial oxygen saturation in the fingertip, Medical and Biological Engineering and Computing, Vol. 18, pp. 27–32.
5. You Z.X., et al. (2007) A design of real-time heart rate variability analysis using saturation of oxygen signal, 2007 Intelligent Living Technology, Taichung, Taiwan, HCD020, pp. 466–469.

Integration of Image Processing from the Insight Toolkit (ITK) and the Visualization Toolkit (VTK) in Java Language for Medical Imaging Applications

D. Gansawat[1], W. Jirattiticharoen[2], S. Sotthivirat[1], K. Koonsanit[1], W. Narkbuakaew[1], P. Yampri[1] and W. Sinthupinyo[1]

[1] National Electronics and Computer Technology Center, Phaholyothin Rd, Klong Luang, Pathumthani 12120, Thailand
[2] Department of computer engineering, Kasetsart University, Bangkok, 10900, Thailand

Abstract — **Image processing and visualization of medical data has become an essential support for clinical diagnosis and treatment planning. The available open source libraries such as the Insight Registration and Segmentation Toolkit (ITK) and the Visualization Toolkit (VTK) with custom designed user interface can help rapid development of medical imaging applications. Both ITK and VTK are written in C++ language with the wrappers for Tcl, Python, and Java languages. Numbers of researchers and developers implement their proposed algorithms with some reusable functions available in ITK and VTK. The ITK offers extensive image filtering techniques for segmentation and registration applications without support of data visualization, while VTK mainly supports the visualization. Therefore, several medical software systems have been implemented using the connection of ITK and VTK. However, the successful connection has been reported only implementing in C++, Tcl and Python languages. The connection of ITK and VTK using Java language is still a problem. However, Java has the advantages of being a less complex, free, and easily portable programming language. Hence, the ability to connect the ITK and VTK classes directly using Java will benefit the rapid development of medical applications and teaching medical image analysis.**

In this paper, we present the method that enables the integration of ITK and VTK libraries together in Java. This integrated ITK/VTK offers more flexible handling and benefits of image processing algorithms from ITK together with the 2-D/3-D visualization from VTK. In the last section, examples of the implementation of the integrated ITK/VTK in Java language on the medical imaging samples are presented.

Keywords — **ITK and VTK in Java, image processing, medical imaging applications**

I. Introduction

The ITK [1] and the VTK [2] are the open-source libraries that are widely used in the applications of image processing and scientific visualization. Several researchers and developers implement their proposed algorithms with the reusable and extendable functions available in ITK and VTK to reduce the amount of time in coding and implementation. The ITK library has the advantage of providing support for numerous standard image processing such as linear and nonlinear filters, image transformations and interpolations, segmentation, morphology and level sets etc., while VTK library offers a variety of visualization algorithms like scalar, vector, texture and volumetric techniques and advanced techniques such as polygon reduction, mesh smoothing, contouring and Delaunay triangulation etc [3].

In medical software and application development, the graphical user interface (GUI) is also important. Java language which is free, less complex programming and easily portable has drawn more attention in application development due to the availability of large standard library and several plug-in tools. Both ITK and VTK libraries are written in C++ language with the wrappers for Tcl, Python, and Java languages, hence the researcher and developers are able to implement and develop prototypes in the language that they are more comfortable with. The integration of ITK and VTK libraries has been reported implementing in C++, Tcl and Python languages, for example, VolView [4] and Slicer [5]. The connection of ITK and VTK libraries using Java language is still a problem for numerous developers as the ConnectVTKITK (direct connection between ITK and VTK library) is not wrapped to be used with Java. Moreover, the documents and technical support about the wrappers for ITK and VTK libraries are limited [6].

This paper presents the method that enables the integration of ITK and VTK libraries together in Java programming language. The compiling processes of ITK, VTK and integrated ITK/VTK for Java are explained in the next section. After that the examples of the integrated ITK/VTK implemented in Java programming on the medical imaging samples are demonstrated.

II. Compiling processes of ITK, VTK and integrated ITK/VTK for Java language

The processes of compiling ITK, VTK and integrated ITK/VTK for Java on Windows platform require CMake [7], C++ compiler and Java SDK. We note that CMake version 2.4 and Java SDK version 1.6 are used in our implementation. In the following subsections, we briefly explain the compilation of VTK, ITK and integrated ITK/VTK for Java respectively.

Chwee Teck Lim, James C.H. Goh (Eds.): ICBME 2008, Proceedings 23, pp. 586–589, 2009
www.springerlink.com

A. Compilation of VTK for Java language

The VTK library written in C++ has its own wrapping facility which is enable to automatically generate Java binding in the same way as the automated wrapping into Tcl as described in [8]. The following steps are carried out for compiling the VTK source code (version 5.0.3 release was used) and generating the Java bindings using the CMake tool. Once the CMake is launched

1. Set the VTK source and the binaries directories
2. Select to build for available C++ compiler
3. Set the following options to ON as the Show Advanced Values option is enable
   - BUILD_SHARED_LIBRARIES to ON
   - ITK_CSWIG_JAVA to ON.
4. Click Configure. There may be some options presented to confirm about the version of Java SDK and click Configure a second time. On the completion, the CMake is automatically closed
5. Open the solution file (VTK.sln) with the C++ compiler and run the Build Solution operation with the Release build configuration. Verify that there are no errors and VTK.jar is built.

Before creating a Java project, the folders that contain compiled VTK library files (DLL files) and VTK.jar must be added to System path.

B. Compilation of ITK for Java language

The ITK can be wrapped using CableSwig or WrapITK [6]. The CableSwig has been developed using a combination of language binding tools such as gccxml[9], CABLE and CSWIG[10]. The WrapITK requires both ITK and CableSwig to have been built firstly. As the WrapITK is still in the development process and mainly supports Python language, hence the wrapping process using CableSwig is recommended. The wrapping can be done by placing CableSwig into the Utilities directory of the ITK source and follow the similar steps as described earlier in compiling the ITK source code and generating the ITK Java bindings.

C. Compilation of integrated ITK/VTK for Java language

The wrapping process for the integrated VTK and ITK is difficult due to the following factors

1. The development of ITK is based on the generic programming (i.e., extensive use of C++ templates), whereas the non-templates are used for VTK.
2. Both ITK and VTK have their own algorithms pipeline.

However, after the thorough study of the ITK and VTK wrapping structures we have proposed the method to wrap the integrated ITK/VTK for Java bindings in the similar way to the integrated ITK/VTK for Tcl language as implemented in 3D Slicer. The project called "vtkDtp" is created by extending the source codes in the vtkITK directory available in the InsightApplications directory. A list of files inside the vtkDtp folder is shown in Fig.1.

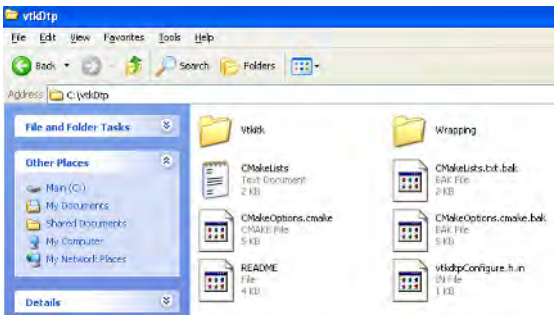


Fig. 1 Files inside the vtkDtp project

The CMakeLists.txt, which is called by CMake tool to compile and build the vtkDtp project, is modified as follows

```
CMAKE_MINIMUM_REQUIRED(VERSION 2.0)
# Set the project name.
#
PROJECT (VTKDTP)
# Load CMake commands that you probably should not modify.
#
INCLUDE (${VTKDTP_SOURCE_DIR}/CMakeOptions.cmake)

# On Visual Studio 8 MS deprecated C. This removes all 1.276E1265
security
# warnings
IF(WIN32)
  IF(NOT BORLAND)
    IF(NOT CYGWIN)
      IF(NOT MINGW)
        IF(NOT
ITK_ENABLE_VISUAL_STUDIO_DEPRECATED_C_WARNINGS)
          ADD_DEFINITIONS(
          -D_CRT_FAR_MAPPINGS_NO_DEPRECATE
          -D_CRT_IS_WCTYPE_NO_DEPRECATE
          -D_CRT_MANAGED_FP_NO_DEPRECATE
          -D_CRT_NONSTDC_NO_DEPRECATE
          -D_CRT_SECURE_NO_DEPRECATE
          -D_CRT_SECURE_NO_DEPRECATE_GLOBALS
          -D_CRT_SETERRORMODE_BEEP_SLEEP_NO_DEPRECATE
          -D_CRT_TIME_FUNCTIONS_NO_DEPRECATE
          -D_CRT_VCCLRIT_NO_DEPRECATE
          -D_SCL_SECURE_NO_DEPRECATE
          )
        ENDIF(NOT
ITK_ENABLE_VISUAL_STUDIO_DEPRECATED_C_WARNINGS)
      ENDIF(NOT MINGW)
    ENDIF(NOT CYGWIN)
  ENDIF(NOT BORLAND)
ENDIF(WIN32)
#
```

```
# Here is where you can list the sub-directories holding your local
# classes. Sorting classes by 'package' type like VTK does (Common,
# Rendering, Filtering, Imaging, IO, etc.) is a good thing and prevents
# numerous dependencies problems.
#

SUBDIRS (
  Vtkitk
)

CONFIGURE_FILE(
  ${VTKDTP_SOURCE_DIR}/vtkdtpConfigure.h.in
  ${VTKDTP_BINARY_DIR}/vtkdtpConfigure.h
)
INCLUDE_DIRECTORIES(${VTKDTP_BINARY_DIR})
```

The subdirectory Vtkitk consists of .cxx and .h files of the integrated VTK/ITK (see inside the Common directory in the vtkITK directory in the InsightApplications directory). Inside the Vtkitk folder also has another CMakeLists.txt, modifying this CMakeLists.txt in the Configure wrappers from Tcl and Python to Java. Next, launch the CMake and set the Cache Values for the project as shown in Fig.2.



Fig. 2 Cache Values Setting for vtkDtp project

Once the vtkDtp project is completely built, the vtkITK.jar can be obtained using the following steps

1. Create folder called “CompileJava”
2. Copy files that have been builded from the VTK project and the vtkDtp project to CompileJava folder. All the files that are copied to CompileJava folder are shown in Fig. 3
3. Use Java JDK tool to pack all the copied file to .jar file. Note that this .jar file contain .class file of VTK and integrated ITK/VTK

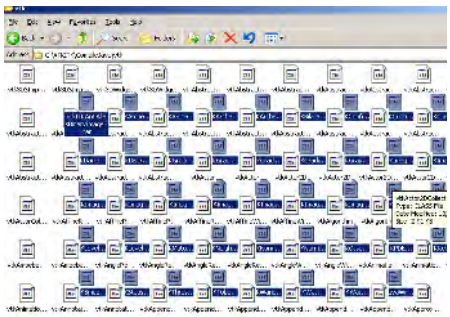


Fig. 3 All the .class file of VTK and integrated ITK/VTK

III. Exerimental Results and Discussion

The following section briefly demonstrates the experimental results of using integrated ITK/VTK in processing and visualizing the input medical images. Fig.4 – Fig.6 illustrate the implemented results using vtkITKOtsuThresholdImageFilter, vtkITKGradientMagnitudeImageFilter, and vtkITKConfidenceConnectedImageFilter classes on the MRI DICOM input respectively.

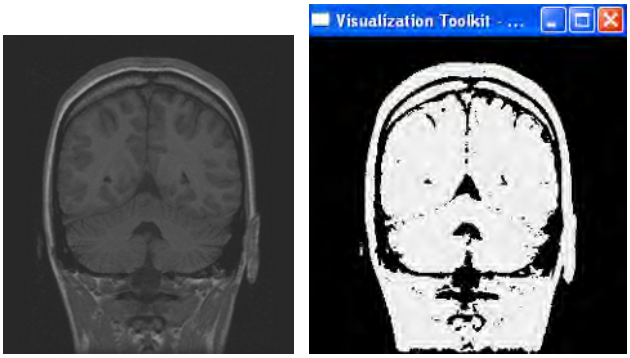


Fig. 4 The implemented result using vtkITKOtsuThresholdImageFilter

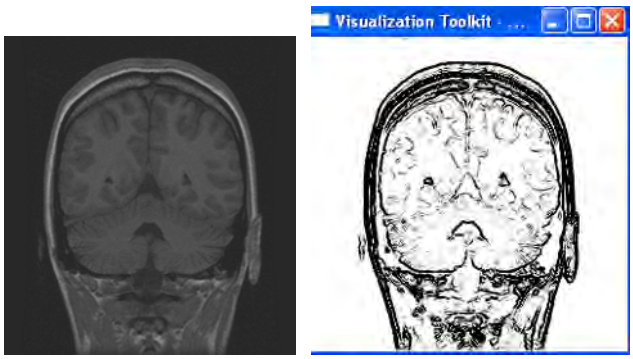


Fig. 5 The implemented result using vtkITKGradientMagnitudeImageFilter

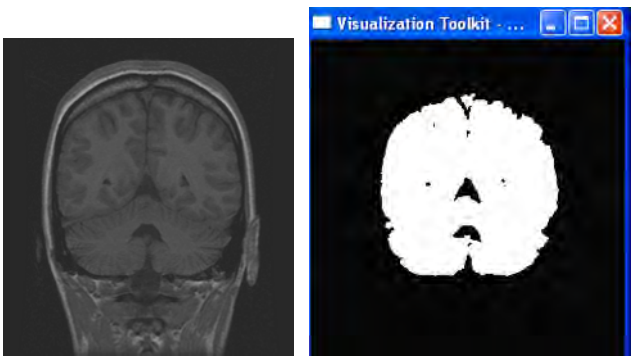


Fig. 6 The implemented result using vtkITKConfidenceConnectedImageFilter

The example of Java code implementing vtkITKGradientMagnitudeImageFilter is as follows

```
package vtkitk_example;
import vtkitk.*;
public class Main {
   static {
      System.loadLibrary("vtkCommonJava");
      System.loadLibrary("vtkFilteringJava");
      System.loadLibrary("vtkIOJava");
      System.loadLibrary("vtkImagingJava");
      System.loadLibrary("vtkGraphicsJava");
      System.loadLibrary("vtkRenderingJava");
      System.loadLibrary("vtkITKJava");
   }
   public Main() {}
   public static void main(String[] args) {
      vtkDICOMImageReader dicomread = new
vtkDICOMImageReader();
       dicomread.SetFileName
("D://DICOM_data/MRI_Series8/I0000437_anon.dcm");
       dicomread.SetDataByteOrderToLittleEndian();

      vtkITKGradientMagnitudeImageFilter Filter = new
vtkITKGradientMagnitudeImageFilter();
      Filter.SetInput(dicomread .GetOutput());
      vtkImageCast cast = new vtkImageCast();
      cast.SetInput(Filter.GetOutput());
      cast.SetOutputScalarTypeToUnsignedChar();

      vtkRenderWindowInteractor renderWindowInteractor= new
vtkRenderWindowInteractor();
      vtkImageViewer viewer = new vtkImageViewer();
      viewer.SetupInteractor(renderWindowInteractor);
      viewer.SetInput(cast.GetOutput());
      viewer.SetColorWindow(255);
      viewer.SetColorLevel(127);
      viewer.Render();
      renderWindowInteractor.Start();
   }
}
```

It can be seen that the proposed method for compiling the integrated ITK/VTK for Java language, has enable the integration of filtering algorithms in the ITK library to the VTK library. There are still numerous filters available in the ITK library that we plan to include in the implementation to make the integrated ITK/VTK library more powerful and available in Java programming language.

IV. Conclusions

In this paper, we present the method that enables the integration of ITK and VTK libraries together in Java language. This integrated ITK/VTK offers more flexible handling the image processing filters in the ITK library into the VTK pipeline. Hence, the rapid development of the applications using the advantages from both VTK and ITK libraries can be achieved.

Acknowledgment

This work is supported by National Electronics and Computer Technology Center (NECTEC) through the DentiPlan (Dental Implant Planning) Software and Dental CT Scanner projects.

References

1. ITK at http://www.itk.org/
2. VTK at http://www.vtk.org/
3. Caban JJ, Joshi A, Nagy P (2007) Rapid Development of Medical Imaging Tools with Open-Source Libraries. Journal of Digital Imaging, vol. 20, pp 83-93
4. VolView at http://www.kitware.com/products/volview.html
5. 3D Slicer at http://www.slicer.org/
6. Lehmann G, Pincus Z, Regrain B (2006) WrapITK: Enhanced languages support for the Insight Toolkit.
7. CMake at http://www.cmake.org
8. Martin K (1996) Automated wrapping of a C++ class library into Tcl" Proceedings of the 4th conference on USENIX Tcl/Tk Workshop, vol. 4, Monterey, California.
9. gccxml at http://www.gccxml.org.
10. CableSwig at http://www.itk.org/HTML/CableSwig.html

ECG Feature Extraction by Multi Resolution Wavelet Analysis based Selective Coefficient Method

Saurabh Pal[1] and Madhuchhanda Mitra[2]

[1] Haldia Institute of Technology, West Bengal, India
[2] University of Calcutta,West Bengal,India

Abstract — **One of the major problems in feature extraction methodologies from ECG is to identify the wave and complex boundaries. Here we present a multiresolution wavelet based approach to identify the boundaries. The wavelet reconstruction coefficients are assessed in terms of shape and size to eliminate the interfering components for better detection of wave boundaries. The relevant coefficients are retained that resembles with the original structure of the wave under investigation. The algorithm suggests different set of reconstruction coefficients for different part of the ECG wave which eliminates the scope of probable interaction between adjacent regions and thus correct identification of wave boundaries are ensured. The QRS complex and T wave duration are measured with the algorithm and validated against some arbitrarily chosen ECG records for lead 1 from Physionet PTB diagnostic database. The measured values are compared with the manually determined values and the accuracy for each evaluation is calculated. The test result shows over 95% accuracy for QRS complex and over 92% accuracy for QT interval and T duration.**

Keywords — **ECG, Feature Extruction, Db6 wavelet, Reconstruction Coefficient**

I. Introduction

The new generation of medical treatment has been suported by computerized processes. Signals recorded from t he human body provide valuable information about the activities of its organs. Their characteristic shape, or temporal and spectral properties, can be correlated with a normal or pathological function. In response to dynamical changes in the behaviour of those organs, the signals may exhibit time-varying as well as non-stationary responses. The QRS complex is the most prominent waveform within the electrocardiographic (ECG) signal, with normal duration from 0.06s to 0.1s [1]. It reflects the electrical activity within the heart for total ventricular muscle depolarization. Its shape, duration and time of occurrence provide valuable information about the current state of the heart. Because of its specific shape, the QRS complex serves as an entry point for almost all automated ECG analysis algorithms. The QRS detection is not a simple task, due to the varying morphologies of normal and abnormal complexes and because the ECG signal experiences several different types of disturbances with complex origin. Once the QRS complex has been identified, a more detailed examination of ECG signal can be performed. The detection of the QRS complex is the most important task in automatic ECG signal analysis [2]. The T wave is another important wave in the ECG waveform. It generates due to ventricular depolarization. In some pathological conditions the morphology of the T-wave may change from beat to beat, the simplest and most easily recognizable change being an amplitude change and the time duration change of the wave. The Q-T interval is measured on the horizontal axis from the onset of the Q wave to the end of the T wave. Since the QRS complex represents ventricular depolarization and the T wave represents ventricular repolarization, the Q-T interval denotes the total duration of ventricular systole. The Q-T interval includes the duration of QRS complex, the length of S-T segment and the width of T wave. Accurate measurement is important as QT prolongation is associated with the risk of ventricular tachyarrhythmia and of sudden cardiac death [3].

II. Discrete wavelet transform

A wavelet is a waveform of effectively limited duration that has an average value of zero. Similar to Fourier series analysis, where sinusoids are chosen as the basis function, wavelet analysis is also based on a decomposition of a signal using an orthonormal (typically, although not necessarily) family of basis functions. Unlike a sine wave, a wavelet has its energy concentrated in time. Sinusoids are useful in analyzing periodic and time-invariant phenomena, while wavelets are well suited for the analysis of transient, time-varying signals (well suited for ECG signals). A wavelet expansion is similar in form to the well-known Fourier series expansion, but is defined by a two-parameter family of functions

$$f(t) = \sum_k \sum_j a_{j,k} \psi_{j,k}(t) \qquad (1)$$

where j and k are integers and the function $\psi_{j,k}(t)$ is the wavelet expansion function. The two-parameter expansion

Chwee Teck Lim, James C.H. Goh (Eds.): ICBME 2008, Proceedings 23, pp. 590–593, 2009
www.springerlink.com

coefficients $a_{j,k}$ are called the discrete wavelet transform (DWT) coefficients of f(t) and the equation given above is known as the synthesis formula (i.e., inverse transformation). The coefficients are given by

$$a_{j,k} = \int f(t)\psi_{j,k}(t)\,dt\,. \tag{2}$$

The wavelet basis functions are a two-parameter family of functions that are related to a function called the generating or mother wavelet by

$$\psi_{j,k}(t) = 2^{j/2}\psi(2^{j}t - k) \tag{3}$$

where k is the translation and j the dilation or compression parameter. Thus wavelet basis functions are obtained by translation and scaling from a single wavelet. This means that given an approximation of a signal using translations of a mother wavelet up to some chosen scale, we can achieve a better approximation by using expansion signals with half the width and half as wide translation steps. The wavelet transform as such decomposes a signal into two subsignals – detail signal and approximation signal. Detail signal contains the upper half of the frequency components and approximation signal contains the lower half. The decomposition can be further repeated on the approximation signal in order to get the second detail and approximation signal. Thus in discrete wavelet domain, multiresolution analysis can be performed.

III. Simulation and Implementation

Here at first we have taken some arbitrarily chosen ECG text data from physionet PTB diagnostic database [4].As the raw ECG signal may be added with some noise, the wave is first denoised using standard technique. Then decomposion of the function is done upto level eight using Daubechies 6 (Db6) wavelet. Here Db6 wavelet is selected as some detail coefficients from multiresolution decomposition shows better resemblance with QRS complex of the ECG wave [5].

The decomposition result along with the original signal is shown in figure 1. This figure shows that coefficients at level three, four and five shows better resemblance with the QRS complex whereas all others appearing to be noisy with respect to the QRS region having most noises at the upper and lower levels. Thus d3, d4 and d5 coefficients are identified for the detection of QRS complex. The plot of the reconstructed wave comprising of d3, d4 and d5 is shown in figure 2. As from figure 2 it is clear that although the QRS region is properly captured but it is difficult to identify R peak due to the oscillatory nature of the graph. So, by simple manipulation, a function e2 is defined as

$$e2 = d4 \times (d3 + d5)/2^{n}\,, \tag{4}$$

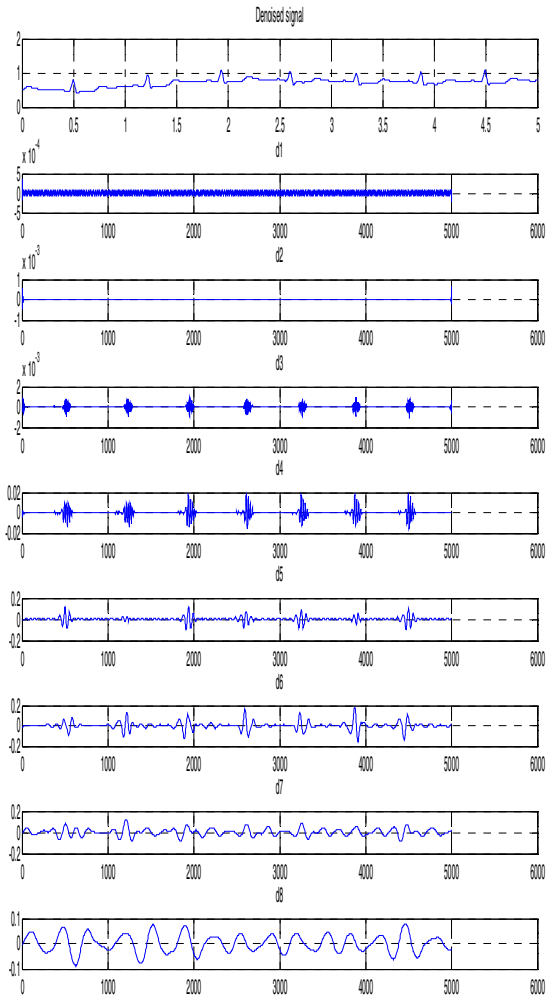


Fig 1: Original signal and multiresolution decomposition using Daubechis 6 wavelet upto level eight

where n is the level of decomposition. Then the modulus of e1 × e2 is done, where

$$e1 = d3 + d4 + d5\,. \tag{5}$$

The corresponding plot is shown in figure 3 along with the original wave. It is seen from plot 3 that the QRS region is not only having sharp peak but is much closely spaced in time also.From this graph the R peak is detected as the highest point. Once the R peak is detected, the Q and S points are to be identified to detect the complete QRS complex. For that decomposition coefficients from d1 to d5 are kept and the reconstructon wave is given by

$$e3 = d1 + d2 + d3 + d4 + d5\,. \tag{6}$$

Then 5 point differentiation on e3 is done to find first two zero slope points on either side of R peak as detected

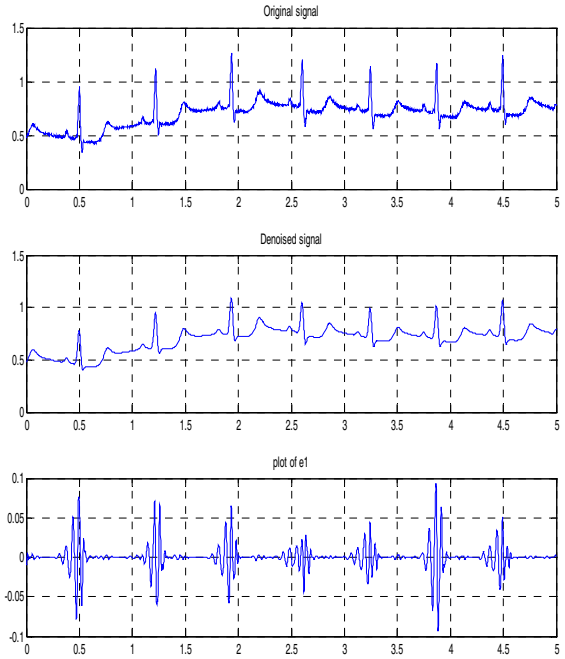


Fig 2: Original signal and polt of e1=d3+d4+d5

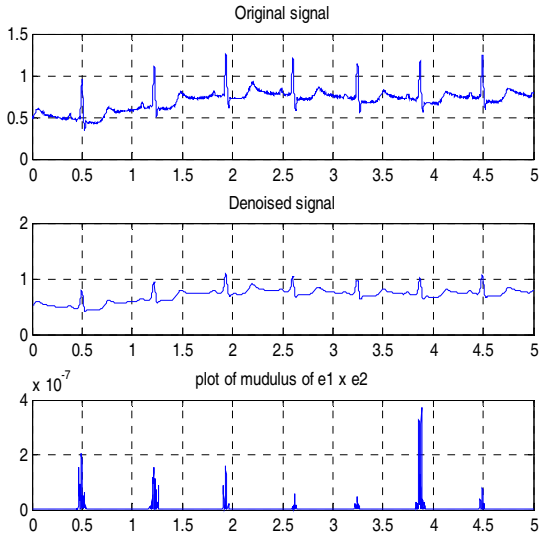


Fig 3: Original signal and plot of modulus of e1 x e2

earlier. The Q point as detected is taken as the J point or zero potential point.

To find out T wave, an inspection has made on the decomposition coefficients and it is seen that T wave is most significant in d4, d5, d6 and d7 coefficients. Hence the reconstructed wave is formed as

$$e4 = d4 + d5 + d6 + d7 \quad (7)$$

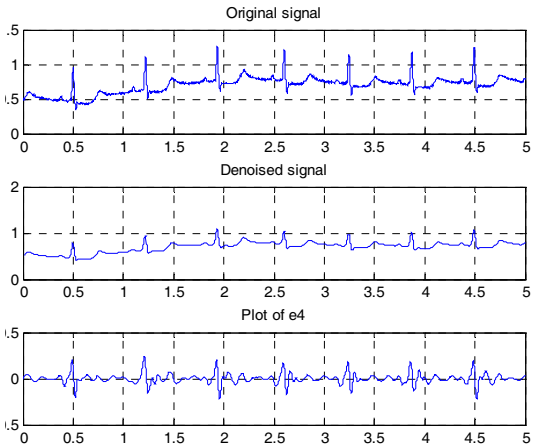


Fig 4: Original signal and plot of e4

Then the T peak is identified as the maxima after the detected S point within a predefined stipulated interval. As the T peak is pointed out, T onset and T offset is found out as the minimum potential crossing points on either side of the T peak. The plot of equation 7 is shown in figure 4. Thus the significant points as Q,R,S and T wave are identified by selective coefficient method.

IV. Result and Analysis

The results are shown in the following figures as per the simulation and implementation discussed in the earlier section. Figure 5 shows the detected QRS complex and T wave for an ECG waveform taken arbitrarily from the physionet database.

Sometimes a serious problem is encountered in automatic ECG feature extraction technique. It is the unpredictable

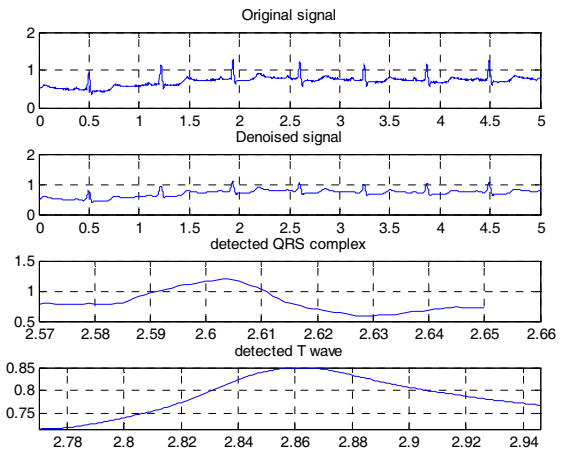


Fig. 5: Plot of Original wave, denoised wave, QRS complex, P wave and NON INVERTED T wave identified by the proposed algorithm.

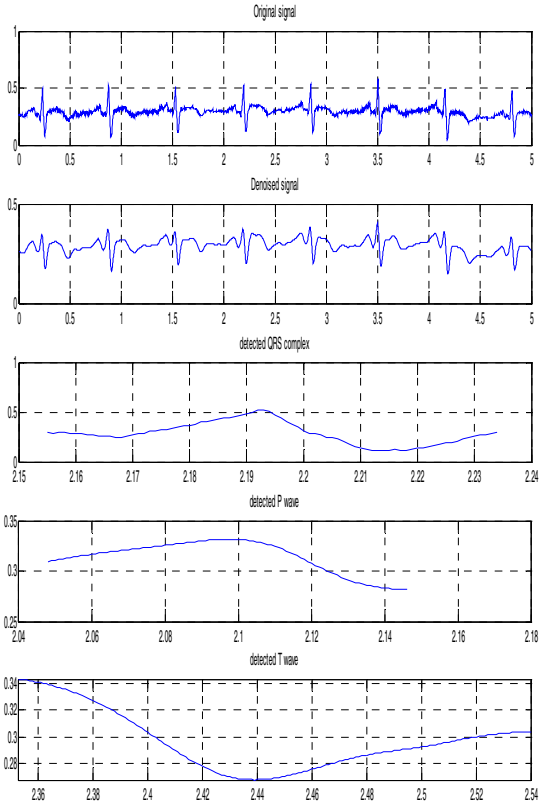


Fig. 6: Plot of Original wave, denoised wave, QRS complex, P wave and INVERTED T wave identified by the proposed algorithm.

shape and slope of T wave specially the inverted T waves. This problem is taken into account here by identifying the type of the T wave at the beginning of the T peak detection algorithm. Here the type of the T wave is detected by comparing the magnitudes within the T wave separated by a predefined interval. An inverted T wave along with corresponding QRS wave is shown in figure 6.

Some arbitrarily chosen data from Physionet PTB diagnostic database are tested by the proposed algorithm and the values of QRS duration, T wave duration and QT internal duration are measured. The results are compared with the manually calculated values for the same database. Some of the results are shown in the following tables.

Table 1: Comparison of QRS duration in automatic and manual mode.

Database	Automatic(sec)	Manual(sec)	Percentage inaccuracy
P61 s210	.079	.077	-2.6
P50 s215	.079	.078	-1.3
P40 s130	.079	.078	-1.3
P42 s 137	.080	.079	-1.3
P32 s106	.057	.059	3.4

Table 2: Comparison of T wave duration in automatic and manual mode.

Database	Automatic(sec)	Manual(sec)	Percentage inaccuracy
P61 s210	.170	.174	2.3
P50 s215	.168	.175	4.0
P40 s130	.173	.177	2.3
P42 s 137	.181	.178	-1.7
P32 s106	.193	.185	-4.3

Table 3: Comparison of QT interval duration in automatic and manual mode.

Database	Automatic(sec)	Manual(sec)	Percentage inaccuracy
P61 s210	.316	.321	1.6
P50 s215	.394	.398	1.0
P40 s130	.394	.383	-2.9
P42 s 137	.300	.314	4.5
P32 s106	.308	.305	-1.0

From the tables it is clear that the proposed algorithm is moderately accurate in terms of the measurement of the durations of QRS complex, T wave and QT interval. Moreover, figure 6 shows that P wave can also be identified by the proposed algorithm.

V. Conclusions

Thus we can hereby conclude that the proposed algorithm based on multiresolution wavelet analysis based selective coefficient method is an easy and accurate one for ECG feature extraction and corresponding analysis. This analysis can further be extended towards automatic disease identification or biometric analysis.

References

1. Principle of Clinical Electrocardiography, M. Goldman, Lange Medical Publication, Drawer L, Los Altos, California 94022
2. C. Li, C. Zheng, C. Tai, Detection of ECG characteristic points using wavelet transforms, *IEEE* Trans. on Biomedical Engineering, vol 42, no. 1, pp. 21- 28, 1995
3. Laguna P, Moody GB, Jane R, Caminal P and Mark RG. Karhunen-Loeve, Transform as a tool to analyze the STsegment– comparison with QT interval. Journal of Electrocardiology,vol 28, pp. 41-49, 1995
4. http://www.physionet.org/
5. S. Z.Mahamoodibad, A Ahmadian, M.D. Abolhasani, ECG feature extraction using Daubechies wavelets, Proceedings of Fifth IASTED International Conference, pp 343-348, 2005

Author: Mr. Saurabh Pal
Institute: Haldia Institute of Technology
Street: BE 45, Bidhannagar east
City: Midnapore
Country: India
Email: spal76@gmail.com

Microarray Image Denoising using Spatial Filtering and Wavelet Transformation

A. Mastrogianni[1], E. Dermatas[1] and A. Bezerianos[2]

[1] Dept. of Electrical Engineering and Computer Technology, University of Patras, HELLAS
[2] Dept. of Medical Physics, School of Medicine, University of Patras, HELLAS

Abstract — **As the aim of using microarray technology is to try to understand fundamental aspects of growth and development as well as to explore the underlying genetic causes of many human diseases, the restoration of the ideal microarray image's properties in a noisy image, is an urgent priority of the image processing procedure. The scope of this work is to describe and evaluate different methodologies for noise reduction in microarray images. In this paper, two basic approaches to microarray image denoising: spatial filtering methods and transform domain filtering methods are presented. The image denoising, with spatial filtering techniques as well as hard and soft thresholding of wavelet coefficients have been tested in microarray images of gene expression profiles of human sarcoma using the Stanford MicroArray Database.**

Keywords — **microarray, image denoising, wavelet, spatial filters**

I. Introduction

Gene expression analysis, using microarrays, targets at the measurement of mRNA abundance as a measure of gene expression activity. In a typical microarray setting, thousands of cDNA clones are robotically spotted onto coated glass slides in a highly condensed array. The output of a single microarray experiment is a digital image [1]. The information extracted from those images comes almost exclusively from the intensities of the spots. Unfortunately, the accuracy of the gene expression depends on the experiment itself, as well as, the image analysis methods.

Due to the nature of the acquisition process, microarray images contain noise, such as dust, fingerprints, small particles, distortions from the optical components and electronic noise, which definitely affect the accuracy of the further data analysis and the validity of the gene mutation prognosis. The noise elimination is a challenging and fundamental problem in microarray analysis and a lot of de-noising methods have already been proposed each one having its advantages and limitations [2, 4].

There are two basic approaches to microarray image denoising: spatial filtering methods and transform domain filtering methods. Spatial filters can be effectively used to remove various types of noise in digital images. Transform domain methods are time consuming and depend on the cut-off frequency and the filter function behavior. Among the most popular transformation methods, wavelet denoising is widely used in microarray analysis [5]. In this paper an overview of various algorithms and analysis is provided and potential future trends in the area of denoising are discussed.

In the next section a presentation of the spatial filtering and wavelet denoising methods is given. In section 3, the microarray database, the experimental results and a number of representative examples are shown. Finally, a short discussion on the results and the on-going work is given.

II. Spatial filtering and wavelet denoising methods

Spatial filters can be classified into non-linear and linear filters. The simplest non-linear filter is the median filter and is effective at reducing impulse noise (i.e. 'Salt&pepper' noise) where the noisy pixels contain no information about their original values. Hsin-Cheng Huang and Thomas C. M. Lee in their work [6] mention a signal and image denoising method using median filter. The linear Wiener filtering method requires the information about the spectra of the noise and the original signal and it performs well only if the underlying signal is smooth. The Wiener filter is the optimal filter for gaussian noise removal in the sense of mean square error.

Wavelet image processing plays a major role in image denoising, especially in the presence of additive Gaussian noise [7]. In medical imaging, wavelet transform were first introduced in 1991 in a journal paper describing an application of noise reduction in MRI images [8]. In 2003, stationary wavelet transform has been used to enhance the quality of microarray images [9], showing superior performance than the discrete wavelet transform and the widely used adaptive Wiener filtering methods.

In this paper we present an overview of microarray image denoising methods, comparing the reconstructed images after using the median filter, the Wiener filter and some of the most commons wavelet families.

All the denoising methods are briefly described in the followed four steps:

- A set of noiseless subarray images are selected from the microarray database.
- Additive 'Salt&pepper' and Gaussian noise are used to distort the selected microarray subarray images.

Chwee Teck Lim, James C.H. Goh (Eds.): ICBME 2008, Proceedings 23, pp. 594–597, 2009
www.springerlink.com

- The evaluated denoising methods are applied and the restored images are created.
- Objective fidelity criteria (PSNR, SNR) are used to evaluate the robustness of the denoising methods.

In the subarray images the noise had been modeled with either a Gaussian (Fig.1), uniform, or Salt&pepper ('impulse') distribution (Fig.2).

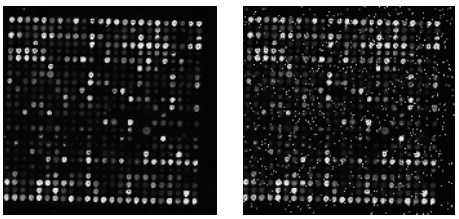


Fig. 1 Microarray image before and after applying Salt&pepper noise of variance 0.04

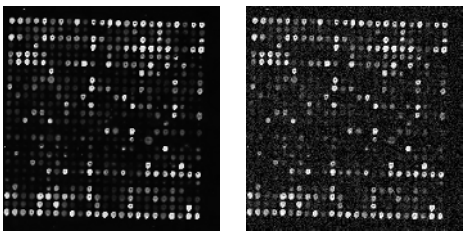


Fig. 2 Microarray image before and after applying Gaussian noise of variance 0.04

Two criteria, the SNR (eq. 1) and the PSNR (eq. 2), are used for quantitating the difference between the noisy microarray and the reconstructed image after applying the denoising method. The higher the PSNR, the better the quality of the reconstructed image.

$$SNR(dB) = 10\log_{10}\left(\frac{P_{signal}}{P_{noise}}\right), \quad (1)$$

where P_{signal} is the power of the signal and P_{noise} is the power of the noise.

$$PSNR(dB) = 10\log_{10}\left(\frac{MAX_I^2}{MSE}\right), \quad (2)$$

where $MSE = \frac{1}{mn}\sum_{i=0}^{m-1}\sum_{j=0}^{n-1}\left\|I(i,j) - K(i,j)\right\|^2$ is the mean square error, I is the $m \times n$ noiseless image and K is the restored image.

III. Experimental results

The implemented denoising methods have been evaluated in 34 microarray images of gene expression profiles of human sarcoma [10], each one containing 32 subarrays. The microarray subarrays are selected according to their level of noise. From the total set of 1088 subarrays included in the Stanford MicroArray Database the less noisy subarrays are selected. In most microarray images extremely noisy background is met but a quite satisfying number of these subarrays (150) had fulfilled our demand for the minimum background noise. The denoising methods were implemented in Matlab computing environment.

In Tables 1 and 2 the mean value of PSNR and SNR of the median and Wiener denoising methods are shown estimated from the evaluation set of 150 subarrays. The median filtering is more effective in case of Salt&pepper noise compared to the PSNR rate achieved in the presence of additive Gaussian noise, as expected. The median filtering is robust in all levels of noise, giving similar PSNR rates in case of Salt&pepper noise. On the contrary, the noise reduction rate using Wiener filtering decreases when the noise level increases in both types of noise.

Table 1: PSNR and SNR for median filtering using four noise levels and two types of noise, in dB.

variance	0.01	0.02	0.03	0.04
		Salt&pepper noise		
PRNR	29.754	29.6907	29.6391	29.54
SNR	9.1173	6.1251	3.9074	3.7803
		Gaussian noise		
PRNR	25.1373	24.4018	23.6430	22.8347
SNR	8.3783	7.7638	7.1149	6.5024

Table 2: PSNR and SNR for Wiener filtering using four noise levels and two types of noise, in dB.

variance	0.01	0.02	0.03	0.04
		Salt&pepper noise		
PSNR	25.3612	23.4316	22.4672	21.8146
SNR	9.0524	6.074	4.2922	3.0927
		Gaussian noise		
PSNR	25.8864	25.1408	24.3024	23.4629
SNR	8.4139	7.7837	7.1569	6.9676

In Tables 3,4,5,6, and 7, the evaluation results of wavelet denoising using five basis-functions (haar, db2, sym2, bior1.1 and coif) are shown. In the case of the wavelet family denoising method, we use both soft and hard thresholding and decomposition level of 2.

Table 3: PSNR and SNR for Wavelet (haar) denoising using four noise levels and two types of noise, in dB

variance	0.01	0.02	0.03	0.04
		Soft thresholding		
		Salt&pepper noise		
PSNR	23.1539	20.0827	18.5035	17.2767
SNR	9.4787	6.3873	4.8059	3.5775
		Gaussian noise		
PSNR	22.5853	21.9917	21.4400	20.8726
SNR	8.9124	8.2366	7.6067	6.9743
		Hard thresholding		
		Salt&pepper noise		
PSNR	22.9704	19.8823	18.2666	17.0274
SNR	9.5296	6.4354	4.8179	3.5775
		Gaussian noise		
PSNR	24.0152	22.5925	22.5737	21.8613
SNR	8.8954	7.6030	7.5845	6.9475

Table 4: PSNR and SNR for Wavelet (db2) denoising using four noise levels and two types of noise, in dB

variance	0.01	0.02	0.03	0.04
		Soft thresholding		
		Salt&pepper noise		
PSNR	23.3335	20.2186	18.5764	17.3499
SNR	9.5811	6.4470	4.8059	3.5815
		Gaussian noise		
PSNR	22.7683	22.2007	21.6923	21.1122
SNR	8.8562	8.2098	7.6150	6.9825
		Hard thresholding		
		Salt&pepper noise		
PSNR	23.1284	19.9345	18.2390	17.0136
SNR	9.6861	6.4859	4.7887	3.5625
		Gaussian noise		
PSNR	23.8110	23.1486	22.4689	21.7760
SNR	8.8499	8.2140	7.5710	6.9433

Table 5: PSNR and SNR for Wavelet (sym2) denoising using four noise levels and two types of noise, in dB

variance	0.01	0.02	0.03	0.04
		Soft thresholding		
		Salt&pepper noise		
PSNR	23.5120	20.2416	18.5013	17.3426
SNR	9.7644	6.4703	4.7309	3.5765
		Gaussian noise		
PSNR	22.7791	22.2002	21.6502	21.1257
SNR	8.9067	8.1963	7.5879	6.9738
		Hard thresholding		
		Salt&pepper noise		
PSNR	22.8751	19.8936	18.0729	16.9887
SNR	9.4322	6.4450	4.6226	3.5377
		Gaussian noise		
PSNR	23.8721	23.1637	22.4682	21.8357
SNR	8.8883	8.2145	7.5745	7.0053

Table 6: PSNR and SNR for Wavelet (bior1.1) denoising using four noise levels and two types of noise, in dB

variance	0.01	0.02	0.03	0.04
		Soft thresholding		
		Salt&pepper noise		
PSNR	23.2565	20.2414	18.5682	17.2156
SNR	9.5811	6.5470	4.8702	3.5169
		Gaussian noise		
PSNR	22.5526	21.9506	21.4118	20.8760
SNR	8.8560	8.2035	7.5753	6.9712
		Hard thresholding		
		Salt&pepper noise		
PSNR	23.0939	20.0136	18.2880	16.8953
SNR	9.6535	6.5668	4.8393	3.4454
		Gaussian noise		
PSNR	23.9939	23.2977	22.5961	21.8731
SNR	8.8515	8.2510	7.6002	6.9584

Table 7: PSNR and SNR for Wavelet (coif) denoising using four noise levels and two types of noise, in dB

variance	0.01	0.02	0.03	0.04
		Soft thresholding		
		Salt&pepper noise		
PSNR	23.3820	20.3825	18.6188	17.3345
SNR	9.5021	6.5016	4.7505	3.4834
		Gaussian noise		
PSNR	23.2661	22.6428	22.1136	21.5362
SNR	8.8533	8.1654	7.5836	6.9728
		Hard thresholding		
		Salt&pepper noise		
PSNR	22.8431	19.8424	18.2491	16.9775
SNR	9.3900	6.3873	4.7940	3.5228
		Gaussian noise		
PSNR	24.1224	23.4018	22.7438	22.0390
SNR	8.8730	8.1969	7.5865	6.9415

The experimental results show that wavelet denoising methods are more effective in the presence of Gaussian additive noise compared to the denoising results derived in case of additive Salt&pepper noise. This figure is valid for both types of thresholding.

In Fig. 3 and 4 two examples of a microarray image denoising processing, using median filter and wavelet bior1.1 transform are given.

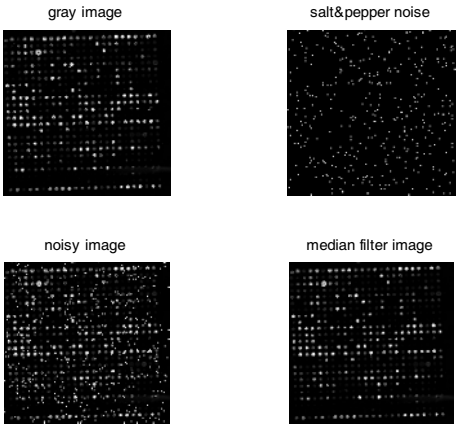


Fig. 3 Example of the median filter denoising method when applying Salt&pepper noise of variance 0.04

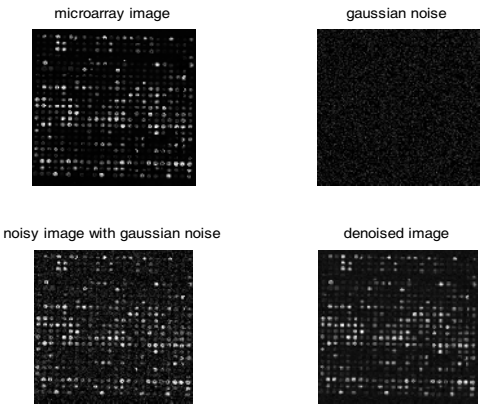


Fig. 4 Example of wavelet bior1.1 denoising method when applying Salt&pepper noise of variance 0.03, soft thresholding and decomposition level of 2

IV. Conclusions

Image denoising is an essential aspect of microarray experiments. The experimental comparison of popular denoising methods in subarray images presented in this paper can be used to implement different denoising methods for different types of noise. The robustness and generalization of the techniques described provide adequate basis to apply the same techniques to nanoarray imaging systems.

Acknowledgment

This paper is part of the 03ED375 research project, implemented within the framework of the "Reinforcement Programme of Human Research Manpower" (PENED) and co-financed by National and Community Funds (20% from the Greek Ministry of Development-General Secretariat of Research and Technology and 80% from E.U.-European Social Fund).

References

1. Stefano Lonardi, Yu Luo, 'Gridding and Compression of Microarray Images', Proc. of Computational Systems Bioinformatics, CSB- 2004
2. Yee Hwa Yang, Michael J. Buckley, Sandrine Dudoit,Terence P. Speed, 'Comparison of methods for image analysis on cDNA microarray data', Journal of Computational & Graphical Statistics, vol. 11, pp.108-136, 2002.
3. Paul O'Neill, George D. Magoulas, Xiaohui Liu, 'Improved Processing of Microarray Data Using Image Reconstruction Techniques', IEEE Transactions on Nanobioscience, vol. 2, no. 4, Dec.2003.
4. J. Quackenbush, 'Computational analysis of microarray data', Nature Reviews Genetics, vol. 2, no. 6, pp. 418-27, 2001.
5. S.Sudha, G.R.Suresh, R.Sukanesh, 'Wavelet based image denoising using adaptive thresholding', International Conference on Computational Intelligence and Multimedia Applications 2007 IEEE.
6. Hsin-Cheng Huang, Thomas C. M. Lee, 'Data Adaptive Median Filters for Signal and Image Denoising Using a Generalized SURE Criterion' IEEE Signal Processing Letters, vol. 13, no. 9, September 2006.
7. Weaver, J. B., Yansun, X., Healy, D. M., and Cromwell, L. D., 'Filtering noise from images with wavelet transforms', Magnetic Resonance in Medicine, vol. 21, no. 2, pp. 288-295, 1991.
8. Weaver, J. B., Yansun, X., Healy, D. M., and Cromwell, L. D., 'Filtering noise from images with wavelet transforms', Magnetic Resonance in Medicine, vol. 21, no. 2, pp. 288-295, 1991.
9. X. H. Wang, Robert S. H. Istepanian, and Yong Hua Song, 'Microarray Image Enhancement by Denoising Using Stationary Wavelet Transform', IEEE Trans. on Nanobioscience, vol. 2, no. 4, Dec. 2003
10. http://smd.stanford.edu

Author: Aikaterini Mastrogianni
Institute: University of Patras
Street:
City: Rion-26500
Country: Greece
Email: kmastro@george.wcl2.ee.upatras.gr

Investigation of a Classification about Time Series Signal Using SOM

Y. Nitta[1], M. Akutagawa[1], T. Emoto[1], T. Okahisa[2], H. Miyamoto[2], Y. Ohnishi[2], M. Nishimura[2], S. Nakane[2], R. Kaji[2], Y. Kinouchi[1]

[1] Faculty of Engineering the university of Tokushima, Tokushima, Japan
[2] School of Medicine the university of Tokushima, Tokushima, Japan

Abstract — **There are various blood purifications. Plasma Exchange(PE) is one of the blood purifications. A patient's circulating blood volume is changing during the PE. Hence, the medical workers must treat to stabilize the circulating blood volume. They are the CLIT-LINE monitor (CLM) to obtain the hematocrit (Ht) values, because the circulating blood volume is calculated by Ht values. Ht value reflects the count of red cells in the circulating blood volume, and Ht values are changed by the urination. They recognize the patient's condition by the classifying the change of Ht values. However, the classifying the change of Ht values is depended on the experience of medical workers. This approach is very subjective. Hence, our purpose is the investigation of the possibility about the classifying the change of Ht value using the Self Organized feature Map (SOM). We used the Ht value that was obtained in the Tokushima University Hospital. The Ht data was greatly changed by urination. At first, the Ht data is divided into the consecutive grouped patterns. We used recurrent neural network (RNN) to treat the change of Ht value in each group. RNN is effective to treat the feature of time series signals, and it was known that the weight values of RNN have some information about the feature of signals. The seconds, the weight values obtained in each group are used as input data to SOM. As a result of SOM, Ht data were divided into 4 groups. One of them was a group into which Ht values were greatly changed by urination. It is thought that other groups show the state that has changed little by little during the PE. As a conclusion, it was supposed that the possibility about the classifying the change of Ht value using SOM.**

I. Introduction

There are various blood purifications. Plasma exchange (PE) is one of the blood purifications. A patient's circulating blood volume is changing during the PE. Hence, the medical workers must treat to stabilize the circulating blood volume. With rapid advances in information technology, computer-aided medical treatments are becoming quite common place in hospitals. Several medical treatments have been evolved by relying on the artificial intelligence [1]-[3]. They use the CLIT-LINE monitor (CLM) to obtain the hematocrit (Ht) values, because the circulating blood volume and Ht value are related. The rate of circulating blood volume ($\Delta BV\%$) is very important during the blood purification including the PE. $\Delta BV\%$ is calculated by the two Ht value. One is the Ht value at the beginning of the PE, and another is the present Ht value. Hence, we thought that the many Ht values in a fixed time showed the more detailed condition of the circulating blood volume. If the characteristics of the Ht values in each fixed time are classified, the doctor has the possibility to treat the patient more safety in blood purifications. Hence, our purpose is the investigation of the possibility about the classifying the change of Ht value using the Self Organized feature map (SOM).

We used the recurrent neural network (RNN) to capture the characteristic of Ht values in a fixed time. We used the weight values obtained in a fixed time as the input data for SOM.

II. Analysys data

Currently, CRIT-LINE monitor (CLM) is one of the popular equipments, specifically due to its ability to obtain the Ht value every 20 seconds. At the Tokushima University Hospital where our study was conducted, CLM is used for obtaining Ht values during blood purification [4].

In this study, Ht values were collected from patient during the PE at the Tokushima University Hospital, after obtaining their consent. Durations of each PE treatment was about 100 minutes, and 4 patients were effectively treated with PE under medical supervision. Fig.1 shows the Ht data for patient A.

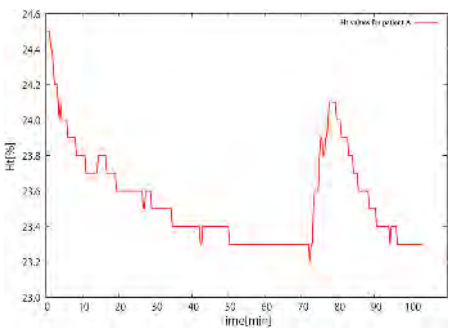


Fig.1 The Ht data for patient A

Chwee Teck Lim, James C.H. Goh (Eds.): ICBME 2008, Proceedings 23, pp. 598–601, 2009
www.springerlink.com

III. METHOD FOR RNN AND SOM

The structure of RNN is 6 units in the input layer and 6 units in the hidden layer. Ht values of first 5 minutes at the beginning of PE procedure were not used. These Ht values were influenced by the saline. In this study, biological time series signals are Ht values, and they are represented as:

$$x_1, x_2, \cdots, x_i, \cdots x_{last} \tag{1}$$

where, x_i is sampled data at sampling time i and x_{last} is the last Ht value. In this study, we used the 30 Ht values as a fixed time to classify the character of the wave. Otherwise, we divided into the consecutive groups the Ht values. A group is defined as:

$$PG_i : x_i, x_{i+1}, \cdots, x_{i+30-1} \tag{2}$$

where, i represents the sampling time as well as the index of the group. The groups were formed by Ht values in the following manner:

$$\begin{aligned} PG_1 &: x_1, x_2, \cdots, x_{30} \\ PG_2 &: x_{31}, x_{32}, \cdots, x_{60} \\ PG_3 &: x_{61}, x_{62}, \cdots, x_{90} \\ &\vdots \end{aligned} \tag{3}$$

The input/output relation of the RNN in the group i is as follows:

$$\begin{aligned} x_i, x_{i+1}, \cdots, x_{i+5} &\mid x_{i+6} \\ x_{i+1}, x_{i+2}, \cdots, x_{i+6} &\mid x_{i+7} \\ x_{i+2}, x_{i+3}, \cdots, x_{i+7} &\mid x_{i+8} \\ &\vdots \end{aligned} \tag{4}$$

The initial weights of RNN in the each group are same values. The initial weights are small random values. Then, the weights trained in each group are inputted to the SOM.

The training method for SOM is shown as follows. The equation (5) shows the method of update the node in SOM.

$$\mathbf{m}(t+1) = \mathbf{m}(t) + ETA \times (\mathbf{w}(t) - \mathbf{m}(t)) \tag{5}$$

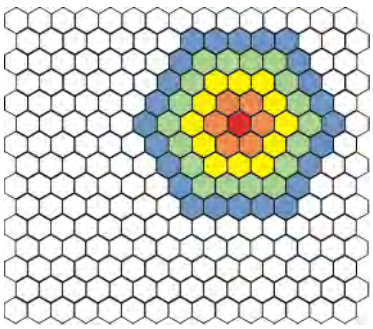


Fig.2 The Self Organized feature Map (SOM)

where, $\mathbf{m}(t)$ is the weights in node fired. $\mathbf{w}(t)$ is the weights of RNN. ETA is the training coefficient. Fig.2 shows the SOM. In this case, the node fired shows the red color, and ETA is 0.1. ETA is 0.05 in the orange nodes. ETA is 0.03 in the yellow nodes. ETA is 0.025 in the green nodes. ETA is 0.02 in the blue nodes.

IV. RESULT

We show the SOMs for each Ht data.

Fig.3 shows the each group for the patient A. Fig.4 shows the node fired. The number in each node fired shows the each group number. The weights of RNN in 1,2,5,6, and 7 groups are fired the same node in the SOM.

Fig.5 shows the each group for the patient B. Fig.6 shows the node fired. The number in each node fired shows the each group number. The weights of RNN in 1 and 2 groups are fired the same node in the SOM. The weight of RNN in 4 and 6 groups are fired the same node in the SOM.

Fig.7 shows the each group for the patient C. Fig.8 shows the node fired. The number in each node fired shows the each group number. The weights of RNN in 1,2,3 and 6 groups are fired the same node in the SOM. The weight of RNN in 4 and 5 groups are fired the same node in the SOM.

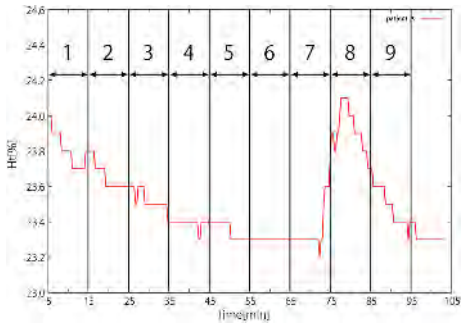


Fig.3 The each group for the patient A

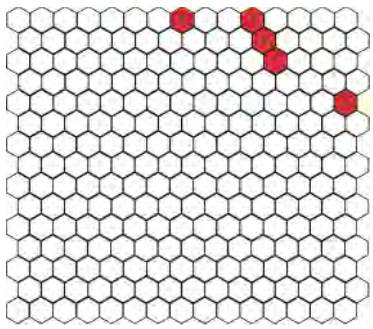


Fig.4 The SOM for patient A

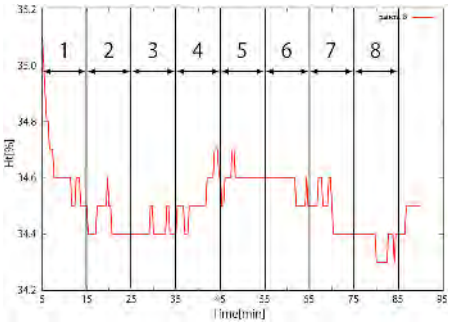


Fig.5 The each group for the patient B

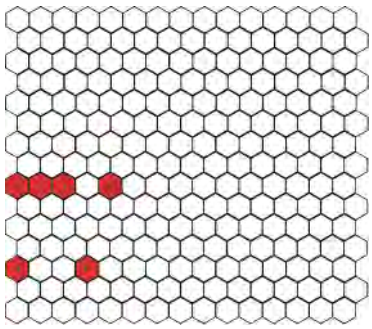


Fig.6 The SOM for the patient B

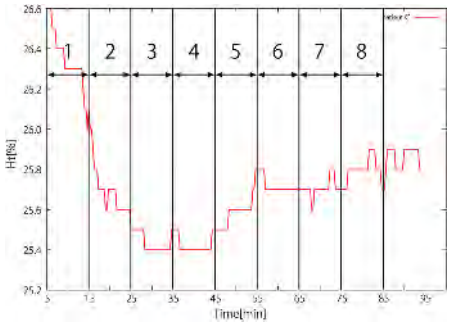


Fig.7 The each group for the patient C

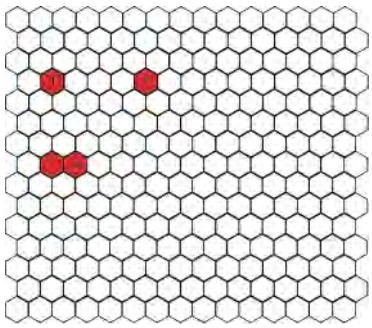


Fig.8 The SOM for the patient C

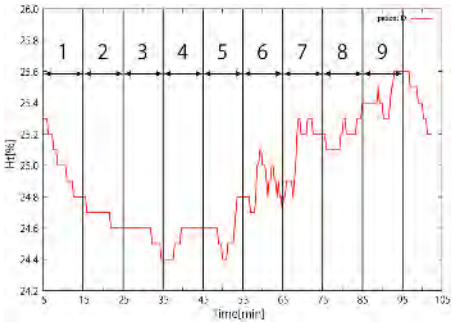


Fig.9 The each group for the patient D

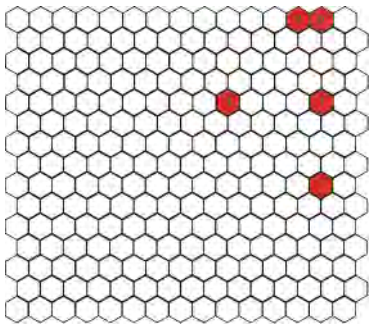


Fig.10 The SOM for the patient D

Fig.9 shows the each group for the patient D. Fig.10 shows the node fired. The number in each node fired shows the each group number. The weights of RNN in 1,2,3 and 6 groups are fired the same node in the SOM. The weight of RNN in 4 and 5 groups are fired the same node in the SOM.

V. Discussion and Conclusion

There was big difference between 8 group and 9 group in Fig.4. The difference was caused by the emiction. The patient A took a leak at the 7 group. The circulating blood volume was changed by this thing. The node fired at the 1 group fired again for the patient A, C and D. It thought that the circulating blood volume returned to the first state.

In this study, we investigated the possibility about the classifying change of Ht values using SOM. Though we investigated the classifying change of Ht values for only 4 patients, we supposed the possibility of the classifying the Ht values using RNN and SOM from the results for 4 patients.

As the future works, we try to investigate the possibility for the many patients and data made by us.

REFERENCES

1. Femandez EA, Naltuille R, Willshaw P, Perazzo CA, Using artificial intelligence to predict the equilibrated postdialysis blood urea concentration, Blood Purification , 19(3), 2001, 271-85
2. K. Papik, B. Mohnar, R. Schaefer, Z. Dombovari, Z. Tulassay, J. Feher, Application of neural networks in medicine – a review, Medical Science Monitor, 4(3), 1998, 538-546
3. L. Gabutti, D. VVadilonga, G. Mombelli, M. Burnier, C. Marone, Artificial neural networks improve the predicion of Kt/V, follow-up dietary protein intale and hypotesion risk in haemodialysis patients, Nephrology Dialysis Transplanttation, 19, May 2004, 1204-1211
4. H.Miyamoto, T.Okahisa, H.Iwaki, M.Murata, s.Ito, Y.Nitta, M.Akutagawa, Y.Kinouchi, Y.Ohnishi, J.Oto, M.Nishimura, Influence of Leukocytapheresis Therapy for Ulcerative Colitis on Anemia and Hemodynamics, Therapeutic apheresis and Dialysis, Vol11, No.1, Feb.2007,16-21

Author: Yoshinori Nitta
Institute: Faculty of Engineering the university of Tokushima
Street: 2-1 Minamijyosanjima cho
City: Tokushima
Country: Japan
Email: nitta@ee.tokushima-u.ac.jp

PCG Spectral Pattern Classification: Approach to Cardiac Energy Signature Identification

Abbas K. Abbas[1], Rasha Bassam[2]

[1] RWTH Aachen University, Aachen, Germany
[2] Biomedical Engineering Dept., Aachen University of Applied Sciences, Juelich, Germany

Abstract — **biomedical data clustering play a principal role in automated aided diagnosis in cardiac auscultation. Therefore different Phonocardiography (PCG) signal classifiers have been used to classify blood flow patterns and adopted to use with Computer Aided Diagnosis (CAD) system. The embedded PCG classifier is widely used in Clinical Decision Support System (CDSS) as well. An Automated PCG clustering module was developed as a base for Auscultation Clinical Assisted Diagnosis (AuCAD). Application of the pattern classification as adaptive k-mean in analyzing normal and pathological heart sound was investigated. The patterns of phonocardiogram signals are used to characterize the abnormalities while detecting non-linearity features in order to improve the diagnostic performance of heart sounds. The index for cardiac work as identified energy signature for the heart. In comparison to the linear clustering of PCG spectrum patterns, the results have shown that adaptive k-mean algorithms reveal difference in PCG analysis indicating non-Gaussian or non-linearity scheme. The intensity-based PCG value and the peaks of Short Time Fourier Transform (STFT) spectrum were efficiently determining cardiovascular dysfunctions affecting PCG trends. Mitral regurgitations and valvular dysfunctions associated with blood flow using CED were inspected. ROC performance test for adapted pattern classifier shows a higher stability with normal and abnormal PCG signal related with a mild decline in energy performance index with agglomerative compartment of PCG spectra. CED represents a robust method to distinguishing different pattern associated with cardiac auscultation. Statistical value from the probability density function of PCG data vectors was derived and verified. Cardiac energy detection (CED) has the affinity to alternate the conventional methods in biosignal patterns categorization.**

Keywords — **Phonocardiography, Pattern classification, Acoustic energy, Hemodynamic, Intensity profile**

I. Introduction

PCG Pattern classification, also known as auscultation pattern recognition, was one of the efficient computer-based methods applied to medical decision making system. PCG Pattern recognition generally is interpreted in two ways. The most general definition includes recognition of patterns in any type of PCG dataset and is called uniform PCG pattern classification this discriminate peaks of heart sounds as excitation source for circulation hemodynamic, and other is called adaptive pattern clustering which magnify and observe spectral characteristics associated with PCG waveform turbulences and differentiate them as clinical diagnostic indices. Fig.1 shows how the eight heart sounds, which are correlated to the physiological and pathophysiological events of the cardiac cycle and corresponding, power spectra.

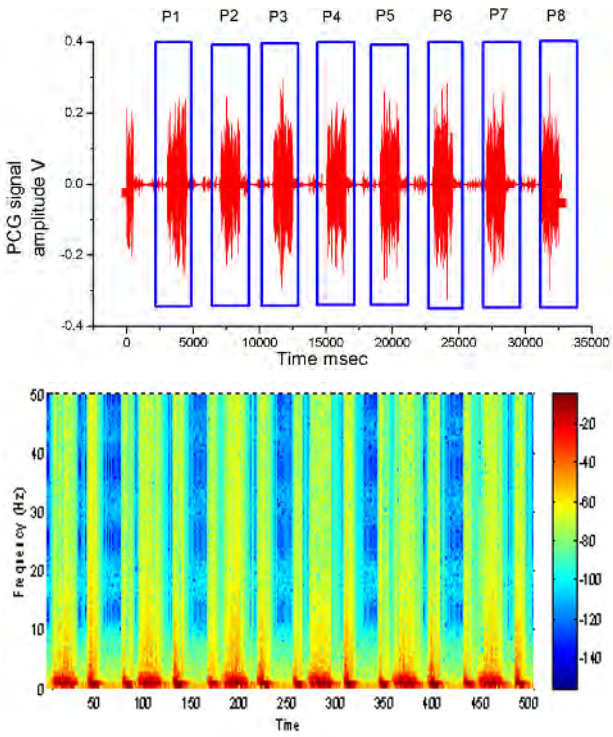


Fig. 1 PCG signal scheme marked with corresponding high intensity spectral peaks.

II. Materials and Methods

The PCG signal was downloaded from Physiobank physiological data bank. Experimental system identification was implemented using MATLAB®. Fig.2 illustrates the experimental setup of PCG signal with k-mean classification algorithm. Spectral estimation was implemented in

Chwee Teck Lim, James C.H. Goh (Eds.): ICBME 2008, Proceedings 23, pp. 602–605, 2009
www.springerlink.com

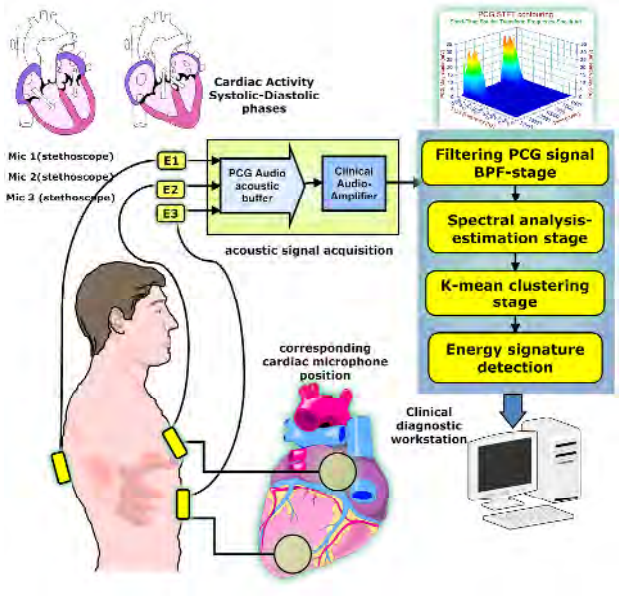


Fig. 2 PCG signal processing system setup based on spectral estimation technique.

computational loop to identify energy signature of cardiovascular activity [1].

III. Cardiac Acoustics Energy

Transducers such as microphones allowed collecting of more accurate acoustical data over a wider range of frequencies. Energy characteristic patterns in PCG data, thus recorded have been associated with conditions affecting hemodynamic patency such as mitral, tricuspid valve insufficiency, angina, malformations and tumors. One common location for recording heart sounds is over mitral valve region, with the sounds recorded referred to as PCG sounds. These sounds are relatively small in amplitude and have a wider range of frequencies than sounds recorded at the chest wall, and also have a close relation to the cardiac circulation [1]. The spectra of these cardiac sounds have been characterized as broad frequency noise with discernible spectral peaks ranging between 8 Hz to more than 23 Hz with a "cut-off"-like frequency of around 13 Hz [2].

IV. Mathematical Method and Computational Implementation

PCG spectra contain vast number of definite harmonics categories that would be useful to be identified as clustering scheme in any data classification algorithms. The majority of these spectra although it belongs to specific valvular pathologies have a distinct energy (intensity) level in STFT plot. This would be attractive point to consider such variation as clustering point; this considerably will orient the classifier algorithm to stable entropy value. The spectral information characteristics of PCG lie within a frequency band of (54-520 Hz) and this band depend on digital stethoscopes interface and resolution of data converters in instrument. This criteria is the basis for pattern classification in which the dependency on frequency (spectral) characteristics. Block diagram for overall spectral classification system is demonstrated in Fig.2 [1]. Several patterns can be derived from the vector input PCG signal, in which they processed with a specific FIR-filter length. The most recognized patterns in PCG are systolic and diastolic and presystolic and post-diastolic peaks of sound (S_1, S_2, S_3, and S_4) which is shown in Fig.1, most of cardiologist prefer the base-diagnosis on two categories of PCG, S_1 and S_2, so that they can discriminate the hemodynamic turbulences in appropriate method[3]. The spectral stamp can be oriented in three schema (supraspectral, infraspectral and mid-spectral) in which are represent the intensity harmonics for PCG waveform, correlation between two intensity peaks of PCG gives a defined index for clustering profile $M_{j\text{-}PCG}$ of PCG signal which in turn apply a segmental cluster for input vector[2]. Systolic and diastolic murmur frequencies are classified according to the frequency band containing the largest power value in the tenth (s) of the systole/diastole corresponding to the found maximum values of SI/DI. If the largest power value is found in one of the two lowest frequency bands (containing frequencies below 125 Hz), the murmur is classified as a low-frequency murmur. If the largest power value is found in one of the eight highest frequency bands (containing frequencies above 250 Hz), the murmur is classified as a high-frequency murmur. If none of the above is the case, the murmur is classified as medium-frequency murmur [5]. The computational steps for PCG energy signature are illustrated below.

1st –step: **PCG Spectral Estimation.**

Spectral Estimation of PCG signal follow the white noise model for identification system parameters in presence of external disturbance.

$$y[n] = (K_{PCG} * g)[n] = \sum_{k=-\infty}^{\infty} K_{PCG}[k]g[n-k]. \quad (1)$$

Extracting the PCG diastolic low frequency components

$$y_{low-PCG(diastolic)}[n] = \sum_{k=-\infty}^{\infty} x_{PCG}[k]g[2n-k] \quad (2)$$

And for PCG systolic high frequency components

$$y_{high-PCG(systolic)}[n] = \sum_{k=-\infty}^{\infty} x_{PCG}[k]h[2n-k] \quad (3)$$

Based on the characteristic features which were derived from PCG-signal, the nature of these signals can be identified using pattern classification techniques. A number of pattern recognition and classification schemes have been implemented for the analysis of heart sounds. Classical pattern recognition techniques include the Gaussian– Bayes classifier and the K-nearest neighbor (k-mean clustering). The Gaussian–Bayes classifier is the most popular parametric technique of supervised pattern recognition. It is considered optimal when the probability density functions (p.d.f) of the patterns in the feature space are known (a pattern is defined as an N-dimensional vector composed of N features)[3,4]. The K-nearest neighbor classifier is a nonparametric approach, which is useful when the p.d.f are difficult to estimate or cannot be predicted [7,5]. The nearest neighbor method is an intuitive approach based on distance measurements, motivated by the fact that patterns belonging to the same class should be close to each other in the feature space. Joo et al [4] illustrated the diagnostic potential of a Gaussian–Bayes classifier for detecting degenerated biocoated prosthetics implanted in the aortic valve [9].

2nd Step: **K-mean Gaussian Clustering**

By applying k-mean clustering for derived PCG spectra, then taking the momentum equation for input vector X_{PCG} to separate the spectral pattern derived from Db-wavelets decomposition algorithm [6].

$$U_{j\,\mathrm{PCG}} = \left(K_{PCG} - \mu_j\right)^T \sum_{j}^{-1} \left(K_{PCG} - \mu_j\right) \tag{4}$$

$$S_{W\,PCG} = \sum_{i=1}^{C} \sum_{x \in X_i} \left(K_{PCG} - m_i\right) \cdot \left(K_{PCG} - m_i\right)^T \tag{5}$$

Where $U_{j\,PCG}$ is the class momentum in *k-space* and it is constructed first to set the separation line for each class, and $S_{W\,PCG\text{-}signal}$ is the segmental pattern derived after integrating the momentum equation (4).

3rd -Step: **Energy signature detection**

The computation of cardiac energy signature based on the following equation.

$$\Psi_{PCG-signal} = \sum_{i=1}^{C} \sum_{x \in X_i} \left| \left(x_{PCG} - m_i\right) \cdot \left(x_{PCG} - m_i\right)^T \right|^2 \tag{6}$$

Through the application of PCG energy equation that was developed by Johnson et al (2003)[10], S1 and S_2 peaks were used as input profile to cardiac energy computation algorithm. The clustered PCG schemes which were identified in the previous step used to correlate result from step two and the result form step three, in order to generate harmonized energy characteristics. In addition to the k-mean clustering, the use of STFT method for detecting intensity-based profile in several mitral valves dysfunction. These findings suggest that there is a potential for these easily-measured tracheal sounds to be used in clinical practice for the diagnosis and monitoring of various respiratory conditions. For such potential clinical applications to be most useful, the relationships between the attributes of these sounds and the underlying anatomy, and ultimately pathophysiology, need to be determined along the computation loop [10, 8].

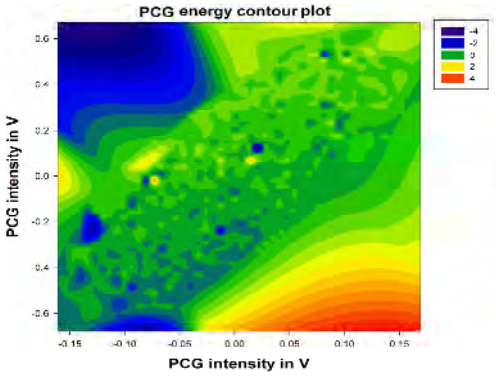


Fig. 3 contouring PCG energy profile that indicated power level of PCG peaks in S_1 and S_2 waveform.

V. PCG SIGNAL INTERPRETATAION

Interpretation of PCG spectral pattern was done through an signal processing toolbox-MATLAB® with spectral generating by Autosignal®; where the vectors of PCG data fed into k-mean-agglomerative cluster kernel and extracted the main classes for $S_1$and S_2 waveform[5]. The computation algorithm presents a stable operation through classification of 11 PCG (8 ♂, 3♀) samples. In Fig.4 the energy index of PCG signal was identified on the basis of correlated amplitude of acquired signal.

In Fig.4, PCG signal classification pattern were identified through k-mean algorithm at which further energy peak definition of PCG power can be localized as energy correla-

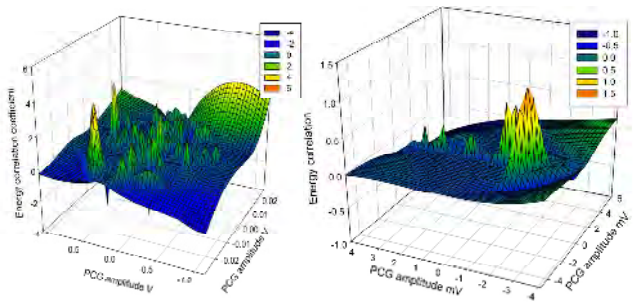


Fig. 4 Energy correlation indices with PCG amplitude, (left) with medium resolution scale (V), the variation index for cardiac hemodynamic (right) with high resolution scale (mV).

tion index versus PCG amplitude which can be noticed in Fig.4, were the correlation index for each PCG was computed in response to intensity amplitude in PCG trace. Hemodynamic parameters of classified PCG signals were illustrated in table.1. X_1, X_2 and X_3 represents the energy value of PCG signal (in watt) after computation of energy signature equation, which indicates for cardiac pathologies.

Table.2 represents estimated paradigm of PCG signal under *k-mean* classification, in which the blood pressure correlation for systolic and diastolic was also computed.

Table 1: Performance index for PCG clustering

Pathology	X1 (watt)	X2 (watt)	X3 (watt)	*K-mean*	*Aggl*	*LMS -Spectral*
Systolic	81	6.1	87	93.0±0.61	88.04	90.02
Diastolic	64	3.6	67	95.5±1.2	89.12	91.49
Murmurs	78	5.7	83	91.7±1.4	90.55	89.32
MS	46	4.2	49	93.9±0.8	92.56	90.16
SSS	67	3.2	46	96.4±0.23	87.04	87.89
Bradycardia	62	2.9	45	96.0±0.53	85.93	90.48
Tachycardia	64	3	46	95.3±1.37	88.67	90.33

Table 2: PCG signal power signature profile with energy correlation technique.

subject	$P_{Systolic}$ mmHg	$P_{Diastolic}$ mmHg	PCG signal estimated paradigm			Estimated freq ω (rad/sec)
			S_1-wave	S_2-wave	S_3-wave	
1	123	76	92.04	87.22	91.21	21.03
2	120	78.4	90.11	86.31	92.07	22.31
3	112	84	92.20	86.04	89.32	21.56
4	119.4	82	88.49	89.18	91.02	23.04
5	119.3	83	86.31	90.63	86.94	20.92
6	117	75	88.28	89.30	85.81	21.54
7	123	80	90.00	88.12	90.00	22.05
8	114	85	91.02	89.47	91.84	23.19
9	117	90	92.7	90.11	90.62	20.72
10	120	94	90.2	91.73	88.23	21.47
11	120.3	84	88.3	90.68	89.34	23.63

VI. Results and discussion

The statistical analysis of cardiac energy signature clustering was achieved based on the 1st and 2nd order regression analysis of the classified PCG. The beat-to-beat interval was also computed from the classified patterns. The number of layers for the k-mean classifier was set to 59 and no of agglomerative classifier was set to 123, and for LMS classifier the layer set to 34 computational layers. Energy cardiac signature was predicted form the (k-mean, agglomerative, LMS) with dynamic computation of spectral pattern for each PCG data batches. The influence of computation layer size will affect on speed and performance of energy signature clustering results.

VII. Conclusions

Cardiac energy signature estimation plays a vital role in quantifying and identifying different hemodynamic pathological cases through pattern classification technique. Well define separation line has been identified and robust S_1 and S_2-spectral patterns. Considerable pathological cases were tested, including different mitral valve regurgitation and systolic hemodynamic abnormalities, stochastic blood flow patterns. A novel method to segment and classified PCG signal into single cycle using spectral pattern decomposition and k-means clustering was achieved. The energy signature identification works well when the heart rate is uniform for the entire sequence of PCG recording. The classification algorithm has shown 91.2% of success. The 29 intensity features of each segmented cycle were reduced to 14 using basic agglomerative clustering. These reduced feature sets were classified by the k-mean clustering into 5 classes. Classification performance for cardiac energy of 95.3% was obtained.

References

1. G. R. Wodicka, K. N. Stevens, H. L. Golub, E. G. Cravalho, and D. C. Shannon, “A model of acoustic transmission in the respiratory system,” *IEEE Trans. Biomed. Eng.*, vol. 36, pp. 925–934, Sept. 1989.
2. H. Pasterkamp, J. Schafer, and G. R. Wodicka, “Posture-dependent change of tracheal sounds at standardized flows in patients with obstructive sleep apnea,” *Chest*, vol. 110, pp. 1493–1498, 1996.
3. R. H. Habib, S. Suki, J. H. T. Bates, and A. C. Jackson, “Serial distribution of airway mechanical-properties in dogs—Effects of histamine,” *J. Appl. Physiol.*, vol. 77, pp. 554–566, 1994.
4. Kudriavtsev VV, Kaelber D, Lazbin M, Polyshchuk VV, Roy DL: New tool to identify Still's murmurs. Pediatric Academic Societies, Annual Meeting [http://www.bsignetics.com/papers/PASStillsMurmur.pdf]. 2006 April 29–May 2.
5. Abbas K. Abbas, Rasha Bassam,”Automated PCC Pattern Classification based on K-mean Clustering", CMBES 31 Canada, June 2008, pp (253-258).
6. Vladimir K., Vladimir P. and Douglas L Roy,”Heart energy signature spectrogram for cardiovascular diagnosis” Biomedical Online Journal, September 2007.
7. Smith J, Jones M Jr, Houghton L et al (1999) Future of health insurance. N Engl J Med 965:325–329.
8. Lock I, Jerov M, Scovith S (2003) Future of modeling and simulation, IFMBE Proc. vol. 4, World Congress on Med. Phys. & Biomed. Eng., Sydney, Australia, 2003, pp 789–792
9. Abbas K. Abbas, Rasha Bassam , Rana M. Kasim , “Prototyping of cardiac clinical decision making based on automated pcg pattern classification”
10. Lang CW, Forinash K: Time-frequency analysis with the continuos wavelet transforms. Am J Phys 1998, 66(9):794-797.

Characteristic of AEP and SEP for Localization of Evoked Potential by Recalling

K. Mukai[1], Y. Kaji[2], F. Shichijou[3], M. Akutagawa[1], Y. Kinouchi[1] and H. Nagashino[1]

[1]The University of Tokushima/Faculty and school of engineering, Tokushima, Japan
[2]Tokushima Bunri University/Tokushima, Japan
[3]Suzue Medical Center/Tokushima, Japan

Abstract — **After it keeps hearing a periodic auditory stimulus, it might be able to be recalled like actual sound even if there is no stimulus. To clarify brain activity at this time, EEG source localization was performed.**

However, in recalling auditory stimulus experiment, when EEG is ensemble averaged, evoked potential may decrease because subject oneself try to recall auditory stimulus according to same timing as periodic stimulus interval.

If SEP can be used as a trigger to recall acoustic stimulus, ensemble average is expected to be applied to attract EP (evoked potential) by recalling. But, because somatosensory evoked potential (SEP) occurs by electric stimulation, it is necessary for SEP and auditory evoked potential (AEP) to be the summation characteristics in order to analyze the simultaneous evoked potential (here, it is defined as S-AEP) of an electric stimulus and auditory stimulus. However, unexpectedly such a summation characteristics is not shown in a past study.

Therefore, it makes comparative study of AEP and EEG which is reduced SEP from S-AEP. First of all, the correlation coefficient of each scalp electrode was examined about AEP and EEG which is reduced SEP from S-AEP. At this time, 1200 ensemble average was done at each stimulus cycle [1/s], and baseline of EEG was the averaging 100 [ms] before the stimulus. Large evoked potential is observed at 300 [ms] after the stimulus and there were high correlation coefficients (from 0.855437[O2 electrode] to 0.975286[C3 electrode]) in all electrodes between AEP and EEG which is reduced SEP from S-AEP. Moreover, in both EEG the topography of N100 and P200 were corresponding.

The summation characteristics of AEP and SEP were able to be shown from the above mentioned result. According to above results summation characteristics of SEP and AEP were confirmed.

Keywords — **somatosensory evoked potential (sep), auditory evoked potential (AEP)**

I. Introduction

The brain has various functions (recognition, memory, thought, consciousness). In addition, those essential functions are caused by innumerable nerve cells. When these nerve cells are active, the chemical mediator released from nerve cells and an electric potential change occurs. Such a phenomenon expresses the information itself and reflects the function of each the territory field of the brain directly. After it keeps hearing a periodic auditory stimulus, it might be able to be recalled like actual sound even if there is no stimulus. In this case it is seemed that a stimulation pattern is memorized and an autonomous signal source with an oscillation pattern like the periodic stimulation is formed in a brain. It was assume that current dipoles as signal sources in the brain. It will be possible to clarify the state of a brain at that time if it is possible to estimate the position and direction of those dipoles with information of EEG that be provided out of the skull at the time of recalling auditory stimulus. Furthermore, it is also thought that Application to the various brain studies such as the study of an ill diagnosis of the brain and the mechanism elucidation of the brain. By the way, the existence of AEP and SEP is shown by past study [1,3]. However, EP (evoked potential) at the time of the recalling is not yet discovered. Therefore, I want to specify evoked potential at the time of the recalling. However, in recalling auditory stimulus experiment, when EEG is ensemble averaged, EP at the time of the recalling may decrease because subject oneself try to recall auditory stimulus according to same timing as periodic stimulus interval. If SEP can be used as a trigger to recall acoustic stimulus, ensemble average is expected to be applied to attract EP by recalling. But, because somatosensory evoked potential (SEP) occurs by electric stimulation, it is necessary for SEP and auditory evoked potential (AEP) to be the summation characteristics in order to analyze the simultaneous evoked potential (here, it is defined as S-AEP) of an electric stimulus and auditory stimulus. However, unexpectedly such a summation characteristics is not shown in a past study. Therefore, it makes comparative study of AEP and EEG which is reduced SEP from S-AEP.

II. Materials and methods

A. Subject

AEP, SEP and S-AEP measurements were performed in a right-handed normal male (27 years old). He was in good health, taking no medication, and without history of hearing loss or neurological diseases. Informed consent was obtained after the experimental procedures were explained.

Chwee Teck Lim, James C.H. Goh (Eds.): ICBME 2008, Proceedings 23, pp. 606–609, 2009
www.springerlink.com

B. Measurement methods

In The measurement of SEP, the median nerve was stimulated with an electrical square wave of 0.3 ms duration at 1.0 Hz. In The measurement of AEP 2000 Hz tone pips of 60ms duration with 10 ms rise and fall times were sequentially delivered to the left and right ear by a speakerphone. This auditory stimulus frequency was 1.0 Hz. In The measurement of S-AEP subject is given each stimulus at the same time. The AEP, SEP and S-AEP were measured with EEG measurement system which consists of an array of 18 electrode by 10-20 system (see Fig. 1). Signals from the 16 electrode scraps are amplified for digitizing on A/D converter by using bio amplifier (NEC BIOTOP 6R12 – 4 / I - BF). The reference electrodes were taken on both ear lobe creases. The software on PC analyzes the EEG signal, and displays its result on the monitor. Simultaneously, measured EEG data is stored into the hard disk for localization after the measurement. The EEG signals were measured in sampling rate 500 [Hz] and filtered from 0.05 Hz to 60 Hz and digitized at 500 Hz. Measured EEG is ensemble averaged to decrease artifact. This averaged EEG data was used for localization.

C. Topography

In 5×5 lattice positions of Fig. 2, the electric potential of the parts of white circles where electrodes are not attached to are estimated with a numerical formula from the electric potential of the electrodes in the circumference to the uniformity. And 50×50 points electric potential around these electrodes is calculated in an equation between the assistant of maintaining the same next with the electric potential value of the electrode of 5×5 lattice positions.

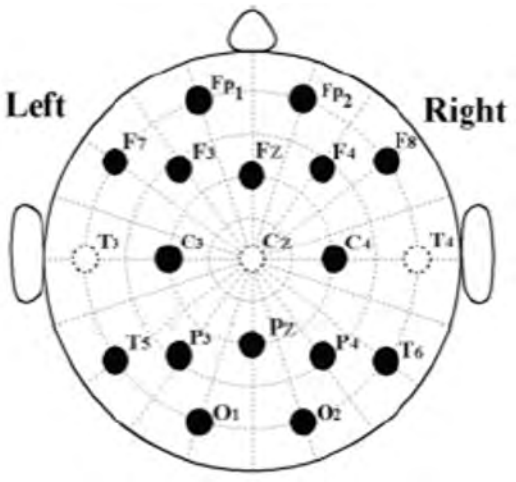


Fig. 1 International standard 10-20 system

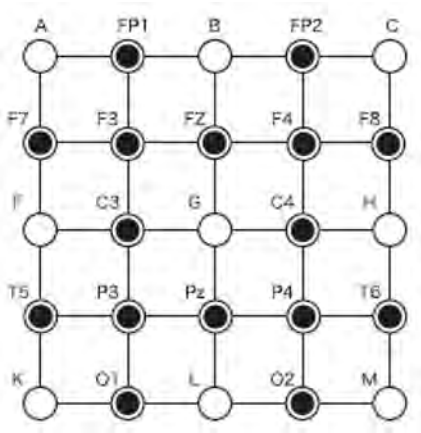


Fig. 2 5×5 lattice positions

The equation in order to calculate the estimate of coordinates except the electrode installation position is as follows;

$$A=\frac{(Fp1+F7)}{k},B=\frac{(Fp1+Fp2)}{2},C=\frac{(Fp2+F8)}{k}$$
$$F=\frac{(F7+F5)}{2},G=\frac{(Fz+C3+C4+Pz)}{4},H=\frac{(F8+T6)}{2} \quad (1)$$
$$K=\frac{(T5+O1)}{k},L=\frac{(O1+O2)}{2},M=\frac{(T6+O2)}{k}$$

But k is different by interpolation function. I applied 4 this time. Interpolation function of k=4 is shown in the next equation by sampling theorem:

$$z=v\cdot\frac{sin(x)}{x}\cdot\frac{sin(y)}{y} \quad (2)$$

III. Result

A. EEG Measurement Result

Fig. 3,4,5 indicate measured EEG that is ensemble averaged AEP, SEP and S-AEP. Furthermore Fig. 6 indicates EEG which is reduced SEP from S-AEP on the front of the head. Horizontal axis is time, and vertical line is EEG value [μ V]. 1200 ensemble average was done at each stimulus cycle [1/s], and baseline of EEG was the averaging 100 [ms] before the stimulus. In AEP data, it seems that the data, the negative peak in the voltage, at time 84[ms] is N100 and the positive peak, minimum in the voltage, at time 158[ms] is P200. Even in Fig. 6 N100 and P200 can identify like evoked potential having been shown with Fig. 3.

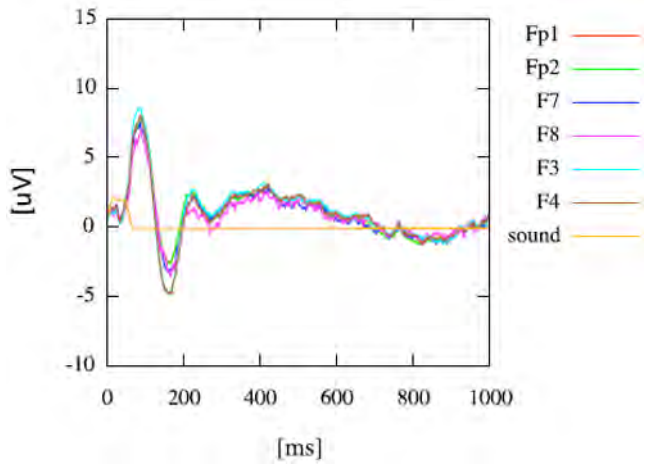


Fig. 3 AEP in the front (1200 ensemble average)

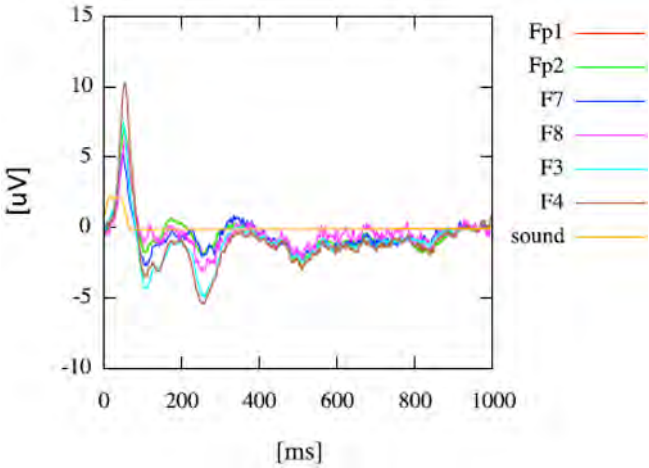


Fig. 4 SEP in the front (1200 ensemble average)

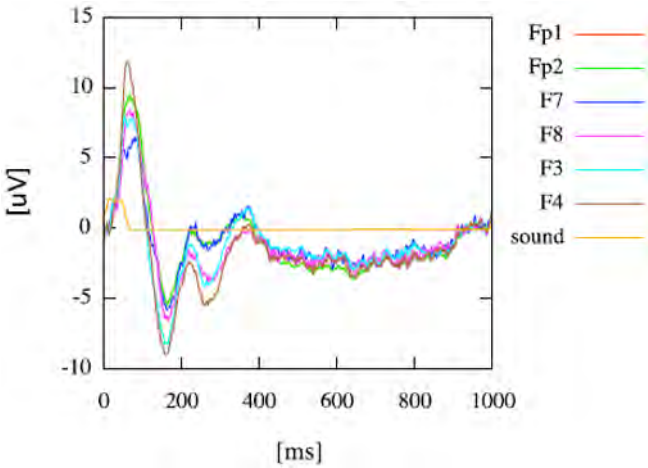


Fig. 5 S-AEP in the front (1200 ensemble average)

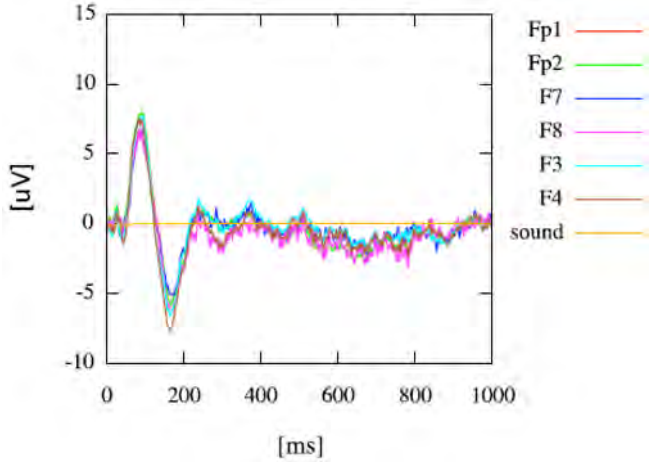


Fig. 6 EEG reduced SEP from S-AEP in the front (1200 ensemble average)

B. Correlation coefficient

Correlation coefficient indicates the strength and direction of a linear relationship between two random variables. A number of different coefficients are used for different situations. The best known is the Pearson product-moment;

$$r_{xy} = \frac{n\sum_{i=1}^{n} x_i y_i - \sum_{i=1}^{n} x_i \sum_{i=1}^{n} y_i}{\sqrt{n\sum_{i=1}^{n} x_i^{\,2} - (\sum_{i=1}^{n} x_i)^2}\sqrt{n\sum_{i=1}^{n} y_i^{\,2} - (\sum_{i=1}^{n} y_i)^2}} \quad (3)$$

Table 1 shows correlation coefficients between AEP and EEG which was reduced SEP from S-AEP in each electrodes at 300 [ms] after the stimulus.). Table 1 indicates that AEP and EEG which is reduced SEP from S-AEP have increasing linear relationship because correlation coefficients of each electrodes were almost +1

Table 1 Correlation Coefficient at 300 [ms] after the stimulus

Pole	Coefficient	Pole	Coefficient
Fp1	0.948320	Fp2	0.947376
F3	0.970904	F4	0.973367
C3	0.975286	C4	0.960479
P3	0.961993	P4	0.935688
O1	0.906088	O2	0.855437
F7	0.968806	F8	0.967107
Fz	0.970577	Pz	0.951431
T5	0.933087	T6	0.906108

Correlation coefficients between AEP and EEG which was reduced SEP from S-AEP in each electrodes.

C. Topography

Fig. 7 represents Topography at N100 (84 [ms]) about each ensemble averaged EEG (AEP, SEP, and S-AEP. EEG which is reduced SEP from S-AEP). Fig. 8 represents Topography at P200 (158[ms]) about each ensemble averaged EEG. Fig. 7 and Fig. 8 indicate that AEP and S-AEP are very similar electric potential distribution.

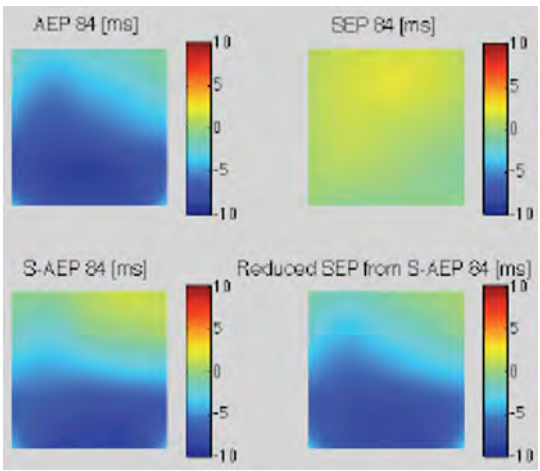


Fig. 7 Topography

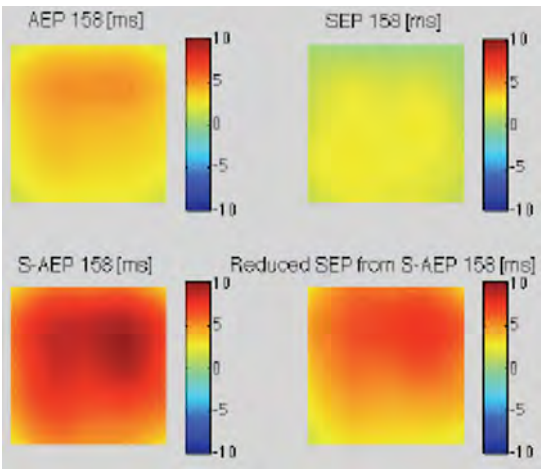


Fig. 8 Topography

IV. Conclusion

It was found that there was strong correlation between AEP and EEG which was reduced SEP from S-AEP by the analysis of EEG data, comparison of Topography, the numerical value of the coefficient of correlation. A linear characteristic of the evoked potential was proved by the above-mentioned result. Therefore, it is thought that application, using SEP as a trigger to recall acoustic stimulus, may be possible for a specific study of the recalling evoked potential as.

Acknowledgment

The authors wish to thank Mr. Shichijou for helpful advice. The author is also deeply indebted to member of the University of Tokushima for their considerable assistance.

References

1. Jewett, D.L., Romans, M.N, et al. Human auditory evoked potentials; Possible brain stem components detected on the scalp, Science, 167 : 1517-1518, 1970.
2. Nobukazu Nakasato, et al. Functional localization of bilateral auditory cortices using an MRI-linked whole head magnetoencephalography (MEG) system, Electroencephalography and clinical Neurophysiology 94 (1995) 183-190.
3. Allison, T. Recovery function of somatosensory evoked responses in man. Electroencephalogr. Clin Neurophysiol., 14 : 331-343, 1962
4. Teruo Okuma, M. D. Rinsho-Nohagaku, Igaku-Shoin Ltd. Tokyo (1991)
5. Arid, R.B. and Adams, J.E. The localizing value and significance of minor differences of homologous tracings as shown by serial electroencephalographic studies. Electoroencephalogr. Clin. Neurophysiol., 3: 487-495, 1951.

Author: Kenta Mukai
Institute: The University of Tokushima
Street: 2-1 Minami Josanjima city Tokushima 770-8506 Japan
City: Tokushima
Country: Japan
Email: mukai@ee.tokushima-u.ac.jp

Automatic Detection of Left and Right Eye in Retinal Fundus Images

N.M. Tan[1], J. Liu[1], D.W.K. Wong[1], J.H. Lim[1], H. Li[1], S.B. Patil[1], W. Yu[1], T.Y. Wong[2]

[1]Institute for Infocomm Research, A*STAR, Singapore
[2]Singapore Eye Research Institute and National University of Singapore

Abstract — **Retinal fundus images are commonly used by ophthalmologists to diagnose and monitor the development of eye diseases. One of the key information in the fundus images is to distinguish between the left and right eye. This work is motivated to provide an accurate and automated method to detect the left and right eye based on the retinal images.**

In current clinical practices, a common method to differentiate left and right eye in the retinal images is via the position of the optic nerve head with respect to the macula. This paper introduces a novel method to automatically detect the orientation of the retina in fundus images from the position of the central retinal artery and veins of the physiologic optic nerve head.

Our method first locates the centre of the optic cup using pixel intensity. A 100 x 100 pixel ROI is then formed based on this centriod. Thresholding by pixel intensity and morphology is then used to segment the optic disc from this ROI to obtain an accurate optic disc and its blood vessels within. The pixel intensity in the green channel of this segmented disc along its horizontal axis is projected. The sum of the pixel intensity in the left half of the disc is then compared to the right half. The prevalence of higher green pixel intensity in either half of the optic disc would then indicate if this is a nasal or temporal sector, which would then indicate if this is a left or right eye.

This method is tested on 194 images collected from patients at the Singapore Eye Research Institute and achieves an accuracy of 92.23%. This method is novel and its results are encouraging to provide an accurate and automatic system to make a distinction between left and right eye from retinal images.

Keywords — **Automated, Detection, Retinal, Pixel Intensity**

I. Introduction

Ophthalmologists often have to identify key anatomical structures (optic disk, macular, retinal vessels) in retinal fundus images. Identification of these structures is important and significant as it would provide localization, annotation and measurement of landmark points and features.

In current clinical practices, there are a number of methods to identify left and right eye in colour fundus images.

One commonly used method is by identifying the relative position of the optic nerve head with respect to the macula[4,5]. The side at which the optic disc lies, with reference to the macula, indicates the corresponding side of the eye in the fundus image. The disadvantage of this method lies in the reliance of a clear definition of the macula. In images where the macula cannot be identified, this method of detection will not be useful.

Another way of categorizing is by analysis and tracking of the parabolic course of the central retinal arteries and veins entering and leaving the optic nerve head to the retinal edges[3]. This technique relies heavily on the following the course of the retinal vessels. The disadvantages of this are that the retinal vessels sometimes may not be captured in the fundus image or that the vessels are blocked by exudates.

An alternative method of identification would be via the position of the central retinal arteries and veins of the physiologic optic nerve head. This method is based on the idea that the retinal arteries and veins are usually found near the nasal edge of the physiological cup[1]. This method is less commonly employed as it is sometimes difficult to visually differentiate which side the retinal vessels are near to.

The above mentioned methods are currently manually visually inspected by physicians and can be time consuming. By means of digital image processing techniques, we propose a novel, unbiased and automatic means of identifying left or right eye image based on the last method introduced, via the retinal vessel structure in relation to the physiological cup, to distinguish left and right eye in fundus images for image annotation and context analysis. The details of the proposed algorithm will be presented in Section II; Experimental results are demonstrated in Section III; Section IV gives a conclusion on this paper; and Section V acknowledges the respective organizations involved in this paper.

II. Methodology

To detect the physiological optic disc, we propose a fast method of localization of the optic disc via pixel intensity and forming a ROI to contain the optic disc. The optic disc is then segmented from this ROI by pixel intensity, pixel counts and morphology. The prevalence of the retinal vessels within the left and right half of the optic disc is then compared. This would result in an indication of the nasal and temporal sector and signify a left or right eye.

Chwee Teck Lim, James C.H. Goh (Eds.): ICBME 2008, Proceedings 23, pp. 610–614, 2009
www.springerlink.com

A. Optic Disc Detection

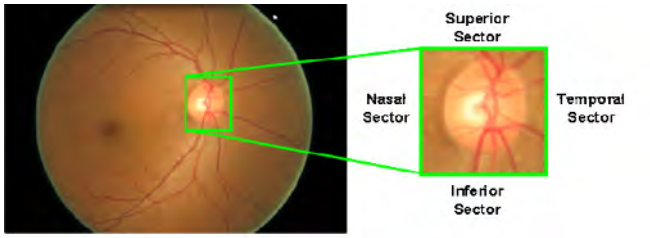


Fig. 1 Retinal Fundus Image. [inset] Optic Disc and its 4 sectors

The optic disc is often the brightest and most distinct feature in a normal patient's retinal colour fundus image. The optic disc can be generally described as a pale-yellow to orange rounded blob, with an embedded optic cup, bright-yellow to white in color, and retinal arteries entering and retinal veins leaving the optic cup.

As shown in Fig. 1, the optic disc, bounded by a green box, has four sectors, Inferior, Superior, Temporal and Nasal. In our approach, we are interested to use retinal vessel information to detect the nasal and temporal sides. This would then reveal if the image is a left or right side. However, segmentation of the optic disc can be tough due to the presence of large number of blood vessels traversing the cup boundary[2], and even more challenging in cases of abnormal retinal images with large areas of exudates[5]. In this paper, we process images in our dataset which are mainly devoid of exudates.

The optic disc detection proposed, an extension of [2], is performed in two steps: patch analysis and disc ROI localization. The fundus image is first divided into 64 8-by-8 patches in its red component channel. Each patch returns the total pixel intensity and a pixel count of the largest mass of threshold blob within itself. An initial patch is selected when it has the highest total pixel intensity among all 64 patches. 'Challenger' patches, patches with the next few highest intensities, are compared against this initial patch. A patch is then selected when it returns the highest threshold pixel count with high pixel intensity. This is done to enhance the accuracy for optic disc detection and obtain a best representation of the optic disc.

The centre of the mass of blob in this selected patch is then used to form a 100x100 pixel candidate area to localize the optic disc. This ROI is set to accurately analyze only the retinal vessels within the optic disc. Pixel intensity is applied to segment the optic disc in this ROI. The threshold for this segmentation is set at the top 2% of highest pixel intensity in the candidate area. A clustering algorithm is then used to fuse nearby blobs and pixels together to form a better representation of the segmented optic disc. The flow of our method is shown in Fig.2.

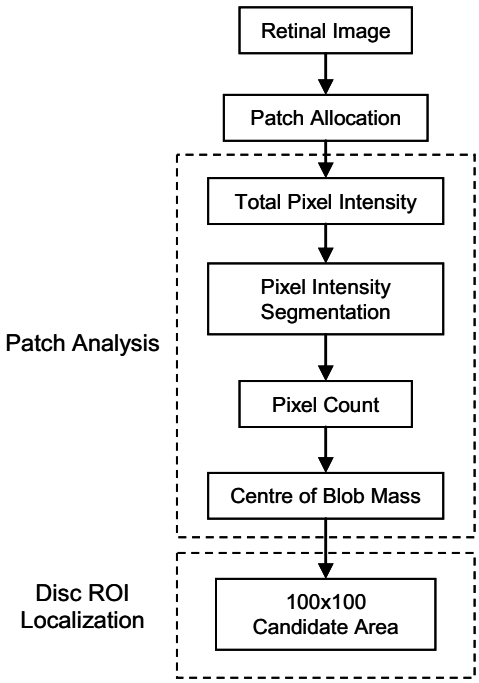


Fig. 2 Optic Disc Detection Workflow

B. Analysis of retinal vessels within optic disc

With the segmented optic disc in the candidate ROI area, we extract the vessel information from the optic disc via its green channel. It is found in our experiments that the central retinal artery and vein are most distinct in this channel. The optic disc is divided into left and right halves. The extracted vessels from the optic disc are then summed up in its columns and projected horizontally across the x-axis. The pixel intensities in each half are compared against each other. The half which indicates lower pixel intensity denotes that it is the temporal sector. If the temporal sector is on the right half, it signifies a right eye, and vice versa.

III. Experimental Results

In this paper, we demonstrate our method on sample 1, a right fundus image, and sample 2, a left fundus image.

Patch allocation and analysis was applied to the sample 1 with results as shown in Fig. 3a. In this sample, majority of the optic disc can be found in the allocated patch. However, as found in our experiments, the optic disc does not necessarily lie fully in the allocated patch as shown in Fig 4a. The

patch which contains the highest total pixel intensity, Fig 4b, may not represent the optic disc at its best. As such, we developed another method to create 'challenger' patches, which takes into account the number of pixels contained in the largest blob after pixel intensity segmentation. As highlighted in the methodology, the threshold is set at the highest 2% of the maximum pixel intensity present in each respective patch. It is important to note that the challenger patches must have a high total pixel intensity before it is compared to the maximum total pixel intensity patch to prevent false detection and unnecessary comparision. After this evaluation, the most suitable patch,Fig 4c, is returned. The centroid of the segmented blob mass, Fig 3c and Fig 4d, is then used as a good centre of origin to create a 100x100 candidate ROI, Fig 5.

Through our experiments, a 100 by 100 pixel ROI is sufficient to contain the optic disc for retinal vessel analysis. The candidate area is first segmented via the red channel as it gives the best outline for the optic disc, Fig. 6. The segmented area is then processed using morphology methods before retinal vessel analysis.

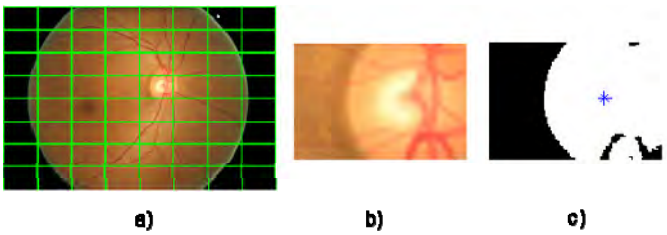


Fig. 3 a) Sample 1 fundus image allocated into patches. b) Selected patch. c) Centre of blob mass after Pixel Intensity Segmentation

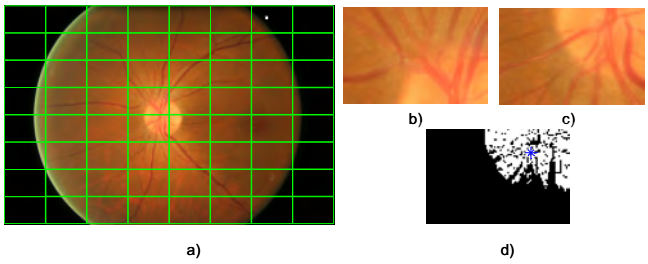


Fig. 4 a) Sample 2 fundus image allocated into patches. b) Max total pixel intensity patch. c) Patch with highest pixel count among high intensity patches. d) Centre of blob mass after Pixel Intensity Segmentation

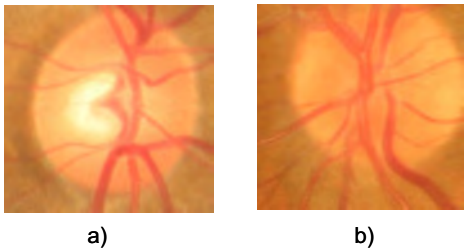


Fig. 5 a) Candidate ROI of sample 1. b) Candidate ROI of sample 2.

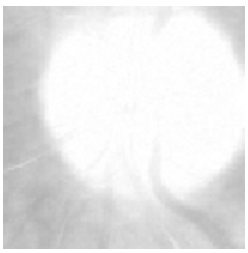


Fig. 6 Red Channel of sample 2 ROI provides a distinct disc boundary.

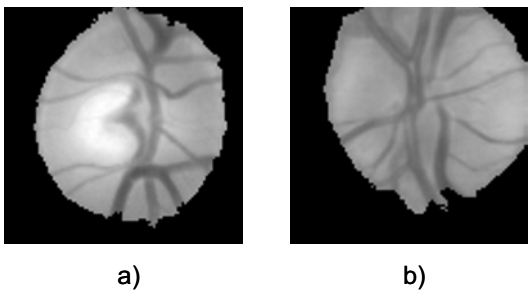


Fig. 7a) Candidate ROI of sample 1. b) Candidate ROI of sample 2.

As shown in Fig. 7, the green channel of this segmented disc provides the clearest information of the retinal vessels. As the retinal vessels are emphasized as the dark regions, they would return a low intensity value. The pixel intensities of the retinal vessels in the optic disc are summed vertically and projected horizontally, Fig 8-9. The optic disc is then divided into left and right halves, and the prevalence of higher pixel intensity in either half would denote the nasal sector of the optic disc. The blue region in Fig 8-9 indicates the temporal sector of the sample images. Sample 1 indicates the temporal sector on the right half, does implying that it is a right eye image. Similarly, sample 2 implies a left eye image. Both results validate our initial claims.

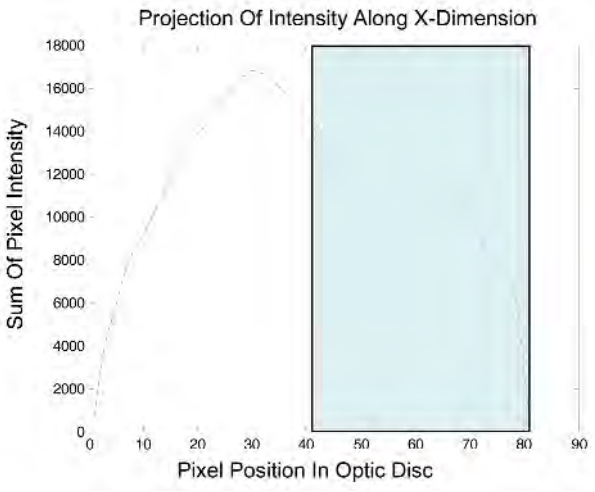


Fig. 8 Projected retinal vessel concentration of Sample 1.

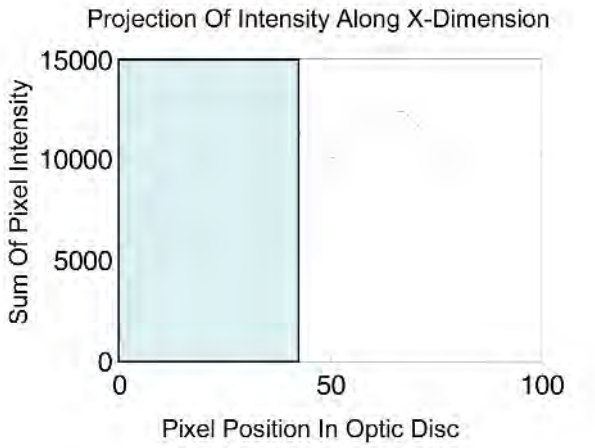


Fig. 9 Projected retinal vessel concentration of Sample 2.

We tested our algorithm on 194 fundus images from the Singapore Malay Eye Study (SiMES)[6]. The SiMES is a research project conducted by Singapore Eye Research Institute(SERI) for determinants of the optic cup to disc ratio in an Asian population. The dataset was first visually inspected and segregated into left and right eyes before the experiments were performed.

As presented in Table 1, our method on 194 images, has achieved a total accuracy of 92.23%. We evaluated our results and found that this approach is highly accurate when the optic disc is accurately detected and segmented.

The failure images were carefully analyzed and we realize that the method is unsuccessful if the optic disc is incorrectly detected and segmented. Retinal images with poorly defined retinal vessels also contribute to inaccurate and unsuccessful detection.

The analysis of the pixel intensity of the retinal vessels confined within the optic disc in the ROI allows the detection to be more robust than analyzing the retinal vessels within the 100x100 ROI area. Our experiments also show that there is no bias for any particular side of the eye.

Table 1 Statistics of Results

Image	# of samples	# correct	Accuracy (%)
Left Eye	97	87	89.69 %
Right Eye	97	92	94.85 %
Total	194	179	92.23 %

IV. Conclusions

In this paper we present a novel method for the fast automatic detection of left and right retinal fundus image. The method is based on using the physiological structure of the retinal vessels in the optic disc. Patch allocation and analysis are performed to provide a fast and accurate means of selecting a candidate ROI for the optic disc. The patch analysis method also consists of a counter check in the form of challenger patches which compete to be selected as the best patch to contain the optic disc. The candidate ROI is subsequently processed to extract the optic disc with its retinal vessels. Retinal vessels are then examined, with their intensity projected along the horizontal axis, giving an indication of the nasal and temporal sector. If the temporal half is on the left, it denotes that the retinal image is a left eye, on the other hand, a right temporal side is a sign that it is a right retinal image.

Our experiments conducted using the 194 images demonstrate an overall accuracy of 92.23%. The results suggest that this is a promising means of detecting left and right fundus images for annotation and subsequent context analysis. We have also established a fast and unbiased method of automatic detection of left and right fundus image. Future work could also be explored to extend this approach to retinal images with exudates.

References

1. Robert Ritch et al. (1989) The Glaucomas. Vol. 1, pp.617-626
2. Wong D.W.K., Liu J., Lim J.H., Jia X., Yin F., Li H., Wong T.Y. (2008) Level-set based Automatic Cup-to-Disc Ratio Determination using Retinal Fundus Images in ARGALI, International Conference of the IEEE Engineering in Medicine and Biology Society, Singapore, 2008.

3. S. Tamura, Y. Okamoto, K.Yanashima(1988) Zero-crossing Interval Correction in Tracking Eye-fundus Blood Vessels, Pattern Recognition, Vol.21, No.3, pp.227-233
4. C. Sinthanayothin, J. F. Boyce, H. L. Cook, T. H. Williamson(1999), Automate3d Location of the Optic Disk, Fovea, and Retinal Blood Vessels from Digital Colour Fundus Images, British Journal of Ophthalmology, Vol. 83(8), pp.902-910
5. H. Li, O. Chutatape(2004), Automated Feature Extraction in Color Retinal Images by a Model Based Approach, IEEE Transactions on Biomedical Engineering, Vol. 51, No.2, pp.246-254
6. Singapore Malay Eye Study(SiMES), at http://www.ncbi.nlm.nih.gov/pubmed/18695105?ordinalpos=2&itool=EntrezSystem2.PEntrez.Pubmed.Pubmed_ResultsPanel.Pubmed_DefaultReportPanel.Pubmed_RVDocSum

Visualizing Occlusal Contact Points Using Laser Surface Dental Scans

L.T. Hiew[1], S.H. Ong[2] and K.W.C. Foong[1]

[1]Department of Preventive Dentistry
[2]Department of Electrical and Computer Engineering, Division of Bioengineering
National University of Singapore

Abstract — **In dentistry, teeth occlusion is the best possible fit between the maxilla (upper teeth) and the mandible (lower teeth). Understanding occlusion is important for diagnosis, prognosis and treatment of occlusal dysfunction and for planning of reconstructive surgery. Teeth occlusion can be determined by a set of occlusal contact points. Due to the complex surface morphology of the maxilla and mandible, identification and localizing this set of contacts, even to the dentist, is not a trivial task. The visualization of occlusal contact points has important significance in providing the dentist a clear picture of the exact locations of these points, which are important in clinical practice when the dentist wishes to recover or maintain a perfect occlusal balance between the maxilla and mandible. This paper presents a method of determining the set of contact points and visualizing them in 3D. We assume that optimal teeth occlusion has been previously obtained. The contacts points are determined by analyzing the difference image between the maxilla and mandible height fields. With a suitable threshold, one can obtain multiple connected contact regions on the difference image. We can further prune the contact points by searching for local minima using an 8-connectivity neighborhood kernel. We then back-project using ray-casting techniques to obtain a pair of contact correspondence for each point. Visualization results are further enhanced by properly positioning the maxilla and mandible models in 3D and joining the contact points by a set of lines.**

Keywords — **occlusal contact points, dental, maxilla, mandible, teeth**

I. Introduction

In dentistry, occlusion is defined as the best possible fit between the maxilla (upper teeth) and mandible (lower teeth). Understanding occlusion is the key to oral function and subsequently the key to restorative oral diagnosis. Critical to the success of determining optimal occlusion is accurate identification and quantification of occlusal contacts.

Conventional approaches of identifying these contacts are determined by an orthodontist or dentist using a color coated, thin plastic sheet known as articulating paper. The patient ``bites'' onto this foil, and the color is then transfered onto patient's tooth surface, thus indicating where teeth have occlusal contacts. Contact information is limited to the width of the foil and requires multiple jaw closures to gather contact information around the around the entire arch [1]. Alternatively, one can use an occlusal registration wax bite. A wax bite can be obtained by inserting a thin sheet of wax into the patient's mouth and having them to bite down on the wax thus leaving a bite mark on both sides of the wax sheet. The dentist can then use the wax bite impression to align both the maxilla and mandible plaster models into its wax bite marks. While wax is commonly used for bite registration, potential problems with wax includes the propensity for wax to warp, bend and/or become brittle, depending on how the wax is handled, stored, and used. A third alternative is to make use of dental impression models which are created separately for the maxilla and mandible using material such as alginate or polyvinylsiloxane (PVS). Once the impression models solidify, they can be mounted on a mechanical articulator which simulates the biting process. The mechanical articulator is accurate, however it is expensive and time consuming in experimental setup. Despite their specific strengths and weaknesses of the three methods that have been discussed earlier, the problem of quantifying the information remains. In the case of a wax bite or silicone impression, transillumination can convert the transparency of the record to digital data. However transillumination is limited because the results are two-dimensional and depend on the orientation of the record to the light source [2].

Having outlined the inconvenience of using conventional methods, this has led to the development of computer-based methods. Advances in 3D digital imaging have allowed the acquisition of more accurate 3D dental data. In this study, we use Minolta Vivid 900 to collect samples of maxilla and mandible of the patients. The scanner allows us to scan the dental impression models quickly and perform occlusal analysis digitally. Due to the fact that, both the maxilla and mandible models are scanned separately at two different instant of time, the relative pose information between the maxilla and mandible that governs the occlusal relationship between them is not captured during the scanning process. An attempt to recover this relative relationship requires occlusal contact registration, which in general is a difficult problem. This requires an optimization over a criterion function that is defined over two separate complex complementary surfaces.

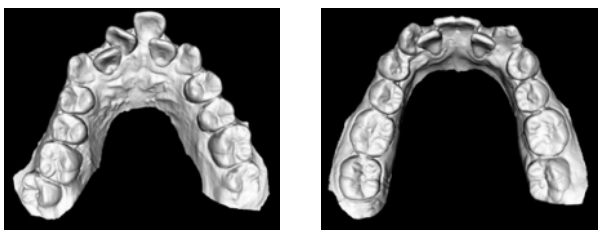
Chwee Teck Lim, James C.H. Goh (Eds.): ICBME 2008, Proceedings 23, pp. 615–618, 2009
www.springerlink.com

II. Related work

The focus of this paper is to present a method to visualize occlusal contacts; however this can only be done only if optimal occlusions between maxilla and mandible models have been recovered. Using laser scanned models, there are published materials relating to the recovery optimal occlusion. R. Delong [3] recovered occlusion by aligning laser scanned maximum intercuspation occlusal record with the dental models. The results are then compared with the conventional gold standards which are the transillumination records, author concluded that both methods are equivalent. Maruyama [4] describe a method to determine and visualize the occlusal contacts using a virtual semi-adjustable dental articulator. However the occlusion is determined based on a user manually identified fix number of contact points. Without using any occlusal records and user manual identification of contact points, Hiew [5] determined the optimal occlusion of teeth using a two step procedure. The first step coarsely aligns the models using key planar structure which can be detected automatically using a planar clustering algorithm. This is follow by applying a fine alignment which uses a variant of the iterative closest point (ICP) algorithm to obtain optimal occlusion. Visualization of occlusal contact is not extensively studies in this work.

III. Data acquisition

A total of 20 pairs of maxilla and mandible, made of alginate impression, are scanned using Minolta Vivid 900 3D scanner. The scanner has a precision of 0.008 mm and X, Y, Z accuracies of 0.22, 0.16 and 0.10 mm, respectively. Individual views were aligned to each other using the Polygon Editing Tool 2.21 [6]. The aligned views were combined into a single data set representing the object (virtual model), rendered as 3D surfaces. Models are stored in either VRML or STL format. Figure 1 shows the scanned results of the maxilla and mandible.



(a) Maxilla (b) Mandible

Fig. 1 Maxilla and mandible scanned using Minolta Vivid 900

IV. Method

A. Searching For Optimal Occlusion

Although mesh representation of the maxilla and mandible is attractive for rendering and display, it is not an efficient and compact representation for the computation of any arbitrary criterion function for searching of optimal occlusion of teeth. We shall first transform the models to a standard canonical coordinate system.

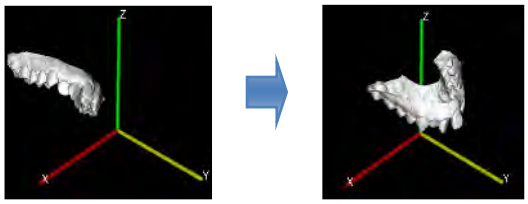
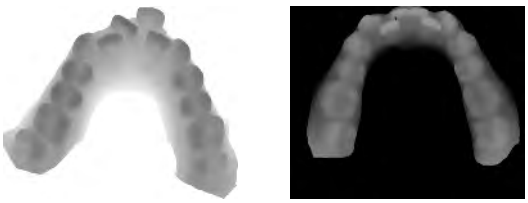


Fig. 2 Canonical transformation of dental models for a more compact and efficient representation

Figure 2 shows one of the models and its world coordinates. Using the principal components of the models, we can adjust the orientation of the models such that the model is parallel to the XY plane. We can then generate a synthetic height field representation of the maxilla and mandible.



(a) Maxilla height field (b) Mandible height field

Fig. 3 Height field representations of the maxilla and mandible

The height fields, also called range images, are generated using a sampling grid of 0.2 mm with linear interpolation by projecting the Z-heights on the XY plane. We transform both the maxilla and mandible such that the Z-heights of the maxilla are always greater than those of the mandible.

Once both models have been transformed in the canonical order, we can search for optimal occlusion. During searching, the mandible is fixed, and only the maxilla is allowed to move in 3D space. A rigid body transformation can be defined by a total of six parameters $\theta = \{t_x, t_y, t_z, r_x, r_y, r_z\}$ which includes both a translation

vector and a rotation matrix. Let $h_u(x,y;\theta)$ and $h_l(x,y)$ be the height fields of the maxilla and mandible generated under transformation θ, respectively.

$$l = \min_{(x,y)}(h_u(x,y;\theta) - h_l(x,y)) \quad (1)$$

$$\hat{\theta} = \max_{\theta} \sum_{(x,y)} e^{-\frac{(h_u(x,y;\theta)-h_l(x,y)-l)^2}{\sigma}} \quad (2)$$

l can be seen as the maximum distance which the maxilla can translate in the Z-axis direction without colliding with the mandible. $\hat{\theta}$ is the optimal solution for optimal occlusion. The summation expression in Equation (2) can be interpreted as a compaction measurement between two complementary surfaces. Optimizing θ will give us the solution to optimal occlusion. Figure 4 shows one of the pair of maxilla and mandibles that are in optimal occlusion determined using the mathematical formulation described in this section.

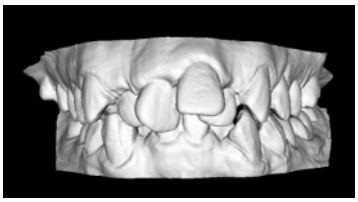


Fig. 4 Maxilla and mandibles in optimal occlusion

B. Identifying Occlusal Contacts

Figure 4 represents one common form of visualizing the maxilla and mandible in optimal occlusion. However if the interest of the dentist is to identify the locations of the contacts, a more effective visualization would be needed. This can be done by first identifying the locations of possible occlusal contacts then displaying them in 3D. In this section, we describe a method of determining the set of occlusal contacts.

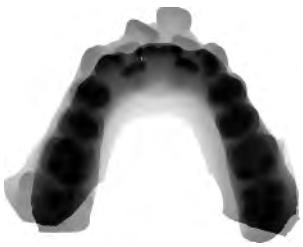


Fig. 5 Height difference image between maxilla and mandible

Given an optimal occlusion parameters $\hat{\theta}$, we can generate corresponding height fields for both maxilla and mandible. The difference between the maxilla and mandible height fields is $h_u(x,y;\hat{\theta}) - h_l(x,y)$.

Let $D = \{d_i \in \Re \mid d_i = h_u(x_i,y_i;\hat{\theta}) - h_l(x_i,y_i)\}$ be the set of height differences. Note that, the lower the values of d_i, the more likely it is that coordinate (x_i,y_i) is an occlusal contact. To determine the locations of occlusal contacts in the image domain, we first sort the values in D, follow by retaining only a certain percentage of the elements in D. In our results, the threshold for this procedure is 2%. We denote this procedure by $T[D_{sort}]$, where T indicates a threshold operation and D_{sort} is the sorted D. The image generated from this procedure identifies the occlusal contact sites in Figure 6 (a).



(a) Occlusal contact sites (b) Superimposed with Fig. 6

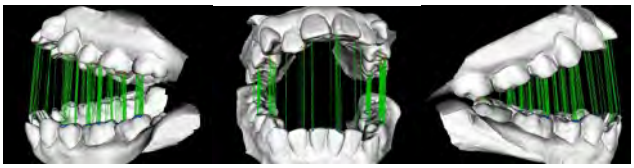
Fig. 6 Height field difference between the maxilla and mandible

Figure 6 (b) also shows an overlay of the contact sites or regions together with the height difference field. Since the contact sites are usually multiply disconnected, we can perform a connected component analysis to identify the number of separate components. In our current example, the components are indicated by different colors in the superimposed image. Contact sites convey region information of the occlusal contacts, it is often desirable to obtain point to point contact information, so that one could display them in 3D. To do so, it is further required to prune down the occlusal contact sites to a finite number of contacting points. In this paper, we make one simple assumption on the occurrence of a true occlusal contact point. We assume that given any point (x_i,y_i) with its corresponding d_i, a point is only a true contact should its value d_i be a local minima in some defined neighborhood. In our experiment, we use the 8-connected neighborhood. Given the true contact points, it is then possible to back project the points to de-

termine their locations on the maxilla and mandible surface model. For each true contact site (x_i, y_i), we have a pair of $h_u(x_i, y_i; \hat{\theta})$ and $h_l(x_i, y_i)$ which defines a 3D line in space. We then determine the intersection of this line with the maxilla and mandible models. The process is similar to ray-casting and the intersection should give two 3D points.



(a) Subject 1



(b) Subject 2



(c) Subject 3

Fig. 7 Visualization of occlusal contact point pairs

For display purposes, we rotate the maxilla and mandible slightly away from the XY plane, so that we can have a full view of teeth. For each contact point pair, we join each of them using green lines as shown in Figure 7. Each column in Figure 7 shows different views of a single human subject. In addition to the model that we use in this paper, we also present another 2 subjects which are shown in Figures 7 (b) and (c).

V. Discussion

We briefly describe the mathematical formulation of optimal occlusion and present a method to visualize the occlusion results. For more details as to how the optimization is being done for Equation (2), readers can refer to one of our earlier works [5]. The main contribution of this paper is to present a fast and efficient method to identify and visualize the occlusal contacts. The algorithm is fast because all processing is done purely in the 2D image domain, and the final output which requires a back-projection to the 3D surface, only involves a small number of points.

In addition to the visualization, it is also possible to measure the number of occlusal contacts, which appear as one of the common measurements in some literature which studies the nature of dental occlusion. We also can obtain a distribution of the number of occlusal contacts over a total of 20 subjects. The weighted average of the number of occlusal contacts is computed as 117.5.

VI. Conclusions

This paper presents a method of obtaining dental occlusion using laser scanned surface models. Instead of using a mesh representation, we use a height field data representation of the maxilla and mandible. Criterion function of arbitrary occlusal configuration can be mathematically formulated using the height fields. Optimal occlusion can now be determined by searching this criterion function. To visualize the occlusal contacts, contacts are first identified using difference of height fields in optimal settings, by applying appropriate thresholds and pruning, we can obtain a sparse number of contact points in the 2D image domain. Points can be back projected using ray-casting techniques to obtain its 3D points on the surface models. One can then visualize the occlusal contact correspondence in virtual 3D. We also quantitatively measure the weight average number of occlusal contacts across a total of 20 human subjects. The weighted average number of occlusal contacts is 117.5.

References

1. W. Mcdevitt, A. Warreth. (1997) Occlusal contacts in maximum intercuspation in normal dentitions. Journal of Oral Rehabilitation 24:725-734.
2. W. Gurdsapsri, M. Ai, K. Baba, K. Fueki. (2000) Influence of clenching level on intercuspal contact area in various regions of the dental arch. Journal of Oral Rehabilitation. 27:239-244.
3. R. Delong, C.-C Ko, G.C. Anderson et al. (2002) Comparing maximum intercuspal contacts of virtual dental patients and mounted dental casts. Journal of Prosthetic Dentistry. 88:622-630. DOI: 10.1067/mpr.2002.129379
4. Tomoaki Maruyama, Yasuo Nakamura, et al. (2006) Computer-aided determination of occlusal contact points for dental 3-D CAD. Medical and Biological Engineering and Computing. 44:445-450 DOI 10.1007/s11517-006-0046-0
5. L.T. Hiew, S.H. Ong, Foong, K.W.C. Foong. (2006) Optimal occlusion of teeth. 9th International Conference on Control, Automation, Robotics and Vision, 2006, ICARCV `06, Singapore. DOI: 10.1109/ICARCV.2006.345476
6. Polygon Editing Tool ver. 2.21 at http://www.konicaminolta.com/instruments/download/software/index.html

Modeling Deep Brain Stimulation

Charles T.M. Choi and Yen-Ting Lee

Department of Computer Science and Institute of Biomedical Engineering, National Chiao Tung University, Taiwan R.O.C

Abstract — **The goal of this project was to develop a quantitative understanding about shape of axonal tissue activated (STA) and stimulation site by deep brain stimulation (DBS) in middle brain like thalamus, subthalamic nucleus (STN), and globus pollidus interna (GPi) to make better stimulation effects. The volume of tissue activated (VTA) can be studied using different electrode dimensions.**

Keywords — **Deep brain stimulation, volume tissue activated, VTA, STA.**

I. Introduction

Deep Brain Stimulation (DBS) is a surgical treatment involving the implantation of a medical device which consists of three components: the implanted pulse generator (IPG), the lead with four platinum iridium electrodes, and the extension. All three components are surgically implanted inside the body. It is an effective, proven therapy for the treatment of Parkinson's disease (PD), essential tremor and dystonia. So far, the mechanisms of deep brain stimulation are still not clear, and DBS patient management is primarily based on trial-and-error. We only know that high frequency DBS directly changes brain activity analogous to those achieved by surgical lesion, its effects are reversible (turn on/ off the electrode can inhibit/recover activity in brain) [1].

The fundamental purpose of DBS is to modulate neural activity with extracellular electric fields, but the technology necessary to accurately predict and visualize the neural response to DBS has not been previously available.

The innovation of this paper is to predict the volume of tissue activated [2][3][4] during stimulation using simple FEM DBS electrode-brain tissue model include myelinated axon. Existing DBS system were adapted from cardiac pacing technology ~20 years old. The original design of the Medtronic 3387/3389 DBS electrode was hindered by limited knowledge of the neural stimulation objectives of the device.

But in recent years, we can use new neural engineering design tools, such as computer modeling techniques in this study. We can improve old DBS electrode design.

While DBS is helpful for some patients, there is also some side effects because there is low threshold in surrounding tissue. These may be temporary and related to correct placement and calibration of the stimulator. In this paper we will also study on this issue and try to improve electrode design to fit the tissue which is activated by using virtual channel [4].

II. Method

A. Quantitative measurement of stimulation region

A quantitative measurement is used in this paper: volume of tissue activated (VTA) and shape of tissue activated (STA) are used to predict a 3-dimensional volume of tissue being activated by the electric field. In this paper a 2-dimensional VTA contour will be used to replace the 3-dimensional VTA because it is more straight forward and convey the similar information. A finite element model (FEM) which includes the brain tissue and special DBS electrode contacts is used to address the effects of deep brain stimulation in a homogeneous isotropic medium. The second derivative of the potential distribution (Activating function) generated in the tissue in our model was used as a predictor of the volume of tissue activated (VTA) and shape of tissue activated (STA) [4][5].

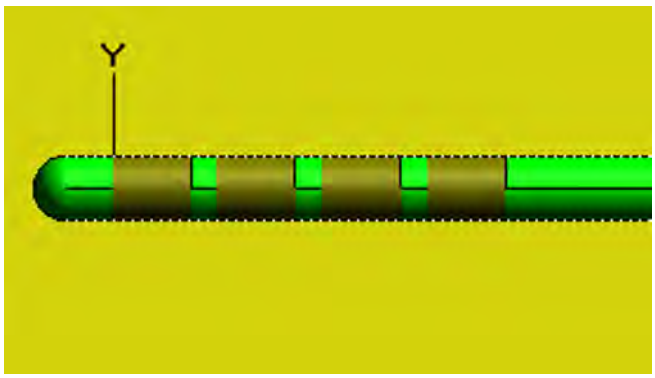


Fig. 1 DBS finite element model (include four contact electrodes and brain tissue). Left to right are electrode 1, electrode 2, electrode 3, and electrode 4.

Chwee Teck Lim, James C.H. Goh (Eds.): ICBME 2008, Proceedings 23, pp. 619–621, 2009
www.springerlink.com

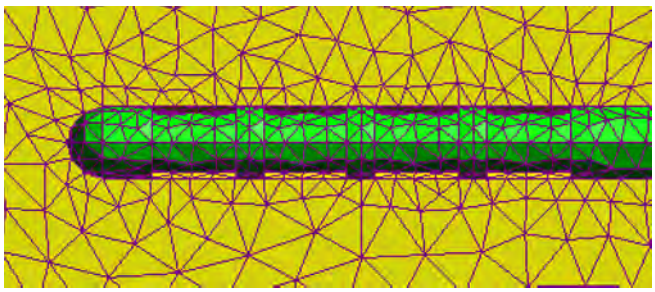


Fig. 2 Finite element meshing model

B. Finite Element model

In our DBS electrode finite element model (Fig. 1, 2), Axisymmetric FEM models of DBS electrodes with approximately 300000 nodes were constructed using Solidwork and ElecNet. The tissue medium was modeled as homogenous and isotropic medium with conductivity $\sigma = 0.3$ S/m. The axisymmetric volume conductor measured 100mm tall by 100 mm wide. Electrode contact dimensions ranged from 0.5mm to 1.5mm in height and 1.27mm in diameter. These dimensions were centered around the Medtronic 3387/3389 quadripolar DBS electrode contact dimensions (1.5mm height, 1.27mm diameter) [6][7]. The electrode lead was modeled as an electrical insulator with the exception of the contact area, which was used for voltage-controlled simulation.

Myelinated axon model [8] is used in conjunction with this FEM model. Under the same power (0.02W), the volume of tissue activated (VTA) was depended on electrode shape (height/diameter) and stimulation site and is relative to the position of electrodes. When we use a DBS electrodes model to simulate STA and VTA, there were also dependent on electrode shape (height/diameter). Stimulation sites were related to the positions of electrode.

C. Simulation Steps

Simulation steps: first, a finite element model is created, then the stimulation waveform is applied to the electrode, and the system is solved using a FEM solver. The result space-dependent voltages are used to calculate activating function thresholds for neural fibers, and the VTA is determined using these thresholds [9][10][11].

III. Result

A. Finite element potential contour and VTA contour

Fig. 3 shows the electrical potential result of DBS finite element model, which contains four-contact platinum electrode and brain tissue. -1V is applied to electrode 2, and others are set to 0V. Fig. 4 shows a VTA contour which shows the volume of tissue being activated.

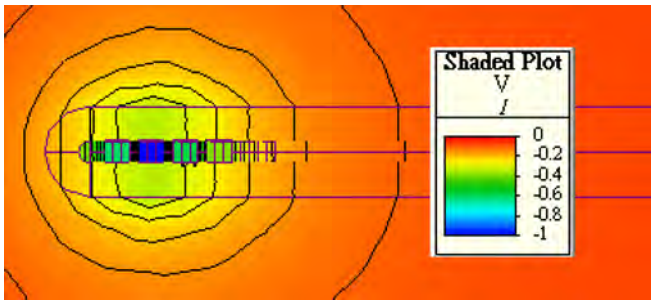


Fig. 3 Finite element potential contour of deep brain electrodes.

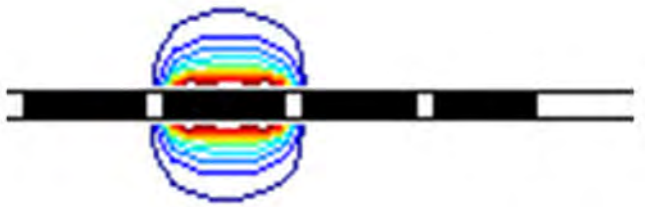


Fig. 4 VTA contour without buffer layer, the region of tissue that would be activated

B. Effect of electrode height, electrode Distance

Fig. 5 shows the relation between electrode height and VTA. When the electrode height is getting larger, VTA is getting longer. It is nearly a direct proportion relationship. The black parts indicate stimulation electrodes in Fig. 5.

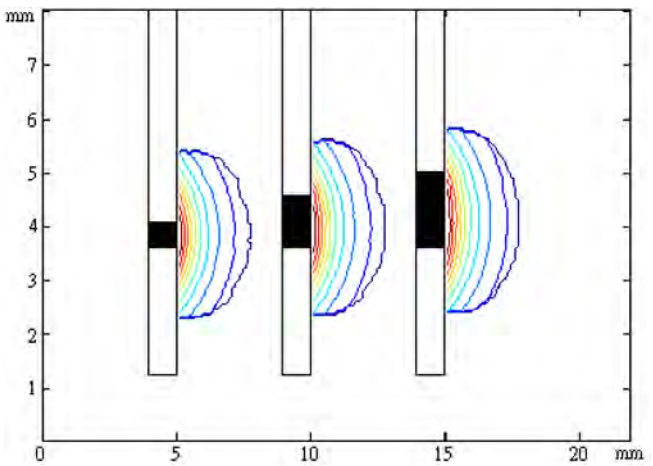


Fig. 5 Relation of electrode height and VTA. VTA contour gets longer with electrode height.

IV. Discussion and conclusion

Volume conduction simulations with typical DBS parameter settings can be used to study VTA and STA for voltage- or current-controlled electrical stimulation [12][13] with various electrode designs. Further, finite element model and neural model for deep brain stimulation can be used in conjunction clinical input parameters and animal models to study the effect of deep brain stimulation and how it is affected by the electric field generated by DBS electrical stimulation.

Acknowledgement

This research was supported in part by National Health Research Institute (NHRI-EX97-9735EI) and National Science Council, (NSC95-2221-E- 009-366-MY3). Taiwan, R.O.C.

References

1. Ashby P, Kim YJ, Kumar R, Lang AE, Lozano AM. Neurophysiological effects of stimulation through electrodes in the human subthalamic nucleus. Brain 1999;122:1919-31
2. McIntyre CC, Thakor NV. Uncovering the mechanism of deep brain stimulation for Parkinson's disease through functional imaging, neural recording, and neural modeling. Crit Rev Biomed Eng 2002; 30:249-81
3. Christopher R buston and Cameron C McIntyre: Role of electrode design on the volume of tissue activated during deep brain stimulation. In: Journal of Neural Engineering. 3(2006) 1-8
4. Ashby P, Kim YJ, Kumar R, Lang AE, Lozano AM. Neurophysiological effects of stimulation through electrodes in the human subthalamic nucleus. Brain 1999;122:1919-31
5. C.T.M. Choi and W.D. Lai, "Modeling Virtual Channels in Cochlear Implant Systems", Proc. of 12th Biennial IEEE Conference on Electromagnetic Field Computation, pp. 329, 200
6. Christopher R buston, Scott E. Cooper, Jaimie M. Henderson, and Cameron C McIntyre: Predicting the effects of Deep Brain Stimulation with Diffusion Tensor Based Electric Field Models
7. Cameron C. McIntyre, Susumu Mori, David L. Sherman, nitish V. Thakor, Jerrold L. Vitek: Electric field and stimulating influence generated by deep brain stimulation of the subthalamic nucleus. In: Clinical Neurophysiology 115 (2004) 589-595
8. McIntyre CC, Grill WM. Excitation of central nervous system neuron by non-uniform electric fields. Biophys J 1999;76: 878-88
9. Moffitt MA, McIntyre CC, Grill WM. Prediction of nerve stimulation threshold: limitations of linear models. IEEE Trans Biomed Eng 2003; (in press)
10. McIntyre CC, Grill WM. Extracellular stimulation of central neurons: influence of stimulus waveform and frequency on neuronal output. J Neurophysiol 2002;88: 1592-604
11. McIntyre CC, Grill WM. Selective microstimulation of central nervous system neurons. Ann Biomed Eng 2000;28:219-33
12. Christopher R buston and Cameron C McIntyre: Tissue and electrode capacitance reduce neural activation volumes during deep brain stimulation. In: Clinical Neurophysiology 116 (2005) 2490-2500
13. McIntyre CC, Grill WM. Finite element analysis of the current-density and electric field generated by metal microelectrodes. Ann Biomed Eng 2001; 29:227-35

Author: Charles T.M. Choi
Institute: Department of Computer Science and Institute of Biomed cal Engineering, National Chiao Tung University
Street: 1001, Ta-Hsueh Road
City: Hsinchu 300
Country: Taiwan
Email: c.t.choi@ieee.org

Implementation of Trajectory Analysis System for Metabolic Syndrome Detection

Hsien-Tsai Wu[1], Di-Song Yzng[1], Huo-Ying Chang[1], An-Bang Liu[2], Hui-Ming Chung[3], Ming-Chien Liu[3] and Lee-Kang Wong[3]

[1]Dept. of Electrical Engineering, National Dong Hwa University No. 1, Sec. 2, Da Hsueh Rd., Shou-Feng, Hualien, Taiwan 974
[2]Department of Neurology, Tzu-Chi General Hospital 707, Sec. 3, Chung-Yang Rd.,Hualien, Taiwan 970
[3]Department of Internal Medicine, Mennonite Christian Hospital, 44 Min-Chuan Rd. Hualien, Taiwan 970

Abstract — **Metabolic syndrome is not only a major public health problem in the United States and other developed countries but also is associated with increased risk for diabetes and coronary heart disease (CHD). This study presents a easy method for metabolic syndrome detection by measuring the digital volume pulse through the finger photoplethysmography (PPG). The trajectory analysis (TA) has been adopted to produce Poincare plots with the PPG signals. The Poincare plots are two-dimensional graphical representations (scatter plots) of PPG signals. The standard deviation along the longitudinal axis (SD2) in the plots are larger for the subjects with metabolic syndrome than who are without metabolic syndrome. SD2 in the Poincare map of finger plethysmographic singnals is a good indicator to detect metabolic syndrome.**

In this study, we hope to develop a simple detecting indicator of metabolic syndrome, and find a simple way to judge metabolic syndrome through the finger pulse infrared sensor for the non-linear analysis of Poincaré plot. The indicator can remind the user to pay attention to their health, control of eating and living habits to reduce future serious chronic diseases at any time.

Keywords — **Plethysmographic signal, Poincare map, Metabolic syndrome**

I. Introduction

Early detection and more intensive management of the metabolic syndrome in order to reduce the long-term risk of cardiovascular disease and diabetes is now possible[1], according to the International Diabetes Federation (IDF) in a global consensus statement presented for the first time today. The statement includes a new, clinically accessible definition of the metabolic syndrome, representing the views of experts in the fields of diabetes, cardiology, lipidology, public health, epidemiology, genetics, metabolism and nutrition from six continents[2].

Building on earlier definitions put forward by the WHO and NCEP ATP III, the new definition is easy to use in clinical practice. It avoids the need for measurements that may only be available in research settings. For a person to be defined as having the metabolic syndrome, the new definition requires they have central obesity, plus two of the following four additional factors: raised triglycerides, reduced HDL cholesterol, raised blood pressure, or raised fasting plasma glucose level. Gender and, for the first time, ethnicity-specific cut-points for central obesity as measured by waist circumference are included. However, noninvasive measuring instruments are now lack for metabolic syndrome detection in hospitals or at home.

In previous studies we had previously developed photoplethysmograpy (PPG) system using infrared sensors at finger tip for detecting the volume change of blood flow at that finger [3-5]. Being able to detect the changes of blood flow volume indicates the capability of endothelial function and arterial stiffness assessment. This infrared PPG system [6] not only has the capacity to record the digital (finger) amplitude signal according to the change of blood flow volume, in addition, it is also capable to calculate the parameters of digital pulse wave.

II. Materials and Methods

One hundred and forty nine examinees were included from a regular healthy check up from the Minot Christine General Hospital. There were 44 patients with metabolic syndrome and 105 age-matched healthy controls. The participants received blood check up of raised triglycerides, reduced HDL cholesterol, raised blood pressure, or raised fasting plasma glucose level and waist circumference.

A. Instruments and Methods

The system comprises two major parts:

(1) Device for Collection of Infrared Ray Finger Plethysmographic Signals: It includes a penetrating infrared sensor, a signal amplifier circuit and an A/D signal converter. Fig. 1 shows the self-developed non-intruding infrared sensor and signal amplifier circuit with simple structures and low costs. The A/D signal converter used in the system is TX-03A, an analog/digital signal switching interface card with the ISA as its interface. The specifications of the interface card are as follows:

Chwee Teck Lim, James C.H. Goh (Eds.): ICBME 2008, Proceedings 23, pp. 622–625, 2009
www.springerlink.com

1. 12-bit resolution;
2. 16 channels;
3. Single electrode;
4. A/D conversion time 60usec/per channel;
5. Input voltage 0-8.5V.

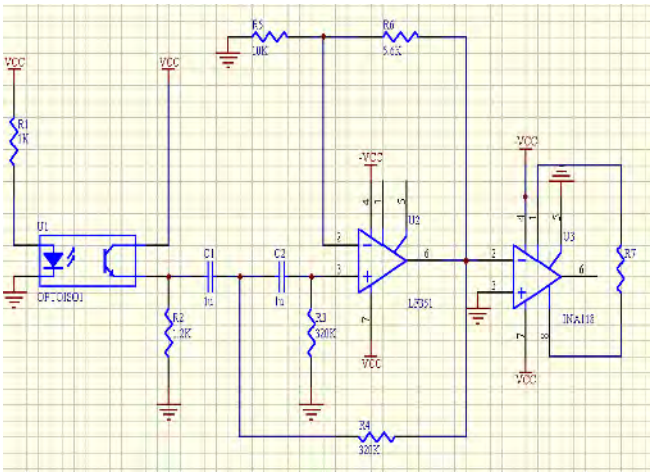


Fig. 1 The self-developed non-intruding infrared sensor and signal amplifier circuit

The hardware comprises (1) a signal collection end and (2) a signal analysis end. At the signal collection end, the signals of the finger capillaries are collected through an infrared sensor with a wavelength of 960nm. The collected signals are then converted to a infrared plethysmographic waveform through a second order differentiating circuit and sent to a low noise amplifier circuit to increase its signal/noise ratio and magnify its power to the level that meets the demand of A/D. The signals are further sent to a buffer circuit for implementing voltage following and impedance matching. The analog volume signals are finally converted to digital signals through the RTX-03A at the signal analysis end.

(2) Poincare Map Interface Analysis:

It can perform Poincare map analysis of plethysmographic signals and Fourier spectrum analysis, and present the different aspect of the plethysmographic strange trajectory. Users may operate the Main Screen to set or adjust parameters to identify the best Poincare maps. The Poincare map interface analysis function of the system has the features of easy operation and excellent expandability.

Signals are sent from the infrared sensor to the hardware circuit for appropriate processing, and then via the signal converter RTX-03A to the software. The software is built in a graphic programming environment created by NI Lab-View8.5. The analog signals collected with a device used to collect the infrared ray finger plethysmographic signals are stored in a file in a real-time manner by RTX-0-3A, driven by an interface controlled data retrieving program. The signals are then read from the file in a real-time manner and form a measure pulse wave diagram. The Poincare map of the STA is presented through the conjunction formed by the trajectory of the sampled signal space of the digital plethysmographic signals and the Poincare plane after the file is read [9]. The input parameter control button is the parameters needed for the input of the STA. Fig.2 shows the Main Screen of the self-developed IRFPS. Fig.2(a) represents original pulsewave from the tester. Fig.2(b) shows poincare map of the pulsewave, and Fig.2(c) is the definition of longitudinal axis,SD1, and the perpendicular direction, SD2.

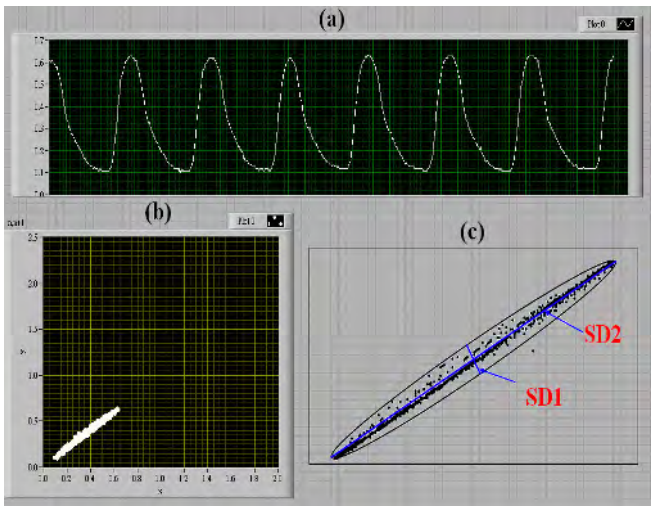


Fig. 2 Main Screen of the self-developed IRFPS

B. Flowchart of STA

The parameters and the actually measured data are read from input and smoothed to draw plethysmographic signals. The signals then undergo a data processing for the drawing of Poincare map conversion used for analysis. The STA follows after the aforementioned steps. Since there are many options for Poincare maps, it depends on the experience of doctors in clinical diagnosis to determine the effective map pattern.

In this study, we address one Poincare map as example for easy description of the study. The value of X/Y-axis of the Poincare map shall be first defined. The value obtained

after the data moves to be the value of X-axis directly. The value gained after the data moves to the parameter delay 1 point is the value of Y-axis. Finally, calculation and storage of the SD1, SD2, SD1*SD2, SD1/SD2, SD2/SD1 will be proceed.

It is the aforementioned observation that motivates us to make the research. We hope that another analysis approach can be provided to doctors and specialists as a reference for their clinical analysis and research to produce an auxiliary effect on diagnoses.

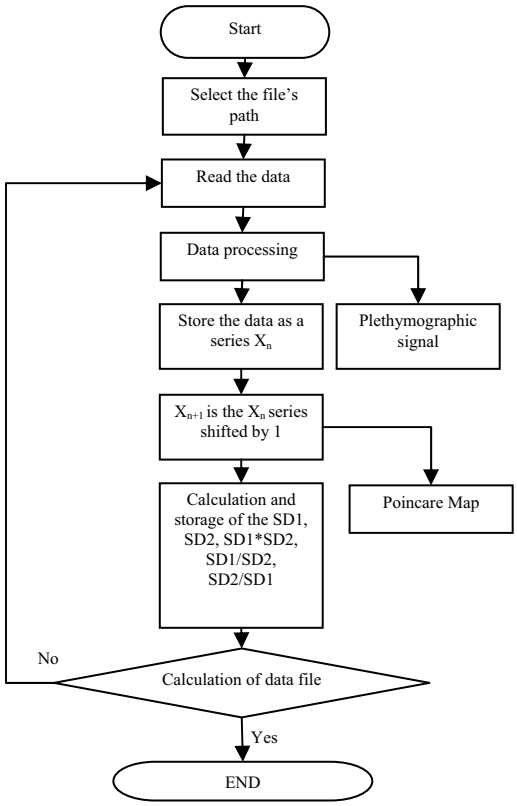


Fig. 3 Flowchart of strange trajectory analysis

III. Results

Among 149 subjects, 44 subjects had metabolic syndrome, and 100 subjects without having the metabolic syndrome. Subjects with metabolic syndrome had significantly higher waistline, weight, systolic and diastolic pressures, blood Glucose, and triacylGlycerol than those without metabolic syndrome, as Table I shown.

However, poincare map shows significant difference of SD2, SD1*SD2 between these two groups. However, there are no significant difference in SD1 and SD2/SD1.

Table I Characteristics of the study population (Mean±SD)

	Metabolic Syndrome N=44	Health N=105	P
Gender(m/f)	13/31	38/67	
Age(years)	61.59±10.74	59.17±11.52	NS
Waistline(cm)	90±7.48	74.23±6.73	p<0.001
Weight(Kg)	67.73±13.03	57.66±8.63	p<0.001
PWV(m/s)	10.42±2.13	9.91±2.31	NS
Systolic(mmHg)	144.89±18.97	122.98±18.29	p<0.001
Diastolic(mmHg)	88.30±12.12	75.50±10.53	p<0.001
Blood Glucose(mg/dl)	120.21±37.73	101.92±21.86	p<0.001
Total Choles-terol(mg/dl)	209.23±38.60	199.17±37.97	NS
TriacylGlyc-erol(mg/dl)	171.16±109.01	90.93±56.94	p<0.001
SD1	0.26±0.11	0.23±0.08	NS
SD2	1.07±0.58	0.86±0.33	p=0.006
SD2/SD1	4.49±2.65	4.02±1.86	NS
SD1×SD2	0.30±0.24	0.21±0.13	p=0.012

IV. Conclusion

Proposed is a self-developed IRFPS retrieving and the STA system. It is expected that many valuable experiences and clinical information will be produced to identify the type of disease to which the system is applicable and its effective Poincare maps. The trajectory analysis (TA) has been adopted to produce Poincare map with a self-developed infrared ray finger plethysmography system(IRFPS) to present one special strange trajectorie of the plethysmographic signal for metabolic syndrome detection. The proposed system can be used as an alternative diagnostic tool for doctors and specialists in an attempt to facilitate metabolic syndrome clinical diagnosis. In addition, the Poincare map of finger plethysmographic singnals is a good indicator to detect metabolic syndrome.

Acknowledgment

This research was supported by the National Science Council under Grant NSC 97-2221-E-259-019, Taiwan, Republic of China.

REFERENCES

[1] J.-P. Despres, P. Poirier, J. Bergeron, A. Tremblay, I. Lemieux, and N. Almeras "From individual risk factors and the metabolic syndrome to global cardiometabolic risk", Eur. Heart J. Suppl., March 1, 2008; 10(suppl_B): B24 - B33.

[2] Lakka HM, Laaksonen DE, Lakka TA, et al. The metabolic syndrome and total and cardiovascular disease mortality in middle-aged men. JAMA. 2002; 288: 2709–2716.

[3] Ju-Yi Chen; Wei-Chuan Tsai; Ming-Sheng Wu; Chih-Hsin Hsu; Chih-Chan Lin; Hsien-Tsai Wu; Li-Jen Lin; Jyh-Hong Chen. Novel Compliance Index Derived from Digital Volume Pulse Associated with Risk Factors and Exercise Capacity in Patients Undergoing Treadmill Exercise Tests. Journal of Hypertension 2007, 25; 1894-1899

[4] Wei-Chuan Tsai, Ju-Yi Chen, Ming-Chen Wang, Hsien-Tsai Wu, Chih-Kai Chi, Yung-Kung Chen, Jyh-Hong Chen, and Li-Jen Lin, "Association of Risk Factors With Increased Pulse Wave Velocity Detected by a Novel Method Using Dual-Channel Photoplethysmography", AJH, 8, pp.1118-1122, 2005.

[5] Philip J. Chowienczyk, Ronan P. Kelly, Helen MacCallum, Sandrine C. Millasseau, Tomas L. G. Andersson, Raymond G. Gosling, James M. Ritter and Erik E. Änggård. Photoplethysmographic assessment of pulse wave reflection: Blunted response to endothelium-dependent beta 2-adrenergic vasodilation in type II diabetes mellitus. J. Am. Coll. Cardiol. 1999;34;2007-2014

[6] Hsien-Tsai Wu, Cheng-Tso Yao, Tsang-Chih Wu and An-Bang Liu, " Development of Easy Operating Arterial Stiffness Assessment Instrument for Homecare", The 29th Annual International Conference of the IEEE Engineering in Medicine and Biology Society, France, 23-26, Aug. 2007, pp5868-5871

[7] Heikki V. Huikuri, Timo H. Mäkikallio, Chung-Kang Peng, Ary L. Goldberger, Ulrik Hintze and Mogens Møller. Fractal Correlation Properties of R-R Interval Dynamics and Mortality in Patients With Depressed Left Ventricular Function After an Acute Myocardial Infarction, Circulation 2000;101;47-53.

[8] Phyllis K, Stein and Anand, Reddy (2005) Non-Linear Heart Rate Variability and Risk Stratification in Cardiovascular Disease. Indian Pacing Electrophysiol J. 2005 Jul–Sep; 5(3): 210–220.

[9] Andreas Voss, Rico Schroeder, Sandra Truebner, Matthias Goerning, Hans Reiner Figulla and Alexander Schirdewan. Comparison of nonlinear methods symbolic dynamics, detrended fluctuation, and Poincare plot analysis in risk stratification in patients with dilated cardiomyopathy, Chaos 17, 015120 (2007); DOI:10.1063/1.2404633.

Diagnosis of Hearing Disorders and Screening using Artificial Neural Networks based on Distortion Product Otoacoustic Emissions

V.P. Jyothiraj[1] and A. Sukesh Kumar[1]

[1]Dept. of Electronics and Communication Engineering, College of Engineering, Trivandrum, India

Abstract — **The auditory system produces low level sound in response to stimulation. Distortion Product Otoacoustic Emissions (DPOAEs) are a series of combination tones generated in the ear when stimulated with two pure tones of frequencies f1 and f2. The most prominent DPOAE is the cubic difference tone at 2f1-f2. The objective of this work is to determine the DPOAE response characteristics from normal and hearing impaired subjects and hearing screening using artificial neural networks (ANN). The data acquisition platform controls the microphone/speaker system which generates the acoustical stimuli for presentation to the ear canal and collects the acoustic responses recorded in the ear canal. Digital signal processing technique involves estimation of weak DPOAE response at the 2f1-f2 frequency, the noise floor and the DPOAE signal to noise ratio (SNR) with f2 at frequencies 1.5, 2, 3, 4, 5 and 6 KHz. The individual pure tone audiometric data are also collected to differentiate ears with normal hearing from impaired ear. DPOAE features and pure tone audiometric data are used to train the ANN classifier. The proposed method is developed and evaluated using a dataset based on 76 hearing subjects. Supervisory learning is used for the training of the classifier. Each hearing subject is classified as normal or abnormal one. The ANN system indicates that the results are comparable to human intervention, with substantial reduction of time and resources. The DPOAE measurement provides detailed frequency specific information on cochlear function; it is a potential tool to find hearing impairment and hearing screening.**

Keywords — **Otoacoustic Emissions, DPOAE, Hearing Screening, Diagnosis, Artificial Neural Networks.**

I. Introduction

Otoacoustic emissions (OAEs) are a low level sound which arises in the ear canal when the tympanic membrane receives vibrations transmitted backwards through middle ear from cochlea as part of the normal hearing process [1], which is discovered by Dr. David Kemp in 1978. The outer hair cell (OHC) system of cochlea is responsible for the generation of OAEs and OHC mobility is the cellular basis of this phenomenon [2] at least for mammals. The generated signal propagates through middle ear and into ear canal, where they can be measured with sensitive microphone placed in the outer ear canal. OAEs are universally present to various degrees in all healthy cochleas, where as they are not generally observed or are greatly reduced in ears with mild hearing losses. This aspect together with the extreme facility to perform the test and the high reproducibility had made the OAEs an increasingly widespread application in diagnosis of hearing impairments.

OAEs are classified according to the type of stimulation to induce them (1) spontaneous otoacoustic emission (SOAEs) (2) evoked otoacoustic emissions (EOAEs). The SOAEs are narrow band and low level signals which are generated without acoustic stimulation, whereas EOAEs occur during or after external acoustic stimulation [3]. There are several subclasses of EOAEs based primarily on the stimuli used to evoke them. These include (i) transient evoked OAEs (TEOAEs) (ii) distortion product OAEs (DPOAEs). TEOAEs are delayed response to acoustic transient stimuli such as clicks or tone burst.

The DPOAEs are inter modulation-distortion response produced by the ear in response to two simultaneous pure tone stimuli referred to as the primary tones f1 and f2 with levels L1 and L2. The primaries are related in frequency separation of f2 from f1 commonly called f2/f1 ratio, i.e., typically 1.22 [4]. The most frequently measured acoustic inter modulation-distortion product is at the frequency 2f1-f2 i.e., the cubic difference tone [4], although the cochlea also produces concurrently DPOAEs at other frequencies (e.g., f2-f1, 2f2-f1, 3f1-2f2) in response to such bitonal stimulation. Indeed, the only emitted distortion component utilized to clinical purpose has been 2f1-f2 because it is the largest DPOAE. The amplitude of a DPOAE depends upon the level of the eliciting stimulus.

The aim of this work is focused (i) to find DPOAE response characteristic of normal and hearing impaired subjects from different age group and (ii) to extract the features from DPOAE measurement data to hearing level for hearing screening using Artificial neural networks. An ANN is computational structure that is inspired by observed processes in natural networks of biological neurons in the human brain. neural net work s have a large number of highly inter connected processing elements that discriminate the ability to learn and generalize from training pattern or data. This work is an extension of author's earlier works [5], [6], [7].

Chwee Teck Lim, James C.H. Goh (Eds.): ICBME 2008, Proceedings 23, pp. 626–630, 2009
www.springerlink.com

II. Materials and methods

A. DPOAE measurement System

A schematic of computer based DPOAE measurement system is shown in the Fig. 1. , which includes a computer, a probe, data acquisition and Digital signal processing (DSP) system. The DPOAE response is measured via a probe that is sealed in the ear canal using a removable rubber or form ear tip. The probe assembly contains two miniature speakers and a low noise microphone. Each speaker is dedicated to delivering a pure tone, either f1 or f2. The f1 and f2 tones are kept separated from each other until they are inserted into the ear canal to minimize the possibility of instrumentation artifacts interfacing with the measurement of the biological response from the cochlea. The DSP platform is the brain of DPOAE system because it is where signal generation, data acquisition and averaging are controlled. The two primary tones f1 and f2 are digitally synthesized are presented to ear canal through digital to analog converter (DAC) and miniature speaker system to elicit DPOAEs. The responses are collected through miniature microphone, after amplification and filtering it is fed to DSP platform through analog to digital converter (ADC) for further signal processing [8]. The signal detected by the microphone includes the primary tone pair, a series of inter modulation products; biological sounds, such as those associated with breathing, blood flow and muscle movements; and room sounds. The challenge for the DPOAE system is to isolate the desired distortion product from the multitude of other frequencies present within the ear canal. Since only the frequencies in the immediate vicinity of the DP frequency (2f1-f2) have the potential of interfering with the measurement of the DP frequency, it is possible to examine the amplitude of these frequencies when calculating the separation of the DP from the noise. The noise floor level is further reduced by using a low noise environment such as a sound proof room for DPOAE measurement.

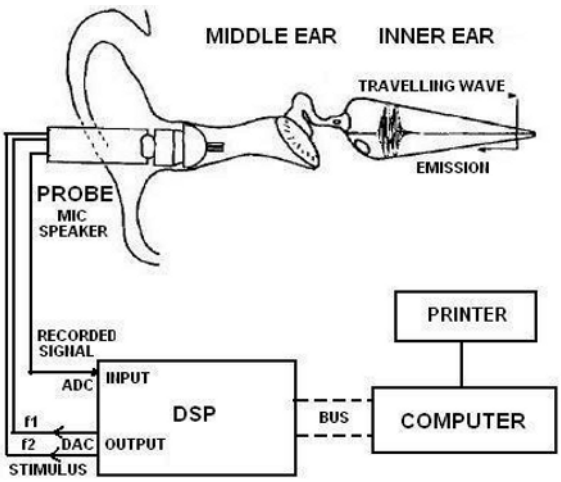


Fig. 1 Schematic of a computer based DPOAE measurement setup

B. DPOAE Acquisition and Analysis

DPOAEs are measured from 76 subjects like normal, hearing impaired, and normal having other diseases. To conduct DPOAE test, two primary tones at frequency f1 and f2 and levels L1 and L2 were presented. The frequency ratio f2/f1 was fixed at 1.22. The stimulus levels were held constant at L1= 65 dBSPL and L2=55dBSPL. These values have been shown to give large amplitude and thus easily detectable.

The recorded DPOAE signal can be formulated as

$$s(n) = \sum_{i=j}^{3} A_i \cos(nw_i + \phi_i) + v(n) \qquad (1)$$

Where $w_i = 2\pi f_i/f_s$ with f_s being the sample rate, and v(n) is the noise. The two sinusoids $A_1 \cos(nw_1+\Phi_1) + A_2 \cos(nw_2+\Phi_2)$ represent the stimulus induced artifact, while $A_3 \cos(nw_3+\Phi_3)$ is the DPOAE component. Because the artifact is about 60 dB larger than the DPOAE, we have $A_1 >> A_3$ and $A_2 >> A_3$. The DPOAE component can be treated as nonrandom signal since the DPOAEs are stable for a long period of time .On the other hand, v(n) is assumed to be uncorrelated Gaussian process with zero mean and variance. In clinical measurement, the signal strength of DPOAEs at f_3 is usually the parameter of interest. Define DPOAE level as $L_{dp}=A_3^2/4$.Since the DPOAEs are tonal; it is possible to obtain L_{dp} by measuring the spectrum of the recorded signal. Conventionally, this is achieved by FFT estimators [9]. The following variables were analyzed**.** (i) the estimated DPOAE level (DP) measured at the 2f1-f2 frequency with f2 at frequencies 1.5,2, 3, 4 ,5 and 6KHz. (ii) the noise level (NF) estimated from the 4 Fourier components nearest to but not including the 2f1-f2 frequency. (iii) the estimated DPOAE signal to noise ratio (SNR) is defined as the difference between estimated DPOAE level and estimated noise level. Fig.2. shows the spectra of ear canal sound pressure detected by microphone.

C. Pure tone audiometric test

In this study, pure tone audiometric data are also collected from the hearing subjects (adults and children)using both air conduction and bone conduction methods in the frequency range1.5 to 6 KHz. Here normal hearing subject is coded as '1', if subject having audiometric mean hearing

level (MHL) less than 30 dB and hearing impaired subject is coded as '0', if MHL greater than or equal to 30dB repetitively. This data are used for ANN training and testing

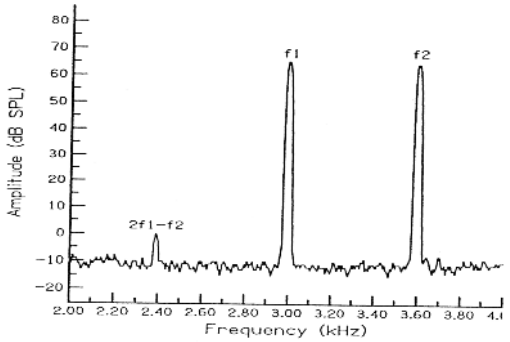


Fig. 2 Spectra of ear canal sound pressure from the ear of a normal hearing adult

D. Artificial Neural Network for Classification

Artificial neural networks are considered to be good classifier due to their adaptive learning, robustness, self organization and generalization capacity. In this work multilayer feed forward network is used for classification (normal or impaired).Fig.3 shows a three layer feed forward network with an input layer, one hidden and an output layer. Where x_i denotes the features vector parameters, 'i' is the number of inputs, k is the number of hidden layers and W_{ik} are the weights between inputs and hidden layers. The number of neurons in the hidden layer is selected by trial and error method. In our case, the final network had 10 inputs, 15 neurons in hidden layer and one neuron in the output layer.

The most popular and well established training algorithm used with the multilayer feed forward network is the back propagation algorithm (BPA), and it is used in this work. The weights were adjusted using Levenberg-Marquardt algorithm during the training procedure. This algorithm has the most rapid convergence properties for network with moderate complexity [10]

The DPOAE features (4Nos), Noise levels (4Nos)of four different f2 frequencies(2 to5KHz), age and sex (1 or 0) of hearing subjects are the input vector for training and pure tone audiometric result (normal and impaired subjects) is the target vector. The network was trained using supervised learning with training set of inputs and targets .This procedure is described by

$$f(x_1,x_2\ldots.x_{10}) = 1 \text{ if } \quad MHL < 30dB$$
$$= 0 \text{ if } \quad MHL \geq 30 \text{ dB} \qquad (2)$$

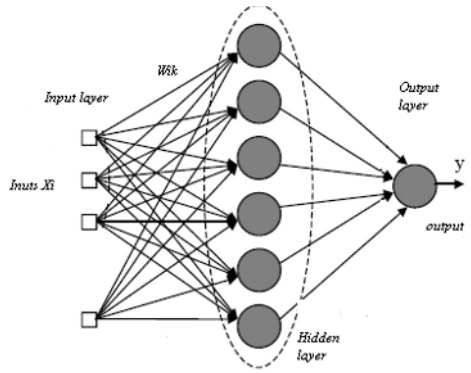


Fig. 3 Schematic representation of a three layer feed forward network

where $f(x_1, x_2,\ldots.x_{10})$ is the discriminate function which have to be determined by the ANN to minimize the mapping error of the features $x_1, x_2,\ldots.x_{10}$ to the targets, the binary values 1 and 0 .These binary value represent the subjects having audiometric MHL in frequency range 2to 5KHz less than 30 dB, and greater than or equal to 30dB respectively. Thus normal hearing subjects are coded '1' and hearing impaired subjects by '0'.

III. Results

The amplitude level of the DPOAE response is depending on the intensity, frequency separation or ratio, and level difference between the tones. The variation of DPOAE level with various stimulus levels for two different frequencies, collected from 6 months old infant with normal hearing is shown in Fig.4. In this graph the emission gradually exceeds the noise floor as the intensity of the primary tones increases. The stimulus increases from 20 to 60 dB, but emission at low intensity levels are difficult to distinguish from the noise floor. At high intensity levels, emissions grow to 15 to 25 dB above noise floor.

Table I gives the DPOAE data of 28 year old female subject with sensorineural hearing loss (left ear) and normal right ear. The result of data analysis shows that the high frequency DP response of the left ear is poorer when compared with that of right ear.

In pure tone analysis behavioral threshold increased significantly with age at and above 3 KHz. The DPOAE amplitude decreased with increasing age at all frequencies. The outcome of analysis for ears is based on 76 subjects for whom both ears are tested; the mean behavioral thresholds are lower in right ear than in left ears for mid frequencies. However the corresponding DPOAE amplitudes did not show any clear difference between right and left ears.

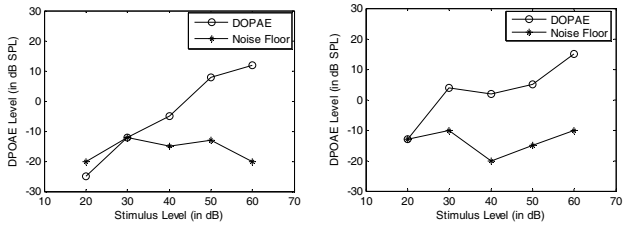


Fig. 4 Variation of DPOAE response level with respect to stimulus level for two different frequencies (a) f2=2KHz and (b) f2=4KHz

Table 1 A sample DPOAE data and Noise floor data

f2 KHz	L1 dB	L2 dB	Left Ear			Right Ear		
			DP dB	NF dB	SNR	DP dB	NF dB	SNR
2	65	55	-4	-17	21	-2	-18	16
3	65	55	-4	-2	16	8	-19	26
4	65	55	-9	-20	11	3	-20	23
5	65	55	-20	-20	0	-3	-20	17

The behavioral thresholds are significantly lower (i.e., better) for women than for men at all frequencies and DPOAE levels are greater for women particularly for frequencies above about 2.5 KHz. DPOAE is a potential tool to find subjects suffering from the noise induced hearing loss, the influence of ototoxic drugs to hearing and cochlear disorders.

An ANN model was trained and applied to classify the normal and pathologic ear using DPOAE response features. For training set 64 normal and 14 pathologic ear data and test set 50 normal and 24 pathologic data were used. The following measures were used to access the performance of classifier i.e. sensitivity, specificity [8] and receiver operating characteristic (ROC) [11]. In this work, ROC points are generated from single trained ANN by systematically varying threshold value for output node Fig.5shows ROC of this ANN model. The ROC, it shows the tradeoff between sensitivity and specificity. The curve closer to left hand border and then the top border of ROC space and away from the 45-degree diagonal of ROC space, i.e. the more accurate the test and approximate area under the curve is more than 80% of ROC space and classifier accuracy is 90.54%.The proposed ANN algorithm is implemented in Matlab.

IV. Conclusions

The ANN classifier transformed a vector of 10 features representing one subjects, into single output. The result

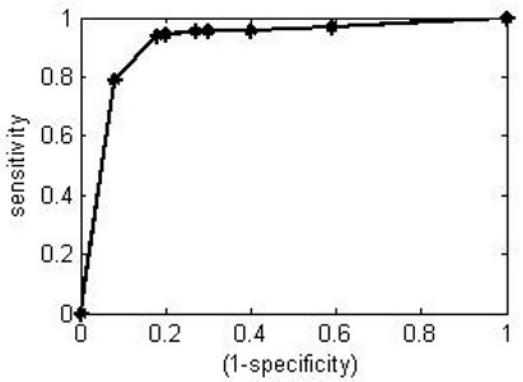


Fig. 5 Receiver operating characteristic of ANN model

concludes that it is possible to classify the hearing subject with the help of 3 layer network driven by BPA. The result shows that the proposed method is effective for classification of hearing subjects with mean accuracy of 90.54%. The ANN system indicates that the results are comparable to human intervention with substantial reduction of time and resources. DPOAE testing is simple, objective and non invasive diagnostic tool in the evaluation of hearing problems and hearing screening.

Acknowledgment

The authors are grateful to the Directors of Kerala ENT Research Foundation (KERF) and National Institute of Speech and Hearing (NISH), Kerala, India for being provided the facility to carry out the above work.

References

1. Kemp D. T (1978) Otoacoustic emissions in perspective, Thiema Medical publishers, New York, pp 1-20
2. Brownwell W E (1990) Outer hair cell electro motility and otoacoustic emissions, Ear.Hear., 11: 82-92
3. Kemp D T (1978) Stimulated acoustic emissions from within the human auditory system, J Acoust. Soc.Am, vol.64,no.5,pp1386-1391
4. Haris F P , Lonsbury, Maertin B L(1989), Acoustic distortion product in human systematic changes in amplitude as a function f2/f1 ratio, *J* Acoust Soc.Am 85: 280-286
5. Jyothiraj V.P, Sukesh Kumar A (2007*)* Computer based Investigation of Hearing disorders through Distortion Product Otoacoustic Emission analysis, MS07, Proc.vol.I,International conference on modeling and simulation, Kolkata,India,pp192-195
6. Jyothiraj V.P , Sukesh Kumar A. (2008) Effect of Stimulus Parameters, Age and Gender on Cubic Difference Distortion Product Otoacoustic Emission Measurement for Hearing Screening and Diagnosis, ICSCN 08, Proc,International Conference on signal processing, communication and networking, Chennai ,India pp225-229

7. Jyothiraj V P, Sukesh Kumar A (2008)Mapping of hearing profile through Evoked otoacoustic emissions,MS08,Proc. International conference on modeling and simulation, Portsaid,Egypt,pp150-162
8. Minghui Du, Chan F H Y, et al, (1998) Design consideration of a multi-function otoacoustic emission measurement system Proc. vol.20,20th Annual International Conference of the IEEE Engineering in Medicine and Biology Society, pp1928-1931
9. Zirani A K, Konard A(2004)A novel method of estimation of distortion product otoacoustic emission signals, IEEE Trans. Biomedical Engg., 51, no.5, pp 864-868
10. Jang J S R, (2004)Neuro-Fuzzy and soft computing, Pearson, India
11. Kevin woods, Kevin W B(1997)Generating ROC curves for Artificial neural networks,IEEE Tran,Medical imaging vol.18:329-337

Author: Jyothiraj V.P
Institute: College of Engineering
Street: Sreekariyam
City: Trivandrum,Kerala
Country: India
Email: vpjr27@yahoo.com

Detection of Significant Biclusters in Gene Expression Data using Reactive Greedy Randomized Adaptive Search Algorithm

Smitha Dharan[1] and Achuthsankar S. Nair[1]

[1]Centre for Bioinformatics, University of Kerala, Thiruvananthapuram, India

Abstract — **In microarray gene expression data, a bicluster is a subset of genes which exhibit similar expression patterns along a subset of conditions. Each bicluster is represented as a tightly co-regulated submatrix of the gene expression matrix. One of the most popular measures to evaluate the quality of a bicluster is the mean squared residue score. Our approach aims to detect significant biclusters from a large microarray dataset through a metaheuristic algorithm called reactive greedy randomized adaptive search procedure (R-GRASP). The method finds biclusters by starting from small tightly co-regulated bicluster seeds and iteratively adds more genes and conditions to it while keeping the mean squared residue score below a predetermined threshold. In R-GRASP, the parameter that defines the blend of greediness and randomness is self adjustable depending on the quality of solutions found previously. We performed statistical validation of the biclusters obtained through p-value calculation and evaluated the results against the results of basic GRASP and as well as with the classic work of Cheng and Church. The experimental results on the Yeast gene expression data indicate that the Reactive GRASP outperforms the basic GRASP and the Cheng and Church approach.**

Keywords — **Gene expression, Biclustering, Mean squared residue score, Metaheuristics, Greedy randomized adaptive search procedure.**

I. Introduction

DNA microarrays have been extensively used for measuring the expression levels of thousands of genes in a genome simultaneously. Gene expression data is typically arranged as an *m x n* data matrix, with rows corresponding to genes and columns corresponding to experimental conditions. The $(m, n)^{th}$ entry of the gene expression matrix represents the expression level of the gene corresponding to row *m* under the specific condition corresponding to column *n.* Cluster analysis plays an important role in the microarray data analysis through the grouping of genes into subsets with similar expression patterns or similar function. However, clustering has its limitations. Mainly, clustering works on the assumption that related genes behave similarly across all measured conditions. But a general understanding of cellular processes expects subsets of genes to be co-regulated and co-expressed only under certain experimental conditions, but behaves almost independently under other conditions [1]. In order to overcome the above shortcoming of clustering, the concept of biclustering is applied to gene expression data.

Biclustering was first introduced by Hartigan [2] and was named as 'direct clustering'. It performs simultaneous row column clustering. Cheng and Church [3] were the first to apply it to gene expression data. In gene expression data, a bicluster is a subset of genes exhibiting a consistent pattern over a subset of conditions. In [3], Cheng and Church proposed a similarity score called *mean squared residue score* as a measure of coherence of the rows and columns in the bicluster. The lower the score, stronger the coherence exhibited by the bicluster, and better is the quality of the bicluster. However, from a biological point of view, the interest resides in biclusters with subset of genes showing similar behavior and not with similar values. Hence the method aims at finding large and maximal biclusters with mean squared residue score below a certain threshold, δ, and the biclusters thus obtained are called δ-biclusters. The value of δ has to be estimated in advance, and it is different for every dataset [4].

In this work, we address the biclustering problem using a metaheuristic technique called *Reactive Greedy Randomized Adaptive Search Procedure* (R-GRASP) which is a variant of *Greedy Randomized Adaptive Search Procedure* (GRASP) [5, 6]. The algorithm makes use of *mean squared residue score* as the cost function to evaluate the quality of the obtained biclusters. We performed statistical validation of the biclusters obtained through p-value calculation and the results are compared against the classic work of Cheng and Church and also with our own work based on basic GRASP [7].

II. Materials and methods

A. Biclustering

A gene expression matrix is an *m x n* matrix, V, whose rows represent the genes, columns the experimental conditions and an element V_{ij} is a real number that represent the expression level of gene i under experimental condition j. Each row corresponds to the expression levels of a particular gene over all *n* experimental conditions and each column corresponds to the expression levels of *m* genes under a specific experimental condition. Fig. 1(a) shows the profile of a sample gene expression matrix where the experimental

Chwee Teck Lim, James C.H. Goh (Eds.): ICBME 2008, Proceedings 23, pp. 631–634, 2009
www.springerlink.com

conditions are represented in the x-axis and the gene expression values are represented in the y-axis. It consists of ten genes and ten experimental conditions. Fig. 1(b) shows the profile of an embedded bicluster containing only five genes and five conditions.

Let G = {g_1, g_2 …, g_m} and C = {c_1, c_2,….., c_n} represent a set of genes and a set of experimental conditions involved in a gene expression matrix, respectively. A bicluster is defined to be a subset of genes that exhibit similar behavior under a subset of experimental conditions, and vice versa. Thus, in the gene expression matrix, a bicluster will appear as a sub matrix of it and represented as a pair A = (I, J) or simply as A_{IJ}, where I ⊆ G and J ⊆ C. The rows and columns of the bicluster need not be contiguous as in the expression matrix.

A group of genes are said to be coherent if their level of expression reacts in parallel or correlates across a set of conditions. Similarly, a set of conditions may also have coherent levels of expression across a set of genes. The degree of coherence of a bicluster is measured using the concept of *mean squared residue score, HScore*, which represents the variance of a particular subset of genes under a particular subset of conditions with respect to the coherence. In [3], Cheng and Church defined the mean squared residue score as follows: It is defined for bicluster A_{IJ} as the sum of the squared residues. R (a_{ij}), the residue of an element a_{ij} in the bicluster $A_{IJ,}$ i ∈ I and j ∈ J, is a measure of how well the element fits into that bicluster. It is defined to be:

$$R(a_{ij}) = a_{ij} - a_{Ij} - a_{iJ} + a_{IJ} \tag{1}$$

Now, *HScore* is defined as in (2):

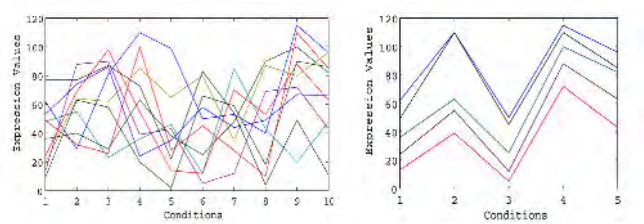
$$HScore = \frac{\sum_{i\in I, j\in J} (R(a_{ij}))^2}{|I| * |J|} \tag{2}$$

where $a_{Ij} = \frac{\sum_{i\in I} a_{ij}}{|I|}$ is the column mean of column j

$a_{iJ} = \frac{\sum_{j\in J} a_{ij}}{|J|}$ is the row mean of row i

$a_{IJ} = \frac{\sum_{i\in I, j\in J} a_{ij}}{|I| * |J|}$ is the mean of bicluster A_{IJ}.

A bicluster is defined to be a δ-bicluster if *HScore (I, J)* ≤ δ, for some δ ≥ 0, where δ is the maximum acceptable mean squared residue. The value of δ has to be estimated in advance, and it is different for every dataset [4]. The *HScore* gives an indication of how the data is correlated in the sub matrix - whether it has some coherence or is random. A matrix of equally spread random values over a range [a, b] has an expected *HScore* of $(b-a)^2/12$ and it is independent of the size of the matrix. A high *HScore* indicates that the data is uncorrelated and a low *HScore* means that there is correlation in the matrix.



(a) (b)

Fig 1. (a) Profile of gene expression data in Table 1. (b) profile of an embedded bicluster.

B. R-GRASP based Biclustering

The bicluster problem is NP-hard as proven by Cheng and Church (2000) [3]. Thus no polynomial time algorithm exists and they might require exponential computation time in the worst-case. In this work, a heuristics based method is adopted for finding the δ-biclusters in reasonable time. The problem is formulated as an optimization problem which aims at minimizing the *HScore*. The algorithm has two major phases. In the first phase, an initial set of seed biclusters are generated. The second is the heuristics based seed growing phase. The R-GRASP metaheuristics, a variant of the GRASP metaheuristics, is used in this phase to refine and enlarge the seeds by adding more rows and columns until their *HScore* reaches a certain predetermined threshold.

Seed generation: A good seed of a possible bicluster is a tightly co-regulated small bicluster whose *HScore* has reached the requirement but the volume may not be maximal. The simplest way to generate quality bicluster seeds is to perform standard one-dimensional k-means clustering on both rows and columns of the expression matrix separately and then combine them to generate different seeds [8, 9]. Finally, the *HScore* of all submatrices are calculated and those having *HScore* less than a threshold value are selected as the seeds.

Seed growing based on R-GRASP: GRASP is a metaheuristic technique, in which each iteration is made up of a construction phase , where a randomized greedy solution is constructed, and a local search phase which starts at the constructed solution. It applies iterative improvement until a locally optimal solution is found. Seed growing is implemented as a two step procedure. Initially, the GRASP iterations are performed over the seed bicluster to enlarge it

column wise and during the second step, another set of GRASP iterations add more rows while keeping the *HScore* below a predetermined threshold.

During the construction phase of each GRASP iteration a set of candidate elements, elements that can be added to the current partial solution without destroying the feasibility are formed. Then a restricted candidate list (RCL) is made from the candidate list according to a greedy evaluation function as shown in (3). The evaluation of the candidate elements by this function leads to the selection of only high quality elements from the candidate list to RCL. i.e. those whose incorporation to the current partial solution results in the smallest incremental costs. The element to be incorporated to the partial solution is randomly selected from those in the RCL. Once the selected element is incorporated to the partial solution, the candidate list is updated and the incremental costs are reevaluated.

$$\text{RCL} \leftarrow \{ s \in \text{C or G} \mid H(\text{Solution} \cup s) \leq \text{Smin} + \alpha(\text{Smax} - \text{Smin})\} \quad \ldots (3)$$

where

$$\text{Smin} \leftarrow \min \{H(\text{Solution} \cup t) \mid \forall\ t \in \text{C or G}\}$$

$$\text{Smax} \leftarrow \max \{H(\text{Solution} \cup t) \mid \forall\ t \in \text{C or G}\}$$

C is the candidate list of conditions
G is the candidate list of genes
H is *HScore*, the cost function to be minimized
α is a threshold parameter, $\alpha \in [0..1]$

The quality of elements in RCL is decided by a threshold parameter $\alpha \in [0..1]$. Since in the case of a minimization problem, $\alpha = 1$ corresponds to pure random construction, as $\alpha \rightarrow 0$; the algorithm behaves more or less like greedy algorithms. Thus the parameter 'α' controls the amount of greediness and randomness in the algorithm. In basic GRASP implementation [7], the same α is used along all iterations and its value is usually determined through experimentation. But in [10], Prais and Ribeiro showed that using a single fixed value for α often hinders finding a high quality solution, which eventually could be found if another value was used. Hence they proposed an extension to GRASP called Reactive GRASP (R-GRASP), in which the parameter α is not fixed, but instead is selected at each iteration from a discrete set of possible values. The solution values used along the previous iterations serve as a guide for the selection process.

During each iteration the value of α is selected from a discrete set of possible values, say $R = \{\alpha_1, \ldots, \alpha_m\}$. Let p_i be the selection probability associated with the choice of α_i, for $i = 1, \ldots, m$. Initially all p_i's are made equal to 1/m. The selection probabilities are periodically reevaluated using information collected during the search. After, each GRASP iteration, with a particular α_i, the difference in the current solution value and the value of the solution obtained in the previous iteration is calculated. Let A_i be the average value of such differences obtained taking $\alpha = \alpha_i$ in the construction phase. The probability distribution is updated after each GRASP iteration by taking $p_i = q_i / \sum_{j=1}^{m} q_j$, with $q_i = 1/A_i$ for $i = 1, \ldots, m$. The value of q_i will be larger for values of $\alpha = \alpha_i$ leading to the best solutions on the average. Larger values of q_i correspond to more suitable values for the parameter α. The probabilities associated with these more appropriate values will then increase when they are reevaluated.

The solution constructed during the construction phase is not necessarily optimal; hence local search is performed over it for further improvements. A first improving local search strategy is adopted for implementation of local search. It considers the neighborhood of the current partial solution and accepts further moves if inclusion of a new row/column improves the current partial solution.

Significance evaluation: The p-values of the biclusters obtained are calculated according to the known classification of genes as follows: suppose prior knowledge classifies m genes into k classes, $C_1, C_2, C_3, \ldots, C_K$. Let B be a bicluster with g genes, out of which g_j belong to class C_j. The *p-value* of B, assuming the most abundant class for B is C_i, is calculated as

$$p(B) = \sum_{k=g_i}^{g} \frac{\binom{|C_i|}{C_k}\binom{m-|C_i|}{C_{g-k}}}{\binom{m}{C_g}} \quad (4)$$

That is, the *p-value* corresponds to the probability of obtaining at least g_i elements of class C_i in a random set of size g.

III. Results

A. Description of the dataset

The proposed biclustering algorithm is implemented in Matlab and tested on the Yeast Saccharomyces Cerevisiae cell cycle expression dataset. The dataset is taken from *http://arep.med.harvard.edu/biclustering* and is based on-Tavazoie et al. [11]. It is a collection of 2884 genes and 17 experimental conditions, having 34 null entries with -1 indicating the missing values. All entries are integers lying in the range 0 to 595. The value of δ is used as an upper limit of allowable dissimilarity among genes and conditions. A higher δ is indicative of diminishing homogenity. Hence in our approach we used a value of 200 for δ.

B. Biclustering using R-GRASP

In R-GRASP, the RCL parameter α is self adjustable based on the quality of solutions found previously. The selection probabilities are calculated accordingly and depending on this, the value of α is selected from a discrete set of possible range [0..1]. In order to ensure the quality of solutions, we have completely eliminated the extreme values. Hence in our implementation of R-GRASP, we have used ten numbers in the range [0.25..0.65]. Since the solution generated by the construction phase is not optimal, local search is performed on these to further improve them.

C. Statistical validation using prior knowledge

For statistical validation, we used the 30 known categories of Yeast genes reported by Tavazoie et al [11]. The p-value of a bicluster signifies how well they match with the known gene annotation. A smaller p-value close to zero is indicative of better match. For a statistical comparison of the biclusters obtained with that of Cheng and church and basic GRASP, the correspondence plot proposed by Tanay et al. [12]. In the plot, the area under the curve shows the approximate degree of statistical significance of the biclusters used to draw the curve [13]. Fig. 2 presents the correspondence plot. It shows the biclusters generated by the R-GRASP tend to be more significant than the basic GRASP and Cheng and Church (CC) approach.

IV. Conclutions

In this paper, the biclustering problem is approached with a bottom up strategy where a tightly co-regulated bicluster seeds consisting of a minimal set of rows and columns are iteratively modified, usually enlarged, until no local improvement is possible anymore. We have proposed a metaheuristic technique- R-GRASP– to enlarge the seeds by adding more rows and columns to increase their size while keeping their mean squared residue below a predetermined threshold. In R-GRASP, the basic parameter that defines the quality of elements in the restricted candidate list is self adjustable depending on the quality of solutions obtained previously. Thus it doesn't require calibration efforts and looks more robust in detecting significant biclusters. We performed statistical validation of the biclusters obtained through p-value calculation and evaluated the results against the results of basic GRASP and as well as with the classic work of Cheng and Church. The results on the Yeast gene expression data indicate that R-GRASP outperforms the others.

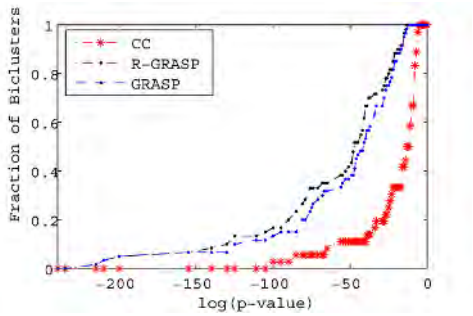


Fig. 2. Correspondence plot

References

1. Madeira SC and Oliveira AL (2004) Biclustering algorithms for biological data analysis: A survey, IEEE Transactions on Computational Biology and Bioinformatics, 1(1): 24-48.
2. Hartigan JA (1972) Direct clustering of a data matrix, J American Statistical Association, 337: 123-129.
3. Cheng Y, Church GM(2000) Biclustering of gene expression data, ISMB Proc.Conf.Intelligent Systems for Molecular Biology, California, USA, 2000, pp 93-103.
4. Jesus S. Aguilar-Ruiz (2005) Shifting and scaling patterns from gene expression data, Bioinformatics, 21(20):3840-3845.
5. Resende MGC, Ribeiro CC(2002) Greedy randomized adaptive search procedures, in Handbook of Metaheuristics, F. Glover and G. Kochenberger, eds, Kluwer Academic Publishers, 219-249.
6. Blum C, Roli A (2003) Metaheuristics in combinatorial optimization : Overview and conceptual comparison, ACM Computing Surveys, 35(3): 268-308.
7. Dharan S, Nair ASN (2008) Biclustering of gene expression data using greedy randomized adaptive search procedure, Proc. IEEE TENCON 2008, Hyderabad, India 2008 " in press".
8. Chakraborty A (2005) Statistical identification of biclusters in gene expression data, Proc. CBGI, 2005, pp 1185-1190.
9. Chakraborty A (2005) Biclustering of gene expression data by simulated annealing, HPCASIA Proc. International Conference on High-Performance Computing in Asia-Pacific Region.
10. Prais M, Ribeiro CC (2000) Reactive GRASP: An application to a matrix decomposition problem in TDMA traffic assignment, INFORMS J Computing, 12:164-176.
11. Tavazoie S, Hughes JD, Campbell MJ, Cho RJ, Church GM (1999) Systematic determination of genetic network architecture, Nat Genet., 22(3): 281-285.
12. Tanay A, Sharan R, Shamir R (2002) Discovering statistically significant biclusters in gene expression data, Bioinformatics, 18: S136-S144.
13. Yoon S, Nardini C, Benini L, De Micheli G (2005) Discovering coherent biclusters from gene expression data using zero-suppressed binary decision diagrams, IEEE/ACM Transactions on Computational Biology and Bioinformatics, 2(4): 339-354.

Author: Smitha Dharan
Institute: Centre for Bioinformatics, University of Kerala
Street: Karyavattom
City: Thiruvananthapuram, Kerala
Country: India
Email: smithadharan@gmail.com

Development of Noninvasive Thrombus Detection System with Near-Infrared Laser and Photomultiplier for Artificial Hearts

S. Tsujimura[1], H. Koguchi[1], T. Yamane[2], T. Tsutsui[3] and Y. Sankai[1]

[1]Systems and Information Engineering, University of Tsukuba, Tsukuba, Japan
[2]National Institute of Advanced Industrial Science and Technology, Tsukuba, Japan
[3]Institute of Clinical Medicine, University of Tsukuba, Tsukuba, Japan

Abstract — **As for artificial hearts generally used in short term, thrombus formation is still a serious issue. To realize effective medical treatment for patients with the artificial heart without increase of anticoagulant agent, it is essential to detect and even predict thrombus formations. The purpose of this study is to develop a noninvasive thrombus detection system for artificial hearts.**

Considering the difference from the optical characteristics of both thrombus and blood, we have developed a thrombus detection system with a near-infrared (NIR) laser and a photomultiplier.

This developed system is composed of a light-emitting device with NIR laser (805 nm), a light receiver with photomultiplier for high measurement accuracy, and a thrombus detection algorithm based on probability statistics. This system is generally attached outside the tubing of the extracorporeal circuit.

To confirm the effectiveness of this system, we performed a thrombus detection test by using this system (light intensity of 2 mW and light path of 6 mm) in the mock circulation loop consisting of the reservoir, the Tygon tubing, and a centrifugal blood pump with hydrodynamic bearings. This circulation loop was filled with sheep whole blood including acid-citrate-dextrose solution. When we intentionally generated thrombus by adjusting activated coagulation time with CaCl2, this thrombus detection system continuously detected floating thrombus, which seemed to be generated around the pump impeller and be moved from there. Moreover this system might have indicated prediction associated with a blood condition conductive to thrombus formation before the thrombus formation was supposed to be generated around the impeller.

In conclusion, we have confirmed the developed thrombus detection system has enough performance to detect floating thrombus and may have the possibility to detect early stages of thrombus formation in the artificial hearts.

Keywords — **Thrombus Detection, NIR Laser diode, Photomultiplier, Artificial heart**

I. Introduction

The development of implantable artificial hearts has made great strides over the past few years [1–3]. However, artificial hearts generally used in extracorporeal circulation still has a serious issue of thrombus formation. To realize effective medical treatment for patients with an artificial heart without increase of anticoagulant agent like heparin, it is essential to detect and even predict thrombus formations.

Noninvasive methods of detecting thrombus in the flowing blood using ultrasound or light have been reported by several researchers [4–6]. Although the method with ultrasound has the ability to detect emboli through material which the light can not go through, the medical device with this method imposes the skill on medical staff and also restrict the patients' movements during the measurement. Moreover, the devices are expensive.

The purpose of this research is to develop a noninvasive thrombus detection system with near-Infrared (NIR) laser diode and photomultiplier for artificial hearts.

Since we apply photomultiplier as the photodetector of the thrombus detection system, the thrombus detection system would have higher sensitivity than the existing method with photodiode [5–6]. Therefore, the higher sensitivity impairs the light emitting power of the thrombus detection system. This system realizes safer measurement during long-term use. Moreover, the thrombus detection system with this sensitivity would have ability to make predictions associated with a blood condition conducive to thrombus formation.

II. Materials and Methods

A. Principle of the thrombus detection method

The red blood cells (RBCs) determine the optical characteristic of blood such as absorption and scattering. The Lambert-Beer law based on the concentration of a solution is usually applied to analyze the optical characteristics of liquid. However, it has been reported that whole blood does not obey the Lambert-Beer law, since there are influences of light scattering by the RBC and reflection between RBCs and plasma. According to the Twersky's theory, total optical density (*O.D.*) for whole blood is a sum of the *O.D.* of linear absorbance and the *O.D.* of scattering [7–8]. Total optical density of blood ($O.D._{total}$) is expressed as follows:

Chwee Teck Lim, James C.H. Goh (Eds.): ICBME 2008, Proceedings 23, pp. 635–638, 2009
www.springerlink.com

$$\begin{aligned} O.D._{total} &= \log_{10}\left(\frac{I_0}{I}\right) \\ &= O.D._{absorb} + O.D._{scatter} \\ &= kDHct - \log_{10}[(1-q)10^{-b} + q] \end{aligned} \quad (1)$$

where I and I_0 are transmitted and incident light intensities respectively; k is absorption coefficient; Hct is hematocrit; D is optical path length; $b = a*D*Hct*(1-Hct)$; a is a constant (<1) that depends on particle size, wavelength, refractive index of particles, and refractive index of suspending medium for plasma; and q is a constant (<1) that depends on particle size, wavelength, refractive index of particles, refractive index of suspending medium for plasma, and the angle of photo detector aperture.

A thrombus differs from the RBCs in the hemoglobin contents, the particle shapes, the particle sizes, and the reflective index.

If the minute quantities of thrombus are contained in a light path, the optical characteristic of the blood will be changed as compared with the case where RBCs are distributed uniformly.

By using the above characteristics, when the NIR laser is irradiated at the blood flowing inside of a cannula and the intensity of the transmitted (forward-scattered) light is observed, it is possible to detect the floating thrombus in the blood.

B. Measurement system

Figure 1 shows a developed thrombus detection system with NIR laser diode and photomultiplier. The NIR laser used as light source has the wavelength of 805 nm, which is known as the isosbestic point. Since the optical absorption ratio of Hb equals to the ratio of HbO2 at the wavelength of 805 nm, this system can eliminate the influence of the oxidization state of the blood such as the difference between venous and arterial blood, the patient's motion, etc.

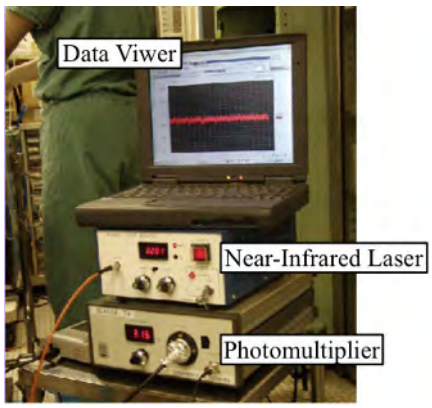


Fig. 1 Photograph of the developed thrombus detection system with a NIR laser and a photomultiplier

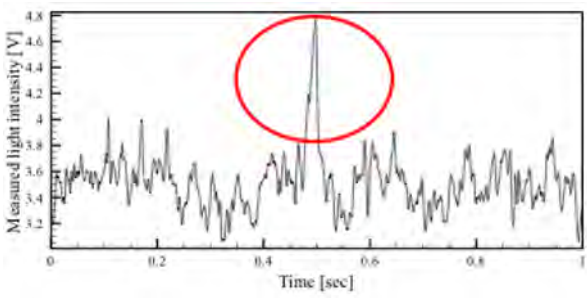


Fig. 2 Light signals of floating thrombus

A photomultiplier with high sensitivity was adopted as the photodetector of the thrombus detection system. Therefore, this system can realize high precision measurement and the noninvasive measurement can be also realized with a low powered laser. The transmitted light signals from the thrombus detection system were recorded by using the computer with 14-bit resolution analog-to-digital converter.

C. Data analysis method

Figure 2 shows transmitted light signals in the case of detecting thrombus by using the developed thrombus detection system. Since the thrombus detection signals are high intensity, the thrombus can be detected by comparison with a threshold value. However, since there are various disturbances such as medications, motions, uneven pulsatile flow of blood and so on, it is too difficult to set the threshold of floating thrombus detection to a constant value, and the credibility of the constant threshold will be low. To solve this problem, it is necessary to develop the method of determining the threshold of the thrombus detection reflecting the ever-changing condition of blood. So, in this research, statistical hypothesis testing is applied to the threshold determination method. As the method of distinguishing the unusual value included in an arbitrary sample (set of data), there is a statistical method called statistical hypothesis testing. The statistical characteristic of the sample $\{x_i\}$ $(i=1, 2, \ldots, n)$ which measured a certain physical value is given by a sample average μ and sample standard deviation σ.

$$\mu = \frac{1}{n}\sum_{i=1}^{n} x_i \quad (2)$$

$$\sigma = \frac{1}{n-1}\sum_{i=1}^{n} (x_i - \mu)^2 \quad (3)$$

This sample x_i shall follow a normal distribution. When a null hypothesis (H_0: $x_k \neq$ unusual value) is made for the *k-th*

data x_k, if the x_k fills a conditional equation (4), this null hypothesis will be rejected with the significant level α.

$$\left|\frac{x_k-\mu}{\sigma}\right| > K_{\frac{\alpha}{2}} \tag{4}$$

$K_{\alpha/2}$ is a constant computed from the significant level α and the standard normal distribution. When sufficient quantity of the measurement data to normal blood is used as a sample, the signals by RBCs follow a normal distribution. On the other hand, when the thrombus is contained in the blood sample of a measurement domain, the abnormal value from which it separates from the distribution of the signal by RBCs based on the difference in the optical characteristic will be outputted. This statistical hypothesis testing is applied to time-series data *y(t)* by which real-time measurement is carried out by the sampling frequency *f* Hz. First, the sample of size *Wf+1* is drawn from the time-series data by using the moving time window of width *W* sec.

$$x_i = \{y((T-W)f), y((T-W)f-1), \cdots, y(T-1), y(T)\} \tag{5}$$
$$i = 1, \quad 2, \quad \cdots, \quad Wf+1$$

The fluctuation of the baseline of *y(t)* by disturbance, such as medication and a pulse, is large. Thus the characteristics of data may not be correctly reflected to the statistics values depending on how to take a moving time window. Then, in order to remove the influence of the baseline fluctuation, the absolute value of the difference of *y(t)* will be used as a sample.

$$D(t) = |y(t) - y(t-1)| \tag{6}$$

At the arbitrary time $t=T$, the deviation $\mu_d(t)$ and standard deviation $\sigma_d(t)$ of the sample $D(t)$ are given as follows:

$$\mu_d(T) = \frac{1}{Wf}\sum_{t=T-Wf}^{T} D(t) = \frac{1}{Wf}\sum_{t=T-Wf}^{T}\{|x(t)-x(t-1)|\} \tag{7}$$

$$\begin{aligned}\sigma_d(T) &= \frac{1}{Wf-1}\sum_{t=T-Wf}^{T}(D(t)-\mu_d(T))^2 \\ &= \frac{1}{Wf-1}\sum_{t=T-Wf}^{T}(|x(t)-x(t-1)|-\mu_d(T))^2\end{aligned} \tag{8}$$

The conditional equation (9) of floating thrombus detection is obtained from equation (4).

$$\left|\frac{D(t)-\mu_d(T)}{\sigma_d(T)}\right| > K_{\frac{\alpha}{2}} \tag{9}$$

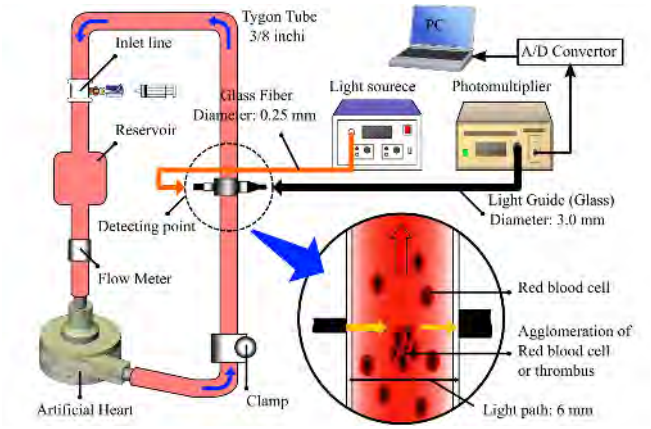


Fig. 3 Mock circulatory loop for the thrombus detection test

If the arbitrary significance level α is determined, it will become possible to solve for the value included in the sample by counting the number of values of *y(t)* that satisfy the conditional equation (9).

We defined the signals separated by this conditional expression (9) as Laser-detected Micro-Embolic Signals (LMES).

D. Thrombus detection test

In order to confirm the validity of the developed system, a thrombus detection test was demonstrated in a mock circulatory loop with sheep blood. The mock circulatory loop was constructed as shown in Figure 3. This mock circulatory loop consisted of a reservoir bag, Tygon tubing, and a centrifugal pump with hydrodynamic bearings (the National Institute of Advanced Science and Technology, Tsukuba, Japan)[9]. The mock circulatory loop was filled with sheep blood as the working fluid. The hematocrit of the blood was approximately 24 %. The thrombus detection system was attached on the surface of the Tygon tubing. The acid-citrate-dextrose solution was previously injected into the sheep blood. The pump flow was set to 5 L/min and the pump speed was set to about 1900 rpm. Then pressure differences across the pump were 100 mmHg. To intentionally generate thrombus formation in the mock circulatory, we adjusted activated coagulation time (ACT) with CaCl2. ACT is an index showing the coagulation property of blood. ACT is shown in the range from 0 sec to 1000 sec, as the time showing that the blood congeals. In this experiment, ACT was used to compare with LMES. The setting conditions of the thrombus detection system were as follows:

- Light emitting power was set at 2mW;
- Light path length between a light-emitting point and a light-receiving point was set at 6 mm;

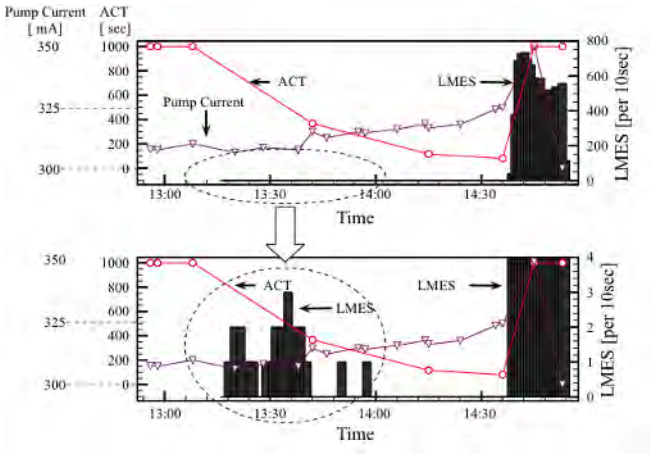


Fig. 4 Result of the thrombus detection test

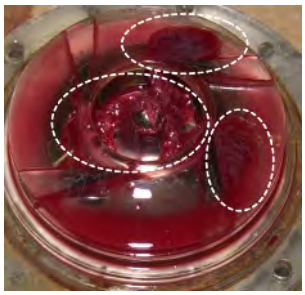


Fig. 5 Thrombus formation around the impeller of the pump in the oval areas

- Sampling frequency was set at 10 kHz;
- Light-trasmitting path was Silica optical fiber (Diameter: 0.25 mm, Length: 3 m);
- Light-receiving path was light guide with glass fiber (Diameter: 3 mm, Length: 2.4 m).

III. Result & Discussion

Figure 4 shows the time-series data which are LMES, ACT, and pump current. The LMES had hardly been detected during ACT of more than 100 sec. After ACT was less than 100, the number of LMES increased from 0 per minute to 80 per minute. And then the number was more than 400 per minute within 1 minute. At the same time, ACT was increased drastically. This would mean that the blood-coagulating factor was used up to generate thrombus in the circulatory loop. After this experiment finished, we checked the impeller and confirmed thrombus formation around this impeller shown in Figure 5. Since there was no thrombus around the reservoir, the Tygon tubing, we think that this thrombus detection system continuously detected floating thrombus, which seemed to originate around the pump impeller and be moved from there. Moreover, this detection system detected a few of the LMES during the period from 13:30 to 14:00. We think that this would indicate prediction associated with a blood condition conducive to thrombus formation before the thrombus formation was supposed to be generated around the impeller because the pump current started increasing after 13:40.

IV. Conclusions

In the present study, we have developed the thrombus detection system with NIR laser and photomultiplier. As a result, we have confirmed the developed thrombus detection system has enough performance to detect floating thrombus and shows the possibility to detect early stages of thrombus formation in the artificial hearts.

References

1. Yamazaki K, Kihara S, Akimoto T et al. (2002) EVAHEART: an implantable centrifugal blood pump for long-term circulatory support. Jpn J Thorac Cardiovasc Surg 50:461–465
2. Dowling RD, Gray LA Jr, Etoch SW, et al. (2004) Initial experience with the AbioCor implantable replacement heart system. J Thorac Cardiovasc Surg 127:131–141
3. Nosé Y, Furukawa K (2004) Current status of the Gyro centrifugal blood pump—development of the permanently implantable centrifugal blood pump as a biventricular assist device (NEDO Project). Artif Organs 28:953–958
4. Giller CA, Giller AM, Landreneau F (1998) Detection of emboli after surgery for intracerebral aneurysms. Neurosurgery 42(3):490–493
5. Solen KA, Mohammad SF, Burns GL et al. (1994) Markers of thromboembolization in a bovine ex vivo left ventricular assist device model. ASAIO J 40(3):602–608
6. Reynolds LO, Mohammad SF, Solen KA, Pantalos GM, Burns GL, Olsen DB (1990) Light scattering detection of microemboli in an extracorporeal LVAD bovine model. ASAIO Trans 36(3):518–521
7. Twersky V. (1970) Interface effects in multiple scattering by large, low-refracting, absorbing particles. J Opt Soc Am A Opt Image Sci Vis 60:908–914
8. Steinke J, Shepherd A (1986) Role of light scattering in spectrophotometric measurements of arteriovenouse oxygen difference. IEEE Trans Biomed Eng 33:729–734
9. Kosaka R, Yamane T Maruyama, O et al (2007) Improvement of hemolysis in a centrifugal blood pump with hydrodynamic bearings and semi-open impeller. Proc. of 29th Annual International Conference of the IEEE EMBS Conference, Lyon, France, 2007, pp 3982–3985.

Author: Shinichi Tsujimura
Institute: Systems and Information Engineering, University of Tsukuba
Street: 1-1-1Tennoudai
City: Tsukuba
Country: Japan
Email: tujimura@golem.kz.tsukuba.ac.jp

Using Saliency Features for Graphcut Segmentation of Perfusion Kidney Images

Dwarikanath Mahapatra and Ying Sun

Department of Electrical and Computer Engineering, National University of Singapore

Abstract — **In this paper we propose a method that uses visual saliency information to segment dynamic kidney perfusion data. Segmenting dynamic data requires the use of temporal information available due to the flow of contrast agent. It is found that although the intensity of the kidney changes due to flow of contrast agent, its saliency profile remains nearly constant. We exploit this characteristic to account for regional information, which we use in a graph cut formulation for segmentation. Our tests on real patient datasets show that our algorithm compares well with other approaches for segmenting dynamic data.**

Keywords — **perfusion MRI, saliency, temporal information, graph cuts.**

I. Introduction

Isolating the kidney from its surrounding organs and tissues is an important step in assessing renal functions. In dynamic perfusion data, intensity at a voxel changes as contrast agent flows through an organ thus providing information on blood flow in different tissues. This temporal information helps in identifying and segmenting organs of interest. Segmentation is a process where image elements representing the same object are grouped together. There have been many useful algorithms for image segmentation such as *snakes* [1], active contours [2] and *geodesic active contours* [3]. Graph cut approaches have also proved to be popular [4].

The graph cut method allows us to find a globally optimal binary segmentation by combining regional and boundary properties in formulating an appropriate energy function. Graph cuts were used by Wu and Leahy in [5] for image segmentation where the image is divided into K optimal parts. Boykov and Jolly use graph cuts to segment an image into object and background and use it for 2D and 3D medical data [6]. Certain points in the image were identified as object and background by the user and information from these 'seed' points are used to classify other points as belonging to the object or the background. Manual selection of seed points allows for imposing hard constraints on the segmentation procedure and at the same time incorporate regional information.

Multidimensional dynamic data presents significant challenges for segmentation techniques. Each volume of data has to be quickly obtained over a short period of time, as a result of which the data sets have relatively low spatial resolution with strong partial volume effects. Many segmentation techniques can easily fail by "leaking" through a large number of weak object boundary segments. Boykov et al. [7] address the difficulties of segmenting dynamic data. In static image data, the regional properties are denoted by intensity histograms for all regions of interest (object and background). Applying these methods to dynamic data poses certain difficulties. Each voxel has an n-dimensional intensity vector instead of a single gray-scale value and it becomes difficult to handle histograms when the dimensionality of data is greater than 4 or 5. To overcome such a difficulty the method in [7] uses temporal Markov model for intensity data. To facilitate calculations it is assumed that the intensity vector is a series of independent observations. However such an assumption does not properly exploit the information present in the time varying intensity data.

We propose a method that uses visual saliency information to facilitate distinguishing between object and background regions. Visual saliency is a concept that states that certain regions in an image are more attractive than their neighbor with respect to low level features. Thus we can say that the saliency value at a voxel (or pixel) is an indicator of its relevance. When the sequence of time series images of a patient are examined it is found that the saliency profile of the kidney region does not change with time even though we see significant intensity change due to flow of contrast agent. This is characteristic of the kidney region and gives us a basis to combine saliency and intensity information. In this paper we propose a method to use this information in a graph cut based formulation to achieve segmentation of the perfusion kidney images.

The rest of the paper is organized as follows: Section II gives a brief description of saliency followed by a short explanation of graph cuts in Section III. Section IV describes saliency and its usefulness in segmenting dynamic image data. Section V describes our experiments and the results and we conclude with Section VI.

II. Saliency

Saliency is a concept which states that there are regions in a scene that are more "attractive" than their neighbors

Chwee Teck Lim, James C.H. Goh (Eds.): ICBME 2008, Proceedings 23, pp. 639–642, 2009
www.springerlink.com

and hence draw attention. Attention can be due to bottom-up cues or top-down influences. A saliency map of an image is a representation of the salient regions of the image. Saliency at a given location is determined primarily by the contrast between this location and its surroundings. The image formed on the fovea of the eye is the central object on which a person is focusing his attention resulting in a clear and sharp image. Regions surrounding the central object have a less clear representation on the retina. To simulate this biological mechanism, an image is represented as a Gaussian pyramid comprising of layers of subsampled and low-pass filtered images. The central representation of the image on the fovea is equivalent to the image at higher spatial scales, and the surrounding regions are obtained from the lower spatial scales. The contrast is thus the difference between these scales. Details of the method can be found in [8]

III. Proposed segmentation framework

A. Graph cuts

Graph cuts are a powerful optimization tool for binary labeling problems because of their ability to obtain a global minimum with a single cut of a graph. The pixels of an image, *P*, are represented as nodes in a graph and in case of binary segmentation problems there are two additional nodes called the source (object) node and the sink (background) node. Pairs of neighboring nodes are connected by a set of edges whose weights are determined by neighborhood information. It is the ability to incorporate both regional and boundary properties that makes graph cut optimization techniques very powerful. An example of the graph used for segmentation is shown in Fig. 1. Consider a neighborhood system in *P* which is represented by a set *N* of all unordered pairs *{p,q}* of neighboring pixels in *P*. Let *L* be the set of labels *{0,1}*, corresponding to kidney and background, respectively. Labeling is a mapping from *P* to *L* and we shall denote the set of labels by $\boldsymbol{f}=\{f_p : p \in P, f_p \in L\}$. Segmentation is achieved by minimizing an energy function that combines region and boundary properties of segments. This function is defined as follows

$$E(f) = \sum_{p \in P} D(f_p) + \sum_{\{p,q\} \in N} V(f_p, f_q) \quad (1)$$

where $D(f_p)$ measures how much assigning a label f_p to pixel *p* disagrees with the pixel intensity i_p. $V(f_p,f_q)$ which represents the penalty of the discontinuity between pixels p and q, incorporates neighborhood information. We shall now explain each of the terms in Eqn. 1.

B. Data Penalty term - $D(f_p)$

The data penalty or the regional term reflects how the intensity of pixel *p* fits into a given intensity model. We selected certain number of points belonging to the object and the background. Information from these points was used to build a model characteristic of the particular region (object or background). It was observed that the saliency profile of the kidney region remains the same even in the face of intensity change due to contrast enhancement and this information proves to be an effective tool to differentiate between kidney and the background. Using the selected seed points, our objective is to formulate a cost function that can clearly distinguish between object and background. A saliency based approach has also been used to register the perfusion image sequences [9].

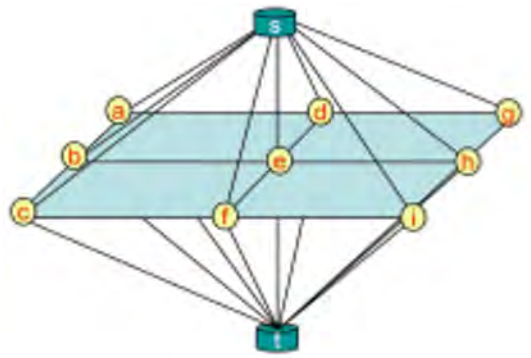


Fig 1. Graph used in image segmentation.

From the seed points belonging to the kidney region we observed that although the intensity of these points changes significantly due to flow of contrast agent, the saliency values remain very nearly the same. We thus define the data penalty term as follows

$$D(f_p) = \frac{\left(\sum_{j=1}^{n}(|\vec{s}_p - \vec{s}_j|) + \in\right) \times \left(\sum_{k=1}^{n}(|\vec{i}_p - \vec{i}_k|) + \in\right)}{n \times n}, \quad (2)$$

where s_p is the saliency value at pixel p and s_j is the saliency value of the j^{th} seed point corresponding to the object (or background), n is the number of seed points chosen for object)or background) . Similarly i_p and i_k are, respectively, the intensity values at pixel *p* and intensity of k^{th} seed point of object (or background). Since the intensity and saliency values of a pixel are vectors the magnitude in eqn. 2 denotes the ℓ_1 norm. Eqn. 2 is thus the product of the saliency and intensity costs.

When pixels belonging to the kidney region are plugged in with the values of the object seed points, the data penalty value is lower and the same is true when background pixels are plugged in with the corresponding parameters of background seed points. To prevent the entire data penalty term from going to zero due to any one value we introduce a small constant ε

C. Neighborhood term - $V(f_p, f_q)$

This term incorporates boundary properties of the image into the segmentation framework. It is a penalty for a discontinuity between p and q. V is large when pixels p and q are similar and V is close to zero when the two are very different. The penalty V can also decrease as a function of the distance between p and q. The penalty may be based on local intensity gradient, gradient direction or other criteria. For our experiments we set the neighborhood term as

$$V(f_p, f_q) = \exp\left(-\frac{(I_p - I_q)^2}{2\sigma^2}\right) \times \frac{1}{dist(p,q)} \quad (3)$$

where *dist(p,q)* is the Euclidean distance between p and q

This function penalizes a lot for discontinuities between pixels of similar intensities i.e. when $|I_p - I_q| < \sigma$. However if pixels are very different, i.e. $|I_p - I_q| > \sigma$, then the penalty is small.

IV. Experimental results

We tested our algorithm on 7 real patient datasets consisting of contrast-enhanced dynamic perfusion MR images of the kidney. The acquired volumes comprised of 40 slices and for each patient 41 volumes were acquired at different time instances.

For each dataset certain points were identified as belonging to the kidney and the background. These seed points have two uses. They provided us with information that is characteristic to the kidney and background, and helps in distinguishing one from the other. Intensity and saliency values of the corresponding points are used in determining the penalty value of each pixel from Eqn. 2 for each label. Besides, the seed points impose hard constraints for the segmentation process. Intensity values of neighboring pixels are used to determine the value of the smoothness term of the energy function given in Eqn. 3.



(a) (b) (c) (d) (e)

Fig 2. Segmentation results: (a)-(c) kidney at different stages of perfusion. (d) kidney segmented by method in [7]. (e) kidney segmented using our approach.



(a) (b) (c) (d) (e)

Fig 3. Segmentation results using an average image: (a)-(c) kidney at different stages of perfusion; (d) kidney segmented by method in [7]; (e) kidney segmented using our approach.

The neighborhood term is useful when the surrounding organs have intensity characteristics that are different from the organ of interest. In many of the datasets, the pre-contrast slices make it difficult to distinguish the kidney from neighboring organs. In such a scenario use of saliency information effectively uses the temporal information increasing the effectiveness of the smoothness term.

In Fig. 2 we show the results of our segmentation algorithm when applied to MR images of the kidney and the results obtained by the method in [7]. The method in [7] assumes Markovian property of the intensity values, i.e. the intensity of a pixel is dependent only on the intensity value at the previous time instant. Fig. 2 (a)-(c) shows slices corresponding to different stages of contrast enhancement and Fig. 2(d)-(e) show, respectively, the results by the approach in [7] and by our method. The segmented region in Fig. 2 (d) includes parts of the liver as well which is not seen by results using our method. This is a typical case of low contrast images for which the method in [7] is not very effective. On the other hand, our approach produces segmentation results that are as good as the one assuming Markovian relationship between intensity values at different time points.

The method in [7] uses negative log likelihood to determine the data penalty values which requires a model histogram for both the object and background. A robust model is possible only when we have a large number of seed points else the segmentation is inaccurate. The use of our penalty term gives accurate segmentation results even when the number of seed points are very few.

An average image of all acquired images shows the kidney having greater intensity. However this is not good enough for segmentation. Certain regions in the image can have noisy characteristics, i.e. regions where there is no flow of contrast agent seem bright, due to noise in the image acquisition process. Thus, in such a scenario use of intensity information alone will be misleading. Using saliency information helps us to avoid such pitfalls. The saliency maps that we get are robust to noise thus ensuring the accuracy of the data penalty values. In Fig 3 we show the results while using an average image. The inaccuracies are expected because of the sole use of intensity information in segmentation.

V. Conclusions

We have proposed a method that can exploit the temporal information present in dynamic contrast enhanced images for efficient segmentation. The saliency information that we use is an effective way to distinguish between the kidney and background in case of dynamic data. We tested our algorithm on real patient datasets and the results obtained were comparable to other methods (e.g. [7]) that deal with segmentation of dynamic data using graph cuts. In some cases where the data is noisy our method outperforms the above mentioned method. From our experiments we also conclude that using the average of the acquired images does not give good results and our approach is especially effective for noisy images.

Acknowledgment

We would like to thank Dr. Vivian Lee of the New York University Langone Medical Center for providing us with the datasets. The work was supported by NUS grant R-263-000-470-112.

References

1. Kass M, Witkin A, Terzolpoulos D. (1988) Snakes: Active contour models. Int J Comp Vis 1(4):321-331
2. Isard M, Blake A, (1998) Active contours. Springer-Verlag
3. Caselles V, Kimmel R, Sapiro G (1997) Geodesic active contours. Int J Comp Vis 22(1):61-79
4. Boykov Y, Funka-lea G (2006) Graph cuts and efficient N-D Image segmentation. Int J Comp Vis 70(2):109-131
5. Wu Z, Leahy R (1993) An optimal graph theoretic approach to clustering: Theory and its application to image segmentation. IEEE TPAMI 15(11):1101–1113
6. Boykov Y, Jolly M-P, (2000) Interactive organ segmentation using graph cuts, LNCS Proc. Vol 1935, MICCAI, Pittsburg, USA, 2001, pp 276-286
7. Boykov Y, Lee V.S, Rusinek H., Bansal R. (2001) Segmentation of dynamic N-D datasets via graph cuts using markov models, LNCS Proc. Vol 2208, MICCAI, Utrecht, The Netherlands, 2001, pp 1058-1066
8. Itti L, Koch C (2000) A saliency based search mechanism for overt and covert shifts of visual attention. Vision Research 40:1489-1506
9. Mahapatra D, Sun Y, (2008) Nonrigid registration of dynamic renal MR images using a saliency based MRF model, LNCS Proc. Vol 5241, MICCAI, New York, USA, 2008, pp 771-779

Author: Dwarikanath Mahapatra
Institute: National University of Singapore
Street: Block E4, Level 5, Room 45, 4 Engineering drive 3
Country: Singapore
Email: dmahapatra@nus.edu.sg

Low Power Electrocardiogram QRS Detection in Real-Time

E. Zoghlami Ayari, R. Tielert and N. Wehn

Microelectronic Systems Design Research Group, Department of Electrical Engineering, University of Kaiserslautern, Germany

Abstract — **A real-time capable, low complexity QRS detection method based on the temporal cross-correlation is presented. Applying a high-resolution QRS template, the new method enables an acceptable under-sampling of the recorded ECG signal. High performance (100%) and standard deviations within the tolerance limits indicate that our method achieves a reliable and accurate QRS detection while reducing the overall energy consumption in the ECG system compared to the use of the classical temporal cross-correlation method.**

Keywords — **Low Power, low complexity, QRS detection, real-time, cross-correlation.**

I. Introduction

The QRS-complex is the dominant waveform within the electrocardiogram (ECG) that corresponds to the depolarization of the ventricles. Its duration, amplitude, and morphology provide much information about the current state of the heart. It is hence useful in diagnosing many cardiac disease states, but also in analyzing the psychological and physiological state of the body, e.g. stress and tiredness. Therefore, QRS detection is a prerequisite procedure in automated ECG signal processing and analysis. The necessity of an accurate and reliable QRS detection algorithm is of great importance. Numerous techniques have been developed for QRS detection. A good review of different techniques for QRS detection can be found in [1].

Energy saving is one of the most crucial requirements to be fulfilled while designing wearable, wireless, and battery-powered ECG systems. Energy in those systems is consumed by three main parts: signal acquisition and conditioning, data communication to a central node, and computational analysis of the signal for features extraction. Most of the existing QRS detection techniques use high sampling rates up to 1kHz [2]-[4], which increases the energy consumption of the analog to digital converter in the signal acquisition and conditioning part of the system.

A wide range of prototyped portable wireless ECG systems can be found in the literature. A mobile-based data acquisition system for real-time health monitoring is developed in [5]. The acquired data are transferred wirelessly in the unlicensed 2.4GHz ISM band to a local PC, or laptop, for storage and further processing. A platform of an ECG sensor conceived for heart patients with needs for home based monitoring is presented in [6]. After digitization, a continuous stream of ECG data are transmitted over IEEE 802.11 and displayed on a PC. The drawback of these systems is the high energy burden on the communication unity due to the transmission of the full signal at a minimum sampling frequency of 200Hz. This energy burden is alleviated in [7] using an on-system integrated wavelet data compression before transmission. However, even though the communication energy is reduced, the energy consumption in the sensing part of the system is still large because of the high sampling rate varying between 150 and 1200Hz.

With aspect of the computational energy consumption, the implementation of a QRS detection algorithm in such an environment requires besides accuracy and stability, low computational load. Whereas different QRS detection techniques show very high detection performance, their shortcoming is the high computational complexity [8], [9].

We propose in this work a low power real-time detection method of QRS-complexes in the ECG signal, which overcomes these limitations and minimizes all of the three parts of the energy consumption in the system. The detection method employs a self-adapting algorithm based on the cross correlation technique, and features the beneficial property of an acceptable under-sampling of the signal. A pre-defined high resolution template is cross-correlated with a dynamically adjustable data set of few samples estimating the location of the QRS complex. The time window of the sampling points is continuously improved after the extraction of the fiducial point.

This paper is organized as follows. Section 2 elaborates on the details of our proposed low power QRS detection method. Section 3 presents the detection results and delineation accuracy of the method. Finally, section 4 concludes the paper.

II. Methods

A. Background

Our QRS detection method is implemented for an ECG system which is dedicated for Ambient Assisted Training, i.e. assisted bicycle training, to optimize the training by monitoring the heart beats of the cyclists [10]. Therefore, normal beats are selected for the evaluation of our method. In this AmI system cyclists and bikes are equipped with a

Chwee Teck Lim, James C.H. Goh (Eds.): ICBME 2008, Proceedings 23, pp. 643–646, 2009
www.springerlink.com

multiplicity of sensors such as an ECG sensor. The bikes are connected to each other and to a coach unit that executes the application, via a wireless network. Each cyclist has his own performance profile and training plan. Two scenarios are suggested, individual training and group training. In the individual training, the training ride has to be controlled in such a way that each cyclist meets his training plan as far as possible. The system enables intervention by the coach during the training, e.g. in cases of too high heart rates of the cyclists, or heart rates below a given threshold value for the obtained pedal power. The scenario of the group training concerns the optimization of the overall performance of the group. The bicycle group is controlled using the stored performance data as well as the actual sensor data, and the condition of the cyclists, so that a given distance must be passed in minimal time by one member of the group.

B. Low Power cross-correlation method for beat detection

The cross-correlation (CC) indicates the strength and direction of a linear relationship between two signals as a function of a time-lag applied to one of them. The CC computes the sum of the products of corresponding pairs of points of the two signals within a specified time window. The CC coefficient measures the degree of similarity between the two signals. The best known is the Pearson product-moment correlation coefficient r_{xy}, which is obtained by dividing the covariance of the two variables by the product of their standard deviations and is defined as:

$$r_{xy}(l) = \frac{\sum_{n=1}^{N}\left(x(n)-\bar{x}\right)\left(y(n+l)-\bar{y}\right)}{\sqrt{\sum_{n=1}^{N}\left(x(n)-\bar{x}\right)^2}\sqrt{\sum_{n=1}^{N}\left(y(n+l)-\bar{y}\right)^2}} \quad (1)$$

where $x(n)$ and $y(n)$ are the values of the two signals to be studied, respectively, at the nth sampling instant; $\bar{x}$ and $\bar{y}$ are their average values; l is the lag between the two signals, and N is the total number of samples.

In ECG signal processing, CC is by far the most widely used alignment technique for ECG records [11]. The ECG signal is matched to a predefined or averaged template. A CC coefficient sequence $r_{xy}(l)$ is computed between the template beat and the time-shifted ECG signal in a temporal window, and the position of the highest value is returned. If this value is greater than a predefined threshold, the lag corresponding to this value is chosen as the alignment point. Many works have successfully reported the use of CC as a means of automated beat detection. In [12] the CC was used for extrasystole rejection and location of fiducial points. Govrin et al. [13] adapted the algorithm in [12] to locate both the P waves and QRS-complexes using CC. In [14] the multi-component based CC approach is introduced, as opposed to a single template CC based approach, for an accurate beat detection. However, the use of the classical temporal CC in signal processing implies the need for the same total number of sampling points in both the analyzed beat and the reference template. Consequently, the ECG signal and the template have to be digitized at the same sampling rate. As the sampling frequency has to be at least higher than the Nyquist frequency, 200 samples are typically required for the QRS alignment at a sampling frequency of 1kHz [11]. This results in a high sensing energy consumption in the system. Moreover, the CC coefficient is typically computed at each sampling instant lag within the time window by shifting the incoming beat one sample point at a time. Thus, 200 computations of the CC coefficient are needed for the above mentioned case to detect the fiducial point, which increases the computational cost.

In order to overcome the drawbacks of the classical CC method regarding to energy consumption, we propose a new low power method based on the cross-correlation for beat detection. The idea of the method is to store the requisite information of the beat to be examined in a high-resolution template, and to reduce the sampling frequency in the recorded signal. The CC coefficient sequence is then computed between the under-sampled beat and a transformed template, which has the same total number of samples as the examined beat. The transformed template is performed in function of the examined beat, the stored high-resolution template, and an estimated lag. Fig. 1 illustrates an example of the low power CC method.

After sampling the ECG signal $y(n)$ within the specified time interval at a lower sampling rate f_S than the typical sampling frequency F_S (>200Hz), an appropriate transformed template is generated. For this aim, time values t_y of the sampled data are shifted by the estimated lag (l=320ms in Fig. 1) building time values of the transformed template t_{x*}, and corresponding data are extracted from the high-resolution template forming the transformed template's data $x*(n)$. If a t_{x*} value doesn't belong to the time range $t_x(n)$, a value of 0 is associated to the corresponding $x*$. Otherwise, an interpolation calculation is made to extract the appropriate data x_{Interp} from the high-resolution template.

$$t_{x*} = t_y - l \quad (2)$$

$$x*[ty-l] = \begin{cases} x_{Interp}[ty-l], & if\,(ty-l) \in t_x[ms] \\ 0 & \end{cases} \quad (3)$$

Our method allows for an acceptable under-sampling of the signal, since the used high-resolution template includes all the waveform information. Consequently, not only the signal sensing energy in our method is reduced by a factor of F_S/f_S compared to the classical cross-correlation method, but also the computational energy by the same factor, since the computational complexity of the algorithm is directly proportional to the energy consumed for its computation.

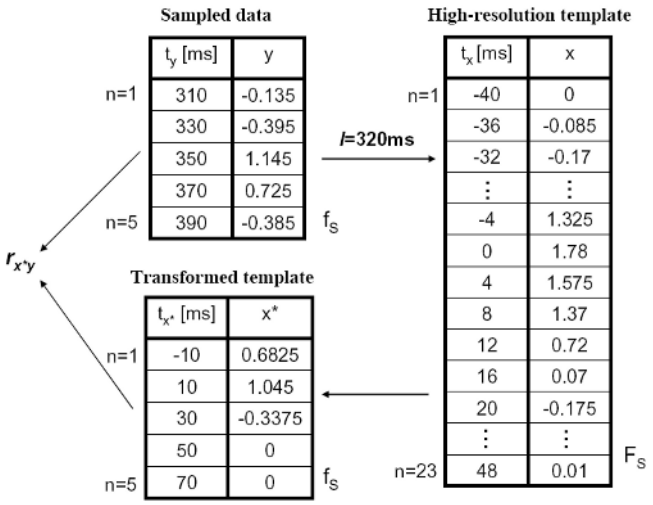


Fig. 1 Example of the Low Power Cross-Correlation

C. Online QRS detection procedure

The Online QRS detection procedure based on our proposed method consists of three stages.

In the *calibration and training stage* a representative high-resolution template of the QRS-complex is manually extracted by an expert from the ECG signal to be analyzed. The ECG signal is sampled at a high frequency of F_S. The QRS template details accurate marker positions of the respective QRS-complex onset and offset. This stage is only once processed for each cyclist on static conditions.

In the *initialization stage* a time period of 2s of the recorded ECG signal is stored, so that at least two consecutive heart beats are available. The goal of this stage is to localize the QRS-complex in the recorded signal, and to obtain an initial time information about the RR-interval. A maximum search is performed in this signal section providing an estimate of the sweep range center of the initial lag to be used for the cross-correlation computation between the QRS template and the signal part around the maximum. An accurate R-peak position is then determined corresponding to the lag with the maximum CC coefficient value. This signal section is sampled at a frequency higher than 200 Hz, so that the result of the maximum search supplies a good estimate of the R-peak position. The time period between the two last extracted R peaks provides an estimate of the QRS sample window center in the next stage.

During the *analysis stage* acquired data from the ECG sensor are online processed for QRS detection and delineation. Positions of the QRS-complexes are dynamically predicted using the last RR-interval. The signal is sampled only in time windows centered around the time corresponding to the last detected R-peak plus the last measured RR-interval. The low power cross correlation is computed within these time windows, where the initial lag corresponds to the first time value of the estimated time window. The lag is not constantly incremented by a sample period, but is increased by a larger step while a low threshold value of the CC coefficient is not attained. After achieving this value, the lag begins to increase by a fine step (sample period). This yields also to a reduction of the algorithm's complexity and thus of the computational energy. The position of the R-peak is chosen as the lag $l_{R\text{-}peak}$ providing the highest value of the CC coefficient computed in the time window. Onset and offset of the QRS-complex are automatically generated from the characteristic lag and the stored QRS template:

$$Onset/Offset[ms] = Onset/Offset_{template} + l_{R-peak} \quad (4)$$

The estimated time windows are continuously adjusted by the algorithm depending on the extracted time position of the R-peak relative to the beginning and end of the actual correlation interval. Information about time distances between the R-peak and the correlation interval's extremities are gained in the training stage according to the time periods between the R-peak and P- and T-waves offset and onset, respectively. Finally, only the online extracted QRS-complex features are transmitted wirelessly to the coach unit. For a heart rate of 60bpm, this reduces the communication energy by a factor of approximately 70 compared to a transmission of the full ECG signal measured at the minimum sample frequency of 200Hz.

III. Results

The proposed algorithm has been first evaluated by a collection of ten ECG recordings from the MIT-BIH Normal Sinus Rhythm Database [15]. The selection of these records was to allow for a comparison with a recent work [4] applying normal ECG beats to a modified "So and Chan" QRS detection method. The comparison results were assessed by the sensitivity metric defined as the ratio between the true positives (TP) and the sum of the true positives and false negatives (FN), where TP denotes the number of the true detected beats, and FN is the number of missed detections.

Table 1 shows that our method outperforms the modified "So and Chan" QRS detection algorithm in [4].

Our QRS detection method has been further tested on approximately 3000 cycles of different ECG recordings sampled at 250 Hz from the standard annotated PhysioNet QT Database [16] to evaluate the accuracy of the QRS boundaries detection. Table 2 lists the mean (me) and standard deviation (SD) of the errors between our QRS detector's annotations and the available manual annotations provided by expert cardiologists. It can be seen that the obtained standard deviations are within the tolerance limits recommended for an automated algorithm.

Table 1 Comparison results of our QRS Detection method with [4]

Dataset	Method	Total # of betas	Sensitivity [%]
16265	[4]	194	100
	proposed		100
16272	[4]	127	99.21
	proposed		**100**
16273	[4]	182	100
	proposed		100
16420	[4]	185	100
	proposed		100
16483	[4]	187	98.98
	proposed		**100**
16539	[4]	163	100
	proposed		100
16786	[4]	142	100
	proposed		100
17052	[4]	147	100
	proposed		100
17453	[4]	168	100
	proposed		100
18184	[4]	175	100
	proposed		100

Table 2 QRS Delineation results following exposure to 3000 cardiac beats

QRS features	me [ms]	SD [ms]	Tolerance SD [ms]
QRS-onset	-1.11	6.44	**6.5**
QRS-offset	-0.11	4.94	**11.6**

IV. Conclusions

A low complexity with reduced energy consumption electrocardiogram QRS detection method in real-time based on the CC has been presented. This method features the beneficial property of an acceptable under-sampling of the signal owing to the use of a high-resolution reference template, which includes the complete signal section information. Therefore, applying this method enables a reduction of the overall energy consumption of the ECG system without compromising its accuracy. High performance (100%) of the method in detecting cardiac cycles, and standard deviations of the extracted features within the tolerance limits are achieved, thus demonstrating the beneficial use of our method including power efficiency, accuracy and simplicity in the detection of QRS-complexes in the ECG signal. The method is, in addition, not restricted on the QRS detection but can be extended to the detection of all the heart waves, and generally to the biosignal processing.

Acknowledgment

This work is sponsored by the research institution "Ambient Systems" at the TU Kaiserslautern.

References

1. Koehler BU, Henning C et al. (2002) Principle of QRS detection. IEEE Eng Med Biol Mag.21: 42-57.
2. Xu X, Liu Y (2004) ECG QRS detection using slope vector waveform (SVW) algorithm, Eng Med Bio Soc. vol. 2, IEMBS'04, San Francisco, USA, 2004, pp 3597- 3600.
3. Raskovic D, et al. (2000) Energy profiling of DSP applications, a case study of an intelligent ECG monitor, Proc. of DSPS Fest 2000, Houston, TX, 2000.
4. Chiu CC et al. (2005) Using correlation coefficient in ECG waveform for arrhythmia detection. Biomed Eng App, Basis & Com 3:147-152.
5. Bobbie PO et al. (2006) Telemedicine: a mote-based data acquisition system for real time health monitoring, Proc Telehealth 512: 50-52.
6. Bobbie PO et al. (2004) Electrocardiogram (EKG) data acquisition and wireless transmission. WSEAS Trans Sys 4: 2665-2672.
7. Jansen D et al. (2004) 24h EKG-Rekorder mit Bluetooth Funkschnittstelle fuer telemedizinische Anwendungen. Horizonte 24: 24-27.
8. Li C, Zheng C et al. (1995) Detection of ECG characteristic points using wavelet transforms. IEEE Trans Biomed Eng. 42: 21-28.
9. Sahambi J S et al. (1997) Using Wavelet transforms for ECG characterization. An on-line digital signal processing system. IEEE Eng Med Biol Mag. 16: 77-83.
10. Ambient Intelligence at http://www.amsys-uni-kl.de/
11. Laciar E, Jane R et al. (2003) Improved alignment method for noisy high-resolution ECG and Holter records using multiscale CC, Trans Biomed Eng, vol. 50, pp. 344-353.
12. Abboud S, Sadeh D (1984) The use of cross-correlation function for the alignment of ECG waveforms and rejection of extrasystoles, Comp Biomed Res, vol.17, pp. 258-266.
13. Govrin O, sadeh S et al. (1985) Cross-correlation techniques for arrhythmia detection using PR and PP intervals, Comp Biomed Res, vol.18, pp. 37-45.
14. Last T et al. (2004) Multi-component based cross correlation beat detection in ECG analysis. BioMedical Eng Online 3: 26-39.
15. NSRD at http://www.physionet.org/physiobank/database/nsrdb/
16. QTD at http://www.physionet.org/physiobank/database/qtdb/

Author: Emna Zoghlami Ayari
Institute: Microelectronic Systems Design Research Group, TU KL.
Street: Erwin-Schroedinger-Straße
City: Kaiserslautern
Country: Germany
Email: zoghlami@eit.uni-kl.de

Analytical Decision Making from Clinical Data- Diagnosis and Classification of Epilepsy Risk Levels from EEG Signals-A Case Study

V.K. Sudhaman[1], Dr. (Mrs.) R. Sukanesh[2], R. HariKumar[3]

[1]U.G Students, ECE, Bannari Amman Institute of Technology, Sathyamangalam
[2]Professor ECE, Thiagarajar college of Engineering, Madurai
[3]Professor ECE, Bannari Amman Institute of Technology, Sathyamangalam

Abstract — **Making decision under certainty is a perennial part of human predicament. In this research, we review the potential of fuzzy modeling technology as a tool for constructing customized decision making function for medical diagnosis, such as classification of epilepsy risk levels. We investigate the optimization of fuzzy outputs in the classification of epilepsy risk levels from EEG (Electroencephalogram) signals using soft decision as post classifier. The fuzzy techniques are applied as a first level classifier to classify the risk levels of epilepsy based on extracted parameters like energy, variance, peaks, sharp and spike waves, duration, events and covariance from the EEG signals of the patient. Soft Decision Trees are identified as post classifiers on the classified data to obtain the optimized risk level that characterizes the patient's epilepsy risk level. The Performance Index (PI) and Quality Value (QV) are calculated for the above methods. A group of ten patients with known epilepsy findings are used in this study. High PI such as 97.87 % was obtained at QV's of 23.31, SDT optimization when compared to the value of 40% and 6.25 through fuzzy techniques respectively. The performance of SDT is lucidly presented in this work. SDT results are validated with standard Multi Layer Perceptrons (MLP) neural networks.**

Keywords — **EEG Signals, Epilepsy risk levels, Fuzzy techniques, Soft Decision trees, MLP Neural networks**

I. Introduction

Epilepsy is a chronic disease characterized from recurrent seizures that cause sudden but revertible changes in the brain functions. Classification of epilepsy risk levels, according to international standard is difficult because individual laboratory findings and symptoms are often inconclusive [1]. Approximately 1% of the people in the world suffer from epilepsy. The electroencephalogram (EEG) signal is used for the purpose of epileptic detection as it is a condition related to the brain's activity. This paper presents the application of Soft Decision Trees (SDT) towards optimization of fuzzy outputs in the classification of epilepsy risk levels. We also present a comparison of SDT and MLP Neural network methods based on their Performance Indices(PI) and Quality Values(QV).

II. Materials and Methods

The EEG data used in the study were acquired from ten epileptic patients who had been under the evaluation and treatment in the Neurology department of Sri Ramakrishna Hospital, Combiatore, India. A paper record of 16 channel EEG data is acquired from a clinical EEG monitoring system through 10-20 international electrode placing method. With an EEG signal free of artifacts, a reasonably accurate detection of epilepsy is possible; however, difficulties arise with artifacts [2]. With the help of neurologist, we had selected artifact free EEG records with distinct features. These records were scanned by Umax 6696 scanner with a resolution of 600dpi. Figure 1 enumerates the overall epilepsy risk level (Fuzzy-SDT/Neural network) classifier system. The motto of this research is to classify the epilepsy risk level of a patient from EEG signal parameters [3],[4],[5].

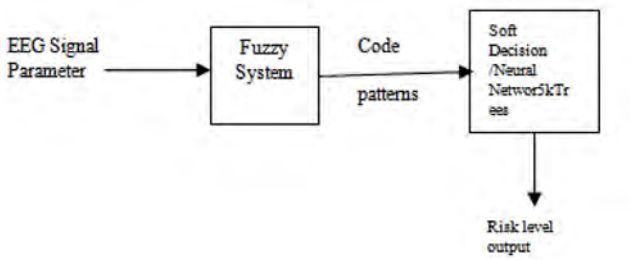


Figure 1. Fuzzy and Soft Decision Tree/ Neural Network Classification

1. The energy in each two-second epoch is given by

$$E = \sum_{i=1}^{n} x_i^2 \qquad (1)$$

Where x_i is signal sample value and n is number of samples. The scaled energy is taken by dividing the energy term by 1000.

2. The total number of positive and negative peaks exceeding a threshold is found.

Chwee Teck Lim, James C.H. Goh (Eds.): ICBME 2008, Proceedings 23, pp. 647–651, 2009
www.springerlink.com

3. Spikes are detected when the zero crossing duration of predominantly high amplitude peaks in the EEG waveform lies between 20 and 70 ms and sharp waves are detected when the duration lies between 70 and 200ms.
4. The total numbers of spike and sharp waves in an epoch are recorded as events.
5. The variance is computed as σ given by

$$\sigma^2 = \frac{\sum_{i=1}^{n} (x_i - \mu)^2}{n} \quad (2)$$

Where $\mu = \frac{\sum_{i=1}^{n} x_i}{n}$ is the average amplitude of the epoch.

6. The average duration is given by

$$D = \frac{\sum_{i=1}^{p} t_i}{p} \quad (3)$$

Where t_i is one peak to peak duration and p is the number of such durations.

7. Covariance of Duration. The variation of the average duration is defined by

$$CD = \frac{\sum_{i=1}^{p} (D - t_i)^2}{pD^2} \quad (4)$$

A. Fuzzy Membership functions

The energy is compared with the other six input features to give six outputs. Each input feature is classified into five fuzzy linguistic levels viz., very low, low, medium, high and very high [6]. The triangular membership functions are used for the linguistic levels of energy, peaks, variance events, spike and sharp waves, average duration and covariance of duration. The output risk level is classified into five linguistic levels namely normal, low, medium, high and very high. Rules are framed in the format.

IF Energy is low AND Variance is low THEN Output Risk Level is low

B. Estimation of Risk Level in Fuzzy Outputs

The output of a fuzzy logic represents a wide space of risk levels. This is because there are sixteen different channels for input to the system at three epochs. This gives a total of forty-eight input output pairs. Since we deal with known cases of epileptic patients, it is necessary to find the exact level of risk the patient. A specific coding method processes the output fuzzy values as individual code. Since working on definite alphabets is easier than processing numbers with large decimal accuracy, we encode the outputs as a string of alphabets. The alphabetical representation of the five classifications of the outputs is as shown below.

Normal U, Low W, Medium X, High Y, Very High Z

A sample output of the fuzzy system with actual patient readings is shown in figure. 2 for eight channels over three epochs. It can be seen that the Channel 1 shows medium risk levels while channel 8 shows very high risk levels. Also, the risk level classification varies between adjacent epochs. The Performance of the Fuzzy method is defined as follows [7]

$$PI = \frac{PC - MC - FA}{PC} \times 100 \quad (5)$$

Where PC – Perfect Classification, MC – Missed Classification, FA – False Alarm, PI= [(0.5-0.2-0.1)/0.5] *100 =40%.

Epoch 1	Epoch 2	Epoch 3
YYYYXX	ZYYWYY	YYYXYZ
YYYXYY	ZZYZZZ	YYYXYZ
YYYYYY	ZZYZZZ	ZYYYZZ
ZYYYZZ	ZZYZYY	YYYXXZ
YYYYYY	YYYXYY	YYYYYZ
YYYYYY	YYYXYY	YYYXYY
YYYYYY	YYYYYY	YYYYYY
ZZYZYZ	ZZYZZZ	ZZYZZZ

Figure 2. Fuzzy Logic Output

The perfect classification represents when the physicians and fuzzy classifier agrees with the epilepsy risk level. Missed classification represents a true negative of fuzzy classifier in reference to the physician and shows High level as Low level. The performance for Fuzzy classifier is as low as 40%. Soft Decision Tree (SDT) optimization technique (post classifier) [8] is utilized to optimize risk level and is given below.

III. Soft Decision Trees (Max-Min) for Optimization of Fuzzy Outputs

Our objective is to merge the epilepsy risk level representation, with approximate reasoning capabilities, and symbolic decision trees while preserving advantages of both: uncertainty handling and gradual processing of the former with the comprehensibility, popularity, and ease of application of the later.

A. Algorithm for SDT Optimization

From a processing point of view, these types of trees are highly recommended [9] [10]. The generic representation of SDT optimization is explained, let W= [P_{ij}] be the co – occurrence matrix with (i,j) elements which represents fuzzy based epilepsy risk level patterns of single epoch. There are 48 (16x3) epochs are available. Now the optimization is a two stage process through SDT, which is explained as below,

1. Deduce the 16x3 matrix epilepsy risk level into 16x1 viz row wise optimization through three types of optimization viz, a) Aggregation method, b) Maximum pattern in the particular row, and c) Minimum element in that particular row.
2. Deduce the 16x1 matrix into one optimum epilepsy risk level through SDT optimization with four levels. Here also we have two decision methods at node level which are Max-min &Min-max combination. Therefore effectively we have six methods of SDT post classifier.

Stage I: The aggregation method converts the column elements of i,j element into a single row element as R_I= 0.4 (P_{ij}(max)+ 0.3(P_{ij}(mid)+ P_{ij}(min)) and the other two methods are self explained in nature. Now the row of three elements is converted into single element. This is repeated for all the 16 rows and the matrix is reduced into 16x1 matrix.

Stage II: Group (16x1) elements as the leaf nodes of the tree. The next level of tree is named as B with eight decision nodes, which is followed by C level with four soft decision nodes. Further level is designated as D level with two nodes and the final level is the E level with single node which is the root of the tree. Perform the following decisions at the each node of the tree as in the case of Aggregation followed by **Max-min method.**

Let R_I , R_{I+1} be the ith and i+1 th leaf to be decided at next level B_I , as

1. B_i=max (R_I,R_{I+1}),& B_{i+1}=min (R_{I+2},R_{I+3}) and at next C_J level, 2. C_i=min (B_I,B_{I+1}) & C_{i+1}=max (B_{I+2},B_{I+3}) and at next D_I level, 3. D_i=max (C_I,C_{I+1}) & D_{i+1}=min (C_{I+2},C_{I+3}) and at next E level, 4. E_I =0.6(D_I) + 0.4 (D_{I+1}).

In the case of **Min –max** procedure the following decisions are taken at the nodes of B, C, D, and E levels

1. B_i=min (R_I,R_{I+1}),& B_{i+1}=max (R_{I+2},R_{I+3}) and at next C_J level, 2. C_i=max (B_I,B_{I+1}) & C_{i+1}=min (B_{I+2},B_{I+3}) and at next D_I level, 3. D_i=min (C_I,C_{I+1}) & D_{i+1}=max (C_{I+2},C_{I+3}) and at next E level, 4. E_I =0.4(D_I) + 0.6 (D_{I+1}).

The obtained singleton results are immensely helpful in devising the therapeutic procedure of the epileptic patients. The pertinent explanation about MLP Neural network is given below.

B. Multi layer Perceptrons (MLP) Neural Network for Risk Level Optimization

Multilayer perceptrons (MLPs) are feed forward neural networks trained with the standard back propagation algorithm. They are supervised networks so they required a desired response to be trained [11]. Most NN applications involve MLPs. They are very powerful pattern classifiers. They have been shown to approximate the performance of optimal statistical classifiers in difficult problems. They can efficiently use the information contained in the input data. The advantage of using this network resides in its simplicity and the fact that it is well suited for online implementation [12]. The Levenberg-Marquardt (LM) algorithm is the standard training method for minimization of MSE (Mean Square Error) criteria, due to its rapid convergence properties and robustness. This error back propagation algorithm is used to calculate the weights updates in each layer of the network. The results of the MLP back propagation neural models trained with the Levenberg-Marquardt (LM) learning algorithm are shown in table I. The gain or learning rate η (0.3), momentum α (0.5), and training epochs are tabulated for each model [13]. The average confidence score for each MLP Network architecture is tabulated in the table. I

Table I. Estimation of MSE in Various MLP Network Architectures

Architecture	**Training Epochs**	**Mean Square Error (MSE) Index**		**Confidence score**
		Training	**Testing**	**C_i=exp(-λε_i^2)**
16-16-1	**38**	**0**	**7.31E-03**	**0.9927**
16-3-1	6	0	2.19E-02	0.9783
8-8-1	283	0	9.13E-03	0.9909
8-4-1	6	0	5.1E-02	0.9503
4-4-1	**9**	**0**	**2.83E-08**	**0.9999**
2-4-2	**8**	**0**	**0**	**1**
1-1-1	4538	1.08E-08	1.2E-08	0.9999

IV. Results and Discussions

To study the relative performance of these Fuzzy techniques STD systems (6 Types), and MLP (2 types), we measure two parameters, the Performance Index and the Quality Value. These parameters are calculated for a group of ten patients and compared.

A. Performance Index

A sample of Performance Index for a known epilepsy data set at average value is shown in table II. It is evident that the STD optimization with [Agg & Max-min] method as well as [Agg &Min-max] method gives a better performance than the fuzzy techniques because of its lower false alarms and missed classifications. The MLP (4-4-1) outperforms the both the methods due to no missed classifications and insignificant false alarm rate.

Table II. Performance Index

Methods	Weighted delay (s)	False-alarm rate/set	Performance Index %	Quality value
Fuzzy logic	4	0.2	40	6.25
Agg&max-min	2.095	1.04	95.88	22.68
Agg&min-max	2.058	1.66	95.88	22.43
Max&max-min	1.9832	2.92	95.88	21.99
Max&min-max	1.942	3.74	95.66	21.66
Min&max-min	2.175	1.25	93.33	21.64
Min&min-max	2.112	1.875	94.1	21.64
MLP Neural Network (16-16-1)	1.92	4.58	96.29	22.05
MLP Neural Network (4-4-1)	1.98	0.624	99.34	24.43

B. Quality Value

The quality value is determined by three factors. Classification rate, Classification delay, and False Alarm rate. The quality value Q_V is defined as [5]

$$Q_V = \frac{C}{\left(R_{fa} + 0.2\right) * \left(T_{dly} * P_{dct} + 6 * P_{msd}\right)} \quad (6)$$

Where, C is the scaling constant, R_{fa} is the number of false alarm per set, T_{dly} is the average delay of the on set classification in seconds, P_{dct} is the percentage of perfect classification and P_{msd} is the percentage of perfect risk level missed. Table III shows the Comparison of the fuzzy, STD optimization techniques, and MLP neural networks. It is observed from table III, that STD (Agg& max-min) and (Agg& min-max) methods are performing well with the higher performance index and quality values. It is compromised to select STD (Agg& min-max) method even though it has low quality value than its predecessors. The SDT results are validated with the standard MLP (16-16-1) and MLP (4-4-1) neural networks, and are also depicted in the table III. Since MLP neural network models are supervised learning in nature and therefore it provides better optimized solution than other two methods.

Table III. Results of Classifiers taken as Average of all ten Patients

Methods	Perfect Classification	Missed Classification	False Alarm	Performance Index
Fuzzy logic	50	20	10	40
Agg&max-min	96.03	2.91	1.04	95.88
Agg&min-max	96.04	2.29	1.66	95.88
Max&max-min	96.04	1.04	2.92	95.88
Max&min-max	95.83	0.416	3.74	95.66
Min&max-min	93.75	4.998	1.25	93.33
Min&min-max	94.37	3.75	1.875	94.1
MLP (16-16-1)	96.42	-	4.58	96.29
MLP(4-4-1)	99.37	-	0.624	99.36

The cost associated with the learning is additional burden with neural networks so that we may select SDT method as a mid path solution to this problem.

V. Conclusion

In this paper, we consider generic classification of the epilepsy risk level of epileptic patients from EEG signals. Since, the fuzzy outputs are highly nonlinear in nature with dynamic probability functions. We have chosen STD based optimization technique to optimize the risk level by incorporating the above goals. Off the six types of STD methods Agg &min-max method performs well with high PI, Quality value and with moderate time delay. Further research is in the direction to compare the STD with unsupervised RBF neural networks model to solve this open end problem.

References

1. Joel.J etal, "*Detection of seizure precursors from depth EEG using a sign periodogram transform*," IEEE Transactions on Bio Medical Engineering, vol, 51 no,4, pp-449-458, April 2004.
2. D.Zumsteg and H.G.Wieser, "*Presurgical evaluation: current role of invavasive EEG*,"Epilepsia,vol.41, No. suppl 3,pp, 55-60,2000.
3. K P Adlassnig, *"Fuzzy Set Theory in Medical diagnosis"*, IEEE Transactions on Systems Man Cybernetics, 16 pp 260-265, March 1986
4. Alison A Dingle et al, *"A Multistage system to detect epileptic form activity in the EEG"*, IEEE Transactions on Biomedical Engineering, 40(12) pp 1260-1268, December 1993.
5. R.Harikumar and B.Sabarish Narayanan, "*Fuzzy Techniques for Classification of Epilepsy risk level from EEG Signals"*, Proceedings of IEEE Tencon – 2003, Bangalore, India, pp 209-213, 14-17 October 2003.

6. R.Harikumar, Dr.(Mrs). R.Sukanesh, P.A. Bharathi, "*Genetic Algorithm Optimization of Fuzzy outputs for Classification of Epilepsy Risk Levels from EEG signals*," I.E. India Journal of Interdisciplinary panels, vol.86, no.1, May 2005.
7. Ronald.R.Yager, *"Hierarichical Aggregation Functions Generated From Belief structures,"* I.E.EE Transaction of Fuzzy Systems,vol.8, no.5, pp 481-490, May 2005.
8. Cezary.Z Janikow, "*Fuzzy Decision Tree: Issues and Methods,"* I.E.E.E Trans SMC,vol.28, no.1, pp 1-14,February1998.
9. S.Rasoul Safavian, David Landgrebe, *"A Survey of Decision Tree Classifier Methodology,"* IEEE Trans SMC,vol.21, no.3, pp-660-674,May 1991.
10. Philippe Salembier, Luis Garrido, *"Binary Partition Tree as an Efficient Representation for Image Processing, Segmentation, and Information Retrieval,,"* I.E.E.E Trans Image processing,vol.9, no.4, pp-561-576, April 2000.
11. Nurettin Acir etal., " Automatic Detection of Epileptiform Events In EEG by A Three-Stage Procedure Based on Artificial Neural Networks,"*IEEE transaction on Bio Medical Engineering,* vol,52,no.1,January 2005 pp30-40.
12. Li Gang etal, "An Artificial –Intelligence Approach to ECG Analysis," *IEEE EMB Magazine*, vol 20, April 2000, pp 95-100.

Magnetic field transducers based on the phase characteristics of GMI sensors and aimed at biomedical applications

E. Costa Silva[1], L.A.P. Gusmão[2], C.R. Hall Barbosa[1], E. Costa Monteiro[1]

[1]Post Graduation Program in Metrology, Pontifícia Universidade Católica do Rio de Janeiro, Brazil
[2]Electrical Engineering Department, Pontifícia Universidade Católica do Rio de Janeiro, Brazil

Abstract — **For the last four years the Laboratory of Biometrology of PUC-Rio has been working in the development of magnetic field transducers to be used in biomedical applications – especially in the three-dimensional localization of needles inserted in the human body and in the measurment of arterial pulse waves. While previous investigations were based on the behavior of the magnitude of the impedance of Giant Magnetoimpedance (GMI) ribbon-shaped sensors, this manuscript presents the preliminary results of a new research that considers the changes in the phase characteristics of GMI sensors due to varying low-intensity magnetic fields. In spite of being less explored in the literature, the work carried out so far indicates that the sensitivity of the phase can lead to more promising results than the ones already obtained with transducers based on the variation of the impedance magnitude. By means of examples showing that the sensitivity of the phase is affected by parameters (amplitude, frequency and DC level) of the AC biasing current that flows throught the sensor, this manuscript discusses how an ideal stimulation condition was derived in order to obtain more sensitive transducers. It is also examined the influence of the ribbon length in the sensitivity. A new conditioning electronic circuit – responsible for the excitation and measurement of the GMI sensor, and designed to work in the 100kHz to 5Mhz range – has been developed and is presented in the manuscript. Simulation studies of the complete transducer, including the conditioning circuit and based on data obtained from measured curves, have shown that an improvement of 10 to 100 times can be expected when compared to the sensitivity of previous magnitude-based transducers.**

Keywords — **Metrology, Biometrology, Giant Magnetoimpedance, Phase Characteristics, Biomedical Transducer.**

I. Introduction

A. Historical context

The department of Metrology for Quality and Innovation (Post-MQI) of PUC-Rio, through the research line in Biometrology and in partnership with the department of Physics of the Federal University of Pernambuco (UFPE), is carrying out studies seeking the implementation of prototypes of magnetometers based in the Giant Magnetoimpedance (GMI) phenomenon [1-2].

The importance of GMI in the world's scientific scenery has been increasing, and several laboratories are accomplishing promising researches in several application areas. A recent example was the concession of the 2007 Nobel Award in Physics to the researchers Albert Fert and Peter Grünberg, who discovered the giant magneto-resistance, GMR [3,4].

The Giant Magnetoimpedance effect started to be studied intensely in the decade of 90. The first results obtained in such studies were interpreted as a variation of the Giant Magnetoresistance effect (GMR), whose experimental behavior is examined with the application of a continuous current and in the presence of a continuous magnetic field. The GMR effect only considers the variation of the resistance, and the phenomenon is explained by the electrons motion change when we act on their spin through the orientation of a magnetization [3]. However, experiments accomplished with samples of amorphous ferromagnetic alloys, using alternating current, have shown a variation of the resistive part as well as of the reactive part with respect both to the external magnetic field and to the frequency of the applied current. Thence comes the name GMI.

B. GMI effect

We focus on a particular case of GMI named Longitudinal Magnetoimpedance (LMI). The phenomenon of LMI is induced through the application of an alternating current (I) along the length of a ribbon (or wire), which is submitted to an external magnetic field ($\vec{H}$) parallel to it. The potential difference (V) is then measured between the extremities of the ribbon, as shown in Figure 1.

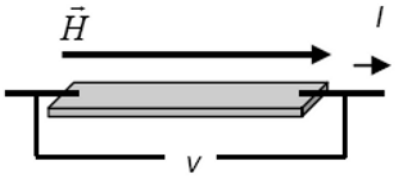


Fig. 1: Typical GMI measurement.

Chwee Teck Lim, James C.H. Goh (Eds.): ICBME 2008, Proceedings 23, pp. 652–656, 2009
www.springerlink.com

Using the phasorial description of the AC tension and current, as well as arbitrating the phase of the current (ϕ_I) as zero, the impedance of the sample can be calculated as:

$$Z=\frac{|V|e^{j\phi_V}}{|I|e^{j\phi_I}}=\frac{|V|}{|I|}e^{j\phi}=|Z|e^{j\phi} \quad (1)$$

Thus, the complex impedance (Z) is defined by two components, a real one and imaginary one:

$$Z=R+jX, \quad (2)$$

where

$$R=|Z|\cos\phi \text{ and } X=|Z|\sin\phi \quad (3)$$

The GMI effect is actually a result of the skin depth dependency with the magnetic permeability, which varies not only with the external magnetic field that is applied to the sample, but also with the frequency and intensity of the current that passes through it. Then, generically, in agreement with the literature [5-6], we can define:

$$Z=(1-i)\frac{L}{2\omega\sigma\delta}\frac{1}{1-e^{-(1-i)/2\delta}}, \text{ and} \quad (4)$$

$$\delta=\frac{c}{2\pi}\sqrt{\frac{1}{2\omega\mu\sigma}}, \quad (5)$$

where L is the length and t is thickness of the ribbon, ω is the frequency of the current and σ is the conductivity of the material.

A. Previous Works

The Laboratory of Biometrology of PUC-Rio has developed, in the recent past, some magnetic field transducers for biomedical applications, all based on the magnitude characteristics of the GMI phenomenon.

As a matter of fact, most of the studies accomplished in the field of GMI has been based in the magnitude characteristics of the samples, being rare those that consider its phase characteristics. Even the most used figure for determination of the GMI percentile variation - as a function of the applied magnetic field - takes into account just the magnitude [5-6]:

$$GMI(\%)=\left[\frac{|Z(H)|-|Z(H_{max})|}{|Z(H_{max})|}\right]10^2, \quad (6)$$

As examples of transducers developed at PUC-Rio, which are based on the magnitude variation of the GMI effect and uses GMI ribbons as sensor elements, it can be mentioned the transducer for localization of needles inserted in the human body shown in Fig. 2 (which sensitivity was 12V/Oe), and the transducer for measurement of arterial pulse waves shown in Fig. 3 (which sensitivity was 1mV/Pa) [1-2, 7-8].

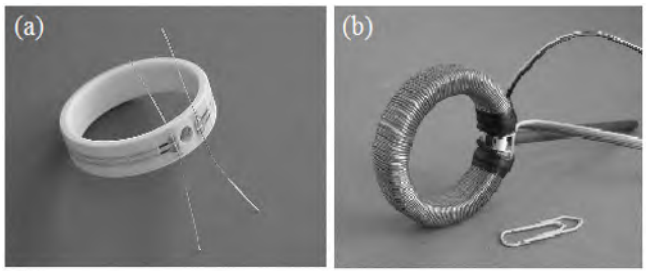


Fig. 2: (a) Partial ring shaped prototype with GMI ribbons fastened; (b) Complete prototype with the excitation coils.

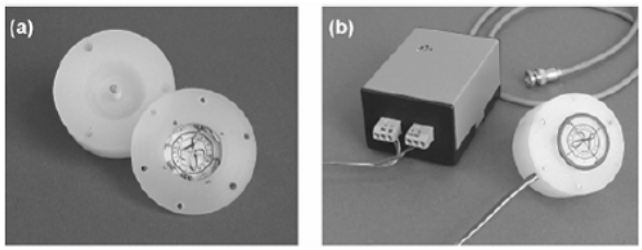


Fig. 3: (a) Opened prototype without the electronic circuit; (b) Complete prototype.

This paper presents the improvements introduced in the foregoing transducers when the phase characteristics of GMI samples started to be considered in place of its magnitude.

II. Experimental Research

A. Phase and Magnitude Characterization

Some initial studies have examined the effect of the frequency and DC level of the excitation current on the sensitivity of the ribbons. All those parameters, as well as the length of the ribbon, affect the magnitude and phase sensitivity in a significant and different way.

Such studies lead to the conclusion that the ribbons presented a maximum sensitivity for DC currents around 80mA, independently of their length or of the AC current frequency. Measurements were accomplished with DC currents of 0mA, 20mA, 40mA, 60mA and 80mA. Due to technical limitations, and to the difficulties imposed by its microelectronic implementation, the sensitivity for higher current values was not tested, but the results should continue to get better.

All of the measurements were made in $Co_{70}Fe_5Si_{15}B_{10}$ ribbon-shaped alloys with an average thickness of 60 mm and an average width of 1.5 mm. The AC current magnitude was kept in 15 mA_p, because it has been previously seen that such variable did not affect the GMI ribbon behavior significantly.

Figures 4 and 5 exemplify, respectively, the magnitude characterization results obtained with 15 cm and 3 cm long ribbons (using an 80 mA DC current), where Z_0 is the value of the magnitude in the case of a null external magnetic field parallel to the ribbon length.

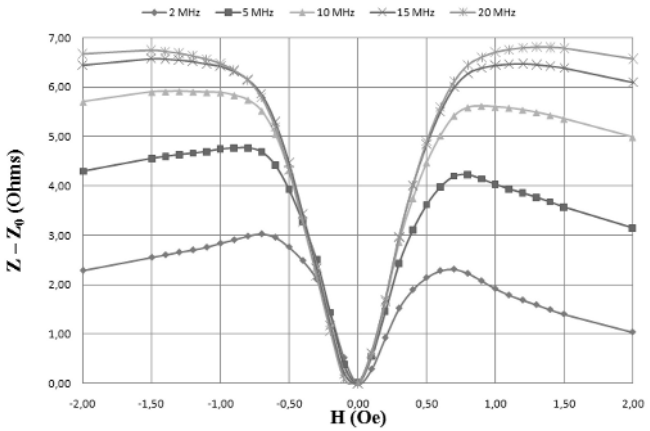


Fig. 4: Magnitude of the impedance of a 15 cm long GMI ribbon submitted to an 80 mA DC current.

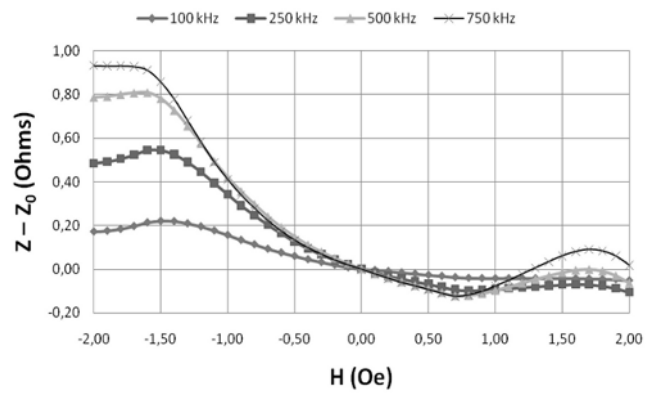


Fig. 5: Magnitude of the impedance of a 3 cm GMI ribbon submitted to an 80 mA DC current.

The best magnitude sensitivity obtained with the 15cm long ribbon was 12.9Ω/Oe at 80mA and 20MHz, while for a 3 cm long ribbon was 0.9Ω/Oe at 80mA and 10MHz.

In spite of the largest value of the sensitivity happening for the highest frequency value tested, it has been noticed that, starting with 10MHz, the sensitivity begins to saturate.

Figures 6 and 7 show, respectively, the results of phase characterization of 15 cm and 3 cm long ribbons, when driven by an 80 mA DC current. θ_0 is the value of the phase in the case of a null external magnetic field parallel to the ribbon length.

The best phase sensitivity obtained with the 15cm long ribbon was 17°/Oe at 80mA and 10MHz, and for a 3 cm long ribbon was 9°/Oe at 80mA and 100kHz.

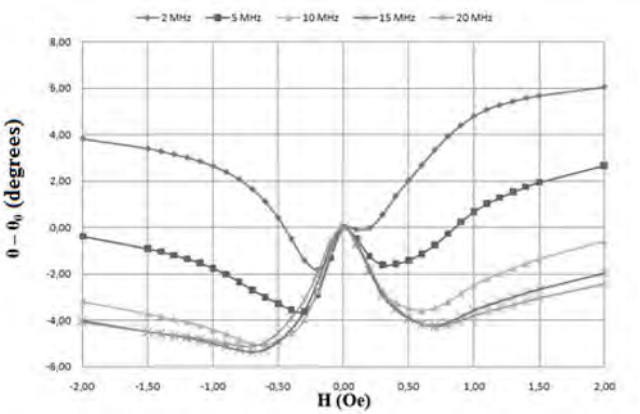


Fig. 6: Phase of the impedance of a 15 cm long GMI ribbon submitted to an 80 mA DC current.

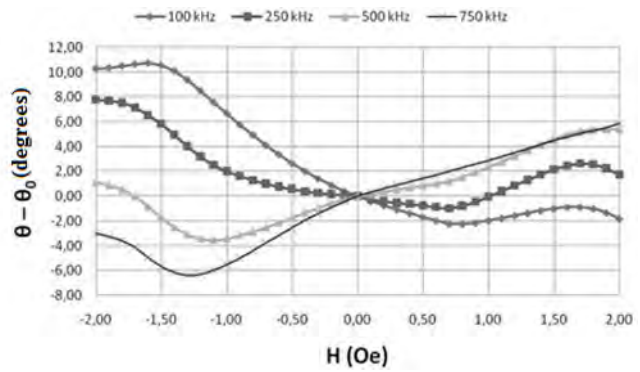


Fig. 7: Phase of the impedance of a 3 cm long GMI ribbon submitted to an 80 mA DC current.

For a fair comparison between the performance of the ribbons with different lengths, the sensitivity value of the 3cm ribbon should be multiplied by five. If this is done, the magnitude sensitivity of the 15 cm long ribbon will be about 2.9 times better than the tripled one, while the phase sensitivity of the cascaded 3 cm ribbons will be about 2.6 times

better than the large one. In other words, the phase sensitivity is improved for smaller lengths of ribbons, while the magnitude sensitivity is reduced as the lenght also reduces. This is clearly an advantage for biomedical applications, where, in general, it is very convenient to work with the smallest possible sensor elements, in order to have a better spatial resolution.

Still, the highest magnitude sensitivities happen for high frequencies (over 2MHz), while a maximum phase sensitivity is obtained in a relatively low frequency (100kHz). Those low frequencies facilitate the implementation of the electronic conditioning circuits, and constitute another advantage of using the phase characteristics of the GMI effect.

B. Electronic circuit

The block diagram of the proposed phase detection and conditioning circuit, to be used in the implementation of the new transducers, is presented in Figure 8.

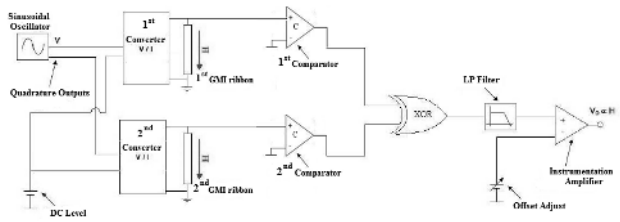


Fig. 8: Conditioning and phase reading electronic circuit.

The idealized circuit is capable of conditioning the ribbon, supplying the AC current (with the appropriate frequency and magnitude) and the specified DC level. It also delivers a voltage output which is proportional to the phase variation of the ribbons ($\Delta\theta$).

Since its final objective is to measure small magnetic fields - to detect small phase variations - the above circuit has to be implemented with fast components (in particular the XOR gate). For this reason, an ECL family XOR - typical propagation delay of 260ps - has been adopted.

The electronic circuit of the arterial pulse waves transducer is similar to the one here presented (fig. 8), except for small alterations. Thus, it won't be shown here for the sake of brevity.

C. Simulations Results

Some simulation studies of the complete transducer circuit have been carried out with the help of a SPICE program. To accomplish this, the GMI ribbons were modeled as a resistance in series with an inductance. The results shown in Table 1 were obtained by the transducers based on the GMI phase characteristics.

Table 1 Transducers Sensitivity

Transducer	Sensitivity
Magnetic Bodies Detection	459 V/Oe
Arterial Pulse Waves Measurement	13.5 mV/Pa

III. Conclusions

The new transducers, based on the GMI phase characteristics, present a significant increase in sensitivity when compared with those based on the magnitude characteristics, approximately 38 times for the Magnetic Bodies Detector and 13 times for the Arterial Pulse Waves Measurement [1-2]. These results indicate, doubtless, that the phase characteristics of the GMI effect deserves to be more studied, especially when it deals with the development of transducers.

It may be also pointed out that the effects of the ribbon length variation should continue to be analyzed, since they can make possible the miniaturization of the sensor elements, especially when using an electronics based in the phase detection.

Acknowledgment

We would like to thank CNPq, FAPERJ and FINEP for the financial support that made this work possible.

References

1. Pompéia F, Gusmão L A P, Hall Barbosa C R, Costa Monteiro E, Gonçalves L A P, Machado F L A (2008) Ring shaped magnetic field transducer based on the GMI effect. Meas. Sci. Technol. at http://www.iop.org/EJ/abstract/0957-0233/19/2/025801/ DOI 10.1088 /0957-0233/19/2/025801
2. Ramos Louzada D, Costa Monteiro E, Gusmão L A P, Hall Barbosa C R (2007) “Medição não-invasiva de ondas de pulso arterial utilizando transdutor de pressão MIG” Proceedings do IV Latin American Congress on Biomedical Engineering, Brazil
3. Fert A (2007) The origin, development and future of spintronics. Nobel Lecture, Stockholm, Sweden, 2007 at http://nobelprize.org /nobel_prizes/physics/laureates/2007/fert_lecture.pdf

4. Grünberg P (2007) From spinwaves to giant magneto magnetoresistence (GMR) and beyond. Nobel Lecture, Stockholm, Sweden, 2007 at http://nobelprize.org/nobel_prizes/physics/laureates/2007/grunberg_lecture.pdf
5. Machado F L A and Rezende S M (1996) A theoretical model for the giant magnetoimpedance in ribbons of amorphous soft-ferromagnetic alloys. J. Appl. Phis. 79:6958–6960 DOI 10.1063/1.361945
6. Knobel V and Pirota K R (2002) Giant magnetoimpedance concepts and recent progress. J. Magn. Magn. Mater. 242–245:33–40 DOI 10.1016/S0304-8853(01)01180-5
7. Costa Monteiro E, Hall Barbosa C R, Andrade Lima E, Costa Ribeiro P, Boechat P (2000) Locating steel needles in the human body using a SQUID magnetometer. Phys. Med. Biol. 45:2389–2402 DOI 10.1088/0031-9155/45/8/323
8. Hall Barbosa C, Costa Monteiro E and Pompéia F (2003) Localization of magnetic foreign bodies in human using magnetic field sensors. 17th IMEKO World Congress, Dubrovnik, Croatia, 2003, pp 22–27

Author: Elisabeth Costa Monteiro
Institute: Pontifícia Universidade Católica do Rio de Janeiro
Street: Rua, Marquês de São Vicente 225; Gávea
City: Rio de Janeiro
Country: Brazil
Email: beth@puc-rio.br

Effects of Task Difficulty and Training of Visuospatial Working Memory Task on Brain Activity

Takayasu Ando[1], Keiko Momose[2], Keita Tanaka[3], Keiichi Saito[3]

[1]Graduate School of Human Sciences, Waseda University, Tokorozawa, Japan
[2]Faculty of Human Sciences, Waseda University, Tokorozawa, Japan
[3]Research Center for Advanced Technologies, Tokyo Denki University, Inzai, Japan

Abstract — **Visuospatial working memory is one of the important cognitive processes and makes it possible to maintain and manipulate the visual information stored in brain systems. In this study, effects of task difficulty and two-week training of visuospatial working memory task on brain activity and its neural mechanisms were investigated.**

We used visuospatial working memory task with 10 or 30 visual targets displayed on a screen. Each target was a numbered white square and subjects were instructed to click the targets sequentially. Brain activity during performance of the task was measured with functional magnetic resonance imaging (fMRI), before and after two weeks task training. Four subjects practiced the task with 30 visual targets 15 times a day for two weeks, and another four subjects were not practiced.

Statistical probability mapping revealed high activity in prefrontal cortex during performance of the task, especially in Brodmann area 10 and 46, which are commonly related to working memory processes. Higher and larger activation was observed for the task with 30 targets than that with 10 targets before training. After training, activated level and area of BA10 and 46 was increased and expanded in tasks with 10.

Keywords — **Visuospatial working memory, fMRI, Brodmann area 10, Brodmann area 46.**

I. Introduction

Recent advances in information technology have provided artificial and digital information environment. Under such environment, we must select necessary information from a lot of digital visual information resources by reading them and saving shortly in our memory.

Working memory (WM) is one of the important functions for such visual information selection, and is thought to be a mechanism of maintenance and the processing of an active memory [1-4]. After Baddeley and Hitch proposed a fundamental framework for the WM [1], many studies on verbal and spatial WM have been presented [2-4]. Neuroimaging studies have shown that the prefrontal cortex is involved in human WM including the central executive system and memory buffers [5-7], and WM is mediated by frontal cortical regions differing in the types of information maintained (e.g., verbal or spatial) [5, 8]. Recent studies have examined the effects of practice, development and aging on cortex activity related to WM [7, 9-12].

In this study, brain activity during visuospatial WM task was investigated to determine how and which cortical regions are involved in the human information processing in the task. Effects of task difficulty (depending on numbers of visual targets displayed) and training (two-week practice) on the brain activity were examined. Preliminary results have already reported [13], but some experimental conditions were improved in this report. The results may give a clue towards understanding the brain function and its relation to the working memory.

II. Methods

A. Subjects

Eight healthy male students (age range, 19-25 years) participated in this study. All subjects were right-handed. A written informed consent was obtained from all subjects.

Subjects were divided into two groups with or without practice: four subjects with practice (group 1), and four subjects without practice (group 2).

B. Visuospatial working memory task and brain activation measurement

We used the same visuospatial working memory (VSWM) tasks, stimulation protocols, and brain imaging methodology that used in our previous report [13].

VSWM tasks with 10 and 30 visual targets (T10 and T30 tasks) were used. The visual target is a numbered white square displayed on black background as shown in Fig.1. Subjects were instructed to sequentially point and to click a visual target by using computer mouse. When subject correctly clicked a target, the target disappeared and next numbered target would appear at another random position of the screen.

Chwee Teck Lim, James C.H. Goh (Eds.): ICBME 2008, Proceedings 23, pp. 657–660, 2009
www.springerlink.com

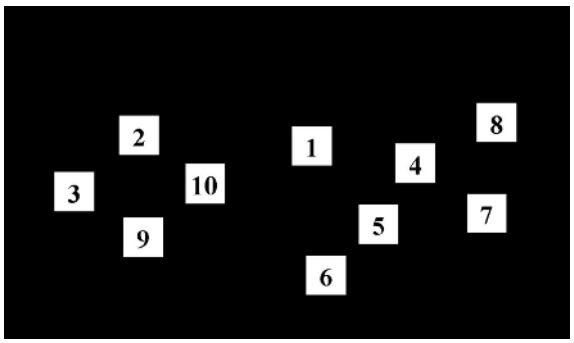


Fig. 1 Stimulus image (T10).

Brain activation during tasks was measured with functional MRI at each end of the two-week the T30 task training. First functional MRI measurement was performed before the training (experiment 1), and second measurement was performed after the training (experiment 2). Subjects in group 1 practiced the T30 task 15 times a day for two weeks after experiment 1. Subjects reported on the score of T30 every day. Subjects in group 2 did no task for two weeks.

Imaging was performed with a 1.5T HITACHI STRATIS MRI scanner equipped with a quadrature RF head coil. Boxcar design which consists of 3 blocks of rest (50 seconds) and task (50 seconds) was employed in this study. Further details are provided in our previous report [13].

C. Statistical analysis

Statistical analysis was performed with SPM99. Functional data sets were realigned and corrected for motion using the first image as the reference, and were normalized to the Talairach space using the EPI template image in SPM99. The normalized data sets were smoothed using an isotropic Gaussian kernel (full width half maximum [FWHM] = 10 mm). For the statistical parametric mapping analysis (SPM), a canonical hemodynamic response function within SPM99 was employed as a basis function. SPM projection maps were generated using the general linear model (GLM) within SPM99.

As for the experiment 1, the brain activation of the 8 subjects conducting T10 task was compared to the brain activation of the same 8 subjects conducting T30 task. Furthermore, for each task, T10 and T30, the brain activation of the experiment 1 and the experiment 2 were compared. Group SPMs were generated using a random-effects model within SPM99 with the individual contrast map. The resulting SPM {t} map was transformed to the unit normal distribution SPM {Z} and threshold at a significance level of $p<0.05$ corrected for multiple comparison, using the theory of Gaussian fields as implemented in SPM99.

III. Results and Discussion

A. Effects of task difficulty (Experiment 1)

Brain activity of T10 and T30 task in experiment 1 are shown in Table 1 and Figure 2. Table 1 shows the analytical result of eight subjects in experiment 1. Figure 2 is a front view of brain areas and the significantly activated areas were displayed with a color code ranging from yellow (high-level) to red (low-level).

Significant activation was observed in right inferior frontal gyrus for both T10 and T30 task. Right inferior frontal gyrus has reported to relate to processing of spatial WM [14] and spatial attention [15], although its role or function is still controversial. Moreover, the Brodmann area 10 (BA10) was significantly activated for both T10 and T30 tasks. BA10 has reported to be the most higher-order functional area in prefrontal cortex [16]. Significant high activity in these areas indicates that both T10 and T30 tasks required spatial processing and attention. In fact, during T10 and T30 tasks, subjects were required to perform visual searching, memorizing of spatial location and spatial motor tasks, in order to click and delete targets sequentially as fast as possible.

However, the highest activity was observed in occipital lobe for both T10 and T30 task, as shown in Table 1. This activation area was large and found in occipital lobe and the cerebellum (this area is not shown in Figure 2). These were because of the visual searching and motor task (computer mouse pointing and clicking).

Table 1 Effects of task difficulty (all subjects' results in experiment 1)

Experiment 1						
Brain region	Hemisphere	Talairach coordinates			Brodmann area	t
		x	y	z		
T10						
Precuneus	R	24	−70	52	7	28.76
Superior Frontal Gyrus	L	−26	58	−2	10	6.03
Parahippocampal Gyrus	R	24	−16	−14		5.53
Superior Frontal Gyrus	R	22	60	0		4.83
Inferior Frontal Gyrus	R	50	40	−2		4.56
T30						
Declive	L	−30	−80	−22		32.41
Middle Frontal Gyrus	R	46	12	30		12.01
Middle Frontal Gyrus	R	38	0	58		11.71
Middle Frontal Gyrus	R	50	44	6	46	7.99
Inferior Frontal Gyrus	R	60	20	6	45	7.23
Middle Frontal Gyrus	L	−44	48	8		5.99
Middle Frontal Gyrus	L	−28	58	20	10	5.33
Inferior Frontal Gyrus	L	−52	22	−8	47	4.49

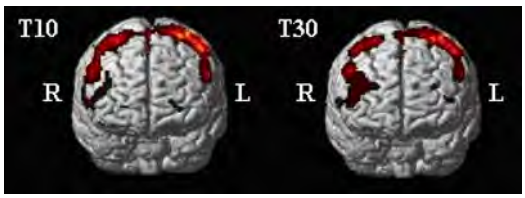


Fig. 2 Significantly activated areas in experiment 1.

Significant high activity was observed in left and right superior frontal gyrus including BA10 for T10 task. In contrast, high activity was observed in left and right middle frontal gyrus for T30 task. This activated area was large and included BA46. Maintenance and manipulation of more visual information in T30 than T10 would lead to the higher and larger activity in T30. Previous study demonstrated that superior frontal gyrus related to visual-spatial WM [17]. It is confirmed that WM task of spatial location activated right middle frontal gyrus and WM task of visual form activated left and right middle frontal gyrus [18]. BA9 and BA46 has considered to be the neural basis of the central executive system in human information processing [5-7], and its activation has confirmed by spatial and verbal task [19]. More visual targets displaying in T30 task would have required the more visual information processing especially on form (numbers on squares) and spatial location.

Table 2 Effects of two-week practice (Group 1)

Experiment 2 – Experiment 1						
Brain region	Hemisphere	Talairach coordinates			Brodmann area	t
		x	y	z		
T10						
Inferior Semi-Lunar Lobule	L	−18	−70	−36		10.32
Middle Frontal Gyrus	R	50	40	24	46	7.6
Superior Temporal Gyrus	R	26	14	−28	38	7.22
Tuber	R	48	−58	−28		6.72
Cerebellar Tonsil	R	40	−48	−42		6.69
Superior Frontal Gyrus	R	30	58	−8	10	6.68
Superior Temporal Gyrus	R	46	6	−22		6.4
Middle Frontal Gyrus	L	−32	58	10		6.24
Parahippocampal Gyrus	L	−22	−26	−18	35	6.16
Superior Frontal Gyrus	R	10	64	18	10	5.91
Inferior Semi-Lunar Lobule	R	26	−68	−40		5.61
Inferior Frontal Gyrus	L	−32	12	−18		5.49
Uvula	R	18	−82	−26		5.33
Middle Frontal Gyrus	L	−56	2	42		5.18
Middle Temporal Gyrus	R	62	4	−12	21	5.06
Superior Temporal Gyrus	R	56	−32	14		4.94
Inferior Frontal Gyrus	R	42	46	2	10	4.93
Declive	R	44	−74	−20		4.83
Inferior Frontal Gyrus	R	40	32	4		4.78
Middle Temporal Gyrus	L	−60	−64	2		4.63
T30						
Inferior Semi-Lunar Lobule	R	34	−68	−38		10.89
Middle Frontal Gyrus	R	44	52	12	10	7.65
Superior Frontal Gyrus	L	−36	52	14		6.81
Superior Frontal Gyrus	R	28	54	−6	10	6.44
Superior Frontal Gyrus	L	−14	22	62	6	6.01
Middle Frontal Gyrus	L	−36	36	−14	11	5.77
Cerebellar Tonsil	R	32	−50	−40		5.62
Inferior Temporal Gyrus	L	−58	−68	0	37	5.59
Middle Temporal Gyrus	L	−52	−76	16	19	5.36
Inferior Temporal Gyrus	R	38	−18	−30		5.01
Declive	R	0	−66	−16		4.92
Middle Frontal Gyrus	R	56	34	24	46	4.86

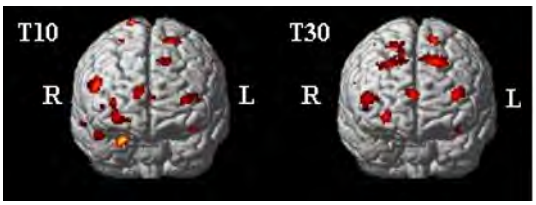


Fig. 3 Areas where their activation level increased after practice weeks in group 1 (with two-week practice).

B. Effects of two-week practice

Practice period of two weeks were determined by referring to the previous other studies [9, 12]. Mean of T10 task score (numbers of correctly clicked targets during fMRI measurement) increased after two weeks practice in group 1 (with two-week practice), from 47.7 ± 5.5 to 53.3 ± 3.3 and that of T30 task score increased from 26.5 ± 1.8 to 28.3 ± 2.5. In group 2 (without practice), the score mean of T10 also increased from 43 ± 3.7 to 45.4 ± 3.0, but that of T30 did not changed (from 25 ± 2.5 to 24.8 ± 2.3). The larger increase of the score in T10 implied the effect of two-week practice. The practice may not be enough to rise the scores of more difficult task T30.

The activated areas in group 1 (with two-week practice) were shown in Table 2 and Figure 3. Those in group 2 (without practice) were shown in Table 3 and Figure 4. Theses results were obtained by the exclusive masking of SPM99. This masking will remove all voxels of the activated areas in the experiment 1 from those in the experiment 2. Masking does not affect p-values of the contrast. In both groups, significant increasing of activity was observed

Table 3 Effects of two-week practice (Group 2)

Experiment 2 – Experiment 1						
Brain region	Hemisphere	Talairach coordinates			Brodmann area	t
		x	y	z		
T10						
Uvula	R	18	−68	−34		9.48
Cerebellar Tonsil	L	−42	−58	−34		7.29
Pyramis	L	−24	−70	−30		7.27
Superior Frontal Gyrus	R	16	50	38	8	6.33
Middle Frontal Gyrus	R	54	8	46	6	5.92
Superior Temporal Gyrus	R	56	4	−4		5.89
Parahippocampal Gyrus	L	−16	−14	−16		5.72
Superior Temporal Gyrus	L	−58	0	2		5.44
Superior Frontal Gyrus	L	−10	38	48	8	5.32
Precentral Gyrus	L	−58	6	30	6	5.23
Medial Frontal Gyrus	R	4	60	2		5.18
Superior Temporal Gyrus	R	26	16	−26		5.18
Middle Temporal Gyrus	R	36	0	−38		4.85
T30						
Pyramis	L	−26	−66	−30		12.98
Superior Frontal Gyrus	R	18	58	0		8.6
Inferior Temporal Gyrus	L	−38	−8	−36	20	6.42
Precentral Gyrus	R	42	−14	52	4	6.37
Medial Frontal Gyrus	R	12	−12	56	6	5.79
Parahippocampal Gyrus	L	−30	−22	−12	Hippocampus	5.75
Inferior Frontal Gyrus	L	−18	18	−16		5.69
Middle Frontal Gyrus	R	56	32	26		5.42
Postcentral Gyrus	R	36	−20	26		4.96
Superior Temporal Gyrus	R	48	−20	8		4.75
Middle Temporal Gyrus	L	−46	−82	20		4.69
Middle Temporal Gyrus	R	68	−12	−6	21	4.68

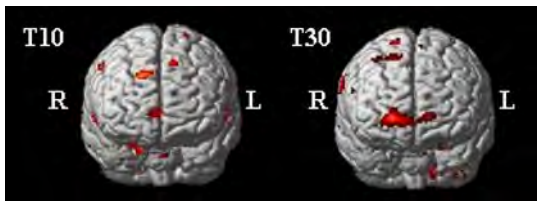


Fig. 4 Areas where their activation level increased after practice weeks in group 2 (without practice).

in the frontal lobe and in the cerebellum. Especially for T10 task in group 1, a lot of activation increased areas were observed, and this would be effects of two-week practice. The activation increase was observed in right middle frontal gyrus and right superior frontal gyrus. In particular, activation in BA46 and 10 increased for T10 task after practice in group 1, but not in group 2. These changes imply that subjects were able to maintain more WM capacities after the practice. In fact their scores actually increased for T10 as mentioned above. The results of activation increase in frontal lobe agreed with previous research [9]. Although no significant increase of activity in BA10 and 46 in group 2, the scores actually increased a little as shown above, so that the reproducibility of task-related brain activity is necessary to be examined in the future.

Moreover, activation increased in the left and right temporal lobe. However, these areas activated in group 1 and group 2. Therefore, it will not be an effect of the practice. We thought the influence of the individual variation.

IV. Conclusions

Effects of task difficulty (number of visual targets) and two-week practice by using visuospatial working memory task were examined. Higher and larger brain activity was observed during the task with more visual targets. Significant activation was observed in BA10 for both T10 and T30 task, and BA46 for T30 task. Results indicate that T30 task required a lot of working memory capacity for the information processing. After two-week practice, the activated area has expanded in the frontal lobe. Effects of practice was observed especially in BA46 and 10 where related to the working memory.

References

1. A.D. Baddeley, G.J. Hitch, (1974) “Working memory” in The Psychology of Learning and Motivation (ed by G. Bower), Academic Press, New York, Vol.18, pp. 47-90.
2. A.D. Baddeley, (1999) Models of Working Memory: Mechanisms of Active Maintenance and Executive Control (eds by A. Miyake, and P. Shah), Cambridge University Press, pp. 28-61.
3. M. Daneman, (1980) “Individual differences in working memory and reading”, J Verb Learn Verb Behav, Vol.19, pp.450-466.
4. M.W. Eysenck, (1994) The Blackwell Dictionary of Cognitive Psychology, Blackwell, Oxford.
5. M. Mimura, Y. Sakamura, (2003) “Recent Advances in Working Memory”, The Japanese Journal of rehabilitation Medicine, Vol40, No5, pp.314-322 (in Japanese).
6. D’Esposito M, Detre JA, Alsop DC, Skin RK, Atlas S. Grossman M. (1995) “The neural basis of the central exective system of working memory.” Nature, 378, pp.279-281.
7. Fletcher PC, Henson RN, (2001) “Frontal lobes and human memory, insights from functional neuroimaging.” Brain 2001, 24, pp 849-881.
8. A.M. Owen, (1996) “Evidence for a two-stage model of spatial working memory processing within the lateral frontal cortex: a positron emission tomography study”, Cereb Cortex, Vol.6, pp.31-38.
9. P.J. Olesen, H. Westerberg, T. Klingberg (2003) “Increased prefrontal and parietal activity after practice of working memory,” Nature Neuroscience, Vol.7, pp.75-79.
10. R.J. Haier, B.V. Siegel Jr., A. MacLachlan, E. Soderling, S. Lottenberg, M.S. Buchsbaum, (1992) “Regional glucose metabolic changes after learning a complex visuospatial/ motor task: a positron emission tomographic study”, Brain Research, Vol. 570, No1-2, pp.134-143.
11. K. Kakoi, H. Tomokiyo, K. Tanaka, G. Wang, K. Yunokuchi, (2004) “Analysis of EEG coherence during working memory with aging”, IEICE technical report. ME and Bio cybernetics, Vol.103, No.637, pp.77-82 (in Japanese).
12. Kirk I. Erickson, Stanley J. Colcombe, Ruchika Wadhwa, Louis Bherer, Matthew S. Peterson, Paige E. Scalf, Jennifer S. Kim, Maritza Alvarado and Arthur F. Kramer, (2007) “Training-Induced Functional Activation Changes in Dual-Task Processing: An fMRI Study”, Cerebral Cortex, 17(1), pp.192-204.
13. T. Takayasu, K. Momose, K. Tanaka, K. Saito, (2007) “Brain Activation during Visuo-Spatial Memory Task: an fMRI study”, ICICIC 2007.
14. Hautzel, H., Mottaghy, F.M., Schmidt, D., Zemb, M., Shah, N.J., Muller-Gartner, H. W., et al. (2002). Topographic segregation and convergence of verbal, object, shape and spatial working memory in human. Neuroscience Letters, 323, 156-160.
15. Curtis, C.E., & D’Esposito, M. (2003). Persistent activity in the prefrontal cortex during working memory. Trends in Cognitive Sciences, 7, 415-423.
16. Burgess PW, Scott SK, Frith CD, (2003) “The role of the rostral frontal cortex (area 10) in prospective memory: a lateral versus medial dissociation.” ,Neurophychologia, 41, pp.906-918.
17. Oliveri, M., Turriziani, P., Carlesimo, G.A., Koch, G., Tomaiuolo, F., Panella, M., & Caltagirone, C. (2001) Parieto-frontal interactions in visual-object and visual-spatial working memory: Evidence from transcranial magnetic stimulation. Cerebral Cortex, 11, 606-618.
18. McCarthy, G., Puce, A., Constable, R. T., Krystal, J. H., Gore, J. C., & Goldman-Rakic, P. (1996) “Activation of human prefrontal cortex during spatial and nonspatial working memory tasks measured by functional MRI.” Cerebral Cortex, 6, pp.600-611.
19. V.Prabhakaran, K. Narayanan, Z. Zhao and J.D.E Gabrieli, (2000) “Integration of diverse information in working memory within the frontal lobe.” Nature Neuroscience , 3, pp.85-90.

Retrieval of MR Kidney Images by Incorporating Shape Information in Histogram of Low Level Features

D. Mahapatra[1], S. Roy[2] and Y. Sun[1]

[1]Department of Electrical and Computer Engineering, National University of Singapore, Singapore
[2]Institute for Infocomm Research, Singapore

Abstract — **Retrieval of medical images from databases is important in the wake of increasing medical image data. Intensity histograms and its variants have proved to be useful features for image retrieval. But in the presence of intensity change due to contrast enhancement in perfusion images, histogram based techniques are not very useful. We propose to use shape context information for retrieval of dynamic perfusion images. Our tests on renal perfusion MR images show that shape context information is a useful approach for the retrieval of such images.**

Keywords — **retrieval, perfusion MR, histogram, shape context, kidney**

I. Introduction

Recent advances in imaging technology have increased the amount of medical data generated and subsequently, automated search and retrieval of images from medical databases has become a very important issue. Traditional medical images are indexed and retrieved using texts only. However the semantic gaps in describing complicated image contents verbally limit the ability of such an approach and affect the performance of content-based image retrieval (CBIR) systems.

Low-level features from the image are used to represent the information content in an image. Although not powerful enough, low-level features are the only information available that can be automatically extracted from images. Low-level features that have been used for image retrieval include color moments [1], color histogram, color correlogram [2] and Gabor wavelet texture feature [3]. These features can be roughly classified into three categories: color, texture or shape. Except for color moment, other features have high dimensionality or the feature extraction algorithm is difficult to implement.

Different features capture different aspects of the semantic contents of images; therefore their combination could be expected to give better results, e.g. color and texture information have been characterized in one feature representation. Yu *et al.* in [4] proposed the color texture moment feature (CTM) to represent image content and Li in [5] derived texture moments from CTM.

Intensity histograms have also been widely used for retrieval applications. However they give a global representation of intensity distributions in an image and incorporating spatial context into the histogram provides a more powerful descriptor [6]. However the spatial histogram cannot capture the similarity information when dealing with contrast enhanced images where there are significant intensity changes.

In dynamic perfusion MRI, the patient body is scanned at regular intervals immediately after the injection of a contrast agent. As the contrast agent flows into the veins and subsequently the kidneys, there is an increase in intensity of the corresponding regions. In such a situation using histograms for image matching tasks does not prove to be very useful. Referring to Fig.1 we see that the histogram for the two images is vastly different. For the post-contrast stage image, where the intensity is higher, the pixels are grouped into higher bins compared to the pre-contrast image. We propose the use of shape context information for retrieval of dynamic renal MR images. Shape context information was proposed by Belongie et al. [7] for digit classification and trademark retrieval among other tasks. The shape context at a reference point captures the distribution of the remaining points relative to it, thus offering a globally discriminative characterization. Such a metric enables us to include shape information into a histogram formulation scheme. We test our proposed metric to retrieve images that best match a given query image

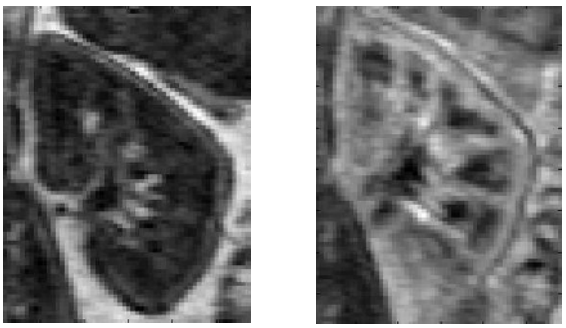
The rest of the paper is organized as follows. Section II discusses the proposed approach. Section III gives details of our experiments and the results are presented in Section IV. Finally we conclude with section V.

II. Our approach

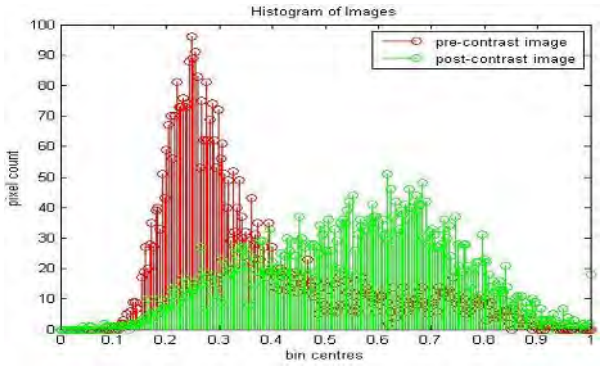
A. Shape Contexts

An object in an image is treated as set of points and the shape is captured by a subset of these points. Practically, a shape is represented by a discrete set of points sampled from the internal or external contours on the object and these can be obtained from the location of edge pixels as

Chwee Teck Lim, James C.H. Goh (Eds.): ICBME 2008, Proceedings 23, pp. 661–664, 2009
www.springerlink.com



(a) (b)



(c)

Fig. 1 Image Histogram: Pre- and post-contrast images with their respective intensity histograms.

found by an edge detector. They need not correspond to key-points like maxima of curvature or inflection points.

Let us consider two shapes P and Q. for each point p_i on the first shape the best matching point, q_j, has to be found on the second shape. This is akin to a correspondence problem and matching becomes easier by using a rich local descriptor. Descriptors that use information from a window of pixels reduce ambiguity in matching. The shape context acts as a rich local descriptor. A set of vectors originating from a sample point to all other points on the shape expresses the configuration of the entire shape relative to the reference point. As the dimension of the vector gets larger more information is captured and representation becomes more exact.

For a point p_i on the shape, a coarse histogram h_i of the *relative coordinates* of the remaining points is generated. This histogram is defined to be the shape context of p_i. The bins of the histogram are uniform in log-polar space, making the descriptor more sensitive to positions of nearby sample points than those to points that are further away. The cost of matching two points p_i and q_j is given by

$$C(p_i, q_j) = \frac{1}{2}\sum_{k=1}^{K}\frac{[h_i(k) - h_j(k)]^2}{h_i(k) + h_j(k)}, \quad (1)$$

where $h_i(k)$ *and* $h_j(k)$ denote the K-bin normalized histogram at p_i and q_j respectively. The cost can also include an additional term based on local appearance similarity at p_i and q_j.

The total cost of matching given by $\Sigma\, C(p_i,q_j)$ has to be minimized in order to get the optimal matching. This is done using a bipartite matching algorithm.

B. Using Shape Contexts for Image Retrieval

The shape context information serves as the feature using which a similarity score between images can be determined. The shape context of the target image is compared with that of the query images using a similarity metric that we describe later.

Using the shape context information we can also identify the most similar slice from the acquired 3D volumes. This is achieved by comparing the shape context measure for all slices in a particular 3D volume.

We also compare the performance of the shape context based method with that of a spatial context based histogram method. To incorporate spatial context into a histogram we make use of the algorithm in [6].

C. Similarity Measure

The measure of similarity between query and target images is defined in the following manner

$$D(p,q) = \sqrt{\sum_{\forall i}\left(p(i) - q(i)\right)^2}, \quad (2)$$

where p and q are the corresponding histograms.

Performance Evaluation: the error of a retrieval task is measured as the sum of actual distances of returns ranked higher than the relevant slice. The performance of retrieval is measured as the average error of all retrieval tasks.

III. Experiments

Our dataset comprised of 5 real patient datasets. For each patient, 41 volumes were acquired at different sampling instances and each volume consisted of 40 slices. The sampling instances corresponded to various stages of contrast enhancement. Regions of interest corresponding to the kidney were cropped from the full abdominal scan of the patients. Our experiments consisted of finding the most rele-

vant images as well as the most similar slice in the scanned volume.

Matching Image:. This task involved identifying the image which is most similar to a template image. To determine the shape context information of an image the locations of the boundary are detected using a canny edge detector to determine the distribution of the relative coordinates.

The shape context information is in the form of a $p \times b$ histogram where p is the number of edge points and b is the number of bins into which the coordinates relative to the current pixel are binned. Distribution of relative coordinates helps to capture shape information even in the face of distortions.

The cost of matching two points as given by Eqn. 1 returns a $p \times q$ matrix, where p and q are the number of points in each edge image. The i^{th} row of the matrix thus gives the matching cost of the i^{th} edge point with all the edge points of the second image. However, to evaluate the effectiveness of the shape context information we need to have a single value. We use Eqn. 3 to get the matching score for two images.

$$score = \sum_{i=1}^{p} \sum_{j=1}^{q} C\left(p_i, q_j\right) \Big/ pq, \qquad (3)$$

where $C(p_i,q_j)$ is obtained from Eqn. 1.

Retrieving Slice: In this set of experiments, we focus on identifying the slice in a 3D image volume that is most similar to a given target slice. Here again we used the score in Eqn. 3 to compare the shape context information between two images.

IV. Results

For the image matching task, we took corresponding slices of different acquired volumes and chose 2 of them as reference. The images were then compared using shape context information. For the image matching task, we had to determine the edge coordinates of the kidney. However for contrast enhanced images it is not an easy task to get an accurate shape contour. Due to the high intensity, the Canny edge detector identifies edges within the kidney cortex as well. To overcome this obstacle we applied connected component analysis to extract the kidney by neglecting the artifacts inside the cortex region. Fig. 2 illustrates the scenario. Although the edge image after pre-processing does not exactly resemble the edge image of pre-contrast images, it is good enough for accurate image matching and in this lies the strength of the shape context based approach. The accuracy of the retrieval task was *73* % using our approach and

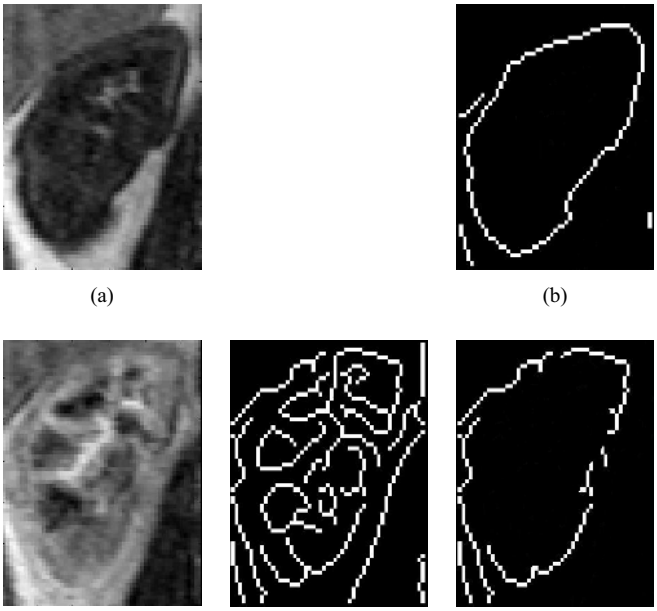


Fig. 2 Artifacts in perfusion images: (a)-(b) pre-contrast image and the corresponding edge map; (c) post-contrast image; (d)-(e) corresponding edge map before and after extraction of connected components.

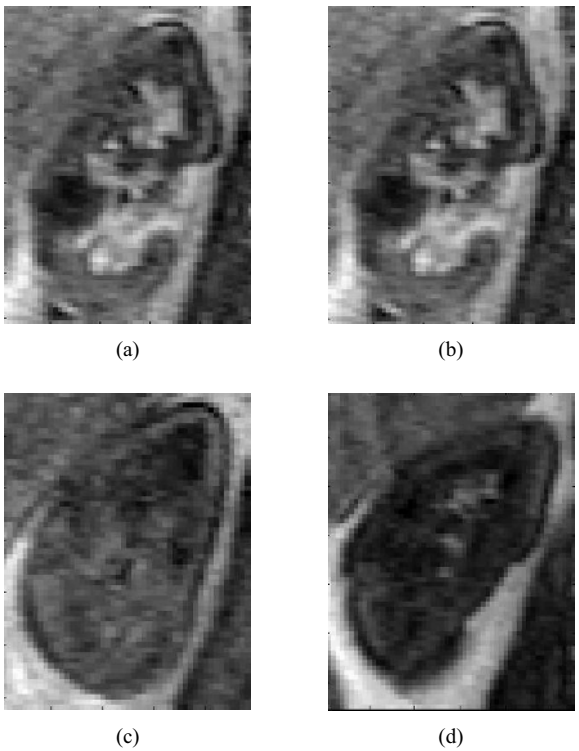
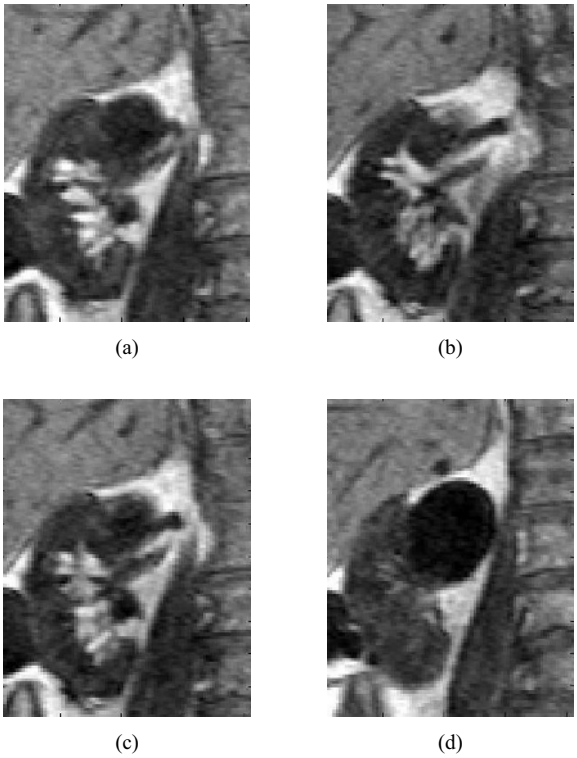


Fig. 3 Image Retrieval Results. (a) reference image; (b)-(d) matched images returned in decreasing order of similarity.



(a) (b)

(c) (d)

Fig. 4 Results for matching slices. (a) reference slice; (b)-(d) matched slices returned in decreasing order of similarity.

60 % using a histogram based approach and a typical case of matched images is shown in Fig. 3.

For the task involving matching slices within the image volume, slices of volumes from the post-contrast stage were subjected to connected component extraction. Fig. 4 shows typical examples of a reference slice and returned matches. The accuracy using shape context information was 85% compared to an accuracy of 61 % using intensity histograms. However it is important to note that the intensity histogram is not an appropriate approach to capture shape information.

V. Conclusion

We proposed the use of shape context information for retrieval of contrast enhanced perfusion images of the kidney. Shape context information helps in identifying the kidney due to change in shape and size of the kidney and also in the face of intensity change due to contrast enhancement, a scenario not addressed by histogram based approaches. The shape of the kidney was identified using connected components. Performance of our approach is comparable to other histogram based techniques for image retrieval. Using shape context information for retrieving appropriate slices shows good performance.

Acknowledgment

The authors would like to thank Dr. Vivian Lee of the New York University Langone Medical Center for providing us with the datasets. The work was supported by NUS grant R-263-000-470-112.

References

1. Stricker M, Orengo M (1995) Similarity of color images. SPIE Proc Vol 2420, Storage and Retrieval for Image and Video databases, San Jose, USA, 1995, pp 381-392.
2. Huang J, Kumar S R et al, (1997) Image inexing using color correlograms. Proc. CVPR 1997, pp 762-768
3. Manjunath B S, Ma W Y, (1996) Texture surfaces for browsing and retrieval of image data. IEEE Trans PAMI 18(8): 837-842
4. Yu M, Li M et al (2002) Color texture moments for content based image retrieval. IEEE Proc. Vol 3 International Conference on Image Processing, 2002, pp:929-932
5. Li M, (2007) Texture moment for content based image retrieval. IEEE Proc. International Conf. Multimedia and Expo, 2007, pp:508-511.
6. Rao A, Hrihari R K, Zhang Z, (1999) Spatial color histograms for content based image retrieval. IEEE Proc ICTAI, Chicago, USA, 1999, pp 183-186
7. Belongie S, Malik J, Puzicha J, (2002) Shape matching and object recognition using shape contexts. IEEE Trans PAMI 24(24) 509-522

Author: Dwarikanath Mahapatra
Institute: National University of Singapore
Street: Block E4, Level 5, Room 45, 4 Engineering drive 3
Country: Singapore
Email: dmahapatra@nus.edu.sg

Performance Comparison of Bone Segmentation on Dental CT Images

P. Yampri, S. Sotthivirat, D. Gansawat, K. Koonsanit, W. Narkbuakaew,
W. Areeprayolkij, W. Sinthupinyo

National Electronics and Computer Technology Center, Phahon Yothin Rd, Klong Luang, Pathumthani 12120, Thailand

Abstract — **Computed tomography (CT) images used in the dental application mainly consist of bone and soft tissue regions. Segmentation of bones from the soft tissues can help clinicians to assess the quality of the patient's jawbone more easily. Moreover, the identifiable bone region can help creating the better results of 3D surface/volume rendering. In the dental CT images, the bone regions are usually surrounded by other regions which are in a larger area and darker colors. The application of Local Entropy Equalization is usually suitable for the images with the mentioned characteristics. It has been reported that different thresholding techniques, namely Otsu and Kittler, are used to segment the bone regions. In this paper, we present the experimental studies for bone segmentation of CT images in the dental application using three different techniques based on i) Otsu's thresholding, ii) Kittler's thresholding, and iii) Local Entropy thresholding. The performances of these three different techniques on the bone segmentation and 3D rendering, which are applied on several CT datasets, are compared and presented. The experimental results show that segmentation of bones using the Local Entropy thresholding technique provides better quality than the Otsu's and Kittler's methods.**

Keywords — **bone segmentation, autometic thresholding**

I. Introduction

Segmentation is a process for dividing a digital image into multiple sets of pixels. It helps selecting the interested region such as a bone boundary in a medical image. In general, the dental CT images include bone and soft tissues. In the case analyses jawbone of patient. If patient has a metal material in his mouth. Such crown with amalgams, the intensity of the image around the location of these materials will be distributed. Thus, this effect is called the metal artifacts. The bone region is difficult to select when the metal artifacts are presented in the data. The result of the manual process may appear the value which is higher or lower than the bone region. Thus, the approximation process for fitting bone is necessary. The thresholding technique is appropriate for using because it is a simple to apply an approximate with volume of CT image data. This paper proposes the case study of an automatic thresholding technique for detecting true bone boundary. It consists of three techniques: Otsu thresholding[1], Kittler thresholding [2] and Local Entropy thresholding[3]. The thresholding technique include creates a histogram of CT images and calculates threshold value from weighting a histogram. However, these concepts are generally used in an automatic threshold technique. In this paper, we compared the performance on bone segmentation of these three thresholding techniques. The result is using the Local Entropy thresholding techniques provides the best results.

II. Segmentation

In CT images, soft tissues and bone regions can be identified through the so-called CT numbers which are in the Hounsfield units (HU). As show in Fig 1

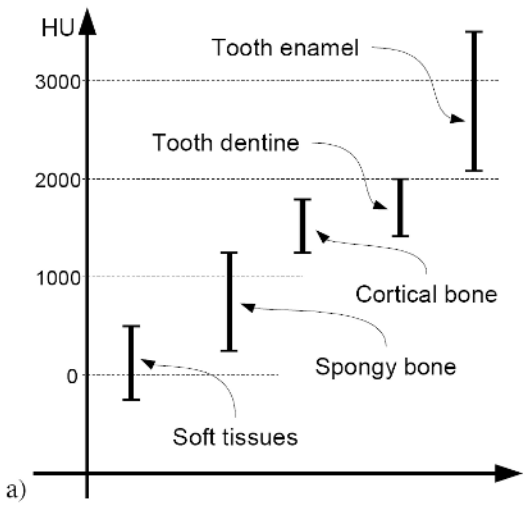


Fig. 1 Typical ranges of different tissues in Hounsfield units

In the case of dental applications we need to perform segmentation of teeth and jawbones. The cortical bone (compact) has the density in range of 1200 to 1800 HU, while the spongy bone the density in the range of 200 to 1200 HU. Teeth consist of two main tissues: enamel and dentine. Enamel is the hardest tissue in human body and has the density in the range of 2100 to 4000 HU. Dentin has the CT number similar to the cortical bone in the range of 1400

Chwee Teck Lim, James C.H. Goh (Eds.): ICBME 2008, Proceedings 23, pp. 665–668, 2009
www.springerlink.com

to 2000 HU. Human soft tissues usually have the density in the range of -200 to 400 HU. Since the CT number of soft tissues and the cortical bone are not overlapping, it is simple to separate them by thresholding or adaptive thresholding. However, spongy bone might be difficult to separate.

III. Threshold techniques

This topic represents the case study of the thresholding techniques for segmenting bone region in CT image. which consist of otsu's thresholding, kittler's thresholding and local entropy thresholding.

A. Otsu's thresholding

In this method, the weight sum between the background and foreground variance (σ_W^2) is computed as follows:

$$\sigma_W^2 = q_1(t)\sigma_1^2(t) + q_2(t)\sigma_2^2(t) \tag{1}$$

where $\sigma_1^2(t)$ is the background variance, which is computed from the value of gray level between at 1 and *t*. as follows:

$$\sigma_1^2(t) = \frac{\sum_{i=1}^{t} [i-\mu_1(t)]^2 P(i)}{q_1(t)} \tag{2}$$

a $\sigma_2^2(t)$ is the foreground variance, which is computed from the gray level between *t+1* and maximum gray level intensity (*l*). as follows:

$$\sigma_2^2(t) = \frac{\sum_{i=t+1}^{l} [i-\mu_2(t)]^2 P(i)}{q_2(t)} \tag{3}$$

where the weights

$$q_1(t) = \sum_{i=1}^{t} P(i) \quad \text{and} \quad q_2(t) = \sum_{i=t+1}^{l} P(i)$$

$$\mu_1(t) = \frac{\sum_{i=1}^{t} iP(i)}{q_1(t)} \quad \text{and} \quad \mu_2(t) = \frac{\sum_{i=t+1}^{l} iP(i)}{q_2(t)}$$

$P(i)$ is the probability of the intensities between i = 1,..*l* and *l* is the maximum gray value.

$$P(i) = \frac{number\{(r,c) \mid image(r,c) = i\}}{(R \times C)} \tag{4}$$

where r = the r[th] row , c = the c[th] column,
R and C values are the number of row and column

The optimal threshold value is selected by searching for the smallest weighted sum. The minimum value of variance must be computed from every intensity value to achieve the minimum value of the weighted sum. This provides the optimal threshold value.

B. Kittler's thresholding

This technique calculates the parameters similar to otsu's thresholding. However, the weighted sum of variance (*H*) is defined as follow:

$$H = \frac{1+log2\pi}{2} - q_1 log(q_1) - q_2 log(q_2) + \frac{1}{2}\left(q_1 log(\sigma_1^2) + q_2 log(\sigma_2^2)\right) \tag{5}$$

This technique finds the threshold value by searching for the minimum value of variance.

C. Local Entropy thresholding

This method represents on the Co-occurrence matrix. The co-occurrence matrix looks like a 2D histogram. This matrix can be created by the equation below.

$$t_{ij} = \sum_{m=1}^{M} \sum_{n=1}^{N} \delta_{mn} \tag{6}$$

where: t_{ij} is the $(i,j)^{th}$ element .
M and N are the number of rows and columns.

$$\delta_{mn} = \begin{cases} 1 \ if \begin{cases} f(m,n) = i \ and \ f(m+1,n) = j \ \ and/or \\ f(m,n) = i \ and \ f(m,n+1) = j \end{cases} \\ 0; \ otherwise \end{cases}$$

We transform an input image to a co-occurrence matrix, which is divided into four quadrants with a threshold value in Fig.2. There four quadrants are defined A, B, C and D. We can calculate variance of each quadrant from these equations.

$$\left.\begin{aligned} P_A^t &= \sum_{i=0}^{t}\sum_{j=0}^{t} p_{ij}, \quad P_B^t = \sum_{i=0}^{t}\sum_{j=t+1}^{L-1} p_{ij}, \\ P_C^t &= \sum_{i=t+1}^{L-1}\sum_{j=0}^{t} p_{ij}, \quad P_D^t = \sum_{i=t+1}^{L-1}\sum_{j=t+1}^{L-1} p_{ij} \end{aligned}\right\} \tag{7}$$

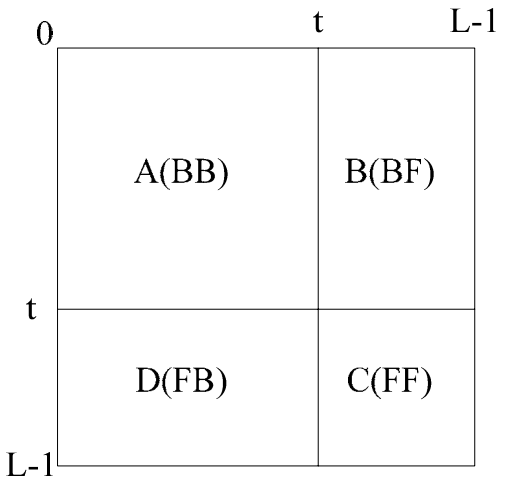


Fig. 2 Co-occurrence matrix

where p_{ij} the probability at element (*i,j*)

p^t_A, p^t_B, p^t_C and p^t_D the probability at quadrant.

$$p^t_{ij|A} = \frac{p_{ij}}{P^t_A},\ p^t_{ij|B} = \frac{p_{ij}}{P^t_B},\ p^t_{ij|C} = \frac{p_{ij}}{P^t_C},\ p^t_{ij|D} = \frac{p_{ij}}{P^t_D} \quad (8)$$

The pixels that have the gray value above the threshold are a foreground. Likewise, the pixels that have the gray value below the threshold are the background. Thus, quadrants A and C are the transition for the background and the foreground we can calculate the local entropy as follows:

$$H_{BB}(t) = -\sum_{i=0}^{t}\sum_{j=0}^{t} p^t_{ij|A} log p^t_{ij|A} \quad (9)$$

$$H_{FF}(t) = -\sum_{i=t+1}^{L-1}\sum_{j=t+1}^{L-1} p^t_{ij|C} log p^t_{ij|C} \quad (10)$$

where $H_{BB}(t)$ is the local entropy value of quadrant A and $H_{FF}(t)$ is the local entropy value of quadrants C. can be calculate total local entropy as follows:

$$H_{LE}(t) = H_{BB}(t) + H_{FF}(t) \quad (11)$$

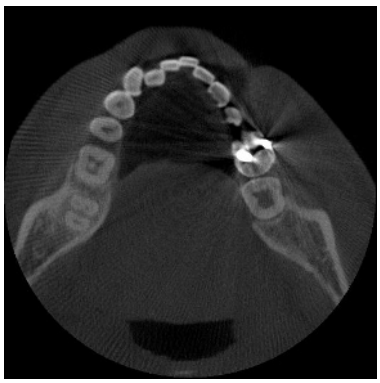
The optimal threshold value can be derived be searching for the minimum value of the total local entropy $(H_{LE}(t))$.

IV. Experiment result

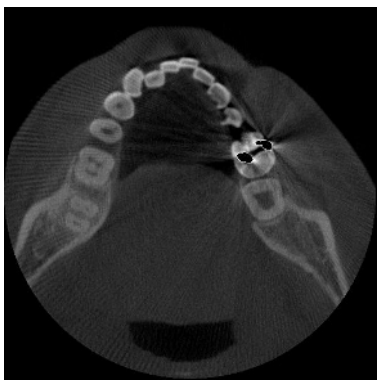
The experimental studies are divided into three parts.

A. Otsu's thresholding

With otsu's thresholding, the bone region cannot be segmented. Only the metal area can be segmented. Thus, automatic thresholding using otsu's thresholding is not suitable for segmentation in CT image.



a.) Original image

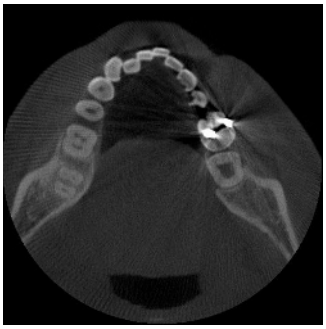


b.) Segment Image

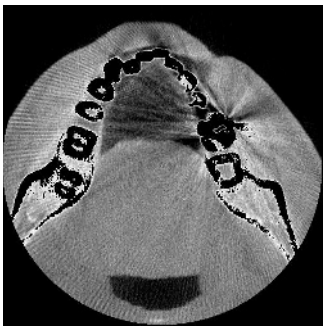
Fig. 3 result of otsu's thresholding

B. Kittler's thresholding

In the Kittler's thresholding technique, only some part of the bone region can be segmented as show in the black area of Fig.4. Both Otsu and kittler thresholding techniques are base on bi model histogram, which is not appropriate for CT images.

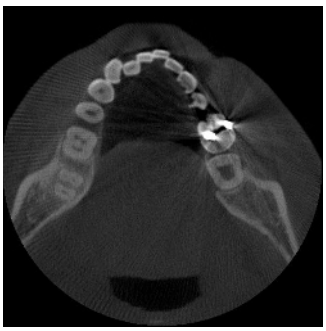


a.) Original image

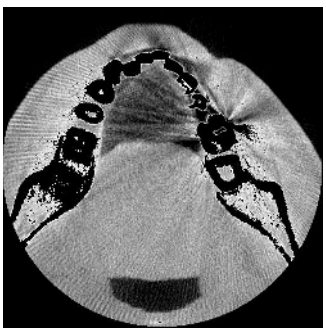


b.) Segment Image

Fig. 4 result of kittler threshold



a.) Original image



b.) Segment Image

Fig. 5 result of Local Entropy threshold

C. Local Entropy thresholding

Unlike the previous two techniques, that are based on bimodal histogram of the image. Local entropy thresholding uses the co-occurrence matrix to calculate the threshold value, it provides better segmentation. The results are show in fig.5.

Table 1 represents the Experimental result to finding threshold value form jawbone. Which it have metal for fit jawbone of each CT-scan machine.

Scan machine	local En-tropy(HU)	Kittler (HU)	Otsu (HU)
Hitachi	1166	1390	3079
ICAT	1359	1500	3095

V. Discussion and conclusion

In this study we have compared three different techniques for segmenting the bone region. Otsu and Kittler thresholding find the threshold values based on the bimodal histogram; however, it is not always true in CT images. The results show that Otsu's thresholding can only segment the metal area. Although the Kittler's thresholding provides better results the Otsu's thresholding, it can partly segment the bone region. With local entropy, the co-occurrence matrix computes the 2D histogram, which is better then 1D histogram as Otsu and kittler methods. The results show that this technique can provide better results than the other.

Acknowledgment

The authors would like to thank the Advanced Dental Technology Center (ADTEC), and the Faculty of Dentistry, Chulalongkorn University for providing CT data.

References

1. Otsu, N., (1979), "A Threshold Selection Method From Grey-Level Histograms", IEEE Transactions on Systems, Man, and Cybernetics, Vol. SMC-9,No.1, pp. 62-66.
2. Kittler, J. and J. Illingworth, (1986), "Minimum Error Thresholding", Pattern Recognition, Vol. 19, No.1, pp.41-47.
3. N. R. Pal and S. K. Pal, "Entropic thresholding," Signal processing, vol. 16, pp. 97-108, 1989.

Multi Scale Assessment of Bone Architecture and Quality from CT Images

T. Kalpalatha Reddy[1], Dr. N. Kumaravel[2]

[1]SKR Engineering College/ ECE, Anna University, Chennai, India
[2]College of Engineering,Guindy / ECE, Anna University, Chennai, India.

Abstract — **The purpose of this study was to develop a methodology for Quantitatively assessing bone Quality and anisotropy based one Texture analysis using curve lets. The curve let approach has the capability to simultaneously examine the images at low and high resolutions to gain information on both global and detailed local features of the bone image. It also allowed us to examine the texture energy at 13 orientations to gain insight about the details of anisotropy. Both histomorphometry and the texture analysis detected significant differences in the trabecular bone of the mandible between the control and abnormal groups. However the texture energy value at all orientations were significantly correlated. Texture analysis was able to assess anisotropy, which could not be extracted from histromorphometric parameters. we conclude that texture analysis is an effective tool for assessing 2-D Jaw Bone images that yields information regarding the Quantity of Bone as well as the orientation of the trabecular structure that can augment our ability to discriminate between normal and pathological bone tissue. The approach consists of two steps: automatic extraction of the most discriminative texture features from regions of interest and compare the features to discriminate between normal and pathological bone tissue. The discriminate power of several curvelet based texture descriptors are investigated.**

Keywords — **Multi – resolution analysis, Texture features curve lets: Computed Tomography**

I. Introduction

Quantitative measures of bone strength, which is dependent on mass, material and architecture, are necessary to investigate factors affecting bone strength.Histomorphometric analysis of trabecular bone has been used to quantity bone mass as well as the rate of bone formation resorption [8]. However, these measures were only designed to assess surface cellular activity, not the quantification of trabecular and cortical bone architecture. Multiple approaches have been utilized in characterizing the structure of trabecular bone from two dimensional images, particularly in describing orientation disparity or anisotropy. Mean intercept length was defined as the ratio between the total line length (in a linear grid) divided by the number of intersections, which when calculated as a function of direction gave information about the anisotropy of a bone sample [8] The MIL method however failed to recognize a visible anisotropy in a simulated images whose pattern had an isotropic interface between the bone and marrow Phases. Volume based methods including the volume orientation (vo) method and star volume distribution (svd) provided measure of trabecular bone around a point in the trabecula and were able to recognize anisotropy when MIL based methods failed, but they only recognized the anisotropy when the correct phase was chosen to avoid the isotropic interface [9].

Our aim is to determine whether a method can be found to characterize and classify the normal and abnormal bone structures and use this to monitor the progression of changes in the bone. The assessment of bone structure / bone quality in live patients is very difficult. Modern clinical methods of assessing bone quality such as QCT, single photon absortionometry, Dual energy radiography depend largely on measurement of bone mineral density. However it has long been acknowledged that the role of bone structure is important in the determination of bone quality and bone mineral density [8].While clinical methods such as the ultrasonic assessment of bone are believed to contain structural information [10], it is not yet known that what contribution this makes to the measured parameters. Other methods used to o obtain structural information are bone biopsies [8],CT imaging [9] [though the high resolutions is necessary to visualize trabecular bone structure require high dosage levels of X – rays], and magnetic resonance imaging [11].MRI is a promising technique but its expense means that any attempt to propose it as a routine method of assessing bone disease must justify its ability over other methods.

Further image analysis has been applied to most of these to extract quantitative information, including histomorphometry[8] and fractal geometry[9],although it has been suggested that the latter method is prone to artifacts. This was a preliminary study designed to test the proposed methods and evaluate their effectiveness in discriminating between different types of bone pathologies.

Chwee Teck Lim, James C.H. Goh (Eds.): ICBME 2008, Proceedings 23, pp. 669–672, 2009
www.springerlink.com

The differences in structure between normal and abnormal bone are often apparent to the unaided eye, but extracting the information contained in images of bone & Quantifying this for classification purpose is not trivial. This study set out to investigate whether changes in bone structure due to disease can be identified by mathematical methods.

In the last decade wavelet theory has been widely used for Texture classification process [2]. A comparative study by Randon & Husoy shows that various filtering approaches yield different results for different images [9] Wavelets are good at catching Zero dimensional or point singularities but two dimensional piecewise smooth signals resembling images have one – dimensional singularities [2]. Multiresolution analysis allows for the preservation of an image according to certain levels of resolution or blurring. Broadly speaking, multiresolution analysis allows for the zooming in and out in the underlying texture structure.

By decomposing the image into a series of high pass and low pass bands, the wavelet transform extracts directional details that capture horizontal, vertical and diagonal activity. However, these three linear directions are limitating and might not capture enough directional information in noisy images, such as medical CT scans which do not have strong horizontal vertical and diagonal elements. To overcome the weakness of wavelets in higher dimensions, Candes & Donoho pioneered a new system of representations named curvelet transform which is designed to handle curve discontinuities well. Here the idea is to partitioning the curves into collections of ridge fragments and then handle each fragment using ridge let transform .Curve lets are proven to be particularly effective at detecting image activity along curves instead of radial directions. Instead of capturing structure along radial lines, the curvelet transform captures this structural activity along radial 'wedges' in the frequency domain.

In this paper the curvelet transform is applied on a set of CT bone images and curvelet statistical features such as mean, variance, energy, entropy and curvelet co-occurrence features are extracted from each of the curvelet sub bands.

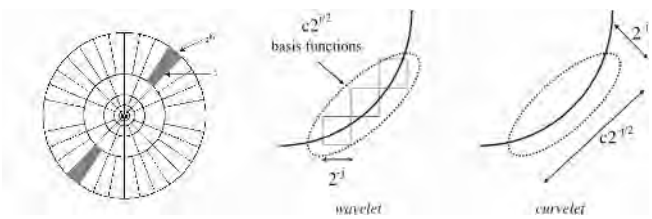


Fig. 1 Curvelet transform

The structural activity extracted from the curvelet transform of the image can be analyzed statistically to generate texture features used in the classifier to create classification rules. Common statistical measures used in texture classification in image processing are mean, standard deviation, energy, entropy, contrast, homogeneity, variance, correlation, max probability ,cluster tendency, cluster shade etc. However since these statistics are being applied to the curvelet transform, which extracts contrast pixel pairs in radial 'wedges', not all of these statistical measures are appropriate. This article introduces the use of several combinations of those descriptors and presents a comprehensive analysis determining the optimal texture descriptors for the curvelet transform as applied to CT scans.

II. Methodology

The texture classification algorithm proposed in this article consists of four main steps: Segmentation of regions of interest, application of the discrete curvelet transform, extraction of texture features and creation of a classifier.

Our tests were conducted on 3D dental CT data extracted from 30 patients consist of 190 2D DICOM consecutive slices for each patient and each of size 512 x 512 having 16-bit grey level resolution. Curvelets, like wavelets are extremely sensitive to contrast in the grey level intensity. Every slice is preprocessed by Gaussian filter and histogram equalization was done for contrast enhancement. The original dental images contain the bone and the background. In order to effectively use curvelet based texture descriptors, it was necessary to eliminate all back ground pixels to avoid mistaking the edge between the artificial background and the tissue as a texture feature. Each slice was therefore further cropped and only square 32 x 32 sub images fully contained in the interior of the anterior & posterior bone region were generated.

The texture features used in the algorithm are derived from the DCT, introduced by Candes & Donoho in [4] .The transform consists of four steps, application of a 2-dimensional Fast Fourier transform of the image, formation of a product of scale and angle windows, wrapping this product around the origin, and application of a 2 - dimensional inverse Fast Fourier transform. The approximate scales and orientations are supported by a generic 'wedge'.

The discrete curvelet transform can be calculated to various resolution or scales and angles. Two parameters are involved in the digital implementation of the curvelet transform: number of resolutions and number of angles at the coarsest level. For our images of 32 x 32, maximum resolution extraction was three levels of resolutions and 16 angles were found to be ideal.

Several features were calculated on the curvelet Coefficients. The most common statistics calculated on wavelet are mean and standard deviation obtained from the histogram of detail matrices. One of the goals of this research was to identify the most effective texture descriptors for medical images. Features such as mean and standard deviation are calculated from histogram of each of these curvelet sub-bands and are stored in the database. In addition to this co-occurrence matrices were also calculated at each detail and level of resolution. Curvelet transform is able to capture multidirectional features, as apposed to the wavelet transform which focuses mainly on horizontal, vertical and diagonal features which are not dominant in medical CT scan images

A co-occurrence matrix captures the spatial dependence of contrast values depending on different directions and distances specified. From the co-occurrence matrix the features such as contrast, cluster shade, cluster-tendency, homogeneity, max-probability are calculated and are stored in the feature data base. For computational efficiency the detail sub bands were binned for the co-occurrence matrix to reduce the size of the matrix

Comparison between the bone texture variables in disease affected and control patients were performed by using the non-parametric regression analysis due to the low number of patients. A value of $r<0.03$ was considered as statistically significant. The results were expressed as mean ± S.D

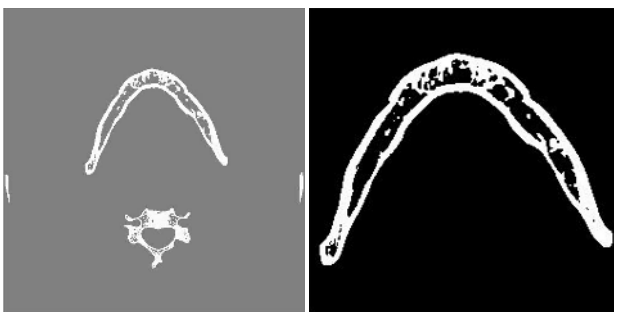


Fig. 2 The Original Jaw bone sample and extracted bone image

Table 1. Statistical Analysis of Significant Parameters

Parameter	Anterior Mandible		Posterior Mandible	
	Normal	Abnormal	Normal	Abnormal
Energy	0.2(0.03)	0.35(0.05)	0.21(0.04)	0.23(0.07)
Entropy	1.83(0.1)	1.31(0.17)	1.74(0.12)	1.71(0.23)
Variance	3.7(1.1)	1.96(0.98)	3.6(1.19)	2.9(0.74)
Mean	3.46(0.39)	2.0(0.34)	3.26(0.398)	2.9(0.56)
Kurtosis	3.78(1.11)	8.49(2.81)	3.94(1.16)	5.04(2.54)
Contrast	14.0(6.15)	4.5(2.8)	11.56(2.95)	10.7(3.3)
Homogeneity	4908(2229)	2302(1215)	2526(2987)	1113(1075)
Cluster Tendency	191.7(122.1)	147.4(60.3)	120.3(57.38)	74.85(56.6)
Maximum propobility	0.048(0.008)	0.426(0.024)	0.09(0.009)	0.142(0.04)

III. Discussion

We developed original methods for the analysis and characterization of bone texture based on numerical processing of Dental CT images. The results of this study indicate that curvelet – based texture analysis is an effective tool that could quantify bone architecture as well as bone density in two dimensional slices. This study set out to investigate whether changes in bone structure due to disease can be identified by mathematical methods. The texture analysis not only detected deficits in the amount of bone following a disuse protocol but the orientations in which the deficit occurred. The most promising structure parameters for CT images are contrast, maximum probability, homogeneity, cluster tendency, energy and variance. The discriminating powers of several resolution levels as well as various feature reduction techniques were analyzed.

A comprehensive analysis was carried out to determine the optional texture descriptors for the curvelet Transform as applied to CT scans. The multi directional features in curve lets prove to be very effective in the texture classification of the more organic textures in medical images. The results indicate that using curvelet based texture descriptors significantly improves the classification of normal and abnormal bone obtained from different patients.

REFERENCES

1. Haralick R.M., Shanmugam K. Dinstein I., Texture features for image classification, IEEE Transactions on System Man Cybernat, Vol, 8, No. 6, 1973, pp. 610-621.
2. Arivazhagan. S and Ganesan. L., Texture classification using wavelet transform, Pattern recognition Letters, 2003, pp. 1513-1521.
3. E.J. Candes L. Demanet D.L Donoho L. Ying " Fast Discrete Transforms" Technical Report, Cal Tech, 2005.
4. L.Ying "CurvelLab 2.0" California Institute of Technology, 2005.
5. Candes, E. and Donoho, D. (1999) Curvelets. Manuscript
6. Candes, E, and Dohono D. (1990) Curvelets a surprisingly effective nonadaptive representation for objects with edges in Curves and Surfaces IV ed. P.J Laurent.
7. Candes E. and Donoho, D. (1999) Curvelet and Linear Inverse Problems mauscript.
8. Yongqing Xiang, Vanessa R. Yingling Comparative assessment of bone mass and structure using texture-based and histomorphometric analysis, Bone 40,2007, pp. 544-552.
9. Chappard D.Retailleau-Gaborit N.Legrand E.Basle MF, Audran M. Comparison insight bone measurement by histomorphometry and microCT.J Bone Miner Res 2005;20:1177-84.
10. Chen J.Zheng B, Chang Y-H, Shaw CC. Towers JD, Gur D. Fractal analysis of trabecular patterns in projection radiographs: an assessment, Invest Radiol 1994;29:624-9.
11. Doughetry G.A Comparison of the texture of computed tomography and projection radiography images of vertebral trabecular bone using fractal signature and lacunarity Med Eng Phys 2001;23:313-21.
12. Lucia Dettori, Lindsay Semlar. A comparison of wavelet, ridgelet and curvelet-based texture classification algorithms in computed tomography, Computer in Biology and Medicine 37 ,2007, 486-498).

An Evolutionary Heuristic Approach for Functional Modules Identification from Composite Biological Data

I.A. Maraziotis, A. Dragomir and A. Bezerianos

Department of Medical Physics, Medical School, University of Patras, 26500 Rio, Greece

Abstract — **Modular structures are key features of the complex biological networks which control the functioning and dynamics of the living cell. In order to unravel this intricate modularity we propose an algorithm having evolutionary features that unveils and optimizes sub-networks within a weighted graph of protein interactions. The graph is enriched by integrating information from gene expression profiles. Functional modules are retrieved by expanding a kernel protein set that originates from 'seed' proteins and validated through biological and topological criteria. The modules obtained are further refined using a framework based on binary particle swarm optimization.**

Keywords — **protein-protein interaction, functional modules, protein interaction network, data integration, particle swarm optimization.**

I. Introduction

Functional modules within protein interaction networks are characterized by the defining property that their members interact to achieve a common biological process, while from the topology point of view, they share more interactions among themselves than with members of other modules [1-2]. The determination of small-scale functional modules, such as protein complexes from large-scale interaction networks is therefore crucial in understanding the relation between the function and organization of a network. With experimental data probing protein interactions available from yeast two hybrid experiments or via immunoprecipitation [3-4], and protein complexes identified from mass spectrometry [5], computational methods are strongly required to fill in the knowledge gap.

Towards this goal, several algorithms ranging from hierarchical clustering [6] to methods considering local topology-based concepts [7] and graph alignment for determining probabilistic motifs [8] have recently been applied for detecting modules in protein interaction networks. These approaches represent the protein network as an unweighted graph, where nodes correspond to proteins and edges to interactions among them. Algorithms based solely on topological aspects manage to capture several features of complex networks. Nevertheless they might prove insufficient when applied at protein interaction networks that include special characteristics like inter-module crosstalk. Additionally, since protein-protein interaction data (PPI) is error-prone and therefore the models derived might be unconfident and misleading, additional measures need to be taken [9].

Various methods have been applied to overcome this. Pereira et al. [10] weighted an interaction based on the number of experiments that support it. Others weighted the distance between two proteins with the minimum shortest path between them [6],[11]. Even though these approaches assign some kind of confidence score to a certain interaction, still they fail to allocate a possible functional association in a pair of proteins. A straightforward solution was to enrich the PPI interactions with information from the corresponding protein-producing genes. The underlying concept is that genes with similar expression profiles are under the same transcriptional control and therefore functionally associated [12]. Despite the inherent noise embedded in expression data, it provides significant information about genes under more perturbations in comparison to PPI data [13]. However, few studies have so far considered gene expression data for weighting the protein interactions graph [14].

Our study introduces a new method for integrating gene expression data and PPI data in order to determine functional modules. Specifically, given a graph describing a set of experimentally determined protein interactions, we assign a weight to each one of these interactions. This weight originates from clustering the gene expression profiles of the corresponding proteins. Subsequently we present a new algorithm for the determination of functional modules within the original PPI graph starting from a kernel protein group that originates from a 'seed' protein. In the final stage, the candidate functional modules are refined within a framework based on Discrete Particle Swarm Optimization, which selects the optimal modules structure by minimizing a fitness function based on the connectivity degree of graph nodes and the weighted density of the graph.

II. Methods

In this section we will describe the procedure we follow to add weights to the interactions of the protein graph as well as the proposed algorithmic approach we have applied to extract functional modules from a given 'seed' protein.

Chwee Teck Lim, James C.H. Goh (Eds.): ICBME 2008, Proceedings 23, pp. 673–677, 2009
www.springerlink.com

A. Assigning weights to Interactions

The weight is based on the GO similarity of the neighbours of proteins sharing the interaction at translational (protein) level and of the gene neighbours (in terms of similar expression profiles) of the corresponding genes at (transcriptional) gene level.

Each one of the proteins p_i and p_j that form a protein interaction u_{ij} is connected to another number of proteins (nodes of the protein graph) called neighbours of the proteins, symbolised as N_i and N_j respectively. Given the fact that each p_i and p_j are neighbours (since they share an interaction) they could have some other common nodes among N_i and N_j; we will symbolize the set of common neighbours as C_{ij} while the sets of the non-common neighbours will be denoted as D_i and D_j respectively. Therefore for the neighbours of the 2 proteins we have:

$$\left|\mathrm{D_i}\right|+\left|\mathrm{D_j}\right|+\left|C_{\mathrm{ij}}\right|=\left|N_{\mathrm{i}}\cup N_{\mathrm{j}}\right| \tag{1}$$

Of course the set C_{ij} could be empty and each one of the proteins forming the interaction is part of the neighborhood set of the other protein. Next step is to check common GO functionality concerning the neighbors of the two proteins based on the sets D_i and D_j (we do not check for functionality on N_{ij} since they are the same proteins for each one the interacting proteins). Specifically, we are considering the set with the minimum number of pairs like:

$$T_{ij}=\min\left(D_i,D_j\right) \tag{2}$$

We check each one of the members in T_{ij} against all of the members in the other set (e.g. that is D_i or D_j, pending on which of the two has the largest number of members) which we will call maximal set (MS), for GO similarity. When we are referring to GO similarity, we mean that the 2 genes having as products the corresponding proteins, share a common GO term. Every time we find a member in T_{ij} having a similar term in MS then we insert this member in the set of similar functionality members named S_{ij}.

The reason for considering the neighborhood set with the minimum number of neighbors instead of the maximum (2) is that there are many proteins that have a very large number of neighbors (these proteins are also known as hubs proteins). The most important reason for this is that a hub protein is a protein involved in many different functions within the cell. Therefore, if we consider the neighbors of such a protein to be compared against some other non-hub protein, then the weight would be degenerated losing information while it shouldn't, since we are interested in the relation between two specific proteins. In other words we are not interested if a specific gene/protein is involved in a large number of cell functions but if a protein is working together even in a fraction of the functions that its hub protein is involved.

Finally the weight for the specific interaction between proteins p_i and p_j is given by:

$$\beta_{ij}^{PPI}=\frac{\left|C_{ij}\right|+\left|S_{ij}\right|}{\left|C_{ij}\right|+\left|T_{ij}\right|} \tag{3}$$

This is the weight of the interaction resulting from the protein level. In an exact similar manner we establish the weight of the gene level. The neighbors of the corresponding gene whose protein product we study each time is determined by a constant number of genes that have the highest degree of similarity with the one under study, concerning their gene expression profiles. As we can derive from (3) the range of the two weights is normalized so as to range from zero to one, namely:

$$0\le\beta_{ij}^{PPI},\beta_{ij}^{GE}\le 1 \tag{4}$$

We now integrate the two weight types to a single weight as:

$$\mathrm{B}_{ij}=n\cdot\beta_{ij}^{PPI}+\left(1-n\right)\cdot\beta_{ij}^{GE} \tag{5}$$

Where n, is a constant ranging from 0 to 1 and determines the importance we impose on the PPI weight, while β_{ij}^{GE} corresponds to gene expression neighbors of the same interaction. In this study we have set the value of n equal to 0.6. The integrated weight B_{ij}, also ranges between 0 and 1 since both of the weights in the right hand side of (5) also have the same range.

B. DMSP

In a recent study we introduced a new method (DMSP – detect modules from seed proteins) for integrating gene expression data and protein-protein interactions in order to determine functional modules [15]. The algorithm operates in two phases as follows: firstly it accepts a 'seed' protein and selects a subset of its most promising neighbors, subsequently expanding this initial kernel to accept more proteins. This expansion is based on certain assumptions, concerning the number of neighbors for the specific protein as well as the weights of these connections.

In the first stage of the algorithm only a certain number of the neighbors of the 'seed' protein are selected. These adjacent nodes are sorted in descending degree of significance and this subset of nodes – proteins is named kernel.

The two criteria (commonly used in graph theory) by which the original kernel is selected are the density of the kernel and the weighted internal and external degrees of it. The objective for selecting the kernel of the seed node is two-fold. Firstly we check that the number of edges of a kernel node within the rest of the kernel is larger or at least equal to the number of the edges that a node has outside the group. At the same time and after we have confirmed that a selected node fulfils the first condition, we request that the same node has smaller weighted internal degree than its corresponding weighted external degree. Nodes that fail to pass the above criteria are discarded, while those that do, are sorted based on the level that each one of them manages to do so.

The second stage of the algorithm receives as input the selected kernel of the 'seed' protein and iteratively adds adjacent nodes based again on two criteria. The first criterion the algorithm checks is the same as the first one of the initial stage of the algorithm. After this criterion has been checked then we select a node to be added to the neighborhood, if it satisfies the condition of having a smaller or equal weight than the weighed internal degree of the kernel node.

C. Evolutionary DMSP

The final step of the algorithm we are proposing is the optimization of the extracted functional modules. In order to accomplish this, we have used a binary discrete version the algorithm particle swarm optimization (PSO). PSO is an algorithm that simulates the social behaviour of organisms, such as birds in a flock [16]. This behaviour can be described as an automatically and iteratively updated system. In PSO, each single candidate solution can be considered as a particle in the search space. Each particle has a position in the search space (which is a possible solution to a given problem) and makes use of its own memory and knowledge gained by the swarm as a whole to find the best solution. All of the particles have fitness values, which are evaluated by a fitness function to be optimized. During movement, each particle adjusts its position by changing its velocity according to its own experience and according to the experience of a neighbouring particle, thus making use of the best position encountered by itself and its neighbour. While there are various different neighbouring schemes for different problems, in this study each one of the particles follows the best position acquired by the flock. Particles move through the problem space by following a current of optimum particles. The process is then iterated a fixed number of times or until a predetermined minimum error is achieved [16].

The procedure of integrating the binary version of PSO (BPSO) and DMSP is the following: initially, we create a predetermined number of particles. The position of each particle is represented by: $X_i = \left(X_{i1}, X_{i2}, \ldots, X_{iN}\right)$ where N is the number of proteins in the module, extracted by DMSP in the 1st stage. Therefore the module is represented by the various particles as a binary string randomly generated; the bit value *{0}* and *{1}* represent a non-selected and selected node/protein, respectively.

The velocity for each one of the particle is given by:

$$v_{ij}\left(t+1\right) = W_I \cdot v_{ij}\left(t\right) + c_1 \cdot \left(B_{ij}^{i} - x_i\left(t\right)\right) + c_2 \cdot \left(B_G^{ij} - x_i\left(t\right)\right) \quad (6)$$

where W_I is known as inertia weight, and c_1, c_2 are called learning or acceleration factors. All of these variables are randomly selected parameters of BPSO ranging between 0 and 1. B^i_{ij} is the best position of the i-th particle and B_G is the best position acquired by the whole swarm.

In every iteration of the algorithm the position of each particle (i.e. the newly formed module based on the one extracted by DMSP) is changed towards an optimum solution which will represent the optimized functional module. In other words the algorithm initiates with a module having an initial number M of proteins and searches for the best subset of these proteins in terms of topological coherency among its members. The fitness function we use for the BPSO is the following:

$$F\left(X_i\right) = D_w\left(G\right) - \frac{1}{N}\sum_{i=1}^{N}\theta\left(G, u_i\right) \quad (7)$$

The fitness function (FF) is built so as to improve, after the end of BPSO, the extracted by DSMP functional module based on topological characteristics of the module within the protein graph. Specifically the FF uses the density $D_w(G)$ of a graph G(V, E), which is generally measured by the proportion of the number of edges in the graph to the number of all possible edges, which is equal to |V|(|V|-1) for an undirected graph. Due to the fact that we work on a weighted graph we are using weighted density of a graph or sub-graph $D_w(G)$, which is the sum of the weights of actual edges over the edges among all nodes in G:

The degree $\theta(G, u_i)$ of a node u_i that is member of a subgraph G of a graph Γ is given as the number of edges of a specific node with the rest of the members of the subgraph, over the total number of edges of the specific node to all other nodes of the graph Γ.

III. Results

Based on MIPS database (http://mips.gsf.de/proj/ppi/) we have created a protein graph of known interactions for yeast. Specifically the protein graph consisted of 4176 proteins and was composed of several smaller isolated subgraphs and nodes (137) consisting of 1 to 5 proteins, and one main sub-graph consisting of 3964 proteins and 11200 interactions among them. For weighting the PPI graph we have used gene expression cell cycle data (http://cellcycle-www.stanford.edu). On the large component we have applied the evolutionary DSMP algorithm.

Table 1 presents some (due to space limitations) of the obtained results. The first column corresponds to the protein given as input 'seed' protein to the algorithm. The second column indicates the protein complex that the algorithm managed to detect, on the third column we provide the number of members detected from the corresponding complex and the true number of members of the complex, in the parentheses there is the number of members of the extracted functional module. Finally the last column gives the p-value which is a commonly used metric for validating results and represents the probability of observing the co-occurence of certain proteins in a protein complex and a detected functional module by chance, based on binomial distribution. The smaller this value is the more remote is the probability of having detected a specific protein complex by chance.

Describing briefly one of the entries in Table 1, we can comment that by entering 'APC11' as a seed protein to the algorithm we have obtained a module of 14 proteins corresponding to the Anaphase promoting complex (APC) which is composed of 11 members. The p-value (<1e-14), signifies that the proposed algorithm (based on the weighted graph we created) managed to adequately detect the protein complex whose member is the provided 'seed' protein.

IV. Conclusions

The technology advances of the last decade triggered an exponential growth in the amount of molecular biology data and created a paradigm shift, from a reductionist view to a systems-oriented one. Therefore the frontier of research moved towards integrated approaches comprising computational analysis and mining large sets of different data types.

The concept of data integration has already been examined by works like [9], which validated the view that protein-protein interaction data are flooded with false interactions and therefore additional sources of data are to be considered in order to provide a more complete and valid models of interaction networks.

In the current study we consider an algorithm that identifies functional modules from weighted graphs derived from PPI by expanding a kernel protein set which originates from 'seed' proteins used as starting point. The functional modules that are obtained are further optimized using an approach based on a particle swarm optimization method. We prove based on data of *Saccharomyces cerevisiae* that our method provides modules with functional and topological consistency.

Table 1 Results obtained using the evolutionary DMSP algorithm

Seed	Complex	Members	p-value
TAF5	SAGA	14/16 (22)	<1e-14
APC11	APC	11/11 (14)	<1e-14
SEC27	COPI	7/8 (10)	<1e-14
ERV46	[550.3.56]	9/10 (11)	<1e-14
SPT7	ADA	6/6(9)	<1e-14
CDC39	NOT	4/5(6)	9.466e-13
RPB11	RNA polymerase II	13/13 (17)	<1e-14
CCT4	TCP RING Complex	8/8(11)	<1e-14

Acknowledgment

This research project (PENED) is co-financed by E.U.-European Social Fund (80%) and the Greek Ministry of Development-GSRT (20%).

References

[1] Hartwell LH, Hopfield JJ, Leibler S and Murray AW (1999). From molecular to modular cell biology. Nature 402: C47–C52

[2] Bork P, Jensen LJ, von Mering C *et al* (2004). Protein interaction networks from yeast to human. Current Opinion Struct. Biol. 14: 292-299

[3] Chien CT, Bartel PL, Sternglanz R and Fields S (1991). The two-hybrid system: A method to identify and clone genes for proteins that interact with a protein of interest. Proc. Natl. Acad. Sci. USA. 88: 9578-9582

[4] Lee TI, Rinaldi NJ, Robert F *et al.* (2002).Transcriptional regulatory networks in *Saccharomyces cerevisiae* Science 298(5594): 799–804

[5] Gavin AC et al (2002). Functional organization of the yeast proteome by systematic analysis of protein complexes. Nature. 415: 141-147

[6] Rives AW and Galitski T (2003). Modular organization of cellular networks. Proc. Natl. Acad. Sci. USA 100: 1128-1133

[7] Radicchi F, Castellano C, Cecconi F *et al.* (2004) Defining and identifying communities in networks. Proc Natl Acad Sci USA 101:2658-2663

[8] Berg J, Lassig M. (2004) Local graph alignment and motif search in biological networks. Proc Natl Acad Sci USA 101:14689-14694

[9] Sprinzak E, Sattath S, Margalit H. (2003) How Reliable are Experimental Protein-Protein Interaction Data?, Journal of Molecular Biology 327, pp. 919-923

[10] Pereira-Leal JB, Enright AJ, Ouzounis CA (2004) Detection of functional modules from protein interaction networks. Proteins 54:49-57
[11] Arnau V, Mars S, Marin I (2005) Iterative cluster analysis of protein interaction data. Bioinformatics 21:364-378
[12] Eisen MB, Spellman PT, Brown PO and Botstein D. (1998) Cluster analysis and display of genome-wide expression patterns. Proc. Natl. Acad. Sci. USA. 95: 14863-14868.
[13] Carlson MR, Zhang B, Fang Z, Mischel PS, Horvath S and Nelson SF. (2006) Gene connectivity, function, and sequence conservation: predictions from modular yeast co-expression networks. BMC Genomics 7:40
[14] Tu K, Yu H and Li YX. (2006). Combining gene expression profiles and protein–protein interaction data to infer gene functions. Journal of Biotechnology 124, 475–485
[15] Maraziotis IA, Dimitrakopoulou K and Bezerianos A (2007) Growing functional modules from a seed protein via integration of protein interaction and gene expression data. BMC Bioinformatics 8: 408
[16] Kennedy J. Eberhart RC, Shi, Y. (2001) Swarm Intelligence. Morgan Kaufman, San Mateo, CA.

An Empirical Approach for Objective Pain Measurement using Dermal and Cardiac Parameters

Shankar K.[1], Dr. Subbiah Bharathi V.[2], Jackson Daniel[1]

[1]Senior Lecturer, Dept. of EIE, National Engineering College, Kovilpatti, Tamilnadu, India
[2]Professor, Dept. of CSE, DMI College of Engineering, Chennai, Tamilnadu, India

Abstract — **As the exact pain measurement is an important prerequisite for pain management, this work aims to measure Pain objectively. As the physiological parameters have significant relationship with pain, we intend to measure ECG, HR, BP and GSR with the equal amount of pain being induced on all the subjects. For this purpose, we have designed an apparatus called Pain Inducer which consists of five discs mounted on a central slot to induce the pain. The experiments (Pre Pain, During Pain and Post pain experiments) were conducted inside the controlled laboratory environment. The parameters have been acquired and analyzed by an instrument called physiograph (RMS Polyrite-D). We have chosen 50 male volunteers of age between 20 and 22 years, for this purpose. The subjects were with normal appetite (food habits) and residing in a confined locality. It is found that both the cardiac parameters and somatic resistance showed significant changes between the 'pain' and 'no pain' conditions. However more experimental studies with additional physiological parameters on large number of subjects in actual clinical setup are required to validate this method. Also, a generalized pain measurement system for all kinds of pain is another challenge to be addressed. Further work on this area may improve the utility of this method in clinical practices for measuring pain objectively. It leads to reduced administration of painkillers.**

Keywords — **GSR, Objective Measurement, Pain, Pain inducer, Physiograph.**

I. Introduction

The onset of the 21st century is an incredibly exciting time in pain research [1]. Information from recent studies in basic pain research is virtually exploding and has revealed numerous novel targets in pain research. The pain offers challenges to both, physician and sufferer [2]. For the sufferer, it is a hurt. He faces huge challenges in getting relieved from pain. For the physician, it offers great challenges in terms of curing sufferer's pain. As the pain is a worldwide clinical problem that causes great suffering for the individual and costs for society, the assessment and evaluation of perceived pain is necessary for diagnosis, choice of treatment, and for the evaluation of treatment efficacy. In order to cure pain, a physician must know the quantity of sufferer's pain exactly. Otherwise, the physician may prescribe a wrong dosage of pain killers; it may lead to adverse effects [3, 4].

Presently, subjective methods (Visual Analog Scale, Verbal Analog Scale, Color Analog Scale, Face Pain Scale, Questionnaire method and Behavioral measures) are being used to assess the pain [5]. As there is no specific standard, we have no accurate terminology for the physician to interpret it. There is an increasing demand for pain measurement especially for infants, mute and people at unexplainable situations. Therefore, it is essential to measure the pain objectively and we need some quantitative indicator of pain.

Though there are many quantitative indicators of pain in the literature [6], we aim to check a response of Galvanic Skin Response (GSR) and Cardiac parameters for the pain. And we checked which one of these parameters could be used as a valid pain indicator.

The term 'pain' in this paper is limited to only for mechanically stimulated pain and not the actual pain. The mechanical pain is induced using 'Pain Inducer' (Fig. 1) designed and fabricated by the 'Pain Experiment Group' (PEG). The parameters of all subjects were measured and analyzed by using a digital physiograph – RMS Polyrite D. The experiments were done in a controlled laboratory set up, not in clinical set up.

II. Methodology

A. Pain Inducer

The pain inducer resembles the "TOWERS OF HANOI" [7]. It consists of discs of diameter of 5cm provided with a central slot. So that weights can be added and the amount of pain can be increased. The base disc is supported with a central rod of 15cm in length. The base of the pain inducer consists of a perfect cube of area 1 X 1 cm. One of the edges of the cube was supposed to be placed on the inner side of the subject's middle finger.

Pain caused (induced):

Pain (pressure) = Force/Area

Chwee Teck Lim, James C.H. Goh (Eds.): ICBME 2008, Proceedings 23, pp. 678–681, 2009
www.springerlink.com



Fig. 1 Pain Inducer setup

Since the cube is of unit area, Area = 1 sq.cm

Therefore, Pain (pressure) = force = mass x gravity

Since gravity is a universal constant, Pain (pressure) is proportional to the applied mass.

By using the pain inducer setup together with the additional discs of 150 grams each, we induce the pain on the subjects. In this setup we could add the weights up to 950 grams. So this pain inducer could cause the pain which is equal to 950 grams / sq.cm.

B. Experiments

The experimental studies in this work involve two types namely (i) Pain-Dermal (PD) and (ii) Pain-Cardiac (PC) experiments. The experiments were conducted in three stages namely 'Pre Pain', 'Pain' and 'Post Pain'. For conducting these experiments, we selected 50 male volunteers of age group between 20 and 22 years. All these 50 volunteers were with normal appetite and healthy. The volunteers were from confined locality also.

Before involving the volunteers in the experiments, the PEG explained all about the experiments including the pain to be induced on them, duration etc. The experiments were conducted only after getting the consent from the volunteers. By conducting these experiments we acquired the dermal and cardiac parameters. Of these parameters the Blood Pressure (BP) alone was measured by using a separate Auto BP module (RMS Phoebus 401 N), simultaneously with other needed parameters.

During the experiments, we followed standard instructions for placing the electrodes on volunteers at desired area of body [8].

III. Results

Experimental studies have been performed to find the effect of certain physiological parameters like GSR, ECG, Heart rate, R-R interval, and Blood pressure when pain was induced on the subjects.

The effect of the pain was analyzed individually related to the noted physiological parameters like blood pressure, Electro cardiogram, and Galvanic Skin response of all the subjects.

A. PD Experiments

The consolidated readings of the average values of Skin resistance (in Kilo Ohms) for each of the subjects are shown in. Table 1.

From these tabulated readings, we come to know that out of fifteen subjects; only one subject has been an exception whereas the rest of the subjects showed a decrease in resistivity, when pain stimuli was induced on them.

The Galvanic skin response introduces an objective element [9], but does not dispose all the problems. But the skin resistivity is a variable and often an unstable phenomenon. Some individuals react too sluggishly; further certain psychic components are involved in GSR analysis. [10].

Table 1 Results of Pain – GSR Analysis

S.No.	Subject	Pre-Pain	During Pain	Post-Pain
1	selva	115.54	93.5	99.87
2	krishnakumar	155.48	110.52	111.42
3	karthikeyan	93.16	51.09	65.77
4	vivek	147.77	143.91	103.37
5	raju	255.75	232.52	242.73
6	kailash	81.38	79.8	102.28
7	p.karthik	87.56	76.09	80.32
8	bijoy	89.03	157.33	165.2
9	sakthivel	132.85	90.567	99.52
10	praveen	130.13	127.73	138.43
11	jone	58.9	53.63	55.59
12	sundar	131.57	97.94	107.65
13	mujibur	155.5917	134.15	136.53
14	nagarajan	126.05	118.9	151.55
15	boopathy	122.66	87.83	112.92

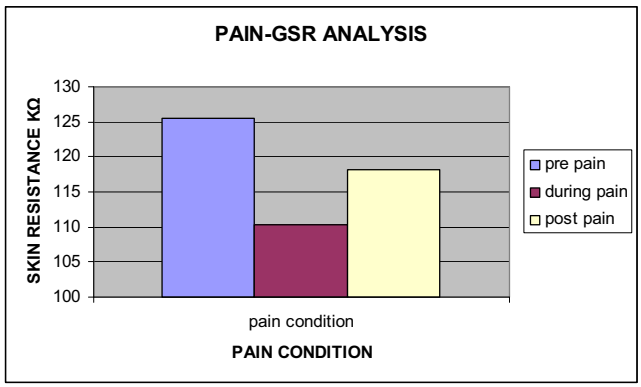


Fig. 2 Average results of Pain – GSR Analysis

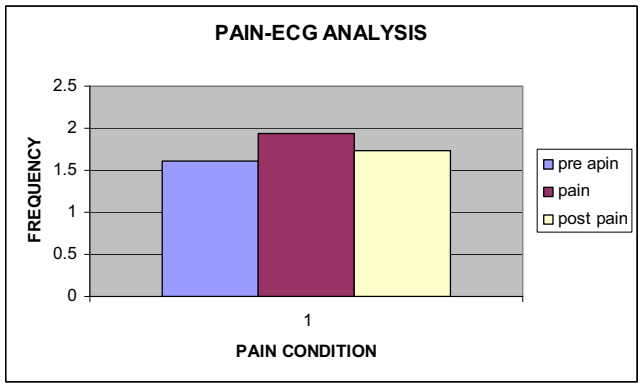


Fig. 3 Average results of Pain – ECG Analysis

On an average, there was a decrease in skin resistance of about 15 kΩ from pre pain to during pain condition and there was an increase in skin resistance of around 8 kΩ when the subject reacts from during pain condition to post pain condition as indicated in Fig. 2.

B. PC Experiments

The influence of pain on the Electro Cardiogram was analyzed in three different time durations of two minutes, each pertaining to the pre pain, during pain and the post pain conditions as in the case of PD experiments.

The Fast Fourier Transform (FFT) analysis was carried out on the recorded readings of the ECG data of all the subjects as shown in the Table 2.

Table 2 Results of Pain – ECG Analysis

S.No.	Subject	Pre-Pain	During Pain	Post-Pain
1	selva	1.311	1.47	1.311
2	krishnakumar	2.95	3.27	3.11
3	karthikeyan	0.98	1.147	0.9
4	vivek	0.98	1.147	0.98
5	raju	0.98	1.147	0.98
6	kailash	1.147	1.47	1.311
7	p.karthik	1.311	1.47	1.311
8	bijoy	1.311	1.47	1.311
9	sakthivel	1.63	1.8	1.47
10	praveen	0.87	0.87	0.87
11	jone	4.42	4.75	4.58
12	sundar	2.26	2.7	2.62
13	mujibur	1.147	1.148	1.147
14	nagarajan	1.51	1.55	1.63
15	boopathy	1.311	3.6	2.45

From this tabulation, we can come to a conclusion that, there has been a sturdy increase of the frequency component of the ECG data of all the subjects when subjected to the pain stimuli, compared with the pre pain and the post pain conditions.

Exceptionally two subjects did not show any significant change in the readings taken during the pre pain, during pain and post pain conditions. And the frequency increased to 4 Hz in one subject, whereas in rest of the subjects the value of frequency was less than 1.8 Hz.

On an average there was a steady increase in the frequency of the ECG wave (Fig. 3) when the subjects were given pain stimuli.

Table 3 Results of Pain – BP Analysis

S.No.	Subject	Pre-Pain		During Pain		Post-Pain	
		S	D	S	D	S	D
1	selva	121	79	124	82	120	80
2	krishnakumar	116	72	122	78	119	76
3	karthikeyan	123	69	129	75	117	72
4	vivek	117	81	120	83	112	80
5	raju	114	75	119	78	111	77
6	kailash	128	61	133	70	122	63
7	p.karthik	133	69	135	71	127	73
8	bijoy	113	68	118	71	116	67
9	sakthivel	125	76	127	79	121	82
10	praveen	129	79	131	81	127	80
11	jone	116	65	122	70	113	68
12	sundar	126	69	130	76	122	74
13	mujibur	105	63	111	72	109	65
14	nagarajan	118	73	126	80	120	75
15	boopathy	122	68	128	74	121	72

In the Pain – Blood pressure analysis, the blood pressure readings (both systolic and diastolic) were sought out from all the subjects and the values were manually entered for the three stages of experiment.

From the Table 3, we can draw to a conclusion that, there is a significant increase in both the systolic and the diastolic blood pressure values of all the subjects. On an average, there has been an increase of 5 mmHg of blood pressure from the pre pain condition to the during pain condition and also there has been a decrease in blood pressure of about 7mmHg from the during pain to the post pain condition (Fig. 4).

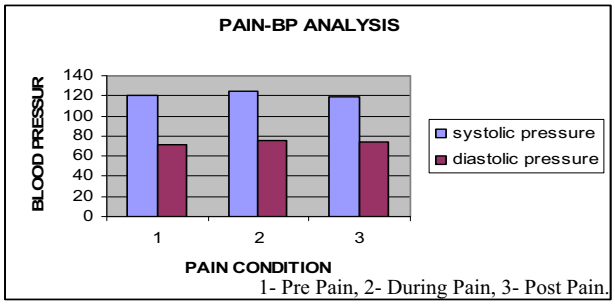


Fig. 4 Average Results of Pain and BP

IV. Conclusion

The specific but future goal of this project is to measure Pain objectively, for which we have taken the cardiac and the dermal parameters to analyze the pain. These results show a clear relation between Pain and GSR also between Pain and other Cardiac parameters like ECG, Blood Pressure and Heart Rate Variability. There is a prominent increase in the value of the R-R interval, which is abruptly seen in the results of HRV analysis.

In the Pain – HRV analysis, the recorded ECG recordings are analyzed both in time and frequency domains. As the cardiac parameters are supposed to be fluctuating under the normal circumstances, for any disturbances, we conclude that there is a scope for measuring pain objectively with a larger reliability on dermal changes.

But it requires a lot of experimental studies with other physiological parameters on many numbers of subjects and could be made to consider this as a method for Objective Pain Measurement. The further work in this area may improve the utility of this method in clinical practices for measuring pain objectively for pain killer management. The future work in this context involves in designing a system to measure all types of pain objectively and guide the physicians in proper administration of painkillers. Further improvements can be made in the reported work by

- Conducting experiments in a clinical setup with actual pain rather than in a laboratory setup with induced pain, and establishing relation between pain and certain other physiological parameters.

- Analyzing the pain responses of larger group of subjects consisting of male and female of different ages may help to determine the precise range of physiological change.

Acknowledgement

The authors thank the students – Mr.Selvamurugan, Mr.Karthik and Mr.Krishnakumar for their help in conducting the experiments.

References

1. Choi PT, Bhandari M, Scott J, Douketis J., (2003), Epidural analgesia for pain relief following hip or knee replacement, The Cochrane Database of Systematic Reviews, Issue 3. Art. No.: CD003071. DOI:10.1002/14651858.CD003071.
2. Ronald Melzack and Patrick D.Wall, The Challenge of Pain, updated 2nd Edition, Penguin Books.
3. Choi PT, Bhandari M, Scott J, Douketis J.,(2003), Epidural analgesia for pain relief following hip or knee replacement, The Cochrane Database of Systematic Reviews, Issue 3.
4. Lee A, Cooper MC, Craig JC, Knight JF, Keneally JP, (2004), Effects of non steroidal anti-inflammatory drugs on post-operative renal function in normal adults, The Cochrane Database of Systematic Reviews, Issue 2.
5. Jensen.M.P, Karoly P, O' Riordan EF, Bland F Jr, Burns RS, (1989), The Subjective Experience of acute pain; an assement of the utility of 10 indices, Clinical Journal of Pain, Jun 5 (2), pp 153 - 159.
6. Ikeda.K.(1995), Quantitative Evaluation of Pain by Analyzing Non Invasively Obtained Physiological Data with Particular Reference to Joint Healing with Continuous Passive Motion, Proceedings RC IEEE-EMBS and 14th BMESI-1955, pp 3.25-3.26.
7. http://www.lawrencehallofscience.org/towerhistory.html.
8. Leslie Cromwell, Fred J.Weibell and Erich A. Pfeiffer, (2001), Biomedical Instrumentation and measurements, 2nd Edition, Printice Hall India Pvt. Ltd.
9. K.Shankar, M.Manivannan, Peter Fernandez, (2008), GSR Analysis of Hypnotic Analgesia, International Journal of Systemics, Cybernetics and Informatics (ISSN 0973-4864), Jan 08-06.
10. Richard A Mularski et al., (2006), Measuring Pain as the 5th Vital Sign Does Not Improve Quality of Pain Management, Journal of General Internal Medicine, Vol.21, Issue 6, pp 607-612.

Corresponding Author:

Author: K.Shankar
Institute: National Engineering College
Street: K.R.Nagar, Kovilpatti
City: Thoothukudi District – 628 503
Country: India
Email: kseie@nec.edu.in

A Diagnosis Support System for Finger Tapping Movements Using Magnetic Sensors and Probabilistic Neural Networks

K. Shima[1], T. Tsuji[1], A. Kandori[2], M. Yokoe[3] and S. Sakoda[3]

[1]Graduate School of Engineering, Hiroshima University, Japan
[2]Fundamental Research Laboratory, Hitachi Ltd., Japan
[3]Graduate School of Medicine, Osaka University, Japan

Abstract — **This paper proposes a system to support diagnosis for quantitative evaluation of motility function based on finger tapping movements using probabilistic neural networks (PNNs). Finger tapping movements are measured using magnetic sensors and evaluated by computing 11 indices. These indices are standardized based on those of normal subjects, and are then input to PNNs to assess motility function. The subject's motor ability is probabilistically discriminated to determine whether it is normal or not using a classifier combined with the output of multiple PNNs based on bagging and entropy. This paper reports on evaluation and discrimination experiments performed on finger tapping movements in 33 PD patients and 32 normal elderly subjects. The results showed that the patients could be classified correctly in terms of their impairment status with a high degree of accuracy (average rate:** 93.1 ± 3.69 **%) using 12 LLGMNs, which was about 5% higher than the results obtained using a single LLGMN.**

Keywords — **Finger tapping movements, magnetic sensors, neural networks, pattern discrimination, diagnosis support**

I. Introduction

To identify neurological disorders such as Parkinson's disease (PD) and quantify motility function by measuring patients' physical movements, various assessment methods have been discussed, including tremor and reaction movements [1] and finger tapping movements [2]. In particular, finger tapping movements have already been widely investigated, and a method to analyze tapping rhythm as well as a method to quantify tapping amplification and velocity [3],[4] have been reported. However, the above evaluations have been performed only for basic analysis such as verification of the feature quantities of PD patients. To realize a diagnosis support system for use in the routine assessment of PD in clinical environments, the features of finger movement need to be extracted numerically for quantitative classification and evaluation.

The classification and evaluation of a subject's movement and symptom severity are equivalent to clustering on measured data distribution. So far, several nonlinear classification methods have been proposed by assuming probabilistic distribution of measured data, and probabilistic neural networks (PNNs) have recently attracted widespread attention [5]. However, the authors are unaware of any reports detailing the use of PNNs to classify motility disturbance.

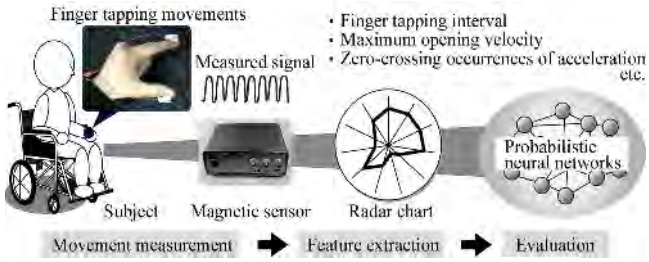


Fig. 1 Concept of the proposed diagnosis support system for finger tapping movements

In this paper, we propose a diagnosis support system employing multiple probabilistic neural networks. The system utilizes a magnetic sensor to measure finger tapping movement and extract its features (such as velocity and rhythm) based on medical knowledge, and then displays the feature indices for doctors' reference on a monitor. Further, the relationships between symptoms and movement features are embedded into the neural networks through learning, and can be used to evaluate motility function by combining outputs of multiple neural networks based on the ensemble learning method of bagging [6]. Since the outcomes of the neural networks indicate probabilities, doctors can intuitively understand the features of finger tapping movements and make quantitative evaluation from the indices or radar chart on the display.

II. Diagnosis Support System for Finger Tapping Movements

The diagnosis support system is shown in Fig. 1. The details of each process are explained in the subsections below.

A. Movement measurement [4]

The magnetic sensor developed by Kandori et al. [3] is utilized to measure finger tapping movements. This sensor

Chwee Teck Lim, James C.H. Goh (Eds.): ICBME 2008, Proceedings 23, pp. 682–686, 2009
www.springerlink.com

can output a voltage corresponding to changes in distance between the detection coil and the oscillation coil by means of electromagnetic induction. First, the two coils are attached to the distal parts of the user's fingers, and finger tapping movements are measured. The distances between the two fingertips (the *fingertip distances*) are then obtained from the output voltage by a calibration model expressed as

$$d(t) = \alpha V^{-1/3}(t) - \varepsilon \,, \tag{1}$$

where $d(t)$ denotes the fingertip distance, $V(t)$ is the measured voltage of the sensors at a given time t, and α and ε are constants computed from calibration [4]. In the calibration process, α and ε are estimated using the linear least-square method for n values of measured output voltages and fingertip distances for each subject. Further, the velocity $v(t)$ and acceleration $a(t)$ can be calculated from the fingertip distance $d(t)$ using differentiation filters.

B. Feature extraction

This paper defines eleven indices for the evaluation of finger tapping movements as follows: (1) *total tapping distance*; (2) *average maximum amplitude of finger taps*; (3) *coefficient of variation* (*CV*) *of maximum amplitude*; (4) *average finger tapping interval*; (5) *CV of finger tapping interval*; (6) *average maximum opening velocity*; (7) *CV of maximum opening velocity*; (8) *average maximum closing velocity*; (9) *CV of maximum closing velocity*; (10) *average zero-crossing occurrences of acceleration*; and (11) *spectral variability of finger taps.*

First, the integration of the absolute value of velocity $v(t)$ through the measurement time is signified as the total tapping distance (Index 1). As feature quantities of the i^{th} tapping, the maximum and minimum amplitude points (dp_i, dq_i) between the interval [T_i, T_{i+1}] are calculated from the measured fingertip distance $d(t)$, and the average (Index 2) and CV (Index 3) of maximum amplitudes $ma_i = dp_i - dq_i$ are computed. Here, T_i (i = 1,2,…,I) is the instant of finger contact, and I is the number of contacts between fingertips. Further, the finger tapping interval It_i, which is the time interval between two consecutive contacts, is applied as $It_i = T_{i+1} - T_i$, and the positive and negative maximum velocity points are defined as the maximum opening velocity vo_i and the maximum closing velocity vc_i, respectively. The averages and CVs of the finger tapping interval, maximum opening velocity and maximum closing velocity are then computed from all the values of It_i, vo_i, and vc_i (Indices 4–9), respectively.

In addition, zc_i, which denotes the number of zero crossings of the acceleration waveform $a(t)$, is calculated from each interval between T_i and T_{i+1}, and the zero-crossing occurrences of acceleration zc_i are defined as the evaluation values of multimodal movements (Index 10). Finally, the time-series finger tapping interval It_i is resampled at f_a Hz by applying the linear interpolation method, and the power spectral density of the data is then estimated using the fast Fourier transform (FFT). The value of the integrated power spectrum from f_b to f_c Hz is defined as the spectral variability of finger taps (Index (11)).

The evaluation indices calculated for the subject are normalized based on the indices of normal subjects to enable comparison of the differences in movement. In this paper, the standard normally distributed variables x_j are converted to the mean and standard deviations of the tapping data from those of the normal subjects using Eq. 2.

$$x_j = (z_j - \mu_j)/\sigma_j \tag{2}$$

Here, j corresponds to the index number, z_j is the computed value in each index, and μ_j and σ_j describe the average and standard deviations of each index in the group of normal elderly subjects respectively. j = 1 represents the total tapping distance, j = 2,…, 9 signify the averages and CVs of maximum amplitude, finger tapping interval, maximum opening velocity and maximum closing velocity, and j = 10 and 11 denote the average zero-crossing occurrences of acceleration and the spectral variability of finger taps. Additionally, the input vector $\boldsymbol{x} = [x_1, x_2, ..., x_{11}]^{\mathrm{T}}$ is defined for the discrimination of finger tapping movements.

C. Evaluation using probabilistic neural network ensembles

The extracted features are discriminated to enable evaluation of motility function. In this paper, a log-linearized Gaussian mixture network (LLGMN) [5] is used as the PNN, and each index is evaluated using the ensemble learning method based on bagging [6] for the LLGMN.

LLGMN [5]*:* The LLGMN is based on the Gaussian mixture model (GMM) and the log-linear model of the probability density function (pdf), and the *a posteriori* probability is estimated based on the GMM by learning. By applying the log-linear model to a product of the mixture coefficient and the mixture component of the GMM, a semi-parametric model of the pdf is incorporated into a three-layer feed-forward PNN. Through learning, the LLGMN distinguishes movement patterns with individual differences, thereby enabling precise pattern recognition for bioelectric signals such as EMG and EEG [5].

Combination rules for LLGMNs: The combination strategy for multiple LLGMNs is shown in Fig. 2. This method consists of the C LLGMN classifiers, corresponding to the number of input vectors, $\boldsymbol{x}_1, \boldsymbol{x}_2, \ldots, \boldsymbol{x}_C$. Each LLGMN out-

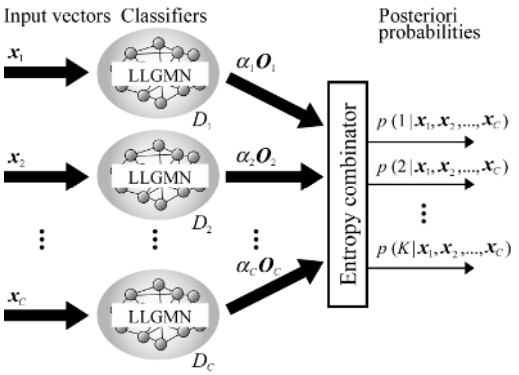


Fig. 2 Combination strategy for LLGMNs

puts the *a posteriori* probability of each learned class, which are then combined based on the ensemble learning method of bagging and entropy. First, each input vector $\boldsymbol{x}_c$ (c = 1,2,…,C) is input to the cth LLGMN, and the *a posteriori* probability vector $\boldsymbol{O}_c$ is calculated by the LLGMN. Here, $\boldsymbol{O}_c$ is defined by Eq. 3 using the *a posteriori* probability $p(k \mid \boldsymbol{x}_c)$ at given value $\boldsymbol{x}_c$:

$$\begin{aligned}\boldsymbol{O}_c &= \left[{}^{(3)}O_1, {}^{(3)}O_2, \ldots, {}^{(3)}O_K\right]^{\mathrm{T}} \\ &= \left[p(1 \mid \boldsymbol{x}_c), p(2 \mid \boldsymbol{x}_c), \ldots, p(K \mid \boldsymbol{x}_c)\right]^{\mathrm{T}}.\end{aligned} \tag{3}$$

The entropy combinator receives the output of each LLGMN weighted by coefficient α_c, and outputs the *a posteriori* probabilities of all classes. Each element of the entropy combinator's input vector $\boldsymbol{y}_c$ is given by

$$y_k(\boldsymbol{x}_c) = \alpha_c p(k \mid \boldsymbol{x}_c), \tag{4}$$

where coefficient α_c $(0 < \alpha_c < 1)$, which denotes the degree of effect of the cth LLGMN's output, is defined as

$$\begin{aligned}\alpha_c &= 1 - H(\boldsymbol{x}_c) \\ &= 1 + \frac{1}{\log K}\left(\sum_{k=1}^{K} p(k \mid \boldsymbol{x}_c) \log p(k \mid \boldsymbol{x}_c)\right).\end{aligned} \tag{5}$$

Here, $H(\boldsymbol{x}_c)$ signifies the entropy of the output of the LLGMN, and denotes the ambiguity of the *a posteriori* probabilities. When these probabilities are ambiguous, the entropy $H(\boldsymbol{x}_c)$ becomes large and α_c approaches 0.

In the entropy combinator, the *a posteriori* probabilities of all classes are calculated by

$$Y_k = p(k \mid \boldsymbol{x}_1, \boldsymbol{x}_2, \ldots, \boldsymbol{x}_C) = \frac{\sum_{c'=1}^{C} y_k(\boldsymbol{x}_c)}{\sum_{k'=1}^{K}\sum_{c'=1}^{C} y_{k'}(\boldsymbol{x}'_{c'})}. \tag{6}$$

In the above method, each pdf for input vector $\boldsymbol{x}_c$ can be estimated and combined, and the networks can be used to calculate the *a posteriori* probability of class k for any given measured data.

For the discrimination of measured data, the entropy of all classes defined by Eq. 7 is used:

$$E = -\sum_{k=1}^{K} Y_k \log Y_k. \tag{7}$$

If E is smaller than discrimination determination threshold value E_d, the class with the highest *a posteriori* probability becomes the result of discrimination. Otherwise, if E exceeds E_d, discrimination is suspended as an obscure class.

Evaluation of finger tapping movements: First, input vector $\boldsymbol{x}_c$ is created from measured finger tapping movements for their evaluation. $\boldsymbol{x}(t_{all}) \in \Re^{11}$ and $\boldsymbol{x}(t_d) \in \Re^{11}$, which are the feature vectors, are computed for the overall measurement time t_{all} and the time interval $[t_d^{st}, t_d^{ed}]$ respectively. Then, the jth elements $x_j(t_d)$ of $\boldsymbol{x}(t_d)$ (d = 1,2,…,D) are used to make the new vector, defined as $\boldsymbol{x}'_j = [x_j(t_1), x_j(t_2), \ldots, x_j(t_D)]^{\mathrm{T}} \in \Re^D$ (j = 1,2,…,11).

The system next measures the finger tapping movements of the patient and those of normal subjects. The feature vectors $\boldsymbol{x}'_j$ and $\boldsymbol{x}(t_{all})$ calculated from these movements are then input to each LLGMN as teacher vectors, and the LLGMNs are trained to estimate the *a posteriori* probabilities of each movement. Thus, the number of LLGMNs is C = 11+1 = 12. After training, the system can calculate similarities between patterns in the subject's movements and trained movements as *a posteriori* probabilities by inputting the newly measured vectors to the LLGMNs.

III. Experiments

A. Method

The subjects were 33 patients with PD (average age: 69.4 ± 8.1, male: 16, female: 17) and 32 normal elderly subjects (average age: 68.2 ± 5.0, male: 16, female: 16). Coils were attached to the distal parts of the thumb and index finger, and the magnetic sensor was calibrated using three calibration values of 20, 30 and 90 mm. The movement of each hand was measured for 60 s in compliance with instructions to move the fingers as far apart and as quickly as possible. The severities of PD in the patients were evaluated by a neuro-physician based on the finger tapping test of the Unified Parkinson's Disease Rating Scale (UPDRS). The calculated indices were standardized on the

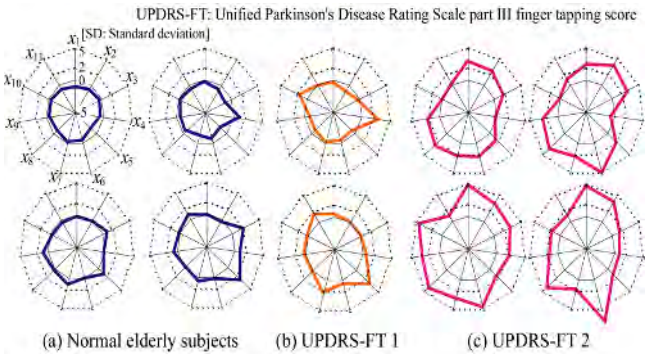


Fig. 3 Examples of radar chart representation of the results of the evaluated indices [4]

basis of the values obtained from the normal elderly subjects. The sampling frequency was 100 Hz. Each index was computed for the overall measurement time t_{all} = 60 and at four pre-specified time intervals of t_1 =[0,30], t_2 = [10,40], t_3 = [20,50] and t_4 = [30,60] and input to the LLGMNs. The measured finger tapping movements were then put into two classes in terms of whether they were normal or not; k = 1: normal elderly; k = 2: PD; K = 2. In addition, fifteen samples of each class were used as teacher vectors for learning.

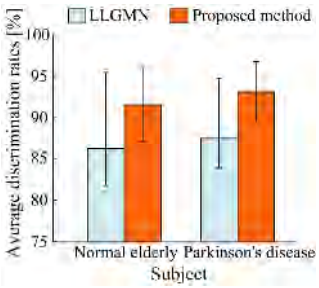


Fig. 4 Discrimination rates of finger tapping movements

B. Results

Radar chart representation of the results of the indices is shown in Fig. 3; (a) to (c) illustrate the charts for normal elderly subjects, PD patients with UPDRS-FT 1 and those with UPDRS-FT 2 respectively. The solid lines describe the average value of each index in the group of normal elderly subjects, and the dotted lines show double and quintuple the standard deviation (2SD, 5SD). The classification results of the finger tapping movements for all subjects are outlined in Fig. 4. This shows the mean values and standard deviations of the discrimination rates for 50 kinds of training set and for the test set, where the initial weight coefficients were changed randomly 10 times in each trial. The average discrimination rates of the normal elderly subjects using a single LLGMN with the proposed method were 86.2 ± 9.24% and 91.6 ± 4.51%, and those of the PD patients were 87.5 ± 7.25% and 93.1 ± 3.69% respectively. Further, each LLGMN's output $y_2(\boldsymbol{x}_c)$ (c = 1,2,…,12), which represents the *a posteriori* probability for PD patients, for all subjects is illustrated in Fig. 5. The subjects shown in this figure are the same as those in Fig. 3.

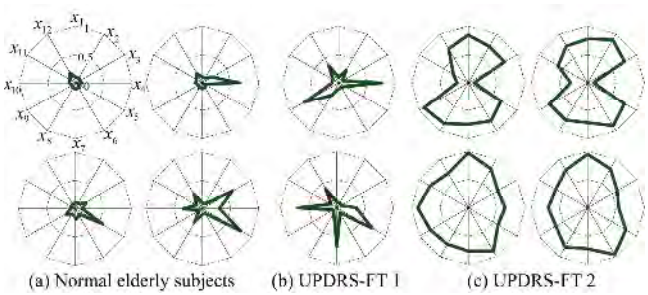


Fig. 5 *A posteriori* probabilities of Parkinson's disease in each index

C. Discussion

From the experimental results, plotting radar charts showing the indices of movements computed and standardized using the basic values obtained from normal elderly subjects revealed that data from normal elderly subjects lie near the average, while those in PD patients' charts become larger according to the severity of their condition. Further, the results of discrimination demonstrated that the patients could be classified correctly in terms of their impairment status using 12 LLGMNs with a degree of accuracy about 5% higher than results obtained using a single LLGMN. Moreover, representing the *a posteriori* probabilities as radar charts confirmed that the values for PD patients become large, and such charts enable quantitative evaluation and description of subjects' motility function. These results indicate that the proposed method is capable of detecting the disease and supporting PD diagnosis.

IV. Conclusions

This paper proposes a diagnosis support system that can quantitatively evaluate motility function for finger tapping movements. From the experiments performed, the finger tapping movements of PD patients were discriminated at a rate of 93.1 ± 3.69 %, demonstrating that the proposed system is effective in the support of diagnosis using finger movements. In future research, we plan to improve the proposed

method to enable diagnosis of the severity of the disease, as well as investigating the effects of aging with an increased number of subjects.

Acknowledgment

This study was supported in part by a Grant-in-Aid for Scientific Research (19 · 9510) from the Research Fellowships of the Japan Society for the Promotion of Science for Young Scientists.

References

1. Holmes G (1917) The symptoms of acute cerebellar injuries due to gunshot injuries. Brain. vol 40, no 4, pp 461–535
2. Okuno R, Yokoe M, Akazawa K et al. (2006) Finger taps acceleration measurement system for quantitative diagnosis of Parkinson's disease. Proc. of the 2006 IEEE Int. Conf. of the Engineering in Medicine and Biology Society, pp 6623–6626
3. Kandori A, Yokoe M, Sakoda S et al. (2004) Quantitative magnetic detection of finger movements in parients with Parkinson's disease. Neuroscience Reseach. vol. 49, no. 2, pp 253–260
4. Shima K, Tsuji T, Kan E et al. (2008) Measurement and Evaluation of Finger Tapping Movements Using Magnetic Sensors. Proc. of the 30th Annual Int. Conf. of the IEEE Engineering in Medicine and Biology Society. 5628–5631
5. Tsuji T, Fukuda O, Ichinobe H and Kaneko M (1999) A Log-Linearized Gaussian Mixture Network and Its Application to EEG Pattern Classification. IEEE Trans. on Systems, Man, and Cybernetics-Part C: Applications and Reviews. vol 29, no 1, pp 60–72
6. Breiman L (1996) Bagging predictors. Machine Learning. vol. 24, pp 123–140

Author: Keisuke Shima
Institute: Hiroshima University
Street: Kagamiyama 1-4-1
City: Higashi-hiroshima
Country: Japan
Email: shima@bsys.hiroshima-u.ac.jp

Increasing User Functionality of an Auditory P3 Brain-Computer Interface for Functional Electrical Stimulation Application

A.S.J Bentley[1], C.M. Andrew[1] and L.R. John[1]

[1]MRC/UCT Medical Imaging Research Unit, University of Cape Town, Faculty of Health Sciences, South Africa

Abstract — **A brain-computer interface (BCI) provides a hands-free means of controlling electrical devices by using signals derived directly from brain activity. Its aim is to provide an additional voluntary channel of output. A P3 BCI utilizes the fact that various stimuli may provide a detection response in the brain's electrical activity to act as a control signal. The aim of this research is to explore different stimulus paradigms in an attempt to develop an accurate, efficient and readily applicable P3 BCI for real task applications. The increased amplitude of a target P3 determines the extent to which it may be detected and thus its efficiency as a signal controller in a P3 BCI. Six different experimental paradigms were explored for feasibility and sustainable applicability. Principal component analysis (PCA) and independent component analysis (ICA) were used to pre-process the data to increase computational efficiency before a linear support vector machine (SVM) was used for categorization. The experimental procedures for single trial detection produced excellent results for visual and auditory stimuli. Visual proved slightly superior overall, but the auditory paradigms were sufficient for real applications. Increasing user functionality decreased the accuracy of the results. It should be noted that accuracies of over 90% were obtained in some instances. Salient results suggest increasing the number of varying stimuli causes minimal differences in speed categorization. The added benefit of a three-stimulus paradigm as opposed to the traditional paradigm is highlighted by its increased user functionality for applications such as functional electrical stimulation (FES). Additionally auditory BCIs do not require the user to avert their visual attention away from the task at hand and are thus more practical in a real environment. Coupled with the proposed three-stimulus procedure, the P3 BCI's capability is vastly improved for people suffering from neurological disorders.**

Keywords — **BCI, FES, P3, auditory, visual**

I. Introduction

Functional electrical stimulation (FES) presents a neuroprosthetic technique that uses changes in potential to activate nerves innervating muscles associated with motor movement [1]. "Neuroprostheses operate through a command interface that measures some modality over which voluntary control is maintained, and translates this to a specific operation of the prosthesis." [2] Devices are developed to restore or improve functionality of an impaired nervous system affected by paralysis [1]. A brain-computer interface (BCI) provides a hands-free means of controlling FES devices. Many patients require the use of their extremities for the intended application and thus it isn't possible to use these in operating a command system. Therefore measured electrical activity in the brain presents a possible control system for FES devices. A BCI is a direct communication pathway between a brain and a reactive device and can operate via mutual interaction between both interfaces [3]. A major aim and incentive of BCIs has been to help users suffering from conditions which inhibit physical control, but which leave intellectual capabilities unhindered. Simplified, BCIs "determine the intent of the user" from various electrophysiological signals in the brain and convert these into responses that enable a device to be controlled [4]. Most BCIs are operated via a visual stimulus or motor imagery [2]. Unfortunately this often distracts the user's attention from the task at hand. Additionally many neurological disorders may lead to loss of vision, especially in the case of patients suffering from a complete locked-in state (CLIS) – voluntary muscular control is lost [5]. Therefore an *auditory* BCI is adopted as the preferred interface between FES and the user.

Although visual stimulus BCIs have proven more accurate than auditory BCIs, their applicability in a clinical setting is limited. A study conducted by Nijboer et al. concluded "that with sufficient training time an auditory BCI may be as efficient as a visual BCI" [6]. Hill et al. suggested that auditory event-related potentials (ERPs) could be used as part of a single trial BCI [7].

Various physiological signals may be used as the control signal for an auditory BCI. However, the associated recorded EEG integrity is affected by passive or active movement of extremities. The P3 presents a robust solution to combating the effects of signal distortion. P3 BCIs provide a means of obtaining cognitive information and communication without relying on peripheral nerves and muscles. For this reason they have widespread use in people with disabilities.

A. P3 (or P300)

It is an ERP component of EEG and indicates a subject's recognition of useful information according to a task. The P3 is one of the most common features of an ERP [8].

Chwee Teck Lim, James C.H. Goh (Eds.): ICBME 2008, Proceedings 23, pp. 687–690, 2009
www.springerlink.com

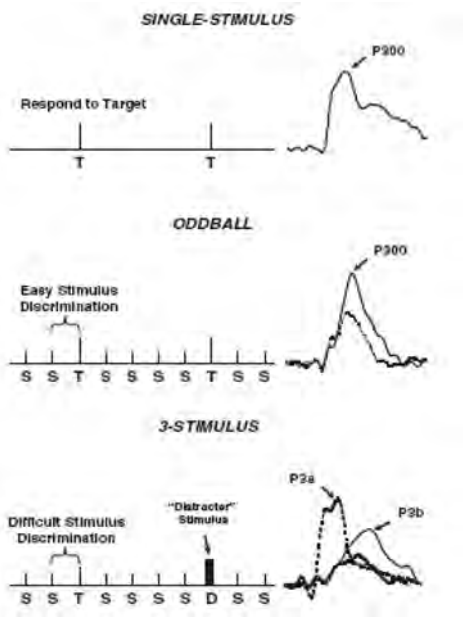


Fig. 1 Schematic illustration of P3 (or P300) waveform [9].

Figure 1 illustrates the three traditional paradigms associated with P3 generation. The target elicits a large positive potential that increases in amplitude and propagates from the frontal to the parietal electrodes of an EEG "and has a peak latency of 300 ms for auditory and 400 ms for visual stimuli in young adults" [9]. Extensive P3 theory is discussed in [9].

A traditional P3 experimental paradigm only allows the user to distinguish between two stimuli – that is, binary selectivity – via a process of weighted probability, whereby the stimulus with the least probability is seen as the target producing a comparable increase in amplitude of the P3. In everyday activity we are confronted with multiple decisions, thus increasing the number of stimuli for P3 production indirectly improves decision making capabilities of an auditory P3 BCI. An attempt must also be made to assess the efficiency with which the proposed system is able to distinguish the target stimulus amongst two other stimuli with the same probability.

B. Principal and Independent Component Analysis

BCI systems employing measurement of cortical areas associated with motor movement are limited by the reliability of the signal for FES applications [5]. The corollary indicates that "using signals outside of motor areas make them less susceptible to disturbance from active or passive movement of limbs" [2].

Most current FES-BCI systems use visual input as a control signal. The reality is that in real-life situations this is not feasible. The pre-processing technique presented by Bentley et al. creates a means of increasing the accuracy and response time of FES-BCI systems for economically viable solutions [5].

P3 waveforms are extracted from EEG signals more often than not by principal component analysis (PCA) or independent component analysis (ICA). *PCA presents an attractive method of data reduction and ICA a means of source extraction* [10]. Importantly PCA is able to compress high resolution data into a format for ICA to extract the required information – increasing computational efficiency. Xu et al. used algorithms based on ICA (with PCA preprocessing) for P3 detection on a 64-channel system by means of anatomical and psychological knowledge of P3 spatio-temporal progression [11].

II. Method

Traditional P3 paradigms consist generally of a two-stimulus experimental technique, whereby decreasing the probability of one stimulus alternately increases the probability of it being distinguished from the other stimuli. These changes in the P3 waveform enable BCIs to differentiate between them. EEG recordings from electrical activity in the brain act as the control method for BCIs. These signals can be generated most effectively by mental imagery and external stimuli produced by vision or hearing. Most of these waveforms (apart from the P3) carry with them complications associated with artifact production and signal echo distortion created by motor movement generated in the motor area of the cortex.

Advantages of auditory stimuli over visual and mental imagery are discussed in Hill et al. [7]. This method of signal control also does not require the extensive training that mental imagery techniques require and the resultant device is not as user specific. It allows the user to focus their attention on the task at hand.

A method using a combination of PCA and ICA techniques discussed in [5] is utilized to pre-process and extract the waveform – the computational efficiency of which is of the utmost importance if it is to be used for FES. The data is spatio-temporally manipulated in the single trial scenario to highlight and enhance the P3 waveforms for classification.

A. Experimental Paradigms

The aim of this research was to investigate increasing user functionality of alternative paradigms associated with the P3.

Materials: It was determined that the use of regular earphones should be utilised for the auditory stimulus so as to replicate a real environment. Electrical noise generated was taken into consideration due to the proximity of the earphones to the high resolution 128-channel Geodesic Sensor Net (GSN).

It was determined that five experiments of 180 trials were to be conducted on 15 subjects (right-handed males between the ages of 21 and 30) using the high resolution system.

The paradigms included visual and auditory stimuli, a requirement for a button to be pushed in certain instances, and a traditional P3 approach. The use of three stimuli of equal probability is assessed for classification accuracy and efficacy so as to simulate multiple decision processes in actual scenarios. It was decided to utilize three different stimuli in an attempt to add extra selective functionality for the user (as opposed to the traditional paradigm utilizing only two differing stimuli).

The five experiments included:

1. presenting the subject with an auditory target stimulus amongst two other stimuli;
2. the same procedure as experiment 1 except that a button is pushed to indicate a target and a separate button is pushed to indicate a non-target;
3. presenting the subject with a visual stimulus amongst two other stimuli;
4. the same procedure as experiment 3 except that a button is pushed to indicate a target and a separate button is pushed to indicate a non-target; and
5. a traditional P3 experiment consisting separately of auditory (indicated by a * in Table 1) and visual stimuli in the single-stimulus paradigm illustrated in Figure 1.

In each case the subject was presented with the target prior to testing to familiarize themselves with the stimulus. All experiments required the subject to focus on a cross-hair and were positioned 0.5 m from the screen.

Auditory stimuli varied only by frequency (volume and time were kept constant throughout). The predetermined sinusoidal tones had frequencies of 500, 1500, and 3500 Hz, which presented the least level of discomfort. These were chosen after subjects indicated from a variety of frequencies which three provided the best discernible differences from a selective range.

Visual stimuli consisted of three arrows of equal size and positioning which only varied by orientation – left, right, and up. The target in each case was randomly selected for cross-validation averaging. In paradigms 1 and 3 the subjects were required to count the number of targets and in instances 2, 4 and 5 they were required to push a button. The paradigms were established according to the ERP technique discussed in [12] and sampled at 200Hz.

B. Processing and Classification

Eye artifacts and bad channels were removed from the recordings and the raw data was 0.1 to 8 Hz band-pass filtered (spectrum analysis reveals that the principal energy of the P3 is in the 1 to 8 Hz band [11], but using high-pass filtering above 0.1Hz tends to attenuate the P3 waveform). A combination of PCA and ICA was used to formulate an independent component (IC) matrix from the training data. This matrix acted as an "unmixing" matrix (W) for single trial data. The ICs of each single trial epoch are then spatio-temporally manipulated to highlight the qualities associated with P3 detection. This method is discussed in [5] and presents an effective and relatively fast classification technique (Figure 2).

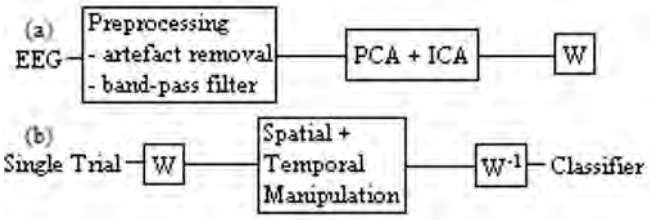


Fig. 2 Algorithm for P3 detection: (a) training and (b) testing phase [5].

A linear support vector machine (SVM) is then used to classify a moving average of the data from 0 to 650ms for a single trial epoch. Thornton's separability index was used to determine the optimal features for classification. A generic subset of features was chosen. The most prominent feature combination was used on all the data in contrast with calculating the index for each test (increased accuracies can be obtained by calculating individual indices).

III. Results

An average of 10 separate cross-validation sets was used to determine the prediction accuracies. It should be noted that certain subjects, presented with the 1500 Hz auditory stimulus, highlighted that identifying the target proved more difficult than in the cases where the higher or lower frequencies were the target. Additionally confusion developed for certain subjects in the visual stimulus paradigm when asked to push a button located on the left when a "right" arrow was displayed and vice versa.

Table 1 Prediction accuracy percentages of cross-validation tests

Subject	Test 1	Test 2	Test 3	Test 4	Test 5
1	68.1	67.2	71.4	74.5	85.0*
2	72.1	71.7	77.3	77.6	83.2
3	72.8	73.1	76.4	78.4	81.5*
4	78.1	75.1	79.1	78.0	81.0
5	65.3	69.6	70.2	68.8	86.2*
6	69.7	68.4	67.5	70.1	90.1
7	72.5	60.2	71.9	77.2	82.3*
8	62.4	68.2	61.3	69.3	77.3
9	73.8	75.4	77.8	76.9	87.7*
10	69.7	70.2	72.3	75.1	87.0
11	58.3	61.4	61.5	62.0	81.6*
12	67.4	66.8	69.9	70.7	78.5
13	73.1	69.9	73.4	71.3	82.2*
14	73.6	71.0	74.5	79.6	91.0
15	70	75.2	74.7	76.1	88.6
Average	*69.8*	*69.6*	*71.9*	*73.7*	*84.2*

Classification accuracies of between 82 and 88% were obtained for auditory P3 single trial traditional paradigms (visual paradigms resulted in accuracies between 77 and 91%). For the four new experimental paradigms (i.e. two stimuli and one target) average accuracies of 70% and 73% were obtained for auditory and visual cases respectively. The results were enhanced by acceptable sensitivity (82%) and specificity (76%) scores for FES compatibility [13].

IV. Conclusions

By using the nominated three-stimulus paradigm, classification accuracies are obtained that may prove acceptable in a clinical environment for FES applications. Greater preprocessing capabilities and classification techniques need to be developed so as to enhance P3 waveform characterization to combat the proportional decrease in P3 differentiation. The traditional P3 paradigm proved superior due to the nature of P3 generation i.e. its increase in amplitude with decreased probability. Visual paradigms proved slightly superior in performance to auditory classification paradigms [4]. However, accuracies obtained from some auditory experiments allow for potential FES implementation [13] and indicated that the traditional button response to stimuli did not prove superior. The speed with which the algorithm may detect single trial P3s is sufficient for the intended application; although the accuracies obtained using the proposed paradigms need to be improved. The lower accuracies result from increased target probability and hence increased task difficulty compared to the traditional paradigm [14].

Acknowledgment

This work was supported in part by the National Research Foundation (NRF) and the Medical Research Council (MRC) of South Africa.

References

1. Crago P, Lan N, Veltink P et al. (1996) New control strategies for neuroprosthetic systems. J Rehabil Res Dev 33:158-172
2. Boord P, Barriskill A, Craig A et al. (2004) Brain-Computer Interface - FES Integration: Towards a Hands-free Neuroprosthesis Command System. INS 7:267-276
3. Levine S, Huggins J, BeMent S et al. (2000) A direct brain interface based on event-related potentials. IEEE T Rehabil Eng 8:180-185
4. Wolpaw J, Birbaumer N, McFarland D et al. (2002) Brain-computer interfaces for communication and control. Clin Neurophysiol 113:767-791
5. Bentley A, Andrew C, John L (2008) An Offline Auditory P300 Brain-Computer Interface Using Principal and Independent Component Analysis Techniques for Functional Electrical Stimulation Application. IEEE EMBS Conf. Proc. in press
6. Nijboer F, Furdea A, Gunst I et al. (2007) An auditory brain-computer interface (BCI). J Neurosci Methods 167:43-50
7. Hill N, Lal T, Bierig K et al. (2005) An Auditory Paradigm for Brain-Computer Interfaces. Advances in Neural Information Processing Systems 17:569-576
8. Sutton S, Braren M, Zubin J et al. (1965) Evoked-potential correlates of stimulus uncertainty. Science 150:1187-1188
9. Polich J, Criado J (2006) Neuropsychology and neuropharmacology of P3a and P3b. Int J Psychophysiol 60:172-185
10. Stone J (2004) Independent Component Analysis: A Tutorial Introduction. The MIT Press, Cambridge, Massachusetts
11. Xu N, Gao X, Hong B (2004) BCI Competition 2003--Data set IIb: enhancing P300 wave detection using ICA-based subspace projections for BCI applications. IEEE T Bio-med Eng 1067-1072 DOI 10.1109/TBME.2004.826699
12. Luck S (2005) An Introduction to the Event-Related Potential Technique. The MIT Press, Cambridge, Massachusetts
13. Bentley A (2005) Design of a PC-based controller for Functional Electrical Stimulation (FES) of Voluntary Muscles. BSc. (Elec.) Eng. thesis, University of Cape Town, South Africa
14. Kok A (2001) On the utility of P3 amplitude as a measure of processing capacity. Psychophysiology 38:557-577

The corresponding author's address details are listed below:

Author: Alexander Bentley
Institute: University of Cape Town
Street: Anzio Road, Observatory, 7925
City: Cape Town
Country: South Africa
Email: alexander.bentley@uct.ac.za

An Electroencephalogram Signal based Triggering Circuit for controlling Hand Grasp in Neuroprosthetics

G. Karthikeyan[1], Debdoot Sheet[2] and M. Manjunatha[2]

[1]Department of Biomedical Engineering, SSN College of Engineering, Chennai, INDIA.
[2]School of Medical Science and Technology, Indian Institute of Technology, Kharagpur, INDIA.

Abstract — **Quadriplegia is a serious problem in the case of patients with neurological disorders. Functional Electrical Stimulation (FES) has been a very good rehabilitation technique to treat this condition and help the patient to lead a near-normal life by aiding him/her to move the limbs of the upper and lower extremities with less difficulty. Various techniques have been proposed to trigger the FES system. In this paper, we describe the design of a novel circuit used to trigger a FES device by a person's EEG signals i.e., by his thoughts. The total project was divided into three modules. The first module was to design a proper interface between the electrodes placed on the scalp and the electronic system which was to be used as a trigger. The second module was to amplify the signal to a sufficient level such that the strength of the signal is high enough to drive the third module which served as the classifier part. The classifier part of the circuit was built out of commercially available IC's and external discrete components. Though there was some tolerance errors induced due to the external components, the error was at a minimal rate when compared with the actual signal considered. The circuit was powered by a 9V battery and the only input to it was the thought waves through EEG signals from the subject/patient considered. The circuit is low power efficient with a wide operational range of ±3V to ±18V.**

Keywords — **Circuit synthesis, Electroencephalography, Electronic equipment, Filters, Instrument amplifiers, Integrated circuits, Logic design.**

I. Introduction

Quadriplegia is a medical condition in which one half of the body is completely paralyzed, greatly reducing mobility of the affected person. In the case of upper extremity paralysis (which is the condition dealt with in this study), the affected person suffers from an inability to move his/her hands, resulting in severe inability to grasp objects and perform normal tasks. The two reasons for occurrence of Quadriplegia are Congenital and Result of a stroke or illness. Though there is little development as of now for treatment of the congenital type of Quadriplegia, recent developments in the field of Functional Electrical Stimulation (FES) have lead to ease in the treatment of the second kind of patients. The treatment of stroke induced Quadriplegia is made possible by a FES system due to the fact that though the Upper Motor Neurons (Connecting the brain with the spinal cord) are damaged, the Lower Motor Neurons (Connecting the spinal cord with the limbs) are healthy. As a result of this, any stimulation given to the nerves connecting the affected limb with the spinal cord stimulates the muscles of the limb and facilitates motion. Recent developments in the acquisition and analysis of Electroencephalogram (EEG) signals have shown that EEG signals are unique for each person and for each thought activity. This property of the EEG has been found to be suitable for usage in Brain- Computer Interface (BCI) applications [1]. Most of the BCI applications use variations in EEG patterns to classify a person's thoughts and make an external device act according to the patterns recognized by the machine [2]. The EEG based trigger circuit developed in this project acts using the same principle as that of a Brain-Computer Interface, detecting patterns in EEG signals using a circuit tailor- made for stimulation of the FES device.

II. Functional electric stimulation: an overview

A Functional Electrical Stimulator is a neuroprosthetic device, the main function of which is to activate the inactive and weak nerves of the upper/lower extremities of the body. Usage of a FES is fruitful in a way that the affected nerves are rejuvenated by continual usage of the device and this helps in restoring movement to the patient. The affected portion of the patient is stimulated whenever movement is required by the patient.

Most of the early FES devices were based upon pure analog designs which rendered the usage and accuracy of usage of the FES device an unpredictable one. But, recent developments in digital technologies and usage of microcontrollers have rendered the usage of FES systems a reliable method of rehabilitation. The schematic of the device used here is shown in Fig. 1 and is controlled using a microcontroller and the output waveform of the circuit is shaped in such a manner that the patient feels negligible fatigue of muscles.

Bio-potentials as a command for FES. Numerous works have been done to study the feasibility of using EEG signals for control of FES. A significant result with regards to this

Chwee Teck Lim, James C.H. Goh (Eds.): ICBME 2008, Proceedings 23, pp. 691–693, 2009
www.springerlink.com

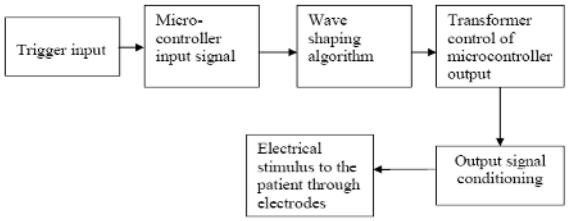


Fig. 1 Block setup of FES

was given by Juul et al (2000) [3] stating that there is a remarkable change in the EEG patterns during preparation of hand or leg movements. This experiment used different kinds of movement trainings to record the Movement Related Potentials (MRPs) for different kinds of movement attempts. Seven recording sites were used according to the 10–20 electrode placement system. The promising results shown by this study prompted us to use C_3 and C_4 recording sites for tapping the Beta waves of the EEG which are the control signals to be used in triggering the FES.

III. Idea of the Circuit

The basic idea of the circuit is divided into two parts- The first part would amplify the circuit to the required level and the second part would classify the amplified signals for triggering of the circuit. The block set up of the total circuit is given is Fig.2 and Fig.3.

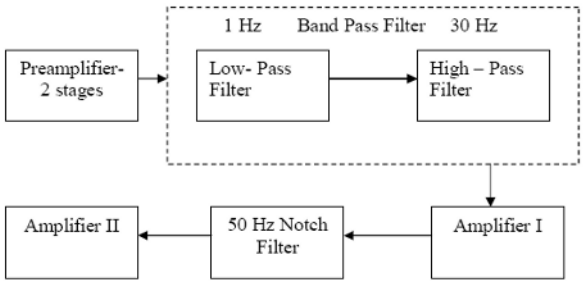


Fig. 2 Amplifier and Preprocessing set up of the circuit

The second portion of the circuit is involved in choosing and classifying the frequencies of interest which would facilitate triggering of the FES device.

The output/ Gain calculation of the amplification portion of the circuit is shown in Table 1.

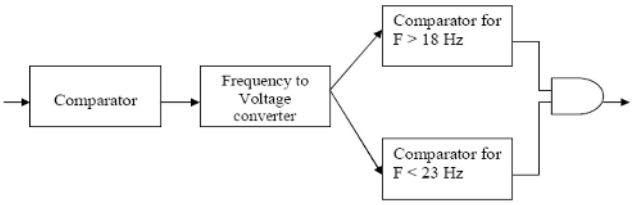


Fig. 3 Classification portion of the circuit

Table 1 Gain of the various stages of the amplification portion of the circuit

Stage	Gain
Preamplifier - I	2.08
Preamplifier - II	74.46
Non-Inverting Amplifier - I	24.33
Non-Inverting Amplifier – II	7.76
Net Gain of circuit in Fig. 2	29358

Voltage dectection and FES triggering using comparators and AND gates: A very critical component of the circuit is the Frequency to Voltage (F–V) converter which is used to convert the various frequencies present in the EEG signal into proportional voltages.

The output of an F–V converter is a voltage signal which would make this portion of the circuit act as a classification precursor stage. The output of the F–V converter is given into two comparators with one comparator being sensitive to voltages corresponding to frequencies greater than F_1 and another comparator being sensitive to frequencies lesser than F_2. The outputs of these comparators are treated as logic levels of 1's and 0's. These logic levels are given as inputs to the AND gate and this AND gate responds to the logic level inputs and gives out an output which is given as a trigger signal to the FES device and the algorithm for the output and input of the comparators and AND gate is as seen in Table 2. The output of the AND gate, is a logic level of 1 or 0 and would be suitable for use as an input to the trigger switch of the FES device.

Table 2 Logic levels of the comparators and AND gate for triggering the FES

Input to AND gate from Comparator 1	Input to AND gate from Comparator 2	Output to the AND gate
0 ($F<F_1$)	0 ($F\geq F_2$)	0
0 ($F<F_1$)	1 ($F<F_2$)	0
1 ($F\geq F_1$)	0 ($F\geq F_2$)	0
1 ($F\geq F_1$)	1 ($F<F_2$)	1

IV. Conclusions

The concept and design of the circuit is in such a manner that it would help quadriplegic and with some fine-tuning, paraplegic patients with foot drop to lead a near- normal life. Though the circuit would help in bringing a near-normal lifestyle back into the life of the patients, it is extremely difficult for any machine to bring a normal life back to the patient at least with present day technology.

The best thing which can be done to improve the lifestyle of disabled people is using rehabilitation techniques such as FES and neural engineering methodologies.

The major drawback with the circuit described above or for that matter any kind of Brain-Computer Interface technologies is the fact that they require cooperation from the patient's side and ultimately however strong the technology developed is, for the technology to be successful, cooperation from the patient side is very much essential.

Acknowledgment

The authors would like to acknowledge the efforts of Mr. Sourajit Das and Mr. Sukanta Kr. Sabut at the Bio-Instrumentation Laboratory, School of Medical Science & Technology, IIT, Kharagpur, for their whole hearted cooperation and assistance.

References

1. Thomas Sinkjaer et al.(2002), "Biopotentials as command and feedback signals in functional electrical stimulation systems," Medical Engineering and Physics.
2. Reinhold Scherer et al.(2007) "The Self-Paced Graz Brain-ComputerInterface: Methods and Applications," Computational Intelligence and Neuroscience
3. Juul PR, Ladouceur M, Nielsen K. D. (2000), "Coding of lower limb muscle force generation in associated EEG movement related potentials: preliminary studies toward a feed-forward control of FES-assisted walking," Proc. 5th Ann. Conf. Int. Funct. Stim. Society, pp. 335–337.
4. Donchin, E., Spencer, K.M., and Wijesinghe, R.(2000), "The mental prosthesis: Assessing the speed of a P300-based brain-computer interface," IEEE Tran. Rehabilitation Engg., vol. 8 no. 2, pp. 174-179,
5. John G. Webster, Medical Instrumentation- Application and Design, Wiley Publications,
6. Analog Devices 620 AN Datasheet at http://www.datasheetcatalog.com
7. Texas Instruments OP07 CP Datasheet at http://www.datasheetcatalog.com
8. Intersil LM339 Quad Voltage Comparators Datasheet at http://www.datasheetcatalog.com
9. Telecom Semiconductors, TC9400 F–V Converter Datasheet at http://www.datasheetcatalog.com
10. Phil Tresadern et al. (2006), "Artificial Neural Network Prediction Using Accelerometers to Control Upper Limb FES During Reaching and Grasping Following Stroke," Proc. 28th IEEE EMBS Ann. Int. Conf., NY US
11. Nai-Jen-Huan et al. (2004), "Classification of mental tasks using fixed and adaptive autoregressive models of EEG signals," Proc. 26th Ann. Int. Conf. IEEE EMBS, San Francisco, CA, USA.
12. Smith J, Jones M Jr, Houghton L et al. (1999), "Future of Health Insurance," N. Engl. J. Med 965:325–329 DOI 10.10007/s002149800025
13. Lock I, Jerov M and Scovith S (2003), "Future of modeling and simulation," IFMBE Proc. vol. 4, World Congress on Med. Phys. & Biomed. Eng., Sydney, Australia, 2003, pp 789–792
14. Keirn Z. A. and Aunon J. I. (1990), "A new mode of communication between man and his surroundings," IEEE Trans. Biomed. Eng., 37 1209–14
15. J.Wolpaw (2006), "Brain-computer interfaces as new brain output pathways," J Physiol, 579:613–619.
16. IFMBE at http://www.ifmbe.org

Corresponding author:

Author: G. Karthikeyan
Institute: SSN College of Engineering
Street: Old Mahabalipuram Road, Kalavakkam,
City: Chennai
Country: INDIA
Email: g.karthikeyan@live.in

A Novel Channel Selection Method Based on Partial KL Information Measure for EMG-based Motion Classification

T. Shibanoki[1], K. Shima[1], T. Tsuji[1], A. Otsuka[2] and T. Chin[3]

[1]Graduate School of Engineering, Hiroshima University, Higashi-Hiroshima, Japan
[2]Faculty of Health and Welfare, Prefectural University of Hiroshima, Mihara, Japan
[3]Hyogo Rehabilitation Center Hospital, Kobe, Japan

Abstract — **To control machines using electromyograms (EMGs), subjects' intentions have to be correctly estimated and classified. However, the accuracy of classification is greatly influenced by individual physical abilities and measuring positions, making it necessary to select optimal channel positions for each subject. This paper proposes a novel online channel selection method using probabilistic neural networks (PNNs). In this method, measured data are regarded as probability variables, and data dimensions are evaluated by a partial KL information measure that is newly defined as a metric of effective dimensions. In the experiments, channels were selected using this method, and EMGs measured from the forearm were classified. The results showed that the number of channels is reduced with 33.33 ± 11.8%, and the average classification rate using the selected channels is almost the same as that using all channels. This demonstrates that the method is capable of selecting effective channels for classification.**

Keywords — **Kullback-Leibler information, partial Wilks' lambda, variable selection method, pattern classification, electromyogram**

I. Introduction

Since electromyograms (EMGs) reflect human intentions and motions, these signals can be used to control various machines estimating these intentions and motions. Recently, neural networks (NNs) to classify EMG patterns have been widely studied, as such networks can represent any nonlinear mapping by learning [1], [2]. In addition, Tsuji *et al*. proposed the Log-Linearized Gaussian Mixture Network (LLGMN) and confirmed its effectiveness in biological signal classification [3].

The number of channels and the measuring positions for EMGs are very important because the accuracy of EMG classification is greatly influenced by the amount of information in measured signals. In the case of EMG classification, effective channel selection methods have been proposed [4], [5] by evaluating all combinations of EMG electrodes. With a very large number of channels, however, computation takes a long time, meaning that real-time applications for human-machine interfaces cannot be achieved. To select effective channels for each subject, it is necessary to evaluate users' EMG patterns and the impact of each channel on the EMG classification with less computational time.

This paper proposes a novel variable selection method based on Kullback-Leibler (KL) information and its application to channel selection for EMG measurement. In this method, measured signals are regarded as probability variables, and their probabilistic density function (pdf) is estimated using probabilistic neural network (PNN) learning based on Kullback-Leibler (KL) information. In addition, a partial KL information measure based on a partial Wilks' lambda is newly defined as a metric of effective dimensions for classification, and dimensions that are not effective are eliminated. As a result, effective channels for each user can be selected using this method without evaluating all channel combinations.

II. Partial KL information measure

A novel metric of dimensions for pattern classification, called the partial KL information measure, is newly defined. Using the partial KL information measure, the most ineffective dimensions can be eliminated.

A. Partial Wilks' lambda [6]

Wilks' lambda is a test statistic used in multivariate analysis of variance. There are N_k samples in the kth class, and each sample x is a vector with L dimensions ($\boldsymbol{x} \in \Re^L$). $\boldsymbol{x}_n^{(k)}$ ($n = 1,2,\ldots,N_k$) denotes the vector of the nth sample in the kth class. Wilks' lambda is defined as follows:

$$\Lambda = |W| / |T|, \tag{1}$$

where $|\cdot|$ denotes the determinant of the matrix, W is the within-class sum of squares,

$$W = \sum_{k=1}^{K} \sum_{n=1}^{N_k} (\boldsymbol{x}_n^{(k)} - \bar{\boldsymbol{x}}^{(k)})(\boldsymbol{x}_n^{(k)} - \bar{\boldsymbol{x}}^{(k)})^{\mathrm{T}}, \tag{2}$$

and T is the total sum of squares,

Chwee Teck Lim, James C.H. Goh (Eds.): ICBME 2008, Proceedings 23, pp. 694–698, 2009
www.springerlink.com

$$T = \sum_{k=1}^{K}\sum_{n=1}^{N_k}(\boldsymbol{x}_n^{(k)} - \bar{\boldsymbol{x}})(\boldsymbol{x}_n^{(k)} - \bar{\boldsymbol{x}})^{\mathrm{T}}, \quad (3)$$

where $\bar{\boldsymbol{x}}^{(k)}$ is the centroid of class k, and $\bar{\boldsymbol{x}}$ is the overall centroid. K is the number of classes, and $(\cdot)^{\mathrm{T}}$ denotes the transpose of the matrix. The smaller the Wilks' lambda, the more classes are separated.

To identify important dimensions for discrimination, a partial Wilks' lambda is then introduced:

$$\Lambda(x_i^* \mid \boldsymbol{x}_{[i]}^*) = \Lambda(\boldsymbol{x}_{[i]}^*, x_i^*) / \Lambda(\boldsymbol{x}_{[i]}^*), \quad (4)$$

where x_i^* is the data set of ith element of $\boldsymbol{x}$, and $\boldsymbol{x}_{[i]}^*$ is the set of vectors that are eliminated in the ith dimension from $\boldsymbol{x}$. Here,

$$F_i = \frac{N-K-(L-1)}{K-1} \cdot \frac{1-\Lambda(x_i^* \mid \boldsymbol{x}_{[i]}^*)}{\Lambda(x_i^* \mid \boldsymbol{x}_{[i]}^*)} \quad (5)$$

performs the same role as the F-statistic in one-way analysis of variance, where N is the number of samples in all classes ($N = \sum_{k=1}^{K} N_k$). This follows an F distribution with K - 1 and N - K - (L - 1) degrees of freedom [7]. In the backward elimination method, the smallest of all the Fi values is eliminated if it is lower than the critical value of Fout. This process is repeated on the remaining dimensions until the smallest F_i value is higher than F_{out}.

However, the partial Wilks' lambda cannot respond to non-Gaussian data since it is based only on data variance. Therefore, it might be difficult to correctly classify the EMG, which is not always Gaussian, for human-machine interfaces after evaluating the dimensions using the Wilks' lambda. To solve these problems, a new metric of effective dimensions referred to as partial KL information is proposed.

B. Partial Kullback-Leibler (KL) information

To classify non-Gaussian and/or non-linear data, it is common to regard them as probability variables and estimate their pdf. It is considered possible to evaluate the dimensions using the estimated distribution.

The KL information represents the difference between two probability distributions [8]. Let $\boldsymbol{x}_n^{(k)}$ be the vector of the nth sample in the kth class, and the probabilities of the kth class in true probability distribution and estimated distribution are $\Pr\{\boldsymbol{x} = \boldsymbol{x}^{(k)}\} = P_k$ and Q_k, respectively. The KL information is calculated by

$$I(\boldsymbol{P}, \boldsymbol{Q}) = \sum_{k=1}^{K} P_k \log \frac{P_k}{Q_k}$$

$$= \sum_{k=1}^{K} P_k \log P_k - \sum_{k=1}^{K} P_k \log Q_k, \quad (6)$$

where $\boldsymbol{P} = [P_1, P_2, \ldots, P_K]^{\mathrm{T}}$ and $\boldsymbol{Q} = [Q_1, Q_2, \ldots, Q_K]^{\mathrm{T}}$, respectively, and the first term on the right side is reduced to a constant; therefore, if the second term becomes the minimum, the KL information becomes the minimum. This means that the estimated distribution is close to the true distribution.

Based on the above concept, this paper defines the partial KL information to evaluate dimensions:

$$I_i = \sum_{n=1}^{N} I_n(\boldsymbol{P}, \boldsymbol{Q}) / \sum_{n=1}^{N} I_n(\boldsymbol{P}_{[i]}, \boldsymbol{Q}_{[i]}), \quad (7)$$

$I_n(\boldsymbol{P}_{[i]}, \boldsymbol{Q}_{[i]})$ is the KL information for the nth sample $\boldsymbol{x}_n$, and is obtained using the probability variable $\boldsymbol{x}_{[i]}^*$ in which the ith element of each variable included is eliminated. If $I_n(\boldsymbol{P}, \boldsymbol{Q}) \equiv I_n(\boldsymbol{P}_{[i]}, \boldsymbol{Q}_{[i]})$, this means that true distribution can be estimated without the dimension x_i.

III. Partial KL Information-Based Variable Selection Using PNN

A novel variable selection method using the partial KL information measure is newly proposed for pattern classification. In this method, KL information is calculated through PNN learning, and redundant dimensions are eliminated one by one.

A. Variable selection using the LLGMN

The LLGMN is based on the GMM and the log-linear model of pdf [3]. By applying the log-linear model to a product of a mixture coefficient and the mixture component of the GMM, the semiparametric pdf model is incorporated into a three-layer feedforward NN. This network can calculate the *a posteriori* probability $Y_k(n)$ for the input pattern $\boldsymbol{x}(n)$ after learning [3].

A simple backpropagation algorithm is feasible when the teacher vector $\boldsymbol{T}(n)$ for the nth input vector $\boldsymbol{x}(n)$ is given. As the energy function J for the network,

$$J = -\sum_{n=1}^{N}\sum_{k=1}^{K} T_k(n) \log Y_k(n) \quad (8)$$

is used, and learning is performed to minimize the KL information for true distribution. This means that a learned network can approximate the data distribution.

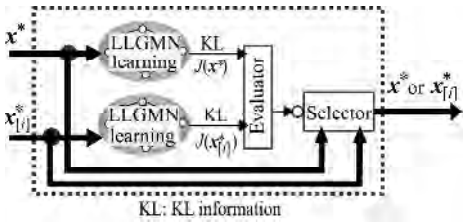


Fig. 1. Variable selector

The variable selection procedure for two input vector sets $\boldsymbol{x}^*$ and $\boldsymbol{x}^*_{[i]}$ is shown in Fig. 1. First, the KL information $J(\boldsymbol{x}^*)$ and $J(\boldsymbol{x}^*_{[i]})$ of two input vector sets are calculated through LLGMN learning. Next, each set of KL information is input to the evaluator. The evaluator outputs the partial KL information calculated based on Eq. (7), where

$$E_i = J(\boldsymbol{x}^*) \ / J(\boldsymbol{x}^*_{[i]}). \tag{9}$$

Based on E_i, two inputs are evaluated, and the more effective one is selected through the selector. The ith dimension for which E_i (i = 1,2,…,L) has the largest value is eliminated by the selector, and ineffective dimensions are then eliminated one by one through repetition of this procedure.

B. Channel selection for EMG classification

Using the partial KL information-based variable selection method, we applied the technique to channel selection for EMG classification. The structure of the channel selection method is shown in Fig. 2.

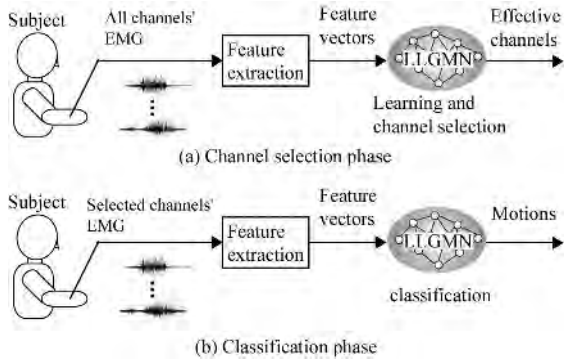


Fig. 2. Structure of the proposed channel selection method

- Feature extraction

First, EMG signals measured from L pairs of electrodes are digitized by an A/D converter (sampling frequency: 1 [kHz]), and are rectified and filtered out through a second- order Butterworth filter (cut-off frequency: 1 [Hz]). These sampled signals are defined as $EMG_l(n)$ (l = 1,2,..., L). Next, the $EMG_l(n)$ values are normalized to make the sum of L channels equal to 1:

$$x_l(n) = \frac{EMG_l(n) - \overline{EMG}_l^{st}}{\sum_{l'=1}^{L} EMG_{l'}(n) - \overline{EMG}_{l'}^{st}} \quad (l = 1,2,..., L) \ , \tag{10}$$

where $\overline{EMG}_l^{st}$ is the mean value of $EMG_l(n)$ while relaxing the muscles. This feature vector $\boldsymbol{x}(n) \in \Re^L$ is input to the LLGMN for channel selection.

- Channel selection

For EMG classification, the effective dimension of the feature vector (i.e., the EMG measurement position) is selected through LLGMN learning. In the channel selection algorithm, ineffective channels are eliminated based on the partial KL information when the termination condition is fulfilled. The algorithm details are as follows:

1. EMG signals are measured from L pairs of electrodes of K motions for LLGMN learning, and the feature vector $\boldsymbol{x}(n)$ is calculated using Eq. (10).
2. The data sets $\boldsymbol{x}^*$, $\boldsymbol{x}^*_{[1]}$, ..., $\boldsymbol{x}^*_{[L]}$ are prepared, and each set is learned by the individual LLGMN.
3. $J(\boldsymbol{x}^*)$ and $J(\boldsymbol{x}^*_{[i]})$ are calculated using Eq. (8), and the partial KL information measure E_i (i = 1,2,…,L) is obtained from Eq. (9).
4. Using each obtained value of E_i, the most ineffective channel is selected. Since the learned network with less partial KL information can approximate the true distribution, therefore, dimension j (for which the partial KL information E_j is the largest) is eliminated. Here, if $E_j \le E_\theta$ (where E_θ is the critical value for the termination condition), the dimension x_j is not eliminated, and the elimination process ends. Meanwhile, if $E_j > E_\theta$, the dimension x_j is eliminated. Then, let $\boldsymbol{x}^* = \boldsymbol{x}^*_{[j]}$ and $L = L - 1$, and return to Step 2.

IV. Channel Selection Experiments

To verify the effectiveness of the proposed channel selection method, we performed EMG-based motion classification experiments.

A. Experimental conditions

The subjects were five normal volunteers (including one person who had experienced EMG control), and six electrodes were attached to each subject's right forearm (see Fig. 3). The subjects performed four motions (K = 4; hand grasping, hand opening, wrist flexion and extension) for a few seconds, and

repeated each motion 10 times. The sampling frequency was 1 [kHz]. One set of the measured data was used for learning and channel selection (learning data), and the other sets were used only for classification (evaluation data). The limit value $E_\theta = 0.8$ was used for channel selection, the number of learning data was $N = 80$, and the number of evaluation data was 4,000 (20 and 1,000 for each motion respectively).

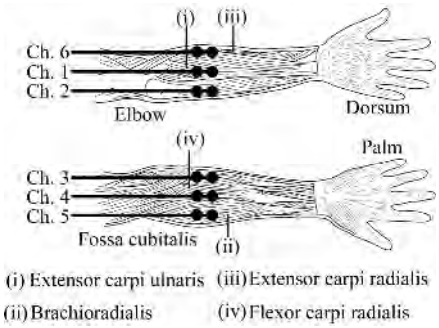


Fig. 3. Electrode positions

B. Results and discussion

Figure 4 shows the relationship between classification rates and KL information when the number of channels for classification is changed. The figure outlines the results of reducing the number of channels using learning data measured from Subject A. In this experiment, the initial weights of the LLGMN were changed 10 times, learning deviations wereand classification were performed in each trial, and the average classification rates and standard obtained. Since the KL information from these results was almost near zero with three to six channels, it is confirmed that the accuracy of classification was high. At this point, three channels were selected by the termination condition of the proposed method (Ch. 2, Ch. 3 and Ch. 6), and the average classification rate was 100%.

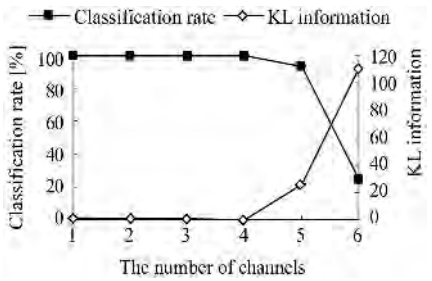


Fig. 4. Relationships between classification rates and KL information (Subject A). Note that the standard deviations are less than 0.27% for the classification rate and 0.06% for the KL information.

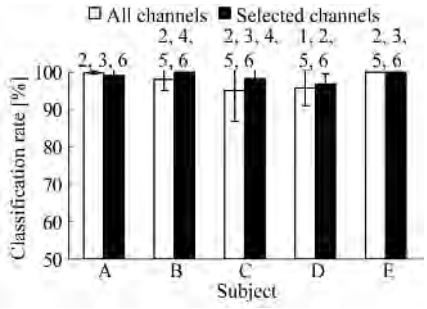


Fig. 5. Classification rates using all channels and selected channels

Next, the average classification rates of the evaluation data using the channels selected with the learning data are shown in Fig. 5. This figure shows the classification results of using all channels' and selected channels' EMG for all subjects. It can be seen that motion could be classified using only the selected channels. The number of channels is reduced with $33.3 \pm 11.8\%$. The classification rates of Subject A, which were calculated using three channels of all combinations from six channels' EMG (i.e. the number of combinations was 6C3 = 20) are shown in Table 1. In this table, the gray zone highlights the outcomes using the proposed method. These results show that the second-highest classification rate was obtained by the proposed method, meaning that semi-optimal channel combination could be selected from all combinations. In the experiments on the other subjects, optimal or semi-optimal channel combinations could also be selected with the highest or second-highest classification rate. These results lead us to the conclusion that effective channel could be selected using the partial KL information measure without evaluating all possible channel combinations.

Table 1. Classification rates using three channels of combinations from all channels (Subject A)

Selected channels	2, 5 ,6	2, 3, 6	2, 3, 4	2, 4, 5	1, 2 ,3
Classification rate [%]	99.16	98.99	97.52	96.96	95.58
Standard deviation	1.75	2.19	4.4	5.27	7.91
Selected channels	1, 3, 5	1, 4, 5	1, 5, 6	1, 2, 4	3, 4, 5
Classification rate [%]	94.97	94.76	94.13	94.06	92.34
Standard deviation	5.16	6.08	5.64	8.6	7.8
Selected channels	1, 2, 5	2, 3, 5	1, 3, 4	1, 3, 6	3, 5, 6
Classification rate [%]	92.24	91.47	90.83	90.78	90.09
Standard deviation	8.96	5.24	8.37	8.08	7.86
Selected channels	1, 4, 6	4, 5, 6	1, 2, 6	3 ,4, 6	2, 4, 6
Classification rate [%]	84.14	81.97	80.91	77.56	75.94
Standard deviation	13.31	19.48	12.5	16.93	17.55

V. Conclusion

This paper proposes a variable selection method using a new metric to select effective dimensions called the partial

KL information measure. In order to confirm its effectiveness, the method was applied to channel selection for EMG classification. In experiments on forearm motion classification, effective channels for classification could be selected for each subject. In future research, we plan to enhance the channel selection method by considering cross-talk EMG and applying the method to training systems for human-machine interfaces using EMG.

Acknowledgment

We would like to cordially acknowledge and express our appreciation to Mr. M. Shigeto for his assistance in the implementation of this research. This work is partially supported by the 21st Century COE Program of JSPS (the Japan Society for the Promotion of Science) on Hyper Human Technology toward the 21st Century Industrial Revolution.

References

1. Hiraiwa, A., Shimohara, K. et al. (1989) EMG pattern analysis and classification by neural network, 1989, Proceedings of IEEE International Conference on Syst., Man and Cybern., pp. 1,113-1,115
2. Kelly, M. F., Parker, P. A. et al. (1990) The Application of Neural Networks to Myoelectric Signal Analysis: A preliminary study, IEEE Trans., Biomedical Eng, Vol. 37, No. 3, 1990, pp. 221-230
3. Tsuji, T., Ichinobe, H. et al., (1995) A Maximum Likelihood Neural Network Based on a Log-Linearized Gaussian Mixture Model, Proc. of IEEE International Conf. Neural Networks, 1995, pp. 2,479-2,484
4. Otoshi, T., Ushiba, J. et al. (2005) Identification of Forearm Movements using Analysis of Electromyographic Signals, IEICE technical report. ME and bio cybernetics, Vol. 104, No. 756, pp. 13-16, in Japanese
5. Nagata, K., Ando, K. et al. (2006) Recognition of Hand Motions based on Multi-channel SEMG Employing the Monte Carlo Method for Channel Selection, BME, Vol. 44, No. 1, pp. 138-147, in Japanese
6. Nath, R., Pavur, R. (1985) A new statistic in the one-way multivariate analysis of variance, Computational Statistics & Data Analysis 2, 1985, pp. 297-315
7. A. C. Rencher. (1995) Methods of Multivariate Analysis, John Wiley & Sons.
8. Kullback, S., Leibler, R. A., (1951) On information and sufficiency, Annals of Mathematical Statistics, Vol. 22, pp. 79-86

Author: T. Shibanoki
Institute: Hiroshima University
Street: Kagamiyama 1-4-1
City: Higashi-Hiroshima
Country: Japan
Email: shibanoki@bsys.hiroshima-u.ac.jp

A Mobile Phone for People Suffering From The Locked In Syndrome

D. Thiagarajan[1], Anupama.V. Iyengar[2]

[1] Sri Sairam Engineering college/Electrical and Electronics Department, Anna university, Chennai, India
[2] Sri Sairam Engineering college/Electrical and Electronics Department, Anna university, Chennai, India

Abstract — **In this paper we have Proposed an idea to design a mobile phone for people suffering from locked-in syndrome using existing technologies. Using this mobile people can code SMS message, compose ring tones, browse and select menu in a commercially available mobile using his/her thoughts.**

Keywords — **Brain computer interfacing, Pattern classification, locked-in syndrome, mobile phone**

I. Introduction

A Brain computer interface (BCI) is a real time communication system designed to allow a user to voluntarily send message or commands without sending them through the brain's natural output pathways [1]. All BCIs have at least four components: Signal acquisition, signal processing, pattern recognition with classification, and external device control.

Locked-In syndrome is a condition, in which a patient is aware and awake, but cannot move or communicate due to complete paralysis of nearly all voluntary muscles in the body. It is the result of a brain stem lesion in which the ventral part of the Pons is damaged.

Applications of BCI systems comprise the restoration of movements, communication and environmental control [2]. However, recently BCI systems have been also used in other research areas such as in the field of virtual reality (VR) [3, 4]

II. Mobile model

Data acquisition: Electrodes are placed on the scalp in the C3, C4 region of the brain according to 10-20 international system.

Signal Processing: The Mu rhythm is amplified filtered and is converted into a digital signal and is transmitted to a mobile phone via a blue tooth.

Pattern recognition: There are many pattern recognition softwares based on MAT LAB, Neural networks, Fuzzy ART map, statistical algorithms like the Bayesian classifier etc and [5] are available commercially. A software compatible with mobile Operating System and is which coded in java can be installed in the mobile phone for classification of signals. We used Java Implementation of Naïve Credal Classifier (JNCC2) open source software for simulation purpose. In real time this software or any software similar to this can be installed in the mobile. The software classifies the signal as left side or right side signal and moves a cursor to the left or right in the mobile screen to navigate and select various options, vertical movements are also possible from classification output. The Figure 1 shows the overall design of the mobile.

The Figure 2 shows the mobile screen, the cursor is represented as arrows in four directions, depending upon the user's imagined direction, the cursor moves horizontally or vertically to select the desired options.

For example if the user chooses 'Message' options by moving the cursor towards it by thought, the message option expands as shown in Figure 3

The message screen consists of three parts. It has a virtual keypad from which the user can select the alphabets from the nine clusters (three alphabets per cluster), the 'dictionary mode' inbuilt in the mobile would coin meaningful words automatically. The user has to keep the cursor on a cluster of alphabets for certain duration for it to get selected. The screen has space for writing the message and a space showing a list of all possible words in that letter combination.

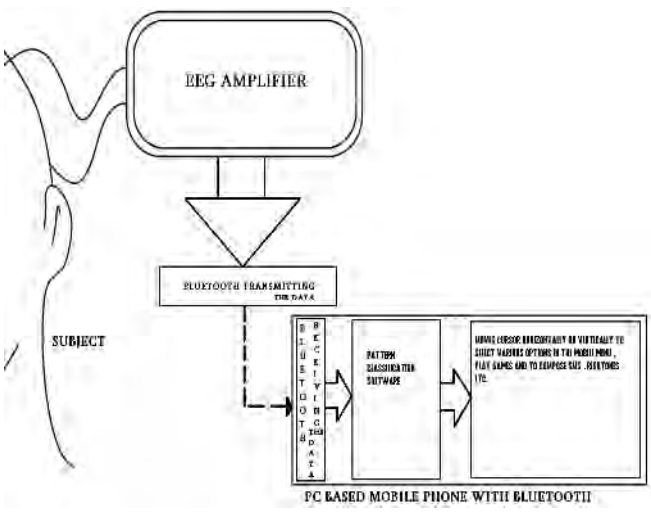


Fig. 1

Chwee Teck Lim, James C.H. Goh (Eds.): ICBME 2008, Proceedings 23, pp. 699–700, 2009
www.springerlink.com

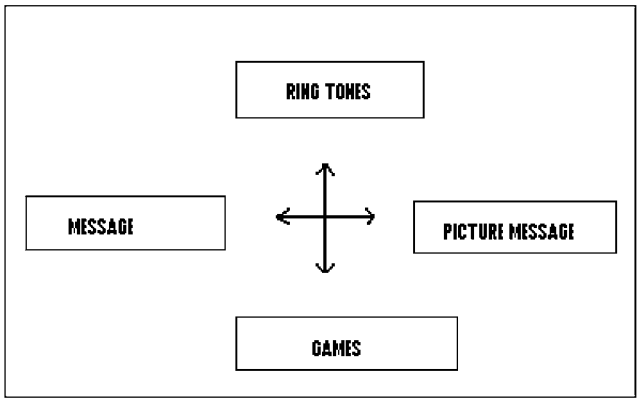


Fig. 2

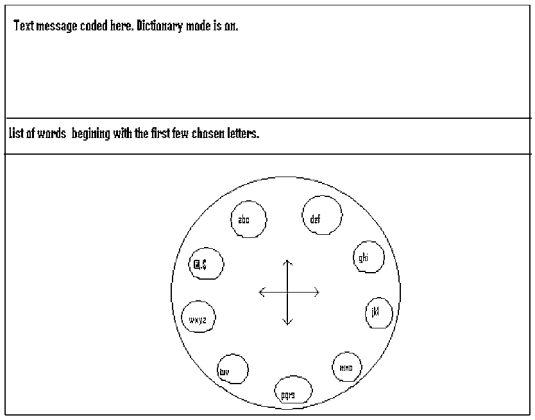


Fig. 3

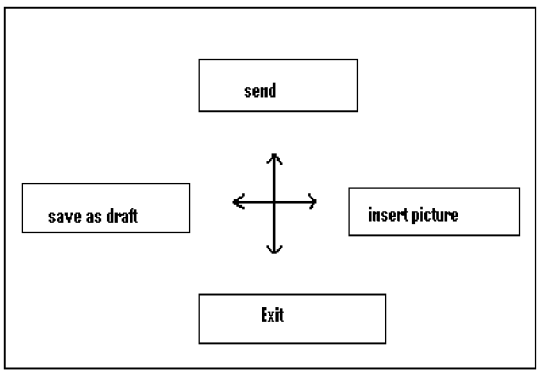


Fig. 4

If the user wants to edit the message he has to select a specific symbol say '@' symbol for a particular duration and if he wishes to navigate back to the main menu, he has to select a specific symbol say '/' for a particular duration of time. The time duration for deletion of message and for navigating backwards to the main menu is different from the duration set for normal selection of words so that a user may use these symbols as text too.

If the user finishes coding the message he has to choose a specific symbol say '#' so that the screen now shows a new screen as shown in Figure 4.

Thus the user can use various options available in a commercial mobile. The picture message options contain some readymade picture templates to display various emotions. The ring tone option consists of symbolic musical notes and the user can select the symbols to compose a tone.

III. Conclusions

BCI is a revolution in technology and would soon find its application in our day to day life. It is in our hands to use it for the betterment of mankind.

References

1. Brenden Allision (2003) P3 or not P3: Toward a better P300 BCI A thesis submitted for the degree of doctorate of philosophy in cognitive science.
2. G. Pfurtscheller, C. Guger, G. Müller, G. Krausz, and C. Neuper,. Brain oscillations control hand orthosis in a tetraplegic. *Neuroscience Letters*, vol. 292, 211-214, 2000.
3. R. Leeb R. Scherer, C. Keinrath, C. Guger, G. Pfurtscheller. Exploring Virtual Environments with an EEG-based BCI through motor imagery. Biomed. Technik, vol. 52, 86-91, 2005.
4. J.D. Bayliss. Use of evoked potential P3 component for control in virtual apartment. IEEE Trans. Neural. Sys. Rehab. Eng., vol. 11(2): 113-116, 2003.
5. P. Bhardwaj; G. Bhateja Composing SMS and Ringtones by though(2006) Brain Computer Interface application Bioengineering Conference, Proceedings of the IEEE 32nd Annual Northeast Volume, Issue , 2006 Page(s):155 – 156

Author: D.Thiagarajan
Institute: Sri Sairam Engineering College
Street: Jyothi Ramalingam Street, Choolaimedu
City: Chennai
Country: India
Email: thiagab4u@gmail.com

Generating Different Views of Clinical Guidelines Using Ontology Based Semantic Annotation

Rajendra Singh Sisodia, Puranjoy Bhattacharya and V. Pallavi

Philips Research Asia, Bangalore, India - 560045

Abstract — **Clinical guidelines comprise collection of medical information related to clinical goals and are used by people having diverse information needs. Commonly users are only interested in information pertinent to their respective goals. Current clinical guidelines are largely textual in form and lack suitable mechanisms for extracting information relevant to different users. This paper proposes a method to extract information from clinical guidelines using a view based approach. Our view generation approach has four steps namely *annotation, view description, view extraction* and *view presentation*. As a case study, we have illustrated the proposed method using the CVD (Cardio-vascular diseases) risk management guideline published by WHO by creating views for different clinical care settings.**

Keywords — **Clinical guideline, View generation, Information extraction.**

I. Introduction

Clinical guidelines are evidence based documents prepared by regulating bodies with the aim of guiding decisions and criteria regarding diagnosis, treatment and management in specific areas of health care. Mostly, it is designed as a multipurpose medical document, which serves different purposes for different users. The principle users include physicians, medical specialists, nurses, medical officers, government health departments, universities and health care industries. All these users have different scopes and purposes. Commonly users are only interested in information pertinent to their respective goals.

Current clinical guidelines are largely textual in form usually written in as a series of paragraphs and lack suitable mechanisms for extracting information relevant to different users. The medical bodies responsible for the publication of guidelines pay more attention to the development of guideline rather than to implementation of guidelines for routine use in clinical settings. There are specific situations when the same information required by different users needs to be adapted for their intended goals. For e.g. a specialist is concerned with only those guidelines that relate to his/her area of specialization. So he/she has to read fewer guidelines and seek finer details in the guideline. However a general practitioner, who treats a range of diseases of multiple domains, will not need the finer details of the diseases as he/she is not a specialist, but will need the macro level details from a large number of guidelines. For these two categories of users, the usage of guideline information for their goals remains the same but differ in terms of details, granularities and entry/exit stage criteria.

If the guideline is not properly indexed getting relevant information becomes a time consuming and tedious task to practitioners for their clinical practices on need basis. In different usage context, the data and control flow within clinical guideline is sequential as defined by the order or textual paragraphs. Hence implementation of any decision support system [[1]] based on clinical guideline is very tedious and prone to error. To address these limitations of the clinical guidelines, this paper proposes a method to extract information from clinical guidelines using a view based approach. Svatek et al. [[2]] developed a document–centric mark–up tool called Stepper, to decompose a clinical guideline formalization process into multiple user–definable steps corresponding to interactive XML transformations. However, this paper does not generate different views of a clinical guideline.

The organization of the paper is as follows. In section II, we present our view based approach and highlight the key steps. Section III discusses our case study for WHO CVD guideline [[3]] for hypertension. We finally conclude and present the future work in section IV.

II. View based approach for information extraction

A view is defined as a collection of information extracted from a guideline and tailored for viewing to the needs of the respective user. Thus, a view could be thought of as a guideline in the user's perspective. It illustrates only the information that the user actually wants to see and omits other details. Views can be of many forms depending on the needs of the users. It could be a list of precautions, or a list of recommendations or the fine details about a particular condition of the disease or any combination of knowledge in guidelines depending on the user's interest.

Chwee Teck Lim, James C.H. Goh (Eds.): ICBME 2008, Proceedings 23, pp. 701–705, 2009
www.springerlink.com

A. Potential Views

In a guideline some views can be predefined based on some particular aspects of treatment which are frequently encountered in the health care. We discuss some of these predefined views and take one as a case study to illustrate our proposed approach.

Disease Condition Specific View: A medical treatment is a sequence of action steps based on a list of evidence. Each action step needs some evidence for execution. Thus the treatment often involves branching of a flow of steps. A view can be defined based on major branches or the special conditions of treatment so that information in other branches not concerning a particular patient can be omitted from the view.

Temporal View: Medical treatment, especially for chronic disease is not done in a single encounter, but is episodic in nature. In many cases, physicians may ask their patients to revisit them after a few days. In this case a view can be described as a set of information related to a particular visit, so that the physician while treating for a particular visit need not look at instructions meant for other visits. The disease management of the guideline in this view looks at the steps needed by practitioner in temporal order.

Resource based View: The healthcare infrastructure, especially in developing and under-developed countries, varies considerably in terms of resource availability. The resource can be lack of facilities, availability of specialized physicians, etc. There can be financial restraint on access to proper medical treatment by patient who may not be able to afford the specialized care and all the recommended medicines. In such cases, it is desirable to have a guideline view based on healthcare resources. For example, in a low resources scenario, the practitioner does not need to look at steps meant for specialized physicians. The assessment and treatment phase should be structured so that guideline recommendations of a are suitable for variable resource settings.

B. View based Approach

In this section we propose our method to extract information from clinical guidelines using a view based approach. Our approach has four steps as shown in Fig. 1 namely annotation, view description, view extraction and view presentation. They are described in the following

C. Semantic Annotation

The first step in our approach is to annotate the textual document of clinical guideline with semantic tags. This step is usually manual and provides additional meta information to be added with the textual clinical guideline thus allowing the process for generating views. The main issues during this step are (i) defining tags for annotation (ii) granularity of annotation (iii) mechanism to annotate.

The selection of tags is influenced by the information of the text to annotate. They should act as keywords and be sufficiently representative of the information they annotate. In trying to keep our tags generic to satisfy the requirements of a variety of users, we restrict ourselves to aspects of common usage of guidelines; in a sense these are kinds of things that users of guidelines try to look for, or relate to in the course of relevant healthcare services. Typical examples include time (such as episodic, stage within each episode, trend), resources (low, medium, high), disease categorization (chronic, acute, risk category, symptoms, observations), workflow (observation, assessment, treatment, referral) etc. The terms to be used for tagging the guideline are assumed from ontology for standardization purposes.

Annotation granularity implies granularity of textual information annotated within the scope of a given tag. Annotation at word level is too granular for any meaningful annotation as the context of the information may get lost whereas annotation at the paragraph level is too broad to generate any useful view. A sentence or phrase level annotation is a good balance between these extremes to capture the context of the information as well as to generate a view, and this has been adopted for the current approach. Annotating mechanism implies the rules and process of annotation. Main issues are (i) whether all text in a guideline should be annotated or some part of the guideline such as background information can be omitted? (ii) whether tags will have nested or overlapping scope? (iii) how tool support can facilitate efficient and effective semi-automated tagging mechanism and reduce the tagging errors? Figure 2 shows our approach for defining tags.

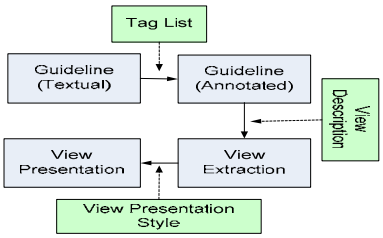


Figure 1: Semantic Annotation Based View Generation

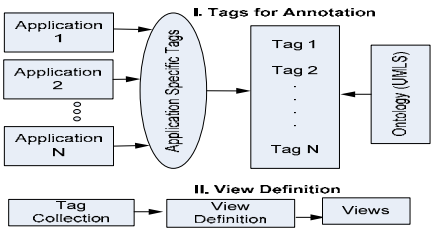


Figure 2: Tag Description

Each tag has a set of attributes to provide more semantic information. In XML, these attributes act as qualifier and can be used for meta information for generating views, organization and presentation.

D. View Description

The second step is to define views according to which the information is extracted. A view is a high level description of logical set of information that a user wants to see in the guideline to fulfill a specific goal. The goal can be different from the medical goals of clinical guidelines. In an ideal case, the logical set of information is a set of continuous or disparate piece of information within a guideline that is sufficient and complete for a user specific goal presented in a logical manner. Operationally, in our approach, a view is a sequence of tagged segments, where each segment satisfies a Boolean function or regular expression of tags.

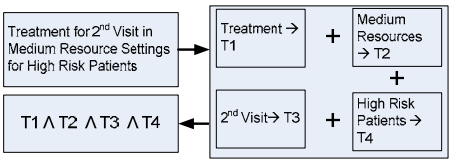


Figure 3: View Description as Boolean Function

Figure 3 describes a specific view for a user who wants to view treatment for second visit of a high risk patient for medium resource settings. The view comprises four aspects *(i)* workflow (treatment**)** *(ii*) resources*,(iii)* episodic (2nd Visit) *(iv*) patient condition assessment (high risk). The annotation tags (T1, T2, T3 and T4) correspond to these aspects to describe the view.

MediumResourceView := <Assessment>$^+$ <Treatment>$^+$
Assessment := <Condition>$^+$<Observation>$^+$
Condition := (<ConditionCriteria><Evaluation>*)$^+$
Observation :=(< ObservationCriteria><Evaluation>*)$^+$
ConditionCriteria := <EpisodicCriteria>$^+$ <RiskCriteria>$^+$
< ResourceSettingCareCriteria>$^+$
ResourceSettingCareCriteria:= 'MEDIUM RESOURCE'
EpisodicCritera := 'SECONDVISIT'
RiskCriteria := 'HIGH'
Evaluation := 'No' |'Yes' |'TRUE' |'FALSE'
Treatment := <Action>|<Advice>
……

Figure 4 : View Description as Regular Expression

The alternative way of describing a view is using a regular expression such as Backus-Naur Form (BNF). In this form (see Fig. 4), the definition of a view is expressed in terms of a set of tags with quantifiers to express the number of their occurrences. The tags composition is recursive in nature and expressed as a function of tags and attributes. We define view using XML schema and XML document type definition (DTD). XML schema is a description of a type of XML document, typically expressed in terms of constraints on the structure and content above and beyond the basic syntactical constraints imposed by XML itself. An example in this form for the same view is as follows

E. View extraction

Once a clinical guideline is annotated with a set of tags and the guideline is annotated by selected subset of tags as discussed in Section C. To illustrate the application of our view generation approach for a specific view: view for low/medium resource settings from specialist settings, we annotated corresponding text with tags to define criteria and context for (i) entry and exit boundary conditions (ii) observation, assessment and treatment for each care settings (iii) tags to qualify the episodic information and patient condition trends. Table 1 shows the annotated text according to our approach. Nested tags define the context and boundary of information. For example, <assessment> tag subsumes <condition> tags to illustrate that within assessment phase, multiple conditions need to be evaluated. For richer semantic information, each tag has set of attributes and their values to add meta information to qualify the tags. For e.g., the <condition> tag <Condition Evaluation= "Observation" Result="No/Yes" Scope=ALL" define attributes to qualify tags to define the evaluation criterion, scope for various care settings and expected results.

Views are defined for the document using a subset of tags structured according to a schema, the next step is to extract the information from the annotated document according to the view. Since we have an annotated document in XML representation, any XML parser [[4]] can provide annotated information for any tags. For a view, we iterate the annotated document to extract information for each tag defined in the view according to the XML schema of the view.

F. View Presentation

The information extracted for the view during view presentation phase is reorganized so that the extracted information is logically relevant. In ideal case, the information extracted in sequential manner from the annotated guideline should be logically relevant as structuring of guidelines is influenced by clinical workflow. For operational purpose we have combined the view extraction and view presentation phase. The XSL [[5]] is used to extract and present the view information. XSL provides a mechanism to select attributes on an XML document using the programming constructs. In any phase of our view generation, we do not modify the content of the guideline and preserve all the

information as it is. The modification in the guideline information during view extraction and presentation is the syntactic change in terms of reorganization of the information rather than any semantic one.

III. Case study

We have applied our proposed approach on WHO CVD Risk Management guideline [3] specifically designed for low and medium resource settings. As a case study we have selected only the high and medium risk assessment and treatment procedure. We omitted details of complicated scenarios of hypertension that are secondary or arises out of complications. The Table 1 shows the annotated guideline for one of the scenario mentioned in the WHO hypertension guideline designed for full specialist care setting. This setting encompasses[1] other care settings with limited resources in terms of facilities and availability of trained personnel. We will discuss how two other views can be generated.

Table 1: Annotated Guideline with Semantic Tags

<Assessment Category=General scope=ALL >
<Condition Evaluation=Risk Value= Medium Scope=ALL Result=" Yes" > [if (SBP 140–179)] < Risk> <Condition>
<Condition Evaluation=Risk Value= High Scope=ALL Result=" Yes"> [if (SBP >=180)] < Risk> <Condition>
<Condition Evaluation= "Patient Details" Value = "Previous_History" Result="No/Yes" Scope=ALL>
[History of heart attack, stroke, TIA, angina, diabetes. Negative urine sugar] <Condition>
<Condition Evaluation= "Observation" Result="No/Yes" Scope=ALL> [Impending hypertensive complications/emergency, Pregnancy, Secondary Hypertension, etc] <Condition>
<Condition Evaluation= "Observation" Result="No/Yes" Scope=GP/Specialist>
[Additional risks factors: Age >60 Smoking Family history of premature CVD ,Obesity] <Condition>
<Condition Evaluation=Risk Value= Medium> [if (DBP >=90)] < Risk> <Condition>
<Condition Evaluation=Risk Value= High> [if (SBP > 220) OR DBP >120] < Risk> <Condition>
<Assessment >
<Action> <Advice category=General scope=ALL >[{*<URL_Identifier:GeneralAdvice1>*}Counsel on cessation of tobacco use, diet and physical activity. <Action>
<Action> <Advice category=General scope=ALL>[<Measure BMI]<Action>
<Action> <Follow-up = "Medium_Risk"> [Review:1–3 months] <Follow-up><Action>
<Action> <Follow-up = "High_Risk"> [Review:2-3 Weeks] <Follow-up><Action>
<Action> <Advice scope= "> Medium_Risk">[Start low-dose Thiazide] <Action>
<Action> <Follow-up = "Medium_Risk"> [Review:1–2 months] <Follow-up><Action>
<Action> <Advice scope= "Medium_Risk/High_Risk" Trend=No_Improvement Episodic=Visit2> [Increase Thiazide] <Action>
<Action> <Advice scope= "Medium_Risk/High_Risk" Trend=No_Improvement Episodic=Visit3> [Maximum Dose of Previous Drugs or add Third Drug] <Action>
<Action> <Advice scope= "High_Risk" Trend=NIL Episodic=Visit1> [Second Drug: beta-blockers or calcium-channel blockers or ACE-Inhibitors] <Action>
<Action> <Advice scope= "High_Risk" Trend=NIL Episodic=Visit1> [compelling indication: appropriate anti-hypertensive] <Action>
<Action> <Advice scope="High_Risk"> {Refer} and {Exit} <Action>
<Action> <Advice scope= "High_Risk/Medium_Risk" Trend=No Improvements Episodic=Visit1> {Refer} and {Exit} <Action>
<Action> <Advice scope= "High_Risk/Medium_Risk" Trend=No Improvements If established CVD and total cholesterol is >5mmol/L (193mg/dl) start statins (if available and affordable) <Advice> <Action>

[1] The third scenario is a superset of the remaining scenarios handling all the complicated cases of CVD which were recommended as referrals in first two care settings.

The view description for medium resource setting is defined in Fig. 4. The view is composed with set of tags with specific value. For e.g., ResourceSettingCareCriteria:= 'MEDIUM RESOURCE' assigns a specific value to the tag and detail the tag composition. The view description schema imposes structural criteria in terms of set of tags and their attributes. e.g., <Assessment>+ <Treatment>+, which are further refined iteratively in terms of their own composition, and ends. The view extraction and view presentation are combined as a single step in the case study. A view specific XSL script is used to extract the relevant tags from the XML complaint annotated document and is transformed into a readable document. In the view extraction step, we define selection and filtering of tags from the complete annotated guideline based on the view description. The view extraction extracts macro level annotated texts encoded within the participant's tags. The specific text within the extracted tags is filtered out during the view extraction stage based on the filtering criteria derived from the attributes and their values. The view presentation step presents the extracted text according to the presentation rules specified in the view presentation style sheet. Table 2 shows the view extracted from the annotated Table 1 for medium resource setting for medium risk CVD patient across multiple episodes.

Table 2: View Presentation for a Specific Criterion

Condition = if (SBP 140–179) && **Assessment** = {No History of heart attack, stroke, TIA, angina, diabetes and Negative urine sugar}
Advice: Counsel on cessation of tobacco use, diet and physical activity
Follow-up : Review:1–3 months
Follow-up:
Condition: If Trend Continuous
Advice: Counsel on cessation of tobacco use, diet and physical activity
Treat with: Start low-dose Thiazide
Follow-up: Review 1–3 months
Follow-up:
Condition: If Trend=No_Improvement
Treat with: Increase Thiazide
Condition: If Trend=No_Improvement
{Refer} and **{Exit}**

IV. Conclusions

In this paper we discussed a view generation approach to extract and present information according to user specific needs. We discussed a four step approach to enrich the clinical guideline with semantic tags, mechanism to define views and extract and present them to a user. Our case study illustrates that our approach can be used to generate different views for accessing information from a clinical guidelines. With tool support, many of the steps can be automated thus enabling wide spread use of clinical guidelines for standard care among various clinical care settings.

Acknowledgment

We would like to thank Gopal Banarwal for his initial investigation on view generation for clinical guidelines.

References

[1] De Clercq P.A., Blom J.A., Korsten H.H.M., Hasman A. Approaches-for creating computer-interpretable guidelines that facilitate decision support, Artificial Intelligence in Medicine, 31 (1), 2004.

[2] Svatek V., Ruzicka M. Mark-up based analysis of narrative guidelines with the stepper tool, Procs. Symposium on Computerized Guidelines and Protocols (CGP-04), 2004.

[3] WHO CVD- risk management package for low and medium resource settings, ISBN 9241545852, http://www.who.int/ cardiovascular_diseases/resources/pub0401/en/index.html

[4] Clark J., expat - XML Parser Toolkit, http://www.jclark.com/xml/expat.html.

[5] Clark J., XSL Transformations (XSLT) Version 1.0, W3C, 1999, http://www.w3.org/TR/xslt.

A High-Voltage Discharging System for Extracorporeal Shock-Wave Therapy

I. Manousakas [1], S.M. Liang [2], L.R. Wan [3]

[1] Department of Biomedical Engineering, I-Shou University, Taiwan
[2]Department of Computer Application, Far East University of Technology, Taiwan
[3]Department of Aeronautics and Astronautics, National Cheng Kung University, Taiwan

Abstract — **Extracorporeal Shock wave therapy has applied by medical doctors on lithotripsy and orthopedics in replacing traditional surgery [1]. For generating shock waves, a high-voltage system of electrical mechanism is necessary to provide [2], and is designed with particular features in this study [3]. In order to build a high-voltage system for an extracorporeal shock wave therapy, some electrical circuits was specially designed and assembled by a charging capacitor system and a discharge control system. The components of the high-voltage system include a power supply, high-voltage resistors, capacitors, a spark gap, a triggering module, and two electrodes. Because the high-voltage power supply is the most decisive device, some electrical components were designed to be protected due to the electromagnetic interference associated with the high- voltage power supply. The high-voltage system can be applied to electromagnetic [4], electrohydraulic and piezolectric shock wave generators that produce shock waves. The details of materials and design methods used will be described. Control procedures for the designed shock wave therapy machine will be explained as flow charts. Schematic diagrams for all designed circuits and dimensions will be illustrated. Each single control procedure for the high-voltage system was validated by a time sequence and profiles of signals captured from an oscilloscope. It is noted that electromagnetic interferences associated with the high-voltage system have been reduced by 99% [5-7] by using well-shielded and optical devices such as optical fibers and infrared modules for controlling signals. Moreover, the mechanical and electrical properties of our designed shock wave generator have been measured. Finally, the positive peak pressure, negative peak pressure, and shock wave intensity were measured by using the pressure sensor of a PVDF membrane hydrophone [8].**

Keywords — **High-voltage, electrohydraulic, Shock wave.**

I. High-voltage system

In order to build an extracorporeal shock wave lithotriptor, a high-voltage system is needed. An important component of a shock wave generator is its electrical circuit. Basically the circuit was assembled by the charging capacitor system and the discharge control system. The components of a high-voltage system include a power supply, high-voltage resistors and capacitors, a spark gap, a triggering module, and two electrodes. Because the high-voltage power supply is the most decisive device, it must have to be used carefully. Thus, a circuit diagram was suggested in the application note of the high-voltage power supply from the Lambda EMI Company. To match practical conditions of our ESWL/ESWT machine, we modified the suggested circuit and added some electrical components to protect the high-voltage power supply. The modified circuit was as shown in Fig. 1.

The principal components of the circuit are a high-voltage power supply model 202A with variable voltage between 0 and 30 kV, a triggered spark gap model GP-12B, a trigger module model TM-11A with 15-30kV output voltage, and several capacitors with different capacitances. The designed circuit of high-voltage power supply as shown in Fig. 1 was used to charge the main capacitor C_2 through a high-voltage resistor R_1. The capacitor C_2 is set to discharge across the underwater spark gap by a triggered spark gap. The trigger spark gap acts as a switch and is held in an off position by a pressurized nitrogen atmosphere which inhibits electrical breakdown. It is turned on when a high-voltage pulse, delivered to a central electrode, ionizes the gas allowing conduction to take place across the spark gap. As a safety reason, the vacuum relay will be kept closed when the high-voltage supply is switched off or any power failure happens so that the capacitor C_2 discharges through the high-voltage resistor R_1 and R_2. Note that capacitor C_1 plays a role as a firewall of high-voltage power supply in this circuit. Power supply will charge the capacitor C_1, and the capacitor C_2 will be charged by the capacitor C_1 right

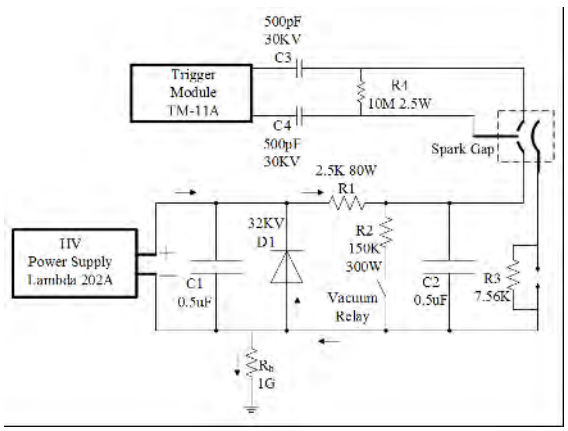


Fig. 1 The high-voltage circuit of our designed ESWL/ESWT machine.

Chwee Teck Lim, James C.H. Goh (Eds.): ICBME 2008, Proceedings 23, pp. 706–709, 2009
www.springerlink.com

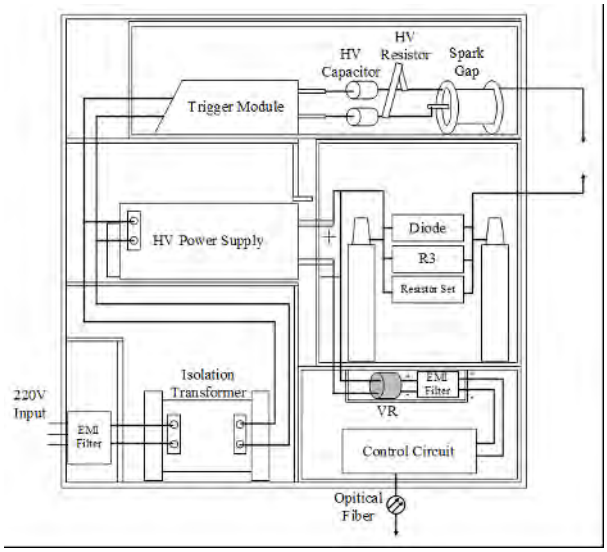


Fig. 2 The settings of a high-voltage system.

after. With this firewall in the front of the high-voltage power supply, any power accident will be blocked by the capacitor C_1 first. Therefore, the high-voltage power supply will be safe. Moreover, the resistor R_3 plays as a damper of discharging. While we trigger the spark gap, an electrical arc will be produced between the two electrodes. At the same time, EMI and signal noise are radiated. With the use of the resistor R_3, most of EMI and noise will be absorbed. This is so-called a soften discharge. Sometimes if a triggered arc failed to discharge between the electrodes, the resistor R_3 will absorb the energy.

To assemble all the high-voltage devices into a high-voltage system, a steel case with several small rooms is needed in order to reduce the electromagnetic radiation. After estimating the size of all the high-voltage devices, a case with the required rooms was designed. For the safety reason, all the small rooms were set with bakelite to prevent any electric shock accident. The designed settings were illustrated in a front view as shown in Fig. 2. The sketch of Fig. 2 also shows the connected wires. The actual circuit can be referred to the circuit diagram in Fig. 1. It is worthwhile to mention that all the separated rooms have their own covers to prevent the electromagnetic radiation. When the covers are closed, most of EMI is blocked by the well-grounded steel case

II. Control System

A. Design of the control circuit

From our experiences, we found that the EMI mainly came from both power and wires or air. To overcome the

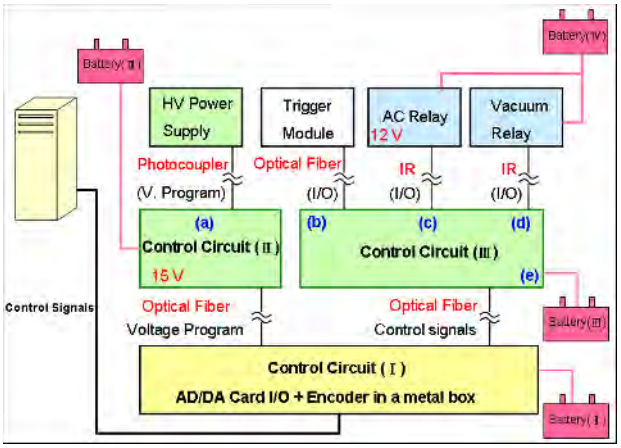


Fig. 3 A sketch of controls.

EMI problem, we insulated the high-voltage device from low-voltage devices for safety. In Fig. 3, a computer was connected to a box, the control circuit (I). This circuit is basically an encoder for controlling signals. These signals were controlled without encoding. A wire looks like an antenna. Connected wires can interfere each other by receiving unnecessary electronic magnetic disturbances. Control signals were encouraged to be transmitted by encoding and decoding processes, resulting in more stable and more safety. Furthermore, the encoded signals can be transmitted through a light transmitting unit without a wire connecting from the control circuit (II) with the control circuit (III). The safety of avoiding electric shock (surge) was guaranteed by separating them completely. Moreover, due to the fact that signals transmitted to the high-voltage power supply should not be interfered by other signals, we separated the control circuit (II) from the control circuit (III) as an independent unit, as shown in Fig. 3.

B. Optical devices applied

Signal transmission by using an optical method could completely avoid the EMI coming from connected wires. Many light transmitting modules were applied in our control system except for signals power. We introduce the main methods we applied in this study.

Optical fiber module: This module consisted of an optical transmitter and an optical receiver. These light transmitting units were manufactured by the EDISON OPTO CORPORATION, and could transmit signals at a high speed of 16 Mbps. Generally speaking, signals were transmitted by a light-transmitter and a light-receiver would receive signals through an optical fiber. The completed control circuit was installed in a metal box as shown in Fig. 4.

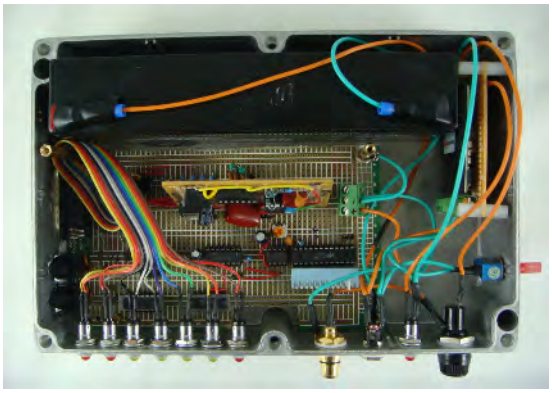


Fig. 4 The assembled control-circuit (II) of high-voltage power supply

Infrared module: The AC relay and the vacuum relay were controlled by control-circuit (III) through an infrared module. Infrared modules were commonly applied in our life. We transmitted the on/off signals with the infrared method and more complicated signals with the optical-fiber method. Here we use two channels of infrared transmission for the AC relay and vacuum relay which were made in a metal box, as shown in Fig. 5. Because the deflection might happen to interfere with each other, an opaque tube was added to limit the infrared passage in the tube. The two tubes shown in Fig. 5 were installed for light limitation.

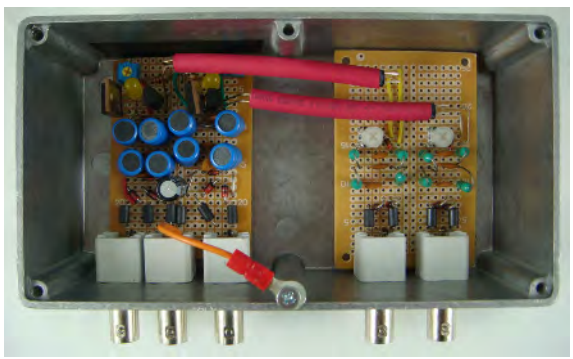


Fig. 5 The infrared signals limited in an opaque tube.

III. Result

A. Result of high-voltage system

According to the design Fig. 2 and 3 we mentioned before a high-voltage system was set up and constructed as shown in Fig. 6. In order to shielding from EMI radiation the room for the high-voltage system was also added with metal covers as their shelter.

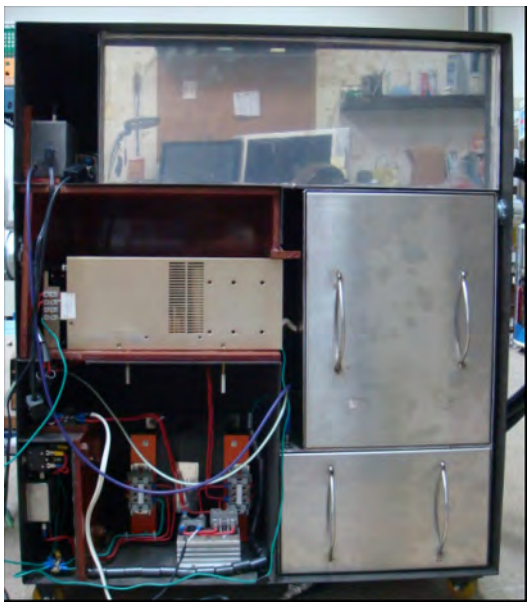


Fig. 6 The high-voltage devices were covered by metal shelters.

B. Results of EMI reducing

The results were measured by using an optical fiber. And the infrared technique was applied in communicating with ACR and VR. All rooms were covered with a metal shelter. Most of high-voltage wires were covered with ferrite cores, too. Fig. 7 shows that the signal without optical device applied and the EMI is about 233V. As shown in Fig. 8 for confirming the result of EMI elimination, resulted pictures of an oscilloscope were captured for several times while the trigger module was triggered. The measured EMI was reduced from about 200V to 2V. The reduction in EMI is approximately 99% by using the present method.

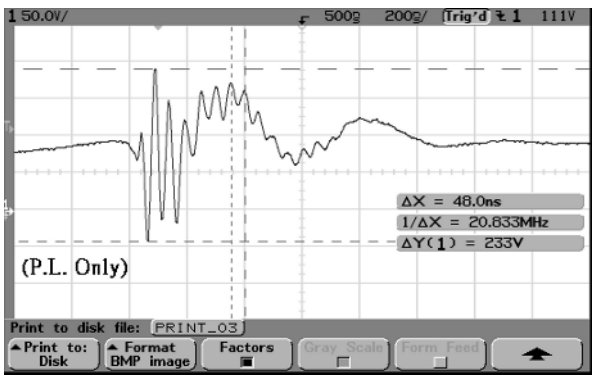


Fig. 7 A signal of EMI before using optical devices.

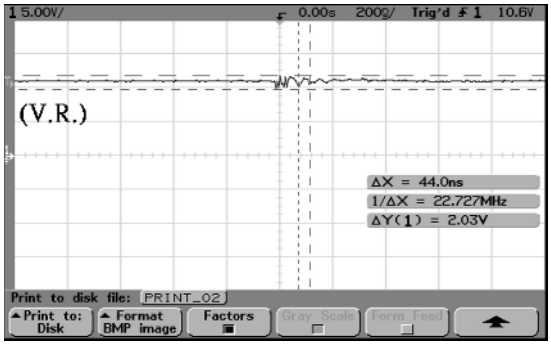


Fig. 8 The resulted signal after using optical devices.

C. Results of output pressure

The focused pressures from our developed ESWL machine were measured by using the pressure sensor of a PVDF membrane hydrophone and a PCB pressure sensor. The profile of the output pressure with its standard deviation was measured at the operation voltage from 10kV to 15kV as shown in Fig. 9. The output pressures were measured by a PVDF membrane hydrophone and each standard deviation were calculated with ten pressure values. Also, the energy density of intensity was calculated from the pressure data as shown in Fig. 10.

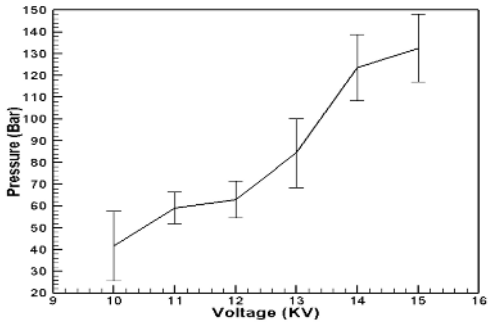


Fig. 9 The measured output pressure from 10kV to 15kV

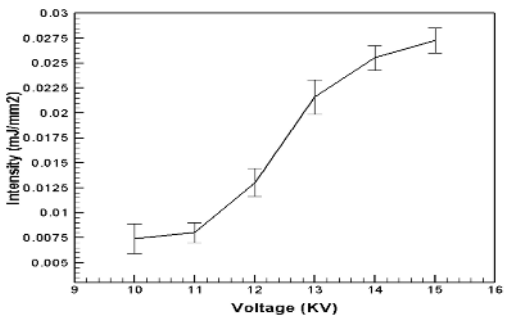


Fig. 10 The profile of intensity from 10kV to 15 kV

IV. Conclusions

The circuit of our high-voltage system has been designed and wired with the aids of the manuals of HVPS. The final test verifies the successful design of our high-voltage circuit. The EMI effects of independent power source, shielding with metal covers and ferrite cores were eliminated, which were found to no longer exist from the captured figures on an oscilloscope. The techniques of using optical module, infrared, encoding and decoding were applied in the controlling system. Circuits and software have been built to communicate signals with the high-voltage device. The test operations of the high-voltage system have successfully passed. The inputted signals would not be interfered by the emitted EMI. All output signals performed clearly and were coincident with expected waveforms. The output pressures at the second focus were measured by a PVDF hydrophone, and the intensity was calculated from the waveform of the output pressures.

References

1. Shrivastava, S.K., and Kailash, "Shock Wave Treatment in Medicine," J. Biosci., Vol. 30, No. 2, pp. 269-75. Mar 2005.
2. Kambe, K., Kuwahara, M., Kurosu, S., Takayama, K., Onodera, O., and Itoh, K., '' Underwater Shock Wave Focousing - An Application to Extracorporeal Lithotripsy,'' Stanford Univ Press, pp. 641-647, 1986.
3. Broyer, P., Cathignol, D., Theillere, Y. and Mestas, J.L.," High-Efficiency Shock-Wave Generator for Extracorporeal Lithotripsy," Medical & Biological Engineering & Computing, Vol. 34, No. 5, pp. 321-328, Sep, 1996.
4. Andriyanov, Yu.V.; Andriyanova, O.N.; Kozodoy, P.V.; Smirnov, V.P. ''The Electromagnetic Type Focusing Shock Wave Generators for Medical and Biology Application'' Pulsed Power Conference, Digest of Technical Papers. 12th IEEE International Vol. 2, No. 27-30, pp. 1410 – 1413, June 1999
5. McDermott, J., "EMI Shielding and Protective Components," EDN, Vol. 24, No. 16, pp. 165-176, Sep 5, 1979.
6. Mitani, T., Shinohara, N., Matsumoto, H., Aiga, M., Kuwahara, N., and Ishii, T., "Noise-reduction Effects of Over Magnetron with Cathode Shield on High-voltage Input Side," IEEE Transactions on Electron Devices, Vol. 53, No. 8, pp. 1929-1936, August, 2006
7. Wang, C., Zhang, Q.H., "EMI and Its Elimination in an Integrated High Voltage Pulse Generator" IECON Proceedings of Industrial Electronics Conference, Vol. 2, pp. 1044-1049, 2000.
8. Etienne, J., Filipczynski, L., Kujawska, T., and Zienkiewicz, B., "Electromagnetic Hydrophone for Pressure Determination of Shock Wave Pulses," Ultrasound in Medicine and Biology, Vol. 23, No. 5, pp. 747-754, 1997.

Author: Ioannis Manousakas
Institute: Dep of Biomedical Engineering
Street: No.1, Sec. 1, Syuecheng Rd., Dashu Township
City: Kaohsiung County 840
Country: Taiwan
Email: i.manousakas@ieee.org

Development of the Robot Arm Control System Using Forearm SEMG

Yusuke Wakita[1], Noboru Takizawa[1] , Kentaro Nagata[2]and Kazushige Magatani[1]

[1] Department of Electrical and Electronic Engineering , Tokai university, Japan
[2] Kanagawa rehabilitation center, Japan

Abstract — **SEMG has many benefits. For example, measurement of SEMG is easy and non-invasive, and especially a characteristic pattern of SEMG is obtained for each body movement. In this research, our objective is the development of a new man-machine interface that is able to control carious equipments by using a characteristic pattern of forearm SEMG. In this paper, we will describe about our developed interface that is controlled by forearm SEMG.**

Keywords — **SEMG, man-machine interface**

I. Introduction

SEMG (Surface Eloctromyogram) is one of the bio-electric signals that is generated from the muscle. There are many kinds of muscles in a human body, and used muscles are different for each body movement. Therefore, body motions can be estimated by analyzing generated SEMG patterns. Our objective of this study is the development of the method that makes perfect estimation of the hand movements possible using SEMG and applying this method to the man-machine interface. In our developed SEMG system, SEMG signals of suitable channels SEMG signals which are measured from a right and left forearm of a subject are used to detect hand motions. And a robot arm is controlled as the results of detecting hand motions.

II. SEMG system

Fig.1 shows a block diagram of our developed SEMG system. In our system, two multi-electrodes that include 48 channels silver electrodes are used to measure left and right forearm SEMG patterns. Measured forearm SEMG signals from a multi-electrode are amplified, filtered and analog to digital converted. In digitization, sampling frequency is 3[kHz], and bit resolution is 16bits. Digitized SEMG data are analyzed in a personal computer.

A block diagram of one channel SEMG amplifier is shown in Fig.2. As shown in this figure, SEMG is amplified about 4400 times and a band width is limited from 10 to 1.5[kHz]. In addition, a SEMG amplifier includes a hum filter which eliminates 50[Hz] in order to be able to use the system in unshielded place. Developed 48 channels SEMG amplifier is also shown in Fig.3.

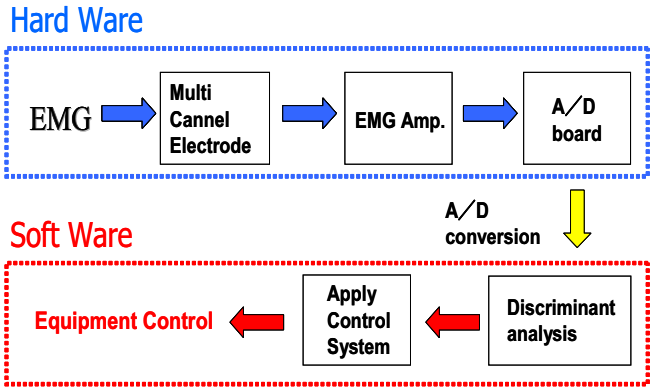


Fig. 1 A block diagram of the SEMG system

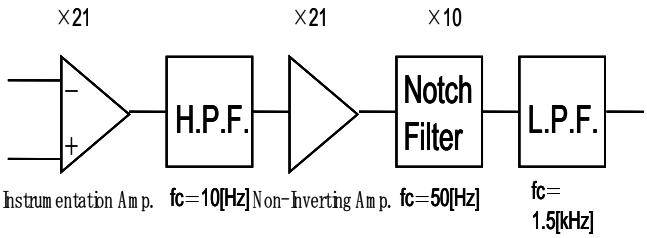


Fig. 2 A block diagram of 1 channel SEMG amplifier



Fig. 3 48 channels SEMG amplifier

A structure of 48 channels surface multi-channel electrode is shown in Fig.4. This multi-channel electrode is composed of 48 silver electrodes (12 x 4). Each electrode is

Chwee Teck Lim, James C.H. Goh (Eds.): ICBME 2008, Proceedings 23, pp. 710–713, 2009
www.springerlink.com

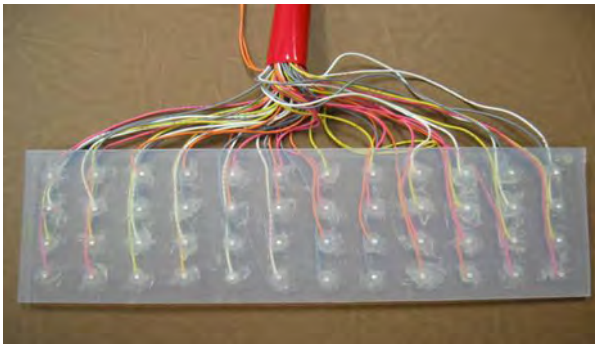


Fig. 4 A multi-channel electrodes

1[mm] in diameter. To fit a forearm bodyline, flexible silicone rubber is used as a base of 48 silver electrodes. A thickness of this silicone rubber is 2[mm].

III. Motion detection

In our system, hand motion detection is done using the method of canonical discriminate analysis. An integrated value while 300[ms] of absolute value of SEMG is used as a SEMG feature extraction. Therefore, each channel's SEMG feature extraction Xi (i = 1, 2, 3, ... , 48) is shown as following formula.

$$X_i = c\sum_{i=1}^{Ti} |x_i(t)|$$

Where C is a constant value for normalization, $xi(t)$ is sampled SEMG value for each channel. Ti is a integration period and this value is set as 300[ms]. As mentioned earlier, sampling frequency of our SEMG system is 3[kHz]. Therefore, one SEMG feature extraction is calculated using 900 data of sampled SEMG.

If we control some equipment using SEMG, the number of using electrodes is important. Of course, using small number of electrode is better. In our system, suitable channels and position of electrodes are estimated by Monte Carlo Method. At first, 48 channels SEMG patterns of a subject are recorded for each hand motion. Next, from 1 to 12 channels electrode sets are evaluated in our system. Positions of electrode are generated randomly for each set in a computer. And recognition rate of each hand motion is calculated for each set by using recorded SEMG patterns. Positions of electrode are generated 1000 times randomly for each set. From results of these trials the suitable number of electrode and suitable positions of electrode are decided for each subject. A flow chart of this deciding process is shown in Fig.5. In our system, canonical discriminate analysis is used for classification of hand motion as mentioned earlier.

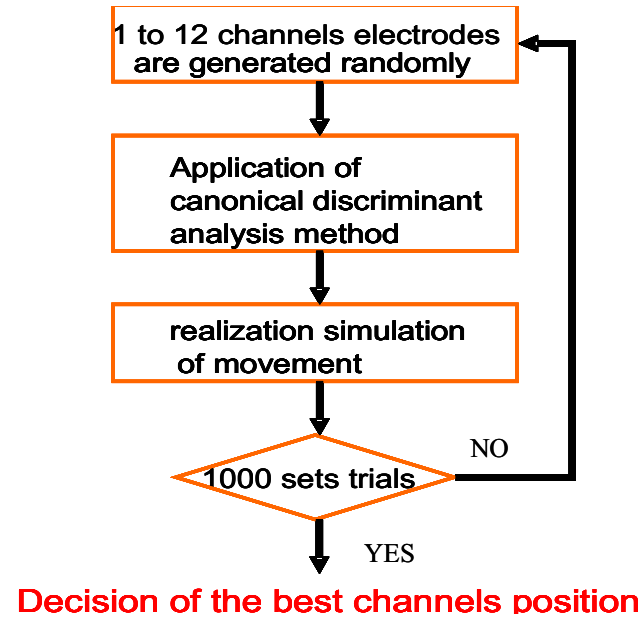


Fig. 5 An algorithm of deciding process for electrode

An example of distribution of classified basic 13 motions of a hand and figures on canonical space are shown in Fig.6. As shown in this figure, all clusters are separated each other. In the case of recognition, the Euclid distance between measured point and mean position of each cluster is calculated, and the motion for the shortest distance is estimated as the real motion.

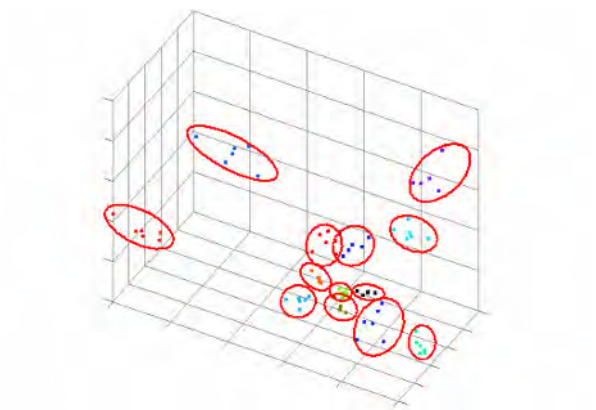


Fig. 6 An example of distribution of hand motion in canonical space

IV. Experiment

At first, the developed system was evaluated for real time motion recognition. In this experiment, basic 8 hand motions and 5 finger motions were tested. Three normal male sub-

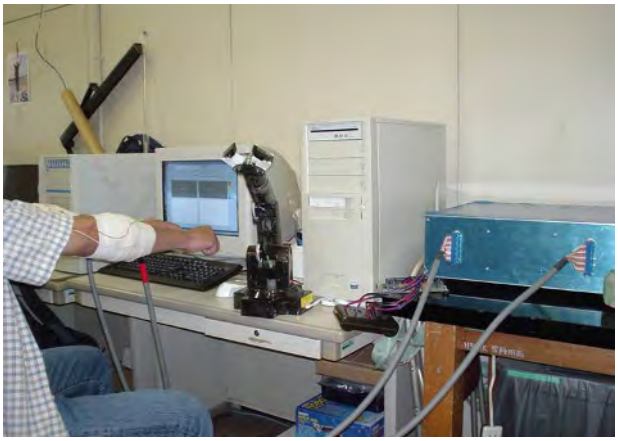


Fig. 7 A scenery of the experiment

jects were studied with our system. Two multi-channel electrodes were attached to subject's right and left forearm. A picture of experiment scenery is shown in Fig.7.

A. Pre-Process

Every subject registered their hand motions to the system and suitable number and position of electrodes were calculated. Then all subjects move their hand 10 times for each 13 hand motions. An example of mean values of the recognition rate is shown in Table 1. This table shows recognition rates of the right hand of one subject for 13 hand motions. As shown in Table 1, for all hand motions, recognition rates were more than 90[%]. In this case, our system selected 6 channels of electrodes as suitable number of electrode. In case of other subject and left hand, recognition rate were also more than 90[%] for all motions. These results indicate that our recognition method worked well.

Table 1 Result of the real time recognition

Motion	Recognition rate [%]
Wrist Flexion	100
Wrist Extension	100
Grasp	90
Release	100
Pronation	100
Supination	80
Radial Deviation	80
Ulnar Deviation	90
Flexion of Thumb Finger	100
Flexion of Index Finger	90
Flexion of Middle Finger	100
Flexion of Ring Finger	100
Flexion of Little Finger	90
Average	94.62

B. Real time recognition using a robot hand

After selecting suitable electrode positions, the number of electrodes, and calculating canonical space, our EMG system are identify hand motions on real time. After these pre processing, a robot arm was tested with our EMG system. One is a robot arm and another is a radio controlled vehicle (tank). Fig.8 shows the toy robot arm which was used in our experiment. This robot arm can operate 10 kinds of motion as shown in Table 2.

Three normal male subjects were tested with this robot arm control system. Their recognition rate was more than 92[%] in all hand motions and he knew this SEMG system very well. They could control the robot arm accurately, and they could transport a small box from one place to another by using this arm. In this experiment, robot arm grasped a box, lifted up it, turned body and release a box on another place.



Fig. 8 Robot arm

Table 2 Correspondence between a robot motion and hand motion

Movement of robot arm	Movement of SEMG
Grasp	Right arm grasp
Release	Right arm release
Counterclockwise of wrist	Right arm pronation
Clockwise of wrist	Right arm supination
Elbow (Up)	Right arm radial deviation
Elbow (Down)	Right arm ulnar deviation
Counterclockwise of base	Right arm wrist flexion
Clockwise of base	Right arm wrist extension
Shoulder (Up)	Left arm wrist flexion
Shoulder (Down)	Left arm wrist flexion

V. Conclusion

In this paper, we talked about our developed SEMG system which can control some equipments using hand motion recognition by SEMG. In our system, suitable electrode positions and number of electrodes are selected from analyzing results of 48 multi-channel SEMG patterns for each subject. The hand motion detection was done using the method of canonical discriminate analysis. In this study, 13 basic hand and finger motions were detected. Recognition rates of this experiment were more than 90[%]. We think this recognition rate is very high and our system works well.

All subjects controlled a robot arm accurately using SEMG patterns which were generated left and right forearm. In this experiment, subjects could transport a small box from one place to another by using this arm. From this experiment, we see that if subjects are experienced for the system, our developed system can control a complex system well.

From these results of our experiment, we have concluded that our new man-machine interface which used SEMG worked perfect and will be a valuable interface in future.

References

[1] Kentaro Nagata, Keiichi Ando, Masafumi Yamada, Kazushige Magatani, "A Classification Method of Hand Movements Using Multi Channel Electrodes", IEEE EMBC 2005 : Proceedings of the 27th Annual International Conference of the IEEE.

[2] Kentaro Nagata, Masafumi Yamada, Kazushige Magatani, "Recognition method for forearm movement based on multi-channel EMG using Monte Carlo method for channel selection", Proceeding of the International Federation for Medical & Biological Engineering Vol.12 (2005).

[3] Keiichi Ando, Kentaro Nagata, Daisuke Kitagawa, Naoki Shibata, Masafumi Yamada, Kazushige Magatani, "Development of the input equipment for a computer using surface EMG", IEEE

Author: Yusuke Wakita
Institute: TOKAI University
Street: 1117 Kitakaname
City: Hiratsuka
Country: Japan
Email: 8adpm039@keyaki.cc.u-tokai.ac.jp

Tissue Classification from Brain Perfusion MR Images Using Expectation-Maximization Algorithm Initialized by Hierarchical Clustering on Whitened Data

Y.T. Wu [1,2,3], Y.C. Chou[1,2], C.F. Lu[1,2] , S.R. Huang[1,2] and W.Y. Guo[4]

[1] Department of Biomedical Imaging and Radiological Sciences, National Yang-Ming University, Taipei, Taiwan, ROC
[2] Integrated Brain Research Laboratory, Department of Medical Research and Education, Taipei Veterans General Hospital, Taipei, Taiwan, ROC
[3] Institute of Brain Science, National Yang-Ming University, Taipei, Taiwan, ROC
[4] Department of Radiology, Taipei Veterans General Hospital, Taipei, Taiwan, ROC

Abstract — **Classification of different perfusion compartments in the brain is important to the profound analysis of brain perfusion. We presents a method based on a mixture of multivariate Gaussians (MoMG) and the expectation-maximization (EM) algorithm initialized by the results of hierarchical clustering (HC) on the whitened data to automatically dissect various perfusion compartments from dynamic susceptibility contrast (DSC) MR images so that each compartment comprises pixels of similar signal-time curves. Monte Carlo simulations have been designed and executed to assess the performance of the proposed method under various signal-to-noise ratios (SNRs). The results of simulations showed that using EM initialized by HC on whitened data produce the best accuracy of segmentation. Five healthy volunteers participated in this study for the validation of this method. The averaged ratios of gray matter to white matter for relative cerebral blood volume (rCBV), relative cerebral blood flow (rCBF) and mean transition time (MTT) derived from 5 normal subjects were 2.196±0.097, 2.259±0.119, and 0.968±0.023 which are in good agreement with those reported in the literature. The proposed method can subserve the diagnosis and assessment of various diseases involving the changes of cerebral blood distribution.**

Keywords — **MR perfusion, expectation-maximization algorithm, hierarchical clustering, whitening, segmentation.**

I. Introduction

Dynamic-susceptibility-contrast (DSC) MR imaging is a widely used tool to record the signal changes embodying different blood supply patterns after intravenous injection of a bolus of contrast agent. With the bolus profile of arterial compartment identified, cerebral hemodynamic parameters, namely, relative cerebral blood volume (rCBV), relative cerebral blood flow (rCBF) and mean transit time (MTT) can be computed based on indicator dilution theory [1].

In order to facilitate the analysis of brain perfusion, we classify the brain tissues into different components based on their specific bolus transit profiles. In this study, a method based on a mixture of multivariate Gaussians (MoMG) and the expectation-maximization (EM) algorithm initialized by the results of hierarchical clustering (HC) on the whitened data is presented to automatically dissect various perfusion compartments. Since the dimension of dynamic MR data is usually far larger than the number of tissue types, we first apply the principal component analysis (PCA) [2] to reduce the data dimension, and the reduced data were further whitened so that the covariance matrix of the whitened data is an identity matrix. The distribution of the whitened data associated with each tissue type is assumed to be a multivariate Gaussian function, and the overall distribution of the whitened data is assumed to be a mixture of multivariate Gaussians (MoMG) [3]. Hierarchical clustering (HC), a multilevel classification method without the need of random initial guess, was applied on the whitened data to segment out each tissue cluster via a hierarchical cluster tree based on a minimum variance algorithm, namely the Ward's method [4]. The results were used to initialize the mean vectors, covariance matrices of the MoMG, and the proportion of each class in the subsequent EM estimation. The number of classes in MoMG model, namely tissue types, is determined by minimizing the information criterion of the minimum description length (MDL) [5]. After comparing values of the resultant posterior probabilities at each pixel, the tissue type that produces the maximal probability will determine the pixel label [6]. To assess the performance of the proposed method, Monte Carlo simulations have been designed and conducted under various noise levels.

II. Material and method

A. Subjects and data recording

Five healthy volunteers aged from 18 to 47 (3 males and 2 females) with body weights between 49 and 70 kg participated in this study. Written informed consent was obtained from each subject before this study. A multi-slice gradient-echo EPI pulse sequence on a 1.5 Tesla scanner (Signa® CV/*i*, GE Medical Systems, Milwaukee,WI, USA) was used to acquire dynamic perfusion images. Imaging used transaxial imaging, TE/TR = 60/1000 ms, flip angle = 90 degree,

Chwee Teck Lim, James C.H. Goh (Eds.): ICBME 2008, Proceedings 23, pp. 714–717, 2009
www.springerlink.com

FOV = 24 cm × 24 cm, matrix = 128×128, slice thickness/gap = 5/5 mm for 7 slices, one acquisition, and 100 images per slice location. Twenty ml of Gd-DTPA-BMA (Omnisacn®, 0.5 mmol/ml, Nycomed Imaging, Oslo, Norway) followed by 20 ml of normal saline were delivered administratively using a power injector (Spectris®, Medrad, Indianola, PA, USA) at a flow rate of 3-4 ml/sec in the antecubital vein. Temporal resolution is one second. Since only dynamic images which have stable baselines and discernibly temporal signal changes are of interest, the first three and last twenty-seven images were removed from a total of 100 images, with seventy images retained per slice location for analysis. All routines were implemented using MATLAB (MathWorks, Inc., Natick, MA) code and carried out on a 2 G-Hz Pentium-based personal computer.

B. Data pre-processing and Dimension reduction using PCA and data whitening

Brain regions were extracted from perfusion images by first setting all pixel values larger than the threshold derived from Otsu's method [7] to one and all values smaller than this threshold to zero. An erosion operation with a 3x3 structure element was applied to the resultant binary mask removing pixels corresponding to skull and scalp areas. This was followed by a dilation operation with a 5x5 structure element filling holes in the brain region. Only the remaining pixels within the extracted brain region were subjected to further classification processing. Assume that the brain region for each image comprises of N pixels, the observation of 70 temporal images can be represented by a $70\times N$ matrix, i.e., each row is an image and each column contains signal intensities of a pixel across 70 time points. To facilitate the subsequent segmentation process, we further reduced the dimension of each data set by PCA [2] to retain most of the data information.

The whitening process is the same as PCA, except that the zero-mean data were transformed by the orthogonal matrix so that the covariance matrix of the whitened data is an identity matrix [2]. In this study, the first *t*-th eigenvectors were selected to form the orthogonal matrix where t was chosen to be between 5 and 12 to condense the data size from $70\times N$ to $t\times N$ so that the sum of the associated eigenvalues interpreted at least 99% of the data variance. The transformed data with reduced dimension resulted from PCA or whitening process were used in the subsequent hierarchical clustering.

C. Initialization: HC on the PCA data or whitened data

Let the compressed data, which were obtained from either PCA or whitening process, be denoted by a matrix $\mathbf{X}$ with size $t\times N$ and each $t\times 1$ column vector in $\mathbf{X}$ be referred to as a feature vector. The objective of HC is to carry out grouping in the data set $\mathbf{X}$ based on a created cluster tree with multilevel hierarchy, where any two nearer clusters at one level are merged into one cluster at the next higher level. The algorithm of HC consists of three major parts: (1) find the dissimilarity between every pair of feature vectors in the data set; (2) group the feature vectors into a binary and hierarchical cluster tree; and (3) determine what level or scale of clustering by cutting the hierarchical cluster tree. Many algorithms are available in regard to the calculation of dissimilarity and the creation of cluster tree [4]. In this work, we employed the Ward's hierarchical clustering method, one of the agglomerative algorithms, for constructing a hierarchical tree. The clustering results on the condensed data $\mathbf{X}$ were used to initialize the mean vectors, covariance matrices of the MoMG, and the proportion of each class for the subsequent EM estimation.

D. Tissue segmentation by the MoMG model with EM algorithm and calculation of rCBV, rCBF and MTT

The tissue segmentation was carried out by EM algorithm by fitting the overall distribution of the whiten data, x_n ($t\times 1$), n = 1, … N, to a mixture of multivariate Gaussian distributions. The EM algorithm is often used for estimation problems in which some of the data are "missing". In this application, the missing data is knowledge of the tissue labels. This algorithm consists of two alternating iterative steps, namely, E-step and M-step. The E-step is to compute the posterior probabilities of tissue classes $p(i\,|\,x_n,\theta^{j-1})$ based on the estimation from previous *(j-1)th* iteration

$$p(i\,|\,x_n,\theta^{j-1})=\frac{\pi_i^{j-1}g_{x_n}[\mu_i^{j-1},\Sigma_i^{j-1}]}{\sum_{l=1}^{K}\pi_l^{j-1}g_{x_n}[u_l^{j-1},\Sigma_l^{j-1}]} \tag{1}$$

where *i=1, ... N* represent labels of tissue classes, $g_{x_n}[\mu_i,\Sigma_i]$ represents the multivariate Gaussian density with the mean vector μ_i and covariance matrix Σ_i of tissue class *i*, π_i denotes the proportion of each class *i* and θ^{j-1} denotes the parameters $\{\mu_i^{j-1}, \Sigma_i^{j-1}, \pi_i^{j-1}\}$ at the *(j-1) th* iteration. The M-step consists of estimating parameters θ^j as follows

$$\mu_i^j = \frac{\sum_{n=1}^{N} p(i \mid x_n, \theta^{j-1}) x_n}{\sum_{n=1}^{N} p(i \mid x_n, \theta^{j-1})},$$
$$\Sigma_i^j = \frac{\sum_{n=1}^{N} p(i \mid x_n, \theta^{j-1}) x_n x_n^T}{\sum_{n=1}^{N} p(i \mid x_n, \theta^{j-1})}, \quad (2)$$
$$\pi_i^j = \frac{1}{N} \sum_{n=1}^{N} p(i \mid x_n, \theta^{j-1})$$

The number of classes K is determined by information criterion of minimum description length (MDL) [4]:

$$\mathrm{MDL}(K) = -\log\left\{ \prod_{n=1}^{N} \sum_{i=1}^{K} \pi_i g_{x_n}[\mu_i, \Sigma_i] \right\} + \lambda J \log(N) \quad (3)$$

where the term $\prod_{n=1}^{N} \sum_{i=1}^{K} \pi_i g_{x_n}[\mu_i, \Sigma_i]$ is the maximum likelihood of $p(x_n \mid \mu_i, \Sigma_i, \pi_i)$ with parameters $\{\mu_i, \Sigma_i, \pi_i\}$ estimated by the EM algorithm, $J = (t \times t + 3 \times t + 2) \times K/2 - 1$ (i.e., tK parameters of μ_i, $(t+1)tK/2$ parameters of Σ_i, and $K-1$ parameters of π_i), and λ is a scalar factor. The tissue label at each pixel was determined by the maximal value of $p(i \mid x_n, \theta^{j-1})$ at that pixel and therefore each tissue type was classified. Once all tissues of interest are identified, the averaged concentration time curves of each tissue type are computed and the AIF is modeled from the averaged concentration time curve of artery to compute the rCBV, rCBF, and MTT maps [8].

E. Monte Carlo Simulation

We conducted the Monte Carlo simulations to assess the performance of the EM-MoMG method. The mean vector and covariance matrice for each cluster were initialized by the following approaches: 1) HC on the whitened data, 2) HC on the PCA data, 3) random selection of columns from the PCA data, and 4) selection of every Kth column (K is the number of cluster) from the PCA data. Sets of simulated dynamic images were first created so that each data set consisted of four to nine hypothetical clusters. The number of pixels and intensity distribution of each hypothetical cluster were generated based on the region of interest (ROI) on one of the raw data sets so that the statistics of the simulated dynamic images can emulate the actual ones. For example, in the case of seven hypothetical tissue clusters, the selected ROIs on the raw data represented artery (Artery 461 pixels), gray matter (GM, 1785 pixels), white matter (WM, 1663 pixels), vein and sinus (vein+sinus, 606 pixels), sinus (104 pixels), cerebrospinal fluid (CSF), choroid plexus (cp, 402 pixels), and artifact (418 pixels), respectively. The ROIs were either merged or split to produce less or more hypothetical clusters. Pixels within each hypothetical tissue area were assumed to be spatially independent, and their intensities across time were assumed to be multivariate Gaussian-distributed. The averaged intensity-time curves, each of which was a 70×1 vector, and covariance matrices of intensities across time, each of which has dimension 70×70, within ROIs on the raw data were employed as the hypothetical parameters for the MoMG model to create a set of noise-free simulated dynamic images using random number generators. Sets of noise-free simulated dynamic images with different numbers of hypothetical clusters were generated in a similar manner. In addition, Gaussian noise was added to each set of noise-free simulated dynamic images to produce the signal-to-noise-ratio (SNR) levels with values of 40 and 70. For each number of hypothetical clusters and SNR level, a Monte Carlo simulation of 1000 runs was performed. Accordingly, the total number of simulated image sets was 6 (number of hypothetical clusters) $\times 3$ (SNR levels) $\times 1000 = 18000$. Each set of simulated dynamic images was rearranged into a $70 \times N$ matrix before classification, where N ($N = 5439$ in the simulation) was the number of pixels representing brain area. Next, PCA and whitening process were applied to condense the $70 \times N$ matrix into two $5 \times N$ matrices in which sum of the 5 largest eigenvalues interpreted 99% of the data variance. The EM-MoMG estimation was initialized by four different initials with number of tissue classes being tested from 3 to 10. After comparing values of posterior probabilities $p(i \mid x_n, \theta)$ at each pixel, the cluster resulting in the maximal probability was identified and the pixel was labeled accordingly. The classification rate for each cluster, denoted by r_i, was defined by the observed proportion of agreements, namely $r_i = f_i / n_i$, where f_i was the number of agreements for the i th cluster and n_i was the total number of pixels in the i th class. The classification rate for a set of simulated dynamic images, denoted by R, was computed by $R = \sum_{i=1}^{K} 100 \times r_i / K$ (percentage), where K is the number of clusters.

III. Results

The results of Monte Carlo are summarized as follows 1) The EM-MoMG method initialized by the results of HC on the whitened data outperformed the other three initializations. Not only the averaged classification rates were much higher, which were between $99.0 \pm 0.39\%$ and $93.6 \pm 1.42\%$ under the noise-free with 4 hypothetical tissue clusters and SNR=40 with 9 hypothetical tissue clusters,

respectively, but also the standard deviations were much smaller (always less than 1.42%), implying accurate and reliable segmentations; 2) The mean classification rates from all methods decreased slightly as the SNR decreased from the noise-free condition to 40. In the case of the proposed EM-MoMG method with whitened+HC initial, the largest decrease and increase of the mean classification rate and standard deviation were merely 0.5% and 0.07%, respectively, namely, from 94.1 ± 1.35% (noise free) to 93.6 ± 1.42% (SNR = 40) in the case of 9 hypothetical tissue clusters; 3) The performances of all methods degraded as the number of hypothetical tissue clusters increased. In the worst case of SNR = 40, although the results obtained from the EM-MoMG method with whitened+HC initial decreased from 98.9 ± 0.40% to 93.6 ± 1.42%, they were far superior to other results in terms of higher classification rates with much smaller standard deviations.

Five normal subjects' data were processed and their perfusion images were segmented into different compartments based on the rule of minimizing MDL. Figure 1 illustrates the segmentation image and its corresponding mean concentration-time curves of one normal subject. Figure 2 illustrates the hemodynamic parametric maps derived from the averaged concentration-time curve of artery.

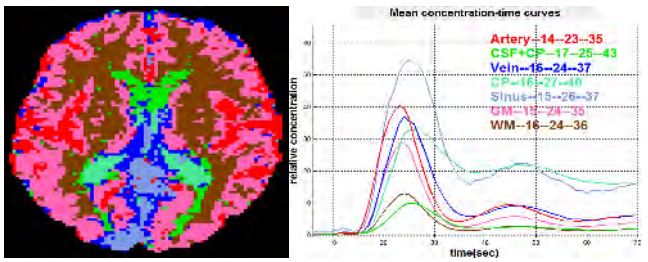


Fig.1 Segmentation results. Left is the composite color-coded image. Right is the corresponding mean concentration-time curves. Seven compartments, namely arteries (red), cerebrospinal fluid +choroid plexus (green), vein (blue), choroid plexus (cyan), sinus (light blue), gray matter (pink) and white matter (brown), were segmented from the whitened dimension-reduced data by EM-MoMG method. The three numbers following each name of tissue type in left-to-right order in the plot stand for the starting time, peak time and ending time of the first pass of contrast.

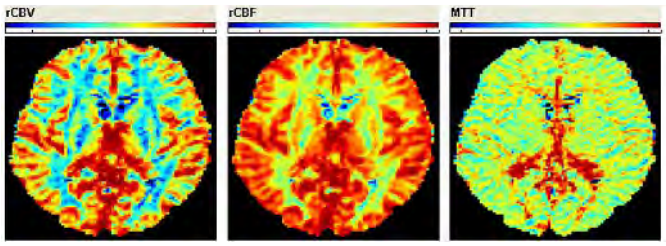


Fig.2 Hemodynamic parametric maps. From left to right are rCBV, rCBF and MTT, respectively.

The average ratios of gray matter(GM) to white matter(WM) for rCBV, rCBF and MTT were 2.196±0.097, 2.259±0.119 and 0.968±0.023, respectively, which are in good agreement with those reported in the literature[9] and it demonstrates the accuracy and feasibility of our proposed method.

IV. Conclusions

The study presents an EM-MoMG method initialized by the HC on the whitened data. This method features several advantages for central hemodynamics studies and clinical applications. First, an AIF can be modeled consistently on the same slice location for the calculation of hemodynamic parametric maps. Second, various tissue compartments on perfusion images can be classified systematically. Third, the bolus transit profiles of these tissues can be well separated.

Acknowledgment

This work was supported in part by NSC96-2628-E-010-015-MY3, NSC 97- 2752-B-010-006-PAE, NSC 97-2752-B-075-001-PAE.

References

1. Zierler KL (1962) Theoretical basis of indicator-dilution methods for measuring flow and volume. Circulation Research 10:393-407
2. Hyvarinen A, Oja E (1997) A fast fixed-point algorithm for independent component analysis. Neural Computation 9(7):1483-1492
3. Bishop CM (1995) Neural networks for pattern recognition. Oxford University Press, Oxford, UK.
4. Wishart D (1969) An algorithm for hierarchical classifications. Biometrics 25:165-170
5. Schwarz G (1978) Estimating the dimension of a model. Ann. Stat. 6:461-464
6. Wu YT, Chou YC, Guo WY et al. (2007) Classification of spatiotemporal hemodynamics from brain perfusion MR images using expectation-maximization estimation with finite mixture of multivariate Gaussian distrubutions. Magn. Reson. Med. 57(1):181-191
7. Otsu N (1979) A threshold selection method froim gray-level histograms. IEEE Trans. Syst. Man Cybern. 9(1):62-66
8. Ostergaard L, Weisskoff RM, Chesler DA et al. (1996) High resolution measurement of cerebral blood flow using intravascular tracer bolus passages. Part I: Mathematical approach and statistical analysis. Magn. Reson. Med. 36(5):715-725
9. Calamante F, Thomas DL, Pell GS et al. (1999) Measuring cerebral blood flow using magnetic resonance imaging techniques. J. Cereb. Blood Flow Metab. 19(7):701-735

Author: Yu-Te Wu
Institute: Department of Biomedical Imaging and Radiological Sciences, National Yang-Ming University,
Street: No.155, Sec.2, Linong Street
City: Taipei
Country: Taiwan, ROC
Email: ytwu@ym.edu.tw

Enhancement of Signal-to-noise Ratio of Peroneal Nerve Somatosensory Evoked Potential Using Independent Component Analysis and Time-Frequency Template

C.I. Hung[1,2], Y.R. Yang[3], R.Y. Wang[3], W.L. Chou[3], J.C. Hsieh[2,4] and Y.T. Wu[1,2,4,*]

[1]Department of Biomedical Imaging and Radiological Science, National Yang-Ming University, Taipei 112, Taiwan, ROC
[2]Integrated Brain Research Laboratory, Department of Medical Research and Education, Taipei Veterans General Hospital, Taipei 112, Taiwan, ROC
[3]Department of Physical Therapy and Assistive Technology, National Yang-Ming University, Taipei 112, Taiwan, ROC
[4]Institute of Brain Science, National Yang-Ming University, Taipei 112, Taiwan, ROC

Abstract — **This study aims to recover the somatosensory evoked potentials (SSEPs) from the smearing electroencephalography (EEG) recordings using independent component analysis (ICA) in conjunction with the proposed time-frequency SSEP template (TF-SSEP). The SSEPs induced from patients with the impaired motor functions exhibit longer latency and lower amplitude than the normal SSEPs and are inevitably contaminated by artifacts and environmental noise. Although ICA has been demonstrated as a novel technique to segregate the EEG into independent sources, the selection of task-related components needs to be further elaborated. The TF-SSEP template, generated by the Morelet wavelet transformation of the averaged SSEPs from three normal subjects, was used to automatically extract the SSEP-related features. The performance of the TF-SSEP template was further validated using EEGs through the left and right peroneal nerve stimulation of four stroke patients. After ICA decomposition, the sources were selected for reconstruction if their correlation coefficients with the TF-SSEP template were higher than the predetermined threshold. On the other hand, the unselected sources were considered as the event-unrelated components or artifacts. Among all patients, the topography maps at four peak times, namely P40, N45, P60 and N75, showed higher contrast in the vicinity of the foot-associated motor area, and the resolved SSEPs demonstrated uncontaminated waveforms in comparison with the conventionally averaging method. This indicated that the proposed method can remarkably suppress artifacts and effectively extracted the SSEP-related features.**

Keywords — **Somatosensory evoked potential (SSEP), Independent component analysis (ICA), Peroneal nerve, Time-frequency template.**

I. Introduction

Evoked potentials are the electrical activities generated by the nervous system in response to external sensory stimuli. Cortical somatosensory evoked potential (SSEP), recorded by electroencephalography (EEG) system, has been applied to assess the functional integrity of the nervous system or to assist in the diagnosis of certain neuropathologic states [1]. Specifically, the morphological characteristics, i.e. latency and amplitude, of SSEP following stimulation of the lower limbs have been used to evaluate the rehabilitation treatment of stroke patients. In comparison with the EEG background rhythm, the evoked potential is much smaller, especially in stroke patients with impaired motor function [2]. The conventional method employs the average of hundreds of trials to increase the signal-to-noise ratio which, however, can only reduce the disturbances of random noise and un-phase-lock brain oscillations. Accordingly, the development of advanced techniques to extract such minute signals is of potentially importance.

EEG recordings are overlapping activities contributed from individual neurons inside the brain as well as the artifacts produced outside the brain [3]. Independent component analysis (ICA) [4-5] is one of the most effective blind-source-separations to separate independent sources from mixing signals, which in turn enables us to resolve features of interest from EEG. ICA has been successfully applied to remove non-physiological artifacts from EEG data [4,5], to segregate Rolandic beta rhythm from magnetoencephalographic (MEG) measurements of right index finger lifting [6], to extract task-related features from motor imagery EEG and flash visual evoked EEG in the study of the brain-computer interface [7,8], to discriminate the concurrent abnormal patterns from EEGs of Creutzfeldt-Jacob disease [9], and to segment spatiotemporal hemodynamics from perfusion magnetic resonance brain images [10].

After ICA decomposition, the signal-to-noise ratio is enhanced by selecting the task-related components for reconstruction, i.e. eliminating the artifact-related or task- unrelated components of the signals. Accordingly, the key step of such ICA-based approaches is the identification of the independent components (ICs) of interest. In this study, we propose a time-frequency-based approach to automatically select the SSEP-related components. We first created a time-frequency (TF) map of the SSEP induced by peroneal nerve stimulation using the Morlet wavelet transformation [11]. The resultant TF-SSEP map was employed as a template to match the TF maps calculated from the EEG independent components of stroke patients. The reconstructed

Chwee Teck Lim, James C.H. Goh (Eds.): ICBME 2008, Proceedings 23, pp. 718–721, 2009
www.springerlink.com

SSEP waveforms obtained from the selected components demonstrated that ICA in conjunction with TF-SSEP template was a robust method to effectively remove the contamination of artifacts.

II. Material and Method

A. EEG recordings

Seven participants (all males), 3 normal subjects and 4 patients with chronic stroke, were recruited for this study. The normal EEG data sets were employed to establish the standard template which consisted of the time-frequency features, i.e. TF-SSEP. The conventional averaging technique and the waveform reconstruction using the separated ICs selected by the TF-SSEP template were applied on the EEGs for performance assessment.

Surface stimulations of the right and left peroneal nerves were performed on the dorsum of the ankle using constant current square wave pulses of 1 ms duration with a stimulation rate of 3 Hz. The stimulus current was set to produce the minimal twitch of the extensor digitorum brevis muscle. Each nerve was stimulated with one session consisting of 1000 stimuli. The EEGs through the peroneal nerve stimulations were acquired using a 32-channel SymAmp EEG system (digitized at 1000 Hz) with Ag/AgCl surface electrodes, placed based on the configuration of the extended international 10-20 system (Fig. 1(A)). The referential montage was applied in the whole head recordings (bandpass filtered between 1 to 450 Hz), and the SSEPs were furthermore calculated from the bipolar derivation, Cpz-Fz.

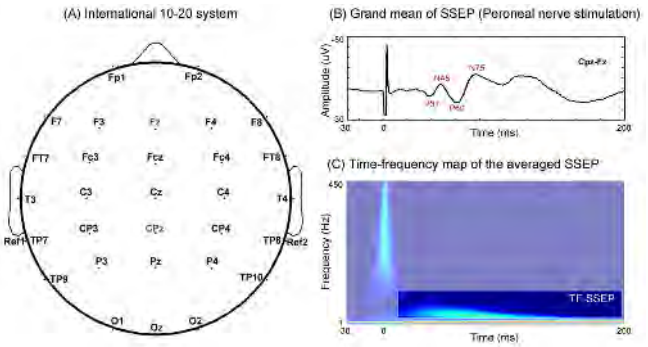


Fig. 1 . (A) The whole scalp of each subject was covered with 32 EEG electrodes placed onto anatomical locations according to the extended international 10-20 system, where Fp, F, C, P, O, and T represent the abbreviations of frontal polar, frontal, central, parietal, occipital, and temporal, respectively. (B) The grand mean of SSEP (gmSSEP) computed from the EEGs through peroneal nerve stimulation, in which P37, N45, P60 and N75 are the four main peak times of interests. (C) The TF map of SSEP produced by the transformation using Morlet wavelet. The darker blue area indicates the feature of interest.

B. Blind source separation by FastICA

ICA is a statistical method that has been developed to extract independent signals from a linear mixture of sources. Let $\underset{m\times n}{X}$ denote the measured data with m and n being the number of channels and the number of data samples, respectively. In the context of ICA, **X** is assumed to be linear combinations of k unknown independent components and can be expressed as

$$\underset{m\times n}{\mathbf{X}} = \underset{m\times k}{\mathbf{A}} \cdot \underset{k\times n}{\mathbf{S}} \tag{1}$$

where **S** contains k independent sources with the same data length as **X**, and **A** is a constant mixing matrix with the k_{th} column representing the spatial weights corresponding to the k_{th} component of **S**. Given the measurement **X**, ICA techniques attempt to recover both the mixing matrix **A** and the independent sources **S**. In the present study, all calculations were performed using the FastICA algorithm [12,13]. The FastICA technique first removes means of the row vectors in the **X** matrix and then uses a whitening procedure, implemented by principal component analysis [13], to transform the covariance matrix of the zero-mean data into an identity matrix. In the next step, FastICA searches for a rotation matrix to further transform the whitened data into a set of components which are as mutually independent as possible. In combination with the previous whitening process, the matrix **X** is transformed into a matrix S via an un-mixing matrix W, i.e.,

$$\underset{k\times n}{\mathbf{S}} = \underset{k\times m}{\mathbf{W}}\ \underset{m\times n}{\mathbf{X}} \tag{2}$$

so that rows of **S** are mutually independent. In this study, the pre-processed epochs were concatenated and arranged across m channels (m=30) and n sampled points (n=231*1000) into a $m\times n$ matrix **X**. The i_{th} row contains the observed signal from the i_{th} EEG channel, and the j_{th} column vector contains the observed samples at the j_{th} time point across all channels. FastICA was applied on the pre-processed and concatenated signals to resolve **W** and **S**. After estimating the un-mixing matrix **W**, we can recover the temporal waveforms of each independent source by applying the inverse matrix of **W** on both sides of equation (2) to yield

$$\underset{m\times n}{\mathbf{X}} = \underset{m\times k}{\mathbf{W}^{-1}} \cdot \underset{k\times n}{\mathbf{S}} \tag{3}$$

where $\mathbf{W}^{-1}$ is the best estimation of the mixing matrix **A** in equation (1). In this study, **S** represents the time sequences of activation sources, i.e. temporal waveforms of ICs, and **A** stands for the weighting of sources recorded

from electrodes. Since **W** is the estimated un-mixing matrix, each column in $\mathbf{W}^{-1}$ represents a spatial map describing the weightings of the corresponding temporal component at each EEG channel. These spatial maps will hereinafter be referred to as IC spatial maps. To determine the number of sources, we simply used the number of channels as the number of sources, as suggested by previous studies [4-10].

C. Criterion for discrimination of ICs

To discriminate the SSEP-related from artifact-related ICs, the TF-SSEP was generated to select ICs. We computed the grand mean of SSEP (Fig. 1 (B)) by averaging the normal SSEPs across all trials and three subjects, which was then transformed into the TF map by using the Morlet wavelet. The window consisted of temporal features within 20 ms to 200 ms after stimulus and frequency information from 10 to 50 Hz (see dark blue area in Fig. 1(C)) was used as the TF-SSEP template

In the present study, the selection criterion for ICs was validated using normal EEGs prior to the processing of EEGs from stroke patients. After ICA decomposition, the correlation coefficients between the templates and ICs were computed. In order to select the SSEP-related ICs, a cutoff value was required. The lower the cutoff value, the more ICs were selected. Since the values of correlation ranged from -1 to 1, we examined cutoff values between -0.5 and 1. The cutoff value, or threshold, for IC selections using the TF-SSEP was determined to be 0.65 so that the correlation coefficients between the reconstructed SSEP (rSSEPs) and the averaged SSEP was as high as 0.9.

III. Results

Figure 2 shows the artifact-suppressed results from the EEGs induced by the right PNS ((A)-(D)) and left PNS ((E)-(H)) of the stroke patients (PT1-4). The averaged SSEPs without using ICA and the rSSEPs using TF-SSEP templates are denoted by green and red waveforms, respectively. It should be noted that the ripple artifacts, which constantly appeared in each trial, cannot be suppressed by the conventional averaging technique (see green spikes and ripples in (B)(C)(D) and (F)(G)(H)). However, as in the normal cases (IC2 in Fig. 4(A)), such contaminations have been successfully separated from the ICA, which in turn can be substantially reduced in the reconstructed results (red curves). The corresponding topographies calculated at the four peak times, labeled 1 (P37), 2 (N45), 3 (P60), and 4 (N80), are displayed in the second and third rows in the upper and lower panels.

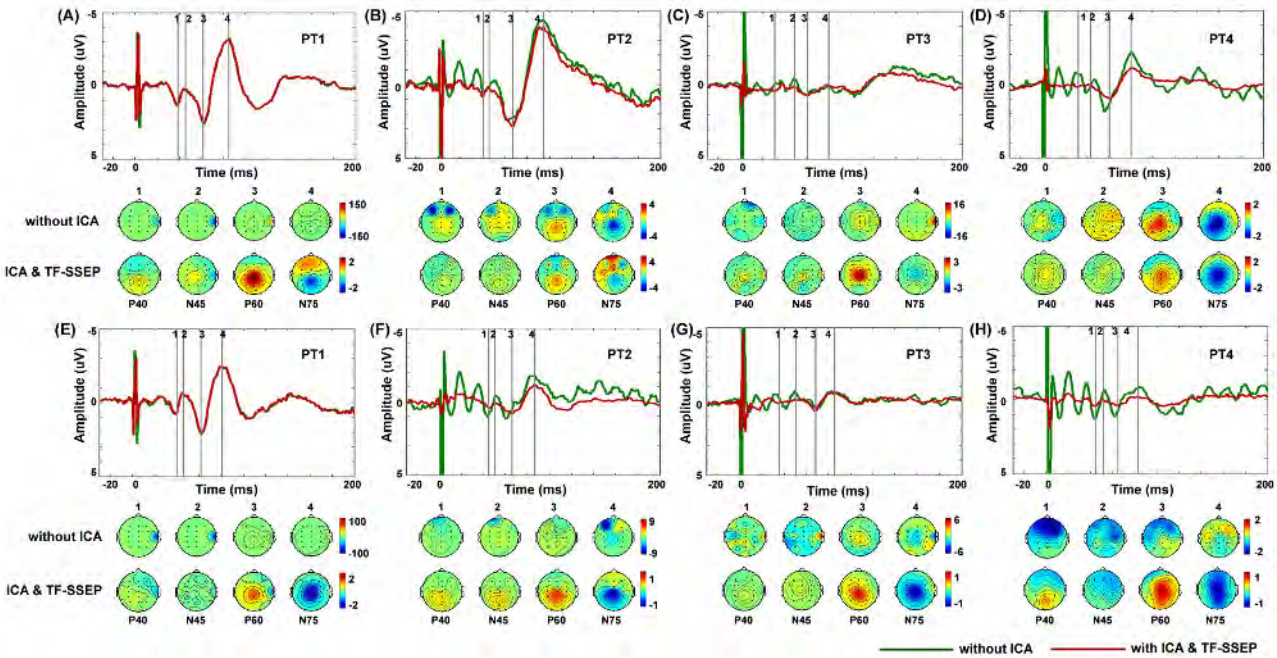


Fig. 2 . The results from the EEGs induced by the right PNS ((A)-(D)) and left PNS ((E)-(H)) of the stroke patients (PT1-4). The green and red curves represent the SSEPs obtained from conventional averaging, and the reconstructed SSEPs using the TF-SSEP templates, respectively. The corresponding topographical maps at P37, N45, P60, and N80 are displayed below the plots of reconstructed SSEPs.

IV. Conclusions

It is worth noting that the signal-to-noise ratio of SSEPs of stroke patients could be much worse than that of the normal, which made the averaging method have difficulty to extract reliable SSEPs from the smearing background (green curves in Figs. 5(B)(C)(D) and (F)(G)(H)). Accordingly, the EEG has seldom been used to investigate reorganization of motor system after stroke in human, although motor recovery assessed by the functional neuroimaging has become an intriguing field over the last decade [14]. Our results demonstrated that the SSEPs embedded in the EEGs of stroke patients can be successfully resolved by ICA with the TF-SSEP template, which sheds the light for the future study of reorganization of motor system for stroke patients.

Acknowledgment

The study was funded by Taipei Veterans General Hospital (V96 ER1-005) and the National Science Council (NSC 96-2221-E-010-003-MY3, NSC 97-2752-B-075-001- PAE, NSC 97-2752-B-010-003-PAE).

References

1. Freye E. (2005) Cerebral monitoring in the operating room and the intensive care unit: an introductory for the clinician and a guide for the novice wanting to open a window to the brain. J. Clin. Monitor. Comp 19:77-168.
2. Misulis K E, Head T C. (2002) Essentials of Clinical Neurophysiology.Butterworth-Heinemann, Boston.
3. Fisch B J. (1999) Fisch and spehlmann's EEG primer.Elsevier Science B.V., Amsterdam.
4. Jung T P, Makeig S, Humphries C et al. (2000) Removing electroencephalographic artifacts by blind source separation. Psychophysiology 37:163-178.
5. Jung T P, Makeig S, Westerfield M et al. (2000) Removal of eye activity artifacts from visual event-related potentials in normal and clinical subjects. Clin. Neurohysiol. 111:1745-1758.
6. Lee P L, Wu Y T, Chen L F et al. (2003) ICA-based spatiotemporal approach for single-trial analysis of postmovement MEG beta synchronization. NeuroImage 20:2010-2030.
7. Hung C I, Lee P L, Wu Y T et al. (2005) Recognition of motor imagery electroencephalography using independent component analysis and machine classifiers. Ann. Biomed. Eng. 33(8):1053-1070.
8. Lee P L, Hsieh J C, Wu C H et al. (2006) The brain computer interface using flash visual evoked potential and independent component analysis. Ann. Biomed. Eng. 34(10):1641-1654.
9. Hung C I, Wang P S, Soong B W et al. (2007) Blind source separation of concurrent disease-related patterns from EEG in Creutzfeldt-Jakob disease for assisting early diagnosis. Ann Biomed Eng 35(12):2168-2179.
10. Kao Y H, Guo W Y, Wu Y T et al. (2003) Hemodynamic segmentation of MR brain perfusion images using independent component, Bayesian estimation and thresholding. Magn. Reson. Med. 49:885-894.
11. Daubechies I. (1992) Ten Lectures on Wavelets.SIAM, Philadelphia, P.A.
12. Vigário R, Särelä J, Jousmäki V et al. (2000) Independent component approach to the analysis of EEG and MEG recordings. IEEE Trans. Biomed. Eng. 47(5):589-593.
13. Hyvärinen A, Karhunen J, Oja E. (2001) Independent Component Analysis.John Wieley & Sons, Inc., New York.
14. Calautti C, Baron J C, FMedSci F R C P. (2003) Functional neuroimaging studies of motor recovery after stroke in adults. Stroke 34:1553-1566.

Author: Yu-Te Wu
Institute: Department of Biomedical Imaging and Radiological Sciences, National Yang-Ming University,
Street: No.155, Sec.2, Linong Street
City: Taipei
Country: Taiwan, ROC
Email: ytwu@ym.edu.tw

Multi-tissue Classification of Diffusion-Weighted Brain Images in Multiple System Atrophy Using Expectation Maximization Algorithm Initialized by Hierarchical Clustering

C.F. Lu[1,7], P.S. Wang[2,3,4], B.W. Soong[2,5], Y.C. Chou[1], H.C. Li[6], Y.T. Wu[1,6,7]

[1] Department of Biomedical Imaging and Radiological Sciences, National Yang-Ming University, Taipei, Taiwan, ROC
[2] The Neurological Institute, Taipei Veterans General Hospital, Taipei, Taiwan, ROC
[3] Department of Neurology, National Yang-Ming University School of Medicine, Taipei, Taiwan, ROC
[4] The Neurological Institute, Taipei Municipal Gan-Dau Hospital, Taipei, Taiwan, ROC
[5] The Faculty of Medicine, National Yang-Ming University, Taipei, Taiwan, ROC
[6] The Institute of Brain Science, National Yang-Ming University, Taipei, Taiwan, ROC
[7] Integrated Brain Research Laboratory, Department of Medical Research and Education, Taipei Veterans General Hospital, Taipei, Taiwan, ROC

Abstract — **Multiple system atrophy (MSA) is a well-known neurodegenerative disorders that present parkinsonism syndrome and autonomic dysfunction. Patients with MSA who have the combination of parkinsonism and cerebellar ataxia are referred to as MSA-C. Brain diffusion-weighted imaging (DWI) offers the potential for objective criteria in the diagnosis of MSA. We aim to develop an automatic method to segment out the abnormal whole brain area in MSA-C patients based on the 13-direction DWI raw data. The whole brain DWI raw data of fifteen normal subjects and nine MSA-C patients were analyzed. In this study, we proposed a novel method to perform tissue segmentation directly based on the directional information of the DWI images, rather than using the parametric images, such as fractional anisotropy (FA) and apparent diffusion coefficient (ADC) as in the previous literatures. Specifically, a hierarchical clustering (HC) technique was first applied on the down-sampled data to initialize the model parameters for each tissue cluster followed by automatic segmentation using the expectation maximization (EM) algorithm. Our results demonstrate that the HC-EM is effective in multi-tissue classification, namely, the cerebrospinal fluid, gray matter, and several areas of white matters, on the DWI raw data. The segmented patterns and the corresponding intensities of thirteen directions of the cerebellum in MSA-C patients showed the decrease of the anisotropy, which were evidently different from the results in normal subjects.**

Keywords — **Multiple system atrophy, diffusion- weighted imaging, hierarchical clustering, expectation maximization algorithm**

I. Introduction

Brain tissue segmentation plays an important role in both structural and functional studies. However, most of the methods in segmentation issues were based on the difference of image intensity in MR structural data, and can be limited due to the field in-homogeneity, partial-volume effect, etc. Diffusion weighted images (DWI), on the other hand, can provide complementary information of tissue contrast to the structural MRI for facilitating the tissue segmentation. In a previous study, Liu et al. have demonstrated that tissue segmentation results based on the parametric images was superior to that in structural MR images [1], but the features of directions of neural fibers have been lost in the parametric images and thus only limited information was utilized.

In this study, we propose a novel method to segment the brain tissue directly on the 13-direction DWI raw data in MSA-C patients so that the direction information can be fully taken into account. To initialize the segmentation for each tissue cluster, the hierarchical clustering (HC) based on a minimum variance algorithm (the Ward's method) [2] was first applied on the down-sampled data. By the assumptions that each tissue type is a multivariate Gaussian function and the overall distribution of the raw data is a mixture of multivariate Gaussians (MoMG) [3], we initialized the parameters of the MoMG and the proportion of each class using the segmented results from HC. Finally, the tissue classifications on the higher dimensional data were given by the expectation maximization (EM) algorithm. Data from fifteen normal subjects and nine MSA-C patients were analyzed. The results illustrated that HC-EM is effective in multi-tissue classification. The segmented patterns and the corresponding intensities of thirteen directions of the cerebellum in MSA-C patients were evidently different from the results in normal subjects.

II. Material and method

A. Subjects and Data Recording

Fifteen normal subjects (9 male and 6 female; range of age, 23-89 years) and nine MSA-C patients (5 male and 4

Chwee Teck Lim, James C.H. Goh (Eds.): ICBME 2008, Proceedings 23, pp. 722–725, 2009
www.springerlink.com

female; range of age, 32-67 years; disease duration, 1-8 years) participated in this study. Written informed consent was obtained from each volunteer before this study. For the DWI settings, A multi-slice gradient-echo EPI pulse sequence on a 1.5 Tesla GE Echo speed scanner system (Signa® CV/i, GE Medical Systems, Milwaukee, WI, USA) was used with the following settings. Sequence: maximum gradient amplitudes: 40 mT/M; square FOV: 240×240 mm; matrix = 128×128; 3 mm slice thickness; no interslice distance; TE: 69.70 ms; TR: 15000 ms; b value: 1000 s/mm^2. DWI images along thirteen non-collinear directions were collected. Whole brain data for about 50 slices, one acquisition, and fourteen images per slice location (one T2 structural image and thirteen directional DWI images).

B. Data Pre-processing

The brain regions were extracted from the diffusion-weighted images slice by slice. We first set all pixel values lower than 15% of the maximum intensity to zero and followed by the erosion (3×3 structure element) and dilation (5×5 structure element) operation. With total $v = \sum_i v_i$ pixels (without air background), v_i stands for the pixels of brain areas on *ith* slice, the observation of 13 directional images can be represented by a $13 \times v$ matrix, i.e., each row is whole brain area and each column contains signal intensities of a pixel across 13 different directions.

In this study, we assume that there are *N* major tissue types presented on DWI images and the overall distribution of the raw data is a MoMG. The raw DWI data with dimension $13 \times v$ was first reduced its dimension to $N \times v$ by whitening process, which is mathematically similar to principal component analysis (PCA). By the limitation of memory capacity, we use the down-sampled data, $N \times v'$ with $v' \le v$, in the following HC step, after such approximate segment by HC, the second step, EM algorithm, would optimize the parameters on the original raw data to carry out the tissue segmentation.

C. Hierarchical Clustering

HC is a means to carry out grouping in a data set based on a created cluster tree with multilevel hierarchy, where clusters at one level are joined as clusters at the next higher level. HC consists of three major parts: (1) find the dissimilarity between every pair of feature vectors in the data set; (2) group the feature vectors into a binary and hierarchical cluster tree; (3) determine what level or scale of clustering by cutting the hierarchical tree. Many algorithms are available in regard to the calculation of dissimilarity and the creation of cluster tree [4]. In this study, we adopted the Euclidean distance to calculate the dissimilarity, which was defined by

$$d_{rs}^2 = (x_r - x_s)^T (x_r - x_s). \tag{1}$$

where d_{rs}^2 is the Euclidean distance between two featured column vectors x_r and x_s. In order to construct the cluster tree, we employed the Ward's method to measure the distance between two clusters which was defined by

$$d^2(p,q) = n_p n_q \frac{\left\| \bar{x}_p - \bar{x}_q \right\|_2^2}{(n_p + n_q)} \tag{2}$$

where $d^2(p,q)$ is the distance between two clusters of featured vectors, n_p and n_q are the numbers of featured vectors in cluster *p* and *q*, respectively, $\| \ \|_2$ is the Euclidean distance, $\bar{x}_p$ and $\bar{x}_q$ and are the centroids of clusters *p* and *q*, respectively, which are defined by

$$\bar{x}_p = \frac{1}{n_p} \sum_{i=1}^{n} x_{pi} \ \text{ and } \ \bar{x}_q = \frac{1}{n_q} \sum_{j=1}^{m} x_{qj} \tag{3}$$

where x_{pi} is the *i*th featured vector in cluster *p* and x_{qj} is the *j*th objects in cluster *q*.

D. Expectation Maximization Algorithm

Let each point in the whiten data be denoted by $x_n (N \times 1)$, $n = 1, \ldots v$. The tissue segmentation was carried out by EM algorithm which fit the overall distribution of the whiten data to a mixture of multivariate Gaussian distributions consisting of two alternating iterative steps, namely, E-step and M-step. The E-step is to compute the posterior probabilities of tissue classes $p(i | x_n, \theta^{j-1})$ based on the estimation from previous *(j-1)th* iteration

$$p(i | x_n, \theta^{j-1}) = \frac{\pi_i^{j-1} g_{x_n}[\mu_i^{j-1}, \Sigma_i^{j-1}]}{\sum_{l=1}^{N} \pi_l^{j-1} g_{x_n}[\mu_l^{j-1}, \Sigma_l^{j-1}]} \tag{4}$$

where *i=1, ... N* represent labels of tissue classes, $g_{x_n}[\mu_i, \Sigma_i]$ represents the multivariate Gaussian density with the mean vector μ_i and covariance matrix Σ_i of tissue class *i,* π_i denotes the proportion of each class *i,* and θ^{j-1} denotes the parameters $\{ \mu_i^{j-1}, \Sigma_i^{j-1}, \pi_i^{j-1} \}$ at the *(j-1)th*

iteration. The M-step consists of estimating parameters θ^j as follows

$$\mu_i^j = \frac{\sum_{n=1}^{v} p(i \mid x_n, \theta^{j-1}) x_n}{\sum_{n=1}^{v} p(i \mid x_n, \theta^{j-1})},$$
$$\Sigma_i^j = \frac{\sum_{n=1}^{v} p(i \mid x_n, \theta^{j-1}) x_n x_n^T}{\sum_{n=1}^{v} p(i \mid x_n, \theta^{j-1})} - \mu_i^j (\mu_i^j)^T, \quad (5)$$
$$\pi_i^j = \frac{1}{v} \sum_{n=1}^{v} p(i \mid x_n, \theta^{j-1})$$

The number of classes N is determined by information criterion of minimum description length (MDL) [3]. The tissue label at each pixel was determined by the maximal value of $p(i \mid x_n, \theta^{j-1})$ at that pixel and therefore each tissue type was classified.

III. Results

A. Normal Subjects

Each DWI raw data set covers whole brain areas (including cerebellum and cerebrum) and Figure 1 displays the fourteen images on a particular slice position for a normal subject.

The final segmentation result based on HC-EM algorithm was depicted by a color-coded composite image (right-lower image in Figure 2). Compared with the segmentation result on structural MR T2 image obtained from Otsu approach (left-lower image in Figure 2), a well-known automatic thresholding method [5], the gray matter (GM, colored in green) classified was obviously over-segmented on the posterior region (white arrows in Figure 2), whereas the GM and cerebrospinal fluid (CSF, colored in brown) were satisfactorily segmented out by our method. These segmentation results show that the intensity-based classification approach, such as Otsu thresholding, would highly depend on the intensity homogeneity of image data and our method could alleviate this disadvantage by taking the directional information into account from 13 directional DWI images. Moreover, the HC-EM algorithm could further divided the anisotropic-white-matter area (colored in red, blue, pink and yellow), into four different clusters according to their different directional primitives. The color map of 1st eigenvectors was calculated to validate our result [6].

Figure 3 shows the corresponding mean signal-direction curves of whole brain areas. The mean signal-direction curves illustrate the variant directional properties of each cluster. For example, the curves of GM (green) and CSF (brown) are less fluctuated than that of other tissues, suggesting the diffusion of these two clusters is less dependent on direction, i.e., isotropic diffusion. Moreover, the mean directional signal intensity between GM and CSF are quite different and therefore classified into different clusters by the EM algorithm.

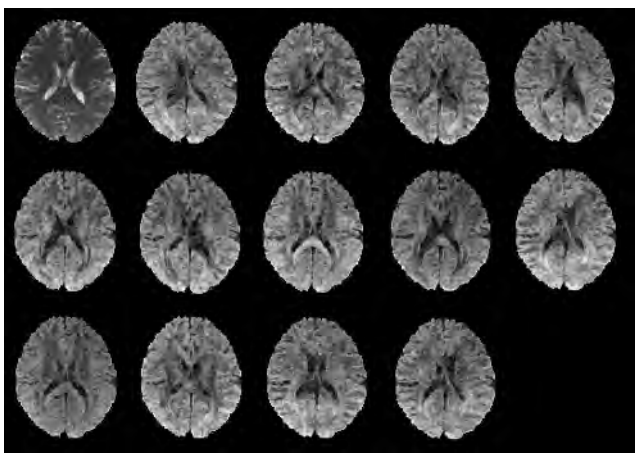


Fig. 1. The 14 images on a slice location consisted of T2 weighted image (upper leftmost one) and 13 directional DWI images.

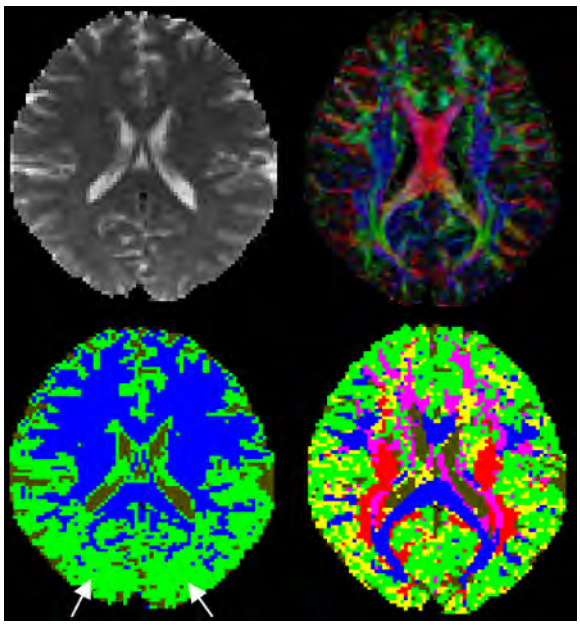


Fig. 2. The structural MR T2 image (upper left), the color map of 1st eigenvectors (upper right), the segmentation result by Otsu thresholding on T2 image (lower left) and the final segmentation result for each tissue type represented by a color-coded composite map by HC-EM algorithm on DWI raw data (lower right). Gray matter is labeled by green, cerebrospinal fluid by orange and white matter is depicted by red, blue, pink and yellow. The white arrows point out the over-segmented area of GM by Otsu method on structural T2 image.

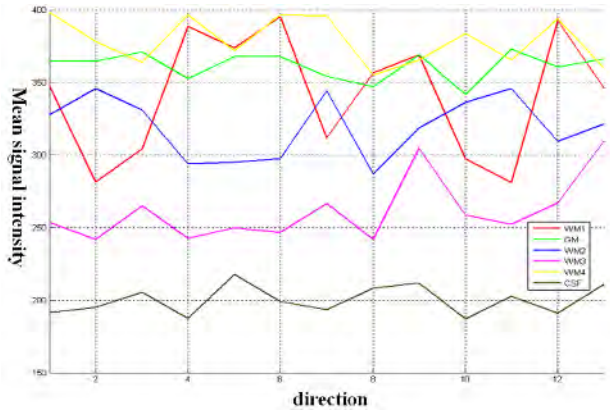


Fig. 3. The mean signal–direction curves of whole brain areas resulted from the HC-EM algorithm.

B. MSA-C patients

In order to show the abnormality in the MSA-C patients, we focused on the slices of the cerebellum areas. Figure 4 illustrates the results of tissue classification using the HC-EM method from a normal subject (left column) and a MSA-C patient (right column). The T2 images on the upper row in Figure 4 exhibited the evident atrophy of cerebellum with large area of high-intensity CSF in the MSA-C patient. In the clustering results on the lowest row, the parenchyma of normal cerebellum were segmented into three major different areas (blue, red and yellow) with averaged intensity ranging from 400 to 500 (Figure 5, left). In contrast, the clustering result in the MSA-C patient only showed one area (blue) in the parenchyma of cerebellum and three different low-intensity CSF areas (Figure 5, right).

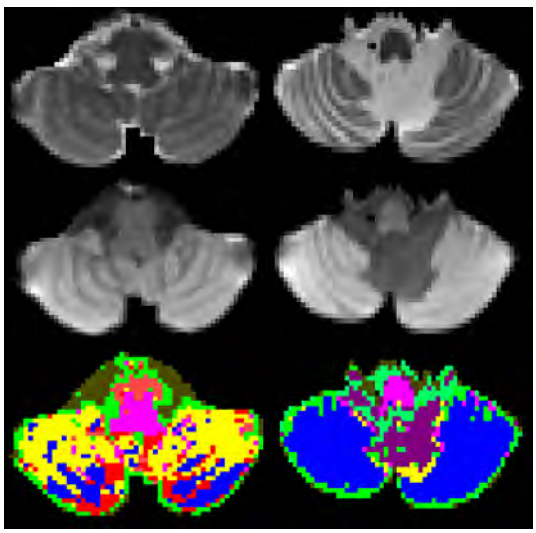


Fig. 4. The left column shows a particular slice of the cerebellum images from a normal subject, and the right column from a MSA-C patient. The upper row presents the T2 images; the middle row presents the averaged images of T2 and 13 directional DWIs; the lower row shows the clustering results using the HC-EM method.

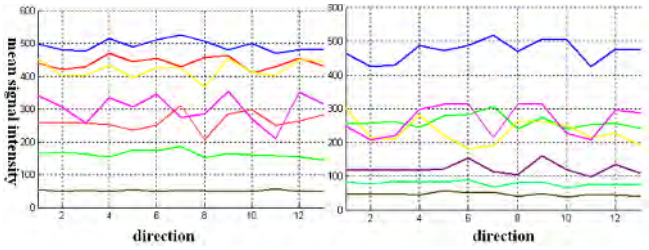


Fig. 5. The signal–direction curves corresponding to the results in Fig. 4 in the normal subject (left) and MSA-C patient (right).

Our results demonstrated that the complexity of the anisotropy in the cerebellum of the MSA-C patient was decreased compared with that of the normal subject. Figure 5 shows the signal-direction curves corresponding to Figure 4 of segmented clusters for the normal subject (left) and MSA-C patient (right).

IV. Conclusions

This study presents a novel HC-EM method for the extraction of different directional dependence tissues from brain diffusion-weighted images. This method features several advantages for using directional information and could be an effective tool for diagnosis of MSA-C.

References

1. Liu T, Li H, Wong K, Tarokh A, Guo L, Wonga TC (2007) Brain tissue segmentation based on DWI data. NeuroImage 38:114-123.
2. Wishart D (1969) An algorithm for hierarchical classifications. Biometrics 25:165-170.
3. Wu YT, Chou YC, Guo WY, Yeh TC, Hsieh JC (2007) Classification of spatiotemporal hemodynamics from brain perfusion MR images using expectation-Maximization estimation with finite mixture of multivariate Gaussian distributions. Magnetic Resonance in Medicine 57: 181-191.
4. Schwarz G (1978) Estimating the dimension of a model. Ann. Statist. 6: 461-464.
5. Otsu N (1979) A threshold selection method from gray-level histogram. IEEE Transactions on Systems, Man, and Cybernetics.
6. Jiang H, Kim J, Pearlson GD, Mori S (2006) DtiStudio: Resource program for diffusion tensor computation and fiber bundle tracking. Computer Methods and Programs in Biomedicine 81:106-116.

Author: Yu-Te Wu
Institute: Department of Biomedical Imaging and Radiological Sciences, National Yang-Ming University
Street: No.155, Sec.2, Linong Street
City: Taipei
Country: Taiwan
Email: ytwu@ym.edu.tw

Small-world Network for Investigating Functional Connectivity in Bipolar Disorder: A Functional Magnetic Images (fMRI) Study

S. Teng[1,2], P.S. Wang[3,4,5], Y.L. Liao[7], T.-C. Yeh[2,6], T.-P. Su[8,9], J.C. Hsieh[2,6], Y.T. Wu[1,2,6]

[1] Department of Biomedical Imaging and Radiological Sciences, National Yang-Ming University, Taipei, Taiwan, ROC
[2] Integrated Brain Research Laboratory, Department of Medical Research and Education, Taipei Veterans General Hospital, Taipei, Taiwan, ROC
[3] The Neurological Institute, Taipei Veterans General Hospital, Taipei, Taiwan, ROC
[4] Department of Neurology, National Yang-Ming University School of Medicine, Taipei, Taiwan, ROC
[5] The Neurological Institute, Taipei Municipal Gan-Dau Hospital, Taipei, Taiwan, ROC
[6] Institute of Brain Science, National Yang-Ming University, Taipei, Taiwan, ROC
[7] National Cheng Kung University, Department of Computer Science and Information Engineering, Taipei, Taiwan, ROC
[8] Division of Psychiatry, School of Medicine, National Yang-Ming University, Taipei, Taiwan
[9] Psychiatric Department, Taipei Veterans General Hospital, Taipei, Taiwan

Abstract — **Small-world network is a highly clustered system but with small mean path length between networks which allow the information transferred with high efficiency. The human brain can be considered as a sparse, complex network modeled by the small-world properties. Once the brain network was disrupted by disease, the small-world properties would be altered to manifest that the information integration was inefficiency and the network was loosely organized. The aim of this study is to investigate the difference of small-world properties of brain functional network derived from resting-state functional magnetic resonance imaging (fMRI) between the healthy subjects and the patients with Bipolar disorder (BD). The functional MRI data was acquired from 5 healthy subjects and 5 patients with Bipolar disorder. All images of each subject were parcellated into 90 cortical and sub-cortical regions which were defined as the nodes of the network. The functional relations between the 90 regions were estimated by the frequency-based mutual information followed by thresholding to construct a set of undirected graphs. Small-world properties, such as the degree and strength of the connectivity, clustering coefficient of connections, mean path length among brain regions, global efficiency and local efficiency, are examined between any pair of functional areas. Our findings indicated that, in comparison with the control subjects, the BD patients presented smaller values of the degree, the strength of the connectivity and the clustering coefficient of connections, whereas larger values of mean path length among brain regions. This suggested the reduced global and local efficiency of the small-world properties for BD patients. In addition, the small-world properties of BD patients were altered significantly in some regions in the frontal lobes and limbic system which were in good agreement with the dysfunction connectivity reported by the previous literatures in the study of bipolar disorder.**

Keywords — **Small-world network, functional connectivity, Bipolar disorder, frequency-based mutual information.**

I. Introduction

A remarkable network between a random network and a regular network is called 'small-word', which is characterized by high cliquishness and short mean path length [1]. The human brain can be considered as a sparse, complex network modeled by the small-world properties, which support rapid integration of information across segregated sensory brain regions, confer resilience against pathological attack, and allow the information transferred between different brain regions with high efficiency. Once the brain network was disrupted by disease, the small-world properties would be altered to manifest that the information integration was inefficiency and the network was loosely organized.

Bipolar disorder (BD) is a category of mood disorders defined by the presence of one or more episodes of abnormally elevated mood. Findings from structural magnetic resonance imaging (MRI) studies suggest that some abnormalities, such as prefrontal sub-region decreased volumes; amygdala and stiatal enlargement and midline cerebellum atrophy. From functional imaging technologies, such as positron emission tomography (PET), single photon emission computed tomography (SPECT) and functional magnetic resonance imaging (fMRI), which are obtained at rest or during cognitive tasks to study specific neural networks, including anterior limbic regions that may underlie bipolar disorder [2,3,4].

These data suggest that activation of 'limbic' prefrontal areas may disrupt of 'cognitive' prefrontal regions. Functional imaging studies support the notion that abnormalities in anterior limbic networks, in which structural and spectroscopic abnormalities have also been reported, appear to underlie the expression of bipolar disorder. The aim of this study is to investigate the difference of small-world properties of brain functional network derived from resting-state

Chwee Teck Lim, James C.H. Goh (Eds.): ICBME 2008, Proceedings 23, pp. 726–729, 2009
www.springerlink.com

functional magnetic resonance imaging between the healthy subjects and the patients with Bipolar disorder.

II. Materials and Methods

A. Data acquisition and preprocessing

The study included 5 patients with bipolar disorder who were recruited from Taipei Veterans General Hospital. Confirmation of the diagnosis for all patients was made by clinical psychiatrists, using the Diagnostic and Statistical Manual of Mental Disorders (DSM). All the five healthy subjects had no history of psychiatric illness. All subjects gave voluntary and informed consent according to the standards set by Taipei Veterans General Hospital.

Imaging was performed on a 1.5 Tesla GE scanner in Taipei Veterans General Hospital. Blood oxygenation level dependent (BOLD) images of the whole brain using an echo planar imaging (EPI) sequence were acquired in 20 axial slices (TR=2000ms, TE=40ms, flip angle=90°, FOV=24cm; 5mm thickness and 1 mm gap). For each subject, the fMRI scanning lasted about 400 seconds. Structural images were obtained using a rapid acquisition gradient echo 3D T1-weighted sequence for each subject (TR=2045ms, TE=9.6ms, flip angle=90°, FOV=24cm). All the preprocessing was carried out using statistical parametric mapping (SPM5). The 200 volumes were first corrected for the acquisition time delay among different slices, and then the all images were realigned to the first volume for head-motion correction. Then, correct differences in image acquisition time between slices. The third step is co-registration: all fMRI images register to the anatomy T1 weighting imaging. The fMRI images were further spatially normalized to the T1 template image.

B. Anatomy parcellation

The registered fMRI data were segmented into 90 regions (45 for each hemisphere, Table1) using the Individual Brain Atlases using Statistical Parametric Mapping Software (IBASPM). For each subject, the representative time series of each individual region was then obtained by simply averaging the fMRI time series over all voxels in this region.

C. Frequency-based mutual information

We applied frequency-based mutual information to each regional time series and estimated the pair-wise inter-regional relations in the specific frequency band (0.01~0.08Hz). We consider the observations of the time series of p points in the brain as finite realizations of a multivariate stationary stochastic process:

$$X(t)=\{X_1(t),X_2(t),...,X_p(t)\},t\in Z \quad (1)$$

We apply the discrete Fourier transform (DFT) to a finite realization of Eq. (1), we have a new set of values

$$Y(\omega_k)=\{Y_1(\omega_k),Y_2(\omega_k),...,Y_p(\omega_k)\} \quad (2)$$

at each $\omega_k(k:1,...,n)$ Fourier frequency. The mutual information between any pair of subsets a, b of Y at frequency ω_k is [5,6]

$$MI_{a,b}(\omega_k)=-1/2\log\left(\left|f_{X_a,X_b}(\omega_k)\right|/\left|f_{X_a}(\omega_k)\right|\left|f_{X_b}(\omega_k)\right|\right) \quad (3)$$

where , $f_{X_a}(\omega_k)$ $f_{X_b}(\omega_k)$and $f_{X_a,X_b}(\omega_k)$are the Hermitian positive definite, (cross-)spectral density matrices of the original processes Xa(t), Xb(t) and {Xa(t), Xb(t)} Symbol $|\ |$ denotes the determinant.

D. Small-world properties

Small-world properties have been described for graphs defined by nodes (brain regions) and undirected edges (functional connectivity). A 90× 90 binary graph can be constructed by applying a threshold T to the frequency-based mutual information. The maximum threshold must assure that each network is fully connected with N= 90 nodes. The minimum threshold must ensure that the brain networks have a lower global efficiency and a larger local efficiency compared to random networks with relatively the same distribution of the degrees of connectivity. The key metrics are the degree and strength of the connectivity, clustering coefficient of connections ,mean path length among brain regions, global efficiency and local efficiency, all defined for each of the i=1,2,3,. . . ,n nodes in the network (Table 1) [7].

Table 1 Small-world indices

Index	Meaning	Formula
K_p	Degree of connectivity	$K_P=\frac{1}{N}\sum_{i\in G}K_i$
E_{corr}	Strength of connectivity	$E_{corr}=\frac{1}{N}\sum_{i\in G}\left(\frac{1}{K_i}\sum_{j\in G_i}\lvert MI(i,j)\rvert\right)$
C_p	Clustering coefficient	$C_P=\frac{1}{N}\sum_{i\in G}\frac{E_i}{K_i(K_i-1)/2}$
L_p	Mean path length	$L_P=\frac{1}{N}\sum_{i\in G}\frac{1}{N-1}\sum_{i\neq j\in G}\min\{L_{i,j}\}$
E_{global}	Global efficiency	$E_{global}=\frac{1}{N(N-1)}\sum_{i\neq j\in G}\frac{1}{L_{i,j}}$
E_{local}	Local efficiency	$E_{local}=\frac{1}{N}\sum_{i\in G}\left(\frac{1}{N_{G_i}(N_{G_i}-1)}\sum_{j,k\in G_i}\frac{1}{L_{j,k}}\right)$

III. Results

The two 90×90 mean functional connectivity matrices shown in Fig.1 were calculated by averaging the frequency-based mutual information matrices of all subjects within the group. The distributions of all the small world properties as a function of threshold from 0.34 to 0.56 within each group are shown in Fig.2. The degree (Kp) evaluates the level of sparseness of a network in Fig.2(A). The strength of the functional connectivity (E_{corr}) of the brain network is shown in Fig.2(B). The cluster coefficient (C_p) measures the extent of a local cluster of the network is shown in Fig2.(C). The mean path length (L_p) measures of the extent of average connectivity of the network is shown in Fig.2(D). The global efficiency (E_{global}) is a measure of the global efficiency of parallel information transfer in the network in Fig.2 (E). The local efficiency (E_{local}) is a measure of the fault tolerance of the network in Fig.2(F). The region analysis for the degree, strength of connectivity, cluster coefficient and mean path length are shown in Fig.3, in which the blue bars and red bars represent healthy subjects and BD patients respectively.

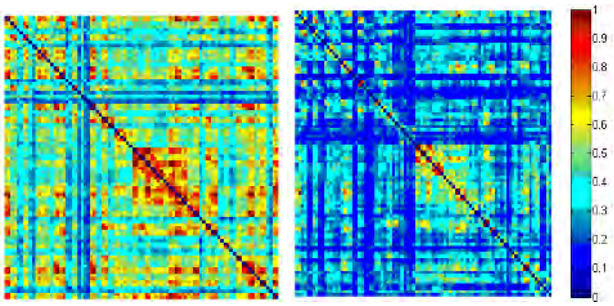


Fig. 1. The mean functional connectivity matrices. Each figure shows 90×90 square matrix, where x and y axes represent the 90 brain regions, and each pixel value indicates the strength of connectivity between each pair of brain regions. The diagonal from upper left to lower right is self-relation, and is set zero. The functional connectivity was stronger in healthy subjects (left) compared with BD patients (right).

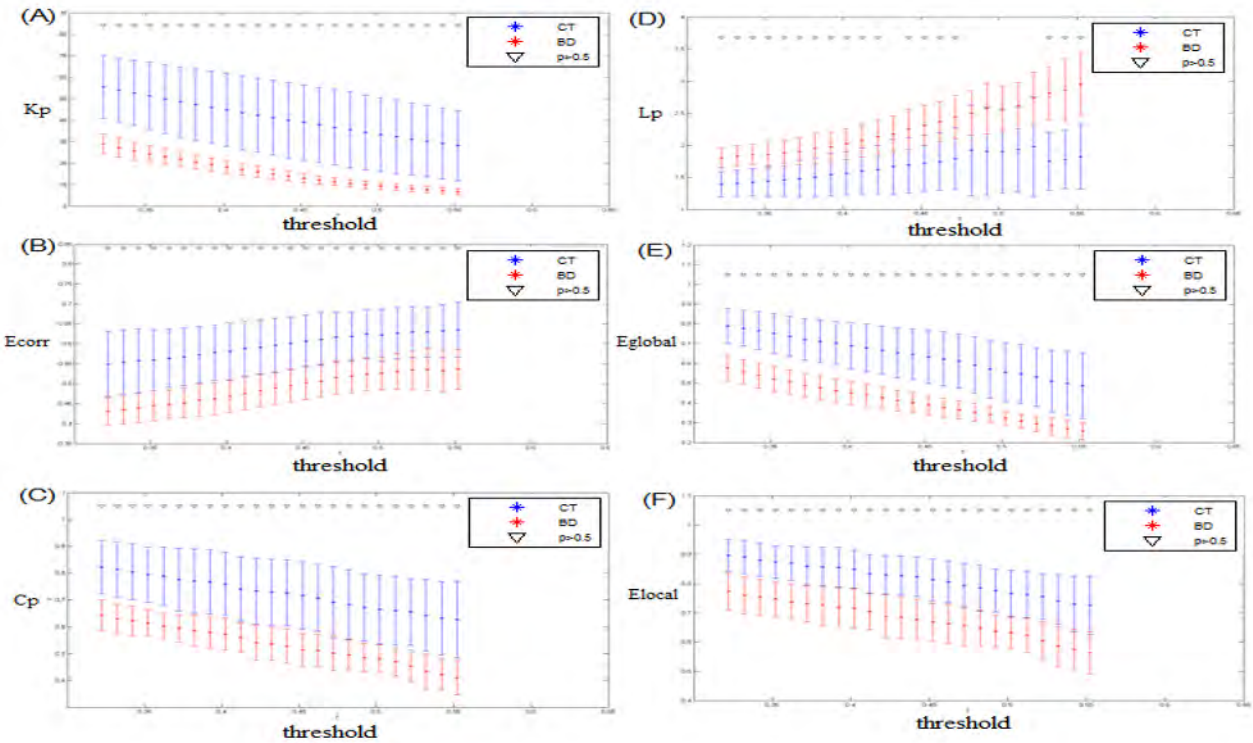


Fig.2. The distributions of all small-world properties. (A) The degree of connectivity (K_p). (B) The strength of connectivity (E_{corr}). (C) The cluster coefficient (C_p). (D) The mean path length (L_p). (E) The global efficiency (E_{global}) (F) The local efficiency (E_{local}). The blue star and red star represent healthy group and BD group, respectively. The black triangle represents the significantly difference between healthy subjects and BD patients.

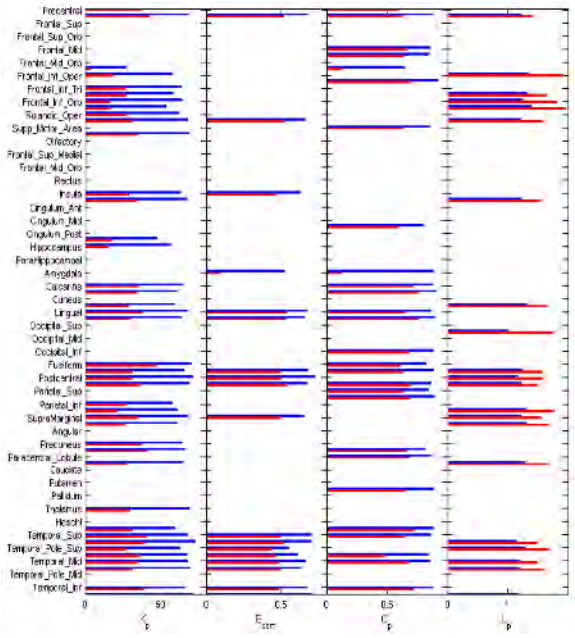


Fig.3 Regional small world properties. The vertical axis is 45 brain regions (both right and left hemispheres), and the horizontal axes are the degree (K_p)., the strength (E_{corr}), the cluster coefficients (C_p) and mean path length (L_p) from left to right in order. Bars indicate the brain region is significantly altered in the relative measurement, and the length of the bar indicates the mean value of the relative measurement between two groups. The blue bars and red bars represent the healthy group and BD group respectively.

IV. Discussion

With an increase in the threshold, the degree (Fig.2(A)) decreases; whereas the strength of the connectivity (Fig.2(B)) increases because increasing the threshold corresponds to eliminate the weaker connections that are more likely to be noisy. Over the whole range of thresholds the degree and strength of connectivity are significantly lower in the BD group. This means the lower connectivity between brain regions in BD patients.

As shown in Fig.2(C) and (D), the higher threshold, the lower cluster coefficient but longer mean path length. The relative lower cliquishness and longer mean path length were presented in BD patients. These results show that the network in BD patients is disrupted.

For all thresholds, both global and local efficiency in Fig.2(E,F) are significantly higher in healthy subjects than BD patients. These results reveal that the information transferred between different brain regions with low efficiency when the brain network was attacked by disease.

We used a two-sample two-tailed t-test to evaluate statistical differences in the four small-world properties between two groups in 90 brain regions at each selected threshold shown in Fig.3. The small-world properties are significantly altered in many brain regions in the frontal, parietal temporal lobes and in limbic system. The similar results in regional analysis show that the brain network in BD patients is sparse and weak connective so that the degree and strength of connectivity are lower. From the lower cliquishness and larger mean path length in BD group indicate the network is loosely organized. Summarize above evidences, the brain network is inefficient in BD patients compared with healthy subjects. Since all thresholds were similar in their trends with respect to the differences in their small-world properties between the BD patients and the healthy subjects, we have chosen to report only one typical threshold (T = 0.34, the top of the threshold range).

V. Conclusion

Our results support the concept that the small-world properties would be altered to manifest that the information integration was inefficiency and the network was loosely organized. These results were in good agreement with the dysfunction connectivity reported by the previous literatures in the study of bipolar disorder. This approach may also be able to be used in other psychiatric disorders such as major depression disease, which can also be taken as a disconnection syndrome and in which abnormal functional connectivity plays a role.

References

1. Duncan J.W. and Steven H.S. (1998) Collective dynamics of small-world' networks. Nature 393:440-442
2. Strakowski S.M., DelBello M.P. and Adler C.M. (2005) The functional neuroanatomy of bipolar disorder: a review of neuroimaging findings. Molecular Psychiatry 10: 105-115.
3. Sophia F. (2006) Functional neuroimaging in mood disorders, Phychiatry 5:5.
4. Hilary P.B., Andres M., Joan K. et al. (2003) Frontostriatal abnormalities in adolescents with Bipolar Disorder_Preliminary observations from functional MRI. Am J Psychiatry 106: 1345-1347
5. Salvdor R., Martinez A., Pomarol-Clotet E. et al. (2008) A simple view of the brain through a frequency-specific functional connectivity measure. NeuroImage 39: 279-289
6. Salvador R., Martinez A., Pomarol-Clotet E. et al. (2007) Frequency based mutual information measures between clusters of brain regions in functional magnetic resonance imaging. NeuroImage 35 :83-88
7. Yong L., Meng L., Yuan Z. et al. (2008) Disrupted small-world networks in schizophrenia. Brain 131(4):945-961.

Author: Yu-Te Wu
Institute: Department of Biomedical Imaging and Radiological Sciences, National Yang-Ming University
Street: No.155, Sec.2, Linong Street
City: Taipei
Country: Taiwan, ROCEmail: ytwu@ym.edu.tw

Fractal Dimension Analysis for Quantifying Brain Atrophy of Multiple System Atrophy of the Cerebellar Type (MSA-C)

Z.Y. Wang[1], B.W. Soong[2,3], P.S. Wang[2,3,4,5], C.W. Jao [6,7], K.K. Shyu[6], Y.T. Wu[1,5,8]

[1] Department of Biomedical Imaging and Radiological Science, National Yang-Ming University, Taipei, Taiwan, ROC
[2] The Neurological Institute, Taipei Veterans General Hospital, Taipei, Taiwan, ROC
[3] Department of Neurology, National Yang-Ming University School of Medicine, Taipei, Taiwan, ROC
[4] The Neurological Institute, Taipei Municipal Gan-Dau Hospital, Taipei, Taiwan , ROC
[5] Institute of Brain Science, National Yang-Ming University, Taipei, Taiwan, ROC
[6] Department of Electrical Engineering, National Central University, Chung-Li, Taiwan, ROC
[7]Department of Holistic Wellness, Chin-Min Institute of Technology, Tao-Fen, Taiwan, ROC
[8] Integrated Brain Research Laboratory, Department of Medical Research and Education, Taipei Veterans General Hospital, Taipei, Taiwan, ROC

Abstract— **Multiple system atrophy-cerebellar (MSA-C) is a degenerative neurological disease of brain. In this study, we used three-dimensional (3D) fractal dimension (FD) method to investigate the structural complexity change of human cerebellum white matter (CBWM) and gray matter (CBGM) for MSA-C disease diagnosis. Twenty patients and twenty-three normal subjects as the control group participated in this study. The T-1 weighted magnetic resonance (MR) images were processed and 3D CBGM and 3D CBGM were analyzed by the FD method. Results demonstrated that the FD values of patients' CBWM and CBGM decreased significantly, and that their CBWM FD values decreased more significant than that of CBGM. Results also showed that the 3D FD method was superior to the conventional volumetric method in terms of better reliability, accuracy, and sensitivity.**

Keywords—**MSA-C, Fractal dimension**

I. Introduction

MSA is a form of sporadic spinocerebellar degeneration characterized by varying degrees of parkinsonism, cerebellar ataxia, and autonomic dysfunction. This disease can be categorized into two subtypes according to dominant clinical features: MSA-C (cerebellar) and MSA-P (parkinsonism). [1,2]. MSA-C is the most common subtype of MSA and also termed as Olivopontocerebellar atrophy (OPCA) [3,4]. In Taiwan, MSA-C is more common than MSA-P. Gait ataxia is the most typically early symptom of this disease and others clinical features consist of dysarthria, unintentional movement, parkinsonian and other extrapyramidal symptoms [5]. Many investigators have reported that the factors of MSA-C are the loss of neurons in the ventral portion of the pons, inferior olives and cerebellar cortex. The fundamental lesions are located in the arcuate, pontine, inferior olivary, pontobulbar nuclei and cerebellar cortex [6].

Magnetic resonance imaging (MRI) is a widely used tool for brain pathology and diagnosis to evaluate demyelinating lesions within the brain and spinal cord, such as MSA [7], motor function impairment [8], epilepsy [9] and tumor detection. The abnormal change of cerebral tissue structure including atrophy, lesions and degeneration could potentially be regarded as disease-diagnosis parameters. Accordingly, the quantification of complexity of the morphological change of cerebral tissue is significant for disease diagnosis.

The FD analysis method applied for cerebrum atrophy diagnosis has been increasing recently. It is an efficiently computational tool for describing the structural complexity and especially suitable for measuring complexity. A fractal is an irregular object in which part of the compartment resemble to the overall shape. Mathematically, FD can condense all the structural details into a single numeric value that summarizes the irregularity of the object, leading to a quantitative measure of morphological complexity [10]. Because the FD analysis is based on the logarithmic scale, small changes in the FD value correspond to large differences in the shape complexity. Smith et al. verified that a difference of 0.1 of FD value representing a doubling of complexity [11].They suggested that the FD analysis would be a useful tool for pathological study. Practically, the FD can serve as an index for quantifying structural complexity of the neural system during the stages of development, degeneration, reorganization, or evolution, because in these processes the FD may be dynamically changing. The conventional volumetric analysis has the defects of less sensitivity and accuracy and often difficult for quantifying the grade of atrophy in the brain and the cerebellum during disease duration. To alleviate this problem, many studies have adopted box-counting method to measure FD of brain structures because of its easy implementation and applicability for objects with or without self-similarity.

Chwee Teck Lim, James C.H. Goh (Eds.): ICBME 2008, Proceedings 23, pp. 730–733, 2009
www.springerlink.com

The aim of this study was to employ 3D FD analysis for investigating the atrophy aliment of GM and WM structures of MSA-C patients. The effectiveness of 3D FD analysis method as an index in quantifying the complexity alteration of CBWM and CBGM in MSA-C patients was assessed.

II. Material and Method

A. Material

Twenty patients (7 males and 13 females, age range 32-77 years), and 23 healthy subjects (10 males and 13 females, age range 32-57 years) were recruited to participate in this study in the Department of Radiology, Taipei Veterans General Hospital (Taiwan) from 2005 to 2007. Written informed consent was obtained from each volunteer before this study. MSA-C, MSA-P and PD were diagnosed according to established guidelines [12]. The patients' illness duration range was from one to 19 years, 17 patients were below 5 years, two patients were above 10 years and the other one patient was in the period between 5 to 9 years.

The axial magnetic resonance (MR) human brain images covering the entire cerebrum and cerebellum were performed on a 1.5-T Vision Siemens scanner (Erlangen, Germany) using a circularly polarized head coil, with the following parameters: 1.5mm axial slices; echo time=5.5ms; repetition time=14.4ms; flip angle 200; field of view 25cm; matrix size=256×256 and the in-plane resolution 1mm×1mm.

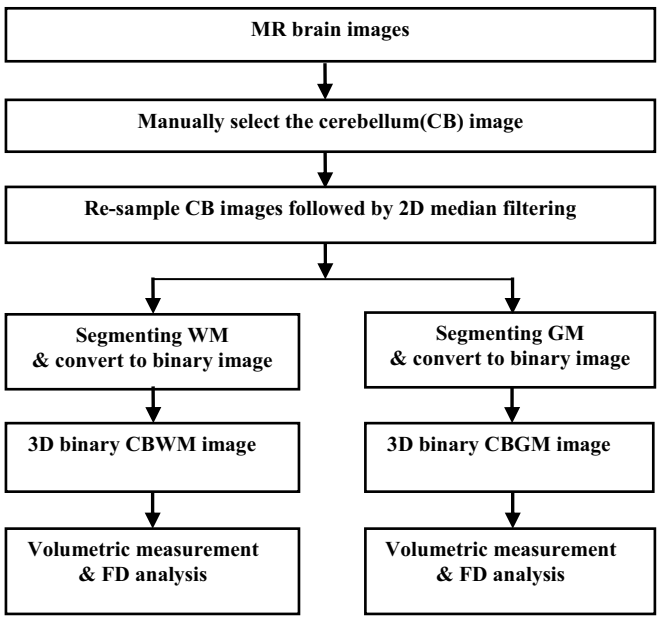


Fig.1 Flow chart of image processing and measuring steps.

B. Method

The processing of MR images and FD measurement consisted of five steps and the flowchart was depicted in Fig.1. It should be noted that the volumes of reconstructed 3D CBWM and CBGM were computed based on the total numbers of pixels within the objects and their units were mm^3. The fractal dimension (FD) is a quantitative indicator of object complexity which condenses all the details into a single numeric value. Let N(r) denote the minimal number of cubes of size r covering the fractal object. The FD of a fractal is defined in the power law relationship [13] $N(r) \propto r^{-FD}$. In this study, the FD analysis was implemented by the box-counting method derived from HarFA software (http://www.fch.vutbr.cz/lectures/imagesci).

The MATLAB 7.0 software was used for the implementation.

There are three steps in the FD measuring procedure: (1) counting the number of boxes to encompass the whole 3-D fractal object in Euclidean space, (2) repeating step (1) with different box sizes, (3) performing the linear regression analysis within the proper range of box sizes to estimate the FD value.

In this study, the FDs of CBWM and CBGM of the normal and patients groups were compared using the t-test for assessing the CBWM and CBGM structural complexity of MSA-C disease. The significant differences were detected at $p<0.01$.

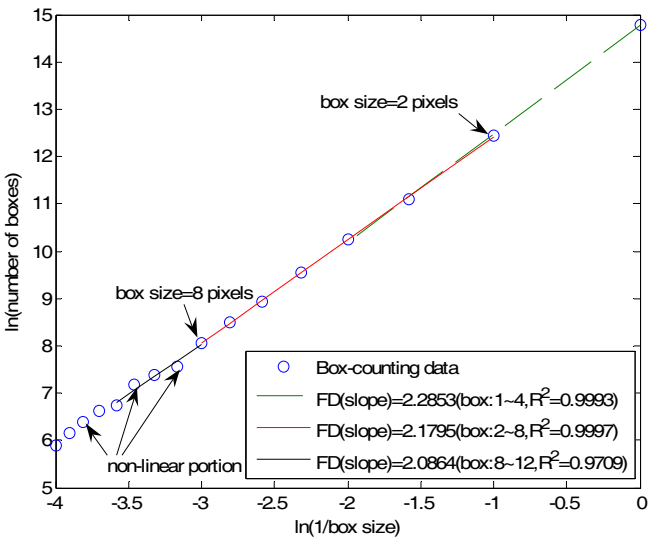


Fig.2 Linear regression analysis to calculate the FD value of CBWM from one patient.

III. Results

Figure 3 displays the MR brain images, CBWM segmented results, and the 3D reconstructed CBWMs from a normal subject and a MSA-C patient, respectively. Compared Fig. 3(c) to Fig. 3(f), the patient's CBWM presented a smaller volume and less folding patterns. The statistical results of FDs analysis and volumes of CBWM and CBGM of all participators were summarized in Table 1. It is worthy to note that the standard deviations of the FDs are much smaller compared with that of the volumes, no matter in control group or patients group. This suggests better reliability of the FD method than the volumetric method. No significant difference was detected between genders of control group (p=0.1592 for CBWM and p=0.6231 for CBGM) and MSA-C patients (p=0.6664 for CBWM and p=0.5562 for CBGM) for both while calculating the FD values of CBEM and CBGM.

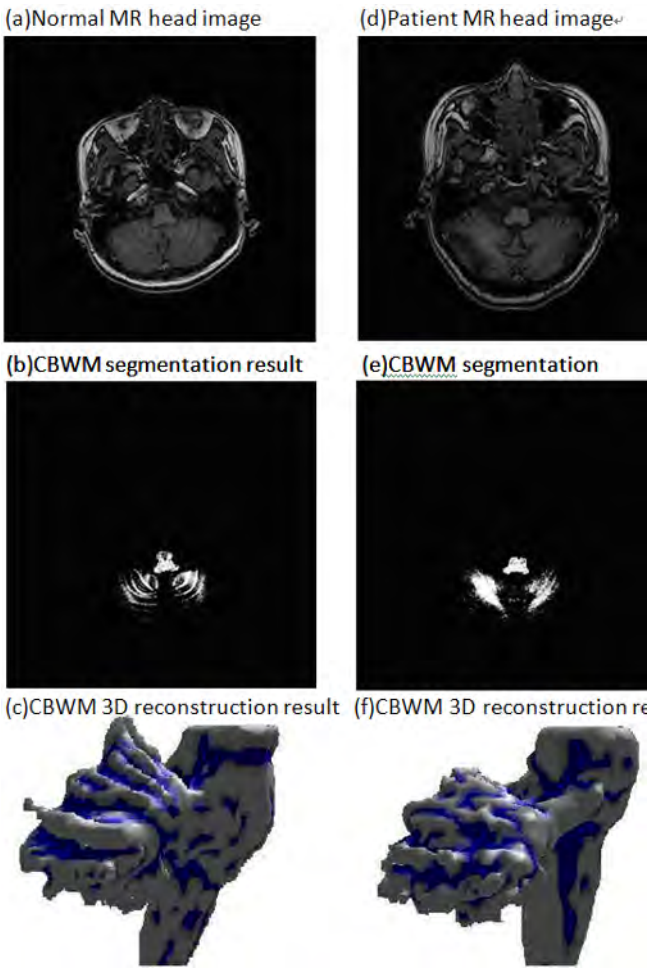


Fig.3 Results of image segmentation and 3D reconstruction for WM from one normal (a-c) and one patient (d-f) subject.

Figures 4(a) and 4(b) displays the statistical results of MSA-C and normal in which the MSA-C patients presented significantly lower CBWM FD values than the normal (p=5.4335e-008,(a)) and the CBGM FD values of MSA-C patients were also lower than the normal (p=6.1139e-005,(b)). The volumes of the cerebellum, including pons and brain stems for the normal subjects, were 172.89±17.05cm^3, and that for MSA-c patients were significant smaller, which were 140.36±26.62cm^3. In addition, the mean value of CBWM volume of the patients was 34.80cm3 which was smaller than that of the control group CBWM (47.48cm^3). The mean value of CBGM volume for patients was 105.57cm^3 which was also smaller that that (125.41cm^3) for the normal subjects. Results were also summarized in Table 1.

Table 1 Statistical results of FDs and volumes of all participators

Groups	MSA-C	Control group	*P*
Age	32~77	30~57	-
Number	20	23	-
Duration(Y)	5.0(1~20)	-	-
FD			
CBWM FD	2.155±0.096	2.267±0.037	<0.01
CBGM FD	2.4999±0.059	2.528±0.027	<0.01
Volume(cm^3)			
CBWM	34.80±8.54	47.48±6.0	<0.01
CBGM	105.57±23.30	125.41±12.73	<0.01
CB	140.36±26.62	172.89±17.05	<0.01

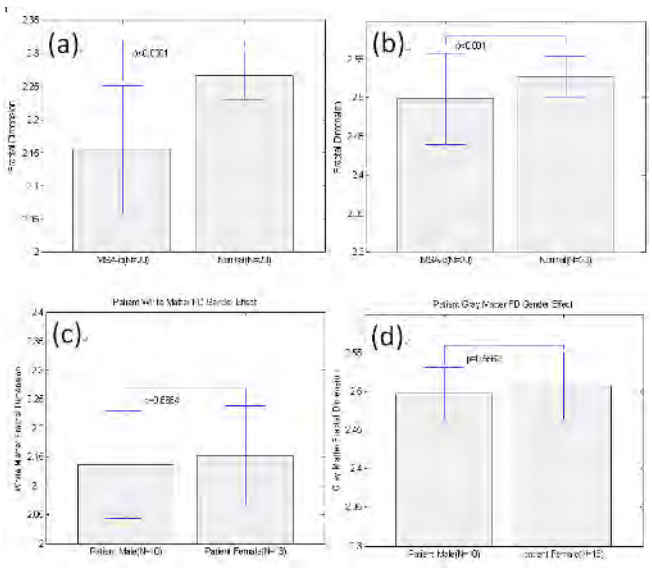


Fig.4 FD comparison between MSA-C and control group

IV. Discussion

Since the 3D cerebellum of MSA-C patients exhibited less folding pattern and smaller volume size, the structures of cerebellum of MSA-C patients were less complicated, and, therefore, smaller FD values. In this study the result confirmed that the FD values of CBWM and CBGM volumetric general structure were decreased in MSA-C patients, and we found that the FD value of CBWM decreased more significant than that of CBGM (p=5.4335e-008 for CBWM; p=6.1139e-005 for CBGM FD values). This suggested that the atrophy phenomena may occurred more seriously in the CBWM region. It is noted that most of the previous studies in brain atrophy disease used the FD analysis to analyze the complexity of surface boundary between WM and GM, and seldom analyze the structural complexity of CBWM and CBGM. In this study, the morphological changes of the CBGM and CBWM of MSA-C patients (Fig.3(c), (f)) have been effectively quantified by FD method. Similar observations have been reported by Specht et al. who applied the VBM analysis to detected WM and GM loss of MSA-C patients and reported that GM degenerated significantly in the cerebellar hemisphere and vermis, and WM degenerated in the pons, middle cerebellar peduncles, mesencephalon and frontotemporal areas.

Although the volumes and FD values of CBWM and CBGM were both smaller for MSA-C patients comparing with the control group, the FD method is superior to the conventionally volumetric method in terms of better reliability, sensitivity, and less gender effect. It can be seen in Table 1 that the percentages of standard deviation of FD values for CBWM and CBGM in the control groups were 2.0% and 1.0%, respectively, which were much smaller than that of volumes (15% and 10.5%, respectively). Volumetric measurement with large variations would make the statistical inference less reliable in comparison with the FD method. In addition, the logarithm-scale based FD measurement is more sensitive to structural change: a small difference in FD value may have a significant impact on the brain structures and their alteration, specifically, a difference of 0.1 of the FD value equivalent to a double of complexity (Smith et al,1989). Zhang et al. have verified that the FD analysis is more sensitive for characterizing WM structural features than the volumetric measurement and capable of describing complexity and variability of WM (Zhang et al., 2007). Moreover, there was no gender effect when the FD values of CBGM and CBWM were evaluated, no matter in the controls or MSA-C patients (Figs. 4(a)(b)(c) and(d)). However, there was a gender effect in evaluating the CBWM volume which could bias the results of volumetric method.

V. Conclusion

We have employed a 3D FD analysis method, which is more accurate and sensitive than the conventional volumetric method, to quantify the atrophy of CBWM and CBGM for MSA-C patients.. Our results showed that the FD of CBWM decreased faster than that of CBGM for the MSA-C patients, suggesting the CBWM degeneration would be the dominate atrophy phenomenon of the disease.

References

1. Papp MI, Kahn JE, Lantos PL.(1989) Glial cytoplasmic inclusions in the CNS of patients with multiple system atrophy (striatonigral degeneration, olivopontocerebellar atrophy and Shy–Drager syndrome). J Neurol Sci 94:79-100.
2. Gilman S, Low P A, Quinn N, et al.(1999) Consensus statement on the diagnosis of multiple system atrophy. J Neurol Sci 163: 94-98.
3. Graham J G, Oppenheimer D R.(1969) Orthostatic hypotension and nicotine sensitivity in a case of multiple system atrophy. J Neuro Neurosurg. Psychiatry 32:28-34.
4. Kuriyama N, Mizuno T, Iida A, et al.(2005) Autonomic nervous evaluation in the early stages of olivopontocerebellar atrophy. Autonomic Neuroscience: Basic and Clinical 123:87- 93
5. Berciano J,(1982) Olivopontocerebellar Atrophy. A review of 117 cases, J Neurol Sci 53:253-272.
6. Pemde H K, Bakhshi S, Kalra V,(1995) Olivopontocerebellar atrophy: a case report, Brain & Development 17:130-132
7. Horimoto Y, Aiba I, Yasuda T, et al.(2000). Cerebral atrophy in multiple system atrophy by MRI. J Neurol Sci 173:109-112.
8. Baloh R W, Ying S H, Jacobson K M,(2003). A longitudinal study of gait and balance dysfunction in normal older people. Arch Neurol.60,835–9.
9. Woermann F G, Steiner H, Barker G J, et al.(2001) A fast FLAIR dual-echo technique for hippocampal T2 relaxometry: first experiences in patients with temporal lobe epilepsy. J Magn Reson Imaging 13:547-55
10. Esteban F J, Sepulcre J, Mendizabal N V, et al.(2007) Fractal dimension and white matter changes in multiple sclerosis. NeuroImage 36:543-549
11. Smith T G Jr, Behar T N, Lange G D, et al.(1989) A fractal analysis of cell images. J Neurosci Methods 27:173-180.
12. Gilman S, Low P A, Quinn N, et al.(1999) Consensus statement on the diagnosis of multiple system atrophy. J Neurol Sci 163:94-98.
13. Mandelbrot BB.(1983) The Fractal Geometry of Nature. New York : W.H. Freeman

Author: Y.T. Wu
Institute: Department of Biomedical Imaging and Radiological Science, National Yang-Ming University
Street: No.155, Sec.2, Linong Street
City: Taipei
Country: Taiwan, ROC
Email: ytwu@ym.edu.tw

A Novel Method in Detecting CCA Lumen Diameter and IMT in Dynamic B-mode Sonography

D.C. Cheng[1], Q. Pu[2], A. Schmidt-Trucksaess[3], C.H. Liu[4]

[1] Department of Radiological Technology, China Medical University, Taichung, Taiwan
[2]Department of Internal Medicine, University Hospital of Bonn, Germany
[3] Department of Prevention, Rehabilitation and Sports Medicine, TU Muenchen, University Hospital, Germany
[4]Department of Neurology, China Medical University, Taichung, Taiwan

Abstract — **n this study, we propose a novel method to detect the intimal layers of the near and far wall of the common carotid artery (CCA) in dynamic B-mode images using dual dynamic programming (DDP). The lumen diameter (LD) can then be measured along a section during a certain time period (1 to 2 seconds.) In addition, the intima-media thickness (IMT) can be measured via detecting the intima and adventitia of the far wall using the same procedure but embedding different anatomic knowledge in DDP. All automatic detection results have been visually confirmed by professional physicians.**

Keywords — **IMT, CCA, dual dynamic programming, lumen diameter**

I. Introduction

Common carotid artery intima-media thickness (**CCA-IMT**) measurements have been confirmed to be an earlymarker of atherosclerosis [1] and have been associated with a higher risk of stroke [2] and myocardial infarction [3]. Recently, it has been shown that an increased CCA-IMT is cross-sectionally associated with a higher risk of brain infarction [4]. The non-invasive sonographic examination has demonstrated its potential in early predicting cardiovascular diseases. The IMT is an important index in modern medicine and can be measured either manually [4] or automatically [5]–[18].

The automatic methods have the potential in reproducing results and eliminating the strong variations in the manual tracings of different observers. Moreover, the processing time can be considerably reduced. The motivation of this study is to develop a confidential system which can identify the intima and adventitia of CCA automatically even under strong speckle noises using dynamic B-mode sonographic images. This system can identify not only the IMT of the far wall and but also the lumen diameter during both systolic and diastolic cycles. Via this system, the dynamic process of CCA can be represented by some parameters such as IMT variation and lumen diameter variation.

The carotid artery stiffness (CS) is one of the important factors for predicting cardio-vascular (CV) events [7]. The factor CS can be measured via measuring the systolic and diastolic carotid diameter on the distal wall of the CCA, 1 to 2 cm beneath the bifurcation with high-precision sonographic modality. Firstly, carotid distensibility (CDist) is estimated through the variations in arterial cross-sectional area and blood pressure (BP) during systole based on the assumption of a circular lumen. CDist is calculated as $\text{CDist}= \Delta A / A \cdot \Delta P$, where A is diastolic lumen area and ΔA is the maximum area change during a systolic-diastolic cycle, and ΔP is the local blood pressure change measured by applanation tonometer. The CDist can be converted to CS by giving $CS = (CDist)^{-1/2}$ [7].

Traditionally, CS is estimated by measuring the lumen diameters in systolic and diastolic states, i.e., only two points. This study provides a new technique in detecting the lumen diameter changes along a section of CCA, which is in general different from previously published works. We propose a novel dual dynamic programming combined with some anatomic knowledge into the algorithm which makes the detection more robust against the speckle noises.

This paper is organized as follows: In section II we firstly introduce how ultrasonic images are obtained. The difficulties of this study are discussed. Afterwards, the feature extraction is stated in details. In section III the results of lumen diameter and IMT detection are demonstrated. We finally issue our conclusion in section IV.

II. Materials, problems, and methods

A. Image acquisition

An Esaote MyLab ultrasound machine with a high resolution transducer was used for the acquisition of the sonographic image sequences. The CCA was examined by turning the neck of the study subject slightly to the left side. The transducer was positioned at the lateral side of the neck without compression on the inner jugular vein. The lumen was then maximized in the longitudinal plane with an optimal image of the near the far vessel wall of the CCA. Thus, both near and far wall of CCA can be observed and the video image sequences were saved on a recorder for off-line proc-

Chwee Teck Lim, James C.H. Goh (Eds.): ICBME 2008, Proceedings 23, pp. 734–737, 2009
www.springerlink.com

ess. All image sequences used in the paper were made in the Department of Prevention, Rehabilitation and Sports Medicine, TU Muenchen, University Hospital, Germany.

B. Problem statement

Figure 1 shows a typical image made by our sonographic modality. The *first* problem is the impact of speckle noises. It is very common that there are speckle noises in the artery lumen. In general, the noises on the near-wall side are stronger than the noises on the far-wall side. It makes the detection of near wall intima much more difficult, comparing to the detection of far wall intima. *Secondly*, some diseases such as atherosclerotic plaques change the structure of IM complex or the intimal layer. Some changes result in strong echoes such as calcification. When the intima is damaged, there are nearly no echoes on the damaged part so that results in an echo hole. All of these problems make the intima detection complex. *Finally*, the target we are processing is moving during the image sequence since it is made by dynamic B-mode sonography. Therefore we have to face the tracking problem. Fortunately, the target we are tracking does not change its shape in a large scale. Moreover, there is no overlapping or shadow problems, which might happen very often in the camera videos. In order to conquer problems listed above, we propose the novel scheme as follows.

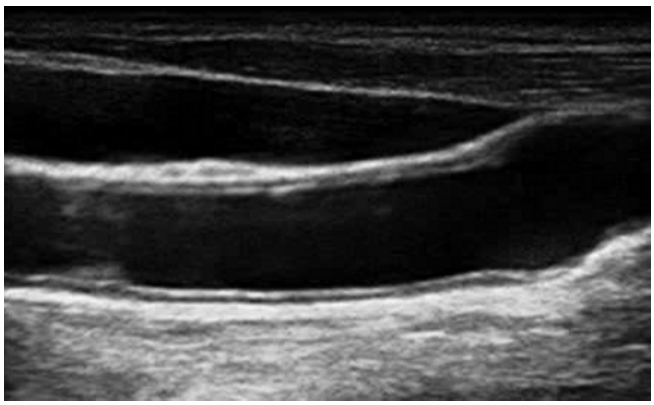


Fig. 1: A typical sonographic image (Esaote MyLab).

C. Image features

The dynamic B-mode image sequences are recorded and converted to several static images saved in BMP format. A graphic user interface (GUI) is designed for the user to select region of interest (ROI) to analyze. The user has only to select a rectangle area which is large enough covering the possible area during a complete systolic and diastolic cycle, when the lumen diameter will be measured. Similarly, the user has to select a smaller rectangle area to cover the intima and adventitia layers on the target to be detected. However, since the IMT does not change too much, the rectangle area is much smaller than the one measuring the lumen diameter.

The image features are extracted only on the selected ROI for the purpose of reducing the computation time. Several operators are used for feature extraction. The first one is MacLeod operator [8]:

$$f_M(x,y) = \exp(-\frac{x^2+y^2}{d_c^2})[\exp(-(\frac{d_{xy}+d_{pk}}{d_{pk}})^2) - \exp(-(\frac{d_{xy}-d_{pk}}{d_{pk}})^2)] \quad (1)$$

where

d_c constant determining rate of radial decay,

d_{pk} distance from axis to peaks in positive and negative weights,

$d_{xy} = x\sin\theta - y\cos\theta$, perpendicular distance of point (x, y) from axis of edge (at orientation θ to horizontal).

The MacLeod operator is in general to detect the gradient in different orientations. In this study, the size of MacLeod operators used in IMT and lumen diameter detection must be different and there are totally four orientations are applied.

One MacLeod operator is insufficient for the intima-adventitia detection since there causes noise layer in the IM-complex [9]. We therefore apply an enhancement operator to degenerate the noise layer in the IM-complex resulted from the MacLeod operator:

$$f_{IMT(far)} = \begin{bmatrix} 0 & \cdots & -1 & \cdots & 0 \\ & & \vdots & & \\ \vdots & & 0 & & \vdots \\ & & \vdots & & \\ 0 & \cdots & 1 & \cdots & 0 \end{bmatrix}, \quad (2)$$

where the size of the operator is determined by the pixelsize and anatomical knowledge. For instance, the IMT of a normal adult is 0.5mm. Therefore, the mask size should not be larger than 11×11. This operator is applied only for IMT detection of the far wall.

Another operator is applied for lumen diameter (LD) detection. The goal of this operator is to inhibit the gradient resulted from the adventitial layer. This is because the adventitia might cause a larger gradient than the intima does. However, the lumen diameter is determined by the intima but not by the adventitia. We thus define the following operator:

$$f_{LD(far)} = \begin{bmatrix} 0 & \cdots & -1 & \cdots & 0 \\ & & \vdots & & \\ \vdots & & 0 & & \vdots \\ & & 1 & & \\ & & \vdots & & \\ 0 & & 0.5 & & 0 \end{bmatrix}, \quad (3)$$

Again, the size of the operator is not fixed. It depends on the pixelsize and the anatomical knowledge. The goal of this operator is to reduce the impact of the gradient resulted from the adventitia. The operator for the near wall LD detection is simply reversed. With this construction, we simply reduce the noise impact and make the lumen diameter detection much easier, the IMT determination as well.

The resultant image feature is the composition of gradient images made by different operators:

$$h' = | I * f_M | + I * f_x, \quad (4)$$

where I is the original sub-image (ROI), f_x is $f_{IMT(far)}$ for IMT determination (far wall) and f_x is $f_{LD(far)}$ for LD determination (far wall). After two terms are summarized, *h'* might have negative values. Therefore, *h'* is shifted to have 0 as the smallest value and then divided by the largest value so that the final h is $0 \le h \le 1$.

D. Dual dynamic programming (DDP)

Structure: An image grid is denoted as $I(x, y)$ of size $M \times N$, where M and N are the number of rows and columns, respectively. Let $g(x, y)$ be the normalized image feature of $I(x, y)$ with $0 \le g(x, y) \le 1$. Suppose the dual curves run from left to right on $I(x, y)$ with two y-coordinates y_1 and y_2 in each column, $1 \le y_1, y_2 \le M$. The node pair is considered instead of the single node as that was done in the traditional dynamic programming. We assume that the dual curves have minimal and maximal distance between each other. Therefore, the anatomical relation is embedded into the dual dynamic programming structure. The details of DDP are described in [10]. The dual dynamic programming is applied on the image feature grid $h(x,y)$ instead of $I(x, y)$ denoted above in this section.

III. Results

Figure 2 shows a typical dynamic B-mode CCA image in one of our image sequence. There are total 84 images in this sequence. The GUI allows the user to select a ROI as shown in the rectangle area. All image features and DDP are executed on the selected ROI.



Fig. 2: The user can select a ROI for LD measurement.

Figure 3 shows the detection results. The parameter settings are: $\omega_1, \omega_2 = 0.1, d_{\min} = 55, d_{\max} = 85, k = 1$, where (ω_1, ω_2) are used to set the stiffness of the curves, $(d_{\min}, d_{\max})$ are the minimal and maximal distance between these two curves, and k denotes how far the neighboring nodes can jump and thus it represents the roughness of the curve. Details of the parameter description are in [10].

The section length of LD analysis is about 1.94 cm (pixelsize=0.0106 cm.) In Fig. 4, the ripple shows there are three systolic-diastolic cycles in this sequence. The middle

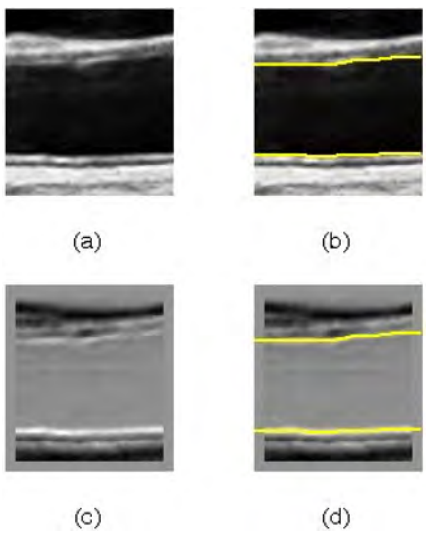


Fig. 3: (a) The selected ROI original sub-image; (b) ROI with detected intimal layers (near and far wall); (c) the feature image; (d) feature image with results.

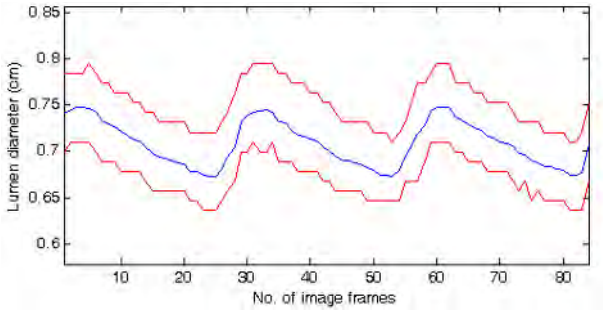


Fig. 4: The detected LD changes along a section. This sequence has 84 images and it lasts more than 2 seconds.

(blue) curve shows the average LD along this section and the upper and lower curves are the maximal and minimal LD changes along this section during the whole cycles, respectively. From the result, we observe that the averaged LD changes from 0.67 cm to 0.75 cm. The ripples of the upper and lower curves might reveal some important information for CV events and it needs a further study to confirm. However, this study provides a practical tool for physicians to analyze the LD along a section of CCA wall for further studies such as finding another factor or information for predicting the CV events.

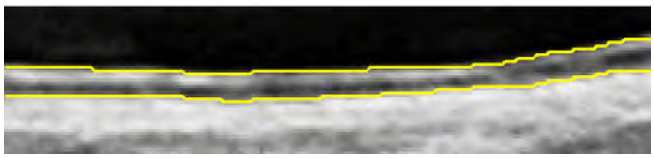


Fig. 5: One detection result of intima-media thickness. There are total 84 images of this analysis.

Figure 5 shows one of the IMT analysis. The length of this section is about 2.18 cm (206 pixels.) From the analysis one can observe the IMT changes along the systolic and diastolic cycles.

IV. Discussion and Conclusion

In section II we have stated three kinds of problem. In this study, we have proposed a novel method in detecting IMT and LD via a dual dynamic programming with a proposed image feature extraction scheme. Through a series of experiments we demonstrate the function and novelty of this proposed scheme which is able to against the speckle noises in the artery lumen. Although the experiment shown in this paper does not include echo holes or calcification, however, we have made some other experiments which reveal that this algorithm is able to solve these kinds of problem. Due to the page limitation, we are not able to demonstrate all experiments we have made.

This system is practical for physicians making further clinical studies such as finding new factors in CV events.

Acknowledgment

This work was supported by the NSC (National Science Council, Taiwan) under Grant NSC 97-2218-E-039-001.

References

1. Bonithon-Kopp C. et al. (1991), "Risk factors for early carotid atherosclerosis in middle-aged french women," Arterioscler Thromb., 11:966–972.
2. O'Leary D., Polak J., Kronmal R., Manolio T., Burke G., and Wolfson S. J. (1999), "Carotid-artery intima and media thickness as a risk factor for myocardial infarction and stroke in older adults," N Engl J Med, 340:14–22.
3. Bots M., Grobbee D., Hofman A., and Witteman J. (2005), "Common carotid intima-media thickness and risk of acute myocardial infarction- The role of lumen diameter," Stroke, 36:762–767.
4. Vemmos K., Tsivgoulis G., Spengos K., Papamichael C., Zakopoulos N., Daffertshofer M., Lekakis J., and Mavrikakis M. (2004), "Common carotid artery intima-media thickness in patients with brain infarction and intracerebral haemorrhage," Cerebrovascular Diseases, 17:280–286.
5. Selzer R, Hodis H., Kwongfu H., Mack W., Lee P., Liu C.R., and Liu C. (1994), "Evaluation of computerized edge tracking for quantifying intima-media thickness of the common carotid artery from b-mode ultrasound images," Atherosclerosis, 111(1):1–11.
6. Gustavsson T., Liang Q., Wendelhag I. et al. (1994), "A dynamic programming procedure for automated ultrasonic measurement of the carotid artery," in IEEE Computers in Cardiology, pp. 297–300.
7. Paini A., Boutouyrie P. , Calvet D., Tropeano A.-I., Laloux B., and Laurent S. (2006), "Carotid and Aortic Stiffness: Determinants of Discrepancies," Hypertension, DOI 10.1161/01.HYP.0000202052.25238.68.
8. MacLeod I. (1972), "Comments on techniques for edge detection," Proc. of the IEEE, vol. 60, p. 344.
9. Cheng D.C., Schmidt-Trucksaess A. Cheng K, Burkhardt H. (2002), "Using snakes to detect the intimal and adventitial layers of the common carotid artery wall in sonographic images," Computer Methods and Programs in Biomedicine, 67:27-37.
10. Cheng D.C. and Jiang X. (2006), "Using dual dynamic programming for artery's inner wall detection in sonographic images," The 1st International Workshop on Computer Vision for Intravascular and Intracardiac Imaging, 138-145, Copenhagen, Denmark.

Acoustic Imaging of Heart Using Microphone Arrays

H. Kajbaf[1] and H. Ghassemian[1]

[1] Electrical and Computer Engineering Department, Tarbiat Modares University, Tehran, Iran

Abstract — **In this paper a novel method for acoustic imaging of heart is proposed. Heart is assumed to be a spread acoustic source which generates sound from its different locations. A simultaneous multisensor recording is used to record the heart sound from human chest wall. By using beamforming techniques the recorded data are combined to form a two or three dimensional representation of heart sound distribution. This map shows the acoustic energy of heart in different locations. Simulations with different array arrangements are done to verify the performance of this system. The heart sound is segmented without any need for other biosignals using an unsupervised method. This procedure is used to separate first and second heart sound. The segmented signal is used in beamforming algorithm. This results in a time-space map of heart sound for different intervals of heart activity. A setup is designed and implemented to record heart sound from human chest. Data are saved on a personal computer for signal processing in order to form a two or three dimensional image. This noninvasive and inexpensive imaging method offers new aspects, which with further studies, can help physicians in more precise diagnosing of heart diseases.**

Keywords — **Microphone array, acoustic imaging, near-field beamforming, heart sounds.**

I. Introduction

Initial diagnosis of heart diseases by listening to heart sound has been a very common method for a long time [1]. Physicians usually listen to the patient's heart sound in different auscultatory areas. Heart sound has different characteristics in different places on the body. This fact recommends an idea that if an electronically recorded heart sound or phonocardiograph (PCG) from different locations in front and at the back of the human chest is used, by combining these data, we can have an acoustic map of the heart.

For this purpose, we need an array of microphones which records the sound simultaneously and sends it to a processing unit. By using an array processing method we can have a spatial filter which helps us to localize the sound source. The configuration of the array and the location of microphones play an important role in array processing. In this research, we investigate different microphone arrangements to find which one is more efficient for heart sound localization.

II. Simulations

Sound is a mechanical wave which propagates through a medium with a speed which depends mainly on the material of medium and ambient conditions. It is generated by a source, travels through a medium and we can sense it with a sensor which is usually a microphone. Heart is a spread sound source which generates sound from its different parts. This source can be estimated with some point sources which generate sound separately [2]. If we estimate each point's signal energy by combining these data, we will have a map which represents the distribution of heart sound through the thorax. As a result, an image is formed that can be named as an acoustic image of heart.

A. Delay-and-sum beamformer

Beamforming is one the most common solutions for sound localization. In this research a delay-and-sum beamformer is used to localize the source. It has been shown that an imaging resolution for human chest cannot be better than approximately 2 cm [3]. So the beamformer scans the total area of the chest by focusing on each point in 1 cm steps. It estimates each point's signal energy and assigns a number between 0 and 1 to that point due to the maximum and minimum of energy in that region.

B. Sound propagation model in human chest

The acoustic properties of human chest are partly known because of its complexity. The speed of sound is varying from 23 m/s to 1500 m/s in human chest [4]. According to some literatures, sound travels as slow as 10m/s in the thorax [5]. Sound speed in chest wall and heart tissue is about 1500 m/s. The large air ways transmit sound with 222 to 312 m/s. Parenchymal sound speed is estimated to be between 23 and 60 m/s depending on air content. Damping is just about 0.5 to 1.0 decibel per centimeter at 400 Hz [3, 4].

Normal heart sound ranges in frequency from 20 to 150 Hz. Other sounds caused by structural abnormality or pathology, have the frequency up to 1200 Hz [4].

In order to verify our algorithm we conducted the simulations on the basis of these assumptions for different sound speeds and different array arrangements. A delay-and-damp model is used in these simulations [6]. In this model the

Chwee Teck Lim, James C.H. Goh (Eds.): ICBME 2008, Proceedings 23, pp. 738–741, 2009
www.springerlink.com

propagating wave is delayed and damped in its way from source to sensors. The delays are according to different times of arrival and are basis criteria in array processing. As mentioned above, damping factor in human chest is relatively low, but by considering it, we can make the model more precise. This model is presented in equation (1) [6]:

$$s\left(t-|x-y|/c\right)=d.|x-y|.r\left(y,t\right)/|x-y|^2 \qquad (1)$$

In this equation s is the recorded signal at each microphone, x is the location of each microphone, y is the location of source in any coordinate system and $r(y,t)$ is source signal. Assuming constant characteristic through the medium, c and d represent speed of sound and damping factor respectively.

C. Array arrangement

Array arrangement plays an important role in array processing. Here, we have a spread sound source which is in the near-field of the array. Our aim is to find a proper arrangement to fit the geometry of human body and at the same time localize the source with least error possible. The simulations are done in two dimensional and three dimensional arrangements. The 2-D arrangement is used for 2-D maps and the 3-D arrangement for the 3-D maps. Several arrangements are tested in each category. Figure 1 shows three typical array arrangements.

A single source of sound is located in a medium with a sound propagation speed of 10, 40 and 344 m/s. 10 m/s is the least propagation sound speed, 40 m/s is an average speed in human body [3] and 344 m/s is the speed of sound in air at room temperature.

The location of the source is changed in 1 cm step size and the error in detecting the location of source is measured as the distance between the detected source and the real source. The total error of each arrangement is defined as the average of these errors. The total error and the standard deviation of the error of each arrangement are shown in tables 1, 2 and 3. The region of interest is set to match the typical human body size. Signal source is a 500 Hz sine as well as a recorded heart sound.

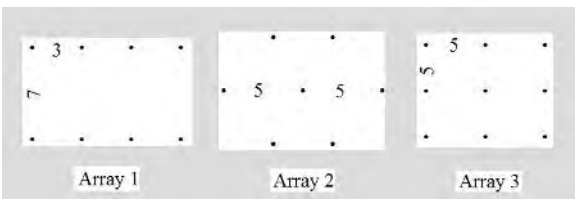


Fig. 1 Array arrangements (distances between microphones are in cm)

Table 1 Total error and standard deviation of the error (speed of sound is 10 m/s)

Array arrangement	Total error (cm)	Error standard deviation (cm)
1	0.02	0.27
2	0.002	0.05
3	0.0	0.0

Table 2 Total error and standard deviation of the error (speed of sound is 40 m/s)

Array arrangement	Total error (cm)	Error standard deviation (cm)
1	0.36	1.57
2	0.35	0.36
3	0.0	0.0

Table 3 Total error and standard deviation of the error (speed of sound is 344 m/s)

Array arrangement	Total error (cm)	Error standard deviation (cm)
1	3.65	2.34
2	4.57	2.60
3	2.31	1.15

The result of simulations for 3-by-3 array at the speed of 40 m/s is presented in figure 2. This array has the least total error and standard deviation of the error among other simulated arrays. It can be seen that the algorithm separated two sources distinctly. In these images points with higher energy are darker and points with lower energy are brighter. Figure 3 shows a three dimensional image. A three dimensional array is used in this case. The array is consist of two 3-by-3 arrays, one in front and one at the back of the chest. So, 18 microphones are used in this array. Because of overlapped voxels, one percent of the points are presented in this image. A side lob can be seen in the image, but it not in the region of interest, so it can be neglected.

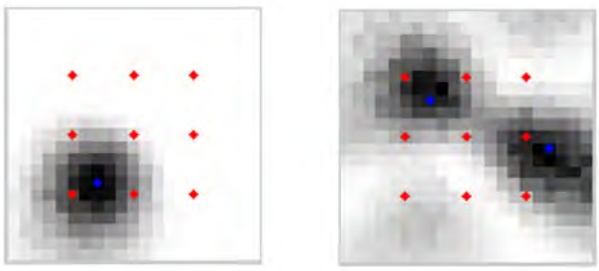


Fig. 2 Localization of one (left) and two (right) acoustic sources (red points indicate microphones location and blue points indicate sources)

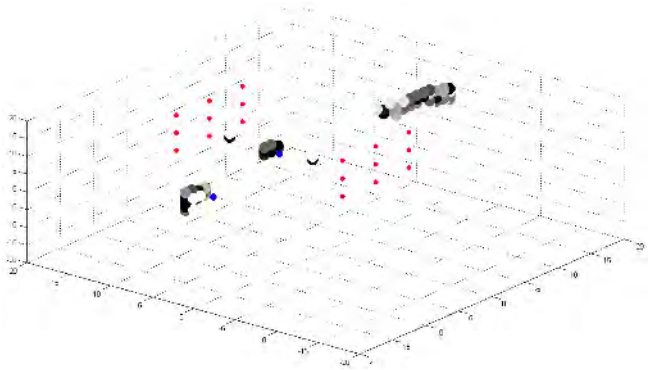


Fig. 3 Three dimensional localization of two acoustic sources (red points indicate microphones location and blue points indicate sources)

III. Segmentation

Heart sound is generated from different places in heart in different intervals [2]. The place of source is different during first heart sound (S1) and second heart sound (S2) so if we separate the sources in time domain, it can help a lot in the problem of source separation and generating the map. We used a heart sound segmentation method presented in [7]. This method doesn't need any extra biological signal (e.g. ECG) as a time guide. More over it overcomes the problem of asynchrony between these extra signals and the phonocardiograph as sometimes occur in certain diseases.

In this method a Morlet bank is used because of its similarity to heart sound. The energy profile of the signal is calculated using this wavelet. Peaks in the energy profile derived from the time-scale representation, are identified and are used to obtain segments containing any activity. Then the singular value decomposition (SVD) of the signal is calculated to determine which segment has a fundamental activity. Due to the following characteristics of PCG the segmented signal is labeled either as S1 or S2: (1) sequential repetition of fundamental activities, (2) the duration of time interval between S1 and S2 (systole) is longer than the duration of time interval between S2 and S1 (diastole), and (3) the heart rate is less than or equal to 160 beat per second. Figure 4 illustrates a PCG signal and its segmented energy profile. These labeled signals are used separately in the beamformer to form time-space maps. More details can be read in [7].

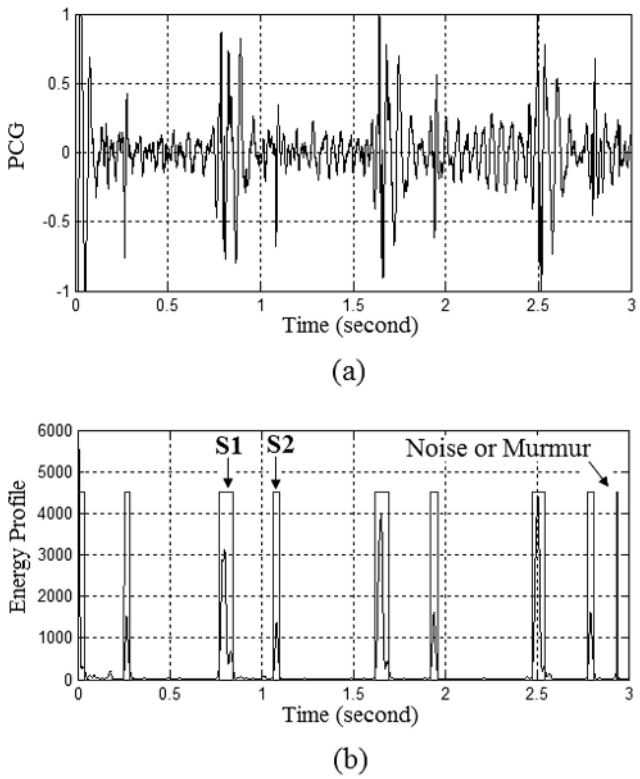


Fig. 4 An example of PCG and its corresponding energy profile. (a) PCG (b) Energy profile

IV. Experimental tests

An experimental setup is prepared for acoustic imaging of heart. It consists of software and hardware units. Software unit process the acquired data to form the acoustic map. Beamforming, segmentation and data presentation are performed in this unit.

Hardware has three major parts: microphone array is made up of Panasonic electret condenser microphones WM-52B, preprocessing unit which amplifies and filters microphone signal in order to enhance sound signal to noise ratio and data acquisition card (DAQ) which is an Advantech PCI-1713 card playing the role of interfacing with a Pentium IV platform PC.

Noise plays an essential role in experiments. In order to eliminate it, firstly we used a low pass filter in the preprocessing circuit with cut-off frequency of 1200 Hz. In software unit the frequencies below 20 Hz are damped with a high pass filter. Some noises such as electricity lines 50 Hz and its higher harmonics and environmental noises such as computer fan noise are inevitable. These noises occur in frequency band that heart sound has information in it and we cannot eliminate them with regular filters. In order to overcome this problem an extra microphone is used to collect noise and subtract it form the main signals adaptively. This method helps enhancing SNR and therefore signal's quality.



Fig. 5 Heart acoustic map for first (left) and second (right) heart sound (red points indicate microphone location)

Experiments are done on a human subject. He is asked to stop breathing at lung resting volume for 3 seconds in order to eliminate breathing sound and heart sound is recorded during this time. According to [3] sound speed in this physiologic condition is near 30 m/s and is closer to the propagation average speed which is 40 m/s. On the other hand overestimation of sound speed causes less artifact and deviation than underestimation [3]. So, experimental tests are done assuming 40 m/s as the propagation speed.

The signals are recorded and saved on a PC, they are segmented using the described method and beamforming is done. Finally a two or three dimensional image is presented on the screen. Figure 5 shows a two dimensional image of heart. It can be seen that heart sound is generated from different locations in different time intervals.

V. Conclusions

The results of this research show that a new imaging method can be introduced and might be helpful. Few clinical researches are done in this field, so there is a need for more investigations to indicate the abilities of this method in diagnosing heart diseases. The most important characteristic of this method is its noninvasive and nondestructive manner. So in future, we may see improvements in acoustic based instruments for heart disease diagnosis.

Some suggestions for improvement of this method are as follow: using more accurate microphones to improve the quality of recorded sound, a more precise estimation of the speed of sound in human chest and designing more complicated array arrangements to eliminate side lobes and to improve the focusing of the array.

References

1. Taplidou S A, Hadjileontiadis L J (2006) Nonlinear analysis of heart murmurs using wavelet-based higher-order spectral parameters, IEEE EMBS Proc. The 28th Annual International Conference, New York City, USA, 2006, pp 4502–4505 DOI 10.1109/IEMBS.2006.259619
2. Bahadirlar Y, Gulcur H O (1998) Cardiac passive acoustic localization: CARDIOPAL. Turkish J Electrical Eng & Computer Sciences 6:243–259
3. Kompis M, Pasterkamz H, Wodicka G R (2001) Acoustic imaging of the human chest. Chest J 120:13091321
4. McKee M, Goubran R A (2005–) Sound localization in the human thorax, IEEE Proc. vol. 1, Instrumentation and Measurement Technology Conference, Ottawa, Canada, 2005, pp 117–122 DOI 10.1109/IMTC.2005.1604082
5. Kawamura Y, Yokota Y, Nogata F (2007) Propagation route estimation of heart sound through simultaneous multi-site recording on the chest wall, IEEE EMBS Proc. The 29th Annual International Conference, Lyon, France, 2007, pp 2875–2878 DOI 10.1109/IEMBS.2007.4352929
6. Kompis M, Pasterkamp H, Oh Y, et al (1998) Spatial representation of thoracic sounds, IEEE EMBS Proc. vol. 3, The 20th Annual International Conference, 1998, pp 1661–1664 DOI 10.1109/IEMBS.1998.747227
7. Rajan S, Budd E, Stevenson M et al (2006) Unsupervised and uncued segmentation of the fundamental heart sounds in phonocardiograms using a time-scale representation, IEEE EMBS Proc. The 28th Annual International Conference, New York City, USA, 2006, pp 3732–3735 DOI 10.1109/IEMBS.2006.260777

Corresponding author:

Author: Hassan Ghassemian
Institute: Tarbiat Modares University
Street: Jalal Al-e-Ahmad Exp.
City: Tehran
Country: Iran
Email: ghassemi@modares.ac.ir

Statistical Variations of Ultrasound Backscattering From the Blood under Steady Flow

Chih-Chung Huang[1], Yi-Hsun Lin[2], and Shyh-Hau Wang[2]

[1)] Department of Electronic Engineering, Fu Jen Catholic University, Taiwan
[2)] Department of Biomedical Engineering, Chung Yuan Christian University, Taiwan

Abstract — **Our previous studies have demonstrated that the statistical distributions of ultrasonic backscattered signals were able to characterize hemodynamic properties of flowing blood associated with red cell aggregation and coagulation. Yet very little is still known about the phenomenon of spatial variation of "black hole" (BH) in the laminar flow with signal statistics of the flowing blood. To further explore this issue, measurements were performed from the porcine blood (with hematocrits of 20 and 50%) circulating in a mock flow loop under various steady laminar flows at mean flow velocities ranged from 1.5 to 12.2 cm/s using a 10 MHz focused ultrasonic transducer. Results showed that the BH phenomenon was apparent for the 50% blood flowing at a low velocity. The BH phenomenon tended to be decreased with the increase of flow velocity and was hardly observed in the 20% blood. The probability density function (PDF) of signals backscattered from flowing blood tended to distribute as pre-Rayleigh statistics with the corresponding mean Nakagami parameter is less than 1. The scaling parameters and Nakagami parameters are respectively decreasing and increasing respectively to the increase of flow velocity. Moreover, larger scaling parameters and smaller Nakagami parameters were obtained respectively from 50% and 20% bloods. The spatial distribution of red cell aggregation and shear rate in the flow tube is a predominant factor leading to the statistical variations of ultrasonic backscattering in the flowing blood and that the formation of BH phenomenon tended to decrease the Nakagami parameter.**

Keywords — **Ultrasonic backscattering, Black hole phenomenon, Nakagami model**

I. Introduction

Several individual red blood cells (RBCs) could aggregate together to form a rouleau depending on blood flow conditions. The red cell aggregation is a reversible physiological process that may increase viscosity and resistance of the flowing blood and further promote blood coagulation [1]. Recently, properties of red cell aggregation associated several factors with blood flows have been studied using ultrasound techniques due to their real-time and noninvasive capabilities [2]. The variation of scatterer size in the flowing blood owing to red cell aggregation may be sensitively detected by ultrasonic backscattering due to that it is scatterer size dependent. Consequently, several previous studies have found that ultrasonic backscattering, corresponding to the formation of RBC aggregation, is affected by the shear rate, hematocrit, and fibrinogen concentration in the flowing blood [2]. An interesting phenonmenon, called "black hole" (BH) phenomenon, was found to form a hypoechoic hole near the center stream of the flow conduit surrounded by a hyperechoic zone discerned by the cross sectional B-mode images, which is presumably resultant from the smaller aggregates at the center stream due to very low shear rate and a maximum aggregation at a certain shear rate [3].

The BH was initially observed by Yuan and Shung [4] in the blood under steady flow and recently that of under pulsatile flow [5]. Many studies indicated that the BH phenomenon is affected by flow velocity, pulsatile condition, entrance length, and hematocrit of the blood. Shehada *et al*. had observed the formation of BH phenomenon from the flowing blood of mean flow velocities ranging from 1.3 to 5.3 cm/s circulated in a rigid tube with a large diameter of 2.54 cm [3]. In addition, a 7 MHz B-mode system was used to image the porcine whole blood at a 28% hematocrit for different entrance lengths circulated in a rigid tube under steady flow conditions, in which results demonstrated that a smaller zone of BH in the center stream was obtained in accordance with the increase of the inlet length of tube [6]. Qin et al. found that the BH was more pronounced corresponding to higher kinetics of RBC aggregation using a 10 MHz Doppler system to measure blood circulated in a 1.27 cm diameter tube under steady flow conditions [7]. Furthermore, the BH phenomenon was investigated with porcine whole blood of different hematocrits under pulsatile flow conditions circulated in a rigid tube of 0.95 cm diameter measured by an ultrasonic scanner with a 7.5 MHz linear array [8]. The results indicated that the formation of BH occurred at hematocrits of blood over 23% and that becomes prominent as that the hematocrit is increased further. Results of these just mentioned investigations showed that the formation of BH phenomenon is related to red cell aggregation in the flowing whole blood.

In this study, the spatial variations of flowing blood including the association of BH phenomenon was explored to better elucidate the relationship between RBC aggregation and backscattering signals statistical behavior. Measurements were carried out on porcine whole blood of 20 and

Chwee Teck Lim, James C.H. Goh (Eds.): ICBME 2008, Proceedings 23, pp. 742–745, 2009
www.springerlink.com

50% hematocrits flowing in a rigid tube of 0.954 cm diameter under various steady laminar flows at mean flow velocities ranged from 1.5 to 12.2 cm/s. The statistical Nakagami parameter and the spatial distribution of backscattering strengths across the whole section of flow tubing were measured and calculated corresponding to different blood properties and flow conditions. The experimental results were analyzed to empirically explore the relationship between BH phenomenon and signal statistics for flowing blood.

II. Materials and Methods

Fresh porcine blood, containing 15% acid citrate dextrose (ACD) anticoagulation solution, was collected from a local slaughterhouse. The impurities of blood, such as hair or fatty tissue, were filtered out using a sponge and that the collected blood was discarded whenever any coagulation was observed. The whole blood was centrifuged at a 2500 rpm for 15 min to separate RBCs from the plasma and other cells. The separated RBCs were subsequently washed twice with saline buffer solution. Whole blood of 20 and 50% hematocrits were obtained by reconstituting the packed RBCs with certain volumes of plasma. The subsequent experiments were performed within 24 h after that the blood sample was collected.

The mock flow phantom, shown in Figure 1, was arranged and calibrated. The flow model comprised a peristaltic pump (Model 7518-00, Masterflex, Cole-Parmer, IL, USA), two reservoirs, and a magnetic stirrer (Cole-Parmer, IL, USA). The blood sample in the conduit was circulated for approximately 20 min before that each data acquisition of an experiment was carried out to eliminate those possible air bubbles and to allow thermal equilibrium with the ambient temperature of 25±1°C. A portion of flow tube was immersed in the degassed water contained in a plexiglass tank to facilitate the transmission and reception of ultrasound waves. The polyurethane flow tube is with an inner diameter of 0.954 cm and thickness of 0.159 cm.

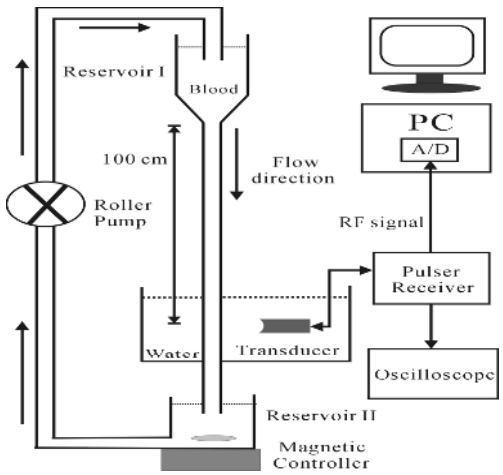


Figure 1, Experimental arrangement.

Prior to each experiment, the flow was calibrated by timing certain flow volumes with respect to the settings on the pump. The mean flow velocities, including 1.5, 3.8, and 12.2 cm/s, were prepared for this study. The inlet length of the tube between the top reservoir and the site of ultrasonic transducer was sufficient (100 cm) to allow a fully developed laminar flow. A wideband 10 MHz focused transducer (A311R, Panametrics, Waltham, Massachusetts, USA) was applied in these measurements. A pulser/receiver (5072PR, Panametrics, Waltham, Massachusetts, USA) was used to drive the transducer for transmitting and receiving ultrasound signals at pulse repetition frequency (PRF) of 100 Hz. The clock signals synchronized with PRF were used to trigger the data acquisition of backscattered echoes at a maximum sampling frequency of 100 MHz by a 14-bit analog-to-digital converter (PCI-5122, National Instruments, Austin, Texas, USA). For all measurements, the sample volume of each collected signal was arranged to be located near the focal zone of the transducer, which was positioned perpendicularly to the flow direction.

A total of 1000 A-lines of radio frequency (RF) backscattered signals were acquired, in which each A-line corresponded to a gated window of 12 μs (assuming the speed of sound in blood is 1540 m/s, and then the length of sample volume is approximately 0.924 cm). The diffraction effect of transducer was subsequently compensated using the axial beam profile of the transducer been measured. The envelopes of those diffraction-compensated backscattered signals for calculating the Nakagami parameter, scaling parameter, and the distribution of backscattering strengths across the flow tube were estimated using Hilbert transform. The M-mode images were obtained for conveniently visualizing the spatial variation of backscattering from flowing whole blood. A total of five porcine blood samples from different animal subjects were used for this study.

The ultrasonic signals backscattered from tissues would result various distributions of PDF, including pre-Rayleigh, Rayleigh, and post-Rayleigh distributions, depending on scatterer concentrations in the sample volume. It thus is feasible to differentiate properties of blood by modeling the PDFs of backscattered envelopes from the blood. The PDFs of the Nakagami distribution (*f*) calculated from the envelope (*R*) of backscattered signals is given by [9],

$$f(R) = \frac{2m^m R^{2m-1}}{\Gamma(m)\Omega^m} e^{\left(-\frac{m}{\Omega}R^2\right)} U(R), \tag{3}$$

where $\Gamma(\cdot)$ and $U(\cdot)$ are respectively the gamma function and unit step function. Both the Nakagami parameter (m) and scaling parameter (Ω) associated with the Nakagami distribution can be calculated as follows:

$$m = \frac{[E(R^2)]^2}{E[(R^2 - E(R^2))^2]}, \tag{4}$$

and

$$\Omega = E(R^2), \tag{5}$$

in which $E(\cdot)$ is the statistical mean. The scaling parameter may directly refer to the average power of the backscattered envelope. In accordance with the resolution cell of the ultrasonic transducer that contains a large number of randomly distributed scatterers, the envelope statistics of the ultrasonic backscattered signals tends to be Rayleigh distributed in which m approached to 1. For that the resolution cell contains scatterers that have randomly varying scattering cross sections with a comparatively high degree of variance, the backscattered envelope tends to be pre-Rayleigh distributed with m less than 1. Further, that the scatterers are located periodically, the corresponding envelope statistics tend to be post-Rayleigh distributed with m larger than 1 [9].

III. Results

Figure 2 is a set of typical M-mode images acquired from flowing whole blood of a 50% hematocrit under different flow velocities ranging from 1.5 to 12.2 cm/s. A tiny hypoechoic region (or black hole) in the center stream of the flow tube surrounded by bright rings was observed associated with flow velocities of 1.5 and 3.8 cm/s shown in Figures 2(a) and (b), respectively. Figure 3 demonstrates respectively the corresponding amplitudes of the backscattered signal envelopes to Figure 2 as a function of radial position in the tube, in which the spatial variation of ultrasonic backscattering from flowing blood could be better delineated. The associated result of Nakagami parameter as a function of flow velocity is in Figure 4, in which the mean Nakagami parameter increased from approximately 0.26 to 0.46 as the flow velocity increased from 1.5 to 12.2 cm/s at a hematocrit of 50 %. As the flow velocity was increased, the corresponding Nakagami parameter tended to increase accordingly.

IV. Discussion and conclusions

Several studies have been undertaken to better comprehend the origin of BH phenomenon [6-7]. As mentioned before, it has been hypothesized that BH phenomenon in the laminar flow was caused partially by the formation of red cell aggregation under the influence of shear rate in the flowing tube. Another study suggested that the very low shear rates around the center of the tube tend to inhibit the

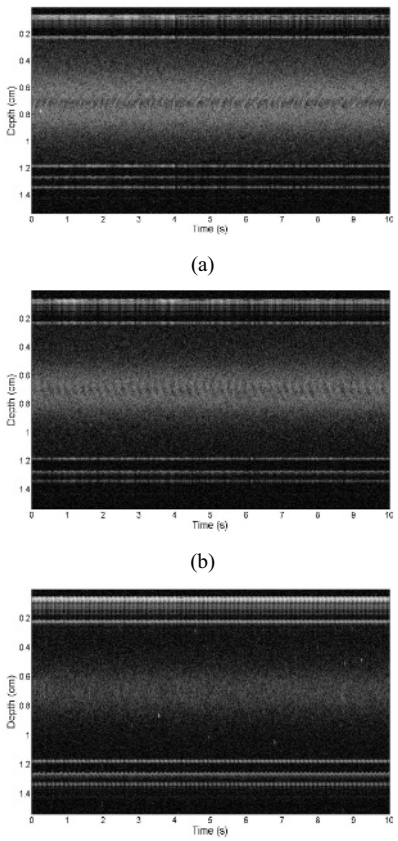


Figure 2, Typical M-mode images associated with whole blood of 50% hematocrit under different flow velocities: (a)1.5 cm/s, (b)3.8 cm/s, and (c)12.2 cm/s.

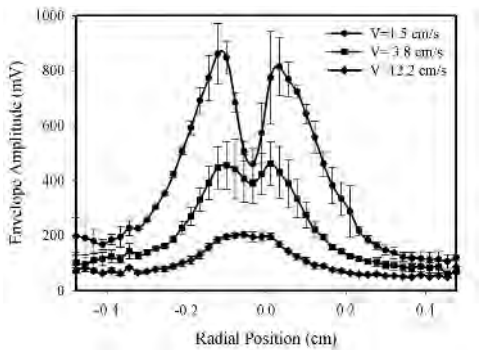


Figure 3, Envelope amplitudes of signals backscattered from a 50% hematocrit blood as a function of radial position in the flowing tube corresponding to different flow velocities.

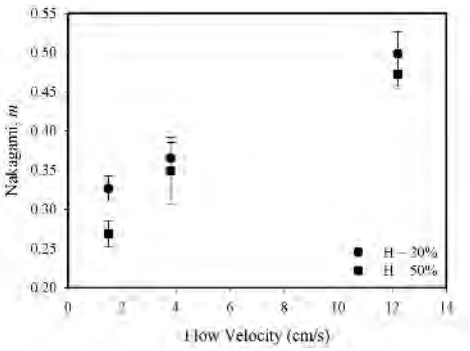


Figure 4, Nakagami parameter of blood of different hematocrits as a function of flow velocity.

formation of large rouleaux whereas higher shear rates in the surrounding region are favorable for the formation of aggregates to produce the BH [8]. However, very little is known about the effect of BH phenomenon on the signal statistics for flowing blood. For this reason, the relationship between blood backscattering behavior and signal statistics should be further established to characterize blood properties with respect to various blood flow conditions.

In general, the BH phenomenon is more likely to appear accordingly to such conditions as the blood flow of lower velocity, the blood of higher hematocrit (over 23%), and a sufficient large flow tube [5]. In this study, the BH phenomenon was able to be created as that the whole blood flowed at very low flow velocities (1.5 to 12.2 cm/s) and circulated in a large tube (diameter of 0.954 cm). The BH in the center stream of the flow tube was observed for blood flowed at velocities of 1.5 and 3.8 cm/s, as shown in Figures 2(a) and (b). As the flow velocity was further increased, the BH phenomenon was diminished. This result well agrees with pervious studies for that the BH phenomenon appeared at a very low velocity [3].

According to results in our pervious study [9], the Nakagami parameter increased from 0.45 to 0.78 as the flow velocities increased from 10 to 60 cm/s. The Nakagami parameter of a blood of 20% hematocrit increased from approximately 0.33 to 0.47 with the increase of flow velocity from 1.5 to 12.2 cm/s, that led PDFs of signal envelopes to pre-Rayleigh distribution. These results imply a correlation could exist between Nakagami parameter and flow velocity. The Nakagami parameter seems to increase with the flow velocity due to the effect of red cell aggregation that varies the size of scatterers in the flowing blood. On the other hand, the PDFs of signal envelopes (50% hematocrit) still exhibited pre-Rayleigh distribution despite the occurrence of BH phenomenon for blood of lower flow velocities from 1.5 and 3.8 cm/s.

In summary, the effects of BH phenomenon in the flowing blood on the backscattering signal statistical behavior using the Nakagami statistical model were investigated. The BH phenomenon was observed obviously associated with the blood of higher hematocrit and that flows at a lower velocity. The experimental results indicated that the Nakagami parameter was smaller than 1 for flowing whole blood due to ultrasonic backscattering of flowing whole blood is spatial variation in the flow tube, resulting in the PDF of the signal envelope being close to pre-Rayleigh distribution. The tendency of decreasing degree of BH phenomenon with respect to the increase of flow velocity is consistent with results obtained from Nakagami parameters.

Acknowledgments

This work was supported by the National Science Council of Taiwan, ROC, under grants: NSC 95-2221-E-033-003-MY3 and NSC 96-2218-E-033-001.

References

1. Vander AJ, Sherman JH, Luciano DS. Human physiology: the mechanisms of body function. Boston, MA: McGraw-Hill; c1998.
2. Shung KK, Cloutier G, Lim CC. The effect of hematocrit, shear rate, and turbulence on ultrasonic Doppler spectrum from blood. IEEE Trans Biomed Eng 1992;39:462-469.
3. Shehada REN, Cobbold RSC, Mo LYL. Aggregation effects in whole blood: Influence of time and shear rate measured using ultrasound. Biorheology 1994;31:115-135.
4. Yuan YW, Shung KK. Echogenicity of whole blood. J Ultrasound Med 1989;8:425-434.
5. Shung KK, Paeng DG. Ultrasound: an unexplored tool for blood flow visualization and hemodynamic measurements. Jan J Appl Phys 2003;42:2901-2908
6. Mo LYL, Yip G, Cobbold RSC, Gutt C, Joy M, Santyr G, Shung KK. Non-Newtonian behavior of whole blood in a large diameter tube, Biorheology 1991;28:421-427.
7. Qin Z, Durrand LG, Cloutier G. Kinetics of the “black hole” phenomenon in ultrasound backscattering measurements with red blood cell aggregation. Ultrasound Med Biol 1998;24:245-256.
8. Cao PJ, Paeng DG, Shung KK. The “black hole” phenomenon in ultrasonic backscattering measurement under pulsatile flow with porcine whole blood in a rigid tube. Biorheology 2001;38:15-26.
9. Huang CC, Wang SH. Statistics variations of ultrasound signals backscattered from flowing blood. Ultrasound Med Biol Ultrasound Med. Biol.(2007) 33:1943-1945.

Employing Microbubbles and High-Frequency Time-Resolved Scanning Acoustic Microscopy for Molecular Imaging

P. Anastasiadis[1], A.L. Klibanov[2], C. Layman[1], W. Bost[3], P.V. Zinin[4], R.M. Lemor[3] and J.S. Allen[1]

[1] Mechanical Engineering, University of Hawaii at Manoa, Honolulu, U.S.A.
[2] Cardiovascular Medicine and Biomedical Engineering, University of Virginia, Charlottesville, U.S.A.
[3] Medical Ultrasound, Fraunhofer-Institute for Biomedical Technology, St. Ingbert, Germany
[4] SOEST, University of Hawaii at Manoa, Honolulu, U.S.A.

Abstract — **Acoustic microscopy offers unique advantages in the investigation of the mechanical properties of biological materials. Ultrasound contrast agents (microbubbles) provide unique acoustic scattering signatures for novel imaging and, in combination with ligands, facilitate molecular imaging capabilities. The potential role and application of microbubble contrast agents at ultra-high frequencies (> 100 MHz) remains an open question. We examine microbubble contrast agents at 200 MHz, 400 MHz and 1.0 GHz in the vicinity of endothelial cells. Visualization of individual microbubbles is demonstrated at 1.0 GHz.**

Keywords — **Ultrasound, Ultrasound Contrast Agents, Endothelial Cells, High-Frequency Acoustic Microscopy, Mechanical Cell Properties.**

I. INTRODUCTION

During the previous decades, on-going research has described the vascular endothelium as an active endocrine, paracrine and autocrine organ, indispensable for the maintenance of vascular homeostasis. Anomalies of the homeostatic state, induced by various stimuli, may cause localized alterations or endothelial dysfunctions, whereby disturbances to molecular and mechanical functions result as direct consequences. The dramatic change of endothelial interaction with blood leukocytes occurring during inflammation provides an example of such an endothelial dysfunction [1]. Furthermore, abnormalities of endothelial function occur in cardiovascular diseases such as atherosclerosis, hypertension, heart failure and organ transplant rejection [2, 3].

The existing techniques for the direct, real-time and non-invasive evaluation of endothelial function *in vivo* have substantial limitations. Acoustically active targeted microbubbles have been applied as a means to non-invasively assess the functional status of the endothelium. Microbubble contrast agents represent an entirely novel family of materials that previously have been used for tissue delineation and perfusion. Their usefulness depends on the compressibility of the interior gas and its associated sound scattering properties which differ from the near-incompressibility of tissue and cells.

Scanning acoustic microscopy (SAM) was employed for the purposes of the current study to examine these acoustic properties at ultra-high frequencies (> 100 MHz).

II. TIME-RESOLVED ACOUSTIC MICROSCOPY

Acoustic microscopy is a significant and promising technique. It depends on the elastic response of the material to waves; and therefore, provides information on local changes in mechanical properties without any physical contact with the specimen. Furthermore, scanning acoustic microscopy (SAM) shows extraordinary advantages such as excellent spatial resolution and minimal invasiveness due to higher sound frequencies, which do not cause damage or disturb the cells [4].

Microbubbles reflect incident ultrasound waves in their response to the alternating compression and rarefaction cycles by changing diameter. This is because their gas content is much more compressible than cells or their surroundings. These oscillations are non-linear for sufficiently high pressure amplitudes. Consequently, this non-linear response alters the character of the reflected signals and hence the

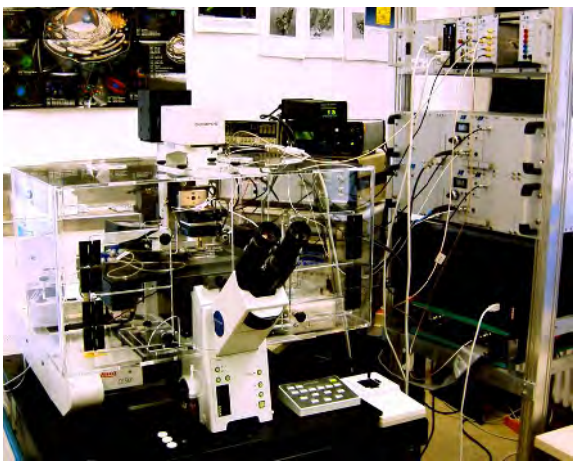


Fig. 1 Scanning acoustic microscope (SASAM, Fraunhofer IBMT, Germany).

Chwee Teck Lim, James C.H. Goh (Eds.): ICBME 2008, Proceedings 23, pp. 746–749, 2009
www.springerlink.com

degree of difficulty of differentiating the received signals is significantly increased.

III. MATERIALS AND METHODS

A. Cell culture

Murine endothelial cells were readily transformed in a single step by the polyomavirus oncogene encoding middle-sized tumor antigen. These cells, bEnd.3 [5], form tumors (hemangiomas) in mice which are lethal in newborn animals [6]. The bEnd.3 cells rapidly proliferate in culture and have an elongated spindle shape (Figs. 2 & 3).

The bEnd.3 cells (obtained from W. Risau, Max Planck Institute) were maintained in Dulbecco's modified Eagle's medium (DMEM) with L-Glutamine (Promochem, 30-2002) containing 10% heat-inactivated fetal bovine serum (Invitrogen) supplemented by 50 i.u./mL of penicillin and 50 µg/mL of streptomycin (Invitrogen).

The cells were dissociated into suspensions of single cells with 0.05% trypsin, seeded at a density of 1-2x10^5 cells/cm^2. The cells were then incubated in a humidified atmosphere of 95% air, 5% CO_2 at a temperature of 37°C. The culture medium was replaced once every 24 hours.

Prior to the experiments, the cells were transferred from culture dishes to Lab-Tek®II (Nunc, GmbH & Co, Wiesbaden, Germany) chambered coverglasses and were then maintained at a temperature of 37°C for 24 to 72 hours. Before conducting high-frequency measurements, the culture medium was replaced by another medium containing 90% DMEM with L-Glutamine supplemented with 10% Fetal Bovine Serum, 40 mM Hepes (Invitrogen), 50 i.u./mL penicillin and 50 µg/mL streptomycin.

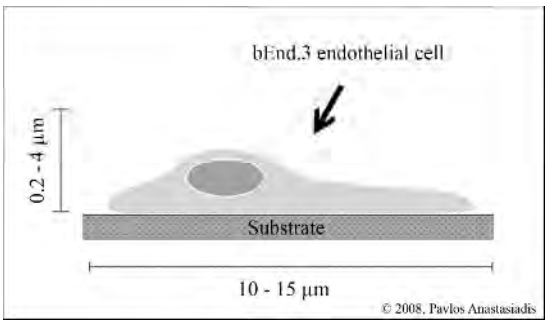


Fig. 2. b.End3 endothelials cells.

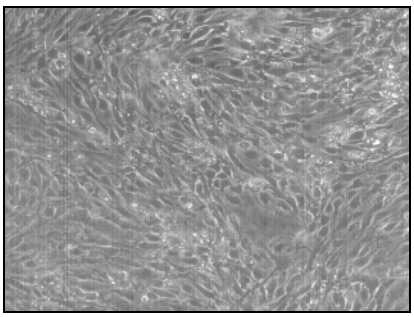


Fig. 3Phase-contrast image of bEnd.3 endothelial cells.

B. Microbubble contrast agents

For the purposes of this study, positively charged lipid-based perfluorocarbon-filled (PFC) microbubbles (Fig. 4) and liquid perfluorohexane emulsion were applied.

The microbubble samples were washed twice in degassed aqueous saline by centrifugation (10^3 rpm for 5 min) to remove the lipids not incorporated in the microbubble shell. The microbubble solution was added along with the degassed saline into a 3 cc syringe equipped with a 3-way luer-lock valve, sealed off with parafilm and subsequently centrifuged. The thin layer of microbubbles that was formed after centrifugation was removed. In the final step, the microbubbles were dispersed onto the adhered bEnd.3 cells.

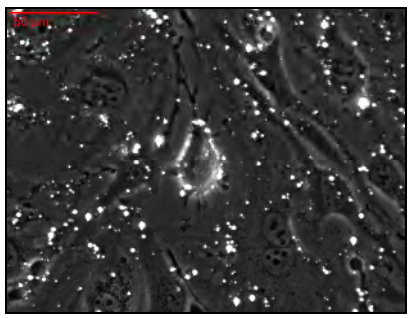


Fig. 4Phase-contrast image of b.End3 cells with microbubbles.

The population of microbubbles used in the study, as determined by an automatic laboratory cell counting apparatus (Casy®, Innovatis Casy Technology, Reutlingen, Germany), was found to be 21.92×10^7 for the PFC-microbubbles per 1 ml solution with a mean diameter of 4.19±1.2 µm, while it appeared to be 11.23×10^7 for the emulsion solution per 1 ml with an average diameter of 4.11±1.2 µm.

C. SAM measurements

Prior to conducting acoustic measurements, the positively charged microbubbles were dispersed into the cell sample chambers as described in the section above. Due to electrostatic forces, they were attracted to either the net negatively charged extracellular matrix (ECM) on the substrate or to the cell surface. Although no systematic quantification

was undertaken, it was observed that most of the microbubble contrast agents remained attached to the extracellular matrix. This might be explained based on electrostatic interactions or simply due to the fact that the substrate corresponds to a substantially larger flat area as opposed to the curved cell surfaces of the sample.

Acoustic measurements were conducted by employing the SASAM scanning acoustic microscope (SASAM, Fraunhofer IBMT, Germany) at frequencies of 200 MHz, 400 MHz and 1.0 GHz. Technical details and applications of SASAM can be found elsewhere [7-9].

IV. RESULTS

A. SAM at 1.0 GHz

Individual bEnd.3 cells were acquired at a frequency of 1.0 GHz at the initial focus position (Z=0) and at different defocused positions above and below the focus position Z (Fig. 5). Microbubbuble contrast agents can be clearly visualized independently of the area of attraction on either the extracellular matrix or the cell surface.

Furthermore, the RF-signals of microbubble A attracted to the ECM and of microbubble B attached to the cell surface (Fig. 6), were compared by plotting the respective power spectra. The power spectra comparison reveals that although a significant overlapping can be observed, there are significant differences at higher frequencies. This discrepancy could be due to the fact that microbubble A is attached to a rigid surface (substrate) as opposed to microbubble B which sits on an elastic surface (cell).

The attenuation of sound in the gigahertz frequency range is high. At the same time, the difference in acoustical impedance between cells and the surrounding medium remains relatively small. The introduction of microbubble contrast agents substantially enhances the amount of backscatter and thus allows for imaging despite the fact that the 1.0 GHz frequency is significantly different from the linear, monopole frequency of the microbubble.

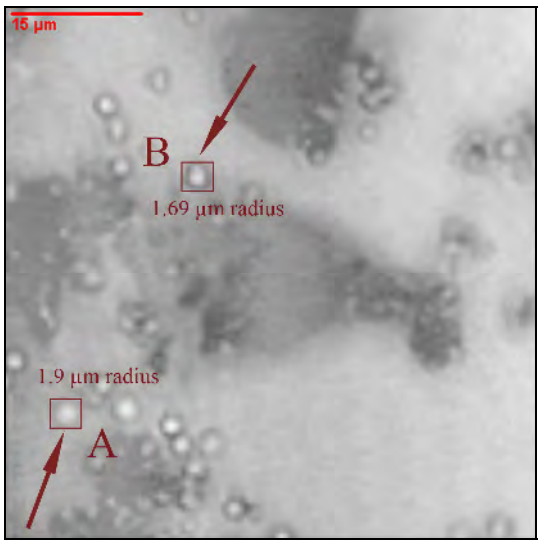


Fig. 6 Visualization of bEnd.3 cells and microbubble contrast agents at 1.0 GHz. The visualization window is 60 µm × 60 µm and the scale bar corresponds to 15 µm.

B. SAM at 400 MHz

Furthermore, bEnd.3 endothelial cells with electrostatically attracted microbubble contrast agents on either the ECM or

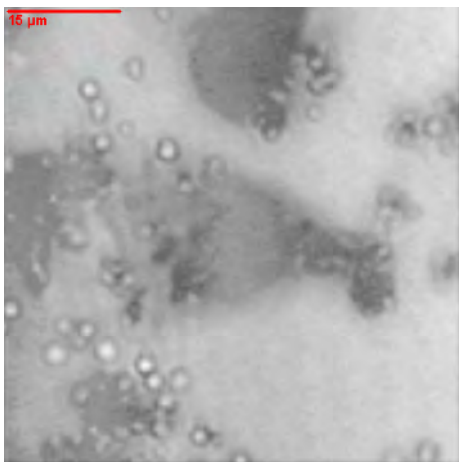


Fig. 5Acoustic microscopy image of bEnd.3 endothelial cells and microbubble contrast agents. The visualization window is 60 µm × 60 µm and the scale bar corresponds to 15 µm.

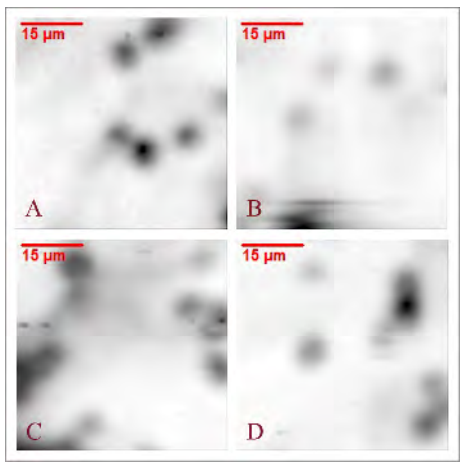


Fig. 7Acoustic microscopy image of bEnd.3 endothelial cells and microbubble contrast agents at 400 MHz. The visualization window is 50 µm × 50 µm and the scale bar corresponds to 15 µm.

the cell surface were imaged ultrasonically at the frequency of 400 MHz (Fig. 7). Although individual microbubbles could be visualized alongside individual cells, the resolution is less than that obtained at 1.0 GHz. This is due to the fact that the resolution at this specific frequency range is approximately 4 μm as opposed to 1.5 μm at 1.0 GHz.

C. SAM at 200 MHz

Visualization of the microbubbles and cells at 200 MHz is limited due to the significant decrease in spatial resolution. However, in Fig. 8 we can discern a cell and microbubbles in the dark region. The cell appears as the darkest semicircular area in the lower left portion. We hypothesize that the regions appear dark due to the defocused position of the acoustic lens.

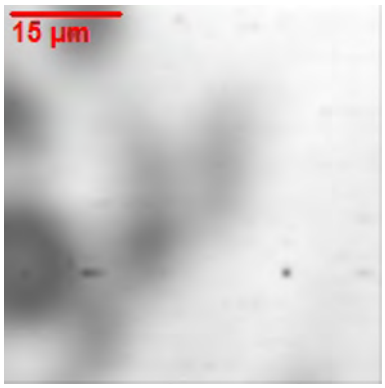


Fig. 8Acoustic image of bEnd.3 endothelial cells and microbubbles obtained at 200 MHz. The visualization window has dimensions 50 μm × 50 μm and the scale bar corresponds to 15 μm.

V. CONCLUSION

Scanning acoustic microscopy equipped with time-resolved analysis provides unique opportunities for real-time monitoring of physiological processes and the assessment of mechanical properties of cells. Furthermore, the combination of SAM and targeted microbubble contrast agents offers the potential to bridge the understanding between the macroscopic factors of cells and their manifestation at the molecular level.

The interaction between microbubbles and ultrasound has been recognized to be fundamental for novel applications in the biomedical field. Nonetheless, the behavior of microbubble contrast agents at ultra-high frequencies remains to be more thoroughly understood.

ACKNOWLEDGMENT

This work was supported by the National Institutes of Health Grant NIH 2 G12 RR0030161-21.

REFERENCES

1. De Caterina R, Libby P, Peng HB, Thannickal VJ, Rajavashisth TB, Gimbrone MA, Jr., Shin WS & Liao JK (1995) Nitric oxide decreases cytokine-induced endothelial activation. Nitric oxide selectively reduces endothelial expression of adhesion molecules and proinflammatory cytokines. *J Clin Invest* **96**, 60-68.
2. Ross R (1999) Atherosclerosis--an inflammatory disease. *N Engl J Med* **340**, 115-126.
3. Tanaka H, Sukhova GK, Swanson SJ, Cybulsky MI, Schoen FJ & Libby P (1994) Endothelial and smooth muscle cells express leukocyte adhesion molecules heterogeneously during acute rejection of rabbit cardiac allografts. *Am J Pathol* **144**, 938-951.
4. Bereiter-Hahn J, Stubig C & Heymann V (1995) Cell cycle-related changes in F-actin distribution are correlated with glycolytic activity. *Exp Cell Res* **218**, 551-560.
5. Montesano R, Pepper MS, Mohle-Steinlein U, Risau W, Wagner EF & Orci L (1990) Increased proteolytic activity is responsible for the aberrant morphogenetic behavior of endothelial cells expressing the middle T oncogene. *Cell* **62**, 435-445.
6. Sheibani N & Frazier WA (1995) Thrombospondin 1 expression in transformed endothelial cells restores a normal phenotype and suppresses their tumorigenesis. *Proc Natl Acad Sci U S A* **92**, 6788-6792.
7. Weiss EC, Lemor RM, Pilarczyk G, Anastasiadis P & Zinin PV (2007) Mechanical properties of single cells. *EEE Transactions On Ultrasonics Ferroelectrics and Frequency Control* **54**, 1-13.
8. Weiss EC, Lemor RM, Pilarczyk G, Anastasiadis P & Zinin PV (2007) Imaging of Focal Contacts of Chicken Heart Muscle Cells by High-Frequency Acoustic Microscopy. *Ultrasound in Medicine and Biology* **33**, 1320-1326.
9. Zinin PV, Weiss EC, Anastasiadis P & M. Lemor RM (2006) "Mechanical properties of HeLa cells at different stages of cell circle by time-resolved acoustic microscope". . *Journal of the Acoustical Society of America* **120**, 3320.

Author: Pavlos Anastasiadis
Institute: Mechanical Engineering, University of Hawaii at Manoa
Street: 2540 Dole Street – Holmes Hall 302
City: Honolulu
Country: U.S.A.
Email: paul.anast@hawaii.edu

Application of Fluorescently Labeled Lectins for the Visualization of Biofilms of Pseudomonas Aeruginosa by High-Frequency Time-Resolved Scanning Acoustic Microscopy

P. Anastasiadis[1], K. Mojica[2], C. Layman[1], M.L. Matter[3], J. Henneman[1], C. Barnes[4] and J.S. Allen[1]

[1] Department of Mechanical Engineering, University of Hawaii at Manoa, Honolulu, U.S.A.
[2] Department of Oceanography, University of Hawaii at Manoa, Honolulu, U.S.A.
[3] John A. Burns School of Medicine, University of Hawaii at Manoa, Honolulu, U.S.A.
[4] Department of Microbiology, University of Hawaii at Manoa, Honolulu, U.S.A

Abstract — **Research on biofilms has benefited from the development of powerful new techniques to investigate their structure, function and morphology. Conjugated lectins combined with microbubbles and high-frequency ultrasound provides unique possibilities to obtain quantitative information on biofilm properties. High-frequency time-resolved scanning acoustic microscopy (SAM) offers a novel means to obtain the structural and material properties of biofilms. Noninvasive measurements were conducted by employing a high-frequency time-resolved scanning acoustic microscope operating at a center frequency of 100 MHz. Fluorescently labeled lectins were used in combination with targeted microbubbles, epifluorescence microscopy and time-resolved SAM for visualization and characterization of carbohydrate-containing extracellular polymeric substances (EPS) in the biofilms of *Pseudomonas aeruginosa*. In addition, ultrasonic reflectivity and transmission experiments were performed on biofilms alone and biofilms with targeted ultrasound contrast agents (UCA) in a water tank at frequencies ranging from 1 to 15 MHz. This data provides measurements of the reflection and transmission coefficients, over a broad frequency spectrum for a range of biofilm growth stages in both the presence and absence of targeted UCA.**

Keywords — **Biofilms, Pseudomonas aeruginosa, High-Frequency Ultrasound, Acoustic Microscopy, Mechanical properties.**

I. Introduction

In natural environments, many bacteria form surface-attached communities known as biofilms [1, 2]. Microbial biofilms are a complex community of sessile bacteria whose behavior is highly differentiated yet coordinated, and are profoundly different from their planktonic counterparts [1, 3]. These three-dimensional heterogeneous assemblages of microbial cells and exopolymeric substances afford bacteria with a protective degree of stability, a primitive circulatory system and a framework for the development of cooperative and specialized cell functions [4, 5]. Notorious for their high level of resistance against all forms of antagonistic chemical treatment; the role of biofilms are of medical interest due to their association with a variety of persistent infections [3, 6, 7].

Numerous methods are available for assessing the formation of biofilms, but their application is often limited by low sensitivity, time intensive intrusive sampling. Rapid, sensitive, and non-intrusive methods are needed for advances in real time monitoring of biofilm research.

Fluorescently labeled lectins, in combination with fluorescencent or confocal laser scanning microscopy, have been used in biofilm research to visualize, localize and biochemically characterize polysaccharides, monitor changes in polysaccharide composition, and to detect cell-cell interactions [8-10]. Despite these successes, the biotechnical and medical potential of using such lectins to identify and localize the presence or absence of a pathogenic biofilm in-situ has not been fully investigated.

The opportunistic pathogen, *Pseudomonas aeruginosa,* often associated with chronic airway infections synthesizes two lectins, LecA and LecB that play an important role in clinical infections [11]. The current study investigates the potential of employing fluorescently labeled lectins in combination with targeted microbubbles and high-frequency time-resolved scanning acoustic microscopy to identify and localize the presence of a *Pseudomonas aeruginosa* biofilm in-situ.

II. Time-resolved acoustic microscopy

Ultrasound imaging is widely used for a range of medical applications. Scanning ultra high-frequency time-resolved acoustic microscopy, in particular, is an emerging and promising technique. A short burst of ultrasound is emitted from a transducer and directed into tissue. Echoes are produced as a result of the interaction of sound with tissue, and some of these are reflected back to the transducer. By timing the period elapsed between the emission of the pulse and the reception of the echo, the system provides information on local changes in mechanical properties without any

Chwee Teck Lim, James C.H. Goh (Eds.): ICBME 2008, Proceedings 23, pp. 750–753, 2009
www.springerlink.com

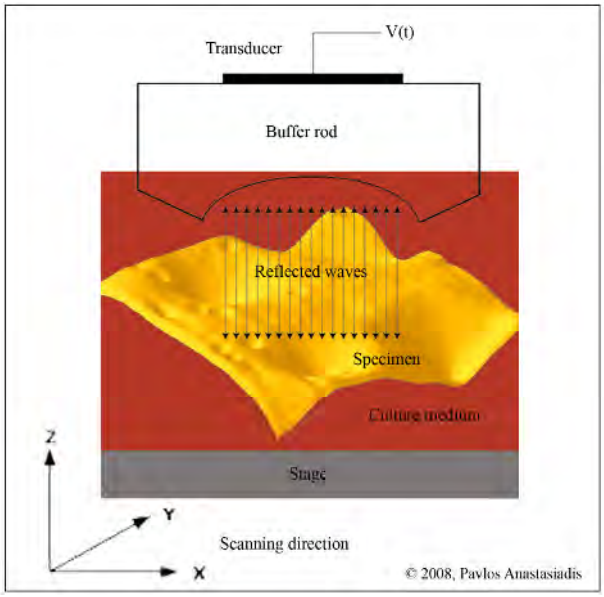


Fig. 1 Scanning acoustic microscope principle.

physical contact with the specimen. Echoes are generated when the propagating ultrasound wave encounters an object with different acoustic impedance. When the sample is significantly smaller than the acoustic wavelength, echo is generated through scattering. This is the origin of the echoes within the biofilm. Finally, if the acoustic wave encounters an interface that is relatively large with respect to the wavelength, then reflection occurs. This is the situation for the substrate/biofilm interface.

Furthermore, microbubble contrast agents scatter incident ultrasound waves in their response to the alternating compression and rarefaction cycles. Their gas content is much more compressible than cells or their surroundings such that they oscillate about their equilibrium radii. This difference in acoustical impedance and compressibility allows for an enhanced ultrasonic image.

III. Materials and Methods

A. Pseudomonas aeruginosa biofilm growth

The bacterial species and strain used in this study was *Pseudomonas aeruginosa* PAO1 (provided by Tung T. Hoang, Department of Microbiology, University of Hawaii at Manoa, Honolulu, USA). A bacterial culture was prepared by inoculating one colony of 1.5 ml *Pseudomonas aeruginosa* strain PAO1 thawed from frozen stock to 100 ml Trypsin Soy Broth growth medium (TSB, T8907, Sigma-Aldrich, St. Louis, USA). The TSB growth medium was diluted in ultrapure water (Alfa Aesar, Ward Hill, MA, USA) and filtrated through a 22 μm filter. Subsequently, the mixture was incubated overnight for twelve hours and kept on the incubator shaker at 37 °C atmosphere and 160 RPM. After the overnight incubation, the culture of *Pseudomonas aeruginosa* was standardized to an optical density at 600 nm (OD_{600}) of 0.05 relative to the TSB growth medium by employing a spectrophotometer (Beckman Coulter, Inc., Fullerton, CA, USA).

Pseudomonas aeruginosa biofilm assays were conducted by adding three microliters of standardized culture in each of the pre-treated cover slips. Cover slips were previously treated with various acids and solutions to enhance hydrophilicity and make them charge neutral to improve biofilm attachment. The cover slips were then kept inside an incubator shaker at 37 °C and 160 RPM continuously for periods of 12, 24, 48, 72 and 96 hours respectively before harvesting the biofilms and image them by confocal scanning laser microscopy and ultrasonically.

B. Microbubble contrast agents and visualization

For the purposes of this study, lipid-encapsulated perfluorocarbon microbubble contrast agents with a mean diameter of 2.5 μm were employed (Targeson, LLC, Charlottesville, VA, USA).

The mircorbubble samples were washed twice in degassed aqueous saline by centrifugation (10^3 rpm for 5 min) to remove the lipids not incorporated in the microbubble shell. The concentration that was used throughout the study was $1\text{-}3\times10^8$ microbubble contrast agents per milliliter.

Prior to ultrasonic and confocal scanning laser microscopy imaging, the microbubble contrast agents were conjugated with 20μL Streptavidin AlexaFluor 568 (Invitrogen).

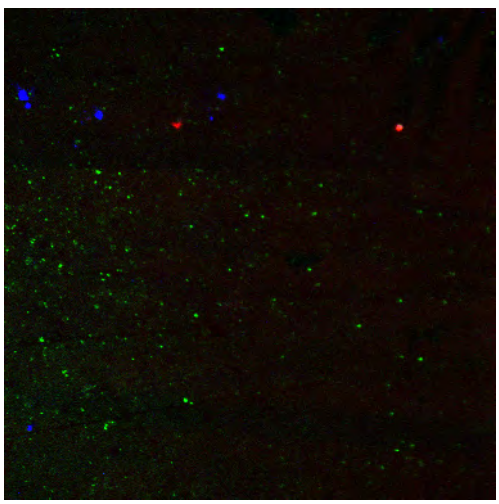


Fig. 2 Confocal scanning laser microscopy image of LecA after 48 hours.

The solution was incubated on ice for 30 minutes. After this time, the excess streptavidin was washed from the microbubbles by adding degassed phosphate buffered saline (PBS) to a 3mL lock-luer syringe attached to a one-way stopcock until a total volume of 2.0 mL within the syringe was reached.

Wheat Germ Agglutinate (WGA) AlexaFluor 488 and Concanavalin A (ConA) AlexaFluor 488 were both used as lectin proteins as both bind different polysaccharides. This is important because *Pseudomonas aeruginosa* biofilms have a tendency to switch polysaccharide makeup of their biofilm production. By using two different lectins that bind to polysaccharides, the chances of biofilm labeling are increased.

The final fluorescent label used was a DAPI, a nucleic acid dye that can be added to TSB media and taken up by the *P. aeruginosa* bacteria. The addition of this nucleic acid dye helps differentiate actual bacteria cells from the polysaccharide matrix of the biofilm.

C. Ultra high-frequency acoustic microscopy

For the purposes of this study a scanning high-frequency time-resolved acoustic microscope with a center frequency of 100 MHz (SASAM, Fraunhofer IBMT, St. Ingbert, Germany) was employed. The transducer mechanically scans laterally over a region of interest, and forms a 2D image using echoes from a series of adjacent transducer beam locations (Fig. 1). The lateral resolution of the system lies in the range of 10-15 μm. At a given beam location, the received ultrasound echo is converted into a brightness scale that is subsequently displayed as one line on the image. The growth medium was refreshed before conducting ultra high-frequency measurements.

D. High-frequency ultrasound measurements

The longitudinal wave data is obtained by the ultrasonic broadband substitution method [12]. This technique provides a means of determining both the attenuation and phase velocity profiles, simultaneously, over a range of frequencies. Briefly, a broadband pulse is generated by a ceramic acoustic transducer (Olympus NDT, Waltham, MA) that is electronically excited by a pulser/receiver (PR5900, Olympus NDT, Waltham, MA). In a water tank, the pulse is either received by another similar ceramic transducer aligned along the wave propagation direction, or received by the same transducer via an aluminum reflecting block. The received signal is digitized by a digital oscilloscope of 500 MHz bandwidth and 5-GHz sampling rate (Waverunner 6051A, Lecroy, Chestnut Ridge, NY). The sample is then inserted between the two transducers (or the single transducer and the reflecting block), allowing the sound beam to propagate, normally, through the sample. The waveform transmitted through the sample is then digitized by the oscilloscope. A complex spectrum is obtained from the sample waveform data, which are then divided by the spectrum from the water, with no sample present. This ratio allows for the determination of the sample's longitudinal phase velocity and attenuation, concurrently. A range of broadband transducers were used to cover the medical relevant ultrasonic frequency range of 1 to 15 MHz.

Biofilms were grown on substrates consisting of 0.003 inch thick TPX polymer films (K-Mac Plastics, Wyoming, MI, USA) and placed in the water bath for insonification, as described above. TPX has an acoustical impedance very similar to that of water and causes virtually no perturbation of ballistic pulse as it travels through the sample/substrate; hence reflection or transmission data can be analyzed without regard to film interference. In order to infer bio-film mechanical properties, acoustic microbubbles are used, which have a high echogeneity where biofilms do not. The micro-bubbles, therefore, act as the necessary coupling agent between the sound and the biofilm. Biofilms with and without attached microbubbles were characterized ultrasonically, in the manner explained above, to quantify the degree of micro-bubble attachment to the films. This quantification can be inferred from the inspection of either the reflected (backscatter) wave amplitude, or conversely by the transmitted (forward scatter) wave amplitude, which is shown over a broad range of frequencies.

IV. Discussion

Microscopy is a highly valuable approach to biofilm investigations, and especially confocal scanning laser microscopy can provide accurate 3D reconstructions. Nonetheless, this technique cannot be used to visualize unstained material or any other matrix which was not specifically treated [13]. Acoustic microscopy provides a non-invasive method which can be applied repeatedly on the same sample after subjecting it to different treatments or materials without the need of any staining or fixing procedure.

Time-resolved acoustic microcopy, in particular, provides a non-invasive visualization method in the field of medicine and biology. Moreover, SAM enables the real-time monitoring of physiological processes in living samples. The observation of changes in the mechanical properties by employing ultrasound with targeted microbubbles in general and ultra high-frequency combined with targeted microbubbles in particular offers the potential to provide new insights at the molecular level and to further assist understanding the complexity of biofilm pathways.

While other studies have focused only on morphology and thickness, this work examines the avenue of ultrasound molecular imaging by employing targeted microbubble contrast agents. Furthermore, it has been shown that high-frequency ultrasound signals can be sensitive to both tissue structure and cells undergoing apoptosis [14]. Thus, examining ultrasound signals reflected from different biofilm types or during growth, after therapy or treatment, may bear useful information and assist advancing considerably the understanding of biofilms.

References

1. Costerton JW Overview of microbial biofilms.
2. Sutherland IW The biofilm matrix--an immobilized but dynamic microbial environment.
3. Donlan Rm Fau - Costerton JW & Costerton JW Biofilms: survival mechanisms of clinically relevant microorganisms.
4. Costerton Jw Fau - Lewandowski Z, Lewandowski Z Fau - DeBeer D, DeBeer D Fau - Caldwell D, Caldwell D Fau - Korber D, Korber D Fau - James G & James G Biofilms, the customized microniche.
5. Hall-Stoodley L Fau - Stoodley P & Stoodley P Biofilm formation and dispersal and the transmission of human pathogens.
6. Baillie Gs Fau - Douglas LJ & Douglas LJ Matrix polymers of Candida biofilms and their possible role in biofilm resistance to antifungal agents.
7. Burmolle M Fau - Webb JS, Webb Js Fau - Rao D, Rao D Fau - Hansen LH, Hansen Lh Fau - Sorensen SJ, Sorensen Sj Fau - Kjelleberg S & Kjelleberg S Enhanced biofilm formation and increased resistance to antimicrobial agents and bacterial invasion are caused by synergistic interactions in multispecies biofilms.
8. Leriche V Fau - Sibille P, Sibille P Fau - Carpentier B & Carpentier B Use of an enzyme-linked lectinsorbent assay to monitor the shift in polysaccharide composition in bacterial biofilms.
9. Strathmann M Fau - Wingender J, Wingender J Fau - Flemming H-C & Flemming HC Application of fluorescently labelled lectins for the visualization and biochemical characterization of polysaccharides in biofilms of Pseudomonas aeruginosa.
10. Wigglesworth-Cooksey B Fau - Cooksey KE & Cooksey KE Use of fluorophore-conjugated lectins to study cell-cell interactions in model marine biofilms.
11. Tielker D Fau - Hacker S, Hacker S Fau - Loris R, Loris R Fau - Strathmann M, Strathmann M Fau - Wingender J, Wingender J Fau - Wilhelm S, Wilhelm S Fau - Rosenau F, Rosenau F Fau - Jaeger K-E & Jaeger KE Pseudomonas aeruginosa lectin LecB is located in the outer membrane and is involved in biofilm formation.
12. Junru W (1996) Determination of velocity and attenuation of shear waves using ultrasonic spectroscopy. *The Journal of the Acoustical Society of America* **99**, 2871-2875.
13. Palmer Jr RJ & Sternberg C (1999) Modern microscopy in biofilm research: Confocal microscopy and other approaches. *Current Opinion in Biotechnology* **10**, 263-268.
14. Czarnota GJ, Kolios MC, Vaziri H, Benchimol S, Ottensmeyer FP, Sherar MD & Hunt JW (1997) Ultrasonic biomicroscopy of viable, dead and apoptotic cells. *Ultrasound in Medicine and Biology* **23**, 961-965.

Author: Pavlos Anastasiadis
Institute: Mechanical Engineering,
University of Hawaii at Manoa
Street: 2540 Dole Street – Holmes Hall 302
City: Honolulu
Country: U.S.A.
Email: pavlos@hawaii.edu

A Comparative Study for Disease Identification from Heart Auscultation using FFT, Cepstrum and DCT Correlation Coefficients

Swanirbhar Majumder [1], Saurabh Pal[2] and Pranab Kishore Dutta [1]

[1] North Eastern Regional Institute of Science and Technology, Arunachal Pradesh, India
[2] Haldia Institute of Technology, West Bengal, India

Abstract — **We present a comparative study for correlation coefficients of three different, but popular transforms of audio signals i.e. Fast Fourier Transform (FFT), Cepstrum and Discrete Cosine Transform (DCT). But this study is done keeping into mind an important application, the heart sound analysis or heart auscultation analysis which manually is done by doctors for disease identification. We present a very simple automated software based approach for first detecting whether the heart is normal or abnormal and then identifying the disease if within the range of diseases for which it has been trained. Here our application has been trained for only three heart diseases, Mitral Regurgitation, Mitral Stenosis, and Splits. Further training might enable our application for identifying other diseases as well. We get better the detection accuracy with the increase of training data. We have taken the help of FBS (Frontiers in Bioscience) online data base for heart sounds for this purpose, and have used their .wav format of heart sound files for our analysis. But along with these we also found out that though Cepstrum is a very important transform for speaker recognition and other audio based application, but here in case of heart sound analysis it is not very user friendly for analysis.**

Keywords — **FFT, Cepstrum, DCT, Mitral Regurgitation, Mitral Stenosis, Splits**

I. Introduction

The heart sounds are generated by mechanical vibration of heart and cardiovascular where they provide abundant information about them while the measurement is noninvasive and low cost. Heart sounds and murmurs are the important parameter used in diagnosing the heart condition and it can be captured by using phonocardiogram or heart auscultation [3]. Classically the sounds made by a healthy heart are conceived as being a nearly periodic signal consisting of four components. These four parts are referred to as the first, second, third and fourth heart sounds as in Fig 1. The first two heart sounds give rise to the familiar 'lub-dup' beating sound of the heart and tend to dominate the Phono-CardioGraphic (PCG) signals [4].

First Heart Sound, S1 is the effect of closing the tricuspid and mitral valve at the beginning of ventricle systolic. There are four components of the first heart sounds. The first component is the effect of ventricular contraction and blood movement towards atrio-ventricular valve. This occurs at beginning of ventricle systolic. The second component is the effect of atrioventricle closure. The third component is reflected the opening of semi lunar valve and the beginning of blood ejection. The fourth and last component represents the maximum blood ejection from ventricle to aorta. Second Heart Sound, S2 represents the vibrations as a result from closure of semi lunar valve at the end of ventricle systolic. Since there are two component of semi lunar valve, the second heart sound is a combination of two components. The aortic valve closed earlier than the closing of pulmonary valve. Third Heart Sound, S3 results from vibration setting by early filling of ventricle during ventricle diastole. Lastly the fourth Heart Sound, S4 is caused by rapid filling of ventricle with blood during atrium systole. It also marked the end of ventricle diastole [8].

Each beat is separated by an interval of the order of around one second, with each heart sound having duration of roughly 50ms. The interval between beats varies even in a patient at rest because of respiration. Similarly the exact nature of each beat varies from beat to beat. The result is a signal which is non-periodic, even though it has a repetitive character.

The heart murmurs occur as the additional components in the PCG signal, most often arising in the interval between the first and second heart sound. Heart murmurs are the result of turbulent blood flow, which produces a series of many vibrations. The murmur signal is often of much smaller amplitude than either of the heart sounds. Many murmurs are described as "whooshing" sounds and are believed to be derived from flow noise. The heart murmurs will produce the abnormal heart sounds. There are four main factor of producing murmurs, firstly high rates of flow through normal and abnormal valves, then forward flow through a constricted or irregular valve or into dilated vessels, next backward flow through an incompetent valve, septal defect, or patient ductus arteriosus and lastly decreased viscosity, which causes increased turbulent and contributes to the production and intensity of murmurs



Fig. 1: Heart Sound Components S4, S1, S2 and S3

Chwee Teck Lim, James C.H. Goh (Eds.): ICBME 2008, Proceedings 23, pp. 754–757, 2009
www.springerlink.com

II. Different techniques

The different techniques we employ are FFT (fast Fourier transform), Cepstrum and DCT (discrete cosine transform). Fourier transform belongs to the family of linear transforms widely used in digital signal processing based on decomposing signal into sinusoids (sine and cosine waves). Usually in DSP we use the Discrete Fourier Transform (DFT), a special kind of Fourier transform used to deal with aperiodic discrete signal. Actually there are an infinite number of ways how signal can be decomposed but sinusoids are selected because of their sinusoidal fidelity that means that sinusoidal input to the linear system will produce sinusoidal output, only the amplitude and phase may change, frequency and shape remain the same. Discrete Fourier Transform changes an Ns point input signal into two Ns/2 +1 point output signals. The output signals representing the amplitudes of the sine and cosine components scaled in a special way as in equations (1) and (2).

$$C_K[i] = \cos(2K\pi/N_S) \quad (1)$$

$$S_K[i] = \sin(2K\pi/N_S) \quad (2)$$

where C_K are Ns/2+1 cosine functions and SK are Ns/2+1 sine functions, index K runs from zero to Ns/2. These functions are called basis functions. Actually zero samples in resulting signals are amplitudes for zero frequency waves, first samples for waves which make one complete cycle in Ns points, second for waves which make two cycles and so on. Signal represented in such a way is called to be in frequency domain and obtained coefficients are called spectral coefficients or spectrum. Frequency domain contains exactly the same information as the time domain and every discrete signal can be moved back to the time domain, using operation called Inverse Discrete Fourier Transform (IDFT). Because of this fact, the DFT is also called forward DFT. The amplitudes for cosine waves are also called real part (denoted as Re [K]) and for sine waves are called imaginary part (denoted as Im[K]). This representation of frequency domain is called rectangular notation. Alternatively, the frequency domain can be expressed in the polar notation. In this form, real and imaginary parts are replaced by magnitudes (denoted as Mag[K]) and phases (denoted as Phase[K]) respectively. The equations (3) and (4) are used for conversion from rectangular notation to the polar notation [7].

$$Mag[K] = \sqrt{(Re[K]^2 + Img[K]^2)} \quad (3)$$

$$Phase[K] = \tan^{-1}\left(\frac{Img[K]}{Re[K]}\right) \quad (4)$$

There are two main reasons why DFT became so popular in digital signal processing. First is Fast Fourier Transform (FFT) algorithm, developed by Cooley and Tukey in 1965, which opened a new era in DSP because of the efficiency of the FFT algorithm. The second reason is the convolution theorem, which states that convolution in time domain is a multiplication in frequency domain and vice versa. This makes possible to use high-speed convolution algorithm, which convolves two signals by passing them through the Fast Fourier Transform, multiplying and using Inverse Fourier Transform computing convolved signal. Here we use the fast Fourier transform to calculate the frequency components of heart sounds.

The Cepstrum [5] is representation of the signal normally having two components that are resolved into two additive parts. It is computed by taking the inverse DFT of the logarithm of the magnitude spectrum of the frame as in equation (5).

$$\text{Cepstrum (frame)}=\text{IDFT}(\log(|\text{DFT(frame)}|)) \quad \textbf{(5)}$$

The process of moving to the frequency domain provides the operation changing from the convolution to the multiplication. Then by taking logarithm, the operation is moving from the multiplication to the addition. That is desired division into additive components. Then it can be applied linear operator inverse DFT, knowing that the transform will operate individually on these two parts and knowing what Fourier transform will do with each part.

The most common DCT definition of a 1-D sequence of length *N* for $\boldsymbol{u} = 0, 1, 2\ldots N$ is:

$$C(u) = \alpha(u)\sum_{x=0}^{N-1} f(x)\cos\left[\frac{\pi(2x+1)u}{2N}\right] \quad \textbf{(6)}$$

Similarly the inverse transformation is defined for $\boldsymbol{x} = 0, 1, 2\ldots N$ is:

$$f(x) = \sum_{u=0}^{N-1} \alpha(u)C(u)\cos\left[\frac{\pi(2x+1)u}{2N}\right] \quad \textbf{(7)}$$

In both equations α(u) is defined as:

$$\alpha(u) = \begin{cases} \sqrt{\frac{1}{N}} \text{ for } u = 0 \\ \sqrt{\frac{2}{N}} \text{ for } u \neq 0 \end{cases} \quad \textbf{(8)}$$

Thus for $\boldsymbol{u} = 0$ we have the DC coefficient and other than that all others are the AC coefficients.

III. SIMULATION AND IMPLEMENTATION

Here we first get the samples of the test samples of normal heart sounds, and the test samples for the three diseases we are analyzing Mitral Regurgitation, Mitral Stenosis, and Splits. Then we go for the first step of detection of the four heart sounds S1, S2, S3, and S4 after undergoing discrete fourier transform on them. Thus based on their values we can detect the condition of heart i.e whether normal or abnormal as well as the heart rate value [2].

Then we take the all the test samples (normal and diseased) and find the FFT (Fast Fourier Transform) of the each one of them. On getting the Fourier coefficients, we get the value of correlation coefficient of each test sample with every other test sample and plot the graphs for normal & the three diseases. This method is replicated for the Cepstrum coefficients as well as the DCT (Discrete Cosine Transform).

Then we go for the analysis of those plots and decide on the specific correlation coefficient values which we can set as threshold for detection. All these operations were built in MATLAB® Release 2008a.

IV. RESULT ANALYSIS

Here firstly for the FFT coefficients we plot 12 test samples of which first three are normal, followed by three each of mitral regurgitation, mitral stenosis and split respectively. Thus figure 2, 3, 4 and 5 give the respective correlation coefficients for the FFT coefficients with each other for normal, mitral regurgitation, mitral stenosis and splits, respectively. Here we see that for each figure the correlation coefficients for the same type of heart sounds are above 0.7, while with others it is less. The analysis is plotted in Table I below for correlation of FFT coefficients.

Correlation coefficients of Cepstrum could not give the same amount of demarcation as provided by FFT coefficients.

Table 1: Analysis of Correlation coefficients of test samples for FFT coefficients

Test Sample	Coefficient	Analysis
Normal	Greater than 0.3	Normal Heart
Mitral Regurgitation	Less than 0.2	Normal Heart
	0.2 to 0.5	Mitral Stenosis
	Greater than 0.65	Mitral Regurgitation
Mitral Stenosis	Less than 0.3	Normal Heart Sound
	0.4 to 0.55	Mitral Regurgitation
	0.5 to 0.6	Splits
	Greater than 0.7	Mitral Stenosis
Splits	Less than 0.3	Normal Heart
	0.25 to 0.4	Mitral Regurgitation
	0.5 to 0.6	Mitral Stenosis
	Greater than 0.7	Splits

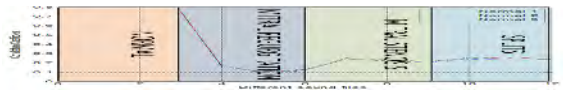


Fig 2: Correlation of FFT coefficients of Normal heart sounds

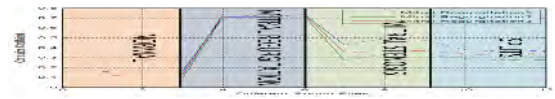


Fig 3: Correlation of FFT coefficients of Mitral Regurgitation heart sounds

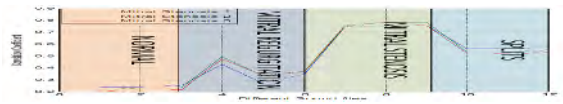


Fig 4: Correlation of FFT coefficients of Mitral Stenosis heart sounds

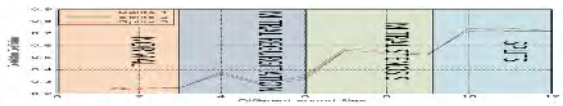


Fig 5: Correlation of FFT coefficients of Splits heart sounds

Though figures 6, 7, 8 and 9 do provide some details but there are some overlapping test sample data which cause conflict in decision making. Any way a partial analysis has been discussed about these plots in Table II based on the correlation of the Cepstrum coefficients with each other. The most alarming problem here is caused by the splits and normal Cepstrum coefficients data as here the splits Cepstrum coefficients give higher correlation with the normal Cepstrum coefficients this leading to erroneous result. Moreover the mitral stenosis based correlation of Cepstrum coefficients does not help in any type of analysis due to their random nature.

Correlation coefficients of DCT coefficients work in a similar pattern as that of FFT coefficients but the range of FFT coefficient was wider than this. Any way it still satisfies our need which can be seen from the figures 10, 11, 12 and 13. The analysis of this is given in Table III, which we can see is of similar type as in case of Table I for analysis of FFT coefficient correlation analysis.

Table 2: Analysis of Correlation coefficients of test samples for Cepstrum coefficients

Test Sample	Coefficient	Analysis
Normal	Greater than 0.87	Normal Heart
	0.7 to 0.85	Splits
	Less than 0.7	Mitral diseases
Mitral Regurgitation	Less than 0.8	May be anything
	Greater than 0.8	Mitral Regurgitation
Mitral Stenosis	Anything	No proper Analysis
Splits	Less than 0.2	Mitral Regurgitation
	0.6 to 0.7	Splits
	0.7 to 0.9	Normal Heart

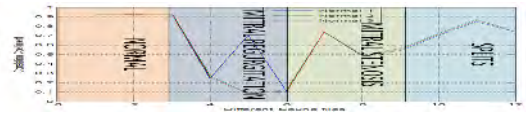


Fig 6: Correlation of Cepstrum coefficients of Normal heart sounds

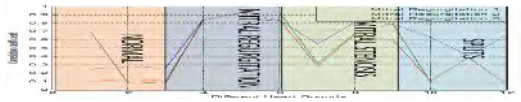


Fig 7: Correlation of Cepstrum coefficients of Mitral Regurgitation heart sounds

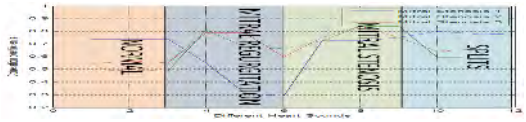


Fig 8: Correlation of Cepstrum coefficients of Mitral Stenosis heart sounds

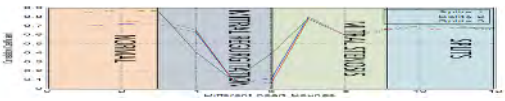


Fig 9: Correlation of Cepstrum coefficients of Splits heart sounds

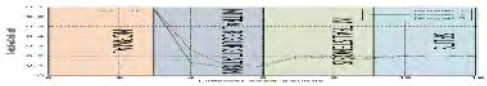


Fig 10: Correlation of DCT coefficients of Normal heart sounds

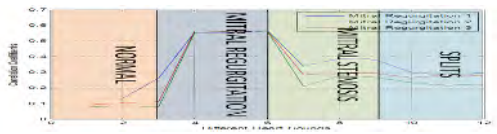


Fig 11: Correlation of DCT coefficients of Mitral Regurgitation heart sounds

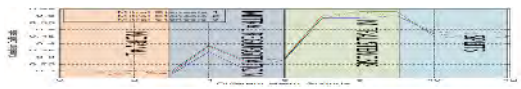


Fig 12: Correlation of DCT coefficients of Mitral Stenosis heart sounds

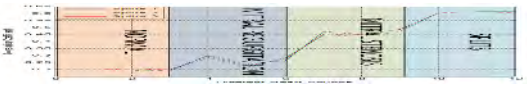


Fig 13: Correlation of DCT coefficients of Splits heart sounds

Table 3: Analysis of Correlation coefficients of test samples for DCT coefficients

Test Sample	Coefficient	Analysis
Normal	Greater than 0.25	Normal Heart
Mitral Regurgitation	Less than 0.2	Normal Heart
	0.2 to 0.4	Mitral Stenosis/Splits
	Greater than 0.5	Mitral Regurgitation
Mitral Stenosis	Less than 0.2	Normal Heart Sound
	0.3 to 0.4	Mitral Regurgitation
	0.4 to 0.5	Splits
	Greater than 0.57	Mitral Stenosis
Splits	Less than 0.2	Normal Heart
	0.25 to 0.3	Mitral Regurgitation
	0.4 to 0.5	Mitral Stenosis
	Greater than 0.6	Splits

V. CONCLUSIONS

Thus we can hereby conclude after analyzing the correlation coefficients of the FFT, Cepstrum and DCT coefficients of different normal and abn006Frmal heart sounds that DCT and FFT give best results for disease identification based on this method.

REFERENCES

1. FBS (Frontiers in Bioscience) online data base for heart sounds. http://www.bioscience.org
2. R Subadar, S Majumder, A D Singh, " Computer Based Heart Auscultation Analysis", Pg 27, proceedings of National Conference on Emerging Trends in Information Technology and its Application for Technical and Management Education, (NETIT^{2}M '08), Alwar, Rajasthan, India.
3. L.G. Durand and P. Pibarot, Digital Signal Processing of the Phonocardiogram:Review of the Most Recent Advancements, Critical Review in Biomedical Eng., Vol 23, pp. 163-219,1995
4. L.G. Durand and G. Cloutier, Comparison of Pattern Recognition Methods for Cornouter-Assisted Classification of Spectra of Heart Sounds h Patients with a Porcine Bioprosthetic Valve Implanted in the Mitral Position, IEEE Trans. on Biomedical Eng., vol. 37, No. 12, pp. 1121-1129.
5. B. P. Bogert, M. J. Healy, and J. W. Tukey, "The frequency analysis of time series for echoes: cepstrum, pseudo- autocovariance, aoss-cepstrum, and saphe cracking," in Time Series Analy¬sir, M. Rosenblatt, Ed. New York: Wiley, 1963, Chap. 15, pp. 209-243.
6. B. P. Bogert and J. F. Ossanna, "The heuristics of cepstrum analysis; of a stationary complex echoed Gaban signal in stationary Gaussian noise," IEEE 7kans. Inform. Theory, vol. IT-12, pp- 373-380, July 1966.
7. F. B. Hilderbrand , "Introduction to Numerical Analysis; TMH edn, pg no: 82-84
8. Wagner, Galen S. Marriott's Practical Electrocardiography, 10th Edition, Copyright ©2001 Lippincott Williams & Wilkins.

Author: Mr. Saurabh Pal
Institute: Haldia Institute of Technology
Street: BE 45 Bidhannagar east
City: Midnapore
Country: India
Email: spal76@gmail.com

Multi Resolution Analysis of Pediatric ECG Signal

Srinivas Kachibhotla[1], Shamla Mathur[2]

[1] Govt.Institute of Electronics, Secunderabad, India (kbhotla_s@yahoo.com)
[2] College of Engg, Department of ECE, Osmania University, Hyderabad, India

Abstract — **This paper investigates the use of Multiresolution technique using Wavelet Transform for analysis of pediatric ECG signals. Wavelets are useful to describe signals at different levels of resolution. By means of multiresolution analysis, a signal can be decomposed into a set of signals (or scales), each scale containing only structures of a given size. The multiresolution approach allows a better understanding of the data values how they are distributed in a signal, and how the signal can be separated from the noise. The main advantage related to wavelet transforms is that they are localized both in the frequency and time domains. This paper presents a useful method based on the wavelet transform, for feature extraction of the Pediatric electrocardiograph (ECG) signals. The ECG signal is first denoised by a soft threshold and then each PQRST cycle is decomposed into a coefficients vector by the bioorthogonal wavelet function.**

Keywords — **The ECG Signal, PQRST cycle, Wavelet Transform, Frequency resolution, Depolarization**

I. Introduction

In signal analysis, there are a number of different functions one can perform on that signal in order to translate it into different forms that are more suitable for different applications. The most popular function is the Fourier transform that converts a signal from time versus amplitude to frequency versus amplitude. This transform is useful for many applications, but it is not based in time. To overcome this problem, mathematicians came up with the short term Fourier transform which can convert a signal to frequency versus time. Unfortunately, this transform also has its shortcomings mostly that it cannot get decent resolutions for both high and low frequencies at the same time. So how can a signal be converted and manipulated while keeping resolution across the entire signal and still be based in time? This is where wavelets come into play. Wavelets are finite windows through which the signal can be viewed. In order to move the window about the length of the signal, the wavelets can be translated about time in addition to being compressed and widened [1].

The Wavelet Transform (WT) is designed to address the problem of non-stationary ECG signals. It is derived from a single generating function called the mother wavelet by translation and dilation operations. The main advantage of the WT is that it has a varying window size, being broad at low frequencies and narrow at high frequencies, thus leading to an optimal time-frequency resolution in all frequency ranges.The WT of a signal is the decomposition of the signal over a set of functions obtained after dilation and translation of an analyzing wavelet [2].

The DWT represents a 1-Decomposition signal s(t) in terms of shifted versions of a low pass scaling function $\varphi(t)$ and shifted and dilated versions of a prototype band pass wavelet function $\psi(t)$.

$$\Psi_{j,k}(t) = 2^{(-j/2)}\, \psi\,(2^{-j}\, t - k) \qquad (1)$$

$$\varphi_{j,k}(t) = 2^{-j}\, \varphi\,(2^{-j}\, t - k) \qquad (2)$$

where: j controls the dilation or translation,
k denotes the position of the wavelet function

Discrete Wavelet Transform is also referred to as decomposition by wavelet filter banks. There are two kinds of data: the sparse data and the detailed data. These coefficients are extracted from the original set of number by using two kinds of filters, high pass (details) and low pass (approximations) The two filters are applied the filtered data from the high pass filter is stored as coefficients for later reconstruction of the signal. The filtered data from the low pass filter is now treated as the original data and the low and high pass filters are then applied to this data. This is repeated until the filtered data from the low pass filter outputs only one number. This is because DWT uses two filters, a low pass filter (LPF) and a high pass filter (HPF) to decompose the signal into different scales. The output coefficients of the LPF are called approximations while the output coefficients of the HPF are called details.The DWT can be calculated at different resolutions using Mallat-algorithm to utilize successive lowpass and highpass filters to compute DWT[8].

The procedure of DWT decomposition of a input signal x[n] is schematically shown in the Figure.1 above. Each stage consists of two digital filters and two down samplers by 2 to produce the digitized signal. The first filter, g[n] is the discrete mother wavelet, which is high-pass filter, and the second, h[n] is low-pass filter. As shown in Fig.2 above the down sampled outputs of first high pass filters and low-pass filters provide the detail, D_1 and the approximation, A_1. The first approximation, A_1 is decomposed again and this process is continued.

Chwee Teck Lim, James C.H. Goh (Eds.): ICBME 2008, Proceedings 23, pp. 758–760, 2009
www.springerlink.com

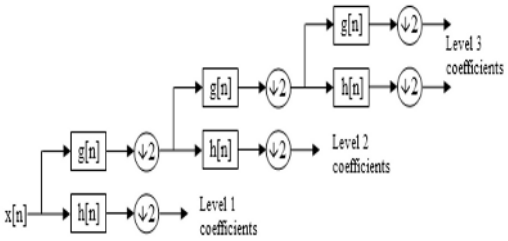


Fig .1 Decomposition of DWT

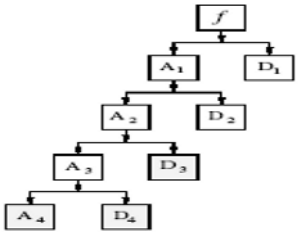


Fig.2 Four level DWT Decomposition

The decomposition of the signal into different frequency bands is simply obtained by successive highpass and lowpass filtering of the time domain signal. The signal decomposition can mathematically be expressed as follows:

$$y_{hi}[k] = \Sigma\, x[n].g[2k-n] \quad (3)$$

$$y_{lo}[k] = \Sigma\, x[n].h[2k-n] \quad (4)$$

II. ECG SIGNAL

The ECG signal, measured with an electrocardiograph, is a biomedical electrical signal occurring on the surface of the body due to the contraction and relaxation of the heart. This signal represents an extremely important measure for physicians, as it provides important information about a patient's cardiac condition and general health [3].Sinus or sinoatrial rhythm is the heart's normal mechanism, the driving impulses arising regularly in the sinus node and driving the heart at a rate between 60 and 100 beats per minute, this does not imply that rates outside this range are abnormal [4].As the heart undergoes depolarization and repolarization, the electrical currents that are generated spread not only within the heart, but also throughout the body. This electrical activity generated by the heart can be measured by an array of electrodes placed on the body surface. The recorded tracing is called an electrocardiogram (ECG, or EKG) [5].

III. RESULTS AND ANALYSIS

The ECG data for the analysis is taken from the MIT-BIH (Massachusetts Institute of Technology-Beth Israel Hospital Arrhythmia Laboratory) ECG arrhythmia database The ECG is of 2 years baby suffering from sepsis. The original Pediatric ECG was shown in Fig.3. We selected Pediatric signal here it is contaminated by noise of artifact and also to prove that bioorthogonal wavelet function which is used for our analysis best suited even under the noisy environment. Initially the signal is denoised as shown in Fig.4 using soft threshold scheme [6].

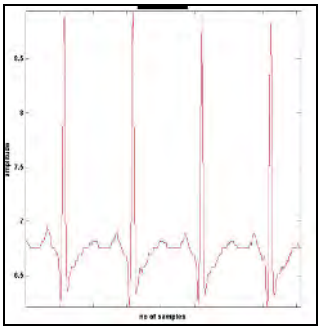


Fig.3 Original pediatric ECG

In the present work 'bior 1.1' wavelet has been used as the mother wavelet. For achieving good time-frequency localization the preprocessed Pediatric ECG signal is decomposed by using the DWT up to the fourth level. The 4-level wavelet decomposition structure is shown in Fig.5 and the resultant uncorrelated five subsets of coefficients are used for further processing. Most of the energy of the ECG signal lies between 0.5 Hz and 40 Hz [7]. It is observed that this energy of the wavelet coefficients is concentrated in the lower sub-bands. The detail information of levels 1 and 2 are discarded, as the frequencies covered by these levels were higher than frequency content of the ECG.

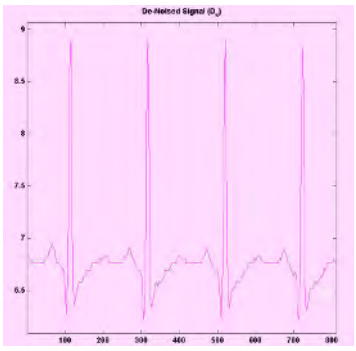


Fig.4 Denoised Pediatric ECG

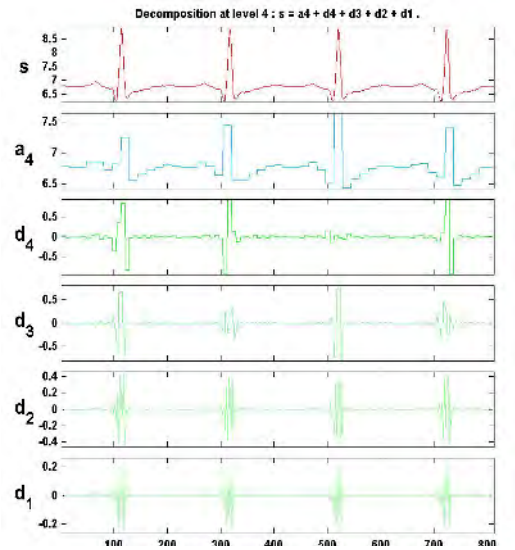


Fig.5.Decomposed Pediatric ECG at Level 4

There are eleven characteristic points in one ECG period.(maximum amplitude of R wave, beginning and maximum amplitude of Q wave, maximum amplitude and end of S wave and beginning ,maximum amplitude and end of P and T waves. Selectable parameters are type of wavelet, order of wavelet and number of decomposition levels.

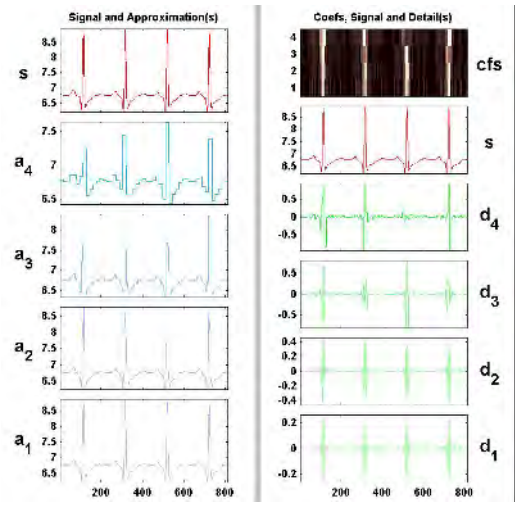


Fig.6 Decomposed signal with approximation and details separately

The characteristic points are found on decomposition of the signal by DWT. Fig.5 shows the original pediatric signal at the top of the plot. Below the signal, the details of all four levels and average value of the fourth level is shown for better illustration. Adding all the details plus remaining signal approximations reconstructs the original signal.Fig.6 shows the all approximations and details at all levels and along with plot of coefficient vectors. R_{max} is found as zero crossing on all details. It is more pronounced in the level1 and level 2 approximations. Q_{peak}, $S_{peak,}$ and S_{offset} also clearly visible and found in a lower levels of details. Finally P and T waves onsets, peaks, offsets are detected in approximations by denosing individual components. Similarly Q and S wave parameters are detected on fourth detail. Unlike the adult ECG features the Pediatric ECG features found in approximation component because of the heart rate of Pediatrics is nearly 120 beats/min.

IV. Conclusions

Selecting a Wavelet function is depends on signal characteristics. In this paper we applied bio-orthogonal wavelet functions which have high reconstructing ability. Bio-orthogonal wavelets are useful when the filters in decomposition require to be asymmetric and our results proved that it is best suited for ECG signal even under the noisy environment and most complicated pediatric signal denoising and feature selection

References

1. S. G. Mallat, "A Theory for Multiresolution Signal Decomposition: A Wavelet Representation," IEEE Transactions on Pattern Analysis and Machine Intelligence, Vol 11, No. 7, July 1989.
2. I. Daubechies, “The Wavelet Transform, Time-Frequency Localization and Signal Analysis, IEEE Trans. Inform. Theory, 961–1005, 1990.
3. Design of an Adaptive Filter with a Dynamic Structure for ECG Signal Processing , International Journal of Control, Automation, and Systems, vol. 3, no. 1, pp. 137-142, March 2005
4. The Heart arteries and veins, International student edition, McGraw-Hill Kogakusha, Ltd, 1974
5. Cardiovascular Physiology Concepts Richard E. Klabunde, Lippincott Williams & Wilkins, 2005
6. “http://ecg.mit.edu.”
7. N. V. Thakor, J. G. Webster, and W. J. Tompkins, “Estimation of QRS complex power spectra for design of a QRS filter,” *IEEE Trans. Biomed. Eng.*, 1984.
8. Tutorials on wavelets By Robi Polikar

Author: Kachibhotla Srinivas
Institute: Govt Institute of Electronics
Street: Eastmarredpally
City: Secunderabad
Country: India
Email: bhotla_s@yahoo.com

3D CT Craniometric Study of Thai Skulls Revelance to Sex Determination Using ogistic Regression Analysis

S. Rooppakhun[1,2], S. Piyasin[2] and K. Sitthiseripratip[3]

[1] School of Mechanical Engineering, Institute of Engineering, Suranaree University of Technology, Thailand
[2] Department of Mechanical Engineering, Faculty of Engineering, Khon Kaen University, Khon Kaen, Thailand
[3] Medical Rapid Prototyping Laboratory, National Metal and Material Technology Center, Pathumthani, Thailand

Abstract— **This study aimed to evaluate the sexual dimorphism in the Thai dry skull based on three-dimensional computed tomography (3D CT) data, and to develop practical a logistic regression model for the sex determination. A total of 21 cranial measurements were investigated from 56-male and 35-female skulls of known sex and race. 3D CT craniometry with identified landmarks and calculated measurements were performed using medical image processing software (MIMICS, Materialise N.V., Leuven, Belgium). According to craniometry, the results indicated that the dimensions of male skull were larger than that of a female. Of 4 cranial measurements displayed non-significant ($p < 0.05$) sexual dimorphism (maximum frontal breadth, anterior interorbitale breadth, nasal breadth, and palatal length). The logit response model was as follows: ln (odds) = Z = 79.759 – 0.392(NA-BA) – 0.200(ZM_l - ZM_r) – 0.520(NA-PR) +0.332(OR-STA). These had the overall accuracy of 92.3% and the accuracy of 92.85%, 91.42% among males and females, respectively (using cut off point for P = 0.5). Using a logistic regression analysis, 3D CT craniometry can be used to determination of sex among Thai.**

Keywords— **Three-dimensional, Craniometry, Thai, Sex determination, Logistic regression analysis.**

I. Introduction

The determination of sex from human skeleton remains is a critical component in forensic anthropological investigation. Normally, the determination of sex has been invented either using a metrical or non-metrical assessment, followed by uni- and multivariate statistical analyses [1, 2]. The accuracy of the sex determination varies considerably between different osteological elements (such as the tibia, femur, humerus, mandible and cranium, etc.), and also between different human populations are reported [1-6].

Normally, the instruments used to measure the skull were osteo metric board, the Mollison's craniophore, and the spreading and sliding calipers [7]. Although, these direct measuring devices can provide accurate and reproducible three-dimensional (3D) surface measurements. But several limitations include the time required for collecting data, as well as storing and reconstructing these data for 3D purpose is reported [7, 10]. With regard to the Thais skull studies, there are almost cranioscopy and craniometry by using either conventional or 3D coordination method. The sexual dimorphism differences in mean and index between genders were reported [12-15].

Currently, the introduced 3D CT software which enables 3D reconstruction and assesses craniofacial morphology is become widely used [8, 9]. Since, it can give much information including complete measurement details which possible to derive linear landmarks, inter-landmark distances, and the special angular measurements. Also these can store in the template file and recall for fast retrieval during subsequent landmark identification which are comparable with the large collection of traditional anthropological data available [10, 11]. In this study, we examined the sexual dimorphism in the skull of Thais based on 3D CT analysis, and developed a logistic regression model for the sexual determination.

II. Meterial and method

A. The reconstructed data acquisition

A CT data base of Thai dry skulls collected in the north-east of Thailand from Department of Anatomy, Medicine, Srinagarind Hospital collections were used. The samples were 56 males and 35 females with age ranging from 26 to 80 years at the time of death. A prepared set of four skulls was created using prepared acrylic box of in each CT scan following a strict protocol axially at 120 kV and 100 mA as shown in Fig 1. The slice thickness was 1.5 mm and the



Fig.1 A prepared set of four skulls for each CT-scanning

Chwee Teck Lim, James C.H. Goh (Eds.): ICBME 2008, Proceedings 23, pp. 761–764, 2009
www.springerlink.com

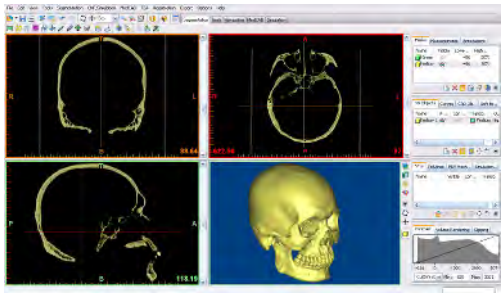


Fig.2 The 3D reconstructed model that can be shown in coronal, axial, and sagittal views

reconstruction interval was 1.0 mm. All CT data set were recorded using DICOM 3.0 format into CD-ROM, and subsequently imported to commercial image-processing package (MIMICS, Materialise N.V.) which saved into *.mcs files (MIMICS project files). Using *segmentation* module, the data were reconstructed into 3D image which manipulated by extract the boundaries of the each skull from the CT data set as shown in Fig 2.

B. 3D CT craniometric analysis

Using *Measure & Analyze* module, the craniometric analysis was performed. The anatomical landmarks were identified into the 3D image which precisely verified their positions on multi-planar layout views as shown in Fig 3. A

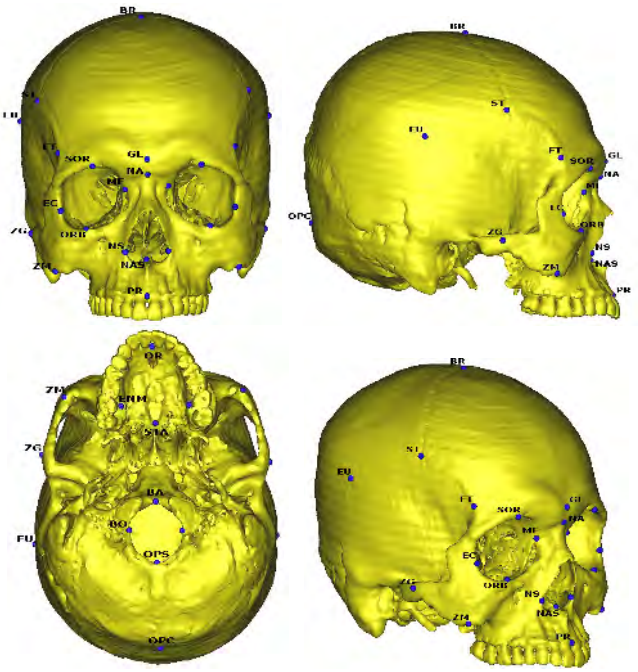


Fig. 3 The anatomical landmarks used in study

total of 21 cranial measurements were calculated and stored into *.xls files (Excel XP^{TM}). Because inter-landmark distances were calculated between the coordinates of the skeletal structure in 3D space, thus the error of magnification or head positioning was avoided.

C. Statistical data analysis

For the descriptive statistics, 3D craniometrical measurement was reported. P-value, difference of mean, and 95% CI of the difference were reported. A 2-tailed p-value of less than 0.05 was examined statistically significant. A binary logistic regression analysis using forward stepwise method was applied to determine logistic response model with the best prediction of gender. Measurements with high colinearity were not excluded in the model fitting process. Statistical data analyses were performed using the SPSS 13.0 software program (SPSS^{TM}, Inc)

III. Results & Discussion

In Table 1, the mean, standard deviation (SD), and standard error of mean (S.E.) of the measurements in both sexes are presented. The analysis of variance (e.g., mean difference, 95% CI diff, and p-value) is used to compare mean measurement values. Examination of the results indicates that males are larger in all dimensions. Of the 21 measurements compared, 17 are shown significantly different ($p < 0.05$); the 4 non-significant measurements are maximum frontal breadth, anterior interorbitale breadth, nasal breadth, and palatal length. And also, the 4 measurements expressing the greatest dimorphism ($p << 0.001$) are nasion-basion length, maximum cranial length, basion-bregma height, and bizygometic breadth.

Using logistic regression analysis, a forward conditional method is used to fit the best discrimination between genders. The logit response function was then calculated and revealed that 4 of 21 from the cranial measurement were significantly predictors ($p < 0.05$). The coefficient (b), standard error, and significant values of each measurement are reported in Table 2. The logit response model was as follows: $\ln(\text{odds}) = Z = 79.759 - 0.392(\text{NA-BA}) - 0.200(ZM_l - ZM_r) - 0.520(\text{NA-PR}) + 0.332(\text{OR-STA})$. From the following logit response function of Z (Table 2), the probability of being a

Table 2 Result of logit response model using logistic regression analysis

Measurements	Coefficient (b)	S.E.	Sig.
Nasion-basion length (NA-BA)	-0.392	0.1157	0.0007
Maxillary breadth (ZMl -ZMr)	-0.200	0.0761	0.0086
Upper facial height (NA-PR)	-0.520	0.1744	0.0029
Palatal length (OR-STA)	0.332	0.1355	0.0141
Constant	79.795	18.1153	0

Table 1 Mean, standard deviation, standard error of mean, and comparison t-test of cranial measurements

Measurement	Sex	N	Mean	SD	S.E.	Difference (M-F)			
						Mean	95 % CI		*p-value*
							Lower	Upper	
Max. cranial length *(GL-OPC)*	M	56	173.1	4.74	0.63	7.94	5.58	10.31	****
	F	35	165.2	6.61	1.12				
Max. cranial breadth *(EU_l-EU_r)*	M	56	144.1	5.45	0.73	3.3	0.97	5.62	**
	F	35	140.8	5.4	0.91				
Min. frontal breadth *(FT_l-FT_r)*	M	56	94.71	4.97	0.66	3.17	1.1	5.25	**
	F	35	91.54	4.64	0.78				
Max. frontal breadth *(ST_l-ST_r)*	M	56	115.6	7.08	0.95	1.93	-1.04	4.89	NS
	F	35	113.7	6.68	1.13				
Basion-brema height *(BA-BR)*	M	56	138.5	4.97	0.66	6.2	4.03	8.36	****
	F	35	132.3	5.18	0.88				
Nasion-basion length *(NA-BA)*	M	56	101.5	3.65	0.49	5.58	4.07	7.09	****
	F	35	95.96	3.33	0.56				
Foramen magnum length *(BA-OPS)*	M	56	36.78	2.14	0.29	2.49	1.54	3.44	***
	F	35	34.29	2.35	0.4				
Foramen magnum breadth *(BO_l-Bo_r)*	M	56	30.71	2.05	0.27	1.81	0.96	2.66	***
	F	35	28.9	1.89	0.32				
Nasion-bregma length *(NA-BR)*	M	56	112.9	4.14	0.55	5.73	3.65	7.81	****
	F	35	107.2	5.84	0.99				
Facial length *(BA-PR)*	M	56	95.95	5.70	0.76	2.89	0.49	5.29	*
	F	35	93.06	5.44	0.92				
Biorbital breadth *(EC_l-EC_r)*	M	56	97.22	3.60	0.48	3.48	1.96	5	***
	F	35	93.73	3.47	0.59				
Bizygometic breadth *(ZG_l-ZG_r)*	M	56	133.2	4.91	0.66	5.9	3.82	7.99	****
	F	35	127.3	4.79	0.81				
Maxillary breadth *(ZM_l-ZM_r)*	M	56	104.5	5.19	0.69	5.72	3.52	7.93	***
	F	35	98.75	5.09	0.86				
Upper facial height *(NA-PR)*	M	56	70.17	4.35	0.58	4.39	2.56	6.21	***
	F	35	65.78	4.13	0.7				
Orbital breadth-left *(EC_l-MF_l)*	M	56	40.95	1.86	0.25	1.6	0.72	2.47	***
	F	35	39.36	2.3	0.39				
Orbital breadth-Right *(EC_r-MF_r)*	M	56	41.43	1.75	0.23	1.76	0.97	2.56	***
	F	35	39.66	2.00	0.34				
Orbital height-left *(ORB_l-SOR_l)*	M	56	36.3	2.35	0.31	1.85	0.83	2.87	***
	F	35	34.45	2.42	0.41				
Orbital height-right *(ORB_r-SOR_r)*	M	56	36.22	2.37	0.32	1.43	0.44	2.41	**
	F	35	34.79	2.17	0.37				
Anterior interorbital breadth *(MF_l-MF_r)*	M	56	21.35	2.09	0.28	0.48	-0.43	1.38	NS
	F	35	20.87	2.16	0.36				
Nasal breadth *(N_l-N_r)*	M	56	27.28	2.08	0.28	0.08	-0.81	0.97	NS
	F	35	27.2	2.07	0.35				
Nasal height *(NA-NAS)*	M	56	52.57	3.02	0.4	3.04	1.8	4.28	***
	F	35	49.53	2.68	0.45				
Palatal length *(OR-STA)*	M	56	41.84	3.79	0.51	0.02	-1.64	1.67	NS
	F	35	41.82	4.00	0.68				
Palatal breadth *(ENM_l-ENM_r)*	M	56	39.03	2.96	0.4	1.2	0.06	2.35	*
	F	35	37.82	2.13	0.36				

Significance: ***$p < 0.001$; **$p < 0.01$; *$p < 0.05$. NS, not significant

male (P) can be calculated through $e^z / (1+e^z)$ ($e = 2.718$). So the probability of being a female is then 1–P. These had the overall accuracy of 94.6% and the accuracy of 93.9%, 95.7% among males and females, respectively.

With regard to sexual determination from the skull, using a stepwise discriminant function analysis, Steyn [4] presented the equations for the sexual dimorphism in the crania and mandible of 91 South African Whites (44 males and 47 females). The average accuracy in correct sex classification ranged from 80% (bizygomatic breadth) to 86 % (cranium). The dimension from the complete cranium provided the best accuracy and the bizygometic were the most dimorphic of measurements. Franklin et. al., [2] presented the function from 322 indigenous South African crania (182 males and 150 females). The facial width (bizygometic breadth) was the strongest discriminating morphometric variable, and cranial length, basi-bregmatic height is the next most significant features. The overall accuracy of sex determination varied between 77 to 80%, with 78% of a single measurement (bizygometic breadth), and 75 to76% of the separate functions (calvaria and face). Dayal et al., [1] proposed the function using discriminant function analysis for sexual assessment in black South Africans skull. The three measurement (bigonial breadth, mandibular ramus height, and total mandibular length) using stepwise analysis from the six mandibular measurements had shown the sex classification rate of 85%. An average accuracy of 80.8%, 80.0 % was obtained for stepwise analysis using cranial and all significantly difference measurements, respectively.

For the study of Thai skull, Sangvichien et.al, [13] presented logistic model which consisted of four craniometry measurements(e.g., nasion-basion length, maximum breadth of the cranium, facial height, and bizygometic breadth) via the forward method. The overall accuracy of correct sex classification was 88.8%, and 82.9%, 92.1% among females and males, respectively. However, Boonkaew [1] recommended that the sexual classification from Krogman's cranioscopy were the best method with an overall accuracy of 91.1%, and 82.9% for females, and 95.5% for males. In comparison to this, our study yielded higher accuracies than the previous study. We attributed our good results to a number of factors. First, most of the previous studies rely on manual measurements using conventionally technique or directly measurement, while we used 3D CT system for indentified landmark and extracted measurements. Second, we established the function from difference sample.

IV. Conclusions

Using 3D CT craniometry, the skulls of Thais have been shown to be sexually dimorphic. Logit response model has also been derived from various combinations of these measureents. The authors suggest that these functions cloud be applied to the Thai population for assessing the skeleton gender.

Acknowledgment

This work is supported by the grant from Thailand Graduate Institute of Science and Technology (TGIST), and Graduate School Khon Kaen University. The author also would like to acknowledge the Department of Anatomy, Faculty of Medicine Srinagarind Hospital for their kindness support the dry skull sample, and the National Metal & Materials Technology (MTEC) of Thailand for their kindness facilitate support.

References

1. Dayal MR, Spocter MA, Bimos MA (2008) An assessment of sex using the skull of black South Africans by discriminant function analysis. HOMO - J Comp Hum Biol, doi:10.1016/j.jchb.2007.01.001
2. Franklin D, Freedman L, Milne N (2005) Sexual dimorphism and discriminant function sexing in indigenous South African crania. HOMO - J Comp Hum Biol 55: 213-228
3. Steyn M, Iscan MY (1997) Sex determination from the femur and tibia in South African whites. Forensic Sci Int 90: 111-119
4. Steyn M, Iscan MY (1998) Sexual dimorphism in the crania and mandibles of South African Whites. Forensic Sci Int 98: 9-16
5. Iscan MY, Shihai D (1995) Sexual dimorphism in the Chinese femur. Forensic Sci Int 74: 79-87
6. Iscan MY, Loth SR, King CA, Shihai D, Yoshino M (1998) Sexual dimorphism in the humerus: a comparative analysis of Chinese, Japanese and Thais. Forensic Sci Int 98: 17-29
7. Park HK, Chung JW, Kho HS (2006) Use of hand-held laser scanning in the assessment of craniometry. Forensic Sci Int 160: 200-206
8. Park SH, Yu HS, et al. (2006) A proposal for new analysis of craniofacial morphology by 3-dimensioal computed tomography. Am J of Orthod and Dento Orthop 129(5): 600e23-34
9. Rooppakhun S, Piyasin S, Sitthiseripratip K (2007) 3D CT Morphological analysis of skull: A method to study on Thai dry skulls. World Congress on Bioengineering, Bangkok, Thailand, 2007, pp 147-152
10. Nagashima M, et al. (1998) Three-dimensional imaging and osteotomy of adult human skull using helical computed tomography. Surg & Radio Anatomy 20(4): 291-297.
11. Olszewski R, Zech F, et al. (2007) Three-dimensional computed tomography cephalometric craniofacial analysis: experimental validation in vitro. Int J Oral Maxillofac Surg 36:828-833
12. Ninprapan A (1996) Three-Dimensional Analysis of Thai Skull collected in Northeast Thailand. A Thesis submitted for M.D., Anatomy Graduates School, Khon Kaen University, Thailand
13. Sangvichien S, Boonkaew K, et al. (2007) Sex determination in Thai skull by using craniometry: multiple logistic regression analysis. Siriraj Med J 59: 216-221
14. Sangvichien S (1971) Physical Anthropology of the skull of Thai. A thesis submitted for M.D., Faculty of Medicine Siriraj Hospital, Mahidol University, Thailand
15. Boonkaew K (2005) Accuracy for sex determination by using cranioscopy and craniometry. A thesis submitted for Master Degree of Science (Anatomy), Faculty of Graduate Studies, Mahidol University, Thailand.

Analysis of Quantified Indices of EMG for Evaluation of Parkinson's Disease

B. Sepehri[1], A. Esteki[2], G.A. Shahidi[3] and M. Moinodin[4]

[1] Department of Mechanics, Islamic Azad university-Mashhad Branch, Mashhad, Iran
[2] Department of Medical Engineering, Shahid beheshti University of Medical Sciences, Tehran, Iran
[3] Department of Neurology, Iran University of Medical Sciences, Tehran, Iran
[4] School of Medical Engineering, Islamic Azad university-Science&Research Branch, Tehran, Iran

Abstract — **In order to find EMG indices that can be used for quantification of rigidity in PD, EMG signal of arm flexor and extensor was recorded for the group of patients consists of 16 persons and group of controls consists of 8 persons. This was repeated in two situations of rest and voluntary contraction. Using statistical methods, correlation of indices and rigidity aspect of qualitative method for evaluation of disease was checked. Although mean values of all indices were different in the groups of controls and patients, no significant statistical difference was seen in most of them between two groups. This could be the result of big variances. Also, the average of maximum amplitudes of rectified signal in rest has the highest correlation with the rigidity examined with the qualitative method. EMG indices of Extensor muscles have the priority for the objective evaluation of Parkinson's disease. This verifies the fact that in Parkinson disease, extensor muscles are more affected than flexor ones.**

Keywords — **EMG, Rigidity, Parkinson's disease, quantification.**

I. Introduction

These Parkinson's disease (PD) is a neurodegenerative disease which is caused by degeneration of cells in a part of brain called substantia nigra[1-3]. PD leads to a range of syndromes which can be divided in three main groups of motion deficits, sensory deficits and emotional deficits. Motion deficits caused by PD are:

1- Tremor at rest which is an involuntary rhythmic movement with a frequency of 6-7 Hz, mostly obvious in hands [1, 2].
2- Rigidity of limbs which is presence in all range of motion and does not decrease with repetition [2].
3- Slowness of motion which leads to problems associated with everyday tasks and is directly related to the passive rigidity of limbs [1].

By the time, subjective method called Unified Parkinson's Disease Rating System, UPDRS is implemented for the evaluation of disease and its level. The method has a qualitative rigidity measure which groups patients from 0 to 4. Zero indicates no unmoral rigidity and four indicates high rigidity and freeze. In some cases surface EMG is performed.

Most of research done on EMG has been goaled at detection between patients and controls [4-7]. Lokhania and co-workers [5] studied the relation of EMG and Movement aspects of UPDRS. Anyhow, no good relation was found.

In the present study, the aim was to consider more indices out of EMGs for more cases. Furthermore, local amplification which was used in this research was considered a way to decrease signal to noise ratio.

II. Material and methos

Data acquisition was performed Using EMG device indexed NOSSX230, manufactured by Biometrics, UK. The device was consisted of skin probes, eight-channel switcher and an amplifier which was connectable to a pc via USB port. Each probe had two skin electrodes and a built in preamplifier with gain of 1000 and band pass of 20-450Hz. Local amplification was considered to minimize noise, because desired signals of about 1 mv. were amplified only [8].Data was monitored and saved using Data Link software which came with the device. The software also had processing items which was used to extract research indices out of EMG data saved.

EMGs of flexor m. m. biceps and lateral head of triceps brachii were simultaneously acquired with two probes in both situations of rest and voluntary contraction. The procedure was performed for 16 parkinsonian referees to neurology clinic of Rasoul hospital, Tehran, Iran and 8 controls. Parkinsonians were 13 male and 3 females with mean age of 57.93 years old and controls were 6 males and 2 females with mean age of 42.37.

As a protocol, for the rest situation, the patient was asked to put his/her arm on a support, with no voluntary contraction and no remarkable mental activity. In contraction mode, patient was asked to flex and extend his/her arm after the "start" command.

In addition to EMG tests, UPDRS rigidity score was measured by the neurologist co-worker for each individual case for later use on. The procedure was the same as what neurologists always do to qualify the patient's rigidity: passive movement of flexion and extension was done

Chwee Teck Lim, James C.H. Goh (Eds.): ICBME 2008, Proceedings 23, pp. 765–768, 2009
www.springerlink.com

on upper limbs of patient to find how rigid they are. Rigidity was measured in two situations of with and without reinforcement. In reinforcement protocol, patient was asked to perform a movement in mirror lime which was examined.

Using Data Link software the following indices [9,10] were calculated out of EMG data saved:

1- Average amplitudes of rectified resting EMG for 5 ms, ARa
2- Maximal amplitudes of rectified resting EMG for 5 ms, Arm
3- Surface integral of rectified resting EMG for 5 ms, Sint
4- Root mean square of resting EMG for 5 ms, RMS
5- Average EMG amplitude on a section with most marked changes in muscle activity under voluntary contraction ,AVCa)
6- Phasic Activation coefficient, PhAC where $PhAC = (AVCa-ARa)/AVCa$

Indices number 3 and 4 have not been studied in previous researches. In particular index number 3 which indicated the mechanical work was considered to be an important index.

Spss-13 software was used for statistic means [11]. Mann-Whitney test was performed to find the significances of differences between control/patients groups and spearman's correlation test was performed to check the correlation of each index and UPDRS levels.

III. Results

Mean values for almost each index were different in groups of control and patients (table1).

Statistic tests showed different significances in different indices (Fig1-3). ARm for both of flexor and extensor had significant difference ($p<0.05$). Other indices including ARa, SInt, RMS and AVCa had significances just for the extensor muscle. PhAc of the extensors in group of patients had negative std. The reason was the negative values of the index in two cases.

Totally, no good correlation ratio was found between indices and UPDRS levels (Fig 3-7). Looking at table1 It can be inferred that high stds in indices has lead to this problem.

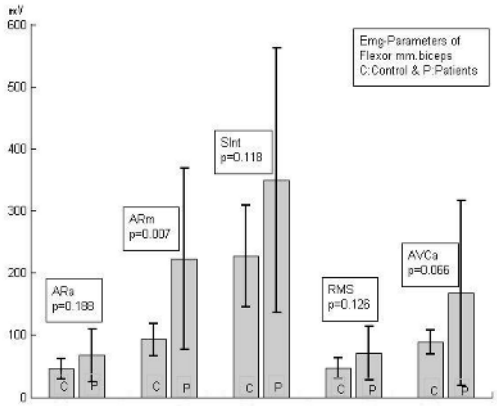


Fig. 1 P-value of Mann-Whitney test for flexor indices

Table1. Mean and std for research indices. UPDRS-R was measured with reinforcement.

	Control				Patients			
	Flexor		Extensor		Flexor		Extensor	
	Mean	Std	Mean	Std	Mean	Std	Mean	Std
ARa	45.38	16.142	43.50	13.959	67.44	42.258	83.31	48.397
ARm	92.63	25.945	95.88	25.085	222.44	145.447	315.94	295.374
SInt	227.63	82.000	225.00	68.958	349.00	212.593	418.75	240.905
RMS	46.63	16.518	44.88	14.357	71.06	43.172	85.50	49.925
AVCa	88.88	19.149	46.75	13.058	167.25	148.480	113.63	75.274
PhAC	.48638	.149422	.07681	.06885	.42956	.458459	.14438	.460850
UPDRS	0	0	0	0	1.13	.871	1.13	.871
UPDRS-R	0	0	0	0	2.219	.9784	2.219	.9784

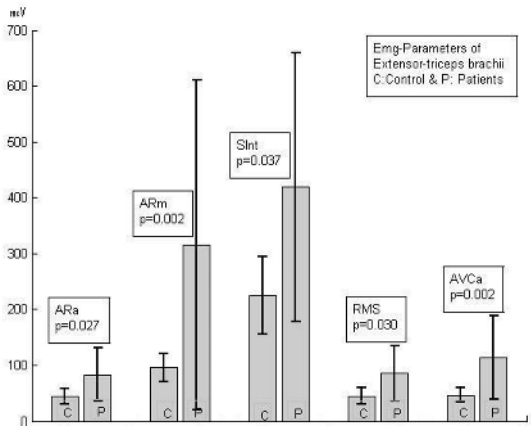


Fig. 2 P-value of Mann-Whitney test for extensor indices

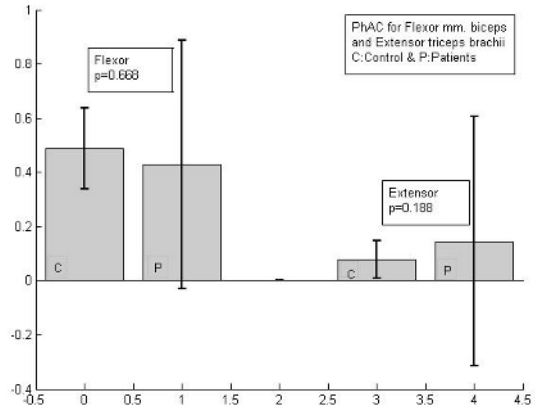


Fig. 3 P-value of Mann-Whitney test for PhAc of extensor and flexor.

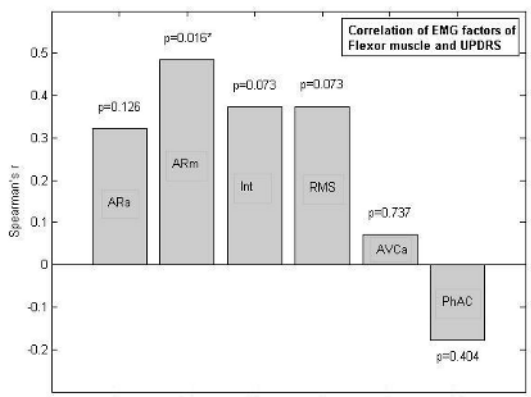


Fig. 4 Correlation ratios of flexor indices and UPDRS measured without reinforcement.

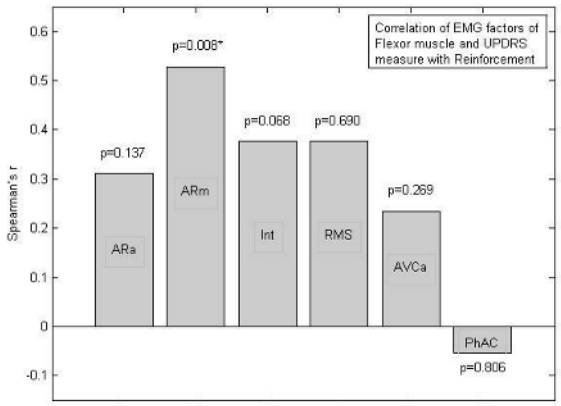


Fig. 5 Correlation ratios of flexor indices and UPDRS measured with reinforcement

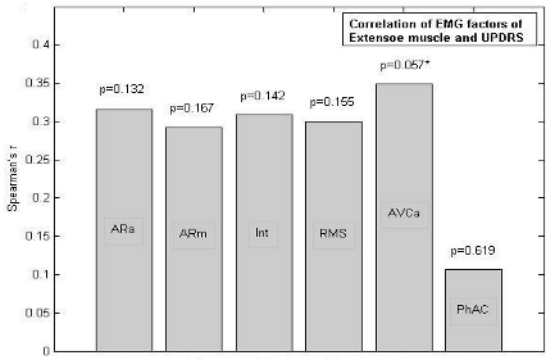


Fig. 6 Correlation ratios of extensor indices and UPDRS measured without reinforcement

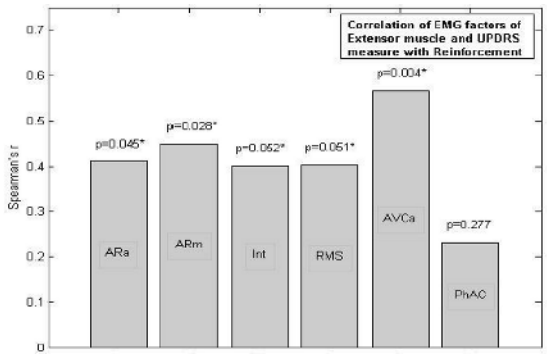


Fig. 7 Correlation ratios of extensor indices and UPDRS measured with reinforcement

IV. Discussion

In the present research, EMG signals of flexor and extensor of the arm was recorded in two groups of controls and parkinsonians. The procedure was done in two situations of rest and voluntary contraction. Statistic tests were performed to find relation between quantified indices of EMG and UPDRS levels measured.

Statistically, indices related to triceps brachii had higher significances than those of m. m. biceps. This finding showed that extensors are more affected by PD than flexors and was reported previously.

Although, indices had different mean values in groups of control and PDs, except for the ARm, there were no good significances in indices of m. m. biceps. This can be addressed to high stds of indices which is a known characteristic of EMG signal.

The highest linear regression ratio to UPDRS was found between ARm and UPDRS measured in reinforced situation (r= 0.528). Totally, regression ratios with UPDRS in reinforced situation were higher than none reinforced situation.

Use of local amplification which leads to decrease in signal to noise ratio was considered in current research. This was previously considered by Flament and co-workers [6]. In the former research the amplification ratio was 10 whilst in present study the ratio was 1000.

Mean values of ARa and ARm measured from m. m. biceps of both control and patients groups in present study were higher than what was previously calculated [5]. Any how in both researches increase in mean values of these two indices for patients than controls were obvious. This had been addressed to damage in relaxation mechanism of PDs [5].

PhAc index of m. m. biceps calculated in this study was closed to what had been reported before [5]. There were no significances related to this index in both researches. In two cases PhAc was calculated negative which was result of higher activity at rest than contraction and was reported in former study [5].

To find a more reliable relation between quantified indices and UPDRS rigidity level, it is suggested to exam more cases and to use more than one neurologist on a case. The later suggestion was previously implemented by Patric and co-workers [12].

V. Conclusion

It can be concluded that direct measurement of rigidity like what had been previously done [12, 14] may better characterize the level of rigidity in PD than what can be done using EMG.

Acknowledgment

Dr. E.Ebrahimi and Dr. F. Khamseh are acknowleged for their part in this research.

References

1. Scenk M. and Venekamp D (2003).Parkinson's Disease," Biomechatronics wb 2432 .
2. Mark Guttman, Stephen J. Kish, Yoshiaki Furukawa (2003) Current concepts in the diagnosis and management of Parkinson's disease. Journal of Canadian Medical Association. • FEB. 4,168 (3): 293-301.
3. Calne D.B. (2001) Parkinson's disease is not one disease. Parkinsonism and Related Disorders 7: 3-7.
4. Lakie M. , Walsh E. G. , and Wright G. W. (1984) Resonance at the wrist demonstrated by the use of a torque motor: An instrumental analysis of muscle tone in man. J. Physiol., vol. 353: 265–285.
5. Lukhaninaa E.P., Kapoustinab M.T. , Karabanb I.N. (2000) A quantitative surface electromyogram analysis for diagnosis and therapy control in Parkinson's disease. Parkinsonism and Related Disorders 6 : 77–86.
6. Flament D. , Vaillancourt D.E. , Kempf T. , Shannon K. , Corcos D.M. (2003) EMG remains fractionated in Parkinson's disease, despite practice-related improvements in performance. Clinical Neurophysiology 114 : 2385–2396.
7. Meara RJ and Cody FW (1992) Relationship between electromyographic activity and clinically assessed rigidity studied at the wrist joint in Parkinson's disease. Brain, Vol 115, Issue 4 :1167-1180, Copyright © 1992 by Oxford University Press.
8. "EMG sensor operating manual", Biometrics Ltd, Cwmfelinfach,Gwent N P11 7HZ UK.
9. Pullman S. L., Goodin D. S., Marquinez A. I., Tabbal S. , Rubin M.(2000) Clinical utility of surface EMG. Neurology 55:171-177.
10. G. L. Soderberg, L. M. Knutsom (2000) A guide for use and interpretation of kinsiologic electromyographic data. Physical therapy Vol. 80, No. 5.
11. Afshani S. A. R. , Norian M. , Hoseini Ramsheh Z. (2005) An introduction to Spss 14", ISBN 964-96471-9-8, Bisheh .
12. Nogaki H. , Kakinuma S., Morimatsu M.(2001) Muscle weakness in Parkinson's disease : a follow up study. Journal of Parkinsonism & Related Disorders 8 : 57-62.
13. Patrick S. K. , Denington A. A., Gauthier M. J. A. , Associate Member, IEEE, Gillard D. M. , Member, IEEE, and Arthur Prochazka, Senior Member, IEEE,(2001) Quantification of the UPDRS Rigidity Scale. IEEE Transactions on Neural Systems and Rrhabilitation Engoneering, VOL. 9, NO. 1: pp31-40
14. Sepehri B., Esteki A., Ebrahimi Takamjani E., Shahidi G. A., Khamseh F. and Moinodin M. (2007) Quantifica-tion of Rigidity in Parkinson's disease. Annals of Bio-medical engineering,vol. 35, no. 12: 2196-2203, 2007.

Author: Behrooz Sepehri
Institute: Azad University-Mashhad Branch
Street: Imamieh Ave.
City: Mashhad
Country: Iran
Email: b_sepehr@mshdiau.ac.ir

A Test for the Assessment of Reaction Time for Narcotic Rehabilitation Patients

S.G. Patil[1], T.J. Gale[1] and C.R. Clive[1]

[1] School Of Engineering, University Of Tasmania, Hobart, Australia

Abstract — **Reaction Time Testing has been successfully used in various areas of research and is potentially a good assessment technique for narcotic rehabilitation patients. However, the number of reaction time samples required from each subject for accurate assessment can be a hindrance in using this test. Therefore in this study we proposed to study the effect of sample size on accuracy and the inter-person differences with normal subjects with a reaction time test of our design. Five normal subjects were tested repeatedly. No significant difference among the mean reaction times of the 5 subjects were found indicating that the test was reliable and the mean of all 5 correlated well with literature values. The test is reliable with normal patients and will be trialed as an assessment tool for use in research with narcotic rehabilitation patients.**

Keywords — **Reaction time test, Narcotic rehabilitation, opioid assessment**

I. Introduction

Reaction time tests have been used in various areas of research including recovery from Althesin anaesthesia, spatial attention after brain damage, etc [1]. We have previously proposed reaction time testing in the assessment of opioid dependent patients [2]. Symptoms of opioid intoxication are the typical symptoms of sedation, including slurred speech, delay in reaction to stimuli and drowsiness.

The test proposed was reaction time to a visual stimulus. Here we describe the test we have designed to evaluate the use of reaction time in the assessment of the levels of intoxication of narcotic dependent patients participating in narcotic replacement program.

In general there are three types of reaction time test. Simple, Recognition and Choice. The simple reaction time test is one reaction to one stimulus, while the recognition reaction time test is either reacting or not reacting depending on the stimulus. The choice reaction test on the other hand has equal numbers of stimuli and responses. In our study we propose to use a simple reaction time test [3].

The number of reaction time samples needed to be acquired as one test set is an important parameter that determines the power of the test in resolving inter and intra person differences. Professional psychologists doing Choice reaction time tests typically employ about 20 people doing 100-200 reaction times each per treatment. [4] recommends an adequate period of practice, and then collection of 300 reaction times per person. This number may not be feasible with narcotic rehabilitation patients as it is very easy for them to feel uncomfortable with such a monotonous test taking such a long time.

For about 120 years, the accepted figures for mean Simple reaction times for college-age individuals have been about 190 ms for light stimuli and about 160 ms for sound stimuli [5, 6]. In addition it was also shown that visual stimuli that are longer in duration elicit faster reaction times [7].

In the present study our aim is to conduct pilot experiments on normal university-age individuals and investigate the effect of sample size on accuracy and the inter-person differences in reaction times using a simple reaction time test of our own design. These results will subsequently help us design tests for assessment of patients undergoing narcotic replacement programs.

II. Method

A. Research Participants

Five subjects were used in this study. The subjects were invited from the School of Engineering, University of Tasmania, who volunteered to participate after being briefed about the aims and procedure of the test. The subject ages were 20, 22, 26, 24 and 29. The subjects were considered as a control group as no obvious signs of abnormality were observed. The subjects were also informed about the test 24hrs before the test was conducted so that they were mentally aware and prepared for the test. The subjects were given a demonstration on how the test works. On the given day the subjects were asked to do their normal daily activity as per routine. The test was conducted on each subject one after the other till all 5 subjects were tested. This procedure was repeated 5 times. Each test lasted approximately 3-5 minutes and after that a gap of 5 minutes to reset the test and prepare the next subject for the test. In between test periods each patient was allowed to do their routine work. Most of them just went back to their desk and continued working until their turn to be tested.

Chwee Teck Lim, James C.H. Goh (Eds.): ICBME 2008, Proceedings 23, pp. 769–773, 2009
www.springerlink.com

B. Test Design

The test was developed in Matlab R2006b (Mathworks, USA). A stimulus was displayed on the background of a grey screen of a 15" SVGA monitor placed at a distance of 80 cm from the eyes. Screen resolution was 1280 X 1024 pixels. A single target, a bright green fluorescent filled square with dimensions 7 cm (height) by 4.5 cm (width) was used as the visual stimulus. The target transforms to green color from grey color at random time intervals during the test. The time between the color change to the clicking of the left mouse button is recorded as the reaction time. The reaction time in milliseconds was displayed in a text box besides the target. The test number increments with each response from the user. The software was designed to record 60 reaction times in one set.

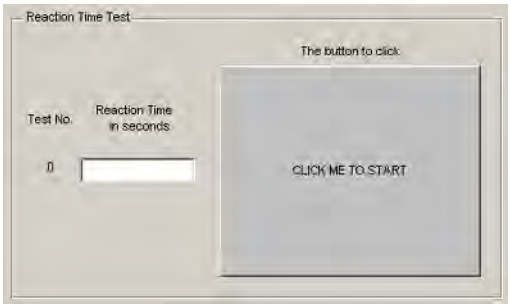
C. Test Procedure

The subjects sat on a chair in a lit room and instructed to look at the monitor and click the left mouse button as soon as, but not before, the stimulus turned green. The computer mouse was kept at the same height used by the subjects in their workplace. To more closely simulate normal conditions, fixation was not required but, to ensure that the participants did not divert their gaze constantly, the background of the monitor was turned to grey, similar as the background of the stimulus when not green. The test was interrupted if the participant slumbered, or distracted, or volunteered to stop, although this was seldom needed.

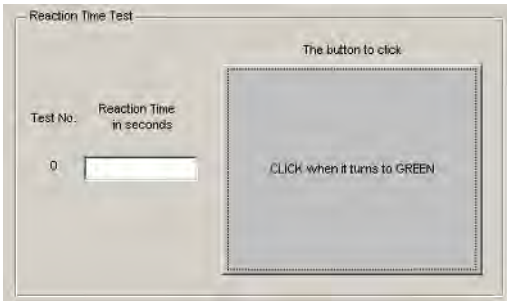
Prior to the initiation of the test, the subjects were shown examples of the working of the test system. Next, they performed a training session of one trial in which targets appeared in random intervals 10 times. Following the trials the participants were asked to do the real test. A few minutes rest was given after each test of 60 responses, during which the subjects were allowed to do whatever they liked but were asked not to eat or drink anything except water.

Fig 1 shows a step wise illustration of one reaction time test. Initially the computer screen as well as the test software is grey in color. The stimulus button or the target to be clicked is clearly seen in rectangular shape with "click me to start" written on it.

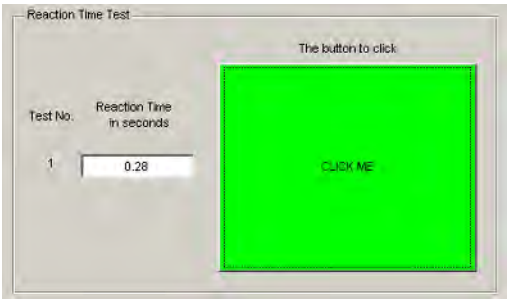
Once the user clicks the left mouse button the test starts. After clicking the target changes the message on it to "CLICK when it turns green". Once the target turns color to green the user has to respond by clicking the left mouse button. The time taken from the target turning green to the user clicking the mouse is considered the reaction time. The time is displayed in the text window besides the target in seconds.



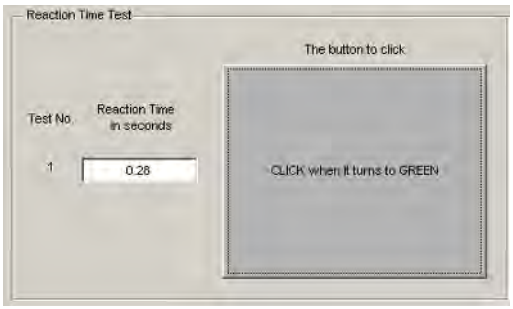
(a)



(b)



(c)



(d)

Fig 1. An illustration of the reaction time test. (a) The screen when the trial starts (b) The screen when the grey button is clicked (c) The buttons turn to fluorescent green (d) The target turns back to grey and repeats (a)(b)(c)

D. Data Collection and Analysis

The test was designed to save the reaction times in a text file. The data obtained was averaged to obtain the mean value for each subject. To test the reproducibility of the technique, the results for each subject were compared using statistical tools in MS Excel. The Mean ± SD of each test and for all tests for each subject were plotted and compared. T-test was used to find any significant differences in inter and intra subject reaction times. A moving average representation of intra-subject data was used to see the trend of reaction times over the course of the test

The data was assumed to be normally distributed and confidence interval of the mean was calculated. The following expression was used to calculate the upper and lower 95% confidence limits

Upper 95% Limit=x+(y*1.96)

Lower 95% Limit=x-(y*1.96)

Where, 'x' is equal to the sample mean, 'y' is equal to the standard error of the sample, and 1.96 is the .975 quantile of the normal distribution.

III. Results

The reproducibility test showed that the reaction time for all subjects agreed well with a mean percentage SD of 10.7%. The intraclass correlation coefficient (correlation of the 5 test sets) for 95% confidence level was r = 0.922 ($p <$ 0.001), which showed a high reproducibility.

The Mean ± SD obtained from all data from the 5 subjects was 0.42± 0.1. The individual Mean ± SD obtained in the 5 subjects is shown in Fig 2. No significant differences were observed between the subjects S1, S2, S4 and S5, however a significant difference ($p<$ 0.01) was observed between S3 and each of the others.

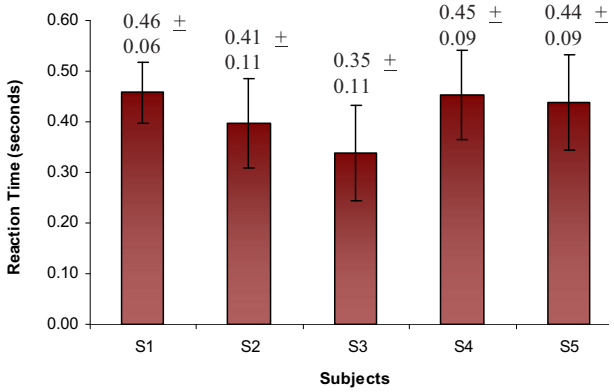


Fig. 2. The Mean ± SD of the 5 subjects participated in the test.

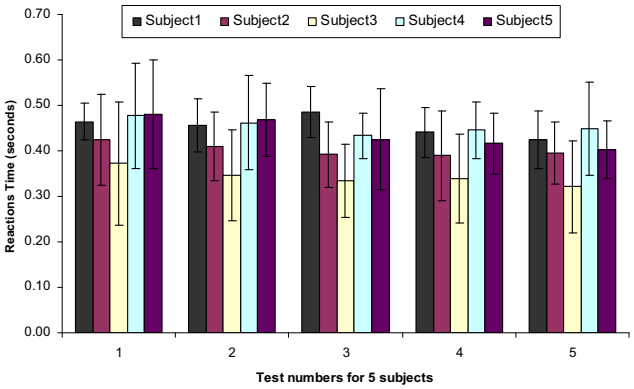


Fig 3 The Mean ± SD of each test for every individual subject.

The Mean ± SD of each test set conducted for each subject is shown in Fig 3. The error lines indicate the variance observed in each test. Fig 4 shows a trend plot (50 point running average) of reaction time in ms against the number of times each subject were tested. The reaction times decrease from test 1 to test 5 for all subjects. Fig 5 shows a typical example of reaction times conducted on one subject (S1). The plot contains of all the data from the 5 test sets carried out by S1. The plot indicates the variance of the data from mean. The variance remained similar for other subjects too. The range of variance observed in Fig 5, between the reaction times, matches with values obtained by [8]. The range of reaction time values found in that study was from 420 ms to 630 ms.

Fig 6 shows a plot of confidence interval versus the number of reaction time taken from all the subjects. Reduction of confidence level can be observed as the number of the samples increases.

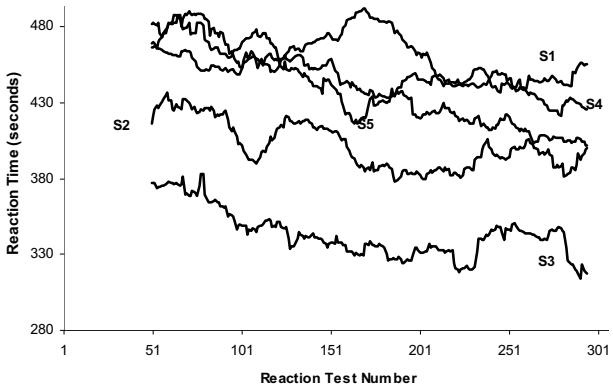


Fig 4. Figure indicates a decreasing trend of reaction time as the test progressed from test set 1 to test set 5 for each subject

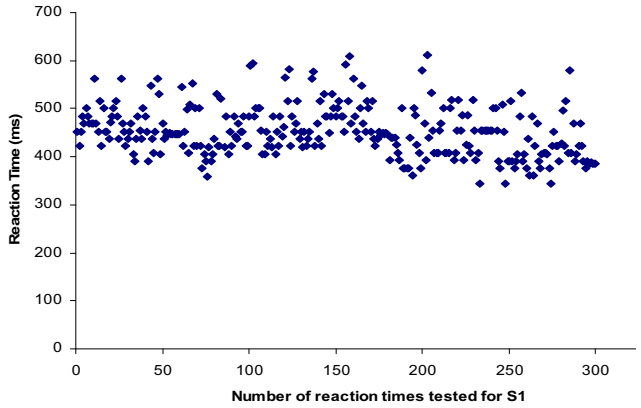


Fig. 5. The graph indicates a typical response of reaction times v/s the number of times tested for subject S1.

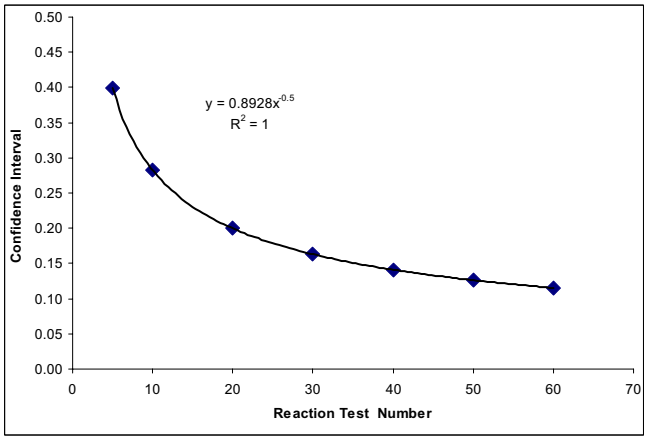


Fig 6. The confidence Interval plot v/s the test number.

IV. Discussion

The means of the 5 subjects were similar except for one subject (S3), all other results being within the range of 0.41s to 0.46s. The difference for S3 can be attributed to the alertness or freshness of the subject. But to confirm this point more samples need to be taken in future. The highest mean reaction time was recorded by S1 (the only female and youngest participant) (0.46 $\pm$ 0.06) which agrees with the result found in few studies in the past [9]. However, one sample is not enough and further test should be carried out according to ages to investigate if sex and age, and their combination can form a significant difference in reaction time test. Studies have shown that age has significant effect on the reaction times. [10] also reported that this age effect was more marked for choice reaction time tasks, and [9] concurred.

System learning capabilities of subjects were also seen during the test. A decreasing trend in reaction time was observed in all the subjects during the first three test sets showing that as the subjects progressed through the test their understanding of the test improved (Fig 4). The difference was noticeable with the maximum difference between the start of the test to the end being 18% however the difference was not statistically significant. The last two sets were mixed with either higher or lower reaction time, however were not significantly different.

Fig 6 shows the confidence interval when more than 40 samples are taken does not change significantly. Considering the above a 40 set test is recommended as a suitably powerful test to discriminate changes in reaction time, without requiring an excessively large number of samples. We plan to use this in future testing of intoxicated narcotic rehabilitation patients.

V. Conclusion

It can be concluded that the reaction time test is reproducible and reliable. Our future work is to use the test with narcotic rehabilitation patients to determine the change in reaction time under methadone intoxication.

References

[1] Deouell L, Sacher Y, Sroker N (2005) Assessment of spatial attention after brain damage with a dynamic reaction time test. J Int Neuropsychol Soc 11: 697-707

[2] Patil S, Gale T, Stack C, (2007) Design of Novel Assessment Techniques for Opioid Dependent Patients, Proceedings of 29th Ann Int conference of IEEE engineering in Med and Bio Soc, Lyon, France, 2007, pp 3737-3740

[3] Luce R (1986) Response Times: Their Role in Inferring Elementary Mental Organization, Oxford University Press, New York.

[4] Sanders A (1998) Elements of Human Performance: Reaction Processes and Attention in Human Skill, Lawrence Erlbaum Associates, Publishers, Mahwah, New Jersey, pp 575

[5] Von F, Huhtala A, Kullberg P et al. (1956) Personal tempo and phenomenal time at different age levels, Reports from the Psychological Institute, no. 2, University of Helsinki

[6] Welford A (1980) Choice reaction time: Basic concepts, In A. T. Welford (Ed.), Reaction Times, Academic Press, New York, pp 73-128

[7] Froeberg S, (1907) The relation between the magnitude of stimulus and the time of reaction, Archives of Psychology, no. 8

[8] Nickerson R (1972) Binary-classification reaction times: A review of some studies of human information-processing capabilities Psychonomic Monograph Supplements, 4:275-318

[9] Der G, Deary I (2006) Age and sex differences in reaction time in adulthood: Results from the United Kingdom health and lifestyle survey, Psychol and Aging 21: 62-73
[10] Luchies C, Schiffman J, Richards L et al. (2002) Effects of age, step direction, and reaction condition on the ability to step quickly, The J Gerontol B Psychol Sci Soc Sci, Series A, 57(4): M246

Author: . G. Patil
Institute: School of Engineering, University of Tasmania
Street: hurchill Avenue, Sandy Bay
City: obart, Tasmania
Country: Australia
Email: gpatil@utas.edu.au

Microdevice for Trapping Circulating Tumor Cells for Cancer Diagnostics

S.J. Tan[1,2], L. Yobas[1], G.Y.H Lee[3], C.N. Ong[4] and C.T. Lim[1-5]

[1]Institute of Microelectronics, A*STAR, Singapore
[2]NUS Graduate School for Integrative Sciences and Engineering, National University of Singapore, Singapore
[3]Singapore-MIT Alliance, Singapore
[4]Life Sciences Institute, National University of Singapore, Singapore
[5]Department of Mechanical Engineering, National University of Singapore, Singapore

Abstract — **Cancer metastasis is the main attribute to cancer-related deaths and early detection is one of the most effective means to treat the disease. Spreading of cancer to distant sites is achieved usually through the circulatory system and the number of circulating tumor cells (CTCs) in peripheral blood is strongly associated to cancer development. Thus detecting CTCs in blood samples will be helpful in identifying susceptible subjects. Here, we propose a label-free technique to isolate these cancerous cells from blood. Using cancer cells spiked in blood samples, isolation efficiency of at least 80% were obtained with high isolation purity. The microdevice also preserved the integrity of the isolated cells to allow further studies to be done on these cells. These results showed a potential effective microdevice for CTCs studies and possible clinical application.**

Keywords — **Cell Isolation, Microfluidics, Circulating Tumor Cells, Cancer Metastasis, Computational Fluid Dynamics (CFD)**

I. Introduction

Early detection is important to effectively treat cancer [1] and advancement in imaging techniques have resulted in faster and more accurate diagnosis. Despite the improving diagnostic aids, cancer remains a leading cause of death globally [2]. This is mostly due to the lack of tell-tale signs until the very late stages of the disease when the cancer has metastasized. Metastasis remains the detrimental part of the disease with tumor cells spreading to distant sites through the body's circulatory system [3,4]. Therefore, analyzing the blood specimens of potential patients is important. Evidence from clinical studies has also showed that the density of cancer cells in blood is directly correlated to disease progression [5,6]. Thus, there is much interest to enrich and enumerate these cells from blood.

Immuno-magnetic separation using various cancer biomarkers followed by immunocytochemistry detection is a leading technique to enumerate circulating tumor cells (CTCs) in peripheral blood [7,8]. However, the sensitivity of the tests varies from different cancer types and is dependent on the biomarkers used [9]. Furthermore, the procedure is tedious involving many complicated steps from sample preparation to immunofluorescence staining of the sample. In the process, viability of the cells are lost, which hold important information about the condition of CTCs whilst in circulation [10]. Having viable cells will also allow further analysis on the CTC subpopulations that might shed insights to the metastatic process.

Here, we present a microdevice that aims to isolate cancer cells from blood using the distinctive difference in biorheology of blood constituents [11,12] and cancer cells [13,14]. Previously, we have reported upon the device to effectively trap breast cancer cells with the ability to maintain the viability of these cells [15]. In this investigation, simulation studies were performed to ensure minimal disturbance to isolated cells that aimed to preserve the condition of the cells during isolation. In addition, we showed that the microdevice was effective for cancer cell types of breast and colon origin. We obtained high isolation purity of the cancer cells in the microdevice which minimizes false positive results and showed that the conditions of isolated cells are preserved. No functional modifications were required in the microdevice. Separation and detection can also be completed in a single step.

II. Methods

A. Microdevice Layout and Fabrication

Numerous crescent structures with gaps are created in the microdevice that aimed to provide effective traps for cancer cells in the sample mixture (Fig. 1a and Fig. 1c). Each trap is positioned with pitch of 50μm which effectively prevents clogging in the device. The gaps of 5 μm in each of the traps ensure that mostly cancer cells are isolated, and allowing other blood constituents to pass through due to their ability to traverse very small constrictions. In this way, white blood cells (WBCs) of comparable size to cancer cells are effectively removed as well. In retrieval of the isolated cells, the inverted isolation structures provide favorable paths that minimized mechanical damage due to physical interactions. For each device, there are a total of 900 cell trap structures.

Chwee Teck Lim, James C.H. Goh (Eds.): ICBME 2008, Proceedings 23, pp. 774–777, 2009
www.springerlink.com

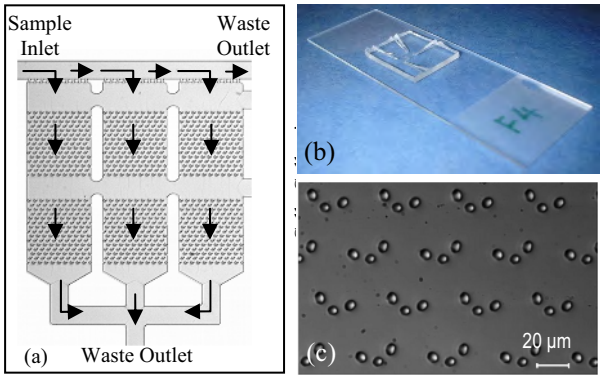


Fig. 1 Microdevice for isolating cancer cells in blood. (a) Device layout. (b) Fabricated microdevice. (c) Crescent isolation structures.

The microdevice was fabricated using soft lithography[16]. An 8 inch silicon substrate was spin coated at 3200 rpm for 45 seconds with SU8-2025 (Microchem Corporation) to get the thickness of 20 μm. Then it undergone an ultraviolet exposure of 120 mJ/cm^2 followed by development. A final hard bake of the master mold ensured better adhesion of the photoresist to the substrate. Polydimethylsiloxane (PDMS, Sylgard 184, Dow Corning) was mixed according to manufacturer's recommendation and poured over the mold. Curing of the PDMS was done in an oven preset at 80°C for 2 hours. Upon careful removal of the patterned PDMS, fluidic ports were created using flat tip needles. The microdevice is completed after subjecting the PDMS pattern structure and a glass slide to oxygen plasma and bonding them together (Fig. 1b).

B. Computational Fluid Dynamics (CFD) Studies

In order to optimize the design of the microfluidic device and visualize the flow profile in the microdevice, 3D computational analyses were simulated on commercial software Fluent (Ansys Inc., Lebanon, NH, USA). Mesh density of approximately 57000 were used in each study with mesh independence ascertained. The flow path as well as the shear stresses of the cells during isolation is of interest so as to maximize isolation efficiency and minimize mechanical damage on cells during isolation.

C. Sample and Apparatus Preparation

Human adenocarcinomas (MDA-MB-231 and HT-29) of breast and colon origin were used in the experiments. Both cell lines were cultured using Dubelcco's Modified Eagle Medium (DMEM) supplement with 10% fetal bovine serum (FBS) and 1% penicillin G / streptomycin / amphotericin. For all apparatus including the microdevices, tubes and fluidic connectors, they were thoroughly sterilized with 70% ethanol prior to experimentation. Sterile phosphate buffered saline (PBS 1×) was then used to remove the ethanol traces and made ready the device for sample injection.

For isolation efficiency characterization, suspended cancer cells were added to PBS 1× at 100 cells per milliliter. By counting the number of escaped and trapped cells over a period of 20 minutes, the efficiency of cell isolation could be obtained. To ascertain the purity of capture, cancer cells were added into whole blood donated from healthy donors at the concentration of 100 cells per milliliter. Isolated cells in the microdevice were stained for EpCAM (Santa Cruz Biotech), CD45 (Santa Cruz Biotech) and DAPI to distinguish between cancer cells and WBCs. For cell viability experiments, isolated cells were retrieved and reseeded back for culture. Their proliferative rate was compared with normal cultures which acted as controls in the experiment.

III. Results and Discussion

The clinical significance of enumerating CTCs is reported to gauge cancer disease progression and also a good measurement for treatment efficacy [17,18]. Having viable CTCs will also help to address issues pertaining to the conditions of CTC in circulation such as their viability, origin and proliferative status [10]. Thus, there is interest to isolate, count the density of cancer cells in blood mixture and preserve the conditions of cells after isolation.

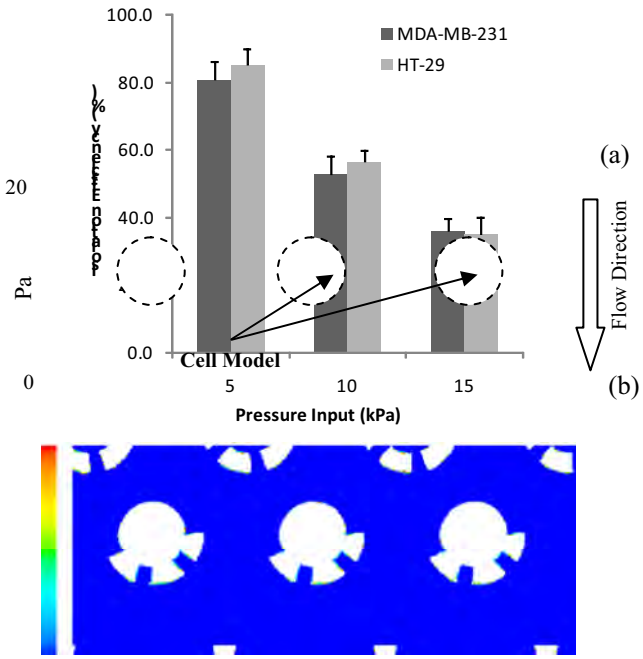


Fig. 2 Microdevice characteristics. (a) Isolation efficiency. (b) CFD studies of shear stress on isolated cells.

Table 1 Isolation purity at different input conditions

Cell Type	5kPa	10kPa	15kPa
MDA-MB-231	85.3%	91.5%	85.3%
HT-29	90.6%	92.0%	87.4%

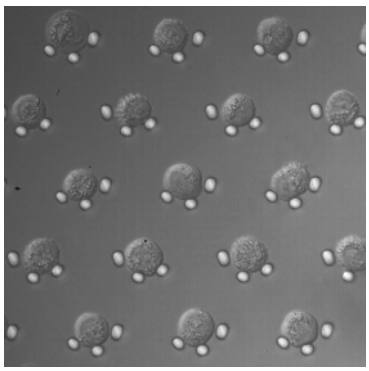


Fig. 3 Isolated HT-29 cells in the microdevice

A pressure driven flow controlled by pressure regulators were used to deliver sample mixtures into the microdevice. Using pressure regulators provided the advantage of precise flow control and allowed real time changes to be made. Isolation via deformability and size of the different cells in the mixture allowed higher capture purity as cancer cells are much stiffer compared to blood constituents which can easily traverse capillaries of 4 μm and smaller. The efficiency of capture is thus likely also to be a determinant of the pressure difference applied in the flow as insufficient pressure applied will retain most WBCs while too much pressure damages the isolated cancer cells and displaces them out of the traps.

Figure 2a showed the investigation of the isolation efficacy over various pressure differential inputs. A general decreasing trend was observed as pressure input was increased for both MDA-MB-231 and HT-29 cancer cell lines. Higher pressure differentials attributed to faster sample processing time but at a reduced isolation efficiency which was not desired. Higher pressure differentials also increased the risk of mechanical damage to isolated cells as the shear forces become excessive due to the flow. Using lower pressure conditions allowed higher isolation efficiencies but at the expense of longer sample processing which might not make the device practical for processing large sample volumes. For our microdevice, at least 80% efficiency was obtained with a pressure setting of 5 kPa for both MDA-MB-231 and HT-29. Our microdevice matches other leading techniques in terms of the enriched cancer cells from blood which can range from 20% to 90% [7,9,19]. Fig 2b showed a simulation study of the shear stresses around an isolated cell at the pressure input of 5kPa. An estimate of the average shear around the isolated cells was still within physiological conditions, highlighting that cells were unlikely to be affected or damaged by the input flow. The proposed optimal condition to operate the device is thus at 5 kPa to attain high isolation efficiency and minimize damage to isolated cells.

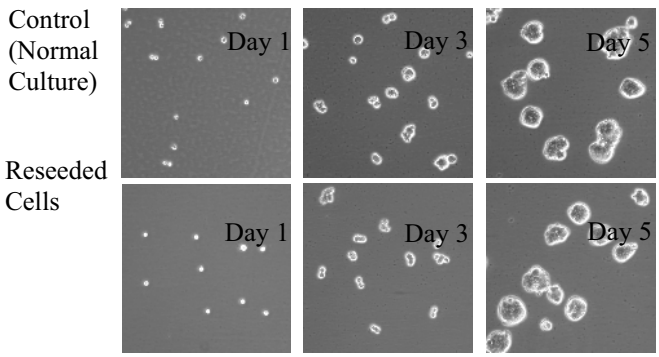


Fig. 4 Cell viability between normal cultures (control) and retrieved HT-29 over a period of 5 days.

To ascertain that the cell isolation was specific only to cancer cells in the blood mixture, immunocytochemistry was performed on the isolated cells in the microdevice for EpCAM, CD45 and DAPI. It is reported that EpCAM is overexpressed in the cancer cells and CD45 is specific for WBCs [20,21]. Thus immunofluorescence staining provided a visual means to quantify the isolated purity over the pressure conditions used. Table 1 summarizes the results of the staining experiments in the microdevice showing a high capture purity of cancer cells from the blood mixture for the range of input pressure used. The high capture purity ensured minimal false positive results giving an accurate assessment of the condition. The uniform arrays of isolation structures also allowed enumeration of isolated cells to be easily processed with image processing software or be counted by visual means under the microscope. As shown in figure 3, most cell traps stores only a single cell and experimental observations saw no more than 3 cells in any isolation structure.

In ensuring the conditions of isolated cells were minimally affected during isolation, the viability and proliferation rate of these cells were studied. Isolated cells were retrieved by reversing the pressure conditions allowing cells to flow to the cell collection port. These cells were reseeded. Figure 4 depicts a typical 5-day culture comparing to normal culture which acted as control. There was no significant difference between the reseeded sample and control, highlighting minimal effects to the cells during isolation. The mechanism to allow retrieval of isolated cells also allows further studies to be undertaken on real clinical samples in subsequent work to better understand the disease.

IV. Conclusions

We had demonstrated a microdevice with an efficient enumeration of viable cancerous cells from blood which has potential in CTCs applications. Neither functional modifications nor complex enrichment processes were required. Separation of cancerous cells from blood utilized their difference in size and cell deformability as cancer cells are stiffer than blood constituents and usually much larger in size. Isolation purity was high which minimized false positive results. Thus a secondary detection mechanism such as immunocytochemistry might not be necessary. The ease of control and handling this microdevice presents an effective means for CTC studies and for evaluation of the cancer status.

References

1. Chambers A F, Groom A C and MacDonald I C (2002) Dissemination and growth of cancer cells in metastatic sites. *Nat Rev Cancer* 2:563-72
2. Lee G Y H and Lim C T (2007) Biomechanics approaches to studying human diseases. *Trends Biotechnol* 25:111-8
3. Steeg P S (2006) Tumor metastasis: mechanistic insights and clinical challenges. *Nat Med* 12:895-904
4. Heyder C, Gloria-Maercker E, Hatzmann W, et al. (2006) Visualization of tumor cell extravasation. *Contrib Microbiol* 13:200-8
5. Cristofanilli M, Budd G T, Ellis M J, et al. (2004) Circulating tumor cells, disease progression, and survival in metastatic breast cancer. *N Engl J Med* 351:781-91
6. Reuben J M, Krishnamurthy S, Woodward W, et al. (2008) The role of circulating tumor cells in breast cancer diagnosis and prediction of therapy response. *Expert Opinion on Medical Diagnostics* 2:339-348
7. Balic M, Dandachi N, Hofmann G, et al. (2005) Comparison of two methods for enumerating circulating tumor cells in carcinoma patients. *Cytometry B Clin Cytom* 68:25-30
8. Cristofanilli M, Broglio K R, Guarneri V, et al. (2007) Circulating tumor cells in metastatic breast cancer: biologic staging beyond tumor burden. *Clin Breast Cancer* 7:471-9
9. Lara O, Tong X, Zborowski M, et al. (2004) Enrichment of rare cancer cells through depletion of normal cells using density and flow-through, immunomagnetic cell separation. *Exp Hematol* 32:891-904
10. Pantel K, Brakenhoff R H and Brandt B (2008) Detection, clinical relevance and specific biological properties of disseminating tumour cells. *Nat Rev Cancer* 8:329-40
11. Shelby J P, White J, Ganesan K, et al. (2003) A microfluidic model for single-cell capillary obstruction by Plasmodium falciparum-infected erythrocytes. 100:14618-14622
12. Mohamed H, McCurdy L D, Szarowski D H, et al. (2004) Development of a rare cell fractionation device: application for cancer detection. *IEEE Trans Nanobioscience* 3:251-6
13. Weiss L (1990) Metastatic inefficiency. *Adv Cancer Res* 54:159-211
14. Weiss L and Dimitrov D S (1986) Mechanical aspects of the lungs as cancer cell-killing organs during hematogenous metastasis. *J Theor Biol* 121:307-21
15. Tan S J, Yobas L, Lee G Y H, et al. (2008) Microdevice for Isolating Viable Circulating Tumor Cells, *International Conference on Biocomputation, Bioinformatics, and Biomedical Technologies, 2008. BIOTECHNO '08.*, Bucharest, Romania, 2008, pp. 109-113
16. McDonald J C, Duffy D C, Anderson J R, et al. (2000) Fabrication of microfluidic systems in poly(dimethylsiloxane). *Electrophoresis* 21:27-40
17. Urtishak S, Alpaugh R K, Weiner L M, et al. (2008) Clinical utility of circulating tumor cells: a role for monitoring response to therapy and drug development. *Biomarkers in Medicine* 2:137-145
18. Dawood S, Broglio K, Valero V, et al. (2008) Circulating tumor cells in metastatic breast cancer: from prognostic stratification to modification of the staging system? *Cancer*
19. Allard W J, Matera J, Miller M C, et al. (2004) Tumor cells circulate in the peripheral blood of all major carcinomas but not in healthy subjects or patients with nonmalignant diseases. *Clin Cancer Res* 10:6897-904
20. Nagrath S, Sequist L V, Maheswaran S, et al. (2007) Isolation of rare circulating tumour cells in cancer patients by microchip technology. *Nature* 450:1235-9
21. Went P T, Lugli A, Meier S, et al. (2004) Frequent EpCam protein expression in human carcinomas. *Hum Pathol* 35:122-8

Corresponding author:

Author: Chwee Teck, Lim
Institute: National University of Singapore
Street: NanoBiomechanics Laboratory, Division of Bioengineering, National University of Singapore, 2 Engineering Drive 3, E3-05-16, Singapore 117576.
City: Singapore
Country: Singapore
Email: ctlim@nus.edu.sg

In-situ Optical Oxygen Sensing for Bio-artificial Liver Bioreactors

V. Nock[1], R.J. Blaikie[1] and T. David[2]

[1] MacDiarmid Institute for Advanced Materials and Nanotechnology, University of Canterbury, Christchurch, New Zealand
[2] Centre for Bioengineering, University of Canterbury, Christchurch, New Zealand

Abstract — **In this paper we present the characterization and application of integrated oxygen sensors to laterally-resolved dissolved oxygen (DO) measurement within a Bio-artificial Liver (BAL) bioreactor device. Sensor patterns were integrated into the PDMS-based bioreactor and calibrated for detection of DO concentration. The intensity signal ratio I_0/I_{100} of the sensor films was optimized to 6.1 by reducing sensor film thickness to 0.6 µm and remained constant for nearly two weeks while covered with type I collagen. Calibration of DO measurement showed linear Stern–Volmer behavior that was constant for flow rates from 0.5 to 2 mL/min. The calibrated sensors were subsequently used to demonstrate detection of transverse oxygen gradients produced by combining multiple flow streams inside the bioreactor. The device has potential applications in shear-dependent cell culture and drug assays with simultaneous monitoring of oxygen tension.**

Keywords — **Laminar flow, bioreactor, PtOEPK/PS sensor, dissolved oxygen, transverse gradient.**

I. Introduction

In a physiological environment, such as in mammalian organs, cellular oxygen is a parameter regulated to within the normoxic range. Values in excess of this range can lead to terminal damage to the cells or, in case of insufficient oxygen supply, to metabolic demise [1]. In contrast, variations within this range have been found to play a significant role in the gradient-induced distribution of functional zones throughout an organ. A prominent example exhibiting oxygen-induced modulation is the mammalian liver, where oxygen gradients (from periportal blood, 84-91µmol/L, to perivenous blood, 42-49µmol/L) have been shown to result in zonal gene expression in hepatocytes [2].

With important biomedical applications, such as liver cell assays and Bio-artificial Liver (BAL) devices, relying on the in-vitro culture of hepatocytes, it is therefore of great interest to study, control and eventually harness the effect of oxygen concentration gradients on cell function. In a BAL bioreactor measurement and control of the dissolved oxygen (DO) level is essential to re-create optimal conditions for in-vivo like liver cell function [3]. Several studies have investigated the relationship between medium flow, oxygen transport and hepatocyte metabolic function [4-7], indicating the importance of DO gradients to liver-specific function of hepatocytes in culture. However, most current experimental approaches featuring parallel-plate reactor geometries are lacking robust control over oxygen graduation. While high-resolution oxidative microgradients have been demonstrated for general, static cell-culture, such graduation relies on potentially hazardous chemical reactions [8].

Previously, we have shown how channel geometry alone can be used to control the fluid shear stress and oxygen gradient experienced by cells cultured within a flow-through bioreactor chamber. A novel analytical model was introduced which can be used to determine the bioreactor shape for a desired oxygen gradient along the reactor length [9]. The model requires only a single inlet stream with an initial oxygen concentration and was validated for the example of linear and constant gradients using computational fluid dynamics [10]. In a further step towards experimental verification, in-situ oxygen sensing was integrated into a prototype of the gradient-producing device. A novel layer-by-layer fabrication process for the integration of platinum(II) octaethylporphyrin ketone (PtOEPK) oxygen sensors, suspended in a microporous polystyrene (PS) matrix, into polydimethylsiloxane (PDMS) based microfluidic devices was developed and sensors were calibrated for detection of DO [11]. In this paper we show how the device can be modified by use of further inlets to yield an additional transverse graduation of DO levels.

II. Fabrication and Experimental

The bioreactor device and the integrated and external gas exchangers were fabricated using micro-lithography and replica-molding in PDMS (Sylgard 184, Dow Corning). Details of the fabrication process and integration of the oxygen sensor layer (PtOEPK, Frontier Scientific; PS, Sigma Aldrich) via soft-lithography are described in [11]. Figure 1 shows a photograph of the complete device with external tubing and two modular gas exchangers attached. The gas exchangers were used to provide a defined oxygen concentration at the bioreactor inlet. Figure 1(b) shows a close-up of the gas exchanger; channels for liquid and gas are separated by a 30 µm thick, gas-permeable PDMS membrane, allowing for bubble-free oxygenation of the liquid. Figure 1(c) indicates the three separate flow streams, with their respective oxygen concentration, converging on the bioreactor chamber. De-ionized (DI) water could be oxy-

Chwee Teck Lim, James C.H. Goh (Eds.): ICBME 2008, Proceedings 23, pp. 778–781, 2009
www.springerlink.com

genated to within a range of 0 to 34 ppm O_2, with 34 ppm being the saturation level for pure oxygen and 8.6 ppm for air (~2_1% O_2) in the gas exchanger.

Oxygen measurements were performed using a standard fluorescence microscope in combination with a digital camera for image acquisition. The change of PtOEPK fluorescent dye intensity in presence of molecular oxygen was analyzed using the image processing module of Matlab and a pre-recorded Stern-Volmer calibration curve, as shown in [11]. A dual syringe pump was used to provide pressure-driven flow for single, dual and triple flow streams. During measurements the device was placed on a microscope stage warmer and held at a constant temperature of 37°C, corresponding to cell-culture conditions. For long-term oxygen measurement experiments a layer of 0.01% (w/v) type I collagen (rat tail, Sigma Aldrich) was deposited onto the PtOEPK/PS film and incubated at room temperature for a duration of 8 hrs. The purpose of this layer is to promote adhesion in subsequent cell culture.

III. Results and Discussion

Observations in vivo have identified oxygen concentration as a major tool to induce metabolic zonation in continuously perfused bioreactors. Concentration gradients parallel to the direction of perfusion can be realized by the use of an integrated gas supply layer [3,4,7] or via the modification of the reactor geometry [10]. Figure 1(c) shows an example of the latter, where the bioreactor shape is designed to provide a nearly constant oxygen concentration along its length. While longitudinal gradient control is of great interest, flow characteristics at the micro scale can be harnessed to implement additional oxygen graduation in the transverse direction.

Due to laminar flow conditions in the bioreactor, and the absence of convective mixing at low Reynolds numbers, diffusion is the predominant transverse transport mechanism. Two or more streams entering the device create a moving interface between the flow streams characterized by the width of the diffusive layer, which, in turn, can be adjusted via the flow rate [12]. Figure 2 shows a schematic of the bioreactor dimensions and corresponding visualization of the oxygen concentration inside the reactor for two inlet streams of water with different DO levels and a flow rate of

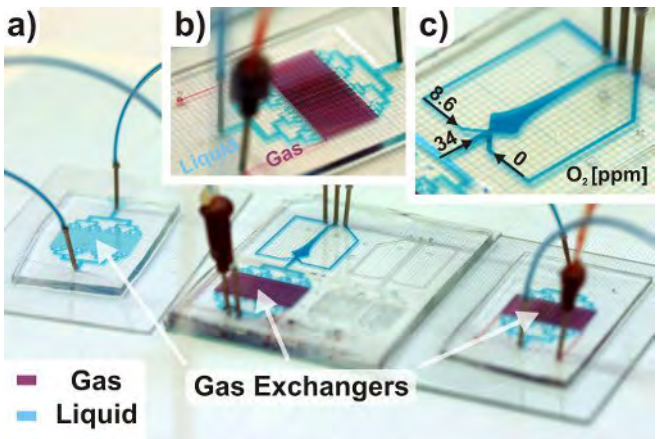


Fig. 1 a) Photograph of the device with two modular gas exchangers. b) Close-up of a single gas exchanger indicating the separate layers for liquid (blue) and gas (red) separated by a thin PDMS membrane. c) Close-up of the central, tapered bioreactor combining three separate flows of water with an oxygen concentration of 8.6, 34 and 0 ppm O_2, respectively. Channels containing liquid were filled with blue (light grey) dye-colored water and those containing gas with red (dark) for illustration purposes.

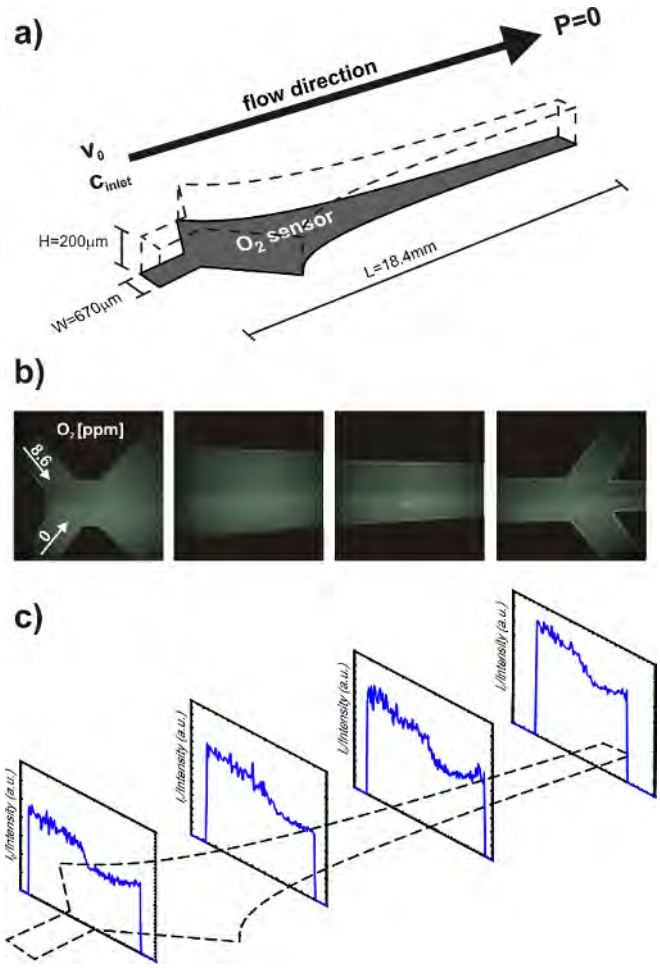


Fig. 2 Illustration of the oxygen measurement process for dual flow conditions: a) Schematic of the bioreactor chamber showing dimensions and flow direction, b) fluorescent intensity images for four positions along the reactor length and two parallel flow streams (8.6 and 0 ppm O_2), and c) plots corresponding to the intensity images overlaid onto the reactor footprint.

0.1 mL/min each. As can be seen from the fluorescence images in Figure 2(b), the difference in intensity of the polymer sensor layer at the bottom surface of the bioreactor indicates the difference in oxygen concentration between the streams. Upon contact the two streams form a stable interface, which remains sharply defined along the reactor length, from the two inlets (left) to the outlet (right). This observation is further supported by plotting the relative intensity I_0/I, where I_0 is the unquenched sensor intensity for 0 ppm O_2, across channel width for the individual intensity images, as shown in Figure 2(c).

The change in sensor signal intensity observed in Figure 2(b) is directly related to the DO concentration of the stream via reversible quenching of the electronic states in the PtOEPK fluorescent dye molecule by O_2. This relationship between intensity and concentration is described by the Stern-Volmer equation

$$\frac{I_0}{I} = 1 + K_{SV}^{S}[O_2] \qquad (1)$$

where K_{SV}^{S} is the Stern-Volmer constant and $[O_2]$ is the oxygen concentration in solution. During fabrication it was observed that the intensity signal ratio I_0/I_{100} of the sensor layer could be optimized to 6.1 by reducing sensor film thickness to 0.6 µm during spin-coating. As shown in Figure 3, this ratio reduced by only 8% over a duration of two weeks while covered with a layer of cell adhesion-promoting collagen to demonstrate its suitability for cell culture.

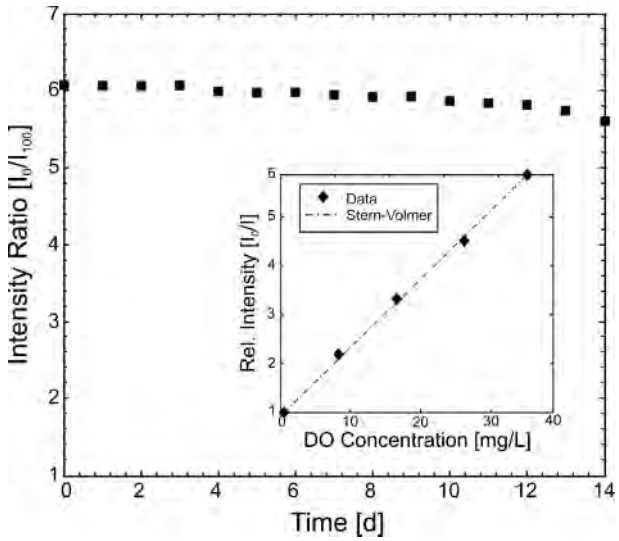


Fig. 3 Plot of the sensor intensity ratio I_0/I_{100} as a function of time in days for a PtOEPK/PS film covered by type I collagen. The inset shows the Stern-Volmer calibration curve for measurement of DO concentration using the same sensor film.

By recording a calibration curve for defined oxygen concentrations, sensor intensity can be translated into corresponding oxygen concentration values. The inset in Figure 3 shows the measured relationship between the relative intensity and five different DO concentrations, as used for calibration. The plot indicates linear Stern–Volmer behavior, which was constant for flow rates from 0.5 to 2 mL/min.

Figure 4 shows the application of the oxygen measurement method by plotting the transverse oxygen concentration profile as a function of the width of the bioreactor. The profiles plotted in Figure 4(a) correspond to the inlet and outlet of the example shown in Figure 2. Dashed lines in the

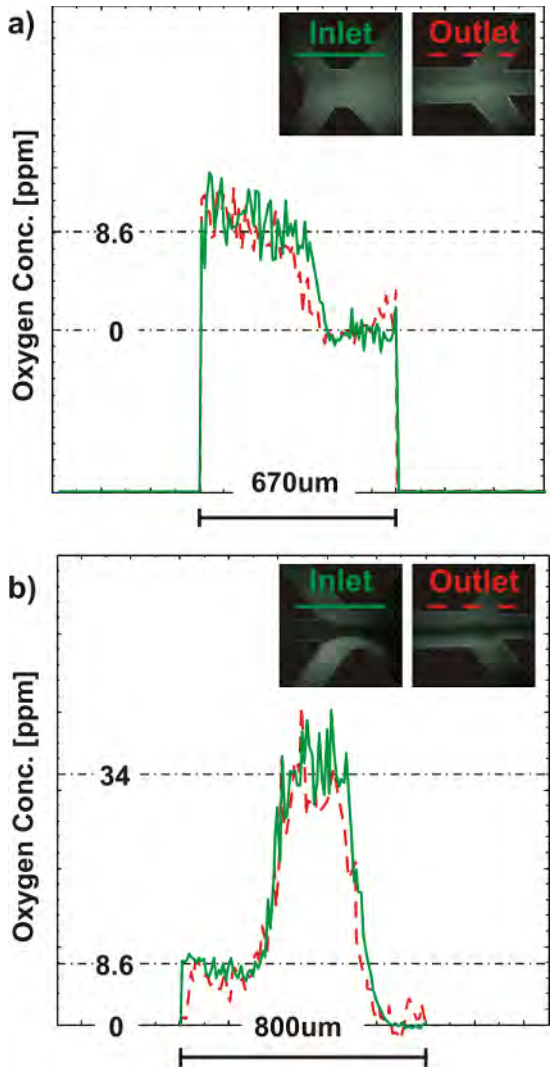


Fig. 4 Plot of the transverse oxygen concentration versus bioreactor width at the inlet (solid) and outlet (dash): a) For two parallel laminar flow streams of 8.6 and 0 ppm O_2, and b) for three streams of 34, 8.6 and 0 ppm O_2. In both cases DI water was used as medium.

graph indicate the 0 and 8.6 ppm DO levels. In Figure 4(b) a third central flow stream was added to the two existing ones via a third inlet connected to an additional gas exchanger. The DO level of this stream was produced by flowing industrial-grade oxygen through the exchanger and represents the upper limit of the attainable range (34 ppm). Custom values in between can be realized by use of an appropriate mixture of nitrogen and oxygen in the gas exchanger.

A further characteristic of parallel laminar flow streams is the development of a diffusive boundary layer between streams of different oxygen concentration. Depending on the flow rate and residence time, oxygen from the oxygen-rich stream diffuses into those with a lower initial DO level. In the transverse concentration plot of Figure 4(a) for example, this is illustrated by a flattening of the initially stepwise transition from inlet to outlet. If undesirable, this effect can be reduced by increasing the flow rate, whereas otherwise it provides a convenient means to determine the diffusion constant of oxygen in the respective medium used for perfusion [13].

The combination of multiple laminar streams with varying DO levels, such as demonstrated here, has the potential for oxygen-dependent treatment of cells without the need for physically separated bioreactors. A similar setup has previously been used to selectively treat cellular microdomains with chemicals [14,15]. However, oxygen concentration, a further parameter with significant effect on cell behavior, was not controlled or monitored for the individual streams used. In contrast, our device enables similar experiments to be performed while simultaneously controlling the DO level of the individual flow stream, thereby increasing the validity of in-vitro experiments.

Concerning BAL devices, the concept of transverse oxygen gradients has the potential, to further understanding of the effect of autocrine signaling on cell metabolic functions and zonation. One such example is the inverse relationship between hormone gradients and those for oxygen, as observed in the liver [2]. Using parallel laminar flow streams, dynamic and simultaneous observation of the effect of different oxygen concentrations on cells located downstream will be possible in a single bioreactor, while at the same time keeping stream-to-stream cross-talk to a minimum.

IV. Conclusions

We have shown the generation and detection of transverse gradients of DO inside a PDMS-based microfluidic device. The oxygen concentration of individual flow streams was controlled, visualized and measured using a polymer-based oxygen sensor layer. Multiple streams were combined in a single bioreactor chamber demonstrating stable inter-stream interfaces. The presented chip provides a novel tool for the parallelization of DO concentration-dependent assays, BAL and tissue engineering applications.

Acknowledgment

The authors would like to thank Helen Devereux and Gary Turner for technical assistance.

References

1. Semenza G L (2001) HIF-1, O2, and the 3 PHDs: How Animal Cells Signal Hypoxia to the Nucleus. Cell 107:1-3 DOI 10.1016/S0092-8674(01)00518-9
2. Jungermann K, Kietzmann T (2000) Oxygen: Modulator of metabolic zonation and disease of the liver. Hepatology 31:255-260 DOI 10.1002/hep.510310201
3. Tilles A W, Baskaran H, Roy P et al. (2001) Effects of oxygenation and flow on the viability and function of rat hepatocytes cocultured in a microchannel flat-plate bioreactor. Biotechnol Bioeng 73:379-389 DOI 10.1002/bit.1071
4. Roy P, Baskaran H, Tilles A W et al. (2001) Analysis of oxygen transport to hepatocytes in a flat-plate microchannel bioreactor. Ann Biomed Eng 29:947-955
5. Allen J W, Bhatia S N (2003) Formation of steady-state oxygen gradients in vitro - Application to liver zonation. Biotechnol Bioeng 82:253-262 DOI 10.1002/bit.10569
6. Allen J W, Khetani S R, Bhatia S N (2005) In vitro zonation and toxicity in a hepatocyte bioreactor. Toxicol Sci 84:110-119
7. Kane B J, Zinner M J, Yarmush M L et al. (2006) Liver-Specific Functional Studies in a Microfluidic Array of Primary Mammalian Hepatocytes. Anal Chem 78:4291-4298 DOI 10.1021/ac051856v
8. Park J, Bansal T, Pinelis M et al. (2006) A microsystem for sensing and patterning oxidative microgradients during cell culture. Lab Chip 6:611-622 DOI 10.1039/b516483d
9. Nock V, Blaikie R J, David T (2007) Microfluidics for Bioartificial Livers. N Z Med J 120:2-3
10. Nock V, Blaikie R J, David T (2007) Micro-patterning of polymer-based optical oxygen sensors for lab-on-chip applications. Proc SPIE 6799:67990Y-10 DOI:10.1117/12.759023
11. Nock V, Blaikie R J, David T (2008) Patterning, integration and characterisation of polymer optical oxygen sensors for microfluidic devices. Lab Chip 8:1300-1307 DOI 10.1039/b801879k
12. Atencia J, Beebe D J (2005) Controlled microfluidic interfaces. Nature 437:648-655 DOI 10.1038/nature04163
13. Nock V, Blaikie R J, David T (2008) Generation and Detection of Laminar Flow with Laterally-Varying Oxygen Concentration Levels. Proc uTAS **In Press**
14. Takayama S, Ostuni E, LeDuc P et al. (2001) Laminar flows: Subcellular positioning of small molecules. Nature 411:1016-1016 DOI 10.1038/35082637
15. Takayama S, Ostuni E, LeDuc P et al. (2003) Selective Chemical Treatment of Cellular Microdomains Using Multiple Laminar Streams. Chem Biol 10:123-130

Author: Volker Nock
Institute: University of Canterbury
Street: Private Bag 4800
City: Christchurch
Country: New Zealand
Email: volker.nock@elec.canterbury.ac.nz

Quantitative and Indirect Qualitative Analysis Approach for Nanodiamond Using SEM Images and Raman Response

Niranjana S., B.S. Satyanarayana, U.C. Niranjan and Shounak De

Manipal Institute of Technology, Manipal, Karnataka, INDIA,576 104.

Abstract — **In the era of nanotechnology, one of the material which seems to be in the forefront, in terms of its application in medical domain is nanocarbon. Various forms of nanocarbon including, carbon nanotubes, nanostructured graphite, nanodiamond, nanowalls, nanocluster carbon, diamond like carbon (DLC) and tetrahedral amorphous carbon(taC) are being studied, for different biomedical applications includes Vacuum based X-ray source, Tribology coating for joints or surgical, Micro/Nano Elcecto Mechanical System (MEMS /NEMS) and Biosensor. Study of nanodiamond grown with Hot Filament Chemical Vapor Deposition(HFCVD) process with various CH4/H2 condition indicates various morphological and compositional properties. The surface based morphology are studied with SEM images provides visual information's. Studied compositional variation using nondestructive and instantaneous approach using Raman response. Reported the mechanism of deposition and the influence of the deposition parameters in terms on the morphology and composition. Designed an insitu applicable software approach for SEM images analysis. The images are initially segmented for enhancing the cluster regions on the substrate and each individual clusters are labeled. Generated histogram using the area estimated for each cluster and analysed it quantitatively. The Raman and SEM based analysis evaluates cluster dimensions, distribution and provides quantitative and indirect qualitative information for evaluating the nanodiamond.**

Keywords — **Nanodiamond,Quantitative analysis, SEM images, Raman Response,**

I. Introduction

Recently miniaturized products have become increasingly dominant in every aspect of life. As per ITRS (International Technology Roadmap for Semiconductor) novel, self aligned nanomaterials which are being developed are the building blocks of future nanoelectronic devices [1-8]. Among the many nanomaterials, nanocarbon is one of the most studied material for nanotechnology applications, in its various manifestations. The various forms of nanocarbon being studied include nanodiamond, Single-walled / Multi-walled carbon nanotubes (SWNT/MWNT), fullerenes (C_{60}), Nanohorns, Nanowalls, Nanowires, Nanofibers, nanocluster or nanostructured carbon. Growing areas of technology were these nanocarbon find applications include Nanoelectronics, Vacuum nanoelectronics, Sensors, Biomedical applications, Novel energy sources, Interconnects in ICs, Novel light, strong and even conducting Composite materials and Flexible electronics [1-8]

Presented here nanodiamond grown using Hot Filament Chemical Vapor Deposition (HFCVD) process under various CH4/H2 condition and its SEM and Raman response based analysis. The morphological information's derived from SEM includes nanostructure distribution ,size and thereby furnishes details for quantitative analysis. The study also provides understanding of the quality of the film. The uniformity of size or distribution of the structure indirectly qualifies the thin films. However the uniform distributed films are more preferred for applications like sensors. Raman Spectroscopic approach of characterization is one of the nondestructive and instantaneous technique used for characterization of nanocarbon in nanotechnology. Raman response as unique signature for nanostructure, is interesting for understanding bonding and dimensional details[9-12].

II. Exeriment

Hot Filament CVD

The heavily n-doped silicon substrate surface was pretreated by polishing to increase diamond nucleation. The nanodiamond deposited using Hot Filament Chemical Vapour deposition[HFCVD]at 1% methane to hydrogen ratio(CH4/ H2) atmosphere for two hours. The filament temperature during the deposition was ranging between 2200 ~ 2300^{o}C and the substrate temperature was between 725 ^{o}C to 925 ^{o}C. Grown nanocrystaline diamond thin films with the variation of methane to hydrogen(CH4/ H2)ratio from 0.5 % to 3 %. Further study was made using the Scanning Electron Microscope(SEM) images, Raman response of the thin films. Typical thickness of the films grown was 500nm.

Further developed , the MATLAB based automated morphology analysis tool for nanostructure size based analysis.

Chwee Teck Lim, James C.H. Goh (Eds.): ICBME 2008, Proceedings 23, pp. 782–785, 2009
www.springerlink.com

III. Result and Discussion

A. Sem Based Analysis

The morphological and dimensional features of various nanocarbons including nanodiamond, carbon nanotube, carbon based nanocluster and nanowalls were studied using Scanning Electron Microscopic images (SEM). Shown in figure1, is the typical SEM images of the nanodiamond considered for the study. The surface morphological study for various sized nanostructures are possible with visual inspection. However automated approach of morphological study is essential for in situ applications. In this approach from the SEM image the nanostructure dimension is estimated. The indirect quality analysis of nanodiamond films are achieved with the histogram plot.

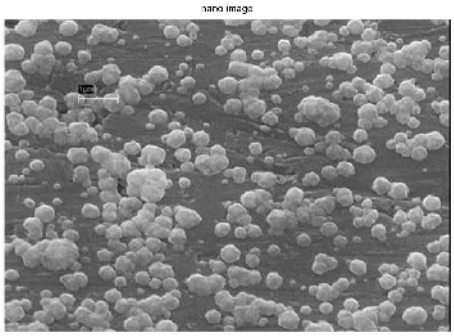


Fig. 1 The original SEM image of Nanodiamond

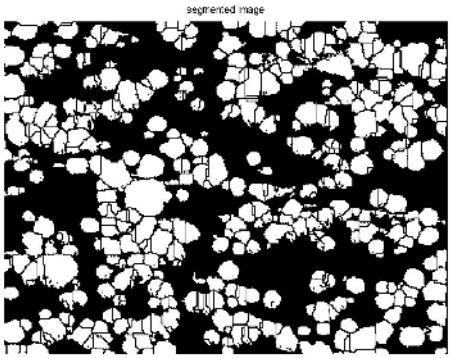


Fig. 2 The segmented SEM image after enhancement

The image based analysis approach includes following steps. Initially the grey image is preprocessed for noise pixel elimination and to enhance the quality.The enhanced binary image is then segmented to get region of interest. Shown in figure2, the image after Watershed segmentation. Estimated area of each nanodimond structure using software and finally plotted the area based histogram for further analysis of the film.

Shown in figure 3, the area histogram plot of nanodimond film plotted considering area along the x axis and count of, nanodiamond structures along y axis. The plot indicates the size distribution of nanodiamond structure around the film surface as well provides the median size or size range

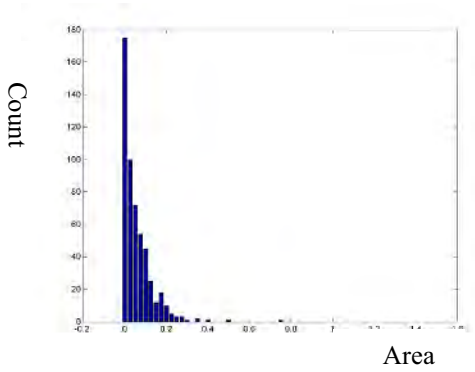


Fig. 3 Histogram plot for the nanodimension indicates Area of structures (along X axis in μm^2, Count (along Y axis)

B. Raman Response Analysis

Raman response of wide variety of nanostructures including carbon nanotube,nanodiamond,nanowall and nanocluste are shown in figure 4. It clearly shows different signature for each individual nanomaterial, promising usage of Raman Response for instantaneous and nondestructive way of nanomaterial understanding approach. In case of Raman studies of nanocarbon, the visible Raman spectrum shows

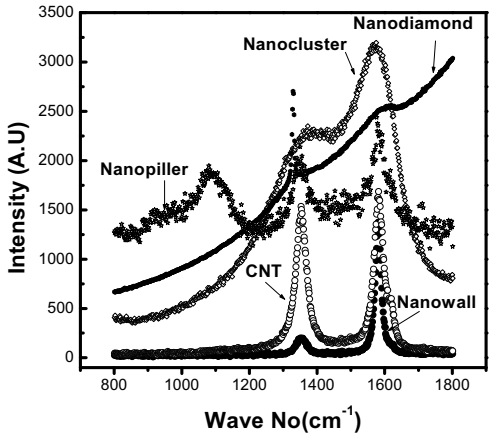


Fig. 4 Raman response of various nanocarbon thin films

two prominent features and some minor modulations. The prominent features are G Peak (Graphite peak around 1580cm^{-1}), and D Peak(Disorder peak around 1330 cm^{-1}) In the case of nanostructured carbon nanowalls we see relatively the narrowest G peak around 1580cm^{-1}, showing the well formed nanowalls. The carbon nanotubes show both the G and D peaks like the nanowalls, but area broader. This shows that the materials have more amorphous phase materials and also clusters with varying dimensions besides the carbon nanotubes. From the Raman response of room temperature grown nanocluster carbon it may be observed that G and D peak are even broader than nanotubes. This indicates that the clusters with vastly varying dimensions and amorphous phase materials.

Especially in case of nanodiamond, the visible Raman spectrum shows two prominent features. The nanodiamond film exhibits a narrow diamond peak around 1332cm^{-1} and a broad peak around 1580cm^{-1}(G peak) showing the presence of graphite like and amorphous phase materials around the grain boundaries. Raman can be used to identify a wide range of material parameters or properties including, if it is amorphous, nanocrystalline or crystalline, the size of the cluster, the nature of bonding: graphite like (sp^2 bonding or π bonding)or diamond like (sp^3 bonding or σ bonds)and the ratio between the two (sp^2/sp^3) types of bonding. Analyzed nanodiamond for understanding its property by using curve fitting approach. Shown in figure 5, curve fitted nanodiamond Raman response. Extracted features from curve fitting includes:D-Peak, G-Peak, Id-Ig Ratio, D peak – G peak Ratio, G-area, D-areas and some statistical values.

Further an effort was made to look at possibility of correlation between the nanocarbon dimension estimated from SEM images to field assisted electron emission properties of theses films finding the FN slope from field emission response and the dimension/size of nanocarbon. The influence of temperature variation also studied between 725 ^{o}C to 975^{o}C for a constant CH4/H2 ratio. Observed the shift of the G peak position towards smaller wave number, with an incremental change of temperature, resulting a more sp3 phase nanodiamond. Based on the experimental data between temperature range 800 ^{o}C -850^{o}C suggests the region of uniform cluster size and distribution.

Shown in figure 6 and figure 7 are some relationship shown with Raman derived parameter Id/Ig. The Figure 6 indicates possibility of some dimension and Id/Ig ratio relation. Similarly shown in figure.7 a plot of process parameter(CH4/H2) ratio dependence along with Raman derived ratio. The results are clearly indicates possibility of usage of Raman response for nanodiamond analysis.

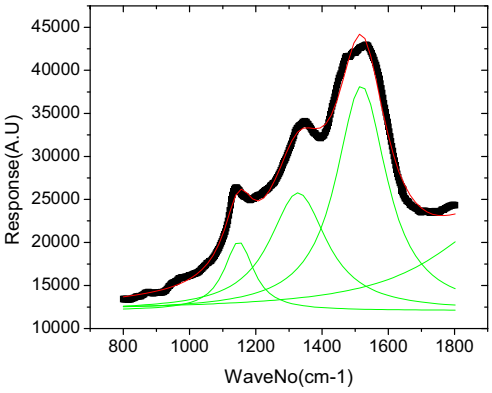


Fig. 5 Curve fitted Raman Response for a nanodiamond film

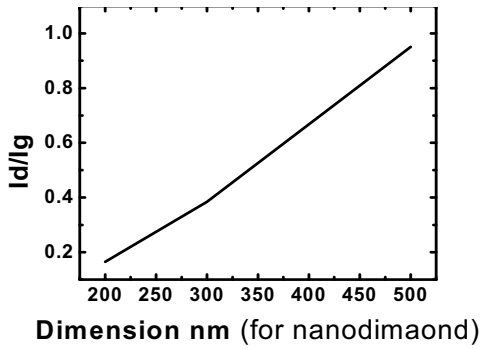


Fig. 6 Size variation of Nanodiamond size with Id/Ig ratio calculated from Raman response.

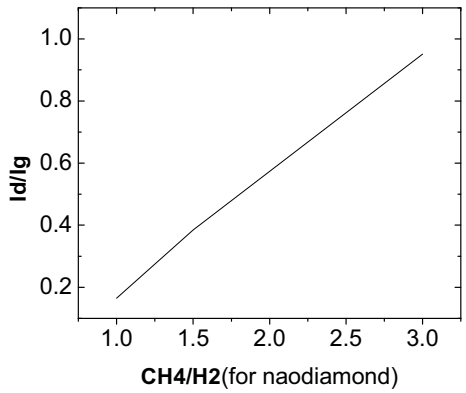


Fig. 7 CH4/H2 ratio variation and Id/Ig ratio for nanodiamond films grown under various conditionsonse.

IV. Conclusion

The study promises the possibility of correlation between dimensions (size) derived from SEM images of nanodiamond and parameters derived from Raman response. Also suggested automated SEM image analysis approach for analysis of nanodiamond SEM image for quantitative analysis. Further the derived parameters from the Raman response are used to evaluate or classify the nanocarbons indirectly with the extracted parameters. However the Raman signature of nanodimond material needs further detailed study to explain conductive or other electronic properties .The work promises the importance of Raman study for qualitative analysis of nonmaterial.

Acknowledgment

The author would like to acknowledge the Innovation Center, Manipal University, Manipal, Karnataka, India, for providing continuous encouragement and support. Also I extend thanks to Dr. Ramesh Galigekere,HOD Biomedical Dept, Dr. V H S Moorthy,E &C Dept and Biomedical Engineering Department for providing the support.

References

1. M.Terones,A.Jorio,M.Endo,A.M.Rao,Y.A.Kim,T.Hayashi,H.Terrones,J.C.Charlier, G.Dresselhaus and M.S.Dresselhaus, "New Directions in Nanotube Science," *MaterialsToday*, Oct, pp 30-45,2004.
2. Walt A De Heer, "Nanotubes and Pursuit of Applications," *MRS Bulletin*,April,2004.
3. Niraj Sinha, JohnT, W.Yellow, "Carbon Nanotubes for biomedical Applications," *IEEE Transaction on Nanobioscience*,Vol.4,No.2, pp180-195, June, 2005.
4. N.S.Xu and S.Ejaz Huq, "Novel cold cathode materials and applications," *Material Science. & Engg*. R 48 ,47-189, 2005.
5. Keat Ghee Ong, Kefeng Zeng, and Craig A. Grimes , "A Wireless, Passive Carbon Nanotube -Based Gas Sensor," *IEEE Sensors Journal,* Vol. 2, No. 2, pp 82- 88 ,APRIL 2002.
6. Seongjeen Kim, "CNT Sensors for Detecting Gases with Low Adsorption Energy by Ionization," *Sensors* 2006*, 6*, 503-513.
7. Niraj Sinha, Jiazhi Ma, and John T. W. Yeow "Carbon Nanotube-Based Sensors," *Journal of Nanoscience and Nanotechnology ASP*, Vol.6, 573–590, 2006.
8. B.S.Satyanarayana, "Room Temperature Grown Nanocarbon based multilayered Field Emitter Cathodes for Vacuum Microelectronics," *11th IWPSD Conference Proceedings*,ed V.Kumar &P.K.Basu, p278,2001.
9. B.S.Satyanarayana, X.L.Peng, G.Adamapolous, J.Robertson, W.I. Milne, and T.W. Clyne, "Very Low Threshold Field Emission from Microcrystalline Diamond films grown using Hot Filament CVD Process," *MRS Symp. Proc.*, Vol.621,Q5.3.1-5.3.7, 2000.
10. B.S.Satyanarayana "The influence of sp3 bonded carbon on field emission from nanostructured sp2 bonded carbon films," *IEEE,18th International Vacuum Nanoelectronics Conference Technical Digest,* Oxford ,p219, 2005.
11. M A Al-Khedher , C Pezeshki, J L McHale and F J Knorr **,** "Quality classification via Raman identification and SEM analysis of carbon nanotube bundles using artificial neural networks", *Nanotechnology,* 18- 355703 (11pp),2007.
12. S. Zhang a,, X.T. Zeng a, H. Xie , P. Hing, "A phenomenological approach for the Id/Ig ratio and sp3 fraction of magnetron sputtered a-C films", Surface and Coatings Technology 123 ,256–260,2000

Author: NIRANJANA .S
Institute: MANIPAL INSTITUTE OF TECHNOLOGY
City: MANIPAL
Country: INDIA
Email: ss_niranjana@yahoo.com; niranjana.s@manipal.edu

Non-invasive Acquisition of Blood Pulse Using Magnetic Disturbance Technique

Chee Teck Phua[1], Gaëlle Lissorgues[2], Bruno Mercier[2]

[1]School of Engineering (Electronics), Nanyang Polytechnic, Singapore
[2]ESIEE – ESYCOM , University Paris Est, France

Abstract — **Blood pulse is an important human physiological signal commonly used for the understanding of the individual physical health. Current methods of non-invasive blood pulse sensing require direct contact or access to the human skin. As such, the performances of these devices tend to vary with time and are subjective to human body fluids (e.g. blood, perspiration and skin-oil) and environmental contaminants (e.g. mud, water, etc). This paper proposes a novel method of non-invasive acquisition of blood pulse using the disturbance created by blood flowing through a localized magnetic field. The proposed system employs a magnetic sensor and a small permanent magnet placed on the artery (major blood vessel) of the limbs. The magnetic field generated by the permanent magnet acts both as the biasing field for the sensor and also the uniform magnetic flux for blood disturbance. As such, the system is able to operate at room temperature, reliable for continuous long term acquisition, compact (small size) and convenient for daily usage. The heart rate obtained from the proposed system when measured through non-conductive opaque fabric, is found to be highly correlated to commercially available cardiac monitoring system such as ECG and pulse-oximetry.**

Keywords — **blood pulse, magnetic biasing, non-invasive, magnetic disturbance**

I. Introduction

A. Context of the study

With the advancement of bioelectronics, portable health monitoring devices are getting popular because they are able to provide continuous monitoring of an individual's health condition with ease of use and comfort. Portable health monitoring devices are increasingly required at places such as home, ambulance and hospital, and at situations including military training and sports.

Pulse rate is a measurement of the number of times the heart beats per minute. The heart pushes blood through the arteries, which expand and contract allowing blood to flow.

Heart or pulse rate is an important parameter subject to continuous monitoring because they are representative in assessing the physical health condition of an individual. Healthcare institutes such as the hospitals and elderly care centers can use this information to monitor the health conditions of their patients. This is particularly important for patients with cardiac arrhythmia whose heart rate variability needs to be monitored closely for early detection of cardiac complications.

Furthermore, pulse rate information of individuals subjected to mentally or physically stressful conditions may be utilized to trigger alert for immediate attention when large changes in heart rate variability indicate potentially fatal events such as heat stroke, cardiac disorder and mental break down. Finally, it can be also important to monitor pulse rate of personnel working in dangerous environments such as deep sea condition (divers), high temperature (fire-fighters), and deep underground (coal miners).

B. State of the art

Current methods of heart or pulse rate acquisition can be classified into electrical [1-2], optical [3,7], microwave [4], acoustic [5,8,11], mechanical [6,9] or magnetic [10,12,13] means. The use of electrical probes to measure heart rate was discovered in 1872. Such a method normally requires good electrical contact with the human skin and the performance is subjective to human body fluids (e.g. blood, perspiration, skin-oil) and environmental contaminants (e.g. mud, water, etc). In most deployment, reference electrodes are usually required to ensure such a system is less susceptible to electrical noise [2]. Recent research [1] had also reported a new method of ECG acquisition using contact free capacitive sensing. However, this method is highly subjective to noise and motion artefact.

Examples of commercially available heart rate acquisition systems include ECG monitoring devices, pulse rate monitoring watches and chest strips. All of these devices require electrical contact between the probes and the human skin.

The use of optical sensors in pulse oximetry [3,7] is getting popular due to its compact nature and the ability to concurrently acquire SpO_2 concentration in blood. The basic operating principle of such a system requires a light source and a sensor where the reflected light content is measured to determine the blood pulse and SpO_2 concentration in blood. Typically, such a system is worn on the tip of the fingers or toes where optical transmittance of the human skin is important to ensure signal quality.

Microwave radar [4] has also been reported for non-invasive detection of heart rate. However, such methods are

Chwee Teck Lim, James C.H. Goh (Eds.): ICBME 2008, Proceedings 23, pp. 786–789, 2009
www.springerlink.com

highly subjective to motion artifacts created due to movement of the subject.

Acoustic method of acquiring heart rate on the human chest was available through the invention of the stethoscope since 1816. Over the years, this method, which has progressed with electronics and innovative signal acquisition systems, is widely reported [5,8,11].

Biomagnetic signal from the heart was detected in 1963 by Baule and McFee. The basic principle involves the mapping of the magnetic field around the thorax while the heart magnetic vector is acquired and is commonly known as magnetocardiogram (MCG). Such a method requires highly sensitive magnetic sensors such as SQUID (Superconducting QUantum Interference Device) and is currently not readily deployed for clinical use as ECG proves to be more reliable, convenient and less expensive.

Another way to measure the blood pulse is based on Hall Effect [10,13]. Such system applies a uni- or bi-directional magnetic field on the human body to create polarization of blood molecules. Electrodes are placed on the human skin near the applied magnetic field to pick up the potential difference created by the induced magnetic signal.

Mechanical methods to acquire heart or pulse rate varies from the use of pressure cuff to piezo-electric materials worn over the limbs or body [6,9]. Such mechanical methods to acquire heart or pulse rate requires the application of localized pressure on the human subject and are not well suited for continuous signal acquisition.

The limitations of each of the above methods to acquire heart or pulse rate motivated the research on a simple and yet reliable magnetic means to acquire blood pulse. Such a method will support the acquisition of blood pulse without the need for a good electrical or optical contact and can be used over a prolonged period of time on the limbs. One of the objectives in developing a non-invasive magnetic based blood pulse acquisition system is to use commercially available magnetic sensors in place of SQUID or electrodes. This will allow the system to operate at room temperature, to be reliable, compact (small size), cheaper, and more convenient for daily usage.

II. Experimental set-up

The experiment on blood pulse acquisition utilizes the concept of placing a magnetic field in the vicinity of the major artery where the blood flowing through the magnetic field will disturb the magnetic field, thus creating a magnetic disturbance. Such a magnetic disturbance is acquired using a magnetic based sensor operating at room temperature as shown in Figure 1. In this experiment, the variation of magnetic field is termed Modulated Magnetic Signature of Blood (MMSB).

The relative position between the magnet (1), sensor (2) and the artery (major blood vessel) was varied and the final set-up for measurement is shown in Figure 2 where the sensor output was sufficiently amplified and then connected to an oscilloscope. The configurations of the sensor on the limbs are illustrated in Figure 3.

To achieve the objective of small size for portability and operation at room temperature, the uniform magnetic field is created by the use of a button-sized permanent magnet (3mm diameter) with magnetic strength of 1000 Gauss. The magnet is placed over the major arteries on the limbs with a magnetic sensor placed in close proximity. The measurements will depend on several aspects: the distance between the sensor and the magnet (approximately 15mm) providing a uniform magnetic field that ensures proper biasing, the magnet strength that does not saturate the sensor, and the appropriate penetration of the magnetic field into the skin tissues.

The magnetic sensor has typical performance characteristics as shown in Figure 4. Magnetic biasing is illustrated in Figure 4 where the sensitivity of the sensor is improved by operating it in the linear region. As such, the sensor is able to amplify any minute changes to the magnetic field due to the flow of pulsatile blood in the uniform magnetic field.

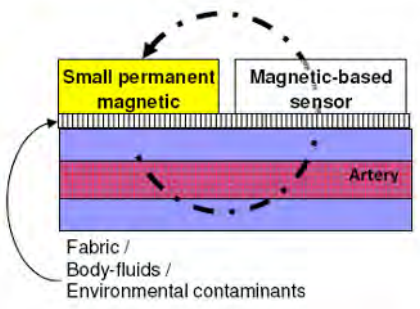


Figure 1. Cross-sectional view of the experimental setup to acquire MMSB

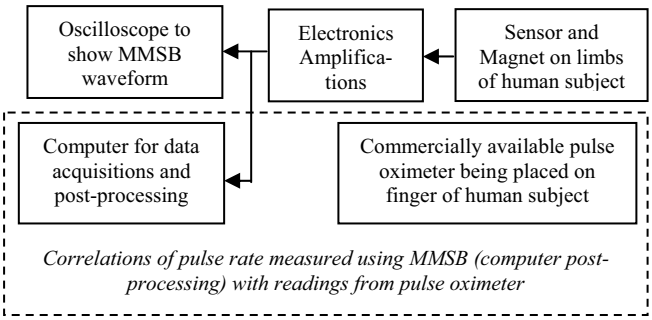


Figure 2. Block diagram of experimental setup to acquire MMSB with correlation of results using commercially available pluse oximeter.

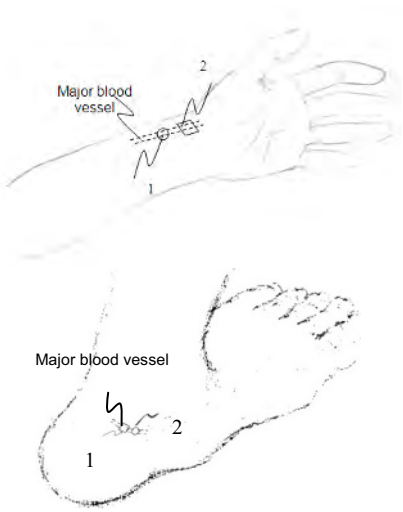


Figure 3. Illustrations of the relative position of the magnet(1), sensor(2) and a major blood vessel

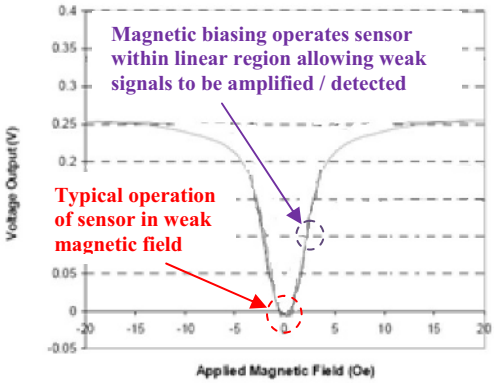


Figure 4. Typical sensor response with illustration of magnetic biasing to increase its sensitivity

III. Results and Discussions

The experimental setup to acquire MMSB on the wrist was done in a laboratory condition where subjects are in a sitting position and their arms are well rested on the table. The magnet is secured on the wrist using a non-magnetic adhesive tape while the sensor is positioned on the artery, near to the magnet. Similar experimental setup to acquire MMSB on the heel was performed on subjects in a sitting position with their heels rested on the floor.

The signal acquired from the sensor on each subject is repeated on at least two separate measurements and found to be repeatable. In addition, these experiments have also been repeated on fifty different subjects and the pulse rates measured are found to be within ±5% of the readings obtained from a pulse oximeter.

A typical waveform acquired from the sensor in this setup is shown in Figure 5 where it can be observed that it is highly periodic and has the pulse width of the subject's heart rate. The waveform obtained is also observed to have high correlations to the MCG reported in [10] as illustrated in Figure 6.

In addition, on the basis of magnetic disturbance of the pulsatile blood flow on a uniform magnetic field, MMSB can also be used to describe the activities of the heart as illustrated in Figure 7. For example, an increase in the measured magnetic disturbance can only be created by an increase in blood flow due to the compression of the heart ventricles. As the ventricles compress to their maximum, the peak of the waveform is reached. Without further force from the heart on the blood flow in the artery, the blood flow rate will reduce as shown in the decreased in amplitude of the waveform. With the relaxation of the ventricles, a back-flow of blood is present in the artery. Finally, the atrium will simultaneously compress, resulting in a small forward flow of blood as shown in the second peak detected in MMSB.

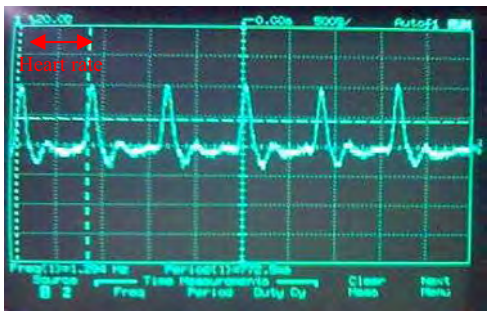


Figure 5. Waveform captured from the sensor output using oscilloscope

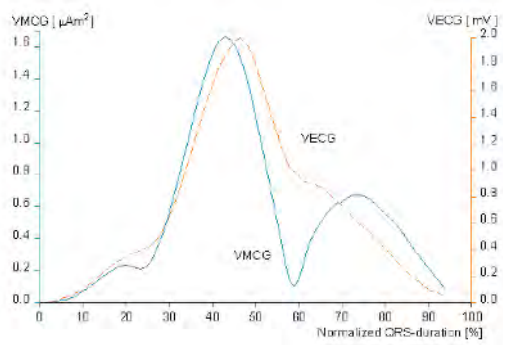


Figure 6. Simultaneous plots of the magnitude curves of the EHV (dashed curve) and the MHV (solid curve) during the QRS complex [10]

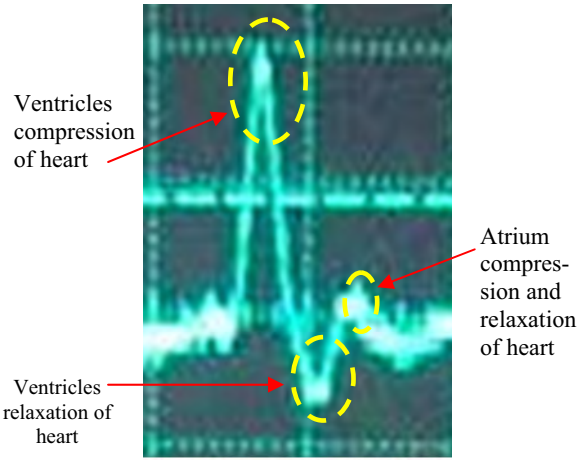


Figure 7. Illustration of MMSB and the activities related to the heart

IV. Conclusions

This experiment demonstrated the concept of magnetic disturbance (MMSB) by the pulsatile blood flowing in a uniform magnetic field. Such magnetic disturbance can be acquired by the use of a button sized permanent magnet and a commercially available magnetic sensor. The waveform obtained is highly correlated to the activities of the heart. It is conclusive that MMSB exists and has the advantage of being contact surface independent which is lacking in existing methods of heart or pulse rate acquisition systems.

Further work will focus on the modelling of the magnetic modulation using blood, to optimise the system sensitivity. This should lead to a reduction in the overall size of the sensing module (i.e. sensor and magnet).

Acknowledgment

The authors would like to thank Nanyang Polytechnic of Singapore for the opportunity to work on this development. In particular, the authors would like to express their gratitude to the School of Engineering (Electronics), Nanyang Polytechnic (Singapore) for the usage of facilities that supported this work.

References

[1] Akinori Ueno, Yasunao Akabane, Tsuyoshi Kato, Hiroshi Hoshino, Sachiyo Kataoka, Yoji Ishiyama (2007) Capacitive Sensing of Electrocardiographic Potential Through Cloth from the Dorsal Surface of the Body in a Supine Position: A Preliminary Study, IEEE Transactions on Biomedical Engineering, Vol. 54, No. 4, April 2007

[2] S. Bowbrick, A. N. Borg. Edinburgh (2006) ECG complete, New York, Churchill Livingstone

[3] S. M. Burns (2006) AACN protocols for practice: noninvasive monitoring, Jones and Bartlett Publishers

[4] Shuhei Yamada, Mingqi Chen, Victor Lubecke (2006) Sub-uW Signal Power Doppler Radar Heart Rate Detection, Proceedings of Asia-Pacific Microwave Conference

[5] G. Amit, N. Gavriely, J. Lessick, N. Intrator (2005) Automatic extraction of physiological features from vibro-acoustic heart signals : correlation with echo-doppler, Computers in Cardiology, Issue September 25-28, pp 299-302

[6] J.L. Jacobs, P. Embree, M. Glei, S. Christensen, P.K. Sullivan (2004) Characterization of a Novel Heart and Respiratory Rate Sensor, Proceedings of the 26th Annual International Conference of the IEEE EMBS

[7] M.N. Ericson, E.L Ibey, G.L. Cote, J.S. Baba, J.B. Dixon (2002) In vivo application of a minimally invasive oximetry based perfusion sensor, Proceedings of the Second Joint EMBS/BMES Conference

[8] Luis Torres-Pereira, Cala Torres-Pereira, Carlos Couto (1997) A Non-invasive Telemetric Heart Rate Monitoring System based on Phonocadiography, ISIE'97

[9] J. Kerola, V. Kontra, R. Sepponen (1996) Non-invasive blood pressure data acquisition employing pulse transit time detection, Engineering in Medicine and Biology Society, Volume 3, Issue 31 Oct-3 Nov, pp 1308 – 1309

[10] J.Malmivuo, R. Plonsey (1995) Bioelectromagnetism – Principles and Applications of Bioelectric and Biomagnetic Fields, New-York, Oxford University Press

[11] Yasuaki Noguchi, Hideyuki Mamune, Suguru sugimoto, Jun Yoshida, Hidenori Sasa, Hisaaki Kobayashi, Mitsunao Kobayashi (1994) Measurement characteristics of the ultrasound heart rate monitor, Engineering in Medicine and Biology Society, Engineering Advances: New Opportunities for Biomedical Engineers. Proceedings of the 16th Annual International Conference of the IEEE Vol. 1, Issue , 3-6 Nov 1994 Page(s):670 - 671

[12] J.R. Singer (1980) Blood Flow Measurements by NMR of the intact body, IEEE Transactions on Nuclear Science, Vol. NS-27, No. 3 June 1980

[13] Hiroshi Kanai, Eiki Yamano, Kiyoshi Nakayama, Naoshige Kawamura, Hiroshi Furuhata (1974) Transcutaneous Blood Flow Measurement by Electromagnetic Induction, IEEE Transaction on Biomedical Engineering, Vol. BME-21, No. 2, Mar 1974

Microfabrication of high-density microelectrode arrays for in vitro applications

Lionel Rousseau[1,2], Gaëlle Lissorgues[1,2], Fabrice Verjus[3], Blaise Yvert[4]

[1]ESIEE, 2 boulevard Blaise Pascal – 93162 Noisy le Grand cedex, France,
[2]ESYCOM, Université Paris-EST, Marne-La-Vallée, France,
[3] NXP Caen, France, [4]CNIC CNRS, Av. des Facultés, F-33402 Talence, France

Abstract — **Micro Electrode Arrays (MEAs) offer an elegant way to probe the neuronal activity distributed over large populations of neurons either in vitro or in vivo. They also give the possibility to deliver specific electrical stimulations to neuronal networks. This paper will present the fabrication of different kinds of 3D electrode arrays based on silicon micromachining: dense 3D arrays with high aspect ratios (up to 1024 probes with a pitch of 50µm and 80µm of height) and 3D probes enabling recording within the depth of the tissues. Stimulation is also possible with these systems, and we have developed a specific MEA to deliver a focal stimulation in the tissue. The 3D-shaped microelectrodes are necessary to achieve better contacts with the neural tissue, the tip of each needle being the recording site. Indeed, we will detail a new technology based on the Deep Reactive Ion etching technique (DRIE) which offers the possibility to manufacture various shapes of electrodes on silicon. Second, alternative geometries with several contacts on each needle will be described, leading to really 3D probes scanning within the depth of the tissues. Such geometry is based on the combination of DRIE and standard etching techniques. Experiments currently performed have shown that both kind of MEAs present a noise level around 10µV, in the same range as available commercial MEAs. In vitro applications will be presented concerning the study of the whole spinal cord of embryonic mousse and we conceived a new configuration to reach a focal stimulation for in vitro and in vivo applications.**

Keywords — **Micro Electrode Arrays, microfabrication, DRIE**

I. Introduction

Although neuroscience has already progressed in the knowledge of the neuronal system with the development of medical imagery (like CT scanner, MRI and nuclear medicine), all those imagery systems only give a global vision of neurons operation. Then Micro Electrode Arrays (MEAs) offer an elegant way to get the recording of large neuronal networks and follow the cellular information, providing a means to record the activity of many cells simultaneously over large networks. Such techniques are using arrays of microelectrodes placed in contact with the neural tissue to probe neuronal electrical activity at several sites simultaneously. In order to be as close to neurons as possible, microelectrodes for in vitro systems are usually shaped as 3D needles, at the tip of which is the recording site.

II. MEA fabrication

A. Standard MEAs

Classically the isotropic etching [1,2], which is a very simple process, is used to etch silicon or glass substrates to fabricate 3D electrodes, Figure 1. Either wet etching (fluorhydric acid, KOH) or dry etching (plasma) is possible.

The major problem of the isotropic etching is due to a large under etch above the protection layer. In isotropic etching, the substrate is etched at the same speed in all directions. The under etch is problematic when you want to fabricate a narrow structure. To obtain a micro needle after isotropic etching we protect the substrate with circular protective layers. Theses circles correspond to the requested diameter of the micro needle.

However, the drawback of such isotropic etching is a dimensioning constraint: the electrode height vs. the electrode pitch. Indeed, the electrode pitch cannot be smaller than twice the electrode height. For example, electrodes with 80 µm of height impose the pitch to be higher than 160 µm. The fabrication of very dense 3D electrode arrays with high aspect ratios is therefore impossible with the standard technique.

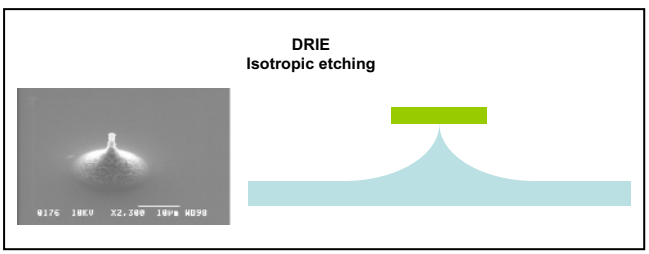


Fig.1. Classical 3D MEAs Process

B. Dense MEAs

The DRIE (Deep Reactive Ion Etching) is an anisotropic etching process and a classical process used to obtain vertical side walls is the Bosch process [3].

Chwee Teck Lim, James C.H. Goh (Eds.): ICBME 2008, Proceedings 23, pp. 790–793, 2009
www.springerlink.com

To get high aspect ratios, a repetitive alternation of etching and insulation steps, see figure 2. This process is composed by two steps performed subsequently: deposition and etching. The sidewall passivation is obtained by teflon-film deposition on the silicon surface and avoids a lateral etching. In plasma etching the ions are oriented vertically to the substrate and etch in priority the bottom of the structures. Consequently the ions firstly etch the teflon-like layer at the bottom before they etch the silicon and leave teflon-like protection on the side walls.

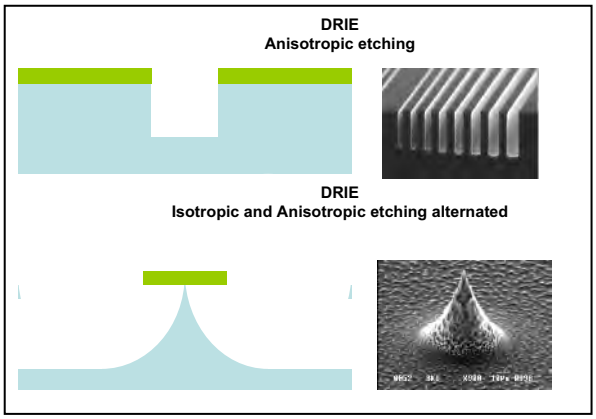
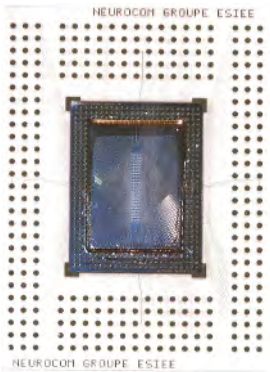


Fig.2. DRIE process adapted to dense MEA fabrication

To prevent the previous limitation of isotropic etching to achieve micro needles, we developed a new technology based on the DRIE technique [4]. We combine anisotropic etching and isotropic etching to give us the opportunity to reduce the diameter of the base micro needle.

a)



b)



Fig.3. An example of a 256 electrode array a) and its position on the whole spinal cord of embryonic mouse b)

We obtained dense MEAs with 64, 256 or 1024 electrodes [5] having a height of 80µm and a pitch of 50 µm, figure 3. This process also offers the possibility to manufacture various shapes of electrodes on silicon, as shown on figure 4.

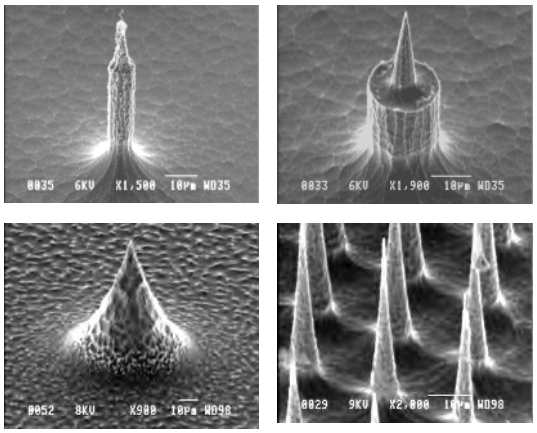


Fig.4. Various shapes of 3D electrodes processed by DRIE

C. 3D needles used in MEAs

The neuronal activity is not distributed on one level but in 3D within the volume of the tissues, i.e. at different depths, as illustrated on figure 5. To achieve a 3D recording, we have fabricated a comb with 4 shafts on which there are 4 electrodes.

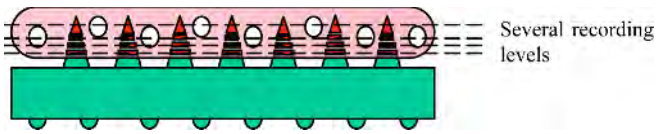
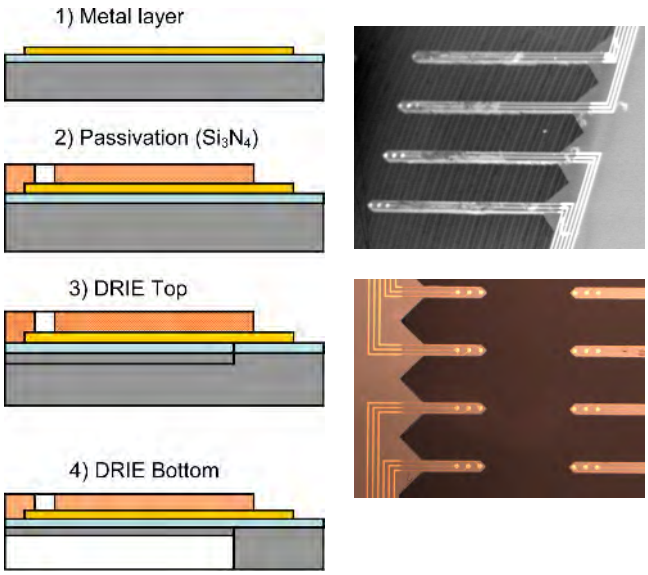


Fig.5. Principle of 3D recording

The fabrication process is again based on DRIE used to release long silicon needles with several recording sites on each, as shown on figure 6 [6].

To manufacture this comb shaft, we started with an oxidation step of a silicon wafer (500 nm). A metallic gold or platinum layer is sputtered to fabricate the micro electrodes. Such noble metal is necessary to prevent degradation of metal in contact with tissues and physiological liquids. A PECVD (Plasma Enhanced Chemical Vapor Depostion) silicon nitride layer is deposited to insulate the leads on the comb shaft from the liquid environment. Top side DRIE is done to define the comb shafts and a second bottom side DRIE to release the structures.



a) process steps b) SEM & top photography

Fig.6. Fabrication process of 3D needles a) and examples of fabricated samples b)

The prototypes are mounted on a PCB support and connected to a specific acquisition system. The first tests have shown that noise level is around 10 µV.

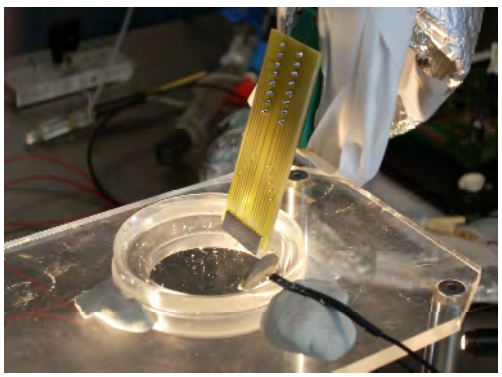


Fig.7. Comb Shaft Mounted on PCB for testing

D. Optimized design for stimulation

Different studies showed that the activation of single neurons may impact the activity of large populations at the networks level [7, 8]. Therefore the precise activation of small groups of neurons is required during stimulation with MEAs. Indeed, each electrode of such array should act as an independent "stimulation pixel", only influencing cells in its close vicinity. Thus an optimized design was elaborated to obtain a more efficient stimulation, which means focal stimulation [9]. The basic idea was to add a ground surface surrounding the electrodes (either a plane or a grid), allowing the whole current delivered by the stimulation electrode to return back directly through this ground surface, figure 8. The induced change in the fabrication technology of the MEA was the addition of one masking level on which a second metallic (Pt) layer is deposited above the passivation layer. The Pt layers can be patterned with a liftoff process. The ground surface was designed as a grid instead of a plane in order to ensure enough transparency of the MEA.

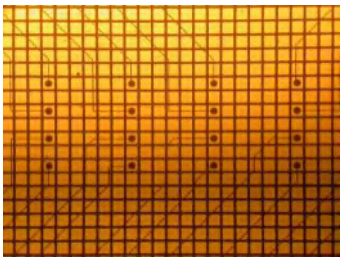


Fig.8. Part of a 4×15 MEA with a grid-like ground surface surrounding all the electrodes

III. In Vitro Measurements

All the presented electrode arrays have been tested by the CNIC laboratory on the whole spinal cord of embryonic mouse, figure 9, and showed performances corresponding to commercially available MEAs. They indeed present a noise level around 10µV.

An example of the improvement obtained during stimulation with the ground surface configuration is illustrated on figure 10.

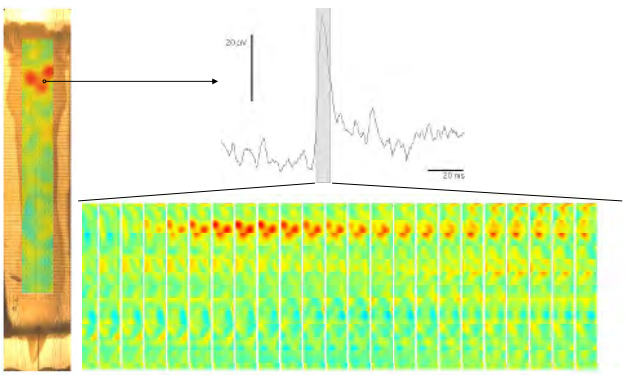


Fig.9. Map of Mouse spinal cord activities (LFP)

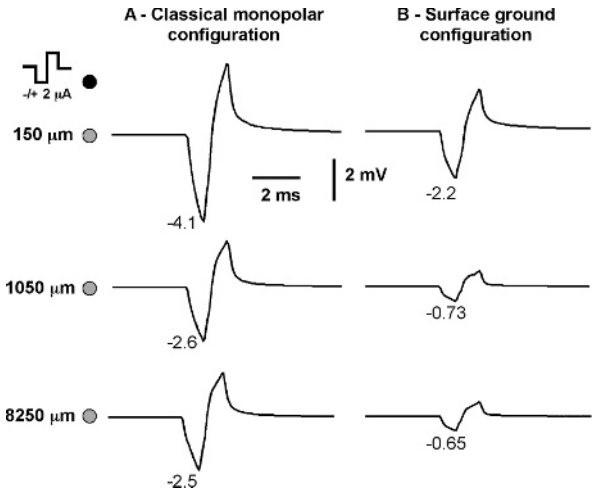


Fig.10. Comparison of field focality between a classical monopolar configuration (A) and the proposed ground surface configuration (B). The potential field is recorded in response to a biphasic stimulation on 3 electrodes located at 3 different distances from the stimulation electrode (150, 1050, and 8250 µm).

IV. Conclusion

In conclusion, we presented the fabrication of different kinds of MEA: very dense 3D microelectrode arrays with high aspect ratios using a specific DRIE process, or real 3D needles to access the volume of the tissues and scan within their depth. We also proposed a new electrode configuration that appears to ensure a good compromise between potential field focality and isotropy, which moreover requires few additional steps in the fabrication process. Such a prototype was micro-fabricated showing that the field focality could be improved.

Acknowledgment

This work was supported by the French Ministry of Technology (Neurocom RMNT project, and MEA3D ANR Blanc). In particular, the authors would like to express their gratitude to SMM-ESIEE for the usage of their clean room facilities.

References

1. Heuschkel MO, Fejtl M, Raggenbass M, Bertrand D, Renaud P, A three-dimensional multi-electrode array for multi-site stimulation and recording in acute brain slices. *J Neurosci Methods* 114, pp.135-148, 2002.
2. N Wilke et al., Fabrication and characterisation of microneedle electrode arrays using wet etch technologies, *Proc. EMN* 2004.
3. F.Laermer and al, Bosch Deep silicon Etching : Improving uniformity and etch rate for advanced MEMS applications, IEEE 1999
4. F.Marty et al., Advanced silicon etching techniques based on deep reactive ion etching for silicon harms and 3D micro- and nanostructures, *Proc. EMN* 2004.
5. L. Rousseau and al, BioMEA : A 256-channel MEA system with integrated electronics, Neurosciences 2006
6. S. Kisban and al, Microprobe Array with Low Impedance Electrodes and Highly Flexible Polyimide Cables for Acute Neural Recording, IEEE EMBS 2007
7. Huber, D., L. Petreanu, N. Ghitani, S. Ranade, T. Hromadka, Z. Mainen, and K. Svoboda, Sparse optical microstimulation in barrel cortex drives learned behaviour in freely moving mice. Nature 451, pp.61-64, 2008.
8. Houweling, A. R. and M. Brecht, Behavioural report of single neuron stimulation in somatosensory cortex. Nature 451, pp.65-68, 2008.
9. Joucla, Rousseau, Yvert. "Matrices microelectrodes". Demande de brevet d'invention français n° 07 07369 du 22 octobre 2007.

Author: Lissorgues Gaëlle
Institute: ESIEE - ESYCOM
Street: BP99 Cité Descartes
City: Noisy-le-Grand 93162
Country: France
Email: g.lissorgues@esiee.fr

A MEMS-based Impedance Pump Based on a Magnetic Diaphragm

C.Y. Lee[1], Z.H. Chen[2], C.Y. Wen[3], L.M. Fu[1], H.T. Chang[3], R.H. Ma[4]

[1]Department of Materials Engineering, National Pingtung University of Science and Technology, Taiwan
[2]Department of Mechanical and Automation Engineering, Da-Yeh University, Taiwan
[3]Department of Aeronautics and Astronautics, National Cheng-Kung University. Taiwan
[4]Department of Mechanical Engineering, R.O.C. Military Academy, Taiwan

Abstract — **In realizing Lab-on-a-Chip systems, micro pumps play an essential role in manipulating small, precise volumes of solution and driving them through the various components of the micro chip. The current study proposes a micro pump comprising four major components, namely a lower glass substrate containing a copper micro coil, a microchannel, an upper glass cover plate, and a PDMS-based magnetic diaphragm. A Co-Ni magnet is electroplated on the PDMS diaphragm with sufficient thickness to produce a magnetic force of the intensity required to achieve the required diaphragm deflection. When a current is passed through the micro coil, an electromagnetic force is established between the coil and the magnet on the diaphragm. The resulting deflection of the PDMS diaphragm creates an acoustic impedance mismatch within the microchannel, which results in a net flow. The performance of the micro pump is characterized experimentally. A deflection of 30 μm is obtained by supplying the micro coil with an input current of 0.6A, and results in a flow rate of 1.5 μl/sec when the PDMS membrane is driven by an actuating frequency of 240 Hz.**

Keywords — **electroplating, impedance pump, magnetic diaphragm, micro coil, micro pump**

I. Introduction

The rapid advances achieved in micro-electro-mechanical systems (MEMS) techniques over the past decade have enabled the development of a wide variety of microfluidic devices for use in the industrial, chemical, biological and medical fields. Typically, these devices are designed to perform specific functions such as sample injection, cell sorting and counting, polymerase chain reaction (PCR), species mixing, and so forth. As the characteristic size of such devices has reduced, researchers have demonstrated the feasibility of integrating two or more micro devices on a single chip to construct so-called micro-total-analysis systems (μ-TAS) capable of performing a complete biochemical assay of solutions. In realizing such systems, micro pumps play an essential role in manipulating small, precise volumes of solution and driving them through the various components of the micro chips.

Broadly speaking, micro pumps can be classified as either mechanical or non-mechanical, depending upon their mode of actuation. Non-mechanical micro pumps are typically actuated using electrohydrodynamic, magnetohydrodynamic or electroosmotic techniques. However, such devices are not fully compatible with many biological systems and suffer a number of practical problems such as electrolytic bubble formation (in the magnetohydrodynamic type) [1] or a solution-dependent flow response (electroosmotic type) [2]. Mechanical micro pumps can be classified as either reciprocating (i.e. diaphragm-based) or peristaltic. Most commercially-available mechanical micro pumps tend to be of the former type since they are generally more easily controlled, more reliable and more effective than their peristaltic counterparts. Furthermore, reciprocating micro pumps resolve many of the problems associated with non-mechanical pumps and are easily integrated with other micro devices to construct large-scale microfluidic networks. Gong *et al.* [3] developed reciprocating micro pumps incorporating a pressure chamber and a system of mechanically-operated inlet and outlet passive check valves. While the results showed that the pump successfully drove fluids, the use of mechanical valves rendered the pump prone to clogging and to leakage at high driving pressures. In an attempt to resolve these problems, researchers have proposed a variety of valveless micro pump schemes based on peristaltic effects [4,5] or the use of reciprocating diaphragms and integrated nozzles/diffusers [6,7]. Some researchers have also presented impedance-based micro pumps comprising an elastic section connected at either end to a rigid body. In such pumps, the elastic section is compressed asymmetrically to create an acoustic impedance mismatch within the microchannel, which prompts a net flow through the pump. Rinderknecht *et al.* [8] proposed a novel valveless, substrate-free impedance-based micro pump driven by an electromagnetic actuating force. The performance of the pump was found to be highly sensitive to the waveform, offset, amplitude and duty cycle of the excitation force. Wen *et al.* [9] presented a planar valveless micro impedance pump in which a PZT actuator was used to drive a thin Ni diaphragm at its resonance frequency of 34.7 kHz. The resulting large-scale displacements of the diaphragm created a significant driving pressure, and yielded a substantial net flow. In their study, the pump was composed of an elastic section con-

Chwee Teck Lim, James C.H. Goh (Eds.): ICBME 2008, Proceedings 23, pp. 794–798, 2009
www.springerlink.com

nected at the ends to rigid sections and a mismatch in acoustic impedance was used to drive fluid flow. By independently compressing the elastic section periodically with the PZT actuator at one asymmetric position from the ends, traveling waves emitted from the compression combined with reflected waves at the impedance-mismatched positions and generated a typically pulsatile flow. It was also found that a flow reversal happened in some range of actuating frequency. However, the device required a high actuating voltage and therefore consumed an excessive power.

Reviewing the literature, it is found that many alterative actuation mechanisms have been proposed for micro pumps, including piezoelectric [9], thermopneumatic [10], electrostatic [11], electromagnetic [12] and others [13]. Of these various methods, electromagnetic actuation has a number of major advantages, including an extended working range, a rapid response time and a low actuating voltage. These characteristics render electromagnetic actuation an appealing choice for applications in which large diaphragm deflections and a straightforward structural integration is required. Among them, Lee *et al.* [12] developed a micro pump comprising a micro coil and a permanent magnet mounted on a PDMS diaphragm. When a current was passed through the micro coil, an electromagnetic force is established between the coil and the magnet. The resulting deflection of the PDMS diaphragm created an acoustic impedance mismatch within the microchannel, which resulted in a net flow.

Accordingly, the current study develops an impedance-based micro pump utilizing an electromagnetic actuation technique. The major components of the device include a lower glass substrate containing an electroplated planar copper micro coil, a glass microchannel, a glass cover plate and a PDMS diaphragm with a magnet diaphragm electroplated on its upper surface. In the pumping operation, fluid is driven through the pump by applying a current to the micro coil such that an electromagnetic force is established between the coil and the magnet causing a resulting deflection of the PDMS diaphragm. The performance of the pump is evaluated experimentally. It is shown that the maximum diaphragm deflection is approximately 30 μm and is attained using an actuating current of 0.6 A. Under these operating conditions, a flow rate of 1.5 μl/sec can be achieved by driving the diaphragm at a frequency of 240 Hz.

II. Design

As shown in Fig. 1, the micro pump comprises four basic layers, namely a lower glass substrate containing a planar micro coil, a microfluidic channel, a glass cover plate, and a PDMS diaphragm with a magnet electroplated on its upper surface. The pump body has overall dimensions of 26 mm × 15 mm × 2.5 mm (length × width × height), while the microchannel measures 11.35 mm × 4 mm × 50 μm (length × width × height). The flow rate of the impedance pump is determined by the volume change induced in the microchannel each time the diaphragm deflects and the frequency at which the diaphragm is actuated [9]. Therefore, in theory, the flow rate can be enhanced by increasing the stroke volume of the diaphragm (i.e. increasing its displacement) or increasing the excitation frequency.

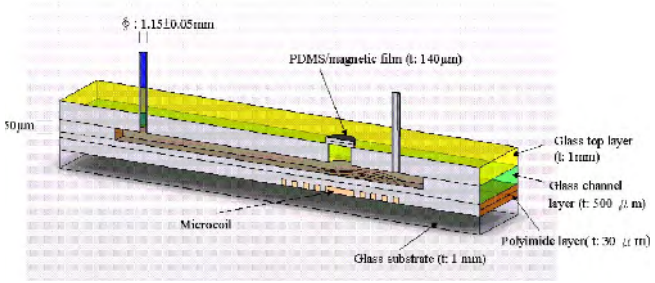


Fig. 1 Schematic illustrations of valveless micro impedance pump

III. Fabication

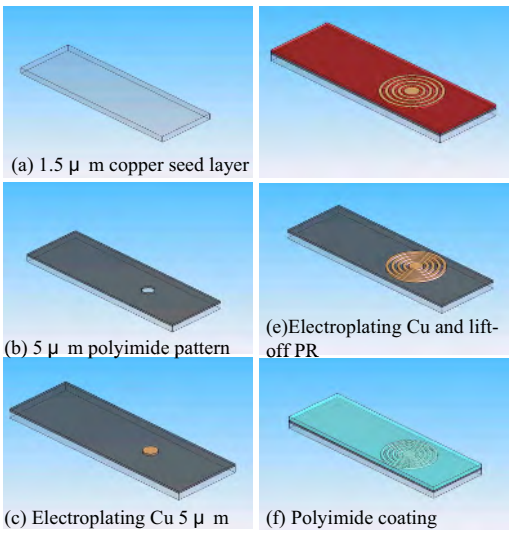


Fig. 2 Major steps in micro coil fabrication process.

The micro pump developed in this study was fabricated using photolithography, vacuum evaporation, electroplating and wet etching microfabrication techniques. The fabrication process involved the following basic procedures: (1) electroplating the micro coil on the lower glass substrate (Fig. 2), (2) etching the microchannel configuration into a second glass substrate, (3) bonding the lower glass substrate

and the etched substrate, (4) fabricating the PDMS diaphragm, (5) electroplating the magnet of Co-Ni alloy on the PDMS diaphragm, (6) attaching the PDMS diaphragm to an upper glass substrate, and (7) bonding the upper and lower substrate layers to form a sealed microchannel (Fig. 3).

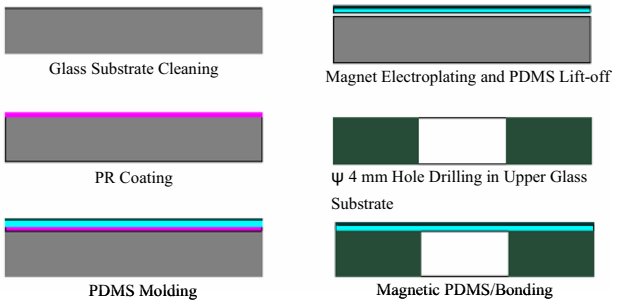


Fig. 3 Major steps in upper plate fabrication process.

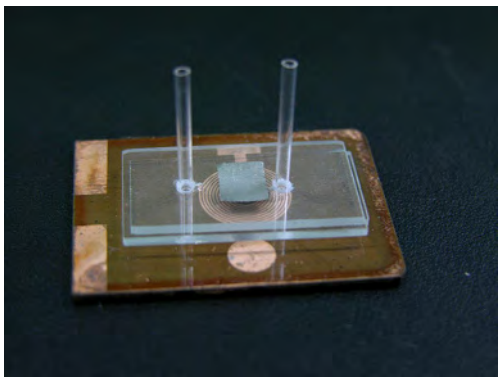


Fig. 4 Photograph of completed micro pump.

IV. Results and Discussion

The flux density characteristics of the micro coil were measured using a Tesla meter (TM-401, KANETEC, Japan). In the characterization tests, the coil was supplied with an input current of 0.2, 0.4 and 0.6 A, respectively, and the variation of the flux density was measured in the vertical direction along the central axis. The experimental results are presented in Fig. 5. Figure 6 presents the experimental results for the rate of change in the magnetic flux density along the vertical centerline of the micro coil. As discussed previously, to optimize the performance of the electromagnetic actuator, the magnet should be positioned at a height corresponding to the maximum rate of change of the magnetic flux. From an inspection of Fig. 6, it is found that the magnet should therefore be positioned 500 μm above the micro coil.

The displacement characteristics of the diaphragm were evaluated experimentally using a laser displacement meter (LC-2400A + 2430, Keyence, Japan) powered by a PR8323 power supply (ABM, Taiwan). The displacement was measured at the central area of the diaphragm, i.e. the position of maximum deflection, at micro coil currents in the range 0.1-0.5 A. The experimental results for the variation of the diaphragm displacement with the input current are presented in Fig. 7.

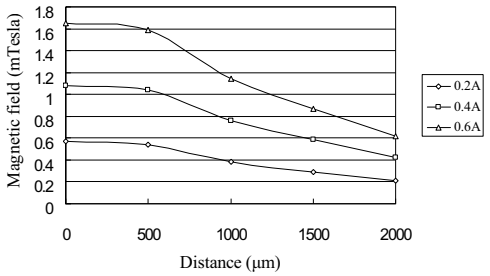


Fig. 5 Experimental results for flux density produced by micro coil.

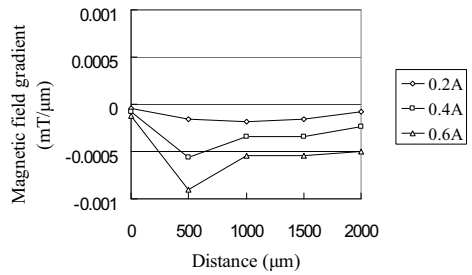


Fig. 6 Experimental results for rate of change of flux density with vertical distance from micro coil

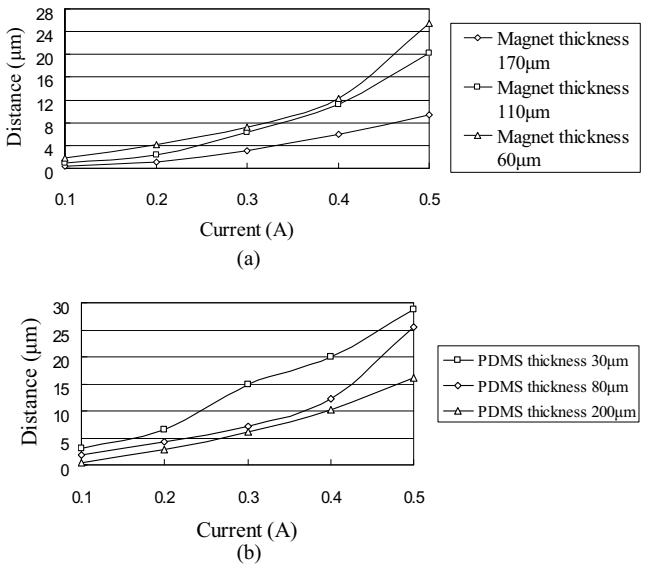


Fig. 7 Experimental results for maximum diaphragm deflection for input current ranging from 0.1 A to 0.5 A. at (a) different magnet diaphragm thicknesses and (b) different PDMS diaphragm thicknesses.

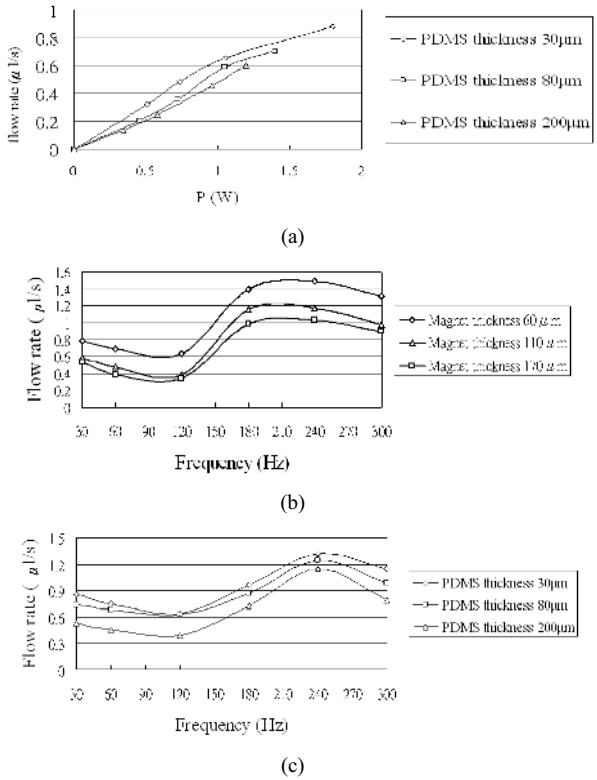


Fig. 8 Experimental results for flow rate given (a) input power ranging from 0 W to 1.8 W at different PDMS thicknesses, (b) actuation frequency raging from 30 Hz to 300 Hz at different magnet diaphragm thicknesses and (c) the same frequency range at different PDMS diaphragm thickensses.

The flow rate characteristics of the micro pump were evaluated by monitoring the difference in the levels of two water columns contained within capillary tubes connected to the inlet and outlet sides of the pump, respectively (see Fig. 4). Figure 8(a) illustrates the variation in the flow rate with different input powers. The results indicate that the flow rate increases linearly with an increasing input power on the coil. From inspection, the maximum operational flow rate (i.e. the flow rate at a coil power of 1.8 W) is found to be around 0.9 μl/s as the PDMS diaphragm thickness is 30 μm and the actuation frequency is 30 Hz. Maintaining a constant coil current of 0.6 A, the flow rate was evaluated for excitation frequencies ranging from 30~300 Hz at different magnet diaphragm and PDMS diaphragm thicknesses. The corresponding results are presented in Fig. 8(b) and (c), and indicate that the maximum flow rate is obtained at a frequency of 240 Hz.

V. Conclusions

This study has designed and fabricated a novel micro valveless impedance pump. The experimental results have shown that the actuator mechanism, comprising a micro coil, a PDMS diaphragm and an electroplated magnet, provides a large diaphragm deflection and a low power consumption. The micro pump is fabricated using MEMS techniques, has a planar structure and can therefore be readily integrated with other microfluidic devices to create a Lab-on-a-Chip device. It has been shown that the maximum diaphragm deflection is approximately 30 μm and is attained using an actuating current of 0.6 A. The corresponding flow rate is found to be 1.5 μl/sec at an actuating frequency of 240 Hz. Overall, the experimental results indicate that the micro pump presented in this study represents an ideal solution for microfluidic systems in which miniaturized pumps are required.

Acknowledgment

The authors would like to thank the financial support provided by the National Science Council in Taiwan (NSC 97-2221-E-020-03, NSC 97-2218-E-006-012 and NSC 96-2218-E-006-004).

References

1. Jang J and Lee S S (2000) Theoretical and experimental study of MHD (magnetohydrodynamic) micropump, Sensors Actuators A 80, pp. 84–89.
2. Brechtel R *et al.* (1995) Control of the electroosmotic flow by metal-salt-containing buffers, J. Chromatogr. A 716, pp. 97–105.
3. Gong Q L *et al.* (2000) Design, optimization and simulation on microelectromagnetic pump, Sensors and Actuators A 83, pp. 200-207.
4. Berg J M *et al.* (2003) A two-stage discrete peristaltic micropump, Sensors and Actuators A 104, pp. 6-10.
5. Husband B *et al.* (2004) Investigation for the operation of an integrated peristaltic micropump, Journal of Micromechanics and Microengineering 14, pp. S64-S69.
6. Olsson A *et al.* (1996) A valve-less planar pump isotropically etched in silicon, Journal of Micromechanics and Microengineering 6, pp. 87-91.
7. Andersson H *et al.* (2001) A valve-less diffuser micropump for microfuidic analytical systems, Sensors and Actuators B 72, pp. 259-265.
8. Rinderknecht D *et al.* (2005) A valveless micro impedance pump driven by electromagnetic actuation, Journal of Micromechanics and Microengineering 15, pp. 861-866.
9. Wen C Y *et al.* (2006) A valveless micro impedance pump driven by PZT actuation, Materials Science Forum 505-507, pp. 127-132.
10. Cooney C G, Towe B C (2004) A thermopneumatic dispensing micropump, Sensors and Actuators A 116, pp. 519–524.

11. Teymoori M M, Abbaspour-Sani E (2005) Design and simulation of a novel electrostatic peristaltic micromachined pump for drug delivery applications, Sensors and Actuators A 117, pp.222-229.
12. Lee C Y et al. (2008) A planar valveless micro impedance pump for micro-fluidic systems, Journal of Micromechanics and Microengineering 18, pp. 1-9.
13. Makino E. et al. (2001) Fabrication of TiNi shape memory micropump, Sens. Actuators A 88, pp. 256–262.

[corresponding author]
Author: Prof. Chia-Yen Lee
Institute: National Pingtung University of Science and Technology
Street: No.1, Shuehfu Rd.
City: Neipu, Pingtung
Country: Taiwan
Email: leecy@mail.npust.edu.tw

Sample Concentration and Auto-location With Radiate Microstructure Chip for Peptide Analysis by MALDI-MS

Shun-Yuan Chen, Chih-Sheng Yu, Jun-Sheng Wang, Chih-Cheng Huang, Yi-Chiuen Hu

[1] Instrument Technology Research Center, National Applied Research Laboratories, Taiwan

Abstract — **A new micro-scale radiate chip was demostrated for matrix assisted laser desoption/ionization mass (MALDI-MS) sample concentration and auto-location. While mass spectrometry is nowadays an important tool for analyzing and characterizing large biomolecules of varying complexity, sample preparation has become a key point within the whole experiment, and sample concentration is a most often used procedure to improve MALDI sensitivity. Here we demonstrated another simple method in concentrating samples for MALDI mass spectrometry analysis by using a micro-scale structure chip. Samples applied around the chip could auto-located to the center and deposited on the central zone after air dried. It showed that all the samples applied on the chip were concentrated and confined precisely to the central zone, even up to 30 micro liters. Sample spots formed on our chip were much smaller than those on an unmodified plate with the same total volume. With standard MALDI/MS sample preparation procedure, we found that matrix samples were precisely concentrated in our chip and significant enhanced results were obtained by MALDI/MS.**

Keywords — **MALDI, mass spectrometry, concentrate, chip, auto-location.**

I. Introduction

While mass spectrometry is nowadays an important tool for analyzing and characterizing large biomolecules of varying complexity, sample preparation has become a key point within the whole experiment. Sample concentration is the most often used procedure to improve the sensitivity of matrix assisted laser desorption/ionization mass (MALDI/MS). Different kinds of methods have been reported and used, like nano-material added, plate surface modified, hydrophobic surface deposition, and so on. Different kinds of functional plates were made by using the concepts of nanotechnologies with unreveal materials that could precisely control the deposition of sample on the surface. The dried spots would be precisely restricted within the less than 300um diameter central zone after vacuum sublimation. With appropriate modification on the surface, the plate could even isolate and purify specific proteins.

Another continuing challenge in MALDI MS is the spread of matrix and sample cocrystalline structures required for effective ionization. Typically, in MALDI MS, the analyte is distributed unevenly throughout the sample spot, or "sweet spot". To search for these sweet spots is time consuming for high-throughput or automated processes. Hence, the ability to concentrate and localize samples is advantageous, especially for low concentration of analyte.

Different methods, like chemical treatment and nanotechnology have been developed to change the surface hydrophobic characters. Although these methods may have good performance, but the processes of manufacture are minute and complicate. Here we demonstrated a new method for peptide sample preparation. Micro-scale radiate chip was manufactured by photolithography process, and could apply directly to the MALDI/MS. Added sample could auto-located to the center of the chips and deposited on the central zone after dried. After analysis by mass spectrometer, the results showed that our chip really had better performance in sample concentration and deposition than conventional MALDI/MS plate.

II. Materials and methods

A. Reagents and Materials

All test materials were reagent grade or better. A-cyano-4-hytdroxycinnamic acid (CHCA) matrix was purchased from Waters Corporation. Acetonitrile (ACN), ethanol, 0.1% trifluoroacetic acid, ammonium citrate, and human albumin were purchased from Sigma-Aldrich. The peptides adrenocorticotropic hormone (ACTH) fragment were used as reference standard and purchased from Bruker Corporation, ACTH (18-39)_[M+H]+_mono with a molecular weight of 2465.199 Da and ACTH(7-38)_mono with 3657.929 Da.

B. Methods

Sample preparation

CHCA matrix working solution was prepared as followed. 5 mg/ml CHCA was dissolved in the solution of 90:10 acetonitrile : 0.1%TFA. Peptides were dissolved in distilled water to a final concentration of 1 mg/ml. Human albumin was dissolved to 5mg/ml solution before use.

Chwee Teck Lim, James C.H. Goh (Eds.): ICBME 2008, Proceedings 23, pp. 799–801, 2009
www.springerlink.com

Micro-scale chip fabrication

The radiate microstructure chip was manufactured by photolithography process, and was deposited with C4F8 in Plasma-thermo Parallel Plate Plasma Etcher. Finally, chips was adhered to the stage of the ABI Vayager mass spectrometer.

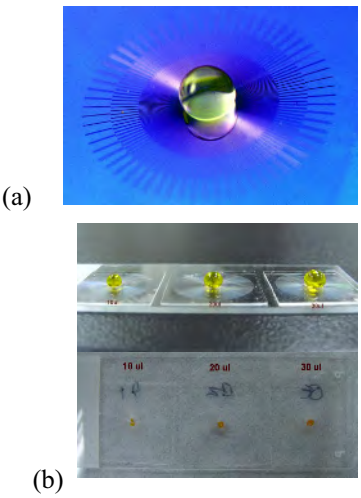
The MALDI/MS experimental process

First, we applied 1 micro litter peptide sample on the plate or chip, and added another 1 micro litter matrix solution immediately without mixing. The mixture solution was dried down in ambient conditions for about few minutes. Finally, the analyte/matrix mixture had been analysis by the mass spectrometer. The time is a function of an ion's mass-to-charge (m/z) ration, enabling an ion's mass to be derived from its TOF.

III. Results

Radiate Microstructure Chip

The chip manufactured by photolithography was illustrated as figure 1. All lines were radiates from the central circle zone which has different diameter. After applied appropriate volume of samples around the chip, the sample droplet would run into the center without any external force and deposited on the central zone. Here we demonstrated 5 mg/ml albumin as sample, and separately added 10, 20, 30 microliter to each chip. The sample droplets were confined to the central zone by the radiated lines. After about four hours, all samples were dried and concentrated into the central zone.



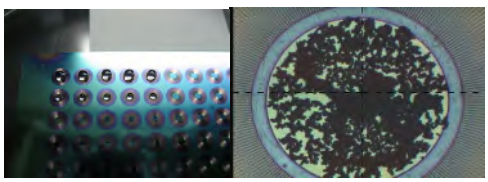
(a)

(b)

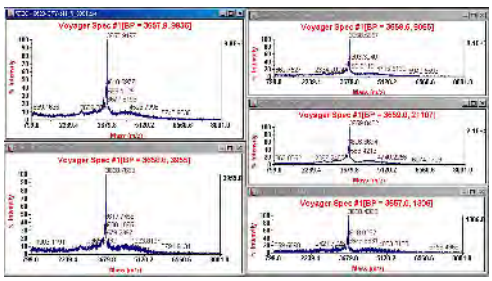
Fig. 1 The appearance of the radiate microstructure chip which applied (a)10 µl H_2O on silicon substrate, (b) 10 µl, 20 µl, 30 µl human albumin (from left to right) on PDMS substrate.

Cocrystalline on the central zone

In order to analyze by the mass spectrometer, sample mixed with organic matrix needed to apply to the stainless plate for electricity conduction. For this reason, we used the silicon chip as substrate. After applied 2 microliter peptide/matrix mixed sample on the chip, cocrystalline was formed in a short time and concentrated on the central zone. Figure 2a showed that peptide/matrix mixed droplet applied on the silicon chip and the observation of cocrystalline from the microscopy. After cocrystalline was formed, chips were analyzed by ABI voyager MALDI/MS. Figure 2b are the peptide mass maps from 1 pmole ACTH with different central zone size. Each zone size all has a significant signal from MALDI/MS.



(a)



(b)

Fig. 2 (a) The appearance of radiate microstructure chip used for MALDI and the peptide/matrix cocrystalline observed by optical microscopy. (b) The peptide mass map of ACTH(7-38)_mono (3657 Da) based on the radiate microstructure chip.

Matrix optimization

In order to find out the optimum condition in our chip, different concentrations of CHCA in matrix were used. We applied 1ul of 1mg/ml ACTH on the chip, and then added another 1ul of matrix immediately. Figure 3 showed the ACTH peptide mass map separately with 10mg/ml, 2mg/ml, 1mg/ml, 0.5mg/ml, 0.1mg/ml CHCA as matrix. It looks that even with low concentration of matrix, the signal from MADLI/MS was still significantly.

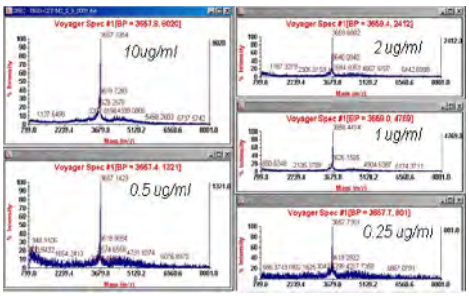


Fig.3 The effects of different CHCA concentration on ACTH peptide mass analysis.

Sample Concentrate on Microstructure Chip

To verify the effect of concentrate on our chip, the original ABI stainless sample plate was used as the control. We used different concentration of ACTH as sample, which was applied separately to the ABI plate and on our chip. Then added equal volume of matrix immediately and waited till dried. All experimental conditions, like laser pulse intensity, were the same. After collected from mass spectrometer, the data were showed as figure 4. It looks that the sensitivity and signal intensity have remarkable performance on our chip than original stainless plate.

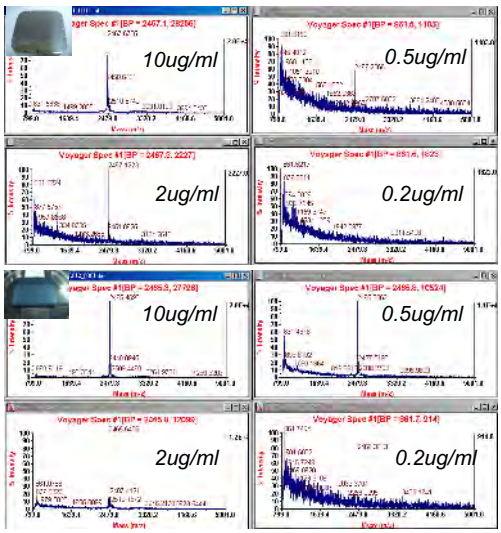


Fig.4 The comparison of ACTH peptide mass maps between conventional mass stage (upper) and radiate microstructure chip (below).

IV. CONCLUSIONS

Silicon-based substrate used for the MALDI/MS has been reported by A. Kraj et al. They developed porous silicon to improve the sensitivity of low molecular weight sample. Here we demonstrated the on-chip concentration with our chip. The radiate silicon chip could concentrate and auto-deposit sample, and used for MALDI/MS is just one of our applications. The results from our experiments showed that to use the microstructure silicon chip as the substrate for mass spectrometer was a feasible way. With appropriate design for the radiate lines, sample/matrix would centralize and cocrystallize to the central zone of our chip. And analyzed by the mass spectrometer, the sensitivity and intensity of our chip showed better than original stainless plate.

The sensitivity and speed of MALDI-MS analysis have led to its being used for the majority of protein and oligonucleotide analysis in high-throughput proteomics and genomics projects. Our chip provides a novel direction to concentration and deposition in MALDI/MS sample preparation, and make the automated process to be more feasible.

ACKNOWLEDGMENT

The authors thank M.C. Tseng (Institute of Chemistry, Academia Sinica, TW) for her technical supported.

REFERENCES

1. Rebekah LG, Edward R, Kole TP et al (2005) Disposable hydrophobic surface on MALDI targets for enhancing MS and MS/MS data of peptides. Anal Chem 77:6609-6617.
2. Lee J, Mysuimi HK, Soper SA et al (2008) Development of an automated digestion and droplet deposition microfluidic chip for MALDI-TOF MS, J Am Soc Mass Spectrom.
3. Juri R, Marc M, Michael LN et al (2003) Experiences and perspectives of MALDI MS and MS/MS in proteomic research. Int J Mass Spectrom 226:223-237.
4. Benito C, Daniel LF, Antonio RF et al (2006) Mass spectrometry technologies for proteomics, Brie Func Geno Proteomics 4:4:295-320.

Author: Shun-Yuan Chen
Institute: Instrument Technology Research Center, National Applied Research Laboratories
Street: R&D Rd. VI
City: Hsinchu
Country: Taiwan
Email: jcchen@itrc.org.tw

The Synthesis of Iron Oxide Nanoparticles via Seed-Mediated Process and its Cytotoxicity Studies

J.-H. Huang[1], H.J. Parab[1,4], R.S. Liu[1,*], T.-C. Lai[2], M. Hsiao[2], C.H. Chen[2], D.-P. Tsai[3] and Y.-K. Hwu[4]

[1] Department of Chemistry, National Taiwan University, Taipei 106, Taiwan
[2] The Genomics Research Center, Academia Sinica, Taipei 115, Taiwan
[3] Department of Physics, National Taiwan University, Taipei 106, Taiwan
[4] Institute of Physics, Academia Sinica Taipei 115, Taiwan

Abstract — **The development of a seed-mediated growth method for synthesis of iron oxide nanoparticles with tunable size distribution and magnetic properties is reported. The detailed investigation of the size distribution of seed as well as iron oxide nanoparticles during the growth process has been carried out using transmission electron microscopy (TEM). It was observed that the distribution of size gradually becomes narrow with time via the intra-particle ripening process and Oswald ripening process. The monodispersed iron oxide nanoparticles with sizes between 5 - 10 nm were fabricated using this method by varying the experimental parameters. The magnetic nanoparticles showed well-defined superparamagnetic and blocking temperature due to the size effects in consistent with the TEM images. The thermogravimetric analyses exhibited the size-dependent weight loss of the magnetic nanoparticles. The in vitro cytotoxicity tests were also performed in order to determine the cell viability as a function of size and concentration of the magnetic nanoparticles. The as-prepared iron oxide nanoparticles showed biocompatibility and nontoxicity against the normal as well as cancerous cell lines.**

Keywords — **magnetite, Fe_3O_4, nanoparticles, cytotoxicity and biomaterial**

I. Introduction

The magnetic nanoparticles have been researched extensively for magnetic resonance image, drug targeting, magnetic separation and catalytic applications. [1-3] The size effect of particles have the influence on their electrical, magnetic and chemical properties. Hence, it is really important to obtain monodispersity-distribution size during the fabrication of the nanoparticles to increase the sensitivity of these particles for the various applications such as cell image. Generally, the synthesis of magnetic nanoparticles, using methods such as chemical coprecipitation [4] and hydrothermal treatment [5-7], produces broad size distribution of particles. Hence, the development of novel methods have been the focus of recent research to fabricate uniform and highly monodispersed nanocrystals by thermal decomposition method.

Herein, we report the development of a seed-mediated growth method for the synthesis of iron oxide nanoparticles with tunable size distribution and magnetic properties. A simple method has been illustrated to fabricate the monodispersed iron oxide nanoparticles from 5 to 10 nm with varying the experimental parameters. It was observed that the seed-mediated growth method for iron oxide nanoparticles is advantageous since it is a non-injection or heating-up method with easily controllable growth process. The iron oxide nanoparticles were characterized by X-ray diffraction (XRD) and thermogravimetric analysis (TGA). The synthesis of iron oxide nanoparticles was found to be reproducible with the tunable properties. The *in vitro* cell viability analysis were also performed for these iron oxide nanoparticles in order to determine their cytotoxic effects.

II. Materials and methods

A. Experimental section

Synthesis of iron oxide nanoparticle seeds. The seeds were prepared by following a procedure reported in literature. [8] Briefly, The mixture of the $Fe(acac)_3$ (2 mmol), oleic acid (6 mmol), oleylamine (6 mmol), 1,2-tetradecanediol (10 mmol) and 20 mL of phenyl ether were magnetically stirred in a three-net-round flask under nitrogen atmosphere. The mixture was slowly heated at 265 °C to reflux for 30 min, then followed by cooling under room temperature. The iron oxide nanoparticles were washed using ethanol and collected in solid form after centrifugation at 9000 rpm. The product was further washed several times by hexane to remove the residual solvent. Finally, 5.4 nm iron oxide nanoparticles were obtained after drying in the oven, which were redispersed into hexane. The different size iron oxide nanoparticles in growth solution was synthesized. The synthesis of iron oxide nanoparticles of different sizes involved an initial formation of iron oxide nanoparticles as seeds and subsequent growth of the particles in the presence seeds at high temperature. The concentration of growth solutions prepared by adjusting the concentration of

Chwee Teck Lim, James C.H. Goh (Eds.): ICBME 2008, Proceedings 23, pp. 802–805, 2009
www.springerlink.com

$Fe(acac)_3$ and phenyl ether/ benzyl ether were 0.028, 0.056, 0.084, 0.112 M. The mixture of 0.08 g seeds and 20 mL growth solution in the presence of 1,2-tetradecanediol, oleic acid and oleylamine was heated to 265 °C at a rate of 4 °C/min under nitrogen atmosphere and then was kept at this temperature for 30 to 90 min for complete growth of nanoparticles. After the growth of the nanoparticles, the reaction mixture was cooled down to room temperature followed by the addition of ethanol. The brown precipitate thus formed was redispersed into hexane.

B. Cytotoxicity assay

Considering the increasing applications of the magnetic nanoparticles in the biomedical fields, the in vitro cell viability studies were performed in presence of the magnetite nanoparticles synthesized by the above method. The normal breast epithelial cell (H184B5F5/M10) and the three type of breast cancer cells (SKBR3, MB157 and T47D) were used for cytotoxicity tests. These cells (2000 cells per 90 μL) with 10 μL of different concentrations of nanoparticles (in 0.l, 1, 10, 100 μg/mL) were seeded into different wells and were incubated for 72 h followed by the addition of 20 mL of MTS (3 - (4,5-dimethylthiazol-2-yl) -5 - (3-carboxymeth oxyphenyl) -2-(4-sulfophenyl)- 2 H- tetrazolium, inner salt) in each well. The optical density (OD) of the resultant solutions were determined (λ= 490 nm) by using microplate absorbance reader (SpectraMAX 340pc, Molecular Devices, CA).

III. Results and Discussion

Figure 1 shows the standard deviation (σ) of nanoparticles size distribution after refluxing for different time scales. In the beginning, the σ value increases with increasing refluxing time owing to the result of size difference between the small nuclei and the growth particles. The maximum value has been observed between 30 and 60 min and then it begins to drop and deviates from the original trend. As a result the amount of small particles decreases and the distribution of particle size start to focus. The rapidly decreasing σ value in high concentration solution shows the small particles dissolves easily due to the relatively large critical radius. By controlling the reaction time and various concentrations of growth solution, it was possible to produce monodispersed nanoparticles with particle sizes of 6.8, 7.6, 8.2 and 8.3 nm. The TEM images of the particles along with the seed are shown in Figure 2. The figure 2 (F) is the table of calculated average size of the particles by using corresponding TEM images of the samples.

Figure 3 shows the concentration-dependent seed growth after reacting for 90 min in different solvents such as benzyl ether and phenyl ether. The boiling temperature of benzyl ether is higher than that of phenyl ether, so the system in benzyl ether product the high temperature condition than in phenyl ether. It was observed that the size of as prepared seeds in benzyl ether is larger than in phenyl ether, because the amount of monomers induced by thermal energy increases with temperature. The growth curve finally reached the saturation value due to the high concentration of solvents. The maximum value was observed at around 8.2 and 10.2 nm for phenyl ether and benzyl ether, respectively. Although the higher concentration causes faster seed growth, some part of monomers also form small particles and grow over the level of critical radius to compete with as-prepared seeds. Hence, the final particle concentration is contributed partial from primary nucleation of the particles, so that the particle size is limited. Thus, by tuning the parameters such as temperature and concentration, the series of monodis-

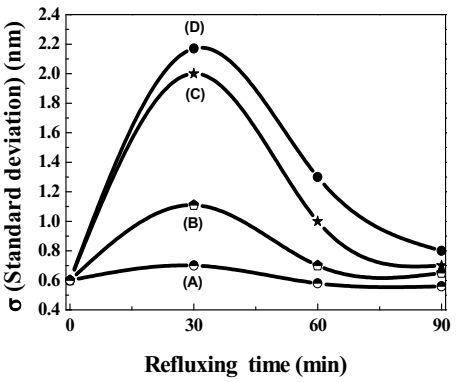


Fig. 1 Standard deviation in size distribution in (A) 0.028 M, (B) 0.056 M, (C) 0.084 M and (D) 0.112 M growth solution.

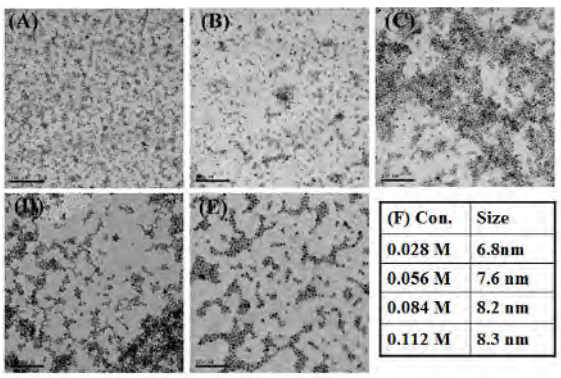


Fig. 2 TEM images of seed solution (A) and iron oxide nanoparticles after growth in different concentrations of growth solution such as (B) 0.028 M, (C) 0.056 M, (D) 0.084 M, (E) 0.112 M and (F) Final particle size of iron oxide nanoparticles in different concentrations of growth solution.

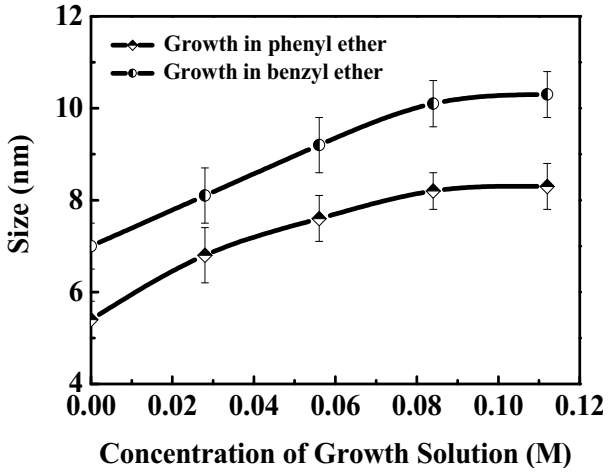


Fig. 3 The concentration-dependent seed growth in phenyl ether and benzyl ether.

persed nanoparticles in the range of 5.4 to 10.2 nm are synthesized successfully.

Figure 4 shows the XRD patterns of iron oxide nanocrystals of 5.4, 6.8, 7.6, 8.2 nm and the standard Fe_3O_4 and αFe_2O_3. The peak positions and relative intensities of nanoparticles agree well with XRD patterns of standard Fe3O4, which confirms the well-known inverse spinel structure of the magnetite materials. The average size of the iron oxide nanoparticles are deduced from Sherrer's equation as shown in Table 1, which is consistent with the result obtained from the transmission electron microscopy (TEM) analysis.

The weight loss in TG analysis for 5.4, 6.8 and 7.6 nm iron oxide nanoparticles are shown in Figure 5. The TGA curve displays a weight loss from room temperature to 250°C and a sudden drop between 250 ~ 350°C and 550 ~

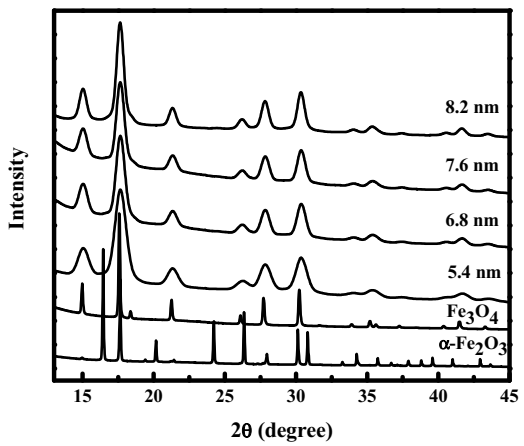


Fig. 4 XRD patterns of iron oxide nanocrystals of 5.4, 6.8, 7.6, 8.2 nm sizes and the Fe_3O_4 and α-Fe_2O_3 standard.

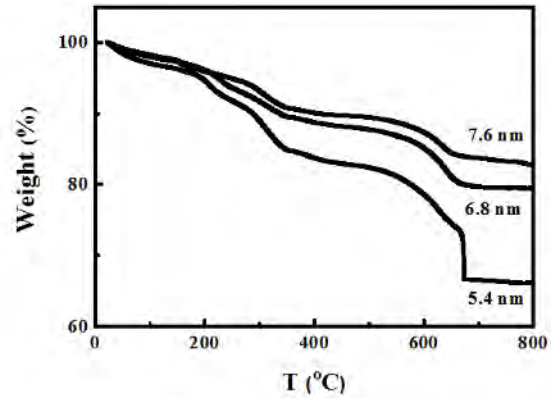


Fig. 5 TG analysis for 5.4, 6.8 and 7.6 nm iron oxide nanoparticles

650°C, respectively. The weight loss in the low temperature region results from the evaporation of free oleic acid and the solvent, phenyl ether. However, the weight loss at relative high temperatures can be attributed to the decomposition of oleic acid bound tightly to the surface of nanoparticles. These results suggest the two dissociation regions of oleic acid, owing to the two kinds of interactions between iron oxide nanoparticles and oleic acid. The decomposition at higher temperatures can be attributed to the chemical bonding between Fe^{2+}/Fe^{3+} and carbonyl group of ligand. Since the smaller nanoparticles provide more binding sites on the surface for surfactant than larger ones, the amount of weight loss is related to the particle size due to higher surface area to volume ratio of nanoparticles. Thus TG analyses offer the important quantitative analysis for different particle sizes of magnetic nanoparticles.

For the biomedical applications of iron oxide nanoparticles such as magnetic resonance imaging, it is necessary to modify the hydrophilic ligand on the nanoparticles surface to promote the suspension of nanoparticles in aqueous media. In the present studies, we have modified the nanoparticles surface by replacing the oleate species using the tetramethyl- ammonium 11-aminoundecanoate ligand to promote hydrophilicity. [8] The carboxylate group of the

Table 1 Comparison of particle size of iron oxide nanoparticles using TEM and XRD analysis

Concentration of growth solution (M)	Particle Size (nm)	
	TEM Analysis	XRD Analysis
Seed	5.4	5.1
0.028	6.8	6.5
0.058	7.6	7.2
0.084	8.2	7.9

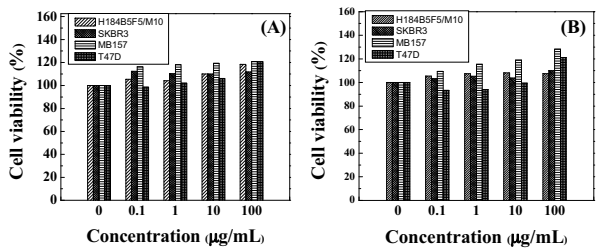


Fig. 6 The cytotoxicity tests for breast epithelial cell (H184B5F5/M10) and the three type of breast cancer cells using (A) 5.4 nm (B) 7.4 nm iron oxide nanoparticles.

ligand binds to the surface iron and exposes the hydrophilic amino group to aqueous media. For analyzing the biocompatibility, the hydrophilic nanoparticles of size 5.4 nm and 7.6 nm in the concentrations range of 0.1, 1, 10 and 100 μM were treated with the normal breast epithelial cells (H184B5F5/M10) and the three types of breast cancer cells (SKBR3, MB157 and T47D) for 72 h. Figure 6 shows the cell viability results for normal as well as breast cancer cells using 5.4 nm and 7.4 nm nanoparticles. The cytotoxicity studies revealed that there is no obvious change in cell viability in the studied concentration range of magnetic nanoparticles, although the 100 μM nanoparticle concentration is considered to be far higher than the normal use. Thus, the as-prepared nanoparticles showed biocompatibility and nontoxicity against the normal as well as cancerous cell lines.

IV. Conclusions

In summary, we have synthesized the iron oxide nanoparticles with monodispereity using the seed-mediated method combined with thermal decomposition. The size evolution has been demonstrated by understanding the growth process for the formation of monodispersed nanoparticles. It is also possible to control the distribution and size of the particles by tuning the temperature and the concentration of growth solution. Under the high concentration condition, the nucleation and growth process compete with each other to consume the monomers, whereas the temperature can affect the degree of dissociation of precursor for the further growth of nanoparticles. Hence, we modified these factors to get the monodispersed iron oxide nanoparticles with standard deviation ($\sigma < 1$). The TG analyses showed that the surface of nanoparticles were occupied by different amount of ligands via physical absorption and chemical binding, which changes with particle size, owing to the surface area to volume ratio. The as-prepared iron oxide nanoparticles showed biocompatibility and nontoxicity against the normal as well as cancerous cell lines.

Acknowledgment

The authors would like thank the National Science Council of Taiwan for financially supporting this research under Contract Nos. NSC 97-2113-M-002-012-MY3, NSC 97-2120-M-002-013 and NSC 97-2120-M-001-006.

References

1. Song H T, Choi J S, Huh Y M et al. (2005) Surface Modulation of Magnetic Nanocrystals in the Development of Highly Efficient Magnetic Resonance Probes for Intracellular Labeling. J Am Chem Soc 127: 9992-9993.
2. Jun Y W, Huh Y M, Choi J S et al. (2005) Nanoscale Size Effect of Magnetic Nanocrystals and Their Utilization for Cancer Diagnosis via Magnetic Resonance Imaging. J Am Chem Soc 127:5732-5733.
3. Weizmann Y, Patolsky F, Katz E et al. (2003) Amplified DNA Sensing and Immunosensing by the Rotation of Functional Magnetic Particles. J Am Chem Soc 125, 3452-3454.
4. Gass J, Poddar P, Almand J, et al. (2006) Superparamagnetic Polymer Nanocomposites with Uniform Fe3O4 Nanoparticle Dispersions. Adv Funct Mater 16:71-75.
5. Daou T J, Pourroy G, Be´gin-Colin S (2006) Hydrothermal Synthesis of Monodisperse Magnetite Nanoparticles. Chem Mater 18:4399-4404.
6. Park J, Lee E, Hwang N-M et al. (2005) One-Nanometer-Scale Size-Controlled Synthesis of Monodisperse Magnetic Iron Oxide Nanoparticles. Angew Chem Int Ed 44: 2872-2877.
7. Park J, An K, Hwang Y et al. (2004) Ultra-large-scale syntheses of monodisperse nanocrystals. Nat Mater 3:891-895.
8. Sun S, Zeng H, Robinson D B et al. Monodisperse MFe2O4 (M = Fe, Co, Mn) Nanoparticles (2004) J Am Chem Soc 126:273-279.

The address of the corresponding author:

Author: Ru-Shi Liu
Institute: Department of Chemistry, National Taiwan University
Street: Sec. 4, Roosvelt Road
City: Taipei, 106
Country: Taiwan
Email: rsliu@ntu.edu.tw

Characterization of Functional Nanomaterials in Cosmetics and its Cytotoxic Effects

J.-H. Huang[1], H.J. Parab[1,3], R.S. Liu[1,*], T.-C. Lai[2], M. Hsiao[2], C.H. Chen[2] and Y.K. Hwu[3]

[1] Department of Chemistry, National Taiwan University, Taipei 106, Taiwan
[2] Genomics Research Center, Academia Sinica, Taipei 115, Taiwan
[3] Institute of Physics, Academia Sinica Taipei 115, Taiwan

Abstract — **The ultraviolet (UV) rays from sun are generally divided in three types such as UVA (315~400 nm), UVB (280~315 nm) and UVC (100~280 nm). Among these, the UVC rays with the highest energy get absorbed completely as they pass through the atmospheric layer. The UVA and UVB rays which penetrate through the atmospheric layer pose a threat for the humankind due to its carcinogenic nature to human skin. Hence it is necessary to develop the cosmetics which absorb the UV rays to prevent the damage of the skin. Generally, the Tinosorb M (2,2'Methyl-enbis[6-(2H benzotriazol-2-yl)-4-(1,1,3, 3-tetra-methylbutyl) phenol]) is mixed in the cosmetics which absorb UVB rays. But almost 97% of the UV rays consist of UVA rays which are mainly responsible for the damage of skin. Recently, the sun-screening cosmetics containing the nanoparticles such as ZnO and TiO_2 nanoparticles or nanorods have attracted great attention for protecting skin from UVA by reducing the amount of UVB penetrating into the skin due to the reflection and scattering. Therefore, it is necessary to investigate the risk factors involved in the usage of these nanoparticles in cosmetics. The present studies involve the characterization of cosmetics containing TiO_2 and ZnO nanoparticles and its comparison with the commercial samples. The absorbance measurements in the range of UVA were performed in order to determine the absorption efficiency of nanoparticles extracted from the cosmetics samples. The transmission electron microscopic analysis revealed the morphology of the nanoparticles. The in vitro cell viability tests were performed as a function of particles size in order to determine the cytotoxicity of the nanoparticles.**

Keywords — **sun-screening cosmetics, zinc oxide, titanium oxide, nanoparticles and cytotoxicity analysis.**

I. Introduction

The nanoscience and nanotechnology have already been offered the new industrial and health related applications of nanoparticles for the commercial product such as cosmetics, food additive and medicine reagent, because it is attributed to the unique properties for nanoparticles in comparison with the their relative bulky materials. [1-4] The sun-screening cosmetics containing the additive of nanoparticles are useful way to protect the human skin from the exposure to the UVA by the result of scattering and reflection physical properties. The nanoparticles such as zinc oxide, titanium oxide etc. with smaller size than the wavelength of light provide the excellent scattering and absorption ability in the range of UVA, but there are many uncertain risk factors formed such as the penetration of nanoparticles for skin and the exposure of nanoparticles to the lung. [5-7] Hence, it is necessarily for scientist to investigate the properties of manufactured commercial product.

In the present studies, the properties of commercial product of sun-screening cosmetics containing the nanoparticles has been investigated, including of the determination of their percentage content and the identification of nanomaterials, by using extraction method to separate the part of nanoparticles from sun-screening cosmetics. We offer and confirms the exact the nanoparticles component for further quantitatively/qualitative analysis and bio-analysis such as cytotoxicity assay. The cytotoxicity analyses of different commercially available nanoparticles are performed with different cell lines including S-G (transformed oral keratinocyte), OMF (oral mucosa fibroblast) and WI-38 (lung fibroblast) to investigate the particles size effect on cell viability.

II. Materials and Methods

A. Experimental section

The sun-screening cosmetics were purchased from the five companies. (SH, ES, KA, LA and CL) Nano-scaled commercially available TiO_2 nanoparticles (AFDC; 161 nm spherical irregular particles and M212; 20 nm width/ 50 nm length nanorods) were purchased from Top Rhyme International Company. Acetone (>99.5%, Sigma-Aldrich), ethanol (99%, Riedel-deHean) and n-hexane (99%, Riedel-deHean) were used as purchased without further purification.

The 1.5 g sun-screening cosmetics was dispersed into 50 mL solvent such as ethanol, hexane or acetone followed by sonification for 20 min. Supernatant was removed using centrifugation at the rate of 9,000 rpm and then white powder was collected and dried in the oven at 70^{o}C for 10 min. Repeating the above steps several times to complete re-

Chwee Teck Lim, James C.H. Goh (Eds.): ICBME 2008, Proceedings 23, pp. 806–809, 2009
www.springerlink.com

moval of the organic species from the sample. Finally, the pure white powders were obtained which was characterized by XRD (X-ray powder diffraction; PANalytical X' Pert PRO), UV/visible spectroscopy, SEM (scanning electron microscope; Tecnai-G2-F20) and TEM (transmission electron microscope; JEOL JSM-1200EX II).

B. Cytotoxicity assay-MTS assay

Three normal cell lines were employed in this study including S-G (transformed oral keratinocyte), OMF (oral mucosa fibroblast) and WI-38 (lung fibroblast). S-G and OMF were cultured in Dulbecco's modified Eagle' medium (DMEM, Gibco, Grand Island, NY, USA). WI-38 was cultured in Minimum essential medium (MEM, Gibco, Grand Island, NY, USA). All mediums supplemented with 10% (v/v) FBS (Hyclone, CA, USA), 2mM glutamine (Gibco, Grand Island, NY, USA), 100 units/mL penicillin (Gibco, Grand Island, NY, USA), and 100 mg/mL streptomycin (Gibco, Grand Island, NY, USA). All cell lines were incubated in a 37°C humidified atmosphere (95% air and 5% CO_2).

In the first day, 2000 cells were seeded to each well in 96-well plate and incubated overnight at 37 °C in 5% CO_2.In the second day, replaced the medium with variant amounts of titanium dioxide which was suspended in 200 µL growth medium. The doses of titanium dioxide (AFDC and M212) were followed: 13000, 300, 80.3, 20.8, 5.2 and 1.3 µg/mL. After 72 hrs incubation, 20 µl MTS was added into each well and incubated for one to three hours. The cell viabilities were determined by the absorbance of OD_{490nm} which were measured by ELISA reader.

III. Results and Discussion

The morphology of the nanoparticles extracted from the sun-screening cosmetics was analyzed using TEM. The images of TEM are shown in figure 1(a) ~ 1(e). The morphology image of the nanoparticles exhibits the irregular spherical shape for the SH and ES cosmetics, the mixture shape of irregular spherical, long rod and short rod for KA cosmetics and only rod shape for LA cosmetics. The morphology of the CL nanoparticles reveals that the shape of the uniformly distributed core-shell structures, which is quite different from others. The TEM images show all the nanoparticles were of the nano-scale size except the figure 1(e) and the morphology of nanoparticles are different due to the nature properties of materials such as the preference orientation for crystallization growth. The nano-scale size of particles satisfies the scattering requirements for the wavelength of UV (100 nm ~ 400 nm) and absorption peak found

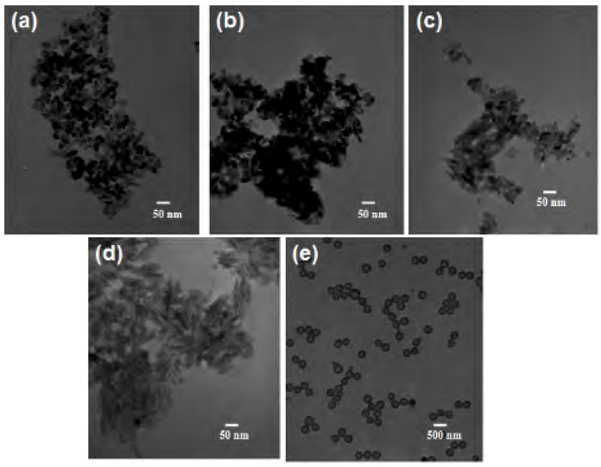


Fig. 1 The TEM images of nanoparticles extracted from the commercial products of (a) SH, (b) ES, (c) KA, (d) LA and (e) CL companies.

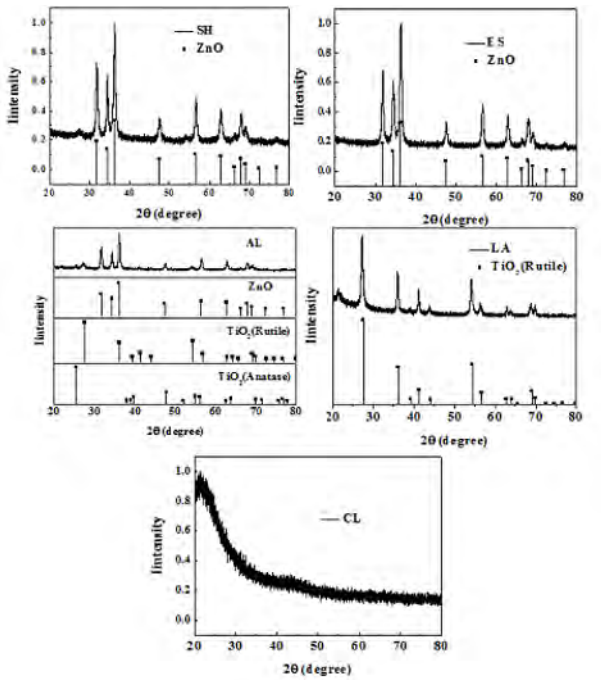


Fig. 2 XRD patterns of nanoparticles and standard of zinc oxide and titanium oxide in the form of rutile and anatase

in the range of UVA, as the nanoparticles size is smaller than the wavelength of incident light and the absorption position of energy shifts to UV range due to size effect. Hence, The TEM images also support that the size of nanoparticles are responsible for the physical sun-screening. Figure 2 reveals the several characterization peaks for the nanoparticles. The XRD peaks of SH nanoparticles are agreed well with the standard zinc oxide pattern and the

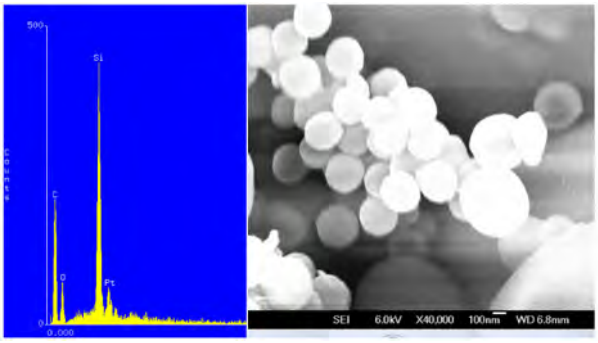


Fig. 3 SEM-EDS and SEM image of nanoparticles extracted from the commercial product of CL company.

same is found for ES nanoparticles, so these contains zinc oxide nanopartcles as the physical sun-screen component. Because the XRD pattern of AL nanoparticles consists of the standard pattern of zinc oxide and titanium oxide in the rutile and anatase forms, the AL nanoparticles being composed of three type nanoparticles, which are responsible for more absorption positions in the range of UVA and UVB than only single material. The XRD peaks for LA nanoparticles appear only the characterization of titanium oxide in the form of rutile. Finally, the crystalline of CL nanoparticles is amorphous, because there is no any peak appeared in the XRD pattern of CL nanoparticles. In figure 3, SEM image revealed the surface morphology of CL nanoparticles, which was found in form of smooth spphere and SEM-EDS analysis show all of its composition is silica. Low refractive indexed non-crystalline components of CL sun-screen make it transparent and high reflection due to the bulk material. In the table 1, it displays the of nanoparticles size for five products calculated by using the Scherrer equation. The zinc oxide nanoparticles sizes are consisted with the TEM image around 20 nm for the SH, ES and AL nanopaticles. However, the titanium oxide in the anatase form for AL cosmetics shows the larger size than others due to the length of nanorod. For titanium oxide in the rutile form, it appears the

Table 1 Nanomaterials size are deduced using scherrer equation.

	SH	ES	AL	LA	CL
ZnO	16.0 nm	16.6 nm	22.8 nm	-	-
TiO_2 (Rutile)	-	-	12.2 nm	16.9 nm	-
TiO_2 (Anatase)	-	-	41.3 nm	-	-

Table 2 Weight percentage of solid component of cosmetics

	SH	ES	AL	LA	CL
Powder (wt%)	20%	16.6%	16%	5.2%	5.5%
Others (wt%)	80%	83.4%	84%	94.8%	94.5%

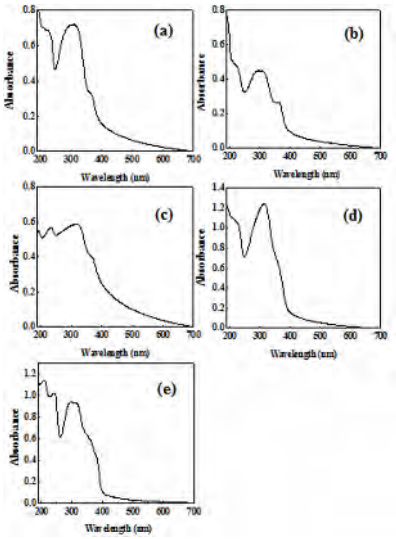


Fig. 4 UV/vis spectroscopy of (a) SH, (b) ES, (c) AL, (d) LA and (e) CL cosmetics with anal sized in the range of 200 ~ 700 nm

size is as same as zinc oxide nanoparticles, so it also forms irregular sphere by comparison with the TEM image. There is no specific peak found in XRD pattern for the CL core-shell nanoparticles, so the particles size is only calculated by the TEM or SEM image.

Table 2 show the percentage of content for cosmetics such as the powder and other organic species. Present of 20 wt%, 16.6 wt%, 16 wt%, 5.2 wt% and 5.5 wt% powders were found for the sun-screen cosmetics of SH, ES and AL cosmetics after the extraction procedure. It shows the large amount of powder used as content of cosmetics during the manufacture procedure. Previously, there is no any investigation that includes bio-analysis such as cytotoxicity for these cosmetics. Exposure of such fine particles to human skin or lung is very dangerous. Though the nature of titanium oxide and zinc oxide did not show any toxicity for humankind, the unexpected effects occurred as the particles size decreases to the nano-scale. Base on the data of TEM image and XRD pattern, the major materials of nanoparticles used as sun-screen agent in cosmetics are titanium oxide and zinc oxide and their sizes localize around 20 nm.

The UV/visible spectroscopy are measured for five cosmetics shown in Figure 4. The wavelength range of UVA lies between 315 ~ 400 nm. The absorption peaks for titanium oxide and zinc oxide nanoparticles are found to be at 280 nm and 375 nm, respectively. Therefore, they all appear the characteristic peaks in the range of UV . [7] The characteristic peak for titanium oxide nanoparticles localize at the UVB range with high intensity, but the absorption peak of zinc oxide nanoparticles exhibit in UVA range with low intensity. For the sun-screening in the UVA range, the zinc

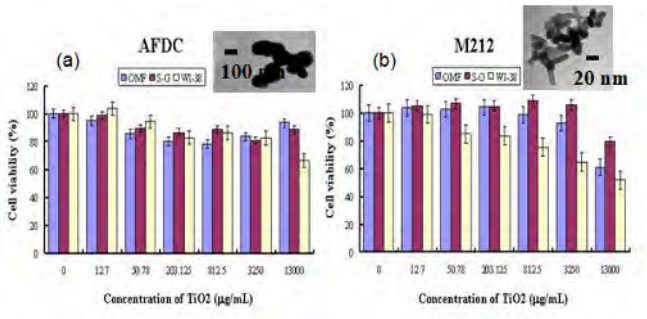


Fig. 5 Cytotoxicity analysis of commercially available titanium oxide with diameter of (a) 161.1 nm and (b) ~20 nm width / 50 nm length nanorod. (The inserts are TEM image of nanoparticles)

oxide nanoparticles is more useful for human skin than titanium oxide nanoparticles, but the intensity is relative low by comparison with each characterization absorption peak. The background for each nanoparticles in figure 4 (a) to 4 (d) is relative higher than the larger particles in figure 4 (e) due to scattering effect by the influence of closed package nanoparticles than larger nanoparticles.

Figure 5 shows the result of cytotoxicity assay of OMF, S-G and WI-38 cell lines incubating in two type nanomaterials as AFDC (161.1 nm nanoparticles) and M212 (20 nm/ 50 nm nanorods). The result reveals that oral keratinocye and fibroblast cells have higher tolerance to the various concentrations of titanium oxide nanoparticles than lung fibroblast, because the cell viability decreases until 13000 μg/mL. For cell lines exposed to M212 nano-materials, the cell viablitity of WI-38 starts to decrease at 50.78 μg/mL. In comparison, the AFDC nano-materials appears less toxic than M212 in cell lines due to the size effect. The mechanisms of the TiO2 to inhibit cell viability remain unknown.

IV. Conclusions

By the analysis of TEM image and XRD pattern, the results reveal that the material of nanoparticles extracted from sun-screening cosmetics is composed of zinc oxide, titanium oxide or mixture of both for the cosmetics of SH, ES, AL and LA companies, but the silica is component for product of CL company by the SEM-EDS. The percentage of content on nanoparticles are 20wt% for SH company, 16.6wt% for ES company, 16wt% for AL company, 5.2wt% for LA company and 5.5wt% for CL company. The datum show quite large amount of nanoparticles used in the sunscreen cosmetics, so the cell in skin and lung will be dangerous to expose to the nanoparticles by the way of contact with flying nanoparticles. The nanoparticles all show the characterization absorption in the range of UV, but only the absorption peak of zinc oxide nanoparticles localize at the range of UVA, and the peak position for titanium oxide nanoparticles place in the range UVB. Hence, the zinc oxide nanoparticles is excellent for sun-screening cosmetics to protect the skin of human kind form the major part of UV, which is UVA. By the cytotoxicity analysis for five cell lines, the high wt% nanoparticles do not benefit the growth environment for the cell and the nano-scale materials suppress the growth of cell due to the size effect.

Acknowledgment

The authors would like thank the Department of Health, Executive Yuan under Contract Nos. DOH97-TD-D-113-97002 and the National Science Council of Taiwan under Contract Nos. NSC 97-2113-M-002-012-MY3 and NSC 97-2120-M-001-006 for financially supporting this research.

References

1. Paul J E, Tatjana P, Stefan V et al. (2007) DNA-TiO_2 nanoconjugates labeled with magnetic resonance contrast agents. J Am Chem Soc 129:15760-15761
2. Bappaditya S, Haoheng Y, Nicholas O F et al. (2008) Protein-passivated Fe_3O_4 nanoparticles: low toxicity and rapid heating for thermal therapy. J Mater Chem 18:1204–1208
3. Aleksandra B D and Yu H L (2006) Optical properties of ZnO nanostructures. Small 2:944 – 961
4. Kazunari O, Shigeyuki N, Yuanzhi L et al. (2007) The surface of TiO_2 gate of 2DEG-FET in contact with electrolytes for bio sensing use. Appl Surf Sci 254:36–39
5. Sang H L, Hyun J L, Hiroki G et al. (2007) Fabrication of porous ZnO nanostructures and morphology control. Phys Stat Sol (c) 4:1747– 1750
6. Qamar R, Mohtashim L, Elke D et al. (2002) Evidence that ultrafine titanium dioxide induces micronuclei and apoptosis in Syrian hamster embryo fibroblasts. Environ Health Perspect 110:797-800
7. Raymond SH Yang, Louis W C, Wu J-P et al. (2007) Persistent tissue kinetics and redistribution of nanoparticles, quantum dot 705, in mice: ICP-MS quantitative assessment. Environ Health Perspect 115:1330-1343

Use macro [author address] to enter the address of the corresponding author:

Author: Ru-Shi Liu
Institute: Department of Chemistry, National Taiwan University
Street: Sec. 4, Roosvelt Road
City: Taipei 106
Country: Taiwan
Email: rsliu@ntu.edu.tw

Design and Analysis of MEMS based Cantilever Sensor for the Detection of Cardiac Markers in Acute Myocardial Infarction

Sree Vidhya[1] & Lazar Mathew[2]

[1] Healthcare Practice, Frost & Sullivan (P).Ltd, Chennai, India
[2] School of Biotechnology, Chemical & Biomedical Engineering, VIT University, Vellore, India.

Abstract — **Piezo-resistive actuation of a microcantilever induced by biomolecular binding such as DNA hybridization and antibody-antigen binding is an important principle useful in biosensing applications. As the magnitude of the forces exerted is small, increasing the sensitivity of the microcantilever becomes critical. In this paper, we are considering to achieve this by geometric variation of the cantilever. The sensitivity of the cantilever was improved so that the device can sense the presence of antigen even if the magnitude of surface-stresses over the microcantilever was very small. We consider a 'T-shaped' cantilever that eliminates the disadvantages while improving the sensitivity simultaneously. Simulations for validation have been performed using Intellisuite software (a MEMS design and simulation package). The simulations reveal that the T-shaped microcantilever is almost as sensitive as a thin cantilever and has relatively very low buckling effect. Simulations also reveal that with an increase in thickness of the cantilever, there is a proportional decrease in the sensitivity.**

Keywords — **Microcantilever, Acute Myocardial Infarction, Cardiac Troponins, Piezo resistive, Thermo Electro Mechanical Analysis**

I. Introduction

This paper presents an analytical modeling of a piezoresistive cantilever used as MEMS based biosensor for the detection of cardiac markers in Acute Myocardial Infarction (AMI).Diagnosis of Myocardial Infarction was achieved by the nanomechanical deflection of the microcantilever due to adsorption of the Troponin I complex. The deflection of the microcantilever was measured in terms of the piezoresistive changes by implanting boron at the anchor point where there is maximum strain due to the adsorption of the analyte molecules. The biochemical interactions between the Cardiac Troponin I (cTnI) complex and the immobilized antibodies would cause change in resistance of the piezoresistor integrated at the anchor point. A 'T' shaped microcantilever design was proposed for the study.

The distal end of the device was coated with gold. The sensitivity of the cantilever was improved so that the device can sense the presence of antigen even if the magnitude of surface-stresses over the microcantilever was very small.

To obtain an application specific optimum design parameter and predict the cantilever performance, Thermo Electro Mechanical (TEM) Analysis using Intellisuite (a MEMS design and simulation package) was performed. The miniaturization of the cantilever-based biosensor leads to significant advantages in the absolute device sensitivity. Precise measurement of the deflection at the end of the cantilever was achieved through this arrangement. Measurement of antigens up to picogram levels can be done using this technique.

II. Materials & methods

A. Theoretical Considerations

The fact that there is no standard procedure to determine the electromechanical parameters of piezo-resistive structures is apparent. In this paper, two different approaches have been used to study the characteristics of the T-shaped microcantilever and to predict its performance during the biomolecular binding process. The first approach uses theoretical relationship between differential surface stress and tip displacement during the biomolecular binding process at the upper surface of the cantilever. In the second approach, FEM simulations by *Intellisuite Software* have been performed on the T-shaped microcantilever.

Piezoelectric materials strain when exposed to voltage and, conversely, electrical charge accumulates on opposing surfaces and produces voltage when strained by an external force. This is due to the permanent dipole nature of these materials. When the biomolecular interaction occurs on the top of the cantilever, the change in the radius of curvature, R and the cantilever deflection z_{max} can be related to the differential surface stress, Δs, by

$$1/R = 6(1 - \nu)\, \Delta s/Et2$$

$$\text{and } z_{max} = 3l\, 2(1 - \nu)\, \Delta s/Et2$$

Where ν is Poisson's ratio, E is Young's modulus for the substrate, t is the thickness of the MC, and l is the cantilever length.

Chwee Teck Lim, James C.H. Goh (Eds.): ICBME 2008, Proceedings 23, pp. 810–812, 2009
www.springerlink.com

B. Microcantilever Design

Silicon is the substrate material used. To use silicon as a substrate material, it has to be pure silicon in a single-crystal form. The Czochralski method appears to be the most popular method among several methods that have been developed for producing pure silicon crystal. A popular method of designating planes and orientations is the Miller indices. These indices are effectively used to designate planes of materials in cubic crystal families. For simulation purposes, we have considered the design parameters given in table 1.

Table 1 Design Parameters

Length of the cantilever	250 µm
Length of the T-arm	100 µm
Width	50 µm
Cantilever thickness	1 µm

Keeping these parameters into consideration a T-shaped microcantilever was designed using IntelliFAB designer. Sequential steps led to the design of the microcantilever model as shown in figure 1.

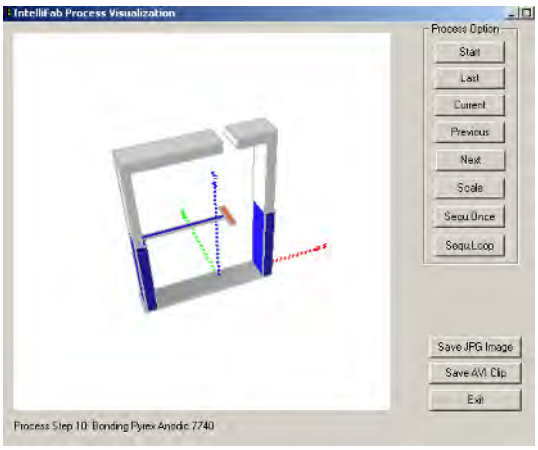


Fig. 1 Cross section of the T-shape micro cantilever design

C. Thermo-electro Mechanical Analysis

Thermo-electro mechanical (TEM) analysis using Intellisuite was chosen as the simulation tool in this study because of its unique capabilities in MEMS design, simulation, and modeling. It has a fully integrated MEMS design environment. The first step (pre-processing) in using TEM analysis module is constructing a model of the structure to be analyzed. The input of a topological description of the structures and geometric features is required in TEM. This is represented in 3D form, using the IntelliFAB designer which gives the virtual prototype of the model. The primary objective of the model is to realistically replicate the important parameters and features of the real model.

Once the geometric model has been created, a meshing procedure is used to define and break the model up into small elements. In general TEM model is defined by a mesh network, which is made up of the geometric arrangement of elements and nodes. Nodes represent points at which features such as displacements are calculated. Elements are bound by set of nodes, and define localized mass and stiffness properties of the model. Elements are also defined by mesh numbers which allow reference to be made to the corresponding deflections or stresses at specific model locations. A fine meshed model of the T-shaped microcantilever used in the analysis is shown in figure 2.

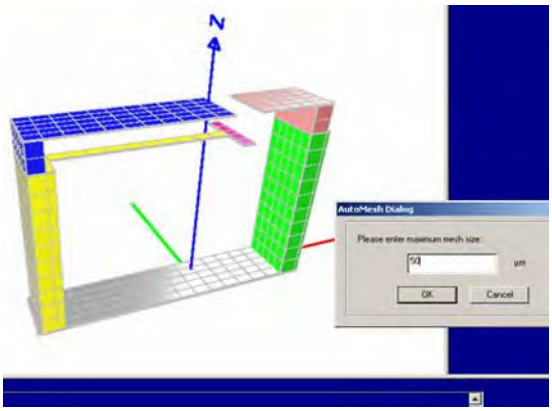


Fig. 2 Intellisuite Auto Mesh With 50 X 50 µ M

III. Simulations and Results

Simulations were performed in order to validate the claim that the T-shaped microcantilever leads to significant advantages in the absolute device sensitivity. Microcantilever with 250µm length x 100µm length of the T-arm x 50µm width x 1µm thickness was used for simulations using INTELLISUITE: material - silicon; Young's Modulus 200GPa; Poisson's ratio 0.22 and mass density of 2.3g cm^{-3}. The effect of the surface stress created by the troponincomplex interactions on the gold coated surface of the cantilever can be effectively simulated by substituting it with a line force (amounting to $15.2x10^{-17}$ MPa) on the edges of the T-arm. Sensitivity has been meas-

ured in terms of the maximum displacement and surface stress undergone by any point on the cantilever as shown in figure 3 & 4.

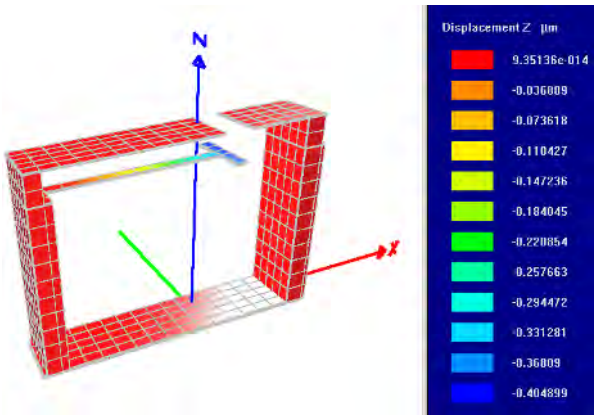


Fig.3 Displacement along Z - axis

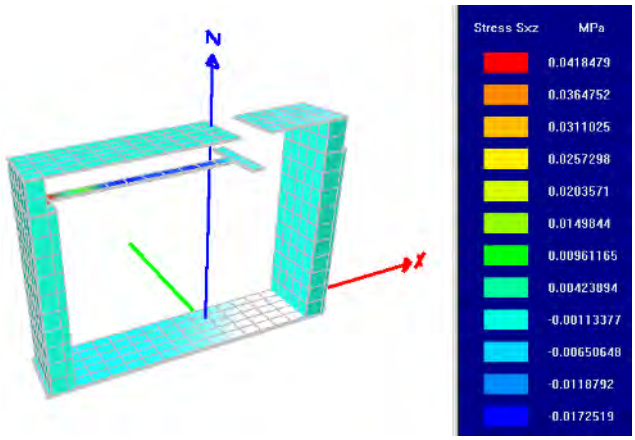


Fig.4 Stress at the anchoring region along Z - axis

IV. Conclusion

Thus a T-shaped microcantilever was designed, analyzed and simulated successfully. Stresses were generated at the anchoring region of the cantilever where Boron was implanted. These stresses were detected by employing piezo-resistive detection method. However, analyses based on the concentration of sample solution may be needed for further research.

References

1. Wu, A.H.B., Feng, Y.J., Contois, J. H. & Pervaiz, J. (1996) Comparison of myoglobin, creatine kinase MB, and cardiac troponin I for diagnosis of acute myocardial infarction Ann. Clin. Lab. ScL 26: 291-300.
2. Wu, Alan, editor. Washington, DC: American Association of Clinical Chemistry (AACC) Press, 1998. – "A review on Cardiac Markers".
3. D. G. Pijanowska, A. J. Sprenkels, W. Olthuis and P. Bergveld,: Chemical, Volume 91, Issues 1-3, 1 June 2003, Pages 98-102.- A flow-through amperometric sensor for micro-analytical systems, Sensors and Actuators.
4. Alansari, S. E. & Croal, B. L. (2004) Diagnostic value of heart fatty acid-binding protein and myoglobin in patients admitted with chest pain Annals of Clinical Biochemistry 41: 391-396.
5. Wei Zhoua, Abdul Khaliq a, Yanjun Tang a, Haifeng Ji a,c, Rastko R. Selmic - Simulation and design of piezoelectric microcantilever chemical sensors.

Integrating Micro Array Probes with Amplifier on Flexible Substrate

J.M. Lin[1], P.W.Lin[2] and L.C. Pan[3]

[1] Chung-Hua University/Department of Mechanical Engineering, Hsin-Chu, Taiwan, R. O. C.
[2] Taipei Medical University/New Business Center, Taipei, Taiwan, R. O. C.
[3] Taipei Medical University/Department of General Education, Taipei, Taiwan, R. O. C.

Abstract — **In this paper a bio-sensing module by integrating a micro-array probes device and a semiconductor amplifier respectively on two flexible substrates is proposed, which utilizes semiconductor processes. The amplifier is formed of bottom-gate thin film transistors (TFT). As such, the signal obtained by the bio-sensing probes can be amplified nearby to improve the signal-to-noise ratio and impedance matching. This module is formed on the flexible substrate such that the bio-probe device can be disposed to conform to the profile of a living body's portion to improve the electrical contact property.**

Keywords — **Bio-sensing probe, thin film transistor amplifier, flexible substrate, signal-to-noise ratio**

I. Introduction

Conventional micro array biological probes are produced on a hard silicon wafer substrate [1-7]. This kind of product is not only heavy and frangible but also high temperature processes needed. Moreover, the conventional micro array biological probes fail to be designed and disposed relying on the profile of a living body's portion, and adversely affecting contact between the biological probes and living body. Besides, after a signal detected from the conventional micro array biological probes, the signal is picked up to process signal-to-noise ratio and impedance matching. Additional devices for signal processing are required.

This research provides a micro array bio-probe device integrated with TFT amplifier formed of bottom-gate thin film transistors [8-9], which utilizes a micro-electro-mechanical process and a semiconductor process to integrate micro array bio-probes and an amplifier, formed of bottom-gate TFTs on a flexible substrate. As such, the signal obtained by the probes can be amplified nearby to improve the signal-to-noise ratio and impedance matching. The micro array bio-probes are formed on the flexible substrate such that the present bio-probe device can be disposed to conform to the profile of a living body's portion so as to improve the electrical contact property.

The organization of this paper is as follows: the first section is introduction. The second one is the fabrication steps of semiconductor amplifier and bio-sensing probe device. The next are microprobe fabrication test and discussion. The last part is the conclusion.

II. Device Fabrication Steps

As in Fig. 1, the bio-sensing probe has a tip end to facilitate thrusting into the living body to decrease the contact impedance. This research can vary the density, occupied area and sharpness of the tip ends of the probes to change the contact impedance so as to meet different needs. In addition this product can be designed for roll-to-roll types to facilitate mass-production.

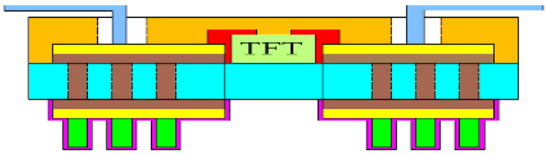


Fig. 1 The side view of the proposed module for micro array bio-sensing probe device integrated with a semiconductor amplifier.

A. Semiconductor Amplifier Design

Step 1: Using mask #1 and Photolithography And Etching Processes (PAEP), some through holes are formed on the flexible substrate for signal conduction between both surfaces. Then remove the Photo Resist (PR). The next is by E-gun evaporator (a low temperature process) to deposit a layer of TiN (0.1 μm) on each side of substrate as seed for electroplating copper (100 μm). The result is in Fig. 2.



Fig. 2 The result of design step 1.

Step 2: By E-gun evaporator deposit an insulating layer of S_iO_2 or Si_3N_4 (2 μm) on the lower surface of substrate. By using mask #1 and PAEP to make vias on those holes made in Step 1 through the insulating layer deposited. Then evaporating a layer of amorphous silicon layer (to be for the four active regions of thin-film-transistors, 2 μm) and using

Chwee Teck Lim, James C.H. Goh (Eds.): ICBME 2008, Proceedings 23, pp. 813–816, 2009
www.springerlink.com

mask #2 with PAEP to left four island regions for making MOS transistor. These regions are going to make two pairs of amplifiers, the left-hand side two regions are for making two N-MOS transistors, and the other two regions are going to make a CMOS transistor amplifier. Finally remove the PR, and anneal the amorphous silicon for re-crystallization by Nd-YAG laser. The result is in Fig. 3.

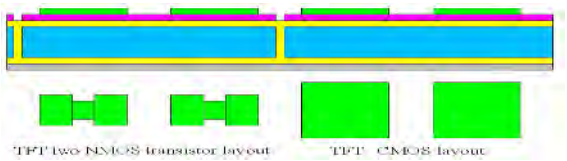


Fig. 3 The result of design step 3.

Step 3: Evaporate layers of S_iO_2 (2μm) and amorphous S_i (2 μm) respectively, and with mask #3 and PAEP to make the gate electrodes of transistors and wirings connecting to the vias. Finally remove the PR, and the result is in Fig. 4.

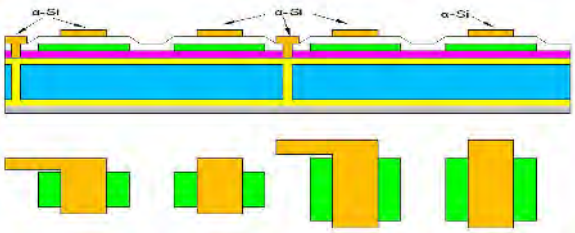


Fig. 4 The result of design step 3.

Step4: Using mask #4 and the PAEP to etch S_iO_2 away at the sources, drains and wirings on the left three N-MOS transistors for phosphorous (N+ donor type) ion implantation. Finally remove the PR, and the result is in Fig. 5.

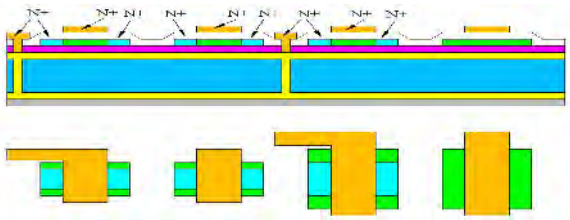


Fig. 5 The result of design step 4.

Step 5: By using mask #5 with the PAEP to etch some regions of S_iO_2 away at the sources, drains and wirings on the right hand side P-MOS transistors for boron (P+ acceptor type) ion implantation. Finally remove the PR, and the result is in Fig. 6.

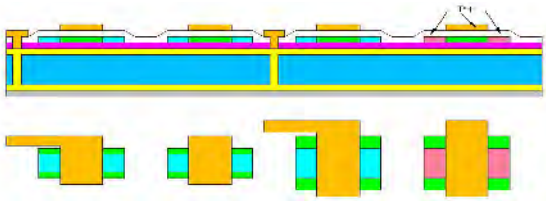


Fig. 6 The result of design step 5.

Step6: Evaporate a layer of Si_3N_4 or SiO_2 (2μm), and with mask #6 and PAEP to make the contact holes for all the electrodes of MOS transistors and wirings. Finally remove the PR, and the result is in Fig. 7.

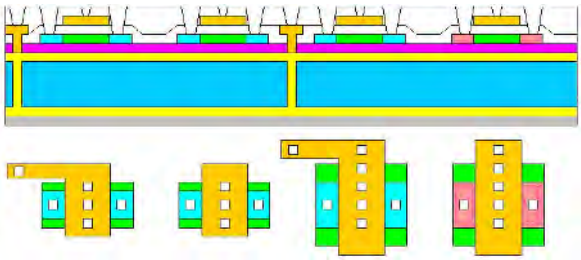


Fig. 7 The result of design step 6.

Step 7: Evaporate a layer of aluminium (2 μm) and with mask #7 and PAEP to make the contact metallization for all the electrodes of MOS transistors and wirings. Finally remove the PR, and the result is in Fig. 8.

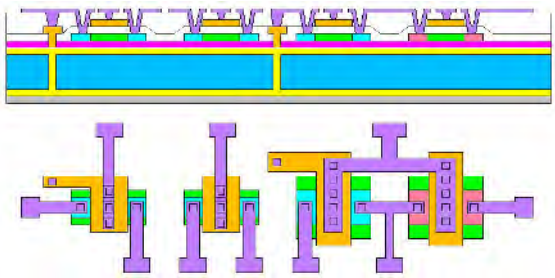


Fig. 8 The result of design step 7.

Step 8: By E-gun evaporator deposit a layer of S_iO_2 or Si_3N_4 (2 μm) for insulation and passivation, using mask #8 with PAEP to make the pad holes for wire bonds. Then electroless plating two layers of nickel and gold. Finally remove PR, and the result is in Fig.9, it is ready for making bumps to connect to the outer circuit by solder screening and the reflow processes. The four transistors are connected as two sets of amplifiers in Fig. 10; they can be used for impedance matching and increasing signal-to-noise ratio.

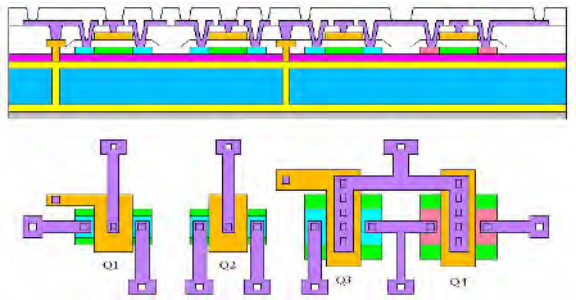


Fig. 9 The result of design step 8.

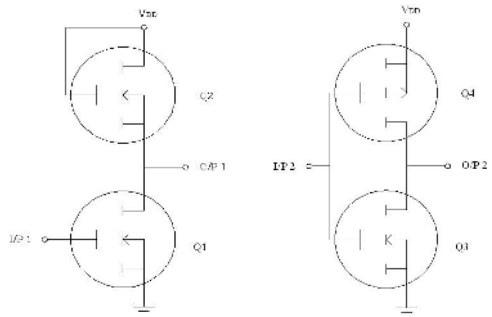


Fig. 10 Four MOS transistors are connected as two pairs of amplifiers

B. Micro Array Bio-Probe Design

Step 1: The conducting vias of the micro array bio-sensing probe is formed by using Nd:YAG laser ablation. Make SU-8 thick photo-resist (500 μm) on each side by using mask #9. The result is in Fig.11.

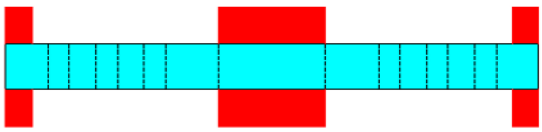


Fig. 11 The result of design step1.

Step 2: Evaporate copper and TiN on each side with thickness 100 μm. Stripe SU-8 photo-resist away. The result is in Fig.12.



Fig. 12 The result of design step 2

Step 3: Forming a layer of Lift-Off-Resist (LOR) with thickness as 500 μm on the back side with mask #10. Make SU-8 PR (500 μm) on back side with mask #3 in Fig. 13.

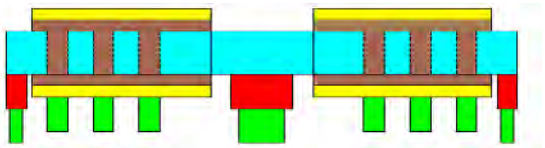


Fig. 13 The result of design step3.

Step 4: By E-gun evaporator deposit a layer of TiN (2 μm). The result is in Fig. 14.

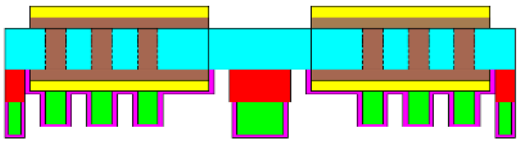


Fig. 14 The result of design step 4.

Step 5: Stripe LOR PR away, then the micro array bio-sensing probe can be formed. The result is in Fig. 15.

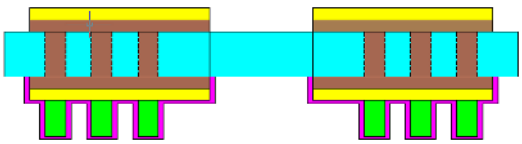


Fig. 15 The result of design step 5.

Step 6: Wire-bonding for electrical signal connection. The result is in Fig. 1.

III. Test and Discussions

The top view and the fabrication result after packaging is shown in Figs.16.and 17. The next step is impedance test [10]. The center line is soldered with the probes while the outer shielding ones connected to the ground of the probe. Then the pig skin in Fig.18 is applied for testing with the equivalent circuit model in Fig.19. The results of pig skin impedance measurements for two cases are shown in Table 1. It can be seen that the resistance obtained by case A is about 330 times larger than that of case B for the same kind of pig skin. The reason is that area of case A is larger, the insertion force may not large enough to penetrate the real skin, and thus the resistance is so much larger. The result of case B is more reasonable.

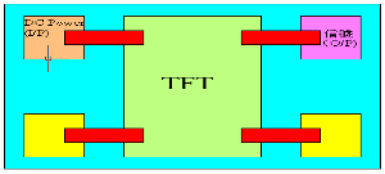


Fig. 16 The top view of the design result.

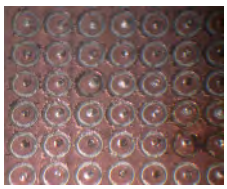


Fig. 17 The result of fabrication.



Fig. 18 The pig skin under test.

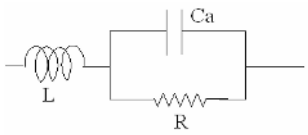


Fig. 19 The equivalent circuit model of pig skin.

Table 1 The results of pig skin impedance measurements for two cases.

Case / Sample	A	B
Length, Width, Thickness (cm)	14 , 14, 0.5	12 , 12, 0.3
Area (cm^2)	196	144
R (Resistance)	11.5261 MΩ	34.9063 KΩ
L (Inductance)	255.366 nH	1.37497 μH
Ca (Capacitance)	8.39747 pF	12.1078 pF

IV. Conclusions

This research employs the MEMS process to integrate TFT amplifiers and micro array biological probes on the flexible substrate. It becomes possible to dispose the bio-sensing probe in conformity with the profile of the living body's portion by forming the bio-probe on the flexible substrate. As such, the contact effect between the biological probes and living body becomes better. On the other hand, the TFT amplifier is also produced on the flexible substrate such that a signal detected from the biological probes can be amplified through a short path. The signal-to-noise ratio and impedance matching are improved.

Acknowledgment

This research was supported by National Science Council Taiwan, R.O.C. with contracts NSC-94-2622-E-216-011-CC3, NSC-95-2622-E-216-CC3 and NSC-96-2622-E-216-005-CC3.

References

1. Lin L, and Pisano, A (1999) Silicon-processed microneedles, *J. of Microelectro-Mechanical Systems,* 18 (1):78–84.
2. Nomura, K, Ohta, H, Ueda, K et al. (2003) Thin-film transistor fabricated in single-crystalline transparent oxide semiconductor, *Science,* 300(5623):1269–1272.
3. Wu Y, Qiu, Y, Zhang S et al. (2008) Microneedle-based drug delivery: studies on delivery parameters and biocompatibility, *Biomedical Microdevices.*
4. Chen B, Wei J , Tay E et al. (2008) Silicon microneedle array with biodegradable tips for transdermal drug delivery, *Microsystem Technologies*, 14/7, pp 1015–1019
5. Zahn J, Talbot N, Liepmann D et al. (2008) Microfabricated polysilicon micro-needles for minimally invasive biomedical devices, *Biomedical Microdevices*,pp 295-303
6. Cormier M., Johnson B, Ameri M, K. et al. (2008) Fabrication and characterization of laser micromachined hollow microneedles, *Journal of Controlled Release,* pp 503–511
7. McAllister D, Cros F, Davis S et al. (2004) Three-dimensional hollow microneedle and microtube arrays, *J. of Micromechanics and Microengi-neering,*14:597–602
8. Meng Z, Wang M, Wong, M (2000) High performance low temperature metal-induced unilaterally crystallized polycrystalline silicon thin film transistors for system-on-panel applications, *IEEE Trans. on Electron Devices*, 47 (2):404–409
9. Wong M, JinZ, Bhat, G, Wong, P et al. (2000) Characterization of the MIC/MILC interface and its effects on the performance of MILC thin-film transistors, *IEEE Tran. on Electron Devices*, 47(5): 1061–1067
10. Rosell J, Colominas, J, Pallas-Areny, R et al. (1988) Skin impedance from 1 Hz to 1 MHz, *IEEE Trans. Bio-med Eng., BME-35:* 649–651.

Author: J.M. Lin
Institute: Chung-Hua University, Dept of Mechanical Engineering
Street: 707, Sec. 2 Wu-Fu Rd.
City: Hsin-Chu
Country: Taiwan, R. O. C.
Email: jmlin@chu.edu.tw

Investigating Combinatorial Drug Effects on Adhesion and Suspension Cell Types Using a Microfluidic-Based Sensor System

S. Arora[1 2], C.S. Lim[1,2,3*], M. Kakran[3], J.Y.A. Foo[14], M.K. Sakharkar[3], P. Dixit[3,5], and J. Miao[3]

[1] Biomedical Engineering Research Centre, Biomedical and Pharmaceutical Engineering Cluster, 50 Nanyang Drive, Research Techno Plaza, 6th Storey, XFrontiers Block, Singapore 637553
[2] School of Chemical & Biomedical Engineering, Nanyang Technological University, 62 Nanyang Drive, Singapore 637459
[3] School of Mechanical & Aerospace Engineering, Nanyang Technological University, 50 Nanyang Avenue, Singapore 639798
[4] Division of Research, Singapore General Hospital, Bowyer Block A Level 3, Outram Road, Singapore 169608
[5] School of Electrical and Computer Engineering, Georgia Institute of Technology, Atlanta GA 30332

Abstract — **Present medical practitioners apply combination drug therapy for faster and effective treatment of diseases. Every individual's reaction to certain drugs or drug combinations is different. Mix and match of drugs is common but they can have adverse complications in the body or sometimes be useful in accelerating the treatment. The uncertainty is very high due to non-linearity of drug interactions. Hence optimization is required, so that the effect of the therapy is useful.**

The present paper discusses a microfluidic-based sensor system that can carry out simultaneous investigations of cell outcomes, exposed to a combination of drugs. It consists of a PDMS based microfluidic-chip that can generate serial combinations of two compounds in a single step and a bioreactor to house the chip, designed to provide favourable conditions for cell growth. The results confirm that the chip can be used for long and short term monitoring of various cell types.

Keywords — **Drug mix, drug interaction, microfluidics, PDMS**

I. Introduction

The fields of biotechnology and microfluidics have witnessed tremendous developments in the past decade. Initially coined by Manz *et. al.* in the early nineties [1] where the concept of "miniaturized total chemical analysis system" or μTAS was first introduced. Since then these systems have been explored for their innumerable advantages, like low volume consumption of reagents and samples, high resolution and sensitivity, economical and short analysis time. Many microfluidic devices that uses combinatorial chemistry to synthesize compounds and/or for culturing cells have been previously reported in literature [2, 3].

In today's age, where infectious diseases are growing rapidly, there is an urgent requirement of effective and long term solutions. Combination drug therapy is often useful, but sometimes one drug may reduce the therapeutic effect of other or even have adverse effects in the body due to drug interactions. One of the reasons for this may be due to the non-linearity of drug interactions with other drugs or herbs which is often difficult to predict for an individual. Hence it is necessary to understand the effects of combination of drugs and/or herbs on various cell types.

In this paper the authors describes a system to monitor and track combinatory drug effects in order to provide a more effective means of accessing drug-drug effects on cell outcomes using various cell types (adhesion and suspension). It consists of a polydimethylsiloxane (PDMS) based microchip for drug mixing and cell culturing and a bioreactor to provide favourable environmental conditions for cell growth in the chip. The results obtained, demonstrates the system to have a strong potential in high-throughput drug-drug analysis on cells.

II. Design Principle

The microchip was aimed at mixing several fluids together to enable rapid mixing ratios to be carried out. As a proof of concept, this work focused on using only two fluids into serial concentration steps of 20% for simplicity. Since microscale flow is laminar (Reynolds number of the order of unity), flow can be controlled more readily, giving:

$$\mathrm{Re} = \frac{\rho V D}{\mu} \tag{1}$$

where, ρ is fluid density, V is fluid velocity, D is characteristic length, and μ is absolute dynamic fluid viscosity [4]. Typical velocity profiles are parabolic in pressure driven flows. Flow can be described by the Stokes equation for incompressible fluids with non-slip boundary conditions. For rectangular channels, height h and width w, pressure drop Δp over length L is related to volumetric flow rate Q by:

$$Q = \frac{w h^3 \Delta p}{12 \mu L}\left[1 - O(h/w)\right] \tag{2}$$

where, the approximate form $O(h/w) = \frac{6(2^5)}{\pi^5}\frac{h}{w}$ gives less then

Chwee Teck Lim, James C.H. Goh (Eds.): ICBME 2008, Proceedings 23, pp. 817–820, 2009
www.springerlink.com

10% error for $h/w \leq 0.7$ [5]. These parameters were used as guidelines to ensure stable laminar flow in the microchannels designed.

The macrowells of the chip were designed at a higher dimension that does not fall in the micro range (~4 mm, see figure 1), to ensure mixing to occur, because the fluid flow is no longer laminar after it enters the wells from the microchannels.

The rationale for microfluidic chip Design I (Figure 1a) entails that the daughter channels have equal cross-sections and were positioned symmetrically with respect to the parent channel upstream. In this respect, each of the channels would receive the same amount of fluid and the flow rate is effectively halved.

The principle of chip Design II (Figure 1b) was based on the distance traveled by a fixed amount of fluid from the parent channel to the daughter channel, for a particular period of time. Each well was filled by each of the opposite two channels from inlets A and B respectively.

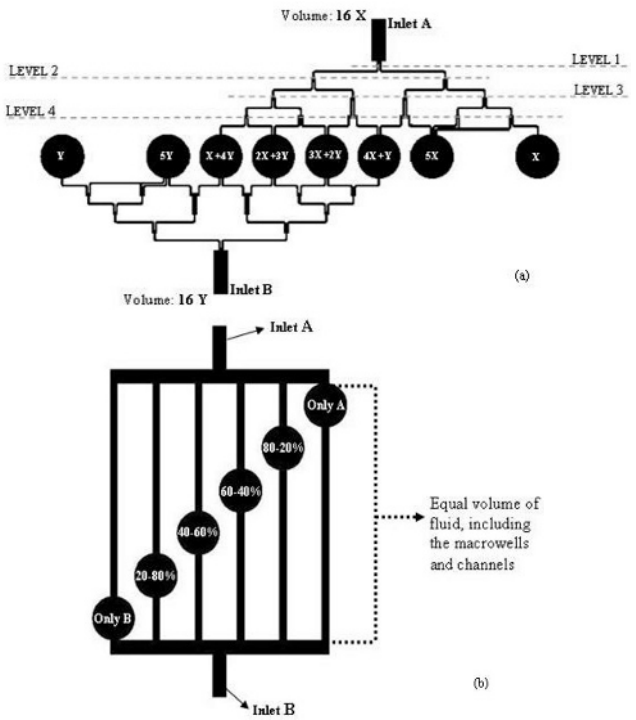


Fig. 1 (a) The layout of design I with the ratio of the fluid mixes denoted as xX + yY ($x \neq y$, X = Y). Volumes of 16X and 16Y enters from inlet A and B respectively. The rectangular microchannel has width of 200 μm except the inlets. (b) The layout for design II with annotations. The percentage mixtures are indicated on the macro-wells as A-B% of fluid volume from inlet A and B respectively. The macrowells measures 4 mm in diameter. Vertical channels are 1mm by 30 mm (excluding wells), horizontal channels are 2mm by 31.5 mm and inlets are 5 mm by 2 mm.

III. Methods and materials

The microchip was fabricated by standard photolithography on four inch silicon wafer (JA Associates, Singapore) and soft lithography on PDMS (Slygard 184 kit, Dow Corning) using SU-8 photoresist (Microchem, USA). This process is well documented in many books and journals and has been used for over a decade for developing PDMS based microchips for biomedical applications [4, 6]. The choice of material was primarily because of its biocompatibility and ease of use and makes the microchip useful for all types of optical detection methods [7]. The final device is shown in figure 2.

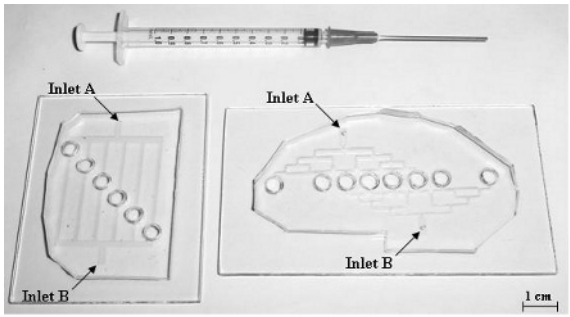


Fig. 2 Final microchips compared to a standard 1 ml syringe. From left to right – Design II and I. The inlets and the wells were punched using 18 gauge blunt needle and 4 mm cork borer respectively. Dimensions: (width × height × thickness) 10 × 6 × 0.6 cm and 6 × 7.5 × 0.6 cm for design I and II respectively.

The depth of the microchannels for both the designs was 150 μm and volume of each well was approximately 50 μl each. For design II, the total volume of each vertical channel is 4.5 mm^3. It is matched with 4.5 μl of fluid in each well. For fluid injection two tubes from both the inlets were connected to standard 1 ml syringes.

The microchips were tested for their performance using water soluble dye, tryphan blue which was simultaneously injected along with DI water from both the inlets of the microchip using syringes and syringe pumps. The concentration was inspected by spectrophotometric studies at 590 nm wavelength (Analytical Instrument Systems Inc., Model DT 1000 CE) as the source and USB2000 (Ocean Optics Inc.) as the detector. The experimental set-up is shown in Figure 3. A control test was done by manually preparing the desired concentrations using the dye and water.

A bioreactor system was designed to house the chip and provide favorable environmental conditions for cell growth and monitoring. The block diagram of the bioreactor is shown in figure 4**.** It consists of a box incubator to house the microchip, integrated with plate heaters and temperature sensors, programmed to maintain the internal temperature at

37 °C using a microcontroller circuitry (ATmega16 chip and AVR® SKT500).

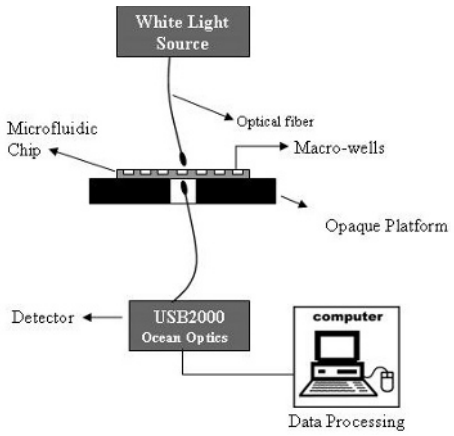


Fig. 3 Experimental setup to perform spectrometric studies on microchip

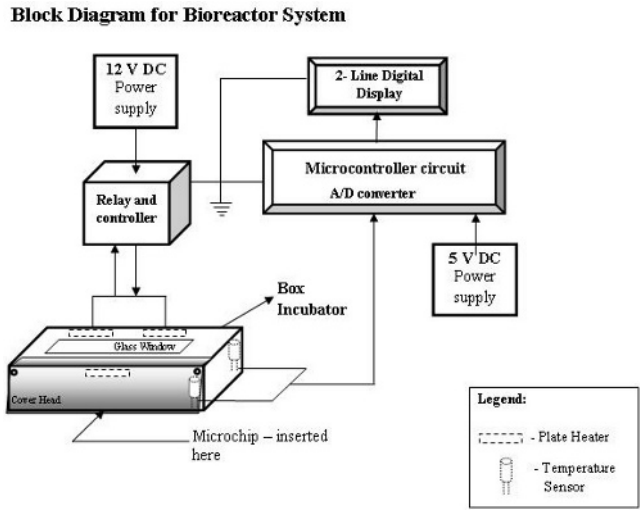


Fig. 4 Block diagram illustrating the components of the bioreactor system. The microchip can be inserted in the box incubator behind the cover-head.

A. Case studies using suspension cells

As one of the prospective application of the diverse microchip, it was used to investigate long term growth of cultures of *Escherichia coli* (*E. coli* strain MC 1061) in the chip wells using Luria-Bertani (LB) broth (Sigma-Aldrich, Singapore) [8]. The chip was incubated in the bioreactor for 18 hours and monitored by optical density (OD) measurement at 600 nm wavelength using the same setup shown in figure 3. The growth curve for bacteria was obtained by plotting absorbance (OD value) versus time.

B. Case studies using adhesion cells

This experiment was performed to check the viability of the microchip and its material for growth and adhesion of mammalian cells. Mouse neuroblastoma or Neuro-2A (N2A) cells were sub-cultured and planted in the wells of the chip and in standard flasks as control to compare the growth. Adhesion was compared by taking images from the test and control after 24 hours of incubation at 37 °C.

IV. Results and Discussion

The result of the dye experiment performed to test the integrity of the microchip is shown in figure 5. The graph was obtained by plotting the averaged absorbance values at 590 nm wavelength versus the concentration of dye in each well of the microchips.

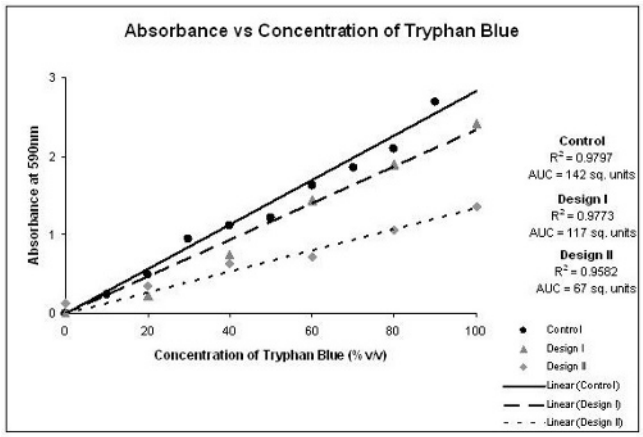


Fig. 5 The graph showing comparison between the microchip results with those of the control (solid line). All the test result data points exhibits an average linear deviation of ± 5 %)

The results obtained were compared with the control for accuracy using R^2 value (coefficient of determination) and area under curve (AUC). R^2 value was used to determine the proportion of variability in a data set [9], whilst AUC was used to establish coherence with the control. The results obtained from the microchip having design I exhibits a near linear graph as compared to design II, also inferred from its high R^2 value of 0.9773. It also reveals that design I presents a high coherence with the control set, with a small AUC difference of 25 square units compared to design II. Hence the design I was the preferred choice for further investigations.

The bacterial growth curve obtained by measuring the OD at 600 nm wavelength in intervals of 3 hours is shown

in figure 6. The growth curve closely matches the standard bacterial growth curves [10] and suggests that the system can be used to monitor long term batch cultures of bacteria.

Mammalian N2A cells that were allowed to incubate for 24 hours before images were taken directly from the chip wells under the microscope, were compared with those taken from the control flasks. The comparison is presented in figure 7 and it clearly suggests good adhesion of the cells onto the bottom of the chip wells as seen also in those taken from the flasks and that the chip wells can sustain mammalian cell for long term monitoring.

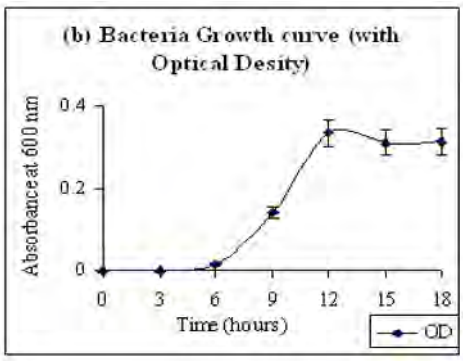


Fig. 6 Growth curve obtained by plotting OD against time with ± 10% error. The error represents average liner deviation of OD.

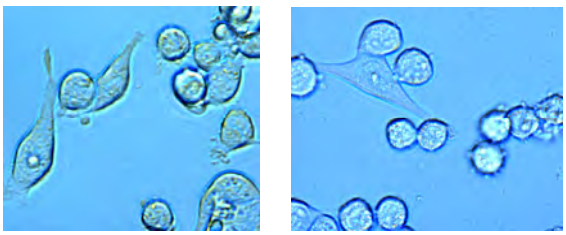


Fig 7. Images show N2A cells at 400 times magnification. The left image was taken from the chip well (test) after 24 hrs of incubation and the right image was taken at the same time from the flask (control).

V. Conclusion

A microfluidic-based sensor system was designed and tested. Case studies were performed by sub-culturing different cell lines into the system and monitored over time. The two microchips designs that were tested with dye solution for accuracy suggested that performance of design I, based on symmetry was superior in terms of reproducibility and accuracy based on the results obtained. This microfluidic platform helped integrate the process of mixing, pipetting and cell screening to perform simultaneous drug-drug investigations on cells *in-vitro*. This in turn results in reduced manpower, time and reagents giving higher accuracy in a single step, compared to conventional mixing techniques.

Microscale mixing problems are not encountered as the mixing occurred in macroscale. Incorporating drugs from the inlets of the microchip would expose the cells directly to various drug-drug combinations that can be monitored over time under microscope or by doing spectrometric studies.

Acknowledgement

The authors of this paper acknowledge the financial support provided by Academic Research Fund (RG 35/06), Ministry of Manpower, Singapore, Biomedical and Pharmaceutical Engineering Cluster and Micromachining Center at Nanyang Technological University, Singapore, for providing facilities to carry out fabrication and experiments.

References

1. Manz, A., N. Graber, and H.M. Widmer, *Miniaturized total chemical analysis systems. A novel concept for chemical sensing.* Sensors and Actuators, B: Chemical, 1990. **B1**(1-6): p. 244-248.
2. Bang, H., et al., *Serial dilution microchip for cytotoxicity test.* Journal of Micromechanics and Microengineering, 2004. **14**(8): p. 1165-1170.
3. Chang, W.J., et al., Poly(dimethylsiloxane) (PDMS) and silicon hybrid biochip for bacterial culture. Biomedical Microdevices, 2003. **5**(4): p. 281-290.
4. Saliterman, S.S., Fundamentals of bioMEMS and medical microdevices. 2006: SPIE. 610.
5. Stone, H.A., A.D. Stroock, and A. Ajdari, *Engineering flows in small devices: Microfluidics toward a Lab-on-a-chip.* Annu. Rev. Fluid Mech., 2004. **36**: p. 381-441.
6. McDonald, J.C. and G.M. Whitesides, *Poly(dimethylsiloxane) as a material for fabricating microfluidic devices.* Accounts of Chemical Research, 2002. **35**(7): p. 491-499.
7. Duffy, D.C., et al., *Rapid prototyping of microfluidic systems in poly(dimethylsiloxane).* Analytical Chemistry, 1998. **70**(23): p. 4974-4984.
8. Ausubel, F.M., *Current protocols in molecular biology*, ed. F.M. Ausubel, et al. 2007 John Wiley and Sons, Inc.
9. Marcello Pagano, K.G., *Principles of Biostatistics*. 2nd ed. 2000, Pacific Grove, CA Duxbury.
10. Singleton, P., *Bacteria in biology, biotechnology and medicine.* 6 ed. 2004: John Wiley and Sons, Ltd. 559.

*Corresponding Author

Associate Professor Lim Chu Sing, Daniel
Division of Manufacturing Engineering,
School of Mechanical and Aerospace Engineering,
Nanyang Technological University,
50 Nanyang Avenue, Singapore 639798.
Email: mchslim@ntu.edu.sg

Organic Phase Coating of Polymers onto Agarose Microcapsules for Encapsulation of Biomolecules with High Efficiency

J. Bai[1], W.C. Mak[3], X.Y. Chang[1] and D. Trau[1,2,*]

[1] Division of Bioengineering and [2] Department of Chemical & Biomolecular Engineering, National University of Singapore, Singapore
[3] Department of Chemistry, Hong Kong University of Science and Technology, Hong Kong, China
*Corresponding Author at: Division of Bioengineering, National University of Singapore, Singapore 117576, Singapore.
Tel: 65 65168052. Fax: +65 65163069. Email Address: bietrau@nus.edu.sg (D.Trau)

Abstract — **The "Matrix-assisted Layer-by-Layer (LbL)" encapsulation technique is one approach to encapsulate biomolecules within hydrogel microcapsules. However, performing "matrix-assisted LbL" encapsulation usually results in low encapsulation efficiency of water soluble biomolecules as these biomolecules leach out into the aqueous phase during the LbL process. To achieve high encapsulation efficiency, the idea of LbL in organic solvents, termed as Reverse-Phase (RP)-LbL, is extended into the "matrix-assisted LbL" encapsulation technique. In this work, agarose microbeads are conferred stability in an organic solvent by fabrication of agarose-based colloidosomes. Next, non-ionized polyelectrolytes (non-ionized poly(allylamine) and non-ionized poly(acrylic acid)) are used to coat the surface of these colloidosomes in organic phase to prevent leakage of preloaded biomolecules from the interior of the colloidosomes. This can allow encapsulation of water soluble biomolecules in agarose microcapsules with high efficiency.**

Keywords — **Layer-by-Layer, colloidosome, hydrogel, polymer capsules, polyelectrolytes**

I. Introduction

Microcapsules, with micrometer dimensions, possess a large surface area to volume ratio and therefore allow efficient diffusion of material into or out of the microcapsules. These allow microcapsules to serve as excellent carriers of biomolecules for many fields. For example, in therapeutics [1,2], micro-bioreactors [3], and bioanalytical applications [4,5]. Hence, different methods to fabricate microcapsules that can encapsulate biomolecules have been developed including colloidosomes [6] and the templated Layer-by-Layer (LbL) polyelectrolyte self-assembly technique [7].

Colloidosomes are capsules formed from self assembled microparticles at an interface. For example, liquid/liquid such as oil/water [8]. However, the requirement of harsh conditions for fixation of the microparticles, such as using a chemical cross-linking reagent or sintering at a temperature of 100 °C [9,10], limits their application for encapsulation of biomolecules.

Another approach to encapsulate biomolecules is via the "Matrix-assisted LbL" polyelectrolyte self-assembly technique. Using this technique, water soluble biomolecules have been encapsulated within hydrogel matrix spheres [11]. The hydrogel spheres contain almost 98% water and can provide both physiological environment for the encapsulated biomolecules and mechanical support for maintaining the shape of the microcapsules. However, low encapsulation efficiency of the pre-loaded biomolecules is usually obtained as the water soluble biomolecules leach out from the spheres during the aqueous LbL process.

As existing hydrogel microcapsules encapsulation methods do not allow high encapsulation efficiency, we extend the idea of LbL in organic phase, termed as Reverse-Phase LbL (RP-LbL) [12], into "matrix assisted LbL" encapsulation technique to allow high encapsulation efficiency of water soluble biomolecules.

II. Experimental section

A. Materials

1-butanol anhydrous 99.8%, mineral oil and N-(3-dimethylaminopropyl)-N'-ethylcarbodiimide hydrochloride (EDC) were purchased from Sigma. Poly(allylamine) (PA) MW 65,000 Da and poly(acrylic acid) (PAA) MW 450,000 Da were purchased from Aldrich. Span® 80, Rhodamine 123 and N-hydroxysuccinimide (NHS) were purchased from Fluka. Carboxylate-polystyrene (carboxylate-PS) microparticles with diameter of 1.0 μm and fluorescent labeled carboxylate-PS microparticles with diameter of 1.0 μm were purchased from Polysciences Inc. PS microparticles with diameter of 20 μm were purchased from microParticles GmbH. Ethanol was purchased from Fisher Scientific. Low melting agarose was purchased Promega. PBS was purchased from 1st BASE. All materials were used as received. Double distilled water (d.d. H_2O) used was distilled using a Fistreem™ Cyclone™ machine.

B. Preparation of Colloidosomes

500 μl of carboxylate-PS microparticles suspension as purchased was aliquoted and centrifuged (4,000 rpm, 6 minutes) and the supernatant was subsequently removed. Ethanol was

Chwee Teck Lim, James C.H. Goh (Eds.): ICBME 2008, Proceedings 23, pp. 821–824, 2009
www.springerlink.com

added and the microparticles were sonicated for 30 minutes to remove any existing surfactants. After sonication, the microparticles were centrifuged (2,000 rpm, 3 minutes) and the supernatant subsequently removed. This sonication procedure was repeated for a total of 3 times. The microparticles were dried, weighted and d.d. H_2O was added to make a suspension of 20 % w/v microparticles. The carboxylate-PS microparticles were subsequently used for fabrication of colloidosomes.

All necessary reagents were pre-warmed and kept at a temperature of 45 °C. A molten solution of 4% w/v low-melting agarose was prepared then mixed with the carboxylate-PS microparticles (20% w/v) to prepare a mixture with a final concentration of 2% w/v carboxylate-PS microparticles in 2% w/v agarose. The agarose/carboxylate-PS mixture was added to prewarmed mineral oil containing 0.1% Span 80 and stirred vigorously for 15 minutes to form water-in-oil (w/o) emulsion droplets. The emulsion droplets were then cooled to 25 °C while stirring for another 10 minutes to allow solidification of the molten agarose core and formation of colloidosomes. The colloidosomes were further stabilized by placing at -20 °C for 5 minutes.

C. Preparation of Agarose Microbeads

Agarose microbeads were prepared with similar procedures as mentioned in the preparation of colloidosomes except no carboxylate-PS microparticles were used in the fabrication step.

D. Self assembly of Non-ionized Polyelectrolytes (niPolyelectrolytes) onto Colloidosomes by Reverse-Phase LbL (RP-LbL)

The RP-LbL coating process was entirely performed in 1-butanol with non-ionized poly(allylamine) (niPA) and non-ionized PAA (niPAA) as niPolyelectrolytes. niPA was prepared by drying the PA solution and dissolving with an appropriate amount of 1-butanol to obtain a concentration of 1 mg/mL. niPAA was prepared by dissolving PAA in 1-butanol to a concentration of 5 mg/mL. To transfer the colloidosomes from mineral oil to 1-butanol, an equal amount of ethanol was shaken with the colloidosomes in mineral oil and centrifuged (1,000 rpm, 2 minutes). The mineral oil and ethanol were then discarded and the colloidosomes were then further washed 2 times with 1-butanol using centrifugation (1,000 rpm, 2 minutes) and redispersion. 1.5 mL of niPA in 1-butanol was used as the initial layer followed by 1.5 mL of niPAA in 1-butanol as the subsequent layer. Each niPolyelectrolyte was coated for 15 minutes with gentle vortexing and excess niPolyelectrolyte was washed away via centrifugation (1,000 rpm, 2 minutes) and redispersion 3 times with 1.5 mL of 1-butanol before coating of the next layer.

E. Self assembly of Non-ionized Polyelectrolytes (niPolyelectrolytes) onto PS microparticles by Reverse-Phase LbL (RP-LbL)

The RP-LbL coating process of niPolyelectrolytes onto PS microparticles is similar to the coating process mentioned in self assembly of niPolyelectrolytes onto colloidosomes except PS microparticles were used in place of colloidosomes.

F. Preparation of Fluorescence niPolyelectrolyte

PAA-Rhodamine 123 conjugate was synthesized with a conjugation ratio of 1:10 (Rhodamine 123 molecules:PAA monomer) using EDC/NHS, purified by dialysis (MWCO of 8,000 Da) and dried at 50 °C. The dry niPAA-Rhodamine 123 was dissolved to a concentration of 0.5 mg/mL in 1-butanol.

III. Results & Discussion

A. Coating of Non-ionized Polyelectrolytes (niPolyelectrolytes) onto PS microparticles by Reverse-Phase LbL (RP-LbL)

To study the RP-LbL coating of niPolyelectrolytes, a fluorescent-labeled niPolyelectrolyte (niPAA-Rhodamine 123) was used in combination with niPAA to coat 20 μm PS microparticles. niPA was coated as the odd layers while niPAA/niPAA-Rhodamine 123 was coated as the even layers.

Figure 1 shows the fluorescence intensity of PS microparticles as a function of the number of coated layers. The fluorescence intensity of PS microparticles after each layer coating was quantified by capturing the fluorescence image

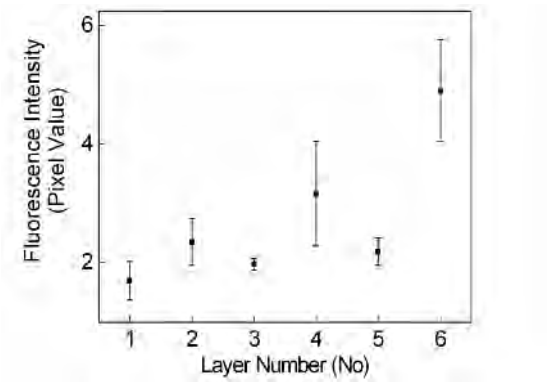


Fig. 1 Fluorescence intensity (pixel value) of PS microparticles against layer number coated onto the microparticles via RP-LbL technique. PAA-Rhodamine 123 was used during coating of even layers as proof of multilayer deposition.

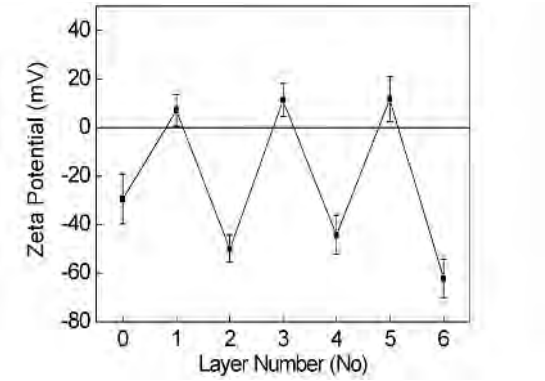


Fig. 2 Zeta potential as a function of layer number (No) for coating of niPolyelectrolytes onto PS microparticles in 1-butanol. Multilayer deposition is demonstrated by the alternating signs of the zeta potential.

of the microparticles and measuring the pixel values of each image using ImageJ. It was noted that the fluorescence intensity of the microparticles increases after each bi-layer coating and this increase in fluorescence intensity is contributed from the accumulation of niPAA-Rhodamine 123 onto the microparticles after each even coating. This result demonstrates that niPA and niPAA can be stepwisecoated onto PS microparticles by RP-LbL.

As further evidence for RP-LbL coating of niPolyelectrolytes onto the PS microparticles, the zeta-potential of the microparticles after each layer coating was measured. All measurements were performed after transferring the PS microparticles from 1-butanol to 0.01x PBS. Figure 2 shows the zeta potential of the PS microparticles after coating of each niPolyelectrolyte layer. The alternating magnitudes of the zeta potential from initially -30 mV (zeta potential of "bare" PS microparticles) to +7, +11 and +12 mV for deposition of niPA layers and -50, -44 and -62 mV for niPAA layers supports evidence for coating of niPolyelectrolytes onto PS microparticles in 1-butanol.

B. Stability & Morphology of Colloidosomes

To improve the mechanical stability of microcapsules and provide a good matrix material to entrap biomolecules, fabrication of microcapsules was done through the use of agarose microbeads – a hydrogel template. Unfortunately, being hydrophilic in nature, the beads are not stable in anhydrous 1-butanol but begin to aggregate (Figure 3A). Hence, microparticles were included into the emulsification phase of agarose microbeads fabrication to produce hydrogel-based colloidosomes [8]. Addition of microparticles was performed to confer dispersion stability to the agarose microbeads in 1-butanol and allow reverse phase (RP)-LbL deposition of polymers. Colloidosomes in 1-butanol were found to be able

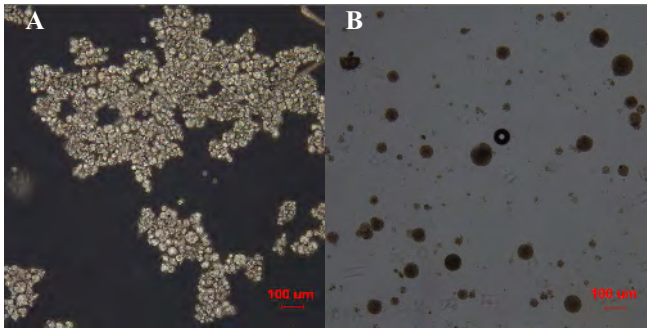


Fig. 3 Optical images of A) Agarose microbeads aggregated in 1-butanol and B) fabricated colloidosomes in 1-butanol. Colloidosomes are stably dispersed and show no aggregation.

to retain their spherical shape (Figure 3B) and colloidosomes fabricated using fluorescent labeled carboxylate-PS beads exhibited a denser population of microparticles lining on the surface of the colloidosomes (Figure 4).

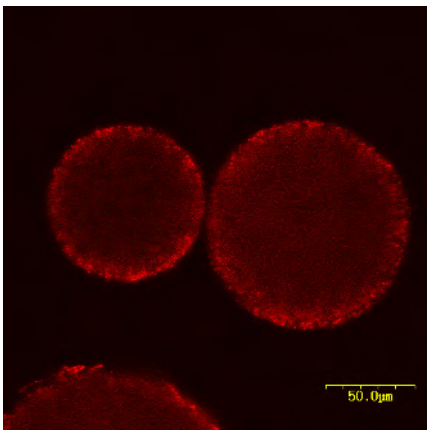


Fig. 4 Confocal Image of colloidosomes fabricated with fluorescent labeled carboxylate PS microparticles. A fluorescence ring can be observed around each colloidosome.

In summary, the inclusion of microparticles for the formation of colloidosomes does allow for the stable dispersion of agarose microbeads in 1-butanol. This stability allows RP-LbL coating of niPolyelectrolytes onto the agarose microbeads for high encapsulation efficiency of water soluble biomolecules.

C. Coating of Non-ionized Polyelectrolytes (niPolyelectrolytes) onto Colloidosomes by Reverse-Phase LbL (RP-LbL)

Encapsulation of preloaded water soluble biomolecules within hydrogel microcapsules with high efficiency requires little or no loss of biomolecules to occur during the LbL

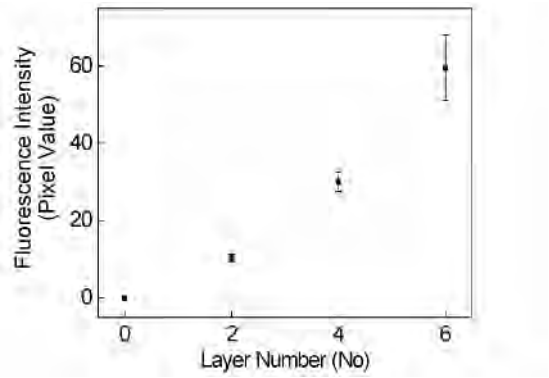


Fig. 5 Fluorescence intensity (pixel value) of colloidosomes against layer number coated onto the colloidosomes via RP-LbL technique. PAA-Rhodamine 123 was used during coating of even layers as proof of multilayer deposition.

coating process. To allow minimal loss of biomolecules, a suitable "coating system" onto the colloidosomes is needed and performing RP-LbL coating of niPolyelectrolytes onto colloidosomes is one suitable approach.

The study of the coating of niPolyelectrolytes onto colloidosomes via RP-LbL was done by using niPAA-Rhodamine 123 as discussed in coating of niPolyelectrolytes onto PS microparticles. Similarly, niPA was coated as the odd layer and niPAA/niPAA-Rhodamine 123 was coated as the even layers. The fluorescence intensity of colloidosomes was also quantified in a similar fashion. Figure 5 shows the fluorescence intensity of the colloidosomes increasing after each bi-layer coating. This increase in fluorescence intensity is due to an accumulation of niPAA-Rhodamine 123 after each bi-layer coating and shows that niPA and niPAA can be coated onto agarose-based colloidosomes by RP-LbL.

IV. Conclusions

niPA and niPAA have been identified as non-ionized polymers that can perform RP-LbL coating of niPolyelectrolytes onto colloidosomes. By coupling this "organic phase coating system" with hydrogel-based colloidosomes, the high encapsulation efficiency of water soluble biomolecules within agarose hydrogel templates has been made possible. We believe that our technology can significantly contribute to the development of microcapsule based bioreactors and bioanalytical system.

Acknowledgment

This work was supported by Research Grant R-397-000-026-112 from National University of Singapore.

References

1. Dai Z, Heilig A, Zastrow H, Donath E, Möwald H (2004) Novel formulations of vitamins and insulin by nanoengineering of polyelectrolyte multilayers around microcrystals. Chem Eur J 10(24):6369-6374
2. De Geest B G, Vandenbroucke R E, Guenther A M, Sukhorukov G B, Hennink W E, Sanders N N, Demeester J, De Smedt S C (2006) Intracellularly degradable polyelectrolyte microcapsules. Adv Mater 18(8):1005-1009
3. Mak W C, Cheung K Y, Trau D (2008) Diffusion controlled and temperature stable microcapsule reaction compartments for high throughput microcapsule-PCR. Adv Funct Mater "in press"
4. Chinnayelka S, McShane M J (2005) Microcapsule biosensors using competitive binding resonance energy transfer assays based on apoenzymes. Anal Chem 77(17):5501-5511
5. Brown J Q, Srivastava R, McShane M J (2005) Encapsulation of glucose oxidase and an oxygen-quenced fluorphore in polyelectrolyte-coated calcium alginate microspheres as optical glucose sensor systems. Biosens Bioelectron 21(1):212-216.
6. Laib S, Routh A F (2008) Fabrication of colloidosomes at low temperature for the encapsulation of thermally sensitive compounds. J Colloid Interface Sci 317(1):121-129.
7. Mak W C, Cheung K Y, Trau D (2008) The influence of different polyelectrolytes on Layer-by-Layer microcapsules properties-encapsulation efficiency, colloidal and temperature stability. Chem Mater 20(17): 5475-5484
8. Cayre O J, Noble P F, Paunov V N (2004) Fabrication of novel colloidosome microcapsules with gelled aqueous cores. J Mater Chem 14(22):3351-3355
9. Velev O D, Furusawa K, Nagayama K (1996) Assembly of latex particles by using emulsion droplets as template. 1. Microstructured hollow spheres. Langmuir 12(10):2374-2384
10. Hsu M F, Nikolaides M G, Dinsmore A D, Bausch A R, Gordon V D, Chen X, Hutchinson J W, Weitz D A, Marquez, M (2005) Self-assembled shells composed of colloidal particles: fabrication and characterization. Langmuir 21(7):2963-2970
11. Srivastava R, Brown J Q, Zhu H, McShane M J (2005) Stable encapsulation of active enzyme by application of multilayer nanofilm coatings to alginate microspheres. Macromol Biosci 5(8):717-727
12. Beyer S, Mak W C, Trau D (2007) Reverse-Phase LbL-encapsulation of highly water soluble materials by Layer-by-Layer polyelectrolyte self-assembly. Langmuir 23(17):8827-8832

LED Based Sensor System for Non-Invasive Measurement of the Hemoglobin Concentration in Human Blood

U. Timm[1], E. Lewis[1], D. McGrath[2], J. Kraitl[3] and H. Ewald[3]

[1] University of Limerick, Optical Fibre Sensors Research Center, Limerick, Ireland
[2] University of Limerick, Graduate Medical School, Limerick, Ireland
[3] University of Rostock, Institute of General Electrical Engineering, Rostock, Germany

Abstract — **In the perioperative area, the period before and after surgery, it is essential to measure diagnostic parameters such as oxygen saturation, hemoglobin (Hb) concentration and pulse. The Hb concentration in human blood is an important parameter to evaluate the physiological condition. By determining the Hb concentration it is possible to observe imminent postoperative bleeding and autologous retransfusions. Currently, invasive methods are used to measure the Hb concentration. For this purpose blood is taken and analyzed. The disadvantage of this method is the delay between the blood collection and its analysis, which doesn't permit a real-time patient monitoring in critical situations. A non-invasive method allows pain free online patient monitoring with minimum risk of infection and facilitates real time data monitoring allowing immediate clinical reaction to the measured data.**

Keywords — **hemoglobin, non-invasive, photoplethysmography**

I. Introduction

In the perioperative area, the period before and after surgery, it is essential to measure diagnostic parameters such as oxygen saturation, hemoglobin (Hb) concentration and pulse[1]. The Hb concentration in human blood is an important parameter to evaluate the physiological condition. By determining the Hb concentration it is possible to observe imminent postoperative bleeding and autologous retransfusions. Currently, invasive methods are used to measure the Hb concentration. For this purpose blood is taken and analyzed. The disadvantage of this method is the delay between the blood collection and its analysis, which does not a permit a real-time patient monitoring in critical situations. A non-invasive method allows pain free online patient monitoring with minimum risk of infection and facilitates real time data monitoring allowing immediate clinical reaction to the measured data. The absorption of whole blood in the visible and near infrared range is dominated by the different hemoglobin derivatives and the blood plasma that consists mainly of water.[2] It is well known that pulsatile changes of blood volume in tissue can be observed by measuring the transmission or reflection of light through it. This diagnostic method is called photo-plethysmography (PPG) The newly developed optical sensor system uses three wavelengths for the measurement of the Hb concentration, oxygenation and pulse. This non-invasive multi-spectral measurement method is based on radiation of near monochromatic light, emitted by light emitting diodes (LED) in the range of 600*nm* to 1400*nm*, through an area of skin on the finger. The sensor assembled in this investigation is fully integrated into a wearable finger clip and allows full wireless operation through on board miniature wireless enabled microcontroller.

II. Measurement method

The new developed sensor device allows a non-invasive continuous measurement of hemoglobin concentration, oxygen saturation and pulse which is based on a multi-spectral measurement method. Thereby the area of skin on the finger is transilluminated by monochromatic light which is emitted by LEDs in the range from 600nm-1400nm.

The arteries contain more blood during the systolic phase of the heart than during the diastolic phase, due to an increased diameter of the arteries during the systolic phase. This effect occurs only in arteries but not in veins.[3]

For this reason the absorbance of light in tissues with arteries increases during systole because the amount of hemoglobin (absorber) is higher and the light passes through a longer optical path length d in the arteries. These intensity changes are the so called PPG-waves.[4] The time varying part allows the distinction between the absorbance due to venous blood (DC part) and that due to the pulsatile component of the total absorbance (AC part). Figure 1 shows the absorption model for light penetrating tissue to sufficient depth to encounter arterial blood. Upon interaction with the tissue the transmitted light is detected non-invasively by photo diodes. Suitable wavelengths were selected for the analyses of relative hemoglobin concentration change and SpO_2 measurement. During the measurement of hemoglobin the absorption should not be dependent on the oxygen saturation. That means that the measurement is only practicable at so called isobestic points where the extinction coefficients of HHb and HbO_2 are identical. One such point is

Chwee Teck Lim, James C.H. Goh (Eds.): ICBME 2008, Proceedings 23, pp. 825–828, 2009
www.springerlink.com

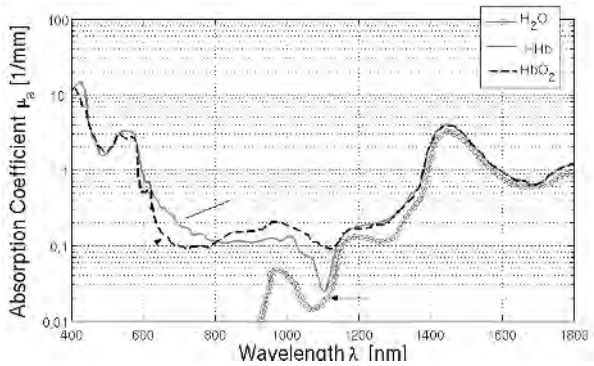


Figure 1: Absorption Spectra of Hemoglobin and Water

known to exist around a wavelength of 810nm.[5] According to the assumption that red blood cells are mainly filled with water, the absorption coefficient of blood is similar to a solution consisting HHb, HbO_2 and water (H_2O) and the absorption of HHb and Hb02 is indistinguishable to the absorption of H_2O above 1200nm, it is necessary to select a wavelength value in this region above the diagnostic window.[6] (Figure 2)

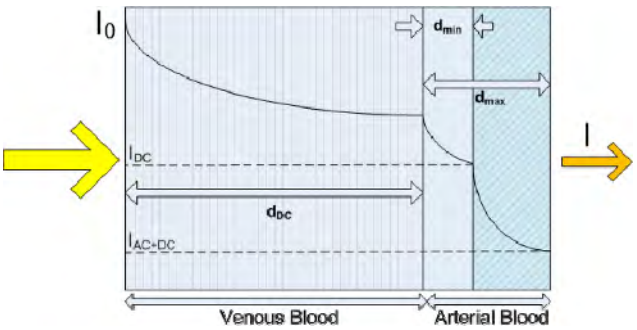


Figure 2: Model of Tissue Layer

Finally the determination of hemoglobin concentration will be performed at the wavelengths λ_1 = 810nm and λ_2 = 1300nm. The AC/DC Values of both wavelengths leads to the quotient H (equation 1):

$$H = \frac{\frac{I_{AC-DC\,810nm}}{I_{DC\,810nm}}}{\frac{I_{AC-DC\,1300nm}}{I_{DC\,1300nm}}} = \ln(10)\frac{\varepsilon_{Hb}\left(\lambda_{810nm}\right)c_{Hb}}{\mu_{H20}\left(\lambda_{1300nm}\right)64500g/l} \quad (1)$$

This theoretical equation results in incorrect values in practise but the fact f(H) is true.[7] Thus, the hemoglobin sensor needs calibration using an external blood stream model including real blood.

III. Sensor Device

The sensor system being developed consists of hardware modules including appropriate light sources and receivers, a microcontroller and a wireless interface. A key component of the sensor system is the low power microcontroller MSP430F1611.[8]

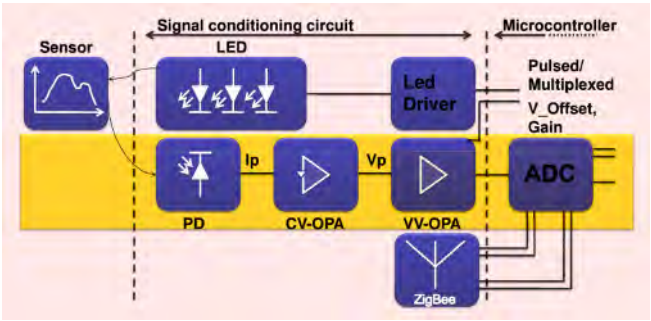


Figure 3: Functional Diagram Sensor Device

This enables software controlled and time multiplexed operation of the light sources and receiver channels. The mean value is calculated and the dark current subtracted in software, and the data is transmitted via serial RS232 or wireless interface. With application software programmed in LabView it is possible to handle the data on a Laptop or PC. The light sources, three LEDs, with centre wavelengths of λ_1= 670nm, λ_2= 810nm and λ_3= 1300nm are installed in the upper part of the clip. The pulsed LED currents are controlled by the microcontroller that allows a change of the light source intensity. To detect the transmission signals of the LEDs a silicon photodiode with a spectral range of 400nm-1100nm was used. For measuring at 1300nm an additional Indium Gallium Arsenide (InGaAs) photodiode with a spectral of 1000nm-1700nm is selected.
Figure 4 shows a photo of the sensor device.



Figure 4: Sensor Head with Photodiodes and Light Sources

IV. Blood Stream Model

The human circulatory system is a fast regulatory transport system. This closed circuit consist of parallel and serially connected blood vessels for which the heart acts as a circulation pump. The mandatory blood circulation is maintained by the contraction of the muscular cardiac wall. The heart is made up of a left and right cardiac half, each of them being a muscular hollow organ. In functional and morphologic terms the circulatory system consists of two serial sections. The heart also can be considered as two serial pumps. The right cardiac side absorbs the deoxygenated blood from the body and transports it to the lungs (lung circuit), where it is re-oxygenated. The oxygenated blood arrives at the left cardiac side, wherefrom the dispensation to various organs takes place (body circuit). The oxygenated blood in the body circuit is pumped from the left ventricle to the aorta and main arteries whose sub branches lead to the tissue and organs. Following the next stage of branching into arteriole and capillary, the oxygen and nutrients and the ingestion of carbon monoxide and intermediate catabolic products are distributed to the tissue and organs of the body. Finally the capillaries terminate into venules and veins which transport the deoxygenated blood back to the right atrium. Figure 5 shows the measuring point for the developed hemoglobin sensor which is located on the finger terminal element.

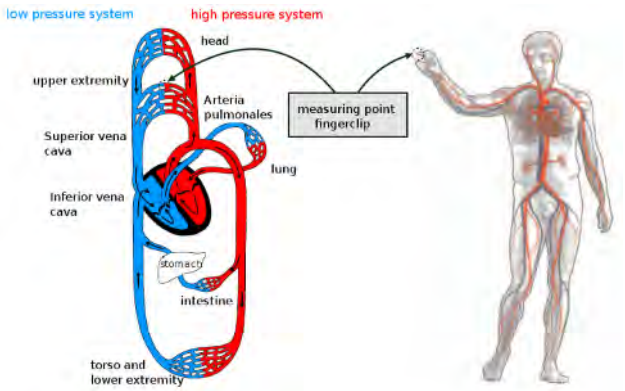


Figure 5: Measuring Point on Circulatory System

Based on human circulatory system a bloodstream model has been designed which is necessary for validation of the measurement method of hemoglobin concentration and the

newly developed optical sensor system. With the help of the model a controlled variation of the blood parameter, hemoglobin concentration and oxygenation are feasible. Thereby both parameters can be changed separately or simultaneously on circulating blood is not representative of the typical physiological state. Therefore a setup for optical measurement on circlulating blood is necessary. By using a circulation system based on a roller pump the blood is circulated through the closed circuit and a pulsatile blood volume is generated. The schematic diagram of the system is shown in Fig. 6.

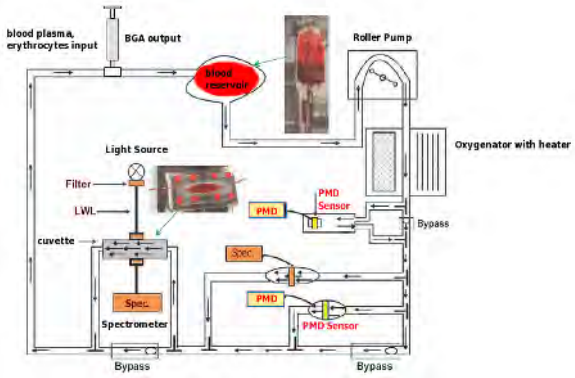


Figure 6: Functional Diagram of the Blood Stream Model

Using this system measurement allowing the accurate assessment of the pulsatile blood portion (AC/DC signal ratio) is possible. The input point is at the same time the blood sample extraction point which will be needed for the reference point measurement. The blood gassing takes place in the oxygenator which allows the precisely controlled introduction of oxygen or carbon monoxide and a separate heated water circuit allows the elevation of the blood temperature to 36°C -37°C

V. Results

Initial measurements of the transmission signals on the finger terminal element have shown variations in light absorption due to the arterial pulse at all three wavelengths. The signal at 1300nm is especially weak and requires further effort in signal processing. However, the signal quality is sufficient to allow analysis of the signals and to calculate the relative attenuation coefficient of the arterial blood. In case of the signal components at 1300nm an evaluation of the relative portions of hemoglobin and water in blood are feasible.[9] On the basis of this measurement technique a pulsed signal for the calculation of the relative attenuation coefficient is required. Decreases of the signal amplitude and therefore the signal to noise ratio caused by vasoconstriction at the extremities is a potential problem. Small signal amplitudes can give rise to inaccurate results.[10] Figure 7 shows the signal at 1300nm and 810nm when light is transmitted through the finger.

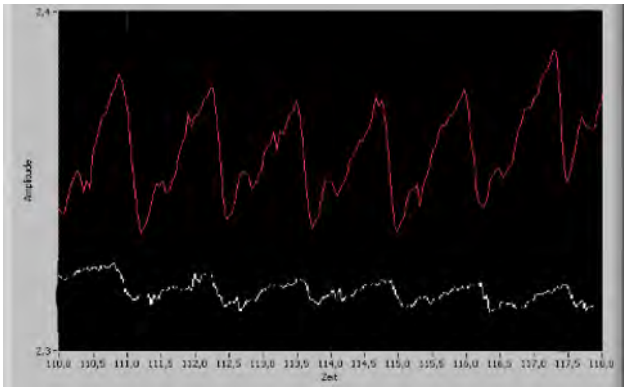


Figure 7: PPG Wave at 810nm and 1300nm

The developed sensor device is suitable for non-invasive continuous online monitoring of one ore biological parameter. The advantage of this measuring technique is independent of blood samples and this allows a minimum risk of infection and it makes possible to react immediately on the measured data.

VI. Conclusions

In this paper a non invasive device for measuring hemoglobin concentration based on multi wavelength light absorption has been reported. The newly developed sensor device is able to measure PPG signals at three independent wavelengths continuously. Future work involves validation of the sensor measurement based on further measurements using an experimental blood stream model and optimisation of the sensor device.

References

1. T. Ahrens and K.Rutherford. Essentials of Oxygenation: Implication for Clinical Practice. Jones & Bartlett Pub, 1993.
2. S. J. Matcher, M. Cope, and D. T. Delpy. Use of the water absorption spectrumto quantifies tissue chromospheres concentration changes in near-infrared spectroscopy. Phys. Med. Biol., 38:177–196, September 1993.
3. Woods AM, Queen, JS, Lawson D., 1991 Valsalva maneuver in obstetrics: The influence of peripheral circulatory changes on function of the pulse oximeter, Anesth. Analg. 73 pp. 765-71
4. Lock I, Jerov M, Scovith S (2003) Future of modeling and simulation, IFMBE Proc. vol. 4, World Congress on Med. Phys. & Biomed. Eng., Sydney, Australia, 2003, pp 789–792
5. Kamal AAR, Hatness JB, Irving G, Means AJ, 1989 Skin photoplethysmography – a review, Comp. Meth.Progr. Biomed., 28, pp 257-69
6. N. Kollias. Tabulated molar extinction coe_cient for hemoglobin in water. Wellman Laboratories, Harvard Medical School, Boston, 1999.
7. Kratil, J., Ewald H., Results of hemoglobin concentration measurements in whole blood with an optical non-invasive method", Photon08, Optics and Photonics, IOP Conference, p 77, Edinburgh UK, 2008
8. U.Timm, E.Lewis, H.Ewald, "Non-Invasive Wireless Sensor System for Measurement of Hemoglobin Concentration in Human Blood", 6th International Forum Life Science Automation (LSA) 2008, September 10th-12th, Rostock, Germany, ISBN: 978-3-938042-17-54
9. Kraitl, J., Ewald H.: None-invasive measurement of hemoglobin concentration with a pulsephotometric method" Proceedings, 5th International Forum Life Science Automation, Washington (DC), USA
10. Yosihida I, Shimada Y, Oka N, Hamaguri K, 1984, Effects of multiple scattering and pheripheral circulation on aterial oxygen saturation measured with pulse type oximeter, Med & Biol. Eng & Comput., 22, pp 475-78

Amperometric Hydrogen Peroxide Sensors with Multivalent Metal Oxide-Modified Electrodes for Biomedical Analysis

Tesfaye Waryo[1,5,*], Petr Kotzian[2], Sabina Begić[3], Petra Bradizlova[2], Negussie Beyene[4], Priscilla Baker[5], Boitumelo Kgarebe[5], Emir Turkušić[3], Emmanuel Iwuoha[5], Karel Vytřas[2] and Kurt Kalcher[1]

[1]Institute of Chemistry-Analytical Chemistry, Karl-Franzens University of Graz, Graz, Austria
[2]Department of Analytical Chemistry, University of Pardubice, Pardubice, Czech Republic
[3]Department of Chemistry, University of Sarajevo, Sarajevo, Bosnia and Herzegovina
[4]Department of Chemistry, Addis Ababa University, Addis Ababa, Ethiopia
[5]SensorLab, Department of Chemistry, University of the Western Cape, P/Bag X17, Bellville 7535, South Africa

Abstract — **An overview of publications (1991 – 2007) on amperometric sensors for hydrogen peroxide (H_2O_2) is presented, with emphasis on carbon electrodes modified with multivalent-metal oxides as electro-catalysts and applications in biosensors.**

Keywords — **Hydrogen peroxide; amperometric sensors; amperometric biosensors; metal oxides; electrocatalyst; carbon electrodes.**

I. Introduction

The development of methods for the detection and quantification of hydrogen peroxide (H_2O_2) in environmental and biological samples is invaluable, particularly as it will also find applications in the indirect determination of several substances of clinical, dietary, and environmental importance [1-4]. H_2O_2 is a by-product of several biochemical reactions and, as a result, it is ubiquitous in the natural biological systems. It has been described as quantitatively the most dominant peroxide in brain cells [4]. Formed via various routes such as superoxide dismutase-catalyzed disproportionation of the superoxide ion [5] and oxidiase enzymes-catalyzed oxidation of biomolecules with oxygen [4,6-8], it is eliminated from the body by the action of catalase and peroxidase enzymes. Peroxidases rely on molecular reducing agents like ascorbates and glutathion [9,10]. Thus, while H_2O_2 by itself is an intesting analyte, the above listed enzymatic reactions in general, and the oxidase catalyzed systems in particular serve as selective biochemical recognition reactions linking H_2O_2 with a number of biomolecules of clinical and dietary interest such as amines, uric acid, glucose, glutamate, lactate, cholesterol, and alcohols [11-15]. Therefore, the development of H_2O_2-detection methods is a catch-all strategy in bioanalytical chemistry.

H_2O_2 can be assayed using various chemical and instrumental methods such as volumetric redox titration [16], spectrophotometry [17], chemiluminometry [18], fluorimetry [19], amperometry/ voltammety and potentiometry [20,21]. *In vivo* and *in vitro*-H_2O_2 determination methods based on indirect spectrophotometric and fluorimetric detections were reviewed by Tarpey and co-workers [22]. Brief reviews on amperometric/ voltammetric sensors for H_2O_2 are widely available [23-27]. Amperometric sensors are interesting since they are suitable for designing portable and multiplex chemical sensor devices with background and interference correction capability. Such H_2O_2 sensors transduce the concentration of H_2O_2 into an electrical current signal via a direct or an indirect electrochemical reduction (cathodic) or oxidation (anodic) of H_2O_2. It is also easy to tailor amperometric sensors in order to suit different real samples by using materials with selective recognition and signal amplification properties towards the analyte of interest [28,29]. Multivalent metal oxides are interesting materials because of the wide spectrum of structure-properties they exhibit. We give an over view of amperometric H_2O_2 sensors in which these oxides function as electrochemical recognition and signal amplification componets. Biosensors developed on sensors for some clinical analytes are also highlighted.

II. Chemically modified electrodes in context

In biomedical analysis, of particular interest is the development of selective amperometric biosensors for in-*vivo* and *in-vitro* applications. Such sensors must be able to function at physiologic pH conditions in the highly complex matrix of undiluted body fluids. For instance, a successful blood serum diagnostics could be anticipated only if the biosensor is developed on an H_2O_2 sensor that responds insignificantly to other common electroactive components at the respective serum concentrations; i.e., less than 1 mM uric acid, ascorbic acid, and acetaminophen; few mM xanthine; 20-40 μM hypoxanthine, Fe, and Cu species [30,31]. Amperometric methods and biosensors based on the detection of H_2O_2 at classic metal electrodes (Pt, Hg, Au) or carbon (C) require very high operating potentials (> 600 or

Chwee Teck Lim, James C.H. Goh (Eds.): ICBME 2008, Proceedings 23, pp. 829–833, 2009
www.springerlink.com

< -600 mV and even outside the range ± 1000 in case of C). Consequently, they are prone to interference [23,24,26] besides surface-fouling complications [26,32]. These limitations could be addressed by different strategies [23,26,33], among which is to lower the operating potential itself by using electrocatalyst-modified electrodes [24]. Chemically modified electrodes have been excellently discussed else where [28,29], and carbon electrodes are the most attractive for modification studies [25,34,35].

Carbon paste (CPE) or thick film (screen printed) carbon electrodes (SPCE) modified with MnO_2 [36], Prussian blue [37], metallophthalocyanins [38], Rh and Ru [24], hexacyanoferrates [39] exhibited significantly reduced operating potentials and improved selectivity. Different enzymes (purified or as-is in tissues) have also been utilized in H_2O_2 biosensors and bi-enzymatic oxidase-biosensors [40,41]. As readily available and robust catalytic materials are preferred, the authors are particularly interested in multivalent metal oxides, which are thermodynamically stable and sparingly soluble under ordinary conditions [42] could yield stable and commercially cheap sensors.

III. Multi-valent metal oxide-modified electrodes

The earliest (1990s) H_2O_2 sensors with electrodes-modified with electrocatalytically active oxides of multivalent metals were based on Mn and Ir oxide films electrochemically deposited on GCE surfaces [43,44], and a Co(II,III) oxide-bulk modified CPE [45]. Since then, amperometric sensors for H_2O_2 based on commercially available powders of MnO_2, Fe_3O_4, CuO, and oxides of platinum metals incorporated into bulk-modified carbon paste and screen printed carbon electrode have been reported [27,46-54]. GCEs modified with electrodeposited films of Ni and Co hydroxides were also reported recently [55,56]. Some Pervoskyte-type oxides, namely $La_{0.6}Ca_{0.4}MnO_3$ and $La_{0.6}Ca_{0.4}CoO_3$ were also tested [57,58]. Zirconia doped with vanadium was also shown to be promising [59]. Polyoxometallates (POMs) [60], especially heteropolytungstates and heteropolymolybdates or their doped and composite versions, are electroctalytic towards H_2O_2 but sensors based on POM-modified electrodes worked only at very low pH conditions [61,62].

Table 1 compiles the multivalent-metal oxide-modified carbon electrodes studied at physiological conditions. Operating potentials, detection limits, and linearity ranges varied markedly with the type of the oxide. The operating potentials of the sensors operated anodically may be compared as follows: nano Co_3O_4 = $La_{0.6}Ca_{0.4}MnO_3$ (+750 mV) > nano MnO_2 > RhO_2 = PdO ≈ RuO_2 (+480 mV) ≈ IrO_2 (+400 mV) ≥ MnO_2 > nano cryptomelane type Mn oxide (+300 mV). Those which were operated cathodically may be ordered according to decreasing operating potential: $VZrO_2$ (-400 mV) = CuO/ Cu_2O ≥ FeO (-200 mV) ≈ Fe_3O_4 ≈ SnO_2 (-170 mV) ≥ PtO_2 (-100 mV).

Table 1. Amperometric H_2O_2 sensors with multivalent metals oxide[§]-modified carbon electrodes demonstrated at physiologic conditions

Sensor	E**/ mV	Mode	DL µM	Linearity, µM	Ref.
MnO_2||SPCE	+480[a]	FIA	0.07	0.1 – 300	[27]
$^{nano}MnO_2$|NaMM||GCE	+650[a]	Stir	0.15	0.5 – 7500	[52]
$^{nano}MnO_2$|DHP||GCE	+650[a]	Stir	0.080	0.10-2000	[53]
Fe_3O_4|C-ink||GCE	-200[c]	RDE	25/3	25 – 1000	[51]
Fe_3O_4|Chitosan|C||GCE	-200[c]	RDE	7.4	25 – 5000	[51]
Fe_3O_4|SPCE	-100[c]	FIA	9	300 – 30000	[48]
FeO|SPCE	-200[c]	FIA	1.2	150 – 60000	[63]
$^{nano}Fe_2O_3$|CPE	-200[c]	Stir	20	Up to 8500	[64]
SnO_2|SPCE	-175[c]	FIA	2.9	150 – 9000	[63]
RuO_2|SPCE	+480[a]	FIA	0.1	29 – 29000	[49]
RhO_2|SPCE	+500[a]	FIA	0.7	3 – 3000	[65]
PdO|SPCE	+500[a]	FIA	24	29 – > 2900	[50]
IrO_2|SPCE	+400[a]	FIA	7	29 – > 2900	[50]
PtO_2|SPCE	−100[c]	FIA	1	29 – > 2900	[50]
CuO|Cu_2O|CPE	-400[c]	Batch	?	?	[54]
$^{nano}Co_3O_4$|Nafion||GCE	+750[a]	CV	0.050	1 – 100	[66]
$^{nano}Co_3O_4$|Nafion||GCE	+750[a]	RDE	$4x10^{-4}$	0.004 – 300	[66]
m-$VZrO_2$||GCE	-400[c]	DPV	1.7	5 – 400	[59]
m-$VZrO_2$||Polyester|C	-400[c]	DPV	2.1	5 – 400	[59]
$^{nano}KMn^{IV}_4Mn^{II}O_{16}$|CPE	+300[a]	Stir	2	100 – 690	[67]
$La_{0.6}Ca_{0.4}MnO_3$||Teflon|C	+750[a]	Stir	?	Up to 500	[57]

[§]Assume microparticles if not specified; "nano" - nanoparticles; **"|"**: bulk-modified, "||": surface-modified; GCE, CPE, and SPCE: glassy, paste, screen printed carbon electrodes; NaMM: sodium montmorillonite; DHP: dihexadecyl hydrogen phosphate; *m*- prefix: monoclinic; ******operating potentials vs. Ag|AgCl or Hg|Hg_2Cl_2 reference; superscripts: a: anodic, c: cathodic; FIA: flow injection analysis; RDE: rotating disc electrode; CV and DPV: cyclic and differential pulse voltammetry; DL: detection limit.

Operated either under hydrodynamic (rotation, stirring, and flowing injection) or voltammetric modes, response times of the sensors were generally described as fast (seconds), but flow rates and voltammetric scan rates obviously determined sample throughput rates. The lowest detection limit (0.4 nM) was reported for nano Co_3O_4-film-modified GCE (rotating disc set-up). However, this was found at high operating potential (+750 mV). The widest linearity range (5 orders) was reported for electrodeposited films of Co_3O_4 and MnO_2. With respect to operational and storage stability, no practical limitations were reported.

SPCEs modified with oxides of Fe and Sn were reported as selective against ascorbic acid, uric acid, acetaminophen,

and xanthine species, possibly because of their low operating potentials. Ascorbic acid, nucleic acid species, and dopamine interfered with MnO_2, RuO_2, and RhO_2-modified electrodes, probably because they were operated at relatively high anodic potentials. Generally, sugars and amino acid species were reported as non-interfering substances. Such data was unavailable for the other oxides.

MnO_2, Fe_3O_4, FeO, RuO_2, RhO_2, IrO_2, PdO_2, and PtO_2 bulk-modified SPCEs have been tested successfully by developing model biosensors using glucose oxidase [48-50,68-70]. A similar demonstration of CuO was also reported [69] using CPEs double bulk-modified with the oxide and glucose oxidase. MnO_2 has seen further applications in which biosensors for sarcosine [71], glutamate [72], and β-ODAP [73] were developed and tested for the determination of these analytes in food samples. In-tissue implantation study with MnO_2-based glucose biosensors was also reported [74]. RuO_2 was tested in a fish quality biosensor [75].

IV. Concluding remarks

A brief account sensors for H_2O_2 with multivalent metal oxide-modified electrodes was presented. Oxides of twelve multivalent metals: Mn, Fe, Co, Ni, Pt, Rh, Pd, Ru, Ir, V/Zr, Cu, and Sn have been identified. Overall, the analytical characteristics of the sensors largely appeared promising.

Acknowledgement

We gratefully acknowledge supports from National Research Fund (NRF, South Africa), Academic Exchange Service (ÖAD – Austria), and Ministry of Education (Czech Republic).

References

1 ECETOC. (1996) Hydrogen peroxide OEL criteria document, special report No. 10, Euopean Center for Ecotoxicology of Chemicals
2 Guwy, A.J., Hawkes, F.R., Martin, S.R., Hawkes, D.L. Cunnah, P. (2000) A technique for monitoring hydrogen peroxide concentration off-line and on-line. Water Research 34: 2191-2198
3 Anglada, J.M., Aplincourt, P., Bofill, J.M. Cremer, D. (2002) Atmospheric formation of OH radicals and H2O2 from alkene ozonolysis under humid conditions. ChemPhysChem 3: 215-221
4 Dringen, R., Pawlowski Petra, G. Hirrlinger, J. (2005) Peroxide detoxification by brain cells. Journal of neuroscience research 79: 157-165
5 Cowan, J.A. (1997) Cell Toxicity and Chemotherapeutic. In Inorganic Biochemistry, an introduction, , pp. 319-356, Wiley-VCH
6 Walters, D.R. (2003) Polyamines and plant disease. Phytochemistry 64: 97-107
7 Ohshima, H., Tatemichi, M. Sawa, T. (2003) Chemical basis of inflammation-induced carcinogenesis. Archives of Biochemistry and Biophysics 417: 3-11
8 Toninello, A., Salvi, M., Pietrangeli, P. Mondovi, B. (2004) Biogenic amines and apoptosis: Minireview article. Amino Acids 26: 339-343
9 Blokhina, O., Virolainen, E. Fagerstedt, K.V. (2003) Antioxidants, oxidative damage and oxygen deprivation stress: A review. Annals of Botany (Oxford, United Kingdom) 91: 179-194
10 Veal, E.A., Day, A.M. Morgan, B.A. (2007) Hydrogen peroxide sensing and signaling. Molecular Cell 26: 1-14
11 Shih, J.C. (2007) Monoamine Oxidases: From Tissue Homogenates to Transgenic Mice. Neurochemical Research 32: 1757-1761
12 Tipton, P.A. (1999) Kinetic studies of urate oxidase. Biomedical and Health Research 27 (Enzymatic Mechanisms): 278-287
13 Wong, C.M., Wong, K.H. Chen, X.D. (2008) Glucose oxidase: natural occurrence, function, properties and industrial applications. Applied Microbiology and Biotechnology 78: 927-938
14 Schwelberger, H.G. (2004) Diamine oxidase (DAO) enzyme and gene. In Histamine: Biology and Medical Aspects (Falus, A., ed.), pp. 43-52
15 De Tullio, M.C., Liso, R. Arrigoni, O. (2004) Ascorbic acid oxidase: an enzyme in search of a role. Biologia Plantarum 48: 161-166
16 Bassett, J., Denney, R.C., Jeffery, G.H. Mendham, J. (1981) In Vogel's Textbook of quantitative inorganic analysis, including elementary instrumental analysis pp. 355, 381, Longman
17 Bailey, R.Boltz, D.F. (1959) Differential spectrophotometric determination of hydrogen peroxide with 1,10-phenanthroline and bathophenanthroline. Analytical Chemistry 31: 117-119
18 Omanovic, E.Kalcher, K. (2005) A new chemiluminescence sensor for hydrogen peroxide determination. International Journal of Environmental Analytical Chemistry 85: 853-860
19 Black, M.J.Brandt, R.B. (1974) Spectrofluorometric analysis of hydrogen peroxide. Analytical Biochemistry 58: 246-254
20 Ho, M.H. (1988) Potentiometric biosensor based on immobilized enzyme membrane and fluoride detection. Sensors and Actuators 15: 445-450
21 Zheng, X.Guo, Z. (2000) Potentiometric determination of hydrogen peroxide at MnO2-doped carbon paste electrode. Talanta 50: 1157-1162
22 Tarpey, M.M., Wink, D.A. Grisham, M.B. (2004) Methods for detection of reactive metabolites of oxygen and nitrogen: in vitro and in vivo considerations. American Journal of Physiology 286: R431-R444
23 Prodromidis, M.I.Karayannis, M.I. (2002) Enzyme based amperometric biosensors for food analysis. Electroanalysis 14: 241-261
24 Wang, J., Lu, F., Angnes, L., Liu, J., Sakslund, H., Chen, Q., Pedrero, M., Chen, L. Hammerich, O. (1995) Remarkably selective metalized-carbon amperometric biosensors. Analytica Chimica Acta 305: 3-7
25 Svancara, I., Vytras, K., Barek, J. Zima, J. (2001) Carbon paste electrodes in modern electroanalysis. Critical Reviews in Analytical Chemistry 31: 311-345
26 O'Neill, R.D., Chang, S.-C., Lowry, J.P. McNeil, C.J. (2004) Comparisons of platinum, gold, palladium and glassy carbon as electrode materials in the design of biosensors for glutamate. Biosensors & Bioelectronics 19: 1521-1528
27 Schachl, K., Alemu, H., Kalcher, K., Moderegger, H., Svancara, I. Vytras, K. (1998) Amperometric determination of hydrogen peroxide with a manganese dioxide film-modified screen printed carbon electrode. Fresenius' Journal of Analytical Chemistry 362: 194-200
28 Martin, C.R.Foss, C.A. (1996) Chemically Modified Electrodes. In Laboratory Techniques in Electroanalytical Chemistry (Kissinger, P.T. and Heineman, W.R., eds.), pp. 403-442, Marcel Dekker

29 Zen, J.-M., Kumar, A.S. Tsai, D.-M. (2003) Recent updates of chemically modified electrodes in analytical chemistry. Electroanalysis 15: 1073-1087

30 Kock, R., Delvoux, B. Greiling, H. (1993) A high-performance liquid chromatographic method for the determination of hypoxanthine, xanthine, uric acid and allantoin in serum. European Journal of Clinical Chemistry and Clinical Biochemistry 31: 303-310

31 Repetto, M.R.Repetto, M. (1999) Concentrations in human fluids: 101 drugs affecting the digestive system and metabolism. Journal of Toxicology, Clinical Toxicology 37: 1-8

32 Maidan, R.Heller, A. (1992) Elimination of electrooxidizable interferant-produced currents in amperometric biosensors. Analytical Chemistry 64: 2889-2896

33 Wang, J., Angnes, L., Sakslund, H., Fang, L., Pedrero, M., Chen, Q. Liu, J. (1995) Mettalized carbons for improved amperometric biosensors. Book of Abstracts, 210th ACS National Meeting, Chicago, IL, August 20-24: INOR-349

34 McCreery, R.L.Cline, K.K. (1996) Carbon Electrodes. In Laboratory Techniques in Electroanalytical Chemistry (Kissinger, P.T. and Heineman, W.R., eds.), pp. 293-332, Marcel Dekker, New York

35 Svancara, I.Schachl, K. (1999) Testing of unmodified carbon paste electrodes. Chemicke Listy 93: 490-499

36 Schachl, K., Alemu, H., Kalcher, K., Jezkova, J., Svancara, I. Vytras, K. (1998) Determination of hydrogen peroxide with sensors based on heterogenous carbon materials modified with manganese dioxide. Scientific Papers of the University of Pardubice, Series A: Faculty of Chemical Technology 3: 41-55

37 Moscone, D., D'Ottavi, D., Compagnone, D., Palleschi, G. Amine, A. (2001) Construction and analytical characterization of Prussian blue-based carbon paste electrodes and their assembly as oxidase enzyme sensors. Analytical Chemistry 73: 2529-2535

38 Linders, C.R., Vincke, B.J. Patriarche, G.J. (1986) Catalase like activity of iron phthalocyanine incorporated in a carbon paste electrode. Analytical Letters 19: 1831-1837

39 Garjonyte, R.Malinauskas, A. (1998) Electrocatalytic reactions of hydrogen peroxide at carbon paste electrodes modified by some metal hexacyanoferrates. Sensors and Actuators, B: Chemical B46: 236-241

40 Kwon, H., Park, I.K. Kim, Y.S. (2004) Amperometric biosensor for hydrogen peroxide determination based on black goat liver-tissue and ferrocene mediation. Journal of the Korean Chemical Society 48: 491-498

41 Wollenberger, U., Wang, J., Ozsoz, M., Gonzalez-Romero, E. Scheller, F. (1991) Bulk modified enzyme electrodes for reagentless detection of peroxides. Bioelectrochemistry and Bioenergetics 26: 287-296

42 Schmuki, P. (2002) From Bacon to barriers: a review on the passivity of metals and alloys. Journal of Solid State Electrochemistry 6: 145-164

43 Taha, Z.Wang, J. (1991) Electrocatalysis and flow detection at a glassy carbon electrode modified with a thin film of oxymanganese species. Electroanalysis 3: 215-219

44 Cox, J.A.Lewinski, K. (1993) Flow injection amperometric determination of hydrogen peroxide by oxidation at an iridium oxide electrode. Talanta 40: 1911-1915

45 Mannino, S., Cosio, M.S. Ratti, S. (1993) Cobalt(II, III) oxide chemically modified electrode as amperometric detector in flow-injection systems. Electroanalysis 5: 145-148

46 Schachl, K., Alemu, H., Kalcher, K., Jezkova, J., Svancara, I. Vytras, K. (1997) Amperometric determination of hydrogen peroxide with a manganese dioxide-modified carbon paste electrode using flow injection analysis. Analyst (UK) 122: 985-989

47 Schachl, K., Alemu, H., Kalcher, K., Jezkova, J., Svancara, I. Vytras, K. (1997) Flow injection determination of hydrogen peroxide using a carbon paste electrode modified with a manganese dioxide film. Analytical Letters 30: 2655-2673

48 Waryo, T.T., Begic, S., Turkusic, E., Vytras, K. Kalcher, K. (2005) Metal Oxide-Based Carbon Amperometric H2O2-Transducers and Oxidase Biosensors. In Sensing in Electroanalysis (K. Vytras and Kalcher, K., eds.), pp. 145-191, University of Pardubice

49 Kotzian, P., Brazdilova, P., Kalcher, K. Vytras, K. (2005) Determination of hydrogen peroxide, glucose and hypoxanthine using (bio)sensors based on ruthenium dioxide-modified screen-printed electrodes. Analytical Letters 38: 1099-1113

50 Kotzian, P., Brazdilova, P., Kalcher, K., Handlir, K. Vytras, K. (2007) Oxides of platinum metal group as potential catalysts in carbonaceous amperometric biosensors based on oxidases. Sensors and Actuators, B: Chemical B124: 297-302

51 Lin, M.S.Leu, H.J. (2005) A Fe3O4-based chemical sensor for cathodic determination of hydrogen peroxide. Electroanalysis 17: 2068-2073

52 Yao, S., Yuan, S., Xu, J., Wang, Y., Luo, J. Hu, S. (2006) A hydrogen peroxide sensor based on colloidal MnO2/Na-montmorillonite. Applied Clay Science 33: 35-42

53 Yao, S., Xu, J., Wang, Y., Chen, X., Xu, Y. Hu, S. (2006) Analytica Chimica Acta 557: 78-84

54 Garjonyte, R.Malinauskas, A. (1998) Amperometric sensor for hydrogen peroxide,based on Cu2O or CuO-modified carbon paste electrodes. Fresensius J. Anal. Chem. 360: 122-123

55 Liu, Y.-q.Shen, H.-x. (2005) Preparation of nickel hydroxide modified glassy carbon electrode and its electrochemical behavior. Fenxi Kexue Xuebao 21: 378-380

56 Liu, Y., Liu, L. Shen, H. (2004) Preparation of a cobalt hydroxide modified glassy carbon electrode and its electrochemical behavior. Fenxi Ceshi Xuebao 23: 9-13

57 Shimizu, Y., Komatsu, H., Michishita, S., Miura, N. Yamazo, N. (1996) Sensing characteristics of hydrogen peroxide sensor using carbon-based electrode loaded with perovskite-type oxide. Sensors and Actuators, B: Chemical B34: 493-498

58 Hermann, V., Muller, S. Comninellis, C. (1998) Oxygen and hydrogen peroxide reduction on La0.6Ca0.4CoO3 perovskite electrodes. Proceedings - Electrochemical Society 97-28: 159-169

59 Domenech, A.Alarcon, J. (2002) Determination of hydrogen peroxide using glassy carbon and graphite/polyester composite electrodes modified by vanadium-doped zirconias. Analytica Chimica Acta 452: 11-22

60 Sadakane, M.Steckhan, E. (1998) Electrochemical Properties of Polyoxometalates as Electrocatalysts. Chemical Reviews 98: 219-237

61 Wang, X., Zhang, H., Wang, E., Han, Z. Hu, C. (2004) Phosphomolybdate-polypyrrole composite bulk-modified carbon paste electrode for a hydrogen peroxide amperometric sensor. Materials Letters 58: 1661-1664

62 Gaspar, S., Muresan, L., Patrut, A. Popescu, I.C. (1999) PFeW11-doped polymer film modified electrodes and their electrocatalytic activity for H2O2 reduction. Analytica Chimica Acta 385: 111-117

63 Kalcher, K.Co-workers. (Unpublished data) Unpublished data. Institute of Chemistry, K.F. University of Graz

64 Hrbac, J., Halouzka, V., Zboril, R., Papadopoulos, K. Triantis, T. (2007) Carbon electrodes modified by nanoscopic iron(III) oxides to assemble chemical sensors for the hydrogen peroxide amperometric detection. Electroanalysis 19: 1850-1854

65 Kotzian, P., Brazdilova, P., Rezkova, S., Kalcher, K. Vytras, K. (2006) Amperometric glucose biosensor based on rhodium dioxide-modified carbon ink. Electroanalysis 18: 1499-1504

66 Salimi, A., Hallaj, R., Soltanian, S. Mamkhezri, H. (2007) Nanomolar detection of hydrogen peroxide on glassy carbon electrode modified with electrodeposited cobalt oxide nanoparticles. Analytica Chimica Acta 594: 24-31

67 Lin, Y., Cui, X. Li, L. (2005) Low-potential amperometric determination of hydrogen peroxide with a carbon paste electrode modified with nanostructured cryptomelane-type manganese oxides. Electrochemistry Communications 7: 166-172
68 Turkusic, E., Kalcher, K., Schachl, K., Komersova, A., Bartos, M., Moderegger, H., Svancara, I. Vytras, K. (2001) Amperometric determination of glucose with an MnO2 and glucose oxidase bulk-modified screen-printed carbon ink biosensor. Analytical Letters 34: 2633-2647
69 Luque, G.L., Rodriguez, M.C. Rivas, G.A. (2005) Glucose biosensors based on the immobilization of copper oxide and glucose oxidase within a carbon paste matrix. Talanta 66: 467-471
70 Waryo, T.T., Begic, S., Turkusic, E., Vytras, K. Kalcher, K. (2005) Fe3O4-modified thick film carbon-based amperometric oxidase-biosensor. Scientific Papers of the University of Pardubice, Series A: Faculty of Chemical Technology 11: 265-279
71 Kotzian, P., Beyene, N.W., Llano, L.F., Moderegger, H., Tunon-Blanco, P., Kalcher, K. Vytras, K. (2002) Amperometric determination of sarcosine with sarcosine oxidase entrapped with Nafion on manganese dioxide-modified screen-printed electrodes. Scientific Papers of the University of Pardubice, Series A: Faculty of Chemical Technology 8: 93-101
72 Beyene, N.W., Moderegger, H. Kalcher, K. (2003) A stable glutamate biosensor based on MnO2 bulk-modified screen-printed carbon electrode and Nafion film-immobilized glutamate oxidase. South African Journal of Chemistry 56: 54-59
73 Beyene, N.W., Moderegger, H. Kalcher, K. (2003) A new amperometric ß-ODAP biosensor. Lathyrus Lathyrism Newsletter 3: 47-49
74 Mang, A., Pill, J., Gretz, N., Kränzlin, B., Buck, H., Schoemaker, M. Petrich, W. (2005) Diabetes Technology and Therapeutics 7: 163-173
75 Brazdilova, P., Kotzian, P. Vytras, K. (2005) Biosensor for control of fish meat freshness. Bulletin Potravinarskeho Vyskumu 44: 75-82

Corresponding author:

Tesfaye Waryo
email: twaryo@uwc.ac.za
Tel: +27-219593079
Fax: +27-219591316

Patch-Clamping in Droplet Arrays: Single Cell Positioning via Dielectrophoresis

J. Reboud[1], M.Q. Luong[1, 2], C. Rosales[3] and L. Yobas[1]

[1] Institute of Microelectronics (IME), Agency for Science Technology & Research, SINGAPORE
[2] National University of Singapore (NUS), SINGAPORE
[3] Institute of High Performance Computing (IHPC), Agency for Science Technology & Research, SINGAPORE

Abstract — **This paper reports a new approach to enable patch-clamp recording from living cells in arrays of droplets placed on a microstructured silicon surface. Single cells were positioned on the lateral patch sites by using dielectrophoresis (DEP) electrical force. This approach simplifies the complex packaging process involved when pressure-driven fluidics are used to guide cells through microchannels towards the patching sites. It also enables direct access to the droplets for fluid exchange, opening the way for the gold standard patch-clamp technique to become compatible with the industry standards of high-throughput liquid handling platforms. The microchips contained two 20µm deep chambers etched in silicon and passivated by silicon oxide, holding the reagent droplets, and separated by a 250µm-long buried microchannel with an aperture of around 1µm in diameter. Simulations of a four-electrode configuration showed that negative DEP could advantageously eliminate the need of any bulk fluid movement and enable single cell positioning in droplets.**

Working DEP parameters (voltage, frequency) were identified using gold microprobes as external electrodes, dipped in the cell droplets. Single cell positioning at the keyhole was achieved at a speed of about 4µm/s for an optimum cell concentration.

Keywords — **patch-clamp, microchip, droplet, microfluidics, dielectrophoresis**

I. Introduction

Patch-clamp is the golden standard technique when studying ion channels in living cells. Contrary to optical assays relying on fluorescence, it enables a direct measurement of the ion transport through the membrane pores of the cells. These ion channels play a fundamental role in cell signaling and are involved in many diseases including epilepsy, cardiac arrhythmia, high blood pressure, and diabetes. Moreover ion channels can be affected by drugs targeted at other mechanisms, which lead the U.S. Food and Drug Administration (FDA) to propose new regulations to study such potential side effects [1]. Conventional patch-clamping uses glass micropipettes terminated by micron-sized apertures to electrically isolate a *patch* of cell membrane (electrical sealing) and record the ionic current flowing through the ion channels it contains. To position the pipettes on the cell and obtain a good seal in the order of gigaohms (Gigaseal) through gentle suction, a skilled scientist uses micromanipulators under a microscope. This technique achieves high precision, but is laborious, and hence, low-throughput.

In an attempt to transform patch-clamp into a high-throughput assay, research groups have been developing microfabricated chips containing arrays of patch apertures to replace the glass micropipettes, either in a planar [2] or lateral[3,4] configuration. In an opposing fashion to the conventional technique in which the micropipette is brought to the cell, the chip-based systems rely on pressure-driven flow of the bulk fluid to position the cell on the patch aperture. The same means are used to gently suck the cell further to obtain the gigaseal. Even though means to achieve pressure-driven actuation on chip have been proposed, a truly integrated system is far from reaching the capabilities of high-throughput assays liquid handling platforms. In addition, fluidic channels opened to air can greatly ease fluidic exchanges [4].

Following a trend put forward by DNA chips and liquid handling machines, droplets have been proposed as bioreactors for cell-based assays [5]. They constitute a completely open-access architecture without any capping, greatly simplifying fluidic integration (Figure 1). Furthermore they use very little volumes of precious samples, such as cells or primary cells, or drug candidates. However surface droplets cannot sustain pressure gradients to position the cells to the patch apertures and obtain a good seal.

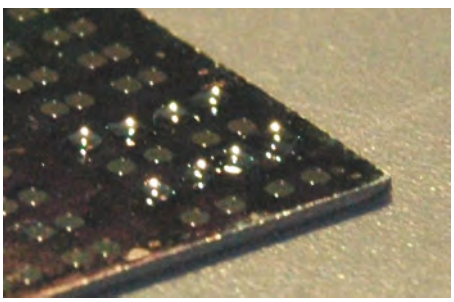


Fig. 1: Silicon microchip for lateral patch-clamping in an array of droplets, without any fluidic channels. Droplets of 0.25µl of cell suspension were manually dispensed onto the microchip

Chwee Teck Lim, James C.H. Goh (Eds.): ICBME 2008, Proceedings 23, pp. 834–837, 2009
www.springerlink.com

Dielectrophoresis (DEP), the electric force arising from the interaction of a particle's polarization and the spatial gradient of the electric field, has been widely used to handle living cells be it in microfluidic flow, or by trapping them in electric field potential wells for example[6,7]. DEP has the advantage of eliminating any bulk movement of the fluid, associated with pressure-driven flow. By carefully designing the geometry of the system, single cells can be captured or directed to specific areas of microsystem, while no measured effects on the cells owing to field exposure have been reported[8].

In this paper, we report a new approach to enable patch-clamp recording from living cells in arrays of droplets placed on a microstructured silicon surface. The patch microapertures (or "keyholes") were fabricated following a technique developed by our group, creating integrated round glass microcapillaries on silicon chips, which has been demonstrated to produce a high success rate of Gigaseals [3]. Using simulations, we studied how negative DEP obtained *via* a four-electrode configuration can control cells in two dimensions and move single cells to the keyhole without liquid flow. This concept is demonstrated by achieving the positioning of single cells to the keyholes at a speed of about 4µm/s.

II. Material and methods

A. Microchip design and fabrication:

The patch micro-apertures were fabricated using a previously reported technique [3] (Figure 2). Briefly, lithographically-defined narrow trenches (2x250x3.5µm cross-section) were etched into a p-type silicon wafer using deep reactive ion etching (RIE). Phosphosilicate glass (PSG) was deposited via plasma enhanced chemical vapour deposition (PECVD) forming a trapped void (''keyhole'') inside the trench, which was rounded after a thermal reflow 1150°C for 30 min.

A second lithography followed by a combination of directional dry etching steps was carried out to create 1mm wide round chambers at both ends of the keyholes and open up the buried capillary. In a final DRIE step the chambers were deepened to 20µm to enable easy access of the cells to the keyhole. The whole surface was finally passivated by silicon oxide.

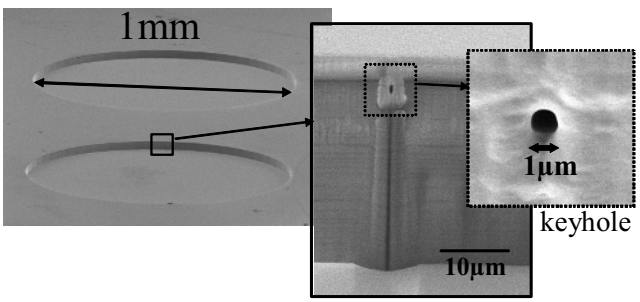


Fig. 2: Scanning Electron Microscope images of a chip, with 2 chambers of 1mm in diameter separated by a 250µm long buried microchannel (or "keyhole").

B. Dielectrophoresis design and simulations:

A 3D model of the microchip was designed in which 4 microelectrodes were placed 2 by 2 on both sides of the keyhole (Figure 2a). The square electrodes shown in Figure 2 represent planar or 3D electrodes that can be microfabricated on the surface of the chip. For ease of computing dimensions were reduced compared to the actual chip. Simulations were performed using depSolver, an Open Source code[9].

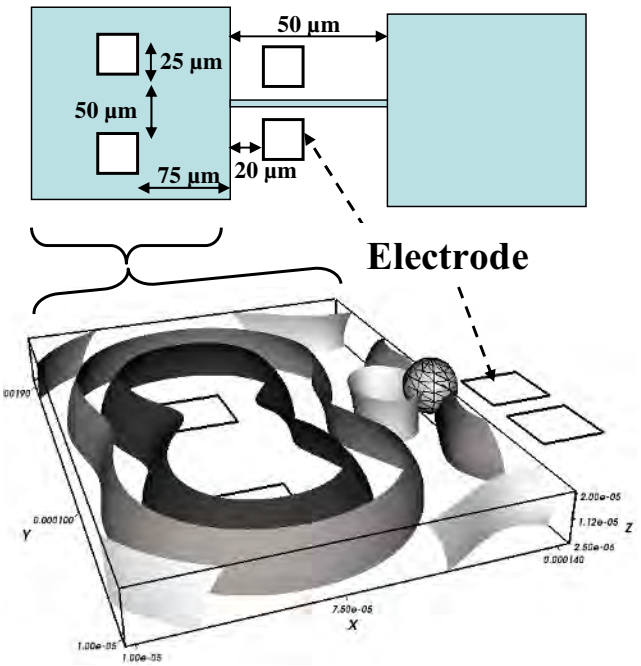


Fig. 3: 3-dimensional simulation of DEP, applied through 4 electrodes (2 right electrodes at the potential +V, left electrodes at –V).
a. Model design used for the simulation. b. Results showing isosurfaces of the DEP force, from dark (intense force) to white (weak).
The sphere represents a particle trapped at the keyhole.

C. DEP application on cells, using external electrodes:

Jurkat T-lymphocytes (ATCC) were maintained following the supplier's protocol. They were harvested and resuspended in Phosphate Buffer Solution (PBS) fresh for every experiment.

Chips were washed with isopropanol (IPA) and water and dried under nitrogen. 0.25µl of the cell suspension solution at the desired concentration were manually dispensed as droplets in the chambers on the chips. The solution formed delimited droplets as seen in Figure 1 above. To prevent evaporation, the droplets were covered with a few microlitres of mineral oil (Sigma-Aldrich, cat#M5904) depending the number of droplets used.

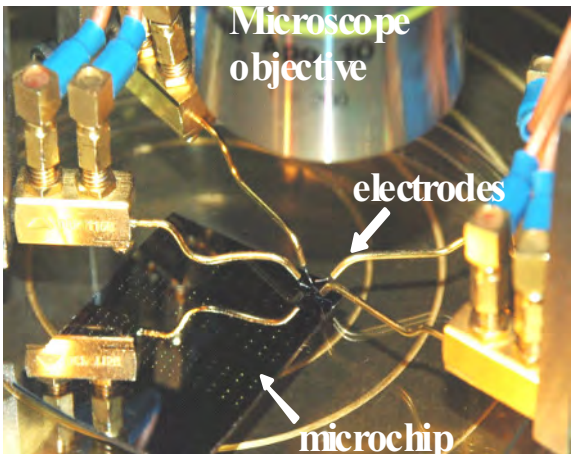


Fig. 4: experimental set-up showing the microchip supporting cell suspension droplets covered in oil. The 4 external gold electrodes are immersed inside 1 droplet on two sides of the keyhole, in a similar configuration as shown in Figure 3.

The chip supporting the droplets in oil were positioned in a probestation (MicrochamberTM alessis REL-6100), which contained 4 micromanipulators, connecting 4 fine-tipped gold microprobes to the electrical circuit. The probes were elongated to allow for liquid contacts. Using the microscope incorporated in the probestation set-up, the tips of the electrical probes were carefully positioned inside the cell suspension droplet in the desired configuration (Figure 4). The use of external electrodes enabled the study of a wide range of configurations and geometries. Voltage (0.2-5MHz, 0.5-20Vpp) was applied to external microprobes to obtain DEP. Movement of the cells was recorded using a digital camera connected to the microscope under a 10X objective.

III. Results and Discussion

A. Dielectrophoresis simulation:

Figure 3 above shows the results of the simulation of the negative DEP force arising from a non-uniform electric field applied from 4 electrodes, placed 2 by 2 on both sides of the keyhole. The isosurfaces presented confirm that the electric field is more intense at the edges of the electrodes. Therefore the minimum of the electric field was located in the middle of the 4 electrodes. Similar configurations had been studied previously, for example for trapping cells moved inside a microchannel by bulk fluid flow[10] and show similar results. Under negative DEP, the cells would be effectively repelled from the electrodes towards the minimum of the electric field. By tuning the distances between each electrode, specific configurations could be found that placed the minimum of the electric field nearest to the entrance of the keyhole (Fig 3.b.).

B. Moving cells in droplets via dielectrophoresis:

In order to confirm the results from the simulations and refine further the configuration of the electrodes onto the microchip, external microelectrodes were used to apply the DEP voltage. The microprobe set-up was flexible so as to allow studying various geometries and configurations without the time-consuming efforts of design and microfabrication of integrated electrodes onto the chip surface. Jurkat cells at relatively high concentrations (around 2 millions cells/ml) were manually dispensed on the microchip in small droplets of 0.25µl, and subjected to DEP voltage. Results from one such experiment are shown in Figure 5 below.

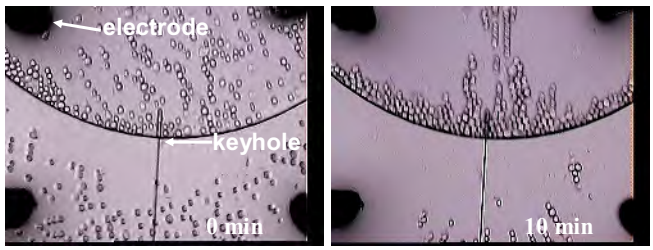


Fig 5: Movement of a high concentration of Jurkat cells under negative DEP towards the keyhole (1MHz, $6V_{RMS}$, in PBS)

The 4 electrodes at the 4 corners of the pictures were placed around the keyhole. The 2 electrodes on top were placed inside the chamber, while the 2 at the bottom were positioned outside the chamber, but still in the cell suspension droplet, that overflowed to keep electrical contact with

the solution. At the beginning of the experiment, cells were distributed throughout the surface. When the DEP voltage was applied, the cells were repelled from the electrodes and moved towards the minimum of the electric field in the center of the 4 electrodes, as was predicted by simulations. Cells accumulated at the border of the chamber because the DEP force was not strong enough to overcome the 20µm deep edge.

C. Single cell positioning:

Patch-clamp recordings are performed on a patch of the cell membrane of a single cell, positioned at the micropipette aperture. Therefore high concentrations of cells between the electrodes such as those used in Figure 5 above, where clusters of cells are connected together at the keyhole, were not suitable for enabling a patch-clamp configuration of interest. A usable concentration would be lower. On the other hand, a concentration where single cells are seldom present in between the electrodes is also damaging. For each configuration of the electrodes, the cell concentration can be optimized so that a single cell will be directed to the keyhole by the DEP force. Figure 5 presents a series of pictures taken during the journey of one cell to the keyhole at a speed of about 4µm/s.

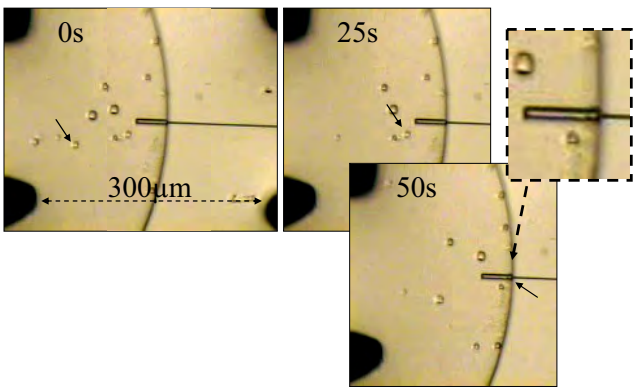


Fig 6: Movement and positioning of a single cell (arrow) to the keyhole ($8V_{RMS}$ at 1MHz). Droplets of 0.5µl containing around 250 cells were manually dispensed

IV. Conclusions

This paper presents a new approach to enable single cell positioning in arrays of droplets placed on a microstructured silicon surface, in order to achieve chip-based lateral patch-clamp experiment. Droplets are completely open-access and will greatly ease fluidic interfaces. Single cells were positioned on the lateral patch sites by using dielectrophoresis, without the requirement of any bulk fluidic movement, which could eliminate the need for pressure driven fluidics limiting the throughput of these assays. The integration of the electrodes onto the microstructured surface will enable greater control on the cell movement.

Acknowledgment

The help of Vijany and her supervisor Martin Buist (NUS/Bioengineering) in conducting DEP experiments is greatly acknowledged.

References

1. Neubert H.-J. (2004) Patch-clamping moves to chips Anal. Chem. Sept 1, 327A-330A.
2. Li, X. H., Klemic K.G, Reed M A., Sigworth F. J (2006) Microfluidic System for Planar Patch Clamp Electrode Arrays, Nano Lett. 6:815-819
3. Ong W.-L., Tang K.-C., Agarwal A, Nagarajan R., Luo L.-W., Yobas L. (2007) Microfluidic integration of substantially round glass capillaries for lateral patch clamping on chip, Lab Chip, 7:1357-1366
4. Lau A. Y., Hung P J., Wu A. R., Lee L. P. (2006) Open-access microfluidic patch-clamp array with raised lateral celltrapping sites, Lab Chip 6:1510–1515
5. Lemaire F. et al. (2006) Toxicity assays in nanodrops combining bioassay and morphometric endpoints. PLoS ONE.2 :e163 17235363
6. Voldman J., (2006) Electrical Forces for Microscale cell Manipulation, Annu. Rev. Biomed. Eng., 8:425-454
7. Frénéa M., Faure S.P., Le pioufle B., Coquet P., Fujita H. (2003) Positioning living cells on a high-density electrode array by negative dielectrophoresis, Mat. Sci. Eng. C, 23 :597
8. Fuhr G., Glasser H., Muller T., Schnelle T. (1994). Cell manipulation and cultivationunder AC electric-field influence in highly conductive culture media. Biochim. Biophys. Acta Gen. Subj. 1201:353–60
9. http://software.ihpc.a-star.edu.sg/projects/depSolver.php: depSolver is an Open Source code developed for the study of dielectrophoretic forces in complex geometries.
10. Voldman J., Toner M., Gray M.L., Schmidt M.A. (2003) Design and Analysis of Extruded Quadrupolar Dielectrophoretic Traps, J. Electrostatics, 57:69

Author: Julien REBOUD
Institute: Institute of Microelectronics
Street: 11 Science Park Road, Science Park II
City: Singapore 117685
Country: Singapore
Email: julien@ime.a-star.edu.sg

Label-free Detection of Proteins with Surface-functionalized Silicon Nanowires

R.E. Chee, J.H. Chua, A. Agarwal, S.M. Wong, G.J. Zhang

Institute of Microelectronics, Agency for Science, Technology and Research, 11 Science Park Road, Singapore 117685.

Abstract — **Semiconducting silicon nanowires (SiNWs) have shown great potential for the electrical detection of human disease biomarkers. The technique for label-free detection using SiNWs allows for fast, efficient and inexpensive detection of biomarkers, unlike current time-consuming methodologies such as fluorescence ELISA or western blot. We demonstrate a proof-of-principle protein detection using biotinylated SiNWs for the detection of ultralow concentrations of streptavidin with a maximum sensitivity of up to 10 fM. Real-time detection of human cardiac troponin T using antibody-functionalized SiNWs is also presented. The possibility of large scale integration paves the way towards the simultaneous detection of a large number of protein biomarkers within a single chip and is of importance to the development of diagnostic tools as well as point-of-care applications.**

Keywords — **silicon nanowire sensor, protein detection.**

I. Introduction

Silicon nanowires (SiNWs) have demonstrated significant potential in its capability for ultrasensitive detection of bio-molecular moieties such as DNAs[1-5], proteins[6,7] and viruses[8]. The biologically gated device owes its sensitive nature to the surface area to volume ratio that the one-dimensional structure confers: unprecedented ultra-sensitivity to biological as well as chemical species. A top-down approach as opposed to nanowire growth techniques elsewhere demonstrated was utilized for which individually addressable silicon nanowires were fabricated[2-5, 7], since reproducible nanowire structures could be mass manufactured and later integrated with external CMOS circuitry for direct electrical readout. The basis of operation of the nanowire device depends on the charge characteristics of the bio-moiety in question. In this case, proteins with various pIs were utilized; surface charges inherent in the protein molecule result in the SiNW operating in either the accumulation or depletion mode depending on the polarity of the charges attached to the target biomolecule.

We investigate the variation of the conductances of the nanowire device where various concentrations of streptavidin and avidin are utilized for covalent attachment, since the pI of streptavidin and avidin are substantially different from the pH of the buffer solution and thus would facilitate the identification of the change between baseline conductances and the conductance after wires have been exposed to a particular protein. These biotinylated wires offer significant advantage over traditional protein identification techniques such as the Western blot or fluorescence ELISA which are both time-consuming and labor-intensive. Furthermore, the bio-FET approach eliminates the need for a fluorescent label, demonstrating high specificity and sensitivity together with rapid response rates, paving the way towards the development of low-cost, sensitive and rapid diagnostic as well as point of care applications which potentially may necessitate the sensing of biomolecules in concentrations of down to 10 fM levels. In addition, the individually addressable array allows for the simultaneous detection of different species in solution, alluding to the devices' capability for multiple detection schemes on a single platform. We also demonstrate the real-time detection of human cardiac troponin-T (cTnT), a significant biomarker for the indication of myocardial tissue necrosis[9-11], which demonstrates the practicable development of biosensors for the identification of patients suffering from acute myocardial infarction.

II. Materials and methods

A. Materials.

EZ-Link™ Sulfo-NHS-LC-Biotin, avidin, and streptavidin were purchased from Pierce Biotechnology, Inc. (Rockford, IL). Mouse anti-human cardiac troponin T and human troponin T were purchased from HyTest Ltd. (Turku, Finland). All other chemicals were purchased from Sigma-Aldrich, Inc. Proteins were used without further purification and diluted to the required concentrations with assay buffer.

B. SiNW device design and fabrication.

SiNW devices were fabricated on a 145-nm buried oxide layer silicon-on-insulator (SOI) substrate that was n-doped on purchase. Deep ultraviolet lithography techniques were used to pattern and etch fins that were later doped and thermally oxidized to form the individual nanowires. Contact metal definition and Si_3N_4/SiO_2 passivation of metal lines were performed and the nanowires released by dry etching of the passivation layers followed by wet etching of the remaining SiO_2 on the device array surfaces. Scanning electron microscopy (SEM) and transmission electron

Chwee Teck Lim, James C.H. Goh (Eds.): ICBME 2008, Proceedings 23, pp. 838–841, 2009
www.springerlink.com

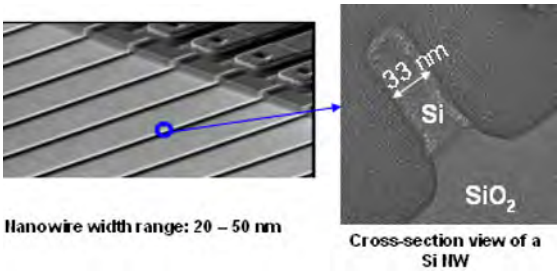


Figure 1. (a) SEM micrograph of SiNW array. (b) TEM image showing the cross-sectional profile of an individual nanowire.

microscopy (TEM) were performed to monitor the uniformity and quality of the resultant devices. Figures 1a and 1b show a SEM micrograph and TEM image of the SiNW array structure, from which the high uniformity of the wire dimension and spacing can be observed.

C. Surface functionalization.

Surface functionalization of the SiNW array chips was carried out using a conventional silane chemistry that has been well documented in the literature[12]. The chips were immersed in a solution of 2% 3-aminopropyltriethoxysilane (APTES) in a 95%/5% mixture of ethanol and deionised water for 2 hrs, resulting in the formation of an amine-terminated surface. A 20 µl aliquot of 10 µg/ml biotin in 1xPBS was applied to the SiNW device clusters and left to incubate in a humidity-controlled environment at room temperature overnight, allowing the N-terminus of the biotin molecules to bind to the amine-terminated SiNW surface. Unbound biotin molecules remaining in the solution aliquot were removed by washing with 1xPBS for 10 minutes, followed by washing in deionised water for 5 minutes. The freshly prepared chips were immediately used for electrical detection experiments, although storage in a 4^0C environment was observed to be possible for short periods of time (< 12 hours) without degradation of the quality of the SiNW devices.

D. Electrical characterization and biomolecular detection.

Electrical characterization of the SiNW devices was carried out with an Alessi REL-6100 probe station (Cascade Microtech, Beaverton, OR). Data was measured and recorded with a HP-4156A parameter analyzer. A controlled voltage of 0.5V was applied across the drain and source electrodes of each individual SiNW device via a two-probe system that referenced one end of the device to ground. The current through the SiNW device was then measured and used to compute the resistance of the SiNW device.

The detection of protein biomolecular species was achieved by measuring the resistance of the SiNW devices at three stages: before chemical functionalization (denoted R_1), after immobilization of biotin probe molecules on the SiNW device surface (denoted R_2), and after the binding of streptavidin or avidin target molecules to the probe-immobilized surface (denoted R_3). The percentage change between R_2 and R_3 was computed and used as the indicator for the binding event.

III. Results and Discussion

A. Theoretical considerations.

Proteins, which consist of long-chain amino acid sequences joined and folded in a specific manner, demonstrate an amphoteric nature in solution due to zwitterion formation between the amine and carboxyl functional groups on the protein molecule. In a solution with a pH less than its iso-electronic point (pI), a protein molecule carries a net positive charge due to the net protonation of its functional groups. Conversely, in a solution with a pH greater than its pI, a protein molecule carries a net negative charge due to the overall deprotonation of its functional groups.

As the SiNW devices used in our experiments are n-doped, the presence of a negative surface charge on the device causes depletion to occur in the SiNW bulk, reducing the effective cross-sectional area for conductance of the SiNW device and thus increasing the resistance of the device. Conversely, the presence of positive surface charge on the SiNW device causes carrier accumulation in the device, increasing its conductance and decreasing its resistance. A positive or negative charge layer on the surface of the devices arise from the charge on the target proteins bound to the antibody-functionalized SiNW surface; thus, by measuring the magnitude and direction of resistance change in the SiNW devices, it is possible to determine with high specificity the type and concentration of biomolecular species present in the analyte solution.

As the strength and specificity of the binding between biotin and the avidin family of proteins is well documented, these biomolecular species were selected for the demonstration of the sensing capabilities of the SiNW devices. The highly specific binding between the antibody and the target molecule ensures that the charge carried by the target molecule is brought sufficiently close to the SiNW surface to affect the resistance changes described above; the presence of a different target protein that does not bind to the biotinylated surface should result in little or no change in SiNW resistance.

B. Streptavidin detection.

Streptavidin (pI = 5.5) has an isoelectronic point that is less than the pH of the assay buffer used, and thus carries a net negative charge in solution. After the immobilization of biotin probe molecules onto the SiNW surface, a 20 µl aliquot of 0.01x PBS solution was applied to the SiNWs and the resistances (R2) of 15 wires on each chip were measured. The buffer solution was then washed away and the dried SiNW chips incubated for ~1hr with a 20 µl aliquot of streptavidin solution in 0.01x PBS solution applied to the SiNWs. Excess streptavidin solution was washed away with 0.01x PBS (3x5min) and deionised water (1x5min) and the chip dried in a stream of dry N_2 gas. Solutions of streptavidin with concentrations of 1 nM, 10 pM, 10 fM and 1fM were used on different devices to investigate the concentration dependence of SiNW device response. The SiNW devices were immersed in a second 20 µl aliquot of 0.01x PBS solution and the resistance (R_3) measured. A box diagram of the responses are given in Figure 2.

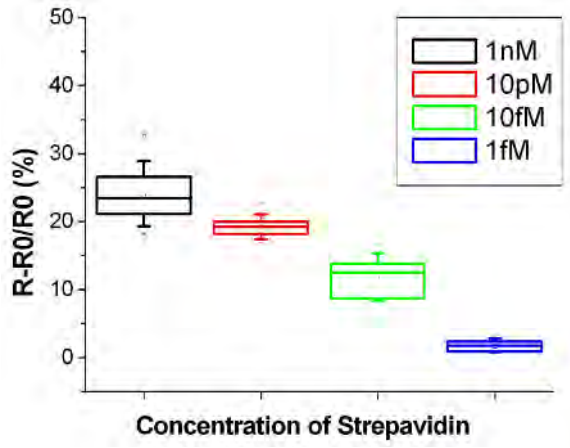


Figure 2. Box diagram of percentage change in resistance of SiNW device with different concentrations of streptavidin solution.

C. Avidin detection.

Avidin (pI = 10.5) has an isoelectronic point that is greater than the pH of the assay buffer used, and thus carries a net positive charge in solution. A 1 nM in 0.01x PBS avidin solution was used to bind avidin target molecules to the SiNW device in the same manner as described above in the section on streptavidin detection. In accordance with theory, a decrease in SiNW resistance was observed from R_2 to R_3 upon binding of avidin. A box diagram of the avidin response plotted with 1 nM streptavidin response for comparison is given in Figure 3.

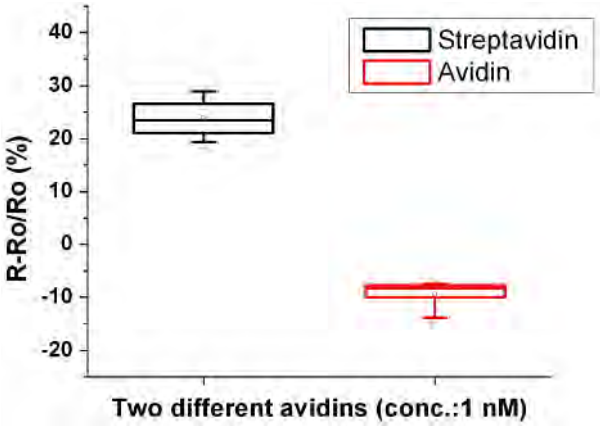


Figure 3. Box diagram comparing the percentage resistance changes of SiNW devices when used to detect 1 nM streptavidin and 1 nM avidin.

D. Detection of human cardiac troponin-T.

In order to demonstrate the applicability of the SiNW array biosensor for medical point-of-care applications, a detection experiment with 1 ng/ml human cardiac troponin-T (cTnT) was performed. Human cTnT is regarded as one of the most cardiac-specific biomarkers and is highly indicative of acute myocardial infarction in heart disease patients. The rapid, real-time and label-free detection of cTnT with the SiNW array biosensor will pave the way for the development of an electrical biosensor for medical point-of-care applications.

A SiNW array device was functionalized with anti-cTnT capture probes in the manner described in section 2.3. Glutaraldehyde, a bifunctional linker, was used to bind the anti-cTnT probe molecules to the amine-terminated SiNW surface as cTnT is unable to directly bind to the amino

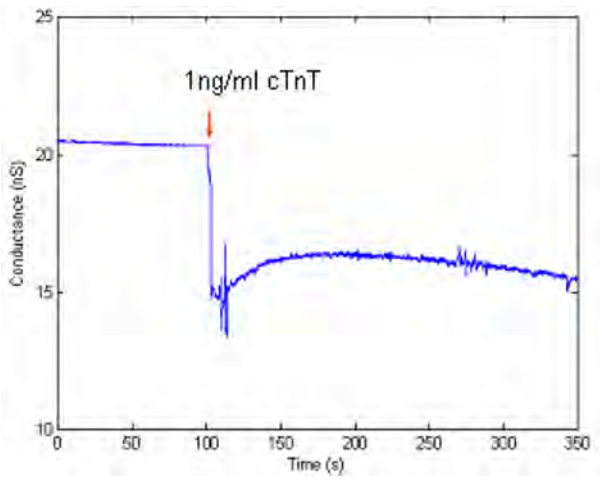


Figure 4. Graph of conductance against time for the real-time detection of 1 ng/ml cTnT in 0.01x PBS.

groups on the silicon surface[13]. Detection was performed by monitoring the baseline current through a SiNW device immersed in 0.01x PBS solution, followed by the addition of an aliquot of 1 ng/ml solution of cTnT in 0.01x PBS. A graph of the conductance against time of the SiNW device is given in Figure 4, and it may be clearly seen that a large and rapid response is obtained upon addition of the cTnT solution. The SiNW conductance decreases and stabilizes quickly to a new, lower baseline level, demonstrating that the binding and detection event has occurred in accordance with theory.

IV. Conclusions

We have demonstrated the sensing capabilities of the silicon nanowires for various proteins, as well as investigated the real-time sensing features of human cardiac troponin-T. The ability to identify ultra-low concentrations of streptavidin in the femtomolar regime attests the sensitive nature of the SiNWs, a feature inherently due to the miniature dimensions of the sensing platform itself. Further work is being carried out to determine the detection limit of troponin-T, but is expected to be comparable to that of streptavidin. The individually addressable nature of the SiNWs alludes to the multiplexing capabilities of the device since each SiNW could be selectively functionalized using a robotic spotter to specifically bind to a specific bio-marker of interest, leading to multiple confirmatory diagnostic investigations on a single platform.

References

[1] Hahm JI, Lieber CM (2004) Direct Ultrasensitive Electrical Detection of DNA and DNA Sequence Variations Using Nanowire Nanosensors. Nano Lett 4(1):51-54.

[2] Li Z, Chen Y, Li X, Kamins TI, Nauka K, Williams RS (2004) Sequence-specific label-free DNA sensors based on silicon nanowires. 4:245-247.

[3] Zhang GJ, Zhang G, Chua JH, Chee RE, Wong EH, Agarwal A, Buddharaju KD, Singh N, Gao ZQ, Balasubramanian N. (2008) DNA Sensing by Silicon Nanowire: Charge Layer Distance Dependence. Nano Lett 8(4):1066-1070.

[4] Zhang GJ, Chua JH, Chee RE, Agarwal A, Wong SM, Buddharaju KD, Balasubramanian N (2008) Highly sensitive measurements of PNA-DNA hybridization using oxide-etched silicon nanowire biosensors. Biosens. Bioelectron. 23:1701-1707.

[5] Bunimovich YL, Shin YS, Yeo WS, Amori M, Kwong G, Heath JR (2006) Quantitative real-time measurements of DNA hybridization with alkylated non-oxidized silicon nanowires in electrolyte solution. JACS 128(50):16323-31.

[6] Cui Y, Wei QQ, Park H, Lieber CM (2001) Nanowire nanosensors for highly sensitive and selective detection of biological and chemical species**.** Science 293(5533):1289-92

[7] Stern E, Klemic JF, Routenberg DA, Wyremebak PN, Turner-Evans DB, Hamilton AD, Lavan DA, Fahmy TM, Reed MA (2007) Label free immunodetection with CMOS compatible semiconducting nanowires. Nature 445(7127):519-22

[8] Patolsky F, Zheng G, Hayden O, Lakadamyali M, Zhuang X, Lieber CM (2004) Electrical detection of single viruses. Proc Natl Acad Sci U.S.A. 101:14017-22

[9] Hamm CW, Ravkilde J, Gerhardt W et al. (1992) Prognostic value of serum troponin-T in unstable angina. N Engl J Med 327:146-50

[10] Adams JE, Bodor GS, Davila-Roman VG et al. (1993) Cardiac troponin I: a marker with high specificity for cardiac injury. Circulation 88:101-6

[11] Ohman EM, Armstrong PW, Christenson RH et al. (1996) Cardiac troponin T levels for risk stratification in acute myocardial ischemia. N Engl J Med 335:1333-41

[12] Zheng G, Patolsky F, Cui Y, Wang WU, Lieber CM. (2005) Multiplexed electrical detection of cancer markers with nanowire sensor arrays. Nat Biotechnology 23:1294-1301.

[13] Zhang, G.J.; Tanii, T.; Kanari, Y.; Ohdomari, I. (2007) Production of nanopatterns by a combination of electron beam lithography and a self assembled-monolayer for an antibody nanoarray. J. Nanosci. Nanotechnol. 7:410-7.

Corresponding author:

G.J. Zhang
Tel: +65-67705390,
Fax: +65-6774-5754,
E-mail: zhanggj@ime.a-star.edu.sg

Bead-based DNA Microarray Fabricated on Porous Polymer Films

J.T. Cheng[1], J. Li[2], N.G. Chen[1], P. Gopalakrishnakone[3] and Y. Zhang[1, 2,*]

[1] Division of Bioengineering, Faculty of Engineering, National University of Singapore, Singapore
[2] Nanoscience and Nanotechnology Initiative, National University of Singapore, Singapore
[3] Department of Anatomy, Yong Loo Lin School of Medicine; National University of Singapore, Singapore

Abstract — **By attaching different biomolecule probes to surface-modified microspheres, a large number of complementary targets labeled with fluorophores can be interrogated simultaneously using the bead-based microarray format. In this work, a new bead-based DNA microarray was fabricated on a porous polymer film with well-ordered array of pores. The well-ordered porous polymer film was prepared using the non-lithographic breath figure method. Different biotinylated DNA probes were conjugated to avidin-modified polystyrene (PS) microspheres. The DNA microarray was fabricated by randomly dispersing DNA probe-conjugated PS microspheres into the pores on the polymer film. Multiplexing detection of DNA was performed using target DNAs labeled with ATTO dyes using a fluorescence microscope imaging system. The Bead-based DNA microarray was constructed for detection of four serotypes of Dengue virus. This technique was demonstrated to be a simple and cost-effective method for rapid detection of DNA targets.**

Keywords — **Pattern, Microspheres, DNA, Microarray**

I. Introduction

DNA microarray technology has been well-known for its tremendous power to conduct parallel analyses of nucleic acids in a single experiment. It has been an extremely important tool in biomedical research and also in diagnostic, treatment and monitoring applications [1]. In a traditional microarray, various DNA probes are immobilized in an array of microscopic spots on a planar substrate [2], such as nylon membrane, glass slide or compact disc. Each type of probes can be spatially addressed, enabling high throughput. However, planar microarrays are restricted by the diffusion-limited kinetics; therefore the amount of probes that can be immobilized on the planar substrate and the amount of targets that can be hybridized on the planar microarray are limited, resulting in low single-to-noise (S/N) ratio.

Instead of using planar surface, bead-based microarrays are applying the non-planar bead surface as the substrate to immobilized probes. The immobilization reaction can take place in a solution with shaking or votexing, resulting in high reaction efficiency. Also, the high surface-to-volume ratio of beads allows a larger amount of probes to be immobilized. Moreover, beads can be fabricated with magnetic, electrical or spectral properties, with various functional groups and of different sizes. Therefore, bead-based microarray format is becoming increasingly popular in nucleic acid analysis.

Various bead-based DNA microarrays have been developed. The most famous are the bead suspension array using flow cytometry [3] for detection and fiber-optic bead-based microarrays [4] from Illumina (San Diego, CA, USA). Facilities such as flow cytometry and the imaging system compatible for the use of optical fibers are needed for these techniques. Other work has been reported on the construction of bead-based DNA microarrays on a platform with patterns fabricated using lithographic methods [5]. However, the need of clean room facilities increases the cost.

Herein, we present a novel technique for the fabrication of bead-based DNA microarrays. This technique applied well-ordered porous polymer films with micrometer-sized pores to serve as the microarray platform. Beads were deposited and confined in the surface pores of the porous films. The porous polymer films were fabricated by the breath figure method, a low-cost non-lithographic technique. Fluorescent microscope equipped with charge-coupled device (CCD) camera was used for the signal detection. In the whole construction of the bead-based DNA microarrays on porous film, only common laboratory facilities were used, resulting in a very simple and cost-effective method. The bead-based DNA microarray was demonstrated for rapid detection of dengue virus.

II. Experimental section

A. Materials

Polystyrene-block-poly(ethylene-ran-butylene)-block-polystyrene (PSEBS, 31wt% styrene) and all solvents were obtained from Sigma-Aldrich. Polystyrene-block-poly(4-vinylpyridine) (PS-b-P4VP, M_n^{PS}= 20.0kg/mol, M_n^{P4VP}= 19.0 kg/mol, M_w/M_n=1.09) was purchased from Polymer Source Inc.

SuperAvidin™ coated polystyrene (PS) microspheres, mean diameter 9.9 μm (1% w/v aqueous suspension; binding capacity: 0.036 μg biotin-FITC/ mg microspheres) were purchased from Bangs Laboratories, Inc.

Chwee Teck Lim, James C.H. Goh (Eds.): ICBME 2008, Proceedings 23, pp. 842–845, 2009
www.springerlink.com

The 25-mer DNA probes were designed according to the sequences of the four serotypes of dengue viruses. Dengue Probes (DP), DP1, DP2, DP3 & DP4 were the capture probes for the Type 1, Type 2, Type 3 & Type 4 dengue viruses, respectively. Their genome positions (GenBank accession No.) are as follows: DP1: 10,550-10,574 (M87512); DP2: 10,557-10,581 (M20558); DP3: 10,530-10,554 (M93130); and DP4: 10,483-10,507 (M14931). All of the four DNA probes were purchased with their 5' end functionalized with biotin. Dengue targets (DT), DT1, & DT2 were the perfect match targets for DP1 & DP2, respectively. All the targets were biotinylated at their 5' end. All the DNA probes and target were purchased from Proligo (Singapore). The sequences of the DNA probes and targets used in the bead-based DNA microarray were listed in Table 1.

Table 1 Sequences of the probes and targets used in the bead-based DNA microarray

Name	Probe sequence
biotin-DP1	biotin-5'-GGGAAGCTGTATCCTGGTGGTAAGG-3'
biotin-DP2	biotin-5'-ATGAAGCTGTAGTCTCACTGGAAGG-3'
biotin-DP3	biotin-5'-AGGGAAGCTGTACCTCCTTGCAAAG-3'
biotin-DP4	biotin-5'-GAGGAAGCTGTACTCCTGGTGGAAG-3'
biotin-DT1	biotin-5'-CCTTACCACCAGGATACAGCTTCCC-3'
biotin-DT2	biotin-5'-CCTTCCAGTGAGACTACAGCTTCAT-3'

Streptavidin labeled ATTO dyes, streptavidin–ATTO 488, streptavidin–ATTO (1mg/ml in 1 x PBS buffer; Molecular Weight = 60.0 k Da) were purchased from Jena Bioscience.

Buffers were prepared as TTL buffer (100 mM Tris-HCl, pH 8.0; 0.1% Tween 20; and 1 M NaCl), TT buffer (250 mM Tris-HCl, pH 8.0; and 0.1% Tween 20) and TTE buffer (250 mM Tris-HCl, pH 8.0; 0.1% Tween 20; and 20 mM EDTA). Hybridization mixture contained 300 M NaCl, 0.5% sodium dodecyl sulfate (SDS) and 30% formamide.

B. Preparation of the polymer porous films

The polymer porous films were prepared by the breath figure method. A mixture of PS-b-P4VP and PSEBS (1/1, w/w) was dissolved in a mixture of toluene and benzene (7/3, v/v) to form a 5~30 mg/ml polymer solution. Equal amount of the solutions were cast onto clean glass substrates (15×15 mm) in a sealed 300 L chamber at room temperature, and then the chamber was immediately vacuumized to an appropriate vacuum level of -50 kPa within about 30 seconds. At the same time, the humidity in the chamber was maintained at 80-85 r.h.%. After dried, porous polymer films were obtained.

C. Patterning of microbeads on the polymer porous films

A glass slide covered with porous polymer films was inserted into a suspension of 9.9 μm polystyrene microbeads in a vial. The vial was then shaken on a shaker to allow beads to settle in the pores by gravity. The settling time is about two hours. After the microbeads were dispensed into the arrayed pores, the surface of the porous films was washed with water to remove the excess beads. The film was then dried at room temperature.

D. Preparation of probe beads and dengue detection

A hundred microliters of avidin-PS beads were washed three times using TTL buffer and resuspended in 20 μl TTL buffer. According to the binding capacity, 0.04 nmol of biotinylated probes was added. Probes were immobilized onto the bead surface via the biotin-avidin coupling by gentle mixing at room temperature for 2 hrs. After probe immobilization, beads were rinsed twice using TT buffer and resuspended in TTE buffer at 80 ^{o}C for 10 min to remove any unstable biotin-avdin coupling. Beads were washed again and resuspended in 100 μl hybridization mixutre.

Twenty microliters of beads conjugated with each type of probes (PS-DP1, PS-DP2, PS-DP3 & PS-DP4) were mixed and diluted to 0.1 wt % using hybridization mixture. Porous film was immersed in the bead suspension in a vial and shaked for 2 hrs. Excess beads were rinsed away.

One microliter 100 μM biotin-DT1 or biotin-DT2 was mixed with 9 μl 1 mg/ml avidin-ATTO 488 or avidin-ATTO550, respectively. The mixture was diluted to 100 μl using TTL buffer and incubated at room temperature for 2 hrs. Twenty microliters of of ATTO-labeled targets from each mixture were mixed and diluted to 800 μl in hybridization mixture. The bead-based DNA microarray on porous film was immersed in the the target solution and incubated at 37 ^{o}C for 1 hr. Array was rinsed with hybridization buffer to remove excess targets thereafter.

III. Results and Discussion

The construction of the bead-based DNA microarray is shown schematically in Figure 1. Firstly, porous polymer films with well-ordered honeycomb structure could be formed when a polymer solution was drop-cast onto a glass slide in a vacuum chamber with moist atmosphere. The vacuum caused a rapid evaporation of the volatile solvent (e.g. toluene and benzene) and subsequently a rapid cooling of the solution, and then sub-micrometer or micrometer sized water droplets were formed on the surface of the cold solution [6]. Convection currents induced by temperature gradients and

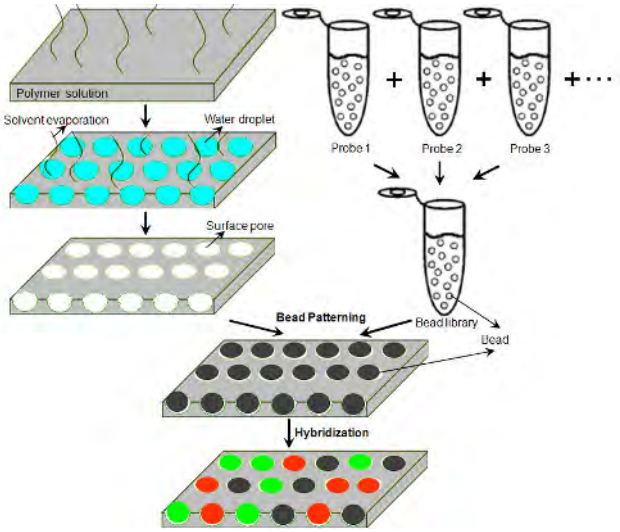


Fig. 1 Schematic design of the bead-based DNA microarray on porous film

capillary forces between the water droplets favored a regular stacking of the water droplets with a narrow size distribution [7]. After the solvent evaporated completely, a polymer film was formed with the water droplets in the film. After the water droplets evaporated, a porous film with well ordered pore structure was formed. Polystyrene (PS) beads with avidin on their surface were mixed with the four types of the dengue probes in separate tubes. An amount of each type of beads, PS-DP1, PS-DP2, PS-DP3 & PS-DP4 was pooled and mixed. The porous film was immersed in the diluted bead mixture to allow settling of beads into the surface pores to form one-bead-in-one-pore pattern. To detect dengue virus, the ATTO-labeled targets were applied on the array to hybridize with the DNA probes immobilized on the bead-based microarray on the porous films.

In order to prepare the porous polymer films for the preparation of the bead-based DNA microarrays, a polymer blend of PS-b-P4VP and PSEBS was dissolved in a solution of mixed toluene and benzene. PSEBS is an elastomer and

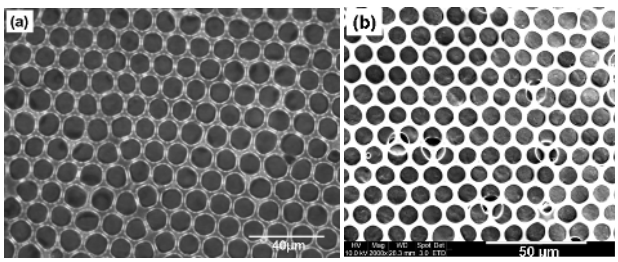


Fig. 2 (a) Optical and (b) SEM images of PS-b-P4VP/PSEBS porous films by the breath figure method. The polymer concentration of preparing the polymer porous films was 15 mg/ml. The relative humidity is 82 r.h.% and the vacuum level is -50 kPa.

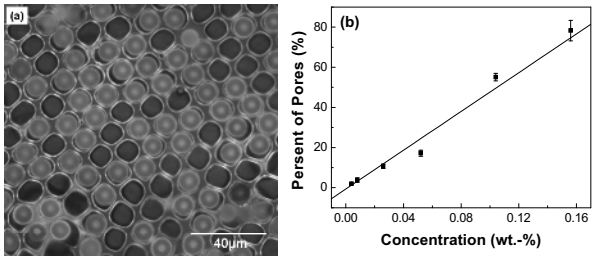


Fig. 3 (a) Optical image of beads-based patterns on the polymer porous films (54%). (b) Bead occupancy as a function of the bead concentration.

the PS-b-P4VP/PSEBS blend polymer has good mechanical properties. Then the porous films with long-range honeycomb structure were prepared in a vacuum chamber with a moist atmosphere. Figure 2 exhibits optical and SEM images of porous polymer films made of a blend of PS-*b*-P4VP and PSEBS. The porous films show two-dimensional and periodical structures with hexagonal array of pores in a long-range order. The pore sizes are on the microscale. The pore sizes of the films were altered by controlling the air humidity and vacuum level in the vacuum chamber. Herein, the pore diameter is 10~12 μm when the vacuum level is about -50 kPa, a polymer concentration is 15 mg/ml and a relative humidity is about 82 r.h.%.

The porous polymer films can be used to pattern beads. Figure 3a exhibits the photograph of beads-based pattern on the porous polymer films. The beads were embedded within the holes on the porous films in a one-bead-in-one-pore format. Figure 3b shows that the bead occupancy on the porous films increased as the bead concentration increased.

DNA probes were immobilized on the bead surface via the biotin-avidin coupling. Equal amount of the four types of probe immobilized beads, PS-DP1, PS-DP2, PS-DP3 & PS-DP4 beads, were pooled and diluted to 0.1 wt % bead suspend in hybridization mixture. A porous film with pore density of 8.38×10^9 pores/m^2 was immersed in the bead suspension in a vial with gentle shaking. The probe beads were settled down in the surface pores to form bead-based DNA microarray on the porous film. Figure 4 shows (a) the

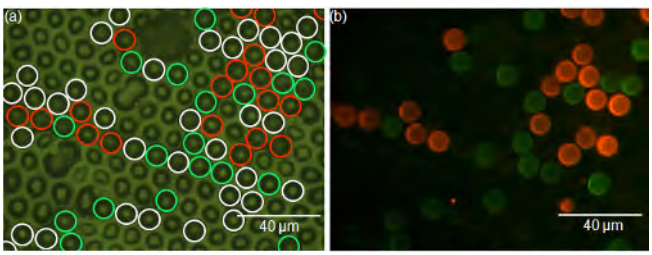


Fig. 4 (a) bright field and (b) fluorescence microscope image of beads-based DNA microarray on the polymer porous films (bead occupancy 50%).

bright field and the fluorescent (b) image of the bead-based DNA microarray after hybridization with ATTO488–DT1 & ATTO550-DT2. On an area of 1.79×10^4 μm^2 on the porous film, shown in the Figure 4, there were 19 replicates for both the detection of DT1 (green beads) and DT2 (red beads). The rest 35 beads (white circled in Figure 4a) were the beads attached with DP3 and DP4. The replicates helped prevent the false-positive or false negative signals. The detection condition could be optimized for even faster analysis and the bead-based DNA microarray could be constructed for the detection of other diseases.

IV. Conclusions

A novel bead-based DNA microarray was constructed on a well-ordered porous polymer film. The porous polymer films were fabricated by the one-step breath figure templating method, a low-cost non-lithographic method. Beads immobilized with DNA probes were patterned on the porous film. The pore size was complementary to the bead size; therefore beads were secured in the pores. These bead-based DNA microarrays were used for the detection of dengue virus. This technique was demonstrated to be a simple and cost-effective method for rapid and high-throughput detection of DNA targets.

Other molecules, such as proteins, peptides or other small molecules can also be immobilized on the bead surface to form a bead-based microarray on porous film. Future work is designed to apply the well-ordered porous films to construct various bead-based microarrays or even cell microarrays.

Acknowledgment

The authors would like to acknowledge the financial support from Agency for Science, Technology and Research, Science & Engineering Research Council, Singapore (A*STAR SERC) (R-398-000-030-305) and the National University of Singapore.

References

1. Venkatasubbarao S (2004) Microarrays – status and prospects. Trends Biotechnol 22: 630-637
2. Schena M, Shalon D, et al. (1995) Quantitative Monitoring of Gene Expression Patterns with a Complementary DNA Microarray. Science 270: 467-470
3. Xu H, Sha MY, et al. (2003) Multiplexed SNP genotyping using the Qbead™ system: a quantum dot-encoded microsphere-based assay. Nucleic Acids Res 31: e43.
4. Ferguson JA, Boles TC, et al. (1996) A fiber-optic DNA biosensor microarray for the analysis of gene expression. Nat Biotech 14: 1681-1684
5. Barbee, KD, Huang X (2008) Magnetic Assembly of High-Density DNA Arrays for Genomic Analyses. Anal Chem 80: 2149-2154
6. Limaye AV, Narhe RD, Dhote AM, et al (1996) Evidence for Convective Effects in Breath Figure Formation on Volatile Fluid Surfaces. Phys Rev Lett 76: 3762
7. Pitois O, Francois B (1999) Crystallization of condensation droplets on a liquid surface. Colloid Polym Sci 277: 574

Address of the corresponding author:

Author: Associate Professor ZHANG Yong
Institute: Division of Bioengineering,
National University of Singapore
Street: Block E3A-04-15, 7 Engineering Drive 1
City: Singapore
Country: Singapore
Email: biezy@nus.edu.sg

Monolithic CMOS Current-Mode Instrumentation Amplifiers for ECG Signals

S.P. Almazan, L.I. Alunan, F.R. Gomez, J.M. Jarillas, M.T. Gusad and M. Rosales

Microelectronics and Microprocessors Laboratory, Department of Electrical and Electronics Engineering,
University of the Philippines, Diliman, Quezon City, Philippines

Abstract — **In this paper, four monolithic current-mode instrumentation amplifier (in-amp) topologies are implemented in 0.25um CMOS process, with positive second-generation current conveyors (CCII+) as building blocks. The in-amp topologies are designed to handle biomedical signals, specifically that of the Electrocardiogram (ECG). Four types of CCII+ are characterized and realized using a rail-to-rail op-amp and different types of current mirrors. The *Op-Amp with Simple Current Mirror* exhibits the highest current swing and the lowest power consumption, and is thus chosen as the optimum CCII+ block to be used in all four in-amps. All current-mode in-amps are implemented using a standard 0.25um CMOS process and yield excellent common-mode rejection ratio (CMRR) greater than 150dB for a differential gain of 100. All four in-amps consumes less than 2.5mW of power for a single voltage supply of 2.5V. However, the *2-Current Conveyor with Op-Amp at the Output (2-CC with Op-Amp)* has adjustable output reference voltage and provides the lowest output impedance among the four in-amps.**

Keywords — **Instrumentation Amplifiers, Current-Mode, Rail-to-Rail Op-Amps, Current Conveyors, ECG**

I. Introduction

The measurement of low-energy bio-potential signals such as the ECG makes the in-amp a significant signal-conditioning block for biomedical systems. With the use of in-amps, it is possible to accurately amplify these weak electric body signals even in the presence of high-amplitude common-mode noise that may tend to corrupt the desired signal. Having this critical application, in-amps are particularly designed to achieve high CMRR to correctly extract and amplify low-amplitude differential signals, and to block unwanted noise potentials that are usually common to the in-amp inputs [1], [2].

Recent works have explored alternative ways to implement in-amps using the current-mode approach to overcome the requirement for matched resistors [3]. One approach is through the use of current conveyors.

Vital parameters for characterization and analysis of in-amps include CMRR, input and output impedance, input and output swing, and power consumption. A simulated ECG signal with common-mode noise is used in simulating these different in-amp circuits to determine which in-amp configuration could best extract these biomedical signals.

II. Current conveyors

A positive second-generation current conveyor (CCII+) is a 3-terminal device with a representation shown in Fig. 1.

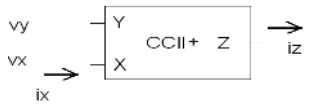


Fig. 1 CCII+ black-box reperesentation

Current conveyor performance relies on its ability to act as a voltage buffer between inputs, and to convey current between two ports that have extremely different impedance levels. To realize this, a CMOS CCII+ can be implemented by a high gain op-amp with a class AB output buffer stage, and connected with a negative-feedback loop, followed by a current mirror [4], as shown in Fig. 2.

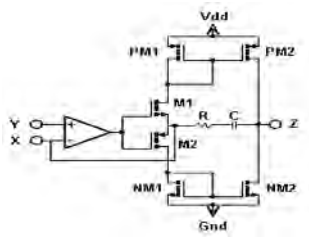


Fig. 2 CCII+ block with series-RC compensation

A. Op-amp block

To implement a CCII+, the *Complementary Differential Pair with NMOS Cascode Load (ComdiffCasc-PN) with Push-Pull Inverter Output Stage* [5] shown in Fig. 3, is the topology used as the op-amp block.

The op-amp has rail-to-rail swing at both the input and output and has fewer stages than the other rail-to-rail op-amp configurations in [4], which makes it more stable. Also, its push-pull output stage further improves the differential gain and provides higher output voltage swing.

Setting all the transistor lengths (L) to 1.2um, the initial op-amp transistor widths (W) may be solved using the current equation, given in Eq. 1, for a MOSFET in saturation.

Chwee Teck Lim, James C.H. Goh (Eds.): ICBME 2008, Proceedings 23, pp. 846–850, 2009
www.springerlink.com

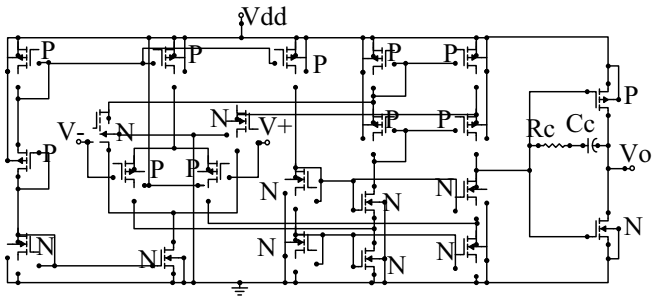


Fig. 3 *ComdiffCasc-PN* with push-pull inverter output stage

The reason for choosing the 1.2um transistor length, instead of the minimum length of 0.25um, is that short-channel effects are more significant at channel lengths less than 1um. Furthermore, submicron lengths for differential input pairs tend to introduce large offset voltage [6]. The tail current (I_{bias}) is set to be 20uA to minimize the total current and to meet the power consumption limits.

$$I_D = \frac{k'}{2}\frac{W}{L}\left(V_{GS} - V_T\right)^2 \tag{1}$$

A width of 5um/20um is used for NMOS/PMOS transistors with $I_{bias}/2$ current. Plugging these values into the schematic produced an op-amp differential voltage gain of less than 10,000, which is below the target gain of at least $1x10^6$. The transistor widths are then resized to increase the gain. A series of simulations aimed at characterizing the op-amp were carried out. The effects of varying the width of each transistor on the op-amp parameters such as differential gain, common-mode gain, 3-dB bandwidth, unity-gain bandwidth and phase margin were studied and plotted. Finally, transistor sizes were assumed to be multiples of 6, to aid in the layout implementation. The compensation resistor (R_C) and capacitor (C_C) used were 10KΩ and 500fF, respectively.

Due to parasitics introduced by metal layers, the total output resistance in the layout simulations increased, as compared to schematic simulations – thus increasing the differential gain. However, slight mismatches in the layout and the lack of symmetry in routing also increased the common-mode gain, hence decreasing the CMRR.

Furthermore, these parasitics introduce more poles, thus decreasing the bandwidth of the op-amp. It was also observed that the phase margin of the layout implementation is 20º lower than that of schematic simulations. As such, it is suggested that the phase margin be set at a relatively high value early in the schematic design stage to ensure stability in the layout stage.

B. Current conveyor block

The designed rail-to-rail op-amp is then connected to an output buffer stage before being paired with four types of current mirrors, which are: *Simple Current Mirror, Cascode Current Mirror, High-Swing Cascode Current Mirror* and *Wilson Current Mirror.* The requirements for the current mirrors to be used for the CCII+ are high output impedance, wide output voltage swing, small input bias voltage, and good high frequency response [7].

Even though the *Op-Amp with Simple Current Mirror* displayed the lowest output impedance among the four CCII+ implementations, it provided the highest current swing and had the least layout area and power consumption (having the least number of transistors) among all designs.

The positive input signal swing is determined by the state of transistor M1 while the negative input signal swing is determined by M2, as shown in Fig. 2. To have a functional output buffer stage, transistors M1 and M2 in Fig. 2 must remain saturated [7]. Therefore, the positive and negative input signal swing is restricted by Eq. 2-3.

$$V_{IN}^{+} = V_{DD} - V_T - V_{DSAT} - V_{DSAT1} \tag{2}$$

$$V_{IN}^{-} = V_{DSAT2} + V_T + V_{DSAT} \tag{3}$$

To minimize the voltage drop across the mirrors, the width of the transistors comprising the current mirrors is increased. This decreases the required V_{GS} for saturation. Hence, decreasing the input bias voltage requirements of the current mirrors increases the input swing at node X in Fig. 2. For uniformity and ease of layout, the widths of all the NMOS and PMOS transistors for the simple current mirrors are set to be 48um and 192um respectively.

III. Current-mode instrumentation amplifiers

Initial simulations on the *Improved 2-Current Conveyor (Improved 2-CC)* in-amp, shown in Fig. 4, verified the functionality of the *Op-Amp with Simple Current Mirror*. The in-amp produced a very high CMRR. However, it was observed from the in-amp's gain plot that the differential gain varies with the differential input voltage by ±10%. This gain irregularity is explained by the current error of the CCII+ (difference in current at the Z and X terminals). Ideally, the current at the output node Z of the conveyor follows the current at the input X but based on simulations, the current error increases as differential input is increased.

Stability was compromised due to the multiple stages employed in the CCII+ implementation. A series-RC compensation was placed between the buffer stage output and the current conveyor output node Z for all the CCII+

blocks used in all the in-amp circuits. The compensating resistor was set to 1KΩ while the compensating capacitor was limited to 2pF due to lay-out area considerations.

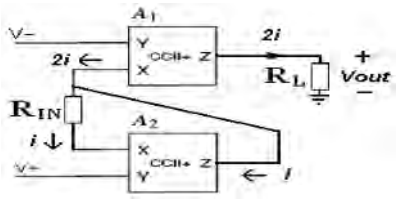


Fig. 4 Improved 2-CC schematic design [8]

The *2-Current Conveyor (2-CC)* is the most basic current-mode implementation of the in-amp. Any voltage difference applied between the in-amp inputs V+ and V- will also be reflected across $R_{IN,}$ forcing a current through it.

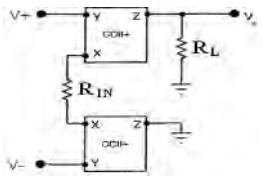


Fig. 5 2-CC schematic design [3]

By the operation of the CCII+, this same current will be conveyed and will then flow through $R_{L.}$ It can be derived that the differential voltage gain of this topology is

$$A_{VD} = \frac{V_{OUT}}{(V-)-(V+)} = \frac{R_L}{R_{IN}} \tag{4}$$

The resistors chosen for this circuit were 50KΩ for R_L (as in the other topologies) and 500Ω for R_{IN} to achieve a gain of 100. A large value of R_L was needed to make the output voltage swing approach the supply rail despite the low current being passed at the output.

The configuration in Fig. 6 is an improvement to the *2-CC* in-amp. As seen, an op-amp is added as an output stage to decrease the output impedance of the in-amp circuit. This op-amp, $A_{3,}$ is chosen to be tied at the output of the conveyor A_2 to produce a positive gain. As in the previous topology, the differential gain is given in Eq. 4.

The cascaded op-amp A_3 is the same op-amp used in the CCII+ implementation, with the same sizing and biasing. However, it was necessary to increase the compensation of the op-amp to make the *2-Current Conveyor with Op-Amp at the Output (2-CC with Op-Amp)* stable. The op-amp's C_C was increased from 500fF to 2pF, while R_C was increased from 10KΩ to 20KΩ.

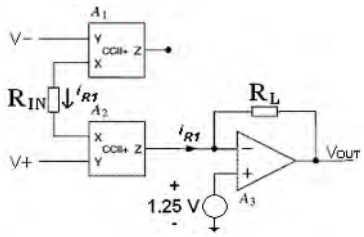


Fig. 6 2-CC with op-amp at the output schematic design [4]

The positive terminal of A_3 must be biased to at least V_{DSAT}, instead of just being grounded. This is to ensure that the output current mirrors of the conveyor A_2 have enough drain-source bias to maintain saturation, and thus enables the conveyor A_2 to properly mirror current $\boldsymbol{i}_{R1}$. In this design, a 1.25V-bias serves two purposes – aside from ensuring that conveyor A_2 effectively mirrors the current $\boldsymbol{i}_{R1,}$ it also raises the in-amp's output reference voltage to 1.25V, placing the output reference exactly between the rails. The 1.25V could be derived from the 2.5 V_{DD} through voltage dividers.

The *Improved 2-CC*, shown in Fig. 4, is typified by a feedback loop from the unloaded output of A_2 to the X terminal of A_1. Effectively, the voltages V- and V+ are imposed on the opposite ends of R_{IN} and determines the value of the current *i*. This same current is forced to flow into the Z terminal of A_2. Therefore, the total current leaving the X and Z terminals of A_1 is 2*i*. A_{VD} can be calculated to be,

$$A_{VD} = \frac{V_{OUT}}{(V-)-(V+)} = 2\frac{R_L}{R_{IN}} \tag{5}$$

The *3-Current Conveyor (3-CC)* topology consists of three CCII+'s and two resistors, with current conveyors B and C cascaded. As seen in Fig. 7, the current entering R_L is twice the current entering R_{IN}, so A_{VD} can be shown in Eq. 5.

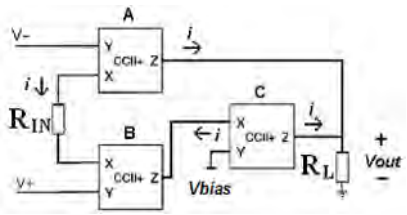


Fig. 7 3-CC schematic design [9]

The CCII+ labeled as C, has V_{BIAS} at its Y terminal instead of being directly grounded. Again, this is to ensure that there is enough V_{DS} at the output current mirrors of conveyor B. As done previously, V_{BIAS} was set to 1.25V.

IV. Representation of the ECG Signal

A representation of an ECG waveform using a piece-wise linear voltage source file is employed to verify the capability of the in-amps to accurately amplify ECG signals amidst common-mode noise. The model used in plotting the signal is adapted from related literature on biomedical signals. In addition, the simulated ECG signal was made to last for only 3 periods, so that simulations would not take much time.

Common-mode noise was added to the ECG signal, as a cascade of 100mV-sinusoids at 60, 120, 180 and 240Hz. A 1.25V DC voltage source was also used as a commode-mode input voltage to maintain correct biasing of the in-amp.

V. Results and Analysis

All the current-mode in-amp topologies achieved the fixed differential gain of 100, a superior CMRR of at least 150dB, and very high input impedance in the GΩ-range. However, the in-amps failed to provide a rail-to-rail input voltage signal swing because of the input signal constraints of the current conveyors. Hence, to allow the uV-range signal level of the ECG as input to the in-amps, the 1.25V DC input common-mode voltage was necessary.

Table 1 Parameters of *2-CC with Op-Amp* vs. INA326

Parameters	*2-CC with Op-Amp*	INA326
Differential gain	102.92	0.1 to 10000
Common-mode gain	4.16E-7	1.995E-04
CMRR	167.87dB	114 dB
Output voltage swing	6.14mV to 2.46V	Vss+10mV to
Input offset voltage	-3.24 uV	100uV
Supply current	798.51uA	2.4mA
Power consumption	1.99mW	Current*(±2.7 to ±5.5)
R_{IN}^+, R_{IN}^-	794GΩ, 792GΩ	100GΩ, 100GΩ
R_{OUT}	58.49Ω	--
3-dB bandwidth	1.26MHz	1KHz
PSRR @ 60Hz	85.68dB	110dB
Settling time	639.28ns	0.95ms
Slew rate	1.9V/us	Filter limited

No significant difference is observed between the *2-CC* and the *Improved 2-CC* in-amps. Both topologies consume less power because they have fewer components compared to the other two topologies. The only difference between them is that the *2-CC* has a greater tendency to suffer crosstalk due to the unused output of one of its conveyor blocks. The *3-CC* in-amp, on the other hand, also produces the same performance despite the additional conveyor. Simulations have shown that aside from failing to produce an evident improvement in results, the third conveyor also degrades the bandwidth of the circuit and consumes more power.

The *2-CC with Op-Amp* in-amp provides the smallest output impedance because of the addition of an op-amp as an output stage. Furthermore, this topology has an easily adjustable output reference voltage.

Shown in Table 1 is the comparison between the achieved parameters of the *2-CC with Op-Amp* and the specifications of the INA326, which is also a current-mode in-amp.

Meanwhile, shown in Fig. 8 is the output plot obtained as the *2-CC with Op-Amp* is applied with the simulated ECG signal and common-mode noise. Clearly, it can be seen that the in-amp has indeed rejected the common-mode signals incorporated in the simulated ECG signal.

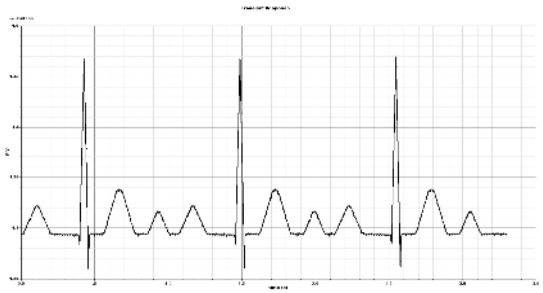


Fig. 8 Output of 2-*CC with Op-Amp* with input ECG signal and noise

VI. Conclusion

In-amp designs should always take into account the trade-off between CMRR and stability. Simulations showed that a decrease in the common-mode gain increases the CMRR, thus compromising stability. Generally, cascading more stages to improve certain parameters, such as CMRR, worsens the stability of a system.

All the current-mode in-amp topologies achieve impressively high CMRR. Hence, any of the implemented current-mode circuits is an outstanding differential amplifier and thus, a potential ECG system block. However, the *2-CC with Op-Amp* provides the lowest output impedance that is essential for connecting the in-amp into a larger system. It also has the advantage of being able to adjust its output reference voltage, allowing it to handle both negative and positive signals with respect to the reference voltage.

References

1. J. G. Webster, *Medical Instrumentation – Application and Design, 3rd ed.,* John Wiley and Sons, Inc., 1998
2. C. Kitchin, L. Counts, *A Designer's Guide to Instrumentation Amplifiers, 3rd ed.* Analog Devices, Inc., 2006

3. C. Toumazou, F. J. Lidgey, and C.A. Makris. "Current-mode instrumentation amplifier," Short Run Press Ltd., Exeter, 1993
4. K. Koli and K. Halonen, "CMRR enhancement techniques for current-mode instrumentation amplifiers," *IEEE Transactions on Circuits and Systems-I: Fundamental Theory and Applications*, vol. 47, no. 5, May 2000
5. M. Lorenzo and A. Manzano, "Design and implementation of CMOS rail-to-rail operational amplifiers," Department of Electrical and Electronics Engineering, University of the Philippines, October 2006
6. P.R Gray, et al., *Analysis and Design of Analog Integrated Circuits, 4th Ed.,* John Wiley and Sons, Inc., 2001
7. A. Sedra and G. Roberts, "Current conveyor theory and practice," *Analogue IC Design: The Current-mode Approach*, Short Run Press Ltd., Exeter, 1993
8. S. J. Azhari and H. Fazlalipoor, "A novel current mode instrumentation amplifier (CMIA) topology," *IEEE Transactions on Instrumentation and Measurement,* vol. 49, no. 6, December 2000
9. A. A. Khan, M. A. Al-Turiagi and M. A. El-Ela, "An improved current-mode instrumentation amplifier with bandwidth independent of Gain," *IEEE Transactions on Instrumentation and Measurement*, vol. 44, no. 4, August 1995

Cells Separation by Traveling Wave Dielectrophoretic Microfluidic Devices

T. Maturos[1], K. Jaruwongrangsee[1], A. Sappat[1], T. Lomas[1], A. Wisitsora-at[1], P. Wanichapichart[2] and A. Tuantranont[1]

[1] 1 Nanoelectronics and MEMS Laboratory, National Electronics and Computer Technology Center, Pathumthani, Thailand
2 Biotechnology Unit, Prince of Songkla University, Songkhla, Thailand

Abstract— **In this work, we present a microfluidic device with a 16 parallel electrode array and microchamber for cell separation by using travelling wave dielectophoretic force. The dielectrophoretic PDMS chamber was fabricated using standard microfabrication techniques. The Cr/Au parallel electrode array of 100 µm wide and 300 nm thick was patterned on a glass slide by sputtering through microshadow mask. In order to test twDEP devices, two different size of polystyrene microspheres suspension in deionized water were used as the tested cells. Each type of polystyrene was tested in both the separated and mixed solution. Cells response to the electric field in various mechanisms depending on the applied voltage and frequency of AC signals. For 4.5 µm polystyrene, cells were forced to locate in the center between electrode array and move along the channel and the traveling wave dielectrophoresis occur, when the applied voltage was 10 V and the frequency of the applied signals is in the range of 50 kHz-700 kHz. For 10 µm polystyrene the twDEP occurs when the applied voltage was 7 V and frequency was in the range 30 kHz-1MHz. For the mixed solution containing equal amount of 4.5 and 10 µm microspheres, the big microspheres were moved under twDEP force when the applied voltage was 7 V and the frequency was in the range 25 kHz-1MHz while the small microspheres were attached to the electrodes. Therefore, the twDEP device can separate the microspheres with different sizes and it can be further applied for cells separation and manipulation.**

Keywords— **Traveling wave dielectrophoresis, cell separation, lab-on-a-chip.**

I. Introduction

Recently, there have been growing interests in using the MEMS technology for biological and medical applications. The use of electrokinetic effects for manipulating microparticles has been shown to be efficient for biological applications. The examples of electrokinetic phenomena include dielectrophoresis, electrorotaion and traveling wave dielec-trophoresis [1-5]. Dielectrophoresis (DEP) is an electrokinetic movement of neutral particles induced by polarization in non-uniform electric field [6]. The time averaged dielectrophoretic force on a dielectric sphere in non-uniform electric fields is represented by

$$F = 2\pi\varepsilon_0\varepsilon_m r^3[\mathrm{Re}(f_{CM})\nabla|E|^2 + (-\frac{2\pi}{\lambda})\mathrm{Im}(f_{CM})E^2]$$

Where ε_0 is the vacuum dielectric constant, r the particle radius, f_{CM} is a Clausius-Mossotti factor, and ε_p^* and ε_m^* are the relative complex permittivity of the particle and the medium, respectively. The positive and negative DEP force is determined by the real part of a Clausius-Mossotti factor. When the dielectric constant of particle is larger than that of medium, the first term is positive; the dielectrophoresis is positive and the particle moves towards the locations with the greatest electric field. In contrast, if the dielectric constant of particle is less than that of medium, the first term is negative, the dielectrophoresis is negative and the particle is repelled from the locations with the greatest electric field [7, 8]. Traveling wave dielectrophoresis (twDEP) is a traveling wave electric field which can be produced when a 90°-phase shift signal sequence is applied to a parallel electrode array. twDEP occurs when the real part of the force equation is much less than the imaginary part [9]. Since the strength of the force depends strongly on the medium, the particle's electrical properties, the particle's shape and size, and the frequency of the electric field, varying of any parameter allows the manipulation of particles with great selectivity which can be applied in many applications.

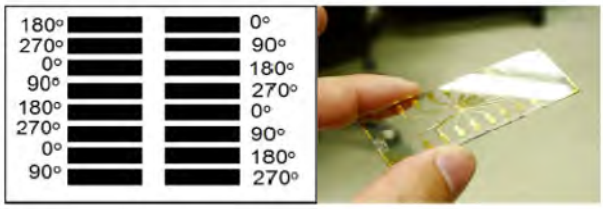
In this work we present a design and fabrication of twDEP device for separation of cells with difference size. The characterization of chip was studied by observing the movement of microparticles under different conditions of applied twDEP.

II. Experimental Study

A. Dielectrophoretic devices

The dielectrophoretic chamber was fabricated using standard microfabrication techniques. A Silicon wafer was cleaned in piranha solution (mixture of 1: 4 of 50% H_2O_2 and

Chwee Teck Lim, James C.H. Goh (Eds.): ICBME 2008, Proceedings 23, pp. 851–854, 2009
www.springerlink.com



(a) (b)

Fig. 1 Electrode geometry and phase applied on the electrode (a) and a photo of the twDEP devices (b)

97% H_2SO_4) at 120 °C for 10 minutes, then carefully rinsed several times in deionized water and dried with a gentle stream of air. After that the silicon wafer was dehydrated by heating at 150-200 °C for 10 minutes. SU-8 photoresist was spin-coated on the silicon wafer using a spin coater (Laurell technologies corp. model WS–400A–6NPP), then soft baked to remove all the solvent in the layer. The photoresist coated wafers were exposed using MJB4 mask aligner (SUSS microtec), then post-baked in order to selectively cross-link the exposed portions of the film. The sample was left in the desiccators to cool down slowly at room temperature for more than 13 hours. Finally, samples were developed and cleaned with deionized water and isopropyl alcohol, and then it was gently dried with air. Spin speed, exposure time, baked time, and developing time were optimized to achieve a smooth surface on mold. The chamber was made from Poly (dimethylsiloxane) (PDMS) by solvent casting and drilling. PDMS was prepared by mixing the precursors sylgard with a curing agent at a ratio of 10:1 by volume. The prepolymer mixture was degassed at 20-50 mTorr at room temperature in desiccators pumped with a mechanical vacuum pump for 10 minutes to remove any air bubbles in the mixture. PDMS mixtures were gradually poured onto the SU8 master mold to the height over the depth of designed chamber. After the PDMS is cured at 100 °C for 30 minutes on a mold, the molded polymer samples are peeled off.



(a) (b)

Fig. 2. The photograph of twDEP chip (a) experimental set up (b)

The mask for fabricating electrode was designed to have 8 parallels bar shape by using L-Edit software as shown in Fig.1. The Cr/Au electrode array of 100 μm wide and 300 nm thick was patterned on glass slide by DC sputtering through microshadow masking. The chromium and gold were sputtering under argon plasma. The sputtering pressure, sputtering current, and time for chromium are $3x10^{-3}$ mbar, 0.2 A, and 2 minutes, respectively. Next, gold was sputtered under the argon pressure of $3x10^{-3}$ mbar and the sputtering current of 0.2 A for 10 minutes. The sputtering was conducted at room temperature. The chamber and electrodes were treated under oxygen plasma (Harrick scientific corp. model PDC –32 G) before being attached to each other.

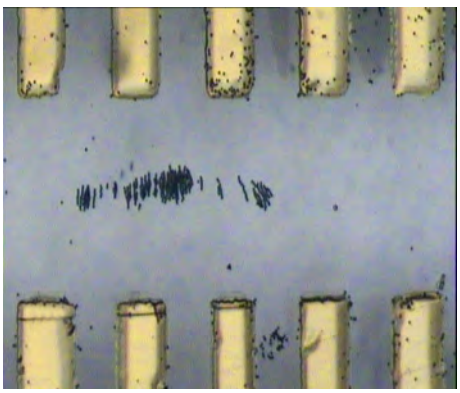


Fig.3 The 4.5 μm microsphere were attached to the center between electrodes array when the applied voltage and frequency to the electrode array was 10 V and 500 kHz

B. Separation test

In order to test the twDEP devices, polystyrene microspheres suspended in water were used as the tested cells. Polystyrene microspheres of 4.5 μm mean diameter and a density of 4.99×10^8 particles per milliliter were purchased from Polysciences, Inc, Warrington, PA, USA. While the 10 μm polystyrene microspheres was purchase from Sigma Aldrich company, USA. The polystyrene solution was dilute 1000 times in deionized water. A 10 milliliter polystyrene solution was dropped in the chamber. The chamber was then closed on top by glass slide. The electrodes were energized with four square wave signals. The cells movements under electric fields were observed by using microscope CX41 (Olympus). Cells respond to the electric field in various mechanisms depending on the frequency of applied AC signals. The experimental setups are shown in Fig.2.

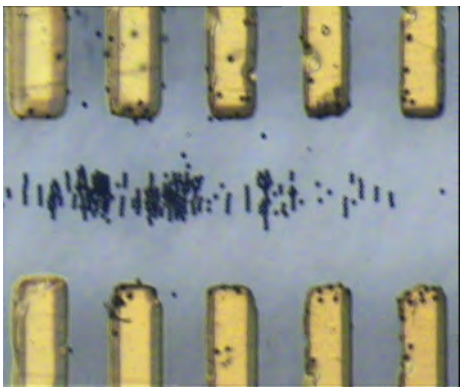


Fig.4 The 10 μm microsphere were attached to the center between electrodes array when the applied voltage and frequency to the electrode array was 7 V and 250 kHz

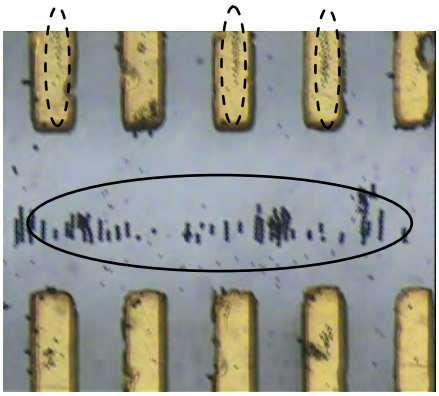


Fig.5 The mixd of two type of microsphere were in the applied voltagae and frequency of 7 V and 25 kHz. The big microsphere were attached to the center between electrodes array (solid line) while the small microspheres were attached to the electrodes (dotted line)

III. Result and Discussion

Two types of cells were tested separately to find the optimum conditions that traveling wave dielectrophoretic occur. For the 4.5 μm microsphere, when the applied voltage and frequency to the electrode array was 10 V and 50 Hz, cells were moved over to the electrode edges in a vertical circular motion and moved faster when the frequency or voltage was increased. When the frequency of the applied signals were more than 350 Hz, cells started moving slowly and tried to move to the center of electrode array. As the frequency of the applied signals was in the range of 50 kHz-700 kHz, cells were attached to the center between electrode arrays and moved slowly along the channel as shown in Fig.3. When the frequency of the applied signals was more than 700 kHz, cells started moving out of the center between electrodes. Therefore, that indicates that the 4.5 μm cells are subjected to the effects of a traveling dielectrophoresis force when the applied voltage was 10 V and the frequency was in the range 50 kHz-700 kHz. These results are consistent with the theory that twDEP occurs when the frequency of applied AC fields is in the range where dielectrophoresis (DEP) is negative so when cells experience twDEP force they were repelled from the electrode rather than being trapped by positive DEP. When applied the proper voltage and frequency to the 10 μm microspheres, the big cells show similar behavior to the small cells. In this case, the twDEP occurs when the applied voltage was 7 V and frequency was in the range of 30 kHz-1MHz, as shown in Fig. 4. For the mixed solution containing equal amounts of 4.5 and 10 μm microspheres, the big cells start moving to the center between the electrode arrays when the frequency reaches 5 kHz. When the frequency was 25 kHz-1MHz, the big cells were attached to the center between electrodes, and moved under twDEP force while the small microspheres were attached to the electrodes as shown in Fig.5. The threshold frequency that the big and small cells have started separating were recorded when the big cells started moving to the center between electrode arrays and the small cells were attached to the electrodes. The threshold frequency at each applied voltage is shown in Fig. 6. It can be seen that at the high applied voltage cells separated at the high applied frequency. However, the best separating condition for the 4.5 and 10 μm microspheres was at the applied voltage and frequency equal to 7 V and 25 kHz-1 MHz, respectively. This result can be further applied in biological and medical application such as motion control and cell selectivity.

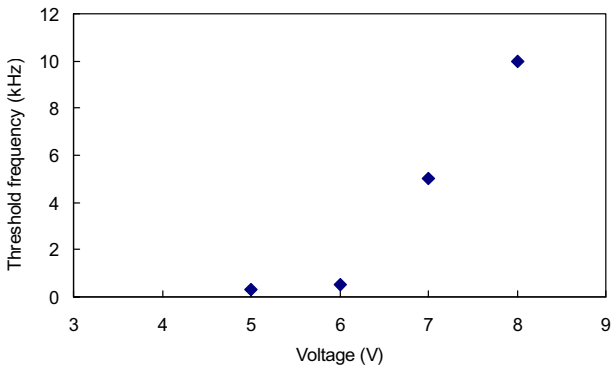


Fig. 6 The relationship between the applied voltage and threshold frequency for cells separation

IV. Conclusions

The traveling wave dielectrophoretic microfluidic devices were successfully fabricated. When energized the electrodes with four square wave signals, cells response to the electric field in various mechanisms depending on the amplitude and frequency of applied AC signals. Cells with different size were subjected to traveling wave dielectrophoresis in the different voltage and frequency range. And the results for the mixed of two type of cells show that at the proper applied voltage and frequency, two cells can be separated. Furthermore, this twDEP separation approach could be applied to the flow system and integrated with other devices for using in biological and medical application.

References

1. Huang, Y., and Pethig, R. (1991) Electrode design for negative dielectrophoresis. J Meas Sci Technol 2: 1142-1146.
2. Wang, X.-B. Huang, Y., Gascoyne, P. R. C Becker, F. F., Hölzel, R. and Pethig, R. (1994) Changes in Friend murine erythroleukaemia cell membranes during induced differentiation determined by electrorotation. Biochimica et Biophysica Acta 1193: 330-344.
3. Schnelle, T., Hagedorn, R., Fuhr, G., Fiedler, S., and Müller, T. (1993) Three-dimensional electric field traps for manipulation of cells-calculation and experimental verification. Biochimica et Biophysica Act 131: 127-140
4. Wang, X.-B. Huang, Y.,Burt, J.P.H., Markx, G.H., and Pethig, R. (1993) J. Phys. D: Appl. Phys. 26: 1278-1285
5. Huang, Y., Wang, X.-B., Tame, J.A., and Pethig, R. (1993) J. Phys. D: Appl. Phys. 26: 1528-1535
6. Pohl, H. A. (1978) Dielectrophoretic. Cambridge, UK.
7. Fu, L. M., Lee, G. B. (2004) Manipulation of microparticles using new modes of traveling-wave-dielectrophoretic force : numerical simulation and experiment, IEEE/ASME Transactions on mechatronics, vol 9, 2004, pp. 377-383.
8. Wang, X.-B., Hughes, M.P., Huang, Y., Becker, F.F., Gascoyne, P. R. C. (1995) Non-uniform spatial distributions of both the magnitude and phase of AC electric fields determine dielectrophoretic force. Biochimica et Biophysica Acta. 1243: 185-194
9. Batchelder, J. S. (1983) Dielectrophoretic manipulator. Rev. sci. Instrum 54: 300-302

A Novel pH Sensor Based on the Swelling of A Hydrogel Membrane

K.F. Chou, Y.C. Lin, H.Y. Chen, S.Y. Huang and Z.Y. Lin

Department of Biomedical Engineering, Yuanpei University, Hsin Chu, Taiwan

Abstract — **A novel pH sensor consists of the pH sensitive hydrogel and conductive polymer layer was developed. The monomers of hydroxyl ethyl methacrylate were polymerized and modified by UV radiation to become the pH sensitive hydrogel. The pH sensitive functional group of poly(HEMA) was created by UV treatment. The sensing principle of the device was based on the piezoresistive effect induced by the swelling behavior of the hydrogel varied with pH value of testing solution on the conductive polymer. The correlation between the sensitivity of the device and UV radiation dosages was investigated. The stree-strain relationship of the polymer membranes and output characteristic of pH sensor were measured, and the computer-aid analysis based on the hyperelastic–viscous model of hydrogel was achieved by using the fine element method. The optimization aspect of pH sensor also was found from the simulating process.**

Keywords — **hydroxyl ethyl methacrylate, pH sensitive, sensor.**

I. Introduction

For past years, a lot of papers on pH sensor based on hydrogel had been published[1-9]. The operating principle of the pH sensors with hydrogel substrate all are based on the bending of flexible matrix induced by the swelling effect of gel. The deformation of geometry structure could be transfer into the change of capacitance or resistance. These similar principles were applied in the design of various sensors. Herber et al.[2] developed a hydrogel biosensor for monitoring the partial pressure of CO_2 in the stomach. Han et al.[1] combinated the pressure transducer and pH sensitive gel to develop a biosensor applied into the measurement of the concentration of glucose in blood. On the other hand, Trinh et al.[9] investigated the effect of polymerization condition on the sensitivity and response time, and predicted the characteristics of the sensor by using Mooney-Rivlin model and finite element method.

Most researchers chose PVA-PAA copolymer as the pH sensitive materials. In our previous study[10,11], the swelling degree of poly(HEMA) exposed by gamma ray in buffer solutions changed with the pH value of buffer. Besides, the pH sensitive behavior could be modified by irradiation dosages. However, in this study, we modified the poly(HEMA) with ultraviolet irradiation but not gamma ray in order to keep the mechanical properties of hydrogel thin film.

II. Material and Method

A. Sensing principle

The sensing device was composed of the pH sensitive hydrogel layer(poly(HEMA)), resistance Ag gel layer and SiO_2 substrate. The operating principle of the sensor was showed as Fig. 1. The swelling of the polymer film induced by absorbing testing solution, and the swelling degree changed with the pH value of solution. The resistance layer under the hydrogel deformed with the swelling of sensitive layer such that resistance changed. The relationship between the resistance variation and strain are linear as formula (1). The resistance layer connected with a Wheatstone bridge. The voltage output of Wheatstone bridge could be measured as the change of the resistance of Ag gel.

$$\frac{\Delta R}{R} = \varepsilon \tag{1}$$

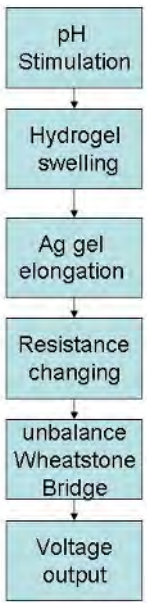


Fig. 1 Operating principle of pH sensor

B. Materials

All chemical reagents were purchased from Tokyo Kasei Kogyo Co. Ltd. and were used as received. Water was dis-

Chwee Teck Lim, James C.H. Goh (Eds.): ICBME 2008, Proceedings 23, pp. 855–858, 2009
www.springerlink.com

tilled and deionized at 18 M resistance. Aqueous solutions (10 wt%) of ammonium persulfate(APS) and sodium metabisulfite (SMBS) were used together as initiators and were made prior to every use. All chemicals were used as received unless otherwise stated. Ethylene demethacrylate (EDMA) were used as crosslinking agent.

C. Polymerization of poly(HEMA)

The monomer mixture was comprised of monomers (HEMA), crosslinking agent (ethylene dimethacrylate, EDMA), and solvent (D. I. water). HEMA monomer diluted with water (HEMA : water = 60 : 40). Next, EDMA, ammonium persulphate and sodium metabisulphite was added into the solution and mixed by ultrasonic machine for 5 min. The polymerization of these monomer mixtures are initiated by APS and SMBS concentrations were 0.5 wt% and 0.2 wt% of the total monomer, respectively. Prepolymerization occurred at 65℃for half hour. Then the prepolymers were spin coated on resistance layer to form the polymer thin film with thickness of 300 μm. After prepolymerization, the specimens were exposed on 360nm UV radiation for 2hr (dosages of 72J/cm^2).

D. Characteristic analysis of the sensitive layer

The chemical structure of poly(HEMA) was determined by FTIR. The hydrogel samples were immersed in various pH buffer solutions. Their weight changes were measured with an electronic balance. The swelling degree of hydrogel was calculated from the result. The definition of swelling degree (SR) listed as equation (2). W_t means the weight of thin film at time t, W_0 is the initial weight.

$$SR = \frac{W_t - W_0}{W_0} \tag{2}$$

E. Fabrication of Sensing Chip

The fabrication process of sensing chip was shown as Fig. 2. The process was divided into three steps (a) two square SiO_2 plates were made up through a PMMA mold, and Ag gel layer was spin coated on SiO_2 substrate. (b) Au conducting electrode was fabricated by sputtering coater, and remove the bump by using acetone. Poly(HEMA) sensitive layer was filled by the principle of siphon effect. (c) The second Ag gel layer was coated on the hydrogel layer.

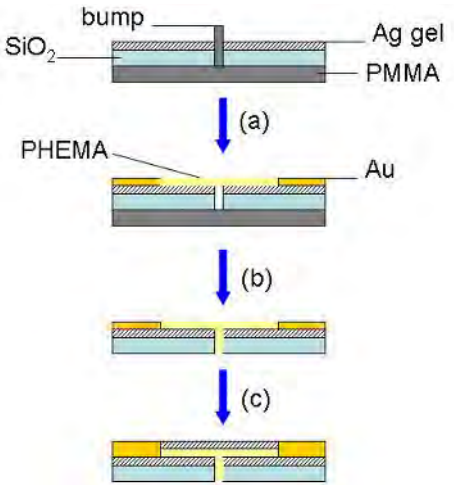


Fig. 2 Fabrication of pH sensor

F. pH measurement system

The infrastructure of pH measurement system was shown as Fig. 3. The pH sensor contains a sensing chip and Wheatstone bridge. In the signal condition part, The output signal are amplified and filtered through AD620 IC. Then, the voltage output converted to digital signal with NI 6024E DAQ. Finally, the curve of pH value versus time is displayed by the panel of virtual instrument.

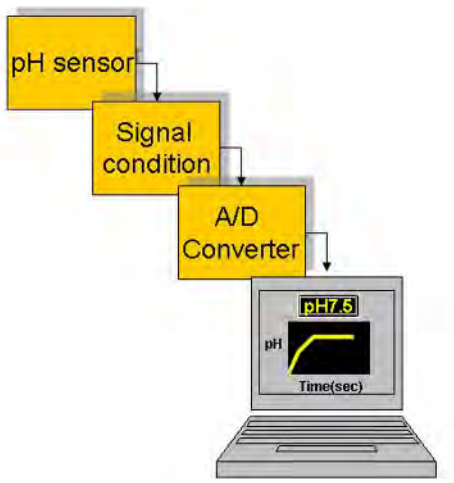


Fig. 3 pH measurement system

III. Results and Discussion

A. Characteristic analysis of the sensitive layer

The effect of UV radiation on the chemical structure of poly(HEMA) was analyzed by FTIR. The spectrum was shown as Fig. 4. Poly(HEMA) thin film exposed on 360nm UV radiation of 72 J/cm^2 presents two significant shift and adsorption at 1244cm^{-1} and 3500cm^{-1}, respectively. The adsorb band at 1244cm^{-1} corresponds to the acrylate group and crosslink structure of EDMA. That implies that UV radiation energy would destroy the crosslink structure and create weak basic groups. On the other hand, the decreasing of restrict force was due to the breaking of crosslink structure. Therefore, the absorption peak of hydrophilic groups was enhanced. This inference was verified by the swelling experimental. Fig. 5 presents the result of the experimental. The swelling degree of poly(HEMA) immersed in acidic solution was higher than base solution, the swelling ratio exponential decays with pH value of buffers.

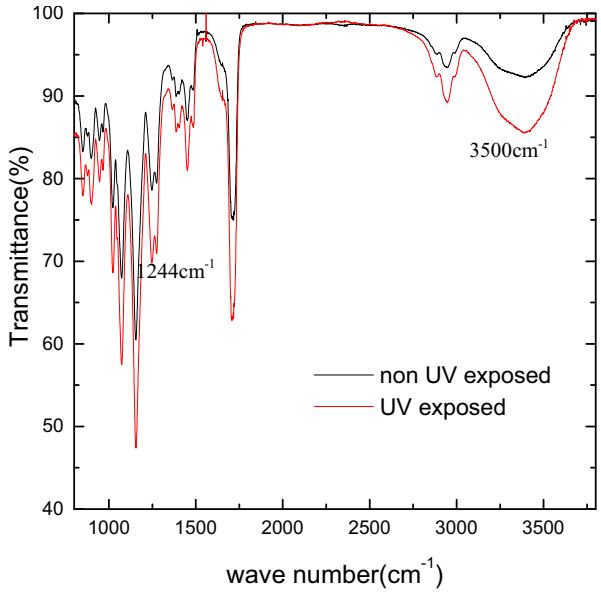


Fig. 4 FTIR spectrum of P(HEMA)

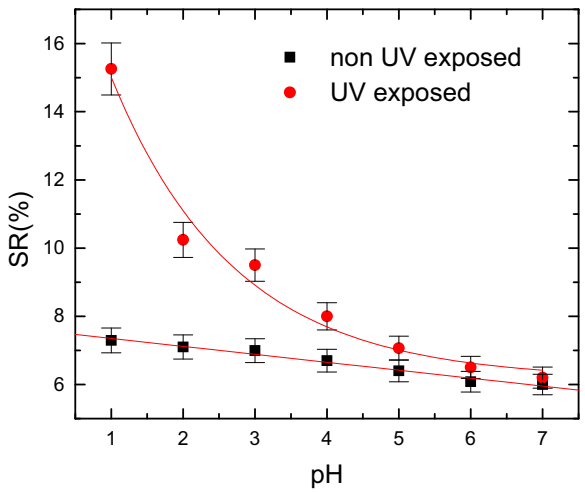


Fig. 5 Plot of swelling degree of P(HEMA) versus pH value of buffers

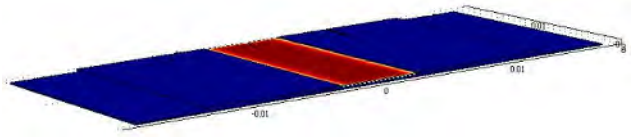


Fig. 6 Stress distribution applied in the P(HEMA) thin film

The Young's modulus of poly(HEMA) was obtained by tensile testing, the value is 0.73MPa. The swelling stress distribution was simulated with Comsol Multiphysics software, shown as Fig. 6. The deformation was limited along axis y and z.

B. Output Characteristic of the resistance Ag gel layer

The plot of resistance of Ag gel layer versus pH value of buffer solutions was shown as Fig. 7. The trend of data could be divided into two stages. The resistance of Ag gel increases with the increasing pH value of buffers in the range of pH1~pH4. However, the trend reverses at pH4. The resistance decreases with the increasing pH value of buffers in the range of pH4~pH7. The characteristic of Ag gel was matched with the swelling behavior of sensitive

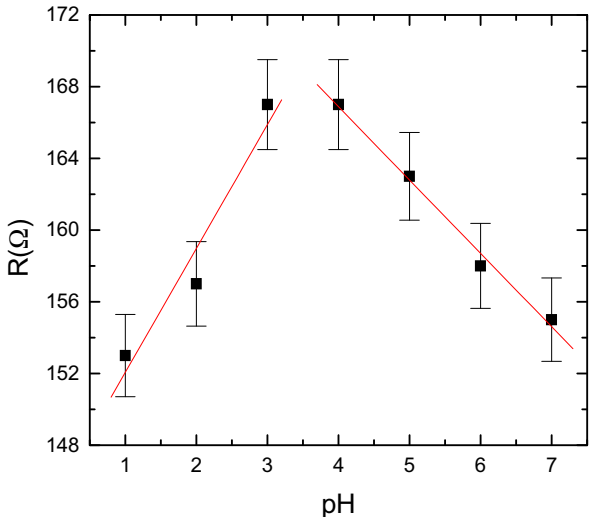


Fig. 7 Plot of resistance of Ag gel versus pH value of buffers

layer as the value of pH>4. Nevertheless, it might be that the moist raises the conductivity of Ag gel, such that the opposite trend was happened as the value of pH<4. This unexpected result should be improved by hydrophobic surface modification of Ag gel.

IV. CONCLUSIONS

This study developed a novel pH sensor based on the swelling of pH sensitive Poly(HEMA). Poly(HEMA) was modified with exposure of UV radiation. A weak basic group was created by the breaking of crosslink structure, such that the swelling degree of Poly(HEMA) exponential decay with the pH value of buffers. Ag gel was made as the resistance layer covered the hydrogel layer. The output characteristic of Ag gel presents two stages. The strain dominated the characteristic of Ag gel in the range of pH4~pH7, so the resistance of Ag gel decreases with the pH value. However, the moist dominated the conductivity of resistance layer in the range of pH1~pH4, such that resistance increases with the pH value of testing solution.

ACKNOWLEDGMENTP

This work was supported by the Ministry of Education, Taiwan (Project No.E-19-012).

REFERENCES

1. Han IS, Han MH, Kim JW, Lew S, Lee YJ, F., Horkay JJ (2002) Biomacromolecules 3:1271–1275.
2. Herber S, Olthuis W, Bergveld P, (2003) Sens. Actuators B 91:378–382.
3. Herber S, Olthuis W, Bergveld P, Van den Berg A (2004) Sens. Actuators B 103:284–289.
4. Gerlach G, Guenther M, Suchaneck G, Sorber J, Arndt KF, Richter A, (2004) Macromol. Symp. 210:403–410.
5. Guenther M, Sorber J, Suchaneck G, Gerlach G, Thong TQ, Arndt KF, Richter A, (2005) Technisches Messen 72:93–102.
6. Gerlach G, Guenther M, Suchaneck G, Sorber J, Arndt KF, Richter A, (2005) Sens. Actuators B:112 555–561.
7. Montheard JP, Chatzopoulos M, Chappard D, (1992) Rev. Macromol. Chem. Phys. C32: 1–34
8. Huglin MB, Sloan DJ, (1983) Br. Polym. J. 15:165–171.
9. Trigo RM, Blanco MD, Teijon JM, Sastre R,(1994) Biomaterials 15:1181–1186.
10. Chou KF, Han CC and Lee S,(2000) Journal of Polymer Science Part B: Polymer Physics, 38: 659-671.
11. Chou KF, Han CC and Lee S, (2001) Polymer, 42:4989-4996

Author: Kuofeng Chou
Institute: Department of Biomedical Engineering, Yuanpei University
Street: Yuanpei Street
City: Hsin Chu City
Country: Taiwan
Email: kuofeng@mail.ypu.edu.tw

Simulation and Experimental Study of Electrowetting on Dielectric (EWOD) Device for a Droplet Based Polymerase Chain Reaction System

K. Ugsornrat[1], T. Maturus[2], A. Jomphoak[2], T. Pogfai[2], N.V. Afzulpurkar[1], A. Wisitsoraat[2], A. Tuantranont[2]

[1]Asian Institute of Technology,Microelectronics, Pahon Yotin Rd, Klongluang, Pathumthani ,Thailand
Email:Kessararat Ugsornrat@ait.ac.th
[2]Nanoelectronics and MEMS Laboratory, National Electronics and Computer Technology Center (NECTEC),
112 Pahon Yotin Rd, Klongluang, Pathumthani, Thailand *Email: adisorn.tuantranont@nectec.or.th*

Abstract — **Polymerase Chain Reaction (PCR) technology has been widely used in molecular biology, forensic analysis, evolutionary and medical diagnostic. PCR requirement for point of care application is shorten reaction time and reduces PCR reagent. If the PCR chip can be done by droplet basis, then the analysis system which minimal amount of fluid will be possible. In this report, we describe the simulation and experimental study of a parallel–plate electrowetting on dielectric (EWOD) based PCR device. The EWOD device is applied to control PCR reagent and sample for a polymerase chain reaction (PCR) system. The EWOD-based PCR system consists of 3.4 mm wide, 15.1 mm long serpentine-shape microheater integrated underneath to maintain temperature at each stage and 370 μm deep microchannel. DNA was driven by moving droplet through each square electrode (dimension 1x1 mm^2) that maintains temperature at denaturation, annealing, and extension region. The fluid dynamics of the device have been modeled by Coventorware®, a commercially available MEMS simulation software, to show temperature distribution on each electrode. In experiment, this work studied contact angle reduction of different droplet because this result can be studied possibility of transporting of PCR reagent for a droplet based PCR.**

Keywords — **Polymerase Chain Reaction (PCR), Electrowetting on Dielectric (EWOD), Droplet, Finite Element Analysis.**

I. Introduction.

The polymerase chain reaction (PCR) is a powerful technique used to make copied DNA sequences of interest through repetitive temperature cycling. For the first report introduce in 1983, PCR has been widely used in molecular biology, medical diagnostic, forensic analysis, evolutionary and medical diagnostic [1]. The temperatures used in PCR are typically 90 - 94°C for denaturation, 50 - 70°C for annealing, and 70 - 75°C for extension. The double-stranded helix of nucleotides, carrying the genetic information, is separated during denaturation, reacts with chemical primers during annealing, and becomes a complete double-stranded DNA helix structure during extension. After about 30-40 thermal cycles, the target is copied into billions copies.

The objective is to design a better PCR device are shorten reaction time and reduces PCR reagent. Currently, most developed PCR system is based on continuous flow system. If the PCR chip can be done by droplet basis, then analysis system with minimal amount of fluid will be possible. In 2003, Zhang et al. reported a theoretical performance of the droplet-based PCR system is better than the continuous flow in terms of performance, simple to design and ease of integration with sample preparation or product detection [2].

Electrowetting is a well known method for moving droplet. The concept of electrowetting process is to alter the wetting properties of a surface by applied electric field. The energy stored in this field can be formulated as equivalent interfacial tension, and thus, related to the large change of contact angle for liquid droplet due to external electric field [3-7].

In 2005, a droplet-based micro oscillating-flow PCR chip was designed and fabricated but this device requires mechanisms to move the sample in the system [8]. Therefore, our research work demonstrates the simulation and experiment of a parallel-plate EWOD device that moves fluid droplets through surface tension effects in microchannel without the use of mechanism to move the sample.

In this work, we show that to achieve a successful device, the shapes of reaction chambers along with the microheaters. In microchannel, PCR was designed by using silicone oil to cover the droplet to prevent evaporation and help reducing voltage to transport droplet [9,10].

II. A droplet based PCR design.

We propose a droplet based PCR by EWOD technique to focus on minimizing reagent consumption and without the use of mechanical mechanism to move the sample in the system. The PCR has a single microchannel because of simplicity and more convenient integration of DNA amplification with product detection. As illustrated in Fig. 1, our design consists of a microchannel and three microheaters.

Chwee Teck Lim, James C.H. Goh (Eds.): ICBME 2008, Proceedings 23, pp. 859–862, 2009
www.springerlink.com

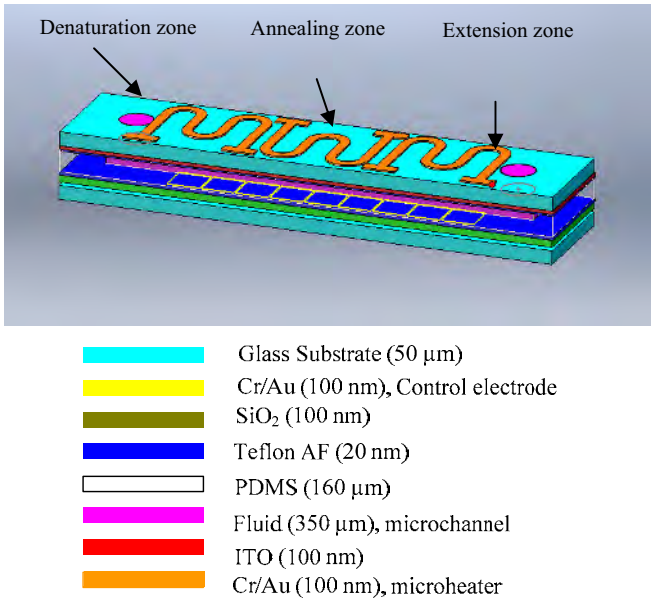


Fig. 1. A droplet based PCR model

Table 1.Charecterization Of State Machine

Configuration No.	E_1	E_2	E_3	E_4	E_5
Step 0.	Off	Off	Off	Off	Off
Step 1.	Off	On	Off	Off	Off
Step 2.	Off	On	On	Off	Off
Step 3.	On	Off	On	Off	Off
Step 4.	Off	Off	Off	On	Off
Step 5.	Off	Off	Off	Off	On
Step 6.	Off	Off	Off	Off	Off
Step 7.	Off	Off	Off	Off	Off
Step 8.	Off	Off	Off	Off	Off
Step 9.	Off	Off	Off	Off	Off
Step 10.	Off	Off	Off	Off	Off
Step 11.	Off	Off	Off	Off	Off

Configuration No.	E_6	E_7	E_8	E_9	E_{10}	E_{11}
Step 0.	Off	Off	Off	Off	Off	Off
Step 1.	Off	Off	Off	Off	Off	Off
Step 2.	Off	Off	Off	Off	Off	Off
Step 3.	Off	Off	Off	Off	Off	Off
Step 4.	Off	Off	Off	Off	Off	Off
Step 5.	Off	Off	Off	Off	Off	Off
Step 6.	On	Off	Off	Off	Off	Off
Step 7.	Off	On	Off	Off	Off	Off
Step 8.	Off	Off	On	Off	Off	Off
Step 9.	Off	Off	Off	On	Off	Off
Step 10.	Off	Off	Off	Off	On	Off
Step 11.	Off	Off	Off	Off	Off	On

On=Applied voltage , Off= Not applied voltage

The main channel is single, straight microchannel with three independent temperature zones for denaturation, annealing and extension zones. Three microheaters maintained at 95ºC, 70ºC, and 60ºC for three temperature zones of single microchannel. A droplet is introduced in the reservoir and is

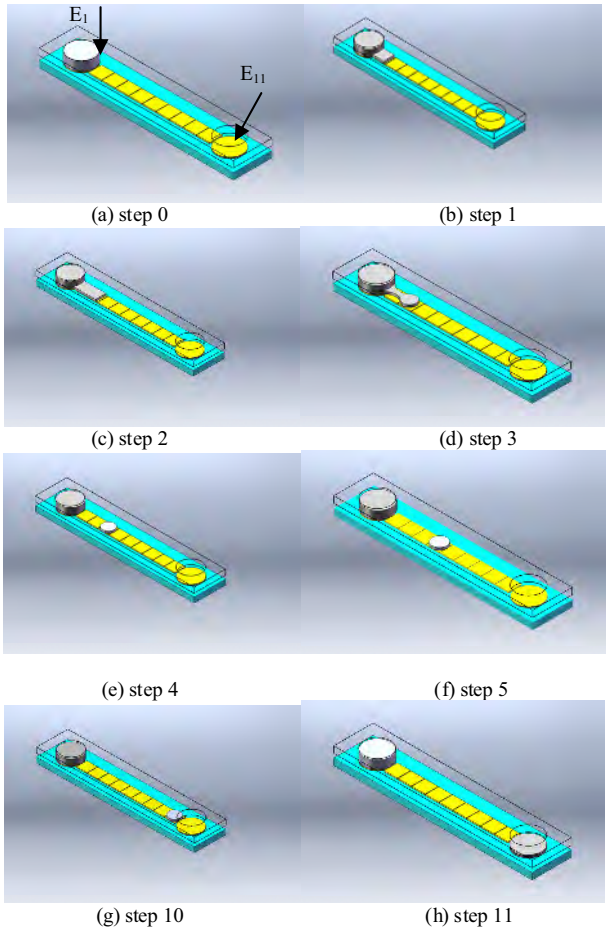


Fig. 2. Schematic of device with voltage pattern used.

moved back and forth along the microchannel by concept of EWOD device. The number of thermal cycles consists of 30-40 cycles in depend on application. Finally the droplet is pushed out of the chip from the outlet hole for analysis.

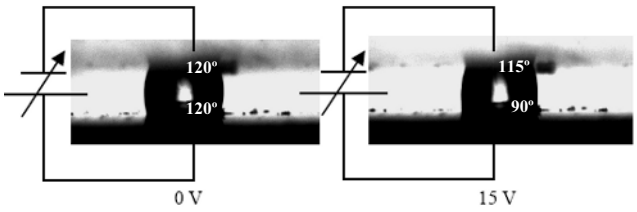
The droplet can be moved in fully controlled manner by applying voltage corresponding to a voltage control scheme shown in Table 1 and Fig 2.

III. Fabrication of EWOD Device.

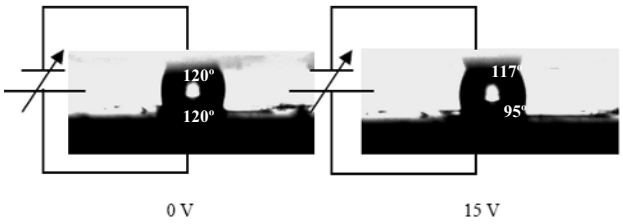
The EWOD device is fabricated with environmental silicone oil and air in microchannel. Initially, 100 nm thick Au electrode is deposited on a glass substrate.A set of device consists of a single linear array of nine control electrodes are fabricated. The first dielectric layer, 100 nm thick silicon dioxide layer is deposited by sputtering technique. Then, a 20 nm Teflon® AF 1601 (Dupont, USA) layer is spin-coated on the silicondioxide layer. This Teflon® AF layer acts as the dielectric layer as well. The entire area of

cover glass is coated with a transparent and conductive ITO film (indium tin oxide, < 15 Ω/square) by sputtering technique as a ground electrode. Then, a 20 nm Teflon® AF layer is also spin-coated on the ITO covered top cover glass to make the surface hydrophobic. Polydimethylsiloxane (PDMS) microchannel used to define the gap between the top and bottom plates in the parallel-plate channel. The droplet was placed and squeezed in microchannel.

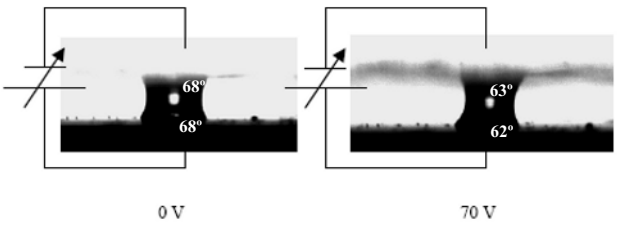
In experiment, the 0.9 µl droplet was dropped on the one electrode of EWOD device (bottom glass, 100 nm SiO_2 and 20 nm Teflon® AF). Contact angle have been determined by image analysis of side views of the droplet using contact angle measurement system (Rame’-hart instrument co. model 200). The contact angle reduction droplet were measured. The reversibility of EWOD actuation is critical to guarantee reliable transportation of droplets.



(a)



(b)



(c)

Fig. 3 Relationship between voltage drop across the dielectric layer and contact angle. (a) Images of de-ionize droplet (b) Images of 0.1 M KCl droplet (c) Images of PCR reagent droplet.

Fig. 3 shows contact angle reduction of droplet at 15 V for de-ionized water, 0.1 M KCl solution and 70 V for PCR reagent. A significant contact angle occurs from 120º/120º to 115º/90º on the top wall/bottom wall for de-ionized water is observed shown in Fig. 3(a). The de-ionized water droplet evaporates at 200 V. The KCl 0.1 M droplet, contact angle change from 120º/120º to 117º/95º on the top wall/bottom wall shown in Fig. 3(b) but the droplet evaporates at 20 V.

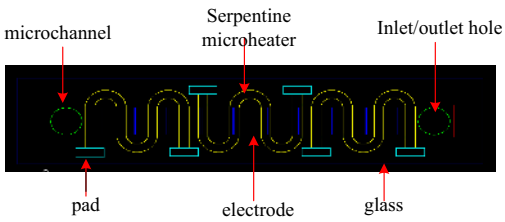
For the droplet of PCR reagent, a significant contact angle change happened at 70 V shown in Fig. 3(c). The characteristic of the PCR droplet is different from de-ionized water and 0.1 M KCl because the contact angle changes from 68º/68º to 63º/62º and droplet evaporates at 200 V.

In microchannel, silicone oil is used to surround the droplet to prevent evaporation. In the experiment, cover glass was coated with silicone oil for contact angle reduction measurement compared with PCR microchip that use air environment. From experimental result, silicone oil helps increase contact angle reduction.

From the result, contact angles of the droplet reduce 3º/2º, 4º/5º and 1º/3º on the top all/bottom wall for de-ionize water, 0.1 M KCl and PCR reagent respectively. The deionized water droplet can be applied by voltage higher than 500 V without evaporation. The droplet of 0.1 M KCl and PCR reagent evaporates in silicone oil at 200 V and 450 V respectively.

IV. Thermal Analysis of a Droplet Based PCR.

A droplet based PCR is first designed using L-edit, commercial 2D layout design software. The 3D EWOD PCR structure is then constructed in CoventorWare® from the 2D layout and predefined PCR fabrication process as shown in Fig. 4 (a) and (b). The 3D structure is then meshed with suitable meshing parameters and simulated for electrothermal behaviors by Etherm module of CoventorWare®



(a)



(b)

Fig. 4 (a) Layout design of a droplet based PCR by EWOD. (b) 3-D model of a droplet based PCR by EWOD.

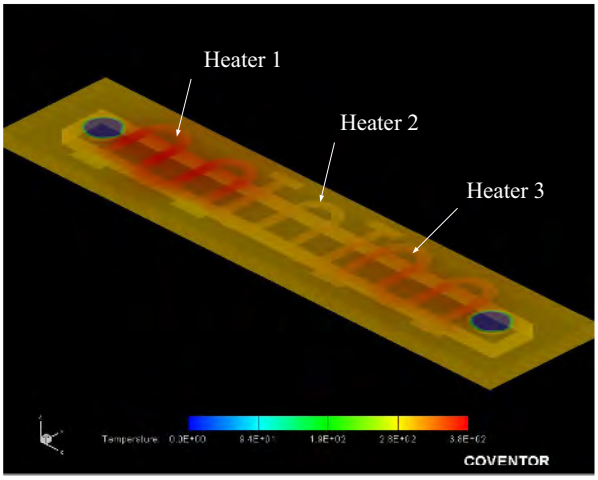


Fig. 5 Temperature distribution of microheaters (with microchannel, inlet and outlet).

In simulation, the PCR were set surface boundary condition into six pad layer for analyzer. To solve temperature distribution of PCR, we vary voltage for each heater. To assess voltage corresponding with temperature in PCR. Heater 1, 2 and 3 are area of denaturation, annealing and extension process. The appropriate voltages for each heater for the required temperatures are 1.19, 0.35, and 0.90 V, respectively as shown in Fig. 5 and Table 2.

Table 2 Temperature vs. applied voltage of three microheaters of a EWOD droplet based PCR.

Heater 1		Heater 2		Heater 3	
Voltage (V)	Temp (°C)	Voltage (V)	Temp (°C)	Voltage (V)	Temp (°C)
1.50	150.35	0.50	78.31	1.00	82.14
1.00	85.34	0.80	75.86	0.90	75.56
1.25	85.63	0.35	60.89	0.50	40.82
1.20	95.92	0.35	58.56	0.60	46.87
1.18	93.6	0.35	61.18	0.80	64.23
1.19	94.9	0.35	61.71	0.90	74.08

Table 3 Temperature vs. applied voltage of three microheaters of a EWOD droplet based PCR that filling channel with silicone oil.

Heater 1		Heater 2		Heater 3	
Voltage (V)	Temp (°C)	Voltage (V)	Temp (°C)	Voltage (V)	Temp (°C)
1.19	93.91	0.35	60.52	0.90	71.82

Table 2 shows temperature vs. applied voltage of microheter of EWOD droplet based PCR system in which microchannel filled with silicone oil. Three microheaters were assessed voltage 1.19, 0.35, and 0.90 V respectively. It can be seen that temperatures of microheaters corresponds to temperature zones of EWOD droplet based PCR slightly lower than in air environment. This result confirms using silicone oil in microchannel slightly change of temperature distribution.

V. Conclusions

A novel EWOD droplet based PCR has been designed, simulated and set up experiment. The EWOD droplet based PCR system consists of two parts, EWOD microchannel and microheater. In addition, contact angle reduction of different droplets by EWOD and silicone oil were studied. The result supports the silicone oil can be used to fill in microchannel to prevent evaporation and reduce contact angle. From simulation result, three microheaters varies applied voltage of 1.29, 0.35 and 0.90 V. The temperature distribution of microheaters correspond to temperature zone of EWOD droplet based PCR both air and silicone oil environment are investigated.

Acknowledgment

This work is supported by Nanoelectronics MEMS Laboratory, National Electronics and Computer Technology Center (NECTEC), National Science and Technology Development Agency, (NSTDA).

References

1. Zhang C, Xu J, Ma W, et al. (2006) PCR microfluidic devices for amplification. Biotechnology.24:243–284
2. Bu M, Melvin T, Ensell G, et al. (2003) Design and theoretical evaluation of a novel microfluidic device to be used for PCR. Journal of Microelectromechanical and Microengineering.13:S125-S130
3. Pollack M G, Fair R G. (2000) Electrowetting-based actuation of liquid droplets for microfluidic application. Applied Physics Letter. 77(11):1725-1726
4. Berthier J, Clementz P, Racurt O, et al. (2006) Computer aids design of an EWOD microdevice. Sensors and Actuators A. 127:283-284
5. Lieneann J, Greiner A, Korvink J G. (2006) Modeling, Simulation and Optimization of Electrowetting. IEEE Transactions on Computer-Aids Design of Integrated Circuits and Systems. 25(2):234-237
6. Walker S W, Shapiro. (2006) Modeling the fluid dynamics of electrowetting on Dielectric (EWOD). Journal of Microelectromechanical Systems. 15(4):986-1000
7. Hu L, Gruner G, Gong J, et al. (2007) Electrowetting devices with transparent single-walled carbon nanotube electrodes. Applied Physics Letters. 90
8. Wang W, Li Z, Lua R, et al. (2005) Droplet-based micro oscillating-flow PCR chip. Journal of Micromechanics and Microengineering. 15:1369-1377
9. Chang Y-H, Lee G-B, Huang F-C et al. (2006) Integrated polymerase chain reaction chips utilizing digital microfluidic. Biomed Microdevices. 8:215-225
10. Zhao Y, Cho S K. (2006) Microparticle sampling by electrowetting-actuated droplet sweeping. Lap Chip.6:137-144

A Label-Free Impedimetric Immunosensor Based On Humidity Sensing Properties of Barium Strontium Titanate

M. Rasouli[1], O.K. Tan[1], L.L. Sun[1], B.W. Mao[2] and L.H. Gan[2]

[1] School of Electrical and Electronic Engineering, Nanyang Technological University, Singapore
[2] Natural Sciences and Science Education, National Institute of Education, Nanyang Technological University, Singapore

Abstract — **A novel signal amplification mechanism for impedimetric biosensors is proposed. The proposed mechanism is based on humidity sensing properties of BST composite film and eliminates the need for application of bioactive labels for signal enhancement in amplified impedimetric biosensors. It suggests a good alternative to conventional impedimetric biosensors by improving the detection limit without adding any extra complexity to the system. It is direct and label-free, and can be employed for detection of a wide range of analytes. The sensing capability of the system was exemplified for detection of anti-BSA protein and a low detection limit of 10 ng/ml was obtained.**

Keywords — **Electrochemical Sensor, Impedimetric Immunosensor, Impedance Spectroscopy, Surface Modification, Barium Strontium Titanate.**

I. Introduction

A biosensor is an analytical device which integrates a biological sensing element with a transducer to produce a signal which is proportional to concentration of a specific analyte or a group of analytes. If antibodies or antibody fragments are applied as the biological element the device is termed immunosensor [1, 2]. Immunosensors have been the subject of an increasing interest during the past few years. That is mainly because of their high selectivity and specificity, short response time, relatively low cost, potential for miniaturization, portability, and ease of use [3, 4].

Immunosensors, as of most of other biosensing devices, involve formation of a biorecognition complex upon the bio-reactions. Formation of the biorecognition complex induces changes in physical properties of the surrounding environment which could be translated to a meaningful electrical signal using various techniques. If impedance features of the system are used for transduction of the immune-reaction, the device will be termed impedimetric immunosensor. Impedimetric immunosensors are attracting increasing interest since they are direct and label free and have many advantages with respect to speed, low driving voltage, simple operation, and the potential for miniaturization and large scale production [5, 6]. However, they still suffer from several drawbacks. One of the major problems of these immunosensors is the relatively small change of the impedance spectra upon direct binding of the analytes to the functionalized electrodes, especially when the analyte concentration is low and the surface coverage of the antigen-antibody complex is far from saturation [7]. This results in low detection limit and low signal to noise ratio. To overcome this problem, the concept of amplified impedimetric immunosensors was introduced. In general, this approach involves the application of enzyme-labels to perform biocatalytic reactions upon the antibody-antigen reactions to amplify the signal [7]. Application of enzyme-labels which could precipitate insoluble products on the sensing interface to increase the interfacial impedance has been reported [7]. Although these signal amplification mechanisms improve the sensitivity of the device, however, they involve application of labels which is not desirable as it increases the cost and complexity of the system.

In this study, a novel label-free signal amplification mechanism for impedimetric immunosensors was proposed, and a prototype immunosensor was fabricated to demonstrate the sensing capability of this sensing mechanism. This method can improve the detection limit by amplifying the generated signal. It also eliminates the need for using harmful redox probes [8], such as $[Fe(CN)_6]^{4-/3-}$, for Faradaic impedance measurements. It is based on humidity sensing properties of Barium Strontium Titanate (BST).

BST is a ferroelectric material with perovskite structure. When water molecules interact with BST grains, the electrical properties of the BST change. As humidity increases, the capacitance of the BST film increases and its resistance decreases. This property has been used for humidity sensing applications [9]. BST can also dissociate the water molecules into H^+ and OH^- ions due to its high polarity [10].

II. Experimental procedures

A. Fabrication of the BST composite film

A modified sol-gel process [11] was applied for fabrication of BST composite films using commercial nano-size

Chwee Teck Lim, James C.H. Goh (Eds.): ICBME 2008, Proceedings 23, pp. 863–866, 2009
www.springerlink.com

BST powder (average grain size: 50 nm, PI-KEM Ltd). The method involved dispersion of BST nano-size powders into BST sol-gel precursor using ball mill technique to form a uniform slurry. The slurry was then deposited onto the platinum coated silicon wafer using the spin-coating technique. Using this method, uniform and crack-free BST composite films with thickness of around 3 μm were synthesized. A part of the BST film was etched off using diluted HF solution to expose the platinum substrate as an electrode.

B. Surface Modification of the BST composite film

BST composite films were functionalized with poly(TMS-*r*-NHSMA) to be able to bind to bio-receptors covalently. A detailed description of the polymer-modification process is reported in [11]. BST composite films were soaked in Nitrogen bubbling DI water for 10 minutes to remove the soluble ions or contaminations, and were dried at room temperature. Clean BST films were treated with phosphoric acid to gain more OH function groups for better polymer modification. Films were immersed into 9.5 % phosphoric acid aqueous solution for 10 minutes and dried at 60 °C for 8 hours, then washed in constant Argon bubbling water for 30 minutes and dried at 60 °C under vacuum condition for 6 hours. Then, the acid modified BST films were immersed in poly(TMS-*r*-NHSMA) methanol solution (8.8 mg/ml) for 10 minutes and dried at 200 °C for 16 hours.

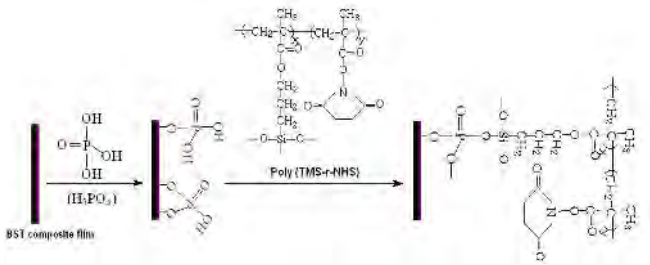


Fig. 1 BST surface modification using phosphoric acid and poly(TMS-r-NHSMA)

C. Immobilization of the biomolecules

To immobilize the Bovine Serum Albumin (BSA) molecules on the surface, polymer modified samples were soaked in BSA solution for 16 hours at 4 °C. The BSA solution was prepared by dissolving BSA in Phosphate Buffer Solution (PBS). Then, the excess protein molecules were removed by rinsing the samples with PBS. The same procedure was applied for immobilization of the anti-BSA molecules.

D. Electrical Characterization

To measure the impedance value, a measurement setup was developed to hold the sample and facilitate the connection between sample's electrodes and electrical probes of the impedance analyzer. The measurement setup consisted of two separate parts: a gold top electrode which was fabricated using e-beam evaporation on a glass substrate, and a platform made of poly-dimethylsiloxane (PDMS) for holding the sample and the top electrode. After fixing the sample on the platform, 10 μl of DI water was dropped onto the sample surface using micropipette. Then, the drop of water was covered by the gold top electrode to form a capacitor structure for impedance measurement. The electrical impedance measurement was carried out using a Solartron SI1260 impedance /gain-phase analyzer in conjunction with SI1296 interface (Solartron Group Ltd, Farnborough England). The impedance spectroscopy was performed over the frequency range of 1 Hz – 1 MHz using ac voltage amplitude of 50 mV. A detailed description of the device structure and the measurement procedure is provided in [11].

III. Results and Discussion

A. Characteristic curve of the immunosensor

Several samples with similar treatment procedure and background impedances were chosen. The samples were first immobilized with BSA solution with concentration of 1 mg/ml, and then were reacted with different concentrations of anti-BSA. Impedance spectroscopy was carried out and differences between impedances of the anti-BSA immobilized samples and impedance of a reference sample were calculated. An interpolated curve of the impedance changes for various anti-BSA concentrations is plotted in Figure 2. As it is shown, higher concentrations of anti-BSA result in higher impedance values. This can be applied for quantifi-

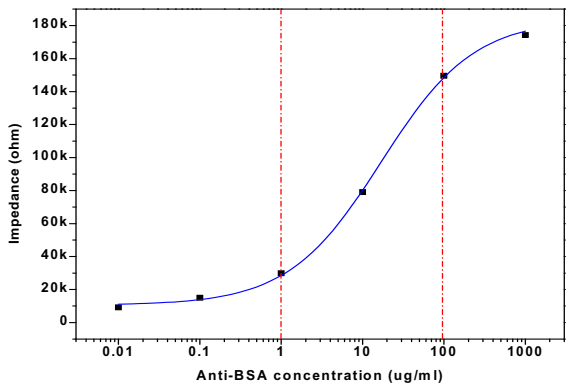


Fig. 2 Characteristic Curve of the immunosensor

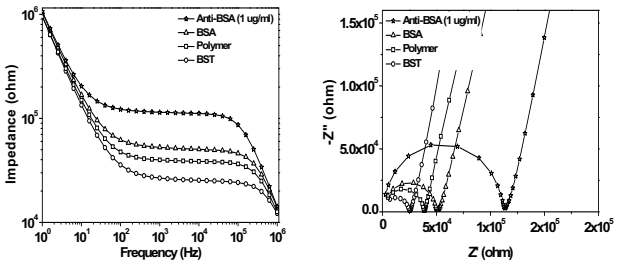
cation of anti-BSA concentration in a solution by calculating the impedance changes upon anti-BSA immobilization and using this characteristics curve.

As it is shown in Figure 2, the relationship is almost linear for anti-BSA concentrations in the range of 1 - 100 μg/ml. The curve tends to saturate at high anti-BSA concentrations. This might be due to the full coverage of all bioreceptors with complimentary analytes (which impedes the binding of further spices). A low detection limit of 10 ng/ml could also be identified, which might be due to the protein association/dissociation constraints at low concentrations.

B. Discussion on sensing mechanism

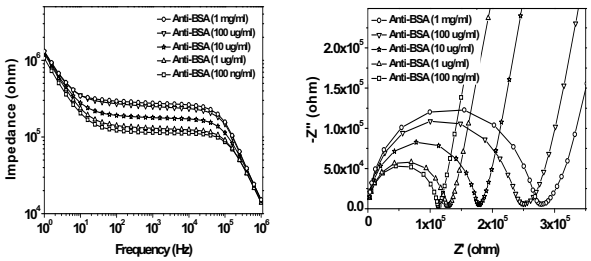
Figure 3 plots the impedance spectra of the bare BST composite film, the poly(TMS-*r*-NHSMA) modified BST composite film, the BSA immobilized film, and the anti-BSA immobilized film (after being immobilized with BSA and reacting with 1 μg/ml anti-BSA solution). After being modified with poly(TMS-*r*-NHSMA), the BST composite film showed higher interfacial resistance. This indicates that the poly(TMS-*r*-NHSMA) could obstruct the charge transfer in the system. After immobilization of BSA molecules, even a further increase in the impedance value was observed which indicates that BSA molecules could further block the surface. A similar behavior was also observed after immobilization of anti-BSA molecules.

An equivalent circuit model was set up to simulate the electrical behavior of the system and obtain a better understanding of the sensing mechanism. The proposed circuit model is illustrated in Figure 5 and includes the ohmic resistance of the water, R_s; resistance of the BST layer, R_m; capacitance of the BST layer, C_m; Warburg impedance (due to diffusion of ions from bulk water to the electrode/water interface), Z_w; the double layer capacitance at the electrode/electrolyte interface, C_{dl}; and charge transfer resistance at the electrode/electrolyte interface, R_{ct}. R_s and Z_w depend on bulk properties of the water and diffusion of dissociated ions, respectively. C_{dl} and R_{ct} represent the impedance features of the electrode/water interface, while R_m and C_m represent the electric properties of the BST layer.



(a) Bode plot (b) Nyquist plot

Fig. 3 Impedance spectra of bare BST film, poly(TMS-r-NHS) modified BST film, BSA immobilized film, and anti-BSA immobilized film



(a) Bode plot (b) Nyquist plot

Fig. 4 Impedance spectra for various concentrations of anti-BSA

Impedance data was fitted to the proposed circuit model and corresponding parameters were extracted. R_s, R_{ct} and R_m increased, and C_{dl} and C_m deceased as the anti-BSA concentration increased from 10 ng/ml to 1 mg/ml. When protein molecules bind to the surface, they will block the surface and reduce the charge transfer at the interface. This results in an increase in the interfacial impedance of the system. The thickness of the interfacial layer also increases which causes a decrease in the capacitance of the double layer and hence an increase in the interfacial impedance of the system. Impedance of the DI water also increases since the dissociation rate of DI water molecules, and hence the amount of charge carriers, decreases. Moreover, the impedance of the BST composite film increases upon prevention of the DI water from penetrating into the BST structure. This is due to the fact that the BST film is a humidity sensor and shows higher impedance values for lower water contents [9].

Figure 6 illustrates the calculated impedances of the DI water, the BST composite film, and the electrode/electrolyte interface. As it is shown, the blockage of the surface after the biorecognition reaction increases the impedance values of all three layers. However, the change in impedance of the BST layer is dominant and can be considered as a significant enhancement to the interfacial impedance changes which is applied in conventional impedimetric biosensors.

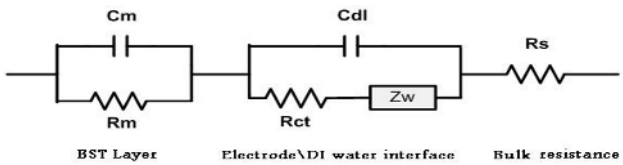


Fig. 5 An equivalent circuit model for analyzing the impedance data, including: R_s, ohmic resistance of the DI water; Z_w, Warburg impedance; C_{dl}, double layer capacitance; R_{ct}, charge transfer resistance; R_m, the BST composite film resistance; and C_m, the BST composite film capacitance

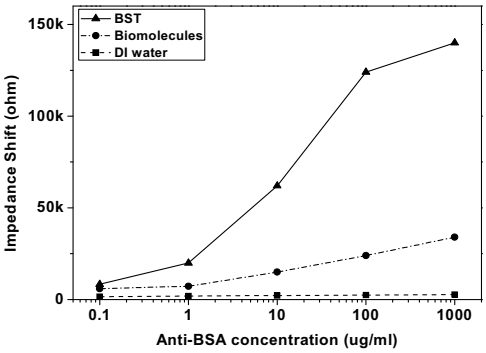


Fig. 6 Impedance changes of the DI water, the BST composite film, and the electrode/electrolyte interface after immobilization of various concentrations of anti-BSA

Thus, the generated signal of the system has been greatly amplified by using this structure.

C. Optimization of the polymer concentration

The effect of polymer concentration on sensing characteristics of the immunosensor was investigated. Several immunosensors with various polymer concentrations were fabricated and the sensitivity of them was measured. The sensitivity was defined as the amount of change in impedance value of the system per decade change in anti-BSA concentration in linear range of the characteristic curve. Figure 7 plots the calculated sensitivity values for various polymer concentrations.

As it is shown, the sensitivity reaches its optimum value at polymer concentration of 8.8 mg/ml. A possible reason for low sensitivity at lower polymer concentrations might be the lack of enough bioreceptors to detect their complementary species. This results in low sensitivity and low device performance. Low sensitivity at high polymer concentrations might be due to two possible factors: 1- difficulty in controlling the modification process which results in different background signals because of cross-sample and sample-to-sample variations, and 2- full blockage of the surface at high polymer concentrations which nullifies the signal amplification mechanism. Further investigations are needed to confirm these possible reasons.

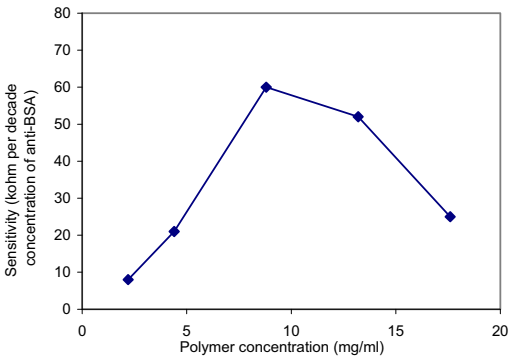


Fig. 7 Sensitivity of the immunosensor for various polymer concentrations

IV. Conclusions

A novel label-free impedimetric immunosensor with a signal amplification mechanism based on humidity sensing properties of BST composite film was introduced. The sensing capability of the fabricated device was illustrated for detection of anti-BSA as a test analyte. The primary results proved that the device could be applied for detection of desired analytes. It suggests a good alternative to conventional impedimetric immunosensors by utilizing a signal amplification mechanism without using any bioactive labels. Moreover, it eliminates the need for using harmful redox reagents for Faradaic impedance measurements.

References

1. Luppa P B, Sokoll L J, Chan D W (2001) Immunosensors: principles and applications to clinical chemistry. Clin Chim Acta 314:1-26
2. Morgan C L, Newman D J, Price C P (1996) Immunosensors: technology and opportunities in laboratory medicine. Clin Chem 42:193-209
3. Cruz H, Rosa C C, Oliva A (2002) Immunosensors for diagnostic applications. Parasitol Res 88:4-7
4. Maquette C A, Blum L J (2006) State of the art and recent advances in immunoanalytical systems. Biosens Bioelectron 21:1424-1433
5. Daniels J S, Pourmand N (2007) Label-Free Impedance Biosensors: Opportunities and Challenges. Electroanalysis 19:1239-1257
6. Guan J G, Miao Y Q, Zhang Q (2004) Impedimetric Biosensors. J Biosci Bioeng 97:219-226
7. Katz E, Willner I (2003) Probing biomolecular interactions at conductive and semiconductive surfaces by impedance spectroscopy: routes to impedimetric immunosensors, DNA-sensors, and enzyme biosensors. Electroanalysis 15:913–947
8. Liang K, Mu W, Huang M et al. (2006) Interdigitated Conductometric Immunosensor for Determination of Interleukin-6 in Humans Based on Dendrimer G4 and Colloidal Gold Modified Composite Film. Electroanalysis 18:1505-1510
9. Agarwala S, Sharma G L (2002) Humidity sensing properties of (Ba, Sr) TiO3 thin films grown by hydrothermal-electrochemical method. Sens Actuators B 85:205-211
10. Chen Z, Lu C (2005) Humidity sensors: a review of materials and mechanisms. Sens Lett 3:274-295
11. Sun L L, Tan O K, Mao B W et al. (2006) A novel Impedimetric immunosensor based on sol-gel derived Barium Strontium Titanate composite film, IEEE Proc., the 5th IEEE conference on Sensors, Daegu, Korea, 2006, pp 482-485

Author: Mahdi Rasouli
Institute: Nanyang Technological University
Street: 50 Nanyang Avenue
Country: Singapore
Email: Mahdi@ntu.edu.sg

Physical Way to Enhance the Quantum Yield and Analyze the Photostability of Fluorescent Gold Clusters

D.F. Juan, C.A.J. Lin, T.Y. Yang, C.J. Ke, S.T. Lin, J.Y. Chen and W.H. Chang*

Department of Biomedical Engineering, Chung Yuan Christian University, Taiwan, R.O.C.
*R&D Center for Membrane Technology, Center for Nano Bioengineering, Chung Yuan Christian University, Taiwan, R.O.C
* whchang@cycu.edu.tw

Abstract — **Generally, there are many significant changes in physical and chemical characteristics such as electronic, magnetic, and optical properties when material size decreases to nanoscale[1]. For example, gold nanoclusters (GNCs) consist of several to tens of atoms which exhibit discrete, electronic states and size-dependent fluorescence. Also, the surface of plasmon resonance peak disappears in these smaller GNCs (< 2nm) [2]. In fact, the preparatory method for colorful fluorescent gold quantum dots was the original theory (which was reported by Dickson group whom) that utilized the dendrimer PAMAM to synthesize and stabilize gold nanodots[3].**

Most nanoparticles were synthesized in organic phase which was not suitable for probe design of cellular imaging. Converting those hydrophobic particles to water phase would be necessary. However, the fluorescent quantum yield will always decrease with the phase transformation. Therefore, the following study should consider how to enhance the fluorescent quantum yield for the use in fluorophore to bio-application, like cellular imaging .

In this study, we focus on how to enhance the fluorescent quantum yield with UV, gel electrophoresis and heat. These physical ways will change the nanoparticles structure or result in the purification of the nanoparticles to disperse. Furthermore, we discuss the appearance of the fluorescence nanoparticles like aging.

Keywords — **gold nanoclusters (GNCs), fluorescence enhance, aging, UV and heating, EDC**

I. Introduction

Wilcoxon observed that the gold nanocluster (< 5 nm) which composed of only a few gold atoms exhibited fluorescence properties in 1998. When we decrease the size of those nanocluster decreases to smaller than 2 nm, a surface plasma effect (SPR) will disappear[2]. These evidences prove the optical and electronic properties of nanocluster which are different from bulk metals.

Monolayer-protected metal clusters (MPCs) in particular have gained much attention as prototype systems to study size-dependent evolution of the electronic structures of metal clusters. One of the recent topics in unique properties of the MPCs is it's photoluminescence (PL). The PL quantum yields of gold MPCs are enhanced by several orders from bulk gold. These PL quantum yield variation can be qualitatively viewed as a consequence of quantization of the electronic levels of the metal cores. But some research reports also indicate the fluorescence property may be the result of the interaction of electron from ligand and the surface of metal, a process we call that "Ligand-Metal Change Transfer" (LMCT).

Based on the MPCs, most studies have been using ligand which includes thiol. The reason is that the thiol ligand has a stronger force (covalent bond) with the surface of GNCs than static electricity.

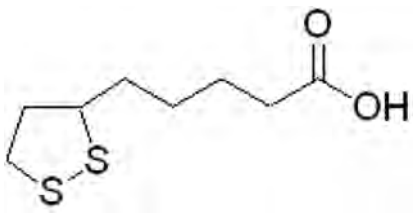
Keeping these in mind, we study lipoic acid (LA) (scheme1.) which also has thiol ligand to cover the surface of the nanocluster and analyze the PL characteristic. Furthermore, we study how to use different kinds of ways to enhance the PL quantum yields.

II. Materials and methods

The protocol of the nanoparticles followed according to Peng in 2003[4]. First, we reduce the $AuCl_3$. Second, we used surfactant to protect the nanoparticles and dissolve them in organic solution (~6 nm). Last, we etch the nanoparticles to be smaller nanoclusters (~2 nm), but the GNCs is not PL at present.

And then, we conjugated the lipoic acid (LA) to the surface of GNCs. Base on LMCT, the interaction between thiol and the surface electron of GNCs produced fluorescence property. However, the reaction is not completed, with the PL presented weakly. In order to improve the reaction, we

Chwee Teck Lim, James C.H. Goh (Eds.): ICBME 2008, Proceedings 23, pp. 867–869, 2009
www.springerlink.com



Scheme1 : lipoic acid

irradiate the UV (365 nm) and heat to 70℃, and the reaction of conjugation becomes more complete. Therefore, we increase the fluorescence characteristic and enhance the PL quantum yields.

III. Results and Discussion

Based on Peng (2003), we synthesized 6 nm gold nano-particles. Also, we add over precursor to etch nanoparticles to become smaller nanoclusters (~2 nm). Fig.1 is the UV-vis absorption spectra shows that gold nanoparticles (~6 nm) have a distinct absorption peak at 520 nm (black wire). When we add the over precursor, the original nanoparticles are etch down to become smaller (~2 nm). As the size is smaller than 2 nm, the surface plasma effect disappeared and the peak on the UV-vis absorption spectra disappeared as well (red wire).

Furthermore, we add lipoic acid (LA) to a solution of gold nanoclusters, and mix it for five minutes. We can observe that the red fluorescence from the solution, but fluorescence is presented weakly. Fig.2 is the fluorescence emission spectra, and there is a peak at 580 nm (black wire). In the following experiment, we paid more attention to the fluorescence enhancement by irradiating UV (365 nm) and heating the GNCs up to 70℃. We can observe that the peak at 580 nm is raised in Fig.2.

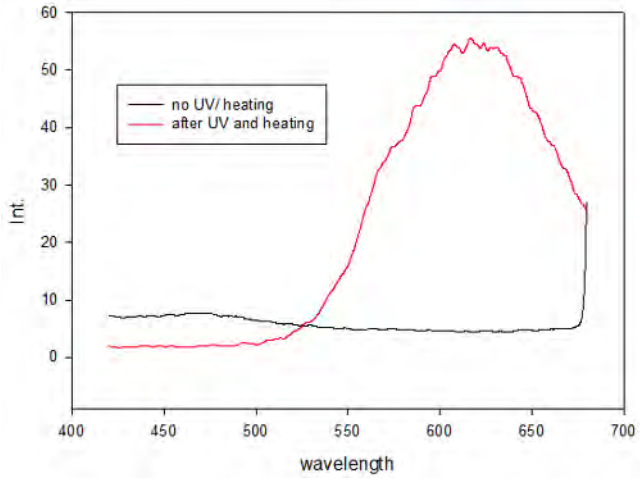


Fig.2 The fluorescence emission spectra of GNCs: a) The black wire is smaller gold nanoclusters b) and the red wire is irradiating UV (365 nm) and heating the GNCs up to 70℃

Another experiment is to add EDC to the solution and mix them for a few minutes. Following this, we found that the fluorescence has a further enhancement (Fig.3).

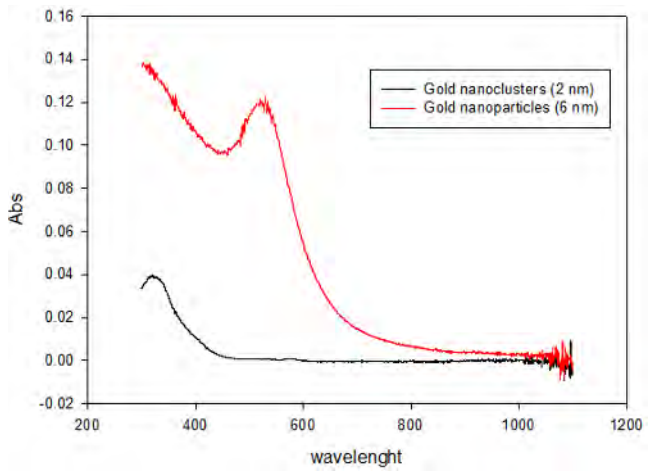


Fig.1 The UV-vis absorption spectra : a) The black wire is gold nano-particles (~6 nm); b) the red wire is smaller gold nano-clusters (~2 nm).

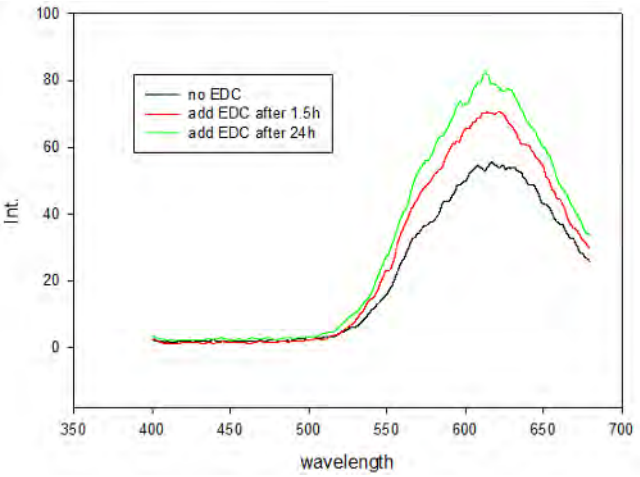


Fig.3 The fluorescence emission spectra of GNCs: a) The black wire is the smaller GNCs; b) the red wire is added EDC and mixed 1.5h; c) the green wire is added EDC and mixed 24h.

After synthesizing GNCs with fluorescence characteristic step by step, GNCs's fluorescence can be maintained for one month at room temperature. After one month, the fluorescence of the GNCs does not decrease but instead increase. We call the phenomenon "aging". Fig.3 is the fluorescence emission spectra, and we can observe the peak at 580 nm increased progressively as time passes.

IV. Conclusion

We conjugated lipoic acid (LA) with thiol ligand to the surface of GNCs using monolayer-protected metal clusters (MPCs). Therefore, we focused more on systems that have a fluorescent characteristic. Furthermore, we developed the way to enhance fluorescence by irradiating UV (365 nm) and heating the GNCs up to 70℃. Finally, we conjugated EDC to the surface of GNCs, and it strengthened the fluorescence signal again.

Follow the above-mentioned, our work provides a new way to get a new clusters with a fluorescent characteristic, and we can enhance its fluorescence signal by UV, heat and EDC, and it is extremely stable. Therefore, we suggest these small metal clusters can work as fluorescent probes to develop biological nanosensors, molecule imaging probe, and optoelectronic nanodevices

We focused on how to develop the molecule imaging probe. The outcome is that GNCs with fluorescence are smaller than quantum dots, and they have better photostability than organic fluorophores at room temperature.

Reference

[1] Lee, T. H.; Gonzalez, J. I.; Zheng, J.; Dickson,R. M. *Acc. Chem. Res.* 2005, 38, 534.

[2] Wilcoxon, J. P.; Martin, J.E.; Parsapour, F.;Wiedenman B,; Kelley, D. F. *J. Chem. Phys*1998, 108, 9137-9143.

[3] Zheng, J.; Zhang, C.; Dickson, R. M. *Phys. Rev.Lett.* 2004, 93, 07740210774024.

[4] Jana, N. R.; Peng, X. J. Am. Chem. Soc.;; 2003; 125(47); 14280-14281

Biocompatibility Study of Gold Nanoparticles to Human Cells

J.H. Fan[1], W.I. Hung[2], W.T. Li[1,3,*], J.M. Yeh[2,4]

[1]Department of Biomedical Engineering, Chung-Yuan Christian University, Taiwan
[2]Department of Chemistry, Chung-Yuan Christian University, Taiwan
[3]Research and Development Center for Biomedical Microdevice Technologies, Chung-Yuan Christian University, Taiwan
[4]Center for Nano-Technology, Chung-Yuan Christian University, Taiwan

Abstract — **Gold nanoparticle (GNP) is one of the most stable and popular nanoparticles, which receives considerable attention due to their applications in biomedical imaging and diagnostic tests. However, its cytotoxicity has not been fully investigated. Here we report the effects on biocompatibility of water-soluble GNPs with different sizes and concentrations to human bone marrow mesenchymal stem cells (hBMSCs) and human hepatoma carcinoma cells (HuH-7). Cytotoxicity was analyzed at different time points using MTT assay after co-culturing with different concentrations of GNPs. Both cells incubated with 71.1 μg/mL 15- and 30-nm GNPs exhibited more than 80 % cell survival. However, cell viability decreased to less than 60% after incubated with 31.6 μg/mL 5-nm GNPs for 5 days. GNP 15 nm in size was chosen for the following experiments. According to Annexin V and propidium iodide (PI) analysis, the percentage of necrotic cells increased gradually with the concentration of GNPs increased. Approximately 1.5 fold increase in the level of reactive oxygen species (ROS) was found, suggesting that necrosis might be triggered by ROS production after GNPs were endocytosed by cells. Alkaline phosphatase activity and calcium deposition of hBMSCs during osteogenic differentiation were inhibited slightly by co-culturing with GNPs. A similar observation was made in adipogenic hBMSCs, in which the accumulation of triacylglycerides was repressed by the addition of GNPs. In conclusion, despite 15- and 30-nm GNPs had little toxicity to hBMSCs and HuH-7 cells, they still had some influence on both osteogenic and adipogenic capabilities of hBMSCs.**

Keywords — **gold nanoparticle, biocompatibility, differentiation, HuH-7, mesenchymal stem cell**

I. Introduction

In the past 30 years, nanomaterials have received considerable attention because of their great potential in nanobiotechnology and drug delivery. Most of the research is focused on nanoparticles. For example, quantum dots are colloidal semi-conductor nanocrystals with unique light emitting optical properties that make them can be used as fluorescent probes for long-term cell targeting and imaging [1,2]. Dextran-coated iron oxide nanoparticles have superparamagnetic core which can be used in magnetic resonance imaging and magnetic biosensors [3]. Gold nanoparticles (GNPs) exhibit scattering light when excited due to surface plasmon resonance [4]. In fact, GNPs are widely used in biomedical imaging and diagnostic tests because they have many advantages over other types of nanoparticles. Besides their characteristics of optical properties, GNPs are chemically inert, easy to prepare and highly stable once synthesized [5]. Conjugation chemistry to biomolecules is simple and well developed in GNPs. Despite the wide application of GNPs, there is a serious lack of information concerning the impact of manufactured GNPs on human health and environment. Because nanoparticles can pass through biological membranes, they can affect the physiology of any cell in human body. This consideration is important for stem cells, where the effect of GNPS on their potential for self-renewal and differentiation is unknown. Here, we report the effect of GNPs on human cells. In addition, the influence on osteogenesis and adipogenesis of human bone marrow mesenchymal stem cells by GNPs treatment was explored.

II. Materials and methods

A. Preparation of GNPs

GNPs were synthesized as described by Turkevich *et al*. [6]. A solution of 1 mM $HAuCl_4$ (Alfa Aesar, MA, USA) was heated to boiling while stirring. After boiling was commenced, 38.8 mM sodium citrate (Mallinckrodt Baker, NJ, USA) solution was added slowly to the $HAuCl_4$ boiling solution. The solution changed color from yellow to dark red within 10 min. The solution was slowly cooled down to room temperature (RT). The resulting particles were coated with negatively charged citrate and were well-suspended. The GNPs solution was stored at 4°C for further use. GNPs of 5, 15 and 30 nm in size were prepared using different ratios of $HAuCl_4$ and sodium citrate solutions.

B. Cell culture

Human hepatoma carcinoma cells (HuH-7, Japanese Collection of Research Bioresources, Japan) were cultured Dulbecco's minimal essential medium (Gibco/BRL, Invitrogen, CA, USA) supplemented with 10 % fetal bovine serum (FBS, Biological Industries, Israel). Human bone marrow

Chwee Teck Lim, James C.H. Goh (Eds.): ICBME 2008, Proceedings 23, pp. 870–873, 2009
www.springerlink.com

mesenchymal stem cells (SV40T- and hTERT-immortalized cells, hBMSCs) were grown in Alpha-minimum essential medium (α-MEM, Gibco/BRL, Invitrogen, CA, USA) containing 10 % lot selected FBS (Hyclone, Utah, USA). Both cells were maintained at 37°C under atmosphere with 5 % CO_2.

C. Cytotoxicity assay

To determine the cytotoxicity of GNPs to HuH-7 cells and hBMSCs, cells (5000 cells/well) were inoculated on a 96-well microplate and allowed to adhere for 24 h. Then, different concentrations of GNPs solution with same volume were added into each well. Cell viability was measured using MTT (3-[4,5-dimethylthiazol-2-yl]-2,5-diphenyltetrazolium bromide) assay after 24, 72 and 120 h incubation. Medium was removed and cells were rinsed with Dulbecco's phosphate buffered saline (PBS, Sigma, MO, USA) twice. The cells were then incubated with MTT solution (0.5 mg/ml) at 37 °C for 4 h. The purple formazan formed in each well was dissolved in 0.1 ml of DMSO for 40 min. The absorbance at 570 nm was monitored using an ELISA reader (Multiskan Spectrum, Thermo Fisher Scientific, Inc., MA, USA).

D. Assessment of necrosis and apoptosis

Annexin V/ Propidium iodide (PI) staining method is commonly used to differentiate necrotic and apoptotic cells. Here, phosphatidylserine externalization and nuclei were stained by the Annexin V-FITC Apoptosis Detection Kit (Sigma, MO, USA). One million HuH-7 cells and hBMSCs were plated on a 60-mm dish. Various concentrations of GNPs15 nm were added to each dish and incubated for 24 h. Cells were trypsinized and resuspended in 1 x binding buffer (0.01 M HEPES, pH 7.4; 140 mM NaCl; 25 mM $CaCl_2$), then incubated with staining solution (Annexin V-FITC : PI = 1 : 2) in darkness for 20 min at RT. Immediately after annexin V/PI staining, the sample was analyzed with Becton Dickinson FACSCalibur flow cytometer (BD Biosciences, NJ, USA).

E. Measurement of ROS formation

Reactive oxygen species (ROS) formation was detected using 2',7'-dichlorofluorescin diacetate (DCFDA, Sigma, MO, USA). Cells (10^6 cells/dish) were seeded a 60-mm dish. Various concentrations of GNPs15 nm were added to each dish. After 24 h incubation, cells were washed with PBS and DCFDA (20 μM) was added into each dish. Cells were washed twice with PBS after 1 h, and lysed by sonication. DCF (2',7'-dichlorofluorescein) fluorescence in cell lysate was analyzed by an ELISA reader (Fluoroskan Ascent FL, Thermo Fisher Scientific, Inc., MA, USA) (ext: 488 nm). The protein amount in each sample was determined by bicinchoninic acid protein assay (Sigma, MO, USA).

F. Differentiation of hBMSCs

To observe the effect of GNPs on osteogenic differentiation of hBMSCs, cells (500 cells/well) were grown on a 96-well microplate and incubated in the osteogenic medium (α-MEM containing 2% FBS, 10 μM β-glycerophosphate, 10^{-7} M dexamethasone and 50 μM ascorbic acid 2-phosphate) containing different concentrations of GNPs 15 nm for 28 days. Fresh medium containing GNPs was replaced every 3 days. Alkaline phosphatase (ALP) activity and calcium deposition of hBMSCs were assessed every week. ALP activity was assayed based on the conversion of *p*-nitrophenyl phosphate (*p*-NPP) into *p*-nitrophenol (*p*-NP) in the presence of ALP. Culture supernant (100 μl) was mixed with 100 μl of 6.7 mM *p*-NPP (Sigma, MO, USA), followed by incubation at 37°C for 30 min. After stopping the reaction with 50 μl of 3 N NaOH, the absorbance at 405 nm of *p*-NP was measured with an ELISA reader. Calcium deposition is a late marker for osteogenic differentiation, which can be stained with Alizarin red S. Cells in each well were stained with 50 μl of 5% (W/V) Alizarin red S. To quantify the amount of mineralization, 50 μl of 5% (W/V) cetylpyridinium chloride (Sigma, MO, USA) was added into each well to dissolve calcium deposition at RT for 3 h. The absorbance at 550 nm was read by an ELISA reader.

To observe the effect of GNPs on adipogenic differentiation, hBMSCs (2×10^4 cells/well) were grown on a 24-well plate for 6 days. Then, the medium was changed into adipogenic medium (α-MEM containing 2% FBS, 0.5 mM 3-isobutyl-1-methylxanthine, 10^{-6} M dexamethasone, 60 μM indomethacin and 5 μg/ml insulin) containing different concentrations of GNPs 15 nm and the medium was replaced every 3 to 4 days. Adipogenesis was assessed by Oil Red-O stain. To quantify the amount of triacylglyceride, 50 μl of isopropanol was added into each well to dissolve Oil Red-O at RT for 10 min. The absorbance at 510 nm was read by an ELISA reader.

III. Results and Discussion

A. Effect of GNPs on cell survival

The results of cell survival of HuH-7 cells and hBMSCs treated with various concentrations (0-75.05 μg/mL) of GNPs with different sizes are shown in Table 1. Cytotoxicity of GNPs was determined by MTT assay that measures

the metabolic activity of survival cells. The LD_{20} value is where the concentration of GNPs that resulted in a 20% reduction in cell survival compared to the untreated control. It is found that cytotoxicity decreased as the size of GNPs increased in HuH-7 cells. GNPs 5 nm in size resulted in less than 80 % cell survival even at low concentrations at day 1. On day 3, the percentages of cell survival for GNPs 15 and 30 nm were higher than 80%, indicating these GNPs had little toxicity to HuH-7 cells. Similar observation was made in hBMSCs, where cell viability increased as the size of GNPs increased. Cytotoxicity of GNPS to HuH-7 cells was higher than that to hBMSCs. Culture media were replaced with fresh media containing GNPs on day 3 (after MTT assay). GNPs endocytosed by cells with GNPs replenished in the fresh medium could lead to increase in total concentration of GNPs, which might be the reason why the LD_{20} values decreased on day 5. To investigate the mechanism of cell death and the effects on hBMSCs differentiation, GNPs 15 nm was chosen for the following experiments.

Table 1 LD_{20} dose of GNPs to human cells

Cell types	Size of GNPs (nm)	LD_{20} (μg/mL)		
		Day 1	Day 3	Day 5
HuH-7	5	0.06	0.70	7.90
	15	14.10	- *	52.21
	30	73.30	-	0.75
hBMSCs	5	16.00	9.31	15.80
	15	45.49	57.70	24.44
	30	-	-	37.53

*The percentage of cell survival was higher than 80% within the range of the concentrations of GNPs tested.

Table 2 Percentages of live, apoptotic, and necrotic cells treated with GNPs

Cell types	Cells gated (%)	GNPs (μg/mL)					
		0	3.56	7.11	17.78	35.55	71.1
HuH-7	Live	99.4±0.1	60.4±2.9	71.5±1.0	78.8±1.3	79.2±4.1	75.4±4.2
	Apoptosis	0±0	0.4±0.2	2.5±0	1.6±0.2	2.2±0.1	3.1±0. 6
	Necrosis	0.6±0.1	39.2±3.0	26.0±0.9	19.6±1.5	18.6±4.2	21.5±4.7
hBMSCs	Live	98.8±0.1	78.2±2.9	83.7±0.4	81.5±0.6	82.3±0.3	86.0±0.3
	Apoptosis	0±0	4.9±0.6	3.9±0.4	3.4±0.6	5.3±0.8	3.4±0.9
	Necrosis	1.2±0.1	17.0±2.3	12.5±0	15.1±0	12.5±1.1	10.6±1.2

B. Apoptosis versus necrosis caused by GNPs

To determine apoptosis and necrosis in HuH-7 cells and hBMSCs treated by GNPs, cells were stained with a combination of Annexin V and PI and subjected to analysis by flow cytometry. As shown in Table 2, both cells treated with 15-nm GNPs were found that the percentage of live cells decreased as the concentration of GNPs increased. Significant increase in necrotic population was observed after treated with GNPs. In contrast, there was no significant increase in apoptotic cells was seen. Our results indicate that GNPs induce cell death in HuH-7 cells and hBMSCs via necrotic process.

C. Effect of GNPs on ROS production

ROS production from HuH-7 cells and hBMSCs was observed (Fig. 1). It was found that the fluorescence intensity increased significantly after treated with GNPs. The level of ROS increased 1.5 fold of the non-treated control. The result suggests GNPs may result in cell death elicited from excessive ROS formation.

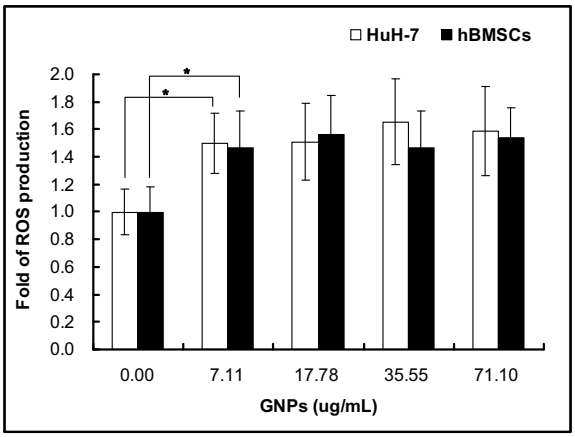


Fig. 1 The effect of GNPs on ROS generation

D. Effect of GNPs on hBMSCs differentiation

Human bone marrow MSCs were subjected to osteogenic induction while treated with GNPs. The osteogenic medium containing GNPs was replaced every 3 days. ALP activity and calcium deposition of MSCs were assessed every week. It was observed that both ALP activity and calcium deposition were significantly inhibited by the addition of GNPs compared with control. ALP activity did not seem to be repressed at early stage of osteogenesis but apparent inhibition was seen at day 14 when GNPs ≧14.78 μg/ml was applied (Fig. 2). Calcium deposition was suppressed at day 28 (Fig. 3). No correlation was found between the decrease of osteogenic differentiation and the concentration of GNPs. Our results suggest that GNPs influence the late stage of hBMSCs osteogenic differentiation.

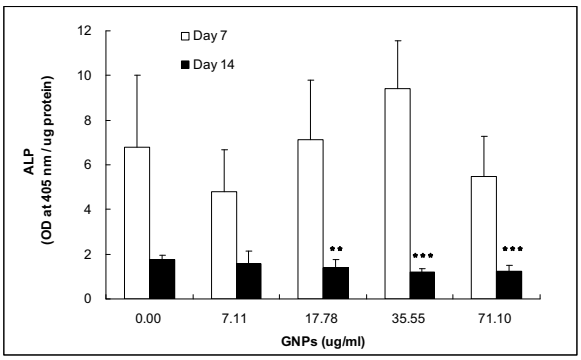


Fig. 2 The effect of GNPs on ALP activity of hBMSCs

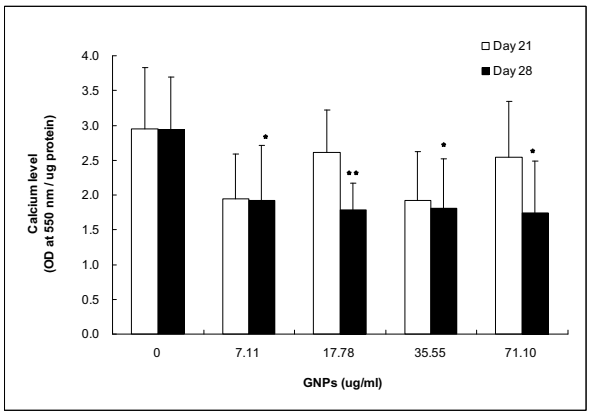


Fig. 3 The effect of GNPs on mineralization of hBMSCs

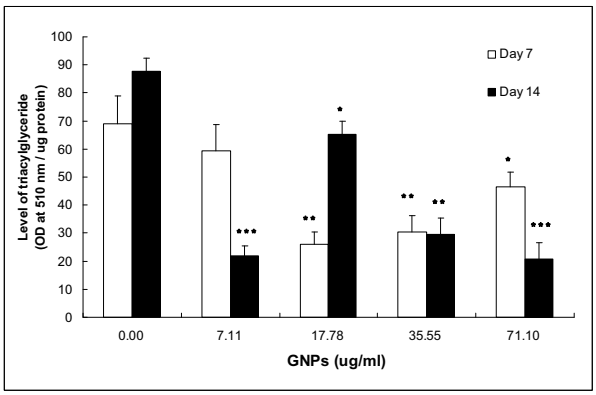


Fig. 4 The effect of GNPs on adipogenesis of hBMSCs

The influence of GNPs on hBMSCs adipogenic differentiation was also studied. It was found that the level of triacylglyceride accumulation decreased as the concentration of GNPs increased during the 14-day period of adipogenesis (Fig. 4). The above results indicate that the addition of GNPs inhibited hBMSCs differentiation despite that hBMSCs showed better tolerance for these nanoparticles.

IV. Conclusions

Our results showed that low concentration of GNPs exhibited more than 80% cell survival in HuH-7 cells and hBMSCs. Cell survival decreased as the size of GNPs increased. GNPs induce cell death via necrotic process, which might be elicited from excessive ROS formation. The addition of GNPs inhibited hBMSCs differentiation despite that hBMSCs showed better tolerance for these nanoparticles. The molecular mechanisms of GNPs toxicity to hBMSCs remain to be explored further.

Acknowledgment

This work was supported in part by the National Science Council, Taiwan, R.O.C. under Grants NSC 96-2218-E-033-001, and NSC 97-2627-M-033-005.

References

1. Chan WH, Shiao NH, Lu PZ (2006) CdSe quantum dots induce apoptosis in human neuroblastoma cells via mitochondrial-dependent pathways and inhibition of survival signals. Toxicol Lett 167:191-200
2. Maysinger D, Lovric J, Eisenberg A, Savić R (2007) Fate of micelles and quantum dots in cells. Eur J Pharm Biopharm 65:270-281
3. Schellenberger EA, Reynolds F, Weissleder R, Josephson L (2004) Surface-functionalized nanoparticle library yields probes for apoptotic cells. Chembiochem 5:275-279
4. El-Sayed IH, Huang X, El-Sayed MA (2005) Surface plasmon resonance scattering and absorption of anti-EGFR antibody conjugated gold nanoparticles in cancer diagnostics: applications in oral cancer. Nano Lett 5:829-834
5. He H, Xie C, Ren J (2008) Nonbleaching fluorescence of gold nanoparticles and its applications in cancer cell imaging. Anal Chem 80:5951-5957
6. Turkevich J, Stevenson PC, Hillier JA (1951) A study of the nucleation and growth processes in the synthesis of colloidal gold. Discuss Faraday Soc 11:55-75

Author: Wen-Tyng Li, Ph.D.
Institute: Chung-Yuan Christian University
Street: 200 Chung-Pei Road
City: Chung-Li
Country: Taiwan, R.O.C.
Email: wtli@cycu.edu.tw

Gold Nanorods Modified with Chitosan As Photothermal Agents

Chia-Wei Chang, Chung-Hao Wang and Ching-An Peng

Department of Chemical Engineering, National Taiwan University, Taipei, Taiwan

Abstract — **Gold nanorods (GNRs) are one of the nanomaterials, which could absorb near-infrared (NIR) light and convert to heat for the application on photothermal therapy. According to literature, Cetyltrimethylammonium bromide (CTAB) is one of the widely used surfactant for the synthesis of GRNs. However, due to cell toxicity of CTAB, it is necessary to modify the surface of gold nanorods for cell-related studies. In this study, thiolated chitosan was employed to replace CTAB on gold nanorods due to its biocompatibility. The absorption spectra ranged from visible to NIR wavelength were tuned by changing the aspect ratio of chitosan-tagged GNRs. We further conjugated chitosan/GNRs with disiloganglioside (GD2) monoclonal antibody which can lead to the functionalized nanomaterials endocytosed into stNB-V1 neuroblastoma cells. After exposure with NIR laser at 808 nm, photothermal destruction of stNB-V1 cells was clearly demonstrated by calcein AM staining.**

Keywords — **gold nanorods, photothermal, neuroblastoma, GD2**

I. Introduction

The use of nanoparticles in medicine is one of the important directions that nanotechnology is taking at this time. Their applications in drug delivery [1], cancer cell diagnostics, and therapeutics [2] have been investigated. Recently, photothermal therapy using the absorption properties of antibody-conjugated gold nanoshells [3] and gold nanospheres [4] has been demonstrated to selectively kill cancer cells.

Gold nanorods (GNRs) have unique optical properties due to their shape [5]. Based on the tissue is friendly penetrated by Near-IR, the optical properties of GNRs are expected to offer a plethora of applications in the bioscience field.

To use long-wavelength (650-900 nm) in laser irradiation that penetrates tissue for in vivo photothermal treatment, the absorption band of the nanoparticles has to be in the NIR region. The synthesis of gold nanorods with various aspect ratios, which enable tunable absorption wavelength in the NIR region is quite simple and well-established. The appropriate size of the nanorods is quite small and is potentially useful in applications such as drug delivery, gene therapy, and recently the noncytotoxicity of gold nanoparticles in human cells has been studied in detail [6].

Neuroblastoma, a neoplasm derived from the sympathetic nervous system, is a common and highly malignant solid tumor of pediatric age [7]. To date, conventional therapy for neuroblastoma includes chemotherapy, radiotherapy and surgical debulking. Despite of aggressive treatment regimens, the overall survival rate of patients with advanced stage neuroblastoma who are older than 1 year at diagnosis has not been prolonged in a satisfactory manner, even if they are treated with high-dose chemotherapy followed by autologous hematopoietic stem cell transplantation [8]. Moreover, anti-neoplastic agents, used in conventional cancer treatments, lack specificity to tumour cells and consequently result in high systemic and organ toxicity [9]. Since the conventional treatments are inefficient, the need of developing novel therapeutic modalities and new selective anticancer drugs with less cytotoxic side effects is indispensable. Several promising approaches have recently emerged to circumvent such treatment failures. For example, it has shown that high-dose, pulse therapy with 13-*cis*-retinoic acid given after intensive chemoradiotherapy significantly improved survival in high-risk neuroblastoma [10]. Anti-GD2 monoclonal antibody immunotherapy has also been shown to dramatically reduce the metastatic spread of neuroblastoma and prolong survival in a dose-dependent manner in a mouse model [11]. Another novel form of therapy for neuroblastoma that has recently been investigated is the targeted delivery of antisense oligonucleotides encapsulated within liposomes. These liposomes were then externally coupled to a monoclonal antibody specific for the neuroectodermal antigen disiloganglioside GD2 resulting in creation of anti-GD2-targeted liposomes. Since disialoganglioside GD2 is expressed on neuroblastoma but is absent in normal tissues [12]. Due to its specific expression on tumor surfaces, GD2 is an attractive targeting ligand for neuroblastoma therapy. In this study, chitosan was covalently grafted with thioglycolic acid (TGA) thiolated chitosan whith was harnessed to replace CTAB originally used to stabilize the suspension of gold nanorods. The biocompatible chitosan-modified gold nanorods (CGNRs) were further functionalized with monoclonal antibody disialoganglioside (anti-GD2) in order to specifically target neuroblastoma (NB) cells which express abundant GD2 on cell surface. The specific binding of anti-GD2 conjugated CGNRs (GCGNRs) against GD2-positive NB cell lines in vitro and the ensuing ingestion of fluorescent

Chwee Teck Lim, James C.H. Goh (Eds.): ICBME 2008, Proceedings 23, pp. 874–877, 2009
www.springerlink.com

labeled GCGNRs were investigated. After GCGNRs nanohybrids are molecularly targeted to neuroblastoma cells and then endocytosed inside the cells, 808nm near-infrared laser system with appropriate intensity and irradiation time was harnessed to excite the energy absorber GNRs, leading to photothermal ablation of NB cells.

II. Materials and methods

A. Materials

Cetyltrimethylammonium bromide (CTAB, Sigma), Chloroauric acid ($HAuCl_4$, Acros), sodium borohydride ($NaBH_4$, Alfa Aesar), ascorbic acid (Sigma), silver nitrate ($AgNO_3$, Showa), 1-Ethyl-3-[3-dimethylaminopropyl] carbodiimide hydrochloride (EDC, Acros), N-hydroxysuccinimide (NHS, Acros), Thioglycolic acid (TGA, Sigma), chitosan (chit5K, MW=5000), rhodamine B (Arcos), mouse anti-human Disialoganglioside GD2 monoclonal antibody (Chemicon international, Inc.), calcein AM (Invitrogen).

B. Instruments

UV-Vis-NIR Spectrometer (JASCO MODEL V-570), ZETASIZER (Malvern Zetasizer 3000 HS), confocal microscope (Leica TCS SP5, Wetzlar), 808-nm laser source (Opto Power Corporation, Tucson, AZ) equipped with , a 15 watt fiber-coupled laser integrated unit, microscopy (Nikon TE2000-U), and transmission electron microscopy (Hitachi H7000).

C. Preparation of gold nanorods

The synthesis of gold nanorods was made according to the seed-mediated method [16], with some modification. First, the gold seed particles were prepared by adding an aqueous of 1mL 0.0005M $HAuCl_4 \cdot 3H_2O$ to 1mL 0.2M CTAB solution. And, then 0.12 mL 0.01M ice-cold $NaBH_4$ was added with gentle mixing, which resulted in the formation of brownish yellow solution. The gold nanorod growth solution was prepared by adding 5mL 0.001M $HAuCl_4 \cdot 3H_2O$ to 5 mL 0.2M CTAB solution. Then, 0.26 mL 0.004M $AgNO_3$, 67 μL 0.0079M ascorbic acid was added respectively. The solution color changed from dark yellow to colorless, while adding the ascorbic acid. Finally, 0.12 μL gold seed solution was added to the above solution. In order to remove the excessive CTAB, the gold nanorod solution was kept in a refrigerator and followed by centrifugation at 3000 rpm for 10 mins.

D. Synthesis of thiolated chitosan

Chit5K dissolved into deionized water was reacted with TGA in the presence of EDC dissolved in 0.1M MES buffer for 24 h at room temperature. The molar ratio of chit5K/EDC/TGA was 1:10:20. The product was dialyzed (3.5 kDa cutoff) against deionized water. The solution containing thiolated chitosan remained in the dialysis tube was freeze-dried and stored for later use.

E. Preparation of chitosan modified gold nanorods

500μl of an appropriate concentration of gold nanorod solution and 5μL ca. 6mg/ml of chit5K-TGA were mixed at room temperature for 2 days. The solution was centrifuged to remove excess chit5K-MAA.

F. Preparation of anti-GD2 conjugated CGNRs

1 μg anti-GD2 were reaction with 5mg EDC and 3mg NHS for 1hr and then adding 500μl ca. 2nM CGNRs further reacted for 3hr at 4 ℃. After the reaction, the mixture was washed with deionized water, and resuspended in MES buffer (PH=6.1) for further use.

G. Endocytosis of anti-GD2 conjugated CGNRs

Neuroblastoma cell line stNB-V1 obtained from Academia Sinica (Taipei, Taiwan) was cultured in DMEM/F12 medium supplemented with 10% FBS. All the cultivation was performed at 37 °C in humidified air containing 5% CO_2. Cells (1×10^6 cells) were plated on T-25 flask for 24 h. Prior to anti-GD2 conjugated CGNRs (GCGNRs) challenge, stNB-V1 and cells NIH 3T3 were separately detached from the T-25 flask by tripsinization and inoculated onto a coverslip-bottomed Petri dishes (MatTek, MA, USA). In each dish, 100 μl of rhodamine B labeled GCGNRs was added.

Neuroblastoma cell line stNB-V1 cells and NIH 3T3 cells were imaged by a confocal spectral microscope (Leica TCS SP5, Wetzlar, Germany).

H. Photothermolysis by NIR

For the laser irradiation experiment, a continuous-wave fiber-coupled laser integrated unit with wavelength 808nm was used. Before the photothermal experiment, neuroblastoma cell line stNB-V1 cells and fibroblast NIH 3T3 cells were cultured in 24-well tissue cultured plate for 24h, then incubation with GCGNRs for 6 hrs. Then, the culture plates were washed thrice with PBS solution prior to the two types of cells exposed to laser source with intensity tuned at

6W/cm^2. After laser irradiation, cells were stained with calcein AM to examine viability under microscopy.

III. Results and Discussion

The surface plasmon absorption of gold nanorods have two bands: a strong long-wavelength band ca. 800nm due to the longitudinal oscillation of electrons and a weak short-wavelength band around 520 nm due to the transverse electronic oscillation. Fig.1 shows the observed optical absorption of GNRs and CGNRs. When thiolated chitosan replace CTAB, the absorbance band shows a little red shift. The optical absorption can be changed by simply adjusting the aspect ratio of gold nanorods.

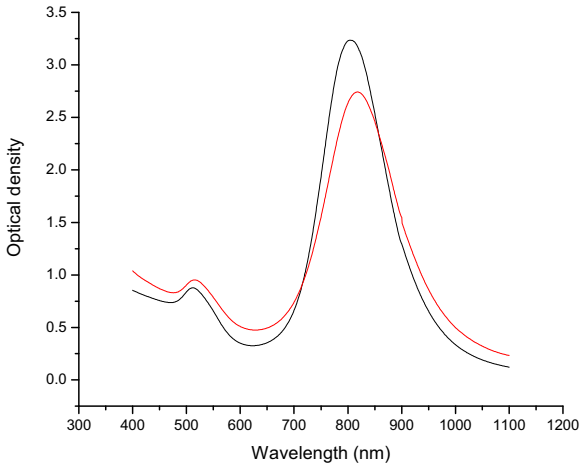


Fig. 1 Absorbance of gold nanorods (-GNRs) and thiolated chitosan modified gold nanorods (CGNRs)

The average size of GNRs and CGNRs were 66 and 84.9 nm, respectively, measured by DLS method and the transmission electron microscopy (TEM) image of the GNRs with an aspect ratio of 3.9 shown in Fig. 2.

GNRs and CGNRs were both positive charges with zeta potential measured to be 28.7 and 26.6 mV, respectively. This is because both of CTAB and chitosan are positively charged substances at neutral pH medium.

The degree of thiolation was determined by qualitative analysis of amount of thiol groups on the modified chitosan with Ellman's reagent. First, 5 mg of thiolated chitosan was dissolved in 2.5 ml of demineralized water. 250µl of 0.5 M phosphate buffer pH 8.0 and 500µl of Ellman's reagent dissolved in 10 ml of 0.5 M phosphate buffer (pH 8.0) were

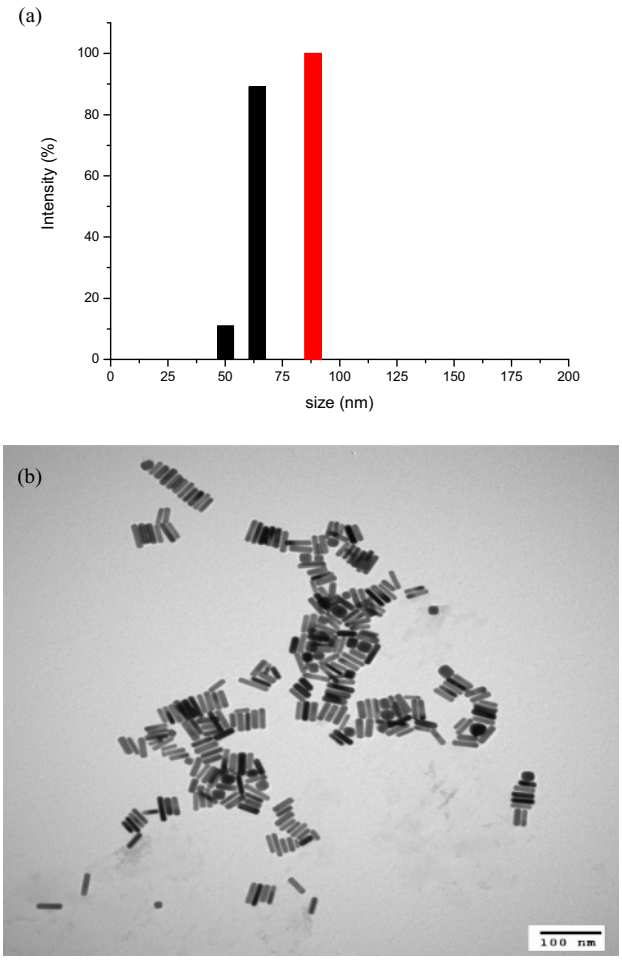


Fig. 2 (a) Size distribution of gold nanorods (-GNRs, shown by two black bars) and thiolated chitosan modified gold nanorods (CGNRs, shown by a red bar), (b) TEM image of GNRs

added. The reaction was allowed to proceed for 2 h at room temperature. Afterwards, the precipitated polymer was removed by centrifugation (18000×g; 5 min) and 1 ml of the supernatant fluid was transferred to a 1 mL cuvette. The absorbance was immediately measured at a wavelength of 412 nm with a UV-VIS spectrometer.

As shown in Fig3, the absorbance of thiolated chitosan was larger than pristine chit-5K at 412nm. This implies that chit-5K was successfully conjugated with TGA. As the molecular weights of chitosan were increased, the absorption values of chitX-TGA/chitX were increasing accordingly. (here X stands for 5K, 12K, 50K).

We used rhodamine B to label GCGNRs, and cultured with stNB-V1 cells and NIH 3T3 cells. The GCGNRs were targeted toward the cell membrane of neuroblastoma stNB-V1 cells which express the high-intensity of GD2. stNB-V1

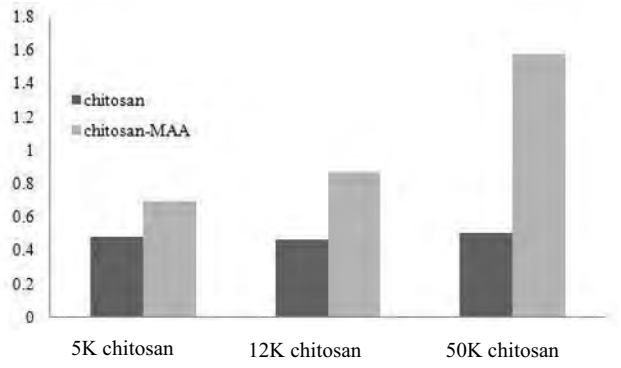


Fig. 3 Thiolated groups of different molecular weight of chitosan determined by Ellman's reagent

cells were observed to be associated with rhodamine B labeled CGNRs in large quantity, in comparison with NIH 3T3 cells after 6 h incubation using confocal microscope. This indicates the anti-GD2 specially interacted with disialoganglioside GD2 abundantly expressed on the extracellular membrane of neuroblastoma cell line stNB-V1.

After cell uptake of GCGNRs, cells remained viable indicating the bioacceptability of GNRs due to the existence of thiolated chitosan on GNRs. To demonstrate the photothermolysis efficacy of GNRs bound with anti-GD2, stNB-V1 and NIH 3T3 cells were exposed with 808 nm, 6W/cm^2 NIR laser separately for 15 min. As shown in Fig 4. stNB-V1 cells went to necrosis while NIH 3T3 cells survived.

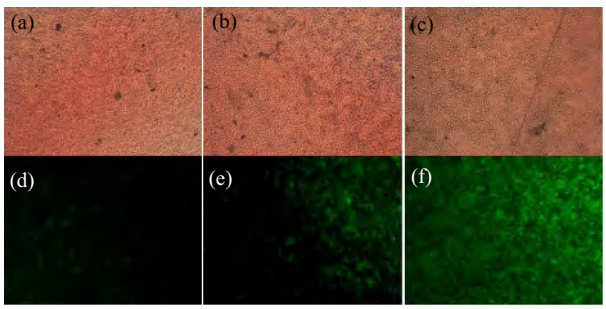


Fig. 4 Images of stNB-V1 cells by laser-beaming range of inside, boundary and outside (a-c). Fluorescent expression of laser-beaming range of inside, boundary and outside under (d-f).

IV. Conclusion

Gold nanorods are better for application in thermal therapy due to the ability to accurately control the absorption maximum to the required wavelength by modulating the aspect ratio with the silver ion concentration added during the gold nanorod growth process. In this study, chit5K-TGA was harnessed to replace CTAB (which is toxic to cells) due to its biocompatibility. CGNRs were further conjugated with anti-GD2 for specific binding to neuroblastoma cells. It was demonstrated that, within NIR laser irradiation zone, cells were not able to be stained in green by calcein AM. In other words, cells were killed via photothermolysis with the aid of internalized or surface bound GNRs. By contrast, cells remained alive (shown green after stained with calcein AM) outside the NIR laser irradiation zone, The above results suggest that CGNR can be used as an efficient photothermal agent for cancer cell therapy.

References

1. West JL, Halas NJ (2003) *Annu. ReV Biomed Eng,* 5: 285-292.
2. Chan WC, Maxwell DJ, Gao X, Bailey RE, Han M, and. Nie S (2002) *Curr Opin Biotechnol,* 13: 40-46.
3. Chen J, Wang D, Xi J, Au L, Siekkinen A, Warsen A, Li ZY, Zhang H. Xia Y, and. Li X. (2007) *Nano lett,* 7: 1318-1322.
4. Loo C, Lowery A, Halas N, West J, Drezek R (2005) *Nano Lett,* 5: 709-711.
5. El-Sayed IH, Huang X., El-Sayed MA (2006) *Cancer Lett,* 239: 129-135.
6. Kelly KL, Coronado E, Zhao LL, Schatz GC (2003) *J Phys Chem B,* 107: 668-677.
7. Sau TK, Murphy CJ (2004) *Langmuir,* 20:6414-6420.
8. Gole A, Murphy CJ (2004) *Chem Mater,* 16: 3633-3640.
9. Connor EE, Mwamuka J, Gole A, Murphy CJ, Wyatt MD. (2005) *Small,* 1: 325-327.
10. Maris JM, Matthay KK. (1999) *J Clincal Oncol,* 17:2264-79.
11. De Bernardi B, Nicolas B, Boni L et al. (2003) *J Clin Oncol,* 21:1592–1601.
1. Hakomori S (2001) *Adv Exp Med Biol,* 491:369-402.
12. Reynolds CP, Matthay KK, Villablanca JG, et al. (2003) *Cancer Lett,* 197:185-192.
13. Raffaghello L, Marimpietri D, Pagnan G, et al. (2003) *Cancer Lett,* 197:205-209.
14. Schulz G, Cheresh DA, Varki NM, et al. (1984) *Cancer Res,* 44:5914-5920.
15. Nikoobakht B, Mostafa A. El-Sayed. (2003) *Chem Mater,* 15:1957-1962.

Author: Ching-An Peng
Institute: Department of Chemical Engineering
Street: No. 1, Sec. 4, Roosevelt Rd.
City: Taipei
Country: Taiwan
Email: chinganpeng@ntu.edu.tw

QDs Capped with Enterovirus As Imaging Probes for Drug Screening

Chung-Hao Wang, Ching-An Peng

Department of Chemical Engineering, National Taiwan University, Taipei, Taiwan

Abstract — **The increasing threats of viral diseases have gained worldwide attention in recent years. Quite a few infectious diseases are still lack of effective prevention or treatment. The pace of developing antiviral agents could be expedited by the availability of quick and efficient drug screening platforms. Enterovirus 71 (EV71) is a highly infectious major causative agent of hand, foot, and mouth disease (HFMD) which could lead to severe neurological complications. There is currently no effective therapy against EV71. In this study, quantum dot (QD), an emerging probe for biological imaging and medical diagnostics, was employed to form complexes with virus and used as fluorescent imaging probes for exploring potential antiviral therapeutics. Inorganic CdSe/ZnS QDs synthesized in organic phase were encapsulated by amphiphilic alginate to attain biocompatible water-soluble QDs via phase transfer. To construct a QD-virus imaging modality capable of providing meaningful information, preservation of viral infectivity after tagging EV71 with QDs is of utmost importance. In order to form colloidal complexes of QD-virus, electrostatic repulsion force generated from both negatively-charged EV71 and QDs was neutralized by various concentrations of cationic polybrene. Results showed that BHK-21 cells infected with EV71 incorporated with QDs exhibited bright fluorescence intracellularly within 30 min. To demonstrate the potency of QD-virus complexes as bioprobes for screening antiviral agents, BHK-21 cells were incubated for one hour with allophycocyanin (APC), C-phycocyanin (CPC) purified from blue-green algae and then infected with QD-virus complexes. Based on the developed cell-based imaging assay, APC and CPC with concentration of 31.25 μg/mL led to extremely weak intracellular fluorescence post-infection of QD/virus complexes for 60 min. That is, the efficacy of anti-enteroviral activity of the algae extract was clearly illustrated by the inorganic-organic hybrid platform constructed in current study.**

Keywords — **Quantum dots, Enterovirus 71, Amphiphilic alginate, Polybrene, Drug screening**

I. Introduction

Enterovirus 71 (EV71) belongs to the family Picornaviridae under the genus Enterovirus and is a human enterovirus A species. It is a positive single-stranded RNA virus with a non-enveloped capsid and a genome size of 7411 nucleotides. It has caused significant mortality worldwide in recent years. EV71-infected children could develop severe neurological complications that lead to rapid clinical deterioration and death. EV71 is one of the main etiological agents of hand, foot, and mouth disease (HFMD). With the emergence of EV71 in Asia as a major causative agent of HFMD fatalities in recent years and the ineffectiveness of anti-enteroviral therapy, there is a need to find a specific antiviral therapy.

In view of the drawbacks of using fluorescent dyes [1, 2], colloidal semiconductor quantum dots (QDs) were investigated in this study to explore the potency of tagging QDs to viral particles. Thanks to excellent photostability, broad adsorption spectra, and narrow emission spectra, QDs have attracted great interests in many areas of research, from molecular and cellular biology to molecular imaging and medical diagnostics [3]. Tri-n-octylphosphine oxide (TOPO)-coated QD suspended in organic solvent was first converted into water-soluble QD employing synthesized amphiphilic alginate surfactants. Complexes between QDs and dengue virus, both possessing a net negative surface charge, will be formed by colloidal clustering, facilitated by positively charged polycationic compound - polybrene. In order to test if QD-virus complexes can be harnessed as diagnostic probes for fast screening potential anti-dengue viral drug candidates, allophycocyanin (APC, a protein-bound pigment) and C-phycocyanin (CPC) purified from a blue-green microalga *Spirulina platensis* was used as the model agent since it has been reported to exhibit anti-EV71 activities [4]. Our results showed that the intensity of green QD images within BHK-21 cells was decreased along with the dosage increase of allophycocyanin up to 125 μg/mL provided one hour prior to the addition of QD-virus complexes. It was clearly illustrated that allophycocyanin possesses anti-enteroviral activity and this can be determined within half an hour after target cells incubated with enteroviruses incorporated with amphiphilic alginate coated QD in the presence of 50 μg/mL polybrene.

II. Materials and methods

A. Synthesis of CdSe/ZnS QDs

To prepare semiconductor CdSe/ZnS QDs, a mixture of 25.7 mg of cadmium oxide (CdO, Sigma, USA), 3.88 g of Tri-n-octylphosphine oxide (TOPO, Sigma), and 2.41 g of hexadecylamine (HDA, Acros, Belgium) was heated to 300-320℃ under a dry nitrogen atmosphere. After the formation

Chwee Teck Lim, James C.H. Goh (Eds.): ICBME 2008, Proceedings 23, pp. 878–881, 2009
www.springerlink.com

of a CdO-HDA complex as indicated by the change of color from reddish to colorless, the temperature of the solution was cooled down to 260℃ and waited for injection. A stock solution with 31.58 mg of Selenium powder (Se, Sigma-Aldrich) dissolved in 5 mL of tri-n-butylphosphine (TBP, Showa, Japan) was quickly injected into the solution under rigorous stirring to nucleate CdSe nanocrystals. After injection, the core solution was grown at 260℃ for approximately 5 s when the color of the mixture turned from colorless to slightly red. The temperature was then cooled to 200℃ for shell growth. The shell solution containing 379.4 mg zinc stearate (J.T. Baker, Netherlands) and 12.8 mg sulfur powder (S, Sigma) dissolved in 5 mL of TBP was heated to 110℃ for 30 min and then cooled to room temperature for injection. The shell solution was added dropwise into the core solution under stirring over a period of 15 min. After addition of shell solution, the core-shell solution was cooled down to 120℃ to anneal for 2 h. The core-shell solution was cooled to room temperature afterwards. The CdSe/ZnS nanocrystals were precipitated by anhydrous methanol (Tedia, USA) and then stored in chloroform (Tedia) for further use.

B. Preparation of amphiphilic alginate surfactant

Sodium alginate solution (Sigma) mixed with 2% weight percent sodium periodate (Acros) in a dark, cold chamber (4℃) for 24h. Exclusion of light was essential for the prevention of side reaction. To obtain oxidized 2,3-dialdehydic alginate, the reaction mixture was extensively dialyzed against distilled water and subsequently freeze-dried. Two milligrams of octylamine (Acros) dissolved in 8 mL methanol was reacted with 0.276 mg 2,3-dialdehydic alginate dissolved in 10 mL phosphate buffer saline (PBS) solution containing 0.1 g sodium cyanoborohydride ($NaCNBH_3$, Acros). The reductive amination proceeded for 12 h with rigorous stirring at room temperature. The reaction mixture was dialyzed and subsequently freeze-dried to obtain the amphiphilic alginate surfactant.

C. QDs encapsulated with amphiphilic alginate

0.4 mg of CdSe/ZnS suspended in 5 mL of chloroform was added with 2 mg of alginate surfactant. The mixture was sonicated in a bath for 10 min, and then the chloroform was removed by a rotary evaporator (Eyela, Japan) at room temperature. At the end of the operation, the mixture was resuspended with PBS solution and filtered through a 0.22-m syringe filter (Millipore, USA) to remove aggregates. The filtrate was freeze-dried to obtain the amphiphilic alginate coated quantum dots in the powder form.

D. Particle size and Zeta potential analysis

QDs encapsulated by amphiphilic alginate (AA-QDs) were thoroughly dispersed in aqueous solution by a sonicator (200 W, 40 kHz; Branson Ultrasonics Corporation, CT, USA) for 10 min and then passed through a 0.22-μm syringe filter to collect non-aggregated AA-QDs which were analyzed for mean particle size and size distribution by the dynamic light scattering (Zetasizer Nano ZS, Malvern Instruments, UK) equipped with a diode-pumped solid-state laser operating at 633 nm wavelength as a light source. (Dispersion Technology Software 5.02, Malvern Instruments, UK). The surface electric charge of AA-QDs, dengue virus, and QD-virus complexes was measured separately by the zeta potentiometer (Zetasizer Nano-ZS, Malvern Instruments, UK) via determining the electrophoretic mobility.

E. Absorption and photoluminescence spectra of AA-QDs

A UV–vis spectrophotometer (Jasco Model V-570, Japan) and a photoluminescence spectrophotometer (Jasco Model FP-6000, Japan) were used to characterize AA-QDs. UV-visible absorption spectrum of QDs was scanned in the wavelength range of 300-700 nm. The photoluminescence of the particles was measured in the wavelength range of 400-700 nm. The spectra were obtained with the data pitch at 5 nm and the scanning speed of 500 nm per min. All samples were placed in quartz cuvettes (1-cm path length) and the optical measurements were carried out using PBS as the reference for AA-QDs.

F. Inhibition of QD/virus infection by algae extracts

AA-QDs suspended in 1 mL DMEM medium were added into 1 mL enterovirus 71-containing medium with multiplicity of infection (MOI) of 0.1, 0.5, and 1.0, respectively. After gentle shaking of the mixed media, polybrene (1,5-dimethyl-1,5-diazaundecamethylene polymethobromide, MW = 5,000 – 10,000, Sigma-Aldrich) stock solution was pipetted into the mixture to reach a final concentration of 10 and 50 μg/mL, respectively. Then, the mixed solution was incubated at 4°C for 1 hour to prevent dengue virus from losing infectivity. After the process of incorporating virus with AA-QDs, 5×10^4 BHK-21 cells in the exponential growth phase were replaced with the QD/virus-containing medium. After treating BHK-21 cells with the QD-virus complexes for various periods of time (30, 60, and 120 min), the cell culture dish was washed with PBS three times and observed under Spectral Confocal and Multiphoton System (Leica TCS SP5, Wetzlar, Germany) with the settings of objective lens 63×, pinhole 1.0, smart gain 380 mV, and 405-nm laser ND 3. The fluorescent intensity of

QDs revealed within the observed BHK-21 cells was quantitatively analyzed by the MetaMorph® imaging software (Version 7.5, Molecular Devices, USA). To determine the efficacy of APC and CPC on preventing enteroviral infection, these algal extracts were added into cell culture plates with various concentrations for pre-selected periods of time prior to the inception of viral infection.

III. Results and Discussion

Colloidal nanocrystal QDs consisting of an inorganic core/shell structure (e.g., CdSe/ZnS) surrounded by a layer of organic ligands (i.e., TOPO) can be converted into hydrophilic nanoparticles by several approaches (Bruchez et al., 1998; Chan and Nie, 1998; Dubertret et al., 2002; Mulder et al., 2006; Pinaud etal., 2004; Zhelev et al., 2006). The commonly used strategy is based on the exchange of the original organic layer with hydrophilic ligands, however the physical properties (i.e., quantum yield) are usually deteriorated through such surface modification. In this study, we demonstrated the first time that amphiphilic alginate can encapsulate CdSe/ZnS by intercalating alginate surfactant's hydrophobic pendant moieties (i.e., octyl chains) into the hydrophobic surfactant layer (i.e., TOPO) on the QD surface, thereby resulting in the phase transfer of hydrophobic QDs from organic solvents to aqueous solution via hydrophilic backbone (i.e., alginate). The average size of water-soluble QDs encapsulated by alginate surfactants was determined to be 23.1 nm in the range of 18.1 to 28.7 nm shown in Fig. 1. As long as the number of pendant groups is sufficient high, the linkage of amphiphilic alginate to the QD surface could be very stable and thereby lead to the physical properties of QD intact. The absorption and emission spectra of QD encapsulated with amphiphilic alginate given in Fig. 2 reveal higher absorbance between 525 and 550 nm and strong photoluminescence with the emission wavelength peaked at 534 nm after excited by UV-light. The inset image in Fig. 2 illustrates the bright green color of AA-QD in aqueous solution.

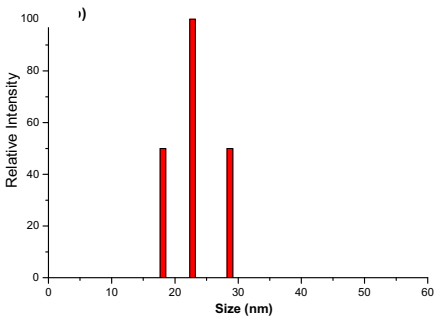


Fig. 1 Particle size distribution of AA-QDs by dynamic light scattering.

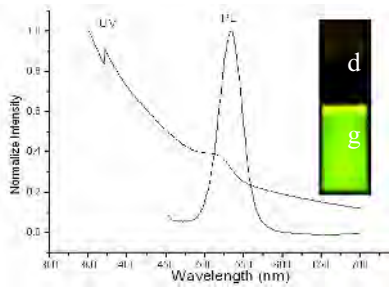


Fig. 2 Photoluminescence and UV/Vis spectra of AA-QDs. Ultraviolet-visible absorption spectrum of AA-QDs was detected in the range of 300-700 nm. The photoluminescence of AA-QDs was measured in the range of 400-700 nm with an excitation wavelength of 390 nm. The photoluminescence with the emission wavelength peaked at 534 nm indicating bright green fluorescence of AA-QDs in aqueous solution shown in the inset photograph.

Fig. 3A showed the photomicrographical images of BHK-21 cells incubated with AA-QDs at various time periods. In Fig. 3A (a)-(b), when the AA-QDs (zeta potential measurement of -7.18 mV) added in cell culture dish without polybrene respectively for 30 and 60 min, AA-QDs were not detected under fluorescent microscopy after remained AA-QDs was washed off with PBS. This is due to electrical repulsion between alginate macromolecule and cell surface which are both negatively charged. However, after 120 min co-culture of AA-QDs and cells without the addition of polybrene, green dots representing QDs were able to be pinpointed within cellular domain (Fig. 3A(c)). It is surmised that, given a longer incubation time (i.e., 120 min), sufficient amount of proteins (ingredients from fetal bovine serum) adsorbed onto the surface of negatively charged AA-QDs triggered nonspecific cell binding and ensuing endocytosis. While, in Fig. 3A(d)-(f), AA-QDs were started to be detected in the intracellular space 60 min post-incubation, in the presence of 10 μg/mL polybrene. This is probably because the electrostatic neutralization effect of polycationic polybrene led to nonspecific adsorption of negatively-charged AA-QDs on negatively charged cell membrane. It is noteworthy that polybrene is a cationic polymer and has been reported to act by neutralizing negative charges on the surface of cells and virions to promote virus attachment and enhance viral transduction rate. Once the concentration of polybrene increased to 50 μg/mL, AA-QDs were able to enter the cell ports within a short period of time and expressed green fluorescence in BHK-21 cells after 30 min of treatment. The QDs encapsulated with amphiphilic alignate surfactants were employed to form colloidal clusters with dengue viruses (zeta potential measurement of -6.04 mV) in the presence of cationic polybrene. To determine the suitable viral concentration for the development of quick and efficient cell-based fluorescent imaging drug screening plat-

form, various MOIs (multiplicity of infection) were employed ranging from 0.1 to 1. As shown in Fig. 3B (a)-(f), green fluorescent intensity expressed within BHK-21 cells due to the entrance of QD-virus was augmented in proportion to the increment of MOI (from 0.1 to 0.5). To confirm the QD/virus complexes were indeed internalized into BHK-21 cells rather than absorbed on cell surface.

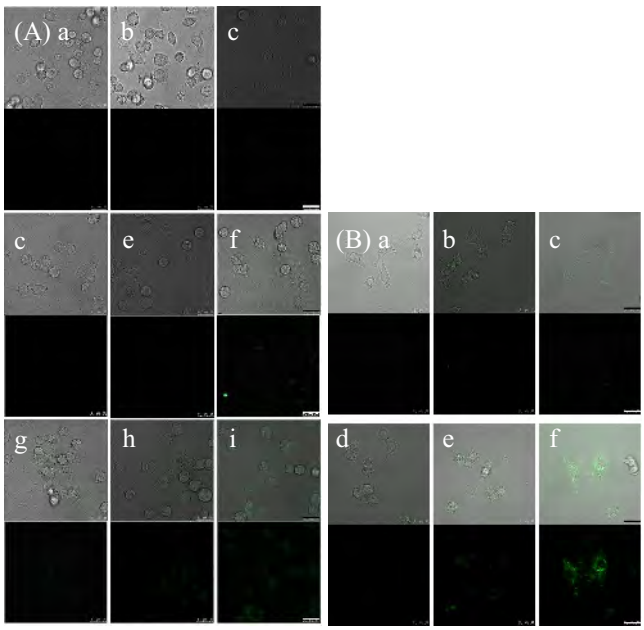


Fig. 3 (A) Photomicrographical images of BHK-21 cells exposed separately to AA-QDs with and without polybrene for various periods of time. (a)-(c) images of BHK-21 cells incubated with QDs without polybrene for 30, 60, and 120 min, respectively. QD was not detected intracellularly under fluorescent confocal microscopy until 120 min post-incubation; (d)-(f) images of BHK-21 cells incubated with QDs in the presence of 10 μg/mL polybrene. QD was not detected intracellularly under fluorescent confocal microscopy until 60 min post-incubation. (g)-(i) images of BHK-21 cells incubated with QDs in the presence of 50 μg/mL polybrene. QD was clearly detected intracellularly under fluorescent confocal microscopy after 30 min post-incubation. (B) Photomicrographical images of BHK-21 cells exposed separately to QD/virus complexes of different MOIs with 10 μg/mL polybrene for various periods of time. (a)-(c) images of BHK-21 cells incubated with QD/virus complexes of MOI being 0.1 for 30, 60, and 120 min, respectively; (d)-(f) images of BHK-21 cells incubated with QD/virus complexes of MOI being 0.5 for 30, 60, and 120 min, respectively. MOI=0.5 and scale bar=25 μm.

As shown in Fig. 4 (a)-(d), (e)-(g) the intensity of green images within BHK-21 cells was decreased along with the dosage increase of APC and CPC provided one hour prior to the addition of QD-virus complexes which were constructed in the presence of 50 μg/mL polybrene for 60 min. It should be noted that cells incubated with QD-virus complexes for only 60 min can give a fairly clear fluorescent intensity decrease with the concentration of APC and CPC up to 125 μg/mL. For cells treated with CPC higher or equal to 31.25 μg/mL for one hour then challenged with QD-virus complexes for 60 min, the diminish of green fluorescence is even astonishing prominent. Compared to other anti-viral agent screening assays, the cell-based QD/virus imaging modality exploited in this study indeed has fast and efficient features for screening antiviral therapeutics.

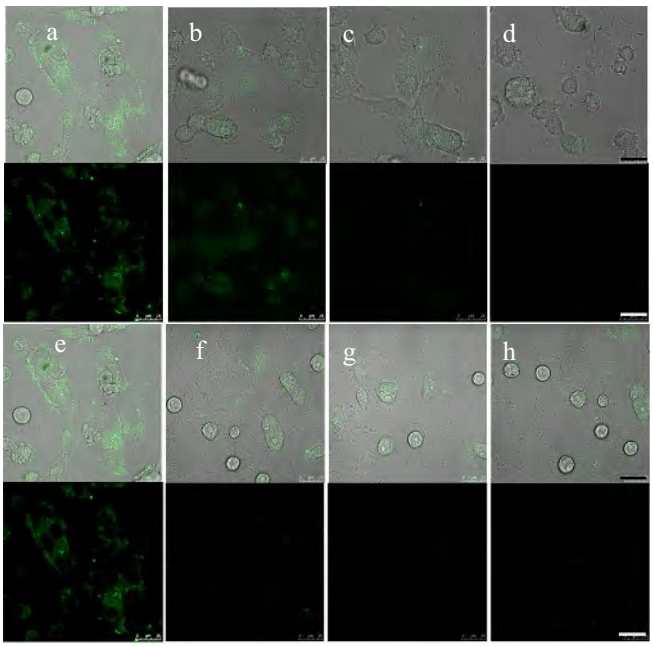


Fig. 4 Photomicrographical images of BHK-21 cells treated with and without allophycocyanin for one hour, then exposed to QD/virus complexes with 50 μg/mL polybrene for various periods of time. (a)-(d) images of BHK-21 cells incubated with QD/virus complexes for 60 min, after cells pre-treated with APC of 0, 6.25, 31.25, and 125 μg/mL, respectively. (e)-(h) images of BHK-21 cells incubated with QD/virus complexes for 60 min, after cells pre-treated with CPC of 0, 6.25, 31.25, and 125 μg/mL, respectively.

References

[1] Chan, W.C.W., Nie, S.M., 1998. Science 281, 2016-18.
[2] Parak, W.J., Pellegrino, T., Plank C., 2005. Nanotechnology 16, R9-25.
[3] Michalet, X., Pinaud, F.F., Bentolila, L.A., Tsay, J.M., Doose, S., Li, J.J., Sundaresan, G., Wu, A.M., Gambhir, S.S., Weiss, S., 2005. Science 307, 538-44.
[4] Shih, S.R., Tsai, K.N., Li, Y.S., Chueh, C.C., Chan, E.C., 2003. J. Med.Virol. 70, 119-125.

Author: Chung-Hao Wang
Institute: Department of Chemical Engineering, National Taiwan University
Street: No. 1, Sec. 4, Roosevelt Road, Taipei, 10617 Taiwan (R.O.C)
City: Taipei
Country: Taiwan
Email: d94524010@ntu.edu.tw

Elucidation of Driving Force of Neutrophile in Liquid by Cytokine Concentration Gradient

M. Tamagawa[1] and K. Matsumura[1]

[1] Kyushu Institute of Technology, Fukuoka, Japan

Abstract — **This paper describes the effects of gradient of cytokine concentration on chemotaxis of neutrophile by observing the motion in liquid with adding cytokine concentration. The aim of this investigation is to control of neutrophile motion in liquid by concentration gradient for drug delivery systems**

Keywords — **Neutrophile, Marangoni effect, Concentration gradient, Chemotaxis**

I. Introduction

Inflammation reaction is very important role as immune response in human body. In this reaction, once the inflammation occurred, the cytokine (chemokine) is delivered from the inflammation place, then neutrophile aggregate at the place to cure. The neutrophile moves the place that has large gradient of cytokine concentration. This is so called chemotaxis of neutrophile, but the driving force of this motion in liquid is not elucidated yet.

In the previous investigations, the motion of neutrophile has been considered to be amebic swimming in liquids as same as amebic motion on solids. Generally, the particulate in liquid on the gradient of concentration has the force by Marangoni effects. So the netrophile has the driving force of the motion in liquids by both amebic motion and Marangoni effects (Fig.1).This mechanism has possibilities to be applied to the drug delivery systems. Once the chemokine or concentration is generated at the affected part, the capsule with chemotactic function moves to this place automatically.

In the previous experiments, the effects of gradient of cytokine concentration on chemotaxis of neutrophile were investigated by observing the motion in liquid with adding cytokine concentration. Then the motion of neutrophile in the physiological salt was taken by CCD camera on microscope. Using PTV measurements, the average velocity of neutrophile was obtained with changing the cytokine concentration.

In this paper, the model of membrane for sensing is discussed by comparing with inorganic particulate model in water. Then the cytokine with fluorescent material (FITC) is observed in the microscope and the motion of neutrophile are analyzed.

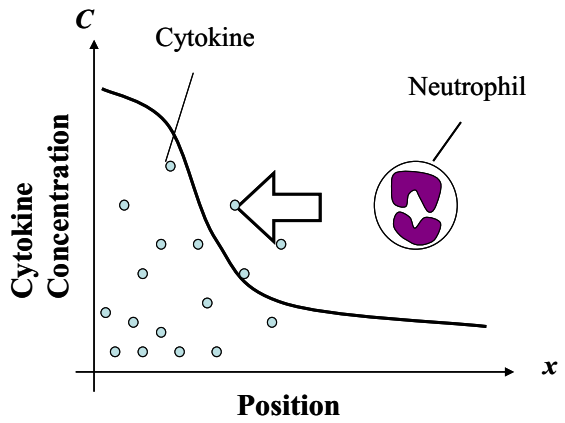


Fig. 1 Concept of chemotaxis using concentration Marangoni effect

II. Driving Force by Surface Tension Gradient

Suppose that the particulate sphere in liquid under the surface tension gradient as shown in Fig.2. The driving force F of particulate in liquid by the surface tension is obtained from the following equation,

$$F = -\nabla G(x) = -4\pi R^2 \left(\frac{d\sigma}{dx} \right)$$

where G indicates kinematic potential. And surface tension on the sphere is generally defined as follows;

$$\sigma = \sigma\left(C(x), T(x)\right)$$

where C and T indicates concentration and temperature.

Then the gradient of surface tension is expressed as follows if the temperature is constant,

$$\left(\frac{d\sigma}{dx} \right) = \left(\frac{\partial \sigma}{\partial C} \right)_T \left(\frac{dC}{dx} \right)$$

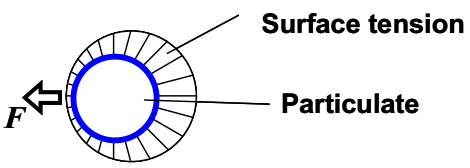


Fig. 2 Driving force by surface tension gradient

Chwee Teck Lim, James C.H. Goh (Eds.): ICBME 2008, Proceedings 23, pp. 882–883, 2009
www.springerlink.com

From this relation the driving force of particulate is dependent on the concentration gradient. Our supposition is that the driving force of neutrophlie is caused by the concentration gradient, so called Marangoni effect.

III. Observation of Concentration Diffusion and Neutrophile Motion by Fluorescence

To prove the neutrophile motion by concentration gradient, the experimental observation was done using the simple system as shown in Fig. 3. In this system, after dropping the cytokine IL-8 at the side of liquid area of neutrophile suspension, the concentration of cytokine diffused to the suspension liquid. The motion of neutrophile is taken by the video movie at the center of the liquid area in Fig.3. The cytokine with fluorescent material (FTTC) is observed as intensity level in CCD image. Figure 4 shows diffusion process of cytokine and motion of neutrophile. It is also found that the high intensity region can be observed around the neutrophile. So it is considered that the cytokine with fluorescence is attached to the

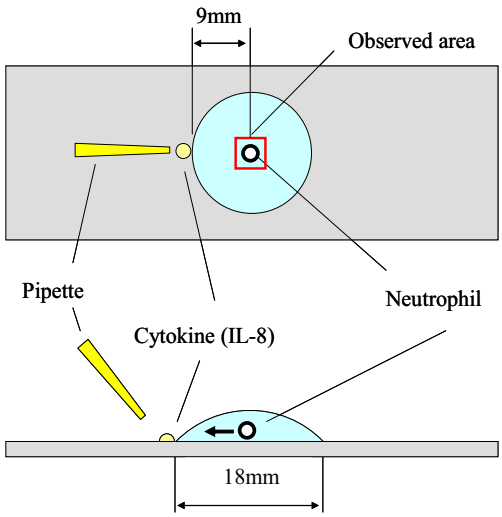


Fig. 3 Observation of neutrophile motion by concentration

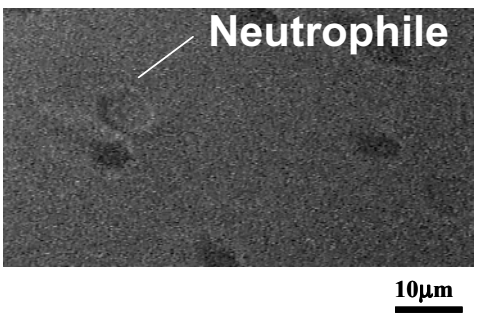


Fig. 4 Observation of neutrophile motion

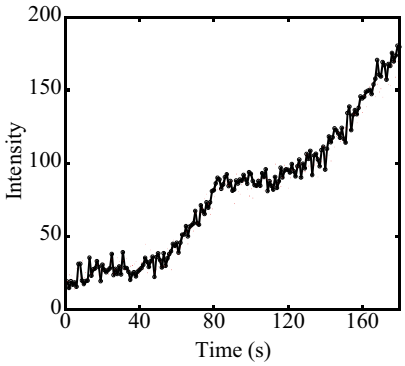


Fig.5 Intensity history at the front of neutrophile

membrane of neutrophile. In Fig.4, the intensity of the point indicated by arrow is measured by CCD image. Figure 5 shows intensity history on this point. From this result, the concentration is increasing suddenly at 50 (s). From this time, the neutrophile begins to move from left to right. These results mean that the surface tension between the membrane and the liquid is different. So the important mechanism of the driving force is hidden in the structure of the membrane of the neutrophile.

Conclusions

From the experiments, the diffusion process of concentration is different between on the membrane and around the membrane. The difference of diffusion process corresponds to the surface tension difference, which leads to driving force by Marangroi effect.

Acknowledgment

We acknowledge the financial support of the grant in aids by a Grant-in-Aid for Scientific Research from the ministry of Education, Culture, Sports, Science and Technology, Japan (Scientific Research (B) (2)19360088, Exploratory Research 19656051).

References

1. Tamagawa M., Mukai, K., Furukawa, Y., Proc. of Fifth East Asian Biophysics Symposium & Forty-Fourth Annual Meeting of the Biophysical Society of Japan, 2006

Author: Masaaki TAMAGAWA
Institute: Kyushu Institute of Technology
Street: Hibikino 2-4, Wakamatsu-ku
City: Kitakyushu
Country: Japan
Email: tama@life.kyutech.ac.jp

Development of a Biochip Using Antibody-covered Gold Nano-particles to Detect Antibiotics Resistance of Specific Bacteria

Jung-Tang Huang[1], Meng-Ting Chang[1], Guo-Chen Wang[1], Hua-Wei Yu[1] and Jeen Lin[1]

[1] Institute of Mechatronic Engineering, National Taipei University of Technology

Abstract — **Detection of bacteria's drug resistance at an early stage not only helps doctors in choosing the appropriate antibiotics, but also prevents antibiotic abuses. The purpose of this research is to develop a simple and efficient method for detecting bacteria and detecting bacteria's drug resistance, which can replace the traditional method. This research used MEMS technology to construct a biochip for detecting the concentration of bacteria in the sample solution. The experiments could be separated into three distinct parts: design of dieclectrophoresis (DEP) electrodes of biochip, the collection and measurement of bacteria, and the detection of bacteria's drug resistance. The detection method primarily used the effect of DEP force to ensure that the bacteria in the solution can be collected within the range of electrodes, increase the validity and accuracy of the detection. Also, this research explored the effect of antibody-covered gold nanoparticles mixed with bacteria in the solution for the detection of bacteria concentration.**

In this experiment, the electrodes of the biochip were fabricated on the glass by a thermal evaporator to deposit a layer of aluminum and then by wet enchant to etch the Al to construct the comb-like electrode pattern which was composed of 7 fingers and surrounded with thick PR to accommodate several μl sample. The width of each finger was 500 μm, and the gap between fingers was 5 μm. The detection based on impedance change among the electrodes.

In this study, the bacteria sample was *Salmonella*, and the results showed that the sensitivity of the biochip could reach to 10^6 CFU/ml. In the experiment of bacteria's drug resistance, the initial concentration of bacteria of 10^5 CFU/ml could be detected after about 2 hrs of bacterial growth period with and without adding ampicillin. The total detection time of this method could be completed within 4 hrs.

Keywords — **nano-gold particles, Bio-chip, antibiotics resistance**

I. Introduction

The impedance change method is one of the most common electrochemical methods for rapid detection of bacteria. It is based on measurement of changes in impedance due to the different concentration of bacteria or the growth of bacteria. This method has been applied to detect different bacteria with appropriate antibodies. DEP force was used to ensure that the bacteria in the solution can be collected within the range of electrodes [1]. Using the specific antibody-covered gold nanoparticles can make sure the selectivity of this method [2-5]. Combining these methods, the biochip can detect the concentration of bacteria and the bacteria's drug resistance.

The purpose of this research is to develop a simple, efficient method for testing bacteria and detecting bacteria's antibiotics resistance, which can replace the traditional method. In order to the target, interdigitated microelectrodes were integrated within the biochip to measure the impedance. Our recent study [6] indicated that impedance change from the concentration of bacteria cloud be measured and the sensitivity could reach to 105 CFU/ml. In this study, the detection of bacteria's antibiotics resistance was explored.

II. Materials and Methods

A. Fabrication of DEP electrodes

The electrodes were fabricated by depositing a layer of aluminum on the glass by a thermal evaporator and then by wet enchant to etch the Al to construct the electrode pattern. The shape of these parallel electrodes was comb-like. Each electrode finger was 10 mm in length and 500 μm in width. The gap between two fingers was 5 μm. The 6 gaps were formed by 7 electrodes. These parallel electrodes were surrounded by a thick photoresist or silicone to form a closed chamber, which has area of 3 mm × 10 mm. (a capacity of 5-10 μl)

B. DEPIM equipment and test setup

The fluidic samples were dropped into the chamber of the chip by a micropipette. The nanoparticles in the system were observed and recorded by using a microscope (Discovery) and a digital camera (Nikon DXM1200). The AC signals were generated by a function generator (TTi, TGA1244), had a frequency ranging from 100 kHz to 800 kHz and a magnitude ranging from 10 to 20 V. The waveforms of the AC signals and the voltage on the chip were monitored by the digital oscilloscope (HP54610B). An equivalent circuit for the DEPIM experiment is shown in Fig. 1 [6-9].

Chwee Teck Lim, James C.H. Goh (Eds.): ICBME 2008, Proceedings 23, pp. 884–887, 2009
www.springerlink.com

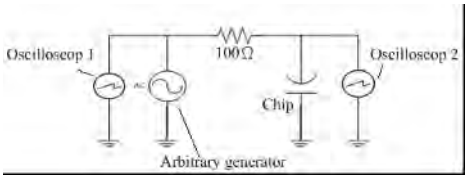


Fig. 1 Schematic diagram of experimental setup

We modeled the impedance of the electrodes on the chip as a capacitive reactance $\frac{1}{\omega C_s}$ serially connected with a resistance R_s. Let a resistor R = 100 ohm to share the supply voltage V_{s_1}. We defined the voltage across the electrodes as V_{s_2}.

$$Vs = \frac{Vs_2}{Vs_1} = \frac{Rs - j\frac{1}{\omega C_s}}{(R + Rs) - j\frac{1}{\omega C_s}} = \frac{\sqrt{Rs^2 + (\frac{1}{\omega C_s})^2}}{\sqrt{(100 + \mathrm{Rs})^2 + (\frac{1}{\omega \mathrm{C}_s})^2}} \quad (8)$$

$$\psi = \tan^{-1}\frac{1}{\omega C_s(100 + R_s)} - \tan^{-1}\frac{1}{\omega R_s C_s} \quad (9)$$

Simultaneously solving the above two equations according to the measured signal from the oscilloscope,

$$Z_{control} = \sqrt{Rc^2 + (\frac{1}{\omega C_c})^2} \quad (10)$$

$$Z_{sample} = \sqrt{Rs^2 + (\frac{1}{\omega C_s})^2} \quad (11)$$

Where Z_{sample} was the magnitude of impedance for the control sample which DI water mixed with antibody-covered gold nano-particles. The Z_{sample} was the magnitude of impedance for a sample which bacteria was coated by antibody-covered gold nano-particles. Then the normalized impedance change, NIC (%), was defined by following formula [10]:

$$\mathrm{NIC}(\%) = \frac{(Z_{sample} - Z_{control})}{Z_{control}} \quad (12)$$

III. Results

Before the drug resistance experiment, it was necessary to know the growth curve measurement from aspect of biotechnology. Measuring T_d (doubling time) of bacteria ensured the repeatability. In the drug resistance experiment, we explored the influence of ampicillin on bacteria growth.

A. Growth curve and Doubling time

The growth of bacteria could divide into four different phases: lag phase, log phase, stationary phase, and death phase. Generally, bacteria were transposed into specific culture medium, they would not grow instantly, which is called "lag phase". In this phase, bacteria did not conduct binary fission. In the log phase, bacteria began to split off, and the total number of bacteria increased geometrically. When the nutrition of culture medium was poor, bacteria did not fission anymore. This phase was called "stationary phase". Finally, bacteria were going dead and the total number of bacteria was decreased. This study just considered the first two phases, lag phase and log phase. Different bacteria had different growth curve. In these experiments, the sample of bacteria was *Salmonella***.**

The experiments were executed in 800 KHz, 10V, and the conductivities of samples were all about 0.005 S/m. As shown in Fig. 2, the lag phase of *Salmonella* was observed from 0 to 1.5 hours and the log phase was from 1.5 to 3 hours. The data showed that the higher concentration of *Salmonella* would get the lower NIC (%) and the magnitude of NIC (%) decreased rapidly in the log phase.

Repeating the same experiment three times, the growth curve of *Salmonella* could be obtained, as shown in Fig .3. Utilizing Interpolation, the doubling time could be obtained. Table 1 indicated the doubling time of *Salmonella*, which was 20 to 25 minutes.

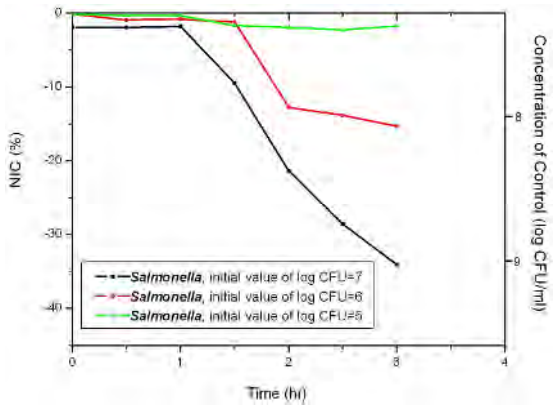


Fig. 2 The growth curve of *Salmonella*, which had different initial concentration about 5, 6 and 7 log CFU/ml

Table 1 Doubling time of Salmonella

	First measurement	Second measurement	Third measurement
log CFU/ml = 7, T_d (mins)	20	23	25
log CFU/ml = 6, T_d (mins)	22	22	24

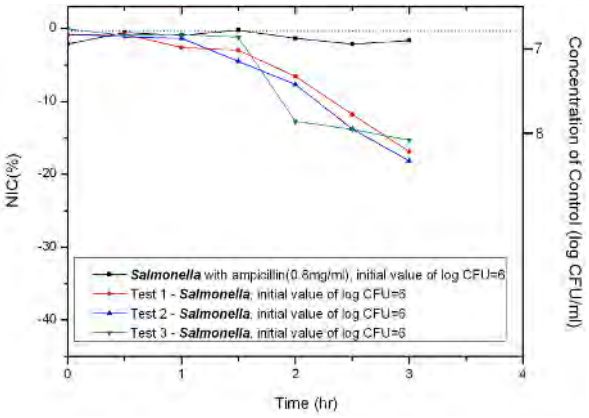


Fig. 3 The growth curve of *Salmonella* with/without ampicillin from 0 to 3 hours

We compared the doubling time that measured by traditional method with ours, and resulted that their doubling time were almost the same. Then, the viability of *Salmonella* could be verified.

B. Growth curve of Salmonella with/without Ampicillin

Measure the changes of the growth curve of *Salmonella* with initial concentration of 6 log CFU/ml. In the same parameters, we added antibiotic, ampicillin with the concentration about 0.8 mg/ml. As a result, we found that the samples with or without ampicillin had different changes of NIC (%), as shown in Fig. 3. The change of NIC (%) of sample without ampicillin was about 20%, and the sample with ampicillin had not large change.

Figure 4 showed that the growth curve of three kinds of initial concentration of *Salmonella* adding with the anti-

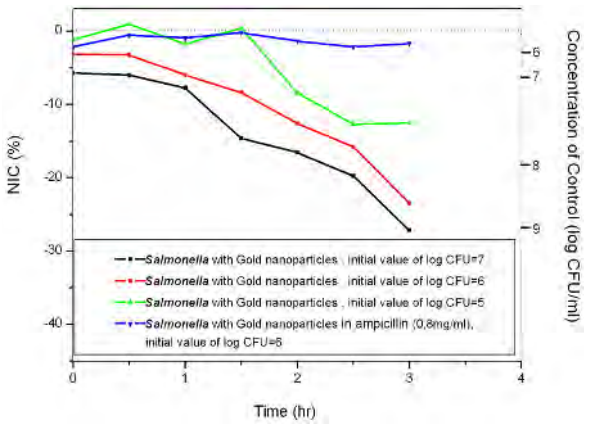


Fig. 4 The growth curve of *Salmonella* mixed with gold nanoparticles with/without ampicillin from 0 to 3 hours. The initial concentration was 5, 6, 7 log CFU/ml.

body-covered gold nanoparticles. Comparing Fig. 4 with Fig. 2 and 3 would know that the sample with gold nanoparticles had the larger change than without gold nanoparticles and therefore the sensitivity could get larger. The deviation between *Salmonella* with and without gold nanoparticles was about 5 to 10 % NIC (%).

As shown in Fig. 5 to 7, observing the *Salmonella* by microscope could found that the number of *Salmonella* with initial concentration of 6 log CFU/ml had different growth situations in the sample with/without ampicillin. The number of *Salmonella* with ampicillin was almost the same with initial, but the number of *Salmonella* without ampicillin had a lot of growing. These observed results were the same as NIC changes.

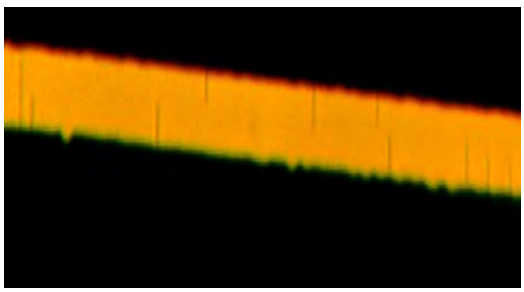


Fig. 5 When the electrode is energized, we observed the initial concentration 6 log CFU/ml by microscope

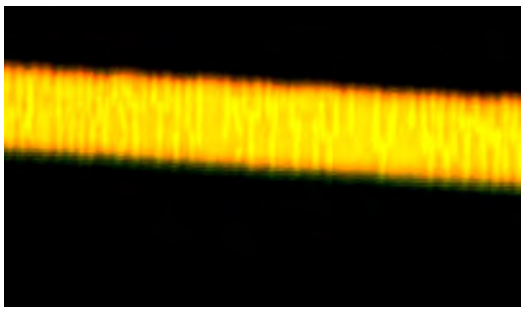


Fig. 6 After 3 hours, the sample without ampicillin was growing up obviously

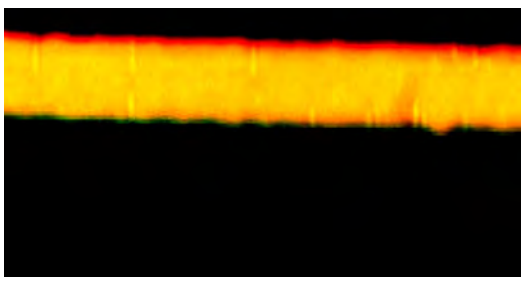


Fig. 7 After 3 hours, the sample with ampicillin *was almost the same as initial*

IV. Conclusions

In this study, impedance biochip based on interdigitated microelectrodes was developed. And this biochip combined with antibody-covered gold nano-particles has been successfully employed to detect the bacteria's drug resistance.

This biochip was used to detect as low as 10^5 CFU/ml of *Salmonella* with antibody-covered gold nanoparticles. The results showed that the initial concentration of bacteria of 10^5 CFU/ml could be detected with and without adding ampicillin after about 2 hrs that because of lag phase. The total detection time of this method could be completed within 4 hrs, which indicated the detection time of bacteria's drug resistance was faster than existing method with the total detection time about 72 hours. If the sensitivity of the biochip could be increased, the detection time would be faster.

V. Acknowledgments

This research is supported by National Health Research Institutes, NHRI-EX97-9628SI. We would like to thank all the fund sponsors.

References

1. J. Suehiro, D. Noutomi, M. Shutou and M. Hara (2003) Selective detection of specific bacteria using dielectrophoretic impedance measurement method combined with an antigen–antibody reaction." *Journal of Electrostatics*, vol. 58, Issues 3-4, pp. 229-246, June 2003
2. Maddocks, S., Olma, T., Chen, S. (2002) Comparison of CHROMagar salmonella medium and xylose-lysine-desoxycholate and Salmonella-Shigella agars for isolation of Salmonella strains from stool samples. J. Clin. Microbiol. 40, 2999-3003. 2002.
3. Perez, J. M., Cavalli, P., Roure, C., Renac, R., Gille, Y., Freydiere, A.M.(2003) Comparison of four chromogenic media and Hektoen agar for detection and presumptive identification of Salmonella strains in human stools" J. Clin. Microbiol. 41, 1130-1134. 2003
4. Henry, J., Anand, A., Chowdhury, M., Coté, G., Moreira, R., Good, T. Development of a nanoparticle-based surface-modified fluorescence assay for the detection of prion proteins." Anal. Biochem. 334, 1-8.
5. Thanh, N. T. K., Rosenweig, Z.(2002) Development of an aggregation-based immunoassay for anti-protein A using gold nanoparticles." Anal. Chem. 74, 1624. 2002.
6. Jung-Tang Huang, Hua-Wei Yu, Shao-Yi Hou, Yu-Huan Lin, Shiuh-Bin Fang, Gau-Chen Wang, Hung-Chang Lee, and Chun-Yan Yeung (2008) Development of a Biochip Using Antibodies-coated Gold Nanoparticles to Detect Specific Bioparticles. *Journal of Industrial Microbiology and Biotechnology, pp. 1-9, 2008*
7. L. Yang, Y. Li (2006) Detection of viable Salmonella using microelectrode-based capacitance measurement coupled with immunomagnetic separation", *Journal of Microbiological Methods* 10 64 9–16. 2006
8. J. Suehiro, R. Yatsunami, R. Hamada and M. Hara (1999) Quantitative estimation of biological cell concentration suspended in aqueous medium by using dielectrophoretic impedance measurement method" *Appl. Phys.* 32 2814–2820. 1999
9. J. Suehiro, Ryo Hamada, D. Noutomi, M. Shutou and M. Hara (2003) Selective detection of viable bacteria using dielectrophoretic impedance measurement method." *Journal of Electrostatics*, vol. 57, Issue 2, pp. 157-168. , February 2003
10. Madhukar Varshney, Yanbin Li (2007) Interdigitated array microelectrode based impedance biosensor coupled with magnetic nanoparticle-antibody conjugates for detection of *Escherichia* O157:H7 in food samples. *Journal of Biosensors and Bioelectronics 22*, pp. 2408-2414

Author: Jung-Tang Huang
Institute: Institute of Mechatronic Engineering,
National Taipei University of Technology
Street: 1, Sec. 3, Chung-Hsiao E. Rd.
City: Taipei
Country: Taiwan, Republic of China
Email: jthuang@ntut.edu.tw

Photothermal Ablation of Stem-Cell Like Glioblastoma Using Carbon Nanotubes Functionalized with Anti-CD133

Chung-Hao Wang, Yao-Jhang Huang and Ching-An Peng

Department of Chemical Engineering, National Taiwan University, Taipei, Taiwan

Abstract — **Despite aggressive multimodality therapy, most glioblastoma-bearing patients relapse and survival rate remains poor. Exploration of alternative therapeutic modalities is needed. Biologically modified materials with intrinsic optical properties, such as multi-walled carbon nanotubes (MWNTs) and gold nanoparticles, have been recently extensively explored for their potential use in biomedical applications. MWNTs revealing strong optical absorbance in the near-infrared region warrant their merits in photothermal therapy. In order to specific target CD133 over-expressed on the surface of glioblastoma cell line GBM S_1R_1, anti-CD133 monoclonal antibody was employed by conjugated to acidified MWNTs pre-modified with N-hydroxysuccinimide (NHS). In order to visualize anti-CD133 tagged MWNTs ingested by GBM S_1R_1 cells, fluorescent dye rhadoamine B was labeled onto MWNTs conjugated with anti-CD133. In comparison with DAOY cells, with negative CD133 expression, confocal images and flow cytometric analysis were showed. After CD133-grafted MWNTs were added into cell culture, GBM S_1R_1 glioblastoma cells and DAOY cells were irradiated separately with 808 nm near-infrared (NIR) laser for 15 minutes under intensity of 6 W/cm^2. Our results showed prominent photothermal damage of GBM S_1R_1 cells, while less necrosis of CD133-negative DAOY cells.**

Keywords — **Multi-walled carbon nanotubes, glioblastoma, CD133, Near-infrared laser**

I. Introduction

Glioblastoma (GBM) is the most common primary brain tumor in adults, without efficient known therapy. Treatment with chemotherapy has been hampered by the apparent resistance of GBM in vivo to various agents and challenges in delivering agents to the tumor cells. This is also due partly to the infiltrating growth pattern of the tumor and the relative resistance of GBM to cytotoxic agents in vitro. The lack of progress in such treatments reflects the need for rapid assays to study the effect of cytotoxic agents on GBM in vitro. It appears now that a new approach for such an assay can be based on the existence of a small fraction of the GBM that can be identified as cancer stem-like cells.

CD133 is a cell surface marker expressed on the progenitors of hematopoietic and endothelial cell lineages. Moreover, several studies have identified CD133 as a marker of brain tumor-initiating cells. In malignant brain tumors, CD133 has been suggested to be a cancer stem cell marker (Singh S. K. et al, 2003 and 2004) since only CD133 positive cells from brain tumor biopsy material were able to initiate brain cancer in a mouse model. Prominin-1 (PROM-1), also called CD133, is a protein with several isoforms of unknown physiological or pathological function, and is localized both in the cytoplasm and at the cell surface [1, 2].

Recently, molecular targeting and photothermal therapy have shown great potential for cancer therapy. Among a plethora of nanomaterials designed and synthesized for biomedical applications, carbon nanotube (CNT) owing to its unique features has been demonstrated to be an alternative option for localized hyperthermia treatment in comparison with nanogold-based materials [3, 4]. There is an increasing interest in exploring all of these properties that CNT possesses for applications ranging from sensors for the detection of genetic or other molecular abnormalities, to substrates for the growth of cells for tissue regeneration, and as delivery systems for a variety of diagnostic or therapeutic agents. For thermal destruction of cancer cells using CNT, Kam et al. (2005) showed CNTs functionalized with folic acid internalized by HeLa cells overexpressed with folate receptors led to cell death under 808-nm near-infrared light exposure. Gannon et al. (2007) [5] further demonstrated that CNTs targeted to cancer cells allowed noninvasive radiofrequency field treatment to produce lethal thermal injury to the malignant cells.

II. Materials and methods

A. Carboxylation of MWNT

In a typical experiment, 10 mg of MWNTs were added to a 20 mL of a mixture of sulfuric acid and nitric acid in a composition of 3/1 by volume. The mixture was sonicated in a bath for 10 min at room temperature. The mixture was then refluxed at 80 ℃ for 48 h. At the end of the reaction, the mixture was washed with deionized water for 5 times. The carboxylated MWNTs were freeze-dried and collected in the powder form. Comparing MWNT and carboxylated MWNT were used by UV/Vis spectrophotometer (Jasco

Chwee Teck Lim, James C.H. Goh (Eds.): ICBME 2008, Proceedings 23, pp. 888–891, 2009
www.springerlink.com

Model V-570, Japan) and X-ray powder diffraction XRD (PANalytical ; X' Pert PRO).

B. Carboxylated MWNT conjugated with anti-CD133 and rhodamine B

10 mg of the carboxylated MWNTs dissolved into DMF were reacted with 4 mg of EDC in the presence of 6 mg of NHS for 1 h at room temperature. After centrifugation for 10 min at 7,690 × g, the modified MWNTs were collected from the bottom layer. Five mL of deionized water were used to suspend MWNTs under sonication for 30 min. Then, 0.5 g of anti-CD133 were added into 10 g of the MWNT-containing tube and reacted for 2 h. For fluorescence observation, 2 g of rhodamine B dissolved in DMF were further used to conjugate anti-CD133 via carbodiimide chemistry at 4 for 8 h. After the reaction, the mixture was washed with deionized water for 3 times to remove excrescent rhodamine B.

C. Endocytosis of anti-CD133-MWNT

Glioblastoma cell line GBM S_1RGlioblastoma cell line GBM S_1R_1 and DAOY obtained from institute of clinical medicine in National Yang-Ming University were cultured in α-MEM medium supplemented with 10% FBS, non-essential amino acids solution, sodium pyruvate, L-glutamine. All the cultivation was performed at 37°C in humidified air containing 5% CO_2. Cells (1×10^6 cells) were plated on T-25 flask for 24 h. Prior to MWNT challenge, GBM S_1R_1 and DAOY cells were separately detached from the T-25 flask by trypsinization and inoculated onto a coverslip-bottomed Petri dishes (MatTek, MA, USA). In each dish, 2.5 g of rhodamine B labeled anti-CD133-MWNTs (CDMWNT) was added. Glioblastoma cell line GBM S_1R_1 cells were imaged by a confocal spectral microscope imaging system (Leica TCS SP5, Wetzlar, Germany). For nucleus staining, 20 g DAPI was added to each dish and allowed to incubate for 1 hr at room temperature before taking confocal images.

D. 808-nm laser irradiation

First, 1×10^5 cells of GBM S_1R_1 cells were cultured in 24-well tissue cultured plate for 24 h. GBM S_1R_1 cells with CDMWNT treatment were exposed to an 808-nm laser source (Opto Power Corporation, Tucson, AZ), a 15 watt fiber-coupled laser integrated unit . Note that all cells were washed with excess MWNTs in the solution removed and placed in fresh solutions after incubation in MWNT solutions and before any of the *in vitro* laser radiation experiments described in this work. The laser beam was delivered to the target through a 1.5m long, 600 μm single core fiber with a numerical aperture of 0.37, followed by a 25-mm focal length fused-silica biconvex lens. The focused spot size was 1.2 cm. After the treatment of laser, cells were stained by 2.5 μM calcein-AM. Cell death was determined by calcein-AM dying cells to determine cell viability.

E. Flow Cytometry.

After the mixed with different ratio of GBM S_1R_1 and DAOY cells and treated by CDMWNT at 6 hr, the mixed cell population were beamed at 15 min by 808-nm NIR laser. Afterwards, the cells were stained by calcein-AM. Finally, the fluorescent intensities of the mixed cells were determined by flow cytometry (Partec CyFlow, Muster, Germany).

III. Results and Discussion

We could obtain the information of that MWNT absorbed the energy of 808-nm laser irradiation according to the peak of 808-nm wavelength and the high intensity about 4.22 in Fig. 1 by UV/Vis. After 808-nm laser beaming, MWNT would enhance the environmental temperature. According to Fig. 2 detected by XRD, the diffraction peaks at 25.9° and 53.6° were assigned to the graphite crystallographic planes (002) and (004) of MWNT and carboxylated MWNT respectively. We could observe that intensity of the planes (002) in the carboxylated MWNT weaken in contrast to MWNT. As shown in Fig. 2, MWNT had the carboxyl group by the mixed solution of a mixture of sulfuric acid and nitric acid in a composition of 3/1 by volume. The carboxylated MWNT was bound with anti-CD133 using NHS to crosslink the carboxylated group of MWNT and the amino group of anti-CD133. The CDMWNT were added into 24-well tissue cultured plate with 0.8 mL medium.

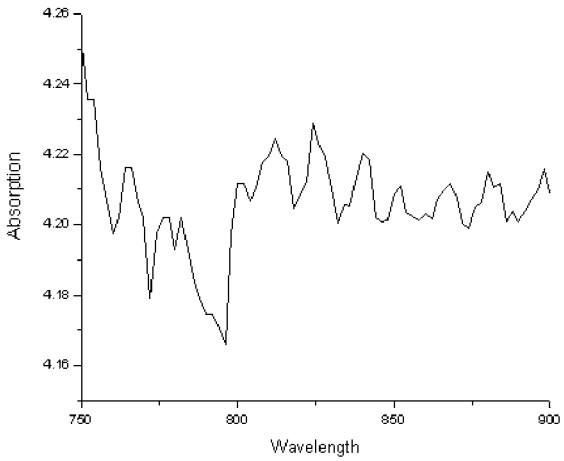


Fig. 1 UV/Vis absorption spectrum of MWNT irradiating by NIR

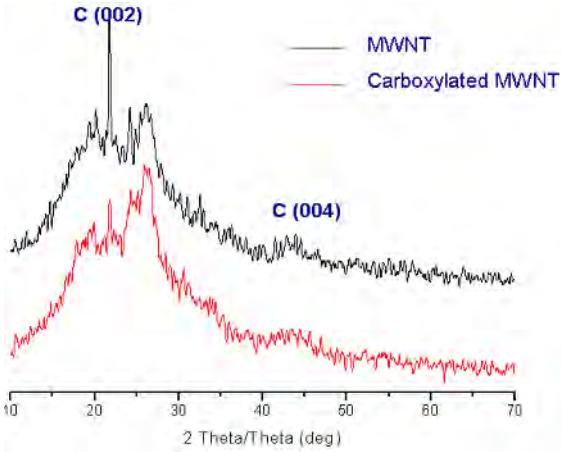


Fig. 2 XRD patterns of MWNT and carboxylated MWNT.

As shown in Fig. 3, after 20 mg, 10 mg, 5 mg of normal MWNT in 2 mL DI water were beamed by 808-nm laser in 12 min, the temperature of solution reached 54 and remained steady.

This situation indicate the anti-CD133 develop the ligand function, make the interaction with the expression of CD133 in the interior of glioblastoma cell line GBM S_1R_1. Monoclonal antibodies CD133 were able to bind to and be internalized by GBM S_1R_1 cells with high affinity. Fig. 4A were showed that the rhodamine B labeled VDMWNTs were targeted toward the cell membrane of glioblastoma GBM S_1R_1 cells to express the high-intensity CD133 receptor. Comparing with DAOY cells in Fig. 4C, GBM S_1R_1 cells could internalize more CDMWNT into cell inside than DAOY cells did. Therefore, anti-CD133 labeled MWNT could selectively target on GBM S_1R_1 cells expressed with the CD133 receptors.

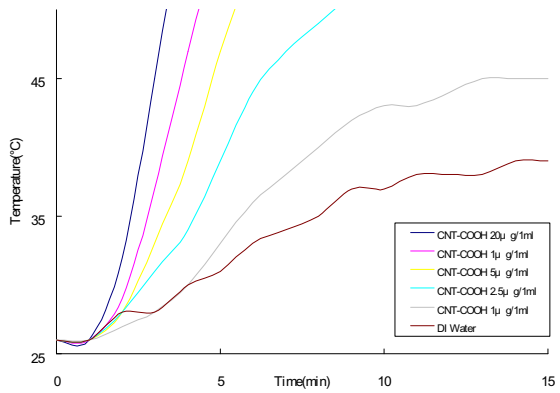


Fig. 3 Temperature curve for the medium with different amount of MWNT.

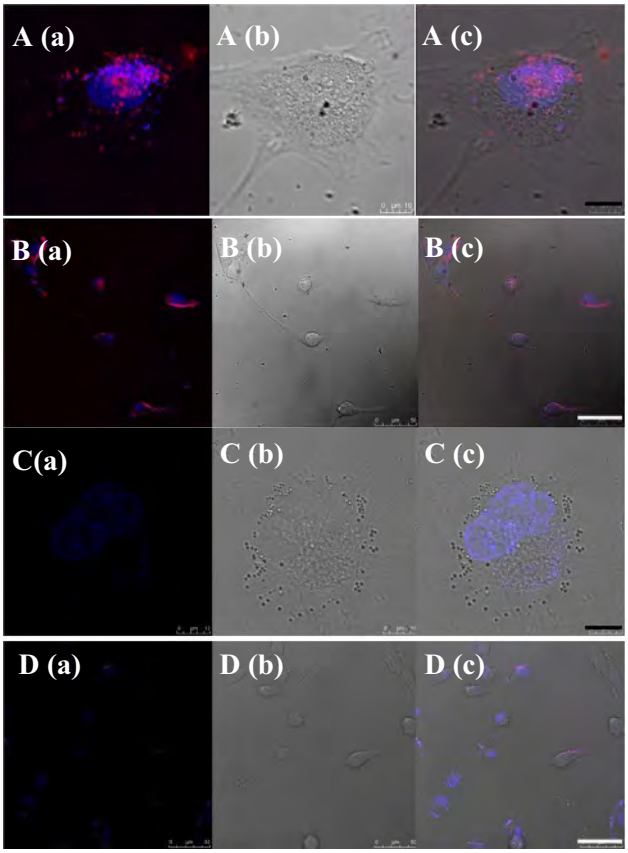


Fig. 4 Confocal images after GBM S_1R_1 cells (A), (B), and DAOY cells (C), (D) were cultured with MWNT-anti-CD133- rhodamine B at 6 hrs in (a) fluorescence with rhodamine B and DAPI, (b) bright view, (c) overlay of (a) and (b) (Block scale bar = 10 μm; white scale bar = 50 μm)

Adding calcein-AM to cells can observe cell death after irradiated with NIR laser. Calcein-AM in common was used to detect the cell viability to make us definitely differentiate the death and living of GBM S_1R_1 and DAOY cells. After dying with calcein-AM then use 496 nm blue light to irradiate the cell, if the cells were alive, it would emit 516 nm green light. If the cells were dead, it would not emit any light. After incubation of CDMWNT for 6 hr, the images of DAOY in the laser-beaming range, boundary and outside were taken and showed in Fig. 5 B (a)-(c). The inside cells appeared darkly to compare cells outside. As shown to the cells dyed calcein-AM in Fig. 5 B (d)-(f), DAOY cells with CDMWNT had the apparent boundary of death and living. GBM S_1R_1 cells with CDMWNT were dead nearly in the region of laser beam. Nonetheless, GBM S_1R_1 cells treated with CDMWNT and beamed with 808-nm laser were observed that the cells would nearly die in Fig. 5 A (d) and wouldn't die in Fig. 5 A (f). In Figure 5 C (d)-(e), the one-by-one ratio mixture of GBM S_1R_1 and DAOY cells wouldn't die absolutely after 808 nm NIR

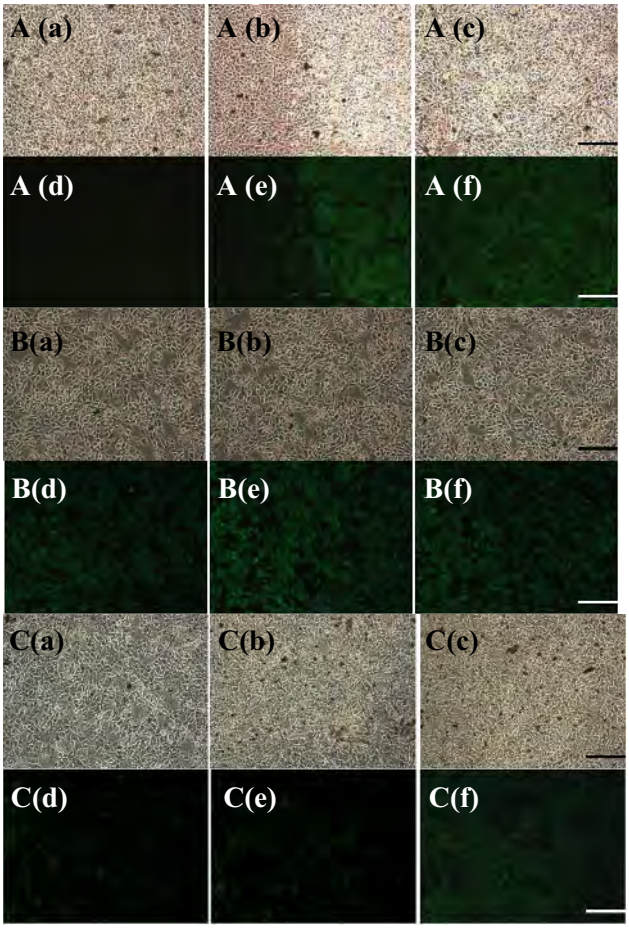


Fig. 5 Photothermal therapy of (A) GBM S_1R_1, (B) DAOY, (C) mixture with GBM S_1R_1 and DAOY cells, ratio was 1 to 1, beamed 808-nm laser. After the incubation with CDMWNT in GBM S_1R_1, DAOY, mixture cells at 6 hr, using 808-nm laser to beam the cells at 15 min. Then, the cells calcein-AM dyed. After dying, Fig. 5 (a-c) were the bright view photos in the wells of laser beaming inside, boundary, and outside. And Fig. 5 (d-f) were the fluorescent photos to dye by calcein-AM in the wells of laser beaming inside, boundary, and outside. (Scale bar = 100 μm.)

beamed. Furthermore, we would make the ratio 1:3 and 3:1 mixture of GBM S_1R_1 and DAOY cells, and use 808 nm NIR to beam. Fig. 6 were showed by flow cytometry that different ratio mixture of GBM S_1R_1 and DAOY cells could be obtained oppositely fluorescent intensity of calcein AM. When the sample including more GBM S_1R_1 cells in Fig. 6 (a) after 808 nm NIR beamed, the fluorescent intensity of lived cell would weaken as compared with Fig. 6 (b). Taken all together, it appears that anti-CD133-tagged MWNTs can specifically target onto GBM S_1R_1 cells, internalized into cells, and photo-theraml ablated by NIR irradiation.

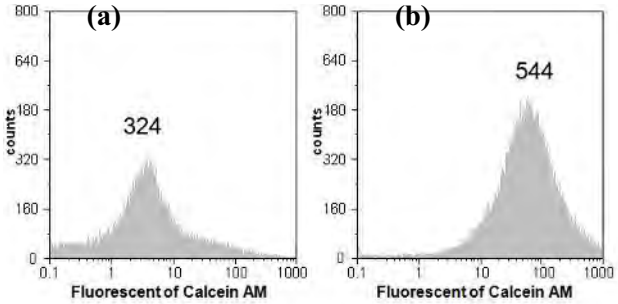


Fig. 6 Flow cytometry of different ratio of mixture with GBM S_1R_1 and DAOY cells beamed 808-nm laser. The ratio of GBM S_1R_1 and DAOY cells were (a) 3 to1 , (b) 1 to 3.

References

[1] Miraglia S, Godfrey W, Yin AH, Atkins K, Warnke R, Holden JT, Bray RA, Waller EK, Buck DW. (1997). Blood 90, 5013–21.
[2] Yu Y, Flint A, Dvorin EL, Bischoff J. (2002) J Biol Chem 277, 20711–16.
[3] Hirsch LR, Stafford RJ, Bankson JA, Sershen SR, Rivera B, Price RE, Hazle JD, Halas NJ, West JL. (2003) *Proc Natl Acad Sci* USA 100,13549.
[4] Tong L, Zhao Y, Huff TB, Hansen MN, Wei A, Cheng JX. (2007). *Adv. Mater.* 19, 3136.
[5] Gannon CJ, Cherukuri P, Yakobson BI, et al. (2007) *Cancer* 110, 2654-2665.

Author: Ching-An Peng
Institute: Department of Chemical Engineering,
National Taiwan University
Street: No. 1, Sec. 4, Roosevelt Road
City: Taipei
Country: Taiwan
Email: chinganpeng@ntu.edu.tw

A Design of Smart Dust to Study the Hippocampus

Anupama V. Iyengar[1], D. Thiagarajan[2]

[1] Sri Sairam Engineering college/Electrical and Electronics Department, Anna university, Chennai, India
[2] Sri Sairam Engineering college/Electrical and Electronics Department, Anna university, Chennai, India

Abstract — **In this paper we have designed a smart dust, which is capable of sensing the neural activity of a human Hippocampus.**

Keywords — **Hippocampus, Nano Generator, Nano Sensor, Volume conduction**

I. Introduction

Hippocampus plays a vital role in the memory formation [4], behavioral inhibition etc. Diseases affecting the brain like the Alzheimer's disease, Amnesia etc involve damage of the hippocampus. Therefore monitoring this region of the brain would deepen our knowledge about the nature of diseases related to it and can save many lives. It would also provide a wealth of information about the memory formation, a phenomenon which still baffles the scientists.

II. Smart dust design

The chip is implanted in any sub-field of the hippocampus, say CA3. The chip is self powered and hence it is devoid of a bulky power supply. The chip consists of a nano sensor, which senses the neuron potential. It is amplified, filtered and is then transmitted to any external interface, like the commercially available motes, MICA2DOT [2] and MICA2 [2]. The neural activity can thus be observed in the computer or through the internet. The design of the power supply has been done by us. The chip uses the property of volume conduction [3] with X- shaped antennas [3] as in other invasive motes used commercially.

The overall design of monitoring the hippocampus is Shown in Figure 1

The smart dust consists of the following parts:

1. Power supply (Nano generator)
2. Nano sensor
3. Amplifier, filter and modulator
4. X- shaped antenna

The Figure 2 shows the overall block diagram of smart dust

Power supply construction and working: The power supply to the chip comes from a nano generator. A set of piezoelectric nano wires are placed in-between the poles of a magnet as shown in the figure 3. The piezoelectric wires contact the neurons and starts vibrating when they receive electrical input from the action potentials of the neurons. When the crystals starts vibrating they cut the magnetic flux between the two poles of the magnet and electrical power is generated by the principle of electro-magnetic induction. We simulated this design using MATLAB.

Nano Sensor: The nano sensor consists of a set of hundreds of gold nano wires which senses the action potentials of hundreds of neuron inside the hippocampus.

Amplifier/filter/modulator: The signal is amplified, high pass filtered, modulated, multiplexed and is sent to the antenna.

X-Shaped Antenna: The x shape antenna forms the exterior parts of the chip and is used for data communication.

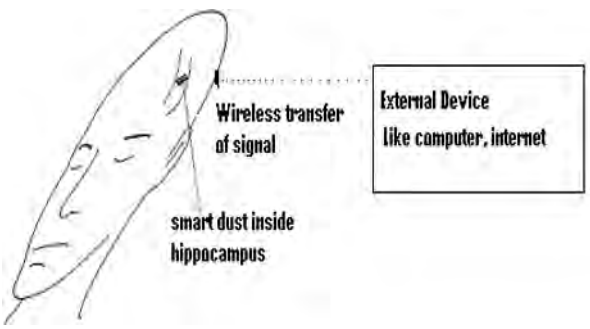


Fig. 1

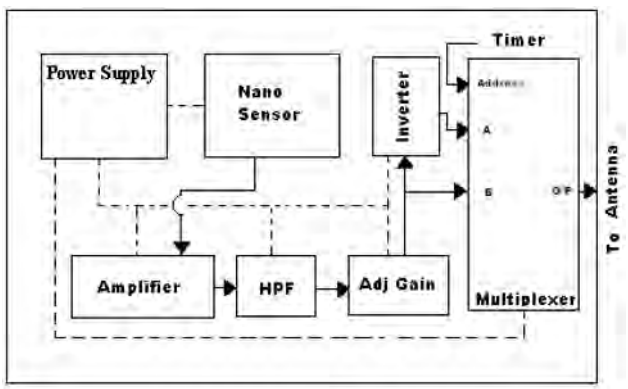


Fig. 2

Chwee Teck Lim, James C.H. Goh (Eds.): ICBME 2008, Proceedings 23, pp. 892–893, 2009
www.springerlink.com

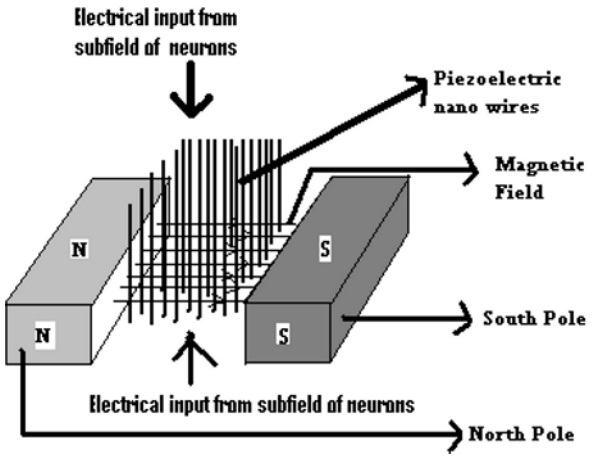


Fig. 3

This type of antenna design has many advantages. It provides a large separation of two antenna surfaces; it occupies little space of the chip and doesn't require a supporting mechanism. Since the chip body acts as an insulator between the antenna, it blocks the formation of shorting current paths and forces the current to take longer paths.

Volume Conduction: The signal is transmitted by the property of *volume conduction. In this system the ionic fluid within the human body passes information between inside and outside the body.* This system has the advantages over Radio Frequency transmission because of lowered frequency operation, the shielding effect of ionic fluid in the body is no longer a problem, instead it is now employed as the information carrier. The volume conduction circuit is simpler than the RF circuit, allowing aggressive size reduction. The system does not require signal conversion to/from RF and is therefore, highly energy efficient. The signal is received by any external interface placed on the scalp like the commercially available motes MICA2DOT and MICA2 and the signal can be observed in a computer or internet.

III. Conclusions

Monitoring hippocampus would answer many unsolved mysteries about the memory formation, behavioral science and cognitive neuro science. We must strive to utilize this technology for the betterment of mankind.

References

1. Theodore.w.Berger, John J.Granaki, Vasilis.Z.Marmarelis, Bing J sheu, Armand.R.Tanguay. Jr "Brain implantable biomimetic electronics as neural prosthetics", proceedings of 25th annual conference of IEEE EMBS, 2003
2. Shahin Farshichi, Istavan Mody and Jack.W.Judy"Tiny wireless based neural interface ", proceedings of 26th international conference of the IEEE EMBS, 2004
3. IEEE ENGINEERING IN MEDICINEAND BIOLOGY Magazine Vol 25 September/October 2006, page no: 22, 40, 41
4. Arthur C. Guyton, John E. Hall "Textbook of Medical Physiology"

Author: Anupama.V.Iyengar
Institute: Sri Sairam Engineering College
Street: Gajalakshmi Nagar, Chromepet
City: Chennai
Country: India
Email: anueinstein1@yahoo.co.in, sadicarnot@rediffmail.com

Determination of Affinity Constant from Microfluidic Binding Assay

D. Tan[1], P. Roy[2]

[1] Graduate Programme in Bioengineering, National University of Singapore, Singapore
[2] Division of Bioengineering, National University of Singapore, Singapore

Abstract — **We present a method of determining the affinity constant of a receptor-ligand pair using equilibrium binding in a microfluidic channel. This technique involves the immobilization of the receptor to the microchannel surface and perfusion of the ligand at a fixed flow rate. The ligand concentration in the eluent is monitored in real time. The break-through time of the ligand is then determined and compared with that of an appropriate, non-binding, reference molecule. The difference in break-through time can then be used in a mathematical model we have developed to determine the affinity constant of the receptor-ligand pair. Using this method, we have determined the equilibrium dissociation constant, K_D, of a rat anti-insulin immunoglobulin and a fluorescein-conjugated human insulin. Fluorescein-conjugated aprotinin was used as the non-binding reference molecule. Our experiments yielded a K_D value of 0.76 μM for this anti-insulin IgG and insulin-FITC pair.**

Keywords — **Receptor-ligand, equilibrium binding, microfluidic, equilibrium constant, mathematical model.**

I. Introduction

Molecules in solution that undergo specific binding are described as receptor-ligand pairs. Since these binding events do not result in covalent bond formation, but rely rather upon the formation of hydrogen bonds, van der Waal's forces and other noncovalent interactions, they are reversible and in the absence of perturbation and mass change, result in an equilibrium bound state. This state comprises the free receptor, free ligand and the receptor-ligand complex co-existing at concentrations characteristic of the system. These concentrations can be expressed as a single parameter – the equilibrium dissociation constant, K_D – which is a useful means of characterizing the receptor-ligand system. The K_D of a receptor-ligand pair is the concentration of free ligand in the system when half of the receptor binding sites have been occupied [1]. K_D is the inverse of the equilibrium affinity constant.

Consider a monovalent receptor, R, undergoing a binding event with the ligand, L:

$$R + L \underset{k_{-1}}{\overset{k}{\rightleftharpoons}} RL \qquad (1)$$

At equilibrium, the forward rate of reaction is equal to the reverse rate of reaction. Defining the forward and reverse reaction rate constants as k and k_{-1} respectively, the equilibrium dissociation constant, $\frac{k_{-1}}{k}$ (K_D) can be expressed as follows:

$$K_D = \frac{[R][L]}{[RL]} \qquad (2)$$

As such, the equilibrium dissociation constant of a system can be determined if the concentration of free ligand, free receptor and receptor-ligand complexes can be measured.

Conventional systems for determining K_D include dialysis, immunoprecipitation or solid-phase binding assays [1-3] wherein the system is allowed to reach equilibrium, after which the free components are separated from the complexes. Where dialysis and immunoprecipitation allow the binding event to occur completely in solution, the solid-phase assays typically involve immobilisation of the receptor on a solid surface, as is employed in enzyme-linked immunosorbent assays [2,3]. In the latter case, the ligand would have to diffuse from the bulk solution to the reaction surface, whereupon they would bind to the immobilized receptors. Subsequently, the concentration of either of the free molecules, or that of the complex may be determined.

To facilitate this determination, either the receptor or the ligand might be labeled with an enzyme or a fluorescent probe. Unlike enzyme probes, which require the addition and enzymatic modification of a substrate to yield a detectable product, a fluorescent probe allows direct measurement of concentration. Mass conservation would then allow the concentration of the other components, and subsequently, the K_D to be calculated.

However, these assays require the use of quantities of receptor or ligand which may be prohibitive in the case where either or both may not be readily available. Adaptation of the solid-phase assay for 96-well plates reduces the necessary reaction volume to 100 μL per microwell and increases the surface area to volume ratio, so improving the efficacy of the system. However, this improvement can be taken a step further by adapting the assay for a microfluidic system [4,5].

Chwee Teck Lim, James C.H. Goh (Eds.): ICBME 2008, Proceedings 23, pp. 894–897, 2009
www.springerlink.com

Microfluidic channels are capillary tubes, typically made of optically transparent material, with at least two of their dimensions being less than a millimeter. A microchannel of 35 μm (H) x 240 μm (W) x 4 cm (L) would have a volume more than 297 times less than that in a microwell. This considerably reduces the volume of reagent needed for each assay. Typically, the receptor molecules are immobilized onto the surface of the microchannel and the ligand in solution is perfused through the microchannel, during which binding occurs. Parameters such as flow rate and perfusion time can then be selected to ensure sufficient time for systems with fast-binding kinetics to attain equilibrium.

Using a fluorescence-labeled ligand, the bound fraction can easily be quantitated by measuring the fluorescence intensity retained in the microchannels. Alternatively, one could monitor the eluent fluorescence intensity and exploit changes in the breakthrough time to calculate K_D.

In the absence of a receptor, the ligand resident time in the microchannel should be dictated only by the flow rate used. The resultant elution profile is a dispersion-induced sigmoid. In contrast, when the receptor is immobilized on the surface of the microchannel walls, binding of the ligand to the receptors increases the residence time, so delaying the breakthrough time. This delay is a function of the system K_D value.

A model was developed to describe the relationship between the shift in breakthrough time, $\Delta T_{50\%}$, immoblised receptor surface concentration (R_T), antigen concentration (L_0) and K_D [6].

Here, we report the use of a polydimethyl siloxane (PDMS) microchannel system to determine the K_D of FITC-conjugated recombinant human insulin and a monoclonal rat anti-insulin immunoglobulin (IgG). FITC-conjugated aprotinin was used as a reference.

II. Materials and Methods

A. Labeling of proteins with fluorescein.

Recombinant, human, insulin (Sigma-Aldrich, USA) and bovine lung aprotinin (Fluka Biochemika, Switzerland), each at 10 mg/mL were prepared in 0.1 M sodium bicarbonate buffer (pH 8.3). Fluorescein isothiocyanate (FITC) succinimidyl ester (Molecular Probes, USA) at 10 mg/mL in dimethylsulfoxide was then added to each protein solution at a FITC to protein molar ratio of 5:1. The reaction mixes were then incubated at room temperature for one hour with gentle agitation at 165 rpm on an orbital shaker. Unreacted FITC was then removed from each reaction mix by ultrafiltration (Vivaspin 500, 3 kDa MWCO, Sartorious, Germany). The protein solutions were then diluted to 500 μL using phosphate-buffered saline supplemented with 0.05% (w/v) sodium azide (PBSA) and the protein concentration of each solution was measured using the bicinchoninic acid assay (Pierce, USA).

B. Conjugation of anti-insulin IgG with biotin.

To immobilize the anti-insulin immunoglobulin (IgG) onto the avidin-coated microchannel surface, it was conjugated with the amine-reactive biotin ester, NHS-PEO-Biotin (Pierce, Rockford, IL). This biotin derivative was selected because it includes a poly(ethylene glycol) (PEO) linker of 29Å between the biotin moiety and the conjugation site [7]. This long and flexible spacer would extend the IgG further into the bulk flow, so minimizing the effects of steric hindrance on the antigen-antibody binding event. Furthermore, the PEO segment would improve the solubility of the biotin succinimidyl ester in aqueous solutions, so allowing the IgG to be conjugated under conditions that would not jeopardize its structure and function. To prepare the reaction mix, 92 μL of D6C4 anti-rodent insulin IgG (Hytest, Finland) at 1.1 mg/mL was added to 8 μL of biotin succinimidyl ester at 0.5 mg/mL (biotin to protein molar ratio of 10:1). The mixture was then incubated at room temperature for one hour, with gentle agitation at 165 rpm on an orbital shaker. The reaction mix was then diluted to 1, 000 μL with PBSA and the unreacted biotin was removed from the mix by ultrafiltration at 12, 000 rcf for 20 min using two Vivaspin 500 ultrafiltration units (50 kDa MWCO, Vivascience, Sartorious, Germany). Each retentate was then diluted to 500 μL and filtered again. This is repeated one more time to ensure complete removal of the unreacted biotin. The final retentates were diluted to a total volume of 400 μL using PBSA. The concentration of the biotinylated IgG was then determined using absorbance at 280 nm.

C. Microchannel fabrication.

Microchannels with a width of 240 μm, a height of 35 μm and a length of 3.7 cm were micromolded from a template using Sylgard 184 (polydimethyl siloxane, PDMS, Dow Corning, USA) at a ratio of 10 parts of PDMS base to one part of cross-linker. A one-millimeter diameter perforation of the PDMS at one end of each microchannel was made to form the outlets. A 4 mm layer of PDMS was separately prepared and both pieces of PDMS were exposed to reactive air plasma for 5 minutes before being bonded together to seal the microchannels. A 1 mm diameter perforation was then made through both layers of PDMS to form the inlets. A piece of PDMS was used to fabricate a flow cell with a PEEK tube from the outlet passing through it and placed in contact with a fiber optic cable via a T-junction.

Another PEEK tube, at the inlet, was carefully perforated and aligned with the microchannel to eliminate impinging flow.

D. Microchannel surface blocking and IgG immobilization.

Immediately after sealing, avidin (Sigma-Alrich, USA) in PBSA at 1 μM was perfused into each microchannel at 5 μL/min for 60 min. The avidin solution was then left in the microchannels for a further one hour at room temperature. The resident blocking buffer was then removed by perfusing the microchannel with PBSA at 10 μL/min for 6.5 hrs to ensure thorough removal of unadsorbed avidin. Biotinylated IgG at 600 nM was then perfused into the microchannels at 1 μL/min for 60 min, and left to incubate in the microchannels for a further 60 min. The microchannels were then re-perfused with 600 nM biotinylated IgG at 1 μL/min for 1 hr, followed by a PBSA wash (1hr at 10 μL/min) to remove IgG that had not bound to the surface-adsorbed avidin. The value of R_T was determined to be 10 pmoles/cm^2 [7].

E. Microchannel binding assay.

Excitation of the eluent in the flow cell was maintained at 490 nm from a LED source (Instech, USA). Fluorescence from the eluent was filtered at 520 nm using a monochromator (DongWoo Optron, Korea) and detected using a photon multiplier tube. The data was then acquired by a PC using the counting board software (Hamamatsu, Japan).

Each microchannel was perfused with wash buffer (polyethylene glycol in PBSA) at 0.20 mL/hr for 30 min before being used for each assay. The reference molecule was then perfused into the microchannel at 0.02 mL/hr and the increase in fluorescence intensity of the eluent was monitored until no further increase was observed. The reference protein was then washed from the microchannel by perfusing wash buffer at 0.20 mL/hr and monitoring the decrease in fluorescence intensity until no further decrease was observed. The sample solution was then perfused into the microchannel at 0.02 mL/hr and monitored as before, for the fluorescence signal.

III. Results and Discussion

The microfluidic competition assay works by entraining the ligand and competitor in laminar flow through a microchannel whose surfaces contain the immobilized receptor. The mathematical model that we have developed [6], incorporates the basic physics describing the microchannel transport and equilibrium binding of receptor and ligand. Although the theory is generally applicable, the results presented here correspond to straight microchannels of rectangular cross section where the Taylor-Aris dispersion theory remains valid [8] ($U \leq 0.39$ cm/s). All experiments were designed to adhere to the conditions prescribed by the theoretical model in order to achieve the best possible agreement.

Aprotinin, with a molecular weight of 6.5 kDa, displays an almost identical elution profile to that of human insulin at 5.8 kDa, likely due to their similar diffusivities. For this reason, aprotinin was used as the reference for elucidating the transport characteristics of the ligand, in the absence of receptor binding. In the presence of surface-immobilised antibody, the model predicts a right-shift of the elution profile, indicating an increased residence time.

Each elution profile has the characteristic sigmoidal shape whose maximum slope is a function of the solute dispersion coefficient [9]. Since dispersion distorts the profile, so making determination of breakthrough time difficult, the time at which the eluent concentration is 50% of that of the inlet was used instead. Any difference between the ligand and reference breakthrough times is then expressed as $\Delta T_{50\%}$, which is the difference between the ligand and reference breakthrough times at 50% of the respective inlet concentrations.

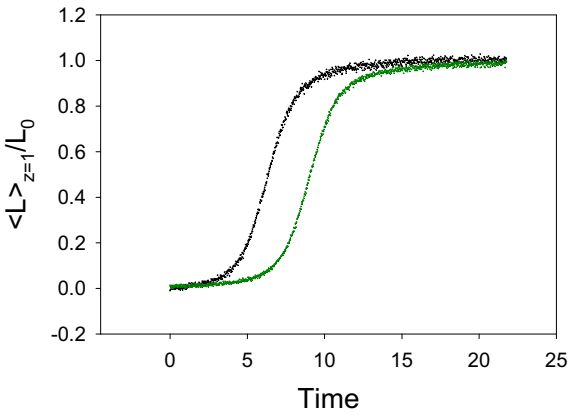


Fig. 1 Average concentration at the outlet ($<L>_{z=1}$) normalized with the inlet concentration (L_0) as a function of dimensionless time, obtained during measurement of K_D corresponding to $\Delta T_{50\%}$=2.7 with aprotinin-FITC (black dots) as the reference and insulin-FITC (green dots) as the ligand.

Figure 1 shows the experimental data for FITC-conjugated human insulin binding to rat monoclonal anti-insulin IgG immobilized in the microchannel. The reference used is FITC-conjugated aprotinin, which has a similar diffusivity. The breakthrough curve for insulin is shifted to the right of the aprotinin curve as expected from the theoretical results. In order to minimize the variation between different micro-

channels, each assay comprising a reference perfusion as well as a ligand perfusion was performed in the same microchannel. Our measured value for $\Delta T_{50\%}$ was 2.7±1.3.

Mathematical simulation of insulin and aprotinin transport phenomena in microchannels coated with anti-insulin IgG demonstrates this trend and also demonstrates how $\Delta T_{50\%}$ changes with L_0/K_D (constant R_T) (Fig. 2). It is seen that an increase in affinity constant increases $\Delta T_{50\%}$ because more binding takes place at the leading front, so depleting the bulk flow to a greater extent.

Our experimentally determined $\Delta T_{50\%}$ allows us to estimate K_D from a plot of $\Delta T_{50\%}$ vs K_D for a fixed L_0 = 2 μM. The value of K_D was found to be 0.76 μM. Further confirmation of this K_D may be achieved by experiments with other L_0 values in the linear part of the binding curve.

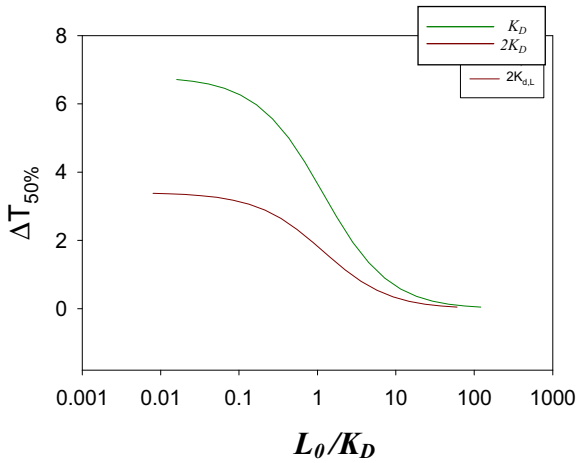


Fig. 2 Binding curves obtained from the numerical simulation showing the change of $\Delta T_{50\%}$ with $L_0/K_{d,L}$ for two different affinity constants.

IV. Conclusions

We have developed a microfluidics-based method of determining the equilibrium dissociation constant of any receptor-ligand pair. This method relies upon determination of the difference in breakthrough times between that of a reference molecule and that of the ligand. The proposed method has the following advantages: 1) uses less reagents than standard ELISA, 2) allows a larger selection of detection techniques, 3) is relatively quicker and, 4) has better mass transfer characteristics than assays in well plates. Furthermore, the theoretical results presented here may also be extended to the study of equilibrium binding (or systems with fast binding kinetics) between the immobilized receptor and competing molecules in solution. This would allow us to develop the system for use in quantitative competition assays. The advances in immobilization methods and linker designs together with low cost microfabrication, makes this a viable and promising technique for large scale adoption.

Acknowledgment

The authors would like to thank Song Ying for assistance with the experimental protocols and Chaitanya Kantak for helping with microchannel fabrication. This study was funded by NUS-FRC research grant R397000015112/101.

References

1. Donald T. Haynie (2001) Biological Thermodynamics. Cambridge University Press, United Kingdom
2. Friquet B et al. (1985) Measurement of the true affinity constant in solution of antigen-antibody complexes by enzyme-linked immunosorbent assays. J Imm Methods 77:305–319
3. Kim B B et al. (1990) Evaluation of dissociation constants of antigen-antibody complexes by ELISA. J Imm Methods 131:213–222
4. Lin F Y H, et al. (2004) Development of a movel microfluidic immunoassay for the detection of helicobacter pylori infection. The Analyst 129:823–828
5. Eteshola E & Balberg M (2004) Microfluidic ELISA: On-chip fluorescence imaging. Biomed Microdev 6(1):7–9
6. P Roy & Darren T C-W. (2008) Microfluidic competition assay via equilibrium binding.Sensors & Actuators (Under review)
7. Ying Song (2007) Binding kinetics of immobilized biomolecules by microchannel flow displacement. Division of Bioengineering, National University of Singapore, Singapore, MS Thesis
8. Rush B M et al. (2002) Dispersion by pressure-driven flow in serpentine microfluidic channels. Ind & Eng Chem Res 41(18):4652–4662
9. Ying S, C-W Tan, P Roy (2007) Dispersion in Microfluidic Channels Measured with an Online Fiber Optic Fluorescence Probe. 3rd WACBE World Congress on Bioengineering, Bangkok, Thailand, July 9-11

Author: Darren Tan
Institute: National University of Singapore
Street: 9 Engineering Drive 2
City: N. A.
Country: Singapore
Email: g0402807@nus.edu.sg

In-Vitro Transportation of Drug Molecule by Actin Myosin Motor System

Harsimran Kaur*, Suresh Kumar*, Inderpreet Kaur*, Kashmir Singh† and Lalit M. Bharadwaj*

*Biomolecular Electronics and Nanotechnology Division
Central Scientific Instruments Organisation, Chandigarh, 160030, INDIA
Phone: +91-172-2657811 Ext. 482, 452, +91-172-2656285 Fax: +91-172-2657267
† Department of Biotechnology, Panjab University, Sector 14, Chandigarh-160014. INDIA
Email: microsimbac@yahoo.co.in, lalitmbharadwaj@hotmail.com

Abstract — **Nanoscale biomolecular motor driven transport systems are the bioinspired alternative for Nanorobotics. With the increasing knowledge within the mechanisms of motor binding and regulation, the appropriate motor components can be modified for micro/nano cargo transportation such as biomolecules, quantum dots, organic molecules, microbeads etc. Our group has already demonstrated transport of such molecules and motor binding tendencies to organic and inorganic drug molecules and regulation is strongly anticipated. Present study explores In-vitro transportation of 5-aminosalicylic acid (5-ASA) by actin myosin motor system. 5-aminosalicylic acid is an anti-inflammatory drug used to treat inflammation of the digestive tract (Crohn's disease) and mild to moderate ulcerative colitis. In this appraoch, binding of 5-ASA to actin filament is achieved by streptavidin-biotin crosslinking. Here, succinimido group of NHS-Biotin will be attached to free amine group present on 5-ASA forming drug-biotin conjugate. Biotinylation of F-actin was attained by capping negative end with biotinylated gelsolin which inturn convert F-actin into biotinylated F-actin. Attachment of drug with actin filament was attained by reacting drug-biotin conjugate with streptavidin. Biotinylated actin filaments were reacted with drug-biotin-streptavidin complex to achieve drug-biotin-streptavidin-actin complex. As streptavidin has four biotin specific sites, two sites will attach to drug-biotin conjugated and remaining two will be available for biotinylated actin filaments. Confirmation and quantitation of attachment of drug was done by UV-vis-spectroscopy, Transmission Electron Microscope, Atomic Force Microscopy and High Performance Liquid Chromatography. Transportation of drug attached to actin filaments was directed by applying a weak electric field. Velocity of actin filaments attached to drug was calculated by tracking program developed in MATLAB. Present study provides insight into the actin-myosin based molecular motor system for drug transportation.**

Keywords — **Actin, 5-Aminosalicylic acid, Biotin, Gelsolin, Streptavidin.**

I. Introduction

Molecular motor protein systems play vital role in actively transporting or moving other molecules or proteins within cellular system. Research during the past several decades has provided a wealth of understanding about nanoscale motor proteins, which generate force and motion in biological systems by hydrolyzing adenosine triphosphate (ATP) as a fuel (1, 2). Examples of these types of proteins are the kinesin motor proteins and actinomyosin motor system. Actin can transport cargo using myosin as a track to run on. Actomyosin motor protein system is an ideal candidate for hybrid nanomechanical systems due to their small dimension and high fuel efficiency (3). The most challenging aspect of using actomyosin motor protein system for drug transportation is to attach a particular drug to actin filaments and then studying their motility on myosin tracks (4). Herein, we present a successful protocol for attaching drug to actin filaments by using biotin-streptavidin conjugate. The binding of biotin to streptavidin (a 60-kDa tetrameric protein) is the strongest noncovalent interaction known (KA~1014M-1) (5). 5-aminosalicylic acid an anti-inflammatory drug used in Crohn's disease was attached to actin filaments. 5-ASA has amine group which forms bond with succinimido group of NHS-Biotin making drug biotinylated. Biotinylated drug inturn will bind to biotinylated actin filaments through streptavidin crosslinking. Drug attached to actin filaments was viewed under flurescence microscope where fluorescence of drug crystals confirms attachment of actin filaments to drug. Velocity of actin filaments carrying drug on myosin tracks was calculated by MATLB software.

II. Materials and Methods

Actin, Myosin of rabbit skeletal muscle, Phalloidin-Tetramethylrhodamine-B-isothio cyanate (Rh-Ph; fluorescent dye) was procured from Sigma-Aldrich. Sulfo-NHS Biotin and Streptavidin were procured from Pierce, USA. 5-Aminosylsalic Acid (5-ASA) was procured from Universal labs. Dimethyl formamide (DMF) was procured from Sigma- Aldrich. All other chemicals used were of molecular and analytical grade unless otherwise stated. All the buffers and solutions were prepared in double distilled deionised (18 MΩ) autoclaved water.

Chwee Teck Lim, James C.H. Goh (Eds.): ICBME 2008, Proceedings 23, pp. 902–905, 2009
www.springerlink.com

A. Polymerization and labeling of actin

G-Actin was polymerized in polymerizing buffer (2 mM $MgCl_2$, 50 mM KCl, 0.25 mM ATP, 0.5 mM DTT, 1 mM EGTA, 0.1 mM $CaCl_2$, 10 mM Imidazole, pH 7.5) prepared in AB buffer (25 mM Imidazole, 25 mM KCl, 1 mM DTT, 1 mM EGTA, 4 mM $MgCl_2$). 25 µg of actin was dissolved in 50 µl of polymerization buffer and incubated for a period of around 4 hrs at room temperature (RT). 500 µl stock solution of Rh-Ph (10 µg/µl) was prepared in methanol. 10 µl of Rh-Ph (10 µg/µl) was transferred in a vial and dried with dry nitrogen stream till the pellet was formed. The pellet was dissolved in 2 µl of ethanol, 290 µl AB buffer and 10 µl of F-actin, stepwise. This was incubated for a time period of 12-16 hrs at 4°C.

B. Biotinylation of actin filaments

0.1mg/ml of gelsolin was dissolved in M buffer (40 mM HEPES, 75mM KCl, 2 mM EGTA, 2 mM $MgCl_2$ pH 7.4). NHS-Biotin (4 µg/ml at a concentration of 0.1 mM) was prepared in Di Methyl Sulfoixide (DMSO). NHS-biotin was mixed with gelsolin at a ratio of 10:1. Mixture was incubated for 2 hours. Biotinylated gelsolin was separated from unbound gelsolin by dialyzing (membrane size: 10,000 MW cutoff) the mixture against M-buffer for 24 hrs at 4°C. 50 µl biotinylated gelsolin was mixed with 50 µl of F-actin (25 µg/ 50 µl), gently mixed and kept for 2 minutes. Biotinylated gelsolin will bind to the minus end of F-actin which will inturn leads to Biotinylation of F- actin.

C. Attachment of 5-ASA with actin filaments by biotin-streptavidin cross linking

10 mg stock solution of 5-ASA was prepared in 1 ml Dimethylformamide (DMF). Stock solution of biotin was prepared by keeping the concentration at 4µg / ml in distill water. For biotinylation of 5-ASA, 20 µl of the biotin (4µg / ml) was taken in 920 µl of distill water. 20 µl of 5-ASA was added to the above suspension and was incubated for 30 minutes. This leads to biotinylation of 5-ASA. To this suspension 20 µl of biotinylated actin was added followed by 20 µl of streptavidin solution (1 mg / ml). Suspension was incubated for 30 minutes.

D. Characterization and quantitation of 5-ASA attached to actin filaments

Quantitative analysis of 5-ASA was done by UV-vis Spectrophotometer (Hitachi U-2800) operating between the ranges of 200 nm to 650 nm. Baseline correction was carried out by water. The morphologies of attached drug to actin filaments were characterized by using Transmission Electron Microscope (Hitachi H- 7500) operating at 80 kV. The samples were prepared by placing a drop of suspension on carbon coated TEM grids (300 mesh, 3 mm, purchased from TAAB Laboratories, England) and viewed under transmission electron microscope. Image analysis of attachment of actin filaments to drug was done by Matlab software. Irfanview software was used to extracts the image frames

E. In Vitro Motility Assay

The micro reaction cell was prepared on 0.1% nitrocellulose coated thin glass slide (25 x 75 x 0.14 mm) Bagga et al., (2005). 100 µl of myosin (40 µg/ml in AB buffer containing 0.6 M KCl) was infused and incubated for 60 sec. 100 µl of AB/BSA solution (0.5 mg/ml of BSA in AB buffer) was infused followed by 100 µl of 5-ASA suspension with actin after incubation for 60 sec. 100 µl of AB/BSA, AB/BSA/GOC (0.3 mg/ml of glucose, 0.1 mg/ml of glucose oxidase and 0.018 mg/ml of catalase in AB/BSA solution), and AB/BSA/GOC/ATP (2 mM of ATP in AB/BSA/GOC solution) was infused subsequently and movement of actin filaments attached wih drugs was recorded on Axiovert 200, USA, Bagga et al.,(2005). Fluorescence images with resolution of 320 x 240 pixels were recorded by 'Camatasia Recorder' at 15 frames per seconds. Irfanview software was used to extracts the image frames from the recorded motility of actin filament in avi format. Images were processed for calculating velocity of individual drug attached with actin filaments by custom built programme in Matlab software.

III. Results

A. Attachment of 5-ASA with actin filaments by biotin-streptavidin cross linkin

G-actin was polymerized to F-actin in polymerization buffer. Length of F-actin filaments as measured were found to be in the range of 1.5 – 5 µm. Attachment of drug for Crohn's disease to actin filaments was achieved by streptavidin-biotin conjugate. As streptavidin biotin linkage is the strongest non covalent linkage hence attachment of drug to actin filaments will be more stable therefore, actin filament can carry 5-ASA on myosin tracks. Attachment of 5-ASA was confirmed by fluorescence microscope and transmission electron microscope (TEM). Figure 1 shows the attachment of 5-ASA to actin filaments.

Figure 1A & 1B represents 5-ASA on actin filaments and actin filaments without drug respectively. Drug molecules are seen as a dots on actin filaments as compare to actin

filaments without drug. Drug crystals were also observed in fluorescence microscope. When drug crystals were viewed with white light on microscope no fluorescence was observed while fluorescent crystal of drug was observed under fluorescent lamp. Flourescence confirming that actin filaments are attached to drug. This is because actin filaments are rhodamine phalloidin labelled which in turn will give fluorescence to drug (Frigure 1C & 1D).

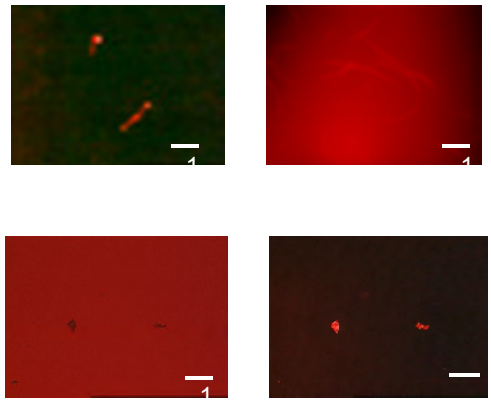


Figure1: Fluorescent images of actin filaments and drug crystals. 1 A & B represents fluorescent image of actin filament with 5-ASA molecule and without drug molecule respectively. 1 C & D shows 5-ASA crystals without fluorescence and with fluorescence which is due to attachment of Rh-PH labeled actin filaments.

Confirmation of drug attachment to actin filament was also done by transmission electron microscope. Similar drug molecules were observed on actin filaments as seen under fluorescent microscope. Actin filaments without drug were observed without any molecules as shown in figure 2A & B.

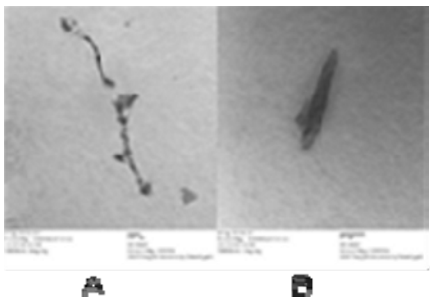


Figure2: TEM images of actin filaments. 3A represents 5-ASA molecules on actin filaments while 3B shows actin filaments without 5-ASA molecules.

Quantitation of attachment of 5-ASA to biotinylated actin filaments was determined UV-VIS spectroscopy. Concentration of biotinylated drug was calculated by using the specific extinction coefficient of 5-ASA at 236 nm as shown below:

Absorbance of 5-ASA at (λmax= 236nm),
$A_{236} = 0.964$
Concentration of drug (c) = 0.1 mM

Molar extinction coefficient of 5-ASA at λmax,
$\varepsilon 236 = A\ 236 / c\ L = 9.64\ (mM\ cm)^{-1}$
Amount of drug attached to biotin (c_1) =

$$\frac{\text{Absorbance of biotinylated drug at 236 nm A'236}}{\varepsilon 236 \text{ X L}}$$

Amount of 5-ASA attached to biotin = 0.07mM

It was calculated that 70 % of 5-ASA drug was biotinylated during incubation. Similarly, we calculated the amount of biotinylated 5-ASA attached to streptavidin and actin filaments was calculated and it was found that >50% of biotinylated 5-ASA attaches to actin filaments through streptavidin cross linking. Absorbance spectra of biotinylated 5-ASA and 5-ASA attached to actin filaments are shown in figure 3 A & B.

B. In Vitro Motility Assay

Sliding velocity measurement is another attempt to confirm non covalent attachment of actin to 5-ASA. Maximum velocity of single bundle of actin filament only on myosin heads was calculated and found to be 4.0-6.0 μm/s (4). The average velocity calculated was found to be 3.59 μm/s. Direction of motile actin

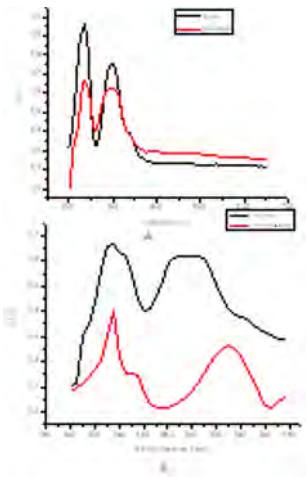


Figure 3: UV-VIS spectra of 5-ASA, biotinylated 5-ASA (A) and biotinylated 5-ASA & actin attached 5-ASA (B). filaments attached to drug was tracked by determining the centroid of actin-drug complex in each frame. After superimposing consecutive frames the path followed by the actin filaments was obtained as shown in figure 4.

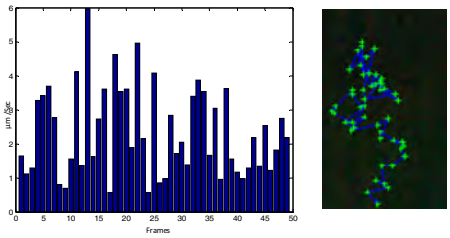


Figure 4: Histogram for velocity of drug attached actin filaments calculated by processing each frame in Matlab (A).The track of motile actin filaments attached to 5-ASA (B).

IV. Discussion & Conclusion

Development of Nano-Robotic devices based on molecular motors (Actin-Myosin) is long anticipated. Attachment of actin to limited cargoes is the pre-requisite to realize such devices. Attachment of actin filaments to drugs by streptavidin-biotin cross linking has not been reported yet. In the present study, we have reported a new methodology to directly attach 5-ASA to actin filaments which is beneficial as load on actin filaments will be reduced. If drug is coating on certain cargoes and then attached t actin filaments then the velocity of actin filament will be reduced as load on filament will be increased. We have calculated the velocity of drug attached actin filaments as 3.59 μm/s which is good enough to carry drug in desired direction. It has been reported that when a polystyrene bead is attached to actin filaments then the velocity reduces to 0.99 μm/s (7). If we will coat drug on these polystyrene beads and then attach them to actin filaments then actin filament will not be able to carry drug. Confirmation of drug attached to actin filament was concluded by fluorescence microscope data where smooth surface of actin filaments get distorted when drug molecules attaches to it as shown in figure 1A & B. Similar structural distortion in actin filaments was also observed in TEM images (figure 2A & B). Quantitation of drug was analyzed by UV-VIS spectroscopy, it was calculated that approximately 50% of the drug in the solution is attached to actin filaments via streptavidin- biotin cross linking. Therefore efficiency of attachment of 5-ASA with this method is not only stable but also efficient.

In the present work, a simple, cheapest and less time consuming method of attachment of drug to single bundle of actin filaments has been reported using biotin and streptavidin as a cross linker. Attached drug can be exploited for transportation for realizing nano-robotic devices in future.

Reference

[1] Mansson A. Sundberg M. Bunk R. Balaz M. Nicholls I A. Omling P. Tegenfeldt J O. Tagerud S. Montelius L. 2005. Actin-based molecular motors for cargo transportation in nanotechnology—potentials and challenges. IEEE Transactions on Advance Packaging. 28: 547-554.

[2] Schliwa M. Woehlke G. (2003). Molecular motors. Nature 422: 759-765.

[3] Månsson A. Sundberg M. Bunk R. Balaz M. Rosengren J P. Lindahl J. NichollsI. Omling P. Tågerud S. Montelius L. (2004). Nanotechnology and actomyosin motility in vitro on different surface chemistries. Biophyisical Journal 86: 58a.

[4] Katsuhisa T. and Ken S. (1991) A physical model of ATP-induced actin-myosin movement in vitro. Biophys. J. 59: 343-356.

[5] Calum S Neish. Robert M Henderson. J Michael Edwardson. Visualisation Of The Streptavidin-Biotin Interaction Using AFM. Biophys. J. (Annual Meeting Abstracts) 82 (1): 337.

[6] Bagga E. Kumari S. Kumar R. Bajpai R. P. Bharadwaj L. M. (2005). Covalent immobilization of myosin for in-vitro motility of actin. Pramana 65: 967-972.

[7] Kaur H. Das T. Kumar R. Ajore R. Bharadwaj L. M. (2008) Covalent Attachment of Actin Filaments to Tween 80 Coated Polystyrene Beads for Cargo Transportation. Biosystems.92:69-75.

Tumour Knee Replacement Planning in a 3D Graphics System

K. Subburaj[1], B. Ravi[1] and M.G. Agarwal[2]

[1]OrthoCAD Network Research Centre, Indian Institute of Technology Bombay, Mumbai, India
[2]Department of Surgical Oncology, Tata Memorial Hospital, Mumbai, India

Abstract — **Limb salvage surgery has replaced amputation as the treatment of choice for sarcomas of the extremities. However, complications such as prosthesis loosening and fracture of bone or prosthesis continue to occur due to poorly aligned prosthesis or unconsidered bone deformities. These can be minimized by detailed implantation planning: intervention, resection, selection, and alignment decisions considering anatomical variations. Previous works employed interactive identification of anatomical landmarks, and prosthesis position planning by superimposing prosthesis drawing on radiographic image, which is cumbersome and error-prone. We present an automated methodology for mega endoprosthesis implantation planning in a 3D computer graphics environment. First, a virtual anatomical model is reconstructed by stacking and segmenting CT scan images. A neighborhood configuration based 3D visualization algorithm has been developed for fast rendering of the volumetric data, enabling a quick understanding of anatomical structures. Key skeletal landmarks used for implantation are automatically localized using curvature analysis of the 3D model and knowledge based rules. Anatomical details (mainly dimensions and reference axes) are extracted based on the landmarks and used in resection planning. A decision support method has been developed for segregating prosthesis components into three sets: 'most suitable', 'probably suitable', and 'not suitable' for a particular patient. The geometrical landmarks of the prosthesis components are mapped with respect to the anatomical landmarks of the patient's model to derive alignment relationships. 3D curved medial axes of both (prosthesis and anatomical models) are used for reference and alignment. A set of selection and positional accuracy measures have been developed to evaluate the anatomical conformity of the prosthesis. The computer-aided methodology is illustrated for tumour knee endoprosthetic replacement. It is shown to reduce the time required for implantation planning and improve the quality of outcome. The 3D environment is also more intuitive and easy-to-use than the traditional approach relying on 2D images.**

Keywords — **tumour knee replacement, virtual 3D reconstruction, prosthesis selection, prosthesis alignment, anatomical understanding**

I. Introduction

Virtual surgery planning is an interdisciplinary contribution of medical and computational knowledge to health sector. The goals of preoperative planning tools are threefold. (i) enable a surgeon to understand the patient's anatomy and the surgical challenges it poses, (ii) help in the development of customized prostheses, alignment of prosthesis components, and evaluation of post-surgical outcomes and (iii) present the data in a way that enables fast and accurate decisions.

Limb salvage surgery (prosthetic replacement after excision of tumour affected bone region) has replaced amputation (excision of lower part of the limb) as the treatment of choice for sarcomas of the extremities (e.g. knee) [1]. However, complications such as prosthesis loosening and fracture of bone or prosthesis continue to occur [2,3]. This can be reduced by detailed implantation planning (intervention, resection, selection, and alignment), which should be carried out bearing in mind that the anatomy of each person is unique [4,5]. A typical prosthesis set, used in massive replacement of distal femur portion of the knee due to primary bone tumour, composes of femoral condyle (FC), space fillers (SF), femoral fork (FK), tibial tray (TT), tibial poly (TP), femoral and tibial stem (FS and TS), and articulation and locking elements (Fig. 1).

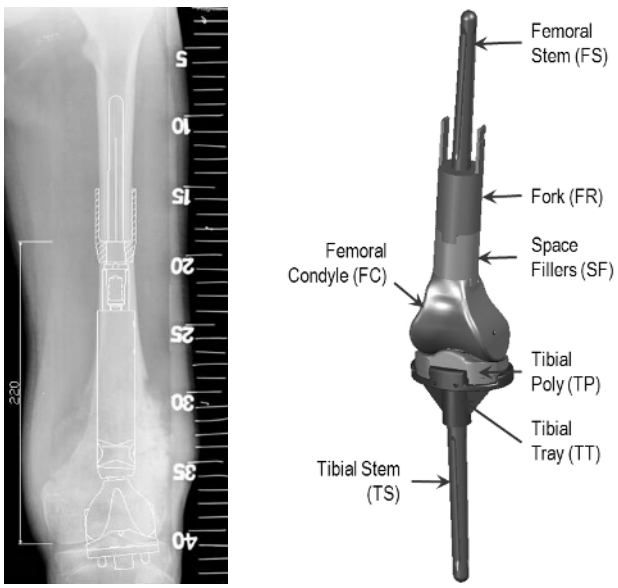


Fig. 1 Endoprosthesis used for reconstructing distal femur/knee after excision of tumour (a) prosthesis design verification using radiographic image (b) typical components of the prosthesis

Chwee Teck Lim, James C.H. Goh (Eds.): ICBME 2008, Proceedings 23, pp. 906–910, 2009
www.springerlink.com

Previous work employed interactive identification of anatomical landmarks and prosthesis positioning by superimposing 2D prosthesis drawing on radiographic image (Fig. 1a). This approach is cumbersome and error-prone, especially for complex anatomical situations, such as total reconstruction of the knee joint [5,6,7]. This can be eliminated by using patient specific 3D computerized anatomical models [4,8]. Even though significant research has been carried out on arthritis knee surgery, 3D solutions for planning are rare especially in tumour knee replacement (TKR). In our knowledge, there is no reported literature on virtual surgery planning of TKR, despite an increasing demand from fields such as computer- and robotic-assisted surgery. In this work, we focus on using 3D computer graphics and geometric reasoning algorithms to aid surgeons in planning tumour knee replacement.

II. Materials and Methods

A. Reconstruction of 3D Anatomical Models

The reconstruction steps of 3D anatomical models start with the imported axial CT images in DICOM (Digital Imaging and Communications in Medicine) format [8]. These images are first processed with filters to reduce the noise while preserving the edge information in the form of intensity gradient. Global thresholding of bony tissue, based on a range of HU values, is carried out in line with local adaptive thresholding, which segments by analyzing 26 neighbors (N_{26}). Next, 3D region growing algorithm is initiated to group the bone data from the thresholded regions. Due to the similarities (overlap) in bone and surrounding tissues, classification only based on thresholding is not feasible. 3D morphological operators (both manual and automatic) are used to close the discontinuities in outer (periosteal) and inner (endosteal) contours. These segmented data are rendered in two modes: direct or volume rendering using transfer functions and surface rendering by fitting triangles using surface tiling.

B. Identification of Anatomical Landmarks

Anatomical landmarks are distinct regions or points on bones with uniqueness in shape characteristics in their vicinity. Manual location of landmarks and related measurements consume time, require a high level of expertise, and may lack in accuracy. Geometrically invariant measures such as curvatures, concavity, and convexity are useful in identifying landmarks on a 3D anatomical model.

We have developed a methodology for automatic localization and identification of anatomical landmarks on a 3D bone model [9]. The model surface is segmented into different regions based on Gaussian and mean curvature gradients, which are then classified as peak, ridge, pit and ravine. These anatomical landmarks are constrained in a spatial relationship that is the same for all the knee models. In order to encode these constraints in a network diagram, we characterize the edges pairs by the positional adjacency of a landmark relative to its neighboring landmarks. Skeletal landmarks are automatically identified by an iterative process using a spatial adjacency relationship matrix formed by these relations between the features. Figure 5 shows the anatomical landmarks on distal femur and proximal tibia which are most distal point of medial and lateral condyles (MC_F and LC_F), medial and lateral epicondyles (ME_F and LE_F), medial and lateral peak of anterior patella tracking edges (MP_F and LP_F), medial and lateral peak on tibial condylar plateau (MP_T and LP_T), tibial tuberosity (TT_T), medial and lateral intercondylar tubercles (MI_T and LI_T), and apex process of fibula (HF).

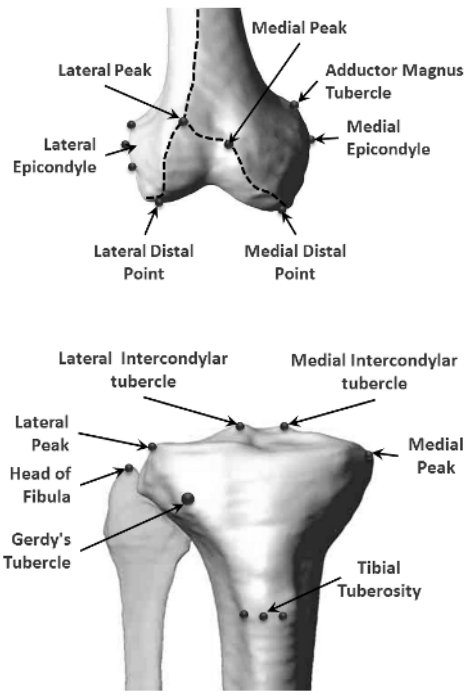


Fig. 2 Anatomical landmarks (a) on distal femur (b) on proximal tibia

C. Assessing Anatomical Parameters

Primary anatomical parameters are extracted using the associated landmarks. These include medio-lateral length

(ML), anterio-posterior length (AP), and inner and outer diameters (d and D) of femur (ML_F, AP_F, d_F, and D_F) and tibia (ML_T, AP_T, D_T, and d_T) bone respectively. Others include femur valgus (V) angle, femur bone curvature (RC_F), and resection length (RL) decided by the surgeon according to spread of disease.

D. Prosthesis Components Selection

Prosthesis components selection is driven by the extracted anatomical details and a decision based methodology. The standard modular prosthesis components are classified into three major categories: *small* (S), *medium* (M), and *Large* (L) according to their sizes (ranges are decided by one of our internal studies on knee morphometry). These components are indexed in terms of their geometric characteristics and design driven parameters to create a database. Critical components (tibial tray, femoral condyle, and tibial poly) are selected independently based on anatomical parameters. Other components (FK, SF, FS, and TS) are selected based on both dimensions and influence of previously selected components. As per this strategy, we found the best selection flow is TT-FC-TP-FK-SF-TS-FS. Remaining components are chosen based on sizes of the mating components.

The selection is performed in two steps: First, the components which are undersized and oversized are eliminated, then the dimensions of components are mapped with the corresponding measured anatomical parameters to form *fuzzy-based-decision-tree* based on the pre-defined rules compiled from surgeons' experience. The TT and FC are first selected based on AP_T and ML_F respectively. The TP is selected based on ML_{FC} and AP_{TT}. The remaining components are selected based on the dimensions of these three. FK is chosen based on D_F and influenced by D_{FC}. FE is chosen based on RL and RCL. Based on d_F and d_T, FS and TS are selected. Each branch of the decision tree is assigned a weight to evaluate its suitability. The choice of prosthesis components are classified with a qualitative tag as: *'most suitable'*, *'probably suitable'*, and *'not suitable'*.

E. Prosthesis Positioning

Positioning of prosthesis components with 3D anatomical model is carried out with reference to anatomical landmarks and reference axes. A set of reference axes of both anatomical (A_A) and prosthesis (A_P) model are generated by computing medial axis. Major reference axes include longitudinal axes of the femur (A_F) and tibia (A_T) bone, and axis of FS (A_{FS}) and TS (A_{TS}). Registering components with corresponding bone is carried out in two steps. First, matching reference axes such as A_F with A_{FS} and A_T with A_{TS}. This is repeated for the entire set A_A and A_P. Next, point to point registration (iterative closest point) with anatomical landmarks on bone model and geometric landmarks on prosthesis components. This include surface matching on both prepared tibial and femoral bone surface with FK and TT respectively. Space fillers are chosen from the 'most suitable' prosthesis components set accordingly after aligning FC, FK, and FS in femoral side, TT, TP, and TS in tibial side. The orientation of the bone is not changed during positioning.

F. Anatomical Suitability Evaluation

Modular prosthetic components may require a little compromise in confirming anatomical shape and size which affects the functional outcome of the joint. A set of anatomical suitability metrics were evolved to evaluate the selected prosthesis components considering their suitability with respect to patient's anatomy (Fig. 3). These measures are: *geometric error* (E_G) (dimensional difference between the resected bone and selected prosthesis components), *curvature error* (E_C) (difference between the measured bone curvature and the obtained curvature after implanting prosthesis with curved stem, with and without osteotomy), *re-*

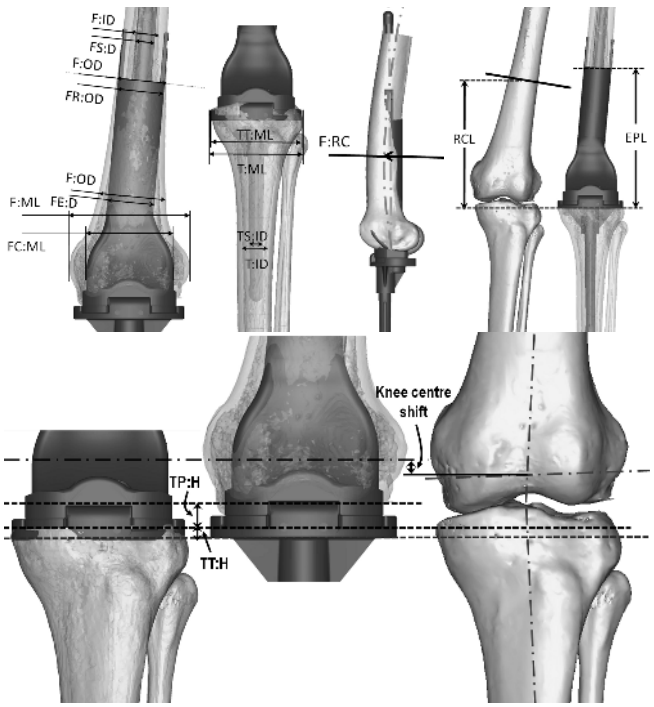


Fig. 3 Anatomical suitability metrics based on (a) geometry (b) bone curvature (c) reconstruction length (a) knee shift

construction length error (E_{RL}) (difference between actual RCL and effective length of the prosthesis (EPL), given by the distance between tibial component's bottom and femoral component's top surface) and *knee centre shift error* (E_{CS}) (difference between the natural knee's articulation centre and the artificial implant's articulation centre after implantation). These metrics are important in deciding whether standard modular prosthesis can be used or customized version is required for the patient.

III. Results

In this study, distal femur knee replacement for a patient (35/M) has been taken as an example to illustrate the methodology. 3D model of the knee joint is reconstructed from 468 CT axial slices in DICOM format (Fig. 4).

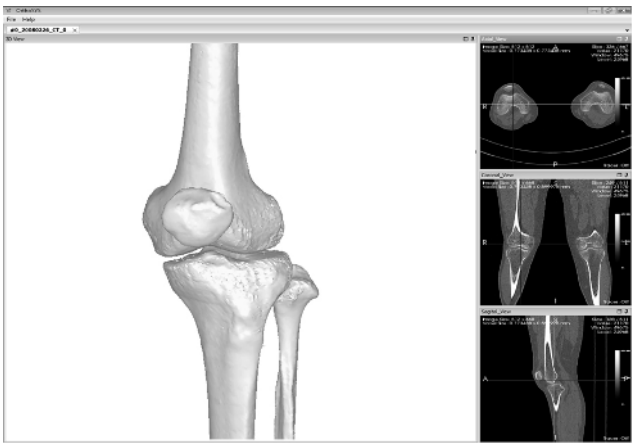


Fig. 4 Reconstructed 3D anatomical model of the knee

Anatomical landmarks and parameters extracted and prosthesis is selected based on these data. In femur (ML:64mm, AP:60mm, D:28-25mm, d:16-13mm, VA: 4.6^0, RL:120mm), tibia (ML:70mm, AP:58mm, d:14mm). The 'most suitable' set is large TT, FC, and TP. Generated reference axes along with landmarks are used in positioning of prosthesis and aligning knee into pre-operative posture (Fig.5). The final suitability metrics are E_G:6mm, E_C:4mm, E_{RL}:3mm, and E_{CS}:4.5mm. The measured metrics are within the limits, which does not affect the gait of the limb.

IV. Conclusions

The implantation planning of knee prosthesis after excision of primary tumour is discussed. The aligned endo-

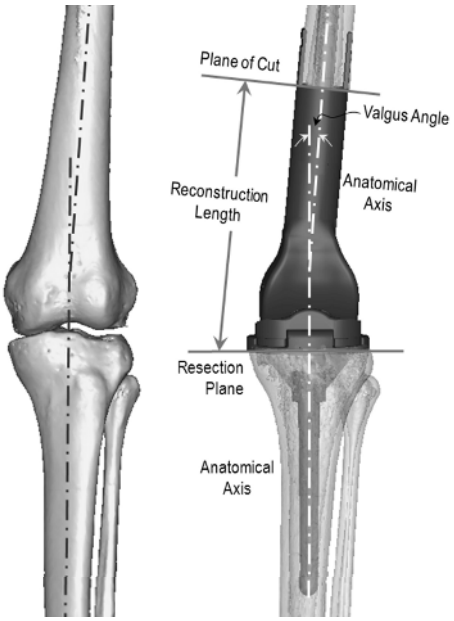


Fig. 5 Aligned distal femur prosthesis in 3D anatomical model

prosthesis is rendered with 3D bone model for visual verification. The suitability metrics indicate a numerical measure to the surgeons to give more attention to error-prone steps during surgical procedure. Integrating 3D geometric reasoning algorithms for anatomical understanding with decision methods makes the system intelligent and independent.

Acknowledgment

This work is a part of the project supported by the Office of the Principal Scientific Adviser to the Government of India, New Delhi.

References

1. Agarwal M (2007) Low cost limb reconstruction for musculoskeletal tumors. Cur Opin Orthop 18:561-571
2. Sim IW, Tse LF, Ek ET et al (2007) Salvaging the limb salvage: Management of complications. Eur J Surg Oncol 33:796-802
3. Malawer MM, Sugarbaker PH (2001) Musculoskeletal cancer surgery: treatment of sarcomas and allied diseases. Kluwer, Netherlands
4. Sutherland CJ, Bresina (1994) Use of general purpose mechanical CAD in surgery planning. Comput Med Img Graph 18:435-442
5. Kendall SJH, Singer GC, Briggs TWR et al (2000) A functional analysis of massive knee replacement after extra-articular resections of primary bone tumors. J Arthroplasty 15:754-760
6. Viceconti M, Testi D et al (2003) An automated method to position prosthetic components within multiple anatomical spaces," Comput Methods Programs Biomed 70:127-127
7. Hewitt B, Shakespeare D (2001) A straightforward method of assessing the accuracy of implantation of knee prostheses. Knee 8:139-44

8. Subburaj K, Ravi B (2007) High resolution medical models and geometric reasoning starting from CT/MR images. Proc. IEEE Int Conf CAD Comput Graph, Beijing, China, 2007, 141-144
9. Subburaj K, Ravi B, Agarwal MG (2008) 3D shape reasoning for identifying anatomical landmarks. Comput Aided Des Appl 5:153-60

Corresponding author:

Author: Dr. Bhallamudi Ravi
Institute: Indian Institute of Technology Bombay
Street: Powai
City: Mumbai
Country: India
Email: b.ravi@iitb.ac.in

Color Medical Image Vector Quantization Coding Using K-Means: Retinal Image

Agung W. Setiawan[1], Andriyan B. Suksmono[2] and Tati R. Mengko[1]

[1]Biomedical Engineering, School of Electrical Engineering & Informatics ITB, Bandung, Indonesia
[2]Telecommunication Engineering, School of Electrical Engineering & Informatics ITB, Bandung, Indonesia

Abstract — **Retinal images play an important role in supporting medical diagnosis. Digital retinal image usually are represented in such a large data volume that takes a considerable amount of time to be accessed and displayed. Digital medical image compression therefore become crucial in medical image transfer and storage in electronic database server. This research is concerned with the development of a color medical image coding scheme using vector quantization. K-means is clustering technique that is applied to create codebook in vector quantization (VQ) coding. This research investigates the performance of each of these clustering technique in four color models: RGB, 4:4:4 YUV, 4:2:0 YUV and HSV. The VQ coding scheme is conducted separately to image components in each channel of the color models. Reconstructed color image is obtained by combining the VQ decoding result of each image components. The VQ coding performance relies on the quality of the utilized codebook. The VQ codebook used in this research was developed from retinal image. The retinal image was processed as a set of four quarter-images. This special treatment is required to cope with the large computational load of the VQ codebook generation, while ensuring the incorporation of the color and texture diversity of the training set in the resulted codebook. The RGB 444 color mode (coding of the red, green, and blue channels by the size of 4×4) produces the best subjective and objective quality of image coding. However, the optimum color models for tele-ophthalmology and electronic medical records are the YUV 4:2:0 and RGB 848 for retinal image.**

Keywords — **Color Medical Image, Retinal Image, Vector Quantization, K-Means.**

I. Introduction

Image is one of the medical data needed in diagnosis. Types of medical image are gray image – for example is Xray image and color image – such as retinal image. These medical images are saved into a medical record database sever. Image compression/coding will be needed to reduce the storage capacity in the server. Without image compression, the size of the images saved in a server will be large. For example, the normal size for a 1600 × 1216 pixels retinal image is 5,701 MB. Therefore, clients will need a lot of time to access such a large file in tele-diagnosis. Meanwhile, the access time also depends on the network bandwidth used. As we know, most of Indonesia rural areas use Public Switched Telephone Networks which have narrow bandwidth capacities.

Tele-diagnosis with asymmetric coding has an advantage, such as the decoding computation in client side is simpler that in the sever side. Thus, vector quantization coding is used in this research because of its lossy-to-lossless capability in sending images in Region of Interest (RoI).

The research aims are to develop a color medical image coding based on vector quantization, to search for an optimal size of codeword in retinal images and to decide a suitable model of color image for quantization vector coding.

One of the most important steps in vector quantization coding is to make a coding book. In this research, coding book is made by K-means algorithm. K-means is an unsupervised learning algorithm which is widely used for data classification. The procedure of its data classification is simple and easy for clustering.

Vector quantization method is commonly used for digital data compression, such as digital image and sound compression. For image compression, vector quantization is computed in adjacent correspondence image pixels. It is likely that the adjacent pixels of pixel P will have the same value as pixel P.

II. Vector quantization

One of the most important steps in vector quantization coding is to make a coding book. In this research, coding

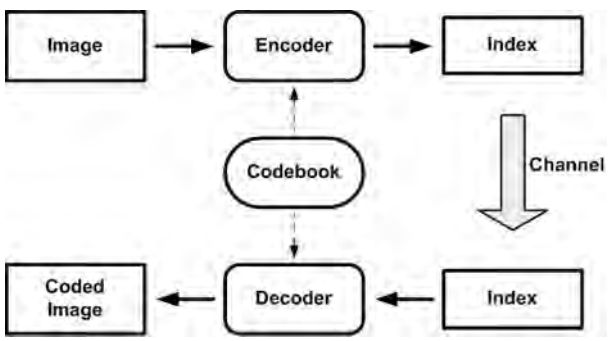


Fig. 1 Vector quantization coding scheme.

Chwee Teck Lim, James C.H. Goh (Eds.): ICBME 2008, Proceedings 23, pp. 911–914, 2009
www.springerlink.com

book is made by K-means algorithm. K-means is an unsupervised learning algorithm which is widely used for data classification. The procedure of its data classification is simple and easy for clustering.

Vector quantization method is commonly used for digital data compression, such as digital image and sound compression. For image compression, vector quantization is computed in adjacent correspondence image pixels. It is likely that the adjacent pixels of pixel P will have the same value as pixel P.

A vector quantizer consists of two parts, encoder and decoder. The function of encoder is to get the input vector and to result the codeword which gives minimum distortion. The most minimum distortion is determined by Euclidian distance between input vector and every codeword in the codebook. Then, this codeword index is saved in a digital data storage or sent through the communication channel. The function of decoder is to change the codeword index received into the codeword form the codebook.

In vector quantization, image coding is done by dividing an image into small blocks of pixels, until it is fit with the codeword dimension, like 2×2, 4×4, etc. The input image in encoder side is divided into small blocks of pixels. The chosen codeword should have the least distance between input vectors. After the codeword has been found, the encoder will result the numbers of codeword index. Then, these process will be repeated until all of the small pixels blocks have their own index numbers.

The encoder reconstructs the image based on the index numbers obtained. A look–up table is needed to produce reconstruction vectors from index numbers. The image encoding – by vector quantization method – is lossy, since it is unsimiliar between the input image and the reconstructed image. These differences are occured because the small blocks of pixels is changed into the codeword which has the least distance with that small pixel block.

III. System Design

The codebook is made by using four retinal images 1600 × 1216 pixels which are cropped until its quarter size. Then, each of these cropped images is combined to be an image in its original size, 1600 × 1216 pixels. This step is effective to decrease the computation load in codebook compilation. Four images chosen are varied in patterns because it is important to obtain a codebook with various values, so that it can be used for various types of retinal images. The tested images can be shown in Figure 2.

There are five color models to be coded, RGB, YUV RGB, YUV 4:4:4, YUV 4:2:0 and HSV. All of those color models have three channels. Codebook is made in each

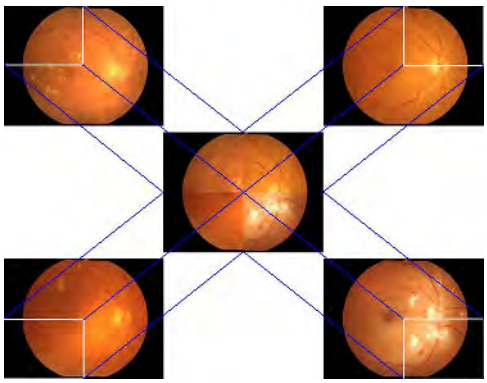


Fig. 2 Retinal image training.

image channels before it is classified by K-means algorithm, which need channels to be extracted. The block diagram is shown in Figure 3.

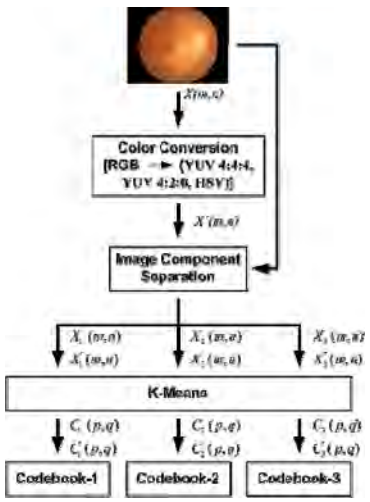


Fig. 3 Codebook generation block diagram.

Coding scheme for RGB, YUV 4:4:4, and YUV 4:2:0 is shown in Figure 6 below. Channel 1 is R & Y channel, channel 2 is G & U channel, and channel 3 is B & V channel. Two types used in this coding are :

1. Input image (RGB) splits directly into channel R, channel G and channel B.
2. Input image (RGB) is changed into color model YUV 4:4:4 and YUV 4:2:0. The converted image then splits into channel Y, channel U and channel V images.

Each of the images channels is coded by using the codebook, and results the index for every channel. To get a coded image, encoding is done by using the same codebook.

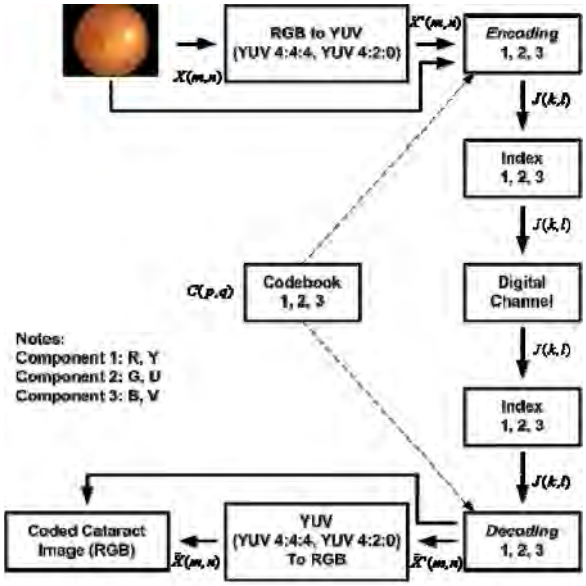


Fig. 4 RGB & YUV image coding scheme.

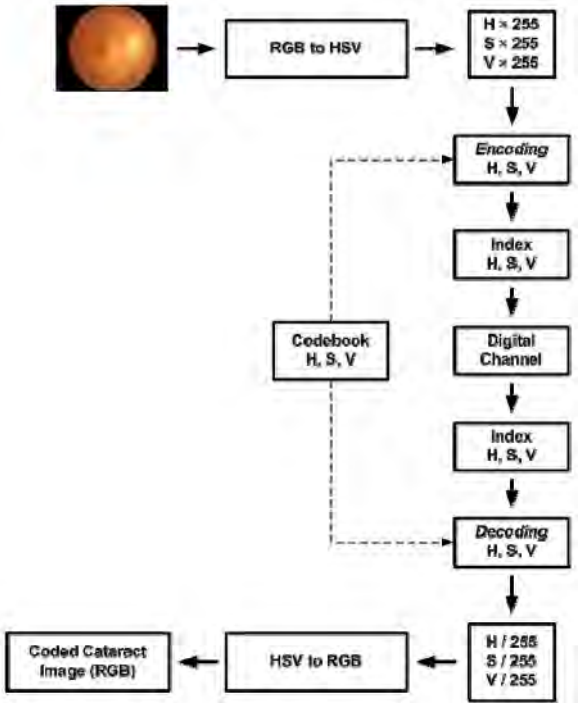


Fig. 5 HSV image coding scheme.

For HSV model, a converted image from RGB has an interval [0,1], so that it must be multiplied by 255 to get an image with interval [0,255]. Therefore, the codebook compilation, encoding process and decoding process will be easier to be done. Otherwise, the computation load will be abundant if the interval is not in [0,255], *out of memory* and the codebook cannot be obtained. Figure 5 shows the coding scheme of HSV model. Before the decoded image is converted into RGB, it is divided by 255 to restore its original interval [0,1].

IV. Experimental Results

We use 10 RGB retinal images of 1600 × 1216 pixels. We tested the system to assess the effectivity of the developed algorithms. Parameter used here is PSNR (Peak Signal-to-Noise Ratio), from RGB coded images with various size of codeword in each color models. PSNR formula for a color image with three channels:

$$\text{PSNR}=10\log_{10}\left(\frac{255^2}{\frac{MSE(1)+MSE(2)+MSE(3)}{3}}\right) \quad (1)$$

Time to produce a codebook of retinal images with 4x4 codeword dimensions is also used as a parameter in this research. This codebook is arranged by classification methods, like K-means. The average PSNR value for retinal images with K-means is in the interval 36,75 – 42,26 dB and can be seen in Figure 6.

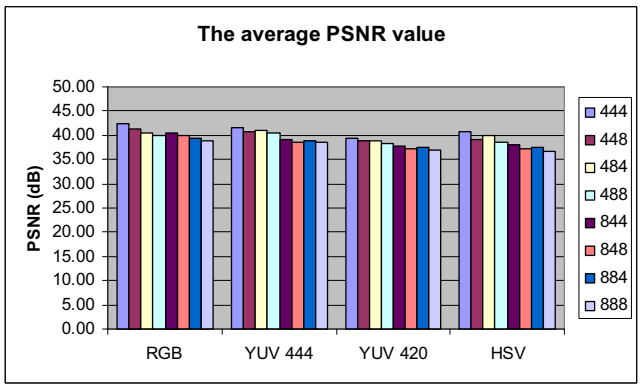


Fig. 6 The average PSNR value.

Tabel 1 gives the size of codebook file and retinal images index with codeword dimension 4×4 and 8×8. It can be shown that all of the channels of RGB, YUV 4:4:4 and HSV have the same size in codebook file and index. The size of codebook file in YUV 4:2:0 is the same as the other channels, but its index file size is different from the other color models. In retinal images, the size of index file in

channel Y is the same as the other color models', but the size of index file in channel U and V for 4×4 dimension codeword is 31 KB and for 8×8 dimension codeword is 9 KB. In

An objective (PSNR values) and subjetive assessment shows that the image quality is not very different/almost similiar with the image quality in other models. The size of index file in channel U and V is small, so that it will be easier to transfer the retinal images in tele-ophthalmology system. Moreover, this advantage will reduce the capacity required for saving the file in electronic medical records server.

Based on the experimental results, an RGB retinal image with combination 848 (red channel is coded in 8×8, green channel is coded in 4×4, and blue channel is coded in 8×8), objectively and subjectively – has a good quality and the coded image can be read. This combination will reduce the size of the codebook and index which will be sent or saved.

Table 1 Size of codebook file and retinal images index

Color Model		Codeword 4 × 4 (KB)		Codeword 8 × 8 (KB)	
		Codebook	Index	Codebook	Index
RGB	R	5	120	17	31
	G	5	120	17	31
	B	5	120	17	31
YUV 4:4:4	Y	5	120	17	31
	U	5	120	17	31
	V	5	120	17	31
YUV 4:2:0	Y	5	120	17	31
	U	5	**31**	17	**9**
	V	5	**31**	17	**9**
HSV	H	5	120	17	31
	S	5	120	17	31
	V	5	120	17	31

V. Conclusions

According to the research results, it can be concluded that :

1. Color model RGB with 444 combination (red, green and blue channel are coded in 4×4) subjectively and objectively (PSNR value) – yields the best quality in retinal and cataract coded images. In tele-ophthalmology application and electronic medical records, YUV 4:2:0 is the most optimal color model for retinal and cataract images since it can reduce the size of the codebook and index which will be sent or saved.
2. A retinal image with RGB 8×8-combination (red channel is coded in 8×8, green channel is 4×4 and blue channel is coded 8×8) subjectively and objectively – has a relatively good quality and its coded image can be read. This combination can reduce the size of the codebook and index which will be sent or saved.

References

1. A.B. Suksmono, U. Sastrokusumo & K. Kondo, "Adaptive image coding based ono vector quantization using SOFM-NN algorithm", Proc. of IEEE-APCCAS '98
2. A.B. Suksmono and U. Sastrokusumo, "A Client-Server Architecture of a Lossy-to-Lossless VQ-Based Medical Image Coding System for Mobile Telediagnosis: A preliminary design and result", Proc. of APT Workshop-MCMT 2002, jakarta. Indonesia.
3. Setiawan, A.W. Design and Implementation of Java™ Distributed Vector Quantization and Huffman Image Coding for X-Ray Medical Image Transfer. Final Project, Department of Electrical Engineering ITB, 2005.
4. A.D. Setiawan, A.B. Suksmono, and B. Dabarsyah, Scalable Radiology Image Transfer and Compression Using Fuzzy Vector Quantization, J. Of eHealth Tech. & Applications, 2007.
5. A.B. Suksmono, T.L.R. Mengko, U. Sastrokusumo, A.D. Setiawan, A.W. Setiawan, R.N. Rohmah, N.S. Surbakti, P. Rahmiati, D. Danudirdjo, A. Handayani, J.T Pramudito, Development of Asymmetric- and Distributed-Image Coding for Telemedicine Applications, Journal. of E-Health Tech. & Applications, 2007.
6. A.B Suksmono, T.L.R Mengko, R. N Rohmah, D Secapawati, J.T Promudito, U Sastrokusumo, Lossy-to-lossless Client Server Medical Image Coding System: Web-based Implementation by Using Java RMI, 2nd APT Telemedicine 2004, New Delhi, India.
7. Hazem Al-Otum. Walid Shahab. Dan Mamoon Smadi. Color Image Compression Using a Modified Agnular Vector Quantization Algorithm. Journal of Electrical Engineering, Vol. 57, No. 4, 2006.
8. Maher.A. Sid-Ahmed. Image Processing: Theory, Algorithms, & Architectures. McGraw-Hill. Singapore: 1995.

Development of the ECG Detector by Easy Contact for Helping Efficient Rescue Operation

Takahiro Asaoka and Kazushige Magatani

Department of Electrical and Electronic Engineering, Tokai University, Japan

Abstract — **When a large-scale disaster occurred, it is expected that much damage occurs. In recent years, various rescue robots are developed as second anti-disaster measures mainly. The realization of a quick rescue operation is expected by these rescue robots. To save life of more victims, it is important that rescuers divide a victim by triage. Effective rescue operations can be realized by it. However, well trained person for the triage can do correct judgment, but it is difficult for other people. Therefore, if rescuers gather bio-signals of the victim when they find or save the victim, they can get a clear criterion. From this, it is thought that many rescuers can evaluate the condition of the victim correctly using bio-signals of the victim. So, we developed the device to detect an electrocardiogram by easy contact in this study. The electrocardiogram is one of the important vital signs in the bio-signal of the human. If we can detect an electrocardiogram, we can diagnose the change of the condition of the person. At the time of the disaster, the diagnosis of the irregular pulse is effective in particular. It is possible to diagnose the irregular pulse by only one detected electrocardiogram. However, the measurement of electrocardiogram at the time of the disaster is difficult, because 12 lead electrocardiogram which is the most general method needs ten electrodes. Therefore we avoid the method to need many electrodes in this way, we aimed for the detection of the electrocardiogram with as few electrodes as possible to be able to measure it at the stricken area. In addition, for the realization of a more effective measurement, I aim at the development of the induction method that is able to detect a electrocardiogram by electrodes which do not touch skin directly.**

Keywords — **ECG (Electrocardiogram), Capacitive coupling, Easy contact**

I. Introduction

As the scale of the disaster becomes big, this widespread damage becomes terrible. And, rescue persons increase together with victims. As this result, there is also possibility that rescue persons receive a serious injury or lose thier life by a second disaster. In order to avoid these situations, robots that engage in rescue operations are being researched and developed. By the introduction of various rescue robots, a quick rescue operation is enabled safely by the people of small number. In addition, the rescue person performs triage after the rescue of the victim. The triage is to choose a priority of the treatment by the state of the victim, but it is necessary training to be able to judge accurately. It is difficult to judge appropriate for other people for that reason. Therefore we developed the device which could detect a bio-signal by easy contact. We think that the detection result of this device helps triage. In addition, if rescue robots have this function, the rescue person can also decide a priority of the help of the victim by this function in the rescue operation. Especially, it is useful in the case of the help of the victim who became burying alive. The survival rate of the victim decreases remarkably after passing 72 hours from buried alive. So, it is desirable to grasp the condition of the victim easily by using this function. Therefore, our goal is the development of a system which can be installed on a rescue robot, measure the victim's vital signs and send these data to medical doctors. In this paper, we describe developed measuring methods for ECG (Electrocardiogram) by using capacitive coupling. In our method, only touching victim's skin with electrodes, a correct victim's ECG is obtained.

II. Methodology

ECG is a bio-signal which is a voltage gap to be lead in two different positions of the heart, and indicates electrical activity of the heart. ECG serves for diagnosis and cure for heart diseases. The heart rate and the existence of the arrhythmia which is helpful on a disaster are obtained by ECG. They are able to be diagnosed from the time relation of each wave of ECG. Therefore, it is possible to estimate them from only one of induction methods of ECG.

There are two leading methods for ECG if we classify them widely. One is the limb leading by bipolar, the other is the precordial leading by unipolar. These leading methods have each merit. However, at the disaster area, we have to select leading method in accordance with the situation. Therefore, we developed the system which can choose either leading method by the situation.

In general, many electrodes are necessary for measuring typical ECG. And to avoid artifacts, the resistance between electrodes and human body surface is fixed on the low resistance value. In other to keep this condition, conductive paste is used between electrodes and body surface. However, it is difficult to measure ECG using these methods at the disaster area. Therefore, new ECG measuring method

Chwee Teck Lim, James C.H. Goh (Eds.): ICBME 2008, Proceedings 23, pp. 915–918, 2009
www.springerlink.com

which needs only two or three electrodes without conductive paste was developed. Using this method we can detect arrhythmia from measured ECG easily.

In our method, ECG is led by capacitive coupling between body and electrode. This principle is explained as following. At first action potential occurs by the heartbeat. By this electric potential, an electric field is formed, and this affects the body surface. This electric field and the electrode form a capacitor. This capacitive coupling between a body surface and the electrode derives ECG signal from a body to the electrode. So, we can obtain ECG without direct touching of electrodes to the body surface. For example, even if electrodes are touched to the victim's clothes, ECG of victim will be able to be measured. Fig.1 shows an equivalent circuit of this principle.

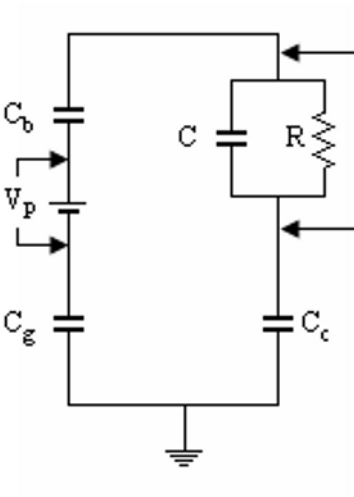


Fig. 1 The equivalent circuit of capacitive coupling.

Where, V_p is the action potential of the heart. V_{out} is the output voltage. C_b is the capacitance between human body and ECG detector. C_g is the capacitance between human body and ground. C_c is the capacitance between ECG detector and ground. C and R are the capacitance and the resistance of the first op-amp respectively. From this figure, a equation of V_{out}/V_p is shown as following.

$$\frac{V_{out}}{V_p} = \frac{1}{\frac{1}{j\omega C_b R} + \frac{C}{C_b} + \frac{1}{j\omega C_g R} + \frac{C}{C_g} + \frac{1}{j\omega C_c R} + \frac{C}{C_c} + 1}$$

III. Detecting device

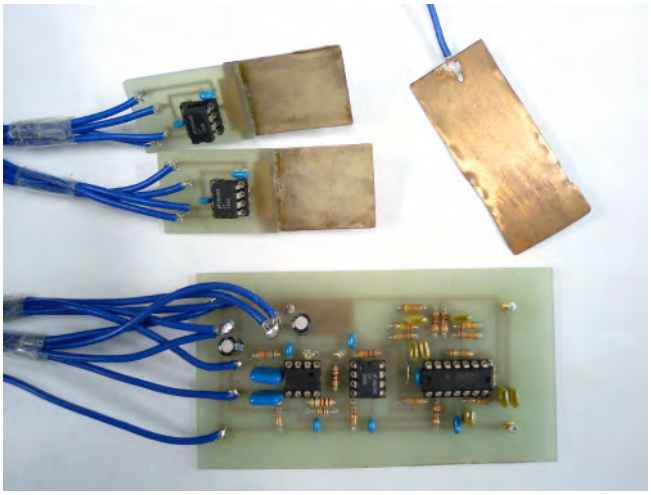


Fig. 2 The ECG electrodes and amplifier.

Fig.2 shows a picture of developed ECG measurement system. As shown in this figure, this system uses three electrodes. One is for the common and others are for leading ECG. In our system, normal detected ECG is measured by using three electrodes. And, capacitive coupled ECG is measured by using only two electrodes. Materials of each electrode are copper sheets. Because of high impedance between a capacitive coupling electrode and body, a voltage follower amplifier is installed on electrode. And low impedance output of a voltage follower is send to the ECG amplifier. The block diagram of our ECG measurement system is shown in Fig.3. As shown in this figure, signals from electrodes are differential amplified by an instrumentation amplifier. Noises in amplified ECG are reduced using filters. B.E.F. removes hum noise.

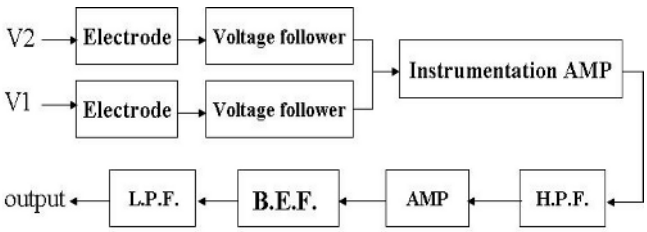


Fig. 3 Block diagram of ECG amplifier.

IV. Experiment and Result

(1) Detection by each lead method



Fig. 4 The ECG wave of the limb lead.



Fig. 5 The ECG wave of the precordial lead with three electrode.



Fig. 6 The ECG wave of the precordial lead with two electrodes.

ECG was experimentally measured about three normal subjects by using each lead method. The detection method of the ECG is mentioned earlier. In all leading methods, ECG was able to detect. As an example, detection results for one subject are showed the following. The result of ECG waveform by limb leading is shown in Fig.4, and Fig.5 shows the ECG for precordial leading. These results were measured by using three electrodes. In these experiments, two electrodes were used for bipolar leading of ECG and one electrode was used for common. A result of ECG for unipolar leading is also shown in Fig.6. This result was acquired by capacitive coupling. As shown in these figure, an amplitude of unipolar leading (Fig.6) is smaller than bipolar leading (Fig.5). In addition, as shown in Fig.5, there are many distortions with ECG waveform. However, measuring ECG using two electrodes is easier than using three electrodes for our objective.

(2) ECG detection through the clothes



Fig. 7 The ECG from the surface of a T-shirt.



Fig. 8 The ECG from the surface of a T-shirt by capacitive coupling.

ECG through the clothes was experimentally measured about one subject by using precordial leading. Fig.7 shows the ECG waveform that is acquired from the surface of a T-shirt by using three electrodes. Fig.8 shows the ECG waveform that is acquired from the surface of a T-shirt by using two electrodes. This result was acquired by capacitive coupling. These results were obtained by higher amplitude than previous experiment result. From these results (especially in Fig.8), a lot of noises are generated in ECG detection through the clothes. So, we think that it is hard to stabilize ECG pattern by using a developed amplifier. So, we are considering about optimal amplitude and filtering of ECG amplifier. And I think that a more accurate filter is necessary to suppress the noises.

V. Conclusion

In this paper, we described about the developed device for measuring vital signs of suffered person under the disaster. ECG measuring system by using capacitive coupling type electrodes was developed. This system can detect ECG by easy contact through textiles. However, the output of this detecting method is unstable, and includes a lot of noises. Therefore, we have concluded that if these problems are improved, our developed system will be useful to rescue sufferers.

References

1. Takahiro ASAOKA, Yoshiaki KANAEDA and Kazushige MAGATANI, “Development of the device to detect human’s bio-signals by easy sensing”, 30th Annual International Conference of the IEEE EMBS (2008)

Author: Takahiro ASAOKA
Institute: TOKAI University
Street: 1117 Kitakaname, Hiratsuka
City: Kanagawa
Country: Japan
Email: 7adpm001@keyaki.cc.u-tokai.ac.jp

A Navigation System for the Visually Impaired Using Colored Guide Line and RFID Tags

Tatsuya Seto[1], Yuriko Shiidu[1], Kenji Yanashima[2] and Kazushige Magatani[1]

[1]Department of Electrical and Electronic Engineering, Tokai University, Hiratsuka, Japan
[2]National Rehabilitation Center for the Disabled, Hiratsuka, Japan

Abstract — **There are approximately 300,000 visually impaired persons in Japan. A navigation system using GPS and point blocks are examples of famous supporting systems for independent activities of the visually impaired. However, these support systems are usually useless in the indoor space (e.g. underground shopping mall, hospital, etc.) and cost a lot of money to spread. Most of the visually impaired in Japan are old and they probably cannot use complex support systems. Therefore, our objective is the development of a simple and inexpensive navigation system for the visually impaired which can use in the indoor space. Our developed instrument consists of a navigation system and a map information system. These systems are installed on a white cane. Our navigation system can follow a colored guideline that is set on the floor. In this system, a color sensor installed on the tip of a white cane senses the colored guideline, and the system informs the visually impaired that he/she is walking along the guideline by vibration. The color recognition system is controlled by a one-chip microprocessor and this system can discriminate 6 colored guidelines. RFID tags and a receiver for these tags are used in the map information system. The RFID tags are set on the colored guideline. An antenna for RFID tags and the RFID tag receiver are also installed on a white cane. The receiver receives tag information and notifies map information to the user by mp3 formatted pre-recorded voice. Three normal subjects who were blindfolded with an eye mask were tested with this system. All of them were able to walk along the guideline. The performance of the map information system was good. Therefore, our system will be extremely valuable in supporting the activities of the visually impaired.**

Keywords — **white cane, RFID tags, colored guideline, color sensor, visually impaired.**

I. Introduction

A white cane is a typical supporting device for the visually impaired. They use a white cane while walking for the detection of obstacles around them. In their known area, they can walk independently using a white cane. However, they cannot walk without help of others in their unknown area, even if they use a white cane. Because, a white cane is a detecting device for obstacles and not navigation device that gives them a route to the destination. Therefore, a navigation system that supports independent activities of the visually impaired is required.

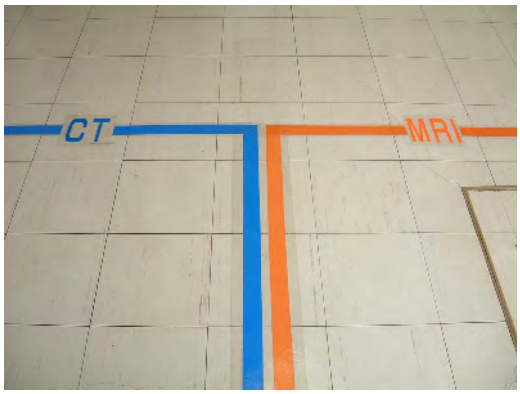


Fig. 1 Example of colored navigation lines

Many navigation systems for the visually impaired are developing. For example, a navigation system using GPS that supports the independent walking of the visually impaired is being developed. However, most of them are for outdoor space and not for indoor. Our objective of this study is a development of the navigation system which can be used in the indoor space and supports independent activities of the visually impaired without help of others.

In Japan, navigation line system is used for the normal person. This system is composed of some colored tapes that set on along the walking route. These colored lines are called colored navigation line. Each color is assigned for each destination. If we walk along one of these navigation lines, we can arrive the destination that corresponds the color of line easily. Fig.1 shows an example of the navigation line system.

II. Methodology

A. Conception

Fig.2 shows the conception of our system. This system is composed of colored navigation lines, RFID tags and an intelligent white cane. A navigation line is set on the floor along the walking route to the destination. If there are many

Chwee Teck Lim, James C.H. Goh (Eds.): ICBME 2008, Proceedings 23, pp. 919–922, 2009
www.springerlink.com

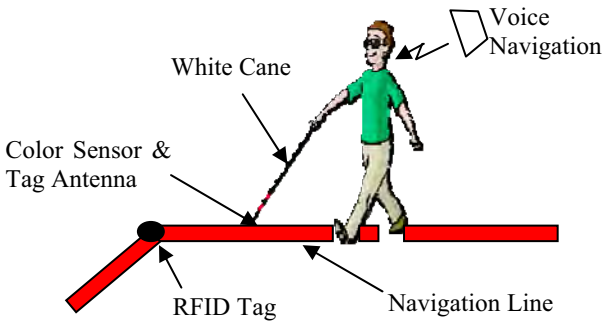


Fig. 2 A conception of the navigation system

destinations, different color is assigned for each route. At the each landmark point of the walking route, an RFID tag that indicates area code is set on a navigation line. An intelligent white cane includes a RGB color sensor, a transceiver for RFID tags, a vibrator and a voice processor. These devices included in a white cane are controlled by one chip microprocessor. A color sensor installed on the tip of a white cane senses the color of a navigation line. A visually impaired user swings the white cane left to right or right to left in order to find a target navigation line. If this sensor catches the target color, the white cane informs the visually impaired that he/she is walking along the correct navigation line by vibration. The white cane also makes communication with a RFID tag at the landmark point of walking route. If the white cane finds a RFID tag, a voice processor notifies area information that corresponds to the received area code by pre-recorded voice. Therefore, a user of this system can obtain the area information and reach the destination, only walking along the selected navigation line by using an intelligent white cane.

B. Color sensing system

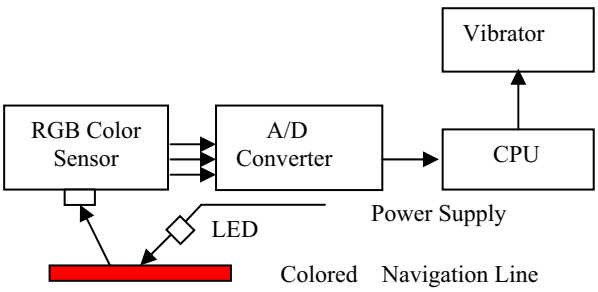


Fig. 3 A block diagram of the color detecting system

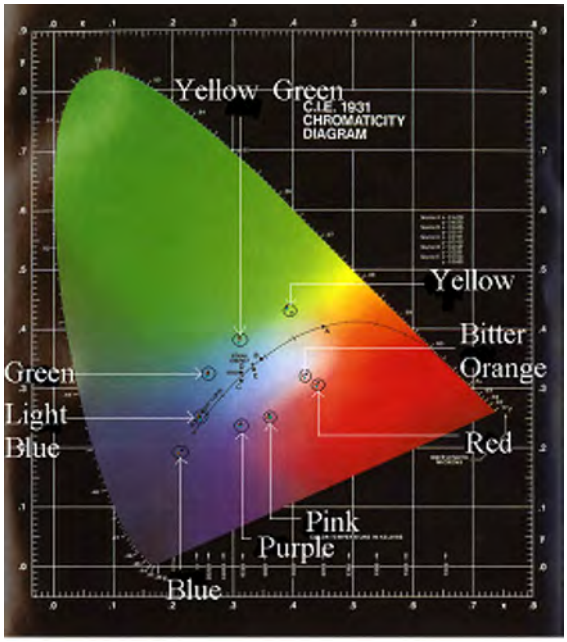


Fig. 4 xy-Chromaticity diagram

A block diagram of a colored line sensing system is shown in Fig.3. In this system a RGB color sensor installed on the tip of a white cane senses the floor color. RGB outputs of this sensor are amplified and noise reduced by a low pass filter. Then these signals are analog to digital converted by 8bit resolution, and then analyzed by a CPU (one chip microprocessor). Intensity of RGB signals change as the circumferential brightness, even if the sensed color is same. However, the ratio of RGB signals dose not change under same color sensing. In our system, digitized RGB signals are transformed to the Yxy notation. A point of one color in x-y coordinate of Yxy notation is located a same point at any condition. Therefore, the system evaluates a line color correctly at any condition by using Yxy notation. The x-y coordinate of Yxy notation is shown in Fig.4.

If a sensed color is the target color, a CPU turns on a vibrator to notify that the user is on the right route. This system can discriminate 6 or more colors of the navigation line.

C. RFID tag system

A block diagram of RFID tag information system is shown in Fig.5. In the navigation route, there are some landmark points where the system has to notify a user of the area information. For example, a corner to turn left or right, an entrance to the elevator, stairs are typical landmark points for the visually impaired. In our previous navigation

system, optical beacons that were set on the ceiling and a receiver for the beacons were used for this objective. From experiments, it is confirmed that the performance of the optical beacon system was good. However, an optical beacon consumes electric power continuously to emit the area code as infrared signals. And a user has to have a receiver for the beacon in addition to a white cane. Therefore, RFID tags are used in our new system. It is not necessary to have own power source for typical RFID tag. The dimension of RFID tag is 8.5cm x 5cm, and the frequency characteristic is 135kHz. The power of RFID tag is supplied from the transceiver that can make communication with RFID tag as radio frequency wave. And RFID tag system can be installed in a white cane. These are the benefit for using RFID tags.

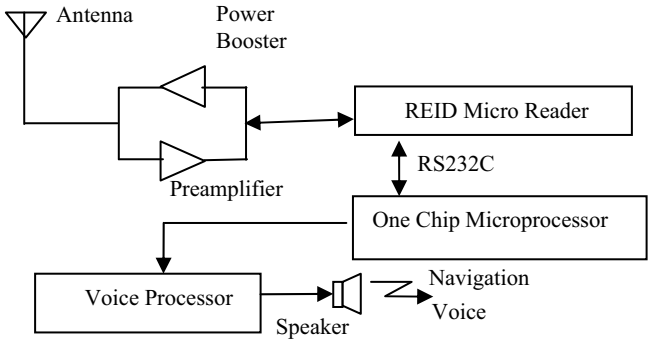


Fig. 5 A block diagram of a RFID tag transceiver and a voice processor

Both receiving sensitivity and output power of ordinary RFID Micro Reader (transceiver) are too small for our system. So, a preamplifier for the receiver and a power booster for the transmitter are developed and equipped in our system. An antenna for the transceiver is also installed on the tip of a white cane. By using this system, communicable distance between an RFID tag and a white cane is about 50cm. Fig.6 shows an RFID tag that is used in our system.

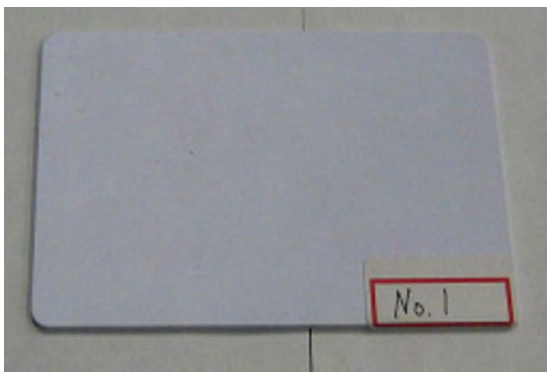


Fig. 6 An example of used RFID tag

The voice processing unit is also necessary for RFID tag system. At a landmark point, it is necessary to notify area information by voice. In our system, a CPU selects and outputs the pre-recorded phrase that corresponds with a received area code. Pre-recorded phrase is encoded in mp3 format and saved in the memory of one chip microprocessor.

III. Experiment

There normal subjects who were blindfolded with an eye mask were tested with our developed system. Two experiment routes were set on the floor and RFID tags were also set at the landmark point of these route. One navigation route was red and another was blue. Start point of both navigation lines were same. A destination of red navigation line is a door to the laboratory and blue is the toilet. Fig.7 shows the schema of experiment route. As shown in this figure, a subject had to turn left to follow red route at the crossing. And a subject had to turn right to follow blue route. RFID tags were set on the navigation lines at the crossing and the destinations. In this experiment, the distance form start point to the destination was about 15m in all routes.

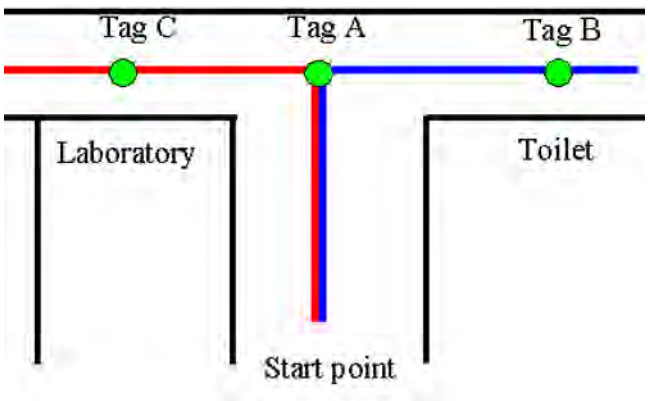


Fig. 7 The schema of experiment route

All subjects could walk along the navigation line correctly, and all colored lines were continuously detected stably. In all cases of this experiment, an intelligent white cane found RFID tag and notify the subject of turning information, and all subjects turned right or left and reached to the destination. Therefore, we think that our navigation system for the visually impaired worked perfect. Fig.8 shows one subject under experiment.



Fig. 8 A subject of the experiment

IV. Conclusion

We described about our developed new navigation system for the visually impaired. A user of this system can obtain the area information and reach the destination, only walking along the selected navigation line by using an intelligent white cane.

We think that our developing method to navigate a visually impaired person using navigation lines worked well. However, previous system was too heavy and huge. So, we developed a new system. These problems were improved in a new system. Therefore, we concluded that our navigation system will be a valuable one for the visually impaired.

References

1. Y. Shiizu, K. Magatani et al.:"Development of an intelligent white cane which navigates the visually impaired", Proceedings of the 29th Annual International Conference of the IEEE EMBS (2007)

Author: Tatsuya Seto
Institute: Tokai University
Street: 1117Kitakaname
City: Hiratsuka
Country: Japan
Email: pop-zgx470akokoro@jcom.home.ne.jp

A Development of the Equipment Control System Using SEMG

Noboru Takizawa[1], Yusuke Wakita[1], Kentaro Nagata[2], Kazushige Magatani[1]

[1]Department of Electrical and Electronic Engineering TOKAI University, Japan
[2]Kanagawa Rehabilitation Center, Japan

Abstract — **SEMG(Surface Electromyogram) is one of the bio-electric signals that is generated from the muscle. There are many kinds of muscles in a human body, and used muscles are different for each body movement. Therefore, any kind of body motions can be detected by analyzing generated SEMG patterns. Our objectives of this study are the development of a method that makes perfect detection of the hand motions possible using SEMG patterns and applying the method to the man-machine interface. In this paper, four channels SEMG signals which were measured from a right forearm of the subject were used to detect right hand motions. And a radio controlled vehicle was controlled as the results of detecting hand motions.**

In our system, suitable electrode positions are selected from analyzing results of 48 multi-channel SEMG patterns for each subject. Measured SEMG signals from electrodes are amplified, filtered and analog to digital converted. Digitized SEMG data are analyzed in a personal computer. The hand motion detection is done using the method of canonical discriminate analysis. In this study, five basic hand movements (wrist flexion, wrist extension, grasp, pronation, supination) were detected and used to control a vehicle. Three subjects were studied with our system. They were male and had not used our system before experiment. After few minutes training, they tried to control a radio controlled vehicle. In spite of first operation, they could control a vehicle almost perfectly and average recognition rate of hand movements were more than 90% for all subjects. From these results of our experiment, we have concluded that our new man-machine interface worked perfect and will be a valuable interface in future.

Keywords — **EMG, Movement identification, Machinery control.**

I. Introduction

SEMG (Surface EMG) is one of the bio-electric signals that are generated from the muscle. There are many kind of muscle in a human body, and used muscles are different for each body movement. Therefore, any kind of body motions can be detected by analyzing generated SEMG patterns. Our objectives of this study are the development of a method that makes perfect detection of the hand motions possible using SEMG patterns, and applying this developed method to the man-machine interface.

In this study, our target machine that is controlled by SEMG is a radio controlled toy vehicle on market. This vehicle and a remodeled radio controller are shown in Fig.1. A user of this vehicle can control five actions (turn left, turn right, go forward, go back, firing) using radio controller. In this study these five actions are controlled by subject's hand movements.

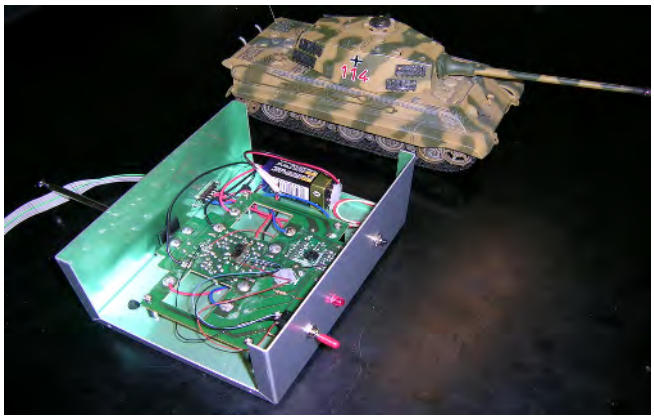


Fig. 1 The vehicle and a remodeled radio controller

II. Methodology

In our system, we tried to use four channels SEMG that were measured a right forearm in order to control a radio control vehicle. It is very important for this objective to select suitable electrode positions. So, we developed a SEMG amplifier and the method that made perfect hand motion detection possible. Fig.2 shows a block diagram of

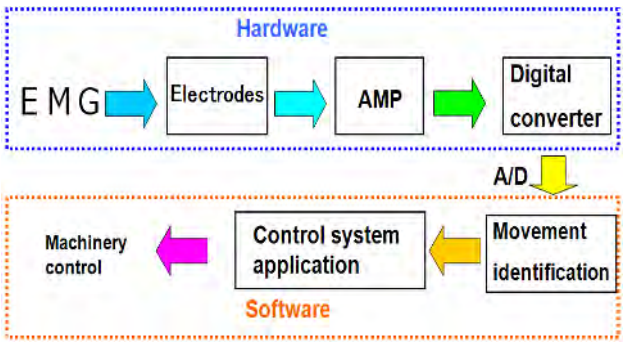


Fig. 2 A block diagram of one channel SEMG amplifier

Chwee Teck Lim, James C.H. Goh (Eds.): ICBME 2008, Proceedings 23, pp. 923–926, 2009
www.springerlink.com

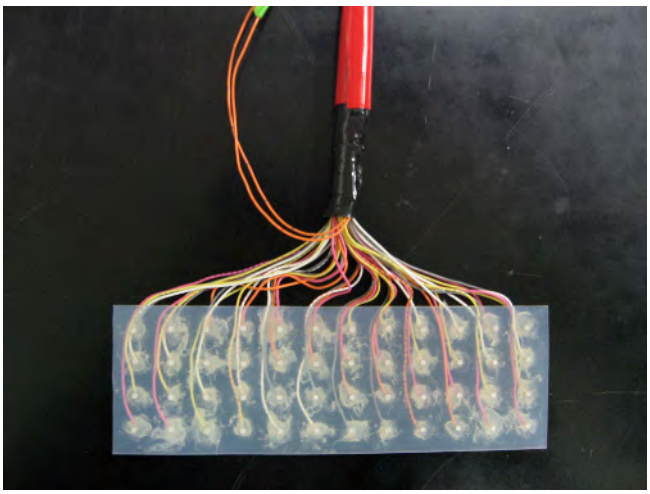


Fig. 3 A multi-channel electrode

one channel SEMG amplifier. As shown in this figure, SEMG measured from a right forearm using an Ag electrode is amplified, noise reduced by a low pass filter and analog to digital converted. And then digitized data is inputted to a personal computer and analyzed in it.

In order to select suitable electrode positions, 48 channels forearm SEMG for each hand motion are measured. A multi-channel electrode that includes 48 channels Ag electrodes is developed for this purpose. Fig.3 shows the multi-channel electrode. As shown in Fig.3, 48 channels Ag electrodes are set on a silicon rubber sheet. This electrode is wrapped around the forearm and 48 channels SEMG are measured form each Ag electrode. Fig.4 shows a 96 channels SEMG amplifier that includes low pass filters. We can

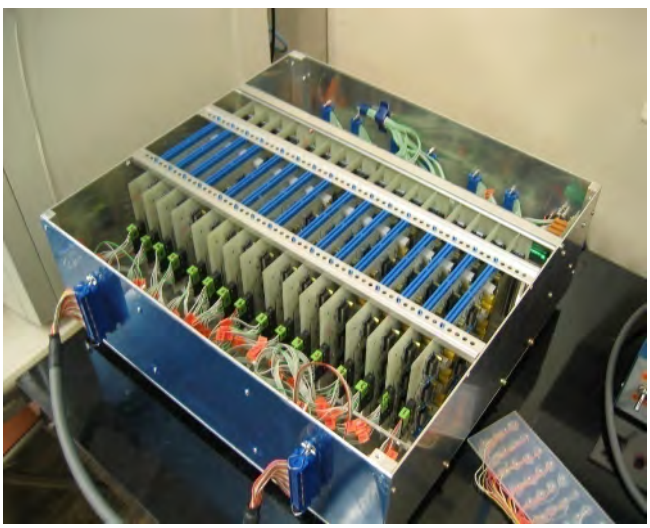


Fig. 4 A SEMG amplifier that include 96 channels

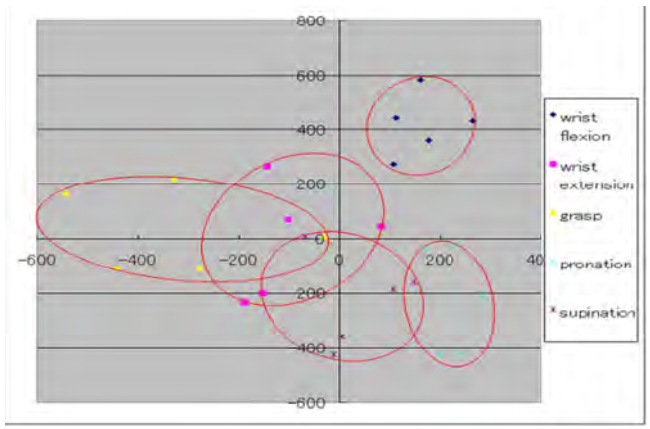


Fig. 5 An example of distribution map

measure 2 forearms SEMG at the same time using this amplifier.

In our system, suitable electrode positions are decided by Monte Carlo method. As mentioned earlier, 48 channels forearm SEMG for each hand motion are measured and digitized at first. 1000 sets of four channel electrodes are generated randomly. And recognition rate of hand motions are calculated and evaluated by canonical discriminate analysis for each electrode set. And finally, the electrode set that achieves highest average recognition rate is selected as the suitable electrode set [1]. Fig.5 shows the an example of distribution map for each hand motion on canonical space. As shown in this figure, cluster of each hand motion are separated each other on canonical space. After deciding electrode set, hand motion analysis is done using selected four channel electrode positions. Fig.6 also shows four channels Ag electrode set that is developed for our objective.

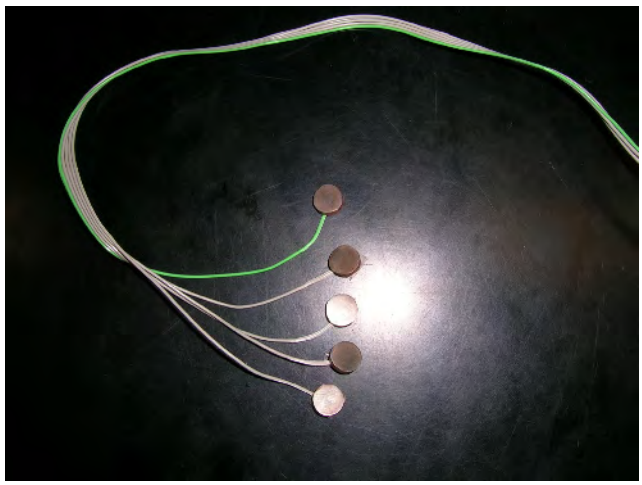


Fig. 6 Four channels Ag electrode

III. Experiment and results

At first, three normal male adult subjects were studied with our SEMG control system. All subjects set a multi-channel electrode on a right forearm and measured 48 channels SEMG for each hand motions. Suitable four channel electrode positions were decided by Monte Carlo method as mentioned earlier. After selecting electrode positions, four channel electrodes (shown in Fig.6) were set on a correct position of right forearm, and real time hand motion recognition test was done. Table 1 shows the correspondence between a hand motion and a motion of a radio controlled vehicle. All subjects moved hand 40 times for each hand motion. And recognition rates of each hand motion were calculated. The result of this experiment is shown in Table 2. As shown in this table, recognition rates for each hand motion are more than 95 % in all subjects. After, this experiment, all subjects tried to control a vehicle by SEMG. In this experiment, all subjects could control the vehicle almost perfect.

Table 1 The correspondence between a hand motion and a vehicle action

Wrist flexion	Go forward
Wrist extension	Go back
Grasp	Firing
Pronation	Turn left
Supination	Turn right

Table 2 recognition rate for each subject

Subject(a)

Movement	Recognition [%]
Wrist flexion	100
Wrist extension	100
Grasp	100
Pronation	96.33
Supination	100
Average	99.33

Subject(b)

Movement	Recognition [%]
Wrist flexion	100
Wrist extension	100
Grasp	100
Pronation	100
Supination	95
Average	99

Subject(c)

Movement	Recognition [%]
Wrist flexion	100
Wrist extension	100
Grasp	96.67
Pronation	96.67
Supination	100
Average	98.67

IV. Conclusion

In this paper, we described about our developed man-machine interface using SEMG. In this system, by using four channels SEMG a radio controlled toy vehicle are controlled. SEMG generated by hand motions are measured and evaluated, and acted hand motion are estimated by measured SEMG. Vehicle's actions are corresponded with estimated hand motions. Therefore, a radio controlled vehicle is able to be controlled by SEMG for each hand motion in our system.

Electrode positions for hand recognition are selected using Monte Carlo method. As using this method, we can obtain suitable set of electrode positions. From our experiment results, recognition rates of hand motions were more than 95% using this method. These results show that our developed method works perfect. In this paper, we described experiment results about three adult subjects. After those experiments, many children were also tested with our system. In spite of the first experience of our system for all children, most of them could control a vehicle perfect. However, our system is too huge to control a small interface. And in real time control by using SEMG, there are

some problems about control timing. Therefore, we concluded that if these problems are improved, our developed system will be a valuable one for the man-machine interface using SEMG.

REFERENCES

1. K. Ando, K. Magatani et al.:"Development of the input equipment for a computer using surface EMG" Proceedings of the 28th IEEE EMBS Annual International Conference (2006)

Author: Noboru Takizawa
Institute: Tokai University
Street: 1117Kitakaname
City: Hiratsuka
Country: Japan
Email: 8adpm025@mail.tokai-u.jp

The Analysis of a Simultaneous Measured Forearm's EMG and f-MRI

Tsubasa Sasaki[1], Kentaro Nagata[2], Masato Maeno[3] and Kazushige Magatani[1]

[1]Department of Electrical and electronic Engineering, Tokai University, Japan
[2]National Rehabilitation Center, Japan

Abstract — **Generally, voluntary muscles are able to be moved freely, if we want to move them consciously. In addition, EMG is generated in a muscle according to contraction of it. If we want control some equipment like an artificial hand by using EMG, a beginner cannot control it without concentration on the motion of equipment. However, if he/she is practiced in operation of the equipment as a result of training, he/she can control it without concentration. In other words, a skilled person has obtained some abilities from training, and these abilities will change brain functions. Making the change of brain function as a result of training clear by using f-MRI is our objective of this study. In our study, 6 channels EMG which are generated from right forearm are measured and basic hand motions are recognized by using them. In our experiment, a subject in a gantry of MRI moves his/her right hand, and generated 6 channels EMG are amplified, filtered and digitized. Digitized EMG data is analyzed and then a recognition result is indicated to a subject as an animation of the recognized hand motion by a LCD projector. A subject trains himself/herself in order to improve the recognition rate. F-MRI is measured while training continuously. In this paper, we will talk about our measurement system and the results of experiment.**

Keywords — **fMRI, EMG, artificial hand, training,**

I. Introduction

Generally, voluntary muscles are able to be moved freely, if we want to move them consciously. In addition, EMG is generated in a muscle according to contraction of it. Therefore, body motions can be estimated by analyzing generated EMG patterns, and the results of estimation are used as the control source for some equipment. If we want to control some equipment like an artificial hand by using EMG, a beginner cannot control it without concentration on the motion of equipment. However, if he/she is practiced in operation of the equipment as a result of training, he/she can control it well without concentration. In other words, a skilled person has obtained some abilities from training, and these abilities will change brain functions. Making the change of brain function as a result of training clear by using f-MRI is our objective of this study.

In our study, 6 channels EMG which are generated from right forearm are measured and basic hand motions (wrist flexion, wrist extension, grasp and release) are recognized by using them. In our experiment, a subject in a gantry of MRI moves his/her right hand, and generated 6 channels EMG are analyzed in a personal computer. The result of recognition is indicated to a subject as an animation of the recognized hand motion by a LCD projector. Therefore, a subject can check the recognition result immediately. All subjects of this experiment are beginners of the EMG recognition and train themselves in order to improve the recognition rate. F-MRI is measured while training continuously. And then, the changes of brain function as a result of training are analyzed by using these f-MRI data.

II. Experiment method

Fig.1 shows a simplified block diagram of our measurement system. As shown in Fig.1, Magnetom-Vision 1.5T(SIEMENS) is used as the f-MRI. 6 channels EMG are measured from right forearm of a subject in a gantry of MRI. Wires of electrodes are shielded and extended to the EMG amplifiers which are set on the outside of the MRI room. A LCD projector in the MRI room projects a result of hand motion recognition to the permeable screen which is set in front of a gantry of MRI. A subject can see the recognition result as an animation of hand motion through a mirror which is set in front of subject's eyes.

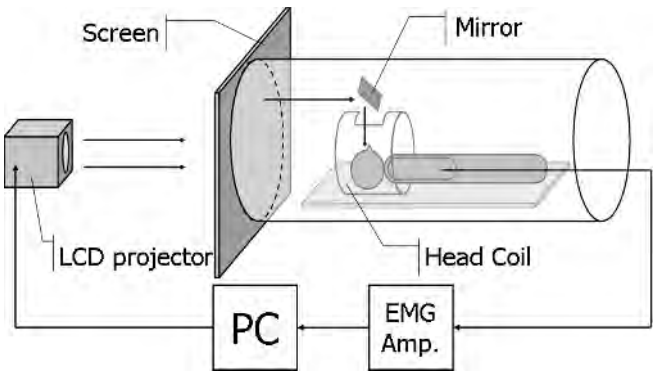


Fig. 1 The Measurement System

Chwee Teck Lim, James C.H. Goh (Eds.): ICBME 2008, Proceedings 23, pp. 927–930, 2009
www.springerlink.com

A block diagram of one channel EMG amplifier is shown in Fig.2. As shown in this figure, SEMG is amplified about 4400 times and a band width is limited from 10 to 1kHz. In addition, a EMG amplifier includes a hum filter which eliminates 50Hz. In digitization of EMG, sampling frequency is 2kHz, and bit resolution is 16bits. Digitized EMG data are analyzed in a personal computer.

Hand motion detection is done using the method of canonical discriminate analysis. An integrated value for 300ms of absolute value of EMG is used as the EMG feature extraction. In our system, suitable position of electrodes is estimated by Monte Carlo method [1], [2]. At first, 48 channels EMG pattern of a subject is recorded for each hand motion. Next, positions of 6 channels electrode are generated 1000times randomly. From results of these trials the suitable position of electrodes is decided. Using this Monte Carlo method, even if we use only 4 channels of EMG, recognition rate of basic 8 hand motions (wrist flexion, wrist extension, grasp, release, radial deviation, ulnar deviation, pronation, and supination) are more than 96%. A 48 channels multi-electrode is shown in Fig.3 (a) and a 48 channels EMG amplifier using detection of suitable position of electrodes is also shown in Fig.3(b).

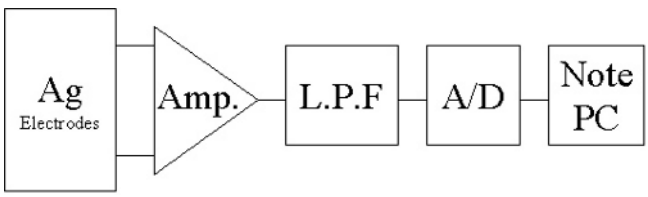
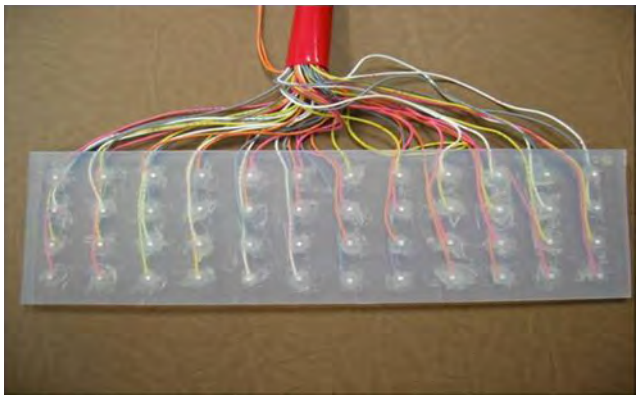


Fig. 2 Machine constitution

A structure of the surface 6 channel multi-electrodes is shown in Fig.4 (a). This multi-channel electrode is composed of 6 silver electrodes. Each electrode is 1mm in diameter. To fit a forearm bodyline, flexible silicone rubber is use as a base of 6 silver electrodes A thickness of this silicone rubber is 2mm. Positions of silver electrodes are set as the results of Monte Carlo method for each subject, as mentioned earlier. The 6 channel EMG amplifier is shown in Fig.4 (b). A 6 channel active low pass filter and a regulated power supply are also shown in Fig.4 (c) and (d). In our system, sometimes ordinary Ag-AgCl electrodes are used. In this case, positions of electrodes are decided as the anatomical position of muscles. Fig.4 (e) shows the shielded Ag-AgCl electrodes. Fig.5 shows the attached multi-electrode on the subject's forearm.

It is well known that many electric noises are generated by MRI. At first, electromagnetic noise from MRI was measured and analyzed. In this experiment, electrodes were



(a) A 48 channels multi-electrode

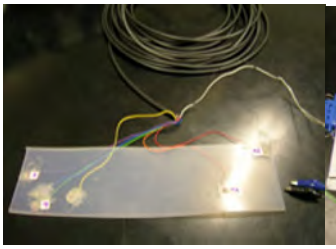


(b) A 48 channels EMG amplifier

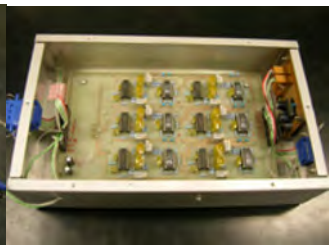
Fig. 3 A suitable position of electrodes detecting system

not attached on a subject's forearm. Each electrode was terminated with 10k ohm respectively, and MRI was measured. Generated noise under MRI measuring was recorded and analyzed. An example of power spectrum for recorded noise is shown in Fig.6. As shown in this figure, 3 peaks of power are observed, and frequencies of all peaks are more than 1kHz. Therefore, noise reduced EMG is obtained by using low pass filter whose cutoff frequency is set under 1kHz. Because of this result, in our system, maximum frequency of amplified EMG signal is limited under 1kHz as mentioned earlier.

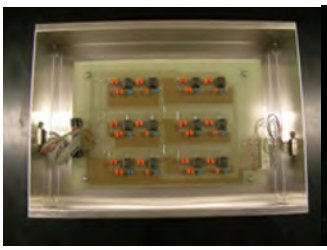
Next, two beginners of the EMG recognition were tested with our system. Multi-channel EMG patterns of all subjects were measured and suitable positions of electrodes were decided before experiment. In this experiment, a subject in a gantry of MRI moved their hand. Because the motion of electrodes and wires of electrodes in accordance with



(a) 6 channels silver electrodes



(b) 6channels EMG amplifier



(c) 6channels active filters



(d) A power supply for the system



(e) Ordinary Ag-AgCl Electrodes

Fig. 4 An EMG measuring system



Fig. 5 An attached 6 channels electrodes

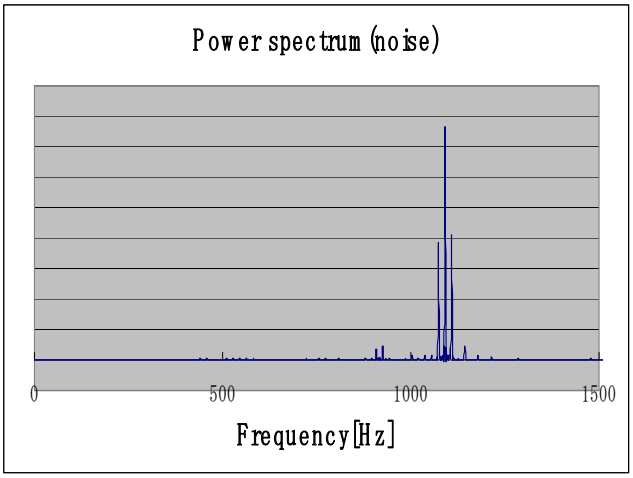


Fig. 6 power spectrum of noise from MRI

hand motions will generate electric noise, basic 4 hand motions (wrist flexion, wrist extension, grasp and release) which do not cause motion artifact are selected as recognized motions.

An example of distribution of classified basic motions of a hand in canonical space is shown in Fig.7 (same colored dot means same motion). As shown in this figure, all clusters are separated each other and we can recognize each hand motion.

Fig.8 shows an example of f-MRI result under EMG recognition test. The subject was a beginner of the EMG rec-

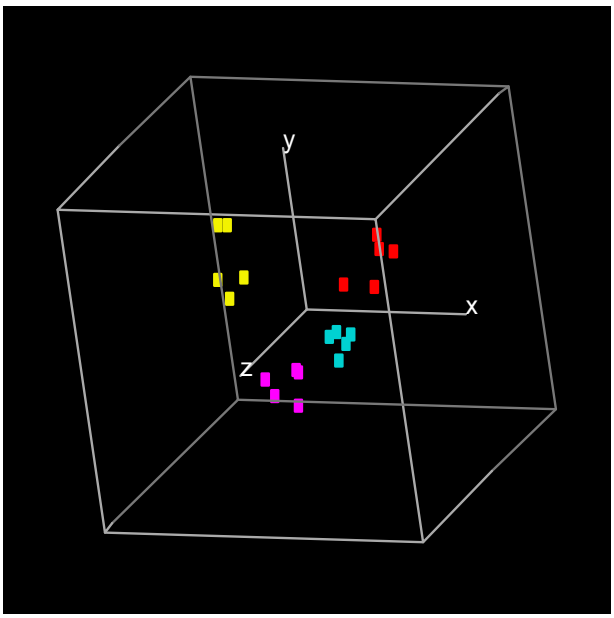


Fig. 7 Distribution result of classified basic motions of hand

ognition, and it was hard for the subject to control EMG pattern. Many activated places are observed in Fig.8. We think that because of inexperience in EMG recognition is the main cause for multi-activation of the brain.

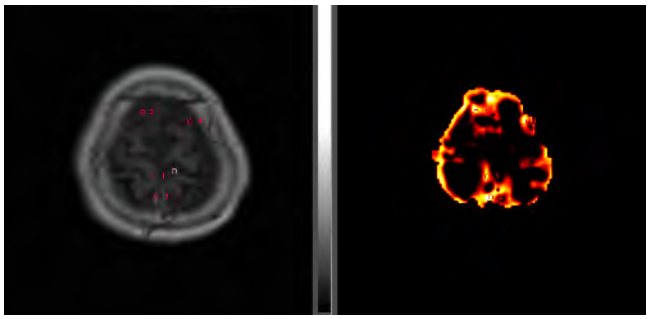


Fig. 8 An example of f-MRI result under EMG recognition test

Fig.9 express signal strengths which can measure at the time of simultaneous acquisition of f-MRI and EMG. As shown in this figure, we can observe activations in a various area of brain that include motor are.

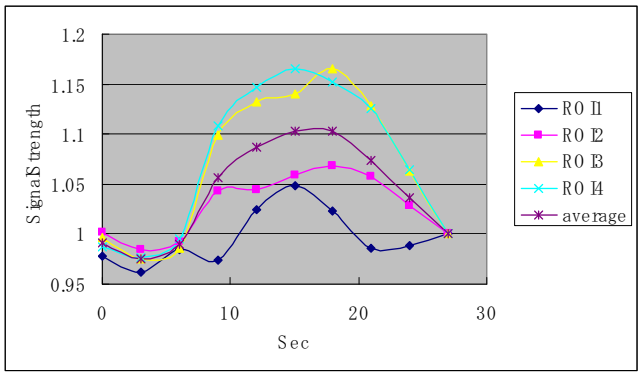


Fig. 9 Signal strength when of f-MRI and EMG simultaneous measured

III. Conclusions

We can use EMG as the control source for some equipment. For example, an artificial hand is controllable using EMG. However, a beginner cannot control it without concentration and skilled person can control it without concentration. A skilled person has obtained some abilities, and these abilities will change brain functions. In order to observe these changes of brain functions, we developed

EMG measurement system which can measure 6 channels EMG and f-MRI simultaneously using canonical discriminate analysis, 4 basic hand motions were recognized from forearm EMG and f-MRI was measured simultaneously. From the results of this experiment, we can see that many places of the brain were activated for a beginner of the EMG recognition. We think that because of inexperience in EMG recognition is the main cause for multi-activation. We would like to trace the change of brain activation in subject's training stage in figure.

References

1. Kentaro Nagata, Masafumi Yamada and Kazushige Magatani, "Recognition method for forearm movement based on multi-channel EMG using Monte Carlo method for channel selection", Proceeding of the International Federation for Medical & Biological Engineering Vol.12 (2005)
2. Kentaro Nagata, Keiichi Ando, Shinji Nakano, Hideaki Nakajima, Masafumi Yamada and Kazushige Magatani, "Development of the human interface equipment based on surface EMG employing channel selection method", Proceedings of the 28th IEEE EMBS Annual International Conference New York City, USA, AUG 30-Sept 3, 2006

Author: Tsubasa Sasaki
Institute: Tokai University
Street: 1117 Kitakaname
City: Hiratsuka
Country: Japan
Email: yoku_sora@hotmail.com

Development of A Device to Detect SPO_2 which is Installed on a Rescue Robot

Yoshiaki Kanaeda[1], Takahiro Asaoka[2] and Kazushige Magatani[3]

[1]Yoshiaki KANAEDA, Tokai Univ., Japan
[2]Takahiro ASAOKA, Tokai Univ., Japan
[3]Kazushige MAGATANI, Tokai Univ., Japan

Abstract — **When a disaster occurs, there is a possibility that a lot of suffering person results. There is also possibility that a rescue person encounters disaster in order to rescue suffering persons. Therefore, there are many researches about rescue robots for the disaster. These robots can find sufferers and rescue them. However, they cannot evaluate sufferer's condition. If we can measure sufferer's vital sign at the disaster area, measured data will be useful for triage. So, we are investigating a measured system which is installed on a rescue robot and can measure the vital sign at the disaster area easily. SPO2 (Arterial blood oxygen saturation degree) is one of the important vital sign of a human. We can evaluate sufferer's state using SPO2. For example, normal level of SPO2 is more than 96%, and under 90% of SPO2 means that he/she is in the fatal condition. SPO2 is able to be measured by using a pulse oxymetry method easily. Therefore, we are developing the easy measuring method of SPO2 of sufferers at the disaster area which is based on pulse oxymetry. Oxy or de-oxy hemoglobin makes change the color of red blood cell. Infrared ray is absorbed in de-oxy hemoglobin and red ray is absorbed in oxy hemoglobin. Therefore, SPO2 can be measured, if light characteristics of blood can be measured. In our method, pulse signal is obtained as the reflection of applied light to the skin. And red ray and infrared ray are used to obtain two kind of pulse. And then, SPO2 is calculated using the amplitude of these two pulses. We developed and assessed a SPO2 measurement system which can measure SPO2 by only easy touching to the skin. Four subjects were studied with our system. In all cases, our developed system was able to measure SPO2 correctly.**

Keywords — **SPO_2, Easy touching, Vital sign, Hemoglobin, Pulse oxymetry.**

I. Introduction

A disaster like a big earthquake usually brings many destroyed buildings and many sufferers are generated in the disaster area. There is also possibility that a rescue person receives a serious injury or loses his/her life by a second disaster. In order to avoid these situations, robots that engage in rescue operations are being researched and developed. By employment of various types of rescue robots, rescuers can search a sufferer under debris, remove obstacles, make a route to him/her, and rescue him/her. However, they cannot measure the sufferer's condition. We think that if they can measure sufferer's vital signs (for example a body temperature, pulses, and so on) at the disaster area, it will be possible to evaluate a sufferer's condition and to realize the effective rescue ability.

So, we developed the device which detected bio-signals. This device helps triage by detecting a bio-signal after rescue with a victim. In addition, if this device is installed in a rescue robot, the rescuer can decide a priority of the help of the victim by bio-signals from this device in the rescue operation. Therefore, our goal is the development of a system which can be installed on a rescue robot, measure the sufferer's vital signs and send these data to medical doctors. In this paper, we describe developed measuring methods for SPO2 using pulse oximetry. In our method, only touching sufferer's skin with a sensor, a correct sufferer's SPO2 is obtained.

II. Methodology

A. SPO2 Detection

SPO2 is an index to show a ratio of oxygen in the body, and is also the thing which expressed the ratio of the oxidation hemoglobin of all hemoglobin by % notation. It is possible to calculate a SPO2 by using 2 types of pulse waves which are measured by infrared rays and red rays respectively. Most of the pulse oxy meter which is a general SPO2 detector is a penetrative type. But, it is difficult to detect SPO2 using penetrative method at disaster areas. So, we developed SPO2 measurement system by using pulse detection of reflection type.

B. Pulse Detection

The pulse is one of the most important vital sign of a human, and it is generated continuously while our life is lasting. The pulse is generated by blood flow that is caused by beats of the heart. In other word, we can observe the pulse as a change of artery diameter from the result of a beat of the heart.

Hemoglobin in the blood absorbs infrared ray. Therefore, if we irradiate infrared ray to a blood vessel, absorption rate of infrared ray will change as increase and decrease of a blood flow. The absorption and reflection of infrared ray inside the blood can be used to detect the pulse. It is possible

Chwee Teck Lim, James C.H. Goh (Eds.): ICBME 2008, Proceedings 23, pp. 931–934, 2009
www.springerlink.com

to detect the pulse by measuring the blood flow of the capillary which is distributing to the skin of human body with infrared ray. In other words, change of reflection rate of infrared ray irradiated a skin of human expresses the pulse.

Then, as two characteristics of infrared ray, infrared ray has permeability to all the substances including the skin, and has a characteristic of absorption toward blood. In our method, the pulse is measured using these characteristics. Infrared ray from an infrared LED is irradiated to the skin. Even if there is one of clothes between the LED and the skin, infrared ray can permeate the clothes completely and reaches the skin surface. A part of this infrared ray is absorbed or penetrates vessels, and the rest is reflected. We can observe the pulse as the intensity change of this reflection.

By the way, red ray is also absorbed into blood. However, infrared ray is mainly absorbed into de-oxy-hemoglobin and red ray is mainly absorbed into oxy-hemoglobin. These characteristics are used to calculate SPO2 in our system. So, we developed a unified sensor which has two types of a pulse sensor. One uses infrared ray (900nm) and the other uses red ray (660nm). Both sensors consist of a LED and a photo sensor. The unified sensor is touched to the human body. It emits infrared and red ray at the same time from each LED, and each photo diodes detect the each reflected ray as electric current.

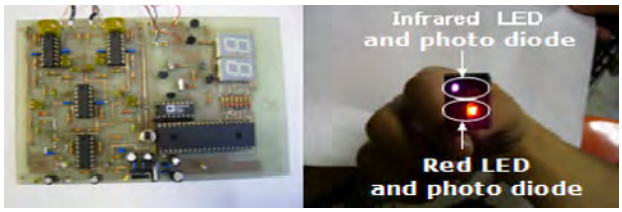


Fig. 1 SPO2 detecting system device and an unified sensor

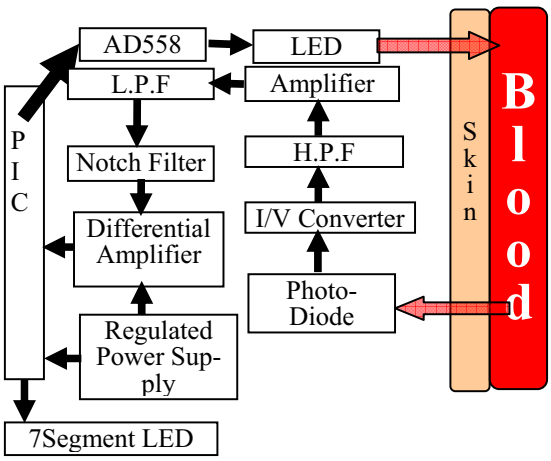


Fig. 2 Block diagram of SPO2 measuring system

Fig.1 shows the view of our system and sensor. Electric current from a photo diode is converted to voltage and then amplified and filtered for noise reduction. Direct contact with human skin of the sensor is the best condition to detect a pulse. However, in many cases at the disaster area, it is difficult to touch a sensor to a skin directly, and there are sufferer's cloths between the sensor and a skin. For such cases, in our measurement system, the brightness of a LED and the amplitude of a photo detector are able to control in order to set their level optimal. These controls of the system are conducted by a one-chip microprocessor (PIC16F877). In our system, intensity of LED is changeable by using a 8bit Digital to Analog converter (AD558). This D/A converter can change the output voltage of a power supply for LED according as a input of the converter. This voltage varies in a range from 0 to 10V by the signal changes in a range from 0 to 255. A block diagram of the system is shown in Fig.2

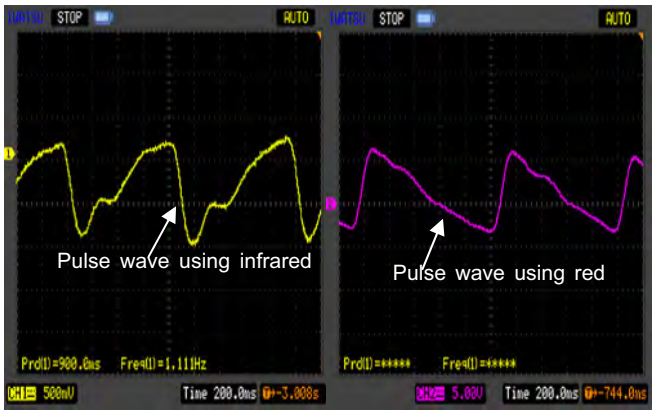


Fig. 3 2 types of measured pulse

Fig.3 shows 2types of measured pulse wave. The pulse by using infrared ray is shown as yellow line and by using red ray is shown as pink line.

C. Calculation of SPO2

It is possible to calculate SPO2 by using these pulse waves. SPO2 expresses the percentage rate of oxy-hemoglobin in blood. This value is one of the most important vital sign of a human. SPO2 reflects the body condition strongly. The body condition for each SPO2 rate is shown in Table I. It is said that about 95% and more of SPO2 is normal level in human. Some medical treatments will need in the condition from 90% to 94% of SPO2. Then, 89% and under-values of SPO2 mean fatal condition, and a correct medical treatment is necessary as soon as possible.

Table 1 Symptom Relation of SPO_2

Oxygen Saturation Blood (%)	Condition	Symptom of body
99 - 95	No damage	Good health
94 - 90	Minor damage	Minor symptom
89 - 75	Middle damage	Cyanosis
74 -	Serious damage	Damage to tissue Cellular death

Hemoglobin is in the red blood cell. And oxy or de-oxy hemoglobin makes the color of red blood cell change. Using this light characteristic of red blood cell, SPO2 can be obtained. In actuality, SPO2 is obtained as a ratio of a magnitude of the pulse for infrared ray and a magnitude of the pulse for red ray. To calculate this value, following formulas were used.

$$\Delta A = \log (I / (I - \Delta I))$$
$$\Delta B = \log (L / (L - \Delta L))$$
$$\Phi = \Delta A / \Delta B$$
$$SPO2 = (Ia/(Ia+La)) \times \Phi \times 100 \quad (1)$$

Where, *I* means the maximum amplitude of infrared pulse signal, and L means the maximum amplitude of red pulse signal. *ΔI* and *ΔL* mean the minimum amplitude respectively. *ΔA* and *ΔB* mean the difference between maximum and minimum amplitude of each signals. And φ is the absorbing light constant. *Ia* and *La* mean the average of pulse wave respectively. SPO2 is calculated by formula (1).

D. Experiment of pulse detection



Fig. 4 The pulse wave through one clothes

Usually, SPO2 is measured from a tip of finger. However, at the disaster area a SPO2 sensor is not always set on a tip of finger. In addition, a sensor is not always set on a skin directly. So, we tried to measure pulse wave from some body places expect a tip of finger, and tried to measure through clothes. In all cases, we could detect pulse wave using our developed system. An example of measured pulse wave (through clothes) is show in Fig.4.

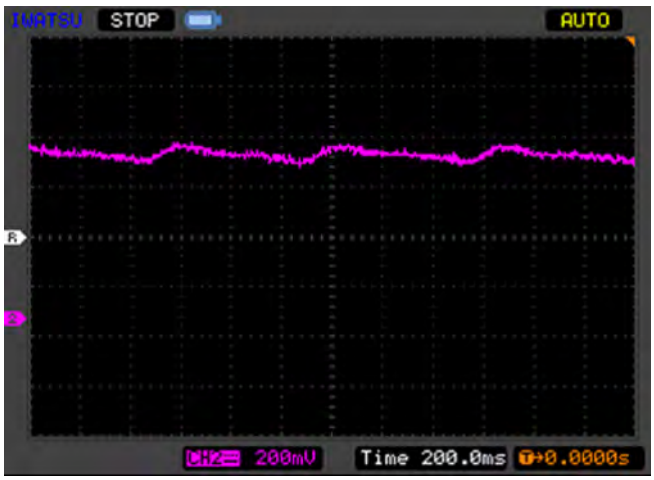


Fig. 5 The pulse wave through two clothes

An example of pulse wave that was measured through two pieces of clothes is shown in Fig.5. In this figure, pulse wave was measured as same as Fig.4. As shown in these figures, it is difficult to measure pulse wave through the clothes. However, if a gain of signed amplifier and brightness of LED is optimal, we can obtain pulse wave through the clothes.

E. Experiment of SPO2 detection

The SPO2 was experimentally measured by using our developed system. Fig.6 shows externals of the comparison experiment. In the experiment, a pulse oxy mater on the market (OLV-3100 Nihon Kohden Ltd.) was also used as a reference. This device's sensor is the penetrating type, but our sensor is the reflection type. In this figure, indicated number by 7segments means calculated SPO2 value. In Fig.6 (Experiment 1), a subject attached the sensor of a pulse oxy mater to the forefinger of the light hand, and the sensor of our device to the forefinger of the left hand respectively. As shown in Fig.6, if brightness of LEDs at set to suitable level, obtained SPO2 value will be correct. However, sometimes errors occurred in our system. Error range of the SPO2 which was measured by our developed system was about from -4% to +4%. We think that a cause of this error is mainly crosstalk between two kinds of light (infra-

red and red ray). We think that it is necessary to develop a new type unified sensor which is able to cancel this cross talk.

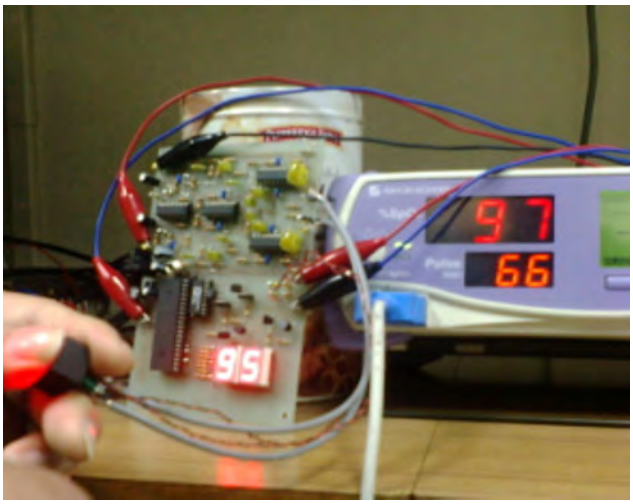


Fig. 6 Experiment 1 and this result

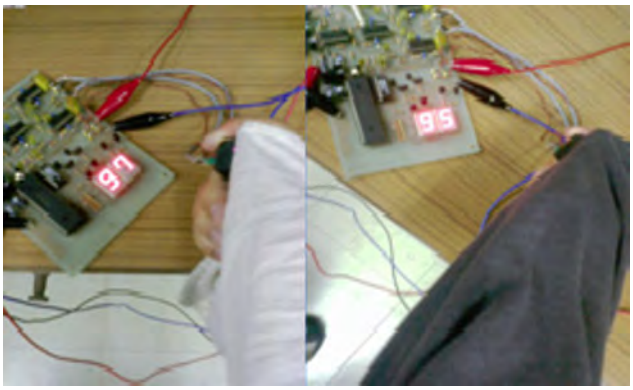


Fig. 7 Experiment 2 and this result

Fig.7 is an experiment result of acquisition on the clothes. From this fig.7, it has been understood to be able to acquire the pulse wave from clothes.

III. Conclusions

In this paper, SPO2 measuring system by using infrared and red ray was developed. This system can detect a pulse on subject's cloths and on many parts of body. And SPO2 value was calculated using measured pulse. This value had some error. Main cause of this error will be crosstalk between photo sensors. Therefore, we have concluded that if these problems are improved, our developed system will be useful to rescue sufferers. And, to install it in the rescue robot, the circuit is miniaturized.

References

[1] Takahiro ASAOKA ,Yoshiaki KANAEDA and Kazushige MAGATANI, "Development of the device to detect human's bio-signals by easy sensing", IEEE EMBS 2008

[2] Yasuhiro SAEKI, Komin TAKAMURA and Kazushige MAGATANI, "The measurement technique of human's bio-signals", IEEE EMBS 2006

[3] Keisuke YASUDA, Koumin TAKAMURA, Takumi MASUDA and Kazushige MAGATANI, "A remote measurement method of the human bio-signals", IEEE EMBS Asian-Pacific Conference on Biomedical Engineering 2003

Author: Yoshiaki KANAEDA
Institute: Tokai University
Street: 1117 Kitakaname Kanagawa
City: Hiratsuka
Country: Japan
Email: 8adpm011@mail.tokai-u.jp

A Estimation Method for Muscular Strength During Recognition of Hand Motion

Takemi Nakano[1], Kentaro Nagata[2], Masahumi Yamada[2] and Kazusige Magatani[1]

[1]TOKAI University, JAPAN
[2]Kanagawa RehabilitationInstitute, JAPAN

Abstract — **In this study, we describe the estimation method for muscular strength during recognition of hand motion based on surface electromyogram (SEMG). Although the muscular strength can consider the various evaluation methods, a grasp force is applied as an index to evaluate the muscular strength. Today, SEMG, which is measured from skin surface, is widely used as a control signal for many devices. Because, SEMG is one of the most important biological signal in which the human motion intention is directly reflected. And various devices using SEMG are reported by lots of researchers. Those devices which use SEMG as a control signal, we call them SEMG system. In SEMG system, to achieve high accuracy recognition is an important requirement. Therefore, conventionally SEMG system mainly focused on how to achieve this objective. Although it is also important to estimate muscular strength of motions, most of them cannot detect power of muscle. The ability to estimate muscular strength is a very important factor to control the SEMG systems. Thus, our objective of this study is to develop the estimation method for muscular strength, and reflecting the result of measured power to the controlled object. Since it was known that SEMG is formed by physiological variations in the state of muscle fiber membranes, it is thought that it can be related with grasp force. We applied to the least-squares method to construct a relationship between SEMG and grasp force. In order to construct an effective evaluation model, four SEMG measurement locations in consideration of individual difference were decided by the Monte Carlo method.**

From the experimental result, the performance of our method using two normal subjects shows that the recognition rate of four motions was perfect and the error rate of the grasp force estimation at that time was less than 5 %.

Keywords — **SEMG, The grip presumption, Operation recognition**

I. Introduction

Electromyography (EMG), is obtained by measuring the electrical signal associated with the activation of the muscle. EMG can be used for a lot of studies (e.g., clinical, biomedical, basic physiological, and biomechanical studies). Recently, in order to describe the neuromuscular activation of muscles within functional movements, kinesiological electromyography deserves attention and is established as an evaluation tool for various applied research. In order to apply it simply, the surface electromyogram (SEMG) which is measured from the skin surface, is widely used as a control source for human interface such as myoelectric prosthetic hands. The SEMG related system has many practical applications in various fields such as human interfaces. Human interfaces are reported by many researchers, and we call them "SEMG interfaces". Our study also aims to develop the SEMG interfaces like myoelectric prosthetic hands. As for a SEMG interface, it is desirable to operate it with the same feeling as the sensations of real body movements In order to achieve this objective, accurate recognition of motions, which is an essential requirement and estimation of muscular strength are both important factors. However, conventional SEMG interfaces have mainly focused on how to achieve the accuracy using sophisticated signal-processing techniques which are represented by a neural network model and a nonlinear one. We think the ability to estimate muscular strength is also an important factor in controlling it. And furthermore, in consideration of simplicity and ease of use in using the SEMG interface, construction of a simple discriminant model with a small number of measurement electrodes has been one of a SEMG interface's main requirement.

In this study, our objective is to develop an estimation method for muscular strength while maintaining the accuracy of hand motion recognition and to reflect the result of the measured power on the controlled object. In order to achieve this purpose, we directed our attention to measuring sufficient amounts of information for SEMG. This is because, the disadvantages of SEMGs are that they have a large detection area and therefore, have more potential for cross talk from adjacent muscles. Each subject's SEMG greatly differed depending on the individual's tissue characteristics, physiological cross talk and so on. Therefore, it is a problem subjects. We think that there is a suitable measurement location for every subject, and it is more effective for solving individual differences than employing strong discriminant simple linear models, and the selection method of optimal electrode configuration for using them effectively. The selection method has been one of our main objectives. As for the number of measurement electrodes, our current work shows "four electrodes"are satisfactory to our objective. In order to perform the selection of an optimal measurement electrode configuration , a 96ch multielec-

Chwee Teck Lim, James C.H. Goh (Eds.): ICBME 2008, Proceedings 23, pp. 935–937, 2009
www.springerlink.com

trode is required to be able to measure an individual's differences for SEMG.

II. Materials and Methods

A. 96ch Multi electrode and SEMG measurement system

The multi electrode is one of the features and the key of our system. This is used in order to detect an individual difference of a measuring SEMG while it is being used by the subject moving their hand. This multi electrode was attached to the forearm and an optimal electrode configuration was selected from it. The structure of this multi electrode is shown in Fig.1. To fit a forearm, we use a flexible silicone gum as the base of 96 silver electrodes. And we also designed the SEMG amplifier, which amplifies an SEMG signal about 3,000 times and the frequency band is limited from 10 Hz to 1,000 Hz. The amplified SEMG signals are sampled by a 16-bit A/D converter at a rate of 2,000 Hz.

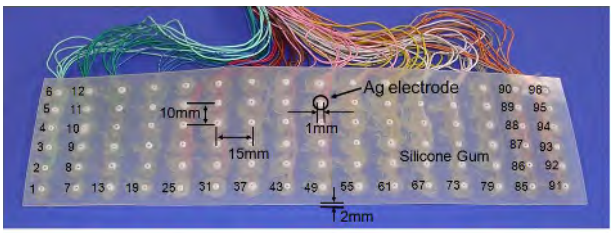


Fig. 1 Structure of 96-channles surface multi electrode. By the side of each electrode is shown the placement number from 1 to 96

B. Grasp force measurement system

In order to estimate a grasp force based on an SEMG signal, it is necessary to determine the relationship between the SEMG characteristic of grasp and a real grasp force for every individual. In the case of most measurement equipment for grasp force, the measured value is indicated by a needle that moves over a dial gauge, and as a result the acquired grasp data cannot be stored into a personal computer (PC). To analyze the relationship using a PC, we developed a grasp force measurement system that provides a real time grasp force measurement and the output data is stored on a PC with the SEMG simultaneously.

A potentiometer is attached to the axis of rotation of the indicator, and translates the indicated value on the dynamometer into a resistance value. The resistance is converted to voltage using a resistance-to-voltage converter which we made. And the analog output voltage is converted to digital for PC input. Most dynamometers indicate only the maximum grasp force, but our equipment directly indicates the change of grasp. Fig.2 shows measuring equipment for grasp force and the resistance-to-voltage converter.



Fig. 2 Grasp force measuring equipment for PC input and the resistance-to-voltage converter

C. Grasp force estimation method

It is well known that there is a close relationship between the muscular force and the EMG signal. However, we used subject-specific models to reduce problems due to intra-subject variation. Thus, our system applies a personal EMG/force relationship depending on the individual's muscle characteristics.

Now, the relationship is written by

$$y_m = \alpha + \beta X_m + \varepsilon_m \tag{1}$$

where y_m is the grasp force data which is performed as the response variable, and X_m is the features of SEGM which is performed as the predictor variables. X_m is the mean value of selected four SEMG. The term ε_m is the residual and it is written by

$$\varepsilon_m = y_m - \hat{y}_m \tag{2}$$

And a SSE is denoted by

$$SSE = \sum_{l=1}^{m} \varepsilon_m^2 \tag{3}$$

The usual method of estimation for the regression model is ordinary least squares. The coefficients α and β are determined by the condition that the sum of the square residuals is as small as possible. Thus, partial differentiation is applied to equation (12), it becomes

$$\begin{aligned} \frac{\partial(SSE)}{\partial\alpha} &= -2\sum_{l=1}^{m}(y_l - \alpha - \beta X_l) = 0 \\ \frac{\partial(SSE)}{\partial\beta} &= -2\sum_{l=1}^{m} X_l(y_l - \alpha - \beta X_l) = 0 \end{aligned} \tag{4}$$

Finally, the regression coefficients are given by

$$\hat{\beta} = \frac{\sum_{l=1}^{m}(X_l - \overline{X})(y_l - \overline{y})}{\sum_{l=1}^{m}(X_l - \overline{X})^2} \qquad (5)$$
$$\hat{\alpha} = \overline{y} - \hat{\beta}\overline{X}$$

where $\overline{X}$ is the mean of the X values and $\overline{y}$ is the mean of the y values. The result of the relationship between the SEMG and the grasp force is shown in Fig.3.

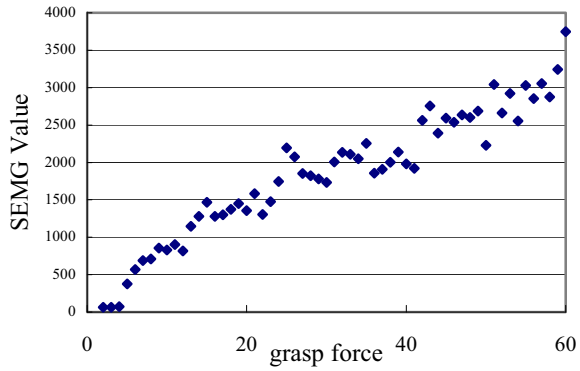


Fig.3 Relationship between the SEMG signals and measured Graspforce

III. Experimental Results and Discussion

We tested two normal subjects to evaluate our system. Requested motions were set to four types which were composed of three motions and one state (Grasp, Release, Pronation, and Rest state). The neutral state is relaxed and there is no motion. This is the initial state and recognition of the three motions is started after this state. The recognition was performed by every 300 ms, and once a grasp motion is recognized, our system moves to the grasp force estimation mode. While a grasp motion is recognized, our system keeps evaluating the grasp force. As for the motions, each subject received training to get used to the control of our system. However, we didn't instruct the subject how to operate the system. Instead, they performed in their own way according to their individual's characteristics.

The experiment was set up as follows:

1 Registration of the SEMG characteristic of the four motions for every subject. This data was used as "predefined data"for the both modeling
2 Selection of best configuration of four measurement electrodes
3 Construction of estimation model and comparison with a real measured grasp data

According to this procedure, the estimation experiment was performed. Fig.4 shows the comparison results of grasp force data between the estimated value and the real measured one. From Fig.4, the estimated value of the grasp force is a good approximation to the real one.

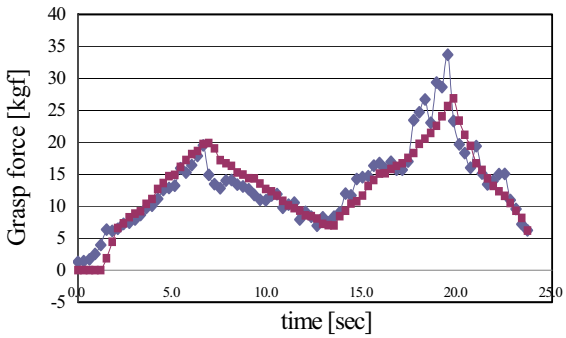


Fig. 4 The grasp force data of estimated value and real measurement value

IV. Conclusion

We have presented an estimation method for muscular strength while maintaining the accuracy of hand motion recognition, and experimental results shows the recognition of four motions were perfect and the grasp force estimated results fit well with the real measured.

The Navigation System for the Visually Impaired Using GPS

Tomoyuki Kanno[1], Kenji Yanashima[2] and Kazushige Magatani[1]

[1]Department of Electrical Engineering, Tokai University, Japan
[2]National Rehabilitation Center for the Disabled, Japan

Abstract — **It is possible for the visually impaired to walk their known area independently by using a white cane. However, in their unknown area, they cannot walk without help of others even if they can use a white cane very well. In such cases, not only a visually impaired person but he/she who assists them receives many stress in dairy activity. Therefore, many types of independent walking assist system for the visually impaired are developing. Our objective of this study is the development of an auto navigation system for the visually impaired which assists independent walking of them. This system measures the position of a visually impaired person (a user) by using GPS (Global Positioning System) and navigates him/her to the destination like as a car navigation system. In our system, a location data is stored in the map database and a position of user are analyzed and optimal route for a user to the destination is calculated. Our system guides a user to the destination along this route, and notifies the user of this route and some information for the safety walking by artificial voice. Three normal subjects were tested with our navigation system. All subjects were blind folded by an eye mask and equipped a navigation system. As a result, our system worked well and all subjects were able to walk to the destination following guidance voice. So, we are developing a new navigation system which is installed on a cellular phone. In Japan, there are some cellular phones that include GPS. And most of application programs for cellular phone are written by JAVA. Therefore, GPS included in a cellular phone will be used and every functions of the navigation system will be written by JAVA. In this paper, we also reports about this new navigation system.**

Keywords — **Visually impaired, GPS, Navigation**

I. Introduction

The objective of this study is the development of the auto navigation system that supports the independent walking of the visually impaired. This system calculates a suitable route to the destination and notifies the user of this route and some information for the safety walking. Fig.1 shows the conception of our navigation system. In our system, the destination is inputted at first. The system obtains the user's position by using GPS and calculates a suitable route to the destination by using map information of the system database. And then, the system guides the user along this route. The voice guidance is used for the notification of a route and some information to user. The action of our system likes a car navigation system. However, there are many different points from a car navigation system. For example, the suitable route is the shortest route in a car navigation system. However, in our system, the suitable route is not the shortest route and is the most safety route for the visually impaired. Therefore, a safety level of each roads are stored in the map database and these information are used in order to calculate a suitable route. And it is important to notify the user of turning and landmark information. In our system, these information is announced by pre recorded voice.

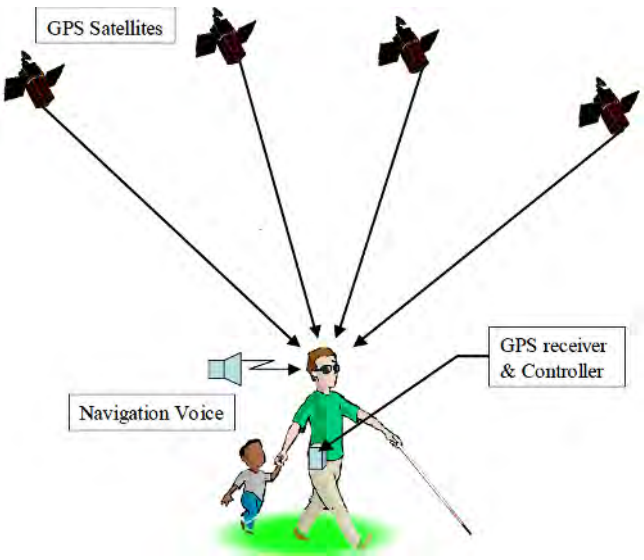


Fig. 1 Navigation system using GPS

II. Methodology

A. GPS

GPS(Global Positioning System) is one of the famous positioning system using satellites. We can obtain the latitude longitude and altitude of the measured position every one second easily. High accuracy data of positioning is able to obtain by using DGPS. In our previous system, DGPS was used in order to measure correct position. However, now we can use GPS without SA, and typical error range of

Chwee Teck Lim, James C.H. Goh (Eds.): ICBME 2008, Proceedings 23, pp. 938–941, 2009
www.springerlink.com

GPS is less than 5m. Therefore, normal GPS is used in our system.

B. Map database

As mentioned earlier, our system has a map database. This database consists of three layers. Latitude and longitude sets of each crossing and landmark are stored in the first layer. Link information between each crossing and landmark are stored in the second layer. And safety levels of each road that is defined the way between one crossing and another are stored in the third layer. In our system, the most likelihood user's position is determined base on GPS and this database information by using map matching method [1]. And the third layer of the database is used in order to obtain a suitable route as following. An example of visualized map information based on a map database is shown in Fig.2.

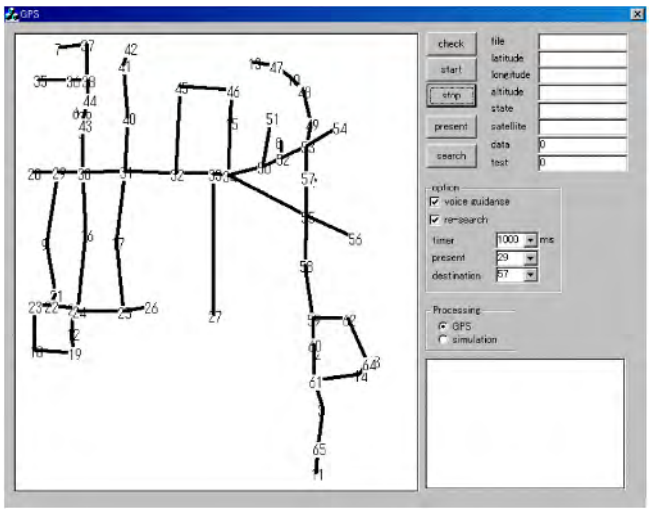


Fig. 2 Digital map

C. Suitable route

Our map database has the safety information of the rode as mentioned earlier. Generally, a rode has many kind of condition and safety. For example, even if the straight road, a rough conditioned rode is not good for the visually impaired. And a road that has stairs or has heavy traffic is not good also. So, the safety levels of each rode for the visually impaired are defined and these levels are stored in the map database. The calculation of a suitable route is based on Dijkstra's method. Generally, the every road distances are used and the suitable route is determined as the shortest distance to the destination in Dijkstra's method. In our system, logical distance of the road is determined as the product of the physical distance and the safety level. Therefore, the logical distance of bad condition road is longer than the physical distance in our system. These logical distances of each road is used for the suitable route calculation. Fig.3 shows a result of the suitable route calculation. In this figure, the system calculated the route form point 1 to point 9. The shortest route is shown in Fig.3. However, in this database the road condition was set as route 34 to 33 was danger for the visually impaired. So, the calculation result is shown in Fig.4. This result is not shortest route, however the road 34 to 33 is avoided.

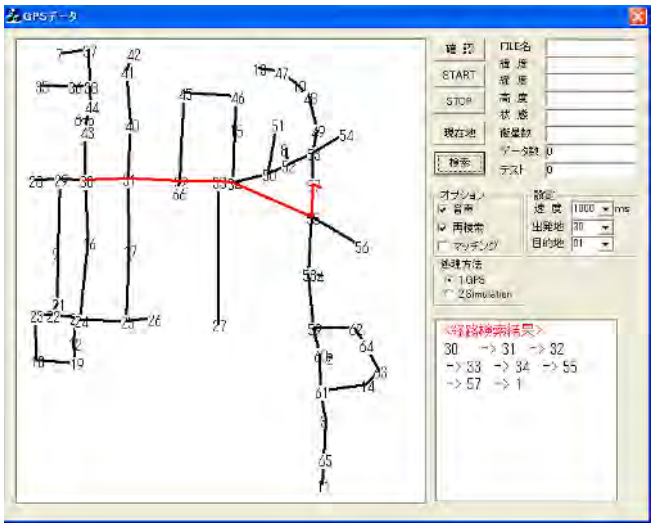


Fig. 3 Shortest route

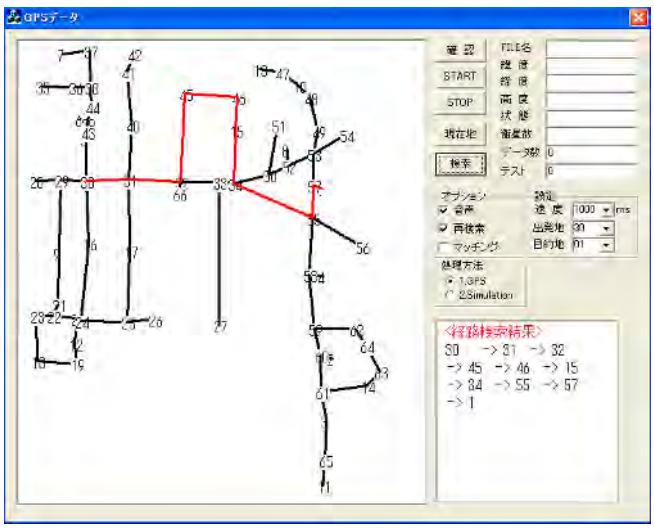


Fig. 4 Suitable route

D. Voice notification

As mentioned earlier, voice processing system is used in order to notify the user to some information of the crossing and the landmark. In our system, the processing of voice guidance is separated into two stages. When an user enters into the landmark point, the system has to notify him/her of the landmark information by pre-recorded voice. In order to avoid miss hearing of this information, voice processing system is separated into two stages. At first stage, when an user enters into the area that is 7.5m away from the landmark, the system notify of the entering to the important area by beep sound. At second stage, after the first stage when an user reach the area that is 5m away from the landmark, the voice notification is started. In our system, first beep sound means "voice guidance point comes soon", and after this warning, the voice guidance is started. The conception of this method is shown in Fig.5.

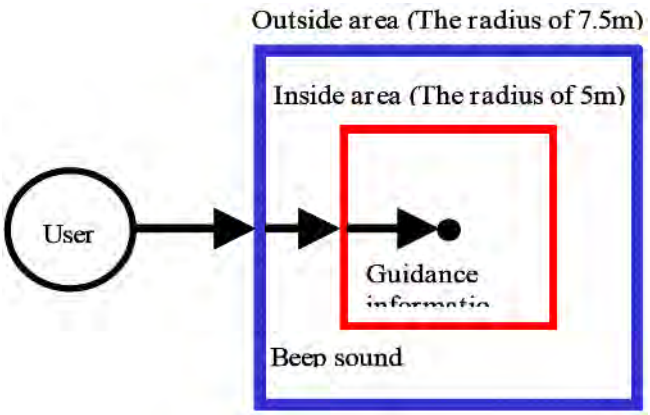


Fig. 5 Voice guidance area

III. Experiment&Results

Five normal subject was tested with our new navigation system. All subjects were blindfolded by an eye mask and equipped the system. The navigation route was set as the point 30 to point 57 and all subjects walked following the guidance voice. A green line of Fig.5 shows that walked on the calculated suitable route. From this experiment, the following characteristics became clear.

(1)All subjects could walk to the destination following the guidance voice.

(2)There are some areas where GPS did not work. Therefore, some system that estimates the position of the user is need.

(3)In some points, voice processing system did not work because of accuracy of GPS.

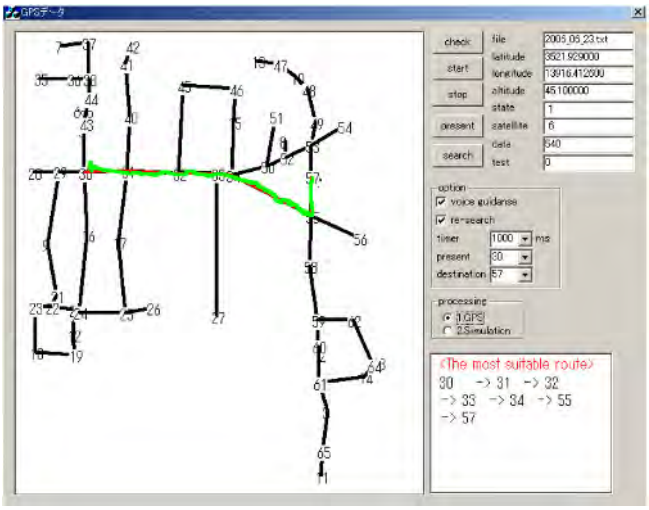


Fig. 6 A result of experiment

IV. Conclusion

In this paper, we described about our developed navigation system for the visually impaired. In this system, suitable route from start point to the destination is calculated by using user's position that is obtained using GPS and a digital map database. In our system, area information is announced by artificial voice at the landmark. Developed navigation system was tested for normal subject. The subject equipped our system and walked along generated suitable route. From this experiments, some problems of our system become clear. However, we think that these problems will be improved near future. And our navigation system will be a very valuable one to support activities of the

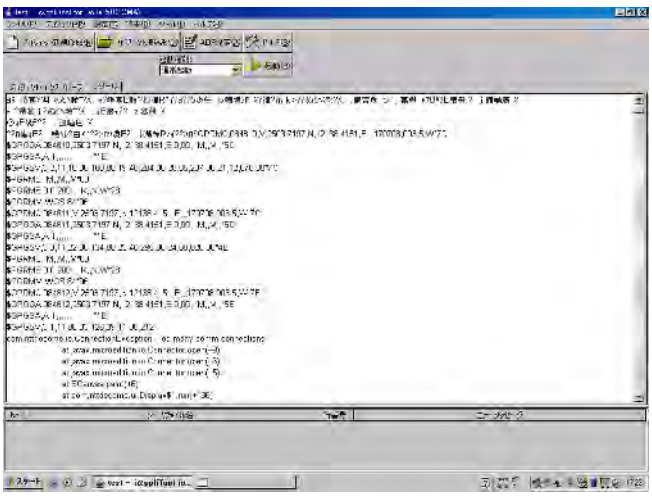


Fig. 7 Location data catched by cellular phone

visually impaired. This study, we propose a navigation system on cellular phone. Cellular phone has high performance processor, high density memory and GPS receiver. It is possible to make more small navigation system for visually impaired. We make an application program written by JAVA language. We test this program, and get location data. Infuture, we will make navigation program on cellular phone.

REFERENCES

1. J.Tanaka, K.Yanashima, K.Magatani "Development of the guidance system for the visually impaired using GPS" Department of Electrical Engineering, Tokai University, Japan

Author: Tomoyuki Kanno
Institute: Tokai University
Street: 1117 Kitakaname
City: Hiratsuka
Country: Japan
Email: 8adpm013@mail.tokai-u.jp

Investigation of Similarities among Human Joints through the Coding System of Human Joint Properties—Part 1

S.C. Chen[1], S.T. Hsu[2], C.L. Liu[2] and C.H. Yu[3]

[1]Department of Physical Medicine and Rehabilitation, Taipei Medical University and Hospital, Taipei, Taiwan
[2]Department of Mechanical Engineering, National Taiwan University, Taipei, Taiwan
[3]Department of Physical Therapy and Assistive Technology, National Yang-Ming University, Taipei, Taiwan

Abstract — **Properties of human joints are essential for orthopedic practice, physical therapy, designing related motion assistive devices, etc. Few studies, however, have ever tried to collect and arrange this knowledge, making researchers need to look up references tiresomely. In view of the above, Hsu et al. [1] proposed a coding system of human joint properties, trying to make reference consulting more convenient and efficient. This coding system includes eight properties of 41 kinds of human joints. The eight properties are locations of joints, numbers of bones involved in joints, functions of joints, shapes of joint surfaces, arthrokinematics of joints, directions of rotation of joints, directions of translation of joints, and numbers of axes of joints. Our work, taking one step ahead, adds one property—the weight bearing of joints—into the original coding system, so as to make the coding system more suitable for medical use. For our newly added property, simple digits are assigned as codes to symbolize the behavior of the 41 kinds of joints. This new property is then joined into the original coding system, and a new coding system with the nine properties is established as a result. In conclusion, this new coding system not only serves as a concise approach to investigating human joint properties, but relatively meets the needs of medical science. We expect that researchers can make further comprehensive studies with this new coding system. Certainly, to upgrade and improve this new classification system, we need specialists' and experts' feedbacks.**

Keywords — **Coding system, weight bearing, property of human joint, human joint.**

I. Introduction

The concern with properties of human joints, which are the essence of orthopedic practice, physical therapy, as well as designing motion assistive devices, has been growing recently. Pertinent studies have focused on properties of such specific joints as the shoulder joint [2], elbow joint [3], wrist joint [4], hip joint [5], and so forth [6, 7], making the related knowledge well developed and human joint properties well understood.

Germane information is so plentiful while works trying to organize it are so rare that reference consulting has been an arduous task. To solve this problem, Hsu et al. [1] collected and arranged this copious knowledge, and proposed a coding system containing eight properties of the 41 kinds of human joints. The eight properties are locations of joints, numbers of bones involved in joints, functions of joints, shapes of joint surfaces, arthrokinematics of joints, directions of rotation of joints, directions of translation of joints, and numbers of axes of joints.

In our work, we attempt to add one more property—the weight bearing of joints, an indispensible factor in the field of rehabilitation—into the original coding system, expecting to enable this system to be more favorable for medical use.

II. Coding procedure for weight bearing

A. Weight bearing of human joints

Weight bearing of joints can be defined as a capability of tissues to bear the compressive force imposed by the weight of the body located above them without being injured or damaged [8]. Besides, joints situated in the lower extremity or in the axial body are generally belonging to weight-bearing joints [8]. Given this point, we categorize the 41 kinds of joints considered in [1] into two groups: weight-bearing joints and non-weight-bearing joints. And those in the lower extremity or axial body are weight-bearing, while others are not. This classification is given in Table 1.

Table 1 Classification of joints according to the property of weight bearing

Weight-bearing joints	Non-weight-bearing joints
Cervical spine, lumbar spine, lumbosacral j't, thoracic spine, atlantoaxial j't, atlanto-occipital j't, symphysis pubis j't, intermetatarsal j't, patellofemoral j't, sacroiliac j't, tarsometatarsal j't, proximal tibiofibular j't, distal tibiofibular j't, subtalar j't, interphalangeal j't (foot), tibiofemoral j't, metatarsophalangeal j't, hip j't, transverse tarsal j't, talocrural j't	Temporomandibular j't, suture j't of the skull, sternocostal j't, intrasternal j't, costotransverse j't, costovertebral j't, 2nd, 3rd carpometacarpal j't, intermetacarpal j't, acromioclavicular j't, humeroulnar j't, interphalangeal j't (hand), proximal radioulnar j't, distal radioulnar j't, metacarpophalangeal j't, 1st, 4th, 5th carpometacarpal j't, sternoclavicular j't, humeroradial j't, glenohumeral j't, scapulocostal j't, radiocarpal j't, midcarpal j't

Chwee Teck Lim, James C.H. Goh (Eds.): ICBME 2008, Proceedings 23, pp. 942–945, 2009
www.springerlink.com

B. Coding rule of the property of weight bearing

Since we are to code the joints and combine the coding result with the ones in [1], the coding rule of the property of weight bearing is required. We define the coding rule as follows: If a joint is a weight-bearing joint, it is coded by 1; if not, it is coded by 0. For instance, the cervical spine in the left column of Table 1 is weight bearing, and thus the code of this property of the cervical spine is 1; on the other hand, the temporomandibular joint in the right column possesses no weight-bearing ability, and thus its code is 0.

C. Codes of weight bearing of joints

Based on the definition given above, all the 41 kinds of joints are then coded. The coding result is given in Table 2, in which the order of the 41 kinds of joints is arranged by their locations: from superior to inferior and from proximal to distal.

Table 2 Codes of weight bearing of joints

Joint	Code of weight bearing
Suture j't of the skull	0
Temporomandibular j't	0
Atlanto-occipital j't	1
Atlantoaxial j't	1
Cervical spine	1
Thoracic spine	1
Lumbar spine	1
Lumbosacral j't	1
Costovertebral j't	0
Costotransverse j't	0
Sternocostal j't	0
Intrasternal j't	0
Sternoclavicular j't	0
Acromioclavicular j't	0
Glenohumeral j't	0
Scapulocostal j't	0
Humeroulnar j't	0
Humeroradial j't	0
Proximal radioulnar j't	0
Distal radioulnar j't	0
Radiocarpal j't	0
Midcarpal j't	0
1^{st}, 4^{th}, 5^{th} carpometacarpal j't	0
2^{nd}, 3^{rd} carpometacarpal j't	0
Intermetacarpal j't	0
Metacarpophalangeal j't	0
Interphalangeal j't (hand)	0
Sacroiliac j't	1
Hip j't	1
Symphysis pubis j't	1
Tibiofemoral j't	1
Patellofemoral j't	1
Proximal tibiofibular j't	1
Distal tibiofibular j't	1
Talocrural j't	1
Subtalar j't	1
Transverse tarsal j't	1
Tarsometatarsal j't	1
Intermetatarsal j't	1
Metatarsophalangeal j't	1
Interphalangeal j't (foot)	1

III. Results

We now combine the codes in Table 2 with the coding system proposed in [1]. The combination, serving as the coding system of nine properties of human joints, is presented in Table 3.

Table 3 Coding system of nine properties of human joints

Joint \ Code	Code of location	Code of number of bones involved	Code of function	Code of shape of surfaces	Code of arthrokinematics	Code of direction of rotation	Code of direction of translation	Code of number of axes	Code of weight bearing
Suture j't of the skull	1	2	1	0	0	0	0	s	0
Temporomandibular j't	1	1	3	2	7	1	4	1	0
Atlanto-occipital j't	2	1	3	4	3	4	0	2	1
Atlantoaxial j't	2	1	3	3	5	5	0	2	1
Cervical spine	2	1	2	0	5	7	0	3	1
Thoracic spine	2	1	2	0	5	7	0	3	1
Lumbar spine	2	1	2	0	5	7	0	3	1
Lumbosacral j't	2	1	2	0	5	7	0	3	1
Costovertebral j't	2	2	2	0	5	1	6	1	0
Costotransverse j't	2	1	2	0	1	2	5	1	0
Sternocostal j't	2	1	1	0	0	0	0	s	0
Intrasternal j't	2	1	1	0	0	0	0	s	0
Sternoclavicular j't	3	1	3	5	5	7	0	3	0
Acromioclavicular j't	3	1	3	1	3	7	0	3	0
Glenohumeral j't	3	1	3	6	6	7	0	3	0
Scapulocostal j't	3	2	3	1	3	2	6	1	0
Humeroulnar j't	3	1	3	2	3	1	0	1	0
Humeroradial j't	3	1	3	6	5	5	0	2	0
Proximal radioulnar j't	3	1	3	3	1	3	0	1	0
Distal radioulnar j't	3	1	3	3	3	3	0	1	0
Radiocarpal j't	3	2	3	4	3	4	0	2	0
Midcarpal j't	3	2	3	5	3	4	0	2	0
1^{st}, 4^{th}, 5^{th} carpometacarpal j't	3	1	3	5	3	4	0	2	0
2^{nd}, 3^{rd} carpometacarpal j't	3	1	1	0	0	0	0	s	0
Intermetacarpal j't	3	1	2	0	3	0	2	0	0
Metacarpophalangeal j't	3	1	3	4	3	4	0	2	0
Interphalangeal j't (hand)	3	1	3	2	3	1	0	1	0
Sacroiliac j't	4	1	2	0	3	1	6	1	1
Hip j't	4	1	3	6	3	7	0	3	1
Symphysis pubis j't	4	1	1	0	0	0	0	s	1
Tibiofemoral j't	4	1	3	2	7	5	0	2	1
Patellofemoral j't	4	1	2	0	3	0	3	0	1
Proximal tibiofibular j't	4	1	2	0	3	c	c	1	1
Distal tibiofibular j't	4	1	2	0	3	c	c	1	1
Talocrural j't	4	2	3	2	3	1	0	1	1
Subtalar j't	4	1	3	1	3	7	0	3	1
Transverse tarsal j't	4	2	2	0	3	7	0	3	1
Tarsometatarsal j't	4	1	2	0	3	4	0	2	1
Intermetatarsal j't	4	1	2	0	3	0	3	0	1
Metatarsophalangeal j't	4	1	3	4	3	5	0	2	1
Interphalangeal j't (foot)	4	1	3	2	3	1	0	1	1

The definitions of the codes of the original eight properties follow those in [1], and are as tabled below.

Table 4 Coding rules of the eight properties of human joints defined in [1]

Property	Code	Definition
Location	1	Skull
	2	Trunk
	3	Upper extremity
	4	Lower extremity
Number of bones involved	1	Simple joint
	2	Compound joint
Function	1	Synarthrotic joint
	2	Amphiarthrotic joint
	3	Diarthrotic joint
Shape of surfaces	0	(Unable to be classified)
	1	Plane joint
	2	Hinge joint
	3	Pivot joint
	4	Condyloid joint
	5	Saddle joint
	6	Ball and socket joint
Arthrokinematics	0	(Unable to be classified)
	1	Spin
	2	Roll
	3	Slide
	4	Spin and roll
	5	Spin and slide
	6	Roll and slide
	7	Spin, roll and slide
Direction of rotation	0	(Unable to be classified)
	1	Rotation around a medial-lateral axis
	2	Rotation around an anterior-posterior axis
	3	Rotation around a vertical axis
	4	Combination of 1 and 2
	5	Combination of 1 and 3
	6	Combination of 2 and 3
	7	Combination of 1, 2 and 3
	a	Dependent rot. around a medial-lateral axis
	b	Dependent rot. around an anterior-posterior axis
	c	Dependent rot. around a vertical axis
Direction of translation	0	(Unable to be classified)
	1	Translation alone a medial-lateral axis
	2	Translation along an anterior-posterior axis
	3	Translation along a vertical axis
	4	Combination of 1 and 2
	5	Combination of 1 and 3
	6	Combination of 2 and 3
	7	Combination of 1, 2 and 3
	a	Dependent trans. alone a medial-lateral axis
	b	Dependent trans. along an anterior-posterior axis
	c	Dependent trans. along a vertical axis
Number of axes	0	Nonaxial joint
	1	Uniaxial joint
	2	Biaxial joint
	3	Triaxial joint
	s	(Unable to be classified)

IV. Discussion

A coding system containing nine joint properties is proposed in this work. For each property, all the 41 kinds of joints are assigned appropriate codes; namely, the joints are expressed by a series of nine digits indicating their nine properties, allowing researchers to learn their needed information through readily consulting the table. Once the code of a certain property is learned, Table 2 and Table 4 can serve as "decoders" to decipher the code, and knowledge of the required properties is then obtained. The coding system, thus, presents an efficient approach to acquiring or gathering pertinent materials.

A. Applications of the coding system

The advantage given above further enables researches to learn these properties simultaneously, for they do not have to consult to different references individually for an individual need anymore. Instead, all the nine properties of these 41 joints can be readily obtained at one time by referring to this system. Thus, a systematical classification of joints, or even an investigation of similarities among joints, is made to be possible. Take the property of the number of axes for example. We can classify the joints according to this property by simply sorting their codes of this property with the help of suitable software. The result classifies all the joints into five groups, as the five ones indicated in the row of Number of Axes in Table 4; joints in the same group possess the similarity regarding the property.

In the same way, similarities among different joints for two or more properties can also be disclosed as well. For instance, if we are interested in finding out all the diarthrotic joints which are also saddle joints, we can focus our attention on the codes of function and shape of surfaces. By searching for the joints with the code of function being 3 (indicating the diarthrotic joint), and the code of shape of surfaces being 5 (indicating the saddle joint), three kinds of joints satisfying this requirement are found; they are the sternoclavicular joint, midcarpal joint, and 1st, 4th and 5th carpometacarpal joint. Other similarities among joints for various combinations of properties can be determined through the same method.

Properties of human joints are the crucial foundation of such pertinent medical fields as orthopedic practice, physical therapy, and designing related motion assistive devices. In addition to these, human joint properties, especially those concerning movement, are also related to the mechanism design for humanoid robots in the mechanical field [9]. It could be beneficial to apply this coding system to this mechanical field. For example, researchers can code the kinematic pairs, which are considered as joints of a kinematic chain [10], according to their pertinent properties. With the two sets of coding systems, relationship between human joints and kinematic pairs will be revealed. Moreover, the equivalent kinematic pairs of human joints, allowing corresponding movements to those of human joints, can also be determined.

B. Interdependence among the properties

The coding system proposed in this study considers nine different properties, six of which are interdependent upon at least one another, and three interdependent cases exist.

The first interdependence occurs among the function, the direction of rotation, direction of translation, and the number of axes. If a joint rotates around one, two, or three axes, its number of axis was one, two, or three. If a joint rotating around no axis allows translations, its number of axis was 0. If a joint allows neither rotation nor translation, then its function is synarthrotic and is coded by "s" in Table 3. The interdependence is denoted by ID1 in Table 5.

The second interdependence occurs among the function and the shape of surfaces. If the code of the function is 1 or 2, the code of the shape of surfaces must be 0; only when the code of the function is 3 can the code of the shape of surfaces be 1 to 6. It agrees with the fact that only diarthrotic joints can be classified according to their shapes [11]. The interdependence is denoted by ID2 in Table 5.

The third interdependence occurs among the function and the arthrokinematics. If the code of the function is 1, the code of the shape of surfaces must be 0; only when the code of the function is 2 or 3 can the code of the shape of surfaces be 1 to 7. It indicates that the synarthrotic joint allows no movement between bones. The interdependence is denoted by ID3 in Table 5.

Except the three sorts of interdependences, other properties are independent of each other.

Table 5 Interdependence among the properties

	Location	Number of bones	Function	Shape of surfaces	Arthrokinematics	Direction of rotation	Direction of translation	Number of axes	Weight bearing
Location	--								
Number of bones		--							
Function			--	ID2	ID3	ID1	ID1	ID1	
Shape of surfaces			ID2	--					
Arthrokinematics			ID3		--				
Direction of rotation			ID1			--	ID1	ID1	
Direction of translation			ID1			ID1	--	ID1	
Number of axes			ID1			ID1	ID1	--	
Weight bearing									--

V. Conclusions

This work proposed a coding system containing nine properties of human joints. The system serves as a concise approach to investigating joint properties, and also meets the needs of medical science. Besides, with this system, comprehensive inspection of information about joints and other interdisciplinary applications are attainable. In the future, feedbacks from specialists and experts are needed, so as to enhance this new classification system.

Acknowledgment

The National Science Council of Taiwan (R.O.C.) is acknowledged for the support of this paper (NSC95-2221-E-038-010-MY3).

References

1. S. T. Hsu, S. C. Chen, C. H. Yu and C. L. Liu (2007) Establishment of the Coding System of Human Joint Properties, Proc. 24th National Conference on Mechanical Engineering of the Chinese Society of Mechanical Engineers, Chungli, Taiwan, 2007, pp 5593-5598
2. G. R. Johnson and J. M. Anderson (1990) Measurement of three-dimensional shoulder movement by an electromagnetic sensor. Clinical Biomechanics, vol. 5, issue 3, pp. 131-136
3. A. P. Vasen, S. H. Lacey, M. W. Keith and J. W. Shaffer (1995) Functional range of motion of the elbow. Journal of Hand Surgery, vol. 20, issue 2, pp. 288-292
4. L. Leonard, D. Sirkett, G. Mullineux, G. E. B. Giddins and A. W. Miles (2005) Development of an in-vivo method of wrist joint motion analysis. Clinical Biomechanics, vol. 20, pp.166-171
5. F. H. Dujardin, X. Roussignol, O. Mejjad, J. Weber and J. M. Thomine (1997) "Interindividual variations of the hip joint motion in normal gait. Gait & Posture, vol. 5, pp. 246-250
6. R. A. Malinzak, S. M. Colby, D. T. Kirkendall, B. Yu and W. E. Darrett (2001) A comparison of knee joint motion patterns between men and women in selected athletic tasks. Clinical Biomechanics, vol. 16, pp. 438-445
7. R. S. Sodhi (2000) Evaluation of head and neck motion with the hemispherical shell method. International Journal of Industrial Ergonomics, vol. 25, pp. 683-691
8. J. E. Muscolino (2006) Kinesiology: The Skeletal System and Muscle Function. Mosby Elsevier, p. 64
9. H. Yussof, M. Yamano, Y. Nash and M. Ohka (2006) Design of a 21-DOF humanoid robot to attain flexibility in human-like motion, the 15th IEEE International Symposium on Robot and Human Interactive Communication (RO-MAN06), 2006, pp. 202-207
10. R. L. Norton (2001) Design of Machinery: An Introduction to the Synthesis and Analysis of Mechanisms and Machines. McGraw Hill Publishing Company, New York, p. 27
11. N. Palastanga, D. Field and R. Soames (2006) Anatomy and Human Movement: Structure and Function. Butterworth Heinemann Elsevier, New York, pp. 23-24

Author: Shan-Ting HSU
Institute: Department of Mechanical Engineering, National Taiwan University
Street: No. 1, Sec. 4, Roosevelt Road, Taipei, 10617
City: Taipei
Country: Taiwan
Email: r94522638@ntu.edu.tw

Investigation of Similarities among Human Joints through the Coding System of Human Joint Properties—Part 2

S.C. Chen[1], S.T. Hsu[2], C.L. Liu[2] and C.H. Yu[3]

[1]Department of Physical Medicine and Rehabilitation, Taipei Medical University and Hospital, Taipei, Taiwan
[2]Department of Mechanical Engineering, National Taiwan University, Taipei, Taiwan
[3]Department of Physical Therapy and Assistive Technology, National Yang-Ming University, Taipei, Taiwan

Abstract — **In rehabilitation engineering and assistive technology, precedent researches have focused on a single characteristic or property of a single joint, while little attention was paid to similarities among joints. This work attempts to investigate similarities among human joints by referring to the coding system of human joint properties proposed in Part 1. To investigate the similarities, eight out of the nine properties in this coding system (except the locations of joints) are divided into five cases. In Case 1, we consider the numbers of bones involved in joints and shapes of joint surfaces. In Case 2, we consider the directions of rotation, directions of translation, and numbers of axes of joints. In Cases 3, 4 and 5, the functions of joints, arthrokinematics of joints, and weight bearing of joints are considered respectively. Similarities among the 41 kinds of joints in this coding system are hereby investigated by sorting the joints' codes in each case. As results, the 41 kinds of joints are classified into 12, 13, 3, 6 and 2 groups in Case 1 to Case 5 in sequence. Regarding the properties discussed in each case, joints in the same group possess similar properties. However, four groups in Case 1, four groups in Case 2, and one group in Case 4 each have only one kind of joint, which is unique, having no similarities with other joints in the properties considered. In conclusion, similarities among human joints are discovered systematically by referring to the coding system proposed in Part 1. These similarities offer an innovative and utile reference for assistive technology device designs and other pertinent research. Similarities beyond these five cases can be further investigated with the same method.**

Keywords — **Similarity among human joints, coding system, property of human joint, sorting, human joint.**

I. Introduction

In the field of rehabilitation engineering and assistive technology, numerous attempts have been successfully made to discover properties of human joints; knowledge of joint properties has been widely understood. These properties are indispensable to pertinent researches in such medicine fields as physical medicine, rehabilitation, assistive technology devices, and so forth. Take continuous passive motion (CPM) for example. It was proved that CPM has a great effect on recovering the range of motion of joints [1, 2], and a considerable number of designs for CPM devices have been proposed for various joints based on their various properties [3, 4]. Besides, many types of artificial joints have also been proposed for different human joints [5, 6]. Another research field related to human joint properties is the mechanism design for humanoid robots. In its designing process, the degrees of freedom (DOFs) of human joints have to be considered, so that the DOFs of humanoid robot joints can approximate to that of human joints [7]. Though properties of human joints are extensively applied in these pertinent fields, most studies have focused on a single property of a single joint; properties of joints have been investigated individually before a designing process begins. Similarity among joints, deserving consideration, has unfortunately hitherto been neglected [8]. If similarities among joints are taken into consideration, one advantage is that, for instance, designers can simply change one existing design of a similar joint to complete a new design fitting their needs. Developing a design in this way thus takes much less time than beginning a completely new one from scratch. On these grounds, the purpose of this paper is to investigate the similarities among human joints.

To achieve this purpose, we attempt to apply the coding system proposed in the first part of our work. One reason for using coding systems, according to Groover [9], is design retrieval—a mechanism for determining whether a similar part exists; if so, an uncomplicated change in an existing part can be made. This is our expectation. Therefore, the coding system is utilized in this part of our work as an approach to investigating similarities among joints.

II. Determination of Cases and Research Method

The coding system proposed in Part 1 considers nine properties, eight of which are of our interests (except the locations). They are categorized into five cases.

In Case 1, the number of bones involved and the shape of surfaces are considered. The two properties are both pertinent to anatomical structures of joints. In Case 2, the direction of rotation, direction of translation, and the number of axes are considered. The three properties are related to the direction of motion allowed at joints. In Case 3, the func-

Chwee Teck Lim, James C.H. Goh (Eds.): ICBME 2008, Proceedings 23, pp. 946–949, 2009
www.springerlink.com

tion of joints is considered. This property has to do with range of motion at joints. In Case 4, we consider the arthrokinematics of joints, which refers to relative movements occurring between joint surfaces. In Case 5, the weight bearing of joints is considered, which is an essential factor widely considered in physical therapy.

The similarities of joints are then investigated based on these five cases. In each case, codes of the considered properties are sorted incrementally by Microsoft Excel®. Similarities among joints can then be determined by the sorting results.

III. Sorting Procedure and Results

For Case 1, the codes of the number of bones involved and the shape of surfaces are to be sorted. We select the codes of the number of bones as the primary codes for sorting, the codes of the shape of surfaces as the secondary codes. And the sorting result is given in Table 1. The result remains constant if we switch "the codes of the number of bones involved" and "the codes of the shape of surfaces" to secondary codes and primary codes respectively.

It is learned from Table 1, from the top, that a group of 16 kinds of joints has similarities concerning the two properties; another group containing two kinds of joints has similarities; still another group containing five ones has similarities, and so on. Altogether, there are 12 groups of joints, among which four groups possess only one kind of joint. Joints in these four groups are unique, sharing no similarities with others in the properties considered.

For Case 2, as given in Table 2, the codes of the direction of rotation, direction of translation, and the number of axes are to be sorted. The codes of the direction of rotation is chosen as the primary codes for sorting, the codes of the direction of translation as the secondary, and the codes of the number of axes as the third. Similarly, the order of sorting has no influence on the result.

As a result of Case 2, joints are classified into 13 groups; those in the same group possess same properties considered in this case. Among the 13 groups, four groups possess only one kind of joint.

Table 1 Similarity among joints and the sorting result regarding the number of bones and shape of surfaces

Joint \ Code	Code of location	**Code of number of bones involved**	Code of function	**Code of shape of surfaces**	Code of arthrokinematics	Code of direction of rotation	Code of direction of translation	Code of number of axes	Code of weight bearing	Number of joints sharing the similarity
Cervical spine	2	**1**	2	**0**	5	7	0	3	1	16
Thoracic spine	2	**1**	2	**0**	5	7	0	3	1	
Lumbar spine	2	**1**	2	**0**	5	7	0	3	1	
Lumbosacral j't	2	**1**	2	**0**	5	7	0	3	1	
Costotransverse j't	2	**1**	2	**0**	1	2	5	1	0	
Sternocostal j't	2	**1**	1	**0**	0	0	0	s	0	
Intrasternal j't	2	**1**	1	**0**	0	0	0	s	0	
2nd, 3rd carpometacarpal j't	3	**1**	1	**0**	0	0	0	s	0	
Intermetacarpal j't	3	**1**	2	**0**	3	0	2	0	0	
Sacroiliac j't	4	**1**	2	**0**	3	1	6	1	1	
Symphysis pubis j't	4	**1**	1	**0**	0	0	0	s	1	
Patellofemoral j't	4	**1**	2	**0**	3	0	3	0	1	
Proximal tibiofibular j't	4	**1**	2	**0**	3	c	c	1	1	
Distal tibiofibular j't	4	**1**	2	**0**	3	c	c	1	1	
Tarsometatarsal j't	4	**1**	2	**0**	3	4	0	2	1	
Intermetatarsal j't	4	**1**	2	**0**	3	0	3	0	1	
Acromioclavicular j't	3	**1**	3	**1**	3	7	0	3	0	2
Subtalar j't	4	**1**	3	**1**	3	7	0	3	1	
Temporomandibular j't	1	**1**	3	**2**	7	1	4	1	0	5
Humeroulnar j't	3	**1**	3	**2**	3	1	0	1	0	
Interphalangeal j't (hand)	3	**1**	3	**2**	3	1	0	1	0	
Tibiofemoral j't	4	**1**	3	**2**	7	5	0	2	1	
Interphalangeal j't (foot)	4	**1**	3	**2**	3	1	0	1	1	
Atlantoaxial j't	2	**1**	3	**3**	5	5	0	2	1	3
Proximal radioulnar j't	3	**1**	3	**3**	1	3	0	1	0	
Distal radioulnar j't	3	**1**	3	**3**	3	3	0	1	0	
Atlanto-occipital j't	2	**1**	3	**4**	3	4	0	2	1	3
Metacarpophalangeal j't	3	**1**	3	**4**	3	4	0	2	0	
Metatarsophalangeal j't	4	**1**	3	**4**	3	5	0	2	1	
Sternoclavicular j't	3	**1**	3	**5**	5	7	0	3	0	2
1st, 4th, 5th carpometacarpal j't	3	**1**	3	**5**	3	4	0	2	0	
Glenohumeral j't	3	**1**	3	**6**	6	7	0	3	0	3
Humeroradial j't	3	**1**	3	**6**	5	5	0	2	0	
Hip j't	4	**1**	3	**6**	3	7	0	3	1	
Suture j't of the skull	1	**2**	1	**0**	0	0	0	s	0	3
Costovertebral j't	2	**2**	2	**0**	5	1	6	1	0	
Transverse tarsal j't	4	**2**	2	**0**	3	7	0	3	1	
Scapulocostal j't	3	**2**	3	**1**	3	2	6	1	0	1
Talocrural j't	4	**2**	3	**2**	3	1	0	1	1	1
Radiocarpal j't	3	**2**	3	**4**	3	4	0	2	0	1
Midcarpal j't	3	**2**	3	**5**	3	4	0	2	0	1

Table 2 Similarity among joints and the sorting result regarding the direction of rotation, direction of translation, and the number of axes

Joint \ Code	Code of location	Code of number of bones involved	Code of function	Code of shape of surfaces	Code of arthrokinematics	**Code of direction of rotation**	**Code of direction of translation**	**Code of number of axes**	Code of weight bearing	Number of joints sharing the similarity
Suture j't of the skull	1	2	1	0	0	**0**	**0**	**s**	0	
Sternocostal j't	2	1	1	0	0	**0**	**0**	**s**	0	
Intrasternal j't	2	1	1	0	0	**0**	**0**	**s**	0	5
2nd, 3rd carpometacarpal j't	3	1	1	0	0	**0**	**0**	**s**	0	
Symphysis pubis j't	4	1	1	0	0	**0**	**0**	**s**	1	
Intermetacarpal j't	3	1	2	0	3	**0**	**2**	**0**	0	1
Patellofemoral j't	4	1	2	0	3	**0**	**3**	**0**	1	2
Intermetatarsal j't	4	1	2	0	3	**0**	**3**	**0**	1	
Humeroulnar j't	3	1	3	2	3	**1**	**0**	**1**	0	
Interphalangeal j't (hand)	3	1	3	2	3	**1**	**0**	**1**	0	4
Talocrural j't	4	2	3	2	3	**1**	**0**	**1**	1	
Interphalangeal j't (foot)	4	1	3	2	3	**1**	**0**	**1**	1	
Temporomandibular j't	1	1	3	2	7	**1**	**4**	**1**	0	1
Costovertebral j't	2	2	2	0	5	**1**	**6**	**1**	0	2
Sacroiliac j't	4	1	2	0	3	**1**	**6**	**1**	1	
Costotransverse j't	2	1	2	0	1	**2**	**5**	**1**	0	1
Scapulocostal j't	3	2	3	1	3	**2**	**6**	**1**	0	1
Proximal radioulnar j't	3	1	3	3	1	**3**	**0**	**1**	0	2
Distal radioulnar j't	3	1	3	3	3	**3**	**0**	**1**	0	
Atlanto-occipital j't	2	1	3	4	3	**4**	**0**	**2**	1	
Radiocarpal j't	3	2	3	4	3	**4**	**0**	**2**	0	
Midcarpal j't	3	2	3	5	3	**4**	**0**	**2**	0	6
1st, 4th, 5th carpometacarpal j't	3	1	3	5	3	**4**	**0**	**2**	0	
Metacarpophalangeal j't	3	1	3	4	3	**4**	**0**	**2**	0	
Tarsometatarsal j't	4	1	2	0	3	**4**	**0**	**2**	1	
Atlantoaxial j't	2	1	3	3	5	**5**	**0**	**2**	1	
Humeroradial j't	3	1	3	6	5	**5**	**0**	**2**	0	4
Tibiofemoral j't	4	1	3	2	7	**5**	**0**	**2**	1	
Metatarsophalangeal j't	4	1	3	4	3	**5**	**0**	**2**	1	
Cervical spine	2	1	2	0	5	**7**	**0**	**3**	1	
Thoracic spine	2	1	2	0	5	**7**	**0**	**3**	1	
Lumbar spine	2	1	2	0	5	**7**	**0**	**3**	1	
Lumbosacral j't	2	1	2	0	5	**7**	**0**	**3**	1	
Sternoclavicular j't	3	1	3	5	5	**7**	**0**	**3**	0	
Acromioclavicular j't	3	1	3	1	3	**7**	**0**	**3**	0	10
Glenohumeral j't	3	1	3	6	6	**7**	**0**	**3**	0	
Hip j't	4	1	3	6	3	**7**	**0**	**3**	1	
Subtalar j't	4	1	3	1	3	**7**	**0**	**3**	1	
Transverse tarsal j't	4	2	2	0	3	**7**	**0**	**3**	1	
Proximal tibiofibular j't	4	1	2	0	3	**c**	**c**	**1**	1	2
Distal tibiofibular j't	4	1	2	0	3	**c**	**c**	**1**	1	

With the identical sorting procedure, joints can be sorted for Cases 3, 4 and 5, and similarities among joints in these cases are then obtained. The results are directly presented in Table 3 to Table 5. Each table gives the codes of the joints belonging to a group as well as the number of the joints sharing the similarity.

Table 3 Similarity among joints regarding the function

Joints	Code	Number of joints
Suture j't of the skull, sternocostal j't, intrasternal j't, 2nd, 3rd carpometacarpal j't, symphysis pubis j't	1	5
Cervical spine, thoracic spine, lumbar spine, lumbosacral j't, costovertebral j't, costotransverse j't, intermetacarpal j't, sacroiliac j't, patellofemoral j't, proximal tibiofibular j't, distal tibiofibular j't, transverse tarsal j't, tarsometatarsal j't, intermetatarsal j't	2	14
Temporomandibular j't, atlanto-occipital j't, atlantoaxial j't, sternoclavicular j't, acromioclavicular j't, glenohumeral j't, scapulocostal j't, humeroulnar j't, humeroradial j't, proximal radioulnar j't, distal radioulnar j't, radiocarpal j't, midcarpal j't, 1st, 4th, 5th carpometacarpal j't, metacarpophalangeal j't, interphalangeal j't (hand), hip j't, tibiofemoral j't, talocrural j't, subtalar j't, metatarsophalangeal j't, interphalangeal j't (foot)	3	22

Table 4 Similarity among joints regarding the arthrokinematics

Joints	Code	Number of joints
Suture joints of the skull, sternocostal j't, intrasternal j't, 2nd, 3rd carpometacarpal j't, symphysis pubis j't	0	5
Costotransverse j't, proximal radioulnar j't	1	2
Atlanto-occipital j't, acromioclavicular j't, scapulocostal j't, humeroulnar j't, distal radioulnar j't, radiocarpal j't, midcarpal j't, 1st, 4th, 5th carpometacarpal j't, intermetacarpal j't, metacarpophalangeal j't, interphalangeal j't (hand), sacroiliac j't, hip j't, patellofemoral j't, proximal tibiofibular j't, distal tibiofibular j't, talocrural j't, subtalar j't, transverse tarsal j't, tarsometatarsal j't, intermetatarsal j't, metatarsophalangeal j't, interphalangeal j't (foot)	3	23
Atlantoaxial j't, cervical spine, thoracic spine, lumbar spine, lumbosacral j't, costovertebral j't, sternoclavicular j't, humeroradial j't	5	8
Glenohumeral j't	6	1
Temporomandibular j't, tibiofemoral j't	7	2

Table 5 Similarity among joints regarding the weight bearing

Joints	Code	Number of joints
Suture j't of the skull, temporomandibular j't, costovertebral j't, costotransverse j't, sternocostal j't, intrasternal j't, sternoclavicular j't, acromioclavicular j't, glenohumeral j't, scapulocostal j't, humeroulnar j't, humeroradial j't, proximal radioulnar j't, distal radioulnar j't, radiocarpal j't, midcarpal j't, 1st, 4th, 5th carpometacarpal j't, 2nd, 3rd carpometacarpal j't, intermetacarpal j't, metacarpophalangeal j't, interphalangeal j't (hand)	0	21
Atlanto-occipital j't, atlantoaxial j't, cervical spine, thoracic spine, lumbar spine, lumbosacral j't, sacroiliac j't, hip j't, symphysis pubis j't, tibiofemoral j't, patellofemoral j't, proximal tibiofibular j't, distal tibiofibular j't, talocrural j't, subtalar j't, transverse tarsal j't, tarsometatarsal j't, intermetatarsal j't, metatarsophalangeal j't, interphalangeal j't (foot)	1	20

IV. Discussion

Five cases of similarities are discovered in this work through the coding system proposed in Part 1. Researchers can determine any other case of similarities based on their needs through the same method. Since the coding system provides us with nine properties of joints, a combination of up to 2^9-1= 511 cases can then be investigated.

The similarities determined in this work may be applied to practical use. Take the atlantoaxial joint, humeroradial joint, and the tibiofemoral joint in Table 2 for example. As indicated in this table, all the three joints possess the same direction of rotation, same direction of translation, and (therefore) the same number of axes. Even if almost all the other codes are different, it could be possible to make a pertinent adjustment in an existing device related to the movement of, for instance, the atlantoaxial joint to produce a fitting device applicable to the humeroradial joint or the tibiofemoral joint.

In this work, joints are sorted by their codes with the help of packaged software. Programs searching the codes or expert systems that help users find out the appointed codes are worth developing. With them, joints possessing the required codes of the appointed properties can therefore be discovered with more efficiency, thus reducing the time for discovering the similarities among joints.

V. Conclusions

In this part of our work, similarities among joints are discovered systematically by sorting their codes proposed in Part 1. The similarities can serve as an innovative and utile reference for assistive technology device designs and other pertinent studies. Similarities beyond these five cases can also be determined with the same method.

Acknowledgment

The National Science Council of Taiwan (R.O.C.) is acknowledged for the support of this paper (NSC95-2221-E-038-010-MY3).

References

1. J. Morris (1995) The value of continuous passive motion in rehabilitation following total knee replacement. Physiotherapy, vol. 81, issue 9, pp. 557-562
2. D. Ring, B. P. Simmons and M. Hayes (1998) Continuous passive motion following metacarpophalangeal joint arthroplasty. The Journal of Hand Surgery, vol. 23, issue 3, pp. 505-511
3. J. H. Saringer and J. J. Culhane (1999) Continuous Passive Motion Device for Upper Extremity Forearm Therapy. United States Patent 5951499
4. A. H. Brook, P. J. Carian, L. Katzin, E. E. Landsinger, J. D. Moore, L. D. Rotter and S. Schreiber (1989) Continuous Passive Motion Devices and Methods. United States Patent 4875469
5. H. C. Amstutz and I. C. Clarke, *Natural Shoulder Joint Prosthesis*, United States Patent 4261062, 1981
6. H. Grundei, J. Henssge and G. Schutt (1980) Endoprosthetic Elbow Joints. United States Patent 4224695
7. H. Yussof, M. Yamano, Y. Nash and M. Ohka (2006) Design of a 21-DOF humanoid robot to attain flexibility in human-like motion, the 15th IEEE International Symposium on Robot and Human Interactive Communication (RO-MAN06), 2006, pp. 202-207
8. S. T. Hsu, S. C. Chen, C. H. Yu and C. L. Liu (2007) Establishment of the Coding System of Human Joint Properties, Proc. 24th National Conference on Mechanical Engineering of the Chinese Society of Mechanical Engineers, Chungli, Taiwan, 2007, pp 5593-5598
9. M. P. Groover (2001) Automation, Production Systems, and Computer-Integrated Manufacturing. Prentice Hall, New Jersey, pp. 420-431

Author: Shan-Ting HSU
Institute: Department of Mechanical Engineering, National Taiwan University
Street: No. 1, Sec. 4, Roosevelt Road, Taipei, 10617
City: Taipei
Country: Taiwan
Email: r94522638@ntu.edu.tw

Circadian Rhythm Monitoring in HomeCare Systems

M. Cerny, M. Penhaker

VSB – Technical University Ostrava, Faculty of Electrical Engineering and Computer Science, Biomedical Engineering Laboratory, Ostrava, Czech Republic

Abstract — **HomeCare system is designed, developed and realized in our laboratory and special Test flat. It is compact remote monitoring system of base life functions primarily. But not only standard biosignals like ECG and others can give us information about changes in state of health of monitored man. One of the possible monitored values can be circadian rhythm.**

The monitoring of the circadian rhythm of people in HomeCare systems is very usable. Each man has own rhythm. This rhythm is periodical for elderly people. In case the life cycle is changed, we can deduce some heath problem will occur.

This article shows our designed a tested technical solutions for circadian rhythm monitoring single elderly man in his flat and methods of interpretation.

Keywords — **ZigBee, HomeCare, Day Activity**

I. Introduction

Elderly people living alone in their own flats have similar day activities. Their own one day cycle is similar for the most of days. There are not so many abnormalities. The personal characteristic circadian rhythm could be calculated from several measured circadian cycles. If any deviation from the characteristic circadian rhythm is detected, it could signify a health problem.

The typical example of day life cycles abnormality could be the typical case of early fall detection during night hours. Old alone living man must regularly visit toilet between second and third hour in the morning. One day he wakes up and goes to the toilet. But he doesn't come back to his bed. The movement monitoring system has found out that he reached the toilet and went away from the toilet. The last found man's position was at the corridor. Another movement had not been detected in other rooms in his flat for a set up time. It could be the sign that he has fallen down. Afterwards the movement monitoring system goes to alarm state. Thanks to the early fall detection his broken leg could be sooner restored to health.

There are two categories of the circadian rhythms deviations. The first type is "short-term" deviation. This type of deviation was described in previous example. It is detection of urgent and accidental changes of circadian rhythm. This detection helps to recognize urgent health problems and accidents.

The second category is "long-term deviation". It means that the evolution of the circadian rhythm is recognized. This evolution could not be strictly pathologic. The degree of pathology has to classify the doctor. Afterwards, this knowledge could be applied to the adaptive and self learning system, which will classify these rhythm changes automatically. The typical example of long term deviation can be the change in the frequency of toilet room visiting.

Of these reasons the monitoring of the personal activity circadian rhythms has information validity in the HomeCare projects.

There are discussed technical solutions for movement monitoring, first. Than there is discussed designed autonomous movement monitoring system.

II. Movement monitoring

The first designed and realized method of the movement monitoring uses standard PIR sensors. These sensors were modified. The communication was realized by ZigBee technology. The measured data were represented in PC by visualization software which was developed in Labview.

This method has some advantages: The hardware is powered by only one CR battery. No wires are required for data transmission. The sensor can work for a long time.

The disadvantage is: The bigger pet could be detected instead of person. In the case that more people will be in the flat, there are misdetections too. These misdetections will influence circadian cycle monitoring. The information about the position is not exact. The area of presence is only found out.

The second designed solution uses the Location Engine solution from Texas Instruments. This engine is included in their single on chip ZigBee chip named CC2431.

The location algorithm used in the CC2431 Location Engine is based on Received Signal Strength Indicator (RSSI) values. The RSSI value will decrease when the distance increases.

Four reference nodes were placed in the flat. The flat user was equipped with special watches, where was mounted the ZigBee chip with location engine.

The advantage of this solution is that the information about position of monitored person is as exact as possible. It

Chwee Teck Lim, James C.H. Goh (Eds.): ICBME 2008, Proceedings 23, pp. 950–953, 2009
www.springerlink.com

isn't possible to detect incorrectly other person or pet in the flat.

This solution has one important disadvantage: The user has to wear an active ZigBee device. This fact could be unacceptable for some elderly people. But the ZigBee chip could be a part of continuously measuring device for ECG measurement which is used in HomeCare system. Thanks to this solution the movement monitoring could be more tolerable for some people.

A. Technical solution discussion

The definitive determination of the human position in the flat can not be done with only one of the introduced movement monitoring technologies. The combination of proposed two technologies has to be used for definitive person's position determination. The additional usage of the optoelectronic bars in the doors will be optimal. Afterwards, the person in the flat can be successfully located. The circadian rhythm could be constructed from these determined person's position data.

III. The Circadian Rhythm Interpretation

The interpretation of the measured data is an important part of this project. It was necessary to define some condition for the data interpretation, respective circadian rhythm construction. There are conditions which are related to long and short term activities representation. From circadian rhythm has to be recognizable person's movement between monitored rooms in his flat. The short time activities have to be recognizable too. The circadian rhythm shall be processed in the microprocessors by the reason of planned movement system autonomy.

A. The mathematical description

The information about human's position in the flat is different for day hours and night hours. In the day hours is active location engine, so measured data are more precise that in the nigh hours, when only the PIR sensor based measurement is active. Actual position of human in the flat could be defined as vector P (eq.1):

$$P = f(x, y, t)$$
$$\textit{where}$$
$$x, y \textit{ are coordinates of persons's position} \quad (1)$$
$$t \textit{ is time}$$

It could be represented by following picture. The displayed flat layout concerns to our HomeCare Testing Flat

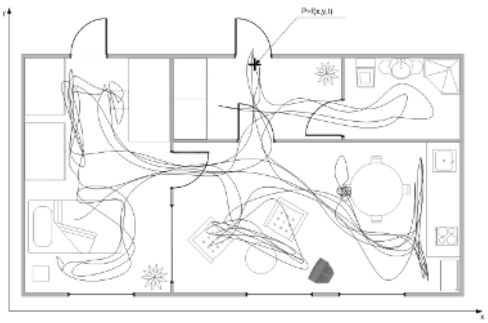


Fig. 1. The movement monitoring during day hours

Information about human's position in the flat is not so exact during night hours due to method of movement monitoring. The PIR based monitoring system purveys only information about area of supposed person's presence. The coordinates of person's position in the P vector are replaced by coordinates of the middle of PIR sensor detection area (see Fig. 2.).

Because the information about person's position given by PIR sensors could be influenced by many errors (misdetection due to for example pets) the additional system of optoelectronic bars controls the validity information.

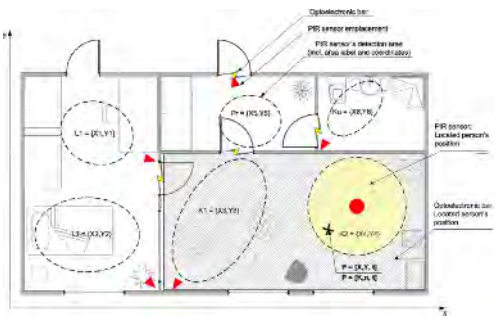


Fig. 2. The movement monitoring during night hours

B. The chronological succession of person's presence in the flat

The simplest method how to represent measured data is the chronological succession of person's presence in the monitored areas of the flat. The circadian rhythm which corresponds to the information about person's movement activity in the flat could be represented by:

$$C = \sum_{t=0}^{24} K[t] \qquad K[t] \in \mathbf{C},\ t \in \mathbf{R}^{+}$$

where (2)

K is a code for monitored area in the flat

The K code for monitored area of the flat could be represented by RGB code. This coding is very useful for next representation of measured data. For each room of flat has been defined own color. Each color is described by the RGB code.

The RGB code definition for each are must be carefully defined. From the RGB coding has to easily be recognizable connections between coded areas. Each room of the flat has one of the RGB code part in maximal values are zeros. The distance from beginning of coordinates system is took into consideration. In the figure 3 is displayed suitable RGB coding for our testing flat. RGB coding is suitable for larger flats too, it is because of number of possible combinations.



Fig. 3. RGB codes for each room of flat and the position vector p

When RGB coding is used the circadian rhythm could be displayed as “chronological succession of RGB codes” .

C. The position matrix

Actual position of monitored person it flat is defined by vector P (eq.1.). When the monitored flat will be represented by matrix, which has the same dimensions as the monitored flat (in the cm) afterwards matrix elements could represent person’s presence in the monitored flat.

$$a_{i,j} = \begin{cases} 0 & \text{for } i \neq x,\ j \neq y \\ 1 & \text{for } i = x,\ j = y \end{cases}$$

where (3)

$a_{i,j}$ *is matrix element*

x, y *are coordinates of person's position*

The actual position of the person in the flat will be represented by one non-zero matrix element in the position matrix. The circadian rhythm *C* could be afterwards represented by the position matrix (eq.4.). This matrix has to be three dimensional matrix, where each two dimensional matrix *M(t)* concerns to one moment (see Fig. 4.).

$$C = \sum_{t=0}^{24} M[t] \qquad \text{where } t \in \mathbf{R}^{+}$$

$$M[t] = \sum_{i=0}^{x_{max}} \sum_{i=0}^{y_{max}} a_{i,j}[t] \qquad (4)$$

$$\text{where } a_{i,j}[t] = \begin{cases} 0 \text{ for } i \neq x_t,\ j \neq y_t \\ 1 \text{ for } i = x_t,\ j = y_t \end{cases}$$

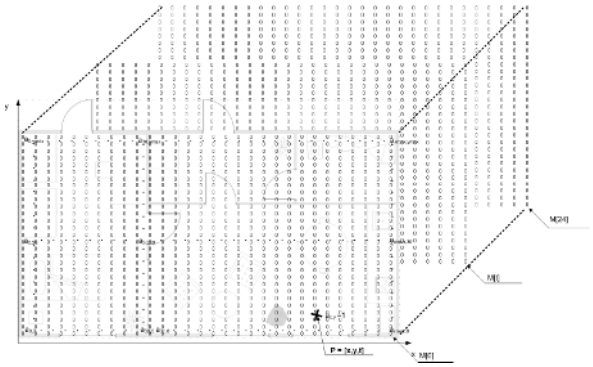


Fig. 4. The position matrix

The position matrix is not suitable for next data processing, and it is not useful for data processing in the microcontrollers, what is one of the conditions defined in the beginnings chapter IV.

D. The position vector

The actual position of the monitored person could be defined as a position vector. This vector is a distance coordinates beginnings and the measured actual position.

The module of this vector could be counted for each measured person’s position (eq. 5.).

$$|\vec{p}| = \sqrt{p_x^2 + p_y^2} \qquad (5)$$

E. The colored vector of position

In the consequence of defined conditions and proposed possibilities of circadian rhythm interpretation it seems to

be most effective to combine "The chronological succession of RGB codes" and "The colored vector of position".

Afterwards can be constructed colored vector of position (Fig. 6.). The x axis is the time axis, the y axis has values of $|\vec{p}|$. The RGB code has been added to each recorded value of position, to we can see, where (in which room) the user was found out. The added RGB code is necessary, because the exact person's position can not be exactly recognized from position vector modulus.

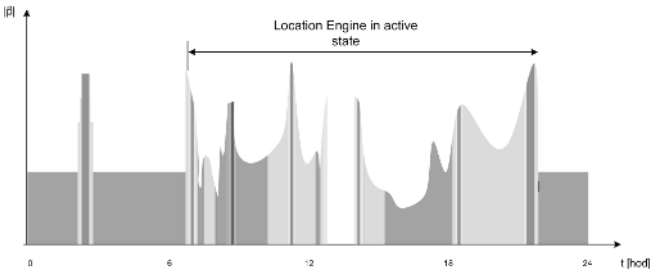


Fig. 5. Colored vector of position (simulation)

This type of interpretation of circadian rhythm concerns to all conditions defined above. The color of vector is very usable for processing of long-term deviations. Personal characteristic long term circadian rhythm can be constructed from the colored vector of position. The values of modulus of position vector are usable for short term deviations detections and classification.

IV. Conclusion

The proposed HomeCare system has been particularly realized and tested in our special HomeCare Testing Flat. The realized measuring devices have been based on Bluetooth technology. The new measuring devices using ZigBee are in progress now and they will be tested in the near future.

The circadian rhythm monitoring system is an important part of our HomeCare system and it is tested in our Testing flat too. The autonomous movement monitoring system was designed and it is in the realization now. The method of the circadian rhythm construction has been specified. The analyze system has to be designed.

The goals of this work could be used in HomeCare systems or in the other circadian rhythms monitoring projects.

Acknowledgment

This work was supported in part by grant GACR 102/05/H525: The Postgraduate Study Rationalization at Faculty of Electrical Engineering and Computer Science VSB-TU Ostrava. This work was supported in part by grant GACR 102/08/1429, Safety and security of networked embedded system applications.

References

1. Noury, N., From Signal to Information : the smart sensor. Applications in Industry and Medicine Habilitation a diriger des recherches, , 2002
2. Bronzino, J. D.: The Biomedical Engineering Handbook, CRC Press 1995
3. Cerny M., Poujaud J.: Movement monitoring in HomeCare, In Acta Electrotehnica, Special issue MediTech 2007, IEEE EMBS conference, 27-29th September, 2007, Editura Mediamira, Cluj-Napoca, Romania, ISSN 1841-3323 str. 99-102
4. Penhaker, M., Imramovský, M., Tiefenbach, P., Kobza, F.: Medical diagnostic devices lectures , ISBN 80-248-0751-3, Ostrava 2004 [czech]
5. Cerny, M.,Penhaker, M.: Biotelemetry lectures, VSB TU Ostrava 2007 ISBN: 978-80-248-1605-0
6. K.Aamodt, CC2431 Location engine, Application note AN042 (rev.1.0), Texas Instruments [online]
7. Penhaker, M., Cerny, M., J., Floder, J., Embedded Biotelemetry System for Home Care monitoring, ICBEM 2007, 6.10 – 19.10 2007, Aizu Wakamatsu, Japan

Author: Martin Cerny
Institute: VSB – Technical University of Ostrava
Street: 17.listopadu 15
City: Ostrava Poruba
Country: Czech Republic
Email: martin.cerny@vsb.cz

Effects of Muscle Vibration on Independent Finger Movements

B.-S. Yang[1,2] and S.-J. Chen[1]

[1]Department of Mechanical Engineering, National Chiao Tung University, Hsinchu, Taiwan
[2]Brain Research Center, National Chiao Tung University, Hsinchu, Taiwan

Abstract — **Previous studies had demonstrated that small amplitude muscle vibration (MV) could increase the motor pathway excitability of the vibrated hand muscle and inhibit the excitability motor pathways of neighboring muscles in healthy individuals. The purpose of this study is to examine whether the vibration-induced neurophysiological changes reflect in the voluntary control of finger movements. We tested the hypothesis that MV to individual hand muscle (abductor pollicis brevis, APB; first dorsal interosseus, FDI; or abductor digiti minimi, ADM) affects the control of finger abduction/adduction. Each fingertip position was captured using a motion capture system during four experiment conditions: no MV, MV to APB, MV to FDI, and MV to ADM. Two consecutive 10-s trials in each condition were tested for each finger. We calculated individuation index (Iind) and index of selective activation (ISA) to compare finger independency with and without MV. The results indicated that muscle vibration could enhance the independency of finger movements.**

Keywords — **Muscle Vibration, Finger independency, Muscle selectivity**

I. Introduction

Lack of finger independency and muscle selectivity is a major contributor to hand dysfunction post stroke [1-4]. Rosenkranz and Rothwell [5] reported that for healthy adults, small amplitude (<0.5mm) muscle vibration to specific hand muscle (abductor pollicis brevis, APB, first dorsal interossei, FDI or abductor minimi digiti muscle, ADM) could increase the motor-evoked potential (MEP) of the vibrated muscle and inhibit or provide no change to the MEPs in other same-hand muscles. Our previous study showed that this vibration-induced neurophysiological modulations might also occur in stroke [6]. The purpose of this study was to explore whether the vibration-modulated neurophyiological changes reflect in the voluntary control of finger movements. We specifically tested the hypothesis that muscle vibration to specific hand muscle affects the individuation of finger movements in healthy adults. If muscle vibration can improve independent finger movement, it may be a useful tool for stoke hand rehabilitation.

II. Materials and methods

A. Subjects

Six healthy subjects (aged 20-25 yrs) without musculoskeletal or motor deficits in upper limbs were studied. The test procedure of this study was approved by the Institutional Review Board of Chang Gung Memorial Hospital. Every subject provided a written consent prior to the experiment.

B. Electromyography (EMG)

Surface EMG recordings were made from the abductor pollicis brevis (APB), the first dorsal interosseus (FDI), and abductor digiti minimi (ADM) using AMT-4 system (Bortec, Alberta, Canada). Signals were sampled at 2 kHz and the raw EMG was filtered with a band-pass of 30 Hz to 1 kHz to analysis afterwards.

C. Muscle Vibration (MV)

Muscle vibration was given to the target muscle using an electromagnetic vibrator (Ling Dynamics System Ltd, United Kingdom) with a 7mm diameter custom-made probe. The vibration frequency was set at 80 Hz and the amplitude was adjusted to just below the threshold for perceiving an illusory movement for each subject [7]. The vibration started 0.5 second before the instructed movement of the finger and lasted till 0.5 second after the end of the movement.

D. Experiment Design

Each subject was comfortably seated beside a table with the forearm and palm of the dominant upper limb positioned on the custom-made device. The shoulder was 30° abduction. Each finger was loosely spread apart to avoid obstructing instructed finger by other fingers during abduction/adduction movements. During experiments, we put some talcum powder on the table to minimize the friction between the fingers and the table. Six-camera motion capture system (Smart-D, BTS Bioengineering, Italy) was used to capture the fingertip movements at 250 Hz.

Chwee Teck Lim, James C.H. Goh (Eds.): ICBME 2008, Proceedings 23, pp. 954–956, 2009
www.springerlink.com

Abduction/adduction movements were tested without and with MV. Subjects were asked to move one finger abduction/adduction cyclically following a metronome timer (40 bpm, 0.67 Hz). Between two closest audio cues metronome, subjects needed to complete one abduction/adduction movement. The instruction for subjects was "move one finger with comfortable range of motion and try to keep the other fingers stationary." Subjects were able to see their finger movements during the test. Before each experiments condition, subjects could practice until they understood the instruction and adapted to the desired movement frequency.

Four conditions were tested: (1) without MV; (2) MV to APB; (3) MV to FDI; (4) MV to ADM of the dominant hand. For each condition, we recorded two consecutive 10s trials for each instructed finger (in the order of thumb, index, middle, ring, and little finger). The sequence of MV conditions was randomized across subjects.

E. Individuation Index (Iind)

An individuation index (Eq. 1), established by Lang and Schieber [3], was employed to quantify the independency of the control of each finger. Motion data were low-pass filtered with cutoff frequency of 10 Hz and the traveled distance of each finger tip was then calculated. The average path distance was defined as the total distance a fingertip traveled in a 10-s trial divided by the number of completed abduction/adduction cycle. The Individuation Index is defined as:

$$H_j = 1 - \frac{\sum_{i=1}^{n} |D_{ij}| - 1}{n-1} \quad (1)$$

Where H_j is the individuation index the j^{th} finger, D_{ij} is the normalized path distance of the i^{th} finger during the j^{th} instructed movement, and n is the number of fingers (here n = 5). For each finger, two Iind values of the same condition would average to get one Iind value. The Iind is unity for an ideal independent movement when the instructed finger moves without any movements in uninstructed fingers.

F. Index of selective activation (ISA)

ISA, adopted from a previous study [3], was used to quantify the selectivity of muscle activation between with and without MV. EMG data were band-pass filtered (30Hz to 1 kHz), rectified, and low-pass filtered with cut-off at 30 Hz. EMG signals of each muscle were then normalized to the highest maximum EMG value recorded from the same muscle within the same test condition. The normalized EMG data were further integrated over a 10-s period. The integrated EMG value was then divided to the cycle number of the instructed finger to obtain an average activation value (A_{ag}, described below). The ISA is defined as:

$$ISA = 1 - [(A_1 / A_{ag} + A_2 / A_{ag} + A_3 / A_{ag} + A_4 / A_{ag}) / 4] \quad (2)$$

Where A_{ag} is the average activation of agonist muscle during the instructed movement, and $A_{1,2,3,4}$ are the average activations of the same muscle during the other four instructed movements. For example, when instructed thumb to move, the A_{ag} is the average activation value of the APB muscle, and $A_{1,2,3,4}$ are average activation values of APB during the instructed movements in the other tested fingers under the same MV condition. Means of two ISA values under the same test condition were used to compare the effects of MV.

III. Results

Fig. 1 shows the individuation index of each finger during no MV versus three different MV conditions. The individuation index of one subject during MV to ADM was not included because some kinematic data were missing.

Regardless MV location, the Iind for the thumb and index finger did not change as compared with no MV condition. The most pronounced effects of MV on Iind were found in ring finger movements. During MV to APB or FDI, the ring finger performed significantly more independent finger movements than those with no MV ($p<0.05$, paired *t*-test). During MV to ADM, the ring finger moved less independently ($p>0.05$, paired *t*-test).

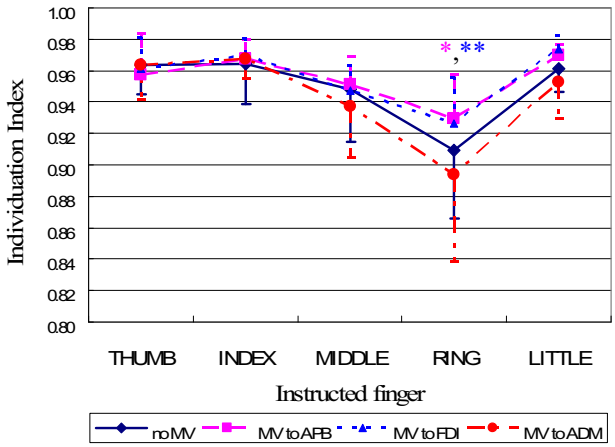


Fig. 1 Group means (error bar: standard deviation) of individuation indices of each instructed finger between different MV conditions when performed abduction/adduction movements. Paired t tests comparing MV with no MV conditions: *: $p<0.05$, MV to APB; **: $p<0.05$, MV to FDI.

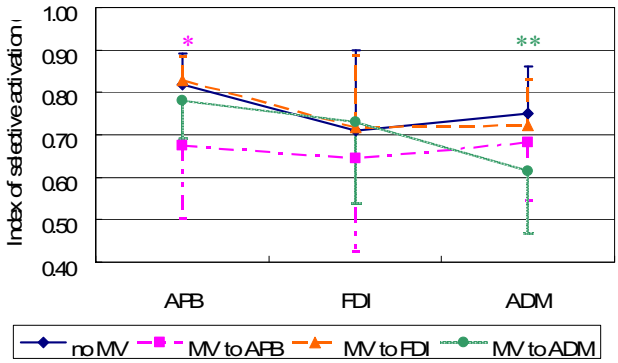


Fig. 2 Group means (error bar: standard deviation) of indices of selective activation for four conditions (no MV and MV to three muscles) when performed abduction/adduction movements Paired *t*-test comparing MV with no MV conditions: *: $p<0.05$, MV to APB; **: $p<0.05$, MV to ADM.

Fig. 2 shows the indices of selective activation of three muscles in four MV conditions. During MV to APB, ISA for APB was significantly smaller than that without MV ($p<0.05$, paired *t*-test). In addition, ISA for ADM was significantly reduced by the MV to ADM as compared to that without MV ($p<0.05$, paired *t*-test).

IV. Discussion

Individual muscle vibration to three hand muscles (APB, FDI or ADM) could affect the independency of finger movements in the same hand, especially the ring finger. Although the vibration-induced improvement in independent control of finger movements is not significant in healthy individuals, we expect to see more pronounced changes in the voluntary control of finger movements modulated by vibration in individuals with less finger independency, such as individuals with neurological disorder [3].

Previous study showed that individual muscle vibration to rested hand could enhance corticomotor excitability of selective motor pathway and inhibit the excitability of motor pathways of other muscles in the same hand in intact or neurological-injured individuals [5, 6]. In this study, we further demonstrated that muscle vibration could modulate voluntary control of finger movements, although the patterns of modulations and disease related effects still need to be studied.

V. Conclusion

Muscle vibration could modify the voluntary control of individual finger movements and the selectivity of hand muscle activation.

Acknowledgment

This study is financially supported by Taiwan National Science Council grant no. NSC96-2221-E-009-MY3.

References

1. Butefisch, C.M., J. Netz, M. Weling, et al. (2003) Remote changes in cortical excitability after stroke. Brain 126: 470.
2. Chae, J., G. Yang, B.K. Park, et al. (2002) Muscle Weakness and Cocontraction in Upper Limb Hemiparesis: Relationship to Motor Impairment and Physical Disability. Neurorehab Neural Re 16: 241.
3. Lang, C.E. and M.H. Schieber (2004) Reduced muscle selectivity during individuated finger movements in humans after damage to the motor cortex or corticospinal tract. J Neurophysiology 91: 1722-1733.
4. Liepert, J., P. Storch, A. Fritsch, et al. (2000) Motor cortex disinhibition in acute stroke. Clin Neurophysiol. 111: 671-676.
5. Rosenkranz, K. and J. Rothwell (2003) Differential effect of muscle vibration on intracortical inhibitory circuits in humans. J Physiology 551: 649-660.
6. Yang, B.–S., Settle, K. and Perreault, E. J. (2006) Vibration-induced modulations of control of finger movements following stroke, Soc. for Neurosci. Ann. Meeting, Atlanta, Georgia, USA.
7. Roll, J.P., J.P. Vedel, and E. Ribot (1989) Alteration of proprioceptive messages induced by tendon vibration in man: a microneurographic study. Exp Brain Res 76: 213-222.

Author: Bing-Shiang Yang, Ph.D., P.E.
Institute: National Chiao Tung University
Street: EE427, 1001 University Road
City: Hsinchu
Country: Taiwan
Email: bsyang@mail.nctu.edu.tw

Modelling Orthodontal Braces for Non-invasive Delivery of Anaesthetics in Dentistry

S. Ravichandran

Faculty, Temasek Engineering School, Temasek Polytechnic, Singapore

Abstract — **It is known that oral and maxillofacial surgeons in collaboration with orthodontist often perform corrective dental procedures and these procedures are carried out after providing local anesthesia adjacent to the site of the lesion. As most of the minor surgical procedures in dentistry do not require general anesthesia, they are carried out with the help of local anesthesia. Local anesthesia is induced when propagation of action potential is to be inhibited from the source of stimulation, such as a tooth, to the sensory areas of the brain. Local anaesthetics work by blocking the entry of sodium ions into their channels, thereby preventing the transient increase in permeability of the nerve membrane to sodium ions for generating an action potential. When a local anaesthetic is injected into soft tissues, it exerts a pharmacological action on the blood vessels in the area. All local anesthetics possess a degree of vasoactivity which may vary depending on the selection of the drug. Development of orthodontal braces for containing the drug for local anaesthetic procedure is one of the emerging areas in biomedical engineering and our research work focuses on the development of one such tool designed for administering anaesthesia non-invasively before dental procedures. Based on the qualitative studies on the nature of the current suitable for the transfer of drug, we have developed the drug delivery system which augments with the orthodontal braces for the delivery of small doses of anaesthetic drug to the target site with the aid of pulse electrical stimulation.**

Keywords — **Orthodontal braces, Local anaesthetic, Non-invasively, Corrective dental procedures**

I. Introduction

A. Anesthesia in Clinical Dentistry

General anesthesia used for major surgical procedures leads to an induced state of unconsciousness, accompanied by partial or complete loss of protective reflexes and also includes the inability to maintain an airway independently and respond purposefully to physical stimulation or verbal command [2]. However, not all dental surgery requires the use of general anesthesia. Some surgical procedures in dentistry are carried out with the help of local anesthesia. It is known that local anesthetics block the entry of sodium ions into their channels, thereby preventing the transient increase in permeability of the nerve membrane to sodium ions for generating an action potential to occur [4, 8, 28, 29].

B. Classification of Local Anesthetics

Local anesthetics can be broadly classified as esters, amides and quinoline. Structurally, local anesthetics have specific fundamental features in common, which include a lipophilic group, joined by an amide or ester linkage to a carbon chain which, in turn, is joined to a hydrophilic group. Most local anesthetics are classified by these amide or ester linkages [8].

C. Neuromodulation of Pain

Pain stimuli receptors are distributed throughout the tissues of the body. These naked nerve endings with no specialist receptor on stimulation initiate a train of action potential [19]. The 'C fibre' receptors are sensitive to many kinds of stimuli including chemicals released from damaged tissue and hence, are also called polymodal receptors [7]. On excitation, a train of action potential travels back to the central nervous system through afferent neurons where processing of the sensory input is completed. The gate control theory of pain, proposed decades ago by Melzack and Wall postulates that information from the vibration and touch receptors located in the skin transmits nerve impulses through A-ß nerve fibers to stimulate inhibitory interneuron in the spinal cord. This in turn acts to reduce the amount of pain signal transmitted by A-delta and C fibers from the skin to second-order neurons that cross the midline of the spinal cord before ascending to the brain [10, 11, 13]. Local anesthetics block the sensation of pain by interfering with the propagation of peripheral nerve impulses. It has been found in the electrophysiological research studies that local anesthetics do not significantly alter the normal resting potential of the nerve membrane but they rather impair certain dynamic responses to nerve stimulation [19,21]. Local anesthetics interfere with Na^+ permeability of the nerve, and its blocking action is characterized by a progressive reduction in the rate and extent of depolarization in the nerve. When depolarization is inhibited, it result in the absence of action potenitial generated from the receptor which in turn results in the absence of nerve conduction leading to the inhibition of transmission of sensory information to the Central Nervous System (CNS) [6].

Chwee Teck Lim, James C.H. Goh (Eds.): ICBME 2008, Proceedings 23, pp. 957–960, 2009
www.springerlink.com

D. Drug Uptake and Biological Interactions

Local anesthetic injected into soft tissues exerts a pharmacological action on the blood vessels in the target area. All local anesthetics possess a degree of vasoactivity which may vary depending on the selection of the drug. A significant effect of vasodilation is an increase in the rate of absorption of the local anesthetic into the blood, which eventually decreases the duration of pain control, while increasing the anesthetic blood level. These effects are also related to the vascularity of the injection site [8]. Local anesthetics cause vasodilatation, which leads to rapid diffusion away from the site of action and results in a very short duration of action when these drugs are administered alone intraorally. This diffusion is reduced to a good extent by adding a vasoconstrictor with the anesthetic [8]. In clinical practice, epinephrine is usually mixed with anesthetic, like Xylocaine, to increase the duration of action of the drug at the target site.

E. Dosing For Safety

High drug levels in the blood can occur due to the result of the single unintended intravascular administration. Table 1 suggests the recommended maximum doses of some of the local anesthetics with vasoconstrictor [5, 27, 29].

Table 1. Recommended doses of local anesthetics

Drug	Maximum Dose
Articaine (4%)	7 mg/kg (up to 500 mg) 5 mg/kg in children
Lidocaine (2%)	7 mg/kg (up to 500 mg)

Lidocaine is a relatively common local anesthetic. It has been studied thoroughly for many years, and has well known effects and side effects. Lidocaine has been used on both adults and children for more than five decades and thus Xylocaine is the drug of choice in our applications [1, 9].

F. Pharmocotherapy

Pharmocotherapy involves the use of electrical fields or acoustic waves for transferring selected chemicals/drugs inside the body. Electrical fields and acoustic waves have been widely used in the delivery of certain ions or drugs inside the body and these processes are more commonly known as iontophoresis and phonophoresis. Iontophoresis has been widely used in the delivery of drugs such as hydrocortisone and methyl salicylic acid for analgesia and anti-inflammatory effect [14, 15]. Phonotherapy is also another effective way of delivering certain drugs through the skin and has been used widely in certain clinical conditions.

G. Phonophoresis

Phonophoresis is the movement of drugs through the skin into the subcutaneous tissues under the influence of ultrasound as ultrasonic vibration has been known to accelerate the movement of drug through the skin. Phonophoresis relies on perturbation of the tissue causing more rapid movement of particles, thus encouraging absorption of the drug. The effects of phonophoresis are those of drug employed combined with the effects of ultrasound [7]. Recent studies using ultrasound applicators for the delivery of selected drugs have shown that this area of noninvasive drug delivery is promising in antithrombotic applications too [22, 23, 26].

H. Iontophoresis

Iontophoresis is a drug delivery method that uses low-level direct current in the milliampere (mA) range to transport drugs and other water-soluble salts through the skin. It is a process of migration of ionized molecules across biological membranes under the influence of mild electric current. Drugs in the form of ions can be transported through the skin or mucus membrane with the aid of small current to the deeper layers of the biological structure [12, 14, 15, 20]. In dentistry, studies have been reported on the use of Lignocaine iontophoresis in small doses for tooth extraction in children [3].

II. Limitations of Iontophoresis in Dentistry

Intolerance to electrical stimulation is one of the major limiting factors in low frequency electro-stimulation. The tolerance to the stimulus has been well investigated in our research program and has been qualitatively documented using Perception Response System (PRS) where the sensation is graded under four perception labels. PRS used in different electro-stimulation studies were found useful in evaluating the tolerance to the electrical currents used in iontophoresis. Recording on this scale involve patient's interaction to classify perception on qualitative basis which is decided on the skin response to the stimulation parameters used in therapy. This qualitative assessment allows the user to choose the right stimulation parameters for treatment which can be selected based on patient's perception to the stimulation. This system thus provides a more reliable guideline in the assessment of stimulation parameters used in the present studies [16, 17, 18].

III. Xylocaine drug delivery system for dentistry

Based on the qualitative studies on the nature of the current suitable for iontophoresis, we have developed the drug delivery system for dentistry to deliver small doses of Xylocaine to the target site with the aid of pulse electrical stimulation. This system, named as "Orthodontal Brace based Drug Delivery System" (OBDDS), is designed around the orthodontal brace and consists of some essential sub modules, such as electrode embedded drug holding cell, and the microcontroller based control system. The control system consists of electrical pulse generator, and interfacing circuit for energizing the electrodes in the drug holding cell. The system architecture of the drug delivery system designed and developed around an orthodontal brace for our application is further discussed.

A. Drug holding cell

The drug holding cell is located at various points of the orthodontal brace and is capable of holding adequate amount of drug for transdermal application. The drug holding cell can be removed and replaced for every application. This drug holding cell is made out of biocompatible polymer and does not cause any adverse reaction.

B. Stimulating electrodes

Use of sensor embedded electrodes have been in practice in our earlier research studies in transdermal delivery of hydrophilic drugs to the target site [24, 25] and based on our earlier experience in designing such electrodes, we have designed the electrodes for this application in dentistry. Wired electrodes were embedded in the drug holding cell and these electrodes are capable of providing the electrical fields for the transfer of drugs from the drug holding cell to the biological tissue under the electrodes. These electrodes are connected to the electronic circuit, providing electrical pulses to stimulate the target site.

C. Control system

This system is programmed for supporting the interface for generating mid frequency pulses ranging from 2 kHz to 10 kHz.

D. Qualitative Studies Based on Perception

Based on the earlier experiments with low frequency currents, we have documented the perception to the pulse current in the frequency range from 2 kHz to 10 kHz. As per the Perception Response Index Scale (PRIS), the tolerance to the currents in the frequency band (2 kHz to 10 kHz) was reported less irritating. It was also observed that the effect of the anesthetic delivery using this method was not any less inferior when compared to the earlier iontophoretic drug delivery protocol. Thus, this developed system is definitely more promising in terms of patient tolerance and usefulness in dentistry.

E. Results and Discussion

It is observed that anesthetized state maintained by quantized delivery of the anesthetic deposited in the target site using a hypodermic needle is usually longer than other methods. This is due to the higher quantity of the medication injected into the target site and also the composition of the anesthetic combined with a vasoconstrictor. With the use of the OBDDS, the duration of the anesthetized state is maintained by quantized delivery of the anesthetic to the target area and is decided only by capillary circulation aided by the electrical pulses. This limits the amount of the anesthesia contained in the target area and thus prevents overdosing which can occur in the conventional method using hypodermic needles.

IV. Conclusion

Avoiding a needle prick for producing anesthesia is a fact appreciated by people who have a strong aversion for injections. Thus, this system will not put off those patients who have a fear for needle pricks and will be useful for dentist to perform minor surgical procedures. However, for major surgical procedures, this method can be a useful prelude to provide the initial dosing non-invasively, before providing larger doses of anesthetics through injections after the initial numbness has set in. Another advantage of this method over the conventional method is that very little drug is required to produce a local analgesic effect. The newly developed OBDDS for providing anesthesia in dental application is definitely a promising tool for pedagogical researchers and professionals in dentistry.

References

1. Blanton PL, Jeske AH; ADA Council on Scientific Affairs; ADA Division of Science. *Avoiding complications in local anesthesia induction: anatomical considerations*. J Am Dent Assoc 2003; 134:888-893.
2. Dr Sean G. Boynes, *Dental anesthesiology: A 2006 guide to the rules and regulations of the fifty united states and the district of Columbia*, Pittsburgh, PA 15220, 2006

3. Geojy Mathew, Sandip B. Tiwari, Design and Development of a Versatile Battery Operated Portable Iontophoretic Module for Application, *Clinical Medicine in Medical Diagnostic Techniques and Procedures*, Narosa Publishing House, 2000, p.497, 499, 500
4. Haas DA, Carmichael FJ. *Local anesthetics. 6th ed.* In: Roschlau WHE, Kalant H, editors. Principles of medical pharmacology. New York: Oxford; 1998. p. 293-302.
5. Haas DA. *Drugs in dentistry. In: Compendium of pharmaceuticals and specialties (CPS). 37th ed*. Canadian Pharmaceutical Association; 2002. p. L26-L29.
6. Jastak JT, Yagiela JA, Donaldson D. *Local anesthesia of the oral cavity. 1st ed*. Philadelphia, Saunders, 1995.
7. John Low, Ann Reed, *Electrotherapy Explained*, Butter Worth, Heine Mann, 1990, 59-60
8. Malamed SF. *Handbook of local anesthesia. 4th ed.* St. Louis: Mosby; 1997.
9. Meechan JG. *Why does local anaesthesia not work everytime?*, Dent Update 2005; 32:66-68, 70-72.
10. Melzack R. From the gate to the neuromatrix. Pain. 1999 Aug; Suppl6:S121-6. Review. PubMed
11. Melzack R, Wall PD. *Pain mechanisms: a new theory. Science*. 1965 Nov 19; 150(699): 971-9. Review PubMed
12. Phipps, J.B., Gyory, J.R., 1992: "*Transdermal Ion Migration*", Adv. Drug. Del. Rev., 12, p. 751-755.
13. Ravichandran S, Narayanan UH and Sujatha UN (1988), *'Transcutaneous Electrical Nerve Stimulation in Pain Management*', Proc. 1988 10th Annual International IEEE/EMBS Conference, New Orleans, USA.
14. Ravichandran S and Raghu Arvind (1989), *'Iontophoresis -- A Tool in Therapy'*, Proc. 1989 Medical Extensions of Electronic Technology, MEET 89, Sponsored by SMLRT and IEE London (Madras Chapter), India.
15. Ravichandran S (1989), *'Iontophoretic Approach in Therapy'*, Proc. 1989 IX and X Annual Conference of Indian Association of Biomedical Scientists, Madras Medical College, Madras, India.
16. Ravichandran S and Prasad G.N.S.(1991b), '*Electrode Array System in Electrokinesy: A Difference Technique in Therapy*', Pro 1991, 13th Annual International IEEE/EMBS Conf. Orlando, Forida, Vol.13,pp0934-0935
17. Ravichandran S and Prasad G.N.S.(1992), '*Advances In Electrokinesy With Macro Electrode Array System'*, Pro 1991, 14th Annual International IEEE/EMBS Conf. Paris, France, Vol.14, pp2320-2321
18. Ravichandran S and Prasad G.N.S. (1994), *'Modelling and Control of Therapeutic System Using Assumption Based Truth Maintenance System'*, Proc. 1994 IFAC Symposium, Galveston Texas, U.S.A., pp.406-407.
19. Roberts DH, Sowray JH. *Local analgesia in dentistry. 3rd edn*. Bristol: Wright, 1987.
20. S Ravichandran, Ng Weili, Lam Hwei Hwei, Yuan Ran Dong, Hong Ka Lic, Lee Chia Yin, Lim Shi Yi Darren, Wu Lie Quan, '*Dedicated controllers for sensor embedded electrode architecture of non-invasive drug delivery system'*, proceedings of the 'IEEE EMBS Asian-Pacific Conference on Biomedical Engineering 2003, Nara, Japan.'
21. Strichartz GR, Ritchie JM. The *action of local anesthetics on ion channels of excitable tissues. Handbook of Experimental Pharmacology, Vol.81*. Berlin, Springer- Verlag, 1987.
22. Subbaraman Ravichandran, Senthil Kumar, Tan Chew Stephanie, Muhammad Zaid Bin Amir, Siti Zubaidah Bt Mohd Akhbar, Naatasha Bt Isahak , Nur Liyana Bte Amrun, *'Modeling therapeutic protocols for non-invasive heparin delivery in the management of subcutaneous microvasculature lesions.'*, proceedings of 'The First International SBE Conference on Bioengineering and Nanotechnology, ICBN 2004, Biopolis, Singapore.'
23. Subbaraman Ravichandran, Senthil Kumar, Tan Chew Stephanie, Muhammad Zaid Bin Amir, Siti Zubaidah Bt Mohd Akhbar, Naatasha Bt Isahak , Nur Liyana Bte Amrun, *'Augmenting "Multilayer Drug Delivery Cells" for Phonophoretic drug delivery procedures using programmable controllers.'*, proceedings of 'The First International SBE Conference on Bioengineering and Nanotechnology, ICBN 2004, Biopolis, Singapore.'
24. Subbaraman Ravichandran, '*Modeling and control of Sensor Embedded Drug Delivery Cells (SEDDC) for long term non invasive drug delivery.*' proceedings of 'The First International SBE Conference on Bioengineering and Nanotechnology, ICBN 2004, Biopolis, Singapore.'
25. Subbaraman Ravichandran, *'Advances in the development of Sensor Embedded Drug Delivery Cells (SEDDC) for long term drug delivery.'* proceedings of 'The First International SBE Conference on Bioengineering and Nanotechnology, ICBN 2004, Biopolis, Singapore.'
26. Subbaraman Ravichandran, Senthil Kumar, Tan Chew Stephanie, Muhammad Zaid Bin Amir, Siti Zubaidah Bt Mohd Akhbar, Naatasha Bt Isahak , Nur Liyana Bte Amrun, *'Modeling of non-invasive heparin delivery system in the management of peripheral vascular lesions.'*, proceedings of '6th Asian-Pacific Conference on Medical and Biological Engineering(APCMBE2005), Tsukuba, Japan.'
27. *United States Pharmacopeial Drug Information Index. 22nd ed.* Greenwood Village (Colorado): Micromedex; 2002.
28. Yagiela JA. Local anesthetics. In: Yagiela JA, Neidle EA, Dowd FJ, editors. *Pharmacology and therapeutics for dentistry. 4th ed*. St. Louis: Mosby; 1998. p. 217-34.
29. Yagiela JA. *Local anesthetics.* In: Dionne RA, Phero JC, Becker DE, editors. Pain and anxiety control in dentistry. Philadelphia: W.B. Saunders; 2002. p. 78-96.

Author: S.Ravichandran
Institute: Temasek Polytechnic
Street: 21 Tampines Ave 1
City: Singapore 529757
Country: Singapore
Emails: subbaram@tp.edu.sg, dr.sun.moon@gmail.com

Assessment of the Peripheral Performance and Cortical Effects of SHADE, an Active Device Promoting Ankle Dorsiflexion

S. Pittaccio[1], S. Viscuso[1], F. Tecchio[2], F. Zappasodi[2], M. Rossini[3], L. Magoni[3], S. Pirovano[3], S. Besseghini[1] and F. Molteni[3]

[1]Unità staccata di Lecco, CNR -IENI,Lecco, Italy
[2]Unità MEG, Ospedale Fatebenefratelli, Isola Tiberina, CNR-ISTC, Rome, Italy
[3]Centro di Riabilitazione Villa Beretta, Ospedale Valduce, Costamasnaga, Italy

Abstract — **Acute post-stroke rehabilitation protocols include passive mobilisation as a means to prevent contractures, but this technique could also help preserve neuromuscular activation patterns through proprioceptive information. This paper presents SHADE, an active orthosis that provides repetitive passive motion to a flaccid ankle by using shape memory alloy wire actuators. SHADE was studied to assess the promoted passive range of motion (PROM), acceptability and cortical effects. PROM and tolerability was assessed on 3 acute post-stroke patients (58±5y/o) by means of optoelectronic cinematic analysis. EEG/MEG instrumentation was utilised to evaluate sensorimotor cortical involvement during passive mobilization induced by SHADE in 7 healthy subjects (30.3±6.9y/o). These data were compared with voluntary movement (VM). SHADE produced good mobilisation across the available PROM (typically, from 5° plantarflexion to 15° dosiflexion). Acceptability in patients was also good. Suitable functional sources were identified for the primary sensorimotor areas. Cortico-muscular coherence was high not only in primary motor but also in primary somatosensory cortex. The cerebral involvement in these regions during the use of SHADE was similar to VM and significantly different from rest. This suggests that passive stimulation with SHADE could have clinical implications in supporting recovery of active functionality in stroke patients.**

Keywords — **Stroke, rehabilitation, orthotics, shape memory alloys, MEG.**

I. Introduction

Ankle rehabilitation techniques are very widespread in the clinical practice, as they are strongly indicated in the treatment of several different neuromuscular diseases. For instance, the distal lower extremities are very often affected by stroke events. After stroke, a rehabilitation program should be performed as soon as the patient's conditions are sufficiently good. Moving the limbs passively can improve circulation, maintain joint flexibility and normal muscle tone, while the patient is unable to exercise actively [1]. Contracture prevention due to passive stretching in the acute phase after CNS injury is also reported [2]. AHA/ASA endorsed guidelines for 2005 [3] indicate that a strong difference in the final treatment outcomes derives from the sheer time spent on physical rehabilitation. This could be improved using robotic devices without much impact on hospital task scheduling.

Passive mobilization [4] may also contrast deafferentation and learned non-use, i.e. directly address impairment of the cortical pathways involved in active limb control. The way this happens is not clear. There is evidence, however, that functional recovery occurs while changes in sensorimotor activation take place in the cerebral cortex.

A simple, user-friendly and safe device for use in the first few weeks after the acute event, during or following manual treatment by a therapist, could lead to great benefits for the patient by preventing the insurgence of severe sequelae and would help limit health service costs. In order to be a reli-

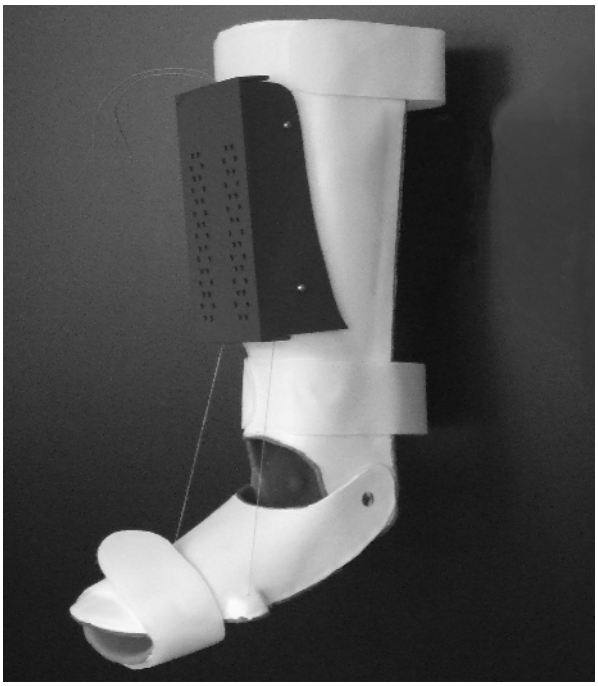


Fig. 1 The SHADE orthosis. Actuators are mounted frontally inside the vented shin housing. Inextensible threads connect them to the foot shell.

Chwee Teck Lim, James C.H. Goh (Eds.): ICBME 2008, Proceedings 23, pp. 961–965, 2009
www.springerlink.com

able device for rehabilitation purposes, this orthosis should comply with a number of clinical and functional requirements, i.e. it should be capable of promoting cyclic mobilization of the ankle joint across at least a range of -5° to 10° (negative is plantarflexion), have suitable repetition times in a physiological range, be thermally and electrically safe for the patient, light-weight and compact to wear. Such a device was designed as a prototype: SHADE (Fig.1).

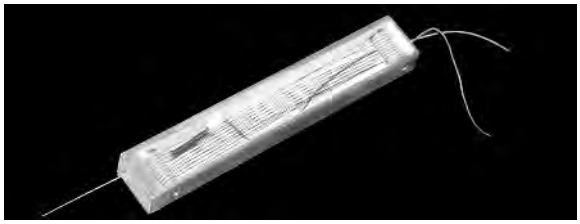


Fig. 2 Actuator mounting 2.5m of NiTi wire between 2 arrays of pulleys.

II. Material and methods

A. Shape memory actuators

Shape memory alloys (typically NiTi alloys) are metal compounds with the unique characteristic of being very deformable at room temperature and fully recovering deformation up to 8% when heated. This behavior is due to a reversible phase transformation occurring in the solid state, from martensite (stable at lower temperatures, more deformable) to austenite (stable at higher temperatures, stiffer). Shape recovery occurs if the alloy is heated above a certain transformation temperature, namely A_f, while on cooling down the material transforms again into martensite below M_f. During shape recovery, these alloys produce force and thus can be utilised to carry out work. For this application, a shape memory NiTi 250µm-diameter commercial wire stabilised for actuation was utilised (M_f= 274K and A_f = 351K) to ensure lasting performance for SHADE and industrial reproducibility. The actuator was designed as a 150mm×20mm×15mm insulated aluminium cartridge wherein 250cm of 0.25mm-diameter NiTi commercial wire is led back-and-forth between two arrays of ten mini-pulleys (Fig. 2). Heating is provided by Joule's effect, while cooling is left to natural convection. Preliminary tests have demonstrated that this actuator can lift 12N through 8cm when activated at 20W for 7s.

B. Orthosis design

A prototype of SHADE was assembled with two thermoplastic shells modelled on a prototype human lower limb of average size. These are hinged together at the ankle and strapped by Velcro® bands on the frontal aspect of the shin and on the foot. Two cartridge actuators are fixed on the front of the upper shell with inextensible threads connecting each NiTi wire to the foot shell. This configuration provides a theoretical maximum angular displacement of 28.67° with maximum force per actuator of around 10N with a foot weighing 12-17N. A dedicated software home-written in LabView (National Instruments, Austin, TX, USA) controls an array of electronic relays (NI9481, National Instruments) that switch on and off a dc-generator providing sufficient power to get shape recovery. All the electric connections and the thermal shielding are suitable to guarantee patients' safety. The performance of the SHADE prototype was tested measuring the angular displacement by means of electrogoniometer SIM-HES-EG 042 (Signo Motus, Messina, Italy). The current pattern was a 7s-step of 1.4A (0.7A per cartridge) and 30s allowed for cooling. The results of these tests showed that the angular displacement is very stable with weight (26.25°±1.5°, mean ± st.dev.), while curves tend to drift towards lower angles (decreasing dorsiflexion) on increasing weights.

C. Pre-clinical assessment

A group of 3 patients (A1, A2, A3) was enrolled to assess the efficacy of SHADE in producing ankle dorsiflexion in accordance with the clinical requirements and to prove short-term tolerability. The selection criteria were: flaccid or slightly spastic (≤1 on the Ashworth Scale) hemiparesis involving the ankle as a consequence of first stroke, no major skin or articular pathologies, no severe cognitive impairment, able to answer questions. The patients' characteristics are presented in Table 1.

Patients were treated according to ethical principles, as approved by the hospital ethical committee, and gave informed consent. They underwent general clinical assessment prior to the start of the treatment. Then they used SHADE in single trials to measure the instantaneous range of motion by means of eight optoelectronic cameras sampling at 100Hz (Elite Gait Eliclinic - BTS, Garbagnate Milanese, Italy). Six IR reflective markers were positioned on the *condyli tibiales*, the *malleoli*, *metatarsi I* and *V*, identifying the ankle angle as the one extending between the central

Table 1 Patients' characteristics (AROM: active range of motion)

	Age	Sex	Time after stroke	Affected side	AROM
A1	63	F	4 y	left	full
A2	53	M	3 y	left	none
A3	58	M	3 mo	left	none

Table 2 EEG left side derivations and mapped areas

EEG derivation	Mapped area
T7-A1	left secondary sensory (S2)
Cpz-C1	left primary sensory (S1)
C1-FC1	left primary motor (M1)
FC1-FZ	left supplementary motor (SMA)

axes of shin and foot. The patients, wearing SHADE, were asked to try and lift the tip of their foot without any cues about to what extent or at what speed the task had to be carried out; irrespective of the results of this active trial, SHADE was then used to elicit passive dorsiflexion twice.

D. Cortical involvement during passive mobilization

EEG and MEG activities were collected bilaterally on 7 healthy subjects (aged 30.3±6.9; 5 male) during rest (REST) and dorsiflexion as produced by voluntary movement (VM) and passive mobilization through the SHADE orthosis (O-PM). Only data from the left hemisphere were analysed. EEG derivations (according to the international 10/20 system) were used as markers of different cortical areas (Table 2). Brain magnetic fields were recorded from a scalp area of 180cm^2 by means of a 28-channel MEG system (Vacuumschmeltze GmbH, Hanau, Germany), centered 2.5cm posteriorly relative to Cz (i.e. in correspondence of Rolandic areas devoted to the lower limb control). Primary sensory and motor areas were then discriminated by Functional Source Separation [5]. The effects of maintaining attention/distraction attitudes during O-PM were also considered. Power spectral density modulation was used to quantify involvement of sensorimotor areas in the different conditions focusing mainly on the α (8-13Hz), β (14-32Hz) and γ bands (33-90Hz).

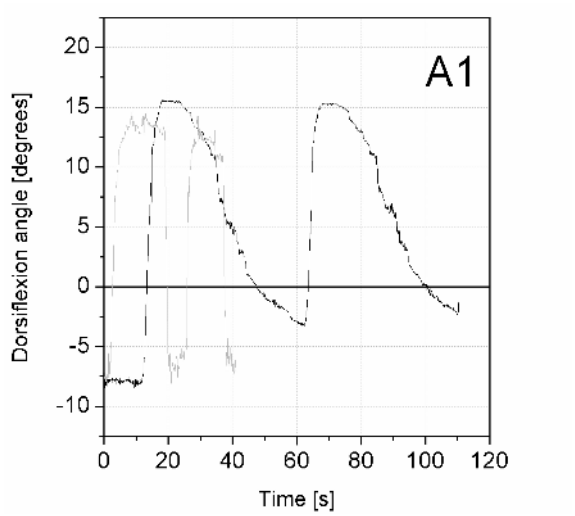


Fig. 3 Results of optoelectronic tracking of ankle motion during the use of SHADE. The black lines represent passive exercise by SHADE; the grey line represent the active ankle motion. Range of motion produced by SHADE is patient-dependent. For patient A1 it is possible to appreciate that dorsiflexion speed (positive slope) is similar to the one spontaneously chosen by the patient. Plantarflexion (negative slope) is limited to 30s by the input current waveform.

III. Results

A. Clinical outcomes

Optoelectronic movement analysis on each patient revealed that SHADE is capable of producing an appropriate range of motion for rehabilitation purposes (Fig. 3). In particular, with patient A3 it elicited motion from -4.5° to +19°, adding up to a total angular displacement of 23.5°, not too far from the theoretical limit. Patient A1 is particularly interesting, as she was able to produce active movements of her own. The speed of passive dorsiflexion, closely matches the one of natural spontaneous motion. Reset speeds and angles are not matched, however. Acceptability was good for all the patients and movement was deemed natural.

B. Cortical correlate of passive movement

Suitable functional sources for S1 (FS_{S1}) and M1 (FS_{M1}) were identified in all subjects. FS_{M1} was correctly found to be more frontal than FS_{S1} (p=0.023). Interestingly, FS_{S1} showed high coherence with ankle muscular activity.

In the β band (Fig. 4), S1 activity during VM and O-PM were both different from the activity during REST (respectively, p=0.015 and p=0.054), while M1 reacted significantly with respect to REST only in VM (p=0.014). Centro-parietal sensory involvement during O-PM was also evident from EEG data (p=0.002, Cpz-C1).

In the γ_1 band (33-60Hz) significant source effect indicated higher power in the primary motor area than in the primary sensory area in all conditions (p=0.04). The same happened also in γ_2 (33-60Hz), with p=0.017. Slightly higher sensory-motor coherence was also observed in γ_2 during attention than no-attention in O-PM (p=0.119).

IV. Discussion

Technical tests were conceived so that the weights and lever arm produced plantarflexion moments in the range of those typical of foot weights (e.g. 15N foot weight × 10cm

lever arm). It is important to notice that with all the tested weights (producing moments 80% to 110% of the reference one) the clinical requirements are always met. Also the clinical tests showed that SHADE can produce dorsiflexion beyond the minimum requirements. The dorsiflexion speed resulted appropriate to generate a natural movement. The reset speed is, on the other hand, much lower than the spontaneous one. This depends on the cooling rate which is rather low, as convection is strongly hindered by the actuator housing walls (albeit they are vented). It was decided that an adjustable reset time of 30s would be allowed during cyclic clinical working. This time is long enough to reach plantarflexion almost completely by means of the sheer foot weight without any forced convection. The chosen reset time, even though it is unnatural, could be suitable for physical rehabilitation because it allows the ankle to remain stretched for as long as 70% of each cycle, which is hoped to avert the development of contractures.

Whereas the applicability of passive mobilisation to maintaining tissue properties and articular suppleness is well referenced in daily clinical practice, any evidence that it affects cortical structures could suggest it might be of some utility in preserving motion planning and control abilities as well. This is certainly hard to tell from a study on healthy control subjects but it was felt to be a good start to prepare a thorough and more to-the-point analysis of post-stroke cases. The experience gained on the chosen acquisition protocol (very scant as to the number of EEG markers and limited MEG-scanned area) suggests that while this MEG paradigm is suitable to study primary motor and sensory cortices, EEG derivations should be increased to monitor more precisely the supplementary, pre-motor and secondary motor areas, whose involvement was not clearly evidenced in this study even during VM but could be of peculiar interest. Furthermore the reconstruction of data from the ipsilateral/contralesional hemisphere (or the right hemisphere in healthy controls) could be included, since cortical remapping and recovery processes can affect both sides in post-stroke patients. On the whole, however, this set-up was able to show significant effects correlating, in particular, somatosensory activation to the use of SHADE, in ways similar to what happens with voluntary movement. If that were true also for post-stroke patients (which will have to be proved), there would be a possibility that passive mobilisation play a role in stimulating appropriate cortical circuitry associated with the execution of ankle motor tasks. For this reason repetitive and prolonged passive mobilisation might be effective in contrasting deafferentation and learned non-use, especially during the post-acute flaccid phase when the patient is unable to carry out active dorsiflexion. The observed slight effect of attention on γ_2 suggests that, through cognitive elaboration of afferent information, patient's awareness might enhance outcomes on cortical stimulation. More subjects are needed to improve significance of these data, however, particularly because constancy of attention levels is difficult to achieve during rather lengthy acquisition sessions.

In sum, it is hoped that the immobilisation-disuse vicious cycle initiated by stroke and the ensuing paresis could be interrupted by a threefold effect of passive mobilisation with SHADE: preserving soft tissue properties; preventing sensorial deprivation and promoting movement rehearsing; modulating remapping by offering constant afferent input.

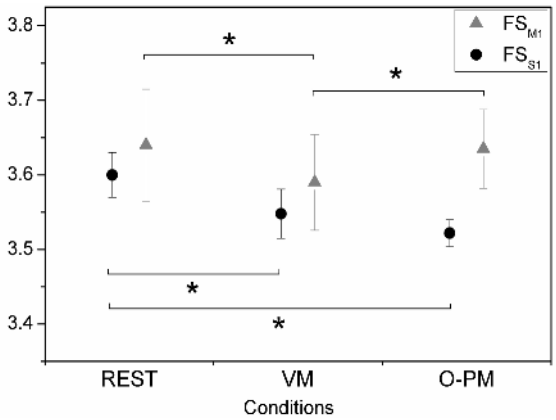


Fig. 4 Power spectral density in the β band in different experimental conditions. VM and O-PM are similar conditions for FS_{S1}.

V. Conclusions

A prototype of SHADE was built and tested, showing good performance even beyond the clinical requirements. Preclinical tests demonstrated that SHADE produces dorsiflexion across a sufficient range of motion from -4.5° up to 19°. During cyclic motion posterior calf muscles remain lengthened for around 70% of the time, ensuring suitable stretch. Acceptability by the patients was very good, but further trials are needed to verify this in longer sessions.

SHADE was proved to stimulate somatosensory cortical areas in a way similar to voluntary ankle motion in healthy subjects. Future work will address the efficacy of passive stimulation in the functional recovery of stroke survivors.

References

1. http://www.ninds.nih.gov/disorders/stroke/poststrokerehab.htm
2. Harvey L, Herbert R (2002) Muscle stretching for treatment and prevention of contractures in people with spinal cord injury. Spinal Cord 40:1–9 DOI 10.1038/sj/sc/3101241

3. Duncan PW, Zorowitz R, Bates B et al. (2005) Management of Adult Stroke Rehabilitation Care. A Clinical Practice Guideline. Stroke 36:e100–e143 DOI 10.1161/01.STR.0000180861.54180.FF
4. Pittaccio S, Zappasodi F, Viscuso S et al. (2008) Cortical correlate of passive mobilisation of the ankle joint by means of the SHADE orthosis. Clin Neurophysiol 119:S20 DOI 10.1016/S1388-2457(08)60078-4
5. Tecchio F, Porcaro C, Barbati G et al. (2007) Functional source separation and hand cortical representation for a brain–computer interface feature extraction. J Physiol 580:703–721 DOI 10.1113/jphysiol.2007.129163

Author: Simone Pittaccio, Ph.D. MSc(Eng)
Institute: CNR – Institute for Energetics and Interphases
Street: corso Promessi Sposi, 29
City: Lecco
Country: Italy
Email: s.pittaccio@ieni.cnr.it

A Behavior Mining Method by Visual Features and Activity Sequences in Institution-based Care

J.H. Huang, C.C. Hsia and C.C. Chuang

ICT-Enabled Healthcare Project, Industrial Technology Research Institute – South, Tainan, Taiwan, R.O.C

Abstract — **This paper proposed a behavior mining method through discriminative visual feature extraction from disabled elder caring. Nursing activities for bed-ridden residents were manually annotated from video data which was collected and provided by a care center. The variation grid sequences are extracted as discriminative features from the difference blobs of successive image frames. The sequential association rules are trained based on the grid sequences for each nursing activity category. A similarity measure between test video segment and related rules is proposed for nursing activity recognition. Through empirical evaluation on annotated video dataset, the proposed approach is very promising for nursing activity discrimination through the sequences of visual features.**

Keywords — **Nursing activity, Behavior mining, Image sequence, Bed-ridden, Institution-based care.**

I. Introduction

With the rapid increasing trends of aging population and chronic diseased or disabled elders, long-term healthcare becomes more and more important. However, the limitation of human resources, including nurses and caregivers, results in caring quality degradation. In the past decade, more efforts have been made to adopt information and communication technology for clinical nursing assist, like nurse call [1], patient monitoring [2], and information system [3] etc.

A lot of healthcare technologies are developed for detecting and monitoring status or behavior of disabled elders. With nursing labor shortage, the lack of professional supervision and possible burn out due to difficulties of nursing care were threats to the caregivers, especially to foreign nursing labor. To reduce the negligence, a reminding system by detecting and recording regular nursing activities is helpful.

Video surveillance system for healthcare is usually used to increase overall security and safety, monitor continuously, and store visual evidence for investigations. Object tracking [4] and fall incident detection [5-6] are hot topics in the last years. However, the complicated environment and light effects are still limited the application.

From the observation of activity of bed-ridden residents, caregivers, and the interaction between them, it can retrieve certain meaningful information from visual features. In this paper, a behavior mining method for nursing activity is proposed. Briefly, the proposed method is composed of two main phases: 1) construction of sequential association rules and 2) discrimination unknown nursing activities with those rules. In next section, we descript the video data which was collected from a care center and introduce the proposed method for behavior mining. Then empirical evaluation of the proposed method is presented. Finally, conclusion is stated in the last part.



(a) (b)

Fig. 1 The view of IP-cameras

II. Material and Method

Video data were collected in the care center using snapshot capturer system with IP-cameras. Two elder subjects participated in. One is 68 years old, recovering from stroke on both sides, especially the left side, and the other is 73 years old, has a stroke on left side and hypertension. The IP-cameras were mounted on the walls. Figure 1 shows the snapshots for the two subjects, (a) for the former and (b) for the latter. The marked regions represent the bed areas.

The snapshot capturer system captures a 320x240 JPEG image from each IP-camera every three to four seconds. The consecutive image sequences of two weeks were collected. The data of the first and second week were used as training and testing set, respectively. Six types of nursing activities were annotated manually and the numbers of annotated activities in training and testing data set are shown in Table 1. “Diaper” means that the caregiver checks is the diaper wet or dirty, and change it. “On Bed” and “Off Bed” means that the caregiver helps residents to get onto and out off the bed. “Reposition” means that the caregiver repositions the residents regularly to reduce pressure sores. “Vital Signs”

Chwee Teck Lim, James C.H. Goh (Eds.): ICBME 2008, Proceedings 23, pp. 966–969, 2009
www.springerlink.com

Table 1 The numbers of annotated activities

Item	1st week		2nd week	
Activity	(a)	(b)	(a)	(a)
1. Diaper	52	52	48	53
2. On Bed	3	16	4	14
3. Off Bed	3	16	4	14
4. Reposition	14	2	19	4
5. Vital Signs	19	20	22	23
6. Food	58	44	58	41

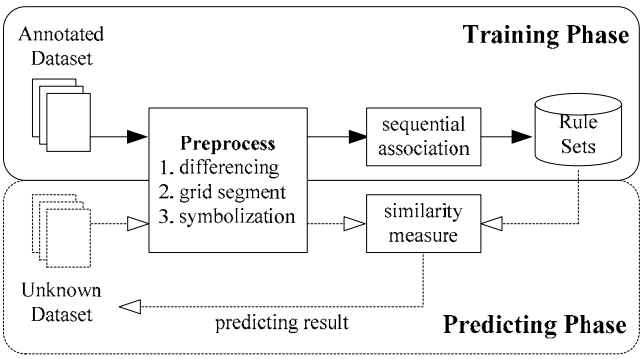


Fig. 2 Flowchart of the proposed method

means that measuring vital signs of the residents, like heart rate, blood pressure, and body temperature. "Food" means that the food and medicine are given to the residents through their nasogastric tube.

Figure 2 depicts the flowchart of the proposed method including training and predicting phases. In visual preprocessing, the changed pixels are extracted for each pixel when the difference between two successive images is larger than a threshold α. The Erosion filter is used to remove random noisy pixels, and the remained changed pixels are clustered into blobs. Only the area of the bed is used for nursing activity modeling and recognition. The bed area is divided into $M \times N$ grids and the variation grid sequence is extracted as the visual features for video segment V_j with $K+1$ image frames.

$$F_j = \left\{ D_1^{(j)}, D_2^{(j)}, ..., D_K^{(j)} \right\} \tag{1}$$

where

$$D_k^{(j)} = \left\{ g_{m,n}^{(j)} \mid grid^{(j)}(k,m,n) = 1 \right\} \tag{2}$$

and

$$1 \le k \le K, \quad 1 \le n \le N, \quad 1 \le m \le M \tag{3}$$



$$F_j = \Big\{ \big\{ g_{1,1}, g_{2,1}, g_{3,1}, g_{1,2}, g_{2,2}, g_{3,2}, g_{1,3}, g_{2,3}, g_{3,3}, g_{1,4}, g_{2,4}, g_{3,4}, g_{1,5} \big\}, \big\{ g_{1,1}, g_{2,1}, g_{1,2}, g_{2,2}, g_{1,3}, g_{2,3}, g_{1,4}, g_{2,4}, g_{1,5}, g_{2,5} \big\}, \big\{ g_{1,1}, g_{1,2}, g_{1,3}, g_{2,3}, g_{1,4}, g_{1,5} \big\} \Big\}$$

Fig. 3 Example of visual feature extraction

The function $grid^{(j)}(k,m,n)$ represents if the grid in location (m,n) contains blobs (equals to 1) or not (equals to 0). Figure 3 gives an example of part of "On Bed" activity for subject (b). The activity contains four image frames. The area of the bed is segmented into 4×5 grids, and red grid denotes that the grid contains blobs. The visual feature is show in the bottom of Fig. 3. Symbolization is a useful method for mining sequences. The same visual features are encoded with the same symbol. An activity can be regarded as a transaction and a transaction contains several symbols viewed as items. The activity-transaction table is established for training and predicting.

A. Training Phase

Input: An activity-transaction table D and minimum support *minsup*
Output: Frequent itemsets F
Algorithm: Gen_FreItems

1. $F_1 =$ scan for each item and get the frequent 1-itemsets;
2. $k = 2$;
3. **while** $F_{k-1} \neq \phi$ **do**
4. **for** $\forall p, q \in F_{k-1}$ **do**
5. **if** $p_1 = q_1 \,\&\, p_2 = q_2 \,\&\, ... \,\&\, p_{k-1} = q_{k-1}$ **then**
6. $r =$ concatenate $\{p_1, p_2, ..., p_{k-1}, p_k, q_k\}$;
7. $C_k = r \cup C_k$;
8. **end if**
9. **end for**
10. $F_k = \{X \mid \sup(X) \ge minsup, X \subseteq C_k\}$;
11. $k = k + 1$
12. **end while**

Fig. 4 Algorithm for generating sequential association rules

From the activity-transaction table, we make use of Apriori-like association mining method [7] to discover the frequent itemsets that sufficiently exceed the presetting minimum support *minsup* , as shown in Fig. 4. These generated frequent itemsets can be viewed as association rules directly since temporal continuities are inherent in them. The difference with Apriori algorithm is the concept of sequence. Keep the order of itemsets in transaction and calculate the support, the number of transactions satisfying the itemsets is measured in each pass. After candidate itemset generation and activity-transaction table scanning, the sequential association rules of each activity are performed.

B. Predicting Phase

For an unknown video segment, the nursing activity is decided based on the similarity to each pre-trained activity rule sets. First, the transaction items of unknown video segment and activity rule sets are be converted into original visual features, which contain $M \times N$ binary attributes. The similarity measure is to accumulate the support of matched rule sets in each activity category. The algorithm by utilizing is shown in Fig. 5. The procedure dist is to get score between two transaction items. The higher score represents more similar. If the number of different visual features is smaller or equals to one, the score is assigned the minimum distance of all the permutations of unmatched visual features of transaction items. Ignore it if the number of different visual features is larger than one. We check if the transaction of unknown video segment contains the rule or not

Input: An unknown activity-transaction $\{a_1, a_2, ..., a_m\}$, an activity rule sets $\{R_1, R_2, ..., R_n\}$ and corresponding support $\{s_1, s_2, ..., s_n\}$

Output: Accumulated support value V

Algorithm: Get_AccSupport

1. **for** $\forall R_i \subset \{R_1, R_2, ..., R_n\}$ **do**
2. let matched number be $M = 0$;
3. **for** $\forall r \subset R_i$ do
4. get corresponding $a \in \{a_1, a_2, ..., a_m\}$
5. **if** dist$(r, a) \le threshold$ **then**
6. $M = M + 1$;
7. **end if**
8. **end for**
9. **if** $M = \text{size}(R_i)$ then
10. $V = V + S_i$
11. **end if**
12. **end for**

Fig. 5 The support accumulation of matched rule sets

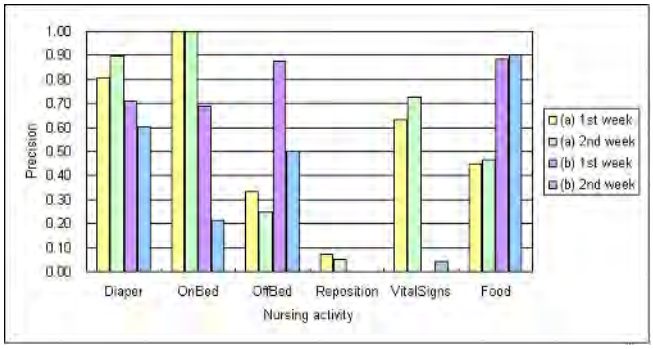


Fig. 6 The precisions of our method

by above method. According to the accumulated support, what activity category does unknown video segment belong to is decided.

III. Results and Discussion

Precision rate is used to evaluate the performance of proposed nursing activity recognition method and is calculated as:

$$\text{Precision} = \frac{\#\text{ of correctly recognized activities}}{\#\text{ of recognized activities}} \quad (4)$$

Figure 6 shows the results for nursing activity recognition. Compared to the chance level, 0.17, the average precision rate of the proposed method is 0.5.

Except for "Diaper" activity, the lower precision of activity "Reposition", the higher part equals to the lower part in the other four. Through the observations on the frequencies and the sequential association rules of activities, we can explain the result of above experiment. First, from the Table 1, the frequencies of activity "Diaper", "Vital Signs", "Food" is larger than the others. The reliability of rules is highly related to the visual features, but the predicting results are not precise in activities "Vital Signs" and "Food". The confusion matrix is shown in Fig. 7. The two activities are not discriminable by rules. The motions of caregiver in "Vital Signs" and "Food" nursing activities are similar to each other. The caregiver always stands near the bedrail and actions on the left-top side of subject. The rules of those two activities are ambiguous. In other words, the sequential association rules are insufficient for discriminating "Vital Signs" and "Food". But duration is an important factor between them. In statistics, the average time spend in vital signs measure is one minute and in feeding is three minutes. Therefore we can use the factor of duration to improve our method. Second, the experimental data are two weeks and number of each activity is not equal, especially "On Bed",

	Diaper	OnBed	OffBed	Reposition	VitalSigns	Food
Diaper	85	1	8	2	4	0
OnBed	0	6	1	0	0	0
OffBed	0	4	2	0	1	0
Reposition	9	3	14	2	4	1
VitalSigns	5	0	0	0	28	8
Food	7	0	0	0	56	53

(a)

	Diaper	OnBed	OffBed	Reposition	VitalSigns	Food
Diaper	69	0	12	0	1	23
OnBed	1	14	1	0	1	13
OffBed	0	1	21	0	4	4
Reposition	0	1	4	0	1	0
VitalSigns	0	0	0	0	1	42
Food	2	1	5	0	1	76

(b)

Fig. 7 Confusion matrices of subject (a) and (b)

"Off Bed" of subject (a) and "Reposition" of subject (b). Nursing activities is not always on schedule. Some nursing activities are taken for the subject if the caregivers think that is helpful for him. Third, the lower precision of "Reposition" is due to the rule sets. For the "Reposition" of subject (a), there are lower support and fewer rules be found. And for the subject (b), the number of training data is just two. Overall, the experiment of "Reposition" is to be no effect.

IV. Conclusions

In this paper, the sequential association rules are mined from visual features and used to discriminate unknown activities. The experimental results show that the proposed method is promising for nursing activity discrimination through the visual features. The goal of nursing activity discrimination is not only alert with daily scheduled nursing activity but also supervise the procedure of nursing activity is being done completely. According the mechanism, reduce the negligence of caregivers, strengthen manpower training, and raised the quality of health care.

Acknowledgment

The experimental data of this paper is provided by a care center in Tainan City, Taiwan, and the dataset were annotated by Professor C. J. Hou, Y.T. Chen and their students, in Southern Taiwan University. We appreciate them for the support of this work.

References

1. E. T. Miller, C.Deets and R. V. Miller (2001) Nurse call and the work environment: lessons learned, Journal of Nursing Care Quality, 15(3):7-15
2. F. de Vibe (2005) Development of a roaming real-time patient monitor, Cand. Scient. Thesis, Depart. of Informatics, Univ. of Oslo
3. Cisco (2008), Clinical connection suite
4. W. Hu, T. Tan, L. Wang and S. Maybank (2004) A survey on visual surveillance of object motion and behaviors, IEEE Trans. on Systems, Man, and Cybernetics – Part C: Application and Reviews, 34(3):334-352
5. J. Tao, M. Turjo, M. F. Wong, M. Wang and Y. P. Tan (2005) Fall incidents detection for intelligent video surveillance, in Proc. of 16th International Conference on Computer Communications and Networks, pp. 1172-1177.
6. C. W. Lin, Z. H. Ling, Y. C. Chang and C. J. Kuo (2007) Compressed-domain fall incident detection for intelligent home surveillance, Journal of VLSI Signal Processing System for Signal, Image, and Video Technology, 49(3):393-408
7. R. Agrawal, T. Imielinski, and A. Swami (1993) Mining association rules between sets of items in large databases, in Proc, ACM SIGMOD Int. Conf. Manage. Data-SIGMOD, pp. 207-216

Chronic Disease Recurrence Prediction Model for Diabetes Mellitus Patients' Long-Term Caring

Chia-Ming Tung[1], Yu-Hsien Chiu[1], Chi-Chun Shia[1]

[1]ICT-Enabled Healthcare Program, Industrial Technology Research Institute – South, Tainan, Taiwan (R.O.C.)

Abstract — **Recurrence and complication prevention is crucial in caring chronic patients. This paper presents a chronic disease recurrence prediction model in long-term caring for diabetes patients. A nursing information system is developed and applied in an institution-based health care center. Values of blood sugar, vital signs, BMI and nursing records of diabetes patients are collected during the daily nursing procedure. Since data are recorded in different time with variable sampling period, a flexible time series analysis method is presented for exploiting seasonal variation and cyclical fluctuation between diabetes and daily-recorded signals. Expert knowledge for chronic disease is built based on domain specific language to extract chronic disease care knowledge from nursing records. Finally, a health surveillance system is developed by integrating multi-modal daily caring information for long-term caring of chronic patients. Several experiments with statistical testing are conducted and the results compare the performance of the proposed method. The expected outcome will build a prediction model to early warning before diabetes will be recurrence.**

Keywords — **chronic disease, diabetes, long-term healthcare, institution-based health care center, nursing information system**

I. Introduction

Taiwan becomes aging society in 1996. 10.33% of population is elder in Taiwan at August 2008 [2]. Elder healthcare is the most important social welfare in the aging society. Taiwan government planned many long-term projects to healthcare. In Taiwan's society, most of the elder live in their home. The elder may have chronic diseases, although not every family could afford enough human resource or knowledge to care the elder. An alternative way is care them at foundational healthcare center for a centralized caring.

Diabetes mellitus is one of the common diseases in elderly human. It is the top four of ten leading causes of death in 2006 [1], and other diseases erupt at the same time, like Cardiovascular disease, Hypertension, Visual disturbance et al. At this time, the best control over diabetes mellitus is to monitor the blood sugar value. The values of blood sugar before or after the meals are measured, and it is now the standard procedure in foundational healthcare center. If patient's status was instable, the blood sugar values are measured once or twice a day. Other signals are also been monitored for diabetes mellitus patients, like vital signs, body mass index (BMI), nursing record, medicine and so on. In healthcare center, nurse or caregiver may not have time to review these measured data. If computer assist tools can help caregiver to monitor these data, caregiver may use these signals to prevent some diseases.

Information and communication technology (ICT) may help caregiver to analysis the nursing record. Jimmy Lin and Dina Demner-Fushman have developed a statistical and knowledge-based automatic medical knowledge extraction [3, 4].

ICT can help caregiver to store and analyze the nursing record. However, ICT can not replace the human resource in healthcare. It can assist human to make the right decision if the knowledge base was built. Back-end database can store interactive result among doctor, nurse or caregiver and patient [5]. Olga Medvedeva, Tamara Knox and Jody Paul present how ICT were utilized to develop assistive software for decision-making in treatment of diabetes [5]. In doctor's view, diabetes mellitus type II is simple to diagnose but difficult to treatment. They develop a web-based application that can help doctor to access data and provide recommendation for patient with better treatment. Software can automatically learn and be applied to medical data diagnosis. The learning algorithm is built and well tuned, the software can automatically learn and diagnosis. The diagnosis result can be verified by human professors [7]. When learning the knowledge, the data type should be considered. Nursing data can be numerals, text, video or sound. Integration of these multi-modal data is helpful [6].

This study prepares to predict the blood sugar value of diabetes mellitus patient. A nursing information system is been applied in a foundational healthcare center for collect the nursing record. Nursing records are collected and analysis by using multiple regression analysis. Two groups' data are categorized to find its own prediction model. Knowledge base was been used to store the predict model.

The prediction models can help caregiver to predict the patient's value of blood sugar. Caregivers don't measure patients' value of blood sugar everyday. Only measure in schedule time or patients' status is not good. The healthcare center can reduce times to measure patients' value of blood sugar. It can use this assist tools to reduce the operation cost, too.

Chwee Teck Lim, James C.H. Goh (Eds.): ICBME 2008, Proceedings 23, pp. 970–973, 2009
www.springerlink.com

II. Materials and Methods

Blood sugar values, vital signs, BMI, text nursing record, and values of SpO_2 are collected and recorded by a nursing information system. These data are measured with different time period. Vital signs, text nursing records are measured and collected everyday. Blood sugar values are measured independently for different patients from twice a week, or once a month. Patient's weight is measured every two-month, and height is measured every half year. The BMI is calculated and recorded every two months. The flowchart of this research is showed in Fig. 1.

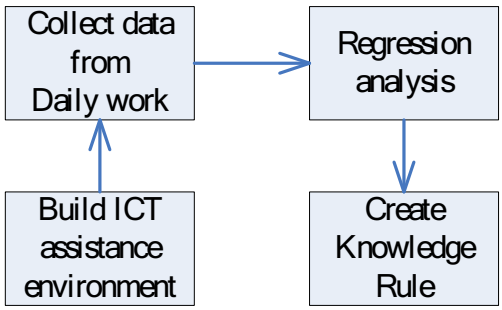


Fig. 1 Research Flow

- ***Build ICT assistance environment***

  Nursing information system (NIS) was deployed into the foundational long-term healthcare center. The NIS system was based on windows application. Design strategy is easy use for caregiver when operating the NIS system. Both mouse and keyboard can be used when input the data.

- ***Collect from daily work***

  Vital signs, values of blood sugar, values of SpO_2, BMI and text nursing record were input into the system. Vital signs and text nursing record were measured everyday for every patient. Values of blood sugar and values of SpO_2 were measured if necessary. BMI was recorded every two months.

  In the other hand, for the cost issue, only diabetes mellitus patients and new entrance patient were measure the blood sugar values.

- ***Regression analysis***

  To understand the relationship among all data, this study used multiple regression analysis to analyze all kinds of data and find out which kinds of data will infect the values of blood sugar.

- ***Create knowledge Rule***

  The prediction model is built based on the results of the multiple regression analysis. Knowledge base can be store in database. Feature, this knowledge could use in expert system like JBOSS Drools.

III. Results

- ***Build ICT assistance environment***

  NIS prototype system was developed and provide user to use and modify the operation flow for ease of use. This study deploys 1 database server and 5 client's user interface in care stations and supervisor's PCs.

- ***Collect from daily work***

  All patients' vital signs were measured every day. The values of blood sugar were not measured for every patient. In the healthcare center, only new patient entrance or the diabetes mellitus patients need to measure the values of blood sugar.

  If the new entrance patient's blood sugar value was normal, the care-giver never tracks the values of blood sugar for this patient.

  The value of blood sugar is measured every Wednesday and Sunday. Some patients ever got the diabetes mellitus before, after treatment the patient was fully recovered from diabetes mellitus. Ever they never need any medicine for treat the diabetes mellitus but doctor still require the caregiver to track these patients values of blood sugar. They only measure value of blood sugar every month.

  Patient's height is measured every 6 months and weight is measure every 2 month. So BMI is calculated every two months.

Table 1 nursing data measure standard

Name	Below	High
Body Temperature	36	37.5
Pulse	60	90
Breath	12	20
Systolic Pressure (SP)	100	130
Diastolic Pressure (DP)	60	85
SpO2	90	100
BMI	18.5	24
Value of Blood Sugar	60 *	100 **
	80 *	120 **

*: Before meal; **: After meal

Table 1 show the measure standard of all nursing records.

This study categorized the diabetes mellitus into two groups. Group 1, patients got both diabetes mellitus and hypertension. Group 2 has diabetes mellitus only or more than two diseases except hypertension. This study didn't use diabetes mellitus type I and type II to separate the diabetes mellitus patients.

- ***Regression analysis***

Both group 1 and group 2 use the same condition. The dependent variable is the value of blood sugar; independent variables are body temperature, pulse, breath, systolic pressure, diastolic pressure, SpO2 and BMI.

Stepwise multiple regression analysis was used to analyze the relationship among value of blood sugar and other data.

Group 1 has 354 numbers of data that selects all data from database when care-giver measures the value of blood sugar and record into database. Group 1's prediction model is below:

$$Y= -0.135_{Breath}+0.155_{BMI}+0.153_{SpO2} \quad (1)$$

Fig.2 showed the Group 1 has not close normal distribute.

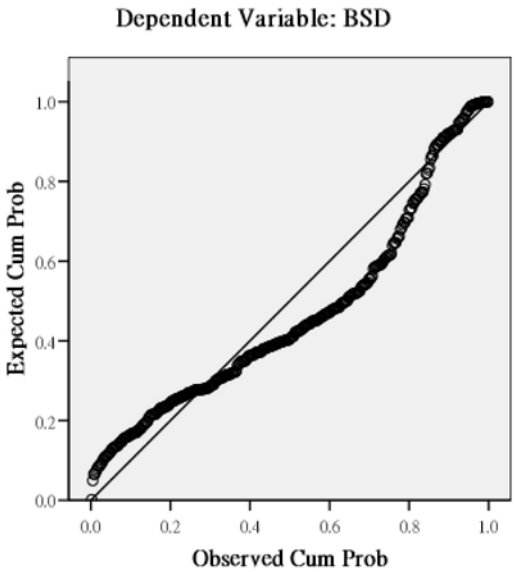


Fig. 2 Normal P-P plot of Regression Standardized Residual for Group 1

Group 2 has 340 numbers of data that selects all data from database when care-giver measures the value of blood sugar and record into database. Group 2's predicting model is below:

$$Y= -0.341_{BMI}+0.259_{SP}-0.205_{DP}+0.120_{Pulse} \quad (2)$$

Fig.3 showed the observed probability was much closed to normal distributes.

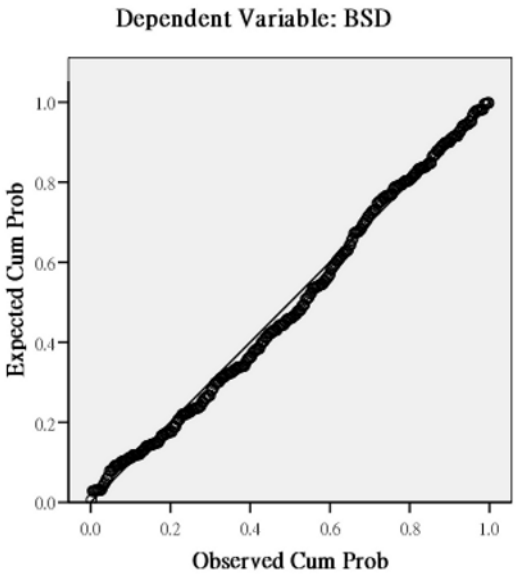


Fig. 3 Normal P-P plot of Regression Standardized Residual for Group 2

- ***Create knowledge Rule***

Two prediction models will be stored in the knowledge base. Excel format is good to store the knowledge rules. The expert system needs the rules and facts to inference the result.

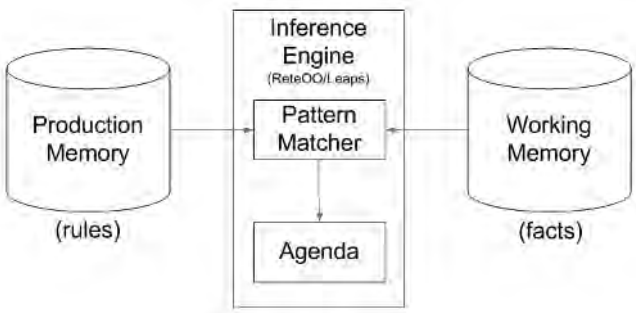


Fig. 4 Expert System common framework

Fig. 4 shows the basic expert system's framework. Rules will be creates by this study's prediction model. Facts will be the data that caregiver

measure with patients. JBOSS Drools is a kind of expert system. In this system, the knowledge rule will be store in Drools or decision table. Decision table can be used excel format. The expert system still be continue to develop. The prediction models will be transfer to domain rule language at that time.

IV. Discussion

Model 1 can predict the value of blood sugar with the patients have both diabetes mellitus and hypertension. Model 2 can predict the value of blood sugar with the patients have diabetes mellitus and other diseases except hypertension. In real condition, some other can cause the value of blood sugar to raise or descent. Like food is the other main reason can influence the value of blood sugar. When family go to healthcare center to visit the elder lived in center. They may take food for the elder. This will break the nutrition plan. The value of blood sugar becomes more difficult to control.

V. Conclusions

The study provides these models to predict the value of blood sugar. If care-giver need, they can measure the value by the standard procedure. Base on these prediction models, the healthcare center can know the patient' value of blood sugar without measure for save the operating cost. But ICT just provide the assist tools, not for replace the human resource. Human determine and experience are the most important than ICT assist tools. For patients' safety, human resource should be the main consideration.

This study just uses numerals to analysis the value of blood sugar. Feature, the multimodal data analysis need to be creates for more correct prediction rate. The more prediction rate, the ICT assist more helpful for care-giver.

References

1. Department of health, Executive Yuan, R.O.C. (Taiwan), http://www.doh.gov.tw
2. Department of statistics, ministry of the interior, R.O.C. (Taiwan), http://www.moi.gov.tw/stat/index.asp
3. Dina Demner-Fushman, Jimmy Lin (2007) Answering Clinical Questions with Knowledge-Based and Statistical Techniques, Computational Linguistics vol.33, issue 1, pp63-103
4. J. H. Gennari et al. (2003), The evaluation of Protégé: An environment for knowledge-based systems development, International Journal of Human-Computer Studies, Vol. 58, pp. 89-123
5. Olga Medvedeva, Tamare Knox, Jody Paul (2007) DiaTrack:web-based application for assisted decision-making in treatment of diabetes, Journal of Computing Sciences in Clooeges vol 23, issue 1, pp154-161
6. Michail Vlachos et al. (2006) Indexing Multidimensional Time-Series, The International Journal on Very Large Data Bases, Vol.15, Issue 1,pp.1-20
7. Zekie Shevked, Ludmil Dakovski (2007), Learning and classification with prime implicants applied to medical data diagnosis, ACM International Conderence Proceeding Series vol 285, Article No. 103

Author: Chia-Ming Tung
Institute: Industrial Technology Research Institute
Street: Bldg. R1, No. 31, Gongye 2nd Rd., Annan District,
City: Tainan City
Country: Taiwan (R.O.C.)
Email: tungcm@itri.org.tw

Author: Yu-Hsien Chiu
Institute: Industrial Technology Research Institute
Street: Bldg. R1, No. 31, Gongye 2nd Rd., Annan District,
City: Tainan City
Country: Taiwan (R.O.C.)
Email: chiuyh@itri.org.tw

Author: Chi-Chun Hsia
Institute: Industrial Technology Research Institute
Street: Bldg. R1, No. 31, Gongye 2nd Rd., Annan District,
City: Tainan City
Country: Taiwan (R.O.C.)
Email: shiacj@itri.org.tw

The Study of Correlation between Foot-pressure Distribution and Scoliosis

J.H. Park[1], S.C. Noh[1,2], H.S. Jang[1], W.J. Yu[1], M.K. Park[1] and H.H. Choi[1,2]

[1]Dept. of Biomedical Engineering, Inje University, Gimhae, Korea
[2]BK21 Bio-Organ Tissue Regeneration Project Team, Inje University, Korea

Abstract — **The foot-pressure while walking represents the status of the geometrical balance of the human's musculoskeletal system. The foot-pressure in unbalanced anatomical position causes physiological disorders to the human body and accumulates stress to the musculoskeletal system. Repetitious abnormal impacts become the direct cause of vertebrae disease. The purpose of this study is to evaluate the correlation between the degree of scoliosis and the foot-pressure distribution in twenty males who have no clinical history of vertebral disease. The F-scan system(Tekscan Inc., USA, 850Hz sampling frequency) was used to measure the foot-pressure. The sole was divided into 7 regions of interest(ROI), and an analysis was performed for these ROIs. The degree of scoliosis was expressed as the angle, calculated with X-ray image, which showed lumbar vertebra number 5 to thoracic vertebra number 7. This angle was used to evaluate the correlations with the result of the foot-pressure analysis. Measurement of foot-pressure on the subjects was executed using the same protocol. The correlation between the measured foot-pressure and the degree of scoliosis was evaluated under a 0.05 level of significance. The results of the evaluation revealed the tendency that, as the degree of scoliosis increases, a difference in foot-pressure also increases. The variables used for analysis showed high correlations. The obtained results will be used to determine the occurrence of vertebra and lower limb disease and to present a qualitative evaluation basis for the rehabilitation of patients with lower limb disease.**

Keywords — **Foot-pressure, F-scan System, Scoliosis**

I. Introduction

Gait is the most common motion of a human being and is learned involuntarily[1]. Gait cycle is a step made by two legs with a line drawn between the on-stance phase and swing period. Normal gait is the repetition of the movement process from the time when one heel reaches the ground to the time for the other heel to reach the ground. Foot-pressure distribution is made by the anatomical and functional status or state of the shoes and road surface while walking[2]. As the standard to reflect the balance of the human body, foot-pressure is one measurement point which is interesting in the clinical and research field of kinematics[3]. The pressure of particular sections of the sole can be observed by measuring foot pressure[4]. The gait pattern by with incorrect posture brings about physiological troubles, fatigues muscles and joints, and is the immediate cause of vertebral disorder because repetitive and abnormal impact is transmitted to the backbone[5].

Typical methods to measure foot-pressure, use a force plate, pressure plate or put pressure sensors in shoes. But methods using a force plate and pressure plate have measuring limits for the pressure of each part of the sole, and are not able to provide variable information about foot pressure[3]. The method of putting pressure sensors in shoes is useful to get information about the change in foot pressure while walking, and it is the primary method of measurement used since the 1990s. As concern about foot health is increasing, the measurement of foot pressure is studied for distribution analysis for patients with leg pain, diabetes, rheumatoid arthritis, and so on[6].

This study was performed to evaluate the relationship between foot pressure distribution and scoliosis. The same protocol for the experiment was given to all subjects and the foot pressure data was acquired and utilized to analyze the relationship between foot pressure distribution and scoliosis.

II. Material and Method

In this study, a F-scan®VersaTek System(Tekscan Inc., USA) was used to measure foot-pressure distribution data and a Research Foot ver 5.23(Tekscan Inc., USA) was used to analyze the data. Subjects were twenty year-old males who had no clinical history of vertebral disease and similar body conditions to minimize variation in measurement. Table 1 is characteristics of the subjects and Figure 1 is the X-ray image of the subjects, showing scoliosis direction and degree. In Figure 1, the scoliosis degree of (a) is 2.25 degrees to the right for the 12th thoracic vertebrae and (b) is 3.96 degrees to the left direction for the 2nd lumbar vertebra. The scoliosis degree of (c) is 1.61 degrees to the left for the 7th thoracic vertebrae and (d) is 3.32 degrees to the left for the 2nd lumbar vertebra.

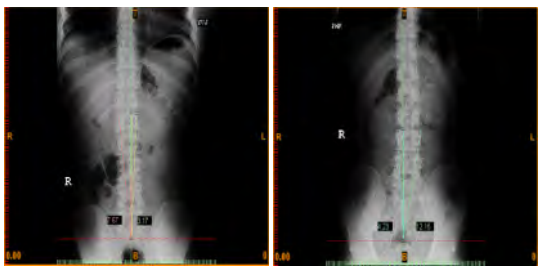
In this study, the F-scan®VersaTek System(Tekscan Inc., USA) was used to measure foot-pressure distribution and consists of sensor assembly, PC interface device and signal process board. Pressure sensor assembly is similar to general foot form, and it is possible to control the size, since

Chwee Teck Lim, James C.H. Goh (Eds.): ICBME 2008, Proceedings 23, pp. 974–978, 2009
www.springerlink.com

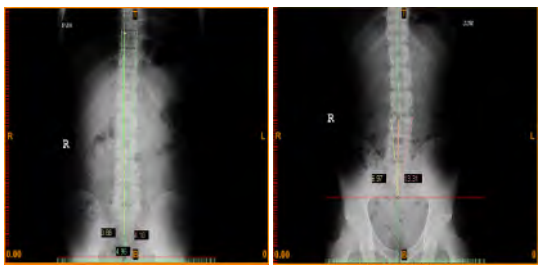
it made of thin material which is easy to shape. The sensor resolution for the foot-pressure measurement was 5mm × 5mm with the array form. The sensor has a cable about 10m long to allow for the free movement of the subjects. The Interface device attaches at ankle. The interface device consists of light material to minimize its affect on foot-pressure when a subject walks. The signal processing board sends the measured foot-pressure signal to a PC and acquires data for 850Hz sampling frequency. Figure 2 shows the foot-pressure measurement system and measuring method.

Table 1 Characteristic of Subjects

Subject	Age(yr)	Stature(cm)	Weight(kg)
1	25	177	84.5
2	26	181	84
3	25	179	84
4	23	180	68



(a) (b)



(c) (d)

Fig. 1 Analysis of Scoliosis using X-ray Image

Before the measuring foot-pressure, sensors were adjusted to fit a subject's foot size. Because the sensitivity of the sensor is influenced by shoes and friction on the road, the best sensitivity is obtained from bare feet. Consequently, foot-pressure was measured by adhering a sensor to the subject's bare foot. Data acquisition was collected separately about both the right and left foot. The reliability of data was assured by using the same measurement protocol and signal processing. For image mapping of the foot, the weight of the subject was entered in to Research Foot ver 5.23 and the subject stood on the foot that the sensor was attached to without moving for 5 seconds to allow for calibration. Following this, all subjects practiced their most natural and comfortable walks at a predesignated space. After the subject is judged to have a adapted himself to the changed environment, he performed ten free walks along a line which was drawn in the experiment space. Of all the acquired data, the first and last data entries were not used. Foot pressure distributions appeared in the same regions by using the mask image. Region of interest were divided into two-sections of prosole(M1, M2), three-sections of midsole(M3, M4, M5) and two-sections of backsole(M6, M7). Figure 3 shows the ROI.



Fig. 2 Measurement Hardware of Foot-Pressure and Measurement Picture

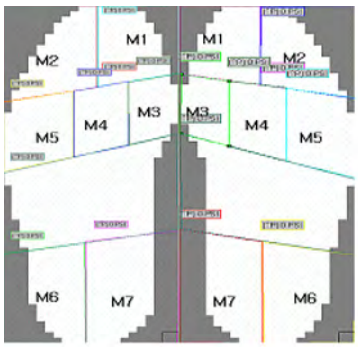


Fig. 3 Demarcation of ROI

III. Discussion & Results

The subjects of this study were healthy people who had never had any spinal disease. Foot pressure data was acquired from form left and right foot for 10 times and the total number was 20. 4~6 pieces of data without errors was

used for analysis of foot pressure. From this data some essential information was found(moving distance, axis point, inclination, direction). The result is Table 2.

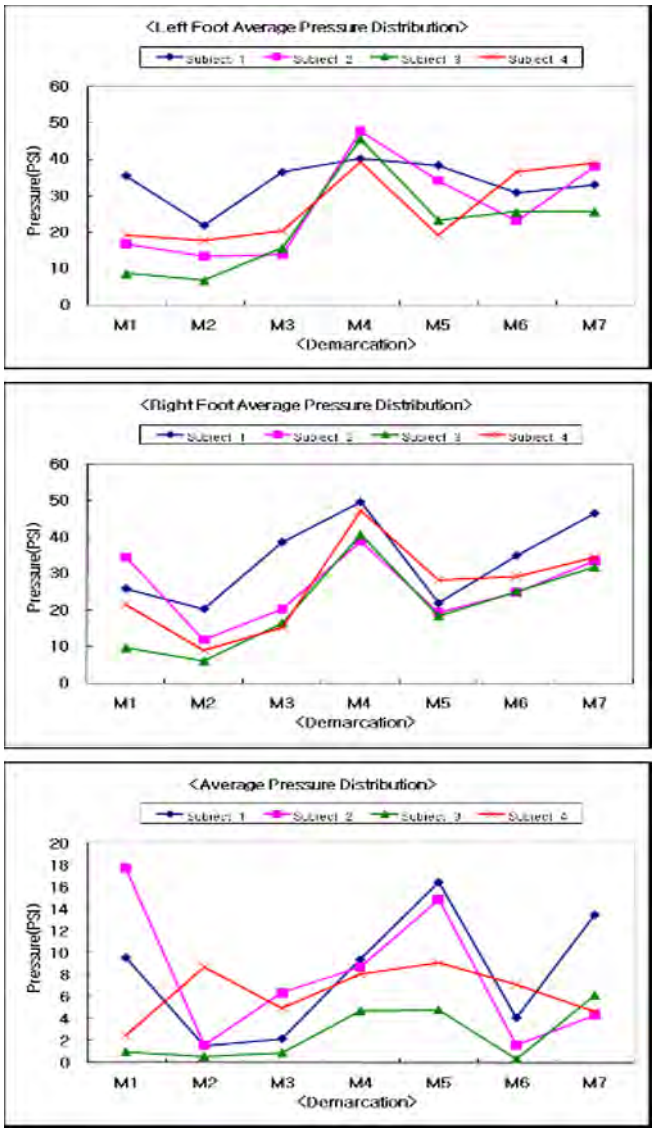


Fig. 4 Average Pressure Distribution; Left Foot(Top), Right Foot(Middle), Difference Pressure(Bottom)

Table 2 Basic Information of Mobility Route in Foot-Pressure

Subject	Distance		Slope		Direction
	Left	Right	Left	Right	
1	194.6±4.2	189.8±3.3	17.16	30.27	inner
2	172.0±5.0	179.5±1.5	27.56	48.38	inner
3	157.0±8.0	174.0±2.0	8.76	7.92	inner
4	162.0±9.6	163.5±9.1	26.38	16.04	inner

Figure 4 and 5 shows the pressure distribution average and maximum pressure. The maximum value showed that there was no difference at the M4 region, but the M5 region has the greatest difference. The area showed the contact status of the sole and the ground. There is a similar value for both the left and right foot while walking, but area of contact subjects who mainly use their mid-outsole and pro-sole when they walk is wider the than area of subjects who mainly use their midsole and backsole. Table 3 shows all the variable that were used for analysis. The vertebra formed "S" shape when viewed from at side and was when viewed from the front. The heavy scoliosis appeared as a sproportion of the body and occurred due to a difference in foot-pressure. In this study foot-pressure was measured during free walks, and the correlation between scoliosis and foot pressure was found by analysis of the variables.

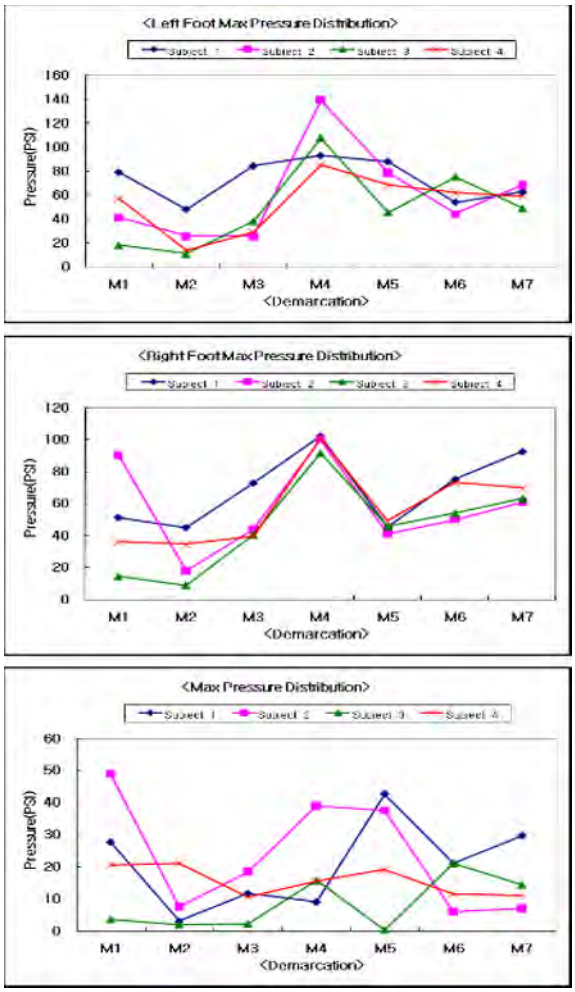


Fig. 5 Max Pressure Distribution; Left Foot(Top), Right Foot(Middle), Difference Pressure(Bottom)

Table 3 Result of Analysis of Foot-Pressure and Scoliosis

Subject	Slope	Area (mm^2)	Average/Max Pressure(PSI)							Scoliosis (°)
			M1	M2	M3	M4	M5	M6	M7	
1	13.11	275.58	9.6/27.7	1.5/3.0	2.17/11.7	9.42/9.0	16.5/42.7	4.1/21.0	13.5/29.7	2.25(R)
2	20.82	322.38	17.8/49.0	1.63/7.5	6.4/18.5	8.75/39.0	14.9/37.5	1.6/6.0	4.4/7.0	3.96(L)
3	0.84	98.75	1.0/3.7	0.6/2.0	0.9/2.3	4.8/15.7	4.8/0.3	0.3/21.0	6.2/14.3	1.61(L)
4	10.34	222.5	2.5/20.5	8.8/21.0	5.0/10.5	8.1/15.5	9.1/19.0	7.1/11.5	4.6/11.0	3.32(L)

Table 4 Result of Correlation Analysis

	Slope	Average Pressure of Demarcation						
		M1	M2	M3	M4	M5	M6	M7
Correlation	.754*	.678*	.247	.563	.444	.410	-.058	-.359
Sig.(2-tailed)	.012	.070	.491	.090	.199	.239	.873	.309
N	10	10	10	10	10	10	10	10
	Different Area	**Max Pressure of Demarcation**						
		M1	**M2**	**M3**	**M4**	**5**	**M6**	**M7**
Correlation	.594	.692*	.218	-.534	-.227	-.594	-.268	-.583
Sig.(2-tailed)	.070	.027	.546	.112	.529	.070	.455	.077
N	10	10	10	10	10	10	10	10

In result, Table 3 shows that as the degree of scoliosis increases, the difference in foot-pressure also increases. Table 4 is the result of analysis of the correlation about all variables used. It was performed by Pearson analysis under the significance 0.05. In the results of the analysis, slope means the numerical value of the mobility route in foot pressure. It showed that as the degree of scoliosis increases, the change in the mobility route is expanded. The significance of the difference area of foot pressure left/right is 0.035. It means scoliosis occurred to the disproportion of the body. Significance of average pressure and maximum pressure distribution in M4(midsole), M6(back-outsloe), M2(a little toe) region was low, and in the case of M4, because all of subjects were used without scoliosis. In the case of M2, it is believed that the significance is low because individual differences appeared because one of the subjects used a little toe when they walked. In the case of M6, the low significance is considered to be due to a foot-pressure distribution difference appearing on the backsole area because of an ankle angle difference while walking. The significance of another area is high and foot-pressure distribution appeared by left/right load difference depending on the degree of scoliosis.

IV. Conclusions

In the study, foot pressure was measured to analyze the correlation between scoliosis and foot pressure. Center mobility route in foot pressure, average and maximum pressure in each ROI, area of on stance phase and degree of scoliosis were used as variables in the analysis. The analysis showed that the directivity of the center mobility route on foot-pressure was similar for all subjects and was not related to scoliosis. In addition, the tendency of the mobility route directivity and length among subjects had no relationship to scoliosis. The numerical values of variables were the proportional relationship with the degree of scoliosis. A high significance level was shown with the exception of three variables(M2,M4,M6) sixteen variables. It was considered that the method using foot pressure and the degree of scoliosis while walking can be used to diagnose the disease from an unbalance in the body. With these result, this study is considered to distinguish vertebral and lower limb disease, and is expected to act as a qualitative evaluation basis for rehabilitation of patients with lower limb disease.

REFERENCES

1. Winter, D.A, (1998): 'mechanics and Motor Control', (University of Waterloo)
2. N. J. Paek. (1997): 'The Path of Center of Pressure(COP) of the Foot during Gait', Korean Acad Rehab Med, 21, pp. 762-770
3. J. S. Noh. (2001): 'Reliability of Plantar Pressure Measures Using the Parotec System', KAUTPT, 8 , pp. 35-41
4. Mann, R. A. (1980): 'Biomechanics of Running, In Symposium on the foot and leg in running sports'. R. P. Mack(ed), st. Louis. The C. V. Mosby Co.; 1-29.
5. Clarke, T. E.(1980): 'The pressure distribution under foot during barefoot gait'. Unpublished doctoral dissertation. The Pennsylvania State University, University park; 25-35.
6. K.H. Lee(1996): 'Analysis of the Stance Phase by Measurement of Plantar Pressure', J Korean Acad Rehab Med, 20, 524-531, 1996

Author: Heung-Ho Choi
Institute: Dept. of Biomedical Engineering, Inje University
Street: #607, Obang-dong
City: Gimhae
Country: Korea
Email: hhchoi@bme.inje.ac.kr

Sensitivity Analysis in Sensor HomeCare Implementation

M. Penhaker[1], R. Bridzik[2], V. Novak[2], M. Cerny[1], M. Rosulek[1]

[1]VSB - Technical University of Ostrava/Department of Measuring and Control, Ostrava, Czech Republic
[2]Video-EEG/Sleep laboratory, Clinic of Child Neurology, University Hospital Ostrava, Czech Republic

Abstract — **The sensing of biological signals is very actual theme. Especially bioelectrical signals are commonly measured for the evaluating a health status of a man. This article is focused on the analysis and design of sensing electrodes by the use of unconventional materials for a long term bioelectric activity measurement with advanced capabilities in a transmission of signal, time-impedance stability and low half cell voltage. The advantages of this matter are in development also the electrodes to build up the sensing element for electrochemical matter detection. The possibility of glucose and cholesterol detection in cheap production process seems to be possible.**

The principle of electrodes is conducting polymers which can be built-up on a textile or other non primary conducting materials.

Keywords — **Biopotential Electrode, Conducting Polymer,**

I. Introduction

Nowadays the sensing of bioelectrical signals with high sensitiveness and long term parameter stability are much needed. Part of them are measured invasively and most of them especially in common medical profession non – invasively. In a long term measurement of bioelectrical activity there should be a problem with standard types of electrodes which has a time variable parameters. [1] [8] [9]

A. Biopotential electrodes

Electrodes (second class leader) have to make a quality conductive connection of these two types' line wires regarding to the fact that the tissue (first class leader) is a conductor of a different type that leads electricity by available ions. That is why the electrodes are supplemented with conductive gels that generate electrolyte to transmit passage electrode – skin. The electrolyte creates surrounding body fluids to undersurface electrodes. [1] [3]

Biopotential electrodes are active sensors – source of an electrical current, source of signal.

General requirements are: high-quality conductive connection skin- instrument, nontoxic and nonirritating for skin, chemical stability, sterility for invasive use, disinfection potentiality.

The biopotential electrode can be as an electrochemical half cell. In contrast of a chemical cell the polarity isn't constant. There are proceeding reducing oxidative reactions. At the electrochemical cell the half cell potential is the goal and instead at biopotential electrodes this is unwanted necessity. During a measurement on a human there is potential difference between electrodes and skin which we would like to measure. Regarding to ignorance and inability to measure the half cell voltage of electrodes exactly the irremovable error is added during measurement. That is why the evaluation of biosignals is not processed absolutely, but also is compared signal from more places and frequency analysis is provided. [2]

II. Methods

Conducting polymers are composed of long repeated constitutional group of chain. Common polymers like polyetylen or polyvinylchloride are non-conducting and they are usually use as an insulating material. However there has been a group of polymers which is chemically conducting.

From that reason of long term monitoring and sensing of biological data there is necessary to find out new materials and conception of sensing to obtain validate data. In this case the conducting materials like textile, polymers and conducting rubber is a way how to realize it. [3] [4]

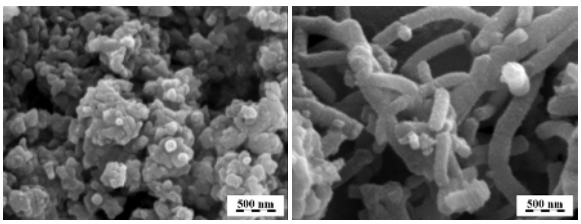


Fig. 1 During polymeration in strong acid environment rising granulation (left). In reduced acidity rising polyaniline nano tubes (right) [6]

Conductive polymers are forming system conjugate dual structures, i.e. in their structure regularly diversify simple and dual bindings Fig.1.

Except conjugation there is another necessary presumption seat electrical conductivity present bearers bullet that the mediating his transport through chains. They are rising which is in an analogy with classical semiconductor given a name geed - up. However substantial discrepancy is between geed - up organic and inorganic semiconductors. In

Chwee Teck Lim, James C.H. Goh (Eds.): ICBME 2008, Proceedings 23, pp. 979–983, 2009
www.springerlink.com

polymers it is for example higher concentration than in inorganic semiconductors. [5]

Table 1 Changes of conductivity during the storage of PANI hydrochloride powder. [4]

Storage time	Conductivity (S cm–1)	
Title	Standard polyaniline	Polyaniline prepared in excess 1 M HCl
3 days	3.20 ±0.04	9.94 ± 0.27
4 months	2.59 ±0.06	12.70 ± 0.34
16 months	1.53±0.03	6.91 ± 0.14
19 months	1.63±0.02	6.87 ± 0.41

Electric conductivity of those group of polymers is at the level 0,01 – 30 $S.cm^{-1}$, i.e. it is compare with conductivity inorganic solid - state materials, as is for example germanium Table 1. Conductivity is then manifold lower in comparison with metals, as is copper or silver, overleaf is but heaps order higher, than it is customary near common polymers. [3] [5]

III. Implementation analysis

The sensor design is a part of the process called implementation analysis. This is set from the implementation layers:

- Knowledge model
- Sensitivity analysis
- Sensor design
- Tests

At the beginning there is necessary to collect the knowledge model. This contains the information about what type of sensor is designed on, what sort of measured variables is measured and the explicit expression of models. Knowledge model is very important for other implementation layers.

The layer of sensitivity analysis consists in an assessment of their relevant changing factors. In the layer of sensor designed is made a list of existing sensors or rules of relevant factors to design new one.

The test layer verifies the quality of the chosen or designed sensor concerning required factors. Also there is a possibility to adjust the knowledge model and sensitivity analysis entry conditions to improve the sensor characteristics.

IV. Knowledge model

Knowledge model specify of physician-expert requirement for measuring the specific biosignals. In our case it is bioelectric signal measure none invasively on the skin. The input information's are: 0,1 – 50mV voltage range, 0 – 1000 Hz frequency range, 40 – 100% humidity range, 2,1 – 7,8 pH range, -40 – 50 °C temperature range etc..

From the physician requirements are not specified the information about accuracy and resolution of bioelectrical signal. These properties have to be linguistic expression and they are input of sensitivity analysis.

V. Sensitivity analysis

Sensitivity analysis establishes an important parameter for sensor selection or new design. In the sensitivity analysis we got layers up from linguistic expression and also from principles of physical measurement. The result is sensitivity level influence of an assigned value. It means that the sensitivity of input/output transmission has the desired value.

Biosignals desired value is deterministic. Most of them are time variable in spite of all regulated fixed factors. That is why it is necessary to reflect some of the criterions like: sensitivity, error, range, resolution, accuracy, time response and others.

In the dependence on a sensor type we can also distinguish from proper and mediate biosignals types, measurement methods and sensor utilization in medical diagnostics.

General requirements on bio-sensors are:

- Explicit input/output sensitivity
- Preferably linear dependence
- Maximal sensitivity
- Acceptable transfer function modality
- Time stability of sensor
- Minimal parasitic dependence
- Minimal measured object stress
- Maximal reliability
- Minimal energy consumption
- Simple construction and maintaining

Sensitivity analysis is mostly done by expert access. Outgoing list then specifies an important respect of sensor selection/design as: speed of response, material, dimension, cable length, impedance and other related aspect for example sensor placement, case making, atc..

A. Deterministic method of sensitivity analysis

Deterministic method is based on partial derivation of input particular parameters implied function.

There can be set a partial derivation in an analytical way for more simple models. For a complex one it can be done by numerical approximation.

By system's analyzing and synthesis there are used mathematical models which are taken to be well known. In reality the real system can not be identified accurately. It is not possible to solve most of tasks without model's simplification. The sensitivity knowledge on parameters change should be necessary piece of every task of identification, analysis, synthesis and also optimization.

Mathematical model is assigned to a certain variable to parameter vector **g.** The variable can be temperature, electrical potential, pH, impedance etc. The parameters are material, response, accuracy, resolution, etc. In certain conditions of continuity assignment can be make out matrix function **S.** This function is sensitivity function. [11]

Vector of parameters is defined by:

$$\mathrm{g}(\mathrm{a}):\mathrm{R}^{m}\times\mathrm{R}^{n}\rightarrow\mathrm{R}^{m} \tag{1}$$

$$\mathrm{g}=\left\{\mathrm{g}_{1}(\mathrm{a}),\mathrm{g}_{2}(\mathrm{a}),\mathrm{g}_{3}(\mathrm{a}),\ldots,\mathrm{g}_{\mathrm{m}}(\mathrm{a})\right\} \tag{2}$$

Sensitivity function is generally defined as Jacobian:

$$S_{i,j}=\frac{\partial g_{i}(\mathrm{a})}{\partial a_{j}}\quad i=1,2,\ldots,m\ and\ j=1,2,\ldots,n \tag{3}$$

The S function is except a parameters also generally dependent on time, frequency, input quantity, etc.. That is why S function is not matrix coefficient but sensitivity function.

For sensitivity function there stand the same rules as for partial derivations. Sensitivity functions in time realm are actually time behaviors of a function. They can be easily simulated by sensitivity models. The functional can be defined to sensitivity functions. They characterize the sensitivity globally by one number that is called sensitivity rate.

VI. Sensors design

A great problem occurs at the ECG measurement. The medical instrument should be transportable and that's why the electrodes has to be part to not to manipulation illimitability. The problem rises how to create the electrodes which can by only put on the skin and not to be stick by conducting stick or gel (dry electrode). As a result it is clear that the designed electrode should be no metal or gel one. For the construction of this kind of electrode the same principles were used as in common electrode. Also the interface skin - electrolyte (gel) – metal. Instead the electrolyte there was used material referred to conducting polymer. It is a mixed conductor. There is neither first-order conductor nor second-order one.

From that reason the polyamide is suitable for making dry bioponetial electrode. Their conductivity is 4 $S.cm^{-1}$ is sufficient because they are settled in thin film form with thickness 100nm.

The production of this type of electrode takes apx. 15 minutes and there is also the need of another 12 hours for desiccation. The production is very cheap and easy to attach for a single use. The price of one polymer electrode realization is apx. 0.25 EUR. For the electrodes manufacturing we can use them with an advantage that there isn't registered any toxic or irritable character.

We can qualify it as a harmless electrode. Another advantage is that the utilization of the material can be manufactured electrode on any matter to resisted acidic medium. Textile materials are easy to use and that is why the electrodes on Velcro fastener were made. Velcro both side fastener is covered by polyaniline. [6], [7]

VII. Results presentation

The testing layer serves for verifying of designed procedures and also for function testing. This can also improve obtaining of valid information about measured value.

During the testing on three leads ECG there was found out that manufactured electrodes are well usability. The measurement were done by ECG being short (pectoral) bipolar placement gained by bioamplifier G.BSamp, 16 channels from G.tec medical engineering GmbH and digitalized by A/D card NI DAQPad-6052E. The results were measured with common attached electrodes on computer at the same time. The measured results were mathematically compared and results were presumable and plausible.

Electrodes were mounted on flexible t-shirt made on elastics fiber. Adherence pressure was too small to well connect skin with electrode and that is why the great interference voltage arose. Consequently there was added the elastic belt on thoraxes to improve adherence pressure of the electrodes.

For impedance characteristics measurement Eval AD5933 module was used. The measurement of impedance was done in frequency range 700 Hz to 15 kHz. The testing voltage was 2 V.

Impedance characteristics measured on AG/AgCl electrode with the gel RED Dot 2570 and Polyaminil covered

textile. Both were measured on six samples each. Results evaluation was compared by value of standard deviation σ (4). The range of σ were between 0,006 to 0,015 Ω.

$$\sigma = \sqrt{\frac{1}{N}\sum_{i=1}^{N}\left(X_i - \bar{X}\right)^2} \qquad (4)$$

where:
X_i - difference between Ag/AGCl and Polyaminil txtile
N - number of values of impedance record (N=14300)

During the tests we designed the electrodes for measuring the glycaemia. The electrodes are silicon (roller) or plastic PVC (wafer) ground. On the Fig. 2. On the matter is 100 nm thin polyamynil thin film. This can be use with the advance of easy and cheap construction of glycaemia strip.

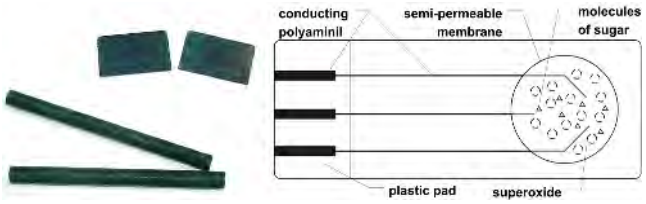


Fig. 2 Semi finished material as silicon (roller) or plastic PVC (wafer for glycemia sensor) ground electrodes covered by polymer and glycemia sensor strip design with polyaniline conducting way

For the biopotential measuring also from plant we designed the process of covering the plant by conducting polymer. The differences between normal matter and plant is in final step of stabilization of the allied substances. In normal process of stabilisation there is used the acid with 5 -7 pH which is absolutely scathing for the plant. That is why we modify the final procedure of stabilizing and we were able to use acid with 2 pH for making the polymer conducting as in dead matter.

VIII. Discussion

We are able to mention that polyamides are suitable material for biopotential electrodes construction from acquired results of our experiments. But there is a need to concentrate on parameters´ measuring and monitoring in long term firmness - both an electro technical and a mechanical. From the point of view the tissue feature that changes its acidity and pH, there can be changes in electrical features of biopotential electrodes in specific circumstances. That is why it is also important to concentrate on materials mechanical resistance.

Also a wide range of sensor design methods can be discussed. Except deterministic method we can use also statistical, graphical and others based on fuzzy, neural network and chaos theory. This has to be verified because probably none of them are multi-purpose for all physical variables.

IX. Conclusions

In the present time the health telemetry systems create an integral part of our everyday lives. The sensors are the primary part of these systems and also the improvement on design, new materials, constructions and sensor disposition are actual nowadays. Our research and tests enabled us to find out that electrochemical allied substances seem to be appropriate for the future applications.

Acknowledgment

Many thanks to Mr. Jaroslav Stejskal PhD. and Mrs. Eleně Konjušenko from Academy of science, The work and the contribution were supported by the project Grant Agency of Czech Republic – GAČR 102/08/1429 Safety and security of networked embedded system applications.

This work was partially supported by the faculty internal project,"Biomedical engineering systems IV"

References

1. Washburn, E.W. et al. (2003) International Critical Tables of Numerical Data, Physics, Chemistry and Technology. 1st Electronic Edition. Knovel,. ISBN 1-59124-491-9.
2. Penhaker, M., Imramovský, M., Tiefenbach, P., Kobza, F. (2004). *Lékařské diagnostické přístroje učební texty*, VŠB – TU Ostrava
3. Stejskal, J., Gilbert, R. G.: Polyaniline. Preparation of a Conducting Polymer, Pure Appl. Chem. 74, 857 (2002).
4. Stejskal, J., Sapurina, I.: Polyaniline: Thin Films and Colloidal Dispersions, Pure Appl. Chem. 77, 815 (2005).
5. Stejskal, J.: Polyaniline conducting polymer, Ústav makromolekulární chemie Akademie věd ČR (2001).
6. Brožová L., Holler P., Kovářová J., Stejskal J., Trchová M.: The Stability of Polyaniline in Strongly Alkaline and Acidic Aqueous Media, Polym. Degrad. Stab. 93, 592–600 (2008).
7. Noury, N., From Signal to Information : the smart sensor. Applications in Industry and Medicine Habilitation a diriger des recherches, Francie: Grenoble, 2002.
8. Randy, F. Understanding Smart Sensors. London: Artech House, 1996. ISBN 0-89006-824-0
9. Julian W. Gardner, Microsensors: Principles and Applications, John Wiley & Sons Ltd, 1999

10. Scanaill, C.N., Carew, S., Barralon, P. Noury, N. Lyons, D. And Lyons, G.M. A Review of Approaches to Mobility Telemonitoring of the Elderly in Their Living Environment Annals of Biomedical Engineering, Vol. 34, No. 4, April 2006 (C_ 2006) pp. 547–563 , ISSN 0090-6964 (Print) 1573-9686 (Online)
11. Martinák, L. Implementační analýza snímačů teploty a pohybu pro použití v telemedicíně, 2006, PhD. thesis,

Author: Ing. Marek Penhaker, Ph.D.
Institute: VSB – TU Ostrava
Street: 17. listopadu 15
City: Ostrava - Poruba
Country: Czech Republic
Email: marek.penhaker@vsb.cz

Fall Detection Unit for Elderly

Arun Kumar, Fazlur Rahman, Tracey Lee

Singapore Polytechnic, Singapore

Abstract — **A fall in case of an elderly person can result in quite serious injuries because of his/her fragile bone structure. In-fact, in one of the recent medical studies on "The Presentation of Elderly People at an Emergency Department in Singapore", published in the Singapore Medical Journal, falls were found to be the second most common cause. Our team has designed and developed a small sized, portable sensor unit that can detect a fall and subsequently send a help request message to the care-giver or a central monitoring station. This unit, which is based on a microcontroller and 3-axis accelerometer, can easily be worn on the waist belt without being obtrusive in a user's normal activities. A number of power saving features have been included in the unit. The signal processing software on microcontroller has been developed to differentiate between the normal movements e.g. sitting, lying down and the movements resulting from a fall. Two different kinds of wireless communication methods, RF and GSM, have been developed and tested in these units. RF communication is useful when a number of persons need to be monitored within a small area using a central monitoring station e.g. in an elderly home. GSM communication has been developed keeping in view the elderly persons staying alone. The GSM based sensor unit is able to send a SMS directly to the caregiver in case a fall is detected. An additional feature, which allows the user to request for help whenever required, has also been incorporated into the unit.**

Keywords — **Fall detection, elderly care, assistive technology, accelerometers, microcontroller based device.**

I. Introduction

This paper describes a hardware device that has been developed to monitor the well-being of elderly persons living alone in home and also for the residents of an old-age home. Generally they are not in the prime of their health; hence keeping a check on their general wellbeing is necessary. Presently most of the monitoring is done by caregivers, nurses or volunteers stationed at the location. If certain parts of these monitoring can be automated, caregivers and others can be relieved of some of their duties and the elderly can lead a more independent life. In the case of the elderly one of the major causes of worry is a fall, because most of the time a fall in their case results in a serious injury because of their fragile bone structure. In fact, in one of the recent medical studies on "The Presentation of Elderly People at an Emergency Department in Singapore", published in Singapore Medical Journal, falls was found to be the second most common cause of injuries [1].

The system developed by our team, is capable of detecting a fall in a user and it can subsequently inform the care giver. The sensor unit is small in size; battery operated with a number of power saving features and can be worn by the user in an unobtrusive manner. The unit is able to communicate wirelessly with a central monitoring station and/or the hand phone of care taking person using RF/GSM communication.

II. System setup

Two different prototypes of the sensor units were designed, developed and tested, with both of them based on a PIC18f4520 microcontroller and 3D accelerometer (Table 1). These prototypes have been described below. Microchip PIC18F4520 was selected because it has low power consumption, is low cost, has powerful development system and can be easily programmed using ICD2 Debugger [2-3].

Table 1: Characteristics of two developed prototypes

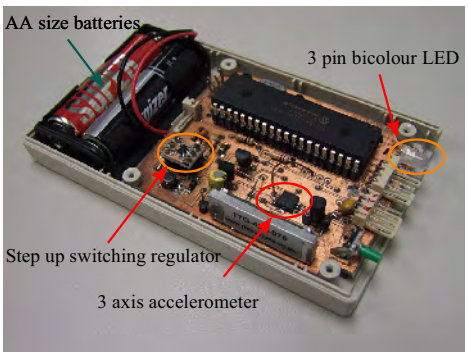
Unit	Sensor Unit Hardware	Sensor Unit Software	Receiver
1	PIC18f4520 microcontroller based unit with a number of power saving features +accelerometer	Program developed to detect fall and transmit the message using RF transmitter.	Computer based GUI program designed - to show data from multiple users. - with option to send out a help request SMS using GSM modem.
2	PIC18f4520 microcontroller based unit + accelerometer	Program developed to detect fall and to interact with a GSM modem to transmit the message using SMS.	Caretaking person's hand phone

Prototype I

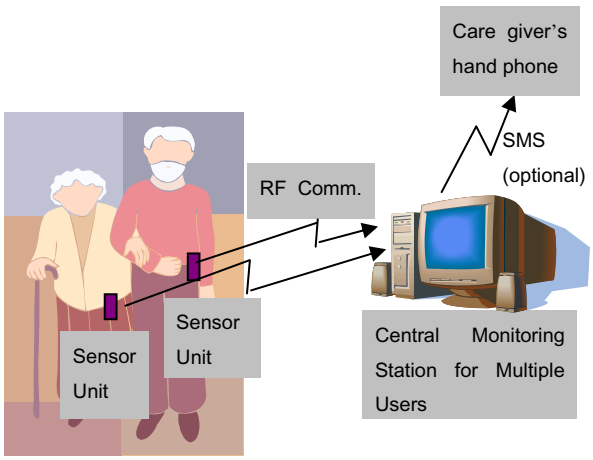
Prototype 1 is based on a microcontroller board which has been designed and developed by our team, with PIC18f4520 microcontroller chip (Figure 1a) [4]. The sen-

Chwee Teck Lim, James C.H. Goh (Eds.): ICBME 2008, Proceedings 23, pp. 984–986, 2009
www.springerlink.com

sor unit (microcontroller board with accelerometers) is programmed to filter and process the accelerometer signal and detect a fall. Three volts battery based supply is used to power up the sensor unit. A wireless (RF-433MHz) transmitter is used to transmit the fall detect signal to a receiver unit.



(a)



(b)

Figure 1: (a) Sensor unit (b) Set up for prototype I

A sensitivity switch is also provided on board to adjust the sensitivity of the unit according to the normal movement pattern of a person. For example, if the person tends to have more abrupt movements normally, the sensitivity of the unit may be lowered to reduce the false alarms. If the person in general has slow movements, the sensitivity can be set to high. In the designed unit, we have allowed the connections for the In Circuit Debugger (ICD), to facilitate programming the device and for debugging. Also the wired connection is retained, as we also may need it to debug the wireless serial link. Finally, we eschewed the use of a connector for the on/off switch and used a PCB mounted switch instead. Also, we have used ST LIS3AL02 3-axis accelerometers to reduce the parts count and also for more efficient usage of space in the unit. We used a specialized boost circuit incorporating the LM2731. This part can provide the voltage even when the combined cell voltages have dropped to 2.2 V. We have opted for a through hole and surface mount (SM) configuration and mounted the SM LM2731 on a special socket. This is in order to avail ourselves of new voltage control technologies as this is currently an active area of development, with the rising price of electrical energy. Some power saving features has been included to make the battery life time longer. The unit does not send the data continuously; instead it sends the data only when the fall is detected. The processor has been programmed in the sleep mode and allows the timer to wake it up during normal operation for saving energy. A LED on the sensor unit has also been programmed to light up whenever the unit recognizes a fall, in order to show the user that a message for his/her help is being sent out. The setup is as shown in figure 1b.

The receiver unit is computer based with a RF receiver (Figure 2), and running the virtual instrumentation (VI) program [5-6].

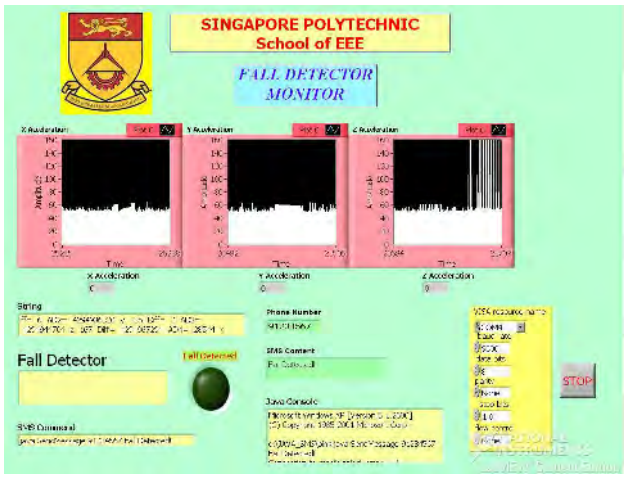


Figure 2: Receiver unit's user interface

The receiver unit is capable of monitoring multiple users at the same time. It is useful when a number of persons need to monitored from a central station e.g. old-age home. Since the range of RF receiver is limited, multiple RF receivers are used around the premises. These multiple receivers are connected to the same monitoring station. The limited range of multiple RF receivers around the old-age home is used in

detecting the location of the elderly. Based on the RF receiver which is receiving the data, we can have some information about the location of the elderly. An option has been provided in the receiver to forward the 'fall detected' message to the caregiver's hand phone, using a GPRS modem, whenever a fall is detected in any one of the users. In this case there is a single modem connected to the receiver unit.

Prototype 2

In this setup, the microcontroller board used is the same as in prototype 1, but instead of the RF transmitter a GSM modem is attached to the microcontroller board (Figure 3). GSM modem is connected to the serial output of prototyped circuit board and a set of *AT commands* are used by the microcontroller board to operate the modem. The microcontroller board is programmed to send a 'help request' SMS whenever it detects a fall. A single unit can also be programmed to send help request to multiple care giving persons, in case required.



Figure 3: Prototype 2

This setup has the advantage that it can be used as a stand-alone unit. It does not require any computer based receiver as used in prototype 1. Prototype 1 is more appropriate in old-age homes, where a number of users need to be monitored centrally. Prototype2 on the other hand is useful for the elderly staying alone at home.

In this setup, the receiver unit is the care giver's hand phone, capable of receiving SMS. The text of the message, e.g. 'Fall Detected', can be set up in the microcontroller program.

III. Conclusions

Two prototypes of small sized fall detection units have been designed, implemented and tested successfully. These units are low cost solutions to detecting falls in elderly and in providing information to the caregivers, resulting in timely aid for the elderly in case of a fall. The system will also be useful in monitoring the dementia patients that get up from bed during night, and also the patients suffering from frequent urination to keep check on number of times they go to toilet. The design of this product proved to be very enlightening for our design group, the electronic and mechanical design re-emphasized the importance of user interface design. The power saving and wireless aspects of the design gave us the experience for future similar ventures.

Acknowledgment

We would like to thank Singapore Tote Board for providing funding for the project.

References

1. Lim KHJ, Yap KS (1999) The Presentation of Elderly People at an Emergency Department in Singapore. Singapore Medical Journal 40(12):742-744
2. Han-Way H (2005) PIC microcontroller: an introduction to software and hardware interfacing. Thomson/Delmar Learning, NY.
3. John Iovine (2000) PIC microcontroller project book. McGraw-Hill, New York.
4. Montrose MI (2000),Printed circuit board design techniques for EMC compliance a handbook for designers, IEEE Press New York
5. Travis J (2007) LabVIEW for everyone : graphical programming made easy and fun, Prentice Hall, Upper Saddle River, NJ
6. Bitter R (2007), LabView advanced programming techniques, Taylor & Francis, Boca, FL.

Address of the corresponding author:

Author: Arun Kumar
Institute: Singapore Polytechnic
Street: 500 Dover Road
City: Singapore
Country: Singapore
Email: arunk@sp.edu.sg

Reduction of Body Sway Can Be Evaluated By Sparse Density during Exposure to Movies on Liquid Crystal Displays

H. Takada[1], K. Fujikake[2], M. Omori[3], S. Hasegawa[4], T. Watanabe[5] and M. Miyao[6]

[1]Department of Radiology, Gifu University of Medical Science, Japan
[2]Institute for Science of Labour, Japan
[3]Faculty of Home Economics, Kobe University, Japan
[4]Department of Information Culture, Nagoya Bunri University, Japan
[5]Aichi Gakuin University, Japan
[6]Information Technology Center, Nagoya University, Japan

Abstract — **Often, people travelling in ships, trains, aircraft, and cars tend to experience motion sickness. It has been reported that even users of virtual environments and entertainment systems experience motion sickness. This visually induced motion sickness (VIMS) is known to be caused by sensory conflict, which is the disagreement between vergence and visual accommodation while observing stereoscopic images. VIMS can be measured by psychological and physiological methods. The simulator sickness questionnaire (SSQ) is a well-known method that is used herein for verifying the occurrence of VIMS. We also quantitatively measure the sway of the centre of gravity of the human body before and during exposure to several types of movies. During the measurement, subjects are instructed to maintain the Romberg posture for the first 60 s and a wide stance (with midlines of the heels 20 cm apart) for the next 60 s. The centre of gravity is projected on a plane that is parallel to the ground. The body sway is recorded as a stabilogram on the plane. According to previous research, a stochastic process is regarded as a mathematical model that generates stabilograms. We propose a method to obtain stochastic differential equations (SDEs) as a mathematical model of the body sway on the basis of the stabilogram. While there are several minimal points of the temporally averaged potential function involved in the SDEs, the stereoscopic images decrease the gradient of the potential function. We have succeeded in estimating the decrease in the gradient of the potential function by using an index called sparse density.**

Keywords — **Visually induced motion sickness (VIMS), Stabilometry, Sparse density, Stochastic differential equation (SDE), Potential.**

I. Introduction

The human standing posture is maintained by the body's balance function, which is an involuntary physiological adjustment mechanism called the 'righting reflex' [1]. In order to maintain the standing posture when locomotion is absent, the righting reflex, centred in the nucleus ruber, is essential. Sensory receptors such as visual inputs, auditory and vestibular functions and proprioceptive inputs from the skin, muscles and joints are the inputs to the body's balance function [2]. The evaluation of this function is indispensable for diagnosing equilibrium disturbances such as cerebellar degenerations, basal ganglia disorders, or Parkinson's disease in patients [3].

Stabilometry has been employed to evaluate this equilibrial function both qualitatively and quantitatively. A projection of a subject's centre of gravity onto a detection stand is measured as an average of the centre of pressure of both feet (COP). The COP is traced for each time step, and the time series of the projections is traced on an xy-plane. By connecting the temporally vicinal points, a stabilogram is composed, as shown in Figure 1. Several parameters such as the area of sway (A), total locus length (L) and locus length per unit area (L/A) have been proposed to quantitize the instability involved in the standing posture, and such parameters are widely used in clinical studies. It has been revealed that the last parameter particularly depends on the fine variations involved in posture control [1]. This index is then regarded as a gauge to evaluate the function of proprioceptive control of standing in human beings. However, it is difficult to clinically diagnose disorders of the sense of balance function and to identify the declines in equilibrial function by utilizing the abovementioned indices and measuring patterns in the stabilogram. Large interindividual differences might make it difficult to understand the results in comparison.

Mathematically, the sway in the COP is described by a stochastic process [4]-[6]. We examined the adequacy of using a stochastic differential equation and investigated the most adequate one for our research. G(x), the distribution of the observed points x, has the following correspondence with V(x), the (temporal averaged) potential function, in the stochastic differential equation (SDE) as a mathematical model of the sway:

$$V(\vec{x}) = -\frac{1}{2}\ln G(\vec{x}) + const. \qquad (1)$$

Chwee Teck Lim, James C.H. Goh (Eds.): ICBME 2008, Proceedings 23, pp. 987–991, 2009
www.springerlink.com

The nonlinear property of SDEs is important [7]. There were several minimal points of the potential. In the vicinity of these points, the SDE shows local stable movement with a high-frequency component. We can therefore expect a high density of observed COP in this area on the stabilogram.

The analysis of stabilograms is useful not only for medical diagnosis but also for explaining the control of upright standing for two-legged robots and for preventing falls in elderly people [8]. Recent studies suggest that maintaining postural stability is one of the major goals of animals, [9] and that they experience sickness symptoms in circumstances where they have not acquired strategies to maintain their balance [10]. Riccio and Stoffregen argued that motion sickness is not caused by sensory conflict, but by postural instability, although the most widely known theory of motion sickness is based on the concept of sensory conflict [10]-[12]. Stoffregen and Smart (1999) report that the onset of motion sickness may be preceded by significant increases in postural sway [13].

The equilibrium function in humans deteriorates when observing 3-dimensional (3-D) movies [14]. It has been considered that this visually induced motion sickness (VIMS) is caused by the disagreement between vergence and visual accommodation while observing 3-D images [15]. Thus, stereoscopic images have been devised to reduce this disagreement [16]-[17].

VIMS can be measured by psychological and physiological methods, and the simulator sickness questionnaire (SSQ) is a well-known physiological method for measuring the extent of motion sickness [18]. The SSQ is used herein for verifying the occurrence of VIMS. The physiological methods measures autonomic nervous activity: heart rate variability, blood pressure, electrogastrography, and galvanic skin reaction [19]-[21]. It has been reported that a wide stance (with midlines of the heels at 17 cm or 30 cm apart) significantly increases total locus length in stabilograms of the high SSQ score group, while the low score group is less affected by such a stance [22].

This study proposes a methodology to measure the effect of 3-D images on the equilibrium function. We assume that the high density of observed COP decreases during exposure to stereoscopic images [14]. Sparse density (SPD) would be a useful index in stabilometry to measure VIMS (Appendix). In this study, we show that reduction of body sway can be evaluated by the SPD during exposure to 2D/3D movies on a Liquid Crystal Display (LCD).

II. Materials and method

Ten healthy subjects (23.6 ± 2.2 year) voluntarily participated in the study. All of them were Japanese and lived in Nagoya and its surroundings. The subjects gave their informed consent prior to participation. The following were the exclusion criteria for subjects: subjects working the night shift, subjects with dependence on alcohol, subjects who consumed alcohol and caffeine-containing beverages after waking up and less than two hours after meals, and subjects who may have had any otorhinolaryngologic or neurological disease in the past (except for conductive hearing impairment, which is commonly found in the elderly). In addition, the subjects must not have been using any prescribed drugs.

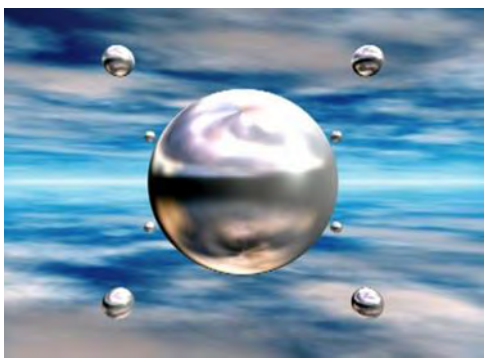


Fig. 1. A scene in the movie.



Fig. 2. The setup of the experiment

We ensured that the body sway was not affected by environmental conditions. Using an air conditioner, we adjusted the temperature to 25 °C in the exercise room, which was kept dark. All subjects were tested from 10 am to 5 pm in the room, which was located in Nagoya University. The subjects were positioned facing an LCD monitor (S1911-SABK, NANAO Co., Ltd.) on which three kinds of images were presented in no particular order: (a) a visual target (circle) whose diameter was 3 cm; (b) a 2-D movie that shows a sphere approaching and going away from subjects irregularly (Fig. 1); and (c) a 3-D movie that shows the same sphere motion as in (b). The distance between the wall and the subjects was 57 cm (Fig. 2).

A. Stabilometry

The subjects stood without moving on the detection stand of a stabilometer (G5500, Anima Co., Ltd.) in the Romberg posture with their feet together for 1 min before the sway was recorded. Each sway of the COP was then recorded with a sampling frequency of 20 Hz during exposure to one of the images. The subjects viewed a movie (image) on the LCD from beginning to end. SSQ was employed before and after this stabilometry.

B. Calculation procedure

We calculated several indices that are commonly used in the clinical field [23] for stabilograms, such as "area of sway," "total locus length," and "total locus length per unit area." In addition, new quantification indices that were termed "SPD" and "total locus length of chain" [24] were also estimated (Appendix).

III. Results and Disscussion

Typical stabilograms are shown in Fig. 3. In these figures, the vertical axis shows the anterior and posterior movements of the COP, and the horizontal axis shows the right and left movements of the COP. The amplitudes of the sway that were observed during exposure to movies (Figs. 3b and 3c) tended to be larger than those of the control sway (Fig. 3a). Although a high density of COP was observed in the stabilograms (Fig 3a and 3b), the density decreased in stabilograms during exposure to stereoscopic movies (Fig. 3c).

A theory has been proposed to obtain SDEs as a mathematical model of the body sway on the basis of the stabilogram. According to Eq. (1), there were several minimal

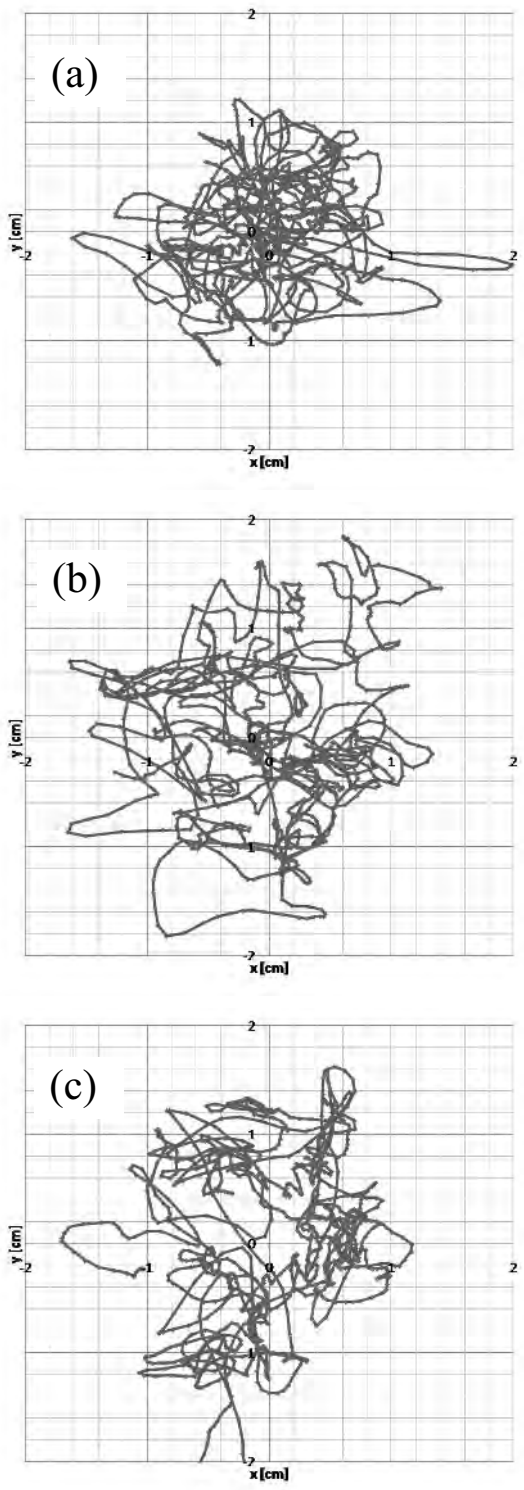


Fig. 3. Typical stabilograms observed when subjects viewed (a) a static circle, (b) the 2-D movie, and (c) the stereoscopic movie.

points of the temporally averaged potential function involved in the SDEs (Fig. 3). The movies, especially stereoscopic images, decrease the gradient of the potential function. 2-D images should reduce the body sway because there is no disagreement between vergence and visual accommodation. The reduction can be evaluated by the SPD during exposure to the movies on the LCD. We have succeeded in estimating the decrease in the gradient of the potential function by using the SPD in accordance with a one-way analysis of variance.

APPENDIX

Here, we describe the new quantification indices, or 'SPD' and 'total locus length of chain' [25].

A. Sparse density (SPD)

SPD was defined by a scaling average of the ratio $G_j(1)/G_j(k)$, where $G_j(k)$ is the number of divisions having more than k measured points; a stabilogram was divided into quadrates whose latus was j times longer than the resolution. If the centre of gravity is stationary, the SPD value becomes 1. If there are variations in the stabilograms, the SPD value becomes greater than 1. In this manner, SPD depends on the characteristics of the stabilogram and the motion process of the COP.

B. Chain

The force acting on the centre of gravity of the body was defined in terms of the difference in the displacement vectors. In particular, we focussed on singular points at which statistically large forces were exerted. On the basis of these forces, chains were eliminated from the stabilogram in the form of a consecutive time series42. If the times measured at these points were in the temporal vi-cinity, these points were connected by segments (sequences). Figures formed by these sequences were called 'chains' because of the shape of the connections. The figures of sequences of points at which large forces were exerted show that the chain had a cusp pattern.

ACKNOWLEDGMENT

Movies shown to subjects in this study were produced Olympus visual communications Co. Ltd.

REFERENCES

1. Okawa T, Tokita T, Shibata Y et al. (1995) Stabilometry - Significance of Locus Length Per Unit Area (L/A) in Patients with Equilibrium Disturbances. Equilibrium Res 55(3): 283-293.
2. Kaga, K. (1992) Memaino Kouzo: Structure of vertigo. Tokyo, Kanehara: pp.23-26, pp.95-100
3. Okawa T, Tokita T, Shibata Y et al. (1996) Stabilometry-Significance of locus length per unit area (L/A). Equilibrium Res 54(3): 296-306.
4. Collins JJ. and De Luca CJ. (1993) Open-loop and closed-loop control of posture: A random-walk analysis of center of pressure trajectories. Exp. Brain Res. 95: 308-318
5. Emmerik REA, Van Sprague RL, Newell KM. (1993) Assessment of sway dynamics in tardive dyskinesia and developmental disability: sway profile orientation and stereotypy, Moving Disorders 8: 305-314.
6. Newell KM, Slobounov SM, Slobounova ES. (1997) Stochastic processes in postural center-of-pressure profiles. 133.
7. Takada H, Kitaoka Y, Shimizu Y. (2001) Mathematical Index and Model in Stabilometry, Forma 16 (1): 17-46.
8. Fujiwara K. Toyama H. (1993) Analysis of dynamic balance and its training effect-Focusing on fall problem of elder persons. Bulletin of the Physical Fitness Research Institute 83: 123-134.
9. Stoffregen TA, Hettinger LJ, Haas MW et al. (2000) Postural instability and motion sickness in a fixed-base flight simulator. Human Factors 42: 458-469.
10. Riccio GE, Stoffregen TA. (1991) An Ecological theory of motion sickness and postural instability, Ecological Physiology, 3(3), pp.195-240
11. Oman C. (1982) A heuristic mathematical model for the dynamics of sensory conflict and motion sickness. Acta Otolaryngologica Supplement 392: 1-44.
12. Reason J. (1978) Motion sickness add –aptation: a neural mismatch model. J Royal Soc Med 71: 819-829
13. Stoffregen TA, Smart LJ, Bardy BJ. (1999) Postural stabilization of looking, Human Perception and Performance. 25: 1641-1658.
14. Takada H, Fujikake K, Miyao M.et al. (2007) Indices to Detect Visually Induced Motion Sickness using Stabilometry, Proceedings of VIMS2007: 178-183.
15. Hatada T. (1988) Nikkei electronics 444: 205-223.
16. Yasui, R., Matsuda, I., Kakeya, H. (2006) Combining volumetric edge display and multiview display for expression of natural 3D images. SPIE proceeding Volume 6055: Stereoscopic Displays and Virtual Reality Systems XIII: 0Y1-0Y9
17. Kakeya, H. (2007) MOEVision:simple multiview display with clear floating image. SPIE proceeding Volume 6490: Stereoscopic Displays and Virtual Reality Systems XIV: 64900J.
18. Kennedy RS, Lane NE, Berbaum KS et al. (1993) A simulator sickness questionnaire (SSQ): A new method for quantifying simulator sickness. International J Aviation Psychology 3: 203-220.
19. Holomes SR, Griffin MJ. (2001) Correlation Between Heart Rate and the Severity of Motion Sickness Caused by Optokinetic Stimulation. J. Psychophysiology 15: 35-42.
20. Himi N, Koga T, Nakamura E et al. (2004) Differences in autonomic responses between subjects with and without nausea while watching an irregularly oscillating video. Autonomic Neuroscience: Basic and Clinical 116: 46-53.
21. Yokota Y, Aoki M, Mizuta K. (2005) Motion sickness susceptibility associated with visually induced postural instability and cardiac autonomic responses in healthy subjects. Acta Otolaryngologia 125: 280-285.
22. Scibora LM, Villard S, Bardy B, Stoffregen TA. (2007) Wider stance reduces body sway and motion sickness. Proceedings of VIMS 2007: 18-23

23. Suzuki J, Matsunaga T, Tokumatsu K. et al. (1996) Q&A and a manual in Stabilometry. Equilibrium Res 55(1): 64-77.
24. Takada H, Kitaoka Y, Ichikawa S. et al. (2003) Physical Meaning on Geometrical Index for Stabilometly. Equilibrium Res 62(3): 168-180.

Author: Hiroki Takada, PhD in Mathematics
Institute: Department of Radiology, Gifu University of Medical Science
Street: 795-1 Ichihiraga Nagamine
City: Seki
Country: Japan
Email: takada@u-gifu-ms.ac.jp

Effects of Phototherapy to Shangyingxiang Xue on Patients with Allergic Rhinitis

K.-H. Hu[1,2,3], D.-N. Yan[2], W.-T. Li[1,4]

[1]Department of Biomedical Engineering, Chung-Yuan Christian University, Chung-Li, Taiwan
[2]Nanjing University of Chinese Medicine, Nan-Jing, China
[3]Department of Otorhinolaryngology, Keelung Hospital, Kee-Lung, Taiwan
[4]Research and Development Center for Biomedical Microdevice Technologies, Chung-Yuan Christian University, Chung-Li,Taiwan

Abstract — **Allergic rhinitis (AR) is a common chronic illness which has a significant impact on patients' quality of life. Current therapeutic options such as avoidance of allergen, medication and immunotherapy are far from ideal due to their adverse effects. The aim of the study was to evaluate the clinical effects of phototherapy to Shangyingxiang Xue on patients with AR. Sixty-one AR patients who met the inclusion criteria were enrolled in this study. Patients were divided randomly into the treating group and control group. Every of them should fill out the informed consent form before treatment and recorded their symptom scores everyday in a diary before and during treatment. Thirty-one patients in the treating group received phototherapy with LED lights consisted of two wavelengths, 660 and 850 nm, applied on bilateral Shangyingxiang Xue. Phototherapy was performed once a day for 7 days. The duration of each treatment was 10 minutes. Thirty patients in the control group received antihistamine (Zyrtec, 10 mg) once a day for 7 days. A symptom score of 0 to 3 was assigned for each of the following rhinitis symptoms: eye itching, nasal itching, nasal obstruction, rhinorrhea, smell impairment, sneezing and size of inferior turbinate. The scores of pre- and post-therapy in both groups were collected after the course of treatments and analyzed by using the paired sample t-test. Scores of the post-therapy were all significantly decreased in the treating group, which means all the symptoms were apparently improved after phototherapy to bilateral Shangyingxiang Xue. Comparing the clinical effects of treating and control groups with repeated measures analysis, no difference was observed except the size of inferior turbinate. In conclusion, phototherapy to Shangyingxiang Xue could relieve the symptoms of allergic rhinitis. It seems to be a safe and effective modality on the treatment of allergic rhinitis.**

Keywords — **allergic rhinitis, phototherapy, Shangyingxiang Xue, infrared, light emitting diode**

I. Introduction

Allergic rhinitis (AR) is a high-prevalence disease in many countries, affecting about 15-30% of the world's population[1]. Unlike most other diseases, which are decreasing in prevalence, AR is on the increase[2]. The clinical symptoms of the nasal allergic response include nasal itching, rhinorrhea, nasal congestion, eye itching, etc. [3]. AR is also an important underlying cause of co-morbidity which includes infective sinusitis and otitis media. Although it is not associated with severe morbidity and mortality, allergic rhinitis has a major effect on the quality of life. Its increasing prevalence, its impact on the individual quality of life and social costs [4,5] and its role as a risk factor for asthma, underline the great need for more and better care of this disease.

The management of allergic rhinitis includes avoidance of the allergen, medication (pharmacological treatment) and allergen immunotherapy. It is no doubt that effective allergen avoidance can lead to substantial relief of symptoms. However, patients are still not able to avoid their confirmed allergens such as mites or atmospheric pollens under many circumstances. Well-established pharmacological therapies with oral and topical H1-antihistamines, topical and systemic glucocorticosteroids, hormones, decongestants and anti-leukotrienes are available for the treatment of the disease. According to the guidelines, oral antihistamines are the first-line therapy [6]-[8]. Intranasal steroids are recommended as first-line treatment in moderate and severe disease, and have been used traditionally to combat nasal congestion, along with the other symptoms associated with allergic rhinitis [9]. Although most of the drugs are effective in treating certain symptoms of AR, they all have limitations due to their adverse effects. Rather than simply to treat the symptoms, immunotherapy has the potential to provide a permanent cure for the disease. However, complete suppression of the clinical symptoms cannot be achieved in most cases with currently managements. Therefore, increasingly, sufferers are seeking alternative therapies for allergic rhinitis

Evidence suggests that acupuncture is a useful complementary or alternative treatment option for people with allergic rhinitis[10]. Treatment for AR may include needling and moxibustion. Low-energy narrow-band illumination has been used as a therapeutic measure in some medical situations. Low-energy narrow-band light in the visible and infrared ranges has various biochemical, cellular, histologic, and functional effects[11]. Although there are some phototherapeutic modalities for the treatment of AR, using both 660 nm and 850 nm as a therapeutic modality has never

Chwee Teck Lim, James C.H. Goh (Eds.): ICBME 2008, Proceedings 23, pp. 992–995, 2009
www.springerlink.com

been reported. The aim of the present study was to investigate the effects of illumination at both 660 nm and 850 nm on the acupuncture point (Shangyingxiang Xue) in the treatment of AR.

II. Materials and Methods

A. Patients

Sixty-one patients (28 male and 33 female, average age 34.1 years) with perennial allergic rhinitis were prospectively enrolled in this study. The patients were randomly assigned to one of two groups: 31 were assigned to the experimental group treated with phototherapy and 30 to the group receiving medication (cetirizine) as a control. The history of most patients reported a long period of daily symptoms (average 6.2 years). Patients with severe deviation of the nasal septum causing bilateral nasal obstruction were excluded from the study. Candidates in whom fibroscopy revealed purulent postnasal drip flowing from an edematous and hyperemic infundibulum or with streaks of purulent discharge flowing across the eustachian tube orifice were diagnosed as suffering from sinusitis and were excluded from the study. Also excluded were patients who were convalescing from an upper respiratory tract infection or had used nasal or oral corticosteroids less than 30 days before the start of the study.

After recording their symptoms in a diary for 1 week, all candidates for inclusion in the study underwent videoendoscopic examination of the nose. Each patient was examined by the use of a rigid endoscope introduced as deeply as possible into the nostril for close examination of the mucosa and intranasal structures. In addition, a flexible endoscope was used to penetrate the narrow intranasal passages not accessible by the rigid endoscope, thus enabling close examination of the nasal cavity.

B. Diagnosis of AR

The diagnosis of allergic rhinitis was based on definite symptoms of nasal itching, rhinorrhea, sneezing, nasal obstruction or mouth breathing, as well as positive reactions to blood tests to antigens, such as house dust mite, cockroach, molds, feathers, grass pollen, weed pollens, sage pollen, and local tree pollens, etc. Criteria for positive skin prick test responses were a wheel of 3 mm or greater diameter with erythema of at least 5 mm. Histamine control skin test was read at 10 minutes, allergen and negative control skin tests were read at 15 minutes.

Table 1. Scoring of symptoms

Scoring of eye itching
0: no eye itching
1: rubbing eyes less than 5 episodes a day
2: rubbing eyes 6-10 episodes a day
3: rubbing eyes more than 10 episodes a day
Scoring of nasal itching
0: no nasal itching
1: rubbing nose less than 5 episodes a day
2: rubbing nose 6-10 episodes a day
3: rubbing nose more than 10 episodes a day
Scoring of nasal stuffiness
0: no nasal stuffiness
1: nasal stuffiness without mouth breathing
2: nasal stuffiness with sporadic mouth breathing
3: nasal stuffiness with predominant mouth breathing
Scoring of rhinorrhea
0: no nasal blowing
1: nasal blowing less than 5 episodes a day
2: nasal blowing 6-10 episodes a day
3: nasal blowing more than 10 episodes a day
Scoring of smell impairment
0: no smell impairment
1: hyposmia with mild smell impairment
2: hyposmia with moderate smell impairment
3: anosmia
Scoring of sneezing
0: no sneezing
1: sneezing less than 5 episodes a day
2: sneezing 6-10 episodes a day
3: sneezing more than 10 episodes a day
Scoring of size of inferior turbinate
0: size less than half of nasal cavity
1: mild swelling, nasal septum and middle turbinate are visible
2: inferior turbinate attached to nasal septum, there is space between inferiot turbinate and nasal floor
3: inferior turbinates attached to nasal septum and nasal floor, middle turbinate is invisible

C. Scoring of Symptoms

A symptom score of 0 to 3 was assigned for each of the following rhinitis symptoms: eye itching, nasal itching, nasal stuffiness, rhinorrhea, smell impairment ,sneezing and size of inferior turbinate. All the patients scored the severity of their symptoms on a four-point scale once a day in a diary; 0 = no symptom, 1 = mild, 2 = moderate and 3 = severe symptom (Table 1). All adverse effects observed during the treatment were recorded.

D. Phototherapy

In this group patients, 13 were male and 18 were female; the average patient's age was 34.3 years. A light emitter was used for phototherapy in this group. The wavelengths of this emitter were 660 nm and 850 nm. The emitter was positioned on the point of bilateral Shangyingxiang Xue. The therapeutic time was 10 minutes everyday for 7 days. All the therapies were performed in the morning during 9 am to 12 pm. During the course of the study, the patients did not receive any other anti-allergic management.

E. Drug therapy

In this group patients, 15 were male and 15 were female; the average patient's age was 33.8 years. The patients received cetirizine in the morning for a period of one week. A dosage of 5 mg/d was administered to patients up to 30 kg in weight and 10 mg/d for patients over 30 kg. All patients in this group did not receive any other drug during study period.

F. Statistical analysis

The effects of phototherapy on the clinical symptoms were analyzed by the paired samples t-test. We compared the mean symptom scores before (pre-therapy) and every time after (post-therapy) the patients completed phototherapy or medicine. To the right of the paired differences, we saw the T, degrees of freedom, and significance. Repeated measures analysis was used to compare the experimental group and control group. A p value of less than 0.05 was considered to be statistically significant.

III. Results and Discussion

A. Effects of phototherapy in the clinical symptoms

Thirty-one patients enrolled in the study completed the phototherapy. Mean values of daily registrations for eye itching, nasal itching, nasal stuffiness, rhinorrhea, smell impairment and sneezing are given in Figure 1. The most severe symptom of the pre-treat patients was rhinorrhea, which the mean value of the symptom score was 2.0, followed by sneezing and nasal stuffiness with scores of 1.84 and 1.55, respectively. The least severe symptom of the pre-treat patients was smell impairment with a mean score of 0.71. After the one-week treatment period, significant improvements were observed in all the symptoms of AR patients. The improved clinical symptoms were usually seen 1 to 2 days after the start of therapy, and thereafter the improvement was continuous. However, the smell impairment did not reveal significant improvement until after the 3th therapy.

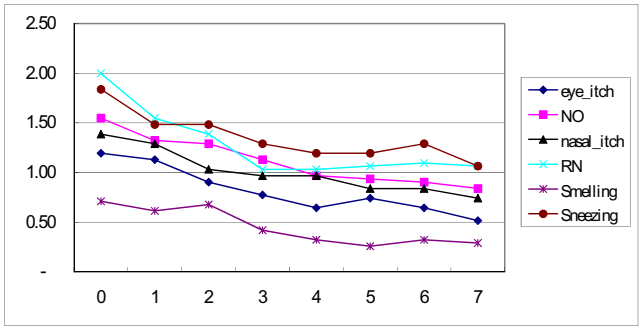


Fig. 1. Mean values of daily scores for symptoms of experimental group by using phototherapy. The score is given on a scale from 0 = no symptom to 3 = severe symptom. The symptom scores decreased over the period of treatment. Pre-treatment (Day 0); during treatment (Day 1-7).

B. Comparison of therapeutic effects between phototherapy and drug

Mean values of daily symptoms of control group are given in Figure 2. Comparison between two groups are shown in Table 2. The results reveal that all the symptoms improved after treatment in both groups. There is no significant difference of therapeutic effect between these two groups except the size of inferior turbinates.

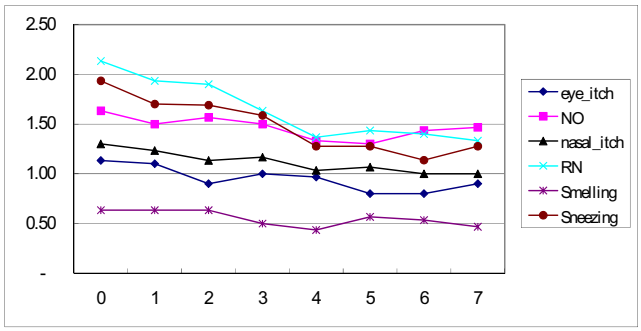


Fig. 2. Mean values of daily scores for symptoms of control group by using drug. The score is given on a same scale as experimental group.

Table 2 Results of comparison between two groups

	eye_itch	NO	nasal_itch	RN	Smelling	Sneezing	IT
Period	S	S	S	S	S	S	S
Group	NS	NS	NS	NS	NS	NS	S

eye_itch: eye itching NO: nasal stuffiness
nasal_itch: nasal itching RN: rhinorrhea
IT: size of inferior turbinate
S: significant difference ($p < 0.05$)
NS: no significant difference ($p > 0.05$)

IV. Discussion and Conclusions

The findings of our study demonstrate that phototherapy to acupuncture point (Shangyingxiang Xue) may improve the clinical symptoms of AR. Most of the symptoms were quickly and significantly improved, however, the smell impairment did not improve until after the 3th therapy. This was probably because the pre-treatment score was lower than the others that there was no much room for decreasing it or phtotherapy to acupuncture point was not so effective on improving olfactory disorder.

Although phtotherapy with combination of 660 nm and 850 nm to Shangyingxiang Xue may therefore be viewed as a useful additional approach in the treatment of AR, the definite mechanism remained unclear. Low-energy illumination therapy has proved effective in some clinical situations such as pain relief and wound healing. Illumination at both the visible and the infrared range were shown to be of therapeutic benefit, but these two types of illumination differ markedly in both photochemical and photophysical properties. The visible light may initiates the cascade of metabolic events at the level of the respiratory chain of the mitochondria, whereas infrared illumination does so by activatin enzymes. Accordingly, on the basis of findings in previous studies, the illumination selected for our study was red light at 660 nm and infrared light at 850 nm.

No adverse side effects of phototherapeutic treatment were observed in this study. During the experimental period, nobody dropped out of this group. We believe that many patients can obtaine relief of symptoms with this new therapeutic protocol. Although there was no much difference of clinical effects between groups of phototherapy and drugs, safety concerns about medical treatment usually pose an important restriction on the use.

In conclusion, AR may be treated effectively and safely by illumination on Shangyingxiang Xue at 660 nm and 850 nm. Further studies are necessary to establish which wavelengths and/or acupuncture points are therapeutically most effective and safe for the treatment of inflammatory disorders of the nasal mucosa.

References

1. A. B. Kay, “Allergy and allergic diseases”. First of two parts, N. Engl. J. Med. vol. 344, no. 1, 30-37,. 2001.
2. N. Aberg, J. Sundell, B. Eriksson et al, “Prevalence of allergic diseases in school children in relation to family history, upper respiratory infections, and residential characteristics”. Allergy. vol. 51, no. 4,.232-237, 1996.
3. K B. Sibbald, “Epidemiology of allergic rhinitis”. Monogr. Allergy. vol. 31, 61-79, 1993.
4. A.W.Law, S.D. Reed, J.S. Sundy, K.A. Schulman, “Direct costs of allergic rhinitis in the United States: estimates from the 1996 Medical Expenditure Panel Survey”. J. Allergy Clin. Immunol. Vol.111, 296-300, 2003
5. D.A. Stempel, R. Woolf, “The cost of treating allergic rhinitis”, Curr. Allergy Asthma Rep. vol.2, 223-230, 2002
6. M. S. Dykewicz, S. Fineman, D. P. Skoner et al, “Diagnosis and management of rhinitis: complete guidelines of the joint task force on practice parameters in allergy, asthma and immunology”. Ann. Allergy Asthma Immunol. vol. 81, 478-518, 1998.
7. P. van Cauwenberge, C. Bachert, G. Passalacqua et al, “Consensus statement on the treatment of allergic rhinitis”. Eur. Acad. Allergol. Clin. Immunol. Allergy. vol. 55, 116-134, 2000.
8. J. Bousquet, P. van Cauwenberge, N. Khaltaev, “Allergic rhinitis and its impact on asthma”. J. Allergy Clin. Immunol. vol. 108, Suppl. 5, . S147-334, 2001.
9. J. M. Weiner, M. J. Abramson, R. M. Puy, “Intranasal corticosteroids versus oral H_1 receptor antagonists in allergic rhinitis, systemic review of randomized controlled trials”. Br. Med. J. vol. 317, 1624-1629, 1998.
10. C.C. Xue, R. English, J.J. Zhang, et al.” Effect of acupuncture in the treatment of seasonal allergic rhinitis: a randomized placebo controlled clinical trial”. Altern Ther Health Med. vol.9, 80-87, 2003
11. I.C. Sallet, S. Passarella, E. Qualiarielio, ”Effects of selective irradiation on mammalian mitochondria”. Photochem Photobiol 45a:433, 1987;

The Study of Neural Correlates on Body Ownership Modulated By the Sense of Agency Using Virtual Reality

W.H. Lee[1], J.H. Ku[1], H.R. Lee[1], K.W. Han[1], J.S. Park[1], J.J. Kim[2], I.Y. Kim[1] and S.I. Kim[1]

[1]Department of Biomedical Engineering, Hanyang University, Korea
[2]Institute of Behavioral Science in Medicine, Yonsei University Severance Mental Health Hospital, Korea

Abstract — **The sense of one's own body as part of the self is a fundamental aspect of self-awareness. The recent distinction between sense of agency and sense of body-ownership has attracted considerable empirical and theoretical interest. In this study, we compared the strength of virtual hand illusion induced by agency controlled movement, to investigate the contributions of visual-motor stimulation and ownership to body using fMRI and behavioral study. In the synchronous conditions, virtual hand angle scaled by a scale factor of real hand angle, while the asynchronous condition showed virtual hand angle didn't correspond to real hand angle. Left precentral gyrus, left SMA, left anterior cingulate cortex and right parahippocampal were significant differences between synchronous condition and asynchronous condition with visual feedback. Left SMA was correlated positively with ownership score. The SMA function is integrated various sensory inputs and optimized action selected and compare body forward model with proprioception, then estimate body image.**

Keywords — **body ownership, sense of agency, left SMA**

I. Introduction

The development of BMI (Brain Machine Interface) technology is able to human brain to communicate with machine, so people can move the prosthesis their intention [1, 2]. To make the prosthetic feel like the subject's own limb, the functional development of prosthesis is important, as well as it also increases the importance of the psychological element (bodily self-awareness) [3]. The sense of agency and the sense of body-ownership jointly constitute the core of our bodily self-awareness [4]. The sense of agency is the sense of intending and executing actions, including the feeling of controlling one's own body movements, and, through them, events in the external environment [5, 6]. The sense of agency involves a strong efferent component, because centrally generated motor commands precede voluntary movement [4, 6]. Body ownership refers to the sense that one's own body is the source of sensations [4, 6]. The sense of body ownership involves a strong afferent component, through the various peripheral signals that indicate the state of the body [7]. The sense of body ownership is present not only during voluntary actions, but also during passive experience. In contrast, only voluntary actions produce a sense of agency [8]. The recent distinction between sense of agency and sense of body-ownership has attracted considerable empirical and theoretical interest [9]. The respective contributions of central motor signals and peripheral afferent signals to these two varieties of body experience remain unknown [10, 11].

In this study, we were interested in the effects of agency controlled (synchronously and asynchronously) movement on brain areas known to be involved in bodily self-awareness.

II. Methods

A. Subjects

Sixteen healthy volunteers (average age: 24.8, range: 21 ~ 31, SD: 2.51), 8 male and 8 female subjects, were recruited for this study. All were free of neurological or psychiatric illness.

B. Experiment Task

Subjects moved the virtual hand corresponded to real hand angle toward randomized target angle with and without visual feedback. We made a MR-compatible device that allowed us to modify the subject's degree of control of the movements of a virtual hand in MR room. The experiment tasks consisted of four agency controlled conditions (Synch 1, Synch 0.5, Synch 2, Asynch) to modulate participants' visual - motor sense (fig. 1). In the Synch 1, virtual hand angle corresponded to real hand angle (real hand angle × 1), while the Synch 0.5, 2 showed virtual hand angle scaled by a scale factor of real hand angle (real hand angle × 0.5, 2). In Asynch, virtual hand angle didn't correspond to real hand angle (agency controlled).

C. Procedure

At the beginning of task, subjects moved the real hand toward target angle without visual feedback to measure baseline hand movement sensation. Then, they performed four blocks corresponded each condition (fig. 2). One block

Chwee Teck Lim, James C.H. Goh (Eds.): ICBME 2008, Proceedings 23, pp. 996–999, 2009
www.springerlink.com

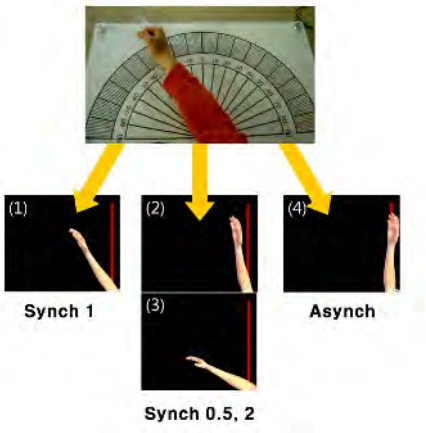


Fig. 1 Consisted of experiment task
(1) Synch 1 : virtual hand angle corresponded to real hand angle (real hand angle × 1), (2,3) Synch 0.5, 2 : virtual hand angle scaled by a scale factor of real hand angle (real hand angle × 0.5, 2), (4) Asynch : virtual hand angle didn't correspond to real hand angle

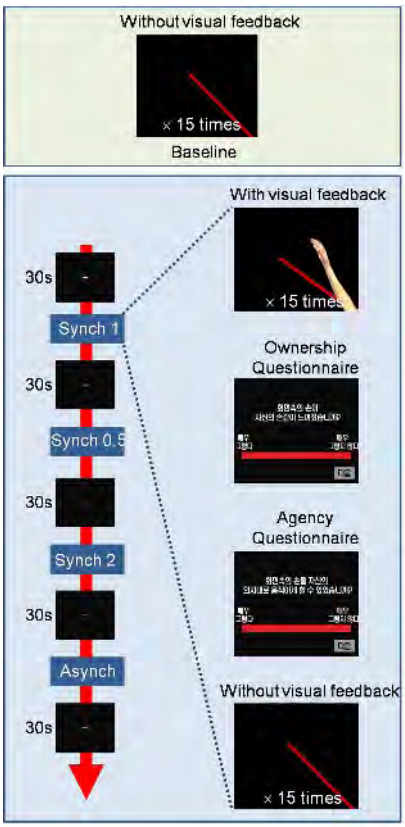


Fig. 2 Experiment procedure
One block consisted of 4 sessions (training session with visual feedback, ownership and agency questionnaire session, test session without visual feedback).

consisted of 4 sessions (training session with visual feedback, ownership and agency questionnaire session, test session without visual feedback). Three kinds of measurement were obtained in this study. One is self-report questionnaire of virtual hand ownership "it seemed like the virtual hand was my hand" and sense of agency "it seemed like I could have moved the virtual hand if I had wanted". Another is the proprioceptive shift, change of hand movement sensation compared baseline with test session (baseline – test session), and the other is brain activity each condition.

D. Data Acquisition

fMRI data was done on a 1.5-T MRI system (Sigma Eclipse, GE Medical Systems). BOLD (blood oxygenation level dependent) signals were obtained using an EPI sequence (Gradient Echo, 64×64×30 matrix with 3.75×3.75×5 mm spatial resolution, TE: 14.3, TR: 2s, FOV: 240 mm, Slice thickness: 5 mm, FA=90, # of slices: 30). A series of high resolution anatomical images was also acquired with a fast spoiled gradient echo sequence (256×256×116 matrix with 0.94×0.94×1.50 mm spatial resolution, FOV: 240 mm, Thickness: 1.5 mm, TR: 8.5s, TE: 1.8s, FA: 12, # of slices: 116).

E. Data analysis

Data analysis was conducted with AFNI (Analysis of-Functional NeuroImages: AFNI, Ver 2007_05_29_1644) freeware developed by R.W. Cox [12]. The first 15 time points in all the time series data were discarded to eliminate the fMRI signal decay associated with magnetization reaching equilibrium. All remaining fMRI data were co-registered to the first remaining time sample to correct for the confounding effects of small head motions during task performance. Then, 'spikes' value are corrected in the 3D+time input dataset despike routine provided in AFNI and performed mean-based intensity normalization. Further processing included temporal smoothing (three-point Low-Pass filter (0.15×(a-1) + 0.7×(a) + 0.15×(a+1)) as well as detrending to remove constant, linear and quadratic trends from the time series data. Spatial Normalization was performed to transform Talairach space using Montreal Neurological Institute (MNI) N27 template provided in AFNI (bilinear interpolation, spatial resolution: 2×2×2 mm^3). Further processing included spatial smoothing (Gaussian filter with 9 mm full-width at half-maximum (FWHM), respectively). After preprocessing, condition-specific effects were estimated according to the general linear model (GLM). According to behavioral data, three synchronously conditions (sync 1, sync 0.5 and sync 2) didn't differ. For this reason, three synchronously conditions data (brain ac-

tivity and behavioral data) averaged one synchronously condition data. We performed a repeated measure ANOVA to test differences in neural activity between synchronously condition and asynchronously condition. Then, correlation analysis conducted between the behavioral data and brain activations.

III. Results

A. Behavioral data

According to the behavioral study, in synchronous condition more felt body ownership and agency score than asynchronous condition. And proprioceptive shift (baseline – test session) was more shifted in synchronous condition (fig. 3).

B. fMRI data

Left precentral gyrus, left SMA, left anterior cingulate cortex and right parahippocampal were significant differences between synchronous condition and asynchronous condition with visual feedback. Left superior orbital gyrus and left hippocampus were significant differences between synchronous condition and asynchronous condition without visual feedback (Table 1, 2).

Table 1 Main effect brain region test differences between synchronously condition and asynchronously condition with visual feedback

Volume	t	x	y	z	region
192	4.4959	-15	-23	68	Left precentral gyrus
160	4.5644	-3	-3	60	left SMA
128	4.4399	-3	39	4	left anterior cingulate cortex
104	4.6158	37	-33	-14	right parahippocampal

Table 2 Main effect brain region test differences between synchronously condition and asynchronously condition without visual feedback

Volume	t	x	y	z	region
176	-4.5188	-11	57	-2	Left superior orbital gyrus
96	4.2105	-27	-21	-2	left hippocampus

C. Correlation analysis

We performed correlation analysis contrasted % signal change (sync – async) with contrasted behavioral data (sync – async). Therefore, left SMA was correlated positively with ownership score (fig. 4).

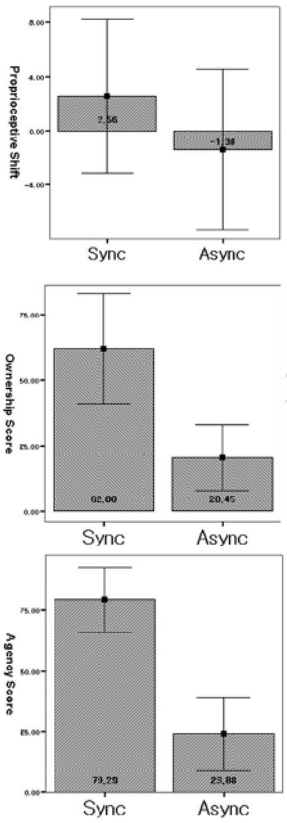


Fig. 3 Behavioral data

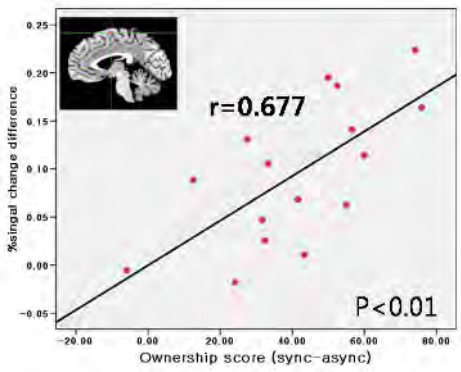


Fig. 4 Correlation with Left SMA % signal change difference (sync – async) and Ownership score difference (sync – async)

IV. Discussion

We investigated the effects of agency controlled (synchronously and asynchronously) movement on brain areas. We particularly focused on the correlation between left

SMA and ownership score. According to few neuroimaging studies, the SMA is implicated in the planning of motor actions and is associated with bimanual control. One could say that the SMA sends a "plan" of the motor action to the primary motor cortex, which executes the action. The SMA is implicated in actions that are under internal control, such as the performance of a sequence of movements from memory [13, 14]. The elicitation of ownership depends on the integration of visual and motor information and the differences between the visual and position sense representations. The period before the ownership develops is critical in this respect, and it probably involves a recalibration of position sense for the hand [15, 16]. Thus, the recalibration of limb position might be a key mechanism for the elicitation of the ownership, and indeed experiencing the ownership has behavioral consequences for arm movements [16]. SMA is one of the region this feature.

REFERENCES

1. Buch E, Weber C, Cohen LG, Braun C, Dimyan MA, Ard T et al. (2008) Think to move: a neuromagnetic brain-computer interface (BCI) system for chronic stroke. Stroke 39: 910-917.
2. Lebedev MA, Nicolelis MA. (2006) Brain-machine interfaces: past, present and future. Trends Neurosci **29**: 536-546.
3. Gallagher II. (2000) Philosophical conceptions of the self: implications for cognitive science. Trends Cogn Sci **4**: 14-21.
4. Tsakiris M, Haggard P, Franck N, Mainy N, Sirigu A. (2005) A specific role for efferent information in self-recognition. Cognition **96**: 215-231.
5. Haggard P. (2005) Conscious intention and motor cognition. Trends Cogn Sci 9: 290-295.
6. Tsakiris M, Prabhu G, Haggard P. (2006) Having a body versus moving your body: How agency structures body-ownership. Conscious Cogn **15**: 423-432.
7. Sato A, Yasuda A. (2005) Illusion of sense of self-agency: discrepancy between the predicted and actual sensory consequences of actions modulates the sense of self-agency, but not the sense of self-ownership. Cognition **94**: 241-255
8. Schwabe L, Blanke O. (2007) Cognitive neuroscience of ownership and agency. Conscious Cogn 16: 661-666.
9. Costantini M, Haggard P. (2007) The rubber hand illusion: sensitivity and reference frame for body ownership. Conscious Cogn 16: 229-240.
10. Tsakiris M, Schutz-Bosbach S, Gallagher S. (2007) On agency and body-ownership: phenomenological and neurocognitive reflections. Conscious Cogn 16: 645-660.
11. Platek SM, Keenan JP, Gallup GG, Jr., Mohamed FB. (2004) Where am I? The neurological correlates of self and other. Brain Res Cogn Brain Res **19**: 114-122.
12. Cox RW (1996). AFNI: software for analysis and visualization of functional magnetic resonance neuroimages. Comput Biomed Res 29: 162-73
13. Shima K, Tanji J. (1998) Both supplementary and presupplementary motor areas are crucial for the temporal organization of multiple movements. J Neurophysiol **80**: 3247-3260
14. Supplementary motor area at http://en.wikipedia.org/wiki/Supplementary_motor_area
15. Naito E, Roland PE, Ehrsson HH. (2002) I feel my hand moving: a new role of the primary motor cortex in somatic perception of limb movement. Neuron **36**: 979-988.
16. Ehrsson HH, Spence C, Passingham RE. (2004) That's my hand! Activity in premotor cortex reflects feeling of ownership of a limb. Science **305**: 875-877.

Author: Jeonghun Ku, Ph. D
Institute: Department of Biomedical Engineering, Hanyang Univesity
Street:
City: Seoul
Country: Korea
Email: kujh@bme.hanyang.ac.kr

Diagnosis and Management of Diabetes Mellitus through a Knowledge-Based System

Morium Akter[1], Mohammad Shorif Uddin[2] and Aminul Haque[3]

[1]Dept. of Computer Science and Engineering, Jahangirnagar University, Savar, Dhaka, Bangladesh
[2]Imaging Informatics Division, Bioinformatics Institute, A*STAR, Singapore
[3]Bangladesh Institute of Health Sciences (BIHS) Hospital, Savar Center, Dhaka, Bangladesh

Abstract — **The chronic disease diabetes mellitus is increasing worldwide. It is caused by absolute or relative deficiency of insulin, and is associated with a range of severe complications including renal and cardiovascular disease as well as blindness. Preventive care helps in controlling the severity of this disease; however, preventive measures require correct educational awareness and routine health checks. Medical doctors help in effective diagnosis as well as treatment of diabetes, although it is associated with high costs. With this view, the purpose of the present research is to develop a low-cost automated knowledge-based system that helps in self-diagnosis and management of this chronic disease for patients as well as doctors. Our knowledge-based system has an easy computer interface, which performs the diagnostic tasks using rules acquired from medical doctors on the basis of patient data. At present our system consists of 26 rules and it has been implemented using Prolog programming. Some real-life experimentations were performed, which confirmed the effectiveness of the developed system.**

Keywords — **Diabetes mellitus, insulin deficiency, disease diagnosis, health care management, knowledge-based (expert) system.**

I. Introduction

In the year 2000, a study [1] among 191 World Health Organization (WHO) member states confirms that 2.8% people for all age groups had diabetes, and this is expected to be 4.4% by the year 2030. This implies that the total number of people with diabetes is projected to rise from 171 million in 2000 to 366 million in 2030. In Bangladesh, diabetes is reaching epidemic proportions; in some sectors of our society more than 10% of people have diabetes [2]. Diabetes causes [3] severe life threatening complications, such as hypoglycemic coma, blurred vision, loss of memory, severe impairment of renal function, insulin allergy, acute neuropathy, etc. Diabetes management requires dietary control, physical exercise and insulin administration. Medical doctors help in effective diagnosis as well as treatment of diabetes. However, it obviously associates with high costs. Despite remarkable medical advances, patient self-management remains the cornerstone of diabetic treatment. Knowledge-based intelligent system has been proven effective in solving many real-world problems requiring expert skills. Hence, to reduce the cost and to improve the early detection as well as self-awareness of diabetes mellitus, automated expert system might be a promising solution. Knowledge-based system for diagnosis can be used in variety of domains: plant disease diagnosis, credit evaluation and authorization, financial evaluation, identification of software and hardware problems and integrated circuit failures etc. [4]-[6].

The main objective of the present research is to develop a low-cost automated knowledge-based system incorporating the skills of medical experts to help the patients in self-diagnosis and management of this chronic disease. Recently, expert systems have been developed in laboratory stage for diabetes awareness and management, and insulin administration [7]-[11]. Compared to these systems, our approach is more simple and pragmatic.

The paper is organized as follows. In Section II the medical knowledge about diabetes is described briefly, Section III presents system architecture, Section IV describes rule-based decision-making process as well as some experimental results, and finally Section V draws the conclusions.

II. Medical knowledge of diabetes

Diabetes mellitus is a clinical syndrome characterized by hyperglycemia, due to absolute or relative deficiency of insulin. [12]

A. Classification of diabetes

1. Type-I (Insulin-Dependent Diabetes Mellitus—IDDM) diabetes tends to occur in the young. Type-II (Non-Insulin-Dependent Diabetes Mellitus—NIDDM) diabetes mellitus occurs more often in older people who are obese and had sedentary lifestyles.
2. Gestational diabetes mellitus (GDM) is a glucose intolerance detected in a pregnant woman who was not known to have these abnormalities prior to conception. [3]

Chwee Teck Lim, James C.H. Goh (Eds.): ICBME 2008, Proceedings 23, pp. 1000–1003, 2009
www.springerlink.com

B. Diagnosis

Diagnosis [13]-[14] is a process, by which a doctor searches for the cause (disease) that best explains the symptoms of a patient. Our knowledge-based system is mainly used for performing diagnosis based on patient data. Patient data can be demographic or clinical. Demographic data relates the information such as patient's age, sex, location, income, etc. Clinical data is divided into physical signs and laboratory results. Physical signs are those detected by a physical examination of patient, like BMI (body-mass index), pulse rate and blood pressure. Laboratory results are those detected via laboratory tests, like blood test, urine test, etc. The diagnosis system is based on following patient data. [12]

1. Test urine for glucose and ketones.
2. Measure random or fasting blood glucose:
   - Fasting plasma glucose >= 7.0 mmol/l
   - Random plasma glucose >= 11.0 mmol/l.
3. Oral glucose tolerance test:
   - Fasting plasma glucose 6.1-6.9 mmol/l
   - Random plasma glucose 7.0-11.0 mmol/l.

C. Method of Treatment

- Diet alone— 50% can be controlled adequately.
- Diet + oral hypoglycemic agent— 20-30% can be controlled.
- Diet and insulin— 30% can be controlled.

III. System Architecture

The computer-based system consists of a user interface, an inference engine, knowledge base, working memory and case history file. The case history file contains the demographic and clinical data of the patient. The knowledge base contains the heuristic knowledge encoded in some form (e.g., rules) for diagnosing diabetes. The working memory contains the (initial) patient data, partial conclusions, data given by user and other information related to the case under consideration. It provides facts and serves as a store for inferences or conclusions.

Inference engine mimics the expert system's reasoning process. It woks on the facts in the working memory and uses the domain knowledge contained in the knowledge base to derive (or infer) new facts as well as conclusions. [5] It achieves this by searching through the knowledge base to find rules whose premises match the facts contained in the working memory. If such a match is found, it adds the conclusion of the matching rule to the working memory. This process continues until the inference mechanism is unable to match any rules with the facts in the working memory. And finally, the user interface allows interaction with the inference engine to diagnose diabetes.

The structure of our expert system is shown in Fig. 1.

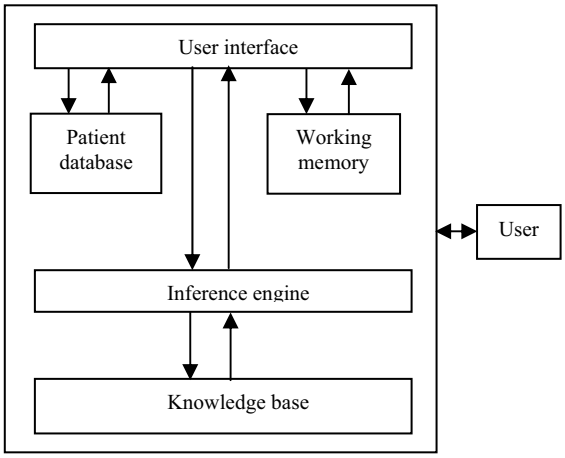


Fig. 1: Architecture of the proposed system.

IV. Diagnostic approach and experimental results

Diagnostic approaches can be grouped into four classes: model-based, rule-based, neural-network based and case-based. The knowledge representation schemes of model-based and rule-based diagnoses can be treated as symbol-oriented, while neural network and case-based diagnoses are instance-oriented. [4] In our system we use rule-based approach. A rule-based expert system is an expert system based on a set of rules that are used to make decisions. [6] To design an expert system a knowledge engineering process is needed, in which the rules used by human experts are accumulated and translated into an appropriate form for computer processing.

In our expert system we divide the treatment of diabetes into three categories.

1. Type-I diabetes— only insulin is used.
2. Gestational diabetes— only insulin is used, and
3. Type-II, where the oral hypoglycemic agent, diet, and sometimes insulin are used. In this category, there are special treatments:
   - The drugs for obese and lean patients.
   - The drugs, which should not used for the patient who have renal diseases, lactic acidosis, liver disease, etc.

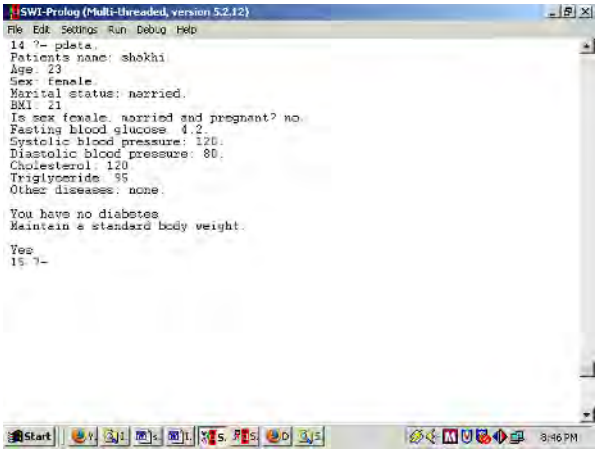


Fig. 2: Sample test result (case1).

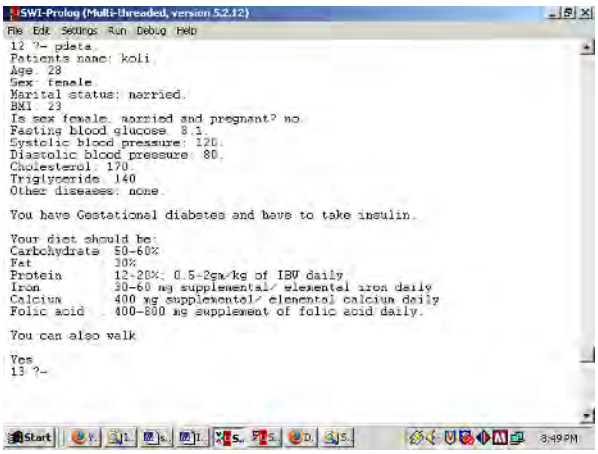


Fig. 3: Sample test result (case2).

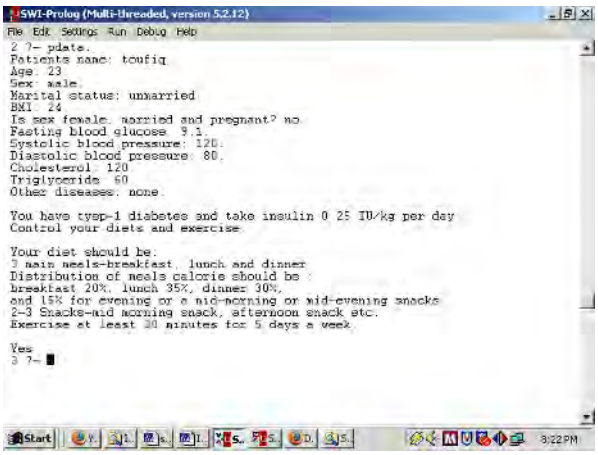


Fig. 4: Sample test result (case3).

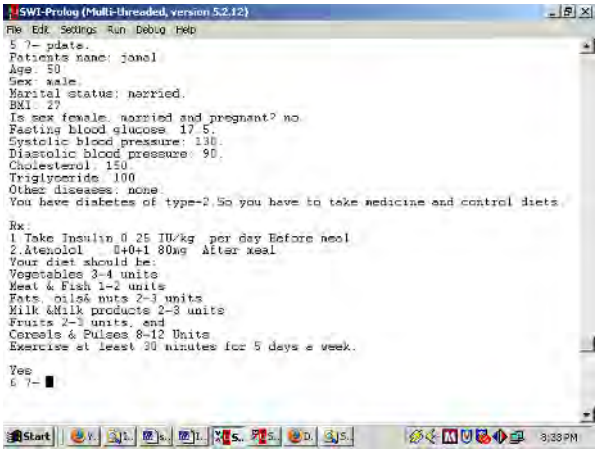


Fig. 5: Sample test result (case4).

At present, the system uses 26 rules and is implemented using Prolog programming language. We did experimentations using data of 100 patients. Some self-explanatory sample test results are shown in Figs. 2- 5.

V. Conclusions

A rule-based expert system for diagnosis of diabetes has been introduced in this paper. The aim of our expert system is to help the diabetes patients in low-cost treatment and management. Some real life experimentations were performed, which confirmed the effectiveness of the proposed system. The system can be used in both home and hospital environments.

There are some limitations in the developed knowledge-based system. For example, the number of rules is not sufficient for a general robust expert system. Moreover, wide real-life experimentations were not performed yet. Rooms are also available for improvement of the expert system on the basis of patients' feedbacks. Our future goal is to overcome the above limitations to make it a robust one.

References

1. S. Wild, G. Roglic, A. Green et al., "Global prevalence of diabetes - estimates for the year 2000 and projections for 2030", *Diabetes Care*, vol. 27, pp. 1047-1053, (2004).
2. Diabetic Association of Bangladesh, "Diabetes Mellitus", 2005 (ISBN: 984-32-2552-X).
3. Hajera Mahtab, Zafar A Latif, Md. Faruque Pathan, "Diabetes Mellitus - A Handbook For Professionals", BIRDEM, 3rd Ed., 2004 (ISBN: 984-31-0100-6).
4. Jie Yang, Chenzhou Ye, Xiaoli Zhang, "An expert system for fault diagnosis", *Robotics*, vol.19, pp. 669-674, (2001).

5. Karthik Balakrishnan and Vasant Honavar, "Intelligent diagnosis systems", available online at http://www.cs.iastate.edu/~honavar/aigroup.html (accessed on December 17, 2007).
6. Costas Papaloukas, I. Dimiritrios, Aristidis Likas, S. Christos Stroumbis, Lampros K. Michalis, "Use of novel rule-based expert system in the detection of changes in the ST segment and the T wave in long duration ECGs", *J. Electrocardiology*, vol. 35, no.1, (2002).
7. V. Ambrosiadou and A. Boulton, "A knowledge-based system for education on management of diabetes", *Proc. IMACS World Congress on Scientific Computation*, 1988, pp. 186-189.
8. Rudi Rudi, and Branko G. Celler, "Design and Implementation of Expert-Telemedicine system for Diabetes Management at Home", *Intl. Conf. on Biomedical and Pharmaceutical Engineering (ICBPE 2006),* pp. 595-599.
9. Diabetes be aware: avbaible online at http://www.hpb.gov.sg/diabetes/ (accessed on July 11, 2008).
10. Kyung-Soon Park, Nam-Jin Kim, Ju-Hyun Hong, Mi-Sook Park, Eun-Jong Cha, Tae-soo Lee, "PDA based Point-of-care Personal Diabetes Management System", *Proceedings of the IEEE 27th Annual Conference on Engineering in Medicine and Biology* (Shanghai, China, September 2005)*,* pp. 3749-3752.
11. V. Ambrosiadou, Diabetes, "An expert system for education in diabetes management", in *Expert Systems Applications*, Sigma Press, UK, pp. 227-238, (1989).
12. Davidson, "Principles and Practice of MEDICINE", Churchill Livingstone, 19th Ed, pp. 644, (2002).
13. G. Gogou, N. Maglaveras, V. Ambrosiadou, D. Goulis, C. Pappas, "A neural network approach in diabetes management by insulin administration", *J. Med. Syst.* Vol. 25, no. 2, pp. 119-31, (2001).
14. Bert Kappan, Wim Wiegerinck, Ender Akay, "Promedas: A clinical diagnostic decision support system", Available online at http://download.intel.com/research/share/UAI03_workshop/kappen/kappen_uai2003.pdf (accessed on June 8, 2007).

Corresponding author:

Mohammad Shorif Uddin
Bioinformatics Institute
30, Biopolis Street, #07-01 Matrix
Singapore 138671
E-mail: msuddin@gmail.com

Modeling and Mechanical Design of a MRI-Guided Robot for Neurosurgery

Z.D. Hong[1], C. Yun[1] and L. Zhao[2, 3]

[1]Robotics Institute, Beihang University, Beijing, China
[2]Harvard Medical School and Brigham and Women's Hospital, Boston, USA
[3]XinAoMDT Technology Co., Ltd., Hebei, China

Abstract — **Magnetic resonance imaging (MRI) has established itself as a standard tool in clinical diagnostics and advanced brain research, and is one of the real time modalities currently being an intra-operative image of neurosurgery. Robots are known to be accurate manipulation device that can share the digital workspace of MR imagers. It is, therefore, conceivable that MRI-guided robot could improve the accuracy of neurosurgery, and provide great assistance for surgeons to execute the planned neurosurgical maneuver in precise manner. This paper deals with a particular hybrid robot developed for keyhole neurosurgery. The kinematics model, dynamic simulation, the control system, and the functional design of the robot are treated, which focus on the necessary actuators' features characterized on the basis of the dynamic simulations.**

Keywords — **MRI, Robot, Neurosurgery, Kinematics and dynamics**

I. Introduction

Magnetic resonance imaging (MRI) is superior to X-ray CT in terms of good soft tissue contrast, lack of ionizing radiation, and functional imaging. MRI which has a relatively wide opening has been developed and spread recently. This kind of MRI is called Open MRI. But the opening is still narrow for sufficient number of surgeons and assistants to stand by the patient. In addition, manual positioning of tools is not as precise as the coordinate information provided by tomography. MRI-compatible robots provide surgeon in attractive way: The robots eliminate hand tremors and enable accurate and dexterous operation; In robotic surgery with MRI-guidance, recurrence of tumors will be reduced because surgeons can confirm the removal of tumor cells and improve the reduction rate of the tumor cells, because MRI can distinguish tumors or other lesions from normal tissues; Furthermore MRI can eliminate exposure to radiation from computer tomography (CT) or positron emission tomography (PET).

A variety of MRI-compatible robots are being developed and reported recently. Chinzei, et al. developed a Cartesian type surgical robot using an X-Y-Z table for use in an intra-operative MRI for biopsy needle or pointing device according to preoperative planning [1]. T. Mashimo, et al. developed a manipulator using a spherical ultrasonic motor which is constructed of three ring-shaped stators and a spherical rotor and has two or three degrees of freedom [2]. S.P. DiMaio, et al. designed a comprehensive robotic assistant system with steady needle placement and high-fidelity MRI imaging [3]. Kerieger et al. presented a 2-DOF passive, unencoded and manually manipulated mechanical linkage to aim a needle guide for transrectal prostate biopsy with MRI guidance [4].

The goal of our project is to design, fabricate, and test an Ultrasonic Motor actuate MR compatible robotic system for automatically and interactively aligning and orienting the surgical needle throughout the intra-operative MRI guided neurosurgical procedures, such as biopsy and brachytherpy. This paper design a particular hybrid robot developed for keyhole neurosurgery. The robot consists of a DELTA parallel mechanism with 3 DOFs and a serial manipulator with 2 DOFs, which function alignments and orienting of the needles respectively. The kinematics model, dynamic simulation, singularity analysis and control system design of the robot are accomplished. The necessary actuators features were characterized on the basis of the multi-body package MSC.ADAMS.

II. Material and method

A. System infrastructure

MRI-guided robotic system requires surgical planning, MR-image acquisition, human-machine interface, navigation, and sensing. To address these components required for MRI-guided intervention, a schematic diagram of the proposed infrastructure is illustrated in Fig.1. The entire system consists of three main subsystems as follows: MRI scanner and its image processing console, navigation computer and monitor, and robot. MR images are transferred across a local area network (LAN) in DICOM format from the MRI console (in the MRI console room) to the navigation computer (inside the operation room). The navigation computer provides pre-operative surgery planning, intra-operative image processing, MRI scanning controls, motion planning, remote actuation, and control of the robotic components. The surgeon is able to control and command the entire system through interactive interface on the navigation consoles.

Chwee Teck Lim, James C.H. Goh (Eds.): ICBME 2008, Proceedings 23, pp. 1004–1008, 2009
www.springerlink.com

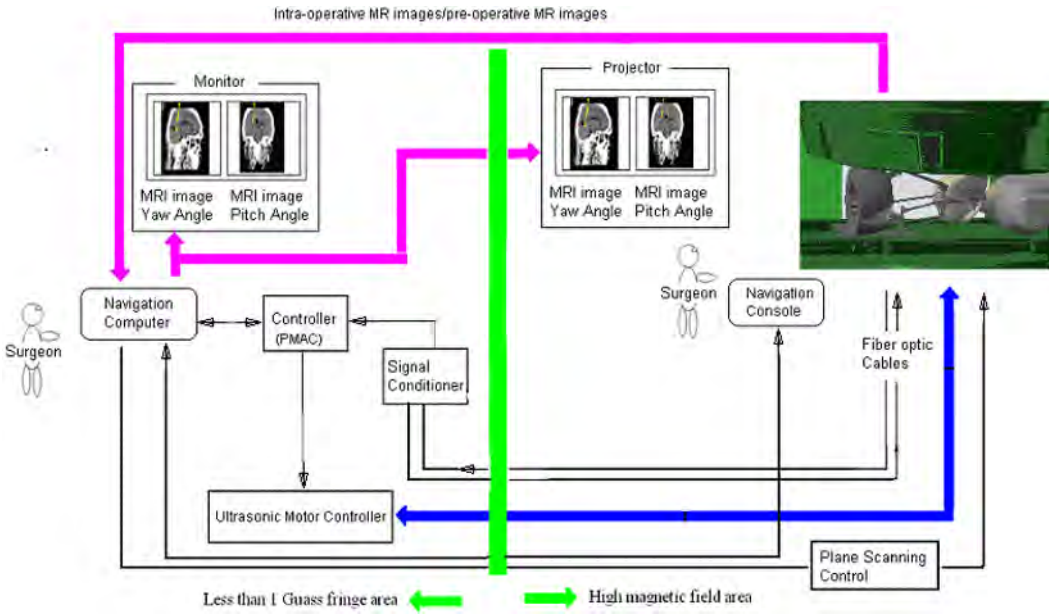


Fig. 1 Entire robot system

B. Mechanical modeling of Robot for neurosurgery

Parametric assembly of the robot, shown in Fig. 2, has been developed by means of the solid modeler NX5.0. The robot comprises DELTA mechanism, developed by L.W. Tsai [5-7], and serial manipulator which function the alignments and orienting of the needles respectively. DELTA mechanism is characterized by three identical kinematical chains, symmetrically placed at 120^0 between each other, which drive a moving platform with respect to a fixed base. The following elements are the elements of the topological structure of one of the three kinematical closed chains, respectively: an engine, an intermediary mechanism with four bars, which are parallel two to two, and finally a passive revolute link connected to the moving platform.

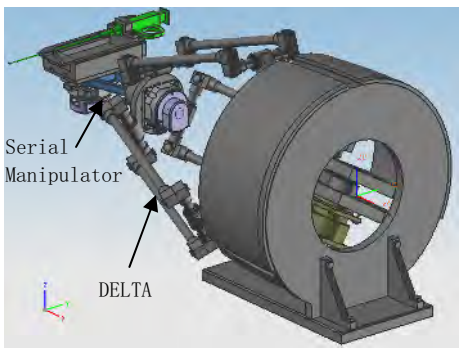


Fig. 2 3D robot model

C. Kinematics analysis

Delta only provides the function as X-Y-Z Cartesian type mechanism [5-7] without any rotation of moving platform. So the equivalent freedoms, labeled in 1 - 6, of the complete robot were described in Fig. 3. $z_i(i=1,2,3)$ are the moving axis of freedom 4, 5, and 6.

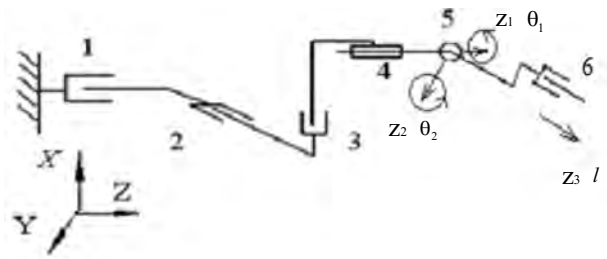


Fig. 3 Equivalent kinematics diagram of the robot

Let O_{XYZ} (Fig. 4) be a fix Cartesian frame, and its origin be set on the center point of the fix platform, and $\phi_0 = 0$. p is set at the center of moving platform, the length of the link connecting with moving platform is l_1, and the offset between serial manipulator and needle is d.

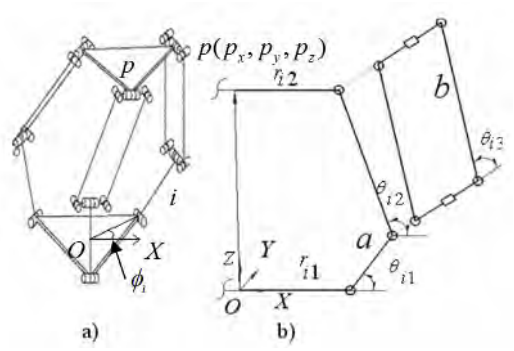


Fig. 4 a) Schematic of the 3 DOF Delta parallel mechanism and b) Description of the joint angles and link lengths for leg i

The direct and inverse kinematical equations of the DELTA were analyzed in [6-7]. The analytical solution proposed by [7] for the direct and inverse kinematical analyses are shown in Eq. 1 and Eq. 2 respectively.

$$ {}^{o}T_p = \begin{bmatrix} 1 & 0 & 0 & x_P \\ 0 & 1 & 0 & y_p \\ 0 & 0 & 1 & z_p \\ 0 & 0 & 0 & 1 \end{bmatrix} \tag{1} $$

$$ \begin{cases} \theta_{i3} = \pm \arccos \dfrac{p_y \cos\phi_i - p_x \sin\phi_i}{b} \\ \theta_{i1} = 2\arctan t_i \qquad ,i = 1,2,3 \\ \theta_{i2} = \arcsin \dfrac{p_z - a\sin\theta_{i1}}{b\sin\theta_{i3}} \end{cases} \tag{2} $$

where $\begin{cases} \mathrm{y_p} = \mathrm{c}\cos\theta_{13} \\ x_p = \dfrac{c}{\sin\phi_2}\left(\cos\theta_{13}\cos\phi_2 - \cos\theta_{23}\right) \\ z_p = k_0\cos\theta_{13} + k_1\sin\theta_{13} + k_2\cos\theta_{23} - k_1\sin\theta_{23} + k_3 \end{cases}$,

$k_i(i=0,1,2,3)$ and $\theta_{i3}(i=1,2)$ are the functions of geometric parameters and positions of DELTA mechanism; $t_i = \dfrac{l1_i \pm \sqrt{l1_i - 4l0_i l2_i}}{2l0_i}$, $l0_i, l1_i, l2_i$ are the function of θ_{i3}, a, b, p_x, p_y, p_z. More details were found in [7].

The direct kinematics of the 2-DOF serial manipulator (Fig. 3) was completed in Eq. 3 based on D-H parameters shown in Table 1, where c_1, c_2, s_1, and s_2 represent $\cos\theta_1$, $\cos\theta_2$, $\sin\theta_1$, and $\sin\theta_2$ respectively. The inverse kinematical model of the 2-DOF serial manipulator was shown in Eq. 4.

$$ {}^{p}T_E = \begin{bmatrix} c_1c_2 & -c_1s_2 & -s_1 & lc_1c_2 \\ s_1c_2 & -s_1s_2 & c_1 & ls_1c_2 + d \\ -s_2 & -c_2 & 0 & -ls_2 + l_1 \\ 0 & 0 & 0 & 1 \end{bmatrix} \tag{3} $$

Table 1 Denavit-Hartenberg parameter of serial manipulator

Link	α_i	a_i	d_i	θ_i
1	0	0	0	θ_1
2	-90^0	0	0	θ_2
3	0	0	l	0

$$ \begin{cases} \theta_1 = \pm \arctan\left(\dfrac{y_E - d}{x_E}\right) \\ \theta_2 = -\arctan\left(\left(\dfrac{z_E}{y_E - d}\right)\sin\theta_1\right) \\ l_2 = -(z_E - l_1)/\sin\theta_2 \end{cases} \tag{4} $$

So the overall direct kinematics ${}^{B}T_N = {}^{B}T_P \times {}^{P}T_N$ is then determined. The overall inverse kinematics was obtained from Eq. 2 and Eq. 4.

When $\theta_{i3} = \begin{cases} 0 \\ \pi \end{cases}$, or $\theta_{i2} - \theta_{i1} = \begin{cases} 0 \\ \pi \end{cases}$, i=1 2 3, innerve singularities of Delta mechanism appeared. The direct singularities are solved analytically, but not all singularities are determined easily. Some typical singularities are $\theta_{i3} = \begin{cases} 0 \\ \pi \end{cases}$, or $\theta_{i2} = \begin{cases} 0 \\ \pi \end{cases}$.

D. Dynamic simulation

The model was exported to the multi-body package MSC.ADAMS, in order to obtain both kinematical and dynamic simulations of the neurosurgery procedures. Moreover, using the FEM analyzer MSC.MARC, the elements' stresses in dynamic conditions were assessed to optimize the detailed design of each component. Finally the necessary actuators' features were characterized on basis of the dynamic simulations.

In Table 2 the maximal torques of all actuators were calculated. The largest torque is 3.5 $N.m$, and the Ultrasonic motor meet the demand (Ultrasonic motor's rate torque is 0.6 $N.m$, ratio of reducer is 20:1).

Table 2 Simulation results

DOF	θ_{11}	θ_{21}	θ_{31}	θ_1	θ_2
Maximum actuator torque (N.m)	3.56	1.22	1.22	0.06	0.001

In Fig. 5 the torque exerted by the actuators at θ_{11} and θ_1 is presented for the cases analysis of maximal torque. The maximal absolute value (dash line) is about 3.56 $N.m$.

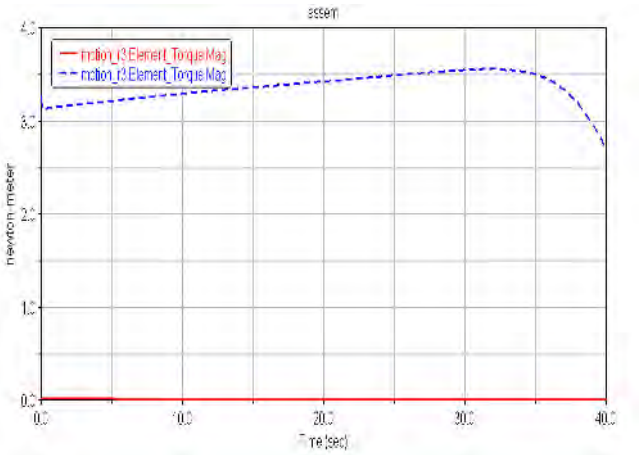


Fig. 5 Actuators' torque of first motor and fourth motor

If a serial mechanical architecture, for example Cartesian, were used to move the same masses along the same trajectories, the requested power would be much greater due to the robot moving masses, which are pre-eminent if compared to the equipment mass.

E. Control system

For the control of the robot the commercial motion controller PMAC has been chosen (8 axes, DSP56303, 40 MHz, endowed with teach pendant). It offers the user the possibility to implement her/his own defined model based control laws and coordinate transformation between the world Cartesian coordinate system and the robot internal coordinate system minimizing the effort of writing interpolating algorithms. The programming environment runs on Windows NT based personal computers and, besides allowing writing compile and debugging the application software, it permits to evaluate the behaviors of the controlled machine and then to choose the vast solution. The control diagram was shown in Fig. 6. PMAC communicate with PC according to RS232 interface. Surgical planning and joint interpolation were conducted in PC and PMAC respectively.

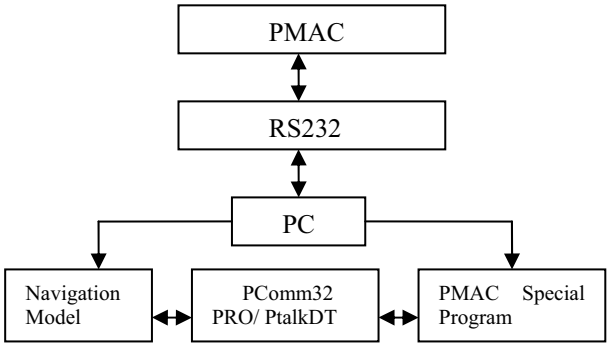


Fig. 6 Control system

III. Conclusions

We are designing a MR-compatible robotic system that can be used for automatically or interactive orientation and alignment of a needle based on the neurosurgical procedure, such as biopsy and brachytherapy, with intra-operative MRI-guidance. The robot has been designed such that it will perform desired tasks inside open MRI scanner. The direct and inverse kinematic equations that describe the robot behaviors can be implemented on a commercial motion controller for robotic application, such as PMAC, and singularities were considered during the design of control system. Ultrasonic motor were selected based on dynamic simulation. Current and future work includes the integration of the robot subsystem and performance of series of experimental test inside the MR scanner using the first physical prototype.

Acknowledgment

The test was performed by XinAoMDT Technology Co., Ltd. (Langfang, Hebei, China). The authors would like to thank XinAoMDT Technology Co., Ltd. for providing help and equipments.

References

1. K Chinzei, R Kikinis, F Jolesz (1999) MR compatibility of mechatronic devices: desighn criteria, MICCAI Proc. vol.1679, Lecture Notes in Computer Science, Cambridge, UK, 1999, pp 1020-1031
2. T Mashimo, S Toyama (2007) MRI-Compatibility of a manipulator using a spherical ultrasonic motor, IFToMM Proc. 12th World Congress, Besancon, France, 2007, pp 1-6
3. S P DiMaio, G S Fischer, S J Haker et al.(2006) A system for MRI-guided prostate interventions, BioRob Proc. 1st International Conference on Biomedical Robotics and Biomechatronics, Pisa, Italy, 2006, pp 68-73

4. A Krieger, R C Susil, C Menard et al. (2005) Design of a novel MRI compatible manipulator for image guided prostate interventions, IEEE Tran. on Biomed. Eng. 52: 306-313
5. Tsai L W.Multi-degrees-of-freedom mechanism for machines tools and the like. U S Patient Pending, 1955. No.08/415
6. Tsai L W, Walsh G C, Stamper R E (1996) Kinematics of a novel three DOR translational platform. ICRA Proc. the 1996 IEEE Int Conf on robotics and Automation, Minnesota, 1996, pp 3446-3451
7. BI Shu-sheng, ZONG Guang-hua (2003) Kinematics of Delta parallel mechanism with offsets. ACTA Aeronautica et Astronautica Sinica. 24(1):84-89

Author: Z. D. Hong
Institute: Robotics Institutes of Beihang Universigy
Street: Xueyuan Road No.37, Haidian District
City: Beijing
Country: China
Email: hongzd2002@sina.com

The Study for Multiple Security Mechanism in Healthcare Information System for Elders

C.Y. Huang[1] and J.L. Su[1]

[1]Department of Biomedical Engineering, Chung Yuan Christian University, 200, Chung Pei Rd., Chung Li, Taiwan 32023, R.O.C.

Abstract — **There were many information systems that were applied to healthcare for recent decades. They were consisted of data, databases, and management tools, etc. and the most important works are going to maintain the security and integrity of system and data. In this study, we have used DICOM 3.0 as the data structure of vital signs and images in order to exchange data easier among heterogeneous system and Web service as the port for database connectivity. We used LDAP in JNDI to set a homepage with username and password to authenticate user has entrance authority or not. Key generation in JCE and X.509 in JCA for digital signature achieved encryption and decryption of personal profile and vital signs/images inside DICOM file for private key at client site and public key at server site to ensure the privacy of personal data and integrity of vital signs/images. All of JNDI, JCE, and JCA are security libraries which provided by Java JDK 1.6. We have tested the system security by user with authority or not, and different keys to verify the correctness of decryption/encryption for personal profile and vital signs/images. The preliminary result shows that the healthcare information system for elders we developed has the abilities to check who has the authority to access the data stored in database, personal profile consists inside the DICOM files will keep privacy except the persons who has correct key to decrypt, and also ensure vital signs or image integrity to display. Finally, the system used Java JDK can be easier to achieve the purposes to maintain authority, privacy, and integrity for data and system.**

Keywords — **Digital Imaging and Communications in Medicine (DICOM), JAVA development kit (JDK), Security, Healthcare Information System (HIS).**

I. Introduction

There were many medical information systems developed in recent decades for specific clinical usage. Such as CoMed system that was a real-time collaborative medical system about images and audio of teleconference and relative information of laryngeal diseases by using a multimedia medical database system [1]. It had gotten better security by distinguished degrees of login level. But just used this matter was not enough to make sure the integrity and privacy of data if someone got these data by abnormal manner. Besides, NEMA of USA has announced DICOM 3.0 PS 15 as the standard of security of medical data and medical information system [2] and the law of medical information security and privacy protection in Taiwan was according to Health Insurance Portability and Accountability Act (HIPAA) [3]. Therefore, data encryption before delivery or communication will be necessary to improve data security and privacy. For this reason, there were many researches focus on privacy or security, e.g. data security about remote vital [4], used security agent to implement interconnection of systems [5], and DICOM-Network Attached server oriented in safety to improve the safety for original server in PACS [6].

The previous study implemented the healthcare information system for elders was focused on DICOM files generation middleware for vital signs, stored into a SQL database, and used ActiveX technique to display on homepage [7]. It was not yet concerned about security and integrity of data and personal privacy. As mentioned above, the personnel profile and facial information encapsulated in DICOM file that can be reconstructed personal face must be encrypt for security and privacy. For this purpose, in this study we used the security components supplied by Java JDK version 1.6 [8] to implement the essential authentication control and achieved the security of contents of file for the purposes of system safety and data privacy. The following sections will descript infrastructure of system, materials and methods used for this study, results, and finally will give some discussions and conclusion.

II. System description

The concept architecture of the healthcare information system for elders was implemented as figure 1. At client site, there are two capture devices including vital signs of electrocardiogram and image for visual light real-time image. These data accumulated by a data accumulation PC located beside elders and operated by users who have essential computer knowledge. Before the work of upload and download files, the data should be encoded and encrypted to transfer into an encrypted DICOM file. Then users need to login the website by username and password that are stored in lightweight directory access protocol (LDAP) server to get authentication. In the end, the files were sent through web server would be decrypted and checked integrity and

Chwee Teck Lim, James C.H. Goh (Eds.): ICBME 2008, Proceedings 23, pp. 1009–1013, 2009
www.springerlink.com

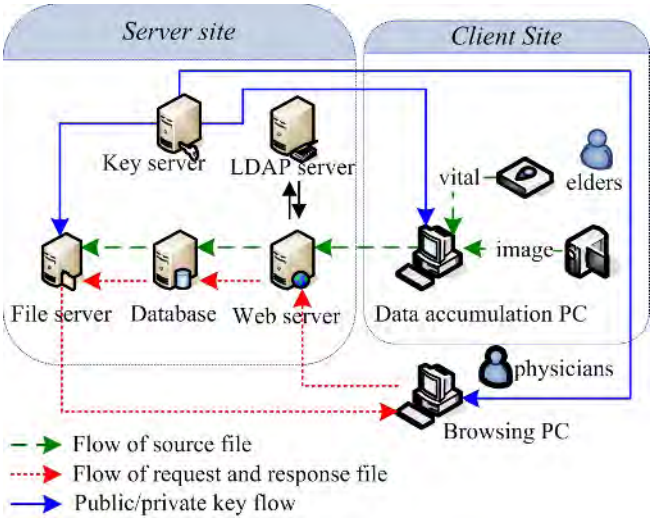


Fig. 1 System architecture

then stored in database/file server. For those who have authorization would review the data about personal profile and other secured profiles by browsing PC.

In this study, we have used the non-encrypted DICOM files included vital signs transferred from MIT-BIH arrhythmia database [9] and visual-light images captured from environment by a real-time USB webcam. The equipments of system were consisted of a Intel® Pentium 1.7 GHz Notebook installed Windows® XP service pack 2 acted as a data accumulation PC and a Intel® Core™ 2 2.4 GHz desktop PC installed Windows® server 2003 acted as web server, database server, and file server. The JSP homepages and Java application were coded both by NetBeans IDE 6.1.

III. Methods

There were many methods used in this study included of JSP, LDAP server, key pair generation, and DICOM encryption/decryption using the keys.

A. DICOM as file format

A DICOM file was constructed of file preamble, 4 chars of 'DICM', and many object groups, e.g. patient, study, series, equipment, image/waveform, etc. and a set of data elements grouped an object. The data elements were consists of tag, optional value representation, value length, and value field. Both of group and element were assigned 2-byte number to consist a specific tag that describes a data element. Then the value length and value field would supply to readout the value of data element correctly. Thus, encryption these object groups were concerned about data security. In this study, we focused on patient profile for privacy and vital/image which were part of analysis data/facial information that were with regard to personal security or integrity.

B. Java server pages (JSP) with Java applications as user interface

For JSP is a server- and platform-independent technology to create dynamic web content. It can change the overall page layout without altering the underlying dynamic content. For the contents of DICOM files are dynamic, JSP would be the adaptive method for implement the Web-based application that is announced by DICOM. Java applications used Java JDK can perform decode/encode, encryption and decryption DICOM files and it will achieve easy implement. Also, the applications can be called and executed by JSP.

C. Security of system and data

- Apache Directory Studio as LDAP server

LDAP server as multi-system entrance has reduced complication for user management by single account/password. Beside, it can distinguish user level and encode data to protect user privacy. Therefore, we used Apache Directory Studio as the role of LDAP server [10]. It provided with LDAP protocol and could run on multi-platform, e.g. Linux and Windows. Using Java naming and directory interface (JNDI) in JDK, JSP and Java application could connect to LDAP server, manage account, and achieve the authentication and authorization service for security of system.

- Key pair generation and Signature certificate

Here we have used Java cryptographic extension (JCE) and Java Cryptography Architecture (JCA), JCE is a part of JCA from JDK 1.4. [11]. Server used KeyPairGenerator to start with key pair generation. First, it decided key length to generate key pair by generateKeyPair() and used getPrivate{}/getPublic{} to get private/public key. The X.509 in JCA used to encode private keys before sent to client by X509EncodedKeySpec Class before transmission and Encoded method returned the key bytes according to the X.509 standard. After that, sent the private key and saved in client to use for DICOM files encryption and the public key was stored in server site for decryption. The digital signature (DS) was generated by using an instance of the Signature class for files in client. Following, file and DS both sent to server site to certificate integrity of data in transmission period.

- Encryption and decryption

As DICOM PS3.15 suggested RSA key pair as the public and private key pair shall be transmitted in an X.509 signature certificate. According to private RSA key encrypts digital signature, there are four tag values shall be embedded into DICOM file including MAC Algorithm (0400,0015) value could be one of "RIPEMD160", "MD5", or "SHA1". Value of Certificate Type (0400,0110) is "X509_1993SIG", Certified Timestamp Type (0400,0305) is "CMS_TSP", and Certified Timestamp (0400,0310) is "Internet X.509 Public Key Infrastructure; Time Stamp Protocols; March 2000".

While accumulation PC got original DICOM files, encryption and transmission progressed. The flowchart for DICOM files encryption and decryption shown as figure 2. In client site, DICOM files encryption would have to decode original DICOM files and then to decide which objects need to be encrypted or non-encrypted. Encrypted-objects were encrypted used private key in encryption process. Finally, all objects would merge with the related public key ID and DS to generate encrypted DICOM files. Then these files transmitted to server through network. When server received encrypted DICOM files, used the public key ID to access the public key stored in server and decoded non-encrypted and encrypted objects simultaneously. Then decrypted the encrypted objects and merged with non-encrypted objects to reconstruct the decrypted DICOM file if DS has certificated correctly.

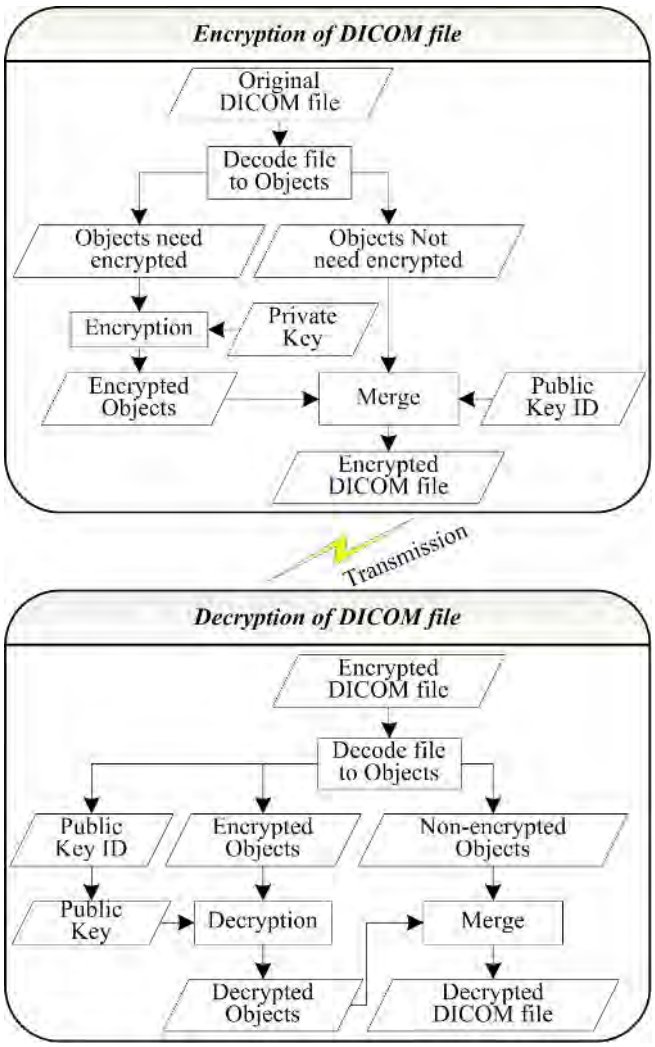


Fig. 2 Flowchart of encryption and decryption of DICOM files

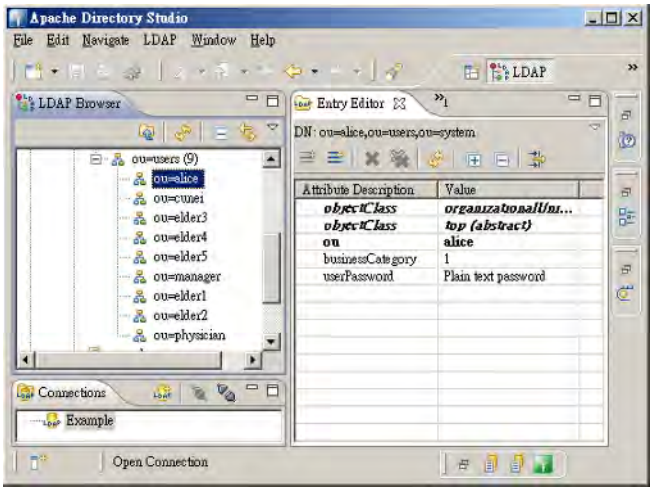


Fig. 3 Apache DS setting for levels of authorization

IV. Results

A. Authentication and Authorization

In this study, we have set three roles of level for users by setting the ApacheDS LDAP server as figure 3 to test authentication for users and about authorization for distinction of data process. Figure 4 shows the implement result of the username and password fields for users to input in main homepage were sent to check coincidence compared to the contents setup in LDAP server by web server. Then it was redirected to achieve the distinguish homepages for levels setting that integrated different functions for Care taker, Care giver, and Management status. It has supplied a mean to authenticate users and give users authorization to achieve the correct procedures resulted from setting LDAP server properly.

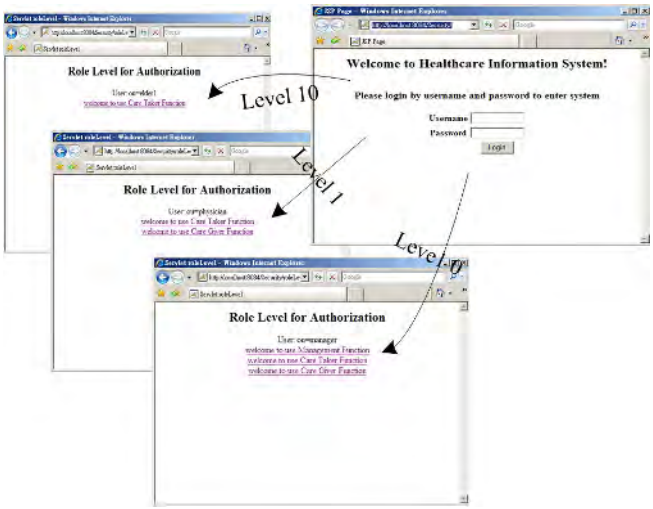


Fig. 4 Homepage for user login with different level to get authorization

B. Encryption and Decryption

There were three kinds of data have been tested for encryption and decryption extracted from DICOM files. They were text-numeric for personal profile, one-dimension vital signs, and two-dimension image. The length of key we used was 512 bits for it was properly for time consumed in CPU operation. Figure 5 was the results have tested by an encryption and decryption Java application. The left side of figure was the original data and right side was decrypted results by corresponding public key about the part of text data as personal profile, graphic vital signs, and environment image. The results of decryption compared by original data and processed data, there were no difference when used the corresponding key of pair but not match when used incongruous keys.

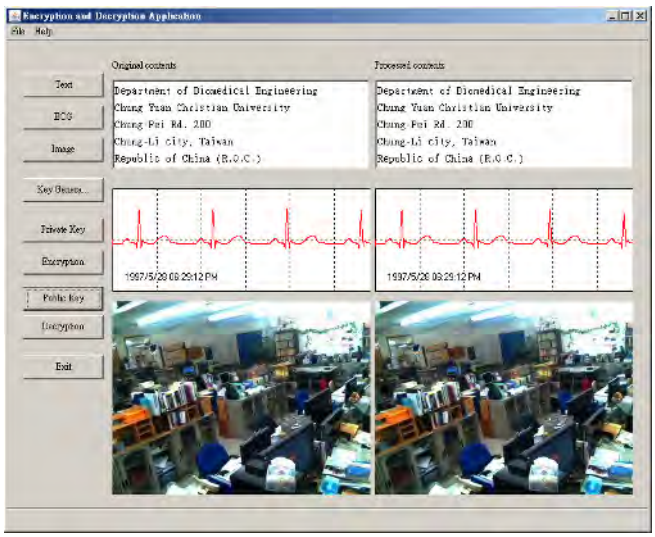


Fig. 5 Test results of encryption and decryption by Java application

V. Discussion

According to the results, we have shown that using Java language and JDK 1.6 supplied by Sun Microsystems® could achieve the purposes of authentication and authorization combined with LDAP server. It means that the levels of users could set and distinguish efficiency. We also could use the LDAP information to enter other information systems only need to connect the LDAP server. Besides, used keys pair generated by JDK security classes would maintain privacy and integrity of data by encryption and decryption worked well by using proper keys length. To combine encrypted data into DICOM files would spread through the heterogeneous healthcare information systems without falsification and readable by users with correct key.

VI. Conclusions

In this paper, we have presented to use JSP and JDK to achieve authentication by connecting LDAP server, keys pair of generation for encryption and decryption to reach the purpose of data privacy and integrity. For development of HIS for elders, next we will focus our efforts on software agents for automatic events detection and upload events with encryption. It is necessary for health care giver to reduce necessary of manpower by avoiding operation of the routine works about reviewing vital signs and images and uploading recorded files.

Acknowledgments

This work was supported in part by National Science Council, Taiwan, R.O.C., under Grant NSC 95-2221-E-033-033-MY3 and NSC 95-2221-E-033-071-MY3.

References

1. Sung MY, Kim MS, Kim EJ et al. (2000) CoMed: a real-time collaborative medicine system. Int J Med Inform 57:117-126
2. Digital Imaging and Communications in Medicine (DICOM) at http://medical.nema.org/
3. Health Insurance Portability and Accountability Act (HIPAA) at http://www.hhs.gov/ocr/hipaa/

4. Gritzalis D and Lambrinoudakis C (2000) A data protection scheme for a remote vital signs monitoring healthcare service. Med Inform 25:207-224
5. Gritzalis D and Lambrinoudakis C (2004) A security architecture for interconnecting health information systems. Int J Med Inform 73:305-309
6. Tachibana H, Omatsu M, and Higuchi K, and Umeda T (2006) Design and development of a secure DICOM-Network Attached Server. Comput Meth Prog Bio. 81:197-202.
7. Huang, CY and Su, JL (2007) A middleware of DICOM and Web service for home-based elder healthcare information system, Proc. of the IEEE/EMBS Region 8, Int. Conf. on Inform. Tech. App. Biomed., ITAB, Tokyo, Japan, 2007, pp 182-185
8. JDK at http://java.sun.com/
9. PhysioNet at http://www.physionet.org/
10. Apache Directory Studio at http://directory.apache.org/studio/
11. Java SE security at http://java.sun.com/javase/technologies/security/

Author: Chang-Yi Huang
Institute: Chung Yuan Christian University/Department of Biomedical Engineering
Street: 200, Chung Pei Rd.
City: Chung Li
Country: Taiwan, R.O.C.
Email: g9302503@cycu.edu.tw
Coauthor: Jenn-Lung Su
Email: jlsu@cycu.edu.tw

Individual Movement Trajectories in Smart Homes

M. Chan[1,2], S. Bonhomme[1,2], D. Estève[1,2], E. Campo[1,3]

[1]LAAS-CNRS ; Université de Toulouse ; 7, avenue du Colonel Roche, F-31077 Toulouse, France
[2]Université de Toulouse ; UPS
[3]Université de Toulouse ; UTM

Abstract — **A project in innovation technology for the advancement of smart home to help elderly is conducted. The aim is to anticipate the dangerous situations that may happen at home (fall, restlessness, fainting, running away etc.) trough individual data collection and analysis of movement trajectories. This paper describes a conceptual space/time model of movement trajectories (beginning, end, stop and move). These models can be used for danger prevention in smart home. Results are presented for apartment scenarios and individual movement trajectories.**

Keywords — **individual movement trajectory, elderly, multisensor home system.**

I. Introduction

The problem of caring for elderly and people with physical disabilities will become more serious when a significant part of the increasing global population is in the 65 or over age group. In addition, the existing welfare model is not able to meet the increased needs. According to Eurostat, 12.1 % of the Europeans will be aged over 80 and 30 % will be over 60 in 2060 [1]. The wish to improve the quality of life for disabled and the rapid growth in the number of elderly has prompted an uncommon effort from both industry and academia to develop smart home technology. Currently, a significant number of dedicated smart home projects are being carried out throughout the industrialized world [2]. It has been shown that the ability to correctly identify mobility of occupants may have significant implications and applications in smart home. For example it may support independent living as people age at low costs [3]. Due to progress in electronics and information technology, one of key components in the development of smart home is detection and recognition of activities or mobility of daily life. For instance, in an attempt to develop a smart home environment, we introduce the concept of individual movement trajectory to monitor the mobility of the occupants. Individual movement trajectories have been considered as the path followed by an individual moving in space and time. Each point in this path represents one location in space and one instant in time. Typically, trajectory data are obtained from devices that capture the location of individual at specific time intervals. The background geographical information on which the individual is moving indoor or outdoor is of fundamental importance for the analysis of trajectory data. In this paper, we define the concept of individual movement trajectory as a set of moves and stops with a beginning and an end and the geographical location [4]. Some examples of movement trajectories of subject living in an institution and the system used to gather raw data are presented. The discovered travel patterns are stored in the movement trajectory database with the events linked to the data, in order to help the user (physician, caregiver, family members) to comprehend, visualize and question movement trajectory pattern relationships of elderly and disabled living alone for safety purpose.

II. Material and Method

A. Case Study

Multisensor system: The system is composed of infrared sensors (S1 to S10) with a binary output, a personal computer (PC), and a communication network connecting the sensors to the PC. Software collects raw data and processes them to assess automatically among variables (getting up, getting out, going to bed, going to washroom, and restlessness in bed or in apartment) the travel patterns of selected residents. The multisensor system is installed in a room of a setting for elderly. Ten areas are defined according to Figure 1. The PC is in the staff room. When a participant travels through the areas of the room, the sensors are activated. In real time the PC through the acquisition card acquires the

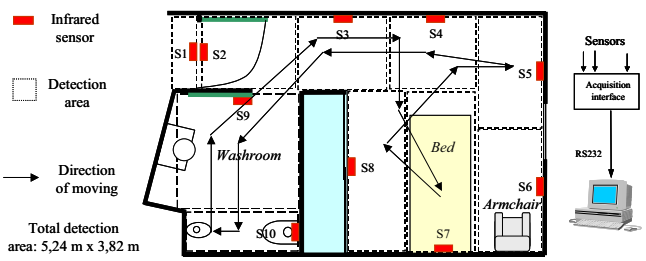


Figure 1. Multisensor system

Chwee Teck Lim, James C.H. Goh (Eds.): ICBME 2008, Proceedings 23, pp. 1014–1018, 2009
www.springerlink.com

data, which are a collection of 10 binary bits (1 or 0) corresponding to the activity of each sensor (on or off). The date of the day is stored with the data [3].

B. Trajectories: Definitions

Definition 1 (Trajectory): A trajectory is a set of ordered stops and moves in a precise geographical location indoor or outdoor, with a beginning and an end.

Definition 2 (Stop): A stop occurs when the subject is motionless. A non-empty time interval represents a stop.

Definition 3 (Move): A move in a trajectory has a time interval; it is preceded by a stop and is followed by another stop.

Definition 4 (Spatial characteristic type): A spatial characteristic type is located in the geographical earth surface indoor or outdoor.

Definition 5 (Sub-trajectory): Each trajectory is a set of sub-trajectories.

C. Sub-trajectories: Definitions

In a movement trajectory, a participant's activity is represented as a sub-trajectory. The participant must be alone; the multisensor system can't distinguish the movements of two participants in the same area. Indeed, the participant doesn't carry any electronic device.

Definition 6 (Going to bed): The participant activates a series of sensors as shown in Figure 1, from stop 1, an area adjacent to bed (S6, S5, S4, S3 or S8) he gets to stop 2, which is bed area.

Definition 7 (Getting up): The reverse procedure of going to bed confirms getting up.

Definition 8 (Getting in): The participant from stop 1 (area 1) gets to stop 2 (area 2).

Definition 9 (Getting out): The participant wanders in the room and then gets out. From stop 1 (area 2), he gets to stop 2 (area 1).

Definition 10 (Going to washrooms): The participant from stop 1 (area 2) gets in stop 2 (area 9).

Definition 11 (Going out to washroom): The participant from stop 1 (area 9) gets in stop 2 (area 2).

Definition 12 (Immobility or stop): The area 0 is artificial or virtual; if the area is 0 in stop 1, that means 10 sensors are in inactive state. In Table 1, from stop 1 (area 0) to stop 2 (area 3), the duration of immobility is 2.5 s. The multisensory system detects the participant at area 3 at 21:19:12.5, but doesn't know where the motionless participant is at 21:19:10.0.

Definition 13 (Restlessness): The multisensor system observes the series of sensor activations as shown in Table 2. In order to optimize data storage, raw data are stored as shown in Table 4. In this case, several stops and moves are in the same area, as shown in Table 3. In this case, a threshold t_s is defined, the participant in a specific area triggers the sensor at t_i and, at t_{i+1}. If $(t_{i+1} - t_i) > t_s$, the participant is quiet, and if $(t_{i+1} - t_i) < t_s$, the participant is restless [5].

Definition 14 (Mobility or move): The participant travels from stop 1 (area 7) to stop 2 (area 3), the time intervals is 50.5s. From stop 1 (area 3) to stop 2 (area 6), the time interval is 4s as shown in Tabs 4 and 5.

Table 1. Immobility sub-trajectory
Duration in seconds

Move	Stop 1	Stop 2	Time Interval (h min s)	Duration
1	0	3	21:19:10.0-21:19:12.5	2.5

Table 2. Restlessness sub-trajectory
Duration in seconds

Move	Stop 1	Stop 2	Time Interval (h min s)	Duration
1	7	7	21:19:10.0-21:19:10.5	0.5
2	7	7	21:19:10.5-21:19:11.0	0.5
3	7	7	21:19:11.0-21:19:11.5	0.5
4	7	7	21:19:11.5-21:19:12.0	0.5
5	7	0	21:19:12.0-21:19:12.5	0.5

Table 3. Restlessness sub-trajectory
Duration in seconds

Move	Stop 1	Stop 2	Time Interval (h min s)	Duration
1	7	0	21:19:10.0-21:19:12.5	2.5

Table 4. Mobility sub-trajectory
Duration in seconds

Move	Stop 1	Stop 2	Time Interval (h min s)	Duration
1	7	0	04:19:10.0-04:19:10.5	0.5
2	0	3	04:19:10.5-04:20:00.5	50
3	3	0	04:20:00.5-04:20:02.5	2
4	0	6	04:20:02.5-04:20:04.5	2

Table 5. Mobility sub-trajectory
Duration in seconds

Move	Stop 1	Stop 2	Time Interval (h min s)	Duration
1	7	3	04:19:10.0-04:20:00.5	50.5
2	3	6	04:20:00.5-04:20:04.5	4

D. Results

A subject of 81 years old took part in the trial. The participant or his family signed an informed consent administered by the nursing staff before the trial. During the eight

months trial, he occupied his apartment in the night and was observed from 9 pm to 7 am. During the day, he was out of his apartment and took part in group activities in the institution. The participant got up 36 nights. Table 6 gives the results obtained with these 36 nights. The nursing staff noticed their getting in and out the participant room and the participant night activities after direct observation. These staff ratings allowed the concordance between staff ratings and automatic data processing to be verified and validated for assessing the resident travel behaviors.

Table 6. 36 night activities

Nights	Activities
28	getting up/wandering in the bedroom/visiting washroom
3	getting up/wandering in the bedroom/visiting washroom/getting out
5	getting up/wandering in the bedroom

Table 7. An example of movement trajectory
Duration in seconds

Move	Stop 1	Stop 2	Time Interval (h min s)	Duration
1	0	7	21:19:10-21:20:11	61
2	7	0	21:20:11-21:20:12	1
3	5	0	21:20:12-21:21:02	50
4	5	6	21:21:02-21:21:04	2
5	6	0	21:21:04-21:21:06	2
6	6	7	21:21:06-21:21:12	6
7	7	5	21:21:12-21:21:17	5
8	5	0	21:21:17-21:21:23	6
9	5	4	21:21:23-21:21:24	1
10	4	3	21:21:24-21:21:26	2
11	3	2	21:21:26-21:21:30	4
12	2	9	21:21:30-21:21:34	4
13	9	10	21:21:34-21:21:39	5
14	10	0	21:21:39-21:23:14	95
15	10	9	21:23:14-21:23:18	4
16	9	0	21:23:18-21:25:00	102
17	9	2	21:25:00-21:25:15	15
18	2	3	21:25:15-21:25:16	1
19	3	8	21:25:16-21:25:18	2
20	8	0	21:25:18-21:25:23	5
21	8	3	21:25:23-21:25:24	1
22	3	2	21:25:24-21:25:26	2
23	2	0	21:25:26-21:25:31	5
24	2	1	21:25:31-21:25:32	1
25	1	0	21:25:32-21:25:37	5
26	1	2	21:25:37-21:25:39	2
27	2	1	21:25:39-21:25:40	1
28	1	0	21:25:40-21:43:59	19
29	1	2	21:43:59-21:44:00	1
30	2	1	21:44:00-21:44:01	1
31	1	0	21:44:01-21:44:05	4
32	1	2	21:44:05-21:44:07	2
33	2	0	21:44:07-21:44:09	2
34	2	3	21:44:09-21:44:14	5
35	3	8	21:44:14-21:44:20	6
36	8	7	21:44:20-21:44:36	16

The movement trajectory as shown in Table 7 includes several sub-trajectories:

- Motionless or stop in area 7 during 61s.
- Restlessness in areas 5, 10, 9 and 8 during respectively 50 s, 95 s, 102s and 16s.
- Going out in area 1 during 19s.
- Going from one area to another area with durations ranging between 1s and 6s.
- For area 5, which is a location adjacent to bed, the participant may remain restless 50s or in his bed. The multisensory system distinguishes with difficulty restless period in bed or in area 5 as shown in Figure 1. A pressure sensor placed in bed could really prove the participant in bed.
- Areas 6, 5, 4, 3, 8 are locations for traveling from one stop to another stop.
- Table 8 shows durations of moves or stops for different areas that the participant traveled.

Table 8. Mobility sub-trajectories

Area	Duration (s)	Mobility/Immobility
9	102	in washroom and restless
10	95	in washroom and restless
7	61	in bed and motionless
5	50	restless
1	19	outside
8	16	restless
9	15	restless
6, 5, 3	6	restless
7, 9, 8, 2, 1	5	restless
3, 2, 1	4	restless and outside (area 1)
5, 6, 4, 3, 2, 1	2	restless and outside (area 1)
7, 5, 2, 8, 1	1	restless and outside (area 1)

Table 9. Duration of stop or move in each area

Area	Duration (s)
1	19, 5, 8, 2 x 2, 1
2	5x2, 4, 2, 4 x 1
3	6, 4, 2 x 2
4	2
5	50, 6, 2, 1
6	6, 2
7	62, 5, 1
8	16, 5, 1
9	102, 15, 5
10	95, 4

Tabs 8 and 9 summarize the results given in Table 7 and shows that the participant got up once from 21:20:11 to 21:44:36. He was in bed in the beginning and immobile (area 0). He was restless in 10 areas and remained restless in 9 and 10, and was probably preparing to get up in 5, he

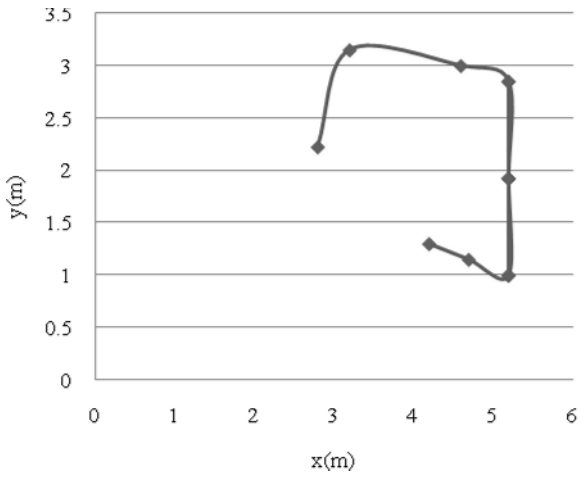


Figure 2. Participant movement sub-trajectories

remained restless during 50s, that was probably the bed area and not really area 5. At 21:21:12, he was in area 7, but probably not in bed.

Figs 2 and 3 show a participant movement trajectories from one location to another location. The location of the beginning is area 7 (Figs 2 and 3) and the location of the end is area 3 (Fig 2) and area 7 (Fig 3). Figure 3 shows 3 activities according to Table 7 (getting up, wandering in the bedroom, going to washroom and going out three times) and most sub-trajectories are direct (from bed to washroom). If it is supposed that from one area to another area, the subject covers approximately 1m. The speed of the move from area 5 to area 2 is 0.23m/s or 830m/h (duration 13s and covered distance 3m according to Table 6). Covered distances and travel speeds could be calculated for sub-trajectories and distance and speed thresholds could be defined for elderly monitoring procedure for safety purpose.

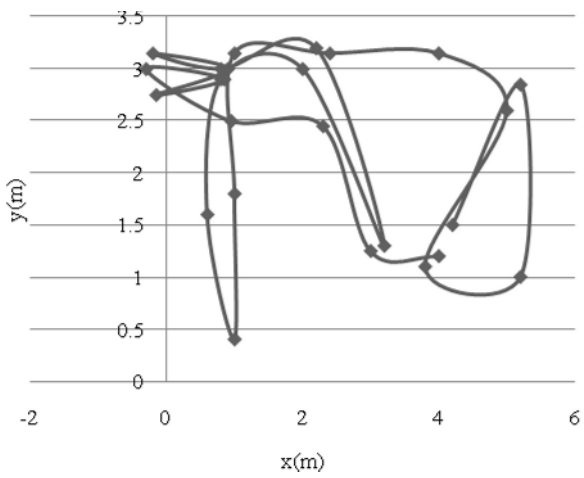


Figure 3. Participant movement trajectory

III. Conclusions

Using a multisensor system allows to collect individual movement trajectory and to estimate covered distances and travel speeds. Due to adjacent areas in the room specifically around the bed (areas 6, 5, 4, 3 and 8), the individual trajectory pattern relationships are hard to be visually identified because the adjacent areas are not easy to be visually identified and can lead to some errors. So a precise location of the infrared sensors is crucial. An attempt to classify different patterns of individual movement trajectories was carried out. Only sub-trajectories were classified [6]. The results show here the participant occupying bed and washroom (respectively 61s, 95s and 102s) and some direct movement sub-trajectories [7]. Choosing a beginning area and an end area for an individual movement trajectory and ordering the durations for moves and stops as shown in Table 8 and Table 9 allow better to comprehend the relationship between stop or move durations and areas in movement trajectories, even covered distances and speeds. Individual movement trajectories could be used to better identify abnormal trajectories in order to ensure security and safety of older individuals living alone instead of condemning then to go to institution and to leave their own home.

Acknowledgment

The authors would like to acknowledge the French Ministry Research New Technology (RNTS) and EDF Research and Development for their support.

References

1. Rodier A. (2008) Union européenne: le défi du vieillissement. In Le Monde September 1st, 2008.
2. Chan M., Estève D., Escriba C., and Campo E. (2008) A review of smart homes—Present state and future challenges. Computer Methods and Programs in Biomedicine 91:55-81.
3. Chan M., Bocquet H., Campo E., Val T., and Pous J. (1999) Alarm communication network to help carers of elderly for safety purposes: a survey of a project. Journal of the Rehabilitation Research 22(2): 131-136.
4. Spaccapietra S., Parent C., Damiani M. L., Antonio de Macedo J., Porto F., and Vangenot C. (2008) A conceptual view on trajectories. Data & Knowledge Engineering 65(1):126-146.

5. Chan M., Campo E., Laval E., and Estève D. (2002) Validation of a remote monitoring system for the elderly: Application to mobility measurements. Technology and Health Care 10:391-399.
6. Chan M., Campo E., and Estève D. (2004) Classification of elderly repetitive trajectories for an automatic behaiour monitoring system. In Proceedings Mediterranean Conference on Medical and Biological engineering "Health in the Information Society" (MEDICON 2004), Island of Ischia, Naples (Italy), July 31 – August 5, 2004, 4p.
7. Martino-Saltzman D., Blash B. B., Morris R. D., and Wynn McNeal L. (1991) Travel behavior of nursing home residents perceived as wanderers and nonwanderers. The Gerontologist 31(5):666-672.

Corresponding author:

Author: Chan Marie
Institute: LAAS-CNRS
Street: 7 avenue du Colonel Roche
City: 31077 Toulouse cedex 4
Country: France
Email: chan@laas.fr

MR Image Reconstruction for Positioning Verification with a Virtual Simulation System for Radiation Therapy

C.F. Jiang, C.H. Huang, T.S. Su

Department of Biomedical Engineering, I-Shou University, Kaohsiung, Taiwan, R.O.C

Abstract — **This paper proposes a systematic method for 3D reconstruction of the MR images of a head to create a virtual radiation target for positioning verification in the treatment planning of radiotherapy. According to different features in the scalp and the brain, two different methods were applied to segment the entities. The scalp was detected by auto-thresholding and the brain was segmented by region-growing. The detected contours were then reconstructed as the 3D polygon meshes and transformed into VRML format to be presented in the virtual simulation environment. This scheme is further implemented as a module embedded in a virtual simulation system of 3D Conformal Radiotherapy (3D-CRT). System verification was achieved by using a full scale AP model of a human head as a target volume for positioning verification. We compared the positioning of the AP model in the real and virtual systems and found that the measurements were very close (difference < 0.3 cm). This state of the art integrates the techniques of image processing, computer graphics and virtual reality. With the assistance of the system, the position verification process may become more efficient and accurate than the conventional positioning toolkit only based on 2D image registration.**

Keywords — **MR image, 3D reconstruction, positioning verification, radiotherapy.**

I. Introduction

Radiotherapy is one of the most important methods to treat cancers nowadays. Since radiation can also damage the normal cells, treatment planning, which includes beam field design and dose calculation prior to radiotherapy is an essential work to reduce the chance of receiving radiation by the normal cells. Patient positioning verification is a routine work to confirm the meet of the radiation target to the planning target, in such a way to reduce the harm of the radiation to the normal tissue and meanwhile to increase the radiation effect to the malignant tissue. Thus patient positioning verification is the first key to a successful radiotherapy.

The three dimensional conformal radiotherapy (3D-CRT) has been introduced to improve the limitation of the regular field shape in the conventional 2D treatment planning system by shaping a target volume in a 3D imaging study, namely, the 3D treatment planning [1]. During the 3D planning, the target shape in MRI images has to be delineated manually on a slice-by-slice basis. After that the target volume is reconstructed and projected into 2D images planes from different angles within a cycle of gantry rotation by using the proprietary software, which is usually bundled with the radiation system. The optimal radiation field is determined by inspecting the target position in the projected image planes from the radiation beam's eye view. Accordingly, the 3D irregular field shape, called prescription volume, which conforms to the target volume can be achieved by figuring the beam portals at each angle and adjusting the length of each leaf in the multi-leaf collimator (MLC). However, the planning process of the 3D-CRT is labor intensive and sometimes need recurring verifications with the patient on site. The overall process can be a physical as well as spiritual torture for a patient. Thus, the 3D-CRT need to encompass a component which can save the labor, accelerate the time, and most importantly decrease the occurrences of patient visits.

Recent works have proposed a collaborative virtual environment as a platform of radiation treatment planning for easy communication in telemedicine [2-3]. In our previous works, we had at first developed a virtual radiation simulator for the training purpose [4]. A virtual linear accelerator associated with a virtual MLC was later integrated with the simulator as a double-platform simulation system [5]. The setting parameters, such as the gantry rotating angle, and the altitude and position of the patient table in the simulation room can be exactly transferred into the treatment room in order to verify the adequacy of both environment setting. However, the target volume used in this prototype is a virtual head, obtained by laser scanning of a full scale 3D solid anthropometric model (AP model) to replace the real patient for positioning and verification in treatment planning. The high-expense and non-deformability of the AP model make it not adapted to case varieties. As a result, the application of the virtual system is restricted to training purposes.

In this study, we propose an MRI image reconstruction scheme based on image segmentation techniques to create a target volume. This scheme is then further integrated into the virtual system as the rendering module of target volume for positioning verification directly in a 3D space. With the

Chwee Teck Lim, James C.H. Goh (Eds.): ICBME 2008, Proceedings 23, pp. 1019–1023, 2009
www.springerlink.com

assistance of this module, the target volume can be generated in an efficient way and the virtual radiation simulation system is prone to an economical solution for clinical application.

II. Methods

A. MR Image Reconstruction

In order to create a 3D polygon mesh of the target, we need to detect the target contours first. Two methods are applied to segment the tissue according to its appearance differentiable by its intensity or by its texture from its surroundings. The MR images used in this pilot study are obtained from the Database of the Virtual Human Project [6]. An example of the original MR image is given in Fig. 3a where the brain is more texture-like, while the head contour is the outmost layer brighter than the background. The segmentation is described in details as follows.

1. Image Segmentation by thresholding

For the tissue with great intensity gradient in the MR images, such as the scalp, we applied the auto-thresholding method developed by Ostu [7] to binarize the image. Due to the double-mode nature of the intensity histogram of MR images, we modified the one-threshold algorithm to a double-threshold one for detection of the head contour. The algorithm derives the optimal thresholds k_1^* and k_2^* to separate objects by maximizing the between-class variance σ_B^2.

$$\delta_B^2(k_1,k_2) = w_0(\mu_0-\mu_T)^2 + w_1(\mu_1-\mu_T)^2 + w_2(\mu_2-\mu_T)^2 \quad (1)$$

$$\delta_B^2(k_1^*,k_2^*) = \max_{1\le k_1<k_2<L} \delta_B^2(k_1,k_2) \quad (2)$$

where w_0, w_1 and w_2 are the probabilities of the three non-overlapping classes in the images, μ_0 , μ_1 and μ_2 are their mean gray values, and μ_T is the mean gray value of the entire image. An optimal set of thresholds k_1^* and k_2^* can be selected by maximizing σ_B^2.

Following that, we used morphological image processing techniques [8] to refine the segmented entity—first using 'fill' to seal the holes inside the head and then 'opening' to remove the resulting binarization debris outside the head.
"fill" operation :

2. Image Segmentation by region growing

For the tissue with its texture different to its surroundings in the MR images, such as the brain, we applied the region growing algorithm for its segmentation [9]. It starts by selecting a seed point, *s*, inside the brain area and forms the grow regions by appending to the seed the four orthogonal neighboring pixels that meet the growing criteria. Two major criteria control the growing process — a similarity criterion that selects the pixel to merge into the region and a stopping criterion that stops the growth of the region. The region growing proceeds with the similarity criterion, which is defined as a limited intensity difference, δ, between the target pixel, *p*, and the seed, *s*.

$$R^i = R^{i-1} \cup \{p \mid I(p) - I(s) < \delta\} \quad (3)$$

The seed, *s*, is updated as the mean intensity of the new growing region for each iteration. The stopping criterion is predefined as the region that exceeds the union of the brain areas manually outlined in the three orthogonal planes.

3. Contour Detection

Once the region of interest (ROI) is segmented by using the pre-described methods, the contours of the regions can be simply detected by searching the first gradient radiating outwards from the centroid of the ROI.

4. Polygon Mesh Creation

Based on these detected contours, the polygons mesh interconnecting the contours can be created by using minimum distance method [10], which is performed by looking the nearest points at the contours in two adjacent slices. The baseline of the first triangle was drawn by joining the first point of each adjacent contour. The next point in each adjacent contour with the minimum distance to the baseline was selected. These three points formed a triangle. The following points are connected together in the same way to form a polygon mesh.

B. Integration into the VSS

The created polygon mesh was transformed into VRML format and its size was adjusted according to the scale ratio predefined by the measures of objects' sizes in real and in virtual. All objects in the system had been scaled down according to this scale ratio. A virtual head holder was created at a fixed position on the table to allocate the virtual target when the VRML file was read into the virtual simulation system.

C. System Verification

System verification was achieved by using the full scale AP model of a human head created in our previous approach [4-5] as a target volume for positioning verification. (Fig.1 and Fig.2) We assumed that if the calibration of the virtual system simulation was correct, when transferring the whole setting in the real environment into the virtual sys-

tem, the position of the isocenter (the center of the beam) in the virtual system should be the same as in the real. There was a minute difference (< 0.3 cm) between these two measurements. This error could be due to the projection bending of the scalar on a head contour in real case (Fig. 1) rather than on a plane in virtual case (Fig. 2).

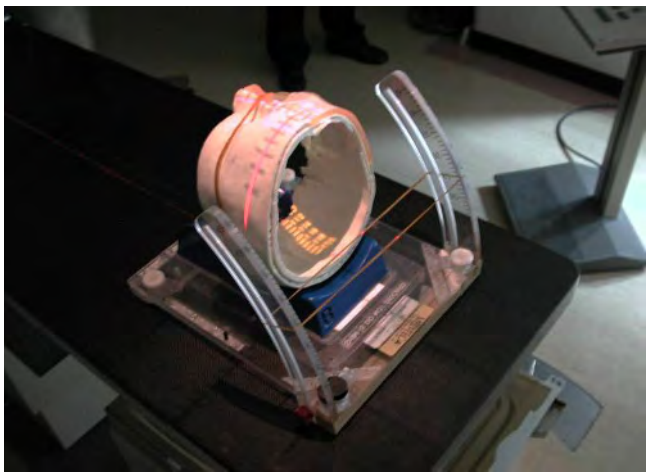


Fig. 1 The position of AP model within the head frame is set to align the tumor (facing inside) with the isocenter.

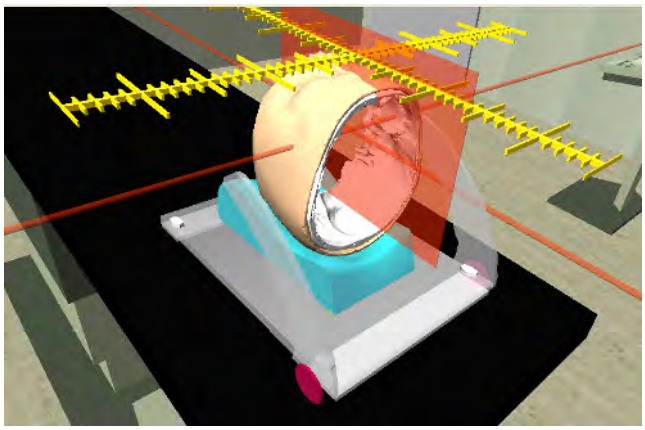


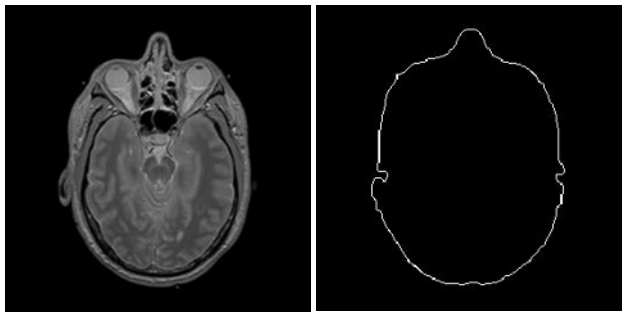
Fig. 2 The calibration in virtual system is verified by the same position setting as in Fig.1 with the virtual scalar on the top of the virtual AP model. The vertical plane at the center is an extension of the laser beam for easy identification of the isocenter location.

III. Results

The results will be presented in two aspects— first regarding the MR image segmentation and reconstruction, and second about integration of the target loading module with the virtual simulation system.

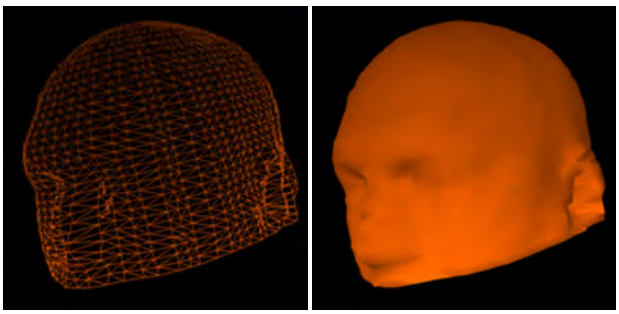
A. Image Processing and Reconstruction

Figure 3b shows the detected contour of Fig. 3a via the double-thresholding technique followed by two-step morphological image processing and maximum gradient detection. Fig. 4a demonstrates the polygon mesh achieved by interconnected the adjacent contours with minimum distance criteria and Fig 4 (b) shows its rendering surface. The same way is applied to generate the brain mesh except the segmentation method that is based on region growing. The two meshes are created separately as two data sets and can be combined together when being loaded by using the target loading module described later.



(a) (b)

Fig. 3 (a) MR image of a head and (b) the corresponding detected head contour (see details in the text.)



(a) (b)

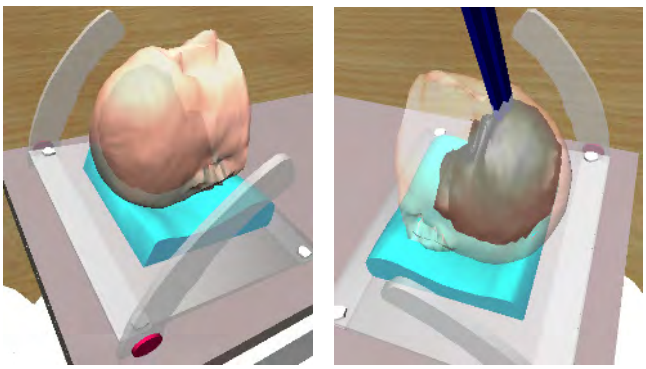
Fig. 4 (a) polygon mesh of the head and (b) surface rendering of the head

B. Integration of the Module into the VS System

In this module, an interface was designed to select and load the polygon mesh files into the VR-scene on the virtual head holder. The VRML-format mesh files can be multi-selected and rendered together as an entity, such as the head with a brain inside (Fig.5a).

The virtual system also provides a MLC configuration function and immediately reveals the 3D beam with color as

the result of the configuration. The visibility of the beam provides an easy way to assure that the 3D radiation beam cover the target volume optimally as shown in Fig.5b. In the position verification, the virtual scalar can be turned on as the reference for the radiation field delineation in comparison with that in the portal film.



(a) (b)

Fig. 5 (a)The reconstructed head with the brain inside had been load into the virtual system; (b) preview of the beam shape and irradiation fields in the virtual system with different rotation angles of the gantry.

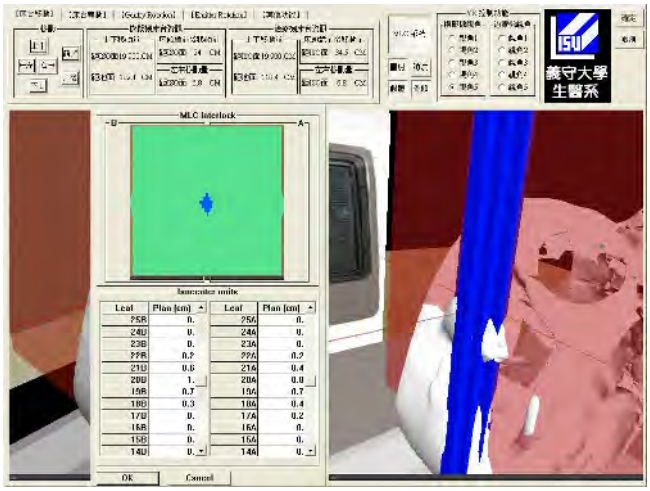


Fig. 6 An example to demonstrate that the VS system also provide a function of on-line MLC design. The result can be viewed immediately with the loaded virtual target.

The intersection of the virtual beam and the target volume can be inspected from different angles as shown in Fig.6 to verify the adequacy of the gantry angle and the MLC configuration.

IV. Discussion and Conclusions

We propose the MR image processing method to reconstruct the target volume for positioning verification in 3D Conformal Radiotherapy. A module with this MR image processing function is integrated into a virtual simulation system previous developed by us in order to load the reconstructed 3D target in this virtual scene such that the commitment between the radiation beam field and the target can be investigated with a 3D global view. The system verification shows the precision less than 0.3 cm. To achieve this precision, the VR system needs to be customized according to the real objects in the radiation treatment room. Nevertheless, this is easy to fulfill by the commercialized computer graphic packages. The key to make this system applicable in clinics is the capability to embed the various target volume of the real patients in this system. In other words, to make a virtual system able to contain a real 3D data from medical images is the aim of this study. Thus we believe that the upgraded system with the newly developed module has the potential for clinical use.

At this stage we only consider the targets in the same image data set; therefore registration is not necessary. However, the image processing module will be further expand is this regards.

Acknowledgment

This work was supported in part by the grant from the National Science Council (NSC 95-2221-E-214-005)

References

1. S. Webb (1993)The physics of three-dimensional radiation therapy, London, U.K: Institute of Physics Publishing,
2. Ntasis, E., Maniatis, T. A., and Nikita, K. S. (2002) Real-time collaborative environment for radiation treatment planning virtual simulation, IEEE Trans. Biomed. Eng. 49(12): 1444-1451.
3. Ntasis, E., et al, (2005) Telematics enabled virtual simulation system for radiation treatment planning, Comput. Biol. Med. 35: 765–781.
4. T.S. Su, D.K. Chen, W.H. Sung, C.F. Jiang, S.P. Sun, and C.J. Wu (2005) Development of a virtual simulation environment for radiation treatment planning, J. Med. Bio. Eng. *25*(2): 61-66
5. T.S. Su, W.H. Sung, C.F. Jiang, S.P. Sun, and C.J. Wu (2005) The development of a VR-based treatment planning system for oncology, Proc. of 27th IEEE Conference of the Engineering in Medicine and Biology Society (EMBC05), 2005.
6. National Library of Medicine. The visible human project, National Institute of Health, U.S., http://www.nlm.nih.gov/research/visible/visible_human.html

7. N. OTSU(1979) A threshold selection method from gray-level histograms. IEEE Trans. SMC,9, 62-66
8. Gonzalez RC, Woods RE. (2002) Digital image processing, Upper Saddle River, NJ, Prentice-Hall Press;.
9. A.P. Dhawan (2003) Medical image analysis, Hoboken, New Jersey, John Wiley & Sons, Inc.
10. A.B Ekoule, F.C. Peyrin, and C.L. Odet (1991) A triangulation algorithm from arbitrary shaped multiple planar contours, *ACM Trans. Graphics, 10*(2), 182-199.

Author: Ching-Fen Jiang
Institute: I-Shou University
Street: No. 1, Sec.1, Hsueh-Cheng Rd, Ta-Hsu Hsiang
City: Kaohsiung
Country: Taiwan, R.O.C
Email: cfjiang@isu.edu.tw

Experimental setup of hemilarynx model for microlaryngeal surgery applications

J.Q. Choo[1], D.P.C. Lau[2], C.K. Chui[1], T. Yang[1], S.H. Teoh[1]

[1]Department of Mechanical Engineering, National University of Singapore, Singapore
[2]Department of Otolaryngology, Singapore General Hospital, Singapore

Abstract — **Mechanical models of the human larynx have been used to validate mathematical vocal cord models, but most lack the applicability for ex-vivo surgical experiments. To our best knowledge, no technical evaluation has been reported using mechanical models to study vocal cord wound closure techniques. We design and develop a customizable and versatile mechanical hemilarynx with direct simulation of vocal cord vibration and airflow that can facilitate ex-vivo surgical experiments on the vocal cord. This setup enables experimental validation on the mechanical stability of novel devices, which are currently developed for epithelial wound closure in microlaryngeal surgery.**

Keywords — **hemilarynx, microlaryngeal surgery, wound closure.**

I. Introduction

Current practices in wound closure following endoscopic surgery to the vocal fold include sutures or tissue adhesives. These methods have proven technically difficult to achieve in such minimal access surgeries or yield less than optimum healing results respectively [1, 2, 3]. Our team is in the process of design and development of novel epithelial wound closure devices that can be easily handled and inserted onto the vocal fold cover with microlaryngeal surgical instruments. These devices must be able to withstand loadings induced by vocal fold vibration and glottal airflow. Experimental validation of these novel wound closure devices via a mechanical larynx model is a crucial and integral step to address limitations and complement results of other analyses, such as Finite Element simulation on these devices.

Many mechanical models of the human larynx have been designed to validate mathematical models of the vocal fold [4, 5]. However, none of these models has been applied in the study of vocal fold wound closure techniques to our best knowledge. These mechanical setups of the larynx lack the applicability and customizability for ex- vivo surgical experiments.

In this paper, we design and develop a simple and customizable mechanical larynx setup for ex- vivo surgical experiments with direct simulation of vocal fold vibration and glottal airflow. This setup serves as a medium to study vocal fold wound closure methods in ex-vivo surgical experiments, with focus on prototype wound closure devices that our team has designed. The efficacies of anchoring and mechanical stability of these devices under flow and vibration conditions can be assessed and evaluated using the model.

A mechanical hemilarynx setup, with one vocal fold replica opposite a flat wall, was designed [4, 6]. The use of a hemilarynx setup eliminates geometrical incongruence that occurs due to inconsistent membrane construction and adhesion on opposing airway walls [6]. This setup correlates most closely with the clinical situation when patients undergo removal of a diseased vocal fold (cordectomy).

II. Materials and Methods

The mechanical hemilarynx consists of a detachable vocal cord piece within a Perspex flow channel. This fits into a wooden casing connected to an external airflow supply.

The components of the Perspex flow channel consist of 2 Perspex boards of thickness, interconnected with a Perspex board of thickness, with a hole serves as an airflow outlet. Four guiding screws of size M5 connect a detachable vocal fold replica piece made of Perspex onto the medial surface of one of the Perspex boards. These screws have partial threads removed, such that the vocal cord piece can slide freely along the screw track. It is assembled as shown in Figure 1. The dimensions of the designed Perspex channel follow closely that of the glottal airway- The depth of the

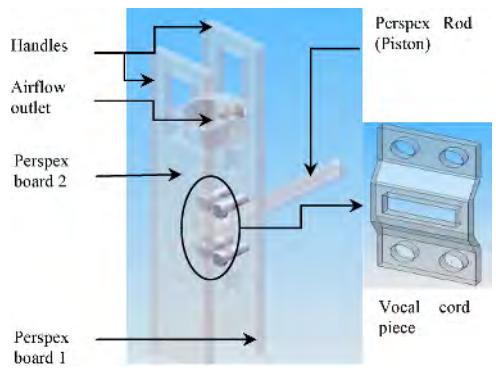


Figure 1: Assembly of Perspex Channel with Perspex rod (piston) and vocal cord piece

Chwee Teck Lim, James C.H. Goh (Eds.): ICBME 2008, Proceedings 23, pp. 1024–1027, 2009
www.springerlink.com

airway channel, enclosed by the sides of the encasing box is 25mm, the width of the channel is 27mm and the length of the channel (from airway entry at the bottom to the top of the vocal fold) is 90mm [4].

The geometrical contour of the detachable vocal fold piece shown in Figure 1 follows that of the outer geometrical contour of the vocal cord described by Alipour et al [4]. This piece is kept to a uniform 2mm in thickness and has a rectangular slot of 15mm by 5 mm removed from its middle section to allow greater clearance for wound closure devices to be inserted without being pushed off by the Perspex rod indicated in Figure 1. The thin structure of the vocal fold piece coupled with the rectangular slot drastically reduces the inertial properties of the vocal fold such that it could slide with ease along the guiding screw tracks.

A single layer of polyurethane film with tensile strength of approximately 3,000psi, tensile break length of 500% is slightly stretched over the detachable vocal fold piece [7]. The top and bottom ends of the sheet are secured to the distal ends of the detachable vocal fold piece using laboratory Parafilm® .This film serves as the primary medium for ex vivo microlaryngeal surgery experiments. It simulates the compressive stresses acting on the novel wound closure devices at the interface areas of contact.

The wooden encase is designed a high degree of versatility and customizability for a wide variety of laryngeal ex vivo surgical experiments on the vocal folds. It is equipped with an I- shaped recess to allow ease of insertion and removal of the Perspex channel. It is also equipped with multiple observation holes for an endoscopic camera system with a stroboscope feature to track the vibration of the vocal cord replica under different flow and vibratory parameters. A portable stroboscope is used in place of the endoscope camera system for this phase of experimentation. A picture of the assembled wooden encase with base supports and a flange that connects to external airflow via a compressor is shown in Figure 2.

A selected prototype of one of the novel wound closure devices is secured onto the film using laboratory forceps. The Perspex channel is then assembled and fitted into the wooden encase as shown in Figure 3. The flat end of the Perspex rod is pushed through corresponding slots on the walls of the wooden encase, Perspex channel and detachable cord piece until it comes into direct contact against the polyurethane sheet. The circular end of the piston is then connected to the core of the linear vibrator, placed on a Perspex stand. A loudspeaker that serves as an external linear vibrator then closed in towards the wooden encase, until that a premade mark of 4mm from the distal flat end of the piston is level with the slot on the slot of the wooden encase. The piston-vibrator system serves as an external simulation of the vocal cord vibration.

A signal function generator, with frequency and amplitude control is calibrated to generate sinusoidal waveforms and is connected to the linear vibrator (loudspeaker). The core of the vibrator then acts as an actuator that pushes the Perspex rod further inwards and draws it outwards in a cyclic motion such that the latex sheet undergoes a forced series of cyclic tension and compression. Air supply is regulated by an air compressor, which can be varied from a few bars to 15 bars. The air is directed through a 3 meter long soft rubber tube fitted into the steel flange at the bottom of the encased box as shown in the Figure 4 below. Finally, a portable stroboscope is placed at a distance of approximately 10cm away from the observation hole as indicated in Figure 4. The stroboscope generates a series of rapidly flashing lights at frequencies prescribed by a dial control to match the frequency of the vocal fold membrane vibration.

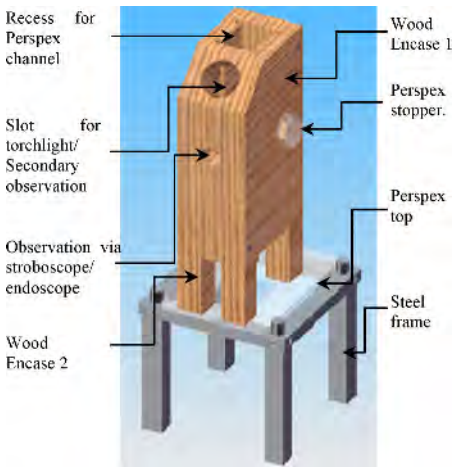


Figure 2: Wooden Encase with Perspex Top Stand

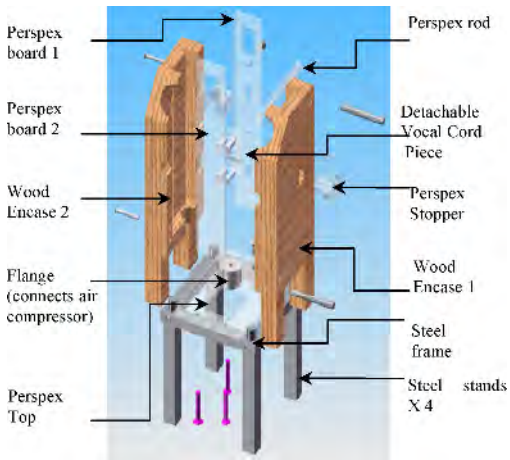


Figure 3: Exploded View of Hemilarynx Model

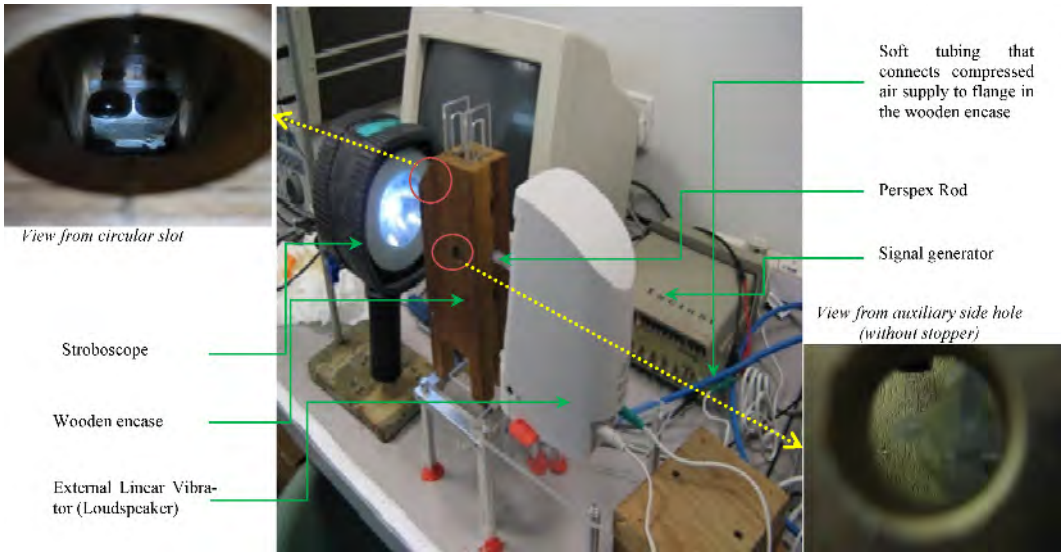


Figure 4: Complete experimental setup with in- experiment views of mock vocal cord with prototype of novel wound closure device during forced vibration and airflow conditions.

III. Results

Experiments are conducted with air supply at constant gauge pressure of 1.5 bars, with low phonation frequencies of 40Hz, 60Hz and 80Hz each with durations of 30 mins [5]. Vibration frequencies of the vocal fold pieces are tallied and validated with stroboscope flash emissions readings.

Observation via the circular slot is conducted at time points of 10 and 30 minutes for all 3 sets of frequencies tested to observe retention of the prototype wound closure device and the tearing of the film at large displacements and high frequencies. Results of the experiment are given in Table 1 below.

Table 1 Ex-vivo experimental trials on stability of novel wound closure device in a hemilarynx model.

Actuator Frequency (Hz)	Stroboscope Frequency (Hz)	Retention of selected prototype on film		Tearing of film observed
		10 (mins)	30 (mins)	30 (mins)
40	40.1	Yes	Yes	No
60	60.3	Yes	Yes	No
80	80.2	Yes	Yes	No

Neither tearing of the polyurethane film nor dislodgment of the selected prototype is observed within a timeframe of 30 minutes for frequencies of 40Hz, 60Hz and 80Hz respectively.

IV. Discussion

Through the ex- vivo experimental setup of the hemilarynx, we are able to validate the dynamic anchoring capabilities of the selected prototype wound closure device, under low frequencies of phonation of 40Hz – 80Hz, characterized by large displacements of the vocal cords. Similarly, the hemilarynx setup is very easily customized to cater for ex-vivo experimentation on other prospective prototype designs of the novel wound closure devices, as well as that involving microsutures and surgical glue. The results of such experimentation with the hemilarynx model will give a good indication of the respective mechanical stability of these materials and devices under vocal cord vibration and subglottal airflow conditions. It will serve to validate and complement other forms of mechanical analysis for epithelial wound closure in microlaryngeal surgery.

The mechanical hemilarynx has several drawbacks compared with an actual human larynx. A single layer polyurethane film is only sufficient to generate compressive stresses along a small area of contact interface with the selected prototype. On the other hand, compressive stresses will act throughout the embedded ends of the selected prototype in an actual larynx due to the presence of the deeper layers of the lamina propria and vocal ligament in a human vocal fold. Viscous and adhesive effects of vocal fold tissue will present shear stresses on the novel wound closure device when it is implanted in a human larynx environment.

In addition, it is difficult to achieve good simulation of subglottal airflow around the vocal fold piece and the wound closure device due to the presence of guiding screws in the Perspex flow channel. Nevertheless, this is not deemed as a major limitation as pressures exerted by vocal cord muscles during phonation far dominate over subglottal airflow pressures [8].

V. Conclusion

The experimental hemilarynx setup is a highly versatile and customizable. It offers direct simulation of vibration of the vocal cords and has been designed to facilitate mechanical means of surgical experimentation on the vocal cords. Most importantly, it has demonstrated good applicability in the evaluation of novel epithelial wound closure devices.

Acknowledgment

This research is funded by an NMRC grant (Development of a vocal cord clip and applicator for laryngeal micro-surgery).

References

1. Woo P. (1995). Endoscopic Microsuture Repair of Vocal Fold Defects. J Voice 9: 332-9
2. Flock S, Marchitto, KS. (2005). Progress toward seamless tissue fusion for wound closure. Otolaryngol Clin N Am 38(2):295-305
3. Fleming D, et. al. (2001). Comparison of mircoflap healing outcomes with traditional and microsuturing techniques: Initial results in a canine model. Ann Otol Rhino Layrngol 110: 707-11
4. Alipour F, Scherer R. (2001). Effects of oscillation of a mechanical hemilarynx model on mean transglottal pressure and flows. J. Acoust. Soc. Am. 110(3):1562-9 DOI: 10.1121/1.1396334
5. Ruty N, Pelorson X, Hirtum A. (2007). An in vitro setup to test the relevance and the accuracy of low- order vocal fold models. J. Acoust. Soc. Am. 121(1): 479-90 DOI: 10.1121/1.2384846
6. Titze I, Schmidtm S, Titze M. (1995). Phonation threshold pressure in a physical model of the vocal fold mucosa. J. Acoust. Soc. Am. 97(5): :3080-4 DOI: 10.1121/1.411870
7. Taller R, McGary J, Charles W. (1987). United States of America Patent No. 468449
8. Zhang K, Siegmund T (2007). A two- layer composite model of the vocal fold lamina propria for fundamental frequency regulation. J. Acoust. Soc. Am. 122(2):1090-101 DOI: 10.1121/1.2749460

Virtual Total Knee Replacement System Based on VTK

Hui Ding, Tianzhu Liang, Guangzhi Wang, Wenbo Liu

Department of Biomedical Engineering, Tsinghua University, Beijing, China

Abstract — **In this paper we present a surgery planning software of total knee replacement (TKR). It was established initially based on the open source package - Visualization Toolkit (VTK). The main innovative feature of this surgery planning system is that it could help the surgeon to choose correct size, orientation and position of the prosthetic components, in order to restore the correct alignment of the mechanical axis of the lower limb. To simulate the multiple degrees of freedom of the embedded prosthesis in operation, such as introversion-extroversion, exterior-interior rotation, flexion-extension, and translations along anatomical axes, in total knee replacement procedure, the appropriate human-machine interactive technology and alignment restrictions were designed to help the operator to perform the virtual cutting and virtual assembly manipulation. Moreover, the clinical commonly used quantitative index contradistinction was provided to assist the doctor to determine the spatial relation of the implantable prosthetic components in 3D space. The function design of the software system was evaluated by the virtual motion analysis of the knee flexion, which obtained a good effect. The process diagram and detailed treatments of virtual operation was provided in this paper. The software of surgery planning plays important roles in preoperative lectotype of the prosthesis and alignment procedure of bone resection and assembly operation.**

Keywords — **Total Knee Replacement, Visualization Toolkit (VTK), Surgery Planning.**

I. Introduction

Total knee replacement (TKR) is a surgical operation in which a surgeon removes a patient's damaged knee joint surface and replaces it with artificial components to restore the disabled knee functions. The purpose of the TKR surgery is to correct the axial alignment of the lower extremity, maintain the joint stability, relieve the pain in the joints and thus restore the whole function of the knee joint.

In order to ensure the good postoperative function of the knee joint, the bone resection position and the placement of the prosthetic components have to be controlled precisely within three dimensional spaces. Therefore, the preoperative planning software of total knee replacement was receiving more and more attention. At present, many institutions have successfully developed total knee replacement surgery planning system [1-3]. Using the planning software, surgeons can virtually simulate the surgical procedures with computer. The system allows them to determine important surgical parameters such as the amount and angle of resection and choose the best artificial knee joint for patient before real operation [1].

As the key procedure to success restore the knee function are the correct selections of prosthesis and put it to the correct location relative to the femur and tibia in TKR surgery. The most import feature of the simulation system is the appropriate human machine interface which provides all kinds of changeable characteristic of the spatial position of the prosthesis in the 3D space. The export of the quantificational indices of operation planning systems provides a significant basis for the establishment of the operation planning.

This paper introduces a TKR planning software which was developed based on Visualization Toolkit (VTK). The preoperative computer tomographic (CT) images of the patient were used to reconstruct 3D bone models. The 3D models of prosthetic components were obtained from 3D laser scan. The appropriate human-machine interactive technology was used to manipulate the 3D model of bones and prosthetic components. Through the simulation of knee flexion of the lower limb models after virtual total knee replacement, the surgeon could observe and evaluate the assembly result from different view point, which help the surgeons to decide the appropriate position of the bone resection and place the embedded prosthesis to desired position. This simulation system is dedicated to assist the surgeon in the preoperative determination of accurate location of the osteotomy, selection of prosthetic implants, as well as the 3D positioning of the implants.

II. Materials and methods

A. *Description of the TKR Planning system*

The basic steps of computer-assisted preoperative planning consist in seven steps: (1) Construct the three dimensional models of limb (femur and tibia) and prosthetic components. The 3D model of lower limbs was constructed from CT images of lower limbs and the 3D model of prosthetic components was from three dimensional laser scan; (2) Identify the limb mechanical axis; (3) Determine the spatial position of prosthetic models in 3D space with re-

Chwee Teck Lim, James C.H. Goh (Eds.): ICBME 2008, Proceedings 23, pp. 1028–1031, 2009
www.springerlink.com

spect to the bones; (4) Pre-assembly of bones and prosthetic components; (5) Quantitatively determine the appropriate bone resection positions and directions; (6) Virtual Cutting; (7) Educe quantitative indicators and save the key index and assembled model.

A block diagram of the planning procedure is illustrated in Fig. 1. The TKA planning system was developed based on the open source platform of Visualization Toolkit (VTK) and development platform of Visual Studio 2005.

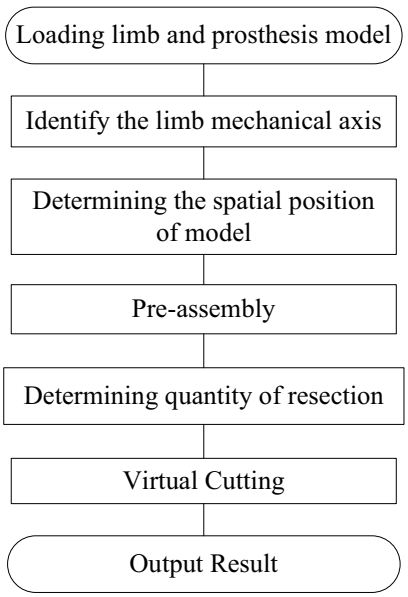


Fig. 1 A block diagram of the TKR planning system

B. Materials

1. Three dimension model of lower limb: The 3D bone models were constructed from computed tomography (CT) scan. Lower limb CT scan was performed with 1mm slice space and image resolution of 512*512. The corresponding pixel size is 0.782*0.782 mm. Slices covers the range from the proximal end to of femur to the distal end of tibia.

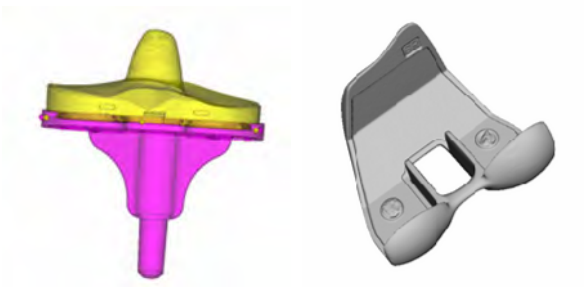


Fig. 2 Three dimension model of the prosthetic components

2. Three dimension model of the prosthetic component: The 3-D prosthetic component models was constructed from three-dimensional laser surface scans, which reverse-engineered the articular surfaces into point clouds with associated point normals. The sampling resolution of the laser scanner used was about 0.5 mm. A 3-D surface model of the prosthetic component is shown in Fig. 2.

C. Realization of the Virtual TKR System

1. Mechanical axis Selection: Osteotomy and prosthesis assembly is based on the mechanical axis of the lower limbs. As a result, lower limb mechanical axes determination is essential in the virtual TKR system. We select the femoral mechanical axis, FMA, from the center of the femoral head to the center of the intercondylar notch of femur, and select the tibial mechanical axis, TMA, from the center of the tibial plateau to the center of the ankle joint.

2. Determining the spatial position of model: Total knee replacement is an extremely "position sensitive" surgical operation [1]. The restoration of correct alignments of lower limb mechanical axes demands precisely positioning manipulation of prosthetic components of femur and tibia in relative with the bones in 3D space. Thus the assembly of tibia and femur prosthetic components may involve multiple degrees of freedom misalignments, such as introversion-extroversion, external-internal rotations, flexion- extension, and translations in all directions.

When we construct the 3D model, each component had its own coordinate system (three orthogonal axes). If we could define the mechanical axes and the flexion axis of the femur and tibia precisely, then the model can be transferred to any desired 3D position with rigid body transformations.

In distal femoral replacement, the bone-cutting of the thighbone basically included the section of distal femoral condyle, the anterior and posterior femoral condyle, and the anterior and posterior bevel of the femoral condyle.

Three steps were designed to determine the position of the thighbone prosthesis. The first step is to choose the anatomical landmarks to determine the mechanical axes of femur and the axis of joint flexion-extension. We palpate a set of points in the surface of femoral head to calculate the center of the femoral head, and pick up the intercondylar notch of femur with the 3D model. Thus the femoral mechanical axis, FMA, from the center of the femoral head to the center of the intercondylar notch was determined. Then we palpate the anterior and posterior femoral condyles to determine the flexion-extension axis of femur.

The second step was to determine the section location of distal femoral condyle. The primal section plane always perpendicular to the femoral mechanical axis and can be adjusted in the direction of proximal-distal. A reference

plane was generated to help the visual inspection of the resection position.

After the initial section plane of distal femoral condyle was determined, the third step could be performed. The flexion-extension axis of femur and the reference plane were used to restrict the flexion-extension of the femoral prosthesis. The cutting planes of anterior and posterior femoral condyle were set parallel to the flexion-extension axis and perpendicular to the reference plane. Moreover, he the cutting planes of anterior and posterior bevel were set parallel to the flexion-extension axis and keep a specific angle to the reference plane. According to the known sizes and angles of the prosthesis, those cutting planes of anterior and posterior femoral condyle can be determined.

The selected landmarks and generated reference plane are show in Fig. 3 and Fig. 4.

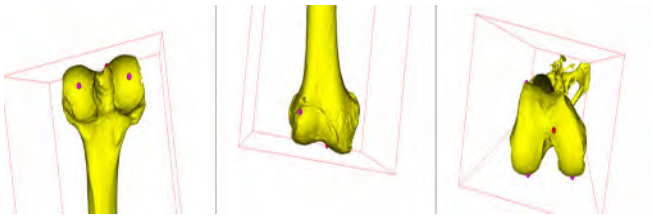


Fig. 3 The palpate of anterior, interior and exterior posterior femoral condyle

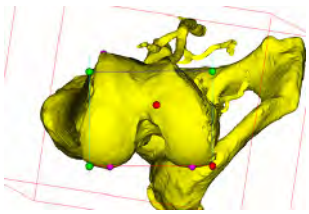


Fig. 4 Reference planes for determine the section of anterior and posterior femoral condyle.

For the tibia, we select the tibial mechanical axis, TMA, from the center of the tibial plateau to the center of the ankle joint. The sagittal plan of tibia was determined by the tibial plateau center, the astragal center and the landmarks interior 1/3 part of the tibial tubercle. With those selection, the restrictions to the tibial prosthesis was applied.

3. Pre-assembly: The pre-assembly of the femur and tibia prosthesis were processed by a sequence of alignments. In the first step, the direction of the prosthetic axis was aligned with the mechanical axis of the thighbone model, and the prosthesis could be moved proximally and distally. Then the inner and outer diameter of the prosthesis was aligned with the thighbone model along the flexion-extension axis. In the third step, through the projection of the center of the femoral condyle notch, the projection of sagittal plane was drawn on the reference plane, and the prosthesis was aligned to make the center of the prosthesis located in this vertical line, with the posterior cutting surface of the thighbone aligning with the posterior cutting line on the reference plane. The similar alignments were performed with the tibial bone and prosthesis.

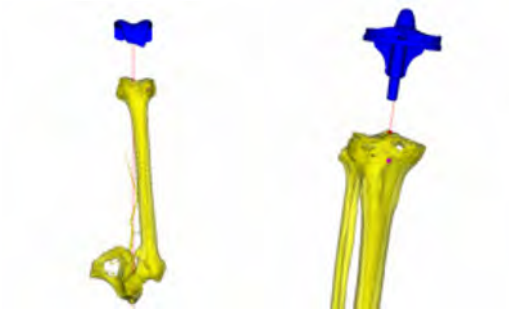


Fig. 5 Pre-assembly of femur and tibia prostheses

4. Determining of the Bone-cutting Quantity: In the operation planning system, the bone-cutting quantity of the distal femoral condyle was calculated by the cross point of the bone-cutting plane of the distal femoral condyle and the thighbone axis. Because the thighbone prosthesis was restricted to move along the mechanical axis of femur, the relative position of the center of prosthesis had no change during the movement. Therefore, the cutting quantity of the distal femur could be determined easily.

In usual cases, if the tibial plateau was perpendicular to the mechanical axis of the tibia, the thighbone prosthesis was in the external rotation position with an angle of 3°. Then bone-cutting quantity of the interior femoral condyle of posterior was longer than that of the exterior femoral condyle of posterior for 2 to 3mm. The cutting quantity of the tibial plateau referred to the distance from the centers of the tibial plateau to the cutting plan of femur. As the mechanical axis of the tibia always past through the centers of the tibial plateau and the bone-cutting surface, the distance between the two centers could be calculated directly as the bone-cutting quantity of the tibial plateau.

5. Virtual resection: The cutting surface of the virtual cutting was realized with the implicit function in the VTK. In the single plane cutting, the implicit function of the virtual cutting was set as the corresponding cutting surface function. However, the virtual cutting of multi-plane was needed in the femur resection, which made it necessary to process the regions of all the cutting surfaces with the "And" operation, and the implicit function of the result

region was set as the implicit function of the virtual cutting to obtain the effect of simultaneous multi-plane cutting.

6. Quantitative indicators of output and save model after assembly: Before the pre-assembly, the models of prosthesis were not in the same coordinate system with the bone models. Therefore, the methods of normal align, rotating align and pan align were selected to complete the alignments between the prostheses, the femur and tibia. The alignments result in accurate assembly of all prosthetic components and bones in the same coordinate system.

D. Virtual motion analysis

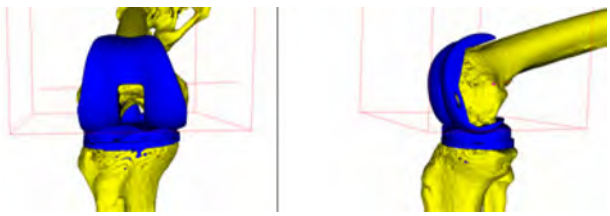
The simulation result of the prosthesis replacement was analyzed initially through the virtual inspection of surgeon. The models can be manipulated to perform rotations along the flexion-extension axis. Fig. 6 illustrated the virtual knee flexion with the 0°, 45° and 75° respectively.



(a) virtual knee flexion with the 0°



(b) Virtual knee flexion with the 45°



(c) Virtual knee flexion with the 75°

Fig. 6 Virtual knee flexion

III. Result and Discussion

This paper mainly dealt with combining the computer simulation technique with the conventional surgery operation process to establish a knee operation planning system. It made full use of the available data obtaining technology including the CT scanning and the laser tridimensional scanning to realize the 3D expression of the virtual objects, and the VTK interaction technology to realize the man-machine interaction.

In present study, we use 3D CT image with 1mm slice distance which generate a good 3D model of the whole femur and tibia. In actual use, the CT scan could be performed only with the hip, knee and ankle joints to build the axes of lower limb, which reduce the number of images.

The article provides a full set of virtual surgery process procedure, it helps the pre-operative prosthesis selection, osteotomy planning, and other assembly simulation to improve the accurate of the surgery.

Further tests will focus on the improvement of simulation procedure and the human-machine interactive. The accuracy of the system will be evaluated and improved through calibration.

Acknowledgment

The work described in this paper has been supported by the National High Technology Research and Development Program of China, under Grant 2006AA02Z4E7 and the National Nature Science Foundation of China under grant 30772195.

The assistance of Dr. Zhou Yixing and Dr. Tang Jing in definition of orthopaedic procedure is gratefully acknowledged.

References

[1] S. H. Park, Y. S. Yoon, L. H. Kim, S. H. Lee, M. Han. Virtual Knee Joint Replacement Surgery System [J]. Geometric Modeling and Imaging, GMAI 2007, Proceedings, 2007: 79-84.

[2] M. Fadda, D.Bertelli, S. Martelli, M.Marcacci, P.Dario, C.Paggetti, D.Caramella, D.Trippi. Computer Assisted Planning for Total Knee Arthroplasty [J]. Computers in Biology and Medicine, 2007, 37(12): 1771-1779.

[3] Nofrini L., La Palombara F., Marcacci M., M.D. Martelli S., F. Iacono F., M.D. Planning of Total Knee Replacement: Analysis of the Critical Parameters Influencing the Implant [J]. Annual International Conference of the IEEE Engineering in Medicine and Biology – Proceedings, 2000, 3: 1861-1863.

Author: Guangzhi Wang
Institute: Department of Biomedical Engineering, Tsinghua University
Street: Medical Science Building, Tsinghua University
City: Beijing
Country: China
Email: wgz-dea@tsinghua.edu.cn

Motor Learning of Normal Subjects Exercised with a Shoulder-Elbow Rehabilitation Robot

H.H. Lin[1], M.S. Ju[2], C.C.K. Lin[3], Y.N. Sun[1] and S.M. Chen[4]

[1]Department of Computer Science and Information Engineering, National Cheng Kung University, Tainan, Taiwan
[2]Department of Mechanical Engineering, National Cheng Kung University, Tainan, Taiwan
[3]Department of Neurology, National Cheng Kung University Hospital, Tainan, Taiwan
[4]Department of Physical Medicine and Rehabilitation, National Cheng Kung University Hospital, Tainan, Taiwan

Abstract — **A shoulder-elbow rehabilitation robot has been developed as clinical treatments to facilitate motor learning and accelerate recovery of motor functions for stroke patients. However, the connection between motor learning and muscle activation patterns for stroke patients remained unknown. This study was tried to fulfill the gap by examining the muscle coordination and motor learning strategies of normal subjects while they interacted with the rehabilitation robot. A Hill-type biomechanical model based on twelve shoulder and elbow muscles was hence constructed for the upper-limb to simulate the interaction. Two normal subjects were recruited to perform upper limb circular tracking movements, clockwise and counterclockwise, on transverse plane at shoulder level in a designed force field generated by the rehabilitation robot. From the inverse dynamics analysis, the interaction was analyzed and the patterns of muscle activation were calculated. EMG signals of eight upper limb muscles were also measured for model validation and muscle coordination observation. The principle component analysis (PCA) was performed to distinguish different groups of muscle co-activation. Results showed that the constructed biomechanical model may be used as a tool for evaluating effects of treatment and be utilized as a blueprint for the design of the training protocol for the stroke patients.**

Keywords — **stroke, rehabilitation, biomechanical model, motor control, optimization.**

I. Introduction

Rehabilitation program is the main stay of treatments for patients suffering from trauma, stroke or spinal cord injury. Conventionally, these programs rely heavily on the experience and manual manipulation by the therapists on the patients' affected limbs. Since the number of patients is large and the treatment is time-consuming, it is a great advance if robots can assist in performing treatments. Recently there have been many researches working on how to use robots in assisting patients in rehabilitation [1-4].

Although many positive outcomes are reported for robot-aided treatment, clinical assessments currently used for stroke patients are based on subjective evaluation of physicians with assessment indices, such as modified Ashworth scale, Brunnstrom's stage and Fugle-Meyer's score, etc. It is hard to describe the individual characteristics of stroke patients with those assessment indices. Hence, there is a need of studies of connection between motor learning and muscle activation patterns for stroke patients. To fulfill the gap, the goal of this research was tried to construct a biomechanical model of the upper limb such that the muscle activations can be estimated for both normal subjects and stroke patients. A better understanding of the motor control and the recovery mechanism of stroke patients during treatments are then provided to physicians. Furthermore, customized treatments for stroke patients may be designed by using the analyses to facilitate the rehabilitation training.

II. Materials and Methods

In our previous studies, a robot was developed for neuro-rehabilitation of the upper extremity [5]. The robot was designed to perform two-dimensional motion on the transverse plane and was able to provide a desired resistive or assistive force to the subjects. Upper limb circular tracking movements, clockwise and counterclockwise, on transverse plane at shoulder level were hence performed in a designed force field.

EMG signals were measured by eight surface electrodes (Delsys, Inc.) from following muscles: pectoralis major (PEC), deltoid (DEL), biceps (BIC), triceps (TRIC), pronator teres (PTm), supinator (SUP), flexor digitorum superficialis (FDS), extensor digitorum (ED). The signals were amplified with a gain of 1000 V/V and band-passed of 20 Hz to 450 Hz and sampled at 2.0 kHz/channel. Signals were processed by full-wave rectification and linear envelope. Smoothed EMG signals were derived after normalizing the signals with the EMG of the isometric contraction and passing the signals through an adaptive filter (cutoff frequency 0.25~2.5Hz) [6].

A Hill-type biomechanical model which includes twelve muscles around shoulder and elbow joints was constructed for the upper-limb to simulate the interaction between subjects and the rehabilitation robot. These muscles includes

Chwee Teck Lim, James C.H. Goh (Eds.): ICBME 2008, Proceedings 23, pp. 1032–1036, 2009
www.springerlink.com

deltoid anterior (DA), deltoid middle (DM), deltoid posterior (DP), teres major (TM), pectoralis major (PM), triceps brachii (TB), biceps brachii (BB), anconeus (ANC), brachialis (BRA), brachioradialis (BRD), pronator teres (PT), and extensor carpi radialis (ECRL). The free body diagram of this model is shown in Fig. 1. According to Fig. 1(c), the dynamic equations of the upper are described as

$$\vec{F}_1 + \vec{F}_2 = m_1\vec{a}_1, \tag{1}$$

$$\vec{L}_1 \times \vec{F}_2 + \vec{\tau}_1 + \vec{\tau}_2 = \vec{L}_{g1} \times m_1\vec{a}_1 + I_1\vec{\alpha}_1. \tag{2}$$

Likewise, the dynamic equations of the forearm as illustrated in Fig. 1(b) are given by

$$\vec{R} + \vec{F}_2 = m_2\vec{a}_2, \tag{3}$$

$$\vec{L}_2 \times \vec{R} + \vec{\tau}_2 = \vec{L}_{g2} \times m_2\vec{a}_2 + I_2\vec{\alpha}_2, \tag{4}$$

where the subscripts 1 and 2 represent the shoulder and elbow, respectively. R is the resistive force imposed at the subject's wrist by the robot. F expresses the force. L is the segment length of the arm. L_g represents the length from the center of the mass to the proximal end. The torque is given by τ. m describes the mass. The acceleration and angular acceleration are symbolized by a and α, respectively. I stands for the moment of inertia.

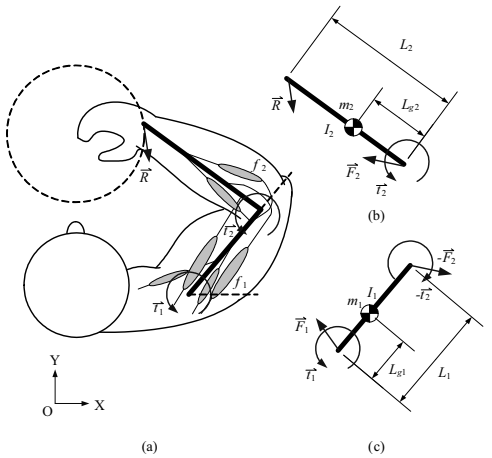


Fig. 1 Free body diagram of the upper-limb biomechanical model

With the measurement data and the muscle-skeleton parameters from the anthropometry, the required forces and torques at the shoulder and elbow for the arm's movements can then be solved by applying the inverse analysis (Fig. 2). In order to solve the load sharing problem for each muscle forces, a nonlinear optimization problem was formulated as in [7, 8]

$$\min J = \sum_{j=1}^{12}\left(\frac{f_j}{PCSA_j}\right)^2 \tag{5}$$

Subject to

$$\sum_{j=1}^{n}\left(\vec{d}_j \times \vec{f}_j\right) + \vec{\tau}_1 = 0, \tag{6}$$

$$\sum_{j=1}^{m}\left(\vec{d}_j \times \vec{f}_j\right) + \vec{\tau}_2 = 0, \tag{7}$$

$$f_j \geq 0, \tag{8}$$

$$f_j - F_{oj} \leq 0, \tag{9}$$

where f_j, d_j, and $PCSA_j$ are the muscle force, moment arm and physiologic cross-sectional area of the muscle j, respectively. n is the muscle number around the shoulder and m is the muscle number around the elbow. F_{oj} represents the optimal muscle force of the muscle j.

With incorporation with the curves of the muscle force-length properties and force-velocity properties, muscle activations were computed by equation below

$$A_j = \frac{f_j}{f_{oj} f_{LT} f_{FV}}, \tag{10}$$

where A_j is the muscle activation of the muscle j, and f_{oj} is the isometric force of the j muscle. The force-length and the force-velocity factors are represented as f_{LT} and f_{FV}, respectively.

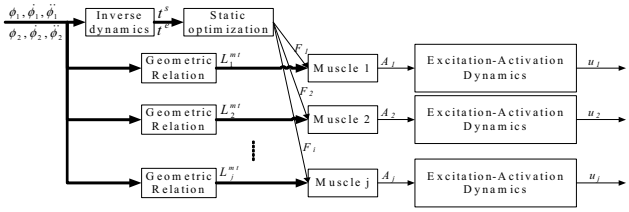


Fig. 2 Inverse analysis of the human-robot interaction

In order to gain a more perspective realization of the co-activation between muscles during a tracking movement, the principle component analysis (PCA) was applied [9]. The purpose of the PCA is to reduce the dimensionality of dependent variables to several orthogonal components. Hence, the data covariance matrix of the calculated muscle activations was formed and then decomposed by computing the corresponding eigenvectors and the eigenvalues. According to the eigenvalues, the number of principle components (PCs) is choose to retain most of the major informa-

tion hidden in data such that different groups of muscles co-activation were distinguished.

III. Results and Discussions

An example of the calculated muscle activations was shown in Fig. 3 for a normal subject tracking in the CW direction. Fig. 4 showed the muscle activations of a tracking cycle in both CW and CCW direction for a normal subject. In this figure, the left and right side plots indicated results in the CW and CCW tracking direction, respectively. From top to bottom, the first plot showed wrist's trajectories in X axis (solid line) and Y axis (dashed line); the second plot showed the angles of shoulder (solid line) and elbow (dashed line). All muscle activations were presented in plots from third to seventh. The muscle activation of TB, BRA, ECRL, TM, and DP were expressed in solid lines; dashed lines are used to showed that of BB, BRD, PT, PM and DM. As for the ANC and DA, dotted lines were used. From this figure, one can find that in the CW direction TB was first activated from 0% to 45% of the cycle and followed by the BB from 35% to 70% and then TB from 70% to 100% again. On the other hand, for the CCW direction, BB was first activated from 0% to 45% and followed by TB from 41% to 95% and then BB from 95% to 100% to complete the cycle. PM and DA were activated at the same time since they are both the prime mover for the horizontal flexion at the shoulder joint. In the constructed model, all muscles were assumed to be mono-articular except the biceps and the triceps which were modeled as bi-articular such that agonist muscles and antagonist muscles can not be activated simultaneously. In contrast, biceps and triceps may have temporary co-activation due to the continuity and correlation of the movements as seen in Fig. 4.

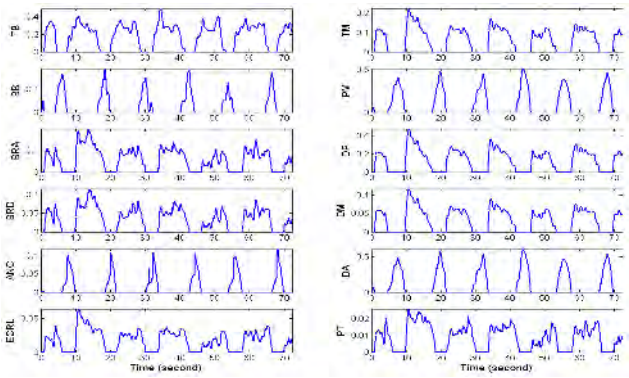


Fig. 3 Example of the calculated muscle activations

The comparisons with measured EMGs for the muscle activations were shown in Fig. 5 for direction CW as an example. The measured EMGs were presented in dotted lines, and the computed muscle activations were shown in solid lines for TB, BB, PM, and DM. The dashed and dashed-dotted lines illustrated muscle activations of DA and DP, respectively. The muscle activation patterns obtained from the biomechanical model were consistent with the EMG signals. However, only one measured EMG signal for the deltoid muscle can be acquired but there are there heads of deltoid muscles constructed in the model. As a result, the estimated muscle activations may provide more detail information than the EMG can offer. The corresponding correlation analysis between the computed muscle and activations and the measured EMGs were shown in the Table 1. The ill-correlation of the PM muscle may result from the noise-contamination of the EMG measurements or the surface electrode may not be placed correctly. For the CCW direction, the calculated muscle activation of DM indicated a short period of activation which may explain the ill-correlation with the measured EMG signals.

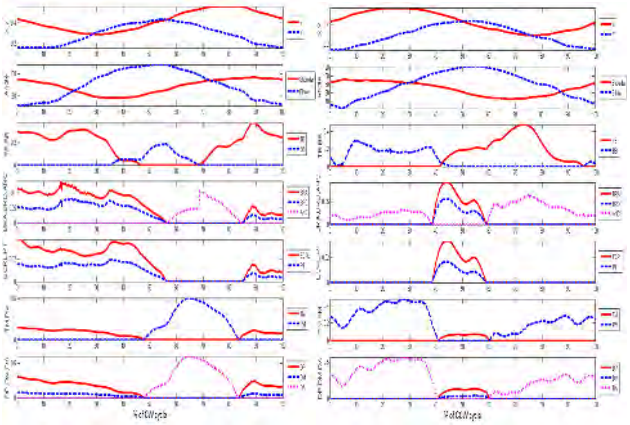


Fig. 4 Muscle activations of a tracking cycle: CW (left), CCW (right)

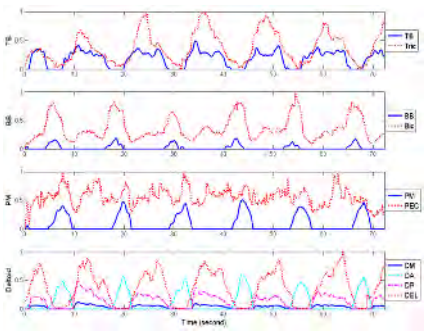


Fig. 5 Comparisons between EMG measurements and calculated muscle activations for a normal subject in the CW direction

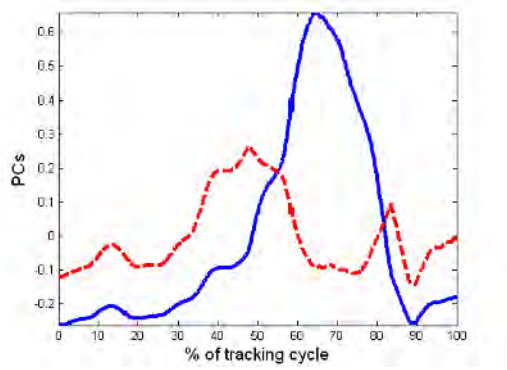


Fig. 6 Values of PC1(solid) and PC2 (dashed) in the CW direction

Fig. 6 showed the results obtained from the PCA analysis for a tracking cycle in the direction CW as an example. Since the first and the second principle component (PC1, PC2) explain 70% and 10% of the data variance, respectively, the analysis is therefore focus on the examination of the PC1 (solid line) and PC2 (dashed line). The coefficients of PC1 and PC2 were indicated in the Table 2. From the plot and the table, one can see that the values of PC1 were positive from around 50% to 82% of cycle and mainly contributed from PM and DA. From 35% to 60% of cycle, the values of PC2 were positive due to the contribution of BB. As for the rest of the tracking cycle, both PC1 and PC2 presented negative values which may be explained by TB and DP. Fig. 7 showed the calculated muscle activation patterns of one cycle for a stroke patient in the CW (left plots) and CCW (right plots) directions while performing circular tracking movements. Observe that the stroke patient performed in-coordinative TB and BB activation for the CW tracking cycle and the secondary movers such as BRA, BRD, ECRL and PT were activated at the early stage of the tracking cycle. Same situation can also be found in the CCW direction. Furthermore, the stroke patient's TB was first activated in the CCW direction. Also, DP and DM were activated in the 0~30% of the cycle, which remained silent for the norm subjects.

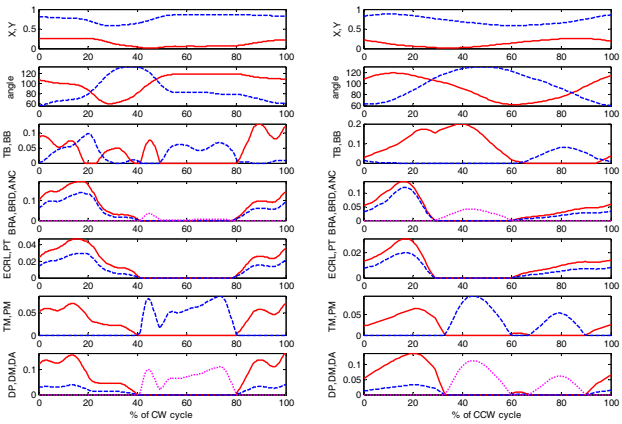


Fig. 7 Muscle activations of a stroke patient in circular tracking movements (left CW, right CCW)

IV. Conclusions

With the help of the biomechanical model, the pattern of the muscle activation of the upper-limb of stroke patients can be estimated. The information may be utilized as a blueprint for the design of the training protocol. In future, time course variation of these muscle activations may provide an assessment tool for the stroke patients during robot-aided rehabilitation.

Table 1 Correlation coefficients between computed muscle activations and the measured EMGs

Muscle	CW	CCW
TB	0.727	0.663
BB	0.798	0.401
PM	0.294	0.676
DM	0.851	-0.025

Table 2 Coefficients of PC values

	TB	BB	ANC	BRA	BRD	ECRL
PC1	-0.3125	0.0646	0.0767	-0.1171	-0.0674	-0.0325
PC2	-0.6796	0.3083	-0.0729	-0.0159	0.0015	0.0138
	TM	PM	DP	DM	DA	PT
PC1	-0.1438	0.5645	-0.2836	-0.0737	0.6689	-0.0171
PC2	-0.2125	-0.2820	-0.4287	-0.1088	-0.3422	0.0049

Acknowledgment

The research is supported by the Ministry of Economic Affairs, Taiwan, under contract 97-EC-17-A-19-S1-053.

References

1. Krebs HI, Hogan N (2006) Therapeutic robotics: A technology push. Proc. of IEEE 94:1727-38, 2006.
2. Hesse S, Werner C, Pohl M, et al. (2005) Computerized arm training improves the motor control of the severely affected arm after stroke - A single-blinded randomized trial in two centers. Stroke 36:1960-1996.
3. Colombo R, Pisano F, Micera S, et al. (2005) Robotic techniques for upper limb evaluation and rehabilitation of stroke patients. IEEE Trans Neural Syst Rehab Eng 13:311-324.

4. Dipietro L, Krebs HI, Fasoli SE, et al. (2007) Changing motor synergies in chronic stroke. J Neurophysiol 98:757-768.
5. Ju MS, Lin CCK, Lin DH, Hwang IS, Chen SM (2005) A rehabilitation robot with force-position hybrid fuzzy controller: Hybrid fuzzy control of rehabilitation robot. IEEE Trans Neural Syst Rehabil Eng 13:349-358.
6. Cheng HS, Ju MS, Lin CCK (2003) Improving elbow torque output of stroke patients with assistive torque controlled by EMG signals. Tran ASME J Biomech Eng 125:881-886.
7. Happee R (1994) Inverse dynamic optimization including muscular dynamics, a new simulation method applied to goal-directed movements. J of Biomech 27:953-960.
8. Challis JH (1997) Producing physiologically realistic individual muscle force estimations by imposing constraints when using optimization techniques. Medl Eng & Physics 19:253-261.
9. Johnson DE (1998) Applied Multivariate Methods for Data Analysts. Duxbury Press, Pacific Grove, CA.

Using Virtual Markers to Explore Kinematics of Articular Bearing Surfaces of Knee Joints

Guangzhi Wang[1], Zhonglin Zhu[1], Hui Ding[1], Xiao Dang[1], Jing Tang[2] and Yixin Zhou[2]

[1]Department of Biomedical Engineering, Tsinghua University, Beijing 100084, China
[2]Beijing Ji Shui Tan hospital, the 4th Medical College of Peking University, Beijing, China

Abstract — **This paper proposed a method of using virtual markers to track the movement of the articular bearing surfaces of femur, tibia and patella simultaneously. With this method, the femur, tibia and patella were treated as three rigid body connected by soft tissue and thus the articular surface moves with corresponding bone in three dimensional (3D) space. The contact kinematics of articular bearing surface can be figured out by track the position and orientation of bones during knee flexion. To perform this method, three sets of tracking marker were attached tightly to femur, tibia and patella to track the 3D motion of lower limb. The articular bearing surfaces of knee joint were digitized to create three groups of registered virtual markers associated to the tracking markers of each bone, respectively. During knee flexion, 3D movement of femur, tibia and patella were tracked by capture the motion of tracking markers. Then the 3D coordinate of each virtual marker was calculated using the registration information of virtual markers. Thus, the trajectory of virtual markers could be tracked during knee flexion which indicates the real kinematics of bearing surfaces of knee joint. Three fresh-frozen lower limbs were tested before and after total knee replacement operation using this technique. The test results show that this method could be used to explore the contact condition of articular bearing surfaces accurately.**

Keywords — **total knee arthroplasty, kinematics, articular surfaces, motion tracking, virtual marker.**

I. Introduction

It is known that the geometry of the articular can affect the location of the contact point during knee motion and ultimately affect the trajectory of the leg. For the total knee arthroplasty (TKA), the position and orientation of the prosthesis components can significantly affect the pattern of knee motion. Surgical implantation strategies, such as placement and sloping of the components, can have dramatic effects on gait. Moreover, the geometry, position and orientation of the prosthesis components affect the mechanics of knee joint which is correlated with the reliability of the TKA. So that, an accurate knowledge of *in vivo* kinematics of the human knee is important in order to improve the treatment of knee pathologies. Knee kinematics had been measured extensively in cadavers and in living subjects [1, 2]. However, direct measurement of contact kinematics of articular bearing surfaces remains technical challenge in biomedical engineering. Previous studies have used various technologies to measure kinematics in human subjects, including video, computerized tomography (CT) and magnetic resonance imaging (MRI) techniques. In recent years, image based 3D model and 2D fluoroscopic image measurements were widely used in the study [3, 4] . Some recent studies have implemented 3D models generated from CT and MRI scans to estimate the motion of the contact points of the femur on the tibial plateau using the bony geometry of the femur and tibia [2, 5]. However, it is hard to obtain the geometry and acquire the motion of the bones simultaneously with the image techniques during knee flexion to quantify tibiofemoral contact in consecutive joint angles.

The object of this study was to quantify the contact kinematics between the tibial and femoral cartilage and/or implanted components during consecutively knee flexion. We use a new methodology to track the movement of virtual markers located on the articular bearing surfaces of femur, tibia and patella simultaneously. Thus the tibiofemoral articular contact of different legs can be compared using the model obtained by digitizing the bony surface geometries of knee joints or using the computer model of artificial knee joint components. The kinematics of articular bearing surfaces before and after the total knee replacement can be compared using this technology.

II. Materials and methods

A. Materials

The three fresh-frozen knee joints specimens (total-femur to midtibia) were used to perform the test. All specimens were anatomically normal, with no varus or valgus deformities. The institutional review board approved the study.

Before the test, three metal screws were inserted into the patella, tibia, and femur. A small X-shaped traceable frame with a marker on each of the four arms was fixed to the metal screw tightly to capture the movement of bones in six degrees of freedom (DOF).

Chwee Teck Lim, James C.H. Goh (Eds.): ICBME 2008, Proceedings 23, pp. 1037–1041, 2009
www.springerlink.com

The specimens were tested before and after implanted with different designed prosthesis such as Simith-nephnew GENESIS II patella preserving and high flexion insert replacement by the same surgeon. Ligament balancing was performed with the femoral and tibial components in their neutral positions.

B. Experiment Setup

1) Weightbearing apparatus: A custom-built Oxford-type weightbearing rig (Fig. 1) actively loaded the knee by moving the femur head to produce continuous flexion and extension to simulate deep knee bends before and post TKA operation. The quadriceps muscles were loaded by dead weights via thin wires which pulling the rope attached to each individual muscle head of the quadriceps. The load was intended to mimic the passive resistance of the quadriceps tendon and to ensure that the patella remained in contact with the femur. The simulated ankle joint allowed rotations about three orthogonal axes and no translations. The simulated hip joint allowed vertical translation, rotation in coronal plane and flexion resulting in one rotational and two translational degrees of freedom. Therefore, the knee retained its full six degrees of freedom.

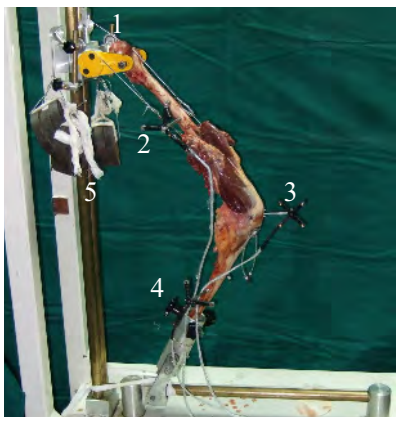


Fig. 1. Weightbearing flexion rig and motion tracking markers. (1) Hip joint, (2) traceable frame fixed to femur, (3) traceable frame fixed to patella, (4) traceable frame fixed to tibia, (5) dead weights.

2) Measurement Devices: To determine the tibiofemoral and patellofemoral tracking characteristics throughout knee flexion and extension, we firmly attached X-shaped traceable frame of marker arrays, each with four infrared-emitting diodes (IREDs) on each of the four arms, to the femur, tibia and patella using metal screws. The three-dimensional position and orientation of bones were tracked with an Optotrak Certus^{TM} optoelectronic camera system (Northern Digital, Waterloo, Canada) via the traceable frames. The root-mean-square (RMS) accuracy for each IRED was 0.1 mm in the plane of flexion and 0.15 mm perpendicular to the plane of flexion. The weight of the patellar tracking frame and associated cable was less than 15g. The effect of this on the kinematics would therefore be easily offset by the quadriceps load.

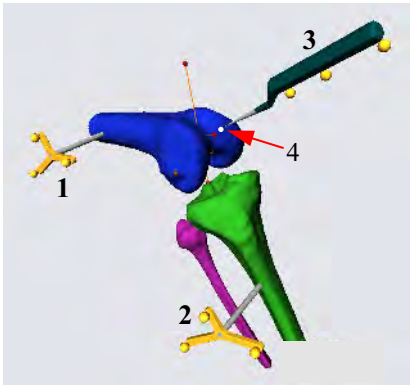


Fig. 2. Traceable frame and digitizer probe for selection of virtual markers. (1) femur tracking frame, (2) tibia tracking frame, (3) digitizer probe, (4) virtual marker.

C. Traceable Markers and Virtual Markers

While the small traceable frame tightly fixed to bones (Fig. 2), 6 DOF movement of each bone can be captured by the Optotrak Certus^{TM} motion capture system. Each bone was regarded as a rigid body moving in 3D space. Thus, any specific point located in the bone will move with the rigid body (bone) and the trajectory of this point in 3D space can be calculated by resolve the rotation and translation of the rigid body. Therefore this specific point can be tracked as if it is a virtual traceable marker. If we define a group of virtual markers on each of the articular bearing surfaces, the 3D movements of articular surface of each bone can be tracked to explore the contact kinematics of bones with consecutively flexion and extension of the knee. A digitizer probe with 3 IRED markers (Fig. 2) was used to digitize the articular bearing surface of femur, tibia and patella. The tip of digitizer probe was calibrated with accuracy of 0.1mm (RMS) before it can be used. The virtual markers located in the articular bearing surface of each bone were obtained by moves the tip of digitizer probe in front of the cartilage while record the 3D location of probe tip and the traceable frame mounted on each bone simultaneously with Optotrak Certus^{TM} system. Then the recorded 3D location of virtual markers with respect to the traceable frame of corresponding bone can be transferred to world coordinate system to analysis the relative motion of the bones.

D. 3D model of articular surfaces of knee joints

For the accurate modeling of the bones, a set of point palpation was performed to sample the coordinates of the articular bearing surfaces of the femur, tibia and patella. Thus, the articular geometries can be represented as point clouds and the 3D surface models could be generated by orderly connect the points to produce mesh grid.

For model the implanted components, we obtained the articular geometries using a three-dimensional laser scanner, which reverse-engineered the articular surfaces into point clouds. The sampling resolution of the laser scanner used was about 0.5 mm.

E. Experiment procedure

Before the TKA procedure, the specimens were set up to the weightbearing rig. Three traceable frames were tightly fixed to the femur, tibia and patella to track the motion of bones. Then, the knee was opened to perform the virtual marker palpation procedure of the articular surfaces using digitizer probe. More than 300 points were obtained for each articular surface.

After suture of the knee, flexion and extension test were performed with the weightbearing rig. 3D movements of the femur, tibia and patella were measured via the traceable frames and recorded at 25 Hz by the Optotrak Certus system during the consecutively knee flexion and extension. Six trials were repeated for each specimen.

After the normal knee flexion test, the TKA procedure was performed by the same surgeon. During the TKA procedure, register points were selected to sample the location of the prosthesis components relative to the traceable frames which was used to register the 3D prosthesis model as the virtual markers. And then, the specimens were tested with the weightbearing rig and Optotrak Certus^{TM} 3D motion tracking system again.

F. Data Processing

1) Coordinate Transformation: When we test the knee, the Optotrak Certus system records the translation vector and rotation matrix of each traceable frame individually. To identify the kinematics of the articular surface, the relative 3D movements of virtual markers need to be resolved. First of all, the virtual markers were defined by digitizing the articular surface with in the traceable frame coordinate system of each bone. So that the 3D coordinates rigid-body transformation is needed to transfer the locations of virtual markers from the frame coordinate system to the world coordinate system. With the rotation matrix $\boldsymbol{R}$ and translation vector $\boldsymbol{T}$ of each traceable frame recorded by the Optotrak Certus system, the coordinate of each virtual marker $\boldsymbol{P_{fi}}$ in traceable frame coordinate system can be transferred to $\boldsymbol{P_{wi}}$ in world coordinate system by equation:

$$P_{wi} = R \cdot P_{fi} + T \tag{1}$$

where, $\boldsymbol{R}$ is an orthogonal rotation matrix and $\boldsymbol{T}$ is displacement vector which indicate the location of the traceable frame in world coordinate system.

2) Re-orientation Process: With the weightbearing rig all the bones moved simultaneously throughout the knee flexion and extension. To represents the kinematics of articular bearing surface of knee joint, the relative movement of tibiofemoral and patellofemoral joint are desired. In this study, relative movements were calculated using a custom-written Matlab program. The kinematics of the joints were determined from the traceable markers and represented as Cardan angles as described by Tupling and Pierrynowski [6]. Translations and rotations of the patella and tibia relative to the femur were calculated from the measured 6D data of the traceable frame.

3) Registration of 3D model and virtual markers: Because the number of virtual markers sampled with digitizer probe is limited, the generated mesh grid is sparse. We obtained the articular geometries from three-dimensional laser scans, which reverse-engineered the articular surfaces into point clouds with higher resolution and generate fine 3D model of the surface. We registered the 3D model of joint components with the virtual markers and transferred the 3D model to the position determined by virtual makers in each joint flexion angle to improve the accuracy of kinematics analysis of the articular surfaces.

4) Kinematics of the 3D Model of Articular Surfaces: In order to compare the kinematics of articular bearing surface at different knee positions and across different subjects, the registered 3D model of bones or implanted components were used to characterize the roll and gliding motion of components in three-dimensional space. By put the motion of 3D model together, the roll and gliding character and contact area of the articular bearing surfaces during knee flexion can be observed.

III. Results

A. Virtual markers and 3D Model of articular surface:

Fig. 3 (left column) depicts samples of virtual markers (point cloud) of the surface of a femoral component obtained by digitizer and 3D laser scanner respectively. The corresponding 3D model of femoral component is recon-

structed by orderly connect the points to construct mesh grid and calculate the associated normals of the surface. The bottom right model was obtained by multiple passes of 3D laser scan.

B. Kinematics of articular bearing surface:

After we obtain the 3D model of articular bearing surface and record the motion of femur, tibia and patella, the kinematics of articular bearing surfaces can by analyzed. The translations and rotations of the patella and tibia relative to the femur were calculated from the measured movement of traceable frame in three-dimensional space.

Fig. 4 illustrates the articular bearing surface of femoral condyle and tibia plateau of two joint flexion angles. The left figure indicates the both side of the femoral condyles balanced contact tibia plateau and the right figure indicates that with more joint flexion the lateral side of femoral condyle is not contact tibia plateau.

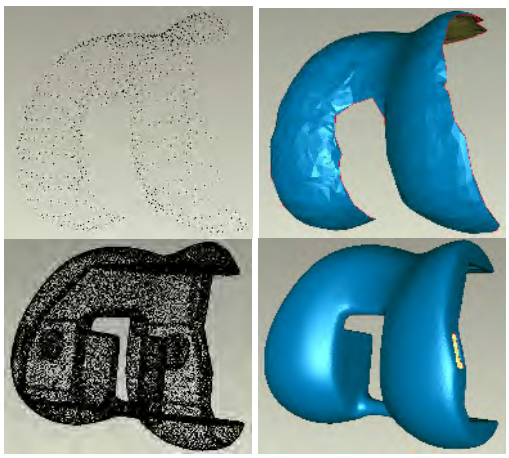


Fig. 3. Point cloud and corresponding 3D surface model. Left column are the virtual markers digitized using 3D probe and point cloud obtained via 3D laser scanner, right column illustrate the corresponding 3D surface model.

Fig. 5 is another example of 3D kinematics analysis of the articular bearing surface. Three surface models were obtained from the virtual markers of femur, tibia and patella joint surfaces using 3D digitizer. The left figure illustrate that in the beginning of knee flexion the patella contacts the femoral condyles in both side. In the middle figure, the patella contacts femoral condyles only in lateral side. The right subplot indicates that with highly knee flexion the patella sink to the deep trochlear groove of the femur and not contact the formal condyles any more.

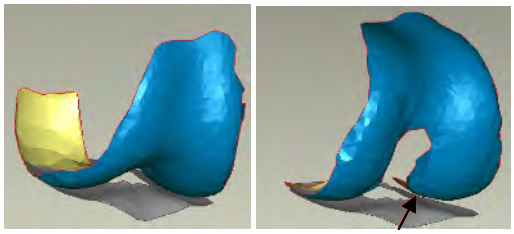


Fig. 4. Contact analysis of articular bearing surface of femoral condyle and tibia plateau in two joint flexion angles.

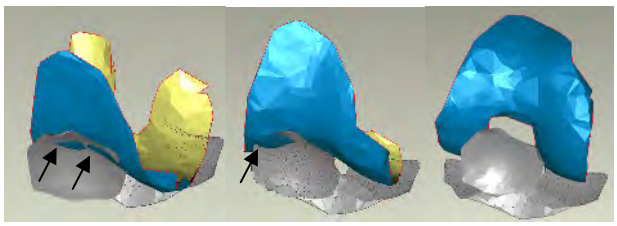


Fig. 5. Contact analysis of articular surface of femoral condyle, tibia plateau and patella with three joint flexion angles.

IV. Discussion and Conclusions

Using virtual marker tracking technique, we tracked the contact kinematics of articular bearing surfaces of femur, tibia and patella simultaneously. Three-dimensional joint kinematics and contact locations were determined with consecutive joint angles. This method is potentially useful in the accurate measurement of joint kinematics. The contact kinematics of tibiofemoral articular with different prosthesis component design can be compared by register the model to the moving virtual markers in consecutive joint angles. The kinematics of articular bearing surfaces before and after the total knee replacement can be compared using this technology.

The accuracy of our method highly depends on the representation of the articular geometry. The virtual marker tracking technique can be used with the CT-based bone model surfaces, and MR-based articular cartilage model surfaces.

Acknowledgment

This work was supported in part by the National High Technology Research and Development Program of China, under grant 2006AA02Z4E7; and the National Nature Science Foundation of China under grant 30772195.

REFERENCES

1. Anglin C., Brimacombe J.M., Wilson D.R. et al. (2007) Intra-operative vs. weightbearing patellar kinematics in total knee arthro-plasty: A cadaveric study. Clin Biomech 23(1):60-70
2. Moro-oka T, Hamai S, Miura H, et al. (2008) Dynamic activity dependence of invivo normal knee kinematics. J Orth Res 26(4): 428-434
3. Li G, DeFrate LE, Park SE, et al. (2005). In vivo articular cartilage contact kinematics of the knee: an investigation using dual-orthogonal fluoroscopy and magnetic resonance image based computer models. Am J Sports Med 33:102–107.
4. Patel V., Hall K, Ries M et al. (2004) A three-dimensional MRI analysis of knee kinematics. J Orth Res 22:283–292
5. Fregly BJ, Rahman HA, Banks SA. (2005) Theoretical accuracy of model-based shape matching for measuring natural knee kinematics with single-plane fluoroscopy. J Biomech Eng 127:692–699.
6. Tupling SJ, Pierrynowski MR. (1987). Use of cardan angles to locate rigid bodies in three-dimensional space. Med Biol Eng Comput 25:527–532.

Author: Guangzhi Wang
Institute: Department of Biomedical Engineering, Tsinghua University
Street: Medical Science Building, Tsinghua University
City: Beijing
Country: China
Email: wgz-dea@tsinghua.edu.cn

Simultaneous Recording of Physiological Parameters in Video-EEG Laboratory in Clinical and Research Settings

R. Bridzik, V. Novák, M. Penhaker

Video-EEG/Sleep laboratory, Clinic of Child Neurology, University Hospital Ostrava, Czech Republic
VSB – Technical University of Ostrava, FEECS, Ostrava, Czech Republic

Abstract — **The possibility of a flexible connection of various diagnostic equipment and seeking for correlations between recordings of different physiological functions is a powerful tool of diagnostics. There are many well-established interconnections, such as video-EEG or video-PSG. However, in some cases we need a combination of parameters "tailored" to the individual patient. Finding solutions for the patient is an interesting competence of the biomedical engineer/EEG technician.**

Keywords — **Video-EEG, pH-metry, device connection, biosignal processing**

I. Introduction

Simultaneous recording of several physiological parameters is often used in diagnostics of many diseases in video-EEG laboratory. Some combinations are fixed – for example the polysomnography comprises recording of EEG, EOG, EMG, respiratory effort, airflow and SpO2.

Many patients need an individualized combination of physiological parameters according to the diagnostic situation. For example, sometimes the correlation between the sleep stage and the moment of urination (wet time) is needed; sometimes the question should be the correlation between respiratory parameters and reflux of the gastric content to the esophagus (detected by esophageal pH-metry).

In case of these individualized combinations of physiological parameters there are some possibilities of quick and flexible approach:

II. Flexible approach

A. Functional addition through the video

This is a very simple, but flexible and fast way. When combining the external measurement with video-EEG equipment, there is a possibility to record the analogue output of the external device on the video. This simple approach is useful especially when the moment of some event should be recorded – for example the LED on urination detector is blinking, when the patient wets. The accuracy is influenced by the resolution and frame-rate of the video.

B. Software association of recordings off-line

It means subsequent combination of digital recordings after the end of measurement. This solution is applicable when the accuracy requirement is about 1 second. It is necessary to compare the internal time clocks of both equipments before and after the measurement. Possible difference should be compensated by linear interpolation. Biological check of synchrony is useful, too. The data format for the measurement interchange depends on the software of the auxiliary device – it should be binary, simple ASCII, European data format (used for EEG/PSG data transfer), or the XML format are the best choice in our opinion.

1) One of the simplest data format appropriate for the data interchange is the ASCII. The data in simple ASCII file are not structured, so it is rather complicated to read and analyze this data (lack of standardization).

2) The XML is a very flexible data format[3]. It has the advantage of a much better possibility to structure the data. The fact that this data format is supported by MS-Excel, web browser etc. is another advantage of the XML. The XML DOM Interface is an ActiveX object supporting the browsing of the XML data by any application using the XML modules[2].

3) The European data format is a widely used data standard[1,4]. Many laboratories use it for EEG data sharing. Unfortunately, it was developed predominantly for the EEG and is not so flexible as the XML.

4) The binary format of the physiological function recording is simple and structured, but with high variability, and there is often a problem with the lack of documentation.

C. Hardware combination of devices

Hardware interconnection is possible in case of analogue output of the secondary device (which should be connected to auxiliary data channel of EEG/PSG machine).

Case report: We have evaluated a case of 3-month-old boy with paroxysmal apnea and convulsions. The EEG and sleep EEG was without epileptic spikes and sharp waves.

Chwee Teck Lim, James C.H. Goh (Eds.): ICBME 2008, Proceedings 23, pp. 1042–1043, 2009
www.springerlink.com

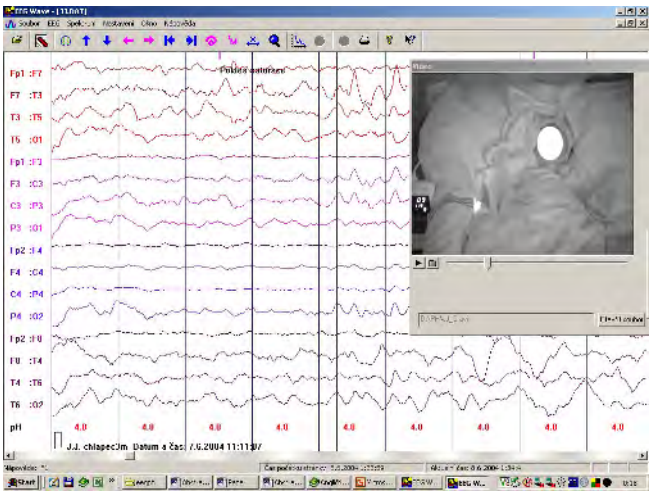


Fig. 1 Combination of 3 devices EEG, SpO2 (in the video-channel) and esophageal pH associated off-line.

The anti-epileptic drugs were ineffective. Because of symptoms of possible gastro-esophageal reflux, we decided to perform a complex recording of several physiological parameters: the video, EEG, ECG, SpO2 and esophageal pH-metry. We had no measurement device for SpO2 with digital output at that time, so we used the analogue output in the video-channel. The data from pH meter were associated after the end of the recording.

The correlation found episodes of the gastro-esophageal reflux with the drop in the peripheral hemoglobin saturation. The diagnosis of the gastro-esophageal reflux disease, not the epilepsy, was established. The child was treated for the reflux and administration of antiepileptic drugs was stopped.

The patient is currently doing well.

III. Conclusions

There are several physiological parameters useful for the correlation in the video-EEG or polysomnographic laboratory. We recommend combining e.g. the pH-metry with the video-EEG. In some cases, it is useful to interconnect the bicycle-ergometer with the detectors of the EEG and cardiologic parameters (ECG, SpO2). In children with nocturnal wetting, the correlation should be between the EEG (sleep stage) and the urination probe. The physician makes the clinical decision, but the engineer provides the technical solution.

In our opinion, the best choice for data interchange between the different equipment in one laboratory and even for the data sharing between laboratories is the XML format[3]. We have developed an XML parser for the biomedical data in the C++ language.

References

1. Kemp B, Värri A, Rosa AC, Nielsen KD, Gade J. A simple format for exchange of digitized polygraphic recordings. Electroenceph. Clin. Neurophysiol. 82, 1992:391-393.
2. Stenback J., Hégaret P.,Hors A. XMLDocument Object Model HTML, W3C, 2003
3. XML at http://www.xmlfiles.com
4. EDF at http://www.edfplus.info

Author: Radim Bridzik
Institute: University Hospital Ostrava
Street: 17. listopadu 1790
City: Ostrava, 708 52
Country: Czech Republic
Email: radim.bridzik@fnspo.cz

Preliminary Modeling for Intra-Body Communication*

Y.M. Gao[1,3], S.H. Pun[1,2], P.U. Mak[1,2], M. Du[1,3] and M.I. Vai[1,2]

[1]Key Laboratory of Medical Instrumentation & Pharmaceutical Technology, Fu jian Province, CHINA
[2]Department of Electrical and Electronics Engineering, Faculty of Science and Technology, University of Macau, Macau SAR, CHINA
[3]Institute of Precision Instrument, Fu zhou University, Fu zhou, CHINA

Abstract — **Intra-Body Communication (IBC) is an interesting and emerging communication methodology in recent years. Beneficial from conductive property of human body, IBC treats human body as transmission medium for sending/receiving electrical signal. As a result, interconnected cable and electromagnetic interference can be greatly reduced for devices communicated within human body. These advantages are significant for home health care system, which abundant of interconnected cables are needed. Furthermore, IBC technology also provides an alternative solution to communicate with implanted devices.**

Currently, pioneer researchers have proposed two general methods for realization of IBC, namely: "Capacitive coupling technique" and "Galvanic coupling/Waveguide type technique". Among the methodologies, the Galvanic technique requires neither return path nor common reference. This feature enables the technology attractive for networking biomedical devices on human body and draws much attention from recent studies. Thus, in this work, a preliminary 3D model of electromagnetic (EM) technique is developed in order to provide insight for electric signal distribution within human body. The development of a mathematical model also facilitates future researches in the aspect of communication theory of IBC, such as: optimizing carrier frequency, identifying channel characteristics, developing suitable modulation/demodulation technique, and etc.

In this paper, a mathematical model, which employs a homogeneous cylinder in analogous to a human limb, is obtained by solving the Laplace Equation analytically. The proposed model is simple and preliminary, yet it encourages further development of better model in the next phase and lays a foundation for future research and development of Intra-Body Communication.

Keywords — **Intra-Body Communication, Body Area Network, Galvanic coupling type/Waveguide type technique.**

I. Introduction

Home health care system and long term physiologic parameters monitoring system are important for chronic disease patients and elderly. They could provide patient and paramedic instant health information and generate alert while emergence. As a result, the research and development of these systems are attracting much attention from researchers. Currently, one of the main research directions is to develop versatile, intelligent, accurate, and convenient system, because it can elevate the performance for the users.

Intra-Body Communication (IBC) is a new communication technique, which employs human body as transmission medium for electrical signal. This is a special type of communication methodology and treats human tissue as a "cable" for electrical signals transmission. The merits of this technique are successful removal of connection cable, reduction of possible electromagnetic radiation, and less probably to be interference by external noise. These features are attracting much interest in the aspect of Body Area Network (BAN); especially, IBC works and relies on the human body. It also can improve home health care system and long term monitoring system, as abundant cables create problems for this kind of system. Thus, these features and advantages motivate the development and advance the research of IBC.

In this article, the authors attempt to present a mathematical model for IBC. In this model, a human limb is generalized as a 5-cm radius homogeneous cylinder with 30-cm long. After applying the quasi-static conditions, the governing equation has been reduced to Laplace Equation and a mathematical model for IBC can be obtained. The proposed model is simple and preliminary, yet it encourages further development of better model in the next phase and lays a foundation for future research and development of IBC.

II. Background

IBC was first introduced by T.G. Zimmerman in 1995[1]. They employed the electrostatic coupling technique to demonstrate the feasibility of the idea and built the first prototype system. The design consisted of a transmitter and a receiver, which had electrodes attached to the human body as depicted in Figure 1. The electric field of the transmitter is induced by the electrodes, coupled to the human body and flowed towards the ground, and then the electrodes of the receiver detected the electric field flowing through the human body with respect to the ground. Normally, only a few potion of electric field flowed to other parts of the body

* The work presented in this paper is supported by The Science and Technology Development Fund of Macau under grant 014/2007/A1 and by the Research Committee of the University of Macau under Grants RG051/05-06S/VMI/FST, RG061/06-07S/VMI/FST, and RG075/07-08S/VMI/FST.

Chwee Teck Lim, James C.H. Goh (Eds.): ICBME 2008, Proceedings 23, pp. 1044–1048, 2009
www.springerlink.com

and detected by the receiver eventually. Thus, the sensitivity of the receiver should be high enough in order to have better and reliable performance.

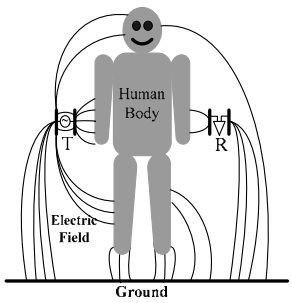


Figure 1 Electrostatic coupling technique

Since the development of the prototype IBC system by Zimmerman, several interesting applications, such as: heart rate and oxygen saturation sensors[2], sensors[3, 4], modeling[5, 6] and various communication techniques: On/Off Keying(OOK)[5], Differential Binary Phase Shift Keying (BPSK), Frequency Shift Keying (FSK)[2, 7, 8] etc. have been employed for improving the performance and stability of IBC.

The Galvanic coupling/Waveguide type technique[9-13] is an alternative configuration for implementation of IBC. As shown in Figure 2, electrodes of the transmitter are attached to one end of the human body while electrodes of the receiver are attached to another end. When electrical signals are applied to the electrodes of the transmitter, the signal will propagate along the human body in analogue to electromagnetic wave propagate along a waveguide. The electrodes of the receiver, which attached on the other end of the body, detect and convert the information from the transmitter. Unlike the electrostatic coupling technique, the electrical signal propagated via ionic fluid and thus, less dependent on the surrounding environment. Since the technique is relative new, the research of galvanic coupling technology mainly focused on application – especially biomedical application. Although the achieved data rate of Galvanic coupling type technique is low, independent of the earth ground and current propagation within human tissue are more attractive than the electrostatic coupling technique. Based on these reasons, the research direction of the authors is focused on the Galvanic coupling type IBC.

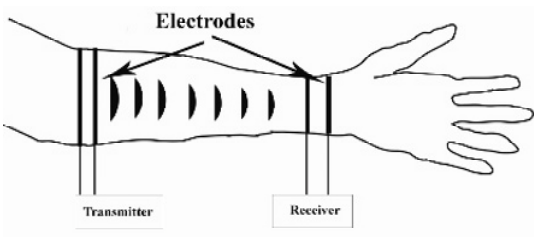


Figure 2 Waveguide type technique

III. Mathemtical model

Since the first report of IBC appeared in 1995, Galvanic coupling technique received much attention from researchers and engineers. During the period, various prototypes and experiments have been built and conducted. Other than demonstrated the feasibility of the method and developed application for IBC, one of the main research goals is to investigate the electrical properties of IBC. Currently, various researchers will employ different carrier frequency, coupling amplitude, encoding scheme, electrode location, and etc. The reasons behind of this phenomenon would be quite complicated; however, lack of good understanding of IBC propagation mechanism may be an explanation. Based on this observation, the authors attempt to develop a model in order to give insight about the electrical and communication properties of Galvanic coupling type IBC.

As the initial attempt of modeling IBC, a human limb is selected and ring-type electrodes are attached to either bands (at $z=z_1$ & z_2) as shown in Figure 2. The irregular geometry of human limb is difficult to be described by mathematics, so, a h=30-cm long homogeneous cylindrical muscle with a=5-cm in radius would be studied instead (as depicted in Figure 3). Then, applying the Maxwell Equations for the simplified problem to study the mechanism of IBC and find out the mathematical model for the problem.

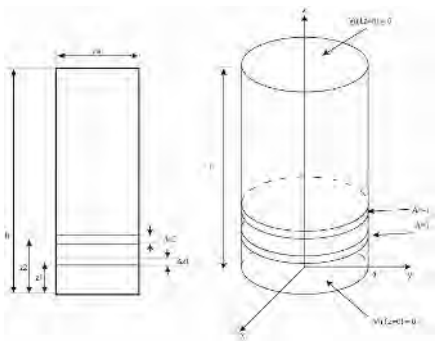


Figure 3 Simplified model with ring electrodes

Additionally, as the material of the IBC problem is biological tissue and is operating at low frequency[9-11], the quasi-static approximation may be used. The quasi-static approximation states that "if the dimension of the studied problem is less than 1 meter and satisfies Eq. (1), the capacitive effect can be neglected" [14, 15].

$$\frac{\omega\epsilon_0\epsilon_r}{\sigma} \ll 1 \tag{1}$$

In Eq. (1), ε_r and σ represent the relative permittivity and conductivity of the tissue and ω denotes the operating angular frequency. In Table 1, the quasi-static approximation with muscle's electrical characteristics[16] is listed.

Table 1 Quasi-static condition

	10kHz	100kHz
Conductivity σ	3.4e-1	3.9e-1
Relative Permittivity ε_r	3.0e4	8.0e3
$\frac{\omega\epsilon_0\epsilon_r}{\sigma}$	≈0.049	≈0.114

From Table 1, for the operating frequency less than 100kHz, the quasi-static could be applied and according to the prior research, the operation frequency of waveguide type technique is typically less than 100kHz[9, 11]. Thus, the governing equation becomes Laplace Equation and, the formulation of the IBC problem can be written as:

$$\nabla^2 V = \frac{1}{r}\frac{\partial}{\partial r}\left(r\frac{\partial V}{\partial r}\right) + \frac{1}{r^2}\frac{\partial^2 V}{\partial \phi^2} + \frac{\partial^2 V}{\partial z^2} = 0 \tag{2}$$

with general side-excited case:

$$\begin{aligned} &V(r,\phi,z=0)=0 \\ &V(r,\phi,z=h)=0 \\ &\frac{\partial V}{\partial r}(r=a,\phi,z)=\frac{J(z)}{\sigma} \end{aligned} \tag{3}$$

where the ring type injected current signal is defined as:

$$J(z)=\begin{cases} J_1 = 1mA/m^2 & z1-\frac{\Delta z1}{2} \le z \le z1+\frac{\Delta z1}{2} \\ J_2 = -1mA/m^2 & z2-\frac{\Delta z2}{2} \le z \le z2+\frac{\Delta z2}{2} \\ 0 & elsewhere \end{cases} \tag{4}$$

By solving the above formulation, an analytical solution for voltage distribution within the cylinder can be obtained.

$$V(r,\phi,z)=\sum_{m'=1}^{\infty} A_{m'} I_0\left(\frac{m'\pi}{h}r\right) sin\left(\frac{m'\pi}{h}z\right) \tag{5}$$

where

$$A_{m'}=\frac{2}{\left[I_0\left(\frac{m'\pi}{h}r\right)\right]'_{r=a}h}\int_0^h J(z)sin\left(\frac{m'\pi z}{h}\right)dz \tag{6}$$

and, I_o represents the modified Bessel function of the first kind of order 0.

With Eq. (5) and Eq. (6), the potential on the surface and within the human limb could be found spatially. From Figure 4, the plot of electrical signal inside the human limb is shown (X-Z sectional view at y=0 of the voltage distribution). Due to the electrode configuration employed in this case, the expected or calculated voltage induced by the electrodes is symmetry with respect to z-axis and the voltage on the same level of z-axis at the surface of the human limb is equal. This suggests that the electrodes of the receiver should not be placed on the same level of z-axis for this parallel ring type electrode case.

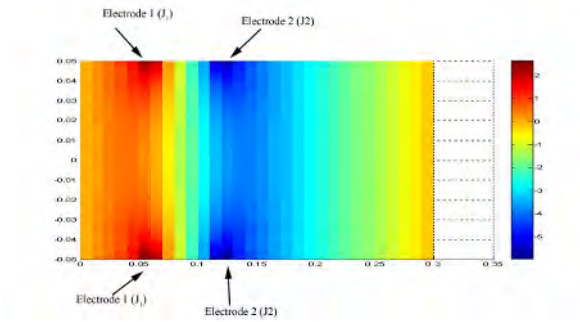


Figure 4 X-Z sectional view (at y=0) of the voltage distribution of the cylinder

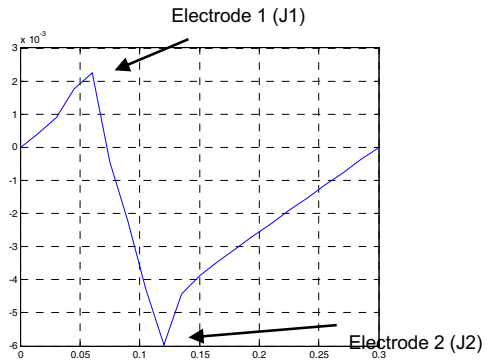


Figure 5 Voltage distribution on the surface of human limb along z-axis

On the other hand, from Figure 5, if electrodes are placed in the direction of z-axis, the voltage difference between electrodes of the receiver will be high (e.g. if the electrodes of receiver located at z=0.2cm and z=0.25cm, the voltage difference would be around 1mV). Thus, according to the mathematical model derived by this paper, the electrodes of the received of IBC would be better placing across z-axis.

IV. Summary

Intra-Body Communication (IBC) is an interesting and emerging communication methodology in these years. Beneficial from conductive property of human body, IBC treats human body as transmission medium for sending electrical signal.

In this paper, a mathematical model, which employs a homogeneous cylinder in analogous to a human limb, is obtained by solving the IBC problem analytically. Through applying the quasi-static approximation, the Maxwell Equation can be simplified to Laplace Equation and the obtained an analytical solution for the voltage distribution can be obtained in certain symmetrical cases. The obtained model reveals the propagation mechanism of the ring type electrodes in human limb and suggests the insight of the configuration of the electrodes placement of the receiver.

The proposed model is simple and preliminary, yet it provides a foundation for analysis and future development of IBC. The obtained model encourages further development of better model in the next phase and lays a foundation for future research and development of Intra-Body Communication.

Acknowledgement

The authors would like to express their gratitude to The Science and Technology Development Fund of Macau and Research committee of University of Macau for their kind support. The authors also appreciate for the continuous support from the colleagues in Institute of Precision Instrument - Fu Zhou University, Biomedical Engineering Laboratory, Microprocessor Laboratory, Control and Automation Laboratory - University of Macau.

References

[1] T. G. Zimmerman, (1995), Personal Area Networks (PAN): Near-Field Intra-Body Communication, in Media Art and Science. Master Thesis: Massachusetts Institute of Technology.

[2] K. Hachisuka, A. Nakata, T. Takeda, Y. Terauchi, K. Shiba, K. Sasaki, H. Hosaka, and K. Itao, (2003), Development and performance analysis of an Intra-Body Communication Device, in The 12th International Conference on Transducers, Solid-State Sensors, Actuators and Microsystems 2003, pp. 1722-1725.

[3] M. Shinagawa, M. Fukumoto, K. Ochiai, and H. Kyuragi, (2004), A Near-Field-Sensing Transceiver for Intrabody Communication Based on the Electroopic Effect, IEEE Transactions on Instrumentation and Measurement, vol. 53, pp. 1533-1538.

[4] A.-i. Sasaki, M. Shinagawa, and K. Ochiai, (2004), Sensitive and stable electro-optic sensor for intrabody communication, in The 17th Annual Meeting of the IEEE Lasers and Electro-Optics Society, 2004 (LEOS 2004), pp. 122-123.

[5] K. Fujii, K. Ito, and S. Tajima, (2003), A study on the receiving signal level in relation with the location of electrodes for wearable devices using human body as a transmission channel, in IEEE Antennas and Propagation Society International Symposium 2003, pp. 1071-1074.

[6] K. Fujii and K. Ito, (2004), Evaluation of the Received Signal Level in Relation to the Size and Carrier Frequencies of the Wearable Device Using Human Body as a Transmission Channel, in IEEE Antennas and Propagation Society International Symposium 2004, pp. 105-108.

[7] E. R. Post, M. Reynolds, M. Gray, J. Paradiso, and N. Gershenfeld, (1997), Intrabody buses for data and power, in First International Symposium on Wearable Computers, 1997, pp. 52-55.

[8] K. Partridge, B. Dahlquist, A. Veiseh, A. Cain, A. Foreman, J. Goldberg, and G. Borriello, (2001), Empirical Measurements of Intrabody Communication Performance under Varied Physical Configurations, in Symposium on User Interface Software and Technology Orlando, Florida, pp. 183-190.

[9] D. P. Lindsey, E. L. Mckee, M. L. Hull, and S. M. Howell, (1998), A new technique for transmission of signals from implantable transducers, IEEE Transactions on Biomedical Engineering, vol. 45, pp. 614-619.

[10] M. Oberle, (2002), Low power system-on-chip for biomedical applications, PhD Thesis vol. ETH NO.14509, IIS/ETH Zurich,

[11] T. Handa, S. Shoji, S. Ike, S. Takeda, and T. Sekiguchi, (1997), A very low-power consumption wireless ECG monitoring system using body as a signal transmission medium, in 1997 International Conference on Solid State Sensors and Actuators, 1997 (TRANSDUCERS '97), pp. 1003-1006.

[12] M. Wegmueller, A. Lehner, J. Froehlich, R. Reutemann, M. Oberle, N. Felber, N. Kuster, O. Hess, and W. Fichtner, (2005), Measurement System for the Characterization of the Human Body as a Communication Channel at Low Frequency, in 27th Annual International Conference of the Engineering in Medicine and Biology Society, 2005 (IEEE-EMBS 2005). , pp. 3502-3505.

[13] M. S. Wegmuller, (2007), Intra-body communication for biomedical sensors networks, in ETH Zurich. vol. Phd Zurich: Swiss Federal Institue of Technology Zurich (ETH).

[14] R. Plonsey, (1995), Volume conductor theory, in The biomedical engineering handbook, J. D. Bronzino, Ed.: CRC Press LLC, pp. 119-125.

[15] R. M. Gulrajani, (1998), Bioelectricity and Bioelectromagnetism: John Wiley & Son, INC.

[16] C. Gabriel and S. Gabriel, (1996), Compilation of the dielectric properties of body tissues at RF and Microwave Frequencies, Occupational and environmental health directorate, Radiofrequency Radiation Division, Brooks Air Force Base, Texas (USA)

Author: Gao Yue Ming
Institute: Key Laboratory of Medical Instrumentation & Pharmaceutical Technology, Fu jian; Institue of Precision Instrument, Fu zhou University
Street: No.523, Gong ye Road
City: Fu zhou, Fu jian
Country: China
Email: fzugym@yahoo.com.cn

Application of the Home Telecare System in the Treatment of Diabetic Foot Syndrome

P. Ladyzynski[1], J.M. Wojcicki[1], P. Foltynski[1], G. Rosinski[2], J. Krzymien[2], B. Mrozikiewicz-Rakowska[2], K. Migalska-Musial[1] and W. Karnafel[2]

[1]Institute of Biocybernetics and Biomedical Engineering, Polish Academy of Sciences, Warsaw, Poland
[2]Department and Clinic of Gastroenterology and Metabolic Diseases, Medical University of Warsaw, Warsaw, Poland

Abstract — **Diabetes is a group of metabolic diseases affecting more than 200 mln people worldwide, which is characterized by elevated blood glucose level. Diabetes causes a number of late complications among which diabetic foot syndrome (DFS) is one of the most dramatic as a major cause of the lower limb amputations. In IBBE PAS the TeleDiaFoS system aimed at monitoring of DFS treatment was developed. In the system, the Central Clinical Server is accessed by the Patient's Module using a wireless internet connection to send the wound pictures, the blood glucose (BG) readings and the blood pressure (BP) values. Clinical verification of the TeleDiaFoS system has been organized as a randomized 90-days trial with the study and the control groups consisting of 10 type 2 diabetic patients, each. Currently, the evaluation of the first patient treated with multi-injection insulin delivery and antibiotic – dalacin therapies has been terminated. Home telecare therapy led to 12-fold reduction of the wound surface (from 356 mm^2 to 29 mm^2). During the whole 90-days period BP was controlled efficiently, however, acceptable BG level has not been maintained. In conclusion, application of the system leads to more effective realization of the DFS therapy and has a positive impact on the patient's comfort.**

Keywords — **Diabetes mellitus, diabetic foot syndrome, telemedicine, wound healing, foot scanner**

I. Introduction

Diabetes mellitus is listed among the most serious and dangerous chronic conditions such as heart disease and stroke (cardiovascular diseases), cancer, asthma and chronic obstructive pulmonary disease that cause 30 mln deaths all over the world each year. The number of diabetic patients has already exceeded 200 mln and it will reach 330 mln cases by the year 2030 according to the predictions.

The International Diabetes Federation and the WHO describe the dramatic increase of the number of cases of diabetes that is occurring throughout the world today as "the most challenging health problem of the 21st century" [1]. Diabetes is characterized by high blood glucose level (hyperglycemia) that impairs the function of the body's proteins leading to a number of late complications related to the microangiopathy, the macroangiopathy and the neuropathy. Among these complications the diabetic foot syndrome (DFS) that is caused by neuropathy, angiopathy or both is one of the most dramatic. DSF is manifested in the form of ulcers, which are unhealing open sores or wounds that most often are located on the sole of the foot. If left untreated these foot ulcers can become infected and may lead to amputation. It is estimated that DSF is a direct cause of more than 50% of all lower limb amputations in the world.

Diabetes has been an incurable disease, so far. Therefore, patients with diabetes require life-long instantaneous monitoring and treatment aimed not only at controlling of the blood glucose level but also at screening for, diagnosing and taking care of the late complications of diabetes. Telemonitoring and telecare have been used to serve these purposes starting from the early 90-ies. First home telecare systems were applied during insulin therapy of diabetic patients for the remote monitoring of the patient's metabolic state, the life-style and the course of the treatment. These systems contributed to an improvement of: the reliability of the data collected and reported by the patients, frequency of the check-ups of the data performed by the physician and different measures of the outcome of the treatment [2-4]. Later, telemedicine usage has spread on screening, monitoring and treating of the late complications of diabetes such as the diabetic retinopathy, the cardiovascular disorders and the DFS. In the last few years, several video consultation services for the DFS patients have been reported, basing on the use of the modern mobile phones integrated with the digital cameras [5-8].

In the first part of the manuscript the design and implementation of the TeleDiaFoS home telecare system developed by the authors is presented. In the second part, a clinical trial validating the feasibility of the system is described and the results of the first clinical application of the TeleDiaFoS system are shown.

II. TeleDiaFoS system

The TeleDiaFoS consists of: the Central Clinical Server (CCS), the Diabetologist's Workstation, the Podiatrist's

Chwee Teck Lim, James C.H. Goh (Eds.): ICBME 2008, Proceedings 23, pp. 1049–1052, 2009
www.springerlink.com

Workstation and a set of the Patient's Modules (PM). The structure of the system is presented in Figure 1.

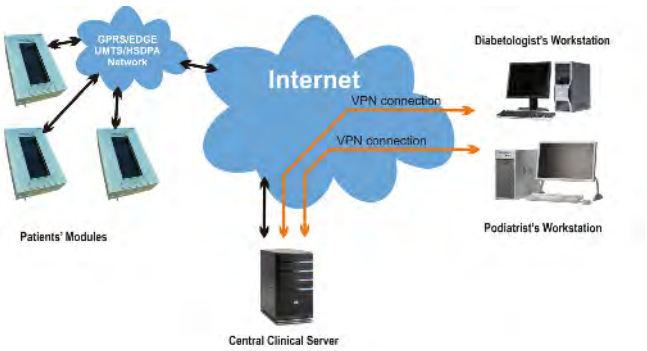


Fig. 1 Structure of the TeleDiaFoS system

The main database of the system is located in CCS. This database [9] contains 5 modules:

- *Patient's Registration,* which groups the standard patient's data like name, address, and telephone number.
- *Examinations*, which collects the data related to the patient's general state, diabetes treatment and diabetic foot examination (vibration sensing test, pressure and temperature sensing test, ankle-brachial index, pedobarographic examination, images from scintillation camera, angio-CT, USG, RTG). In this module there are also results of the tissue evaporative water loss (TEWL) measurements, pH and temperature of the skin and the images of the foot ulcers taken with an optical scanner during routine check-ups in the foot care clinic.
- *Telemedical Data*, which gathers the data sent by the patient using the homecare PM, i.e. blood glucose concentration, arterial blood pressure, heart rate and images of the foot wounds.
- *Graphical Presentation*, which makes it possible to annotate the schematic pictures of the patient's feet by means of marking the location and size of the ulcers and other changes on the foot like tinea pedis, gangrene, pseudomonas aeruginosa and keratosis (see Figure 2). It is also possible to erase parts of the foot image, which corresponds to the amputated parts of the patient's foot. Additionally, the physiological parameters being monitored, i.e. the blood glucose concentration, the arterial blood pressure and the heart rate can be displayed on the time graphs.
- *Options,* which enables to synchronize the database, change the optical scanner, and display short information about the TeleDiaFoS database.

The data can be either entered manually or can be uploaded automatically from the PM, which is a homecare device (see Figure 3).

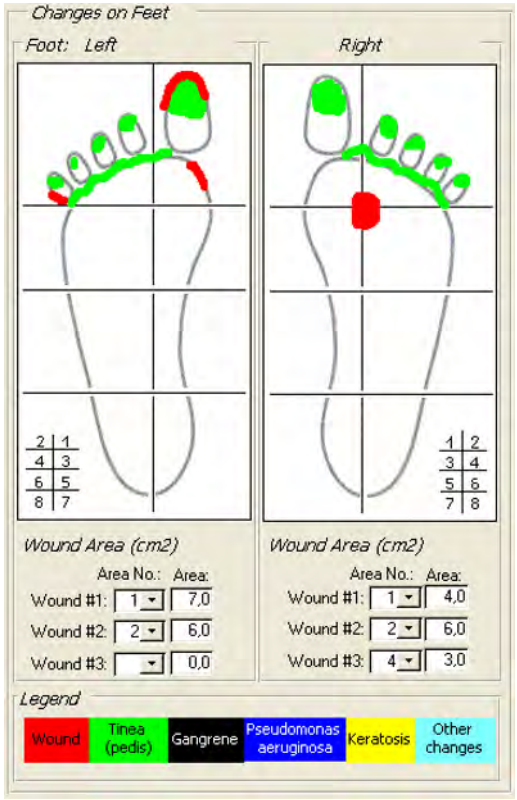


Fig. 2 Exemplary drawing of feet state.
Wounds and tinea pedis are present on both feet.

PM is operated by a patient using a simple two-buttons remote controller. There are four LEDs located on the front panel of PM which signals the current state of the device. The following operations can be performed:

- taking pictures of the sole of the patient's foot with a built-in foot scanner,
- downloading the blood glucose data, the blood pressure recordings and the heart rate values from memory of the external meters connected to PM,
- switching PM on and off.

The Accu-Chek Active glucometer (Roche, Germany) and BP 3BU1-4 blood pressure meter (Taiwan) were selected devices to gather the patients' data. PM is able to communicate with glucometer and to download the data stored in its internal memory using the infrared interface (IrDA). The communication with the blood pressure meter is possible via the RS232 port.

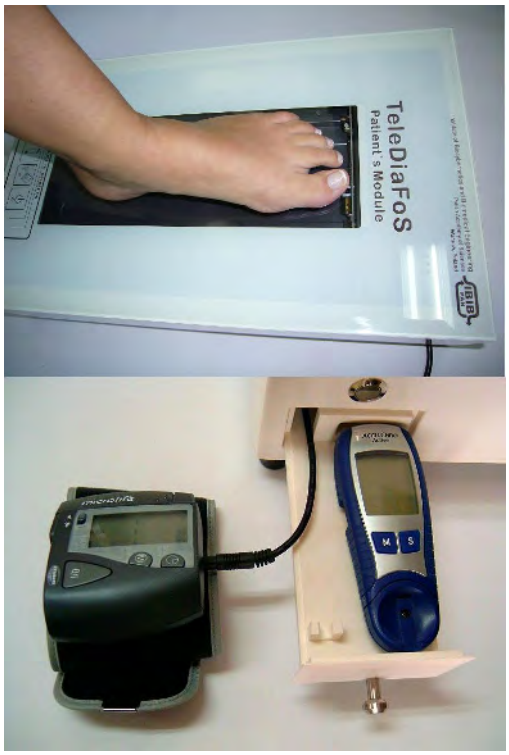


Fig. 3 Patient's module with a foot prepared for scanning (upper picture); glucometer and blood pressure meter connected to PM (lower picture)

It is possible to send the pictures of the foot being scanned together with the blood glucose readings and the blood pressure values being downloaded from the above-mentioned meters to the CCS. The PM is connected to the Internet using the built-in wireless modem, which operates in HSDPA/UMTS/EDGE/GPRS modes. The modem software selects automatically the highest data transfer speed available in the network of the internet provider.

The foot image files and the files containing the data downloaded from the external meters are transferred to the CCS automatically using the ftp protocol. At the server site specialized software service decodes the data and inserts them into the TeleDiaFoS database.

Physicians can access the patients' data using the workstations with locally replicated copies of the main database. The data on the local workstations are synchronized with the data stored in the main database through the virtual private network (VPN).

Proper operation of all building blocks of the TeleDiaFoS and the technical feasibility of the automatic teletransmission of the data from PM were confirmed during extensive laboratory tests. The initial tests in real homecare conditions were performed afterwards with one patient over a period of 32 days. The patient sent 6 pictures of the foot and 6 times was sending the data from measuring devices. No technical problems during the homecare test were identified. The patient has not reported any problems related to the management of PM.

III. Clinical Verification of the TeleDiaFoS

Clinical verification of the TeleDiaFoS system has been organized as a randomized 90-days trial. The study protocol has been approved by the Local Ethical Committee. The target of 10 type 2 diabetic patients in the study group and in the control group has been set. Each patient has to sign the informed consent for participation. The inclusion criteria comprise the ability and willingness of the patient to perform everyday self-monitoring (i.e. blood glucose and blood pressure testing) and control (i.e. insulin injections), age between 45 and 65 years, neuropathic DFS with an ulcer located on the sole of one foot, ankle-brachial index greater than 0.7. Patients are excluded from the study in the case of the proliferative retinopathy and / or maculopathy that require active treatment, kidney dysfunction (creatinine > 2 mg/dL), cardiac insufficiency, cardiac infarction within the last 3 months before the study and mental impairment. The study protocol includes 3 clinical visits at the beginning of the study, after one month and at the end of the study. During the first visit each patient is trained to be able to use the glucometer, the blood pressure meter and to control the PM.

Currently, the treatment of the first patient from the study group (66 years old male with a 9-years history of diabetes, treated with multi-injection insulin delivery and antibiotic – dalacin therapies) has been terminated.

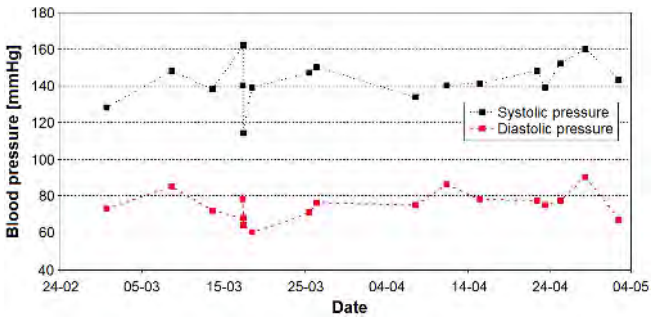


Fig. 4 Blood pressure of the diabetic patient with DFS treated using the TeleDiaFoS

During the monitoring period 13 transmissions of the data were performed (in average once per week). Most of the time blood pressure was controlled satisfactory (see Figure 4). However, acceptable glycemic control has not been maintained (see Figure 5). Despite this, the treatment that

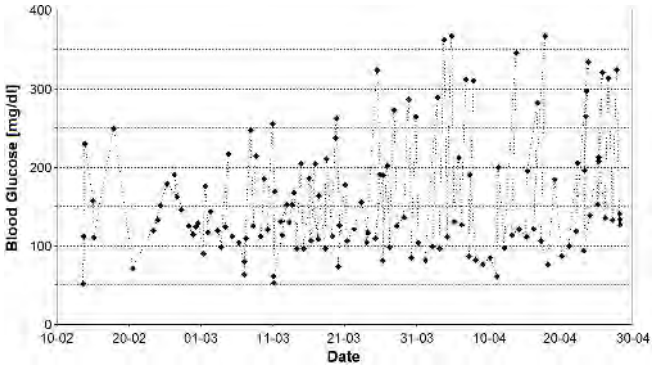


Fig. 5 Blood glucose concentration of the diabetic patient with DFS treated using TeleDiaFoS



Fig. 6 Exemplary pictures of the foot wound sent by the patient at the beginning of the study period (left), 23 days later (in the middle) and at the end of the study (right)

was supported by an application of the TeleDiaFoS system led to more than 12-fold reduction of the wound surface, i.e. from open wound with a surface of 356 mm^2 to minimal change of the skin area measuring 29 mm^2 (see Figure 6).

IV. Conclusions

The TeleDiaFoS system takes the advantage of the wireless telematic technology which enables the physician to monitor and analyze patients' data remotely. Application of the system leads to more effective realization of the DFS therapy and has a positive impact on the patient's comfort eliminating the inconvenience related to regular visits in the outpatient clinic.

Acknowledgment

The work has been financed using funds for the scientific research in the years 2005–2008 in the framework of the research grant from the Polish Ministry of Science and Higher Education (Grant No. 3 T11E049 29).

References

1. International Diabetes Federation at http://www.idf.org
2. Montani S, Bellazzi R, Quaglini S, d'Annunzio G (2001) Meta-analysis of the effect of the use of computer-based systems on the metabolic control of patients with diabetes mellitus. Diabetes Technol Therap 3:347–356.
3. Farmer A, Gibson OJ, Tarassenko L, Neil A (2005) A systematic review of telemedicine interventions to support blood glucose self-monitoring in diabetes. Diabetes Med 22:1372–1378.
4. Ladyzynski P, Wojcicki JM, Krzymien J et al. (2006) Mobile telecare system for intensive insulin treatment and patient education. First applications for newly diagnosed type 1 diabetic patients. Int J Artif Organs 29:1074–1081.
5. Clemensen J, Larsen SB, Kirkevold M, Ejskjaer N (2008) Treatment of diabetic foot ulcers in the home: video consultations as an alternative to outpatient hospital care. Int J Telemed Appl 2008:132890 DOI 10.1155/2008/132890
6. Hsieh CH, Tsai HH, Yin JW et al. (2004) Teleconsultation with the mobile camera-phone in digital soft-tissue injury: a feasibility study Plast Reconstr Surg 114:1776–1782
7. Wilbright WA, Birke JA, Patout CA et al. (2004) The use of telemedicine in the management of diabetes-related foot ulceration: a pilot study. Adv Skin Wound Care 17: 232–238
8. Finkelstein SM, Speedie SM, Demiris G et al. (2004) Telehomecare: quality, perception, satisfaction. Telemed J e-Health 10:122–128
9. Foltynski P, Wojcicki JM, Migalska-Musial K et al. (2006) TeleDiaFoS database for monitoring diabetic foot patients. IFMBE Proc. vol. 14, World Congress on Med. Phys. & Biomed. Eng., Seoul, Korea, 2006, p 4926
10. Foltynski P, Ladyzynski P, Migalska-Musial K et al. (2007) A new device for monitoring of foot wounds healing. Int J Artif Organs, vol. 30, Congress of Europ. Soc. Artif. Organs, Krems, Austria, 2007, p 746.

Corresponding author:

Author: Piotr Ladyzynski, Ph.D.
Institute: Institute of Biocybernetics and Biomedical Engineering, Polish Academy of Sciences
Street: 4 Trojdena Street
City: 02-109 Warsaw
Country: Poland
Email: pladyzynski@ibib.waw.pl

In-vitro Evaluation Method to Measure the Radial Force of Various Stents

Y. Okamoto[1], T. Tanaka[1], H. Kobashi[1], K. Iwasaki[2], M. Umezu[1]

[1]Integrative Bioscience and Biomedical Engineering, Twins, Waseda Univ., Japan
[2]Waseda Institute for Advanced Study, Waseda Univ., Japan

Abstract — **Endovascular treatments of stenosis in carotid artery often utilize a self-expanding stent. There are a variety of stents commercially available. The radial force of a stent is a key parameter to characterize its mechanical property, but there is no reliable evaluation to standardize the force measurement. In measuring the radial force accurately, the stent deformation has to be uniform for the whole structure so as to ensure the force balance. Here we aim to develop such a measuring system of stent radial force, and compare the results with those obtained by conventional techniques.**

A developed device consisted of a tubular stent holder and a load measuring system. The Precise, Protege and Easy Wall stents with a diameter (D) of 10 mm were placed by a delivery system. Radial forces were measured with D = 8, 6, 5, and 4 mm at a temperature of 37 degrees. Maintaining the circular shape of stents was found to influence substantially the magnitude of radial force. The value increased about 80 % at maximum for those measured by conventional techniques. These data show that the radial force has to be uniformly applied in a circumferential direction. Also, the Easy Wall stent showed a distinct tendency in contrast to the Precise and Protege stent. The Easy Wall stent was found to be placed with eliminating the axial variation of mesh geometries.

These results indicate that the radial force measurements of stents have to ensure the uniform mesh geometry in both the axial and circumferential direction. It was concluded that our device can ensure the reliable measurement of stent radial forces.

Keywords **— Stent, Radial force, Self-expanding stent, Mechanical property**

I. Introduction

Endovascular treatments of stenosis using a stent are a common procedure. There are indeed a variety of stents available in market. In clinical practice, however, selection criteria of stents are often obscure, and are determined empirically by surgeons. In order to establish a selection guideline of stents, it is mandatory to understand mechanical properties of stents, such as radial force, and characterize them among a variety of stents in a standardized condition. In doing so, a reliable in vitro evaluation methodology has to be established.

A measurement of stent radial force, such as seen in literatures [1-4], often utilizes a film-type jig to hold a stent tested [1] [2](Fig. 1). In our laboratory, we previously used a comb-type jig (Fig.2). However, these conventional systems have some disadvantages. First, stents tended to show varying patterns of the cross-section in the axial direction according to loading applied. Second, the uniformity of the stent mesh was no longer maintained, resulting in varying mesh intervals locally. Particularly, the large deformation with the irregular mesh was often detected at the edge. In order to solve these problems, we aim to develop a new system for measuring a stent radial force. Here we compare the data with those obtained by our previous measurement system in order to establish a reliable methodology of stent radial force measurement.

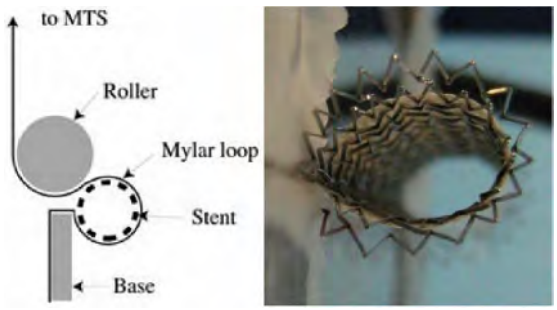


Fig.1 Schema and photograph of film-type jig

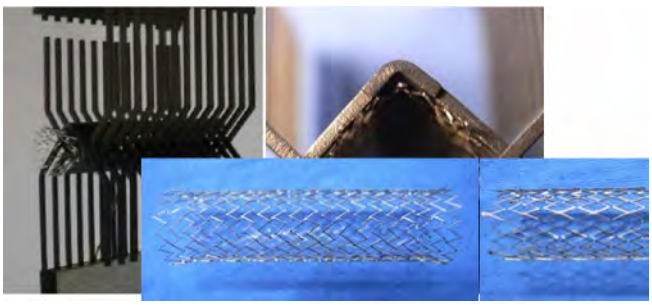


Fig.2 Photograph of comb-type jig

Chwee Teck Lim, James C.H. Goh (Eds.): ICBME 2008, Proceedings 23, pp. 1053–1056, 2009
www.springerlink.com

II. Material and Method

Fig.3 shows a schema of a newly developed device for measuring a stent radial force. It consisted of a U-shaped stent holder and a load measuring system. A pair of stent holders constituted a tubular geometry, in which a stent is placed by a delivery system.

Fig.4 shows a photograph of a stent delivered. As shown in the figure, the cross-section of a stent remained circular, and there is no marked variation of mesh-to-mesh pitches in the axial direction.

Conventionally, the cross-sectional shape of the stent in response to loading applied depends on the geometry of a jig (Fig.2). Also, the edge of the stent tends to be locally deformed. These drawbacks were improved in our current measuring system.

The stent tested comprised three commercially available ones, namely the Precise, Protege and Easy Wall stents with a diameter (D) of 10 mm, as shown in Table. 1. These stents varied in mesh geometry, and the Precise and Protege stents had a similar zigzag shape fabricated by laser cutting of a tubular Nitinol, while the Easy Wall stent was a wire-braided type. Experiments were conducted at a temperature of 37 degrees. Radial forces were measured with D = 8, 6, 5, and 4 mm for three stents, respectively.

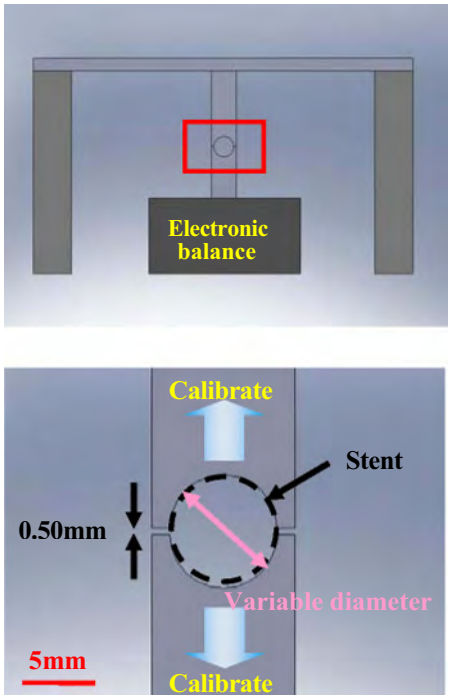


Fig.3 Schema of a developed device for measuring a stent radial force

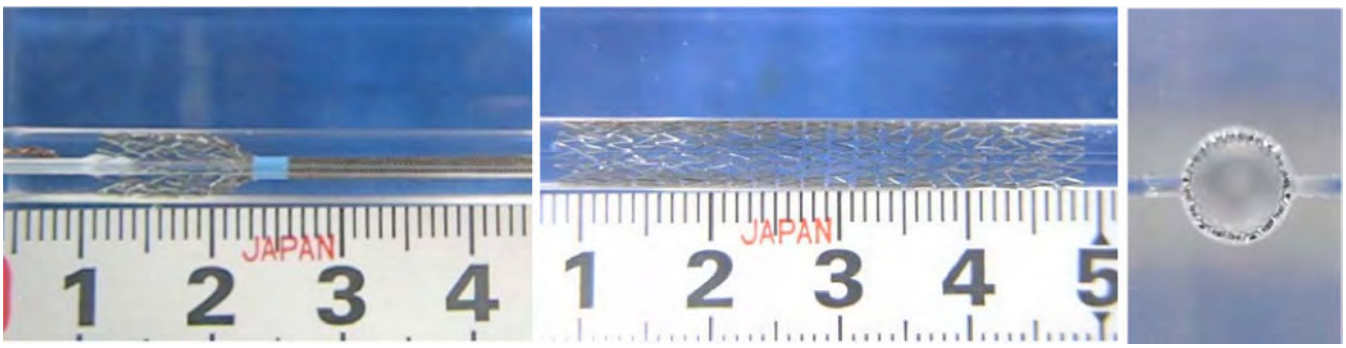


Fig.4 Photograph of a stent delivered

Table 1 Stents (Left: Precise, Center: Protege, Right: Easy Wall)

Stent	Precise	Protege	Easy Wall
Dia.-Length	φ10-40mm	φ10-40mm	φ10-32mm
Material	Ni-Ti	Ni-Ti	Elgiloy
Manufacturer	Cordis / J&J	ev3	Boston Scientific

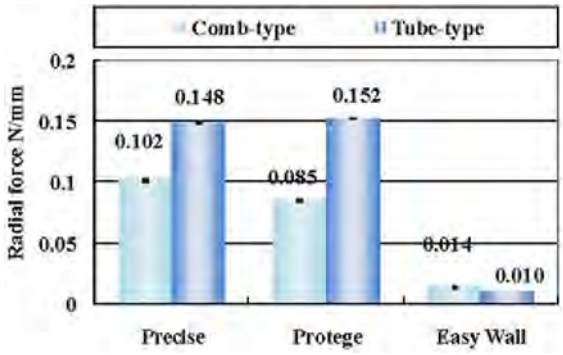


Fig.5 Comparison of radial force between comb-type and tube-type jigs at a diameter of 8 mm
(Left: Precise, Centre: Protégé, Right: Easy Wall)

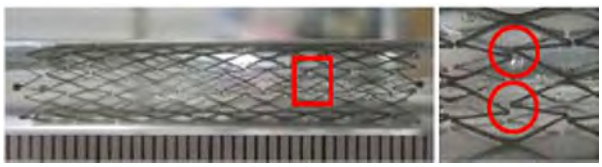


Fig.6 Photograph of irregularities on mesh of the Protege stent (D=8mm)

III. Results and Discussion

Fig.5 compares the results obtained by a comb-type and tube-type jig for the Precise, Protege and Easy Wall stent at a diameter of 8 mm. In the Precise and Protege stents, radial force measured showed 45 %, and 79 % higher for the tube-type jig than those of a comb-type jig. On the other hand, the Easy Wall stent showed an opposite tendency, where the tube-type jig showed 29 % lower value. In the case of the Precise and Protege stent, the elimination of clearance within a jig using the tube-type one elevated the magnitude of the radial force. The comb-type jig had the clearance at the corner, where the stents were deformed locally.

As a result, the zigzag stent segment did not shrink in the circumferential direction, resulting in the lower value of radial force. On the other hand, the Easy Wall stent had a diamond-shaped segment, which released the radial force in the axial direction. This stent structure substantially reduced the radial force. In the comb-type jig, the Easy Wall stent received the counter force due to the mechanical contact at the edge, whereas the tube-type jig had the same cross-sectional shape along with the axis. These results indicate that the present tube-type jig system enables to measure the radial force of stents in a reliable manner.

Also, we used a delivery system to insert a stent inside a jig. Then, we found an interesting phenomenon for the Protege stent. In releasing a stent out of the delivery system, the Precise and Easy Wall stent did not show any mesh irregularities. However, the Protege stent showed a local

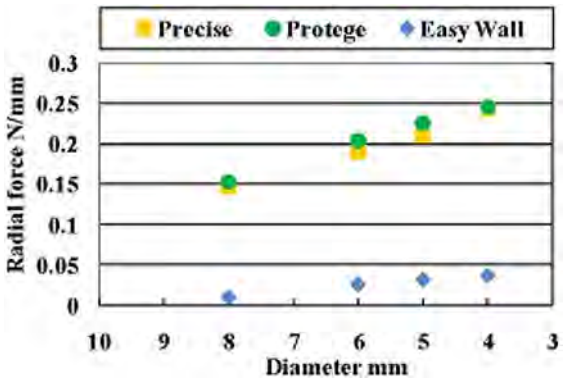


Fig.7 Characteristics of a radial force

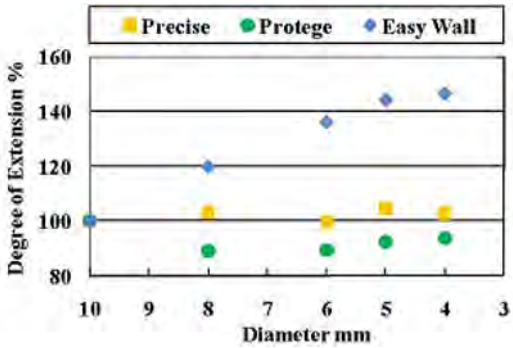


Fig.8 Extensional rate of the stent longitudinal length during radial force measurements

mesh deviation during release as shown in Fig.6. This phenomenon attributes to the mesh design, and the use of a delivery system in testing stent radial force was found to be important.

Fig.7 characterizes a radial force measurement at a diameter of 8, 6, 5, 4 mm for the Precise, Protege and Easy Wall stents. Also, Fig.8 shows the degree of extension of the longitudinal length of stents. By comparing those two figures, there is an interesting trend of stent radial force. In Fig.7, it can be observed that the Easy Wall stent did not even show a marked elevation of radial force under maximum compression. This was caused by the axial extension as shown by Fig.8. Indeed, the axial extension of the Precise and Protege stent did not vary substantially, which in turn led to increase the radial force linearly for the loading applied.

IV. Conclusions

We demonstrated that the present system enabled to measure stent radial force more accurately than previous ones. Also, it was found that the radial force was substan-

tially affected by the mesh structure. These data may provide a useful knowledge to assess the radial force in clinical practice and to establish the selection guideline of stents in endovascular treatments.

ACKNOWLEDGMENT

This research was partly supported by Health Science Research Grant (H20-IKOU-IPAN-001) from Ministry of Health, Labour and Welfare, Japan, Biomedical Engineering Research Project on Advanced Medical Treatment from Waseda University (A8201), and "Establishment of Consolidated Research Institute for Advanced Science and Medical Care", Encouraging Development Strategic Research Centers Program, the Special Coordination Funds for Promoting Science and Technology, Ministry of Education, Culture, Sports, Science and Technology, Japan.

REFERENCES

1. Stephan H, Jakub Wiskirchen, Gunnar Tepe, Michael Bitzer, Theodor W, Dieter Stoeckel, Claus D (2000) ,Physical Properties of Endovascular Stents: An Experimental Comparison, JVIR 11 :pp645-654
2. Dieter Stoeckel, Alan Pelton, Tom Duerig(2003) Self-expanding nitinol stents: material and design considerations, Eur Radiol 14: pp293-301
3. John F.Dyet, William G. Watts, Duncan F. Ettles, Anthony A. Nicholon(2000) Mechanical Properties of Metallic Stents: How Do These Proprtties Infuluence the Choice of Stent for Specifid Lesions?, Cardiovasc Intervent Radiol 23:pp47-54
4. Regis Rieu, Paul Barragan, Catherine Masson, Jean Fuseri Vincent Garitey, Marc Silvestri, Pierre Roquebert, and Joe¨ l Sainsous(1999) Radial Force of Coronary Stents: A Comparative Analysis, Catheterization and Cardiovascular Interventions 46:pp380-391

Author: Y.Okamoto
Institute: Graduate School of Integrative Bioscience and Biomedical Engineering, TWIns, Waseda University
Street: 2-2 Wakamatsu-cho
City: Shinjuku Tokyo
Country: JAPAN
Email: y_okamoto@ruri.waseda.jp

Motivating Children with Attention Deficiency Disorder Using Certain Behavior Modification Strategies

Huang Qunfang Jacklyn[1], S. Ravichandran[2]

[1]Student, Singapore Management University, Singapore
[2]Faculty, Temasek Engineering School, Temasek Polytechnic, Singapore

Abstract — **Attention-Deficit Hyperactivity Disorder (ADHD) is a neurobehavioral developmental disorder and its manifestation during childhood are characterized by a persistent pattern of inattention and/or hyperactivity. ADHD is currently considered a persistent and chronic condition for which no medical cure is available, although medication and therapy can treat symptoms. Children with such mental retardation more often exhibit behavior problems than children without disabilities. Teaching these students is more challenging and is considered as one of the most important functions of special education. Though a common behavior modification strategy is not always useful in dealing with neurobehavioral development, it may be more appropriate to design strategies based on the cognitive ability of the subject undergoing treatment. This paper summarizes the knowledge gained by the authors on designing specific cognitive strategy to deal with children in the age group (8 – 12 year). The strategy discussed in this paper is mostly focused on educating children with attention deficit disorder than treating hyperactivity as hyperactivity is mostly managed by the used of medication. The behavior modification strategy suggested is based on the fact that children within the age group have strong interest in specific activities involving audiovisual stimulus. The strategy aims in motivating the children to learn a specific act such as learning subjects like mathematics. The protocol basically motivates the children to focus and concentrate on solving a problem in order to be rewarded with audiovisual stimulus which are of interest to them. Though it may be beyond the scope of this paper to provide a comprehensive picture on the neuro-cognitive modifications associated with this behavior modification strategy, it provides a realistic picture on the changes reflecting the improvements in the cognitive aspects of the subject.**

Keywords — **ADHD, Behavior modification, Cognitive strategy**

I. Introduction

Attention-Deficit/Hyperactivity Disorder (ADHD) is typically first diagnosed in childhood, with symptoms persisting into adolescence and adulthood [1]. ADHD is characterized by inattention, impulsivity, and hyperactivity. It has recently been estimated to affect 3.5% of school-aged children worldwide and is said to be one of the most common psychiatric disorders of youth [2, 3]. Children with these problems are often unpopular and lack reciprocal friendships, but are not always aware of their own unpopularity [4]. Though these symptoms tend to decline with age, at least 50% of children with ADHD still experience impairing symptoms in adulthood [5]. Despite the vast literature supporting the efficacy of stimulant medication in the treatment of attention-deficit/hyperactivity disorder (ADHD), several limitations of pharmacological treatments highlight the clear need for effective alternative psychosocial treatments. There are also evidences on interventions involving both the school and parents training which have resulted in classifying these as "empirically validated treatments" [6].

II. Definition of ADHD

Most studies on ADHD attribute reasons/explanations on how they affect the cognitive processes of subjects [7, 8, 9]. However the field has not been able to develop an evidence-based intervention based on cognitive-behavioural principles [10]. Indeed, part of the challenge has been the changing conceptualization of the etiology and behavioural profile of ADHD [11]. Based on the pattern of symptoms present, the Diagnostic and Statistical Manual (DSM-IV) distinguishes three subtypes, namely, the inattentive, the hyperactive/impulsive, and the combined subtype [12]. The latter is by far the most common. Children with the inattentive ADHD subtype suffer from rejection by peers. Their social behaviour is of a more subdued nature [4]. Children with ADHD display chronic and pervasive difficulties with inattention, hyperactivity, and impulsivity that result in profound impairments in academic and social functioning across multiple settings (typically, at home, in school, and with peers). Some children with ADHD, despite having difficulties in performing tasks at school, have a healthy social life, while others appear to be unable to connect with peers and other people in a normal way [4].

Chwee Teck Lim, James C.H. Goh (Eds.): ICBME 2008, Proceedings 23, pp. 1057–1060, 2009
www.springerlink.com

III. Neurophychological aspects of ADHD

Explanations on the neuropsychological aspects of ADHD as per available literature imply that the disorder has a pathological basis in descending cortical control systems such as the prefrontal cortex and frontostriatal networks [13].The literature also states that, the prefrontal cortex is believed to bias subsidiary processing implemented by posterior cortical and subcortical regions in accordance with current goals. One of the mechanisms by which the prefrontal cortex is believed to exert its coordinating effects is via the suppression or gating of neural signalling irrelevant to current behaviour or goal [14, 15].

IV. Assessment of ADHD

The use of "Disruptive Behaviour Rating Scale" to obtain parent and teacher ratings of the 18 symptoms of *DSM-IV* ADHD has been reported as a qualitative yard stick to categorize subjects under various types depending on the manifested symptoms [16]. Children were categorized as ADHD only if symptoms were present prior to age seven and if these symptoms caused significant functional impairment. Individuals with six or more symptoms of inattention but fewer than six symptoms of hyperactivity-impulsivity were identified as Predominantly Inattentive Type, participants with six or more symptoms of hyperactivity-impulsivity but fewer than six symptoms of inattention were categorized as Predominantly Hyperactive/Impulsive Type, and individuals with six or more symptoms on both dimensions were coded as Combined Type [17].

V. Changing conceptualization of ADHD

The changing conceptualization of ADHD necessitates the field to constantly evaluate the adequacy of treatment approaches, and the working theory of ADHD has an important impact on treatment approaches. It has been reported that the sensory integration therapy, for use with children with ADHD involves compensatory strategies, such as altering or avoiding certain stimulus characteristics of the physical environment. This therapy is based on the assumption that ADHD is an "input" problem, and that sensory and motor input is processed and interpreted in faulty ways which result in inappropriate responses to sensory stimuli [18]. In ADHD cases, we are dealing more with cognitive deficiencies as opposed to distortions [19].

VI. Treatments currently being practiced

Treatment of ADHD is currently managed through various methods such as pharmacological intervention, behaviour interventions, cognitive behaviour treatment, neural-based intervention. Each treatment has its own merits and demerits and quite often a combination of two interventions is sought by the clinicians in treating ADHD children. We intend not to elaborate on the merits and demerits of each intervention in this paper, but would provide a brief insight into each intervention and focus more on the behaviour intervention and strategies beneficial in motivating children to develop attention for solving problems in education.

A. Pharmacology

Though it is beyond the scope of this paper to discuss the various medications available for ADHD children, developments in the pharmacological management of ADHD mean that there is now a much greater choice of approved medications these days. However, there are limitations to an exclusively pharmacological approach in the treatment of ADHD. These include the limited effects of stimulant medication on problems such as academic achievement and peer relationships, the fact that up to 30% of children do not show a clear beneficial response to stimulants. It is reported that the long term side effects of taking stimulants has been a limiting factor in the used of these medication as children suffer side effects such as insomnia and appetite suppression. [6].

B. Behaviour Interventions

It is seen that the inattentive, hyperactive, and impulsive behaviors that characterize ADHD often contribute to impairment in the parent–child relationship and increased stress among parents of children with the disorder [20, 21]. It follows that one evidence-based component of comprehensive treatment for ADHD involves working directly with parents to modify their parenting behaviours in order to increase positive outcomes with their children [22]. Effectively modifying poor parenting practices is of utmost importance, as poor parenting is one of the more robust predictors of negative long-term outcomes in children with behaviour problems [23]. Parents are taught to identify and manipulate the antecedents and consequences of child behaviour, target and monitor problematic behaviours, reward pro-social behaviour through praise, positive attention, and tangible rewards, and decrease unwanted behaviour through planned ignoring, time out, and other non-physical discipline techniques.

In classroom behaviour management, teachers are instructed regarding the use of specific behavioural techniques, which includes giving praises, planning ignorance etc. Behavioural goals are set at a level that is challenging, yet attainable, and are made increasingly more difficult until the child's behaviour is within developmentally normative levels based on the principle of shaping. Behaviourally based classroom interventions appear to be a very effective means of behaviour change in children with ADHD in the school setting. However, as cooperation of school professionals is necessary for these interventions, some of these challenges exist as with home behavioural programs [6].

C. Cognitive-behavioral Treatments

It has been reported by researchers that studies conducted on cognitive-behavioural approaches which include training in self-instructions, problem-solving, self reinforcement, and self-redirection have helped children to cope with errors. Children were taught a five-step process of problem-solving, including defining the problem, setting a goal, generating problem-solving strategies, choosing a solution, and evaluating the outcome with self-reinforcement. These concepts were reinforced through the use of modelling and role-playing exercises, instructional training, homework, and behavioral techniques, such as social reinforcement and a token system. As observed from the studies, there was a significant decrease in child activity level following CBT than controls [24].

D. Neural-based Interventions

Neurofeedback, based on electroencephalogram biofeedback, is sometimes used as one of the intervention in the management of ADHD children. The theoretical basis of neurofeedback describe ADHD as a disorder of neural regulation and under arousal, and it is assumed under this approach that these neural deficiencies are amenable to change using behavioural methods [25]. Some refer this intervention as a relatively unresearched treatment, and the research that has been conducted has reportedly been inconsistent and problematic. It is believed that this is due to methodological problems such as confounded treatments, inconsistent use of dependent measures, and a lack of clinically meaningful dependent measures [18, 26].

E. Combined behavioural-pharmacological interventions

It has been reported that Medication Management was as effective as Combined Treatment in reducing ADHD symptoms, with no clear incremental benefit of behaviour therapy noted [6]. Also, it is believed that combined treatment may allow for lower doses of medication to be used in conjunction with behaviour management in the home and school settings, resulting in increased satisfaction with treatment [27, 28].

VII. Strategies to improve attention span

The current behaviour modification strategies are based on identifying and manipulating the antecedents and consequences of child behaviour, target and monitor problematic behaviours, reward through praise, positive attention, and tangible rewards. Our focus was more on those subjects who have attention deficit yet who were willing to cooperate with assistances for learning. This group of people has been identified with certain interests in audio-visual stimulus and hence were willing to participate in solving problems leading to positive attention.

VIII. Treatment protocol

Our treatment protocol relies on some of the audio-visual animations which can be played using an available audio-visual system. As it is possible to play a variety of animated audio-visual animations which are of considered fascination by the children, it serves as a reward for every positive step taken by those who cooperate on solving problems, thereby prompting better attention.

IX. Conclusion

Treatment of ADHD is currently managed through various methods such as pharmacological intervention, behaviour interventions, cognitive behaviour treatment, neural-based intervention. Each method has its own merits and demerits and quite often a combination of two interventions is sought by the clinicians in treating ADHD children. No single strategy in the management of ADHD children has been advocated by the clinicians in the past and the success of each strategy depends on the cooperation extended by the subjects in a given setup. The current strategy based on behaviour modification is very attractive due to the fact that it does not relay on pharmacological intervention. However any strategy has its own limitations and in this behaviour modification strategy, the success purely depends on the ability of the subjects to be motivated in learning for rewards given for every positive step in improving their attention span. It is also worth noting that if the reward falls short of the subject’s expectation, it may results in poor attention span of the subjects under this treatment protocol.

REFERENCES

1. American Psychiatric Association. (2000). Diagnostic and statistical manual of mental disorders, 4th edition, Text Revision (DSM-IV-TR). Washington, DC: American Psychiatric Association.
2. Polanczyk, G., de Limas, M. S., Horta, B. L., Biederman, J., & Rohde, L. A. (2007). The worldwide prevalence of ADHD: A systematic review and metaregression analysis. American Journal of Psychiatry, 164, 942−948.
3. American Psychiatric Association (2000). Diagnostic and statistical manual of mental disorders (4th ed., rev.). Washington DC: Author.
4. Nijmeijier, J. S., et al. (2008). Attention-deficit/hyperactivity disorder and social dysfunctioning. Clinical Psychology Review, 28, 692-708
5. Faraone, S. V., Biederman, J., & Mick, E. (2006). The age-dependent decline of attention deficit hyperactivity disorder: a meta-analysis of follow-up studies. Psychological Medicine, 36, 159−165.
6. Chronis, A. M., Jones, H. A., & Raggi, V. L. (2006). Evidence-based psychosocial treatments for children and adolescents with attention-deficit/hyperactivity disorder. Clinical Psychology Review, 26, 486−502.
7. Barkley, R. A. (2006). Attention-deficit hyperactivity disorder: A handbook for diagnosis and treatment, 3rd Edition. New York: Guilford Press.
8. Sonuga-Barke, E. J. S. (2002). Psychological heterogeneity in AD/HD — A dual pathway model of behaviour and cognition. Behavioral Brain Research, 130, 29−36.
9. Sonuga-Barke, E. J. S. (2003). The dual pathway model of AD/HD: An elaboration of neurodevelopmental characteristics. Neuroscience and Biobehavioral Reviews, 27, 593−604.
10. Hinshaw, S. P. (2006). Treatment for children and adolescents with Attention-Deficit/Hyperactivity Disorder. In P. C. Kendall (Ed.), Child and adolescent therapy: Cognitive-behavioral procedures, Third Edition. New York: Guilford Press.
11. Toplak, M.E., et al. (2008). Review of cognitive, cognitive-behavioral, and neural-based interventions for Attention-Deficit/ Hyperactivity Disorder (ADHD). Clinical Psychology Review, 28, 801-823
12. American Psychiatric Association (1994). Diagnostic and statistical manual of mental disorders (4th ed.). Washington DC: Author.
13. Halperin, J. M., & Schulz, K. P. (2006). Revisiting the role of the prefrontal cortex in the pathophysiology of attention-deficit/hyperactivity disorder. Psychological Bulletin, 132, 560–581.
14. Barkley, R. A. (1997). Behavioral inhibition, sustained attention, and executive functions: Constructing a unifying theory of ADHD. Psychological Bulletin, 121, 65–94.
15. Pennington, B. F., Grossier, D., & Welsh, M. C. (1993). Contrasting deficits in attention deficit disorder versus reading disability. Developmental Psychology, 29, 511–523.
16. Barkley, R.,&Murphy, K. (1998). *Attention-deficit hyperactivity disorder: A clinical workbook* (2nd ed.). New York, NY, US: Guilford Press.
17. Shanahan, M. A., et al. (2006). Processing Speed Deficits in Attention Deficit/Hyperactivity Disorder and Reading Disability. Journal of Abnormal Child Psychology 34:585-602 DOI 10.1007/s10802-006-9037-8
18. Waschbusch, D. A., & Hill, G. P. (2003). Empirically supported, promising, and unsupported treatments for children with Attention-Deficit/ Hyperactivity Disorder. In S. O. Lilienfield, S. Jay Lynn, & J. M. Lohr (Eds.), Science and pseudoscience in clinical psychology. New York: Guilford Press.
19. Hinshaw, S. P. (2006). Treatment for children and adolescents with Attention-Deficit/Hyperactivity Disorder. In P. C. Kendall (Ed.), Child and adolescent therapy: Cognitive-behavioral procedures, Third Edition. New York: Guilford Press.
20. Fischer, M. (1990). Parenting stress and the child with attention deficit hyperactivity disorder. Journal of Clinical Child Psychology, 19, 337−346.
21. Johnston, C., & Mash, E. J. (2001). Families of children with attention-deficit/ hyperactivity disorder: Review and recommendations for future research. Clinical Child and Family Psychology Review, 4, 183−207.
22. Pelham,W. E., Wheeler, T., & Chronis, A. (1998). Empirically supported psychosocial treatments for attention deficit hyperactivity disorder. Journal of Clinical Child Psychology, 27, 190−205.
23. Chamberlain, P., & Patterson, G. R. (1995). Discipline and child compliance in parenting. In M. H. Bornstein, & H. Marc (Eds.), Handbook of parenting Applied and practical parenting, Vol. 4 (pp. 205−225) Mahwah, NJ: Lawrence Erlbaum Associates, Publishers.
24. Fehlings, D. L., Roberts,W., Humphries, T., & Dawe, G. (1991). Attention deficit hyperactivity disorder: Does cognitive behavioral therapy improve home behavior? Developmental and Behavioral Pediatrics, 12(4), 223−228.
25. Butnik, S. M. (2005). Neurofeedback in adolescents and adults with attention deficit hyperactivity disorder [Special issue: ADHD in adolescents and adults]. Journal of Clinical Psychology, 61, 621−625.
26. Kline, J. P., Brann, C. N., & Loney, B. R. (2002). A cacophony in the brainwaves: A critical appraisal of neurotherapy for Attention Deficit Disorders. The Scientific Review of Mental Health Practice, 1, 46−56.
27. MTA Cooperative Group. (1999a). A 14-month randomized clinical trial of treatment strategies for Attention Deficit Hyperactivity Disorder (ADHD). Archives of General Psychiatry, 56, 1073−1086.
28. Pelham, W. E., Erhardt, D., Gnagy, E. M., Greiner, A. R., Arnold, L. E., Abikoff, H. B., et al. (submitt for publication). Parent and teacher evaluation of treatment in the MTA: Consumer satisfaction and perceived effectiveness.

Authors: Huang Qunfang Jacklyn[1], S.Ravichandran[2]
Institutes: Singapore Management University[1],
Temasek Polytechnic[2]
Addresses: 90 Stamford Road #04-71[1]
21 Tampines Ave 1[2]
City: Singapore
Country: Singapore
Email: jacklynhuang@gmail.com, dr.sun.moon@gmail.com

Regeneration of Speech in Voice-Loss Patients

H.R. Sharifzadeh[1], I.V. McLoughlin[1] and F. Ahmadi[1]

[1]School of Computer Engineering, Nanyang Technological University, Singapore

Abstract — **This paper considers regeneration of natural sounding speech from whisper-speech, produced by patients with vocal tract lesions affecting the glottis. Such reconstruction is important for both total and partial laryngectomy patients to improve on the monotonous robotized sound typical of electrolarynx devices.**

Reconstruction of speech from whispers has been demonstrated previously, however the resulting speech does not exhibit particularly high intelligibility, and more importantly, sounds un-natural. It is the conjecture of the authors that limited pitch variations in the reconstructed speech contributes most to that lack of naturalness.

In this paper, a method for pitch contour variation in reconstructed speech is presented. This method extracts voice factors which are important to 'naturalness' from the whispered signal and applies these to the reconstructed speech. The method is based upon our previous published work which implemented an analysis-by-synthesis approach to voice reconstruction using a modified CELP codec.

Keywords — **Rehabilitation, Laryngectomy, Speech, Whispers, CELP codec**

I. Introduction

The speech production process starts with lung exhalation passing a taut glottis to create a varying pitch signal which resonates through the vocal tract, nasal cavity and out through the mouth. Within the vocal, oral and nasal cavities, the vellum, tongue, and lip positions play crucial roles in shaping speech sounds; these are referred to collectively as vocal tract modulators [1].

Total laryngectomy patients will have lost their glottis and also the control to pass lung exhalation through the vocal tract in many cases. Partial laryngectomy patients, by contrast, may still retain the power of controlled lung exhalation through the vocal tract. Despite the loss of the glottis including vocal folds, both classes of patients retain the power of vocal tract modulation and therefore by controlling lung exhalation, they have the ability to whisper [2]; in other words, they maintain most of the speech production apparatus.

In normally phonated speech, pitch itself is known to be the major source of important tonal information, alongside the lower formants [3]. Since there is no fundamental pitch present in whispers, other parameters contribute more heavily to perceived tonal variation. These include duration, amplitude, and formant location/bandwidth (whisper-speech formants are both wider and upward shifted compared to normal speech, as it is described in section 2). Although the contribution of amplitude to pitch variation has been studied by others such as [4], neither duration nor formant location have been used for tone reconstruction. The new technique presented in section 4 describes an algorithm which combines the use of formant information, along with amplitude, to estimate pitch contour variations in vowels.

The approach discussed in this paper utilizes a code excited linear prediction (CELP) codec and is based upon our previous published work in [5]. In a standard CELP codec, speech is generated by filtering an excitation signal in which the excitation sequence is selected from a codebook of zero-mean Gaussian sequences and then is shaped by an LTP filter to convey the pitch information of the speech [6]. For the purpose of speech reconstruction from whispers, we need to modify the standard CELP codec which details are described in section 3.

Section 2 outlines whispered speech features regarding formant information in vowels and also in terms of their acoustic and spectral characteristics while section 3 explains the modified CELP codec customized for our purpose of natural speech regeneration. Section 4 discusses our proposed method for pitch contour variation in reconstructed speech and finally section 5 concludes the paper.

II. Acoustic and Spectral Features of Whispered Speech

Whispered speech can be categorized into two different classes: soft whispers and stage whispers [7]. Soft whispers which are also referred to as quiet whisper are produced in certain circumstances to reduce perceptibility, such as whispering into someone's ear in the library and usually used in a relaxed, comfortable, low effort manner [8]. Stage whispers, on the other hand, are a combined kind of whisper one would use if the listener is some distance away from the speaker [7]. In other words, stage whisper is actually a whispery voice in phonetic terms, which is a type of phonation that involves vocal fold vibration [9].

Within this paper, we will concentrate on soft whispers which are produced without vocal fold vibration and not

Chwee Teck Lim, James C.H. Goh (Eds.): ICBME 2008, Proceedings 23, pp. 1065–1068, 2009
www.springerlink.com

only are more commonly used in daily life but also are the same type of whispers produced by laryngectomy patients.

As mentioned, essential physical features of whispered speech include the absence of vocal cord vibrations which leads to the absence of fundamental frequency and consequent harmonic relationships [10]. This is the most significant acoustic characteristic of whispers. By considering a source filter model [11], exhalation can be identified as the source of excitation in whispered speech and the shape of the pharynx is adjusted so that the vocal cords do not vibrate [12]. Thus, turbulent aperiodic airflow is the only source of sound for whispers, and it is a strong, rich, and hushing sound [13].

Regarding spectral characteristics, whispered speech sounds do have peaks in their spectra with roughly the same frequencies as those for normally phonated speech sounds [14]. These formants occur within a flatter power frequency distribution, and there are no harmonics in the spectra corresponding to the fundamental frequency [10].

Whispered vowels differ from normally voiced vowels. All formant frequencies (including the important first three formants) tend to be higher [15], particularly the first formant which shows the greatest difference between two kinds of speech. Lehiste in [15] reported that F1 is approximately 200-250 Hz higher, whereas F2 and F3 are approximately 100-150 Hz higher in whispered vowels.

Furthermore, unlike phonated vowels where the amplitude of each higher formant is less than for lower formants, whispered vowels usually have second formants that are as intense as first formants. These differences mainly in first formant frequency and amplitude are thought to be due to the alteration in the shape of the more posterior areas of the vocal tract including the vocal cords which are held rigid. Although these changes in acoustics are significant, there is only reported to be a small reduction, of 10 percent or less, in the accuracy of vowel identification for whispered speech [16].

As mentioned, since excitation in whisper mode speech is the turbulent flow created by the exhaled air passing through the open glottis, the resulting signal is completely noise excited [12, 16]. One of the consequences of a glottal opening is an acoustic coupling to the subglottal airways. The subglottal system has a series of resonances, which can be defined as the natural frequencies with a closed glottis. The average values of the first three of these natural frequencies have been estimated to be about 700, 1650, and 2350 Hz for an adult female and 600, 1550, and 2200 Hz for an adult male, but there are of course substantial individual differences [17]. Analysis shows that the effect of these subglottal resonances is to introduce additional pole-zero pairs into the vocal tract transfer function from the glottal source to the mouth output. The most obvious acoustic manifestation of these pole-zero pairs is the appearance of additional peaks or prominences in the output spectrum. The influence of zeros can also be seen sometimes as minima in the spectrum [18].

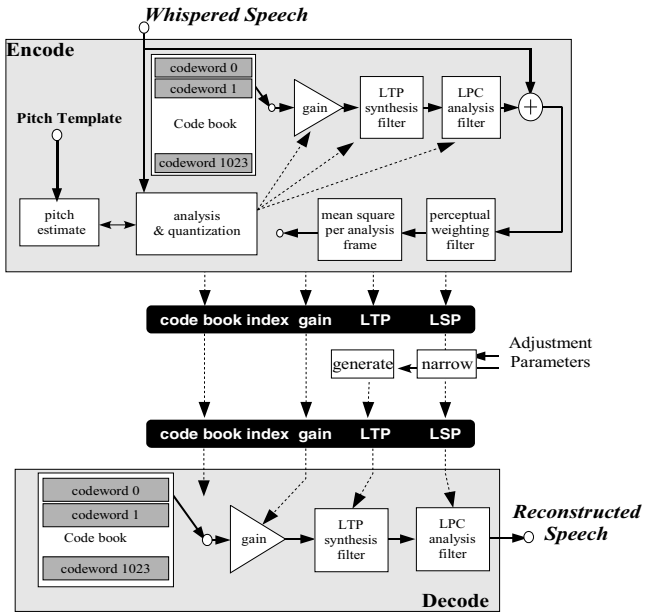


Fig. 1 A block diagram of a modified CELP codec used for speech reconstruction

III. Modified CELP Codec

As described in section 1, the approach used in this project utilizes a code excited linear prediction (CELP) codec in which the excitation sequence is selected from a codebook of zero-mean Gaussian sequences and then is shaped by an LTP filter to convey the pitch information of the speech.

Figure 1 shows a block diagram of the CELP codec as implemented in this paper, with the modifications for whisper-speech reconstruction identified. In comparison with the standard CELP codec, we have added a "pitch template" corresponding to the "pitch estimate" unit while "adjustment parameters" in this model are used to generate pitch factors as well as to apply necessary LSP modifications. The pitch estimate method is described within section 4 while LSP modifications, required for preparing the whispered speech signal to insert pitch into it, is described in the following.

For this research, a 12^{th} order linear prediction analysis is performed on the waveform, which is sampled at 8 kHz. A

frame duration of 20 ms is used for the vocal tract analysis (160 samples) and a 5 ms sub frame duration (40 ms) for determining the pitch excitation.

In the CELP codec, as well as many other low bit-rate coders, linear prediction coefficients are transformed into line spectral pairs (LSPs) [19]. LSPs describe the two resonance states of an interconnected tube model of the human vocal tract. These conditions are those that describe the modelled vocal tract being either fully open or fully closed at the glottis respectively. In reality, the human glottis is opened and closed rapidly during speech and thus the actual resonances occur somewhere between the two extreme conditions. The LSP representation, hence, has a significant physical basis [20]. However, this rationale is not necessarily true for whispered speech (since the glottis does not vibrate), and thus we need to make some adjustments to the model.

In figure 2, the linear prediction spectrum obtained from analyzing a typical segment of a vowel in whispered speech (/a/) is plotted and dashed lines drawn at the LSP frequencies derived from the linear prediction parameters are overlaid on it.

As discussed in [21], spectral peaks are generally bracketed by LSP line pairs, with degree of closeness being dependent upon the sharpness of the spectral peak, and its amplitude. However, as previously discussed in section 2, whispered speech has few significant peaks in the spectrum which implies wider distances between LSP lines. Hence to emphasize formants, it is necessary to narrow the LSP lines corresponding to likely formants, i.e. the 2 or 3 narrowest of them.

Since altering the frequency of lines may lead to formation of unintentional peaks by narrowing the gap between two irrelevant pairs, it is important to choose the pair of lines corresponding to likely formants. As mentioned, this might be done by choosing the three narrowest LSP pairs which works well when the signal has fine peaks (see our previous paper in [5]), but in case of the expansion of formant bandwidths (common in whispered speech), which leads to the increase of distance between the corresponding LSPs, the choice of the 3 narrowest LSPs may not identify the three correct formant locations, particularly for a vowel. The narrowing procedure is, hence, strengthened with the formant position indication based upon the classic approach of finding phases of the poles of vocal tract transfer function. As a matter of fact, the improved algorithm will narrow the LSP pairs which are corresponding to each of the three formants (regardless of the fact they are the narrowest LSP pairs or not). Figure 3 shows the result of LSP narrowing algorithm as described above for the same frame in figure 2.

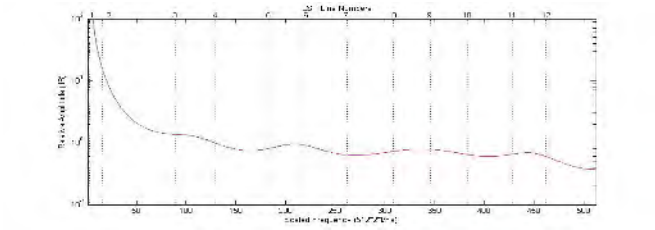


Fig. 2 Plot of LPC spectrum with LSPs overlaid for a whispered vowel /a/

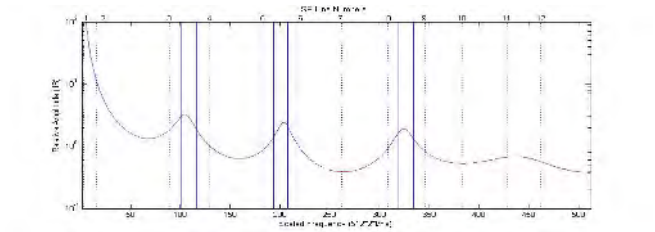


Fig. 3 Reconstructed LPC spectrum after applying improved LSP narrowing procedure for the whispered frame illustrated in figure 2

IV. Pitch Contour Variation Method

The pitch estimation algorithm discussed in this paper is based upon our recent work in [5] in which parameters are extracted from normally phonated speech and is tried to regenerate the excitation based on these parameters using CELP excitation synthesis method, but for improving the method to gain more natural synthesized speech, a novel approach for pitch estimation in terms of formant locations and amplitudes is proposed in this section. (Further details regarding the approach basics and the corresponding LTP filter parameters used in the CELP codec can be found through [5].)

By performing several alteration steps, a whispered vowel segment is converted to a normally phonated segment in a CELP based regeneration method. These steps are mostly being accomplished between the encoding and decoding modules of the CELP codec. As mentioned in section 4, the procedure is commenced by smoothing the LSP parameters to stabilize the formant locations of each segment. The formant bandwidths are also decreased to intensify formant amplitudes. The resulting formants are then shifted down to match the formant locations of normally phonated vowels.

As described in [5], long term predictor delay, *P,* has the main role in pitch determination in the CELP codec. Pitch contour variation, hence, can be achieved by variation of this parameter which, in our proposed method, is based on formant frequencies and amplitude according to (1) as follows:

$$P(n) = \begin{cases} P_{n-1} + \bar{P} + \alpha(\theta_n - \bar{\theta}) + \lambda h + S & h > 0 \\ P_{n-1} + \bar{P} + \alpha(\theta_n - \bar{\theta}) & h < 0 \end{cases} \quad (1)$$

in which n represents the number of current speech frame, h shows the instant amount of $\Delta F1_n \Delta F2_n$ which calculates the covariance of the first and second formants, S is the average value of formants in L previous frames which is calculated based on (2), α and λ are the factors to be set for generating the most natural voice and θ is the gain value in the CELP codec.

$$S = \frac{\sum_{i=n-L}^{n-1} F1_i + F2_i}{2} \quad (2)$$

Figure 4 illustrates the regenerated pitch contours of two samples of whispered vowel /a/ based on (1). Figure 5 demonstrates F1, F2, and pitch contour of a whispered and corresponding reconstructed vowel.

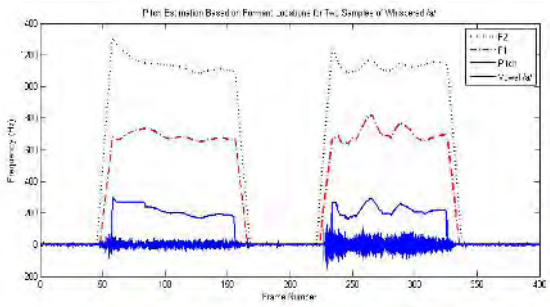


Fig. 4 Pitch estimation based on the first 2 formants of whispered vowel /a/

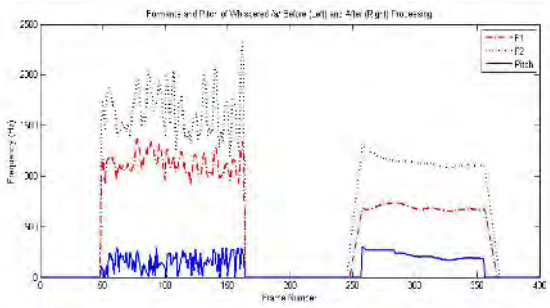


Fig. 5 Formants and pitch values for whispered vowel /a/ before and after enhancement

V. Conclusion

A method for real time synthesis of normal speech from whispers through an analysis-by-synthesis CELP codec with concentration on natural pitch generation in vowels has been proposed. By extraction of voice factors including formant location and amplitude, this method tried to regenerate natural pitch contours particularly in vowels.

By consideration of formant locations as well as amplitudes, a formula for generating pitch parameters in CELP codec was proposed. The results of the current work could highly contribute to natural speech regeneration for voice-loss patients.

References

1. Vary P, Martin R (2006) Digital speech transmission, John Wiley & Sons Ltd, West Sussex
2. Pietruch R, Michalska M, Konopka W, Grzanka A (2006) Methods for formant extraction in speech of patients after total laryngectomy, Biomedical Signal Processing and Control, Vol. 1, pp. 107-112
3. Plack C J, Oxenham A J (2005) Pitch: neural coding and perception, Springer Handbook of Auditory Research, New York
4. Morris R W, Clements M A (2002) Reconstruction of speech from whispers, Medical Engineering and Physics, vol. 24, pp. 515-520
5. Ahmadi F, McLoughlin I V, Sharifzadeh H R (2008) Analysis-by-synthesis method for whisper-speech reconstruction, IEEE Asia Pacific Conference on Circuits and Systems (APCCAS 2008), China
6. Atal B S (1982) Predictive coding of speech at low bit rates, IEEE Transaction on Communications, pp. 600-614
7. Weitzman R S, Sawashima M, Hirose H (1976) Devoiced and whispered vowels in Japanese, Annual Bulletin, Research Institute of Logopedics and Phoniatrics, vol. 10, pp. 61-79
8. Solomon N P, McCall G N, Trosset M W et al. (1989) Laryngeal configuration and constriction during two types of whispering, Journal of Speech and Hearing Research, vol. 32, pp 161-174
9. Esling J H (1984) Laryngographic study of phonation type and laryngeal configuration, Journal of the International Phonetic Association, vol. 14, pp. 56-73
10. Tartter V C (1989) What's in whisper?, Journal of Acoustical Society of America, vol. 86, pp. 1678-1683
11. Fant G (1960) Acoustic theory of speech production, Mouton & Co, The Hague
12. Thomas I B (1969) Perceived pitch of whispered vowels, Journal of the Acoustical Society of America, vol. 46, pp. 468-470
13. Catford J C (1977) Fundamental problems in phonetics, Edinburgh University Press, Edinburgh
14. Stevens H E (2003) The representation of normally-voiced and whispered speech sounds in the temporal aspects of auditory nerve responses, PhD Thesis, University of Illinois
15. Lehiste I (1970) Suprasegmentals, MIT Press, Cambridge
16. Kallail K J, Emanuel F W (1985) The identifiability of isolated whispered and phonated vowel samples, Journal of Phonetics, vol. 13, pp. 11-17
17. Klatt D H, Klatt L C (1990) Analysis, synthesis, and perception of voice quality, variations among male and female talkers, Journal of Acoustical Society of America, vol. 87, pp. 820-857
18. Stevens K N (1998) Acoustic phonetics, The MIT Press, Cambridge
19. Goalic A, Saoudi S (1995) An intrinsically reliable and fast algorithm to compute the line spectrum pairs in low bit-rate CELP coding, In proceedings of IEEE International Conference on Acoustics, Speech and Signal Processing, pp. 728-731
20. McLoughlin I V (2007) Line spectral pairs, Signal Processing Journal, pp. 448-467
21. McLoughlin I V, Chance R J (1997) LSP-based speech modification for intelligibility enhancement, In proceedings of 13th International Conference on DSP, vol. 2, pp. 591-594

Human Gait Analysis using Wearable Sensors of Acceleration and Angular Velocity

R. Takeda[1], S. Tadano[1], M. Todoh[1] and S. Yoshinari[2]

[1]Division of Human Mechanical Systems and Design, Graduate School of Engineering, Hokkaido University, Sapporo, Japan
[2]Human Engineering Section, Product Technology Department, Hokkaido Industrial Research Institute, Sapporo, Japan

Abstract — **This work proposes a method for measuring human gait posture using wearable sensors. The sensor used consist of a tri-axial acceleration sensor and three gyro sensors aligned on three axes. These are worn on the abdomen and the lower limb segments (both thighs, both shanks and both feet) to measure acceleration and angular velocity during walking. Three dimensional positions of each lower limb joint are calculated from segment lengths and joint angles. Segment lengths are calculated by physical measurement and joint angles can be estimated mechanically from the gravitational acceleration along the anterior axis of the segments. However, the acceleration data during walking includes three major components; translational acceleration, gravitational acceleration and external noise. Therefore, an optimization analysis was represented to separate only the gravitational acceleration from the acceleration data. Because the cyclic patterns of acceleration data can be found during constant walking, a FFT analysis was applied to obtain some characteristic frequencies. A pattern of gravitational acceleration was assumed using some parts of these characteristic frequencies. Every joint position was calculated from the pattern under the condition of physiological motion range of each joint. An optimized pattern of the gravitational acceleration was selected as a solution of an inverse problem. Three healthy volunteers walking straight for 20 seconds on a flat floor were measured. For comparison reflective markers were also placed on the volunteers for camera recordings. As a result, the characteristic three-dimensional walking of each volunteer could be expressed using a stick figure model. The trajectories of the knee joint in the horizontal plane were checked by images on PC. Therefore, this method provides important quantitive information for gait diagnosis.**

Keywords — **gait analysis, wearable sensor system, gravitational acceleration.**

I. Introduction

Gait analysis is an important clinical tool for diagnosing patients with walking disabilities. Currently, the main method for gait analysis is done by tracking a patient's movement through camera-based analysis systems, like the Vicon motion analysis system (Vicon Motion Systems, Inc.). Camera-based systems can provide three-dimensional position of body segments, but use of these systems is generally indoors in laboratories.

An alternate method for measuring human motion is by wearing small acceleration sensors on the body [1]. Wearable sensor systems are useful because it allows measurements outside the laboratories [2] [3]. However, wearable acceleration sensors can not provide position data directly. Therefore, many works in the past using wearable sensors systems have been limited to monitoring gait events [4] or comparing raw acceleration data [5].

A popular method for measuring three-dimensional position from acceleration is by double integrating the acceleration data. However integrating acceleration data accumulates error causing drift. Instead of integrating acceleration data, this work will use the gravitational acceleration measured by a wearable sensors system to calculate tilt angle of body segments. A optimization analysis was developed to estimate the gravitational acceleration included in acceleration data. This analysis used cyclic patterns of acceleration data during constant walking and physiological motion range of each joint to estimate only the gravitational acceleration. Gaits of three healthy volunteers were measured and the acceleration data of every lower limb segment was measured simultaneously. As a result three-dimensional walking established in this method could be visualized by using a stick figure model.

II. Method

A. Sensor System

A sensor system consisting of a tri-axial acceleration sensor (H34C, Hitachi Metals, Ltd.) and three single axis gyro sensors (ENC-03M, muRata Manufacturing Co., Ltd.) was used for this investigation. The axes of both acceleration and gyro sensors were orthogonally aligned. The sensor system also contained a data logger that simultaneously recorded the 3 axis acceleration and 3 axis angular velocity data for a maximum of 150 seconds at a sampling rate of 100Hz. Sensors were placed on seven segments (abdomen (AB), left and right thigh (LT, RT), left and right shank (LS, RS), left and right foot (LF, RF)) as shown in Fig. 1.

Chwee Teck Lim, James C.H. Goh (Eds.): ICBME 2008, Proceedings 23, pp. 1069–1072, 2009
www.springerlink.com

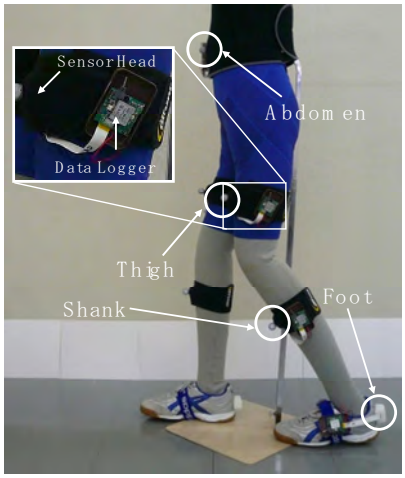


Fig. 1 Sensor attachment location. Sensors are attached to the abdomen (AB), both thighs (LT, RT), both shanks (LS, RS), both feet (LF, RF).

B. Acceleration and Gyro Sensor Measurement

The three-dimensional position of lower body joints can be calculated from orientation and length of each body segment. We presumed that the orientation of the segment is equal to the orientation of the attached acceleration sensor.

$$\theta^{\alpha} = \sin^{-1}\left(\frac{a_x^{\alpha}}{g}\right) \quad (1)$$

Here, a_i^{α} is the acceleration measured along x axis direction of segment α (LT, RT, LS, RS, LF, RF). During static state the gravitational acceleration is the only acceleration for a_i^{α}, therefore the orientation angle θ^{α} is the orientation against the direction of gravity. Gyro sensors were used to measure the horizontal rotation of the abdomen. Rotation θ^{AB} can be calculated by integrating the angular velocity ω, measured from the gyro sensor placed on the abdomen.

$$\theta^{AB} = \int \omega \, dt \quad (2)$$

C. Gravitational Acceleration Estimation

Data collected by the acceleration sensors during gait has three major components: translational acceleration, gravitational acceleration, and external noise [6]. Therefore a method was developed to separate out the gravitational acceleration to obtain segment orientation using Eq. 1.

The thin line in Fig. 2 shows the raw data taken from the anterior axis of an acceleration sensor of the RS. Noise is removed from this data by using cyclic acceleration patterns during gait. Cyclic patterns have been reported in the movement of body segments during constant walking [7] [8]. Fast Fourier transformation was applied to the acceleration data to investigate the frequencies of these cyclic patterns. The frequency analysis results are shown in Fig. 3. Peaks at certain frequencies were found. The first peak is the same frequency as the gait frequency and defined as the primary GF (gait frequency). This work focused on the first three frequencies in Fig. 3, the primary GF, secondary GF, and tertiary GF. The acceleration data of these GFs were extracted from the original acceleration data using low-pass and band-pass filters. As shown in Fig. 2, the composite data coincides with the original acceleration data with the noise removed. Since the heavy line in Fig. 2 still contains both gravitational acceleration and translational acceleration, wave decomposition was performed.

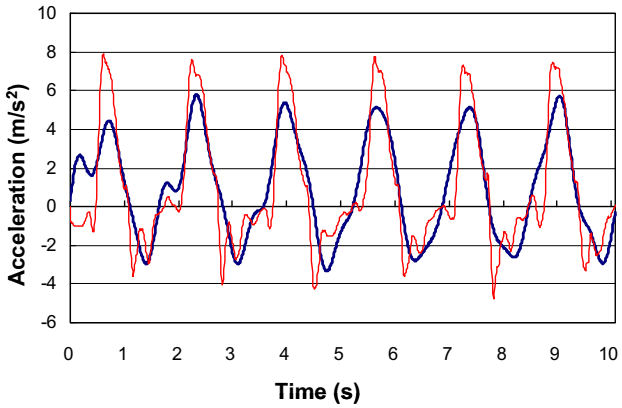


Fig. 2 Anterior axial acceleration data of right shank. Thin line represents raw acceleration data and Heavy line represents composite data of primary, secondary and tertiary GFs.

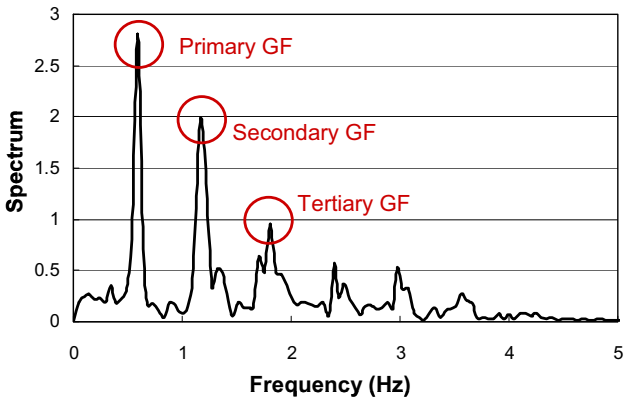


Fig. 3 Frequency analysis of anterior axial acceleration during constant gait. The primary, secondary and tertiary frequencies are circled in red.

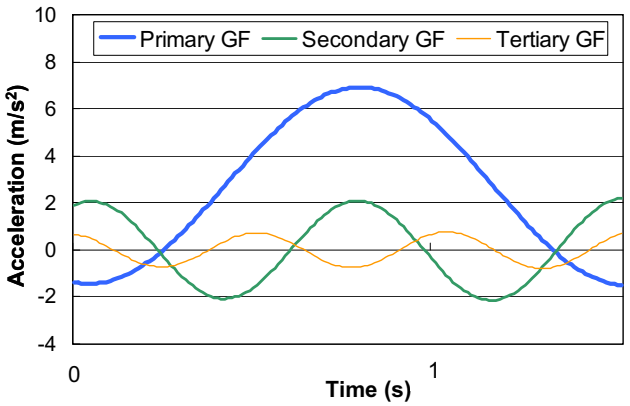


Fig. 4 The extracted primary, secondary and tertiary GF acceleration data. One primary GF cycle is equal to two secondary GF cycles and three tertiary GF cycles.

Wave decomposition divided the secondary and tertiary acceleration data into peaks and valleys. Since one primary GF cycle is equal to two secondary GF cycles and three tertiary GF cycles, the secondary was divided into 4 peaks and valleys and the tertiary GF was divided into 6 peaks and valleys, with 0 as the threshold. The gravitational acceleration was assumed to be a combination of these peaks and valleys.

There are $2^4 = 16$ combination for the secondary GF, and $2^6 = 64$ combinations for the tertiary GF, giving a total of $16 \times 64 = 1024$ combinations for each sensor. In this work, normal walking was assumed to be bilaterally-symmetric, meaning that right and left leg acceleration combinations are the same. Therefore, the total number of combinations was limited to 16,777,216 (1024 for the foot × 1024 for the shank × 16 for the thigh).

An optimization algorithm was developed to establish the gravitational acceleration within the 16,777,216 combinations. First, one combination is considered and the orientation of each body segment is calculated using Eq. (1), then the ankle, knee and hip joint positions can be calculated from the tilt angle and length of segments. Next, the range of motion of flexion-extension of the hip and knee and plantar flexion-dorsal extension for the ankle were checked (hip: -20°to 90°, knee: 0° to 120°, ankle: -30° to 50°). Afterwards, the ankle and hip position during heel contact was checked to remove any combinations that showed inadequate posture.

Within the combinations that fulfilled the conditions above, one combination with the least amount of vertical position error for the left and right ankle during heel contact was taken as the gravitational acceleration. Using the selected gravitational acceleration a stick figure model was created to visually confirm the lower limb posture.

D. Experiment Process

Three volunteers, 2 male and 1 female, participated in the experiment. None of the volunteers had any past history of disabilities or injuries. Along with sensors reflective markers are placed on the volunteers for analysis with video camera. In addition lower body measurements of each volunteer were taken.

Volunteers were asked to walk a flat straight corridor; the gait velocity was at the discretion of the volunteers. To avoid errors caused by attachment, measurements of each sensor were measured before and after trials.

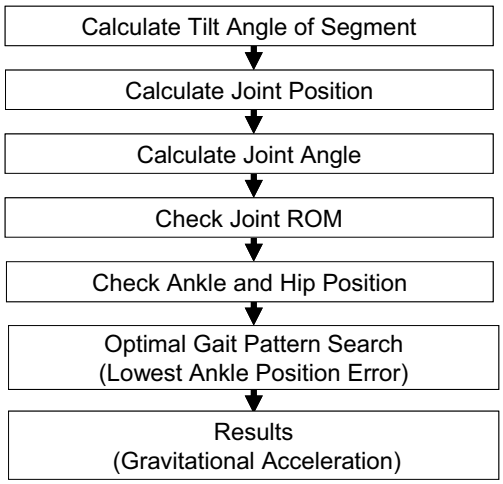


Fig. 5 Gravitational acceleration estimation algorithm. Combination created from primary, secondary and tertiary GF are used to estimate optimal gravitational acceleration.

III. Results and Discussions

Figure 6 and 7 are a comparison of the calculated hip and knee joint angles with this method and the angles determined using camera images. The horizontal axis represents percent in a gait cycle and vertical axis represents joint angle in degrees. There are differences in the swing phase for the hip joint, but the maximum and minimum peak values and joint angles during heel contact were similar. In the knee joint angle results shown in Fig. 7, the peak flexion angle was 10 degrees different.

The differences in the results may be caused by several reasons. Since the acceleration data are larger at the end segments of the limb some frequencies containing high amplitude acceleration data at the shank or foot could have been excluded by the low-pass and band-pass filters. These high frequencies could be the reason why there were differences in the peak flexion angles in the knee joint but not so much in the hip joint.

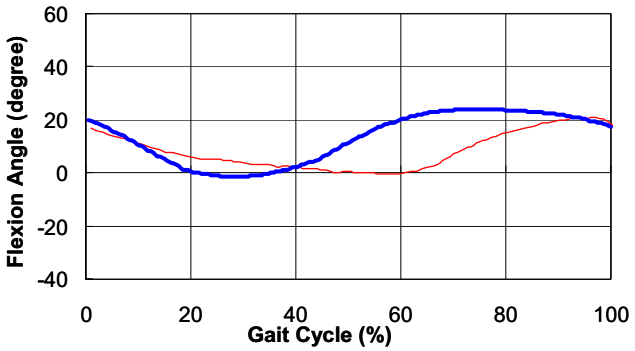


Fig. 6 Hip joint flexion angle comparison. Thin line represents joint angles measures by camera and heavy line represents those of this method.

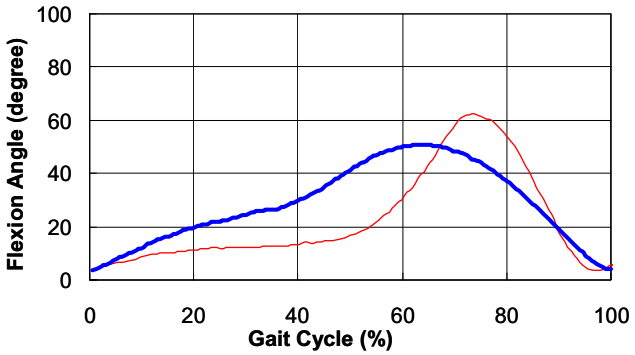


Fig. 7 Knee joint flexion angle comparison. Thin line represents joint angles measures by camera and heavy line represents those of this method.

Another reason is because the gravitational acceleration estimated by this method was optimized for heel contact, and the pattern may not have been optimal for the swing phase, where the maximum knee flexing occurs.

A Stick figure representation of a volunteer using this method is shown in Fig. 8.

IV. Conclusions

This work showed that the acceleration patterns during gait can be used to estimate lower body posture. We developed an optimization analysis that estimated the gravitational acceleration. The estimated gravitational acceleration was used to calculate the orientation of each body segment and gait of the subjects could be visually confirmed by stick figure model.

However, there are some limitations to this work. Because this method uses the cyclic acceleration pattern, this can only target constant movements such as gait, running and climbing of stairs.



Fig. 8 .Stick figure lower limb representation of a subject during gait.

Future works will be to improve estimation of gravitational acceleration with consideration for swing phase. In addition, conduct experiments on patients with lower limb disabilities to verify effectiveness for gait diagnosis.

Acknowledgment

The authors would like to express their thanks to M. Morikawa and M. Nakayasu of formerly master course students of Laboratory of Biomechanical Design (Division of Human Mechanical Systems and Design, Hokkaido University), for their support and cooperation to experiment and computer data analysis of this study

References

1. Morris J.R.W. (1973) Accelerometry - A technique for the measurement of human body movements. J Biomechanics 6: 729-736.
2. Veltink P.H., Bussmann HansB.J., de Vries W. et al. (1996) Detection of static and dynamic activities using uniaxial accelerometers. IEEE Trans Rehab Eng 4: 375-385.
3. Bouten C.V.C., Koekkoek K.T.M., Verduin M. et al. (1998) A triaxial accelerometer and portable data processing unit for the assessment of daily physical activity. IEEE Trans Biomed Eng 44: 136-147.
4. Jasiewicz J.M., Allum J.H.J., Middleton J.W. et al. (2006) Gait event detection using linear accelerometers or angular velocity transducers in able-bodied and spinal-cord injured individuals. Gait Pos 24: 502-509
5. Kavanagh J.J., Barrett R.S., Morrison S. (2004) Upper body accelerations during walking in healthy young and elderly men. Gait Pos 20: 291-298.
6. Luinge H.J. (2002) Inertial sensing of human movement. PhD. thesis, Twente University Press.
7. Grossman G.E., Leigh R.J., Abel L.A. et al (1988) Frequency and velocity of rotational head perturbations during locomotion. Exp Brain Res 70, 470-476.
8. Lamoth C.J.C., Beek P.J., Meijer O.G. (2001) Pelvis-thorax coordination in the transverse plane during gait, Gait Pos 16: 101-114.

Author: Ryo Takeda
Institute: Hokkaido University
Street: Kita 13 Nishi 8, Kita-ku
City: Sapporo
Country: Japan
Email: takeda@mech-me.eng.hokudai.ac.jp

Deformable Model for Serial Ultrasound Images Segmentation: Application to Computer Assisted Hip Athroplasty

A. Alfiansyah[1,2], K.H. Ng[2] and R. Lamsudin[3]

[1]Faculty of Industrial Engineering, Islamic Indonesian University, Indonesia
[2]Department of Radiology, Faculty of Medicine, University of Malaya, Malaysia
[3]Faculty of Medicine Islamic Indonesian University, Indonesia

Abstract — **In this paper, we present a segmentation method for ultrasound images acquired serially for intra-operative data acquisition in computer assisted total hip athroplasty application. To extract the bone surface from ultrasound image, we propose a method based on model deformable (snake) with integration of local intensity variable around the evolved contour. We also proposed an adaptive additional force calculated from image gradient vector flow in narrow band around the contour. In this serial image segmentation, we utilized the segmentation result of previous image as an input of next image segmentation. Finally, we perform a post treatment of the final contour to select exclusively the real points on the bone surface. This point selection is based on intensity criteria, so that we only keep the points having strong intensity amongst the points on the final contour. Validated on a fresh cadaver and a health subject, we found that the precision of this method is applicable for the input of registration method in computer assisted orthopedic surgery. Despite of its possibility to be applied in off line manner, the needed time calculation is acceptable for intra-operative application.**

Keywords — **ultrasound images, segmentation, model deformable, gradient vector flow, computer assisted surgery.**

I. Introduction

Image guided surgery proposes intra-operative navigation for the surgeons in performing minimally invasive surgery. Using this navigation, some medical interventions that considered as too dangerous before, it becomes a daily routine in operating room nowadays. Computer assisted surgery also proposes better result of surgical procedure, shorten post-operative recovery needed times and lower overall cost motivated the emergence of computer assisted surgery. Using this approach, surgeon can design a pre-operative planning based on available images acquired pre-operatively. This planning is then integrated to the operating room by performing a registration between intra-operative images data with the preoperative ones. This registration process determines the spatial relationship between pre-operative and intra- operative datasets.

The needed intra-operative data are usually obtained by sliding a three dimensional pointer on the anatomical part using. This method is fast, easy, and accurate; but it has twofold important drawbacks: *invasive*; acquisition area is *limited* in the exposed anatomical part and cause additional pain. In the other hand, the lack of dataset in some areas may affect the registration accuracy.

For orthopedic application, CT scan is commonly used as pre-operative data and implanted fiducially markers, optically tracked sensor data, or localized X ray data as intra-operative ones. Since past few years, ultrasound images have also been used as intra-operative modality because of its non-invasive, inexpensive, and real-time character. But due to the poor image quality (speckle, delayed echoes, reverberation…), ultrasound images are very difficult to analyze in order to obtain an accurate segmentation result.

Besides of segmentation result quality, to achieve accurate registration result, sufficient amounts of intra-operative data are also required. The more data are utilized for registration, the more accurate registration result can be obtained. These additional data sets can be gathered from a set of serial ultrasound images in the interested area. However, the complexity of ultrasound images analysis will significantly increase the needed intra-operative time. This intra-operative additional time is critical to reduce the blood loss and infection risk. Thus, we need a fast serial ultrasound image segmentation algorithm applicable in surgical intervention and require minimum user interactions.

This paper focuses on an automatic bone surface detection method applied for serial ultrasound images acquired intra-operatively. The proposed method based on a deformable model (snake), with an additional force derived from the gradient vector flow. These serial segmentation results of such images are then applied as an input for a registration processes for orthopedic surgery, especially total hip athroplasty for our case.

II. Method

To extract the bone surface from ultrasound images, we follow the expert reasoning described in [1,2]. As shown in figure 1, bony structures can be characterized by a strong intensity change from a bright pixel group to a global dark

Chwee Teck Lim, James C.H. Goh (Eds.): ICBME 2008, Proceedings 23, pp. 1073–1076, 2009
www.springerlink.com

area below, because bones high absorption rate generates an acoustic shadow behind. The segmentation method should produce a smooth contour, because discontinuities are normally not present on the bone. Some artifacts might be generated below the bone structure when ultrasound probe position is close to the bone surface during acquisition.

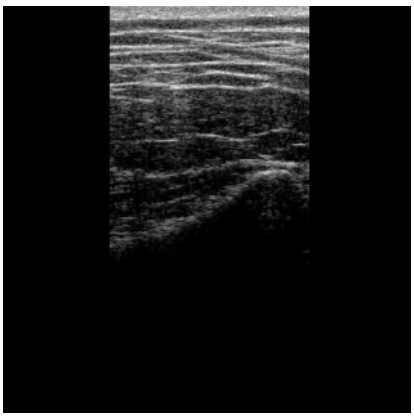


Figure 1: Ultrasound image of iliac.

Considering all that, we applied a method based on open active contour represented as a set of discrete points, initialized as a simple contour placed near to the bone surface. This contour is then evolved until meets the bone surface.

A. Model deformable

We propose previously in [1, 2], an automatic bone surface detection method for single ultrasound images based on deformable model. The method also includes region based energy for detecting the image local contrast; and intensity based posteriori point selection to select only the real bone.

Model deformable: The active contours are generally modeled as the sum of *internal energy*, that imposes the regularity of the curve; and *external energy* that attracts the contour toward the image significant features. The segmentation process is then achieved by minimization of the following total energy function [3]:

$$E(s) = \underbrace{\int_{\Omega}(\alpha|v'(s)|^2 + \beta|v''(s)|^2)ds}_{InternalEnergy} + \underbrace{\int_{\Omega}P((v))ds}_{ExternalEnergy} \quad (1)$$

$v'(s)$ and $v''(s)$ represent the derivative of the model, and $P(v)$ is an image potential associated with the image force.

We proposed an open contour active model with two free extremities to make it move easily. From the given initial contour, the model is evolved to find the minimum energy. The minimization process is estimated via finite elements method. For each step in time discretization, the evolved snake contour is updated using this equation:

$$V_t = (\tau A + I)^{-1} + (V_{t-1} + P(V_{t-1})) \quad (2)$$

where V_t is evolved contour at discretized time step t, A and I are pentadiagonal matrices express the contour rigidity and identity matrix respectively.

Implementing this snake using that numerical scheme, bring us to linear system, so we have to solve a pentadiagonal banded symmetric positive system. We can compute the solution using a LU decomposition of $(\tau A + I)$ need to be computed only once.

Regional energy integration: in classical snake, $P(v)$ is defined as negative of gradient image to stop the evolution in the image border. In our case in bone detection from ultrasound images, we need to integrate the local intensity variation, so that the contour detects only a group of bright-to-dark intensity variation, and not in the opposite contrast. The final contour should be placed about in the middle of the bright intensity stripe.

To handle this local image intensity change automatically, we propose to integrate the regional energy around the evolving contour. We defined this term as difference of mean intensity between the regions above (V_{up}), below (V_{down}) and at the considered location (V_{middle}) as illustrated at figure 2. So, it can be formulated as follows:

$$Dif(v_i) = 2 \times V_{middle} - V_{down} - V_{up} \quad (3)$$

if the difference is negative a penalization is applied.

$$E_{regional} \begin{cases} k & \text{if } Dif(v_i) < 0 \\ Dif(v_i) & \text{otherwise} \end{cases} \quad (4)$$

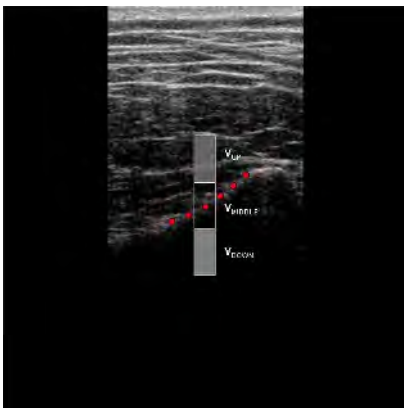


Figure 2: Regional energy definition.

The final external energy is then incorporated to the contour actives as the multiplication result between this region-based measurement and the original gradient term.

$$E'_{regional} = E_{regional} \times E_{external} \quad (5)$$

B. Gradient Vector Flow (GFV)

In order to simplify the snake initialization and avoid local minimum solution, in previous implementation we followed Cohen [4] who proposed an additional force in the contour normal direction. This force pushes the contour evolved upward since the initial contour is placed below the edge to be detected from ultrasound image.

In the context of serial images segmentation, we propose to use the segmentation result of the previous image as the initial contour of next image segmentation process. It is possible because the bone positions in two consecutive ultrasound images are normally not so distance. This approach will accelerate the overall segmentation method, since contour active requires only some amount of iterations to find the bone surface. Unfortunately, this initialization technique might give false segmentation result when the initial contour from previous image placed above the desired bone surface. In such position, the contour active will never find the correct result situated below, because the additional force push always upward.

To overcome this drawback, we proposed an adaptive additional force that capable of pulling the evolved contour toward the edge, even its position is above. This additional force is derived from image *Gradient Vector Flow* (GVF) [5, 6] as an energy that regularizes the potential gradient in order to improve active contours facing the weak image intensity and boundary concavities. GFV improves active contour to converge to long, thin boundary indentations and extend the capture range. In our context, this force is integrated to pull the contours toward the edge to be detected where ever its position is.

This method replaces the external force term $P(v)$ with a gradient vector field, $gvf(I)$, derived from the equilibrium state of this partial differential equation:

$$gvf_t = g(|\nabla f|)\left|\nabla^2 gvf\right| - h(|\nabla f|)(gvf - \nabla f) \quad (5)$$

The first term in that equation is referred to as *smoothing term* since it produces a smoothly varying vector field. The second term $(gvf - \nabla f)$ is referred to as the *data term*, since it encourages the vector field $gvf(I)$ to be close to ∇f. The weight functions *g(.)* and *h(.)* are applied to the both of smoothing and data terms. We propose the following weight functions:

$$g(|\nabla f|) = e^{-\frac{|\nabla f|}{K}}$$

$$h(|\nabla f|) = 1 - e^{-\frac{|\nabla f|}{K}}$$

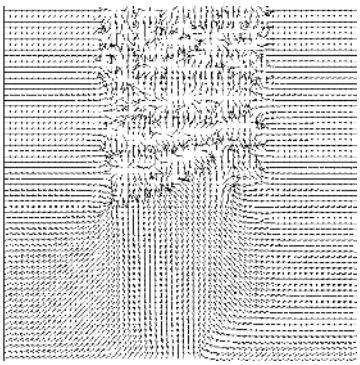


Figure 3: Gradient Vector Flow of the image in figure 1.

Using these weight functions, GVF field will conform to the distance map gradient near the relevant features, but vary smoothly away from them. The constant K determines the extent of the field smoothness and the conformity gradient. This additional force gives the desired edge a capability to pull the contour active downward when it is situated above, without loss its capability to push the contour upward in the other situation.

GVF calculation is a time and memory consuming process. To reduce the needed computation time and memory for computing of this force, we proposed to calculate only in the narrow band area around the evolved contour. We expect that the initial contour (comes from previous segmentation) is situated in this defined narrow band. This is the often the case in the images acquired serially, due to the similarity of two consecutives images of this type.

C. Posteriori selection.

Since the active contour initialization goes from one side to the other of the image, and considering that the real bone contour does not always do so, we need to perform a posterior point selection procedure. Amongst all points on the final contour, only those statistically having high enough intensity are retained.

D. Implementation issue

To integrate both of two methods effectively, but at the same time respect the operating room time constraints, we perform this segmentation in offline manner instantaneously after the images acquisition. For the first images, the addi-

tional force is fixed like a balloon force in vertical direction. When it reaches the convergence, we start the segmentation process using the previous contour as initialization and images energy and GVF calculation in the range of 15 pixels around the contour. For each images, we evolved the snake in fixed number iteration without convergence detection. In our experiences, 70 iterations are sufficient to put the contour in the desired edge.

Once all of the images have been segmented, we perform a posteriori selection to detect the real points on the bone surface.

III. Validation

To perform the validation of segmentation method quantitatively, we utilize an approach presented by Chalana [7] that compares the difference between the manual segmentation and automatic one. Measured as *Mean Sum of Distance* (MSD), the method calculates the mean of closest points in two compared curves as error measurement. The method was validated on three fresh cadavers and two healthy subjects (25 images for each) by comparing the result of automatic segmentation results with the manual ones. The images were acquired in the hip bone area, as we are interested particularly to apply the method for hip athroplasty application. The result this validation is presented in table 1.

Table 1 MSD between automatic and manual segmentation (in mm)

Subject	MSD	Max
Cadaver iliac wing (3 set)	0.46±0.39	1.34
Cadaver symphis (3 set)	0.57±0.43	0.82
Cadaver ischium (3 set)	0.85±0.54	1.40
Cadavre knee (3 sets)	0.53±0.30	0.81
Healthy iliac wing (2 set)	0.56±0.89	1.34
Healthy symphis (2 set)	0.63±0.22	0.90

From that table, we can see that almost of the segmentation result on the total hip surgery acquisition areas is acceptable as the input of computer assisted surgery. On ischium, this error is rather big due to its poor images quality on this anatomical area. Although the method is not intended to perform a real time bone contour extraction, but in average it needs less than 1 second giving the final results for each image.

Despite of its capability to describe the segmentation error precisely, MSD also prone to the segmentation error performed manually that utilized as gold standard. Furthermore, in serial images there are a big amount of images to be analyzed, thus manual segmentation might then becomes a hard, tedious and labor intensive task for the operators. The other error source might also comes from the inter- and intra-operator variation during segmentation. Further work, we plan to investigate this variability for validating the segmentation method.

IV. Conclusions

We presented this paper that focused on segmentation method applied on ultrasound images acquired serially for computer assisted orthopedic surgery. The segmentation result is then utilized as enhanced input of geometric based registration between CT scan and ultrasound image for total hip athroplasty. The method extract the bone surface from ultrasound image based on model deformable (snake) with integration of local intensity variation information around the evolved contour. We also proposed an adaptive additional force calculated from image gradient vector flow in narrow band around the contour. In this serial image segmentation, we consecutively utilize the segmentation result of previous image as the input of next image segmentation. And finally, we perform a post-treatment on the final contour to select exclusively the real points situated on the bone surface. This point selection is based on point's intensity criteria, so that, we only keep the points having strong intensity amongst the points on the final contour.

Validated using some different object, we found that the precision of this method is acceptable and quite fast for real clinical application in computer assisted surgery.

References

1. Alfiansyah A., Streinchenberger R., Kilian P., Bellemare ME., Coulon O. *'Automatic segmentation of hip bone surface in ultrasound images using an active contour,'* in: CARS 2006 Computer Assisted Radiology and Surgery, June 2006.
2. Alfiansyah A.,*'Integration of intra-perative ultrasound images in Computer Assisted Orthopedic Surgery',* Ph.D Dissertation, Universite de la Mediterranne, 2007.
3. M. Kass, A. Witkin, and D. Terzopoulos. *'Snakes : Active contour models'*. International Journal of Computer Vision, 1:321−332, 1988.
4. Laurent D. Cohen, *On active contour models and balloons*. Computer Vision, Graphics, and Image Processing: Image Understanding (CVGIP:IU), 53(2):211218, March 1991
5. C. Xu and J. L. Prince. *Snakes, shapes, and gradient vector flow.* IEEE Transactions on Image Processing, 7(3):359-369, 1998.
6. C. Xu and J. L. Prince. *Generalized gradient vector flow external forces for active contours*. Signal Processing, 71(2):131_139, December 1998.
7. V. Chalana and Y. Kim. *A methodology for evaluation of boundary detection algorithms on medical images.* IEEE Trans. Med. Imaging, 16(5):642_652, 1997.

Author: Agung ALFIANSYAH
Institute: Islamic Indonesian University/University of Malaya
Email: agung.alfiansyah@univmed.fr

Bone Segmentation Based On Local Structure Descriptor Driven Active Contour

A. Alfiansyah[1,2], K.H. Ng[1] and R. Lamsudin[3]

[1]Faculty of Industrial Engineering, Islamic Indonesian University, Indonesia
[2]Department of Radiology, University of Malaya, Malaysia
[3]Faculty of Medicine Islamic Indonesian University, Indonesia

Abstract — **In this paper we present a method to segment the bony structures from CT scan data using active contour guided by image local descriptor derived from 3D Hessian matrix that encodes important local shape information. Eigen-values decomposition of 3D Hessian matrix measures the maximum changes in the normal vector (gradient vector) of the underlying intensity iso-surface in a small neighborhood. Thus, the eigen-values of the Hessian matrix can be explored to locally describe whether the underlying iso-surface behaves a form like a sheet, a tube, and a blob. Inspired by this fact, we propose a novel filtering method capable in estimating the sheet-ness measure that enhances the bony structures in the image but capable to remove the noise. We choose a segmentation method based on geometric active contour for the reason of its robustness against noises often presence in images, and also its capability to automatically handle the topological change. To incorporate this Hessian based local structure descriptor, we utilized the sheet-ness measure to drive the surface evolution in geodesic contour active toward the sheet like structure, lower for tube like region and zero for the others. We do not define the tube-like elimination term, as the curved end of the bone structure have a behavior that is both sheet-like and tube like. The contour active is implemented by following the surface evolution using level-set implementation in a narrow band area around the evolved surface to make the computation faster and more efficient.**

Keywords — **CT scan image, segmentation, model deformable, Hessian filter, local descriptor.**

I. Introduction

Segmenting the bony structure from Computer Tomography Scanner (CT scanner) images plays the roles important in computer assisted surgery, not only for reconstructing three dimension model in intra operative navigation, but also for pre-operative surgical planning. Methodologically this segmentation method is also important for feature based registration, where CT scan is commonly utilized as pre-operative data. In almost conventional technique, the segmentation of such data type is done using a method based on application of threshold value of the bony anatomy in CT scan. To enhance the result, this method is then followed by large connected component detection or sometimes a manual post-processing. This segmentation of bone using thresholding approach is a fairly successful procedure, since the CT values for bone are higher than that of surrounding soft tissues.

Although the CT value for bone is well-known (as Hounsfield value) and can be considered as constant for each images acquisition thanks to image modality pre-calibration, a discrimination based on these values does not always work well in practice for all areas of anatomical bone at all different condition of patient. In orthopedic surgery, it is often that the CT scan images are polluted by the noises comes from metallic object implanted to the patient before. Furthermore, some different anatomical bones are often situated near each other, that make the segmentation gives the false result.

This paper, we present a segmentation algorithm to be applied in bony anatomical extraction using contour active geodesic. To enhance such deformable model, we applied a local descriptor based on second-order local shape operator. Such local descriptor is useful to determine the anatomical bone structures, as they have a specific geometrical form that near to the sheet and tube. Our proposed filter is also capable to reduce the presence of the noise in the image by detecting the other local structure different from that in the anatomical bone.

The remaining of this paper is organized as follows: Section 2 introduces the proposed method that includes the local structure descriptor based on image's Hessian filter and brief theory of geodesic active contour. The filter method and model deformable integration strategies as well as our numerical implementation scheme are also detailed in this section. Section 3 presents the experimental results of the application of the method. And finally, Section 4 concludes this paper.

II. Method

A. Local structure descriptor

One of the common approaches to analyze the local behavior of an image I by consider its Taylor expansion in the neighborhood of a point x_0

Chwee Teck Lim, James C.H. Goh (Eds.): ICBME 2008, Proceedings 23, pp. 1077–1081, 2009
www.springerlink.com

$$I(x_0 + \Delta x) \approx I(x_0) + \Delta x^T \nabla I(x_0) + \Delta x^T H(x_0) + \ldots$$

where ∇I is the gradient vector and H denotes the Hessian matrix.

Both the gradient and the Hessian matrix are usually used separately. The gradient vector is widely used as a normal to an implicitly defined iso-surface and its magnitude provides edge detector information, while the Hessian matrix encodes the shape information description of how the normal to iso-surface changes. We want to take the profits of this local shape information by defining a Hessian matrix based image filter. This Hessian based filter is a voxel based filter, meaning that each voxel is calculated for a filter response. In 3D image I , this second order derivative of the intensity values to form a Hessian matrix for each voxel can be calculated as:

$$H = \nabla^2 I = \begin{bmatrix} I_{xx} & I_{xy} & I_{xz} \\ I_{yx} & I_{yy} & I_{yz} \\ I_{zx} & I_{zy} & I_{zz} \end{bmatrix} \quad (1)$$

Then, from this Hessian matrix we can compute the three eigenvalues ($|\lambda_1| \geq |\lambda_2| \geq |\lambda_3|$) that each of them encodes the local shape information. This eigenvalue decomposition measures the maximum changes in the normal vector (gradient vector) of the underlying intensity iso-surface in a small neighborhood.

Some previous works are interested particularly on eigenvalues and eigenvectors exploitation of the Hessian matrix based analysis. Sato [1] and Frangi [2] independently employed these eigenvalues to design a filter for vessel enhancement in 3D medical digital images. Later then, Sato *et al.* [3] generalized their previously introduced concept to enhance tubular, blob, and sheet–like anatomical structures. The relationship between different combinations of the eigenvalues of Hessian matrix and their corresponding possible 3D local structure can be observed at Table 1.

Table 1 Eigenvalue decomposition from Hessian matrix to determine the the local structure description ($|\lambda_1| \geq |\lambda_2| \geq |\lambda_3|$)

Eigenvalues	Likeness local structure
$\lvert\lambda_1\rvert \approx \lvert\lambda_2\rvert \approx 0;\ \lvert\lambda_3\rvert >> 0$	Sheet-like
$\lvert\lambda_1\rvert \approx 0;\ \lvert\lambda_2\rvert \approx \lvert\lambda_3\rvert >> 0$	Tube-like
$\lvert\lambda_1\rvert \approx \lvert\lambda_2\rvert \approx \lvert\lambda_3\rvert >> 0$	Blob-like
$\lvert\lambda_1\rvert \approx \lvert\lambda_2\rvert \approx \lvert\lambda_3\rvert \approx 0$	Noises-like

For our application, we are particularly interested to apply this local descriptor in segmenting the bony structure, in which propose a sheet-ness measure that enhances bone structures and then use it to guide a deformable model that stops at bone boundaries on the image. Thus at every voxel, we determine whether the underlying iso-intensity surface behaves like a sheet. In this case, we know that the eigenvectors corresponding to the null eigenvalues span the plane of the plate structure and the other eigenvector is perpendicular to it.

To determine such structures, we define firstly three ratios, R_{sheet}, R_{blob}, R_{noise}, that describe the structure likeness of an iso-surface to the some geometry form to differentiate the sheet-like structures from others. They are defined as:

$$\begin{aligned} R_{sheet} &= \left(|\lambda_1| + |\lambda_2|\right) / |\lambda_3| \\ R_{blob} &= \left|\left(2|\lambda_3| - |\lambda_2| - |\lambda_1|\right)\right| / |2 \cdot \lambda_3| \\ R_{noise} &= \sqrt{\lambda_1^{\,2} + \lambda_2^{\,2} + \lambda_3^{\,2}} \end{aligned} \quad (2)$$

We utilize these three ratios to determine a score measures the structure sheet-ness to decide whether a structure should be kept during segmentation, as it have a sheet-like structure, or be removed because it is considered as having the blob-like and noise structures. The structure sheet-ness S can be calculated follows:

$$S = \begin{cases} 0 & \text{if } \lambda_3 > 0, \\ \exp\left(-\dfrac{R_{sheet}^{\,2}}{2\alpha^2}\right) & \\ \left(1 - \exp\left(-\dfrac{R_{blob}^{\,2}}{2\beta^2}\right)\right) & otherwise \\ \left(1 - \exp\left(-\dfrac{R_{noise}^{\,2}}{2\gamma^2}\right)\right) & \end{cases} \quad (3)$$

Each term of the equation 2 has a different function that depends on the characteristics of Table 2.

Table 2 Properties of ratios defined from the Hessian eigenvalue for different local structure form in image.

Ratio	Sheet	Tube	Blob	Noise
R_{sheet},	0	1	1	Undefined
R_{blob}	1	1	0	Undefined
R_{noise}	λ_3	$\sqrt{2\lambda_3}$	$\sqrt{3\lambda_3}$	0

Each term in equation (3) correspond to a filtering process that enhance specific geometric structure, but remove the others. Each of them is:

- $\exp\left(-\frac{R_{sheet}^{\ 2}}{2\alpha^2}\right)$ corresponds to a sheet structure enhancement term, that will be maximum value in the sheet like structure, but minimum for others.
- $\left(1-\exp\left(-\frac{R_{blob}^{\ 2}}{2\beta^2}\right)\right)$ is a term to remove the blob and noise structure, because it having zero value for both, but high value for sheet.
- $\left(1-\exp\left(-\frac{R_{noise}^{\ 2}}{2\gamma^2}\right)\right)$ is background and noise reduction term that high only in the present of structure.

Using our defined term, we do not define a tube elimination term, thus this structure will be kept during segmentation. We decided to design our filtering method like that because sometimes the curved ends of bony structures have a behavior that is both tube-like and sheet-like. Thus, to accommodate this form, the sheet-ness measure is designed to be maximum for sheet-like voxels, lower for tube-like regions, and zero for other structures.

The advantage of this approach is that after the sheet-ness computation, we have a confidence score denotes the sheet-like at each voxel, and in addition, for high score locations, we can estimate the thickness of the sheet as well as the normal vector to the plane.

B. Contour Active Geodesic

Firstly motivated in majority part by the classical parametric snakes introduced by Kass *et al.* [4], at nowadays, the deformable model is widely utilized for segmentation in many computer vision applications. This method was elaborated extensively by so much research in medical image analysis and computer vision, and then the corresponding literature is very rich. We are specifically interested to a type of this deformable model known as contour active geodesic, which has been extended from the original model to naturally handle changes in topology due to the splitting and merging of contours during evolution. We begin by describing the active contour itself, and then, we will integrate local descriptor later as we move forward.

Let $C(p,t)$ be a family of closed curves where t parameterizes the family and p the given curve, where $0 \le p \le 1$. We assume that $C(0,t) = C(1,t)$ and similarly for the first derivatives for closed curves.

The curve length functional can be defined as:

$$L(t) = \int_0^1 \left\| \frac{\partial C}{\partial p} \right\| dp \tag{4}$$

By taking the first variation of the length functional, we obtain a curve shortening flow, in the sense that the Euclidean curve length shrinks as quickly as possible when the curve evolves:

$$\frac{\partial C}{\partial p} = \kappa \vec{N} \tag{5}$$

where κ is the local curvature of the contour, and $\vec{N}$ is the inward unit normal. The detailed this derivation can be found in [5].

For the intrinsic property of being closed, the curve under the evolution of the curve shortening flow (5) will continue to shrink until it vanishes. By adding a constant ν, which we will refer to as the “inflation term", the curve tends to grow and counteracts the effect of the curvature term when ν is negative [6]:

$$\frac{\partial C}{\partial p} = (\kappa + \nu)\vec{N} \tag{6}$$

The image influence can be introduced to the above framework by changing the ordinary Euclidean arc-length function along the curve C given by:

$$\partial s = \left\| \frac{\partial C}{\partial p} \right\| \partial p \tag{7}$$

to a geodesic arc length

$$\partial s_\phi = \phi \cdot \partial s = \phi \cdot \left\| \frac{\partial C}{\partial p} \right\| \partial p \tag{8}$$

by multiplying a conformal factor ϕ, where $\phi = \phi(x,y)$ is a positive differentiable function that is defined based on the given image $I(x,y)$.

We now take the first variation of the following geodesic curve length function:

$$L_\phi(t) = \phi \int_0^1 \left\| \frac{\partial C}{\partial p} \right\| dp \tag{9}$$

and reach a new evolution equation combining both the internal property of the contour and the external image force:

$$\frac{\partial C}{\partial t} = \phi \kappa N - \nabla \phi \tag{10}$$

As in equation (6), we also add an inflation term to this curve evolution model:

$$\frac{\partial C}{\partial t} = \phi(\kappa + \nu)N - \nabla\phi \tag{11}$$

More details of the geodesic active contours explication can be found in the work of Caselles *et al.* [7,8], Kichenassamy *et al.* [6], and Yezzi *et al.* [9].

C. Integration scheme

The generic numerical implementation of geodesic active contour using level set formulation [10, 11] of Equation 11 is (that now become standard):

$$\frac{\partial \psi}{\partial t} = \phi\left(div\left(\frac{\nabla\psi}{|\nabla\psi|}\right) + \nu \right)\cdot|\nabla\psi| + \nabla\phi\cdot\nabla\psi \tag{12}$$

where ψ is the level set function, usually initialized as a signed distance function to be updated in each time step, and $div\left(\frac{\nabla\psi}{|\nabla\psi|}\right)$ essentially the curvature κ of the level sets of ψ. Classically, ϕ is usually associated to a decreased function of gradient intensity having near to 0 value on the region with high gradient, but it will be 1 in the region with constant intensity variation. This value is applied to stop the implicit active contour from evolving at image boundaries or salient features.

To incorporate the Hessian filter into model deformable, we modified ϕ so that it depends not only to the image gradient, but also to the sheet-ness measurement defined previously. Thus for each voxel in equation 12, ϕ function should be redefined as:

$$\phi = S \cdot e^{\left(\frac{\nabla I}{K}\right)^2} \tag{12}$$

where S and ∇I denotes the sheet-ness measure calculated from equation 3 and image gradient respectively.

D. Implementation issue

To make the computation efficient, the proposed contour active is implemented using the zero level set of a signed distance function in the narrow band around the evolved contour. The derivative term $\nabla\psi$ is calculated using central different method as $\nabla\psi$ is relatively smooth. For $\nabla\phi$, we applied a second-order essentially non-oscillatory scheme to capture the image gradient that sometimes sharp.

The method is initialized using a surface issued from image binarisation by applying the threshold value of the bony anatomy in CT scan. This result is then enhanced using large connected component to remove the remaining speckle in the binary volume.

III. Experiences

At this moment the validation is performed qualitatively. In evaluating the segmentation results, we have particularly focused on CT scan hip bone image for our application in computer assisted total hip athroplasty. We utilized two CT scan image with different conditions: a clear and noise polluted CT scan images.

For our application context, the method segments the CT scan image much better than conventional binary segmentation of bones; in which sometimes missing the segmentation and incapable in removing the remaining noise issued by metallic object in CT scan data for the patient with implanted prothese due to their previous surgery.

IV. Conclusions

We proposed a segmentation method which combines the capability of Hessian filter in detecting specific local structure in images to drive a geodesic contour active in segmenting structures having sheet-like form. We introduced a generalization of sheet-ness measurement derived from the Hessian shape operator property that robust enough facing the noise present in image. This sheet-ness operator is directly integrated to the image energy in geodesic contour active.

In current work, we are not only validating the method with different CT image data set but also better integrating this Hessian filter to the deformable by taking into account the direction of the sheet-ness measure and its normal vectors.

References

1. Sato Y, et al, "*Three-dimensional multi-scale line filter for segmentation and visualization of curvilinear structures in medical images",* Medical Image Analysis, vol. 2, no. 2, pp. 143-168, 1998..
2. A. F. Frangi, Wiro J. Niessen, Koen L. Vincken, and Max A. Viergever, *"Multiscale vessel enhancement filtering,"* Lecture Notes in Computer Science, vol. 1496, pp. 130–138, 1998..
3. Sato Y, et al, "*Tissue classification based on 3D local intensity structures for volume rendering",* IEEE Transactions on Visualization and Computer Graphics, vol. 6, no. 2, pp. 160-180, 2000.
4. Kass, M., Witkin, A., and Terzopoulos, D., *"Snakes: Active Contour Models"*, International Journal of Computer Vision, (1988), pp. 321-331.

5. Tannenbaum, A., *"Three Snippets of Curve Evolution Theory in Computer Vision"*, Mathematical and Computer Modelling, 24, (1996), pp. 103-119
6. Kichenassamy, S., Kumar, A., Olver, P., Tannenbaum, A., and Yezzi, A., *"Conformal Curvature Flows: From Phase Transitions to Active Vision,"* Archive of Rational Mechanics and Analysis, 134 (1996) pp. 275-301.
7. V. Caselles, F. Catte, T. Coll, et F. Dibos. *"A geometric model for active contours."* Numerische Mathematik, 66:1-31, 1993.
8. V. Caselles, R. Kimmel, et G. Sapiro. *"On geodesic active contours."* International Journal of Computer Vision, 22(1):61-79, 1997.
9. Yezzi, A., Kichenassamy, S., Kumar, A., Olver, P., and Tannenbaum, A., *"A geometric Snake Model For Segmentation of Medical Imagery,"* IEEE Trans. on Medical Imaging, 16 (1997) pp. 199-209.
10. Osher, S. and Fedkiw, R., *"Level Set Methods and Dynamic Implicit Surfaces"*, Springer-Verlag, 2003.
11. Sethian, J., *"Level Set Methods and Fast Marching Methods"*, Cambridge University Press (1999)

Author: Agung ALFIANSYAH
Institute: Islamic Indonesian University/University of Malaya
Email: agung.alfiansyah@univmed.fr

An Acoustically-Analytic Approach to Behavioral Patterns for Monitoring Living Activities

Kuang-Che Liu[1], Gwo-Lang Yan[2], Yu-Hsien Chiu[1], Ming-Shih Tsai[3], Kao-Chi Chung[4]

[1]ICT-Enabled Healthcare Program - Industrial Technology Research Institute, Tainan, TAIWAN
[2]Department of Computer Science and Information Engineering, Southern Taiwan University, Tainan, TAIWAN
[3]Potz General Hospital , Chiayi, TAIWAN
[4]Institute of Biomedical Engineering, National Cheng Kung University, Tainan, TAIWAN

Abstract — **Risk prevention and alarm are crucial for home care of aged people who live alone. In this paper, an acoustically-analytic approach is proposed to extract behavioral patterns for modeling and monitoring living activities. An experimental environment was established for collecting sound tracking data of behaviors from daily activities. Each sound tracking data was transcribed to the corresponding sound event sequences by caregivers and psychologists. A living activities mining algorithm is applied to extract meaningful sequences of sound event as behavioral patterns. Then K-means algorithm is adopted to classify events into several fuzzy clusters relating to living activities for modeling behaviors in daily activities. An experimental database consists of 150 sound tracking data was established by collecting three guided behaviors included rolled out of bed to drink water, go to the toilet and watch the fish jar from 5 subjects in two weeks. 476 meaningful sequences of sound events were explored and clustered into 32 quasi-activities. These quasi-activities were further concluded into 5 kinds of behavioral patterns for modeling living activities. The preliminary result shows the potential for modeling and proactively detecting abnormal behaviors or changes of the aged.**

Keywords — **Aged people, Living Activities, behaviorism**

I. Introduction

Advancement of medical technologies and living quality extend global human life. According to the official report from United Nations, the percentage of aged people population has reached to 7% in 2004, and it will arrive to 21% in 2050 in official estimation [1]. Due to the aging society, aged people's care and its related services are getting common recently. Consequently, concerns of aged people's safety and life quality are more important. For issue of improving aged care and aged people's life quality, apply well-developed information communication technology (ICT) into aged people care service is the tendency.

Monitoring living activities of the aged people can prevent accidents and increase safety in their daily lives [2, 3, 4]. Currently, most common approaches to monitor the safety of aged persons are via wireless networks [5, 6]. Patients wear portable wireless sensors for monitoring their daily safety. If any abnormal conditions such as dizzy, heart attack or falling down occur, the information will be reported to healthcare staffs or nursing stations for providing first aid or further assistances. However, this approach will not work if the patients do not want to wear portable wireless sensors.

In this research, an acoustically-analytic approach is proposed to extract behavioral patterns for modeling and monitoring living activities. A living activities mining algorithm, which utilizes an event matching algorithm and K-means algorithm [7], is proposed to process the sequences of sound events to explore living activity models Discovered living activity models provide references about living models and behavioral prediction of aged people. These behavior models also can assist caregivers at home or care centers to prevent accidents of the aged people effectively and increase their quality and satisfaction.

II. Materials and methods

Humans' behaviors express their inner thoughts and desires. Through monitoring and observing daily actions of humans, the personal behavior model can be concluded and effective to predict the future behaviors.

According to behaviorism from Edwin Ray Guthrie [8], Human has a tendency to duplicate the successful movements. This process is called canalization [9] which is key factor for human to form a habit. When human comes across the same issue daily, he/she defers to the custom movement to respond and carry out the same issue. Behaviors in human life will produce sounds; these sounds will be appropriate sources for behavior mining due to the issue of privacy. For example, people will feel humiliated and their privacies are violated if they are monitored in video while they are taking a shower or toileting.

In this research, an approach of behaviors mining via sound data was proposed. Figure 1 shows the framework of

Chwee Teck Lim, James C.H. Goh (Eds.): ICBME 2008, Proceedings 23, pp. 1082–1085, 2009
www.springerlink.com

this research. It consists of three phases, which are development of sound tracking data collecting pilot environment, tagging sound tracking data to sequences of sound event and living activities mining and behavior model exploring algorithms.

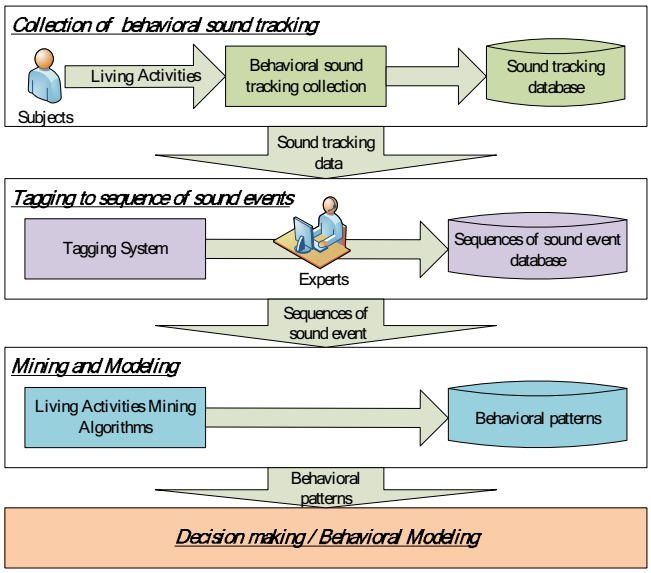


Fig. 1 Research framework of the proposed system for mining and modeling the aged people's behaviors

A. Collection of behavioral sound tracking

A sound tracking data collecting environment was established to simulate real bedroom, lavatory and kitchen of aged peoples' daily living environment. Figure 2 illustrates the sound tracking data collection environment. Five Omni-directional capacitance microphones with -65dB +- 3dB sensitivity at 1000Hz and frequency response range 50 ~ 18000 Hz are set up in proper positions to clearly record sound data of aged people. The sound data was recorded in wave format with 8 kHz sample rate and 8 bits resolution. Real-time sound tracking data is sent to the data center by the network, which is build up in the ceilings. Figure 3 illustrates the network deployment of sound data collection environment. Network protocol in this environment is control area network (CAN) 2.0 with sample rate 1 megabps [10]. Sound data captured by omni-directional capacitance microphones and transfer to data server via Ethernet for database establishment. In this research, the sound tracking data collected from three habits of daily life was recorded in the environment for further processing in the second phase.

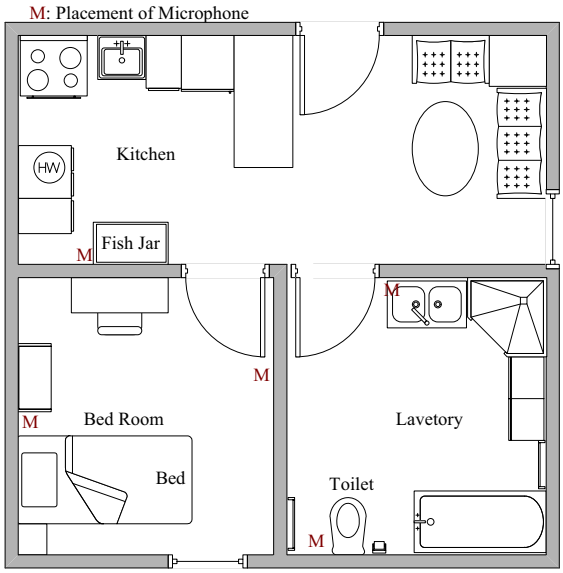


Fig. 2 Sound tracking data collection environment

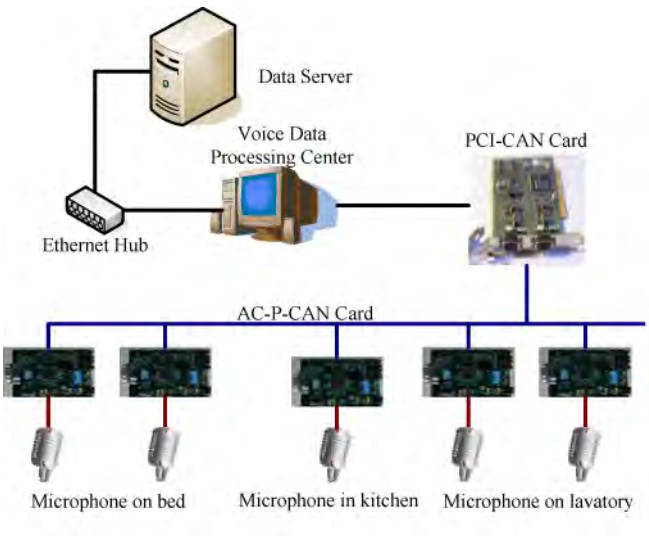


Fig. 3 CAN Network deployment for sound tracking data collection

B. Sound tracking data tagging process

In the phase, sound tracking data which was collected from the phase A was been analyzed according to two different habits of daily life and tagged into the corresponding sequences of sound events. The experts such as caregivers and psychologists of behavior were invited to tag the sequences of sound events with possible activities according

to the behavior conditions of the subjects manually. Figure 4 shows the tagging system interface. Those tagged sound event sequences provide information about subjects' daily behaviors.

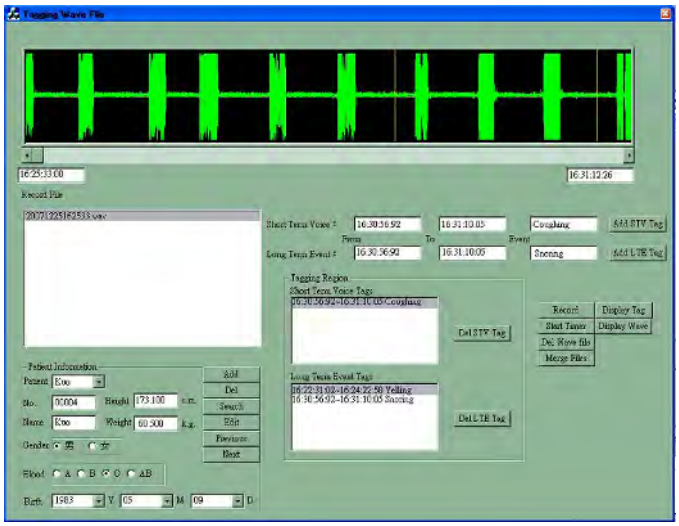


Fig. 4 Sound data tagging system interface

C. Mining and Modeling Process

For the issue of canalization, individual living activities will be reduplicated in the daily life. In this phase, a living activities mining algorithm, which utilizes a event matching algorithm and K-means algorithm[11], is proposed to explore sequences of sound event that are representative of daily activities and classify those sound event sequences to several categories according to the similarities.

The steps of living activities mining algorithm is:

Step 1: Apply the event matching algorithm to explore meaningful behavioral patterns B_1~B_M from sound event sequences S_1~S_N, mutually which are trivial sound segments tagged from phase B.

Step 2: Set length constrain for filtering behavioral patterns from step 1 to form B_1~B_O.

Step 3: Calculate the probability of each behavioral pattern by

$$prob(B_i) = \frac{N(B_i)}{C_2^N}$$

Then set constrain of probability to over 0.05 for filtering behavioral patterns from step 2 to B_1~B_P.

Step 4: Apply K-means algorithm to classify behavioral patterns from step 3 to M categories according to the similarities of behavioral patterns.

Each category discovered from the above algorithm represents a behavioral model. An example of event matching mining string exploring algorithm can be described as:

Assumed there are three data blocks:

Data block 1: ABABC
Data block 2: ABAAC
Data block 3: CCBAC

The probability of each behavioral pattern discovered from above data blocks is shown as following.

$$prob(ABA) = 0.333$$
$$prob(BA) = 0.667$$

With proposed algorithm and set the length constrain is 2, data segment ABA and BA will be explored to represent a meaningful behavioral patterns.

III. Results and Discussion

In the experiment, five subjects who are over sixty years old were brought into the sound data collecting environment to collect the testing database. They were guided by the working staffs with the two instructed behaviors of drinking water and toileting in the way of instruct-to-action. 150 sound tracking data was recorded and tagged into sequences of sound event by the caregivers and psychologists of behavior for different behaviors. 11,175 sequences of sound event were tagged totally. After processed living activities mining algorithm, 476 meaningful sequences of sound event were explored. Those sequences of sound event were processed by the living activities extraction algorithm to conclude behavioral models. The experimental result is shown in Table 1.

Table 1 Expected and experimental classified results

Expected Result	Experimental Result
Drinking water	Drinking water on bed
	Drinking water in kitchen
Watching fish jar	Watching fish jar in kitchen
Toileting	Washed hands after finished
	Finished with lavatory door closed
	Finished with lavatory door open

Figure 5 shows a state diagram example for one of the selected behavioral model of daily activities - toileting, which includes the states of door-opening, flushing, and door-closing. These states would be executed in sequence if no specialized condition happened. However, different

outcome of action and sound would result from different conditions. State transfer diagram could be used for modeling human action and exploring action changing and accidents.

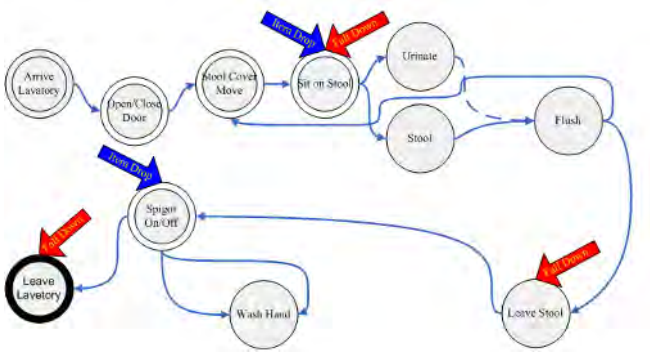


Fig. 5 A state diagram example for daily activities - toileting

In this research, three expected behavioral models of living activity should be explored, but there were six different sound traces found in the experiment. This is because that the subjects have the action variation in their daily lives. Although the subjects were guided by the same instructions, they would act for different actions which represented different sound event sequences. These six different experimental results were further analyzed and found that they actually could be concluded into three kinds of behaviors as shown in Table 1. Those results gave us a great encouragement that the proposed algorithm is feasible to explore living activities correctly.

IV. Conclusions

In this research, an acoustically-analytic approach is proposed to extract behavioral patterns for modeling and monitoring living activities of aged people. A sound tracking data collecting environment was established to simulate real bedroom, lavatory and kitchen of aged peoples' daily living environment. The sound data was analyzed by two different habits of daily lives and tagged into the corresponding sequences of sound events by experts. Then living activities extraction algorithm was adopted to analyze the sequences of the sound events to explore living activities. These living activities were further induced into individual behavior models, which can be applied to alarm abnormal and dangerous conditions in aged care. The experimental result shows the proposed living activities mining algorithm could explore living activity models correctly and effectively. This result also shows the aged people's behavior detection system via sound traces is feasible. In the future, the proposed algorithm needs more sound data with no limitation for providing more effective and reliable activity modeling.

Acknowledgment

The authors would like to thank the National Science Council, Republic of China, for financial support of this work, under Contract No. NSC 96-2221-E-218-051-MY3.

References

1. UN Population Division at: http://www.un.org/esa/population
2. Y. T. Gross, et al. "Why do they fall? Monitoring risk factors in nursing homes", J Gerontol Nurs, 1990. 16(6):p. 20-5.
3. A. H. Myers, et al. "Risk factors associated with falls and injuries among elderly institutionalized persons", Am J Epidemiol, 1991, 133(11):p. 1179-90.
4. L. Z. Rubenstein, K. R. Josephson, A. S. Robbins "Falls in the nursing home", Ann Intern Med, 1994. 121(6)"p. 442-51.
5. J. Yao, "A Wearable Point-of-Care System for Home Use That Incorporates Plug-and-Play and Wireless Standards", IEEE Transactions on Information Technology in Biomedicine, v 9, n 3, September, 2005, p. 363-371.
6. H. Harry Asada, Phillip Shaltis, Andrew Reisner, Sokwoorhee, Reginald C. Hutcinson, "Mobile Monitoring with Wearable Photoplethysmographic Biosensors", IEEE Engineering in Medicine and Biology Magazine, 2003 ,p. 28-40.
7. A. M. Fahim, A. M. Salem, F. A. Torkey "An Efficient Enhanced k-means Clustering Algorithm", *Journal of Zhejiang University Science*, Vol. 10, pp. 1626-1633, 2006.
8. S. Smith, E. R. Guthrie "General Psychology in Terms of Behavior 1921", Nov. 2007, ISBN: 0-548-74745-8.
9. G. Gottleb "Experiential Canalization of Behavioral Development: Theory", *The American Psychological Association, Inc.*, Vol. 27, No. 1, pp. 4-13, 1991.
10. "CAN Specification Version 2.0", Robert Bosch GmbH, 1991.
11. L. Rabiner and B.H. Juang (1993) : 'Fundamentals of Speech Recognition' , (Prentice-Hall, New Jersey), pp 125-128

Implementation of Smart Medical Home Gateway System for Chronic Patients

Chun Yu[1], Jhih-Jyun Yang[2], Tzu-Chien Hsiao[3], Pei-Ling Liu[4], Kai-Ping Yao[2], Chii-Wann Lin[1,5]

[1]Institute of Biomedical Engineering, National Taiwan University, Taiwan, ROC.
[2]Department of Psychology, National Taiwan University, ROC
[3]Department of Computer Science/Institute of Biomedical Engineering, National Chiao Tung University, Taiwan, ROC.
[4]Institute of Applied Mechanics, National Taiwan University, Taiwan, ROC
[5]Institute of Biomedical Electronics and Bioinformatics, National Taiwan University, Taiwan, ROC.

Abstract — **Because of the rapid aging population in Taiwan and the trend of fewer children, people are looking into technical solutions for continuous/intermittent monitoring of vital signs in the home setting environment and the interactions between family members. In this study, we have designed and implemented a home medical gateway system to connect the home-care side and the health informatics side. The home-care part provides five vital signs monitoring and on-line feedback message. Users are allowed to browse their records and read the received health information (e.g. physical checkup, health education, preventive inoculation…etc.) on the Flash based interface. This study also evaluated the practicability of the home gateway system. The number of interviewees is twenty. The analysis results show the positive user feedback of the system, and have high potential to promote the quality of patient's life. An example case of obstructed sleep apnea (OSA) patient has been studied with this system. The result shows that the gateway system can help the OSA patient to monitor and improve their sleep quality.**

Keywords — **Smart medical home, home gateway, telehomecare, telemedicine**

I. Introduction

Being the fastest aging nation in the world, Taiwan is now facing challenges of changing society structure, house hold style, and national expanses on health care. According to the definition of population structure of the United Nations, the Aging Population Society is that over 7% of total population is exceeding 65 years old. The Extra-aging Population Society is that over 20% of total population is exceeding 65 years old. In terms of the population statistic in Taiwan in 2008, the populace of older over 65 years is 2.34 million, which is 10.21% of total population. This already exceeded the threshold of the Aging Population Society [1]. It is inevitable to development Smart Medical Home to decrease the expenditure of medical service price.

For those who live in the cities and urban areas, we normally can access the health care facilities quite efficiently. It would thus require more emphasis on the quality of long term health care, especially for the home care sector of whole social care system. In view of the possible causes of deteriorating life quality can be simply age related or as complicated as disease related, the development of "Smart Medical Home" will have to cover deep thoughts of both humanity and medical needs [2-4]. These include possible disabilities caused by losses of sensory and motor functions, pains and discomforts caused by physical and metabolic changes, and psychological stresses due to self awareness and lack of knowledge about the health status and possible progresses.

Since 1990, there are more and more researches and development focus on the new technologies which could apply in the home care service [5-7]. There are also many researches focus on the cost and social impact with the home care service, but the real evaluation still lack [8,9].

This study focuses on the design and planning of a smart medical home gateway system which provide convenient home health care services. This study integrated several medical care services in the gateway system, including the biosignal record and monitor, physiology check records, health and hygiene education, and social welfare information. The health care services are designed for the chronic patients, elder and parents. The user could manage their families' and their self's health, and get health information and welfare from public resource more conveniently. In order to evaluate the practicability of the home gateway system, this study investigated and analyzed the user feedback by paper survey.

II. Method

A. Architecture of the home gateway system

This study focuses on the design and planning of a smart medical home gateway system which provide convenient home health care services. The assignment of the home gateway system is transmitting the biosignal to the server, information exchanging with hospital and social welfare canter, and a health manager interface for the user. The architecture of the smart medical home gateway system is shown in figure 1. The biosignal would transmit to server through the home gateway way. The home gateway also

Chwee Teck Lim, James C.H. Goh (Eds.): ICBME 2008, Proceedings 23, pp. 1086–1089, 2009
www.springerlink.com

provides the function of security monitor, which will send the emergency massage for the user. Moreover, the home gateway system transmits the health information from public resource and display on the user interface which was made in this study.

The server in this smart medical home gateway system was developed by MySQL Database. MySQL database could edit and modify through Microsoft Access conveniently. The interface was designed and made by Flash in this study. The user could use all function in the user interface through a touch screen.

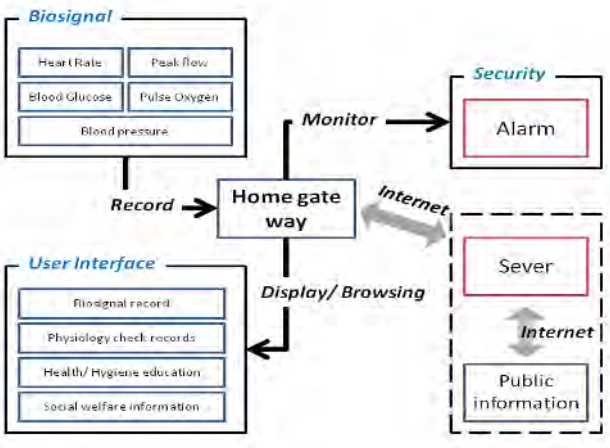


Fig. 1 The architecture of the home gateway system

B. Biological signal measurement

The biosignal measurement items involved in this home gateway system are shown in table 1, which including blood pressure, blood glucose, heart rate, pulse oxygen (SpO_2) and peak flow. All of the biosignal were collected by wearable devices which have wireless transmission function. The wireless technology used in this study is Bluetooth. Blood pressure and blood glucose could be measured by 2-in-1 device which made by Tibac technology Inc. The measured results could be sent and record in the server through home gateway after per measurement. Heart rate and SpO_2 are also measured by 2-in-1 device which was made in this study. Heart rate, pulse and SpO_2 value are real-time transmitted to the home gateway system and be monitored for emergency. Peak flow meter was designed for asthma patients controlling and monitoring their asthma condition. The principal measure theory of peak flow meter is heat lose on the sensor surface. The peak flow curve and calibrated value were transmitted to home gateway by Bluetooth after per measurement automatically.

In this system, user could choose the biosignal device following up the physicians' indication. The safe range of each biosignal should be sat to suit for personal health condition.

Table 1 The characters of medical devices

Item	Biosignal	Safe range	Transmission rate
Blood pressure monitor	Blood pressure	S: 85~95 mmHg D:120~140 mmHg	1dataset after measurement
Blood glucose monitor	Blood glucose	<140 mg/dl	1 dataset after measurement
Heart rate monitor	ECG or Pulse	50 ~ 110 beat/min	1024 data points/ sec
Pulse oximeter	Pulse	95 ~ 100 %	1024 data points/ sec
Peak flow meter	Respiratory flow	-	1 dataset after measurement

C. Evaluation

In order to evaluate the practicability of the home gateway system, this study investigated and analyzed the user feedback by paper survey. The survey questions are shown in table 2. The theme of questions are separated into three parts, these are the feedback of device operation, the interface and the acceptability conception. There are 20 interviewees in this study. The interviewees would finish the survey after experience the home gateway system. In order to let interviewees realize and respond the questions quickly, all question are positive item. The feedback score is 1 to 5, and the middle point score is 3. If user's feedback score higher 3 means it has positive feedback. The survey results were analyzed by T-test. The analysis software is SPSS.

Table 2 User Feedback Survey items

No.	Question
	Device Operation
1	Ease to use
2	Benefit for personal health care
3	Suitable for home use
4	Suitable for elder
	Friendly Interface
5	Simple and clear information display
6	Ease to use
	Health Homecare Conception
7	Match further needs
8	High potential in the market
9	Reduce medical cost
10	Promote the quality of health life

III. Results and Discussion

The health care services in this home gateway system have three categories, those are physiology signal real-time monitor, health record and health related information. This study designed a "health manager interface" which provides a friendly interface allow user browsing the health record and health related information conveniently. The interface was designed and made by Flash. The design concept of this interface is simple and instinctive operation. The information shown in the interface including the physiology measurement record, personal physiology check and health service record, hygiene education, and children electronic protective inoculation record. The health manager interface is shown in figure 2. Each family member has their own physiology measurement record and personal physiology check. The safe range of each biosignal would suit for the personal physiology condition. This interface also allow user appointing next physiology check through the system.

There are 20 interviewees in this study. The career and background of interviewees are all related to the "home care service" subject. There are 45% of interviewees are the industrial research and development workers, 45% of interviewees are the savant, another 10% are unsigned. The analysis results of the survey are shown in figure 3. SMEAN(VAR00001) to SMEAN(VAR00010) are the number code of questions which are list in table 2. Column "Sig. (2-tailed)" shows the T-test result and expresses significant difference with mean (under 95% confidence intervals). In other words, the results show the positive feedback of all questions. Interviewees are of the opinion that the operation of the interface is simple and instinctive for elder, the home care service is helpful for manager the personal health, and the information communication service is clear and convenient. Question 7 (match further needs) and 8 (High potential in the market) have highest score.

An application case of the smart medical home gateway system is the home care of obstructive sleep apnea (OSA) patient. The physiology real-time monitor and health record services were used in this study. This physiology real-time monitor applied in this application case is SpO_2 monitor. In 2000 Vázquez et al utilized the oximeter to estimate the apnea hyperpnoea index (AHI), which has potential to monitor the physiological condition of OSA patient [10]. Figure 4 shows the SpO_2 monitor result of an OSA patient during sleeping. This clinical measured data were obtained from Apex Medical Corporation. Dark black line is breath (refer to left scale) flow which was measured by resistance belt, and grey line is SpO_2 concentration curve (refer to right scale) which was measured by pulse oximeter. After the OSA patient decreased the breath frequency (or no breath), the SpO_2 concentration start to decrease. Low SpO_2 concen-



Fig. 2 The health manager interface. Top two figure show the biosignal record, bottom two figure show the children protection inoculation and physiology check.

One-Sample Test

One-Sample Statistics					Test Value = 3		
					t	df	Sig. (2-tailed)
	N	Mean	Std. Deviation	Std. Error Mean	Lower	Upper	Lower
SMEAN(VAR00001)	20	3.8421	.74432	.16644	5.060	19	.000
SMEAN(VAR00002)	20	4.2500	.63867	.14281	8.753	19	.000
SMEAN(VAR00003)	20	4.1053	.55200	.12343	8.954	19	.000
SMEAN(VAR00004)	20	4.0000	.85840	.19194	5.210	19	.000
SMEAN(VAR00005)	20	3.8333	.74339	.16623	5.013	19	.000
SMEAN(VAR00006)	20	4.0000	.64889	.14510	6.892	19	.000
SMEAN(VAR00007)	20	4.4000	.50262	.11239	12.457	19	.000
SMEAN(VAR00008)	20	4.4000	.59824	.13377	10.466	19	.000
SMEAN(VAR00009)	20	3.8500	.93330	.20869	4.073	19	.001
SMEAN(VAR00010)	20	4.3000	.65695	.14690	8.850	19	.000

Fig. 3 The analysis result of survey by SPSS software.

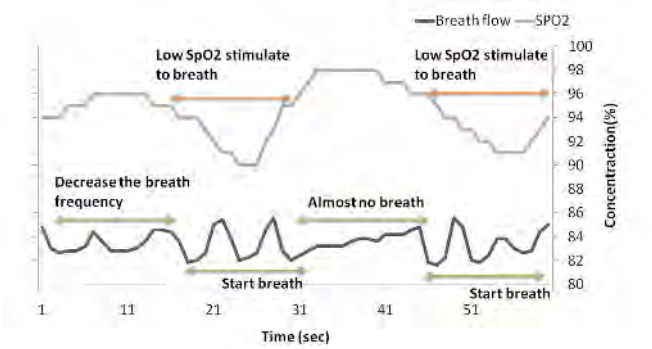


Fig. 4 The SpO_2 monitor result of an OSA patient during sleeping.

tration stimulates the patient breathing. In this application case, the home gateway system could record the frequency of low SpO_2 concentration during sleeping and providing a reference to medical treatment. If low SpO_2 concentration continues a long time, the system will trigger the alarm to notify other families to check the condition. For the future integration of mechanical ventilator, physician could adjust the treatment level through the gateway system. The OSA patient also could track the covering by themselves through the gateway system. The physiology real-time monitor and health record services could provide positive feedback control for the treatment.

IV. Conclusion

During the processing of this study, we have several discussion meeting and requirement interview with related social welfare centers. We have modified the detail of the smart medical home gateway system clearly. The smart medical home gateway system already provides the services of biosignal record and monitor, physiology check records, health and hygiene education, and social welfare information. The preliminary test shows that the system could monitor the OSA patient's sleeping quality and providing references for treatment. This study also evaluated the practicability of the hardware and software of this system. The result shows the positive user feedback of the system, and has high potential to promote the quality of patient's life.

Acknowledgment

The authors would like to thank the National Science Council of the Republic of China, Taiwan, for financially supporting this research under Contract and No. NSC 96-2627-E-002 -002 and No. NSC 97-2218-E-002-010. The authors also would like to thank the Apex Medical Corporation for financially supporting this research under clinical data collection.

References

1. The service of the Department of Statistics, Ministry of the Interior, ROC. The report of Taiwan demographic statistics (2008) Available at http://www.moi.gov.tw/stat/index.asp
2. K. Roback and A. Herzog (2003) Home informatics in healthcare: Assessment guidelines to keep up quality of care and avoid adverse effects. Technology and Health Care, vol. 11, no. 3, pp. 195-206
3. A. Dickinson, J. Goodman, A. Syme, R. Eisma, L. Tiwari, O. Mival and A. Newell (2003) Age-old Question(naire)s. Utopia, In-home requirements gathering with frail older people, 10th International Conference on Human - Computer Interaction HCI, pp. 22-27
4. J. Rodin (1986) Aging and Health: Effects of the Sense of Control, Science, vol. 233, no. 4770, pp. 1271-1276
5. J. Yao, R. Schmitz, and S. Warren (2005) A Wearable Point-of-Care System for Home Use That Incorporates Plug-and –Play and Wireless Standards, IEEE TRANSACTIONS ON INFORMATION TECHNOLOGY IN BIOMEDICINE, vol. 9, no.3, pp. 363-371
6. D. O. Kang, H. J. Lee, E. J. Ko, K. Kang and J. Lee (2006) A Wearable Context Aware System for Ubiquitous Healthcare, Proceedings of the 28th IEEE EMBS Annual International Conference NY, USA Aug, pp. 5192-5195
7. H. J. Lee, S. H. Lee, K. S. Ha, H. C. Jang, W. Y. Chung, J. Y. Kim, Y. S. Chang, D. H. Yoo (2008) Ubiquitous healthcare service using Zigbee and mobile phone for elderly patients, Internation Journal of Medical Informatics, (article in press)
8. L. Magnusson, E. Hanson (2005) Supporting frail older people and their family carers at home using information and communication technology: cost analysis, Journal of Advanced Nursing, 51(6), pp. 645–657
9. S. Koch (2006) Home telehealth – current state and future trends, International Journal of Medical Informatics, no. 75, pp. 565—576
10. J. Vazquez, W. Tsai, W Flemons, A. Masuda, R. Brant, E. Hajduk, W. Whitelaw, and J. Remmers (2007) Automated analysis of digital oximetry in the diagnosis of obstructive sleep apnoea, Thorax, no. 55, pp. 302-307

Author: Chii-Wann Lin
Institute: Institute of Biomedical Engineering, National Taiwan University
Street: No.1, Sec. 4, Roosevelt Road
City: Taipei
Country: Taiwan
Email: cwlinx@ntu.edu.tw

A Comparative Study of Fuzzy PID Control Algorithm for Position Control Performance Enhancement in a Real-time OS Based Laparoscopic Surgery Robot

S.J. Song[1,2], J.W. Park[3], J.W. Shin[3], D.H. Lee[3], J. Choi[1] and K. Sun[1,4]

[1]Korea Artificial Organ Center, Korea University, Seoul, Korea
[2]Department of Biomedical Engineering, Brain Korea 21 Project for Biomedical Science, College of Medicine, Korea University, Seoul, Korea
[3]Biomedical Engineering Branch, Research Institute, National Cancer Center, Goyang-si, Korea
[4]Department of Thoracic and Cardiovascular Surgery, College of Medicine, Korea University, Seoul, Korea

Abstract — **Position control in joint space is a basic problem in robot control where the goal is to make the manipulator joint track a desired trajectory. A number of globally asymptotically stable position control algorithms are available in the literature. Among them, an application of intelligent fuzzy PID controller to position control of robot system is studied in this paper. The robot system used is the laparoscopic surgery robot of the National Cancer Center, Korea. The intelligent fuzzy control algorithms consist of rule-based fuzzy PID and learning fuzzy schemes. The results of the experiments for the rule-based fuzzy PID controller and the learning fuzzy controller are compared with results using conventional PID controller. Various performance indices like the RMS error, IAE, ISE and etc. are used for comparison. It is observed that the learning fuzzy controller gives the best performance. Further refinement of the proposed algorithm for the control performance enhancement is under way.**

Keywords — **Fuzzy PID Control, Position Control, Learning Control, Rule-based Fuzzy PID control, Real-time OS, Laparoscopic surgery, Surgical robot, Telesurgery.**

I. Introduction

The conventional linear PID controllers are still the majority of the regulators used in industrial control systems because of their simple structure and robust performance in a wide range of operating conditions. However, the linear PID controllers using fixed gain coefficients are limited in the control techniques when they are applied to the nonlinear or time variant systems with delay. In particular, in case of the medical robot systems such as laparoscopic surgery robot, the precision control of the surgical tool is required to perform accurate surgical task. When conventional PID controller is used in the control of the multi-DOF (degree-of-freedom) manipulator with nonlinearity, large time delays, strong coupling, and with fixed PID gain parameters, it is difficult to fully satisfy performance requirement of tracking the target in real-time and precisely. In order to systemically tune parameters of conventional PID controller, many research have been done [1][2].

In this paper, we applied methods of the rule-based fuzzy PID controller and the learning fuzzy PID controller. Also, this control algorithm is compared with a linear PID controller and rule-based fuzzy PID controller.

II. System Configuration of Laparoscopic Surgery Robot

A laparoscopic surgery robot is composed of a surgery robot (master robot) and a control robot (slave robot) that telesurgery operation is available through a controlling laparoscope and surgical instrument in an abdominal cavity(Fig. 1). A surgical instrument in a slave robot is inserted in trocar that penetrates an abdominal skin and a muscle layer, and then is operated. A surgical instrument that is inserted to trocar does five drives of such operation as a pitch axis operation, yaw axis operation, rotation axis operation, translation axis operation and actuation axis operation. A master robot must realize 5 degrees of freedom corresponds to equally these, and each joint structure in the proposed system designed to be corresponded one to one by the same structure as a structure of slave robot [3].

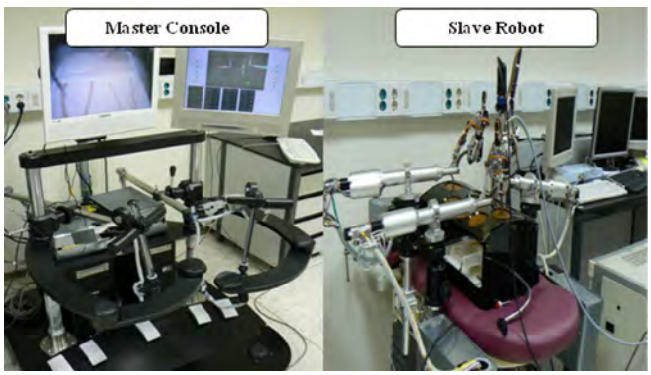


Fig. 1 Basic configuration of the laparoscopic telesurgery robot system

Chwee Teck Lim, James C.H. Goh (Eds.): ICBME 2008, Proceedings 23, pp. 1090–1093, 2009
www.springerlink.com

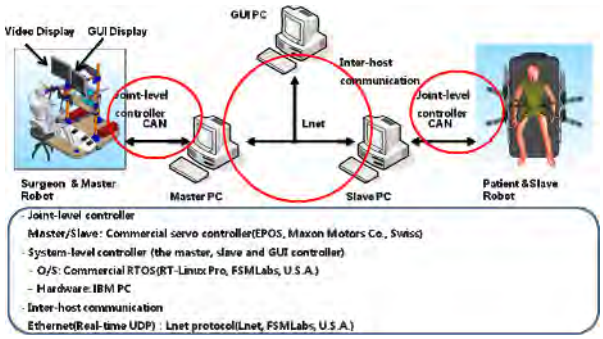


Fig. 2 Total system block diagram by constructing to master robot, slave robot and GUI

III. Controller Design

A. Rule-based fuzzy PID controller design

A generally rule-based fuzzy PID controller is a control method of creating a control signal with summing a proportional, integral and derivative signal about an inference input of tracking error and change of error(Fig. 3). In the initially of a system, a control gain coefficient of PID controller is tuned by a rule-based fuzzy PID controller. However, a proportional gain coefficient is retuned by a newly created control rule by the learning controller. Then, an integral and derivative gain coefficient corresponding it is retuned by the ***Ziegler-Nichols*** tuning method [4].

Two input variables(error($e(n)$) and change of error($\Delta e(n)$) of fuzzy PID controller are defined as:

$$E(n) = Pcmd(n) - Presp(n), \quad \Delta e(n) = e(n) - e(n-1) \qquad (1)$$

where, n is an event, P_{cmd} is a transferred control input value from master, and P_{resp} is a feedbacked response value from each robot axis of slave.

A control input value transmitted from the master composed to transmits a normalized fuzzy section value to the slave as a section of a universal set [-1, 1], and then this value was directly used as a fuzzy input value of fuzzy PID controller. An output value was directly performed to normalizing work by size conversion to a section of a universal set.

The fuzzy control rules were the most performed by **IF-Then** rules in ***Mamdani*** controller. Because the input variables are individually designed for seven input membership function, total 49 of fuzzy rules can be made.

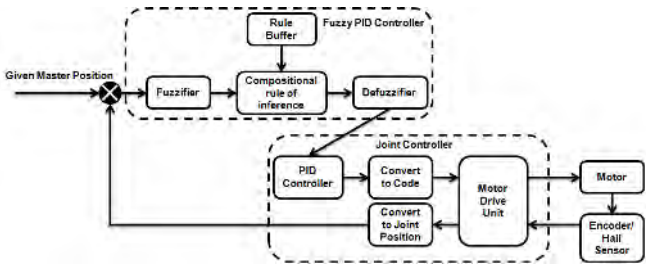


Fig. 3 Structure of a linear PID controller

Table 1 The proposed fuzzy rule buffer

Δe / e	NB	NM	NS	ZO	PS	PM	PB
NB	ZO	PS	PS	PM	PM	PB	PB
NM	PS	ZO	PS	PS	PM	PM	PB
NS	PS	PS	ZO	PS	PS	PM	PM
ZO	PM	PS	PS	ZO	PS	PS	PM
PS	PM	PM	PS	PS	ZO	PS	PS
PM	PB	PM	PM	PS	PS	ZO	PS
PB	PB	PB	PM	PM	PS	PS	ZO

This paper applied the simplified reasoning method by ***Mizumoto*** that is classified as one of the linear reasoning methods in product-sum-gravity method [5].

B. PID control gain coefficient

In this paper, the rule-based fuzzy produces readjustment values for the proportional PID gains only. The corresponding values of the fuzzified integral gain coefficient and the fuzzified derivative gain coefficient are calculated using Ziegler-Nichols method. In the deffuzifier block the fuzzy signal KP_I, is outputted and is added to the proportional gain coefficient K_P in the PID gains block to readjust the values.

$$KP(After\text{-}Apps) = KP(Before\text{-}Apps) - KPI \cdot KCP \qquad (2)$$

where, I is the sampling instant, $K_{P(After\text{-}Apps)}$ is the proportional PID gain after the application of the rule-based fuzzy PID controller. $K_{P(Before\text{-}Apps)}$ is the proportional PID gain before the readjustments. K_{CP} is the descaling factor coefficient for the proportional PID gains.

The integral and derivative gain coefficients are calculated using the ***Ziegler-Nichols*** method from the readjusted proportional gain coefficient.

C. Learning fuzzy PID controller design

The learning fuzzy PID controller is in effect the rule-based fuzzy PID controller with an addition of the rule creation and modification (figure 8). The rule creation and modification are composed of the linguistic rule table, the fuzzified past K_P buffer and the rule reinforcement [6][7].

Table 2 Comparative table of performance criteria about step response

Controller	RMS Error	Steady State Error	Settling Time	Maximum Overshoot	Delay Time	Rise Time	Fall Time	IAE	ISE	ITAE	ITSE
PID	0.032085	0.100439	0.316	0.93	0.1	0.108	0.156	6.19462	0.462212	5.599202	0.414848
Rule-Based Fuzzy PID	0.023906	0.100231	0.264	0.22	0.068	0.068	0.116	3.62758	0.256601	3.011748	0.199133
Learning Fuzzy PID	0.019042	0.100173	0.24	0.17	0.052	0.056	0.072	2.30881	0.1628	1.599909	0.106816

In the proposed learning fuzzy PID controller, the present control result is decided to have a cause in the past n samples of manipulated quantity and then this controller tunes the rules using in the past n sample before the present sample. By the values of $K_{Prop}(I\text{-}N)$ and K_{PC}, the new control rules is created in the rule reinforcement block, and these rules are applied to the rule buffer of rule-based fuzzy PID controller.

$$K_{Prop}(I) = K_{Prop}(I\text{-}N) + K_{PC} \tag{3}$$

where, $K_{Prop}(I\text{-}N)$ is the proportional PID gain from the fuzzified past K_{Prop} buffer block, N is number of past samples before the present samples and I is sampling instant. K_{PC} is a value of gain correction.

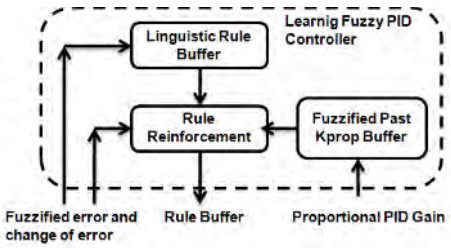


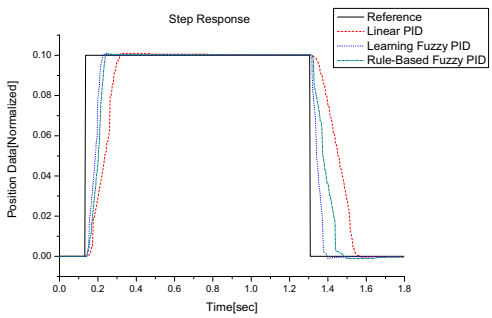
Fig. 4 Learning fuzzy control algorithm

Number of samples in the present system are defined the number in conjunction with the delay time and set up 6.

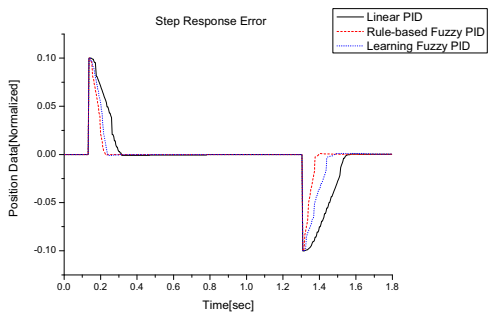
IV. Experimental Comparative Analysis

For the comparative testing the reliability and stability of the fuzzy PID controllers and a linear PID controller, a trial performance test is performed by applying the controller in the slave robot of the surgery robot system. Also, we are compared control performance through the test results. In the 5 axis of a slave robot, a translation axis that the surgical instruments are really set up have each different weight through the kinds of surgical instruments and the types of operation are various. Through these test, we compared to the control performance due to the various performance parameters such as RMS error, steady state error, settling time, maximum overshoot, delay time, rising time, IAE, ISE, ITAE, ITSE and etc..

Fig. 5 is the test result of the position tracking performance of the translation axis about the unit input of slave robot with step position command of master robot. A position tracking of translation axis of slave robot through a rapid change of translation axis of master robot verified a possibility about more fast tracking in the learning fuzzy PID controller. For numerical evaluating the system's response and comparing with the controllers, the various performance criteria were used. In Table 2, we summarized the values.



(a) Tracking result



(b) Positioning error

Fig. 5 Result of the position tracking performance of the translation joint with step position command

V. Conclusions

In this paper, the rule-based fuzzy PID controller and the learning fuzzy PID controller are both applied to a laparoscopic surgery robot, currently developing. The learning fuzzy PID controller is realized through the design of fuzzy rules and membership functions. Through the experiments applying to translation axis of a laparoscopic surgery robot prototype, currently developing, the learning fuzzy PID controller was compared with conventional PID controller and typical rule-based fuzzy PID controller and was proved to have better performance through the comparative analysis. Also, through all types of experiments under load and dynamic condition similar to surgery, a tracking performance of the system confirmed that is a suitable level. Accordingly, we will be going to process not only the experiments about the translation axis but also the experiments of the other axis. The complementary measures for the various additional function and the improved accommodation and stability are necessary hereafter, and the related developments are now under way.

Acknowledgment

This work was supported in part by the grant (No. R01-2006-000-11368-0) from the Basic Research Program of the Korea Science & Engineering Foundation.

References

1. P.J. Gawthrop and P.E. Nomikos, "Automatic tuning of commercial PID controllers for single-loop and multi-loop applications," IEEE Control System Magazine, vol. 10, No. 1, pp. 34-42, January 1990
2. Y. Nishikawa, N. Sannomyya, T. Ohta and H. Tanaka, "A methods for auto-tuning of PID control parameters," Automatica, vol. 20, No. 3, pp. 321-332, 1984
3. S. J. Song, Y. Kim, J. Choi, " A Study of a RealTime OS Based Control System for Laparoscopic Surgery Robot", The 34th Kosombe Conference on, 2006, pp. 65-68
4. J.G. Ziegler and N.B. Nichols, "Optimum settings for automatic controllers," Transactions of ASME, vol. 64, pp. 759-768, November 1942
5. M. Mizumoto, "Realization of PID controls by Fuzzy Control Methods", IEEE International conference on, vol. 4, pp.709-715, March 1992
6. H.B. Kazemian, "Development of an intelligent fuzzy controller," IEEE International Conference on Fuzzy Systems, vol. 1, pp. 517-520, December 2001
7. H.B. Kazemian, "Study of learning fuzzy controllers," Expert Systems: The International Journal of Knowledge Engineering and Neural Networks, vol. 18, No. 4, pp. 186-193, September 2001

Author: K. Sun
Institute: Department of Biomedical Engineering, Brain Korea 21 Project for Biomedical Science, College of Medicine, Korea University, Seoul, Korea.
Department of Thoratic and Cardiovascular Surgery, College of Medicine, Korea University, Seoul, Korea.
City: Seoul
Country: South Korea
Email: ksunmd@kumc.or.kr

Investigation of the Effect of Acoustic Pressure and Sonication Duration on Focused-Ultrasound Induced Blood-Brain Barrier Disruption

P.C. Chu[1], M.C. Hsiao[2], Y.H. Yang[2], J.C. Chen[3], H.L. Liu[1]

[1]Department of Electrical Engineering, Chang-Gung University, Taoyuan, Taiwan
[2]Department of Medical Image and Radiological Sciences, Chang-Gung University, Taoyuan, Taiwan
[3]Department of Physiology and Pharmacology, Chang-Gung University, Taoyuan, Taiwan

Abstract — **The purpose of this study is to investigate the influence of the ultrasound peak pressure and sonication duration on blood-brain barrier (BBB) disruption, and also seek for the optimized sonication parameter to introduce BBB-opening with minimal hemorrhagic damage. Twelve SD rats were sonicated. During sonication, the 309 kHz focused ultrasound was employed to deliver burst-mode low-pressure ultrasound to animal brains in the presence of microbubbles to introduce local and temporal BBB disruption. Different ultrasonic peak pressures and sonication durations were tested, and the BBB-disruption and accompanied hemorrhage were confirmed by brain section and histological examinations. Our results showed that the peak pressure is the major factor to generate BBB disruption, where as the sonication duration can be utilized to moderately regulate the accompanied hemorrhagic damage. We also found that the low-pressure long-duration ultrasound exposure may be beneficiary to reduce hemorrhage than high-pressure short-duration mode.**

Keywords — **Focused ultrasound, blood-brain barrier, histology**

I. Introduction

The blood-brain barrier (BBB) is a specialized structure of blood vessel walls that limits the free transportation and diffusion of molecules from the vasculature to the surrounding neurons. Many methods have been developed to enhance the BBB permeability to assist the penetration through the tight junction for therapeutic purpose, but most of the existing approach all induce a systemic BBB disruption, and was also fail to achieve the targeting drug delivery to a specific brain region.

High-intensity focused-ultrasound (HIFU) was first developed a half century ago, and has been shown with the potential to increase BBB permeability[1,2]. Recently, Hynynen et al showed that the BBB can be selectively disrupted with a reduced ultrasound energy exposure, which minimized the parenchyma damage with the use of low-power burst mode HIFU sonications under the presence of Optison® (GE Healthcare, Milwaukee, WI, USA), an ultrasound contrast agent to enhance the BBB-disruption effects[3,4].

Although the burst mode was already used during the HIFU sonication to lower the damage of surrounding tissue, hemorrhage still can be observed and becomes the major adverse effect of this approach. Intracerebral hemorrhage may be hazardous when intending to use this approach to locally deliver therapeutic molecules into brain. Therefore, exploring the safety ultrasound exposure only disrupts BBB but not causing any hemorrhage becomes a major task to make this treatment modality more promising. Therefore, the optimization of the sonication becomes essential in order to make this approach more secure.

On the optimization of delivered acoustic parameters into brain, current literatures reports that operating frequency, burst-tone ultrasonic wave output, and the concentration and administration of ultrasound microbubbles are all relevant. At the ultrasound burst-tone wave deliver design, most of the reports emphasize on the effect of peak acoustic pressure, and the role of sonication duration on BBB disruption was regards to be only play a secondary but not a major role and are rarely investigated.

In this study, therefore, we aim to investigate the sonication parameter take into account the pressure and the sonication time in order to optimize the quality of focused ultrasound induced BBB disruption. A 400-kHx focused ultrasound was selected in this examination based on its good skull-bone penetration capability. The accompanied tissue damages were evaluated by histological approach.

II. Methods

A. Animal preparation

Adult male Sprague-Dawley rats (300–350 g) were purchased from the National Laboratory Animal Breeding and Research Center (Nan-Kang, Taipei, Taiwan). The experiments conducted in this study were approved by the Institutional Animal Care and Use Committee of Chang Gung University and adhered to the experimental animal care guideline.

Chwee Teck Lim, James C.H. Goh (Eds.): ICBME 2008, Proceedings 23, pp. 1094–1097, 2009
www.springerlink.com

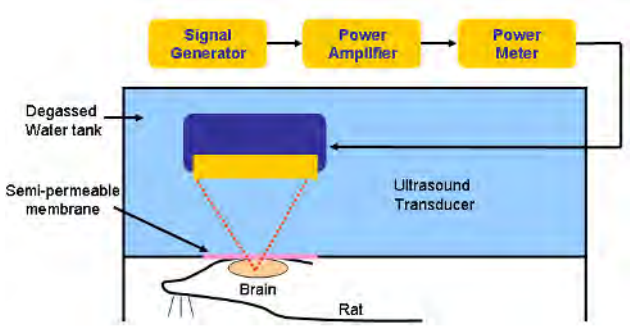


Fig. 1 Experimental setup

In the preparation of the experiments, animals were anesthetized using Chlorohydrate (300 mg/kg) through IP injection. Craniotomy was performed before the ultrasound sonication to reduce distortion of the ultrasound focal beam. A cranial window of approximately 7×7 mm2 was opened with a high-speed drill and a PE-50 catheter was placed in the jugular vein. The skull defects were covered with saline-soaked gauze to prevent dehydration and infection during the process.

B. Ultrasound Sonication

Figure 1 shows our experimental setup. The ultrasonic focal beam was generated by a 1-3 Piezocomposite focused ultrasound transducer (Imasonics, France. Diameter = 60 mm, Curvature radius = 80 mm, Frequency = 400 kHz, electric-to-acoustic efficiency = 40%). An arbitary-function generator (33220A, Agilent, USA) was used to generate the driving signal that was fed to a radio-frequency power amplifier (100A250A, Amplifier Research, USA) and the energy of signal delivered to the transducer was monitored by a power meter (Model 4421, Bird, USA). Another acrylic water tank was used for animal experiment, which had a window of approximately 4×4 cm^2 at its bottom that was sealed with a thin film to allow the entry of ultrasound energy. The animal was placed directly under the water tank with its head tightly attached to the thin-film window. The animals were prepared for the experiment as described above and placed below the water tank as figure 1.

Micro-bubbles also presented during the HIFU treatment to enhance the efficiency of BBB opening. SonoVue® (Bracco, Milan, Italy. SF_6 coated with mean diameter = 2.0-5.0 μm) was injected through the catheter 10 seconds prior to the sonications. (Each bolus injection contains 10 μl).)

On the acoustic parameter design, the pressure of 0.3,0.4,0.56 MPa and the sonication duration of 15, 30, 60, 90, 120, 150, and 180s were employed respectively. The burst length were fixed at 1%, and the pulse-repetition frequency were fixed to 1 Hz.

C. Pathologic Examinations

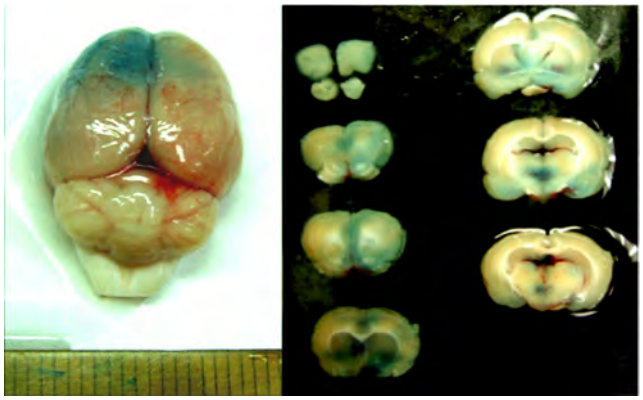
Animals were sacrificed about 3-4 hours after HIFU sonication. The brains were immediately removed and frozen in an OCT compound (Tissue-Tek®, SAKURA, USA). The tissues were sectioned using a Microtome (Model 3050S, Leica, German). The slices were preserved and stained with hematoxylin and eosin (H&E). The results were classified into 4 categories as figure 2, it depends on level of hemorrhage and cell damage. The neuronal cell damage and hemorrhage were evaluated quantitatively by four different grades. The grade 0 was defined as neither tissue damages nor erythrocyte extravasations were observed after sonication. In grade 1, a few small extravagated erythrocytes were occasionally observed, but H&E staining showed neither neuronal loss nor cell structure changed. In grade 2, there is continuous and extensive hemorrhage, accompanying neuronal loss, or apoptotic cell death. Grade 3 was the most severe damage in tissue, it has observed neuronal cell necrotic death besides grade 2.

Besides of HE staining, the terminal deoxynucleotidyl transferase biotin-dUTP nick-end labeling (TUNEL) staining from selected slides on the neighboring sections of the H&E plane were used to detect the apoptotic neurons. The histology evaluations were performed by personnel blinded to the ultrasound parameters but was informed of the specific sonication brain side.

The neuronal cell damage and hemorrhage were evaluated quantitatively by four different grades. The level 0 was defined as neither tissue damages nor erythrocyte extravasations were observed after sonication. In level 1, a few small extravagated erythrocytes were occasionally observed, but H&E staining showed neither neuronal loss nor cell structure changed. In level 2, there is continuous and extensive hemorrhage, accompanying neuronal loss, or apoptotic cell death. Level 3 was the most severe damage in tissue; it has observed neuronal necrotic or apoptotic cell death.

III. Results

First we demonstrate the histological examination of the tissue been sonicated by focused ultrasound. Figure 2 demonstrates a typical brain section after the focused ultrasound exposure (peak pressure = 0.3MPa, sonication duration = 60s). Brain tissue stained by the blue dye was caused by the dye leakage into the parenchyma. From the observation of the brain sections, it shows that the focal energy can be well steered and well penetrate the unilateral brain.



(a) (b)

Fig. 2 Typical example showing the animal brain section after undergo the focused ultrasound exposure. (a) Outlook appearance; (b) Brain tissue sections.

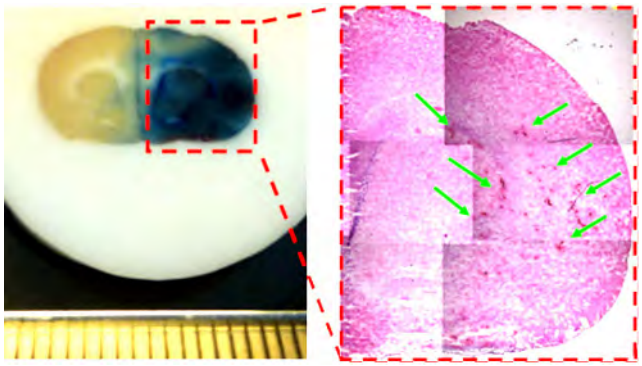


Fig. 3 HE stain examination at the sonication region

Figure 3 demonstrate typical HE stained section showing that intracerebral hemorrhage could be induced when excessive ultrasonic energy were delivered (0.3MPa, 150s). In the BBB disruptive region, there are a number of micro hemorrhage region was be detected (pointed by green arrows).

Figure 4 further demonstrate that the apoptotic cell detection by using TUNEL staining. No apoptotic cell was found when a lower parameter was delivered (0.3MPa, 15s) as shown in Fig. 4(a). When the sonication energy increased (0.3MPa, 150s), apoptotic cells can be stained in brown color (pointed by arrows) as shown in Fig. 4(b). This shows that even under the same peak pressure, the variation of sonication duration can also induced a variety of tissue damage.

Next we analyze the focused ultrasound induced brain damage in a parametric way by testing the sonication parameter with varied peak pressure and sonication time. A series of sound pressure ranging from 0.3 to 0.56 were employed, and the sonication duration ranged from 15 to 180s.

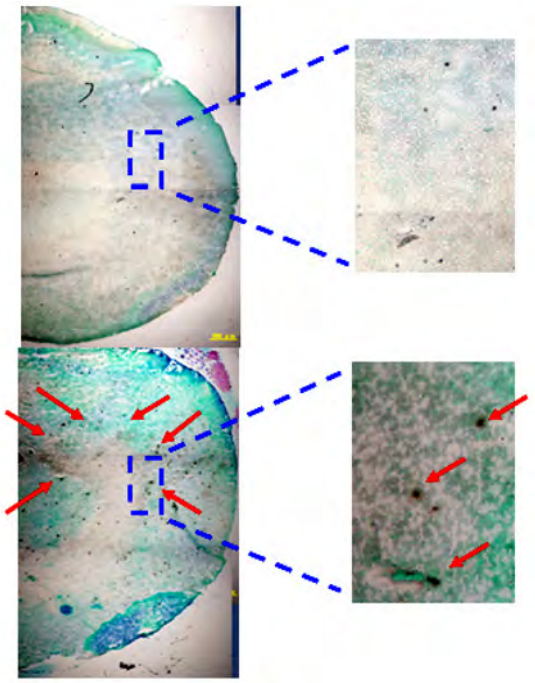


Fig. 4 TUNEL stain examination at the sonication region.

Figure 5 shows the brain tissue damage level after examine the sonicated brain sections both in HE and TUNEL (. The threshold of BBB disruption under the operating frequency was characterized to be (60s, 0.3 MPa), (30s, 0.4 MPa), and (15s, 0.56 MPa). Figure 6 demonstrate the similar information as Fig. 5 but only 0.3 and 0.56 MPa sonication were shown. When analyzing the data from Figs. 5 and 6 together, it can be observed that as the sonication duration decreased, the required peak pressure seems to be higher. On the other hand, when higher pressure was employed, tissue damage were more apparent and the damage level was characterized to be increased accordingly.

From the point view of exposure ultrasonic energy, the delivered power of two cases listed in Fig. 6 were 2 W and 10 W respectively. For example, 0.3 MPa/ 75s (the data were not present but should be located at the range between 60s and 90s cases) and 0.56 MPa/ 0.56 MPa and 15s contains identical exposure energy (power × time) but the higher pressure one contributes to a severer tissue damage.

When looking into the brain tissue section in detail (see Fig. 7), 0.3 MPa/ 60s can well disrupt the BBB region with and only take a few portion of active area been damaged (i.e., intracerebral hemorrhage); on the other hand, for high pressure sonication (0.56 MPa/ 15s), The focused ultrasound induced intracerebral hemorrhage covering all the BBB disruptive region (In some cases, the hemorrhagic areas was larger than the BBB-disruptive area). This sup-

ports that under the same standard of energy exposure, the combination of low pressure/ long sonication time would be superior than high pressure /short sonication time in inducing BBB disruption and at the same time reduce the hemorrhage as could as possible.

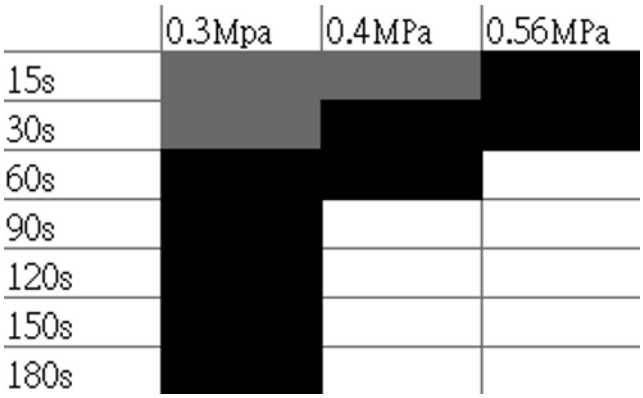


Fig. 5 BBB disruption threshold investigated under different acoustic pressures and sonication times. Gray = no BBB disruption was found; black = BBB disruption was detected.

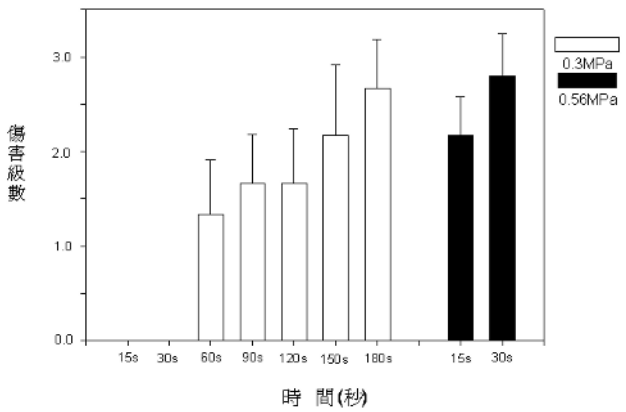


Fig. 6 Histological analysis under different sonication

IV. Conclusions

In this paper, we have successfully analyzed a more comprehensive sonication protocols study that includes not only the major factor, peak pressure, but also one of the important factors, sonication time. We have proposed to reach the requirement of BBB disruption and at the mean time reduce the brain damage, a combination of low-pressure long sonication time may be better. This approach could be benefiting the focused ultrasound brain drug delivery from the view point of increasing the safety of this technology. The future study will include a more precise and comprehensive parameters investigation to further optimize the focused ultrasound energy delivery for brain drug delivery.

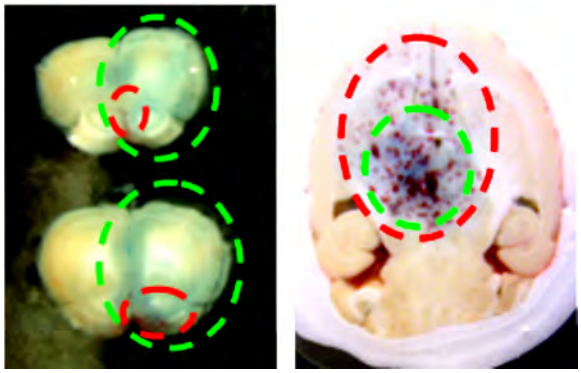


Fig. 7 Brain tissue damage when sonicating with the energy at (a) 0.3 MPa, 60s and (b) 0.56 MPa, 15s. Red regions represents the BBB disruptive region and the green region represents the hemorrhagic occurrence coverage.

Acknowledgment

The project has been supported by the National Science Council (NSC-95-2221-E-182-034-MY3) and the Chang-Gung Memorial Hospital (CMRPD No. 34022, CMRPD No. 260041).

References

1. Mesiwala, A.H., et al., (2002) High-intensity focused ultrasound selectively disrupts the blood-brain barrier in vivo. Ultrasound Med Biol, 2002. 28(3): pp. 389-400.
2. Sun, J. and K. Hynynen, (1999) The potential of transskull ultrasound therapy and surgery using the maximum available skull surface area. J Acoust Soc Am, 1999. 105(4): pp. 2519-27.
3. Hynynen, K., et al., (2005) Local and reversible blood-brain barrier disruption by noninvasive focused ultrasound at frequencies suitable for trans-skull sonications. Neuroimage, 2005. 24(1): pp. 12-20.
4. Hynynen, K., et al., (2003) The threshold for brain damage in rabbits induced by bursts of ultrasound in the presence of an ultrasound contrast agent (Optison). Ultrasound Med Biol, 2003. 29(3): pp. 473-81.

Design and Implementation of Web-Based Healthcare Management System for Home Healthcare

S. Tsujimura[1], N. Shiraishi[1], A. Saito[1], H. Koba[1], S. Oshima[1], T. Sato[1], F. Ichihashi[1] and Y. Sankai[1]

[1]Systems and Information Engineering, University of Tsukuba, Tsukuba, Japan

Abstract — **For safe and effective home healthcare, a network system monitoring one's vital signs and evaluating one's health conditions is highly desirable. In our laboratory, we have developed a vital sensing system for home healthcare. The purpose of this study is to design and implement a prototype web-based healthcare management system (WBHMS) to make effective use of the data that are measured by the vital sensing system.**

In system design, we adopted a platform-independent web-based system for its easy use. Then we considered security and privacy because the personal data were handled via the Internet. Moreover, we considered that the users were able to check not only the data from the vital sensing system but also the analyzed report as feedback.

From the above design specifications, we implemented a prototype WBHMS. This WBHMS consisted of a web server with Apache, an application server with Tomcat, a database server with PostgreSQL, and a web application with JAVA technologies. This web application had a data viewer function, an analysis function, and a feedback function. The data viewer function provided graphs of physiological data, which were body temperature, blood pressure, pulse wave (PW), and electrocardiograph (ECG), measured by the vital sensing system. The analysis function estimated parts of the users' health conditions by two indexes. One was pulse wave velocity reflecting arteriosclerosis and was calculated from both PW at the tips of one's finger and ECG. The other was an index reflecting autonomic nervous activity and was estimated based on power spectrum analysis of RR interval of ECG. The feedback function provided advice based on both the measurement data and the results of the analysis function.

Through performance tests, we have confirmed that the prototype WBHMS has the ability to make effective use of the measurement physiological data for home healthcare.

Keywords — **Home healthcare, Web-based healthcare management system, Data viewer function, Analysis function, Feedback function,**

I. Introduction

Disease such as stroke, heart disease, and cancer are generally related closely to lifestyle [1-3]. Therefore, it is essential for people to improve their daily lifestyle to prevent and reduce the diseases. To realize the improvement, we think it most desirable that people can easily know their health conditions and can obtain adequate advice based on evidence from their physiological data.

In our laboratory, we have developed a vital sensing system which can measure users' physiological data easily in order to improve home healthcare [4]. This vital sensing system mainly consisted of two sensor units and data viewer software. These sensor units are called "smart telecom unit" and can measure blood pressure, electrocardiograph, pulse wave, and body temperature. Moreover, these sensor units had a Bluetooth module in order to transmit wirelessly the above data to a personal computer with the data viewer software. Users can check the data by using the software.

Although this vital sensing system can measure one's physiological data and display the data, it is essential to develop a data management system in order to make effective use of the data.

The purpose of this study is to design and implement a prototype WBHMS to make effective use of the data that are measured by the vital sensing system.

A vital sensing network composed of a vital sensing system and a WBHMS is shown in Figure 1.

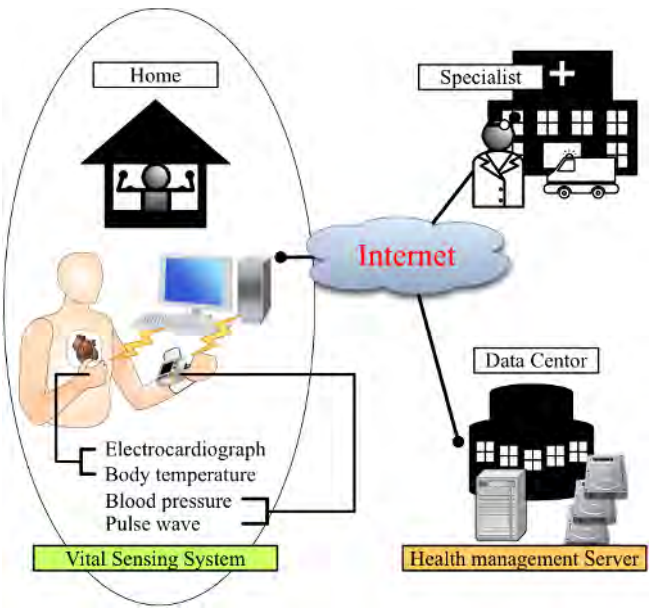


Fig. 1 Architecture of a vital sensing network composed of a vital sensing system and a web-based healthcare management system

Chwee Teck Lim, James C.H. Goh (Eds.): ICBME 2008, Proceedings 23, pp. 1098–1101, 2009
www.springerlink.com

Since we develop a prototype WBHMS which enables users to share the data with specialist via the Internet and supports the specialist giving advice based on both the data and the analysis report of the data, the WBHMS would contribute to improve the users' daily lifestyle.

II. Design of healthcare management system

We adopted a platform-independent web-based system for its easy usage and effective utilization of our vital sensing system. Therefore, we considered security and privacy because the personal data were handled via the Internet. Moreover, we considered that the users were able to check not only the data from the vital sensing system but also the analyzed report as feedback.

A. Privacy and security for web-based healthcare management system

There are various envisioned security threats such as the leakage or falsification of private information and virus attacks on a WBHMS. In each case, the fundamental security attributes of the information, namely integrity (prevention of unauthorized modification), availability (prevention of unauthorized withholding), and confidentiality (prevention of unauthorized disclosure) must be protected [5]. The most important security threats are shown as follows:

- Central information server attacks: Personal data are stored in a data server, and can be accessed over the Internet by remote users. Even though such systems are useful for users, they put the confidentiality and integrity of stored data at risk. The related security incidents are unauthorized access, technical failure of the server system, denial of service, and the threat of computer viruses.

- Communication lines monitoring and tampering: Since data have personal information, we may detect unauthorized access to the data, which is compromising the confidentiality of the data, by monitoring communication lines. The related security incidents are the infiltration and falsification of communication data.

- Authorization problems among diverse environments: Users have access to the WBHMS from a remote site. Ensuring that only authorized persons can access the personal data becomes increasingly difficult and complex. The related security incidents are masquerading user identity, unauthorized use of an application and password theft.

B. Functions of web-based healthcare management system

Our vital sensing system can measure the users' physiological data and show the data to users. However, for the people that don't have correct knowledge about the disease or are indifferent about their health would hardly utilize the system. Therefore, considering such a situation, we decided to design the three following functions:

1. Data viewer function: This function enables users to check their physiological data not only from their home but also from everywhere via Internet every day. They also can review own past records easily. Moreover, since specialist can confirm users' long-term condition via the Internet, the specialist gives some proper advice about users' health to the users.

2. Analysis function: This function estimates invisible physiological condition from the data measured with the vital sensing system. Moreover, it is expected that this function would support diagnosis by specialist.

3. Feedback function: The advice by the specialist is useful for the users. This function enables the specialist to give proper advice according to each user. Moreover, the users don't have to go to the hospital frequency in order to consult their health with the specialist. This function is also convenient for users who have no time to go to the hospital.

III. Implementation of a prototype web-based healthcare management system

We constructed a prototype WBHMS based on the design specifications in Section 2. The configuration of this system is shown in Figure 2.

This system was composed of a broadband router, three server computers, and open source software installed in these computers. The broadband router allowed only Hypertext Transfer Protocol Security (HTTPS) as communication protocol to go through. The HTTPS encrypts the information dealt between server and client for security. Apache for web server, Tomcat for application server, and PostgreSQL for database server were installed on the server computers (OS: Fedora6, CPU: AMD Opteron 2350, Memory: 2 GB). Moreover, a web application composed of Java Server Pages and Servlet was deployed on the application server. In the database server, redundant arrays of inexpensive disk (RAID) and disk backup were carried out in order to prevent disk failure. The latest software update and setting for security were executed after all the required software was installed.

The home users and specialist can easily access this system via the Internet wherever and whenever they want.

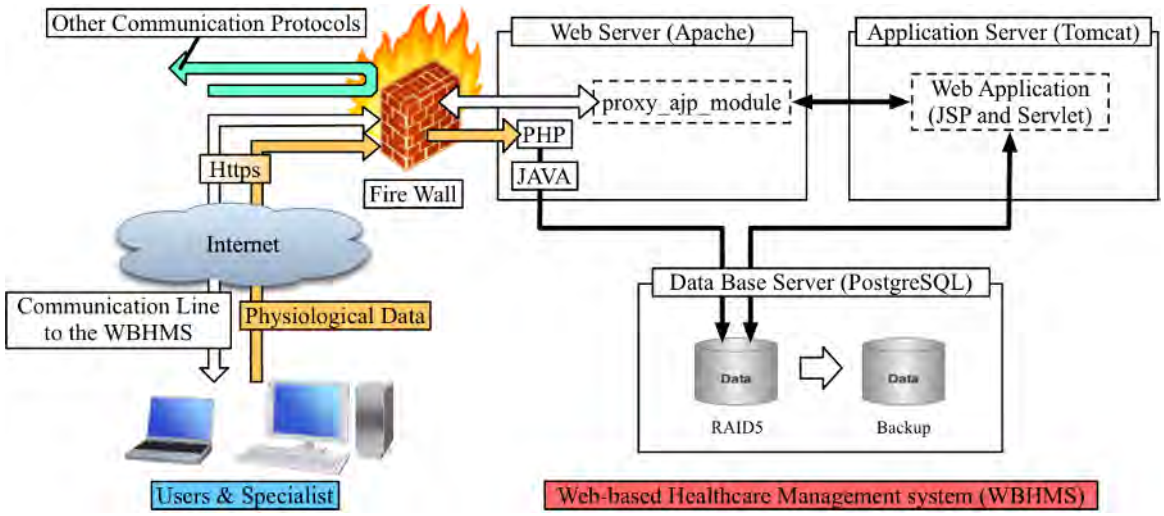


Fig. 2 Configuration of the prototype web-based healthcare management system

IV. Web Application with Java Technologies

The web application was deployed on the application server. When users access the web server, the users' request is transferred to the application server via the web server. This web application was developed by JAVA technologies and provide available service according to the users' requests. The users utilize this web application system on the web browser without the install of any special software. This web application supplied three functions composed of data viewer, feedback, and analysis.

A. Data viewer function

Sample screenshots of the data viewer function are shown in Figure 3. This data viewer function provided graphs of physiological data, which were body temperature, blood pressure, pulse wave (PW), and electrocardiograph (ECG), measured by the vital sensing system. This viewer function also provided the graphs of monthly data and the graphs of daily data. These graphs were generated by JFreeChart, which is one graph generation library, on the web application.

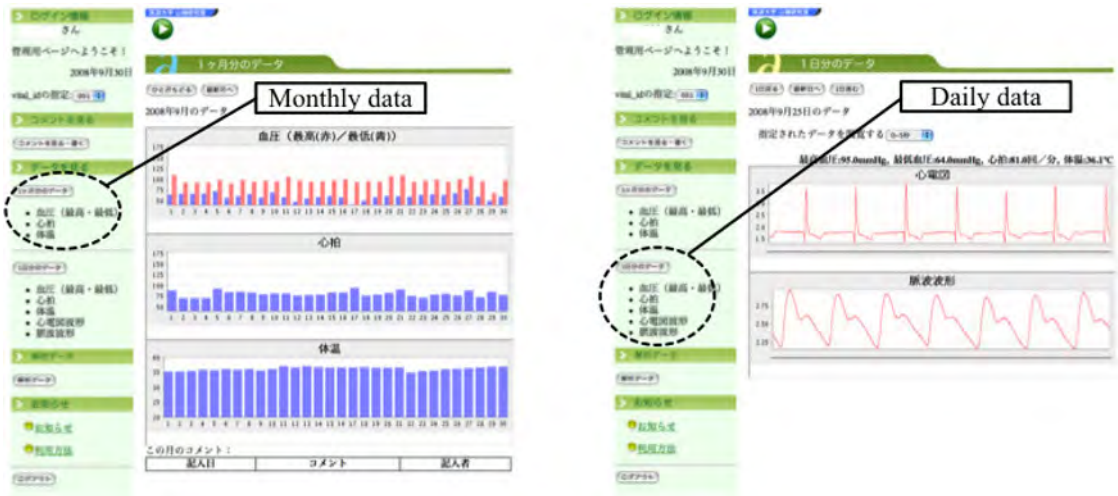


Fig. 3 Sample screenshots of measurement data shown in the data viewer function

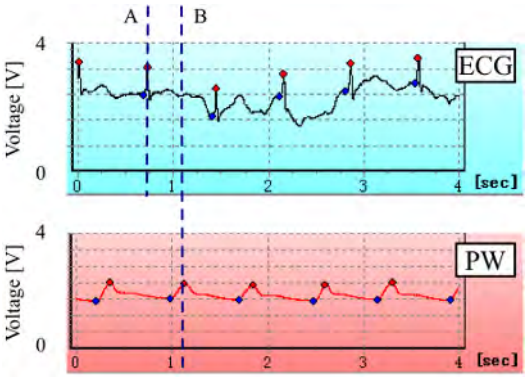


Fig. 4 Sample screenshots of the analysis function



Fig. 5 A sample screenshot of feedback function

B. Analysis function

Sample screenshots of the analysis function were partly shown in Figure 4. This analysis function estimated parts of the users' health conditions by two indexes.

One was pulse wave velocity (PWV) reflecting arteriosclerosis. We calculated the PWV from both ECG at the tips of one's finger and PW as follows:

1. Peak points of both ECG and PW were detected as both point A and point B in Figure 4.
2. The time difference from point A and point B was calculated.
3. Body length was divided by the time difference. Then, PWV was calculated.

The other was an index reflecting autonomic nervous activity and was estimated from two power spectrum frequency components (0.04 to 0.15 Hz and 0.15 to 0.4 Hz) of RR interval of ECG.

C. Feedback function

A sample screenshot of the feedback function is shown in Figure 5. The feedback function provided advice based on both the measurement data and the results of the analysis function. If specialist gives some advice to users at regular intervals, this advice would supports improvement in user's lifestyle.

V. Conclusion

In this study, we have designed and implemented the prototype WBHMS in order to make effective use of the data measured by the vital sensing system.

We have operated this WBHMS for more than 6 months through basic performance tests. We confirmed that this system has the ability to make effective use of the measurement physiological data for home healthcare.

At present, we assume our vital sensing system is used at user's home. However, there are a few people who don't have the Internet environment or even personal computers. Therefore, we are planning to introduce this system to public establishment such as community center. This would promote not only home healthcare but also community health.

References

1. Lakatta EG, Levy D (2003) Arterial and cardiac aging: major shareholders in cardiovascular disease enterprises, part I: aging arteries: a "set up" for vascular disease. Circulation 107:139–146
2. Najjar SS, Scuteri A, Lakatta EG (2005) Arterial aging: is it an Immutable Cardiovascular Risk Factor? Hypertention 46:454–462
3. Eyre H, Kahn R, Robertson RM et al. (2004) Preventing cancer, cardiovascular disease, and diabetes: a common agenda for the American Cancer Society, the American Diabetes Association, and the American Heart Association. Stroke 35(8):1999–2010
4. Ichihashi F, Sankai Y (2007) Development of a Portable Vital Sensing System for Home Telemedicine, Proc. of 29th Annual International Conference of the IEEE EMBS, Lyon, France, 2007, pp 5873–5878
5. Gritzalis S, Lambrinoudakis C, Lekkas D, and Deftereos S (2005) Technical guidelines for enhancing privacy and data protection in modern electronic medical environments. IEEE Trans Inf Technol Biomed 9 (3):413–423

Author: Shinichi Tsujimura
Institute: Systems and Information Engineering, University of Tsukuba
Street: 1-1-1Tennoudai
City: Tsukuba
Country: Japan
Email: tujimura@golem.kz.tsukuba.ac.jp

Quantitative Assessment of Left Ventricular Myocardial Motion Using Shape–Constraint Elastic Link Model

Y. Maeda[1], W. Ohyama[1], H. Kawanaka[1], S. Tsuruoka[1], T. Shinogi[1], T. Wakabayashi[1] and K. Sekioka[2]

[1]Graduate School of Engineering, Mie University, Tsu, Japan
[2]Sekioka Clinic, Minami–Ise, Japan

Abstract — **We propose a novel technique to track the motion of the left ventricular myocardium on a sequence of transthoracic two–dimensional echocardiogram. Although the proposed method is generally based on the traditional correlation based motion tracking, the tracking accuracy and stability are improved by the introduction of new objective function. In our method, the objective function is defined from the model where multiple Regions of Interest (ROIs) are connected to each other with elastic links. The elastic links reflect both elastic and shape properties of myocardium. The proposed method is implemented and evaluated using ten clinical subjects. The experimental results show that the tracking accuracy of the proposed method is higher than that of the conventional method.**

Keywords — **echocardiogram, motion tracking of myocardium, connected multiple ROIs**

I. Introduction

The echocardiogram is an essential tool for diagnosis and treatment of cardiovascular diseases. The use of echocardiograms for clinical diagnosis serves clinicians and doctors with multifold advantages including noninvasiveness of diagnosis and real–time imaging. Recent technical innovations of ultrasonic diagnosis equipment reclaim their new availabilities in clinics. These novel modalities require clinicians or doctors to track a specific tissue of myocardium by hand to keep their focus on a relevant tissue to evaluate. Manual tracking not only be tedious and time consuming but also leads subjective diagnosis and significant variability within clinicians. Therefore, an automated, computer–based objective tracking of myocardium is necessary for quantitative diagnosis.

Several approaches have been proposed to quantify the motion of myocardium from two dimensional (2–D) echocardiograms[1, 2, 3, 4]. The quantified velocity or motion itself is not of direct use for the diagnosis. In order to track the relevant regions of myocardium, we must define a region of interest (ROI) that typically corresponds to the myocardium and track the ROI in time by using the quantified velocity field.

In the tracking stage, the displacement of ROI is estimated from quantified tissue velocity and then it is accumulated on the position of ROI. In this context, the error of estimated displacement is also accumulated, hence it sometimes corrupts the tracking. The incorrect estimation of displacement occurs frequently due to the low quality of echocardiogram degraded by image noise such as speckle. Furthermore, the error causes that a tissue tracked by a ROI is not equivalent between consequent image frames. Once the error deflects the ROI form original tissue displacement, it is quite difficult to correct this disagreement between original tissue and tracking ROI.

We propose a novel algorithm to track motion of relevant regions in myocardium from high spacial resolution 2–D echocardiograms. These high resolution echocardiograms are generated from the ultrasonic radio frequency (RF) signals not using any low–pass filters. The proposed algorithm employs a modified version of the correlation method where ROIs are connected each other by elastic links. The conventional cross–correlation approach proposed for estimation of velocity field in images employs an objective function which measures the similarity of speckle patterns in two images. Instead of this objective function, we use an objective function in which we add terms evaluating the spacial relationship of ROIs.

The paper is organized as follows. We describe the motion tracking algorithm in Section II. In Section III, availability of the proposed method is evaluated using clinical echocardiograms. And finally, we conclude the paper in Section IV.

II. Myocardial motion tracking

We describe here how to estimate the velocity field and how to track the motion of relevant regions in echocardiograms by the proposed method.

A. High spacial resolution echocardiograms

An ultrasonic radio frequency (RF) signal captures the motion of left ventricular myocardium for one heartbeat. The signal is digitized with high spatial resolution and input to a PC. The one heartbeat length ultrasonic signal is separated into N frames corresponding to the frame rate of echo-

Chwee Teck Lim, James C.H. Goh (Eds.): ICBME 2008, Proceedings 23, pp. 1102–1106, 2009
www.springerlink.com

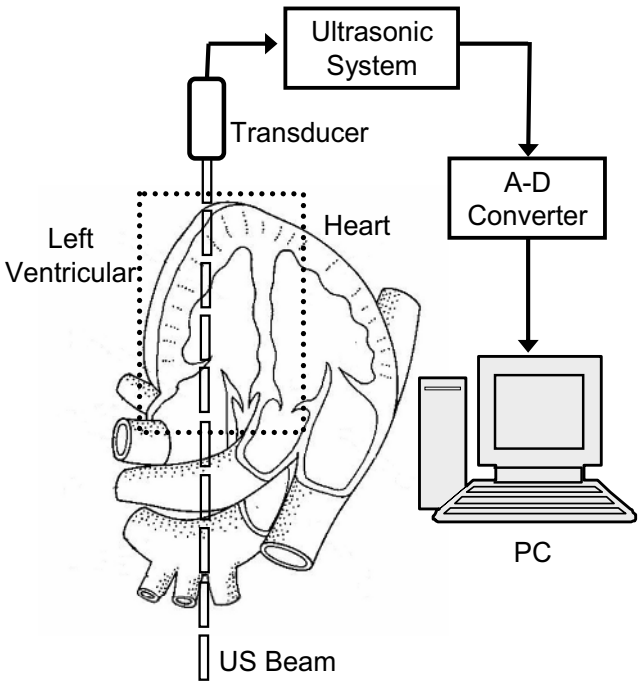


Fig. 1 Diagram of ultrasonic system for data acquisition

cardio-gram. The RF signal in each frame consists of L scan-lines. Same as in the diagnosis equipment, these scan-lines are aligned pertinent to the direction of themselves in the frame buffer and interpolated to derive the echocardio-gram. Creating images from acquired RF signal instead of using echocardiogram generated by diagnosis equipment allows us to control the spacial resolution of the resultant images. This means that we are able to obtain echocardio-grams with intended resolution.

Fig.1 illustrates the block diagram of the data acquisition process.

B. Image representation

We handle the echocardiogram derived above as a high–resolution gray-scale raster image. We show here some definitions and representation related to images used in the following contents.

Let $p = (p_x, p_y)$ and $f(p,i) = f(p_x, p_y, i)$ denote the pixel at (p_x, p_y) and the pixel value corresponding the pixel p. An echocardiogram of i-th frame is represented as a grayscale image, which is a vector where a pixel value is an element,

$$F_i = (f(p,i) \mid p \in R_{ALL}), \tag{1}$$

where $R_{ALL} = ([1, W], [1, H])$ denotes the region containing entire image surface. We denote a rectangular sub region of which p is the center and w and h are the width and height as,

$$R(p,w,h) = \left(\left[p_x - \frac{w}{2}, p_x + \frac{w}{2} \right], \left[p_y - \frac{h}{2}, p_y + \frac{h}{2} \right] \right). \tag{2}$$

A sub–image cropped by the subregion $R(p,w,h)$ from the entire image F_i is represented by,

$$\begin{aligned} f_i(R(p,w,h)) &= (F_i \mid R(p,w,h)) \\ &= (f(p,i) \mid p \in R(p,w,h)). \end{aligned} \tag{3}$$

The parallel translation of a pixel is defined as an add operation for vectors,

$$\begin{aligned} p' &= p + q \\ &= (p_x, p_y) + (q_x, q_y) \\ &= (p_x + q_x, p_y + q_y), \end{aligned} \tag{4}$$

then, the distance between two pixels p and q is obtained by,

$$\begin{aligned} d(p,q) &= \|p - q\| \\ &= \sqrt{(p_x - q_x)^2 + (p_y - q_y)^2}. \end{aligned} \tag{5}$$

And the angle of the line segment connecting p and q is defined as,

$$\theta(p,q) = \tan^{-1}\left(\frac{p_y - q_y}{p_x - q_y} \right) \tag{6}$$

C. Connected Multiple ROIs

In the motion tracking method, we should fist define an objective function to optimize. A well–defined objective function is required to give a good evaluation for displace-ment between two images and be robust for image noise. Our former research[5] shows that an objective function based on the residual instead of the cross– correlation de-rives good performance for the myocardial motion tracking in echocardiograms.

The basic idea of the method in [5] is that elastic links which connect adjacent ROIs can reduce tracking errors due to velocity estimation error. Fig. 2 shows that the model of this idea. The connecting multiple ROIs increase the com-plexity of objective function.

Let $P = \{p_1, p_2, \cdots, p_n\}$ and $Q = \{q_1, q_2, \cdots, q_n\}$ represent a set of tracking point on the i-th frame and i + 1-th frame respectively. The objective function for P and Q is defined as,

$$h(P,Q) = \sum_{j=0}^{n} \left\{ \gamma(p_j, q_j) + \frac{k}{2}(L(p_j) - L(q_j))^2 \right\}, \tag{7}$$

$$L(p_j) = \begin{cases} d(p_{j+1}, p_j), & 1 \le j \le n-1 \\ d(p_0, p_j), & j = n \end{cases}, \tag{8}$$

where $L(p_j)$ denotes a distance between the i-th and i + 1-th tracking points. The parameter k reflects the elastic property of myocardium and controls change of distance between tracking points. A large k constrains tracking points not to change the distance between each other.

The objective function in (7) is based on the assumption where the elastic property of myocardium is homogeneous. This assumption sometimes results tracking errors in [5]. In order to adopt this assumption on the real property of myocardim, we modify (7) by introducing heterogeneous elastic parameters.

$$h'(P,Q) = \sum_{j=0}^{n} \left\{ \gamma(p_j, q_j) + \frac{k_j}{2} \left(\frac{L(p_j) - L(q_j)}{L(p_j)} \right)^2 \right\}. \tag{9}$$

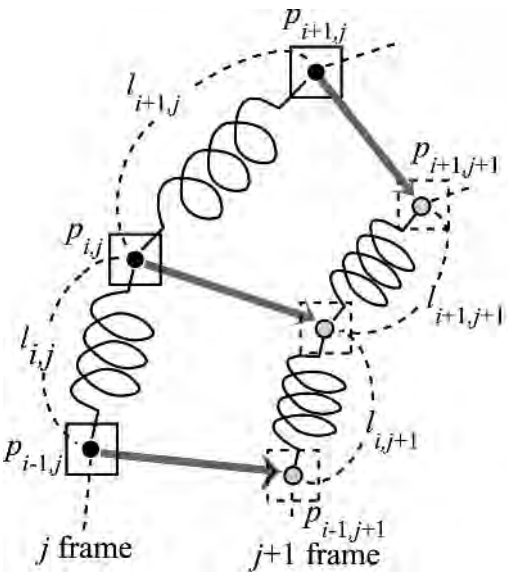


Fig. 2 Model of the objective function in the proposed method

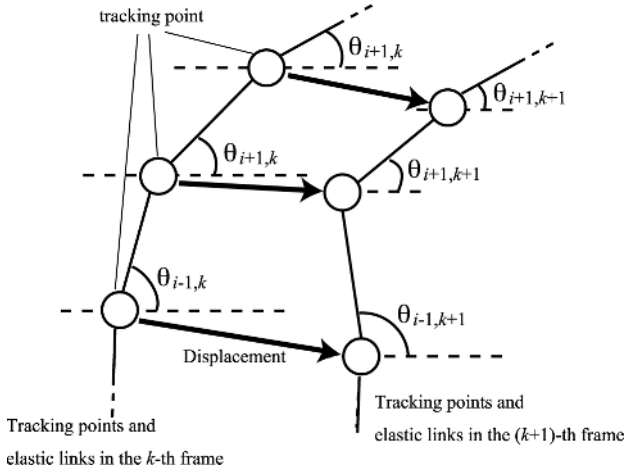


Fig. 3 Shape–constraint elastic link model

The each parameter k_j in $K = \{k_1, k_2, \cdots, k_n\}$ reflects the elastic property of link corresponding to the tracking point. The proposed method minimizes the (9) by using a dynamic programming approach.

D. Shape–Constraint Elastic Link Model

The motion property of myocardium in the long–axis B–mode scan is different from that in the short–axis scan. For instance, in the long–axis the shape of left ventricular endocardium does not changed while the cavity of left ventricle does, during systole and diastole cycle. Motivated by this property, we introduce the shape–constraint elastic link model (SCEL) into the objective function of motion tracking.

The basic concept of SCEL model is illustrated by Fig.3. The model considers the angle of each elastic link not only the length of them. The model constraints the angle change between two consequent frames. The objective function considering the SCEL model is expressed as,

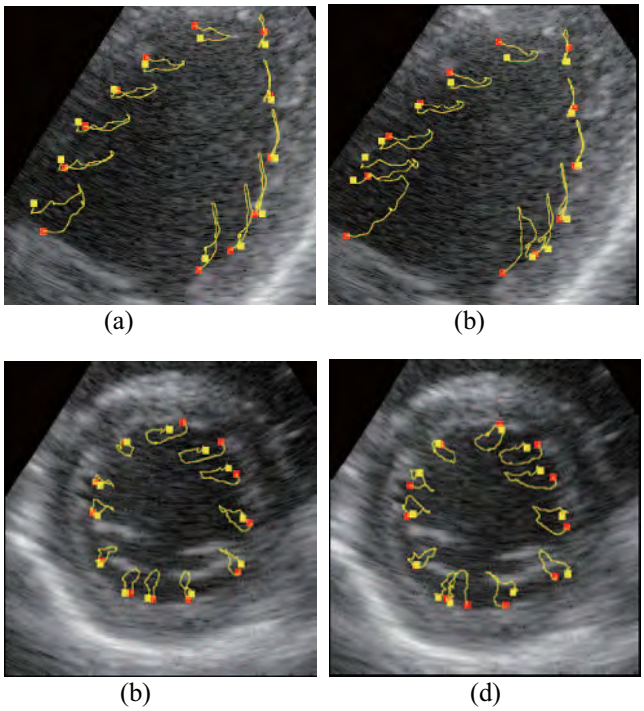
$$h''(P,Q) = \sum_{j=0}^{n} \left\{ \gamma(p_j, q_j) + \frac{k_j}{2} \left(\frac{L(p_j) - L(q_j)}{L(p_j)} \right)^2 + v_j (\theta(q_{j+1}, q_j) - \theta(p_{j+1}, p_j))^2 \right\}. \tag{10}$$

Where, the angle change between frames, $\theta(q_{j+1}, q_j) - \theta(p_{j+1}, p_j)$, are calculated by equation (6).v_j is weighting factors which control the importance of shape–constraint in the objective function. At this point, we defined the weighting factors experimentally. For minimi-

zation of the objective function (10), we can also employ dynamic–programming approach.

E. Determination of weighting factors k_j and v_j

To track myocardial motion accurately using SCEL, we have to determine a suitable combination of weighting factors k_j and v_j . These parameters control the level of importance of the image correlation, distance change between tracking ROIs and angle consistency in the objectivefunction (10).



(a) (b)

(b) (d)

Fig. 4 Examples of tracking result by the proposed and the conventional methods. (a),(c) and (b),(d) are results by the proposed and conventional methods respectively.

The determination of the weighting factors is quite important; however it is almost impossible to determine a suitable combination of factors to a particular echocardiogram. From this reason, we determine the value of factors employing the following exploratory experiment. At first, three sequences of echocardiogram are selected randomly for the exploratory experiment. The myocardial motion contained in the three sequences is tracked by manual. Next, a range of kj and vj is defined within that the values do not corrupts the motion tracking.

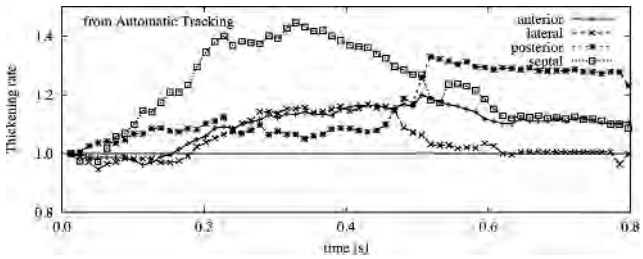


Fig. 5 An example of myocardial wall thickening assessment using motion tracking result

III. Experiments and Results

We use ultrasonic diagnosis equipment (Hitach–medical EUB–6500) to acquire ultrasonic RF signals. The signals capture the motion of left ventricular myocardium in short– and long–axis view. Ultrasonic data from ten normal subjects are used for verification of the proposed method. High spacial resolution echocardiograms are created from the RF signals. Initial tracking points are defined by manually on the first frame.

Fig. 4 illustrates the examples of tracking result. In the figure, (a),(c) and (b),(d) show the result by the proposed method (10)and the conventional CMR one (9) respectively. Since we use one heart beat length signals, the tracking points is expected to return at the position of initial ones. From these results, it is obvious that the proposed method is able to track the myocardial motion more reliable than the conventional one.

Fig.5 shows an example of application of the proposed result. This figure illustrates change of myocardial thickening during one heart cycle. The myocardial thickening of four myocardial region, anterior, lateral, posterior and septum, are calculated using the motion tracking result by the proposed method.

Conclusions

In this paper, we propose a new modality to track the myocardial motion from 2–D echocardiogram. The experimental results with clinical subjects show that the performance of the proposed method is empirically superior to the conventional methods.

Further study topics include (1) further improvement of tracking accuracy, (2) define an effective procedure to define the elastic parameters kj and vj in (10) and (3) detailed performance evaluation with enough number of clinical data.

REFERENCES

[1] B. Lucas and T. Kanade. An iterative image restoration technique with an application to stereo vision. Proc. DARPA IUWorkshop, pages 121–130, 1981.

[2] Y. Chunke, K. Terada, and S. Oe. Motion analysis of echocardiograph using optical flow method. Proc. IEEE Int. Conf. Systems, Man, and Cybernetics, 1:672–677, 1996.

[3] P. Baraldi, A. Sarti, C. Lamberti, A. Prandini, and F. Sgallari. Evaluation of differential optical flow techniques on synthesized echo images. IEEE Trans. Biomed. Eng, 43(3):259–272,1996.

[4] Michael S¨uhling, Muthuvel Arigovindan, Christian Jansen, Patrick Hunziker, and Michael Unser. Myocardial motion analysis from b–mode echocardiograms. IEEE Transactions on Image Processing, 14(4):525–536, 2005.

[5] Wataru Ohyama, Masaki Inami, Tetsushi Wakabayashi, Fumitaka Kimura, Shinji Tsuruoka, and Kiyotsugu Sekioka. Automatic tracking for regional myocardial motion by correlation method with connecting multiple rois. IEEJ Trans. EIS, 124(10):2079–2086, 2004.

Assessment of Foot Drop Surgery in Leprosy Subjects Using Frequency Domain Analysis of Foot Pressure Distribution Images

Bhavesh Parmar

Ramrao Adik Institute of Technology, Navi Mumbai, India

Abstract — **Foot problems in leprosy subjects are of major concern. Quantitative assessment of corrective foot drops surgery in detecting effectiveness of recovery after surgery overtime having prime importance. This paper quantifies and distinguishes between the foot pressure images of leprotic subject for preoperative as well as different duration of post-operative and of normal foot. Detailed analysis is performed on walking foot pressure distribution image in the frequency domain. Power ratio (PR) (ratio of power in higher spatial frequency components to the total power in the power spectrum) is used to distinguish between the foot pressure image pattern in preoperative and postoperative over different time duration. Statistical Analysis involving calculation of 'p' using Welch ANOVA test followed by post Dunnett's test and Kruskal-Wallis test has been carried out on mean PR to understand the progress of recovery after surgery from preoperative state and with normal state in all the foot sole areas. It is observed that the postoperative stages are the one with increase sensitive feet and decrease PR. These results could help in early detection of recovery and/or defect of surgery, and thereby help orthopedic surgeons for early corrective action for preserving or restoring normal foot function.**

Keywords — **Foot drop surgery, Foot pressure images, Frequency domain Image Analysis, Leprosy, Power ratio.**

I. Introduction

Leprosy, a disease as old as mankind, has been a public health problem to many developing countries. Leprosy has always and everywhere been regarded as a special disease. It has stimulated studies in various fields, such as pathology, histology, immunology and rehabilitation. Of them rehabilitation of the victims has assumed prime importance as its focus is on prevention of further advancement of deformities. This paper aims to understand the pressure distribution patterns under the foot-soles of leprotic subjects at different stages of curing of leprotic disorder with different time duration after surgery with new foot pressure parameter PR (ratio of power in higher spatial frequency components to the total power in the power spectrum of the foot pressure image) developed by Prabhu et al., 2001[1]. This work could help the orthopedic surgeons in detecting the effectiveness of surgery with time duration after correction of leprotic feet and thereby in taking early corrective action for curing of the feet disorders of the disease as well as the functional rehabilitation of the leprosy feet, in time.

Section II describes the foot pressure measurement system used for acquiring the data and image processing methodology. Section III describes the frequency domain analysis of walking foot pressure images. In section IV results with analysis is been discussed. At last conclusions with the scope for the future extension are discussed in section VI.

II. Foot pressure measurement system

The Foot pressure measurement system involves the use of an optical pedobarograph developed earlier [2] in the Biomedical Engineering laboratory, IIT, Madras.

Standing foot pressure measurements gives only a fraction of the potential information regarding the functionality of the foot. More valuable information would result from the dynamic distribution of pressures and loads, particularly since many abnormalities of the foot only reveal themselves in dynamic (walking) measurements while remaining hidden on a fairly detailed static (standing) analysis [3].

The size of the individual footprint is varying and these foot print images are divided into ten standard regions as per the method indicated in Patil et al [4]. Now each plantar area is obtained manually, from the corresponding frames of distinct phase of walking cycle, i.e., area 1 and 2 from heel–strike; area 4 from mid–stance and area 5 to 10 from push–off phases of walking cycle.

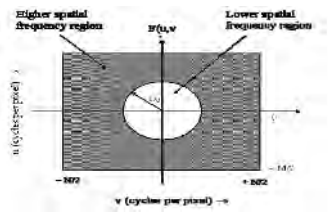


Figure 1 The Fourier spectrum, *F(u,v)* of an image showing the higher and lower spatial frequency regions.

$$LFP = \left\{ \sum_{D(u,v)=0}^{D_0} |F(u,v)|^2 \right\} - |F(0,0)|^2 \quad (1)$$

$$HFP = TP - LFP \quad (2)$$

Chwee Teck Lim, James C.H. Goh (Eds.): ICBME 2008, Proceedings 23, pp. 1107–1111, 2009
www.springerlink.com

$$PR = \left(\frac{HFP}{TP} \right) \text{ x } 100 \quad (3)$$

Frequency domain analyses of these images corresponding to all the plantar areas are performed, and the PR (ratio of high frequency power to the total power in an image) is calculated using equations (1-3).

III. Frequency domain analysis.

The frequency domain analysis, of walking foot pressure light intensity images, is done for 12 leprotic subjects. Comparisons of PR values are made between normal and leprotic subjects pre and post corrective foot drop surgery.

A. Results

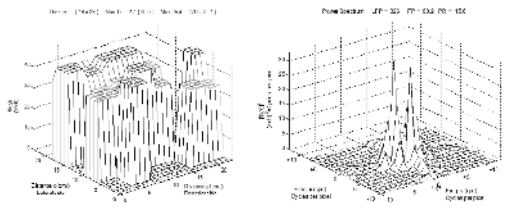
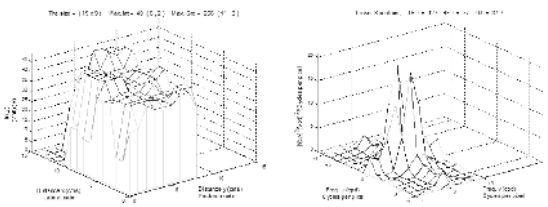


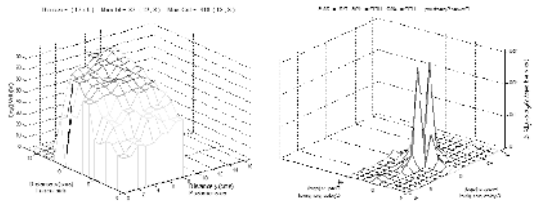
Figure 2 (a) The walking foot pressure image intensity (spatial) distributions; the directions of x and y axes are from medial to lateral and posterior to anterior side and (b) power spectrum after deleting the DC component, in area 2 for a normal subject, respectively.



(a) (b)

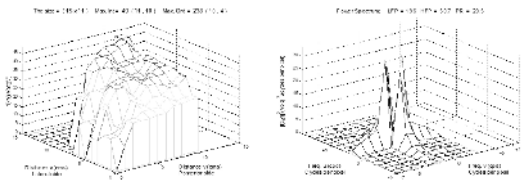
Figure 3 (a) The walking foot pressure image intensity (spatial) distributions; the directions of x and y axes are from medial to lateral and posterior to anterior side, respectively, and (b) the power spectrum (after deleting the DC component), in area 2 of the left foot for a leprotic subject before corrective foot drop surgery.

Figures 2(a) and 3(a) show the spatial variation of intensity distribution in area 2 (lateral heel) for a normal and leprotic subject (with foot drop and claw toes) before the corrective foot drop surgery. It is observed that the spatial intensity variation distribution for a leprotic foot is not uniform (Figure 3a) compared to that of a normal foot (Figure. 2a). The power spectrum of these intensity distributions are shown in Figures 2(b) and 3(b), respectively. The power spectrum of foot pressure image intensity for a leprotic foot before corrective surgery (Figure 3b) shows higher relative value of high spatial frequency power in the total power spectrum distribution compared to that of a normal foot (Figure 2b), giving rise to higher value of PR (37.7) in that area of the foot for the leprotic subject before the surgery.



(a) (b)

Figure 4 (a) The walking foot pressure image intensity (spatial) distributions; the directions of x and y axes are from medial to lateral and posterior to anterior side, respectively, (b) the power spectrum after deleting the DC component, in area 2 of the left foot for the same subject, (as in Fig 3) after corrective foot drop surgery (41-60 days after correction).



(a) (b)

Figure 5 (a) The walking foot pressure image intensity (spatial) distributions; the directions of x and y axes are from medial to lateral and posterior to anterior side, respectively, and (b) the power spectrum after deleting the DC component, in area 2 of the left foot for the same subject) (as in Figs. 3 and 4) after corrective foot drop surgery (above 210 days after correction).

Similarly the spatial variation of intensity distribution in area 2 (lateral heel) for the same leprosy subject after corrective surgery (41-60 days duration after surgery and 210 days after surgery) are shown in Figures 4(a) and 5(a), respectively. The corresponding power spectrums are shown in Figures 4(b) and 5(b), respectively. It is observed, from Figures 4(a) and 5(a), that the foot pressure spatial intensity distribution is becoming nearly uniform, giving rise to lower relative value of high spatial frequency power in the total power spectrum compared to the corresponding value before corrective foot drop surgery, thus decreasing the value of PR (28.5 and 20.5, respectively) towards normalization.

B. Analysis of Results

The Figures 6 and 7 show summary of variations of values of PR in different foot sole areas for two typical leprotic

subjects before and after different durations of the foot drop corrective surgery in comparison with normal subjects. It is observed from the Figures, that the PR values are very high prior to surgery in heel, first and second metatarsal head and second to fifth toes. The high values of PR observed in the heel area could be due to the foot drop and in the mid foot areas due to lateral shift of walking pattern observed in foot drop subjects. The high values of PR in second to fifth toes could be due to claw toes exerting high pressure distributions. There is general recovery (after foot drop surgery) in the heel to fore foot regions, as shown in decrease of average PR values in all foot areas (fig. 6) from 28-30 (before surgery) to 18-22 as the recovery process takes from 40-60 days to 210 days. The values in the second to fifth toes did not reduced due to non correction of claw toes in all the leprotic subjects. From comparison of both the Figures 6 and 7, it is observed that the recovery pattern is different in both the subject. In Fig. 6 the recovery is faster than the Fig 7, form that we can say that the recovery of foot sole parameter may also depend on the type of corrective surgery.

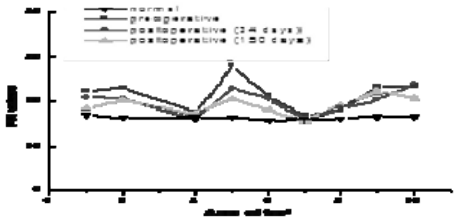


Figure 6 Variations of mean values of PR in the different areas of the foot sole for leprosy subjects before and after the foot drop correction with varying recovery time.

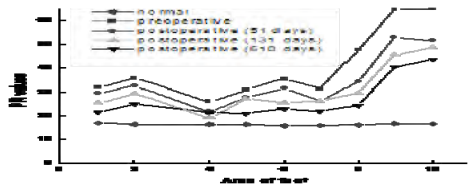


Figure 7 Variations of mean values of PR in the different areas of the foot sole for leprosy subjects before and after the foot drop correction with varying recovery time.

The mean PR values, for all leprosy subjects in preoperative and postoperative stage of corrective surgery-with different time durations of recovery compared to corresponding normal feet, are shown in first group for all the specified foot sole areas.

The above Figure 8 shows summary of variations of mean values of PR in different foot sole areas for all the leprosy subjects before and after different durations of the foot drop corrective surgery in comparison with normal subjects. It is observed that the PR values are very high prior to surgery in heel, second metatarsal head and second to fifth toes. The high values of PR felt in the heel area in mid-stance phase, could be due to the foot drop and in the lateral mid foot area due to lateral shift of walking pattern observed in foot drop subjects. The high values of PR in second to fifth toes could be due to claw toes exerting high pressure distributions. There is gradual recovery (after foot drop surgery) in the heel to fore foot regions, as shown decrease of average PR values in all foot areas from 30-35 to 20-22 as the recovery process takes from 40-60 days to 210 days. The values of PR after 210 days being very nearly equal to normal subject values. The values in the second to fifth toes did not reduce due to non correction of claw toes in all the leprotic subjects.

C. Statistical Analysis

A statistical study was carried out on PR values obtained from the foot image data of normal and leprosy subjects

Table 1 Values of mean difference and significance level (p) for different group taking normal as a control group for all foot sole areas.

Group	Areas of foot								
	1	2	4	5	6	7	8	9	10
Preoperative	-16.955**	-16.939**	-9.119**	-14.885**	-23.899**	-10.175**	-14.25**	-31.136**	-28.595**
Postoperative (40-60 days)	-10.471*	-9.785**	2.189§	-11.403**	-16.022**	-10.158**	-9.864**	-25.071**	-25.645**
Postoperative (90-110 days)	-2.885§	1.220§	1.465§	-5.357§	-7.976§	-4.939§	-6.284§	-21.750+	-22.250+
Postoperative (111-150 days)	-10.747§	3.179*	0.647§	-6.319§	-9.763§	-6.244*	-7.903*	-20.520+	-19.150+
Postoperative (>210 days)	-6.876§	2.184§	1.718§	-6.912§	-8.124§	-3.928§	-6.437§	-24.100+	-25.833+

** Very significant ($0.001<p<0.01$), * significant ($0.01<p<0.05$), § not significant ($p > 0.05$), + Dunn's test could not performed due to small sample size.

(before and after the corrective foot drop surgery). To know the difference of mean values of PR in all the standard foot sole areas, comparisons were made between different groups. If the data is parametric, it will be tested by Welch ANOVA test followed by Dunnett's C test. For non-parametric data relevant Kruskal-Wallis test has been performed followed by Dunn's test.

Normal group is found to be significantly different ($0.001<p<0.01$) from preoperative group and ($0.01<p<0.05$) postoperative group for40-60 days after surgical correction of foot drop. Table 1 shows the details of these tests and respective level of significance (p) and mean differences for all groups belonging to different foot sole areas.

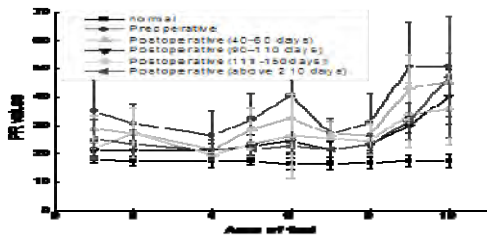


Figure 8 Mean values of PR in the different areas of the foot sole for normal and all the leprosy subjects before and after the foot drop correction. The bars indicate the standard deviations in every foot sole areas.

IV. Discussion

It is observed that the percentage of power in higher spatial frequency components, is more in the foot pressure images corresponding to before the corrective foot drop surgery for the leprotic feet than those of the images of the normal feet in all the corresponding foot sole areas, giving rise to higher value of PR. This may be due to the non uniform variations of the spatial intensity in the foot pressure image of the leprotic feet (Figure 3a) as compared to a more smoother intensity distributions, in a normal feet (Figure 2a). Variation of the spatial intensity reduces to nearly uniform after the corrective foot drop surgery of the leprotic surgery in their recovery period (Fig. 4a and 5a). It is also observed that when the duration of recovery period for the corrective surgery increases, the power ratio also decreases, tending to near normal value. From comparison of the recovery pattern in different subjects, it is observed that the recovery is faster (Fig. 6) in some of the subjects than other (Fig 7). There is gradual recovery in the heel to fore foot regions, as shown by decrease of average PR values in all foot areas from abnormal to nearly normal (Fig. 8) as the recovery period increases. The values of PR after 210 days are found to be very nearly equal to normal subject values.

Statistical results shows that the mean values of the parameter PR, for all leprotic subjects before corrective foot drop surgery, compared to the corresponding values of PR of normal feet are found to be significantly higher with 'p' values < 0.001 for all the areas of the foot sole.

V. Conclusions

Walking foot pressure patterns of normal and leprotic subjects before and after the foot drop correction have been analyzed in frequency domain to understand the change taking place in the pressure distribution patterns under the foot-soles of leprotic subjects before and after undergoing corrective foot drop surgery. The foot pressure parameter PR shows the difference between its values before and after corrective foot drop surgery and hence help to detect the effectiveness of the corrective foot drop surgery.

It is observed that the relative values of higher spatial frequency power in the total power spectrum of foot pressure is more, in the images of leprotic subjects before corrective foot drop surgery and in initial stage of recovery after corrective surgery, than those of the images of the normal feet in all the foot sole areas, giving rise to higher value of PR. This may be due to the non uniform variations in spatial intensity of foot pressure image in the leprotic feet as compared to a smoother intensity distribution, in normal feet. Variation of the spatial intensity of foot pressure image reduces nearly to uniform level in the later stage of recovery after the corrective foot drop surgery. It is also observed that when the progress of recovery, for the corrective surgery increases the power ratio PR also decreases towards normal values, showing the degree of recovery from foot drop. After the corrective foot drop surgery with different durations of recovery, the mean values of the parameter PR reduces nearly to normal value for all leprotic subjects, in all foot sole areas except toe areas.

The different durations of recovery processes observed after foot drop corrective surgery, may help the orthopedic surgeons to assess, quantitatively, the procedures used by them in selecting the insertion points, quality, lengths and tension used for the Tibialis Posterior tendon transfer in foot drop corrective surgery.

References

1. Prabhu, G.K., K.M. Patil and S. Srinivasan (2001) Diabetic feet at risk: a new method of analysis of walking foot pressure images at different levels of neuropathy for early detection of plantar ulcers, Medical and Biological Engineering and Computing, 39, 288-293.
2. Alexander, I. J., E. Y. S. Chao and K. A. Johnson (1990) The assessment of dynamic foot-to-ground contact forces and plantar pressure distribution: A review of the evolution of current techniques and clinical applications, Foot and Ankle, 11, 152–167.

3. Bauman, J.H. and P.W. Brand (1963) Measurement of pressure between foot and shoe, Lancet, 1, 629-632.
4. Betts, R. P. and C. I. Franks (1980a) Static and dynamic foot-pressure measurements in clinical orthopedics, Med. Biol. Eng. Comput., 18, 674–684.
5. Bhatia, M. M. (1996) Online imaging system for acquisition and analysis of barefoot pressure patterns of normal and leprosy patients, M.S Thesis, IIT, Madras, India.

Author: Bhavesh Parmar
Institute: Ramrao Adik Institute of Technology
Street: Dr. D. Y. Patil Vidyanagar,Sector7, Nerul
City: Navi Mumbai 400706
Country: India
Email: bhparmar@gmail.com
Website: http://mail.rait.ac.in/~bhavesh

The Development of New Function for ICU/CCU Remote Patient Monitoring System Using a 3G Mobile Phone and Evaluations of the System

Akinobu Kumabe[1], Pu Zhang[1], Yuichi Kogure[1], Masatake Akutagawa[1], Yohsuke Kinouchi[1], Qinyu Zhang[2]

[1]Graduate School of Advanced Technology and Science, the University of Tokushima, Japan
[2]Shenzhen Graduate School, the Harbin Institute of Technology, China

Abstract — **Telemedicine plays a more and more important role in supporting doctors and taking care of people's daily health. Recently, the 3G mobile phone progressed rapidly. It is possible to use the 3G mobile phone for telemedicine. In this paper, new functions are developed for ICU/CCU Remote Patient Monitoring System using a 3G mobile phone and the system was evaluated.**

This system consists of three parts: Patients Monitoring System, Remote Information Server which are built in the hospital and Java-enable 3 G mobile phones. Patients Monitoring System consists of bedside monitors in ICU/CCU and central monitors installed in the place where medical staffs gather. Commonly, several patients' information which was measured with bedside monitor can be stored in the database of central monitor. Remote Information Server plays an important part. It can extract specific data from central monitor and send it to the 3G mobile phone. Via the Internet and 3G mobile network, the Java application on the 3G mobile phone receives the data and displays the visual information on the screen of the mobile phone to the doctor. Even from the outside of the hospital, by using this system the doctor can monitor the vital biosignals of patients in ICU/CCU, such as ECG, SpO2, RESP, and so on. The doctors can monitor graph trend data as well as real-time data, list rend data and patient information. Graph trend application is useful to watch the past of change of the patient. This application took about 23 seconds till the doctor displayed graph trend data. However, this delay time was decreased for 8 seconds by compressing data with algorisms.

The proposed system can provide high level patient monitoring to doctors and do a powerful supporting to save patient's lives when doctors are outside the hospital.

Keywords — **telemedicine, 3G mobile phone, java, ICU/CCU**

I. Introduction

In late years, with the spread of the Internet and the development of the mobile technology, we can get information anywhere anytime. This progress affects the field of medical care and the study of the telemedicine using a mobile phone is reported much in the world. In North America and Europe, there is the reports that they collects the measurement data in the server via Bluetooth equipped with a PDA and a mobile phone [3][4]. In Japan, with TV phone, the system knowing the state of patient are reported [2]. In this way, the studies of telemedicine are performed actively in the world.

The mobile phone is expected as a platform for the ubiquitous society in Japan. The total number of the subscribers of mobile phone (including PHS) is more than 104 million. The big market is mainly shared by three carrier companies. More than 53 million users belong to NTT docomo Inc., 30 million users belong to KDDI Corporation, and 19 million users belong to SoftBank Corporation [7]. The diffusion rate is more than 84%. From this data, it may be said that each person in Japan has a mobile phone in hand.

Nowadays, mobile phone has become more than a tool only for talking with other people. Multi-functions, such as Internet browser, one-segment broadcasting, Java application, Camera, Bluetooth/infrared connection, GPS, multitasking and so on make it more and more powerful and indispensable. Furthermore, third-generation(3G) mobile communication networks combine standardized streaming with a range of unique services to provide high-quality Internet contents. Packet communication via WCDMA networks provided by NTT docomo and SoftBank can reach 144kbps when high speed moving, 384kbps when walking while 2Mbps when being stillness (downlink speed) as that via CDMA 2000 provided by KDDI can reach the limit of 2.4mbps(down link speed). Therefore, the mobile phone is possible to transfer large amount of data, such as photos, movies and application.

For the medical scene, the doctor contacts medical staffs with a mobile phone routinely. When a patient had an accident, and there is a doctor outside a hospital, the medical staff in the hospital telephones the mobile phone of the doctor and tells it about the situation. The method to know the condition of the patient then is only conversation with the partner of telephone.

we started the development of the ICU/CCU Remote Patient Monitoring System which supported a doctor by adding visual information. We improve utility more by adding a new function to a current system.

Chwee Teck Lim, James C.H. Goh (Eds.): ICBME 2008, Proceedings 23, pp. 1112–1115, 2009
www.springerlink.com

II. Method

A. System architecture

The overview of ICU/CCU Remote Patient Monitoring System is shown in Fig. 1. This system consists of three parts: Patient Monitoring System, Remote Information Server which are built in the hospital and Java-enable 3G mobile phones. Patient Monitoring System consists of bedside monitors in ICU/CCU and central monitors installed in the place where medical staffs gather. Commonly, several patients' information which was measured with bedside monitor can be stored in the database of central monitor. Remote Information Server plays an important part. It can extract specific data from central monitor and send it to the 3G mobile phone. Via the Internet and 3G mobile network, the java application on the 3G mobile phone to the doctor. Even from the outside of the hospital, by using this system the doctor can monitor the vital biosignals of patients in ICU/CCU, such as ECG, SpO2, RESP, and so on.

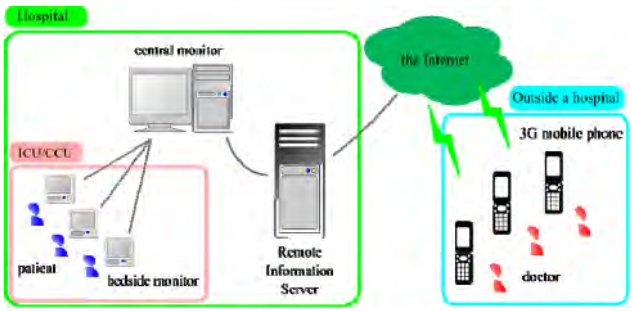


Fig. 1 The system architecture

The model of bedside monitor is DS-7100, and central monitor is DS-5700. They are both provided by Fukuda Denshi Co., Ltd. The bedside monitor can measure ECG, RESP, IBP, NIBP, TEMP, SpO2 and EtCO2. The central monitor memories 96-hour waveform and simultaneously monitors up to 16 patients. The connection is up to bedsides and 16 patients [5][6].

Remote Information Server is Apache web server on a SUSE Linux operating system. This server is running the PHP Hypertext Preprocessor (PHP) application.

We use mobile phone F901iC released by NTT docomo Inc., which is biggest mobile communication carrier in Japan. The java application we made uses jiglet application which jig.jp company offers [8]. This application can work on in not only NTT docomo's i-mode platform but also ezweb platform of KDDI Corporation and S! platform of SoftBank Corporation. In other words, it can be used on all the mobile phones in Japan, no matter which carrier company they are belong to.

B. Protocol and Data Format

Session between the application of mobile phone and Remote Information Server is transited by HTTP communication. If doctors want to check some information, they can get necessary information by appointing a specific parameter in URL of PHP application.

Data format is based on XML (Extensive Markup Language). The mobile phone analyzes the tag of the data which received from Remote Information Server and extracts necessary data. This data format can acquire necessary data just to appoint a tag, but depends on the quality of performance of the mobile phone in processing time.

For example, the format of the URL used to get the data needed is as http://xxx.server.xxx/realtime.php?time=xxx&pati=0&data=ECG1&type=HR&length=10&scale=6. And the received data is shown as following: <time>xxx</time><id>0</id><name>ECG1</name><type>HR</type><meas>60</meas>. The time of the data received is "xxx", the patient ID is "0", the name of the waveform is "ECG1", type of the measurement is "HR", and the number of HR is "60".

III. Results

A. Examples of Monitoring Application

There are four functions in the Remote Patient Monitorig application. They are real-time waveform monitoring, list trend Monitoring, patient information checking and graph Trend Monitoring.

Fig.2 shows three monitoring application: Real-time monitoring, List trend monitoring and Patient information

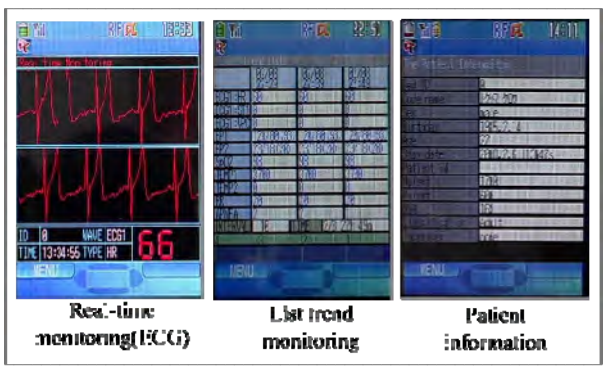


Fig. 2 Monitoring application

checking. Real-time Monitoring shows the real-time waveform of ECG, SpO2, RESP and so on. The bottom of the screen also shows the basic information of the waveform, the time shown on the bed side monitor and the average value. Fig. 2 shows "HR=66". List trend monitoring shows the patient's numeric data of the last 4 days. Doctors can check several value of the patient in the hospital. Patient information displays the basic information of the patient. This information displayed in this function on the mobile phone corresponds to the data registered with the bedside monitor.

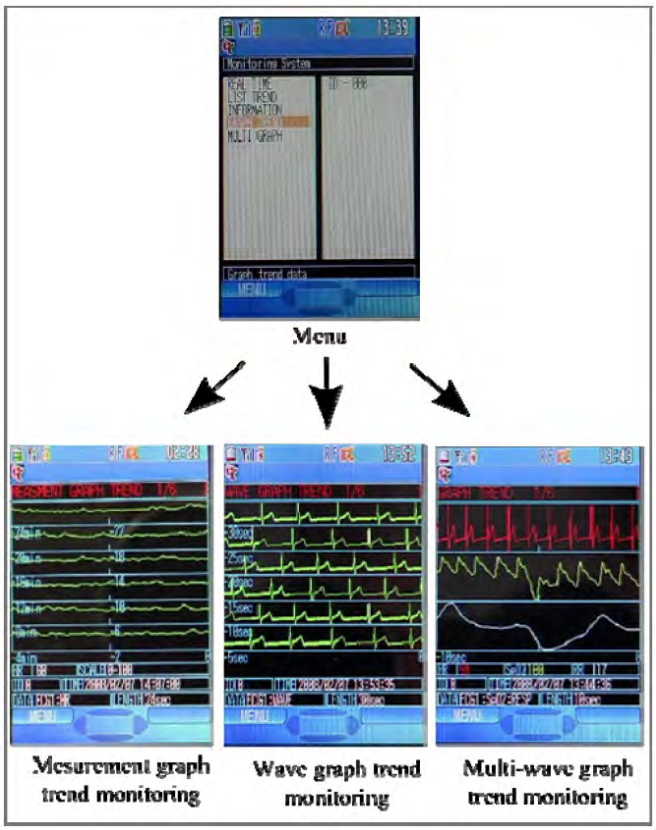


Fig. 3 Graph trend application

There are three modes in graph trend application, as shown in Fig. 3. The first is measurement graph trend monitoring mode that can display measurement data for 24 minutes to the screen on the mobile phone. The second is wave graph trend monitoring mode that can display wave data for 30 seconds to the screen. The last is the multi-graph trend fashion that can display three wave patterns at a time.

B. System Evaluation

Table 1 shows received data size and delay time before acquiring some information with FOMA F901iC.

Table 1 Size of data and delay time

Item	HTTP + PHP processing time[s]	Mobile phone processing time [s]	Size of data[Kbyte]
To get real-time waveform at the beginning	0.42	4.29	1.30
To get list trend data	0.52	6.50	3.24
To get the patient's information	0.27	3.47	0.196
To get the wave graph trend data	1.44	37.3	51.7
To get the multi – wave graph trend data	0.66	23.3	26.3
To get the measurement graph trend data	0.43	7.88	5.07

As is showed in Table 1, the time used for transferring is related to the size of data. And processing time that HTTP communication and PHP application is negligible compared with the processing time of the mobile phone. The processing time of mobile phone costs the most of delay time. Wave graph trend data and multi-wave graph trend data acquiring the waveform of the long time is big size of data and it take much time till mobile phone is displayed it. Therefore we compressed it to reduce delay time.

C. Compression Algorisms

A simple method to reduce the size of data is to decrease sampling rate of the original data. However, this method isn't adequate method for a complicated wave pattern such as the ECG. ECG wave appears in turn a wave that changes suddenly (Q-wave, R-wave, S-wave) and a wave that changes slowly (P-wave, T-wave). If Sampling rate is matched with Q,R and S-wave, it is redundant that P and T-wave do a sample of wave in this sampling rate. Therefore, with the following method, we compressed it.

1. Original data is made the resolution that match with the width and height of the screen of the mobile phone.
2. It is similar to the data by a straight line, and the point that is necessary for drawing is chosen.
3. The chosen data are drawn on the screen of mobile phone as the waveform.

Table 2 Data size and delay time after having compressed

Item	Delay time [s]	Size of data [Kbyte]
To get the wave graph trend data	12	15
To get the multi-wave graph trend	8. 5	8. 30

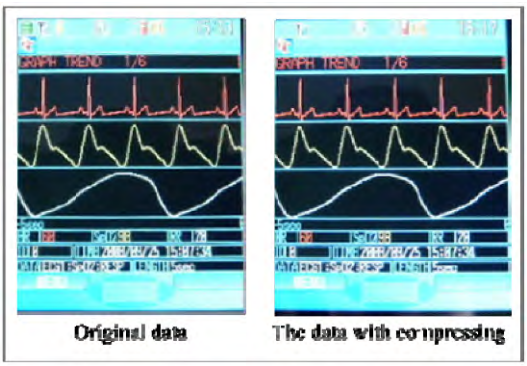


Fig. 4 Comparison with original data and the compressed data

As is showed in Table 2, size of wave graph trend data and size of multi-wave graph trend data was decreased for about 15 Kbyte and 8.30 Kbyte each by compressing data with algorisms. And each delay time was able to decrease. As is showed in Fig. 4, it is said that compressing waveform is almost not different from original waveform. Delay time was able to be decrease, but it cannot be yet said that it is displayed smoothly. Therefore, more attention should be put on the improvement of the performance of the application, including adopting new compressing algorithms and so on.

IV. Conclusion

In this paper, new function “graph trend application” and compressing algorithms are introduced to the Remote Monitoring System for ICU/CCU by a 3G mobile phone to make the system more useful and quickly. The proposed system can provide high level patient monitoring to doctors and do a powerful supporting to save patient’s lives when doctors are outside the hospital.

Acknowledgment

The authors wish to thank Professor Yohsuke Kinouchi and Lecturer Masatake Akutagawa for their helpful advice. Thanks are due to my many colleagues with whom I have discussed this work.

References

1. Yuichi Kogure, Hiroki Matsuoka, Masatake Akutagawa, Yoshihiro Shimada and Yosuke Kinouchi, (2006) The Applications of Remote Patient Monitoring System using a Java-enabled 3G mobile phone, IFMBE Proceedings WC2006 World Congress on Medical Physics and Biomedical Engineering, vol.14, 2006, pp.3522-3525
2. Hisao oka, Hiroki okada, Kiyouhiko Okayama, Nariyoshi Yamai, Masaharu Hata, Takuji Okayama, Hiromi Kumon, (2007) Telemedicine by movie transmission using TV mobile phone, Symposium on Mobile interactions, pp.101-102
3. H. nazeran, S. Setty, e. Haltiwanger, V. Gonzalez, (2004) A PDA-based flexible telecommunication system for telemedicine applications, Proc. 26th Ann. Int. conf. IEEE EMBC, pp.2200-2203
4. M. F. A. Rasid, B.Woodward, (2005) Bluetooth Telemedicine Processor for Multi-channel Biomedical signal Transmission via Mobile Cellular Networks, IEEE Trans Inf Technol Biomed, vol.9, pp.35-45
5. Fukuda Denshi, Introduction to Bedside Monitor DYNASCOPE DS-7100 System, http://was.fukuda.co.jp/medical/products/catalog/ patient_monitor/ds_7100.html
6. Fukuda Denshi, Introduction to Central Monitor DS-5700 System, http://was.fukuda.co.jp/medical/products/catalog/patient_monitor/ds_5700.html
7. Telecommunications carriers Association, japan, Number of subscribers by carriers, http://www.tca.or.jp/japan/database/daisu/yymm/0808matu.html
8. Jig browser, http://br.jig.jp/pc/index.html

Author: Akinobu Kumabe
Institute: the University of Tokushima
Street: 2-1 Minami-josanjima-cho
City: tokushima
Country: Japan
Email: kumabe@ee.tokushima-u.ac.jp

Development of Heart Rate Monitoring for Mobile Telemedicine using Smartphone

Hun Shim[1,3], Jung Hoon Lee[1,3], Sung Oh Hwang[2,3], Hyung Ro Yoon[1,3], Young Ro Yoon[1,3]

[1]Department of Biomedical Engineering, Yonsei University, Wonju, Republic of Korea
[2]Departments of Emergency Medicine, Yonsei University, Wonju College of Medicine, Wonju, Republic of Korea
[3]Home Healthcare Management Research Center, Wonju, Republic of Korea

Abstract — **The point of this study is on the development of wireless patient monitoring system that can monitor heart rates in real time environments. The entire system consists of a portable photoplethysmography device, a healthcare server and a Smartphone for healthcare information reports. The portable device collects heart rate information from the patients and sends the data to home healthcare server. This device is designed to be easily worn and have low power consumption. The role of the healthcare server is to analyze the collected biomedical signals. The result of the analysis is displayed on the Smartphone through the CDMA networks. The application program on Smartphone gives the healthcare information to patients and doctors. This system would be useful for patients who have chronic heart disease.**

Keywords — **Heart Rate, Photoplethysmography (PPG), Smartphone, Personalized Comment Service, Telemedicine**

I. Introduction

The recent progress in personal healthcare device such as blood pressure monitor, electrocardiogram (ECG) monitor, pulse oximeter and blood sugar monitor has made ubiquitous healthcare easier. Now, there are lots of devices which are portable and easy-to-use in that field. It has been developed with multiple functions not only real time monitoring but also doing signal analysis and signal transfer to doctors using wireless communication technology. It means that patient can receive healthcare services such as prevention, diagnosis and prognosis management at any time and in any place [1] with the help of small personalized monitoring devices. Furthermore, it could be performed without visiting hospital regularly.

However, people may feel the lack of personalized healthcare comment service contents, in spite of efforts to develop of various personal healthcare devices for health monitoring under ubiquitous healthcare management environment.

We propose a heart rate (HR) monitoring system model that aims to easily measure of HR, and to provide personalized comment service in daily life. This system integrates Smartphone into giving meaningful information and Bluetooth™ technology, CDMA (Code Division Multiple Access) network for healthcare data transferring. In this paper, the Smartphone based monitoring system has been preliminary evaluated. This system is focused on enhancing the quality of healthcare service for people who do not visit their physicians on a regular basis in medical interpreting aspects.

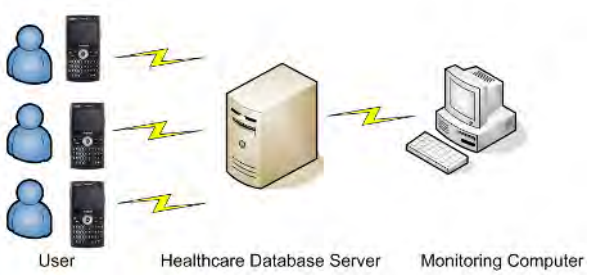


Fig. 1 Proposed scenario using Smartphone

II. System Design and Implementation

The aim of this study is to design and implement a mobile system can monitoring heart rate. This Smartphone based system provides general healthcare comment of heart rate. It not only provides healthcare comment to user but also send the physical data of user to physician for review and consultation. Fig. 1 shows the architecture of the proposed application in this study. The heart rate caring system consists of three parts which include a heart rate measurement module to acquire the user's physiological data, and a Smartphone based mobile unit for data review with programmed physician's comment and healthcare database server for data recording and backup.

A. Heart Rate Measurement Module Description

ECG is widely used as one of the most simple and effective methods of continuously monitoring the heart for telehealthcare and conventional medical care [2]. Although it has been used widely for heart rate monitoring however, it has some uncomfortable aspect when people without have sufficient medical knowledge use this device. For instance, at least 3 electrodes will be required for heart rate measure-

Chwee Teck Lim, James C.H. Goh (Eds.): ICBME 2008, Proceedings 23, pp. 1116–1119, 2009
www.springerlink.com

ment [3] and user has to know the proper placement of each electrode.

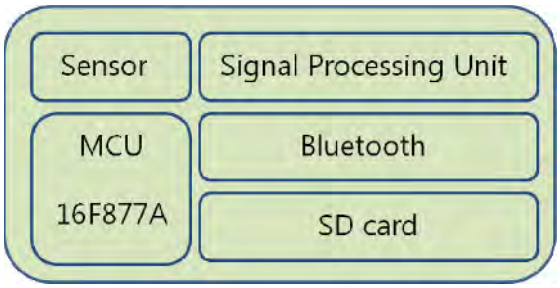


Fig. 2 The Scheme of PPG module

In contrast to ECG, photoplethysmography (PPG) is a simple and low cost optical technique that can be used to detect blood volume changes in the microvascular bed of tissue [4]. The most recognized wave form feature is the peripheral pulse, and it is synchronized with each heartbeat [5]. According to recent research, the component of PPG pulse is synchronous with the beating heart. The pulse rate based on finger photoplethysmography always agreed with the heart rate based on the ECG [6]. Therefore the pulse of PPG can be a source of heart rate information.

In accordance to previous study result, the analog circuitry of the HR measurement module was designed based on the photoplethysmography and a CHUNJIIN oxygen sensor (CJ002R, finger probe type) was used to measure the PPG signals. This module consists of an analog circuit for photoplethysmography, secure digital (SD) memory module (SD-COM-RTC, ELPOT Co.) for raw data storage, serial communication module and Bluetooth™ module (FB155BC, Firmtech Co.) for data transmission.

The main control unit of this module is an 8-bit microcontroller, PIC16F877A, which has 10-bit multi-channel Analog-to-Digital converter. It digitizes the signals with a sampling frequency of 200Hz for heart rate estimation. The heart rate measurement module transmits the estimated HR data to the Smartphone through Bluetooth™. Fig. 2 illustrates the heart rate measurement unit.

B. Mobile Healthcare Module Description

The Smartphone (Samsung, SPH-M6200) was used as the user's heart rate data review device. Basically, this user terminal device performs HR data analysis. It transmits data of biomedical signal between Smartphone and healthcare data server by CDMA network. We developed an application program in C#. In the proposed design, it adapted for client-server architecture, with Smartphone unit serving as the client end and the healthcare server unit serving as the server end. Through this architecture, doctor could review the HR data of multi users. In this system, Smartphone works as a HR information provider, so the users can review their daily physiological data to get a personalized description and prescription by programmed classification.

C. Diagnosis of Heart Rate Status by Rule Based Algorithm

Rule based algorithms were applied to this system for determine the heart status of the user. Through this method, we could offer the descriptions and prescriptions of heart rate case-by-case. The rule based algorithm was verified by the medical doctor in Wonju College of Medicine, Yonsei University. A classification program, developed by Microsoft Visual Studio™ 2005 (Microsoft, USA), was installed on the Smartphone and healthcare database server to provide heart rate review result respectively.

The automatically provided description and prescription is dependent on user's present and past data. Consequently, collecting and reconstructing data of heart rate is essential. The information of heart rate status is generated by the following series.

1. Current Heart Rate State Classification

The classification of current heart rate status was reorganized according to '2005 American Heart Association Guidelines for Cardiopulmonary Resuscitation and Emergency Cardiovascular Care [7]' and clinical experiences. We suggested HR state to emergency, alert, abnormal, normal1 (slow) and normal2 (fast). Fig. 3 shows the classification of heart rate present status.

2. Classification of Heart Rate Up and Down State

This part represents the comparison between present state of HR and their mean value during first week in the previous month. It has three classification of up, same, and down. Fig. 4 shows the classification of up and down status.

3. Variation Steps in Classification of Heart Rate Up and Down State

The step variation of up and down is defined as the step difference between present data during the period of seven days in the previous month. There are in total of eight steps in this part. Fig. 5 shows the step variations in heart rate status.

4. Heart Rate Status Information Provider

Almost of available HR status and the possibility were checked by physicians. The information is assigned according to the available HR status. Provided information consist of two parts. The first part is the objective explanation of the present HR data, and the second part is the medical

doctor's suggestion or comment on each one of the different HR data state combinations.

5. Selected Examples of Description and Prescription

- Your current heart beat is extremely slow. You have bradycardia.
- It is hard to maintain the blood pressure when the heart beat is 40 or lower because the amount of blood pumped out of the heart decreases significantly. You need to get test as soon as possible.
- Heart beat is affected by autonomic nerve, so it constantly changes according to our bodily conditions.
- Heart beat of 50 or lower could result from temporary rest, other medicines, and heart diseases. If there are no evident symptoms, no special treatments are required. However, if you have breathing problems, vertigo, emesis, nausea, chest pain, then a checkup is needed.

D. Healthcare Database Server

The healthcare data includes personal information, heart rate. It was collected at Smartphone first and then sent to healthcare database server at hospital. The respective data from each user's Smartphone are sent through TCP/IP communication or CDMA network. The physician in charge could get their patient form this server. This, though a simple application program, could allow them review the healthcare data.

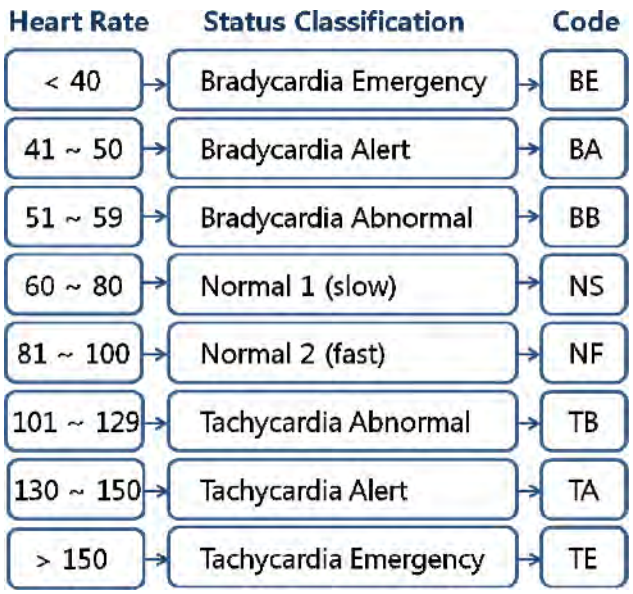


Fig. 3 Classification of heart rate present status

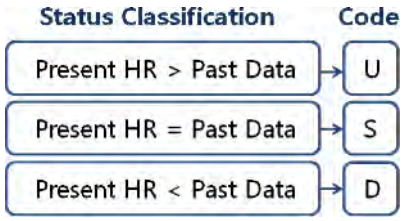


Fig. 4 Classification of up and down status

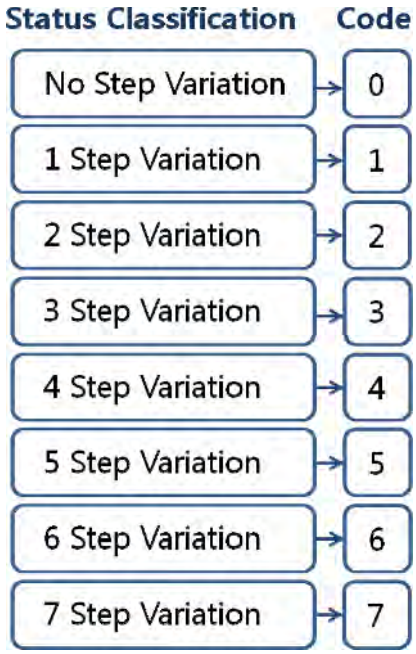


Fig. 5 Step variations in heart rate status

III. Conclusions and Discussion

In this preliminary study, we proposed a heart rate caring service for user using Smartphone. In these days Smartphones are reasonably priced and are becoming increasingly popular with powerful functions on it, not to mention its large storage space. Thus, a Smartphone based telemedicine system without doctor is cost effective solution in a range of medical applications [8]. It is a suitable for daily self-checking user's health parameters.

Knowing the physical change of oneself while they live is very important. It prevents and allows for an early treatment strategy that makes the health management systematic and stable.

This proposed system has two major advantages. Firstly, it offers a chance to review of heart rate changes to general user in medical interpreting aspect. Secondly, it provides

personalized comment of heart rate to user based on case-by-case analysis.

ACKNOWLEDGMENT

This study was supported by a grant from the Korea Health 21 R&D Project, Ministry of Health & Welfare, and Republic of Korea (A020602). The authors would like to thank Mr. Kim Oh Hyun and Ms. Park Mi Jung in Wonju Christian Hospital, Wonju, and Republic of Korea for their help in medical consultation. The authors would also like to thank Mr. Uh Soo Yong for help in research assistance.

REFERENCES

1. T.S Lee, J.H Hong, M.C Cho (2008) Biomedical Digital Assistant for Ubiquitous Healthcare. Proceedings of the 29th Annual International Conference of the IEEE EMBS 1790-1793
2. J.M Kang, T.W Yoo, H.C Kim (2006) A Wrist-Worn Integrated Health Monitoring Instrument with a Tele-Reporting Device for Te-lemedicine and Telecare. IEEE Transactions on Instrumentation and Measurement 1655-1661
3. Y. Sakaue, M. Makikawa (2007) Development of Wireless Biosignal Monitoring Device. 60th International Special Topic Conference on ITAB 306-308
4. A.V. Challoner, C.A Ramsay (1974) A photoelectric plethysmograph for the measurement of cutaneous blood flow. Phys. Med. Biol. 19:317-328
5. J. Allen (2007) Photoplethysmography and its application in clinical physiological measurement, Physiol. Meas. 28: R1-R39 DOI:10.1088/0967-3334/28/3/R01
6. T. Kageyama, M. Kabuto, T. Kaneko et al. (1997) Accuracy of Pulse Rate Variability Parameters Obtained from Finger Plethysmogram: A Comparison with Heart Rate Variability Parameters Obtained from ECG. J Occup Health 154-155
7. http://circ.ahajournals.org/content/vol112/24_suppl/
8. Y. H. Lin, I.C. Jan, P. C. I. Y.Y. Chen et al. (2004) A Wireless PDA-Based Physiological Monitoring System for Patient Transport. IEEE Transactions on Information Technology in Biomedicine. 8:439-447

Address of the corresponding author:

Author: Young Ro Yoon
Institute: Dept. of Biomedical Engineering, Yonsei University
Street: #201 Techno Tower for Medical Industry, Maeji, Heungup
City: Wonju
Country: Republic of Korea
Email: yoon@yonsei.ac.kr

Cognitive Effect of Music for Joggers Using EEG

J. Srinivasan[1,2], K.M. Ashwin Kumar[3] and V. Balasubramanian[4†]

[1]TATA Consultancy Services Ltd. Innovation Lab, Scientist, Bangalore, India
[2]IIT Madras, Rehabilitation Bioengineering Group, Department of Biotechnology, Research Scholar, Chennai, India
[3]IIT Madras, Rehabilitation Bioengineering Group, Department of Biotechnology, under graduate student, Chennai, India
[4]IIT Madras, Rehabilitation Bioengineering Group, Department of Biotechnology, Assistant Professor, Chennai, India
[†]Email: chanakya@iitm.ac.in

Abstract — **This study aims to investigate the effect of music on human central nervous system fatigue during his various activities. In general, fatigue is viewed as an unavoidable and negative consequence of physical activity, since the outcome almost exclusively results in reduced performance and function. Fatigue can occur in two basic mechanisms, central and peripheral fatigue. Even though peripheral fatigue plays a role in reducing the efficiency of performance, here in this study our interest is central fatigue. For simplicity in investigation, we executed the study with jogging, using EEG as a tool to quantify the parameter.**

Eleven male volunteers with a mean age of 22.45 years (range 18 – 24 years) and mean weight of 70.45 Kg (range 52 to 92 Kg) participated in the study. EEG signals were acquired while an individual undergo jogging on a treadmill until individuals feel tired. Experiment was divided into two set: in first experiment individuals used to jog without hearing music and during second experiment they were jogging with music. The data was preprocessed and ANOVA tests were performed to determine the relation between the mental fatigue during absence of music and the presence of music. The results is evident that, hearing music while jogging significantly decreases the mental fatigue and thus the overall duration of jogging has been elongated

Keywords — **Electroencephalogram, Cognitive fatigue, Jogging, Effect of music, Stochastic analysis**

I. Introduction

Walking and jogging is a form of trotting or running at a slow or leisurely pace. The main intention is to increase fitness with less stress than actually running, instead of competition. Jogging is an excellent means of improving cardiovascular health, bone density, and physical fitness. In contrast, in endurance performances for hours or even minutes without any break, an incline in performance will occur. The sustained muscular contractions externally associated will not being able to maintain certain force, lead to physiological fatigue, tremor or pain, localized in the specific muscle. This is called muscular fatigue [1].

Fatigue can occur in two basic mechanisms, central and peripheral [2]. In central fatigue, proximal motor neurons of the brain and spinal chord are involved. However in peripheral fatigue motor units of peripheral nerves, motor endplates and muscle fibers are affected [3]. In this study, central fatigue plays a key role and central fatigue is defined as, the failure to sustain concentration tasks and physical activity as opposed to external stimulation [4], which exists in the absence of any clinically detectable motor weakness or dementia.

Today advancement in technology people got habituated to hear music during almost all activity in their day to day life. Does really music play a predominant role for effective work? We have chosen jogging a one of the activity for such analysis, since it plays major role in fitness and rehabilitation centre.

Often music claim to and is believed to have favorable psychological and physiological effects on human beings and other animals [5]. Such effect of music on human central nervous system can be quantitatively studied using Electroencephalography (EEG).

EEG is the measurement of electrical activity of the brain. The resulting collection of traces is known as an electroencephalogram [6]. The frontal and the temporal lobes of the brain are involved in the motion and hearing activity respectively; so, we aim to study the activity of brain in these regions.

To the author's best knowledge there is a little data pertaining to the effect of music on CNS while jogging. This study aims to; examine whether music helps in reducing the mental fatigue while jogging and thus helping the person to jog for a much longer period time than there normal duration.

II. Methodology

A. Subjects

Eleven male volunteers with a mean age of 22.45 years (range 18 – 24 years) and mean weight of 70.45 Kg (range

Chwee Teck Lim, James C.H. Goh (Eds.): ICBME 2008, Proceedings 23, pp. 1120–1123, 2009
www.springerlink.com

52 to 92 Kg) participated in the study. Subjects were chosen randomly to include a right mixture of persons who are not much involved in jogging or other physical activities and athletes to whom jogging is part of their daily life. All the subjects were healthy during the time of conducting the experiment.

B. Protocol

It was observed during the experiment that the people who do not get involved in much of physical activities get tired very fast when compared to the athletes. However, since we are interested in studying the effect of music on the brain while jogging, we consider a well mixed population.

Subjects were instructed not to participate in any heavy training or physical activity 24 hours prior to their clinical assessment or testing day. They were informed not to apply hair oil before the EEG experiment. They were asked to jog on a Treadmill model –720T for a time period of 15 minutes with an average speed of 6kmph through out the experiment. The EEG signals were recorded two times for each subject. First time when subjects were not listening to music and the second time when were subjects listening to music while jogging. Music digitized at CD quality was played using Nokia N73 MP3 player at an identical intensity for all subjects. The choice of music is decided by the subject itself. Few subjects selected Bollywood music and few selected rock music based on their interest.

The EEG signals were recorded from five surface electrodes (F3, F4, T3, T4 and Cz) placed according to the standard 10-20 system of electrode placement configuration using a battery-powered, MITSAR-20 EEG amplifier instrument. A plastic mesh is placed on the subject's scalp to identify the positions of signal electrodes and then the electrodes were pasted on the required positions. In addition to the proposed positions 2 electrodes (A1, A2) one to each ear and one neutral is also connected. The EEG gel is used to paste the electrodes which act as an excellent conductor.

The EEG is activity is captured by WINEEG software using sampling rate of 250 Hz and gain of 3000 EEGs were acquired at identical hours of the day for all subjects. This time of the day was chosen, based on the results of a campus-wide survey, to coincide with the hours of maximum physical activity. All experimental data were recorded at the Rehabilitation Bioengineering Group (RBG) laboratory, IIT Madras.

C. Analysis

EEG raw data were contaminated with noise, which had to be eliminated through a pre-processing procedure. Generally, the raw signals of the EEG larger than 50–70 μV were treated as artifact. Under this assumption, the artifacts were removed through Independent Component Analysis (ICA) with the help of WINEEG software.

The pre-processed data were separated into θ (4–8 Hz), α (8–13 Hz), and β (13–22 Hz) bands with the help of MATLAB. The δ (0.5–4 Hz) band was not included in our analysis. The powers of alpha, beta and theta are calculated at time intervals 30–50 sec, 4 min–4min 20 sec, 8 min–8min 20 sec, 11 min–11min 20 sec and 14 min–14min 20 sec.

$$P_{\alpha} = 100 \times \frac{\text{Power Range 8-13Hz}}{\text{Total Spectral Power}}$$

Using these powers the overall increasing or decreasing slopes with respect to time were calculated using a linear fit. The presence of music, position of the electrode and subjects were the other variables in calculating the slope of these powers additional to the wave form (α, β, θ) itself being a variable.

D. Statistical Analysis

The results obtained are further analyzed statistically using the N-way ANOVA toolbox in MATLAB to find whether there is any significance difference in these powers with respect to the presence of music.

III. Result

Sample power spectrum of EEG acquired from the five different electrodes before and after pre processing is shown in figure 1 and 2

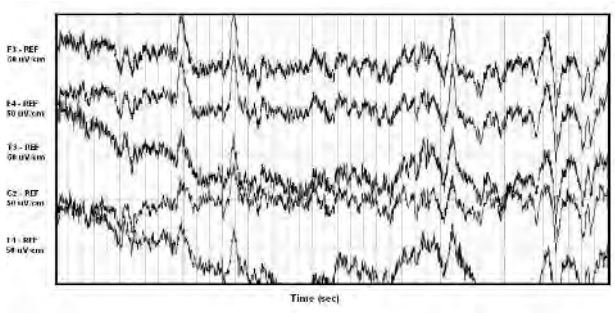


Figure 1 Raw EEG data of the 5 electrodes in the order F3, F4 T3, Cz, T4 with respect to time.

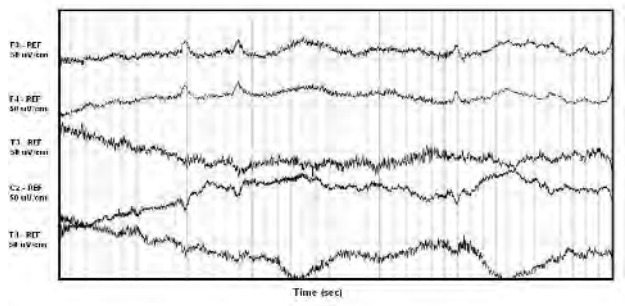


Figure 2 EEG data of the electrodes after the removal of artifacts using the Independent Component Analysis

A sample of the linear fit of the Power of α vs. Time is shown in the Figure 3.

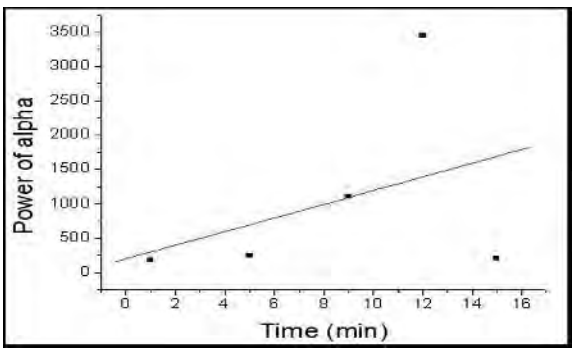


Figure 3 Linear Fit Power of α Vs Time for a subject at Cz electrode position

Table 1 N-way Analysis of Variance (ANOVA)

Source	Mean Sq	F	Prob>F
Electrode	8.27E+006	0.97	**0.4286**
Wave	1.07E+007	1.26	**0.2905**
Subject	2.03E+007	2.39	**0.0156**
Music	3.43E+007	4.03	**0.0481**
Electrode + wave	8.49E+006	1	**0.4451**
Electrode + Subject	9.2	1.08	**0.3783**
Electrode + Music	1.01E+007	1.23	**0.3065**
Wave + Subject	1.69E007	1.99	**0.0168**
Wave + Music	2.21E+007	2.59	**0.0812**
Subject + Music	1.76E+007	2.07	**0.0369**
Electrode + Wave + Subject	8.52E+006	1	**0.5002**
Electrode + Wave + Music	8.48E+006	1	**0.4461**
Electrode + Subject + Music	8.96E+006	1.05	**0.4156**
Wave + Subject + Music	1.57E+007	1.84	**0.0295**
Error	**8.52E+006**		

Table 1 shows the statistical analysis of the data using n-way ANOVA.

IV. Discussion

Music has been believed to have favorable physiological and psychological effects such as reducing stress, increasing the degree of calm *etc*. Many studies [7–9], have been conducted in the past to verify the validity of music while performing various physical activities mostly followed an approach in which the brain activity was not studied. However it was evident from their research that music definitely has a positive effect and enhances the performing of the activity. In our experiment, we considered the study of the EEG activity of the brain which also revealed that music definitely has a significant affect on the brain while jogging.

Previous studies used analysis of subjective information. Rauscher *et.al*. [10] used various spatio-temporal cognition tasks. Steel *et.al*. [11] tested the performance of subjects on backward digit span. Bridgette *et. al*. [12] used a mathematical test. Stratton [13] used the stress perceived while waiting as an indicator. In our study, the notable difference is that the analysis was quantitative and used well developed statistical techniques. While processing the signals obtained, the signals are filtered to remove any out-of-band noise and artifacts, further decomposition of the signals into independent components or the application of other noise cancellation methods were not undertaken since the study was looking for differences between correlated pair-wise samples of activities before and during exposure to music. In addition to analysis, we also targeted an activity in which much of the physical motion of the subject is involved as physical fatigue of the subject is also related to the brain activity.

The Multivariate analysis of variance (MANOVA) result infers that, there is a significant ($p < 0.0168$) difference between EEG waves (alpha, beta and theta) with subjects. With-in subject, our result infers that there is significant ($p<0.0369$) different between with and with out music. An existence of the trend can be observed for the music*wave interaction effect with a significance of $0.081 < 0.1$. MANOVA result shows that significant difference we seen in EEG rhythms (alpha, beta and theta), subject with and without music during jogging.

V. Conclusion

This study helps us to understand the effect of music on the brain while jogging. From the results, it is evident that

music definitely has a significant effect on the human brain while jogging; however our study does not reveal whether listening to music has a decrease or increases the mental fatigue. Therefore a further study can be conducted to find out whether music really decreases the mental fatigue and thus helping the person to jog for a much longer period of time.

ACKNOWLEDGMENT

The authors wish to thank all the members of Rehabilitation Bioengineering Group (RBG) at IIT Madras and the volunteers who participated in this study.

REFERENCES

1. Basmanjian J.V., Delica C.J. (1985) 'Muscles Alive. Their functions revealed by Electromyography' (William and Wilkins, Baltimore), 1985
2. Srinivasan.J and Venkatesh Balasubramanian (2005), 'Low Back Pain and Muscle Fatigue due to Road Cycling – A sEMG Study', Journal of Bodywork and Movement Therapy, Elsevier Publication,Vol-1,Issue-3,pp;260-266Muscle
3. Asmussen E. 1979. Muscle fatigue. Medicine and Science in Sports, 11: 313–321
4. Chaudhuri A. and Behan P. 2000a. Fatigue and basal ganglia. Journal of Neurological Sciences 179: 34–42
5. SMITH D.S, Editor (2000): 'Effectiveness of Music therapy Procedures-Documentation of Research and Clinical practice', (Third Edition, American Music Therapy Association)
6. Rangayyan Rangaraj M. (2002): 'Biomedical Signal Analysis – A case-Study approach', (J. Wiley and Sons, New York, IEEE Press Series on Biomedical Engineering)
7. Brownley.K.A., Robert.G.McMurray, Anthony.C.Hackney (1995) Effects of music on physiological and affective responses to graded treadmill exercise in trained and untrained runners, International Journal of Psychophysiology 193-201.
8. Anil Bharani, Ashutosh Sahu, Vivek Mathew (2004) Effect of passive distraction on treadmill exercise test performance in healthy males using music, International Journal of Cardiology, vol. 97, 305– 306.
9. Lorna Seath, Moorcsg Thou (1995) The Effect of Music on the Perception of Effort and Mood During Aerobic Type Exercise Physiotheraphy , vol. 81, no 10.
10. Bridgett D.J., Cuevas J. (2000): 'Effect of listening to Mozart and Bach on the performance of a mathematical test', Percept Mot Skills, 90: pp.1171-1175
11. McCutcheon L.E. (1993): 'Another failure to Generalize Mozart effect', Psychol. Rep., 87: pp.325-330
12. Creutzfeldt O., Ojemann G. (1989): 'Neural activity in the human temporal lobe III-Activity changes during music', Exp. Brain Res., 77: pp. 490-498
13. Kenealy P. (1988): 'Validation of a music mood induction procedure: Some preliminary findings', Cognition and emotion, 2: pp. 11-18.

System for Conformity Assessment of Electrocardiographs

M.C. Silva[1], L.A.P. Gusmão[2], C.R. Hall Barbosa[1] and E. Costa Monteiro[1]

[1]Post Graduation Program in Metrology, Pontifícia Universidade Católica do Rio de Janeiro, Brazil
[2]Electrical Engineering Department, Pontifícia Universidade Católica do Rio de Janeiro, Brazil

Abstract — **Safety and performance assessment are essential for most medical devices. In some countries they are mandatory at least prior to the launch of the equipment in the market. Aiming at contributing with the assurance of the metrological reliability of analog and digital electrocardiographs (ECGs), this work presents the development of a system for ECG conformity assessment according to IEC 60601-2-51 and OIML R90 standards. The proposed system has been calibrated with traceability to SI units and is structured in two subsystems: evaluation of electrical safety and evaluation of performance. The first subsystem performs grounding tests, leakage current tests and insulation tests, and is based on commercial equipment. The second subsystem evaluates the metrological characteristics of ECGs and is composed by software in LabVIEW, a digital-to-analog converter and three signal conditioners. The system has been evaluated using two digital ECGs in use in a public hospital of Rio de Janeiro. The tests performed indicate that the system complies with the requirements of IEC 60601-2-51. It has been observed a maximum error on the standard signals lower than 1% during the calibration of the equipment that integrates the performance evaluation subsystem. The non-conformities observed during the system validation by means of ECG essays were probably due to the high noise level present in the hospital environment, being necessary the continuous use of digital filters. Also, limitations on the system concerning common-mode rejection ratio, temperature drift and reticulate of time and amplitude have been observed and solutions are being studied.**

Keywords — **Metrology, Electrocardiograph, Metrological Reliability, Conformity Assessment, Biometrology.**

I. Introduction

The measuring instruments used for biomedical application need metrological evaluation in order to guarantee their reliability concerning safety and performance [1].

The International Organization of Legal Metrology (OIML) elaborates international recommendations for measuring instruments as a base for the metrological regulation used by a specific National Metrology Institution (NMI). Concerning health, there are about 13 OIML metrological recommendations, being three of them already adopted by the Brazilian NMI.

Despite the fact that (pre-sales) type approval and (post-sales) periodic verifications are routinely used in legal metrology for the metrological control of measuring instruments, medical electrical equipment are usually only required to go through type approval. Type approval for medical electrical equipment (MEE) usually involves compliance with the IEC 60601 standard series, containing prescriptions of safety and performance for MEE.

Particularly, for electrocardiographs (ECGs), although existing a specific international metrological recommendation from OIML (R-90 for analog ECGs)[2], it has not been adopted as a metrological regulation by the Brazilian NMI. By means of the study of the R-90 and of the IEC 60601-2-51 Standard [3, 4], containing the particular requirements for safety and essential performance of recording and analyzing single channel and multichannel electrocardiographs, the present work has developed a preliminary system for ECG conformity assessment, aiming to contribute with the elaboration of a specific metrological regulation for ECGs [5].

II. Materials and Methods

The IEC 60601-2-51 standard classifies electrocardiographs as recording ECGs and analyzing ECGs. The recording ECGs are divided into analog and digital without automated measurement. The analyzing ECGs are digital devices with automated measurement of electrocardiograms, including or not the automated signal interpretation.

IEC 60601-2-51 divides the performance evaluation in two kinds of tests:

Accuracy of operating data (section 50): this test aims at evaluating the reliability of analyzing ECGs measurements.

Protection against hazardous output (section 51): this test evaluates the essential characteristics of all kinds of ECGs.

The system presently developed contains qualitative and quantitative analysis and has been divided in two subsystems: electrical safety and performance evaluations.

The *electrical safety evaluation subsystem* evaluates the protection against electric shock hazard (IEC 60601-1). In order to perform these tests, a commercial equipment has been used (601 Pro Series$_{XL}$ International Safety Analyzer).

Chwee Teck Lim, James C.H. Goh (Eds.): ICBME 2008, Proceedings 23, pp. 1124–1127, 2009
www.springerlink.com

By means of this equipment, grounding, leakage current and insulation tests have been performed.

The performance evaluation subsystem evaluates metrological characteristics of ECG. It comprises software in LabView, a digital-to-analog converter and three signal conditioners. This subsystem evaluates ECGs according to section 50 and 51 of IEC 60601-2-51.

Since the procedures and conditioners used for the correspondent tests of section 50 and 51 are very different, this subsystem has been divided in two parts: *part 1- evaluation of operating data accuracy* and *part 2 - evaluation of protection against hazardous output.*

The part 1 of the performance evaluation subsystem *(operating data accuracy)* includes:

Database: It provides the characteristics of the signals to be generated by the software ECG/MPD. It is based on the database adopted by the IEC 60601-2-51 standard and includes signals to cover sub-sections 51.107 and 51.109;

Software ECG/MPD: This software has been developed in LabView and is used to simulate the ECG recordings and signals, in order to cover sub-sections 51.107 and 51.109;

D/A converter: Converts digital signals to be used by the analog ECG conditioner.

ECG conditioner: Conditioner circuit that attenuates and adjusts the analog signals to be directly connected to the patient cable.

The part 2 of the performance evaluation subsystem (*protection against hazardous output*) comprises qualitative and quantitative evaluations. For the quantitative tests it was developed an equipment including 5 parts:

Signal Generator Software: developed in LabView, it generates sinusoidal, triangular, square and pulse signals.

D/A converter: the same used for the part 1 of the performance subsystem;

MPD/Signal Generator conditioner: it simulates the signals of the *Software Signal Generator* and is used together with the ECG/MPD software to simulate signals to cover sub-sections 51.107 and 51.109;

E-P Conditioner: it simulates the electrode-skin impedances, in order to evaluate noise and common mode rejection ratio;

Mains Voltage Noise Simulator: Simulates the noise due to the mains voltage that is superimposed to the heart's electrical potential and the capacitive impedance between the patient and the ground terminal.

In order to perform the preliminary evaluation of the developed system for conformity assessment of ECGs, measurements have been done in two recording ECGs (brands A and B) in use in a public hospital of Rio de Janeiro. Since the test of *operating data accuracy* described in the section 50 of IEC 60601-2-51 applies only to analyzing ECGs, procedures have been developed for the accuracy evaluation of the amplitude of recording ECGs using the IEC database and the amplitude specification indicated in the OIML R-90 recommendation [2].

Table 1 shows the sensitivity-setting, database and leads used to perform the ECG evaluation.

The maximum permissible limits used for conformity assessment were the ones specified in the IEC 60601-2-51 standard (±25 μV for reference values lower than or equal to 500 μV, or more than 5% or ± 40 μV – the highest – for reference values above 500 μV).

Table 1 Sensitivity-setting, Database and Leads used during accuracy evaluation of the amplitude of ECG

Sensitivity-setting (mm/mV)	Database	Leads
20	CAL05000 CAL10000	I, aVL V1, V2
10	CAL10000 CAL20000	II, aVF V3, V4
5	CAL20000 CAL40000	aVR, V5 V6, aVL

During the ECGs evaluation, the gains used in LabView were related to the attenuation values adjusted at the moment of measurement (Fig.1).

In order to guarantee the metrological reliability of the developed system and the results obtained with both ECGs, the system has been calibrated with traceability to SI, at the Metrology Laboratory of the Electronics Material Depot of the Air Force at Rio de Janeiro (PAME-RJ). This calibration has been performed in the ECG Conditioner and in the MPD/Signal Generator Conditioner [5].

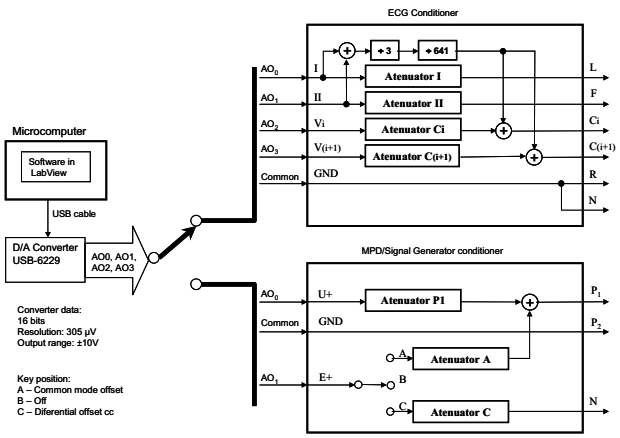


Fig. 1 Block diagram of the calibrated system

In Figure 1 are shown the 6 outputs of ECG Conditioner to be connected to the ECG being evaluated. In this conditioner, each electrode has a connection previously established, except for the chest electrodes. In this last case the evaluation is performed in pairs: C1 and C2, or C3 and C4, or C5 and C6. In the case of the *MPD/Signal Generator Conditioner*, the evaluation is performed between two electrodes or a set of electrodes, whose connections change as a function of the test described in section 51 of the Standard.

During the calibration of the developed system, the level of attenuation was measured in each attenuator

III. Results

By means of the study of the IEC 60601-2-51 standard, the best positions to measure the attenuation level and to perform the calibration of the *ECG conditioner* and of the *MPD/Signal Generator Conditioner* were identified and are presented in Table 2.

Table 2 Attenuation levels measured for the attenuators of Fig. 1.

Attenuator	Attenuation level during ECG evaluation	Measured attenuation level	Error (%)
I	650	650.8	-0.12
II	650	653.4	-0.52
C_i	650	650.7	-0.11
$C_{(i+1)}$	650	652.2	-0.34
P_1	1001	1008	-0.69
A	28	28.23	-0.81
C	28	28.65	-2.27

Since the error between the attenuation level used during the ECGs evaluation and during calibration was lower than 1% for attenuators I, II, C_i, $C_{(i+1)}$ e P_1, this error has been disregarded in order to facilitate the analysis of results.

The ranges used to perform the ECG conditioner calibration were between 100 µV and 5000 µV and between -100 µV and -5000 µV. The maximum values of error and uncertainty [6, 7] are presented in Table 3. The smallest uncertainty observed in the conditioner outputs was 0.40µV.

Table 3 Values obtained during calibration of the ECG Conditioner

Output	Largest Error		Largest Uncertainty	
	RV (µV)	Error (%)	RV (µV)	$U_{95,45\%}$ (µV)
L	-100	-0.64	-4000	±0.52
F	-100	0.48	-4000	±0.52
C_i	333.33	-0.65	-6666.67	±0.56
$C_{(i+1)}$	-166.67	0.54	-6666.67	±0.56

RV – Reference value; $U_{95,45\%}$ - Expanded uncertainty for a 95.45% level of confidence

The ranges used to perform the MPD/Signal Generator Conditioner calibration were between 50 µV and 4500 µV and between -50 µV e -4500 µV for the U+ input; and between -300 mV and 300 mV for the E+ input. The maximum values of error and measurement uncertainty are presented in Table 4. The smallest uncertainty observed in this conditioner outputs was 0.32 µV for the U+ input and 0.0040 mV for the E+ input.

Table 4 Values obtained in the calibration of the MPD/Signal Generator conditioner

Output	Largest error		Largest uncertainty	
	RV	Error (%)	VR	$U_{95,45\%}$
P_1-P_2/U+	50 µV	-0.41	-3000 µV	±0.54 µV
P_1-P_2/E+	200 mV	0.29	-300 mV	±0.0065 mV
N-P_2/E+	-300 mV	0.09	-300 mV	±0.0167 mV

RV – Reference value; $U_{95,45\%}$ - Expanded uncertainty for a 95.45% level of confidence

Both ECGs evaluated were compliant to electrical safety requirements according to the IEC 60601-1 standard.

By evaluating the amplitude accuracy, it has been observed that the ECG of brand A presented better results with the digital filters turned off, and the one of brand B using the digital filters (Table 5). Nevertheless, both ECGs presented non-conformities for the sensitivity setting of 5mm/mV.

Since the IEC 60601-2-51 standard does not define anything about the use of digital filters during measurements of protection against hazardous output, in all of these tests the result analysis had to be performed with these filters turned on and off. In general, the recordings presented a high noise level, hindering the evaluation that proceeded with a sequential introduction of filters until achieving an adequate signal to noise ratio (Table 6).

Table 5 Non-conformities identified in the ECGs for the sensitivity-setting of 5 mm/mV during amplitude accuracy evaluation

Brand	Amplitude (µV)	Database	Derivation	Error (µV)
A	-4000	CAL40000	V6	-260
	4000	CAL40000	V6	360
B	-400	CAL20000	aVR	40
	400	CAL20000	V5	-40
	800	CAL40000	V6	-70
	400	CAL40000	aVL	-67

Table 6 Summary of results for the evaluations performed in the two ECGs regarding protection against hazardous output

Sub-section	Evaluation	Conform. Brand A	Conform. Brand B
101	Insp. of the minim. config. and lead sel. nomenclat.	A	A
	Verification of electrodes polarity	A	A
	Insp. of Goldberger and Wilson derivation networks	A	A
	Recovery time after the application of a 300 mV cc signal	A	A
102	Input impedance	*R*	*R*
103	Inspection of the calibration signal description in the manufacturer manual	A	A
104	Verification of stability and accuracy of the sensitivity	*R*	A
105	Common mode rejection ratio	NV	NV
	Overload tolerance	A	A
	Electrocardiogram filter indication	A	A
106	Drift control	NA	NA
	Temperature drift	NV	NV
	Base-line stability	A	A
	Noise level	*R*	*R*
	Recording speed and base-line width	A	A
	Interchannel Crosstalk	NA	*R*
	Sensitivity/baseline drift	NA	NA
107	High frequency response	*R*	*R*
	Low frequency response (impulse)	A	*R*
	Linearity and dynamic range	*R*	*R*
	Minimum signal response	A	A
	Sampling rate	A	A
	Amplitude quantization level	*R*	A
108	Recording and patient identification	NA	NA
	Recording time	NA	A
	Rectangular coordinates and alignment of writing dot	NA	A
	Time and event markers	NA	NA
	Effective recording width	A	A
	Recording speed	A	A
	Reticulate of time and amplitude	NV	NV
109	Electrocardiogram distortion – First part	A	A
	Electrocardiogram distortion – second Part	A	A
	Visible pacemaker pulses	A	*R*

A - Approved; R - Rejected; NA - Not Applicable; NV - Not Verified

IV. Discussion

The measurements performed in two ECGs using the system developed for conformity assessment have shown non-compliances with the performance standard requirements for both equipments.

Concerning the accuracy of amplitude evaluation, the results indicate non-compliances that might have been caused by limitations such as: high noise level in the measurement environment; the necessity of the use of filters during tests, which can generate an error in the measurement of the ECG output signals.

In order to make a complete performance analysis of the ECGs it has been necessary to complement the IEC 60601-2-51 requirements and technical guide with the OIML R-90 recommendation. The latter is directed to a single type of recording ECG (the analog ECG) but the detailed information of this recommendation has been used for accuracy evaluation of the amplitude and in some tests of protection against hazardous output.

V. Conclusions

The system developed for conformity assessment of ECGs complies with the requests of IEC 60601-2-51 for the evaluation of recording ECGs, and partially, of analyzing ECGs. The observed limitations concerning the common-mode rejection ratio, temperature drift and reticulate of time and amplitude have been characterized and solutions are being studied.

After solving the detected limitations and increasing the number of outputs of the D/A board to eight outputs, the system will be able to perform all essays of IEC 60601-2-51, making it possible to evaluate all types of ECG.

Acknowledgment

We would like to thank FINEP, CNPq and FAPERJ for the financial support that made this work possible.

References

1. Costa Monteiro, E (2007) Biometrologia: Confiabilidade das biomedições e repercussões éticas. Metrologia e Instrumentação. vol. 49, pp. 6-12
2. OIML (1990) R-90: Electrocardiographs Metrological characteristics – Methods and equipment for verification. Paris
3. ABNT (2005) NBR IEC 60601-2-51: Equipamento eletromédico – Parte 2-51: Prescrições particulares para segurança, incluindo desempenho essencial de eletrocardiógrafos gravador e analisador monocanal e multicanal
4. IEC (2003) Medical electrical equipment - Part 2-51: Particular requirements for safety, including essential performance, of recording and analysing single channel and multichannel electrocardiographs
5. Silva M C, Costa Monteiro E, Barbosa C R H (2008) System for Conformity Assessment of Electrocardiographs. Rio de Janeiro, 2008. 175 p. MsC Thesis – Pos-graduation Program in Metrology. Pontifical Catholic University of Rio de Janeiro
6. ABNT INMETRO (2003) Guia para a expressão da incerteza de medição. 3rd edition, Rio de Janeiro, Brazil
7. ISO/IEC (1995) Guide to the Expression of Uncertainty in Measurement

Author: Elisabeth Costa Monteiro
Institute: Pontifícia Universidade Católica do Rio de Janeiro
Street: Marquês de São Vicente 225
City: Rio de Janeiro
Country: Brazil
Email: Beth@puc-rio.br

The Development and Strength Reinforcement of Rapid Prototyping Prosthetic Socket Coated with a Resin Layer for Transtibial Amputee

C.T. Lu[1], L.H. Hsu[1], G.F. Huang[2], C.W. Lai[1], H.K. Peng[1], T.Y. Hong[1]

[1]Department of Mechanical Engineering, National Cheng Kung University, Tainan, Taiwan
[2]Department of Physical Therapy, Fooyin University, Kaohsiung, Taiwan

Abstract — **This article proposed a computer-aided engineering process that is to fabricate a prosthetic socket using rapid prototyping technology. Moreover, since current RP machines use a layer-based process to manufacture products, this result in RP products liable to break along layers once bending moment is applied. To prevent RP prosthetic socket from breaking, this study proposes wrapping a layer of unsaturated polyester resin (UPR) around the prosthetic socket to reinforce its strength. Factors affecting the strength of the resin-reinforced RP socket include thickness and forming orientation of the preliminary RP socket, thickness of the UPR layer, and type of material used to make the preliminary RP socket. This study employed Taguchi experimental design method to design a series of test specimens for use by the 3-point bending test. Based on analysis of the results of the bending strength test, the design parameters for a resin-reinforced transtibial socket of appropriate strength can be determined. The preliminary RP socket for a specific transtibial amputee is fabricated using an FDM machine and then wrapped with a reinforcing layer of UPR.**

To confirm the applicability of the resin-reinforced socket developed in this study, the measurement of interface pressures between the residual limb and the socket was implemented. Analysis of the result of this measurement would assist a prosthetist to realize the distribution of interface pressures at the pressure-tolerant (PT) and pressure-relief (PR) areas of the residual limb while the resin-reinforced RP socket is being worn. The result of this study demonstrates that by integrating a CAD system, reverse engineering and RP technologies, a qualified resin-reinforced RP socket can be fabricated that meets the requirements of a transtibial amputee. The quality uncertainty of sockets can be improved if the proposed socket and the corresponding production procedure are adopted to replace the traditional manual method of fabrication.

Keywords — **Prosthetic socket, Transtibial amputee, Rapid prototyping, Resin reinforcement.**

I. Introduction

Introducing the contemporary technologies involving rapid prototyping (RP) and CAD systems provides an alternative means to overcome the shortcomings of the conventional process of fabricating prosthetic sockets. Since the emergence of rapid prototyping technology, a variety of prosthetic sockets have been designed and fabricated using various types of RP machines that include stereolithography (SLA), selective laser sintering (SLS), fused deposition modeling (FDM), and droplet/binding [1,2]. Although RP technology has been employed to develop prosthetic sockets for almost two decades, no RP prosthetic socket provided by prosthesis industry has really ever been used in daily life. That is because any object fabricated by current layer-based RP machines is liable to break along the forming layer. Therefore, a method of wrapping a carbon fiber layer was proposed to reinforce the strength of RP sockets [3]. Fuh et al. [4] also suggested that coating a reinforced layer on the RP socket would improve its strength.

A project aimed to develop a plaster-free process (Fig. 1) that employed the contemporary technologies including a scanner, CAD systems together with RP machines [5]. That

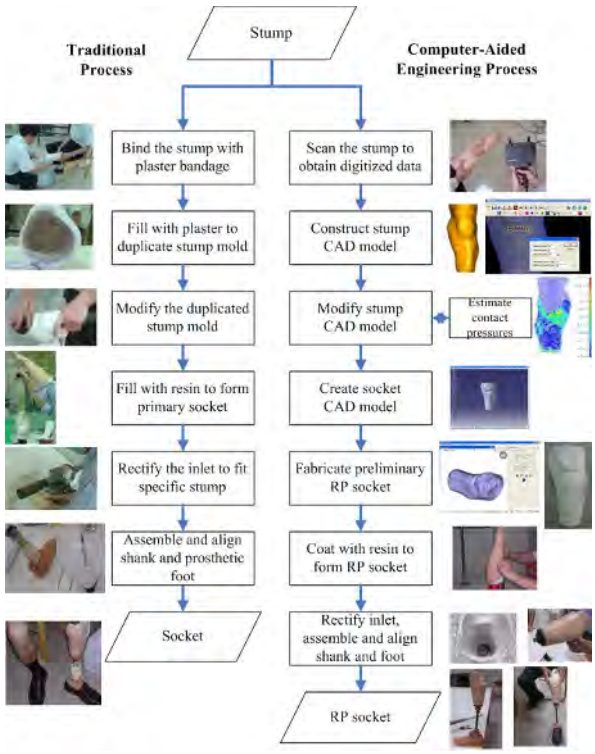


Fig. 1 Comparison between traditional and computer-aided approaches

Chwee Teck Lim, James C.H. Goh (Eds.): ICBME 2008, Proceedings 23, pp. 1128–1131, 2009
www.springerlink.com

project concluded that prosthetic sockets fabricated by RP machine are liable to break along forming layer during the implementation of testing RP prosthetic socket. To prevent RP prosthetic socket from breaking, wrapping a layer of unsaturated polyester resin (UPR, a widely adopted material in conventional socket manufacturing process) around the prosthetic socket to reinforce its strength is then proposed. This idea also raised the problem of determination of factors affecting the strength of the resin-reinforced RP socket. The bending strength of this proposed socket might need to be validated by a testing process such as the three-point testing method. An experiment reported in this paper is to determine the appropriate parameters including RP material, thickness of the RP layer, forming orientation of the preliminary RP socket, thickness of the UPR layer coating for building resin-reinforced RP prosthetic sockets of proper flexural strength.

II. METHOD

A. Three-point bending test and Taguchi experiment method

To confirm the parameters that affect the strength of RP socket a series of bending strength tests are implemented. We apply the Taguchi method to data analysis of the bending test in order to find out the best parameters of the RP prosthetic socket, including thickness of the RP layer, thickness of the UPR layer, the RP material and RP fabricating orientation, and the relationship illustration is shown in Fig. 2. Based on the ASTM D790 [6], a standard method for testing the flexural properties of reinforced plastics, the specification of a testing specimen is designed and an MTS universal tensile testing system is used (Fig. 3). To simplify the experiment, the Taguchi method [7] helps to compare all the parameters.

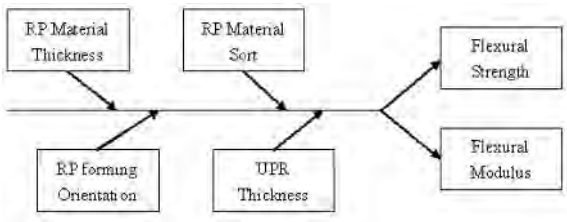


Fig. 2 The relationship of the parameters

Based on the expertise of a prosthetist and RP techniques, the level values of the parameters are determined as follows: RP materials selected in this study including ABS, PC and gypsum; the thickness of specimen made by RP machine designated as 1.5 mm, 2.0 mm and 2.5 mm; the thickness of

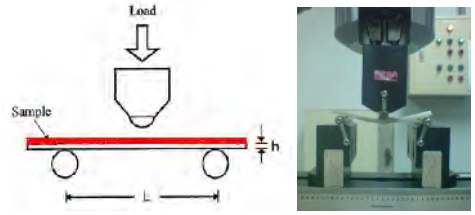


Fig. 3 The layout and a MTS machine used for three-point bending test

UPR layer coated onto RP specimen 2.0 mm, 2.25 mm and 2.5 mm; the forming orientation of RP specimen. Taguchi method provided the appropriate orthogonal array (L_9 in this study) is selected to carry the reasonable number of experiments. According to the calculation values of the flexural strength and flexural modulus from the MTS testing data, the ratio of signal and noise can be estimated the best performance parameters as shown in Table 1.

Table 1 Best collocation of the prosthetic socket fabricated by FDM and 3D printing

RP type	FDM	3D printing
RP Thickness	1.50 mm	2.00 mm
UPR Thickness	2.50 mm	2.50 mm
RP Material	ABS	Gypsum
Forming orientation	Horizontal	Lie down

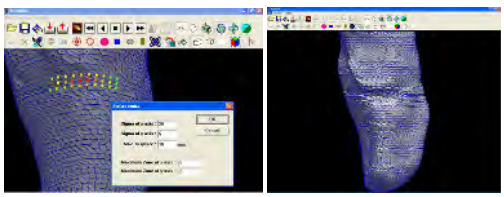
The results shown in Table 1 are then used to design socket, two kinds of sockets will be fabricated. The first one is fabricated by FDM, and the other is fabricated by 3D-printer.

B. Design and fabrication of a resin-reinforced socket

Based on the principles of designing a prosthetic socket to achieve the criteria of a qualified prosthesis in terms of comfort, sufficient strength, and good performance, the sensitive (or pressure-relief, PR) areas on a residual limb should not bear too much load either at standing or during the stance phase of the prosthesis. The weight should be supported on pressure-tolerant (PT) areas while the amputee is walking and standing. The PR areas are moved outward and PT areas indented inward according to the expertise of the prosthetist so that the interface pressures between stump and socket can be properly distributed. The shape modification will be proceeded iteratively until biomechanical assessment of the interface pressures on all PT/PR areas meets the load-bearing ability of the amputee. The modified stump shape (Fig. 4) will then be used to design a socket for the specific amputee. With the parameters illustrated in Table 1

to achieve better flexural strength and flexural modulus, the designed socket model with a thickness of 1.5 mm (Fig. 5a) is then acquired and its data in STL format transferred to an FDM machine. A preliminary RP socket with ABS material is fabricated as shown in Fig. 5b.

To reinforce the bending strength of a socket made by RP, covering the preliminary RP socket with six layers of cotton socks, the liquid UPR mixed with hardener was then filled and uniformly squeezed by hand around the socket to allow UPR to infiltrate into the socks' fiber layers (Fig. 5c). The thickness of the resin-reinforced layer is approximate 2.5 mm according to the three-point test specimen. The proximal brim of that resin-reinforced socket is manually trimmed to fit the shape of the stump (Fig. 6).



(a) (b)

Fig. 4 Shape modification during socket design

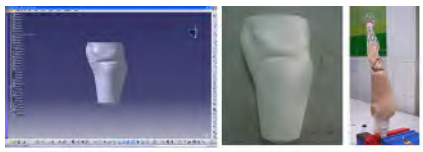


Fig. 5 A socket CAD model, its preliminary RP socket and infiltration of the resin-layer



Fig. 6 Trimming the proximal brim, assembling components and fitting the stump

C. Measurement of interface pressures and results

To verify the applicability of resin-reinforced RP socket fabricated by following the procedure proposed as shown in Fig. 1, interface pressures between socket and stump were measured using socket sensors (Fig. 7). A male volunteer (whose residual limb is the stump used in this study) weighing 60kg with a left below-knee amputation was selected in this experiment. A Pliance mobile system® [8] was employed to measure the local pressure distribution at the residual limb and socket interface. The procedure of the measurement for interface pressures is shown in Fig. 7. Due to the preliminary RP socket made of gypsum was brittle and avoiding its rough surface harm to stump, the layer of gypsum was removed. That means the preliminary RP socket fabricated by using a 3D printing machine was used as mold for producing a UPR socket. The measurement results (Fig. 8) showed that the interface pressures either on main PT areas or PR areas have similar distribution.

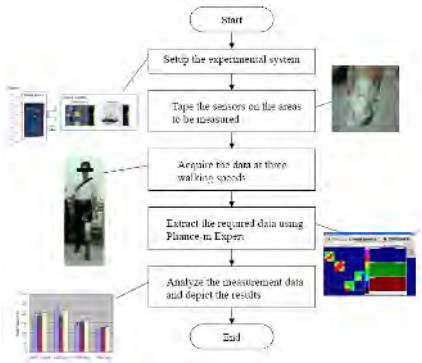
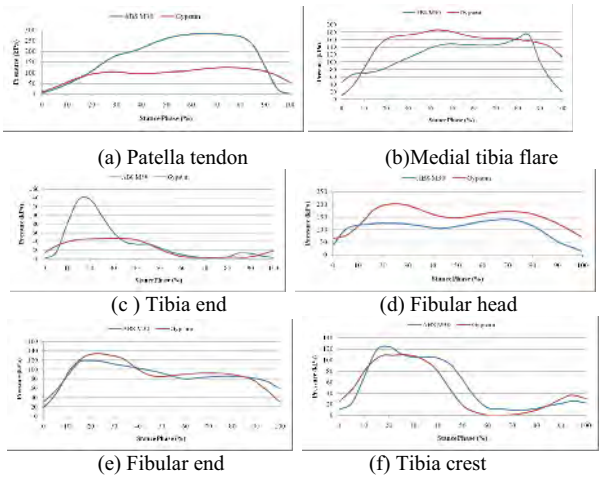


Fig. 7 Procedure for the measurement of interface pressures



(a) Patella tendon (b)Medial tibia flare

(c) Tibia end (d) Fibular head

(e) Fibular end (f) Tibia crest

Fig. 8 The interface pressures measured on some PT/PR areas

III. Conclusions

Using the Taguchi experimental design method and ASTM three-point bending test standard, the parameters that influence the flexural strength of the RP prosthetic

socket coated with a UPR layer could be determined. Based on the better parameters, including thickness of the RP layer, thickness of the UPR layer, the RP material and RP fabricating orientation, the resin-reinforced RP prosthetic sockets fabricated by FDM and 3D-printer RP machines can be normally used by volunteer amputee for walking and implementing the interface pressure measurement.

Two RP-based sockets have been designed and fabricated based on the computer-aided process proposed in this study. This process reduced the quality uncertainty and labor intensity, and also the level of discomfort experienced by the amputee, which are pitfalls of the conventional manual method. An assistant interface used in the proposed process also helps to shorten training time for prosthetists and to modify pressure-tolerant and pressure-relief areas more precisely.

Although the resin-reinforced RP prosthetic socket proposed in this study has primarily shown the applicability for the specific amputee, a long period of trial should be conducted for a durability test. Furthermore, investigation on the trial use of more subjects is needed for testing effectiveness of using this socket type.

Acknowledgment

The authors would like to thank the National Science Council Taiwan for its support through grant No. 97-2212-E-006-105.

References

1. Gibson I, editor. (2005) Advanced manufacturing technology for medical applications: reverse engineering, software conversion and rapid prototyping. John Wiley & Sons.
2. Rogers B, Bosker GW, Crawford RH, Faustini MC, Neptune RR, Walden G, Gitter AJ. (2007) Advanced trans-tibial socket fabrication using selective laser sintering. Prosthet Orthot Int 31(1):88-100.
3. Herbert N, Simpson D, Spence, W, Ion, W. (2005) A preliminary investigation into the development of 3-D printing of prosthetic sockets, J Rehabil Res Dev 42(2):141-146.
4. Fuh JYH, Feng W, Wong YS. (2005) Modelling, analysis and fabrication of below-knee prosthetic sockets using rapid prototyping. In: Gibson I, editor, Advanced manufacturing technology for medical applications: reverse engineering, software conversion and rapid prototyping. John Wiley & Sons. p. 207-226.
5. Hsu LH, Huang GF, Lu CT, Chen YM, Yu IC, Shih HS. (2008) The application of rapid prototyping for the design and manufacturing of transtibial prosthetic socket. Materials science forum. Switzerland: Trans Tech Publications; 594: 273-280.
6. Taguchi G, Yokoyama T, chief editor, (1993) Taguchi methods :design of experiments , Yuin Wu, technical editor for the English edition, Dearborn, MI :ASI Press ; Tokyo, Japan :Japanese Standards Association.
7. ASTM D790, (2007) Standard Test Methods for Flexural Properties of Unreinforced and Reinforced Plastics and Electrical Insulating Materials, American Society of Material Testing.
8. Novel. 2008. Pliance application on prosthesis system. [cited 2008 Aug 15] Available from: http://www.novel.de/productinfo/systems-pliance-prosthesis.htm.

The address of the corresponding author:

Author: L.H. Hsu
Institute: Department of Mechanical Engineering, National Cheng Kung University
Street: No. 1, University Street
City: Tainan, 70101
Country: Taiwan
Email: lhhsu@mail.ncku.edu.tw

A New Phototherapy Apparatus Designed for the Curing of Neonatal Jaundice

C.B. Tzeng[1], T.S. Wey[1], M.S. Young[2]

[1]Department of Electronic Engineering, Kun Shan University, Tainan, Taiwan, R.O.C.
[2]Department of Electrical Engineering, National Cheng Kung University, Tainan, Taiwan, R.O.C.

Abstract — **In this paper, we propose the prototype of a new phototherapy apparatus that ensures a safe and effective therapy against neonatal jaundice. It use the high power LED (with the wavelength within a specified range) as the light source and allows the medical care personnel to adjust the light intensity and the place of the body to be irradiated according to the symptom and jaundice index. The light intensity of each module is adjustable separately at each therapy stage to treat the patient in an orderly way. The current status of the therapy can be monitored by the medical care personnel on the monitor to make appropriate adjustments.**

According to the test and the measurement of the photocharacteristics, the 100% luminance of this system is 2.5 times the luminance of a blue lamp and its wavelength is fixed at 460nm. Therefore, this proposed LED phototherapy apparatus is better than others.

Keywords — **Neonatal Jaundice, Phototherapy, High power LED, Luminance, Light intensity**

I. Introduction

About 80% to 90% new born babies suffer from the "neonatal hyper-bilirubinemia", also known as the "neonatal jaundice", because the liver function of neonates has not been completely developed and, thus, the bilirubin in the blood can not been excreted naturally, resulting in yellow skin and eyes. More than 60% of the neonates and more than 80% of the premature babies suffer from this disease.

The neonatal jaundice may disappear gradually within two weeks and no side effects will be left. This is the so-called physiologic jaundice. If the symptom does not disappear within two weeks, it is reasonable to suspect the occurrence of "pathologic jaundice" that might be brought about by other factors. Excessive bilirubin will damage brain cells and may lead to cerebral palsy or even death. [1-6]

The normal serum bilirubin value of a newborn baby is between 0.2mg/dl and 1.4mg/dl. When it exceeds 5mg/dl, jaundice appears in the skin, fingernail or sclera. The symptom of hyper-bilirubinemia appears when the serum bilirubin value is between 15mg/dl and 20mg/dl. A newborn baby is diagnosed with kernicterus when the serum bilirubin value is higher than 20mg/dl. [2, 4, 5]

Depending on the severity of the disease, the treatment by medicine, phototherapy, and blood exchange are usually used to cure jaundice, among which the phototherapy is the most commonly used approach. It irradiates the skin of the patient with a special light to decompose the bilirubin structure and excrete it through organs. The phototherapy apparatus commonly used by many hospitals at the present, use a timer to control the duration of the therapy and the light source (such as fluorescent lamp) with fixed luminance. With this type of apparatus, the duration of therapy is controlled manually or through a timer, without the possibility to adjust the light intensity and the time of the irradiation cycle depending on the symptom. Therefore, newborn babies may be hurt by excessive light intensity at the initial stage. This and other factors affect the efficacy of phototherapy.[6-10]

After analyzing the disadvantages and problems of current phototherapy apparatus, we propose a "design of phototherapy apparatus with multiple operation modes and automatic light adjustment mechanism" for medical personnel as an alternative. The new design features customized light intensity, adjustable therapy duration, and periodical change of the light intensity that can effectively minimize the side effect of phototherapy. [11-14]

Normally in phototherapy, the apparatus uses a high-voltage fluorescent lamp as the light source. This design not only brings potential hazard to the medical personnel and the treated newborn baby, but also brings about direct or indirect injury to newborn babies who fail to adapt to the apparatus. [15-17] The main objective of this study is to make improvement of the following designs:

1. Replacement of the traditional fluorescent lamp with LED

The high-power blue LED with a wavelength between 460nm and 475nm (medical literature reviews suggest the best wavelength for treatment of jaundice is between 425nm and 475nm) is used for this new design. [6, 7, 9, 14] Instead of the high voltage for traditional fluorescent lamps, low voltage is used to control the irradiation of the LED.

2. Adjustable irradiation intensity

Irradiation of the LED is controlled with a pulse width modulation (PWM), so that the medical care personnel can adjust the intensity of the irradiation depending on the symptom of the disease.

Chwee Teck Lim, James C.H. Goh (Eds.): ICBME 2008, Proceedings 23, pp. 1132–1135, 2009
www.springerlink.com

3. Pre-set irradiation time to avoid carelessness and mistakes

The time of irradiation can be set via the human-machine interface to disable the machine at the end of the therapy to reduce the cost of human resources.

4. Selectable irradiation intensity for each module place

The modular design allows the user to set the intensity and time of irradiation for each module via the human-machine interface.

Accordingly, this phototherapy apparatus provides more functions for medical care personnel, such as customized light intensity, duration of the irradiation, and periodical adjustment of the light intensity, to reduce the side effects of phototherapy.

II. System Design

To remove the disadvantages of traditional phototherapy apparatus, the system suggested in this study provides the following basic functions: (1) the high-power LED is used to replace the traditional fluorescent lamp; (2) intensity of the irradiation is adjustable depending on the symptom; (3) the irradiation time can be set in advance to reduce the need for manpower; (4) the volume to be irradiated is selectable; and (5) the easy-to-use human machine interface.

The structure of the system is shown in Fig. 1. It comprises a human machine interface (running on PC), a control system (Embedded microcomputer ARM 7), an irradiating module (Embedded MCU, constructed by Toshiba MCU chip TMP87C202), and a power supply (POWER).

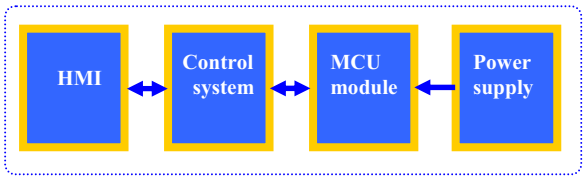


Fig. 1 Block diagram of this proposed system.

The control system (Embedded microcomputer ARM 7) is the core of the system for status display (showing the connection between the PC and embedded MCU), command transmission (transmitting commands to the controlled node for execution of specified actions), reading data (reading the signal detected at the controlled node and its status), manual control (implementing manual control without connection to the PC), and communication interface (providing a communication interface between the PC and embedded MCU).

The picture of this proposed apparatus is shown in Fig. 2.



Fig. 2 Photo of a LED Jaundice Phototherapy Device, designed by our research team in Kun Shan University.

A. Measurement Results of the Proposed Phototherapy System

The Japanese TOPCON spectroradiometer (Model SR-3) is used for measurement of the exposure and spectrum. The TOPCON SR-3 is a spectrum measurement instrument to measure the FPD and visible light source, as well as the luminance and hue of a single point. It has a resolution up to 1nm and is suitable for the laboratory that needs highly-accurate and highly-precise analysis of visible light spectrums. It is installed with standard software applications for easy analysis and storage of the measured data. The SR-3 instrument can display 2D color drawings; it can also measure extremely small light dots through using a close-up lens. TOPCON SR-3 can measure the luminance value up to 0.1 cd/m^2.

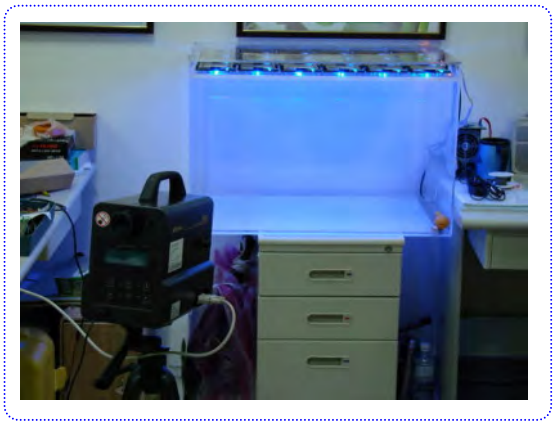


Fig. 3 Measuring instrument.

Fig. 3 shows the simulated phototherapy environment and a spectroradiometer is used to measure the data. The CS-900 measurement software is used for collection of measured data. Excel software is used for comparison of the

measurement results. The items to be measured include (1) background measurement (without a doll) with light pollution (with the fluorescent lamp on); (2) background measurement (without a doll) without light pollution (with the fluorescent lamp off); (3) simulated measurement (with a doll) and with light pollution (with the fluorescent lamp on); and (4) simulated measurement (with a doll) without light pollution (with the fluorescent lamp off). 11 luminance values are applied to each measurement item. They are 0%, 10%, 20%, 30%, 40%, 50%, 60%, 70%, 80%, 90%, 100%.

III. Conclusions

A. Comparison with the Current Phototherapy Apparatuses

To prove the advantages of this system that current phototherapy apparatuses do not provide, we use the SR-3 spectroradiometer to measure the three phototherapy apparatuses, including the ones using the blue or white fluorescent lamps, for the intensity of their wavelength. The measurement results are shown in Fig. 4. The blue fluorescent lamp /max. luminance is at the wavelength 435nm/intensity 0.003683107 (top diagram), the white fluorescent lamp /max. luminance is at the wavelength 435nm/intensity 0.002954492 (middle diagram), and the blue LED/max. luminance is at the wavelength 460nm/intensity0.009041377 (bottom diagram).

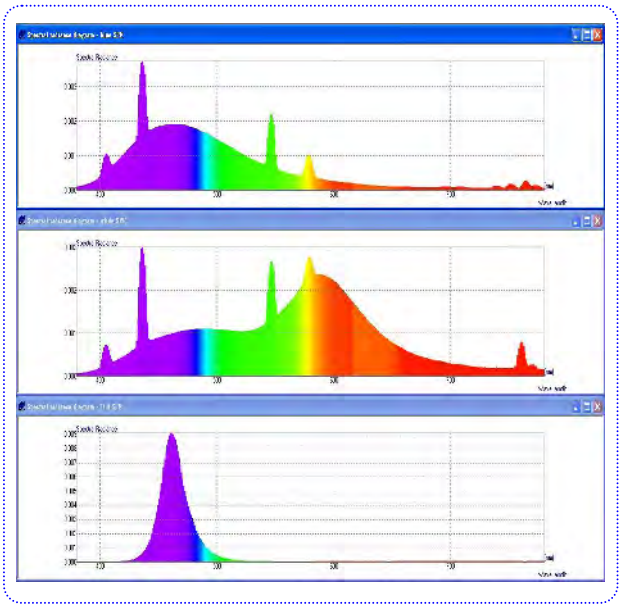


Fig. 4 Intensity of different phototherapy apparatus.

The Excel data is shown in Fig. 5. These three apparatuses meet the requirements for treatment of neonatal jaundice with the wavelength within the optimal photo range (425~475nm). However, the color gamut of the visible light of the white fluorescent lamp is too wide and the intensity of the blue fluorescent lamp is only 40% of the LED. The 100% luminance of this system is 2.5 times the luminance of a blue lamp. Its wavelength is about 460mm. The design of this proposed LED phototherapy apparatus is better than the traditional systems.

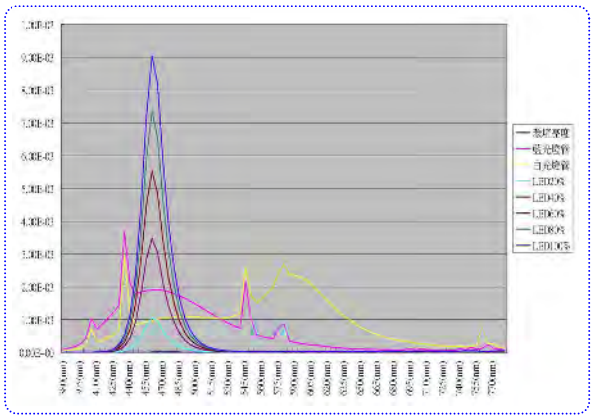


Fig. 5 Intensity comparison of different phototherapy apparatus.

B. Advantages and Development of the Proposed System

As the measurement result of TOPCON SR-3 shows, the wavelength of this system is within the range of 460~475nm, as indicated on the specifications of high-power LED. As these figures shown, this phototherapy system has a wavelength that is within the ideal range of the wavelength required for the treatment of neonatal jaundice (about 425~475nm).

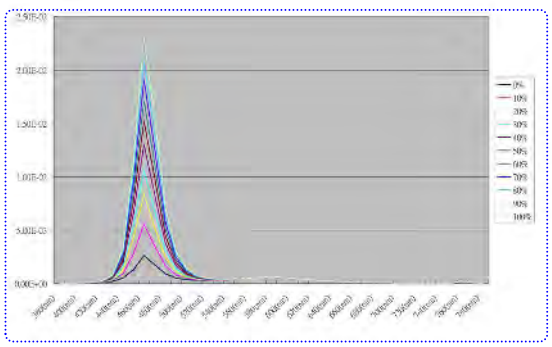


Fig. 6 Comparison of background and luminance with light pollution.

After importing SR-3 data in the Excel, comparison is made using a fold-line chart for each luminance from 0% to 100% at an interval of 10%. As shown in Fig. 6, the intensity of the irradiation is adjusted via the human-machine interface and the exposure rises accordingly, indicating that the system can provide the performance as expected.

The "auto therapy control panel" of the human-machine interface allows the setting of the treatment time, intensity, and module block to be used for the treatment. The medical care personnel can adjust the intensity, time and affected area of the irradiation depending on the symptom and jaundice index of the patient. They can view the treatment and adjust it at any time.

Scientists have found that LED of different colors has different efficacies for human bodies. For example, the red/blue light: relief of inflammation, anti-allergy, anti-acne, treatment of sinusitis; ultraviolet: disinfection. The most popular IPL therapy also applies LEDs.

Accordingly, this system is applicable to other fields only by replacing the blue LED of the modular photo board with the LED of other wavelength. In addition to treatment of neonatal jaundice, this system can be applicable to the daily life of us in many different areas.

Acknowledgment

The authors wish to acknowledge the National Science Council for the support of researched project NSC96-2622-E-168-005-CC3.

References

1. P. A. Dennery, D. S. Seidman, and D. K. Stenvenson (2001) Neonatal Hyperbilirubinemia. New England Journal of Medicine, No. 344, pp.580-589.
2. J. C. Martinez, H. O. Garcia, G. S. Drummond, and A. Kappas (1999) Control of Severe Hyperbilirubinemia in Full-term Newborns with the Inhibitor of Bilirubin Production in Sn-mesoporphyrin. Pediatrics, No. 103, pp.1-5.
3. J. F. Ennever (1990) Blue Light, Green Light, White Light, More Light: Treatment of Neonatal Jaundice", Clin. Perinatol., No. 17, pp.467-479.
4. G. K. Suresh, and R. E. Clark (2004) Cost-effectiveness of Strategies That Are Intended to Prevent Kernicterus in Newborn Infants. Pediatrics, No. 114, pp.917-924.
5. S. Ip, J. Lau, M. Chung, J. Kulig, R. Sege, S. Glicken, and R. O'Brien (2004) Hyperbilirubinemia and Kernicterus: 50 years later. Pediatrics, No. 114, pp.263-264.
6. H. J. Vreman, R. J. Wong, and D. K. Stevenson (2004) Phototherapy: Current Methods and Future Directions. Semin. Perinatol., No. 28, pp.326-333.
7. A. K. Brown, M. H. Kim, P. Y. Wu, and D. A. Bryla (1985) Efficacy of Phototherapy in Prevention and Management of Neonatal Hyperbilirubinemia. Pediatrics, No. 75, pp.393-400.
8. H. S. Lopes, E. J. Netto, and B. Wang (1989) Microprocessor-based Phototherapy Monitoring Station. Proceedings of the V Mediterranean Conference on Medical & Biological Engineering, pp.298-299.
9. P. Eggert, C. Stick, and H. Schroder (1984) On the Distribution of Irradiation Intensity in Phototherapy: Measurements of Effective Irradiance in an Incubator. Eur. J. Pediatrics, No. 142, 1984, pp.58-61.
10. F. J. Walther, P. Y. Wu, and B. Siassi (1985) Cardiac Output Changes in Newborns with Hyperbilirubinemia Treated with Phototherapy. Pediatrics, No. 76, pp.918-921.
11. Newman, and J. Gregory (2000) Bilirubin Measurements in Neonates. Proceedings of SPIE – The International Society for Optical Engineering, Vol. 3913, pp.25-33.
12. M. Pezzati, R. Biagiotti, V. Vangi, E. Lombardi, L. Wiechmann, and F. F. Rubaltelli (2000) Changes in Mesenteric Blood Flow Response to Feeding: Conventional versus Fiber-optic Phototherapy. Pediatrics, No. 105, pp.350-353.
13. J. H. Olsen and H. Hertz (1996) Childhood Leukemia Following Phototherapy for Neonatal Hyperbilirubinemia. Cancer Causes & Control, Vol. 7, No. 4, pp.411-414.
14. N. O. Osaku and H. S. Lopes (2006) A Dose-response Model for the Conventional Phototherapy of the Newborn. J. of Clinical Monitoring and Computing, No. 20, pp.159-164.
15. G. R. Mostnikova, V. A. Mostnikov, V. Y. Plavskii, A. I. Tret'yakova, S. P. Andreev, and A. B. Ryabtsev (2000) Phototherapeutic Apparatus Based on an Argon Laser for the Treatment of Hyperbilirubinemia in Newborns. Journal of Optical Technology, Vol. 67, No. 11, pp.981-983.
16. V. P. Zharov, K. I. Kalinin, Y. A. Menyaev, G. N. Zmievskoy, A. A. Savin, I. D. Stulin, R. K. Shihkerimov, A. V. Shapkina, L. Z. Veisher, and M. L. Stakhanov (2001) Phototherapeutic Treatment of Patients with Peripheral Nervous System Diseases by means of LED Arrays. Proceedings of SPIE – The International Society for Optical Engineering, Vol. 4244, pp.143-151.
17. A. H. Farouk, and L. Bernard (2003) Polychromatic LED Therapy in Burn Healing of Non-diabetic and Diabetic Rats. Journal of Clinical Laser Medicine and Surgery, Vol. 21, No. 5, pp.249-258.

Address of the corresponding author:

Author: C. B. Tzeng
Institute: Department of Electronic Engineering, Kun Shan University
Street: No. 949, Da Wan Rd.
City: Tainan
Country: Taiwan, R.O.C.
Email: cbtzeng@ms17.hinet.net

Study to Promote the Treatment Efficiency for Neonatal Jaundice by Simulation

Alberto E. Chaves Barrantes[1], C.B. Tzeng[2] and T.S. Wey[2]

[1]Department of Mechanical Engineering, Kun Shan University, Tainan, Taiwan, R.O.C.
[2]Department of Electronic Engineering, Kun Shan University, Tainan, Taiwan, R.O.C.

Abstract — **In this paper, we promote effectiveness, by using light simulation software, which we are able to simulate the propagation of the light, and we design a baby dummy (which it's sizes are close to a real baby), where we can measure the effectiveness of the light over the skin surface.**

With this method we show the results of an actual device and also propose a new design to use as an example for improving the effectiveness. Using this software we can get better results and hoping developers use this method for exchanging the phototherapy device performance, which babies patients are the ones who have the benefits.

Keywords — **Jaundice, Bilirubin, Phototherapy, Simulation software, Device performance.**

I. Introduction

The aim of phototherapy is to curtail rising serum bilirubin and prevent its toxic accumulation in the brain, where it can cause the serious, permanent neurological complication known as kernicterus. Phototherapy has greatly reduced the need for exchange transfusion to treat hyperbilirubinemia. Phototherapy is used in 2 main ways: prophylactically and therapeutically.

The photoisomerization of bilirubin begins almost instantaneously when the skin is exposed to light. Unlike unconjugated bilirubin, the photoproducts of these processes are not neurotoxic. Therefore, when faced with a severely hyperbilirubinemic infant, it is important to begin phototherapy without delay.

The normal serum bilirubin value of a newborn baby is between 0.2 mg/dl and 1.4 mg/dl. When it exceeds 5 mg/dl, jaundice appears in the skin, fingernail or sclera. The symptom of hyperbilirubinemia appears when the serum bilirubin value is between 15 mg/dl and 20 mg/dl. A newborn baby is diagnosed with kernicterus when the serum bilirubin value is higher than 20 mg/dl.

The most effective light sources for degrading bilirubin are those that emit light in a relatively narrow wavelength range of 458 nm. At these wavelengths, light penetrates the skin well and is maximally absorbed by bilirubin.

Irradiance is the light intensity, or number of photons, delivered per square centimeter of exposed body surface. The delivered irradiance determines the effectiveness of phototherapy; the higher the irradiance, the faster the decline in serum bilirubin level. Spectral irradiance, quantities as $\mu W/cm^2/nm$, largely depends on the design of the light source. It can be measured with a spectral radiometer sensitive to the effective wavelength of light. Intensive phototherapy requires a spectral irradiance of 30 $\mu W/cm^2/nm$, delivered over as much of the body surface as possible.

The gallium nitride LED is a recent innovation in phototherapy. These devices provide high irradiance in the blue to blue-green spectrum without excessive heat generation. Light-emitting diode units are efficient, long-lasting, and cost-effective. The latest models incorporate amber LEDs to counteract the blue hue effect that can irritate caregivers.

LED have shown that are more efficient both in energy consumption than ordinary fluorescent lamps; but above else deliver more energy in the skin for breaking up the bilirubin (Yun-Sil Chang and Jong-Hee, 2005).

We will study further more about the principle of an LED phototherapy unit, which this project really appreciated Kun Shan University's LED phototherapy unit. (Fig. 1 shown)



Fig. 1 Photo of a LED Jaundice Phototherapy Device, designed by our research team in Kun Shan University.

II. Research methodr

So as promoting the efficiency for a jaundice treatment, we will focus in 2 parts of effectiveness :

(1) Energy saving : we can predict with the software, the amount of irradiance in the baby's skin. This means that if we had a light source of 6W light power, we can set a

Chwee Teck Lim, James C.H. Goh (Eds.): ICBME 2008, Proceedings 23, pp. 1136–1139, 2009
www.springerlink.com

minimum of power so the light is above the minimum the bilirubin breaks (> 30 μw/cm^2).

(2) Expose at maximum the skin's surface : we are going to be able to see how much of the skin surface we will cover with the light, so this means, if more skin is covered, a better treatment we will provide to the patient. For this study work, we will study the behavior of an actual device, from Kun Shan University, Department of Electronic Engineering.

Using Trace Pro simulation software, requires these steps to perform a study in it *:*

(1) Creating a Solid Model : Here in the first step, we create the 3D model of the light source (LED) and later we create the "Dummy Baby" which is a dummy with actual sizes from a new born baby, so we can simulate the light behavior in a planar surface and with the dummy.

(2) Defining Properties : This step is very important, where we define the physical properties of each part of the LED, planar surface and "Dummy baby".

(3) Applying Properties: This step is a continue from previous one, we select different types of properties as well we set the light source and its properties (5W, 458nm, 30000 rays, radiometric measurement).

(4) Ray Tracing: we finally trace the rays, the computer works, to get our simulation results.

(5) Analysis: finally, when we get the results, we can analyze all we need to study.

First study: Planar surface

We first begin with studying the behavior of the light, with just a planar surface, this surface have skin properties (Tissue, Epidermis).

Second study: with "Dummy baby"

We already know how the jaundice phototherapy device behaves, but just with a plane surface, which we can wonder: "It works the same with a baby inside the phototherapy device ?"

This section, we construct without software what I called Dummy baby, which is a design, not real baby, but is a body which have the basic properties: (1)Extremities (legs: 170mm long, 57mm radius; arms: 145mm long, 15mm radius), (2)Head (62 mm radius), (3)Thorax (chest, waist and shoulders all average: 360 mm radius).

This is not all, how about the measurements; well we get them from babies' average sizes for all these basic properties. So finally, designing our Dummy baby, so for final design, to study the behavior of the jaundice phototherapy device.

Result and discussion

Starting with a full power LED in Fig. 2 and Table 1, (Fig. 2(a) 5W LED), we can see the power absorbed is too high, with an average of 367.51 μW/cm^2, which means the required amount of light power (over 30 μW/cm^2) is surpassed by more than ten times! This means we can still lower the light power by ten and still have good results with the jaundice phototherapy device. So for conclusion, we waste energy with full power LED.

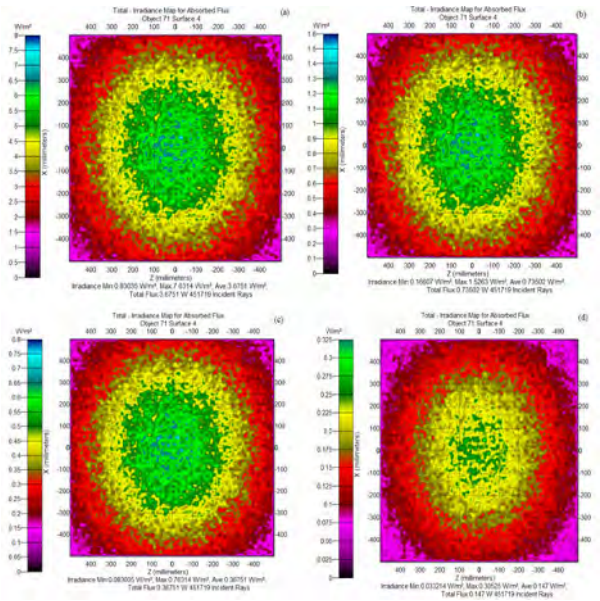


Fig. 2 Results of study of a planar surface without any customized LED pattern, results on Table 1; (a) 5W, (b) 1W, (c) 0.5W, (d) 0.2W.

With 1W we drastically reduce the LED power by 80% (Fig. 2(b) 1W LED), also is very good to see that all surface is over the minimum (over 30 μW/cm^2), average of 73.502 μW/cm^2, so this part we still have good results with the baby patient jaundice and also the device won't consume a lots of power (reduce from 175W to 35W) which becomes efficient. But we can still see many parts of the surface above the 100 μW/cm^2, so we still going to reduce the power, so we can save even more energy!

With Fig. 2(c), for 0.5W LED power, we again reduce the power to 50%, having as result an average of 36.751 μW/cm^2, clearly above of the minimum power we need to have the phototherapy device to do its job. But also we can see that the area can do the job, is only concentrate in the center and the borders remain under the minimum, which makes this light pattern inefficient.

For Fig. 2(d), with 0.2W LED power, an average of 14.7 μW/cm^2, this power is not enough for the objective of the

jaundice device, just only in the middle we can see have power over the minimum required.

So from these figures (Fig. 2 (a), (b), (c) and (d)) we can appreciate, the best light pattern is for 1W, which is low power and almost cover all surface above the minimum required.

Table 1 Results of study, without any customized LED pattern

Figure (Fig. 2)	**Total LED power**	%LED power	Irradiance Over 30μW/cm^2	**Average Irradiance Power**
5W(Fig.a)	**175W**	100%	100%	**367.51 μW/cm^2**
1W(Fig.b)	**35W**	20%	92%	**73.502 μW/cm^2**
0.5W(Fig.c)	**17.5W**	10%	60%	**36.751 μW/cm^2**
0.2W(Fig.d)	**7W**	4%	4%	**14.7 μW/cm^2**

Then, we customize 3 different LED light power pattern to increase energy saving by reducing LED power and having same great results. On Figure 3 and Table 2, we compare the best LED uniform light pattern (1W) with two customized light pattern.

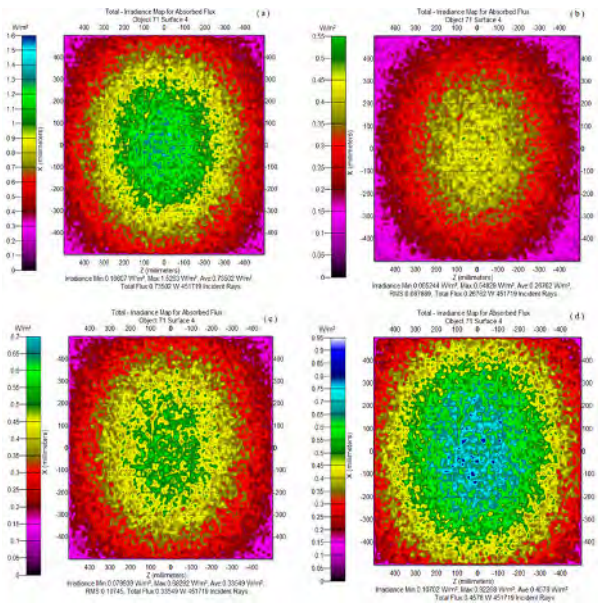


Fig. 3 Results for planar surface with a customized LED pattern, results on Table 5; (a) 1W, (b) light pattern # 1, (c) light pattern # 2, (d) light pattern # 3.

First, we know 1W is very efficient, delivers good amount power over the surface (73.502 μW/cm^2, of average), but also we know many parts of the surface, special in the middle, where the amount of power still high and I change the light pattern to change the values around the surface.

The first LED customized light pattern (Light pattern #1), we put an out ring of 0.5W, which we know in the borders the irradiance goes down and in the middle goes a power of 0.2W. We choose this pattern, because we want to try to get the minimum LED possible power pattern. So we know before, 0.2W in the middle we will have barely enough power to get it over the minimum required (over 30 μW/cm^2), and for the edges, we increase the power to 0.5W. In the Fig. 3(b), we see we get an irradiance barely surpass the minimum required, but also we can see we still get a ring of irradiance power bellow the minimum required. So for this reason we create the custom patter number two.

Custom pattern number two, in the corner's LED and the out-middle LED we increased the power to 1W, this way we intend to increase the outer irradiance ring that was below with the minimum irradiance power required. So as final result, with the light custom pattern # 2, we have good irradiance, which the average is 33.549 μW/cm^2, which is good to break the bilirubin and covers most of the plane surface and we don't need to much power (1W light patterns requires 35W total LED power, custom LED # 2 requires just 17W LED power to do the same job) so this means we will have the same results with less power.

Then, last pattern # 3, I increase the power for the outer LEDs to 1W (Light pattern # 3), so finally we can get the same amount of coverage (92% of surface is greater than 30 μW/cm^2) as if we put the all LED to 1W, so finally we can get same coverage and average over 30 μW/cm^2 but with much less power.

Table 2 Results for planar surface with customized light pattern

Figure (Fig. 3)	**Total LED power**	%LED power	Irradiance Over 30μW/cm^2	**Average Irradiance Power**
1W(Fig.a)	**35W**	20%	92%	**73.502 μW/cm^2**
Light pattern #1 (Fig.b)	**13W**	7.42%	30%	**26.762 μW/cm^2**
Light pattern #2 (Fig.c)	**17W**	9.7%	76%	**33.549 μW/cm^2**
Light pattern #3 (Fig.d)	**23W**	13.14 %	92%	**45.78 μW/cm^2**

III. Conclusions

For conclusion, with our project, we want to state that our main goal is to promote the light simulation software in the steps of designing a neonatal jaundice phototherapy apparatus, this way we can improve the device's performance.

Energy Saving and Performance

With an energy saving program, we can get a cheaper device, which will be able to do the main goal of the jaundice phototherapy device (bilirubin breaking) with less energy, as for the designers with this they can reduce cost on:

- Have less light sources, but with great performance.
- Use a reliable light sources, we can be able to use cheap LED as light sources, omitting expensive ones, if can do good performance.
- Reduce manufacturing cost, by placing less light sources if with less LED we can have a great performance.

Enhance the phototherapy

Enhancing the phototherapy, as we know, the most skin we can cover with the minimum light irradiance power, the most effective therapy we will get, by reducing the timing the baby patient will stay for therapy and this way the hospital or clinic can reduce cost for energy, less hours and the number of times the equipment can be used in a period of time.

As for final statement, we hope developers really can see the importance of simulation software in the design steps, as we prove we can have better results from saving energy and performance enhance.

As for recommendations, to improve the reliable of the results from the simulation software, we will need to pay attention to the following issues:

(1) Close communication between the Jaundice phototherapy device designers and the light source manufactures. This because important information we can't see in the data sheet, that we will need! (For example: the range of working wavelengths, the loss power by heat and noise, etc). So this way we can reduce the errors on the final result we get from the light simulation software.

(2) When designing a better baby model (if it uses) remember the software cares and we get the result just one surface at time. This means we need to construct a irradiance map (total surfaces together) to have a good analysis.

ACKNOWLEDGMENT

The authors wish to acknowledge the International Cooperation and Development Fund (Taiwan ICDF) for the financial support provided during this study. In addition, the authors wish to acknowledge the National Science Council for the support of researched project NSC96-2622-E-168-005-CC3.

REFERENCES

1. Vreman HJ (1998) Light-emitting diodes: a novel light source for phototherapy. Pediatric Research, 44(5):804-809.
2. Yun Sil Chang, Jong Hee Hwang, Hyuk Nam Kwon, Chang Won Choi, Sun Young Ko, Won Soon Park, and Son Moon Shin (2005) In vitro and in vivo Efficacy of New Blue Light Emitting Diode Phototherapy Compared to Conventional Halogen Quartz Phototherapy for Neonatal Jaundice. Journal of Korean Medical Science, 20: 61-64.
3. Ching-Biau Tzeng, Tsuu-Shiang Wey, Chih-Chieh Huang, and Tsung Yu Su (2007) Design and Implementation of a New Phototherapy Apparatus for the Curing of Neonatal Jaundice", Proceedings of the 2007 3rd National Electronics Design Creative Contest, 301-308.
4. Frank A. Osk (1990) Principles and Practices of Pediatrics. Lippincott Company, 34-42.
5. James G. Hughes, and John F. Griffith (1984) Sypnopsis of Pediatrics. The Mosby Company, 6th edition , 76-78.
6. Rita G. Harper, and Jing Ja Yoon (1987) Handbook of Neonatology. Yearbook Medical Publisher, 2nd edition, 123-131.
7. Shannon Munro Cohen (2006) Jaundice in the Full-Term Newborn. Pediatric Nursing, 32(3):202-208.

Author: C. B. Tzeng
Institute: Department of Electronic Engineering, Kun Shan University
Street: No. 949, Da Wan Rd.
City: Tainan
Country: Taiwan, R.O.C.
Email: cbtzeng@ms17.hinet.net

Low Back Pain Evaluation for Cyclist using sEMG: A Comparative Study between Bicyclist and Aerobic Cyclist

J. Srinivasan[1,2] and V. Balasubramanian[3]

[1]TATA Consultancy Services Ltd. Innovation Lab, Scientist, Bangalore, India
[2]IIT Madras, Rehabilitation Bioengineering Group, Department of Biotechnology, Research Scholar, Chennai, India
[3]IIT Madras, Rehabilitation Bioengineering Group, Department of Biotechnology, Assistant Professor, Chennai, India
Email:chanakya@iitm.ac.in

Abstract — **Despite of wide use of surface electromyography (EMG) recorded during dynamic exercises; the reproducibility of sEMG variables has not been fully established in cycling exercise. As an extension of our previous study, this study aims to examine, muscle fatigue of bicyclist and aerobic-cyclist on biceps brachii medial, trapezius medial, latissimus dorsi medial, and erector spinae muscles within low back pain (LBP) group using bilateral surface EMG (sEMG).**

Five male volunteers with LBP were chosen and sEMG was recorded bilaterally from selected muscle groups for 30 minutes of ride of each subject. The collected sEMG signals were filtered using Butterworth filter with a pass band of 20–400 Hz and stop band of 47–49 Hz. Statistical tests were performed to determine the difference in fatigue, using MPF difference. No significant result was found for aerobic–cyclist. Whereas, in case of bicyclists in LBP group showed a significantly fatigue in biceps brachii medial, right trapezius medial and erector spinae.

From the results, it is evident that LBP can worsen significantly by cycling than aerobic cycling; for subjects who have previous injury to lower back. These inferences could be used when deciding fitness and rehabilitation regimes.

Keywords — **Surface Electromyography, Low Back Pain, Bicycling, muscle fatigue, repetitive motion disorder.**

I. Introduction

This paper is an extension of our previous study; muscle fatigue analysis for bicycle and aerobic cycle riders [1, 2]. Cycling serves both, as a mode of transportation and as training equipment in fitness and rehabilitation. Cycling utilizes a reciprocating vertical motion similar to walking, hence cycling plays equivalent important in fitness and rehabilitation centres. As there is little data pertaining to the development of LBP and shoulder pain in cyclists, this study aims to examine whether difference in muscle activity existed between aerobic–cyclists and bicyclist of LBP using sEMG. Our previous study on road cyclist infers that, there is a higher muscle fatigue in the back muscles of LBP group when compared to non LBP group of bicycle riders. However for aerobic–cyclist there was no significant result found.

sEMG has been used to display muscle activation patterns and is extensively employed to interpret both dysfunction and functional muscle recruitment patterns related to cycling activity [3]. The sustained muscular contractions externally associated with not being able to maintain a certain force, lead to physiological fatigue, tremor or pain, localized in the specific muscle. This is called muscular fatigue [4], associated with a compression of the power spectral density (PSD) of the sEMG towards lower frequency [5], measured by MF computed from the sEMG PSD.

The spectral analysis of the sEMG was widely used to detect and quantify the electrical manifestations of muscle fatigue [6]. It was well known that during a sustained muscle contraction, the power spectrum of the sEMG is scaled toward the lower frequency end. At this time, the spectral scaling is most reliable sign of localized muscle fatigue; and some researchers rely on it for studying the variations of the excitability of the membrane of muscle fatigue during sustained contractions.

In our study, we concentrate on peripheral muscle fatigue. The development of muscle fatigue during exercise is associated with a decrement in their performance. Mechanisms of muscle fatigue depend on the exercise conditions and the subject's level of physical fitness. The decrements in skeletal muscle power output are also related to neural drive reductions and may also lead to muscle fatigue in prolonged exercise [1]. In general, fatigue is viewed as an unavoidable and negative consequence of physical activity.

In summary, one could infer that bicycling can induce higher muscle fatigue in individuals with LBP than aerobic–cycling. As a support of our result, we have performed a 10 point visual-analogue scaling test.

II. Methodology

A. Subjects:

Five male volunteers with a mean age of 26.20 years (range 23 – 29 years) and mean weight of 60.17 Kg (range

Chwee Teck Lim, James C.H. Goh (Eds.): ICBME 2008, Proceedings 23, pp. 1140–1143, 2009
www.springerlink.com

45 to 68 Kg) participated in the study. LBP group had a history of low back pain (1 year < LBP > 3 years).

B. Protocol

Subjects were instructed not to participate in any heavy training or physical activity 24 hours prior to their clinical assessment or testing day. All activities were explained to the subject before the experiment. Subjects rode their own road bicycles on outdoor within the institute campus and were instructed to sit and keep a posture of their comfort. They were also instructed to cover a distance of 6 km in 15 minutes. While riding, cyclists were exposed to vibration and force during which several muscles will be activated. On the other hand, aerobic–cycling experiment was done as indoor experiment for 30 minutes and data were collected at initial and after 30 minutes of aerobic cycling. Indoor experiment and outdoor experiment were carried on different day, so that they do not have influence on each other. In our study, we considered the biceps brachii medial (BBM), trapezius medial (TM), latissimus dorsi medial (LDM), and erector spinae (ES) muscle group, bilaterally. Signals from these groups of muscles were collected using EMG. (Delsys, Inc., USA).

Before placement of the electrode, the site was shaved, abraded with sandpaper, and cleaned with ethanol to avoid impedance mismatch and movement artifact. Ag/AgCl differential electrode was adhered to the skin along the muscle fiber orientation. Care was taken to place electrodes on the midline of muscle belly, between the myotendonous junction and the nearest innervation zone. Detection surface was oriented perpendicularly to the length of muscle fibers.

Bagnoli-8^{TM} machine with an amplifier gain setting of 1000 was used to acquire the myolectric signal. Customized program was written in LabVIEW^{TM}, National Instruments, Inc. This was used to sample sEMG at the rate of 1000 Hz. Each subject was asked to exert MVC and the sEMG were recorded for 10 seconds, before cycling. sEMG was also collected at three intervals for all the subjects as they underwent psychophysical tests to determine MVC. The three intervals were, a) before cycling, b) after 15 minutes of cycling, and c) after 30 minutes of cycling. All experimental data were recorded at the Rehabilitation Bioengineering Group (RBG) laboratory, IIT Madras

C. Analysis

Raw sEMG signals were filtered using eighth-order Butterworth filter with a pass band of 20–400 Hz. A second order notch filter with a band stop of 47–49 Hz was used to eliminate AC line interference. Filtered signals were normalized with respect to mean, and then full–wave rectified. sEMG signals were analyzed in frequency domain using power spectrum. The power spectrum of the sEMG has been reported to change under influence of muscle fatigue [7]. As muscle fatigues, there is a concomitant change in the power spectrum of sEMG signals; there is an increase in the amplitude of the lower frequency band and a relative decrease in higher frequency band. Decrease in mean power frequency (MPF) from sEMG profiles is a recognized method of determining fatigue in an isometric muscle action [8]. However the methods employed to calculate MPF and the groups of muscles selected vary with requirement. In this study, hamming–windowed algorithm was applied on rectified sEMG signals and MPF was extracted from the power spectrum. Fatigue difference was calculated using MPF. These were used to determine the level of muscle fatigue.

$$\text{MPF difference} = (\text{MPF}_{\text{after}} - \text{MPF}_{\text{before}}) \quad [1]$$

D. Statistical Analysis

Skewness test performed on the features extracted from sEMG signals showed that they were not normally distributed. Hence a non-parametric test, Mann–Whitney 'U' test, was used to determine the significant difference in EMG activation between bicycle riders and aerobic–cycle riders, before and after 30 minutes of cycling.

III. Result

Sample power spectrum of EMG acquired from erector spinae muscle of LBP subjects is shown in Figure 1.

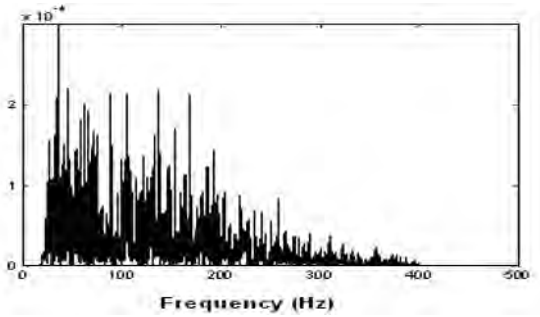


Figure 1 Power spectrum of erector spinae of LBP group

MPF difference was able to significantly differentiate ($p<0.05$) EMG activity in right trapezius medial and erector spinae muscles of LBP group than control group of bicyclist from the same muscle groups. Table 1 shows the compari-

son of MPF difference on right and left Biceps Brachi medial of LBP group.

Table 1 Comparison of MPF difference on Biceps Brachii Medial of LBP and control group

Subject	LBP Group MPF Difference of Biceps Brachii Medial	
	Left	Right
1	31.71	18.40
2	8.39	10.01
3	-1.04	5.18
4	-27.88	-15.76
5	-13.79	-4.22

Table 2 Comparison of MPF difference on Right Trapezius Medial and Right Erector Spinae for LBP group of bicyclist and aerobic – cyclist

Subject	MPF Difference			
	Right Trapezius Medial		Right Erector Spinae	
	Bicycle riders	Aerobic–cyclist	Bicycle riders	Aerobic – cyclist
1	-17.7218	-25.0269	8.4057	55.8728
2	19.8030	-7.9963	8.8680	-67.8936
3	2.9325	2.0581	15.1752	-4.5040
4	-2.9845	-17.2942	4.0484	-16.4673
5	5.0577	0.3370	-3.4990	6.7107

Table 2 shows the Comparison of MPF difference on Right Trapezius Medial and Right Erector Spinae for LBP group of bicyclist and aerobic – cyclist.

Visual Analogue Scale Result: LBP subjects were admitted based on entry criteria and their severity of LBP was quantified after 30 minutes of cycling using a 10 point visual-analogue scale.

The result of 10 point visual-analogue scale, infers that LBP groups of aerobic cyclist have a mean of 6.20 (±0.49), while bicyclist have a mean of 7.80 (±0. 86).

Result infers that there is a significant difference existed between the aerobic –cyclist and bicyclist.

IV. Discussion

This study demonstrates the difference in muscle activity of LBP individuals who uses aerobic and road cycle for fitness, using a statistical test. Still to our surprise, we found that there were no differences between LBP and control group; during a dynamic exercise on an aerobic cycle. It also states that there were no significant fatigue occurred for LBP groups of bicyclist and aerobic–cyclist; during a dynamic exercise on an aerobic cycle. LBP subjects, with a previous history of existence of back pain for a period of 1 to 3 years only, were chosen for this study. Subjects were instructed to use similar models of bicycles.

Limitation of this pilot study was the duration; the experiment duration was determined after the initial screening test made on sample subject. Screening test infers that, subjects were not able to maintain the speed after 30 minutes of cycling. As a result of this, our experiment duration was fixed as 30 minutes.

A few previous studies have examined the changes in lower extremity muscle activities during cycling in indoor environments and lower extremity only [9 –11, 3]. In our study, we consider the back muscle and upper extremity; also compare the rode bicycle riders and aerobic–cyclist.

Chaffin, DB *et al.* (1978), reported isometric strength testing provides information which can be used to predict occupational injuries associated with dynamic lifting tasks. Hunter *et al* (2001) reported that MVC produce highest levels of EMG and therefore will be more effective in describing maximal muscle recruitment activity. They suggest that MVC can be used as a normalization procedure for dynamic cycling activity. Therefore, during this study, a psychophysical test for dynamic lifting task was performed to determine MVC of the required muscles for each subject.

Hunter *et al* (2001) also demonstrated that MVC produced greater MPF activity, which indicates a higher rate of motor units firing or recruitment of a greater number of motor units. As generally reported, MPF decreases as muscle fatigue progresses. Although central and peripheral factors are responsible, the main factor contributing to the MPF shift towards lower values may be peripheral, i.e. a slowing of the muscle action potential conduction velocity. In our study, MPF of LBP group shows a steady decrease when compared to control group.

Hoeven *et al* (1993) performed linear regression analysis on sEMG. Our study used MPF difference to significantly differentiate the fatigue of muscle before and after 30 minutes of cycling. In the literature, gender difference in muscle fiber compositions are still discussed controversially. Most authors found no statistically significant differences between genders [12]. Hence this study had only male participants.

V. Conclusions

This study helps us to understand the consequences of cycling. From the results, it is evident that there is no significant result was found for aerobic–cyclist. Whereas, in case of bicyclists in LBP group showed a significantly fa-

tigue in biceps brachii medial, right trapezius medial and erector spinae than those in the control group. From the results, it is evident that LBP can worsen significantly by cycling than aerobic cycling; for subjects who have previous injury to lower back.

These inferences should be used when deciding the use of bicycle as an option in fitness and rehabilitation, instead of walking for LBP individuals.

ACKNOWLEDGMENT

The authors wish to thank all the members of Rehabilitation Bioengineering Group (RBG) at IIT Madras and the volunteers who participated in this study.

REFERENCES

1. Srinivasan.J and Venkatesh Balasubramanian (2005), 'Low Back Pain and Muscle Fatigue due to Road Cycling – A sEMG Study', Journal of Bodywork and Movement Therapy, Elsevier Publication,Vol-1,Issue-3,pp;260-266Muscle
2. Srinivasan.J and Venkatesh Balasubramanian (2008), Surface EMG based muscle activity analysis for aerobic cyclist'. doi:10.1016/j.jbmt.2008.03.002
3. Gregor,R.J, J.P.Broker and M.M.Ryan (1991) 'The biomechanics of cycling. Exerc.Sport' Sci. Rev.19; 127-169, 1991
4. Basmanjian J.V., Delica C.J. (1985) 'Muscles Alive. Their functions revealed by Electromyography' (William and Wilkins, Baltimore)
5. Stulen F.B., Deluca C.J. (1981) 'Frequency parameters of the myoelectric signal as measure of muscle conduction velocity', IEEE Transactions on Biomedical Engineering, col.BME-28, No.7, pp.515-523, 1981
6. Marco knaflitz and Filippo Molinari (2003) 'Assessment of muscle fatigue during biking', IEEE transaction of neural systems and rehabilitaion engineering, vol.11, no. 1, pp 17 –23
7. J.H. Van der Hoeven, T.W.Van Weerden, M.J.Zwarts, (1993).'Long-Lasting Supernormal Conduction Velocity after Sustained Maximal Isometric Contraction in Human Muscle', Muscle Nerve, 16, pp 312-320
8. G.T.Allison, T. Fujiwara, (2002). 'The Relationship between SEMG Median Frequency and Low Frequency Band Amplitude Changes at Different Levels of Muscle Capacity', Clinical Biomechanics, 17, pp 464 -469
9. Angus M. Hunter, Allan St Clair Gibson, Michael Lambert and Timothy D. Noakes. May (2002) EMG normalization method for cycle fatigue protocols. Medical & Science in sports & Exercise:.857-861
10. Prilutshky BI and Robert J Gregor Sep (2000) Analysis of muscle coordination strategies in cycling IEEE Transaction on Rehabilitation Engineering 8,3: 362 – 370
11. Singh VP, Kumar DH, Djuwari D, Polus B, Frase S, Hawlwy J, and S Lo Giudice (2004) Strategies to identify muscle fatigue from SEMG during cycling ISSNIP 547 – 551
12. Christoph Anders, Susanne Bretschnedier, Annette Bernsdorf, Kerstin Erler and Wolfgang Schneider (2004) 'Activation of shoulder muscles in healthy men and women under isometric conditions'. Journal of Electromyography and Kinesiology

3D Surface Modeling and Clipping of Large Volumetric Data Using Visualization Toolkit Library

W. Narkbuakaew, S. Sotthivirat, D. Gansawat, P. Yampri, K. Koonsanit, W. Areeprayolkij and W. Sinthupinyo

National Electronics and Computer Technology Center, Phahon Yothin Rd, Klong Luang, Pathumthani 12120, Thailand

Abstract — **A 3D surface model of human anatomy is widely used in medical imaging software to increase visualization of volumetric data in 3D. In the first part of the paper, we present a process for fast 3D surface reconstruction with high quality from large volumetric data. The subsampling technique is used to support large volumetric data. After constructing the contours, we apply the smoothing technique to smooth out the polygon mesh. Specifically, in this study, we focus on the subsampling and smoothing parameters that affect the quality of the 3D surface model and the efficiency of the computation time. In addition to 3D surface reconstruction, 3D surface clipping is also useful for visualization because it allows one to see detail structures inside the surface model. In the second part of the paper, we propose another process to perform 3D surface clipping on volumetric data. Clipping along an arbitrary plane requires the position and orientation of that clipping plane. Since, with clipping only, the corresponding clipped surface produces empty holes, a texture mapping technique is used to cover the holes by placing the cut image data of that clipping plane on top of the clipped surface. Our proposed processes in this paper are based on the Visualization Toolkit (VTK) library.**

Keywords — **3D Surface Modeling, Surface Clipping and Visualization Toolkit (VTK)**

I. Introduction

3D Surface Modeling is one of volumetric data representations. It is represented in a form of polygon meshes, which consist of a large number of vertexes and normal vectors. These vertexes and normal vectors can be exported into a graphic file format without the original volumetric data for constructing a physical model. This is an advantage of 3D surface model because the physical model is useful in some applications. For example, it is used for printing a surgical guide in dental implantology by a rapid prototyping machine. Another good advantage of 3D surface modeling is an ability to view an interested section by a clipping method. This paper is divided into two parts: a 3D surface modeling or reconstructing process and a 3D surface model clipping method. In addition, all processes are developed and based on the Visualization Toolkit (VTK) [1] library, which is an open source library for computer graphics, image processing and visualization.

In the first part, a 3D surface reconstruction process is proposed to solve a problem of reconstruction from large volumetric data. This problem is usually solved by high efficient hardware. For example, John G. Torborg [2] applied a parallel processing technique to provide floating point computation, which handled complex models, and preserved basic operations, such as transforming and clipping. Although these algorithms are effective, they will be difficult to implement in practical if the resources of hardware, such as random access memory (RAM) and computer processing unit (CPU), are limited. Consequently, we proposed a process for reducing resources requirement and reconstructing a 3D surface model by basic algorithms. The proposed process uses subsampling technique to reduce the resolution of volumetric image data. This technique helps reducing memory and computation time usages. The proposed process applies the Marching Cubes algorithm [3] to extract contours from volumetric data. Furthermore, it uses polygon decimating to reduce memory for handling poly data, and polygon smoothing is applied to adjust the quality of a 3D surface model.

In the second part, 3D surface clipping method is proposed. This method requires a clipping plane for defining a clipped location, and we use texture mapping technique for covering empty holes at a cut surface after clipping a 3D surface model.

This paper is organized as follows. The next section discusses a concept of the Marching Cubes and describes the proposed process for reconstructing 3D surface model. Then, a concept of clipping and the 3D surface clipping method are explained. We will show the experimental results of the proposed processes. Finally, the conclusion is discussed in the last section.

II. Marching cubes algorithm and 3D surface reconstruction

Marching Cubes is a popular algorithm for extracting a contour from volumetric image data, and the contour is constructed by matching between voxel and cube patterns.

Chwee Teck Lim, James C.H. Goh (Eds.): ICBME 2008, Proceedings 23, pp. 1144–1148, 2009
www.springerlink.com

These patterns are generated from the consideration of edges and vertexes in each cube, and they can be summarized into 15 patterns [3], which are shown in Figure 1. Each vertex is considered to turn on when its weight is higher than the defined threshold. In addition, the position of contour that passes through each edge is defined by linear interpolation between two vertexes.

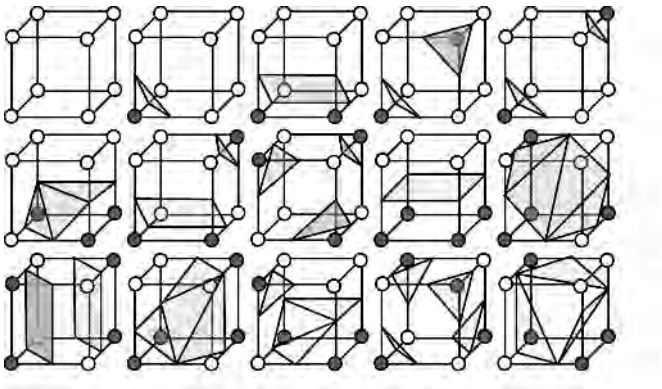


Fig. 1 The 15 patterns of Marching Cubes Algorithm

The Marching Cubes algorithm is supported by the vtkMarchingCubes class in the VTK library. The input of this class is vtkDataObject that is a general representation of visualization data, such as volumetric image data, and its output is vtkPolyData that is the data set of vertexes, lines, polygons, and triangle strips. Therefore, we should adjust and improve the image data before applying the vtkMarchingCubes class. Moreover, the quality of polygon mesh can be improved after reconstructing. Specifically, the proposed process for reconstructing a 3D surface can be divided into six steps as shown in Figure 2.

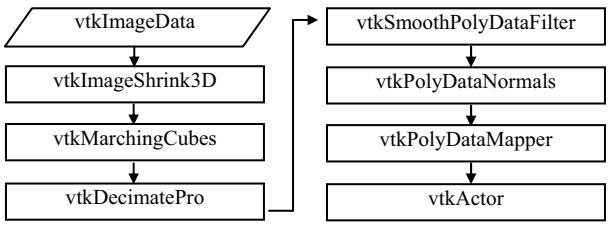


Fig. 2 The 3D Surface Reconstruction Process

The first step starts by applying the subsampling techniqued that is supported by the vtkImageShrink3D class. We use the subsampling technique to reduce the effect of large volumetric data. In the next step, vtkMarchingCubes class is selected to reconstruct the contour or polygon mesh. Hence, we apply the mesh decimation for reducing the number of the triangle mesh, and it is served by the vtkDecimatePro class. This step helps us to reduce memory usage for interacting with the polygon mesh. In the next step, the polygon mesh is smoothed by the vtkSmoothPolyDataFilter class that uses Laplacian smoothing. Then, the vtkPolyDataNormals class is applied to calculate the normal vector of the polygon mesh, and the vtkPolyDataMapper class is applied to map poly data into basic graphic data by the setMapper method of the vtkActor class. The vtkActor is an object format that is allowed to add in the vtkRenderer for display.

III. 3D SURFACE CLIPPING

Surface clipping is a basic operation for dividing the polygon mesh from one piece into two pieces. The divided pieces are based on the implicit function, which divides all points into negative scalar values on one side and positive scalar values on the other side. This operation is served as the vtkClipPolyData class. In addition, the points that make the implicit function to be zero are defined as the cut edge. This operation is called cutting, and it is supported by the vtkCutter class. When 3D performs surface clipping, the empty holes may exist. One approach to covering these holes is by replacing with an image at the clipped-plane position. This enables one to see the detail at cut surface.

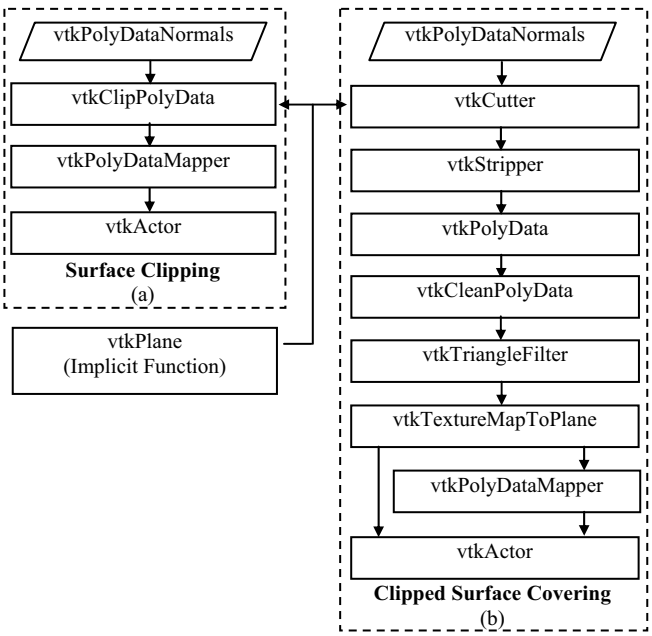


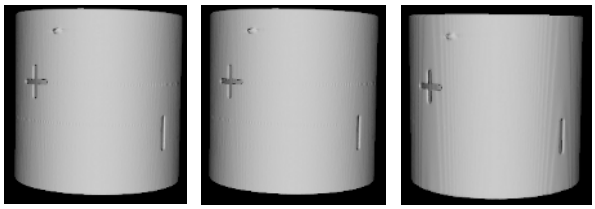
Fig. 3 The 3D Surface Clipping Method: (a) Surface Clipping Process and (b) Clipped Surface Covering

The proposed 3D surface clipping method can be divided into two parts as shown in Figure 3. In the first part, 3D surface clipping is performed by the vtkClipPolyData class, which includes the implicit function of a plane. The position and orientation of the corresponding plane must be defined for clipping. In addition, we use the output of the vtkPolyDataNormals class as an input of the vtkClipPolyData class. Then, the output of vtkClipPolyData is prepared for display by the vtkPolyDataMapper and the vtkActor classes. In the second part, the cut surface is covered by finding the cut edge of 3D surface using the vtkCutter class. The output of this class is poly data; however, it does not contain any points and lines data. Thus, the vtkStripper class is needed for reconstructing points and lines. After that the vtkPolyData class can be applied to create poly data through the SetPoints and SetPolys methods. The result of this step requires the vtkCleanPolyData class for removing unused points and merging duplicated points. The vtkTriangleFilter class is applied to convert the poly data into triangle polygons. These triangle polygons are used as an input to the vtkTextureMapToPlane class for generating texture coordinates by mapping points to a plane. Finally, the output of vtkTextureMaptoPlane class is applied to vtkPolyDataMapper for converting poly data into basic graphic data. To set the texture of actor, we use the SetTexture method of the vtkActor class.

IV. Experiment and Result

A. 3D Surface reconstruction experiment

In this section, we tested on the cone beam CT data of a cylinder phantom. These data contain 324 axial slices. Each slice consists of 400x400 pixels, and the data spacing is 0.4 mm. The proposed process was tested on Java environment, and based on Pentium D CPU 2.80 GHz, 504 MB of RAM, and Intel(R) 82865G Graphics controller. In addition, this study defined the threshold value for reconstructing from 200 to 31692 Hounsfield units (HU) to extract the cylinder and metal areas. We defined the reduction factor (r) of the vtkDecimatePro class to be 0.1, and studied the effect of the computation time on three parameters: the subsampling factors of vtkImageShrink3D class, and the number of iterations (n) and the relaxation factor (σ) of vtkSmoothPolyDataFilter class. The reduction factor is used to reduce the data set. If the reduction factor is set to 0.6, the data set will be reduced 60 percents. The subsampling factors (δ) are defined in three dimensions as x: y: z axes. The number of iterations and the relaxation factor for smoothing polygon mesh will be set to a high value if we want more smoothing. However, we cannot set them too large because the polygon mesh may distort excessively. The effect of these parameters on computation time usages can be shown on the Tables 1-3. Figure 4 shows that the quality of a 3D suface model was not reduced when we little adjusted the reduction factor of the vtkDecimatePro class and smoothing parameters of the vtkSmoothPolyDataFilter as shown in Figure 4(b). However, when we increased the subsampling factors, the quality of the 3D surface model was reduced as appeared in Figure 4 (c).



(a) (b) (c)

Fig. 4 Examples of the quality of the 3D surface model:
(a) δ = 1:1:1(400x400x324), r = 0, n = 1, σ = 0, Time = 33.11 s,
(b) δ = 1:1:1(400x400x324), r = 0.2, n = 3, σ = 0.3, Time = 29.20 s, and
(c) δ = 2:2:2(200x200x162), r = 0.2, n = 3, σ = 0.3, Time 6.65 s.

Table 1 Computation time usages when varying the subsampling factors. (n = 1, σ = 0.01)

Subsampling Factors	Time (s)	Subsampling Factors	Time (s)	Subsampling Factors	Time (s)
1 : 1 : 1 (400x400x324)	33.11	1 : 1 : 2 (400x400x162)	16.30	1 : 2 : 2 (400x200x162)	8.74
2 : 1 : 1 (200x400x324)	23.12	2 : 2 : 1 (200x200x324)	12.05	2 : 2 : 2 (200x200x162)	6.54
1 : 2 : 1 (400x200x324)	21.35	2 : 1 : 2 (200x400x162)	8.86		

Table 2 Computation time usages when varying the number of iterations for smoothing. (δ = 1:1:1 (400x400x324), σ = 0.01)

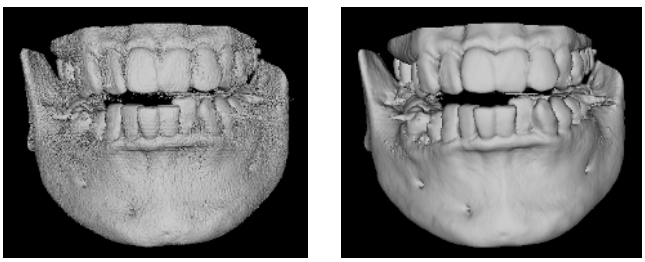
Number of Iteration	Time (s)	Number of Iteration	Time (s)	Number of Iteration	Time (s)
1	33.11	7	33.36	50	38.33
3	35.00	10	31.23	70	40.67
5	36.57	30	35.20		

Table 3 Computation time usages when varying the relaxation factor. (δ = 1:1:1 (400x400x324), n = 1)

Relaxation Factor	Time (s)	Relaxation Factor	Time (s)	Relaxation Factor	Time (s)
0.01	33.11	0.07	26.35	0.5	28.37
0.03	27.29	0.1	25.80	0.7	25.19
0.05	26.24	0.3	25.86	1.00	25.62

Table 1 shows that the time usages of subsampled reconstruction are about two times less than the non-subsampling case when subsampling by two in one direction. With subsampling by a factor of two in two directions, the computation time was about three times faster than the non-subsampling case. Likewise, the time usage of subsampling by a factor of two in all directions was about five times less than the non-subsampling case. Table 2 shows that the computation time usages are increased slightly when we defined the number of iterations to be a large value. The difference of the computation time when varying the relaxation factor in Table 3 is inexplicit.

In addition, we applied the proposed process to reconstruct a 3D surface from another CT volumetric data. It was acquired from Hitachi CB MercuRay CT scanner. These data contain 300 axial slices with the image size of 512x512 pixels, and data spacing of 0.2 mm. We defined the threshold boundary as 200 to 2000 HU, and the 3D surface results are shown in Figure 5. In addition, Table 4 shows the computation time when we adjusted some reconstruction parameters.



(a) (b)

Fig. 5 Examples of the 3D surface model: (a) δ = 1:1:1 (512x512x300), r = 0, n = 1, σ = 0, Time = 67.54 s, (b) δ = 2:2:2 (256x256x150), r = 0.2, n = 3, σ = 0.3, Time = 28.65 s.

Table 4 Computation time usages with different reconstruction parameters.

Subsampling Factors	Reduction Factor of Decimation	Number of Iteration	Relaxation Factor	Time (s)
1 : 1 : 1 (512x512x300)	0.0	1	0.0	67.54
1 : 1 : 1	0.2	3	0.3	96.98
1 : 1 : 1	0.3	3	0.3	106.36
1 : 1 : 1	0.2	5	0.3	106.85
1 : 1 : 1	0.2	5	0.5	106.03
2 : 2 : 2 (256x256x150)	0.2	3	0.3	28.65

Figure 5 (b) shows that the quality of the 3D surface barely differs from the 3D surface reconstructed with the original size (Figure 5 (a)), although we subsampled by two in all directions. In contrast, the computation time of the subsampling case is about two times less than the non-subsampling case. Table 4 shows that the computation time increases when the number of iterations for smoothing is increased, whereas the reduction factor of decimation and the relaxation factor have a little effect on computation time usages.

B. 3D Surface Clipping Result

In this section, we used the 3D surface model acquired from a Hitachi CB MecuRay CT scanner to study the clipping method. We used the subsampling factors of two in all directions. The reduction factor of decimation was 0.2, the number of iterations for smoothing was 3, and the relaxation was 0.3. The results in Figure 6 show that the proposed method can cover the holes that occur on the cut surface.



(a) (b)

Fig. 6 Examples of the 3D Surface Clipping when defining the position and the normal vectors of the clipping plane: (a) position was 0, 0, and 29.79, and normal vector was 0, 0, and 1 (b) position was 44.6, 102.4, and 0, and normal vector was -0.9, -0.3, and 0.

V. Discussion and Conclusion

In this research, we propose a process for reconstructing a 3D surface model from large volumetric image data, and a method for clipping a 3D surface model. All steps are based on the pipeline of VTK. The first experiment shows that the subsampling factors are the main parameters to reduce the computation time while the reduction factor of polygon decimation, the number of iterations for smoothing, and the relaxation factor have little effect. In contrast, the number of iterations will be significant if the polygon mesh has a large size. However, the quality of 3D surface may reduce when increasing the subsampling factors. The second experiment shows that the proposed method achieves the clipping of the 3D surface model without holes at the cut surface. With the proposed processes, reconstructing and clipping the 3D surface model can be implemented on the limited resource.

Acknowledgment

The authors would like to thank the Advanced Dental Technology Center (ADTEC), and the Faculty of Dentistry, Chulalongkorn University for providing CT data.

References

1. Will Schroeder, Ken Martin, and Bill Lorensen. *The Visualization Toolkit: An Object-Oriented Approach to 3D Graphics*. Prentice Hall 2006.
2. John G. Torborg, "A Parallel Processor Architecture for Graphics Arithmetic Operations,"*ACM SIGGRAPH Computer Graphics*, Vol. 21, No. 4, pp. 197-204, July 1987.
3. William E. Lorensen and Harvey E. Cline, "Marching Cubes: A High Resolution 3D Surface Construction Algorithm," *ACM SIGGRAPH Computer Graphics,* Vol. 21, No. 4, pp. 164-169, July 1987.

The Effects of Passive Warm-Up With Ultrasound in Exercise Performance and Muscle Damage

Fu-Shiu Hsieh[1], Yi-Pin Wang[2], T.-W. Lu[3], Ai-Ting Wang[1], Chien-Che Huang[1], Cheng-Che Hsieh[1]

[1]Department of Physical Education and Health, Taipei Physical Education College, Taiwan
[2]Department of Physical Therapy & Rehabilitation, Shin Kong Wu Ho-Su Memorial Hospital
[3]Institute of Biomedical Engineering, National Taiwan University, Taiwan
Web: http://oemal.bme.ntu.edu.tw, Correspondence: Lu, T.-W. E-mail: twl@ntu.edu.tw

Abstract — **Background: Warm-up before exercise could increase blood flow of whole body, increase muscles and skin temperature, prevent injury within exercise. Passive warm-up can increase temperature of muscles as active warm-up do, but it won't cause the muscle fatigue. To use heat packs or to apply ultrasound is the way for passive warm-up. Purpose: To determine the effects of two different modalities of passive warm-up and exercise without warm-up on exercise performance and recovery on muscle damage. Methods: Eight volunteers were participated in this study (age =23.88±5.06 y/o), and all of them were involved into three groups as control group (CON), heat packing group (HP) and ultrasound group (USD). CON never received any warm-up protocol before eccentric exercise, HP received 15 minutes of superficial heat with electrical heat pack before exercise, and USD received 7 minutes of deep heat with ultrasound diathermy before exercise. Each subject processed 30 repeated bouts of eccentric exercise with 80% MVC level. Serum CK, MVC, ROM and CIR were measured before, immediately after exercise and at 2nd, 4th, 7th, and 10th days post-exercise. Results: When measuring serum CK and CIR, there were no significant difference between CON, HP and USD (p>0. 05). When measuring ROM and MVC, there were significant difference between CON, HP and USD (p<0. 05). Conclusion: USD and HP have better muscle strength and performance than CON. According to the recovery procedure, USD took lesser damage on muscles than HP and CON. USD had lesser swelling then HP and CON in recovery stage after exercise.**

Keywords — **Passive warm-up, Muscle damage, Ultrasound**

I. Introduction

Sports injuries are common problems in clinic, especially for muscle damage. [1-7] The clinical features of muscle damage include increased activation of creatine kinase (CK), muscle dysfunction, decreased muscle power, muscle fatigue, decreased range of motion of involved joint, muscle swelling and delayed onset muscle sorenessoccured.[8,9] Many evidences revealed that adequate warm up before exercise, not only decreased muscle damage occurred but also elevated skin and body temperature through increased whole blood volume in athletes, and improve exercise performance .[10-14] There are two types of warm up. Active warm up and passive warm up. Active warm up means use sub maximal intensity before exercise to elevate deep muscle temperature, such as jogging, yoga, swimming. And passive warm up means elevate muscle and core temperature by external modality, without cause energy diminish, such as hot pack, bath or massage. [11,13,15] So it is interesting to discuss that passive warm up could increase blood flow in major muscle group and prevent energy consumption. Hot pack and ultrasound are common heat modalities in clinics, but few studies investigate the recovery effect when apply in muscle damage. The goals of our study are to compare the effect of different heat modality in recovery after muscle damage. And we use swelling of joints, range of motion of joint, muscle swelling and creatine kinase (CK) in blood as indirected makers after eccentric exercise.[16-23]

II. Method

There are 8 physical educational college students involved the study. The mean age was 23.88±5.06. All of them need to accept 3 different intervention, which included control group(CON), ultrasound intervention before eccentric exercise(USD), and hot pack apply before eccentric exercise(HP). The interval between each session was 18 days to make sure total recovery.[24,25] All of the subjects were examined the upper arm circumference of nondominant side(CIR),we measured 4 cm and 8 cm above elbow joint (CIR-4,CIR-8), and maximal voluntary isometric contraction (MVIC) of biceps, active range of motion(AROM) of elbow joint, and blood sample analysis before test. The eccentric exercise mode included that subjects eccentric elbow flexor with 80% load of maximal voluntary isometric contraction of biceps, and repeat 30 times. The contraction time of each eccentric exercise was 5 seconds and the rest interval between each contraction was 45 seconds. [26] Subjects were examined the upper arm circumference of nondominant side, MVIC of biceps, AROM of elbow joint immediately after eccentric exercise, repeat the above measurements and CK analysis on 2nd,4th,7th,10th day after exercise to examined the recovery state after muscle damage.

Chwee Teck Lim, James C.H. Goh (Eds.): ICBME 2008, Proceedings 23, pp. 1149–1152, 2009
www.springerlink.com

III. Result

CK. There were no significant difference between 3 groups at each time (p>0.05)(fig.1), and all the groups showed elevation the concentration of CK after 2nd day post exercise, and peak on 4th day then gradually recovery. CK on 4th day post exercise had significant difference from pre-test in CON and HP groups, but not revealed in USD group.

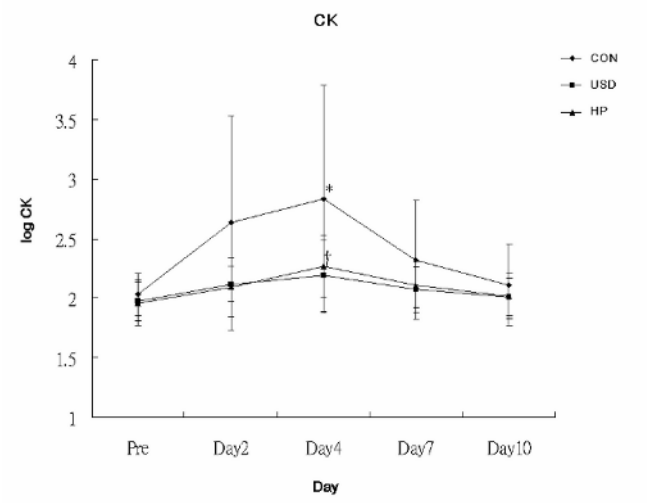


Fig. 1 CK response to eccentric exercise in CON, HP and USD groups. * means significant difference compared with pre-test in CON group ($p < 0.05$), † means significant difference compared with pre-test in HP group ($p < 0.05$)

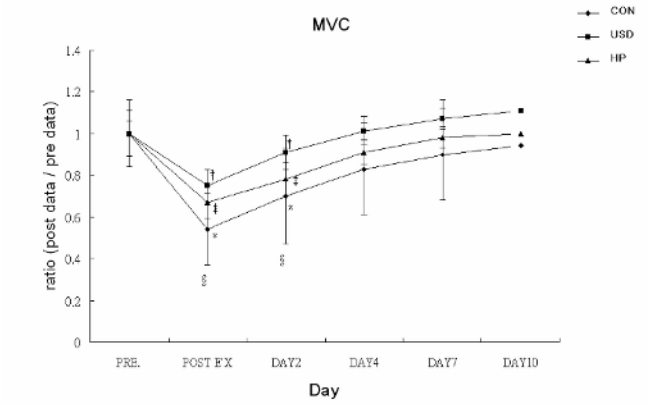


Fig. 2 MVIC response to eccentric exercise in CON, HP and USD groups. * means significant difference compared with pre-test in CON group ($p < 0.05$),† means significant difference compared with pre-test in USD group ($p < 0.05$),‡ means significant difference compared with pre-test in HP group ($p < 0.05$),§means significant difference between CON and USD group ($p < 0.05$).

MVIC. It sowed significant less MVIC post exercise in 3 groups ($p < 0.05$) (fig.2), especially in CON group, and less in USD group. It recovered after 2nd day post exercise, but had significant difference from pre-test. The MVIC of USD showed significant higher than CON group at post exercise immediately and 2nd day after exercise.

ROM of elbow joint. All the groups showed significant decrease after eccentric exercise ($p < 0.05$) (fig.3), especially the CON group. USD and HP groups showed significant decrease after eccentric exercise only on 2nd day post exercise. There were significant difference between USD and the other two groups on 2nd,4th,7th,10th day.

CIR. There were no significant difference between CON, USD and HP group at each measurement in upper arm proximal part, and all the groups showed significant increase after eccentric exercise even on 2nd day post-exercise. Only CON group had significant swelling persist on 4th day post-exercise (fig.4). In the distal part, it revealed significant swelling on 4th day post-exercise in CON and HP groups (fig.5).

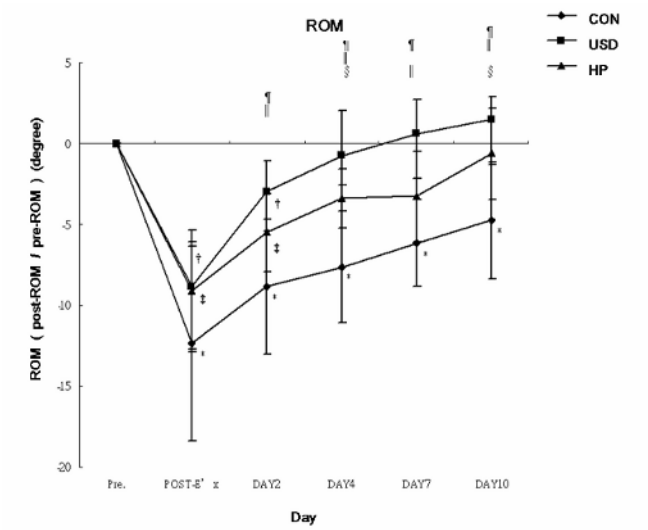


Fig. 3 ROM response to eccentric exercise in CON, HP and USD groups. * means significant difference compared with pre-test in CON group ($p < 0.05$),† means significant difference compared with pre-test in USD group ($p < 0.05$),‡ means significant difference compared with pre-test in HP group ($p < 0.05$) , §means significant difference between CON and USD group ($p < 0.05$),¶ means significant difference between USD and HP group ($p < 0.05$).

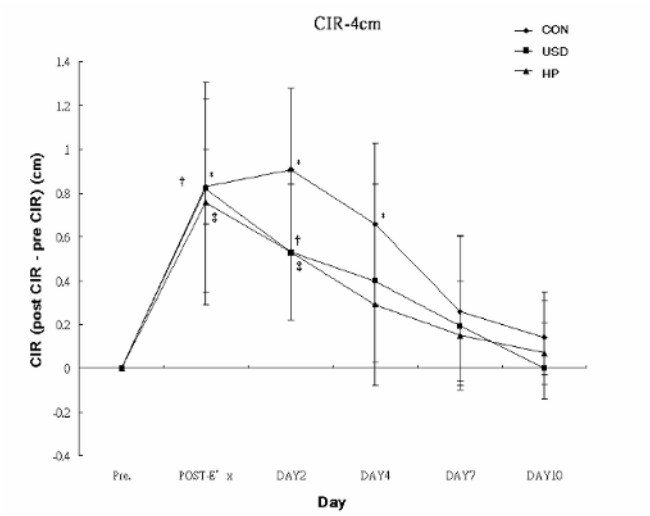


Fig. 4 CIR-4 response to eccentric exercise in CON, HP and USD groups. * means significant difference compared with pre-test in CON group ($p < 0.05$),† means significant difference compared with pre-test in USD group ($p < 0.05$), ‡ means significant difference compared with pre-test in HP group ($p < 0.05$).

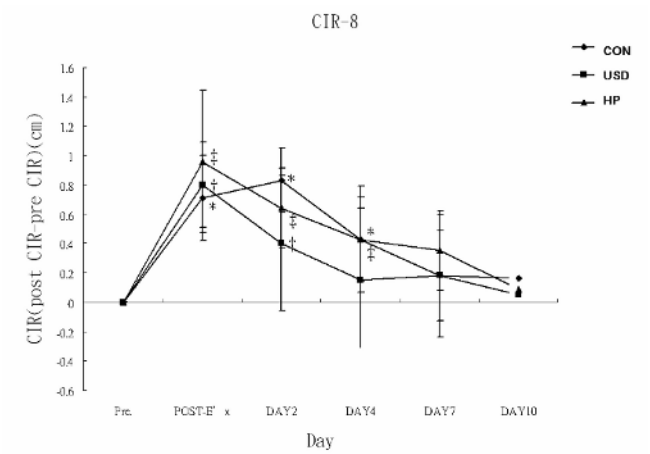


Fig. 5 CIR-8 response to eccentric exercise in CON, HP and USD groups. 。* means significant difference compared with pre-test in CON group ($p < 0.05$),† means significant difference compared with pre-test in USD group ($p < 0.05$),‡ means significant difference compared with pre-test in HP group ($p < 0.05$).

IV. Discussion

USD showed significant effect in decrease muscle damage and improve muscle recovery. In our study, CK data revealed that USD applied before exercise could decrease muscle damage, but there were no significant difference between all three groups. We hypothesized that the reason was due to insufficient work load. Some studies used the mode of 100% MVIC and repeat for 12 times could lead muscle damage, [25,29] but 80% MVIC and repeat for 30 times in our study didn't show the result. Further study is needed to make sure how intensive eccentric exercise program will induce muscle damage. USD and HP groups showed better recovery after eccentric exercise, and it means that passive warm up before exercise could less muscle damage from exercise. Though some authors compared the effect of microwave with coldpack, and found no difference between each other. The effect of hot mechanism before exercise still be doubted.[17,29,30] More study could focus on local blood flow change after passive warm up and find the link between temperature and muscle damage. In our study we found that there were no difference persist in three conditions, and it was different from other studies. The reason may be due to insufficient precise tool to exam. The Dopplar ultrasound maybe need to consider to detail detect microchange in cross section of muscle fiber in future study.[31,32]

V. Conclusion

USD and HP have better effect than CON. According to the recovery procedure, USD took lesser damage and swelling than HP and CON in recovery stage after exercise.

References

1. Wood K, Bishop P, Jones E. Warm-up and stretching in the prevention of muscular injury. Sports Med 2007;37:1089-99.
2. Brown S, Day S, Donnelly A. Indirect evidence of human skeletal muscle damage and collagen breakdown after eccentric muscle action. J Sports Sci 1999;17:397-402.
3. Newham DJ, Mcphail G, Mills KR, Edwards RHT. Ultrastructural changes after concentric and eccentric contractions of human muscle. J Neurol 1983;61:109-22.
4. Clarkson PM. Eccentric exercise and muscle damage. Int J Sports Med 1997; 10: S314-7.
5. Evans RK, Knight KL, Draper DO. Effects of warm-up before eccentric exercise on indirect markers of muscle damage. Med Sci Sports Exerc 2002;34:1892-9.
6. Sorichter S, Puschendorf B, Mair J. Skeletal muscle injury induced by eccentric muscle action: muscle proteins as markers of muscle fiber injury. Exerc Immunol Rev 1999;5:5-21.
7. Symons TB, Clasey JL, Gater DR, Yates JW. Effects of deep heat as a preventative mechanism on delay onset muscle soreness. J Strength Cond Res 2004;18:155-61.
8. Sayers SP, Clarkson PM, Rouzier PA, Kamen G. Adverse events associated with eccentric exercise protocols: six case studies. Med Sci Sports Exerc 1999;31:1697-702.
9. Kasper CE, Talbot LA, Gaines JM. Skeletal muscle damage and recovery. AACN Clin Issues 2002;13:237-47.

10. Bishop D. Warm up I: potential mechanisms and the effects of passive warm up on exercise performance. Sports Med 2003a;33:439-54.
11. Bishop D. Warm up II: performance changes following active warm up and how to structure the warm up. Sports Med 2003b;33:483-98.
12. Hajoglou A, Foster C, De Koning JJ, Lucia A, Kernozek TW, Porcari JP. Effect of warm-up on cycle time trial performance. Med Sci Sports Exerc 2005;37:1608-14.
13. Shellock FG, Prentice WE. Warming-up and stretching for improved physical performance and prevention of sports-related injuries. Sports Med 1985;2:267-78.
14. Stewart IB, Sleivert GG. The effect of warm-up intensity on range of motion and anaerobic performance. J Orthop Sports Phys Ther 1998;27:154-61.
15. Reisman S, Walsh LD, Proske U. Warm-up stretches reduce sensations of stiffness and soreness after eccentric exercise. Med Sci Sports Exerc 2005;37:929-36.
16. Lin YH. Effects of thermal therapy in improving the passive range of knee motion: comparison of cold and superficial heat applications. Clin Rehabil 2003;17:618-23.
17. Rennie GA, Michlovitz SL. Thermal agents in rehabilitation (3rd ed.). Philadelphia, PA: FA. Davis;1996.
18. Laufer Y, Zilberman R, Porat R, Nahir AM. Effect of pulsed shortwave diathermy on pain and function of subjects with osteoarthritis of the knee: a placebo-controlled double-blind clinical trial**.** Clin Rehabil 2005;19:255-63.
19. Gray S, Nimmo M. Effects of active, passive, or no warm-up on metabolism and performance during high-intensity exercise. J Sports Sci 2001;19:693-700.
20. Knight CA, Rutledge CR, Cox ME. Effect of superficial heat, deep heat, and active exercise warm-up on the extensibility of the plantar flexors. Phys Ther 2001;81:1206-14.
21. Rodenburg JB, Steenbeek D, Schiereck P, Bär PR. Warm-up, stretching and massage diminish harmful effects of eccentric exercise. Int J Sports Med 1994;15:414-9.
22. Clarkson PM, Hubal MJ. Exercise-induced muscle damage in humans. Am J Phys Med Rehabil 2002;81:S52-69.
23. Lee J, Goldfarb AH, Rescino MH, Hegde S, Patrick S, Apperson K. Eccentric exercise effect on blood oxidative-stress markers and delayed onset of muscle soreness. Med Sci Sports Exerc 2002;34:443-8.
24. Brown S, Day S, Donnelly A. Indirect evidence of human skeletal muscle damage and collagen breakdown after eccentric muscle action. J Sports Sci 1999;17: 397-402.
25. Nosaka K, Clarkson PM. Influence of previous concentric exercise on eccentric exercise-induced muscle damage. J Sports Sci 1997;15:477-83.
26. Nosaka K, Newton M, Sacco P. Muscle damage and soreness after endurance exercise of the elbow flexors. Med Sci Sports Exerc 2002;34:920-7.
27. Clarkson PM, Byrnes WC, McCormick KM, Turcotte LP, White JS. Muscle soreness and serum creatine kinase activity following isometric, eccentric, and concentric exercise. Int J Sports Med 1986;7:152-5.
28. Wu AH, Perryman MB. Clinical applications of muscle enzymes and proteins. Curr Opin Rheumatol 1992;4:815-20.
29. Nosaka K, Sakamoto K. Influence of pre-exercise muscle temperature on responses to eccentric exercise. J Athl Train 2004;39:132-7.
30. Michlovitz SL. Thermal agents in rehabilitation (3rd ed.). Philadelphia, PA: FA. Davis; 1996.
31. Clarkson PM, Sayers SP. Etiology of exercise-induced muscle damage. Can J Appl Physiol 1999;24:234-48.
32. Mair J, Koller A. Effects of exercise on plasma myosin heavy chain fragments and MRI of skeletal muscle. J Appl Physiol 1992;72:656-63.

Author: Lu, T.-W.
Institute: Institute of Biomedical Engineering, National Taiwan University, Taiwan
Street: No. 1, Sec. 4, Roosevelt Road
City: Taipei
Country: Taiwan (R.O.C.)
Email: twl@ntu.edu.tw

Capacitive Interfaces for Navigation of Electric Powered Wheelchairs

K. Kaneswaran and K. Arshak

Department of Computer and Electronic Engineering, University of Limerick, Limerick, Ireland

Abstract — **This paper presents the design of capacitive interfaces, developed on standard printed-circuit boards, which allow persons with muscular weakness the ability to navigate an electric powered wheelchair by small finger movements. The goal was to develop a high-quality and reliable capacitive-sensor interface that was easy to use, met ergonomic requirements and reduced the mobility requirements needed by that of a standard joystick user. Usability and acceptability criteria were also considered. An Assistive Device Platform was also developed to allow the sensors to interface to a wheelchair platform. The sensors were connected to the platform through an I^2C connection. The platform can also accommodate for other sensors such as accelerometers and switch interfaces requiring digital interfaces such as SPI, parallel and serial connections thus accommodating for a wider range of motor disabilities. The platform has been tested by able and non-able bodied users.**

Keywords — **Assistive Technology Device, Electric Powered Wheelchair, Capacitive Sensors, Joystick, Electric field sensing.**

I. Introduction

The successful integration of capacitive touch sensors into everyday consumer products, e.g. mobile phones, has led to improved user interfaces and aesthetic look of the products. Although these new intuitive interfaces have been designed for a mass portable device market their non mechanical nature may have more relevant use in Assistive Technology Devices (ATD).

As a standard, a power wheelchair system is normally supplied with a master joystick. For persons with severe immobility and conditions which limit range of movement the use of a joystick to control navigation of a powered wheelchair may not be possible. In this case a secondary joystick is provided and usually consists of a sip-and-puff, chin or a head control device. However, a clinical survey in 2000 [1] of 200 practicing clinicians in the U.S presented that 40% of patients who used the secondary joysticks found steering and maneuvering tasks difficult or impossible. The paper outlined the requirement for more "independent mobility controllers"; controllers which allow even the most severely immobile person the ability to navigate a powered wheelchair. The Assistive Device Platform (ADP) together with the use of capacitive sensors is designed to alleviate some of the problems associated with the use of secondary joysticks by making them easier to use, non mechanical in nature and aesthetically more pleasing. The current state of the art device, the VIC-CCD [1], uses a mixture of capacitive technology and infrared sensing. The problems found with infrared sensing is that strong sunlight can affect the CCD elements. This problem is rectified by using capacitive based touch pads. This paper outlines the design of the ADP for use with printed circuit board (PCB) based capacitive sensors and their application to Assistive Technology Devices (ADT).

II. Assistive device platform design

A. Microcontroller and Wheelchair interface

The ADP is based around the ADuC842 microprocessor [3], which boasts a plethora of peripheral support allowing us to interface a wide range of sensors to the system. Some of the common on-chip interfaces are UART, $I^2C^{©}$, SPI I/O, an 8 channel 12 bit 420 kSPS ADC, two 12 bit DAC's, two PWM sigma delta DAC's, three 8-bit bi-directional digital ports and one 8-bit digital input port.The microcontroller is an optimized 8052 core offering up to 20 MIPS peak performance. Three different memory options are available offering up to 62 kBytes of nonvolatile Flash/EE program memory. Four kBytes of nonvolatile Flash/EE data memory, 256 bytes RAM, and 2 kBytes of extended RAM are also integrated on-chip. The on chip data retention allows code to run from internal memory without the need for an external memory IC reducing board size and power consumption. A unique feature of the ADuC842 is that it allows both the I^2C and SPI bus access simultaneously. The Analog Device range of Capacitive Sensing IC's gives the option of I^2C or SPI interface. This makes the system more versatile as the code can be included for both interface types allowing several devices to be run simultaneously.

A main component of the Assistive Device Platform is the General Purpose SLIO Board (GPSB), figure 1. This is an interface board which allows us to connect to the Wheelchair controller unit on almost all Dynamic Ltd controller powered wheelchairs. The GPSB allows the designer to control the wheelchair by use of four analog channels two of which are direction channels and two mirror channels.

Chwee Teck Lim, James C.H. Goh (Eds.): ICBME 2008, Proceedings 23, pp. 1153–1157, 2009
www.springerlink.com

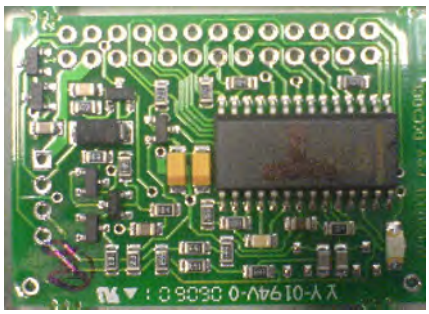
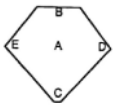


Figure 1: General Purpose SLIO Board (GPSB).

The four channels must be used in a dual decode format with all voltages with respect to half rail for correct interface. Table 1 outlines the dual decode voltage specification. The voltage speed mirrors are used for error control, when a change in voltage occurs on the directional channel a corresponding voltage change occurs on the mirror channel. The mirror voltage changes in proportion by 5 - 10% of the direction value voltage. The voltage speed mirror value never exceeds ±.17 of the half rail voltage value.

Table 1: Voltage Specifications Dual Decode.

	Stick Position		V_{DIR}	V_{SPD}	V_{DIR}	V_{SPD}
	A	0°	0	±.05	0	±.05
	B	17.5°	1.3	±.06	0	±.16
	C	-20°	-1.5	±.16	0	±.16
	D	20°	0	±.17	1.5	±.17
	E	20°	0	±.17	-1.5	±.16

All voltages are with respect to mid rail.

Under fault conditions, for example due to a short on the directional or speed mirror channels, the GPSB will detect a direction channel and mirror channel mismatch and issue a speed mirror fault to the DX© Controller stopping the wheelchair motor system. However the wheelchair will operate without the use of the speed mirror channels. If the speed mirror channels are not used they should be tied to the mid-rail voltage as with the current assistive device platform.

The ADuC842 has two 12 bit DACs and two PWM sigma delta DAC's. The first two DAC's are used to control the motion of the wheelchair; the second two DAC's can be used to generate the speed mirror faults but are not implemented in the current design. The output of the DAC's are buffered through op-amps and connected to a resistor network before connection to the GPSB. The resistor network reduces the current input and gain of the signal to the GPSB keeping the output range of a dual decode joystick between .05v and 4.5 volts. This is the recommended connection method for any dual decode joystick.

Power is supplied to the ADP by the GPSB which has the ability to supply a 20mA regulated or 200mA unregulated source for the remote joystick design. The ADP uses a 5v regulator connected to the SB+D output of the GPSB to supply power for the microprocessor, serial output port interface circuitry and capacitive IC's. The diagram in figure 2 depicts the typical configuration of the master and secondary joysticks for DX© controlled wheelchairs.

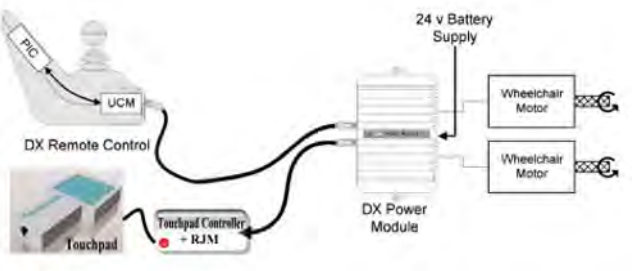


Figure 2: Prototype System.

B. Capacitive based sensors for touch control

Three touchpad designs were developed for use with the ADP and were based around the new range of Analog Devices Capacitive to Digital IC's. The AD7142 [3] was chosen for our first design but later upgraded to the AD7147 [4]. The main difference between the two is that the AD7142 required a transmit electrode to create an electric field that the receiver electrodes could detect. The AD7147 however used a single electrode to create transmit and sense the electric field. This simplified board design and reduced the pin count and size of the IC.

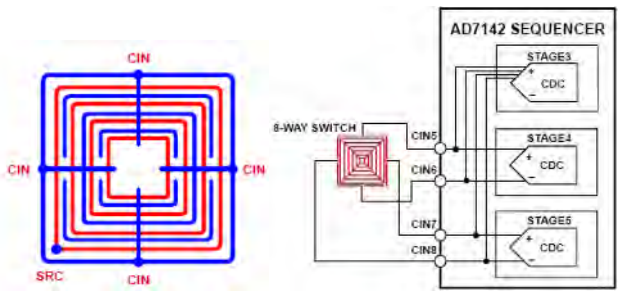


Figure 3: 8-way Switch and connections.

Figure 3 shows the use of the AD7142 to create a simple 8 point switch. It requires the use of 4 sensors each pair connected differentially, this way there can never be a false touch as the response of the system can only be from two of the sensors. This sensor type can have dimensions ranging

from 8 mm square up to 15 mm square, and requires four inputs to the AD7142. The 8-way switch gives eight positional outputs: north, south, east and west, as well as the diagonal positions: northeast, southeast, southwest, and northwest. Users move their finger in a gliding motion around the 8-way switch to change the output position. The 8-way switch is constructed from four virtual 'buttons' that are routed in an intertwined fashion. The top and bottom buttons are connected internally in the AD7142 to a CDC (Capacitance to Digital Converter) as a differential pair, as is the left and right buttons. The connections for the 8-way switch are shown in Figure 3. The 8-way switch also requires an activation measurement; this measurement detects if the 8-way switch is active before determining the direction of movement. The measurement requires a connection to the sequencer of the AD7142, as shown in Figure 3, Stage 3. The inputs from all four elements of the 8-way switch sensor sum together at the positive CDC input to determine if the sensor is active. When the user activates the 8-way switch in any direction, status bits in the status registers are set. The ADP can read back data from the AD7142 to determine which status bits are set. Four status bits on the AD7142 are used to determine all eight positions from the 8-way switch. To make the sensor interface mimic a proportional joystick the values of stage 4 and stage 5 CDC outputs are scaled accordingly and limited to the maximum input range of the Wheelchair interface hardware. The sensor board was connected to the ADP using I^2C connections.

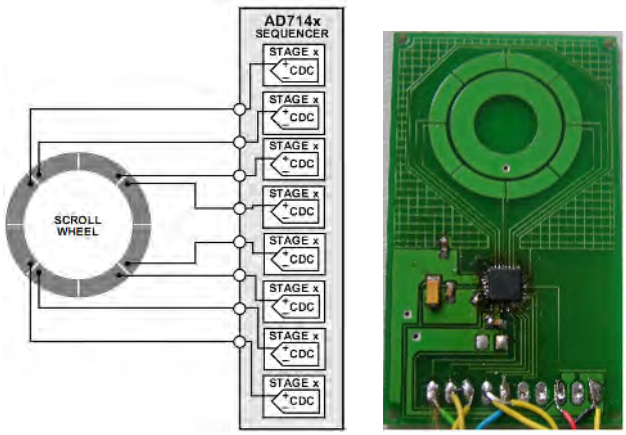


Figure 4: Scroll wheel connections and prototype PCB.

The second design the AD7142 as a scroll-wheel device much like that of the IPod. This required that 8 segments were connected to the AD7142 inputs and internally to 8 positive CDC inputs as shown in Figure 4. An algorithm supplied by Analog Devices was used to determine the finger position on the pad. The algorithm read 8 stages from the CDC sequencer and used these values to determine whether the persons finger was scrolling, the position on the scroll wheel, whether there were one or two fingers being used, and gave a switch output if the finger was stationary in either up, down, left or right positions. The algorithm results were found by reading the status of a 16 bit register, table 2, containing the positional information. The switch output was used to drive the wheelchair while the scroll status was used to change the profiles on the DX Controller. The sensor board was connected to the ADP using I^2C connections.

Table 2: Status Register for Scroll-wheel

Status Bits 15 - 8							Position 8 bits		
Activation	Tapping	Go up	Go Down	Touch Error	Touch Error	Not used	Bit7	<->	Bit0

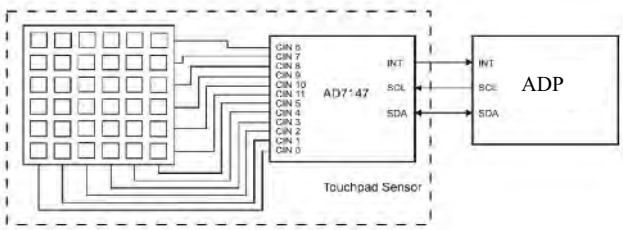


Figure 5: Touchpad connections.

The final sensor interface design was a 23mm x 23mm touchpad. The AD7147 IC was used as it was smaller, required less external components and used single electrode sensors to detect electric field disturbances. Fig 5 shows the connections for the touchpad, while figure 6 shows the actual touchpad used for testing. The touchpad requires 12 connections, 6 for the x-axis and 6 for the y axis, each con-

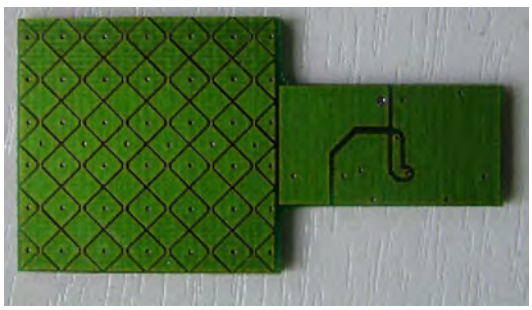


Figure 6: 23mm x 23mm Touchpad PCB design.

nected to a positive input of the CDC per stage using a total of 12 stages. After the ADP reads the 12 stages from the AD7147 the algorithm produces four 16 bit registers containing positional and status information

The status of the register can is decoded using Table 3.The extra functionality is exploited by using the tap function to increase and decrease the profile number of the DX© Controller. A tap in the upper quadrant raises the profile number while a tap in the lower quadrant decreases the profile number.

Table 3: Status Registers for 23mm x 23mm touchpad.

Bit	Register 0	Register 1	Register 2	Register 3
15	Active	Active	Not used	Not used
14	Tap	Tap	Not used	Not used
13	Go Left	Go Up	Not used	Not used
12	Go Right	Go Down	Not used	Not used
11	2 Fingers	2 Fingers	Not used	Not used
10	Large finger	Large finger	Not used	Not used
9	Touch error	Touch error	Not used	Not used
8	Touch error	Touch error	Not used	Not used
7	8 bit position	8 bit position	8 bit position	8 bit position
↓	↓	↓	↓	↓
0	Range 0 -199	Range 0 -199	Range 0 -127	Range 0-127

C. DAC Output.

The DAC outputs on the ADuC842 control the motor on the wheelchair by sending voltages to the GPSB in proportion to the movement of the user's finger across each of the touch pad designs. The range that the GPSB will accept before issuing a fault is between .05v and 4.5v. The DAC output can be set to either 8 or 12 bit. By using 8 bit we can reduce the number of calculations needed to scale the final voltage output and also issue an update to DAC in one write operation.

III. Experiment

For each sensor a user was seated in an Invacare Cruiser Plus wheelchair with the ADP connected as a secondary joystick. The DX© Controller was reprogrammed to accept the secondary joystick on the three lower profiles each programmed to control the motors at different proportions to full speed. Profile one allowed a maximum speed of 40% of the max value, profile 2 was set to 50% while profile 3 was set to 60%. The user was then asked to navigate the electric powered wheelchair using the three different profiles around a room full of obstacles such as bollards, tables and chairs.

IV. Results

Through general discussion and visual inspection it was clear to see that the users found it easier to drive the wheelchair with the proportional systems, 8 way switch and touchpad. The users found that there was no necessity for the scroll-wheel on the second design unless they were in need of controlling an environmental unit or detailed menu system much like it was designed for in MP3 players. The size and shape of these touch controllers in general were a major improvement over the VIC-CCD controller as users found it bulky and cumbersome affecting their mental attitudes and willing to accept it as an assistive device. All users were successfully able to change from profile to profile on each design. Some found the touchpad design to be more responsive than a commercial joystick with respect to obstacle avoidance as the smaller finger movements could be completed quicker than a wrist movement when pushing a joystick.

Furthermore, the ability to attach a small metal rod to any moveable part of the body meant the wheelchair could be controlled by any moveable limb expanding the range of users who can avail of this device. The touchpad design was also controlled by use of the tongue.

V. Conclusion

This paper demonstrates how technology already available can be used to improve accessibility and independence for persons with severe immobility. The paper outlines several designs than can be used to control navigation of an electric powered wheelchair. However, further testing is scheduled before the ADP platform and capacitive sensors can be used to control a wheelchair system on a day to day basis.

Acknowledgements

The authors would like to acknowledge and thank the following suppliers: Dynamic Europe Ltd, Stonebridge Cross Business Park, Droitwich, UK and Analog Devices, Raheen Industrial Estate, Limerick, Ireland. This research has been carried out under the Enterprise Ireland Commercialization Fund

REFERENCES

1. M. W. E. L. Linda Fehr, Phd;Steve B.Skaar,Phd, "Adequacy of power wheelchair control interfaces for persons with severe disabilities: A clinical survey," Journal of Rehabilitation Research and Development, vol. 37, pp. 353 - 360, 2000
2. VIC-CCD Finger Controller, http://www.hmc-products.com/fileadmi
3. n/products/inputdevices/0002-8001a-0201b.pdf
4. Analog Devices, ADuC842 Datasheet, http://www.analog.com/en/
5. analog-microcontrollers/ ADUC842/products/product.html.
6. Analog Devices, ADuC842 Datasheet, http://www.analog.com/en/
7. analog-to-digital-converters/capacitance-to-digital-converters/ad7142/products/product.html
8. Analog Devices, ADuC842 Datasheet, http://www.analog.com/en/
9. analog-to-digital-converters/capacitance-to-digital-converters/ad7147/products/product.html

Author: Kelly Kaneswaran
Institute: University of Limerick
Street: Limerick
City: Limerick
Country: Ireland
Email: Kelly.kaneswaran@ul.ie

Health Care and Medical Implanted Communications Service

K. Yekeh Yazdandoost and R. Kohno

Medical ICT Institute, National Institute of Information and Communications Technology, Yokosuka, Japan

Abstract — **The medicine day by day and more and more is associated with and reliant upon concepts and advances of electronics and electromagnetics. Numerous medical devices are implanted in the body for medical use. Tissue implanted devices are of great interest for wireless medical applications due to the promising of different clinical usage to promote a patient independence. It can be used in hospitals, health care facilities and home to transmit patient measurement data, such as pulse and respiration rates to a nearby receiver, permitting greater patient mobility and increased comfort. As this service permits to remote monitoring of several patients simultaneously it could also potentially decrease health care costs. Advancement in radio frequency communications and miniaturization of bioelectronics are supporting medical implant applications. This paper discusses the issues related to health care via Medical Implanted Communications Service (MICS) and presents guidelines for addressing these issues.**

Keywords — **Implant medical device, in-body radio communications, electromagnetic wave, thermal effect, security and privacy.**

I. Introduction

The use of implantable wireless communication device is growing at a remarkable rate for human medical and clinical applications such as cardiac pacemaker, blood glucose sensing, pain management and epileptic seizures, because the Medical Implant Communications Service (MICS) is replacing inductive communication for radio frequency implanted device. Therefore everybody can benefits of the best healthcare service irrespective of their geographic location.

Implantable medical devices have a history of great success in the treatment of many diseases, such as heart diseases and neurological disorders. Pacemakers are the oldest and most successful example of implantable medical device. Today's aging population is driving wide scale demand for more advanced healthcare treatments, including wireless implant devices that can deliver ongoing and cost effective monitoring of a patient's condition.

Using MICS, a healthcare provider can set up a wireless link between an implanted device and a base station, allowing physicians to establish high-speed, easy-to-use, reliable, short-range access to the patient health data in real-time. Innovation in wireless communications aligned with the MICS band of frequencies is fueling the growth. The frequency band for MICS operations is 402-405 MHz [1], [2].

From a regulatory viewpoint, the establishment of the MICS band began in the mid 1990s when Medtronic petitioned the Federal Communication Commission (FCC) to allocate spectrum dedicated to medical implant use. After gaining wider industry support, the 402–405 MHz MICS band was recommended for allocation by International Telecommunication Union Radiocommunication Sector Recommendation (ITU-R) SA1346 in 1998. The FCC established the band in 1999, and similar standards followed in Europe. The common standards will eventually allow patients with implantable devices to obtain care worldwide.

Recognizing the level of international support for the use of MICS, international travel of patients fitted with MICS devices should not pose any problem.

The IEEE 802.15 WPAN Task Group 6 (TG6) was formed with the charter of drafting a standard for Body Area Network (BAN) [3]. There are more than 25 companies, including R&D centers and universities from around the world. According to the IEEE 802.15.TG6 group, there is a need for a communication standard optimized for low-power devices and operation on, in or around the human body to serve a variety of applications including medical, consumer electronics and personal entertainment. What is unique in this wireless standard is the presence of a body, which impacts the radio frequency channel model.

The growing complexity of implant devices has led to the need to transfer greater amounts of data during a communications session; the use of MICS devices with bandwidth up to 300 KHz can support these and future development. A typical communications distance for a MICS device is intended to be around 2 meters, allowing greater patient mobility during communications sessions.

Implanted medical devices are usually driven by two primary requirements. First, it must consume very little power so that they can last on battery power for a long period of time. Second, Implanted medical devicess must often be added to other low-cost, small-sized components such as sensors. This consideration requires that MICS radios be low cost, have a simple design.

The design of implanted medical devices is challenged by the following basic requirements:

- Low power consumption

Chwee Teck Lim, James C.H. Goh (Eds.): ICBME 2008, Proceedings 23, pp. 1158–1161, 2009
www.springerlink.com

- Form factor
- Thermal effect
- Antenna and body loss
- Reasonable data rate
- High reliability
- Security

The above challenges are more crucial when to know that, between 1990 and 2002, over 2.6 million pacemakers and implantable cardioverter defibrillators were implanted in patients in the United States [4].

II. Wireless communications

The use of implanted medical devices is not without many significant challenges, particularly, the increasing of propagation losses in biological tissue. Therefore, to ensure the efficient performance of body implanted wireless communication the channel model need to be characterized and modeled for reliable communication system with respect to environment and antenna.

An important step in the development of a wireless MICS is the characterization of the electromagnetic wave propagation from devices that are inside the human body. The complexity of the human tissues structure and body shape make it difficult to drive a simple path loss model for MICS. As the antennas for MICS applications are placed inside the body, the MICS channel model needs to take into account the influence of the body on the radio propagation.

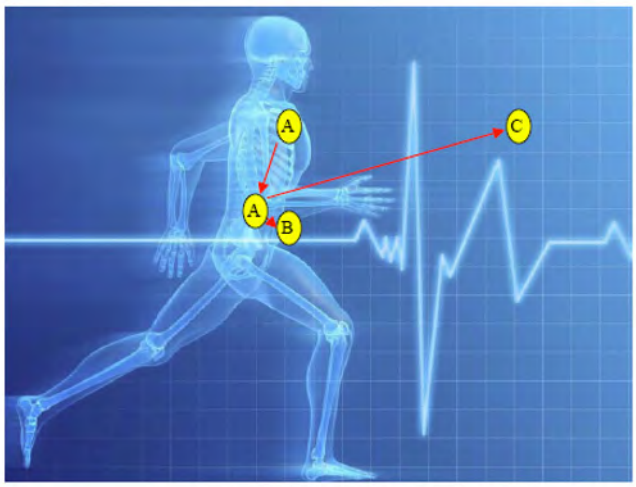


Fig. 1 Possible communication links for medical implanted devices

For wireless communication inside the human body, the tissue medium acts as a channel through which the information is sent as electromagnetic radio frequency waves. A propagation model is necessary to determine the losses involved in the form of absorption of electromagnetic wave power by the tissue. Absorption of electromagnetic waves by the tissues, which consists of mostly water, accounts for a major portion of the propagation loss.

Fig. 1 shows possible communication links for medical implanted communications service; implanted device to the implanted device (A to A), implanted device to the body surface (A to B), and implanted device to 2 meters a way from the body (A to C).

Indeed, the need for small sized antennas and RF front ends with compromising performance has emerged as a key driver in implanted medical wireless devices.

III. Body tissues and radio frequency

Understanding the human body's effect on RF wave propagation is complicated by the fact that the body consists of components that each offer different degrees, and in some cases different types, of RF interaction. The liquid nature of most body structures gives a degree of RF attenuation, whereas, the skeletal structure introduces wave diffraction and refraction at certain frequencies.

The human body is not an ideal medium for radio frequency wave transmitting. It is partially conductive and consists of materials of different dielectric constants, thickness, and characteristic impedance. Therefore depending on the frequency of operation, the human body can lead to high losses caused by power absorption, central frequency shift, and radiation pattern destruction. The absorption effects vary in magnitude with both frequency of applied field and the characteristics of the tissue, which is largely based on water and ionic content. It is very difficult to determine the absorption of electromagnetic power radiated from an implanted source by the human body. Although quite a few investigation has been done to determine the effect of human body on radiated field [5], [6], and almost all of these studies have been based on external sources.

When the wavelength of a signal is significantly larger than the cross-section of the human body being penetrated, there is very little effect of human body on the signal. These wavelengths occur at frequencies below 4 MHz. Above 4 MHz the absorption of RF energy increases and the human body may be considered to be essentially dense until roughly 1 GHz when the dielectric properties of the human body begin to introduce a scattering effect on the RF signal.

Table 1 shows the electrical properties of muscle, fat, and skin at frequency of 403.5 MHz [7]-[9]. Where ε is the

dielectric constant, σ is the conductivity, δ is the penetration depth.

Table 1 Electrical properties of the body tissues at 403.5 MHz

Tissue	ε	σ[S/m]	δ[m]
Muscle	57.1	0.7972	0.0525
Fat	5.5783	0.0411	0.3085
Skin	46.7060	0.6895	0.0551

IV. Thermal effects

The heating effect of microwave destroys living tissue when the temperature of the tissue exceeds 43^o C. Accordingly; exposure to intense microwaves in excess of 20 mW/cm2 of body surface is harmful.

For the safety reason of human body to the radiation, in-body radiation is restricted to certain level. There is a relatively extensive body of published literature concerning the biological effects of RF radiation. The FCC regulations limit the Maximum Permissible Exposure (MPE) to non-ionizing radiation based on the amount of temperature rise that will occur. The regulation limits the temperature rise to 1 degree of Celsius. This limit is being determined by the specific heat of the tissue. The IEEE C95.1 [10] defines that the body exposure to radiation from implanted medical device is considered as partial body exposure in an uncontrolled environment. In such a case, the general provisions of the standard should not be violated, which is whole-body averaged SAR during localized exposure. The limits for partial body exposure are specified in terms of maximum limits on the Specific Absorption Rate (SAR). The average SAR over the whole body is to be lower than 0.08 W/Kg and the spatial peak value of the average SAR over any 1 g of tissue (define as a tissue volume in the shape of cube) is to be less than 1.6 W/Kg. The spatial peak SAR shall not exceed 4 W/Kg over any 10 g of tissue in wrists, ankle, hands and feet. The relationship between radiation and SAR is given by

$$SAR = \frac{\sigma |E|^2}{\rho} \quad (W / Kg) \tag{1}$$

where σ is the electrical conductivity of the tissue, E is the induced electric field, and ρ is the density of tissue. Experiments show exposure to an SAR of 8 W/Kg in any gram of tissue in the head or torso for 15 min may have a significant risk of tissue damage [11].

V. Low power consumption

For a long-term implantable device, minimizing the device power consumption is the most critical requirement. For an implant device with a desired battery life of seven to 10 years, every joule of energy must be carefully conserved. Power consumption determines the life of the implant as well as the battery size. The battery can be the largest component in a medical device where a minimal device size is another critical requirement.

Energy is largely consumed during data transmission. The transceiver's output power amplifier must be capable of broadcasting data relatively quickly over a reasonable distance. The smaller the transmission range and the slower the data can be sent, the lower the power consumption. Furthermore, the tiny antennas used in an implanted device are inefficient, requiring a further boost in power. And, as noted earlier, the human body is a good attenuator of an electromagnetic signal.

Fortunately, implant transmissions are usually infrequent, so MICS-band transceivers squeeze power savings by turning off as many circuits as possible. An obvious approach to saving power is to keep the power-hungry transmitter circuits powered off when not required. Most radio circuits are designed to operate in a receive mode when not transmitting, both because the radio is constantly looking for an asynchronous transmit request and because the receiver circuits generally consume less power.

A more effective technique is to periodically power-down the receiver circuits to conserve additional power. The trick is to periodically wake the receiver up to check for an asynchronous transmit request. The power-up timing must be done quickly enough to catch the transmitted message with just enough time left to acquire the portion of the message containing the information.

VI. Security and privacy risk

Wireless technology gives many benefits but these may come with unanticipated risks. The patient's private medical information stored on pacemakers or implantable cardiac defibrillators could be extracted and their devices reprogrammed without the patient's authorization or knowledge.

Security typically involves protecting data and protecting the network from pinching or destruction. Protecting data ensures that it arrives at the destination as it was transmitted and that no other entity was able to receive and decode the data. Protecting the network ensures that external attacks do not adversely affect network performance [12].

Implantable medical device such as pacemakers and implantable cardiac defibrillators can save lives and greatly

improve a patient's quality of life. But, as these devices begin to interoperate in vivo and to use wireless communications with out side the body, the need to address security and patient privacy.

There has never been a reported case of a patient with an implantable cardiac defibrillator or pacemaker being targeted by hackers.

When considering implantable medical device security and privacy, it is important to draw distinctions between classes of devices that have different physical properties and healthcare goals.

The range of applications supported by MICS technology is quite wide, from patient condition monitoring to control of body functions. Likewise, the degree to which the patient will need security and protection of privacy will also vary.

VII. Conclusions

The use of implantable devices in the treatment of a number of chronic diseases and disorders including pain management is growing at a remarkable rate. Advances in low-power semiconductor design and manufacturing processes are enabling longer battery life. Innovations in wireless communications aligned with the Medical Implant Communication Service band of frequencies are fueling the growth. Furthermore, clinical research continues to identify new indications for implantable devices, applications that will benefit from the ever-improving sensor electronics that will optimize patient therapy in real-time. Finally, physicians are recognizing the advantages of implantable devices over traditional methods of treatment. There are a number of problems that could surely benefit from MICS, such as; deafness, blindness, paralysis, Parkinson's disease, and epilepsy. Indeed, the medical implant communications service is going to make a significant impact on health care in the coming next few years.

References

1. Fcc, Medical implant communications, at http://wireless.fcc.gov/services/index.htm?job=service_home&id=medical_implant
2. ERC recommendation 70-03 relating to the use of Short Range Device (SRD), European conference of postal and telecommunications administrations, CEPT/ERC 70-03, Tromsø, Norway, 1997
3. IEEE802.15.TG6 at http://www.ieee802.org/15/pub/TG6.html
4. Maisel W.H., Moynahan M., Zuckerman B. D. et al (2006) Pacemaker and ICD generator malfunctions: Analysis of Food and Drug Administration annual report, J. American Med. Ass., 295:1901-1906
5. Scanlon W. G., Evans N. E. (1997) RF performance of a 418 MHz radio telemeter packaged for human vaginal placement, IEEE Trans. Biomed. Eng., 44:427-430
6. Scanlon W. G., Burns J.B., Evans N. E. (2000) Radio wave propagation from a tissue implanted source at 418 MHz and 916 MHz, IEEE Trans. Biomed. Eng., 47:527-534
7. Gabriel C., Gabriel S., Compilation of the dielectric properties of body tissues at RF and microwave frequencies, AL/OE-TR-1996-0037at http://www.brooks.af.mil/AFRL/HED/hedr/reports/dielectricReport/Report.html
8. Duney C. H., Massoudi H., Iskander M..F., Radiofrequency radiation dosimetry handbook (1986), USAF School of Aerospace Medicine
9. Dielectric properties of body tissues at http://niremf.ifac.it
10. IEEE standard for safety levels with respect to human exposure to radio frequency electromagnetic field, 3 KHz to 300 GHz, IEEE Std C95.1, 1999
11. Tang Q., Tummala N., Kumar S. et al. (2005) Communication scheduling to minimize thermal effects of implanted biosensor networks in homogeneous tissue, IEEE Trans. on Biomed. Eng., 52:1285-1294
12. Baker S. D., Hoglund D. H. (2008) Medical-grade, mission-critical wireless network, IEEE Eng. In Med. And Bio. Mag., 86-95 DOI 10.1109/EMB.2008.915498

Author: Kamya Yekeh Yazdandoost
Institute: National Institute of Information and communications Technology
Street: 3-4 Hikarino-oka
City: Yokosuka 239-0847
Country: Japan
Email: yazdandoost@nict.go.jp

MultiAgent System for a Medical Application over Web Technology: A Working Experience

A. Aguilera, E. Herrera and A. Subero

Faculty of Sciences and Technology, University of Carabobo, Valencia, Venezuela

Abstract — **At present, many medical applications are limited to storing basic information concerning patients, such as, their medical history, diagnostic issued by specialists, reviews, etc. But the medical work is not easy when considering complex cases involving different experts and require a high degree of coordination and cooperation. Traditionally communication between experts takes place across consultations involving large amounts of resources (money, time, etc.). MultiAgent Systems (MAS) are a branch of artificial intelligence distributed to adequately address problems of coordination and communication (among others) where several decision-making agents are involved. The objective of this work is the design and implementation of MAS that allows coordinate the workflow of a medical center. We have implemented a management tool for medical records and requests for medical services based on Web technology. The application made available to doctors all the information necessary for carrying out timely diagnosis, through electronic medical records. Regarding the tasks of coordination mentioned: assigning tasks to doctors, requests for reviews, delivering results, among others, using technologies such as text messaging, e-mail messages and on-line. To design agents and their roles, tasks and plans using the "Software Agent Architecture Pattern" the which is based on a set of classes organized for the encoding software components with agents that are integrated into Web applications, in addition to use as MAS commonKADS Methodology development of MAS. Currently have an application robust and stable. It is worth mentioning that this approach used specifically in the medical field is extended to other areas that require coordination distributed.**

Keywords — **MultiAgent Systems, Web technology, MAS-commonKADS, Medical Application.**

I. Introduction

Agent-based systems technology has recently generated plenty of research work because it has been considered as a new paradigm for conceptualizing, designing, and implementing software systems. It is particularly attractive for software development that operates in distributed and open environments. Central to the design and effective operation of such MAS is a core set of issues and research questions that have been studied over the years by the distributed artificial intelligent community [19]. An intelligent MAS includes a number of software agents interacting to each other to solve a problem. Various agents are responsible for planning different tasks. These tasks should be coordinated to solve complex problems [10, 11, 13].

Particularly in health care environments, agents have the potential to assist in a wide range of activities [16]. They can keep the autonomy of the collaborating participants, integrate dissimilar operating environments, and coordinate distributed data, such as patient's records filed in different hospitals (private and public) or in different medical departments, and other organizations involved in health care systems such as insurance companies and government organizations. The agents at a MAS may run associated with different locations, such as the departments of a medical center [15] or the file of a single person included in a health care program from a certain community [3]. The autonomy of each agent in a MAS keeps the independent views of each modeled actor. For example, each agency involved in the provision of health care to a community, such as social workers, health care professionals and/or emergency services may have different private policies determining their relationship between their individual decisions and other agents [3]. Agents can also handle the complexity of solutions through decomposition, modelling and organization of relationships among components; improve patient management through distributed patient scheduling using cooperating intelligent agents; provide remote care monitoring and information for such groups as the elderly and chronically ill; undertake hospital patient monitoring; supply diagnosis decision-support; improve medical training and education in distance-learning tutoring systems [20]; gather, compile and organise medical knowledge available on the Internet [2,23]; and enable intelligent human-computer interfaces to adapt medical data and users requirements and visualise medical data [9,10,11,21]; medical decision making [14], medical e-learning [5]; medical workflow [6,7] .

II. Medical case study

Physicians treat different diagnostic cases, and some of them are considered obvious (classical cases). This happens because the nature of the illness under study is simple or

Chwee Teck Lim, James C.H. Goh (Eds.): ICBME 2008, Proceedings 23, pp. 1162–1165, 2009
www.springerlink.com

because the physician's experience is significant. There are other less obvious cases for which it is not easy to establish a satisfactory diagnosis directly (complex cases). There are many reasons for this: (1) a number of available judgment elements may not be enough, (b) the illness has not evolved enough for certain signs to appear; and/or (3) an incidental nonschematized cause may appear. The diagnosis in these cases can then involve great difficulties and require a complex procedure [1]. This procedure can implement several clinical maneuvers (exploration of various organs or systems, complementary tests, and sometimes, a further patient observation) which are repeated several times [17].

In the daily practice, the care of a particular patient is often shared by several different clinicians who are located in a variety of physically distributed health care settings [11]. In addition to this interorganizational coordination, there is also a need to ensure that the activities within an organization are effectively and coherently managed. In a hospital, for instance, health care typically involves execution of interrelated tasks by medical doctors, nurses, pharmacists, laboratory analysts, and resource management departments. Shared care is a situation where in which clinicians (GPs and specialists) jointly treat the same patient. Patients requiring shared care are, for example, patients undergoing chronic disorders, such as diabetes mellitus, obstructive pulmonary diseases, and/or cardiological diseases [24]. They may also be, or patients who receive palliative care at home or patients with a multisystemic pathology where physiopathology and etiology are necessary to examine the results of several diagnostic procedures. A clinical case illustrating this type of work is shown in fig. 1 (A more detailed explanation is found in [18]). In this case, we can observe the interaction among a GP, a radiologist and a pathologist.

The provision of medical care typically involves a number of individuals, located in a number of different institutions, whose decisions and actions need to be coordinated if care is to be effective. In doing so, shared care requires structured coordination of medical activities, where physicians know the kind of guidelines or protocols will follow and where physicians trust each other's actions and interventions. When different providers are involved in a patient's care without proper coordination, care process may not be meaningfully integrated; a patient receiving such a care under such conditions may be subject to two conditions: unjustified interventions and/or justified actions not performed. To provide an adequate software support for such a coordinated health care management it was decided to adopt an agent-based approach [1].

Clinical case

A 40 year-old male patient, non-smoker, without any obvious particular antecedents in his past medical history. He attended his GP with a non-productive cough of a three-month evolution . His physical tests normal. GP recommended him a palliative treatment and some laboratory and paraclinical tests (Postero-anterior chest x-ray).



x-ray result : circumscribed 2-3 cm nodule located in the right upper lobe of the lung with the presence of interior calcifications of non-specified type. Heart and rest of study without obvious modifications. Scanner recommended.

CAT Lung scanner: It indicates a 2 x 3 cm mass with non-epimacular aspect located in the right upper lobe of the lung with non-specified calcifications. There is no affectation of Mediastinum lymphatic ganglia. There are no other masses in the thorax.

Pulmonary biopsy: macro and microscopic analysis of post-operative piece.

Diagnosis: ENDOBRONCHIAL HAMARTHOMA.

The patient left the hospital and considering the benign origin of the pathology, the doctor recommended an annual check up with his general practitioner.

Fig. 1. A clinical case

III. Design and Implementation of the System

We defined system architecture with a three-level structure [1]: the collaborator level or users (human agents), computer systems agents (software agents) and the data level (databases and knowledge bases). For design and develop of system, we follow the procedure showed in Fig. 2. We used a model-view-controller and a web agent pattern [4] to our design. The first task consists in identifying and defining model elements. Then, these elements are coded and tested individually. Finally, system functionality is checked and validation tests are executed with the real user.

At design level, we have used a pattern architecture based in the model-view-controller (MVC) to our web application. For the agent design, we have used an experimental framework called WAF [4]. This framework has been used successful in the developing of several theses in the University of Carabobo- Venezuela with web technology. In this framework, each agent has its own directory (following Tomcat's structure), and each agent is also structured in directories according to WAF. Each directory (environment,

behavior, resource and communication) contains the implementation of Java classes. The communication among agents is made by message passing thanks to javax.mail library and to the implementation of a blackboard.

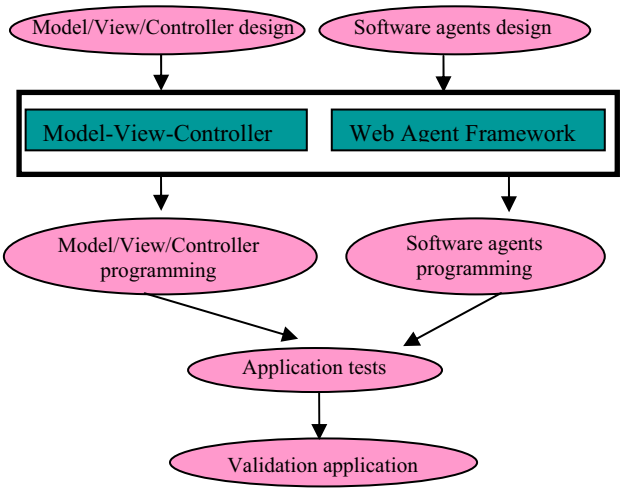


Fig. 2. Procedure of design and develop system

The aim of our web application is to facilitate data exchange and communication among the medical specialists in medical solving problems. This system offers the specialists adequate interfaces for storage and updating of medical histories; it also allows us the dynamic construction of our medical case base. At the level of construction, the system was conceived to allow an easy incorporation of software agents. These agents have the objective to coordinate medical work, control medical doctors' workload, control appointments, and so on. The idea is to provide to the users a working and portable tool easy to install and integrate with other applications.

At develop level, we used a client-server communication model based on Sun Microsystems technology. This model is the base of high level views of JAVA™: servlets and JavaServer Pages (JSPs). In the context of our application, JSPs constitute the views of application according to model MVC; they allow communication with users; servlets constitute the models and one special servlet is the controller. JSPs and servlets are coded in XHTML and Java respectively. TOMCAT server is our web server and PostgreSQL is our database system. In the agent's case, each one constitutes a thread program by extending the Thread class in Java. Each agent runs as an independent process on the server side [8].

IV. System validation

The system is conceived as a web application. The system validation is based on user and functionality tests. The web application is composed of a number of services, most of which a user can interact with through the use of a web accessible graphical user interface.

a. User validation

The validation approach is based on expert inspection and user tests. The aim of the user tests is to verify the user behavior in front of the system. The user has to test different services and use them in the daily work.

Test plan :

1. Selection of functionalities to be tested by users.
2. Construction of a questionnaire with functionalities and query evaluation.
3. Selection of a complex case with medical aid.
4. Request of medical specialists concerned with the medical case.
5. Random selection of other specialist physicians.
6. Gathering of information from specialists.
7. Analysis of result.

The services of the system to be tested are:

• User access and security of the system.

• Updating patient data: personal data, familiar data, past history.

• Updating case data: consultations, establishment of actual clinical context.

• Management of patients.

Test Results: We worked on a real case in the «Enrique Tejera » hospital, Venezuela (Valencia). 5 physicians were asked. Additional functionalities by specialty were required. In general, our application is successful and each of the services defined for the system can be successfully completed. The main difficulty is related to specialist availability.

b. Usability test

The aim of this test is to evaluate the quality of the interface with computer specialists.

Test plan:

1. Selection of instruments from ISO/IEC 9126 norm [12].
2. Preparation of questionnaires.
3. Random selection of computer specialists.
4. Request from computer specialists.
5. Information gathering from physician specialists.
6. Analysis of result.

Test Instrument: Some basic principles of usability from ISO/IEC 9126 standard [12]. P10 - Principles of dialogue, P11 - Usability of system, P12 – Visual display of information, P13 - Guidance to users, P14 - Dialogues menu styles,

P15 - Dialogues for process control languages, P16 - Dialogues by direct handling, P17 - Dialogues for the filling of forms.

Test results: 3 expert users have been inquired. Improvements are necessary on the following aspects: User feedback; Possibilities of interface personalization; Presentation of windows; Information on the state of the system; Reduction of errors.

V. Conclusions

Multi-agent systems have shown their effectiveness to develope distributed systems on different areas. We used this approach to address the medical knowledge acquisition problem. A web application has been developed for distributed management of patients having critical disorders. Preliminary evaluation of this application shows that in real-life clinical application settings the procedure followed in building dynamically knowledge bases is effective. Internet is a technology that makes applications highly portable and accessible. The method followed in this development can easily integrate with other existing applications.

Acknowledgment

We are grateful to FONACIT, Venezuela, under Project No G-2005000278, which has sponsored this work.

References

1. Aguilera A. , “Construction Dynamique d’une Base de Connaissance dans le Cadre du Diagnostic Médical Multi-Experts”, PhD. Thesis, Université de Rennes I, France, 2008.
2. Baujard O., Baujard V., Aurel S., Boyer C., Appel R. D., “MARVIN, a multi-agent softbot to retrieve multilingual medical information on the Web”, Medical Informatics, Vol. 23 (3), 1998, pp. 187-191.
3. Beer D., W. Huang, A. Sixsmith, “Using agents to build a practical implementation of the INCA-Intelligent Community Alarm- system, Intelligent Agents and their applications”, L.C.Jain, Z.Chen and N.Ichalkaranje (Eds.), Springer Verlag, pp. 320-345, 2002.
4. Cataffi R., “Waf: Un Framework para el Desarrollo de Componentes con Agentes de Software”, Master Thesis, University Central of Venezuela, Venezuela, 2008.
5. Farias A., Arvanitis T. N., “Building Software Agents for Training Systems: A Case Study on Radiotherapy Treatment Planning. Knowledge-Based Systems”, Vol. 10, 1997, pp. 161-168.
6. Heine C., R. Herrler, M. Petsch, C. Anhalt, “ADAPT - Adaptive Multi Agent Process Planning & Coordination of Clinical Trials”, Proceedings of AmCIS2003, Tampa, Florida, USA, 2003.
7. Heine C., R. Herrler, S. Kirn, “ADAPT@Agent.Hospital: Agent-Based Organization & Management of Clinical Processes”, International Journal of Intelligent Information Technologies, Vol. 1, No. 1, 2005.
8. Herrera E. , “Sistema Multiagente para una Aplicación Médica bajo Tecnología Web”, Enginieer thesis, University of Carabobo, Venezuela, 2008.
9. Huang J., Jennings N. R., Fox J., “An Agent Architecture for Distributed Medical Care, Intelligent Agents”, M. J. Wooldridge and N.R. Jennings (Eds.), Lecture Notes in Artificial Intelligence, 1995, Springer Verlag, pp. 219-232.
10. Huang J., Jennings N. R., Fox J., “An Agent-based Approach to Health Care Management”, Applied Artificial Intelligence: An International Journal, Vol. 9 (4), 1995, pp. 401-420.
11. Huang J., Jennings, N.R. Fox, J. : Intelligent agents for distributed patient care, In: IEEE Colloquium on Artificial Intelligence in Medicine, No: 1996-031, 1996.
12. ISO International Organization for Standardization, "ISO 9000 and ISO 14000", WWW: http://www.iso.org/iso/iso_catalogue/management_standards/iso_9000_iso_14000.html
13. Jenders R., Sailors R. M., “The Arden Syntax for Medical Logic Systems”, An ANSI Standard Sponsored By Health Level Seven, 1998, WWW: http://cslxinfmtcs.csmc.edu/hl7/arden/
14. Larsson J. E., Hayes-Roth B., “Guardian: An Intelligent Autonomous Agent for Medical Monitoring and Diagnosis”, IEEE Intelligent Systems, 1998, pp. 58-64.
15. Moreno A., Isern D., “Accessing distributed health-care services through smart agents”, in Proc. of 4th IEEE Int. Workshop on Enterprise Networking and Computing in the Health Care Industry – HealthCom, France, 2002.
16. Nealon J. L., Moreno A., “The Application of Agent Technology to Health Care”, 2002. WWW: http://citeseer.ist.psu.edu/nealon02application.html
17. Paolaggi, J. B., Coste, J.: Medical reasoning, from science to medical practices, Ed. ESTEM, 2001.
18. Quintero, J.: Collaborative decision in medicine. Analysis of a case diagnosis, In Proceedings of the Sciences of Electronic, Technology of Information and Telecommunications, SETIT, Sousse, Tunisia, 2003, paper R228137.
19. Sycara, K.: MultiAgent Systems. In: AI Magazine 19(2), 1998.
20. Triantis A.G., Kameas A.D., Zaharakis I. D., et al., “Towards a generic Multi-Agent Architecture of Computer-Based Medical Education”, 1999. WWW :http://citeseer.ist.psu.edu/456846.html.
21. Turcka F., J. Decruyenaereb, P. Thysebaerta, S. Van Hoeckea, B. Volckaerta, et al., “Design of a flexible platform for execution of medical decision support agents in the intensive care unit”, Computers in Biology and Medicine, Elsevier Science, Vol. 37, pp. 97 – 112, 2007.
22. Vázquez-Salceda J., Cortés U., “Using Agent- Mediated Institutions for the distribution of Human Tissues among Hospitals”, Advanced Course on Artificial Intelligence - ACAI-01, Praga, 2001, pp. 205-209.
23. Walczak S., “A Multiagent Architecture for Developing Medical Information Retrieval Agents”, Journal of Medical Systems, Vol. 27, No. 5, pp. 479 - 498, October 2003.
24. Musen M.A., “Handbook of Medical Informatics”, Stanford University, Stanford, WWW: http://www.mieur.nl/mihandbook/r_3_3/handbook/home.htm.

Author: Ana Aguilera
Institute: University of Carabobo
Street: Dep. of Computer Science-Bárbula
City: Valencia
Country: Venezuela
Email: aaguilef@uc.edu.ve

Collaborative Radiological Diagnosis over the Internet

A. Aguilera, M. Barmaksoz, M. Ordoñez and A. Subero

Department of Computer Science, Faculty of Science and Technology, University of Carabobo, Valencia, Venezuela

Abstract — **Nowadays in many cities, there is a high concentration of general and specialized physicians working in areas of highest population density. Additionally, the large number of patients who come from rural medical centers to hospitals and others medical centers is increasing. For this reason, it is necessary to create, as an alternative, mobile care centers, in order to reduce the patients in the main hospital centers. The objective of this is to develop a collaborative web application to assist the radiological medical diagnosis at distance. This application combines the web, the case based and the collaborative technologies. The application design was made with XP methodology including own elements of the Case Based Reasoning (CBR) and Computer supported Cooperative Work (CSCW). In the specification phase, we used interviews with experts and non-experts users. At the implementation level, case bases and collaborative tools have been developed to help the medical inter-consultations. We built a practical implementation of system with all these elements. This application offers to radiologists: an online help, a case base with cases solved in the past and collaborative tools. Thus, we offer the possibility of inter-consultations with others radiologists using chat, audio, video and pointers. The fuzzy similarity function was used to querying and to adapting the case base. All these functionalities have been integrated in the same application to user's comfort and use facilities. In this way, the radiologist diagnoses efficiently and with more precision. Our application was validated by the user and functionality tests and the network performance tests to obtain: average transfer rate and latency with several possibilities of communication. The user's acceptation is good and the network tests give us the better platform to implantation.**

Keywords — **Radiological Diagnostic, Collaborative Work, Case Based Reasoning, Web Medical Application.**

I. Introduction

With the introduction of high speed networks, high-resolution computers and connectivity to internet and advanced techniques on images processing, the changing phase of the health care is creating a demand of support tools of effective decisions. All of this, to help to the medical practitioners with the overload of information when they is providing high-quality patient care with effective costs. These tools not only must demonstrate a behavior based on knowledge to assist in the resolution of the medical problem but that also they must provide intelligent, intuitive and interactive interfaces that allow the users to execute their tasks effective and efficiently. Additionally with the initiation of the radiology departments in these technological aspects, the development of viable computer systems comes to be incrementally important. Medical diagnostic imaging instrument and electronic networks have resulted in accumulation and online availability of large collections of digital medical images. The radiological diagnosis is subjective by nature. The computational systems make efforts for improving the precision / fidelity in the diagnosis and the consistency of the diagnostic final decision and the resulting reproducibility in the image interpretation. It is necessary to design an appropriately defined and organized notation that enables to the clinicians to externalize, reflect on and share diagnostic knowledge. The specialty of radiology, in common with most of medicine, is gradually developing a more systematic approach to training, replacing the traditional mixture of ad hoc apprenticeship and formal lectures with a combination of structured tuition and case-based experimental learning.

Artificial Intelligence has been applied in numerous applications in the domain of health sciences. In the late 1980's, followed by ground laying work done by Koton [9], and Bareiss [3], Case-Based Reasoning (CBR) appeared as an interesting alternative for building medical AI applications, and then it has been used in the field. Case-Based Reasoning (CBR) is a recognized and well established method for building medical systems. Many works have been developed [1], [5], [7], [13] etc. The intention of these works is a) to help medical students improve their knowledge by solving practice cases and b) to help in the construction of medical knowledge base systems to support of medical decision making.

Consultation between radiologists and referring physicians is part of routine medical practice. These collaborative acts are important both for clinical decision-making concerning diagnosis and treatment, and for the training of student and novice physicians. In medical domain, there are many works related to collaborative technology (groupware), the most of them are oriented to Computer Support Collaborative Work (CSCW). These systems are able to support the collaborative multi-expert acts with the technical infrastructure [4], [6], [12], etc. Others works are oriented to the workflow systems like [2], [8], [10], etc.

The aim of our work is to carry out the implementation of a collaborative application for radiological diagnostic aid.

Chwee Teck Lim, James C.H. Goh (Eds.): ICBME 2008, Proceedings 23, pp. 1166–1170, 2009
www.springerlink.com

This application integrates a case-based reasoning mechanism and some techniques computer support collaborative work. The case based reasoning give us to selecting a case similar to the actual case. The CSCW techniques give us the possibility of real time interconsultations between specialists using text messaging, video conferencing and an electronic whiteboard.

II. Radiological diagnostic process

Once the imaging procedure has been performed, the radiologist analyzes the images to identify pertinent features and integrates the imaging findings and their clinical context to determine the diagnosis or a set of diagnostic possibilities. Then, the radiologist communicates the results of the procedure to the referring physician, and may offer recommendations about further investigation. Each of these steps requires informed decision making. Some times, the radiologists have doubts about to a diagnosis. In this case, he/she can a) to querying the academic medical knowledge and b) to ask another radiologist about this diagnosis.

In general, the radiological diagnostic process can be resumed in the following steps (Fig. 1) [11]:

1. Patient evaluation and imaging study selection. Initiated by the referring physician, this process can benefit from access to clinical guidelines, consultation, and decision support.
2. Request for examination. The information tasks involve communication and require provision of appropriate definition of the problem and clinical information.
3. Performance of the examination. This involves adaptation to the problem and patient- specific requirements as well as modification based on intermediate findings, post processing, and analysis of image data for presentation and interpretation.
4. Identification of findings. The tasks are both perceptual and cognitive and include use of decision aids and education resources.
5. Interpretation of patterns and formation of diagnostic assessment. Interpretation requires integration of findings, other patient-specific information, and general knowledge.
6. Communication of results and recommendations. The tasks are those of creating a narrative report, direct contact, an image review and consultation.
7. Improving process. The radiological process requires continual monitoring and control, research database development, process and outcomes analysis, and cost-effectiveness evaluation.
8. Education and training. Information needs are for methods of carrying out all of the processes involves in

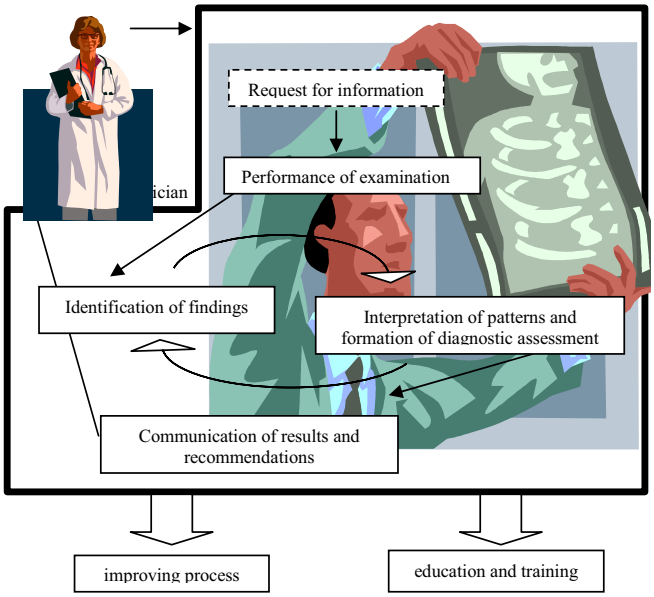


Fig. 1 Diagnostic Process

radiological practice as well as for the knowledge to support them.

Information is the sine qua non of decision making. In radiology, such information includes clinical data (presenting symptoms, signs, laboratory data, results of prior imaging studies) and clinical knowledge (general facts about diseases, how to choose imaging studies, how to perform and interpret radiological examinations). Radiologists also must consider the risks, benefits, and costs of the available actions, and the desirability, or “utility,” of each potential outcome of the decision, both from the perspective of society and that of the individual patient. Computer systems can aid radiologists in these tasks by providing patient-specific information, recalling general medical knowledge, and integrating such information to recommend a course of action. First, decision making requires accurate and ample patient-specific clinical data. Unfortunately, radiologists often lack information (patient-specific clinical data.) to determine if the requested procedure is appropriate, to perform the procedure safely, and to interpret the results accurately. Second, physicians must draw upon a large, rapidly growing body of medical knowledge. Organizing, storing, and retrieving this knowledge is a daunting task. Third, optimal decision making requires an understanding of the “utility” — that is, the relative value — of all possible outcomes of the available plans. Utility can include consideration of costs, mortality, morbidity, and the patient’s preferences. The utility of diagnostic tests such as radiological procedures reflects their potential informative ness and their

role in the overall management of the patient's illness. Decision making is a process, not a single action. For example, to resolve a question raised by an imaging finding, additional imaging procedures may be needed. Or, if a particular imaging finding is present, one may need to re-analyze the image for additional features to confirm or refute a diagnostic hypothesis. A radiologist may need to seek additional clinical information, either from the patient's records or by further examination of the patient. Thus, it is crucial to integrate the various aspects of the decision-making process, whether computer-aided or not, and to integrate knowledge of imaging procedures, findings and diagnoses with pertinent patient-specific information. In diagnostic radiology, a decision aid is required when interpretation demands specialist expertise, when many images are generated or when interpretation is especially difficult.

III. Collaborative radiological application

The application is called SICADIR (System for Collaborative Support Radiological Diagnostics). This is design over Internet with the advantage of increased its availability. The main goal considered in the system design was to build a tool which facilitates the processes of interaction between specialists and the support of physicians' knowledge based in experiences. The design of the architecture includes the following subsystems:

1) Database management subsystem. This is responsible for the maintenance of databases (insertion and deletion of data): patient history and images (Fig. 2). Also, it controls update and query processes. The medical information of patients and the cases are structured in an entity relationship model.

Entities: CASE (id_case, title, problem, solution, sex, age); IMAGE (id_case, image)]; SIMILARITY (id_case similarity, age); HISTORY (id_patient, firstname, secondname, sex, age, instruction_level, civil_state, address, telephone, year, month, day, country, state); USERS (login, password, names, email)

Relationships: SEARCH (login, id_case); HAVE (id_case1, id_case2); CREA (login, id_patient); HAVE2 (id_case1, id_case2)

2) Case base management subsystem. The medical knowledge representation is done with a case base, where the knowledge provided by the medical practice/experience is reflected through a wide repository of cases. This subsystem provides retrieve, adaptation, verification and learning processes for the case base. We retrieved all cases which satisfy certain parameters. These parameters include the patient's medical condition (signs and symptoms) and her/his age. We use an evaluation function to find the best neighbor (if any) that match the case of entry. This function does a search across the case base to show cases with a certain similarity with the actual case. Other element considered is a range of -3, +3 at the age of the patient. The appropriate indexes were built to identify the case in the case base.

3) CSCW subsystem. This contains the basic tools to support of collaborative work: chat, videoconference, common blackboard, facilities to share applications and files. These tools are integrated in a single application being able to access to her at the moment that is desired.

The flow through the system can be illustrated with this short example: a general physician seeing a patient with pulmonary distress could access selective clinical data, x-rays, etc. searching for clinical and therapeutic guidelines, and also patient-oriented educational resources correlated to this problem, from the information resources contained in the system or in the web. When the physician is faced with taking a clinical decision, he/she can request assistance from the system using the user interface. This interface then communicates with the support decision-making subsystem which will assist the decision-making process. This subsystem will try to give answers to the requirement accessing the present knowledge in the system by means of the case base. If this knowledge is not sufficient to fulfill the user's requirements, this subsystem will establish a collaborative session with other physicians. In order to do this, the processes contained in the CSCW subsystem will be activated Fig. 3.

Application implementation

For the implementation of SICADIR, we used the Web Server Apache and the application was developed in PHP with the database manager MySQL. For the CSCW, we used the NetMeeting application which is a client of multipoint videoconference VoIP. It is included in many versions of Microsoft Windows (from Windows 95 OSR2 to Windows XP). It utilizes the H.323 protocol to make the conferences, and it is interoperable with clients based on OpenH323 like Ekiga, as well as Internet Locator Service (ILS) like reflector. Also, it uses a soft modified version of protocol ITU T.120 for the electronic blackboard, the sharing of applications, the remote desktop sharing (RDS) and the transferences of files. The secondary electronic blackboard in NetMeeting 2.1 (and later) uses the H.324 protocol.

Test phase

Following the eXtreme Programming methodology, we have applied the unitary tests (using scripts of tests) to verify the soundness and consistence of each one of the functionalities in the application. Also, a general test of the system was made in order to verify its stability and capacity of answer in the context of the requirements. On the other

hand, a heuristic evaluation of the Web site associated to application SICADIR was made, with the purpose of verifying the fulfillment of the basic principles of usability. Also, the user and acceptability tests were applied to verify if the different functionalities from the application are offered to the user of safe way, reliable and friendly. We asked the radiologist in the "Enrique Tejera-Venezuela" hospital about our application. They have accepted our system and they have given a feedback including recommendations to improve it.

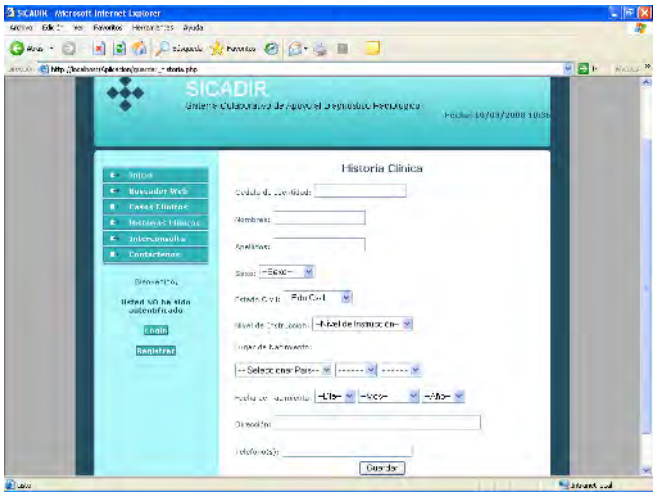


Fig. 2 Patient interface

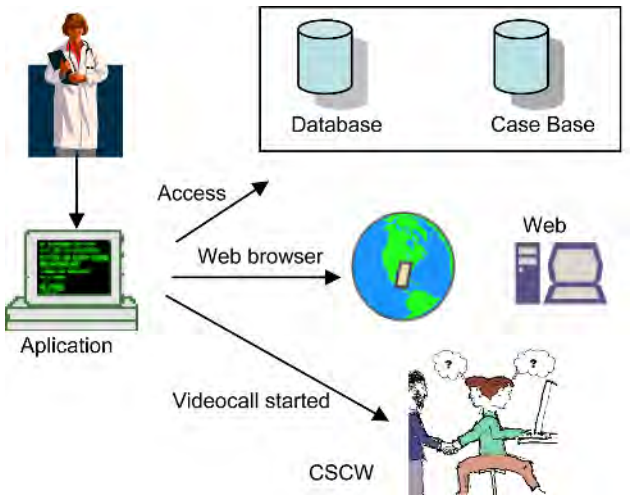


Fig. 3 The flow through the system

IV. Conclusions

A web application for a support to medical decision making in radiological diagnosis has been presented. This application includes three important elements: the database management, the case base management and the CSCW tools. Several tests have been done and we have the good results. Several technologies have to be combined to get to the new medical challenges. The internet is field which offer many advantages for developing of more accessible application. The security and confidentiality of data remain to explore and to implement.

Acknowledgment

We are grateful to FONACIT, Venezuela, under Project No G-2005000278, which has sponsored this work.

References

1. Aguilera A. , "Construction Dynamique d'une Base de Connaissance dans le Cadre du Diagnostic Médical Multi-Experts", PhD. Thesis, Université de Rennes I, France, 2008.
2. Ardissono L., Di Leva A., Petrone G., et al., "Adaptive Medical Workflow Management for a Context-Dependent Home Healthcare Assistance Service". In Electronic Notes in Theoretical Computer Science, Elsevier, 2005.
3. Bareiss, E. R. Exemplar-Based Knowledge Acquisition: A unified Approach to Concept Representation, Classification and Learning. 300 North Zeeb road, Ann Arbor, MI 48106-1346: UMI, 1989.
4. Barnes M., Oliver D., Barnett G., et al., "InterMed: An Internet-based medical collaboratory", Proceedings of the Nineteenth Annual Symposium on Computer Applications in Medical Care. New Orleans, LA: American Medical Informatics Association, Vol. 1023, 1995.
5. Bichindaritz, I., and Sullivan, K. "Generating practice cases for medical training from a knowledge-based decision-support system", In Workshop Proceedings, 3–14. ECCBR'02, 2002.
6. Chronaki C.E., Katehakis D.G., Zabulis X.C., et al., "WebOnCOLL: medical collaboration in regional healthcare networks", IEEE Transactions on Information Technology in Biomedicine Vol. 1, Issue 4, pp. 257 – 269, 1997.
7. Evans-Romaine K., and Marling C. "Prescribing exercise regimens for cardiac and pulmonary disease patients with cbr", In Workshop on CBR in the Health Sciences, 45– 52. ICCBR'03, 2003.
8. Han M., Thiery T., Song X., "Managing exceptions in the medical workflow systems", Proceedings 28th International Conference on Software Engineering, pp. 741 – 750, 2006.
9. Koton, P. A., "Using Experience in Learning and Problem Solving", MIT Press 1988.
10. Quaglini S., Stefanelli M., Lanzola G., et al., "Flexible guideline-based patient careflow systems", Artificial Intelligence in Medicine, 22, 1, pp. 65-80, 2001.
11. Quintero J., Le processus diagnostique en radiologie, rapport interne de recherche, Juin 2002, Département d'Image et Traitement de l'information, ENST-Bretagne.

12. Reddy R., Jagannathan V., Srinivas K., et al. "ARTEMIS: a research testbed for collaborative health careinformatics", 1993. Proceedings Second Workshop on Enabling Technologies: Infrastructure for Collaborative Enterprises, Vol. 20, Issue 22 pp.(s):60 – 65, 1993.
13. Schmidt R., and Gierl L. "Prognostic model for early warning of threatening influenza waves", In German Workshop on Experience Management, 39–46. GWEM'02, 2002.

Author: Ana Aguilera
Institute: University of Carabobo
Street: Dep. of Computer Science-Bárbula
City: Valencia
Country: Venezuela
Email: aaguilef@uc.edu.ve

HandFlex

J. Selva Raj[1], Cyntalia Cipto[2], Ng Qian Ya[3], Leow Shi Jie[3], Isaac Lim Zi Ping[3] and Muhamad Ryan b Mohamad Zah[3]

[1]Singapore Polytechnic, Section Head-Energy Systems School of Mechanical and Manufacturing Engineering, Singapore, Singapore
[2]Project Group Leader Diploma in Bioengineering, School of Mechanical and Manufacturing Engineering, Singapore Polytechnic
[3]Project Group Member Diploma in Bioengineering, School of Mechanical and Manufacturing Engineering, Singapore Polytechnic

Abstract — **This device will be capable of working as a wrist and finger exerciser to aid stroke patient recovery. This assistive device will be linked via an appropriate wireless protocol to a PC game engine. It is envisaged that this link via interacting with the game will trigger visual stimuli neurons that will accelerate recovery of patients. The many challenges in conceptualizing of the abovementioned device are addressed by the use of "smart materials" or "muscle wires" and ultra compact power sources. It is hoped that the presentation of the paper will create a greater awareness on the recent quantum improvements in materials technology and design. The portability of the device will enable ease of use for patients at home, a speedy and measurable recovery and freeing the rehabilitation resources of orthopedic departments.**

Keywords — **muscle wire, rehabilitative engineering, passive hand motion, strokes.**

I. Introduction

Handflex aims to work as an assistive device for stroke patients and aids the recovery of the finger and wrist mobility. Stroke is the paralysis of the muscles in the body. We will focus on hemiplegic and embolic stroke. There are several causes that lead to the occurrence of these two incidents. One of the causes is the formation of blood clots or the breakage of blood vessels leading to the disruption of blood flow. The other is the paralysis in the muscles due to injury to the brain's motor centers.

This device will assist patients by providing passive motion to each finger of the hand. The stimuli, administered within a systematic program, we proposed will realize demonstrable recovery. Muscle wires are embedded into a glove. The heat generated when an electric current is present would cause flexion and extension of the muscle wires. The movement of the muscle wires generate passive motions which will enables rehabilitation process. It is hoped that computer gaming sessions requiring psychomotor will encourage neural activity between the hand and brain via visual stimulus will further speed up the healing process.

II. Anatomy of hand

The human hand is very unusual in human anatomy. The hand is required to be flexible in order to position the fingers and the thumb. It must have adequate strength to provide for normal hand functions. In addition, hand must also be coordinated to perform fine precision motor tasks.

The human hand consists of several different structures. The most important structures of the hand are the bones & joints, ligaments & tendons, muscles, nerves and the blood vessels. In this report, we will only focus on the bone, joints and muscles.

A. Bones and joints

The human hand consists of 27 bone segments that are connected together to each other through the joints. In the wrist, there contains 8 small bones which are called the carpals. Further in to the palm, the carpals are connected to the metacarpals. Besides this, there are also small bone shafts known as phalanges that will line up to form each finger and thumb. These are shown in the Figure 1 below.

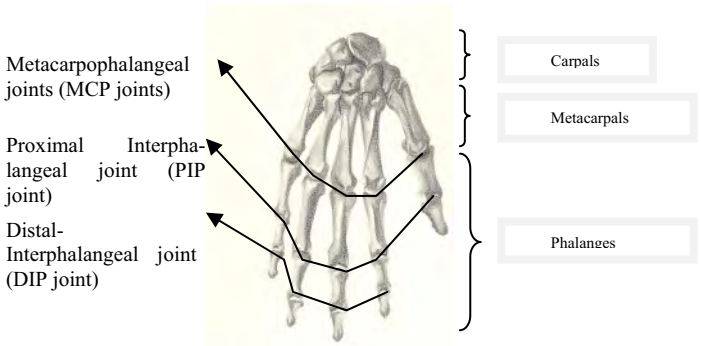


Figure 1 Bone structures on the hand

Chwee Teck Lim, James C.H. Goh (Eds.): ICBME 2008, Proceedings 23, pp. 1171–1174, 2009
www.springerlink.com

The carpal bones of the human hand are generally arranged in 2 rows namely the proximal[1] and the distal [2]rows. The distal carpals will articulate with the 5 metacarpals.

The 5 metacarpals will also articulate with the proximal phalanges, and the proximal phalanges will join up with the middle phalanges which will then articulate with the end-sections of the fingers which are known as distal phalanges. However, the thumb is an exception as it lacks a middle phalange.

The main knuckle joints are formed by the connections of the phalanges to the metacarpals. These joints are called the metacarpophalangeal joints (MCP joints). As for the 2 joints that connect the 3 phalanges in each finger are called the interphalangeal joints (IP joints).The one closest to the MCP joint is called the proximal IP joint (PIP joint) and the joint that is nearer to the end of the finger is called the distal IP joint (DIP joint) [1]. However for the thumb, it only has 1 interphalangeal joint between the 2 thumb phalanges [1]. The types of joints that have been mentioned above are shown in Figure 1.

B. Hand Muscles

There several different types of muscles in the hand that assists the hand to articulate. The muscles in the hand are separated in to 2 main portions. The 2 main portions are the intrinsic [3] muscles and the extrinsic [4] muscles. Under the intrinsic muscle, this can be further classified in to the dorsal and the volar muscle [2]. The extrinsic muscles, can be further classified in to the extensors and the flexors muscle groups.

In the dorsal intrinsic muscle group, there are the dorsal interossei and the abductor digiti minimi muscles [2]. In asimilarly way the volar intrinsic muscle group, there are 2 layers which are the superficial layer and a deep layer. The superficial layer consists of the lumbricals, flexor digiti minimi and the thenar muscles [2]. The volar extrinsic deep consists of the palmar interossei and the opponens digiti minimi. Next, the extrinsic extensors are divided into the muscles whose primary action is on the wrist extension and the muscles whose primary action is at the digits. However, we will only focus on those muscles whose primary action is at the digits. The muscles whose primary action is at the digits are the abductor pollicus longus, extensor pollicus brevis, extensor pollicus longus, extensor indicis, extensor digiti minimi and the extensor digitorium [2].

The extrinsic flexors muscles are arranged in 3 layers. They are the superficial muscles, intermediate muscles and deep muscles. The primary effect of these 3 layers of muscle is at the wrist, digits and the palm. The types of muscles at these 3 layers are the flexor carpi radialis, Palmaris longus, flexor carpi ulnaris, flexor digitorum superficialis, flexor pollicus longus and the flexor digitorium profundus [2].

III. Causes of paralysis in body parts

In this section, we will discuss the conditions that have caused certain parts of the body to become paralysed. The 2 conditions are Hemiplegia and the Embolic Stroke.

Hemiplegia refers to paralysis or abnormal movements on one side of a person, either the right or left.

Hemiplegia affects people differently but the most obvious result is a varying degree of weakness and lack of control in one side of the body. It will also cause specific learning difficulties such as dyslexia [5] , perceptual and concentration problems [4]. There are several different causes of Hemiplegia. One of the most common causes will be stroke. Stroke occurs either when a blood clot forms and obstructs normal blood flow or when a blood vessel breaks, cutting off or disrupting blood flow [5].

Embolic stroke occurs when a blood clot or other particle form in a blood vessel away from the brain is swept through the bloodstream to lodge in narrower brain arteries [6].

A blood clot is called an embolus. This is caused by irregular beating in the heart's 2 upper chambers. This abnormal heart rhythm can lead to poor blood flow and the formation of a blood clot [6]. Paralysis of the muscle thus occurs.

IV. Muscles wires

Muscle wires[6]are thin strands of a special nickel-titanium alloy that actually shorten in length when electrically powered. They are easy to use, and they can lift thousands of times their own weight. The direct linear motion of muscle wires offers the type of motion that is very similar to that of a human muscle.

A. Properties

The bending ability [8] of the muscle wires is determined by the wire's diameter (Figure 2). Therefore, the minimum bend radius is the smallest bend that the muscle wire can make without being damaged.

[1] Nearer to the body
[2] Further from the body
[3] Originate at wrist and hand structures
[4] Origins are located proximal to the wrist
[5] Impaired ability to learned to read
[6] Muscle wire is also referred by its trade name Flexinol

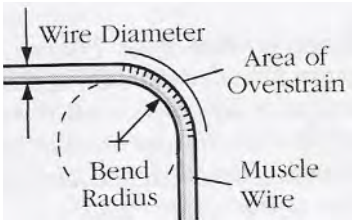


Figure 2 Minimum bend radius[7]

The electrical properties [8] of the muscle wires follow the basic equations derived from Ohm's law. The three equations are:

$$V = I \times R^{8}$$

$$W = I \times V^{9}$$

$$W = I^{2} \times R^{10}$$

When an electrical current [8] is passed through the muscle wires, the resistance in the wire causes it to dissipate part of the current as heat. As the result, the temperature of the wire increases. As it reaches a level that is high enough, the wire will undergo shape memory effect phase. The activation and relaxation temperature of the muscle wires is dependent on the formulation of the alloy. There are two types of alloys; namely the low temperature alloy and high temperature alloy.

The speed at which muscle wires can contract and relax depends on several factors. This includes the circuit that drives the wires, the surrounding condition, and the wires formulation. However, the total time for contract and relax action of the wire depends on the composition, the electrical power applied, and the local cooling conditions. To reiterate, local cooling conditions are important to shorten the relaxation speed. Therefore, the more quickly the muscle wires can be cooled, the faster its cycle time.

Muscle wires exhibit two types of microstructure for heating and cooling respectively. During heating, muscle wires contracts. During full contraction, microstructure formed is harder austenite phase. When wire cools, it changes to martensite phase. Thus, the wires relax and lengthen to its original length. The change in microstructure provides the muscle wires with unique shape memory effect.

[7] Figure from Muscle Wires Project Book[8]
[8] Voltage (in volts) equals current (in amperes) times resistance (in ohms)
[9] Power (in watts) equals current (in amperes) times voltage (in volts)
[10] Power (in watts) equals current (in amperes) squared times resistance (in ohms)

B. Shape memory effect

The shape memory effect for muscle wires is the ability of the wires to recover to its original shape. Upon heating, wire will undergo plastic deformation resulting in contracting and bending of the wire (Figure 3).

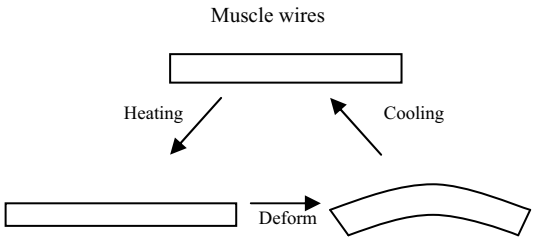


Figure 3 Shape memory effect

V. Muscle hand

The muscle hand consists of muscle wires embedded on the casing of the wearable glove (Figure 4). The purpose of this design is to provide movement to the phalanges and protect the user's hand from the heat produced during the process of contraction. This design is based on the fundamental movements of the hand. The glove concentrates mostly on the flexion and extension of the DIP joint, PIP joint and, the thumb MCP and IP joint.

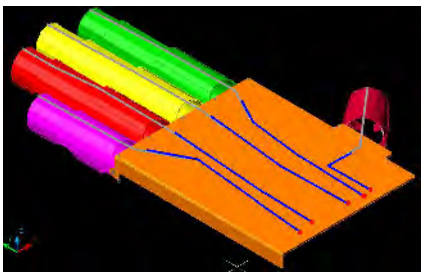


Figure 4 Muscle hand

The designed 'V-shape joint system' comes close to duplicating the functionality of the hand (Figure 5). The V-shape joint is located between the two fingers of the wearable glove. It is capable of providing a wide range of motions such as abduction and adduction for the fingers. Hence, this provides a firm and flexible support for ease of movement. This design will not hinder the natural movement of the phalanges.

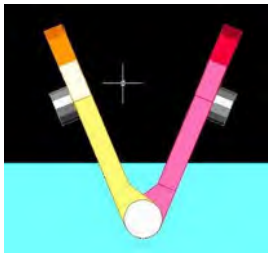


Figure 5 Joint system

The hinge joint segment system is located at the joints of the fingers (Figure 6). It enables the glove to replicate the natural joints. This promotes flexion and extension of the fingers. In addition, it serves as a guide while the muscle wire acts as the movement generator for the injured phalanges. This would allow natural movements to the phalanges.

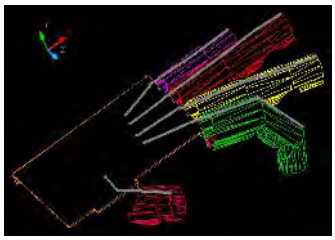


Figure 6 Segment system

The limitations posed by the use of the muscle wire are the heat produced, calling for the need to protect the hand from this heating effect. Also any additional detailed movement to the phalanges requires a very complex layout of muscle wires. In basic finger movements such as extension and flexion two muscle wires are used to move a phalange.

VI. Discussion

While designing the wearable glove type robotic "muscle hand" prototype, our groups faces several problems. One of the stumbling blocks was the difficulty in purchasing muscle wires. All the muscle wires suppliers are from overseas. The only way of getting the wires is through internet purchases. While purchasing the muscle wires, we face some difficulties.

Next, there is also an absence of information on how to embed muscle wires into the designed prototype. The first prototype was fabricated by 'trial and error'. Since then, we have improved on our designs to enable different sequence of finger movement.

The activation start temperature of the muscle wires poses many challenges in the design. In addition, insulation conditions surrounding the muscle wires can greatly affect the performance. Quicker the wires cools, faster it relaxes and reverts to its initial length thus the shorter the cycle time. Therefore, the cooling method used is critical to effectively operate the muscle hand.

The areas we have yet to research and focus on will be the nature of the recovery process from the stroke to a point where the patient can confidently independent. There is also an absent of information on how to establish our device to stimulate re-growth and restore the brain cell functions.

VII. Conclusion

Muscle wire is the best candidate for our "muscle hand". However, problems of heat generation and rapid cooling required, poses challenges for a ventilated version of the muscle hand.

Finally, it is hoped that this project will heighten attention and interest in this domain of rehabilitate engineering. The inclusion of game based activity will further enhance our horizon to achieve our desired goals.

Acknowledgments

As a group, we would like to thank Mr Gribson Chan of St. Luke's Hospital for initiating this project and keeping us on track in our research. We would also like to thank Dr Boey Siek Yeng and Dr Ong Fook Rhu from the Singapore Polytechnic's School of Mechanical and Manufacturing Engineering for their invaluable assistance and support in throughout this project. Not forgetting thanking Singapore Polytechnic for being able to fund the project and participate in this conference.

References

1. A Patient's Guide to Hand Anatomy at http://www.eorthopod.com/public/patient_education/6606/hand_anatomy.html
2. Hand Kinesiology at http://classes.kumc.edu/sah/resources/handkines/kines2.html
3. Alfred B. Swanson (1995) Rehabilitation of the Hand. St. Louis, Mosby
4. An introduction to epilepsy for people with childhood hemiplegia at http://organizedwisdom.com/helpbar/index.html?return=http://organizedwisdom.com/Hemiplegia?url=http://www.epilepsynse.org.uk/pages/info/leaflets/hemiplegia.cfm
5. What are some causes of Hemiplegia at http://www.wisegeek.com/what-are-some-causes-of-hemiplegia.htm
6. Nervous System at http://www.mayoclinic.com/health/stroke/DS00150/DSECTION=causes
7. Muscle Wires at http://www.mondotronics.com/
8. Roger G.Gilbertson (1992) Muscle Wires Project Book Mondo . Tronics ISBN: 1-879896-14-1

Treatment Response Monitoring and Prognosis Establishment through an Intelligent Information System

C. Plaisanu[1], C. Stefan[1]

[1]SC IPA SA, Bucharest, Romania

Abstract — **Numerous medical statistics confirm the extremely high incidence of genital area neoplasia. Although the incidence of this type of cancer is growing, currently, in the oncology field, negative aspects such as ignorance, diagnosis fear and lack of sanitary education are still dominant. This article presents a framework for developing a decisional system for monitoring treatment response at genital area cancer patients as well as the assessment of their life expectancy and prognosis. The decisional system is being developed by an undergoing national research project - NEOSIM - and will be implemented at The Oncology Institute of Bucharest.**

Keywords — **genital neoplasia, decisional system, data acquisition, prognosis**

I. Introduction

In Romania, at the present time, there is no virtual system for research, diagnosis and medical prognosis in oncology. This article would present the main objectives and achievements of an undergoing national research project, characterised by an important degree of originality and novelty and implemented in a main Romanian oncology institute.

The fundamental idea of this project is to elaborate an intelligent informational system for monitoring, treatment modification and prognosis elaboration, in order to assist oncology experts in supervising their patients.

It is of great importance to mention that, in the oncology area, the effect of treatment generates the possible extension of a patient's lifespan. It other words, it would be essential to forecast the most probable life expectancy, taking into account all the changes in clinical and paraclinical parameters and, also the prescribed treatment.

This research also includes the monitoring and analysis of some tumoral markers that are considered to be more accurate in prognosis establishment, an innovative approach regarding disease evolution (for example the level of telomerase, enzyme involved in DNA replication).

II. Description of system architecture

In order to achieve the proposed main objectives, it would be necessary to design and implement a virtual information platform, based on a decision support system. This intelligent informational system will have five main components; a brief presentation of these components will be made as follows.

A. Oncological Warehouse Module

This module is actually a medical knowledge database. It has the role of storing relevant medical information, obtained from oncology specialists and experts, but also from other medical sources. As it name suggests, this module contains a large amount of medical data, such as: patient general information, clinical and paraclinical parameters, genic expression category parameters (telomerase), imagistic data, facts, rules, solving methods, heuristics, complete information about genital area neoplasia, clinical studies, etc.

B. System Reasoning Core Module

This module is an application that holds the control knowledge and represents an inference engine. In order to obtain the required information regarding the evolutional state of the disease and the efficiency of the treatment, the medical database would be exploited with the purpose of reasoning generation. Through this module, the oncology clinician will obtain additional information for treatment adjustment and prognosis forecasting.

C. The Dialogue Interface

This interface also called NEOSIM Façade, will allow communication of oncology specialists within the advising steps. It would also make possible the on-line access of medical experts to the knowledge base. Together with Medical Knowledge Spring module, it also has the role of adding and updating information into the system.

Chwee Teck Lim, James C.H. Goh (Eds.): ICBME 2008, Proceedings 23, pp. 1175–1178, 2009
www.springerlink.com

D. Medical Knowledge Spring

This module would permit the knowledge acquiring. Therefore, oncology specialists would be able to insert medical data in a form recognized by the system and, also, to update the complex medical data base;

E. The Knowledge Interpreter

This knowledge interpreting and explicative module has the purpose to explain to the medical personnel, the information level of the intelligent system, the reasoning processes and the results obtained from advising sessions among oncology specialists. This module will also display the results obtained from the evaluation of changes suffered by analyzed parameters, the solution for treatment adjustment and prognosis;

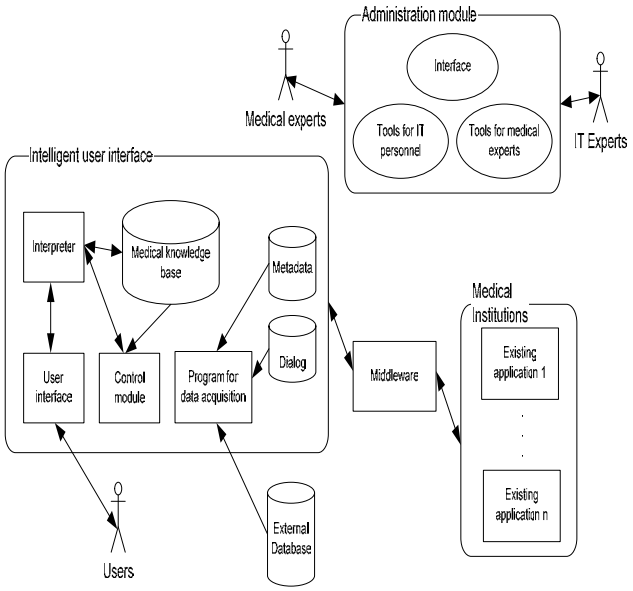


Fig. 1 System architecture and main user groups

The intelligent system also contains a module that ensures the interoperability with existing information systems from the medical institutions where it would be implemented. Medical and IT experts will have access to a management module in order to assure the proper functioning of the platform.

The latest technologies for medical information management will be used for the design of the intelligent information system. In order to increase safety and integrity of data it is necessary to use technologies like semantic web and ontologies.

The system will also be based on open standards like web services (SOAP, UDDI, WSDL) or XML to ensure interoperability and integration of various applications and information systems that exist or will be developed in the future. [1]

III. Presentation of main user groups

The intelligent system contains three categories of user groups: medical experts specialized in the oncology domain, the IT experts that supervise the proper technological functioning of the system and the general users that are oncology doctors or resident doctors involved in health-management of cancer patients [2].

A. Medical experts

In order for the system to contain all the medical information that are necessary, medical experts will access the intelligent system in the purpose of creating descriptive models that will define the main characteristics of different types of genital area neoplasia and, also, the parameters and investigations necessary for evaluating such pathologies. Furthermore, there will be defined sets of parameters and features (clinical and paraclinical parameters, imagistic aspects, parameters in the genic expression category) whose utility will be materialized in elaborating the decision to modify the treatment and the prognosis.

B. General users

The general users are the oncology field doctors that are practically involved in clinical supervision of cancer patients. They would establish a dialogue with the system in order to optimize their clinical decision. In the medical practice, and especially in the oncology field, it is essential to know whether the prescribed treatment is working or not, the main problem being the large quantity of variables that a doctor has to deal with. In this regard, the intelligent system would manage properly this situation, helping the doctor to optimize his decision or to obtain additional information. The system also facilitates the dialogue and the advising among the oncology specialists through the elaboration of a virtual community.

C. IT experts

The IT experts have an important role in the system their purpose being the continuous monitoring and management, in real time, of the execution environment from the technical-functional point of view.

IV. System objectives

The main objective of this intelligent informational system is to improve the treatment and life expectancy of patients diagnosed with genital area cancers. This is realized by monitoring and properly analyzing the disease evolution based on the evaluation of treatment response and health changes reflected by medical imagistic aspects and clinical and paraclinic parameters.

A. Main medical objectives

The most important medical aspect is considered to be the prognosis establishment through a complex analysis of tumoral markers variability from the diagnosis moment and over the treatment period. There are two types of genital area neoplasia that are most common nowadays, uterine and ovarian cancers, and an accurate modality of prognosis prediction would by the tracking of high sensitivity tumoral markers such as CA 125, SCC, CEA and TPA [3].

These markers can indicate the primary tumor at the moment of diagnosis and, if the administrated treatment hasn't been efficient, they can indicate a recidivating tumor. In addition to these markers, the Bucharest Oncology Institute research team is also conducting an innovative study of gene expression category markers such as DNA- replication enzyme telomerase. About this enzyme it is known that it becomes active in the evolution of cancer and if it's found very early, it becomes a marker for diagnosis. Telomerase can tell if the disease is very advanced and also can establish the prognosis of the patient [4], [5].

The intelligent system would manage a large amount of data regarding tumoral markers variations and would correlate them to the clinical status and life expectancy of the patient.

B. General objectives

This project consists of numerous and complex activities, combining fundamental research, application research and support activities, all involving four main Romanian institutes- one University, an important Oncology Institute and two IT Institutes. There are six phases of the research project, all the objectives accomplished through them being presented above [6].

Phase 1: Creation of conceptual models for medical decision and computerized models for medical data - clinical parameters, tumoral markers and gene expression parameters and imagistic aspects.

Phase 2: Design of system architecture, object orientated models for specifying system's functions, specifications for realization of an identification model of the main characteristics genital area cancers, a specific model for monitoring gene expression category parameters and a project presentation site.

Phase 3: Database and data knowledge structure design, specification of the intelligent monitoring, treatment change and diagnostic elaboration system, (inference engine, dialog interface, knowledge acquisition module, explicative and interpretative module) and also software specifications for information system module component (administrative module, middleware, virtual community).

Phase 4: Elaboration of programs for information system component modules (administration modules, middleware to existing system connection application, application for elaborating a virtual community) and the programs and algorithms for the intelligent monitoring, treatment change and diagnostic elaboration system (medical knowledge base, inference engine, dialog interface, knowledge acquisition module, explicative and interpretative module).

Phase 5: Scientifically research is conducted in order to realize the testing methodology, the functional testing of algorithms, data bases and intelligent system's component modules. There is also realized the evaluation methodology and intermediary evaluation report of activity.

Phase 6: This phase refers to demonstrations, scientific communications and articles. There will also be a manual for presentation and utility of the project. The phase ends with the final evaluation report.

V. Implementation of the system

The main outcome of this systems implementation is essential for the patient: it would made possible for the oncology doctor to answer the most common question that the suffering patients have – has the administrated treatment been efficient and, what is the life expectancy from the moment of the diagnosis ? In other words, one of the main effects that the system would have is to ensure the patient that all the variables in his health status are complete and correct monitored therefore, his life quality and prognosis would be improved.

The system assures a high level of certitude in prognosis assessment due to computerized analysis of a large quantity of data regarding complex genetic parameters and tumoral markers.

The most important aspect regarding this systems implementation concerns the social area. It would improve the life quality and life expectancy of genital area neoplasia patients and reduce medical errors by access to relevant medical data.

The system would also generate a continuous professional forming of medical specialists based on scientific

knowledge and on the best practice and would be an important education and research support in the medical field.

In the technical area, the project intends to use the most recent informational technologies low cost, meaning the web services, the ontology, the semantic web, advanced programming languages, which respect the newest development tendencies of the informational society and in which the information access is not restricted by temporal or geographic barriers.

Regarding the financial aspect, the project would generate savings throw the growth of efficacy of the clinical decision process, by reducing the number of hours spent for diagnosis and treatment and there for also reducing the financial costs.

VI. Conclusion

This project would create a complex virtual journal of disease evolution in which there will be included concrete data on the respective patient but, also, medical analysis, imagistic aspects as well as values of some clinical parameters, tumoral and genetic markers.

In the medical world, the research aims at discovering new methods for prognosis assessment and treatment response evaluation. In the field of oncology an element of special interest is represented by life expectancy and prognosis. In this way, the project brings an innovative element: monitoring the evolutional state of the disease by tracking and analysing the levels of some tumoral markers and gene expression category markers.

Regarding the medical practice, the system offers the oncology doctor a sufficient and complete data volume about the patient, the reduction of the work volume with the help of modern informatics and telecommunication techniques, the increase of the analysis speed of the medical information based on a virtual interpretation system of medical data, as well as the improvement of the patient's life quality.

References

1. Bredemeyer Consulting, Software Architecture and Related Concerns, 1999.
2. H. Hofmann, H. Lehner, Requirements Engineering as a success Factor in Software Projects, IEEE Software, 2001.
3. L.L. Gunderson, J.E. Tepper, Clinical Radiation Oncology, Philadelphia, 2000..
4. Shelly Cummings, Current Perspectives in Genetics: Insights and Applications in Molecular, Classical, and Human Genetics, Brooks Cole, 2000.
5. Xueli Zhu, Rakesh Kumar, Mahitosh Mandal, Neeta Sharma, Harsh W. Sharma, Urvashi Dhingra, John A. Sokoloski, Rongshen Hsiao, and Ramaswamy Narayanan; Cell cycle-dependent modulation of telomerase activity in tumor cells; Proceedings of the National Academy of Sciences, Vol. 93
6. Olivé, Antoni; Conceptual Modeling of Information Systems, ISBN: 978-3-540-39389-4, 2007.

A Surgical Training Simulator for Quantitative Assessment of the Anastomotic Technique of Coronary Artery Bypass Grafting

Y. Park[1,2], M. Shinke[1], N. Kanemitsu[1], T. Yagi[1,3], T. Azuma[4], Y. Shiraishi[5], R. Kormos[2] and M. Umezu[1]

[1]Integrative Bioscience and Bioengineering, TWIns, Waseda University, Tokyo, Japan
[2]Heart, Lung and Esophageal Surgery Institute, University of Pittsburgh Medical Center, Pittsburgh, U.S.A.
[3]CSIRO Minerals, Melbourne, Australia
[4]Dept. of Cardiovascular Surgery, Tokyo Women's Medical University, Tokyo, Japan
[5]Institute of Aging and Cancer, Tohoku University, Sendai, Japan

Abstract — **Here we describe a personal training simulator that improves manual dexterity required for the anastomotic technique of Coronary Artery Bypass Grafting (CABG). The simulator-based surgical training is termed "DRY Lab". The system evaluates surgical skill hydrodynamically as well as visually. This report focuses on the effects of regular DRY Lab for an inexperienced surgeon.**

A cardiac surgeon with no experience in CABG volunteered for the DRY Lab. The model of a coronary artery consisted of a three-layered silicone rubber tube. To ensure its suitability for suturing, the tearing strength of the tube was 0.14N. In the course of training, the surgeon made 62 anastomosis in 80 days. During this time, we recorded the number of sutures, operation time, and hydrodynamics of the anastomosis made early and late in the training sessions. Hydrodynamic testing measured the pressure difference due to suturing in steady flows. At a flow rate of 100ml/min, the Reynolds number was 350.

On the period of the training, the mean number of sutures was 16.9 ± 2.5. Thereafter, it decreased gradually, converging to 14.0 ± 0.0 on the last day. This indicated that the surgeon eventually established own particular design of an anastomosis throughout the trainings. Pressure loss of the anastomosed model in the final training was 65.8% lower than that in the initial training. The difference appeared to be due to the stenosed effective orifice area of the anastomosis.

In sum, the findings suggest that quantitative assessment of simulator-based surgical training is an effective way to improve anastomotic technique in CABG.

Keywords — **Surgical Training, Skill Assessment, Self Training, Pressure loss, Coronary Artery Bypass Grafting**

I. Introduction

Surgeons need a large volume of high-quality experience to improve or maintain their skill. It was reported that patients undergoing selected cardiovascular or cancer procedures can significantly reduce their risk of operative death by selecting a high-volume hospital [1]. Especially in a field of cardiac surgery, the operators' individual techniques are important to reduce the mortality [2] [3]. However, the situation has been more difficult to provide enough operating cases for trainee cardiac surgeons. The number of CABG cases was 20,095 for 2,937 registered cardiac surgeons in Japan [4]. "WET Lab" was adopted as a surgical training method that experts instruct trainees on defrosted porcine hearts. Although the WET Lab has advantages such that enable to avoid malpractice and good fidelity of the organs, it is high-cost for instructors, organizers and trainees.

Our group proposes the "DRY Lab" stage, before the WET Lab stage to brush up fundamental surgical techniques by their own using simulators. It is demanded by both experts and trainees that the simulators must include quantitative assessment functions to keep the motivation. Ideally, the quantitative assessment can be done instantly while the training. We have developed coronary artery model named "YOUCAN" and beating heart simulator "BEAT". Then the first trial of the quantitative assessment was done with original mock circulatory simulator. The anastomotic technique of an expert and inexperienced trainee cardiac surgeon was hydrodynamically assessed by selected parameter of an energy loss [5][6]. This Report focuses on the short-term effects of regular DRY Lab training on an inexperienced surgeon.

II. Method

A. DRYLAB training

A cardiac surgeon who inexperienced CABG clinical cases volunteeered for the regular DRY Lab training. The trainee made 62 anastomosis in 80days. Fig.1 shows the models of vessels consisted of three-layered silicone rubber tube. To ensure its suitability for for suturing, tearing strength was measured. Fig.2 shows measurement apparutus for the measurement. The coronary artery model and defrosted porcine coronary were tested. The specimens were sized to square shape (5mm × 5mm) by a scalpel. The

Chwee Teck Lim, James C.H. Goh (Eds.): ICBME 2008, Proceedings 23, pp. 1179–1182, 2009
www.springerlink.com

specimens were sutured by surgical strings (PROLENE 8-0, ETHICON). Tensile testing mashined recorded the load where the model was torn by strings. The value of tearing-strrength were obtained as 0.14N (model) and 0.27N (pig).

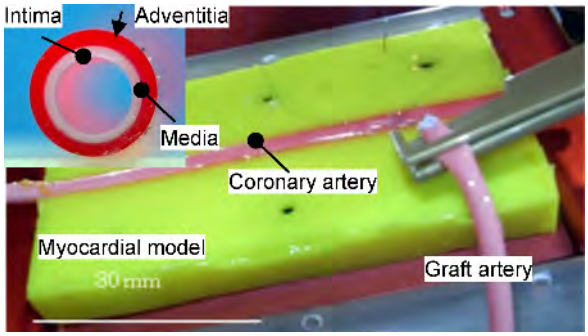


Fig. 1 Silicone tubular models of coronary artery and graft artery: "YOUCAN"

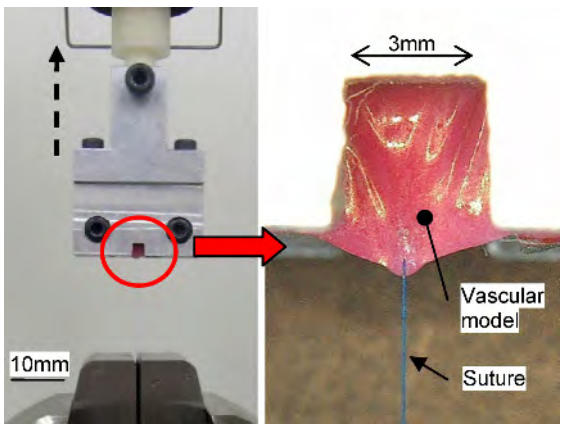


Fig. 2 Measurement of the tearing strength

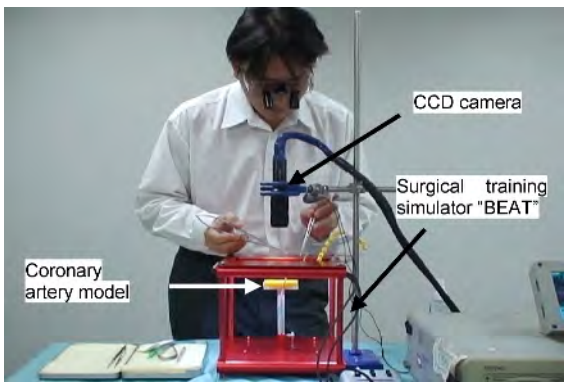


Fig. 3 Training apparatus; coronary artery model has been mounted on the "BEAT".

The tearing strength of the model was adjusted about half of poricin artery. Because it was reported that porcine coronary artery has three times of elasticity compared to human coronary artery [7]. Fig.3 shows apparatus for the DRY Lab training. The coronary artery model was mounted on the BEAT. Although the BEAT could simulate myocardial pulsatile motion, the trainings were done under off-beating condition to study the training effects within initial phase. We recorded the number of stitches and time to complete an anastomosys with a CCD camera (VH-6300, KEYENCE, 0.9 Mpixel). The trainee was received feedback consultations with assessment reports at the beginning of each trainings.

B. Hydrodynamic assessment of an anastomotic technique

Fig.4 shows an experimental apparatus to assess an anastomotic technique hydrodynamically. This open-circuit was designed to simplify the assessment procedure. A manometer was installed at inlet and outlet of the test section. The pressure difference was measured under steady flow condition where flow rate of 100ml /min and the Reynolds number of 350 (simulated coronary circulatory flow at the peak). Anastomosed models were selected from early and late in training sessions.

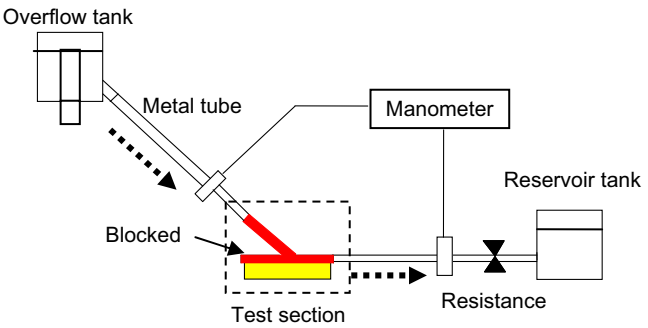


Fig. 4 In-vitro mock circulatory simulator for hydrodynamic assessment of the anastomosed models.

C. Analysis of surgical operation in clinical cases

Clinical operations of on-pump CABG that operated by a registered cardiac surgeon, a cardiac fellow and a resident was recorded by digital video camera (at UPMC Passavant hospital, Pittsburgh, USA in 2008). The number of experienced case was >10,000, >700 and 0 cases, respectively. Total time and rhythm was calculated from the visual records. Then, it was examined that characteristics of the DRY Lab training comparing to surgical operation in a clinical case.

III. Results and Discussion

Fig. 5 shows changes anastomotic design during the DRY Lab trainings. On the first day, number of stitches to make an anastomosis was counted as 16.9 ± 2.5 (mean ± S.D.). Thereafter, it has decreased gradually then converged to 14.0 ± 0.0 on the last day. This results indicated that there exists two phases during the training. The earlier is the trial phase that understanding and solving the technical problems (see fig.5 A). The later can be understood as fixing phase to fix the established technique (see fig.5 B). It was suggested that continuous feedback is needed for a trainee especially in an initial stage.

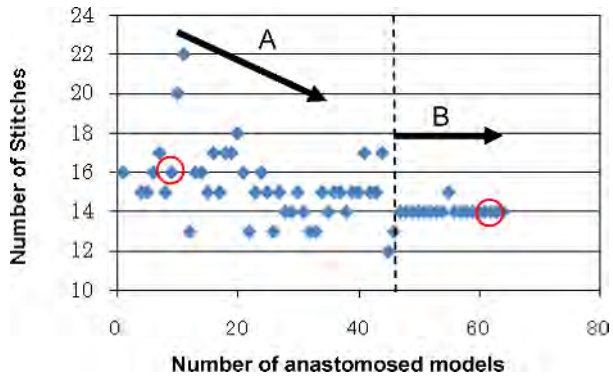


Fig. 5 Changes of anastomotic design were observed during the DRY Lab training. (A: trial phase, considering suitable design for an anastomosis, B: fixing phase after the design was established)

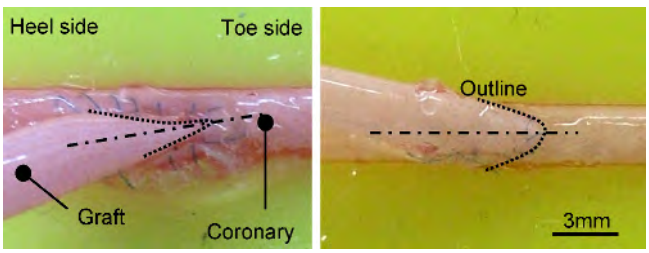


Fig. 6 Outcomes of anastomosed models (left: the first day, right: the last day)

Next, we selected the best model based on a comment of the trainee from the first and the last day. Fig. 6 shows the comparative visual inspection. Initial model was observed as more likely collapsed rather than the later model as shown with dotted line in Fig.6. Irregular stitches may be caused of stenosis. Graft artery of the initial model was more twisted compared to the later model. The orientation of stitches in later model was found as close to a shape of an eclipse.

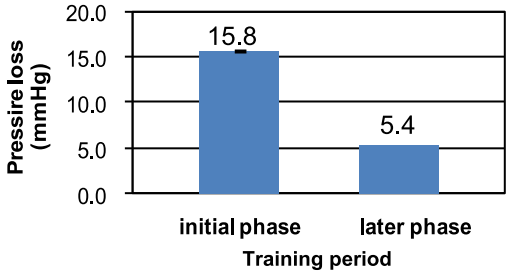


Fig. 7 Comparison of pressure loss of anastomosed models (the initial vs. the end of the training)

Fig. 7 shows the result of hydrodynamic assessment anastomosed models. The values of pressure loss in the initial and the later day model were 15.8 ± 0.1 mmHg and 5.4 ± 0.0 mmHg, respectively. The mean flow rate in each condition was 28.0 g/min and 27.8 g/min. The pressure loss of later training was 65.8% lower than the initial. Then energy loss was calculated by equation (1), using following parameters: pressure gradient ΔP and flow rate $Q_{in.}$

$$E_{loss} = \oint (\Delta P \cdot Q_{in}) dt \quad (1)$$

The energy loss of the initial and the later models were 0.98 ± 0.01 mJ and 0.34 ± 0.00 mJ, respectively. The energy loss of later model was less than 65.7% lower than the initial model. The difference appeared to be due to stenosed effective orifice area of the anastomosis. This result could indicate following two thoughts. (a) An anastomotic technique of a trainee surgeon has been significantly improved, (b) measurement of pressure difference is effective method to distinguish the phase of a trainee. It still needs further studies to establish the evaluation index for an anastomotic technique.

Table 1 shows timing data for an anastomosis, which was obtained by image analysis of the on-pump CABG operation. Fig. 8 shows a time chart to finish one anastomosis. It was found that total time of the experienced group (expert and fellow) was clearly lower than resident and the DRY Lab trainee. It was also clarified the DRY Lab trainee took more time to do parachuting technique compared with the resident. It can be thought that the silicone vascular models were fragile. Therefore it has taken more time for parachuting to avoid tearing the coronary artery model. Further improvements of the models were expected. The total time of DRY Lab trainee without parachuting time was 8.3 min. it was lower than the time of the resident. Fig. 9 shows time for each single suture to make one anastomosis. The value of standard deviation of the time for respective stitches can be understood as a rhythm of suturing during an anastomosis. This value of the DRY Lab trainee was higher as 65.5 (s) comparing to that expert and fellow were 6.9 (s) and 9.7 (s), respectively.

Table 1 Comparison of the time for anastomosis

	Total time (min)	Rhythm: time of respective stitches (sec) (mean ± S.D.)
Expert	4.8	16.0 ± 6.9
Fellow	5.9	19.2 ± 9.7
Resident	14.6	62.4 ± 31.6
DRY Lab	16.0	68.6 ± 65.5
DRY Lab (except parachuting time)	8.3	52.1 ± 22.7

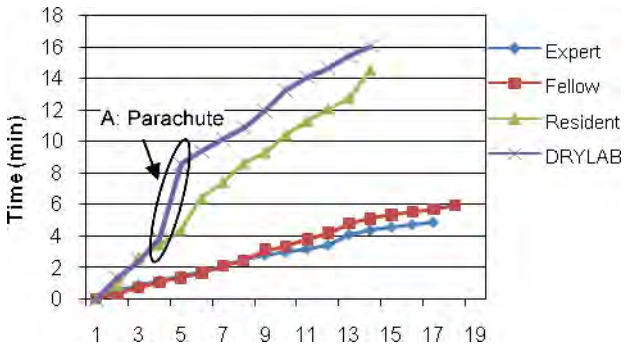


Fig. 8 Time chart to finish one anastomosis (clinical case vs. DRY Lab, A: time for parachute)

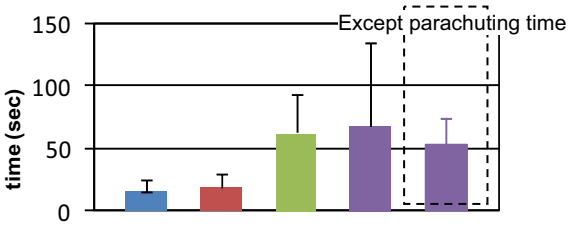


Fig. 9 Quantification of a suturing rhythm during an anastomosis (clinical cases vs. DRY Lab

IV. Conclusions

In this study, the DRY Lab, a simulator-based surgical training, has been proposed as a new approach to overcome the recent severe situation to train the cardiac surgeons. 62 anastomosis have been made by a trainee cardiac surgeon within 80 days. A hydrodynamic assessment of an anastomotic technique has been suggested by using mock circuit. It has been confirmed that measurement of pressure loss is effective to distinguish the learning phase of the trainee. An anastomotic technique also has been quantified by timing the respective sutures during a clinical operation. In sum, the findings suggest that quantitative assessment of simulator-based surgical training is an effective way to improve anastomotic technique in CABG.

Acknowledgment

This work was partly supported by "the robotic medical technology cluster in Gifu prefecture", Knowledge Cluster Initiative, Ministry of Education, Culture, Sports Science and Technology, Japan, partly supported by the Global Center of Excellence (GCOE) Program "Global Robot Academia", Waseda University, Tokyo, Japan and also partly supported by Health Science Research Grant (H20-IKOU-IPAN-001) from Ministry of Health, Labor and Welfare, Japan.

References

1. J. D. Birkmeyer, A. E. Siewers, D. E. Wennberg et al. (2002) Hospital volume and surgical mortality in the United States, N Engl J Med, Vol.346, No. 15 1128-1137
2. R. E. Clark and the Ad Hoc Committee on cardiac surgery credentialing of the Society of Thoracic Surgeons (1996) Outcome as a function of annual Coronary Artery Bypass Graft volume, Ann Thorac Surg 61:21-26
3. J. H. Shuhaiber and S. A. M. Nashef et al. (2008) Impact of cardiothoracic resident turnover on mortality after cardiac surgery: a dnamic human factor, Ann Thorac Surg 86:123-31
4. The ministry of health, labor and welfare (2002) statistical survey on medical doctors
5. Y. Park and M. Umezu et al., Quantitative Evaluation for Anastomotic Technique of Coronary Artery Bypass Grafting by using In-vitro Mock Circulatory System, EMBS 2007. 29th Annual International Conference of the IEEE, Aug. 2007 Page(s):2705 - 2708
6. M. Umezu, J. Kawai, H. Niinami et al. (2004) Biomedical engineering analysis on the effectiveness of cardiovascular surgery: anast, omosis methods for coronary artery bypass grafting, 7th Polish – Japanese seminar on new technologies for future artificial organs, pp.80-86
7. C. J.Andel, Teter V. Pistecky and C. Borst (2003) Mechanical properties of porcine and human arteries: implications for coronary anastomotic connectors, Ann Thorac Surg 2003; 76:58-65

Y. Park, M. Shinke, N. Kanemitsu, T. Yagi and M. Umezu are with the Umezu Laboratory from Graduate School of Integrative Bioscience and Biomedical Engineering, Waseda University, Tokyo, Japan (Corresponding author: Y. Park, youngpark@moegi.waseda.jp

Development of Evaluation Test Method for the Possibility of Central Venous Catheter Perforation Caused by the Insertion Angle of a Guidewire and a Dilator

M. Uematsu[1,2], M. Arita[2], K. Iwasaki[2], T. Tanaka[2], T. Ohta[2], M. Umezu[2] and T. Tsuchiya[1]

[1]Division of Medical Devices, National Institute of Health Sciences, Tokyo, Japan, [2] TWIns: Tokyo Women's Medical University/Waseda University Joint Institution for Advanced Biomedical Sciences, Waseda University, Tokyo, Japan

Abstract — **The Seldinger technique is a well-established medical procedure to insert an indwelling device into blood vessel. Although the method is widely performed, various adverse effects due to the procedure have been reported. In order to improve safety, some hospitals originally compiled important reminders based on their experiences in an operation manual. The aim of our research is to provide evidences supporting failure behaviors with a mock system to promote awareness in clinical practice. This paper presents results of a newly developed test method to evaluate the possibility of perforation while inserting the dilator to the cervical vein after the guidewire placement.**

A tensile tester (AGI-250kN, Shimadzu Corp.) equipped with a load cell (SLBL-50N, Shimadzu Corp.) was utilized to measure the insertion force of a dilator to vein. The porcine vein was prepared to be aligned with 15mm and to be cut opened to expose the medial wall, and it was mounted on a custom-made device. A guidewire and a dilator were vertically suspended from the upper side of the tensile tester. During the dilator was approaching down to the vein through the guidewire at the constant velocity, the insertion force was measured and the tissue surface was observed simultaneously. The perforation force was examined in relation to the insertion angle from 15degrees to 60degrees.

While veins were pressed only by a guidewire, perforation was not identified at all degrees. After inserting a dilator, veins were torn at 45degrees and at 60degrees more than 10N. It was suggested that vessel wall could be thinner and be torn by multiple insertion. It is concluded that the usage situation of a guidewire and a dilator was assessed objectively and the angle-load relationship was quantified. The test would be helpful to propose safe approach for patients.

Keywords — **Risk assessment, Central venous catheter, Perforation, Guidewire, Dilator.**

I. Introduction

Central venous catheters are routinely utilized to measure hemodynamic values, to deliver medications, and to offer nutrition. The catheter skill is required of doctors as basic procedure. However, central veins are located in deep except the external jugular. Doctors should search the inserting position blindly.

In order to approach a central vein, there are several methods: 1) catheter over the needle (conventional), 2) catheter over the guidewire (recently popular), 3) catheter through the needle or the catheter thorough cannula (less popular). Among them, the Seldinger technique (above 2) is a well-established medical procedure that allows catheters to be placed in the vein through a guidewire path.

Although the method is widely performed, various adverse effects due to the procedure have been reported[1-4]. The major complications are arterial puncture, bleeding, cardiac arrhythmias, etc. They have the following possible causes: 1) patient, 2) operator, 3) technique characteristics, 4) equipment available.

Many researchers have studied about the rate of catheter-related complications with respect to each factor. In order to improve safety, some hospitals originally compiled important reminders based on their experiences in an operation manual. Moreover, some doctors recommend using the ultrasonography to target the vein accurately by supporting visual information.

The aim of our research is to provide evidences supporting failure behaviors with a mock system to promote awareness in clinical practice. This paper presents results of a newly developed test method to evaluate the possibility of perforation while inserting the dilator to the cervical vein after the guidewire placement.

II. Materials and Methods

A. Seldinger technique

The system is designed for Seldinger technique. The technique is pursued as follows.

1. Insert the guidewire through the needle tube into the vessel
2. Remove the needle with indwelling the guidewire in the vessel
3. Pass a dilator through the guidewire into the vessel and expand the puncture hole with the dilator
4. Insert the central venous catheter via the guidewire and advance to the desired position

Chwee Teck Lim, James C.H. Goh (Eds.): ICBME 2008, Proceedings 23, pp. 1183–1186, 2009
www.springerlink.com

This testing method fulfills the condition as expressed above in 4.

B. Test apparatus

To examine the acceptable load for central vein while using the guidewire and the dilator under clinical situations, a mock system was developed. It was composed of a tensile tester and a vein-fixation jig. As shown in Fig.1, a load-cell (SLBL-50N, Shimadzu Corp.) was equipped on the top of the tensile tester (AGI-250kN, Shimadzu Corp.). Also, the vein-fixation jig was attached below the tester.

The porcine vein was prepared to be aligned with 15mm and to be cut opened to expose the medial wall as shown in Fig.2. And, it was mounted on a custom-made device with tucking the vein as shown in Fig.3.

A testing guidewire was passed through the dilator, and the dilator was chucked to the top of the tensile tester. Then, the guidewire was suspended from the ceiling and lay the part of it on the vein. During testing, veins were moistured with saline.

C. Test process

C-1. Perforation force: Measure the loading force with varying the angle θ that is formed between the vein and the dilator.

1. Adjust the jig to set the angle (θ=15, 30, 45, 60 [degrees]) between the vein and the dilator.
2. Advance the head of the dilator to about 10mm from the vein as a default position.
3. Measure the loading force with 20Hz sampling rate, while shifting the dilator downward in a vertical direction by 500mm/min until perforating the vein or moving 20mm from default position.
4. Repeat 1-3 by varying θ. The angle is registered as θ_p, if the vein starts to be perforated.

C-2. Slip angle (θ_s): Identify the angle θ when the guidewire is slipped away with no perforation.

1. Adjust the jig to set the angle ($\theta=\theta_p$-15, θ_p-7.5, θ_p [degrees]) between the vein and the dilator. The angle θ is set to the perforation angle θ_p+7.5degrees.
2. Advance the head of the dilator to about 10mm from the vein as a default position.
3. Measure the loading force with 20Hz sampling rate, while shifting the dilator downward in a vertical direction by 500mm/min until perforating the vein or moving 20mm from default position.
5. Repeat 1-3 by varying θ. The maximum loading force is registered as F_s, and also the angle is as θ_s, if the vein remains not to be perforated.

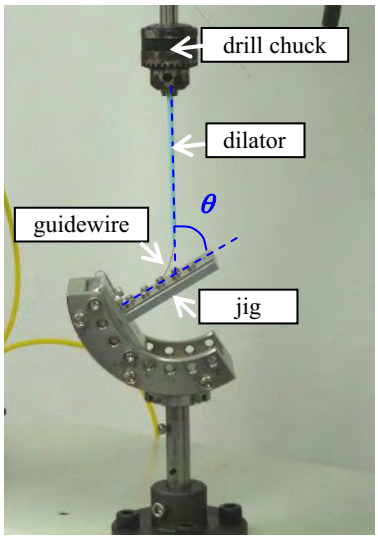


Fig. 1 Test apparatus

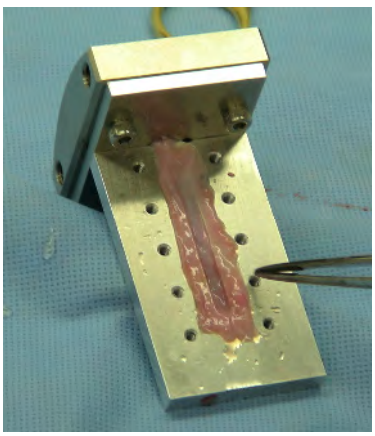


Fig. 2 Porcine vein

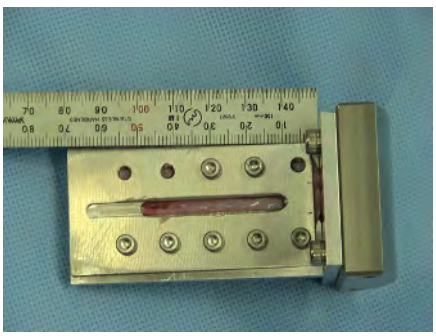


Fig. 3 Attachment jig

D. Experiment

The testing methods were applied for the porcine cervical vein. The details are as follows.

(a) θ=15 degrees, 4 trials (*C-1*)
(b) θ=30 degrees: 5 trials (*C-1*), 1 trials (*C-2*)
(c) θ=45 degrees: 4 trials (*C-1*), 2 trials (*C-2*)
(d) θ=60 degrees: 1 trials (*C-1*)
(e) $\theta=\theta_s$ degrees: 1 trials (*C-2*)

III. Results

A. Perforation force and slip angle

While veins were pressed only by a guidewire, perforation was not identified at all degrees. After inserting a dilator, veins were torn at 45degrees and at 60degrees more than 10N.

Fig.4 (a)-(d) show the loading force to the displacement of the dilator while changing the angle by 15degrees. Fig.4 (e) shows at the angle of 37.5degrees that was determined as the angle between 30degrees and 45degrees.

(a) θ=15 degrees
- Vein perforation was not observed.
- Dilator was just slipping over vein.

(b) θ=30 degrees
- Vein perforation was not observed.
- Dilator was slipping over vein, and deformed to follow the shape of vein.

(c) θ=45 degrees
- Vein was stretched thin, and perforated.
- Vein was started to be split over 10N.

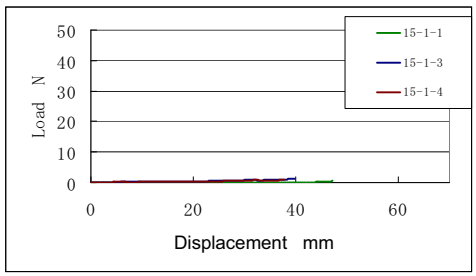
(d) θ=60 degrees
- Vein perforation was observed at 30N.
- Vein was perforated due to pushing the head of the dilator.

(e) θ=37.5 degrees
- Vein perforation was not observed.

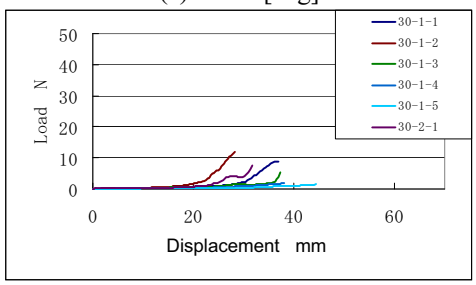
B. Relationships between loading force and angle

Table 1 and Fig.5 show the results of perforation force to insertion angle for all cases. At 45degrees, for three trials, vein was started to be split at 10.9±1.4N. For the other three trials, veins tore loose from the jig. At 60degrees, vein was entirely perforated at 30.4N. At 37.5degrees, perforation was not observed at more than 45N.

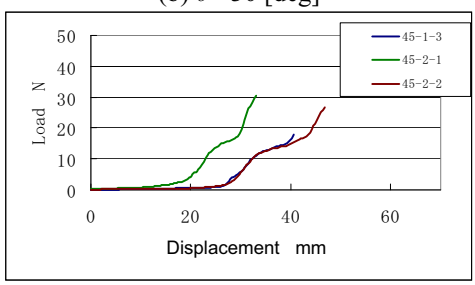
In Fig.5, measurement value was indicated in round, and average value was marked in asterisk.



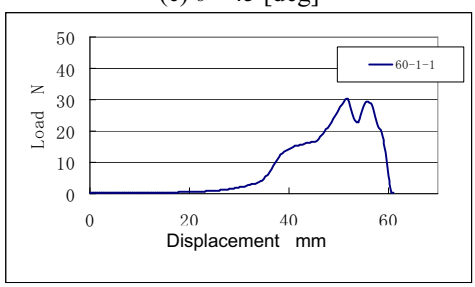
(a) θ =15 [deg]



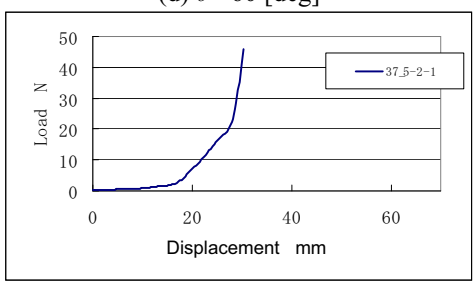
(b) θ =30 [deg]



(c) θ =45 [deg]



(d) θ =60 [deg]



(e) θ =37.5 [deg]

Fig. 4 Loading force to displacement of the dilator

Table 1 Perforation force to insertion angle

θ [deg]	Num. of trials	Num. of data obtainable	Num. of perforation	Perforation force Av.±Dev.[N]
15	4	3	0	N.A.
30	6	4	0	N.A.
45	6	6	3	10.9±1.4
60	1	1	1	30.4
37.5	1	1	0	N.A.

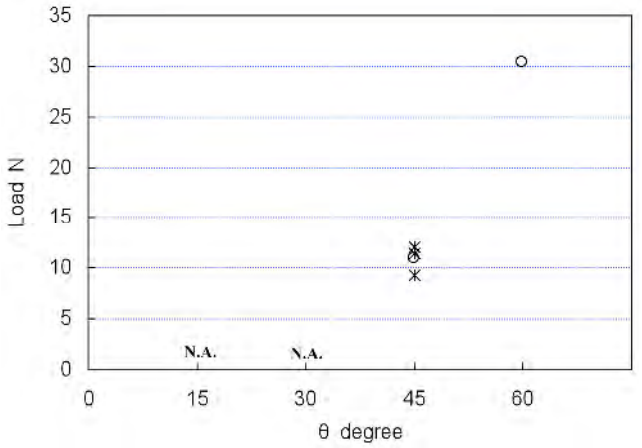


Fig. 5 Perforation force to insertion angle

IV. Discussion

During the insertion, dilator proceeded in 5 steps as follows: 1) dilator was slipping over the vein, 2) dilator was bending to fit the guidewire path, 3) dilator was pushing onto the vein, 4) dilator was bending to fit the guidewire path (same as 2), 5) guidewire was kinked by dilator and vein perforation was identified.

As shown in Fig.5-(d), after guidewire kinking, the loading force was decreased drastically. It was caused by vein perforation. Fig.5-(c) shows that no force-decreasing point was identified, but vein was stretch to thin and perforated. Fig.5-(e) shows that there were neither force-decreasing point nor perforation. Thus, the pushing force to the vein would make vascularized tissue be thinner and be destroyed.

As described in the conventional manual[5], this experiment exhibited the insertion angle was suitable at 30degrees to 45degrees. Under the general operation, 10N as inserting force is larger than anticipated. However, caution should be exercised in multiple insertions of the guidewire and the dilator.

V. Conclusion

It is concluded that this newly-developed evaluation method was achieved as follows: 1) the usage situation of a guidewire and a dilator was assessed objectively. 2) The angle-load relationship was quantified. The test would be helpful to propose safe approach for patients.

Acknowledgment

This swork was supported by Health Labour Sciences Research Grant (H19-iyaku-ippan-015).

References

1. David C. McGee, Michael K. Gould (2003) Preventing Complications of Central Venousss Catheterization. N Engl J Med 348:1123–1133
2. Mansfield PF, Hohn DC, Fornage BD et al (1994) Complications and failures of subclavian-vein catheterization: N Engl J Med 331:1735–1738
3. T. Andrew Bowdle (2002) Central line complications from the ASA Closed Claims Project: an update: ASA Newsletter. 66:11-2, 25
4. Denys BG, Uretsky BF (1991) Anatomical variations of internal vein location: impact on central venous access: Crit Care Med. 19:1516–9
5. William C. Shoemaker, George C. Velmahos, Demetrios Demetriades(2003) Procedures and Monitoring for the Critically Ill, WB Saunders Co, Philadelphia

Author: Miyuki UEMATSU
Institute: National Institute of Health Sciences
Street: Kamiyoga 1-18-1, Setagaya-ku
City: Tokyo
Country: Japan
Email: uematsu@nihs.go.jp

The Assessment Of Severely Disabled People To Verify Their Competence To Drive A Motor Vehicle With Evidence Based Protocols

Peter J. Roake

European Mobility Group, Hemel Hempstead, England

Abstract — **Objectives. The demographics of the disabled and aging populations who are demanding to maintain their independence and mobility are testing the driver licensing authorities to ensure that physical and cognitive difficulties are measured to an acceptable standard.**

The highways are becoming more congested with an ever increasing population which is likely to continue for many years to come. It is therefore important to ensure that the disabled and elderly populations are accurately assessed of their competence to drive for the safety of all.

Assessment procedures which take account of the client's limitations, innovative adaptations to vehicles and the latest range of vehicles available should result in a solution which satisfies the national regulations and the aspirations of disabled and elderly people.

Methods. In North America, Europe and Scandinavia this task is being carried out by a team of professionals such as Occupational Therapists, Clinicians and Engineers. Assessment centres are being developed throughout these countries working to national and local standards utilising part time and voluntary staff in an effort to keep costs down.

The need for evidence based assessment reports is becoming an essential requirement to justify the costs of funding an adapted vehicle, especially if a drive from the wheelchair solution is deemed necessary.

Results. It is clear that a common approach to assessment methods is required and new EU initiatives are being developed such as PORTARE and CAPI projects (Refer: Fit to Drive International Congress in Prague June 19th – 20th 2008) which will result in an EU handbook of Driving Assessment and Protocols for adapting vehicles.

Discussion. Will it be possible for countries who take their population demographics seriously to participate in these EU initiatives and benefit from the research to ensure that their disabled and aging people will be able to drive safely on the road?

Keywords — **Disability, Assessment, Driving, Simulator, Wheelchair**

I. Introduction

Advances in medical provision have resulted in an ever increasing aging population throughout most developing countries, coupled with the expectations of the disabled community to maintain their mobility is leading to extra ordinary demands on driver licensing authorities to decide on driving entitlement.

In the USA and E.U./Scandinavian countries the decision on the ability of a person to drive after acquiring a disability is taken by a doctor using guidelines developed over a period of time reflecting agreed standards of safety for the territory concerned.

These guidelines are not consistent [1] throughout these countries making it difficult to extend these guidelines to the developing world, however they can provide a good platform to start from if standard regulations do not exist.

However certain common sense rules apply which govern items such as visual and cognitive ability being two of the most written about subjects when considering testing for the driving ability of the elderly and disabled and are readily referenced.

It is anticipated that the aging and disabled populations will continue to expand in line with the technological advances in the vehicle adaptation field such that more people will expect to maintain their mobility and independence.

In many countries including Australia rules/laws exist to ensure people who reach a certain age have to retake their national driving test [2] the results of which are not always conclusive as many older drivers adapt their method of driving to compensate for infirmity.

It is important to have in place a recognised method of performance measurement/test that can determine their ongoing mobility with regard to driving a motor vehicle. This can consist of a theory test combined with a practical road test reflecting the latest demands on drivers. Some elderly people may find this discrimative and be reluctant to subject themselves to a driving test of this sort, especially as some may be only using their vehicles for short journeys. This was the case for the group of disabled people in the U.K. who were given a special three wheeled vehicle funded by the U.K. government.

This group rarely completed more than 1000 miles per year and when they were eventually transferred into specially adapted standard cars it was found that their average annual mileage more than quadrupled as they became familiar with the benefits of driving the modern car albeit no additional driving test was thought necessary further high-

Chwee Teck Lim, James C.H. Goh (Eds.): ICBME 2008, Proceedings 23, pp. 1187–1190, 2009
www.springerlink.com

lighting the possible need for additional driver testing when changing from one type of driving system to another.

A. Static simulator

This method of assessment is usually carried out in a semi clinical environment utilising simulators or test rigs with a video screen or some method of stimulus to impart a dynamic element into the evaluation experience. Some of these simulators include the sound of a car's engine, ability to change gear and vibration to make the test more realistic.

Other methods rely on visual stimulus using a variety of light patterns to test the cognitive ability with regard to decision making accuracy.

These types of clinical tests are usually carried out indoors and can be regarded as a "sorting process" prior to road testing however the value of utilising the static simulator is that severe cognitive difficulties can be identified without endangering the disabled person or driving examiner which could be the outcome when road testing.

Borderline cases will need to be subjected to a live road test in an effort to extend their cognitive ability to recognise instructions given by the driving examiner and observing road signs in an all encompassing driving test which takes into consideration visual acuity and the ability to remember items such as road signs. In some countries this process is videoed to provide evidence of the performance of the road test.

B. Disability examples.

When an individual acquires a disability from a road traffic accident, medical negligence or other source a significant element of their recovery/rehabilitation is awareness of their mobility prospects.

These disabilities can include Tetraplegia, Hemiplegia, Polio, Muscular Dystrophy and Thalidomide being just a small sample of catastrophic impairments that can inhibit mobility. Some of these disabilities can result in it being necessary to drive a vehicle from an electric wheelchair where the following considerations should be made.

C. Driving from an electric wheelchair.

People presenting in an electric wheelchair at the assessment centre are some of the most difficult to assess as the integrity and crash worthiness of the wheelchair needs to be considered along with the everyday special needs of the disabled person. This reduces the selection of wheelchairs considerably to ensure compatibility of the wheelchair with a suitable vehicle and wheelchair tie down system.

A wheelchair assessment including a driver option can result in an expensive solution which may need the support of external or third party funding agencies as these specialised wheelchairs can cost up to (Euro) €20,000.

In the USA and E.U./Scandinavian countries drive from the wheelchair has been available for over 20 years utilising large electric wheelchairs and van derived vehicles with automatic transmission such as the Dodge Day Van, Mercedes Sprinter, Ford Transit Van, VW Caravelle and Chrysler Voyager Entervan which have entry possibilities through either the side or rear doors. In E.U. countries there has been a trend towards the smaller van derivatives such as the Renault Kangoo and VW Caddy types with automatic transmission and usually entry into the vehicle through the rear doors as the demand for this type of solution is increasing in line with the demographics outlined earlier.

Crash testing of wheelchairs and wheelchair tie downs to National Standards are now mandatory in these territories which provide a sense of security and confidence for users, funding agencies and insurance companies.

D. Driving criteria.

The criteria for safe driving is no different for a disabled person to that of an able bodied person and in most countries where drive from the wheelchair has been legislated the demands of being able to operate the primary and secondary controls are no different.

Servo systems have been developed to compensate for reduced ability to enable severely disabled people to drive safely and pass the standard driving test. Part of the assessment process is to determine the essential demands of the driving test and the approval of a doctor and/or oculist is essential in this process where cognitive and visual acuity has been tested and approved.

The hands on driving of the vehicle needs to be established so that the appropriate servo systems can be prescribed.

E. The Steering system.

In the case of high lesion tetraplegia, with a cervical break at, say C5/6, where loss of muscle tone, ligament control and nerve responses may have been compromised it may be necessary to determine work effort, range of movement and speed of movement of the hands and arms to determine a satisfactory steering solution.

The results of which can range from a reduction of the steering efforts and fitting a special quad grip device to the

steering wheel rim to fitting a joystick steering device in lieu of the steering wheel.

The assessment process needs to test these parameters at least 20 times, to inflict a measure of fatigue and record the results in a clinical format which can be stored on a computer to be included in the assessment report.

F. Braking and accelerator.

These two features are considered together as it is necessary to determine the minimum time taken to effect an emergency stop from a designated speed. A typical emergency stop reaction time could be measured from a speed of 48k/h to a point in time when all road wheels are locked up (i.e. sufficient brake load to stop the vehicle in the designated stopping distance), (say 100Nm), in the quickest possible time.

This stopping distance has no particular international standard however a nominal figure of 0.75 seconds is generally accepted as a satisfactory stopping time to pass a driving test.

For most high lesion tertraplegics this can only be achieved by adding servo assisted brake and accelerator systems into the vehicle such as Electronic Brake and Gas device (E.B.G.).

The assessment process should include access to a static simulator or test rig which is wheelchair compliant and enables the individual to attempt this via a joystick control or hand control which is directly connected to transducers which can undertake both force and time measurements which are then processed by a computer to provide a direct read out of the resulting performance.

Stimulus can be by light or sound or both with a minimum number of 20 tests once the person has become familiar with the tasks involved [3].

G. Fatigue Allowance.

It is necessary to determine the fatigue boundary of the person being assessed so that an accurate conclusion of their capabilities is made. This can involve repeating the steering and emergency stop reaction tests until the work effort and or reaction times deteriorate to an unacceptable level or beyond the technology available to adapt the vehicle.

This will be seen on the output graphs and be useful to include in the conclusions of the assessment report. It is important for the assessor to be able to recommend a driving solution which is able to extend a disabled persons range of mobility bearing in mind that most journeys consist of two directions i.e. going out and getting back.

Budgetary constraints can sometimes result in inadequate driving controls be prescribed which have great demands on the driver and result in fatigue which can lead to a loss of confidence in attempting the journey resulting to false economy and frustration for all concerned.

H. Servo Systems Development

Devices for interfacing with the vehicles primary and secondary controls are always under development to support the competitive nature of the vehicle adaptation industry. This type of development engineering is an ongoing feature of the automotive industry with the release of "concept cars" which sometimes include electronic joystick devices to operate steering, braking and accelerator along with infra red or wireless systems to interface with vehicle electronic systems such as Multiplex and Can Bus electronic systems.

Research and development by the automotive industry is not always directed at the less able and more targeted at improving sales, however it is clear that in recent years the development of on board computers and much improved vehicle electronic systems that a considerable spin off has benefited the disabled driver such as digital signals monitoring and controlling most of the vehicles primary and secondary systems. Specialist adaptation companies throughout the E.U. and Scandinavia have been spearheading the interface devices to enable the severely disabled to regain a measure of independence and mobility.

With the co operation of the industry as a whole the new interface devices are able to comply with stringent type approval demands of the Vehicle Construction and Use Regulations both in the USA and E.U./Scandinavian countries.

I. Disabled Driver Statistics.

The most severe of disabilities such as those mentioned earlier which represent the smallest population but reflect the highest cost due to the low volume and high technical content whereby a drive from the wheelchair solution for a high lesion tertraplegics could cost in the region of (Euro) €120.000. These levels of cost are regularly reflected in litigation cases or supported by governmental/charitable funding activities.

The vast majority of special needs mobility funding will be required to support people with lesser disability but also life threatening conditions such as Hemiplegia (stroke) where relatively simple vehicle adaptations will be required (e.g. left foot accelerator pedal or simple hand controls for operating the brake and accelerator) which subject to assessment may be all that is required.

There is a need for ongoing assessment of people who have progressive disabilities such as Multiple Sclerosis (M.S.), Muscular Dystrophy (M.D.) and Motor Neurone Disease (M.N.D.) where the condition can deteriorate to a point where safe driving can be compromised e.g. in some M.S. cases the ability to positively transfer the right foot from the accelerator pedal to the brake pedal to stop the car become difficult to achieve. However if hand controls are used which are operable within the peripheral vision of the driver then the confidence to stop the car is regained and generally the overall emergency stop time is reduced to an acceptable level.

The responsibility for reassessment is not clear in many countries and in some territories relies on the integrity of the driver to report his/her condition to the authorities and determine a solution for continuance of driving or alternatively stop driving altogether.

J. European Initiatives.

There are two projects being conducted by professional bodies in the E.U. to self regulate the assessment process (PORTARE) and the vehicle adaptation process (CAPI) in an effort to standardise these activities across all countries of the E.U. and Scandinavia.

The outcomes will be a set of standards and quality procedures which should be available for publication during 2009/10. This work will enable developing countries that recognise the importance of making mobility for all a priority in their governmental strategies to put into practise at a beneficial budget.

II. Conclusions.

The assessment of older drivers is complicated by various changes associated with the aging process, including cognitive, morbidity and differences in individuals to adjust to impairments and road testing may be the most appropriate method of reviewing driving competence [4].

However when assessing the severely disabled (who may be confined to a wheelchair) competences to drive a motor vehicle there are many facets to consider such as the suitability of the wheelchair, effects of gravitational forces and the type of servo systems that are required to meet the national driving regulations. It is clear that in the western countries that driving regulations exist according to the territory and not necessarily on U.S. or E.U. wide basis.

There is massive scope to standardise the methods of assessment throughout the world to ensure that severely disabled people are not excluded from being able to extend their mobility as far as possible.

The work of the E.U. POTARE and CAPI groups are an attempt to meet these criteria and countries who are considering an inclusive legislation for their elderly and disabled drivers could benefit from this research.

An agreed set of standards/rules need to be developed with the possibility of flexing them to meet with local conditions may provide a framework to base the research on.

This research should include the vast amount of literature available for assessing the cognitive and sensory perception that may affect driving [5] amongst others whose literature contribution has provided a set of international data to compare with including [6]

In addition to the development of international standards for assessment methods there is a need to set out standards for vehicle adaptation methods which take into account the design, crash worthiness and national standards such ISO, Construction and Use regulations for motor vehicles and the criteria set out by testing authorities such as German TUV organisation (short for Technischer Überwachungs-Verein, Technical Monitoring Association in English) and in the USA Society of Automotive Engineers (SAE).

This research will benefit developing countries that will be looking for agreed standards that encompass good working practices coupled to high quality engineering at a cost that is affordable.

Acknowledgment.

This research was supported by the European Mobility Group and the UK Forum of Assessment Centres. The author also wishes to acknowledge the support of the SIM University in Singapore and industry partners: Steering Developments Ltd in the UK and the University of Greenwich in London.

References

1. White S O'Neill D. (2000) Health and Re-Licensing Policies for Older Drivers in the European Union, Gerontology, Vol.46, pp. 146-152
2. Langford J, Fitzharris M,Newstead S,Koppel S. (2004) Some Consequences of Different Older Driver Licensing Procedures in Australia, Accident Analysis and Prevention, Vol. 36, No. 6, pp. 993-1001.
3. Morrison RW, Swope JG, Halcomb CG. Movement Time and Brake Pedal Placement, Human Factors 1986; 28:241-246.
4. Coeckelbergh T, Brouwer W, Cornelissen F, Kooijman A. (2004) Predicting Practical Fitness to Drive in Drivers with Visual Field Defects Caused by Ocular Pathology, Human Factors, Vol.46, No. 4, pp. 748-760.
5. Marottoli and Drickamer, 1993; Stelmach and Nahom, 1992.
6. Bohensky, Megan, Charlton, Judith, Odell, Morris and Keeffe, Jill (2008) Implications of Vision Testing for Older Driver Licensing', Traffic Injury Prevention, 9:4,304-313

Viscoelastic Properties of Elastomers for Small Joint Replacements

A. Mahomed[1,2], D.W.L. Hukins[1], S.N. Kukureka[2] and D.E.T. Shepherd[1]

[1] School of Mechanical Engineering, University of Birmingham, Birmingham, UK
[2] School of Metallurgy and Materials, University of Birmingham, Birmingham, UK

Abstract — **In the first part of this paper, the *E'* (storage modulus) and *E''* (loss modulus) values of six cylindrical specimens of Silastic® Q7-4780 medical grade silicone (suitable as a 90 day implant material), immersed in containers with physiological saline solution at 37°C, were measured using dynamic mechanical analysis. The results were compared with previous published data of a medical grade silicone, suitable as a 29 day implant material. The moduli of Q7-4780 were frequency-dependent as expected and were not significantly different from the shorter-term implant material. In the second part of this paper, the *E'* and *E''* values of Elast-Eon™ 3, a polyurethane with poly(dimethylsiloxane) (PDMS) and poly(hexamethylamine oxide) (PHMO) segments, were measured before and after accelerated aging in an oven at 70°C for 38 days. The moduli of six cylindrical specimens of Nagor® medium hardness medical grade silicone were also investigated using the same aging conditions. The results showed, that both the *E'* and *E''* of the Elast-Eon™3 were affected by accelerated aging. However the properties of Nagor® silicone were not affected.**

Keywords — **Silicones, Polyurethanes, Elast-Eon™, Viscoelastic, Accelerate aging, Dynamic Mechanical Analysis**

I. Introduction

Rheumatoid arthritis and osteoarthritis can destroy the natural metacarpophalangeal (MCP) and proximal interphalangeal (PIP) joints in the hand [1, 2]. As a result, patients will experience pain and loss of function of the hand [3, 4]. In many cases, the best option available to restore the function of the hand is to replace the destroyed joint with an artificial joint [4, 5, 6].

One of the most popular artificial joints used is the one-piece silicone joint developed by Alfred B. Swanson in the 1960s [5]. Since the development of the Swanson joint (Wright Medical Technology, Arlington, TN 38002, USA), other designs have been produced, such as the soft skeletal hand implants (Small Bone Innovations, Inc, Morrisville, PA 19067, USA) and the NeuFlex finger joint (DePuy Orthopaedics, Inc, Warsaw, IN 46581, USA) [6].

Silicones are used because they are biocompatible, durable, flexible and allow the necessary range of movements. However, the joints fracture prematurely *in vivo* [6]. The highest fracture rate reported is 82% by Kay et al. [7].

Silicones are viscoelastic i.e. their properties are time (or frequency) and temperature-dependent [8]. It has been suggested by Mahomed *et al*. [9] that there is the possibility that the behaviour of the silicone joint may be frequency-dependent.

Mahomed *et al*. [9] investigated the viscoelastic properties of 3 medical grade silicones intended for 29-day implantation (short-term). During the tests, the silicones were immersed in physiological saline solution at 37°C. The properties were measured using dynamic mechanical analysis (DMA) over a frequency range, *f*, of 0.02–100 Hz. It was concluded that the viscoelastic properties of these silicones depended on frequency and appeared to be undergoing the onset of a transition from the rubbery to the glassy state at above about 0.3 Hz. As a result, above about 0.3 Hz, the three silicones grades used in their study could experience a reduced life-time and dissipate more energy through fractures [9].

Apart from the short-term silicone, silicones intended for 90-day implantation (medium-term) are also available from the supplier (Dow Corning Limited, Allesley, Coventry, UK) for research. It is not known whether the implantation time will affect the viscoelastic properties of the material. The aim of the first part of this paper is to investigate this possibility using the same experimental procedure as Mahomed *et al*. [9].

More recently, another viscoelastic material, Elast-Eon™ has been suggested as a possible substitute for silicone in the implants [10]. Elast-Eon™ is a polyurethane elastomer with poly(dimethylsiloxane) and poly(hexamethylamine oxide) segments [11].

The properties of materials such as Elast-Eon™ that are suitable to be implanted in the body should not deteriorate while *in vivo*. It is possible to subject the materials to elevated temperatures, known as "accelerated aging", to determine whether deterioration is likely to occur [12, 13]. It is not known whether accelerated aging will affect the modulus of the material. However, the properties of polyurethane has been reported to degrade as a result of accelerated aging [14, 15, 16], but not those of poly(dimethylsiloxane) [14, 17].

The aim of the second part of this paper is to compare the effect of accelerated aging on the modulus of Elast-Eon™ and of Nagor® medical grade silicone; a poly(dimethylsiloxane).

Chwee Teck Lim, James C.H. Goh (Eds.): ICBME 2008, Proceedings 23, pp. 1191–1194, 2009
www.springerlink.com

II. Theory

The modulus of a viscoelastic material is represented by a complex number [8].

$$E^* = E' + iE'' \quad (1)$$

Where E' is the storage modulus (elastic) and E'' the loss modulus (viscous).

Aging of a material can be accelerated by a factor of

$$f = 2^{\Delta T/10} \quad (2)$$

by increasing the temperature by an increment ΔT [12, 13]. For example, if a material is maintained at 70°C for 38 days, this is the same as aging it for 38 × 2(70-37)/10 = 380 days, i.e. aging for ≈ 13 months, at 37°C [12, 13].

III. Materials and Methods

The experiments were performed on a Silastic® Q7-4780 Silastic® silicone (medium-term implant material from Dow Corning Ltd, Coventry, UK). The material was supplied in two parts, Part A and B. A Schwabenthan Berlin two-roll-mill (Engelmann & Buckham Ltd, Alton, Hampshire, GU34 1HH, UK) was used to mix the parts together. Ten cylindrical specimens (29 mm in diameter and 13 mm thick), were pressed into a mould and cured in exactly the same way as described previously [9]. Since these silicones are intended to be implanted for a maximum of 90 days, they were kept in physiological saline solution (9.5 g L^{-1} NaCl in water) at 37°C for 90 days to simulate *in vivo* conditions before undergoing compression tests.

Nagor® medium hardness medical grade silicone was supplied as a cured 17 mm thick carving block with dimensions (70 x 20 mm) from (Nagor Limited, Isle of Man, IM99 1AX, British Isles). The original carving block was cut into six cylindrical silicone specimens (15 mm diameter, 6 mm thickness).

The Elast-Eon™ 3 was supplied by the manufacturer (AorTech Biomaterials Pty Ltd, Frenchs Forest, Australia) as a cured cylinder of material. The original cylinder was cut into six cylindrical specimens (diameter 5 mm, thickness 2.2 ± 0.2 mm).

Six specimens of the Nagor® and Elast-Eon™ 3 cylinders were immersed in containers with physiological saline solution and put into a Carbolite natural convection laboratory oven (Carbolite, Hope Valley, S33 6RB, UK) at 70°C for 38 days. This is the same as aging them for ≈ 13 months at 37°C.

Each sample was immersed in physiological saline at 37°C and subjected to sinusoidal cyclic compression tests under a static load of 40 N in the frequency range 0.02-100 Hz, using a BOSE ElectroForce 3200® Series testing machine (BOSE Corporation, ElectroForce Systems Group, Minnesota, USA) [9]. The peak for the sinusoidal cyclic load was ± 5 N. All tests were controlled using the BOSE WinTest DMA software.

IV. Results

The results for Silastic®, in Fig. 1, show that E' is fairly constant, at ≈ 7 MPa, at loading frequencies below 0.3 Hz (log$f$ value of -0.5). Above this, E' increases, eventually attaining a value of about 13 MPa. E'' also shows similar frequency-dependent behavior. Therefore, the medium-term implant material (silicone Grade Q7-4780) appears to undergo a glass transition above ≈ 0.3 Hz. Below this frequency it behaves like a rubber and above it, it starts to behave more like a glass.

Results for Elast-Eon™ 3, in Fig. 2, show that both E' and E'' of Elast-Eon™ increased with frequency i.e. showed frequency-dependent behavior. The moduli also increased after accelerated aging. The upper and lower 95% confidence intervals (shown as error bars) did not overlap throughout the frequency range, i.e. accelerated aging had a significant effect. The appearance of the specimens changed after accelerated aging. Before aging, they were transparent with a slight yellow coloration, but after aging, they became darker and more opaque.

Fig 3. shows that for the Nagor® silicone both the E' and E'' increased with frequency i.e. showed frequency-dependent behavior. The E' increased slightly but not significantly after accelerated aging i.e. the confidence intervals (shown as error bars) overlapped thought the frequency range.

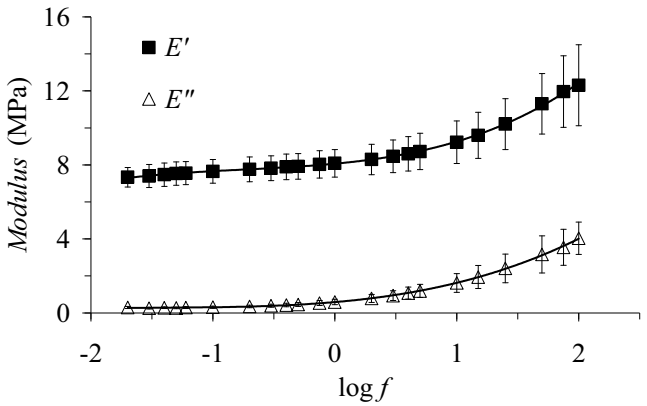


Fig. 1 E' and E'' of Silastic® Q7-4780 plotted against $\log_{10}$ of frequency

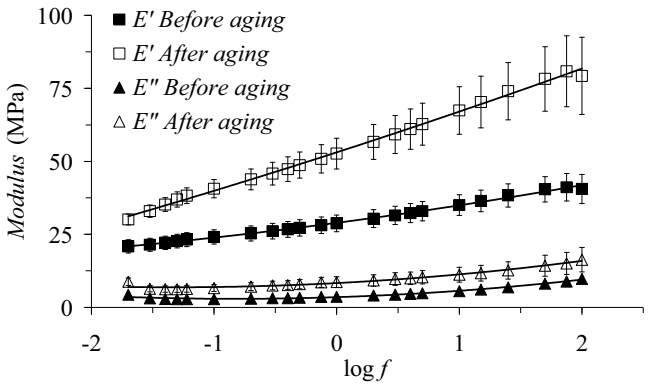


Fig. 2 *E'* and *E''* of Elast-Eon™ 3 plotted against $\log_{10}$ of frequency

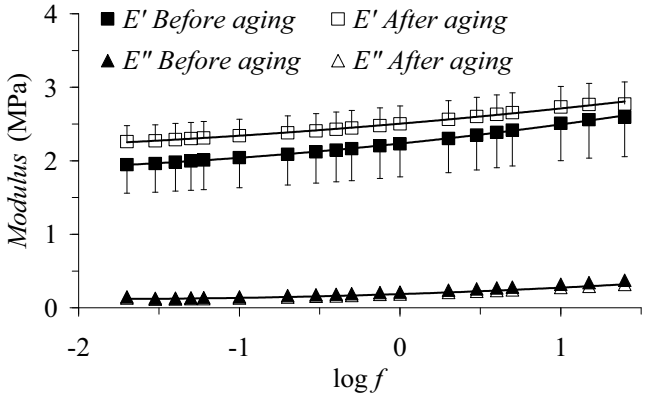


Fig. 3 *E'* and *E''* of Nagor® silicone plotted against $\log_{10}$ of frequency

V. Discussion

When the results in Fig.1 were compared with published data [9] from a short-term implant material (silicone Grade C6-180) using 95% confidence intervals, the confidence intervals throughout the frequency range overlapped, i.e. implantation time had no significant effect on *E'* and *E''* values. The frequency-dependent behavior of Silastic® Q7-4780 is consistent with the previous studies by Mahomed *et al*. [9] and Murata *et al*. [18].

Accelerated aging (70°C for 38 days) significantly affected the viscoelastic properties of Elast-Eon™ 3. As no previous study has investigated this, it is not possible to compare this result with other studies. However, Elast-Eon™ is a derivative of polyurethane and previous studies [14, 15, 16] have suggested the polyurethanes will degrade as a result of accelerated aging. It is recommended that before Elast-Eon™ 3 is used as a substitute for silicone in finger and wrist implants, further studies are required to determine its effectiveness as an implant material. In particular it would be interesting to age Elast-Eon™ at 37°C for a year and measure its properties before and after aging.

The viscoelastic properties of Nagor® medium hardness medical grade silicone were not affected by accelerated aging (70°C for 38 days). This result is consistent with previous studies [14, 17].

VI. Conclusions

- *E'* and *E''* of Silastic® Q7-4780 are frequency-dependent.
- The *E'* and *E''* of Silastic® Q7-4780 is not significantly different ($p < 0.05$) when compared with Grade C6-180 investigated by Mahomed et al [9]. Implantation time does not affect the properties.
- *E'* and *E''* of Elast-Eon™ 3 and Nagor® medium hardness medical grade silicone are frequency-dependent, before and after accelerated aging has occurred.
- *E'* and *E''* of Elast-Eon™ 3 increased after accelerated aging (at 70°C for 38 days) and were significant different ($p < 0.05$) when compared to the moduli before aging. After accelerated aging, the colour of Elast-Eon™ 3 darkens and the opacity increases.
- *E'* of Nagor® medium hardness medical grade silicone increased slightly but not significantly after accelerated aging.

Acknowledgments

We thank: Mr Derek Boole, Mr John Lane, and Mr Peter Hinton for help and advice in making the equipment; the Engineering and Physical Sciences Research Council for a research studentship for Aziza Mahomed; Dow Corning Limited for the medical grade silicone elastomers; the Arthritis Research Campaign for funds for the testing equipment.

References

1. Beevers D J, Seedhom B B (1993) Metacarpophalangeal joint prostheses: a review of past and current designs. Proc Inst Mech Eng [H] 207:195-206
2. Pylios T, Shepherd D E T (2007) Biomechanics of the normal and diseased metacarpophalangeal joint: implications on the design of joint replacement implants. J Mech Med Bio 7:163-174
3. Alderman A K, Ubel P A, Kim H M et al. (2003) Surgical management of the rheumatoid hand: Consensus and controversy among rheumatologists and hand surgeons. J Rheum 30:1464-1472
4. Mandl L, Galvin D H, Bosch J P et al. (2002) Metacarpophalangeal arthroplasty in rheumatoid arthritis: What determines satisfaction with surgery? J Rheum 29 2488-2491

5. Swanson A B (1968) Silicone rubber implants for replacement of arthritic or destroyed joints in hand. Surg Clin N Am 48:1113-1127
6. Joyce T J (2004) Currently available metacarpophalangeal prostheses: their designs and prospective considerations. Exp Rev Med Dev 1:193-204
7. Kay A G, Jeffs J V, Scott J T (1978) Experience with Silastic prostheses in the rheumatoid hand. A 5-year follow-up. Ann Rhuem Dis 37:255-258
8. Ferry J D (1961) Viscoelastic properties of polymers. John Wiley & Sons Inc, New York and London
9. Mahomed A, Chidi N M, Hukins D W L et al. (2008) Frequency dependence of viscoelastic properties of medical grade silicones. J Biomed Mater Res [B] In press
10. Shepherd D E T, Johnstone A J (2005) A new design concept for wrist arthroplasty. Proc Inst Mech Eng [H] 219:43-52
11. Gunatillake P A, Martin D J, Meijs G F et al. (2003) Designing biostable polyurethane elastomers for biomedical implants. Aust J Chem 56:545-557
12. Hemmerich K J, (1998) Accelerated aging. General aging theory and simplified protocol for accelerated aging of medical devices. Med Plast Biomat 16-23
13. Hukins D W L , Mahomed A, Kukureka S N (2008) Accelerated aging. General aging theory and simplified protocol for accelerated aging of medical devices. Med Eng Phys In press
14. Yu R, Koran A 3rd, Craig R G (1980) Physical properties of maxillofacial elastomers under conditions of accelerated aging. J Dent Res 59: 1041-1047
15. Craig R G, Yu R, Koran A 3rd (1980) Elastomers for maxillofacial applications. Biomaterials 1:112-117
16. Goldberg A J, Craig R G, Filisko F E (1978) Polyurethane elastomers as maxillofacial prosthetic materials. J Dent Res 57: 563-569
17. Wagner W C, Kawano F, Dootz E R et al. (1995) Dynamic viscoelastic properties of processed soft denture liners: Part 2-effect of aging. J Prosth Dent 74:299-304
18. Murata H, Hong G, Hamada T et al (2003) Dynamic mechanical properties of silicone maxillofacial prosthetic materials and the influence of frequency and temperature on their properties. Int J Prostho 16:369-374

Corresponding author:

Miss Aziza Mahomed
School of Mechanical Engineering
University of Birmingham
Edgbaston
Birmingham
B15 2TT
United Kingdom
Email: axm503@bham.ac.uk

Synergic Combination of Collagen Matrix with Knitted Silk Scaffold Regenerated Ligament with More Native Microstructure in Rabbit Model

Xiao Chen[1], Zi Yin[1], Yi-Ying Qi[1], Lin-Lin Wang[1], Hong-Wei Ouyang[1,2 *]

[1] Ccenter for stem cells and issue Engineering, School of Medicine, Zhejiang University; China
[2] Department of Orthopaedic Surgery, Sir Run Run Shaw Hospital, School of Medicine, Zhejiang University; China

Abstract — **A number of researches on ligament and tendon tissue engineering scaffold have been carried out. However, a scaffold which simultaneously possesses optimal strength, porous structure and biocompatible microenvironment is yet to be developed. This study aims to design a new practical ligament scaffold by synergic incorporation of silk material, knitting structure and collagen matrix.**

Physical properties and biocompatibility of the knitted silk-collagen sponge scaffolds were evaluated in vitro and in mice model. Their efficacy for in situ ligament tissue engineering was investigated in New Zealand White rabbit model with a 6-mm gap defect of the medial collateral ligament (MCL). The histology, microstructure, biochemical composition, matrix genes expression and strength of the ligament repair of different groups were evaluated at 2, 4 and 12 weeks.

In vitro data show that cells on collagen matrix expressed higher collagen I and decorin genes at 3 and 5 days than that on silk substrate. The study in mice model demonstrated that silk scaffold caused little inflammatory reaction after subcutaneous implantation, the strength of scaffolds decreased to 25.9% of original value at 3 month and increased to 33.5% at 6 month. In the MCL repair study, silk-collagen treated MCLs had more connective bands of collagen matrix formed and more collagen deposition compare to those in silk treated MCLs at 2 ,4 and 12 weeks. Moreover, silk-collagen treated MCLs possessed better mechanical property, larger diameter of collagen fibrils and stronger scaffold-ligament interface healing at 12weeks.

These results proved that the knitted silk-collagen sponge scaffold possessed optimal internal space, biocompatible environment and mechanical strength. It could improve the structure and function of ligament repair by regulating ligament matrix genes expression and collagen fibril assembly. The findings suggested that knitted silk-collagen sponge scaffold is a promising candidate scaffold for practical ligament and tendon tissue engineering.

Keywords — **ligament, tissue engineering, knitted silk scaffold, collagen matrix**

I. Introduction

Ligaments and tendons are frequently damaged during sports and other rigorous activities [1,2]. Significant dysfunction and disability can result from suboptimal healing of ligament injuries. At present, the therapeutic options to treat tendon and ligament injuries include autografts, allografts, xenografts and prosthetic devices However, no ideal replacement have been able to adequately restore function for the long term [1,2]. Clearly, more advantageous alternative grafts are yet to be developed.

Recent advances in biomaterials provide the possibility of developing biodegradable grafts for ligament and tendon tissue engineering and reconstruction. However no scaffold that simultaneously possesses optimal strength, a porous structure and a biocompatible microenvironment has not been developed [3]. This study aimed to design a new practical ligament scaffold by the synergistic incorporation of silk fibers, a knitted structure, and a collagen matrix, in which silk fibers provided mechanical strength, the knitted structure provided internal connective space, and a collagen matrix initially occupied the internal space of the knitted scaffold for neo-ligament tissue ingrowth as well as the capacity to modulate neo-ligament regeneration by regulating matrix gene expression and the assembly of collagen fibrils. This study was conducted to assess: 1) the effect of collagen and silk on ligament matrix gene expression; 2) the degradation and biocompatibility of a knitted silk scaffold in a mouse model; and 3) the effect of a knitted silk+collagen scaffold on in situ ligament repair in a rabbit model.

II. Materials and Methods

The warp knitted scaffold was fabricated using 12 yarns (1 filament/yarn) of silk fibers on a knitting machine. Plain knitted silk scaffolds were manufactured with 21 stitches per centimeter. The pore size was approximate 1 × 1 mm. Then the knitted scaffolds were processed to extract sericin. The sericin-extracted knitted silk mesh was moderately stretched and immersed in an acidic collagen solution and frozen at -80°C for 12 h. It was then freeze-dried under a vacuum for 24 h to allow the formation of collagen microsponges. Then the scaffolds were crosslinked by dehydrothermal treatment. All subsequent analyses were carried out to evaluate these hybrid scaffolds.

Rabbit BMSCs (3.5×10^4 cells/cm^2) were seeded on silk, collagen films and normal plates. Cells were cultured in

Chwee Teck Lim, James C.H. Goh (Eds.): ICBME 2008, Proceedings 23, pp. 1195–1198, 2009
www.springerlink.com

DMEM supplemented with 10% FBS and harvested after 3 or 5 days for analysis of gene expression. Medium was exchanged after 3 days.

Sericin-free and 1% collagen-modified knitted silk were used. Fifteen ICR mice weighing 20-25 g were anesthetized with 10% chloral hydrate. A 1-cm dorsal midline skin incision was made on the back of each mouse and two subcutaneous pockets were created by dissection. Implants were inserted into each pocket individually, taking care to prevent any contact between them. Specimens were harvested at15 or 60 days histological evaluation and 30，60days for mechanical evaluation.

Animal model: In twenty skeletally mature female New Zealand White rabbits., a MCL gap defect was e was created according to the method used by Musahl *et al* [4]. In brief, from a medial incision, a piece of the MCL midsubstance, 6 mm in length, was transected and removed. In the right leg, a hybrid scaffold (10×4×1 mm) was then secured on top of the gap using a non-resorbable suture (6-0 nylon) at each of the four corners (n =14). Silk was sutured in the left leg for control. In the remaining animals (n = 6), right MCLs were not cut and a gap injury was surgically created in the left leg and remained untreated. In all animals, the tension on the repaired tendon was returned to approximately normal. The wound was then irrigated and fascia and skin were closed. Post-operatively, animals were allowed free cage activity. Specimens were harvested at 2, 4 and 12 weeks for histological, Masson trichrome staining, collagen content, matrix genes expression and strength of the ligament analysis. At 12 weeks, two randomly-selected rabbits in each group were used for transmission electron microscopy (TEM) and about 1000 collagen fibrils were measured to assess the collagen fibril diameter. The interface healing between engineered ligament and host tissue was also examined.

III. Results

A. Morphological characterization, in vivo degradation and cytotoxicity of scaffold

SEM observation of the silk+collagen hybrid scaffold demonstrated that collagen microsponge was formed in the interstices of the knitted silk scaffold (Fig. 1 B).Histology results (Fig. 1 C-E) showed that tissue ingrowth by fibroblasts between the fibers of the scaffolds with little vascularization was observed at 15 and 60 days after subcutaneous implantation. A few inflammatory cells were found around silk fibers.

The knitted silk scaffold exhibited a 19.6% (p <0:05) decrease in ultimate tensile strength (from 46.5 ± 9.2 to 37.4 ±3.8 N) as an effect of sericin removal when compared with the raw fibers and retained 25.9% of its original tensile strength at 3 months, and 33.5% at 6 months.

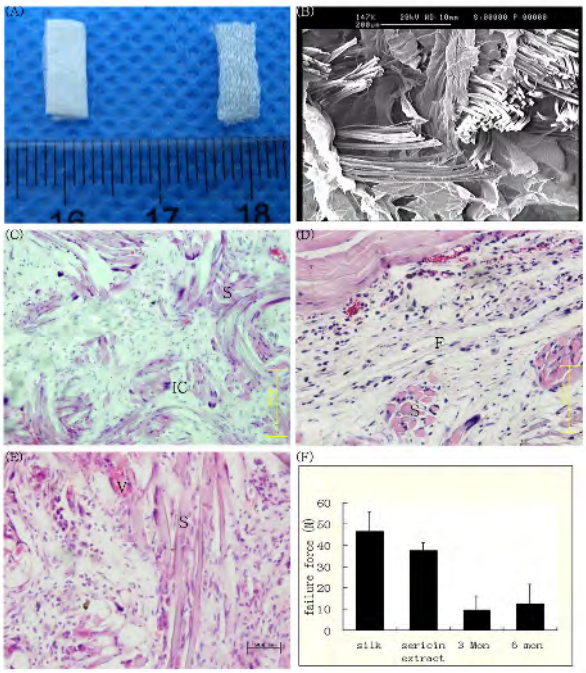


Fig. 1. Characterization of scaffold: The gross (A) and SEM images (B) show combined silk scaffolds showing collagen sponge formed in the knitted silk scaffold . Cellular response of sericin-free silk scaffolds (C,D) and hybrid scaffold (E) to subcutaneously implanted at 15 (C), 60 days (D, E), post-surgery. F. The changes in the mechanical stress of knitted silk scaffold after sericn extraction and subcutaneously implanted at 3 months and 6 months. S indicates silk scaffold in all forms; F indicates .broblasts with capsulation; IC indicates in.ammation cells; V indicates vascular formation. Scale bars 200 um (B,C), 100 um,(D) and 50 um(E).

B. BMSC response on collagen and silk film

At both 3 and 5 days, the mean level of collagen I and decorin expression after cell seeding on the collagen film was elevated (Fig. 2). A decrease of collagen III was found in the silk film specimen, at 3 days. At 5 days, the mean levels of collagen III were similar in the three groups.

C. Results of MCL repair

The defects in MCLs treated with hybrid scaffold (14/14), silk scaffold (13/14) and those without treatment (3/6) showed good attachment of the scaffold to the proximal and distal ends of ligament. The volume of spacefilling fibrous tissue and enveloping soft tissue increased at hybrid scaffold treated groups. The CSAs of both treatment groups (silk+collagen-treated group: 6.4 ± 0.9 mm2 and silk-treated

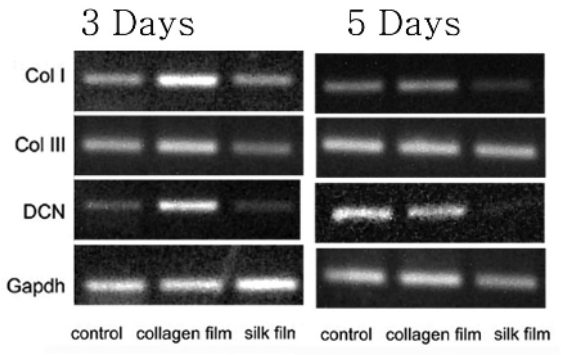


Fig. 2. RT-PCR analysis of collagen I, collagen III and decorin gene expressions of MSCs seeded ion collagen and silk films at 3 and 5 days. Col I: collagen I, Col III: collagen III, DCN: decorin.

group: 4.2 ± 1.0 mm2) were nearly twice as large as that of normal MCLs (2.4 ± 0.1 mm^2) ($p < 0.05$).

The histology and Masson trichrome staing of silk+collagen treated groups showed that more collagen fibers with a larger number of cells exhibiting spindle-shaped morphology along the axis of tensile load were formed in the silk+collagen group than in the silk-treated group at 2 and 4 weeks (Fig. 3). At 12 weeks, all the regenerated tissues showed organized bundles of highly crimped fibers. However, more collagen bands were ingrowth into the scaffold at cross section and the interface of one (out of 3) silk+collagen-treated ligament was interspersed with adi pose connective tissue, while 2/3 silk-treated ligaments had similar adipose tissues (data not show).

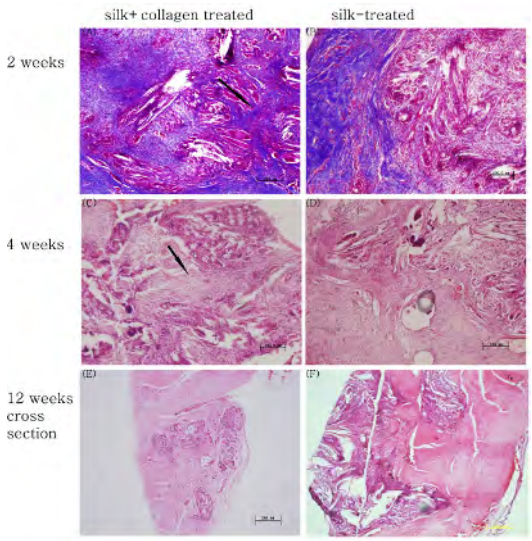


Fig. 3. Repaired MCLs at 2, 4 and 12 weeks. Scale bars 100 um (A-D), 200 um(E, F).

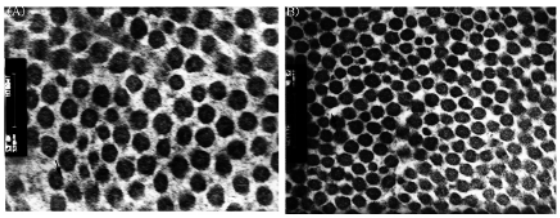


Fig. 4. Ultrastructure of the repaired MCLs 12 weeks. A. silk–collagen-treated MCLs, B.the silk-treated MCLs. Magnification 73 000X.

Both the silk+collagen-treated and silk-treated MCLs had much smaller collagen fibrils than native ligament, but the diameters were larger in the silk+collagen-treated group (65.8 ± 11.8 nm *vs.* 51.2 ± 9.8 nm)(Fig. 4). All samples from silk-treated ligaments had lower collagen content than silk+collagen-treated MCLs. At 4 and 12 weeks, the collagen I expression of silk+collagen-treated MCLs was higher at 4weeks and lower at 12 weeks compare to silk-treated MCLs. The mean level of decorin expression in silk-treated MCLs was elevated at 4 and 12 weeks (data not show).

Mechanical character of repaired MCL: In terms of the failure model, all normal (6/6), silk+collagen-treated (5/5), and half of the silk-treated MCLs (3/5) failed by tibial avulsion. Two specimens of silk-treated MCLs failed at the scaffold-ligament interface, and the remaining one broke in the midsubstance. These results were in accord with the histology results and indicated that normal ligament and silk+collagen-repaired ligament were stronger than the MCL insertion at the tibia. The stiffness of the MCLs in the treated groups was similar (24.3±2.9N/mm vs. 21.7±8.4 N/mm, respectively, $p > 0:05$). The ultimate load of the MCL for the Silk-collagen treated group was 31% higher than that of silk-treated groups, although the difference was not found to be significant ($p > 0.05$) .It may due to the relative small sample size(n=5).The energy absorbed at failure for the silk-collagen -treated group was 90% higher than that of the silk-treated group, the $P>0.05$ may due to the small number of the samples. Both were significantly less than that for the normal (147± 97 Nmm, $p < 0:05$).

IV. Discussion

The results of the study showed that that the addition of collagen matrix led to the formation of larger collagen fibrils in MCL repair by regulating matrix gene expression and the assembly of endogenous collagen fibrils. It highlighted the important role of biomaterials in modulating ligament regeneration processes. Although the collagen fibril diameters in the MCL repair were still smaller than those in native ligaments, the average diameters of fibrils in

the silk+collagen-treated MCLs were significantly larger than in the silk-treated MCLs at 12 weeks, and this was consistently related to the better histology and mechanical properties of the silk+collagen-treated MCLs.

To understand the mechanisms by which collagen and silk regulates the assembly of collagen fibrils in MCL repair, we tested ligament matrix gene expression effected by the silk and collagen both in vitro and in vivo. Cells on collagen had higher matrix gene expression compare to those on silk. The different expression levels of different matrix genes caused by the collagen and silk may be one of the reasons for the change in fibril diameter. Previous studies reported that decorin decreases collagen fibril diameter both in vitro and in vivo [5]. In the in situ MCL repair study, the lower expression of collagen I and the higher expression of decorin may cause the smaller collagen fibers in silk-treated MCLs.

The present work showed that knitted scaffold has much internal connective space to allow large bands of collagen fibers with proper orientation and crimp pattern to form within the scaffold. However, the internal space decreases when the knitted scaffolds are put under heavy physical loading. In order to utilize the excellent biocompatibility of collagen matrix while preserving the internal space of the knitted silk scaffold, collagen sponge was chosen to fill the pores of the scaffold. The histology showed that the space filled by collagen sponge facilitated cell infiltration and connective tissue formation in the scaffold, at 2 weeks and 4 weeks after operation. The mechanical strength of the silk+collagen treated MCLs were also stronger than the silk treated MCLs.

Moreover, it is worthy of note that healing at the scaffold-ligament interface was improved by the hybrid collagen+silk scaffold. This may be explained by the fact that silk+collagen-treated MCLs synthesize more collagen ($P < 0.05$). It indicated that the structural/functional unit of the MCL was improved by enhancing neoligament tissue formation as well as interface healing between neoligament and native ligament.

Silks are naturally occurring protein polymers that have an excellent strength that have mechanical characters similar to the human ACL [3]. Our data showed that the knitted sericin-free silk and silk+collagen scaffolds were biocompatible and retained 25.6% of their tensile strength after 3 months implanted subcutaneously in mice. The tensile strength increased to 33.5% after 6 months which may be due to the ingrowth of new tissue. The knitted silk scaffold-treated MCLs reached 50% of normal failure force; this is higher than the peak force in vivo [2]. These data demonstrate the strong potential for knitted silk scaffolds in ligament regeneration.

V. Conclusions

In conclusion, this study highlight the important biological roles of biomaterials in ligament regeneration and the concept of an "internal-space-preservation" scaffold for the reconstruction of tissues which need to resist heavy physical loading. The knitted silk-collagen sponge scaffold, which possessed optimal internal space, a biocompatible environment, and mechanical strength, is a promising candidate for practical ligament and tendon tissue engineering.

Acknowledgement

This work was supported by the National Natural Science Foundation of China (30600301, 30600670, U0672001) and Zhejiang Province grants (R206016, 2006C 14024, 2006C 13084).

References

1. Woo SL, Debski RE, Zeminski J et al. 2000. Injury and repair of ligaments and tendons. Annu Rev Biomed Eng 2:83-118.
2. Butler DL., Juncosa-Melvin N., Boivin GP, et al. 2008. Functional tissue engineering for tendon repair: A multidisciplinary strategy using mesenchymal stem cells, bioscaffolds, and mechanical stimulation. J Orthop Res 26:1-9.
3. Altman GH, Horan RL, Lu HH, et al. 2002. Silk matrix for tissue engineered anterior cruciate ligaments. Biomaterials 23:4131-4141.
4. Musahl V, Abramowitch SD, Gilbert TW, et al. 2004. The use of porcine small intestinal submucosa to enhance the healing of the medial collateral ligament--a functional tissue engineering study in rabbits. J Orthop Res 22:214-220.
5. Nakamura N, Hart DA, Boorman RS, et al. 2000. Decorin antisense gene therapy improves functional healing of early rabbit ligament scar with enhanced collagen fibrillogenesis in vivo. J Orthop Res 18:517-523.

Author: Ouyang Hongwei
Institute: Zhejiang university
Street: 388# Yu Hang Tang Road
City: Hang Zhou
Country: China
Email: hwoy@zju.edu.cn

Preparation, Bioactivity and Antibacterial Effect of Bioactive Glass/Chitosan Biocomposites

Hanan H. Beherei[1], Khaled R. Mohamed[1], Amr I. Mahmoud[2]

[1]Biomaterials Department, National Research Centre, Dokki, Giza, Egypt
[2]Medical Biochemistry Dept., National Research Centre, Dokki, Giza, Egypt

Abstract — **In this study, we prepared BG filler powder containing some ions such as copper or zinc via sol gel method and their loading onto chitosan polymeric matrix for improving their bioactivities as well as their effect onto microorganisms such as Staphylococcus aureus bacteria were studied. The produced biocomposites characterized using X-ray diffraction (XRD), Fourier transformer infrared spectra (FT-IR), Thermogravimetric (TGA) analyses and Scanning electron microscope. Bioactivity behavior carried out in simulated body fluid (SBF) at 37 ºC and pH 7.4 for the biocomposites to verify the formation of apatite layer onto their surface. The results proved the presence of integration and homogeneity between BG and chitosan polymeric matrix. The results showed that BG/chitosan composite containing zinc ions had high ability effect onto Staphylococcus aureus compared to other composites. The in-vitro study confirmed the formation of apatite layer onto the surface of chitosan polymeric matrix and its composites with BG proving the vital role of chitosan to precipitate the ions of calcium and phosphate onto the composite surface. The conclusion show that BG/chitosan composite had ability to induce the bone-like apatite layer and anti-bacterial properties especially those containing zinc ions. Therefore, these biocomposites are promising to use as bone grafting, in tissue engineering as scaffolds and antibacterial applications.**

Keywords — **Sol-gel, chitosan, Antibacterial, In-vitro, Biocomposites**

I. Introduction

The formation of the hydroxyl-carbonate apatite (HCA) layer on the surface of bioactive glasses (BG) performed and a hydrated silica gel layer formed during the reactions [1]. Recently, the ionic products of BG dissolution exert a genetic control over the osteoblast cell cycle and the rapid expression of genes that regulate osteogenesis and the production of growth factors [2]. BG knows for their bone regeneration ability [3]. Certain bioactive glasses show to exert an antibacterial effect when challenged with bacteria [4]. Bioglass exerts an antibacterial effect on certain oral bacteria, possibly by virtue of the alkaline nature of its surface reactions. This may reduce bacterial colonization of its surface in vivo [5]. There are two types of antibacterial material containing either organic or inorganic substances such as chitosan [6] or silver, copper, and zinc [7]. Several interesting biological properties have reported for chitosan such as wound healing, immunological activity and antibacterial effects [8-10]. An interesting advance in technology has been to trap silver or zinc ions within inorganic ceramics and to apply these compounds to various materials as long lasting antimicrobial treatments [11]. The antimicrobial and anti -inflammatotory potency of these materials originate from the release of the Zn, Cu, Ag ions which react with proteins by combining the SH groups and leads to the inactivation of such proteins [12]. The zinc component results in the formation of a fibrous collagen capsule around the zinc polycarboxylate cement in vivo, which compromises the strength of the intermediate region between the bone and the cement [13]. In this study, we prepared the preparation of new composites from chitosan and BG containing cupper or zinc elements. The prepared composites characterized by XRD, TGA, FT-IR and SEM. These composite samples were soaked in SBF for different times. In addition, their bioactivities were characterized measurement of calcium and phosphorus, FT-IR, and SEM.

II. Materials and Methods

A. Materials

The polymer material used in this study was chitosan (High molecular weight and Brookfield viscosity: 800,000 cps) and 2-hydroxyethylmethacrylate (HEMA) were purchased from (Aldrich). Cerric ammonium nitrate initiator (CAN) was provided from (BDH, England). The starting materials used in this method to prepare (BG) were $Ca(NO_3)_2$ $4H_2O$ (Merk), triethylphosphate (Merk), tetraethylorthosilicate (Merk) and Sodium hydroxide.

B. Methods

B.1a. Preparation of BG filler

The bioactive glass material (BG) (45S5) was prepared in weight percentage: 45: SiO_2, 24.5: Na_2O, 24.5: CaO and 6: P_2O_5 using sol-gel method according to Li et al. [14]. Briefly, preparation of BG powder using sol-gel method was carried out via addition of $Ca(NO_3)_2$ $4H_2O$,

Chwee Teck Lim, James C.H. Goh (Eds.): ICBME 2008, Proceedings 23, pp. 1199–1203, 2009
www.springerlink.com

triethylphosphate, tetraethylorthosilicate and NaOH to de-ionized water at 25°C in the presence of nitric acid. After mixing, the resulting sol was aged at 60°C and dried at 130°C. The dried gel stabilized at 450°C, ground and sieved up to 50 μm. Other two types of glasses BG-Zn and BG-Cu were prepared by addition of tetraethylorthosilicate, $Ca(NO_3)_2$ $4H_2O$, triethylphosphate and $ZnNO_3$ or Cu $(NO_3)_2$ to deionized water at 25°C in the presence of nitric acid. The mix composition, expressed in weight % was as follows: 60% SiO_2; 26% CaO; 4% P_2O_5; and 10% of either ZnO or 10% of CuO. After mixing, the resulting sol was aged at 60°C and dried at 130°C. The dried gel stabilized at 450°C, ground and sieved below 50 μm.

B.1b. Preparation of BG/polymeric composite samples

Fixed weight (1.5 g) filler powder dispersed, well mixed with the copolymer mixture after 2.5 h from copolymerization process from the previous experiment and kept at 40 °C in water bath for 30 min to complete the copolymerization process in the presence of the filler. The BG/grafted chitosan composites left overnight at room temperature and then the mixture was washed with hot ethanol with stirring for 2 h to remove the homopolymer. The composite mixture filtered, collected and dried at 60°C overnight. The grafting yield of the grafted chitosan in the presence of BG filler powder calculated according to the following equation:

$$\text{The grafting yield} = (W_f\text{-}Wi/\ W_i) \times 100$$

Where: W_f is the weight of grafted chitosan in the presence of 1 g of filler and Wi is the weight of original chitosan. The produced BG/grafted chitosan composites denoted as BG composite. The same experiment was repeated with BG-Cu filler (1.5 g) to produce BG-Cu/ grafted chitosan composite that denoted as BG-Cu composite and repeated with BG-Zn filler (1.5 g) to produce BG-Zn/grafted chitosan composite that was denoted as BG-Zn composite.

B.2. Characterization

The thermal properties of the starting fillers and their composites were evaluated by thermogravimetric analysis (TGA) using a Perkin–Elmer, 7 series thermal analyzer at a heating rate of 10°C/min. The phase analysis of samples examined by X-Ray diffractometer (Diana Corporation, USA) equipped with CoK_α radiation. The FT-IR spectra measured using KBr pellets made from a mixture of powder for each sample and assessed from 400 to 4000 cm^{-1} using a Nexus 670, Nicloet FT-IR spectrometer, USA. SEM micrographs of the composites were also studied using SEM Model Philips XL 30, with accelerating voltage 30K.V. and magnification 10x up to 400.000x.

B.3. Bacterial test

The test microorganism was Staphylococcus aureus. Antibacterial test has carried out as follows: 40 ml of the agar medium inoculated with 200 micro liter of the test microorganism prepared inoculums and poured in 15 cm diameter Petri dish and solidified. After placing the disks of the tested materials on the surface of the solidified agar and let it to diffuse in the medium, the plates incubated at 37°C for 24 hours. The observation of the Halo zones carried out to assess the antimicrobial activity.

B.4. Bioactivity test

In order to study the bioactivity, the samples were soaked in SBF, proposed by Kokubo et al. [16] at the body temperature (37°C) and pH = 7.4 for several periods. After the immersion periods, the solutions were analyzed by spectrophotometer (Shimadzu, Japan) using biochemical kits (Techo Diagonstic, USA) to detect the total calcium ions $(Ca)^{2+}$ at λ= 570 nm and phosphate ions (PO_4^{3-}) concentrations at λ= 675 nm.

III. Results and Disccussion

A. The grafting yield (G) and thermo-gravimetric analysis (TGA)

The G of the BG-Cu composite recorded the maximum value (1390) compared to BG composite (1057) and BG-Zn composite (1097), respectively. This result is due to the presence of Cu doped with BG resulted in the enhancement of the affinity of BG-Cu filler particles to the co-polymeric matrix compared to other composites. The TGA results show that the destruction of three BG/ BG-Cu/ BG-Zn composites started at 168, 159 and 104°C and ended at 470, 557 and 557°C, respectively. The total weight loss of the three composites were 28.18, 46.13 and 38.35%, respectively, as a result of the release of all CO_2, NH_3 gases and water molecules [15] (Fig.1). The attached copolymer onto the filler particles was calculated by subtracting the weight loss of BG filler powder from the total weight loss of the prepared composite, whereas, the weight loss of BG filler recorded 3.78% due to the release of absorbed water proving its stability. Therefore, the order of the attached layer of copolymer onto the surface of BG particles was mentioned as follows: BG-Cu composite> BG-Zn composite >BG composite (42.35> 34.57> 24.30%, respectively). It noted that BG powder containing 10% copper oxide as in BG-Cu composite had high affinity to the copolymer compared to other composites and this result is coincided with the grafting data.

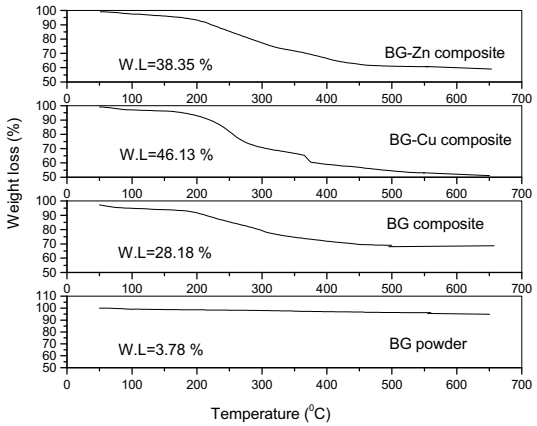


Fig. 1 TGA analysis of the BG composites compared to BG filler powder

B. Characterization of composites

B.1. Phase analysis

The XRD patterns of BG filler, copolymer, BG powder and their composites shown in Fig.2. In case of copolymer, there is a broad hump in the range of 2θ (12–25)° attributing to the structure of chitosan polymer (Card No.39-1894) as a result of interaction between HEMA monomer onto chitosan polymer (Fig.2a) For BG filler powder, the amorphous nature characterizing BG structure appears as a broad peak in the range of 2θ (30–40°). This broad peak which appears in the BG spectrum is still persisted in three BG composites with the disappearance of copolymer peak proving the effect of the filler particles onto the polymer sites as well as the amorphous nature of the copolymer matrix [17] (Fig.2b, c and d).

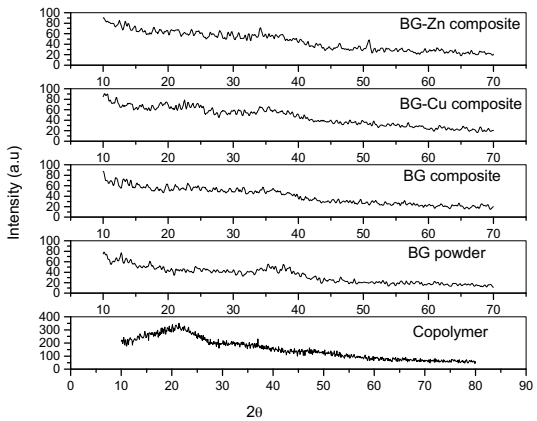


Fig. 2 XRD patterns of the prepared samples

B.2.FT-IR analysis

The FT-IR spectra of copolymer, BG filler and their composites show in Fig.3. After the loading of the BG filler powder onto the co-polymeric matrix,for the three composites, the optical density (O.D) of polymer bands were reduced compared to original copolymer proving effect of BG particles onto these sites especially as in BG and BG-Zn composites. Also, the O.D of phosphate and/or Si-O-Si at 1060 cm^{-1} and OH at 3450 cm^{-1} appearing into the spectra of the three composites were reduced compared to original BG filler denoting effect of coating onto these site bands especially as in BG-Cu composite (Fig.3). This result is coincided with the grafting and TGA results.

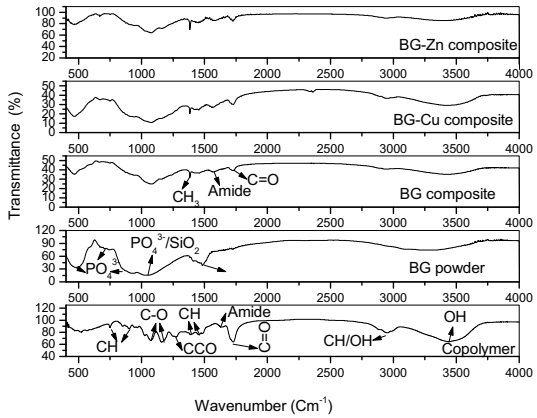


Fig. 3 FT-IR spectra of the prepared samples

C. Bacterial effect

The effect of the prepared composites onto bacteria (Staphylococcus aureus bacteria) show that the inhibition zone was 1.1, 2.05 and 2.2 cm for BG/, BG-Cu/ and BG-Zn/ composites, respectively (Fig.4). This result proves that the BG-Zn composite or BG-Cu/composites releases Zn or Cu ions which react with proteins in the micro-organism via the combination of SH groups resulting in the inactivation of proteins.



Fig. 4 Effect of the prepared composites on bacteria (Staphylococcus aureus) as in a) BG composite, b) BG-Cu/composite and c) BG-Zn/composite

D. Bioactivity behavior

D.1. In vitro test

D.1a. Total calcium ions (Ca^{++})

Concentration of Ca^{++} ions recorded higher values at all periods for three composites than control especially BG-Zn composite proving release of Ca^{++} ions from the composite surface into the media (Fig.5). This result proves that the presence of chitosan polymeric matrix containing BG particles leads to acceleration of the release of Ca^{++} ions from the surface especially for BG-Zn composite.

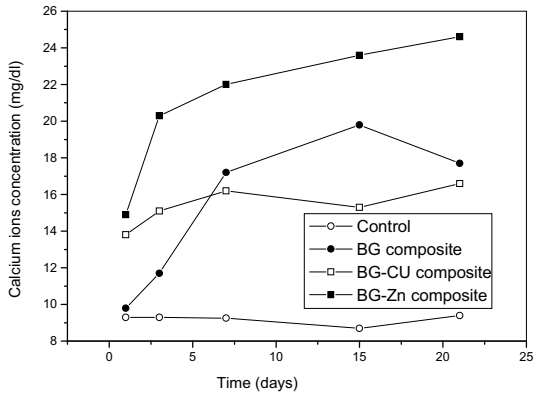


Fig. 5 Concentration of calcium ions in SBF post-immersion of three composites for different periods compared to control

D.1b. Phosphate ions (PO_4^{3-})

Concentration of PO_4^{3-} ions post-immersion for all tested composites recorded lower values than control especially BG and BG-Cu composites at all periods proving mineralization of PO_4^{3-} ions onto the composite surface and the interaction between phosphate ions in SBF and amino groups of chitosan into the composite (Fig.6). This result confirms that the presence of copolymer matrix containing BG or BG-Cu fillers enhanced the deposition process of phosphate ions.

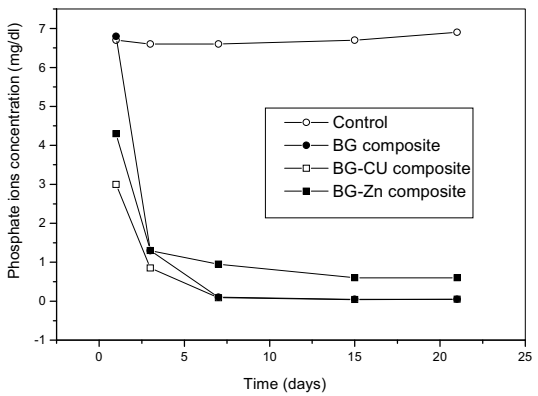


Fig. 6 Concentration of phosphate ions in SBF post-immersion of three composites for different periods compared to control

D.2. Solid Characterization

D.2a FT-IR analysis

Fig.7 shows that the O.D of OH at 2950 and 3450 cm^{-1} and phosphate groups at 470 and 1070 cm^{-1} into the spectra of three composites are enhanced post-immersion after 21 days compared to pre-immersion (Fig.3) proving mineralization of phosphate ions onto the surface. For BG composite, new bands appeared at 805, 880 and 1440 cm^{-1} that are assigned to carbonate group's post-immersion proving formation of carbonated apatite layer. For BG-Cu composite, new bands appeared such as phosphate band at 910 cm^{-1} and carbonate groups at 1400-1470 cm^{-1} denoting formation of carbonated apatite layer. For BG-Zn composite, new band appeared for carbonate group at 1460 cm^{-1} denoting formation of carbonated apatite layer. Additionally, it noted that the three composites had ability to form the carbonated apatite layer onto their surfaces.

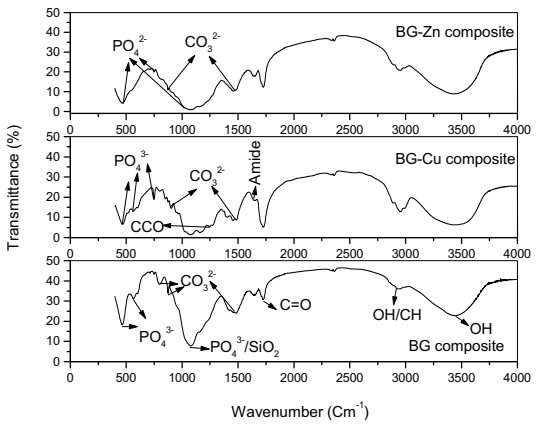


Fig. 7 FT-IR patterns of BG, BG-Cu and BG-Zn composites post-immersion for 21 days in SBF

D.2b. Microstructure of composites

For BG composite, pre-immersion (Fig.8a), SEM shows the appearance of smooth surface containing BG particles that are connected to each other and coated proving high homogeneity, while post-immersion (Fig.8b), SEM shows abundance of spherical shapes with some clusters having small particles indicating nucleation of apatite layer.

For BG-CU composite, pre-immersion (Fig.8c), SEM shows the presence of smooth surface containing some pores having irregular shapes proving coating and integration. Post-immersion (Fig.8d), SEM shows the presence of larger spherical shapes appearing onto the

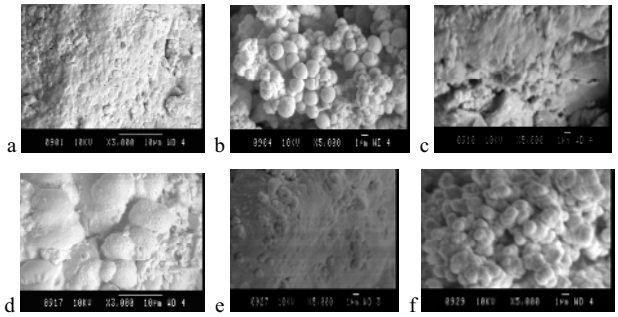


Fig. 8 SEM of BG composite a) pre- and b) post-immersion, BG-Cu composite c) pre- and d) post-immersion and BG-Zn composite e) pre- and f) post-immersion for 21 days in SBF

composite surface compared to post-immersion of BG composite indicating the role of Cu additive into the BG composite on the shape of the formed apatite layer. For BG-Zn composite, pre-immersion (Fig.8e), SEM shows the presence of smooth surface containing BG-Zn particles. Post-immersion (Fig.8f), SEM indicates the appearance of spherical particles which accumulated and connected to each other onto the surface proving high nucleation of a bone-like apatite layer.

IV. Conclusion

The results prove the presence of integration and homogeneity between BG and chitosan polymeric matrix. The data prove that BG/chitosan composite containing zinc ions had high ability effect onto Staphylococcus aureus compared to other composites. The in-vitro study confirmed the formation of apatite layer onto the surface of BG chitosan composites proving the vital role of chitosan to precipitate the ions of calcium and phosphate onto the surface. The results show that BG/chitosan composite had ability to induce the bone-like apatite layer and anti-bacterial effect especially those containing zinc ions in their structure. Therefore, these biocomposites are promising to be used as bone grafting, in tissue engineering as scaffolds and antibacterial applications.

References

[1] Hench LL, Wheeler DL, and Greenspan DC (1998). J of Sol Gel Sci and Tech 13: 245.
[2] Xynos ID, Edgar AJ, Buttery LDK et al. (2001). J of Biomed Mat Res 55, 151.
[3] Jie Q, Lin K, Zhong J, Shi Y, Li Q et al. (2004). J of Sol-Gel Sci and Tech 30: 49–61.
[4] Stoor P, Soderling E, Salonen JI (1998). Acta Odontol Scand 56:161-5.
[5] Allan I, Newman H, Wilson M (2001). Biomaterials 22: 1683-1687.
[6] Jung BO, Lee YM, Kim JJ, Choi YJ et al. (1999). J. Korean Ind Eng. Chem 10:660-5).
[7] Kim TN, Feng Q L, Kim JO, Wu J et al. (1999). J. Korean Ind. Eng. Chem 10:660-5).
[8] Rabea EI, Badawy ET, Stevens CV, Smagghe G, Steurbaut W (2003). J Bio-macromol. 4:1457-65.
[9] Huh MW, Kang IK, Lee DH, Kim WS, Lee DH, Park LS, et al (2001). J Appl Polym Sci 81:2769-78.
[10] Kim CH, Choi JW, Chun HJ, Chio KS (1997). Polym Bull 38:387-93.
[11] Inoue, Y., M. Hoshino, H. Takahashi, T. Noguchi, T et al. (2002). J Inorg Biochem 92:37-42.
[12] Lehning Al, Nelson DL and Cox MM (1993). Principles of biochemistry.2nd NewYok, Worth, USA.
[13] Peters WJ, Jackson RW, Iwano K and Smith DC (1972). J Clin Orthop 88: 228.
[14] Li P, Clark AE, and Hench LL (1992). In chemical processing of advanced material, Hench L.L and West J.K (eds), Wiley, New York, pp. 627-633.
[15] Mohamed K R, El-Bassyouni G T, Beherei H H (2007). J App Polym Sci 105: 2553-2563.
[16] Kokubo T, Kim H M, Kawashita M, Takadama H et al. (2001). Glastech Ber Glass Sci Tech 73: 247-254.
[17] Prashanth KVH, Tharanathan RN, Hu Q, Li B, Wang M, Shen J (2004). J Biomat 25:779-785.

Author's address:

Dr. Khaled Rezk Mohamed, National Research Centre,
33 El Behooss, Egypt, E-mail: Kh_rezk@yahoo.com

Biocompatibility of Metal Sintered Materials in Dependence on Multi-Material Graded Structure

M. Loderova[1], J. Rybnicek[1], J. Steidl[1], J. Richter[2], K. Boivie[3], R. Karlsen[3], O. Åsebø[3]

[1] Czech Technical University in Prague, Department of Materials Engineering, Prague, Czech Republic
[2] Institute of Microbiology of the Academy of Sciences of the Czech Republic, Czech Republic
[3] SINTEF, Norway

Abstract — **Rapid prototyping of real products, which are customized to the needs of individual patients, became very successful in the field of biomaterials recently. But meanwhile the production is increasing, demands for the newly developed materials and new approaches became more and more important. In this respect multi-material functionally graded sintering has been introduced into production of materials. Certain combinations of materials with different mechanical properties tend to be promising in the field of bio-implants production as well as the Rapid prototyping methods such as Selective Laser Sintering (SLS) and 3D printing (3DP). In this study a possibility of application of functionally graded metal structures was evaluated. The two materials, CoCr alloy and Ti6Al4V alloy, were joined together by multi-material sintering procedure. Both materials are known to be used in orthopedics because of their excellent biocompatibility. In this case the testing samples were made as graded structures, having CoCr alloy on one end and Ti6Al4V alloy on the other end. Different sintering temperatures were applied. The obtained samples were tested in terms of biocompatibility where the manufacturing conditions, especially the sintering temperature, and surface structure were taken into account. The used cells were Balb/c Mouse Fibroblasts and the viability was assessed by MMT test. Samples were further examined for influence on PBMC (Peripheral Blood Mononuclear Cells) by Flow Cytometry analysis (FACS).**

Keywords — **functionally graded, biomaterial, rapid prototyping**

I. Introduction

The implantation of integrated biomedical devices to the human body provides challenges to the engineering materials science and technology. Because the production has rising tendency, new materials and innovated approaches are still required [1]. In this respect multi-material functionally graded sintering has been introduced into production.

In the multi-material functionally graded implants the mechanical, physical and chemical properties change from one side of the product to the other. Biomaterials with excellent osseointegration and low Young's modulus on one side of the implant and other materials with perfect mechanical properties such as hardness, abrasion resistance etc. on the other side, are advantageous for various bio-applications. For example, the disadvantage of joint requirements in bioimplants can thus be eliminated and the risk of screw connections or corrosion of welding avoided [2]. These appliances can also present contrasting adhesive requirements over very short distances along the same structure [3]. The additional requirements such as simplicity of manufacture, low cost production and individual demands such as design which can differ from patient to patient should be met as well [1].

Fundamental materials which are recommended especially for joint and bone implants and can withstand complex operating conditions are pure Ti, Ti-6Al-4V alloy and Co-28Cr-5Mo alloy [4, 5]. Especially titanium and its alloys currently constitute the most favored implant materials for joint replacement [6]. Moreover the powder metallurgy is involved in improving the bone-implant contact by making the implant structure porous and thus friendlier to bone cell anchorage [7]. In comparison to other metallic implant materials, titanium is characterized by a high biocompatibility, a good workability and corrosion resistance with suitable mechanical properties (low Young's modulus - high strength) [1]. Ti and Ti-6Al-4V alloy also perform a highly inert behavior while they develop a very sable oxide layer when exposed to air or to aqueous media [8]. Among all implant materials, Co-Cr-Mo alloys demonstrate the most useful balance in strength, fatigue and wear along with resistance to corrosion. Powder Metallurgy (P/M) route offers additional advantages [9]. It has been shown, that the extent of bone growth in implants where powder metallurgy was used was markedly greater, attributed to the microstructure of these implants [10].

There are numerous manufacturing processes employed nowadays in the Powder Metallurgy (P/M) field. The most promising ones are Selective Laser Sintering (SLS), Three-Dimensional Printing (3DP) or Metal Printing Process (MPP). These processes build components ready for use directly from metal powders using layer manufacturing principles. By changing the powder in the powder reservoir form layer to layer, graded materials can be thus produced [11].

Chwee Teck Lim, James C.H. Goh (Eds.): ICBME 2008, Proceedings 23, pp. 1204–1207, 2009
www.springerlink.com

II. Materials and methods

A. Materials

Ti6Al4V and CoCr alloys were supplied in a powder form by Arcam AB. The powder was produced by a gas atomization process and particle sizes laid within a size range from 10 to 70 μm. Multi-material functionally graded samples of CoCr alloy and Ti6Al4V alloy were manufactured by the MPP. They consisted of one part of CoCr and one part of Ti6Al4V, see Fig. 1. These were built in the shape of disks (30mm diameter, 3mm thickness) by the successive application of 10 to11 pattern layers of CoCr and Ti6Al4V on a foundation of pure Ti6Al4V powder, consolidated at various temperatures as derived in Fig. 1. For comparison, one sample of pure CoCr alloy and one of pure Ti6Al4V alloy where also manufactured by a similar procedure. The consolidation took place in a protective atmosphere of 95% Ar and 5% H, while the compaction pressure during consolidation was set to 170 MPa.

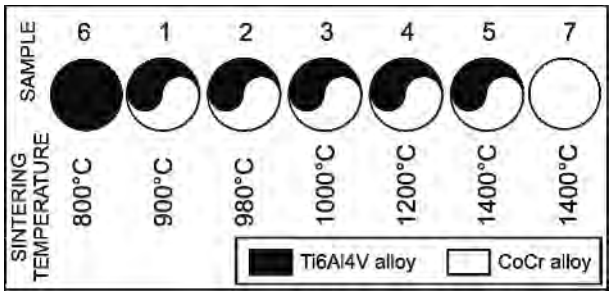


Fig. 1 Layout of testing samples

B. Mechanical Properties

Hardness was measured with the help of Brinell test, where the hardened steel ball-shape indenter was used. The diameter of indenter was 2.5mm and the applied load was 612.9N for 10 seconds. Specimens were measured at Ti6Al4V part and CoCr part three times to determine an average value.

Contact Angle was measured by Surface Energy Evaluation System. The samples were ultrasonic cleaned in ethanol bath and dried with agitated air. The sessile drop technique was used to measure the water contact angle using the See System software. The contact angle was measured three times on each part of the samples.

Surface topography was evaluated using the JEOL JSM 5410 Scanning Electron Microscope. Images were taken to show the most realistic information about the surface topography of the samples.

C. Biocompatibility

Viability: The Balb/c Mouse Fibroblast cell line was used in this study. For the precise evaluation of number of live cells the MTT test was used. The cytotoxicity level (see Table 1) was evaluated on the basis of cells viability in culture with presence of tested material extraction compared with control culture without presence of any cytotoxic material.

Table 1 Evaluation of cytotoxicity level

Viability	Cytotoxicity evaluation	Cytotoxicity level
>80%	Non-toxic	0
80-60%	Slightly toxic	1
60-40%	Moderately toxic	2
<40%	Highly toxic	3

In-vitro cultivation with PBMC: Isolated leukocytes were cultivated with the selected samples on 24-well cultivation plate for 18 hours in H-MEMd cultivation medium. $5x10^5$ cells from each specimen were then stained with Hoechst 33258 five minutes prior to measurement for exclusion of dead and damaged cells. Samples were measured on BD LSRII flow cytometer. Data were evaluated by TreeStar FlowJo software.

III. Results

A. Mechanical Properties

Hardness results are shown in Fig. 2. It can be seen, that the hardness of both materials increases with increasing sintering temperature. The hardness of CoCr alloy is generally higher than hardness of Ti6Al4V.

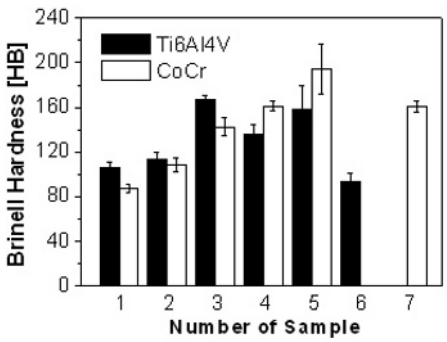


Fig. 2 Brinnel hardness results

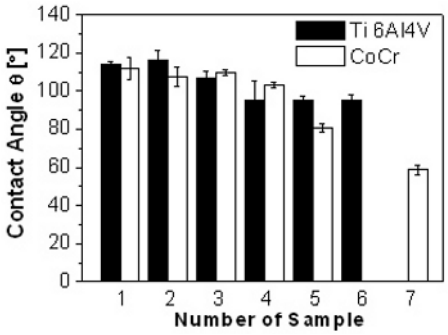


Fig. 3 Contact angle results

Contact angle results are shown in Fig. 3. The contact angle decreases with increasing sintering temperature. This applies for both materials, but the contact angle of Ti6Al4V is generally smaller than that of CoCr alloy.

Surface topography results are shown in Fig. 4a-g. The porous structure can be seen within all samples, but the best consolidation can be seen within the sample number 5 (Fig. 4e), where the interface between the two materials is also most visible.

B. Biocompatibility

Viability for different dilutions was evaluated and the results are shown in Table 2. The most favorable multi material sample is number. Numbers 4 and 5 exhibited high toxicity only in the presence of 100% extract; with the 50% extract they were non-toxic. The most adverse reaction can be seen within sample number 1. Sample number 6 proved the great biocompatibility of Ti6Al4V alloy.

In-vitro cultivation with PBMC results are shown in Fig. 5. The percentage of live cells after 18 hours incubation with presence of the samples was evaluated by FACS analysis of each of the samples. Also the micrographs of cells reaction are shown in Fig. 6a-h. For comparison, a control sample without presence of any of the materials was included into the results (Fig. 6h).

Table 2 Cytotoxicity levels for different extract dilutions

	Cytotoxicity Level			
Sample	100% extract	50% extract	25% extract	10% extract
1	3	3	3	0
2	3	1	0	0
3	0	0	0	0
4	3	0	0	0
5	3	0	0	0
6	0	0	0	0
7	2	0	0	0

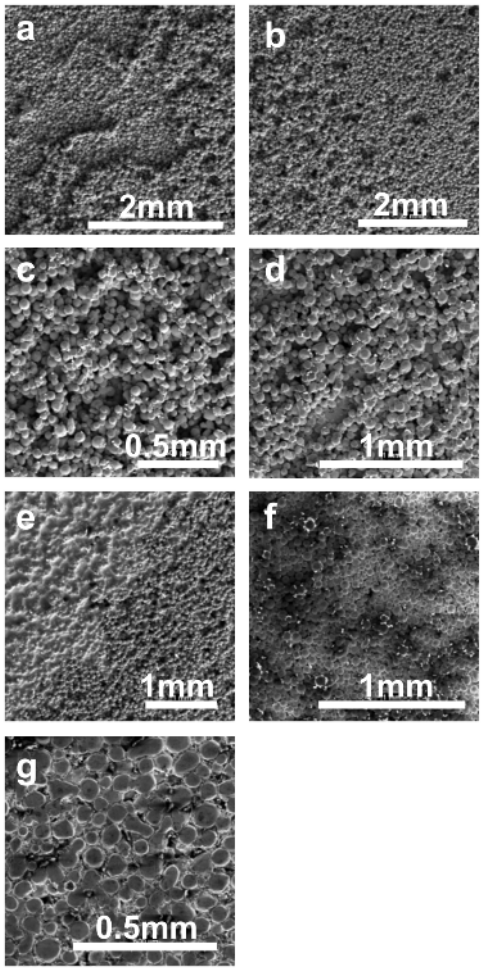


Fig. 4 SEM image of sample surface - interface between CoCr and Ti6Al4V alloy: (a) sample no.1, (b) sample no.2, (c) sample no.3, (d) sample no.4, (e) sample no.5, (f) sample no.6, (g) sample no.7

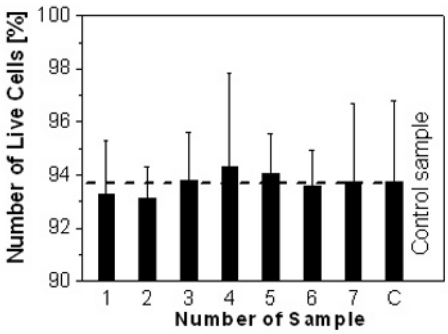


Fig. 5 Percentage of live cells within each sample obtained by FACS

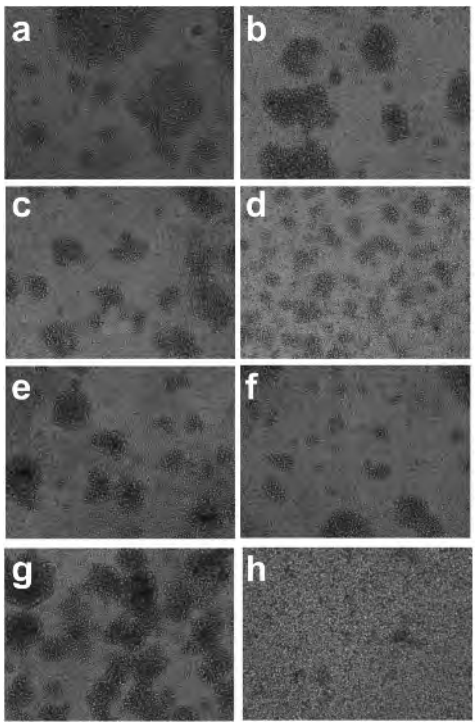


Fig. 6 Images of PBMC proliferation (magnification 10x): (a) sample no.1, (b) sample no.2, (c) sample no.3, (d) sample no.4, (e) sample no.5, (f) sample no.6, (g) sample no.7, (h) control sample

From the Fig. 5 and 6 it can be concluded, that the presence of samples has negligible influence on the cell behavior. No significant mortality or proliferation of cells has been reported by the FACS analysis. Only the micrographs show a slight agglomeration of PBMC.

IV. Discussion

Increase in hardness with increasing sintering temperature is favorable for further wear resistance properties.

As well as the decrease of the contact angle with increasing sintering temperature, which promises better cell anchorage and proliferation and better access of cell nutrients.

The functionally graded samples sintered at lower temperatures did not reach full density during consolidation but had a remaining porous structure. This condition was however improved with increased temperature. The higher was the temperature the better was the consolidation of particles, which promises better mechanical properties in general. It is also likely that further improvement would come with an increase in compaction pressure.

Also the viability of Balb/c cells was better within those samples, where the particles were consolidated more compactly. Nevertheless more detailed study in terms of biocompatibility would be required in order to state this type of material as fully applicable in bioimplant manufacturing.

Damage or proliferation of PBMC was negligible in relation to the control sample. Even though there was significant agglomeration of cells in presence of samples, materials are not likely to cause a strong immune reaction.

V. Conclusions

In this study a possibility of application of functionally graded metallic materials was studied. From the obtained results it can be stated that such combination of materials is likely to be applicable in the field of bioimplants. Samples where the higher temperatures of sintering were applied are recommended for further testing in order to meet high requirements on mechanical properties and biocompatibility.

References

1. Frosch K H, Sturmer K M (2006) Metallic Biomaterials in Skeletal Repair. Eur J Trauma 32: 149-159
2. Lodererova M, Steidl J, Rybnicek J, Hornik J, Godlinski D, Dourandish M (2007) Structure of Multi-Layer Metal Materials, Proc. 27th International Conference of Sampe Europe 2007, Paris, France, 2007
3. Baier R (2006) Wiley Encyclopedia of Biomedical Engineering, John Wiley & Sons, Inc
4. Becker B S, Bolton J D (1995) Production of porous sintered Co-Cr-Mo alloys for possible surgical implant applications Part II: Corrosion behaviour. Powder Metall 38:305-313
5. Long M, Rack H J (1998) Titanium alloys in total joint replacement-a materials science perspective. Biomaterials 19:1621-1639
6. Rack H J, Qazi J I (2005) Titanium alloys for biomedical applications. Mater Sci Eng C in press
7. Ryan G, Pandit A, Apatsidis D P (2006) Fabrication methods of porous metals for use in orthopaedic applications. Biomaterials 27:2651-2670
8. Deligianni D D, Katsala N, Ladas S et al. (2001) Effect of surface roughness of the titanium alloy Ti-6Al-4V on human bone marrow cell response and on protein adsorption. Biomaterials 22:1241-1251
9. Dourandish M, Godlinski D, Simchi A et al. (2007) Sintering of biocompatible P/M Co–Cr–Mo alloy (F-75) for fabrication of porosity-graded composite structures. Mater Sci Eng in press
10. Hunta J A, Callaghana J T, Sutcliffeb C J et al. (2005) The design and production of Co–Cr alloy implants with controlled surface topography by CAD–CAM method and their effects on osseointegration. Biomaterials 26:5890-5897
11. van der Eijk C, Mugaas T, Karlsen R et al. (2004) Metal Printing Process Development of a New Rapid Manufacturing Process for Metal Parts. Proc. World PM2004 Conference, Vienna, Austria, 2004

Author: Michaela Lodererova
Institute: Czech Technical University in Prague
Street: Karlovo namesti 13
City: Prague 2, 12135
Country: Czech Republic
Email: michaela.lodererova@fs.cvut.cz

PHBV Microspheres as Tissue Engineering Scaffold for Neurons

W.H. Chen[1], B.L. Tang[2] and Y.W. Tong[3]

[1] National University of Singapore/NGS-GPBE, Singapore
[2] National University of Singapore/Biochemistry, Singapore
[3] National University of Singapore/ChBE, Singapore

Abstract — **Polymeric microspheres are versatile tissue engineering scaffold, suitable for simultaneous drug delivery and surface modification. They are small units that can be individually tailored for different cell types and purposes, then assembled with various compositions and shapes. In addition, they provide a 3D environment for cell-cell and cell-material interactions. Poly(3-hydroxyburate-co-3-hydroxyvalerate) (PHBV, 8% PHV content), a biodegradable and biocompatible microbial polyester, was used to fabricate microspheres using an oil-in-water emulsion solvent evaporation technique. As PHBV is biodegradable, the eventual construct will consist of only natural tissues, avoiding chronic complications. The versatility of microspheres is useful in neural therapies which require several cell types and various biomolecular signals to overcome inflammation, glial scarring, and inhibitory signals, as well as to promote repair and regeneration. Due to cell source limitations, neuronal expansion might have to be carried out on the microspheres to yield enough neurons for therapies. Also, a key requirement for engineered neural tissue would be its functional integration into host tissue. Thus, the suitability of PHBV microspheres as neural tissue engineering scaffolds was investigated using neuro2a neuroblastoma cells as a model for proliferating neurons and primary mouse fetal cortical neurons as a model for functioning neurons. Scanning electron microscope (SEM) imaging, and confocal laser scanning microscopy were used to observe morphologies of cells cultured on PHBV microspheres. Also, DNA Quantification and cell viability assay (MTT assay) were carried out. Neuro2a cultures on PHBV microspheres showed a growth trend comparable to that in 2D culture plate controls, in both assays. Also, through immunoflourescence staining for beta-III tubulin, primary neurons were found to extend neurites on PHBV microspheres. The results showed that PHBV microspheres are suitable scaffolds for neural tissue engineering, as they support the neural cells' adhesion, growth, proliferation and differentiation.**

Keywords — **Neural Tissue Engineering, Polymeric microspheres, Poly(3-hydroxyburate-co-3-hydroxyvalerate)**

I. Introduction

Cell replacement, drug delivery, and cell delivery therapies are being developed for neurodegenerative diseases and traumatic injuries to the nervous systems. Some challenges for an effective therapy include avoiding further inflammation, providing neuroprotection, stimulating tissue regeneration, overcoming inhibitory cues, and promoting functional recovery [1, 2, 3, 4].

Polymeric microspheres have been widely used for drug delivery. Their sizes, surface morphology and drug delivery profiles can be controlled [5, 6, 7]. Being small, they can also be injected into the defect site via less invasive surgical methods [8, 9]. Furthermore, microspheres made from biodegradable polymers, such as PLGA and PHBV, would disappear from the implant site thus avoiding long term complications.

PHBV is a polyhydroxyalkanoate produced by microorganisms for energy storage. It has been produced commercially and in large quantities from engineered microorganisms, and is considered a renewable resource [10, 11]. Furthermore, PHBV was found to be biodegradable [12] and biocompatible [13]. Thus, PHBV has potential as an environmentally-friendly material for tissue-engineering scaffolds in the form of microspheres. However, PHBV does not seem to be among the biomaterials studied for use in neural tissue engineering [14].

For PHBV microspheres to be useful neural tissue engineering scaffolds, they would have to support neural proliferation due to cell source limitations [15], and maturation of the cells to provide function [16]. In this work, neural proliferation was studied using neuro2a neuroblastoma cell line, and neuronal maturation was investigated using mouse fetal cortical neurons.

II. Materials and methods

A. Materials

Poly(3-hydroxyburate-co-3-hydroxyvalerate) (PHBV, 8% PHV) was purchased from Sigma-Aldrich. Chloroform and Poly (vinyl alcohol) (PVA, Mw 6000) were acquired from Fluka (Steinheim, Germany) and Polysciences (Warrington, PA, USA) respectively. Neuro2a cells were a gift from Associate Professor Too Heng Phon (National Univer-

Chwee Teck Lim, James C.H. Goh (Eds.): ICBME 2008, Proceedings 23, pp. 1208–1212, 2009
www.springerlink.com

sity of Singapore/Biochemistry, Singapore). C57/BL6 mice were obtained from Animal Holding Unit (AHU, National University of Singapore). All medium components were purchased from Invitrogen. All other chemicals were purchased from Sigma-Aldrich unless otherwise stated.

B. Microsphere fabrication

Poly(3-hydroxyburate-co-3-hydroxyvalerate) (PHBV) microspheres were fabricated using the water-in-oil-in-water (w/o/w) double emulsion solvent evaporation technique [17]. 0.6 g PHBV was dissolved in 12 ml chloroform at 60 °C to form the oil phase, while 0.15 g poly(vinyl alcohol) (PVA) was dissolved in 300 ml phosphate buffer saline (PBS) to form the water phase. The first water-in-oil emulsion was formed by sonicating (SONICS Vibra-Cell™, Boston, Massachusetts, USA) a mixture of 1 ml water phase in the oil phase. The second water-in-oil-in-water emulsion was obtained by adding the first emulsion into the remaining water phase and stirring the mixture at 300 rpm using a mechanical stirrer (RW20, Ika Labortechnik, Staufen, Germany) for 4.5 hours. This final mixture was maintained at 37°C using a water bath on a magnetic hotplate stirrer (Cimarec2, Barnstead/Thermolyne, Iowa, USA). The formed microspheres were collected and wash 5 times with deionised water, then freezedried (Alpha 1-4, Martin Christ, GmbH, Germany) for 36 hours.

C. Scanning Electron Microscope imaging of microspheres

The microspheres were characterized by measuring their sizes and imaging their surface morphology using a scanning electron microscope (SEM) (JSM-5600VL, JEOL, Tokyo, Japan). Freezedried microspheres were mounted onto brass stubs using carbon tape. The microspheres were then coated with platinum using a sputter coater (JFC-1300, JEOL, Tokyo, Japan). The coated samples were viewed under the SEM and patches of microspheres were captured to provide sample sizes of no less than 100 microspheres per fabricated batch. Representative images of the spheres' surface morphology were taken at various magnifications. The diameters of the microspheres were measured from the SEM images using the software Smile View.

D. Neuro2a cell culture

The neuro2a cells were cultured in Hyclone hi-glucose DMEM with 10 % fetal bovine serum and 1% penicillin-streptomycin added. The medium was changed at 50% every 24 hours.

E. Mouse fetal cortical neuron culture

Primary cortical neurons were harvested from E16 embryos (mouse C57/BL6) and cultured in Neurobasal medium supplemented with B27 and L-Glutamine.

F. Cell Seeding

Before seeding, microspheres were treated by overnight soaking in medium (uncoated microspheres) or 0.01w/v% poly-L-lysine solution (PLL-coated microspheres) at room temperature. Glass coverslips were also soaked overnight in PLL. 5 mg of treated microspheres were placed into each well of 24-well plates. Neuro2a cells were seeded onto the microspheres at 3 X 10^4 cells per well. Cortical neurons were seeded at 5 X 10^5 cells under similar conditions. In addition, cortical neurons were seeded onto PLL-treated coverslips at 1.5 X 10^5 cells per well.

G. MTT assay

The assay is based on the transformation of yellow water-soluble tetrazolium (MTT) salt, by viable cells' mitochondrial succinic dehydrogenases, to water-insoluble purple formazan crystals of which quantity is proportional to the number of viable cells [18]. Medium from culture wells was replaced with serum-free medium and MTT chemical at 9:1 ratio. The cultures were then incubated for 3 hours at 37˚C. Following this, the solution was removed and 500µl of DMSO was added into each well to dissolve the formed purple crystals. The resulting solutions were transferred into 96-well plates, and measured for absorbance (560 nm) with reference wavelength (620 nm) using a microplate reader (Tecan GENios, Switzerland).

H. Total DNA quantification

The assay measures cell numbers by quantifying the amount of DNA using Hoechst 33258 [19]. Cultures were washed twice with PBS and the cells lysed in ultrapure water through 3 freeze-thaw cycles. The cell lysates were mixed with 1 µg/ml Hoechst 33258 in 10mM TrisHCl (pH 7.4), 1mM EDTA and 0.2M Nacl fluorescence assay buffer, then incubated in the dark for 30 minutes. The fluorescence was read at 465 nm using a microplate reader with excitation at 360 nm.

I. Immunoflourescence staining

Immunoflourescence staining was carried out to label various biomolecules and structures in the cells. Cultures

were fixed with 4% paraformaldehyde for 20 minutes, then washed once with PBS, twice with 100mM NH_4Cl in PBS, and once more with PBS. Following this, permeabilisation of the cells was carried out for 15 minutes in 0.1 w/v % saponin in PBS. Primary antibodies were diluted 150 times in blocking buffer consisting of 5% fetal bovine serum and 2 % bovine serum albumin in PBS. The saponin was removed from the culture samples and the samples were incubated in this primary antibody solution for 1 hour. After the incubation, samples were washed 3 times with PBS, and incubated for 1 hour in secondary antibody solution consisting of fluorophore-conjugated secondary antibodies diluted 150 times in blocking buffer. Finally, the samples were washed 4 times in PBS, placed onto glass coverslips, and viewed under Laser Scanning Confocal Microscopes:

- TCS SPE, Leica Microsystems GmbH. Wetzlar, Germany
- Axiophot microscope, Carl Zeiss Inc., Thornwood, NY, USA
- C1 system, Nikon Singapore, Singapore)

J. Statistical analysis

All data is presented as mean ± standard deviation of 3 replications.

III. Results

A. Microsphere characterization

Table 1 shows the size distribution of the 4 microsphere batches fabricated for this study. Figure 1 shows a representative SEM image of microspheres from the 4 batches fabricated. The microspheres are generally spherical, and have similar surfaces with nano-sized features and pores.

Table 1: Microsphere sizes

Batch	a	b	c	d
Mean diameter	189.2	209.9	218.4	203.2
Standard deviation	37.9	48.7	55.3	77
Sample size	145	138	139	152



Figure 1: SEM image of microsphere morphology

B. Growth curve of neuro2a model

Figure 2 shows the growth curves of neuro2a cultures on uncoated, and PLL-coated microspheres, in comparison to tissue culture plate well. The growth curves were measured through the MTT (a) and TDQ (b) assays. Both sets of growth curves show comparable cell growth and proliferation on the 3D microspheres compared to standard 2D culture wells up to 9 days in vitro.

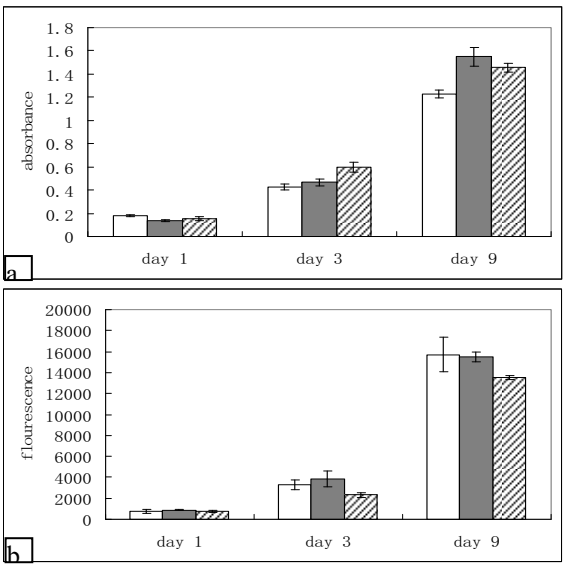


Figure 2: MTT results of neuro2a cultures on uncoated ■, and PLL-coated ▨ microspheres, in comparison to tissue culture plate well □.

C. Primary neuron differentiation on PHBV microspheres

Figure 3 shows neurite extension from mouse fetal cortical neurons as verified by beta-III tubulin staining. The cortical neurons were cultured for 3 days on PLL-coated microspheres. They were stained with Hoechst (blue) for nuclei, and anti-beta-III-tubulin (red) for neurites.

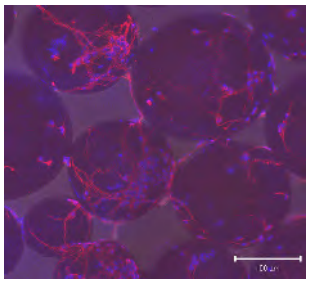


Figure 3: CLSM image of primary neurons on microspheres

IV. Discussion

Due to cell shortages, neuron populations would have to be expanded in vitro to yield enough cells for tissue engineering applications and research [15]. Thus, it is important for scaffolds to support neuronal proliferation. Neuro2a is a neuroblastoma cell line and was used as a model for neuronal proliferation in this study. Neuro2a proliferated on PHBV microspheres at a rate comparable to standard 2D cultures (figure 2). As neuro2a is a neuron-like, the results suggest that neuronal cells such as Neural Stem Cells and Neural Progenitor Cells can proliferate on PHBV microspheres too.

One final aim of neural tissue engineering is to restore function. Thus, scaffold should support neuronal differentiation essential for functional development and restoration. Neuronal differentiation involves formation of cellular structures which include neurites at early stages of maturation. Due to their innate capacity for differentiation, primary mouse fetal cortical neurons were chosen for investigating neuronal differentiation on PHBV microspheres.

Antibodies to beta-III-tubulin were used to stain for neurites. Beta-III-tubulin is found in the microtubules of neurites [20]. Thus, beta-III-tubulin's presence (figure 3) suggests that neurons were extending neurites which could be or could develop into axons and dendrites, and form functional networks on PHBV microspheres.

V. Conclusions

PHBV microspheres have been shown to support neuronal proliferation and differentiation. Thus, PHBV microspheres have potential as neural tissue engineering scaffold.

Acknowledgment

The first author would like to thank Ms Chen Yanan for her mentorship and help in harvesting the primary neurons.

References

1. Ofira E, Tamir BH. The changing face of neural stem cell therapy in neurologic diseases. Arch neurol 2008; 65(4): 452-456.
2. Guzman R, Choi R, Gera A, Angeles ADL, Andres RH, Steinberg GK. Intravascular cell replacement therapy for stroke. Neurosurg Focus 2008; 24 (3&4): E14.
3. Eftekharpour E, Karimi-Abdolrezaee S, Fehlings MG. Current status of experimental cell replacement approaches to spinal cord injury. Neurosurg Focus 2008; 24 (3&4): E18.
4. Chen CP, Kiel ME, Sadowski D, McKinnon RD. From stem cells to oligodendrocytes: Prospects for Brain Therapy. Stem Cell Rev 2007; 3: 280-288.
5. O' Donnell PB, McGinit JW. Preparation of microspheres by the solvent evaporation technique. Adv Drug Deliv Rev 1997; 28: 25-42.
6. Xu XJ, Sy JC, Prasad SV. Towards developing surface eroding PHAs. Biomaterials 2006; 27(15): 3012-3030.
7. Chen J, Davis SS. The release of diazepam from poly(hydroxybutyrate-hydroxyvalerate) microspheres. J Microencapsul 2002: 19(2): 191-201.
8. Van Tomme SR, Van Steenbergen MJ, De Smedt SC, Van Nostrum CF, Hennink WE. Self-gelling hydrogels based on oppositely charged dextran microspheres. Biomaterials 2005; 26(14): 2129-2135.
9. Payne RG, Yasko AW, Yaszemski MJ, Mikos AG. Temporary encapsulation of rat marrow osteoblasts in gelatin microspheres for bone tissue engineering. Materials Research Society Symposium – Proceedings (2001).
10. Wong MS, Causey TB, Mantzaris N, Bennett GN, San KY. Engineering poly(3-hydroxybutyrate-co-3-hydroxyvalerate) copolymer composition in E. Coli. Biotechnol Bioeng 2008; 99(4): 919-928.
11. Squio CR, Marangoni C, De Vecchi CS, Aragao GMF. Phosphate feeding strategy during production phase improves poly(3-hydroxybutyrate-co-3-hydroxyvalerate) storage by Ralstonia eutropha. Appl Microbiol Biotechnol 2003; 61: 257-260.
12. Hankermeyer CR, Tjeerdema Rs. Polyhydroxyburate: plastic made and degraded by microorganisms. Rev Environ Contam Toxicol 1999; 159: 1-24.
13. Gürsel İ, Korkusuz F, Türesin F, Alaeddinoğlu N.G, Hasırcı V. In vivo application of biodegradable controlled antibiotic release systems for the treatment of implant-related osteomyelitis. Biomaterials 2001; 22: 73-80.
14. Willerth SM, Sakiyama-Elbert SE. Approaches to neural tissue engineering using scaffolds for drug delivery. Adv Drug Deliv Rev 2007; 59: 325-338.
15. Kallos MS, Sen A, Behie LA. Large scale expansion of mammalian neural stem cells: a review. Med Biol Eng Comput 2003; 41: 271-282.
16. Schmidt CE, Leach JB. Neural tissue engineering: strategies for repair and regeneration. Annu Rev Biomed Eng 2003; 5: 293-347.

17. Yang YY, Chia HH, Chung TS. Effect of preparation temperature on the characteristics and release profile of PLGA microspheres containing protein fabricated by double-emulsion solvent extraction/evapouration method. J Control Release 2000; 69: 81-96.
18. Ciapetti G, Cenni E, Pratelli L, Pizzoferrato A. In vitro evaluation of cell/biomaterial interaction by MTT assay. Biomaterials 1993: 14(5): 359-364.
19. Rago R, Mitchen J, Wilding G. DNA fluorometric assay in 96-well tissue culture plates using Hoechst 33258 after cell lysis by freezing in distilled water. Anal Biochem 1990; 191: 31-34.
20. Moskowitz PF, Oblinger MM. Sensory neurons selectively upregulate synthesis and transport of the beta-III-tubulin protein during axonal regeneration. J neurosci 1995; 15(2): 1545-1555.

Corresponding author:

Author: Tong Yen Wah
Institute: National University of Singapore
Street: 10 Kent Ridge Crescent
City: Singapore
Country: Singapore
Email: chetyw@nus.edu.sg

Fabrication of Three-Dimensional Tissues with Perfused Microchannels

Katsuhisa Sakaguchi[1], Tatsuya Shimizu[2], Kiyotaka Iwasaki[1], Masayuki Yamato[2], Mitsuo Umezu[1], Teruo Okano[2]

[1] Graduate School of Advanced Science and Engineering, Waseda University, Twins, Tokyo, Japan
[2] Institute of Advanced Biomedical Engineering and Science, Tokyo Women's Medical University, Twins, Tokyo, Japan

Abstract — **Recently, researchers have challenged to create three-dimensional (3-D) tissues with tissue engineering technology in order to establish in vitro models and new therapy for damaged organ. We have developed cell-sheet based tissue engineering and successfully fabricated pulsatile 3-D myocardial tissues both in vivo and in vitro by layering cardiac cell sheets. However, in vitro scaling up of 3-D cell-dense tissues is limited due to lack of blood vessels supplying oxygen and nutrition and removing waste molecules. In this study, we have developed novel bioreactor culturing layered cell sheets on collagen-based microchannels and examined cell behavior between tissues and channels. Rat cardiac cells including endothelial cells were cultured on temperature responsible culture dishes for 4 days. By lowering temperature, confluent cardiac cells were harvested as an intact cell sheet and two cardiac cell sheets are layered. Collagen-based microchannels were engineered by gelling collagen around parallel stainless wires and extracting the wires. The double-layer cell sheets were put on the microchannels and the constructs were connected to the novel perfusion bioreactor. After 5 days of cultivation, the tissue sections were stained with Hematoxylin-Eosin and endothelial cell specific Isolectin B4. HE staining demonstrated that layered cell sheets tightly connected onto the collagen microchannels. The microchannels maintained their patency during culture period. The cardiac cells migrated into collagen gel and the number of migration increased flow-rate dependently. At higher flow-rate, some cardiac cells reached to microchannels and covered over their inner surface. Isolectin B4 staining showed endothelial cells formed networks within the cell sheets and also played as migrating cells. We have successfully fabricated 3-D tissues with perfused microchannels and tissue-originated cells migrated and communicated with the microchannels. These results showed new insights regarding in vitro vascular formation and indicated the possibility for fabricating vascularized 3-D tissues.**

Keywords — **Tissue engineering, Cell sheet, Bioreactor, 3-D myocyte tissues, Vascular formation**

I. Introduction

For end stage heart failure, cardiac transplantation is the most effective treatment, but transplantation is limited by sever shortage of donors. Therefore myocardial tissue engineering to supplement impaired heart tissue is expected alternatively, and has been investigated by various researchers [1]. The conventional approach of tissue engineering is to construct 3-D tissues by using biodegradable scaffolds as alternatives for ECM. In contrast to using biodegradable scaffolds, our group has developed a novel method to fabricate tissues by layering cell sheets. The layered cell sheets were connected tightly, and electrical communications were established between the layered cell sheets [2], layered cell sheets macroscopically beat like heart both in vitro and in vivo [3]. This method has high potential to fabricate functional cell-dense myocyte tissues. However, in the reconstruction of cell-dense myocardial tissue, hypoxia and nutrient insufficiency and waste accumulation limit the final size of viable constructs.

In this study, we developed novel perfusion bioreactor to fabricate 3-D tissues with collagen-based microchannels to overcome those limitations during tissue culture. Cell migration and communicate with the microchannels were examined.

II. Materials and Method

A. Preparation of neonatal rat cardiac cell sheets

Neonatal rat myocytes were isolated from ventricles of 1-day-old rat (CLEA Japan Inc, Tokyo, Japan) as previously described procedures [4]. Briefly, ventricles were minced and digested in Ca^{2+} -Mg^{2+} -free Hanks' balanced salt solution (Sigma, St. Louis, Mo) with 200U/mL collagenase (Class II, Worthington Biochemical, freehold, NJ) at 37°C for 4 cycles of 10 min. Isolated myocytes were cultured in medium with 6% fetal bovine serum, 40% medium 199, 1% penicillin-streptomycin solution, and 54% balanced salt solution containing 166mM NaCl, 1.0mM NaH_2PO_4, 0.8mM $MgSO_4$, 26.2mM $NaHCO_3$, 0.9mM $CaCl_2$, and 5mM glucose. The cell suspensions were seeded at a density of 2.4×10^6 cells/dish on UpCell dish (φ35mm, Type-E, CellSeed Inc, Tokyo, Japan) . The dishes were incubated in 5% CO2 atmosphere for 4 days at 37°C. To detach confluent cell as a cell sheet, culture dishes were incubated in another CO2 incubator set at 20°C for 1 hour.

Chwee Teck Lim, James C.H. Goh (Eds.): ICBME 2008, Proceedings 23, pp. 1213–1216, 2009
www.springerlink.com

B. Creation of collagen-based microchannels

The stainless wires (φ300μm) were inserted into the holes (φ400μm) of the acrylic frame made from Rapid Prototyping (EDEN, Objet Geometries Ltd, Israel) (Fig. 1B). Neutralized liquid collagen was poured into the acrylic frame surrounding the stainless wires set at parallel position (Fig. 1C). To make collagen harden, the collagen was incubated for 30 minutes at 37°C. After collagen gelling, extracting of the wires yielded 300-μm-diameter channels in the collagen gel (Fig. 1D). Neutralized collagen solution consisted of 10% decuple-concentrated cardiac cell culture medium described above, 10% balanced solution containing 10mM Hepes (Sigma, St. Louis, Mo), 15mM $NaHCO_3$, and 80% collagen Type1 (IAC-05, KOKEN Co. LTD, Tokyo, Japan). At the same time as collagen gelling, the double-layer cell sheets were put on the collagen based-microchannels for attachment. The distance from microchannels to cell sheets was approximately 600μm.

C. Assembly of bioreactor

The collagen-based microchannels with cardiac cell sheets were cultured statically at 37°C for 24 hours to make collagen gel stabilized. To perfuse the microchannels, the acrylic frame was connected to the connector of the microsiring pump (KDS270, KD Scientific, USA). All bioreactor devices were putted in the culture box (As one, Tokyo, Japan) maintained at 37°C by the fan heater (Sankei, Tokyo, Japan) and supplied with mixed gas (5% CO_2, 95% Air). The perfusion rate was set to 0.3mL/min, 0.5mL/min, and 0.7mL/min. During the experiment, the performance of bioreactor was observed by the monitoring system (Power Lab, AD Instruments, NZ). The pH and oxygen of culture media were measured by the optic chemical sensors (Presens, Regensburg, Germany) and the inlet pressure of channels was measured by a disposable pressure transducer (Truwave, Edwards Lifesciences, CA., USA) (Fig. 2).

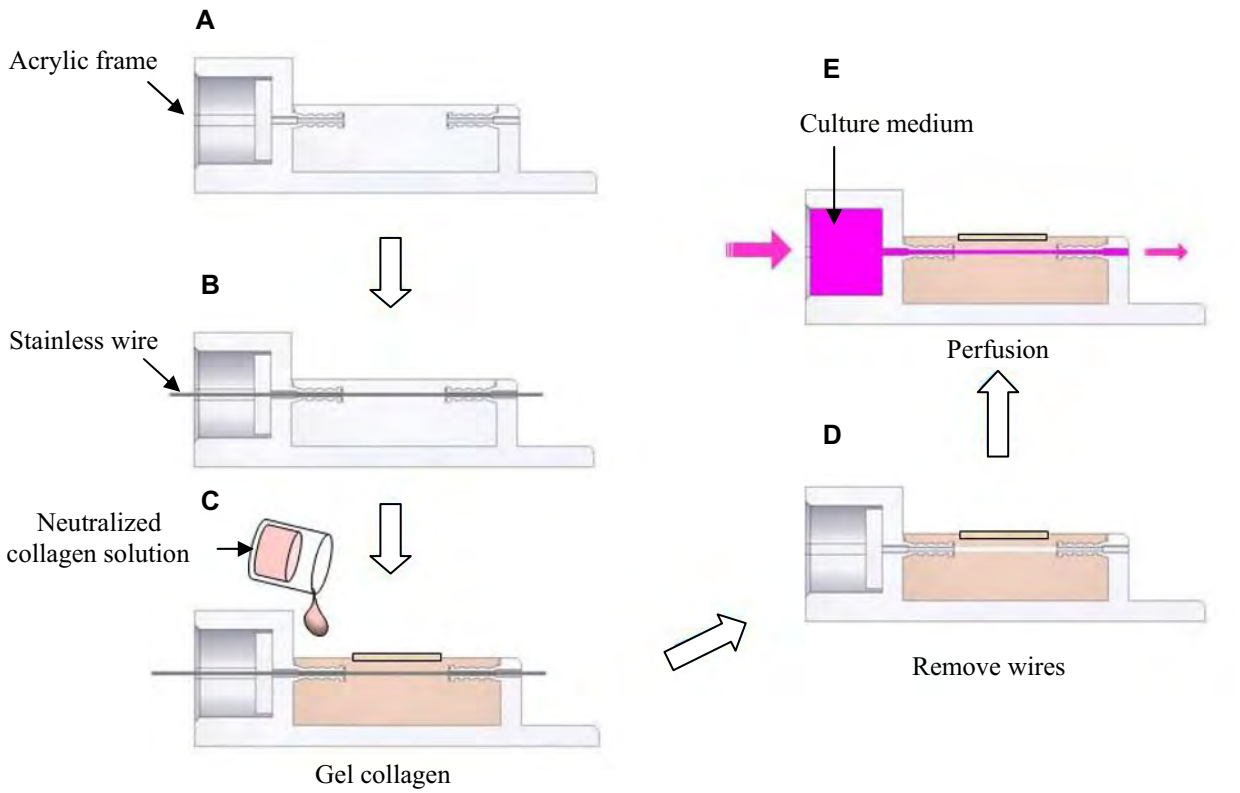


Fig. 1. Schematic diagram of fabricating collagen-based microchannels. The Acrylic frame served as a gel holding device (A). The stainless wires (φ300μm) were inserted into the holes (φ400μm) of the acrylic frame (B). Neutralized liquid collagen gel was poured into the device surrounding the stainless wires putted in parallel position. At the same time as collagen gelling, the double-layer cell sheets were put on the collagen based-microchannels (C). After collagen gelling, extracting of the wires yielded 300-μm-diameter channels in collagen gel (D). After 24hours, culture medium was perfused through the microchannels (E).

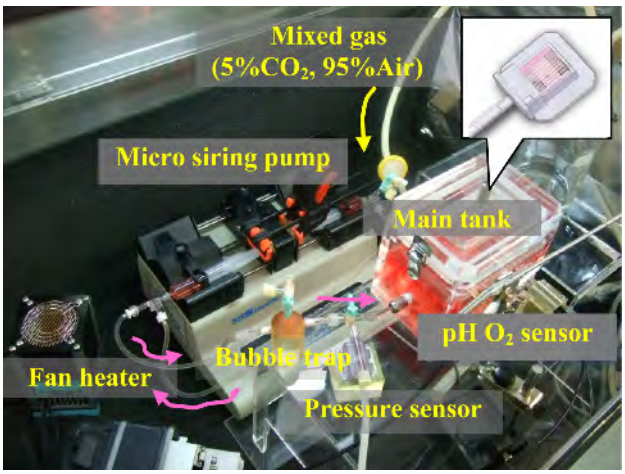


Fig. 2. The perfusion bioreactor was set in the stainless box. In this box, temperature was kept at 37°C.

D. Histological analysis

After perfusion culture, the construct was fixed in 4% paraformaldehyde (Wako Pure Chemicals, Osaka, Japan) and routinely processed into 10-μm-tick paraffin-embedded sections. Hematoxylin and eosin and Azan staining were performed by conventional methods. Fluorescence cells were labeled with Griffonia Simplicifolia Lectin I Isolectin B4 (Vector Laboratories inc, Burlingame, USA), and selected slides were nuclear-stained with 1:500 dilution of Hoechst 33342.

III. Result

During our experiments, the constant flow was realized in the bioreactor system (Fig. 3A-C). The flow within collagen-based microchannels was checked by black ink immediately prior to the fixation. No medium leakage was observed from the microchannels. After perfusion culture for 5days, the HE staining demonstrated that the inner diameter of the collagen-based microchannels did not change at any flow.

In the first place, the distance between cell sheets and the microchannels set at approximately 600μm and the media flow was changed. At flow-rate of 0.3mL/min, the cell migration form the cell sheets was not observed (Fig. 3D). However, at the rate of 0.5mL/min, the cardiac cells migrated into the collagen gel, the distance of migration was approximately 100μm, and the cells just above each microchannel tended to migrate more (Fig. 3E). In the case of 0.7mL/min, the cardiac cells migrated into the

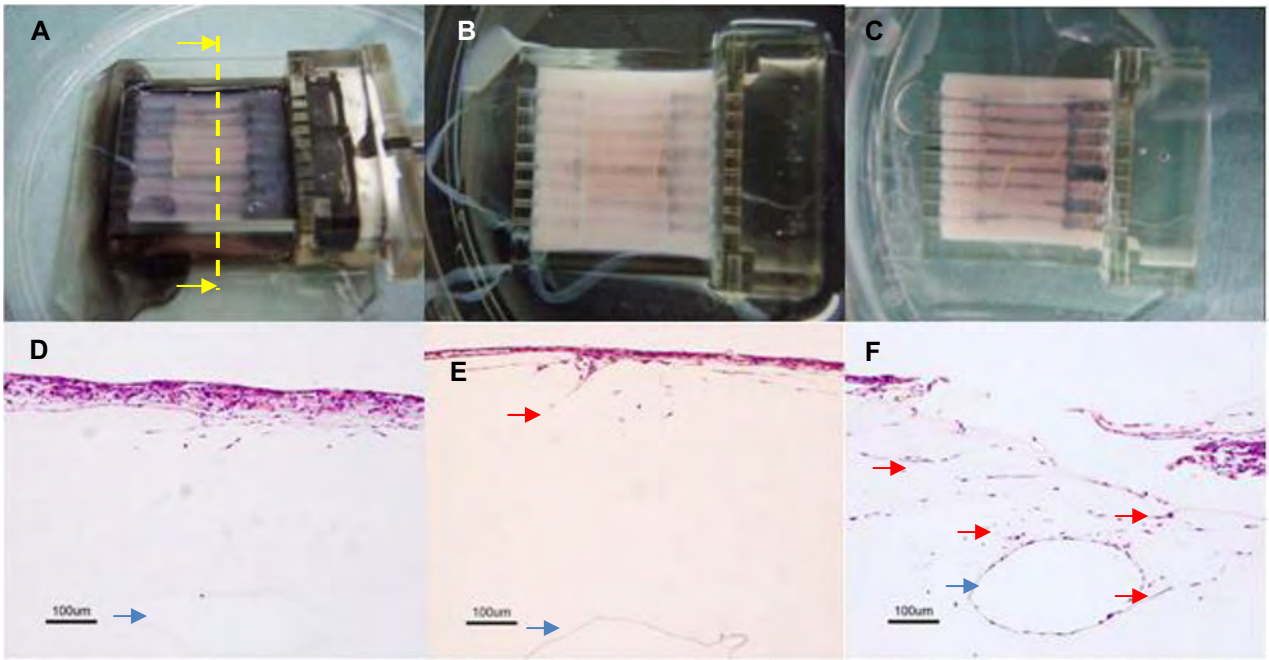


Fig. 3. Collagen-based microchannels after perfused culture. The microchannels were media flowed with 0.3mL/min flow rate. The yellow arrows indicate cross section of HE strain slide (A). 0.5mL/min flow rate (B). In case of 0.7mL/min, the layered cell sheet detach from the collagen gel (C). Demonstration of the morphology with hematoxylin and eosin stain of A (D), in the case of B (E), and C (F). The blue arrows indicate microchannels, and the red arrows indicate migration cells.

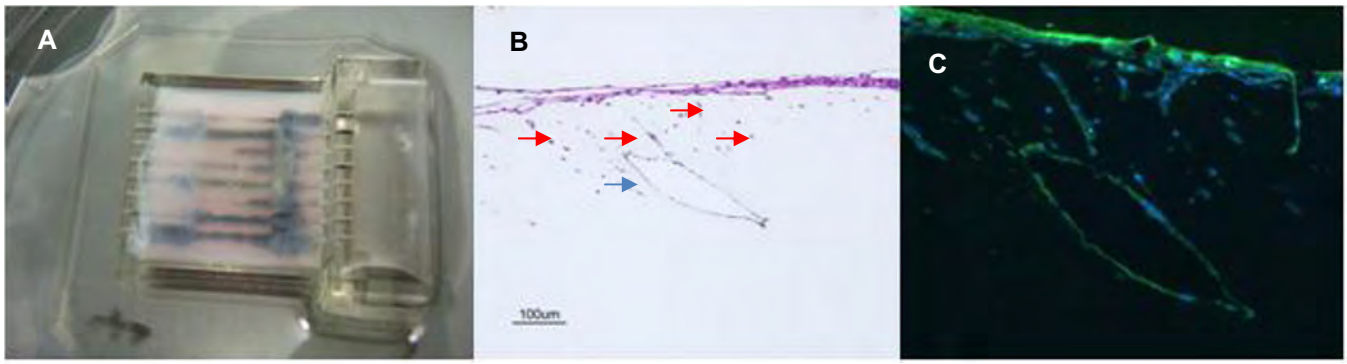


Fig.4. Novel collagen-based microchannels (A). To accelerate the bridge between cell sheets and microchannels without cell sheet delamination, the distance between them was made shorter to approximately 200μm and flow rate was fixed at 0.5mL/min. In result, the cardiac cells migrated and communicated with microchannels. Further more migrating cells covered over the inner surface (B). Isolectin B4 staining showed those migrating cells included endothelial cells (C).

microchannels more deeply and reached to the microchannels (Fig. 3F). However, the higher flow rate caused greater media permeation through collagen gel and the cell sheets finally detached from the gel, (Fig. 3C). Over 0.7mL/min flow-rate, cell sheets detached from the first.

To accelerate the bridge between cell sheets and microchannels without cell sheet delamination (Fig. 4A), the distance between them was made shorter to approximately 200μm and flow rate was fixed at 0.5mL/min. In result, the cardiac cells migrated and communicated with microchannels. Further more migrating cells covered over the inner surface (Fig. 4B). Isolectin B4 staining showed those migrating cells included endothelial cells (Fig. 4C).

IV. Conclusions

We have successfully fabricated cardiac tissues with perfused microchannels and tissue-originated cardiac cells migrated and communicated with the microchannels, and covered over their inner surface. Endothelial cells also contributed to 3-D tissue reconstruct. These results showed new insights regarding in vitro vascular formation and indicated the possibility of fabricating vascularized cardiac tissues.

Acknowledgment

This work was supported by the New Energy and Industrial Technology Development Organization, Japan, Health Science Research Grant (H20-IKOU-IPAN-001) from Ministry of Health, Labor and Welfare, Japan, and Biomedical Engineering Research Project on Advanced Medical Treatment from Waseda University (A8201).

References

1. Thomas Eschenhagen Wolfram H. Zimmermannl (2005) Engineering Myocardial Tissue. Circ Res 97:1220–1231
2. Tatsuya Shimizu et al. (2002) Fabrication of Pulsatile Cardiac Tissue Grafts Using Manipulation Technique and Temperature-Responsive cell culure. Circ Res 90:e40-e48
3. Tatsuya Shimizu et al. (2006) Polysurgery of cell sheet grafts overcomes diffusion limits to produce thick, vascularized myocardial tissues. FASEB J. 20(6):708-10.
4. Kinugasa K et al.(1997) Transcriptional Regulation of inducible nitr oxide synthase in cultured neonatal rat cardiac myocyte. Cir Res 81:911-921

Author: Katsuhisa Sakaguchi
Institute: Graduate School of Advanced Science and Engineering, Waseda University
Street: 8-1, Kawata-cho, Shinjyuku-ku
City: Tokyo
Country: Japan
Email: Katsuhisa@toki.waseda.jp

The Effects of Pulse Inductively Coupled Plasma on the Properties of Gelatin

I. Prasertsung[1,3], S. Kanokpanont[1], R. Mongkolnavin[2,3] and S. Damrongsakkul[1,3]

[1] Department of Chemical Engineering, Faculty of Engineering, Chulalongkorn University, Bangkok, Thailand
[2] Department of Physics, Faculty of Science, Chulalongkorn University, Bangkok, Thailand
[3] Plasma Technology and Fusion Energy Research Unit, Chulalongkorn University, Bangkok, Thailand

Abstract — **Plasma treatment is a technique that can be used to modify the surface of materials. It has been widely used in applications such as surface cleaning, activation, etching, and coating. In this work, pulse inductively coupled plasma (PICP) device is introduced for treatment of crosslinked gelatin film. The effects of plasma on the properties of gelatin film were investigated. Type A gelatin film crosslinked by dehydrothermal (DHT) was treated by N_2 plasma. PICP device produces plasma by discharging large electrical current around a cylindrical quartz tube. The operating pressure of N_2 was 5 Pa and the number of pulse applied was varied from 1 to 10 pulses. The surface properties of crosslinked gelatin were characterized by water contact angle and atomic force microscopy (AFM). The preliminary results showed that, the water contact angle of crosslinked gelatin treated by N_2 plasma were decreased compared to untreated crosslinked gelatin film. This implied that, N_2 plasma could introduce hydrophilic groups onto the surface of crosslinked gelatin. The result from AFM revealed that, enhanced surface roughness of crosslinked gelatin film when much number of pulses applied. *In vitro* test using L929 mouse fibroblast revealed that, the number of cells adhere and proliferate on plasma-treated samples was higher than that on untreated samples. The results implied that PICP has a high potential to modify the surface of gelatin for greater cell affinity.**

Keywords — **Pulse inductively coupled plasma, Surface modification, Plasma treatment, Gelatin**

I. Introduction

One of significant challenges for tissue engineering is to design and fabricate suitable scaffolds from biodegradable materials favorable to cell adhesion, growth, proliferation and differentiation [1]. Commonly, cell attachment and growth are considered as two important factors of cell affinity because they will directly influence cell capacity to proliferate and differentiate [2]. Surface characteristics of material such as hydrophilicity/hygrophobicity, charge property and surface roughness greatly influence cell attachment and growth on the material [3].

Gelatin is a protein biopolymer derived from partial hydrolysis of native collagens, the most abundant structural proteins found in skin, tendon, cartilage and bone of animal. Due to a wealth of merits such as biological origin, nonimmunogenicity, biodegradability, biocompatibility, and commercial availability at relatively low cost, gelatin has been widely used in pharmaceutical and medical fields. Recently, Ratanavaraporn [4] has reported that gelatin could be used to partly replace collagen in scaffold fabrication without losing great biological properties of collagen. Since gelatin is water soluble, dehydrothermal crosslinking was employed to prevent its solubility so that it could be used in tissue culture. However, crosslinked gelatin exhibited hydrophobicity property which was not favorable to cells adhesion [5].

Many approaches have been developed to improve cell affinity of hydrophobic polymers, including surface and bulk modification. Surface modification can be performed by combining some functional groups that are biologically active onto surface of the materials. Surface coating is a simple and general approach for surface modification, but bioactive molecules usually are not able to spread well on the hydrophobic substrate, and thus the surface is unstable [5]

Plasma treatment is a method that can be employed to modify the surface of material since reactive groups or chains can be easily introduced onto the surface of material. Cold plasma such as radio frequency (RF) generated plasma has been reported to modify surface of biomaterials such as poly (lactide-co-glycolide) (PLGA) [5]. However, this plasma generating process is continuous, therefore the controls of heat accumulation and plasma exposures are difficult. Pulse inductively coupled plasma (PICP) method, on the other hand, eliminates heat accumulation problem as well as producing higher energy plasma. PICP device generates plasma by applying large electrical discharge around cylindrical quartz tube. The plasma produced provides high energy ions and electrons that they can be used to modify material surface [6,7]. PICP is discontinuous therefore the plasma exposure can be relatively easy to control.

In this study, PICP was introduced to enhance cell affinity of crosslinked gelatin film. The plasma-treated gelatin was then characterized by water contact angles measurement and atomic force microscopy (AFM). The cell affinity of plasma-treated gelatin was evaluated and compared with that of untreated gelatin using mouse L929 fibroblast as a model cell *in vitro*.

Chwee Teck Lim, James C.H. Goh (Eds.): ICBME 2008, Proceedings 23, pp. 1217–1219, 2009
www.springerlink.com

II. Materials and methods

Type A Gelatin from porcine skin was obtained from Nitta Gelatin, Japan. Dulbecco's modified Eagle's medium (DMEM) and trypsin/EDTA from Sigma Aldrich Chemical Co. were used as received.

A. Preparation of crosslinked gelatin film

Type A Gelatin was dissolved in deionized water to achieve 10% w/w solution. The solution was cast into a teflon mould. After solvent evaporation at room temperature, the film was removed from the mould and crosslinked by dehydrothermal treatment (DHT) at 140°C for 48 hr to obtain crosslinked gelatin (GA-DHT).

B. Plasma treatment

The plasma treatment was done by PICP device using nitrogen gas. Crosslinked gelatin film with a diameter of 14 mm was placed inside a cylindrical quartz tube. The tube was evacuated to less than 2 Pa before filling with nitrogen gas. After the pressure was stabilized at 5 Pa, glow discharge plasma was produced by electrical discharge from a network of electrical energy storage that was charge to a potential of 20 kV. A single pulse discharge and a multiple pulse discharge, in this case up to 10 pulses, were applied to the samples and were coded as GA-DHT-1 and GA-DHT-10, respectively.

C. Characterization of plasma treated gelatin

Determination of water contact angle: Contact angles of crosslinked gelatin films were investigated at room temperature using a Contact Angle Meter Model CAM-PLUS MICCRO equipped with an optical microscope from TANTEC INC. Deionized water was used as liquid media. The contact angle of the samples was averaged from 5 measurements.

Surface topography: Surface topography of the samples was examined by Atomic Force Microscopy (AFM) in contact method. Three-dimensional images and surface topography parameter data were acquired using Nanoscope image-processing software.

D. In vitro cell culture

Plasma treated crosslinked gelatin and untreated crosslinked gelatin were placed into 24-well tissue culture plates and sterilized in 70% (v/v) ethanol for 30 min. To remove ethanol, the samples were rinsed with phosphate-bufferd saline (PBS). L929 mouse fibroblast cells were seeded at a density of $2x10^4$ cells per well in DMEM containing 10% fetal bovine serum and incubated at 37°C in 5% CO_2 incubator. After cultured for 6, 24 and 72 hr, the culture media was replaced with 3-(4,5-dimethylthiazolyl)-2,5-diphenyltetra zolium bromide (MTT) (0.5 mg/ml) and incubated for 30 min to establish cell viability. Dimethylsulfoxide (DMSO) was used to elute complex crystals and the absorbance of solution was measured at 570 nm using a spectrophotometer. The same treatment of the films without cells was used as control. All data were expressed as mean ± standard deviation (n=3).

III. Results and discussion

Water contact angles of untreated and plasma-treated crosslinked gelatin film were shown in Fig. 1. It could be seen that water contact angle of plasma-treated crosslinked gelatin film was lower than that of untreated samples. The water contact angle of plasma-treated crosslinked gelatin film was decreased with increasing a number of pulses applied. This could be due to the introduction of hydrophilic groups by nitrogen plasma onto the surface of crosslinked gelatin [8].

The surface topography of crosslinked gelatin films before and after nitrogen plasma treatment was investigated by AFM. The three-dimensional images of AFM were shown in Fig. 2 and the quantitative data of surface roughness parameters were presented in Table 1. The surface of the untreated crosslinked gelatin was smooth (Fig. 2a) and the value of mean surface roughness (Ra) was 0.603 nm. However, after treated by plasma for 1 pulse, the sample surface became obviously rough and irregular (Fig. 2b).

Table 1 Surface parameter of crosslinked gelatin film before and after plasma treatment

Surface parameter	Treated and untreated gelatin		
	GA-DHT	GA-DHT-1	GA-DHT-10
Ra (nm)	0.603	0.628	0.787

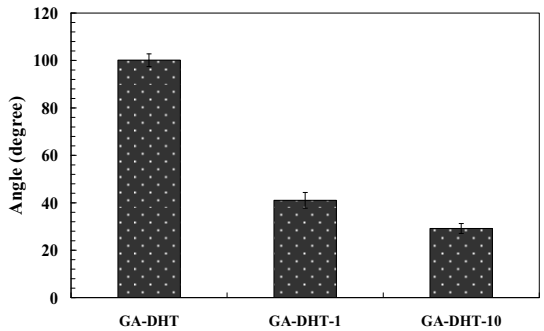


Fig. 1 Water contact angle of untreated and plasma-treated gelatin films

The mean surface roughness was increased to 0.628 nm. When further increasing the nitrogen plasma pulses applied to 10 pulses, the roughness of the gelatin film was remarkably enhanced (Fig. 2c). These results revealed that, enhanced surface roughness of crosslinked gelatin film could be obtained by increasing the number of pulses applied.

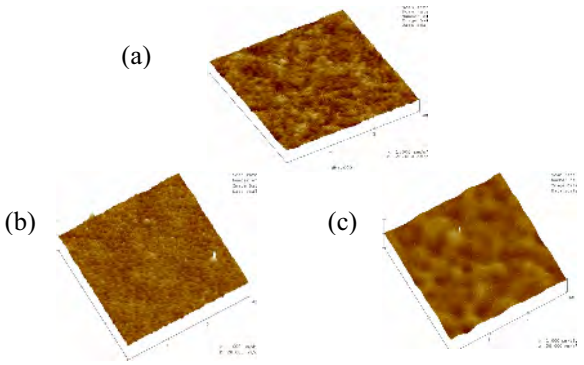


Fig. 2 AFM images of crosslinked gelatin films before and after plasma treatment: (a) untreated; (b) treated with 1 pulse; (c) treated with 10 pulses

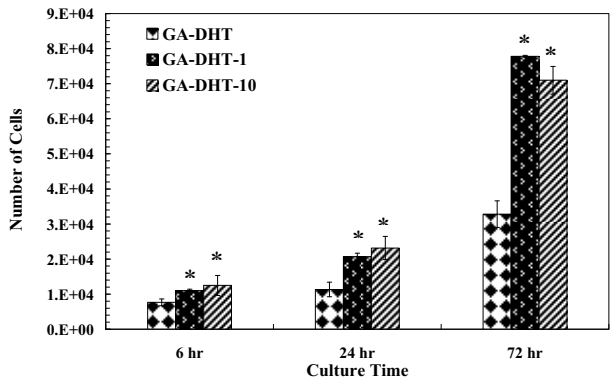


Fig. 3 Number of L929 cells on plasma-treated and untreated crosslinked gelatin film after 6, 24 and 72 hr culture. * represented a significant difference at P<0.05 relative to GA-DHT.

The results on *in vitro* L929 cell attachment and proliferation on plasma-treated and untreated crosslinked gelatin film were shown in Fig. 3. It was notice that the number of adhere cells (after 6 hr of culture) and proliferated cells (after 24 and 72 hr of culture) on PICP-treated gelatins was significantly higher than that on untreated samples. This implied that, increasing in the hydrophilic property and surface roughness of PICP-treated crosslinked gelatin can improve cell adhesion and proliferation.

IV. Conclusions

In this study, PICP was introduced to treat the surface of crosslinked gelatin film. It was found that hydrophilicity and surface roughness of PICP-treated gelatin was promoted in comparison to untreated samples. From *in vitro* L929 cell culture, it was shown that cells could adhere and proliferate on PICP-treated samples greater than that on untreated samples. The results implied that PICP method has potential to modify the surface of crosslinked gelatin for tissue engineering application.

Acknowledgment

The authors would like to acknowledge the grant provides by The Royal Golden Jubilee Ph.D Program, Thailand Research Fund and Chulalongkorn University through the Ratchadaphiseksomphot Endowment Fund.

References

1. Langer R, Vacanti JP. (1999) Tissue engineering. Science. 260:920–926
2. Anselme K. (2000) Osteoblast adhesion on biomaterials. Biomaterials. 21:667–81.
3. Daw R, Candan S, Beck AJ, Devlin AJ, et al. (1998) Plasma copolymer surfaces of acrylic acid/1,7 octadiene: surface characterization and the attachment of ROS 17/2.8 osteoblast-like cells. Biomaterials. 19:1717–25.
4. Ratanavaraporn, J. Physical and biological properties of collagen/gelatin scaffolds. Master thesis Department of Chemical Engineering Chulalongkorn University, 2005.
5. Hong S., Hu X., Yang F., Bei J., Wang S. (2007) Combining oxygen plasma treatment with anchorage of cationized gelatin for enhancing cell affinity of poly(lactide-co-glycolide). Biomaterials 28:4219-4230
6. Kan C.W., Chan K., Yuen C.W.M., Miao M.H. (1998) Surface properties of low temperature plasma treated wool fabric. Journal of Materials Processing Technology. 83:180-184
7. S. Chuenchon, P. Kamsing, R. Mongkolnavin, V. Pimpan and C. S. Wong (2007) Surface modification of rayon fiber using pulsed plasma generated from theta pinch device. Journal of Science and Technology in the Tropics , 3:21-26
8. Carmen Almazán-Almazán M., Paredes J.I., Pérez-Mendoza M., Domingo-García M., López-Garzón F.J., Martínez-Alonso A., Tascón J.M.D. (2006) Surface characterisation of plasma-modified poly(ethylene terephthalate). Journal of Colloid and Interface Science. 293:353-363

Author: Siriporn Damrongsakkul
Institute: Chulalongkorn University
Street: Phayathai
City: Bangkok
Country: Thailand
Email: siriporn.d@chula.ac.th

Dosimetry of ^{32}P Radiocolloid for Radiotherapy of Brain Cyst

M. Sadeghi[1,2,*], E. Karimi[2]

[1] Agricultural & Medical & Industrial Research School, P.O. Box 31485/498, Karaj, Iran
[2] Faculty of Engineering, Research and Science Campus, Islamic Azad University, Tehran, Iran

Abstract — **In the radionuclide treatment of some forms of brain tumors such as craniopharyngiomas, the selection of the appropriate radionuclide for therapy is a key element in treatment planning. The aim of present study was to study the influence of ^{32}P in the radionuclide therapy of cranio-pharyngioma cysts by considering to its dose rate to sites of the diseased tissues. Dosimetry calculations were performed by utilizing the MCNP4C radiation transport code. Analytical dosimetry was additionally performed using the Loevinger formula in MATLAB software for ^{32}P. Each result was compared under identical conditions. The needed activity for injection according to the cyst volume was also obtained in the case of ^{32}P. At the range of 200-300 Gy dose, changes of activity was studied too. Increasing desired dose for therapy results in growth of essential activity for treatment.**

Keywords — **MCNP4C, MATLAB, Craniopharyngioma, Loevinger, Dosimetry**

I. Introduction

Intracavitary radionuclide instillation offers an alternative method for delivering to a focal area in a brain relatively larger radiation dose rate in comparison to external radiation therapy.

Craniopharyngioma is a cyst that develops in the area of the brain called the hypothalamus that is close to the pituitary gland. It is usually found in children [1] or young adults and accounts for around 10% of all brain cysts in young people. It can however be diagnosed at any age. Craniopharyngiomas are nearly always benign but can cause symptoms once they press upon neighboring structure of the brain [2]. Consequently they are often quite large when they are detected and may range in size from 2.5 to 10 cm in diameter [3].

Chromic phosphate (^{32}P) suspension is supplied as a sterile, nonpyrogenic aqueous suspension in a 30% dextrose solution with 2% benzyl alcohol added as preservative. According to this fact that ^{32}P is a beta emitter with half-life 14.2 days, it is used in the form of colloid to treatment craniopharyngioma cyst. The maximum energy of beta spectrum ^{32}P is about 1.71 MeV with average energy o.695 MeV.

Various simulations have been done in the case of brachytherapy using PENELOPE code by Sánchez-Reyes et al [4] etc. The cyst and its surrounding medium were simulated by Rojas et al [5] using PENELOPE code. In this work the dosimetry of the cyst for ^{32}P were done based on the Loevinger and Berger formula and the MCNP4C radiation transport code. Calculation and simulation were done by assuming volume spherical distribution of the radiocolloid [5].

II. Material and methods

A. Loevinger analytic formulas

Loevinger's formula is one of the useful formula calculated dose rates in the case of cyst therapy using beta emitter radionuclide. The basic equation was suggested for a beta emitter point source in uniform medium [6], but by calculating for a spherical volume distribution following formula obtains [5]:

Which the normalization constant B is evaluated by forcing all emitted energy to be absorbed in a very large sphere, and

$$D_{\beta}(x) = A\left\{\begin{array}{l}\frac{\pi Bt}{2x}\left(t\left[12x-11t+4(t-R)\exp(\frac{t+R-x}{t})\right]+3R^2+2Rx-5x^2+2(R^2-x^2)\ln(\frac{t}{x-R})\right)\theta(R+t-x)+\\ 2\frac{\pi Bz^2}{x}\exp(\frac{z-R-x}{z})\left[R+z+(R-z)\exp(\frac{2R}{z})\right]\end{array}\right\}\theta(x-R) \quad (1)$$

is given by:

$$B = \frac{1}{4\pi}\rho v^2 \alpha \overline{E}_{\beta}, \quad (2)$$

With

$$\alpha = \left[3c^2-(c^2-1)\exp(1)\right]^{-1} \quad (3)$$

and $\overline{E}_{\beta}$ is the average energy per disintegration.

The formula changes when the dose rate at the inner surface of the wall is desired (means x=R) [5]:

Chwee Teck Lim, James C.H. Goh (Eds.): ICBME 2008, Proceedings 23, pp. 1220–1223, 2009
www.springerlink.com

$$D_\beta = A\left\{\left(\frac{\pi B t^2}{2R}(4R(3-\exp(\quad))-t(11-4\exp(\quad))\right)+\frac{2\pi B z^2}{x}\times\exp(\frac{z-R-x}{z})\times(R+z+(R-z)\exp(\frac{2R}{z}))\right\} \quad (4)$$

All above equations, the relation between activity and the decay time were used in our analytical calculation for estimating dose rate at any desired distance of the cyst wall. According to volume of the cyst, amount of radiopharmaceutical for injection was calculated too; diameters of the cyst were obtained via MRI images.

The average diameter is approximately 3 cm. The best condition for treatment is achievement 200-300 Gy dose to the interface wall of the cyst [7].

The activity according to desired dose in inner surface of the wall obtains by following formula:

$$A_{inj}=1.355\times10\text{^}(-2)\times D_c\times V_{cyst}\times\rho/(f_1\times f_2\times\bar{E}_\beta\times T_{eff}) \quad (5)$$

A_{inj} is given in μCi and V_{cys} is in cm³. $\bar{E}_\beta$ average energy of radioisotope, T_{eff} effective half-life, ρ density of the cyst (g/cm^3) and D_c is desired dose rate for treatment. Coefficients f_1 defines as the ratio of the dose at radius R from a finite size sphere of radius R to the dose at the center of the cyst [7] and f_2 is equal to 0.455 for cyst with diameter bigger than 1 cm. Activity for 250 Gy dose by using ^{32}P obtain as below:

$$A_{inj} = 75.01\times V_{cyst} \quad (6)$$

(A_{inj} is given in μCi and V_{cys} is in cm³).

By assuming spherical shape for cyst, following formula used for a cyst volume:

The necessary radiocolloid volume was obtained by considering the initially volume and existence activity before injection:

$$V_{inj} = \frac{A_{inj}}{A_o}\times V_o \quad (7)$$

Which V_o is the initially volume of the ^{32}P and A_o is existent activity.

In this work density which used for soft tissue wall was 1.00 g/cm^3 (equal to water) either for inner volume and also the cyst wall.

B. MCNP4C calculation (Monte Carlo N-Particle) [8]

In order to quantify the accuracy of the Loevinger formulas introduced in the preceding section the calculation was done using a full Monte Carlo simulation technique. The cyst was simulated by numerous spherical shells. The $^*F_8$ Tally gives the energy deposition in each point of the cyst in units of MeV. There are four possible source types:

1. Fixed (or general source) source.
2. MCNP generated surface source.
3. Criticality Source.
4. User supplied source.

A particle source has an intensity, energy, direction, shape and temporal characteristics and needs to be positioned somewhere within the phase space of the problem.

The density used in this work is illustrated in Table 1.

Table 1 Composition of different material used in the MCNP4C simulation performed in this paper

	Soft tissue (Rojas, 2003)	Perspex
Density [g/cm^3]	1.0	1.15
H	10.117	8.050
C	11.100	59.98
N	2.600	
O	76.183	31.96

Because of more accurate simulation by MCNP4C code, at the case of soft tissue, density of the inner volume fluid was assumed equal to water. Surrounding medium was simulated by assuming Perspex density.

The condition to compare the result for each radionuclide was created similar: a cyst with radius 1.75 cm and wall thickness 1 mm. The Inner volume of the cyst was layered with a distance of 0.25 mm separating each layer (Fig. 1).

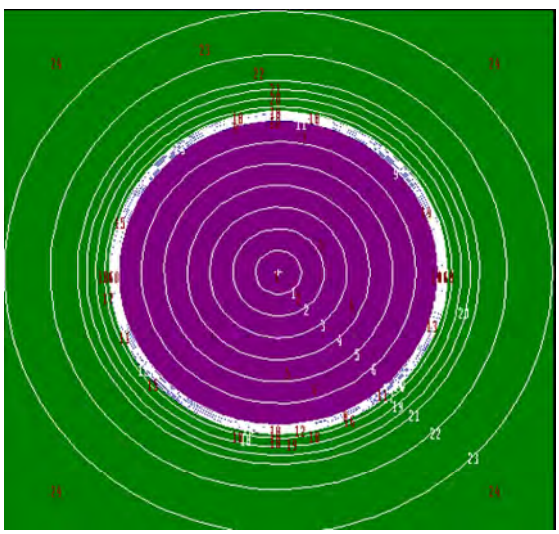


Fig.1 Schematic of the cyst with 1.75 cm radius and 1 mm wall thickness, the distribution of the radiocolloid versus r.

The data were calculated regarding 1 MBq/cm^3 activity concentration of radiocolloid.

^{32}P beta spectrum was inserted according to the intensity of the energy in the range of 0-1.71 MeV.

The spherical deposition of radionuclide can be shown by the following formula:

P=dV/V $P(r) = r \times p$,

$$P(r) = r(\frac{dV}{V}) = r.(\frac{3r^2}{R^3})$$

R: radius of the Cyst

In simulation by MCNP4C code, the spherically distribution of ^{32}P at inner volume of the cyst was indicated by considering above equation (means r^3).

III. Results and Discussion

For a cyst with radius 1.75 cm and wall thickness 1 mm, MCNP4C results and Loevinger's formula calculation consequences were obtained and compared with each other. All the activity concentration of the radiocolloid is 1 MBq/cm^3. Two densities of the wall were used in simulation: soft tissue and compact bone. Inter fluid density considered equal to water for soft tissue wall and same as gel for compact bone wall, the density of surround medium was considered as Perspex density. In analytical calculation based on Loevinger's equation for ^{32}P the mean density was used for compact bone case, and for soft tissue wall was considered as same as simulation.

The parameters which used in computing were:

I. 3 diameter of the cyst in cm
II. Point of interest for Dosimetry in cm
III. Desired dose
IV. Initially volume (the volume which is mentioned on the vial) mL
V. The day passed after production in day
VI. Primary activity (the activity which is mentioned on the vial) in mCi

First estimating dose rate was done based on 250 Gy total dose at inner surface of the cyst wall. In Table 2 MCNP4C results have been mentioned based on 1 MBq/mL concentration activity of ^{32}P.

The results of calculation based on Loevinger's formula at same condition have been compared with MCNP4C data. The results of simulation by MCNP4C code and analytical calculation (MATLAB program) have a good corresponding (Fig. 2). The relative errors were less than 9%.

The contrast between MCNP4C code and MATLAB program results with PENELOPE data for soft tissue [5] according to Table 3 and Figure 3 shows some differences. All the facts were based on 1 MBq/mL concentration ^{32}P. In this work simulation was done based on energy spectrum of ^{32}P.

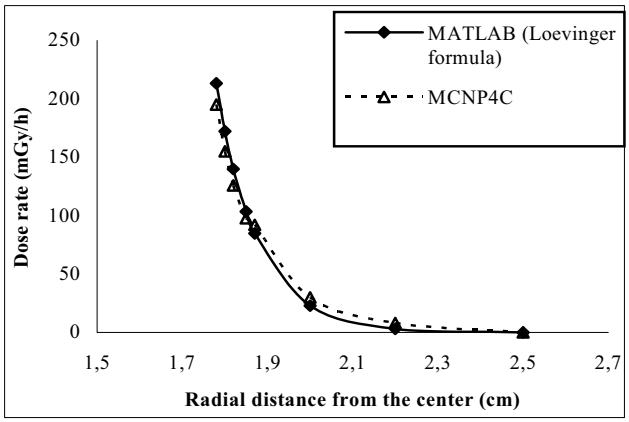


Fig. 2 Comparison between Mon Carlo and MATLAB program data of ^{32}P radionuclide for soft tissue wall

Table 2 Monte Carlo data used tally *F8 for a cyst with1.75 cm radius and 1 mm soft tissue wall thickness tissue for ^{32}P

Radial distance from the interface [cm]	Mass [g]	Energy deposition [MeV]	MeV/g	Dose [Gy/h|MBq]
1.00E-02	4.03E-01	1.73E-03	0.0043	0.00248
2.00E-02	4.07E-01	1.55E-03	0.0038	0.00219
3.00E-02	4.12E-01	1.40E-03	0.00339	0.00195
4.00E-02	4.16E-01	1.27E-03	0.00305	0.00175
5.00E-02	4.21E-01	1.15E-03	0.0027	0.00155
6.00E-02	4.26E-01	1.06E-03	0.0024	0.00138
7.00E-02	4.31E-01	9.75E-04	0.0022	0.00126
8.00E-02	4.35E-01	8.89E-04	0.002	0.00115
9.00E-02	4.40E-01	8.17E-04	0.0018	0.00103
1.00E-01	4.45E-01	7.54E-04	0.0017	0.000979
1.50E-01	2.54042	3.89E-03	0.00153	0.00088
2.50E-01	5.49632	2.86E-03	0.00052	0.0003
3.50E-01	6.0748	8.49E-04	0.00014	0.00008
4.50E-01	6.68133	1.74E-04	0.000026	0.0000015
7.50E-01	2.40E+01	2.62E-05	0.000001	0.00000057

Table 3 Comparison of dose rate (mGy/h|1MBq mL) for 3 kind of calculate and simulation for soft tissue wall with 1 mm thickness and 1.75 cm radius

Radial distance from center [cm]	MATLAB, 250-300 Gy Loevinger's formula [mGy/h|1MBq mL]	MCNP4C, 250-300 Gy [mGy/h|1MBq mL]	PENELOPE, 200 Gy (Rojas, 2003) [mGy/h|1MBq mL]
1.78	213.2	195	168
1.8	172.3	155	140
1.82	140	126	93
1.85	103.6	98	78
1.87	84.7	92	65
2	22.9	30	20
2.2	3.5	8	4
2.5	0.0154	0.017	0.001

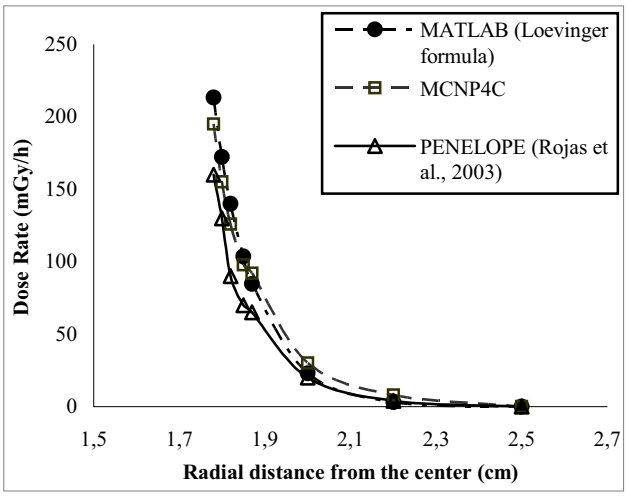


Fig. 3 Comparison between Monte Carlo and MATLAB data with PENELOPE data of ^{32}P radionuclide

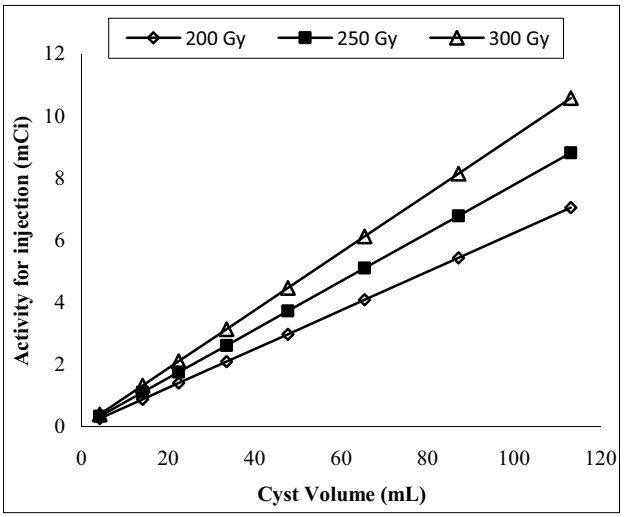


Fig. 4 Differences of needed activity for injection by changing the desired dose for therapy

Three desired doses that have more probable chance in therapy were seen: 200, 250 and 300 Gray and so according to these values, the injection activity for different volume of the cyst was calculated for ^{32}P (Fig. 4). Increasing desired dose causes increasing at necessary injection activity in therapy, also changing in volume of the cyst has direct effect on activity.

IV. Conclusion

In this work, the dosimetry for radiocolloid therapy of cystic craniopharyngiomas was investigated. The ideal assumed in the calculation was a spherical cyst (R=1.75 cm) with 0.1 cm thickness. The cyst and its surrounding medium have been simulated by spherical shells. The results obtained with the analytical expression have been compared with calculations performed with the MCNP4C code for ^{32}P. The calculation shows a nice agreement. In the range of 200-300 Gy for different volume, activity obtained for ^{32}P.

Refrences

1. Shapiro K, Till K , Grant N (1979) Craniopharyngiomas in childhood. J Neurosurg 50: 617–623
2. Shahzadi S, Sharifi G, Rashin A et al (2008) Management of Cystic craniopharyngiomas with Intracavitary Irradiation with ^{32}P. Archives of Iranian Medicine 11: 30-34.
3. Karavitaki N, Cudlip S, Adams C B T et al (2006) Craniopharyngiomas. Endocrine Reviews 27(4): 371-397
4. Sánchez-Reyes A, Tello J J, Guix B et al (1998) Monte Carlo calculation of the dose distributions of two ^{106}Ru eye applicators. Radiother Oncol 49: 191–196.
5. Rojas E L , Al-Dweri F M O, Lallena A M et al (2003) Dosimetry for radiocolloid therapy of cystic craniopharyngiomas. Med Phys 30: 2482-2492
6. Loevinger R, Japha E M, Brownell G L (1956) Discrete radioisotope sources. I. Beta-radiation, in radiation dosimetry, edited by Hine , G. J. and Brownell , G. L. Academic, New York , pp 694-754
7. Janicki C, Seuntjens J (2003) Re-evaluation of the dose to the cyst wall in P-32 radiocolloid treatments of cystic brain tumors using the dose-point-kernel and Monte Carlo methods. Med Phys 30: 2475-2481
8. Briesmeister J F Ed (2000) MCNP4C A General Monte Carlo N-Particle Transport Code System Version 4C. Los Alamos National Laboratory, LA,13709.

Mahdi Sadeghi
Agricultural & Medical & Industrial Research School
P.O. Box 31485/498
Karaj
Iran
E-mail adress: msadeghi@nrcam.org (M. Sadeghi)

Overcoming Multidrug Resistance of Breast Cancer Cells by the Micellar Drug Carriers of mPEG-PCL-graft-cellulose

Yung-Tsung Chen[1], Chao-Hsuan Chen[1], Ming-Fa Hsieh[1,*], Ann Shireen Chan[1], Ian Liau[2], Wan-Yu Tai[2]

[1]Department of Biomedical Engineering and Master Program in Nanotechnology, Chung Yuan Christian University, Chungli, Taiwan
[2]Institute of molecular science, National Chiao Tung University, Hsinchu, Taiwan

Abstract — **The amphiphilic block copolymers methoxy-poly (ethylene glycol)-poly (ε-caprolactone) (mPEG-PCL) was grafted to 2-hydroxyethyl cellulose (HEC) to produce water-soluble copolymers. Doxorubicin (DOX)-loaded nanoparticles were prepared by dialysis method and the sizes of nanoparticles were determined by dynamic light scattering (DLS) in solution. The size of the nanoparticles was in the range of 197.4 to 340.7 nm. Rhodamine 123 was used to probe the relative P-glycoprotein (P-gp) expression in human breast cancer cell lines MCF-7/WT and MCF-7/ADR. Confocal laser scanning microscopy (CLSM) showed a difference between the fluorescence images of DOX-loaded micelles and free DOX. For a quantitative basis, flow cytometry was done on both cell lines treated with DOX-loaded micelles and free DOX to compare a difference in effect. The amount of DOX-loaded micelles in MCF-7/ADR increased compared to that in the MCF-7/WT cells. This gives insight into how the micellar system developed in this study overcomes the multidrug resistance (MDR) effect.**

Keywords — **methoxy-poly (ethylene glycol), poly (ε-caprolactone), multidrug resistance, P-glycoprotein**

I. Introduction

One of the most common problems encountered in chemotherapy is the lack of specificity in treatment which leads to many unpleasant and detrimental side effects. Furthermore, clinical chemotherapy of breast carcinoma is considered insufficient mainly due to drug resistance. The multidrug resistance (MDR) of breast carcinoma is associated with the expression of P-glycoprotein (P-gp) on the plasma membrane, leading to activation of P-gp efflux which causes a reduction of the intracellular drug concentration [1]. Expression of P-gp confers drug resistance to numerous antitumor agents, including the drug doxorubincin (DOX). High drug accumulation in solid tumors was achieved by prolonged circulation in blood as well as the enhanced permeability and retention effect [2]. To achieve this advantage, drug carriers play a key role. Amphiphilic block copolymeric micelles having nano range of particle size possess the core-shell architecture where the core provides the space for drug loading [3]. We have developed the biodegradable block copolymers as micellar-type carrier. For example, poly (ethylene glycol)-block-poly (ε-carprolactone) (PEG-PCL) in which PEG is hydrophilic segment and PCL is hydrophobic one. This sort of amphiphilic block copolymer can self-assemble in the aqueous solution to form micelles where hydrophobic anti-tumor drug is entrapped. In the present study, we synthesized comb-like copolymer PEG-PCL-graft-cellulose for the application of drug carrier. Then, Rhodamine123 (Rh123) was used to display the efflux pump P-gp in human breast cancer cell lines [4], and the cellular uptake of DOX released from the micelles was performed using flow cytometry. The intracellular distribution of cell-associated DOX was observed under confocal laser scanning microscope.

II. Materials and methods

A. Materials

Monomethoxy-PEG (mPEG, M_W=5000) was purchased from Scientific polymer products. Inc. ε-caprolactone and stannous 2-ethyl hexanoate (SnOct) were purchased from A Johnson Matthey Company. The mPEG was purified by re-crystallization on the dichloromethane/diethyl ether system, and ε-caprolactone was dried using CaH_2 and distilled under reduced pressure. 2-hydroxyethyl cellulose (HEC) was purchased from Aldrich Chem. Co. Inc., USA. DOX in aqueous solution (DOX.HCl, 2 mg/mL) was purchased from the Sigma Chem. Co. Inc., USA.

For cell culture experiments, human breast cancer cell lines, MCF-7/WT (Adriamycin-sensitive cell line) and MCF-7/ADR (Adriamycin-resistant cell line). The medium was composed of DMEM, 10% FBS, 1% antibiotic-antimycotic. Rhodamine123 (Rh123) was purchased from Sigma.

B. Synthesis of mPEG-PCL-g-HEC copolymers

The mPEG-PCL diblock copolymer was synthesized by ring opening polymerization of ε-caprolactone in the presence of mPEG as a macro initiator with SnOct as catalyst at 130°C for 24 h [5, 6]. Carboxylic acid terminated mPEG-PCL (0.35 g) was dissolved in THF and stirred at room temperature for 30 min. Then DCC (0.01 g) and DMAP

Chwee Teck Lim, James C.H. Goh (Eds.): ICBME 2008, Proceedings 23, pp. 1224–1227, 2009
www.springerlink.com

(0.015 g) were added sequentially. The HEC (4.125 g) was dissolve in DMSO (10 ml) and introduced to the reaction mixture. The resulting mixture was stirred for 12 h at room temperature under nitrogen atmosphere. The THF was removed in a rotary vacuum evaporator. The mixture was dialyzed to remove DMSO then extracted with dichloromethane to eliminate unreacted mPEG-PCL. The product was frozen and lyophilized to give the solid product.

C. Doxorubicin loading in mPEG-PCL-g-HEC

The micelle solution was prepared by direct dissolution of copolymer in aqueous solution, due to good water solubility of mPEG-PCL-*g*-HEC copolymer. Unlike its hydrophobic drug, DOX.HCl is hydrophilic so it was modified with PBS buffer (pH 9.4) prior to dissolution in THF. This was dropped into the aqueous solution of mPEG-PCL-*g*-HEC copolymer in glass vial, which was allowed to stand overnight to remove THF solvent, then was transferred to a dialysis bag and dialyzed against 500 mL of double distilled water using cellulose dialysis membranes (molecular weigh cut off 50,000 Da). The nanosphere solution was centrifuged, then filtered with a syringe filter (pore size 0.45μm) to eliminate unloaded DOX and aggregated particle.

D. Particle size measurements

The mean diameter and size distribution of the micelles were determined by dynamic light scattering (DLS) method. The instrument was operated at fixed angle of 90°, 628 nm and 25°C. Mean and standard deviation of particle sizes were calculated by assuming a lognormal distribution, and the measured intensity autocorrelations function of scattered light was corrected using Stokes-Einstein equation.

E. P-glycolprotein overexpression assay

Both wild-type and adriamycin-resistant MCF-7 cells (cell number = 2×10^5) were incubated in 2ml DMEM media with Rh 123 (0.5μg/ml) for 30mins at 37 °C. Cells were then washed with PBS, and incubated at 37 °C for another 50mins. The cells were washed with cold PBS and harvested with trypsin. Finally Rh123 fluorescence in cell pellets was measured by flow cytometry (FACS200, BD) and fluorescence microscopy.

F. Cellular uptake and distribution of DOX

The cellular uptake experiments were performed using a flow cytometer. The cells were seeded in six-well culture plates (1×10^5 cells per well) and incubated for 24 hours. The cells were then incubated at 37°Cwith free DOX or DOX-loaded polymer micelles (DOX concentration of 10μg/ml). 24 hours later, the DOX uptake by cells was measured in a flow cytometer which detected the fluorescent DOX in the cell [7]. In addition the intracellular distribution of DOX was observed under confocal laser scanning microscope (CLSM) [8]. The cells were seeded in MatTek glass bottom dish and incubated with free DOX and DOX-loaded micelle for 2 hours and 24 hours, respectively. After ward, the cells were washed with cold PBS and then observed under a confocal laser scanning microscope (FluoView FV300, *Olympus*).

III. Results and discussions

A. Particle size of micelles

The hydrodynamic diameters of copolymer micelles were measured with DLS at 25°C. In our experiments, samples were prepared and analyzed in a concentration range of 3.0mg/ml which is above its critical micelle concentration (0.045mg/mL). The DOX-free micelle and DOX-loaded micelles sizes were found to be around 197.4 nm and 231.5 nm, respectively. It was found that the particle size of DOX-loaded micelles was higher than that of DOX-free micelles.

B. P-glycoprotein overexpression of MCF-7/WT and MCF-7/ADR

Since Rh 123 has been considered to be a relatively specific substrate for *mdr 1* gene-encoded efflux pump P-gp, the release of this fluorescent dye from the cells is an indication of the overexpression of the membrane-bound protein. Fig. 1 shows that the adriamycin-resistant cells revealed a significant rhodamine efflux compared with wild-type breast cancer cells. This assay displayed that the cells used in the present study retain its phenotype of P-glycoprotein during the experiment. Fig. 2 shows the histogram of Rh 123 fluorescence for MCF-7/WT and MCF-7/ADR, respectively. The cells without Rh123 treatment were used as a control and showed only the auto-fluorescence of the cells. The MCF-7/WT showed higher fluorescence intensity than MCF-7/ADR. This evidences confirmed the overexpression of P-gp in MCF-7/ADR cells. found in fluorescence microscope image (Fig. 1). There is therefore a need to address the drug resistance found in this cell line.

C. Cellular uptake and distribution of DOX

In order to visualize the cellular uptake of DOX, the distribution of DOX by MCF-7/WT and MCF-7/ADR cells were observed by confocal microscopy. Since DOX emits

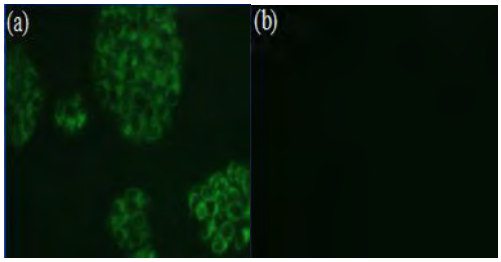


Fig. 1 Fluorescent Rhodamine 123 images of the human breast cancer cell lines. (a) MCF-7/WT (b) MCF-7/ADR

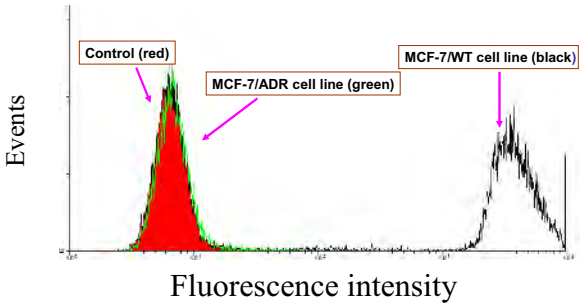


Fig. 2 Flow cytometry histogram profile of Rhodamine 123 efflux for human breast cancer cells.

red fluorescence, its distribution in the cells can be easily observed under CLSM. For free DOX (Fig. 3a and b), the drug was concentrated only in the nuclei but not the cytoplasm [9]. In the case of the micelle formulation, red fluorescence was observed in the cytoplasm, indicating that the large DOX-loaded micelles were internalized by the cells in an endocytotic process. Literature showed that, following cellular uptake, nanoparticles could escape the endo-lysosomal pathway and enter the cytoplasm [10]. After entry into cells, nanoparticles are retained in the cytoplasm for a sustained period of time. When MCF-7/WT cells were exposed to micelles for 24 hours, there was no significant increase in the DOX fluorescence unlike that of cells treated with free DOX. In contrast, with micelle-treated MCF-7/ADR, more intense DOX fluorescence was observed in the cytoplasm after 24 hours. Fig.4 shows the histogram of cell-associated DOX fluorescence for MCF-7ADR and MCF-7/WT cells.

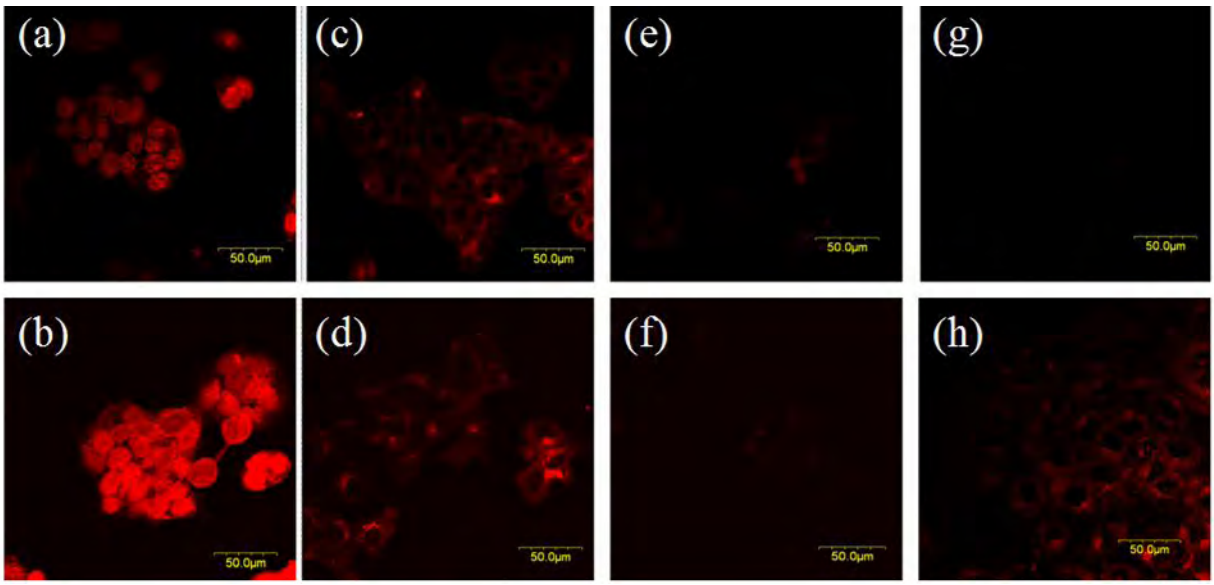


Fig. 3 Confocal images of human breast cancer cell lines treated with different DOX formulations at 10μg/ml concentration. MCF-7/WT cells treated with free DOX for 2h (a) and 24h (b), and with DOX-loaded micelles for 2h (c) and 24h (d). MCF-7/ADR cells treated with free DOX for 2h (e) and 24h (f), and with DOX-loaded micelles for 2h (g) and 24h (h).

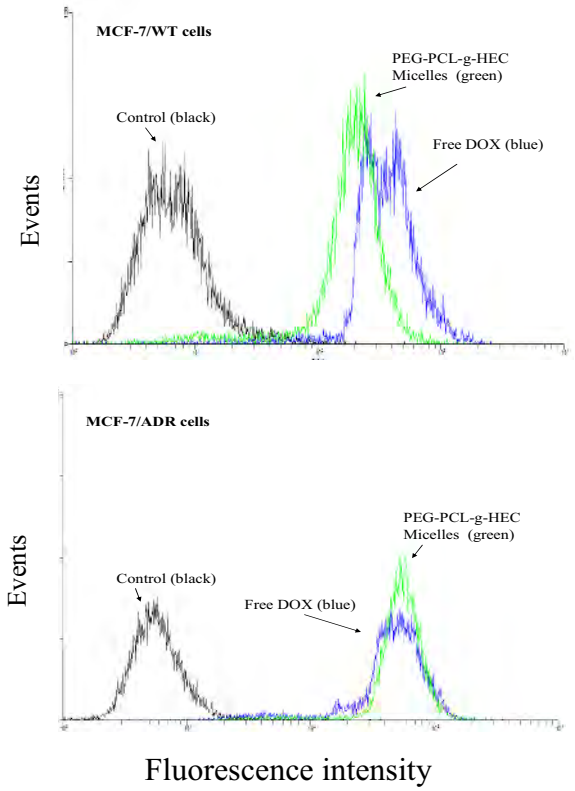


Fig. 4 Flow cytometry histogram profiles of human breast cancer cell lines treated with different DOX formulations at 10μg/ml concentration

For MCF-7/WT cells, the free DOX shows higher fluorescence intensity than DOX-loaded micelles. This indicates that free DOX penetrates the drug-sensitive cell line more efficiently than the DOX-loaded micelles. As for the MCF-7/ADR cells, the cell uptake of DOX-loaded micelles is slightly higher than the free DOX. This result confirms that the cellular uptake of micelles can be enhanced for MDR cells. Hence, the present study suggests that mPEG-PCL-*g*-HEC copolymers may enhance the therapeutic efficacy of DOX in MDR tumor cells.

IV. Conclusions

In this study, the amphiphilic block copolymers methoxy-poly (ethylene glycol)-poly (ε- caprolactone) was grafted to 2-hydroxyethyl cellulose to produce the water-soluble copolymers. The size of the nanoparticles formed by the copolymer was in the range of 197.4 to 340.7 nm. DOX-loaded micelles can accumulate mostly in the cytoplasm while free DOX can diffuse into the nuclei for both MCF-7/WT and MCF-7/ADR. The confocal images further revealed that DOX-loaded micelles entered MCF-7 cells through endocytosis process. The fluorescence intensity of DOX-loaded micelles in MCF-7/ADR cells is higher than that of free DOX. The micellar system of mPEG-PCL-*g*-cellulose was found to be effective to overcome MDR of breast cancer cells. Thus, we expect to carry out in-vivo study in the near future in order to confirm the efficacy of this system to treat breast cancer patients.

Acknowledgement

The authors thank Dr. Y. H. Chen of School of Pharmacy, College of Medicine National Taiwan University for providing the breast cancer cells. The study was sponsored by National Science council of Republic of China under grant numbers: NSC 96-2218-E-033-001, 96-2221-E-033-049.

References

1. Mahesh DC, Yogesh P,Jayanth P. Susceptibility of nanoparticle-encapsulated paclitaxel to P-glycoprotien-mediated drug efflux. Int. J. Pharm 320:150-156
2. Xintao S, Hua A, Norased N, Saejeong K, Jinming G. (2004) Micellar carriers based on block copolymers of Poly(ε-caprolactone) an Poly(ethylene glycol) for doxorubicin delivery. J. Controlled release 98:415-426
3. Radoslav S, Laibin L, Adi E, Dusica M. Micellar nanocontainers distribute to defined cytoplasmic organelles. Science 300:615-618
4. Ulrike S, Wolfgang W, Margit L, Helga N, Iduna F. (1997) Development and characterization of novel human multidrug resistant mammary carcinoma lines in vitro and in vivo. Int. J. Cancer 72:885-891.
5. MF Hsieh ,Nguyen VC, CH Chen, YT Chen, JM Yeh, (2008) Preparation and Characterizations of Block Copolymers of Methoxy Poly(ethylene glycol)-Poly(ε-caprolactone)-Graft-2-Hydroxyethyl Cellulose for Doxorubicin Delivery. J. Nanosci. Nanotechnol.8(5):2362-2368
6. MF Hsieh, TY Lin, RJ Gau, HT Chang, YL Lo, CH Lai, (2005) Biodegradable polymeric nanoparticles bearing stealth PEG shell and lipophilic polyester core. J. Chin. Inst. Chem. Engrs., 36(6):609-615.
7. Yilwoong Y, Jae HK, Hye-Won K, Hun SO, Sun WK, Min HS. (2005) A polymeric nanoparticle consisting of mPEG-PLA-Toco and PLMA-COONa as a drug carrier: improvements in cellular uptake and biodistribution . Pharm Res.22(2):200-208
8. Haizheng Z, Lin YLY. (2008) Selectivity of folate conjugated polymer micelles against different tumor cells. Int. J. Pharm. 349:256-268
9. Kenji K, Chie K, Nobuyuki H, Eiko N, Katsuyuki K, Shinobu W, Atsushi H. (2008) Preparation an cytotoxic of poly (ethylene glycol)-modified poly (amidoamine) dendrimers bearing adriamycin. Biomaterials 29:1664-1675.
10. Panyam J, Zhou WZ, Prabha S, Sahoo, SK, Labhasetwar V. (2002) Rapid endo - lysosomal escape of poly (DL - lactide - co - glycolide) nanoparticles : implications for drug and gene delivery. FASEB Journal 16(10): 1217-1226.

Individual 3D Replacements of Skeletal Defects

R. Jirman[1], Z. Horak[2], J. Mazanek[1] and J. Reznicek[2]

[1] Charles University in Prague, 1st Faculty of Medicine/Department of Stomatology, Prague, Czech Republic
[2] Czech Technical University in Prague, Faculty of Mechanical Engineering/Laboratory of Biomechanics, Prague, Czech Republic

Abstract — **In this work several clinical cases of production of individual bone defect replacements will be presented. Special replacements were produced on the basis of 3D geometric models designed from available diagnostic imaging methods (CT and MRI), and their following computer processing. For production of implants by conventional CNC machining were used in clinical practice commonly used biomaterials (titanium, PEEK, UHWMPE), which can be easily machined. The implants were produced for a particular patient individually with millimetre accuracy so that not only fully functional, but also aesthetic defect replacements were achieved**

Keywords — **skeletal defect, individual replacement, defect reconstruction**

I. Introduction

The objective of a skeletal defects reconstruction using individual implants is achievement of comparable function and perfectly natural physiognomy for the patient. There is effort to replace the lost anatomic structures, to renew the disturbed function, and in case of aesthetic surgery, to improve the physiognomy of the patient. At present, the worldwide prosthesis production follows the trend to individualize the prosthesis for a particular patient instead of unified sizes and shapes. Such approach can be applied in various disciplines: neurosurgery, dental surgery, orthopaedics, but also aesthetic surgery [2, 5]. To achieve high-quality osseointegration, it is necessary to ensure optimum conditions for integration of the implant. The success of the reconstruction of the defect using individual implants depends on thorough examination of the patient supplemented with professional diagnostic imaging, proper indication and choice of treatment, and perfect surgery together with prosthetic treatment. Very close cooperation between the surgeon, technician, producer and also the patient is essential not only during the treatment, but also during the patient's convalescence and rehabilitation.

The aim of the project was to devise a fast, accurate and effective method for designing and production of skeletal implants using appropriate commonly used biomaterials, which can be used to replace the defect, and in conclusion, to conduct several clinical studies demonstrating construction of these individual implants together with postoperative RTG verification.

II. Methods and materials

The method of designing and fabrication of individual implants is in data processing and transfer from available diagnostic imaging methods (CT and MRI), and their following transformation to 3-D geometric models. From 3-D models fabricated in this way, it is possible to make a shape reconstruction of the defect with satisfactory accuracy, and subsequently design an individual implant. The model of the defect for planning of the surgery can be made using the rapid prototyping technology (RPT), and the implant itself using the available conventional CNC machining methods (CAD/CEM). For fabrication of individual implants are, with regards to the health and technological possibilities, available metal (titan Ti6Al4V, chirurgic steel) and plastic (PEEK, UHWMPE) materials. The choice of used material must respect the size of the defect, possible force loading and the implantation method.

The geometries of individual prostheses were designed on the basis of the defect models obtained from the CT image files of the individual patients. The models of bone defects were built in the Laboratory of human biomechanics, CTU in Prague, using segmentation of image data executed in the programme Mimics (Materialise). CT images were made on the Siemens Emotion 16 device with resolution 512x512, the size of pixel was 0.682 mm and the distance of individual sections was 1 mm. The following shape adjustments of the individual prostheses were made using the modelling programme Rhinoceros®, and subsequently verified together with the surgeon on a plastic model of the defect on skeletal part created using the Rapid Prototyping technology. The final geometric models of individual augmentations were exported to an STL file, on the basis of which the prosthesis was finally fabricated.

The individual prostheses were fabricated by the DUO CZ engineering company together with companies MEDIN Orthopaedics and ELLA-CS, from plastic materials Chirulen 1020 (UHWMPE polyethylen, MediTech) and PEEK Optima (polyetheretherketone, Invibio), and also from titanium alloy Ti6Al4V ELI, which is commonly used for joint implant prosthesis. The ultimate input for the fabrication was the data file of the individual prosthesis 3-D model. Using the CAD (Computer Aided Design) volume designer, the size and position of the semi-finished product were

Chwee Teck Lim, James C.H. Goh (Eds.): ICBME 2008, Proceedings 23, pp. 1228–1231, 2009
www.springerlink.com

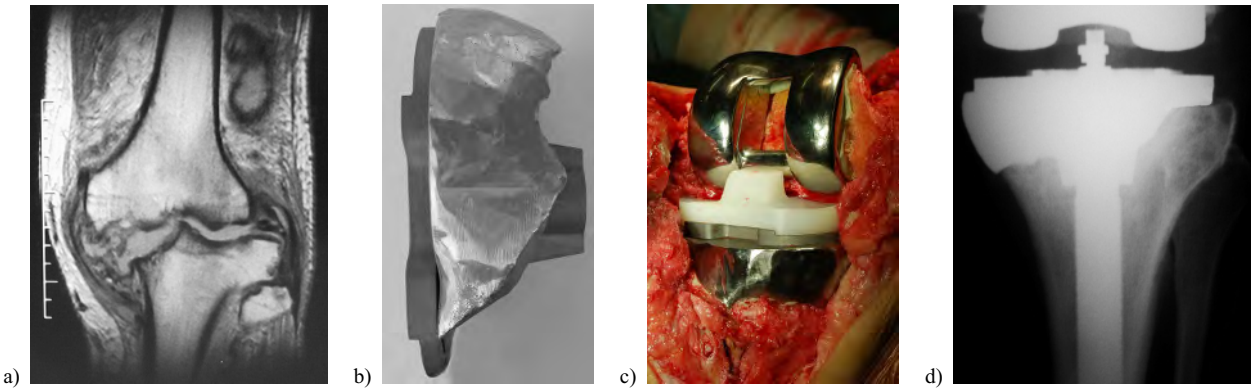


Fig. 1: a) MRI image of the knee defect, b) arrangement of the total replacement of the knee joint together with individual implant (image is rotated by 90°), c) image of an individual implant together with standard prosthesis of knee joint after surgery, d) X-ray images of a patient's knee after surgery with implanted prosthesis.

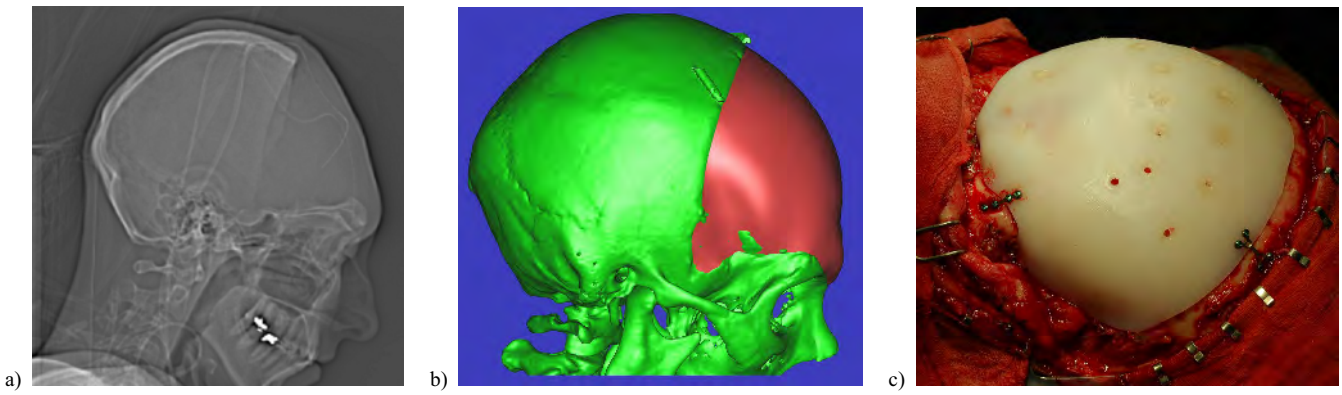


Fig. 2: a) RTG image of the patient's head with defect, b) computer reconstruction of the defect with individual implant, c) implanting the prosthesis to the patient

determined together with fixing aids enabling effective fixation of the material. The machining programme for the CNC (Computer Numerical Control) device was created in the programme CAM (Computer Aided Manufacturing) generating the NC code using the post-processor, which was then adjusted to the particular machining tool. The final prostheses were fabricated by traditional CNC machining (see. Fig. 1a, 2c, 3b). In the following part, some clinical cases will be presented.

Case 1: Tibia defect

The patient is a 65-year-old man with psoriatric arthritis cured for more than 20 years. He was sent by a regional rheumatologist to an orthopaedic consultation with filling of his right knee, serious dysbalance, especially in the frontal plane, and deepening varus deformity. In the X-ray image, there was evident large destruction of the medial condyle of tibia, which extended over the central line far into the lateral condyle. The depth of the defect from the level of the joint was more than 34 mm. Also symmetric usuration of the distal part of both condyles of the femur. The CT examination with 3-D reconstruction showed the actual size of the defects. While it was possible to cure the defects on femur with standard augmentations, the depth and shape of the defect on tibia made using commonly supplied tibial augmentations impossible. It was possible to solve the situation with a custom-made implant, or a custom-made tibial augmentation adapted on a commonly supplied tibial component. After considering all the conditions, the second option was chosen.

Case 2: Defect of os frontale and os temporale

In 2007, a 33-year-old woman in the 37 week of pregnancy arrived at the Neurosurgery clinic of the 1st Medical Faculty of the Charles University and Central Military Hospital in Prague to be examined for deterioration of mental

a) b) c)

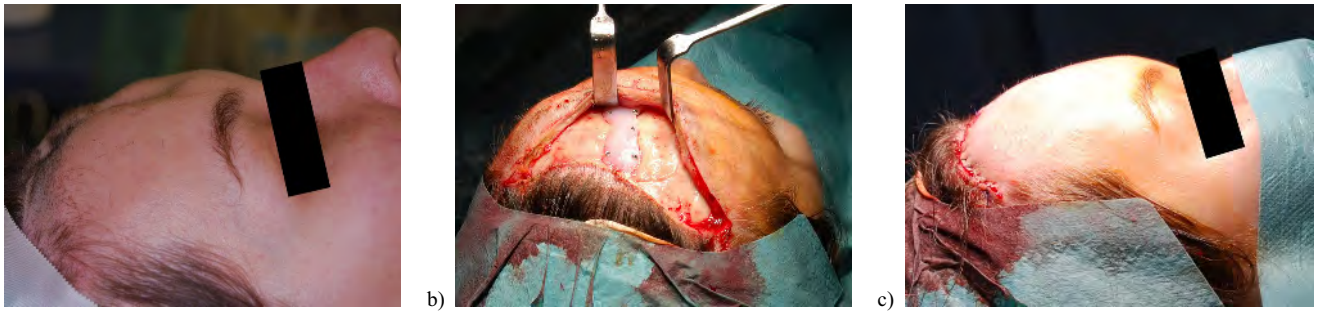


Fig. 3: a) patient with forehead defect, b) fixed implant in the place of the defect, c) patient after the surgery

functions, and symptoms of intracranial hypertension (headaches, vomiting). The imaging method detected a large meningiom on the anterior fossa skull base, size of 76x58x57 mm, with large collateral brain edema. As removing the intracranial tumour is in similar situation usually fatal, due to the vital indication the posterior decompression was performed: the frontal and temporal bones were removed and the dura mater was wide open. After this procedure, the reaction of pupils was immediately adjusted, subsequently after the anti-edema treatment in artificial ventilation the CT finding improved (the brain stem was unblocked), and consciousness was coming back. Only on day 6 after the decompression, it was possible to proceed to the radical resection of the tumour. The anti-edema ventilation regime was still in effect. Two weeks after, a cranial plastic surgery was performed using bone cement, i.e. the large bone defect was modelled from acrylic resin. During healing, there was an inflammatory infiltration of the augmentate, therefore the cement implant was removed, which was the only effective method of solving the situation. Then the inflammation healed. The new implant was fabricated from a block of super-molecular polyethylene Chirulen 1020, and grafted on to the skull using self-tapping titanium screws.

Case 3: Os frontale defect

In 1998, the patient suffered a serious polytrauma as a front-seat passenger, together with fronto-basal injury with defect fracture of the frontal bone in the size of 7x3x2 cm. The patient was repeatedly cured by conventional augmentation procedures using a solid bioceramics replacement covered by resorbable membrane, or using bioactive bone granules separated from the soft tissue by a resorbable membrane Bioguide. Due to the unsatisfactory form and character of the prosthesis, the implant was rejected, which was followed by seamed surrounding tissue. The new individual implant was fabricated from a block of super-molecular polyethylene Chirulen 1020.

III. Discusion and conclusions

Large implants using bone homografts causes problems connected with their integration and resistance to infection; commonly supplied augmentations often do not have satisfactory size or shape. Heavy implants made from bone cement are mechanically and biologically unsatisfactory, and they fail very soon. The way out of these situations are custom-made implants or their components [5]. Replacing large bone defects on tibia is a very difficult task for far-gone knee destructions, and especially during revision surgeries [7].

The main advantage of an individual augmentation, in comparison with commonly supplied modular components, is its optimum shape and the maximum size of the contact surface between the implant and the bone. An individual implant follows exactly the shape of the surface created at the place of the defect, and thus enables even distribution and transfer of loading. The optimum distribution of the loading affects conveniently the structure of the bone tissue, which is loaded evenly on the whole surface, and so there is only minimum reconstruction in the place where the replacement is implanted. The risk of local concentration of loading, which would result in degradation of the bone tissue [6], is reduced considerably. Another indisputable advantage of this approach is minimizing of the bone tissue resection, which is necessary when implanting the standard modular augmentations. The individual augmentation also enables to get over the defects, which might not be possible to treat well using the common augmentations due to their shape or size. The layer of the used bone cement is minimized, and in the future we can predict applying of microporous spray on its contact surface, enabling direct osteointegration.

In case of plastic implants, it is possible to take advantage of their low weight, especially of the skull replacements, but at the same time high degree of their safety in case of a damage (injury, splitting fracture), where the created individual fragments of the ground implant do not form

sharp edges, which might cause deeper injury of the soft tissue (CNS). The chemical structure of these plastic materials enables the surgeon to make fine adjustments (holes, refining the edges) directly in the operating theatre using commonly available millers and drills.

The disadvantage of using the individual augmentation is its higher demand for fabrication, resulting in the higher price. The higher demands for the implant fabrication are especially in the necessity to design a 3-D model of the individual implant and the defect in order to plan the surgery and to check the final set up [3, 8]. The second point is the expenses for preparation of the necessary software, machining time, and the tools for machining the hard material on a special machine tool. Another disadvantage is the necessity of thorough pre-operation planning and a certain latency period between the order for fabrication and the surgery. Standardizing the procedures for taking the measuring data, preparing the software, and the fabrication itself, will allow reducing the period only to several days.

Using of the individually produced augmentation is one of the possibilities how to cure larger bone defects. In case of implants produced in this way, the distribution of the loading on the surface of the neighbouring bone improves. The suitable material for fabrication of these implants is currently commonly used titanium and high molecular polyethylene, but prospectively also PEEK, which is easier to machine, and its mechanical features are closer to the bone tissue. The disadvantage of using individual augmentations is more difficult fabrication, higher price, and high demands for preparation and planning of the surgery.

Acknowledgment

The work was supported by the grant GACR 106/07/0023: Application of synthetic biomaterials for replacement of orofacial parts of skull.

References

1. Delépine F., Jund S., Schlatterer B., de Peretti F. (2007): Experience with Poly Ether Ether Ketone (PEEK) cages and locking plate for anterior cervical fusion in the treatment of spine trauma without cord injury. Rev Chir Orthop Reparatrice Appar Mot., 93: 789-97.
2. Harrysson O.L.A., Hosni Y.A., Nayfeh J.F. (2007): Custom-designed orthopedic implants evaluated using finite element analysis of patient-specific computed tomography data: femoral-component case study. BMC Musculoskeletal Disorders, 8: 1-10.
3. Jiankang H., Dichen L., Bingheng L., Zhen W., Tao Z. (2006): Custom fabrication of composite tibial hemi-knee joint combining CAD/CAE/CAM techniques. Proceedings of the Institution of Mechanical Engineers, Part H: Journal of Engineering in Medicine, 220: 823-830.
4. Kulkarni A., Hee H., Wong H. (2007): Solis cage (PEEK) for anterior cervical fusion: preliminary radiological results with emphasis on fusion and subsidence. The Spine Journal, 7: 205-209.
5. Lee M.Y., Chang Ch.Ch., Lin Ch.Ch., Lo L.J., Chen Y.R. (2002): Custom implant design for patients with cranial defects. Engineering in Medicine and Biology Magazine, 21: 38-44.
6. Pascale V., Pascale W. (2007): Custom-made Articulating Spacer in Two-stage Revision Total Knee Arthroplasty. An Early Follow-up of 14 Cases of at Least 1 Year After Surgery. Hospital for the Special Surgery Journal, 3: 159-163.
7. Rozkydal Z., Janik P., Janicek P., Kunovsky R. (2007): Revision knee prosthesis after asseptic unlocking. Acta Chir. Orthop. Traum. Čech., 74: 5-13.
8. Starly B., Fang Z., Sun W., Shokoufandeh A., Regli W. (2005): Three-Dimensional Reconstruction for Medical-CAD Modeling. Computer-Aided Design & Applications, 2: 431-438.

Address of the corresponding author:

Author: R. Jirman
Institute: Charles University in Prague, 1st Faculty of Medicine, Department of Stomatology
Street: Katerinska 32
City: Prague 2
Country: Czech Republic
Email: radek.jirman@seznam.cz

Brain Gate as an Assistive and Solution Providing Technology for Disabled People

Prof. Shailaja Arjun Patil

Electronics & Telecommunication department, RCPIT, Shirpur Dist: Dhule, Maharashtra, INDIA

Abstract — **A range of applications and products with a combination of nanotechnology, biotechnology, and information technology are under development to directly improve the lives of people with severe injuries or medical conditions. Solutions range from better implants and prosthetics to brain-machine interfaces and they already are in the early stages of development and have working prototypes.**

Nanomedical and bionic products that could directly improve sensory, motoric and other functions cover all aspects of the human body. These visions go far beyond the current implant technologies (bionic ears and limbs, neural and retinal implants, artificial muscles etc) under development.

The best solution we could find for the disabled and elderly people is the use of brain gate. The technology gives the disabled people the opportunity to live a quasi-normal life inspite of being not able to move their body parts. Infact this technology is a boon for physically disabled and elderly people. So, here is a brief introduction of BRAIN GATE.

Keywords — **Basic Principle behind Brain Gate, Need for Brain Gate, Experiment on Human Being, Brain machine interface, Brain gate human neural interface system**

I. Introduction

People who are paralyzed have been given new hope by stem cell research, championed by the late Christopher Reeve P'02. But researchers in neuroscience are looking at other, less controversial ways of restoring independence to people with disabilities.

The Brain Gate System is based on Cyberkinetics' platform technology to sense, transmit, analyze and apply the language of neurons. The System consists of a sensor that is implanted on the motor cortex of the brain and a device that analyzes brain signals.

A. Basic Principle Behind Brain Gate:

The principle of operation behind the Brain Gate System is that with intact brain function, brain signals are generated even though they are not sent to the arms, hands and legs. The signals are interpreted and translated into cursor movements, offering the user an alternate "BrainGate pathway" to control a computer with thought, just as individuals who have the ability to move their hands use a mouse.

B. Need For Brain Gate:

The device was designed to help those who have lost control of their limbs, or other bodily functions, such as patients with amyotrophic lateral sclerosis (ALS) or spinal cord injury. ALS is a degenerative disease in which people eventually lose the ability to perform the most basic movement tasks, including twitching a cheek muscle or blinking an eye. The System consists of a sensor that is implanted on the motor cortex of the brain and a device that analyzes brain signals. So one can easily move a cursor on the computer screen also one can use the robotics arm or any other devices in the case of failure of the limbs.

A team of neuroscientists have successfully implanted a chip into the brain of a quadriplegic man, allowing him to control a computer.

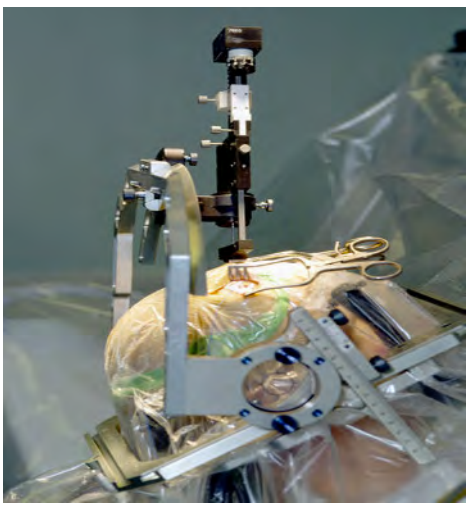


Fig 1. Implantation of brain chip

The chip, called Brain Gate, is being developed by Massachusetts-based Neurotechnology Company Cyberkinetics, following research undertaken at Brown University; Rhode Island.Results of the pilot clinical study will be presented to the Society for Neuroscience annual conference in San Diego, California, on Sunday. Up to five more patients are to be recruited for further research into the safety and potential utility of the device.

Chwee Teck Lim, James C.H. Goh (Eds.): ICBME 2008, Proceedings 23, pp. 1232–1235, 2009
www.springerlink.com

C. Experiment On Human Being

SAN FRANCISCO -- Any geek worthy of the moniker has dreamed of connecting his or her brain directly to a computer for blissful freedom from keyboard and mouse. For quadriplegics, that ability would give life a whole new dimension. If people with physical handicaps could control a computer by just thinking, they could also operate light switches, television, even a robotic arm -- something the 160,000 people in the United States who can't move their arms and legs would surely welcome.

Work in that brain-computer interface, or BCI, technology has ramped up considerably in the past five years. More than half of the scientific papers on the topic were published in just the past two years. Also, by connecting their patients' brains directly to a computer, researchers have seen improvement in patients' ability to control a cursor.Cyberkinetics is leading research on BCIs in the private sector. Last year the company enrolled its first patient, Matthew Nagle, in a clinical trial to test its Brain Gate system. From his wheelchair, Nagle can now open e-mail, change TV channels, turn on lights, play video games like Tetris and even move a robotic hand, just by thinking.

The device, which is implanted underneath the skull in the motor cortex, consists of a computer chip that is essentially a 2-mm-by-2-mm array that consists of 100 electrodes. Surgeons attached the electrode array like Velcro to neurons in Nagle's motor cortex, which is located

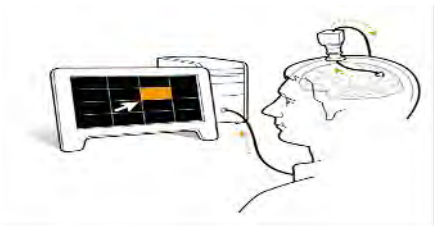


Fig 2.

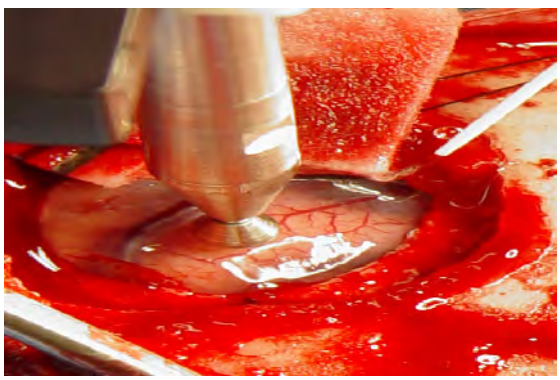


Fig 3. Insertion

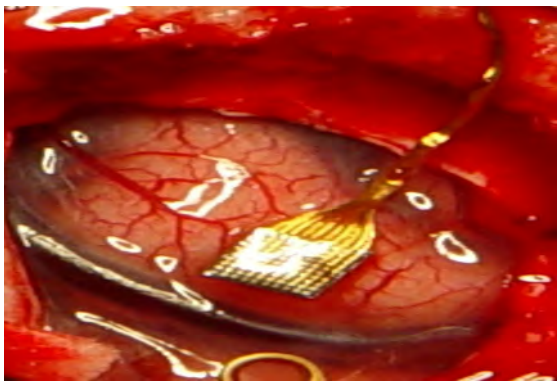


Fig 4. Computer Chip

in the brain just above the right ear. The array is attached by a wire to a plug that protrudes from the top of Nagle's head.

The electrodes transmit information from 50 to 150 neurons through a fiber-optic cable to a device about the size of a VHS tape that digitizes the signals. Another cable runs from the digitizer to a computer that translates the signal.

The Matrix-like device protruding from Nagle's head seems little price to pay for the new abilities he's gained thanks to Brain Gate.

But other researchers are working on simpler, noninvasive BCIs. Jonathan Wolpaw, a professor at the Wadsworth Center in New York, published a paper in December 2004 in the Proceedings of the National Academy of Sciences showing that his noninvasive electroencephalogram, or EEG, cap could pick up brain signals at least as well as Cyberkinetics' invasive technology.

Both patients and their doctors would prefer not to open the skull to implant a BCI, but it's not yet clear whether a BCI sitting outside the head will be as good at picking up brain waves as an implanted device. Experts generally thought the answer was no until Wolpaw published his results.

II. Brain machine interface

Modifying the human body or enhancing our cognitive abilities using technology has been a long-time dream for many people. Nano-bio-info-cogno-synbio (NBICS) is now reaching a critical stage where it could lead to the fulfillment of that dream.

An increasing amount of research tries to link the human brain with machines allowing humans to control their environment through their thoughts. It is said: "Ultimately the technology will be used for people whose spinal cords



Fig 5.

are destroyed in accidents or those handicapped by strokes." Scientists demonstrated in 2002 that human thoughts can be converted into radio waves and used by paralyzed people to create movement. "Scientists in Australia have developed a mind switch that enables people to activate electrical devices (e.g. turn on a radio or open doors) by thinking."

The IDIAP Research Institute (formerly the Institute Dalle Molle d'Intelligence Artificially Perceptive/Dalle Molle Institute for Perceptual Artificial Intelligence) is developing non-invasive brain machine interfaces.

The Institute states in a recent publication: "Brain activity recorded non-invasively is sufficient to control a mobile robot if advanced robotics is used in combination with asynchronous EEG analysis and machine learning techniques. Until now brain-actuated control has mainly relied on implanted electrodes, since EEG-based systems have been considered too slow for controlling rapid and complex sequences of movements. We show that two human subjects successfully moved a robot between several rooms by mental control only, using an EEG-based brain-machine interface that recognized three mental states. Mental control was comparable to manual control on the same task with a performance ratio of 0.74."Many researchers are working on brain machine interfaces.

Cyberkinetics Neurotechnology Systems, Inc. of Fox borough, Massachusetts, received FDA approval to test the "Brain Gate." The company started with people with spinal cord injuries and is now recruiting patients for BrainGate ALS trials, according to deal.com.

Researchers at Duke University Medical Center in Durham, North Carolina, are developing a wireless neuroprosthetic that could potentially be used to control robotic limbs for quadriplegics. Dr. Miguel Nicolelis of the university's Department of Neurobiology has a variety of articles on his webpage. A 14 year-old boy plays space invaders using thoughts alone, as a grid connected to his brain measures his electrocortigraphic activity.

The device was developed by Dr. Eric C. Leuthardt, an assistant professor of neurological surgery at the School of Medicine, and Dr. Daniel Moran, assistant professor of biomedical engineering at Washington University in St. Louis. They connected the patient to a sophisticated computer running a special program known as BCI2000 developed by collaborator Gerwin Schalk at the Wadsworth Center, New York State Department of Health in Albany, which displays a video game linked to an electrocorticographic (ECoG) grid. The primary purpose of the grid was to facilitate treatment for epilepsy.

In Austria, the Graz University of Technology has a brain-computer interface lab. In Japan, Hitachi has joined forces with university researchers. In Finland the Proactive Computing Research Programme (PROACT) is funded by the Academy of Finland and led by Academy Professor Mikko Sams. IST has funded the Presencia project under its Fifth Framework Programme - Future Emerging Technologies Presence Research.

III. BRAINGATE HUMAN NEURAL INTERFACE SYSTEM

Cambridge Consultants' Virtual Helmet can link brain wave patterns to a virtual reality system, allowing the wearer to enter an illusory world of movement. Researchers at Nippon Telegraph & Telephone Corporation in Japan have developed galvanic vestibular stimulation -- a technology that can compel a person to walk along a route in the shape of a giant pretzel, in effect creating remote-controlled humans.

Researchers at Columbia University have combined the processing power of the brain with computer vision to develop a novel device that allows people to search through images ten times faster than they can on their own. The cortically coupled computer vision system -- known as C3 Vision -- turns the brain into an automatic image-identifying machine. The project is funded by the US Defense Advanced Research Projects Agency. The Air Force has long been interested in "alternative control technology" that will allow its pilots to fly planes hands-free.

A ***robotic hand*** controlled by the power of thought alone has been demonstrated by researchers in Japan. It mimics the movements of a person's real hand, based on real-time functional magnetic resonance imaging of brain activity. This is seen as another landmark in the advance towards prosthetics and computers that can be operated by thought alone. The system was developed by Yukiyasu Kamitani and colleagues from ATR

Computational Neuroscience Laboratories in Kyoto, and researchers from the Honda Research Institute in Saitama. Subjects lying inside an MRI scanner were asked to make "rock, paper, scissor" shapes with their right hand. The scanner recorded brain activity and fed data to a connected computer. After a short training period, the computer was able to recognize the brain activity associated with each shape and command the robotic appendage do the same.

A brain-activity interpretation contest organized by the University of Pittsburgh provided entrants with functional MRI scanner data and behavioral reports recorded when four people watched two movies. Competitors were asked to create an algorithm that used the brain activity to predict what viewers were thinking and feeling as the film unfolded.

The crunch test came from a third film. Competing researchers were shown the brain activity only, and had to predict the behavioral data -- what the viewers had reported seeing and feeling during the film on a moment-by-moment basis. The rules are here and the results are here.

Although brain–machine interfaces are often talked about in relation to disabled people, we can expect they will also be used by the non-disabled as a means to control their environment -- especially if the devices are non-invasive and no implants are needed.

To date there has not been much public discussion of the implications of brain machine interfaces, the amount of public R&D funding they receive, and control, distribution and access to these devices.Paralyzed patients dream of the day when they can once again move their limbs. That dream is making its way to becoming a reality, thanks to a neural implant created by John Donoghue and colleagues at Brown University and Cyberkinetics Neurotechnology Systems.

In 2004, Matthew Nagle, who is paralyzed due to a spinal-cord injury, became the first person to test the device, which translated his brain activity into action (see "Implanting Hope," March 2005, and "Brain Chips Give Paralyzed Patients New Powers"). Nagle's experience with the prosthetic was exciting but very preliminary: he could move a cursor on a computer screen and make rough movements with a robotic arm. Now Donoghue and team are pushing ahead with their quest to develop a commercially available product by testing the device in two new patients, one with a neurodegenerative disease and the other suffering the effects of a stroke.

With spinal-cord injuries and some types of stroke and neurodegenerative disease, the information-relay system between the brain and muscles is disrupted. The Cyberkinetics device consists of a tiny chip containing 100 electrodes that record signals from hundreds of neurons in the motor cortex. A computer algorithm then translates this complex pattern of activity into a signal used to control a computer cursor, robotic arm, and, maybe eventually, the patient's own limb.

The researchers have now tested the device in two new patients, one with ALS, a progressive neurodegenerative disease, and the other with brain-stem stroke, a particularly devastating type of stroke that paralyzes the body but leaves the mind intact.

IV. Conclusion

So, this was a brief introduction to brain gate and various applications of brain gate. These are some of the opportunities we can provide to disabled peopled using the brain gate. Though these technologies are in the preliminary stage of their development they are some of the most widely used assistive technologies of the future. With more demand it will become some of the most affordable and house hold assistive technology.

Reference

1. R. Borgolte, R. Hoelper, H. Hoyer, H. Heck, W. Humann, J. Nezda, I. Craig, R. Valleggi and A. M. Sabatini. Intelligent control of a semi-autonomous omni-directional wheelchair. In *Proceedings of the 3rd International Symposium on Intelligent Robotic Systems `95 (SIRS `95)*, pp. 113-120, Pisa, Italy, July 10-14, 1995.
2. D. Miller and M. Slack, Design and testing of a low-cost robotic wheelchair prototype, *Autonomous Robots,* **2**(1): 77-88, 1995.
3. S. J. Sheredos, B. Taylor, C. B. Cobb and E. E. Dann, Preliminary evaluation of the helping hand electro-mechanical arm. *Technology and Disability*, **5**(2): 229-232, 1996.
4. Teenager moves video icons just by imagination, press release, Washington University in St Louis, 9 October 2006.
5. Warwick,K, Gasson,M, Hutt,B, Goodhew,I, Kyberd,P, Andrews,B, Teddy,P and Shad,A:"The Application of Implant Technology for Cybernetic Systems", Archives of Neurology, 60(10), pp1369-1373, 2003.
6. Cyberkinetics.com

Author: Prof. Shailaja Arjun Patil
Institute: R.C.Patel Institute of Technology,Shirpur
City: Shirpur, Tal: Shirpur, Dist: Dhule, Maharashtra.
Country: India
Email: shailajadp@yahoo.co.in

Compressive Fatigue and Thermal Compressive Fatigue of Hybrid Resin Base Dental Composites

M. Javaheri[1], S.M. Seifi[1], J. Aghazadeh Mohandesi[1], F. Shafie[2*]

[1] Department of Metallurgical Engineering Amirkabir University of Technology, Tehran, Iran
[2] Department of Dentistry, Tehran University of Medicine Science, Tehran, Iran
*: Corresponding author

Abstract — **The object of this paper is to investigate the compressive and thermal-compressive fatigue behaviour of four hybrid resin base dental composites. Cylindrical specimens (6mm in length ×3 mm in diameter) were made considering manufacturers' recommendation and stored for 48 hours in distilled water at 37°C. The compressive fracture strength was measured and fatigue tests under frequency of 10 Hz were carried out. For thermal-compressive fatigue test a cyclic flowing cold and hot-water set designed. The compressive strength of the four materials KURARY® Clearfill AP-X (AP-X), 3M ESPE® Supreme, SAREMCO® Extra Low Shrinkage (ELS) and Tetric® Ceram were obtained. Supreme showed the highest compressive fracture strength and thermal compressive strength while ELS was the lowest. The compressive fatigue strengths obtained using staircase method for 100,000 cycles under sinusoidal loading and based on compressive fracture strength, the acquired data were analyzed using ANOVA and Weibull statistics. The results indicate that the Supreme and ELS composites hold the highest and lowest fatigue strengths, respectively. This seems to be caused by the superior matrix properties associated with the different type of fillers alongside the highest ratio of Vol%/ Wt%.**

Keywords — **Dental composites, Thermal compressive fatigue, Compressive fatigue, Fracture Mechanism**

I. Introduction

Light-cured hybrid composites resins are an important group of restorative materials in dentistry and can be used to restore shape and function of anterior and posterior teeth.Since the very first dental resin composites were developed, many efforts to improve their clinical performance have been undertaken. Research on the resin matrix is mainly based on the development of new monomers while studies on the filler content focus on loading, particle size, silanation [1] and on the development of new particles. Such studies are of high importance because the mechanical properties of dental composites depend highly on the concentration and particle size of the filler. The compressive strength and compressive fatigue limit increase with the amount of inorganic fraction while the polymerization shrinkage is said to decrease [1]. Dental composite restorative materials consist of an organic matrix, ceramic fillers, and the interface' between the inorganic fillers and the matrix. Fatigue fractures of resins after years of clinical use were found to be a common failure reason. Braem *et al.* [2] (1994) reported that fatigue is a major factor in determining the life expectancy of resin composite restorations.

Lohbauer *et al*. [3] (2003), evaluating the mechanical properties of contemporary conventional and packable composites under flexural strength and flexural fatigue limits concluded that the fatigue behaviour of the materials does not correlate with initial strength values.

Since the properties of the composites for the restoration of posterior teeth are controversial while clinical and fatigue studies are scarce and also in the oral cavity, prosthetic reconstructions are usually under conditions of thermal variation and loading conditions. Such thermal cycling and cyclic loading may cause fatigue fractures during long-term clinical use, the objective of the present study was to characterize the inorganic fraction and to measure and compare the mechanical properties, compressive strength, compressive fatigue strength and thermal compressive fatigue strength, of four commercially available hybrid composites.

II. Materials and methods

A. Material selection and specimen fabrication

The substances and materials used in this study are presented in Table 1.

Cylindrical specimens, 3 mm in diameter and 6 mm long, were according to the manufacturers' recommendations. The specimens were then stored in distilled water at 35 ± 2°C for 2 days. The quantity of specimens for compressive and fatigue tests were 5 and 15 respectively.

B. Experimental process

The compressive strength tests were carried out under the compressing rate of 0.5 mm/min according to ASTM-D695.

Chwee Teck Lim, James C.H. Goh (Eds.): ICBME 2008, Proceedings 23, pp. 1236–1240, 2009
www.springerlink.com

Table 1: Characteristics of used materials

No	Type	Resin	Filler fraction Vol%/Wt%	Filler type
1*	Micro-hybrid	BIS-GMA UDMA BIS-EMA	59.5/78.5	Zirconia-Silica
2*	Micro-hybrid	BIS-GMA TEGDMA	71/85.5	Barium glass Colloidal silica
3*	Fine particle-hybrid	BIS-GMA UDMA TEGDMA	60.5/78	Barium glass Ytterbium triflorid Ba-Al fluorosilicate
4*	Micro-hybrid	BIS-GMA BIS-EMA	73/82	Barium glass

* 1: Supreme, 2: Clerfil AP-X, 3: Tetric® Ceram, 4: ELS

For the fatigue tests, the mechanical test machine was programmed to operate in force mode, producing 100,000 at a frequency of 10 Hz. During the thermal compressive fatigue testing, the specimens were immersed in cyclic flowing cold (5^0 C) and hot (55^0 C) water with period of 8seconds. The compressive fatigue limit was determined using the "Staircase" method described by Draughn [4] (1979). The initial stress was 60% of the static compression strength mean, calculated for each material.

The specimens were loaded to 100,000 cycles or until specimen fracture. When the specimen resisted to 100,000 cycles, it was tested with a fixed tension increase of 8 MPa of the initial stress. If the specimen failed before reaching 100,000 cycles, it was tested with a load reduction of 8 MPa of the initial stress. Thus, the further values varied (higher or lower), depending on the event of failure or non-failure.

C. Statistical analysis

Mean compressive fatigue strength (CFS) is given by Equation (1) as follows:

$$CFS = x_0 + d\left(\frac{\sum in_i}{n_i} \pm 0.5\right) \quad (1)$$

Where x_0 is the lowest load level considered in the analysis and d is the fixed stress increment. To calculate CFS, data analysis was carried out based on the least frequent event (failures *versus* non-failures). The lowest stress level considered was designated as i=0, the next stage as i=1, and so on until n_i, which was the number of failures or non-failures at a given stress level. According to the assumption of the weakest link, the fracture load of brittle materials would be limited by the longest crack size in the loaded volume. Hence, a distribution of crack lengths resulted in a strength distribution, which was commonly described by Weibull distribution as follows:

$$P_f = 1 - \exp\left[1 - \left(\frac{\sigma_c}{\sigma_0}\right)^m\right] \quad (2)$$

Where σ_0 is the load level at which 63.2% of the specimens failed and m is the Weibull modulus determined by a maximum likelihood approach. P_f is the probability of failure, varying from 0 to 1.

III. Results

A. Compressive fatigue strength

Table 2 presents and figure 1 illustrates the results of mechanical tests.

Table 2: Results of the tests

No	*Compressive Fracture strength (MPa)*	*m*	*CFS (MPa)*
*1**	*376*	*11*	*259*
*2**	*300*	*10.9*	*230*
*3**	*296*	*10.4*	*218*
*4**	*270*	*8.9*	*210*
No.	Thermal CFS (MPa)	Decrease of CFS (%)	CFS / Compressive fracture (%)
*1**	*241*	*7*	*69*
*2**	*201*	*13*	*76*
*3**	*183.3*	*16*	*74*
*4**	*197*	*6*	*77*

1: Supreme, 2: Clerfil AP-X, 3: Tetric® Ceram and 4: ELS

It could be seen that the fracture strength of Supreme was higher than the others, with Clearfil AP-X and Tetric® Ceram composites ranking as second and third respectively. As for the fracture strengths of ELS, it was lower than the other dental composites. Table 2 also presents the results of the compressive fatigue test obtained *via* staircase method based on Equation (1). The compressive fatigue strength (CFS) of the studied composites (for 100,000 cycles) followed an identical pattern as the fracture strength. Fairly uniform microstructures were revealed during microstructure analysis, hence indicating a proper curing procedure.

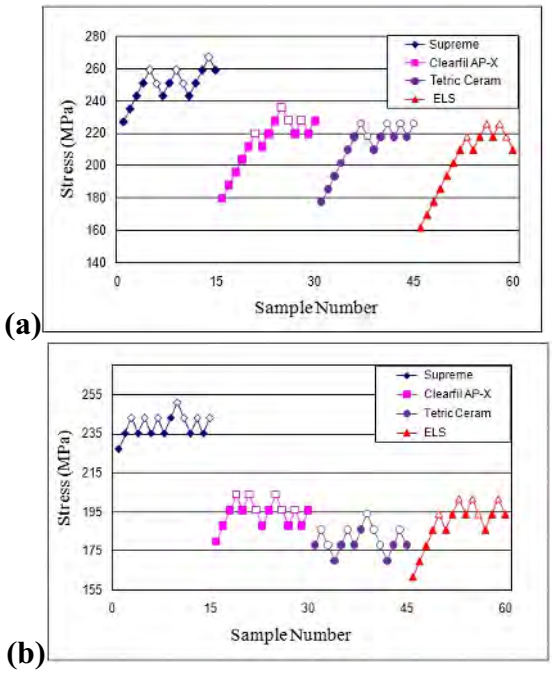


Fig. 1 Comparison of a) fatigue strength, b) thermal fatigue strength, obtained by Staircase method for 15 samples of each composite studied. The non-filled marks are illustrating failed specimens, and filled marks are illustrating non-failed specimens.

B. Thermal compressive fatigue

Table 2 and figure 1 present the results of mean thermal compressive fracture strength, at a fracture probability P_f 63.2%.

The parameter, Decrease of CFS (D.CFS), is the percent of decline of compressive fatigue strength under thermal cycling and is calculated by Equation (3).

$$\text{D.CFS} = \frac{\text{CFS - Thermal CFS}}{\text{CFS}} \times 100 \qquad (3)$$

IV. Discussion

A. Compressive fatigue

To evaluate a material's behaviour related to its reliability on compressive fracture strength, Weibull analysis, together with modulus (m), must be considered. Composites with high compressive fracture strength coupled with high Weibull modulus are better than low compressive fracture strength with low Weibull modulus. In the present study, Supreme and ELS revealed the highest and lowest Weibull module respectively. In other words, fatigue strength result obtained for ELS revealed some dissimilarity in relation to its compressive fracture strength and Weibull modulus. It should be mentioned that in general, high compressive fatigue strength with a low Weibull modulus (m) might be worse than low compressive fracture strength with high Weibull modulus. As seen from Table 2, the compressive strengths of Supreme and ELS composites ranked the highest and lowest respectively. The high compressive strength of Supreme might be attributed to its superior polymer matrix coupled with a favourable filler composition — which was based on a zirconia-silica system. As a result, a very uniform microstructure was obtained. As for the influence of filler volume fraction, previous studies indicated that a chief means of increasing the compressive strength of dental composites was to increase the amount of filler particles . However, results of the present study did not indicate a strong correlation between compressive strength and filler volume fraction.

In a work by Ikejima *et al*. [1], they clearly demonstrated the effects of filler content, filler particle size, and filler silanization on the mechanical properties of dental composites. With the increase of filler volume fraction by up to about 50%, flexural strength, flexural modulus, and shear strength were also increased. However, any further increase in filler volume fraction above 50% did not cause any further increase in flexural strength nor shear strength. On the contrary, there was some evidence that strength started to decline at very high filler levels (>60 Vol %). It should also be noted that the modulus of elasticity continued to increase as more filler particles were incorporated. In the present study, all composites — except Supreme which had a filler volume fraction below 60% and which belonged to the Ultrafine Midway-Filled composites — had a filler volume above 60% and they belonged to the Ultrafine Compact-Filled composites according to the classification of Willems *et al*. [5].

As shown in Fig. 1, Supreme exhibited the highest fatigue strength by virtue of its resin matrix and a zirconia-silica filler type at the highest density. It has been reported that for hybrid composites, increasing the volume fraction of filler particles in a dental composite would heighten the probability of increasing the local energy for crack growth. In other words, an advancing crack would need more energy to move through the particles. In hybrid composites, the direction of crack growth continually changes at it encounters particles. Consequently, the rate of crack growth decreases and more particles are sheared because of higher volume fraction of filler particles.

This thus explained the higher strength in Tetric® Ceram and Clearfil AP-X, which were hybrid composites in comparison to the old composites. As for the ELS composite, its low fatigue resistance under cyclic loading has been confirmed by other similar *in vitro* studies, which

highlighted that 20% of composites filled by microfilled particles failed after two years.

Apart from the type of filler content, the composition of resin matrix also influenced the mechanical properties of composites. With Supreme, the fundamental component was Bis-GMA, but part of the solvent monomer TEGDMA was substituted by UEDMA and Bis-GMA. Asmussen & Peutzfeldt [6] showed that the replacement of Bis-GMA and TEGDMA by UEDMA was instrumental for the increase in both tensile and flexural strengths of the matrix. This could be attributed to the degree of conversion of the polymer matrix or due to the ability of the urethane linkage to form hydrogen bonds in the copolymer, which presumably resulted in restricted sliding of the polymer segments relative to each other.

Asmussen [7] pointed out that composites which utilized a Bis-GMA/TEGDMA blend exhibited a higher degree of conversion when the quantity of TEGDMA was increased. This thus explained the lower strength of ELS (Bis-GMA/Bis-EMA) composites when compared to the other composites in this study which contained TEGDMA.

It is also noteworthy that fatigue cracks may initiate from defects and impurities — especially those located in areas of high stress. As shown in Fig. 2, a primary crack nucleated from a large inclusion located near the specimen edge, causing a fracture at the tip of the Tetric® Ceram composite specimen. Additionally, two secondary cracks which were not nucleated from the inclusion are visible in the picture. The primary crack initiated from a large inclusion had a remarkable effect on fatigue life reduction. For the specimen shown in Fig. 2, it experienced only 1071 cycles under a stress of 225 MPa before fracture. However,

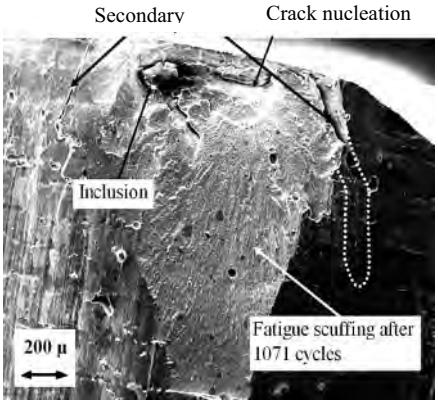


Fig. 2 Fracture surface of Tetric® Ceram composite, illustrating fatigue crack initiation from a large inclusion in the composite and two secondary cracks.

when the fatigue test was repeated under the same stress with a similar Tetric® Ceram composite, a fatigue life of 14320 cycles was obtained (*i.e*., a fatigue life reduction of nearly 90%).

B. Thermal compressive fatigue

Internal stresses due thermal variations can have destructive effects on toughness of the specimen [8]. Thermal shock occurs on the surface of filled or restored area and cause to sudden expansion and contraction on the surface while internal layers remain without any change. Effective factors on thermal expansion coefficient of resin composites contains: amount of filler particles in resin matrix, thermal properties of filler, kind of junction between filler and matrix, matrix composition, amount of polymerization and water absorption. Some efforts have been done with the aim of nomination the degrader factors in composites structures in which the majority have shown water absorption by polymeric matrix as the degrader factor. Presence of water and other liquids cause protuberance and existing of some stresses. Water absorption can has softening effect on the polymeric matrix and also disjoining of filler and matrix. Water also is the author of filler and matrix hydrolysis descending or fracturing the junctions between filler and matrix. Exertion of thermal cycles by water had negative effects on the fatigue limits of all of materials, although, the amount of this descending was not very effective on the fatigue strength of Supreme and ELS. According to the mentioned points these decreasing in fatigue strength can be due to the expansion, contractions and microstructure destruction which is due of water absorption. This weakening intensified for the cases of Clearfil AP-X and Tetric® Ceram. In resin composites there is an inverse relation between the volume percent of filler and thermal expansion coefficient, of course, it is not the only determinant parameter, but can be utilized for the low decreasing of fatigue limit of ELS. Softening of the polymers depends on presence of water, temperature of the polymer and the amount of the difference between it and glassing temperature (T_g). More difference between the polymers temperature and T_g cause more brittleness of them. Whatever this difference is lesser, the polymers become softer. Also in the same reference T_g for Bis-GMA and TEGDMA have been mentioned as 223^0 C and 100-120^0 C respectively. This can strongly justify the more descending of Tetric® Ceram and Clearfil fatigue limits than two other materials under thermal-compressive fatigue tests.

V. Conclusions

The compressive fatigue strength of Supreme and ELS composites posses the highest and lowest fatigue strength, respectively, this is due to superior matrix properties associated with fewer voids in the uniform microstructure seemingly in the wake of the highest ratio (Vol% / Wt %) of different filler particles in Supreme.

Thermal cycling reduced the compressive fatigue limits of the materials' specimens. This matter was due to the secondary stresses in specimen which were existed by expansions and contractions due of the water used for the thermal cycling.

Thermal cycling was more effective on Tetric Ceram' compressive fatigue strength due to the existence of TEGDMA in the composition of the matrix of Tetric Ceram.

References

1. Ikejima I, Nomoto R, McCabe JF. Shear punch strength and flexural strength of model composites with varying filler volume fraction, particle size and silanation. Dent Mater 2003; 19:206–11.
2. Braem M, Lambrechts P, Vanherle G. Clinical relevance of laboratory fatigue studies. J Dent 1994; 22:97-102.
3. Lohbauer U, von der Host T, Frankberger R, Krämer N, Petschelt A. Flexural fatigue behavior of resin composite restorative materials. Dent Mater 2003; 19:435-40.
4. Draughn RA. Compressive fatigue limits of composite restorative materials. J Dent Res 1979; 58: 1093- 1096.
5. Htang A, Ohsawa M, Matsumoto H. Fatigue resistance of composite restorations: effect of filler content. Dent Mater 1995; 11: 7-13.
6. Asmussen E, Peutzfeldt A. Influence of UEDMA, BisGMA and TEGDMA on selected mechanical properties of experimental resin composites. Dent Mater 1998; 14: 51-56.
7. Asmussen E. Factors affecting the quantity of remaining double bonds in restorative resin polymers. Scand J Dent Res 1982; 90: 490-496.
8. Ashby MF, Hallam SD. The failure of brittle solids containing small cracks under compressive stress states. Act Mater 1986; 34: 497-510.

Author: Dr. Farhad Shafie
Institute: Department of Dentistry,
Tehran University of Medicine Science
Street: Ghods St, Enghelab St.
City: Tehran
Country: Iran
Email: Faradent@Yahoo.com

Development of Amphotericin B Loaded PLGA Nanoparticles for Effective Treatment of Visceral Leishmaniasis

M. Nahar, D. Mishra, V. Dubey, N.K. Jain*

Pharmaceutics Research Laboratory, Department of Pharmaceutical Sciences, Dr. H. S. Gour University, Sagar 4 70003, India

Abstract — **Aim of present investigation was to develop novel nanoparticulate carrier of Amphotericin B (AmB) for effective treatment of visceral leishmaniasis. PLGA nanoparticles (PNPs) were prepared with emulsion solvent evaporation method. Prepared nanoparticles were characterized for size, polydispersity index (PI), shape, morphology, surface charge, and drug release. *In vitro* antileishmanial potential of AmB loaded PNPs was assessed on GFP transfected parasite (promastigote model, Dd8 strain) and infected macrophages (amastigotes macrophages model) cell line (J774.A1 murine macrophage-like cell line) using FACS and geimsa staining method, respectively and results were compared with marketed liposomal formulation (AmBisome®). The developed PNPs were found to be of nanometric size (168 nm), having low polydispersity index (0.15) and good entrapment efficiency (53.0%). Transmission electron microscopy (TEM) showed that the PNPs were spherical in shape. The zeta potential of AmB loaded PNPs, surface was found to be -46.7 mV. PNPs showed biphasic release characterized by an initial burst followed by controlled release. *In vitro* antileishmanial activity against promastigote model showed about 85% inhibition and with insignificant difference amontgst plain drug, AmBisome® and PNPs. The activity of AmB (1μM) as plain drug, AmBisome® and PNPs against *L. donovani* in intraamstigote macropage model showed percent inhibition 71.77%, 83.03%, 84.06%, respectively. Accordingly, PNPs showed potential antileishmanial activity and is equivalent to marketed AmBisome®. Results suggest that developed novel nanoparticulate carrier could provide controlled, safe, effective and economical delivery of AmB for effective treatment of visceral leishmaniasis as an alternative to lipid based formulations.**

Keywords — **PLGA, nanoparticles, amphotericin B, visceral leishmaniasis**

I. Introduction

Visceral leishmaniasis (kala-azar) is a protozoal infection disseminated by the parasite called *Leishmania donovani,* transmitted by sandfly bite, in which macrophages of the liver, spleen, lymph node and bone marrow are preferentially parasitized and support intracellular replication. Visceral leishmaniaisis maintaining its status as "most neglected disease", occurs in more than in 80 countries in Asia and Africa (*Leishmania donovani*), Southern Europe (*L. infantum*) and South America (*L. chagasi*)[1].

The development of new antiparasitic drugs to market level is a very rare and costly event. The drugs currently in use against leishmaniasis are highly toxic and have serious adverse effects that limit their clinical application. Therefore, parasite- and disease-specific formulations and delivery systems should be explored, enhancing efficiency and reducing side effects of available drugs at relatively low cost. Various polymers have been exploited for formulating the nanoparticualte carrier system but poly (lactic acid) (PLA), poly (glycolic acid) (PGA) and their copolymers poly (lactide-co-glycolide) (PLGA) have been extensively employed because of their biocompatibility, biodegradability, versatile degradation kinetics, FDA approved and commercial available[2,3].

Therefore, in the present investigation, we attempted to develop alternative delivery system i.e. PLGA nanoparticles (PNPs), which may overcome the severe side effects of existing AmB formulations by controlled delivery and provide effective treatment of visceral an alternative to lipid based formulations.

II. Materials and Methods

Amphotericin B was generously gifted by Dabur India Ltd. (Ghaziabad, UP, India). Poly(lactic-co-glycolic) acid (PLGA) with a lactic to glycolicratio of 50:50 (RG502, Mw=12kDa) were received from Boehringer Ingelheim (Ingelheim,Germany), amberlite XAD 16 resin were purchased from Sigma Chemical Co. (St Louis, MO, USA)., Dimethyl sulfoxide (DMSO) and acetonitrile were purchased from Central Drug House (New Delhi, India). All others chemicals were of analytical grade and used as received.

A. Preparation of PNPs

The nanoparticles were prepared by the emulsion solvent evaporation (o/w emulsification) technique [4]. Initially, specified amounts of polymer was dissolved with or without drug in 2 mL of DCM, vortexed and emulsified in 20 mL of a 0.1% sodium cholate solution in a sonicator (Sonics-Vibra Cell, BC-130, Ultra sonic processor, CT, USA) at 20 W output for 1 min. The organic solvent was evaporated at

Chwee Teck Lim, James C.H. Goh (Eds.): ICBME 2008, Proceedings 23, pp. 1241–1243, 2009
www.springerlink.com

room temperature for 4 h. The nanoparticles were then recovered by centrifugation (33,900 x g, 20min, 4°C; Remi, India), washed twice with water and unentrapped drug removed by using amberlite resin XAD 18 and lyophilized [5].

B. Characterization of PNPs

The particle size, surface charge and PI were determined by using a Malvern Zetasizer (NanoZS, Malvern Instruments Inc., Worcestershire, UK). Particle size and PI of PNPSs were determined by light scattering method based on laser diffraction at angle 135^0. PNPSs surface charge was determined by laser doppler anemometry. Transmission Electron Microscopy (TEM, H7500**,** Hitachi Ltd., Tokyo, Japan) was used for determination of shape and size of PNPs. Dialysis membrane method was used to determine the release of AMB from the nanoparticulate formulations.

C. In vitro intrinsic antileishmanial activity (promastigotes assay)

In vitro antileishmanial screening was performed with 100 µL (10^6 cells per mL) of the parasite suspension (WHO reference strain, *L. donovani* (MHOM/IN/80/Dd8) promastigotes), and plates were incubated at 27°C in an atmosphere of 95% air/5% CO_2 for 1 h prior to addition of formulation. AmB loaded plain and PNPs were added to each well to obtain the final concentration of 0.05, 0.1, 0.2, 0.5 and 1 µM equivalent AmB. Each concentration was screened in triplicate. After a 3-day incubation period at 27°C in the dark and under a 5% CO_2 atmosphere, the viability of promastigotes was checked using FACS by obtaining mean fluorescence intensity of 10,000 counts. Percentage inhibition was calculated considering untreated parasite as control [6].

D. Ex vivo antilieshmanial activity (intramacrophages amastigote model)

Macrophages J774A.1 (10^5 cells/well) in 16-well chamber slides (Nunc, IL, USA) were infected with promastigotes (*L. donovani,* Dd8) at multiplicity of infection of 10:1 (parasites/macrophages) and incubated at 37 ± 1°C in 5% CO_2 for 12 h. Different concentrations of various PNPs formulations in RPMI-1640 medium (Sigma, USA) were added to wells in triplicate and examined for intracellular amastigotes after washing, methanol fixing and Giemsa staining of the slides. At least 100 macrophages nuclei were counted per well for calculating percentage infected macrophages and number of amastigotes per 100 macrophages. The untreated infected macrophages were used as control. Percent parasite inhibition in treated wells was calculated using the following formula [7].

$$\text{Percentage Inhibition} = 100 - \frac{T}{C} \times 100$$

where, T the number of parasites in treated samples/100 macrophages nuclei, and C is the number of parasites in control samples/100 macrophages nuclei. The 50 % inhibitory concentrations (IC_{50}) were determined by using sigmodal regression analysis and expressed in µM ± S.D.

III. Results and Discussion

PNPs were prepared with solvent evaporation method using sodium cholate as surfactant. Sodium cholate is very effective in reducing the size and only low amount remained associated with nanoparticles surface [4]. The unloaded and AmB loaded PNPs were characterized for particle size, shape and surface charge using various techniques (Table 1). TEM photomicrograph reveals the spherical shape of PNPs (Fig.2).

Table 1: Characterization of PLGA nanoparticles

Parameters*	Unloaded PNPs	AMB loaded PNPs
Particle Size	146 ± 26 nm	168 ± 16 nm
Polydispersity index	0.081 ± 0.031	0.152 ± 0.015
Zeta potential	−43.04 ± 1.40 mV	-46.7 ± 0.55mV
% Yield	84.0 ± 1.20	68.50 ± 3.4
Percent drug entrapment (%)	-	53.0 ± 1.5
Drug content (%)	-	2.81 ± 1.1

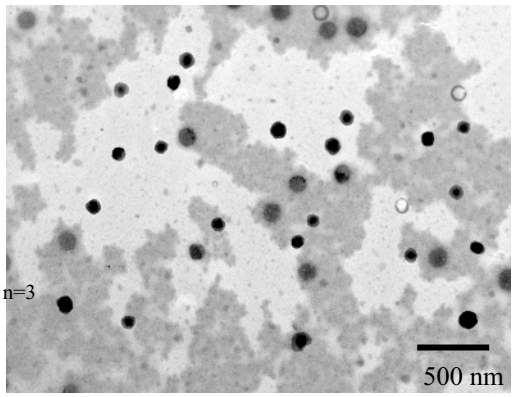


Fig. 1 TEM photo micrograph of PNPs

Drug release from the PLGA nanoparticles prepared by the dialysis method using DMSO was almost complete within 6 days as shown in figure 2.

The profile showed a fast release of the active drug during the first 4 h of incubation. This type of profile is charac-

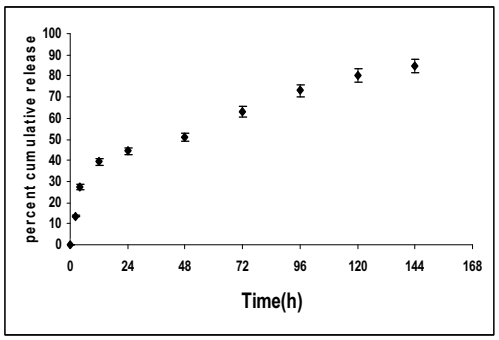


Fig. 2 Percent cumulative release of AmB from PLGA nanoparticles in PBS 7.4 (5% v/v DMSO)

teristic of a burst-release, which suggests that AMB may be in the vicinity of the nanoparticles surface. The fast release is followed by sustained release to 144 h where 86% of entrapped drug is released. The release profile observed with AmB suggested pseudo-zero order release kinetics.

The effect of various concentrations of plain (free) and encapsulated AmB was evaluated against *L. donovani* extracellular promastigote using FACS and the results depicted concentration-dependent inhibition. Maximum percent inhibition obtained with plain AmB, AmBisome®, PNPs (1μM equivalent AmB) were 85.71± 3.69, 87.37± 2.43, and 87.10 ± 2.48, respectively. On the contrary, percent inhibition obtained in amastigote model were 71.77± 1.23 %, 83.03 ±1.32 % and 84.06 ± 1.2 %, with plain AmB, AmBisome®, PNPs (1 μM equivalent AmB), respectively. The result suggests increased activity of PNPs in intramastigote macrophage model that could account for more efficient uptake of particles in comparison to plain (free) drug by macrophages. Moreover, IC_{50} of various formulations and pure drug were calculated in both experimental models (Table 2). The result suggests that a higher IC_{50} was obtained with PNPs while a significantly low value obtained with plain AmB and AmBisome®($p < 0.001$) in extracellular promastigote model. The probable reason for such contrary results is that this parasitic genus has two main forms (promastigotes and amastigotes) with different morphological and biochemical characteristics, including energy metabolism and transport across membranes and their access to therapeutic moiety. The extracellular promastigotes showed a significant higher inhibition with pure AmB and also with AmBisome® and could be ascribed for accessibility of drug to promastigotes and lipidic nature of AmBisome® that can fuse with promastigotes membrane.

Table 2. Antileishmanial activity of various formulations against promastigotes and intracellular amastigotes (IC_{50} values)

Formulations	IC_{50} against promastigotes (μM) by FACS assay*	IC_{50} against intracellular amastigotes (μM) by Geimsa staining method*
AmB	0.091± 0.004	0.21 ± 0.01
AmBisome®	0.082 ± 0.002	0.061 ± 0.02
PNPs	0.079 ± 0.002	0.059 ± 0.03

*Values represent mean ± SD (n = 3)

IV. Conclusion

PLGA nanoparticles were developed, characterized and evaluated for antileishmanial potential. The developed novel nanoparticulate carrier could provide controlled, safe and efficient delivery of AmB for effective treatment of visceral leishmaniasis as an alternative to lipid based formulations.

Acknowledgment

One of author (Manoj Nahar) is thankful to Indian council of medical research (ICMR) for providing financial support.

References

1. Yamey G (2002) The world's most neglected diseases. Br Med J 325: 176–177.
2. Nahar M, Dutta T, Murugesan S, Asthana A, et al. (2006) Functional polymeric nanoparticles: an efficient and promising tool for active delivery of bioactives. Crit Rev Ther Drug Carrier Syst 23,: 259-318.
3. Mittal G, Sahana DK, Bhardwaj V, Ravi Kumar M.N.V(2007) Estradiol loaded PLGA nanoparticles for oral administration: Effect of polymer molecular weight and copolymer composition on release behavior in vitro and in vivo. J Contr Rel 119: 77–85.
4. Senthilkumar M, Subramanian G, Ranjitkumar A, Nahar M, Mishra P, Jain NK (2007) PEGylated Poly (Lactide-co-Glycolide) (PLGA) nanoparticulate delivery of Docetaxel: synthesis of diblock copolymers, optimization of preparation variables on formulation characteristics and in vitro release studies. J Biomed Nanotech1:52-60.
5. Venier-Julienne M, Benoit J (1996) Preparation, purification and morphology of polymeric nanoparticles as drug carriers. Pharm. Acta Helv 71, 121–128.
6. Dube A, Singh N, Sundar S, Singh N (2005), Refractoriness to the treatment of sodium stibogluconate in Indian kala-azar field isolates persists in *in vitro* and *in vivo* experimental models. Parasitol Res 96, 216–23.
7. 7. Guru PY, Agarwal AK, Singhal, UK, Singhal A, Gupta CM (1989) Drug targeting in Leishmania donovani infections using tuftsin bearing liposomes as drug vehicles. FEBS Lett 245: 204–208.

*Corresponding author

Prof. N. K. Jain
Department of Pharmaceutical Sciences
Dr. H. S. Gour University, Sagar 470003, India
Tel / Fax: +91 7582 264712
Email address: jnarendr@yahoo.co.in; mnjnahar@yahoo.co.in

Swelling, Dissolution and Disintegration of HPMC in Aqueous Media

S.C. Joshi and B. Chen

School of Mechanical & Aerospace Engineering, Nanyang Technological University, Nanyang Avenue, Singapore 639798

Abstract — **This paper contains the work on monitoring the swelling, dissolution, and disintegration processes for hydroxypropyl methylcellulose (HPMC) tablets fabricated under 400, 1000, 2000 kg/cm^2 pressures. The density and porosity of tablets of three grades of HPMC (6, 40, 4000 mPa.s viscosity of 2 wt% aqueous solution at room temperature) were measured to identify the effect of different physical/chemical properties on the swelling and the subsequent processes involved. The process observations were conducted at human body temperature of 37ºC to understand drug release. The cumulative swelling curve showed that particle size and their distribution in HPMC powder, and density and porosity of the formed tablets have influence on the swelling kinetics. The strength and thickness the gelated layer formed during the swelling process influenced by the chemical structure of HPMC ultimately determined the behavior during the swelling, dissolution and disintegration of the HPMC tablets. The possible mechanism leading to these changes was proposed. The detailed kinetic simulation of the integrated process was also discussed, which seemed to follow power-law formulations.**

Keywords — **HPMC, swelling, dissolution, kinetic**

I. Introduction

Nowadays cellulose and its derivates in the form of agglomerates of porous particles are regarded as the most useful filler for direct compression tablets.[1, 2] With improvement in water solubility and affinity, HPMC has been the important vectors in the drug release systems for its high swellability and thermal gelation properties.[3-6]

Among various dosage forms in medicine, tablets still account for 80% of the drug delivery systems administered to human.[7] Physicochemical properties of various grades of HPMC are some of the critical factors that influence swelling, dissolution and disintegration behavior of HPMC tablets in aqueous media.

As a common item in swellable matrix for drug release systems, HPMC tablets had been investigated in various aspects. SEM and NMR were used to monitor the swelling process for HPMC tablets.[8,9] Gel-layer structure was studied by optical imaging.[10] Subsequent dissolution of the gelated layer of the tablets during eroding and moving swelling front was investigated using ultrasound technique.[11] The common mechanism of swellable HPMC was assigned to the glassy-rubbery transition, and swelling kinetics was expressed in power law without consideration to dissolution during swelling.[12] But if the aqueous medium was absorbed into the tablets, the "moving-boundary" would cause heterogeneous swelling of the gelated layer and big deviants from the empirical power relation with time.[13] Most theoretical models did not examine detailed effect of physical and chemical parameters, although these parameters for various HPMC vectors influenced their behavior in aqueous media.[14,15]

The objective of the work was to monitor swelling, dissolution and disintegration process in an aqueous medium for three grades of HPMC tablets formed under 400, 1000, 2000 kg/cm^2 direct compression respectively. Various parameters, like particle size and distribution, density and porosity of the formed tablets, were considered in the process of direct compression formation of tablets and subsequent interaction with aqueous medium. Kinetic studies were derived from the cumulative swelling data of HPMC tablets. The possible mechanism and simulation of the integrated process were discussed.

II. Materials and methods

A. Materials

Different grades of HPMC powders (2 wt% aqueous solution with viscosity as 6, 40-60, 4000 mPa.s at 20 °C), referred as HPMC A, B, and C respectively, were supplied by Sigma. Deionized water was produced from Mill-Q system.

B. Preparation of Tablets

Initially, HPMC A, B, and C powders were dehydrated in vacuum at 60°C. The tablets were prepared using the direct-compression method for 1 minute compression under 400, 1000, 2000 kg/cm^2 pressure at room temperature using Carver Laboratory Press (2518 series). The tablets were stored in the dry box before use.

C. Morphology of HPMC Powder by Scanning Electron Microscopy (SEM)

Pre-dried samples of HPMC powders were mounted on the sample holder using a double-side tape and coated gold.

Chwee Teck Lim, James C.H. Goh (Eds.): ICBME 2008, Proceedings 23, pp. 1244–1247, 2009
www.springerlink.com

The samples were examined wyith a SEM (Leica S360) at different accelerating voltage according to various samples.

D. Density and Porosity of Tablets

The true density of HPMC powder was determined by a pycnometer using nitrogen (Accupyc 1330, Micrometrics). The packed density of tablets was calculated based on the Archimedes Law, and the measurements were repeated three times to minimize errors.

Porosity of the formed tablets was calculated based on equation:

$$\Phi = 1 - \left(\rho_b \Big/ \rho_p \right) \quad (1)$$

Where Φ represents the porosity of tablets, ρ_b and ρ_p represent the density of the formed tablets and the true density of a HPMC powder.

E. Swelling and Dissolution in Deionized Water

Three full-sized tablets of each of HPMC A, B and C were weighed accurately before loading them individually into a porous paper bag soaked in a 50 ml deionized water at 37 °C. The swelling ratios were calculated using equation:

$$\alpha = \frac{w_t - w_{t0}}{w_{t0}} \times 100\% \quad (2)$$

where α represents the swelling ratio, W_t and W_{t0} represent weight of tablets at a certain time and its original weight respectively. The values of α were averaged over three readings for each type of tablet.

III. Results and Discussion

A. Morphology of HPMC Powders

Morphology of three HPMC powder is shown in Figure 1. HPMC A and C showed an irregular rod-like shape with the fibrous appearance, while HPMC B appears oblong in shape. All three types of HPMC powders had a quite broad particle size distribution in the range 20-250 μm.

B. Porosity of HPMC Tablets

With a broad particle size distribution, all three type of HPMC tablets were fabricated under 400, 1000, 2000 kg/cm^2 respectively, and porosity of the formed tablets was shown in Figure 2.

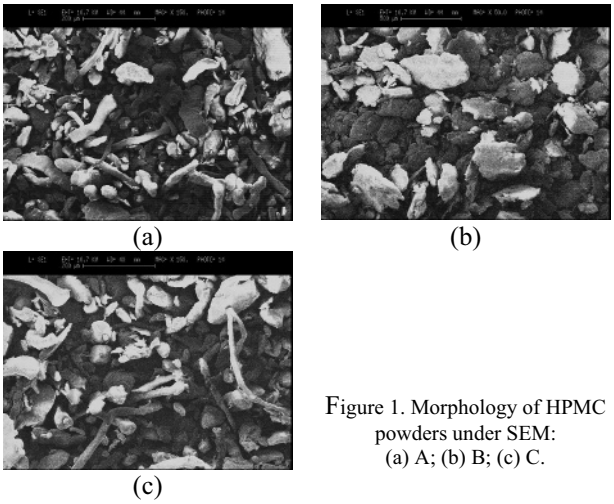


Figure 1. Morphology of HPMC powders under SEM: (a) A; (b) B; (c) C.

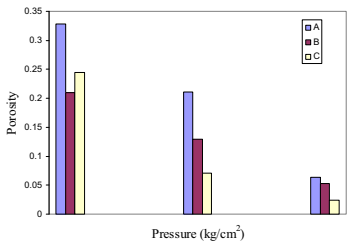


Figure 2. Porosity of tablets of HPMC A, B, and C under various tablets.

With increase in the pressure from 400 to 2000 kg/cm^2, the porosity decreased from 0.3 to ~0.05. Without precisely known average particle size and due to the broad particle size distribution, it was hard to describe relationship between powder size and porosity formed thereof. Nevertheless, the order of porosity of the tablets under the same process pressure indicated that the physical properties of various HPMC powders definitely determined aggregation patterns in the tablet form.

C. Kinetics of Sweeling and Dissoution Process

In general, HPMC tablets, like other swellable matrix would experience different stages when soaked in aqueous media: first, water as plasticizer would penetrate into the tablets to induce a glassy-rubbery transition; then a gel layer would be induced until to the saturation state of water absorption. With further interactions with the aqueous medium, association of the entangle polymer chains in the gelated layer would dismantle leading the structure of the tablets to dissolve and disintegrate.[16] The swelling and dissolution curves for three HPMC tablets are shown in Figure 3.

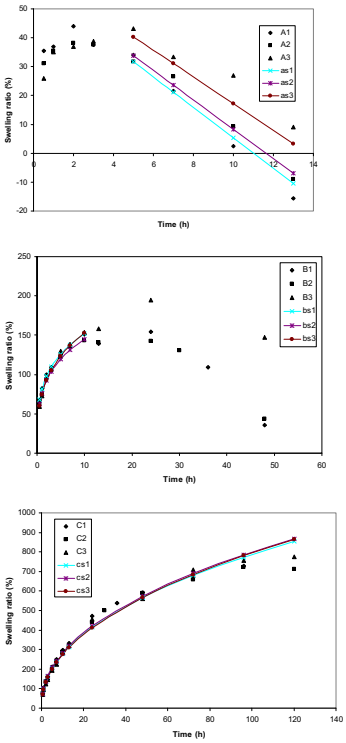


Figure 3. Swelling and simulation curves for tablets of HPMC (a) A; (b) B; (c) C at 400 (1), 1000 (2), 2000(3) kg/cm^2 respectively.

In the case of HPMC A (Fig 3a), tablets formed under the three pressures showed a similar trend. The initial swelling reached its maximum swelling ratio (<40%) in less than 5 h, and the dissolution process dominated after 5h.. The fabrication pressure seemed influencing the swelling process in a limited way with no apparent influence in the dissolution stage. As far as HPMC B tablets were concerned (Fig 3b), the maximum swelling reached around 10 h with a much higher value (>150%), and dissolution rates decreased with the increase in the fabrication pressure. The integrity of the tablets could be kept until a late stage of the whole process. With the highest viscosity of three specimens, HMPC C tablets had the highest swelling ratio (Fig 3c) to almost 800%, and the tablets maintained their integrity during the whole experiment and time scale chosen.

Based on the cumulative swelling curves, simulation results for the process are given in Table 1. For HPMC A, kinetic equations of tablet dissolution at 400, 1000 kg/cm^2 shared a similar trend, while tablets at 2000 kg/cm^2 showed some deviation. For HPMC B specimens, the swelling process obeyed almost the same law, while swelling/dissolution stage showed a reversible trend with the increase in the compression pressure. In the case of HPMC C, the whole process followed a similar trend with the power of the order of 0.45 indicating that the swelling/ dissolution process was a diffusion-control type based on the ideal cylinder geometry.[17]

The rate of the formation, the thickness and the strength of the gelated layer determine the behavior of a swellable hydrophilic matrix. [18] As a type of porous hydrophilic matrix, HPMC tablets would involve three processes when soaked in aqueous media, namely; free water transfusion into the porous tablets, swelling and gelation under water induction of glass-rubbery transition, and dissolution with further water uptake.

Table 1. Summary of simulation results for the process

Material	Swelling time scale in hours (tablet forming pressure in kg/cm^2)	Parameters	
		a	b
HPMC A	5-13 (400)	-5.37	58.12
$\alpha = a*T+b$	5-13 (1000)	-5.09	59.22
	5-13 (2000)	-4.62	63.39
HPMC B	0.5-10 (400)	81.62	0.27
$\alpha = a*T^b$	0.5-10 (1000)	76.04	0.28
	0.5-10 (2000)	74.75	0.31
HPMC C	0.5-120 (400)	99.07	0.45
$\alpha = a*T^b$	0.5-120 (1000)	100.49	0.45
	0.5-120 (2000)	95.68	0.46

α represent swelling ratio, T for the time involved.

As the kinetic-related process of the transfusion of water into the tablets, porosity determined by the particle size and distribution, and the compression pressure, play important roles in the initial swelling process. When the gelated layer formed, the chemical structure of different grade of HPMC chain would be the dominating factor to determine the rate of gelation, and the thickness and strength of the gel layer, thus to decide whether it later affected by dissolution and disintegration process.

Hydrophobic interactions between methyl groups and water were the main driving forces to the spontaneous swelling process and self-aggregation to form gelated layer of different grades of HPMC. The different chain structures and the formed ordered network were determined by the density of methyl groups in the entanglement of polymer chains. As shown in Table 2, HPMC A had the physical cross-linking sites formed by clustering of methyl groups in the swollen state. The formed cluster of physical cross-linking was easy to dismantle, thus shown a dominating dissolution process at the late stage. HPMC B had the lowest substitution ratio of methyl groups, but in a higher molecular weight range (longer polymer chains) resulting in a loosely formed network. HPMC C had the longest polymer chains and the higher ratio of methyl group

substitution. This induced formed network with the highest density of physical cross-linking sites.

Table 2. Specific parameters for different grades of HPMC

HPMC	Viscosity (mPa.s)	% CH_3 content	% HPMC content	M_n
A	6	60-67	7-10	10000
B	40-60	28-30	7-12	22000
C	4000	60-67	7-12	86000

Density of the physical-crosslinking sites determined the strength of gelated layers and subsequently controlled the disintegration behavior of the direct-compressed tablets with time elapsing in aqueous media. As shown in Figure 4, HPMC A had the weakest network that disintegrated into small parts much earlier than HPMC B. HPMC C showed the strongest network and stable shape even after absorbing considerable amount of the aqueous media. Due to the different strength of the gelated layer for various grades, the low viscosity HPMC appeared to be more suitable as a short-time delivery vector or a fast disrupting capsule, while high viscosity HPMC can be used as materials for coating tablets or long-duration delivery vectors.

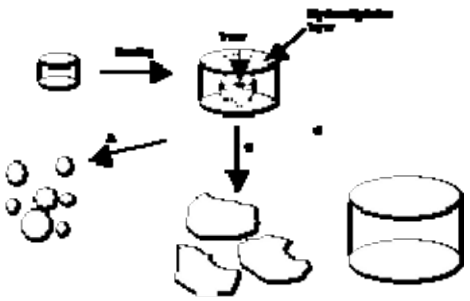


Figure 4. Schematic depicting swelling and dissolution process for tablets with time.

IV. Conclusions

Based on investigated swelling, dissolution and disintegration behaviors of tablets of three different grades of HPMC in aqueous media, physical parameters such as the particle size and distribution and the processing conditions as the pressure and porosity found to have limited influence in the initial swelling stage. The dominating factor that determined the behavior during the whole process was the formation and strength of the gelated layer determined by the chemical structure of the various HPMC. The processes seemed to follow power law formulations.

References

1. Shangraw, R. F. and Demarest, D. A. (1993). Pharmaceutical. Technology, 17: 32–38.
2. Armstrong, N. A. (1997). Pharmaceutical Technology Europe, 9: 24–30.
3. Velasco, M. V., Ford, J. L., Rowe, P., Rajabi-Siahboomi, A. R.(1999) J. Control. Release 57: 75-85.
4. Colombo, P. (1993) Adv. Drug Deliv. Rew. 11: 37-57.
5. Freely, L. C., Davis, S. S. (1988) Int. J. Pharm. 44: 131-139.
6. Xu, G., Lee, P. I. (1995) Chem. Pahrm. Bull. 43: 483-487.
7. Jivarij M., Martini, L. G., and Thomson, C. M. (2000). Pharm.Sci.Tech. Today, 3: 58-63.
8. Melia, C. D., Rajabi-Siahboomi, A. R., Davies, M. C.(1992) Proc. 19th Int. Symp. Control. Rel. Bioact. Mater. 19: 28-29.
9. Rajabi-Siahboomi, A. R., Bowtell, R. W., Mansfield, P., Davies, M. C., Melia, R. W. (1996) Pharm. Res. 13: 376-380.
10. Gao, P., Meury, R. H., J. (1996) Pham. Sci. 85: 725-731.
11. Konard, R., Christ, A., Zessin, G., Cobet, U. (1998) Int. J. Pharm. 163: 123-131.
12. Ritger, P. L., Peppas, N. A. (1987) J. Control. Release 5: 37-42.
13. Lin, C. C., Metters, A. T. (2006) Adv. Drug Deliv. Rev. 58: 1379-1408.
14. Lombardi, C., Zema, L., Sangalli, M. E., Maroni, A., Giordano, F., Gazzaniga, A. (1998) Proc. World Meet. APGI/APV 2: 39-73.
15. Zema, L., Sangalli, M. E., Pavesi, P., Vecchio, C., Giordano, F., Gazzaniga, A. (1998) Proc. World Meet. APGI/APV 2: 333-334.
16. Pepps, N. A. (1987) Hydrogels in Medicine and Pharmacy Vol 3 CRC Press.
17. Siepmann, J., Peppas, N. A. (2001) Adv.. Drug Deliv.. Rev., 48: 139-157.
18. Colombo, P., Bettini, R., Santi, P., Peppas, N. A. (2000) PSTT, 3: 198-204.

A Comparative Study of Articular Chondrocytes Metabolism on a Biodegradable Polyesterurethane Scaffold and Alginate in Different Oxygen Tension and pH

S. Karbasi

Medical Physics and Biomedical Engineering Department, School of Medicine, Isfahan University of Medical Science, Isfahan, Iran

Abstract — **There are some different methods in the literatures that used for healing and repairing of cartilage. One of the methods for increasing of regeneration and metabolism in cartilage, is stimulating physicochemical parameters on cell-polymer systems, as cartilage based cells. In this research, two physicochemical parameters, oxygen tension and pH, was changed to measure the lactate production after 1, 2 and 3 days culture and GAG(glycosaminoglycan) production after 3, 7 and 14 days culture of chondrocytes on DegraPol®, as a biodegradable polyurethane scaffold (BPUS), and alginate scaffolds. The results finally were compared on both scaffolds. The results showed that physicochemical parameters like oxygen tension and pH could change cell metabolism. In fact, the physicochemical parameters could affect lactate production and GAG content of chondrocyte cells and it does not depend on the type of scaffold. The best condition of the articular chondrocytes metabolism was for 5% O2 and pH=7.4($p<0.001$). The comparison between BPUS and alginate scaffold is showing that the results are better for alginate beads ($p<0.001$). In fact, hydrophilicity of alginate causes better cell distribution and nutrition than BPUS; because the cells are able to transfer the ions and the products through the medium easily.**

Keywords — **Chondrocyte, physicochemical parameters, DegraPol®, alginate, Tissue engineering**

I. Introduction

Articular cartilage is avascular and communicates with the rest of the body only by limited processes of diffusion of solutes to and from blood vessels in the underlying bone and through contact with the synovial fluid which washes across the articular surface intermittently, propelled by the movement of the joint [1]. Because of the long diffusion pathway involved, provision of glucose and especially oxygen into the cartilage may be particularly critical [2-4].

Even so, oxygen plays a role in chondrocytes physiology which is not well understood. Oxygen concentration may influence inflammation associated with cartilage injury and disease [2]. It is shown that concentrations of dissolved oxygen rang from 45 to 57 mmHg at the cartilage surface to less than 7.6 mmHg in the deep zone, and exteracellular pH ranges from 6.8-7.1[2]. Under these physiological conditions, cartilage has only a small capacity to repair structural damage. In contrast, articular chondrocytes exposed to relatively higher concentrations of dissolved oxygen and extracellular pH actively synthesized extracellular matrix (ECM) when cultured on 3D biodegradable scaffolds [5, 6]. In all of these researches, it is appearing that in similar physicochemical conditions, chondrocyte metabolism is different. It means that the type of scaffold, as the major parameter in tissue engineering, could also affect cell metabolism [7]. One of the 3D substrates that recently are used in articular cartilage tissue engineering is DegraPol® as a biodegradable polyesterurethane scaffold, BPUS [8-10]. BPUS is a new elastic, highly biocompatible and degradable synthesis polymer [8]. It is block copolyester, predominantly based on β-(R)-hydroxy-butyrate and hydroxyl-alkanoate (93% by weight), and linked with TMDI (trimethylhexamethylene diisocyanate) units (7% by weight) [8]. The degradation time can be adjusted between a few weeks and years through the chemical composition of the material. It has low polymer fraction (void volume about 95%) with pore size in about 50-300 μm. Also the elasticity can be varied from highly elastic and expandable from tough to brittle [8-10]. It might be the main reason of using BPUS in articular cartilage tissue engineering. But, we don't find any report about the effect of physicochemical parameters, such as oxygen tension and pH on articular chondrocyte metabolism in BPUS. However, we recently had a comparative study between cell viability of chondrocytes on BPUS and alginate (as a common material for study on chondrocyte metabolism) in different oxygen tension and pH [10]. We have shown that cell viability on alginate beads, in all physicochemical conditions is more than that of BPUS, after 3 days cell culture. We reported that the best conditions for cell viability is 5% oxygen tension and pH=7.4.

The goal of the present study is to investigate the effects of oxygen tension and pH on chondrocytes metabolism for two different scaffold material, BPUS and alginate beads, useful for articular cartilage tissue engineering. This study could answer the reasons of different chondrocyte metabolism on these two scaffolds.

Chwee Teck Lim, James C.H. Goh (Eds.): ICBME 2008, Proceedings 23, pp. 1248–1251, 2009
www.springerlink.com

II. Materials and methods

A. Material preparation

The BPUS scaffolds, as round disks were obtained from Zurich University (Institute of polymers). Its dimension was 15 mm in diameter and 1mm in thickness. The pore volume was about 95% and the pore size was about 50-300 μm. The modulus of elasticity was about 40 MPa. The samples were sterile by ethylene oxide method [8-10] and then suspended in distilled water and medium solution over night and then degassed under vacuum.

The alginate solution, as a natural biodegradable polymer, was prepared with the following method [10]. The 1.2% alginate solution was prepared by adding 240 mg alginic acid (Fluka, Biochemica) to 20 mL of 0.9% NaCl and stirring and then was steriled through 0.22 filters.

B. Cell culture method

There were two different methods for cell seeding, depend on the scaffolds. After harvesting of chondrocyte cells from metacarpophangeal joints of 6-9 month-old steers, for BPUS samples, the samples were put into the bottom of a 24 well-plate and then 0.1 mL of cell-medium suspension with 4×10^6 cell/mL concentration was added to the top of the samples for cell attachment [8]. After 2 hours incubation under different physicochemical conditions, the medium (DMEM, 6%v/v FBS, 1%v/v AA) was changed with 2 mL new medium and the plate was put into the incubator again, at the same condition.

For alginate samples; first, the actual amount of alginate solution was added to the pelleted cells to obtain a suspension with 4×10^6 cell/mL of alginate [10]. Then this suspension was mixed thoroughly and transferred to a syringe with 22 G needle and dropped to a sterile 102 mM $CaCl_2$ solution for formation of beads. After dropping all the cell-alginate suspension to the $CaCl_2$ solution, $CaCl_2$ was aspirated and the beads were washed with 0.9% NaCl and DMEM 3-4 times to remove all $CaCl_2$ from the beads.

C. Oxygen tension and pH condition

The experiments was done in three different oxygen tension; 21%, 5% and 1%. Briefly, BPUS and alginate samples was divided to three 6 well-plate. In one row, 2 mL of medium with pH=7.4 and in another row, 2mL of the medium with pH=6.5 was added. Then each 6 well-plate was put into the oxygen chamber. Oxygen was blown in different percents, 21%, 5% and 1%, into the three chambers and finally the chambers were put into the incubator at 37°C and 5 % CO_2. The old medium was replacing with 2 mL of the new medium with the same pH and oxygen, everyday.

D. Determination of lactate production

In this study, after 1, 2 and 3 days culture, for both scaffold and in different oxygen tension and pH, the medium was replaced with 0.5 mL new medium for 4 h [2]. Then the medium (per each sample) was transferred to an eppendorf. 10 *mL* of each medium sample was added to one well of 96 well-plate and 100 *mL* of lactate reagent (Sigma, UK) was added to each well. Finally, the absorbance of each medium sample (in each well) was measured by ELIZA reader (enzyme linked immune absorbent assay) at 540 nm. The standard curve was derived by the same method and the amounts of lactate production were determined for each sample by equation derived from the standard curve.

E. Determination of GAG production

The amount of GAG was measured by DMMB (dimethylmethylene blue, Aldrich) assay in day 3, 7 and 14 of cell culture in different oxygen tension and pH [11]. Briefly, the scaffolds were put separately in papain solution at 60-65°C over night. The papain solution was made with mixing of 20 mM sodium phosphate buffer (pH=6.8), 1 mM EDTA(Sigma, UK), 300 μg papain (Sigma, UK) and 10 mM cysteine-HCl (Sigma, UK). Then, 20 μL of each digested sample were added into a disposable spectrophotometer cuvette. Finally, 1 mL of DMMB was added to each cuvette and absorbance was measured at 595 nm by spectrophotometer. The standard curve was obtained by the same method and the amounts of GAG production for each sample were determined by the equation derived from standard curve. Statistical analysis in all experiments was based on student t-test.

III. Results

A. Lactate production

As shown in figure 1, there is a significant difference between the amounts of lactate production in pH=6.5 and pH=7.4 for BPUS scaffold ($p<0.001$).The results were the same for Alginate.It means that the pH=7.4 is a physiological condition for cell metabolism on both scaffolds. On the other hand, the chondrocytes were producing adenosine triphosphate (ATP) and subsequently, faster cell proliferation. Figures 1 also is showing the increasing lactate production with time in pH= 7.4. In pH=6.5, not only the amount of lactate production is not increasing with time, but also is decreasing for both scaffolds. In general, decreasing pH could reduce the cell volume and reduction of cell volume could change the normal mechanism of transferring

ions like glucose into the cells and reduce lactate production [2-5].

Figure 3 are showing the effect of oxygen tension on lactate production for BPUS scaffold. In this figure, it dose appear that the lactate production in 5% O2 atmosphere is maximum and there is significant difference between these three oxygen tension ($p<0.01$). The results were the same for Alginate. It means that the lactate production is maximized at optimum value of oxygen tension and increased with time. On the other hand, changing of oxygen tension could change cell volume and finally affect the cell metabolism [2-5].

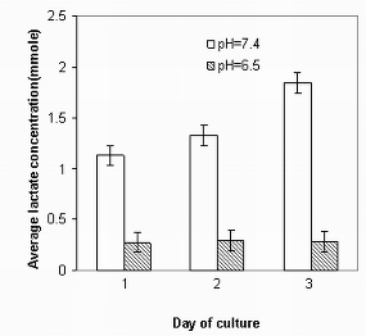


Fig. 1 Effect of pH on lactate production in different days of culture for BPUS (Osm. =380, 21% O_2) (n=9, mean ± SD, P<0.001)

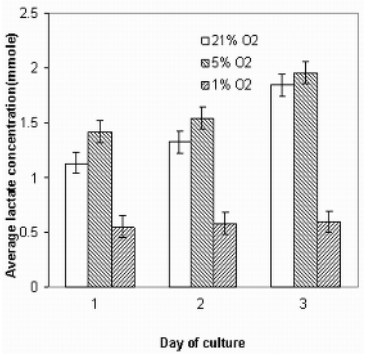


Fig. 2 Effect of oxygen tension on lactate production in different days of culture for BPUS (Osm. =380, pH=7.4) (n=9, mean ± SD, P<0.01)

B. GAG production

The results repeatedly showed here that the highest GAG production is in pH=7.4 and 5% oxygen tension. Figure 3 is showing that GAG production is increasing with time significantly for BPUS scaffold in pH=7.4($p<0.01$). The results were the same for Alginate.

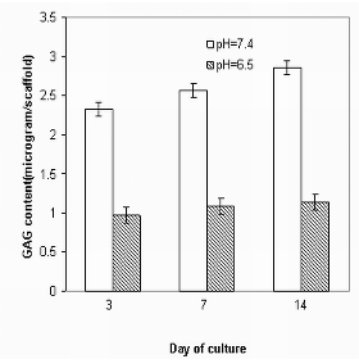


Fig. 3 Effect of pH on GAG production in different days of cell culture for BPUS (Osm. =380, 21%O2) (n=9, mean ± SD, p<0.01)

It is also appear in figure 4 that the amount of GAG production for BPUS scaffold is increased significantly with increasing the time of cell culture at 5% oxygen tension, as Alginate beads($p<0.05$). These results generally shown that the changing of pH and oxygen tension could change cell volume and finally affect the cell metabolism for both scaffolds.

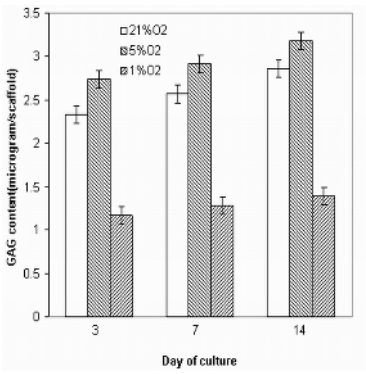


Fig. 4 Effect of oxygen tension on GAG production in different days of cell culture for BPUS (Osm. =380, pH=7.4) (n=9, mean ± SD, p<0.05)

IV. Discussion

The cell–polymer system can be used to identify and control various biochemical and physical factors that are expected to influence cell function and tissue growth [12]. In this study, the comparison between BPUS and alginate scaffold is showing that the results are better for alginate beads. It is shown in figure 5 that average lactate production in constant pH, oxygen tension and Osmolarity, is higher for alginate scaffold ($p<0.001$).

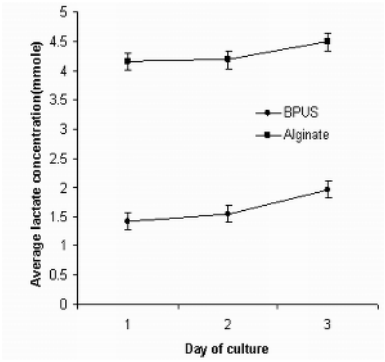


Fig. 5 Comparison between average lactate production for BPUS and Alginate in different days of cell culture (Osm. =380, pH=7.4, 5%O2) (n=9, mean ± SD, p<0.001)

This is also the same for GAG production (p<0.001) (figure 6).

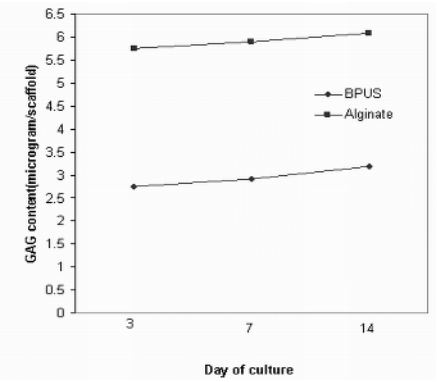


Fig. 6 Comparison between GAG production for BPUS and Alginate in different days of cell culture (Osm. =380, pH=7.4, 5%O2) (n=9, mean ± SD, p<0.001)

It seems likely that there are some factors in alginate that cause these differences. One of these factors is high hydrophilicity of alginate. This property causes good cell distribution and nutrition; because the cells are able to transfer the ions and the products through the medium easily [10]. But, BPUS is not hydrophilic. It has some interconnected porosity that can help cell nutrition and cell metabolism. In static culture, cell seeding is just putting the cells on top of the scaffold. Therefore, in rigid scaffolds like BPUS, cells can not distribute inside the bulk of the scaffold. Also, some of the cells can go through the pores, slowly; but because of the situation in the static culture, medium content can not reach the diffused cells and the cells will die. Therefore, in rigid scaffolds like BPUS that are not hydrophilic and just have some porosity, the best way for increasing the cell metabolism is to find a method for nutrition of the cells in entire part of the scaffold. One of these methods is perfusion culture. Perfusion culture is a method for perfusing the cells through the scaffold [12]. It seems that this method could improve the results for BPUS, significantly.

V. Conclusion

In rigid scaffolds like BPUS that are not hydrophilic and just have some porosity, the best way for increasing the cell metabolism is to find a method for nutrition of the cells in entire part of the scaffold. One of these methods is perfusion culture. It seems that this method could improve the results for BPUS, significantly.

References

1. Lee RB, Urban JPG (1997) Evidence for a negative Pasteur effect in articular cartilage. Biochem J 321: 95-102.
2. Lee RB, Urban JPG (2002) Functional replacement of oxygen by other oxidants in articular cartilage. Arthritis & Rheumatism 46: 3190-3200.
3. Lee RB, Wilkins RJ, Razaq S, Urban JPG (2002) The effect of mechanical stress on cartilage energy metabolism. Biorheology 39: 133-143.
4. Urban JPG (1994) The chondrocytes: A cell under pressure. Br J Rheumatol 33: 901-908.
5. Freed LE, Hollander AP, Martin I et al. (1998) Chondrogenesis in a cell-polymer bioreactor system. Exp Cell Res 240: 58-65.
6. Obradovic B, Carrier RL, Vunjak-Novakovic G (1999) Gas exchange is essential for bioreactor cultivation of tissue engineered cartilage. Biotechnol Bioeng 63:197-205.
7. Hardingham T, Tew S, Murdoch A (2002) Tissue engineering: chondrocytes and cartilage. Arthritis res 4: 63-68.
8. Yang L, Korom S, Weder W et al. (2003) Tissue-engineered cartilage generated for human trachea using Degrapol scaffold. Eur J Cardiothoracic Surg 24: 201-207.
9. Raimondi MT, Falcone L, Colombo M et al. (2004) A comparative evaluation of chondrocyte/scaffold constructs for cartilage tissue engineering. J Applied Biomat & Biomech 2: 55-64.
10. Karbasi S, Mirzadeh H, Orang F, Urban JPG (2005) A comparison between cell viability of chondrocytes on a biodegradable polyesterurethane scaffold and alginate beads in different oxygen tension and pH. Iranian Polym J 14: 823-830.
11. Farndale RW, Buttle DJ, Barrett AJ (1986) Improved quantitation and discrimination of sulphated glycosaminoglycans by use of dimethylmethylene blue. Biochimica et Biophysica Acta 883: 173-177.
12. Novakovic GV, Abradovic B, Martin I et al. (1998) Dynamic cell seeding of polymer scaffolds for cartilage tissue engineering. Biotechnol Prog 14: 193-202.

Author: Saeed Karbasi
Institute: Isfahan University of Medical Science
Street: University Street
City: Isfahan
Country: Iran
Email: karbasi@med.mui.ac.ir

Effect of Cryopreservation on the Biomechanical Properties of the Intervertebral Discs

S.K.L. Lam, S.C.W. Chan, V.Y.L. Leung, W.W. Lu, K.M.C. Cheung and K.D.K. Luk

Department of Orthopedics and Traumatology, The University of Hong Kong, Hong Kong SAR

Abstract — **Intervertebral Disc (IVD) allograft transplantation is presented to be a practical treatment of severe Degenerative Disc Disease (DDD). Limited availability of fresh allograft tissues necessitate the establishment of tissue banking for long-term storage. However, the effects of the cryopreservants on the mechanical properties of the IVD remains unknown. We hypothesize that the appropriate use of cryopreservants can preserve the mechanical properties of the IVD. In this study porcine discs were cryopreserved in different cryopreservative agent (CPA) concentration following a stepwise freezing protocol. After four weeks of storage in liquid nitrogen, dynamic viscoelastic properties of the IVDs were tested using uniaxial compression at different frequencies. Compared to fresh IVDs, no significant differences were found in the elastic modulus (E'), viscous modulus (E") and loss tangent (E"/E') in the discs cryopreserved with 0-20% CPA. However, cryopreservation at 20% CPA mixture resulted in lower E'and E". Our data suggest properly cryopreserved IVD is able to maintain both elastic and viscous characteristics and distribute loads as of a normal IVD.**

Keywords — **Degenerative Disc Disease, Intervertebral Disc, Allograft, Cryopreservation, dynamic viscoelastic**

I. Introduction

Total disc replacement by intervertebral disc (IVD) allograft transplantation has been reported as a possible treatment for severe Degenerative Disc Disease (DDD) [1-3]. Recent clinical trial indicates that IVD allografts are able to preserve motion and stability of the spinal segment [3]. However, limited availability of fresh allograft tissues and the need for size matching during transplantation necessitate the establishment of cryopreserved IVD tissue bank. To date, little is known about the effects of cryopreservants (CPA) on the mechanical properties of the IVD although the mix effects of freezing on the IVD have been previously reported [4-5]. Bass et al. (1997) reported that frozen storage of porcine intervertebral discs alters the compressive creep behaviour and that the frozen disc do not represent fresh behaviour. However, in another study, no significant alteration in the creep response of human lumbar disc were found following frozen storage [5]. Since frozen storage may have some effects on the behaviour of the disc, it is hypothezied that the appropriate use of cryopreservant is required to maintain the integrity of IVD matrix and hence preserve the mechanical properties of the IVD during disc cryopreservation. The objective of this study is to test if cryopreservation with or without CPA can affect the dynamic viscoelastic properties of the IVD.

II. Method

Porcine lumbar IVDs of diameter 22-25mm were randomly assigned to undergo a stepwise freezing protocol using 0% CPA, 10% CPA, or 20% CPA (5 samples each) and stored in liquid nitrogen at -196°C. After 4 weeks of storage the IVDs were fast-thawed at 37°C in a saline bath. All specimens were radiographed by Faxitron (Faxitron X-Ray Corporation, Wheeling, IL) and the lateral and anteroposterior widths of the discs were measured from the radiographs using Image Pro Plus (Media Cybernetics, Inc., Bethesda, MD), and disc cross-sectional area was computed as an ellipse using the formula $\Pi/4 \times d1 \times d2$, where d1 and d2 were the lateral and anteroposterior widths.

Non-destructive uniaxial compression testing was performed using MTS 858 Bionix Testing Machine (MTS System Inc., Minneapolis, MN). The samples were placed on a porous puck inside a 37°C saline bath and then another porous puck, connected to the loading shaft, was loaded onto the samples. A basal compressive load of 10N was applied so as to maintain contact between the puck and the samples during the unloading cycle of the test. Dynamic viscoelastic properties of the IVDs were tested by uniaxial compression as previously described [6] using 6 frequencies of loading (0.05Hz, 0.1Hz, 0.2Hz, 0.5Hz, 1Hz and 2Hz) with 10% strain amplitude. Each frequency test was performed using one cycle of sinusoidal strain followed by 3-minute recovery. The complex modulus $|E^*|$ was determined by $|E^*|=\sigma/\varepsilon$, where stress σ = force (F) / cross-sectional area (A), strain ε = change in disc height (ΔDH) / disc height (DH) [6]. The elastic modulus E' was determined by $E'=|E^*|\cos\delta$, the viscous modulus by $E''=|E^*|\sin\delta$, and the loss tangent by $\tan\delta=E''/E'$.

One-way ANOVA followed by LSD post-hoc test was used to evaluate the statistical difference with $p < 0.05$ considered as significant.

Chwee Teck Lim, James C.H. Goh (Eds.): ICBME 2008, Proceedings 23, pp. 1252–1254, 2009
www.springerlink.com

III. Results

The elastic modulus (E'), viscous modulus (E") and loss tangent (E"/E') of the fresh control and different treatment groups over the range of testing frequencies are presented in Figure 1.

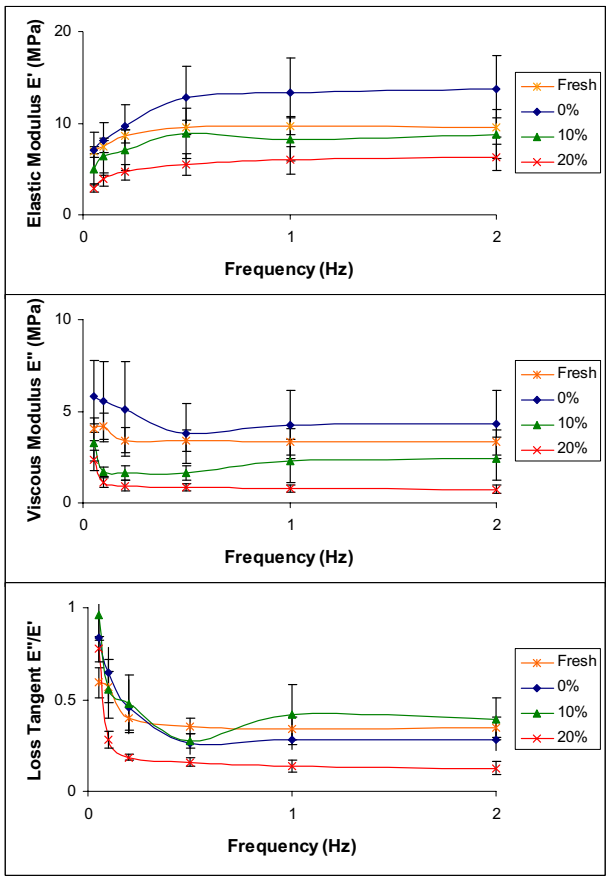


Figure 1: Effects of cryopreservation with or without CPA on the elastic modulus (E'), the viscous modulus (E") and the loss tangent (E"/E') of porcine IVD (Mean±SEM).

The 0% CPA group had the highest E'and E" properties at all frequencies among all the groups, while, the 20% CPA group recorded the lowest E', E" and E"/E' properties at all frequencies out of all the treated groups. Relative to fresh IVD, cryopreservating the IVD 0% CPA resulted in higher E' and E", whilst, IVD cyropreserved with 10% CPA retained the closest E'and E" properties to fresh IVD and IVD cryopreserved with 20% CPA resulted in lower E, E", and E"/E'. No significant differences were found in the E', E" and E"/E' between the fresh control group and the treatment groups.

IV. Discussion

Higher values of apparent modulus attained in the 0% CPA group suggests freezing without CPA have a detrimental effect to the elastic properties of IVD and that the use of CPA can affect the mechanical performance of the IVD during freezing. The full extent of the effects of CPA on the cryopreservation of the disc has yet to be studied.

The use of CPA could be a vital component to cryopreservation of the discs as suggested by other groups [2, 4]. The use of appropriate CPA and freeze-thaw protocol can prevent cell death associated with freezing and reduce ice crystal formation and nuclear expansion which can reduce the potential disruption of the annulus [4, 5]. Although the differences between groups were not significantly, however, the use of CPA in cryopreservation of the IVD can affect other parameters such as cell viability which was not tested in this study. We postulate that the maintenance of mechanical properties of the cryopreserved IVD is related to the preservation of IVD structure due to attenuation of extracellular ice crystal formation with the use of cryopreservants and stepwise freezing protocol.

V. Conclusions

This study demonstrated that the cryopreservation with CPA would not affect the dynamic viscoelastic properties of the IVD. Preservation of the dynamic viscoelastic properties in the IVD allograft would facilitate the kinematics and distribute loads of the spine following the IVD allograft transplantation.

Acknowledgment

This project is support by The Univeristy of Hong Kong: CRCG grant and Tai Sai Kit Endowment Fund.

References

1. Luk KD, Ruan DK, Lu DS, Fei ZQ et al. (2003) Fresh frozen intervertebral disc allografting in a bipedal animal model. Spine 28:864-9
2. Matsuzaki H, Wakabayashi K, Ishihara K, Ishikawa H, Ohkawa A et al. (1996) Allografting intervertebral discs in dogs: a possible clinical application. Spine 21:178-83
3. Ruan D, He Q, Ding Y, Hou L, Li J, Luk KD et al. (2007) Intervertebral disc transplantation in the treatment of degenerative spine disease: a preliminary study. Lancet 369:993-9
4. Bass E, Duncan NA, Hariharan JS, Dusick J, Bueff HU, Lotz JC et al. (1997) Frozen storage affects the compressive creep behavior of the porcine intervertebral disc. Spine 22:2867-2876

5. Dhillon NM, Bass E, Lotz JC et al. (2001) Effect of Frozen Storage on the Creep Behavior of Human Intervertebral Disc's. Spine 26:883-888
6. Miyamoto K, Masuda K, Kim JG, Inoue N, Akeda K, Andersson GBJ, An HS et al.. (2006) Intradiscal injections of osteogenic protein-1 restore the viscoelastic properties of degenerated intervertebral discs. The Spine Journal 6:692-703

Corresponding Author: Prof. Keith D K Luk
Institute: The University of Hong Kong
Street: L9-06, 9/F, Laboratory Building,
21 Sassoon Road, Pokfulam
City: Hong Kong
Country: Hong Kong SAR
Email: hrmoldk@hku.hk

A Serum Free Medium that Conserves The Chondrogenic Phenotype of *In Vitro* Expanded Chondrocytes

Saey Tuan Barnabas Ho[1,2], Zheng Yang[1,3], Hoi Po James Hui[1], Kah Weng Steve Oh[4], Boon Hwa Andre Choo[4] and Eng Hin Lee[1]

[1]Department of Orthopaedic Surgery, Yong Loo Lin School of Medical and NUS Tissue Engineering Program, National University of Singapore, Singapore 119074
[2]Division of Bioengineering, Faculty of Engineering, National University of Singapore, Singapore 119260
[3]Faculty of Dentistry, National University of Singapore, Singapore 119074
[4]Stem Cell Group, Bioprocessing Technology Institute, A*STAR, Singapore 138668

Abstract — **Objective: The success of autologous chondrocyte implantation hinges on several factors. One of which is that sufficient chondrocytes with a conserved phenotype is required for the procedure. This proves to be a challenge with conventional cell culturing which is dependent on animal serum. The authors propose a serum free media that not just enhance cell growth but also preserve the chondrogenic phenotype during expansion.**

Design: Chondrocytes were harvested from human articular cartilage biopsies and cultured either in serum supplemented media or in the serum free formulation. To promote cell attachment, collagen or fibronectin coating was coupled to the use of the serum free media. During expansion, cell attachment and proliferation were evaluated, while key chondrogenic markers were assessed in the later redifferentiation phase.

Results: Promising results were observed with superior long term proliferation as compared to the FBS supplemented cultures. When these cells were redifferentiated, aggrecan and collagen II were expressed especially so for the cells cultured on collagen coated surfaces under serum free conditions. These cartilage ECM molecules were either reduced or absent in the FBS group. The serum free formulation also lowered collagen X gene expression which was indicative of a reduced likelihood of the cells undergoing hypertrophy.

Conclusion: The work represents one of the first attempts in the in *in vitro* expansion of human chondrocytes independent of serum or its derivatives. The findings indicate that serum free media on collagen and fibronectin substrates supported higher cell proliferation and better chondrogenic phenotype compared to serum supplemented media.

Keywords — **Serum free, Chondrocytes and Autologous chondrocyte implantation**

I. Introduction

Functionally viable chondrocytes in sufficient quantity is crucial for the success of autologous chondrocyte implantation. This is difficult with conventional methods as chondrocytes dedifferentiate during 2D expansion with the loss of their chondrogenic phenotype [1]. Moreover established protocols are dependent on the use of animal serum (especially FBS) which is not without its drawbacks. These would include inconsistency in outcomes due to the variability in serum lots and the transmission of pathogens. This study sought to address the issue by evaluating a newly developed serum free media which is capable of encouraging cellular growth while conserving the chondrogenic phenotype. The investigation was conducted by culturing chondrocytes plated on either human collagen I (hCol1) or fibronectin (hFN) coated surfaces and maintained using a serum free formulation. Comparisons during proliferation and re-differentiation were made against FBS supplemented cultures.

II. Materials and Methods

Biopsies of articular cartilage were taken from the knee joints of young patients who underwent reparative surgery following knee trauma. Chondrocytes were subsequently isolated via enzymatic treatment and expanded. At P2, the cells were cultured under 3 different conditions : Serum free with hCol 1, serum free with hFN and FBS supplemented media which served as a control. The serum free media consisted of 10% Knockout SR (Invitrogen), 2 ng/ml FGF-2, 2 ng/ml PDGF-AB, 2 ng/ml EGF and 10^{-8} M dexamethasone. Cell proliferation was examined at P2, while major chondrogenic markers such as collagen I, II, X and aggrecan were evaluated via real time PCR or histological staining for the P3 redifferentiated pellet cultures.

III. Results and Discussion

The serum free culturing enhanced cell proliferation over long term as compared to the FBS cultures as shown in figure 2A. The usage of FBS has resulted in a severe loss of chondrogenic phenotype as reported by other investigators

Chwee Teck Lim, James C.H. Goh (Eds.): ICBME 2008, Proceedings 23, pp. 1255–1257, 2009
www.springerlink.com

[2]. This effect can be countered under serum free conditions. When redifferentiated, the serum free groups exhibited better chondrogenic phenotype with higher deposition of aggrecan and collagen II (figure 1). Moreover there was a reduced tendency of undergoing hypertropy as indicated by the lower collagen X gene expression in the serum free cultures. When the substrate coatings were compared, hCol 1 appeared to be preferable with superior aggrecan secretion and collagen II gene expression. Despite of the promising results with the serum alternatives, the prevalence of collagen I across all groups proved that there was a general loss of hyaline phenotype which could not be completely arrested with the serum free formulation.

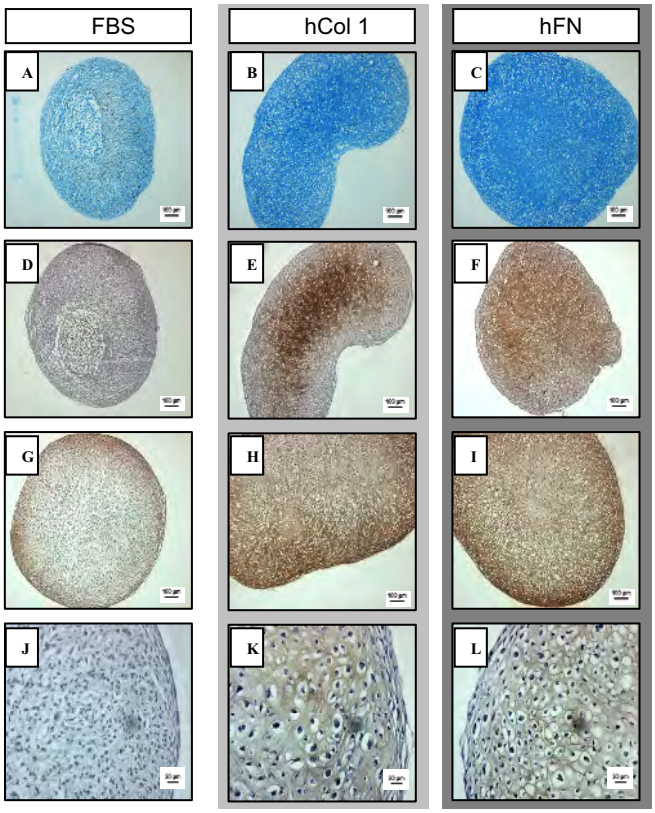


Figure 1. Alcian blue staining (A – C), aggrecan (D – F), collagen I (G – I) and collagen II (J – L) immunostaining of redifferenitated chondrocyte pellets cultured for 14 days. Prior to redifferentiation, the cells were expanded under the 3 different conditions : FBS supplemented media (A, D, G and J), serum free with hCol 1 (B, E, H and K) or hFN (C, F, I and L). All isotype controls were stained negative, while collagen X was absent in all groups (results not shown).

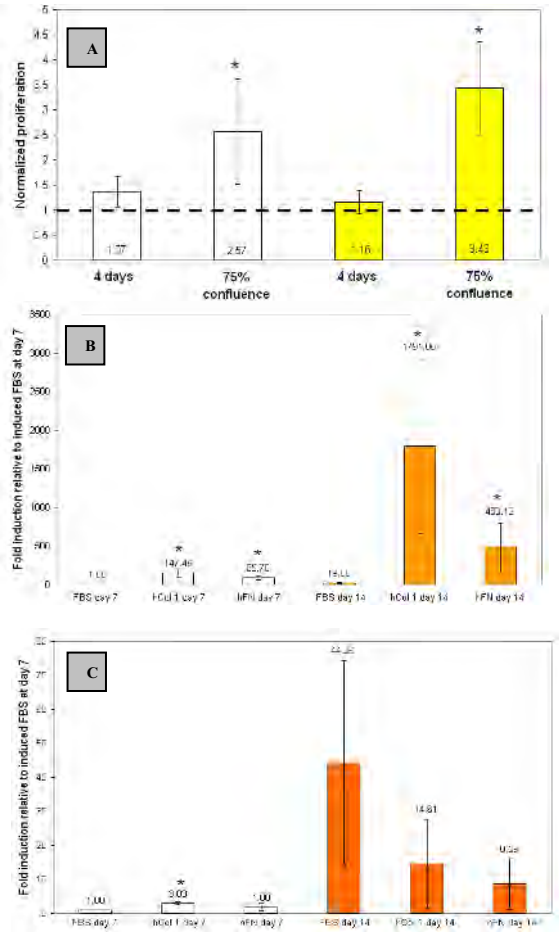


Figure 2. Cell proliferation over 4 days and at 75% confluence is as shown in A. Proliferation in serum free media with hCol 1 or hFN was normalized to that of FBS cultures as indicated by the dotted line. N = 4 for 4 days and N = 3 for 75% confluence. * indicates significant difference when compared to the FBS group at the same time point ($P<0.05$). Collagen II (B) and collagen X (C) gene expression of the redifferentiated chondrocyte pellets derived from the expansion in FBS supplemented media, serum free with hCol 1 or hFN. The results were normalized to that of the 7 days pellet derived from the expansion with FBS. * indicates significant difference ($p< 0.05$) with the FBS group at the same time point. There is no statistical difference ($p> 0.05$) between the serum free groups within the same time point.

IV. Conclusion

The presented work proves the feasibility of maintaining human chondrocytes in a serum free environment. Moreover the findings have shown that the serum free media promoted superior cell growth with a better conserved chondrogenic phenotype as compared to serum supplemented cultures.

Acknowledgment

This study was supported by the Singapore National Medical Research Council, NMRC grant R175000074213. The work would not have been possible without valuable contributions from Chong Sue Wee, Chan Shzu Wei, Lim Shu ly and Dr Ouyang Hong Wei.

References

1. Von der Mark K, Gauss V, Von der Mark H and Muller P. (1977) Relationship between cell shape and type of collagen synthesized as chondrocytes lose their cartilage phenotype in culture. Nature, 267 (5611), pp. 531 – 532.
2. Giannoni P, Pagano A, Maggi E, Arbico R, Randazzo N, Grandizo M, Cancedda R and Dozin B. (2005) Autologous chondrocyte implantation (ACI) for aged patients : development of proper cell expansion conditions for possible therapeutic applications. Osteoarthritis and cartilage, 12, pp. 589 – 600.

Corresponding author : Eng Hin Lee

Institute: Department of Orthopaedic Surgery, Yong Loo Lin School of Medical and NUS Tissue Engineering Program, National University of Singapore, Sinapore 119074
Street: National University of Singapore,
Kent Ridge, 27 Medicine drive.
City: Singapore
Country: Singapore
Email: dosleeeh@nus.edu.sg

High Aspect Ratio Fatty Acid Functionalized Strontium Hydroxyapatite Nanorod and PMMA Bone Cement Filler

W.M. Lam[1], C.T. Wong[1], T. Wang[1], Z.Y. Li[1], H.B. Pan[1], W.K. Chan[3], C. Yang[2], K.D.K. Luk[1], M.K. Fong[1], W.W. Lu[1]

[1] Department of Orthopaedics and Traumatology, The University of Hong Kong, China
[2] Department of Chemistry, The Hong Kong University of Science and Technology, China
[3]Department of Chemistry, The University of Hong Kong, China

Abstract — **High aspect ratio strontium hydroxyapatite nanorod significant enhances the mechanical strength of bioactive bone cement, due to its fiber like nature. However, incompatibility between resin matrix and strontium hydroxyapatite (Sr-HA) reduce the maximum filler loading and excessive strontium release leads to cytotoxicity problem. The aim of this study is to design a high aspect ratio hydroxyapatite nanorod with good resin compatibility and acceptable strontium release rate.**

In this study four C-18 fatty acids with different degree of unsaturation on nanorod morphology were investigated. These include stearic(n=0), oleic(n=1), linoleic(n=2), and linolenic acid(n=3). Functionalized strontium hydroxyapatite nanorod was synthesized by Liquid Solid Solution Method at 160°C for 15 hours.

From TEM analysis, the aspect ratio of linoleic (22.00±11.86) and oleic acid (22.47±6.20) were larger than linolenic(4.76±1.73) and stearic acid (6.14±2.57). Hydrophobic FTIR pattern was shown in linolenic, linoleic and stearic acid functionalized nanorod. The reinforced bone cement has lower setting temperature than PMMA counterpart.

Based on MTT and BrdU assay on mouse fibroblast (L929), proliferation rate of linoleic acid> linolenic acid> oleic acid> stearic acid. Exclude oleic acid all functionalized nanorod has higher relative growth rate than untreated strontium hydroxyapatite nanorod. From Hank immersion study and rat implantation study, the reinforced bone cement showed good bioactivity.

In this study, high aspect ratio strontium hydroxyapatite nanorods can be fabricated by using linoleic and oleic acid. Linoleic acid functionalized strontium hydroxyapatite showed optimal aspect ratio, proliferation rate, cytotoxicity profile and good resin compatibility. New bone cement has lower setting temperature, better match stiffness and high bioactivity; these properties enhance the safety of vertebroplasty application.

Keywords — **Strontium hydroxyapatite, nanorod, high aspect ratio, biocompatibility**

I. Introduction

PMMA bone cement has excellent workability and stability that allow it as the only market player in cement prosthesis fixation for more than four decades. However this product suffers the difficulties such as lack of bioactivity, highly exothermic reaction and monomer toxicity. During recent ten years, such problems could be partially resolved by the addition of bioactive filler [1], bioactivity of the bone cement was improved setting temperature was reduced.

Our group has also developed strontium containing bioactive bone cement since release of strontium can suppress osteoclast proliferation and promote osteoblast differentiation. Due to stimulatory effect of strontium enhance bony ingrowth on the cement surface can stabilize the bone - cement mantle interface. This hypothesis had been proven by goat femur model. [2] High aspect ratio Sr-HA nanorod enhances the mechanical strength of bioactive bone cement via fiber reinforcement mechanism. [3] Based on previous study, we found that adding high aspect ratio Sr-HA nanoparticle dramatically improved the bending strength of bone cement by 78%. However, the incompatibility between resin matrix and Sr-HA reduced the maximum filler loading. In addition, release of high aspect ratio Sr-HA nanoparticle leaded to cytotoxicity. Therefore, surface treatment with silane agent e.g. A174 is a common solution to reduce the particle release. However, silanized filler can release cytotoxic silane agent due to presence of not crosslinked silane. Therefore replacement of silane with biocompatible surface treating agent may improve the bioactivity of bone cement.

C-18 fatty acid is cell membrane component and exists in droplet in human body to store energy. Fatty acid surface treatment is well adopted in polymer industry to reduce the aggregation problem in polymer processing.

Liquid-solid solution method [4] was reported in synthesizing hydrophobic calcium hydroxyapatite nanorod. Fatty acids with different chains geometry have been reported to influence particle morphology and phase purity.[5]

Therefore, the aim of this study is to design a high aspect ratio Sr-HA nanorod with good resin compatibility and good biocompatibility.

Chwee Teck Lim, James C.H. Goh (Eds.): ICBME 2008, Proceedings 23, pp. 1258–1262, 2009
www.springerlink.com

II. Material and Method

C-18 fatty acids with different degree of un-saturation on Sr-HA nanorod morphology were investigated. Stearic(n=0), oleic(n=1), linoleic(n=2), and linolenic acid(n=3) were also included in this study. 5 g of octadecylamine, 40 g of fatty acid and 160ml of ethanol were mixed by agitation. Strontium nitrate solution was prepared by dissolving 6.44g into 75ml distilled water. Strontium nitrate solution was added to the octadecylamine fatty acid-ethanol mixture. 5 g sodium phosphate was dissolved in 75 ml distilled water and added to above mixture. The mixture was agitated for about 10 minutes and then transferred to a 500ml Teflon lined autoclave, which was sealed and treated at 160°C for 15 hours. The precipitates were washed by distilled water, 70% ethanol and dehydrated with absolute ethanol.

Transmission electron microscopy

Particle size and morphology were characterized by measuring 100 particles by Technai G2 transmission electron microscopy.

X-ray diffraction pattern

The composition and phase purity of the fatty acid functionalized strontium hydroxyapatite and strontium hydrogen phosphate impurity was characterized by X-ray diffraction. The peaks were indexed and matched with Joint Committee on Powder Diffraction Card.

Fourier Transform Infrared Spectroscopy

Fatty acid adsorption mode has significant influence on load transfer from bone cement resin matrix to functionalized nanorod. Functionalized nanorod was mixed with KBr and analyzed with BIO-RADFTS-7 at $4cm^{-1}$ resolution.

Thermal gravimetric analysis

The amount of fatty acid adsorbed on Sr-HA nanorod surface was determined by Thermogravimetric analysis (TGA) (TA, Q5000 TA Instruments, New Castle, DE) under air-stream at a heating rate of 20°C/min. Sample gas flow rate was 25ml/minutes.

MTT and BrdU assay

Functionalized nanorod suspension was prepared by dispersing 200μg of nanorod in DMEM culture medium with the assistance of ultrasound. Mouse fibroblast (L929) was used to determine the cytotoxicity of suspended nanorod. Relative growth rate was determined by MTT assay according to Dojino guideline. Proliferation assay was performed to determine whether functionalized nanorod retain stimulatory effect on osteosacroma cell (Sa-OS2). Functionalized strontium hydroxyapatite was compared with untreated strontium hydroxyapatite and calcium hydroxyapatite nanorod.

Bone cement compressive strength

Compressive strength and modulus of bone cement was evaluated by MTS 858 according to ISO 5833 standard.

Hank solution immersion test

After immersion in Hank solution at 37°C for 7 d, the bone cement was observed under SEM Leo 1530 at 5kV and 20kV respectively.

Rat tibia implantation study

In vivo response of linoleic acid functionalized strontium hydroxyapatite reinforced bone cement was evaluated by rat tibia model.

III. Result

Particle morphology and aspect ratio

Fig. 1 a-d, aspect ratio of linoleic (22.00±11.86) and oleic acid (22.47±6.20) were larger than linolenic (4.76±1.73) and stearic acid (6.14±2.57).

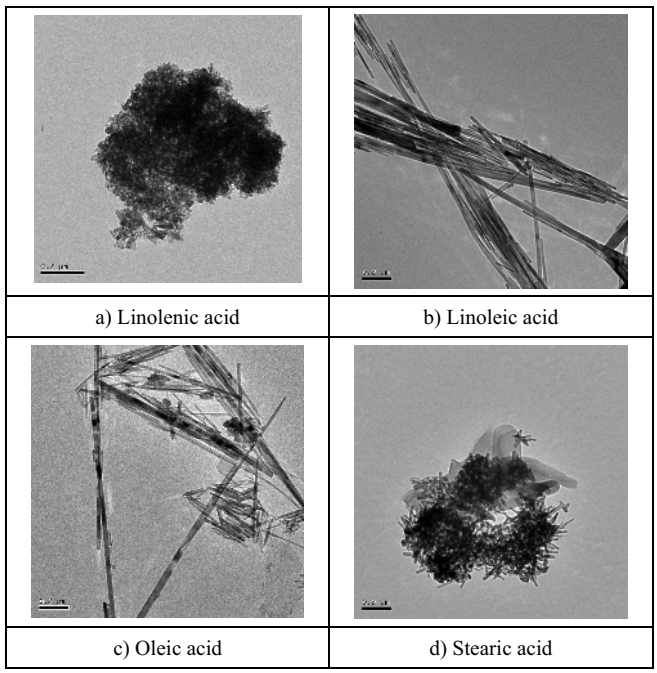


Fig 1. Nanorod functionalized by different fatty acid a) linolenic acid, b) linoleic acid, c) oleic acid d) stearic acid.

Phase purity and chemical composition

From **Fig. 2** linoleic, oleic and stearic acid functionalized nanorod, matched the pattern of strontium hydroxyapatite. Stearic acid functionalized nanorod suffered minor contamination of sodium strontium phosphate hydrate. In addition the particle size was also calculated according to Scherer Equation. The particle size of linolenic acid functionalized Sr-HA (256.68nm) < linoleic acid (453.96nm) < oleic acid (690.8nm) < stearic acid (845.13nm)

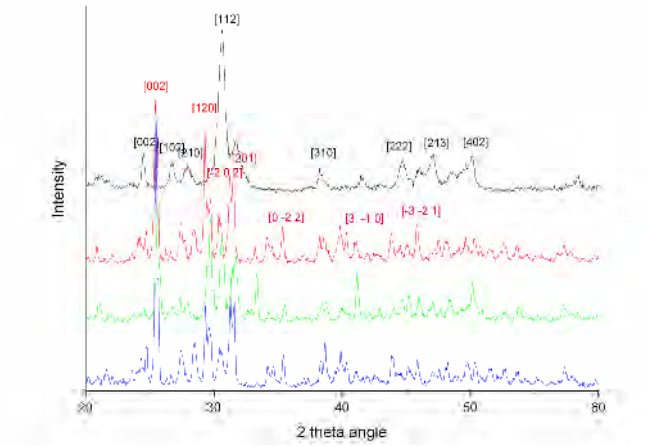


Fig. 2 X-ray diffraction pattern of nanorod functionalized by linolenic (black), linoleic (red) oleic (green) and stearic acid (blue).

Fatty acid adsorption mode

From **Fig. 3** presence of C=O stretching group (1710cm^{-1}) suggests the fatty acid was chemical boned on nanorod surface. In the FTIR spectrum of pure liquid fatty acid was absent. High CH_3 and CH_2 intensity in stearic acid

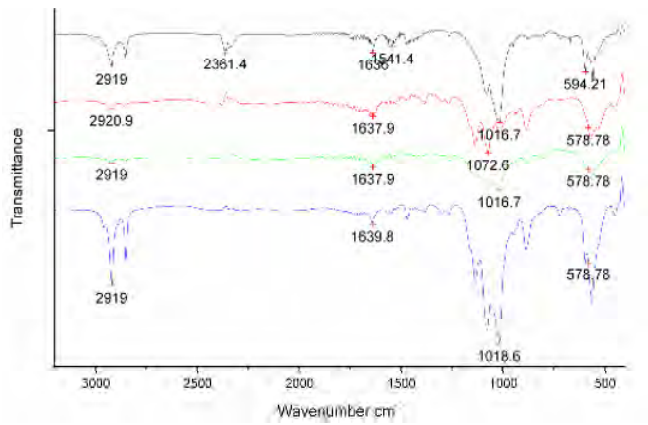


Fig. 3 FTIR spectrum of linolenic (black), linoleic (red), oleic (green) and stearic acid (blue) functionalized nanorod.

functionalized strontium hydroxyapatite suggest significant amount of stearic acid was adsorpted as intercalated layer. Intercalated fatty acid layer tends to weaken the mechanical strength of the reinforced bone cement due to lubricant like effect. TGA pattern found that the presence of intercalated layer in stearic acid functionalized Sr-HA.

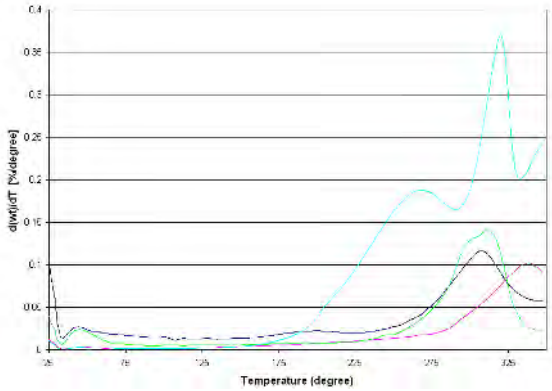


Fig. 4 TGA graph of linolenic (deep blue), linoleic (red), oleic (green) and stearic acid (blue) functionalized nanorod.

Aggregate size determination

Aggregation of filler is the key factor affecting bone cement mechanical strength. Thus, the aggregate size distributions of fatty acid functionalized Sr-HA were determined by Mastersizer 2000E based on laser scatter method by Mie method. Functionalized nanorod was dispersed by ultrasound and stirred by Hydro 2000MU (Malvern Instruments, UK). 5 consecutive tests were performed again to determine the size distribution. The d(0.9) value represent largest 10% particle. Particle size of linolenic acid functionalized Sr-HA d(0.9) =1149.524μm is significant higher than linoleic acid d(0.9) = 35.394μm oleic acid d(0.9) = 31.905μm and stearic acid functionalized hydroxyapatite d(0.9) = 21.544μm.

Cytoxicity of fatty acid functionalized nanorod

Relative growth rate of linolenic acid functionalized nanorod was (81.65±4.71)> linoleic acid functionalized nanorod (79.19±5.98)> stearic acid functionalized nanorod (70.54±15.68) > Sr-HA (68.12± 2.65) > oleic acid functionalized nanorod (51.03±1.38). Except oleic acid group, all functionalized Sr-HA is less cytotoxic than untreated counterpart. Proliferation rate of linoleic acid was (1.5188 ± 0.1400)> linolenic acid (1.5008 ± 0.1085) > oleic acid (1.3727 ± 0.1211)> Sr-HA (1.3398 ± 0.1769) stearic acid (1.1506 ± 0.1769). From BrdU result functionalized nanorod was slightly better than untreated counterpart.

Compressive strength

Compressive strength and modulus of reinforced bone cement was 81.81±1.56MPa and 3385.71±559.89MPa respectively. The bone cement setting temperature is less than 60°C.

Hank solution immersion test

After immersion in Hank solution at 37°C for 7 d, the Osteo-G bone void filler surface was covered with a hydroxyapatite(Hap) like coating. From EDX, the coating Ca/P ratio was around 1.68, close to the stoichiometric ratio of HAp at 1.68, indicating HAp-like material was formed. (**Fig 5**).

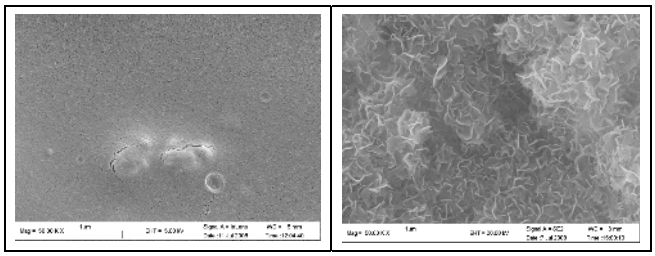


Fig. 5 SEM image of linoleic acid functionalized Sr-HA nanorod before immersion (left) after immersion in Hank solution (right).

Rat tibia μ*CT*

From Fig. 6 significant bone growth was observed near the bone cement implanted area.

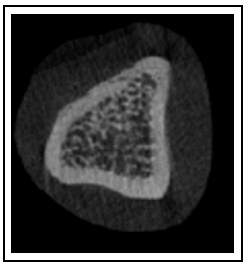


Fig. 6 microCT image of bone cement boundary area after 4 weeks implantation.

IV. Discussion

The kink on linoleic and oleic acid decrease the packing efficiency on the strontium hydroxyapatite nanorod surface that favors higher directional growth along c-axis. During hydrothermal treatment process oleic acid polymerization reduce oleic acid concentration leading to formation of both low aspect ratio and high aspect ratio nanorod. From dynamic light scattering analysis, linolenic acid functionalized nanorod has aggregate size larger than 1μm. Highly branched linolenic acid cannot stabilize the strontium hydroxyapatite nanorod by steric hindrance due to poor packing.

Oleic acid on the strontium hydroxyapatite surface was thermal polymerized to form a single layer polymer layer under hydrothermal condition. This layer is not biocompatible that lead to increase cytotoxicity of oleic acid functionalized Sr-HA.

Due to presence of two double bonds, the kinky linoleic acid is less susceptible to thermal polymerization. The thermal polymerized oleic acid lead to higher cytotocity of oleic acid functionalized Sr-HA nanorod.

V. Conclusion

High aspect ratio Sr-HA can be synthesized with linoleic and oleic acid. After soaking in Hank solution, HAp-like material was formed, thus indicating the cement is bioactive. Linoleic acid functionalized strontium hydroxyapatite nanorod showed optimal aspect ratio, proliferation rate, and cytotoxicity profile. Hydrophobic coating on functionalized nanorod improved resin compatibility. Addition of linoleic acid functionalized nanorod filler reduces the setting temperature and monomer release from the reinforced bone cement.

After 2 months of implantation, no inflammatory response was observed. From μCT images significant bone growth was observed near the cement implanted area. This suggests Sr-HA nanorod reinforced bone cement can stimulate bone growth via local release of strontium ions.

Lower setting temperature and stiffness also improve the safety in using this new cement in compressive dominant application such as vertebroplasty.

Acknowledgment

Present study was supported in part by Innovation Technology Fund (GHP 009-06) and Research Grant Council (RGCHKU7147/07E). We thank Electron Microscopy Unit for TEM analysis.

REFERENCES

1. Goto K, Tamura J, Shinzato S, Fujibayashi S, Hashimoto M, Kawashita M, et al. (2005) Bioactive bone cements containing nano-sized titania particles for use as bone substitutes. Biomaterials 26(33):6496-6505.
2. Ni GX, Choy YS, Lu WW, Ngan AHW, Chiu KY, Li ZY, et al. (2006) Nano-mechanics of bone and bioactive bone cement interfaces in a load-bearing model. Biomaterials 27(9):1963-1970.
3. Xu HHK, Burguera EF, Carey LE. (2007) Strong, macroporous, and in situ-setting calcium phosphate cement-layered structures. Biomaterials 28(26):pp3786-3796.
4. X. Wang (2006) Liquid-Solid-Solution Synthesis of Biomedical Hydroxyapatite Nanorods.. Adv. Mater 18:p. 2031-2034. DOI:10.1002/adma.200600033.
5. Lu HB, Ma CL, Cui H, Zhou LF, Wang RZ, Cui FZ. (1995) Controlled crystallization of calcium phosphate under stearic acid monolayers. Journal of Crystal Growth 155(1-2):pp120-125.

The HIV Dynamics is a Single Input System

M.J. Mhawej[1], C.H. Moog[1] and F. Biafore[2]

[1] IRCCyN, UMR-CNRS 6597, Ecole Centrale de Nantes, France
[2]National University of San Martin, School of Science and Technology, Argentina

Abstract — **Modeling, identification and control issues for the HIV infection are challenging issues since the infection spreads worldwide at an alarming rate. Based on real clinical data, the analysis of the impact of antiretroviral therapy on the HIV dynamics shows that the system is essentially a single input system in the sense that one single parameter is mostly affected by the drugs. This result has a strong implication on the design of control strategies.**

Keywords — **HIV, non linear systems, control inputs, therapy effect, parameter identification**

I. Introduction

Treatment of human immunodeficiency virus (HIV) remains a major challenge and it is reported that in 2007, 33.2 million of people were living with HIV/AIDS, 2.5 million people were newly infected and 2.1 million people died due to development of AIDS [1].

Most of the currently available anti-HIV drugs fall into one of two categories: Reverse Transcriptase Inhibitors (RTIs) and Protease Inhibitors (PIs). From a system theoretic approach, these families of drugs represent independent "control inputs" whose role is detailed hereafter. On one hand, RT inhibitors prevent HIV RNA from being converted into DNA, thus blocking integration of the viral code into the target cell. On the other hand, protease inhibitors affect the viral assembly process in the final stage of the viral life cycle, preventing the proper structuring of the viral proteins before their release from the host cell. Highly Active Antiretroviral Therapy (HAART) is the most prevalent treatment strategy for HIV infected patient. It uses two or more drugs, typically one or more RTI and one PI. However, these drugs have a number of side effects on vital human functions. Mathematical models may become an important tool in the quest for optimal dosage strategies because of their ability to predict the response of the average patient to medication.

Analysis and control of HIV dynamics gets an increasing interest from control engineers during these recent years [2], [3]... Optimization of the therapy and the minimization of the costs are open problems. In [4], Kirschner et al. derive an optimal control law which maximizes the population of healthy CD4 cells and minimizes the treatment side effects and costs. On another hand, Shim et al. propose in [5] a control scheme which stimulates the precursors CTLs to drive the patient to the state of a long-term non progressor (LTNP) which doesn't develop AIDS. Many other contributions to therapeutical strategies design may be found, such as model predictive control [5], [6], structured treatment interruptions [7], exact linearization and feedback linearization [8].

The majority of previous studies consider the HIV dynamics as a system with two independent control inputs, each input being related to one of the two drug types *i.e* RTIs and PIs. To the best of our knowledge, it is not confronted to real clinical data. The aim of this work is to check the accuracy of this scheme which is taken for granted in a wide range of contributions [5], [7], [9], [10], [11]. This kind of studies has a great impact on control laws design. In fact, as, said earlier, many control schemes are being developed for the HIV dynamics but their application remains questionable due to the validation of the model. In this paper, we show that the two families of drugs essentially act on one same single model parameter. Thus, the HIV dynamics reduces to a single input system. This conclusion follows from real clinical data analysis.

In Section II, we recall the basic third order model which is used. Section III describes the identification technique used in the paper. Section IV presents the major result of this paper. It states that the HIV dynamics is a single input system based on real clinical data analysis. In Section V we show that the single input system is accessible and fully linearizable by state feedback. Full and partial linearization are also detailed in this section. Section VI concludes.

II. Modelling the infection dynamics

The basic modelling of the HIV/AIDS dynamics is described by a 3-dimensional (3D) continuous-time model ([12], [9]). This model, given by equation (1), includes the dynamics of the uninfected CD4+ T-cells, the infected CD4+T-cells, and the virions.

$$\begin{cases} \dot{T} = s - \delta T - \beta TV, \\ \dot{T}^* = \beta TV - \mu T^*, \\ \dot{V} = kT^* - cV. \end{cases} \tag{1}$$

Chwee Teck Lim, James C.H. Goh (Eds.): ICBME 2008, Proceedings 23, pp. 1263–1266, 2009
www.springerlink.com

T (CD4/mm^3) represents the amount of uninfected CD4+ T cells, T*(CD4/mm^3) represents the amount of the infected CD4+ T cells and V (RNA copies/ml), the free virions. Healthy CD4+ T-cells are produced at a constant source rate s. Free virus particles infect uninfected cells at a rate proportional to T and V (βTV) and are produced at a rate proportional to T* (kT*). δ, μ and c are the death rates of the uninfected CD4+ cells, infected CD4+ cells and the virus.

III. Parameter identification

According to identifiability theory presented in [13], it is shown that the presented 3D model (1) is algebraically identifiable from output measurements, namely the viral load (V) ant the total CD4 count (T + T*) ([14], [15], [16]).

The identification of all the parameters of the 3D model from standard clinical data was first introduced in [17]. This approach was based on the nonlinear simplex optimization method. A new estimation method was introduced in [18]. It is based on a Monte-Carlo approach which is heuristic and relies also on the simplex optimization algorithm. This method enables having stable and robust results even for ill conditioned problems as it is the case for HIV dynamics. It is implemented in a software available at [19]. The estimations results presented in section IV were directly obtained with this software. The reader can refer to [18], [14], [15], [16] for further details.

IV. Control inputs

A. Parameters sensitivity to therapy: State of the art

Commonly, an HIV/AIDS therapy includes some RTIs and some PIs. The action of RTIs is to block the production of new viral particles since they inhibit the reverse transcription of viral RNA into viral DNA. According to [9], [7], [10], [5], and [11], their action is on parameter β. On another hand, the PIs affect the natural life cycle of the virus by prohibiting the maturation of new virions. As a result, the newly produced virions are defectuous. The PIs effect is admitted to be on parameter k ([9], [7], [10], and [11]). Parameters s, δ, μ and c are usually assumed not to be affected by drugs which is coherent with their biological meaning. When therapy effects are taken into consideration, model (1) reads as follows:

$$\begin{cases} \dot{\mathrm{T}} = \mathrm{s} - \delta \mathrm{T} - \overline{\beta}\mathrm{TV}, \\ \dot{\mathrm{T}}^* = \overline{\beta}\mathrm{TV} - \mu \mathrm{T}^*, \\ \dot{\mathrm{V}} = \overline{\mathrm{k}}\mathrm{T}^* - \mathrm{cV}. \end{cases} \quad (2)$$

where $\overline{\beta} = (1-\eta_{\mathrm{RTI}})\beta$ and $\overline{\mathrm{k}} = (1-\eta_{\mathrm{PI}})\mathrm{k}$ with η_{RTI} and η_{PI} denoting the effectiveness of RTIs and PIs respectively. Thus, the HIV dynamics is a two control inputs system. To the best of our knowledge, little work has been done to validate the above theoretic modelling. The aim of the next section is to show how drugs affect model parameters, based on clinical data from the CHU de Nantes.

B. Parameters sensitivity to therapy: Clinical data results

1. For each of the six patients involved in this study, identification of model parameters was performed twice. The first set of parameters was evaluated using the pre-treatment clinical data and the second using the post-treatment clinical data. Results are depicted in Table (1).Calculation shows that parameters β and k are most sensitive to treatment and that parameter k is much more sensitive to treatment than parameter β.

Table 1 Pre and Post treatment values of parameters k and β

ID	Pre-treatment values		Post-treatment values		Ratio	
	β	k	$\overline{\beta}$	$\overline{\mathrm{k}}$	$\beta/\overline{\beta}$	$\mathrm{k}/\overline{\mathrm{k}}$
P1	1.22E-6	167	5.46E-7	35.1	2.23	4.76
P2	9.05E-7	663	6.66E-7	405	1.36	1.64
P3	8.98E-7	360	2.37E-7	0.037	3.79	9729.7
P4	8.7E-7	79.6	5.94E-7	0.197	1.46	404.6
P5	9.63E-7	633	8.29E-7	64.70	1.16	9.78
P6	1.79E-6	390	1.04E-6	129	1.73	3.02

2. Case of a 7th patient
   This patient started regular therapy for two weeks and then entered in a non-observance phase. Parameters evaluated for this patient are illustrated in Table (2). which confirms that parameter k, *i.e* the production rate of virus, is more sensitive to treatment than parameter β. We argue from the real clinical data analysis that the HIV dynamics system is a single input system.

Table 2 The specific case of patient 7

Regular treatment		Non-observance Phase	
$\overline{\beta}$=1.88E−7	$\overline{\mathrm{k}}$=56	β=1.75E−7	k=1300

C. Discussion

From the results above, one can conclude that

- RTIs and PIs effects can not be considered to be decoupled, at least on the 3D model (1).
- Therapy (*i.e* the combination of the RTIs and the PIs) affects parameter k much more than parameter β.

This conclusion yields to the following single input system:

$$\begin{cases} \dot{T} = s - \delta T - \beta TV, \\ \dot{T}^* = \beta TV - \mu T^*, \\ \dot{V} = (1-u(t))kT^* - cV. \end{cases} \quad (3)$$

where u(t) ($0 \le u(t) \le 1$)denotes the single input affecting parameter k. It represents the efficacy of the whole therapy.

V. Analysis and Control of the Single Input Model

A. Accessibility of the single input HIV 3D model

Definition 1: Accessibility of a nonlinear system

Let $\dot{x} = f(x) + g(x).u$, be a nonlinear system, where f and g are analytic functions. The system is accessible [20] if there exists a positive integer k such as $\forall i \ge k, H_i = \{0\}$, where $\begin{cases} H_1 = \text{span}\{dx_i, 0 \le i \le n\} \\ H_k = \text{span}\{\omega \in H_{k-1}, \dot{\omega} \in H_{k-1}\}, \text{for } k \ge 2 \end{cases}$

For system (3), $H_4 = \{0\}$ if $\delta \ne \mu$ .Thus system (3) is accessible and fully linearizable since all integrability conditions are fulfilled.

B. Feedback linearization

Input-output linearization is a common approach used in controlling nonlinear systems. Let

$$\begin{cases} \dot{x} = f(x) + g(x)u \\ y = h(x) \end{cases} \quad (4)$$

be a nonlinear system. Using the nonlinear geometric control theory, the procedure consists on finding a change of variables (diffeomorphism) $z = P(x)$ and a state feedback, $u(t) = a(x) + b(x)v$ that transforms the nonlinear input-output system to an equivalent linear form. Then, a controller v is designed for the obtained linear system.

Definition 2: Relative Degree

The SISO system given by (4) is said to have a relative degree r if $\begin{cases} L_g L_f^k h(x) = 0 \text{ for all } k \le r-1 \\ L_g L_f^{r-1} h(x) \ne 0 \end{cases}$

Considering this definition of relative degree, the relative degree of system (4) can be considered as the number of times we have to differentiate the output y to have an explicit dependence on the input u.

For the controlled model (3) we have:

$$f(x) = \begin{bmatrix} s - \delta T - \beta TV \\ \beta TV - \mu T^* \\ kT^* - cV \end{bmatrix}, g(x) = \begin{bmatrix} 0 \\ 0 \\ -kT^* \end{bmatrix} u(t) \quad (5)$$

The goal of the control input u(t) is to keep the system around the equilibrium point $\left(T_0 = s/\delta, T_0^* = 0, V_0 = 0\right)$. Although the full linearization of system (3) is theoretically possible, simulation of its implementation was extremely sensitive to initial conditions and parameter values. Moreover, the complexity of the computations generated several numerical problems. To reduce this complexity and prevent initial conditions and parameters sensitivity, a partial linearization of the system is proposed hereafter, which also leads to the desired equilibrium point.

- Partial linearization

Let $y = h(x) = T - T_0$ be the linearizing output. In this case, the system has a relative degree equal to 2 and is partially linearizable. Consider the following change of coordinates $z = \begin{bmatrix} z_1 \\ z_2 \end{bmatrix} = \begin{bmatrix} h(x) \\ L_f h(x) \end{bmatrix}$ and the input $u(t) = \dfrac{v - L_f^2 h(x)}{L_g L_f h(x)}$. To complete the coordinate change we choose $\varphi = T^*$. Thus, system (3) is equivalent to the linear system (6) associated to the zero dynamics $\dot{\varphi}$.

$$\begin{bmatrix} \dot{z}_1 \\ \dot{z}_2 \end{bmatrix} = \begin{bmatrix} 0 & 1 \\ c_1 & c_2 \end{bmatrix} \begin{bmatrix} z_1 \\ z_2 \end{bmatrix}, \ (\dot{z}_2 = v = c_1 z_1 + c_2 z_2)$$
$$\dot{\varphi} = \beta TV - \mu\varphi = \beta(z_1 + T_0)\left[\frac{z_2 - s + \delta(z_1 + T_0)}{-\beta(z_1 + T_0)}\right] - \mu\varphi \quad (6)$$

Constants c_1 and c_2 are chosen to ensure the stability of (6) at $z_1 = z_2 = 0$. In this case, $\dot{\varphi}\big|_{z_1 = z_2 = 0} = -\mu\varphi$, and the zero dynamics is asymptotically stable. The input u(t) is depicted on Figure 1. Treatment starts at day 50 and ends by day 375. Figure 1 is a simulation of the partial linearization feedback control after suitable pole placement.

One major advantage of this control scheme is its ability to minimize the viral load by the means of a time-varying effectiveness of the drugs. This means that if the effectiveness of the drug is related to its dosage, no full dosage is needed all the time.

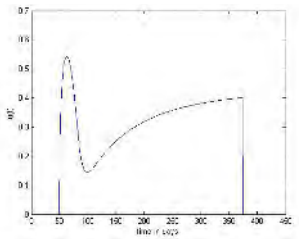


Fig. 1 The control input

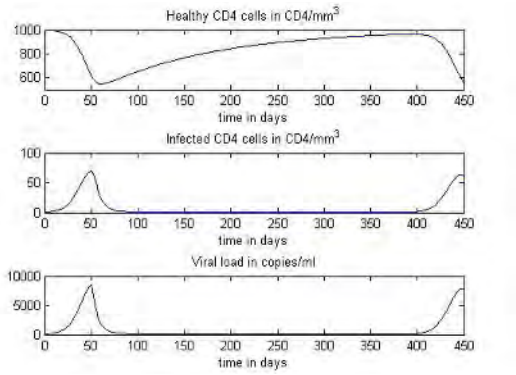


Fig. 2 Infection evolution

VI. Conclusion and perspectives

The main point in this paper was to show that the HIV dynamics is a single input system, based on clinical data analysis. The main contributions of this work are:

- the confrontation of the literature assumptions to real clinical data to get some hints about therapy effects on model parameters
- the proposition of a simplified model, with one single input describing the therapy effect
- the design and simulation of a linearizing control law as an illustration of the feasability of common control strategies on the proposed model.

One perspective of this work is to include pharmacokinetics and pharmacodynamics of antiretroviral drugs.

Acknowledgment

This work was supported by a CNRS-INRIA/MINCyT project.

References

1. UNAIDS and The World Health Organization. AIDS epidemic update. 2007.
2. R. Zurakowski and D. Wodarz. Treatment interruptions to decrease risk of resistance emerging during therapy switching in HIV treatment. In 46th IEEE Conference on Decision and Control, New Orleans, LA, USA, December 2007.
3. A. Chang, H. Astolfi. Immune response's enhancement via controlled drug scheduling. In 46th IEEE Conference on Decision and Control, New Orleans, LA, USA, December 2007.
4. D. Kirschner, S. Lenhart, and S. Serbin. Optimal control of the chemotherapy of HIV. J. Math. Biol, 35:775–792, 1997.
5. H. Shim, S.-J. Han, H. Shim, S.W. Nam, and J.H. Seo. Optimal scheduling of drug treatment for HIV infection: Continuous dose control and receding horizon control. International Journal of Control, Automation, and Systems, 1(3), September 2003.
6. R. Zurakowski and R.A. Teel. A model predictive control based scheduling method for HIV therapy. Journal of Theoretical Biology, pages 368–382, July 2006.
7. M.A. Jeffrey, X. Xia, and I.K. Craig. When to initiate HIV therapy : A control theoretic approach. IEEE Transactions on Biomedical Engineering, 50(11):1213–1220, 2003.
8. F. Biafore and C.E. D'Attellis. Exact linearisation and control of an HIV-1 predator-prey model. In 27th Annual International Conference of the IEEE Engineering in Medecine and Biology Society, Shanghai, China, September 2005.
9. A.S. Perelson and P.W. Nelson. Mathematical analysis of HIV-1 dynamics in vivo. SIAM Review, 41(1):3–44, 1999.
10. I. Craig and X. Xia. Can HIV/AIDS be controlled? IEEE Control sytems Magazine, pages 80–83, February 2005.
11. B.M Adams, H.T. Banks, Hee-Dae Kwon, and Hien T. Tran. Dynamic multidrug therapies for hiv: Optimal and sti approaches. Mathematical Biosciences and Engineering, 1(2), september 2004.
12. M.A. Nowak and R.M. May. Virus dynamics: Mathematical principles of immunology and virology. Oxford University Press, 2002.
13. X. Xia and C.H. Moog. Identifiability of nonlinear systems with application to HIV/AIDS models. IEEE Transactions on Automatic Control, 48(2):330–336, February 2003.
14. D.A. Ouattara and C.H. Moog. Modelling of the HIV/AIDS infection: an aid for an early diagnosis of patients. In Biology and control theory: current challenges, volume Springer Series in Lecture Notes in Control and Information Sciences (LNCIS). Springer Verlag, 2007.
15. D.A. Ouattara. Modélisation de l'infection par le VIH, identification et aide au diagnostic. PhD thesis, Ecole Centrale de Nantes & Université de Nantes, Nantes, France, September 2006.
16. D.A Ouattara, M.J Mhawej, and C. Moog. Clinical tests of therapeutical failures based on mathematical modeling of the hiv infection. Joint special issue of IEEE transactions on circuits and systems and IEEE transactions on Automatic Control, Special issue on systems biology, pages 230–241, jan 2008.
17. R.A. Filter and X. Xia. A penalty function to HIV/AIDS model parameter estimation. In 13th IFAC Symposium on System Identification, Rotterdam, 2003.
18. D.A. Ouattara. Mathematical analysis of the HIV-1 infection: Parameter estimation, therapies effectiveness, and therapeutical failures. In 27th Annual International Conference of the IEEE Engineering in Medecine and Biology Society, Shanghai, China, September 2005.
19. D.A. Ouattara, M.-J. Mhawej, and C.H. Moog. IRCCyN web software for the computation of hiv infection parameters. Available at http://www.irccyn.ec-nantes.fr/hiv.
20. G. Conte, C. H. Moog, and A. M. Perdon. Algebraic Methods for Nonlinear Control Systems. Springer, London, U.K., 2nd edition, 2006.

Marie-José Mhawej
IRCCyN, Ecole Centrale de Nantes, Bat S bureau 212
1, rue de la Nöe BP 9201, 44321 Nantes Cedex 03-France

Evaluation of Collagen-hydroxyapatite Scaffold for Bone Tissue Engineering

Sangeeta Dey, S. Pal*

School of Bioscience and Engineering, Jadavpur University, Kolkata-700032, India

Abstract — **The regeneration of diseased or fractured bones is the challenge faced by current technologies in tissue engineering. Tissue engineering is a new and exciting technique which has the potential to create tissues and organs *de novo*. It involves the *in vitro* seeding and attachment of human cells onto a scaffold. These cells then proliferate, migrate and differentiate into the specific tissue while secreting the extracellular matrix components required to create the desired tissue.Hydroxyapatite and collagen composites (Col-HA) have the potential in mimicking and replacing skeletal bones. In this study, Type I collagen isolated from animal tendons and synthesized Hydroxyapatite were used in different proportions. SDS-PAGE characterization results of protein extracted and purified has showed that bovine type I collagen was successfully obtained. Scaffolds were prepared by controlled freezing and lyophylization of corresponding composite solutions and cross linked using glutaraldehyde (0.3%). The properties of collagen and its composite scaffolds, such as microstructure, chemical, physical, swelling mechanical and degradable properties were studied. Compared to a single component scaffold, the addition of hydroxyapatite to collagen decreased the mean aperture but increased the swelling ability,mechanical stability,biodegradability In enzymatic degradation test, crosslinked scaffolds showed significant enhancement of the resistance to collagenase activity in comparison with non-crosslinked scaffolds. Hydroxyapatite could significantly prolong the biodegradation of collagen-HA scaffolds. FT-IR indicated the presence of bonds between Ca^{2+} ions of HA and R-NH_2 ions of collagen in the composite scaffolds The FTIR spectra result shows that addition of HA in the scaffolds does not alter the structure of collagen. Hence, the novel developed biocomposites have high potential to be used for rebuilding small lesions in bone tissue engineering.**

Keywords — **collagen, Hydroxyapatite, scaffolds, tissue engineering, bone substitute**

I. Introduction

Tissue engineering aims to produce biological substitutes which may overcome the limitations of conventional clinical treatments for damaged tissues or organs. One of the principle methods behind tissue engineering involves growing the relevant cell(s) in vitro to form the required tissue, or organ, before inserting into the body. To achieve this goal the cells must attach to a three dimensional (3D) substrate, known as a scaffold. The scaffold provides the initial extra-cellular matrix required to support the cells and may also define the micro- and macro-structure of the desired-engineered structure [1].The scaffold therefore is a key component of tissue engineering. Several requirements have been identified as crucial for the production of tissue engineering scaffolds. These are that the scaffold should: (1) have appropriate surface chemistry to favour cellular attachment, differentiation and proliferation; (2) be made from a biodegradable or bioresorbable material, that degrades at an appropriate rate with no undesirable byproducts, so that tissue will eventually replace the scaffold; (3) possess adequate mechanical properties to match the intended site for implantation and handling, (4) be easily fabricated into a variety of shapes and sizes and (5) possess interconnecting porosity so as to favour tissue integration and vascularisation [2].

Bone tissue engineering is aimed at repairing diseased or fractured bone, which cannot be replaced naturally. Skeletal tissue is a highly organised structure comprising mainly type I collagen, nanometre sized carbonate-substituted hydroxyapatite crystals, water and various other non-collagenous proteins. Alike many extracellular matrix proteins, collagen type I presents natural binding sites such as the Arg-Gly-Asp (RGD) and the Asp-Gly-Glu-Ala (DGEA) peptide sequence that modulates the adhesion of osteoblasts and fibroblasts [3, 4]. On the other hand, hydroxyapatite is osteoconductive and a good source of calcium and phosphate ions necessary for the survival and proliferation of cells. Although collagen and apatite-based products have been widely used individually in biomedical applications, their combination should prove beneficial for bone tissue engineering due to their natural biological resemblance and properties [5].

II. Material and methods

Collagen Isolation: In this study, Type I collagen was extracted from Sprague dawley rat tail tendon according to the method of Liu *et al*. Sprague Dawley rat tails obtained from the animal house of IICB. This was based on the protocol followed by Liu *et al*[6] with slight modifications. Hydroxyapatite was prepared by synthesis of microwave.

Determination of collagen purity: The purity of isolated collagen was analysed using sodium dodecyl sulphate poly-

Chwee Teck Lim, James C.H. Goh (Eds.): ICBME 2008, Proceedings 23, pp. 1267–1270, 2009
www.springerlink.com

acrylamide gel electrophoresis (SDS-PAGE) according to the method of lammelli.[7].

Fabrication of scaffolds: The differently proportioned Hydroxyapatite -collagen scaffolds were prepared by controlled freezing and lyophylization of corresponding composite solutions

Cross-linking: For cross-linking, the fabricated porous scaffolds were immersed in cross-linking bath with glutaraldehyde of concentration of 0.3%, pH 8 for 2 h at room temperature, then washed by distilled water and lyophilized.

Table-1.Collagen-HA composites compositions

Specimen	Collagen: Hydroxyapatite (w/w)	Concentration of collagen solution (w/v) in acetic acid
Collagen	-	0.5%
CH1	1:2	0.5%
CH2	1:4	0.5%
CH3	1:6	0.5%

Characterization of scaffolds

SEM Study: The surface microstructures of the scaffolds in the cross-section positions before and after cross-linked with glutaraldehyde were observed under scanning electron microscope (SEM, Jeol Jsm 5200) operated at an accelerating voltage of 2-15 kV. The mean pore size of the scaffolds was determined by analysis of the SEM images by importing data to image-J software. Ten apparent pores were measured. The pores were measured in a perpendicular direction through the long axis and the minor axis. Then the average values were calculated and taken as the mean pore size.

Mechanical testing: The tensile strength of the scaffolds were evaluated on an Instron Material tensile testing machine 4204, UK using pneumatic grips with load cell 500N at room temperature. The cross-head speed was set at 1 mm min^{-1}. Four samples were tested for each composition. The specimens were of rectangular shape and the dimensions were measured with a dial calipers as per general practice. Three readings were taken at different positions and mean values were used to calculate the cross-section.

Swelling Study: The water absorption capacities of collagen-HA scaffolds were determined by equilibrium swelling studies [8]. Swelling studies of the scaffolds were carried out in PBS over 3 h periods until equilibrium was reached. Four scaffolds were taken from each specimen. The dry weights of the scaffolds were taken and dipped in 30 ml PBS solution in Petri dishes. The wet weights were taken at every 10 min interval upto 2 h. At each immersion interval, the samples were removed and the absorbed water gently removed with filter paper as much as possible. The samples were weighed accurately on a microbalance to 0.01 mg. The initial sample weight before immersion was recorded as W_o and the sample weight after each immersion interval was recorded as W_e. The percent swelling at equilibrium E_{sw} was calculated from the Flory-Huggins swelling formula:

$$E_{sw}= [(W_e - W_o)/ W_o)]\times 100$$

Infrared spectroscopic measurement and analysis: Infrared spectra were obtained in absorption mode using a FTIR spectrometer (Nicolet™ Thermo 380) from collagen-HA scaffolds.

Biodegradability Testing: In vitro degradation test of cross-linked collagen-HA scaffolds were performed using bacterial collagenase obtained from *Clostridium histolyticum* (EC 3.4.24.3, Sigma Chemical Co., St. Louis, MO. USA) with a collagenase activity of 300 units/mg. The *in vitro* degradation of collagen and its composite scaffolds were carried out at 37°C in 10 ml phosphate buffered solution (pH 7.4) containing collagenase in CO_2 incubator (Lishen –HF151UV). The dynamic degradation of the scaffolds of four different compositions with known dry weights were incubated at different concentrations of collagenases (0.1mg, 0.5 mg, 1 mg, 2 mg) for 24 h incubation and different variation of day.

Hemocompatibility Testing: The percentage Hemolysis of blood was measured using UV-VIS spectrophotometer by comparing the optical densities of the test and control group. The control was a standard biocompatible material. The optical densities were measured at 545 nm. The test was conducted according to ASTM protocol.

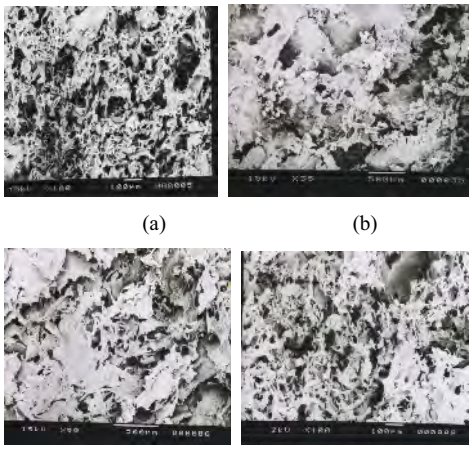
III. Results and Discussion

Characterization of composite scaffolds

The different tests were performed on collagen-hydroxyapatite scaffolds to evaluate its characteristics the results were discussed under following tests.

Microstructure evaluation: Figure 1(a), (b) and (c), (d) are Scanning Electron Microscope (SEM) photographs of the surface morphology and pore structure of single collagen and its composite scaffolds. Each scaffold demonstrated an open pore microstructure with a high degree of interconnectivity. Single collagen scaffolds appeared to be macro porous and the collagen-HA scaffolds appeared to have the same morphology but not so regular. The collagen scaffold showed an aperture of 50–100 μm while the composite scaffold showed a smaller aperture of 10–40 μm. of open

pore microstructure with a high degree of interconnectivity. These three-dimensional scaffolds provided a cellular matrix analog that could function as a necessary substrate for host cells to infiltrate and a physical support to guide the differentiation and proliferation of cells toward the targeted functional tissue or organ [9].



(a) (b)

(c) (d)

Fig 1. SEM of 4 different crosslinked & composite scaffolds
(a) collagen scaffold; (b) collagen HA (1:2),
(c) collage: HA (1:4); (d) collagen: HA (1:6)

Mechanical study: The scaffolds for bone tissue engineering should be mechanically stable to keep their structural integrity during the tissue regeneration. Compared with pure collagen (0.246 MPa), the ultimate strength of porous collagen-HA composites increases significantly (0.265 MPa for CHI, 0.323 MPa for CH2, 0.416 MPa for CH3 shown in figure. With the amount of HA incorporated into the collagen matrix increasing, the ultimate strength increases.

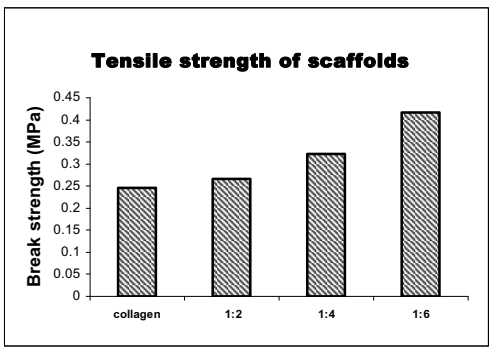


Fig 2. Ultimate strength of scaffolds with various collagen: HA (wt ratio)

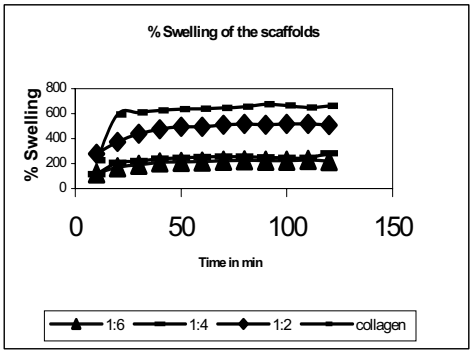


Fig 3. Percent swelling of scaffolds at different immersion intervals

Swelling Study: The swelling results of collagen scaffold was found to be 614 %, and that of the collagen-hydroxyapatite scaffolds of different compositions was decreasing (476.7 % for CH1, 237.3 % for CH2, 208.5 % for CH3) which was much less than that of collagen scaffolds. So by incorporation HA in collagen scaffolds drastically reduced the swelling. This reduction is expected as hydroxyapatite absorb negligible amount of water. Comparison of swelling of collagen and collagen–hydroxyapatite composite scaffolds is shown in figure3.

Infrared Analysis: Infrared spectrum of a composite scaffold after freeze drying is presented in Fig. 4. The FTIR spectra of composite scaffolds showed peaks at 3485.6 cm^{-1} and 1529.57 cm^{-1} due to -NH stretching and N-H bending of secondary amide of collagen I. The antisymmetric phosphate band (1200–1000 cm^{-1}) is characteristic of hydroxyapatite [10]. The data shows the phosphate stretching peaks at (1203.5 cm^{-1}) for hydroxyapatite. So the results indicate the presence of both collagen Type I and hydroxyapatite respectively in the composite scaffolds. It is also important that the HA does not affect the chemistry of collagen, as cells are shown to attach to a higher degree to surfaces containing natural binding sites [11]

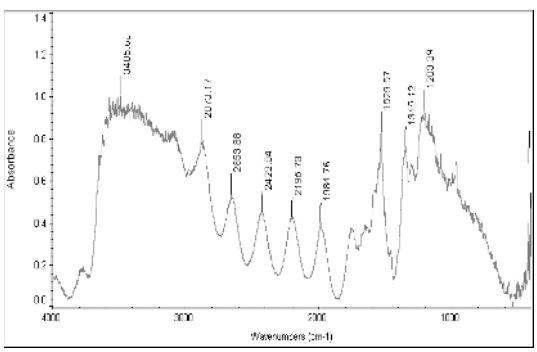


Fig 4. FTIR spectra of collagen-hydroxyapatite scaffold

Biodegradability Testing: In all of the collagenase solutions, crosslinked collagen-HA scaffolds have greater resistances to biodegradation than crosslinked collagen scaffolds The resistance of chemically modified collagen-HA scaffolds was greater than non-cross-linked samples, which was so easily dissolved in the collagenase solution that the degradation test of the scaffolds could not be performed. The dynamic degradation was found to be much faster between 2-6 days. After that the degradation was almost linear, because the activity of enzyme reduced significantly after that. It can depict that HA incorporation can provide collagen-HA scaffolds with improved mechanical property, as well as a reduced biodegradation rate.

Hemocompatibility Testing: The hemocompatibility of collagen and its composite scaffolds were evaluated by this hemolysis study. Blood compatibility is most important requirement for the blood interfacing biomaterials. The implants should not damage the proteins, enzymes or elements of blood (red blood cell, white blood cell and platelets). The results showed that by addition of HA into porous structure of collagen the % of hemolysis increased. The results indicated that collagen-HA composite scaffolds show less hemocompatible than the single collagen scaffolds.

IV. Conclusion

The results obtained in this work clearly showed that collagen and Hydroxyapatite are worthwhile perspectives for the development of composite scaffolds for bone tissue engineering. The biopolymer composite seems to be appropriate for the purpose of generating multifunctional solid surfaces triggering intensive bone cell growth.

Acknowledgment

The Indian Institute of Chemical Biology, Kolkata for providing the facilities for conducting the various tests, specially Dr .P. Das and his scholars

References

1. Langer R, Vacanti JP. Tissue engineering. Science 1993; 260: 920–6.
2. Hutmacher DW. Scaffold design and fabrication technologies for engineering tissues: state of the art and future perspectives. J Biomater Sci Polym E 2001; 12:107–24.
3. Dedhar S, Ruoslathi E, Pierschbacher MD (1987). A cell surface receptor complex for collagen type 1 recognizes the Arg-Gly-Asp sequence. *J. Cell Biol.* **104,** 585-593.
4. Staatz W. D.Fok K.F,Zutter M.M,Adams SP,Rodriguez BA,Santaro SA(1991)., Identification of a tetrapeptide recongnition sequence for the alpha 2 beta 1 integrin in collagen *J. Biol. Chem.* **266** (1991) 7363-7367
5. Lawson AC and Czernuszka JT (1998). Collagen–calcium phosphate composites. *Proc. Instr. Mech. Engg* **212 (11)**, 413–425.
6. Liu XD, Skold.'M.Umino T. Zhu Y.K, Romberger DJ, Spurzem JR, Rennard SI (2000). Endothelial cell-mediated type I collagen gel Contraction is regulated by hemin. J. Lab. Clin. Med. 136(2), 100-109.
7. Laemmli UK. Cleavage of structural proteins during the assembly of the head of Bacteriophage T4. Nature 1970; 227:680Ð5.
8. Shanmugasundaram, N., Ravichandran, P., Reddy, P.N., Ramamurthy, N., Pal, S. and Rao, K.P. (2001). Collagen–Chitosan Polymeric Scaffold for the In Vitro Culture of Human Epidermoid Carcinoma Cells, Biomaterials, 22:1943–1951.
9. Hutmacher, D.W. Goh, J.C.H. and Teoh, S.H. (2001). An Introduction to Biodegradable Materials for Tissue Engineering Applications, Ann. Acad. Med. Singapore., 30: 183–191.
10. Rehman I and Bonfield W (1997).Characterizations of hydroxyapatite and carbonated apatite by photo acoustic FTIR spectroscopy. J. Mater. Sci. Mater. Med. 8, 1.
11. Boyan BD, Hummert TW, Dean DD, Schwartz Z (1996). Role of material surfaces in regulating bone and cartilage cell response. Biomaterials 17, 137-146.

Author: Prof (Dr) Subrata Pal
Institute: Jadavpur University
Street: 188, Raja S.C. Mullick Road, Kolkata-700032
City: Kolkata
Country: India
Email: spalbme@yahoo.co.in

Effect of Sintering Temperature on Mechanical Properties and Microstructure of Sheep-bone Derived Hydroxyapatite (SHA)

U. Karacayli[1], O. Gunduz[2], S. Salman[2], L.S. Ozyegin[3], S. Agathopoulos[4], and F.N. Oktar[5,6]

[1] Oral Surgery Department, GATA, Ankara, Turkey
[2] Metal Education Department, Marmara University, Istanbul, Turkey
[3] Dental Technology Department, Marmara University, Istanbul, Turkey
[4] Material Science and Engineering Department, Ionnina University, Ionnina, Greece
[5] Radiology Department, Marmara University, Istanbul, Turkey
[6] Industrial Engineering Department, Marmara University, Istanbul, Turkey

Abstract — **Hydroxyapatite (HA) is currently one of the most attractive materials for human hard tissue implants because its close crystallographic resemblance to bones and teeth, conferring HA with excellent biocompatibility. Because of that fact as well as economic and time-saving reasons, we have stressed the need for safe production of HA-powders and ceramics from natural resources, such as animals' bones and teeth, or hydrothermal transformation of shell's aragonite.**

Nevertheless, the applications of pure HA-ceramics are limited to non load-bearing implants, because of HA's poor mechanical properties. Our research group has dedicated a lot of effort to achieve enhancement of mechanical strength and the fracture toughness of sintered HA-ceramics, mainly with HA-powder of natural origin, by fabricating composite materials of HA doped with various types of biocompatible oxides.

This work aims to present that bulk ceramics of pure HA (i.e. with no incorporation of any reinforcing phase), derived from sintered HA–powder obtained from calcinated (at 850°C) bones of sheep (SHA), exhibit the best mechanical properties ever measured for sintered HA ceramics (pure and composites) using naturally (i.e. animal bone) derived HA. The characterization of the new HA-ceramics comprised measurements of density and mechanical properties, namely compressive strength and Vickers microhardness, along with microstructure observation with scanning electron microscopy (SEM). The best mechanical properties were achieved in the samples sintered between 1200°C-1300°C; the highest value of compression strength was achieved after sintering at 1300°C, 180.75 MPa. SEM observations in conjunction with density measurements confirmed the good sintering ability of the SHA-powders to highly condense bulk HA-ceramics.

Keywords — **Hydroxyapatite, sheep derived hydroxyapatite, mechanical properties**

I. Introduction

Skeletal deficiencies, due to trauma, tumors, or abnormal growth, are quite common. Surgical intervention and grafting are usually applied to restore mechanical function and reconstruct the damaged areas. Approximately 500,000 bone grafting procedures are annually performed in the USA. Autogenous grafts feature the problems of the limitation of the available graft area and the fact of extra surgery. Synthetic or naturally derived hydroxyapatite (HA) is the most popular biomaterial for skeletal reconstructions. HA attracts considerable interest over the past two decades due to its excellent biocompatibility [1]. HA, which is the main mineral of bones and teeth, is among the leading grafting biomaterials [2]. Biological HA features several substitutions at the Ca^{2+}, PO_4^{3-}, and OH^- sites of its lattice, which also accommodates several trace elements of high importance in the biological performance of HA after implantation [3] during the osseointegration process [4]. Nevertheless, the brittleness of pure HA materials narrows their application only to low-load bearing applications, such as tooth root substitutes, filling of periodontal pockets, cystic cavities, regions adjacent to implants, spinal fusions, contour and malformation defects and nonunions of long bones [5]. Hence, the incorporation of other phases in HA matrix is indicated as a solution for expanding HA application in hard tissue biomaterials [2]. On the other hand it is well known that the incorporation of a ceramic reinforcement (i.e. fibres, whiskers, platelets or particles) in a ceramic matrix improves the mechanical properties. Nevertheless, with respect to monolitic matrix behavior, the presence of a reinforcement phase opposes somehow sintering process since a second phase is inserted in the matrix. In general, sintering is the term used to describe the consolidation of the product during firing. Consolidation implies that in the product, particles have joined together into strong aggregate. The term sintering is often interpreted to imply that shrinkage and densification have occurred [6]. It is now well recognized that the microstructure and properties of ceramics critically depend on processing routes and densification parameters [7].

HA can be produced chemically or from natural resources, such as hydrothermal converted aragonite from corals or with various methods from bones from humans or animals [8, 9]. There is no harm effect reported from HA which was prepared through chemical means [8]. Synthetic

Chwee Teck Lim, James C.H. Goh (Eds.): ICBME 2008, Proceedings 23, pp. 1271–1274, 2009
www.springerlink.com

HA is the most frequently used, but it does not completely match the chemical composition of bone [10]. HA materials which are prepared from bovine and human resources can be very safe when all safety procedures are sufficiently followed. The latter materials are prepared by treating them with diluted HCl acid, which de-mineralizes and freeze-dries the tissues. However, some diseases can survive all controlled processes. Prions, for example, which can alter themselves into very dangerous incurable forms, can survive such processes. Calcination at high temperature can solve this possible disease transmission problem. The deadly prions can not survive calcination temperatures as high as 850ºC [8]. Moreover, sintered BHA is absolutely safe from potentially transmitted diseases like bovine spongiform encephalopathy (BSE) and others [11]. BHA features advantages namely low production costs and high safety regarding elimination of any risk of transmitting of the fatal prion diseases [3]. Furthermore, since years the mad cow disease and others were never seen in many developed countries (including Turkey that this work was performed [12-15]).

There are very few papers in the open literature reporting on the composition of sheep bone. Jan *et al.* have completed some studies about distribution of some organic pollutants in sheep dental tissue and bone [16, 17].

Bellof *et al.* have conducted a study about the major components of bone tissue as Ca 12.92%, P 4.68%, Mg 2.22%, Na 1.20%, and K 9.56% [18].

The histological appearance of the long bone cortical bone of mature sheep is similar to that of goats. In mature goats, the long bone cortical bone consists of both plexiform and Haversian bone tissue. Ribs of mature sheep also display a mixture of secondary and primary tissue, with Haversian tissue serving as a replacement for plexiform tissue. The Haversian canals within the secondary tissue are classified as medium in size and irregular in shape. Hilliar and Bell have demonstrated that differentiation of human from certain nonhuman species is possible, including small mammals exhibiting Haversian bone tissue and large mammals exhibiting plexiform bone tissue. Pig, cow, goat, sheep, horse, and water buffalo exhibit both plexiform and Haversian bone tissue and where only Haversian bone tissue exists in bone fragments, while differentiation of these species from humans is not possible. Haversian system diameter and Haversian canal diameter are the optimal diagnostic measure to use [19].

This study aims, for the first time in the literature (to the knowledge of the authors) to determine the influence of sintering temperature on densification, the development of microstructure and the mechanical properties of sheep derived HA (SHA).

II. Materials and methods

The HA powder used in this study was derived from fresh sheep bones (SHA) which, after cutting into pieces and chemical de-mineralization, was calcined at 850ºC and finally milled into fine powder, according to the method described earlier by Oktar *et al.* [20]. 120 cylindrical compacts of BHA-powder (10 samples for each set of testing conditions) were prepared by dry uni-axial pressing in a steel die, according to British Standards (height = 11 mm, diameter = 11 mm). The compacts were sintered at 1000ºC, 1100ºC, 1200ºC, and 1300ºC for 4 h in air in an electric furnace (Nabertherm HT 16/17, Lilienthal, Germany), at a heating rate of 4 K/min. After sintering, the samples were let to slowly cool down inside the furnace. Measurements of density (using the Archimedes method), Vickers microhardness (200 g load) and compression strength were carried out on the sintered samples (The presenting average values and their standard deviation have been obtained from 10 different independent measurements made with 10 different samples). Compression tests were done with a universal test apparatus (Instron 1195, USA), with a crosshead speed of 2 mm/min. Microstructural observations at fracture surfaces (after chemical etching with acetic acid) were carried out by Scanning Electron Microscope (SEM, S-4100, HITACHI, Japan).

III. Results and discussions

The high temperature of calcination during SHA production (850ºC, [20]) implies that any possible disease existing in the original bone has been completely eliminated. Furthermore, earlier reports have suggested that interesting bioceramics could be produced from high-temperature calcined BHA. This has also been confirmed by cell culture and animal studies [21].

The SEM images of Figures 1 and 2 indicate typical densification of HA ceramics, suggesting that SHA behaves as a typical HA material. In particular, the samples largely maintain the features of the initial powder compact after firing at 1000ºC, suggesting poor sintering (Fig. 1). A completely different microstructure of high density, no porosity and big grains is developed after sintering at 1300ºC (Fig. 2). There is no evidence of glassy phase formation at large extent, which may cause brittleness of the material. Table 1 summarizes the experimental results of density, compression strength and Vickers microhardness of the SHA samples sintered at the four investigated temperatures. The results agree fairly well to the SEM images of Figures 1 and 2 since the denser samples were obtained after sintering at

the highest tested temperatures. Moreover, the denser samples exhibited the higher values of mechanical temperatures.

For comparison purposes, results reported in earlier studies [21-23] for bovine derived HA (BHA) materials sintered at the same temperatures are presented in the Tables 2 and 3. Similar results, where BHA was reinforced with 5% and 10% addition of commercial inert glasses (CIG), are also presented in the Tables 4 and 5, respectively [24].

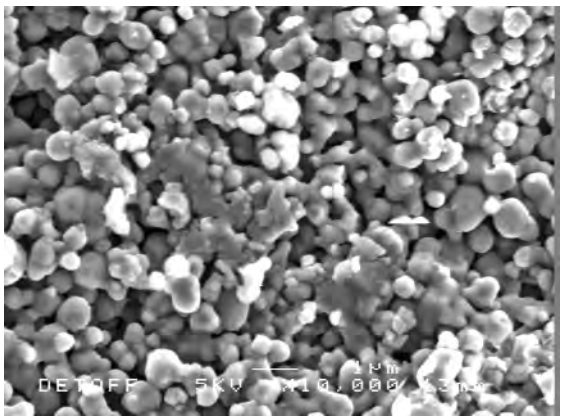


Fig. 1 Microstructure of SHA sintered at 1000°C.

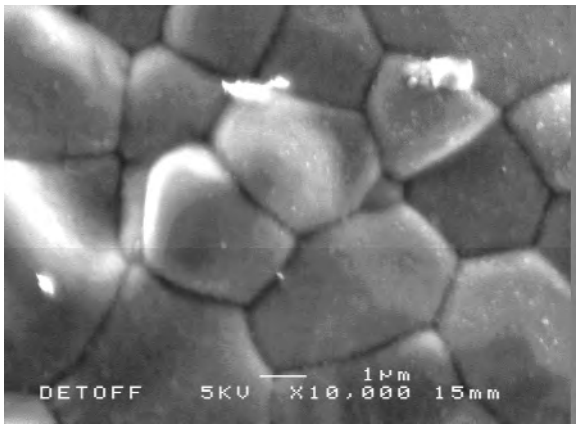


Fig. 2 Microstructure of SHA sintered at 1300°C.

Table 1 Density, compressions strength and Vickers microhardness of sheep derived hydroxyapatite (SHA) samples sintered at different temperatures.

T (°C)	d (g/cm^3)	σ (MPa)	$HV_{0.2}$
1000	2.019	30.1	95
1100	2.367	52.9	166
1200	2.841	118.7	262
1300	2.861	180.7	331

Table 2 Density, compressions strength and Vickers microhardness of bone derived hydroxyapatite (BHA) samples reported in Refs. 22 and 23.

T (°C)	d (g/cm^3)	σ(MPa)	$HV_{0.2}$
1000	2.46	50	85
1100	2.34	22	70
1200	2.59	80	150
1300	2.48	70	130

Table 3 Density, compressions strength and Vickers microhardness of bone derived hydroxyapatite (BHA) reported in Ref. 21.

T (°C)	d (gr/cm^3)	σ (MPa)	$HV_{0.2}$
1000	1.98	12	42
1100	2.59	23	92
1200	2.62	67	138
1300	2.72	60	145

Table 4 Density, compressions strength and Vickers microhardness of composites made of bone derived hydroxyapatite (BHA) matrix and reinforced with 5% additives of commercial inert glasses (CIG) reported in Ref. 24.

T (°C)	d (gr/cm^3)	σ (MPa)	$HV_{0.2}$
1000	2.52	48.3	98
1100	2.42	43.9	149
1200	2.48	67.6	202
1300	2.63	104.8	227

Table 5 Density, compressions strength and Vickers microhardness of composites made of bone derived hydroxyapatite (BHA) matrix and reinforced with 10% additives of commercial inert glasses (CIG) reported in Ref. 24.

T (°C)	d (gr/cm^3)	σ (MPa)	$HV_{0.2}$
1000	2.40	64.0	54
1100	2.41	77.0	135
1200	2.55	133.0	506
1300	1.77	6.9	307

The comparison of the results of the present study (Table 1) with the values of the Tables 2 and 3 suggests that SHA exhibited superior compression strength than the BHA materials. Similar conclusions are suggested for the microhardness as well.

From our reported earlier experience at reinforcing HA matrices, the addition of commercial inert glasses (GIC, 5% and 10%) in BHA resulted in composites with the best values of mechanical properties that we had ever measured (Tables 4 and 5 [23, 24]). Accordingly, the results of the

present study with SHA are even better than values obtained via the concept of producing composite materials. Moreover, SHA completely eliminates the addition of other phases, which may complex sintering processing and also may both jeopardize the biocompatibility of the resultant material and produce fragile phases due to the reaction between HA and the reinforcing phase.

IV. Conclusions

The results of this study indicate SHA as a very promising HA type of biological origin for producing biomaterials that may be successfully bear high loads. The highly dense and homogenous microstructure obtained after sintering at 1200°C and 1300°C resulted in superior values of compression strength and hardness, better even from values obtained by reinforced HA-composites.

Acknowledgments

This study was carried out with the financial support of the Turkish Republic Government Planning Organization in the framework of the Project "Manufacturing and Characterization of Electro-Conductive Bioceramics" (No 2003 K120810). This paper is also a result of collaboration between Marmara University and Georgia Institute of Technology, College of Engineering where Prof. S. Salman spends a sabbatical year. O. Gunduz acknowledges the support of Prof. M. Edirisinghe from University College London where he spends a sabbatical year.

References

1. Oktar FN (2006) Hydroxyapatite–TiO_2 composites. Mater Lett 60: 2207–2210.
2. Gunduz O, Daglilar S, Salman S et al (2008) Effect of Yttria-doping on Mechanical Properties of Bovine Hydroxyapatite (BHA). J Composite Mater 42: 1281-1287.
3. Gunduz O, Erkan EM, Daglilar S et al. (2008) Composites of bovine hydroxyapatite (BHA) and ZnO. J Mater Sci 43:2536–2540.
4. Rocha JHG, Lemos AF, Agathopoulos S et al. (2005). Scaffolds for bone restoration from cuttlefish. Bone 37: 850–857.
5. Goller G, Oktar FN (2002) Sintering effects on mechanical properties of biologically derived dentine hydroxyapatite. Mater Lett 56: 142–147.
6. Oktar FN, Goller G (2002) Sintering effects on mechanical properties of glass-reinforced hydroxyapatite composites. Ceram Int 28: 617–621.
7. Nath S, Sinha N, Basu B (2008) Microstructure, mechanical and tribological properties of microwave sintered calcia-doped zirconia for biomedical applications. Ceram Int 34: 1509–1520.
8. Goller G, Oktar FN, Ozyegin LS et al. (2004) Plasma-sprayed human bone-derived hydroxyapatite coatings: effective and reliable. Mater Lett 58: 2599– 2604.
9. Kurkcu M, Benlidayı ME, Ozsoy S, et al. (2008) Histomorphometric evaluation of implants coated with enamel or dentine derived fluoride-substituted apatite. J Mater Sci: Mater in Med 19: 59-65.
10. Carvalho AL, Faria PEP, Marcio Grisi MFM et al. (2007) Effects of granule size on the osteoconductıvıty of bovine and synthetic hydroxyapatite: A histologic and histometric study in dogs. J Oral Implant 33: 267-276.
11. Ozyegin LS, Oktar FN, Goller G et al. (2004) Plasma-sprayed bovine hydroxyapatite coatings. Mater Lett 58: 2605– 2609.
12. http://www.oie.int/eng/info/en_esbmonde.htm. Last update: 27 July 2007 (fr)
13. http://www.oie.int/eng/info/en_esbcarte.htm. Geographical Distribution of Countries that reported BSE Confirmed Cases since 1989. Last update: 04 January 2007
14. http://www.europa.eu.int/comm/food/fs/sc/ssc/outcome_en.html. Final Report on the assessment of the Geographical BSE-risk of Turkey 27 June 2002
15. Opinion of the Scientific Steering Committee on the Geographical Risk Of Bovine Spongiform Encephalopathy (GBR) in Turkey Adopted by the SSC on 27 June 2002
16. Jan J, Vrecl M, A. Pogacnik A, Gaspersic D (2001) Bioconcentration of lipophilic organochlorines in ovine dentine. Arch Oral Bio 46: 1111–1116.
17. Jan J, Milka V, Azra P et al. (2006) Distribution of organochlorine pollutants in ovine dental tissues and bone. Environ Toxic Pharma 21: 103–107.
18. Bellof G, Most E, Pallauf J(2006) Concentration of Ca, P, Mg, Na and K in muscle, fat and bone tissue of lambs of the breed German Merino Landsheep in the course of the growing period. J Animal Physio Animal Nut 90: 385–393.
19. Hillier ML, Bell LS (2007) Differentiating Human Bone from Animal Bone: A Review of Histological Methods. J Forensic Sci 52: 69-72
20. Oktar FN, Kesenci K, Piskin E (1999) Characterization of processed tooth hydroxyapatite for potential biomedical implant applications. Artif Cell Blood Subs Immob Biotech 27: 367-379.
21. Goller G, Oktar FN, Agathopoulos S et al. (2006) Effect of sintering temperature on mechanical and microstructural properties of bovine hydroxyapatite (BHA). J Sol-Gel Sci Techn 37: 111–115.
22. S. Goren, Gokbayrak H, S. Altintas (2004) Key Eng Mater 264–268: 1949-1952
23. H. Gokbayrak, Production of hydroxyapatite ceramics, M.S. Thesis, Bogazici University, 1996.
24. Salman S, Oktar FN, Gunduz O et al. (2007) Sintering Effect on Mechanical Properties of Composites Made of Bovine Hydroxyapatite (BHA) and Commercial Inert Glass (CIG). Key Eng Mater 330-332: 189-192.

Author: Umut Karacayli
Institute: GATA Oral Surgery Department
Street: General Teyfik Saglam Street
City: Ankara
Country: TURKEY
Email: ukaracayli@gmail.com

Flow Induced Turbulent Stress Accumulation in Differently Designed Contemporary Bi-leaflet Mitral valves: Dynamic PIV Study

T. Akutsu[1], and X.D. Cao[2]

[1] Dept. of Mech. Eng., Kanto Gakuin Univ., Yokohama, Japan
[2] Graduate School of Engineering, Kanto Gakuin Univ., Yokohama, Japan

Abstract — **Fluid stresses and duration of it on the blood component are considered influential to the cause of hemolysis, thromboembolic complications, and platelet activation. This experimental study was conducted to analyze the accumulated turbulent stresses generated by the differently designed prosthetic heart valves using Dynamic PIV system. Four bi-leaflet valves, the St. Jude Medical (SJM) and the On-X (OX) valves with straight leaflets and the Jyros (JR) and the MIRA (MIRA) valves with curved leaflets were used in the mitral position under pulsatile-flow condition. Dynamic PIV system was employed to trace the particular particle simulating blood element and to analyze the accumulated turbulent stresses on the particular particle by analyzing the time-resolved flow fields affected by the leaflet shapes, valve designs.**

Keywords — **Dynamic PIV, Bi-leaflet valves, Stress accumulation**

I. Introduction

Fluid stresses and duration of it on the blood component are considered influential to the cause of hemolysis, thromboembolic complications, and platelet activation. Experimental study was conducted to analyze the accumulated turbulent stresses generated by the differently designed prosthetic heart valves using Dynamic PIV system.

II. Models and Method

The study was carried out using a cardiac simulator [1] in conjunction with a high-speed (1000 frames/s) and high resolution (1024x1024) Dynamic PIV system for the mapping of the time resolved velocity and the turbulent stress distribution inside the simulated ventricle (Fig.1). Operating condition was simulating normal adult at resting condition: 120/80 mmHg at 72BPM. Saline solution was used as working fluid. Operating waveforms were the sinusoidal waveform.

Four bi-leaflet valves (Fig.2), the St. Jude Medical (SJM) and the On-X (OX) valves with straight leaflets and the Jyros (JR) and the MIRA (MIRA) valves with curved leaflets were tested in the mitral position under pulsatile-flow condition. Dynamic PIV system was used to trace the movement of the fluid particle and investigate the influence of the valve design differences of each valve on the accumulated turbulent stresses for traced particles using Dynamic PIV system.

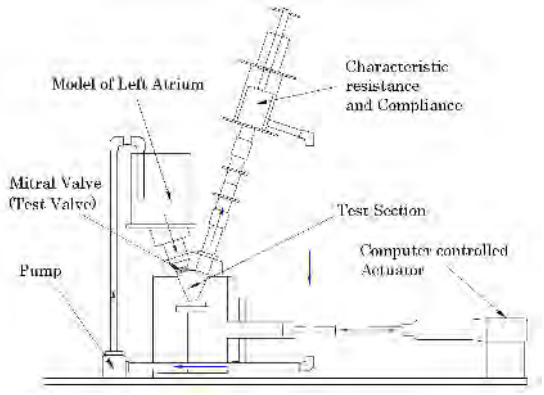
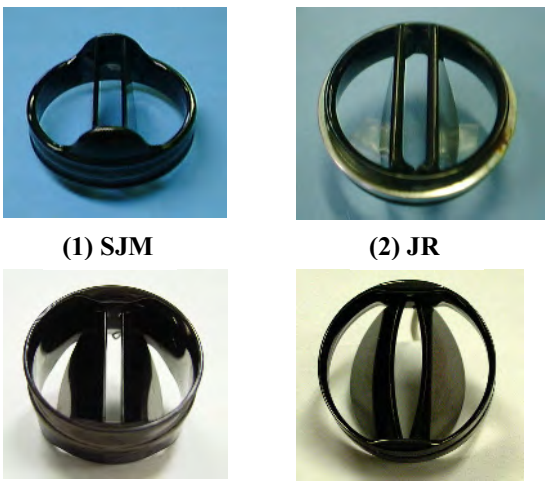


Figure 1 Schematic diagram showing the test facility



(1) SJM **(2) JR**

(3) OX **(4) MIRA**

Figure 2 Photographs showing the test valves: (1) the SJM valve, (2) the JR valve, (3) the OX valve, and (4) the MIRA valve

Chwee Teck Lim, James C.H. Goh (Eds.): ICBME 2008, Proceedings 23, pp. 1275–1278, 2009
www.springerlink.com

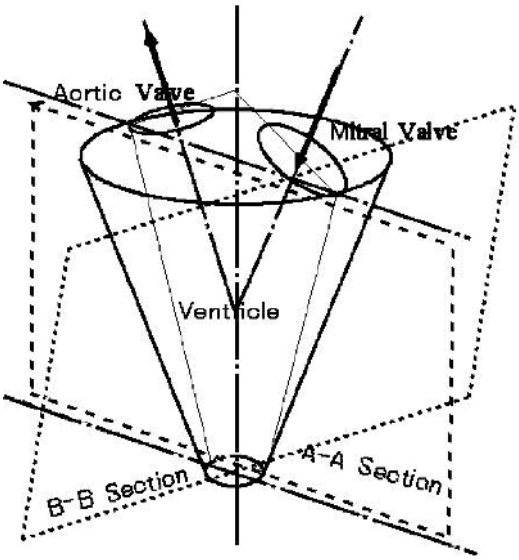


Figure 3 Two slit light sheet locations used for measuring velocity field

Since the flow inside the ventricle is three-dimensional in nature, two vertical planes were selected for PIV measurement (Fig.3). One measuring plane which passes through the centers of the aortic and the mitral valves (A-A section). The other measuring plane is normal to the previous plane and directly downstream of the mitral valve (B-B section).

III. Results and discussion

All valves showed distinct sideway flows immediately after the valve was opened, however, timing of the opening and degree of flow deflection differed widely among different designs. Noticeable differences on the three-dimensional flow were observed during the opening and accelerating flow phase of the valve (Fig.4). Straight leaflet of the OX valve did not deflect the flow when it fully opened, while curved leaflet of the JR and the MIRA valves deflected the flow sideway even the valve was fully opened. The OX and the MIRA valves open quickly and utilize central orifice more effectively than older designs. On the A-A section, flow near the ventricle wall (right flow on Fig. 5) tends to show higher accumulated stress level (Table 1). Because of these characteristic differences, the JR and the MIRA valves with curved leaflet on the B-B section tend to show higher accumulated stress at peripheral area (right flow on the Fig. 6), while the SJM and the OX valves with straight leaflet tend to show higher accumulated stress at more central area (Table 2). Newer valves also showed higher accumulated stress level.

Table 1 Averaged stress values for the SJM, the JR, the OX, and the MIRA valves: during period between accelerating to peak flow phase anti-anatomical orientation, A-A section

	Left flow stress (Pa)	Center flow stress (Pa)	Right flow stress (Pa)
SJM valve	1.63	3.722	5.887
JR valve	0.798	1.870	5.973
OX valve	6.492	5.839	9.887
MIRA valve	3.117	4.058	2.196

Table 2 Averaged stress values for the SJM, the JR, the OX, and the MIRA valves: during period between accelerating to peak flow phase anti-anatomical orientation, B-B section

	Right center flow stress (Pa)	Right mind flow Stress (Pa)	Right flow stress (Pa)
SJM valve	7.742	9.641	2.040
JR valve	7.004	3.448	16.407
OX valve	7.903	19.244	10.871
MIRA valve	7.249	15.306	21.394

IV. Conclusions

Newer designs open quickly and utilize central orifice more effectively than older designs but also showed higher accumulated stress level.

Acknowledgment

This work is partly supported by a Grant-in Aid for Scientific Research from the Japan Society for the Promotion of Science (Grant C-17591491).

References

1. Akutsu T, Saito J (2006) Dynamic particle image velocimetry flow analysis of the flow field immediately downstream of bileaflet mechanical mitral prostheses. J Artificial Organs 19: 165-178

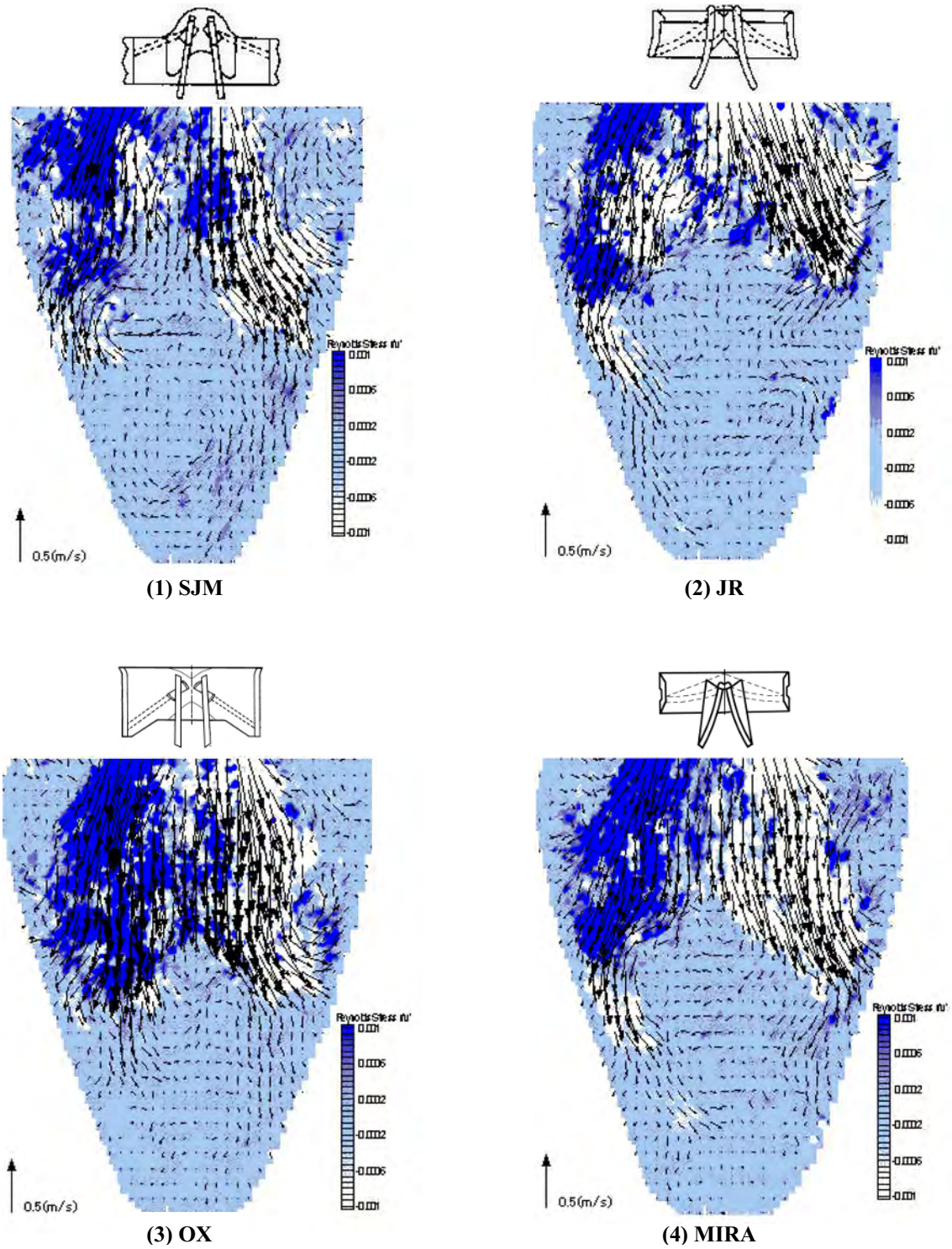
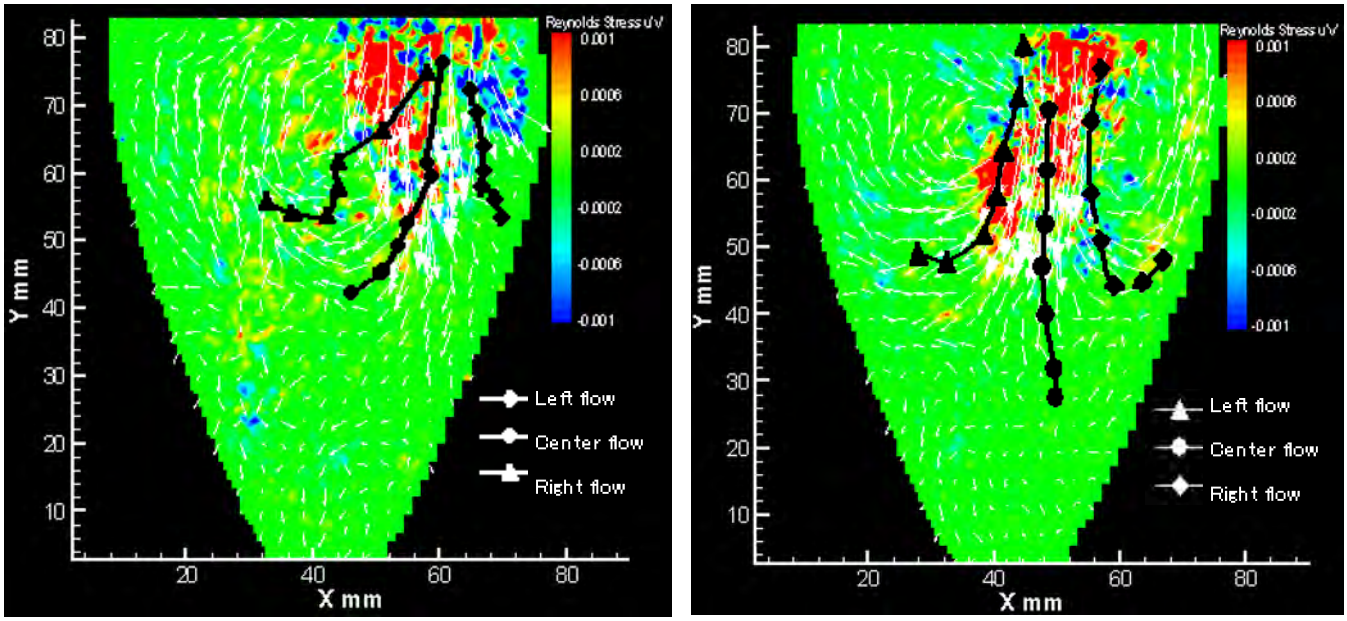
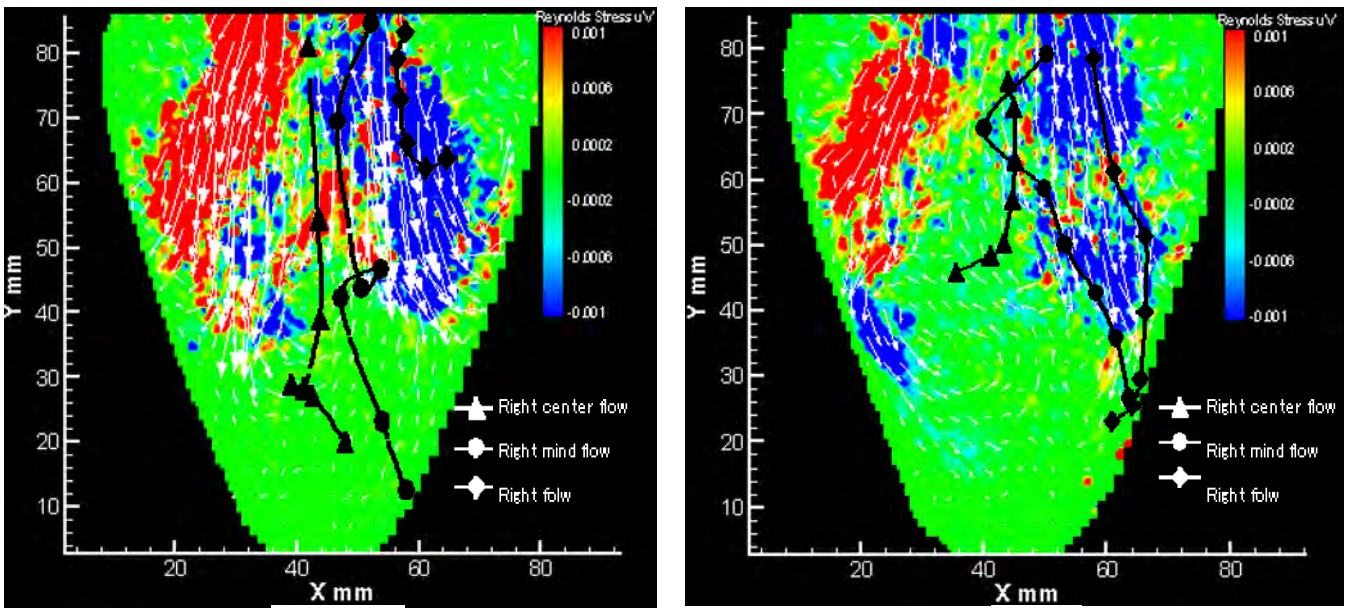


Figure 4 Figures showing the typical velocity and turbulent stress distribution at B-B section inside the simulated ventricle with the mitral valves in the anti-anatomical position during the late acceleration flow phase: (1) the SJM valve, (2) the JR valve, (3) the On-X valve, and (4) the MIRA valve (72BPM, Sinusoidal waveform, Saline solution)



SJM **JR**

Figure 5 Figures showing the typical velocity and turbulent stress distribution at A-A section inside the simulated ventricle with the mitral valves in the anti-anatomical position during the late acceleration flow phase: superimposing lines and symbols indicate the trace of particle through corresponding orifice locations; (left) the SJM valve, and (right) the JR valve (72BPM, Sinusoidal waveform, Saline solution)



SJM **JR**

Figure 6 Figures showing the typical velocity and turbulent stress distribution at B-B section inside the simulated ventricle with the mitral valves in the anti-anatomical position during the late acceleration flow phase: superimposing lines and symbols indicate the trace of particle through corresponding orifice locations; (left) the SJM valve, and (right) the JR valve (72BPM, Sinusoidal waveform, Saline solution)

A Biofunctional Fibrous Scaffold for the Encapsulation of Human Mesenchymal Stem Cells and its Effects on Stem Cell Differentiation

S.Z. Yow[1], C.H. Quek[2], E.K.F. Yim[3], K.W. Leong[2, 4], C.T. Lim[1, 3]

[1] National University of Singapore, Graduate Program in Bioengineering, Singapore, Singapore
[2] Duke University, Departments of Biomedical Engineering and Surgery, North Carolina, USA
[3] National University of Singapore, Division of Bioengineering, Singapore, Singapore
[4] Duke-NUS Graduate Medical School, Singapore, Singapore

Abstract — **We report a collagen based fibrous scaffold for the encapsulation and seeding of human mesenchymal stem cells. The scaffold was fabricated through interfacial polyelectrolyte complexation (IPC) of an anionic synthetic terpolymer and a cationic methylated collagen in aqueous conditions. The collagen in the fibers was labeled with quantum dots and was found to be evenly distributed in each fiber strand. Encapsulating human mesenchymal stem cells (hMSCs) into these collagen based fibers and maintaining the viability are steps towards the creation of a biofunctionalised scaffold and the existing problems of the lack of cell infiltration in scaffolds and effective nutrient/waste exchange can be overcome. This cell encapsulation in scaffolds technique is simple and least toxic compared to existing fabrication techniques. hMSCs were seeded onto the fibrous scaffold and compared with hMSCs encapsulated within the scaffold. The cytoskeletal organization of seeded hMSCs and encapsulated hMSCs were different and the results were correlated to the gene expressions of both samples.**

Keywords — **Stem Cell, Cell Encapsulation, Polyelectrolyte Complex Fibers, Collagen, Biomimetic Scaffold**

I. Introduction

Tissue development requires the effective infiltration of cells into the scaffolds and typically, seeded cells migrate into the scaffold by either displacing individual scaffolding fibers or digesting them, both of which require extended culture period and appropriate chemotactic factors present within the scaffold [1,2]. Cell infiltration into scaffolds becomes hindered significantly when scaffold thickness increases and pore size decreases. To address this problem, various strategies [3-9] have been proposed and they are based on a common hypothesis: that scaffolds embedded with cells in a controlled spatial distribution can address the current problem of limited cell infiltration and achieve a highly cellularized tissue construct. Despite making significant progress, the said processes are often complex and detrimental to cell viability and therefore, a simpler and milder cell encapsulation technique is desirable.

We introduce a new fiber forming technique, interfacial polyelectrolyte complexation (IPC) [10-12] where stable fibers can be produced at the interface of oppositely charged polyelectrolytes. The polyelectrolyte complex (PEC) fibers are produced in room temperature and aqueous medium and thus, cells can be encapsulated into the newly formed PEC fibers easily without compromising its viability. Here, we study the complexation of a cationic methylated collagen with an anionic terpolymer to produce a hybrid fibrous scaffold that might possess the favourable biological properties of collagen and the tunable physical properties of a synthetic polymer. hMSCs were encapsulated into the PEC fibers and cultured in proliferation medium and the cytoskeletal organization and gene expressions of the encapsulated hMSCs were studied.

II. Materials and methods

Materials: Methyl methacrylate (MMA), hydroxyethyl methacrylate (HEMA) and methacrylic acid (MAA) monomers and 2,2'-Azobisisobutyronitrile (AIBN) were purchased from Sigma-Aldrich Chemicals Ltd. (Singapore). The monomers were purified by vacuum distillation and AIBN was recrystallized in ethanol before use. Collagen Type I (Nutragen, 100mL) was purchased from Nutacon Netherlands. hMSCs were purchased from Cambrex (Poietics; Lonza, Switerzland), cultured and expanded in mesenchymal stem cell growth medium (MSCGM^{TM}). The cells used in the experiments were between passages 4 and 7.

Terpolymer synthesis: The terpolymer was synthesized as described [12]. Briefly, MMA, HEMA and MAA monomers were charged into a 250mL round bottom flask at a molar ratio of 25:25:50 with 0.25 wt% of AIBN as an initiator. The reaction mixture was immersed in a hot silicone oil bath for a 24 hour polymerization process. The terpolymer was precipitated and vacuum dried before it was dissolved in 1M NaOH and dialyzed against deionized water.

Collagen Methylation: 15 mL of collagen was precipitated in 400 mL of acetone and redissolved in 200 mL of methanol containing 0.1 M HCl. The mixture was stirred for

Chwee Teck Lim, James C.H. Goh (Eds.): ICBME 2008, Proceedings 23, pp. 1279–1281, 2009
www.springerlink.com

2 days at room temperature before it was dialyzed against deionised water (Spectrapor MWCO = 3,500) until the external reservoir reached a pH of 5.5. The methylated collagen was lyophilized and stored at -80°C before use.

Encapsulating hMSCs into PEC Fibers: hMSCs were encapsulated in PEC fibers as described in [12]. Briefly, 3 X 10^5 cells/mL of cell suspension in collagen were used to produce a hMSC-encapsulated fiber (see Fig. 1) and the fibers were collected and cultured in a 6 well Transwell plate and incubated at 37°C with 5% CO_2.

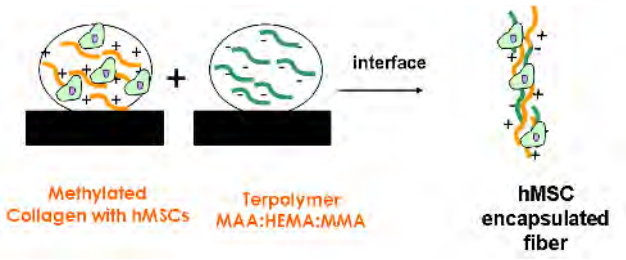


Figure 1: Schematic diagram of cell encapsulation in PEC fiber

Immunofluorescence Staining: PEC fibers encapsulated with hMSCs were fixed and stained with TRITC phalloidin and DAPI before viewing with a confocal microscope.

Gene expression studies: The samples were stabilized with RNAlater RNA stabilization reagent (Qiagen, Singapore) and homogenized with QIAshredder. The RNA was isolated with RNeasy Minikit. Synthesis and amplification of cDNA were carried out with Qiagen One-Step RT-PCR with primers (designed in-house) at an annealing temperature of 60°C for 33 cycles. The PCR products were resolved in 1.2% agarose gel.

III. Results

The (MMA-HEMA-MAA) terpolymer was converted to an anionic polyelectrolyte with the addition of NaOH at the end of the polymerization reaction. The conversion of the sodium carboxylic acid functional groups in MAA to a sodium salt gave the terpolymer a net negative charge at neutral pH. Native collagen proteins were methylated to produce a cationic polyelectrolyte at neutral pH. PEC fiber was formed upon charge neutralization at the interface of the oppositely charged polyelectrolytes and a pair of tweezers was used to draw the PEC fiber up from the interface.

Collagen distribution in PEC fibers: The collagen present in the PEC fibers were labeled with quantum dot 605 nm (Invitrogen) as shown in Fig. 2. The results showed uniform distribution of collagen in the main fiber.

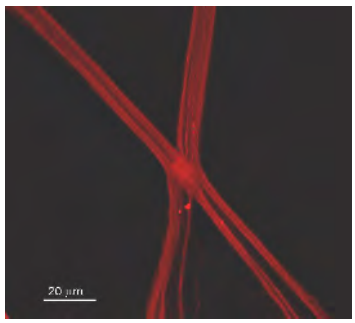


Figure 2: Quantum dot labeling of collagen in PEC fibers

Cytoskeletal Organization and Gene Expressions of Encapsulated hMSCs: To observe the cytoskeletal changes and the resulting gene expressions in encapsulated hMSCs, hMSCs were seeded onto PEC fibers and hMSCs cultured on TCPS (hMSC control) were used for comparison. hMSCs encapsulated in PEC fibers were mostly elliptical and they were observed in different z planes of the scaffold. hMSCs seeded onto the PEC fibers were elongated and found to extend along the fiber axis. The gene expressions showed upregulation of Noggin in both hMSC-encap and hMSC-seeded samples and MAP2 gene in hMSC seeded samples by 14 days.

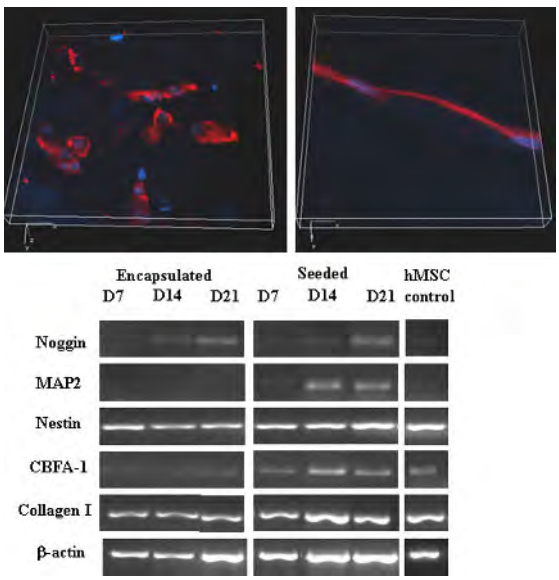


Figure 3: F-Actin/DAPI labeling of encapsulated and seeded cells and the respective gene expressions between day 7 to day 21 of culture

IV. Discussion

The PEC fibers used in this study are a hybrid of synthetic and natural polymers and its inception was based on the desire to produce a fibrous material that has the complementary properties of both polymer types. The process in which such fibers were produced was carried out in aqueous conditions, thus giving PEC fibers additional advantage where biological incorporation into scaffolds is of interest. The uniform collagen distribution in PEC fibers has been verified by immunofluorescence labeling and the mechanical properties of these fibers have been shown to be superior to native collagen fibers and alginate-chitosan PEC fibers [12].

Encapsulated and seeded hMSCs maintained the early markers of chondrogenesis, osteogenesis, adipogenesis and neurogenesis, suggesting that hMSCs when conformed to different morphologies in our PEC fibers did not undergo spontaneous differentiation and maintained its pluripotency for at least 7 days.

MAP2 was downregulated in encapsulated hMSCs and upregulated in seeded hMSCs and this observation could be explained by the elongation of seeded cells along the PEC fibers which could have determined, stabilized the dendritic shape of cells [13] and signaled the expression of this gene. MAP 2 is a dendrite-specific microtubule-associated protein found specifically in dendritic branching neurons [14] and was thought to be involved in microtubule assembly which is an essential step in neurogenesis.

V. Conclusions

The PEC fibers have been shown to support the encapsulation of cells and where mesenchymal stem cells are concerned, the multipotency is maintained at least for the first 7 days of culture despite being conformed to different morphologies. Changes in neuronal gene expressions were observed from 14 days of culture. Fabrication of cell-encapsulated fibers allows the 3D patterning of cells within a matrix and this is a first step towards the creation of a complex biological construct.

Acknowledgments

The author would like to thank NUS for her research scholarship, NUS Life Science Institute and Duke-NUS Graduate Medical School for their financial support.

References

1. Cao X and Shoichet M S (2002) Photoimmobilization of biomolecules within a 3-dimensional hydrogel matrix. *J Biomater Sci Polym Ed* 13:623-36
2. Nam J, Huang Y, Agarwal S, et al. (2007) Improved Cellular Infiltration in Electrospun Fiber via Engineered Porosity. *Tissue Engineering* 13:2249-2257
3. Almany L and Seliktar D (2005) Biosynthetic hydrogel scaffolds made from fibrinogen and polyethylene glycol for 3D cell cultures. *Biomaterials* 26:2467-77
4. Fedorovich N E, De Wijn J R, Verbout A J, et al. (2008) Three-Dimensional Fiber Deposition of Cell-Laden, Viable, Patterned Constructs for Bone Tissue Printing. *Tissue Engineering Part A* 14:127-133
5. Nahmias Y, Arneja A, Tower T T, et al. (2005) Cell patterning on biological gels via cell spraying through a mask. *Tissue Eng* 11:701-8
6. Stankus J J, Guan J, Fujimoto K, et al. (2006) Microintegrating smooth muscle cells into a biodegradable, elastomeric fiber matrix. *Biomaterials* 27:735-744
7. Townsend-Nicholson A and Jayasinghe S N (2006) Cell electrospinning: a unique biotechnique for encapsulating living organisms for generating active biological microthreads/scaffolds. *Biomacromolecules* 7:3364-9
8. Vermonden T, Fedorovich N E, van Geemen D, et al. (2008) Photopolymerized thermosensitive hydrogels: synthesis, degradation, and cytocompatibility. *Biomacromolecules* 9:919-26
9. Xu T, Gregory C A, Molnar P, et al. (2006) Viability and electrophysiology of neural cell structures generated by the inkjet printing method. *Biomaterials* 27:3580-3588
10. Wan A C, Yim, E. K., Liao, I. C., Le Visage, C., Leong, K. W. (2004) Encapsulation of biologics in self-assembled fibers as biostructural units for tissue engineering. *J Biomed Mater Res A* 71:586-95
11. Yim E K F, Wan, A. C.,Le Visage, C.,Liao, I. C.,Leong, K. W. (2006) Proliferation and differentiation of human mesenchymal stem cell encapsulated in polyelectrolyte complexation fibrous scaffold. *Biomaterials* 27:6111-22
12. Yow S Z, Quek, C. H., Yim, E. K. F., Lim, C. T., Leong, K. W. (2008) Collagen-based Fibrous Scaffold for Spatial Organization of Encapsulated and Seeded Human Mesenchymal Stem Cells. *Biomaterials (submitted)*
13. Bossolasco P, Cova L, Calzarossa C, et al. (2005) Neuro-glial differentiation of human bone marrow stem cells in vitro. *Experimental Neurology* 193:312-325
14. Chen Y, Teng F and Tang B (2006) Coaxing bone marrow stromal mesenchymal stem cells towards neuronal differentiation: progress and uncertainties. *Cellular and Molecular Life Sciences (CMLS)* 63:1649-1657

Author: Chwee Teck, Lim
Institute: National University of Singapore
Street: NanoBiomechanics Laboratory, Blk E3, #05-16,
2 Engineering Drive 3, S117576
City: Singapore
Country: Singapore
Email: ctlim@nus.edu.sg

Potential And Properties Of Plant Proteins For Tissue Engineering Applications

Narendra Reddy[1] and Yiqi Yang[1,2,3]

[1] Department of Textiles, Clothing and Design
[2] Department of Biological Systems Engineering
[3] Nebraska Center for Materials and Nanoscience
University of Nebraska-Lincoln, Lincoln, NE, USA

Abstract — **Fibers produced from plant proteins such as zein, soyprotein and wheat gluten, glutenin and gliadin have good mechanical properties, excellent water stability and biocompatibility that make them suitable for tissue engineering and other medical applications. Although animal proteins such as collagen are used for medical applications, materials developed from collagen do not have the properties desired for tissue engineering applications. Materials developed from collagen have poor wet strength and also have the risk of carrying diseases. The plant protein fibers developed in our laboratory have better water stability than PLA and collagen fibers in water and films developed from wheat gluten, gliadin and glutenin without using any crosslinking agents have strength, water stability and biocompatibility required for medical applications. The plant protein fibers developed were characterized for their morphological and physical structures, mechanical properties and stability under various physiological conditions. Different types of animal cells were cultured on the fibers and the cytocompatibility and attachment, growth and proliferation of cells on the fibers was studied. It was found that plant proteins fibers supported the attachment, growth and proliferation of animal cells and the fibers were stable in pH 7.2 water for at least 30 days. Some of the plant proteins show better cell attachment and proliferation than PLA. In this paper, we will present the properties and potential of using various plant protein fibers for tissue engineering and other medical applications.**

Keywords — **Plant proteins, Fibers, Tensile Properties, Tissue engineering**

I. Introduction

Proteins are preferred for medical applications due to their biocompatibility, ability to support the attachment, growth and proliferation of cells and presence of various functional groups that facilitate the absorption of different types of drugs for controlled drug release [1]. Collagen and silk fibroin are the two most commonly used proteins for medical applications. However, both collagen and silk have several limitations that limit their use in tissue engineering and other medical applications [1]. Collagen is mostly derived from animal sources and carries the risk of contamination by prions and viruses [1]. In addition, it is difficult to obtain collagen with consistent properties, cannot be autoclaved and products made from collagen have poor mechanical properties when wet [2,3]. Silk fibroin needs to be separated from sericin, has long degradation rates that make it unsuitable for some applications and it has been recently discovered that fibroin can cause amyloidosis, a chronic inflammatory reaction [4].

Compared to collagen and silk, plant proteins such as zein, soyproteins and wheat gluten are abundant and inexpensive proteins that can be made into fibers and films with properties suitable for tissue engineering and other medical applications. However, limited studies have been conducted on understanding the potential of using plant proteins for medical applications. So far, zein and soyproteins have been made into films and used as substrates for tissue engineering [5,6]. It has been reported that zein and soyproteins are biocompatible proteins and have good potential for tissue engineering [5, 6]. Recently, we have reported that fibers made from wheat gliadin are suitable for tissue engineering applications [7].

Fibers are more preferable for tissue engineering applications because fibers are stronger than films, more closely imitate the structure of the extracellular matrix and can guide tissue regeneration. Except for gliadin fibers, the potential of using the other plant proteins for tissue engineering applications has not been studied.

This paper presents an overview of the potential of using plant proteins for tissue engineering applications. Zein, soyproteins, wheat gluten and gliadin have been made into fibers and the properties of the fibers developed and the ability of the fibers to support cell attachment, growth and proliferation has been studied.

II. Materials and Methods

Materials

Zein (F4000) was purchased from Freeman Industries, Tuckahoe, NY. Soyproteins (Profam) were supplied by Cargill Inc and Wheat gluten (WHETPRO 80) was supplied by Archer Daniels Midlands Company.

Chwee Teck Lim, James C.H. Goh (Eds.): ICBME 2008, Proceedings 23, pp. 1282–1284, 2009
www.springerlink.com

Methods

Fiber production: Zein fibers were produced by dry spinning according to the method previously described [8]. Briefly, the required concentration of zein was dissolved in 70% aqueous ethanol and the solution was aged for a particular time. The zein solution was then extruded onto a rotating drum. Fibers formed were collected on the drum after evaporating the ethanol. Soyproteins, wheat gluten and gliadin were dissolved in aqueous urea solution in the presence of sodium sulfite as the reducing agent. The protein solution was aged and later extruded into a coagulation bath consisting of acids and salt solutions. The precipitated fibers were washed several times and water and later dried [7,9].

Drawing and Annealing: The fibers produced were drawn by hand to about 200 to 300% of their original length by dipping the fibers in water. The drawn fibers were later annealed at 125 °C for about 90 minutes. Drawing and annealing were done to improve the mechanical properties of the fibers.

Tensile Properties: The breaking tenacity, breaking elongation and Young's modulus of the fibers was determined using an Instron tensile testing machine according to ASTM standard 3822. A gauge length of 1 inch and crosshead speed of 18 mm/min was used for testing.

Water stability: The stability of the wheat gluten, gliadin and soyprotein fibers was studied in water at various temperatures and physiological conditions. Fibers were dipped in pH 7.2 PBS solution at 50 °C for several days. The strength loss of the fibers in water was compared to the untreated fibers and to PLA fibers. The stability of the fibers was also tested in pH 3 to 11 solutions at 50 °C and the strength loss was determined.

Cell culture: Mouse fibroblasts cells were used to study the potential of using the wheat protein fibers for tissue engineering. The fibrous substrates were placed on the bottom of a 12, 24 or 48 well culture plates ensuring that the bottom of the plates are completely covered. Cells with passage numbers less than 20 were be seeded on the substrates at concentrations of about 1.2 x10^5 cells/ml in Dulbecco's Modified Eagles Media (DMEM) containing 10% (w/w) fetal bovine or calf serum, 3-5% L-glutamine and 1% (w/w) penicillin-streptomycin. The initial concentration of the cells will be determined by counting using a hemacytometer and also by measuring the optical density (OD). The culture plates were then incubated at 37 °C and 5 % CO_2 for the required time.

SEM analysis: The attachment and proliferation of the cells on the protein fibers was observed using a SEM. The cells after the desired duration of growth on the fibers were fixed using glutaraldehyde (2.5% in PBS) and later with osmium tetroxide. After fixation, the substrates were rinsed several times in PBS and then with deionized water and later dehydrated by successively washing with 50, 75, 95 and 100% ethanol. The samples were later dried using critical point drying, coated with gold palladium and then observed under the SEM.

III. Results and discussions

Tensile properties: The tensile properties of the plant protein fibers are compared with collagen and wool in Table 1. As seen from the table, the plant protein fibers have similar strength and elongation to wool fibers. The dry strength of the plant protein and wool fibers is lower than that of collagen. However, the wet strength of collagen is very low. Both gliadin and gluten fibers have good wet strength, similar to the wet strength of the crosslinked collagen fibers. The wet strength of the plant protein fibers can also be increased by crosslinking. Except for zein fibers, the other plant protein fibers have breaking elongation and Young's modulus similar to that of wool.

Table 1 comparison of the tensile properties of the plant protein fibers with wool and collagen

Fiber	Breaking Tenacity, MPa		Breaking Elongation, %	Modulus, GPa
	Dry	Wet		
Gliadin	120 ± 10	23 ± 3	25 ± 3.2	4.2 ± 0.4
Wheat gluten	115 ± 7	17 ± 2	23 ± 2.7	5 ± 0.2
Zein	36-60	-	1.8-5.0	-
Wool	174-260	-	30-40	4.3-6.5
Collagen	224 ± 19	2.4	24	-
Collagen (Crosslinked)	175-197	17-24	15-18	1.7-2.0

Water stability: Wheat gluten and gliadin fibers have better stability in water than PLA fibers in pH 7 water at 50 °C as seen from Figure 1. The gliadin fibers show a increase in strength after treating in water whereas the wheat gluten fibers show a steady decline in strength up to 7 days and the strength loss later stabilizes. The gliadin fibers show no loss in strength even after being in water for 40 days. The PLA fibers show continuous decrease in strength and were very brittle and could not be tested after 20 days in water. The plant protein fibers were also found to have good stability when treated in pH 3 to 9 water at 90 °C for 1 hour.

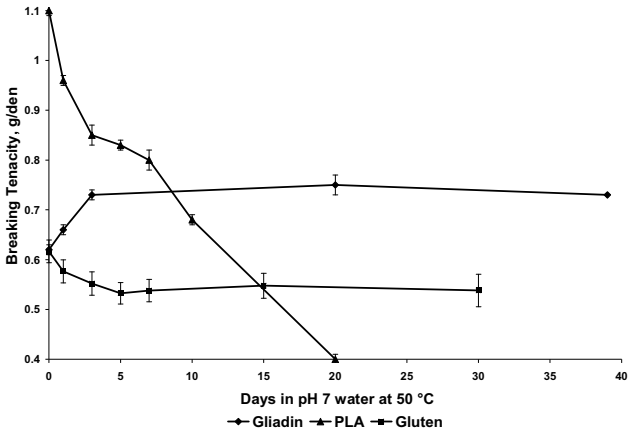


Figure 1 Changes in the breaking tenacity of wheat gluten, gliadin and PLA fibers after treating in pH 7 water at 50 °C for various periods of time.



Figure 2 Mouse fibroblasts showing attachment, growth and spreading on soyprotein fibers, five days after incubation

Cell growth and proliferation: Fibroblasts grown on soyprotein fibers showed good attachment, growth and proliferation. Figure 2 shows an SEM image of mouse fibroblasts grown on soyprotein fibers, five days after seeding. As seen from the figure, the cells have polygonal shapes, are firmly attached and the spreading of the filaments can also be seen. This demonstrates that the soyprotein surface is conducive for cell attachment, growth and proliferation.

IV. Conclusions

Our research demonstrates that plant proteins can be made into fibers with better wet mechanical properties than collagen fibers and better water stability than PLA fibers. The fibers made are conducive for cell attachment, growth and proliferation. Plant proteins could be novel biomaterials suitable for tissue engineering, drug delivery and other medical applications.

Acknowledgment

The authors wish to acknowledge the Nebraska Wheat Board, Nebraska Soybean Board, The Consortium for Plant Biotechnology Research Inc by DOE prime agreement No. DE-FG36-02G012026, Archer Daniel Midland Company, USDA Hatch Act, the Agricultural Research Division at the University of Nebraska-Lincoln and Multi State Research Project S-1026 for funding this project. The financial sponsors do not endorse the views expressed in this publication.

References

1. Malafaya P B, Silva G A, Reis R L, (2007) Natural origin polymers as carriers and scaffolds for biomolecules and cell delivery in tissue engineering applications, Adv Drug Del 59:207-233
2. Cavallaro J F, Kemp P D, Kraus K H, (1994) Collagen fabrics as biomaterials, Biotechol Bioengg 43(8):781-791
3. Friess W, (1998) Collagen-biomaterials for drug delivery, Eu J Pharma Biopharma 45:113-136
4. Hakimi O, Knight D P, Vollrath F, Vadgama P, (2007) Spider and mulberry silks as compatible biomaterials, Composites B 38:324-337
5. Vaz C M, Fossen M, Tuil R F , Graaf L A, Reis R L, Cunha A M, (2003), Casein and soybean protein-based thermoplastics and composites as alternative biodegradable polymers for biomedical applications, J Biomed Mat Res 65A(1):60-70
6. Gong S, Wang H, Sun Q, Xue S, Wang J, (2006), Mechanical properties and in vitro compatibility of porous zein scaffolds, Biomaterials 27:3793-3799
7. Reddy N, Yang Y, (2008), Self-crosslinked gliadin fibers with high strength and water stability for potential medical applications, J Mat Sci Mat Med, 19:2055-2061
8. Yang Y, Wang L, Li S, (1996), Formaldehyde-free zein fiber preparation and characterization, J Appl Polym Sci 59:433-441
9. Reddy N, Yang Y, (2007), Novel protein fibers from wheat gluten, Biomacromolecules 8(2):638-643

Author: Yiqi Yang
Institute: University of Nebraska-Lincoln
Street: 234, HECO Building, East Campus
City: Lincoln, Nebraska
Country: United States of America
Email: yyang2@unl.edu

Comparison the Effects of BMP-4 and BMP-7 on Articular Cartilage Repair with Bone Marrow Mesenchymal Stem Cells

Yang Zi Jiang[1], Yi Ying Qi[1], Xiao Hui Zou[1], Lin-Lin Wang[1], Hong-Wei Ouyang[1,2 *]

[1] Center for stem cells and issue Engineering, School of Medicine, Zhejiang University; China
[2] Department of Orthopaedic Surgery, Sir Run Run Shaw Hospital, School of Medicine, Zhejiang University; China
[3] Zhejiang Women's Hospital, School of Medicine, Zhejiang University, Hangzhou, China

Abstract — **To compare the potential effects of bone morphogenetic proteins 4 and 7 (BMP-4 and BMP-7) on the chondrogenic differentiation of mesenchymal stem cells(MSCs) for articular cartilage regeneration in vitro and in vivo.**

In the in-vitro experiment, MSCs were derived from bone marrow. The chondrogenic effects of BMP-4 and BMP-7 were compared at the gene expression level. In the in-vivo experiment, full-thickness cartilage defects (diameter = 4 mm, thickness =3 mm) in the patellar grooves of male New Zealand white rabbits were chosen as model of in-situ cartilage repair. MSCs were treated with BMP4(group II) / BMP7 (group III) in a bilayer collagen scaffold (n=11/group). Full-thickness cartilage defects without treatment was regarded as a control (group I) (n=11). The rabbits were sacrificed at 6 and 12 weeks after operation. The repaired tissues were processed for histology and for mechanical test.

In-vitro study showed increased expression levels of cartilage-related genes after MSCs were treated with BMP4 or BMP7 in culture medium. In-vivo study showed both BMP4 and BMP7 group increased new cartilage formation at 6 and 12 weeks than that of control group. BMP4 group had the largest amounts of cartilage tissue, which restored larger surface area of the cartilage defects. Moreover, BMP4 group had higher ICRS histological scores and more type II collagen in the neo-cartilage matrix than those in other two groups ($p<0.05$). The Young's modulus of the repaired tissue in group III can reach 30% of normal hyaline cartilage tissue, which were significantly higher than group II and group I ($p<0.05$).

Our data indicate that both BMP4 and BMP7 may induce MSCs chondrogenesis and increase the expression of cartilage-related genes. BMP-4 is more potent than BM7 in inducing chondrogenesis, and more inclined to form the hyaline cartilage in vivo.

Keywords — **Mesenchymal stem cells, Bone Morphogenetic Proteins 4, Bone Morphogenetic Proteins 7, cartilage repair, tissue engineering**

I. Introduction

Articular cartilage is lack of self-repair capability due to lack of blood supply and limited innervationits vasul less. When damaged and if the defect size was larger than two to four millimeters in diameter, it rarely healed if leave untreated [1]. Unhealed articular cartilage lesions can induce mechanical instability of the joint and often lead to osteoarthritis further [2].Current therapies include microfracture[3], abrasion, drilling[4], osteochondral grafting[5] and autologous chondrocyte implantation (ACI) [6]. Because of the capacity for self-renewal , the potential for multidifferentiation, and their accessibility, mesenchymal stem cells (MSCs) become an attractive option in tissue-engineering approaches to cartilage repair.

Growth factors are very important for bMSCs and chondrocytes proliferation and differentiation, which can be used to improve the quality of cartilage repair. Previours study show that several growth factors, including transforming growth factor b (TGFb), bone morphogenetic proteins (BMPs) and basic fibroblast growth factor (bFGF) can promote chondrocyte proliferation and extracellular matrix (ECM) synthesis in vitro and in vivo [7–10].Studies performed in vitro and in the developing skeleton have led to the identification of bone morphogenetic proteins 4 (BMP-4) as a promising candidate for the promotion of chondrogenesis [11–13]. Previous researches reported that local delivery of BMP4 gene at joint cartilage defect not only enhance the regeneration of subchondral bone but also induce the regen-eration of hyaline-like cartilage in as short a period as 6 weeks [14].BMP7 as a growth factors were used as a osteogeneration in clinical and adipolineage differentia-tion[15] ,has also shows a great effect of the potential for chondrolineage differentiation[14] . However, no evidence is available to correlate those findings and chose optimal BMPs for cartilage repair and regeneration.

This study aimed to compare the efficacy of BMP4 and BMP7 for cartilage regeneration on an established animal cartilage repair model. The findings might be useful for the choice of BMPs for enhancing the therapeutic efficacy of microfracture on articular cartilage repair.

II. Materials and methods

Cell culture: Isolation of rabbit marrow MSCs and differentiation assay in vitro. MSCs were derived from bone marrowaspirates of 4-week rabbit taken from the distal femur. Each aspirate was combined with 25 ml of MSCs

Chwee Teck Lim, James C.H. Goh (Eds.): ICBME 2008, Proceedings 23, pp. 1285–1288, 2009
www.springerlink.com

growth medium consisting of 89% DMEM–low glucose (Gibco BRL/Life Technologies Inc., Gathersburg,MD), 10% fetal bovine serum (HyClone Laboratories, Inc., Logan, UT) and 1%antibiotic and 1% antimycotic (Gibco). Growth medium was changed every two days. To characterize the pluripotential of MSCs, we induced MSCs towards adipocytes, chondrocytes and osteoblasts formation(data not shown).

BMP4(Stemcell.) and BMP7(Stem cell.) were add into the culture medium at the concentration of 10ng/ml to test the effect of chondrogenesis of MSC.

RNA Isolation and RT-PCR: Total cellular RNA was isolated by lysis in TRIZOL (Invitrogen) followed by one-step phenol chloroform- isoamyl alcohol extraction as described in protocol. 200 nanogram of total RNA was reverse-transcribed into complementary DNA (cDNA) by incubation with 200 U of reverse transcriptase in 20 μL of reaction buffer at 37 centi-degree for 1h. One microliters of the cDNA was used as a template for the PCR. Semi-quantities RT-PCR of the Collagen I, III, decorin and GAPDH was proceeded as previous described [17]. The semiquantitative measurement of the band density was calculated by using Glyko Bandscan (Glyko, Inc., USA). The band intensity was normalized to the band intensity of GAPDH in the same sample. The results were repeated for 3 times. The following 5′ and 3′ primers (listed respectively) were used to evaluate gene expression: collagenII, ATGGACATTGGAGGGCCTGA, and TGTTTGACACGGAGTAGCACCA; Sox9, GGTGCTCAAGGGCTACGACT, and GGGTGGTCTTTCTTGTGCTG; collagen X,GAAAACCAGGCTATGGAACC,and GCTCCTGTAAGTCCCTGTTGTC and; GAPDH, TCACCATCTTCCAGGAGCGA and CACAATGCCGAAGTGGTCGT.

Animal model: Thirty-eight knee joints of male New Zealand White Rabbits (2-2.5 kg) were used in this study. Rabbits were maintained separately in stainless-steel cages. The rabbits were anesthetized by an intramuscular injection. The knee joints were opened with a medial parapatellar approach. The patella was dislocated laterally and the surface of the femoropatellar groove was exposed. A full-thickness cylindrical cartilage defect of 4 mm in diameter and 3 mm in depth was created in the patellar groove using a stainless-steel punch. The defects were either untreated (group I, n=11) or treated with MSC in a bilayer collagen matrix with BMP4(250ng/ml) (group II, n=11), and MSC in a bilayer collagen matrix with BMP7(250ng/ml) (group III, n=11). Sample and time point was arraged as Table.1 shown.

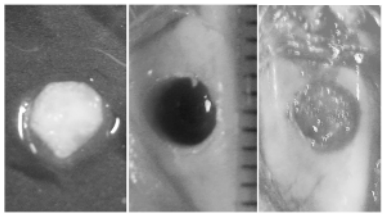


Fig. 1. Animal model of cartilage defect.The MSC were seeding on the collagen scaffold,and implanted into a Afull-thickness cylindrical cartilage defect which was 4 mm in diameter and 3 mm in depth.

All the animals were operated according to the standard guidelines approved by Zhejiang University Ethics Committee.

Table 1 Animal experiment, Samples(N=)

Time points	Normal control	Control group	BMP4 group	BMP7 group
6w		3	3	3
12w	5	8	8	8

Gross morphology and histology: At 6 and 12 weeks post-surgery, the rabbits were sacrificed by intravenous overdose of pentobarbital. The harvested samples were examined and photographed for evaluation. After gross examination, samples were fixed in 4% formalin, decalcified in 10% formic acid, then embedded in paraffin and cut to 7μm thick sections. Sections were stained with Safranine-O for GAG distribution. According to the area of positive Safranine-O staining, the percentage of cartilage tissue in the area of defect was calculated. For the overall evaluation of the regenerated tissue in the defects, the repaired tissues were graded using the International Cartilage Repair Society (ICRS) Visual Hisological Assessment Scale by one blinded observer according to the strategy of previous study [16].

*Mechanical evaluation:*Mechanical evaluation protocol was adopted from previous study [10]. Before testing, samples were placed in Phosphate Buffered Saline (PBS) at room temperature for 3-4 hours to equilibrate. Compressive mechanical properties of the cartilage layer after a long-term (12 weeks, n=5 samples) period in vivo were determined using a 2 mm diameter cylindrical-shaped indenter to compressively load the cartilage tissue in Instron Testing machine (model 5543, Instron, Canton, MA).

Statistical analysis: Histological scoring data and biomechanical test data were assessed for statistical differences using a paired t-test to compare experimental characteristics to control.

III. Results

A. Chondrogenic effects of BMP-4 and BMP-7 on MSC at the gene expression level

Add BMP4 and BMP7 in to the MSC culture medium for three days ,test the gene exprssion level of chondrogenesis. The chondrogenesis marker gene type II collagen,Aggrecan and Sox9 show a positive expression after three days treated with BMP4 and BMP7.

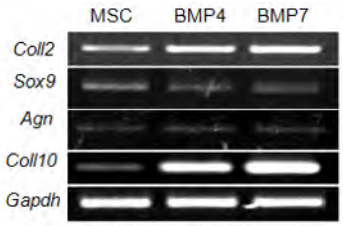


Fig. 2. RT-PCR analysis of collagen II, SOX9,Aggrecan,collagenX gene expressions of MSCs treated with BMP4 and BMP7 for 3days.Col II: collagen II,Sox9:Sox9; AGN:aggrecan;Coll X: collagen X.

B. Gross morphology

The gross examinations of knee joints showed that there were no abrasions on the opposing articulating surfaces and no inflammation at both 6 and 12 weeks time point. (Fig.3)The defects remained empty in small parts at 6 weeks after transplantation

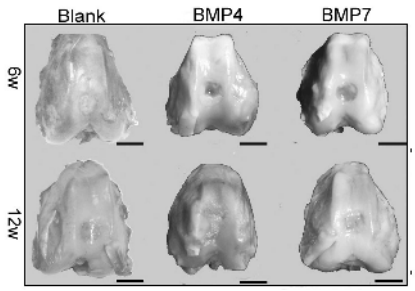


Fig. 3. Animal model of cartilage defect.The MSC were seeding on the collagen scaffold,and implanted into a Afull-thickness cylindrical cartilage defect which was 4 mm in diameter and 3 mm in depth.

C. Results of Histological examination and ICRS

At 6 weeks after transplantation, the defects in group I (n=3) were filled with fibrous tissue (Figure 4.). In group II (n=3) and group III (n=3), the defects were repaired with mixture of fibrous tissue and cartilage-like tissue as shown by Safarnine-O staining. The amounts of chondrocyte-like cells and cartilage-like extracellular matrix in group II were more than those of group III as observed (Figure 4,6w,BMP4,BMP7). At 12 weeks after transplantation, the defects in group I (n=3) were almost filled with fibrous tissue and a little cartilage-like tissue at the margins of the defects (Figure 4,12w,Control). Group III had lager amounts of hyaline cartilage (Figure4,12w,BMP7). Group II has the largest amounts of hyaline cartilage tissue(Figure4,12w,BMP4). The total ICRS histological scores of the specimens at 6 and 12 weeks revealed differences between the three groups. The scores for the repaired tissue of group II were significantly higher than those for other two groups ($p < 0.05$). The histological scores of the specimens at 12 weeks were higher than those of specimens at 6 weeks.

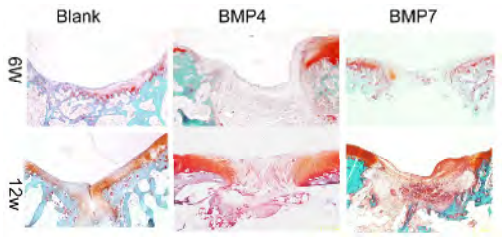


Fig. 4. Histological examination of the three groups at 6 weeks and 12weeks post-surgery.Left is the microfracture group .Middle are the microfracture with MSC and BMP4 in collagen matrix group. Right is the microfracture with MSC and BMP7 in collagen matrix group. Safranine-O staining. Original magnification 40x. Scale is as indicated (bar=500 micrometer).

D. Results of Biomechanical evaluation

The From the indentation test, the Young's modulus of repaired tissues from the three groups (12 weeks) were determined and compared with each other while the tissues from normal rabbit knee joint were used as normal control. At 12 weeks, the compressive modulus of the repaired tissue in group II and group III samples showed greater improvement compared with specimens from group I ($p<0.05$). However, the modulus of repaired tissue in both group II and group III was inferior to that of normal cartilage (0.52 +/- 0.01Mpa) ($p< 0.05$).The Young's modulus of the repaired tissue in group III can reach 30% of normal hyaline cartilage tissue, which were significantly higher than group II and group I ($p<0.05$).

IV. Discussion and Conclusions

Our data indicate that both BMP4 and BMP7 are able to induce MSCs chondrogenesis and increase the expression of cartilage-related genes. This finding is consistent with previous studies [18]. More importantly, it was found that

BMP-4 is more potent than BM7 in inducing chondrogenesis, and more inclined to form the hyaline cartilage in vivo.

Previous study reported that BMP7 significantly inhibited Runx2 expression,and activated UCP gene expression-whereas BMP4 had no effect[15].

Cellular responses to BMPs have been shown to be mediated by the formation of a hetero-oligomeric complex of the type 1 and type 2 BMPs.BMP-4 and BMP-7 bind to the same type II receptors (BMP type II receptor/activin type IIA receptor) and to several common type I receptors ALK-3 and ALK-6. BMP7 binds to different type I receptors ALK-2 [19]. We speculate that the similarity of the chondrogenic responses induced byBMP-4 and BMP-7 reflects the commonality of their receptors ALK3,6, and that the different responses elicited by BMP-7 bespeak the occupation and activation of another set of receptors ALK-2 and the triggering of an alternative signaling pathway.

In summary, we have demonstrated that BMP-4 and BMP-7manifest different potentials for the chondrogenic differentiation of MSCs and induce the formation of cartilaginous tissue with different characteristics. The findings are useful for future application of BMP for cartilage repair. It is of worthy to note that neither BMP-4 nor BMP-7 alone is capable of inducing the complete cartilage repair with MSCs.

A further refinement of the stimulation conditions is needed.

ACKNOWLEDGEMENT

This work was supported by National Natural Science Foundation of China (30600301, 30600670, U0672001) and Zhejiang Province grants (R206016, 2006C14024).

REFERENCES

1. Akeda, K, An, H. S., Okuma, M.; Attawia, M. et al. (2006) Platelet-rich plasma stimulates porcine articular chondrocyte proliferation and matrix biosynthesis. Osteoarthritis Cartilage 14(12):1272-1280
2. Breinan, H. A.; Martin, S. D.; Hsu, H. P.; Spector, M. (2000) Healing of canine articular cartilage defects treated with microfracture, a type-II collagen matrix, or cultured autologous chondrocytes. J Orthop Res 18(5):781-789
3. Buckwalter, J. A. (1998) Articular cartilage: injuries and potential for healing. J Orthop Sports Phys Ther 28(4):192-202
4. Buma, P.; Pieper, J. S.; van Tienen, T. et al. (2003) Cross-linked type I and type II collagenous matrices for the repair of full-thickness articular cartilage defects--A study in rabbits. Biomaterials 24(19):3255-3263
5. Chen, G.; Sato, T.; Tanaka, J. et al. (2006) Preparation of a biphasic scaffold for osteochondral tissue engineering. Materials Science and Engineering: C 26(1):118-123
6. Dzioba, R. B. (1988) The classification and treatment of acute articular cartilage lesions. Arthroscopy 4(2):72-80
7. Gelse K, von der Mark K, Aigner T, et al. (2003) Articular cartilage repair by gene therapy using growth factor-producing mesenchymal cells. Arthritis Rheum 48:430–41.
8. Glansbeek HL, van Beuningen HM, Vitters EL,(1997) Bone morphogenetic protein 2 stimulates articular cartilage proteoglycan synthesis in vivo but does not counteract interleukin-1_1alpha effects on proteoglycan synthesis and content. Arthritis Rheum;40:1020–8.
9. Morales TI, Roberts AB.(1988) Transforming growth factor beta regulates the metabolism of proteoglycans in bovine cartilage organ cultures. J Biol Chem;263:12828–31.
10. Sellers RS, Peluso D, Morris EA. (1997) The effect of recombinant human bone morphogenetic protein-2 (rhBMP-2) on the healing of full-thickness defects of articular cartilage. J Bone Joint Surg Am;79:1452–63.
11. Ryosuke Kuroda,Arvydas Usas, Seiji Kubo et al. (2006) Cartilage Repair Using Bone Morphogenetic Protein 4 and Muscle-Derived Stem Cells. Arthritis Rheum 2006;54:433-442.
12. Semba I, Nonaka K, Takahashi I, et al. (2000) Positionally-dependent chondrogenesis induced by BMP4 is co-regulated by Sox9 and Msx2. Dev Dyn;217:401–14.
13. Kramer J, Hegert C, Guan K et al. (2000) Embryonic stem cell-derived chondrogenic differentiation in vitro: activation by BMP-2 and BMP-4. Mech Dev 2000;92:
14. Nahoko Shintani and Ernst B. Hunziker (2007) Chondrogenic Differentiation of Bovine Synovium Bone Morphogenetic Proteins 2 and 7 and Transforming Growth Factor-1 Induce the Formation of Different Types of Cartilaginous Tissue.Arthritis Rheum 56: 1869-1879.
15. Yu-Hua Tseng, Efi Kokkotou, Tim J. Schulz, (2008) New role of bone morphogenetic protein 7 in brown adipogenesis and energy expenditure.Nature. 454:10.1038.
16. Sciore P, Boykiw R, Hart DA.(1998) Semiquantitative reverse transcription-polymerase chain reaction analysis of mRNA for growth factors and growth factor receptors from normal and healing rabbit medial collateral ligament tissue. J Orthop Res;16:429-437.
17. Mainil-Varlet, P.; Aigner, T.; Brittberg, M.; (2003) Histological assessment of cartilage repair: a report by the Histology Endpoint Committee of the International Cartilage Repair Society (ICRS). J Bone Joint Surg Am 85-A Suppl 2:45-57; 2003.
18. Xin Zhang , Zhuozhao Zheng, Ping Liu et al.(2008) The synergistic effects of microfracture, perforated decalcified cortical bone matrix and adenovirus-bone morphogenetic protein-4 in cartilage defect repair.Biomaterials.2008.inpress.
19. Yigong Shi and Joan Massague,(2003)Review-Mechanisms of TGF-b signaling from cell membrane to the nucleus.Cell.113:685-700.

Author: Ouyang Hongwei
Institute: Zhejiang university
Street: 388# Yu Hang Tang Road
City: Hang Zhou
Country: China
Email: hwoy@zju.edu.cn

Local Delivery of Autologous Platelet in Collagen Matrix Synergistically Stimulated In-situ Articular Cartilage Repair

Yi Ying Qi[1,3], Hong Xin Cai[2], Xiao Chen[1], Lin Lin Wang[1],Yang Zi Jiang[1], Nguyen Thi Minh Hieu[4], Hong Wei Ouyang[1, 2, 3*]

[1] Center for stem cells and issue Engineering, School of Medicine, Zhejiang University; China
[2] Department of Orthopaedic Surgery, Sir Run Run Shaw Hospital, School of Medicine, Zhejiang University; China
[3] Institute of Cell Biology, School of Medicine, Zhejiang University; China
[4] Division of Bioengineering, National University of Singapore; Singapore

Abstract — **Objective: Microfracture is a routine therapy to release bone marrow from subchondral bone for in-situ cartilage repair. However, it can only treat small cartilage defects (< 2 cm^2). The study aims to investigate whether autologous platelet rich plasma (PRP) transplantation in collagen matrix can synergistically improve the in-situ bone marrow-initiated cartilage repair.**

Experimental design: Full-thickness cartilage defects (diameter = 4 mm, thickness =3 mm) in the patellar grooves of male New Zealand White rabbits were chosen as model of in-situ cartilage repair. They were treated with bilayer collagen scaffold (group II), PRP and bilayer collagen scaffold (group III) and untreated (group I) respectively (n=11). The rabbits were sacrificed at 6 and 12 weeks after operation. The repaired tissues were processed for histology and for mechanical test.

Results: The results showed that at both 6 and 12 weeks, group III had the largest amounts of cartilage tissue, which restored larger surface area of the cartilage defects. Moreover, group III had higher histological scores and more glycosaminoglycans (GAGs) content than those in other two groups ($p<0.05$).The Young's modulus of the repaired tissue in group II and group III were significantly higher than that of group I ($p<0.05$).

Conclusion: Autologous PRP and bilayer collagen matrix synergistically stimulated the formation of cartilage tissues. The findings implicated that the combination of microfracture with PRP in collagen matrix may repair certain type of cartilage defects larger than 2 cm2 which currently require the complex autologous chondrocyte implantation (ACI) or osteochondral grafting. number of researches on ligament and tendon tissue engineering scaffold have been carried out. However, a scaffold which simultaneously possesses optimal strength, porous structure and biocompatible microenvironment is yet to be developed. This study aims to design a new practical ligament scaffold by synergic incorporation of silk material, knitting structure and collagen matrix.

Keywords — **Articular cartilage defect, PRP, collagen matrix, microfracture**

I. Introduction

Articular cartilage has a very limited self-repair capability. When the defect size is larger than 2-4mm in diameter, the damaged cartilage is rarely healed if left untreated [1]. Unhealed articular cartilage lesions can induce mechanical instability of the joint and often lead to osteoarthritis[2]. Current therapies include microfracture[3], abrasion, drilling[4], osteochondral grafting[5] and autologous chondrocyte implantation (ACI) [6]. It is generally agreed that ACI and osteochondral grafting are used for treating lager defect (>2 cm^2) while microfracture is for treating small cartilage defect (< 2 cm^2). However, ACI and osteochondral grafting are complex and costly.

Microfracture is a routine simple arthroscopic technique. It is showed to have good results on small cartilage treatment by penetrating the subchondral bone to induce fibrin clot formation and the migration of progenitor cells from the bone marrow into the defective cartilage region [7]. As a result, chondral resurfacing is enhanced by taking advantage of human body's self-healing capacity[8].

However, the number of bone marrow stem cells (bMSCs) is limited. Moreover, bMSCs might leak from the hole since there is no stable scaffold to hold the cells. In addition, the fibrin clot is not always mechanically stable and can not cover larger defect. Hence addition of a scaffold may provide an optimal microenvironment for endogenous MSCs infiltration, proliferation and differentiation[9]. A variety scaffolds have been studied and used [10-14].Among them, collagen-based scaffold is the most promising biomaterial due to its excellent biocompatibility, biodegradability and mechanical properties.

The quality of cartilage repair can be improved by growth factors, which are important for bMSCs and chondrocytes proliferation and differentiation. Endogenous growth factors are often utilized since exogenous grow factors have not been approved for clinical cartilage repair. Platelet-rich plasma (PRP), which can be easily obtained from autologous blood is a natural source of autologous growth factors. PRP has been used successfully in clinical

Chwee Teck Lim, James C.H. Goh (Eds.): ICBME 2008, Proceedings 23, pp. 1289–1292, 2009
www.springerlink.com

practice. PRP contains many growth factors, such as platelet-derived growth factor (PDGF), transforming growth factor (TGF-beta1, TGF-beta2), insulin-like growth factor (IGF-1, IGF-2) and vascular endothelial growth factor (VEGF)[15]. It has been proven effective for bone defects repair both in experimental and clinic studies [16-18]. It was also demonstrated that PRP could stimulate chondrocytes proliferation and matrix biosynthesis in vitro[19].

To explore a strategy of utilizing body's self-healing capacity for larger cartilage defect repair, the present study hypothesized that the delivery of autologous PRP in collagen matrix can improve the in-situ Bone marrow-initiated cartilage repair. Full-thickness cartilage defects were treated by collagen matrix with and without PRP. The quality and resurfacing area of cartilage defect repair were investigated. The results might be useful to enhance the therapeutic efficacy of microfracture on articular cartilage repair.

II. Materials and Methods

Fabrication of bilayer collagen scaffolds: The biodegradable collagen scaffolds which are used in this study comprised of two layers: a dense layer and a loose layer. The diameter of the scaffolds was 4 mm and the thickness was 3 mm. Insoluble type I collagen was isolated and purified from pig Achilles tendon using neutral salt and dilute acid extractions (21).Then collagen was dissolved in 0.5 M acetic acid (1.0 wt%). The collagen solution was added to a dish (thickness = 4mm) and frozen at -70 °C. Then it was lyophilized in a freeze dryer (Heto Power Dry LL1500) and compressed mechanically. Collagen solution was added onto the compressed collagen matrix and was frozen-dried again. After that, the bilayer scaffold was ready for use. Scanning electron microscope (SEM) photographs revealed that the dense layer had microspores and the loose layer had macrospores. The average pore size in the loose and dense layer of the scaffold was measured as 100-200 μm and 10-50 μm respectively. The relatively small pore size in the dense layer can efficiently prevent cells from leaking. All the pores around the unit area were measured by observation using internal standard (bar), and the average was calculated manually. The scaffold was cross-linked by severe dehydration (dehydrothermal cross-linking) (17). Then the scaffold can be used for the following implantation.

Preparation of platelet-rich plasma (PRP): Prior to surgery, approximately 5 ml of venous blood of a rabbit was drawn into a sterile pipe containing sodium citrate as an anticoagulant for processing PRP. The platelets were enriched by a two-step centrifugation process. During the first centrifugation at 200 ×g for 10 minutes in a Refrigerated Centrifuge 5415R (Eppendorf Corporation, German), the components of blood were separated into two phases: one phase comprises of PRP and the other comprises of erythorocytes and leukocytes. The samples of PRP underwent a second centrifugation at 560 × g for 15 minutes that allowed the precipitation of the platelets, which thereafter were re-suspended in 0.05ml of plasma. Samples of PRP and whole blood were analyzed in an automatic counter (Sysmex F-820). 0.05 ml PRP was loaded onto the scaffold immediately before the insertion into the cartilage defect.

Animal model: Thirty-three knee joints of male New Zealand White Rabbits (2-2.5 kg) were used in this study. Rabbits were maintained separately in stainless-steel cages. The rabbits were anesthetized by an intramuscular injection. The knee joints were opened with a medial parapatellar approach. The patella was dislocated laterally and the surface of the femoropatellar groove was exposed. A full-thickness cylindrical cartilage defect of 4 mm in diameter and 3 mm in depth was created in the patellar groove using a stainless-steel punch. The defects were either untreated (group I, n=11) or treated with bilayer collagen matrix (group II, n=11), and with PRP and bilayer collagen matrix (group III, n=11). 5 knee joints were used as normal control for biomechanical evaluation. The animals were returned to their cages and allowed to move freely without joint immobilization. At 6 and 12 weeks after transplantation, cartilage defect was evaluated histologically (n=3 at each time point of each group). In addition, mechanical properties were evaluated at 12 weeks (n=5).

All the animals were operated according to the standard guidelines approved by Zhejiang University Ethics Committee.

III. Results

A. Platelet concentration in the PRP characterization

The average amount of PRP for transplantation was 0.05ml after processing. The average platelet concentration in whole blood was 2.44 +/- 0.46×105/μl before processing, while it reached to 18.25 +/- 1.21×105/μl in the final PRP for transplantation. In other words, the platelet concentration increased more than seven-fold after processing.

B. Gross morphology

The gross examinations of knee joints showed that there were no abrasions on the opposing articulating surfaces and no inflammation at both 6 and 12 weeks time point. The defects remained empty in small parts at 6 weeks after transplantation (Figure 1. a, e, f).

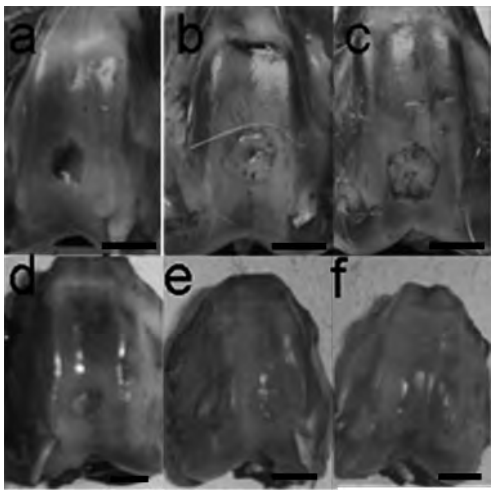


Fig. 1. Macrophotograph shows that the defects in the three groups at 6 weeks (a,b,c) and 12 weeks (d,e,f) post-surgery. a,d the microfracture group (group I); b, e the microfracture with collagen group (group II); c, f the microfracture with PRP in collagen matrix group (group III).

C. Results of Histological examination

At 6 weeks after transplantation, the defects in group I (n=3) were filled with fibrous tissue (Figure 2.). In group II (n=3) and group III (n=3), the defects were repaired with mixture of fibrous tissue and cartilage-like tissue as shown by staining and Safarnine-O staining. The amounts of chondrocyte-like cells and cartilage-like extracellular matrix in group III were more than those of group II as observed from Safranine-O staining (Figure 2,6w).

At 12 weeks after transplantation, the defects in group I (n=3) were almost filled with fibrous tissue and a little cartilage-like tissue at the margins of the defects (Figure 2,12w). Group II had lager amounts of hyaline cartilage (Figure2,12w). Group III has the largest amounts of hyaline cartilage tissue. It was found that hyaline cartilage tissues were formed at the surrounding area of the defects while the fibrous tissues were located at the central part of defects.

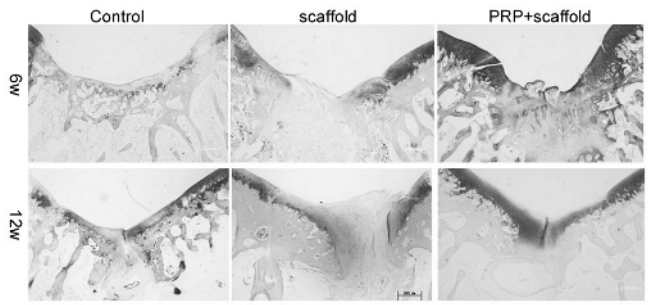


Fig. 2. Histological examination of the three groups at 6 weeks and 12weeks post-surgery.Left is the microfracture group .Middle are the microfracture with collagen matrix group. Right is the microfracture with PRP in collagen matrix group. Safranine-O staining. Original magnification 40x. Scale is as indicated (bar=500 micrometer).

The total ICRS histological scores of the specimens at 6 and 12 weeks revealed differences between the three groups. The scores for the repaired tissue of group III were significantly higher than those for other two groups ($p < 0.05$). The histological scores of the specimens at 12 weeks were higher than those of specimens at 6 weeks.

D. Results of Biomechanical evaluation

From the indentation test, the Young's modulus of repaired tissues from the three groups (12 weeks) were determined and compared with each other while the tissues from normal rabbit knee joint were used as normal control. At 12 weeks, the compressive modulus of the repaired tissue in group II and group III samples showed greater improvement compared with specimens from group I ($p<0.05$). However, the modulus of repaired tissue in both group II and group III was inferior to that of normal cartilage (0.52 +/- 0.01Mpa) ($p< 0.05$). It was found that the difference between the group II and group III has no statistical significance, which may be caused by the limitation of mechanical test. As the diameter of defect was 4 mm and the diameter of the indenter was 2 mm, the compressive test was carried out at the central area of those defects which were mainly fibrous tissue.

IV. Discussion

The present study demonstrated that autologous PRP and collagen matrix synergistically stimulated the formation of cartilage tissues, [20,21]which significantly improved body's self-healing capacity for larger cartilage defect repair by providing scaffolds and growth factors for in-situ bone marrow progenitor cells. The results were useful to enhance the therapeutic efficacy of microfracture on articular cartilage repair. It implicated that the combination of microfracture with PRP in collagen matrix could repair certain type of cartilage defects (larger than 2 cm2) which currently require the complex autologous chondrocyte implantation or osteochondral grafting. Moreover, this study was the first to present that cartilage tissue formation was initiated at the surrounding area of the defects and crept to cover the central part of defects with time. It was different from the format of simultaneous or random cartilage tissue formation at the cartilage defect after ACI, which implicated that the cells or signals from the edge of native cartilage tissue played a crucial role in inducing the bone marrow stem cells for cartilage formation.

V. Conclusions

In summary, autologous PRP and bilayer collagen matrix acted synergistically in stimulating the formation of cartilage tissues in articular cartilage defects. PRP can be easily obtained from autologous blood, and the operation procedure is simple and safe. It appeared that the combination PRP with scaffold might have great potential in clinical application to improve the therapeutic efficiency of microfracture on articular cartilage repair.

Acknowledgement

This work was supported by National Natural Science Foundation of China (30600301, 30600670, U0672001) and Zhejiang Province grants (R206016, 2006C14024).

References

1. Akeda, K.; An, H. S.; Okuma, M et al. (2006) Platelet-rich plasma stimulates porcine articular chondrocyte proliferation and matrix biosynthesis. Osteoarthritis Cartilage 14(12):1272-1280
2. Breinan, H. A.; Martin, S. D.; Hsu, H. P et al. (2000) Healing of canine articular cartilage defects treated with microfracture, a type-II collagen matrix, or cultured autologous chondrocytes. J Orthop Res 18(5):781-789
3. Buckwalter, J. A (1998) Articular cartilage: injuries and potential for healing. J Orthop Sports Phys Ther 28(4):192-202
4. Buma, P.; Pieper, J. S.; van Tienen, T et al. (2003) Cross-linked type I and type II collagenous matrices for the repair of full-thickness articular cartilage defects--A study in rabbits. Biomaterials 24(19):3255-3263.
5. Chen, G.; Sato, T.; Tanaka, J et al. (2006) Tateishi, T. Preparation of a biphasic scaffold for osteochondral tissue engineering. Materials Science and Engineering: C 26(1):118-123
6. Dzioba, R. B. (1988) The classification and treatment of acute articular cartilage lesions. Arthroscopy 4(2):72-80
7. Fan, H.; Liu, H.; Zhu, R.(2007) Comparison of chondral defects repair with in vitro and in vivo differentiated mesenchymal stem cells. Cell Transplant 16(8):823-832
8. Frisbie, D. D.; Trotter, G. W.; Powers, B. E.; et al. (1999) Arthroscopic subchondral bone plate microfracture technique augments healing of large chondral defects in the radial carpal bone and medial femoral condyle of horses. Vet Surg 28(4):242-255
9. Hunziker, E. B. (2002) Articular cartilage repair: basic science and clinical progress. A review of the current status and prospects. Osteoarthritis Cartilage 10(6):432-463
10. Kandel, R. A.; Grynpas, M.; Pilliar, R. et al. (2006) Repair of osteochondral defects with biphasic cartilage-calcium polyphosphate constructs in a Sheep model. Biomaterials 27(22):4120-4131
11. Kitoh, H.; Kitakoji, T.; Tsuchiya, H. et al. (2007) Transplantation of culture expanded bone marrow cells and platelet rich plasma in distraction osteogenesis of the long bones. Bone 40(2):522-528
12. Kramer, J.; Bohrnsen, F.; Lindner, U. et al. (2006) In vivo matrix-guided human mesenchymal stem cells. Cell Mol Life Sci 63(5):616-626
13. Ma, Z.; Gao, C.; Gong, Y et al. (2005) Cartilage tissue engineering PLLA scaffold with surface immobilized collagen and basic fibroblast growth factor. Biomaterials 26(11):1253-1259
14. Mainil-Varlet, P.; Aigner, T.; Brittberg M et al. (2003) Histological assessment of cartilage repair: a report by the Histology Endpoint Committee of the International Cartilage Repair Society (ICRS). J Bone Joint Surg Am 85-A Suppl 2:45-57
15. Marx, R. E.; Carlson, E. R.; Eichstaedt, R. M et al. (1998) Platelet-rich plasma : Growth factor enhancement for bone grafts. Oral Surg Oral Med Oral Pathol Oral Radiol Endod. 85(6):638-646
16. Matsusue, Y.; Yamamuro, T.; Hama, H. (1993) Arthroscopic multiple osteochondral transplantation to the chondral defect in the knee associated with anterior cruciate ligament disruption. Arthroscopy 9(3):318-321
17. Ming-Che, W.; Pins, G. D.; Silver, F. H. (1994) Collagen fibres with improved strength for the repair of soft tissue injuries. Biomaterials 15(7):507-512
18. Newman, A. P. (1998) Articular cartilage repair. Am J Sports Med 26(2):309-324
19. O'Driscoll, S. W. (1998) The healing and regeneration of articular cartilage. J Bone Joint Surg Am 80(12):1795-1812
20. Richardson SM, Walker RV, Parker S et al. (2006). Intervertebral disc cell-mediated mesenchymal stem cell differentiation. Stem Cells 24:707-716.
21. Shapiro F, Koide S, Glimcher MJ.(1993) Cell origin and differentiation in the repair of full-thickness defects of articular cartilage. J Bone Joint Surg Am75:532-553.

Author: Ouyang Hongwei
Institute: Zhejiang university
Street: 388# Yu Hang Tang Road
City: Hang Zhou
Country: China
Email: hwoy@zju.edu.cn

Bioactive Coating on Newly Developed Composite Hip Prosthesis

S. Bag[1] & S. Pal[2]

[1] JIS College of Engineering, Kalyani, West Bengal, India
[2]School of Bioscience & Engineering, Jadavpur University, Kolkata, India
[1]Corresponding author, email: sandip_bag76@yahoo.co.in

Abstract — **Conventional metal prostheses carry the major joint load and cause stress shielding and bone become osteoporotic due to lack of physiological stress flow in a common hip replacement. To develop suitable hip prosthesis having properties similar in terms of density and modulus of elasticity of bone, ceramic reinforced polymer composite material would be an ideal material as bone is also a composite material consisting of collagen fiber matrix and embedded hydroxyapatite mineral. With this idea in mind we developed a composite material using UHMWPE and alumina ceramic in various proportion whose properties are similar to that of bone and tried to integrate it with bone using hydroxyapatite and bio-glass separately leading to new osseous tissue generation for fixation when in intimate contact with bone in animal model.**

Keywords — **Bioactive coating, Composite prosthesis, hip prosthesis, UHMWPE, alumina**

I. Introduction

Hip joint is one of the most vulnerable joint in human body requiring replacement surgery. It has become the most widely accepted procedure for the treatment of disabling hip arthritis in modern orthopedic surgery [1]. Currently hip prostheses made of stainless steel (316L) are widely used for their good load bearing properties [2]. The density of this metal is heavier by 6-7 times compared to bone, the density of which ranges between 0.8-2.1gm/cc. similarly the modulus of elasticity of surrounding bone (3-30 GPa) is nearly 10-20% that of stainless steel (stainless steel exhibits a modulus of elasticity of 200GPa) [3,4]. So the applied load is mostly transferred through the metal not to the bone [5]. This results in the bone being inadequately loaded and consequently it resorbs and also changes the biomechanical environment [6].

To make suitable hip prosthesis in terms of density and modulus of elasticity ceramic reinforced polymer composite material would be the ideal material as bone itself is a composite material [7,8]. Hip replacement is a common phenomenon in advanced orthopedic surgery. Since hip joint is a load bearing joint, so it is replaced only by the material having load bearing capacity. Generally hip prosthesis is made of stainless steel 316L because it has good load bearing property.

The hip prosthesis must be anchored securely within the narrow cavity of femur for good function. The loose sitting hip prosthesis is painful and such loose hip is also stiff [9](Hirsch C, 1974).

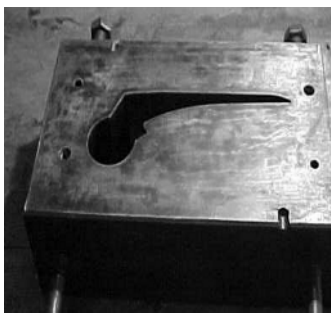
II. Materials and Methods

A. Design and development of Hip prosthesis mould

Hip prosthesis mould was designed in consultation with a local Industrial consultant and developed by us as per the standard size and shape of Austein Moore metallic hip prosthesis. These were highly specialized job. EDM and program controlled wire cut technology were used. The system contains heating arrangement inside the mould. The design & fabrication and machining of the mould were shown in Fig1a& Fig1b respectively.



(a)



(b)

Fig-1: Three-piece hip prosthesis mould a) shows the two components of the mould and b) shows the main Die with heating coil.

Chwee Teck Lim, James C.H. Goh (Eds.): ICBME 2008, Proceedings 23, pp. 1293–1296, 2009
www.springerlink.com



(a)



(b)

Fig-2: Machining of Hip Prosthesis mould using numerically controlled EDM technology (a) Shows the copper EDM spark cutter for the mould which mimics the shape and (b) shows the total machining set up in a chamber, to be filled with dielectric fluid, kerosene.



Fig-3: Mould of Hip prosthesis along with heating arrangement placed in compression machine.

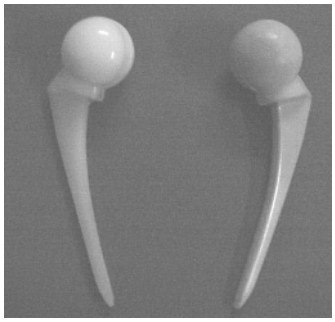


Fig-4: UHMWPE and UHMWPE-alumina ceramic composite Hip prosthesis.

B. Preparation of Polymeric and composite Hip Prosthesis

The UHMWPE (GUR 4020) and UHMWPE-alumina ceramic composite hip prosthesis was prepared in the 3 piece hip mould using compression moulding technique. The accurately weighed UHMWPE powder (50 gms) and mixture of UHMWPE and alumina ceramic powders (65 gms) were taken and placed inside the mould. Initially by pressing the top part of the mould over the powder, the structure of hip prosthesis was made and the top part kept intact. The total assembly was placed between the two plates of a compression machine (ALMIL-make hydraulic press of capacity 2000kN). The powder was cold compressed repeatedly for 5-10 minutes under a pressure of (10 MPa) in order to expel the air entrapped between the mixtures. The temperature of the thermocouple-programmed controller was set to 160^0C and held constant for sufficient time to melt the powder material properly. Heating time of very short duration results in inadequate plasticization. This may be detected by finding a white core in a vertical section through the produced sheet.

After plasticization air-cooling was applied to the compression mould. As the shrinkage of the material progresses, pressure is gradually increased and brought up to 8-10 MPa (load-300KN). This pressure is maintained constant until the total mass came back to ambient temperature. Then the mould was taken out from the press and the desired prosthesis was removed from the mould.

C. Bioactive material coating on hip prosthesis

Since the stem of the composite hip prosthesis were very smooth so surface modification was required to improve the coating adherence to the smooth composite stem. The surface treatment processes of the stem included sand blasting and acid etching. After that the hip prosthesis was cleaned with ethyl alcohol and distilled water to remove the sand particle and acid from the prepared surface. The coating was applied by air spray technique.

The coating solution was prepared by pouring the powder (hydroxyapatite or bio-glass) in ethyl alcohol water mixture at volume ratio (1:1) and continuously stirred to get a homogeneous suspension. The suspension was sprayed in a thin layer over the composite stem surfaces with the help of a spray gun (spray gun was attached to the compressed air) and then dried at room temperature. Several fine layers were applied as per the required thickness. After that the spray coated composite material was placed again in the hip pros-

thesis mould box and compressed at 8 MPa pressure after heating at 95-100°C for 30 min. The load is maintained constant until the total mass came back to ambient temperature. After cooling the mould was taken out form the press and finally we get a bioactive material coated stem of a composite hip prosthesis. The mechanism behind this coating is polymer matrix of the composite was softened during heat treatment and enhanced the coating adhesion to the substrate by mechanical anchoring through loading.

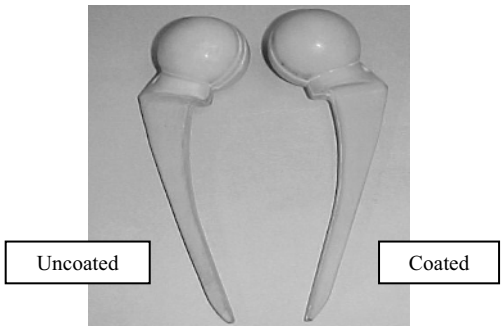


Fig-5: Uncoated and coated hip prosthesis.

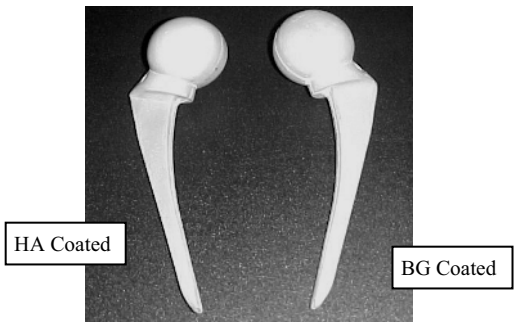


Fig-6: Hydroxyapatite(HA) and Bio-glass(BG) coated hip prosthesis.

III. Coating characterization

After successful deposition of bioactive (HA and Bio-glass) coating over composite hip stem, the coating layer were analyzed using the following methods

A. Surface roughness measurement

The roughness values of both the coated and uncoated stem was measured using Handysurf surface roughness measuring instrument (Handysurf E-30A, made by TSK, Japan). Roughness of the coated stem was measured in longitudinal and transverse directions.

Cells are shown to attach to a higher degree to surfaces containing natural binding sites [11].



Fig-7: Surface roughness measurement by Handysurf E-30A

B. Coating Thickness measurement

Ultra-sonic coating thickness gauge (Quintsonic PRO, Electro-Physik GmbH & Co., Germany) was used to measure the coating thickness of hydroxyapatite and bio-glass coated composite plate.



Fig-8: Coating Thickness measurement by Quintsonic Coating Thickness Gauge

C. Coating strength measurement

The coating strength of the coated hip stem was measured by scratch adhesion testing method using a special tooling for the purpose. . A qualitative adhesion test was carried out to measure the adhesive strength of bioactive coating to the stem.

IV. Results

The average roughness value of the coating over composite hip stem was directly noted from the display screen of Handysurf E-30A, made by TSK, Japan. The surface roughness (Ra) value of the uncoated stem is 0.4050 ±

0.0686μm. After coating, the roughness value of the stem increases. The roughness value of the HA coated stem was 4.2955 ± 0.2508 μm and BG coated stem was 2.1055 ± 0.1882 μm.

The thickness of the bioactive coating layer was measured using ultrasonic coating thickness gauge. The mean coating thickness of the HA coating is 36.1 ± 2.4244 μm and for Bio-glass coating the thickness value is 26.2 ± 2.4855 μm.

In scratch test, it was found that a sufficient scrapping force was to remove the thin bioactive coating from the composite stem. The mean coating strength of HA coating was measured as 618±5.9798 MPa whereas in case of BG coating it was 612 ± 3.3626 MPa.

V. Discussion

Bioactive hydroxyapatite and bio-glass coating over the stem of the composite hip prosthesis has been successfully achieved using combination of spray deposition and compression moulding technique. The quantity of the bioactive particles embedded on the composite surface was controlled by the concentration of the bioactive suspension and the applied coating layers. The mean coating strength was measured as 618 ± 5.9798 MPa and 612 ± 3.3626 MPa respectively for HA and BG coating and will not easily remove from the composite surface. The surface roughness of the coating layer was found 4.2955 ± 0.2508 μm for HA coated stem and for BG coated stem is 2.1055 ± 0.1882 μm and it will influence the bone cell to deposit over it. The coating thickness is sufficient for bone bonding and long term stability. The above mentioned bioactive coating adhere to the surface of the implant, binds with both implant and bone, promotes the formation of new bone and extends the implant life [10,11].We also did some animal study which indicated the integration of the of the implant with the bone[12].

Acknowledgement

This work was funded by DRDO-New Delhi, Govt. of India to the 2nd author.

Reference

1. Beckenbaugh RD, Ilstrup DM (1978): Total hip arthoplasty. *J. Bone Jt. Surg*. 60-A: 306-313
2. Skinner H B (1988): Composite Technology for total hip arthoplasty-*Clinical orthopaedics and related Research* 235: 224-36.
3. Greesink R G T (1989): Experimental and clinical experience with HA-coated hip implants. *Orthopaedics*, 12 (9): 1239-1242.
4. Ratner B D, Hoffman A S, Schoen F J, Lemons J E. (1996): Biomaterials Science: An introduction to materials in medicine. 1st edition. *Elsevier Science*. San Diego.
5. Karachalios T, Tsatsuaronis C, Efraimis G, Papadelis P, lyritis G, Diakoumopoulos G. (2004): The long-term clinical relevance of calcar atrophy caused by stress shielding in total hip arthroplasty-A 10 year postoperative, randomized study. *Journal of Arthroplasty* 19: 469-475.
6. Greesink R G T (1990): HA-coated total hip prostheses: Two-year clinical and roentgenographic results of 100 cases. *Clin. Orthop*., 261: 39-58.
7. Farling, G M and Greer K (1978): An improved bearing material for joint replacement prostheses: Carbon-fiber reinforcement UHMWPE.
8. Bonfield W (1988): In vivo evaluation of hydroxyapatite reinforced polyethylene, in Materials Characteristics Vs *In vivo* Behaviour, eds. P.Ducheyne & J.E.Lemons, New York Academy of Sciences, p 173.
9. Hirsch, C. (1974): Clinical problem of total hip replacements*, J. Biomed. Mat. Res:* Symposium, No**.5**, 227.
10. Anderson O H, Karlsson K H and Kangasniemi K (1990): *J. Non-Cryst. Solids*. `Vol-112, pp 290.
11. Hench L L (1991): *J. Am. Ceram. Soc*., Vol-74, pp-1487.
12. Ph.d thesis sandip bag-"Development and Characterization of Bioactive Coating on Polymer & its Composite",2006

1st Author: Dr. Sandip Bag

Institute: JIS College of Engineering
Block-A, Phase-III
City: Kalyani
Country: India
Email: sandip_bag76@yahoo.co.in

2nd Author: Prof (Dr) Subrata Pal
Institute: Jadavpur University
Street: 188, Raja S.C. Mullick Road, Kolkata-700032
City: Kolkata
Country: India
Email: spalbme@yahoo.co.in

Development and Validation of a Reverse Phase Liquid Chromatographic Method for Quantitative Estimation of Telmisartan in Human Plasma

V. Kabra[1], V. Agrahari[1], P. Trivedi[2]

[1] Department of Pharmacy, Shri G. S. Institute of Technology & Science (SGSITS), Indore, India
[2] School of Pharmaceutical Sciences, Rajiv Gandhi Technical University (RGTU), Bhopal, India

Abstract — **A sensitive, rapid, reverse phase and isocratic high-performance liquid chromatography (HPLC) method has been developed for the estimation of telmisartan in human plasma. Sample detection was carried out at 297 nm using an Ultraviolet (UV)-PDA detector. Plasma sample pretreatment consist of protein precipitation extraction with methanol. The compounds were separated using a mobile phase of sodium dihydrogen phosphate buffer (pH 3.0): acetonitrile (ACN) (42:58, v/v) on a Phenomenex LUNA C_{18}, column (250×4.6 mm i.d., 5µm) at a flow rate of 1.2 ml/min. The total run time for the assay was 4.2 min. The method was validated over the range of 40-1600 ng/ml. The lowest limit of quantification and limit of detection was found 40 and 2.8 ng/ml respectively. The recovery for low, medium and high quality control samples were found 81.13, 79.96 & 82.40 % respectively. The method was found to be accurate and precise. Stability data of analytes revealed that they are stable in plasma under different stability conditions. The results observed conclude that the developed method is very appropriate and applicable for antihypertensive research programs of telmisartan.**

Keywords — **High performance liquid chromatography, telmisartan, plasma, reverse phase, stability**

I. Introduction

Bioanalytical method is the qualitative and quantitative analysis of drug substances in biological fluids or tissues. It plays a significant role in the evaluation & interpretation of bioavailability, bioequivalence and pharmacokinetic data. The sensitivity and selectivity of the bioanalytical methods are essential to the success of preclinical and clinical studies during all phases of the drug development process, i.e. from the initial preclinical phase to the final clinical phases.

Telmisartan, [1,1-biphenyl]-2-carboxylic acid, 4-[(1, 4 -dimethyl-2-propyl[2,6-bi-1H-benzimidazol]-1-yl)methyl] (Fig. 1) is an angiotensin II receptor antagonist that lowers blood pressure through blockade of the rennin-angiotensin-aldosterone system and shows non-competitive inhibition, used in the treatment of hypertension [1]. A few analytical methods for the determination of telmisartan have reported [2-11]. However no methods have been reported for the determination of telmisartan in plasma by HPLC with ultraviolet detection. All these reported methods have some drawbacks such as use of extensive sample preparation methods, excess quantity of sample requirement, long run time and higher cost of sample analysis due to the use of sensitive detectors which is a tedious and costly job for lab scale analysis of telmisartan. In this paper, we describe a sensitive, isocratic & simple HPLC–UV method for the determination of telmisartan in human plasma which includes short run time & small plasma sample volume. The method was validated for different parameters. On the basis of the results obtained it can be said that the method described here would be suitable for determination of pharmacokinetic profiles, drug monitoring and in bioequivalence studies of telmisartan.

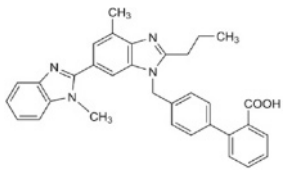


Fig. 1 The chemical structure of telmisartan (TLMS)

II. Experimental

A. Reagents and Chemicals

Telmisartan was kind gift sample from Dr. Reddy's laboratories ltd., Hyderabad, India. Methanol and Acetonitrile (ACN) were of HPLC grade and purchased from Merck ltd., New Delhi, India. Human plasma was kindly obtained from blood bank department, Bhopal Memorial Hospital & Research Centre (BMHRC), Bhopal, India. All other chemicals were of analytical grade and used without further purification.

B. Instrumentation

The HPLC system (Shimadzu Corporation, Japan) consisted of a LC-10AT VP pump, SPD-10AT VP photo diode array (PDA) detector. A manual injector attached with a 20 µl sample loop was used for sample loading. Class LC10/M10A work station was used for data collection

Chwee Teck Lim, James C.H. Goh (Eds.): ICBME 2008, Proceedings 23, pp. 1297–1300, 2009
www.springerlink.com

and acquisition. The analytical column was Phenomenex Luna C_{18} (250mm X 4.6mm, 5µm), protected by Phenomenex HPLC guard cartridge system.

C. Chromatographic conditions

The chromatographic separations were performed at ambient temperature with an isocratic elution. The mobile phase composed of sodium dihydrogen phosphate buffer (pH 3.0, adjusted with orthophosphoric acid): ACN (42:58 v/v) and was set at a flow rate of 1.2 ml/min. The chromatogram was monitored with UV detection at a wavelength of 297 nm. The mobile phase was prepared daily, filtered & sonicated before use.

D. Sample extraction procedure

Protein precipitation technique was used for extraction of telmisartan from plasma samples by using methanol as a precipitating agent. The satisfactory values for recovery for each plasma sample with single extraction were observed when 1:4 ratios of plasma & methanol were mixed thoroughly and vortexes at room temperature. It was then centrifuged at 10,000 rpm for 10 min at 4 ^{0}C. The decanted clear supernatant liquid was filtered through 0.45µ syringe filter and injected into HPLC system by using a small sample volume (20µl).

E. Preparation of standard stock solution and quality control samples (QC)

Standard stock solution of telmisartan (100µg/ml) was prepared in methanol and stored at 4°C. Serial dilution of the standard stock solution with methanol, lead to solution of concentration of 40-1600 ng/ml. For the preparation of calibration samples, 0.8 ml was taken from the standard stock solution and diluted up to 10 ml with blank plasma to give standard spiked plasma stock solution of 8 µg/ml. From the standard spiked plasma stock solution different concentrations were prepared by taking 0.05, 0.1, 0.2, 0.4, 0.8, 1.2, 1.6 & 2.0 ml and the volume of each was made up to 2 ml with blank plasma. 8 ml of precipitating agent (methanol) was added in all to obtain the final concentration of 40, 80, 160, 320, 640, 960, 1280 and 1600 ng/ml of telmisartan in plasma respectively. After that these different concentrations were followed to sample extraction procedure as described above, and the supernatant was filtered, directly injected into HPLC column for each concentrations. QC samples at different levels of high quality control (HQC, 1600 ng/ml), middle (MQC, 640 ng/ml), low quality control (LQC, 80 ng/ml) and lowest limit quality control (LLOQ, 40 ng/ml) samples were selected to perform various validation parameters.

F. Limit of detection (LOD) and lowest limit of quantification (LLOQ)

LOD was defined as the concentration that yields a signal-to- noise ratio of 3. LLOQ was the smallest analytical concentration which could be measured with defined accuracy and precision under the given experimental conditions. LLOQ was calculated to be the lowest analyte concentration that could be measured with a signal-to-noise ratio of 10. The LLOQ & LOD was found to be 40 ng/ml & 2.8 ng/ml respectively.

G. Linearity

Calibration plots for the analytes in plasma were prepared by spiking drug-free plasma with standard stock solutions to yield concentrations of 40–1600 ng/ml (40, 80, 160, 320, 640, 960, 1280 and 1600 ng/ml) for telmisartan. Five replicate injections (n =5) of each concentration were performed. The linear regression data analysis was used for the calculation of intercept, slope and correlation coefficient (r^2) which were then used to calculate the analytes concentration in each sample.

H. Selectivity

The ability of an analytical method to differentiate and quantify the analyte in the presence of other components in the sample is termed as selectivity. For selectivity, blank sample of the plasma was prepared from six different sources.

I. Accuracy

The accuracy of an analytical method describes the closeness of mean test results obtained by the method to the true value of the analyte. The mean value should be within ± 15% of the actual value except for LLOQ, where it should not deviated by more than ± 20%. It is determined by calculating the percent difference (% bias) between the mean concentrations and the corresponding nominal concentrations. The accuracy samples were analyzed for five replicates (n =5) of LLOQ, LQC, MQC and HQC.

J. Precision

The precision of an analytical method describes the closeness of individual measure of an analyte. Precision of the assay in plasma was determined by assaying all quality

control samples including LLOQ in five replicate (n =5). To determine different precision parameters sample was analyzed within the same day (repeatability of precision), on other day (inter day precision) & by other analyst (analyst to analyst precision). Precision was reported in terms of percent relative standard deviation (% RSD).

K. Recovery

Recovery analysis should be performed by comparing the analytical results of extracted samples with unextracted samples for HQC, MQC & LQC samples which representing 100% recovery. The percentage of the drug recovered from the plasma samples was determined by comparing the peak height ratio after extraction with those of unextracted methanolic solution containing same concentration of telmisartan as in plasma.

L. Stability

Stability analysis should evaluate the stability of the analytes during sample collection and handling after long-term and short-term (bench top) storage at room temperature and after going through freeze and thaw cycles. The different stability conditions are described are Stock solution stability (SSS), Short term (bench top) storage stability (BTS), Post-Preparative Stability (PPS), Freeze–thaw stability (FTS), Long term storage stability (LTS).

III. Results and discussion

A. Selection of HPLC chromatographic conditions

Various combinations of different solvents were tried & investigated to optimize the mobile phase composition to performance and peak shape. The separation of telmisartan and plasma were affected by the composition and pH of the obtain good results for the separation, sensitivity, column mobile phase. Peak shape and run time were improved by adjusting the pH of water to 3.0 with orthophosphoric acid (OPA). Under the chromatographic conditions described above, blank plasma sample did not give any peak at the retention time of telmisartan (Fig. 2) i.e. the peaks were well separated. The retention times of plasma and of telmisartan were 1.78 ± 0.3 min and 3.5 ± 0.3 min, respectively (Fig. 3).

B. Validation of the optimized method

1. Selectivity

No interfering endogenous compound peak was observed at the retention time of blank plasma and telmisartan. Thus the method was selective for analysis of telmisartan in plasma.

2. Linearity

Linearity was determined over the concentration range of 40–1600 ng/ml, which display good linear response to the method. The calibration curves were fitted by linear least-square regression and the correlation coefficient was found to be 0.9998.

3. Recovery of the method

Recovery for telmisartan was evaluated. The overall mean value of recovery was found to be 81.16%. The recovery of the extraction procedure at HQC, MQC and LQC samples of telmisartan were found to be 82.4 %, 79.96 % and 81.13 % respectively (Table 1).

4. Assessment of stability

Telmisartan was found stable under different storage and processing conditions. The stability data of telmisartan under various storage conditions was shown in Table 2.

5. Accuracy and precision measurement

The accuracy (% N conc.) for telmisartan was found to be 100.93 101.30, 103.99 & 108.05 for HQC, MQC, LQC & LLOQ samples respectively (Table 1). The precision data for HQC, MQC, LQC & LLOQ samples were analyzed in replicates of five (n = 5) and were shown in Table 1. For intra-day it was found 1.31 %, 1.53 %, 4.68 % & 7.40 %, for inter-day 1.50 %, 4.82 %, 3.20 % & 5.71 % and for analyst to analyst precision it was found 2.15 %, 1.89 %, 4.67 % & 5.53 % for HQC, MQC, LQC & LLOQ samples respectively. The results were within the acceptance criteria for precision and accuracy, i.e., deviation values were within ± 15% of the authentic values, except for LLOQ, which could show a ± 20% deviation.

Table 1 Accuracy, precision & recovery of the developed method

QC samples **r**	Accuracy		Precision (% RSD)			Mean Recovery (%)
	% N.Conc.[a]	% Bias	Intra day	Inter day	Analyst-to-analyst	
LLOQ[b]	108.05	8.05	7.40	5.71	5.53	-
LQC[c]	103.99	3.99	4.68	3.20	4.67	81.13
MQC[d]	101.30	1.30	1.53	4.82	1.89	79.96
HQC[e]	100.93	0.93	1.31	1.50	2.15	82.40

[a] % Nominal concentration; [b] lowest limit of quantitation; [c] low quality control; [d] medium quality control; [e] high quality control.

Table 2 Stability of the developed method at various conditions

Stability Conditions	Telmisartan			
	LQC		HQC	
	% N. Conc.	% Change	% N. Conc.	% Change
SSS[a]	93.60	5.28	103.20	3.08
BTS[b]	102.40	1.81	94.63	8.57
PPS[c]	98.42	4.73	92.65	6.10
FTS[d]	103.30	2.70	107.96	4.70
LTS[e]	110.57	-5.60	112.40	2.96

[a] stock solution stability; [b] bench top stability; [c] post processing stability; [d] freeze & thaw stability; [e] long term stability.

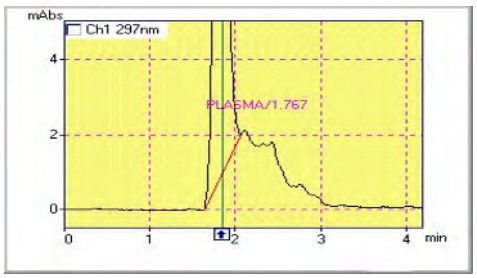


Fig. 2 The representative chromatogram of blank plasma

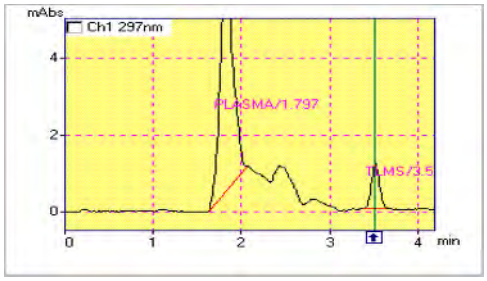


Fig. 3 The extracted chromatogram of telmisartan from plasma

IV. Conclusion

A rapid, sensitive, selective and validated assay for the quantitative determination of telmisartan in human plasma was described. The result observed from this study concludes that the developed method is very appropriate for quantitative analysis and applicable for toxicokinetic, pharmacokinetic, bioavailability, bioequivalence, therapeutic drug monitoring (TDM) and routine plasma monitoring studies of telmisartan in hypertensive patients.

Acknowledgement

The authors are grateful to Prof. P. B. Sharma (Ex-Vice Chancellor, RGTU, Bhopal, India) for providing generous access to laboratory facility to perform this study, and to the blood bank department, Bhopal Memorial Hospital & Research Centre, Bhopal, India for providing plasma samples. This work was also supported by a grant from the Ministry for Human Resource Development (MHRD), New Delhi, India.

References

1. Wienen, W, Entzeroth M, Stangier, J et al. (2000) A Review on Telmisartan: A Novel, Long-Acting Angiotensin II-Receptor Antagonist. Cardiovasc Drug Rev 18:127-154
2. Hillaert S, Bossche W V D (2002) Optimization and validation of a capillary zone electrophoretic method for the analysis of several angiotensin-II-receptor antagonists. J Chromatogr A 979:323-333
3. Su C A, Stangier J, Fraunhofer A et al. (2000) Pharmacokinetics of acetaminophen and ibuprofen when coadministered with telmisartan in healthy volunteers. J Clin Pharmacol 40:1338-1346
4. Stangier J, Schmid J, T¨urck D et al. (2000) Absorption, metabolism, and excretion of intravenously and orally administered telmisartan in healthy volunteers. J Clin Pharmacol 40:1312-1322
5. Stangier J, Su C A, Van H et al. (2001) Inhibitory Effect of Telmisartan on the Blood Pressure Response to Angiotensin II Challenge. J Cardiovasc Pharmacol 38:672-685
6. Torrealday N, Gonzalez L, Alonso R M et al. (2003) Experimental design approach for the optimisation of a HPLC-fluorimetric method for the quantitation of the angiotensin II receptor antagonist telmisartan in urine. J Pharm Biomed Anal 32:847-857
7. Xu M T, Song J, Li N (2003) Rapid determination of telmisartan in pharmaceuticals and serum by the parallel catalytic hydrogen wave method. Anal Bioanal Chem 377:1184-2650
8. Xu M, Song J, Liang Y (2004) Rapid determination of telmisartan in pharmaceutical preparations and serum by linear sweep polarography. J Pharm Biomed Anal 34:681-687
9. Chen B M, Liang Y Z, Wang Y L et al. (2005) Development and validation of liquid chromatography–mass spectrometry method for the determination of telmisartan in human plasma. Anal Chim Acta 540:367-373
10. Li P, Wang Y W, Wang Y et al. (2005) Determination of telmisartan in human plasma by liquid chromatography–tandem mass spectrometry. J Chromatogr B 828:126-129
11. Hempen C, Schwarz L G, Kunz U et al. (2006) Determination of telmisartan in human blood plasma: Part II: Liquid chromatography-tandem mass spectrometry method development, comparison to immunoassay and pharmacokinetic study. Anal Chim Acta 560:41-49

Author: Ms. Vibhuti Kabra
Institute: Department of Pharmacy, Shri G. S. Institute of Technology & Science (SGSITS)
Street: 23-Park Road
City: Indore
Country: India
Email: vibhuti.kabra@rediffmail.com

Response of Bone Marrow-derived Stem Cells (MSCs) on Gelatin/Chitosan and Gelatin/Chitooligosaccharide films

J. Ratanavaraporn[1], S. Kanokpanont[1], Y. Tabata[2] and S. Damrongsakkul[1]

[1] Department of Chemical Engineering, Chulalongkorn University, Phaya Thai Road, Phatumwan, Bangkok 10330, Thailand
[2] Institute for Frontier Medical Sciences, Kyoto University, 53 Kawara-cho Shogoin, Sakyo-ku, Kyoto 606-8507, Japan

Abstract — **In this study, we investigated the effects of gelatin, chitosan and chitooligosaccharide on the biological response of bone marrow-derived stem cells (MSCs). Chitosan (CH, MW 1,000 kDa) and chitooligosaccharide (COS, MW 1.4 kDa) were produced from alkaline deacetylation and free radical degradation with hydrogen peroxide (H_2O_2) processes, respectively. Films of gelatin/CH and gelatin/COS with various blending ratios were prepared by solution casting and dehydrothermal crosslinking techniques. MSCs isolated from 3-week-old Wistar rat were cultured on the films to assess cell attachment, proliferation and osteogenic differentiation including alkaline phosphatase (ALP) activity and calcium content. On the 1st day after seeding, it was noticed that spreading areas of MSCs attached on blended gelatin/CH and gelatin/COS films were larger than those on pure gelatin, CH and COS films. It was observed that the morphology of MSCs attached on pure CH films was round compared to those on pure gelatin and COS. The number of MSCs attached and proliferated on gelatin/CH and gelatin/COS films, particularly for the films containing 70% CH and COS, were significantly higher than those on pure gelatin, CH and COS films. Along period of culture, the lowest number of MSCs was found on pure CH film, implying the toxicity of CH. After 7 days of culture under osteogenic differentiation condition, higher amount of ALP and calcium released from MSCs cultured on pure gelatin film were noticed. It was interesting that less ALP and calcium were observed on pure COS film compared to CH film. It could be concluded from the results that chitooligosaccharide was more favorable to the proliferation of MSCs compared to high molecular weight chitosan. On the other hand, high molecular weight chitosan had higher potential to promote osteogenic differentiation of MSCs than chitooligosaccharide.**

Keywords — **mesenchymal stem cells, gelatin, chitosan, proliferation, osteogenic differentiation**

I. Introduction

Three strategies required for the approach of bone tissue engineering consist of osteogenic cells, osteoconductive scaffolds and osteoinductive signaling molecules. Stem cells have potentials of proliferation and differentiation into various cell lineages [1, 2]. Mesenchymal stem cells (MSCs) isolated from bone marrow are most used stem cells in research field and clinical applications due to their high potential of differentiation [3, 4].

Scaffolds used in bone tissue engineering are designed to mimic natural bone matrix which consist of organic and inorganic materials. Usually, materials used to form organic part of bone scaffolds should be biocompatible and biodegradable. Among various types of candidates, gelatin and chitosan are ones of most widely used materials due to their appropriate biological characteristics. Gelatin, a denatured collagen, possesses biocompatible, biodegradable, non-immunogenic and non-antigenic properties and contains Arg–Gly–Asp (RGD)-like sequence that promotes cell adhesion and migration [5-7].

Chitosan, a deacetylated derivative of chitin, is an amino polysaccharide consisting of β-(1,4)-2-acetamido-2-deoxy-D-glucose and β-(1,4)-2-amino-2-deoxy-D-glucose units. It shows antimicrobial, antitumor, and haemostatic properties [8, 9]. In addition, chitosan is reported to accelerate wound healing and enhance bone formation [10]. The molecular weight of chitosan can be varied in a wide range, resulting in different effect on the scaffolds properties and cell response. Our previous study has shown that the molecular weight of chitosan had significant influences on the mechanical and biological properties of collagen/chitosan scaffolds [11]. It was reported that low molecular weight chitosan was more effective to promote the proliferation of mouse fibroblasts.

In this study, we thus prepared high MW chitosan (CH) and water-soluble chitosan called chitooligosaccharide (COS) in order to investigate MW effects on the response of MSCs in the system of blended gelatin/CH and gelatin/COS. To study cell response on such materials without the effect of scaffold morphology, 2-dimensional films of gelatin/CH and gelatin/COS were prepared instead of the scaffolds. Attachment, proliferation and osteogenic differentiation of MSCs on the films were evaluated.

II. Material and Methods

A. Materials

Type A gelatin (pI 9) was purchased from Nitta Gelatin Co., Osaka, Japan. Chitosans (CH) was produced from deacetylation process while chitooligosaccharide (COS)

Chwee Teck Lim, James C.H. Goh (Eds.): ICBME 2008, Proceedings 23, pp. 1301–1304, 2009
www.springerlink.com

was produced from free radical degradation using hydrogen peroxide (H_2O_2) oxidizing agent. Molecular weight (MW) and deacetylation degree (%DD) of CH and COS were presented in Table 1.

Table 1 Chemical characteristics of CH and COS

Sample	MW (kDa)	DD (%)
CH	1,000	82
COS	1.4	80

B. Methods

Preparation of G/CH and G/COS films: G/CH and G/COS films with various blending ratios were prepared by solution casting and dehydrothermal crosslinking techniques. Sample solutions were cast on glass slips and dried overnight. Dried films were crosslinked by dehydrothermal treatment at 140°C for 24 h in a vacuum oven.

Isolation of MSCs: Marrow-derived stem cells (MSCs) were isolated from the bone shaft of femurs of 3-week-old female Wistar rats according to the technique reported by Tabata *et al*. [6]. The medium was changed on the 4th day after isolation and every 3 days thereafter. The cells of the second- and third-passages at subconfluence were used for all experiments.

Attachment and proliferation tests by MTT assay: MSCs ($2x10^4$ cells/film) were seeded onto the films and cultured in proliferating medium (α-MEM supplemented with 15% FBS) at 37°C, 5% CO_2. The numbers of cells attached on the 1st day and cells proliferated on the 3rd and 5th days after seeding were quantified by MTT assay.

Measurement of cell spreading area: Photographs of at least 100 cells attached on the films at the 1st day after seeding were taken at 10X magnification. Cell spreading area was determined using Metamorph program (Universal Imaging Systems) [12].

Osteogenic differentiation of MSCs on G/CH and G/COS films: Osteogenic differentiation of MSCs cultured on the films under osteogenic differentiation induction was assessed. MSCs ($3.6x10^5$ cells/film) were seeded on the films and cultured in proliferating medium. After one day of seeding, the medium was changed into osteogenic medium (α-MEM supplemented with 10% FBS, 10 mM β-glycerol phosphate, 50 μg/ml L-ascorbic acid and 10 nM dexamethasone) and changed every 2 days thereafter. After 7 days culture in osteogenic medium, ostognic differentiation markers including alkaline phosphatase (ALP) activity and calcium release were determined by *p*-nitrophenyl phosphate and O-cresolphythalein methods, respectively [6].

Statistical analysis: All statistical calculations were performed using MINITAB (Statistical software, version 13.2, PA, USA). The differences of data analyzed using 2 sample t-test were considered at $p < 0.05$ and $p < 0.01$.

III. Results

Fig. 1 demonstrated the number of MSCs attached and proliferated on G/CH and G/COS films. It was observed that MSCs tended to attach and proliferate well on the blended films, particularly for the films containing 70% CH and COS. It was also noticed that the number of MSCs proliferated on pure CH film were significantly lower than the others, indicating the toxicity of CH. In contrast, the number of MSCs attached and proliferated on pure COS film were comparable to those on pure gelatin film, implying less toxicity of COS.

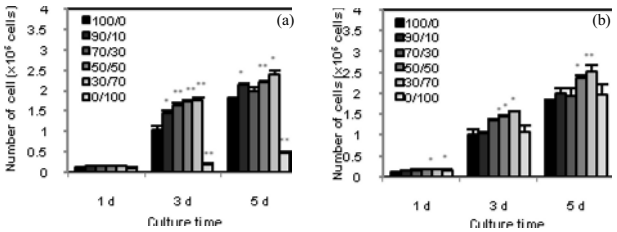


Fig. 1 Number of MSCs attached (1 day after seeding) and proliferated (3 and 5 days after seeding) on G/CH and G/COS films at different blending ratios (a) G/CH films and (b) G/COS films (* and ** presented significant difference at $p<0.05$ and $p<0.01$ relative to gelatin within each group).

Spreading areas of MSCs attached on different films on the 1st day after seeding were presented in Table 2. It was found that area of MSCs attached on the blended films were larger than those on pure gelatin film. Also, it was noticed that areas of MSCs attached on pure CH film were significantly smaller than those on the others. The cell morphologies attached on pure CH film were rounded which was markedly different from those on the other.

ALP activities of both stem cells cultured on different films for 7 days under osteogenic medium were demonstrated in Fig. 2. ALP activities of MSCs cultured on gelatin film were highest. In addition, it could also be noticed that ALP activity on CH surface was significantly higher than this on COS.

Fig. 3 showed calcium released from both stem cells cultured on different films for 7 days under osteogenic differentiation induction. Similar to the results of ALP activity, calcium released from MSCs cultured on pure gelatin and CH films were significantly higher than those on COS film.

Table 2 Spreading area of MSCs attached on G/CH and C/COS films at different blending ratios.

	Cell area (μm^2)	
	G/CH	G/COS
100/0	45.17 ± 8.66	
90/10	66.45 ± 14.95 **	53.77 ± 10.97 **
70/30	65.61 ± 12.37 **	91.44 ± 18.69 **
50/50	83.52 ± 16.78 **	99.90 ± 19.99 **
30/70	97.91 ± 21.13 **	99.32 ± 18.06 **
0/100	12.72 ± 3.84 **	69.73 ± 15.95 **

* and ** presented significant difference at $p<0.05$ and $p<0.01$ relative to gelatin.

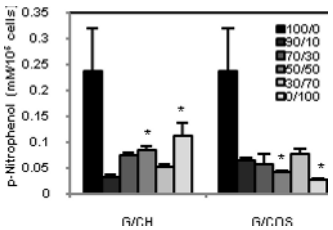


Fig. 2 ALP activity of MSCs cultured on G/CH and G/COS films at different blending ratios for 7 days in osteogenic medium (* presented significant difference at $p<0.05$ between G/CH and G/COS at same blending ratio).

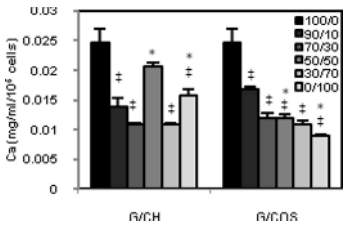


Fig. 3 Calcium release of MSCs cultured on G/CH and G/COS films at different blending ratios for 7 days in osteogenic medium (* presented significant difference at $p<0.05$ between G/CH and G/COS at same blending ratio and ‡ presented significant difference at $p<0.05$ relative to pure gelatin films within each group).

IV. Discussion

MSCs tended to attach and proliferate well on the blended films, particularly for the films containing 70% CH and COS. This was because the interactions of carboxyl (COOH) and amino (NH_2) groups with the cell surface could induce the activation of cells [13]. Therefore, blended G/CH and G/COS would introduce more of free COOH and NH_2 groups than the crosslinked pure gelatin, resulting in better cell affinity. The toxicity of high MW chitosan found in this study corresponded to several works reported. Simon *et al.* also reported that a variety of chitosans were cytotoxic and haemolytic and the extent was being dependent upon their molecular weight, degree of deacetylation and salt form [14]. Toxicity increased with increasing molecular weight and chitosan hydrochloride was the most toxic form. Subsequent studies using lower molecular weight chitosan showed that toxicity could be substantially decreased [15]. Morphologies of MSCs attached on pure CH film were rounded which was markedly different from those on the other, corresponded to the results observed by Tillman *et al.* [16]. They found that spreading area of mouse embryonic fibroblasts showed significant reduction on 2-D chitosan surfaces, compared to tissue culture plastic surfaces. In contrast, areas of MSCs on pure COS film were comparable to other films. This confirmed more toxicity of CH than the COS.

In term of osteogenic differentiation, gelatin was found to be the most preferable material for *in vitro* osteogenic differentiation in this study. This could be due to the hydrophobicity of crosslinked gelatin described previously. Saldana *et al.* have reported that osteoblast-specific activities including ALP activity and mineralization of human MSCs were clearly exhibited when cultured on the hydrophobic Zr-based surfaces [17]. Some studies reported that $–NH_2$- and SH-modified surfaces which showed more hydrophobic property could promote and maintain osteogenic capability when compared to less hydrophobic CH_3-, OH- and COOH-surfaces [18].

Comparing between CH and COS, CH films showed higher potential to induce osteogenic differentiation of MSCs than COS. Kim *et al.* reported the inhibitory effect of COS on activation and expression of matrix metalloproteinase-2 (MMP-2) in primary human dermal fibroblasts [19]. The MMP-2 belongs to a larger family of proteases known as the metzincin superfamily and plays a major role on cell behaviors such as cell proliferation, migration, differentiation and angiogenesis. Another possible reason could be attributed to the higher protein adsorption on highly positive charged of high MW chitosan. This could promote cell differentiation, as found by Amaral *et al.* and Hu *et al.* [20].

V. Concludions

This study presented that system of gelatin/chitosan and gelatin/chitooligosaccharides, except the pure of high MW chitosan, could effectively promote attachment and prolife ration of MSCs. Furthermore, chitooligosaccharide could enhance the proliferation of MSCs as good as gelatin. However, gelatin was the most preferable material for *in vitro* osteogenic differentiation in this study.

Acknowledgment

The financial support from the Chulalongkorn University Dutsadi Phiphat Scholarship is gratefully acknowledged.

References

[1] Toma J. G., Akhavan M., Fernandes K. J. et al. (2001) Isolation of multipotent adult stem cells from the dermis of mammalian skin. Nat. Cell Biol. 3: 778-784

[2] Joon Y. L., Zhuqing Q. P., Baohong C. et al. (2000) Clonal isolation of muscle-derived cells capable of enhancing muscle regeneration and bone healing. J. Cell Biol. 150: 1085-1100

[3] Mark F. P., Alastair M. M., Stephen C. B. et al. (1999) Multilineage potential of adult human mesenchymal stem cells. Science 284: 143 – 147

[4] Giuliana F., Gabriella C., De A. et al. (1998) Muscle regeneration by bone marrow-derived myogenic progenitors. Science 279: 1528 – 1530

[5] Feng Z., Grayson W. L., Teng Ma et al. (2006) Effects of hydroxyapatite in 3-D chitosan–gelatin polymer network on human mesenchymal stem cell construct development. Biomaterials 27: 1859–1867

[6] Yoshitake T., Masaya Y., Yasuhiko T. (2005) Osteogenic differentiation of mesenchymal stem cells in biodegradable sponges composed of gelatin and b-tricalcium phosphate. Biomaterials 26: 3587–3596

[7] Yan H., Stella O., Mbonda S. et al. (2005) In vitro characterization of chitosan–gelatin scaffolds for tissue engineering. Biomaterials 26: 7616–7627

[8] Liu H., Du Y., Yang J. and Zhu H. (2004) Structural characterization and antimicrobial activity of chitosan/betaine derivative complex. Carbohydr. Polym. 55: 291-297

[9] Madihally S. V. and Matthew H. W. T. (1999) Porous chitosan scaffolds for tissue engineering. Biomaterials 20: 1133-1142

[10] Park D. J., Choi B. H., Zhu S. J. et al. (2005) Injectable bone using chitosan-alginate gel/mesenchymal stem cells/BMP-2 composites. Journal of Cranio-Maxillofacial Surgery 33: 50-54

[11] Chalonglarp T., Sorada K., Neeracha S. et al. (2007) The influence of molecular weight of chitosan on the physical and biological properties of collagen/chitosan scaffolds. J. Biomater. Sci. Polymer Edn 15: 147–163

[12] Hannah S., Mustafa O. G., Suha N. A. et al. (2007) Supramolecular crafting of cell adhesion. Biomaterials 28: 4608–4618

[13] Mattioli B. M., Lucarini G., Virgili L. (2005) Mesenchymal stem cells on plasma-deposited acrylic acid coatings: An in vitro investigation to improve biomaterial performance in bone reconstruction. J. Bioact. Compat. Polym.20: 343-360

[14] Richardson S. C. W., Kolbe H. V. J. and Duncan R. (1999) Potential of low molecular mass chitosan as a DNA delivery system: biocompatibility, body distribution and ability to complex and protect DNA. Int. J. Pharm.178: 231–243

[15] Heller J., Liu L. S., Duncan R. (1996) Alginate: chitosan microporous microspheres for the controlled release of proteins and antigens. Proc. Int. Symp. Control. Release Bioact. Mater. 23: 269–270

[16] Jeremy T., Annett U., Sundararajan V. M. (2006) Three-dimensional cell colonization in a sulfate rich environment. Biomaterial 27: 5618–5626

[17] Laura S., Antonio M. V., Ling J. et al. (2007) In vitro biocompatibility of an ultrafine grained zirconium. Biomaterials 28: 4343–4354

[18] Judith M. C., Rui C. and John A. H. (2006) The guidance of human mesenchymal stem cell differentiation in vitro by controlled modifications to the cell substrate. Biomaterials 27: 4783–4793

[19] Moon-Moo K. and Se-Kwon K. (2006) Chitooligosaccharides inhibit activation and expression of matrix metalloproteinase-2 in human dermal fibroblasts. FEBS Letters 580: 2661–2666

[20] Hu S. G., Jou C. H. and Yang M. C. (2003) Protein adsorption, fibroblast activity and antibacterial properties of poly(3-hydroxybutyric acid-co-3-hydroxyvaleric acid) grafted with chitosan and chitooligosaccharide after immobilized with hyaluronic acid. Biomaterials 24: 2685–2693

Manufacturing Porous BCP Body by Negative Polymer Replica as a Bone Tissue Engineering Scaffold

R. Tolouei[1], A. Behnamghader[2], S.K. Sadrnezhaad[2], M. Daliri[3]

[1] Biomedical Engineering Faculty, Science and Research campus, Islamic Azad University, Tehran, Iran
[2] Materials and Energy Research Center, Tehran, Iran
[3] National Institute of Genetic engineering and Biotechnology, Tehran, Iran

Abstract — **The porous calcium phosphate scaffolds with defined pore-channel interconnectivity were successfully prepared via negative replica method. The internal channel architecture was achieved using a water-insoluble polyurethane sponge. The PU sponge was first filled with aqueous slurry of biphasic calcium phosphate material containing pore forming agent. After drying at room temperature, a heat treatment was employed to remove all organic material. The bodies were finally sintered at the temperature of 1200°C. The phase composition and chemical structure of bodies were determined by X-ray diffraction (XRD) and FT-IR methods. Scanning electron microscopy (SEM) was used to study the pore size and distribution and pore-pore and pore-channel interconnectivity. The scaffold bodies were principally composed of HA and β-TCP with some traces of α-TCP. No residue of polymer replica or pore agent was remained. The scaffolds contained an interconnected pore-pore and pore-channel structure with a pore size less than 500 µm. The company of desired phase composition and pore-channel structure here increases the hope for the production of more effective biodegradable scaffolds for hard tissue engineering.**

I. Introduction

The importance of pore characteristics such as their size and interconnectivity along with the biodegradability of scaffold materials have been widely studied in tissue engineering domain [1,2]. The pore size and distribution, pore-channel interconnectivity and fenestration size are thought to play an important role in deep colonization and fast osseointegration of functional porous materials [3,4].

Calcium phosphate (CaP) bioceramics are known as the attractive biomaterials used in hard tissue surgeries [5, 6]. Among the different CaP compounds, mixtures of two or more calcium phosphates such as biphasic calcium phosphates (BCP) containing more stable hydroxyapatite (HA) and more bioactive tricalcium phosphate (TCP) have attracted a growing interest for use as scaffold materials [7]

The BCP compounds exhibit good *in vitro* and *in vivo* biocompatibility but the degree of bioactivity is found to be depended on the proportions of TCP to HA constituents in the mixture. The bodies composed of higher TCP/HA ratios are generally used to achieve high-level resorption and to promote osteoconduction. [8]. BCP powder can be synthesized in different methods such as simple mixing of HA and TCP, solid-state reactions, and co-precipitation [9]

The aim of this study was to prepare the scaffolds using polymeric foam and a pore forming agent. The objective of use of these agents was to produce microcapillaries allowing circulation of biological fluid and pores for seeding and stable cell proliferation during in vitro or in vivo experiments.

II. Materials procedures

The HA and tricalcium phosphate (TCP) powders used in this study were prepared from Merck (Darmstadt, Germany). Porlat (Zschimmer and Schwarz GmbH, Germany) was employed as pore forming agent, with a particle size range of 150-400 µm.

Based on own experiences and reported researches [10], the as received HA and TCP powders were firstly subjected to a calcination process conducted at temperatures of 1000 and 1200 °C respectively. Then, they were mixed with a weight ratio of 50:50. The dough was prepared with the following chemical composition: 16.7 wt% demineralized water and 80 wt% BCP powder, 1.5 wt% ammonia solution (33%, Merck Eurolab BV), 1.5 wt% defloculant (Dolapix, zschimmer and Schwarz GmbH, Germany) and 0.15 wt% binder.

After milling, the dough was injected into the cavities of PU foam through a syringe. This porous polymer structure is substantially insoluble in water, and is thermally decomposable into gaseous residues. After drying overnight, a heat treatment at a controlled heating performed to removal of pore agents and PU foam. After elimination of all organic components, up to 500°C, samples were finally sintered at 1200°C for 5 h in air.

To optimize the heating profile, simultaneous thermal analysis (STA) was performed on Porlat-contained dried dough. The phase composition and chemical structure of the scaffold products were determined by X-ray diffraction (XRD) and FT-IR analyses respectively. Scanning electron microscopy (SEM) was used to investigate the pore size and

Chwee Teck Lim, James C.H. Goh (Eds.): ICBME 2008, Proceedings 23, pp. 1305–1308, 2009
www.springerlink.com

distribution and the effect of PU foam on the pore-channel architecture.

III. Results and Discusion

The viscosity of dough was taken into account to optimize the solid to liquid proportion in the dough preparation step. The different solid to liquid proportions ranging from 40% to 80% were studied and the optimum condition was found at a proportion equal to 80% (Fig. 1). The viscosity of dough prepared from 0.5, 1 and 1.5% defloculant showed an almost the same value for the 0.5 and 1.5% whereas the sample prepared from 1% defloculant was so thick that it was not possible to inject properly through a syringe.

To fix an appropriate thermal treatment process, the thermal behavior of dried dough with a solid to liquid proportion, defloculant and pore agent amounts of 80%, 1.5% and 10% respectively, was investigated. The weight loss of 20% at about 120°C is related to remained water and pore agent removal.

The exothermic peak seen at 330-360 °C accompanied by a slight weight loss in the TGA curve can be attributed to the burnout of remained polymeric constituents (Fig. 2). Based on the reports of Mothe [11] and Song [12], Polyurethane foams present a thermal decomposition at 300-500°C. It seems that the heat treatment at 500 °C with a holding time of 90 min has been long enough to remove all polymeric residues (Fig. 3).

The XRD analysis revealed the scaffold sintered at 1200°C composed principally of HA and β-TCP phases (36% and 57% respectively) and some trace of α-TCP phase (7%) (Fig. 4).

The increase in the amount of β-TCP phase and the appearance of α-TCP phase are due to HA→α-TCP and β-TCP→α-TCP phase transformations during sintering [13].

Based on the results obtained from FT-IR analyses of dried dough containing defloculant and pore former and powdered sintered body, no residue of polymeric constitu-

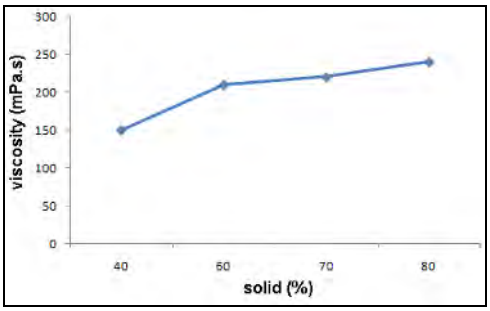


Fig. 1 Viscosity of BCP dough for different solid percentages

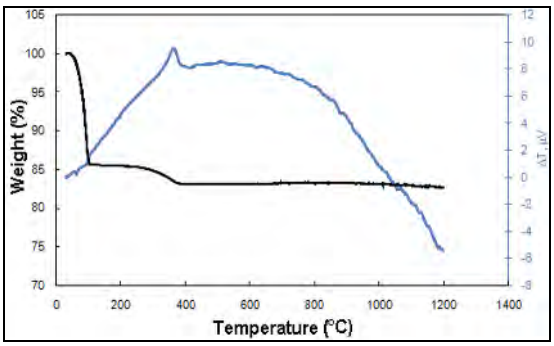


Fig. 2 STA of dried dough

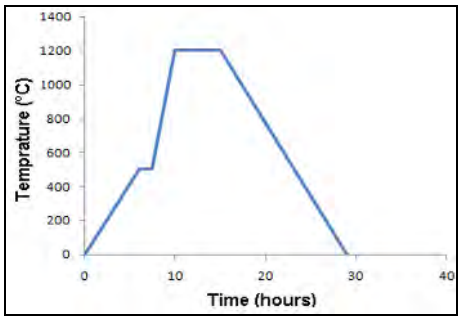


Fig. 3 Flowchart of heat treatment process for dried sample

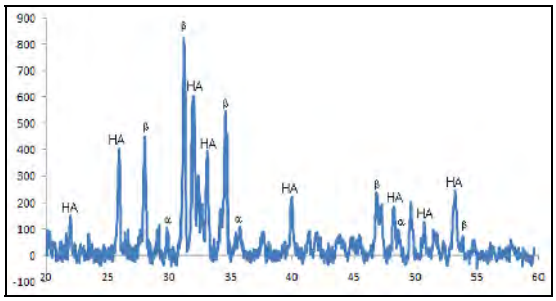


Fig. 4 XRD pattern of sintered scaffold

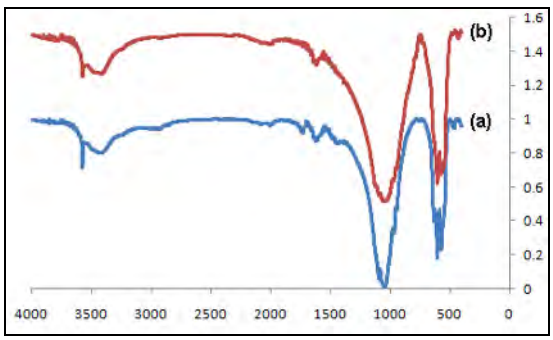


Fig. 5 FT-IR spectra of dried dough containing defloculant and pore former (a) and sintered scaffold (b)

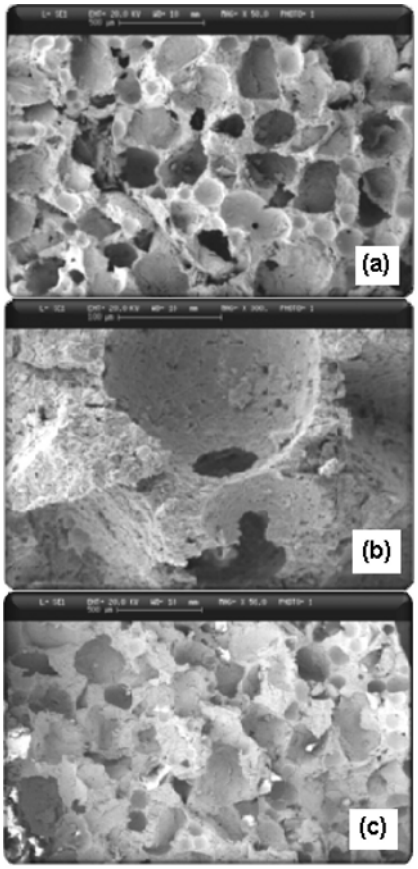


Fig. 6 SEM fracture surface images of the scaffolds

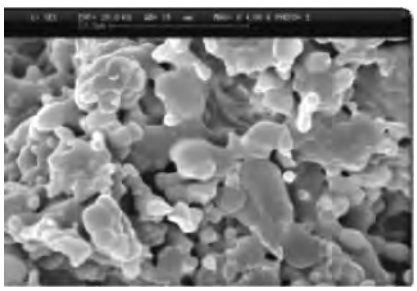


Fig. 7 SEM image of the pore wall microstructure

ents (PU foam, defloculant and pore former) was identified in the resulting sintered scaffolds. Moreover the O-H characteristic peak of hydroxyapatite at 3520 cm^{-1} decreased through HA to TCP phase transformation (Fig. 5) [13].

The theoretical density and porosity percentage of scaffolds were 0.9 and 74% respectively. The SEM images of figure 6 (a and b) taken from fracture surface revealed the scaffolds contained a pore amount of about 70% with a size ranging from 100 to 450 μm which is consistent with the size range of macroporosity-inducing agent Porlat used in this study. The pore wall thickness was about 30-60 μm. About 40% of pores are interconnected to the channels with a mean diameter size of 50 μm. A pore-capillary connection is clearly shown in the figure 6-b. To determine the effect of PU foam on the pore-channel architecture, the SEM images of the scaffolds were compared with those of samples without the PU foam (Fig 6-c). The pores in the scaffolds were connected through the channels and seemed deeper whereas in the absence of PU foam, the pores were found to be isolated.

The SEM image of scaffold body shown in the figure 7 was taken from the pore wall illustrating a sintered granular microstructure with a grain size of 0.8-4 μm. No grain growth was happened through the sintering.

IV. Conclusions

The porous BCP scaffolds were successfully prepared via negative polyurethane replica method. The pore-channel architecture was obtained using polyurethane foam. The X-ray diffraction revealed the scaffold bodies were principally composed of HA and β-TCP with some traces of α-TCP. Any trace of polymer replica, pore agent and PU foam was detected in FT-IR analysis. The XRD results about HA to TCP phase transformation during the sintering was confirmed by the results of FT-IR analysis when O-H hydroxyapatite characteristic peak was taken into account.

The scaffolds contained an interconnected pore-pore and pore-channel structure. The theoretical porosity and that evaluated from SEM images of scaffolds were about 70-74%. Pore sized from 100 to 450 μm and the pore wall thickness was about 30-60 μm. The results obtained in this research showed the use of PU foams was effective to promote the connection of pores through the channels. SEM studies revealed a typical granular microstructure of sintered bodies without any grain growth during the sintering.

Acknowledgment

The authors gratefully acknowledge support for studies reported in this paper provided by Materials and Energy Research Centre (Merck, Iran).

References

1. Hollister SJ, Maddox RD, Taboas JM. “Optimal design and fabrication of scaffolds to mimic tissue properties and satisfy biological constraints”. Biomaterials 2002; 23:4095–103.
2. Hutmacher DW. “Scaffolds in tissue engineering bone and cartilage”. Biomaterials 2000; 21:2529–43.

3. R. Langer and J.P. Vacanti, Tissue engineering. Science 1993; 260: 920–926.
4. K. Anselme “Osteoblasts adhesion on biomaterials” Biomaterials 2000 [21]7: 667-681.
5. L.L. Hench, “Bioceramics: from concept to clinic”. J Am Ceram Soc. 1991; [74]7:1487–1510.
6. L.L. Hench, “Bioceramics”. J Am Ceram Soc. 1998; [81]7: 1705–1728.
7. J. Peña and M. Vallet-Regí “Hydroxyapatite, tricalcium phosphate and biphasic materials prepared by a liquid mix technique”. Journal of the European Ceramic Society. 2003; 23[10]: 1687-1696.
8. N. Passuti, J. Delecrin and G. Daculsi, “Experimental data regarding macroporous biphasic calcium phosphate ceramics”. Eur J Orthop Surg Traumatol 1997; [7]: 79–84.
9. Youn-Ki Jun and Seong-Hyeon Hong. “Effect of Co-Precipitation on the Low-Temperature Sintering of Biphasic Calcium Phosphate”. J. Am. Ceram. Soc., 2006; 89[7]: 2295–2297.
10. Giuliano Gregori, Hans-Joachim Kleebe , Helmar Mayr, Gunter Ziegler. “EELS characterization of β-tricalcium phosphate and hydroxyapatite”. Journal of the European Ceramic Society. 2006; [26]:1473–1479.
11. C.G. Mothe, C.R. de Araujo. “Properties of polyurethane elastomers and composites by thermal analysis”. Thermochimica Acta. 2000; [357-358]:321-325.
12. L. Song, Y. Hu, Y. Tang, R. Zhang, Z. Chen and W. Fan, “Study on the properties of flame retardant polyurethane/organoclay nanocomposite”. Polym Degrad Stab. 2005; 87: 111-116.
13. A. Behnamghader, N. Bagheri, B. Raissi, F. Moztarzadeh. "Phase development and sintering behavior of biphasic HA-TCP materials prepared from hydroxyapatite and bioactive glass". Journal of Material Science: Materials medicine. 2008; 19: 197-201.

Author: Ranna Tolouei
Institute: Biomedical Engineering Faculty, Science and Research campus, Islamic Azad University
Street: Ponak Sq.
City: Tehran
Country: Iran
Email: Ranna.tolouei@gmail.com

Synthesis and Characterizations of Hydroxyapatite-Poly(ether ether ketone) Nanocomposite: Acellular Simulated Body Fluid Conditioned Study

Sumit Pramanik[1] and Kamal K. Kar[1,2*]

Advanced Nano-Engineering Materials Laboratory
[1]Materials Science Programme and [2]Department of Mechanical Engineering
Indian Institute of Technology Kanpur, Kanpur-208016, INDIA
*Corresponding Author (kamalkk@iitk.ac.in); Fax # 0512-2597408, Phone # 0512-2597687

Abstract — **Development of prosthesis materials is a great challenge in biomedical fields. However, no material has been developed successfully for long-term orthopedic implantations. In this context the present investigation is being tried to develop a prosthesis material using apatite-thermoplastic nanocomposites. Hydroxyapatite (HAp) synthesized by sol-gel technique and commercial graded poly(ether ether ketone), PEEK, were used as apatite and thermoplastic, respectively. The HAp-PEEK nanocomposite was made by phase separated precipitation technique. The morphology and component distribution were performed by scanning electron microscopy (SEM) and atomic force microscopy (AFM). The functional groups present in composite materials were evaluated by Fourier transformation infrared spectroscopy. The biocompatibility performance was evaluated through acellular simulated body fluid (SBF) tests of HAp and PEEK-HAp nanocomposite using freshly prepared SBF at physiological condition of 37^{o}C temperature and pH of 7.0. The compositional studies were carried out by x-ray diffraction (XRD) technique. The coating of SBF crystal after SBF study was characterized by SEM, FTIR and XRD techniques. The sintered HAp-PEEK nanocomposite shows higher compressive strength (143 MPa) and modulus (2 GPa) values than that of human cancellus bone and also crosses the lower limit of corticle bone.**

Keywords — **Hydroxyapatite, Poly(ether ether ketone), Nanocomposite, Sol-gel, Simulated body fluid**

I. Introduction

Hydroxyapatite [$Ca_{10}(PO_4)_6(OH)_2$, HAp] is a best mineral constituent for hard tissue among all the synthetic apatites. It is used in hard tissue implantations since its capability of undergoing bonding osteogenesis and chemical stability for long- term *in-vivo* applications [1]. However, pure HAp material can not be directly used for hard tissue replacement due to its brittleness as reported in our previous work [2]. Hence, several composites of HAp have been tried to improve the mechanical properties for particular biomedical applications. In 1980s, Bonfield et al. has first introduced the concept of bioactive particulate reinforced polyethylene (PE) polymer composite as bone analogue [3]. Then several polymers have been used in bioactive HAp-polymer composites. However, in recent years, the poly(ether ether ketone) [PEEK], -[-O-C_6H_4-O-C_6H_4-CO-C_6H_4-]-, polymer is being started to use in the biomedical field, especially in the area of load-bearing orthopedic fields [4,5,6] due to its good bioinert property, high glass transition temperature (T_g =145^{o}C), and high melting temperature (335-400^{o}C), depending upon grade of polymer [7]. But none of them has been succeeded for long-term applications to date.

Therefore, the aim of this study is to develop high strength materials using apatite-thermoplastic nanocomposites for long-term prosthetic applications. The major objectives of this present work are focused on the synthesis of composites by novel method and to investigate the biocompatibility of the synthetic materials using acellular simulated body fluid (SBF). HAp synthesized by sol-gel technique is used as apatite and commercial grade PEEK is used as thermoplastic. The phase separated precipitation technique is used to fabricate the HAp-PEEK nanocomposite.

II. Materials and methods

A. Materials

All commercial grade chemicals (supplied by M/S Glaxo Smith Kline Pharmaceuticals Ltd., India) like orthophosphoric acid (H_3PO_4), ethanol (C_2H_5OH), and calcium nitrate [$Ca(NO_3)_2$] were used to synthesize the hydroxyapatite in sol-gel technique. The employed thermoplastic polymer was commercial grade PEEK powders (supplied by Gharda Chemicals Ltd., India). Methanol (CH_3OH) was used as a media to prepare composite by phase separation technique.

B. Methods

i. Preparation of hydroxyapatite

The hydroxyapatite was prepared by sol-gel technique as reported in other study [8]. The employed steps for synthesis of HAp are given below.

Chwee Teck Lim, James C.H. Goh (Eds.): ICBME 2008, Proceedings 23, pp. 1309–1312, 2009
www.springerlink.com

A solution-1 was prepared by using 1:5 (v/v) of H_3PO_4 and C_2H_5OH in addition to 60 ml distilled H_2O. A solution-2 was made separately using 1:4 (w/v) of $Ca(NO_3)_2$ and C_2H_5OH in 60 ml distilled H_2O. Then the each solution was vigorously stirred for 24 h at 27°C. The P^{5+} solution (solution-1) was added over Ca^{2+} solution (solution-2) drop wise and stirred vigorously for 4 h at 25°C to prepare a sol. Then the sol was kept for 48 h at 25°C with out any stirring. Further, this sol was stirred at 40°C for 16 h to produce gel. Finally, the remaining gel was soaked at 220°C for 6 h to get a solid form of HAp. The solid HAp was further sintered at 1000°C for 1.5 h followed by powdering with the help of hand mortar to make composite.

ii. Preparation of HAp-PEEK nanocomposite

The HAp-PEEK nanocomposite was prepared by phase separated precipitation technique, which is quite similar with other reports [9,10]. In this technique, 40:60 (w/w) of sintered HAp (SHAp) powder and as received PEEK powder were mixed homogeneously. The composition of 40 wt% SHAp was chosen to get the good mechanical properties for hard tissue implantations, which have been reported for HAp-PEEK composite [6]. Then 15 gm of the dry solid mixture was added in 200 ml of CH_3OH with stirring at 25°C for 16 h in a closed vessel. Here the HAp was partially dissolved in CH_3OH and made a coating slowly on the PEEK particles to form composite. In this time solid phases were separated from the liquid solution and precipitated as a composite paste. Finally, the composite paste was dried at 110°C for 5 h. Then the composite was pelletized by powder metallurgical technique using uniaxial pressure followed by liquid phase sintering at 350°C for 1.5 h. The sintered HAp-PEEK composite (SHAp-PEEK) samples were used for various characterizations. Preparation of specimen for mechanical characterization was made in a suitable mold using uniaxial pressure of about 200 MPa followed by liquid phase sintering.

iii. Preparation of simulated body fluid

The SBF solution was prepared by a technique reported in earlier works [2, 11]. The major chemical component in SBF was highly pure sodium chloride (NaCl) [2,11]. The freshly prepared aqueous SBF solution without using any living cell at physiological conditions of pH 7.0 and 37°C temperature was used to evaluate the acellular SBF conditioned study for the SHAp and SHAp-PEEK nanocomposite specimens.

C. Experimental

The morphology and component distribution were performed by scanning electron microscope (FBI make, model: QUANTA-2000) and atomic force microscope (Molecular Imaging Ltd., USA, model: Pico Scan). The functional group present in composite materials was evaluated by spectroscopic absorption study using Fourier transformation infrared (FTIR) analyzer (Bruker make, model: Vector 22).

The biocompatibility or SBF conditioned study of HAp and SHAp-PEEK nanocomposite pellets was carried out by freshly prepared SBF at a temperature of 37°C and pH of 7.

The SBF crystal was characterized by scanning electron microscope, FTIR and x-ray diffractometer (Seifert Diffractometer make, England, model: ISO Debyeflex-2002).

Mechanical properties are essential criteria for hard tissue engineering, was evaluated by compression test on cylindrical specimens of 7mm diameter and 14 mm height at a crosshead speed of 1 mm/min using Zwick/Roell-Z010 Universal Testing Machine.

III. Results and Discussions

The morphology and component distribution of unsintered HAp and SHAp-PEEK particles are measured by scanning electron microscopy (SEM) and shown in Figs. 1(a) and (b), respectively. Less than 100 nm size HAp particles are found in SEM study.

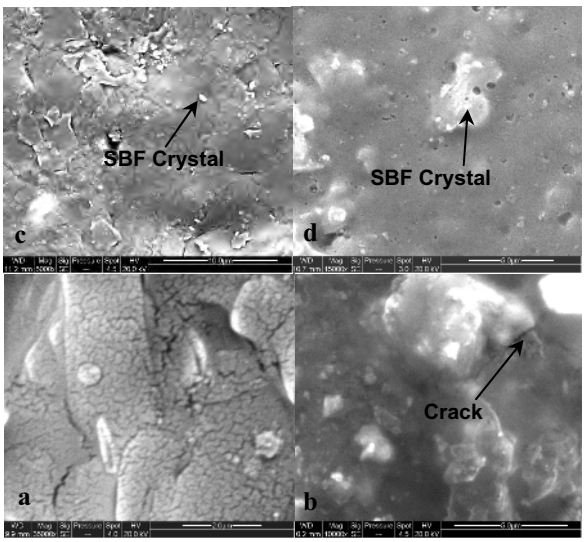


Fig. 1 SEM images of (a) unsintered HAp, (b) SHAp-PEEK, (c) SBF conditioned-SHAp and (f) SBF conditioned-SHAp-PEEK

The good interfacial bond between HAp and PEEK is observed in SHAp-PEEK nanocomposite as shown in the SEM image (Fig. 1(b)). A very few particles of ceramics (HAp) has come out from the polymer matrix (PEEK) during sintering, is also revealed in Fig. 1(b). A very few mi-

cro-cracks are also formed during sintering as indicated in Fig. 1(b). It is also observed in AFM image as shown in Fig. 2(a). This is probably due to the evaporations of gases, which are coming out from the absorbed moisture of HAp. The 50-100 nm size HAp particles have agglomerated with micron size PEEK particles during liquid phase sintering. The SEM images of SBF conditioned -SHAp (after acellular SBF conditioned study of SHAp nanocomposite for 30 days) and SBF conditioned-SHAp-PEEK (after acellular SBF conditioned study of SHAp-PEEK nanocomposite for 30 days) samples after dipping for 30 days in SBF solution are shown in Figs. 1(c) & 1(d), respectively. A layer of SBF crystals on the SHAp-PEEK nanocomposite is observed. The macro porous HAp has shown a good compatibility with PEEK matrix. The detail of the SBF conditioned study is to be discussed in later section.

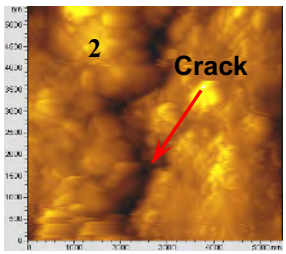


Fig. 2 AFM image (2-D Topography) of SHAp-PEEK nanocomposite

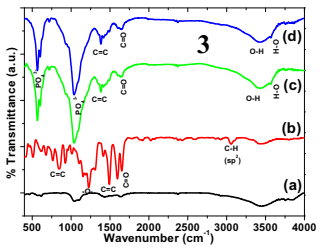


Fig. 3 FTIR spectra of (a) SBF crystal, (b) PEEK, (c) SHAp-PEEK and (d) SBF conditioned-SHAp-PEEK

The characteristic peaks of existing functional groups in PEEK, SHAp-PEEK and SBF conditioned-SHAp-PEEK are characterized by FTIR analysis and shown in Figs. 3(b), (c) & (d), respectively. However, there is no sharp characteristic peak for SBF crystal has been observed in Fig. 3(a). In SHAp-PEEK and SBF conditioned-SHAp-PEEK, the IR absorption peaks at around 1050 and 565 cm^{-1} are attributed for PO_4^{3-} vibration mode of SHAp [2,11,12]. The small sharp peak at around 3600 - 3530 cm^{-1} is attributed to the stretching vibration of molecular OH^- and the broad band at around 3500-3100 cm^{-1} is attributed to the absorbed water (H_2O) or hydrated OH^-. All IR peaks of various functional groups present in PEEK are shown in Fig. 3(b). The peaks at 846 and 1490 cm^{-1} are attributed for aromatic (C=C) group. Other peaks at 1226, 16452 and 3062 cm^{-1} are due to the aromatic ether (-O-), carbonyl (C=O) and aromatic hydrogen (C-H, sp^2) respectively [13].

The characteristic XRD peaks of the virgin PEEK (see Fig. 4(a)) at around 2θ = 18-23° and the sintered HAp (JCPDS Card No. 09-0432) (see Fig. 4(b)) at around 30-35° have found in SHAp-PEEK nanocomposite (see Fig. 4(c)). The XRD pattern of pure PEEK is similar to the other report [14]. The major XRD peaks of SBF crystals are obtained due to its main component NaCl crystals (PDF No. 05-0628) (see Fig. 4(f)). The peaks of SBF crystals are also revealed in SBF conditioned-SHAp and SBF conditioned-SHAp-PEEK as shown in Figs. 4(d) and (e), respectively.

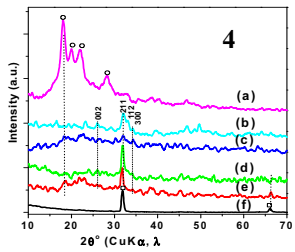


Fig. 4 X-ray diffraction pattern of (a) PEEK, (b) SHAp (JCPDS Card No. 09-0432), (c) SHAp-PEEK, (d) SBF conditioned-SHAp, (e) SBF conditioned-SHAp-PEEK and (f) SBF crystal (PDF No. 05-0628)

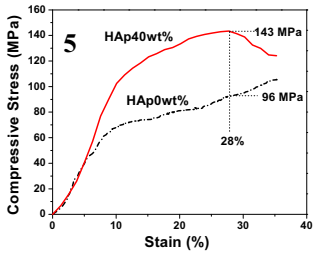


Fig. 5 Compressive properties of PEEK and SHAp-PEEK nanocomposite

The mechanical characterization of SHAp-PEEK nanocomposite and pure sintered PEEK is performed to compare the compressive strength and modulus. In compression test the ultimate strength of SHAp-PEEK nanocomposite is found to be 143 MPa, which is noticeably higher than the pure sintered PEEK (96 MPa) at the same elongation of 28% as shown in Fig. 5. However, modulus (2 GPa) of this nanocomposite has not improved significantly compare to pure PEEK matrix. This is might be due to the porous nature of HAp particles. But both the compressive strength and modulus values of this SHAp-PEEK nanocomposite are still much higher than cancellus bone and also it has crossed the lower limit (120 MPa) of corticle bone [3].

The SBF conditioned study is evaluated by freshly prepared acellular SBF solution. The SHAp and SHAp-PEEK nanocomposite pellets were dipped into the SBF solution for 15 and 30 days. Thereafter, the gradual weight change of the each sample is observed using the equation (1) and shown in Table 1.

$$W_c = 100 \times (W_d - W_i)/W_i \ \% \qquad (1)$$

Where, W_i is initial weight of sample, W_d is dry weight after dipping, and W_c is dry weight change after dipping.

Water absorption property of SHAp-PEEK has improved compare to pure sintered HAp. The amount of absorbed water is lower in SHAp-PEEK as compared to pure SHAp. Also the amount of SBF particles deposited on the top surface of SHAp-PEEK specimen is significantly less compare to pure nano HAp ceramic. As a result the low value of W_c for SHAp-PEEK is observed as illustrated in Table 1. Hence, the bioinert property is improved in SHAp-PEEK nanocomposite produced by phase separation technique as compared

Table 1 Weight change of sintered HAp and sintered HAp-PEEK nanocomposite after dipping in SBF for 15 and 30 days

Sample	Initial weight of sample Wi (gm)	Wet weight after dipping W_w (gm)	Dry weight after dipping W_d (gm)	Dry weight change after dipping W_c (%)	Dipping time T (day)
SHAp	0.536	0.902	0.695	29.66	15
		0.925	0.772	44.03	30
SHAp-PEEK	0.502	0.784	0.642	27.89	15
		0.806	0.678	35.06	30

to pure nano SHAp synthesized by sol-gel method. Therefore, the long term effect of biomaterials may be improved by increasing the bioinert property of a material.

The growth of SBF crystals is observed as a thin film coating on the SHAp and SHAp-PEEK materials as shown in Fig. 1(c) & (d), respectively. The major peaks of the SBF crystals are remain unaltered in SBF conditioned-SHAp-PEEK nanocomposite and SBF conditioned-SHAp as shown in Figs. 4(e) & (d), respectively. The growth of SBF crystal on the SHAp-PEEK nanocomposite is similar to the growth of host tissue on the porous implants as *in-vivo* applications. Hence, this nanocomposite can also enhance the osteoconductive effect due to the presence of HAp.

IV. Conclusions

The HAp was synthesized by a sol-gel technique. The HAp-PEEK nano composite was made by phase separation technique. The good interfacial bond between PEEK and HAp particle in SHAp-PEEK nanocomposite is observed in SEM and AFM micrographs. The observed compressive strength (143 MPa) and modulus (~2 GPa) values of this nanocomposite are higher than the human cancellus bone and also crossed the lower limit of corticle bone. The growth of SBF crystal on the SHAp-PEEK nanocomposite may enhances the osteoconductivity due to the presence of HAp. The less deposition of SBF crystals on the SHAp-PEEK nanocomposite through acellular SBF conditioned study shows that the bioinert property of this composite is better than that of pure HAp. This combined effect of bioinert property and osteoconductive effect of SHAp-PEEK nanocomposite may serve the long-term implantations, which is a main objective of this research.

Acknowledgement

Authors gratefully acknowledge Department of Biotechnology (DBT), India for financial support and Gharda Chemicals Limited, India for providing PEEK polymer. The authors also extend their thanks to the Unit on Nano Science and Technology (UNANST-DST), IIT Kanpur for allowing them to use the atomic force microscope for this work.

References

1. Ruys AJ, Wei M, Sorrell CC, Dickson MR, Brandwood A, and Milthome BK. (1995) Sintering effects on the strength of hydroxyapatite. Biomaterials 16:409-415
2. Pramanik S, Agarwal AK, Rai KN, and Garg A. (2007) Development of high strength hydroxyapatite by solid-state-sintering process. Ceramics International 33:419-426
3. Bonfield W, Grynpas MD, Tully AE, Bowman J, and Abram J. (1981) Hydroxyapatite reinforced polyethylene - a mechanically compatible implant material for bone replacement. Biomaterials 2:185–186
4. Barton AJ, Sagers RD, and Pitt WG. (1996) Bacterial adhesion to orthopaedic implant polymers. J Biomed Mater Res 30:403–410
5. vander Sloten J, Labey L, van Audekercke R, and vander Perre G. (1998) Materials selection and design for orthopaedic implants with improved long-term performance. Biomaterials 19:1455–1459
6. Abu Bakar MS, Cheng MHW, Tang SM, Yu SC, Liao K, Tan CT, Khor KA, and Cheang P. (2003) Tensile properties, tension–tension fatigue and biological response of polyetheretherketone–hydroxyapatite composites for load-bearing orthopedic implants. Biomaterials 24:2245–2250
7. Clayden NJ. (2000) 2H NMR spin relaxation study of the molecular dynamics in poly(oxy-1,4-phenyleneoxy-1,4-phenylenecarbonyl-1,4-phenylene) (PEEK). Polymer 41:1167–1174
8. Byung-Hoon K, Ju-Hyun J, Young-Sun J, Kyung-Ok J, and Kyu-Seog H. (2007) Hydroxyapatite layers prepared by sol–gel assisted electrostatic spray deposition. Ceramics International 33:119-122
9. Ma PX, Zhang R, Xiao G, and Franceschi R. (2001) Engineering new bone tissue in vitro on highly porous poly(alpha-hydroxyl acids)/hydroxyapatite composite scaffolds. J Biomed Mater Res 54:284-293
10. Hu Y, Zhang C, Zhang S, Xiong Z, and Xu J. (2003) Development of a porous poly(L-lactic acid)/hydroxyapatite/collagen scaffold as a BMP delivery system and its use in healing canine segmental bone defect. J Biomed Mater Res Part A 67A:591-598
11. Ding SJ, Ju CP, Chern-Lin JH. (2000) Morphology and immersion behavior of plasmasprayed hydroxyapatite/bioactive glass coatings. Journal of materials science: materials in medicine 11:183-190.
12. Yamashita K, Owada H, Nakagawa H, Umegaki T, and Kanazawa T. (1986) Trivalent-Cation-Substituted Calcium Oxyhydroxyapatite", J Am Ceram Soc 69:590-594
13. Perng LH, Tsai CJ, and Ling YC. (1999) Mechanism and kinetic modelling of PEEK pyrolysis by TG/MS. Polymer 40:7321–7329
14. Small RWH. (1986) A method for direct assessment of the crystalline/amorphous ratio of polyetheretherketone (PEEK) in carbon fibre composites by wide angle x-ray diffraction. Eur Polym J 22:699-701

Address of the corresponding author:

Author: Dr. Kamal K. Kar
Institute: Indian Institute of Technology Kanpur
Street: Kanpur
City: Kanpur
Country: India
Email: kamalkk@iitk.ac.in

Microspheres of Poly (lactide-*co*-glycolide acid) (PLGA) for *Agaricus Bisporus* Lectin Drug Delivery

Shuang Zhao[a], Hexiang Wang[a], Yen Wah Tong[b,c,*]

[a] State Key Laboratory for Agrobiotechnology, Department of Microbiology, China Agricultural University, Beijing, China 100094
[b] Department of Chemical & Biomolecular Engineering, National University of Singapore, 21 Lower Kent Ridge Road, Singapore 119077
[c] Division of Bioengineering, National University of Singapore, 21 Lower Kent Ridge Road, Singapore 119077

Abstract — **Due to their unique properties, polymers are potential vehicles for drug delivery and a popular choice among researchers. In this study, a double emulsion technique was used to fabricate PLGA microspheres that encapsulate ABL. It was also found that PLGA microspheres as a delivery vehicle can increase the residence time and improve the therapeutic efficiency of ABL toward cancerous cells Hep3B, KB and MCF-7. Thus, this delivery system using a PLGA microsphere is an efficient vehicle for overcoming the limitations of ABL in drug applications.**

Keywords — **Drug delivery, *Agaricus bisporus* lectin, PLGA, microsphere, cancerous cells**

I. Introduction

ABL is a lectin from an edible mushroom *Agaricus Bisporus*, and it recognizes TF antigen or T antigen which are hidden in healthy cells but are exposed in a high percentage of human carcinomas and other neoplastic tissue [1]. ABL can potentially inhibit cell proliferation in diverse cell lines via a non-cytotoxic mechanism: interfering with nuclear pores and blocking nuclear protein import [2]. Due to the unique properties of ABL, it could be a more suitable agent for inhibiting the proliferation of cancer cells as compared to toxic chemicals. The antiproliferative effects of ABL are reversible. The reversibility of the anti-proliferative effects of ABL is associated with its release from cells after internalization [3]. This limitation requires ABL to be frequently injected or administrated in order to fulfill its functions as a drug. In order to circumvent this, ABL needs a system that can release it at a sustained rate for extended periods.

The purpose of the current work is to investigate the effect of ABL-loaded PLGA microspheres on the inhibition of tumor cells proliferation. This combination will have advantage over other chemical drugs in terms of toxic side effects as ABL is a natural drug from mushroom without any apparent cytotoxicity. Based on the different release speed with different lactic to glycolic acid monomer ratio, we chose PLGA 5050DL as a vehicle for encapsulating the drug. The novelty of this work lies in the use of ABL as a drug that is conjugated with PLGA polymer. In this way, it can make ABL expressing its function in control of proliferation in optimal medicinal effects.

II. Materials and methods

Poly (lactide -*co*-glycolide acid) (PLGA, 5050DL) was purchased from Lakeshore Biomaterials (Birmingham, AL, USA) Chloroform and Poly (vinyl alcohol) (PVA) (Mw 6000) were acquired from Fluka (Steinheim, Germany) and Polysciences (Warrington, PA, USA) respectively. All other chemicals were purchased from Sigma-Aldrich unless otherwise stated.

A. Preparation of protein-loaded PLGA microspheres

A water-in-oil-in-water (w/o/w) emulsion solvent evaporation technique was used to fabricate microspheres as well as to encapsulate the proteins [4]. Briefly, PLGA was first dissolved in chloroform. Then, a mixture of BSA, ABL and phosphate-buffered saline (PBS, 0.01M, pH=7.4) solution was added. Emulsification was carried out using an ultrasonic processor for 40s. The homogenized mixture was immediately dropped into PBS with 0.1 w/v% PVA. After which, the solution was placed under continuous mechanical stirring for 4h to evaporate the organic solvent. The microspheres produced were then washed with deionized water five times to remove the solvent before being placed in a freeze dryer for 36 hours to remove any remaining solvent and water droplets and to get a constant weight of porous microspheres.

B. Preparation of release medium

Base on the data of the release studies in Figure 1, the release medium for culturing cells was prepared. 100mg of the encapsulated microspheres was suspended in 5ml of serum free medium and incubated at 37°C, in a circulating water bath. At pre-determined times, the microspheres were centrifuged, and the resultant supernatant was sterilized with a filter and then stored in a -80°C fridge till bioactivity analysis [5].

Chwee Teck Lim, James C.H. Goh (Eds.): ICBME 2008, Proceedings 23, pp. 1313–1315, 2009
www.springerlink.com

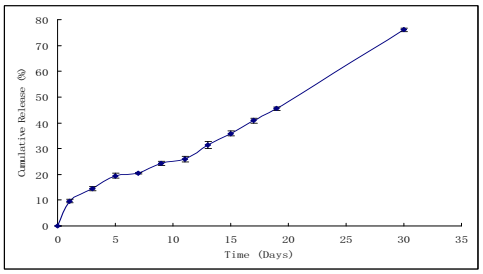


Fig. 1 *In vitro* accumulated protein release of the protein-loaded PLGA microspheres. Values represent means ± SD, n=3

C. Bioactivity assays for the released ABL

The bioactivity of the released ABL from PLGA microspheres was evaluated using cell proliferation inhibition assays. Hep3B liver cells [6, 7], KB human mouth epidermal carcinoma cells [8] and MCF-7 breast cancer cells [9] were cultured in their own medium with 10% serum. The serum-free (SF) medium was defined similarly as the above mentioned serum-medium except that FBS was not added. Cells were seeded in 96-well plate at a density of 8×10^3 cells/well in culture medium and incubated for 6 hours. The medium was aspired out and replaced by the release medium containing ABL. SF medium and SF medium with 20μg/ml and 100μg/ml ABL were used as positive and negative controls respectively. After incubation for 24 hours, MTT quantification assays were used to measure the proliferation. Hep3B cells have well-known cell functionalities, such as P-450 activity, which may be affected by ABL's inhibitory effects. To investigate this, the changes in these cell functionalities were measured. The P-450 activity (CYP1A1/2) represents the detoxification ability of liver cells, which was measured using an ethoxyresorufin-o-deethylase (EROD) assay.

III. Result and Discussion

The bioactivity of ABL/BSA released from PLGA microspheres was assessed by culturing Hep3B, KB and MCF-7 cells in the medium from the release study and studying the inhibitory effects of ABL on them. Cell viability, were used as an indicator of bioactivity by comparing to a positive control (SF medium) and two negative controls (SF medium supplemented with 20 μg/ml and 100 μg/ml ABL respectively). The medium from microspheres encapsulated with BSA alone served as a control for both the effects of released BSA on cell proliferation and any potential cytotoxicity effects of the polymer degradation products [10].

The MTT and EROD results are shown in Figure 2. Generally, the cell proliferation was significantly inhibited by released ABL in these three types of cell as compared to positive controls. Some results at time points with low inhibitory effect may be attributed to the lower amount of ABL released. However, more ABL was released as the PLGA microspheres degraded, and the degraded product of PLGA may also improve the therapeutic efficiency of ABL. Considering the results of the released BSA without cytotoxic, it can be concluded that the inhibitory effect was due mainly to the released ABL. The acidic degraded product of PLGA may stimulate the variation of the molecular conformation of ABL in order to improve its penetration ability such that it may get into the cell more easily so as to achieve the same inhibitory level with a lower concentration of ABL, and thus magnify the inhibitory effect in the process. The results indicated that the bioactivity of ABL released from PLGA microspheres was preserved for at least 30 days, and this proved to be an efficient way to increase the residence time of ABL. It also can overcome the limitation of reversible inhibition and increase ABL's potential application value. Furthermore, the results also implied that PLGA microspheres can serve as vehicles for drug delivery of ABL.

The bioactivity of ABL was also assessed by measuring the cytochrome P-450 activity of Hep3B cells, which is an important hepatic function. It was interesting to draw from the EROD result that the cytochrome P-450 activity of the cells cultured in ABL containing medium was higher than that cultured in the positive control. Although the viability of Hep3B decreased significantly, the cytochrome P-450 activity remained at a relatively stable level. From Figure 2(D), it was observed that cytochrome P-450 activities in the medium containing ABL at every 5 days interval were slightly higher than those in the medium containing only BSA. It was due to ABL stimulation that promoted cell differentiation during the inhibition process of cell proliferation. Therefore, the cytochrome P-450 activity can be maintained at a high level without any sharp decrease, which is consistent with other findings that showed that cells with lower proliferation rates may have higher differentiated functions [11]. At the same time, it verified that ABL inhibited the proliferation of cancerous cells without any cytotoxic effects.

IV. Conclusion

PLGA microspheres, prepared for the potential application for ABL drug delivery, can increase the residence time and improve the therapeutic efficiency of ABL. Through the co-encapsulation investigation, we found BSA was effective as a protector as it can prevent ABL from denaturation or degradation during the fabrication process. The system has

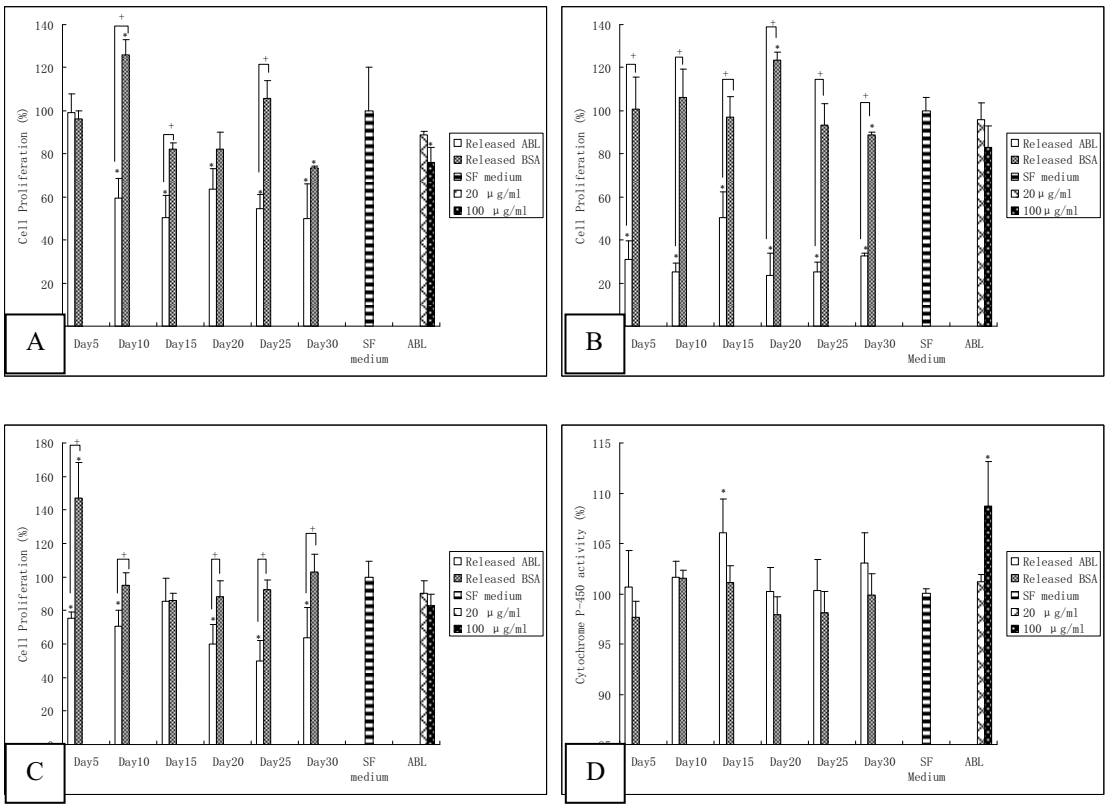


Fig. 2 Assays of incubation with released medium for 24 hours. The results of MTT assays are (A) Hep3B, (B) KB, (C) MCF-7. (D) Hep3B is the result of EROD assay. Value represent means ±SD, n=3. Statistical significance (*$p< 0.05$) were determined by one-way ANOVA with Tukeys's HSD post hoc analysis as compared to the positive control, while ($^{+}P< 0.05$) was determined between the two samples

proven to be a useful vehicle for improving on the limitations of ABL as a drug in application.

References

[1] M. E. Carrizo, S. Capaldi, M. Perduca, F. J. Irazoqui, G. A. Nores, and H. L. Monaco, The antineoplastic lectin of the common edible mushroom (Agaricus bisporus) has two binding sites, each specific for a different configuration at a single epimeric hydroxyl, Journal Of Biological Chemistry 280 (2005) 10614-10623.

[2] D. Kent, C. M. Sheridan, H. A. Tomkinson, S. J. White, P. Hiscott, L. Yu, and I. Grierson, Edible mushroom (Agaricus bisporus) lectin inhibits human retinal pigment epithelial cell proliferation in vitro, Wound Repair And Regeneration 11 (2003) 285-291

[3] L. G. Yu, D. G. Fernig, and J. M. Rhodes, Intracellular trafficking and release of intact edible mushroom lectin from HT29 human colon cancer cells, European Journal Of Biochemistry 267 (2000) 2122-2126.

[4] X. H. Zhu, C. H. Wang, and Y. W. Tong, Growing tissue-like constructs with Hep3B/HepG2 liver cells on PHBV microspheres of different sizes, Journal Of Biomedical Materials Research Part B-Applied Biomaterials 82B (2007) 7-16.

[5] C. H. W. X.H. Zhu, Y.W.Tong, In vitro characterization of hepatocyte growth factor release from PHBV/PLGA microsphere scaffold, Journal of Biomedical Materials Research Part A (2008).

[6] S. T. Khew, and Y. W. Tong, The specific recognition of a cell binding sequence derived from type I collagen by Hep3B and L929 cells, Biomacromolecules 8 (2007) 3153-3161.

[7] P. P. Wang, J. Frazier, and H. Brem, Local drug delivery to the brain, Advanced Drug Delivery Reviews 54 (2002) 987-1013.

[8] H. Z. Zhao, L. Yue, and L. Yung, Selectivity of folate conjugated polymer micelles against different tumor cells, International Journal Of Pharmaceutics 349 (2008) 256-268.

[9] Z. P. Zhang, S. H. Lee, and S. S. Feng, Folate-decorated poly(lactide-co-glycolide)-vitamin E TPGS nanoparticles for targeted drug delivery, Biomaterials 28 (2007) 1889-1899.

[10] X. D. Cao, and M. S. Shoichet, Delivering neuroactive molecules from biodegradable microspheres for application in central nervous system disorders, Biomaterials 20 (1999) 329-339.

[11] X. H. Zhu, S. K. Gan, C. H. Wang, and Y. W. Tong, Proteins combination on PHBV microsphere scaffold to regulate Hep3B cells activity and functionality: A model of liver tissue engineering system, Journal Of Biomedical Materials Research Part A 83A (2007) 606-616.

Hard Tissue Formation by Bone Marrow Stem Cells in Sponge Scaffold with Dextran Coating

M. Yoshikawa[1,2], Y. Shimomura[1], N. Tsuji[1], H. Hayashi[1], H. Ohgushi[2]

[1] Department of Endodontics, Osaka Dental University, 5-17, Otemae 1-chome, Chuo-ku, Osaka 540-0008, Japan
[2] Tissue Engineering Research Group, Research Institute for Cell Engineering, National Institute of Advanced, Industrial Science and Technology, 3-11-46 Nakouji, Amagasaki, Hyogo 661-0974, Japan

Abstract — **A scaffold is necessary for bone regeneration, because the structure of hard tissue is three-dimensional. For application in dentistry, it is desirable for the scaffold to be modified the geometry easily according to the defect. Therefore it is thought that a sponge is suitable as a scaffold. A sponge (Polyvinyl formal®: PVF) was purchased for this study. The sponge was made from polyvinyl alcohol (PVA) with formalin preparation. In this study, the PVF sponges were coated with dextran, because dextran may affect cell adhesion. The effect of dextran for hard tissue formation by bone marrow stem cells in the PVF scaffold was examined *in vivo*. PVF scaffolds (5×5×5 mm) were immersed in each dextran solution of 10 kDa (2 g/dl) and 500 kDa (4 g/dl) and air dried. The coating for the PVF scaffolds by dextran was confirmed by SEM. Rat femur bone marrow cells of 1×10^7 were seeded in PVF scaffolds. They were implanted for four weeks in rat dorsal subcutaneous tissue. In removed scaffolds, hard tissue formation was examined histologically. Bone formation was conspicuously found in the scaffold coated with 10 kDa of dextran. Value of ALP activity measured biochemically in the scaffold was 58.5 mM/scaffold. By immunochemical examination, it was measured that quantity of osteocalcin in the scaffold was 25.9 ng/scaffold and that of Ca was 129.2 μg/scaffold. These values showed a significantly higher in comparison with those of the scaffold with 500 kDa dextran coating and without coating. It was suggested in this study that coating of the scaffold with dextran induce increase of quantity of hard tissue formation in PVF scaffold *in vivo*. It is concluded that 10 kDa dextran coating of PVF scaffolds effectively contribute to adhesion of bone marrow cells in the scaffold.**

Keywords — **bone marrow cells, polyvinyl alcohol, scaffold, sponge, dextran**

I. Introduction

Multifunctional undifferentiated mesenchymal cells are present in bone marrow [1]. It is reported that this mesenchymal stem cells differentiates to osteoblasts, chondrocytes, adipocytes or nerve cells [2]. In dentistry, regeneration of a part of defect or total teeth is attempted [3, 4]. Tooth and the bone should be regenerated three dimensionally. Therefore scaffold is necessary for these regeneration. In the scaffold, stem cells proliferate and differentiate to blast cells. Generally, porous hydroxyapatite (HA) is used as a scaffold for bone regeneration [5, 6]. The defects in tooth are varying in the configurations and in size from small to large. It is desirable that the scaffold can adjust to the geometry of the defect. Therefore, use of the sponge as a scaffold was considered. Polyvinyl alcohol (PVA) treated with formalin is purchased as a sponge (Polyvinyl formal: PVF). The sponge was used in this *in vivo* study.

Bone marrow cells were seeded for osteogenesis in PVF sponges. For effective osteogenesis in a PVF sponge by seeding of undifferentiated mesenchymal stem cells from bone marrow, a number of undifferentiated mesenchymal stem cells should adhere to an inner structure of the scaffold. Dextran, a kind of polysaccharide, was selected for adherent of bone marrow cells in the scaffold. To obtain a larger quantity of osteogenesis in the scaffolds, they were coated by the compound.

The purpose of this study was to examine effectiveness of the PVF sponge as the scaffold and influence of dextran coating to the scaffold for osteogenesis in the scaffold by attachment of bone marrow cells.

II. Materials and Methods

A. Rat bone marrow cell isolation and preparation of the cell suspension

Bone marrow cell isolation: To prepare a rat bone marrow cell suspension, seven-week-old male Fischer 344 rats were used. Rat bone marrow cells were obtained from the bone shaft of femora of seven-week-old male Fischer 344 rats after euthanasia by intraperitoneal overdose of sodium pentobarbital. Minimum essential medium supplemented with 15% fetal bovine serum and antibiotics (100 units/ml penicillin, 100 μg/ml streptomycin, and 0.25 μg/ml amphotericin B) was used as a culture medium. Primary culture for the cell proliferation was performed for 1 week. The culture medium was subsequently renewed two times afterward.

Preparation of the cell suspension: After the primary culture, confluent rat bone marrow cells in the T75 culture flasks were released from their culture substratum using trypsin-EDTA solution (0.5 mg/ml trypsin, 0.53 M/ml EDTA). The rat bone marrow cells were resuspended in the

Chwee Teck Lim, James C.H. Goh (Eds.): ICBME 2008, Proceedings 23, pp. 1316–1319, 2009
www.springerlink.com

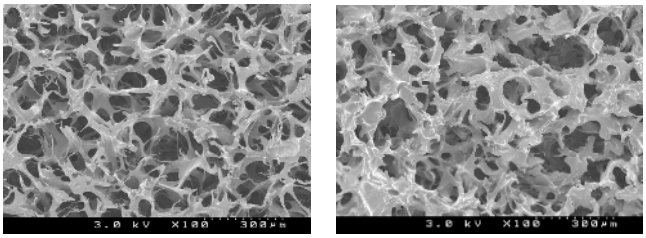


Fig. 1. SEM images of PVF sponge with and without immersion in dextran solution
Left: Inner construction of PVF without immersion in dextran solution. Right: Inner construction of PVF with immersion in dextran solution.

culture medium at a density of 1×10^8 cells/ml for *in vivo* experiment.

B. PVF scaffold

Preparation of dextran solution: Dextran with 10kDa and 500 kDa of molecular weight was purchased. Dextran of 10 kDa molecular weight was prepared at 2 g/dl concentration of solution, and that of 500 kDa was at 4 g/dl concentration. SEM images of PVF scaffold with and without immersion in dextran solution was shown in Fig. 1. Accumulation of substance on the internal structure surface of the sponge with immersion in dextran was clearly observed.

PVF scaffolds: PVA is water-soluble [7]. PVA processed with formalin was commercially available. PVF cross-linked with formalin is insoluble. Commercially available PVF sponges used in this study were purchased. Scaffold of 5×5×5 mm was made from a sheet of PVF. Those pore size was 100 to 130 μm in an average.

Dextran coating of PVF scaffold: The scaffolds were divided into three groups of four each. They were immersed in dextran solution of each concentration for twenty-four hours and then were air dried in clean condition for three days. Four PVF sponges immersed in 10 kDa molecular weight of dextran solution were abbreviated to PVF-A. Other four PVF sponges immersed in 500 kDa of dextran solution was abbreviated to PVF-B. The others without immersion in every dextran solution were abbreviated to PVF-C.

Seeding of bone marrow cells in PVF scaffolds: In each PVF scaffold, 1×10^7 of bone marrow cells (0.1ml of sell suspension/scaffold) were seeded. They were kept in an incubator for three hours before use *in vivo* examination.

C. Osteogenesis in PVF scaffold in vivo

Dorsal subcutaneous implantation of scaffolds: The scaffolds with rat bone marrow cells were implanted in the dorsal subcutis of seven-week-old male Fischer 344 rats. They were removed from the subcutis four weeks post-operatively. Some of the removed PVF scaffolds were decalcified in 10% formic acid and made of 6μm serial section for histological examination. Others were used for immunochemical and biochemical examination.

Histological examination of implanted scaffolds: The scaffolds removed from dorsal subcutaneous tissue of rats were respectively embedded in paraffin, and 6 μm serial sections were made according to the routine histological methods. All sections were stained with hematoxylin-eosin and examined bone formation in the pores of scaffold under an optical microscope.

Immunochemical and biochemical examinations for osteogenesis in implanted scaffolds: The removed scaffolds were homogenized in 1 ml of 10-fold concentration of TNE solution (pH7.4, 10mM Tris-HCl, 1mM EDTA, 100mM NaCl). They were centrifuged for one minute at 16,000×g. Absorbance of the supernatant reacted with *p*-nitrophenylphosphate-substrate at 37°C for thirty minutes was measured at 405 nm for measuring ALP activity. The value was represented as ALP activity per one scaffold. The supernatants were also used for immunochemical quantitative analysis of osteocalcin using Rat Osteocalcin ELISA kit DS (DS Pharma Biomedical Co., Ltd., Osaka, Japan). The precipitation was immersed into 1ml of formic acid and quantity of calcium was measured. Each data was presented as mean ± standard deviations. The results were statistically analyzed respectively using two-way unrepeated ANOVA followed by post hoc analysis using Tukey-Kramer's test. Differences of $p<0.05$ were considered significant.

III. Results

Histological findings of implanted PVF scaffolds: Optical microscopic images of osteogenesis in scaffolds are shown in Fig. 2. Bone was found in many pores in PVF-A. The number of pores including bone in PVF-A was remarkably large in comparison with ones of PVF-B. In PVF-B, a little of pores contained bone were observed. Bone formation in the pores was scarcely seen in PVF-C.

Value of ALP activity, quantity of calcium and osteocalcin in implanted scaffolds: Value of ALP activity, calcium level and quantity of osteocalcin were shown in Fig. 3. Value of ALP activity measured in PVF-A was significantly higher than that of PVF-B and PVF-C. Between ALP activity measured in PVF-B and PVF-C, there was no significant difference. The value of ALP activity in PVF-A was 58.5 mM/scaffold. The calcium level detected in PVF-A scaffolds was 129.2 μg/scaffold. It showed significant differences with that in PVF-B and PVF-C. There were statistically significant differences between molecular weight of

dextran. A quantity of osteocalcin detected in PVF-A was 25.9ng/scaffold. The level of osteocalcin in PVF-A was significantly different from that in PVF-B and PVF-C.

IV. Discussion

Regeneration of a partial or complete tooth has been halfway developed [2, 3]. Scaffold should be used for tooth regeneration. The configuration of tooth and the defect is various. A sponge would be suitable for regeneration of hard tissue with various configurations. PVA is one of the materials of the scaffold for osteogenesis [8]. PVA treated with formalin was used in this study. It was confirmed from the results of this *in vivo* study that PVF sponge shows excellent biocompatibility. However, no bone-like tissue was formed in the pores of PVF-C, which was not immersed in dextran solution. The result showed that few bone marrow stem cells adhered to the PVF scaffold. So the PVF is hydrophilic [9], it is generally hard for the cells to adhere to such a material.

Hydrogels have some unique properties that make them highly biocompatible. They have a low interfacial tension with surrounding biological fluids and tissues. This minimizes the property for protein adsorption and cell adhesion [10]. Therefore it was thought that scaffolds should be coated with a chemical agent for cell adhesion. For the use as the sponge, PVA might be processed with formalin because the PVA was water-soluble. The PVF cross-linked with formalin should be insoluble. It was not proved that the sponge is hydrophobic. In this study, no bone was observed in PVF-C. The result suggested that the sponge was hydrophilic. On the other hand, it was also sure that a dextran, which coated on PVF scaffolds, played a role to attach bone marrow cells and maintained the cells in PVF-A and PVF-B for osteogenesis. It was reported that dextran agglutinated cells [11]. Bone formation in PVF-A and PVF-B would be induced after dextran and bone marrow cell conjugate.

In vitro preliminary experiment, the concentration of dextran solution for use of immersion of scaffold in this study was decided from the result of bone formation level.

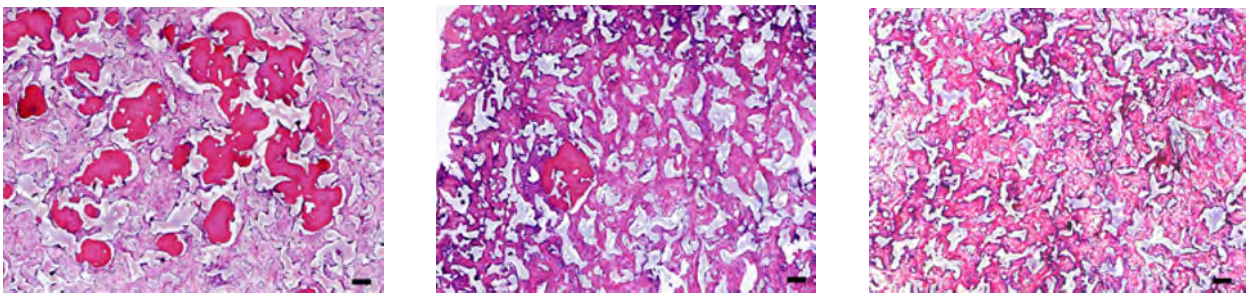


Fig. 2. Optical microscopic images of PVF scaffold implanted *in vivo*
Left: Bone are seen in many pores of PVF-A. (Bar=100μm) Center: A few pores containing bone are seen in PVF-B. (Bar=100μm) Right: There is little bone formed in pores of PVF-C. (Bar=100μm)

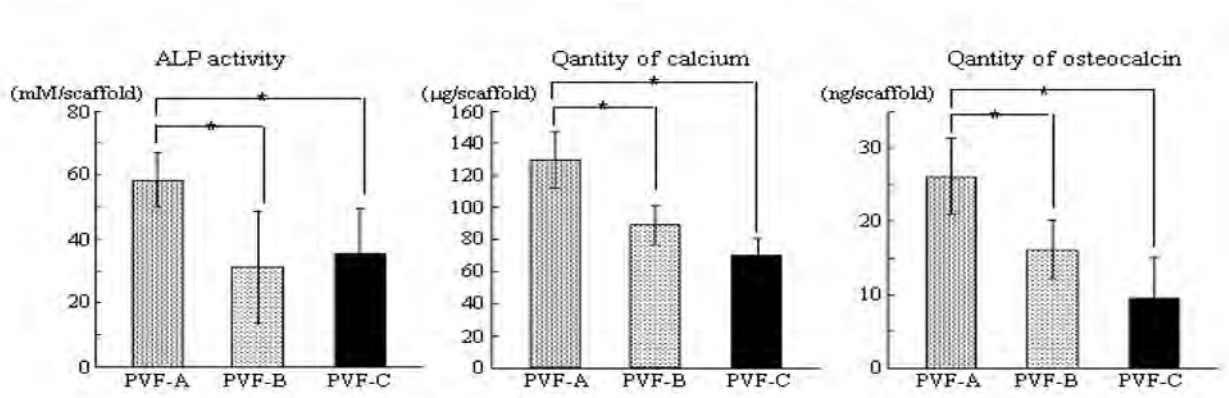


Fig. 3. Biochemical and immuno-chemical measurement of ALP activity, quantity of calcium and osteocalcin in implanted scaffolds (* $p<0.05$)

It could not be confirmed in this experiment that induction of bone marrow stem cell aggregation with a small amount of dextran coated on the scaffold. However, it was thought from this result, that bone marrow stem cells adhered to dextran on the inner structure of PVF and aggregate mutually there. It was also suggested that bone marrow stem cells proliferated and differentiated to osteoblasts in the scaffold immersed in 10 kDa of dextran solution.

On the other hand, molecular weight of dextran should be related closely to osteogenesis in the scaffold. PVF-B showed less formation of bone in the scaffold than PVF-A in this experiment. It was suggested that low molecular weight dextran was effectively form bone in the pores. By dextran of 10kDa molecular weight, many pores with bone were observed in this *in vivo* experiment.

The pore size of the PVF sponge is 100-130μm. The pore size is a suitable dimension for hard tissue formation in the scaffold [12]. Bone marrow cells seeded in the scaffolds with the pores of an appropriate diameter might be almost located in all pores, and supplied nutrition from the subcutaneous surrounding tissue should arrive to the cells in the pores.

Scaffolds made of sponge have some advantages. For application to a defect, the sponge scaffolds can be cut easily. It is easy for the scaffold to adjust the shape to a defect that should be restored. The manufacturing cost for the sponge scaffold may be low than that of HA scaffolds. However, there are several problems for the sponge scaffolds to be improved for clinical use. Biodegradable sponge scaffold has been developed. The biodegradable scaffold may be unsuitable for teeth or bone regeneration from the viewpoint of hardness. Regenerated bone or tooth have to bear a large load. The structural hardness for the scaffolds to bear the load is required.

V. Conclusions

PVF sponge was immersed in dextran solution to promote osteogenesis by bone marrow cells. The sponge was implanted in subcutis and estimate osteogenesis *in vivo*.

Conclusions obtained from the results of this study were as follows:

1) No bone would be formed in the PVF sponge.
2) Osteogenesis occurred in the PVF sponge with immersion in dextran solution.
3) Quantity of osteogenesis in the PVF sponges was under the influence of the molecular weight of dextran.
4) Bone was formed in many pores of PVF sponges immersed in a dextran solution with low molecular weight.

Acknowledgment

This study was performed in the Morphological Research Facilities, Low Temperature Facilities, Tissue Culture Facilities, Laboratory Animal Facilities and Photograph-Processing Facilities, Institute of Dental Research, Osaka Dental University.

This study was supported in part by a 2008 (C:20592246) Grant-in-Aid for Scientific Research (C) from the Japan Society for the Promotion of Science.

References

1. Couble LM, Farges CJ, Bleicher F et al. (2000) Odontoblast differentiation of human dental pulp cells in explant culture. Calcif Tissue Int 66: 129–138.
2. Kawano S, Saito M, Handa K et al. (2004) Characterization of dental epithelial progenitor cells derived from cervical-loop epithelium in a rat lower incisor. J Dent Res 83: 129–133.
3. Gronthos S, Brahim J, Li W et al. (2002) Stem cell properties of human dental pulp stem cells. J Dent Res 81: 531–535.
4. Kawano S, Saito M, Handa K et al. (2004) Characterization of dental epithelial progenitor cells derived from cervical-loop epithelium in a rat lower incisor. J Dent Res 83: 129–133.
5. Yoshikawa T, Ohgushi H, Uemura T et al. (1998) Human marrow cells-derived cultured bone in porous ceramics. Biomed Mater Eng 8: 311–320.
6. Ohgushi H, Caplan AI (1999) Stem cell technology and bioceramics: From cell to gene engineering. J Biomed Mat Res 48: 913–927.
7. Kakinoki A, Kaneo Y, Tanaka T et al. (2008) Synthesis and evaluation of water-soluble poly(vinyl alcohol)–paclitaxel conjugate as a macromolecular prodrug *Biol Pharm Bull* 31: 963–969.
8. Nuttelman RC, Mortisen FD, Henry MS et al. (2001) Attachment of fibronectin to poly(vinyl alcohol) hydrogels promotes NIH3T3 cell adhesion, proliferation, and migration. J Biomed Material Res 57: 271-223.
9. Knabe C, Howlett CR, Klar F et al. (2004) The effect of different titanium and hydroxyapatite-coated dental implant surfaces on phenotypic expression of human bone-derived cells. J Biomed Mater Res A 71: 98-107.
10. Cascone G M, Maltinti S, Barbani N (1999) Effect of chitosan and dextran on the properties of poly(vinyl alcohol) hydrogels. J Mater Sci Mater Med 10: 431-435.
11. Thébaud NB, Pierron D, Bareille R et al. (2007) Human endothelial progenitor cell attachment to polysaccharide-based hydrogels: a prerequisite for vascular tissue engineering. J Mater Sci Mater Med 18: 339-345.
12. Tsuruga E, Takita H, Itoh H et al. (1997) Pore size of porous hydroxyapatite as the cell-substratum controls BMP-induced osteogenesis. J Biochem 121: 317-324.

Author: M. Yoshikawa
Institute: Department of Endodontics, Osaka Dental University
Street: 5-17, Otemae 1-Chome, Chuo-ku
City: Osaka
Country: Japan
Email: yosikawa@cc.osaka-dent.ac.jp

Inactivation of Problematic Micro-organisms in Collagen Based Media by Pulsed Electric Field Treatment (PEF)

S. Griffiths[1,2], S.J. MacGregor[2], J.G. Anderson[2], M. Maclean[2], J.D.S. Gaylor[1] and M.H. Grant[1]

[1] Bioengineering Unit, University of Strathclyde, Wolfson Building, 106 Rottenrow, Glasgow, UK
[2] Robertson Trust Laboratory for Electronic Sterilisation Technologies (ROLEST), University Of Strathclyde, Royal College Building, 204 George Street, Glasgow, UK

Abstract — **The potential of pulsed electric field (PEF) treatment as a novel/safe method of decontaminating collagen based biomatrices was investigated. Collagen gels (0.3% w/v) were seeded at a concentration of 10^6 CFU/ml with either *Escherichia coli* or *Staphylococcus epidermidis* and then treated with 100 pulses at ~45 kV/cm, using a static PEF chamber. To investigate if the collagen gel had a "protective" effect on the bacteria, PEF inactivation was also investigated in phosphate buffered saline (PBS) and melted collagen gel (heat-treated, 10 min at 80°C, and as a result not set as a gel). When subjected to PEF, different levels of inactivation were observed with *E. coli* and *S. epidermidis* seeded in the different media. In all three media *E. coli* was more susceptible to PEF treatment than *S. epidermidis*. *E. coli* cell counts were reduced by ~3.3 logs in PBS, 2.6 logs in collagen gel and least inactivation (~1.5 log reduction) was observed in melted gel. *S. epidermidis* also showed higher inactivation levels in PBS compared to native collagen gel and melted collagen gel. Current results have established that PEF treatment can inactivate different types of bacteria seeded in collagen gels. However, complete inactivation was not achieved in any of the different types of suspending media, possibly due to the high seeding densities utilized. Previous results have established that PEF does not adversely affect the collagen structure. Future work is required to optimize microbial inactivation levels and to fully establish whether PEF treatment may offer a novel biomatrix decontamination method, which achieves sterility without damaging labile biological components.**

Keywords — **Collagen gel, microbial inactivation, pulsed electric field, sterilization, biomatrices**

I. Introduction

Collagen is a fibrous structural protein and the most abundant protein in mammals. Hence collagen based biomatrices have numerous potential applications within the fields of tissue engineering and regenerative medicine. The use of these biomatrices for clinical applications requires a compatible sterilization method and this is problematic as conventional methods of sterilization (ethylene oxide, gamma irradiation) have been shown to cause detrimental effects on the collagen structure or can produce mutagenic and carcinogenic products [1, 2]. Pulsed electric field (PEF), initially investigated for use in the food industry, is a non-thermal treatment that causes bacterial inactivation through irreversible rupture of microbial cell membranes [3]. Previous work has established that PEF treatment can achieve complete bacterial inactivation of *E. coli* in collagen gel at low levels of contamination [4]. It has also been demonstrated that PEF does not affect the structure of the collagen molecule or its ability to support cell culture[5]. However, when high bacterial densities were seeded in collagen gel complete inactivation was not achieved, one explanation proposed was the protective effect that collagen gel may provide to bacteria suspended within its gel matrix. The present study aims to investigate how the viscosity of the suspending medium affects microbial inactivation. The media examined included collagen gel, melted collagen gel and phosphate buffered saline (PBS), and the PEF inactivation of two different bacteria suspended within these media was investigated.

II. Materials and Methods

A. Microbial inactivation

Two different types of bacteria were chosen for the present study, one a Gram negative rod, *Escherichia coli* National Collection of Type Cultures (NCTC) 9001 and the other a Gram positive coccus *Staphylococcus epidermidis* NCTC 11964. *E. coli* and *S. epidermidis* populations were grown by incubating at 37 °C under rotary conditions for 18 h, in nutrient broth and brain heart infusion broth (Oxoid) respectively. Inocula used to seed the different media were produced at densities of ~10^8 colony forming units (CFU) per milliliter by diluting with PBS.

PEF treatments were performed in three types of suspending media - PBS, melted collagen gel and collagen gel. Collagen gels (0.3% w/v) were prepared by mixing collagen solution (4.29 mg/mL), a mixture of 10X Dulbecco's minimal essential medium (DMEM) and 0.4 mol/l NaOH (2:1), and acetic acid (1:1000 v/v) at a ratio of 7:2:1[6]. The above

Chwee Teck Lim, James C.H. Goh (Eds.): ICBME 2008, Proceedings 23, pp. 1320–1324, 2009
www.springerlink.com

collagen mixture was seeded with inoculum and vortexed, prior to being set to a gel with 0.5 mol/l NaOH. Melted collagen gel was produced by taking collagen gels (as above but with no inoculum) set in a universal and liquefying them by placing in a water bath at 80 °C for 10 min. The melted gels were seeded once they had attained ambient temperature. PBS samples were seeded in the same manner. Once seeded, all media had a final concentration of ~ 10^6 CFU/ml.

Sterile electroporation cuvettes with 4mm electrode spacing and 800µl volume (Bio-Rad Laboratories) were loaded with 700µl of test sample and topped with 200µl of Tween 80 (covering the top surface of the electrodes and hence preventing any electrical breakdown). The different media when overlaid with Tween had similar conductivities that ranged between 6.0-8.8 ms/cm at 15°C. The cuvette was placed in the chamber which was then pressurized with air to 4 bar. Samples were subjected to high-intensity pulsed electric fields (pulse duration 1 µs, at ~ 45 kV/cm) using the test arrangement illustrated in Fig. 1. A low pulse frequency and water cooling were employed to maintain the treatment medium below 30°C. The pulse frequency was set to 0.1 Hz and 1 min breaks were taken after every 10 pulses to ensure that there were no thermal inactivation effects associated with the energy dissipated in the test chamber. Water cooling (15°C) was controlled by a thermostatic regulator and supplied to the earth connection which was situated along the side of the cuvette. The voltage waveforms generated across the samples were monitored throughout all experiments using a 1,000:1 Tektronix high-voltage probe connected to a Tektronix digital oscilloscope. This also enabled calculations of any temperature increases and provided confirmation that these were insufficient to cause thermal inactivation effects.

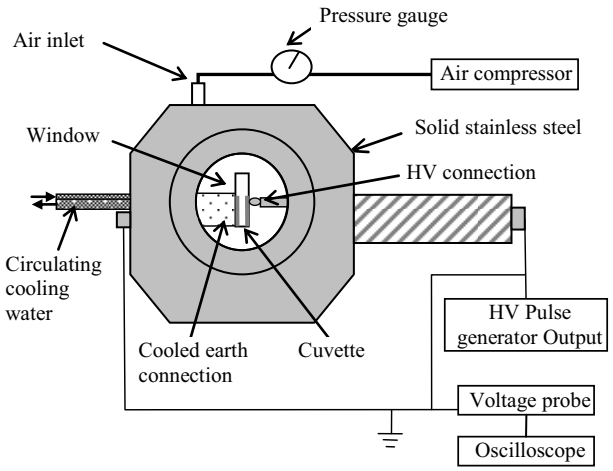


Fig. 1 Schematic of pressurized static PEF chamber.

The level of microbial inactivation was assessed post treatment by removing samples from the cuvette and diluting with PBS prior to plating in triplicate. To recover bacteria from collagen gel, samples were stomached with PBS (using a Colworth Stomacher) prior to further dilutions. The surviving populations, expressed as $\log_{10}$ CFU/ml, were enumerated from duplicate experiments, following incubation for 24 h at 37°C on nutrient agar and brain heart infusion agar, respectively. Where applicable, statistical analysis was carried out using Minitab 14. A one-way ANOVA, combined with Dunnett's comparison was utilized, with a significance level of 95 %.

B. Viscosity Measurements

All measurements were taken at 25°C using a Wells-Brookfield cone and plate viscometer (Brookfield Engineering Laboratories). The system was calibrated with a Newtonian calibration oil (4.4 mPa s at 25°C). Viscosity measurements were carried out on melted collagen gel, PBS and for comparison on collagen solution (3.58 mg/ml), a 50% mixture of glycerol/water and olive oil. Torque values (Nm) were taken over a range of shear rates (s^{-1}) and corresponding shear stresses (Pa) were calculated.

C. SDS-PAGE of melted collagen gel

Sodium dodecyl sulfate polyacrylamide gel electrophoresis (SDS-PAGE) analysis was used to determine the integrity of the collagen molecules after the collagen gel was melted. Samples analyzed included melted collagen gel (heat treatment at 80°C for 10 min), collagen solution (heat treated as above), a positive control (collagen solution heat treated at 90°C for 1h) and a negative control (non-treated collagen solution). Collagen samples were adjusted to a concentration of 1 mg/ml, prepared in Laemmli buffer, and subjected to SDS–PAGE. Coomassie Brilliant Blue was used to stain the bands obtained.

III. Results and Discussion

The results shown in Fig. 2 compare the effect of different suspending media on PEF inactivation of *E. coli*. The data show *E. coli* populations before and after PEF treatment. After 100 pulses *E. coli* populations were significantly decreased, at the $P < 0.05$ level, in all three types of media. *E. coli* was most susceptible to PEF treatment when suspended in PBS, where a ~3.3 log reduction was observed

compared to 2.6 logs in collagen gel and least inactivation (~1.5 log reduction) was observed in melted gel.

The results of Fig. 3 show the inactivation of *S. epidermidis* when suspended in different media. Significant population decreases ($P < 0.05$) were seen in PBS and collagen gel. The results showed that the greatest inactivation (~0.9 log reduction) occurred in PBS, and then collagen gel (~0.3 log reduction) but no significant decrease was observed for *S. epidermidis* when suspended in melted collagen gel.

Greater inactivation was observed with *E. coli* in all three types of media compared to *S. epidermidis*. The same trend was seen with both organisms, i.e. greater inactivation in PBS compared to native collagen gel and lower inactivation in melted collagen gel compared to native collagen gel.

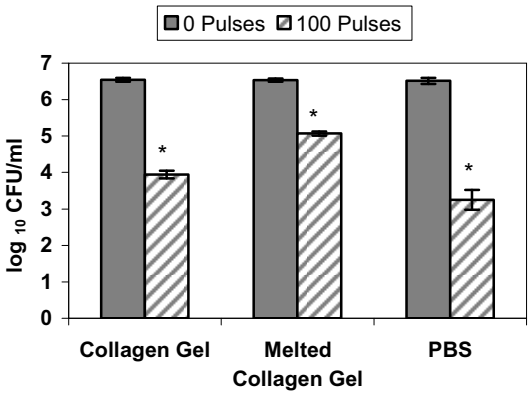


Fig. 2 The effect of suspending media on PEF inactivation of *E. coli*. n=6, data points show mean ± standard deviation. * Significant difference at the P<0.05 level.

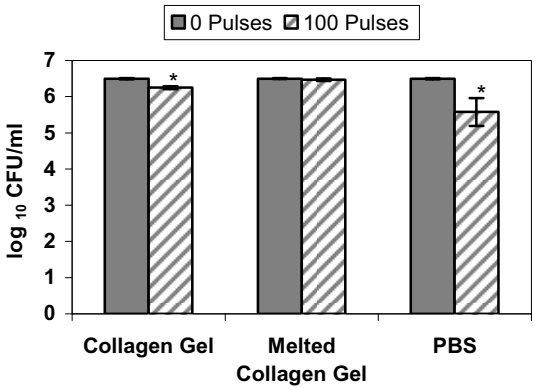


Fig. 3 The effect of suspending media on PEF inactivation of *S. epidermidis*. n=6, data points show mean ± standard deviation. * Significant difference at the P<0.05 level.

Previously it had been thought that suspending bacteria in a gel could possibly provide protective interactions with collagen fibres [4]. By melting the collagen gel and breaking the cross-linked fibres formed during the gelling process and creating a liquid it was considered that greater inactivation might be achieved. In fact, the results showed the opposite effect since less inactivation was observed in melted collagen gel compared to native collagen gel.

The results of SDS-PAGE analysis, Fig. 4, show that there was no obvious sign of damage to the collagen monomer in melted gel samples. The banding pattern seen for the melted gel was similar to that of the negative control with no detectable occurrence of low molecular weight components. These intact fibres when in a liquid suspension may potentially form better interaction with the suspended bacteria and hence provide greater protection from pulsed electric fields. It has also been reported that *S. epidermidis* has the ability, possibly through extracellular lipases to bind to collagen [7]. This may explain why *S. epidermidis* is particularly difficult to inactivate when suspended in collagen gel as shown in these studies.

In order to further understand the differences in cell inactivation (particularly in PBS and melted collagen gel) rheology experiments were conducted in order to establish any substantial difference in fluid viscous properties. Fig. 5 shows the shear stress versus shear rate (of which the gradient is the apparent viscosity) of PBS, melted collagen gel and other sample liquids showing a range of viscosities.

All the fluids tested exhibited Newtonian behaviour as demonstrated by the linear plots. The results for PBS and melted collagen gel have similar gradients and hence viscosities, particularly compared to other (more viscous)

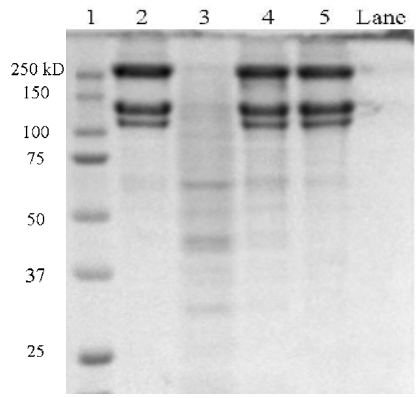


Fig. 4 SDS-PAGE of collagen samples. Lane 1 molecular weight marker, lane 2 negative control (non-treated collagen solution), lane 3 positive control (collagen solution heat treated at 90°C for 1h), lane 4-collagen solution (treated at 80°C for 10 min), lane 5-melted collagen gel (treated at 80°C for 10 min).

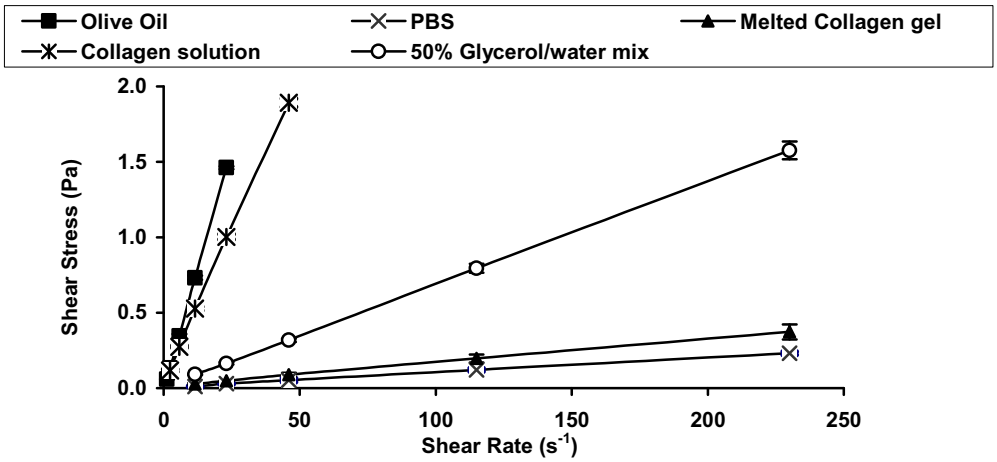


Fig. 5 Viscosity measurements of melted collagen gel and a range of other media at 25 °C, n=7 data points show mean ± standard deviation.

liquids such as collagen solution and olive oil. Due to the similar results for PBS and melted collagen gel, viscosity was not considered to be a major factor influencing bacterial inactivation by PEF treatment.

Limited information is available in the PEF literature on studies comparing liquid and gel suspending media and their effect on microbial inactivation levels. One study has reported that PEF reductions of *E. coli* were lower in skimmed milk than in a buffer solution, potentially due to the presence of proteins [8]. The results of the present study are in agreement, showing bacterial inactivation in PBS was superior when compared to that in collagen gel. However complete inactivation at high contamination levels was not achieved with any of the three suspending media used. Results of the present and previous studies indicate that PEF may be more successful treating low levels of contamination, particularly in collagen gel.

IV. Conclusions

The study has shown that suspending media can affect microbial inactivation by PEF. The "protective" effect associated with collagen is not thought to be the due to the physical properties of the gel itself but to the collagen monomer, as least inactivation was seen in liquid melted collagen gel. Significant decreases in bacterial populations were achieved when seeded in collagen gel. However, to fully establish whether PEF treatment can offer a novel biomatrix decontamination method, further research is necessary. Future investigations will concentrate on optimization of microbial inactivation levels and extending the investigation to include other problematic bacterial species as well as yeast and mould contaminants.

Acknowledgment

SG is supported by an EPSRC Doctoral Training Centre in Medical Devices studentship. The authors would like to David Currie and Catherine Henderson for their excellent technical assistance.

References

1. Gorham S D, Srivastava S, French D A, et al. (1993) The effect of gamma-ray and ethylene oxide sterilization on collagen-based wound-repair materials. J. Mater. Sci. - Mater. Med. 4(1): p. 40-49.
2. Yunoki S, Ikoma T, Monkawa A, et al. (2006) Influence of irradiation on the mechanical strength and in vitro biodegradation of porous hydroxyapatitecollagen composite. J. Am. Ceram. Soc. 89: p. 2977-2979.
3. Wouters P C, Bos A P and Ueckert J (2001) Membrane permeabilization in relation to inactivation kinetics of Lactobacillus species due to pulsed electric fields. Appl Environ Microbiol. 67(7): p. 3092-3101.
4. Griffiths S, Smith S, Macgregor S J, et al. (2008) Pulsed electric field treatment as a potential method for microbial inactivation in scaffold materials for tissue engineering: the inactivation of bacteria in collagen gel. J Appl Microbiol. DOI 10.1111/j.1365-2672.2008.03829.x.
5. Smith S, Griffiths S, Macgregor S, et al. (2008) Pulsed electric field as a potential new method for microbial inactivation in scaffold materials for tissue engineering: The effect on collagen as a scaffold. J Biomed Mater Res A. DOI 10.1002/jbm.a.32150.

6. Kataropoulou M, Henderson C and Grant M H (2005) Metabolic studies of hepatocytes cultured on collagen substrata modified to contain glycosaminoglycans. Tissue Eng. 11(7-8): p. 1263-1273.
7. Bowden M G, Visai L, Longshaw C M, et al. (2002) Is the GehD Lipase from Staphylococcus epidermidis a Collagen Binding Adhesin? J Biol Chem. 277(45): p. 43017-43023.
8. Martin O, Qin B L, Chang F J, et al. (1997) Inactivation of Escherichia Co*li* in skim milk by high intensity pulsed electric fields. J. Food Process Eng. 20(4): p. 317-336.

Author: M. Helen Grant
Institute: Bioengineering Unit, Strathclyde University
Street: Wolfson centre, 106 Rottenrow
City: Glasgow, G4 0NW
Country: UK
Email: m.h.grant@strath.ac.uk

Development, Optimization and Characterization of Nanoparticle Drug Delivery System of Cisplatin

V. Agrahari[1], V. Kabra[1], P. Trivedi[2]

[1] Department of Pharmacy, Shri G. S. Institute of Technology & Science (SGSITS), Indore, India
[2] School of Pharmaceutical Sciences, Rajiv Gandhi Technical University (RGTU), Bhopal, India

Abstract — **Purpose: Polymeric nanoparticles are frequently employed for drug delivery systems to perform a sustained release behavior of incorporated drug. These polymeric nanoparticles can be used for site specific targeting of encapsulated drug. The objective of present study was to develop a poly (lactide-co-glycolide) (PLGA) nanoparticles drug delivery system of anticancer drug cisplatin with higher therapeutic efficacy, lesser side effects, and with further development to advances in targeted chemotherapy. PLGA nanoparticles were prepared by double emulsion solvent evaporation method and characterized by their morphology, size, polydispersity index, zeta potential, drug encapsulation efficiency and *in-vitro* drug release in phosphate buffer saline (pH 7.4). The influences of several process parameters on the nanoparticles were observed. The results obtained from studies showed that nanoparticles developed in this study could be the nanoparticles for application in the controlled delivery of cisplatin for cancer therapeutics and may be considered promising in targeted therapy of cancer.**

Keywords — **Poly (lactide-co-glycolide), nanoparticles, cisplatin, controlled release, targeted chemotherapy**

I. Introduction

Controlled drug delivery technology represents one of the frontier areas of science. These delivery systems offer numerous advantages compared to conventional dosage forms like improved efficacy, reduced toxicity and improved patient compliance & convenience. Such systems often use biodegradable polymers as drug carriers. [1-3].

Biodegradable polymer, poly (lactide-co-glycolide) (PLGA) is one of the most useful polymers for drug delivery applications. The preparation methods for nanoparticles depend on the nature (hydrophobic or hydrophilic) of the drug to encapsulate. A surfactant is required to stabilize the system [4,5]. Sodium cholate (SC) is one of the most commonly used polymeric stabilizer.

There are different methods for the preparation of polymeric nanoparticles. Among them emulsification solvent evaporation technique is most useful because of simple, fast and economic and also has the advantage of employing non toxic solvents. It may be single emulsion method if the drug is hydrophobic and double emulsion if hydrophilic. In the single emulsion method, PLGA and the drug were dissolved in an organic solvent, which was then emulsified in an aqueous (aq) phase (w) containing stabilizer to make an o/w emulsion. In the double emulsion method the drug was dissolved in an aq phase (w_1) which was emulsified in the PLGA solution (o_1) to make w_1/o_1 single emulsion. This emulsion was again emulsified in an outer aq phase containing stabilizer (w_2) to form a $w_1/o/w_2$ double emulsion. Organic solvent in both of the methods was removed by solvent evaporation technique [6,7].

Cisplatin, an anticancer drug is one of the most potent & effective anticancer drug available today but have limited applications because of the serious side effects produced by the drug [8,9]. Targeted delivery of cisplatin to the specific cancer cells is thus required because it could provide a means of modifying the distribution of cisplatin *in -vivo* and of increasing its concentration in the target sites, thereby improving efficacy and reducing toxicity. Several strategies have been described in the literatures for selective cisplatin drug delivery. Some of these attempts include the administration of cisplatin by its water soluble conjugates, such as with poly (amidoamines) [10] and poly (amidoamines) dendrimers [11]. Anticancer activity of cisplatin entrapped PLGA-methoxy poly (ethylene glycol) nanoparticles on LNCaP prostate cancer cells and the *in vitro* nanoparticle degradation, *in vitro* drug release & *in vivo* drug residence in blood properties of PLGA-methoxy poly (ethylene glycol) nanoparticles of cisplatin have also been investigated [12,13]. Although there was no details available for the effect of change in processing parameters on the characteristics of nanoparticles of cisplatin.

The aim of this study was to define the parameters determining an optimized yield of monodisperse, nanosized particles of cisplatin by using PLGA as a polymer, dichloromethane as an organic solvent and sodium cholate as a surfactant (stabilizer). Experimental parameters such as the polymer concentration (conc), sonication time, internal & external aq phase volume and stabilizer concentration were investigated for surface morphology, particle size, zeta potential, drug encapsulating efficiency, *in-vitro* drug release profile and polydispersity index of nanoparticles. The preparation parameters leading to particles with well-defined characteristics were identified.

Chwee Teck Lim, James C.H. Goh (Eds.): ICBME 2008, Proceedings 23, pp. 1325–1328, 2009
www.springerlink.com

II. Materials and methods

A. Materials

Poly (lactide-co-glycolide) 50/50 (mol. wt. 17,000) was kind gift sample from Sun Pharmaceuticals Ltd., Vadodara, India. Cisplatin was received as a gift sample from Cipla Pharmaceutical Ltd., Mumbai, India. Sodium Cholate (SC) was purchased from S d fine chemicals Ltd., Mumbai, India. Other chemicals used were of reagent grade.

B. Optimization of processing parameters

Different batches of nanoparticle formulations were prepared and the parameters controlling the formation of nanoparticles were systematically varied and optimized to produce small & stable nanoparticles. The influence of the different parameters on the nanoparticle characteristics were observed & summarized in Table 1-5.

C. Preparation of PLGA nanoparticles of cisplatin

Nanoparticles were prepared by a double emulsion solvent evaporation technique. The primary emulsion (w/o) was formed between an organic solution (o) of the polymer (50 mg of PLGA in 2 ml of dichloromethane) and an aq solution (w) of drug (5 mg of cisplatin in 2 ml of distilled water) by using sonication (probe sonicator, Frontline®) for 5 min. Then this primary emulsion was again sonicated in 50 ml of an aq solution (w_1) of sodium cholate (0.5% w/v solution in distilled water) to obtain the double emulsion ($w/o/w_1$). After wards, the solvent evaporation was carried out by gentle magnetic stirring at room temperature. Nanoparticles were recovered by centrifugation (at 20,000 rpm for 1 hr at -4^{o}C), washed with distilled water, lyophilized & stored at cool temp (2-8 ^{o}C).

D. Surface morphology

Scanning electron microscopy (SEM) and atomic force microscopy (AFM) were performed to evaluate the surface morphology of nanoparticles. A JEOL Model-6400 Field Emission Scanning Electron Microscope and a Contact Mode Nanoscope E version Digital Instrument were used to evaluate SEM and AFM respectively.

E. Measurement of nanoparticle size and zeta potential (ζ)

The particle size (nm), zeta Potential (mV) and polydispersity index (PDI) were determined by using a Zetasizer apparatus (Malvern Instruments Ltd, UK) equipped with the Malvern photon correlation spectroscopy (PCS) software (version 4.1). Mean values of these parameters for three batches are illustrated in Table 1-5.

F. Drug encapsulation efficiency

5 mg of the nanoparticle preparation was dissolved in 10 ml of dimethylformamide (DMF). The drug content of this solution was determined by measuring the absorbance at 308 nm with a Shimadzu®-1700 pharmaspec UV/visible spectrophotometer and quantitatively determined by comparison with a standard curve. Percent loading ((% loading) of cisplatin was evaluated by using the following equation 1.

$$\% \text{ loading} = \frac{W_{ds} \times 100}{W_s} \quad (1)$$

Where,

W_{ds} = Amount of drug (mg) found in the sample of lyophilized nanoparticles

W_s = Theoretical amount (mg) of the drug used

G. In-vitro drug release study

The *in-vitro* cisplatin release of the nanoparticle was determined by dialysis method. 2 ml of nanoparticle sample was sealed in cellulose dialysis membrane. The dialysis bag was submerged in 100 ml of phosphate buffer saline (PBS, pH 7.4) and incubated at 37 ^{0}C. At definite time intervals 1 ml sample from the incubation medium was drawn and analyzed for cisplatin. After sampling, the incubation medium was always replaced by the same quantity of fresh PBS solution. Samples were drawn at each day after the start of release study and thereafter for 7 days. The release of drug was observed by using Shimadzu®-1700 pharmaspec UV/visible spectrophotometer after proper dilution and quantitatively analyzed by comparing with a standard curve of cisplatin in DMF.

III. Results and discussion

A. Optimization of processing parameters

The preparation study was carried out at room temperature (excess temperature may cause degradation to encapsulated drug). From the results observed by changing the processing parameters, it was found that an increase in polymer concentration results in to increase in the size of the nanoparticles. The optimum concentration of the polymer selected was 25 mg/ml (Table 1).

An increase in the concentration of stabilizer in the external aq phase can results in an increase in the residual amount of sodium cholate in nanoparticles, which cannot be removed easily during the washing of nanoparticles. For instance, with a concentration of sodium cholate equal to 0.5 %, nanoparticles with size of 199 nm were obtained (Table 2). Other characterization parameters were also found as required.

An increase in drug encapsulation efficiency was found with increase in internal aq phase volume, but excess of internal aq phase volume produced particles with larger size. The volume of 1 ml used in the nanoparticle preparation was good enough to produce particles with smaller size and having satisfactory results for other characterization parameters (Table 3).

On the other hand, an increase in the external aq phase volume could lead to a decrease in the particle size of nanoparticles. The volume (50 ml) of external aq phase selected for the preparation of nanoparticles was sufficient to produce appropriate results (Table 4). There was no prominent effect of external aq phase volume observed on the drug encapsulation efficiency of nanoparticles.

Sonication is an important parameter for the emulsification and size reduction of nanoparticles. Sonication for much more time can cause in rupture of the nanoparticles. The optimum time for sonication was found 5 min at which satisfactory results were obtained (Table 5).

B. Surface morphology of nanoparticles

AFM (Fig. 1) and SEM (Fig. 2) analysis were used to investigate the surface morphology of nanoparticles. The nanoparticles appear spherical and almost no aggregation was observed as illustrated in the respected Figures.

C. Entrapment efficiency & In-vitro drug release study

The entrapment efficiency of cisplatin in the nanoparticles was found up to 24.95 %. As shown in Fig. 3, nanoparticles produced a biphasic cisplatin release profile with an initial burst effect within the first 48 hr. This fast release is related to drug adsorbed on the nanoparticle surface. After this phase a constant slow release of cisplatin was observed for 7 days of study period.

Table 1 Effect of polymer concentration

Polymer conc (mg/ml)	Size (nm)	Polydispersity index (PDI)	Zeta potential (mV)
25	199	0.04	-13.7
30	225	0.06	-14.0
40	265	0.06	-13.8

Table 2 Effect of stabilizer concentration

Stabilizer conc. (%w/v)	Size (nm)	Polydispersity index (PDI)	Zeta Potential (mV)
0.5	199	0.04	-13.7
1	225	0.06	-14.0
2	265	0.06	-13.8

Table 3 Effect of internal aqueous phase volume

Internal aq phase volume (ml)	Size (nm)	Polydispersity index (PDI)	Zeta potential (mV)	Encapsulation efficiency (%)
0.5	195	0.04	-13.0	20.15
1.0	199	0.04	-13.7	24.95
2.0	241	0.06	-13.0	25.17

Table 4 Effect of external aqueous phase volume

External aq Phase volume (ml)	Size (nm)	Polydispersity index (PDI)	Zeta potential (mV)	Encapsulation efficiency (%)
10	291	0.1	-13.0	24.21
25	235	0.7	-16.0	23.45
50	199	0.04	-13.7	24.95

Table 5 Effect of sonication time

Sonication time (minutes)	Size (nm)	Polydispersity index (PDI)	Zeta potential (mV)
2	238	0.07	-13.6
5	199	0.04	-13.7

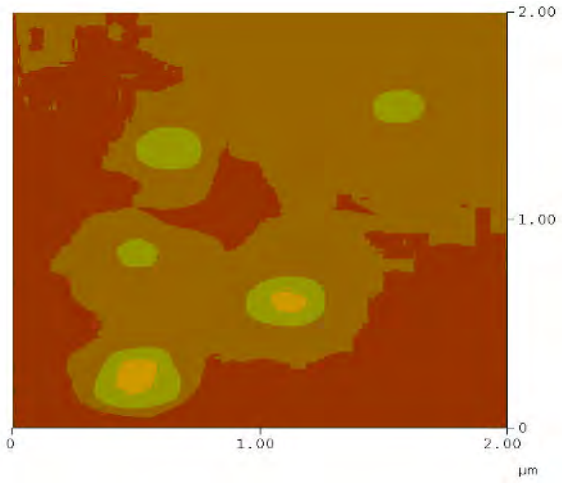


Fig. 1 AFM image of nanoparticle

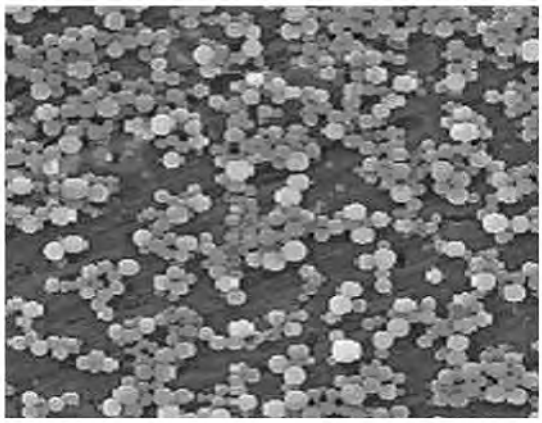


Fig. 2 SEM image of nanoparticle

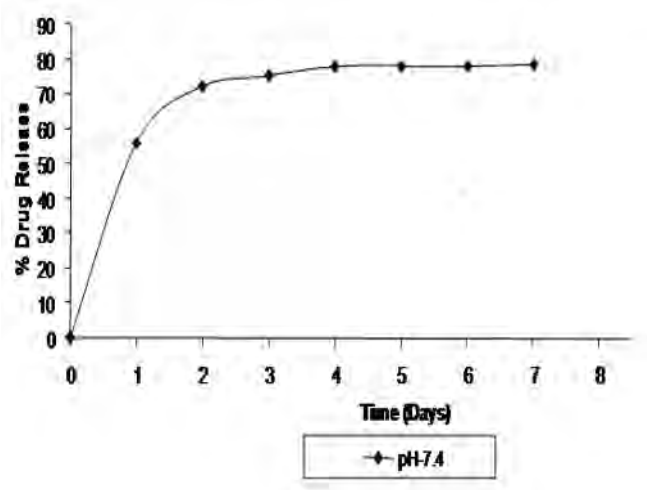


Fig. 3 *In-vitro* release profile of cisplatin

IV. Conclusions

We have developed and optimized a simple and rapid process to produce polymeric nanoparticles by varying the different processing parameters. The influences of several parameters on the preparation of PLGA nanoparticles were shown. The results obtained for different studies showed that PLGA nanoparticles developed in this study could be the nanoparticles for application in the controlled delivery of cisplatin for cancer therapeutics.

Acknowledgement

The authors would like to thank Prof. P. B. Sharma (Ex-Vice Chancellor, RGTU, Bhopal, India) for providing generous access of lab facility to carryout this research work. This work was supported by grants from the Ministry for Human Resource Development (MHRD), New Delhi.

References

1. Peppas L B, Blanchette J O (2004) Nanoparticle and targeted systems for cancer therapy. Adv Drug Deliv Rev 56:1649-1659
2. Moghimi S M, Hunter A C, Murray J C (2001) Long-circulating and target-specific nanoparticles: Theory to practice. Pharmacol Rev 53:283-318
3. McNeil S E, Frederick S (2005) Nanotechnology for the biologist. J Leuk Biol 78:1-10
4. Anderson J M, Shive M S (1997) Biodegradation and biocompatibility of PLA and PLGA microspheres. Adv Drug Deliv Rev 28:5-24
5. Park T G (1995) Degradation of poly (lactic-co-glycolic acid) microspheres: effect of copolymer composition. Biomaterials 16:1123-1130
6. Soppimath K S, Aminabhavia T M, Kulkarnia A R et al. (2001) Biodegradable polymeric nanoparticles as drug delivery devices. J Controlled Release 70:1-20
7. Hans M L, Lowman A M (2002) Biodegradable nanoparticles for drug delivery and targeting. Current Opinion in Solid State and Materials Sci 6: 319-327
8. Rosenberg B (1985) Fundamental studies with cisplatin. Cancer 55: 2303-2316
9. Sedletska Y, Giarud-Panis M J, Malinge J M (2005) Cisplatin is a DNA damaging antitumour compound triggering multifunctional biochemical responses in cancer cells: importance of apoptotic pathways. Curr Med Chem Anticancer Agents 5:251-265
10. Ferruti P, Ranucci E, Trotta F et al. (1999) Synthesis, characterization and antitumour activity of platinum (II) complexes of novel functionalised poly(amidoamine)s. Macromol Chem Phys 200:1644-1654
11. Malik N, Evagorou E G, Duncan R (1999) Dendrimer-platinate: a novel approach to cancer chemotherapy. Anticancer Drugs 10:767-776
12. Gryparis E C, Hatziapostolou M, Papadimitriou E et al. (2007) Anticancer activity of cisplatin-loaded PLGA-mPEG nanoparticles on LNCaP prostate cancer cells. Eur. J Pharm Biopharm 1-8
13. Avgoustakisa K, Beletsia A, Panagia Z et al. (2002) PLGA–mPEG nanoparticles of cisplatin: In vitro nanoparticle degradation, in vitro drug release and in vivo drug residence in blood properties. J Controlled Release 79:123–135

Author: Mr. Vivek Agrahari
Institute: Department of Pharmacy, Shri G. S. Institute of Technology & Science (SGSITS)
Street: 23-Park Road
City: Indore
Country: India
Email: vivek.agrahari@rediffmail.com

Physics underling Topobiology: Space-time Structure underlying the Morphogenetic Process

K. Naitoh

Waseda University, Faculty of Science and Engineering, Tokyo, Japan

Abstract — **Development processes of multi-cellular systems have attracted attention for a long time. One particular aspect of interest is the fusion of the symmetric and asymmetric cell divisions in space. We clarify the physical principle for determining whether asymmetric cell divisions occur in living beings or not. Then, we also reveal the physical reason why the organs such as arms, legs, lungs, vertebrae, and kidneys are left-right symmetric, while the heart and the liver are asymmetric. Next, we examine the temporal aspects underlying the morphogenetic processes. The macroscopic model having six categories of molecules shows that the antagonism between the negative controllers and the positive replication factors induces bifurcations in stem and pluripotent cells at rhythmic intervals comprising about six divisions. This cycle of six divisions, i.e., branching time between periodic bifurcation events, corresponds to the emergence timings of blast cysts, embryos, germ layers, tissues, and organs, which can be observed for about every six cell divisions. Finally, we show that the evolution of negative controllers brings longer non-coding regions in DNA and higher-organisms.**

Keywords — **Morphogenesis, Organs, Topobiology, Cyto-fluid dynamic theory, Asymmetry**

I. Introduction

Development processes of multi-cellular systems can be examined separately from two viewpoints of space and time.

The symbiotic concept of symmetry and asymmetry is a key for understanding the spatial structures in living organisms. Stem cells show asymmetric and symmetric divisions. [1, 2, 3, 4] A left-right symmetric distribution of the eyes, nose, ears, arms, and legs is observed in outward appearance, although the inner body, including the heart and the liver, is asymmetric. We reveal the physics underlying the fusion of asymmetry and symmetry.

Next, let us see the temporal characteristics. It is well-known that each cycle of six cell divisions is the basic morphogenetic cycle determining the bifurcation points of organs in human beings. [5] For example, about six cell divisions of a fertile egg produce blast cysts and the next six divisions lead to the new stage with the complex structures of ectodermal and endoderm cells. In the later part of the morphogenesis of human beings, hands and legs also emerge at six divisions after the first heart beat. Thus, in this report, we will reveal the temporal mechanism promoting the cycle of six cell divisions, "six-stroke engine", by proposing the nonlinear equation derived based on the molecular biology.

II. Spatial structure

The cyto-fluid dynamic theory for describing the deformation and motions of connected cells [6, 7] is used to examine the relation between the type of motion and cell size. The dimensionless deformation rate x of each cell dependent on dimensionless time t can be described as

$$d^2x/dt^2=(e-1)(dx/dt)^2+(e^3-3)x+q(t), \quad (1)$$

where the parameter e and the term $q(t)$ denote the size ratio of the two cells connected under equilibrium conditions and the time-dependent force generated by the other connected particles, respectively. When the particles are spheres under equilibrium conditions, x is zero. A symmetric ratio of 1.0 (e=1) makes the first term on the right-hand side of the equation zero, while an asymmetric ratio of $\sqrt[3]{3}$ around 1.5 (e^3=3) makes the second term zero. Life is relatively quasi-stable because d^2x/dt^2 becomes relatively smaller, when the size ratio of cells connected takes these values of e=1 and e^3=3. The first and second terms also show that *symmetric (e=1) and asymmetric (e^3=3) cell divisions are more stable for the small disturbance of motion (dx/dt) and cell deformation x, respectively.* (Fig. 1.) (Losick et al. writes the review paper that small fluctuations of cells are important for determining the morphogenetic processes. [8] Living microorganisms such as bacteria move round with fine motion, although dead ones are stationary. This fine motion will bring small deformations of cells inside agglomerate of cells. Thus, analysis based on Eq. (1) is important to examine the processes.)

This relation between small deformation and asymmetric division leads to an understanding of the aggregation of cells such as those in a colony. Let us separate cell aggregation into two parts, the internal side around the center of the aggregation and the external side close to the surface. External cells close to the surface move relatively easily under the influence of inhomogeneous force, because one part of the cell is free without any connection to other cells. However, internal cells often receive homogeneous forces from

Chwee Teck Lim, James C.H. Goh (Eds.): ICBME 2008, Proceedings 23, pp. 1329–1332, 2009
www.springerlink.com

many directions due to the presence of other cells, making it relatively difficult for them to move relative to the origin on the earth. Thus, inner cells deform relatively easily without any translational motion of the gravity center. (Fig. 2.) As a result, the inner and outer cells determine whether cell divisions are asymmetric or symmetric, respectively. [9]

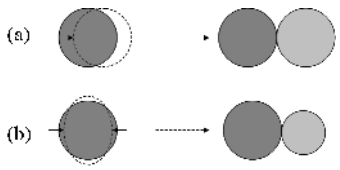


Fig. 1. **Symmetric and asymmetric divisions.**

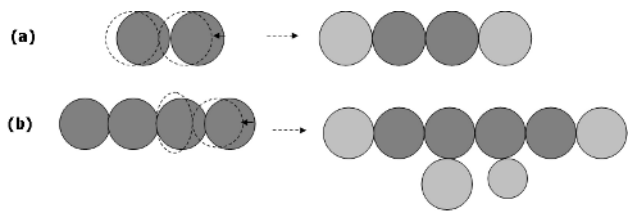


Fig. 2. **Division pattern related to neighboring states of cells.**

Let us examine the cell division process of yeast (Saccharomyces cerevisiae), because symmetric and asymmetric size ratios are also observed at the cell level of microorganisms. Saccharomyces cerevisiae was cultivated at a constant temperature of 37 degrees Celsius on a warm plate and was observed continuously under a microscope until eight cells were formed. Figure 3 shows that internal mother cells (black) generate child cells in asymmetric division, while external mother cells (gray) produce symmetric ones.

The present analysis also clarifies the reason why the left-right symmetric distribution of arms and legs is observed in outward appearance, although the inner body, including the heart and the liver, is asymmetric. It is posited that the lungs are symmetric because of contact with the outer air during breathing. [9] It is clear that the spatial distribution pattern of organs such as the lungs is sensitive to connections with the outer environment, as is also seen in the emergence of the respiratory passage and pulmonary circuit just after birth. (The lungs will be open even before the birth, while filling with water.) The kidneys are symmetric because of continuous contact with outer water in the form of urine owing to the fact that the amniotic fluid of fetus is fetal urine.

The reason why vertebrae in the center of mammals are symmetric is related to the fact that water containing Ca ions enters the inner region when gastrulation occurs, because the primordial gut is also in the outer part of water.

Blood vessels are closed and must not be open to the outer world in order to prevent virus infections. Thus, the heart and liver filled with blood are asymmetric due to the process similar to buckling behavior.

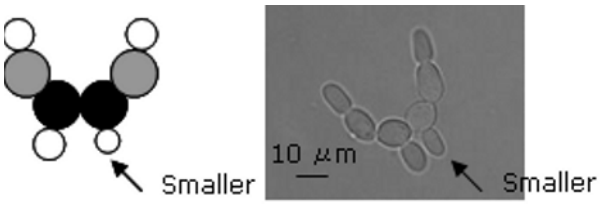


Fig. 3. **Cell division process of Saccharomyces cerevisiae.**

Classification based on the concept of Ectoderm, mesoderm, and endoderm is not deficient for the question whether the organs are left-right symmetric or not. Both asymmetric heart and symmetric kidney come from the mesoderm as an example.

A lot of leaves in plants also have the left-right symmetry in the outer shapes and also in the main vein in the leaf center, although the branch veins in the middle are asymmetric.

It is stressed that the center and outer parts of DNA such as centromere and telomere have symmetric arrays of bases, while the middle part of DNA has asymmetric arrays.

The human body has over 10 trillion cells. *Nature generates the physical rule of self-organization whereby open organs become symmetric, while closed organs show asymmetry. As a result, trillions of cells in human beings can be generated by only forty cell divisions.*

III. Temporal structure

A. 4-cylinder engine

All of the molecules are classified into some categories, based on their representative physical characteristics.

At least two types of molecular categories (enzyme systems), which are for replicating gene groups and enzyme systems, are necessary for achieving a closed reaction cycle. Examples of the former and latter are DNA-replicase and ribosome protein, respectively. This leads to the conclusion that two types of gene groups are also inevitable and serve to code the two enzyme systems. The core cycle for self-replication can be modeled by these four molecular categories, two gene groups and two enzyme systems (Categories D1, D2, R1, and R2). (Fig. 4)

Here, Di and Ri for i = 1 and 2 also denote the density of each molecular category. We assume that the production

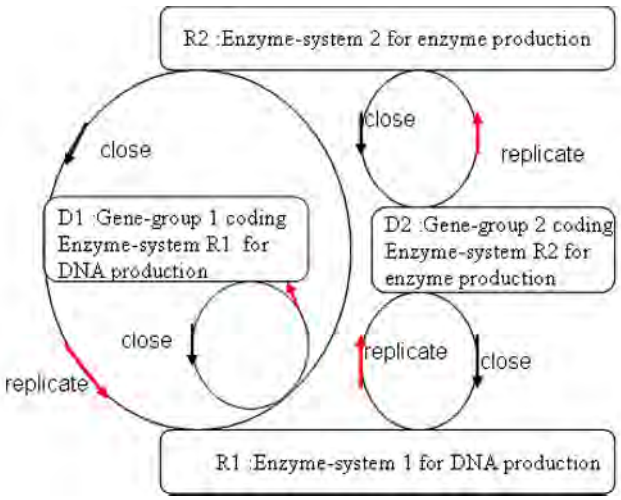


Fig. 4. **Four categories of molecules for minimum replicator.** (D1: Gene group 1 that codes enzyme system R1 for DNA production, D2: Gene group 2 that codes enzyme system R2 for enzyme production, R1: Enzyme system 1 for DNA production, which includes DNA polymerases, topoisomerase, helicases, ligases, and primases, R2: Enzyme system 2 for enzyme production, which includes ribosomes with rRNAs and ribosome proteins, RNA polymerase, mRNAs, and tRNAs)

rate of a category due to the reaction of categories Dj and Rj is restricted by the smaller one of Dj and Rj.

Then, we can describe the densities of four categories averaged over all the cells at generation *N* by Eq. (2).

$$D_i^{N+1} - D_i^N = \alpha_{ij} D_i^N \otimes R_j^N, \quad i = 1, 2,\ j = 1, 2 \tag{2}$$

where $D_i \otimes R_j$ and α_{ij} denote $\min(D_i, R_j)$ and a constant, respectively.

This system of D1, D2, R1, and R2, the 4-cylinder engine for life, can replicate each other. (Fig. 4.) [9]

B. 6-cylinder engine

The negative enzyme system and its gene group (D3 and R3) are then incorporated into the foregoing core cycle of 4-cylinder, because the morphogenetic process of multi-cellar systems in mammals must include negative controllers such as Oct-4 and SOX2 for producing tissues and organs. [10, 11, 12] D3 and R3 can be defined as follows.

D3: Gene group 3 that codes protein system R3 for suppressing D2 gene expressions

R3: Protein system 3 for suppressing D2 gene expressions, which includes the proteins of the transcription factors such as those of Oct-4 and SOX2. (Only the protein system generated in Category R3, a negative controller, attaches to the positive gene group D2**.** Thus, the production rate of R2 can be re-written in the form of min (D2-R3, R2).)

We can describe the densities of six categories averaged over all the cells at generation *N* by the following equations.

$$D_i^{N+1} - D_i^N = \alpha_{i1} D_i^N \otimes R_1^N, \quad i = 1,2,3 \tag{3}$$

$$\begin{aligned} R_1^{N+1} - R_1^N &= \alpha_{12} D_1^N \otimes R_2^N \\ R_2^{N+1} - R_2^N &= \alpha_{22} \delta(D_2^N - R_3^N) \otimes R_2^N \\ R_3^{N+1} - R_3^N &= \alpha_{32} D_3^N \otimes R_2^N \end{aligned} \tag{4}$$

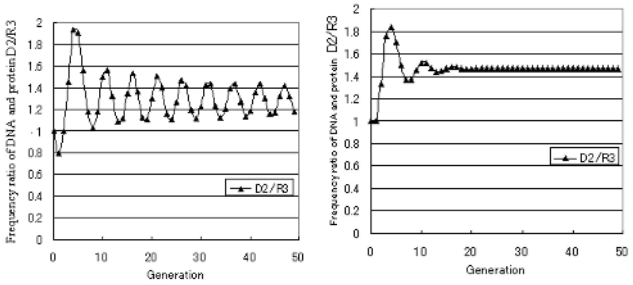
where $D_i \otimes R_j$ denotes $\min(D_i, R_j)$ for i=1-3 and j=1-3, and also where $\delta(x)$ denotes the larger one of *x* or 0, i.e., max (x, 0). (Here, the constant α_{ij} includes the influences of many types of molecules in the category and the molecule movements on reaction probability. There is an important constraint, i.e., the densities of D1, D2, and D3 are identical, because the three gene groups 1, 2, and 3 are in one set of DNA in each generation. Thus, α_{i1} for D1, D2, D3 is a set having the identical value of 1.0. Initial densities of D1, D2, D3, R1, R2, and R3 are set to be 1.0, respectively.)

Let us denote the number of cell divisions after the mother cell generation as N. Generation N is less than 50, because an adult human body can be generated by about fifty cell divisions from a fertilized egg. Accordingly, the number of cells at generation N is defined as P(N). There are many types of cells among P(N) such as somatic and stem cells. A cell must have one set of DNA. Thus, the number of cells, P(N), is equal to D_i^N.

Broadly speaking, computational results obtained by Eqs. (3) and (4) show nearly exponential or hyperbolic increases of Di and Ri. *Then, the antagonism between the negative controller R3 and the positive replication factors R1 and R2 induces bifurcation events in the stem and iPS cells at rhythmic intervals constituting about six divisions, although the intervals are slightly chaotic and the vibrational amplitude is attenuated. It is stressed that this cycle of six divisions, i.e., branching time between periodic bifurcation events, corresponds to the emergence timings of blast cysts, embryos, germ layers, tissues, and organs, which can be observed for about every six cell divisions.* (Fig. 5a.)

The flexible shapes of transcription factors may give the parameters of α_{i2} various values. However, emphasis is placed on the fact that three system parameters, α_{i2}, have less influence on the time cycle of bifurcations. The cycle of about six divisions is stable. (Fig. 5b.)

The condition of D2/R3 > 1.0 means that a part of D2 is not covered by R3. This implies that several types of proteins in D2 emerge and also several types of somatic cells



(a) (b)

Fig. 5. **Time histories of D2/R3 during 50 generations of the morphogenetic process.** (a) $\alpha_{i2} = 1.5$ and (b) $\alpha_{i2} = 1.0$

are produced to make organs and tissues. The condition of D2/R3 < 1.0 means that D2 is completely blocked by redundant R3, which implies stem or induced pluripotent stem (iPS) cells. This oscillation of D2/R3, which implies the amount of D2 uncovered by protein group R3, will lead to the changes in the gene combination for expressions. This corresponds to the fact that iPS cells can be reprogrammed by the presence of much Oct-4.

Averaged value of D2/R3 is around 1.30. This means that the amount of genes in D2 expressing is about 30 percents and also the 70 percents in D2 are suppressed. The large amount of suppression in D2 may imply non-coding regions such as introns and junk. This also corresponds to the fact that microorganisms without R3 have less introns and junk.

As R3 becomes more effective according to increasing α_{32}, introns and junk become longer according to depression of D2. It is stressed that effective R3 (increasing $\alpha 32$) reduces the dissipation of the D2/R3-oscillation, leading to larger sizes of multi-cellular organism. (Fig. 5) Effective R3 leads to the longer oscillation of six cycles, which produce larger life having more types of organs.

Analysis based on Eqs. (3) and (4) also shows that D2/R2 is large during the early stage before N = 6, indicating a small density of protein R2. This small density of R2 produces fewer proteins and enzymes at the early stage, while gene groups of Di can be generated more. This leads to decreasing cell sizes with each succeeding generation, as is seen in actual blastocysts.

IV. Conclusion

Small deformation of cell shape brings the molecular deformation in DNA and proteins inside cell. This leads to the replacement of the genes expressed. Asymmetric cell division promoted by the fluid-dynamical stability is fixed by the asymmetric usage of genes at molecular level.

The early cell divisions of fertile egg and the cerebral development can also be explained by using fluid-dynamics. [14, 15]

Acknowledgment

The author thanks Mr. K. Ogata and Mr. R. Kubo of Waseda University for their help on the photographs of Yeast.

References

1. Beckmann J, Scheitza S, Wernet P, Fischer JC, Giebel B. (2007) Asymmetric cell division within the human hematopoietic stem and progenitor cell compartment: identification of asymmetrically segregating proteins. *Blood* **109**- 12: 5494-501
2. Scott C. (2006) Stem Cell Now, pp1-267 (Kawade Shobo Shinsha Publisher, Tokyo)
3. Thomas P, Zwaka A, James A Thomsona B (2005) Differentiation of human embryonic stem cells occurs through symmetric cell division, *Stem Cells* **23**: 146-149
4. Plusa B. et al. (2005) The first cleavage of the mouse zygote predicts the blastocyst axis, Nature **434**: 391-395
5. Nishikawa S (Ed.) (2008) Ultimate Stem Cell, Newton 6: 12-55
6. Naitoh K (1999) Cyto-fluid Dynamic Theory for Atomization Processes, Oil & Gas Science and Technology, Vol. 54, No. 2: 205-210
7. Naitoh K (2001) Cyto-fluid Dynamic Theory, Japan Journal of Industrial and Applied Mathematics **18**-1: 75-105
8. Losick R and Desplan C (2008) Stochasticity and Cell Fate, Science, 320: 65-68
9. Naitoh K (2008) Stochastic determinism underlying life, to be published in Artificial Life and Robotics **13** [selected from among Proceedings of 1st European Workshop of Artificial life and Robotics, 2007]
10. Edelman G (1988) Topobiology, pp1-371(Basic Books Inc., New York)
11. Niwa HJ, Miyazake, Smith A (2000) Quantitative expression of Oct3/4 defines differentiation, dedifferentiation, or self-renewal of ES Cells. Nature Genetics **24**: 372-376
12. Takahashi K, Yamanaka S (2006) Induction of Pluripotent Stem Cells from Mouse Embryonic and Adult Fibroblast Cultures by Defined Factors, *Cell* **126**: 663-676
13. Homma K, Hastings JW (1989) Cell growth kinetics, division asymmetry and volume control at division in the marine dinoflagellate Gonyaulax polyedra. J. of Cell Science **92**: 303-318
14. Naitoh K (2008) Fluid Dynamics underlying Morphogenesis, Proc. of 13th Int. Sym. on Artificial Life and Robotics
15. Naitoh K (2007) Engine for cerebral development, Proc. of 1st European conference of Artificial Life and Robotics (also in Artificial Life and Robotics, in press.)
16. Naitoh K (2006) Gene engine and machine engine, Springer-Japan, pp1-251
17. Naitoh K (2008) Physics underlying Topobiology, Abstracts of the Annual Meeting of JSIAM (in Japanese)

Corresponding Author: Ken Naitoh
Institute: Waseda University, Faculty of Science and Engineering
3-4-1 Ookubo, Shijuku, Tokyo, Japan,
Email: k-naito@waseda.jp

The Properties of Hexagonal ZnO Sensing Thin Film Grown by DC Sputtering on (100) Silicon Substrate

Chih Chin Yang, Hung Yu Yang, Je Wei Lee and Shu Wei Chang

Department of Microelectronics Engineering, National Kaohsiung Marine University, Kaohsiung, 81143 Taiwan, Republic of China

Abstract — **This research was proposed to utilize sputtering system to fabricate sensing material of electronics nose of humidity sensor, and expected to use it in nano and multiple biosensor system with intelligent functions in new generation. The first test was material measurement for zinc oxides (ZnO) deposited on (100) Si substrate in variable thin film thickness and epitaxial growth time. The second test was that the variable growth time will be selected to study characteristics of the sensing material in humidity sensors by measurement of resistance and capacitance. The ZnO nanostructure-like were synthesized on silicon wafer with native buffer layer by the DC sputtering method, and the optimum growth conditions based on growth temperature, oxygen flow rate, and growth time, have been found. We discussed some issue of growth rate, resistivity of thin film, and crystalline of nanostructure, and also explained the sensing mechanism of ZnO hexagonal nanostructure in impedance measurement. It is experimentally demonstrated that the ZnO hexagonal nanostructures have potential growth by DC sputtering growth method on silicon wafer with native oxidation at room temperature. This grown ZnO epitaxial layers would be used in application of sensors.**

Keywords — **ZnO, Sputtering system, Sensing material, Humidity sensor**

I. Introduction

Humidity, gas and temperature measurements are very important concerns in environment fields, such as medical applications for human comfort and industrial uses [1]. Therefore, the requirement for cheap, reliable, and sensitive humidity, gas and temperature sensors are urgent. For the humidity sensor and gas sensing devices, an ideal coating material should adsorb the moisture efficiently and easily. Until now, many nano-materials have exhibited excellent molecular adsorption properties. ZnO nanostructures, in particular, are being considered as prime material for the moisture adsorption due to their large specific surface area.

The ZnO material is also a versatile II-VI semiconductor, with numerous applications ranging from blue and ultraviolet optical devices such as light emitting diodes and laser diodes in the ultra violet range to chemical sensors because of its distinctive optical [2-4], electronic, and chemical properties [5-8]. It has a hexagonal wurtzite structure, with lattice parameters of a=3.2498Å and c=5.2066Å. Among them, ZnO has been receiving considerable attention because of its wide and direct band-gap energy (3.34 eV~3.37 eV at room temperature) and high exaction binding energy (~60 meV). In fact, the high exaction binding energy of ZnO, compared with that for GaN (28 meV) and ZnSe (19meV), would allow for excitonic transitions even at room temperature, which could lead to a higher radiation recombination efficiency for spontaneous emission as well as a lower threshold voltage for laser emission [9]. In order to realize these devices, it is indispensable to grow high-quality ZnO films with p-type conductivity. Undoped ZnO expitaxial films normally exhibit strong n-type conductivity due to intrinsic defects such as interstitial Zn and oxygen vacancies. These intrinsic defects make it very difficult to grow low resistively p-type material. Although ZnO based oxide semiconductors in the area has been grown, a number of problems remain, including difficulties associated with p-ZnO growth and the lack of high quality ohmic or schottky contacts for n type or p type ZnO.

ZnO thin films have been grown using several different deposition techniques, including pulsed laser deposition (PLD) [10-12], spray pyrolysis (SP) [13], molecule beam epitaxy (MBE) [14], atomic layer epitaxy (ALE), metal organic vapor phase epitaxy (MOCVD) [15-16], and electron cyclotron Resonance (ECR) [17]. ZnO has been deposited on various substrates, such as silicon [18], gallium arsenic (GaAs) [19], indium phosphor (InP) [20], diamond on silicon [21], and sapphire (Al_2O_3) [22]. In this study, ZnO thin film materials were fabricated on silicon (100) substrates using native silicon dioxide buffer layers with a hexagonal wurtzite structure similar to that of zinc oxide, with lattice parameters of a=3.11Å and c=4.98Å, by using the DC sputtering growth method. For sensor applications, a greater resistively is necessary. The aim of our works was to find out the sputtering conditions which allow the deposition of ZnO films at high deposition rates with a high electrical resistively without any doping and heating processes. Zinc oxide thin films can be grown on buffer layer by means of lattice-matching epitaxy, since the lattice misfit between these two materials is smaller. On the other hand, epitaxial growth of zinc oxide on a silicon substrate with native oxidation buffer layer is necessary to integrate these films with sensing function.

Chwee Teck Lim, James C.H. Goh (Eds.): ICBME 2008, Proceedings 23, pp. 1333–1336, 2009
www.springerlink.com

II. Experiments

The high quality ZnO nanostructures were fabricated by a dc reactive ion sputtering technique. The system has been constructed with a turbo-molecular pump, a throttle valve pressure controller feedback from the gauge. The load-lock allowed the growth system and zinc target to remain constantly under vacuum. The films were deposited on silicon substrates of (100) orientation. The epitaxial structure consisted of an about 40-400 nm thick un-doped ZnO sensing layer and silicon dioxide layer with native oxidation of silicon. In this experiment, the growth temperature was arranged at room temperature. The sputtering conditions were with zinc target of 2" diameter, sputtering mode of bottom-up, distance of 60 mm between target and substrate, gas of both 50% oxygen source and 50% argon source, and the total gas process pressure on the order of 10^{-5}Torr. The argon flow rate is fixed at 10 sccm with a dc power of 50 W. Many products with different resistively and impedance were obtained using different growth time on silicon substrate. The growth period was 1 to 10 minutes and all the films reported here were grown on silicon substrates degreased and cleaned prior to loading in the growth system.

Film thickness was determined by scanning electron microscopy (SEM, JEOL-JSM- T330A)**.** The film thickness was carefully controlled so that the film had a thickness of 1 μm less. The average size of hexagonal crystallites of the film was estimated to be smaller. The structure and orientation of the zinc oxide films were also investigated by XRD. The XRD patterns were measured using CuKα X-rays from a rotating cathode operated at 40 kV and 180 mA. The carrier concentration and mobility of the ZnO layers were measured at room temperature by Hall effect measurements of van der Pauw method. The sensing impedance values of humidity were measured using LCR meter of Agilent – E4980A.

III. Results and discussion

The XRD measurements of ZnO thin film grown on silicon substrate all show the same characteristics with a preferred (002) orientation indication. The c-axis of the hexagonal ZnO structure is perpendicular to the substrate. Fig.1 shows typical XRD of ZnO sample, well oriented with all crystallites having (002) planes parallel to the growth surface. As we improve the quality of our ZnO films by modification of the growth chamber and investigation of the optimum growth conditions, the (002) peaks become sharper indicating a good quality a material with a single orientation. In this study, single crystalline ZnO films oriented along [002] were successfully grown even on (100) Si

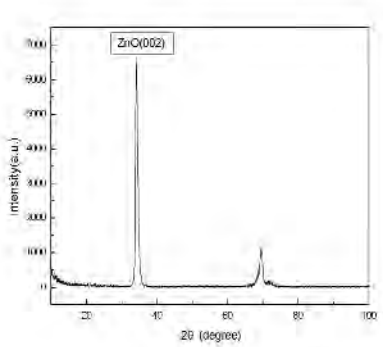


Fig. 1 XRD pattern of ZnO thin film deposited at room temperature.

substrate. Under growth of room temperature, the full width at half maximum (FWHM) of their x-ray diffraction became narrower with low growth temperature. An increase of growth time may improve crystalline of the ZnO films by providing activation energy for ad-atoms to occupy the positions of potential minima and enhancing re-crystallization due to the coalescence of islands by increasing the surface and volume diffusion, resulting in the improvement of the electrical properties with increasing growth time.

The film thickness was carefully controlled so that the film had a thickness of 1 μm less. The average thickness of hexagonal crystallites of the film was estimated to be about 100 nm. ZnO films were deposited on (100) silicon substrates at growth of room temperature. Fig.2 shows a typical scanning electron microscopy image of cross section of the ZnO grown on the silicon substrate at growth of room temperature. Almost the interface of between silicon and ZnO had well-defined shape. The growth rate about 9.6nm/min was obtained by calculation of SEM measurement.

Linear increase in film thickness of ZnO with grown flow rate of 10 sccm at oxygen was observed with increasing growth time as shown in Fig.3. The variation of thickness was performed in the absence of temperature, and the result is also shown in Fig.3.

Interestingly, the resistively variation of ZnO thin films with different growth time was displayed in Fig.4. The resistively is decreased with increased growth time. When a small growth time was utilized in growth of ZnO thin film, the resistively of ZnO thin film exhibited more 260 Ω-cm and the variation of ZnO film thickness had no significant over larger growth time above 5 minute due to the saturation of oxygen in ZnO crystal. All the ZnO films showed n-type conduction. The carrier concentration is of the order 10^{16}cm^{-3}, and almost independent of the substrate temperature. The Hall mobility increases smoothly from 69.9 cm^2/V-s for films deposited at a substrate of room temperature to 2.4×10^2 cm^2/V-s at growth temperature of 400^{o}C.

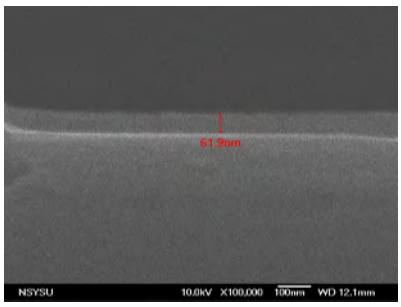


Fig. 2 SEM image of cross section for ZnO thin film.

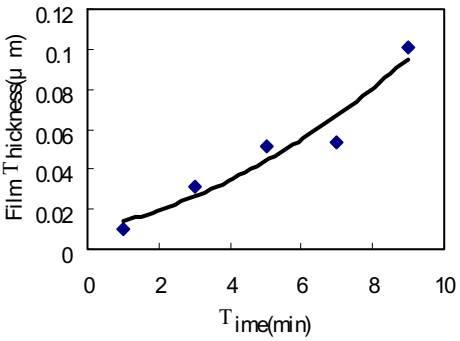


Fig. 3 The deposited time versus film thickness for ZnO thin film in the oxygen flow 10 sccm and the substrate didn't heat.

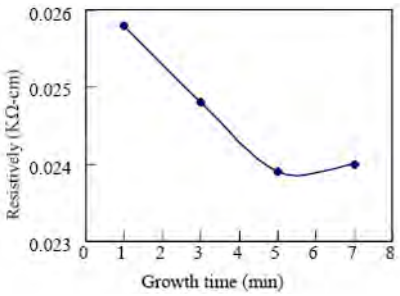


Fig. 4 The deposited time versus resistively for ZnO thin film in the oxygen flow 10 sccm.

The humidity sensing device with finger electrode is fabricated by lithographic method as shown in Fig.5. Concerning the impedance-type sensor, I-V characteristics measured in the relative humidity of 12% and 97% indicate an almost impedance behavior, and evidence a resistance and capacitance strongly dependent on relative humidity, as shown in Fig.6. The ZnO thin film is added moisture on the thin film surface, Fig.6 shows some different for the measurement of the resistances and capacitances by the measurement of LCR Meter. The ZnO epitaxial layers would be successfully in applications of humidity sensor.

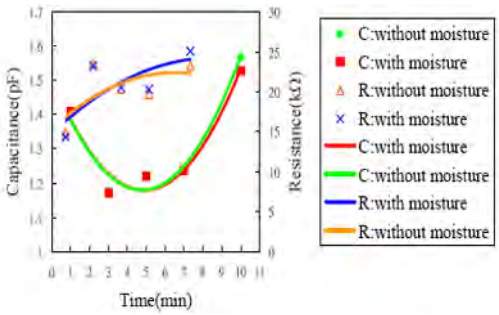


Fig. 5 The resistance and capacitance of ZnO humidity sensor versus growth time in different moisture environment.

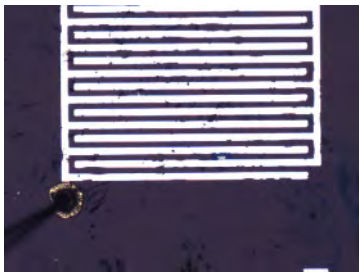


Fig. 6 The ZnO humidity sensor with finger electrodes.

IV. Conclusions

To better understand the influence of the growth process on the sensing characteristic of ZnO humidity sensor on silicon substrate, ZnO films were grown on silicon (100) substrates without initial processing of buffer layer growth. Without initial processing, the ZnO film tended to be grown with crystallographic orientations of (002), though the orientation could be controlled by increasing the growth time but keeping the temperature below the ZnO dissociation temperature. The measurements showed that the carrier concentration and Hall mobility are 10^{16} cm^{-3} and the order of $10^{2}cm^{2}/V$-s, respectively. The film thickness increased with increased growth time linearly. A maximum growth rate of 9.6nm/min was obtained at O_2 flow rate of 10 sccm. At this O_2 flow rate it also displayed a higher preferential and the narrowest FWHM of x-ray. However, with increase in the growth time, the resistively is first started to decrease significantly. While a large growth time, it exhibited less change in resistively and no significant variation is observed above growth time of 7 min. The result shows some different for the measurement of the resistances and capacitances by the measurement of LCR meter in the variation of moisture. The ZnO humidity thin film sensor is successfully fabricated by lithographic method with the use of finger electrodes.

ACKNOWLEDGMENTS

The authors wish to thank National Science Council (No.NSC95-2815-C-022-003-E) and National Kaohsiung Marine University for support of this research. The authors are also grateful to Mr. P. C. Wu for her technical help to carry out the experiments of wire bonding.

REFERENCES

1. Yamazoe N, Shimizu Y (1986) Humidity sensors: principles and applications. Sensor. Actuat. 10:379-398
2. Guo X L, Choi J H, Tabata H, Kawai T (2001) Fabrication and opto-electronic properties of a transparent ZnO hemostructural light-emitting diode. Jpn. J. Appl. Phys. 40:L177-L179.
3. Liang S, Sheng H, Liu Y, Hou Z, Lu Y, Shen H (2000) ZnO schottky ultraviolet photo-detectors. J. Cryst. Growth 225:110-113.
4. Kim H, Gilmore C M, Horwitz J S, Pique A, Murata H, Kushto G P, Schlaf R, Kafafi Z H, Chrisey D B (2000) Transparent conducting aluminum-doped zinc oxide thin films for organic light-emitting devices. Appl. Phys. Lett. 76:259-261.
5. Burda C, Chen X, Narayanan R, El-Sayed M A (2005) Chemistry and properties of nanocrystals of different shapes. Chem. Rev. 105:1025-1102.
6. Ohtomo A, Kawasaki M, Sakurai Y, Ohkubo I, Shiroki R, Yoshida Y, Yasuda T, Segawa Y, Koinuma H (1998) Fabrication of alloys and superlattices based on ZnO towards ultraviolet laser. Mater. Sci. Eng. B56:263-266.
7. Makino T, Chia C H, Segawa Y,Kawasaki M, Ohtomo A, Tamura K, Matsumoto Y, Koinuma H (2002) High-throughput optical characterization for the development of a ZnO-based ultraviolet semiconductor-laser. Appl. Surf. Sci. 189:277.
8. Segawa Y, Ohtomo A, Kawasaki M, Koinuma H, Tang Z K, Yu P, Wong G K L (1997) Growth of ZnO thin film by laser MBE: Lasing of exciton at room temperature. Phys. Status Solid B202:669-672.
9. Thomas D G (1960) Fine structure in the optical absorption edge of anisotropic crystals, J. Phys. Chem. Solids 15:97.
10. Jin B J, Im S, Lee S Y (2000) Violet and UV luminescence emitted from ZnO thin films grown on sapphire by pulsed laser deposition. Thin Solid Films 366:107-110.
11. Bae S H, Lee S Y, Kim H Y, Im S (2000) Comparison of the optical properties of ZnO thin films grown on various substrates by pulsed laser deposition,". Appl. Surf. Sci. 168:332-334.
12. Ong H C, Dai J Y, Li A S K, Du G T, Chang R P H, Ho S T (2001) Effect of microstructure on the formation of self-assembled laser cavities in polycrystalline ZnO. J. Appl. Phys. 90:1664-1666.
13. Studenikin S A, Golego N, Cocivera M (1998) Optical and electrical properties of undoped ZnO films grown by spray pyrolysis of zinc nitrate solution. J. Appl. Phys. 83:2104-2111.
14. Hongm S K, Chen Y, Ko H J, Wenisch H, Hanada T, Yao T (2001) ZnO and related materials: Plasma-assisted molecular beam epitaxial growth, characterization, and application. J. Electron. Mater. 30:647-658.
15. Wang X, Yang S, Wang J, Li M, Jiang X, Du G T, Liu X, Chang R P H (2001) Nitrogen doped ZnO film grown by the plasma-assisted metal organic chemical vapor deposition. J. Cryst. Growth. 226:123-129.
16. Lau C K, Tiku S K, Lakin K M (1980) Growth of epitaxial ZnO thin films by organometallic chemical vapor deposition. Journal of the Electrochemical Society: Solid State Science and Technology, 128:1843-1847.
17. Moeller F, Buff W (1992) Electromagnetic feed through in Si/ZnO-SAW-Devices, Proceedings of the 1992 IEEE Ultrasonics Symposium, 1992, pp. 245-248.
18. Kim Y, Hunt W D, Hickernell F S, Higgins R J, Jen C K, (1995) ZnO films on {011}-Cut<110>-propagating GaAs substrates for surface acoustic wave device applications. IEEE Transactions on Ultrasonics, Ferroelectronics and Frequency Control, 42:351-361.
19. Chang S J, Su Y K, Shei Y P (1995) High quality ZnO thin films on InP substrates prepared by radio frequency magnetron sputtering II. Surface acoustic wave device fabrication. Journal of Vaccum Science and Technology A13:385-388.
20. Dreifus D L, Higgins R J, Henard R B, Almar R, Solie L P (1997) Experimental observation of high velocity pseudo-SAWs in ZnO/Diamond/Si multilayers., Proceedings of the 1997 IEEE International Ultrasonics Symposium, 1997, pp.191-194.
21. Koike J, Tanaka H, Ieki H (1995) Quasi-microwave band longitudinally coupled surface acoustic wave resonator filters using ZnO/Sapphire substrate. Japanese Journal of Applied Physics. 34:2678-2682.
22. Ieki H, Tanaka H, Koike J, Nishikawa T (1996) Microwave low insertion loss SAW filter by using ZnO/Sapphire substrate with Ni dopant. 1996 IEEE MTT-S Digest, 1996, pp.409-412.

Author: Chih Chin Yang
Institute: Department of Microelectronics Engineering,
National Kaohsiung Marine University
Street: No.142, Haijhuan Rd., Nanzih District
City: Kaohsiung City 81143
Country: Taiwan, Republic of China
Email: chchyang@mail.nkmu.edu.tw

Multi-objective Optimization of Cancer Immuno-Chemotherapy

K. Lakshmi Kiran, D. Jayachandran and S. Lakshminarayanan

Department of Chemical and Biomolecular Engineering, National University of Singapore, Singapore 117576

Abstract — **Relentless research efforts in the recent past have led to the discovery of various cancer treatment modalities. However, there is no specific or absolute therapy for cancer treatment. As a result, doctors/researchers are proposing and employing unprecedented and promising strategies that synergistically combine different therapies to cure cancer. The timing and dosage levels at which the different therapies need to be administered for optimally treating cancer remains not only an interesting research problem but also one that is clinically relevant. In this work, we use a mathematical model comprising of ordinary differential equations to study how immunotherapy and chemotherapy can be optimally employed in cancer treatment. The model elucidates the dynamics of tumor cells, immune cells and therapeutic agents. Our aim is to minimize the tumor size via the optimum application of therapeutic agents. To this end, we use a multi-objective optimization strategy to design an immuno-chemotherapy plan that treats the cancer using minimum therapeutic intervention. We will also compare the best possible single therapy results with the best possible combination therapy protocol.**

Keywords — **Cancer, Mathematical model, Immunotherapy, Chemotherapy, Optimization**

I. Introduction

Presently, cancer is the second lethal disease next to heart disease. The numbers of cancer patients are increasing drastically year by year. According to World Health Organization (WHO) in 2005, about 13% (7.6 million) of the total deaths (58 million) in world were caused by cancer. WHO also speculates that around 9 million and 11.4 million people will die due to cancer by 2015 and 2030 respectively. These figures are alarming and motivate researchers to come up with effective treatment strategies to combat cancer.

Cancer is caused by the external factors such as UV radiations, carcinogenic chemicals as well as transfer of the cancer prone genes from parents. When a normal cell interacts with these external factors, its information system (DNA) gets damaged and the normal cell transforms to a cancer cell. The main characteristics of the cancer cell are its uncontrolled and unregulated growth [1, 2]. Initially, the clump of the cancer cells is confined to particular location and it is regarded as being benign. If the cancer is not diagnosed and treated in the benign stage, it will change into a malignant form, and the cancer cells could migrate to different parts of the body and ultimately may lead to the death of the patient. So, it is better for the cancer patients to be provided suitable treatment at the early stages itself so as to prolong and enhance the quality of their life.

In the past 50 years, many cancer treatment modalities have been discovered. The most common of these are surgery, chemotherapy, radiation therapy, and immunotherapy. However, there is no specific therapy for all types of cancer and each therapy has its own shortcomings. Usually, surgery is favored to remove the tumors. However, the complete clearance of the tumor cells is not assured with surgery. As a result, surgery is followed by chemotherapy or radiation therapy to suppress further tumor growth. In the case of chemotherapy and radiation therapy, precise care should be taken to avert the damage of normal tissue. Among these two therapies, chemotherapy is preferred because it is systemic therapy. In systemic therapy, the drug flows throughout the body and destroys the migrated cancer cells along with residual cancer cells near the surgery location.

Chemotherapy is always given as a course in cycles based on the patient health status rather than as a one-time treatment. This is done so as to maintain the drug concentration within the dosage limits in the body and kill the remaining cancer cells in the subsequent treatments [3] . However, the side effects of the chemotherapy are significant and sometimes they become serious than the disease itself. In this regard, combination of chemotherapy with immunotherapy can be a better alternative. Additionally, immunotherapy has fewer side effects, because, typically, patient's own cells are modified and used as therapeutic agents in contrast to chemotherapy and radiation therapy. Thus, in this paper we focused on immuno-chemotherapy.

The prime objectives of any therapy are to keep the number of cancer cells below a lethal level and avoid the side effects of the therapeutic agents. This can be achieved by optimal scheduling and the optimal administration of the therapeutic agents. Here, we applied multiobjective optimization strategy on the immuno-chemotherapy mathematical

Chwee Teck Lim, James C.H. Goh (Eds.): ICBME 2008, Proceedings 23, pp. 1337–1340, 2009
www.springerlink.com

model to achieve the optimal dosage and scheduling of the immune cells and chemotherapeutic drug.

II. Mathematical model and problem formulation for the multi-objective optimization

The model is adapted from [4] and it describes the growth of the tumor cells and its interaction with the immune cells. The model assumes that tumor cells are immunogenic and do not metastasize. In the other words, tumor cells are recognized and attacked by the cytotoxic effector cells. The interactions between the effector cells and the tumor cells are described by a kinetic scheme and are presented as simple equations. The parameters of the model were obtained by using the experimental data presented in [5]. The activity of chemotherapeutic drug is also included in this model [6] . Equation (3) explains the pharmacokinetics and the term *L (T, M)* in equation (2) corresponds to the pharmacodynamics of the drug. *J(M)* is the term related to the death of effector cells due to the excess chemotherapeutic drug.

$$\frac{dE}{dt} = s + \frac{pET}{g+T} - mET - d_1E + s_1 - J(M) \quad (1)$$

$$\frac{dT}{dt} = aT(1-bT) - nET - L(T,M) \quad (2)$$

$$\frac{dM}{dt} = u - \gamma M \quad (3)$$

$$L(T,M) = k(M - M_{th})H(M - M_{th})T$$
$$J(M) = K_l(1 - e^{M})H_1(M - M_{\max}) \quad (4)$$

Where, H and H_1 are the Heaviside functions:

$$if\ (M - M_{th}) < 0, then\ \ H = 0,$$
$$if\ (M - M_{th}) \geq 0, then\ \ H = 1$$
$$if((M - M_{\max}) \geq 0), then\ H_1 = 1$$
$$if((M - M_{\max}) < 0), then\ H_1 = 0$$

$$E(0) = 1\times10^6,\ T(0) = 1\times10^6,\ M(0) = 0$$

In the above model, the states E(t), T(t) and M(t) refer to the effector cells, tumor cells and concentration of chemotherapeutic drug respectively. In equation (1) 's' represents the rate of flow of the inherent effector cells to the tumor location, which is dependent on the number of lymphocytes in the body. The effector cells accumulate at the tumor sites because of events such as release of cytokines and it is proportional to the number of tumor cells. The total degradation of the effector cells is due to its natural degradation and its interaction with the tumor cells. 's_1' is the externally given modified immune cells. The model assumes that tumor growth follows the logistic equation with the constants 'a' and 'b' in the absence of immune interactions. The total decay of tumor cells is the result of interactions with the effector cells and the chemotherapeutic drug. In equation (4), 'u' is the drug delivery rate and 'γ' is the decay parameter of the drug. Equation (4) shows that drug can kill the tumor cells and immune cells only when its concentration is above the threshold limit 'M_{th}' and 'M_{max}' respectively. The three assumptions related to the drug delivery are: (i) infusion of the drug; (ii) spontaneous mixing of the drug with the plasma; and (iii) immediate reach of the drug to cancer site. In this paper, the two contradictory objectives to be minimized are the total number of cancer cells and the total amounts of the therapeutic agents. The time horizon considered to implement the multi-objective optimization is 500 days. Objective 1 is given by equation (5) which is the summation of the running load and final load of tumor cells. Objective 2 is given by the equation (6) and is the combination of the running load of the chemotherapeutic drug and summation of all inputs of the immune cells. We used MATLAB's [7] implementation of genetic algorithm to solve this multi-objective optimization problem. The algorithm starts with an initial population of possible solutions and in each generation, the solutions are updated based on genetic principles. In this work, we considered population number as 100 and the maximum number of generations as 100. The decision variables in the problem are injection times, administration of number of immune cells and amount of drug.

PROBLEM FORMULATION:

Objective 1: $$\min_{u(t_i),s_1(t_i)} \int_0^{t_f} T(u(t_i),s_1(t_i))\,dt + T(t_f) \quad (5)$$

Objective 2: $$\min_{u(t),s_1(t)} \int_0^{t_f} M(u(t_i),s_1(t_i))\,dt + \sum_{i=1}^{10} s_1(t_i) \quad (6)$$

t_f is the final time i.e. the planning horizon
t_i is the ith time injection of the therapeutic agents

Constraints:
Equations (1) through (4) i.e. the mathematical model

$$0 \leq M(t) \leq M_{\max}$$
$$50(i-1) \leq t_i \leq 50i\ \ , i = 1,2....,10$$

Table 1
Parameter values in the model

parameter	value	unit
a	0.18	day^{-1}
b	2.0×10^{-9}	$cells^{-1}$
n	1.01×10^{-7}	$day^{-1}cells^{-1}$
k	8.4×10^{-3}	$day^{-1}[D]^{-1}$
M_{th}	10	[D]
γ	0.27	day^{-1}
s	1.3×10^{4}	cells day^{-1}
p	0.1245	day^{-1}
g	2.019×10^{7}	cells
m	3.422×10^{-10}	$day^{-1}cells^{-1}$
d_1	0.0412	day^{-1}
M_{max}	50	[D]
U_{max}	51	$[D]day^{-1}$
S_{1max}	1e8	cells
K_1	0.6	day^{-1}

[D] is concentration of the drug

III. Results and Discussions

Figure 1 show that the evolution of tumor cells is oscillatory with decreasing amplitude and finally reaches a steady value. It also confirms that only chemotherapy to the patient does not bring down the steady state value of the tumor cells. However, it is clear that the drug lowers the amplitude of the oscillation. While the steady state value of the tumor cells can be brought down (compared to the no treatment case) through increased infusion of the drug, the concentration of the drug may cross the allowable limits and it is undesirable for the patient.

Figure 2 shows that, the combination therapy is better than chemotherapy alone in controlling the growth of the tumor cells. The solutions of injection times for all generations of the genetic algorithm are projected in figure 3. This gives us an idea about the tendency of solutions towards the optimal schedule with the generations. Information on the injection time and the administration of immune cells and chemo drug can be acquired from Figures 3, 4 and 5.

Figures 3, 4 and 5 describe the decisive impact of administration of maximum number of immune cells and maximum amount of drug to the patient at the initial time. Recall that our objective is to minimize the tumor cells with an optimal amount of therapeutic agents. Hence, once the

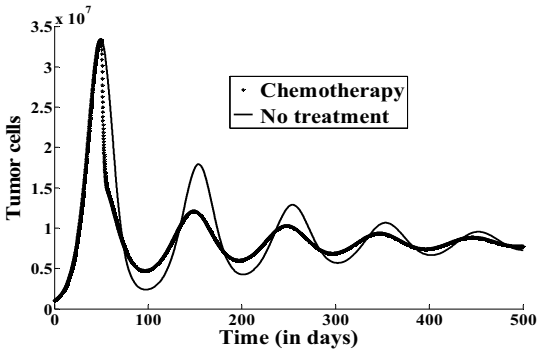


Figure 1: Evolution of tumor cells for chemotherapy only

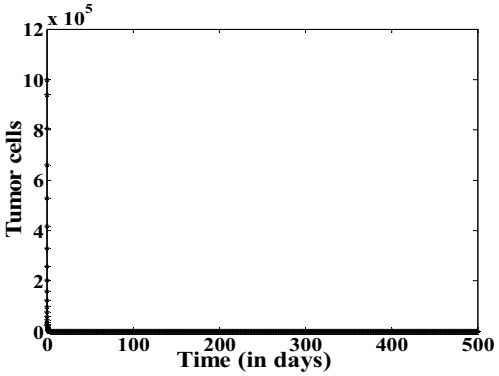


Figure 2: Evolution of tumor cells for combination therapy

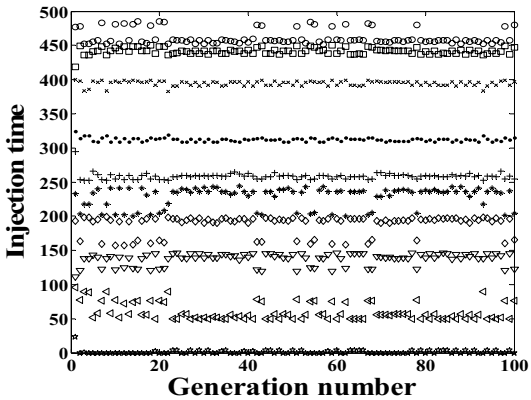


Figure 3: Variation of schedule with generations of the algorithm

tumor cells are reduced with the initial input, lesser number of immune cells and lesser amount of drug is enough in the subsequent time instants to control the tumor cells. Another important feature observed in figures 4 and 5 is that, in many cases, when one therapeutic agent is decreased from its previous input value, the other therapeutic agent is increased. This shows that the optimization procedure prop-

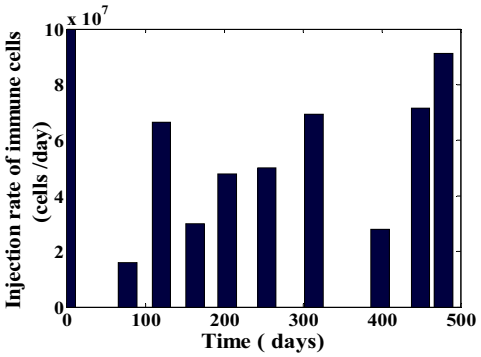


Figure 4: Optimal input of immune cells in combination therapy

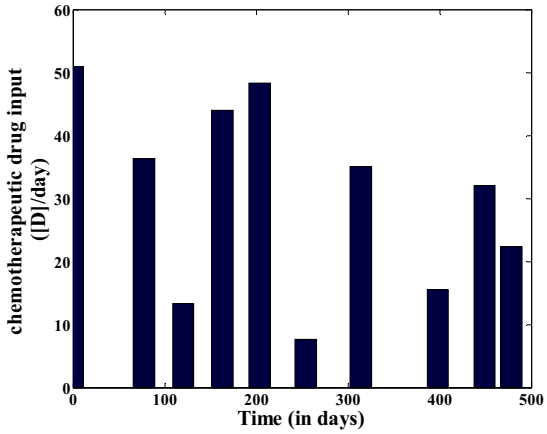


Figure 5: Optimal input of chemotherapeutic drug in combination therapy

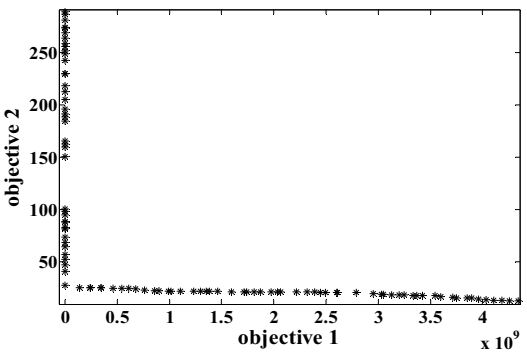


Figure 6: Optimal Pareto solutions for the multi-objective optimization problem

erly balances the administration of therapeutic agents. Figure 6 summarizes the Pareto optimal solutions between the extreme values of the two objectives. Here, we considered the solution when the values of the objective 1 and objective 2 are 3.814e+005 and 2.88e+002 respectively.

IV. Conclusions

We applied multi-objective optimization to find the optimal schedule as well as optimal dosage of the therapeutic agents. A major advantage of the multi-objective optimization method is that we get a set of best solutions and we have the freedom to choose any one solution as per the requirements. The result obtained proves that immunochemotherapy is very much significant than chemotherapy alone in controlling the tumor cells. The obtained protocol design can guide caregivers in treating cancer patients.

Acknowledgements

This work was supported by the National University of Singapore in the form of a research scholarship to the first author.

References

1. Hanahan, D. and R.A. Weinberg (2000), The Hallmarks of Cancer. Cell 100(1): p. 57-70.
2. Martins, M.L., S.C. Ferreira Jr, and M.J. Vilela (2007), Multiscale models for the growth of avascular tumors. Physics of Life Reviews 4(2): p. 128-156.
3. Dua, P., V. Dua, and E.N. Pistikopoulos (2008), Optimal delivery of chemotherapeutic agents in cancer. Computers & Chemical Engineering. 32(1-2): p. 99-107.
4. Kuznetsov, V.A., et al. (1994), Nonlinear dynamics of immunogenic tumors: Parameter estimation and global bifurcation analysis. Bulletin of Mathematical Biology 56(2): p. 295-321.
5. Siu, H., et al. (1986), Tumor dormancy. I. Regression of BCL1 tumor and induction of a dormant tumor state in mice chimeric at the major histocompatibility complex. J Immunol 137(4): p. 1376-1382.
6. Martin, R.B. (1992), Optimal control drug scheduling of cancer chemotherapy. Automatica 28(6): p. 1113-1123.
7. MATLAB 7.4.0.287, Release 17, (2007) The MathWorks Inc., Natick, MA

Author: Dr. Lakshminarayanan S
Institute: National University of Singapore
Street: 4 Engineering Drive 4, E5-02-23
City: Singapore
Country: Singapore
Email: chels@nus.edu.sg

Dip Coating Assisted Polylactic Acid Deposition on Steel Surface: Film Thickness Affected by Drag Force and Gravity

P.L. Lin[1], T.L. Su[1], H.W. Fang[1*], J.S. Chang[1], W.C. Chang[2]

[1] Department of Chemical Engineering & Institute of Biotechnology, National Taipei University of Technology, Taipei, Taiwan
[2] Bio-Invigor Corporation, Taipei, Taiwan

Abstract — **Dip coating process has the potential of providing an easier and economical way to form a polylactic acid (PLA) layer on metal surface for various applications. The effects of dip coating operating parameters such as the withdrawal velocity, concentration, and viscosity of the solution on the film thickness were investigated in this study. Our experimental results show that the increase of withdrawal velocity leads to the increase of PLA film thickness at the relatively low withdrawal velocity regime. However, at the relatively high withdrawal velocity regime of the dip coating process, it was observed that the PLA layer thickness starts to decrease with increasing withdrawal velocity. It is suggested that the competition of drag force and gravity during the dip-coating process dominates PLA film formation. A mechanism was proposed to explain this special behavior which was never observed in the dip coating process.**

Keywords — **Coatings, Polymers, Deposition, Dip coating, Polylactic acid, Film thickness**

I. Introduction

Polylactic acid (PLA) based materials have been applied in biomedical applications due to their bioresorbable properties [1–3]. Deposition of biodegradable PLA layer on medical implant surface may assist on drug release and tissue regeneration applications. The dip coating process involves by dipping substrate into reservoir of solution for some time until the substrate is completely wetted, and then withdrawing the substrate from the solution bath [4]. The dip coating process has been applied in various applications such as thin films in sol–gel technology [5], photoresists films [6] and lubricant layers for magnetic hard disks [7]. Not only that the process itself, space required, and equipment used can be simple enough, but it also can be applied to coat thin films onto plates, slabs, or almost any irregular shaped objects.

The purpose of this study is to observe how the dip-coating operating parameters affect the deposited film thickness. Various concentrations of PLA solutions and different withdrawal velocities were applied in the dip coating experiments to see their effects on PLA film thickness. In addition, by comparing the results with the dip coating models in the literature, it is expected to obtain the critical information for further optimization of the dip coating process from practical viewpoint.

II. Materials and methods

A. Materials

Medical grade poly (DL-lactic) acid with an inherent viscosity of 0.55 dl/g was obtained from Bio-Invigor Corporation (Taipei, Taiwan). Three different solution concentrations (15%, 20%, 30%) of PLA solutions were prepared by dissolving PLA into acetone. The rheological properties of the PLA solutions were measured with cone/plate viscometer (Brookfield LVDVIII ultra rheometer) at 25 °C. The medical grade 316 stainless steel disks (3 mm thick, 15 mm in diameter) were prepared as substrate materials for dip coating process. The surfaces of the 316 stainless steel disks were polished to mirror surface with the roughness of Ra=0.11 μm.

B. Dip coating process

The schematic of the dip coating process is shown in Fig.1. A self developed controller was used in the experiment for the dip coating process. The instrument can move clamp vertically at constant speeds between 4 to 100 mm/s. cover lid with designed small slot was designed to prevent solvent evaporation from the surface of the solution. The 316 stainless steel disks were then immersed into the solution and kept an uncoated area on the top of the disk. The disk was then withdrawn from the bath at prescribed withdrawal velocity. The drying process of the coated disk is done by leaving the disk in its natural vertical position in the hood at room temperature.

C. Dip coating process

A surface profilometer (Mahr, Germany) was used to measure the surface profile of the coated 316 stainless steel disks after the dip coating process. The tracing probe was traveling across the boundary of the uncoated and PLA coated areas on the steel plate. The movement of the probe

Chwee Teck Lim, James C.H. Goh (Eds.): ICBME 2008, Proceedings 23, pp. 1341–1343, 2009
www.springerlink.com

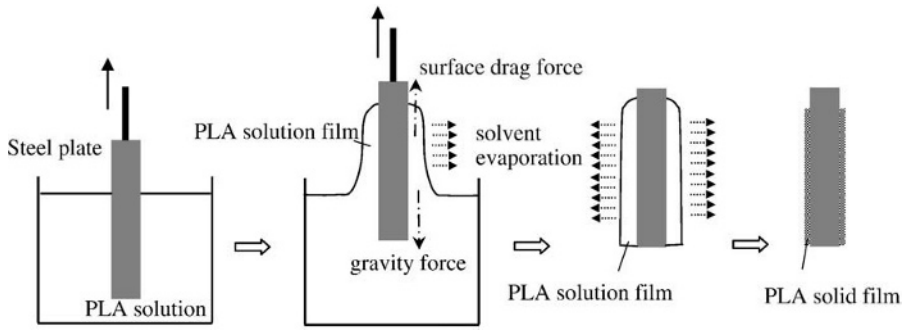


Fig. 1. Schematic of dip coating assisted PLA deposition on steel plate and the factors affecting the solid PLA film formation in a dip coating process.

is recorded for film thickness determination. The PLA film thickness defined in this study presents the gap between the uncoated area and the coated area far from the coating boundary. The measurement was at least repeated 3 times at different locations on the disk to obtain the average film thickness.

III. Results and Discussion

A. Materials

Results of shear stress of the PLA solutions with different concentrations were measured under various shear rates between 1~60 (s^{-1}). It is observed that the viscosity is independent of shear rate. The viscosity of the PLA solution increases with the increase of solution concentration. The average viscosities of the PLA solutions with 15%, 20% and 30% concentrations are 11.2 cp, 20.2 cp, and 107.7 cp respectively.

B. Film thickness

The experimental results of the film thickness versus the withdrawal velocity of dip coating process for PLA solutions with concentrations of 15%, 20% and 30% are shown in Fig. 2. In section I of the plot, the film thickness, h, increases with increase of withdrawal velocity. This trend is expected since the viscous pull drag of steel plate surface on PLA solution is proportional to the withdrawal velocity. With a higher velocity, a greater amount of the liquid is pulled which results in a thicker film. It is also observed from Fig. 2 that a higher concentration of PLA solution leads to the increase of film thickness, h. It is due to the viscosity (pull drag) is larger for high concentrations as indicated in Section I. In other words, at the same withdrawal velocity, the amount of PLA solution moving upwards with the steel plate is larger for a more viscous liquid according to the fact that the drag force is proportional to the solution viscosity.

Section II of Fig. 2 indicates the decrease of film thickness with increase of the withdrawal velocity. We call the point in which the withdrawal velocity creates the maximum PLA film thickness as. The value of differs with each solution and is smaller for PLA solutions with smaller concentrations. We recall that in section I the thickness of the coating film increases as the viscous pull drag is proportional to withdrawal velocity. However as υ further increases in section II, an abundant amount of solution is pulled up with a comparative shorter time. With the lack of sufficient evaporation time, the gravity force of the PLA solution film leads to solution film moving back the solution pool before the solid PLA film formation on steel surface. The outcome of the competition between drag force (solution film moving upward) and gravity (solution film moving downward) as shown in Fig. 1 determines the variation of final solid PLA film thickness while increase of withdrawal velocity during the dip coating process.

C. Model fitting and gravity affect

Landau et al. provided the earliest analysis of the dip coating process [4]. Their model was a one-dimension infinite long plate drawn out of a wetting bath. The analysis was based on the hydrodynamics equations of Newtonian fluid. The relationship between the film thickness and withdrawal velocity is given as,

$$h \propto \upsilon^{0.667} \tag{1}$$

where h is the thickness of the coated layer and υ is the withdrawal velocity. Eq. (1) however is based on the above theoretical situation and for practical purposes and process conditions the above relation is modified as,

$$h \propto \upsilon^{x} \tag{2}$$

in which the power term of 0.667 is replaced with x.

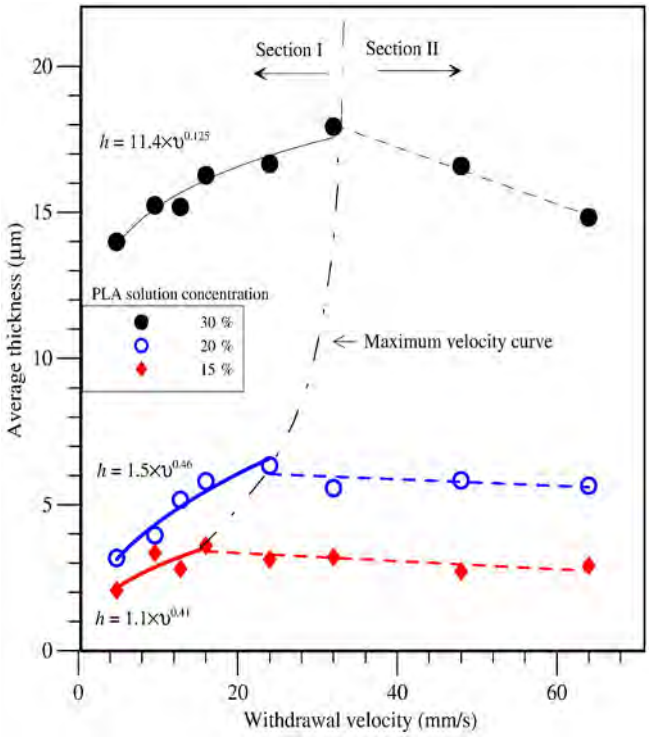


Fig. 2. Solid PLA film thickness as a function of withdrawal velocity with different concentration solutions.

Table 1
υ_{max} and percentage of thickness loss caused by gravitational effect under 3 different concentrations of PLA solutions

Concentration (wt.%)	υ_{max}	Maximum thickness	Percentage of h loss at
		h_{max} (μm)	$2\times\upsilon_{max}$
15.0	16.0	3.6	5.1%
20.0	24.0	6.3	8.0%
30.0	32.0	18.0	17.3%

According to the mathematical expressions of Eqs. (1) and (2), it indicates that there exists a limitation of film thickness increase while $0< x <0.667$. However, the above equations do not show the decreasing effect as the withdrawal velocity is increased. Table 1 lists and the percentage loss compared to the maximum thickness of each concentration.

As shown in Table 1, we have measured a loss of up to 17% of film thickness during the dip coating production. This kind of waste needs to be prevented in practical applications by controlling the operation withdrawal velocity of the dip coating process not exceed to υ_{max}. Control of the solid PLA film thickness can be reached by combined selections of appropriate PLA solution concentration and withdrawal velocity during the dip coating process.

IV. Conclusion

The results indicated that the gravity effect must be considered when dealing with the dip coating process for PLA. The outcome of the competition between drag force (solution film moving upward) and gravity (solution film moving downward) determines the variation of final solid PLA film thickness while increase of withdrawal velocity during the dip coating process. The findings of this study can contribute to the optimization of the dip coating assisted PLA deposition process on medical implant surface in order to improve the functionality.

Acknowledgment

The authors are pleased to acknowledge the financial support from National Taipei University of Technology (NTUT 97-140-3) and National Science Council, Taiwan (94-2622-E-027-011-CC3).

References

1. Lin P, Fang H, Tseng T, Lee W. Mat Lett 2007;61:3009–13.
2. Vainionpaa S, Rokkanen P, Tormaala P. Prog Polym Sci 1989;14:679–716.
3. Tschakalo A, Losken H, Lalikos J. J Craniofac Surg 1993;4:223–7.
4. Landau L, Levich B. Acta Physicochim URSS 1942;17:42–54.
5. Brinker C, Frye G, Hurd A, Ashley C. Thin Solid Films 1991;201: 97–108.
6. Gibson M, Frejlich J, Machorro R. Thin Solid Films 1985;128: 161–70.
7. Gao C, Lee Y, Chao J, Russak M. IEEE Trans Magnet 1995;21: 2982–4.

Author: Dr. Hsu-Wei Fang, Ph.D., Associate Professor
Institute: Department of Chemical Engineering & Institute of Biotechnology, National Taipei University of Technology
Street: 1, Sec. 3, Chung-Hsiao E. Road
City: Taipei, 106
Country: TAIWAN
Email: hwfang@ntut.edu.tw

Some Properties of a Polymeric Surfactant Derived from Alginate

R. Kukhetpitakwong[1], C. Hahnvajanawong[2], D. Preechagoon[1] and W. Khunkitti[1]

[1] Faculty of Pharmaceutical Sciences, Khon Kaen University, Khon Kaen 40002, Thailand
[2] Faculty of Medicine, Khon Kaen University, Khon Kaen 40002, Thailand

Abstract — **The aim of this study was to prepare a polymeric surfactant from alginate, to evaluate the properties of this surfactant for pharmaceutical application and to study the effect of the surfactant on immune response. The polymeric surfactant was prepared by the method previously reported. Surface tension of its solution was determined by maximum pull force technique. Proliferation of splenocytes was performed by the measurement of 5-bromo-2-deoxyuridine (BrdU) incorporation during DNA synthesis. The proliferative response of splenocyte to the surfactant was compared to quillaja saponin. The surface tension of the surfactant in water was decreased to 30.37 mN/m. Critical concentrations for micelle formation in water, 5% dextrose, phosphate buffered saline and 0.9% NaCl were 2.95 mg/ml, 3.07 mg/ml, 1.55 mg/ml and 1.52 mg/ml, respectively. The surfactant at the concentration higher than 1.5 mg/ml showed significantly reduction of splenocyte proliferation. The highest stimulation was found at a concentration of 0.75 mg/ml. The alginate-derived polymeric surfactant seems to form micelles in aqueous solutions and to stimulate immune responses. These results indicated that the polymeric surfactant could be a potential vaccine adjuvant.**

Keywords — **alginate, polymeric surfactants, surface tension, splenocyte proliferation**

I. Introduction

Alginate is a linear polysaccharide present in the cell walls of the fronds of various seaweeds, including the giant brown kelp (*Macrocystis pyrifera*), horsetail kelp (*Laminaria digitalis*), and sugar kelp (*L. saccharina*). It consists of 1,4-β-D-mannuronic and 1,4-α-L-guluronic acid residues [1]. Alginate plays important role in product development such as to improve drug stability and to prolong drug release. It is regarded as biocompatible, non-toxic, non-immunogenic and biodegradable which make it widely used for biomedical applications as drug delivery systems for living cells, protein and DNA [2-5]. Recently, alginate has been chemically modified to increase its hydrophobicity for delivery protein [6-12].

Therefore, the goal of this study was to investigate the properties and potential uses of a modified alginate as an adjuvant. The article reports on the surface activity of the modified alginate in aqueous solution. In addition, it was tested in stimulation of splenocyte proliferation in comparison with quillaja saponin.

II. Materials and methods

A. Materials

Sodium alginate was from Carlo Erba Reagenti, Italy. Saponins from quillaja bark (QS) as partial purified extract with 25% of sapogenin content and octylamine were purchased from Sigma Chemical Co., USA. Cell proliferation ELISA, BrdU (colorimetric) kit was purchased from Roche Diagnostics, Germany. All other chemicals were of grade AR.

B. Animals

BALB/c mice, 6–8 weeks old, were purchased from the National Laboratory Animal Center, Thailand. The animals were housed under standard conditions at 25±2°C and were provided with chow pellets and tap water ad libitum. The procedures applied to the mice were approved by the Animal Ethics Committee of Khon Kaen University, in accordance with the requirements of the Ethics of Animal Experimentation of the National Research Council of Thailand.

C. Preparation of alginate-derived polymeric surfactant

Alginate-derived polymeric surfactants were prepared by oxidation and reductive amination [13]. Briefly, one gram of sodium alginate was dissolved in a solution containing 40 ml of water and 10 ml of 1-propanol. Sodium peroxidate was added and the reaction mixture was stirred at 1250 rpm in dark condition at ambient temperature for 24 h [14]. Alginate was partially oxidized to yield 30% oxidized 2,3-dialdehydic alginate. Then, 1 ml of ethylene glycol was added and the mixture was stirred at 400 rpm for 2 h. Sodium chloride (0.5 g) was added and dissolved in the reaction mixture. After addition of 96% ethanol (50 ml), the reaction mixture was centrifuged at 4000 rpm for 5 min. Pellets were re-dissolved in 50 ml of water before adding NaCl (0.05 g) and 96% ethanol (200 ml). The mixture was

Chwee Teck Lim, James C.H. Goh (Eds.): ICBME 2008, Proceedings 23, pp. 1344–1347, 2009
www.springerlink.com

stirred at 300 rpm for 30 min and then centrifuged as the above condition and pellets were collected. Oxidized 2,3-dialdehydic alginate was dried under vacuum at 40ºC.

Oxidized 2,3-dialdehydic alginate (0.404 g) was dissolved in 20 ml of phosphate-buffered saline, pH 7. Then, 0.092 g of sodium cyanoborohydride ($NaCNBH_3$) was weighed under fume hood and added. The solution was mixed with 10 ml of methanol containing octylamine. The reductive amination was performed for 12 h at room temperature [13]. The mixture was centrifuged at the same condition as described above. Supernatant was used and 96% ethanol (20 ml) was then added. Precipitate was washed three times with 20 ml of 96% ethanol and dried under vacuum at 40ºC.

D. Surface tension measurement

Solutions of the modified alginate were prepared at the concentration of 10 mg/ml in deionized water, 5% dextrose, phosphate buffered saline (PBS), pH 7 or 0.9% NaCl. Serial 2-fold dilutions of the solution were performed to obtain 11 concentrations. Fifty microliters of each sample were added into a conical bottom 96-well microplate. Surface tension of the solutions was measured by using a multi-channel microtensiometer (Delta-8, Kibron Inc. Oy, Germany) at 20°C.

E. Splenocyte proliferation assay ex vivo

Mouse splenocytes were prepared as a method previously reported [15]. The proliferation of splenocytes was performed by the measurement of 5-bromo-2-deoxyuridine (BrdU) incorporation during DNA synthesis in proliferation cells [16]. Briefly, 50 µl of splenocytes (1×10^6 cells) were seeded in 96-well plates. Then 50 µl of various concentrations of the modified alginate or controls were added. After incubation at 37ºC in CO_2 incubator for 3 d, 10 µl of BrdU labeling reagent were added to each well and the plates were incubated for a further 24 h before centrifugation at 2000 rpm for 15 min at 4ºC. After that the culture medium was removed and 200 µl of FixDenat solution were then added to each well. After 30 min, 100 µl of mouse anti-BrdU were added and incubated for 90 min at 37ºC. The plates were washed three times. Then, 100 µl of substrate solution were added and incubated for 30 min at room temperature. Then, the reactions were stopped by incubation with 25 µl of 1M H_2SO_4 for 5 min. The absorbance (Abs) was measured at 450 nm using an ELISA reader. The stimulation index (SI) was calculated as the following equation.

$$SI = \frac{(Abs_{Treated\ cultures} - Abs_{Background})}{(Abs_{Untreated\ cultures} - Abs_{Blank})} \quad (1)$$

F. Statistical analysis

Statistical significance of the differences among stimulation index of various concentrations on the proliferative response of mouse splenocytes were analyzed by one-way analysis of variance (ANOVA) followed by the Tukey multiple comparison test. P-values of less than 0.05 were considered to be statistically significant.

III. Results

Surface activity of the modified alginate: The effect of modified alginate concentration on surface tension of aqueous solutions at 20°C is shown in Fig. 1. The critical micellar concentrations (CMC) of the modified alginate in water, 5% dextrose, phosphate buffered saline (PBS) and 0.9% NaCl were 2.95 mg/ml, 3.07 mg/ml, 1.55 mg/ml and 1.52 mg/ml, respectively. The surface tension of the modified alginate in PBS (29.55 mN/m) and 0.9% NaCl (29.94 mN/m) was lower than those in water (30.37 mN/m). However, its surface tension in 5% dextrose (30.76 mN/m) was closed to those in water.

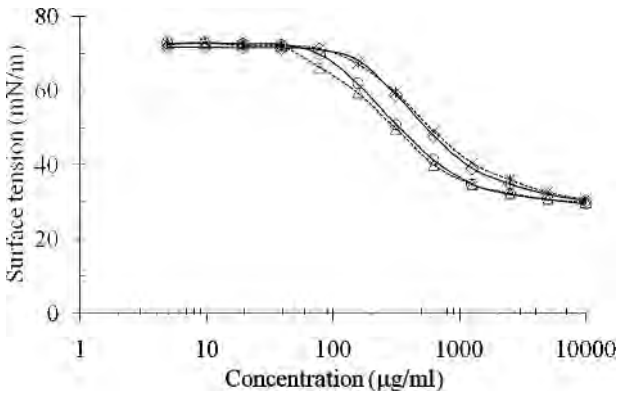


Fig. 1 Critical micellar concentration of modified alginate in (◇) water, (✳) 5% dextrose, (○) PBS, pH 7 and (△) 0.9% NaCl

Effect of the modified alginate on splenocyte proliferation: A spleen was removed from specific pathogen-free BALB/c mouse to prepare a single cell suspension. The proliferative responses were determined by BrdU ELISA. The effect of the modified alginate on splenocyte proliferation is shown in Fig. 2. The highest splenocyte proliferation was found at a concentration of 0.75 mg/ml with the stimulation index (SI) of 1.99±0.21 (mean ± standard error of mean, n=6). The modified alginate at the concentrations higher than 1.5 mg/ml induced splenocyte proliferation significantly less than the modified alginate at the concentration of 0.75 mg/ml did ($p<0.001$).

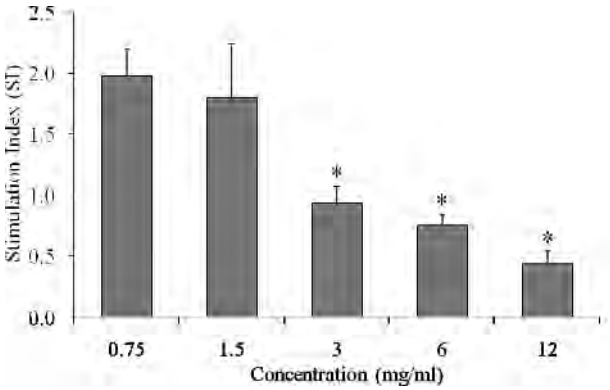


Fig. 2 Effect of the modified alginate on lymphoproliferation.

IV. Discussion

The lowering of water surface tension and the formation of self-aggregates clearly represented amphiphilic character of the modified alginate. The critical micellar concentration is a principal thermodynamic parameter for polymer aggregation and is usually used to evaluate the thermodynamic stability of the aggregates in aqueous solutions [17-19]. The CMC value of modified alginate in 0.9% NaCl and PBS was lowered to about 1.5 mg/ml. These finding suggested that in the presence of strong electrolytes, modified alginate could form micelles like surfactants at the lower concentration [20]. In contrast, the CMC of modified alginate in a solution containing nonelectrolytes such as 5% dextrose was similar to those of in water. This phenomenon could be explained by electrostatic repulsion. Since the carboxylic groups of sodium alginate on the β-D-mannuronate and α-L-guluronate residues were partially modified, the modified alginate had electrostatic repulsion of the charged headgroups in the periphery of ionic micelles. The addition of salts reduces these repulsive forces, lowering the CMC of the anionic surfactant [21]. Nonelectrolytes dissolve in water as intact molecule therefore they might not effect on micellar formation of the modified alginate.

In this study, quillaja saponins were used as positive control for stimulation of lymphoproliferation. Their structure consisted of a hydrophobic aglycone and hydrophilic sugar chains [22]. The usefulness of saponins as adjuvant could be able to induce sufficient both protective humoral- and cell-mediated immune responses [23]. The SI value of quillaja saponin (100 μg/ml) was 1.78±0.29 whereas the SI value of the modified alginate (0.75 mg/ml) was 1.99±0.21. These revealed that the modified alginate at the concentration of 0.75 mg/ml could be an adjuvant. In addition, it could stimulate proliferation of splenocyte at the concentration closed to the critical micellar concentration as found in case of saponins [15].

V. Conclusions

Alginate-derived polymeric surfactant with a linear alkyl group of octylamine were synthesized by oxidation followed by reductive amination of 2,3-dialdehydic alginate. It could aggregate by itself in aqueous solutions. For biomedical application, it might be useful for protecting drugs from hydrolysis and for encapsulating hydrophobic drugs as self-assembly in aqueous solution. In addition, it could be used as vaccine adjuvant. However, further studies on vaccine delivery systems of the modified alginate need to be investigated

Acknowledgment

The authors would like to acknowledge the significant role of Professor Dr.Jörg Kreuter for his advice. We also thank the staff at Institute for Pharmaceutical Technology, University of Frankfurt, Germany for their generous support and providing multi-channel microtensiometer facilities.

References

1. Braccini I, Pérez S (2001) Molecular basis of Ca^{2+}-induced gelation in alginates and pectins: The egg-box model revisited. Biomacromolecules 2:1089-1096.
2. Chung TW, Yang J, Akaike T et al (2002) Preparation of alginate/galactosylated chitosan scaffold for hepatocyte attachment. Biomaterials 23:2827-2834.
3. Lemoine D, Wauters F, Bouchend'homme S et al (1998) Preparation and characterization of alginate microsphere containing a model antigen. Int J Pharm 176:9-19.
4. Bhowmik BB, Sa B, Mukherjee A (2006) Preparation and *in vitro* characterization of slow release testosterone nanocapsules in alginates. Acta Pharm 56:417-429.
5. Ghiasi Z, Sajadi Tabasi SA, Tafaghodi M (2007) Preparation and *in vitro* characterization of alginate microspheres encapsulated with autoclaved Leishmania major (ALM) and CpG-ODN. Iranian J Basic Med Sci 10:90-98.
6. Broderick E, Lyons H, Pembroke T et al (2006) The characterization of a novel, covalently modified amphiphilic alginate derivative, which retains gelling and non-toxic properties. J Colloid Interface Sci 298:154-161.
7. Leonard M, Rastello De Boisseson M et al (2004) Hydrophobically modified alginate hydrogels as protein carriers with specific controlled release properties. J Controlled Release 98:395-405.
8. Leonard M, Rastello De Boisseson M et al (2004) Production of microspheres based on hydrophobically associating alginate derivatives by dispersion/gelation in aqueous sodium chloride solutions. J Biomed Mater Res A 68:335-342.
9. Bu H, Nguyen GTM, Kjøniksen A-L (2006) Effects of the quantity and structure of hydrophobes on the properties of hydrophobically modified alginates in aqueous solutions. Polym Bull 57:563-574.

10. Liu XM, Pramoda KP, Yang YY et al (2004) Cholesteryl-grafted functional amphiphilic poly(*N*-isopropylacrylamide-co-*N*-hydroxylacrylamide): synthesis, temperature-sensitivity, self-assembly and encapsulation of a hydrophobic agent. Biomaterials 25:2619-2628.
11. Yang L, Zhang B, Wen L et al (2007) Amphiphilic cholesteryl grafted sodium alginate derivative: synthesis and self-assembly in aqueous solution. Carbo Polym 68:218-225.
12. Babak VG, Skotnikova EA, Lukina IG et al (2000) Hydrophobically associating alginate derivatives: surface tension properties of their mixed aqueous solutions with oppositely charged surfactants. J Colloid Interface Sci 225:505-510.
13. Kang H-A, Shin MS, Yang J-W. (2002) Preparation and characterization of hydrophobically modified alginate. Polym Bull 47:429-435.
14. Bouhadir KH, Hausman DS, Mooney DJ (1999) Synthesis of cross-linked poly(aldehyde guluronate) hydrogels. Polymer 40:3575-3584.
15. Kukhetpitakwong R, Hahnvajanawong C, Homchampa P et al (2006) Immunological adjuvant activities of saponin extracts from the pods of *Acacia concinna*. Int Immunopharmacol 6:1729-1735.
16. Porstmann T, Ternynck T, Avrameas A (1985) Quantitation of 5-bromo-2-deoxyuridine incorporation into DNA: an enzyme immunoassay for the assessment of the lymphoid cell proliferative response. J Immunol Methods 82:169-179.
17. Kataoka K, Harada A, & Nagasaki Y (2001) Block copolymer micelles for drug delivery: design, characterization and biological significance. Adv Drug Deliv Rev 47:113–131.
18. Tian L, Yam L, Zhou N et al (2004) Amphiphilic scorpion-like macromolecules: design, synthesis, and characterization. Macromolecules 37:538–543.
19. Yang L, Zhang B, Wen L et al (2007) Amphiphilic cholesteryl grafted sodium alginate derivative: synthesis and self-assembly in aqueous solution. Carbo Polym 68:218-225.
20. Priyadarsini KI, Mohan H (2003) Effect of NaCl on the spectral and kinetic properties of cresyl violet (CV)-sodium dodecyl sulphate (SDS) complex. Proc Indian Acad Sci 115:299-306.
21. Gennaro AR (1995) Remington: the science and practice of pharmacy. Mack Publishing:Pennsylvania.
22. Kensil CR, Patel U, Lennick M et al (1991) Separation and characterization of saponins with adjuvant activity from *Quillaja saponaria* Molina cortex. J Immunol 146:431-437.
23. Cox JC, Coulter AR (1997) Adjuvants-a classification and review of their modes of action. Vaccine 15:248-258.

Author: Mrs.Ratiya Kukhetpitakwong
Institute: Faculty of Pharmaceutical Sciences, Khon Kaen University
Street: 123 Mittraphap Highway
City: Khon Kaen
Country: Thailand
Email: ratkom@kku.ac.th

Nano-Patterned Poly-ε-caprolactone with Controlled Release of Retinoic Acid and Nerve Growth Factor for Neuronal Regeneration

K.K. Teo[1], Evelyn K.F. Yim[1,2]

[1] Division of Bioengineering, Faculty of Engineering, National University of Singapore, Singapore
[2] Department of Surgery, Yong Loo Lin School of Medicine, National University of Singapore, Singapore

Abstract — **A combination of nanotopography and controlled release could be a potential treatment for damages to the central and peripheral nervous system. Synergistic effects of both physical and chemical guidance were more effective than individual cues in the directional promotion of neurite outgrowth[1]. Hypothesizing that synergistic effect will enhance neuronal differentiation of human mesenchymal stem cells (hMSCs), a fabrication method for neurotrophic factors encapsulation in a nanopatterned (350nm-gratings) poly-ε-caprolactone (PCL) film was developed. Nanotopography directs hMSCs into neuronal lineage while controlled release of neurotrophic factors presents biochemical signals with temporal and spatial control. Preliminary results demonstrated synergistic effect on hMSC cultured on substrates with both nanotopographical and biochemical cues.**

The protein/drug encapsulated PCL films were fabricated by modified solvent casting methods in which the biologics were 'sandwiched' between two layers of PCL on a nanopatterned polydimethylsiloxane mold. Bovine serum albumin (BSA), RA and NGF were encapsulated into the films using this sandwich approach. BSA was first encapsulated to optimize the sustained release. Among different fabrication methods in BSA optimization, encapsulating solid BSA between 2 PCL layers resulted in most sustainable release. Surface topography remained intact after 10 days incubated in PBS with controlled release, verified through SEM.

Continuous release of bioactive RA and NGF was observed over the 1 week release period. Human MSCs aligned and elongated along the nano-patterned films. Enhanced upregulation of neuronal gene such as microtubule associated protein (MAP2) and neurofilament (NFL) was observed in hMSCs cultured on combination cues, as compared to individual cues. Using quantitative PCR analysis, upregulation of MAP2 in hMSCs on the nanogratings with controlled release NGF was verified, highlighting the synergistic effect of both biochemical and nanotopographical cues in directing hMSC differentiation. This fabrication methodology will allow the delivery of multiple therapeutic cues for potential applications in neural regeneration.

Keywords — **Controlled release, synergistic, differentiation, NGF, nanotopography, human mesenchymal stem cells**

I. Introduction

Nanotopography regulates cellular activities and directs human mesenchymal stem cells (hMSCs) into neuronal lineage [2, 3] while controlled release of neurotrophic factors presents biochemical signals with temporal and spatial control. The synergistic effects of both physical and chemical guidance were also more effective than individual cues in the directional promotion of neurite outgrowth [1]. A combination of nanotopography and controlled release could be a potential treatment for damages to the central and peripheral nervous system.

Hypothesizing that the synergistic effect will enhance neuronal differentiation of hMSCs, a fabrication method for neurotrophic factors encapsulation in a nanopatterned (350nm gratings) poly-ε-caprolactone (PCL) film was developed. Preliminary results demonstrated a synergistic effect on hMSC cultured on substrates with both nanotopographical and biochemical cues.

II. Materials and methods

A. Fabrication of nanopatterned film with controlled release of Retinoic acid (RA) or Nerve Growth Factor (NGF)

Poly-ε-caprolactone (PCL, Sigma) films were fabricated on nanopatterned polydimethylsiloxane (PDMS) mold by solvent casting. Bovine serum albumin (BSA, Sigma), RA (Sigma) and NGF (R&D Systems) were encapsulated into the films using a sandwich layer approach.

BSA was first encapsulated to optimize the sustained release. To characterize the controlled release profile of the encapsulated biochemical cues, supernatant obtained from PCL films incubated in phosphate buffered saline (PBS) was quantified for BSA, RA and NGF using BCA assay (Pierce), UV spectrophotometry and β-NGF ELISA (R&D Systems), respectively. Bioactivity of the released RA and NGF was tested for using the PC12 assay.

Chwee Teck Lim, James C.H. Goh (Eds.): ICBME 2008, Proceedings 23, pp. 1348–1351, 2009
www.springerlink.com

The surface topography of the film before and after controlled release was examined by scanning electron microscopy (SEM).

B. Synergistic effects in hMSC differentiation

RNA was isolated from hMSCs (Lonza) cultured on the polymer substrates at day 7. RNA isolated from hMSCs cultured on unpatterned PCL film and tissue culture polystyrene served as controls. Human β-actin was used as the endogenous control. Gene expression was measured by RT-PCR and real time PCR. Synthesis and amplification of DNA were performed with Qiagen One-step RT-PCR kit for RT-PCR. For real-time PCR, PCR was performed using TaqMan Universal PCR Mix with human MAP2 Taqman Gene Expression Assay primer and probes and human β-actin as endogenous control (Applied Biosystems).

III. Results and Discussion

Modified solvent casting methods were used for fabrication of the protein / drug encapsulated films, in which the biologics were 'sandwiched' between two layers of PCL. Among the different fabrication methods in BSA optimization, the most sustainable release profile methodology (arrow in Fig. 1) was achieved by encapsulating BSA in solid form between the two PCL layers.

SEM images showed that surface topography of the PCL substrates, with or without encapsulated protein or RA, remained intact after 10 days incubation in phosphate buffered saline (PBS) (Fig. 2).

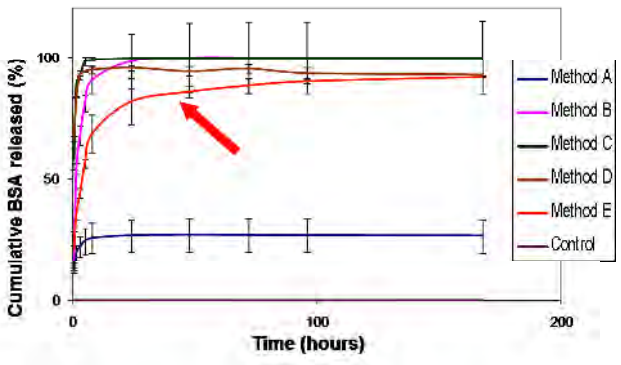


Fig. 1. Cumulative control release profile of bovine serum album (BSA) over a 7 day period.

RA was mixed with the PCL solution for solvent casting, while NGF was encapsulated into the PCL using the sandwich method optimized by the BSA encapsulation. Burst release was observed in both of the RA and NGF-encapsulated film, but continuous release was observed over the 1 week release period. Fig 3 shows the cumulative release profile of the NGF over 7 days incubation. Released

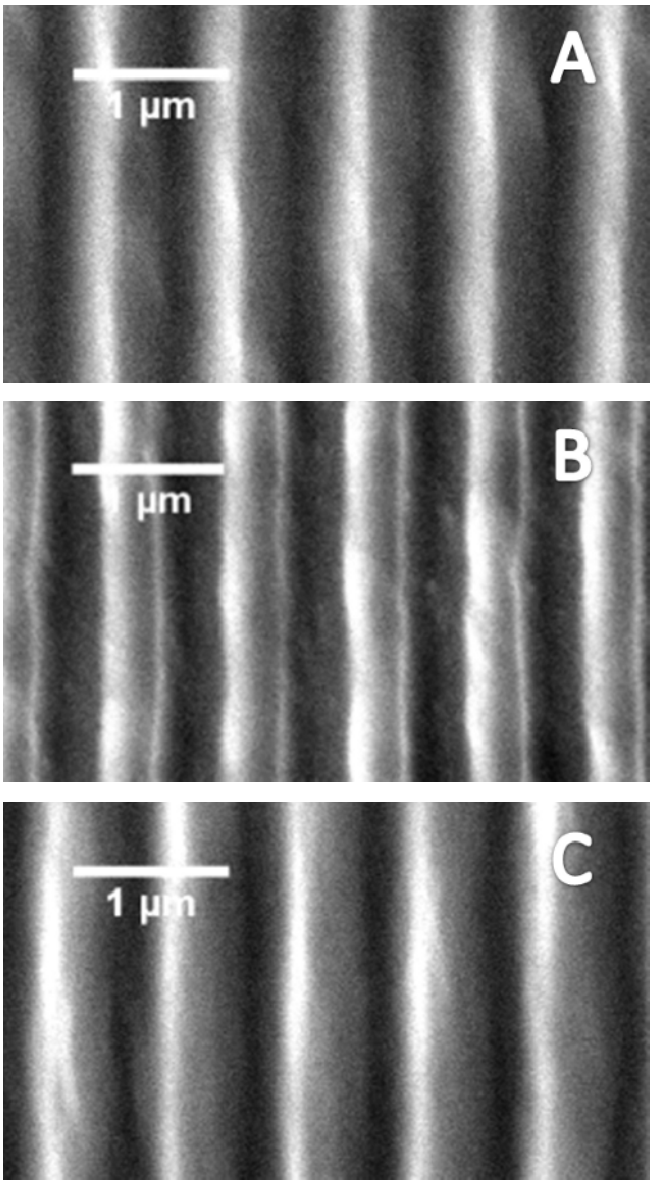


Fig. 2 Scanning electron micrographs of poly(ε-caprolactone) nano-gratings (A) without NGF encapsulation incubated with PBS, (B) with encapsulated retinoic acid incubated with PBS, and (C) with encapsulated NGF incubated with PBS.

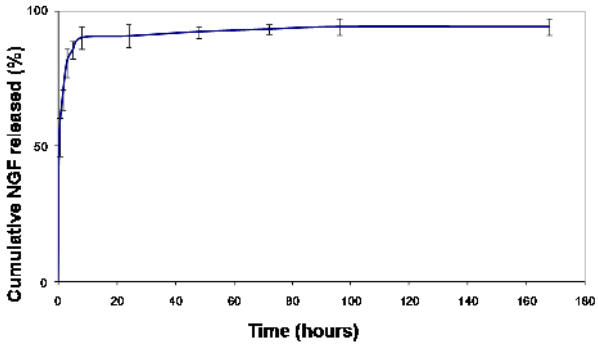


Fig. 3 Cumulative nerve growth factor (NGF) release over a period of 7 days.

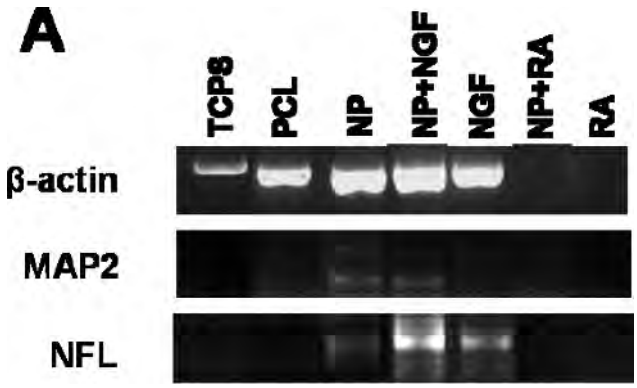


Fig. 4A Gene expression of neuronal markers MAP2 and neruofilament (NFL) in hMSCs cultured on nano-patterned (NP) substrates with or without NGF or RA, and also unpatterned PCL and TCPS controls.

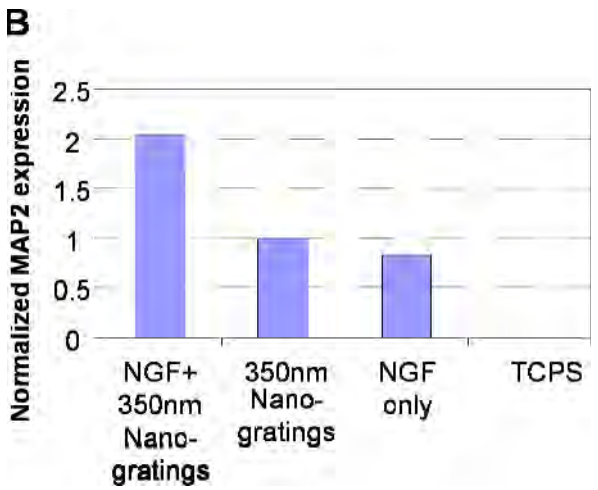


Fig. 4B Quantitative analysis of microtubule associated protein 2 (MAP2) expression in hMSCs on nanogratings with encapsulated NGF (NGF+350nm nanogratings), nanogratings without encapsulation (350nm nanogratings), tissue culture polystyrene with NGF (NGF only) and without NGF (TCPS).

RA and NGF remained bioactive demonstrated through the induction of PC12 neurite outgrowth.

Human MSCs were aligned and elongated along the nano-patterned films. In addition to changes in morphology, enhanced upregulation of neuronal gene such as microtubule associated protein 2 (MAP2) and neurofilament (NFL) was observed in hMSCs on nanopatterned substrates with controlled release of NGF, as compared to individual cues (Fig. 4A). The RNA isolated from the hMSCs cultured on RA-encapsulated substrates, with or without nanogratings, was low. The low yield could be due to the high RA concentration released from the RA-encapsulated substrate, interfering with the RNA isolation and quantification. A slow growth rate was also observed in the hMSCs cultured on the RA-encapsulated substrates; the lower cell density could also decrease the RNA isolation yield.

The quantitative PCR analysis verified the upregulation of MAP2 in hMSCs on the gratings with controlled release NGF (Fig 4B), compared to controls of nano-gratings alone and soluble NGF, highlighting the synergistic effect of biochemical and nanotopographical cues in directing stem cell differentiation.

IV. Conclusions

The fabrication methodology allows bioactive neurotrophic factors, such as the hydrophilic nerve growth factor and the lipophilic retinoic acid, to be released from a nanopatterned substrate, effectively delivering multiple therapeutic cues. The preliminary results showed enhanced neuronal marker upregulation, which suggested that they exerted a synergistic effect on the neural differentiation of hMSCs. The applications of such a multi-functional drug delivery platform have potential for the augmentation of neural regeneration.

Acknowledgement

The authors would like to acknowledge the Singapore Ministry of Education for the financial support from Academic Research Fund Tier 1 R-397-000-047-133.

References

1. Miller, C., S. Jeftinija, and S. Mallapragada (2001) Synergistic effects of physical and chemical guidance cues on neurite alignment and outgrowth on biodegradable polymer substrates. Tissue Eng 8(3): 367-378

2. Curtis, A.S., M. Dalby, and N. Gadegaard (2006) Cell signaling arising from nanotopography: implications for nanomedical devices. Nanomed 1(1):67-72
3. Yim, E.K., S.W. Pang, and K.W. Leong (2007) Synthetic nanostructures inducing differentiation of human mesenchymal stem cells into neuronal lineage. Exp Cell Res 313(9):1820-1829

Address of the corresponding author:

Author: Evelyn K.F. Yim
Institute: National University of Singapore
Street: 7 Engineering Drive 1
City: Singapore
Country: Singapore
Email: eyim@nus.edu.sg

Exposure of 3T3 mouse Fibroblasts and Collagen to High Intensity Blue Light

S. Smith[1,2], M. Maclean[2], S.J. MacGregor[2], J.G. Anderson[2] and M.H. Grant[1]

[1]Bioengineering Unit, University of Strathclyde, Glasgow, UK
[2]Robertson Trust Laboratory for Electronic Sterilisation Technologies (ROLEST), University of Strathclyde Glasgow, UK

Abstract — **The field of tissue engineering is continually expanding and advancing with the development of hybrid biomaterials incorporating active biomolecules, such as mammalian cells and DNA, into scaffolds. Sterilization of these biomaterials for clinical use has become an issue as the most common methods of sterilizing biomaterials, gamma radiation and ethylene oxide treatment, not only have a detrimental effect on the base scaffold, but are also incompatible with biological molecules. There has been long standing interest in the effect of light on biological cells and tissues. Recently, exposure to blue light has become of interest for applications including skin treatment (acne vulgaris) and for the inactivation of problematic microorganisms. High-intensity blue light in the 405 nm region has previously been shown to be an effective bacterial decontamination method and may have a potential application for biomaterials. This study investigated the effect of blue light treatment on both the structure of collagen, the most widely used scaffold for tissue engineering applications, and on the viability of a mammalian cell line (3T3 mouse fibroblasts). Type I collagen solution was treated with the blue light (405 nm) at 10 mW/cm^2 for 1 hour and SDS-PAGE analysis used to determine the effect on the gross structure of the collagen monomer. To determine the effect of the blue light exposure (1.0 mW/cm^2 for 1 hour) on mammalian cell viability the following methods were used: MTT and Neutral Red microplate assays, measurement of reduced glutathione and protein content, and leakage of cytoplasmic lactate dehydrogenase (LDH) activity. Results show that blue light treatment, for the power densities detailed above, had no noticeable effect on the gross structure of the collagen monomer, nor did it affect the viability, redox state, growth rate or LDH leakage of 3T3 cells.**

Keywords — **Blue-light, collagen, 3T3 fibroblasts, cell viability, redox status**

I. Introduction

Tissue engineering is becoming a major area of medical research with the potential to facilitate culture of cells and tissue for transplant surgery [1]. Advances within the field have resulted in the development of complex hybrid biomaterials that incorporate active biomolecules, such as mammalian cells and DNA. For clinical applications such biomaterials must be sterilized. Currently, gamma irradiation and ethylene oxide (EtO) treatment are the most common decontamination methods used for biomaterials, but both are known to cause detrimental effects to the physiochemical and biochemical properties of the biomaterial [2,3], and neither is compatible with many active biomolecules.

Exposure of biological cells and tissue to blue light has recently become of interest for areas such as skin treatment (acne vulgaris) and for the inactivation of problematic organisms. *Propionibacterium acnes* irradiated with blue-light results in photosensitization of intracellular porphyrins, generating reactive oxygen species and therefore causing cell death [4]. Blue-light in the 405 nm region has also been shown to be an effective decontamination method for *Staphylococcus aureus* [5]. Blue-light therefore shows good potential as a decontamination method for hybrid biomaterials, and its biocompatibility was assessed in this study.

To determine the effect of the blue light exposure on collagen structure, SDS-PAGE analysis was carried out. Its effect on mammalian cell viability was measured by MTT and Neutral Red (NR) microplate assays, reduced glutathione (GSH) and total protein content, and leakage of cytoplasmic lactate dehydrogenase (LDH) activity.

II. Materials and Methods

High intensity blue light source: A grid of 9 narrow-band light-emitting diodes (LED) with peak emissions at 405 nm was used. Although LEDs have minimal heat dissipation, a heatsink was integrated to ensure a stable operating temperature was maintained. The LEDs and heatsink combination were mounted on a PVC housing.

Collagen solution: Type I collagen, derived from rat-tail tendon [6], was used at a concentration of 5.25 mg/ml. It was treated with 10 mW/cm^2 blue-light for 1 hour before the effect on its structure was assessed.

Cell culture: 3T3 cells (mouse fibroblast cell line), in Dulbecco's modified Eagles medium (DMEM) supplemented with 10 % foetal calf serum, were seeded on tissue culture polystyrene at 2x10^4 cells/cm^2 and then incubated for 18-24 hr prior to treatment, unless otherwise stated. For treatment, the medium was removed from the cells and replaced with phosphate buffered saline (PBS). Cells were treated at 1.0 mW/cm^2 for 1 hour. On completion of the treatment, the PBS was replaced with medium. For positive control, cells were incubated in 250 μM H_2O_2 in PBS for 1

Chwee Teck Lim, James C.H. Goh (Eds.): ICBME 2008, Proceedings 23, pp. 1352–1355, 2009
www.springerlink.com

hour, and both positive and negative controls were incubated in the dark.

Sodium dodecyl sulphate polyacrylamide gel electrophoresis (SDS-PAGE) analysis: Gels were prepared and analyzed as previously described [7]

MTT microplate assay: The culture medium was removed from each well, and MTT solution (10 mM in PBS, pH 6.75) added. After 4 hours incubation (37 °C) the MTT solution was removed and the product dissolved in DMSO. Absorbance was read at 540 nm.

Neutral Red (NR) Assay: The culture medium was removed and the NR solution (5mg Neutral Red powder in 100ml PBS) added. After an incubation period of 3 hours (37 °C) the excess NR stain was removed, and intracellular NR dissolved with NR destain until a homogenous color was obtained. Absorbance was read at 540 nm.

Cell growth rate, lactate dehydrogenase (LDH) leakage and GSH content: Growth rate was determined by measuring total protein according to the method of Lowry et al [8]. LDH activity in the medium was measured by the method of Bergemeyer et al [9], and GSH content by the fluormetric method as described by Hissin and Hilf [10].

Statistics: ANOVA followed by Dunnett's test, at the 95% level, was carried out to determine significant difference, where applicable.

III. Results

SDS-PAGE analysis of the collagen gel shows that the light treatment with 10 mW/cm^2 did not appear to have any noticeable effect on the gross structure of the collagen monomer (Fig. 1). The pattern of protein bands and the optical density profiles obtained from treated and untreated collagen is similar (Fig. 2).

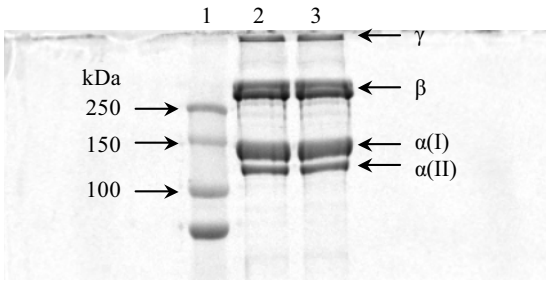


Fig. 1 SDS-PAGE gel; Lanes 1-3 are molecular weight marker, untreated control, and blue-light treated sample, respectively.

The results from MTT and NR show that the blue-light treatment had no significant effect on the viability of the 3T3 cells, compared to the untreated control cells (Fig. 3). The cells treated with H_2O_2 (positive control) showed a 72 % and 78 % decrease in viability from the MTT and NR assays respectively, compared to the untreated cells.

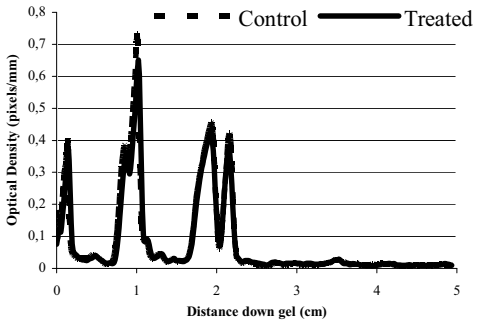


Fig. 2 Optical density profile of the SDS-PAGE gel in Fig. 1

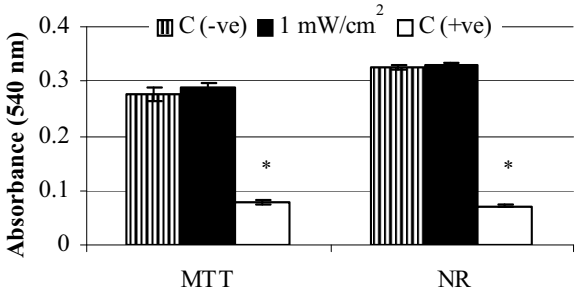


Fig. 3 MTT and NR absorbance for treated and control cells, 24 hours after treatment (n=48, +/- SEM, $p < 0.05$).

The growth rate of the 3T3 cells was assessed by measuring the total protein content of the 3T3 cells, at 24, 48, 72 and 96 hours after treatment. The results showed that the growth rate of the cells appears to be unaffected by the treatment (Fig. 4). Both the control and the treated cells showed a drop in protein content on the fourth day. This drop was due to the cells having reached confluence on the surface of the tissue culture well. Where the cells had been treated with H_2O_2, the total protein measured was significantly less than the untreated cells at all time-points. The protein content at day 1 was similar to that at day 4 for the H_2O_2 treated cells, which shows that the growth rate of the cells had been significantly affected by the treatment.

The LDH leakage into the medium was used to determine the membrane integrity of the 3T3 cells during the post treatment incubation period. Figure 5 shows that LDH leakage from the light treated cells follows the same pattern as the untreated control cells, suggesting that the treatment had no significant effect on the integrity of the cell membrane. The results also show that the media recovered from

the H_2O_2 treated cells had significantly higher levels of LDH leakage, compared to the untreated cultures for the first 3 days, demonstrating that the H_2O_2 treatment had significantly compromised the integrity of the cell membranes.

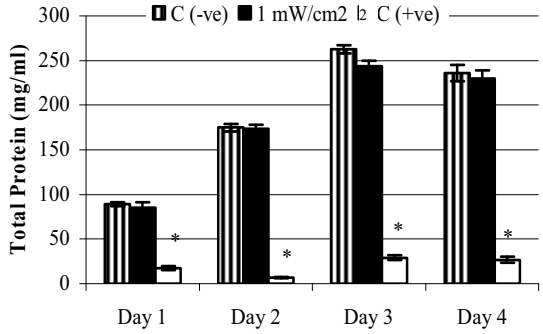


Fig. 4 Total protein content of 3T3 cells (n=4, +/- SEM, $p < 0.05$)

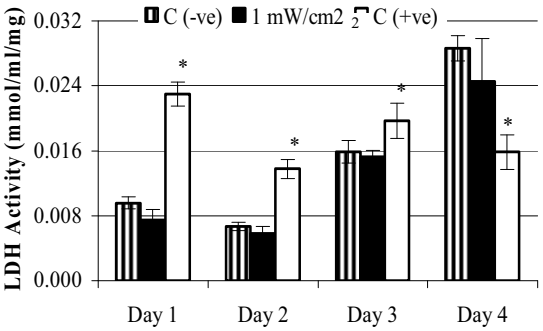


Fig. 5 LDH activity of 3T3 cells (n=4, +/- SEM, $p < 0.05$)

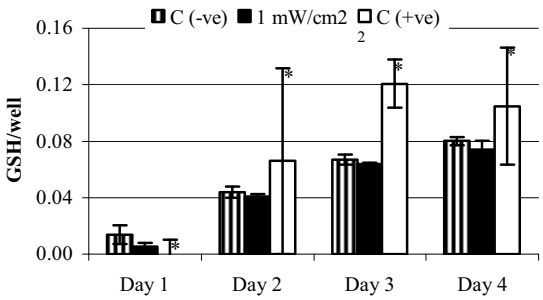


Fig. 6 GSH activity of 3T3 cells (n=4, +/- SEM, $p < 0.05$)

The amount of GSH, a cytoprotective antioxidant that reacts with free radicals and organic peroxides and provides essential redox balance, was measured at each time-point. The results show that with the exception of day 1, where the treated cells show a decreased GSH level, the blue-light treated cells show GSH levels that were not significantly different from those of the untreated (negative) control (Fig. 6). The results for the positive control were very different, showing an almost complete depletion of GSH on day 1, and then increased levels of GSH for the remaining 3 days, when compared with the untreated negative control.

IV. Discussion

Collagen is one of the most widely used biomaterials in tissue engineering and medicine, and can be processed in many forms including sheets, sponges, and injectable solutions [11]. Medical applications include grafts for corneal replacement and shields as corneal bandages in ophthalmology, sponges to promote healing of burns/wounds, subcutaneous injection of soluble collagen for the repair of dermatological defects, and drug loaded inserts (cut from films or as molded rods) for prolonged drug delivery [11,12,13].

It is difficult to sterilize collagen biomaterials without causing detrimental effects. Currently, the most common sterilization methods are gamma irradiation and ethylene oxide treatment. Gamma irradiation, which kills microorganisms by disrupting DNA thus preventing cell division, causes alpha chain fragmentation and/or cross-linking of collagen biomaterials, altering their mechanical properties and degradation rate. Ethylene oxide (EtO) has less of an impact on the physical properties of collagen biomaterials, but is known to cause decreased stability of the collagen molecule triple-helix. It also requires up to 2 weeks post treatment aeration, as the EtO itself is mutagenic and carcinogenic.

It is therefore important to ascertain the impact that blue light treatment has on the collagen monomers. The intensities used in the present study are of the same order as the narrow-band blue light used previously [5] to inactivate *S. aureus*. The results of the SDS-PAGE demonstrate that the blue-light treatment does not cause any noticeable damage to the structure of the individual alpha-chains. This method has previously been used to demonstrate collagen monomer fragmentation as a result of heat degradation [7].

Having established that blue-light treatment offers a potential decontamination method that is compatible with collagen, its impact on the viability of mammalian cells was determined. The incorporation of mammalian cells into novel hybrid biomaterials is an expanding area of regenerative medicine. Compatible sterilisation technologies are being sought to facilitate clinical use of such biomaterials. Broad-band violet-blue light (400-490 nm) has previously been shown to be toxic to mammalian cells, and disrupts cellular processes, such as mitosis, mitochondrial function, and DNA integrity [14].

The purpose of this work was to look at the effects of a narrow-band blue-light (405 nm) on mammalian cell viability and redox state. After treatment at 1.0 $mWcm^2$, the viability of the 3T3 cells was not significantly different to that of the untreated control cells, as ascertained by a combination of the MTT and NR assays. This suggests that blue-light treatment does not have a major effect on the cell viability. This is supported by the results of the LDH assay, which demonstrated that treatment with H_2O_2 significantly compromises the integrity of the 3T3 cell membrane, but blue-light does not appear to have any significant effect.

Treatment with blue light had no significant effect on the GSH levels in the cells, demonstrating that blue-light treatment also does not cause any disturbance to the redox status within the cell. This was an important result as it has previously been reported that violet-blue light toxicity is due to light-induced reactive oxygen species (ROS) generated from excitation of endogenous photosensitizers; the most likely ones being porphyrin ring structures and flavins [14, 15]. Although the results show that blue-light does not disturb the redox state of the cell, it is important to note that it has been suggested that the oxidative stress response may be cell-type-specific [14], and may depend on the energy consumption of the specific cell [16]. GSH is a crucial thiol within cells and is involved in regulation of cell division and function. When cells suffer oxidative stress, they work hard to replenish cellular GSH levels; therefore cell GSH levels may be linked to the cell-specific ability to cope with oxidative stress.

It has previously been suggested that blue light exposure, from dental curing sources, can inhibit cell proliferation [17]. In this present study, cells treated with blue-light had a similar growth rate to that of the untreated control cells for up to 4 days post-treatment, suggesting that the treatment has no effect on cell proliferation. This indicates that blue light could be used to sterilize cell-seeded matrices for tissue regeneration. There is much work yet to be carried out to demonstrate that the technology does not affect cell function or differentiation.

V. Conclusions

Blue-light treatment shows good potential for use as a decontamination method for complex hybrid biomaterials as the results demonstrate its compatibility with both collagen and mammalian cells. This work is being expanded to investigate the limits of the tolerance intensities and durations, and the effect of the blue-light treatment on the decontamination of problematic bacteria, such as *Staphylococcus aureus* and *Staphylococcus epidermidis*, is also being investigated.

Acknowledgments

SS is supported by a studentship from the EPSRC Doctoral Training Centre in Medical Devices. We thank Mrs Katie Henderson for her help with cell culture.

References

1. Oh S, Oh N, Appleford M, et al (2006) Bioceramics for tissue engineering applications – A review. Am J Biochem Biotechnol 2(2):49-56
2. Shearer H, Ellis M, Oerera S, et al (2005) Sterilization of PGLA flat sheet and hollow fibre tissue engineering scaffolds. Eur Cell Mater 10 (Suppl. 2):4
3. Holy C, Cheng C, Davies J, et al (2000) Optimizing the sterilization of PLGA scaffolds for use in tissue engineering. Biomat 22:25-31.
4. Kawada A, Aragane Y, Kameyama H et al (2002) Acne phototherapy with a high-intensity, enhanced, narrowband, blue light source: An open study and in vitro investigation. J Derm Sci 30:129-135
5. Maclean M, MacGregor SJ, Anderson JG, et al (2008) High-intensity narrow-spectrun light inactivation and wavelength sensitivity of *Staphylococcus aureus*. FEMS Microbio Let 285(2): 227-232
6. Elsdale T, Bard J (1972) Collagen substrata for studies on cell behaviour. J Cell Biol 54(3):626-637
7. Smith S, Griffiths S, MacGregor S, et al (2008) Pulsed electric field as a potential new method for microbial inactivation in scaffold materials for tissue engineering: The effects on collagen as a scaffold. J Biomed Mater Res A: Early View (DOI: 10.1002/jbm.a.32150)
8. Lowry O, Rosebrough NJ, Farr AL et al. (1951) Protein measurement with the folin phenol reagent. J Biol Chem 193(1):265-275
9. Bergemeyer HU, Bernt E and Hess B (2003) Lactate dehydrogenase. In Methods of enzymatic analysis, Chemie, Weinhein.
10. Hissin PJ and Hilf R (1976) A fluorimetric method for determination of oxidized and reduced glutathione in tissue. Anal Biochem 74:214-226
11. Freiss W (1998) Collagen – biomaterial for drug delivery. Eur J Pharma Biopharm 45(2): 113-136
12. Lee C, Singla A, Lee Y (2001) Biomedical applications of collagen. Int J Pharm 221(1-2): 1-22
13. Pachence JM (1996) Collagen-based devices for soft tissue repair. J Biomed Mater Res A 33: 35-40
14. Lewis JB, Wataha JC, Messer RLW, et al (2004) Blue light differentially alters cellular redox properties. J Biomed Mater Res A 72B(2):223-229
15. Hockberger PE, Skimina TA, Centonze VE, et al (1999) Activation of flavin-contaning oxidases inderlies light-induced production of H2O2 in mammalian cells. Proc Nat Acad Sci USA 96:6255-6260
16. Wataha JC, Lewis JB, Lockwood PE, et al (2004) Blue light differentially modulates cell survival and growth. J Dent Res 83(2):104-108
17. Taoufik K, Mavrongonatou E, Eliades T, et al (2008) Effects of blue light on the proliferation of human gingival fibroblasts. Dent Mater 24:895-900

Author: Prof. M. Helen Grant
Institute: University of Strathclyde
Street: 106 Rottenrow
City: Glasgow
Country: UK
Email: m.h.grant@strath.ac.uk

Preparation of sericin film with different polymers

Kamol Maikrang, M. Sc.[1], Pornanong Aramwit, Pharm.D., Ph.D.[2]

[1] Department of Materials Science and Engineering, Faculty of Science, Mahidol University, Bangkok, Thailand
[2] Department of Pharmacy, Faculty of Pharmaceutical Sciences, Chulalongkorn University, Bangkok, Thailand

Abstract — **Silk sericin (SS) is a natural protein derived from silkworm *Bombyx mori*. It is applicable as an antioxidant in the field of medicines, cosmetics, foods, and food additive SS protein can be blended with polymers, to produce materials with improved properties. SS films were prepared using different polymers which are polyvinyl alcohol (PVA), polyoxyethylene-polyoxypropylene block copolymer (Plu) and glycerine (G) and fixed concentration of SS (3.0% w/v). The physical properties and some structure characteristics of siricin films were analyzed. The result showed that SS films prepared by cast method containing 3.0 % w/v SS with 2%PVA+1%G, 2%PVA+2%G, 0.2%Plu-F68+1%G, 0.2%Plu+2%G, 2%PVA and 1%G showed good film property from observation. The solubility studies showed that SS was rapidest released from film containing 3%SS+2%PVA which released all SS content within 10 minute whereas other films released all SS content within 1 hour. Humidity-absorption studies of SS film showed that 3%SS+2%PVA+2%G film had the highest moisture absorption rate after incubated in 70-80% humidity environment.**

Keywords — **sericin, silk, polymers**

I. Introduction

In the cocoon shell of silkworm *Bombyx mori* composes of two proteins named fibroin, held together by a gum-like protein called "sericin" (SS). SS is a water-soluble globular protein and its molecular weight ranges from 10 to 310 kDa[1]. SS protein is made of 18 amino acids, especially rich in aspartic acid (~19%) and serine (~32%) [2], which has a high content of the hydroxyl group. SS is applicable as an antioxidant in the field of medicines, cosmetics, foods, and food additive [3]. The protein is also used as a coating material for natural and artificial fibers, which can prevent abrasive skin injuries, the development of rashes and antibacterial for the products such as diapers, diaper liners, and wound dressing [4]. SS is particularly useful for improving polymer materials such as polyesters, polyamide, polyolefin, and polyacrylonitrile. Moreover, it can also be applied to degradable biomaterials, biomedical materials, functional bio-membrane materials and functional fibers [4, 5]. We have blend SS with different polymers and investigated their physical properties.

II. Materials and methods

A. Sericin extrction

The cocoon shells of *Bombyx Mori* were cut into pieces (about $1cm^2$) and then immersed in water in ratio 1:30 by weight. Aqueous SS solutions were extracted with hot water under pressure at 121º C for 1 hour using an autoclave. The solution was then filtrated to remove fibroin and impurities. Finally, the solution was freeze dried by Heto PowerDry LL3000 Freeze Dryer (Thermo electron corporation). SS sample powder was white in color.

B. Preparation of SS film with different polymers.

SS films were prepared using different polymers which are polyvinyl alcohol (PVA), polyoxyethylene-polyoxypropylene block copolymer (Plu) and glycerine (G) and fixed concentration of SS (3.0% w/v). Polymers were heated at 80ºC until they were melted and then 3.0% w/v SS was added. The solutions were poured and casted at room temperature for 1 hour. The SS/polymers were dried at 60ºC for 24 hours in oven.

C. The solubility studies

SS films were immersed in phosphate buffer pH 7.4 and stirred. The samples were then sampling collected at different time points to analyze protein concentration by Pierce® BCA Protein Assay Kit.

D. Humidity-absorption studies

SS films were exposed to water vapor from different salts sush as potassium acetate, potassium carbonate, sodium bromide, sodium chloride and potassium chloride in desiccators. Then, the weight of films were measured at different time point until the weight of films were constant.

III. Results and discussion

A. The solubility studies

Table 1 shows the solubility results of SS films prepared by casting method containing 3.0 % w/v SS with

Chwee Teck Lim, James C.H. Goh (Eds.): ICBME 2008, Proceedings 23, pp. 1356–1358, 2009
www.springerlink.com

2%PVA+1%G, 2%PVA+2%G, 0.2%Plu-F68+1%G, 0.2%Plu+2%G, 2%PVA and 1%G. The solubility studies showed that SS with 2% PVA has the fastest released from film, which released all SS content within 10 minute, as shown in Fig. 1. Other SS films released all SS content within 1 hour.

Table 1 Solubility of SS films

Films	Protein concentration at steady state (μg/ml)
3%SS+2%PVA	3596.96
3%SS+1%G	1807.70
3%SS+0.2%Plu+1%G	1638.04
3%SS+0.2%Plu+2%G	1590.63
3%SS+2%PVA+1%G	1097.30
3%SS+2%PVA+2%G	1074.33

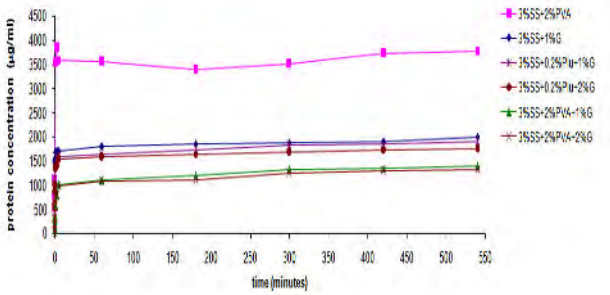


Fig. 1. Solubility of SS films.

The component of 3%SS+2%PVA film had PVA that is a water-soluble synthetic polymer[6]. The water solubility of polyvinyl alcohol films can be regulated and weakly soluble in cold water[7]. It may be dissolved rapidly and released SS much faster compared to other films.

B. Humidity-absorption studies

The reference values of relative humidity of each salt is shown in Table 2 [8]. SS films composed of 3%SS+2%PVA+2%G film had the highest moisture absorption rate after incubated in 70-80% humidity environment, as shown in Fig 2 whereas the weight of SS films in other humidity environment did not change from initiate weight.

Table 2 Relative humidity of salts [8]

Salts	Relative Humidity
Potassium acetate	22.51±0.32
Potassium carbonate	43.16±0.39
Sodium bromide	57.57±0.40
Sodium chloride	75.29±0.12
Potassium chloride	84.34±0.26

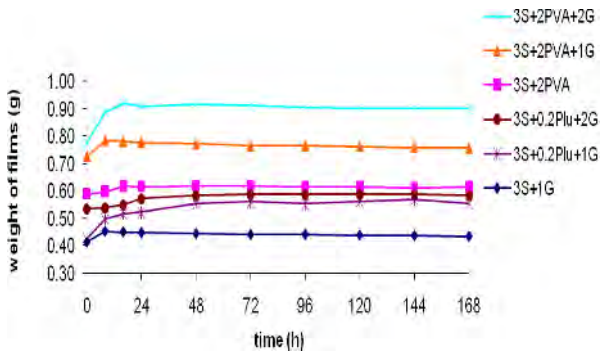


Fig. 2. The weight of SS/polymers films in chamber of potassium chloride.

SS can absorb water [4]. PVA and glycerine are the main components to reinforce the moisture absorbtion of 3%SS+2%PVA+2%G film. The result is similar to previous reports by other researchers that PVA left at high humidity environment could absorb more moisture [6, 7]. Moreover, glycerine can even make the films moisturized.

IV. Conclusions

We study the solubility and humidity-absorbtion properties of SS/polymers film. SS with PVA films show good physical property. SS can be released from film at different rate, depending on type and concentration of polymers.

Acknowledgment

This work was supported by The Thailand Research Fund, Thailand.

REFERENCES

1. Wu, J.-H., Z. Wang, and S.-Y. Xu, *Preparation and characterization of sericin powder extracted from silk industry wastewater.* Food Chemistry, 2007. **103**(4): p. 1255-1262.
2. Cho, K.Y., Moon,J.Y., Lee,Y.W., et al., *Preparation of self-assembled silk sericin nanoparticles.* International Journal of Biological Macromolecules, 2003. **32**(1-2): p. 36-42.
3. Kato, N., Sato,S., Yamanaka,A., et al., *Silk protein, sericin, inhibits lipid peroxidation and tyrosinase activity.* Biosci Biotechnol Biochem, 1998. **62**(1): p. 145-7.
4. Zhang, Y.-Q., *Applications of natural silk protein sericin in biomaterials.* Biotechnology Advances, 2002. **20**(2): p. 91-100.
5. Zhang, Y.-Q., Tao,M.L., Shen,W.D., et al., Immobilization of -asparaginase on the microparticles of the natural silk sericin protein and its characters. Biomaterials, 2004. **25**(17): p. 3751-3759.
6. Mark, J.E., *Polymer Data Handbook*. 1998: Oxford University Press, Inc., p. 890-909.
7. Gooch, J.W., *Encyclopedic Dictionary of Polymers*. 2007, Atlanta, USA: Springer Science+Business Media, LLC., p. 772.
8. Greenspan, L., *Humidity fixed points of binary saturated aqueous solutions*, Journal of research of the National Bureau of Standards. A, Physics and chemistry, 1977. **81a**(1): p. 89-96.

Author: Kamol Maikrang
Institute: Department of Materials Science and Engineering, Faculty of Science, Mahidol University
Street: Rama VI
City: Bangkok
Country: Thailand
Email: MAIKRANG@HOTMAIL.COM

Fabrication and Bio-active Evolution of Mesoporous SiO_2-CaO-P_2O_5 Sol-gel Glasses

L.C. Chiu[1], P.S. Lu[1], I.L. Chang[2*], L.F. Huang[3], C.J. Shih[*1]

[1]Faculty of Fragrance and Cosmetics, Kaohsiung Medical University, Kaohsiung 807, Taiwan
[2]Department of Orthopaedic surgery, Chang-Hua Christian Hospital, Changhua, Taiwan
[3]Faculty of Pharmacy, college of Pharmacy, Kaohsiung Medical University, Kaohsiung 807, Taiwan

Abstract — **In the bio-medical materials category, the bone tissue material is receives people to take. The bone tissue material not only substitutes for the human body skeleton supports (scaffolds), but also stimulates the cell to grow, to paste attaches and to split up. It drives the bone tissue researches from the originally organization replacement to the nowadays organization regeneration.**

Surfactant tri-block copolymer (F127) was used as the structure-directing agent for synthesis of mesoporous SiO_2-CaO-P_2O_5 sol-gel glasses. The specific surface area and crystallite size of mesoporous SiO_2-CaO-P_2O_5 calcined at different temperature were evaluated. The phase structure, N_2 adsorption/desorption isotherm and powder morphology were analyzed by XRD, BET and HRSEM.

The powders with high specific surface area (224.6m^2/g) and pore size of ~5.5 nm mesoporous structure were used as tissue generation materials directly. Basic effects of the nature of the bio-active evolution of these materials were discussed.

Keywords — **bioactive glasses, mesoporous, sol-gel, scaffolds, in vitro test**

I. Introduction

In recent years, mesoporous materials have attracted the attention of many scientists, mainly due to their unique structural properties which have high surface area, pore volume and pore size, with narrow pore diameter distribution. For the reasons, applications in the field of catalysis, inductors, sensors, lasers, carriers, etc. have been proposed and developed.[1-2]

Zhao et al. successfully synthesized highly hexagonally ordered mesoporous bioactive glasses by template with a non-ionic tri-block copolymer, $EO_{20}PO_{70}EO_{20}$ (P123). That made hydroxylcarbonate apatite changed into mesoporous materials which accumulated the enhancement of specific surface areas, promoted the speed of growth and reduced bone tissue has formed the time in the clinical treatment.[3]

In the present study, the mesoporous SiO_2-CaO-P_2O_5 sol-gel glasses powders with high specific surface area (224.6m^2/g) and pore size of ~5.5 nm mesoporous structure were used as tissue generation materials directly. Basic effects of the nature of the bio-active evolution of these materials were discussed.

II. Materials and methods

A. Materials

Calcium nitrate $Ca(NO_3)_2{\cdot}4H_2O$ was purchased from SHOWA, Japan. Triethyl phosphate(TEP) was purchased from Fluka, China. Tetraethyl orthosilicate (TEOS) was purchased from ACROS, U.S.A.

B. Preparation of mesoporous bioactive glasses

In sol-gel synthesis, 4.0g of F127 was dissolved in 60g of ethanol (EtOH). Stock solutions, which were prepared by mixing 1.4g of calcium nitrate $Ca(NO_3)_2{\cdot}4H_2O$, 6.7g of tetraethyl orthosilicate (TEOS), 0.73g of triethyl phosphate(TEP) and 1.0g of HCl (0.5 mol/L), stirred at room temperature for one day, and then were aged at room temperature for 72 h to form sol state. After that, sols dried at 50°C for 24 h. The calcination of the powder sample was conducted in an Al_2O_3 boat in a temperature range of 500–600°C. The temperature was increased at a heating rate of 5°C /min to the preset temperature and held for 5 h. The calcined sample was cooled to room temperature at a rate of 5°C/min. Finally, the calcined powders were obtained.[2][4]

C. Assessment of in vitro bioactivity

The calcined powders were immersed in simulated body fluid (SBF). The chemical composition of SBF was similar to that of human plasma. Afterward, the solution put in shaker under 160 rpm/min for one day and was kept at 37°C. Then, the powders were taken out with filtering, washed three times with acetone, and dried in air for further characterization.[5-6]

III. Results and discussion

The relation between textural and calcined temperature of the synthesized SiO_2-CaO-P_2O_5 powders has been examined earlier by Brunauer-Emmett-Teller (BET) method. The nitrogen adsorption/desorption isotherm of the 500°C, 550°C, 600°C shown in Figure 1. The samples were all identified as typical type IV isotherms with the same hys-

Chwee Teck Lim, James C.H. Goh (Eds.): ICBME 2008, Proceedings 23, pp. 1359–1361, 2009
www.springerlink.com

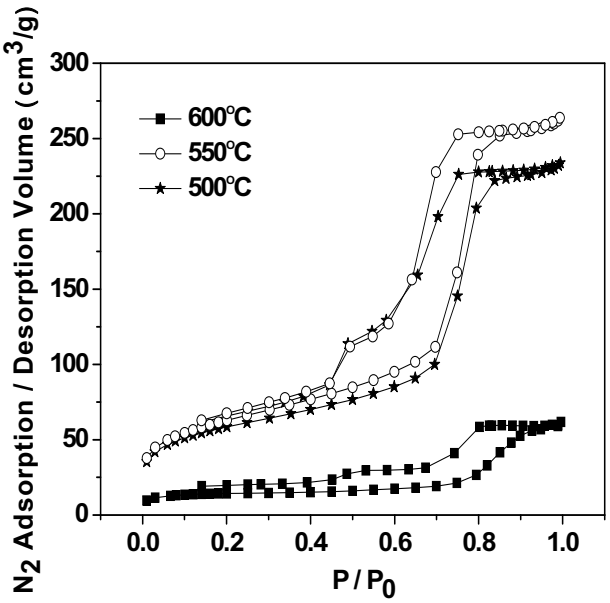


Fig. 1 Nitrogen adsorption/desorption isotherms of the SiO_2-CaO-P_2O_5 precursor powders precipitated at various temperatures for 5h.

teresis loops of H1 type. It reveals that mesoporous structure formed in this temperature range.

To elucidate what is responsible for it, the Textural Properties of Mesoporous SiO_2-CaO-P_2O_5 Sol-gel Glasses are shown in Table 1. It indicate that after calcined at 500°C and 550°C for 5 h, the calcined powders all with high specific area in the range of 208.3~224.6 m^2/g. Further heating of the precursor powders decreased sharp to 49.5 m^2/g. Pore volumes were calculated and illustrated a same trend. After calcined at 500°C and 550°C for 5 h, the calcined powders all with high pore volumes ~0.4g/cm^3. Further heating of the precursor powders decreased sharp to ~0.1g/cm^3. [4][7-8]

Therefore, powder of 500 ^oC and powder of 550^oC both have high BET specific surface area and pore volumes.

The XRD patterns of SiO_2-CaO-P_2O_5 glasses soaking in simulated body fluid (SBF) at various times (a) 0h (b) 24h (c) 48h. It indicates a sharp reflection peak of around 32^O appeared, While the sample after soaking in SBF for 24h, which can be ascribed to (211) and (112) reflections of hydroxylapatite [3][5][7-9].

The in vitro bioactivity of the powder has been investigated by soaking them in simulated body fluid (SBF). HRSEM images of the powder before and after soaking in SBF for 24h are shown in Figure 3a, 3b.

The smooth surface was shown in Figure 3a, after being soaked in SBF for 24h, small stick-liked deposits of about 200nm on the surface of the powders were visible. The small stick-liked deposits were becoming more according to

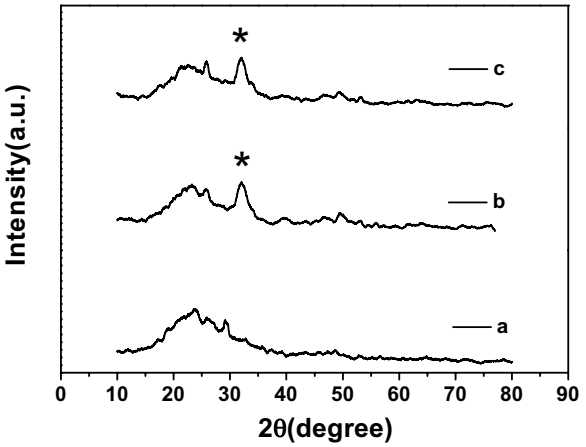


Fig. 2 XRD patterns of SiO_2-CaO-P_2O_5 glasses soaking in simulated body fluid (SBF) at various times (a) 0h (b) 24h (c) 48h.

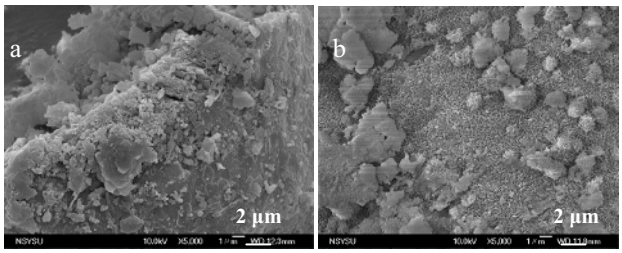


Fig. 3 HRSEM micrographs of SiO_2-CaO-P_2O_5 glasses soaking in simulated body fluid (SBF) at various times (a) 0h (b) 24h.

Table 1 The data list of nitrogen adsorption/desorption isotherms of the SiO_2-CaO-P_2O_5 precursor powders precipitated at various temperatures.

Calcinated Temperature	Specific Surface Area	Pore Volume
500 ^oC	208.3 m^2/g	0.4 cm^3/g
550 ^oC	224.6 m^2/g	0.4 cm^3/g
600 ^oC	49.5 m^2/g	0.1 cm^3/g

the length of soaked time, as also indicated by the wide-angle XRD.[3][6][8]

The nitrogen adsorption/desorption isotherm of SiO_2-CaO-P_2O_5 glasses soaking in simulated body fluid (SBF) at various times, 0h, 4h, 6h, 24h as Fig.4 shown. They were identified as type IV isotherms with the same hysteresis loops of H1 type and means identical in the type of mesopores even after immersing in SBF.

The Textural Properties before and after soaking in SBF for 4 h, 6 h and 24 h shown in table 2. It revealed that BET specific surface area is in the range of 270.2m^2/g ~ 283.4m^2/g and pore volume is in the range of 0.5cm^3/g ~0.6 cm^3/g. There is the same condition of distributed pore size.

They show the length of soaking time do not influence BET specific surface area a lots. For further observation of

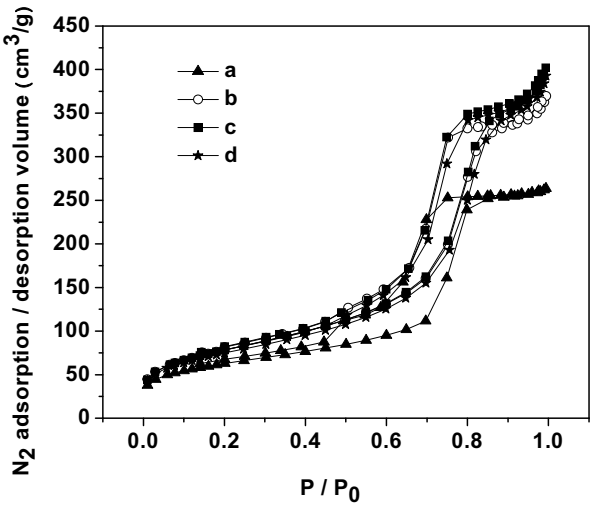


Fig. 4 Nitrogen adsorption/desorption isotherms of SiO_2-CaO-P_2O_5 glasses soaking in simulated body fluid (SBF) at various times (a) 0h (b) 4h (c) 6h (d) 24h.

Table 2 The data list of nitrogen adsorption/desorption isotherms of the SiO_2-CaO-P_2O_5 precursor powders soaking in simulated body fluid (SBF) at various times.

Soaking Time	Specific Surface Area	Pore Volume
0 h	224.6 cm^3/g	0.4 cm^3/g
4 h	282.9 cm^3/g	0.5 cm^3/g
6 h	283.4 cm^3/g	0.6 cm^3/g
24 h	270.2 cm^3/g	0.6 cm^3/g

the microstructure of hydroxylapatite, the HR-SEM micrographs before and after soaking were shown in Fig. 3. The surface of the sintered pellets prior to soaking (a) was smooth, and after soaking for 24h, the surface was covered by nanometric needles.

IV. Conclusions

In the system regulation, calcined temperature is the main factor to affect bioactive glasses (BG) specific surface area , pore volume, pore size. The BG calcined at 550 ^oC own high specific surface area 224.66 cm^3/g, 5.5nm of the pore size, and the pore volume is 0.354 cm^3/g. XRD and FESEM both indicated that the BG powder soaked in simulation body fluid(SBF)for 24h could succeed in the growth of hydroxycarbonate apatite (HA)crystallization.

References

[1] Larry L. Hench, Julia M Polak, Science 295, 1014(2002)
[2] Antonio J. Salinas, Maria Vallet-Regi, Z. Anorg. Allg. Chem. 633, 1762(2007)
[3] Hui-suk Yun, Seung-eon Kim, Yong-teak Hyeon, materials letters 61(2007)4569-4572
[4] X.X. Yan, H.X. Deng, X.H. Huang, G.Q. Lu, S.Z. Qiao, D.Y. Zhao, C.Z. Yu, Journal of Non-Crystalline Solids 351, 3209(2005)
[5] Wei Xia, Jiang Chang, Joural of Controlled Release 110, 522(2006)
[6] Xia Li, Xiupeng Wang, Hangrong Chen, Peng Jiang, Xiaoping Dong, Jianlin Shi, Chem. Mater. 19, 4322(2007)
[7] Hui-suk Yun, Seung-eon Kim, Yong-teak Hyun, Solid State Sciences**(2007)1-10
[8] Jenny Andersson, Sami Areva, Bernd Spliethoff, Mika Linden, Biomaterials 26,6827(2005)
[9] Qihui Shi, Jianfang Wang, Jinping Zhang, Jie Fan, Galen D. Stucky, Adv.Mater. 18, 1038(2006)

The Influences of the Heat-Treated Temperature on Mesoporous Bioactive Gel Glasses Scaffold in the CaO - SiO_2 - P_2O_5 System

P.S. Lu[1], L.C. Chiou[1], I.L. Chang[2,*], C.J. Shih[1,*], L.F. Huang[3]

[1]Faculty of Fragrance and Cosmetics, Kaohsiung Medical University, 100 Shi-Chuan 1st Road, Kaohsiung 807, Taiwan
[2]Department of Orthopaedic surgery, Chang-Hua Christian Hospital, Changhua, Taiwan
[3]Faculty of Pharmacy, College of Pharmacy, Kaohsiung Medical University, 100 Shi-Chuan 1st Road, Kaohsiung 807, Taiwan

Abstract — **Mesoporous bioactive glasses (MBGs) have been successfully synthesized by templating with a block co-polymer.**

The specific surface area and crystallite size of mesoporous bioactive gel glasses scaffold calcined at different temperature are evaluated. The phase structure, N_2 adsorption/desorption isotherm and powder morphology were analyzed by XRD, BET and FE-SEM.

The influences of the heat-treated temperature on pore morphology and specific surface area of the cubic ordered MBGs Scaffold were very important.

High Specific Surface area Mesoporous Bioactive Glasses (MBGs) scaffold successful fabricated by calcined the co-precipitated dry gel at 500°C and dwell 2h. After soaking these MBGs scaffolds in simulated body fluid (SBF) for 24 h, it can be observed that the formation of needle shape hydroxylapatite (HAP) crystal on the surface of the MBG scaffolds.

Keywords — **Calcined Temperature, Scaffold, Mesoporous Bioactive Glasses**

I. Introduction

Current clinical procedures for the repair of bone defects are transplantation or implantation [1]. However, there are some disadvantages of the abilities to self-repair, maintain a blood supply, and modify their structure and properties in response to environmental factors.

Bioactive glasses(BGs) have attracted much attention in recent years because such materials not only chemically bond to and integrate with living bone in the body, but also used in regenerative medicine to restore diseased or damaged bone to its natural state and function[2].

A hierarchical bioactive glass scaffold exhibits enhanced bioactivity and resorbability, due to its macropore (larger than 100μm) and mesoporous texture (pore diameters in the range of 2-50nm) [3]. It raise the adsorption rates of bone tissues due to the advantages of mesopore [4], including high specific surface area, uniform and pore controllability [5]. That would be very helpful to form the bonding with hydroxylapatite, promote to repair and regenerate, and then shorten the recover time [6].

In sol-gel process, the different thermal temperatures lead to changes in the structural and textural properties.

In the present study, mesoporous bioactive gel glasses scaffold have been successfully synthesized in temperature range of 400–700°C. The preparation technique, crystal structure, as well as thermal temperatures behavior of Mesoporous Bioactive Gel Glasses Scaffold have been discussed in detail.

II. Experimental section

A. Prepared of MBGs

The hierarchical bioactive glass scaffolds were synthesized by using nonionic block copolymer $EO_{100}PO_{65}EO_{100}$ (F127) and polyurethane (PUF) as the template. In typical synthesis, a ternary MBGs (CaO - SiO_2 - P_2O_5) were prepared by mixing 4.0g of F127, 6.7g of tetraethyl orthosilicate (TEOS), 1.4g of $Ca(NO_3)_2$. $4H_2O$, 0.73g of triethyl phosphate (TEP), the molar ratio of Si:Ca:P is 80:15:5, and 1.0g of 0.5m HCl were dissolved in 60g of ethanol , then stirred at room temperature for one day. PUF were then immersed into the sol and dried for one day. The same procedure was repeated several times, and then dried at 100°C for 24h. The calcination of precursor scaffold was conducted in an Al_2O_3 boat in a temperature range of 400–800°C and dwell for different times (2 h, 3 h, 5 h, 7 h). The scaffold was obtained as Fig. 1 shown.



Fig. 1 Image of precursor scaffold calcined at 500°C for 3h.

Chwee Teck Lim, James C.H. Goh (Eds.): ICBME 2008, Proceedings 23, pp. 1362–1365, 2009
www.springerlink.com

B. Bioactivity tests

The bioactivity of the scaffold in vitro was tested by immersing the samples in SBF at a solid: liquid ratio of 1 mg/mL at 37°C and 160 rpm for 24h. Afterward, the scaffold washed with acetone, and dried in air for further characterization.

III. Results and Discussion

The samples were identified in Fig.2 as type IV isotherms with the same hysteresis loops of H1 type. The surface area values decrease with temperature in the range of 400°C to 800°C.

To quantify it, we therefore consider the specific surface area of 400°C as 100%. These other specific surface areas were then normalized. Fig. 3 shows normalized surface area of the precursor scaffold calcined at various temperatures for 2h. The specific surface area decreased with calcined temperature, and trends a two-step drop-off. At the calcined temperature below 600°C, the Normallized surface area decreased from 100% to 87%, further heating of the precursor scaffold decreased sharp to 1.3%.

To identify what is responsible, pore volumes were calculated and illustrates a same slow descending trend in the first step. As Table 1 shown, the pore volume decreased only from 0.6 cm^3/g to 0.46cm^3/g. It reveals that that the crystallinity is improved with increasing calcination temperature at this stage.

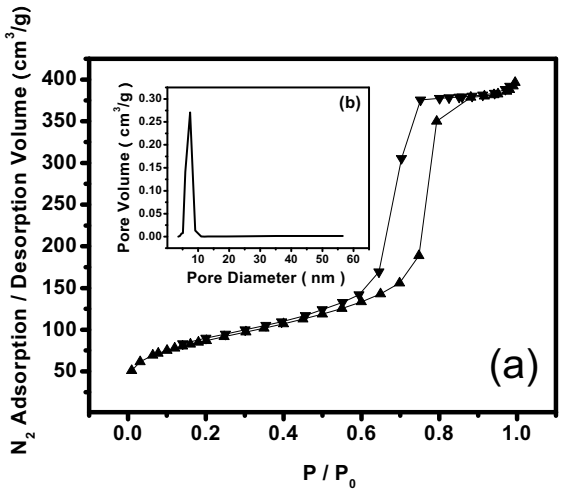


Fig. 2 The typical nitrogen adsorption/desorption isotherms of MBGs.

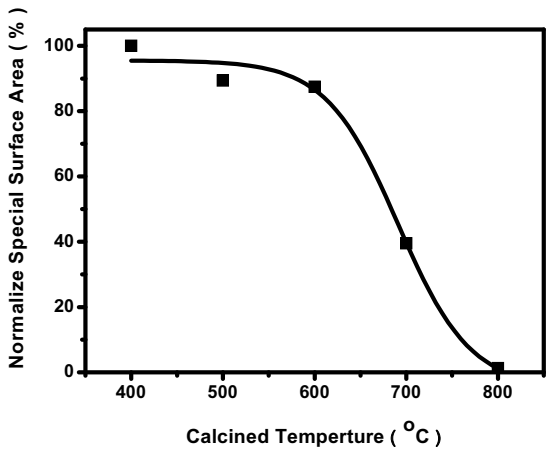


Fig. 3 Normalized surface area of the precursor scaffold calcined at various temperatures for 2h.

Table 1 Textural Properties of mesoporous Bioactive Glasses

Temperature (°C)	Specific Surface Area (cm^2/g)	Pore Volume (cm^3/g)
400	311.4	0.60
500	278.1	0.34
600	272.3	0.46
700	123.1	0.19
800	3.6	0.003

In the second step, the thickness of the pore wall were large enough to fill the pore[7,8]. These results can be proved from the pore volume decreased from 0.46 cm^3/g to 0.003 cm^3/g when calcined temperature increased from 600°C to 800°C.

Considering the high specific surface area and all residual species were removed, used 500°C as heat-treated condition to analyze the textural properties at different dwell time (2 h, 3 h, 5 h,). Regarding the specific surface area of 500°C -2h as 100%, these value were normalized.

Temperature dependence of the time was shown as Fig. 4, illustrating the specific surface area of the MEGs decrease with time.

Moreover, there was the high specific surface area in the dwell for 2h. That would be not only effective to promote cell adhesions and tissue ingrowths, but also shorten the process of preparing bioactive glass materials. For these reasons, dwell for 2h is the best condition.

The specific surface area, pore size and the residual species remove would be considered, the sample under the condition of 500°C -2h, which was measured as the best, was chosen for bioactivity test. The values of textual prosperity (specific surface area, pore size and residual species remove) were 236 cm^3/g, 6.5 nm, 0.46 cm^3/g.

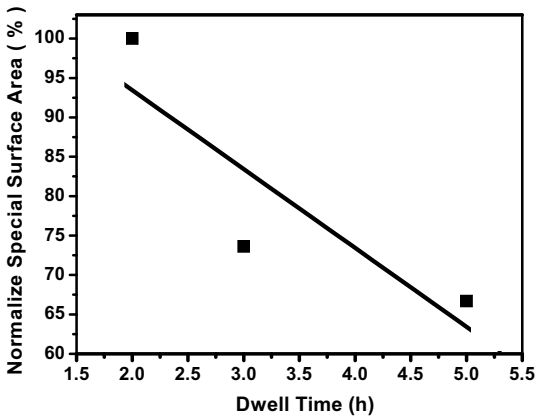


Fig. 4 Normalized surface area of the precursor scaffold calcined at 500°C for different times.

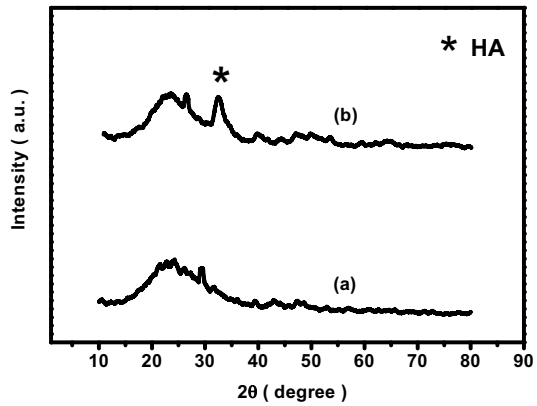


Fig. 5 XRD patterns of MBG_S before (a) and after (b) soaking in SBF for 24h.

Table 2 EDS analysis of scaffold before and after soaking in SBF for 24 h.

Element	Wt%	
	Before soaking	After soaking
Si	21.70	13.06
P	12.93	22.06
Ca	15.87	25.01
O	49.50	39.06
Total	100.00	100.00

The XRD patterns of the bioactive glass scaffold and after soaking in SBF for 24h of sample (b) are shown in Fig. 5.

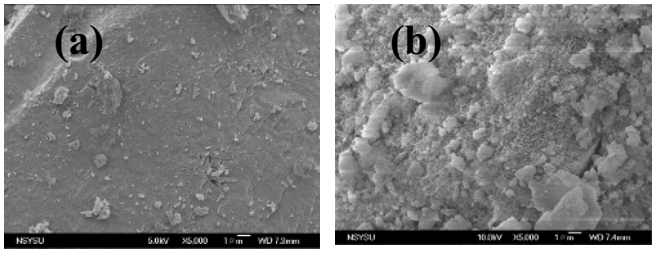


Fig. 6 FE-SEM micrographs of scaffolds before (a) and after (b) soaking in SBF for 24 h.

It indicates a sharp reflection peak of around 32° appeared, While the sample after soaking in SBF for 24h, which can be ascribed to (211) and (112) reflections of hydroxylapatite [9].

The semi-quantitative element had been examined by Scanning Electron Microscope and Energy Dispersive X-Ray Spectrometer (SEM/EDS) shown in Table 1. The variation of nominal composition (Si: Ca: P = 80: 15: 5) of the samples before and after soaking in SBF were measured by weight percentage. After soaking in SBF, Si diminished from 22% to 13%, while Ca and P became predominant, separately raise from 16% to 25% and 13% to 22%. That is, the content after soaking in SBF of MBGs changed, which Ca and P increased but Si decreased, indirectly proved the growths of hydroxylapatite [9].

For further observation of the Microstructure of hydroxylapatite, the FE-SEM micrographs before and after soaking were shown in Fig. 6. The surface of the sintered pellets prior to soaking (a) was smooth, and after soaking for 24h, the surface was covered by nanometric needles. Needle size was in the range of 300 nm.

IV. Conclusions

Mesoporous bioactive gel glasses scaffold have been successfully synthesized in temperature range of 400–700°C. The best bioactive glass scaffolds in ternary CaO - SiO_2 - P_2O_5 system which have both macropores and mesopores is being heat-treated at 500°C for 2h. The specific surface area, pore size, pore volume were 236cm^3/g, 6.5nm, 0.46cm^3/g.

The specific surface area decreased with calcined temperature, and trends a two-step drop-off. At the calcined temperature below 600°C, the Normallized surface area decreased from 100% to 87%, further heating of the precursor scaffold decreased sharp to 1.3%.

The MBGs scaffold after soaking in SBF for 24h can be observed the length ~300nm hydroxylapatite needles.

REFERENCESES

[1] A. J. Salinas and M.Vallet-Regi,Z. Anorg. Allg. Chem., 633, 1762-1773 (2007)
[2] D. Arcos, D.C. Greenspan, and M. Vallet-Regi, Chem. Mater., 14, 1515-1522 (2002)
[3] X. Li, X. Wang, H. Chen, P. Jiang, X. Dong, and J. Shi, Chem. Mater., 19, 4322-4326 (2007)
[4] W. Xia, and J. Chang, J. Control. Release, 110, 522-530 (2006)
[5] A. Lopez-Noriega, D. Arcos, I. Izquierdo-Barba, Y. Sakamoto, O. Terasaki, and M. Vallet-Regi, Chem. Mater., 18, 3137-3144 (2006)
[6] X. Yan, C. Yu, X. Zhou, J. Tang, and D. Zhao, Angew. Chem. Int. Ed., 43, 5980-5984 (2004)
[7] J. R. Jones, L. M. Ehrenfried, L. L. Hench, Biomaterials, 27, 964-973 (2006)
[8] X. X. Yan, H. X. Deng, X. H. Huang, G. Q. Lu, S. Z. Qiao, D. Y. Zhao, and C. Z. Yu, J. non-cryst. solids, 351, 3209-3217 (2005)
[9] A. Rainer, S. M. Giannitelli, F. Abbruzzese, E. Traversa, S. Licoccia, and M. Trombetta, Acta Biomater., 4, 362-369 (2008)

Influence of Surfactant Concentration on Mesoporous Bioactive Glass Scaffolds with Superior in Vitro Bone-Forming Bioactivities

L.F. Huang[1], P.S. Lu[2], L.C. Chiou[2], I.L. Chang[3,*], C.J. Shih[2,*]

[1]Faculty of Pharmacy, College of Pharmacy, Kaohsiung Medical University, 100 Shi-Chuan 1st Road, Kaohsiung 807, Taiwan
[2]Faculty of Fragrance and cosmetics, Kaohsiung Medical University, 100 Shi-Chuan 1st Road, Kaohsiung 807, Taiwan
[3]Department of Orthopaedic surgery, Chang-Hua Christian Hospital, Changhua , Taiwan

Abstract — **Hierarchically 3D porous mesoporous bioactive glasses (MBGs) scaffolds with advantages of both macroporosity and mesoporosity have been successfully synthesized through evaporation-induced self-assembly (EISA) in the presence of a nonionic block copolymer $EO_{100}PO_{65}EO_{100}$ (F127) and polyurethane (PUF) as co-templates.**

Higher pore volume and uniform mesopore sizes are formed when F127 concentration over the critical micelle concentration (CMC).

After soaking these MBGs scaffld in simulated body fluid (SBF) for 4 h, it can be observed that the formation of hydroxyl apatite (HAP) on the surface of the MBG scaffolds.

Keywords — **Critical Micelle Concentration, Mesoporous Bioactive Glass Scaffolds, Bioactivity**

I. Introduction

Recently, mesoporous bioactive glasses have shown to be excellent candidates for biomedical applications. It is well known that mesoporous materials have the attractive feature of large surface area, ordered mesoporous structure, tunable pore size and volume. Due to these properties, mesoporous materials have been expanded into the field of biomaterials science. Increasing the specific surface area and pore volume of BGs is especially important to accelerate the kinetic deposition process of hydroxycarbonate apatite and therefore enhance the bone-forming bioactivity[1]. MBGs with three-dimensional (3D) porous structures provide more advantages than the normal powder or granules, because ideal 3D scaffolds consist of an interconnected macroporous network to allow cell migration, nutrient delivery, bone ingrowth, and eventually vascularization, thereby allowing them to have better in vivo bioactivity[2,3].

The formation of a long-range cubic mesostructure are known largely depends on the concentrations of F127[4]. In this study, we investigated the influence of the concentration of the surfactant on mesoporous bioactive glass scaffolds, and the assessment of in vitro bioactivity of the MBGs scaffolds was carried out in a SBF solution to monitor the formation of hydroxyl apatite (HA) on the surface of the MBG over time.

II. Materials and Methods

A. Preparation of the MBGs scaffolds

In a typical synthesis, different amounts of F127 ($EO_{100}PO_{65}EO_{100}$, BASF) were dissolved in ethanol (EtOH) with HCl solution. Afterward tetraethyl orthosilicate (TEOS, ACROS), $Ca(NO_3)_2{\cdot}4H_2O$ (SHOWA), and triethyl phosphate (TEP, FLUKA; 80:15:5 Si:Ca:P molar ratio) were added and stirred at room temperature for 1 day. Then the polyurethane foam was completely immersed into the sol and compressed in order to force the sol to migrate into all pores; the excess sol was then squeezed out. After 1day of drying, the same procedure was repeated, and then dried the samples at 100°C for 24 h. When the samples were completely dry, they were calcined at 500°C (ramp of 10°C/min) for 5 h. This stage was aimed to decompose and burn out the polyurethane foam support without collapsing the scaffold[7].

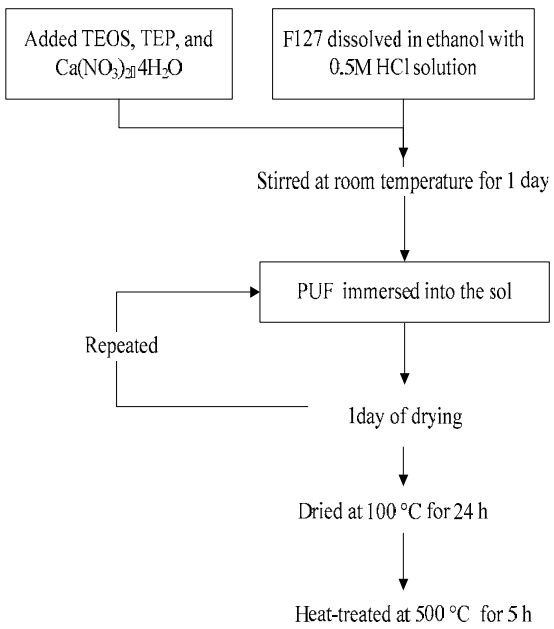


Fig. 1. Process flow chart of MBG materials.

Chwee Teck Lim, James C.H. Goh (Eds.): ICBME 2008, Proceedings 23, pp. 1366–1368, 2009
www.springerlink.com

B. Assessment of in Vitro Bioactivity

The bioactivity of the scaffold in vitro was tested by immersing the scaffold samples with a dimension of 5 × 5 × 5 mm^3 in simulated body fluid (SBF) at a solid:liquid ratio of 1 mg/mL at 37 °C in 160 rpm/min to monitor the formation of hydroxyapatite on the surface of the sample every 0, 4, 6 and 24 h. Afterward, the scaffold was taken out, washed three times with acetone, and dried in air for further characterization.

III. Results and Discussion

A. The influence of the concentration of F127 on mesoporous structure

In this study, it was found that the weight ratio of the triblock copolymer, F127, significantly affects the formation of the mesostructure. Using a low weight ratio of F127 (F127/total solution = 2.1 wt%; the concentration < Critical Micelle Concentration) induces heterogeneous reactions between F127 and the inorganic species, which lead to the inferior pore textural properties (Fig. 2) . As the result, 2.1 wt% F127 has a low specific surface area of 41.46 m^2 g^{-1} and large pore size, which comes from its having large slit-like pores between the particles rather than a mesostructure. Increasing the weight ratio of F127 allows homogeneous reactions to take place between the templates and inorganic species, and subsequently leads to mesostructure formation. The sample with an amount of F127 greater than 5.42 wt% (CMC) finally formed a 3D ordered mesostructure, shows an H2-type hysteresis loop[8]. The specific surface area increases to 262.3 m^2 g^{-1}, but the pore volume is relatively low. A mesostructure with a better and longer range arrangement was formed by increasing the weight ratio of the F127 from 5.42 wt% up to 9.11 wt%. It exhibits a type IV isotherm with a sharp capillary condensation step at high relative pressures and an H1 hysteresis loop in the mesopore range, that is indicative of uniform and homogeneously distributed mesopores. In particular, the mesopore volume of the scaffold with 9.11 wt% F127 was considerably increased about 31.8%.

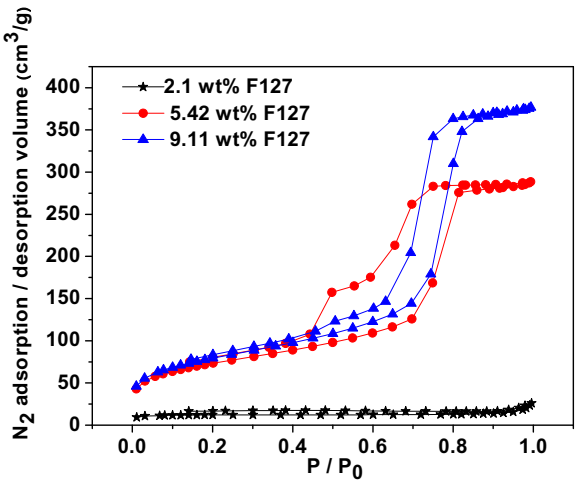


Fig. 2. N_2 adsorption–desorption isotherms of the MBGs scaffolds with different weight ratio of F127

B. In Vitro Bioactivity Tests

It has been accepted that the bioactive characteristic of the scaffold biomaterials is their ability to bond with living bone through the formation of an apatite layer on their surface both in vitro and in vivo. The XRD patterns can be used to evaluate the changes on the scaffold surfaces. Fig.3~5 shows the XRD patterns of the MBGs scaffolds with different weight ratio of F127 after soaking in SBF for

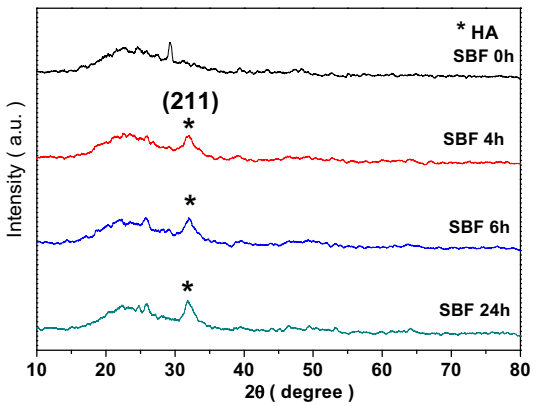


Fig. 3. XRD patterns of the 2.1 wt% F127 MBGs scaffold after soaking in SBF for 0, 4, 6 and 24 h.

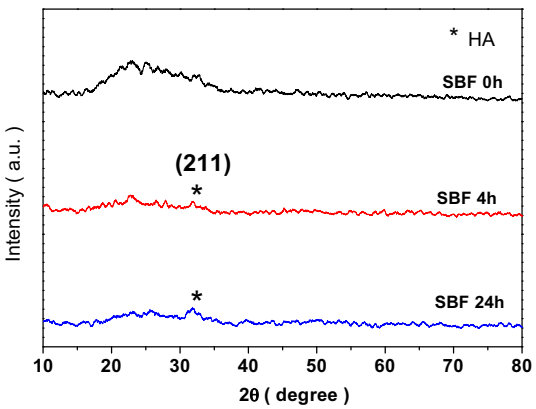


Fig. 4. XRD patterns of the 5.42 wt% F127 MBGs scaffold after soaking in SBF for 0, 4 and 24 h.

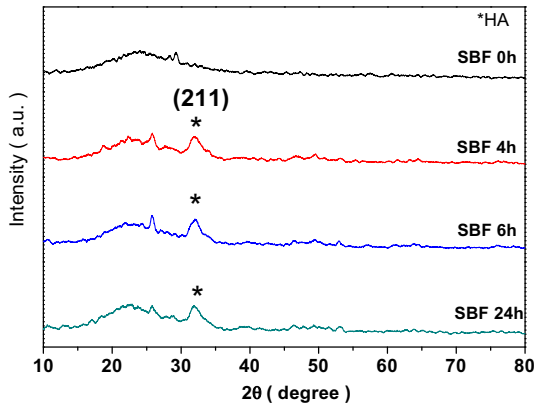


Fig. 5. XRD patterns of the 9.11 wt% F127 MBGs scaffold after soaking in SBF for 0, 4, 6 and 24 h.

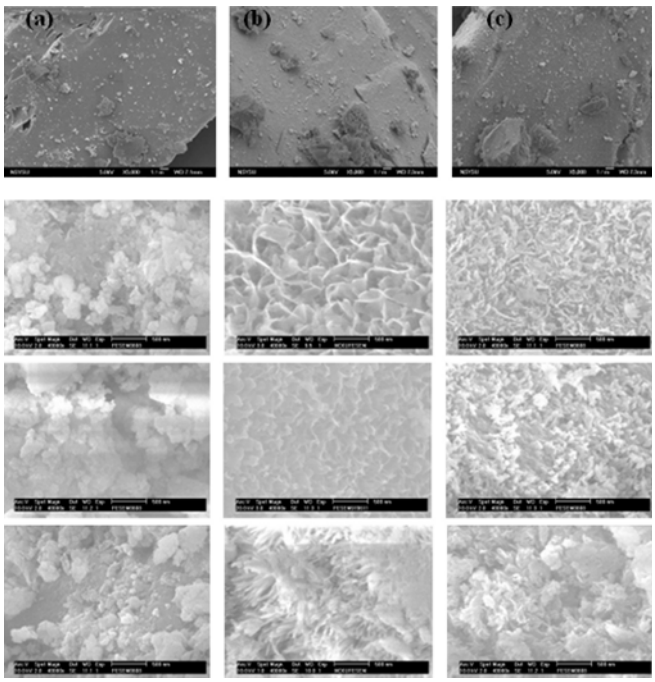


Fig. 6 FE-SEM images of the MBGs scaffolds with different weight ratio of F127 (a) 2.1 wt% (b) 5.42 wt% (c) 9.11 wt% after soaking in SBF for 0, 4, 6, and 24h.

0, 4, 6, 24 h. It can be observed that there are only one broad reflection in the 2θ range of 15-40° before soaking. After soaking these MBGs scaffolds in simulated body fluid (SBF) for 4 h, the XRD patterns show several new diffraction peaks, which are the characteristic peaks of apatite phase[9] (Standard card number: JCPD 24-0033).

Fig. 6 shows the FE-SEM image of the MBGs scaffolds with different weight ratio of F127 after soaking in SBF for 0, 4, 6, 24 h. The scaffolds before soaking show a smooth and homogeneous surface. The FE-SEM image reveals that the surface of the MBG undergoes important changes during the reaction with SBF. The scaffold with 2.1 wt% F127 after soaking for 4 h, although it has no mesostructure but the surface was covered by roundish nanoparticles. And the scaffold with 5.42 wt% F127 after soaking for 4 h, the surface was covered by flower-like deposited layer. The amount of the deposited layer increased with increasing soaking time. When the scaffold with 9.11 wt% F127, it can be observed that a layer composed of needle-shaped crystallites fully covered the surface. Furthermore, the thickness of the needlelike crystallites increase is subsequently observed after 24 h.

IV. Conclusions

(1) When the concentration of F127 is 9.11 wt%, shows an H1 hysteresis loop in the mesopore range with uniform and homogeneously distributed mesopores.

(2) The concentration of F127 and the time of scaffolds soaking in SBF are important factors to influence the morphology of HA in human bones.

(a) When the concentration of F127 is 2.1 wt%, although the scaffold has no mesostructure but the surface was covered by roundish nanoparticles.

(b) The scaffold with 5.42 wt% F127 after soaking for 4 h, the surface was covered by flower-like deposited layer.

(c) The scaffold with 9.11 wt% F127, it can be observed that a layer composed of needle-shaped crystallites fully covered the surface after soaking for 4 h.

References

[1] M. Vallet-Regı ´, C.V. Ragel, A.J. Salinas, Eur. J. Inorg. Chem. (2003) 1029.
[2] X. Yan, C. Yu, X. Zhou, J. Tang, D. Zhao, Angew. Chem., Int. Ed. 43 (2004) 5980.
[3] A. Lo ´pez-Noriega, D. Arcos, I. Izquierdo-Barba, Y. Sakamoto,O. Terasaki, M. Vallet-Regı ´, Chem. Mater. 18 (2006) 3137.
[4] D. Zhao, Q. Huo, J. Feng, B.F. Chmelka, G.D. Stucky, J. Am. Chem. Soc. 120 (1998) 6024.
[5] C. Jeffrey Brinker, Y. Lu, A. Sellinger, and H. Fan, Adv. Mater., 11, 579-585(1999)
[6] S. Angelos, M. L. E. Choi, J. I. Zink, Chem. Eng. J., 137 (2008) 4–13
[7] Y. J. Lee, J. S. Lee, Y. S. Park, and K. B. Yoon, Adv. Mater., 13, (2001)1259-1263
[8] M. Lu. Nanoporous Materials – Science and Engineering, College Press, 317 (2004)
[9] A. Rainer, S. M. Giannitelli, F. Abbruzzese, E. Traversa, S. Licoccia, M. Trombetta, Acta biomater., 4 (2008) 362–369

Human Embryonic Stem Cell-derived Mesenchymal Stem Cells and BMP7 Promote Cartilage Repair

Lin Lin Wang[1], Yi Ying Qi[1], Yang Zi Jiang[1], Xiao Chen[1], Xing Hui Song[1], Xiao Hui Zou[1,4], Hong Wei Ouyang[1,2,3*]

[1]Center for Stem Cell and Tissue Engineering, School of Medicine, Zhejiang University, Hangzhou, China
[2]Institute of Cell Biology, School of Medicine, Zhejiang University, Hangzhou, China
[3]Department of Orthopedic Surgery, Sir Run Run Shaw Hospital, and School of Medicine, Zhejiang University, Hangzhou, China
[4]Zhejiang Women's Hospital, School of Medicine, Zhejiang University, Hangzhou, China

Abstract — **ESCs are pluripotential, but their application for cartilage regenration has not been explored. Our study was designed to explore a strategy of using human embryonic stem cell-derived mesenchymal stem cells(hESC-MSCs) with BMP7 in collagen scaffold to improve the therapeutic efficacy of cartilage defect repair. Full-thickness cartilage defects (diameter=2mm, thickness=2 mm) were made in the patellar grooves of male SD rat and randomly divided into four groups: No treatment group, collagen scaffold group, hESC-MSCs in collagen scaffold group or hESC-MSCs with BMP7 in collagen scaffold group, respectively (n=11 in each group). The rats were sacrificed at 4 and 8 weeks after operation. The repaired tissues were processed for histology and for mechanical test. The histological results showed that the group treated with hESC-MSCs had more amounts of hyaline cartilage, higher ICRS histological scores and Young's modulus of the repaired cartilage tissue. Moreover, hESC-MSCs with BMP7 group had the highest histological scores and Young's modulus of the repaired cartilage tissue. The amounts of hyaline cartilage were significantly higher than those in hESC-MSCs group. Our results demonstrated that hESC-MSCs can improve the regeneration of cartilage tissue. It acts synergistically with BMP7 in stimulating the formation of hyaline cartilage tissues. These findings suggested that the combination of hESC-MSCs with BMP7 in collagen matrix may be used to improve the quality of cartilage repair.**

Keywords — **hESC-MSC, BMP7, collagen scaffold, Cartilage defect**

I. Introduction

Human adult bone marrow mesenchymal stem cells(BMSCs) are known to possess the capability to differentiate into chondrocytes[1], but the availability of tissues for MSCs isolation remains limiting and requires invasive procedures, and expansion of MSCs is finite. Morever, chondrogenic potential of MSCs declines with age and MSCs caused ectopic bone formation[2]. Recently, it is realiazed that ESCs could potentially be an source of consistently uniform MSCs for therapeutic applications. These human ESC-derived MSCs (hESC-MSCs) have similar cell surface markers, differentiation potentials, and immunological properties to adult BMSCs[3]. However, the application of hESC-MSCs for cartilage regenration has not been explored.

In recent years, BMP-7 has become the subject of major research aimed at therapeutic strategies for the treatment of cartilage defects[5] despite that BMP7 have osteoblastic and adipogenic differentiation potential[5]. Interestingly, BMP-7was proved to be a key regulator in the regenerative response to ischemia,which is similar to hypoxia and low serum condition in knee joint. Thus, we speculate that hESC-MSCs combines with BMP7 may promote chondrocyte regeneration.

The present study tested the hypothesis that hESC-MSCs promote the therapeutic efficacy of cartilage defect repair and they act synergistically with BMP7 in stimulating the formation of hyaline cartilage tissues. Therefore, hESC-MSCs with or without BMP7 in collagen scaffold were implanted into defects in a rat model. The quality and resurfacing area of the cartilage repair were investigated.

II. Materials and methods

A. Cell Culture and cell labeling

Human embryonic stem cell (Hues9) derived mesenchymal stem cells were used. hESC-MSCs were cultured in DMEM medium containing 10% fetal calf serum, 100 U/mL penicillin, and 100 mg/mL streptomycin at 37°C in 5% CO_2. 90% confluent cells were digested and incubated with DiI (1μg /mL) at 37°C for 5 minutes. hESC-MSCs labeled with DiI were washed 3 times with Phosphate Buffered Saline (PBS) before loading in collagen scaffolds.

Chwee Teck Lim, James C.H. Goh (Eds.): ICBME 2008, Proceedings 23, pp. 1369–1372, 2009
www.springerlink.com

B. Collagen scaffold fabrication and cell loading

Insoluble type I collagen was isolated and purified from pig Achilles tendon using neutral salt and dilute acid extractions. The diameter was 2 mm and the thickness was 2 mm. DiI- hESC-MSCs (5×10^5) were resuspened in 3 % alginate acid solution with or without human recombninat BMP7 (500ng/ml, R&D system, Inc.USA). And then each scaffold immerged into the suspension and incubated at 37°C in 5% CO_2 for 30 minute. Finally, they were added into 102 mM $CaCl_2$ solution to get the gels for experiment.

C. Animal model

Male SD rats (230-250g) were immunodepressed with cyclophosphamide (150mg/Kg) three days before experiment. A full-thickness cylindrical cartilage defect of 2 mm diameter and 2 mm depth was made in the patellar groove of the bilateral knees using a stainless-steel punch (Figure 1.a). The experiment consisted of the following three treatment groups as in Table 1. hESC-MSCs or hESC-MSCs with BMP7 in scaffold was implanted to the defects (Figure 1.b). The rats were sacrificed at 4 and 8 weeks after transplantation.

Table 1: Design of experimental groups

groups	4 weeks	8 weeks
Group I: Defect with collagen scaffold	n=3	n=8
Group II: Defect with hESC-MSCs in collagen scaffold	n=3	n=8
Group III: Defect with hESC-MSC and hBMP7 in collagen scaffold	n=3	n=8

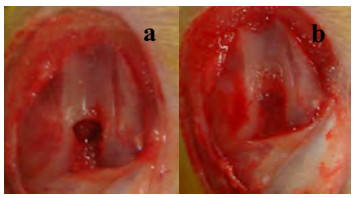


Fig. 1. Macroscopic photograph showing a full-thickness cartilage defect of 2 mm diameter in a patellar groove(a). The defect was covered with the scaffold (b)

D. Gross morphology and histology

At 4 and 8 weeks post-surgery, the rats were sacrificed by intravenous overdose of pentobarbital. Three harvested samples of each group were examined and photographed for evaluation. After gross examination, the survival of the transplanted hESC-MSCs was demonstrated by the presence of fluorescence from DiI-labeled cells (KODAK Image Station In-Vivo FX.USA). Samples were fixed in 4% formalin, decalcified in 10% formic acid, then embedded in paraffin and cut to 5μm thick sections. Sections were stained with Hematoxylin and Eosin (H&E) for the study of morphological evaluation. For the overall evaluation of the regenerated tissue in the defects, the repaired tissues were graded using the International Cartilage Repair Society (ICRS) Visual Histological Assessment Scale[6] by one blinded observer.

E. Mechanical evaluation

Compressive mechanical properties of the cartilage layer following long-term (8 weeks, n=5 samples) period in vivo were determined using a 1 mm diameter cylindrical-shaped indenter to compressively load the cartilage tissue in Instron Testing machine (model 5543, Instron, Canton, MA) fitted with a 10 N maximum load cell. The ratio of equilibrium force to cross-sectional area was divided by the applied strain to calculate the equilibrium modulus (in MPa).

F. Statistical analysis

Histological scoring data and biomechanical test data were assessed for statistical differences using a paired t-test to compare experimental characteristics to control.

III. Results

A. Gross morphology

The gross examinations of knee joints showed that there were no abrasions on the opposing articulating surfaces and no inflammation at both 4 and 8 weeks time point. The defects remained empty in small parts at 4 weeks after transplantation (Fig.2). Red fluorescence in the defect areas are clearly photographed in all of the 4-week samples and in most of the 8-week samples (Fig.2g). The posibility in 8-week samples is about 3/4.

B. Histological examination

At 4 weeks after transplantation, the defects in group I (n=3) were filled with fibrous tissue (Fig. 3a). In the group II (n=3) and group III (n=3), the defects were repaired with the mixture of fibrous tissue and cartilage-like tissue as shown by H&E staining. The amounts of chondrocyte-like cells and cartilage-like extracellular matrix in the group III were more than those of group II by means of H&E staining (Fig. 3b,3c). At 8 weeks after transplantation, the defects in group I (n=3) were almost filled with fibrous tissue and a little cartilage-like tissue at the margins of the defects

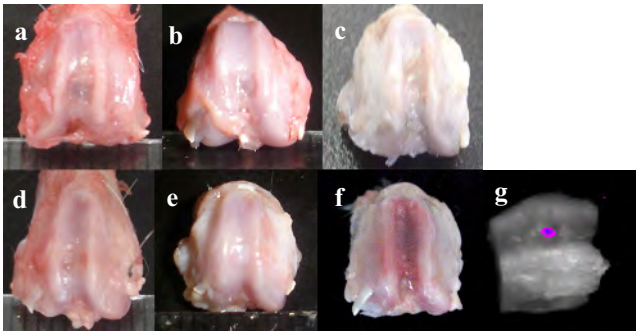


Fig. 2. Macrophotograph shows that the defects in the three groups at 4 weeks (a, b, c) and 8 weeks (d, e, f) post-surgery. a, d group I; b, e group II; c, f. group III. G. Red area indicates the fluorescence in the defect areas in 8-week sample.

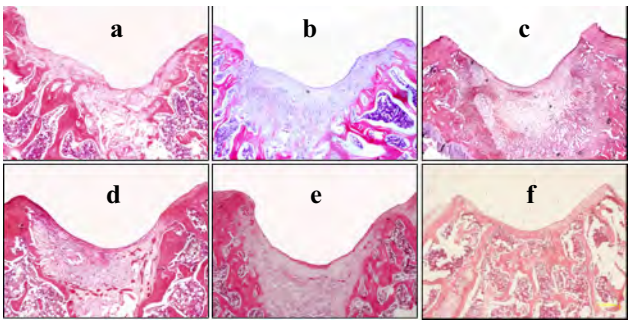


Fig. 3. Histological examination of the three groups at 4 weeks (a,b,c) and 8 weeks (d,e,f) post-surgery. a, b. Group I; b, e. Group II; c, f. Group III.

(Fig. 3d). Group II had lager amounts of hyaline cartilage (Fig. 3e). The group III has the most amounts of hyaline cartilage tissue (Fig. 3f). It was found that hyaline cartilage tissues were formed at the surrounding area of the defects while the fibrous tissues were located at the central part of defects.

The total ICRS histological scores of the specimens at 8 weeks revealed differences between the three groups (Table 2).The scores for the repaired tissue of group III were significantly higher than those for other two groups (#p < 0.05).

Table 2: Comparison of the total ICRS histological scores (Total scores are 18 points)

groups	ICRS histological scores
Group I	5.52±1.15
Group II	9.17±1.34
Group III	11.12±0.32

C. Biomechanical evaluation

Biomechanical analysis of the repaired tissues at 8 weeks post-surgery (n = 5 in all groups). At 8 weeks post-surgery, as shown in Table 3, the compressive modulus of the repaired tissue in group II and group III samples showed greater improvement compared with specimens from group I (**p<0.01). The compressive modulus in group III showed significant higher than that in specimens from group II (*p<0.05).

Table 3: Summary of biomechanical evaluation

groups	Young’s modulus (MPa)
Group I	0.0397±0.0087
Group II	0.0528±0.0072
Group III	0.0634±0.0072

IV. Discussion

The present study demonstrated that hESC-MSCs can existed in the defect area at least 8 weeks as evidenced by tracing the red Dil labed hESC-MSCs (Fig.2g). hESC-MSCs improved the regeneration of cartilage tissue in vivo model. The histological results showed that the group treated with hESC-MSCs had more amounts of hyaline cartilage, higher ICRS histological scores. More importantly, the Young's modulus in group II increased to 0.0528±0.0072 Mpa at 8 weeks, which was significantly higher than 0.0397±0.0087 Mpa in group I. These findings suggested that hESC-MSCs can be one of the seed cells for cartilage tissue engineering.

Although it is not clear about the detail mechanism, the improvement effects could be explained by possibility of the chondrogenesis of hESC-MSCs. The local environment in the defect area may facilitate chondrogenic differentiation in hESC-MSCs, such as hypoxia[7] and the change of the cartilage matrix[8].

Nevertheless, recent reports have suggested that the reparative effects associated with MSC transplantation are not mediated by direct differentiation of MSCs but by paracrine factors secreted by MSCs. hESC-MSCs may secrete a variety of cytokines, which inhibit apoptosis in hypoxia and low serum condition of knee joints, enhance differentiation of stem cells or cartilage-intrinsic reparative.

In present study, BMP7 and hESC-MSCs acted synergistically. BMP7 significantly improved the efficacy of hESC-MSCs in promoting the formation of hyaline cartilage tissues as shown in Fig. 2 and Fig.3. Combination of BMP7

with hESC-MSCs in collagen matrix also increased the function of cartilage as evidenced by the elevation of Young's modulus (0.0634±0.0072Mpa), which was the highest level among these three groups. Thus, we demonstrated that BMP7 with hESC-MSCs promote new hyaline-like cartilage formation in vivo. This finding is consisted with the report in MSCs [9].

BMP7 has positive influence on the cartilage matrix environment, which is reported to regulate the chondrogenic differentiation[10]. BMP7 increases the synthesis of aggrecan , type II collagen, proteoglycan, hyaluronan synthase-2 and hyaluronan production[11]. However, the detail relationship between BMP7 and hESC-MSCs are not clear. For example, whether BMP7 has direct effect on hESC-MSCs or not? Further studies are needed to focus on the mechanism of hESC-MSCs and BMP7, including the relationship between them.

In this experiment, the degradable alginate gel was designed to contain hESC-MSCs and BMP7 in the defect areas to prevent the loss of implanted cells and cytokine. Moreover, the use of degradable alginate gel loaded with BMP-7 in collagen scoffold might offer the advantage of a better distribution and a prolonged delivery of BMP7 within the tissueengineered site and consequently an enhanced effect both on the differentiation of hESC-MSCs and on the metabolism of the host's chondrocytes, by which promote the repair of cartilage defect.

V. Conclusions

This study demonstrated that hESC-MSCs can improve the regeneration of cartilage tissue. The combination of hESC-MSCs with BMP7 in collagen scaffold may have greater potential to repair larger cartilage defects. But the underlying mechanism are remained to be elucidated.

References

1. Lisignoli G, Cristino S, Piacentini A, et al. (2005) Cellular and molecular events during chondrogenesis of human mesenchymal stromal cells grown in a three-dimensional hyaluronan based scaffold. Biomaterials 26: 5677-5686.
2. Harris MT, Butler DL, Boivin GP, et al. (2004) Mesenchymal stem cells used for rabbit tendon repair can form ectopic bone and express alkaline phosphatase activity in constructs. J Orthop Res 22: 998-1003.
3. Trivedi P, Hematti P (2008) Derivation and immunological characterization of mesenchymal stromal cells from human embryonic stem cells. Exp Hematol 36: 350-359.
4. Chubinskaya S, Hurtig M, Rueger DC (2007) OP-1/BMP-7 in cartilage repair. Int Orthop 31: 773-781.
5. Neumann K, Endres M, Ringe J, et al. (2007) BMP7 promotes adipogenic but not osteo-/chondrogenic differentiation of adult human bone marrow-derived stem cells in high-density micro-mass culture. J Cell Biochem 102: 626-637.
6. Mainil-Varlet P, Aigner T, Brittberg M, et al. (2003) Histological assessment of cartilage repair: a report by the Histology Endpoint Committee of the International Cartilage Repair Society (ICRS). J Bone Joint Surg Am 85-A Suppl 2: 45-57.
7. Khan WS, Adesida AB, Hardingham TE (2007) Hypoxic conditions increase hypoxia-inducible transcription factor 2alpha and enhance chondrogenesis in stem cells from the infrapatellar fat pad of osteoarthritis patients. Arthritis Res Ther 9: R55.
8. Gotting C, Prante C, Kuhn J, et al. (2007) Proteoglycan biosynthesis during chondrogenic differentiation of mesenchymal stem cells. ScientificWorldJournal 7: 1207-1210.
9. Cook SD, Patron LP, Salkeld SL, et al. (2003) Repair of articular cartilage defects with osteogenic protein-1 (BMP-7) in dogs. J Bone Joint Surg Am 85-A Suppl 3: 116-123.
10. Vats A, Bielby RC, Tolley N, et al. (2006) Chondrogenic differentiation of human embryonic stem cells: the effect of the microenvironment. Tissue Eng 12: 1687-1697.
11. Nishida Y, Knudson CB, Eger W, et al. (2000) Osteogenic protein 1 stimulates cells-associated matrix assembly by normal human articular chondrocytes: up-regulation of hyaluronan synthase, CD44, and aggrecan. Arthritis Rheum 43: 206-214.

*corresponding Author: Hongwei Ouyang
Institute: Center for Stem Cell and Tissue Engineering,
School of Medicine, Zhejiang University
Street: 388 Yu Hang Tang Road
City: Hangzhou
Country: China
Email: hwoy@zju.edu.cn

Novel Composite Membrane Guides Cortical Bone Regeneration

You Zhi Cai[1], Yi Ying Qi[1], Hong Xin Cai[1], Xiao Hui Zou[1,4], Lin Lin Wang[1], Hong Wei Ouyang[1,2,3] *

[1]Center for Stem Cell and Tissue Engineering, School of Medicine, Zhejiang University, Hangzhou, China
[2]Institute of Cell Biology, School of Medicine, Zhejiang University, Hangzhou, China
[3]Department of Orthopedic Surgery, Sir Run Run Shaw Hospital, and School of Medicine, Zhejiang University, Hangzhou, China
[4]Zhejiang Women's Hospital, School of Medicine, Zhejiang University, Hangzhou, China

Abstract — **Current treatment options for restoring large bony defects due to trauma or tumor ablation are limited by the host bone tissue availability and donor site morbidity of bone implantation. Creation of implantable functional bone tissue that could restore bony defects may be a possible solution. Previously, many *in vitro* studies have indicated the potential of using electrospun nanofibrous scaffolds for tissue repair. However, few studies demonstrated their utility in tissue repair models. We hypothesized that the electrospun nanofibrous membrane improves the efficacy of currently-used collagenous guided bone regeneration (GBR) membrane in repairing large cortical bony defect. A practical biodegradable nanofibrous poly-L-lactic-acid (PLLA) membrane honeycombed with one layer of collagen matrix was developed. Bone defect with 10 × 15 mm^2 area was covered by nanofiber-reinforced bi-layer membrane or collagenous membrane. 3 and 6 weeks after operation, bone defect healing was assessed radiologically and histologically. The radiolographic data showed that the group treated with nanofiber-reinforced bi-layer membrane had more bony tissue formation at 3 weeks. The histology results were consistent with that of radiographic findings at 3 weeks. Moreover, the defects treated with bi-layer membrane were repaired perfectly by dense cortical bone at 6 weeks, while whose treated with collagenous membrane were filled with spongy bone and fibrous tissues. The results demonstrated that electrospun nanofibrous membrane can be combined with collagenous GBR membrane to improve guided bone regeneration technology. And this type of membrane may provide implantable functional bone tissues for patients with large bone defects.**

Keywords — **Tissue engineering, Electrospun nanofiber, Guided bone regeneration, Bone defect**

I. Introduction

Guided bone regeneration (GBR) is a standard procedure to protect a tissue defect from the ingrowth of surrounding fibrous tissue. Biodegradable GBR membranes, such as collagen and synthetic biodegradable polymers, have been developed [1]. Among these, collagen-based membranes have been well-accepted by clinicians [2-4]. However, although the excellent biodegradability and biocompatibility of collagenous membrane has been demonstrated *in vitro* [5], the same positive results have not been evident *in vivo* [6]. Collagenous membrane is mechanically weak, making it difficult to shield a bone defect efficiently. In addition, the rapid degradation time does not match with that of the bone-healing process. So, further investigations are needed to overcome these disadvantages.

In recent years, electrospinning technology has been used to produce nanofibrous scaffolds, which are superior in surface area, mechanical strength, and biomimetic properties. Numerous studies have shown that nanofibrous architecture is beneficial to the proliferation and differentiation of cells [7-8]. These special properties may be utilized to overcome the disadvantages of the collagenous GBR membrane.

The present study tested the hypothesis that electrospun nanofibrous membrane improves the efficacy of currently-used collagenous GBR membrane for large bony defect repair. Therefore, a novel degradable bi-layer guided bone regeneration (GBR) membrane consisting of an electrospun nanofibrous membrane and a collagenous membrane was designed for bone defect repair, with the aim of developing a more efficient GBR membrane.

II. Materials and methods

A. Fabrication of the membranes

Nanofibrous poly-L-lactic acid (PLLA) fibers were fabricated by electrospinning [9]. All electrospun fibrous membranes were stored in desiccators for several days before use. Collagen was extracted and purified from tendons [10]. The solution was then dialysed, frozen and freeze-dried to obtain the collagen. The collagen was dissolved again in 10 mg/ml 0.5 M HAc and placed onto the nano-PLLA membrane. The composite was freeze-dried and treated at 110°C under vacuum for 48 h to cross-link the collagen matrix. Consequently, a bi-layer membrane was produced (Fig. 1a). Collagenous membrane, as a control, was also produced using the same procedure without the nanofibrous membrane. The properties of 12 specimens (6 PLLA and 6 collagenous membranes) were characterized using a mechanical testing machine (Instron 5530, USA) and scanning electron microscopy (SEM).

Chwee Teck Lim, James C.H. Goh (Eds.): ICBME 2008, Proceedings 23, pp. 1373–1376, 2009
www.springerlink.com

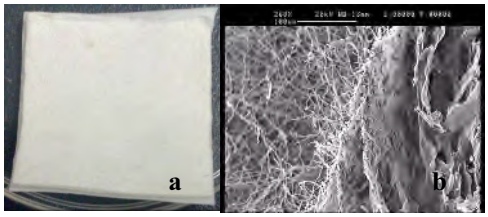


Fig. 1. (a) Optical image of bi-layer membrane. (b)The SEM image of the bi-layer membrane (side view).

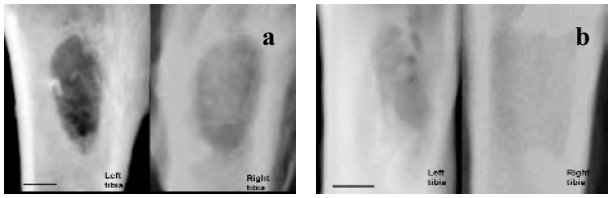


Fig.2. Radiographs Obtained at 3 weeks(a) and 6 weeks (b). (bar = 0.5cm).

B. In vivo studies

Eight adult male NZW rabbits weighing 2.59 ± 0.35 kg were randomly divided into two groups of 4, and anesthetized before surgery. A defect 10 mm wide and 15 mm long in the anteromedial cortex of the proximal tibia, starting 5 mm below the joint line, was created using a micro-burr and saline irrigation to minimize thermal damage. With this method, bilateral defects were created, and collagenous membrane (control group), or the bi-layer membrane (experimental group) of 10 × 15 mm^2 was placed into left or right defect respectively. The incision was then closed. Four animals were sacrificed at 3 and 6 weeks respectively. The region surrounding the implant was harvested and processed for X-ray evaluation and histological analysis.

C. Bone score

The degree of new bone formation during the healing period was estimated from the sections, using a semiquantitative score from 0 to 4. The score values were defined as follows: 1 = few and isolated centers of ossification; 2 = more, but still discontinuous new bone formation; 3 = beginning, but incomplete bridging of the defect. The scores were added to estimate the overall bone formation in the defect at a given time.

III. Results

A. Physical properties of bi-layer membrane and collagenous membrane

SEM examination of the bi-layer membrane (Fig. 1b) revealed excellent integration of the two layers, without any PLLA nano-fibers melting on the collagen scaffold. The elastic modulus of PLLA was 83.55 ± 18.82 MPa, while that of collagen was 1.68 ± 0.30 MPa.

B. X-ray evaluation

At 3 weeks, new bone formation was detected in the experimental and control groups. But in the control group, the medial region of the defect contained little mineralized bone, which was only seen at the margin of the defect (Fig. 2a). No radiographic differences were detected in the defects filled with collagenous membrane alone or bi-layer membrane at 6 weeks (Fig. 2b).

C. Histological assessment

No infiltration of multinucleated cells was found at 3 or 6 weeks. The location of the defect was easily recognizable by the degraded membrane (Fig. 3).

At 3 weeks in the experimental group, nano-fibers were seen to guide a layer of newly formed bone as a bridge over the defect. New bone formation was observed around the periphery of the defect, and intense remodeling was seen in the adjoining cortical bone. But in the control group at 3 weeks, the defect was filled with a few islands of newly-formed bone dispersed among a mass of fibrous connective tissue, and no bone bridges over the defect were found.

At 6 weeks, only the bi-layer membrane-treated bone defects displayed nearly complete regeneration of cortical bone tissue with a physical contour. The newly-formed bone tightly contacted the residual nanofibrous membrane. In the control group, the quantity of newly-formed bone increased greatly with time. However, this new bone was disorganized and appeared to be spongy rather than cortical bone. Moreover, the contour of the tibial defect was not restored, due to the evident invasion of fibrous tissue.

D. Bone score

Table 1 summarizes the results of bone score evaluation. New bone formation in the bi-layer membrane group was significantly greater than that in the collagenous membrane control at 3 weeks ($p<0.01$). At 6 weeks, defect closure was

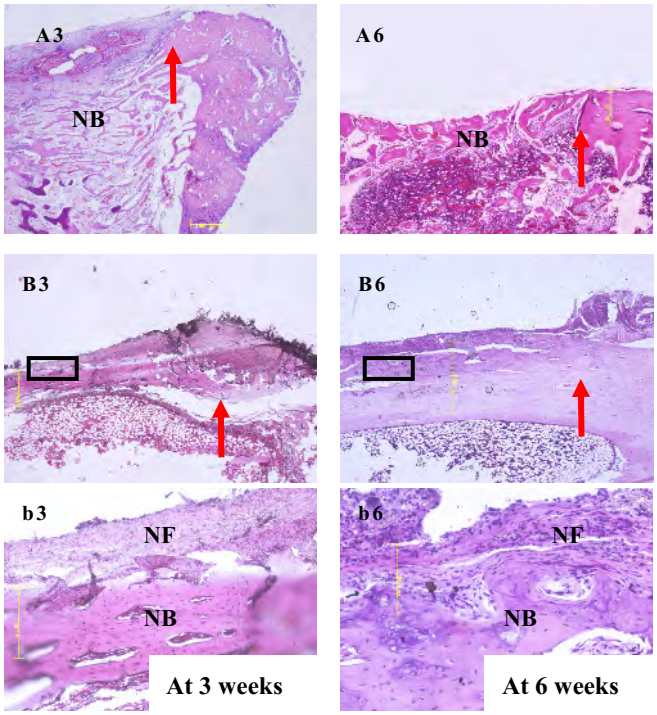


Fig.3. Representative photomicrographs of defect sites. (A = Control group; B = Experimental group; red arrowhead = defect margin; NB = newly formed bone; NF = nanofibers; H–E stain; original magnification: 40x (A3, 6 and B3, 6), 400x (b3 and b6).

significantly greater in the bilayer membrane group than in the collagenous membrane control ($p<0.01$).

Table 1: Summary of bone score evaluation

groups	3 weeks	6 weeks
Bi-layer membrane	3.60±0.58	3.65±0.50
Collagen membrane	1.78±0.50	2.55±0.58

IV. Discussion

The present study describes a novel bi-layer nano/micro-porous GBR membrane in which a pliable and substantially cell-impermeable nanofibrous membrane was honeycombed with cell-permeable collagenous membrane. The bi-layer GTR membrane allowed physical cortical bone formation with normal contour in a rabbit model. This is the first demonstration that nanofibrous membrane improves the efficacy of collagenous GBR membrane in creating a satisfactory biological environment for accelerating new bone growth at a large bone defect. Moreover, it is worth emphasizing that the bi-layer GBR membrane led to cortical bone formation rather than the spongy bone found in collagenous GBR membrane-treated defects. These results are of considerable interest for improving current GBR technology.

Some studies have demonstrated nanofiber-induced bone tissue growth *in vitro* when seeded with bone cells or stem cells [11-13]. However, little is known about the effects of nano/micro-porous bi-layer membrane on bone wound healing in animal models. By *X-ray evaluation* and histological analysis, the ratio of new bone formation increased in the control group and became comparable to that of the bi-layer membrane group at 6 weeks. This can be explained by the fact that there was a great deal of new bone formation in the first 3 weeks, but subsequently bone remodeling rather than bone formation became the major repair process in the bi-layer membrane group. This indicates that bi-layer membrane improved the quantity of new bone tissue at early stages, and the quality of bone repair at later stages.

Collagen has relatively poor mechanical strength and is rapidly degraded. The early absorption of membrane results in reduced bone formation and incomplete bone filling [14]. The bi-layer GBR membrane had good biomechanics and a relatively slow degradation rate, providing enough space to selectively guide cells in growth, and acting as a periosteum-like scaffold.

In the present study, resorption and distortion of the nanofiber membranes were seen 3 weeks after they were grafted onto the tibia defects. Previous data has indicated that biodegradation through hydrolysis can have adverse effects [15-16]. But this bi-layer membrane did not elicit a severe local or systemic inflammatory response *in vivo*. One of the reasons may be due to its specific characteristics, including the rate of degradation, the large surface area, and the surface chemistry. Another may be due to the composite of collagen and PLLA in the bi-layer GBR membrane, which only contained a few micrograms of PLLA polymer.

In order to study the efficiency of this bi-layer GBR membrane for relatively large bone defect healing, we created the full-thickness defect (10x15 mm^2) in the proximal tibia. It is bigger than those critical defects of 5mm wide and 15 mm long reported by previous studies [17-18]. In our pilot study, it was found that the defect can not be even bigger without fractures.

Further studies are needed to investigate more intelligent, functionally degradable multi-layer GBR membranes. Moreover, nano-PLLA/micro-collagenous membranes incorporating osteoinductive factors are yet to be investigated.

V. Conclusions

This study demonstrated that the nanofiber-reinforced bi-layer membrane repaired a large tibial bone defect with physical cortical bone tissue and normal contour. Therefore, this type of membrane might be able to act as a novel GBR membrane, and provide implantable functional bone tissues for patients with large bone defects.

Acknowledgment

This work was supported by China NSF grants (30600301, U0672001) and ZheJiang Province grants (2006C13084, 2006C14024, R206016).

References

1. Imbronito AV, Todescan JH, Carvalho CV, Arana-Chavez VE. (2002) Healing of alveolar bone in resorbable and non-resorbable membrane-protected defects. A histologic pilot study in dogs. Biomaterials 23:4079-4086.
2. Mattson JS, McLey LL, Jabro MH. (1995) Treatment of intrabony defects with collagen membrane barriers. Case reports. J Periodontol 66:635-645.
3. Hammerle CH, Lang NP. (2001) Single stage surgery combining transmucosal implant placement with guided bone regeneration and bioresorbable materials. Clin Oral Implants Res 12:9-18.
4. Brunel G, Brocard D, Duffort JF, Jacquet E, Justumus P, Simonet T, Benque E. (2001) Bioabsorbable materials for guided bone regeneration prior to implant placement and 7-year follow-up: report of 14 cases. J Periodontol 72:257-264.
5. Rothamel D, Schwarz F, Sculean A, Herten M, Scherbaum W, Becker J. (2004) Biocompatibility of various collagen membranes in cultures of human PDL fibroblasts and human osteoblast-like cells. Clin Oral Implants Res 15:443-449.
6. Park J, Lutz R, Felszeghy E, Wiltfang J, Nkenke E, Neukam FW, Schlegel KA. (2007) The effect on bone regeneration of a liposomal vector to deliver BMP-2 gene to bone grafts in peri-implant bone defects. Biomaterials 28 (17):2772-2782.
7. Chen VJ, Smith LA, Ma PX. (2006) Bone regeneration on computer-designed nano-fibrous scaffolds. Biomaterials 27:3973-3979.
8. Li WJ, Tuli R, Huang X, Laquerriere P, Tuan RS. (2005) Multilineage differentiation of human mesenchymal stem cells in a three-dimensional nanofibrous scaffold. Biomaterials 26:5158-5166.
9. Zhang YZ, Ouyang HW, Lim CT, Ramakrishna S, Huang ZM. (2005) Electrospinning of gelatin fibers and gelatin/PCL composite fibrous scaffolds. J Biomed Mater Res B Appl Biomater 72:156-165.
10. Miller EJ, Rhodes RK. (1982) Preparation and characterization of the different types of collagen. Methods Enzymol 82 Pt A:33-64.
11. Stevens MM, George JH. (2005) Exploring and engineering the cell surface interface. Science 310:1135-1138.
12. Xin X, Hussain M, Mao JJ. (2007) Continuing differentiation of human mesenchymal stem cells and induced chondrogenic and osteogenic lineages in electrospun PLGA nanofiber scaffold. Biomaterials 28:316-325.
13. Shin M, Yoshimoto H, Vacanti JP. (2004) In vivo bone tissue engineering using mesenchymal stem cells on a novel electrospun nanofibrous scaffold. Tissue Eng 10:33-41.
14. Becker W, Dahlin C, Becker BE, Lekholm U, van Steenberghe D, Higuchi K, Kultje C. (1994) The use of e-PTFE barrier membranes for bone promotion around titanium implants placed into extraction sockets: a prospective multicenter study. Int J Oral Maxillofac Implants 9(1):31-40.
15. Rocha LB, Goissis G, Rossi MA. (2005) Biocompatibility of anionic collagen matrix as scaffold for bone healing. Biomaterials 23(2):449-456.
16. Bostman O, Pihlajamaki H. (2000) Clinical biocompatibility of biodegradable orthopaedic implants for internal fixation: a review. Biomaterials 21:2615-2621.
17. William R. Walsh_, Frank Vizesi, Dean Michael, Jason Auld, Andy Langdown,Rema Oliver, Yan Yu, Hiroyuki Irie, Warwick Bruce. (2008) β-TCP bone graft substitutes in a bilateral rabbit tibial defect model. Biomaterials, 29: 266–271.
18. D. Stubbs,M. Deakin,P. Chapman-Sheath,W. Bruce,J. Debes, R.M. Gillies,W.R. Walsh. (2004) In vivo evaluation of resorbable bone graft substitutes in a rabbit tibial defect model. Biomaterials 25: 5037–5044.

*corresponding Author: Hongwei Ouyang
Institute: Center for Stem Cell and Tissue Engineering,
School of Medicine, Zhejiang University,
Street: 388 Yu Hang Tang Road
City: Hangzhou
Country: China
Email: hwoy@zju.edu.cn

Morphology and *In Vitro* Biocompatibility of Hydroxyapatite-Conjugated Gelatin/Thai Silk Fibroin Scaffolds

S. Tritanipakul[1], S. Kanokpanont[1], D.L. Kaplan[2] and S. Damrongsakkul[1,*]

[1] Department of Chemical Engineering, Chulalongkorn University, PhayaThai Road, Phatumwan, Bangkok 10330, Thailand
[2] Department of Biomedical Engineering, Bioengineering Center, Tufts University, 4 Colby Street, Medford, MA 02155, USA

Abstract — **Silk fibroin from *Bombyx mori* silkworm is one of attractive biomaterials for tissue engineering because of its excellent mechanical properties, biocompatibility and slow biodegradation. Silk fibroin from Thai yellow cocoon "Nangnoi-Srisaket 1" was employed to prepare aqueous-derived fibroin scaffolds via salt leaching method. The porous structure of scaffolds could be regulated by the size of granular NaCl used. Surface of Thai silk fibroin scaffolds were modified by gelatin conjugation. Furthermore, scaffolds were immersed in $CaCl_2$ and Na_2HPO_4 solutions alternately in order to deposit hydroxyapatite into the scaffolds. After alternate soaking, hydroxyapatite was observed on the porous surface of scaffolds. The comparison between Thai silk fibroin and conjugated gelatin/Thai silk fibroin scaffolds exhibited that the deposition of hydroxyapatite in Thai silk fibroin scaffolds was more than in conjugated gelatin/Thai silk fibroin scaffolds. Gelatin conjugation and hydroxyapatite deposition could enhance the compressive modulus of Thai silk fibroin scaffolds. *In vitro* biocompatibility of Thai silk fibroin-based scaffolds using rat bone-marrow derived mesenchymal stem cell (MSCs) showed that the number of proliferated MSCs, determined by DNA assay, in conjugated gelatin/Thai silk fibroin scaffolds and hydroxyapatite-conjugated gelatin/Thai silk fibroin scaffolds were higher than pure Thai silk fibroin scaffolds, possibly due to RGD sequence contained in gelatin. As gelatin conjugation and hydroxyapatite deposition could alter the morphology of Thai silk fibroin scaffolds and promote the proliferation of MSCs on the scaffolds, these scaffolds have a potential to be applied in tissue engineering applications.**

Keywords — **silk fibroin, gelatin, hydroxyapatite, scaffold, tissue engineering**

I. Introduction

Three-dimensional scaffolds having appropriated porous structure, mechanical integrity, and good biocompatibility are required to promote cell and tissue growth [1]. Various types of biomaterials have been extensively used to fabricate scaffolds for *in vitro* study of cell–scaffold interactions. The scaffold material, as well as the three-dimensional structure of the scaffold, have significant effects on cell activity. They act as a physical support structure and a regulator of biological activity that affects cell response such as migration, adhesion, and proliferation.

Silk fibroin is a major constituent of raw silk fiber from *Bombyx mori* silkworm which has been used in many biomedical applications because of its impressive mechanical properties and biocompatibility [2]. Recent studies showed the benefits of RGD coupling growth and gelatin conjugation to silk fibroin surface on the osteoblasts, fibroblasts and bone marrow mesenchymal stem cell [3-4]. Furthermore, the surface modification with hydroxyapatite is known to have high affinity for various types of cells. Especially when hydroxyapatite is implanted in bone defectes, bone formation between the implanted hydroxyapatite and host cell is reportd [5].

In this study, silk fibroin scaffolds were prepared from Thai silk fibroin via salt leaching method. Gelatin conjugation and hydroxyapatite deposition was introduced to modify the porous surface of Thai silk fibroin scaffolds. The influences of both gelatin conjugation and hydroxyapatite deposition on the morphology and *in vitro* biocompatibility of the scaffolds were evaluated.

II. Materials and methods

Cocoon of Thai silkworm "Nangnoi-Srisaket 1" from Nakhonratchasima province, Thailand, and type A gelatin from Nitta Gelatin, Japan, were used as raw materials. All chemicals used were analytical grade.

A. Preparation of Thai silk fibroin scaffolds.

Thai silk fibroin fibers were prepared as described by Kim *et.al* [1]. Briefly, cocoons were boiled for 20 min in an aqueous solution of 0.02M Na_2CO_3 and then rinsed thoroughly with deionized water to extract the sericin. The degummed Thai silk fibroin was dissolved in 9.3M LiBr solutions at 60°C for 4 h to form 25wt% solution. The solution was dialyzed in deionized water at room temperature for 2 days. The final concentration of Thai silk fibroin aqueous solution was 6.5wt%. Thai silk fibroin scaffolds were prepared by adding 9 g of NaCl (particle size: 600 – 710 μm) into 3 ml of Thai silk fibroin solution in a container. The containers were left at room temperature for

Chwee Teck Lim, James C.H. Goh (Eds.): ICBME 2008, Proceedings 23, pp. 1377–1380, 2009
www.springerlink.com

24 h. Then, salt was leached out by water and left to be dried overnight. The Thai silk fibroin scaffolds were punched into 11mm in diameter, 2mm in height.

B. Preparation of conjugated gelatin/Thai silk fibroin scaffolds (CGSF)

Conjugated gelatin/Thai silk fibroin scaffolds (CGSF) were prepared by coating Thai silk fibroin scaffolds with 0.5wt% gelatin solution, followed by conjugation via dehydrothermal treatment at 140°C for 48 h in a vacuum oven. After that, the scaffolds were treated with carbodiimide solution (14mM 1-ethyl-3-(3-dimethyl aminopropyl) carbodiimide hydrochloride (EDC) and 5.5mM N-hydroxysuccinimide (NHS)) under vacuum for 2 h [6].

C. Preparation of hydroxyapatite/Thai silk fibroin (SF4) and hydroxyapatite-conjugated gelatin/Thai silk fibroin scaffolds (CGSF4)

The alternate soaking process was used to deposit hydroxyapatite into the scaffolds [7]. First, Thai silk fibroin scaffolds and conjugated gelatin/Thai silk fibroin scaffolds were immersed in 0.2M $CaCl_2$ solutions for 30 min, followed by immersing in 0.12M Na_2HPO_4 solution for another 30 min. This was considered as one cycle of alternate soaking. The alternate soaking was performed for 4 cycles to allow the deposition of hydroxyapatite into the scaffolds. The weight percentage of hydroxyapatite deposited was determined from the weight increased after alternate soaking as followed

$$\%HA = \frac{W_{HA} - W_0}{W_0} \times 100$$

Where W_{HA} and Wo is the weights of dried scaffold after and before alternate soaking, respectively. The reported values were the mean±standard deviation (n=5).

D. Morphological observation

The morphology of scaffolds was investigated by scanning electron microscopy (SEM).

E. Mechanical test

The compression tests were performed using a universal testing machine (Instron 5567) at the constant compression rate of 0.5 mm/min. The compressive modulus reported was the mean±standard deviation (n=5).

F. In vitro cell culture

The scaffolds were placed into 24-well tissue culture plates and were sterilized using ethylene oxide. After sterilization, the scaffolds were immersed in phosphate buffered saline (PBS) for 24 h. Rat bone-marrow derived mesenchymal stem cells (MSCs) were seeded at a density of 2×10^4 cells per scaffold onto each scaffold placed in medium (α-MEM containing 10% FBS and 50 U/ml penicillin streptomycin) and incubated at 37°C in air containing 5% CO_2. After cultured for 6 h, 1, 3, 7 and 14 days, the number of cells were determined by DNA assay. The samples were washed with PBS and lysed in SDS lysis buffer at 37°C in air containing 5% CO_2 for 24 h. Hoechst 33258 dye was added into the cell lysate and the fluorescent intensity of the solution was measured in a fluorescence spectrometer at the excitation and emission wavelengths of 355 and 460 nm, respectively [8]. All data were expressed as mean±standard deviation (n = 3).

III. Results and Discussion

A. Morphological observation

Fig. 1 showed the cross sectional morphology of Thai silk fibroin-based scaffolds. Porous structure with smooth surface of SF scaffolds was noticed as illustrated in Fig. 1(a). The pore size of scaffold structure corresponded to the size of salt crystals used. Gelatin conjugation could form fibers inside the porous structure of fibroin scaffolds (Fig.

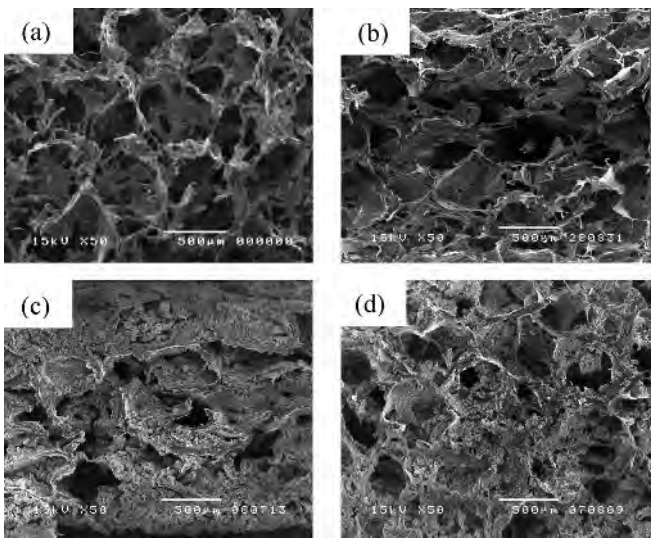


Fig. 1 SEM micrographs of (a) silk fibroin scaffolds, (b) conjugated gelatin/silk fibroin scaffolds, (c) hydroxyapatite/Thai silk fibroin scaffolds and (d) hydroxyapatite-conjugated gelatin/Thai silk fibroin scaffolds.

Table 1 The percentage of hydroxyapatite deposited in silk fibroin scaffolds (SF) and conjugated gelatin/silk fibroin scaffolds (CGSF).

Scaffolds	%HA
SF	130.3±12.8
CGSF	102.5±9.3

1(b)). After alternate soaking, hydroxyapatite/Thai silk fibroin scaffolds (SF4) and hydroxyapatite-conjugated gelatin/Thai silk fibroin scaffolds (CGSF4) exhibited the deposition of hydroxyapatite inside the pore of the scaffolds as shown in Fig. 1(c) and (d), respectively. The deposition of hydroxyapatite in SF was greater than in CGSF as shown in Table 1. This could be a result from a difference in the morphology. Gelatin conjugation caused less pore volume of scaffolds which could limited the deposition of hydroxyapatite into the scaffolds.

B. Mechanical Property

The compressive modulus of SF, CGSF, SF4 and CGSF4 shown in Figure 2 indicated that the compressive modulus of CGSF was higher than that of SF. This could be a result from the conjugation reaction by dehydrothermal and EDC treatments. Dehydrothermal brings about chemical bonding between the amino and carboxyl groups within molecules of polypeptide. Further treatment with EDC, the primary amines on the peptides formed a stable amide bond between the peptide of gelatin and silk fibroin [9]. After hydroxyapatite deposition, compressive modulus of SF increased by 52.3% while that of CGSF increased by 19.4%. The results indicated that gelatin conjugation and hydroxyapatite deposition enhanced the compressive modulus of Thai silk fibroin scaffolds.

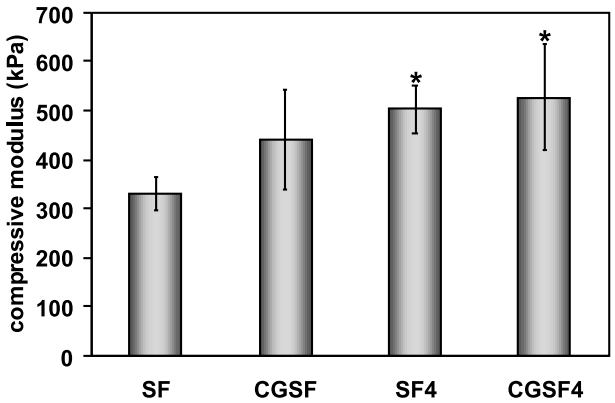


Fig. 2 Compressive modulus of silk fibroin scaffolds (SF), conjugated gelatin/silk fibroin scaffolds (CGSF), hydroxyapatite/Thai silk fibroin scaffolds (SF4) and hydroxyapatite-conjugated gelatin/Thai silk fibroin scaffolds (CGSF4).
* represent the significant difference ($p<0.05$) relative to silk fibroin scaffolds.

C. In vitro cell proliferation tests

Fig. 3 presented the number of MSCs determined by DNA assay after 6 h, 1, 3, 7, and 14 days of the culture. It could be noticed that there were no significant differences between the cell adhered on SF, CGSF, SF4 and CGSF4 after 6 h of seeding. After 1 day of seeding, CGSF showed the highest number of MSCs. At longer culture time, the number of proliferated cells on CGSF continuously increased, compare to other scaffolds. The number of cells on SF, CGSF, SF4 and CGSF4 after 14 days of cell seeding was about 3.4, 4.2, 3.2 and 3.5 folds of those after 6 h of seeding. This could be the result of arginine-glycine-aspartic (RGD) sequence contained that in gelatin that was reported to promote cell adhesion and migration [10]. SF4 and CGSF4 tended to have a slightly fewer proliferated MSCs compared to SF and CGSF, respectively. This might be attributed to the different morphology of scaffolds. Hydroxyapatite deposited on the surface of scaffolds might obstruct the cell migration into the scaffolds.

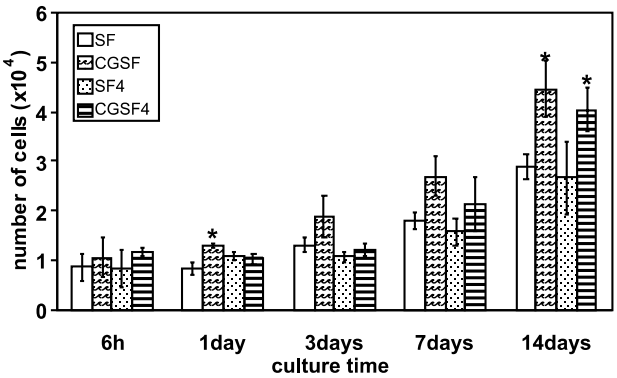


Fig. 3 Number of MSCs on silk fibroin scaffolds (SF), conjugated gelatin/silk fibroin scaffolds (CGSF), hydroxyapatite/Thai silk fibroin scaffolds (SF4) and hydroxyapatite-conjugated gelatin/Thai silk fibroin scaffolds (CGSF4) after 6 hours, 1, 3, 7 and 14 days of the culture.
* represent the significant difference ($p<0.05$) relative to silk fibroin scaffolds at each culture time.

IV. Conclusions

Gelatin conjugation and hydroxyapatite deposition influenced on the morphology and compressive modulus of salt-leached Thai silk fibroin scaffolds. The morphology of the scaffolds was more fibrous after gelatin conjugation. Hydroxyapatite deposition on both silk fibroin scaffolds, with and without gelatin conjugation, resulted in less pore volume. *In vitro* study revealed that the conjugated gelatin/Thai

silk fibroin and hydroxyapatite-conjugated gelatin/Thai silk fibroin scaffolds supported the proliferation of bone-marrow derived mesenchymal stem cell. The results on the physical, mechanical and biological properties of hydroxyapatite-conjugated gelatin/Thai silk fibroin scaffolds implied that the scaffolds had a potential to be applied in tissue engineering.

Acknowledgements

Financial supports from the National Research Council of Thailand are acknowledged.

References

1. Kim UJ, Park J, Kim HJ, Wada M, Kaplan DL (2005) Three-dimensional aqueous-derived biomaterial scaffolds from silk fibroin. Biomaterials 26:2775–2785
2. Vepari C, Kaplan DL (2007) Silk as a biomaterial. Progress in Polymer Science 32:991
3. Wang Y, Kim HJ, Novakovic GV, Kaplan DL (2006) Stem cell-based tissue engineering with silk biomaterials. Biomaterials 27:6064-6082
4. Chamchongkaset1 J, Kanokpanont1 S, Kaplan DL, Damrongsakkul S (2008) Modification of Thai Silk Fibroin Scaffolds by Gelatin Conjugation for Tissue Engineering. Advanced Materials Research 55-57:685-688
5. Tanaka T, Hirose M, Kotobuki N, Ohgushi H, Furuzono T, Soto J (2007) Nano-scaled hydroxyapatite/silk fibroin sheets support osteogenic differentiation of rat bone marrow mesenchymal cells. Materials Science and Engineering C 27:817-823
6. Taguchi T, Kishida A, Akashi M (1998) Hydroxyapatite Formation on/in poly(vinyl alcohol) hydrogel matrices using a novel alternate soaking process. Chemistry Letters:711-712
7. Tachaboonyakiat W, Serizawa T, Akashi M (2001) Hydroxyapatite formation on/in biodegradable chitosan hydrogels by an alternate soaking process. Polymer Journal 33:177-1181
8. Takahashi Y, Yamamoto M, Tabata Y (2005) Osteogenic differentiation of mesenchymal stem cells in biodegradable sponges composed of gelatin and β-tricalcium phosphate. Biomaterials 26:3587–3596
9. Sofia S, McCarthy MB, Gronowicz G, Kaplan DL (2001) Functionalized silk-based biomaterials for bone formation. Journal of Biomedical Materials Research 54:139–148
10. Calvert JW, Marra KG, Cook L, Kumta PN, Dimilla PA, Weiss LE (2000) Characterization of osteoblast-like behavior of cultured bone marrow stromal cells on various polymer surfaces. Journal of Biomedical Materials Research 52:279

Author: Siriporn Damrongsakkul
Institute: Chulalongkorn University
Street: Phayathai
City: Bangkok
Country: Thailand
Email: siriporn.d@chula.ac.th

Development of a Silk-Chitosan Blend Scaffold for Bone Tissue Engineering

K.S. Ng[1], X.R. Wong[1], J.C.H. Goh[2] and S.L. Toh[1]

[1] Division of Bioengineering, National University of Singapore, Singapore
[2] Department of Orthopaedic Surgery, National University of Singapore, Singapore

Abstract — **There is a pressing need for bone graft substitutes to augment bone regeneration in patients with damaged or diseased bone tissues. Currently, autologous bone graft is the gold standard but its use is limited by supply and donor site morbidity. Consequently, tissue engineering is seen as a solution to the shortage of functional bone graft substitutes. In the scaffold-guided approach to bone tissue engineering, it requires the development of a three-dimensional scaffold to mimic the native 3D environment of the bone cells. In addition, the scaffold material would need to be biocompatible, biodegradable, and possess the appropriate mechanical properties similar to that of the native tissue.**

In this study, silk and chitosan were combined to produce a blended scaffold using the lyophilization technique. The resulting scaffolds were seeded with bone marrow derived mesenchymal stem cells and subjected to osteogenic stimulation. Results were shown to support cell growth and proliferation, eventually resulting in a mineralized extracellular matrix. It is hoped that the resulting scaffold would become a highly functional bone graft substitute and further optimization work will be done to achieve this goal.

Keywords — **Silk, Chitosan, Bone marrow derived mesenchymal stem cells, Freeze drying, Bone Tissue Engineering**

I. Introduction

There is a great need for bone graft substitutes in the repair and replacement of damaged or diseased bone tissues. Currently, autologous bone grafts remain as the current gold standard as it possess osteogenic, osteoconductive and osteoinductive properties, without the undesirable immune rejection experienced when allogenic bone grafts are used. However, autografts are associated with donor site morbidity and a limited supply. Tissue engineered bone could provide an answer to the shortage of bone grafts.

Tissue engineering is the use of a combination of cells, engineering and materials methods and suitable biochemical and physico-chemical factors to improve or replace biological function [1]. More specifically, suitable materials favorable for survival and normal function of relevant cells are used to fabricate scaffolds. These scaffolds then serve as templates for tissue construction, mechanical support for the cells and a source of multi-factorial cues necessary for cellular functions. Eventually, the scaffold materials will degrade and be replaced by extracellular matrix. With the critical choice of cells and materials, tissue engineering provides the prospects of an autogenic, osteogenic, osteoconductive and osteoinductive bone graft.

In this study, silk and chitosan are the materials chosen to fabricate scaffolds for bone tissue engineering. Desirable characteristics of scaffolds include biocompatibility, adequate pore size, high porosity, interconnected architecture, appropriate mechanical strength and biodegradability [2, 3]. Silk has long been used in biomedical applications as suture materials. It is a viable material because of its permeability to oxygen and water, cell adhesion and growth characteristics, relatively low thrombogenicity, low inflammatory response, protease susceptibility, and high tensile strength [4, 5]. Furthermore, silk can be subjected to aqueous or organic solvent processing and can be chemically modified to cater for a wide range of applications. Recent bone tissue engineering studies performed using silk scaffolds resulted in extensive mineralization, alkaline phosphatase activity (an early marker for osteoblast differentiation) and cortical mineralized network [6, 7]. This indicates that silk is indeed a favorable material for use in bone tissue engineering.

On the other hand, chitosan is a partially deacetylated product of chitin, a crystalline polysaccharide found in crustaceans and insects, which is structurally similar to glycosaminoglycans (GAG) [8]. Chitosan can be fabricated to form porous, interconnected structures and the cationic nature of chitosan allows for pH dependent electrostatic interactions with anionic GAG and proteoglycans [9]. Other desirable characteristics of chitosan include wound healing properties, non-toxicity, and minimal foreign body response with accelerated angiogenesis [9]. Like silk, chitosan also has biomedical applications as wound dressings and drug delivery systems.

There are already several studies investigating the characteristics of silk-chitosan blend hybrid material [10, 11]. A recent study by She *et al* investigated the HepG2 cell culture behavior of the silk-chitosan scaffolds [11]. The aim of this study is to develop a silk-chitosan scaffold cultured with bone marrow derived mesenchymal stem cells (BMSCs). The investigators seek to determine the morphology and structure of the blended scaffold, and to study the response of the BMSCs-loaded scaffolds under osteogenic stimulation.

Chwee Teck Lim, James C.H. Goh (Eds.): ICBME 2008, Proceedings 23, pp. 1381–1384, 2009
www.springerlink.com

II. Materials and methods

A. Silk fibroin and Chitosan Dissolution

Bombyx mori silk fibers (local name: "Nang Lai" silk fibers) were used in this study. Raw silk fibers were immersed in a degumming solution of 0.25% (w/v) Na_2CO_3 and 0.25% (w/v) sodium dodecyl sulfate (SDS) between 98°C and 100°C for 30 minutes. After 30 minutes, the solution was refreshed. This process was repeated until most of the sericin has been removed. The degummed silk was then rinsed with distilled water for 1 hour to remove the residual degumming solution before leaving them to air dry. The degummed silk was then dissolved in $CaCl_2$–C H_3CH_2OH–H_2O (molar ratio = 1:2:8) at 65°C with continuous stirring. The resulting silk solution was dialyzed against distilled water using a SnakeSkin Pleated Dialysis Tubing (PIERCE, MWCO 3500). The concentration (w/v) of the dialyzed solution was determined and adjusted to 3% w/v by using distilled water to dilute or by concentrating the solution at 60°C.

Chitosan solution was prepared by dissolving chitosan from crab shells (minimum 85% deacetylation: Sigma-Aldrich) at 3% (w/v) in 2% acetic acid. Chitosan powder was added slowly with continuous stirring to obtain a viscous solution.

B. Silk-Chitosan Blend Scaffold Fabrication

An equal volume of the same concentration of silk was added to prepare a 50:50 blend and allowed to mix for 15 minutes. The blended solution was then poured into polypropylene molds (diameter, 17 mm; height, 15 mm), frozen in a -80°C freezer for 1 hour, followed by lyophilization for 18 hours. The dried sponges were removed from the molds and treated in a 50:50 (v/v) methanol: sodium hydroxide (1N) solution for 30 minutes, to induce an amorphous to silk II conformational change in the silk-chitosan sponges to prevent resolubilization in the cell culture medium. The NaOH was removed by soaking the sponges in phosphate buffered solution (1x PBS) with solution changes every hour until the pH had equilibrated to 7.4. The sponges were freeze-dried for another 18 hours to remove the water before finally cutting them into individual scaffolds (diameter, 17 mm; height, 3 mm). Prior to seeding, the scaffolds had to be sterilized in 70% ethanol, followed by washing in PBS.

C. Determination of the Optimal Concentration of Silk-Chitosan Scaffold

For vascularization purposes, the pore size range of the scaffolds should be about 300μm or slightly larger for angiogenesis. Yet, the mechanical properties of the scaffold should be adequate for bone tissue engineering. Various concentrations (2%, 2.5%, 3% and 3.5%) of the silk-chitosan blends were fabricated to determine the optimal pore size and mechanical properties.

D. Scaffold Characterization

For characterization, the dried scaffolds were coated with gold using a Sputter Coater (JEOL, JFC 1600). The morphology was observed by a scanning electron microscope (Quanta FEG 200) operated at a voltage of 10 kV. Sagittal and transverse views of the scaffolds were obtained by cryosectioning and observed using light microscopy.

E. Isolation of Rabbit BMSCs

Rabbit BMSCs were obtained from whole bone marrow aspirates from New Zealand white rabbits and culture expanded according to procedures previously described [12]. Rabbit MSCs were isolated from fresh whole bone marrow aspirates from New Zealand White Rabbits (8 weeks old), culture expanded in low glucose culture medium containing Dulbecco's modified Eagle's medium (LG-DMEM; Gibco, Invitrogen, CA), 15% v/v fetal bovine serum (HyClone, Logan, UT), penicillin and streptomycin. Nonadherent cells were removed upon first passage of the cells. When primary MSCs became near confluent, they were detached using trypsin (0.25%) /1mM ethylenediamine-tetraacetic acid (EDTA) and replated at a 1:3 ratio. The second passage cells were then used for further study. All cell cultures were maintained at 37oC in an incubator with 5% humidified CO_2. The cultures were replenished with fresh medium at 37°C every 3 days.

F. Cell seeding and Culture

BMSCs were pre-cultured in a T175 flask with osteogenic medium (DMEM supplemented with 50μg/ml ascorbic acid-2-phosphate, 10nM dexamethasone and 10mM β-glycerolphosphate). The cells were harvested upon reaching 80% confluence and seeded onto the scaffolds with a density of $2x10^6$ cells / scaffold. Two methods were used, static and perfusion seeding. Static seeding is via pipetting 100μL of the cell suspension dropwise onto the scaffold. Perfusion seeding is achieved using a setup which pumps the cell suspension from the medium reservoir into the scaffolds, which are loaded in a bioreactor. The seeded scaffolds are then cultured in-vitro on non-treated 6-well plates in a 5% CO_2 incubator at 37°C. Culture period was 2 weeks and medium was changed every 3 days.

G. Proliferation and Differentiation Assays

The viability of the cells present within the scaffold was determined using the Alamar Blue (Invitrogen, CA) colorimetric assay. Briefly, the cells were incubated in medium supplemented with 10% (v/v) Alamar Blue dye for 3 hours. Two hundred microliters of medium from each sample was read at 570/600nm in a microplate reader (Tecan). Medium supplemented with 10% Alamar Blue dye was used as a negative control and the percentage of Alamar Blue reduction was calculated according to the formula provided by the vendor.

H. Histological Analysis

Samples were fixed in 4% formaldehyde, dehydrated and embedded in paraffin, and 10µm sections were cut. To identify mineralization, Von Kossa staining was done.

III. Results and Discussion

A. Morphology of the scaffold

To restate, the pore size range of the scaffolds was chosen to be about 300µm for vascularization purposes. It was observed that the scaffolds fabricated using 2% and 2.5% were not mechanically strong and the scaffold architecture was disrupted when the sponge was cut into the desired dimensions. The mean pore size of the fabricated scaffolds using 3% and 3.5% blends were 311µm and 282µm respectively. Hence, a 3% silk-chitosan blend was chosen because a pore size range of 300-400µm has been suggested to be the optimal pore size for attachment, differentiation and growth of osteoblasts and vascularization [13, 14].

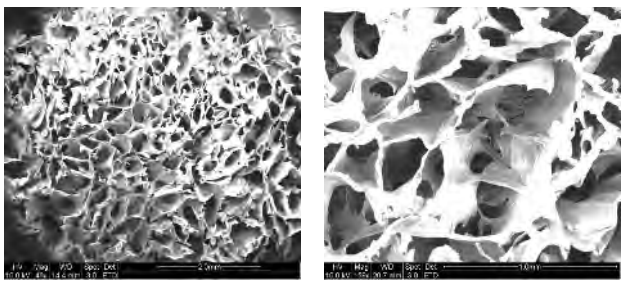


Figure 1: SEM images of silk-chitosan scaffolds (45X and 158X)

Figure 1 shows that the overall pore architecture was rather homogenous. Heterogeneous scaffold architectures could lead to variable cell adhesion and influence the ability of the cell to produce a uniform distribution of extracellular matrix proteins [15]. Therefore, it is important that the freeze-drying process is fine-tuned to produce scaffolds with homogenous pore architecture.

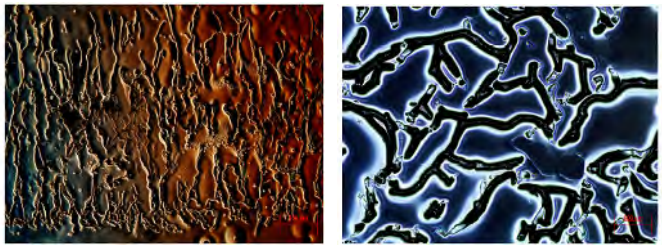


Figure 2: (A) Sagittal and (B) Transverse sections of the scaffold

The scaffolds were section vertically to reveal the sagittal cross sections of the scaffolds. This was done using the cryostat. From Figure 2(A), the width of the channels of similar dimensions suggests similar pore sizes with depth. The presence of pore interconnectivity was investigated by taking horizontal cross sections to reveal the transverse cross sections of the scaffolds. The light microscopic image of Figure 2(B) shows that each pore opens up to another, suggesting highly interconnected pores in the 3% silk-chitosan scaffolds.

B. BMSC-Scaffold Construct in Static Culture

From Figure 3, it can be seen that the cells were still capable of proliferating after seeding onto the scaffolds. Although samples that underwent static seeding cannot be compared to those that underwent perfusion seeding (due to different basal metabolic activities as a result of different culture treatments), it was interesting to note that the percentage reduction actually dipped in the later phase of the culture. This trend was observed in several repeats of the experiment. This suggested that static seeding might have caused cells to be localized at or near the surface of the scaffolds. Over time, the competition for nutrients and the accumulation for metabolites might have limited the proliferation capacity of the cell population. Nevertheless, the findings showed that BMSCs were still able to proliferate after seeding onto the silk-chitosan scaffolds.

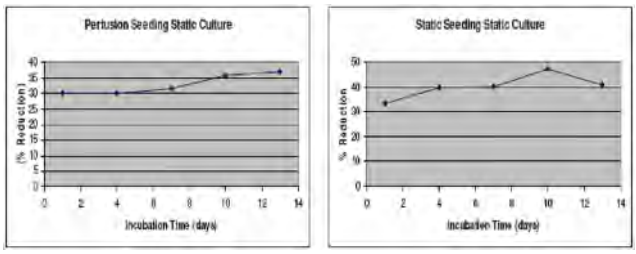


Figure 3: Proliferation studies after perfusion and static seeding

C. Deposition of bone minerals

Von Kossa technique stains calcium minerals black. Hence differentiation potential can be qualitatively determined from light microscopic images of the stained sections because the ability to deposit minerals is the marker for mature osteoblasts.

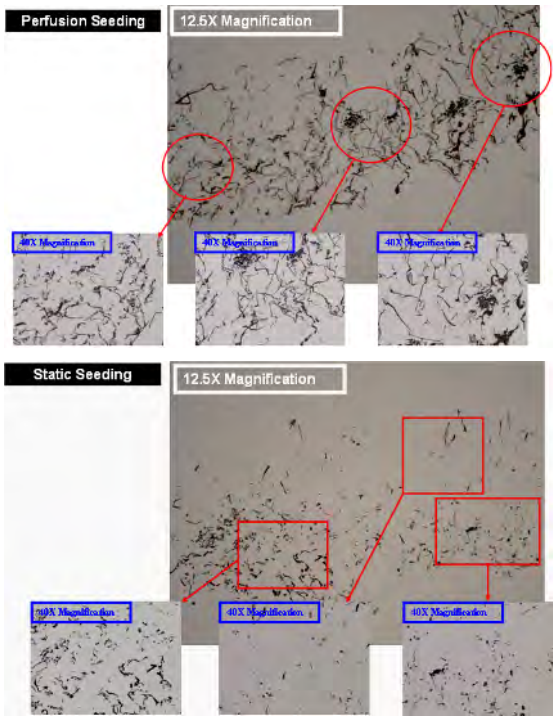


Figure 4: Von Kossa sections, showing signs of mineralization

From Figure 4, it can be seen that the BMSCs that were seeded into the silk-chitosan scaffolds remain differentiated and went into the mineralization phase to deposit mineralized extracellular matrix, which was detected in this procedure.

IV. Conclusion

This study demonstrated the potential of silk-chitosan scaffolds for bone tissue engineering application. Coupled with BMSCs, which is a good source of autologous osteogenic cells, this scaffold may be able to provide highly functional substitutes of native tissues. Future studies on gene expression of bone markers will be carried out to determine the expression level of bone markers such as alkaline phosphatase, osteocalcin and osteopontin. More work also needs to be done to better quantify the DNA and calcium content within the cell-scaffold constructs.

References

1. Langer R, Vacanti JP. (1993) Tissue engineering. Science 260(5110):920-926.
2. Hutmacher D.W. (2000) Scaffolds in tissue engineering bone andcartilage. Biomaterials 21:2529-2543.
3. Khan Y, Yaszemski MJ, Mikos AG *et al*. (2008) Tissue Engineering of Bone: Materials and Matrix Considerations. The Journal of Bone & Joint Surgery 90 (Suppl 1): 36-42.
4. Altman GH, Diaz F, Jakuba C *et al*. (2003) Silk-based biomaterials. Biomaterials 24:401-416.
5. Gotoh Y, Minoura N, Miyashita T. (2002) Preparation and characterization of conjugates of silk fibroin and chito-oligosaccharides. Colloid Polym. Sci. 280:562-568.
6. Meinel L, Karageorgiou V, Hofmann S *et al* (2004) Engineering bone-like tissue in-vitro using human bone marrow stem cells and silk scaffolds. J Biomed Mater Res A 71(1):25-34.
7. Uebersax L, Hagenmuller H, Hofmann S *et al* (2006) Effects of scaffold design on bone morphology in-vitro. Tissue Engineering 12(12):3417-3429.
8. Kumar MNVR. (2000) A review of chitin and chitosan applications. React. Funct. Polym. 46:1-27.
9. Kim IY, Seo SJ, Moon HS *et al*. (2008) Chitosan and its derivatives for tissue engineering applications. Biotechnology Advances 26:1-21.
10. Gobin AS, Froude VE, Mathur AB. (2005) Structural and mechanical characteristics of silk chitosan blend scaffolds for tissue regeneration. J Biomed Mater Res. 74A(3):465-473.
11. She Z, Jin C, Huang Z *et al*. (2008) Silk fibroin/chitosan scaffold: preparation, characterization, and culture with HepG2 cell. J Mater Sci: Mater Med 19(12):3545-53.
12. Liu H, Fan H, Wang Y *et al*. (2008) The interaction between a combined knitted silk scaffold and microporous silk sponge with human mesenchymal stem cells for ligament tissue engineering. Biomaterials 29(6):662-74.
13. Tsuruga E, Takita H, Itoh H *et al*. (1997) Pore size of hydroxyapatite as the cell-substratum controls BMP-induced osteogenesis. J Biochem. 121(2):317-24.
14. Laschke MW, Harder Y, Amon M *et al*. (2006) Angiogenesis in tissue engineering: Breathing life into constructed tissue substitutes. Tissue Engineering 12(8):2093-2104.
15. Zeltinger J, Sherwood JK, Graham DA *et al*. (2001) Effect of pore size and void fraction on cellular adhesion, proliferation and matrix deposition. Tissue Engineering 7(5):557-72.

Corresponding Author: Siew Lok, TOH
Institute: Division of Bioengineering, National University of Singapore
Country: Singapore
Email: bietohsl@nus.edu.sg

Effects Of Plasma Treatment On Wounds

R.S. Tipa, E. Stoffels

Department of Biomedical Engineering, Eindhoven University of Technology, PO Box 513, 5600 MB, Eindhoven, The Netherlands

Abstract — **Cold plasma treatment of wounds is gaining much interest, because it will offer a non-contact, painless and harmless therapy to manage large-area lesions (burn wounds, chronic ulcerations). One of the important issues in plasma wound healing is the safety of the method. In this work we study in vitro the effects of plasma treatment on cell death, proliferation and wound healing. Many methods have been developed to study the cell viability and proliferation, but one of the most appreciated ones is the MTT Assay. There are many advantages of using this method such as: the method is safe, fast and convenient, and allows simultaneous analysis of many samples (e.g. cell samples prepared in 96 well plates). Viable cells transform the added MTT tetrazolium salt into purple formazan, which is detected by colorimetric methods. The amonut of viable cells is proportional to the amount of formazan. We performed a parametric study of plasma-treated 3T3 fibroblast cells. For the treatment, a cold atmospheric plasma needle (13.56 MHz micro-jet in helium) was used. The influence of plasma on cell viability was measured using the MTT assay. We observed the long-term effects of plasma on cell viability, dependent on the dosage of plasma treatment. Under high doses cell suffered damage that led to decreased viability. Cell death by apoptosis and necrosis was considered.**

Keywords — **MTT assay, spectrophotometry, cell proliferation**

I. Introduction

Cold plasma treatment of wounds is gaining much interest, because it will offer a non-invasive method (the plasma needle operates without incision in the skin), painless and harmless therapy to manage large-area lesions (burn wounds, chronic ulcerations), shorter time for wound healing and also disinfection of the wound.. One of the important issues in plasma wound healing is the safety of the method. In this work we study *in vitro* the effects of plasma treatment on cell death and proliferation and also the model of the wound.

When the skin is damaged, in the body there are chemical and biological processes that are helping the skin to repair the area that has been exposed to a traumatism. The process of wound repair is starting with the inflammatory phase (remove of bacteria) and continues with the releasing factors for helping the proliferative phase (angiogenesis, collagen deposition, epithelialization, wound contraction), maturation and remodeling phase [1]. The current research tries to get more deep in the effects of plasma to the cells, focusing on the healing time for the wound after plasma treatment.

II. Experimental set – up

A. The plasma needle

For our experiments we used a small-size cold atmospheric plasma source, having the frequency of 13.56 MHz. The gas used is Helium, as a matrix, because is inert (non-toxic), has a low breakdown voltage and high heat conductivity. The voltage of the system is 200-400 V p.p, and the power consumption is bellow 100 mW [2]. Compared with other types of plasmas, the plasma needle has also the advantage of working at the room temperature (non-destructive), and also allow the treatment without overheating the cells which will lead them to die. After some other fundamental studies will be done, our main goal is to have the plasma needle working on same parameters for in vivo experiments, where are expected promising results. In Figure 1 is presented the plasma needle with the glow that appears at the tip of the needle when plasma is working.

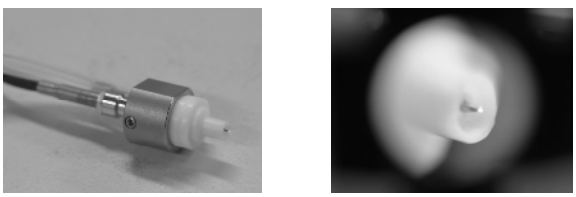


Figure 1 Appearance of the plasma glow – the way plasma appears at the tip of the needle before treatment of the samples

For being able to create cold atmospheric plasma the 13.56 MHz voltage is applied to a sharp metal needle so the plasma is being created at the tip of the needle. The diameter of the needle is about 0.3 mm and is inserted in a Teflon tube with the inner diameter of 0.4 cm. The helium bottle is connected to Brooks series 5850E so the flow can be setted to 1 l/min. The diagram of the experimental set-up is shown in Figure 2.

Chwee Teck Lim, James C.H. Goh (Eds.): ICBME 2008, Proceedings 23, pp. 1385–1388, 2009
www.springerlink.com

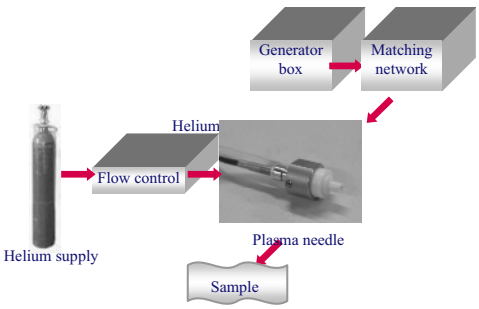
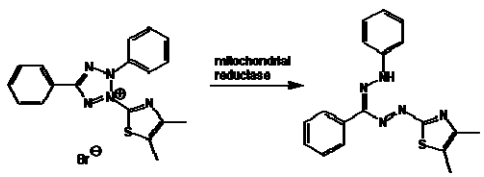


Figure 2 The diagram of the experimental set-up for the plasma needle; we can see the plasma needle confined in a Teflon tube, the connection with the matching box, the Helium supply

B. MTT Assay

Many methods have been developed to study the cell viability and proliferation, but one of the most appreciated ones is the MTT Assay. There are many advantages of using this method such as: the method is safe, fast and convenient, and allows simultaneous analysis of many samples (e.g. cell samples prepared in 96 well plates). Viable cells transform the added MTT tetrazolium salt into purple formazan, which is detected by colorimetric methods. The amount of viable cells is proportional to the amount of formazan.



We performed a parametric study of plasma-treated 3T3 fibroblast cells. For the treatment, a cold atmospheric plasma needle (13.56 MHz micro-jet in helium) was used. The influence of plasma on cell viability was measured using the MTT assay. We observed the long-term effects of plasma on cell viability, dependent on the dosage of plasma treatment. Under high doses cell suffered damage that led to decreased viability. The component for the assay is (3- [4,5-dimethylthiazol-2-yl]-2,5-diphenyl tetrazolium bromide) or MTT. For being able to use the MTT assay, the cultured cells were washed two times with PBS, then added the MTT solution and incubated between 2-4 hours, period in which the purple formazan crystals are formed. After incubation is added isopropanol (to solubilize the crystals) and in the end the absorbance was readed, using the plate reader.

III. Plasma Treatment of the Wounds. Results and Discussions.

A. Cell treatment

The aim of the experiment is to see in time the effects of plasma to the cells in the model of the wound. One of the most important to think of are that we are interested in getting a faster healing of the damaged area, avoiding the side effects like overheating the cell membrane which will lead the cytoplasm out of the cell and causing in the end necrosis. For the experiment, we used 3T3 cells. Those cells lines are the most common fibroblast cultures in the laboratory and were established from disaggregated tissue of an albino Swiss mouse (Mus musculus) embryo. The shape of the cells can be seen in the Figure 3.

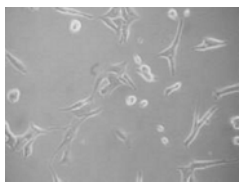


Figure 3 3T3 cells after a few hours of incubation

The 3T3 line was established by George Todaro and Howard Green in 1960. For our experiment, the 3T3 cells were cultured in T75 flasks for 2-3 days and then transferred into 6 well plates. The medium for growing the 3T3 cells contain Dulbecco's modified Eagle's medium with 4.5 g/L glucose (100%), L-glutamine (1%), FBS (10%), Penicillin / Streptomycin (1%). Before culturing the cells in the well plate, they were counted and then the medium was added. In within 3 days, the tissue tends to fill the whole surface, but the best results are when we have 80% confluent cells. In the case of 100% confluence, the growing of the cells is reduced and also can appear the die of the cells. After the tripsinization process, when the cells are round, in time they change the shape and try to adhere of the surface they are cultured on. The fibroblast locomotion is due both lamellipodia and filopodia (lamellipodia is a cytoskeletal actin projection on the mobile edge of the cell. It contains a two-dimensional actin mesh; the whole structure pulls the cell across a substrate (Alberts, et al, 2002). Within the lamellipodia are ribs of actin called microspikes, which, when they spread beyond the lamellipodium frontier, are called filopodia (Small, et all, 2002). The lamellipodium is born of actin nucleation in the plasma membrane of the cell (Alberts, et al, 2002) and is the primary area of actin incur poration or microfilament formation of the cell.)[3]. The cells are ready for treatment when most of them had an

elongated shape and are adherent of the area they are cultured on.

For plasma treatment we used the setup from Figure 4. The plasma power is in the range of 50-250 mW, the voltage 200-400 V p.p and the range of time used for plasma treatment to the cells between 10 - 30 s (the optimal time of treatment, when we got the best results were between 10 – 15 s). in the case of applying a higher voltage or long time treatment, one can see necrosis of the cells. The necrotic cells detached of the surface and are floating like some clouds at the surface of the liquid. This result is due to the fact that the membrane brake and the internal structure is leaking.

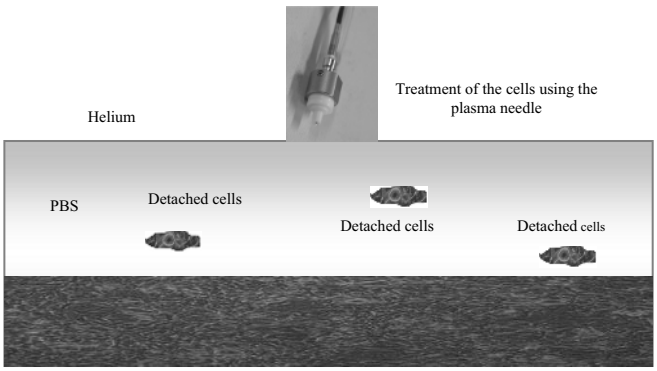


Figure 4. Treatment of the cells using the plasma needle

The graph from Figure 5 is showing cell growing after 24 hours of incubation for plasma treated samples and untreated samples. We can see that the plasma treated samples has a higher rate of growing compared with the untreated samples The method used for analysis is the MTT Assay.

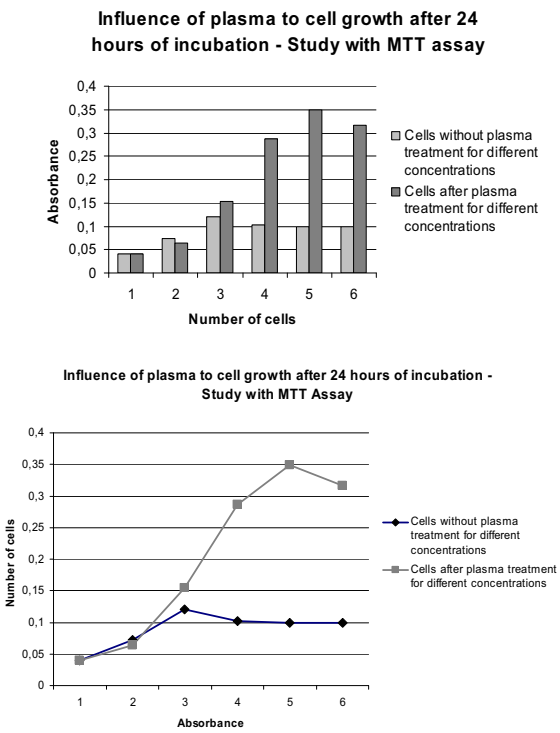


Figure 5. Influence of plasma to the cell growth after 24 hours of incubation

B. Model of wound

In order to create the model of the wound, we used the 3T3 fibroblast cell line. To prepare the samples for the experiment, cells were trypsinized for 5 minutes, then added 10 ml culture medium containing contain Dulbecco's modified Eagle's medium with 4.5 g/L glucose (100%), L-glutamine (1%), FBS (10%), Penicillin / Streptomycin (1%). Then the cells were centrifuged for 5 minutes, the medium was extracted and then to the palette of cells added 1 ml medium. After that cells were counted and recultured in 6 well plates for 2 days in an incubator containing 5% CO_2, at 37ºC. When the cells become 80% confluent they were rinsed 2 times with PBS and inside every plate made scratch using a cell scrapper. In the end, the scratched area was treated using the plasma needle. The treatment time varied between 5 – 30 sec. We could see that the best treatment time operates in the range of 5 – 15 sec. After plasma treatment, the cells were again incubated using the same conditions as described above and the results of the treatment were checked every day. The results of analysis are shown in Figure 6.

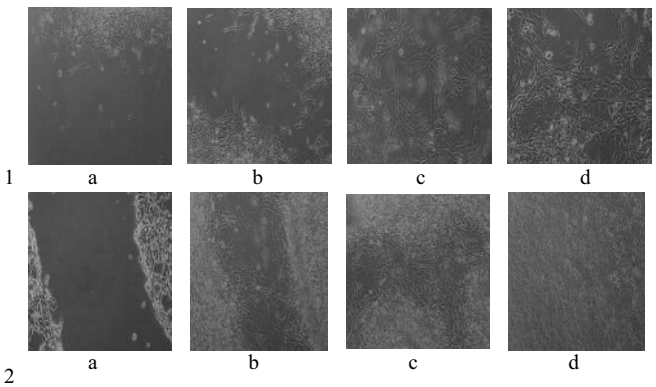


Figure 6. The model of the wound for untreated samples (1) and treated samples (2) – measurements after 0 hours of incubation (a), 24 hours of incubation (b), 48 hours of incubation (c) and 72 hours of incubation (d).

The period for data analysis was between 0 hours (immediately after treatment) and 3 days of incubation. The period of 3 days was chosen because the cells become 100% confluent and the cells are starting to detach and die. From data analysis we can see that for the plasma treatment in case of a wound is more efficient, the complete healing process is faster due to the plasma. In the case of untreated samples, the complete healing process takes longer, about 5 days.

IV. Conclusions

The experiment shows that plasma treatment has a non-destructive effect when we apply plasma treatment for a short time, cells are not dying but growing faster. This is an important feature for our future research regarding the plasma treatment of wounds. How is plasma influencing the healing process? How fast is the healing if we use the plasma treatment? At this question we can answer after doing some additional experiments and we will be able to explain more detailed how this mechanism are working and what is the influence of plasma to the biochemical reactions inside the cells.

During plasma treatment we could see that some of the cells are detaching, but not dying. If we transfer the detached cells to a new plate and adding new medium, after a while cells are starting to attach again.

References

[1] http://en.wikipedia.org/wiki
[2] Stoffels, E., Sladek, R.E.J., Kieft, I.E., Physica Scripta, T107, 79-82 (2004)
[3] http://www.microscopyu.com/articles/livecellimaging/fpintro.html
[4] Stoffels, E., Sladek, R.E.J., Kieft, I.E., J. Phys. D: Appl. Phys. **36**, 2908-2913 (2003)

Author: R.S. Tipa , E. Stoffels
Institute: Department of Biomedical Engineering,
Eindhoven University of Technology
Street: PO Box 513, 5600 MB
City: Eindhoven
Country: The Netherlands
Email: r.s.tipa@tue.nl

Effects of the Electrical Field on the 3T3 Cells

E. Stoffels[1], R.S. Tipa[1], J.W. Bree[2]

[1] Department of Biomedical Engineering, Eindhoven University of Technology, PO Box 513, 5600 MB, Eindhoven, The Netherlands
[2] Department of Electrical Engineering, Eindhoven University of Technology, PO Box 513, 5600 MB, Eindhoven, The Netherlands

Abstract — **This article surveys the application of using the electrical field for cell growing. The design of the experimental setup for generating the electrical field will be described and the procedure used for the biological tests that have been made. In the end are shown the results of the tests that confirm the fact that the electrical field has a positive influence on 3T3 cells, helping them to grow faster in time.**

Keywords — **electrical field, fibroblasts, cell growth**

I. Introduction

Many papers have been published relating that cells are affected by an electric field. This method is generally called electroporation which means that the permeability of the membrane increases. Electroporation occurs when a external electric field is applied to a biological cell. Depending on the charging time of the membrane either electroporation occurs at the cell membrane or at the intracellular membrane. The first kind of electroporation is well known and probably the best understood. When electroporation occurs at the cell membrane, protein channels in the cell membrane will open, figure 1, causing a change in ion concentration.

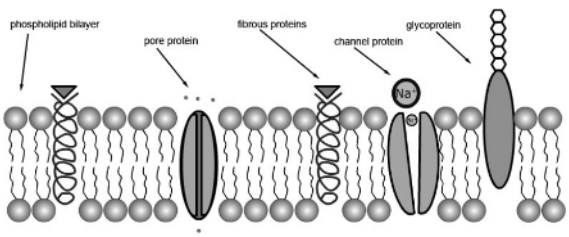


Fig. 1 Cell membrane

This change in ion concentration will cause cell stress. When the electric field is not too high (so that the voltage over the membrane is around the critical threshold of 1 Volt) and of relative short duration the cell will recover itself. Electroporation can be applied for example in gene transport and drug delivery[1][2]. Higher electrical fields, higher voltage across the cell membrane, and of longer duration causes irreversible damage to the cell and eventually cell death. This method is under investigation for applications as cold pasteurization and sterilization[3]. The critical voltage to affect the cell membrane is at least 1V. Since the size of a eukaryote is around 10^{1}m, a externally applied field in the order of 1KV/cm over the cell membrane is needed. A often used electrical model to simulate the voltage across the cell membrane in a conducting fluid is made by Dr. Schoenbach, figure 2. Dr. Schoenbach has done a lot of research in the area of cell treatment with pulsed electric fields [4]. The effects on a cell with an externally applied field can be described by a conductive body (cytoplasm) surrounded by a dielectric layer(membrane). The fluid outside the cell is represented by capacitors(Cs) and resistor(Rs). The membrane and its permeability is represented by capacitors(Cm). Resistor(Rc) represents the cytoplasm (interior) of the cell. The electric parameters for biologic cells are known from literature and it is therefore possible to calculate these electrical equivalent values [5]. The protein channels are modeled as voltage dependable conductance in series with voltage sources.

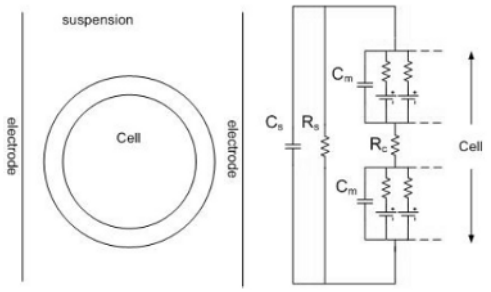


Fig. 2 Equivalent model of the cell

The charging time of the cell membrane is determined by the following formula [1].

$$\tau_m = ((\frac{1+2V}{1-V})\frac{\rho_s}{2} + \rho_c)C_m a$$

$$C_m = \frac{\epsilon_0 \epsilon_r}{d}$$

The required membrane voltage to affect the cells intracellular membrane is found to be of the same order as for the cell membrane and is therefore 1 Volt. The dimensions of the intracellular structures are roughly a factor 10 smaller compared to the cell size so the electric field must be

Chwee Teck Lim, James C.H. Goh (Eds.): ICBME 2008, Proceedings 23, pp. 1389–1392, 2009
www.springerlink.com

around 10kV/cm. To affect the intracellular membrane the cell membrane must be transparent. This is done by applying a pulse much shorter then the charge time of the cell membrane. Various effects have been observed after applying ultra short pulses to cells such as apoptosis (programmed cell death) and intracellular calcium release (indication for intracellular perturbation) [6][7]. However it is still unclear what exactly happens when these microsecond electric fields are applied.

II. Materials and methods

A. Description

The 3T3 cells were cultured in T75 flask and then transferred to well plates before the experiments. The incubator used for the cells had a constant temperature of 37º C and a 5% concentration of CO2. The medium used for the cell culture was DMEM (Dulbecco's modified Eagle's medium) on which we added 10 % fetal bovine serum (FBS), 1% glutamine and 1% penicillin / streptomycin. After 2-3 days in culture (when the cells reached a 80% confluence) the cells were counted and transferred to Ependorf tubes to be tested.

B. Exposure of the 3T3 cells in the electric field

In order to study the effects of the electrical field on the cells, the tubes containing the cell culture were exposed in the electrical field using the following set up. The electrical field is induced in the single winding coil. For the practical implementation of the RLC circuit, the setup used in the paper 'Multiple-gap spark gap switch' was first considered without the trigger circuit[8]. This would give a good impression about the capabilities of a low self inductance RLC series circuit.

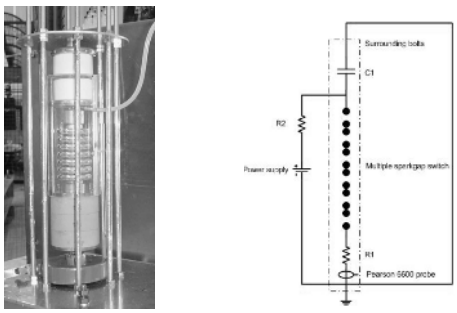


Fig. 3 Multiple spark gap

The article shows that an increasing number of spark gaps (keeping the total gap distance the same) and a coaxial structure give a very short rise time. Instead of the trigger circuit a dc voltage source was connected directly to the capacitor. Picture 12 shows the setup. The single winding coil wasn't placed in the circuit yet since this wouldn't increase the self inductance significantly. From top till bottom two capacitors, with high voltage cable to charge them, followed by the multiple spark gap and resistor can be seen. The Pearson 6600 current probe on the bottom was used to measure the current. Rise times of several tens of nanoseconds and a current of 600 Amps were measured. Although the article claims that an increasing number of spark gaps will decrease the rise time, own measurements showed that no significant difference in rise time were measured between two and six spark gaps (keeping the total distance the same). This is probably because an increasing number of spark gaps increases the height of the setup and will therefore increase the self inductance of the circuit. An increasing self inductance will then cause a longer rise time. Given this information decided was to use a spark gap consisting of two gaps so that the height of the circuit should be as short as possible and that the eight bolts surrounding the circuit would be replaced by a brass tube. In order to keep the height of the setup as short as possible the setup could be pressurized so that the distance between the spark gaps could be kept to a minimum. An air pressure of 8 bar and an voltage source of 50KV were available which means that the total distance between the gaps could be 2mm.

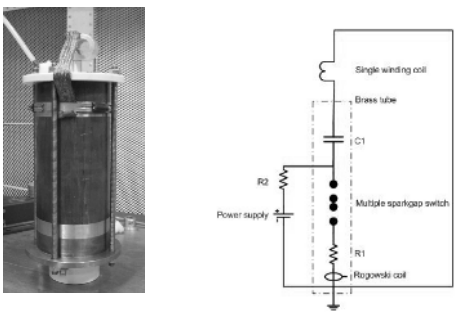


Fig. 4 The new set up

The new setup is practically the same as the former one, except that the tube is sealed with two flanges that keep the pressurized air inside the tube. The top flange had to be made out of an isolator since not only the single winding coil connection but also the high voltage and compressed air outlet had to go through the top flange. The material Ertalyte was chosen as isolator since is has a high breakdown voltage, 22KV/mm.

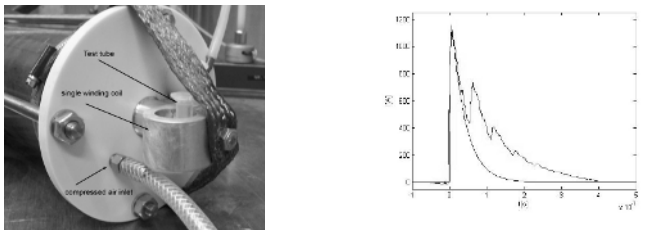


Fig. 5 Test tube in single winding coil and current measured during treatment

III. Results

The pictures taken of the cells treated between 1 and 5 minutes show an increase in cell growth as compared to the control sample.

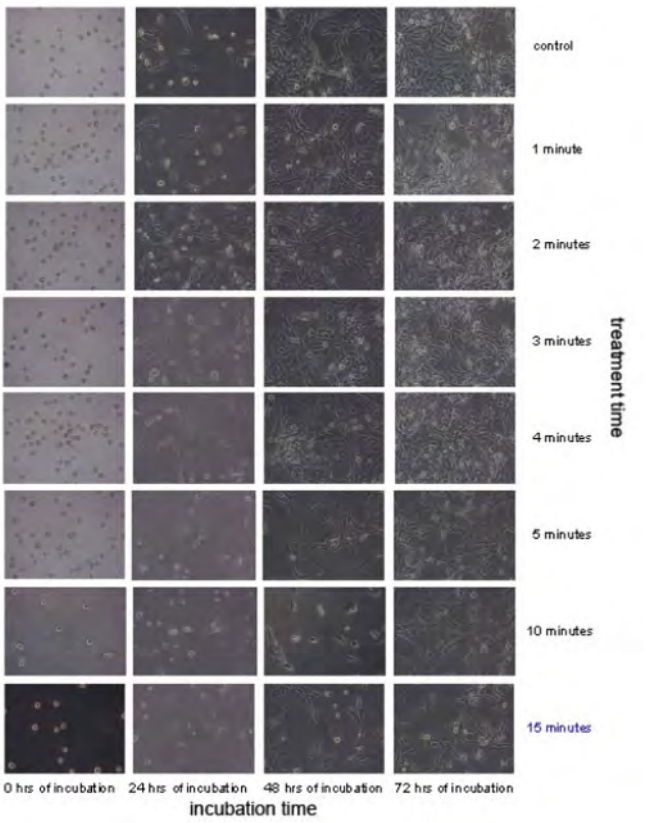


Fig. 6 Pictures of the samples after treatment (incubation time between 0-72 hours of incubation)

If we take a look to the graph from Figure 7, we can see that even if the treatment is longer, the number of dead cells is the same as for the case of untreated samples.

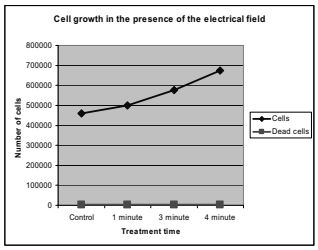
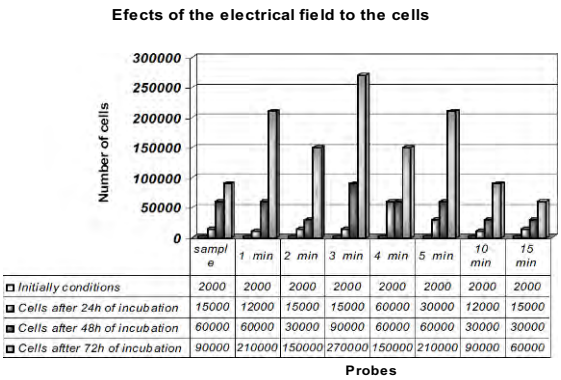


Fig. 7 Effects of the electrical field to the cells

Experiments of cells treated between 10 and 15 minutes show a decrease in cell growth compared to the control sample. Figure 7 shows the number of cells from 4 different pictures taken of the same sample, after a treatment time up to 15 minutes. This figure again shows an increase of the number of cells at a treatment time of 3 and and a decrease of the number of cells at a treatment time of 10 and 15 minutes.



	sample	1 min	2 min	3 min	4 min	5 min	10 min	15 min
Initially conditions	2000	2000	2000	2000	2000	2000	2000	2000
Cells after 24h of incubation	15000	12000	15000	15000	60000	30000	12000	15000
Cells after 48h of incubation	60000	60000	30000	90000	60000	60000	30000	30000
Cells after 72h of incubation	90000	210000	150000	270000	150000	210000	90000	60000

Fig. 8 Cells growth in time (The first 4 columns represent the cell growth for the untreated samples and the next ones the cell growth in time for cells exposed in the electrical field)

IV. Conclusions

The 3T3 cells are clearly affected by the pulsed electric field. Depending on the treatment time a noticeable effect on the cell growth was observed. For treatment times of about 2-5 minutes the cell growth increases as compared to the control samples. For longer treatment times(10-15 minutes) the cell growth significantly reduces, as compared to the control samples. More tests must be done to determine how significant these effects are. The underlying mechanism of these findings is not known, further research is necessary to obtain more insight.

REFERENCES

1. M. Benninger S. Li. Aplications of muscle electroporation gene therapy. Current Gene Therapy, 2:5, (2002).
2. J. Gehl. Electroporation: theory and methods, perspectives for drug delivery, gene therapy and research. Acta Physiologica, 177:11, (2003).
3. M.W. Gri±ths K. Smith, G.S. Mittal. Pasteurization of milk using pulsed electrical field and antimicrobials. Journal of Food Science, 67:4, (2006).
4. R. W. Alden S. J. Beebe K. H. Schoenbach, F. E. Peterkin. The effect of pulsed electric fields on biological cells: experiments and applications. IEEE transactions on plasma science, 25:2, (1997).
5. G. Shama B. M. Novac I. R. Smith P. R. Chalise, S. Permni and M. G. Kong. Lethality mechanisms in escherichia coli induced by intense sub-microsecond pulses. Applied physics letters, 89:2, (2006).
6. J. F. Kolb R. J. Swanson A. L. Garner J. Yang R. P. Joshi Nianyong Chen, K. H. Schoenbach and S. J. Beebe. Leukemic cell intracellular responses to nanosecond electric fields. Biochemical and biophysical research communications, 317:7, (2004).
7. R. R. Smith E. S. Buescher and K. H. Schoenbach. Submicrosecond intense pulsed electric field effects on intracellular free calcium. IEEE Transactions on plasma science, 32:4, (2004).
8. G.J.J. Winands A.J.M. Pemen E J.M. Van Heesch Z. Liu, K. Yan and D.B. Pawelek. Multiple-gap spark gap switch. REVIEW OF SCIENTIFIC INSTRUMENTS, 77, (2006).
9. J. W. Bree, The generation of a nanosecond Pulsed Electric Field for the manipulation of biological cells, Master reportSmith J, Jones M Jr, Houghton L et al. (1999) Future of health insurance. N Engl J Med 965:325–329

Author: R.S. Tipa, E. Stoffels
Institute: Department of Biomedical Engineering,
Eindhoven University of Technology
Street: PO Box 513, 5600 MB
City: Eindhoven
Country: The Netherlands
Email: r.s.tipa@tue.nl

^{99m}Tc(I)-tricarbonyl Labeled Histidine-tagged Annexin V for Apoptosis Imaging

Y.L. Chen[1], C.C. Wu[1], Y.C. Lin[1], Y.H. Pan[1], T.W. Lee[2] and J.M. Lo[1,3]

[1]Department of Biomedical Engineering and Environmental Sciences, National Tsing Hua University, Hsinchu 30013, Taiwan
[2]Institute of Nuclear Energy Research, Longtan 32546, Taiwan
[3]Institute of Nuclear Engineering and Science, National Tsing Hua University, Hsinchu 30013, Taiwan

Abstract — **Annexin V labeled with a γ emitter can be used for the imaging of apoptosis. ^{99m}Tc is very suitable for clinical imaging with its 140-keV γ ray, 6-h half life and economical availability from a ^{99}Mo-^{99m}Tc generator. In this study, we have constructed a form of annexin V with a N-terminal extension containing six histidine residues. The histidine-tagged annexin V (his-annexin V) can be directly labeled with ^{99m}Tc(I) tricarbonyl ion, $[^{99m}Tc(OH_2)_3(CO)_3]^+$.**

In labeling, $[^{99m}Tc(OH_2)_3(CO)_3]^+$ was freshly synthesized and incubated with his-annexin V at 37°C for 1 h. The resultant ^{99m}Tc(I)-his-annexin V was assayed by high performance liquid chromatograph (HPLC) with size exclusion column. The labeled yield was ≥ 87%. ^{99m}Tc(I)-his-annexin V was evidenced to be stable in PBS and serum. From the work, ^{99m}Tc(I)-his-annexin V has been characterized as a potent apoptosis imaging agent.

Keywords — **annexin V, his-annexin V, ^{99m}Tc(I) tricarbonyl ion, ^{99m}Tc(I)-his-annexin V, imaging agent for apoptosis**

I. Introduction

Apoptosis is initiated by externalization of phosphatidylserine (PS) from the inner leaflet of the cell membrane. Annexin-V, a human endogenous protein (35.8 kDa), binds selectively with nanomolar affinity (Kd=0.5-7 nM) to the membrane-bound, externalized PS. A γ-emitting nuclide labeled annexin V is applicable as an agent for imaging apoptosis.

Clinical experience has been taken with the ^{99m}Tc-labeled annexin V complex modified with a hydrazinenicotinamide ligand (^{99m}Tc-HYNIC-annexin V) [1]. However, there is still a need to improve ^{99m}Tc labeling annexin V with high specific activity, radiostability and bioactivity. ^{99m}Tc(I) tricarbonyl ion, $[^{99m}Tc(OH_2)_3(CO)_3]^+$ has recently been explored as a potent precursor for ^{99m}Tc labeling of biomolecules [2]. Histidine is capable of forming complex of very high stability with $[^{99m}Tc(OH_2)_3(CO)_3]^+$ [3]. In this study, annexin V with a N-terminal extension with peptide sequences containing six histidines was constructed for ^{99m}Tc labeling. By the method, the ^{99m}Tc(I) labeled histidine-tagged annexin V (^{99m}Tc(I)-his-annexin V) may most likely retain its membrane binding affinity and protein folding [4]. pETBlue-1-his-annexin V plasmid was constructed and transformed in *E. coli* and the his-annexin V protein expressed was extracted and purified by an affinity chromatography. Efficient labeling of his-annexin V with $[^{99m}Tc(OH_2)_3(CO)_3]^+$ and stability of the radiolabeled product, ^{99m}Tc(I)-his-annexin V in PBS and serum were demonstrated in the work.

II. Methods and meterials

A. Construction and verification of plasmid

1. Polymerase chain reaction (PCR)

A plasmid was constructed to express mutant form of human annexin V in *E. coli* under control of the phage T7 promoter. The forward primer Anx V-*Eco*R V-his-F: 5'-GATATCATGGCCCATCATCATCATCATCACGCTC-3'was designed with a *Eco*R V cutting site and six histidine DNA sequences. The forward primer was designed as previously described [4]. The primer Anx V-*Eco*R I-R : 5'GAATTCTTAGTCTTAGTCATCTTCTCCACAGAGC AGCAG - 3' was designed with a *Eco*R I cutting site. PCR of the template pOTB7 (Invitrogen) which encodes wild-type annexin V, was performed with proofreading *Pfu* DNA polymerase (Invitrogen) and with three steps of amplification as follows : 94°C for 30 sec, 53°C for 45 sec, 68°C for 45 sec each with 30 cycles. The PCR product was subjected to electrophoresis in 2% agarose gel and purified by gel extraction kit (Qiagen).

2. Digestion with restriction enzyme

The PCR product was ligated into pETBlue-1 vector (Novagen). 4 μL of appropriate 10X restriction enzyme buffer (25mM Tris-Acetate, 100mM potassium acetate, 10mM magnesium acetate, 1mM DTT), 1μL *Eco*R V, 1μL *Eco*R I , 3μg insert DNA or pETBlue-1 plasmid DNA, and sterile water were added to a final volume of 40 μL. The solution mixture was incubated at 37°C for 1 h. The product was cleared up by PCR purification kit (Qiagen).

Chwee Teck Lim, James C.H. Goh (Eds.): ICBME 2008, Proceedings 23, pp. 1393–1396, 2009
www.springerlink.com

3. Ligation reaction

1 μL 10X T4 DNA ligase buffer (300 mM Tris-HCl , 100 mM $MgCl_2$, 100 mM DTT and 10 mM ATP), 1μL of T4 DNA ligase (Promega), 50 ng of vector DNA and 500 ng of insert DNA were added and adjusted to a total volume of 10 μL by sterile water. The mixture was incubated overnight at room temperature and then kept on ice for transformation.

4. Transformation

One tube of ECOS™ competent cells (Yeastern Biotech Co.,Ltd) frozen at -70°C was taken out and put on ice for liquefaction until 1/3 volume was thawed. 100μL of the competent cells was mixed with 5 μL of the ligation product. The mixture was incubated on ice for 30 min and heat-shocked the cells in a 42°C water bath for 45 sec and incubated on ice for 2 min again. The cells were spread over the surface of the pre-warmed LB agar containing 50 μg/mL carbenicillin, 70 μg/mL X-gel, and 80 mM IPTG. The plate medium was incubated overnight at 37°C. Plasmid DNA was prepared from white carbenicillin-resistant colonies and screened by PCR and restriction mapping for the presence of the desired insert. Finally the positive clones were subjected to Protech Technology Enterprise Co., Ltd. to verify the presence of the desired insert.

B. Expression and purification of the protein

1. Protein expression

pETBlue-1/his-annexin V plasmid was transformed into the *E. coli* strain, Tuner(DE3)pLac I (Novagen). Each clone was grown overnight at 37 °C with shaking in Terrific Broth (Invitrogen) containing carbenicillin (50 μg/mL). The cells were separated from culture medium by centrifugation for 20 min at 6000*g* and washed in ice-cold buffer **1** (50 mM Tris-HCl, 150 mM NaCl, pH8.0). Bacteria were ruptured by sonication in ice-cold buffer **2** (50 mM Tris-HCl, pH 7.2, 10 mM $CaCl_2$), being every 10-sec sonication following every 10-sec pause time in ice bath, with a total sonication time of 20 min. Then the mixture was centrifuged for 40 min at 16000 *g*. The supernatant was discarded, and the annexin V bound to bacterial membranes was released by resuspending the pellet in EDTA buffer (50 mM Tris-HCl, pH7.2, 20mM EDTA). Bacterial membranes were removed by centrifugation for 40 min at 16000*g*; the supernatant containing annexin V was filtered with a 0.45 μm filter and then dialyzed against binding buffer (20 mM Tris-HCl,0.3 M NaCl, and 5 mM imidazole, pH 7.9) at 4 °C.

2. Purification of the protein

A 10 mm diameter plastic column tube was packed with 6 mL of Ni^{2+} sepharose 6 fast flow (GE Healthcare). The Ni^{2+} sepharose column was equilibrated with 50 mL binding buffer (20 mM Tris-HCl, 0.3 M NaCl, and 5 mM imidazole, pH 7.9) and then loaded with the dialysand of his-annexin V. The bound protein was eluted steppedly with 20 mL pH 7.9 buffer (20 mM Tris-HCl, and 0.3 M NaCl) containing increasing concentrations of imidazole (20 mM, 40 mM, 80 mM, 100 mM, 150 mM, 300 mM, and 500 mM, respectively). The eluate containing his-annexin V was collected and dialyzed against 20 mM HEPES, pH 7.4, 100mM NaCl. The dialyzed product was concentrated by Amicon® Ultra-15 Centrifugal Filter Devices using a 10 kDa cutoff membrane and stored at -70°C.

3. SDS-Page and immunoblotting

Samples were taken from the different elutions during purification and subjected to 10% SDS-PAGE gel. The separated protein was stained with Commassie brilliant blue R-250 or electroblotted on nitrocellulose for Western blotting analysis. After being blocked with 5% non-fat milk in PBS, the membrane was washed four times with PBS for 15min and incubated further with a 1:2000 dilution of his-tag monoclonal antibody (Novagen) to his-annexin V for 1 h. The membrane was washed with 0.05% Tween/PBS for 10 min and incubated with a 1:5000 dilution of horseradish peroxidase (HRP)-labeled goat anti-mouce IgG (Novagen). The membrane was washed four times with 0.05% Tween/PBS for 15 min and was visualized by the addition of the G: BOX (SYNGENE) and exposure to for 5–10 min.

C. Radiolabeling of his-annexin V with $[^{99m}Tc(OH_2)_3(CO)_3]^+$

1. ^{99m}Tc(I) Tricarbonyl Ion Labeling His-annexin V

$[^{99m}Tc(OH_2)_3(CO)_3]^+$ was prepared as previously described [5]. Labeling of $[^{99m}Tc(OH_2)_3(CO)_3]^+$ to his-annexin V was carried out by adding 50 μg (50 μL) of his-annexin V to 100 μL (20 mCi) of $[^{99m}Tc(OH_2)_3(CO)_3]^+$ solution, and the solution mixture was heated at 37°C for 1 h. The resultant ^{99m}Tc(I)-his-annexin V product was purified with a Sephadex G-25 packing column, using normal saline as the eluent at a flow rate of 1 mL/min. Non-reacted $[^{99m}Tc(OH_2)_3(CO)_3]^+$ was simultaneously removed from the separation method. The purity of ^{99m}Tc(I)-his-annexin V was checked by high performance liquid chromatography (HPLC) on a size exclusion column(Ultrahydrogel™ 250 7.8×300 mm column) using PBS as the eluent at a flow rate of 0.8 mL/min.

2. Stability Test for ^{99m}Tc(I)-his-annexin V in PBS and Serum

The purified ^{99m}Tc(I)-his-annexin V eluate as described above was diluted 10 times and 0.1 mL of the solution was

incubated with 0.9 mL of PBS or serum at 37°C. The stability of the radiolabeled annexinV in PBS or serum was assayed by radio-HPLC after incubation for 0.5, 1, 2, 4 and 6 h.

III. Results and Discussion

A. Construction of recombinant expression plasmid

The Anx V-*Eco*R V-his-F primer and Anx V-*Eco*R I-R primer were used to amplify a 984 bp fragment (Fig. 1), which contained the entire wild type coding region, six histidine coding region, and endonuclease sites . The fragment was ligated into pETBlue-1 plasmid at *Eco*R V/ *Eco*R I sites to create a recombinant molecule pETBlue-1/his-annexin V (Fig. 2). The result of the sequence analysis of the insert DNA of the positive clone indicates that it contains 984 nucleotides and its amino acid sequences (data not shown).

pETBlue-1/ his-annexin V was transformed into *E. coli* strain Tuner(DE3)pLac I, which supplied sufficient *lac* repressor from the compatible pLacI plasmid and screened in Terrific broth containing carbenicillin (50 μg/mL). The plasmid extracted from positive clone was further investigated by the restriction endonuclease cutting and DNA sequencing.

It was observed that there existed a very intensely staining protein band with an apparent molecular mass of 36 kDa (Fig. 3, lane 1), as indicated by scanning the protein density of the SDS–PAGE gel. The harvested cells were sonicated in ice-cold buffer **2** on ice and centrifuged. SDS–PAGE analysis showed that almost all expressed his-annexin V was precipitated by addition of calcium ion, with little his-annexin V remaining in the supernatant (Fig. 3, lane 2). Soluble rh-his-annexin V was released effectively by resuspending the precipitate in the EDTA buffer (Fig. 3, lane 5). The major proportion of target protein was found in the supernatant, accounting for over 50% of the total soluble cellular protein as estimated by densitometric analyses, while little target protein appeared as inclusion body in the pellet (Fig. 3, lane 4).

A single-step affinity chromatography with Ni^{2+} sepharose column was performed for further purification. His-annexin V was eluted at eluent buffer contaning 40 mM and 80 mM imidazole (Fig. 4, lane 2 and 3). Single protein band exhibiting a molecular mass of 36 kDa was present in SDS–PAGE gel (Fig. 5A, lane 1). The antigenicity of his-annexin V was confirmed by Western blot analysis with a his-tag monoclonal antibody (Fig. 5B, lane 1). The final yield of protein was approximately 39 mg of protein/L of culture with a purity of ~98% as judged by SDS-PAGE.

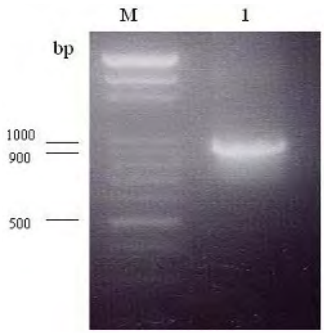


Fig. 1 Agarose gel electrophoresis of PCR product of his-annexin V. M, DNA marker; 1, PCR product.

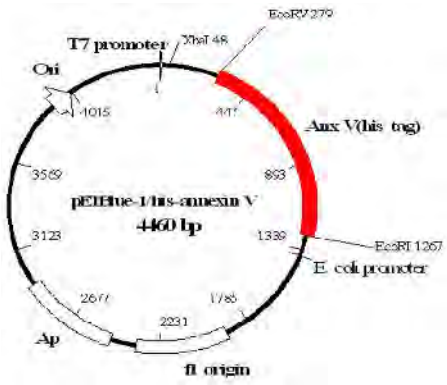


Fig. 2 Schematic representation of pETBlue-1/his-annexin V expression.

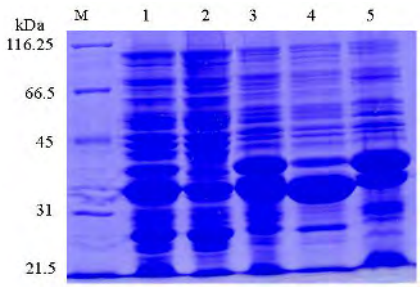


Fig. 3 Expression of cloned his-annexin V. Tuner(DE3)pLac I containing expression vector pETBlue-1/his-annexin V was disrupted by sonication. The soluble and precipitated fractions were separated by centrifugation and applied to 10% SDS-PAGE gel stained with Coomassie blue R-250. Lane M, molecular weight markers; lane 1, total protein of E. coli incubated overnight at 37 °C; lane 2, supernatant of Escherichia coli sonicated in calcium buffer; lane 3., precipitated fraction after being sonicating; lane 4, his-annexin V released from the pellet by EDTA buffer; lane 5, remaining protein in the pellet after being treated with EDTA buffer

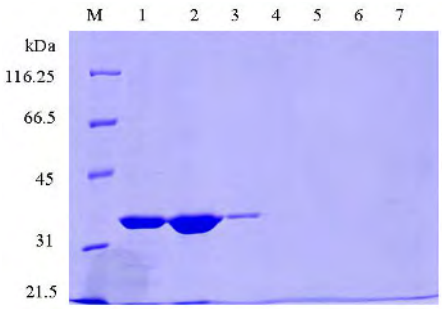


Fig. 4 SDS–PAGE analysis of the purity of rh-his-annexin V during the purification process. Elute the bound protein with various concentration imidazole eluent buffer. Lane M, molecular weight markers; lane 1, 20 mM imidazole; lane 2, 40 mM imidazole; lane 3, 80 mM imidazole; lane 4, 100 mM imidazole; lane 5, 150 mM imidazole; lane 6, 300 mM imidazole; lane 7, 500 mM imidazole.

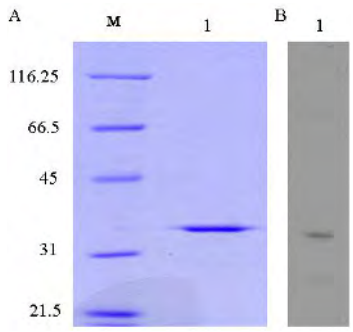


Fig. 5 SDS-PAGE analysis and Western blot analysis of mutant proteins. Recombinant mutant annexin V molecule was analyzed on a 10% gradient gel and stained with Commassie Brilliant Blue. Molecular mass standards (with Mw in parentheses) were *β*-galactosidase (116.25 kDa), albumin (66.2 kDa), ovalbumin (45 kDa), carbonic anhydrase (31 kDa), soybean trypsin inhibitor (21.5 kDa).

B. Labeling his-annexin V with ^{99m}Tc(I)-tricarbonyl ion

The preparation of his-annexin V labeled with $[^{99m}Tc(OH_2)_3(CO)_3]^+$ was assayed by HPLC on a size exclusion column using phosphate buffer saline(PBS) as the eluent. The retention time of ^{99m}Tc(I)-his-annexin V was approximately at 9.1 min as detected by a radio-detector (Fig. 6). The radiolabeled yield of ^{99m}Tc(I)-his-annexin V was estimated to be greater than 87%.

The radiochemical purity of ^{99m}Tc(I)-his-annexin V maintained at greater than 95% when incubated either in PBS or serum at room temperature even for as long as 6 h. The ^{99m}Tc(I)-his-annexin V was evidenced to be stable in PBS and serum.

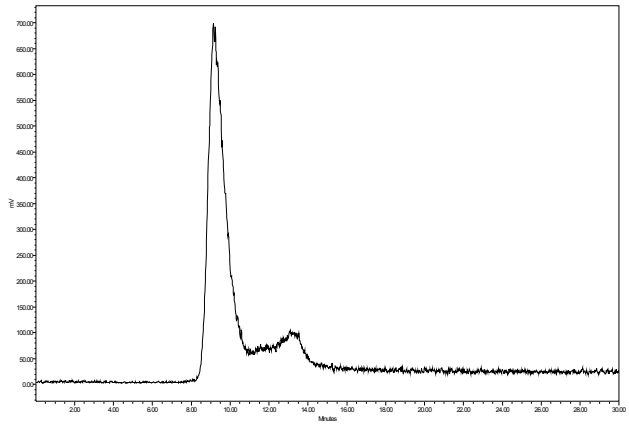


Fig. 6 Size exclusion HPLC of 99mTc(I)-his-annexin V with radio-detection

Acknowledgment

We are indebted to the National Science Council of Taiwan for support under No. NSC 95-2113-M-007-033-MY3.

References

1. Blankenberg F G, Katsikis P D, Tait J F et al. (1999) Imaging of apoptosis (programmed cell death) with ^{99m}Tc annexin V. J Nucl Med 40(1):184-91.
2. Alberto R, Schibli R, Egli A et al. (1998) A novel organometallic aqua complex of technetium for labeling of biomolecules. J. Am. Chem. Soc. 120:7987-7988.
3. Egli A, Alberto R, Tannahill L et al. (1999) Organometallic ^{99m}Tc-aquaion labels peptide to an unprecedented high specific activity. J Nucl Med 40(11):1913-7.
4. Tait J F, Smith C, Gibson D F. (2002) Development of annexin V mutants suitable for labeling with Tc(I)-carbonyl complex. Bioconjug Chem, 13(5):1119-2
5. Chen W J, Yen C L, Lo S T et al. (2008) Direct ^{99m}Tc labeling of Herceptin (trastuzumab) by ^{99m}Tc(I) tricarbonyl ion. Appl Radiat Isot. 66: 340-5.

Author: J.M. Lo
Institute: Department of Biomedical Engineering and Environmental Sciences, National Tsing Hua University, Hsinchu
Street: Kuang-Fu Rd
City: Hsinchu
Country: Taiwan
Email: jmlo@mx.nthu.edu.tw

Cell Orientation Affects Human Tendon Stem Cells Differentiation

Zi Yin[1], T.M. Hieu Nguyen[2], Xiao Chen[1], Hong-Wei Ouyang[1*]

[1]Center for Stem Cells and Tissue Engineering, School of Medicine, Zhejiang University, China
[2] Division of Bioengineering, National University of Singapore, Singapore
Corresponding author: Dr HW Ouyang, Email: hwoy@zju.edu.cn

Abstract — **Tendon is a specific connective tissue composed of parallel collagen fibers. The effect of matrix orientation on tendon differentiation has not been investigated. The recent discovery of tendon stem cells (TSPCs) [1] provided an ideal cell model for tendon biology study. This study focused on investigating the effect of cell orientation, which induced by aligned electrospun poly (L-lactic acid) (PLLA) nanofibers, on human TSPCs differentiation..**

The multipotency and stem cell surface markers of the fetal human TSPCs were identified. The TSPCs were then seeded onto the aligned and randomly oriented PLLA scaffolds. Cell morphology, tendon specific genes expression were evaluated by SEM, and RT-PCR. The degree of extra cellular matrix (ECM) production was evaluated by comparing the amount of collagen on aligned and randomly oriented scaffolds.

TSPCs on the aligned nanofibers were spindle-shaped and oriented in the direction of the nanofibers. The SEM micrograph also revealed the appearance of filament-like structures, which were suspected to be focal adhesions, connected between cells and nanofibers. The expression of tendon specific or bone specific genes was upregulated in the TSPCs growing on random nanofibers, while tendon specific genes but not bone specific genes were upregulated in aligned nanofibers, suggesting that nanofibers structure can influence TSPC differentiation.

In conclusion, cell orientation has effect on hTSPCs differentiation, moreover, the aligned nanostructures of biomaterials provides an instructive microenvironment to modulate and guide TSPCs differentiation ranging from cell orientation to gene expression and could be serve as proper scaffolds for tendon tissue engineering.

Keywords — **TSPCs, differentiation, aligned nanofibers**

I. Introduction

Tendon injuries are common clinical problems due to the poor regeneration ability of tendons. The tendon stem cells (TSPCs), which are derived from human tendon, exhibit universal stem cells characteristics such as clonogenic, self-renewal and multipotency[1]. This cell population resides within an in vivo niche that comprises primarily of ECM. In the same study, it is also showed that human TSPCs formed tendon-like tissue in vivo 8 weeks after transplantation with HA/TCP and Matrigel carriers. Hence, the identification of such cells promises a great potential for tendon repair. However, induction of TSPCs into mature tenocytes has become a major challenge of tendon tissue engineering.

In this study, we attempt to culture TSPCs on aligned nanofibers scaffolds. Nanofibers have been proven a promising biomaterial for bone tissue engineering [2].Moreover, human ligament fibroblasts (HLFs) cultured on aligned nanofibers is showed to have similar morphology to ligament fibroblasts in vivo. They are spindle-shaped and oriented on the fiber direction. The aligned structure also induced an increase in ECM production rate [3]. Based on those researches, we hypothesize that nanofibers alignment induces the differentiation of TSPCs. This study focused on investigating the potential of aligned electrospun poly(L-lactic acid) (PLLA) nanofibers on teno-lineage differentiation of human TSPCs and their performance with randomly oriented PLLA nanofibers is compared as well.

II. Materials and methods

Cell culture: After isolation from human fetal tendon, the TSPCs are cultured in a control medium contains Dulbecco's Modified Eagle Medium (DMEM, low glucose) with 10% fetal bovine serum (FBS) and 1% penicillin-streptomycin (P/S). Media change is performed every 3 days. After 8-10d, the colonies that formed are visualized using methyl violet staining. Monocloning selection is conducted and 6 clones are obtained.

Monocloning selection: hTSPCs passage 2 were used for cloning. After subculture, the cells were counted using a hemacytometer. Then, 1000 cells were plated on a 10cm dish for mono-cloning selection. In addition, two 6 cm dish were with the density of 300 and 1000 cells per dish were also used to assess the colony forming efficiency of hTSPCs. The cells were cultured in DMEM-LG containing 20% FBS and 1% P/S. The medium was changed every 3 days. The individual clones are allowed to develop until they reach several mm in diameter. The locations of clones to be removed are then marked on the lids of the dishes. After 12 days, 4 clones were selected by using pipette and tip to detach cells in the circles marked previously under a microscope. The cultured room was sterilized under UV 30min prior to selection. After that, the clones were trans-

Chwee Teck Lim, James C.H. Goh (Eds.): ICBME 2008, Proceedings 23, pp. 1397–1400, 2009
www.springerlink.com

ferred to four 3.5cm dishes and continue to be cultured in DMEM-LG medium with 10% FBS and 1%

Methyl violet staining: 10 days after cloning, methyl violet staining was performed to visualize the colonies in the 6cm dish that initially contained 1000 cells. First, the medium was discarded and the cells were washed with PBS. After that, methyl violet was added to the dish which was then incubated at room temperature for 10 min. After methyl violet was removed, the cells were washed with PBS again till the clones were visualized. Approximately, there were 50 clones formed.

Fluorescence-activated cell sorting (FACS) analysis: Cells ($5x10^5$) were incubated with 1 μg of PE- or FITC-conjugated mouse specific to human monoclonal antibodies for 1 h at 4 ºC. PE-or FITC-conjugated isotype-matched IgGs (BD Pharmingen) were used as controls. After two washes with PBS containing 1% FBS, the stained cells were subject to FACS analysis (Coulter Epics XL). The percentage of the cell population in each quadrant was calculated. All antibody conjugates were purchased from Pharmingen/BD Biosciences unless specifically mentioned, which include FITC-conjugated mouse specific antibodies to human CD18 (clone 6.7, IgG1, κ), CD34 (581, IgG1, κ),CD90 (5E10, IgG1, κ), and PE-conjugated mouse specific antibodies to human CD44 (515, IgG1, κ). For non-conjugated mouse specific antibody to human CD105, they were incubated with 1 × 106 cells for 1 h 4ºC. After washing, the cells were incubated with rabbit anti-mouse IgG-FITC conjugated for 45 min on ice. After washing, the samples were analyzed using a Coulter Epics XL flow cytometer**.**

Multipotent differentiation: We studied the *in vitro* multidifferentiation potential of the hTSPCs toward osteogenesis, adipogenesis and chondrogenesis as described previously[4][5][6].

von Kossa staining: The cells are rinsed on 100-mm^2 plates with phosphate-buffered saline and fixed in 4% paraformaldehyde for 1 h at room temperature. They were then incubated in 5% silver nitrate for 30 min in the dark, after which they were rinsed with distilled water and exposed to ultraviolet light for 1 h.

Oil Red O staining: The cells are rinsed on 100mm plate with PBS and fixed in 10% formalin for 1h. They are then stained with propylene glycol (2x5min), Oil Red O (1x7min) then agitate and 85% propylene glycol (1x3min) respectively. After rinsed in distilled water, they are continually stained with Hematoxylin in 1 minute, rinsed again then mouted with aqueous mounting media, Glycerin Jelly.

Safranin O staining: The cells are rinsed on 100 mm plate with PBS and fixed in 10% neutral buffered formalin for 1h at room temperature. The cells are then embedded in paraffin. The pellet sections are then deparaffinized in xylene (3x3min), 100% ethanol (2x3min), 95% ethanol (2x3min) and 70% ethanol (1x3min). Stain the sections in Weigert's iron hematoxylin for 4 mins, then destain in fresh acid alcohol (1ml concentrated HCl in 100ml 70% ethanol) and rinse in tap water. Continue stain in 0.02% aqueous fast green FCF fro three minutes, then wash in 1% acetic acid for 30s. Finally, the sections are stained in 0.1% aqueous Safranin-O for 5 mins then dehydrated in 95% ethanol (2x5min), 100% ethanol (3x5min), then xylene (3x5min).

Scanning electron microscopy: 2 days after seeding cells on nanofibers scaffold, the cell morphology and distribution are visualized using SEM. Specimens are fixed in 0.25% glutaraldehyde solution, then rinsed in phosphate-buffered saline 3 times, 30 minutes each time The specimens were immersed in OsO_4 for 40 min and then rinsed in phosphate-buffered saline (PBS; Gibco) 3 times, 30 minutes each time and dehydrated in increasing concentrations of acetone (from 30%-50%-70%-80%-90%-95%-100%-100%-100%, 10 mins for each concentration). After drying, the specimens were mounted on aluminum stubs and viewed in a Hitachi S-3000N SEM with an accelerating voltage of 15 kV.

RNA Isolation and Semiquantitative Reverse Transcription-Polymerase Chain Reaction (RT-PCR): Total cellular RNA was isolated by lysis in TRIZOL (Invitrogen) followed by one-step phenol chloroform- isoamyl alcohol extraction as described in protocol. 200 nanograms of total RNA was reverse-transcribed into complementary DNA (cDNA) by incubation with 200 U of reverse transcriptase in 20 μL of reaction buffer at 37 centi-degree for 1 h. The semiquantitive measurement of the band density was calculated by using Glyko Bandscan (Glyko, Inc., USA).

*Collagen assay:*1, 4 and 7 days after seeding, the amount of deposited collagen in the scaffold and the collagen in medium were quantified using two collagen assay kits and following the manufacturer's protocol (Jiancheng Ltd., Nanjing, China).

III. Results

Study the characteristics of hTSPCs

In order to demonstrate tendon-derived cells are stem cells, we isolated and cultured single-cell suspensions to do colony-forming assay. Fig. 1, A shows the morphology of hTSPCs. After 10-12d, colonies which had formed from single cells were visualized by methyl violet staining (Fig1 B, C). Two independent experiments showed that the colony-forming efficiency was 5%~10%. The results from methyl violet staining proved the stem characteristics: clonogenic and self-renewal of hTSPCs

We determined the multidifferentiation potentials of hTSPCs toward adipogenesis, osteogenesis and chondro-

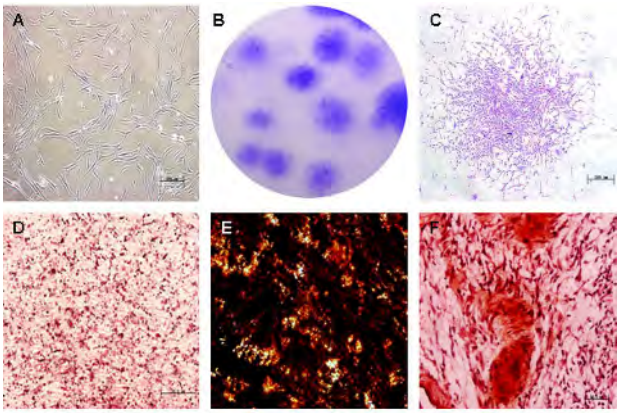


Fig. 1 Characteristics of hTSPCs. (A) morpholosy of hTSPCS. (B, C) colony formation of hTSPCs. (D-F) shows the multipotential of the hTSPCs

genesis. 3 weeks after adipogenic induction, Oil Red O staining was performed to visualize the lipid drops which indicate the differentiation of adipocytes (Fig.1, D). Von kassa staining was performed to give evidence of successfully osteogenic differentiation (Fig.1, E). Chondrogenic differentiation after 4 weeks induction in chondrogenic medium was assessed in pellet culture by Safranin O staining of the proteoglycan-rich ECM (Fig.1, F).

In this study, flow cytometric analysis was used to examine the presence of surface antigens on hTSPCs. Five CD markers were used: CD34 (hematopoietic stem cell marker), CD44, CD90, CD18 (bone marrow stem cell markers) and CD105. The results showed that hTSPCs were positive with CD90, CD105, and CD44 and negative with CD34 and CD18. This results, which were consistent with previous reports [1], further confirmed that hTSPCs was tendon stem/progenitor cells (TSPCs).

Scaffold and cell morphology characterization

Aligned and random poly (l-lactic acid) (PLLA) scaffolds were fabricated by electrospining to assess the effect of cell orientation on hTSPCs differentiation. After fabrication, SEM micrographs (Hitachi S3000N, 15kV) of both aligned and randomly oriented nanofiber scaffolds were taken to assess the degree of alignment (Fig.2, A, B). The results showed that the diameters of the nanofibers of the aligned nanofiber scaffolds and randomly oriented nanofiber scaffolds were comparable. The majority of the fibers in the aligned scaffolds formed angles from 0 to 10°with respect to the vertical axis. Hence, the fibers can be considered to be parallel with each other.

Before the scaffolds were used, the toxicity test was conducted to ensure the PLLA nanofiber scaffolds were nontoxic and could be used to accommodate hTSPCs. The next day after seeding cells on the nanofibers, the cell morphology on the scaffolds was observed under a scanning electron microscope (Fig. 2, C, and D). The SEM micrograph showed that the cells on the aligned nanofiber scaffolds were spindle-shape and oriented in the direction of the nanofibers whereas they look different on the randomly oriented scaffolds. The cells secrete ECM (extra cellular matrix) in both scaffolds.

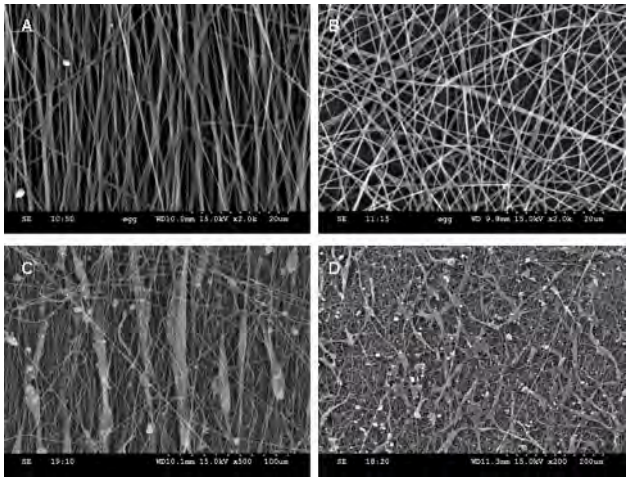


Fig. 2 SEM micrographs of aligned nanofibers (A) and random nanofibers (B). SEM images show the hTSPCs orientation on nanofibers (C) and random nanofibers (D)

Semi-quantities RT-PCR and collagen assay analysis

The gene expression changes of hTSPCs cultured on scaffolds were evaluated by Semiquantitative RT after 3 days, 7 days, and 14days. A and R indicates the gene expression of cells cultured on aligned nanofibers and randomly oriented nanofibers, respectively. A general increase in expressions of tendon specific genes (six 1, eya2) and matrix genes (collagen I and collagen III) was observed when cell grown on nanofibers, when compared to the cells before seeding on the nanofiber scaffold (Fig. 3). Moreover, we noticed the expression level of an osteogenic marker, Runx 2, was significantly upregulated in hTSPCs on ran-

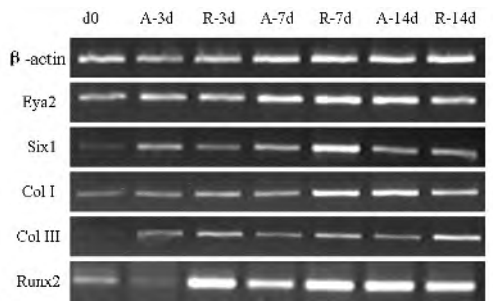


Fig. 3 semiquantitive RT-PCR analysis. A, aligned scaffold; R, random scaffold.

domly oriented nanofibers compared with that on aligned ones (Fig. 3).

We also examined the total collagen secreted by hTSPCs in the medium and on the scaffolds. The hTSPCs cultured on aligned nanofibers produced more collagen than the cells on random oriented ones at 1d, 4d and 7d (data not shown) .

These results shows aligned nanofibers, which can promote hTSPCs tendon-lineage differentiation whereas inhibit osteogenesis, are suitable for tendon tissue engineering.

IV. Discussion

The present study indicate that hTSPCs cultured on the aligned nanofibers were similar with tenocytes in vivo and could be serve as proper combination for tendon tissue engineering.

Adult hTSPCs, which had been reported by Bi, Y et al, had great tendon-formation potential. However, the fetal TSPC may be optimal seed cells as the tendon regeneration potential of fetal cells [1]. As showed in the results, fetal cells had similar morphology with tenocytes and high efficiency of colony formation. The phenotype and multipotency is similar with BMSC and adult TSPC. Therefore, fetal TSPC could provide as optimal seed cells for tendon tissue engineering.

Aligned PLLA nanofibers were fabricated using a simple rotating collector. The diameter and the arrangement of the aligned nanofiber scaffold is a biomimetic structure that is similar with collagen fibers of tendon. Previous work demonstrated that the structure and materials of the scaffold play an important role in cell differentiation and tissue repair and is suitable for ligament cell proliferation and overall ligament and tendon strength [3].

To evaluate the differentiation and ECM production of hTSPCs seeded on aligned nanofibers, we assessed cellular responses, tendon and bone specific gene expression and ECM production. hTSPCs attached to the nanofibers through the small filaments connect to the scaffold. Cells seeded on aligned nanofibers become spindle-shaped that similar with tenocytes in vivo. Gene expression of the hTSPCs shows that the tendon-related genes, such as six1, collagen III were upregulated after seeding on nanofibers.

However, osteocytes also express those genes. hTSPCs seed on random fibers showed higher runx2 expression compare to cells seeded on aligned scaffold. Moreover, those cells seeded on aligned nanofibers showed lower runx2 expression than those of normal cells and the effect was reversed after 7 days culture. It indicated that the nanofibers may induce the osteogenesis and the aligned nanofibers may inhibit this effect and induce tenogenesis by inducing the hTSPCs as spindleshaped tendon-like oriented cells . Those results indicated that the hFTSCs and aligned nanofibers could serve as an optimal material for tendon tissue engineering. However, we did not know the mechanism of this phenomenon. A future study should be explored to find out the mechanism.

V. Conclusions

In conclusion, cell orientation has effect on hTSC differentiation, moreover, the aligned nanostructures of biomaterials provides an instructive microenvironment to modulate and guide TSCs differentiation ranging from cell orientation to gene expression and could be serve as proper scaffolds for tendon tissue engineering.

Acknowledgment

The authors thank Chen Han ming for the SEM observations. This work was supported by the National Natural Science Foundation of China (30600301, 30600670, U0672001) and Zhejiang Province grants (R206016, 2006C 14024, 2006C 13084).

References

1. Bi, Y., Ehirchiou, D., Kilts, T. M., Inkson, C. A., Embree, M. C., Sonoyama, W., Li,L., Leet, A. I., Seo, B. M., Zhang, L., *et al.* (2007). Identification of tendon stem/progenitor cells and the role of the extracellular matrix in their niche. *Nature Medicine 13(10): 1219-1227.*
2. Yoshimoto H., Shin Y.M., Terai H., Vacanti J.P. (2002). A biodegradable nanofiber scaffold by electrospinning and its potential for bone tissue engineering. *Biomaterials 24: 2077–2082*
3. Lee C.H., Shin H. J., Choa I. H., Kang Y. M., Kim I. A., Park K. D., Shin J. W. et al. (2004). Nanofiber alignment and direction of mechanical strain affect the ECM production of human ACL fibroblast. *Biomaterials 26: 1261–1270*
4. Bi, Y. et al. Extracellular matrix proteoglycans control the fate of bone marrow stromal cells. *J. Biol. Chem. 280, 30481–30489 (2005).*
5. Gimble, J.M. et al. Bone morphogenetic proteins inhibit adipocyte differentiation by bone marrow stromal cells. *J. Cell. Biochem. 58, 393–402 (1995).*
6. Johnstone, B., Hering, T.M., Caplan, A.I., Goldberg, V.M. & Yoo, J.U. In vitro chondrogenesis of bone marrow–derived mesenchymal progenitor cells. *Exp. Cell Res. 238, 265–272 (1998).*
7. Sciore P, Boykiw R, Hart DA. Semiquantitative reverse transcription-polymerase chain reaction analysis of mRNA for growth factors and growth factor receptors from normal and healing rabbit medial collateral ligament tissue. J Orthop Res 1998;16:429-437.

Author: Ouyang Hongwei
Institute: Zhejiang university
Street: 388# Yu Hang Tang Road
City: Hang Zhou
Country: China
Email: hwoy@zju.edu.cn

Synthesis and Characterization of TiO_2+HA Coatings on Ti-6Al-4V Substrates by Nd-YAG Laser Cladding

C.S. Chien[1,4], C.L. Chiao[2], T.F. Hong[3], T.J. Han[1], T.Y. Kuo[5]

[1]PhD Student, Institute of Biomedical Engineering, National Cheng Kung University, Tainan 710, TAIWAN
[2]Master Student, Department of Mechanical Engineering, Southern Taiwan University, Tainan 710, TAIWAN
[3]Assistant Professor, Department of Materials Engineering, National Pingtung University of Science and Technology, Pingtung 912, TAIWAN
[4]Attending Orthopaedic Surgeon, Chimei Foundation Hospital, Tainan 701, TAIWAN
[5]Professor, Department of Mechanical Engineering, Southern Taiwan University, Tainan 710, TAIWAN

Abstract — **Hydroxyapatite (HA) coatings are usually used to improve the bonding abilities between implants and surrounding bone tissues. By means of a novel laser cladding technology, a good quality metallurgy bonding interface can be successfully formed between coatings and titanium-based materials. However, dissipation of phosphorous (P) from HA during laser cladding process is a main concern, because the alteration of Ca/P ratio may cause bioactivity degradation of the coatings. The aim of this study is to overcome this problem and enhance the bioactivity of the coatings. Two biocompatible titanium oxides (TiO_2) with different crystal structures (anatase and rutile) were added with HA powders in the initial stage, and these mixtures were then coated on the Ti-6Al-4V plates by the Nd-YAG laser. All the samples were characterized by a range of techniques for investigating and evaluating how these TiO_2 additives affected the microstructure, chemical composition, Ca/P ratio and bioactivity of the coating products.**

Keywords — **laser cladding, hydroxyapatite, TiO_2, Ti-6Al-4V**

I. Introduction

Hydroxyapatite (HA) is the major coating material on biomaterial applications. In recent HA laser cladding research works, most efforts are devoted on promoting the adhesion between the coating layer and substrates [1-2]. However, due to the melting point of phosphorous (P) in HA is relatively low, it is easily vaporized during the melt-coating process and cause the bioactivity degradation of produced coatings [3]. For eliminating this phenomenon, bioactive powder materials were added in HA coatings for improving the bioactivity of final products [4-5]. Titanium dioxide (TiO_2) is one of the attractive candidates, due to its bioactivity and also helps to enhance the adhesion strength between the coating layer and substrate [6-7].

TiO_2 is also called titanium white, which can be categorized into anatase, rutile, and brookite by its crystal structure. Anatase has the best bioactivity but relatively lower strength among three structures. It can effectively attract protein molecules and reduce the formation of connective tissue after implantation [8]. Rutile has a relatively lower bioactivity but better strength than anatase [9], after mixing with HA, which acts as an important role for improving the coating strength. In most bioactivity studies on adding TiO_2 into HA, are focused on the adhesive between the coatings and substrates, and the bonding between the coating layers and surrounding bone tissues. Allen [10] utilized a sol-gel method to coat a TiO_2 layer on Ti-6Al-4V substrate and tested its bioactivity in calcium phosphate liquid and simulated body fluid (SBF), respectively. It was found that the produced TiO_2 coatings were able to attract Ca and P ions, and the following formed HA can help the growth of osteoclast. Kim [11] coated HA+TiO_2 layers on Ti, and found TiO_2 transferred from the bioactive anatase into rutile after heat treatment. It was also observed that the adhesive between the coating and substrate is increased with the increase of TiO_2 addition in HA [11-12].

Laser cladding technology has been applied on HA coatings in previous study. Although the recent developed laser coating method can get a better quality of metallurgical bonding, it still has not solved problems such as non-stoichiometric composition of coatings that degrades in bioactivity. The aim of this study is to overcome this problem and improve the bioactivity of the coating layers. Anatase and rutile were added with HA powders, respectively, in the initial stage, and these mixtures were then coated on the Ti-6Al-4V plates by the Nd-YAG laser. All the samples were characterized by a range of techniques for investigating and evaluating how these TiO_2 additives affected the microstructure, chemical composition, Ca/P ratio and bioactivity of the coating products.

II. Experiment procedures

Ti-6Al-4V substrate was prepared into plates with dimensions of 100mm×60mm×3mm. Its chemical composition can be seen in Table 1. In order to remove the surface oxidation, the plates were grinded by #120 SiC paper, cleaned by acetone, and then dried in an electric oven. 50 wt.% HA+50 wt.% anatase (HA+A) and 50 wt.%

Chwee Teck Lim, James C.H. Goh (Eds.): ICBME 2008, Proceedings 23, pp. 1401–1404, 2009
www.springerlink.com

HA+50 wt.% rutile (HA+R) powder mixtures were used as coating materials, respectively. The powder mixtures were stirred well with water glass (WG, $Na_2O{\cdot}nSiO_2$) binder and then applied 0.9mm thickness on Ti-6Al-4V substrates via pre-place method. The laser cladding experiment was conducted in continuous wave (CW) mode by Nd-YAG laser of 5° incident angle and 15mm defocus length in an Ar shielded atmosphere with 25 l/min flow rate. The travel speed was 200, 360, 480 and 600 mm/min, respectively, and the laser output power was 850W. The microstructure of the specimens was characterized via optical microscopy (OM) and scanning electron microscopy (SEM). Their chemical composition was analyzed by energy dispersive spectroscopy (EDS) and X-ray diffraction (XRD). Their adhesive strength was determined by the crack formed by the diamond pyramid of Vickers hardness tester.

Table 1 Chemical composition of Ti-6Al-4V used in the study (in wt.%)

Al	V	O	Fe	C	N	H	Ti
6.1	4.24	0.152	0.16	0.017	0.008	0.0006	Bal.

III. Results and Discussion

A. Cross section morphology and bead profile of the weldment

Fig.1 shows the cross section morphology of weldments under different cladding factors. The fusion zone can be classified into coating layer and transition layer. It can be observed that the area of the fusion zone, heat affected zone (HAZ) and the penetration depth were decreased with the increase of laser travel speed. This is due to the average input heat was decreased with the travel speed. On the other hand, porosity and cracks can be found in the fusion zone in both HA+A and HA+R specimens. Since the solidification speed of melts is relatively high, the vaporized WG were trapped in the melts and the pores were formed in the structure afterwards [13]. Furthermore, some white particles were observed on the upper coating layer of HA+A and HA+R specimens, show in Fig.2. From their identified chemical composition, it is assumed that they are compounds from melted WG+TiO_2.

B. Ca/P value and microstructure characterization of coating layer

Ca/P value analysis was obtained from the top, center and bottom area of coating layer. The results reveal show in Fig.3, that the Ca/P value is higher than HA due to the dissipation of P from HA during laser cladding process. It is also observed that the center area has a highest Ca/P value and the top area has a lowest value. Moreover, it is found that the Ca/P value in the HA+A specimens is decreased with the increase of laser travel speed, but the one in the HA+R counterparts shows an opposite trend.

Laser power (W)	Travel speed (mm/min)	Coating layers	
		HA+Anatase	HA+Rutile
850	200		
	360		
	480		
	600		

Fig. 1 The morphology of weldments with different TiO_2 addition in HA

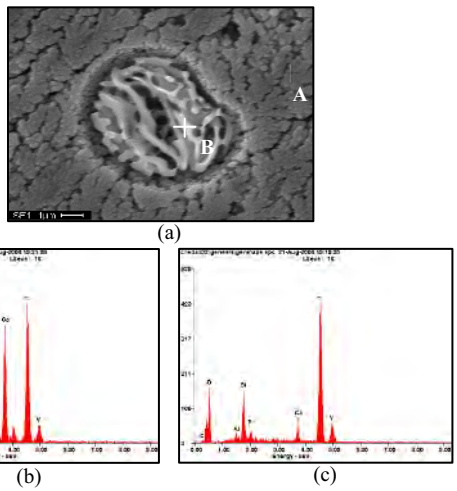


Fig. 2 Characterization of white particles on the top of coatings: (a) SEM image of HA+TiO_2 coating, (b) the EDS analysis of Ca-Ti-O rich phase at point A, and (c) the EDS analysis of Si rich phase at point B

The SEM images in Figs. 4 and 5 show the coral-shaped microstructure (top view) of HA+A and HA+R coatings, respectively. The white areas (points 5A and 6A) were identified as Ti-O rich phases, whereas the dark areas (points 5B and 6B) were identified as Ca-Ti-O rich phases. It is supposed that the Ca-Ti-O phases are composed of the dissipated Ca from HA, and Ti and O from the TiO_2.

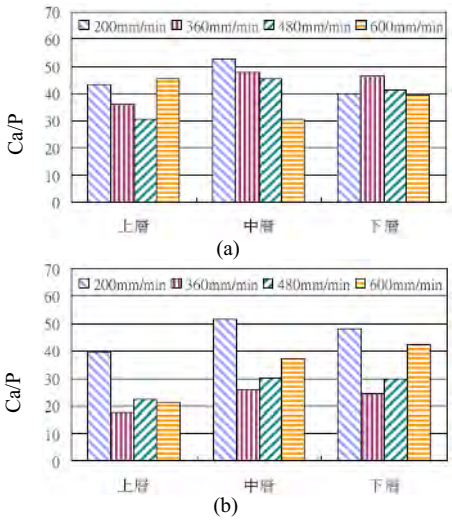


Fig. 3 The Ca/P value comparison of coatings with different TiO_2 addition and laser travel speed: (a) HA+A, and (b) HA+R

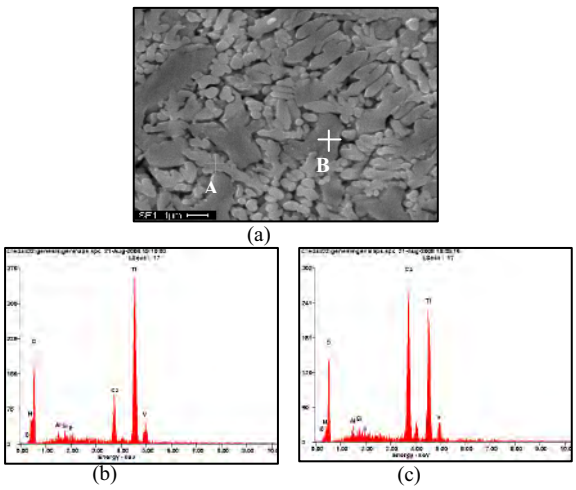


Fig. 4 Characterization of HA+A coating: (a) SEM image of HA+A coating, (b) the EDS analysis of Ti-O rich phase at point A, and (c) the EDS analysis of Ca-Ti-O rich phase at point B

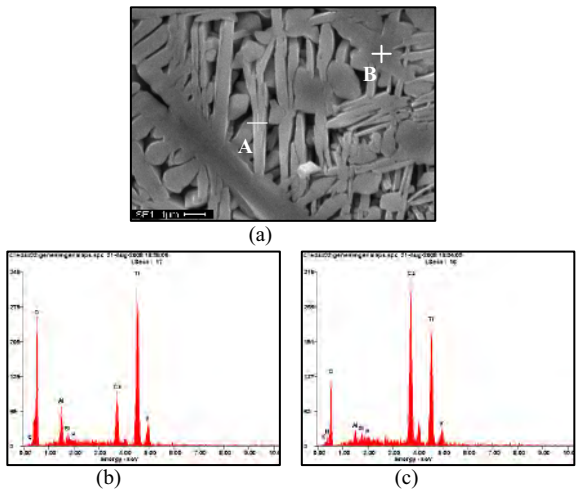


Fig. 5 Characterization of HA+R coating: (a) SEM image of HA+R coating, (b) the EDS analysis of Ti-O rich phase at point A, and (c) the EDS analysis of Ca-Ti-O rich phase at point B

C. XRD analysis of coating layers

The results of XRD analysis can be seen in Fig. 6. Anatase, rutile, HA, β-$Ca_3(PO_4)_2$, $CaTiO_3$ and $CaCO_3$ were found in the HA+A specimen; whereas rutile, HA, Ti_2O_3, $CaTiO_3$ and $CaCO_3$ were found in the HA+R specimen. These phases are supposed to be synthesized from the decomposed HA+TiO_2 precursors during laser cladding, where the rutile (high temperature phase) found in the HA+A specimen was originally from the anatase (low temperature phase).

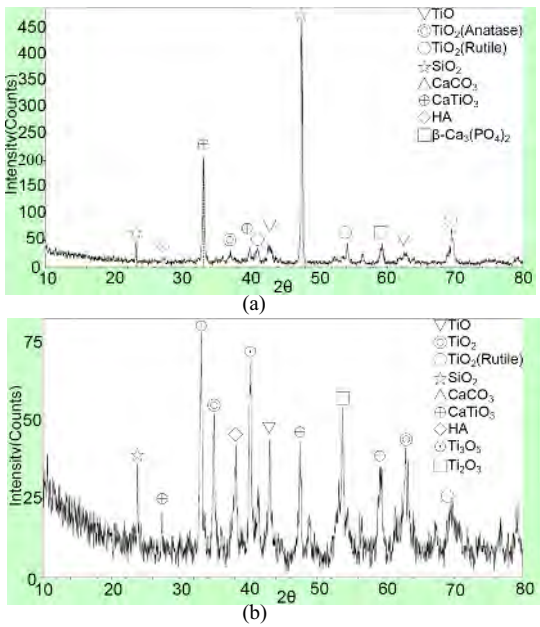


Fig. 6 The XRD analysis of: (a) HA+A coating, and (b) HA+R coating

D. Interface bonding analysis

Currently, tensile test and HV hardness test are the two methods to evaluate the bonding strength between the coating layer and substrate. HV hardness method was adopted in this study and the results can be seen in Fig. 7. It is revealed that no crack was observed from all specimens of different cladding factors and coating precursors, which indicates a sufficient bonding strength of coating is obtained by adding TiO_2 into HA.

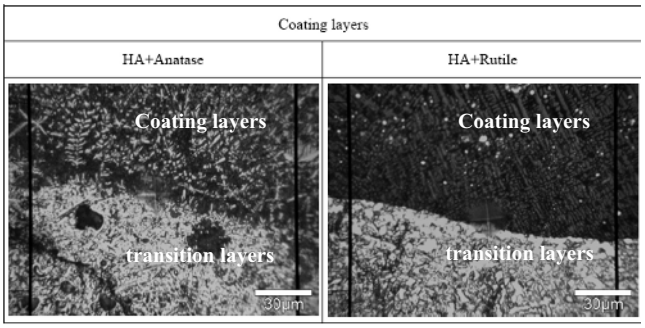


Fig. 7 The OM images of the interface between different coatings and substrate after HV hardness tests

IV. Conclusions

1. The morphology of weldments reveals the area of the fusion zone, HAZ and the penetration depth were decreased with the increase of laser travel speed. More pores and cracks were observed in the HA+A coating than HA+R counterpart.
2. HA+A coating has a higher Ca/P value than HA+R counterpart. All the coatings show that the center area has a highest Ca/P value and the top area has a lowest value. The coatings revealed a coral-shaped microstructure, which is believed that favorable for the attachment and growth of cells.
3. The XRD analysis shows all coatings have HA, $CaTiO_3$ and $CaCO_3$ phases. Additionally, β-$Ca_3(PO_4)_2$, which has good bioactivity was found in the HA+A coating, whereas Ti_2O_3 was observed in the HA+R coating, respectively.
4. The interface bonding strength evaluation revealed that no crack was observed from all specimens of different cladding factors and coating precursors, which indicates a sufficient bonding strength of coating is obtained by adding TiO_2 into HA.

Acknowledgment

The authors would like to thank Ya-Chung Industrial Co., Ltd. for providing TiO_2 powder; Ruhnyu Industrial Co., Ltd. for providing WG; and Chimei Foundation Hospital for the grant support of this work.

References

1. Sen Y. and Hau C.M., Fabrication of bioactive HA/Ti composite coating by laser cladding, Key Engineering Materials, 2007, pp.569-572.
2. Chen C.Z., D.G. Wang, P. Xu et al., Microstructure of laser cladding hydroxyapatite bioceramic gradient coatings, Zhongguo Jiguang/Chinese Journal of Lasers, 2004, pp. 1021-1024.
3. Chen C. Z., Wang D. G., Bao Q. H. et al., Composition and structures of laser synthesizing calcium phosphorous bioceramic coatings on the surface of titanium .Biological Orthopaedics Materials and Clinical Application, 2003, 16 (1) : p51-54.
4. Leonor I.B., Ito, A., In vitro bioactivity of starch thermoplastic/hydroxyapatite composite biomaterials: an in situ study using atomic force microscopy, Biomaterials , 2003, 24,579-585.
5. Zhang Yaping, Effect of Y_2O_3 on Bioceramic Coating by Laser Cladding. Digitized Periodical, 1999, No.10.
6. Li H., Khora K.A., P. Cheang, Impact formation and microstructure characterization of thermal sprayed hydroxyapatite / titanium composite coatings, Biomaterials, 2003, 24, 949-957.
7. X Nie, A Leyland, A Matthews, Deposition of layered bioceramic hydroxyapatite/TiO_2 coatings on titanium alloys using a hybrid technique of micro-arc oxidation and electrophoresis, Surface and Coatings technology, 2000, p407-414.
8. N. Huang, P. Yang and X. Cheng, Blood compatibility of amorphous titanium oxide films synthesized by ion beam enhanced deposition, Biomaterials, 19, 1998, pp771-776.
9. Li Panjian, Paul Ducheyne, Quasi-biological apatite film induced by titanium in a simulated body fluid, J Biomed Mater Research, 1998, 41, pp341-348.
10. Allen, Preparation and Characterization of Ti-6Al-4V alloy Coated Titanium Oxide and Hydroxyapatite, National Chung Hsing University, Master degree thesis, 2005.
11. Kim Hae-Wo ，Kim Hyoun-Ee. Hydroxyapatite and Titania Sol-Gel Composite Coatings on Titanium for Hard Tissue Implants: Mechanical and In Vitro Biological Performance. J Biomed Mater Research Part B: Applied Biomater, 2005.72B:1-8.
12. Lu Yu-Peng, Li Mu-Sen, Li Shi-Tong et al., Plasma-sprayed hydroxyapatite+titania composite bond coat for hydroxyapatite coatingon titanium substrate, Biomterial,25, 2004,p4393-4403
13. Han Tsung-Jen, Investigations of HA coating on Ti-6Al-4V substrates with Nd-YAG laser, Southern Taiwan University, Master degree thesis, 2008.

Corresponding author:

Author: T.Y.Kuo
Institute: Department of Mechanical Engineering, Southern Taiwan University
Street: No.1 , Nan-Tai
City: Yung-Kang, Tainan
Country: Taiwan
Email: tykuo@mail.stut.edu.tw

Computational Fluid Dynamics Investigation of the Effect of the Fluid-Induced Shear Stress on Hepatocyte Sandwich Perfusion Culture

H.L. Leo[1], L. Xia[1,2], S.S. Ng[3], H.J. Poh[4], S.F. Zhang[1,2], T.M. Cheng[1,5,6], G.F. Xiao[7], X.Y. Tuo[1,5,8], H. Yu[1,5]

[1]Institute of Bioengineering and Nanotechnology, ASTAR, Singapore
[2]Graduate Program in Bioengineering, National University of Singapore, Singapore
[3]Institute of Molecular and Cell Biology, ASTAR, Singapore
[4]Institute of High Performance Computing, ASTAR, Singapore
[5]Department of Physiology, National University of Singapore, Singapore
[6]Department of Gastroenterology, Nanfang Hospital, Southern Medical University, Guangzhou China
[7]Department of General Surgery, Xiang Ya Hospital, Hunan, China
[8]Department of Burns and Plastic Surgery, The First Affiliated Hospital of PLA General Hospital, Beijing, China

Abstract — **Primary hepatocyte *in vitro* culture is a challenging area in liver tissue engineering. Hepatocyte viability and functions drop significantly after isolation step. The perfusion culture is a promising culture method to maintain cell viability and function *in vitro* for long term. Hepatocytes cultured in perfusion condition have better oxygen and nutrient supply due to improved mass transfer. The metabolite wastes excreted by cells can also be removed effectively in the perfused flow, avoiding local accumulation of these wastes which deteriorates cell functions. However, hepatocytes are sensitive to shear stress associated with the flow rate in perfusion culture and are shielded by sinusoidal endothelial cells in the liver to avoid direct exposure to shear stress. Fluid-induced high shear stress in perfusion culture may cause detrimental effect on hepatocyte viability and functions. In the current study, we simulated the profile of fluid-induced shear stress under different flow rate in our sandwich perfusion bioreactor using computation fluid dynamics (CFD) method, and investigated the effect of shear stress on the cell function. The results indicated that hepatocyte function can be maintained in long term under moderate shear stress in perfusion culture.**

Keywords — **Liver failure, hepatocytes, fluid shear, bioreactor, CFD**

I. Introduction

Patients with fulminant hepatic failure (FHF) have a mortality rate of more than 80% [1]. Transplantation remains the only curative option for patients with liver failure [1,2]. However, liver transplantation is constraint by cost, donor scarcity and compatibility [1]. Recently, bio-artificial liver devices are emerging as one of the promising solution in bridging for transplantation and/or liver regeneration [1,2,4]. These artificial liver devices make use of isolated liver cells, i.e. hepatocytes, either of allogeneic or xenogeneic origin to replace the liver-specific functions of patients with FHF.

Of the myriad of culturing techniques currently employed by today's bio-artificial liver devices, sandwich culture method has demonstrated excellent ability of re-establishing hepatocytes polarity with long-term maintenance of specific-liver functions and viability [3]. Studies have indicated that the hepatocytes culture in sandwich configuration generally provide better control in terms of the uniformity of cell distribution and the regulation of microenvironments mimicry of that found *in vivo* [3].

Perfusion bioreactor provides an ideal solution to the support and culturing of vast liver cell mass (in the range of 100×10^6 - 2×10^9) through efficient transport of essential nutrients and gases to the cell surfaces. However, it remains that one of the major engineering concerns facing bioengineers in the development of bio-artificial liver is the effect of fluid-induced shear stress on the hepatocytes [3,4]. Studies have shown that fluid shear stress exceeding 0.5 dynes/cm^2 is detrimental to the viability of the hepatocytes culture [4]. Computational fluid dynamics (CFD) technique provides an efficient and reliable means to assess the flow characteristics in the perfusion bioreactors, with the technique gaining wide acceptance among present day tissue-engineers in the optimization of bioreactor design [4].

At present, the characteristics of fluid-induced shear stress in sandwich culture have not been adequately addressed. Through computational modeling, the current study set out to investigate the effect of fluid shear on the hepatocytes sandwich culture.

II. Methods

A. Perfusion Bioreactor

The bioreactor used in the current study is shown in Figure 1. It consisted of a circular culture chamber (15 mm dia.) with inlet and outlet ports for medium perfusion.

Chwee Teck Lim, James C.H. Goh (Eds.): ICBME 2008, Proceedings 23, pp. 1405–1408, 2009
www.springerlink.com

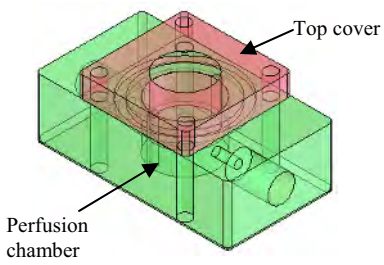


Fig. 1 Schematic of the perfusion bioreactor

B. Computer Model

Figure 2 shows the 3D fluid volume of the bioreactor. Half model of the fluid volume was solved since the flow characteristics through the culture chamber are considered symmetric about the stream-wise plane.

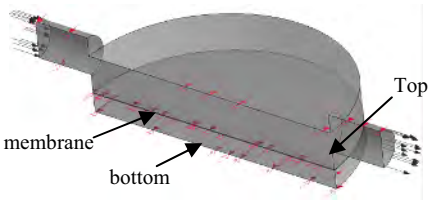


Fig. 2 Half-model of fluid volume of bioreactor

The 3D fluid model comprises of three domains; 1) top, 2) porous membrane, and 3) bottom domains. The top domain consisted of the inlet and outlet conduits. The porous membrane consisted of the membrane with an experimentally derived permeability value. The bottom domain is where the sandwich cell culture is located. The thickness of the porous polycarbonate membrane is 50 μm, while the height of the flow channel in the top and bottom domains are 2 and 1 mm, respectively. The 3D model was first created using Solidworks (Solidworks, Singapore) before being discretized using ANSYS meshing software ICEM CFD (ANSYS, Singapore). Tetrahedral meshing was used for the volume discretization resulting in a total of 408,952 nodes and 2,209,336 elements.

C. Modeling Fluid Flow

A finite element approach was adopted in order to evaluate the distribution of fluid shear stress on the cell surface through the porous membrane at various flow rates. To simulate the flow, the commercial CFD package (ANSYS Inc, Singapore) was used to numerically solve the steady-state Navier-Stokes equations. Fluid properties were set to those of the culture media and the culture medium was modeled as an incompressible, isothermal, Newtonian fluid with a density of 1000 kg/cm^3 and a dynamic viscosity of 0.889 mPa s. Flow rates of 0.1, 0.06, 0.03 (with and without membrane) and 0.018 mL/min were simulated for comparison. The selection of 0.03 mL/min to study the effect of membrane on cell functions is based on our preliminary *in vitro* experiments flow rate optimization, which demonstrated enhanced liver-specific functions at flow rate of 0.03 mL/min compared to other flow rates. Outlet boundary condition was set at zero pressure outflow, while the no-slip walls boundary conditions were used along the walls of the model.

D. Experimentally Derived Permeability Value, α (1/m^2)

The porous membrane may be considered as a momentum sink that contributes to the pressure drop in the porous media, which is composed of two parts, a viscous loss term (Darcy's law) and an inertia loss term (kinetic loss):

Momentum sink, Si = Viscous loss + Inertia loss

$$Si = \nu(\frac{\mu}{\alpha}) + \frac{1}{2}(C\,\rho\,\nu^2)$$

where Si is the momentum sink or pressure drop per unit membrane thickness (Pa/m), ν is the fluid velocity (m/s), μ is the fluid viscosity (Pa s), α is the fluid membrane permeability (m2), ρ is the density of the fluid (kg/m3) and C is the inertial resistance factor. Under laminar flow, pressure drop is directly proportional to velocity and the viscous loss is dominant, thus C can be considered to be zero. The membrane permeability α was thus derived from measuring the pressure drop per unit thickness across the membrane and the output flowrate as shown in Figure 3.

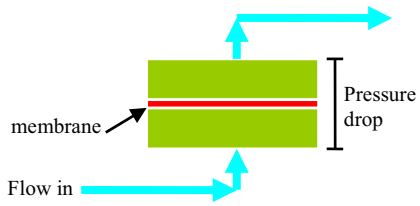


Fig. 3 Schematic of setup to measure the permeability of porous membrane experimentally

From the slope as shown in Figure 4, (μ/α) = 1 x 10^7 m^2 Pa^{-1}s^{-1} and taking μ = 8.81 x 10^{-4} Pa s, thus α = 8.81 x 10^{-11} m^{-2}. The simplified porous membrane momentum sink equation with empirically derived α was used in the CFD model to simulate the shear stress at different flowrates.

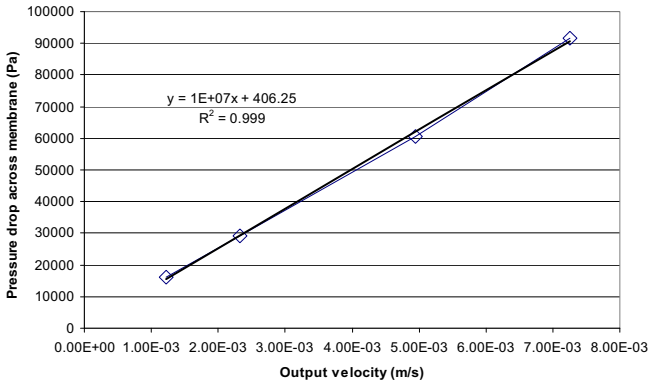


Fig. 4 Permeability of the polycarbonate membrane is measured as the slope of pressure drop vs output velocity

III. Results

Table 1 tabulates the mean shear stress, velocity and Re with corresponding flow rates. The mean shear stress experienced by the cell surface at flow rate of 0.03 mL/min is lower at 0.70 dynes/cm^2 with membrane compared with that without membrane at 0.85 dynes/cm^2.

Figure 5 shows the shear strain distribution across the cell surface below the porous membrane. Elevated fluid shear values were observed in the stream-wise plane while those of lower values were observed along the edge of the culture chamber.

Table 1 Mean shear stress, velocity and Re with corresponding flow rates

Flow rates (ml/min)	Mean shear stress (x 10^{-3} dynes/cm^2)	Re	Velocity (m/s)
0.100	2.10	3.136	5.3276E-04
0.060	1.13	1.882	3.1978E-04
0.030	0.70	0.941	1.5989E-04
0.018	0.37	0.564	9.5935E-05
0.030 (w/o) membrane	0.85	0.934	1.5941E-04

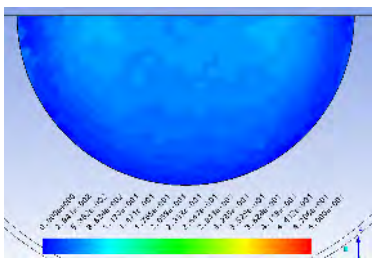


Fig. 5 Shear strain contour plot at flow rate of 0.03 mL/min (with membrane)

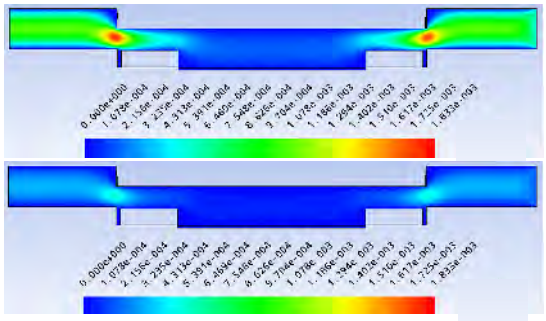


Fig. 6 Velocity contour plot at flow rates of flow of 0.1 and 0.03 L/min

Higher flow velocity was observed at inlet and outlet ports of the chamber as a result of the constriction of flow area in these regions (Fig. 6). Low recirculating regions were typically observed at the sudden expansion and contraction regions within the chamber as a result of the flow separation.

Figure 7 compares the stream-wise shear strain profile across the cell surface below the porous membrane. The profile was characterized by two peaks along the flow

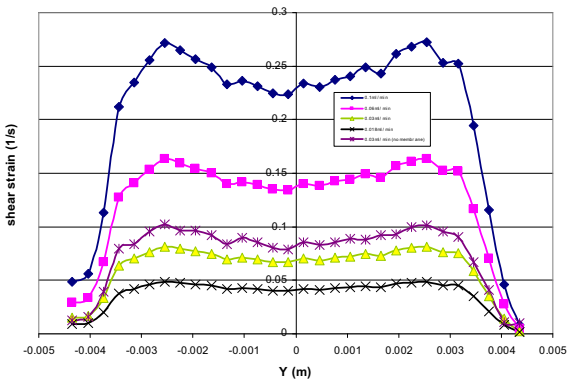


Fig. 7 Shear strain across the cell surface at different flow rates

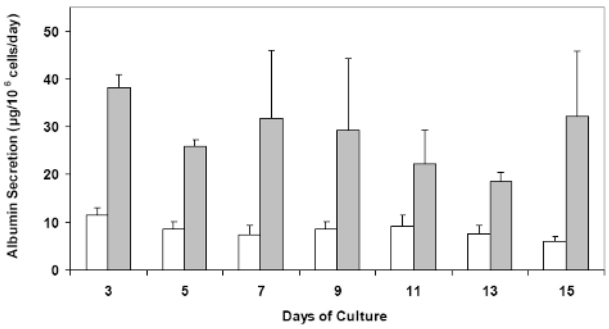


Fig. 8 Albumin secretion function of sandwich perfusion culture at flow of 0.03mL/min compared with sandwich static culture.

stream. These were due to the boundary layer detachment at inlet port and its subsequent attachment within the culture chamber (Fig.8). Both Table 1 and Figure 7 show that the fluid shears generated by the different flow rates were well below the threshold value of 0.33 dynes/cm^2 [4]. Figure 8 albumin secretion function of sandwich perfusion culture at flow rate of 0.03mL/min, which is optimized using CFD simulation of the shear stress to be well below the threshold value. The function of perfusion culture was maintained for 15 days and was consistently higher than that of static culture.

IV. Discussions

Fluid-induced shear stress is an important consideration in bioreactor designs. Hepatocytes in native liver are arranged in plates, separated and shielded from the direct effect of fluid shear by layer of sinusoidal cells. Studies have shown that primary hepatocytes cultures are sensitive to external flow conditions [1,2,4]. Two opposing fluid associated conditions may determine the outcome of the hepatocytes cultures, namely, the shear stress and the transport of nutrients and oxygen. Higher flow rates invariably improve the convective transport of oxygen to the cell surfaces but the corresponding elevated shear stress values could prove detrimental to viability of the cell culture. Conversely, lower flow rates could lead to inadequate supply of oxygen, even though the shear stresses are well below the critical threshold value.

Several innovative bioreactor designs have been suggested to regulate the wall shear stress experienced by the hepatocytes. One such device is developed by J. Park *et al* in which micro-fabricated concentric grooves in glass are used to shield the monolayer hepatocytes culture from the effect of fluid flow without compromising on the supply of nutrients and oxygen to the cell surface [4]. Our preliminary *in vivo* experiments with sandwich configuration showed that hepatocytes culture perfused at the rate of 0.03 mL/min demonstrated enhanced liver-specific functions and viability compared to those at other flow rates. The shear stresses experienced by the hepatocytes with and without the membrane at 0.03 mL/min were 0.7 x 10^{-3} and 0.85 x 10^{-3} dynes/cm^2, respectively. Our computational study has also demonstrated the sensitivity of hepatocytes cultures to the different flow conditions. The difference between mean shear stresses at flow rates of 0.06 and 0.03 mL/min was ~0.4 x10^{-3} dynes/cm^2, while that between the flow rates of 0.03 and 0.018 mL/min was ~0.30 x10^{-3} dynes/cm^2.

The top membrane in a sandwich culture, besides providing an anchorage for the hepatocytes attachment, also acts as a shield to protect the hepatocytes from the direct effect fluid flow. Comparison of the hepatocytes cultures at 0.03 mL/min showed only a difference of 0.7 x10^{-3} dynes/cm^2 and 0.85 x10^{-3} dynes/cm^2 for cultures with and without membrane, respectively. Effectively, the 50 μm thick membrane was able to reduce the shear stress by ~0.1 x10^{-3} dynes/cm^2. However, it should be noted that our current study did not include a layer of coated collagen on the membrane when measuring its permeability. The coating of an additional layer of collagen onto the membrane should further reduce the shear stress experienced by the cell surface. But a corresponding reduction in the transport of nutrients and oxygen should be expected.

V. Conclusions

The study has demonstrated the sensitivity of the hepatocytes to fluid-induced shear stresses. The membrane in sandwich culture is able to act as a shield for the hepatocytes from the direct effect fluid flow. However, a compromise between the transport of oxygen and nutrient and magnitude of shear stresses need to be considered when using sandwich culture. Hepatocyte functions were well improved in the perfusion culture at optimized flow rate by CFD simulation.

Acknowledgment

Institute of Bioengineering and Nanotechnology, ASTAR, Singapore

References

1. Allen, J. W., Hassanein, T. and Bhatia, S. N. (2001) Advances in bioartificial liver devices, Hepatology vol. 34, no. 3, 447-454
2. Strain, A. J. and Neuberger, J. M. (2002) A bioartificial liver--state of the art, Science Feb 8;295(5557):1005-9
3. Du Y, Han R, Wen F, Ng San San S, Xia L, Wohland T, Leo HL, Yu H. (2008) Synthetic sandwich culture of 3D hepatocyte monolayer. Biomaterials. 2008 Jan;29(3):290-301.
4. Park, J., Li, Y., Berthiaume, F., Toner, M., Yarmush, M. L. and Tilles, A. W. (2008) Radial flow hepatocyte bioreactor using stacked microfabricated grooved substrates, Biotechnol Bioeng. Feb 1;99(2):455-67

Author: H. L. Leo
Institute: Institute of Bioengineering and Nanotechnology
Street: 31 Biopolis Way, The Nanos, #04-01, S
City: Singapore
Country: Singapore
Email: hlleo@ibn.a-star.edu.sg

Preliminary Study on Interactive Control for the Artificial Myocardium by Shape Memory Alloy Fibre

R. Sakata[1], Y. Shiraishi[2], Y. Sato[1], Y. Saijo[3], T. Yambe[2], Y. Luo[2], D. Jung[2], A. Baba[4], M. Yoshizawa[5], A. Tanaka[6], T.K. Sugai[3], F. Sato[3], M. Umezu[1], S. Nitta[2], T. Fujimoto[4], D. Homma[6]

[1] Graduate School of Integrative Bioscience and Biomedical Engineering, Waseda University, Tokyo, Japan
[2] Institute of Development, Aging and Cancer, Tohoku University, Sendai, Japan
[3] Graduate School of Biomedical Engineering, Tohoku University, Sendai, Japan
[4] Shibaura Institute of Technology, Tokyo, Japan
[5] Cyber Science Center, Tohoku University, Sendai, Japan
[6] Fukushima University, Fukushima, Japan

Abstract — **The authors have been developing a sophisticated artificial myocardium for the treatment of heart failure, which is capable of supporting contractile function from the outside of the ventricle. The purpose of this study was to construct the control methodology of functional assistance by an artificial myocardium using small active mechanical elements composed of shape memory alloy fibres (Biometal). In order to achieve a sophisticated mechanical support by using shape memory alloy fibres, the diameter of which was 100 microns, the mechanical response of the myocardial assist device unit was examined by using PID (Proportional-Integral-Derivative) control method. Prior to the evaluation of dynamic characteristics, the relationship between strain and electric resistance of the shape memory alloy fibre and also the inditial response of each unit were obtained in the electrical bridge circuit. The component for the PID control was designed for the regulation of the myocardial contractile function. An originally-designed RISC microcomputer was employed and the input or output signals were controlled by pulse width modulation method in respect of displacement controls. Consequently, the optimal PID parameters were confirmed and the fibrous displacement was successfully regulated under the different heat transfer conditions simulating internal body temperature as well as bias tensile loading. Then it was indicated that this control methodology could be useful for more sophisticated ventricular passive or active restraint by using the artificial myocardium on physiological demand interactively.**

Keywords — **Artificial myocardium, shape memory alloy fibre, PID control, dynamic characteristics**

I. Introduction

In general, ventricular assist devices (VADs) such as artificial hearts are used for the surgical treatment of the final stage of severe heart failure. However, it is anticipated that the interface between artificial materials and blood might cause severe complications from thrombosis or hemolysis in the application of blood flow pumps. On the other hand, the direct ventricular mechanical assistance is well known for the effective cardiac support from outside of the heart without thrombogenicity on the surface of the device. We have been developing an original artificial myocardial assist system, which is shown in Figure 1, for the treatment of severe heart failure by using a sophisticate shape memory alloy fibre. In order to achieve the effective cardiac assist on physiological demand for the patients' quality of life, the sophisticated mechanical control should be considered in the device. The special features of the shape memory alloy fibre which we employed in this study are along with its high durability and controllability. The purpose of this study was to evaluate its basic dynamic characteristics and parameters for proportional-integral-derivative (PID) feedback control for more sophisticated and effective mechanical assistance in our artificial myocardial assist system.

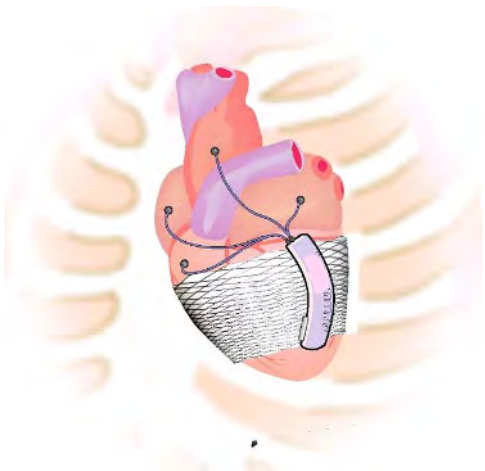


Fig. 1 Schematic illustration of our artificial myocardial assist system using shape memory alloy fibres (Biometal)

Chwee Teck Lim, James C.H. Goh (Eds.): ICBME 2008, Proceedings 23, pp. 1409–1412, 2009
www.springerlink.com

II. Material and Methods

A. Mechanical structure of the artificial myocardium using shape memory alloy fibres

Special features of the shape memory alloy fibre (Biometal®) which was to be employed as the actuator of the artificial myocardium were as follows: a) composition of covalent and metallic bonding structure, b) 4-7 % shortening by Joule heating induced by the electric current input, c) linear characteristics of electric resistance against shortening, d) strong maximum contractile force of 10N with 100um-fibre, e) high durability of over one billion cycles, f) contractile frequent response by 1-3 Hz, g) selectable maltensitic temperature by fabrication processing from 45 to 70 Celsius, and h) elective diameter size smaller than 30um.

The myocardial assist system consisted of a shape memory alloy band unit as shown in Figure 2. The diameter of each fibre employed in this study was 100 microns, and it was contracted by the Joule heating. In general, Ti-Ni alloy is well known as a material with the shape-memory effect[13]-[15]. The fibre material is able to be covered with a silicone tubing (diameter: 150um).

B. Examination of dynamic characteristics of the shape memory alloy fibre

The basic dynamic characteristics for the sophisticated PID parameters of the artificial myocardium were examined in the setup as shown in Figure 3. The heating conditions for each shape memory alloy fibre unit could be determined by the driver which consisted of a microcomputer and a power MOS-FET, and the driving signal for the contractile procedure of the unit was programmed and installed into the controller.

In order to obtain the dynamic characteristics, the length and displacement of the fibre were measured by using a laser displacement sensor (Keyence, LB-01), which was connected to the edge of the bias spring as shown in Figure 3 (bottom). The changes in the voltage between terminals of the fibre was also derived by the operational amplifier (Analog Devices, AD623), and the electric resistance was calculated by each voltage. Those data was digitally recorded simultaneously by the sampling rate of 1kHz.

As shown in Figure 4, the parameter of 'e0' could be calculated as the resistance of the shape memory alloy fibre unit (BMF), when the resistance ratio in the Wheatstone bridge was set to be constant as follows:

$$e_0 = (1 + \frac{100 \times 10^3}{R_G}) \times \frac{R_1 R_2 - R_{BMF} R_3}{(R_{BMF} + R_1)(R_2 + R_3)} E \qquad (1)$$

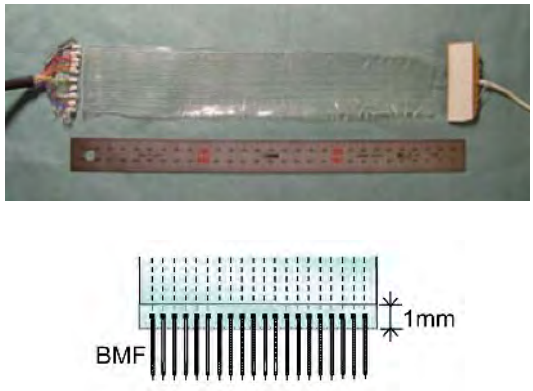


Fig. 2 Whole view of an artificial myocardial assist device (top) and schematic illustration of its cross sectional structure (bottom); each shape memory alloy fibre was covered by a silicone rubber tubing.

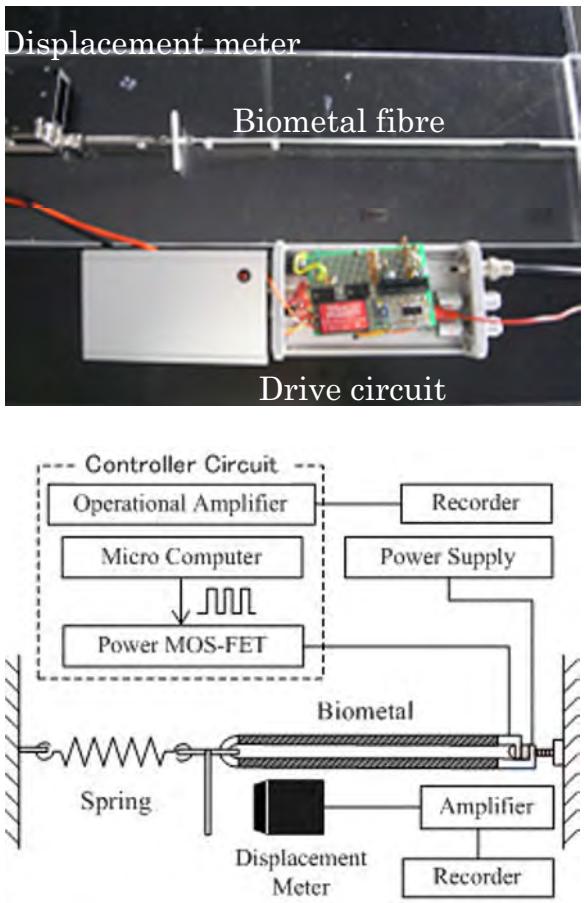


Fig. 3 Whole view of the test apparatus for the examination of dynamic characteristics for artificial myocardium units (top), and the schematic drawing of the circuit for the test of a single shape memory alloy fibre (bottom).

III. Results and Discussion

A. Dynamic characteristic evaluation of the shape memory alloy fibre for the artificial myocardium

As shown in Figure 7 and 8, the changes in displacement as well as the electric resistance of each fibre could be obtained. And the PID control parameters could be defined by the three components, floating time 'T', time constant 'L', and process gain 'K' under the conditions of different electric voltage supplied for each fibre as shown in Table 1. The PID control parameters were also calculated as shown in Table 2.

Table 1 Font sizes and styles

Floating time T	Time constant L	Process gain K
0.061	0.043	1.0

Table 2 PID parameter calculated

Proportion gain K_P	Integral time T_I	Derivative time T_D
1.2T/KL	2L	1.5L

B. Interactive control without displacement sensor

As the precise structural characteristics of the fibre material remains to be seen from the metallic materials science point of view, the dynamic change at the strain range over around 4.5 % could not be expressed by the linear relationship between strain and resistance. On the other hand, it was possible to write those relations as a linear function at the strain range of 4% or less. Figure 9 was an example of the application of PID control for the same unit, and it was indicated that this specific method would be useful to implement interactive control to the artificial myocardium without displacement sensors.

IV. Conclusions

The improvement of an artificial myocardial control using the sophisticated covalent shape memory alloy fibres could be achieved with the implementation of PID control method. And the linearity of the material enables us to establish more sophisticated procedure of contraction by using PID control method. As the load of this myocardial system, which was generated by the natural cardiac function, could be estimated by measuring the electrical resistance of the shape memory alloy fibre, the mechanical myocardial assistance might be effective for heart failure conditions according to the cardiovascular physiological demand.

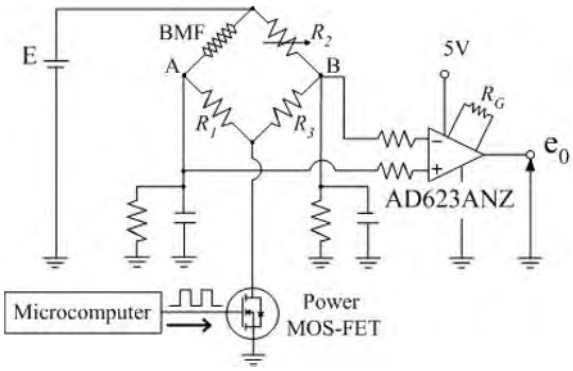


Fig. 4 Schematic drawing of the electric circuit; the shape memory alloy fibre (BMF) was connected to the portion of the Wheatstone bridge, and the changes in voltage between the terminal of the fibre as 'e0'.

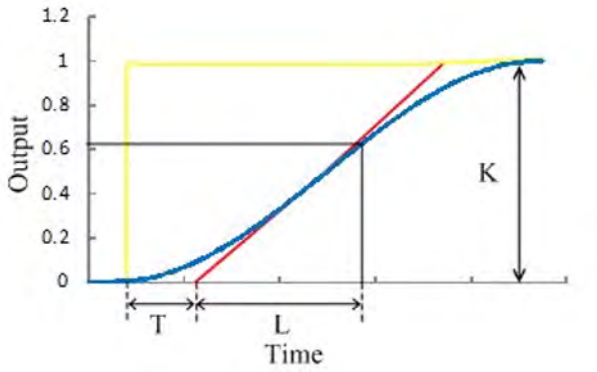


Fig. 5 Schematic illustration for the typical changes in the displacement of the shape memory alloy fibre obtained by step response examination; 'T' as the floating time, 'L' as the time constant, and 'K' as the process gain were calculated for the determination of PID control parameters.

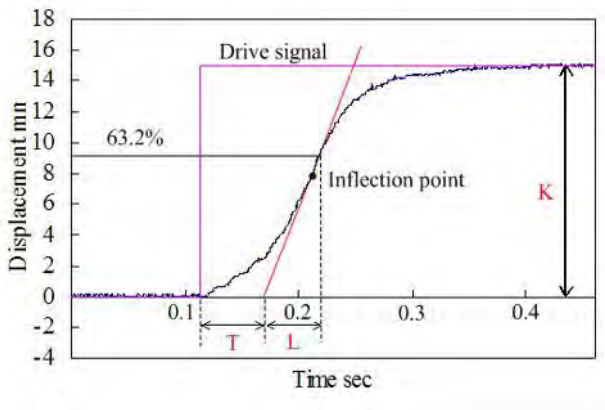


Fig. 6 Changes in the displacement obtained at the shape memory alloy fibre under the terminal voltage condition of 36 Volts.

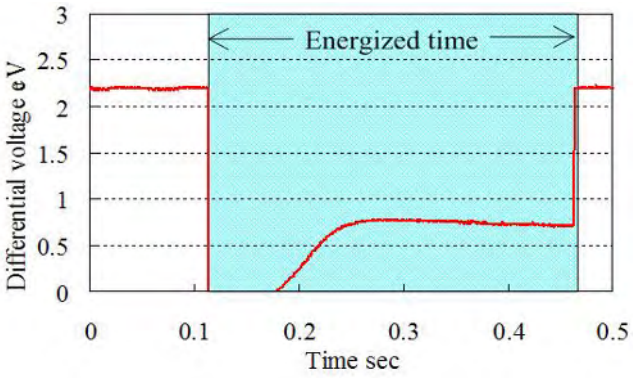


Fig. 7 Relationships between the electric 'step' input and the changes in the displacement obtained at the shape memory alloy fibre; the contraction change was saturated and stabilized against the stress of the bias spring.

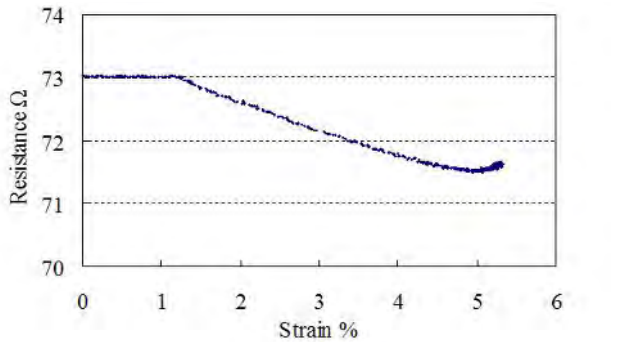


Fig. 8 Dynamic characteristics obtained at the displacement range of 0 to 5% of the single unit measured by the Wheatstone bridge circuit; the particular characteristics of this material could be investigated over 4% shortening, which might be caused by the structural changes in metallic bonding and crystallization in the shape memory alloy material.

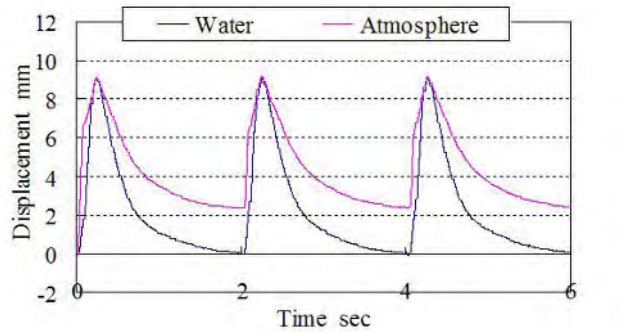


Fig. 9 An example of the application with PID control for the contraction in the shape memory alloy fibre as a unit of artificial myocardium

Acknowledgment

The authors acknowledge the support of Grand in Aid for Scientific Research of and Ministry of Education, Culture, Sports, Science and Technology (17790938, 19689029, 20659213).

References

1. Hosenpud JD, et al., "The registry of the international so-ciety for heart and lung transplantation: fifteenth offi-cial report–1998," J Heart Lung Transplant, 17, pp. 656–68, 1998
2. Rose EA, et al., "Long-term use of a left ventricular assist device for end-stage heart failure," New Eng J Med, 345, pp. 1435-43, 2001.
3. Long JW, et al., "Long-term desitination therapy with the Heartmate XVE left ventricular assist device: improved outcomes since the REMATCH study," Congest Heart Fail, 11, pp.133-8, 2005.
4. Drakos SG, et al., "Effect of mechanical circulatory support on out-comes after transplantation," J Heart Lung Transplant, 25, pp. 22-8, 2006.
5. Shimizu T, et al., "Fabrication of pulsatile cardiac tissue grafts using a novel 3-dimensional cell sheet manipulation technique and tempera-ture-responsive cell culture surfaces," Circ Res, 90(3), e40, Feb 2002.
6. Shiraishi Y, et al., "Development of an artificial myocardium using a covalent shape-memory alloy fibre and its cardiovascular diagnostic response," Proc of 2005 IEEE 27th EMBS 0-7803-8740-6/05, 2005
7. Yambe T, et al., "Addition of rhythm to non-pulsatile circulation," Biomed Pharmacother, 58 Suppl 1:S145-9, 2004.
8. Yambe T, et al., "Artificial myocardium with an artificial baroreflex system using nano technology," Biomed Pharmacother, 57 Suppl 1:122s-125s, 2004.
9. Wang Q, et al., "An artificial myocardium assist system: electrohy-draulic ventricular actuation improves myocardial tissue perfusion in goats," Artif Organs, 28(9), pp. 853-857, 2004..
10. Anstadt GL, et al., "A new instrument for prolonged mechanical massage," Circulation, 31(Suppl. II), p.43, 1965.
11. Anstadt M, et al., "Direct mechanical ventricular actruator," Resusci-tation, 21, pp. 7-23, 1991.
12. Kawaguchi O, et al., "Dynamic cardiac compression improves con-tractile efficiency of the heart," J Thorac Cardiovasc Surg, 113, pp. 923-31, 1997.
13. Buehler WJ, Gilfrich J, Wiley KC, "Effect of low-temperature phase changes on the mechanical properties of alloys near composition TiNi," J Appl Phys, 34, p.1465, 1963.
14. Homma D, Miwa Y, Iguchi N, et al., "Shape memory effect in Ti-Ni alloy during rapid heating," Proc of 25th Japan Congress on Materials Research, May 1982.
15. Sawyer PN, et al., "Further study of NITINOL wire as contrctile artificial muscle for an artificial heart," Carrdiovasc Diseases Bull. Texas Heart Inst 3, p. 65, 1976.

Author: Ryo Sakata
Institute: Graduate School of Integrative Bioscience and Biomedical Engineering, Waseda University
Street: 5-17-1-408, mizonokuchi, Takatsu-ku
City: Kawasaki, 213-0001
Country: Japan
Email: ryosakata314@yahoo.co.jp

Synthesis, Surface Characterization and In Vitro Blood Compatibility Studies of the Self-assembled Monolayers (SAMs) Containing Lipid-like Phosphorylethanolamine Terminal Group

Y.T. Sun, C.Y. Yu and J.C. Lin

Department of Chemical Engineering, National Cheng Kung University, Tainan, TAIWAN

Abstract — **Creating a surface with structure mimicking the phospholipid configuration, the most abundant component of the cell membrane, has been considered as one of the important methods to improve the blood compatibility of artificial surfaces. In this study, self-assembled monolayers (SAMs) formed by alkanethiol with phospholipid terminal group, 11-mercaptoundecanephosphorylethanolamine (PE), were explored as the potential surface modification technique to vary the blood contacting characteristics of metallic biomaterials.**

The surface characteristics and blood contacting properties of the SAMs formed from different solvents and concentrations are evaluated in this study. It was noted that the SAMs with phosphorylethanolamine terminal functionality is more hydrophilic, especially the ones formed using PBS as the solvent, than those with methyl terminate and the non-modified pure gold. ESCA analyses have suggested these phosphorylethanolamine terminated SAMs are less- ordered, likely due to the steric hindrance as well as the charging effects caused by this terminal end. This less-ordered configuration might explain the surface hydrophilicity of phosphorylethanolamine terminated SAMs was not as high as expected from its chemical structure. In addition, the ESCA analyses have shown that unbound thiols were noted within the SAMs, resulted from the steric hindrance caused by these bulky phospholipid-like terminal ends. Blood-contacting property evaluation has shown that parts of the SAMs surfaces exhibited platelet activation and aggregation while others didn't as compared to those prepared from the alkanethiol with methyl terminal end. Further study is undergoing to explore this unique blood contacting phenomena.

Keywords — **self-assembled monolayers, solvent effect, surface property, blood compatibility, ESCA**

I. Introduction

It is believed that creating a structure that is biomembrane-mimicking can improve the biocompatibility of materials. Biomembrane are composed of phospholipids and protein. Phospholipid is a fatty-like compound, but one of the fatty acid is replaced by phosphate, like phosphatidylcholine and phosphatidylethanolamine. Previously, there were numbers of studies submitted ideas to improve blood compatibility. For example, phospholipid could be copolymerized [1,2] or graft onto copolymer chains. But phase separation and function groups embedded for polymers were serious problems to overcome. Therefore, to discuss surface property and blood compatibility, a well-defined surface by self-assembled monolayers method was explored in the present study.

Self-assembled monolayers (SAMs) prepared by organosulfur compounds on metal surfaces have been extensively studied because of the wide varieties of potential applications. In particular, alkanethiol SAMs on gold have been thoroughly studied due to their highly reproducibility, well-defined and highly stable structure, as well as ease of preparation. The surface properties of the SAMs can be tuned by varying the terminal functionalities of the monolayers. In the view of energy, the well-ordered surface structure is formed by the interactions among head group, alkyl chain, and terminal ends. Numbers of topics have been studied, such as tilt angle between SAMs and substrate [3], intermolecular energy [3], chain length effect [4], solvent effect [5], wetting properties [6], kinetic of adsorption [4], and microstructure of surfaces [7,8]. The potential applications of SAMs were in protection of corrosion, biomimetics, and biosensors, to name a few.

Generally, the solvent used in preparation of SAMs was ethanol, because it is cheap, low toxicity, high purity, and doesn't act with SAMs [4]. There were studies with different solvents [9,10], and it was found that solvents did affect the structure of SAMs. In the present study, different solvent was used in order to explore its likely effects on the surface properties and blood-contacting characteristics of the SAMs prepared.

II. Materials and methods

A. Materials

11-Undecylenyl alcohol (98%, Aldrich), phosphorus oxychloride (99%, RDH), triethylamine (TEDIA), 4-Dimethylamino-pyridine (99%, Sigma), triisopropylbenzenesulfonyl chloride (>98%, Fluka), ethanolamine hydrochloride (>99%, Aldrich), thioacetic acid (95%, Fluka), and 2,2′-Azobis (2-methylpropionitrile) (98%, Showa) were all of analytical reagent grade and were used as received.

Chwee Teck Lim, James C.H. Goh (Eds.): ICBME 2008, Proceedings 23, pp. 1413–1417, 2009
www.springerlink.com

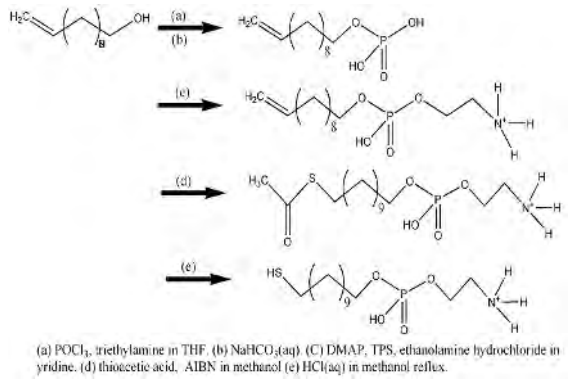


Fig. 1 Synthesis scheme for 11-mercaptoundecanephosphorylethanolamine

B. Synthesis of 11-mercaptoundecanephosphoryl ethanolamine

Alkanethiol with phospholipid terminal group, 11-mercaptoundecanephosphorylethanolamine (PE) was synthesized by the scheme shown in Figure 1.

C. Preparation of gold substrates and SAMs

Silicon wafers (1.5 cm × 5 cm) were cleaned by dipping into the Piranha solution (70 % H_2SO_4 and 30% H_2O_2) for an hour at 90°C. These substrates were rinsed with deionized water and ethanol several times and were then dried with nitrogen. The substrates were prepared by thermal evaporation of 300 Å titanium as an adhesion layer onto silicon wafer, followed by 2000 Å of gold. The PE SAMs formation was carried out by immersing gold substrates into methanol (MeOH), ethanol (EtOH0, deionized water (H_2O), and PBS at the concentration of 1mM and 0.1mM thiol solution for 24hrs. The CH_3-terminated thiol dissolved in ethanol solution at concentration of 1mM and 0.1mM (named as $1CH_3$ and 0.1 CH_3, respectively) were used as comparison. After the immersion, the samples were rinsed with deionized water and ethanol to remove physically adsorbed thiol, and dried with nitrogen. The nomenclature for the PE SAMs prepared was as follow: xxYY, where xx is the thiol concentration while YY is the solvent used.

D. Surface characterization and in vitro platelet analysis

The surface hydrophilicity was measured by sessile drop method (Face CA-A, Kyowas Kaimenkagaku Co. Ltd, Japan). Deionied water was used as the wetting liquid. The same-sized liquid drops were extruded to contact the SAMs surface, and the contact angles were determined on averaging the results obtained on three to five spots.

Electron spectroscopy for chemical analysis (ESCA or XPS) spectra were obtained by PHI Quantera SXM spectrometer under monochromatic AlKα source (hν=1486.6 eV) and the take-off angle was set at 45°.

Scanning electron microscope (SEM, S-2500, Hitachi, Japan) was to determine the morphology of the SAMs prepared as well as the adhered platelets. The 1000× image was used to calculate number of platelets adhered while 2000× one was used for platelets activation observation. Human platelet–rich plasma (PRP, 3.5×10^{10} platelets/mL) was used for *in vitro* platelet adhesion assay.

III. Results and Discussion

It was clearly noted that the SAMs prepared from PBS at 0.1mM (0.1PBS) and 1mM (1PBS) concentration were the most hydrophilic ones with contact angle values less than 10° (Figure 2). However, for other PE SAMs prepared, the contact angle values were all greater than the reported value for $–PO_3H_2$ terminated SAM, 37° [12], except those prepared by ethanol. The contact angle of CH_3-terminated SAMs and the bare gold was consistent with the literature values [13,14]. The small contact angle values noted on the SAMs prepared from PBS are very likely resulted from the adsorption of salt ions, as indicated by the existence of salt ions on the ESCA spectra. As for the high contact angle values for other PE SAMs, this can be attributed to the less-ordered structure resulting from the steric hindrance effect caused by the bulky PE terminal ends.

The surface elemental composition was determined from the XPS survey spectra. The atomic concentration of S2p is smaller than the theoretical one (Table 1). This is due to the inelastic collisions of sulfur photoelectrons prior arriving the detector. Such results indicated that the sulfur was resid-

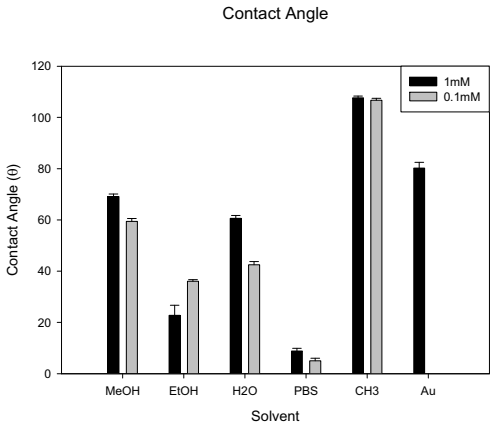


Fig. 2 The contact angle of PE SAMs prepared from different solvent and concentration as compared to the CH_3-terminated SAM and non-treated bare gold

Table 1 Atomic composition of PE SAMs
(the number within parentheses indicates the theoretical value)

Solvent	At%				
	C_{1s}	O_{1s}	N_{1s}	P_{2p}	S_{2p}
1MeOH	61.1 (65.0)	26.2 (20.0)	4.6 (5.0)	5.1 (5.0)	3.0 (5.0)
0.1MeOH	60.3	26.7	4.7	5.3	3.3
1EtOH	61.1	25.8	4.7	5.7	2.6
0.1EtOH	62.0	25.3	4.9	5.5	2.4
$1H_2O$	61.6	26.4	4.4	5.5	2.2
$0.1H_2O$	62.4	24.8	4.4	5.5	3.0
1PBS	63.4	23.1	4.1	5.9	3.5
0.1PBS	64.0	23.3	4.7	5.4	2.7
$1CH_3$	80.3 (90.9)	17.3 (0.0)	--	--	2.3 (9.1)
$0.1CH_3$	85.8	10.2	--	--	4.0

ing within the deeper layer of the SAM, implicating the thiolate (Au-S) was formed. The atomic percentages as well as the N/S and P/S ratios were all similar to each other. In addition, the N/S and P/S ratios were all greater than the theoretical ones (i.e. 1.0). This finding suggested that the PE SAMs formed were not quite ordered. The $–NH_3^+$ terminal ends can either be exposed at the surface or buried within the monolayer randomly.

Figure 3 depicted the N1s spectra, which can be curve-fitted into two peaks, $-NH_2$ (~399.8 eV) and NH_3^+ (~401.5 eV). The $–NH_2$ peak was resulted from the deprotonation of NH_3^+ during SAM formation stage or after washing steps. The amount of $–NH_2$ within the N1S peak is around 10-35%. This value, however, cannot be related to the ionization capability of the solvent used.

The S2p spectra shown in Figure 4 can be resolved into bound and unbound thiol centered at ~162 eV and 164 eV, respectively. In addition, peak representing oxidized sulfur ($-SO_x$, ~167.8 eV) was noted on the PE SAMs prepared from methanol at 0.1 mM and 1mM as well as that from ethanol at 1 mM. The notation of oxidized sulfur likely resulted from the oxidation of the –SH terminal ends that exposed to ambient environment due to the formation of bilayer structure through the ionic interactions between the

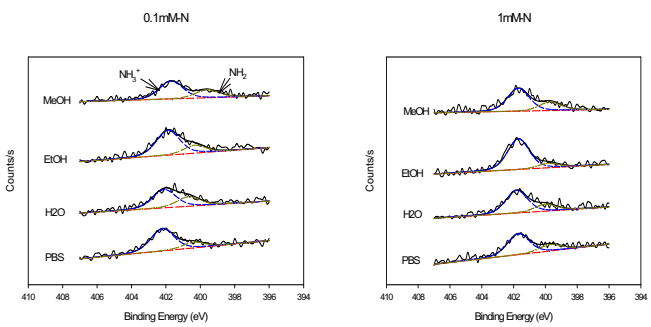


Fig. 3 XPS N1s spectra for PE SAMs prepared.

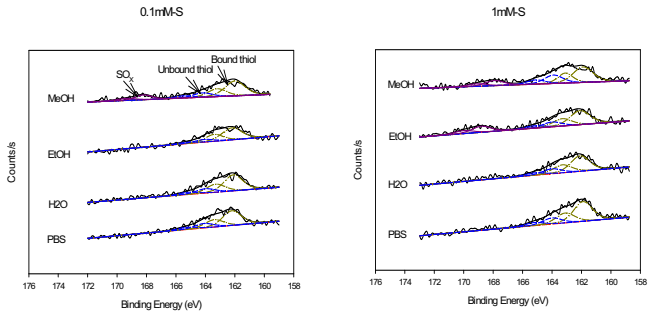


Fig. 4 XPS S2p spectra for PE SAMs prepared.

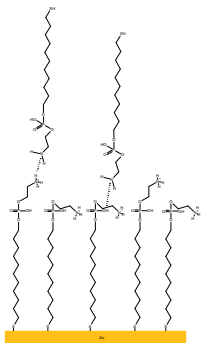


Fig. 5 Schematic representation of bilayer formation during PE SAM formation

ionic PE ends of adsorbed thiol and free one within the solution (Figure 5). In addition, the area ration for the unbound thiol was about 17-28%. These unbound thiols should be resulted from the steric hindrance as well as the hydrogen bonding and ionic interactions associated with the phosphorylethanolamine functionalities. In contrast, no unbound thiol and oxidized sulfur peak were noted on SAMs prepared from thiol with small $–CH_3$ terminal ends.

The morphology of adhered platelets on different PE SAMs, $-CH_3$ terminated SAM and non-treated gold control was shown in Figure 6. Generally, these PE SAMs can be classified into two categories: I. Significant activation and aggregation of platelets. This phenomenon was noted on 0.1MeOH, 1EtOH, $0.1H_2O$, $1H_2O$ and 0.1PBS samples. II. Slight activated platelets, sometimes, with pseudopod extension on surface. These samples include 1MeOH, 0.1EtOH and 1PBS. With same numerating procedure, the number of platelets adhered was shown in Figure 7. In combine of the two abovementioned observations for the platelets adhered, these PE SAMs exhibited better platelet-contacting property as compared to the $–CH_3$ terminated SAM and non-treated gold control, in which significant platelet activation (i.e. fully spreading platelets) was noted.

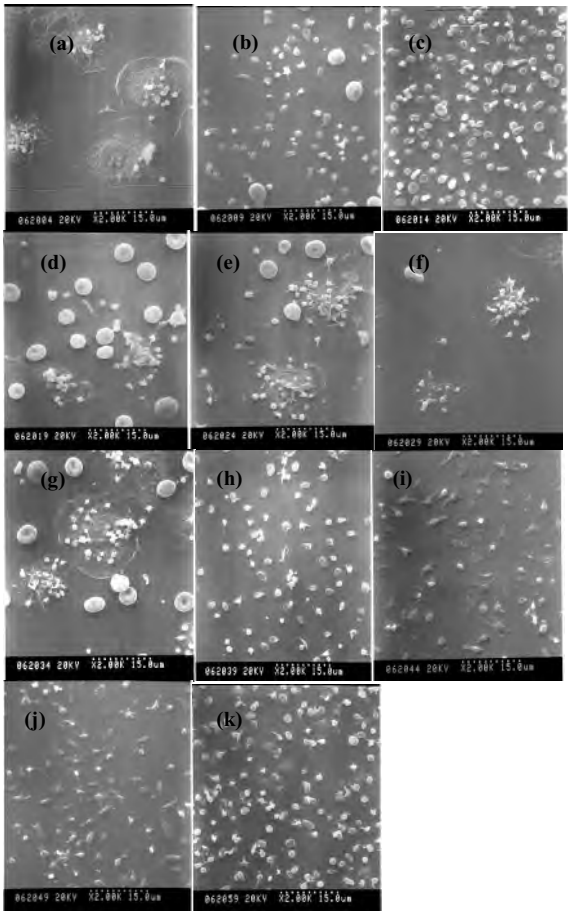


Fig. 6 SEM micrographs of platelets adhesion study (2000×): (a) 0.1MeOH; (b) 1MeOH; (c) 0.1EtOH; (d) 1EtOH; (e) 0.1H2O; (f) 1H2O; (g) 0.1PBS; (h) 1PBS; (i) 0.1CH3; (j) 1CH_3; (k) pure gold substrate

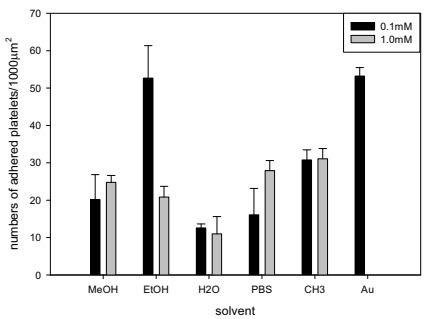


Fig. 7 Platelets adhesion density on various SAMs

IV. Conclusions

The surface properties and blood-contacting characteristics of the phospholipid-mimicking PE SAMs have been shown to be affected by the solvent and concentration used. The PE SAMs prepared were less platelet-activating than the methyl-terminated SAM ad non-treated gold control.

Acknowledgment

We thank the Tainan Blood Donation Center for providing human platelet-rich plasma.

References

1. Li YJ, Bahulekar R, Chen TM et al. (1996) The effect of alkyl chain length of amphiphilic phospholipid polyurethanes on haemocompatibilities. Macromol Chem Phys 197:2827-2835
2. Ishihara K, Aragaki R, Ueda T et al. (1990) Reduced thrombogenicity of polymers having phospholipid polar groups**.** J Biomed Materi Res 24:1069-1077
3. Nuzzo RG, Dubois LH, Allara DL (1990) Fundamental studies of microscopic wetting on organic surfaces. 1. Formation and structural characterization of a self-consistent series of polyfunctional organic monolayers. J Am Chem Soc 112:558-569
4. Bain CD, Troughton EB, Tao YT et al. (1989) Formation of monolayer films by the spontaneous assembly of organic thiols from solution onto gold. J Am Chem Soc 111:321-335
5. Bain CD, Evall J, Whitesides GM (1989) Formation of monolayers by the coadsorption of thiols on gold: variation in the head group, tail group, and solvent. J Am Chem Soc 111:7155-7164
6. Laibinis P E, Whitesides GM, Allara DL et al. (1991) Comparison of the structures and wetting properties of self-assembled monolayers of n-alkanethiols on the coinage. J Am Chem Soc 113:7152-7167
7. Himmelhaus M, Gauss I, Buck M et al. (1998) Adsorption of docosanethiol from solution on polycrystalline silver surfaces: an XPS and NEXAFS study. J Electron Spectros Relat Phenomena 92:139-149
8. Samant M G, Brown CA, Gordon JG (1991) Structure of an ordered self-assembled monolayer of docosylmercaptan on gold (111) by surface x-ray diffraction. Langmuir 7:437-439
9. Lee SL, Noh J, Ito E et al. (2003) Optical and electrical properties of Si nanocrystals embedded in SiO_2 layers. Jpn J Appl Phys 42:236-241
10. Dannenberger O, Wolff JJ, Buck M (1998) Solvent dependence of the self-assembly process of an endgroup-modified alkanethiol. Langmuir 14:4679-4682
11. Inagaki N, Tasaka S, Horikawa Y (1989) Nafion-like thin film plasma-polymerized from perfluorobenzene/SO_2 mixture. J Polym Sci 27:3495-3501
12. Tanahashi M, Matsuda T (1997) Surface functional group dependence on apatite formation on self-assembled monolayers in a simulated body fluid. J Biomed Mater Res 34:305-315

13. Arima Y, Iwata H (2007) Effect of wettability and surface functional groups on protein adsorption and cell adhesion using well-defined mixed self-assembled monolayers. Biomaterials 28:3074-3082
14. Martins CL, Ratner BD, Barbosa MA (2003) Protein adsorption on mixture of hydroxyl- and methyl-terminated alkanethiols self-assembled monolayers. J Biomed Mater Res-Part A 67:158-171

Corresponding author:

Author: Jui-Che Lin
Institute: Dept. of Chem Engr, National Cheng Kung University
Street: 1, University Rd.
City: Tainan
Country: Taiwan
Email: jclin@mail.ncku.edu.tw

Surface Characterization and *In-vitro* Blood Compatibility Study of the Mixed Self-assembled Monolayers

C.H. Shen and J.C. Lin

Department of Chemical Engineering, National Cheng Kung University, Tainan, TAIWAN

Abstract — **Self assembled monolayer (SAM) of the long-chain alkanethiols ($HS(CH_2)_nX$, n=10) with variant terminal functionalities adsorbed on Au substrate can serve as a well-oriented surface with a broad range of chemical configuration for studying the blood-material interactions. The mixed SAM can be produced by adsorption from mixtures of two alkanethiols with different types of terminal groups and the complicated microstructures of this surface can be explored and tailored to mimic the physiological microenvironment associated with variant biological entities.**

In this study, two different mixed SAMs by mixing lab-synthesized sulfonic acid terminated alkanethiol, which carried heparin-like chemical structure, with the methyl terminated alkanethiol or hydroxyl terminated one were prepared. Surface characterization results showed that the contact angle was gradually decreased with the increase the solution mole fraction of $–SO_3H$ thiol ($\chi_{SO3H,soln}$) on $–SO_3H/-CH_3$ mixed SAMs. On $–SO_3H/-OH$ mixed SAMs the surfaces were hydrophilic. The surface composition of the $–SO_3H$ thiol ($\chi_{SO3H,surf}$) was analyzed by X-tray photoelectron spectroscopy (XPS) and the adsorption behavior of two mixed SAMs was all presented as "$-SO_3H$ poor". The surface charge was evaluated by streaming potential and the charge of these mixed SAMs was all negative in PBS (pH 7.4). *In vitro* platelet adhesion assay indicated that the amount of adhered platelets was similar on both mixed SAMs, except on the pure –OH SAM. The adhered platelets on $–SO_3H/-CH_3$ mixed SAMs were more activated than on $–SO_3H/-OH$ mixed SAMs. This finding suggested that the surface wettability and surface charge could affect the material's platelet compatibility synergistically.

Keywords — **alkanethiol, mixed SAMs, surface charge, platelet adhesion**

I. Introduction

Thrombus formation, induced by a series protein adsorption, and platelet adhesion and activation is still an obstacle for biomaterial scientists to develop a truly blood compatible synthetic materials [1]. Some factors noted in interfacial reactions between synthetic materials and biological environment can affect these materials' blood compatibility. Henceforth, to optimize the surface properties of the artificial biomaterials has become the major research theme.

Self-assembled monolayers technique can provide a densely packed, well-defined, and highly ordered surface [2]. Alkanethiol assembled on gold is widely used due to easy preparation and forms such a strong covalent bonding between the head group of sulfur atom and gold layers that it can be stable even in harsh environment. Among these applications, the long chain alkanethiol with variant functional groups adsorbed on Au substrates has been widely used to study the blood-material interactions [3-5]. But SAMs prepared by pure alkanethiol have some limitations because of the high surface density of specific functional ends as well as the likely steric hindrance effect caused by bulky terminal ends. Mixed SAMs composed two or more alkanethiols on gold may solve the problems. By modulating the solution mole fraction of the alkanethiol, chain length of the thiol and solvent, different physicochemical property of surfaces can be produced [6]. In this study, we prepared two different series of mixed SAMs, which composed the mixture of the sulfonic acid terminated alkanethiol with the methyl and the hydroxyl terminated one, respectively. Surface characterization and *in vitro* platelet adhesion test were evaluated to investigate the roles of surface microstructure related to platelet adhesion characteristics. In addition, the concentration of the mixture alkanethiol solution has been chosen as either 2mM or 0.1mM in order to analyze the likely "concentration" effect on the SAM packing quality.

II. Materials and Methods

A. Synthesis of 10-mercaptodecanesulfonic acid

The alkanethiol with $–SO_3H$ functional group was synthesized by the strategy illustrated in Figure1 [1]. The spectral data for identifying this structure was as follows: ^{1}H NMR(300 MHz,D_2O): δ1.25-1.33 (overlap, 13H), 1.5-1.57 (m, 2H), 1.64-1.69 (m, 2H), 2.44-2.49 (t, 2H), 2.78-2.83 (t, 2H).

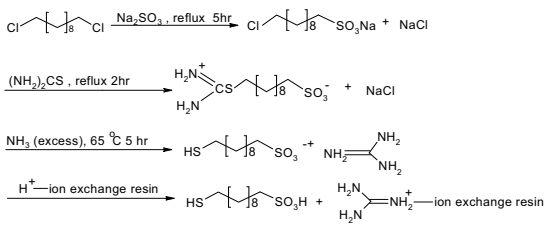


Fig. 1 Synthesis procedure of $–SO_3H$ terminated alkanethiol

Chwee Teck Lim, James C.H. Goh (Eds.): ICBME 2008, Proceedings 23, pp. 1418–1421, 2009
www.springerlink.com

B. Preparation of gold substrates and SAMs

The Si wafers was used as substrate for preparing SAM for contact angle experiments, X-ray photoelectron spectroscopy (XPS) and *in vitro* platelet adhesion analysis. The Si strips were cut in moderate size and were cleaned by immersion in piranha solution at 90°C for 2 hours. The surface was rinsed with a large amount of deionized water and absolute ethanol thoroughly and then blown dry with nitrogen. The gold substrates were prepared with thermal evaporator by pre-depositing Ti (100 Å, 1 Å/s) to improve the adhesion and then Au (1000 Å, 5 Å/s) was deposited onto Si strips. The fresh gold substrates were immediately immersed into two different series of mixed alkanethiol solutions, containing the mixture of the 10-mercaptodecanesulfonic acid with 1-dodecanthiol or with 11-mercapto-1-undecanol in absolute ethanol at room temperature for 24 hours. The total concentration of thiol solution was 2mM and 0.1mM. Upon removal, these strips were rinsed with absolute ethanol and deionized water and blown dry with nitrogen.

The mixed SAM formed on the cover glasses as substrates were used for zeta potential determination. The preparation of gold coated cover glasses and mixed SAMs was similar to that onto the Si strips mentioned above.

C. Surface characterization and in vitro platelet analysis

The contact angle measurement was carried out by sessile drop technique after the SAMs preparation and the probing liquid was deionized water. The surface composition of these mixed SAMs was characterized by XPS. Zeta potential measured by streaming potential technique was used to determine the surface charge of the mixed SAMs in PBS at pH 7.4. Human platelet–rich plasma (PRP, 3.5×10^{10} platelets/mL) was used for *in vitro* platelet adhesion assay. The experimental procedure is similar to our previous reported study [1].

III. Results and Discussion

A. Contact angle

The contact angle value of $-SO_3H/-CH_3$ mixed SAMs prepared from 2mM and 0.1mM as the function of solution mole fraction of the $-SO_3H$ terminated thiol ($\chi_{SO3H,soln}$) was shown in figure 2-(a). With the increase of $\chi_{SO3H,soln}$, the contact angle was gradually decreased. This was resulted from the increase of the $-SO_3H$ functional ends within the mixed SAMs. Furthermore because of the variations in surface assemblies at nano-scale the contact angle values of the $-SO_3H/-CH_3$ mixed SAMs prepared from 2mM were similar to those prepared from 0.1mM, except at $\chi_{SO3H,soln}$= 0.7 and 1.

For the $-SO_3H$/-OH mixed SAMs, the contact angle indicated that all surfaces were all hydrophilic. (Fig.2-(b)) In addition, the contact angle for the $-SO_3H$/-OH mixed SAMs prepared from 2mM was all lower than that of pure $-SO_3H$ SAMs ($\chi_{SO3H,soln}$ =1) and pure $-CH_3$ SAMs ($\chi_{SO3H,soln}$ =0), but for those prepared from 0.1 mM the contact angle was gradually decreased with the increase of $\chi_{SO3H,soln}$. Such phenomena were likely resulted form the hydrogen bonding or polar interactions among the hydrophilic ends of alkanethiol.

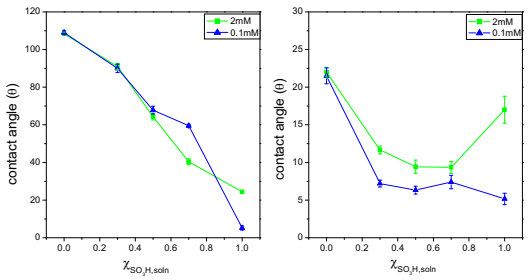


Fig. 2 The contact angle of (a) $-SO_3H/-CH_3$ mixed SAMs and (b) $-SO_3H$/-OH mixed SAMs prepared from 2 mM and 0.1 mM as the function of the mole fraction of $-SO_3H$ thiol in the ethanolic solution.

B. XPS

The surface composition determination of these two series of mixed SAMs was carried out by XPS. The relationship between surface composition of the $-SO_3H$ SAMs and solution mole fraction of the $-SO_3H$ terminated thiol was presented in Figure 3. All of these mixed SAMs showed "negative derivation" (i.e. below the 45° diagonal line) and indicated that they were "$-SO_3H$ alkanethiol poor" on these SAMs. It was likely due to the differences in solvation capability of the alkanethiol within the ethanolic solution. A higher solubility of the $-SO_3H$ terminated thiol than the $-CH_3$ terminated thiol and the –OH terminated one was suggested. Therefore, the variations in adsorption rate and thiolate formation rate might result in this observation.

C. Zeta potential

Because the surface charge of these mixed SAMs couldn't be directly measured, it was represented by the zeta potential, which was the charge on the shear plane. The electrolyte solution was chosen as PBS at pH 7.4 because of the close similarity to the body fluid.

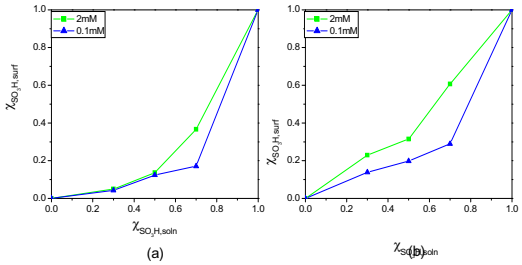


Fig. 3 Surface composition *vs* solution composition of the (a) $–SO_3H/-CH_3$ and (b) $–SO_3H/-OH$ mixed SAMs.

The zeta potential of $–SO_3H/-CH_3$ mixed SAMs in PBS at pH 7.4 as prepared form 2mM and 0.1mM with various $\chi_{SO3H,soln}$ was shown in Figure 4. The zeta potential of all these mixed SAMs was negative. On the apolar surface without dissociated sites, like pure $–CH_3$ SAMs, the negative surface charge might be resulted from the highly oriented water molecules near the surfaces and this structure makes anions preferentially adsorbed. [7-8] The zeta potential of the $–SO_3H$ SAMs was negative in PBS at pH 7.4 because sulfonic acid functionality was a strongly dissociated acid group at this pH.

Statistical analysis using ANOVA (analysis of variance) and Tukey method revealed that the zeta potential of $\chi_{SO3H,soln}$ =0 (pure $–CH_3$ SAMs) was similar to $\chi_{SO3H,soln}$ =1 (pure $–SO_3H$ SAMs), but was significantly more negative than others as prepared from 2mM mixture solution.

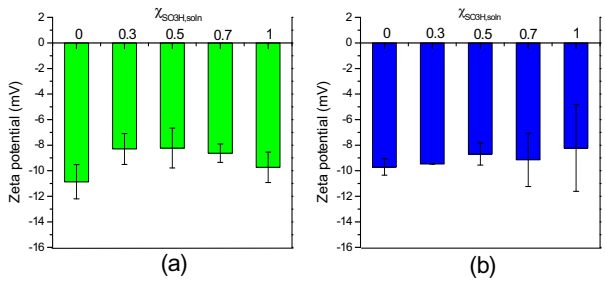


Fig. 4 The zeta potential of $-SO_3H/-CH_3$ mixed SAMs prepared from (a) 2 mM and (b) 0.1mM as the function of the mole fraction of $–SO_3H$ thiol in the ethanolic solution as determined in PBS pH 7.4.

Figure5 showed the zeta potential of the $–SO_3H/-OH$ mixed SAMs prepared from 2mM and 0.1mM in PBS at pH 7.4. The zeta potential of these mixed SAMs was also negative. Since the –OH functionality was polar but not dissociated in PBS at pH 7.4, the negative zeta potential might be caused by the preferentially anions adsorption. As compared to the apolar hydrophobic pure $–CH_3$ SAM, less negative surface charge on pure –OH SAM was noted. It was due to the loosely ordered water molecules near surfaces that resulted in less anions adsorbed.

As determined from the statistical analysis, $\chi_{SO3H,soln}$ =0 (pure –OH SAMs) has less negative zeta potential than others which contained $–SO_3H$ terminated alkanethiol for SAMs prepared from all concentrations. However, the negative charge didn't varied significantly with the amount of $–SO_3H$ terminated thiol added in the solution.

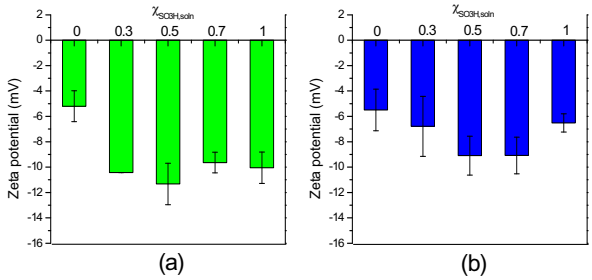


Fig. 5 The zeta potential of $-SO_3H/-OH$ mixed SAMs prepared from (a) 2 mM and (b) 0.1mM as the function of the mole fraction of $–SO_3H$ thiol in the ethanolic solution as determined in PBS pH 7.4.

D. In vitro platelet adhesion analysis

The platelet adhesion density on $–SO_3H/-CH_3$ mixed SAMs prepared from 2mM and 0.1mM is shown in Figure6. By statistical analysis with ANOVA and Tukey methods, pure $–CH_3$ SAMs ($\chi_{SO3H,soln}$ =0) exhibited the highest platelet adhesion density while others showed similar adhesion platelet density among each other. Moreover the adherent platelets on $\chi_{SO3H,soln}$ =0 was highly activated but with the increase of the $\chi_{SO3H,soln}$, the platelets adhered were less activated.

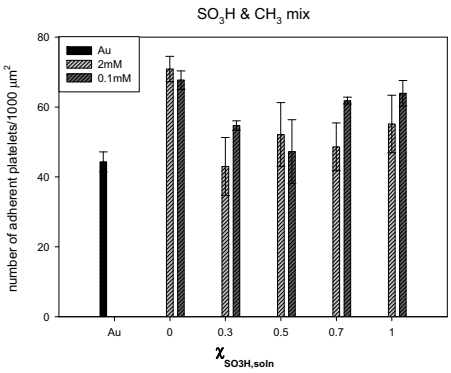


Fig. 6 Number of adherent platelets on $–SO_3H/-CH_3$ mixed SAMs prepared from 2mM and 0.1mM.

Figure 7 showed the platelet adhesion density on –SO_3H/-OH mixed SAMs prepared from 2mM and 0.1mM. In contrast to the –SO_3H/-CH_3 system, statistical analyses revealed that the –OH SAMs ($\chi_{SO3H,soln}$ =0) adhered the least amount of platelets. For other mixed SAMs, the platelet adhesion density was similar to each other. Moreover, SEM analyses have shown that the platelets adhered on –SO_3H/-OH mixed SAMs was less activated.

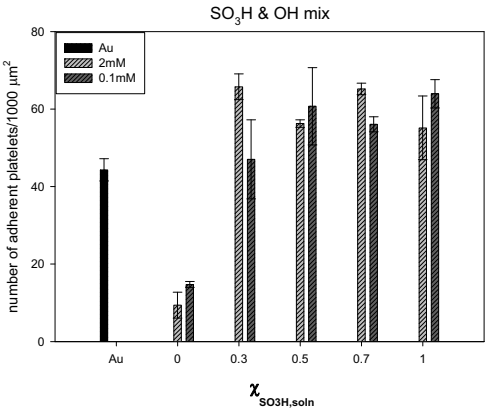


Fig. 7 Number of adherent platelets on –SO_3H/-OH mixed SAMs prepared from 2mM and 0.1mM.

IV. Conclusions

In this study, the surface properties and platelet-contacting properties of two different mixed SAMs series were examined. The surface wettabilities of –SO_3H/-CH_3 mixed SAMs varied from hydrophobic to hydrophilic with the increase of $\chi_{SO3H,soln}$ while all surfaces were hydrophilic on –SO_3H/-OH mixed SAMs. XPS results revealed that –SO_3H/-CH_3 mixed SAMs and –SO_3H/-OH ones were "-SO_3H alkanethiol poor" during SAM formation. All of the surface charge of these two mixed SAMs was negative in PBS pH 7.4 and the pure –OH terminated SAM was the least negative surface charged among the samples tested. *In vitro* platelet adhesion assay indicated that these two mixed SAMs exhibited similar amount of platelets adhered except for pure –CH_3 (the highest platelet adhesion density) and –OH (the lowest platelet adhesion density) terminated SAMs. Therefore the less negative surface charge might lead to the fewer platelets adhered, likely due to the differences in the amount of protein adsorbed as well as the variation in its conformation after adsorption.

Acknowledgment

We thank the Tainan Blood Donation Center for providing human platelet-rich plasma.

References

1. Lin JC, Chuang WH (2000) Synthesis, surface characterization, and platelet reactivity evaluation for the self-assembled monolayer of alkanethiol with sulfonic acid functionality. J Biomed Mater Res 51:413-423
2. Ulman A (1996) Formation and structure of self assembled monolayers. Chem Rev 96:1533-1554
3. Prime KL, Whitesides GM (1991) Self-assembled organic monolayers-model systems for studying adsorption of proteins at surfaces. Science 252:1164-1167
4. Tidwall CD, Ertel SI, Ratner BD et al. (1997) Endothelial cell growth and protein adsorption on terminally functionalized, self-assembled monolayers of alkanethiolates on gold. Langmuir 13:3404-3413
5. Lòpez GP, Albers MW, Schreiber R et al. (1993) Convenient methods for patterning the adhesion of mammalian cells to surfaces using self-assembled monolayers of alkanethiolates on gold. J Am Chem Soc 115:5877-5878
6. Bain CD, Evall J, Whitesides GM (1989) Formation of monolayers by coadsorption of thiols on gold: variation in the head group, tail group, and solvent. J Am Chem Soc 111:7155-7164
7. Welzel PB, Rauwolf C, Yudin O et al. (2002) Influence of aqueous electrolytes on the wetting behavior of hydrophobic solid polymers-low rate dynamic liquid/fluid contact angle measurements using axi-symmetric drop shape analysis. J Colloid Interf Sci 251:101-108
8. Hermitte L, Thomas F, Bougaran R et al. (2004) Contribution of the comonomers to the bulk and surface properties of methacrylate co-polymers. J Colloid Interf Sci 272:82-89

Corresponding author:

Author: Jui-Che Lin
Institute: Dept. of Chemical Engineering,
National Cheng Kung University
Street: 1, University Rd.
City: Tainan
Country: Taiwan
Email: jclin@mail.ncku.edu.tw

Microscale Visualization of Erythrocyte Deformation by Colliding with a Rigid Surface Using a High-Speed Impinging Jet

S. Wakasa[1], T. Yagi[1,2], Y. Akimoto[1], N. Tokunaga[1], K. Iwasaki[3] and M. Umezu[1]

[1] Integrative Bioscience and Biomedical Engineering, Twins, Waseda Univ., Japan
[2] CSIRO Minerals, Melbourne, Australia
[3] Waseda Institute for Advanced Study, Waseda Univ., Japan

Abstract — **Erythrocyte deformation by colliding with a rigid surface using a high-speed impinging jet was studied with microfluidic techniques. We aim to investigate the relevance of colliding erythrocytes with hemolysis. A micro-channel chip was made of polydimenthyl-siloxane (PDMS), which comprised a T- and Y-shaped junction with a micro-nozzle and diffuser in order to attain a high-speed microflow with a jet velocity of m/s scale. A high-speed camera with a microscope imaged colliding erythrocytes by shadow imaging. Porcine erythrocyte with a hematocrit of 0.5 % in phosphate buffer saline was utilized. At the Y-junction, erythrocytes showed buckling due to an impulsive, longitudinal, compressive deformation. Such anomalous phenomena were not detected at the T-junction, where erythrocytes underwent sequential compressions as approaching the colliding surface. Erythrocyte after buckling showed a hazy membrane while being released from the colliding surface, suggesting the ejection of hemoglobin out of the pore on a membrane. Flow-induced hemolysis has been considered as a model of viscous shear stress and exposure time. From our data, however, it was suggested that hemolysis due to a high-speed impinging flow characterized by mechanical heart valve flows may arise as an impulsive failure of erythrocyte membrane upon collision.**

Keywords — **Hemolysis, erythrocyte, microfluidics, heart valve, turbulence**

I. Introduction

Prosthetic mechanical heart valves require a mandatory drug therapy including anticoagulation. Blood cell damage, such as hemolysis and platelet activation, is one of the relating phenomena. Such damage can be observed by shearing flows in a rotating viscometer and a turbulent jet [1-5]. Likewise, blood flow in mechanical heart valves is widely accepted to promote damage of flowing cells, but the underlying phenomena remain to be fully understood due to the complexity of actual flows. Indeed, a number of studies revealed abnormal streams characterized by transient high shear, turbulence, squeezing flow and cavitation [6-9]. These flows require verifications in a cellular scale to elucidate their anomaly with the relevance of blood cell damage.

We propose a new challenge termed *macroscale modeling and microscale verification*. From our previous study of macroscale modeling [10], we hypothesize that turbulence promotes an impinging flow, which then causes the collision of erythrocytes. The similar knowledge can be applied to valve closure, where erythrocytes impulsively collide with a rigid leaflet upon closure. Herein we aim to investigate such an erythrocyte deformation upon collision using high-speed microfluidic techniques in order to verify the involvement of impinging flows with hemolysis.

II. Method

The overview of an experimental setup is shown in Fig.1. A micro-channel was set on a linear stage. A flow was driven by a syringe pump (SP-70, NIPRO Corp., Japan). An imaging system comprised a high-speed camera (FASTCAM-1024PCI, Photron, Japan) and a metal halide lump. The camera was equipped with a zooming microscope (DZ-3, Union Optical Co., Ltd., Japan). The light source was aligned as shadow imaging. Experiments were made in a temperature-controlled box at 37 degrees.

A micro-channel geometry was shown in Fig.2. These channels were fabricated by polydimenthyl-siloxane (PDMS). In order to attain microscale high-speed flows, channels had a micro-nozzle and diffuser at the upstream and downstream of a test section, respectively. A flow rate was set at 18 and 36 mL/h to make a desired flow condition, in the T- and Y- shaped channel, so that a bulk jet velocity at the nozzle outlet could reach 1 m/s in both channels.

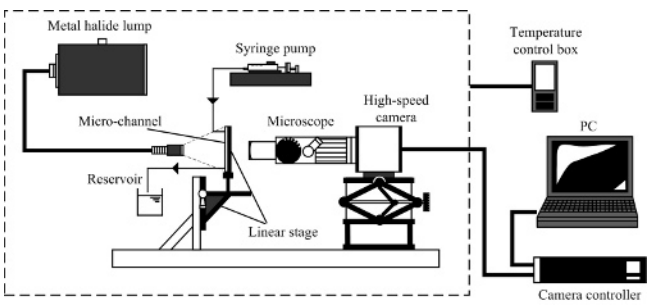


Fig. 1 Schema of experimental set-up

Chwee Teck Lim, James C.H. Goh (Eds.): ICBME 2008, Proceedings 23, pp. 1422–1425, 2009
www.springerlink.com

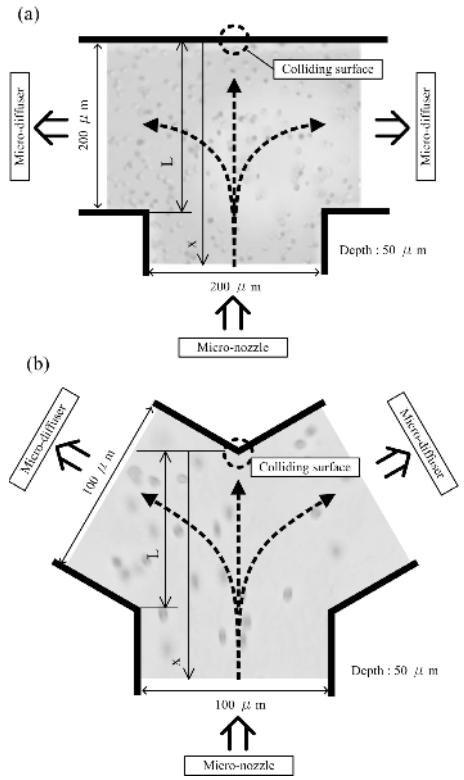


Fig. 2 Schema of micro-channels with a T- and Y-shaped junction

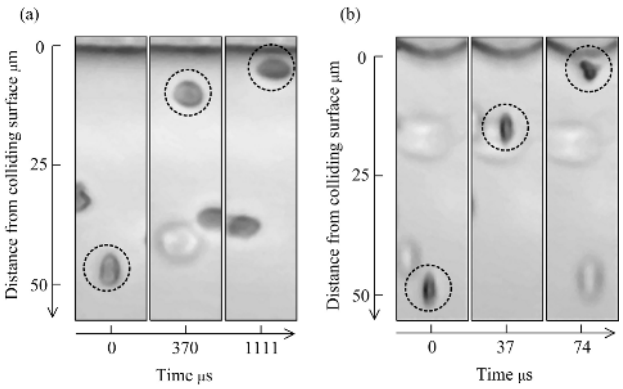


Fig. 3 Erythrocyte deformation upon collision at a T- and Y- shaped junction (a,b)

Fresh porcine blood was collected and was immediately centrifuged at 1000 g for 5 min. The plasma and buffy coat containing white blood cells and platelets were removed, and erythrocytes were washed three times in phosphate buffer saline (PBS). Porcine serum albumin (Sigma Aldrich, U.S.A.) was added at a concentration of 5.5×10^{-2} [g/dL]. A hematocrit was adjusted to be 0.5 % by suspending erythrocytes in the PBS solution.

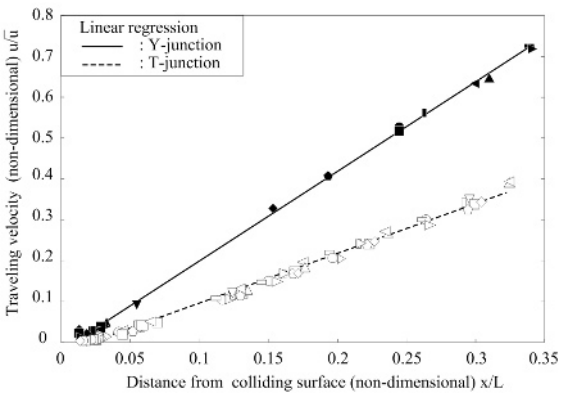


Fig. 4 Traveling velocity of erythrocytes in the vicinity of a colliding surface

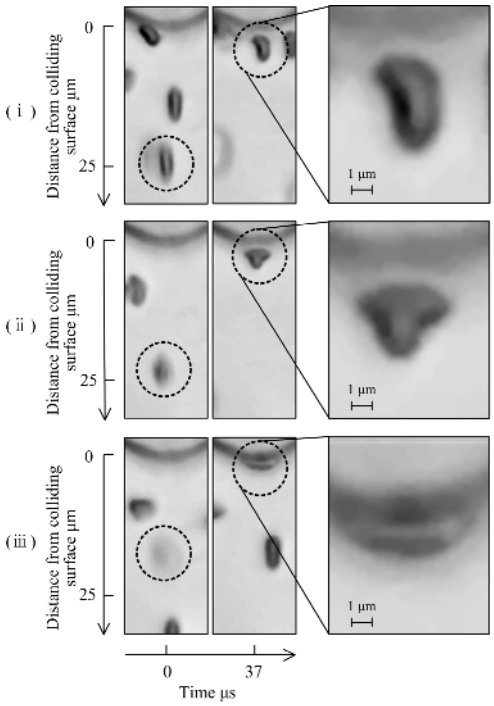


Fig. 5 Characteristic deformation of erythrocyte upon collision at a Y-junction

III. Results and Discussion

A. Comparison of colliding erythrocytes between T- and Y-shaped channels

We first compared the deformation pattern of erythrocytes upon collision between T- and Y-shaped junctions (Fig.3 (a), (b)). We limit herein ourselves to describe the erythrocytes that collided with a surface at a test section (Fig.2). Other erythrocytes appearing in Fig.3 were those

disappeared without collision. In the T-junction, flowing erythrocytes were elongated at a far field from a colliding surface, became spherical as approaching the surface, and were laterally deformed in the vicinity of the surface. The lateral deformation, though affected by rotating effects, indicated a compression of erythrocyte upon collision.

On the other hand, colliding erythrocytes in the Y-junction showed an impulsive deformation (Fig.3(b)). The erythrocytes maintained their elongated shapes further as they approach the colliding surface, and then they abruptly altered the shapes upon collision without showing a sequential deformation seen in the T-junction. These include impulsive bending and buckling as characterized by the longitudinal deformation unlike lateral one in the T-junction, and will be detailed later. Here, the varying collision dynamics between T- and Y-shaped junction is considered. Fig.4 shows the traveling velocity of erythrocytes. The velocity was non-dimensionalized using a bulk flow velocity at the outlet of the micronozzle (1 m/s). The velocity plot in the Y-junction showed the greater deceleration. The corresponding slope was about 1.8 times higher. These velocity differences attributed to varying degrees of stagnation. It was believed that the T-junction had a blunt pressure field, whereas the Y-junction had a sharp field. As a result, erythrocytes at the Y-junciton maintained the higher speed towards the colliding surface, resulting in the impulsive, longitudinal and compressive deformation upon collision.

B. Buckling of erythrocytes upon collision

At a Y-junction, we observed some abnormal erythrocytes at the same flow conditions. Fig.5 summarized their characteristics; (i) and (ii) show a significant bending upon impingement, and (iii) was similar to that observed in a T-junction. The impulsive bending of erythrocytes indicated that erythrocytes underwent buckling due to an impulsive longitudinal compression. Furthermore, such erythrocytes often showed a hazy membrane while being released out of the collision (Fig.6). These anomalous phenomena may indicate the ejection of hemoglobin out of the membrane pore, as illustrated in Fig.7. These locations more likely corresponded to a stretched part of membrane, rather than bending. It was suggested that the erythrocyte membrane received an impulsive stress with a structural instability upon buckling and this phenomenon resulted in the pore formation. Such impulsive phenomena have not been observed at a T-junction, suggesting the geometrical significance of the colliding surface.

IV. Conclusions

The present study utilized high-speed microfluidic techniques to study colliding erythrocytes on a rigid surface. A Y-shaped junction caused the buckling of erythrocytes due

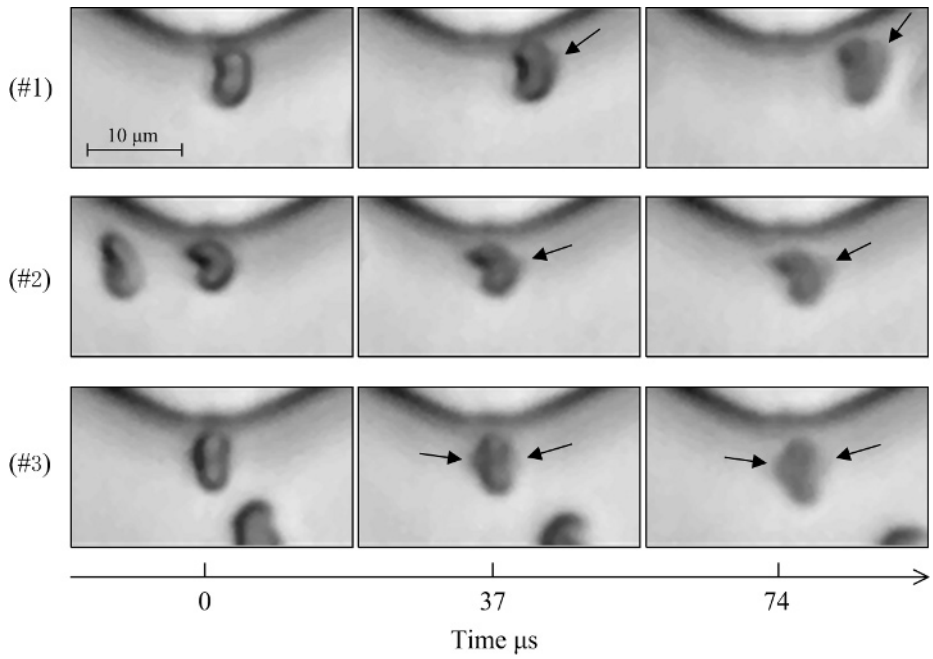


Fig. 6 Anomalous erythrocytes after undergoing buckling.
A hazy membrane indicated by an arrow suggests hemoglobin released out of erythrocyte membrane.

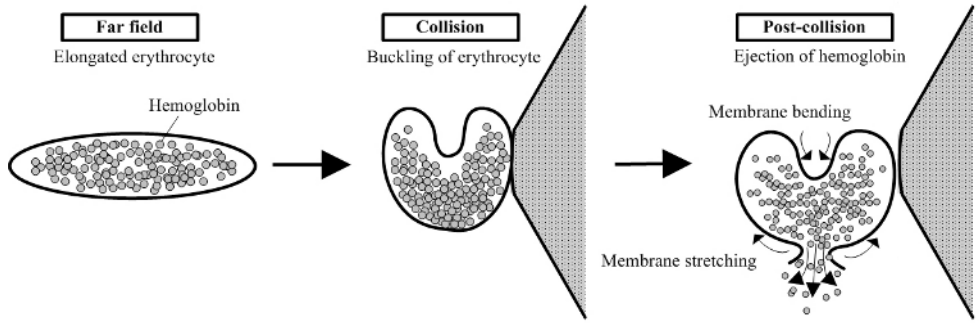


Fig. 7 Model of erythrocyte deformation by colliding with a Y-shaped junction

to an impulsive, longitudinal, and compressive force upon collision. Anomalous erythrocytes included those showed a hazy membrane at a post-collision phase, suggesting the ejection of hemoglobin from a membrane pore. These results deserve further microscale verifications of impinging flows with the relevance of hemolysis. Particularly, the effect of hematocrit is of prime importance. Actual valve flows were all transient with a velocity scale reaching a few m/s, where impinging flows further elevate an impulsive force upon collision according to our previous study of macroscale modeling. Conventionally, flow-induced hemolysis has been considered as a model of viscous shear stress and exposure time. From our data, however, it was suggested that hemolysis in actual valve flows may arise rather instantaneously as an impulsive failure of erythrocyte membrane upon collision.

Acknowledgement

This research was partly supported by Health Science Research Grant (H20-IKOU-IPAN-001) from Ministry of Health, Labour and Welfare, Japan, Biomedical Engineering Research Project on Advanced Medical Treatment from Waseda University (A8201), and "Establishment of Consolidated Research Institute for Advanced Science and Medical Care", Encouraging Development Strategic Research Centers Program, the Special Coordination Funds for Promoting Science and Technology, Ministry of Education, Culture, Sports, Science and Technology, Japan.

References

1. Leverett LB, Hellums JD, Alfrey CP, Lynch BC. (1972) Red blood cell damage by shear stress. Biophysical Journal 12: 257-273.
2. Sallam AM and Hwang NH. (1984) Human red blood cell hemolysis in a turbulent shear flow: contribution of reynolds shear stresses. BiorBiorheology 21: 783-797.
3. Ikeda Y, Handa M, Kawano K, Kamata T, Murata M, Araki Y, Anbo H, Kawai Y, Watanabe K, Itagaki I, Sakai K and Ruggeri ZM. (1991) The role of von Willebrand factor and fibrinogen in platelet aggregation under varying shear stress. Journal of Clinical Investigation 87: 1234-1240.
4. Paul R, Apel J, Klaus S, Schugner F, Schwindke P and Reul H. (2003) Shear stress related blood damage in laminar couette flow. Artificial Organs 27(6): 517-529.
5. Kameneva MV, Burgreen GW, Kono K, Repko B, Antaki JF, and Umezu M. (2004) Effects of turbulent stresses on mechanical hemolysis experimental and computational analysis. ASAIO Journal 50(5): 418-23.
6. Yoganathan AP, Woo Y and Sung H. (1986) Turbulent shear stress measurements in the vicinity of aortic heart valve prostheses. Journal of Biomechanics 19(6): 433-442.
7. Akutsu T, Bishop WF and Modi VJ. (1994) Hydrodynamic study of tilting disc valves (Effect of valve orientations) 60(577): 121-127.
8. Simon HA, Leo HL, Carberry J, Yoganathan AP. (2004) Comparison of the hinge flow fields of two bileaflet mechanical heart valves under aortic and mitral conditions. Annals of Biomedical Engineering 32(12): 1607-17.
9. Bluestein D, Yin W, Affeld K and Jesty J. (2004) Flow-induced platelet activation in mechanical heart valves. The Journal of Heart Valve Disease 13: 501-508.
10. Yagi T, Ishikawa D, Sudo H, Akutsu T, Yang W, Iwasaki K, Umezu M. (2006) Real-time planar spectral analysis of instantaneous high-frequency stress on blood cells downstream of an artificial heart valve, CD-ROM Proceedings of the 12th International Symposium on Flow Visualization, Gottingen, Germany 9: 10-14.

Author: Takanobu Yagi, Ph.D.
Institute: Integrative Bioscience and Biomedical Engineering, TWins, Waseda Univ.
Street: 2-2 Wakamatsu-cho, Shinjuku
City: Tokyo
Country: Japan
Email: Takanobu-yagi@akane.waseda.jp

Development of an Implantable Observation System for Angiogenesis

Y. Inoue[1], H. Nakagawa[2], I Saito[2], T. Isoyama[1], H. Miura[2], A. Kouno[1], T. Ono[1], S.S. Yamaguchi[1], W. Shi[1], A. Kishi[3], K. Imachi[4] and Y. Abe[1]

[1] Graduate School of Medicine, the University of Tokyo, Tokyo, Japan
[2] RCAST, the University of Tokyo, Tokyo, Japan
[3] Graduate School of Medical Science, Kitasato University, Japan
[4] Graduate School of Biomedical Engineering, Tohoku University, Japan

Abstract — **A miniaturized video camera system integrated with a scaffold for blood vessels and tissue induction that is implantable into an animal body was developed. A small auto-focus camera with USB interface was used as an imaging device. A close-up lens was added to reduce the focusing point. Also 45-degree reflecting prism was added for the compact system design. A spongy polyglycolic acid sheet of 0.3 mm thickness was used as a scaffold. The observation area was about 8 x 6 mm and the tissue was induced from sideways. The camera was implanted into a muscular layer of a goat for more than 60 days to observe the skeletal muscle induction. Tissue induction to the scaffold started from second week and it took about 5 weeks to cover the entire area by the tissue, Vigorous angiogenesis was observed at the front region of tissue induction resulting dense distribution of capillary vessels and red blood cells. The density of capillary vessels reduced considerably behind the front region and arterioles and venules started to appear.**

Keywords — **Implantable microscope, Angiogenesis, Tissue regeneration**

I. Introduction

Recent progress in biotechnology is astonishingly successful. Not only one can predict the various disease risks from gene diagnosis, one may even create genetically identical individuals from stem cells. From the viewpoint of regenerative medicine, however, the success is limited. One can create many square meters of skin by cultivating epidermal cells for several weeks. Or one can create a cardiac muscle cell sheet, which beat spontaneously. But we are not successful in generating an entire heart or any other functioning organs for regenerative medicine. The cultivation is limited to a two-dimensional structure with a single cell species. The most of human organs are of three-dimensional structure with several cell species. Two major obstacles hampered the artificial generation of three-dimensional functioning organs;

1. One has to supply nutrients and oxygen to cells deep inside the structure.
2. Plural cell species have to be cultivated in a harmonized manner to achieve the desired function.

In naturally formed organs, the blood cells and vessels supply nutrients and oxygen. Angiogenesis or vessel formation could be a crucial process for the 3-D structure formation. We are hoping that the observation of structure formation, in vivo, provide crucial information for the artificial realization of functioning organs. So, we were small and were high resolution and developed implantable microscope camera system.

II. Experimental Method

A. System design

Figure 1 shows a cross-section of the camera system. A small CMOS camera (Hitachi Maxell, PM7, Tokyo, Japan) with USB interface is used as an imaging device. The imaging device that has 1.3 mega pixels and has 1/3-inch CMOS sensor was mounted on a printed circuit board together with the auto-focus lens was taken out from original case and used. Extra close-up lenses were added to shorten the focal length. Further 45-degree prism was inserted to reduce the

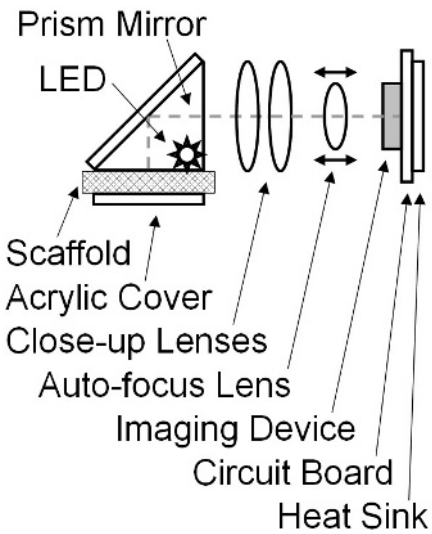


Fig. 1 Cross-section of the camera system

Chwee Teck Lim, James C.H. Goh (Eds.): ICBME 2008, Proceedings 23, pp. 1426–1429, 2009
www.springerlink.com

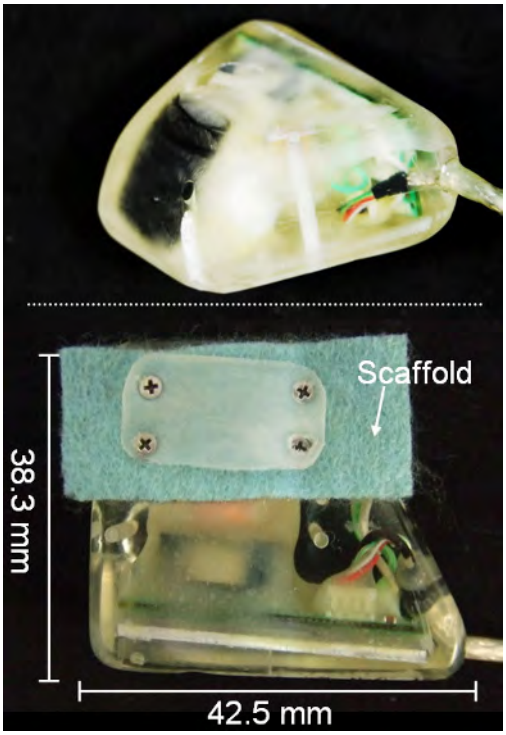


Fig. 2 The camera system with a scaffold sheet

system size. And this design, the device can be implanted with out stress. A scaffold sheet was directly attached to the bottom of the prism. The scaffold is made of poly glycol acid (PGA: Gunze, NV-N-015N, Kyoto, Japan), and the hickness is 0.3mm. The scaffold type and thickness were selected by basic research. A white-color LED device (Nichia-kagaku, NSPW500BS, Tokushima, Japan) was placed at the side of the prism for scaffold illumination. Entire system except the scaffold was embedded in transparent medical epoxy resin and the camera system can be implanted into an animal body. The scaffold at the bottom of the prism is sandwiched with an acrylic plate, so the cells can be induced from the sides. Figure 2 shows the picture taken from the bottom. This system is small (W 42.5mm x D38.3mm x H18mm) enough to implant. This system can record high resolution picture (1280 x 1024 pixels: SXGA) and movie (1280 x 1024 : 15fps, 640 x 480 : 30fps).

B. Animal experiment

We implanted the camera system into an animal and observed vessel generation and tissue induction process. We used the goat (female, ~50kg) as experimental animals. We implanted the system between the skeletal muscle (latissimus dorsi) and skin at the side of the body. Figure 3 shows implantation of camera system on the muscle.

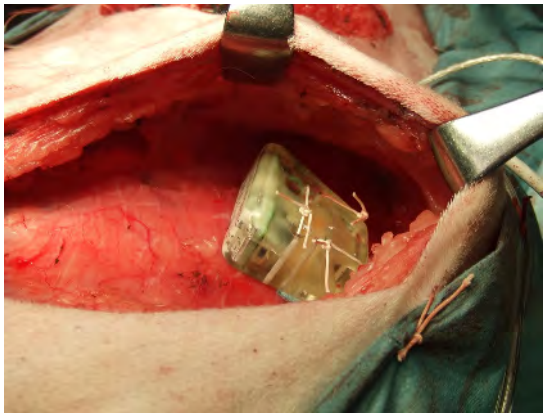


Fig. 3 Operation of camera system on the muscle

We record the picture (1280 x 1024 pixels) every 30 minuets with a personal computer. The camera system was connected to the PC by USB2.0 interface. This experiment was continued for nine weeks.

C. Tissue Extraction

At the end of experiment, camera system and regenerated tissue were extracted from the body. The tissue was stained with hematoxylin eosin for histological analysis.

III. Result and Discussion

A. Regenerating pictures

We implanted the device into the goat and we observed regenerating tissues and vessels.

Figure 4A-D shows regenerating pictures by the camera system for 6weeks. No induction was observed under the camera view for the 2 weeks. We observed at initial stage, the blue section is a scaffold.

The tissue induction in the camera view was started in the third week (Figure 4-A). We observed scaffold almost all camera view and we observed many small capillary at the right and left side in the view.

Figure 4-B shows result at 4th week. Vessels and tissue were regenerating from last week. At front section have many capillary, and at the rear section, capillary disappered, and have some big vessels.

Figure 4-C shows result at 5th week. Most scaffolds were hydrolyzed. Regenerated tissue from both sides were growing and connecting at the centre of the camera view. At front regenerating section have many capillary. At middle regenerated section have some vessels branched from big vessels. At rear section the density of capillary vessels were reduced.

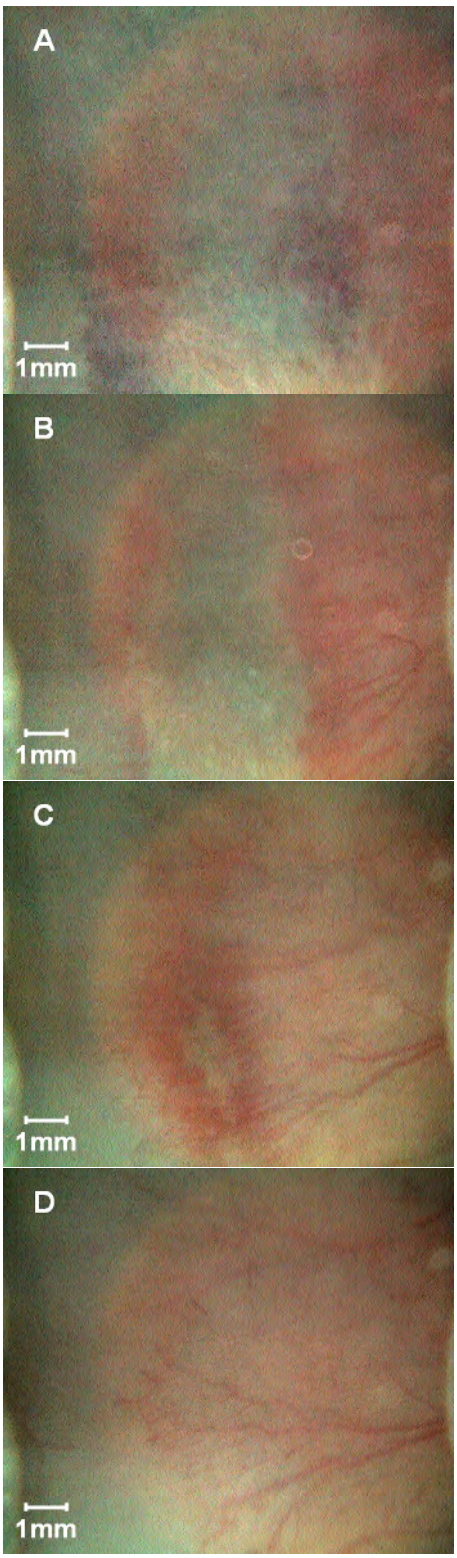


Fig. 4 Regenerating vessels and tissues pictures (A - D)

Figure 4-D shows result at 6th week. The blood vessels and tissue have covered on the whole camera view. Growth rate was within the range of 0.15-0.20mm/day through the whole experiment.

After the 6th week, the camera view did not have big change. We continued this experiment for nine weeks.

B. Tissue extraction

At the end of experiment, camera and regenerated tissues were extracted from the body. And the tissue was stained with hematoxylin and eosin for histological analysis.

Figure 5 shows the generated tissue which it sliced in parallel to the PGA scaffold plane. We observed the small vessels branched from large vessel. With higher magnification, we observed red blood cells in the vessels. We were not able to observe the PGA scaffold any where, because it was hydrolyzed.

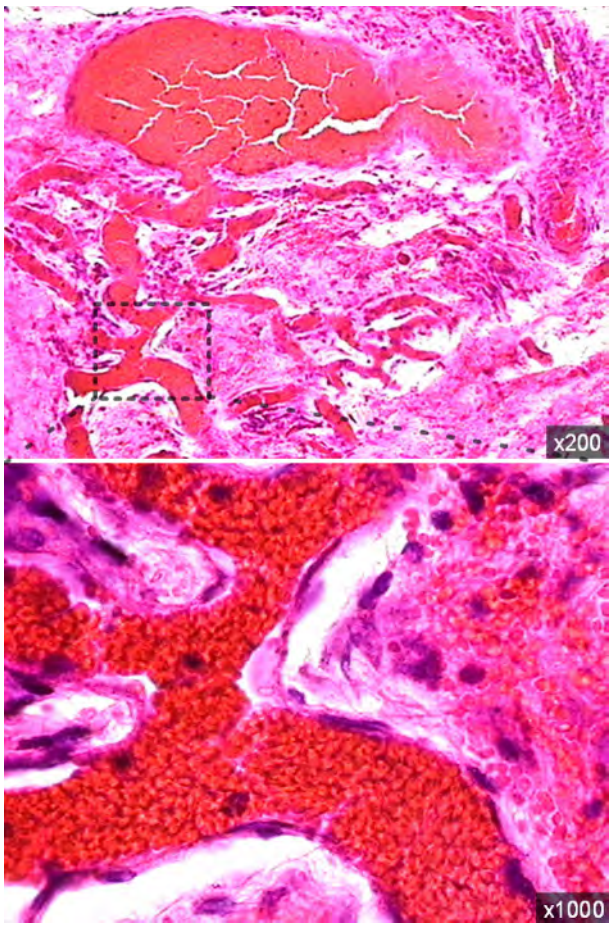


Fig. 5 H.E. stained generated tissue (Parallel slice)

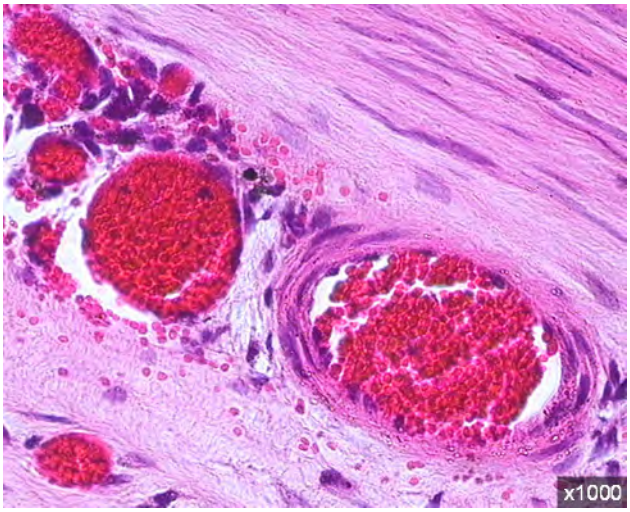


Fig. 6 H.E. stained generated tissue (Vertically slice)

Figure 6 shows the generated tissue which it sliced in vertically to the PGA scaffold plane. We observed cross sections of several vessels. We observed small artery which have thick wall. And we observed veins beside the artery.

IV. Conclusions

We developed the implantable small camera with scaffold for tissue and vessels induction observation. The device is small enough to implant. And the device had high resolution and function so as to observe regenerated tissue.

We observed blood vessels when 2weeks after an experiment start. Many blood vessels were observed at front section of new tissue. Almost all capillaries were disappeared at rear section where growth rate decreased, but arterioles and venules were generated. At the 6th weeks the generated tissues have covered on the whole camera view. Exchange of interconnection points among arterioles were observed. Hierarchical branchings of vessels were frequently observed.

At end of an experiment, we dyed generated tissues with H.E. staining. We observed active generation of capillaries at the front section. And we observed small artery and small vein.

We developed the real-time observation device. In future, we will intend to continue experiment with this device.

New challenge for studying flow-induced blood damage: macroscale modeling and microscale verification

T. Yagi[1,2], S. Wakasa[1], N. Tokunaga[1], Y. Akimoto[1], T. Akutsu[3], K. Iwasaki[4], M. Umezu[1]

[1]Integrative Bioscience and Biomedical Engineering, Waseda University, TWIns, Tokyo, Japan
[2]CSIRO Minerals, Melbourne, Australia
[3]Dept. of Mechanical Engineering, Kanto Gakuin University, Yokohama, Japan
[4]Waseda Institute for Advanced Study, Waseda University, Tokyo, Japan

Abstract — **Prosthetic heart valves often induce blood cell trauma, but its mechanism is not clearly understood due to the complexity of dynamical flows. We herein propose a new challenge, termed *macroscale modeling and microscale verification.* This report is the former, and here we aim to clarify the physical interpretation of Reynolds stress for flowing cells. One polymer and two mechanical valves are compared, and the Reynolds stress is visualized using a novel analytical technique including time-resolved particle image velocimetry and continuous wavelet transform. The method enables to analyze the dynamics of Reynolds stress in a spatial and temporal domain. As a result, it is found that the Reynolds stress should be considered as an indicator of impinging flows for circulating cells. Such flows may impulsively apply a colliding force on a membrane of flowing cells. As microscale verification based on this new hypothesis, we are currently investigating such collision phenomena of flowing cells using high-speed microfluidic techniques.**

Keywords — **turbulence, hemolysis, heart valve, collision, impinging flow**

I. Introduction

Prosthetic heart valves often require a mandatory drug therapy including anticoagulation. Blood damage, such as hemolysis and platelet activation, is one of the underlying phenomena. Such damage can be observed in controlled flows, such as shearing flows and turbulent jets [1-3]. However, actual flows are dynamically complex including transient high shear, turbulence, squeezing flow, hinge flow and cavitation [4-7]. Currently, understanding a mechanism of causing blood trauma in dynamical flows is still immature. These aspects indicate the necessity of *verifying* the anomaly of flows in a cellular scale in an effort to detect the most critical phenomenon for blood trauma. Here, we propose a new challenge termed *macroscale modeling and microscale verification*. This study is the former, and herein we aim to make a physical model of turbulence for flowing cells. Reynolds stress has been used as an indicator of turbulence, but it is also known as apparent stress in fluid dynamics. Due to the limitation of classical fluid dynamics, the physical interpretation of Reynolds stress for flowing cells remains controversial [8-9], which is of prime interest in modeling turbulence in a cell scale and verifying the relevance with blood cell damage.

II. Method

We made a pulsatile flow circuit to reproduce a physiological aortic flow at a pump outlet (Fig.1). A working fluid consisted of glycerol and water with a volume fraction of 44 and 56 %, respectively. And its kinematic viscosity and density was ν=3.3 cSt and ρ=1100 Kg/m^3 at room temperature. The flow had a 5L/min mean rate and 80-120 mmHg pressure variation at a pulse rate of 70 bpm. Reynolds number and Womersley parameter was approximately 1600 and 14.9, respectively. The Jellyfish polymer valve (JF), the St. Jude Medical bileaflet valve (SJM), and the Medtronic Hall

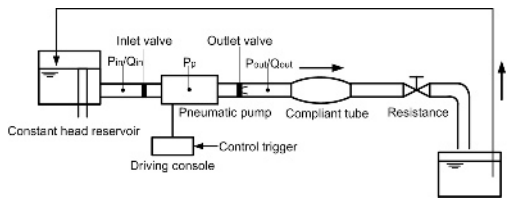


Fig.1 Schema of experimental rig

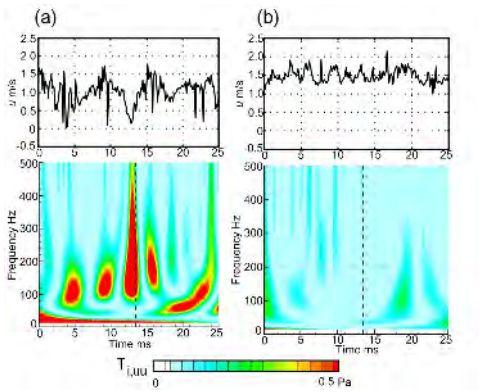


Fig.2 Continuous wavelet transform of turbulent jet in a prosthetic heart valve (a: shear layer, b: downstream)

Chwee Teck Lim, James C.H. Goh (Eds.): ICBME 2008, Proceedings 23, pp. 1430–1433, 2009
www.springerlink.com

monoleaflet valve (MD) were compared, and their flows were quantitatively visualized using Time-resolved 2D Particle Image Velocimetry (TR-PIV). A 1.5 mm-thick laser light sheet was symmetrically aligned passing through a valve center. Temporal and spatial resolution of TR-PIV was 7400 Hz and 0.64×0.64 mm^2, respectively.

Then, continuous wavelet transform was made using the following equation,

$$T(a,b) = \frac{1}{\sqrt{a}} \int_{-\infty}^{\infty} u(t)\psi^*\left(\frac{t-b}{a}\right)dt \quad (1)$$

where T denotes wavelet coefficient, $u(t)$ is a velocity signal as a function of time, and ψ^* is a complex conjugate of a wavelet function. In this study, the streamwise velocity was selected. Parameters a and b indicate scaling in dilating and translating the wavelet function, respectively. $1/\sqrt{a}$ is a weighting function. The wavelet coefficient was computed using the Mexican hat wavelet,

$$\psi(t) = \frac{2}{\sqrt{3}\sqrt[4]{\pi}}(1-t^2)e^{-t^2/2} \quad (2)$$

and its admissibility constant C_g is equal to $4\sqrt{\pi}/3$ [10]. A wavelet turbulent spectrum was calculated using the following formula,

$$\tau_i(f,t) = \frac{\rho}{\Delta f_c C_g}\left|T(f,t)\right|^2 \quad [\text{Pa}] \quad (3)$$

where Δ is a sampling period and f_c is a characteristic frequency of the wavelet (f_c=0.251Hz) [10]. A wavelet frequency is defined as follows.

$$f = \frac{f_c}{a \cdot \Delta} \quad (4)$$

Note that if the wavelet spectrum is integrated over time and frequency, it becomes equal to the magnitude of conventional Reynolds stress. Fig.2 illustrates examples for better understanding. Times-resolved velocity series were transformed to a time-frequency domain, where the color contour corresponded to the magnitude of turbulent spectrum, namely *instantaneous Reynolds stress*. All above computations were carried out using an in-house MATLAB code.

III. Results and Disucussion

A. Reynolds stress during systole

Fig.3 compares mid-systolic flows. Wavelet transform was carried out for time-resolved 2D velocity data sets, and the stress field was colored by representing the magnitude at

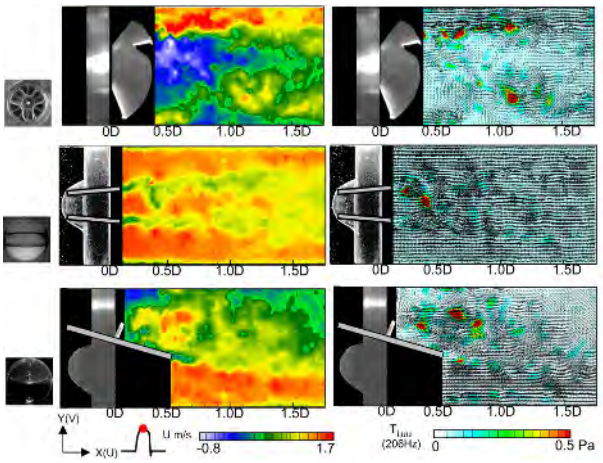


Fig.3 Instantaneous velocity field (left) and Reynolds stress (right) during peak phase (top: JF, mid: SJM, bottom: MD)

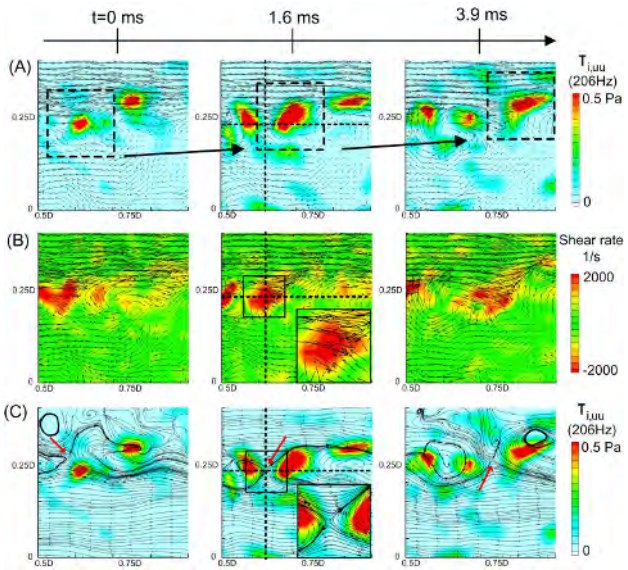


Fig.4 Dynamics of turbulent cell in a shear layer (A: Reynolds stress, B: Shear rate, C: Streamline). Streamlines were obtained in a relative coordinate by subtracting the traveling speed of the turbulent cell. Dotted-line squares showed incipient, growinges by tracking a single cell, and solid-line squares corresponded to zoomed views of colliding surface as indicated by red-colored arrows.

a frequency of 206 Hz. This stress mapping enabled to visualize the dynamic motions of Reynolds stress in a spatial and temporal domain. The Reynolds stress emerged in a mixing process of varying magnitude of momentum, which was observed along with shear layers and at the downstream of expanding flows. Fig.4 illustrates a spatio-temporally evolving Reynolds stress along with the shear layer. The Reynolds stress begun to be spatially organized (t=0), grew by entraining the ambient fluid (t=1.6 ms), and elongated its

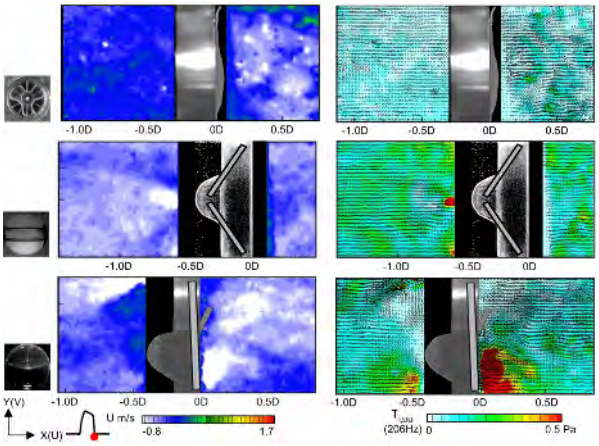


Fig.5 Instantaneous velocity field (left) and Reynolds stress (right) immediately before valve closure (top: JF, mid: SJM, bottom: MD)

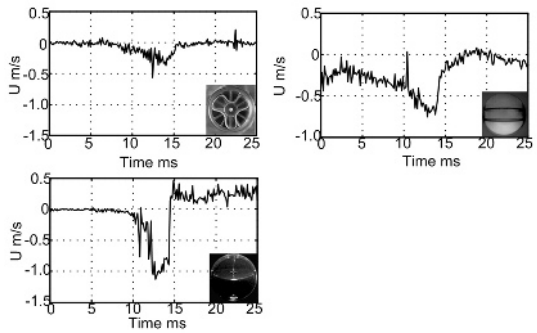


Fig.6 Streamwise velocity profile upon valve closure. The value was represented in the vicinity of a closing leaflet. A spike-like signal indicated an impact of valve closure.

structure (t=3.9 ms). In the further downstream, the Reynolds stress was decayed and finally disappeared by diffusing. This spatially organized pattern of Reynolds stress is termed *Turbulent cell (T-cell)*. Interestingly, while the T-cell traveled downstream with a certain speed, it was followed by a cluster of shear rate (Fig.4). In order to understand their relationship, streamlines were obtained in a relative coordinate, where the velocity in a fixed coordinate was subtracted by the traveling speed of the T-cell (see Section C). Then, we found that streamlines from the upstream and downstream were collided within the shear cluster. In other words, the incoming jet impinged with the T-cell because the traveling speed of T-cell was substantially smaller than the convective jet velocity. Since the T-cell grew by entraining the ambient weak flow, this impinging flow was observed with a large velocity fluctuation, such as seen in Fig.2 (a), which is exactly a core of Reynolds stress analyzed conventionally. By entraining the ambient flow periodically along with the shear layer, a core jet was collapsed and diffused. During this process, the velocity profile became blunt, such as seen in Fig.2 (b). Taken together, it can be said that the physical interpretation of Reynolds stress during systole is an indicator of impinging flows.

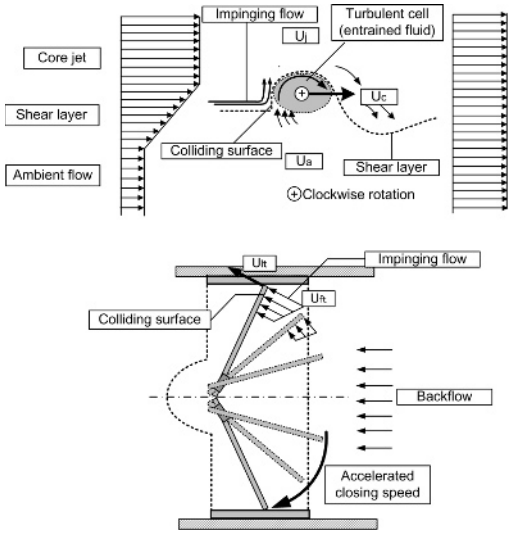


Fig.7 Model of impinging flow
(top: Shear layer, bottom: Valve closure)

B. Reynolds stress during valve closure

Fig.5 compares Reynolds stress immediately before valve closure. The Reynolds stress appeared impulsively with a sudden halt of valve leaflet, and the varying magnitude observed among three valves attributed to the distinct closing mechanics. The polymer valve was closed more smoothly thanks to the flexible leaflet and the central backflow that promoted the closing motion of the leaflet. In contrast, the closing speed of mechanical valves was accelerated by an adverse pressure gradient. In addition, the leaflet was impulsively halted by the hinge mechanics. Since the closing leaflet speed may reach an order of m/s immediately before closure, the instant of valve closure had a spike-like velocity profile (Fig.6), resulting in the impulsive and extensive formation of the Reynolds stress (Fig.5). Herein as well, the Reynolds stress can be considered as an indicator of impinging flows.

C. Physical interpretation of Reynolds stress

Fig.7 summarizes illustrations for above cases. In both cases, Reynolds stress can be considered as an indicator of impinging flows. At the shear layer, the core jet entrains the ambient flow impulsively (*entrainment*). The traveling velocity of entrained fluid U_c is substantially lower than that of the jet convective velocity. This finding was already described by pioneers in 1966 [11]. Thus, the colliding

velocity U_{col} becomes $U_{col}=U_j-U_c$, which declines sharply towards the colliding surface as indicated by a cluster of shear rate (Fig.4). The traveling velocity of a T-cell in Fig.4 was approximately 0.6 m/s at t=0 to 1.6 ms and 1.3 m/s at t=1.6 to 3.9 ms. Since the jet velocity reached as high as 1.7 m/s approximately (Fig.4), the colliding velocity may reach an order of m/s. On the other hand, during valve closure, the closing leaflet speed is equal to the fluid velocity nearby (Fig.7). The closing speed of mechanical valves is exponentially accelerated, and the terminal velocity may reach an order of m/s at the tip of leaflet. At this instant, the leaflet tip speed U_{lt} becomes equal to the fluid convective velocity U_{ft} in the vicinity. This elevated fluid momentum impulsively collided with a leaflet upon closure ($U_{col}=U_{lt}=U_{ft}$)

To the best of our knowledge, there are little studies done to investigate the relevance of impinging flows with blood trauma. So far, the most popular parameter to study hemolysis and platelet activation is a bulk viscous shear stress τ and exposure time t_{exp}. Paul et al. [1] reported that a measurable damage increase was not detectable below τ=425 Pa and t_{exp}=620 ms. This order of shear stress corresponded to a shear rate of 85,000 1/s, indicating a velocity difference of 0.85 m/s per 10 μm. This level of shear rate is overwhelming. Indeed, the shear rate observed during systole was in the order of several thousands. Although the present study did not rigorously investigate the hinge flow, the recent studies done by Simon et al. [6] indicated that the hinge jet velocity was around a few m/s with a hinge gap of several hundred of micrometers. Thus, the shear rate does not appear to reach a critical value. In addition, the phenomenon is transient, thus the time scale being extremely small in contrast to t_{exp}=620 ms. As summary, it was concluded that an impulsive loading system upon collision should be considered in elucidating turbulent-induced hemolysis in artificial heart valves.

IV. Conclusions

The present study served as *macroscale modelin*g of prosthetic heart valve flows, where we utilized time-resolved PIV and continuous wavelet transform to obtain the physical interpretation of Reynolds stress. As a result, the Reynolds stress was found to be an indicator of impinging flows for circulating cells. Impinging flows may apply an impulsive force on a cellular membrane upon collision. The knowledge of impinging flows as a cause of blood cell damage has yet to be accumulated. We are currently investigating such phenomena using high-speed microfluidic techniques as *microscale verification*.

Acknowledgement

This research was partly supported by Health Science Research Grant (H20-IKOU-IPAN-001) from Ministry of Health, Labour and Welfare, Japan, Biomedical Engineering Research Project on Advanced Medical Treatment from Waseda University (A8201), and "The Robotic Medical Technology Cluster in Gifu Prefecture", Knowledge Cluster Initiative, Ministry of Education, Culture, Sports Science and Technology, Japan.

References

1. Paul R, Apel J, Klaus S, Schugner F, Schwindke P, Reul H (2003) Shear stress related blood damage in laminar couette flow. Artificial Organs 27(6): 517-529
2. Sallam AM, Hwang NH (1984) Human red blood cell hemolysis in a turbulent shear flow: contribution of reynolds shear stresses. Bior-Biorheology 21: 783-797
3. Kameneva MV, Burgreen GW, Kono K, Repko B, Antaki JF, Umezu M (2004) Effects of turbulent stresses on mechanical hemolysis experimental and computational analysis. ASAIO Journal 50(5): 418-23
4. Yoganathan AP, Woo Y, Sung H (1986) Turbulent shear stress measurements in the vicinity of aortic heart valve prostheses. Journal of Biomechanics 19(6): 433-442
5. Akutsu T, Bishop WF, Modi VJ (1994) Hydrodynamic study of tilting disc valves (Effect of valve orientations) 60(577): 121-127
6. Simon HA, Leo HL, Carberry J, Yoganathan AP (2004) Comparison of the hinge flow fields of two bileaflet mechanical heart valves under aortic and mitral conditions. Annals of Biomedical Engineering 32(12): 1607-17
7. Bluestein D, Yin W, Affeld K, Jesty J (2004) Flow-induced platelet activation in mechanical heart valves. The Journal of Heart Valve Disease 13: 501-508
8. Jones SA (1995) A relationship between Reynolds stresses and viscous dissipation: implications to red cell damage. Annals of Biomedical Engineering, 23: 21-28
9. Liu JS, Lu PC, Chu SH (2000) Turbulence characteristics downstream of bileaflet aortic valve prostheses. Journal of Bimedical Engineering 122: 118-124
10. Addison PS (2002) The illustrated wavelet transform handbook, Institute of Physics Publishing
11. Townsend AA (1966) The mechanism of entrainment in free turbulent flows. Journal of fluid mechanics, 26: 689-715.

Author: Takanobu Yagi, Ph.D.
Institute: Integrative Bioscience and Biomedical Engineering, TWIns, Waseda Univ., Japan
Email: takanobu_yagi@akane.waseda.jp

Pollen Shape Particles for Pulmonary Drug Delivery: *In Vitro* Study of Flow and Deposition Properties

Meer Saiful Hassan and Raymond Lau

Nanyang Technological University (NTU), School of Chemical and Biomedical Engineering (SCBE), Singapore

Abstract — **Pollen shape hydroxyapatite (HA) particles have been synthesized in this study. The flow and deposition properties of these pollen shape particles are compared with needle, cube and plate shape particles of similar size range of around 5 µm. The flow properties of the particles are characterized by the angle of slide (θ) method. The deposition properties of the particles are studied *in vitro* by using an eight-staged Anderson cascade impactor with a Rotahaler®. Pollen shape particles exhibits better flow behavior, higher emitted dose and higher fine particle fraction compare to particles of other shapes. The surface structure of the pollen shape particles increases the distance between particles, hence reduce the interparticle forces and aggregation tendency.**

Keywords — **Pulmonary drug delivery, pollen shape particles, cascade impactor, emitted dose, fine particle fraction**

I. Introduction

Pulmonary drug delivery has been gaining considerable interests as an alternative route of drug administration. Most studies are focused on the effect of particle size on the efficiency of drug delivery. Drug particles with an aerodynamic diameter (d_a) with a range 1-5 µm were found to have the highest delivery efficiency [1,2]. Crowder et al [3] found an increase in respirable fraction by lowering the aerodynamic diameter of the particles through surface treatment and turn the particles into elongated shape. Theoretically, shape can affect drag force and terminal settling velocity of the particles, which would also affect the aerodynamic behavior of the particles [2,3]. Particle shape also affects the dispersion property of the particles, which is directly related to the design of inhalation devices. However, the study of particle shape on delivery efficiency or dispersion property is limited. It is believed that a pollen shape structure can increase the effective distance, reduce the contact area and van der Waals force between two particles [4]. It would be ideal to design drugs with a pollen shape structure to increase the dispersion property and delivery efficiency.

In this study, the flow and deposition properties of pollen shape particles are compared with needle, cube and plate shape particles of similar size range. The particle flow property is characterized by the angle of slide method. The deposition properties of the particles are determined in vitro using an Anderson cascade impactor.

II. Experimental

A. Materials and Method

Pollen shape hydroxyapatite (HA, $Ca_5(PO_4)_3(OH)$) particles are synthesized by hydrothermal reaction using KH_2PO_4, $Ca(NO_3)_2{\cdot}4H_2O$, poly(sodium-4-styrene-sulfonate) (PSS), and urea [5]. 30 ml of KH_2PO_4 (0.02 M) solution is mixed with 50 ml of Ca $(NO_3)_2.4H_2O$ (0.02 M) solution. PSS and urea are then added to the mixture to get the respective concentration of 40 g/liter and 7.5 M. The solution mixture is poured into an autoclave and kept in an oven at 200°C for 6-12 hours. Finally, the precipitated product is collected, washed and then dried at 70°C.

Plate shape calcium oxalate (CaC_2O_4) is synthesized by precipitation reaction of $Na_2C_2O_4$ and $CaCl_2$ using Poly-(styrene-alt-maleic acid) (PSMA) as surfactant [6]. 0.8 ml of $Na_2C_2O_4$ (0.1 M) solution is added to 80 ml aqueous solution of PSMA (0.5 g/liter) and adjust the pH to 4 by adding dilute HCl. Then 0.8 ml of $CaCl_2$ (0.1 M) is added and kept the mixture at 25°C under static condition for 24 h. The product is then collected, washed and dried.

Cube shape calcium carbonate ($CaCO_3$) is produced by precipitation reaction of Na_2CO_3 and $CaCl_2$ using CTAB as surfactant [7]. 1.28 ml of Na_2CO_3 (0.5 M) solution is added to 80 ml aqueous solution of CTAB (1 g/liter) and then adjust the pH at 10 by adding NaOH. 1.28 ml of $CaCl_2$ (0.5 M) solution is added. The mixture is kept at 80 °C under static condition for 24 h before the final produced is collected.

Needle shape $CaCO_3$ particles are synthesized by precipitation reaction of $KHCO_3$ and $CaCl_2$ [8]. Equal volume of 0.1M $KHCO_3$ and $CaCl_2$ are brought to boiling temperature. Then, they are added together to get carbonate precipitate. The precipitate is then filtrated, washed, and dried at 110 °C.

B. Mean Particle Diameter and Particle Shape

Images of the four types of particles used are taken using scanning electron microscope (SEM) (JEOL JSM-5600). The SEM images are taken randomly from different area of the sample. The dimensions of the particles are determined based on the SEM images. At least two hundred particles are measured to get the average volume equivalent diameter

Chwee Teck Lim, James C.H. Goh (Eds.): ICBME 2008, Proceedings 23, pp. 1434–1437, 2009
www.springerlink.com

of the particles. The surface morphologies of the particles are assessed qualitatively based on the SEM images. The bulk (ρ_{bulk}) and tap (ρ_{tap}) densities of all the samples are measured according to Shi et al. [11].

C. Powder flowability

The flowability of the particles of different shapes is characterized by the angle of slide method [9]. A fixed volume of particle sample is placed on a dry glass plate. A lab jack is used to tilt the slide vertically upwards until the major portion of the powder slides. The angle between the tilted plane and horizontal (angle of slide, θ) is then measured.

D. In Vitro Deposition Property

An eight staged Anderson cascade impactor (ACI) (Copley, UK) is used to determine the emission and deposition properties in vitro. The experiment is carried out with a preseparator at an air flow rate of 30 liter/min. In each experiment, 8 ml of the dissolving solvent (2% HNO_3) is poured inside the preseparator and a coating of 1% w/v solution of silicon oil in hexane is used on the impaction plates to prevent particle bounce and re-entrainment. A Rotahaler® (GSK, U.K.) is used to aerosolize the powder inside the impactor. 20mg of each sample is loaded into a hard gelatin capsule (Gelatin Embedding Capsules, size 4, 0.25 cm^3, Polysciences, Inc., Warrington, PA) manually. An actuation time of 20 seconds is allowed for each capsule to completely disperse all the particles. Experimental runs are conducted in triplicate. The emitted dose (ED) and fine particle fraction (FPF) are determined.

III. Results and Discussion

A. Particle characteristics

The SEM images of the four particles used in this study are shown in Fig 1. The physical properties of the particles are listed in the table 1. The pollen shape particles has petal like surface structure and an average geometric diameter of 5.7 μm. The plate shape particles are rectangular shape with a length of 3.1-5 μm and width of 1.8-3.2 μm. The thickness of these particles is approximately 0.5 μm. The cube shape $CaCO_3$ particles have a uniform side length of around 3 μm. Needle shape $CaCO_3$ particles have a length of 12.5-25 μm and a width of 1.25-2 μm. From table 1 it can be seen that all the four particles are in similar equivalent diameter range. The bulk densities of the particles are also comparable in the range of 0.275-0.346 g/cm^3.

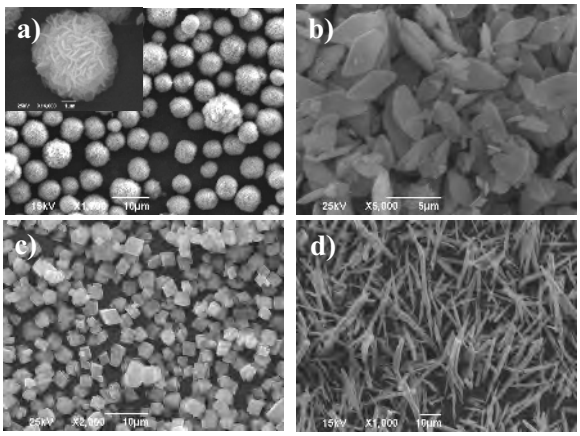


Fig. 1 SEM images of different shape particles, a) Pollen shape, b) Plate shape, c) Cube shape and d) Needle shape.

Table 1 Physical properties of different shape particles

Shape	d_{eq} range (μm)	ρ_{bulk} (g/cm^3) (n=0)	ρ_{tap}(g/cm^3) (n=2500)	θ (°)
Pollen shape	3.9-6.9	0.346	0.719	35.3±2.3
Plate shape	1.8-2.3	0.392	0.661	51.0±6.1
Cube shape	1.6-4.1	0.286	0.617	55.7±5.5
Needle shape	2.0-3.0	0.275	0.458	40.7±1.5

B. Flow property

The flow property of the particles is measured by the angle of slide method. θ values of the four particles are listed in Table 1. θ indicates the ability of particle flow in the presence of shear. The lower the θ, the better the shear flow property. It can be seen that pollen shape particles has the lowest θ compared with the other particles. As the density and size of the particles are comparable, the interparticle forces would be proportional to the area of the contact surface. The surface asperities of pollen shape particles result in small contact area between particles and hence low aggregation tendency. Plate and cube shape particles have the highest contact surface and indeed shows the largest θ. The angle of slide test does show that pollen shape particles have better shear flow property compared with particles of other shapes.

C. In Vitro deposition Property

ED and FPF of the different shape particles are determined in an eight staged Anderson cascade impactor. ED is defined as the mass percentage of particles delivered from the inhaler. FPF is defined as the mass percentage of the particles deposited in stage 2 or lower in the cascade impactor. Though ED and FPF both indicate the flow property of

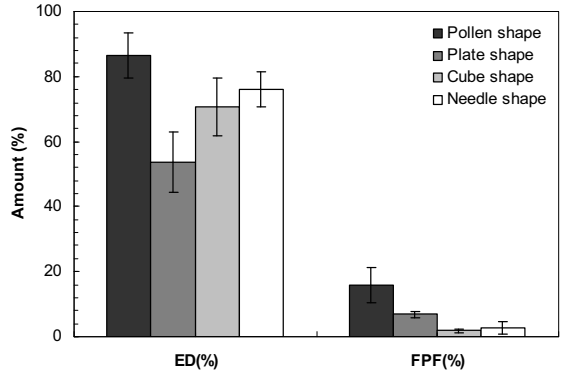


Fig. 2 Comparison of ED and FPF of the different shape particles.

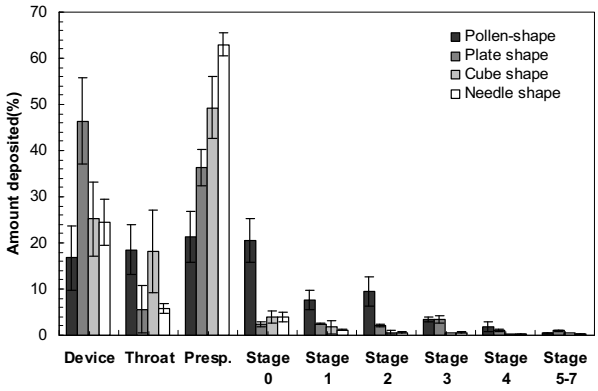


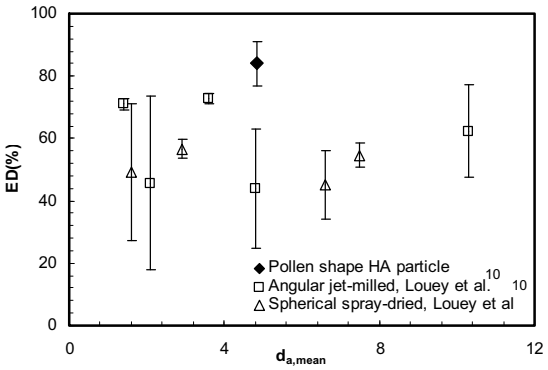
Fig. 3 Percent deposition of the samples in different stages of cascade impactor.

particles, they show different aspects of particle flows. As the particles are discharged from the capsule, fraction of the particles will be dispersed and flow with the gas stream. The rest of the particles will remain in the chamber and the capsule and entrained by gas flow. Therefore ED takes into account both the dispersion ability of particles as well as shear flow property. FPF, on the other hand, considers only the flow property of dispersed particles. A comparison of the ED and FPF of the different shape particles is shown in Fig. 2. The pollen shape particles have both higher ED and FPF than the particles in other shapes. For pollen, needle and cube shape particles, θ, ED and FPF correlates well with each other. Pollen shape particles are superior in all the three parameters while cube shape particles are inferior in θ and FPF. Plate shape particles, however, show poor shear flow ability (θ) and poor dispersion in gas flow (ED). Nonetheless, once the particles are dispersed, the flow of plate shape particles in a gas stream is better than cube and needle shape particles, though not as good as pollen shape particles. This may be owing to the plate shape structure that let the particles to glide along the gas flow and enhances the FPF.

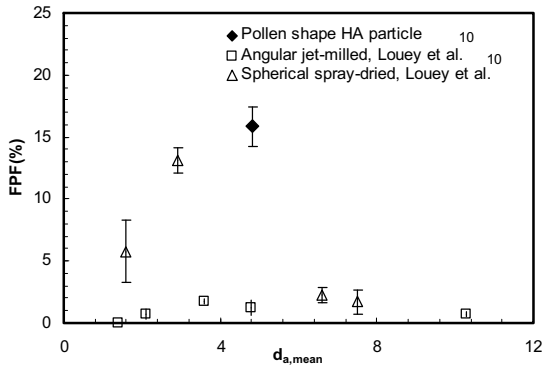
Fig 3 shows the detailed breakdown of the regional deposition of the different particles. A high percent deposition in the inhaler device and preseparator is observed for the plate, needle and cube shape particles. Though these three types of particles has different regional deposition percentage in the inhaler and preseparator, the high deposition percentage in the region would indicate a substantial loss of particles in these regions and would not be ideal for drug delivery. The pollen shape particles have low and uniform deposition percentage in the inhaler and preseparator region. This is a good indication that pollen shape particles have good dispersion property in gas flow and the deposition is independent of flow geometry. In general, particle size, density and material would also play important role in the deposition behavior. In this case, the size and density of the four particles are in a similar range. All the materials ($CaCO_3$, CaC_2O_4 and $Ca_5(PO_4)_3(OH)$) are inorganic derived with calcium metal. All the properties of the different particles can be considered similar except the shape. Therefore, the difference in ED and FPF result among the particles indicates a strong dependence of deposition behavior on the particle shape. In this case, pollen shape is found to exhibit the best flow and deposition property in terms of ED and FPF among other shapes.

Aerodynamic diameter is generally used as the characterizing property of aerosol particles. The aerodynamic diameter is defined as the diameter of a sphere of unit density that has the same terminal settling velocity as the particle under consideration, $d_a = d_g\sqrt{\frac{\rho_e}{\lambda\rho_p}}$ where ρ_s= 1 g/cm^3, d_g is the particle geometric diameter, ρ_e is the effective particle density and λ is the particle shape factor [2,3]. The effective density can be approximated by the tap density, ρ_{tap}. The shape factor of the particles is estimated based on the dimensions obtained from the respective SEM images. The ED and FPF of the pollen shape HA particles are compared with some prior studies as a function of mean aerodynamic diameter.

There is limited ED and FPF result using single particle formulation in cascade impactor. The ED of the HA particles are compared with angular jet milled and spherical spray dried mannitol particles with aerodynamic diameter lower than 10 μm [10]. The mannitol particles were aerosolized at an air flow rate of 60 liter/min whereas the flow rate used in this study is 30 liter/min. Despite the lower air flow rate, the HA particles show higher ED than the angular and spherical particles as shown in Figure 4(a). An increase in flow rate can substantially increase the total particle emission from an inhaler [11]. It is anticipated that the HA particles would exhibit even higher ED at a flow rate of 60 li-



(a)



(b)

Fig. 4. Comparison of (a) ED and (b) FPF of pollen shape HA particles with angular jet-milled and spherical spray-dried particles.

ter/min. The FPF of the HA particles is also compared against the FPF of the mannitol particles. A clear improvement is observed in FPF of pollen shape HA particles over the FPF of the mannitol particles. It is apparent that pollen shape HA particles are highly effective in improving the ED and FPF of drug particles in inhalation delivery.

IV. Conclusions

The flow and deposition properties of pollen shape HA particle is investigated along with particle of other shape. Plate shape particles have poor shear flow and dispersion property but good FPF. Pollen shape particles exhibit better flow and deposition property in angle of slide, ED and FPF. A comparison ED and FPF of pollen shape particles with other particles in literature indicates that pollen shape is effective in improving delivery efficiency.

Acknowledgment

The authors are grateful to the financial support of NTU/SUG Grant. The authors would also like to express their appreciation to Prof. Xu Rong and Dr. Yongsheng Wang for their help in particle synthesis.

References

1. Hicky A J (2004) Pharmaceutical Inhalation Aerosol Technology, Marcel Dekker, Inc., New York.
2. Edwards D A (2002) Delivery of biological agents by aerosols. AIChE Journal 48(1):2-6.
3. Crowder T M, Rosati J A, Schroeter J D et al. (2002) Fundamental Effects of Particle Morphology on Lung Delivery: Predictions of Stokes' Law and the Particular Relevance to Dry Powder Inhaler Formulation and Development. Pharm Res 19(3):239-245
4. Visser J (1989) Van der Waals and other cohesive forces affecting powder fluidization. Powder Technol 58(1):1-10
5. Wang Y, Gunawan P, Xu R (2008) Polyelectrolyte-mediated formation o hydroxyapatite microspheres: From anisotropic to isotropic growth. Submitted
6. Yu J, Tang H, Cheng B et al. (2004) Morphological control of calcium oxalate particles in the presence of poly-(styrene-alt-maleic acid). J Solid State Chem 177(10):3368-3374
7. Yu J, Lei M, Cheng B et al. (2004) Facile preparation of calcium carbonate particles with unusual morphologies by precipitation reaction. J Cryst Growth 261(4):566-570
8. Lucas A, Gaude J, Carel C et al. (2001) A synthetic aragonite-based ceramic as a bone graft substitute and substrate for antibiotics. Int J Inorg Mater 3:87-94
9. Shi L, C J Plumley, C Berkland (2007) Biodegradable Nanoparticle Flocculates for Dry Powder Aerosol Formulation. Langmuir 23(22):10897-10901
10. Larhrib H, Martin G P, Marriott C et al. (2003) The influence of carrier and drug morphology on drug delivery from dry powder formulations. Int J Pharmaceutics 257(1-2):283-296
11. French D L, Edwards D A, Niven R W (1996) The influence of formulation on emission, deaggregation and deposition of dry powders for inhalation. J Aerosol Sci 27:769-783

Author: Lau Wai Man, Raymond
Institute: Nanyang Technological University
Street: 62 Nanyang Drive, N1.2-B3-13
City: Singapore
Country: Singapore 637459

Effect of *Tephrosia Purpurea* Pers on Gentamicin Model of Acute Renal Failure

Avijeet Jain, A.K. Singhai

Natural Product Research Laboratory, Dept of Pharmaceutical Sciences, Dr H S Gour Vishwavidyalaya, Sagar, MP, India

Abstract — ***Tephrosia purpurea*** **leaves were studied for its protective and curative effect against gentamicin-induced acute renal injury in albino rats of both sexes. The maximum free radical scavenging activity of ethanolic extract was made the basis of selection of this extract for in vivo study. In study, gentamicin intoxication caused significant increase in blood urea (69.48 ± 4.34) and serum creatinine (3.017 ± 0.208) from normal levels 33.72± 1.92 and 0.818 ± 0 .073, respectively, in control group. In the preventive regimen, the extract (200 mg/kg) showed significant reduction in the elevated blood urea (45.44 ± 1.88) and serum creatinine (1.84 ± 0.192), respectively. Histopathological changes were in line with biochemical findings. In the curative regimen (200 mg/kg) blood urea was found to be 41.21 ± 2.28 and serum creatinine level was 1.42 ± 0.122, which revealed significant curative effect. In vivo antioxidant activity was also determined. Reduced glutathione (GSH) level was significantly (P< 0.05) increased in the extract treated groups whereas malondialdehyde (MDA) was reduced significantly (P< 0.05). The findings suggest that the ethanol extract of *Tephrosia purpurea* leaves possesses marked nephroprotective and curative activities without any toxicity. The proposed mechanisms of activities are antioxidant activity and inhibition of overproduction of NO and Cox-2 expression. It is further concluded the activities may be attributed to phenolic and flavonoidal compounds like quercetin. Our study reveled that *Tephrosia purpurea* could offer a promising role in the treatment of acute renal injury caused by nephrotoxin like gentamicin.**

Keywords — ***Tephrosia purpurea,*** **blood urea, serum creatinine, neproprotective, nephrocurative**

I. Introduction

Tephrosia purpurea (Linn.) Pers. (Leguminosae), commonly known in Sanskrit as Sharapunkha is a highly branched, sub-erect, herbaceous perennial herb [1]. According to Ayurveda literature this plant has also given the name of *" wranvishapaka "* which means that it has the property of healing all types of wounds [2]. It is an important component of some preparations such as Tephroli and Yakrifit used for liver disorders [3]. In Ayurvedic system of medicine various parts of this plant are used as remedy for impotency, asthma, diarrhoea, gonorrhoea, rheumatism, ulcer and urinary disorders. The plant has been claimed to cure diseases of kidney, liver spleen, heart and blood [4]. The dried herb is effective as tonic laxative, diuretics and deobstruents. It is also used in the treatment of bronchitis, bilious febrile attack, boils, pimples and bleeding piles. The roots and seeds are reported to have insecticidal and piscicidal properties and also used as vermifuge. The roots are also reported to be effective in leprous wound and their juice, to the eruption on skin. An extract of pods is effective for pain, inflammation and their decoction is used in vomiting [5]. The ethanolic extract of seeds has shown significant in vivo hypoglycaemic activity in diabetic rabbits [6]. The ethanolic extracts of *Tephrosia purpurea* (TP) possessed potential antibacterial activity. The flavanoids were found to have antimicrobial activity [7]. The phytochemical investigations on TP have revealed the presence of glycosides, rotenoids, isoflavones, flavanones, chalcones, flavanols, and sterols [8].

Acute renal failure refers to the sudden and usually reversible loss of renal function, which develops over a period of days or weeks. Among the causes of acute renal failure, acute tubular necrosis, which occurs due to ischemia or nephrotoxins like cisplatin and gentamicin, is most common, accounting for 85% of the incidence. There is a continuous search for agents, which provide nephroprotection against the renal impairment caused by drugs like cisplatin and gentamicin for which allopathy offers no remedial measures. Thus, it is imperative that mankind turns towards alternative systems of medicine for treatment. Hence, the present study is an attempt to screen TP leaves for its nephroprotective and curative activities.

In the ethnobotanical claims, TP plant (mentioned above) is used for the treatment of renal diseases. To the best of our knowledge there is no scientific report is available in support of the nephroprotective activity of TP leaves. Therefore, to justify the traditional claims we have assessed the nephroprotective and curative effect of TP leaves using gentamicin intoxicated rats.

Free radical scavenging and in vivo antioxidant activities were also determined. Ethanolic extract with maximum free radical scavenging activity was selected for in vivo studies.

II. Material and methods

A. Collection

The plant of *Tephrosia purpurea* was collected from the forest around Dr. H.S. Gour Vishwavidyalaya, Sagar in the month of September 2006 and identified at Department of Botany, Dr. H.S. Gour Vishwavidyalaya, Sagar (M. P.).

Chwee Teck Lim, James C.H. Goh (Eds.): ICBME 2008, Proceedings 23, pp. 1438–1442, 2009
www.springerlink.com

B. Preparation of extracts

The TP dried leaves were coarsely powdered and defatted with petroleum ether in soxhlet (72 h). The defatted drug was soxhlet extracted with various solvents chloroform, ethyl acetate and ethanol for 48 h. Water extract was prepared by decoction method. Percentage yield was calculated for each extract after drying under vacuum. The percentage yield of chloroform, ethanol, ethyl acetate and water extract were 4.1, 5.7, 10.14, and 8.9%, respectively.

C. Phytochemical Screening

All the extracts were subjected for phytochemical screening.

D. Animals

Healthy adult albino rats (100–150 g) of both sex aged 60–90 days were used for the study. The rats were housed in polypropylene cages and maintained under standard conditions (12-h light: 12-h dark cycle; 25 ±3 .C; 35–60% humidity). The animals had free access to standard lab chow (Hindustan Lever Ltd., Mumbai, India) and water *ad libitum*. Study was conducted after obtaining institutional animal ethical committee clearance (412/01/ab/CPCSEA, India).

E. Acute toxicity studies

The ethanolic extract was suspended in gum acacia (2% w/v) and administered to animals in increasing dose levels. The dose of the extract was calculated as 1/10th of the maximum tolerated dose (2000 mg/kg b.w.).

F. Superoxide free radical scavenging activity

This was determined by the NBT (Nitro Blue Tetrazolium) reduction method. The assay was based on the capacity of sample to inhibit blue formazan formation by scavenging the super oxide radical generated in riboflavin-light-NBT system. The reaction mixture contains EDTA, riboflavin, Nitro Blue Tetrazolium, various concentrations of extracts (1-100 μg/ml) and phosphate buffer pH (7.6) in a final volume of 3 ml. The tubes were uniformly illuminated with an incandescent lamp for 15 min and absorbance was measured at 590nm before and after illuminated. The percentage inhibition of super oxide generation was measured by comparing absorbance value of control and those of test [9].

G. DPPH free radical scavenging activity

A stock solution of 0.1 ml of DPPH was prepared in ethanol. This solution was mixed with equal volume of solutions (different concentrations) of compound A in ethanol. The reaction was allowed to complete in the dark for about 20 minutes. The absorbance was taken at 517 nm. Experiment was repeated three times. The difference in absorbances between the test and the control was calculated and expressed as percentage scavenging of DPPH radical [10].

H. Total antioxidant activity

Total antioxidant activity of all the extracts was measured in concentration of 10 -1000 μg/ml [11]. Briefly, peroxidase (4.4 unit/ml, 0.2 ml), H_2O_2 (50 mM, 0.2 ml), ABTS [2,2'-azino-bis(3-ethylbenzothiazoline-6-sulfonic acid), 100 mM, 0.2 ml] and distilled water (1.4 ml) were mixed and kept in dark for 1 h to form a bluish green complex. After adding the various concentrations of the tested extracts (1 ml), the absorbance at 734 nm was measured.

I. Gentamicin-induced renal damage

Test samples were prepared in the distilled water. Weighed quantity of the ethanolic extract was suspended in distilled water by trituration. Extract was taken in pastel motor and triturated continuously to get homogenous suspension. Suspension was stored in airtight bottle in cool and dry place.

The animals were divided into 4 groups of 6 rats each and all testing drugs were administered orally at the calculated dose.

Group I: control to which neither drug or gentamicin was administered

Group II: Treated with only gentamicin (40mg/kg b.w.) s.c.

Group III (Preventive): Treated with ethanolic extract suspension (200 mg/kg/day b.w.) 30 minute before the gentamicin administration.

Group IV (Curative): Treated with ethanolic extract suspension (200 mg/kg/day b.w.) 7 days onwards the gentamicin administration.

In preventive groups, dose of gentamicin and extracts were given once a day, whereas in curative regimen gentamicin was administered twice a day. After16 days animals were scarified by cervical dislocation and blood samples were collected from the inferior vena cave. To get serum from the blood sample, freshly drawn blood was centrifuged at 2500 rpm for 30 minute and placed in refrigerator.

J. Biochemical determinations

Blood urea concentration in the blood was estimated by enzymatic method using urease enzyme kit by modified Berth Elot method [12]. Absorbance was read using UV-240 Vis spectrophotometer (Shimadzu Corporation, Japan).

Serum creatinine level in serum was estimated by the alkaline picrate method using creatinine kit [13]. Absorbance was read by UV-240 Vis spectrophotometer.

K. In vivo antioxidant activity

Reduced glutathione (GSH) and malondialdehyde (MDA) were estimated to access in vivo antioxidant activity. Methods of Ellamn Georg [14] with some modification and Uchiyama and Mihara [15] were used respectively.

L. Histopathological examination

Animals from each group were sacrificed on the day of blood withdrawal and kidneys were isolated. Tissue samples were immersed in 10% formalin for histopathological studies. Samples were embedded in paraffin, sectioned and stained with haematoxylin and eosin.

M. Statistical analysis

Results are given as mean ±SEM. Data were analyzed using one-way ANOVA. The statistical significance of difference was taken as $P<0.05$.

III. Results

A. Phytochemical study

All the extracts were subjected for phytochemical studies. Ethanolic extract showed positive test for flavonoids, glycosides, phenolic compounds, alkoloids, carbohydrates and amino acids etc.

B. Super oxide scavenging activity

NBT method was applied for screening of super oxide free radical scavenging activity. All the extracts were screened in concentration of 1-100 µg/ml. Ethanolic extract showed maximum percent reduction followed by aqueous, ethyl acetate and chloroform extracts. This activity was dose dependent in all cases.

C. DPPH free radical scavenging activity

Ethanolic extracts at 1000 µg/ml showed maximum inhibition. Other 3 extracts showed results in similar pattern.

D. Total antioxidant activity

All the extracts were screened in concentration of 10-1000 µg/ml. Ethanolic extract showed maximum inhibition amongst all the extracts.

In vitro antioxidant activity screening was made basis for the selection of extract for further studies and as results revealed ethanolic extract was subjected for in vivo studies.

E. Acute toxicity studies

In acute toxicity ethanolic extract was found to be safe up to a dose of 2000 mg/kg.

F. Gentamicin induced renal damage

Gentamicin induced renal injury that was evidenced by the elevated blood urea and serum creatinine levels. Table 1 shows the results of biochemical estimation in various groups, where blood urea and serum creatinine estimations are reported to access nephroprotective and curative activities of ethanolic extract. Study has reveled increased level of blood urea (69.48 ± 4.34) and serum creatinine (3.017 ± 0.208) in gentamicin intoxicated animals compare to control 33.72± 1.92 and 0.818 ± 0 .073, respectively. On other hand, it was observed that 16 days administration of the extract (200 mg/kg) prior to gentamicin administration (40 mg/kg, single dose) in the prophylactic regimen, provided marked protection against gentamicin induced renal injury. Similarly, in the curative regimen of the gentamicin model, the ethanol extract recovered the renal damage induced by gentamicin suggesting that it has nephrocurative activity in gentamicin models of renal injury. Histopathological studies supported the results

G. In vivo antioxidant activity

Activity was accessed by estimation of reduced glutathione (GSH) and malondialdehyde (MDA). Results are cited in Table 2. Results of study clearly revealed increase in the levels of MDA in gentamicin intoxicated rats (462±4.3) compare to control group (197.7±2.1). Treatment with extracts significantly prevented and as well recovered this raise in levels. GSH has significantly increased in extract treated groups whereas gentamicin intoxicated group has shown significant decrease in levels compare to control group. Curative groups have shown better results.

H. Histopathological studies

In histopathological studies, gentamicin intoxicated group showed definite signs of nephrotoxicity, when compared to the control groups. The intoxicated group has shown presence of peritubular and glomerular congestion, tubular casts, epithelial degeneration, interstitial edema, blood vessel congestion and infiltration by inflammatory cells, which are features of acute tubular necrosis observed

Table 1 Determination of blood urea and serum creatinine in Serum of rats

Groups	Treatment regimen	Blood urea mg/dl	Serum creatinine level mg/dl
Group I	Control (Vehicle)	33.72± 1.92	0.818 ± 0 .073
Group II	Control (Gentamicin)	69.48 ± 4.34***	3.017 ± 0.208***
Group III	TP 200 + Gentamicin (Preventive)	45.44 ± 1.88**	1.84 ± 0.192***
Group IV	TP 200 + Gentamicin (Curative)	41.21 ± 2.28***	1.42 ± 0.122***

All the values are expressed as Mean± SEM. *P<0.05, **P<0.01, ***P<0.001 shows level of significance compare to control group

Table 2 Determination of blood urea and serum creatinine in rats.

Groups	Treatment Regimen	Blood urea mg/dl	Serum creatinine level mg/dl
Group I	Control (Vehicle)	33.72± 1.92	0.818 ± 0 .073
Group II	Control (Gentamicin)	69.48 ± 4.34***	3.017 ± 0.208***
Group III	TP 200+ Gentamicin (Preventive)	45.44 ± 1.88**	1.84 ± 0.192***
Group IV	TP 200 + Gentamicin (Curative)	41.21 ± 2.28***	1.42 ± 0.122***

All the values are expressed as Mean± SEM. *P<0.05, **P<0.01, ***P<0.001 shows level of significance compare to control group

in the histopathological sections and indicative of the extent of damage done at the tissue level whereas control group shows normal architecture. All the preventive and curative groups have shown sign of recovery.

IV. Discussion

Gentamicin, an aminoglycoside antibiotic is used as an effective agent against gram negative infections. Its chemical stability, rapid bactericidal action has made it a first-line drug in a variety of clinical situations. However, nephrotoxicity is the major side effect of amino-glycosides accounting for 10 - 15% of all cases of acute renal failure [16]. Studies have also shown that 30% of the patients treated with gentamicin for more than 7 days show signs of nephrotoxicity [17]. It has been shown that the specificity of gentamicin renal toxicity is related to its preferential accumulation in the renal convoluted tubules and lysosomes [18].

In present study, ethanolic extract of TP leaves was selected based on its in vitro antioxidant activity for screening of nephroprotective and nephrocurative activities using Gentamicin induced nephrotoxicity. In preventive and curative regimens, the ethanol extract at dose levels of 200 mg/kg, significantly recovered the raised blood urea, serum creatinine compare to control group and supported by histopathology. Thus results suggest nephroprotective and curative activities of TP.

In various studies it have been reported that gentamicin activates phospholipases and alters the lysosomal membrane in addition to oxidative stress [19]. Although the mechanism of gentamicin-induced nephrotoxicity is not completely known. However, studies have implicated reactive oxygen species particularly superoxide anion radical in the pathophysiology of gentamicin nephropathy [20]. It has been demonstrated that gentamicin administration increases renal cortical lipid peroxidation, renal nitric oxide generation and mitochondria H_20_2 generation [21, 22]. Ethanolic extract has shown good superoxide radical scavenging, DPPH scavenging and total antioxidant activity along with significant in vivo antioxidant activity. In treated groups, GSH has been significantly increased whereas MDA level, results from lipid peroxidation has been significantly reduced. Previously, *Aerva lenata* has been reported for nephroprotective activity due its antioxidant activity i.e. free radical scavenging activity [23].

Natural and synthetic antioxidants and free radical scavengers are claimed to provide nephroprotection in gentamicin renal injury. Vitamin C, Vitamin E, selenium, etc are among the natural free radical scavengers. Previously, Natural antioxidants ascorbic acid and alpa-tocopherol have also been found nephroprotective in animal model [24]. Flavonoids and phenolic compounds are well known potent antioxidant and free radical scavengers. Renoprotective effects have been reported for polyphenols such as quercetin [25]. Previously presence of quercetin in TP is well documented and our chromatographic studies have also reveled its presence in the extract. Phytochemical study revealed that flavonoids and phenolic compounds are present in the extract. Various in vitro models have shown significant free radical scavenging activity of TP. Significant increased in GSH level and reduction in MDA level revealed its vivo antioxidant activity. Hence, the probable mechanism of nephroprotection by TP may be attributed to its antioxidant and free radical scavenging property, while free radical scavenging activity may be attributed to flavonoids and phenolic compounds like quercetin.

In addition, it has been already demonstrated an increased NO production during ischemia and gentamicin-induced renal failure [26, 27]. NO has been reported as oxidant in presence of superoxide anions. Both of these react and produce peroxynitrite, which is a potent and versa-

tile oxidant [28]. GSH is the natural antioxidant present in the renal tissues. In our study it is clearly reveled that pre and post treatment with the ethanolic extract is able to recover the reduced GSH level. It is also evidenced that extract reduces the lipid peroxidation. Quercetin, one of the most abundant flavonoids, is a potent oxygen free radicals scavenger and a metal chelator [29]. In addition, several studies indicate that quercetin inhibited the expression of COX-2 and (Inducible nitric oxide synthesis) iNOS [30]. Thus it is able to reduce overproduction of NO. In vitro experimental systems also showed that flavonoids possess anti-inflammatory properties [31]. Hence, another probable mechanism of nephroprotective and curative activities of TP may be ability to maintain GSH level and inhibit overproduction of NO and inhibition of Cox-2 expression due to presence of quercetin and other flavonoidal and phenolic compounds.

V. Conclusions

To conclude, our studies have shown that leaves of *Tephrosia pururea* possesses marked nephroprotective and nephrocurative activities without any toxicity and thus has a promising role in the treatment of acute renal injury induced by nephrotoxins especially gentamicin. It is further concluded that mechanisms involved probably are antioxidant activity and inhibition of overproduction of NO and Cox-2 expression. We also conclude that the activities are attributed to phenolic and flavonoidal compound specially quercetin. Further isolation of active components and its role in renal diseases is being targeted. Further work is in process with few more models.

Acknowledgements

Authors sincerely thank Indian Council of Medical Research, New Delhi, for providing fellowship for this work. The authors also sincerely thank Dr. Bagdi, Department of Pathology, India for providing assistance in histopathological study.

References

1. Chopra, RN, Nayer SL, Chopra IC (1956) Glossary of Indian Medicinal Plants. Council of Scientific and Industrial Research. New Delhi, India.
2. Despande SS, Shah GB, Parmar NS (2003). Indian Journal of Pharmacology 35:168–172.
3. Sankaran JR (1980). The Antiseptic 77:643-646.
   Shifow AA, Kumar KV, Naidu MUR, et al. (2000). Nephron 85:167-169.
4. Kirtikar KR, Basu BD (1956). Indian Medicinal Plants. Lalit Mohan Basu. Allahabad, India:
5. The Wealth of India, (1976) A Dictionary of Indian Raw Materials and Industrial Product. Publication and Information Directorate, CSIR. New Delhi, India:
6. Rahman H, Kashifudduja M, Syed M.et al. (1985). Indian Journal of Medical Research 81:418-422.
7. Gokhale AB, Saraf MN (2000). Indian Drugs 37 :553-557.
8. Pelter A., Ward RS, Rao EV, et al. (1981). Journal of Chemical Society. Perkin Trans 1: 2491-2495.
9. Baugl S, Millind K, Natarajan S, et al. (2005). Indian Journal of Experimental biology 43**:**732-734.
10. Hemant R Jadhav Bhutani KK (2002). Phytotherapy Research 16:771-772.
11. Liu CT, Yi Wu C, Weng YM, Tseng YC (2005). Journal of Ethnopharmacology 99:293-297.
12. Bonses RW, Taussky HH (1945). Journal of Biological Chemistry158:581-584.
13. Coulambe GG, Favrean LA (1965). Clinical chemistry11:624-626.
14. Ellman Georg L (1959). Archives of Biochemistry and Biophysics 82:70-74.
15. Uchiyama M, Mihara M (1978). Analytical Biochemistry 8:6271-6275.
16. Shifow AA, Kumar KV, Naidu MUR, et al. (2000). Nephron 85:167-174.
17. Mattew TH (1992). Medical Journal of Australia 156:724-726.
18. Nagai J, Takano M (2004).Drug Metabolism and Pharmacokinetics 19:159-161.
19. Laurent G, Kishore BK, Tulkens PM (1990). Biochemical.Pharmacology, 40:2383-2387.
20. Cuzzocrea E, Mazzon LI, Dugo Serraino R, et al. (2002). European Journal of Pharmacology 450**:** 67-69.
21. Parlakpinar H, Tasdemir S, Polat A, et al. (2005) Toxicology 207:169-172.
22. Yang CL, Du XH, Han YX (1995). Renal Failure 17:21-24.
23. Shirwaiker A, Issac D, Malini S (2004). Journal of Ethnopharmacology 90:81-85.
24. Ajith TA,Usha S, Nivitha V (2007). Clinica Chimica Acta 375: 82-86.
25. Ishikawa Y, Kitamura M (2000). Kidney International, 58:1078-1084.
26. Rivas Cabanero L, Rodryguez Lopez AM, Martynez Salgado C, et al. (1997). Exp Nephrol 5:23-27.
27. Valdivielso JM, Crespo C, Alonso JR, et al. (2001). Am J Physiol: Regul, Integ. Comp Physiol 280:R771-774.
28. Beckman JS Koppenol WH (1996). Am Physiol Soc C1424.
29. Jovanovic SV Steenken S. Simic MG, et al. (1998). Flavonoids in Health and Disease. Marcel Dekker INC , New York:
30. Liang YC, Tsai SH, Tsai DC,et al. (2001). FEBS Lett 496:12-14.
31. Middleton Jr E. (1998). Adv Exp Med Biol 439:175-177.

Avijeet Jain
Natural Product Research Laboratory,
Dept of Pharmaceutical Sciences,
Dr H S Gour Vishwavidyalaya, Sagar, 470001
MP, India
E mail- avijeet_9826275340@rediffmail.com

Successful Reproduction of In-Vivo Fracture of an Endovascular Stent in Superficial Femoral Artery Utilizing a Novel Multi-loading Durability Test System

K. Iwasaki[1,2], S. Tsubouchi[2], Y. Hama[2], M. Umezu[2]

[1]Waseda Institute for Advanced Study, Waseda University, Tokyo, Japan
[2]Integrative Bioscience and Biomedical Engineering, Graduate School of Waseda University, Tokyo, Japan

Abstract — Aim: High rates of stent fracture have been reported in the treatment of diseased superficial femoral artery (SFA). Understanding of in-vivo mechanical-loading environments, therefore, draws serious attention. We have developed a novel multi-loading durability tester which can apply cyclic twist and stretch on stents. Here, in-vitro stent fracture patterns were compared with stent fracture observed in vivo. Methods: The angle of cyclic twist as well as cyclic stretch exerted to the stents was regulated to physiologic conditions by utilizing referenced data of MR angiography of SFAs obtained in the spine and fetal position. Stiffness of the silicone vessel models were regulated to that of SFAs. As the SFAs are intrinsically stretched in vivo, stents were tested not only in the non-stretched vessel model but also in the 50% pre-stretched vessel model, respectively. The simultaneous cyclic multi-loads were exerted to the stents under the mean luminal pressure of 100mmHg at 60 cycles per minute. Considering the data that average Japanese walk 7378 steps per day, the cyclic numbers of the in-vitro durability tests were converted to the equivalent durability in vivo. Results: Only minor fracture was observed at the stent strut after one-year-equivalent duration when the stents were tested using the non-stretched vessel models. However, employment of the novel pre-stretched vessel model resulted in complete stent fractures in the middle of longitudinal direction in 2-months-equivalent duration. Moreover, the fracture pattern was clearly coincident with the stent fracture in vivo. Conclusions: This is the first demonstration that the pre-stretch of vessel model is a requisite condition in durability tests of stents for SFA. Moreover, these results indicated that reproduction of multi-loading environments including cyclic twist and stretch is of great significance in order to obtain reliable durability data of endovascular stents for SFA.

Keywords — **Stent fracture, Superficial femoral artery, Accelerated durability test, Regulatory science, Endovascular stent**

I. Introduction

Maintaining patency after recanalization of stenotic superficial femoral artery (SFA) is one of the most challenging themes in endovascular therapy. Stenting in SFA yielded frequent stent fractures, for example 64 of 261 implanted stents (24.5%) after mean follow-up of 10.7 months. Moreover it became evident that stent fractures were associated with restenosis or reocclusion [1] as shown in Fig.1. Therefore, establishment of practical in-vitro durability test system and reliable methodologies become high priority for not only medical companies but also governments [2]. SFA receives multiple forces such as bending, twist, compression, stretch / shortening in response to daily life activities (Fig.2) [3]. However, there is no practical durability test system as well as reliable methodology to predict in-vivo performance of endovascular stents. We, here, developed a novel durability

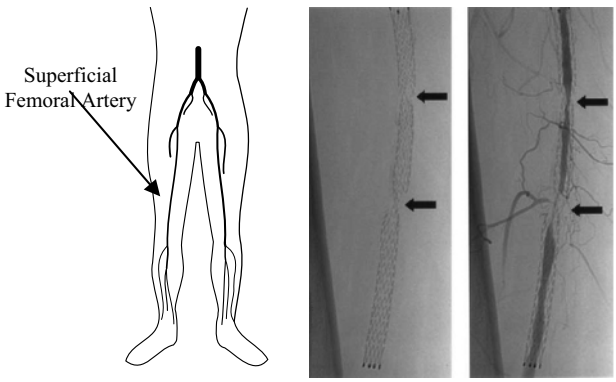


Fig.1 A nitinol stent 9 months after implantation showing severe stent fractures and reocculusion

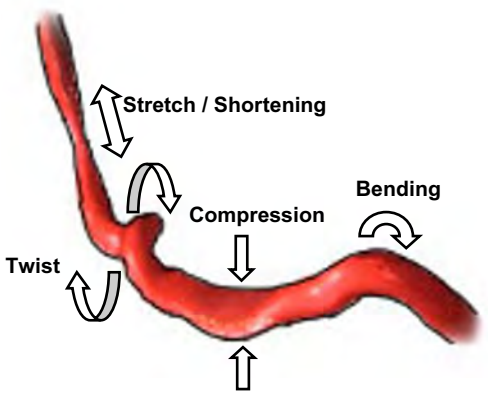


Fig.2 Mechanical loads exerted to the superficial femoral artery in daily life activities

Chwee Teck Lim, James C.H. Goh (Eds.): ICBME 2008, Proceedings 23, pp. 1443–1446, 2009
www.springerlink.com

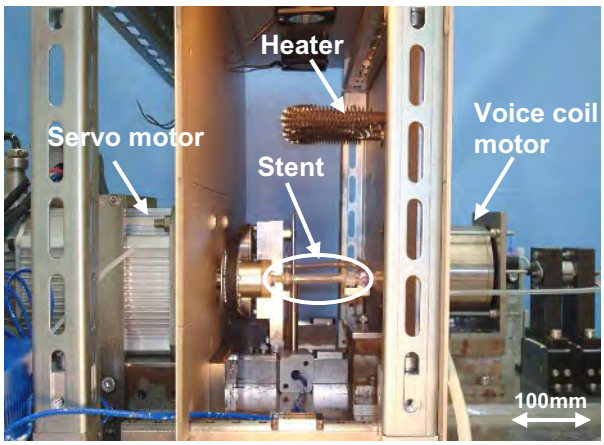
test system which can mimic in-vivo multi-loads environment for testing endovascular stents. Then, influences of loading conditions on stent fractures were investigated. Moreover, we investigated, for the first time, the influence of pre-stretch of the vessel model before stent implantation on durability, because the artery is kept stretched in human body.

II. Method

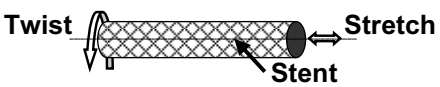
Understanding of mechanical loads exerted to SFA is essential to determine the specification of durability test system. We referenced the in-vivo deformation data of SFA in the supine and fetal position (Table1) [4]. It was shown that during the transition of supine and fetal positions, cyclic twist and stretch forces are exerted to SFA. Therefore, we developed the novel durability tester which can apply the multi-loads of twist and stretch forces to the stents installed in a blood vessel model (Fig.3). The durability test system consists of a servo-motor for producing twist force, and a voice coil motor for producing stretch force, a heater for regulating environmental temperature to 37°C, and a vessel model for incorporating the stents. Because the SFA is present in stretched condition, investigation of its influence on durability was included in the durability tests. Figure 4 shows a schematic representation of the test condition that the silicone vessel model is pre-stretched before stent placement. The SFA model with stiffness of 19.8, which matches to that of human SFA, was manufactured. In the experiment using the pre-stretched vessel model, the stiffness of the vessel model after pre-stretch was adjusted to 19.8. In order to apply the exact amount of twist force as well as stretch force to the stents, both the ends of the stents were fixed to the force generators. Typical simultaneous waveforms of cyclic twist, stretch, and pressure in the durability test in accordance with the maximal deformation of SFA among 8 volunteers were shown in Fig.5. The twist and stretch forces were exerted to stents 60 times per minute.

Table 1 Deformation of superficial femoral arteries in the supine and fetal positions

	Twist	Stretch
Average	2.8°/cm	13%
Maximum	5.3°/cm	18%



(a) The multi-loading durability test system



(b) Cyclic twist and stretch forces exerted to the stent.

Fig.3 The novel multi-loading accelerated durability test system for the endovascular stents. Cyclic twist, stretch, and pressure coincident with in-vivo practical environment can be exerted.

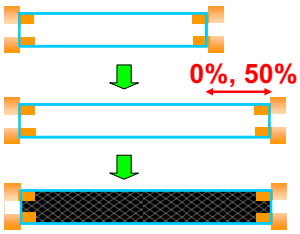
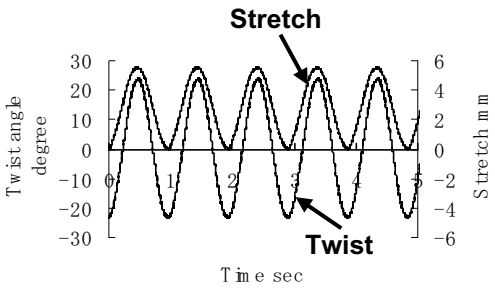
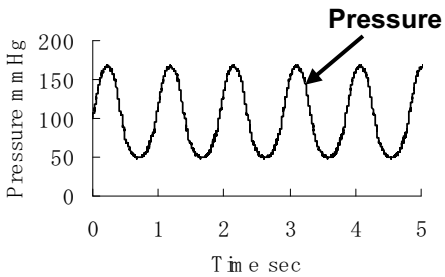


Fig.4 The schema of pre-stretch of the vessel model before installing the stent



(a) Cyclic twist and stretch



(b) Pressure

Fig.5 Simultaneous loads waveforms in the durability test

According to the data of Annual Reports of Health and Welfare in Japan [5], the average Japanese walk 7378 steps per day, therefore, 1.3 x 10^6 cycles (7378steps/2legs x 365days) were considered as one-year-equivalent cycles. The durability tests were conducted for one-year-equivalent duration, except for termination by the incidence of stent separation.

III. Results

The durability tests were conducted in the following three typical conditions. In the first experiment, cyclic twist and stretch forces were regulated to those consistent with the maximal data among 8 volunteers. The conventional non-stretched vessel models were used. In 5.5 x 10^5 cycles (equivalent to 5 months in vivo), a single strut fracture was observed at the middle area of the stent (Fig.6) However, further fracture did not occur until the termination in one-year-equivalent test. The second experiment was conducted using the pre-stretched vessel model. The loads condition was regulated to that of the average data of 8 volunteers. In 2.2 x 10^5 cycles (equivalent to 2 months), 6 strut fractures were observed at the middle area of the stent. Multiple strut fractures were observed after one-year-equivalent test (Fig.7). The third experiment was conducted using the pre-stretched vessel model. The loads condition was regulated to that of the maximal data of 8 volunteers. In 1.1 x 10^5 cycles (equivalent to 1 month), a single strut fracture was observed. In 1.5-months-equivalent duration, the number of strut fractures reached over 10. Complete separation of the stent eventually occurred in 2-months-equivalent duration (Fig.8).

IV. Discussion

Even though the maximal loads of twist and stretch among 8 volunteers were exerted, only one strut fracture occurred when the non-stretched vessel models were used. However, complete separation of the stents was induced when the pre-stretched vessel model was employed under the identical maximal-loads environment. These investigations demonstrated that employment of the pre-stretched vessel model strongly affects on the durability of the stents. We, for the first time, demonstrated that employment the pre-stretched vessel model is requisite parameter in the durability tests of endovascular stents. The stent fractures rapidly propagated in response to increase in loads. Iida et al. reported that patients with a habit of walking > 5000 steps per day had higher fracture rates than the patients who did not exercise [6]. These clinical data do match with our in-vitro accelerated durability test results. In this study, we used Wallstent (Boston Scientific, Natick, MA). Scanning electron microscope examination revealed

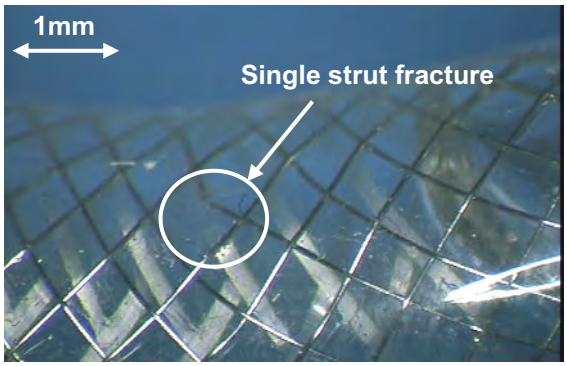


Fig.6 Single strut fracture after one-year-equivalent durability test. The maximal loads among 8 volunteers were exerted to the stent placed in the conventional non-stretched vessel models.

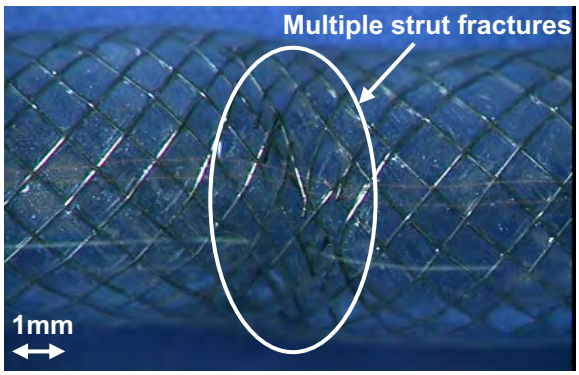


Fig.7 Multiple strut fractures after one-year-equivalent durability test. The average loads among 8 volunteers were exerted to the stent. The novel pre-stretched vessel model was employed.

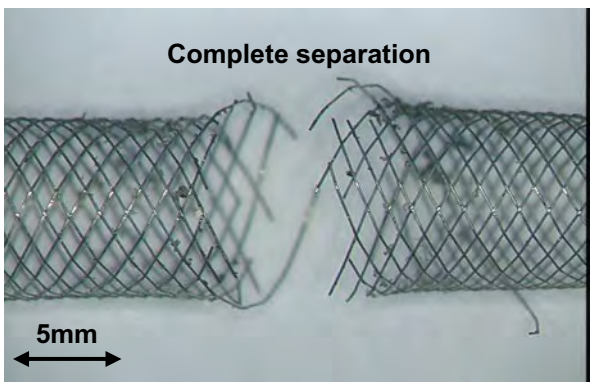
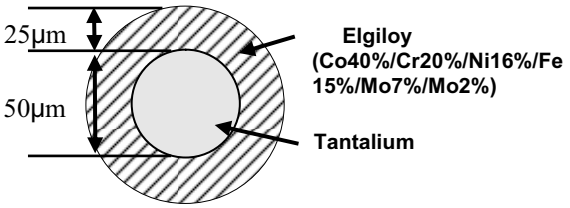


Fig.8 Complete separation of the stent after 2-months-equivalent durability test. The maximal loads among 8 volunteers were exerted to the stent placed in the pre-stretched vessel model.

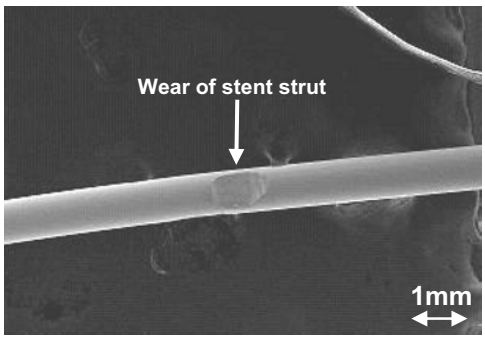
the fracture pattern of Wallstent. As shown in Fig.9, Wallstent consists of a center core made of Tantalium, and Elgiloy covering the core. It was found that stent fracture occurred when wear of Elgiloy region reached to the Tantalium.

V. Conclusions

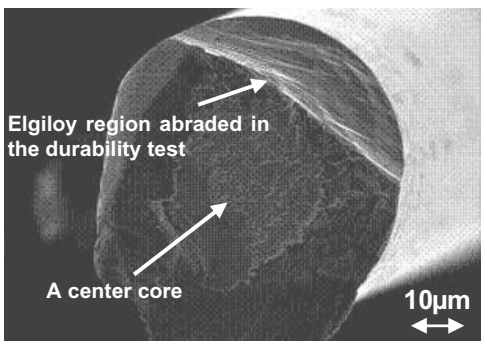
We developed the novel multi-loading durability test system, which can reproduce in-vivo equivalent mechanical environments. It was demonstrated that cyclic twist and stretch forces are important parameters in the durability test of endovascular stents. Moreover, to our knowledge, this is the first demonstration that pre-stretch of the vessel model before stent placement is requisite in order to produce the similar fracture pattern as observed in clinical reports. These efforts will contribute to establishment of a reliable durability testing methodology for endovascular stents.



(a) Composition of Wallstent used throughout the study



(b) Wear of the stent at the crossing region of struts



(c) Fracture surface of Wallstent

Fig.9 Scanning electron microscopic examination for investigating fracture mechanism of Wallstent

Acknowledgement

This study was partially performed as part of the Tenure Track Program at Waseda Institute for Advanced Study, supported by the "Promotion of Environmental Improvement for Independence of Young Researchers" activities under the Special Coordination Funds for Promoting Science and Technology provided by the Ministry of Education, Culture, Sports, Science and Technology, Japan. In addition, it was also supported by Health Science Research Grant (H20-IKOU-IPAN-001) from Ministry of Health, Labour and Welfare, Japan, Biomedical Engineering Research Project on Advanced Medical Treatment from Waseda University (A8201), and "The Robotic Medical Technology Cluster in Gifu Prefecture", Knowledge Cluster Initiative, Ministry of Education, Culture, Sports, Science and Technology, Japan.

References

1. Scheinert D, Scheinert S, Sax J et al. (2005) Prevalence and clinical impact of stent fractures after femoropopliteal stenting. J Am Coll Cardiol 45(2):312-315
2. Drisko K (2004) Characterizing the unique dynamics of the SFA : the RESIStent program. Endovasc Today oct :6-8
3. Jaff MR (2004) The nature of SFA disease. Endovasc Today oct :3-5
4. Cheng CP, Wilson NM, Hallett RL (2006) In vivo MR angiographic quantification of axial and twisting deformations of the superficial femoral artery resulting from maximum hip and knee flexion. J Vasc Interv Radiol 17:979-987
5. Annual report on Health, Labour and Welfare (1995), Japan
6. Iida O, Nanto S, Uematu M et al. (2006) Effect of exercise on frequency of stent fracture in the superficial femoral artery. Am J Cardiol 98(2):272-274

Author: Kiyotaka Iwasaki , Ph.D.
Institute: Waseda Institute for Advanced Study, Waseda University
Street: 2-2 Wakamatsu-cho, Shinjuku
City: Tokyo
Country: Japan
Email: iwasaki@waseda.jp

Star-Shaped Porphyrin-polylactide Formed Nanoparticles for Chemo-Photodynamic Dual Therapies

P.S. Lai

Department of Chemistry, National Chung Hsing University, Taichung, Taiwan

Abstract — **One potential way to overcome the side effects of chemotherapy is to develop therapeutic drug delivery systems that can enhance tumor cytotoxicity but reduce the adverse effects to the normal cells. Recently the studies of nanoparticle formulation of anticancer devices via drugs associated with synthetic polymers have been used as delivery systems for this purpose. In this study, we attempt to synthesize a novel star-shaped biodegradable polylactide (PLA) with chemo-photodynamic dual therapeutics for cancer treatments.**

The branched star porphyrin-PLA (BSPPLA) conjugate was synthesized by ring-opening polymerization of lactides from porphyrins with benzyl alcohol. The doxorubicin-loaded BSPPLA nanoparticles with 59.8±21.4 nm were fabricated by a modified solvent evaporation/extraction technique. Intracellular distribution, cell viability and phototoxicity of this novel BSPPLA nanoparticle were evaluated *in vitro*. The results show that BSPPLA nanoparticles, mainly localized in endosome/lysosome compartments, was non-toxic below 10 μM, but significantly induced cell death after suitable irradiation in MCF-7 cells. Furthermore, the photodynamic treatment obviously improved the cytotoxicity of doxorubicin-loaded BSPPLA nanoparticle through synergistic effects by median effect analysis. In conclusion, doxorubicin loaded BSPPLA nanoparticle showed considerable potential as a bimodal biomaterial for chemo-photodynamic drug delivery system for cancer therapy.

Keywords — **Photodynamic therapy, chemotherapy, Doxorubicin, polylactide, nanoparticles**

I. Introduction

Photodynamic therapy (PDT) is a treatment that utilizes the combined action of photosensitizers (PSs) and specific light sources for the treatment of various cancers. Following the activation of PSs by photochemical reaction, reactive oxygen species (ROS) are generated from molecular oxygen and act to destroy cancer cells [1, 2]. Important advantages of PDT over other therapies are that it is a precisely targeted treatment through selective illumination, it can be repeated in the same site if needed and it is less invasive than surgery. Despite these significant advantages, the biodistribution of PSs is unfavorable, and phototoxicity to the skin, mainly caused by existing agents' hydrophobicity and non-selectivity, is a considerable limitation of their use [3]. An ideal photosensitizer should be non-toxic if it has not been irradiated and should induce a large amount of damage to cells when exposed to a specific light source of long wavelength, which has advantages in the treatment of deeper lesions; fast accumulation in the target tissue, rapid clearance and tumor selectivity must also be considered [1, 4, 5].

In recent years, nanomaterials such as polymer–drug conjugates [6], liposomes [7], nanoparticles [8] and polymeric micelles [4, 5] have been considered as potential carriers for hydrophobic drug delivery that may resolve the aforementioned problems. Polymeric micelles composed of amphiphilic block copolymers demonstrate a series of attractive properties in drug delivery systems, such as good biocompatibility and high stability *in vitro* and *in vivo*, and can be successfully used for various poorly-soluble agent encapsulations. These nanosized micelles consist of a hydrophilic outer shell and a hydrophobic inner core that can be used to incorporate lipophilic drugs in aqueous solution [9-11]. Recently, potential micelle composed of terminal-modified amphiphilic copolymers for PDT has been developed in our lab.

In this study, a porphyrin-centered, 4-armed star poly(L-lactide) (PLA) was synthesized and its potential as a drug delivery carrier evaluated. Hydrophobic chemotherapeutic agents, such as doxorubicin (Dox), can then be encapsulated into the core region of this nanoparticle, presenting a combined chemotherapy/PDT strategy in one delivery system. Our results show that the cytotoxicity of the Dox-loaded micelle can be further enhanced after combination with PDT technology. Besides, Dox-resistance in MCF-7 breast cancer cells can be overcome by this carrier. This star-shaped PLA nanoparticle can be a promising biomaterial for dual therapies.

II. Materials and Methods

A. Synthesis of meso-tetra-(p-hydroxymethylphenyl) porphyrin

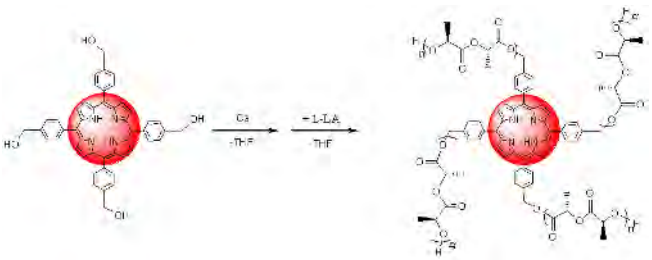
To a suspension of 0.28 g of lithium aluminium hydride in 15 ml. of tetrahydrofuran (THF)(dry and distilled over lithium aluminium hydride) was added slowly 200mg of meso-tetra-(p-carbomethoxyphenyl)porphyrin dissolved in 85 ml of dry THF and refluxed for an hour. Another 50ml

Chwee Teck Lim, James C.H. Goh (Eds.): ICBME 2008, Proceedings 23, pp. 1447–1450, 2009
www.springerlink.com

portion of dry THF was added to the reaction mixture and refluxing was continued for an additional 30 minutes. To unreacted lithium aluminium hydride was decomposed with most ether at 0 °C and filtered through a celite bed. Since the filtrate was almost colorless (indicating that the celite bed absorbed all the porphyrin), the celite was repeatedly extracted with pyridine. The combined pyridine extracts were distilled under reduced pressure, and the residue was triturated with acetone and filtered. The purple solid was dried in vacuo.

B. Synthesis of branched star porphyrin- PLA (BSPPLA)

The schematic representation of BSPPLA was shown in Scheme 1. BSPPLA was synthesized by ring-opening polymerization (ROP) of lactides with *meso*-tetra-(p-hydroxymethylphenyl) porphyrin as an initiator under $(DAIP)_2Ca]_2$·(THF) calcium complex (where DAIP-H = 2-[(2-dimethylamino-ethylimino)methyl]phenol) catalyst [12]. The molecule weight of BSPPLA obtained from ^{1}H NMR analysis is 19800 and the polydispersity index is 1.4 (measured by GPC).



Scheme 1 Synthesis of BSPPLA

C. Preparation of Dox encapsulated BSPPLA nanoparticles

The nanoparticles with 0.1mg Dox were prepared by solvent evaporation/extraction technique (the single emulsion technique). Typically, 1μl TEA and 2mg of BSPPLA were dissolved in 1ml acetone. The solution of organic phase was slowly poured into the stirred 5ml ddH_2O of 0.03% TPGS. The formed oil-in-water (O/W) emulsion was gently stirred at room temperature by a magnetic stirrer for overnight to evaporate the organic solvent.

D. Cell line and culture conditions

Human breast adenocarcinoma (MCF-7) cells and doxorubicin-resistant cells (MCF-7/ADR) were obtained from Dr. Lou of the Department of Otolaryngology, National Taiwan University Hospital. The cells were maintained in DMEM supplemented with 10% heat-activated fetal bovine serum (FBS), 2 mM L-glutamine and 1% antibiotics. The MCF-7/ADR cells were maintained continuously in 0.25 μM Dox.

E. Cytotoxicity of Dox or BSPPLA/Dox- mediated PDT

The cytotoxicity of Dox to MCF-7 and MCF-7/ADR cells was assessed by incubating the cells for 6h in medium containing different concentrations of Dox, followed by washing of the cells 3 times, incubation in fresh culture medium and then subjecting the cells to viability assays using MTT method.

The effect of PDT was assessed by incubating the cells with various concentrations of BSPPLA or BSPPLA/Dox for 6h at 37°C, washing the cells 3 times followed by incubation in phenol red-free medium for a further 48h. Then the cells were exposed to the light source with dose from 0.7J to 2.1J/cm^2 and subsequently subjected to the cell viability assays.

III. Results

A. Characterizations of BSPPLA or BSPPLA/Dox nanoparticles

The BSPPLA nanoparticles without or with Dox loading were prepared by solvent evaporation method. As shown in Table 1, BSPPLA nanoparticles exhibited a uniform size around 51 nm. After Dox loading, the size of BSPPLA nanoparticle decreased to 45.5 nm with PDI ~ 0.243. The encapsulation efficiency is almost 90% at polymer/Dox ratio = 10/1.

Table 1 Characterization of BSPPLA and BSPPLA/Dox nanoparticles (polymer/drug = 10/1 (w/w)

Nanoparticles	Size (nm)[a]	PDI	EE%[b]
BSPPLA	51.1	0.151	--
BSPPLA/Dox	45.5	0.243	89.8

[a] determined by DLS
[b] EE%[encapsulation efficiency] = (actual drug loading /theoretical drug loading)×100%

B. Cytotoxicity and phototoxicity of BSPPLA nanoparticles

Fig. 1 shows the cytotoxicity of BSPPLA nanoparticles without or with irradiation in MCF-7 cells. Obviously, more than 83 % of cells survived after BSPPLA nanoparticles incubation. After irradiation, the increased phototoxicity of BSPPLA nanoparticles was observed in MCF-7 cells as the light dose increased. It indicates that the BSPPLA exhibited successfully the PDT effects after irradiation.

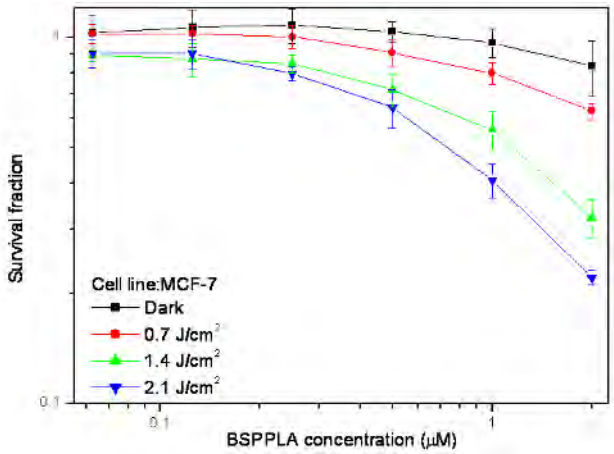


Fig. 1 Cytotoxicity and phototoxicity of BSPPLA in MCF-7 cells.

C. Cytotoxicity and phototoxicity of BSPPLA/Dox nanoparticles

Fig. 2 shows the cytotoxicity of BSPPLA/Dox nanoparticles without or with irradiation in MCF-7/ADR cells. Obviously, the cell viability in the dark was inhibited about 17% by Dox alone and 84% by BSPPLA/Dox at the highest Dox concentration (10μM) for 24 hours. These results reveal that Dox-loaded nanoparticles showed enhanced cytotoxic activity in MCF-7/ADR cells. After 2.1 J/cm^2 light irradiation, more than 95% of cells were killed by BSPPLA/Dox at 10 μM Dox concentration, whereas there was no conspicuous difference with Dox alone. Interestingly, Dox combined with PDT can improve the cytotoxicity of BSPPLA/Dox at a Dox concentration of 0.5375 μM from slight toxic (more than 85% cell survival) to toxic (55% cell survival). This enhancement of cytotoxicity may be due to the effect of photochemical internalization (PCI). PCI, a specific branch of PDT, is a novel technology for the site-specific release of macromolecules within cells. The mechanism of PCI is based on the breakdown of the endosomal/lysosomal membranes by photoactivation of photosensitizers [13]. The micellar photosensitizing agent can be taken by cells via endocytosis and entrapped into the endosome/lysosome. After irradiation, PCI can disrupt the endocytic vehicles and enhance drug release to the cytosol [14-16].

D. Intracellular localization of free Dox and BSPPLA/Dox without or with PCI

Fig. 3 shows the intracellular distribution of Dox or BSPPLA/Dox nanoparticles in MCF-7/ADR cells. After uptake by MCF-7/ADR cells, doxorubicin was localized in discrete granules in the cytosol. Interesting, Dox was observed in nuclei after BSPPLA/Dox nanoparticles treatment for 12 hours without PCI. This may result in the cell toxicity of BSPPLA/Dox nanoparticles. However, the detail mechanism is not clear. After PCI, the Dox was obviously translocated from cytosol to nuclei that can cause the cell death.

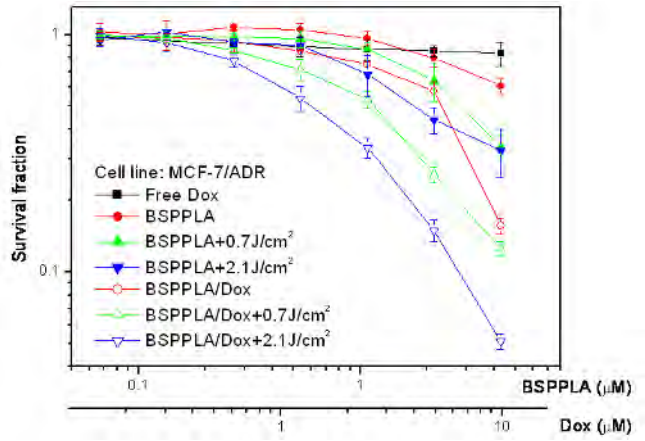


Fig. 2 Cytotoxicity and phototoxicity of BSPPLA/Dox in MCF-7/ADR cells.

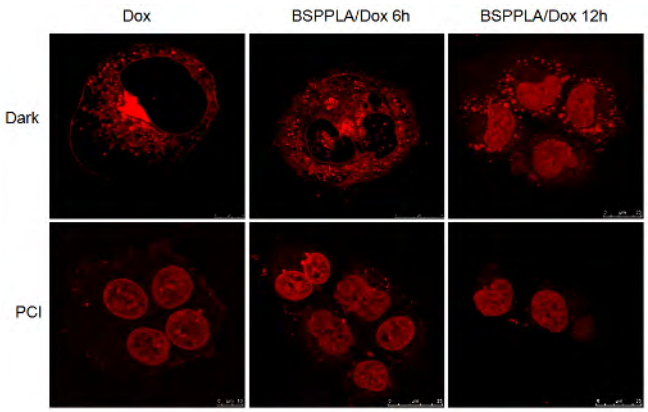


Fig. 3 Intracellular distribution of BSPPLA/Dox without or with irradiation.

IV. Conclusions

In this study, 4-armed star-shaped porphyrin-cored PLA were synthesized and characterized. These porphyrin-cored PLA could self-assemble to form nanoparticle using solvent evaporation method, which act as nanosized photosensitizing agents for PDT and further encapsulate hydrophobic drugs such as doxorubicin. Our results showed that these nanoparticles can improve the cytotoxicity of Dox significantly in MCF-7/ADR cells after irradiation in a synergistic effect. This functionalized nanoparticle delivery system is a potential dual carrier for the synergistic combination of

photodynamic therapy and chemotherapy for the treatment of cancer.

Acknowledgment

This research was supported by grants from Ministry of Education of the Republic of China under the ATU plan and National Science Council of the Republic of China (NSC 97-2113-M-005-002).

References

1. Dolmans D, Fukumura D, Jain RK (2003) Photodynamic therapy for cancer. Nature Rev Cancer 3:380-387.
2. Snyder JW, Greco WR, Bellnier DA et al., (2003) Photodynamic therapy: A means to enhanced drug delivery to tumors. Cancer Res 63:8126-8131.
3. Zhang GD, Harada A, Nishiyama N et al., (2003) Polyion complex mi-celles entrapping cationic dendrimer porphyrin: effective photo-sensitizer for photodynamic therapy of cancer. J Control Release 93:141-150.
4. Ideta R, Tasaka F, Jang WD et al., (2005) Nanotechnology-based photodynamic therapy for neovascular disease using a supramolecular nanocarrier loaded with a dendritic photosensitizer. Nano Lett 5:2426-2431.
5. Jang WD, Nakagishi Y, Nishiyama N et al., (2006) Polyion complex micelles for photodynamic therapy: Incorporation of dendritic photo-sensitizer excitable at long wavelength relevant to improved tissue-penetrating property. J Control Release 113:73-79.
6. Kopecek J, Kopeckova P, Minko T et al., (2001) Water soluble polymers in tumor targeted delivery. J Control Release 74:147-158.
7. Takeuchi Y, Ichikawa K, Yonezawa S, et al., (2004) Intracellular tar-get for photo sensitization in cancer antiangiogenic photodynamic therapy mediated by polycation liposome. J Control Release 97:231-240.
8. Vargas A, Pegaz B, Debefve E et al., (2004) Improved photo-dynamic activity of porphyrin loaded into nanoparticles: an in vivo evaluation using chick embryos. Int J Pharm 286:131-145.
9. Liu JB, Xiao YH, Allen C. (2004) Polymer-drug compatibility: A guide to the development of delivery systems for the anticancer agent, Ellipticine. J Pharma Sci 93:132-143.
10. Shuai XT, Merdan T, Schaper AK et al., (2004) Core-cross-linked polymeric micelles as pac-litaxel carriers. Bioconjug Chem 15:441-448.
11. Torchilin VP. (2004) Targeted polymeric micelles for delivery of poorly soluble drugs. Cell Mol Life Sci 61:2549-2559.
12. Chen HY, Tang HY, Lin CC. (2007) Ring-opening polymerization of L-lactide catalyzed by a biocom-patible calcium complex. Polymer 48:2257-2262.
13. Berg K, Selbo PK, Prasmickaite L et al., (1999) Photochemical internalization: A novel technology for delivery of macromolecules into cytosol. Cancer Res 59:1180-1183.
14. Lai PS, Lou PJ, Peng CL et al., (2007) Doxorubicin delivery by polyamidoamine dendrimer conjugation and photochemical internali-zation for cancer therapy. J Control Release 122:39-46.
15. Lai PS, Pai CL, Peng CL et al., (2008) Enhanced cytotoxicity of saporin by polyamidoamine dendrimer conjugation and photochemi-cal internalization. J Biomed Mater Res: Part A 87A:147-155.
16. Peng CL, Shieh MJ, Tsai MH et al., (2008) Self-assembled star-shaped chlorin-core poly(ε-caprolactone)-poly(ethylene-glycol) dib-lock copolymer micelles for dual chemo-photodynamic therapies. Biomaterials 29:3599-3608.

Author: Dr. Ping-Shan Lai
Institute: Department of Chemistry,
National Chung Hsing University
Street: No. 250, Kuo-Kuang Road
City: Taichung 402
Country: Taiwan
Email: f89548003@gmail.com

Enhanced Cytotoxicity of Doxorubicin by Micellar Photosensitizer-mediated Photochemical Internalization in Drug-resistant MCF-7 Cells

C.Y. Hsu[1], P.S. Lai[1], C.L. Pai[2], M.J. Shieh[2], N. Nishiyama[3] and K. Kataoka[3,4]

[1] Department of Chemistry, National Chung Hsing University, Taichung, Taiwan
[2] Institute of Biomedical Engineering, National Taiwan University, Taipei, Taiwan
[3] Center for Disease Biology and Integrative Medicine, the University of Tokyo, Tokyo
[4] Department of Materials Engineering, the University of Tokyo, Tokyo

Abstract — **Multiple drug resistance (MDR) is a major clinical problem that seriously reduces the efficacy of many chemotherapy agents. In doxorubicin-resistant breast cancer cells, drugs accumulate only within discrete cytoplasmic organelles and almost none is detectable in the nuclei, the target of anthracycline drugs. Photochemical internalization (PCI), a specific branch of photodynamic therapy, is a novel technology utilized for the site-specific release of macromolecules within cells. In this study, the phototoxicity of dendrimer phthalocyanine (DPc)-encapsulated polymeric micelle (DPc/m) combined with doxorubicin was studied in drug-resistant MCF-7 cells. After photoirradiation with a LED (670 nm), the internalized DPc/m showed unique photochemical processes inside of the cells that can disrupt the endosomal/lysosomal membrane and thereby cause the doxorubicin release from the lysosome to nuclei. In conclusion, DPc/m-mediated PCI destroyed endosomal/lysosomal membrane efficiently that can reverse the MDR phenotype of doxorubicin resistant MCF-7 cells. The technique is a promising new approach to overcome the drug-resistance in breast cancer cells.**

Keywords — **Doxorubicin, drug-resistance, photochemical internalization, micelle**

I. Introduction

Photodynamic therapy (PDT) is an effective strategy for treatment of solid tumors via systemic administration of porphyrin- or phthalocyanine-based photosensitizers (PSs), followed by local irradiation with the light of a specific wavelength [1, 2]. Upon photoirradiation, PSs generate reactive oxygen species (ROS) such as singlet oxygen, leading to photochemical destruction of tumor vessels and tumor tissues. PDT is a recognized therapeutic modality for the treatment of a variety of human pre-malignant and malignant diseases. Photochemical internalization (PCI), a specific branch of PDT, is a novel technology utilized for the site-specific release of macromolecules within cells. The mechanism of PCI is based on the breakdown of the endosomal/lysosomal membranes by photoactivation of photosensitizers, aluminum phthalocyanine disulfonate ($AlPcS_{2a}$) or disulfonated meso-tetraphenylporphyrin ($TPPS_{2a}$), that localize on the membranes of these organelles [3]. The PCI strategy has been utilized to release macromolecules such as toxins, DNA delivered as a complex with cationic polymers or dendrimer-doxorubicin conjugates from endocytic vesicles to the cytosol [4-6].

The PSs applied on PDT/PCI are small molecules that may have several drawbacks *in vivo*. The development of tumor-selective PSs and their formulations is expected to restrain unfavorable side effects and improve the PDT efficacy against intractable tumors. In this context, the use of long-circulating nanocarriers such as polymer-drug conjugates [6, 7] and polymeric micelles [8-10] are a promising way to improve the tumor-selectivity of PSs based on the enhanced permeability and retention (EPR) effect [11]. Recently, the highly efficient ionic dendrimer photosensitizers with the core of porphyrin or phthalocyanine for PDT were developed by Prof. Kataoka [9, 12]. These dendrimer PSs can be encapsulated into polyion complex (PIC) micelles with remarkably high photocytotoxicity against cancer cells and successful treatment for experimental disease models of choroidal neovascularization in rats [8]. As previous study, DPc/m was accumulated in endosome/lysosome via endocytosis and disrupted the endosomal/lysosomal membrane successfully after irradiation that cause the enhancement of transgene expression [13]. DPc/m exhibited similar transfecion activity of $AlPcS_{2a}$-mediated PCI but without inevitable phototoxicity.

Multiple drug resistance (MDR) is a major clinical problem that seriously reduces the efficacy of many chemotherapy agents. In doxorubicin-resistant breast cancer cells, drugs accumulate only within discrete cytoplasmic organelles and almost none is detectable in the nuclei, the target of anthracycline drugs [14, 15]. This leads to increased drug sequestration in acidic vesicles, followed by transport to the outer cell wall and extrusion into the external medium as the protonation, sequestration, and secretion (PSS) model [16]. Recently, this plight can be overcome successfully via the disruption of endosomal/lysosomal membrane by $TPPS_{2a}$-mediated PCI *in vitro* [17]. However, $TPPS_{2a}$ exhibited several drawbacks including lower exciting wavelength, inevitable phototoxicity and poor tumor selectivity, DPc/m

Chwee Teck Lim, James C.H. Goh (Eds.): ICBME 2008, Proceedings 23, pp. 1451–1454, 2009
www.springerlink.com

provides an obvious deeper penetrating of light, passive targeting ability and lower phototoxicity that can specific destabilize the endosomal/lysosomal membranes for further PCI application.

In the present paper, we have studied *in vitro* photocytotoxicity of DPc/m combined with doxorubicin when drug-resistant MCF-7 cells were photoirradiated by a light emitting diodes (LEDs, 670 nm), and found that DPc/m showed unique photochemical processes inside of the cells to induce endosomal/lysosomal membrane and thereby cause the doxorubicin release from the lysosome to nuclei.

II. Materials and methods

A. Cell line and culture conditions

Human breast adenocarcinoma (MCF-7) cells and doxorubicin-resistant cells (MCF-7/ADR) were obtained from Dr. Lou of the Department of Otolaryngology, National Taiwan University Hospital. The cells were maintained in DMEM supplemented with 10% heat-activated fetal bovine serum (FBS), 2 mM L-glutamine and 1% antibiotics. The MCF-7/ADR cells were maintained continuously in 0.25 μM doxorubicin.

B. Cytotoxicity with doxorubicin and DPc/m mediated PDT given separately

The cytotoxicity of doxorubicin to MCF-7 and MCF-7/ADR cells was assessed by incubating the cells for 6h in medium containing different concentrations of doxorubicin, followed by washing of the cells 3 times, incubation in fresh culture medium and then subjecting the cells to viability assays using MTT method.

The effect of PDT was assessed by incubating the cells with various concentrations of DPc/m for 18h at 37^{o}C, washing the cells 3 times followed by incubation in phenol red-free medium for a further 6h. Then the cells were exposed to the light source with dose from 10J to 40J/cm^2 and subsequently subjected to the cell viability assays.

C. Stability assay of lysosomal membrane after DPc/m-PCI treatments

To evaluate the efficiency of different PCI strategies on endosomal/lysosomal membrane, acridine orange (AO) was utilized as an intracellular indicator of acid organelles in MCF-7/ADR cells. When normal cells were excited by blue light, highly concentrated lysosomal AO emitted an intense red fluorescence, while nuclei and cytosol showed weak diffuse green fluorescence [6]. In this study, cells were grown overnight on glass slides in 35-mm petri dishes and then treated with different concentrations of DPc/m for 18 hours. For 'light before' strategy, cells were irradiated by light source with 10 J and then the cultures were then incubated with 6 μM AO for 15 minutes. For 'light after' experiment, cells were incubated with 6 μM AO for 15min and then photoirradiated with 10J. After PCI and staining, the fluorescence of AO was immediately imaged by Leica-SP5 confocal laser scanning microscope.

D. Intracellular localization of doxorubicin after DPc/m-PCI treatments

To evaluate the influence of PCI on the intracellular distribution of doxorubicin, MCF-7/ADR cells were documented before and after the photochemical treatment by confocal laser scanning microscope. In brief, cells were grown on glass-based 35-mm petri dishes. After overnight, cells were incubated with 15 μM of DPc/m for 18 hours. For 'light before' strategy, cells were irradiated by light source with 10 J and then the cultures were then incubated with 5 μM doxorubicin for 1 hour. For 'light after' experiment, cells were incubated with 5 μM doxorubicin for 6 hours and then photoirradiated by LED light source at 10J. After treatment, the intracellular distribution of doxorubicin was assessed immediately by Leica-SP5 confocal laser scanning microscope.

E. Cytotoxic effects of PCI combined with doxorubicin

For the PCI studies (doxorubicin plus PDT), the cells were treated with various concentrations of DPc/m plus light dose from 10J to 40J/cm^2 as described above. Doxorubicin (2.5μM) was applied to the cultures immediately after light delivery for an incubation period of 6h, as the results from the experiments on intracellular drug localization showed that this was more effective than giving the doxorubicin before the light.

III. Results

A. Doxorubicin treatment in MCF-7 or MCF-7/ADR cells

Fig. 1 shows the cytotoxicity and intracellular localization of doxorubicin in MCF-7 or MCF-7/ADR cells. It is obviously that almost 90% MCF-7 cells were killed after 2.5 μM doxorubicin treatment for 24 hours, meanwhile, more than 80% MCF-7/ADR cells survived with 10 μM doxorubicin incubation. As shown in Fig. 1B, doxorubicin was accumulated only within discrete cytoplasmic organelles and almost none is detectable in the nuclei. Therefore,

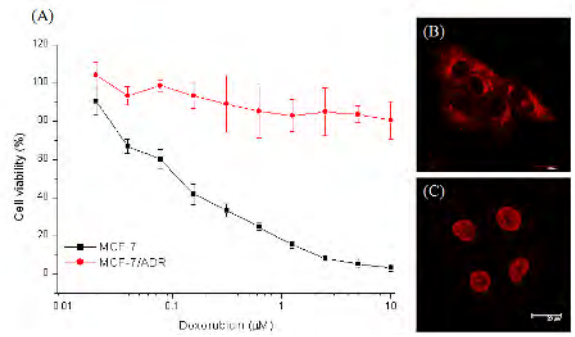


Fig. 1 Cell viability and intracellular localization of doxorubicin in MCF-7 and MCF-7/ADR cells

doxorubicin-resistance was observed. However, doxorubicin was localized in nuclei after 6 hours incubation in MCF-7 cells (Fig. 1C) that will cause the cell death.

B. Photochemical disruption of the endosomal/lysosomal membrane

To assess whether DPc/m could disrupt the endosomal/lysosomal membrane and could help doxorubicin escape from the lysosomes after irradiation, AO was utilized as a marker to trace the integrity of the endosomes/lysosomes. Without treatments, endosome/lysosome can be labeled as red spots (Fig. 2A). For "light after" PCI at 10 J/cm^2 light dose, red spots decreased with 1.5 μM DPc/m (Fig. 2E) and almost disappeared with a 3 μM DPc/m (Fig. 2G). However, red spots were almost non-detectable with 1.5 μM DPc/m "light before" PCI (Fig. 2F) at 10 J/cm^2 light dose. These results demonstrated that the endocytozed DPc/m, which accumulated in the endosomes/lysosomes, could destabilize the endosomal/lysosomal membranes and cause a rapid loss of AO staining of acidic organelles after

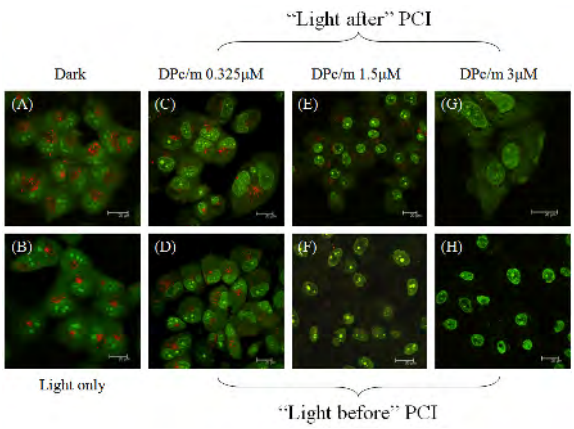


Fig. 2 Estimation of lysosome disruption capability of DPc/m with 10 J/cm^2 irradiation.

irradiation. Moreover, "light before" PCI strategy seems more efficient than "light after" PCI.

C. Intracellular localization of doxorubicin combined with DPc/m-PCI

Fig. 3 shows the distribution of doxorubicin in MCF-7/ADR cells without or with PCI. After uptake by MCF-7/ADR cells, doxorubicin was localized in discrete granules in the cytosol (Fig. 3A). After PCI, the distribution of doxorubicin in MCF-7/ADR cells was apparently changed. For "light after" PCI, red spots in cytosol decreased and slight fluorescence of doxorubicin increased in the nuclei. For "light before" PCI, no red spots can be observed in the cytoplasma and the doxorubicin was translocated from cytosol to nuclei. It is evidently that "light before" PCI is more efficient in endosomal/lysosomal disruption and enhancement of nuclear accumulation of doxorubicin than "light after" PCI.

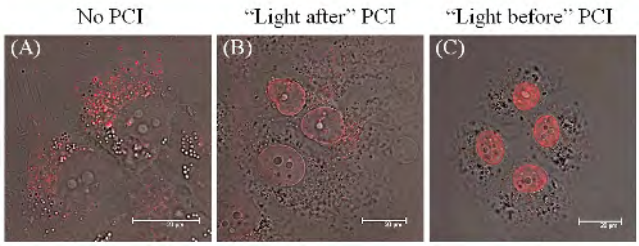


Fig. 3 The intracellular distribution of doxorubicin before and after PCI.

D. Cytotoxicity of doxorubicin combined with DPc/m-PCI

Fig. 4 shows the dose-dependent nature of the cytotoxicity and phototoxicity of DPc/m with or without doxorubicin treatment in MCF-7/ADR cells. It is obvious that the cytotoxicity of doxorubicin can be enhanced after 0.3125 μM DPc/m-mediated PCI at 20 or 40 J/cm^2 light dose. This enhancement of cytotoxicity may be due to the effect of PCI. The micellar photosensitizing agent can be taken by cells via endocytosis and entrapped into the endosome/lysosome. After irradiation, PCI can disrupt the endocytic vehicles and enhance doxorubicin translocation to nuclei.

IV. Conclusions

Drug-resistance is a major problem of clinical chemotherapy. We demonstrated that the DPc/m is a promising biomaterial to overcome the drug resistance based on PCI effect. Moreover, "light before" PCI strategy is more efficient to improve the cytotoxicity of doxorubicin in MCF-7/ADR cells. As PDT is becoming increasingly used for

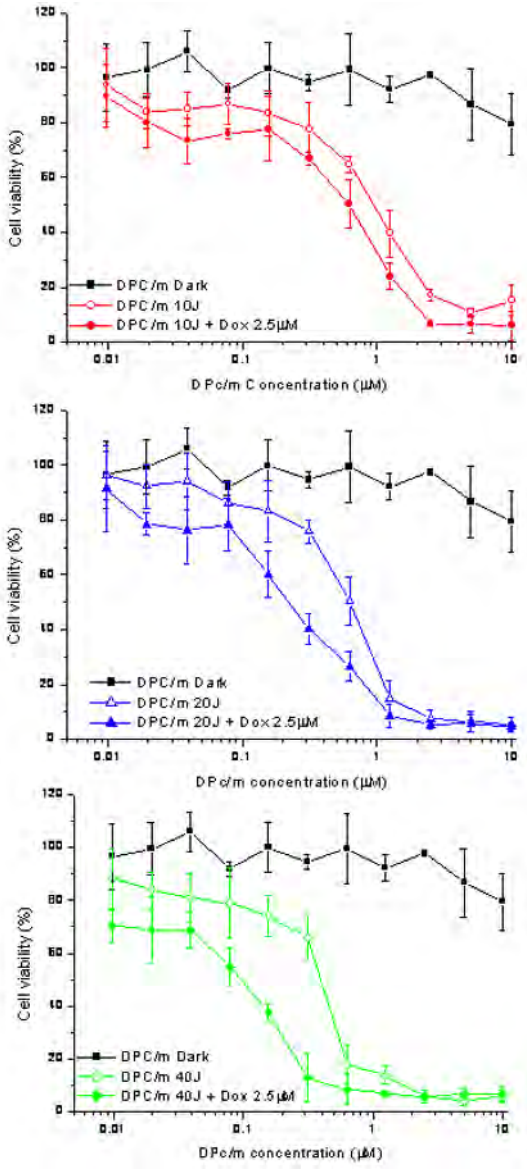


Fig. 4 Cell survival of doxorubicin combined with "light before" PCI in MCF-7/ADR cells.

cancer treatment, these findings may have important implications for the use of chemotherapy agents like doxorubicin in patients with drug resistant cancers.

Acknowledgment

This research was supported by grants from Ministry of Education of the Republic of China under the ATU plan and National Science Council of the Republic of China (NSC 97-2113-M-005-002).

References

1. Dolmans D, Fukumura D, Jain RK (2003) Photodynamic therapy for cancer. Nature Rev Cancer 3:380-387.
2. Snyder JW, Greco WR, Bellnier DA et al., (2003) Photodynamic therapy: A means to enhanced drug delivery to tumors. Cancer Res 63:8126-8131.
3. Berg K, Selbo PK, Prasmickaite L et al., (1999) Photochemical internalization: A novel technology for delivery of macromolecules into cytosol. Cancer Res 59:1180-1183.
4. Lai PS, Lou PJ, Peng CL et al., (2007) Doxorubicin delivery by polyamidoamine dendrimer conjugation and photochemical internalization for cancer therapy. J Control Release 122:39-46.
5. Lai PS, Pai CL, Peng CL et al., (2008) Enhanced cytotoxicity of saporin by polyamidoamine dendrimer conjugation and photochemical internalization. J Biomed Mater Res: Part A 87A:147-155.
6. Shieh MJ, Peng CL, Lou PJ et al., (2008) Non-toxic photo-triggered gene transfection by PAMAM-porphyrin conjugates. J Control Release 122:200-206.
7. Kopecek J, Kopeckova P, Minko T et al., (2001) Water soluble polymers in tumor targeted delivery. J Control Release 74:147-158.
8. Ideta R, Tasaka F, Jang WD et al., (2005) Nanotechnology-based photodynamic therapy for neovascular disease using a supramolecular nanocarrier loaded with a dendritic photosensitizer. Nano Lett 5:2426-2431.
9. Jang WD, Nakagishi Y, Nishiyama N et al., (2006) Polyion complex micelles for photodynamic therapy: Incorporation of dendritic photosensitizer excitable at long wavelength relevant to improved tissue-penetrating property. J Control Release 113:73-79.
10. Peng CL, Shieh MJ, Tsai MH et al., (2008) Self-assembled star-shaped chlorin-core poly(ε-caprolactone)-poly(ethylene-glycol) diblock copolymer micelles for dual chemo-photodynamic therapies. Biomaterials 29:3599-3608.
11. Maeda H, Wu J, Sawa T et al., (2000) Tumor vascular permeability and the EPR effect in macromolecular therapeutics: a review. J Control Release 65:271-284.
12. Arnida, Nishiyama N, Kanayama N et al., (2006) PEGylated gene nanocarriers based on block catiomers bearing ethylenediamine repeating units directed to remarkable enhancement of photochemical transfection. J Control Release 115:208-215.
13. Nishiyama N, Arnida, Jang WD et al., (2006) Photochemical enhancement of transgene expression by polymeric micelles incorporating plasmid DNA and dendrimer-based photosensitizer. J Drug Target 14:413-424.
14. Coley HM, Amos WB, Twentyman PR et al., (1993) Examination by laser scanning confocal fluorescence imaging microscopy of the subcellular localization of anthracyclines in parent and multidrug-resistant cell lines. Br J Cancer 67:1316-1323.
15. Gervasoni JE, Fields SZ, Krishna S et al., (1991) Subcellular distribution of daunorubicin in P-glycoprotein-positive and -negative drug-resistant cell lines using laser-assisted confocal microscopy. Cancer Res 51:4955-4963.
16. Altan N, Chen Y, Schindler M et al., (1998) Defective acidification in human breast tumor cells and implications for chemotherapy. J Exp Med 187:1583-1598.
17. Lou PJ, Lai PS, Shieh MJ et al. (2006) Reversal of doxorubicin resistance in breast cancer cells by photochemical internalization. Int J Cancer 119:2692-2698.

Author: Dr. Ping-Shan Lai
Institute: Department of Chemistry, National Chung Hsing University
Street: No. 250, Kuo-Kuang Road
City: Taichung 402
Country: Taiwan
Email: f89548003@gmail.com

Amino Acid Coupled Liposomes for the Effective Management of Parkinsonism

P. Khare and S.K. Jain*

Department of Pharmaceutical Sciences, Dr H. S. Gour University, Sagar (M.P.)-470003 INDIA

Abstract — **Purpose: The Blood Brain Barrier restricts the brain uptake of many valuable hydrophilic drugs and limits their efficacy in the treatment of brain diseases because of the presence of tight junctions, high metabolic capacity, low pinocytic vesicular traffic and efficient efflux mechanisms. Parkinson's disease is a brain disorder caused due to deficiency of dopamine-HCl (Neurotransmitter). In the present project, amino acid coupled liposomes bearing dopamine-HCl were prepared to deliver the drug to the brain for the management of Parkinsonism utilizing receptor-mediated transcytosis. Method: Uncoupled liposomes were prepared by cast film method using phosphatidylcholine and cholesterol whereas coupled liposomes were prepared using phosphatidylcholine, cholesterol and lysine stearylamine conjugate (LSC) in the film. These liposomes were characterized for entrapment efficiency, vesicle size, shape, in vitro drug release and in vivo studies. The vesicle size was found to increase upon coupling of liposomes, whereas percent entrapment efficiency was reduced from 38.40±1.94% to 34.15±1.70% after coupling of liposomes. The in vitro percent cumulative drug release studies exhibited 58.7% drug release for uncoupled liposomes and 43.9% drug release for coupled liposomes at the end of 24 hours. These selected formulations were subjected for in vivo performance, which was assessed by periodic measurement of drug (Chlorpromazine) induced catatonia in albino rats (Wistar strain) and fluorescence microscopy studies of the rat brain using fluorescent marker. The results were compared with plain dopamine-HCl solution. Conclusion: Studies revealed that dopamine-HCl can be effectively delivered to the brain via lysine-coupled liposomes and exhibited superiority of coupled liposomal formulation over uncoupled formulation.**

Keywords — **Brain targeting, Parkinsonism, Catatonia, Liposomes**

I. Introduction

The drug delivery to the brain in effective concentration is a challenging task due to the presence of blood brain barrier. It is well established that blood brain barrier (BBB) is a unique membranous barrier that tightly segregates the brain from the circulating blood [1, 2]. The BBB is formed by brain capillary endothelial cells, which are linked to each other by tight junctions and lack in fenestrations. Hence the delivery of many essential substances is dependent on carrier mediated transport systems that are present on the membrane of brain capillary endothelial cells [3]. Metabolic substrates such as glucose and some amino acids have insignificant lipid solubility and penetrate the BBB rapidly by means of specific carrier transport systems. Numerous strategies have been developed for the effective transport of drug molecule across the BBB [4]. Among these strategies receptor mediated endocytosis is one of the specialized methods.

Liposomes have been widely used as drug carriers which are self assembled vesicles composed of a lipid bilayer that forms a closed shell, surrounding an internal aqueous phase and able to entrap hydrophilic and hydrophobic molecules [5,6]. Also they are non-toxic, biodegradable and composed of natural biomolecules. Increasing interest in receptor mediated targeting of liposomes has led to development of a variety of procedures for the coupling of ligands to preformed liposomes [7-9]. The reagents employed during coupling may destabilize or penetrate the vesicle bilayers and inactivate or modify entrapped agents. This problem can be avoided by the coupling of ligands to lipids, which are then incorporated into liposomes. The brain capillary endothelial cells of BBB are rich in amino acid transporters and hence L-lysine coupled liposomes bearing dopamine-HCl were developed to facilitate the transport of drug across BBB via receptor-mediated endocytosis. The dopamine-HCl is a drug of choice for treatment of Parkinsonism. But it does not cross BBB and is degraded in systemic circulation. Thus, its therapeutic use for treatment of the disease is limited. Hence the drug was encapsulated in the L-lysine coupled liposomes to facilitate its delivery across the BBB as well as to protect its degradation in the systemic circulation.

II. Experimental section

Materials

Phosphatidyl choline (PC), Cholesterol (CH), Stearylamine, L-lysine, Triton X-100 and Dicyclohexylcarbodiimide (DCC) were procured from Sigma chemicals, St Louis, MO, USA. Dopamine-HCl was generously supplied by Troikka Labs, Ahemdabad (Gujarat), INDIA, as gift sample. All the solvents used were of analytical grade.

Chwee Teck Lim, James C.H. Goh (Eds.): ICBME 2008, Proceedings 23, pp. 1455–1458, 2009
www.springerlink.com

A. Synthesis of L-Lysine Stearylamine Conjugate

The conjugate was prepared in two steps via carbodiimide reaction, first di-BOC-lysine was synthesized and then amino acid-stearylamine conjugate was synthesized. The formation of conjugate was confirmed by IR-spectroscopic study of the conjugate.

B. Preparation of liposomes

Liposomes were prepared by film cast method. Uncoupled liposomes were prepared by taking phosphatidylcholine and cholesterol in ratio 7:3 (PC: CH, optimized ratio) whereas coupled liposomes were prepared by using phosphatidylcholine, cholesterol and L-lysine stearylamine conjugate in a ratio of 7:3:1.5 (PC: CH: LSC, optimized ratio). The lipid components were dissolved in chloroform and methanol mixture (2:1) and the solvent was evaporated to cast a thin film on the inner surface of round bottom flask using a rotary vacuum evaporator. The dried film was hydrated with phosphate buffer saline (PBS) of pH 7.4 containing dopamine-HCl. All the preparations were briefly sonicated for a period of 30 seconds. Coupled and uncoupled formulations were characterized for vesicle size, percentage entrapment efficiency and in vitro drug release**.** Entrapment efficiency of the coupled and uncoupled liposomes was determined using the method described by Fry, et al. [10]. Drug content was analyzed spectrophotometrically at 280 nm using the method reported in USP [11]. The *in vitro* drug release from the coupled and uncoupled liposomal formulations was analysed using dialysis method.

C. In vivo studies

The *in vivo* efficacy of the coupled and uncoupled formulations was assessed by measuring the reduction in the degree of drug-induced catatonia in albino rats (wistar strain). The study was approved by University Animal Ethical Committee. The performance of plain drug solution, uncoupled formulation and coupled formulation was compared.Twenty-four animals were selected, weighed and divided in four groups, with six rats in each group. First group was kept as control while second, third and fourth group animals were intravenously (i.v) administered plain dopamine-HCl solution of (1mg/ml), uncoupled formulation and coupled formulation, respectively. The Chlorpromazine (5mg/kg) was injected intravenously to all the animals 30 minutes after the drug treatment. The reduction in the degree of catatonia was recorded periodically.The reduction in degree of catatonia was assessed by scoring the animals periodically. Difficulty in moving and changing the posture by the animals was evaluated by alternately placing the paw of the rat on a 3-cm-and 9-cm-high block.

D. Fluorescence Microscopic Study

The fluorescence microscopy was performed in order to confirm the brain delivery of the coupled liposomes and uncoupled liposomes. 6-carboxyfluoroscein was used as fluorescence marker, which was encapsulated into the coupled and uncoupled liposomes. The formulations were administered to albino rats intravenously. Rats were sacrificed after 30 minutes and brain from these animals was excised Then microtomy was done with the help of microtome and ribbons of sections obtained were fixed on slides using egg albumin solutions as fixative.

III. Results and Discussion

The L-lysine coupled liposomes were prepared by incorporation of L-lysine Stearylamine conjugate (LSC) in the lipid film, which was synthesized using carbodiimide chemistry. The conjugate was characterized by IR spectroscopy, which revealed different peaks (Fig.1).

Peaks at 3343cm^{-1} (N-H stretching), 1465cm^{-1} (N-H bending), and 1683cm^{-1} (C=O stretching) revealed the formation of amide bond between L-lysine and stearylamine, which confirmed the formation of Lysine stearylamine conjugate (LSC). Peaks at 2921 cm^{-1}, 2851 cm^{-1}, 1465 cm^{-1}, 722 cm^{-1} show different methyl and methylene group vibrations.

Shape of liposomes was found to be spherical in both uncoupled and coupled formulations (Fig. 2).

The average vesicle size of the uncoupled and L-lysine coupled liposomes was determined and found to be in the range of 1.25±0.06 to 0.36±0.04 μm and 1.56±0.09 to

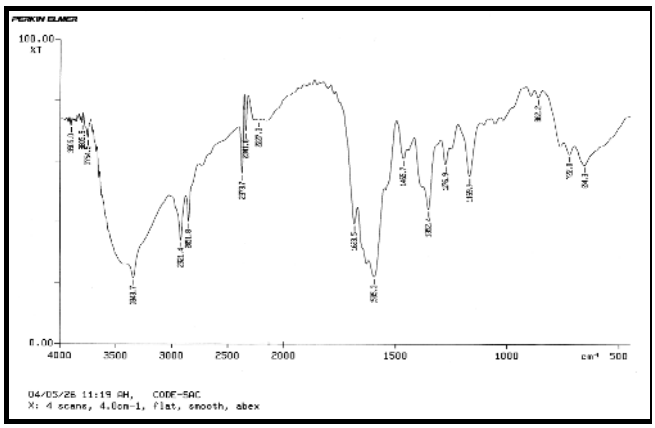


Fig.1. IR of L-Lysine Stearylamine Conjugate (LSC)

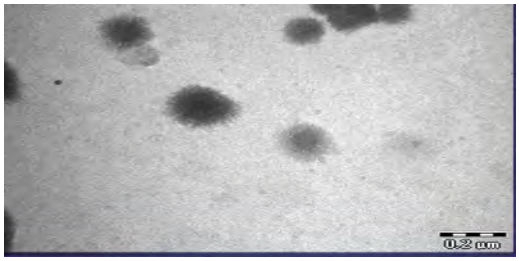


Fig.2. TEM photomicrograph of Coupled liposomes

Table 1: Characterization of liposomal formulation

Formulation code	PC: CH: Molar ratio	Lipids: LSC ratio	Vesicle size (µm)	Percent encapsulation efficiency
			Initial/ After coupling	Initial/ After coupling
LIP-A	9:1		1.25±0.06	43.56±2.17
LIP A-C		9:1:0.5	1.86±0.09	36.23±1.81
LIP-B	8:2		1.05±0.05	41.45±2.07
LIP B-C		8:2:1	1.65±0.08	34.93±1.71
LIP-C*	**7:3**		**0.41±0.04**	**38.40±1.94**
LIP C-C*		**7:3:1.5**	**0.56±0.06**	**34.15±1.70**
LIP-D	6:4		0.36±0.04	35.89±1.79
LIP D-C		6:4:2	0.52±0.05	22.14±1.10

Values are mean±sd, where n= 3. * Optimized parameter

0.52±0.05 µm, respectively. The increase in size for coupled liposomes was due to the inclusion of L-lysine stearylamine conjugate in the liposomal bilayer. The percentage entrapment efficiency was found to be 38.40±1.94% for uncoupled formulation and 34.15±1.70% for coupled formulation (Table 1). This could be due to change in the bilayer statistics and less available space for entrapment.

The *in vitro* drug release was analysed by calculating percentage cumulative drug release. It was found to be 58.7±2.94% for uncoupled formulation whereas it was 43.9±2.18% for coupled formulation, at the end of 24 hours. The lower value for coupled formulation could be due to the retardation of drug release caused due to the incorporation of LSC in the liposomal bilayer, which enhanced the structural integrity of the bilayer (Fig. 3).

The *in vivo* performance of the plain dopamine solution and the liposomal formulations was evaluated by measuring reduction in drug-induced catatonia in albino rats. Observations are tabulated in Table 2. Results revealed that dopamine-HCl solution did not show any reduction in degree of catatonia (score 3.5 after 180 minutes) while the animals in the third group which received uncoupled liposomal formulation showed partial reduction in catatonia (maximum score 3.5 for 4 animals and 1.5 for 2 animals).

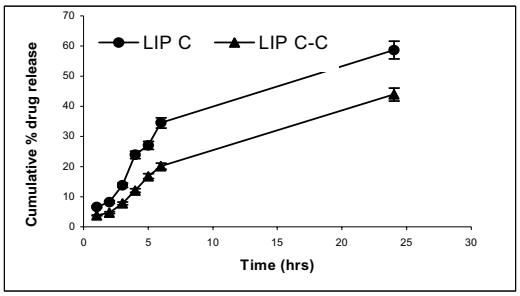


Fig.3. Cumulative Percent Drug Released after i.v. administration of coupled and uncoupled liposomes

Table 2: Effect of different formulations on the drug-induced catatonia in albino rats.

Action	Dopamine-HCl Solution (100mg/kg)	LIP C	LIP C-C (100mg/kg)
No reduction	6	4	None
Partial reduction	None	2	2
Complete reduction	None	None	4

The animals of the fourth group, which received coupled formulations showed almost complete reduction in catatonia (maximum score 1.5 for 2 animals and 0.5 for 4 animals). This could be due to enhanced uptake of L-lysine coupled liposomes through amino acid transporters present at BBB surface with subsequent delivery of dopamine-HCl to the brain effectively (Table 2).

Furthermore Fluorescence microscopy was performed to establish a qualitative over view of the liposomal targeting to brain and to confirm the brain uptake of lysine coupled liposomes by using 6 CF (6-carboxyfluoroscien) as fluorescence marker (Fi. 4). Fluorescence microscopic studies exhibited no fluorescence in the brain tissue when plain dye solution was administered and fluorescence was observed only in the blood vessels whereas on administering uncoupled liposomes, the fluorescence was observed in the adjoining area of the blood vessels of the brain which could be due to the entry of a little amount of the uncoupled liposomes containing 6 CF which might have gained entry through the Jonula occludence of the endothelium, crossing the nervous tissue. On the other hand lysine coupled liposomes containing 6 CF showed uniform intensity of fluorescence in the neuroglia and cerebral spinal fluid while uncoupled liposomes did not access these parts of the brain.

Therefore, it can be concluded that lysine coupled liposomes can localize efficiently in the brain and can subsequently deliver the therapeutics to the brain as compared to the uncoupled liposomes.

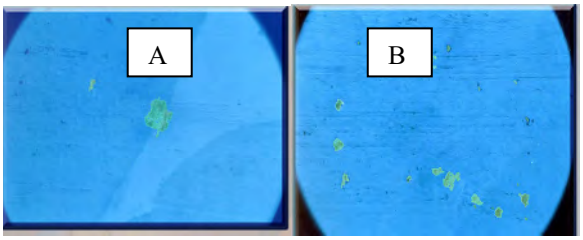


Fig. 4. Fluorescent photomicrographs of brain sections.
A: Photomicrograph after administration of Unoupled liposome.
B: Photomicrograph after administration of Coupled liposome.

IV. Conclusions

Conclusively it can be stated that dopamine-HCl can be delivered effectively through L-lysine coupled liposomes to the brain for effective management of Parkinsonism. Also, they hold great potential for targeting of therapeutics across BBB. However, a deep pharmacokinetic and clinical assessment is needed to establish their efficacy and quality.

Acknowledgements

The authors wish to acknowledge Head Department of Pharmaceutical Sciences, Dr. H.S. Gour Vishwavidyalaya, Sagar, India for providing necessary facilities.

References

1. Rahman, A.; Treat, J.; Roe, J. K.; Potkul, L. A.; Alvord, W.G. Phase I clinical trial and pharmacokinetic evaluation of liposomal encapsulated doxorubicin. *J Clin Oncol* 8: 1093-1100, 1990
2. Begley, D. J. The blood brain barrier: principles for targeting peptides and drugs to the central nervous system. *J Pharm Pharmacol* 48: 136-146, 1996
3. Schlossauer, B.; Steuer, H. Comparative anatomy, physiology and in vitro models of the blood brain and blood retina barrier. *Curr Med Chem* 2: 175-186, 2002
4. Gabizon, A.; Chemla, M.; Tzemach, D.; Horowitz, A. T.; Goren, D. Liposome longevity and stability in circulation: effects on the in vivo delivery to tumors and therapeutic efficacy of encapsulated anthracyclines. *J Drug Target* 3: 391-398, 1996
5. Sakamoto, A.; Ido, T. Liposomes targeting to rat brain effect of osmotic opening of the blood brain barrier. *Brain Res* 629: 171-175, 1993
6. Lasic, D. Liposomes. *American Sci* 80: 20-31, 1992
7. Gregoriadis, G.; Florence, A. T. Liposomes in drug delivery. *Drugs* 45: 15-28, 1993
8. Woodle, M. C.; Lasic D. D. Sterically stabilized liposomes. *Biochim Biophys Acta* 1113: 171-192, 1992
9. Gupta, Y.; Soni, V.; Chourasia, M. K.; Jain, A.; Khare, P.; Jain, S. K. Targeted drug delivery to brain via transferrin coupled liposomes. *Drug Del Tech* 5: 66-71, 2005
10. Fry, D.W.; White, J.C.; Goldman, I.D. Rapid separation of low molecular weight solutes from liposomes without dilution. *J Anal Biochem* 90: 803-812, 1978
11. United States Pharmacopoeia, 23ed ed., Asian edition, The United States Pharmacopoeial Convention, Inc., Rockville, MD. 1995.

*Corresponding author

Prof. S. K. Jain
Department of Pharmaceutical Sciences
Dr. H. S. Gour University, Sagar 470003, India
Tel / Fax: +91-7582-225782
Email address: drskjainin@yahoo.com

Corrosion Resistance of Electrolytic Nano-Scale ZrO_2 Film on NiTi Orthodontic Wires in Artificial Saliva

C.C. Chang[1] and S.K. Yen[2]

[1]Department of Dental Technology, Shu Zen College of Medicine and Management, Kaohsiung , Taiwan
[2]Department of Materials Science and Engineering, National Chung Hsing University, Taichung, Taiwan

Abstract — **Nano-Scale ZrO_2 films were produced on NiTi alloy orthodontic wires using electrolytic deposition to prevent corrosion and nickel ion release. Nickel ion release was observed in cyclic potentiodynamic test in artificial saliva at 310K. The amount of the nickel ion release was measured by inductively coupled plasma-atomic emission spectroscopy (ICP-AES), and for the Electrolytic ZrO_2 films samples, the nickel ion release level was 58 ppb. The ZrO_2 film reduced the nickel ion release level by 78%. The cyclic potentiodynamic test results showed the lower corrosion density of electrolytic ZrO_2 film than uncoated.**

Keywords — **Corrosion Resistance, Ion Release, Electrolytic Deposition, ZrO_2, NiTi Wires**

I. Introduction

Ti and Ti alloys have been widely used for dental applications due to their good mechanical properties, corrosion resistance, and biocompatibility. However, corrosion of Ti and Ti alloys still occur in some clinical circumstances. The release of metal ions from dental alloys may have adverse biological effects, depending on the ion species and its concentration. In conventional orthodontic treatment, NiTi alloy, which contains about equi-atomic Ni and Ti, is one of the most common orthodontic wires applied clinically due to its good working and mechanical properties [1].

Ni is capable of eliciting toxic and allergic responses [2,3]. In vivo study, NiTi alloys show cytotoxic reactions [3]. It is clear that the potential risk associated with corrosion, in the use of NiTi orthodontic wires, comes from the biological side effects of Ni.

Recently, electrolytic Al_2O_3 and ZrO_2 coatings on metal have been verified to improve the corrosion resistance and wear resistance [4-6] of biomedical alloys. This method has several potential advantages, including the cheap deposition technology, low preparation temperature, high purity of deposits, the ability to cover complex shapes of various materials and the application of multi-component oxides [7]. Especially, the film thickness can be controlled under 300 nm [8] which is required for the orthodontic wires. Electrolytic deposition is achieved via hydrolysis of metal ions or complexes by electrogenerated base to form hydroxide or peroxide deposits on cathode substrates. Hydroxide and peroxide deposits can be converted to corresponding oxides by thermal treatment [7,8].

In this study, the electrolytic nano-scale ZrO_2 film has been deposited on NiTi wires in $ZrO(NO_3)_2$ aqueous solutions. The characteristics of the film have been examined corrosion resistance.

II. Experimental

Materials: An equiatomic NiTi (Rematitan® Life, Dentaurm, Prorzheim, Germany) wire with a diameter 0.016 inch was employed in experiments.

Electrolytic Deposition: The electrolytic ZrO_2 film was deposited on NiTi wire in 0.03125 M $ZrO(NO_3)_2$ aqueous solution at voltage -1.2 V for 500 and 1000s at room temperature, using an VersaSTAT^3 potentiostat (Princeton Applied Research). The sample was the cathode, graphite bars (φ= 5 mm, l= 55 mm) were the anode and saturated Ag/AgCl was the reference electrode. The coated specimens were then naturally dried in air and annealed for 3 h at 723K.

SEM: The surface morphology of coated specimens was observed by scanning electron microscopy (SEM, JEOL, JSM-5400, Japan).

Polarization Test and ICP-AES: The corrosion resistance of the ZrO_2 film was evaluated by an electrochemical cycle dynamic polarization test in artificial saliva (Table 1) at

Table 1 The composition of artificial saliva

composition	mg/L
NaCl	400
KCl	400
$CaCl_2 \cdot 2H_2O$	795
$NaH_2PO_4 \cdot H_2O$	690
KSCN	300
$Na_2S \cdot 9H_2O$	5
Urea	1000

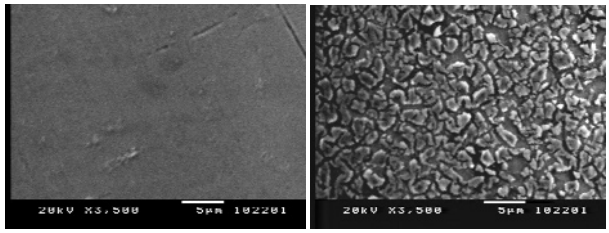
Chwee Teck Lim, James C.H. Goh (Eds.): ICBME 2008, Proceedings 23, pp. 1459–1461, 2009
www.springerlink.com

310K, also by using VersaSTAT[3]. After the open-circuit potential became steady, the cyclic polarization test was from -0.2 V (vs. open-circuit potential) to 1 V (Ag/AgCl), then back to open-circuit potential at a scanning rate of 0.167 mV/s. The first oxidation-reduction equilibrium potential E_{01} was derived when current density equaled zero during the applied voltage increased (forward cycle). If oxidation is due to the corrosion of electrode, this potential is also named corrosion potential E_{corr}, and the corrosion current density i_{corr} can be calculated at this potential. The second oxidation-reduction equilibrium potential E_{02} was derived when current density was back to zero again during the applied voltage decreased (backward cycle). If the oxidation is decreased abruptly at some passivation potential E_{pass}, because of the formation of passivation films and corrosion rate falls to very low, and the beginning current density is named the critical passive current density i_{crit}, and the stable current density is named the passive current density i_{pass}. If the oxidation is increased abruptly at some pitting potential E_{pit} because of the breakdown of passive film and the localized corrosion of the electrode, the crossover of the backward cycle and the forward cycle on the anodic polarization region will be found because of repassivation and defined as protection potential E_{pp}.

The amount of the nickel and Ti ions release after cycle dynamic polarization test was measured by inductively coupled plasma-atomic emission spectroscopy (ICP-AES, ICAP 9000, Jarrell-Ash, USA).

III. Results and Discussion

Surface Morphology: The SEM observations of specimens coated at -1.2V for 500 and 1000 s after annealed at 723K are show in Fig. 1(a) and (b), respectively. No cracks are found in Fig. 1(a), but they are found for a longer deposition time or thicker film, as shown in Fig 1(b). These cracks occur because the evaporation rate of H_2O from the coating surface is higher than the diffusion rate of H_2O from the bulk of coating, during drying in air. Thus, a tension effect will be found on the film surface due to shrinkage as it contains less H_2O than the bulk. SEM cross sectional observation of the ZrO_2 film specimen is shown in Fig. 2. The thickness of ZrO_2 film was approximately 150 nm.



(a) (b)

Fig. 1 SEM observations of specimens coated at V = -1.2 V: for (a) 500 s and (b) 1000 s annealed at 723 K for 3 h.

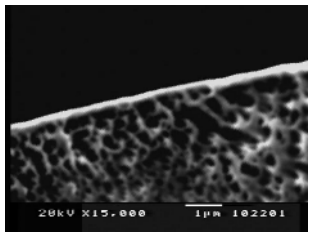


Fig. 2 SEM Cross-sectional observation of ZrO_2 coated for 500s after annealed at 723K for 3 h.

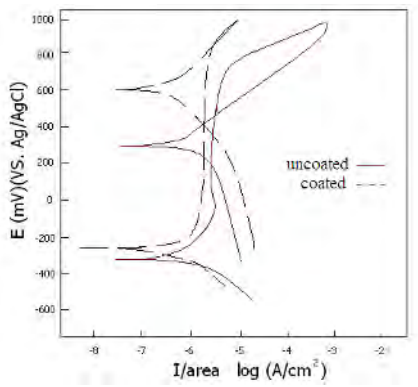


Fig. 3 Polarization curves of the uncoated and ZrO2 coated specimens in artificial saliva at 310 K.

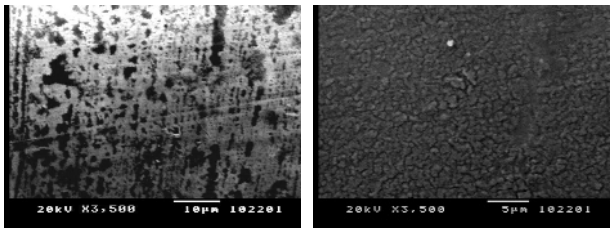
Corrosion Resistance: Electrochemical cycle polarization curves of the uncoated and coated specimens in artificial saliva at 310 K are show in Fig. 3. From the forward curves, E_{01} (or E_{corr}), i_0 (or i_{corr}), E_{pass}, i_{crit}, i_{pass} and E_{pitt} were analyzed, and from the backward curves E_{02} and E_{pp} were measured, as given in Table 2. The ZrO_2 film specimens

Table 2 List of the first redox potential E_{01} (E_{corr}), exchange current density i (i_{corr}), critical passive current density $i$crit, passive current density i_{pass}, pitting potential E_{pit}, the second redox potential E_{02} and protection potential E_{pp} of the uncoated and ZrO_2 coated specimens, derived form the polarization tests in artificial saliva

Specimens	E_{01} (E_{corr}) (mV)	i(i_{corr}) (10^{-6}A/cm^2)	i_{crit} (10^{-6}A/cm^2)	i_{pass} (10^{-6}A/cm^2)	E_{pitt} (mV)	E_{02} (mV)	E_{PP} (mV)
NiTi wire	-322	0.92	51	18	772	322	462
ZrO_2/NiTi wire	-250	0.45	-	37	854	604	840

revealed the higher E_{corr}, E_{pitt}, and lower i_{corr} and i_{pass}. After polarization tests in 3.5% artificial saliva, the large area corrosion on the uncoated was observed, as shown in Fig. 4a, but none on the coated, as shown in Fig. 4b.

Table 3 show the concentration of Ni and Ti ions in artificial saliva after the electrochemical cycle polarization tests that had been released from wires. As a result of the electrochemical cycle polarization tests, the ZrO_2 film coating reduced the amount of the Ni and Ti ions release by 78% and 76%, respectively. That is presumably due to these properties of ZrO_2 film, the Ni ion release from the orthodontic wires was reduced. The primary concern with NiTi orthodontic wires is a possible influence of Ni ion release on biocompatibility. Applications of the ZrO_2 film to prevent the Ni ion release problem are very appropriate.



(a) (b)

Fig 4. SEM observations of (a) the uncoated and (b) ZrO_2 coated specimens after polarization test in artificial saliva at 310 K.

Table 3 Concentration of Ni and Ti ions released from the NiTi wires

Specimens	Ni concentration (ppb)	Ti concentration (ppb)
NiTi wire	264	374
ZrO_2/NiTi wire	58	88

IV. Conclusions

In this study, ZrO_2 film was deposited on NiTi wires and the effects of ZrO_2 film coating on the Ni ion release from orthodontic wires were investigated. Using electrolytic deposition process, ZrO_2 films were deposited on NiTi wires successfully. In the electrochemical cycle polarization test, it was observed the amount of the Ni and Ti ions release were reduced by 78% and 76%, respectively. Applications of the ZrO_2 film to prevent the Ni ion release problem of NiTi wires are very appropriate.

References

1. Huang H. H., Chiu Y. H., Lee T. H. et al. (2003) Ion release from NiTi orthodontic wires in artificial saliva with various acidities, Biomaterials 24:3585-3592
2. Kerosuo H., Kulla A., Kerosuo E. et al. (1996) Nickel allergy in adolescents in relation to orthodontic treatment and piercing of ears. Am. J. Orthod. Dentofac. Orthop. 109:148-154
3. Berger-Gorbet M., Broxup B., Rivard C. et al. (1996) Biocompatibility testing of NiTi screws using immunohistochemistry on sections containing metallic implants, J. Biomed. Mater. Res. 32:243-248
4. Hsu H. C. and Yen S. K. (1998) Evaluation of metal ion release and corrosion resistance of ZrO_2 thin coatings on the dental Co-Cr alloys, Dental Mater. 14:339-346
5. Yen S. K., Wu S. J. and Wu C. H. (2003) Electrolytic Al_2O_3/ZrO_2 coating on Co-Cr-Mo implant alloys, Mater. Sci. Forum, 426-432:2509-2514
6. Yen S. K., Guo M. J. and Zhan H. Z. (2001) Characterization of electrolytic ZrO_2 coating on Co-Cr-Mo implant alloys of hip prosthesis, Biomaterials 22:125-133
7. Zhitomirsky I. (1999) Electrolytic deposition of oxide films in the presence of hydrogen peroxide, J. Euro. Ceram. Soc. 19:2581-2587
8. Chang C. C. and Yen S. K. (2004) Characterization of electrolytic ZrO_2/Al_2O_3 double layer coatings on AISI 440C stainless steel, Surf. Coat. Tech., 182:242-250

Author: C. C. Chang
Institute: Department of Dental Technology,
Shu Zen College of Medicine and Management
Street: No. 250, Huen-chiu Rd.
City: Luchu, Kaohsiung
Country: Taiwan
Email: ccchang@szmc.edu.tw

Stability of Polymeric Hollow Fibers Used in Hemodialysis

M.E. Aksoy[1], M. Usta[2] and A.H. Ucisik[3]

[1] Istanbul City Health Management, Author, Istanbul, Turkey
[2] Gebze Institute of Technology, Department of Material Sience and Engineering, Co-author, Kocaeli, Turkey
[3] Bogazici University, Institute of Biomedical Engineering, Department of Prostheses Materials and Artificial Organs, Co-author, Istanbul, Turkey

Abstract — **High flux dialysis the first choice of therapy for hemodialysis patients within the last decade due to its clinical outcome. In this study the effect of dialysis environment on the mechanical and structural stability of high flux dialyzers containing polysulfone membranes were investigated. Dialysis sessions were performed on a certain group of patients with dialysis ages less than two years and without any other accompanying disease. Mechanical data and XRD results revealed the differences in material characteristics between virgin and used membranes obtained from polysulfone membranes. With the help of tensile tests it was shown that the mechanical properties used membranes were reduced in terms of ultimate tensile strength. XRD experiments revealed that the degree of crystallinity of the polysulfone dialysis membranes were raised. It was concluded that high flux dialyzer membranes are becoming more brittle and having more crystallinity after dialysis session. By this way the membranes are more prone to mechanical defects during dialysis. The degree of crytallinity increases under cyclic loading which resembles the changing of the pump speed or transmembrane pressure during dialysis in case of clinical situations like hypotension during dialysis. This issue is very important for dialysis centers performing reuse procedures for dialysis centers, because any damage to dialysis membranes would cause very serious clinical complications.**

Keywords — **High flux, hemodialysis, x-ray diffraction, mechanical properties**

I. Introduction

Due to their clinical outcome high flux dialyzers containing new generation of dialyzer membrane materials have been widely used for patients with chronic renal failure within the last decade [1]. Improved survival for hemodialysis patients was reported for synthetic, high-flux compatible membranes [2,3]. Dialyzer membranes are more prone to damage to the harsh environment during high flux dialysis. Reuse of dialyzers has advantages such as better biocompatibility and lower cost. Any damage of the dialyzers membrane during reuse of the dialyzers can also cause very serious clinical complications. Therefore; reuse of the dialyzers is an issue that has to be approached more cautiously [4]. In this study polysulfone dialyzer membranes were investigated in terms of mechanical properties and changes in crystallinity before and after dialysis sessions. Internal and external pressures are applied to the dialysis fibers by the pump of the hemodialysis machine, dialysate and blood. The dialysis membrane has to withstand these pressures during hemodialysis because any damage in any part of the hemodialysis membrane will cause changes in the material exchange properties of the membrane. Dialysis sessions were performed on five patients with dialysis ages less than two years and without any other accompanying disease at the Hemodialysis Department of Istanbul Haydarpasa Numune State Hospital.

II. Materials and method

A. Tensile Test Studies and SEM Studies

Many factors contribute to the differences in fiber tensile behavior, including fiber geometrical shape, morphological structure and fiber fracture mechanism [5].

In order to have more information about the mechanical behavior of the dialysis membranes tensile testing studies were performed. As dialysis membranes are produced as hollow fibers with thousands of pores on each fiber, this structure can not be ignored from fracture mechanics point of view. Under loading condition, circular shape of the pores may be converted into elliptical shape. At the end of major axes of ellipse high amount of stress concentration is expected. The pore sizes of virgin polysulfone membranes and used polysulfone membranes after tensile test can be compared on figures 1 and 2.

These experiments were performed by using Instron tensile testing machine. All tests were run at room temperature and in laboratory atmosphere and the load cell, which was used for the experiments was 50 kilograms. Crosshead speed was kept constant (50 mm/min) and the gauge length was always 40 mm for all tensile testing studies.

In this study virgin and used hollow fibers originating from dialyzers with polysulfone membranes were used. For virgin fibers tensile test with monotonic loading until fracture was performed. For used fibers two different tensile testing methods were performed:

Chwee Teck Lim, James C.H. Goh (Eds.): ICBME 2008, Proceedings 23, pp. 1462–1465, 2009
www.springerlink.com

Experiment 1: Tensile test with monotonic loading until fracture of a used fiber
Experiment 2: Cyclic test with 90% of the maximum stress required for fracture for a used fiber followed by tensile test with monotonic loading until fracture.

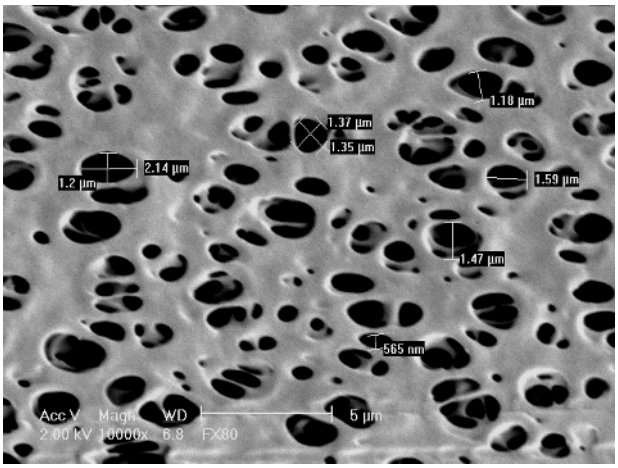


Fig. 1 Pore sizes of a virgin polysulfone membrane.

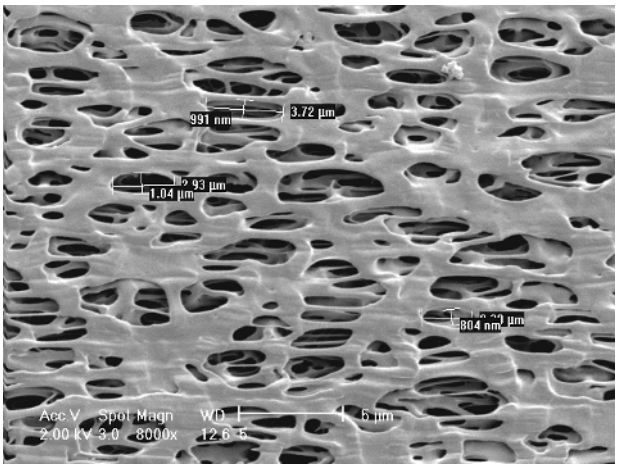


Fig. 2 Pore sizes of a used polysulfone membrane after tensile test.

B. XRD (X-Ray Diffraction) Studies

X-ray diffraction (XRD) is one of the most powerful technique for qualitative and quantitative analysis of crystalline compounds. A polymer can be considered partly crystalline and partly amorphous. Many polymers can be identified by using the XRD method. Polymers are, at least in part, crystalline or pseudo-crystalline with partially ordered structures. The degree of crystallinity can be quantified with this nondestructive, analytical technique. If the degree of crystallinity is increased in a material, it becomes more brittle [6]. The crystallinity parts give sharp narrow diffraction peaks and the amorphous component gives a very broad peak [7].

Following XRD studies have been performed for virgin and used polysulfone membranes, which were used for five different patients. The patients were chosen among the patients with dialysis ages less than two years. Following XRD experiments were performed:

XRD studies on virgin polysulfone membranes
XRD studies on used polysulfone membranes after dialysis
XRD studies on used polysulfone membranes after tensile testing.
XRD studies with used polysulfone on which cyclic tests were applied before continuous monotonic loading until fracture

XRD studies were performed with Rigaku Dmax 2200 XRD instrument. The d-spacing value was 1,54059 Å. X-Ray voltage and current values were 40kV and 40mA. Copper x-ray tube was used for XRD the experiments.

III. Experimental Results

A. Tensile Test Results

Depending on the results of the tensile tests performed it was concluded that virgin polysulfone membranes can resist higher loads compared to used ones. After one dialysis session ultimate tensile strength of a used polysulfone membrane lowers by approximately 30,94 % compared with the values virgin membranes, but it was also observed that the strain required for fracture of a used polysulfone membrane was 38,12% higher than virgin ones. It can be observed that membranes are becoming more ductile after first use and can only resist lower loads (Fig.3).

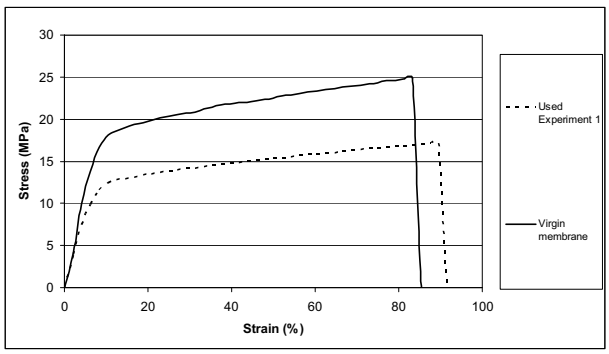


Fig. 3 Tensile testing results of virgin and used polysulfone hollow fibers.

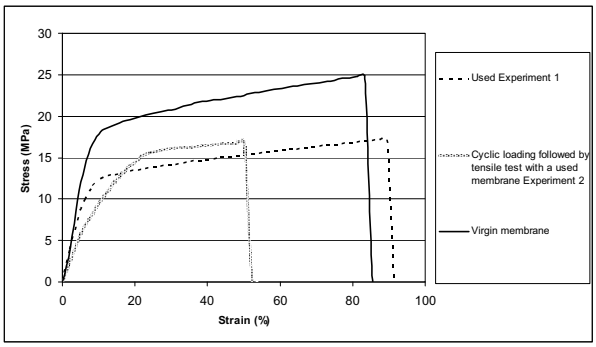


Fig. 4 Tensile testing results of virgin and used polysulfone hollow fibers (Experiment1 and 2)

The second types of tensile testing experiments included cyclic tests with 90% of the maximum stress required for fracture for a used fiber followed by tensile test with monotonic loading until fracture It was observed that the ultimate tensile stress value is near to the one of the used membrane, but this value was 35,89 % lower than to the ultimate tensile stress value of a virgin membrane. Cyclic loading followed by tensile test cause a 7,1 % reduction in stress values of the polysulfone membranes compared to used ones The reduction in strain values after cyclic loading followed by tensile test was 28,75% compared to virgin membranes. When the tensile test data of used membranes are compared a 48,4% reduction in strain values can be observed (Fig.4). These data show us that membranes are becoming more brittle with loading and unloading processes.

B. Results of the XRD Studies

After the XRD experiments it has been observed that there are three main intensity peaks in virgin polysulfone membrane and four main intensity peaks in used polysulfone membranes. The first three peaks at 2θ =14, at 2θ = 17 and at 2θ = 27 are present in the XRD data of both virgin and used polysulfone membranes, but the fourth peak at 2θ = 33 is only observed in used membranes (Fig.5).

The intensity values of all the peaks are getting their highest values when the membrane after cyclic loading followed by continuous monotonic tensile test. In used membranes the mean intensity value at 2 θ = 27 is 44,4 % higher compared to the same intensity value of a virgin membrane. The mean intensity value of used polysulfone membranes at 2θ = 17 is 20 % higher than the XRD value of a virgin membrane. At the intensity of 2 θ = 27 data obtained from XRD studies of used membranes are 40 % higher than the data from virgin membranes.

When cyclic loading followed by continuous monotic tensile test is applied to used membranes, the intensity values elevated between 59% - 70% compared with the values of virgin membranes.

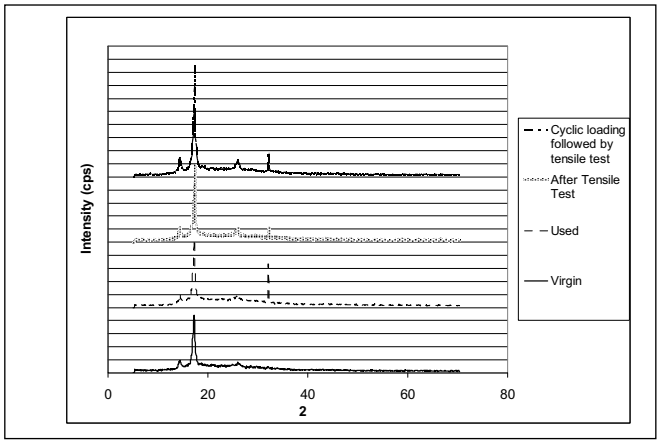


Fig. 5 Overview of the XRD results virgin and used fibers originating from patient M.D.

IV. Discussion

High flux dialysis has already proven itself with its superior clinical outcomes compared to low flux dialysis. Membranes for high flux hemodialysis have to resist a much more harsh environment due to factors such as increased flowrates compared to low flux dialysis. Depending on the results of the tensile test and XRD experiments the membranes are becoming more ductile and more brittle after the first use. The problem worsens when cyclic loading is applied to the polysulfone membranes. During hemodialysis the pump speed or the transmembrane pressure is lowered, when patients have a severe hypotension periods. When the clinical status of the patient stabilizes, the pump speed or transmembrane pressure is slowly elevated by the physicians. From the mechanical point of view this situation resembles the cyclic loading procedure performed during our experiments. Depending on the study by Lameire there is no significant risk between using new or reused membranes for hemodialysis [8]. But depending on the data obtained in our experiments the reuse issue with high flux membranes is still a question that has to be further investigated.

References

1. Ahrenholz P,, Tiess M. (2002) Removal characteristics of synthetic high flux dialyzers in pre- and postdilution hemodiafiltration. J Am Soc.Neph.;13:239-240
2. Woods HF, Nandakumar M. (2000) Improved outcome for hemodialysis patients treated with high flux membranes. Nephrol Dial Transplant; 15:36-42

3. Port F, Wolfe R (2001) Mortality risk by hemodialyzer reuse practice and dialyzer membrane characteristics; results from the usrds dialysis morbidity and mortality study. Am J Kidney Dis ;37;276-86
4. Konduk BA, Ucisik AH. (2002) A study on the characterization and biostability of used and virgin dialysis membranes and biocompatibility of composite biomaterials. Aust. Ceram. Soc;37:63-82.
5. Zhang Y, Wang PN. (2002) Weibull analysis of the tensile behavior of fibers with geometrical irregularities. J. Mat. Sci ;37:1401 – 1406
6. Murthy NS. Recent developments in polymer characterization using x-ray diffraction (2004) Rigaku J;21-1:15-24
7. Xrd Basics at http://epswww.unm.edu/xrd/xrdbasics.pdf
8. Lameire N. Management of the hemodialysis patient: A European perspective. Blood Purif. ;20:93-102.

Author: M. Emin Aksoy
Institute: Istanbul City Health Management
Street: Peykhane cad. No.10 34400
City: Istanbul
Country: Turkey
Email: dreminaksoy@gmail.com

Estimation of Blood Glucose Level by Sixth order Polynomial

S. Shanthi[1], Dr. D. Kumar[2]

[1] Asst. Prof, Department of ECE, J.J. College of Engineering and Tech, Tiruchirappalli, Tamilnadu, India
[2] Prof & Head, Department of ECE, Periyaar Maniammai University,Vallam,Tanjore, Tamil nadu, India ,613 403

Abstract — **An accurate method of blood glucose measurement for Diabetes patients is presented in this paper. The people affected with Diabetes Mellitus use Glucometers for measuring their blood glucose level. The present days Glucometers use the principle of Reflective Colorimetry for calculating the Glucose concentration in the capillary blood applied over the Test Strips. This measurement has an accuracy of plus or minus 20 variations. This variation could be reduced if we apply the Sixth order polynomial for conversion of glucose concentration in the capillary blood into current value which is shown in the display unit of Glucometer. The analysis of Blood Glucose is very important in self monitoring, since by proper monitoring and control , we can delay the onset and slow down the progressing of Diabetes complications. Recent clinical studies have shown the correlation between the glucose variability and the long-term diabetes related complications. The method proposed in this paper has been validated with simulated datas and tested with success in the retrospective analysis of real patient's data sets. The feasibility of this method to normalize blood glucose concentrations is demonstrated.**

Keywords — **Estimation of blood glucose level, Glucometers, Reflective Colorimetry, Polynomial Equations**

I. Introduction

Diabetes Mellitus is a disorder of carbohydrate metabolism, usually occurring in genetically predisposed individuals, characterized by inadequate production or utilization of insulin and resulting in excessive amounts of glucose in the blood and urine, excessive thirst, weight loss, and in some cases progressive destruction of small blood vessels leading to such complications as infections and gangrene of the limbs or blindness. It is a disorder of the metabolism characterized by the inability of the pancreas to secrete sufficient insulin which plays a key role in regulating glucose level in blood stream. The complications could be reduced by proper monitoring and control of blood glucose level (BGL). People use Glucometers for this monitoring of BGL.

II. Self monitoring blood glucometers

Multilayer thin film dry technology is adopted in most of the handheld Glucometers. A Colorimeter slide as shown in

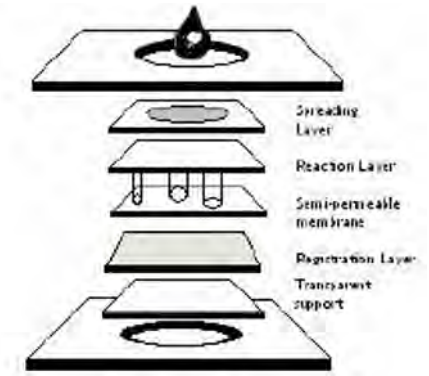


Fig 1: Colorimeter Dry Slide

Figure.1 comprises several layers coated on transparent plastic support. The sample is applied to the top of the spreading layer. This ensures uniform dispersion. It is also a micro filter, removing small particulate material and large molecules, such as proteins. It also contains a white diffuse reactant which acts as a reflecting medium during colorimetry made through the transparent support.

Various underlying layers have different functions. They include a reaction layer which usually contains an enzyme catalyst and a registration layer where colored dye is formed in proportion to the analyte concentration. The color density is measured by a reflection spectrometer. Other layers may include physical barriers such as semi permeable membranes and scavenger layers which chemically alter potentially interfering endogenous substances. Interferences are thus minimized.[4-5]

For each test a mathematical function is stored in the analyzer's central processor. It is used to convert the dye density into analyte concentration. The function is a third degree polynomial. Its three coefficients are determined during calibration.[6]

III. Problem definition

These glucometer readings do have a variation of plus or minus 20 from the actual value. The polynomial equations of higher orders (Sixth order) give better, accurate and quicker results compared to lower order polynomials (Third order).

Chwee Teck Lim, James C.H. Goh (Eds.): ICBME 2008, Proceedings 23, pp. 1466–1468, 2009
www.springerlink.com

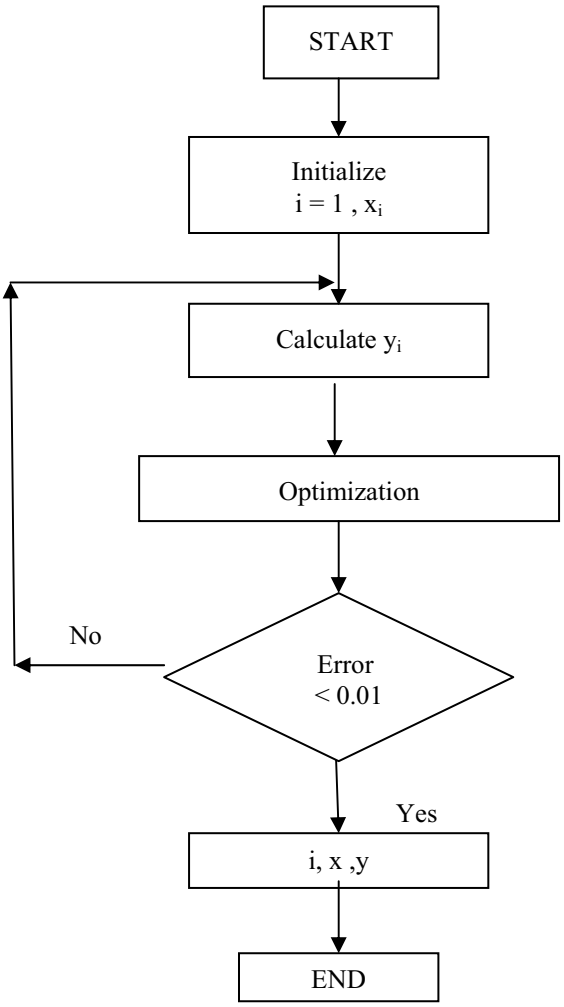


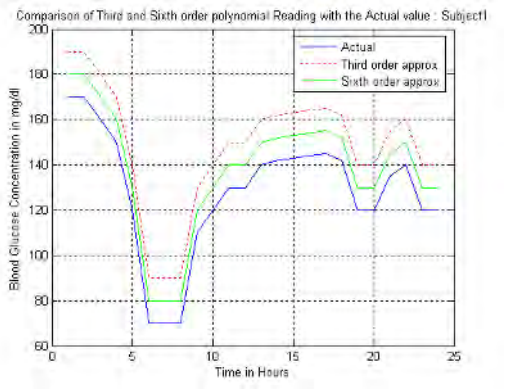
Fig. 2: Flow chart to calculate y

A. Methodology

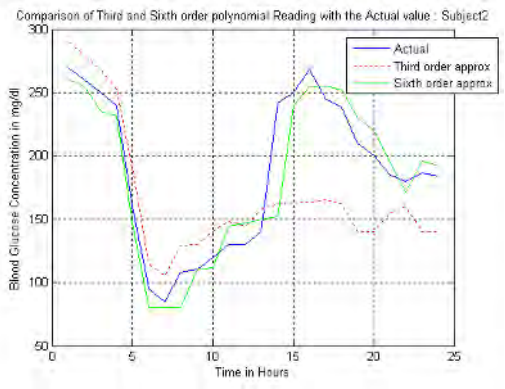
The formulas of a predictive model have normally been used only for calculating the future values of predicted variables. The polynomial theory proposes to use predictive polynomials as the basic means for the general investigation of dynamic system. The polynomial theory enable us to obtain polynomial description of a component by observing their inputs and outputs during a comparatively short time. The polynomial description does not require any information about initial condition.

For measuring the concentration of Blood Glucose, the Saturation(x) values obtained for various known concentrations of Glucose (y) are fit into an m^{th} order polynomial equation.[6]

$$y = a_m x^m + a_{m-1} x^{m-1} + \ldots\ldots + a_2 x^2 + a_1 x + a_0$$



(a)



(b)

Fig. 3: Comparison of actual values with 3rd and 6'th order polynomial for two (a and b) different subjects

From this equation, (m+1) simultaneous equations will be generated. Solving these (m+1) simultaneous equations using Cramer's rule, the value of the unknowns a_m to a_0 can be calculated.

This polynomial equation is suitable for non linear responses also. Once this polynomial equation is ready then the saturation (x) of the unknown Glucose concentrated assay can be substituted and the unknown Glucose concentration (y) can be estimated. Calculation of y is given in flow chart as shown in figure 2.

B. Results

A third order polynomial equation and a sixth order polynomial equation have been taken and are used to estimate the Blood Glucose level of two subjects for a 24 hour day. The readings have been compared with the actual laboratory measurement value.

The reading obtained from the sixth order polynomial has a lesser variation than that of the third order polynomial

from the actual value. The error is less than plus or minus 10.

These observations have been simulated using the MATLAB.

IV. Conclusion

We perceive that this system will prove useful when integrated into whole body glucose homeostasis simulators. The Sixth order polynomial has proved to converge in lesser no of iterations than the Third order polynomial when both are solved by Newton Raphson method.

References

[1] A.Sivanantha Raja, K.Sankaranarayanan: "Use of RGB Color Sensor in Colorimeter for better Clinical measurement of Blood Glucose". BIME Journal, Volume (06), Issue (1), Dec 2006.

[2] Vallera Da, Bissel M G Barron W: "Accuracy of portable Glucose monitoring. Effect of Glucose level and prandial state", Journal of Clinical Pathology, Feb 95(2).

[3] Robbert J Slingerland. Kor Miedema: "Evaluation of portable Glucose meters. Problems and recommendation", Journal of Clinical Pathology, Sep 2003.

[4] Carol Rados: "Safety Alerts on Blood meters ", FDA Consumer, Proquest Science Journals, Volume No.40:2, March / April 2006.

[5] Monika Mehta et al.:"Emerging Technologies in Diabetes Care", U.S Pharmacist,Vol No.27:11,Nov 2002.

[6] IEEE TRANSACTIONS ON BIOMEDICAL ENGINEERING,VOL 54, MAY 2007 Glucose concentration can be predicted ahead in Time From Continuous Glucose monitoring Sensor Time Series .Giovanni Sparacino, Francesca Zanderigo, Stefano Corazza, Alberto Maran, Andrea Facchinetti, and Claudio Cobelli, Fello IEEE

Dirty Surface – Cleaner Cells? Some Observations with a Bio-Assembled Extracellular Matrix

F.C. Loe[1], Y. Peng[1], A. Blocki[1], A. Thomson[2], R.R. Lareu[1,3], M. Raghunath[4]

[1] Tissue Modulation Laboratory, Division of Bioengineering, National University of Singapore, Singapore
[2] Genome Institute of Singapore, Singapore
[3] NUS Tissue Engineering Program and Department of Orthopaedic Surgery, Yong Loo Lin School of Medicine, National University of Singapore, Singapore
[4] Department of Biochemistry, Yong Loo Lin School of Medicine, National University of Singapore, Singapore

Abstract — **Conventional human mesenchymal stem cells (hMSC) cultures are carried out on tissue culture polystyrene (TCPS) surfaces while human embryonic stem (hES) cells are normally propagated on feeder layers or Matrigel™. However, TCPS culture of MSCs lead to senescence [1] and decreased self-renewal [2, 3]; while hES cells cultured on xenogenic feeder layers or Matrigel™ express immunogen which presents a xenogenic risk thus hampering transplantion [4]. Culture of MSCs on TCPS does not emulate the natural stem cell microenvironment, which consists of soluble factors, neighbouring cells and extracellular matrix. The extracellular matrix (ECM) is a complex supramolecular assembly of various proteins, some of which binds growth factors like FGF-2 and TGFβ1 [5]. We have directed ECM deposition by human fibroblasts through application of excluded volume effect (EVE) [6, 7] followed by detergent lysis to achieve a cell-free matrix. The matrix obtained contained proteins such as collagens, fibronectin, glycoproteins, proteoglycans and growth factors, FGF-2 and TGFβ1. Proteins within the matrix were analysed by gel electrophoresis, and the protein profile obtained highlighted its complexity. Matrix propagation was observed to enhance the proliferation rate of hMSCs, resulting in more cells in a shorter time compared to TCPS controls. In addition, hMSCs pre-cultured on matrix prior to adipogenesis showed increased differentiation compared to TCPS control based on flow cytometry and adherent cytometry , indicating better retention of differentiation capabilities despite long term culture. The population doubling rate of hES cells cultured on matrix surpassed those on feeder-free culture on Matrigel™ in defined culture medium in just 3 weeks, while maintaining similar expression of pluripotency marker Oct4 as Matrigel controls. In conclusion, we demonstrate that the application of EVE to obtain a collagen-rich fibroblasts layer followed by detergent lysis results in a cell-rich matrix rich in diverse proteins. Culture of hMSCs on such a matrix increases their proliferation rate while still retaining differentiation potential. hES cells grown on matrix also proliferated faster with retention of stem cell markers.**

Keywords — **Extracellular matrix, macromolecular crowding, mesenchymal stem cell, human embryonic stem cell**

I. Introduction

Complex cell–ECM interactions play an integral role in modulating stem cell development and function *in vivo* by providing signals via growth factors and integrin interactions. However, current culture practices neglect this aspect. hMSCs extensively propagated on TCPS show a more differentiated progeny with reduced capacity for self-renewal [1-3]; while hES cells are cultured on mouse embryonic fibroblasts (MEFs) or murine Matrigel with MEF-conditioned medium which introduce a xenogenic threat [4]. Such culture conditions result in progressive loss in the ability of stem cells to differentiate into multiple lineages. Cells present in the initial culture undergo unsymmetrical division during expansion to produce a vast progeny of committed and differentiated daughter cells which progressively dilutes the original stem cell population, resulting in a heterogeneous population [8].

In view of this, such imperfect systems could be replaced by development of an ECM made by human fibroblasts, the professional ECM producer. We hypothesize that the application of such an *in vitro* human derived bio-assembled matrix could recapitulate these interactions *in vitro* thus providing a more physiologically relevant environment to (i) retain multipotentiality of human mesenchymal stem cells by delaying senescence during extensive *ex vivo* expansion and (ii) sustain growth and maintain pluripotency of human embryonic stem cells (hES). The ability to engineer such a specialized microenvironment would be of great benefit for tissue engineering applications involving stem cells.

To generate our bio-assembled ECMs, we applied macromolecular crowding on human fibroblasts culture with Dextran Sulfate 500kDa (DxS) which has been shown to enhance deposition of collagen I and fibronectin in aggregates [6,7]. To render the ECM cell-free, *in situ* detergent (sodium deoxycholate; DOC) lysis was employed to remove the fibroblasts without complete solubilization of the ECM proteins.

In our study, we focused on characterizing the composition of our decellularised matrix and the effect of propagat-

Chwee Teck Lim, James C.H. Goh (Eds.): ICBME 2008, Proceedings 23, pp. 1469–1472, 2009
www.springerlink.com

ing the two types of human stem cells – human embryonic stem cells (hES) and mesenchymal stem cells (hMSCs) on matrix, in comparison to their regular systems.

II. Materials and methods

A. Generating Bio-assembled Matrices

Embryonic lung fibroblasts, WI-38 (CCL-75) obtained from American Type Culture Collection were routinely cultured up to passage 22 in Dulbecco's Modified Eagle Medium supplemented with 10% fetal bovine serum which was changed every 3-4 days. At confluency, fibroblasts were seeded at a ~25,000 cells/cm^2 in either 24- or 6-well culture plates. After 24 hours, adhered cells were supplemented with 0.5% fetal bovine serum and 30μg/ml of L-ascorbic acid, with or without 500kDa Dextran Sulfate (USB; DxS) at 100μg/ml. After 3 days incubation, cell layers were lysed with 0.5% DOC to remove cellular components.

B. Characterising Bio-assembled Matrices

Immunostaining for ECM and cellular components: Immunofluorescence was used to detect retained key ECM proteins- Collagen I and fibronectin; and also to verify the complete removal of cellular debris – nuclei, endoplasmic reticulum (ER) and the F-actin filaments. Briefly, monolayers were fixed with 4% methanol-free formaldehyde for 15mins at 37°C, permeabilized with 0.2% Triton X-100 then blocked with 10% normal goat serum in PBS. Col I was detected by mouse anti-human collagen I (1:1000); fibronectin was stained by rabbit anti-human fibronectin (1:100); F-actin filaments were stained using AlexaFluor 594 phalloidin (50U/ml); ER was stained by mouse anti-protein disulfide isomerase (1:1000) while cell nuclei were counterstained with DAPI. Images were captured with an IX71 inverted fluorescence microscope (Olympus).

SDS-PAGE quantitation of Col 1 retained in matrices: Soluble procollagen was removed together with culture medium while intact cell layers and DOC-lysed matrices were pepsin-treated (0.25mg/ml; Roche) to isolate collagens. Digested samples were separated by SDS-PAGE and the protein bands were quantified by silver-staining and densitometry.

C. Matrix propagation of stem cells

Human embryonic stem cells (hES): (WiCell Research Institute, WA09) received at passage 49 were adapted to mTeSR1 culture medium (StemCell Tech). For propagation, cells were passaged every 5-7 days using 1mg/ml collagenase in Dulbecco's Modified Eagle Medium – Nutrient Mixture F-12 and reseeded onto 6-well plates coated with either matrix or Matrigel as a control. Medium was changed daily. During subsequent passages, respective hES cells were seeded onto fresh matrices. For cell counting at every passage, 3 replicate wells of a 24-well plate were plated in parallel and resuspended with TrypLE to obtain single – cell suspensions.

Human Mesenchymal Stem Cells (hMSCs) were obtained commercially (Cambrex) at passage 2 and propagated in low glucose Dulbecco's modified Eagle's medium (Gibco) supplemented with Glutamax and 10% fetal bovine serum on either 100mm regular tissue culture polystyrene plates (TCPS) or matrix-coated TCPS plates (Matrix). After 4 passages, hMSCs were trypsinised, reseeded into 24-well TCPS plates (50,000/well) and adipogenically induced with the addition of 3-Isobutyl-1-methylxanthine (0.5 mM), dexamethasone (10^{-7}M) and indomethacine (0.2 mM) in high glucose Dulbecco's modified Eagle's medium (HG DMEM, Gibco-BRL) supplemented with 10% fetal bovine serum [9].

D. Characterizing hMSCs post matrix-propagation

hMSC growth kinetics: hMSCs seeded at 350,000 per 100mm plates (BD) ± matrix were passaged at confluence (~7-10 days) using Collagenase IV (0.5mg/ml) followed by 0.5% trypsin/1mM EDTA; viability was assessed by trypan blue exclusion prior to hemocytometer counting. Cells are then re-seeded at 350,000/plate and allowed to re-grow to confluence. Population doubling was calculated based on the increase in number of cells at confluence as a measure of time to attain confluence.

Nile Red Adherent Cytometry: Mature adipocytes are characterized by cytoplasmic lipid droplets detected by the lipophilic dye, Nile red. Briefly, monolayers in 24-well plates were rinsed with PBS, fixed in 2.5% paraformaldehyde (PFA) then co-stained with Nile red (0.05mg/ml in PBS; 1hr) and DAPI (0.5μg/ml; 30min). Fluorescence was accessed in a montage of 9 sites within each well (Metamorph); absolute amount of lipid droplets in each well was quantified from thresholded fluorescent events and normalized to cell number based in DAPI fluorescence. End data correspond to total amount of lipid droplets present per well relative to cell number.

Nile Red FACS: Monolayers were washed twice in PBS, trypsinized then resuspended in 350ul of Nile red (0.05mg/ml in PBS) for 15min followed by the addition of 150ul of 0.5% PFA. Fluorescent events were detected using a FACScan flow cytometer (BD).

E. Characterizing hES cells post matrix-propagation

OCT-4 Flow Cytometry (FACS): hES cells were trypsinized to obtain single-cell suspensions and fixed with 4% methanol-free formaldehyde at 37°C for 15 mins. Samples were immunostained with goat anti-Oct4 (Santa Cruz), AlexaFluor 488 chicken anti-goat (Molecular Probes) and DAPI. Flow cytometry was done on a CyAn ADP High-Performance Flow Cytometer (Dako cytomation).

III. Results

A. Characterizing Bioassembled matrices

Immunofluorescence co-staining of matrices for Collagen I, Fibronectin, DAPI, phalloidin and actin confirmed that lysis had retained extracellular matrix proteins while completely removing intracellular structure (data not shown). To determine the retention of Collagen I, densitometry on SDS-PAGE of pepsin digests of intact cell layers and lysed matrices was performed. By comparing the densities of collagen α1(I) bands, we observed that DOC treatment of DxS-crowded matrix retained about 20% of the collagenous material compared to the cell layer samples (Fig.1).

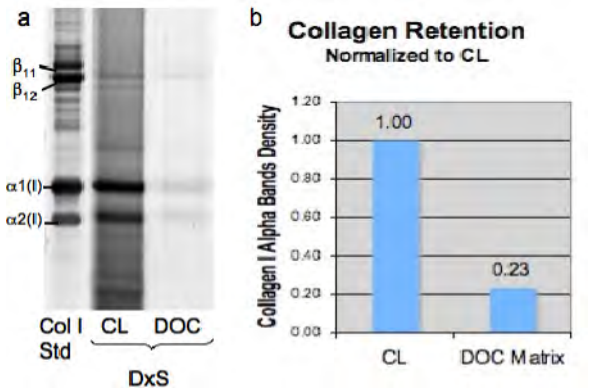


Fig. 1 Treatment with DxS yields more insoluble collagen I deposited on the cell layer by fibroblasts. (a) SDS-PAGE (b) Densitometry analysis of collagen I alpha bands

B. Matrix enhanced proliferation of hMSCs

hMSC growth kinetics during expansion was investigated over 58 days, where cumulative cell doublings of the populations were plotted against time in culture. It was observed that hMSC on plates without matrix (TCPS) had a cumulative population doubling of 11.9 while those on matrix had attained nearly double that, at 20.3 population doublings (Fig.2).

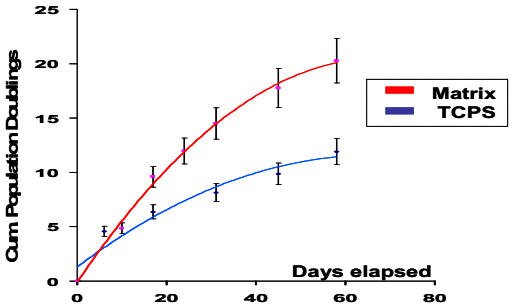


Fig. 2 hMSC growth kinetics with propagation on either TCPS or Matrix for 58 days.

C. Pre-propagation on matrix enhanced adipogenic differentiation of hMSCs

The effect of pre-propagation on either TCPS or matrix for 4 passages prior to hMSC adipogenesis was examined via Nile Red adherent cytometry and FACS. We observed that with pre-propagation on matrix, cytoplasmic lipid accumulation increased from 18.9% to 22% (Fig.3).

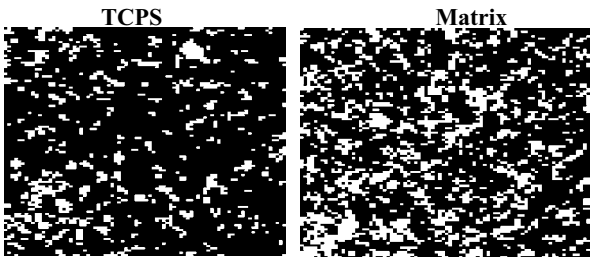


Fig. 3 Nile Red stained adipocytes post-propagation on either TCPS or matrix, white patches indicates lipid droplets. (2x)

Flow cytometry also demonstrated that pre-propagation on matrix increased the percentage of the population that differentiated from 12.47% to 22.9% (Fig.4), in agreement with adherent cytometry.

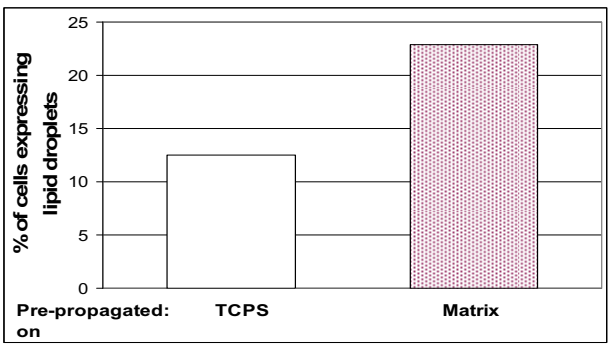


Fig. 4 Flow cytometry of nile red stained adipocytes post-propagation on either TCPS or matrix.

D. Matrix restrains hES spontaneous differentiation

To analyze for spontaneous differentiation, hES cells were stained for the pluripotency marker, Oct-4, then analyzed by FACS and immunostaining. We observed from FACS that there was a dramatic increase in the number of hES cells expressing Oct-4 on matrix compared to matrigel control (17.81million versus 3.88 million; Fig. 4). This is also reflected in OCT-4 immunostaining of hES colonies after 2 weeks of propagation (data not shown).

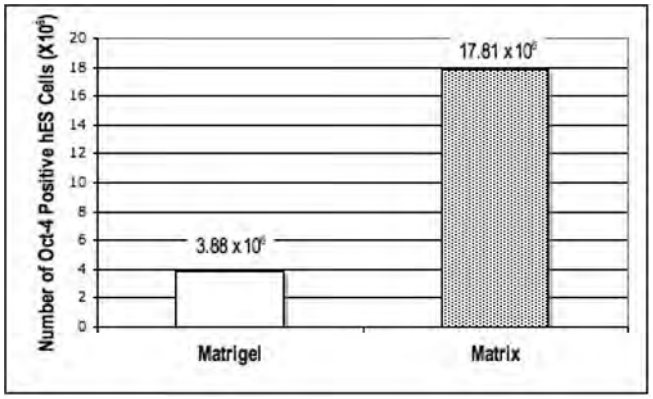


Fig. 5 Flow Cytometry of hES cells propagated on either Matrigel or matrix immunostained for Oct-4.

IV. Discussion

Current culture systems inadequately sustain stem cell self-renewal during expansion, this presents a major bottleneck in the downstream use of these stem cells for translational tissue engineering where large numbers of cells still capable of differentiating into multiple lineages are required. We hypothesize that this is due to the absence of complex cell-ECM signals which are present *in vivo*. To tackle this issue, we have introduced the use of a human derived bio-assembled matrix to recapitulate these physiological signals *in vitro*. We demonstrate that our bio-assembled matrix retains the key ECM proteins, collagen I and fibronectin, in their native forms. The propagation of hMSCs on this matrix was shown to substantially increase their population doubling rate compared to the current expansion system, while pre-propagation on matrix prior to adipogenic induction was observed to retain a greater differentiation capability. Similarly, propagation on matrix substantially increased population doubling for hES cells but this exceptional increase in proliferation did not result in a proportionate increase in spontaneous differentiation based on percentage of cells still expressing the pluripotency marker OCT-4. This indicates that the hES cells on matrix were obtained through self-renewal rather than differentiation into daughter cells. The results obtained will lay the foundation for the further development of improved *ex vivo* stem cell culture systems based on a bio-assembled matrix for translational tissue engineering, enabling the expansion of stem cells in a manner that is based on symmetric self-renewal thus reducing heterogeneity and retaining differentiation capacity.

References

1. Banfi A, Muraglia A, Dozin B, et al. Proliferation kinetics and differentiation potential of ex vivo expanded human bone marrow stromal cells: Implications for their use in cell *therapy Exp Hematol.* **28**,707-71, 2000.
2. DiGirolamo CM, Stokes D, Colter D et al. Propagation and senescence of human marrow stromal cells in culture: A simple colony-forming assay identifies samples with the greatest potential to propagate and differentiate. *Br. J. Haematol*. **107**, 275–281, 1999.
3. Baksh D Song L, Tuan RS. Adult mesenchymal stem cells: characterization, differentiation, and application in cell and gene therapy. *J Cell Mol Med* **8**,301-316, 2004.
4. Martin MJ, Muotri A, Gage F, Varki A. Human embryonic stem cells express an immunogenic nonhuman sialic acid. *Nat Med.* **11(2),**228-32, 2005.
5. Raghunath M, Unsöld C, Kubitscheck U, Bruckner-Tuderman L, Peters R, Meuli M. The cutaneous microfibrillar apparatus contains latent transforming growth factor-beta binding protein-1 (LTBP-1) and is a repository for latent TGF-beta1. *J Invest Dermatol*. **111(4),** 559-64, 1998.
6. Lareu RR, Arsianti I, Subramhanya KH, Peng YX, Raghunath M. In vitro enhancement of collagen matrix formation and crosslinking for applications in tissue engineering –a preliminary study. *Tissue Eng.* **13**, 385–391, 2007.
7. Lareu RR, Subramhanya KH, Peng Y, Benny P, Chen C, Wang Z, Rajagopalan R, Raghunath M. Collagen matrix deposition is dramatically enhanced in vitro when crowded with charged macromolecules: the biological relevance of the excluded volume effect. *FEBS Lett.* **581**, 2709-14, 2007.
8. Bruder SP, Jaiswal N, Haynesworth SE. (1997) Growth kinetics, self-renewal, and the osteogenic potential of purified human mesenchymal stem cells during extensive subcultivation and following cryopreservation. J Cell Biochem. **64**:278-94.
9. Pittenger MF, Mackay AM, Beck SC, Jaiswal RK, Douglas R, Mosca JD, Moorman MA, Simonetti DW, Craig S, Marshak DR (1999) Multilineage potential of adult human mesenchymal stem cells. Science **284**:143-7.

Quantitative Immunocytochemistry (QICC)-Based Approach for Antifibrotic Drug Testing *in vitro*

Wang Zhibo[1], Tan Khim Nyang[1] and Raghunath Michael[1,2]

[1] Tissue Modulation Laboratory, Division of Bioengineering, Faculty of Engineering, NUS
[2] Department of Biochemistry, Yong Loo Lin School of Medicine, NUS

Abstract — **Aim: Chemicals that can reduce extracellular collagen accumulation and inhibit the transdifferentation of fibroblast into myofibroblasts marked by expression of α-SMA (α-smooth muscle actin) will be promising antifibrotic drugs. We developed a QICC-based approach using microplate-reader to quantify the deposited collagen and α-SMA for antifibrotic drug testing. Methodology: Fibroblasts IMR-90 were cultured under standard and EVE (excluded-volume effect) conditions. "Footprints" were revealed by removing cells with detergent. TSA (trichostatin A) with or w/o TGF-β1 or CPX (ciclopirox olamine) was added under EVE conditions. Collagen I and α-SMA were labeled by immunocytochemistry. The fluorescence signal was quantified by BMG PHERAstar with a focusing lens system. Biochemical evaluation of collagen production served as a benchmark. Results: The QICC-based assay detected 7-fold enhanced collagen deposition under EVE condition and "footprints" was 40% of total collagen matrix, well comparable with that of biochemical assay. Dose-dependent inhibition of TGF-β1-induced collagen production and α-SMA expression by TSA and 90% decrease of collagen production by CPX were successfully detected by QICC-based approach. Conclusion: We have shown, for the first time, the feasibility of QICC-based approach using microplate-reader to quantify collagen deposition and α-SMA *in vitro*, thus enabling screening for candidate drugs that are likely to prevent scarring.**

Keywords — **Quantitative immunocytochemistry, fibroblasts, antifibrosis, collagen, α-SMA**

I. Introduction

Excessive accumulation of collagen in extracellular matrix and contractile myofibroblasts trans-differentiated from fibroblasts are two hallmarks of fibrotic diseases and peri-implantational fibrosis [1, 2]. Peri-implantational fibrosis is the end stage of foreign body reaction generated by host to implants. Fibrosis can severely impair organ function and compromise the performance of implants. Chemicals can reduce collagen accumulation and/or inhibit the transdifferentiation of fibroblast into myofibroblasts will be promising antifibrotic drugs.

Quantification of the deposited collagen and/or expression of α-SMA is the essential technique for potential antifibrotic drug testing. However, current methods for collagen quantification, such as amino acid analysis, hydroxyproline determination or radioactive labeling and Sircol™ dye assay, are labor and time-consuming without type-sorting. Immunoblot for collagen and α-SMA fail to retrieve morphology information.

Moreover, current methods measure procollagen in medium or intracellularly due to the tardy enzymatic processing of procollagen into collagen by N- and C-propeptidases in standard cell culture condition. Our group has accelerated collagen deposition by EVE [3]. Here, we developed a QICC-based approach using PHERAstar microplate-reader with a focusing lens system to quantify collagen matrix and α-SMA *in vitro*. The antifibrotic potential of Histone deactylases inhibitor TSA was investigated in fibroblast cultures under EVE conditions.

II. Methods

A. Cell culture and treatment

Lung Human embryonic lung fibroblasts IMR-90 (10, 000/well) were cultured in 96-well plate (Greiner Bio-one Lumox™) in 0.5% FBS DMEM under standard and EVE conditions (100μg/ml DxS) which was described in [3]. Different concentrations of TSA with or w/o TGF-β1 (5ng/ml) were added to IMR-90 cultured under EVE conditions.

B. QICC

Prior to ICC, "footprints' were revealed by lysing the cells with 0.5% sodium deoxycholate (w/v). ICC was done by adding mouse monoclonal anti-collagen type I antibody (Sigma) or mouse monoclonal anti-α-SMA (Dako) as the primary antibody, followed by Alexa Fluor 594 (AF594) goat anti-mouse antibody (Invitrogen) as the secondary antibody. The fluorescent stain 4', 6-diamidino-2-phenylindole (DAPI) (Invitrogen) was used to visualize nuclei. The fluorescence intensity (FI) of the AF594 dye as well as that of DAPI was quantified by PHERAstar microplate reader with a focusing lens system (BMG LABTECH). The ratio of FI of AF 594 to FI of DAPI was used to represent collagen deposition or α-SMA per cell.

Chwee Teck Lim, James C.H. Goh (Eds.): ICBME 2008, Proceedings 23, pp. 1473–1475, 2009
www.springerlink.com

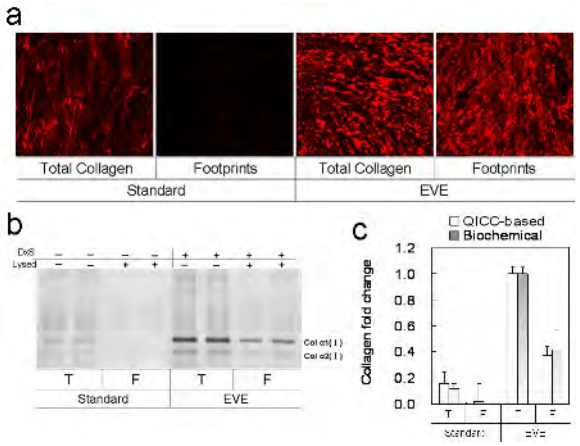


Fig.1 Total collagen deposition and "footprints" were quantified by QICC-based approach and biochemical assay. (a) Representative pictures of deposited Col (I) from QICC-based assay (b) Representative SDS-PAGE from biochemical assay. (c) Comparison of collagen deposition fold changes between two approaches.

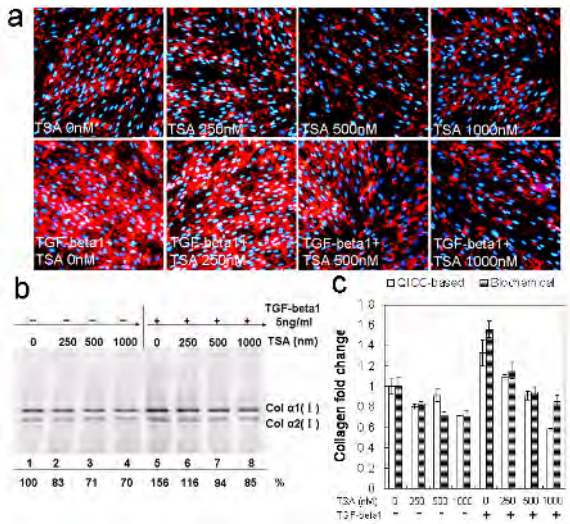


Fig.2 Antifibrogenesis effect of TSA was detected and visualized by QICC and biochemical assay. (a) Representative pictures from QICC-based approach (b) Representative gel from 3 independent experiments. The quantification result from QICC-based approach (c) Comparison of collagen fold changes between two approaches.

Quantitative biochemical evaluation of collagen production was done by pepsin digestion followed by SDS-PAGE. Collagen bands were visualized by silver staining (Silver-Quest, Invitrogen).

III. Results

Around 6-7 folds enhanced total collagen deposition under EVE can be detected by QICC-based approach and the "footprints" were around 40% of total deposited collagen under EVE, which was well-comparable with that of biochemical assay (Fig.1)

Antifibrogenic effect of TSA was quantified by QICC-based approach. TSA can dose-dependently inhibit TGF-β1 induced collagen production. TSA 500nM can bring collagen production to basal level in IMR-90 treated with TGF-β1. TSA alone modified the normal collagen synthesis modestly (Fig.2).

Dose-dependent inhibitory effect of TSA on TGF-β1 induced α-SMA expression was quantified by QICC-based approach. TGF-β1 induced the expression of α-SMA which is a marker of myofibroblasts to 5-6 folds. The expression of α-SMA was inhibited by an increasing concentration of TSA (Fig.3).

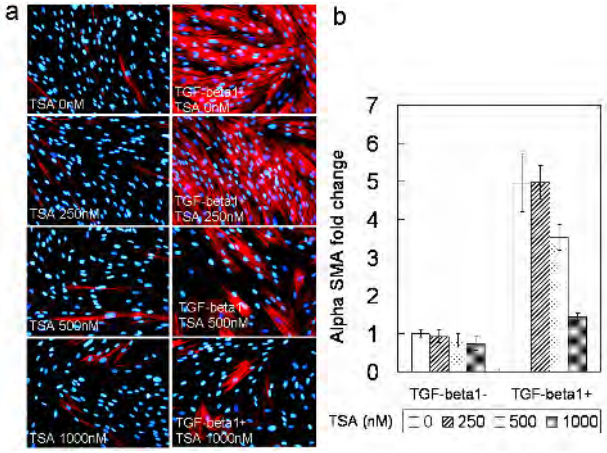


Fig.3 Dose-dependent inhibition of TGF-β1 induced α-SMA by TSA was detected by QICC-based approach. (a) Representative pictures of α-SMA expression (b) α-SMA expression fold changes.

IV. Conclusions

We have shown, for the first time, the feasibility of QICC-based approach using microplate-reader to quantify collagen deposition and α-SMA *in vitro*, thus enabling screening for candidate drugs that are likely to prevent scarring.

Acknowledgment

We thank the NUS Tissue Engineering Program (NUSTEP) for the help and support for this study.

REFERENCES

1. Ratner BD, Bryant SJ. (2004) Biomaterials: where we have been and where we are going. Annu Rev Biomed Eng 6:41-75.
2. Tuan TL, Nichter LS. (1998) The molecular basis of keloid and hypertrophic scar formation. Mol Med Today 4:19-24
3. Lareu RR, Arsianti I, Subramhanya HK, Peng YX, Raghunath M. (2007)In vitro Enhancement of Collagen Matrix Formation and Crosslinking for Applications in Tissue Engineering: A Preliminary Study. Tissue Eng 13, 385-391.

Author: Wang Zhibo
Institute: National University of Singapore
Street: 27, Kent Ridge, Medical drive
City: Singapore
Country: Singapore
Email: g0500817@nus.edu.sg

Fusion Performance of a Bioresorbable Cage Used In Porcine Model of Anterior Lumbar Interbody Fusion

A.S. Abbah[1], C.X.F. Lam[2], K. Yang[1], J.C.H. Goh[1], D.W. Hutmacher[3], H.K. Wong[1]

[1] Department of Orthopaedic Surgery, National University of Singapore, Singapore
[2] Division of Bioengineering, National University of Singapore
[3] Division of Regenerative Medicine, Queensland University of Technology Australia

Abstract — **The use of metallic fusion cages in lumbar interbody fusion is often associated with serious complications including implant subsidence and corrosion. A bioresorbable scaffold with distinct architectural design has recently been fabricated from medical grade polycaprolactone and beta-tricalcium phosphate (mPCL-TCP) for bone tissue engineering at weight bearing sites. Porous mPCL-TCP scaffolds demonstrate mechanical and biological properties comparable to cancellous bone and have been shown to enhance new bone formation at ectopic and cranio-facial sites. In this study, we evaluated the fusion performance of mPCL-TCP implants in a porcine model of anterior interbody lumbar fusion (ALIF). Twenty two pigs underwent a two-level (L3/4 and L4/5) ALF surgery in four experimental groups namely, standalone scaffolds, scaffolds + stem cells, scaffolds + rhBMP-2 and bone autograft. Results indicate a significant enhancement in stiffness of motion segments implanted with scaffolds + rhBMP-2 compared to other groups including autografts as early as three months ($p<0.01$). A trend of increasing mineralization was also observed over six months with significant bone ingrowth in scaffolds loaded with rhBMP-2 as well as stem cells compared to standalone scaffolds ($p<0.05$). Finally, accurate radiographic assessment was not hampered by this radiolucent scaffold on follow-up. This is the first time that mTCP-PCL has been used as a fusion cage in a large animal, weight bearing condition for bone healing.**

Keywords — **bone tissue engineering, spinal reconstruction, scaffold design, bone morphogenetic protein, stem cells**

I. Introduction

Low back pain is a common problem in many clinics around the world. In one study, low back pain was reported to represent more than half of the musculoskeletal impairments reported in the USA annually [1]. When conservative treatment fails, a vast majority of these patients require spinal fusion (arthrodesis) with over 200,000 procedures performed annually in the USA alone.

The gold standard procedure for spinal arthrodesis involves the use of metallic fusion cages packed with moserlized autologous bone grafts harvested at time of surgery. There are several problems associated with both the harvesting of autogenous bone [2] and the implantation of metallic devices [3]. Donor site morbidities such as chronic pain and visceral hernia as well as difficulties with radiographic assessment due to metallic interference are some of the common drawbacks in addition to cage subsidence or outright implant migration. To overcome some of the shortcomings of current techniques, allograft bone materials have been used as an alternative to autograft bone. However, the inherent risk of disease transfer and rejection remarkably limit the use of fresh frozen allografts [4].

The evolution of bone tissue engineering has stimulated the development of "tailor made" bioresorbable implant materials capable of significantly enhancing repair and regeneration at bone healing sites. Bioabsorbable fusion cages (biocage) offer many distinct advantages over conventional metallic fusion cages including biological and mechanical compatibility with host bone [3]. Furthermore, polymer cages could act as delivery systems for potent growth factors and osteogenic cells thus abrogating the need for autogenous bone graft incorporation.

Despite these and other stated advantages, the use of biocages in spinal reconstructive surgery has been limited because of the need to tailor cage porosity with adequate mechanical strength required for weight bearing and stabilization of the healing bone ends. Many previous studies have described bioresorbable materials for use in orthopaedic tissue engineering however, many of these materials are fabricated from polymers that leave toxic degradation products and lead to chronic inflammatory reaction that eventually result in failure of joint fusion [3]. In the present study, mPCL-TCP polymer device was implanted into the lumbar intervertebral space of SPF Yorkshire pigs in combination with either bone marrow stem cells (MSCs) or recombinant human bone morphogenetic protein type 2 (rhBMP-2). The main aim of this study was to evaluate the efficacy of the novel mPCL-TCP bioresorbable scaffolds as a fusion cages when used in combination with MSCs and rhBMP-2.

Chwee Teck Lim, James C.H. Goh (Eds.): ICBME 2008, Proceedings 23, pp. 1476–1479, 2009
www.springerlink.com

II. Materials and methods

A. Materials

Bioresorbable scaffolds fabricated from medical grade polycaprolactone and tricalcium phosphate mPCL-TCP (80:20) was from Osteopore International (Singapore) (Fig. 1). The morphological and topological parameters of the scaffolds used are as listed in Table 1. Pedicle screws and rods were purchased from DePuy Orthopaedics, Inc. Winterthur, Switzerland. Recombinant human bone morphogenetic protein-2 (rhBMP-2) was from Medtronic INFUSE® Sofamor Danek. Twenty two male SPF Yorkshire pigs aged 6 months old and weighing 50-60 kg were used in this study. All animal related procedures were in accordance with the principles of laboratory animal care [National Institutes of Health (NIH) publication no. 86-23, revised 1985] and were approved by the institutional review committee on the use of laboratory animals. Animals were randomized into four groups for interbody fusion surgery (L3/4, L4/5) according to implants used viz: 1) standalone bioresorbable scaffolds (n = 6) 2) bioresorbable scaffolds wrapped with autogenous mesenchymal stem cells treated with dexamethasone to differentiate into osteogenic lineage over a 14-day in vitro culture period (n = 6); 3); bioresorbable scaffolds filled with 0.6mg rhBMP-2 (n = 6); 4) autologous iliac crest bone graft (n = 4). Pedicle screws fixation was performed for both levels on all pigs

SCAFFOLD PREPARATION

In order to improve cell-scaffold interaction, the surface of all scaffolds was modified by soaking in 1M sodium hydroxide for 3 hours to enhance their hydrophilicity followed by thorough rinsing in distilled water and drying in an oven at 40^{o}C overnight as described previously [5]. The scaffolds were sterilized in 70% ethanol and lyophilized with bovine collagen (Symatese, France) to enhance biocompatibility and create a mesh structure within the scaffold pores for enhanced cell seeding, attachment and proliferation.

IMPLANTATION PROCEDURE AND FOLLOW UP

Surgeries were performed under strict aseptic conditions. The pigs were anesthetized with ketamine (15mg/kg) and maintained with inhalational anesthesia (halothane). After identification of disc levels of interest, the discs were completely removed, adjacent endplates were decorticated and disc space was distracted using a Casper distractor for insertion of appropriate fusion models. Prophylactic parenteral antibiotics (Ampicillin/Cloxacillin 500mg/500mg) and analgesics (intramuscular injection of ketorolac (1mg/kg) for 3 days) were administered routinely. After surgery, pigs were housed individually. Stock diet and tap water were available *ad libitum*. Daily activity and wound conditions were monitored. At designated time points, animals were sacrificed with an overdose of pentobarbital injected intravenously. Subsequently, the spine segments were harvested from L1 to sacrum, cleaned of excess soft tissues, and functional spine unit of interest were dissected out for freezing at -80 C until examination.

COMPUTED TOMOGRAPIC ANALYSES (μ-CT)

The microstructural morphology of harvested specimen were evaluated using a μ-CT system (Shimadzu, SMX-100 CT, Kyoto Japan). Isotropic slice data obtained by the system were used for 2D image reconstruction employing 3D Studio Max software version 1.2 (Volume Graphics GmBH, Germany). From each section, a 10 X 8 X 2 mm^3 volume of interest (VOI) was selected at implant site. The VOIs were represented in 22 x 22 x22 mm^3 voxels and segmented using an individually optimized density threshold value. These images were further compiled and used to reconstruct 3D images for quantitative bone ingrowth parameters.

MECHANICAL TESTING

After thawing at room temperature overnight, specimen were prepared for mechanical testing as described previously [6]. Soft tissues and facet joints of each harvested motion segment were removed so that only the fusion mass was left connecting the two vertebrae. Following embedding in polymethylmethacrylate (PMMA) bone cement, the segments were tested in flexion and extension, left and right lateral bending and axial rotation at a constant loading rate (1.0°/s) using a servo-hydraulic materials-testing system (MTS 858 MiniBionix, MTS Corp., Eden Prairie, MN).

STATISTICAL ANALYSIS

Data obtained were analyzed by SPSS software package (SPSS, Inc., Chicago, IL). All values are reported as means ± standard deviation (SD). Unpaired *t* tests were used to compare mean values among groups. $P < 0.05$ was considered significant.

III. Results

All segments treated with mPCL-TCP scaffolds loaded with rhBMP-2 showed radiographic fusion at three months as opposed to only 25% of animals receiving autograft bone, (Table 2). At six months, 50% of animals receiving autograft bone showed radiographic fusion. However, animals who had received scaffolds alone as well as those with scaffolds + MSCs did not show any radiographic evidence of fusion even at six months (Fig. 1).

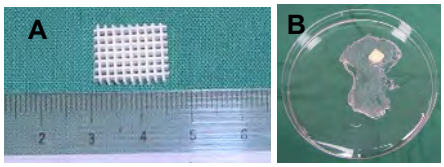


Figure 1: An mPCL-TCP scaffold prior to implantation (A) and (B) *in vitro* differentiated mesenchymal stem cell sheet is wrapped around the scaffold for implantation.

Table 1: Architectural design parameters of mPCL-TCP scaffolds used in bone regeneration at weight bearing sites

Morphology parameter	Value
Pore interconnectivity	100%
Pore size range	350-500μm
Scaffold porosity	65%
Lay-down pattern	0/90°
Cage dimension	15 x 12 x 10˜

Micro-CT analysis revealed significant bone ingrowth in all groups except groups receiving scaffolds alone (Fig. 2 and 3). Over the course of six months, mineralized tissue deposition increased in all groups thus making the scaffold denser.

Table 2: Spine fusion on x-ray assessment. Fusion was observed in all segments receiving rhBMP-2 loaded cages as early as 3 months

Groups	3 m	6 m
Scaffolds	0/6 (0%)	0/6 (0%)
Scaffold + MSCs	0/6 (0%)	0/6 (0%)
Scaffolds + BMP	6/6 (100%)	6/6 (100%)
Autograft	1/4 (25%)	2/4 (50%)

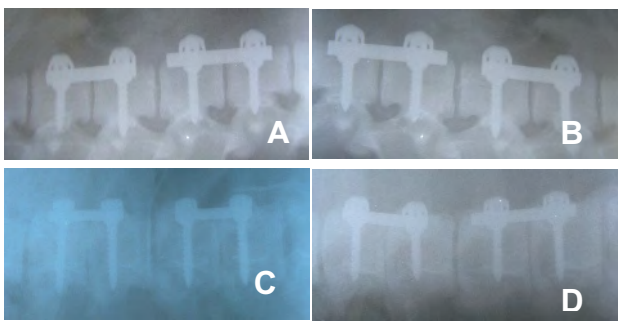


Figure 2: Representative x-ray photographs (lateral view) of segments with scaffold alone (A); scaffolds + MSCs (B); scaffolds + rhBMP-2 (C) and autograft bone (D) at 3 months.

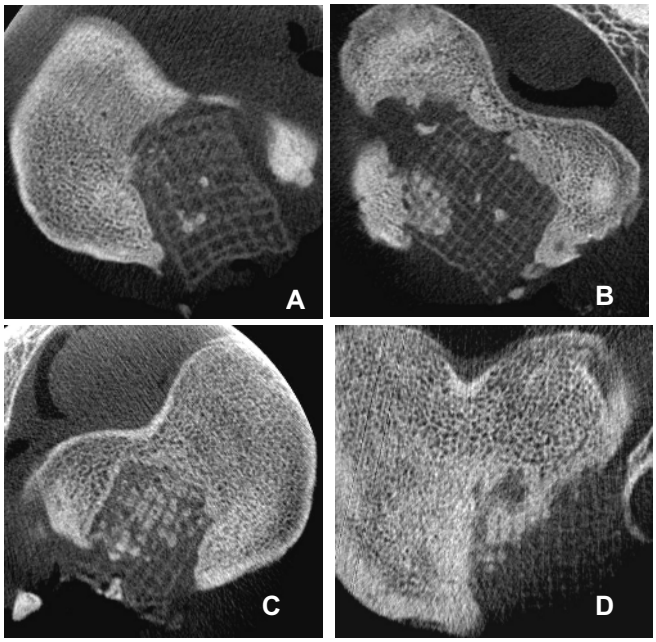


Figure 3: Micro-CT assessment of bone ingrowth after 3 months at implant sites. Notice minimal bone ingrowth among scaffolds alone (A) as compared with improved ingrowth with scaffolds + MSCs (B), scaffolds + rhBMP-2 (C) and autograft bone (D). New bone was laid down in a squared pattern similar to the 0/90° topology of the scaffolds.

Morphometric analysis indicates statistically significant increase in bone ingrowth volume among motion segments treated with bioresorbable mPCL-TCP scaffolds loaded with rhBMP-2 compared to autograft bone ($p<0.05$) as well as standalone scaffolds and scaffold + cells ($p<0.01$) at 3 months (Fig. 4).

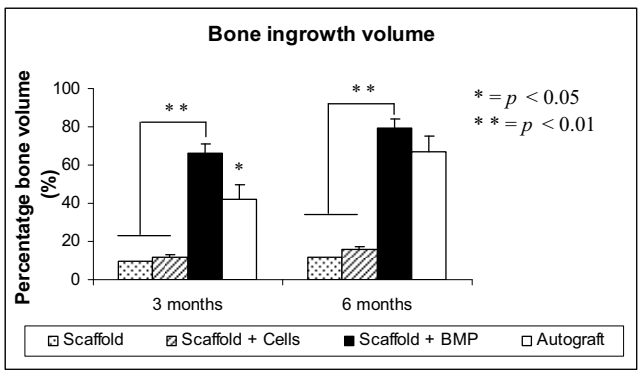


Figure 4: Bone ingrowth at 3 and 6 months into defects created at sites of implantation.

At 6 months this increase in bone volume was not statistically significant between autograft group and scaffold + BMP group.

Similarly, stiffness analysis revealed significantly stiffer motion segments in the group treated with mPCL-TCP scaffolds loaded with rhBMP-2 when compared with cell seeded scaffolds, autograft bone and standalone scaffolds (Fig. 5).

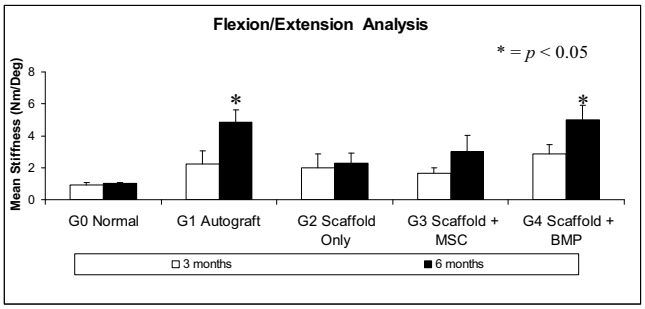


Figure 5: Flexion/extension analysis at 3 and 6 months compared with intact (non-operated) segments to determine fusion.

IV. Discusion

Anterior lumbar interbody fusion (ALIF) represents a challenging micro-environment for bone healing because of the complexity of compressive and torsional forces acting on this site. The need for a stable environment in bone healing has necessitated the use of metallic cages despite the high risk of associated complications [7].

Our results show bone ingrowth as early as three months in mPCL-TCP scaffolds incorporating low dose rhBMP-2 (Fig. 2 and Table 2). Furthermore, radiographic and mechanical fusion was demonstrated in scaffolds receiving rhBMP-2 as compared to intact bone. These findings suggest that the customized mPCL-TCP scaffolds are mechanically and biologically suitable for bone healing at a partial weight bearing site.

Absence of fusion in the standalone scaffold group was to be expected as the influence of an osteoinductive component in tissue engineered constructs has been recognized in several recent studies. The osteoconductivity of mPCL-TCP scaffolds reported in previous study was not sufficient to support fusion at this bone healing site [8]. Failure of early fusion after seeding of in vitro differentiated stem cells could indicate a less than optimal environment in the construct for stem cells after implantation or that the appropriate number of cells had not been implanted. However, the increasing quantity of mineralized tissue formation suggests that prolonged implantation could result in increased new bone formation and that may eventually lead to bone bridging and spine fusion. Moreover, the radiolucent feature of this scaffold offers unobstructed x-ray follow-up assessment.

V. Conclusion

In conclusion, low dose rhBMP-2 loading unto surface modified mPCL-TCP scaffolds promoted early fusion compared to autograft materials in this large animal multi-level anterior lumbar interbody fusion model.

Acknowledgment

This work was supported by a grant from the Biomedical Research Council (BMRC) Singapore.

References

1. McBeth J, Jones K. (2007) Epidemiology of chronic musculoskeletal pain. Best Pract Res Clin Rheumatol. 21:403-425.
2. Arrington ED, Smith WJ, Chambers HG, Bucknell AL, Davino NA. (1996) Complications of iliac crest bone graft harvesting. Clin Orthop Relat Res.329:300-309.
3. Ames CP, Crawford NR, Chamberlain RH, Cornwall GB, Nottmeier E, Sonntag VK. Feasibility of a resorbable anterior cervical graft containment plate. Orthopedics. 2002;25(10 Suppl):s1149-55
4. Ehrler DM, Vaccaro AR. (2000) The use of allograft bone in, lumbar spine surgery. Clin Orthop Relat Res.;371:38-45
5. Rai B, Teoh SH, Ho KH, Hutmacher DW, Cao T, Chen F, Yacob K. (2004) The effect of rhBMP-2 on canine osteoblasts seeded onto 3D bioactive polycaprolactone scaffolds. Biomaterials 25: 5499-5506
6. Kai T, Shao-qing G, Geng-ting D. (2003) In vivo evaluation of bone marrow stromal-derived osteoblasts-porous calcium phosphate ceramic composites as bone graft substitute for lumbar intervertebral spinal fusion. Spine 28:1653-1658
7. Rutherford EE, Tarplett LJ, Davies EM, Harley JM, King LJ. (2007) Lumbar spine fusion and stabilization: hardware, techniques, and imaging appearances, Radiographics. 27:1737-1749
8. Rai B, Oest ME, Dupont KM, Ho KH, Teoh SH, Guldberg RE (2007). Combination of platelet-rich plasma with polycaprolactone-tricalcium phosphate scaffolds for segmental bone defect repair. J Biomed Mater Res A. 81:888-899

Corresponding author:

Author: Professor Wong Hee-Kit
Institute: Department of Orthopaedic Surgery,
Yong Loo Lin School of Medicine,
National University of Singapore
Email: doswhk@nus.edu.sg

Composite PLDLLA/TCP Scaffolds for Bone Engineering: Mechanical and *In Vitro* Evaluations

C.X.F. Lam[1], R. Olkowski[2], W. Swieszkowski[3], K.C. Tan[4], I. Gibson[5], D.W. Hutmacher[1,6,7]

[1] Division of Bioengineering, National University of Singapore, Singapore
[2] Department of Biophysics and Human Physiology, Medical University of Warsaw, Poland
[3] Faculty of Materials Science and Engineering, Warsaw University of Technology, Poland
[4] Temasek Engineering School, Temasek Polytechnic, Singapore
[5] Department of Mechanical Engineering, National University of Singapore, Singapore
[6] Department of Orthopaedic Surgery, National University of Singapore, Singapore
[7] Division of Regenerative Medicine, IHBI, Queensland University of Technology, Australia

Abstract — **Bone tissue engineering scaffolds have two challenging functional tasks to play; to be bioactive by encouraging cell proliferation and differentiation, and to provide suitable mechanical stability upon implantation. Composites of biopolymers and bioceramics unite the advantages of both materials resulting in better processibility, enhanced mechanical properties through matrix reinforcement and osteoinductivity. Novel composite blends of poly(L-lactide-co-D,L-lactide)/tri-calcium phosphate (PLDLLA/TCP) were fabricated into scaffolds by an extrusion deposition technique customised from standard rapid prototyping technology.**

PLDLLA/TCP composite material blends of various compositions were prepared and analysed for their mechanical properties. PLDLLA/TCP (10%) was optimised and fabricated into scaffolds. Compressive mechanical properties for the composite scaffolds were performed. In vitro studies were conducted using porcine bone-marrow stromal cells (BMSCs). Cell-scaffold constructs were induced using osteogenic induction factors for up to 8 weeks. Cell proliferation, viability and differentiation capabilities were assayed using phase contrast light microscopy, scanning electron microscopy, PicoGreen DNA quantification, AlamarBlue metabolic assay; FDA/PI fluorescent assay and western blot analysis for osteopontin.

Microscopy observations showed BMSCs possessed high proliferative capabilities and demonstrated bridging across the pores of the scaffolds. FDA/PI staining as well as AlamarBlue assay showed high viability of BMSCs cultured on the composite scaffolds Cell numbers, based on DNA quantitation, was observed to increase continuously up to the 8th week of study. Western blot analysis showed increased osteopontin synthesis on the scaffolds compared to tissue culture plastic. Based on our results the PLDLLA/TCP scaffolds exhibit good potential and biocompatibility for bone tissue engineering applications.

Keywords — **Composite, bioresorbable scaffolds, PLDLLA, tissue engineering, bone**

I. Introduction

In the clinical setting, bone graft substitutes are commonly used in the treatment of bone injuries and diseases where the host bone tissue needed to be removed. Autogenous and allogeneous bone grafts are the most common, they also entail many shortcomings. The demand for alternative bone graft has been growing dramatically. Selection of an effective bone graft substitute is paramount for the repair of bone defects and fractures; revision surgeries should be avoided as they would lead to higher risks, costs and even increased non-onion chances.

Some major drawbacks associated with bone regeneration are the lack of a suitable scaffold and materials to meet the mechanical and functional requirements at the defect site. An ideal scaffold should be biocompatible, bioresorbable, able to retain the shape and structure of the defect site while providing mechanical support, be porous and osteoconductive for bone regeneration to occur [1, 2]. It should also be a suitable carrier for cells or growth factors which could be included to enhance the bone regeneration therapy.

Bone tissue engineering scaffolds made of polymers or ceramic have extensively reported [3-7]. However, polymers and ceramics individually have several shortcomings, and by creating polymer-ceramic composite scaffolds, advantageous properties from both materials could be harnessed to improve on mechanical and biological properties to improve cell proliferation and differentiation [8-11]. Novel composite blends of poly(L-lactide-co-D,L-lactide)/ tri-calcium phosphate (PLDLLA/TCP) were fabricated into scaffolds by an extrusion deposition technique customised from standard rapid prototyping technology and characterised in the paper.

II. Materials and methods

Polylactide (PLA) generally has superior mechanical properties as compared to polycaprolactone (PCL), and has vastly different degradation rates and processibility chal-

Chwee Teck Lim, James C.H. Goh (Eds.): ICBME 2008, Proceedings 23, pp. 1480–1483, 2009
www.springerlink.com

lenges. Tri-calcium phosphate bioceramic is a common and typical bone filler material used in bone grafting. Composite scaffolds were intricately designed and fabricated with these novel biopolymer-bioceramic composite materials with superior mechanical properties [2]. Poly(L-lactide-co-D,L-lactide) (PLDLLA) was purchased from Boehringer Ingelheim GmbH and β-Tri-Calcium Phosphate (TCP) from Progentix BV.

A composite material blend was mixed together using an in-house screw-extruder and various compositions were prepared for the pilot material analysis. The particle size distribution of the TCP particulates were determined on a laser diffraction particle size analyzer (Partica LA-950, Horiba; range 0.01-3000μm) and averaged 15μm. This novel composite blend was prepared into dumb-bell shaped specimen for tensile tests by injection molding.

An in-house rapid prototyping (RP) system, namely the screw extrusion system (SES) was developed between Temasek Polytechnic, Singapore (TP) and National University of Singapore (NUS). This customised system allows for exploratory novel polymeric-based materials to be extruded into porous three-dimensional (3D) scaffolds. The working principle of the SES is similar to the FDM [2, 12, 13]. The final composition for scaffold fabrication was PLDLLA (90%wt) and TCP (10%wt).

Scaffolds ($5\times5\times10mm^3$) were cut from larger blocks which were fabricated with a 0-90° lay-down pattern, for mechanical studies. Tensile and compression tests were conducted on an Instron 4302 Material Testing System, operated by Series IX Automated Materials Tester v. 7.43 system software, with a 1 kN load cell. For tensile test, the specimens were pulled in tension at a rate of 1mm/min until break; while for the compression test, the compression rate was 1mm/min up to a strain level of 0.6. The stress–strain (σ –ε) curves were obtained to evaluate the elastic/stiffness (modulus) and compressive yield strength of the scaffolds. The modulus was calculated from the stress–strain curve as the slope of the initial linear portion of the curve, with any toe region from the initial settling of the specimen neglected. A sample size of n = 5, was tested for each group.

Thinner scaffold sheets of $5\times5\times4mm^3$ with a 0-60-120° lay-down pattern were also prepared for the in vitro cell culture study. The scaffolds were treated with 5M sodium hydroxide for 10 minutes and rinsed with 5 changes of de-ionised water; this would yield a more hydrophilic and corrugated material surface for cell culture. The scaffolds were then sterilized in 70% ethanol for 2 hours and under UV light for 20 minutes for each side.

Each scaffold was seeded with 100 000 primary porcine bone marrow stem cells (BMSC) expanded from our frozen stock (passage 3-4) in growth media: Dulbecco's Modified Eagle medium (DMEM) with 10% fetal bovine serum (FBS), 1% penicillin and 1% streptomycin (all from Gibco). The seeded cells were cultured up to 8-weeks in static culture supplemented with osteogenic media comprising of DMEM growth media with 10 nM of dexamethasome, 50 μM of ascorbic acid 2 phosphate and 10 mM of β-glycerolphosphate (all from Sigma).

The cell-scaffold constructs were observed and analysed at various time points with phase contrast light, confocal laser microscopy (CLM) and scanning electron microscopy (SEM). The BMSC proliferation and development was examined on a phase-contrast light microscopy. For CLM analysis, the cells within the scaffold construct was stained using fluorescent dyes, fluorescein diacetate (FDA) and propidium iodide (PI) (both from Molecular Probes Inc) and viewed on a confocal laser microscope (Olympus IX70-HLSH100 Fluoview). Viable cells were stained green (FDA) while apoptotic cells were stained red (PI). The samples were then fixed in 3.7% formaldehyde, dehydrated over a graded ethanol series and samples gold sputtered for SEM observation at 15 kV accelerating voltage (Philips XL30 FEG).

Semi-quantitative measurements were also done with the AlamarBlue assay (Biosource) and PicoGreen dsDNA quantification assay (Molecular Probes Inc), to investigate the metabolic activity (n=5) and cell numbers (relative to DNA content, n=5) over various time points. At each time point, culture medium was aspirated and mixed with 5% AlamarBlue. The mixture was incubated for 2 h at 37°C in and absorbance was measured on a plate reader (Safire^2 – Tecan) at wavelengths of 560nm and 600nm, together with blank controls using medium with reagent and medium only. Cell-construct metabolic activity was directly correlated to the percentage reduction of AlamarBlue reagent. For dsDNA quantification, specimens were subjected to freeze-thaw cycles of 1 hour each (between -80°C and 37°C) for 3 cycles to breakup the cell and nuclear membranes to obtain a homogenous cell suspension. 100μl of PicoGreen working solution was added to 100μl of specimen and incubated at room temperature for 5 minutes. Fluorescence was then measured with a plate reader (Safire^2 –Tecan) at excitation and emission wavelengths of 480nm and 520 nm, respectively. The amount of DNA was calculated by extrapolating a standard curve.

Western blot analysis was performed to observe presence of osteogenic proteins synthesized in the constructs. Pro-

teins from specimen were isolated in a lysis buffer (5mM MgCl2, 150mM NaCl, 1% triton-100, pH7.5) at 4°C for 20 minutes after rinsing in cold PBS three times. Lysates were collected after centrifugation at 12 000g at 4°C, for 5 minutes. The total amount of protein obtained was quantified with the Micro BCA kit (Pierce) with a standard curve derived from bovine serum albumin (Sigma). Polyacrylamide gel electrophoresis (SDS–PAGE) was performed and the separated proteins were then transferred to nitrocellulose membranes and incubated with of rabbit anti human osteopontin antibody (OPN-Abcam) and rabbit anti human β-actin (Delta Biolabs) as control. The protein bands on the membrane were detected by chemiluminesence (SuperSignal West Pico-Pierce) and the intensity measured with a densiometer (BioRad VersaDoc 5000).

III. Results and Discussions

The tensile test of the composite material with increasing percentage of TCP revealed that reinforcing the polymer matrix resulted in an increase of stiffness for the new composite material (Figure 1). However, with higher TCP contents the processibility of the material becomes a challenge as the overall viscosity of the material increases.

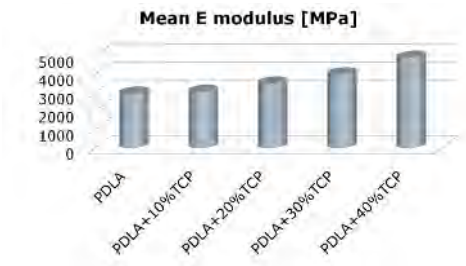


Figure 1. Modulus of dumb-bell shaped test specimen of PLDLLA and composite PLDLLA/TCP.

The SES fabricated PLDLLA/TCP (10%) scaffolds have a highly porous three-dimensional structure manufactured by the deposition of individual layers of struts in two angles (Figure 2). Gross morphological observations show good strut fusion between the layers, homogeneity and consistency of the deposited struts (average diameter ~400μm). The pores created were also regular and coherent to the design. The scaffold gross morphology had a neat spatial arrangement of pores and channels which were fully interconnected throughout the whole scaffold.

The compression tests revealed that the 2-angled scaffold design (0-90°) had a compressive stiffness of about 80MPa and a maximum compressive strength of 3MPa (Figure 3). These values are near and in the range of normal cancellous bone which had a reported stiffness of 90 - 400MPa and strength of 2-5MPa [14]. These mechanical properties indicate the potential application of these scaffolds in the field bone engineering. For load-bearing tissues, especially bone and cartilage, the 3D scaffold platform should be bioresorbable and provide adequate mechanical stability over the required period of time to withstand the *in vivo*.

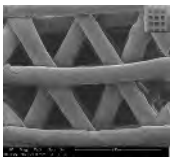


Figure 2. Plan view of an SEM micrograph of a 3-angle scaffold with picture of a 2-angle scaffold inset (*top right*).

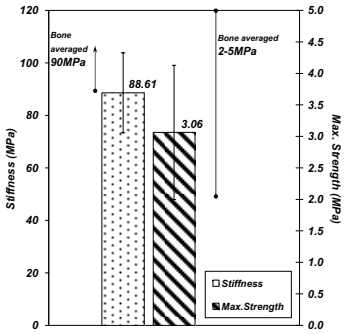


Figure 3. Compression stiffness (modulus) and maximum strength of the PLDLLA/TCP scaffolds. Arrowed and bulbed indicators indicate range of values for cancellous bone [14].

The importance of scaffold interconnectivity and porosity is essential for cell proliferation and exchange of nutrient and waste products [1]. Its effects and relation to mechanical stability has also been clearly defined. As porosity increases, a decrease in scaffold material, its mechanical properties would suffer correspondingly. Zein *et al.* [13] and Lam *et al.* [15] have demonstrated the dependence of mechanical properties on scaffold porosity when designing and fabricating scaffolds via rapid prototyping. The relationship of increasing porosity and declining mechanical properties has been found to follow a power law relationship [16]. The high dependence of mechanical properties on scaffold porosity had also been reported by Thomson *et al.* [17] and de Groot *et al*. [4]. Reinforcement through incorporation of filler material into the polymer matrix is one alternative of increasing the mechanical properties.

Cell-scaffold constructs cultured in static conditions up to 8 weeks showed a promising scaffold with suitable surface characteristics and architecture for cell proliferation and growth. AlamarBlue assay revealed increasing metabolic activity from day 0 to day 28, when the peak was reached (Figure 4). Phase contrast microscope observation and SEM observations concurred with the cell proliferation

in the scaffold and forming layers and sheets covering the scaffold struts and bridging the pores (Figure 4). Confocal laser microscope observations confirmed the cell morphology and distribution of viable cells in the cell-scaffold construct. DNA quantification with the PicoGreen assay also confirmed the increase in cell population. Subsequent western blot analysis for osteopontin revealed presence of the osteo-protein, indicating differentiation capability and plasticity of the BMSCs on the composite scaffolds.

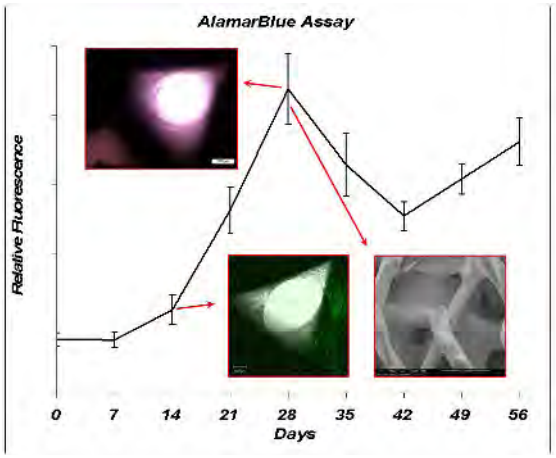


Figure 4. Composite pictures of PLDLLA/TCP scaffold on a graph showing the observed AlamarBlue relative fluorescence readings, metabolic activity on the uptrend; dipping slightly after day 28 and continue to increase shortly after. Inset images: Microscope image at day 28; pBMSC has proliferated and formed dense sheets adhering to the PLDLLA/TCP scaffold struts and structures. They also form bridging over the open pores (*Top*). Confocal microscope image showing majority of viable cells (*green*) already bridging the pores at day 14; dead cells would fluoresce red (none observed) (*bottom left*). SEM image at day 28 showing dense cell sheets spread over the pores and struts of the scaffold architecture (*bottom right*).

IV. Conclusions

These results demonstrate the PLDLLA/TCP scaffolds exhibit good biocompatibility and potential, for both functional mechanical and biological role requirements, as a scaffold for bone tissue engineering applications or bone graft substitute.

Acknowledgment

This work has been supported by SERC-A-star (R397-000-038-305) and the Polish Ministry of Science and Higher Education.

References

1. Hutmacher DW. Scaffolds in tissue engineering bone and cartilage. Biomaterials 2000 Dec;21(24):2529-2543.
2. Hutmacher DW, Schantz JT, Lam CX, Tan KC, Lim TC. State of the art and future directions of scaffold-based bone engineering from a biomaterials perspective. Journal of tissue engineering and regenerative medicine 2007 Jul-Aug;1(4):245-260.
3. Chu TM, Orton DG, Hollister SJ, Feinberg SE, Halloran JW. Mechanical and in vivo performance of hydroxyapatite implants with controlled architectures. Biomaterials 2002 Mar;23(5):1283-1293.
4. De Groot JH, Kuijper HW, Pennings AJ. A novel method for fabrication of biodegradable scaffolds with high compression moduli. Journal of Materials Science-Materials in Medicine 1997 Nov;8(11):707-712.
5. Ishaug SL, Crane GM, Miller MJ, Yasko AW, Yaszemski MJ, Mikos AG. Bone formation by three-dimensional stromal osteoblast culture in biodegradable polymer scaffolds. J Biomed Mater Res 1997 Jul;36(1):17-28.
6. Ramay HR, Zhang M. Biphasic calcium phosphate nanocomposite porous scaffolds for load-bearing bone tissue engineering. Biomaterials 2004 Sep;25(21):5171-5180.
7. Chistolini P, Ruspantini I, Bianco P, Corsi A, Cancedda R, Quarto R. Biomechanical evaluation of cell-loaded and cell-free hydroxyapatite implants for the reconstruction of segmental bone defects. J Mater Sci Mater Med 1999 Dec;10(12):739-742.
8. Schumann D, Ekaputra AK, Lam CXF, Hutmacher DW. Biomaterials/Scaffolds - Design of Bioactive, Multiphasic PCL/collagen Type I and Type II - PCL-TCP/collagen Composite Scaffolds for Functional Tissue Engineering of Osteochondral Repair Tissue by Using Electrospinning and FDM Techniques. In: Hauser H, Fussenegger M, editors. Tissue Engineering (Methods in Molecular Medicine). 2nd ed. New Jersey: Humana Press, 2007. p. 101-124.
9. Kim HW. Biomedical nanocomposites of hydroxyapatite/polycaprolactone obtained by surfactant mediation. J Biomed Mater Res A 2007 Mar 27.
10. Liao S, Wang W, Uo M, Ohkawa S, Akasaka T, Tamura K, et al. A three-layered nano-carbonated hydroxyapatite/collagen/PLGA composite membrane for guided tissue regeneration. Biomaterials 2005 Dec;26(36):7564-7571.
11. Zhou YF, Hutmacher DW, Varawan SL, Lim TM. In vitro bone engineering based on polycaprolactone and polycaprolactone-tricalcium phosphate composites. Polym Int 2007 Mar;56(3):333-342.
12. Hutmacher DW, Schantz T, Zein I, Ng KW, Teoh SH, Tan KC. Mechanical properties and cell cultural response of polycaprolactone scaffolds designed and fabricated via fused deposition modeling. J Biomed Mater Res 2001 May;55(2):203-216.
13. Zein I, Hutmacher DW, Tan KC, Teoh SH. Fused deposition modeling of novel scaffold architectures for tissue engineering applications. Biomaterials 2002 Feb;23(4):1169-1185.
14. Athanasiou KA, Zhu C, Lanctot DR, Agrawal CM, Wang X. Fundamentals of biomechanics in tissue engineering of bone. Tissue Eng 2000 Aug;6(4):361-381.
15. Lam CXF, Teoh SH, Hutmacher DW. Comparison of Degradation of PCL & PCL-TCP scaffolds in Alkaline Medium. Polym Int 2007;56(6):718-728.
16. Gibson LJ, Ashby MF. Cellular Solids: Structure and Properties 2nd ed ed: Cambridge University Press, 1997.
17. Thomson RC, Yaszemski MJ, Powers JM, Mikos AG. Fabrication of Biodegradable Polymer Scaffolds to Engineer Trabecular Bone. Journal of Biomaterials Science-Polymer Edition 1995;7(1):23-38.

Effects of Biaxial Mechanical Strain on Esophageal Smooth Muscle Cells

W.F. Ong[1], A.C. Ritchie[1*] and K.S. Chian[1]

[1] School of Mechanical and Aerospace Engineering, Nanyang Technological University, Singapore

Abstract — **Esophageal cancer has one of the highest mortality rates compared to other types of cancer. Tissue engineering promises a bio-artificial prosthesis for enhanced surgical treatment. To facilitate the tissue engineering of the esophagus, a bioreactor capable of two-dimensional mechanical strain was designed and fabricated. Esophageal smooth muscle cells are seeded onto oxygen plasma treated polyurethane sheets and mechanically stimulated for 3 days at 420 cycles/day. The cells are then assessed for cell alignment by phase contrast microscopy and cell proliferation by MTS assay. After mechanical stimulation, the smooth muscle cells showed alignment under varying biaxial strain conditions in different regions of the bioreactor while the cell proliferation assay suggests the possibility of the change in the metabolic and phenotypic state of the cells over the 3 days of mechanical stimulation.**

Keywords — **bioreactor, mechanical stimulation, smooth muscle cells, esophagus tissue engineering**

I. Introduction

Esophageal cancer has one of the highest mortality rates compared to other types of cancer [1, 2]. Although the survival rate of esophageal cancer has been increasing over the years, the overall survival rate is still considered low [2]. Epidemiological studies have shown that esophageal cancer is 10 to 100 times more prevalent in Asia and Africa when compared to the United States [1-3]. The most common treatment method for managing esophageal cancer is surgical resection [3-6]. This results in a significant decrease in the quality of life for the patient after surgery [7, 8]. In cases where surgical treatment is not possible, artificial devices and the intraesophageal stent have been used to manage the disease with limited success [9]. The biocompatibility of the materials used is still far from ideal [10, 11].

Tissue engineering may provide a viable alternative for the treatment of esophageal cancer [10, 12]. *In vitro* studies on vascular cells have shown that mechanical stimulation is able to improve the structural and functional properties of cell/scaffold constructs for the purpose of tissue engineering organ replacements [13, 14]. However as previous studies have focused on vascular and cardiac cell types [15], their results may not be representative of the cell types found in the esophagus. This study aims to investigate the effects of mechanical stimulation on esophageal smooth muscle cells to develop a tissue engineered esophagus.

II. Materials and Methods

A. 2-Dimensional strain bioreactor

A bioreactor capable of providing biaxial mechanical strain by out-of-plane circular substrate distention [16] was designed and fabricated. A schematic drawing of the bioreactor design is shown in Figure 1. Figure 2 shows the complete system. The 2-dimensional strain bioreactor is actuated using a microprocessor controlled syringe pump to provide fluid displacement to induce mechanical strain on a flexible polyurethane membrane held between the top and bottom chambers.

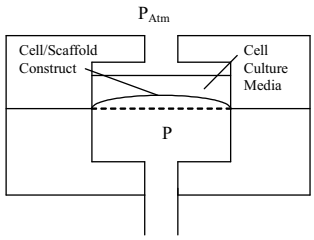


Fig. 1. Schematic drawing of 2-D strain bioreactor

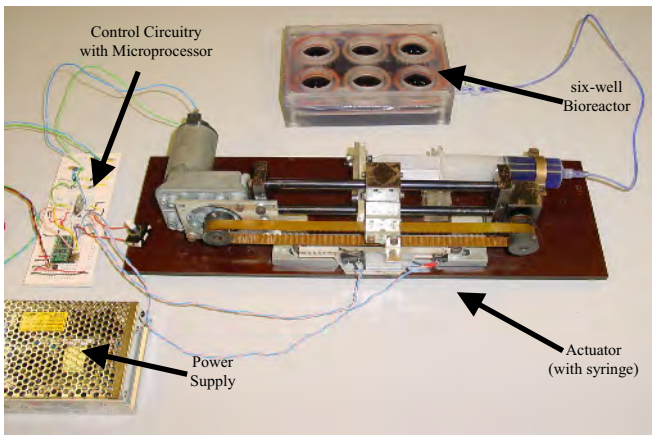


Fig 2. Two-dimensional strain bioreactor system

B. Fabrication of polyurethane membrane

Flexible polyurethane membranes were fabricated using Chronoflex® AL80-A pellets (CardioTech International)

Chwee Teck Lim, James C.H. Goh (Eds.): ICBME 2008, Proceedings 23, pp. 1484–1487, 2009
www.springerlink.com

dissolved in 1,4-dioxane (Merck). The polyurethane-dioxane solution was then cast onto a glass mould with a wet thickness of 2mm and air dried. The polyurethane sheet is then extracted from the glass mold and vacuum dried for 3 days at 24°C to extract residual solvents. The prepared polyurethane sheet is then treated with oxygen plasma to facilitate cell attachment prior to the experiment.

C. Culture of esophageal smooth muscle cells

Esophageal smooth muscle cells were isolated from the muscle layer of fresh porcine esophagus using enzymatic dissociation with collagenase. The isolated smooth muscle cells were then allowed to grow to confluence in a humidified 5% CO_2 incubator (Sanyo) at 37°C and passaged at a split ratio of 1:5 every 7 days. Smooth muscle cells from passages 4 to 6 were used for the bioreactor experiments. The isolated smooth muscle cells are cultured using Dulbecco's Modified Eagle's Medium (Hyclone) with 10% Fetal Bovine Serum (Hyclone) and 1 % Antibiotic Antimycotic Solution (Sigma).

Cells were seeded onto the polyurethane sheet within the bioreactor at a density of ~2.6×10^4 cells/cm^2 and left to attach for 24 hours before commencement of the mechanical strain regime. Control experiments were carried on oxygen plasma treated polyurethane sheets in static culture.

D. Mechanical strain regime

Mechanical strain (2% magnitude) was applied to the smooth muscle cells for 420 cycles at a rate of 5 cycles per minute every 24 hours for 3 consecutive days, as shown in figure 3. This mechanical stimulation wave form is designed to closely resemble the mechanical forces experienced by the cells *in vivo* based on the pressure waveform generated by the esophagus during ingestion of solid food.

E. Assessment of cell response to 2-dimensionalmechanical strain

Cell alignment

After mechanical stimulation for 3 days, alignment of the smooth muscle cells was observed using phase contrast microscopy. Three regions of the polyurethane sheet were examined due to their different states of strain.

MTS assay

To determine the effects of 2-dimensional mechanical strain, a cell proliferation assay was performed using CellTiter96® AQ_{ueous} One Solution Reagent (Promega) by mixing 1 part of MTS reagent to 4 parts of fresh culture medium. The light absorbance was then measured at a wavelength of 490nm using a GENios micro plate reader (TECAN).

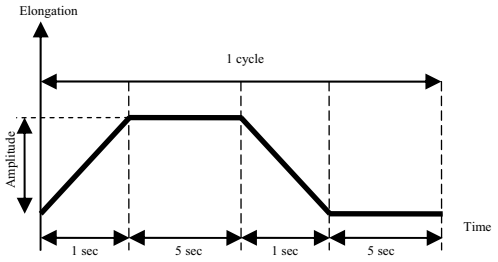


Fig. 3. Mechanical strain cycle for esophageal smooth muscle cells

III. Results and Discussion

A. Cell alignment

The 2-dimensional bioreactor imparts a complex state of strain on the polyurethane sheet. Due to the deformation geometry of the polyurethane sheet during mechanical stimulation, the polyurethane sheet changes from a flat sheet to a spherical cap[17]. As a result of this deformation, the radial strain remains constant throughout the polyurethane sheet as determined by its curvature, while the tangential strain is at a maximum at the centre of the bioreactor and would decrease to zero at its edge. Figure 4 shows the state of strain at the 3 locations of interest: well centre (A), mid radius (B) and well edge (C).

After 3 consecutive days of mechanical stimulation, the smooth muscle cells grown on the polyurethane membrane were observed using phase contrast microscopy. Figure 4 shows the phase contrast micrographs of the mechanically stimulated smooth muscle cells at the 3 locations of interest compared to the cells grown on polyurethane sheet control.

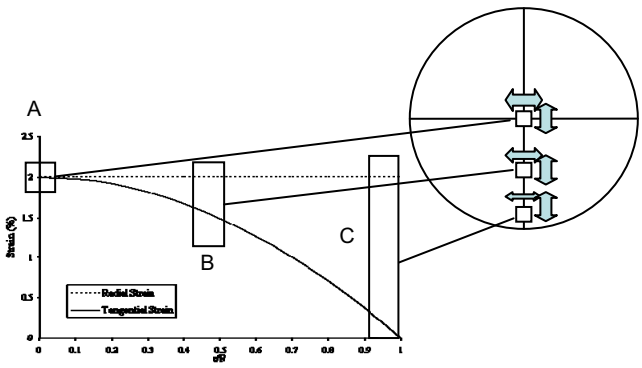
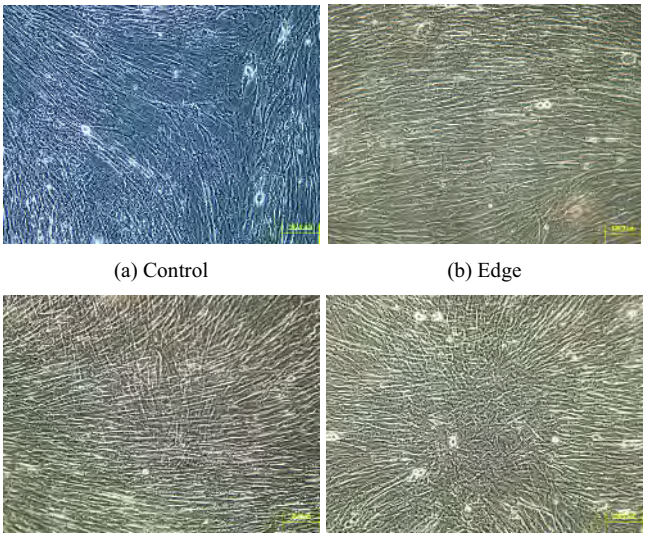


Fig 4. Profile of state of strain within the polyurethane sheet



(a) Control (b) Edge

(c) Mid radius (d) Centre

Fig 5. Phase contrast micrographs of esophageal smooth muscle cells at different locations of the bioreactor (20× objective)

The phase contrast micrographs presented in Figure 5a shows that the esophageal smooth muscle cells in static conditions exhibit random alignment. The characteristic hill and valley growth and pattern is observed as it reaches confluence in all areas. Although small domains of local alignment of the smooth muscle cells can be observed, the cell alignment is still random on a macroscopic scale. This phenomenon is also exhibited by smooth muscle cells cultured on other tissue culture surfaces [18, 19].

Mechanically stimulated esophageal smooth muscle cells exhibited varying alignment in all 3 locations of interest. At the well edge (Figure 5b), the cells are aligned perpendicular to the radial strain in the absence of tangential strain. This result corresponds to previous work on smooth muscle cells subjected to uniaxial strain [13, 20-25]. Buck [25] postulated that smooth muscle cells align perpendicular to the direction of applied strain to minimize mechanical stress by moving the long axis of the cell away from the direction of applied strain, preserving their existing focal adhesion points.

At the mid radius of the bioreactor, the state of strain is predominantly radial with some tangential strain (Figure 5c). Most of the smooth muscle cells align perpendicular to the radial strain while some cells align parallel to it. This may be due to the presence of the tangential strain component, which increases from the edge to the centre. When both radial and tangential strains are present, the cell must align perpendicular to one of the principal strains to minimize the stress it experiences. At the centre of the bioreactor, smooth muscle cells were observed to align perpendicular to one another. At this location, the radial strain and the tangential strain are equal. From the geometrical perspective, the equi-biaxial state of strain is created by a series of radial strains passing through the central axis of the bioreactor well. The cells are observed to align parallel to the radial strain, radiating outwards from the bioreactor centre (Figure 5d) as there is little difference between the radial and tangential strain in the areas just outside the bioreactor centre.

B. MTS Assay

To investigate the effects of cyclic two-dimensional mechanical strain on esophageal smooth muscle cells, a cell proliferation assay was conducted using CellTiter® AQ_{ueous} One Solution Reagent. The MTS assay was performed after each day of stimulation to determine the effects of mechanical stimulation on cell proliferation. Figure 6 shows the light absorbance values of the stimulated esophageal smooth muscle cells compared to the static controls.

The light absorbance of the MTS assay reveals that the mechanically stimulated cells display consistently lower light absorbance for all 3 days when compared to the control cells.

The MTS light absorbance for the static controls can be seen to increase to confluence on days 2 and 3 (Figure 6) while the mechanically strained cells show a sudden decrease after 1 day of stimulation. On days 2 and 3, the MTS values have increased significantly.

As the MTS assay measures cell numbers through the metabolic conversion of the reagent to a soluble formazan colored product [26], the metabolic state and phenotype of the cells used in this assay must be generally similar to make a valid comparison. In these experiments, mechanical

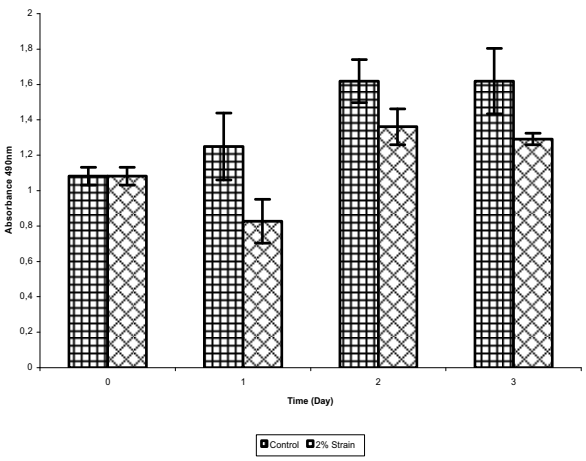


Fig 6. MTS cell proliferation assay between mechanically stimulated and control

stimulation may induce a change in cell metabolism and a change in phenotype. Under high strain magnitudes and cyclic frequency, cells are known to detach from smooth surfaces due to their poor attachment [25]. The sudden drop in MTS values may be due to a shift in the cell metabolism after the sudden shock of the commencement of mechanical stimulation. There may also be loss of poorly attached cells from the surface. After the 2nd day of mechanical stimulation, the MTS values for the strained cells reach a plateau, possibly indicating differentiation.

IV. Conclusion

From the results obtained from this study, biaxial mechanical strain stimulation is shown to be able to induce alignment of the esophageal smooth muscle cells. In addition, the MTS assay results obtained have suggest the possibility of metabolic changes of the mechanically strained cells and also a possible phenotypic change.

The two-dimensional mechanical strain bioreactor has demonstrated that differential biaxial strain would cause the smooth muscle cells to align to one of its principal stress axis to minimize the mechanical stresses on the cell.

The two-dimensional mechanical strain bioreactor has demonstrated that it is able to induce alignment in smooth muscle cells and may induce differentiation of the smooth muscle cells. This knowledge will be used for mechanical stimulation of a tubular 3 dimensional scaffold to facilitate the tissue engineering of a clinically functional esophagus.

Acknowledgment

The authors would like to acknowledge the support of the School of Mechanical and Aerospace Engineering, Nanyang Technological University.

References

1. http://www-dep.iarc.fr/: GLOBOCAN, 2002
2. http://www.cancer.org/: What are the key statistics about the cancer of the esophagus?, 2005
3. Pazdur R: Cancer management : a multidisciplinary approach : medical, surgical, & radiation oncology, 8th ed. New York: Oncology Publishing Group; 2004.
4. Allum WH, Griffin SM, Watson A, Colin-Jones D: Guidelines for the management of oesophageal and gastric cancer. Gut 2002, 50 Suppl 5(90005):v1-v23.
5. http://www.cancer.gov/: What you need to know about: Cancer of the esophagus. 2002.
6. http://www.upmccancercenters.com/: Esophageal cancer: General information about esophageal cancer. 2004.
7. http://patienteducation.upmc.com/: Diet after an esophagectomy. 2004.
8. http://www.virginiamason.org/: Esophagectomy and Quality of Life. 2005.
9. Nakamura T, Shimizu Y: Tracheal, Laryngeal, and Esophageal Replacement Devices. In: The biomedical engineering handbook. Edited by Bronzino JD, 2nd edn. Boca Raton, FL: CRC Press; 2000.
10. Fuchs JR, Nasseri BA, Vacanti JP: Tissue engineering: a 21st century solution to surgical reconstruction. Ann Thorac Surg 2001, 72(2):577-591.
11. Saltzman WM: Cell Interactions with Polymers. In: Principles of tissue engineering. Edited by Lanza RP, Langer RS, Vacanti J, 2nd edn. San Diego: Academic Press; 2000: 221-235.
12. Langer R, Vacanti JP: Tissue engineering. Science 1993, 260(5110):920-926.
13. Kim BS, Nikolovski J, Bonadio J, Mooney DJ: Cyclic mechanical strain regulates the development of engineered smooth muscle tissue. Nature Biotechnology 1999, 17(10):979-983.
14. Martin I, Wendt D, Heberer M: The role of bioreactors in tissue engineering. Trends Biotechnol 2004, 22(2):80-86.
15. Petrosko P, Acarturk TO, Dimilla PA, Johnson PC: Muscle Tissue Engineering. In: Frontiers in tissue engineering. Edited by Patrick CW, Mikos AG, McIntire LV, 1st edn. Oxford, U.K. ; New York, NY: Pergamon; 1998: 495-513.
16. Gooch KJ, Tennant CJ: Mechanical forces : their effects on cells and tissues. New York: Springer; 1997.
17. Williams JL, Chen JH, Belloli DM: Strain fields on cell stressing devices employing clamped circular elastic diaphragms as substrates. J Biomech Eng 1992, 114(3):377-384.
18. Chamley-Campbell J, Campbell GR, Ross R: The smooth muscle cell in culture. Physiol Rev 1979, 59(1):1-61.
19. 147. Fallier-Becker P, Rupp P, Fingerle J, Betz E: Smooth muscle cells from rabbit aorta. In: Cell culture technique in heart and vessel research. Edited by Piper HM. New York: : Springer-Verlag; 1990: 247-267.
20. Kanda K, Matsuda T, Oka T: Two-dimensional orientational response of smooth muscle cells to cyclic stretching. ASAIO J 1992, 38(3):M382-385.
21. Kanda K, Matsuda T, Oka T: Mechanical stress induced cellular orientation and phenotypic modulation of 3-D cultured smooth muscle cells. ASAIO J 1993, 39(3):M686-690.
22. Kanda K, Matsuda T: Mechanical stress-induced orientation and ultrastructural change of smooth muscle cells cultured in three-dimensional collagen lattices. Cell Transplant 1994, 3(6):481-492.
23. Kakisis JD, Liapis CD, Sumpio BE: Effects of cyclic strain on vascular cells. Endothelium 2004, 11(1):17-28.
24. Cha JM, Park SN, Noh SH, Suh H: Time-dependent modulation of alignment and differentiation of smooth muscle cells seeded on a porous substrate undergoing cyclic mechanical strain. Artif Organs 2006, 30(4):250-258.
25. Buck RC: Behavior of vascular smooth muscle cells during repeated stretching of the substratum in vitro. Atherosclerosis 1983, 46(2):217-223.
26. Berridge MV, Tan AS: Characterization of the cellular reduction of 3-(4,5-dimethylthiazol-2-yl)-2,5-diphenyltetrazolium bromide (MTT): subcellular localization, substrate dependence, and involvement of mitochondrial electron transport in MTT reduction. Arch Biochem Biophys 1993, 303(2):474-482.

Author: Alastair Campbell Ritchie
Institute: Nanyang Technological University
Street: 50 Nanyang Avenue Singapore 639798
City: Singapore
Country: Singapore
Email: macritchie@ntu.edu.sg

Characterization of Electrospun Substrates for Ligament Regeneration using Bone Marrow Stromal Cells

T.K.H. Teh[1], J.C.H. Goh[1,2], S.L. Toh[1,3]

[1] Division of Bioengineering, National University of Singapore, Singapore
[2] Department of Orthopedic Surgery, National University of Singapore, Singapore
[3] Department of Mechanical Engineering, National University of Singapore, Singapore

Abstract — **Challenges persist in the tissue engineering and regeneration of ligaments. Of the various aspects contributing to the success of ligament tissue engineering (such as the scaffold, cell source and stimulatory biochemical and mechanical cues), architecture and material involved in scaffold design remain as a significant area of study. Essentially, the scaffold for ligament regeneration, especially the cell-seed substrate, should be viable for cell attachment, promotes nutrient and waste transfer, be mechanically viable, and stimulates initial cell proliferation and ECM production. In this study, electrospun substrates using the silk fibroin (SF) and PLGA material, with different electrospun fiber arrangements (aligned (AL) and random (RD)) were compared for their ability to promote MSC attachment and subsequent differentiation down the ligament fibroblast cell lineage. The rationale for such characterizations lies in the hypothesis that SF, being a natural protein, provides significantly more favorable surface chemistry for cell attachment and differentiation than synthetic polymers such as PLGA. On the other hand, the aligned electrospun fiber arrangement will mimic the native ligament ECM environment, to guide MSCs down the fibroblast lineage. Electrospun PLGA and SF substrates were fabricated by first dissolving the respective material in HFIP (7-10% w/v). Following which, aligned PLGA and SF substrates were collected from a rotational electrospin setup, while the random types were collected from a grounded plate. These four groups of substrates (SF-AL, SF-RD, PLGA-AL, PLGA-RD) were then characterized in terms of cell adhesion, proliferation, viability and function via post-seed cell counting, AlamarBlue™ assay, Fluorescence Microscopy, Sircol® Collagen Assay and SEM. Results from this characterization show that cells remained viable when cultured on these substrates, with the AL types being mechanically stronger and promoted increased proliferation and collagen production as compared to the RD types. SF substrates promoted cell attachment and differentiation, as inferred from the increased collagen production.**

Keywords — **Scaffold, Electrospin, Alignment, PLGA, Silk**

I. Introduction

In the pursuit of functional tendon/ligament tissue engineering, several factors have been identified by various groups as essential. [1, 2] They include the various aspects of the scaffold, cell source and stimulatory biochemical/mechanical cues. Of the different aspects involved for scaffold design, the architecture and material used remain significant.

In view of the surface topology at which cells are exposed to in their native environment, a scaffold architecture involving aligned ultra-fine fibers is envisioned. The fabrication method of choice is electrospinning, which produces non-woven fibrous structures of different fiber orientations, including the aligned and random fiber arrangements. With diameters in the range of nanometers to microns, integrating to produce structures with interconnected pores and high surface area to volume ratio, electrospun fibers can mimic the native extracellular matrix (ECM) to serve as a suitable seeding substrate for tissue engineering.

Using electrospinning, aligned fibers are produced to act as guidance structures for cells. Lee et. al. carried out assessments of cellular responses, histological observation, proliferation and ECM production of human ACL fibroblasts (HLF). They found that HLFs on the aligned fibers were spindle-shaped and aligned in the direction of the fibers. Such HLFs formed tissue like, oriented bundles, which were confluent over the surface. Significantly more collagen was produced on aligned fiber sheets than on randomly oriented sheets. [3] Xu et. al. compared the cell-cell adhesion and proliferation of human coronary artery smooth muscle cells (SMC) on TCP, plane polymer film and aligned polymer fiber. They observed that SMCs migrated along the axis of the aligned fibers and expressed spindle-like contractile phenotype. [4] Mauck et. al. employed fibrous scaffolds for the tissue engineering of the meniscus. They seeded mesenchymal stem cells (MSC) on aligned and random fibers. Results showed that aligned fibrous scaffolds serve as a micro-pattern for directed tissue growth and that when seeded with MSCs, produce constructs with improved mechanical properties compared to random scaffolds. [5] These studies have shown the potential of aligned fibers as tissue engineering scaffolds/substrates. However further optimization should be carried out and applied for ligament regeneration. Assessements for the differentiative potential down the ligament fibroblast cell lineage by aligned substrates have also not been conclusive.

Chwee Teck Lim, James C.H. Goh (Eds.): ICBME 2008, Proceedings 23, pp. 1488–1491, 2009
www.springerlink.com

From the scaffold material aspect, PLGA has been identified as a suitable candidate for electrospinning of fibrous scaffolds. Mao et. al. had produced PLGA fiber scaffold with an architectural morphology similar to those of natural ECM. Such scaffolds were cytocompatible with hMSCs and their osteoblast and chondrocytes lineage. [6]

Apart from synthetic polymers, recent efforts have been spent on using natural materials such as silk for electrospinning. As a potential material for tissue engineering, silk displays properties of enhanced environmental stability due to extensive hydrogen bonding and significant crystallinity. Min et. al. have produced silk fibers which have been shown to promote cell adhesion and spreading of type I collagen. They also discussed the possibility of surface modification of the nanofibers with ECM proteins. [7]

As such, this study is set to perform a comparative study between electrospun substrates using silk fibroin (SF) and PLGA material. It is hypothesized that SF, being a natural protein, provides significantly more favorable surface chemistry for cell attachment and differentiation than synthetic polymers such as PLGA. On top of that, different electro-spun fiber arrangements will be compared for their ability to promote rabbit MSC attachment and subsequent differentiation down the ligament fibroblast cell lineage.

II. Materials and Methods

A. Substrate Fabrication

Silk Degumming: Sericin, the antigenic part of raw silk, was first removed prior to dissolving for electrospinning purposes. Bombyx mori raw silk (Thailand), was soaked in degumming solution, containing aq. Na_2CO_3 and Sodium dodecyl sulphate (SDS), 0.25%(w/v) each (Sigma Chemicals) at 98~100^{o}C for 30 mins and thereafter rinsed in distilled water for 30 mins.

Electrospin Solution Preparation: PLGA (85:15) polymer pellets were dissolved in hexafluoro-2-propanol (HFIP) (Fluka) at 7% w/v to obtain PLGA solution. To obtain electrospinnable SF solution, degummed silk was first dissolved in saturated aq. lithiumthiocyanate (LiSCN) (Sigma Chemicals) solution, and upon full dissolution, dialyzed in distilled water for 3 days. The dialyzed aq. SF solution was then lyophilized to obtain regenerated SF sponge. The SF sponge was then dissolved in HFIP at 10%w/v to obtain the electrospinnable SF solution.

Electrospinning: Aligned electrospun fibers were obtained using a customized rotational electrospin setup involving a combination of positive electric field plates and a rotating collector device. Using such a setup, the path of the polymer jet is restricted such that highly aligned electrospun fibers can be obtained on the grounded rotating frame. Randomly arranged electrospun fibers were collected from a grounded metallic collector. Four groups of substrate: PLGA random (PLGA-RD), PLGA aligned (PLGA-AL), SF random (SF-RD) and SF aligned (SF-AL) were collected on 40 x 22mm glass slides for characterization purposes.

Sterilizations: Prior to cell seeding, the scaffold substrates were sterilized by means of formaldehyde (37%) (JT Baker) gassing for 24 hours. All other equipment was sterilized by autoclaving.

B. Cell Culture

Bone marrow stromal cells (BMSC) extracted from New Zealand white rabbits were cultured in DMEM culture medium (Sigma) with fetal bovine serum (FBS) (Hyclone) of 15% v/v concentration. P3 cells cultured at 70% confluence were used for all the four groups of substrates.

C. Characterization of Electrospun Fiber Substrate

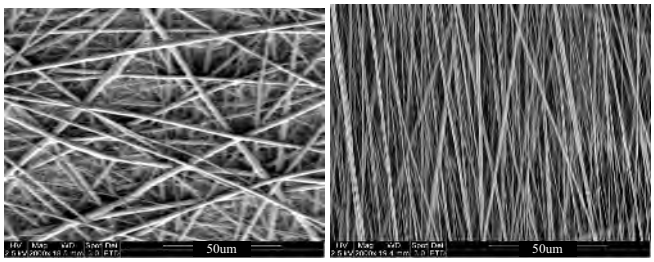
Substrate Gross Morphology: SEM images of the electrospun fibers were taken to observe the morphology of the fibers. To measure the fiber diameters and degree of alignment in the fibers, the software ImageJ (U.S. National Institutes of Health) was used. The angles from the vertical of each individual fiber (n=30) were measured and given a value from -90° to 90°. The distribution of the angles from the vertical was plotted for both aligned and random fibers.

Cell Seeding Efficiency: After incubating the cell-seeded substrates (n=3, $0.7x10^6$ cells/substrate) for 36 h, the culture medium was collected from the wells and cell count of unattached cells performed. The cell seeding efficiency was expressed as a percentage of the number of attached cells to the number of cells seeded.

Cell Proliferation Assay: Alamar Blue™ (Biosource) assay was used to assess cellular proliferation. The assay was carried out at D1, 3, and 7, whereby seeded substrates (n=3 each) were exposed to 10% Alamar Blue™ reagent in DMEM for 3h. The percentage reduction of Alamar Blue™ reagent was computed and taken to be an indication of cell proliferation levels.

Collagen Production Assay: The amount of collagen synthesized and deposited onto the substrate structure was determined by SirCol Assay (Biocolor) at D3, 7 and 14. Substrates from the four groups (n=3 each) were sacrificed and digested in pepsin from porcine mucosa (4000U/mg, Sigma) in 0.5M acetic acid (100ul) to isolate the sample collagen triplehelix from all non-collagenous protein.

Cellular Alignment and Morphology: DAPI and phalloidin (Invitrogen) staining were carried out on the nuclei and actin filaments of the cells respectively at D7 and D14.



a b

Fig. 1 SEM images: (a) randomly oriented and (b) aligned electrospun fibers. (2000x Magnification)

Staining was carried out on BMSCs-seeded substrates to observe the morphology and orientation. Briefly, the seeded substrates at the respective timepoints were fixed and permeabilized in 0.1% Triton X-100 (Sigma). Staining was carried out subsequently.

D. Statistical Analysis

Data were expressed as means ± standard deviation (SD). Single factor analysis of variance (ANOVA) technique was used to assess the statistical significance of results between groups. For pair-wise comparisons, two-tailed, unpaired Student's t tests were used. A $p<0.05$ was considered statistically significant.

III. Results

A. Substrate Gross Morphology

SEM imaging was performed on the aligned and random electrospun fibers (Fig. 1). From the images, the measured diameters of the electrospun fibers were of the range of 400-800nm. As observed from the histograms (results not shown), nanofiber alignment was achieved using the rotating electrospin setup. In contrast, no specific orientation was observed from the randomly deposited fibers.

B. Cell Seeding Efficiency

The cell seeding efficiency was found to be as follows. PLGA-AL: 95.4±1.11%, PLGA-RD: 94.1±1.35%, SF-AL: 97.3±0.90%, and SF-RD: 96.6±0.68%.

C. Cell Proliferation Assay

Fig. 2 shows the percentage Alamar Blue™ reduction by the four groups of cell-seeded substrates. There was significant proliferation when BMSCs were cultured in the substrates from D1 to D7. Within each timepoint, no significant difference ($p>0.05$) was found in Alamar Blue™ reduction between the two materials. However, BMSCs seeded onto the aligned substrates proliferated significantly faster ($p<0.05$) than the random counterparts by D7.

D. Collagen Production Assay

The amount of insoluble collagen synthesized increased over the 14 days experimental period for all the four groups of substrates (Fig. 3). There was significant difference ($p<0.05$) in the amount of collagen deposited between the substrates with aligned fibers and that with randomly oriented fibers from D7 onwards. Significantly more collagen ($p<0.05$) was also deposited for the silk substrates as compared with the PLGA type substrates after D7.

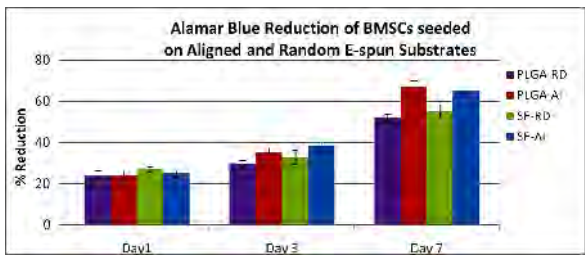


Fig. 2 Proliferation rates as represented by the Alamar Blue reduction by BMSCs seeded electrospun substrates

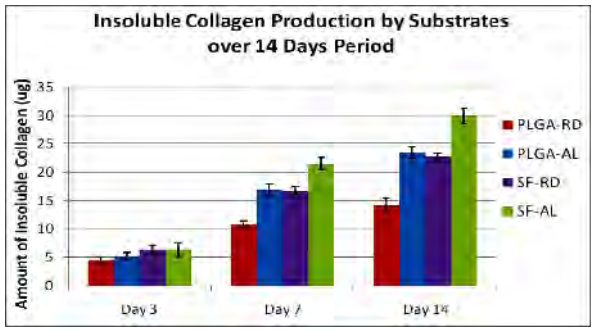
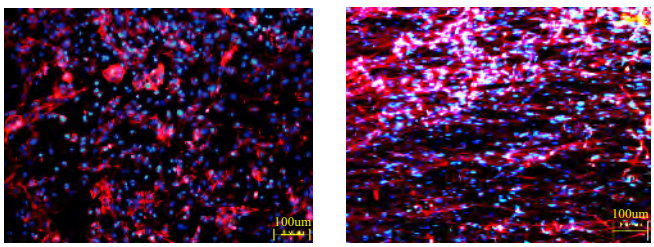


Fig. 3 Insoluble collagen produced by BMSCs seeded electrospun substrates



a b

Fig. 4 Fluorescence micrograph of BMSCs (actin: Red, nucleus: Blue) after 14 Days culture on random (a) and aligned (b) electrospun substrates

E. Cellular Alignment and Morphology

Fig. 4 illustrates the alignment and morphology of BMSCs after 14 days of culture on substrates with different fiber orientation. Cells assumed a more rounded morphology when cultured on randomly arranged electrospun fibers, while cells are elongated and aligned along the fiber direction when cultured on the substrates with aligned fibers. Cellular alignment was determined by the presence of aligned actin filaments in the aligned fiber substrates. Such alignment was not apparent in the random fiber substrates.

IV. Discussion

The aligned surface topology has been shown by several groups to have a positive effect on cell proliferation and collagen production. [3, 4, 8] Specifically, Lee et. al. had suggested that such cellular responses are likely due to a cell-cell interaction or cell-matrix interactions. [3] Yim et. al. had also presented a comprehensive review of the interaction of cells with nanoscale topography. Their findings indicate that cells respond to topography of synthetic substrates in the nanometer range in terms of adhesion, proliferation, migration and gene expression. [8]

This study further exemplifies these phenomena and demonstrates a method of producing aligned electrospun fibers that is suitable for the application of tendon/ligament tissue engineering. The advantage of such a structure lies in the biomimicry of the aligned electrospun fibrous substrate to native tissue environment of the tendon/ligament, where there is a high level of ECM and fibroblasts cellular alignment. This is evident from the proliferation and insoluble collagen assays, which show that the aligned substrates, regardless of materials, stimulated significantly higher proliferation and collagen deposition after D7 of experimentation.

Other than the architectural effect, the substrate material used also affects cellular responses. BMSCs seeded on SF substrates synthesized significantly more collagen than those seeded on PLGA substrates after 7 days culture. Although there was no significant effect on proliferation, the use of SF as seeding substrate material did improve collagen deposition. This is likely due to the increased number of protein binding sites, which facilitated the deposition of synthesized collagen. Further studies will be required to ascertain the types of collagen that are bound and the efficiency involved.

The use of aligned SF electrospun fibers (SF-AL) is thus shown to be advantageous as seeding substrate for tendon/ligament tissue engineering whereby higher proliferation and improved collagen deposition is desired.

V. Conclusion

A method of producing aligned electrospun submicron fibers of PLGA and SF was described. Aligned fibers as such stimulated increased proliferation and collagen depostion. SF type fibers provided a suitable surface for ECM deposition as indicated by the increased insoluble collagen deposited. Aligned SF electrospun fiber mesh was thus shown to be a promising seeding substrate for tendon/ligament regeneration.

Acknowledgment

This study is funded by the National University of Singapore, under Grant R-397000041112.

References

1. Petrigliano FA, McAllister DR, Wu BM (2006) Tissue engineering for anterior cruciate ligament reconstruction: a review of current strategies. Arthroscopy 22(4):441-51
2. Goh JC, Ouyang HW, Teoh SH, Chan CK, Lee EH (2003) Tissue-engineering approach to the repair and regeneration of tendons and ligaments. Tissue Eng 9 Suppl 1:S31-44
3. Lee CH, Shin HJ, Cho IH, Kang YM, Kim IA, Park KD, et. al. (2005) Nanofiber alignment and direction of mechanical strain affect the ECM production of human ACL fibroblast. Biomaterials 26(11):1261-70
4. Xu CY, Inai R, Kotaki M, Ramakrishna S (2004) Aligned biodegradable nanofibrous structure: a potential scaffold for blood vessel engineering. Biomaterials 25(5):877-86
5. Baker BM, Mauck RL (2007) The effect of nanofiber alignment on the maturation of engineered meniscus constructs. Biomaterials 28(11):1967-77
6. Xin X, Hussain M, Mao JJ (2007) Continuing differentiation of human mesenchymal stem cells and induced chondrogenic and osteogenic lineages in electrospun PLGA nanofiber scaffold. Biomaterials 28(2):316-25
7. Min BM, Lee G, Kim SH, Nam YS, Lee TS, Park WH (2004) Electrospinning of silk fibroin nanofibers and its effect on the adhesion and spreading of normal human keratinocytes and fibroblasts in vitro. 25(7-8):1289-97.
8. Yim EK, Leong KW (2005) Significance of synthetic nanostructures in dictating cellular response. Nanomedicine 1(1):10-21.

Corresponding Author: Siew-Lok Toh
Institute: Division of Bioengineering,
National University of Singapore
Street: 7 Engineering Drive 1, Block E3A #04-15,
Singapore 117574
City: Singapore
Country: Singapore
Email: bietohsl@nus.edu.sg

Cytotoxicity and Cell Adhesion of PLLA/keratin Composite Fibrous Membranes

Lin Li[1], Yi Li[1*], Jiashen Li[1], Arthur F.T. Mak[2], Frank Ko[3] and Ling Qin[4]

[1]Institute of Textiles and Clothing, The Hong Kong Polytechnic University, Hong Kong, China
[2]Department of Health Technology and informatics, The Hong Kong Polytechnic University, Hong Kong, China
[3]Department of Materials Engineering, AMPEL, The University of British Columbia, Vancouver, Canada
[4]Dept of Orthopaedics and Traumatology, The Chinese University of Hong Kong, Hong Kong, China

Abstract — **Fibrous membranes composed of wool keratin and Poly-L-Lactide (PLLA/keratin) were prepared using wool keratin particles, with the weight ratios of PLLA/keratin at 2:1, 1:1, 1:2, 1:4 and 1:8. In vitro cytotoxicity tests and cell adhesion experiments were performed on these fibrous membranes using osteoblasts for assessment of the cytocompatibility of the membranes. The cytotoxicity of the PLLA and PLLA/keratin fibrous membranes changed as the concentration of wool keratin increased. PLLA/keratin at a ratio of 2:1 or 1:1 was nontoxic to the cells, while 1:4 and 1:8 PLLA/keratin membranes were remarkably cytotoxic. In addition, cell adhesion was influenced by the keratin concentration. Cell adhesion to the membranes decreased when keratin concentration increased. These results suggest that high concentration of wool keratin can be cytotoxic, and the concentration of wool keratin particles influences the cell adhesion on PLLA/keratin fibrous membranes significantly.**

Keywords — **Wool keratin, PLLA, Cytotoxicity, Cell adhesion, Tissue engineering**

I. Introduction

Tissue engineering employs natural and synthetic polymers to fabricate biomedical scaffolds [1-12]. Two basic preconditions are necessary for biomedical materials which support cell proliferation for tissue regeneration. Firstly, they should be non-cytotoxic [13] and secondly, they should allow cell proliferation [1, 6-9].

Arising from different compositions such as silk, collagen, chitin, chitosan, and other proteins, polymers play a pivotal role as biomaterials for tissue engineering [4-6, 8, 12, 14-22]. Poly-L-Lactide (PLLA), which is a kind of biodegradable polymer with high biocompatibility, was thought to be suitable for potential biomedical applications in the human body [5, 12, 23].

From our previous investigation, wool keratin/PLLA composite fibrous membranes were found to improve cell proliferation [24]. Thus, in this study, in vitro cytotoxicity tests and cell adhesion experiments were undertaken to assess the effects of PLLA/keratin composite fibrous membranes on cell proliferation.

II. Materials and Methods

A. Materials

Poly-L-Lactide (PLLA) (IV6-8) was purchased from Purac, Netherlands Ltd. Wool fibres were purchased from the Nanjing Wool Market. Wool keratin particles were obtained by using spray drier (Buchi, B-290) and wool keratin emulsion which was prepared according to a patent-pending technique [25].

B. Fabrication of PLLA/keratin Fibrous Membranes

Nano wool keratin particles and PLLA were added into an organic solvent mixture composed of chloroform and N, N-dimethylformamide (DMF) (10:1, w/w) and subjected to electrospinning to obtain PLLA/keratin fibres at weight ratios of 2:1, 1:1, 1:2, 1:4 and 1:8 (Pk21, Pk11, Pk12, Pk14 and Pk18 respectively) [26].

C. Cytotoxicity Test

According to the standard, EN ISO 10993-12:2007, sterilized membranes were rinsed with PBS three times, then immersed into culture medium at the ratio of 0.1g/mL and kept in the incubator at 37°C for 24 hr to get the extractions. The extractions of the membranes were applied for cell culture. Meanwhile, PLLA extraction was used as a negative control. Cells (25μl) at a density of 4×10^5 cells/ml were seeded in a 96-well plate, to which was added membrane extraction and normal culture medium. Morphological changes of the cells were observed through an inverted microscope [27].

D. Cell Adhesion

Osteoblasts (MC3T3, ATCC) used in this study were maintained in Dulbecco's Modified Eagle's Medium (DMEM) with 10% foetal bovine serum (FBS, Invitrogen, USA) in a 37°C and 5% CO_2 incubator. The medium was replaced twice weekly. All of the membranes were sterilized by ultraviolet irradiation for 20 minutes after being immersed in 70% ethanol for 1 hour. Each membrane was

Chwee Teck Lim, James C.H. Goh (Eds.): ICBME 2008, Proceedings 23, pp. 1492–1495, 2009
www.springerlink.com

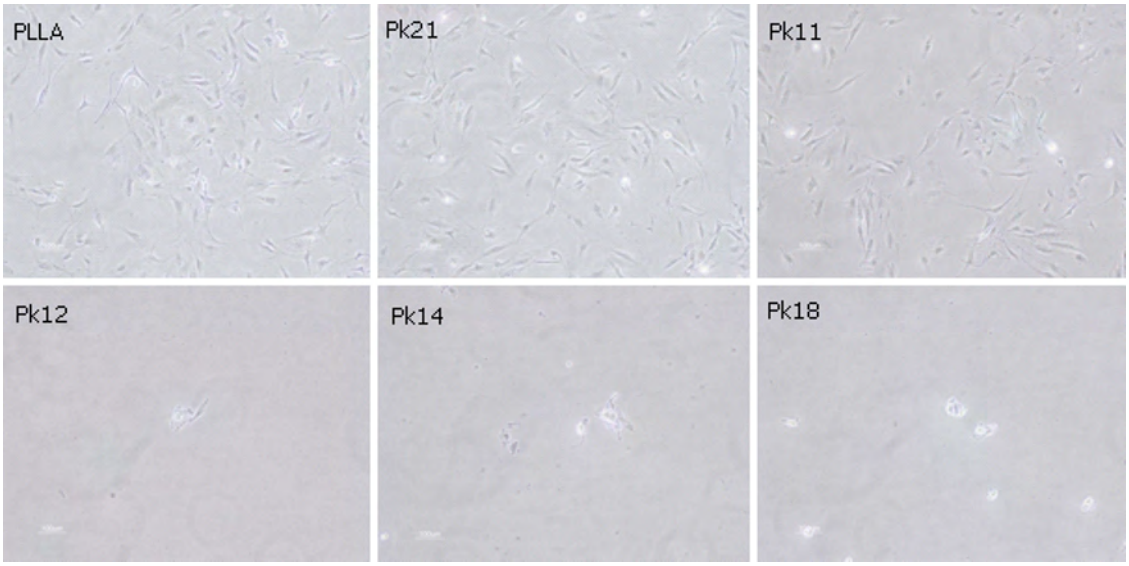


Fig.1. Morphological changes of cells cultured with different extractions of PLLA/keratin fibrous membranes. Morphological changes and detachment of the cells were observed in the extractions of Pk12, Pk14 and Pk18 membranes through the inverted microscope.

seeded with 2×10^4 cells and kept in the incubator for one day. An MTS assay was employed to assess the cell adhesion on membranes.

E. Scanning Electron Microscopy (SEM)

Electrospun fibrous membranes with cells were coated with gold and then their morphologies were observed by scanning electron microscopy (JEOLJSM-6335F, 20kV).

F. Statistical Analysis

Values were expressed as means ± standard deviations. Statistical differences were determined by one-way Analysis of Variance (ANOVA). *P* values of less than 0.05 were considered to be statistically significant.

III. Results

A. Cytotoxicity of PLLA and PLLA/keratin Membranes

To determine the cytotoxic effects of the PLLA/keratin fibrous membranes, cytotoxicity tests were performed using the membrane extractions.

The morphological changes and detachment of the cells were observed through an inverted microscope. As shown in Fig.1, the Pk12, Pk14 and Pk18 membranes inhibited cell proliferation. The Pk21 and Pk11 membranes did not change the cell morphology significantly, which implies that these two membranes are suitable for cell proliferation.

B. Cell Adhesion

Cells were cultured on PLLA and PLLA/keratin membranes for one day before applying an MTS assay for checking cell adhesion (see Fig.2 which compares PLLA and PLLA/keratin fibrous membranes).

As shown in Fig. 2, the cell adhesion of Pk21 is significantly higher than that of the other Pk membranes, and there

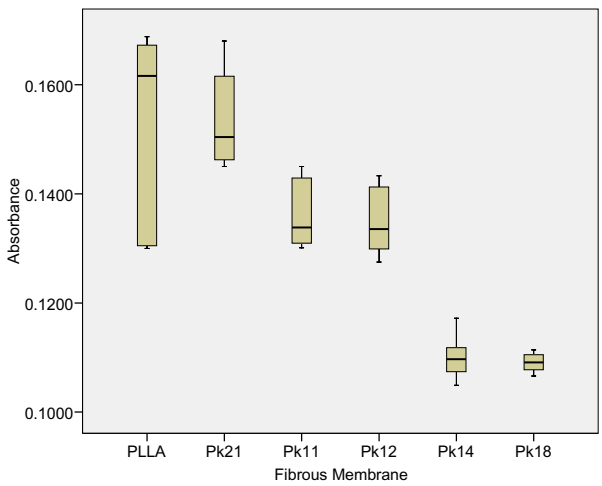


Fig.2. MTS assay results of cell adhesion on PLLA and PLLA/keratin fibrous membranes. Pk21 is significantly higher than that of the other Pk membranes and there is no significant difference between the Pk21 and PLLA membranes.

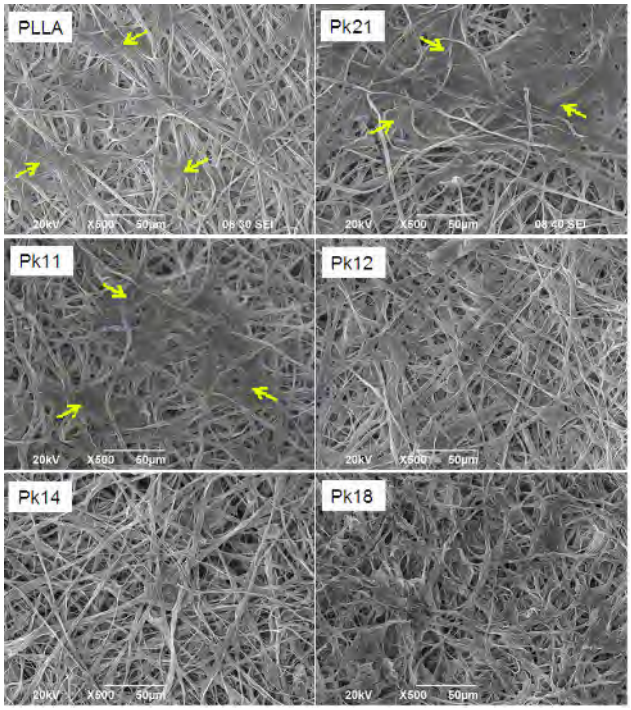


Fig.3. SEM images of PLLA/keratin fibrous membranes with cells cultured for three days. Cells can be seen stretched and spread like translucent films on PLLA, Pk21 and Pk11 membranes (arrows), few cells can be seen on the Pk12, Pk14 and Pk18 membranes.

is no significant difference between the Pk21 and PLLA membranes.

In addition, cells had been cultured on membranes for three days for observing cell adhesion through SEM. In accordance with the MTS assay results, confluent cells were found to stretch and spread spanning the fibers as translucent films on PLLA, Pk21 and Pk11 membranes (Fig.3, arrows), while confluent cells were hard to be seen on the other Pk membranes.

IV. Discussion

Tissue engineering matrices for loading cells have to fulfill two preconditions. Firstly, they must not be cytotoxic [13]. Secondly, they must be suitable for cell adhesion [7, 18]. In this study, PLLA/keratin fibrous membranes were assessed to discover whether they fulfilled these two preconditions.

In vitro cytotoxicity tests were firstly performed using the extractions of the membranes to determine which membranes were cytotoxic. The Pk12, Pk14 and Pk18 membranes were found to inhibit cell proliferation. The cells cultured in the extractions of these three membranes underwent significant morphological changes, and very few cells could be seen through the inverted microscope. These observations suggested that high concentrations of wool keratin can be cytotoxic.

In addition, the cell adhesion result for the Pk21 membrane was significantly higher than those of the other Pk membranes. Although it was not obvious in one day cell adhesion experiment, the Pk11 membrane showed the potential for cell adhesion in SEM images. These results imply that the level of cell adhesion is one of the important factors for successful cell proliferations on Pk membranes.

Tachibana *et al*. reported that wool keratin scaffolds would be useful for long-term and high-density cell culture [19, 20]. Our previous study also found that the Pk membranes improved cell proliferation significantly [24]. As a degradable material, PLLA could provide a good matrix for long-term cell culture scaffolds with a non-cytotoxic wool keratin concentration. So, PLLA/keratin composite membranes are reasonable scaffolds for tissue engineering.

In summary, wool keratin can influence the cell adhesion on PLLA/keratin fibrous membranes significantly, and using the right concentration will avoid the problem of cytotoxicity.

V. Conclusions

High concentrations of wool keratin can be cytotoxic, and the concentration of wool keratin particles influences cell adhesion on PLLA/keratin fibrous membranes significantly. Thus, PLLA/keratin membranes of the correct ratio can provide a non-cytotoxic surface for cell adhesion.

Acknowledgments

We would like to express our gratitude to the Hong Kong Research Grant Council, the Technology Innovation Commission/HKRITA and the Hong Kong Polytechnic University for supporting this research through projects PolyU 5281/03E, ITP-001-07-TP and G-YE51.

References

1. Moroni L, Licht R, de Boer J et al. (2006) Fiber diameter and texture of electrospun PEOT/PBT scaffolds influence human mesenchymal stem cell proliferation and morphology, and the release of incorporated compounds. Biomaterials 27: 4911-4922.
2. Li WJ, Laquerriere P, Laurencin CT et al. (2002) Electrospun nanofibrous structure: A novel scaffold for tissue engineering. Journal of biomedical materials research 60: 613-621.
3. Li WJ, Tuli R, Huang XX et al. (2005) Multilineage differentiation of human mesenchymal stem cells in a three-dimentional nanofibrous scaffold. Biomaterials 26: 5158-5166.

4. Putthanarat S, Eby RK, Kataphinan W et al. (2006) Electrospun Bombyx mori gland silk. Polymer 47: 5630-5632.
5. Bos RRM, Rozema FR, Boering G et al. (1991) Degradation of and tissue reaction to biodegradable poly (L-lactide) for use as internal fixation of fractures: a study in rats. Biomaterials 12: 32-36.
6. Tomihata K, Ikada Y. (1997) In vitro and in vivo degradation of films of chitin and its deacetylated derivatives. Biomaterials 18: 567-575.
7. Kwon IK, Kidoaki S, Matsuda T. (2005) Electrospun nano- to microfiber fabrics made of biodegradable copolyesters: structural characteristics, mechanical properties and cell adhesion potential. Biomaterials 26: 3929-3939.
8. Sukigara S, Gandhi M, Ayutsede J et al. (2003) Regeneration of Bombyx mori silk by electrospinning. Part 1. Processing parameters and geometric properties. Polymer 44: 5721-5727.
9. Ji Y, Ghosh K, Shu XZ et al. (2006) Electrospun three-dimensional hyaluronic acid nanofibrous scaffolds. Biomaterials 27: 3782-3792.
10. Reneker DH, Chun I. (1996) Nanometre diameter fibres of polymer, produced by electrospinning. Nanotechnology 7: 216-223.
11. Xin XJ, Hussain M, Mao JJ (2007). Continuing differentiation of human mesenchymal stem cells and induced chondrogenic and osteogenic lineages in electrospun PLGA nanofiber scaffold. Biomaterials 28: 316-325.
12. Noh HK, Lee SW, Kim JM. (2006) Electrospinning of chitin nanofibers: Degradation behavior and cellular response to normal human keratinocytes and fibroblasts. Biomaterials 27: 3934-3944.
13. Alt V, Bechert T, Steinrucke P. (2004) An in vitro assessment of the antibacterial properties and cytotoxicity of nanoparticulate silver bone cement. Biomaterials 25:4383-4391.
14. Venugopal JR, Zhang YZ, Ramakrishna S. (2006) In vitro culture of human dermal fibroblasts on electrospun polycaprolactone collagen nanofibrous membrane. Artificial Organs 30: 440-446.
15. Ayutsede J, Gandhi M, Sukigara S. (2006) Carbon nanotube reinforced bombyx mori silk nanofibers by the electrospinning process. Biomacromolecules 7: 208-214.
16. Li MY, Mondrinos MJ, Gandhi MR et al. (2005) Electrospun protein fibers as matrices for tissue engineering. Biomaterials 26: 5999-6008.
17. Sukigara S, Gandhi M, Ayutsede J et al. (2004) Regeneration of Bombyx mori silk by electrospinning. Part 2. Process optimization and empirical modeling using response surface methodology. Polymer 45: 3701-3708.
18. Chen Y, Cho MR, Mak AFT et al. (2008) Morphology and adhesion of mesenchymal stem cells on PLLA, apatite and apatite/collagen surfaces. J Mater Sci: Mater Med 19: 2563-2567.
19. Tachibana A, Furuta Y, Takeshima H et al. (2002) Fabrication of wool keratin sponge scaffolds for long-term cell cultivation. Journal of Biotechnology 93:165-170.
20. Tachibana A, Kaneko S, Tanabe T et al. (2005) Rapid fabrication of keratin-hydroxyapatite hybrid sponges toward osteoblast cultivation and differentiation. Biomaterials 26: 297-302.
21. Katoh K, Tanabe T, Yamauchi K. (2004) Novel approach to fabricate keratin sponge scaffolds with controlled pore size and porosity. Biomaterials 25: 4255-4262.
22. Ye P, Xu ZK, Wu J et al. (2006) Nanofibrous poly (acrylonitrile-co-maleic acid) membranes functionalized with gelatin and chitosan for lipase immobilization, Biomaterials 27: 4169-4176.
23. Chen VJ, Ma PX. (2006) The effect of surface area on the degradation rate of nano-fibrous poly (L-lactic acid) foams. Biomaterials 27: 3708-3715.
24. Li L, Li Y, Li JS et al. (2008) The Effects of PLLA/keratin Composite Fibrous Scaffolds on the Proliferation of Osteoblasts, TBIS Proceedings, International Symposium of Textile Bioengineering and Informatics, Hong Kong, China, 2008, pp 696-699.
25. Li Y, Xu T, Hu et al. (2004) Preparation of nano functional wool protein crystallites (colloid crystal) by nano- emulsification method. China Patent, CN1693371.
26. Li JS, Li Y, Li L et al. (2008) Preparation and Degradation of PLLA/keratin Electrospun Membranes. TBIS Proceedings, International Symposium of Textile Bioengineering and Informatics, Hong Kong, China, 2008, pp 654-658.
27. Li L, Li Y, Li JS et al. (2008) Antibacterial and non toxic nano silver PLLA composites for tissue engineering. International conference on Multi-functional Materials and Structures, Hong Kong. 28 July-31 July, 2008. Advanced Materials Research 47-50: 849-852.

Author: Yi Li
Institute: Institute of Textiles and Clothing,
The Hong Kong Polytechnic University
Street: Hung Hom
City: Hong Kong
Country: China
Email: tcliyi@inet.polyu.edu.hk

Tissue Transglutaminase as a Biological Tissue Glue

P.P. Panengad[1], D.I. Zeugolis[2] and M. Raghunath[3]

[1]Tissue Modulation Laboratory, Division of Bioengineering, Faculty of Engineering, National University of Singapore, Singapore
[2]National Center for Biomedical Engineering Science, National University of Ireland, Galway, Ireland
[3]Tissue Modulation Laboratory, Division of Bioengineering, Faculty of Engineering, & Department of Biochemistry, Yong Loo Lin School of Medicine, National University of Singapore, Singapore

Abstract — **Surgeons have long sought an efficient biological method of wound repair that requires little time and minimizes discomfort for their patients, yet produces a good cosmetic outcome. Our aim is to develop a biological tissue glue based on the extracellular matrix stabilizing enzyme transglutaminase 2 to covalently bond tissue layers to promote suture-less closure of surgical wounds. We used human skin tissue as a model to test our hypothesis. Human skin samples were studied for endogenous transglutaminase activity and probed for target structures for commercial enzyme using standardized histochemistry. Tissue bonding between two skin sections was monitored under phase contrast microscopy.**

Keywords — **Transglutaminase, biological tissue glue, skin, histochemistry**

I. Introduction

Transglutaminases (TGases) constitute a family of enzymes that stabilize protein assemblies by Gamma-glutamyl Epsilone-lysine crosslinks [1]. Six different gene products are so far known in the human genome, of which at least three play important roles in the skin. TGase 2 (tissue TGase) is likely to be involved in crosslinks anchoring fibrils of the dermoepidermal junction [2] and is active during different phases of wound healing and can function to promote wound repair [4]. We hypothesize that primary closure of wounds by covalent transamidation cross linking of extra cellular matrix proteins will achieve wound repair at molecular level, efficient primary intention healing and thereby prevention of scarring, due to high biocompatibility.

II. Methods

A. Assay of native Transglutaminase activity

Cryostat sections (5μm) of human skin were assayed for native transglutaminase activity as described earlier [3].

B. Assay of exogenous Transglutaminase activity

Cryosections (5μm) of human skin were air-dried for 10 min at room temperature (RT), incubated with 10 mM solution of TGase inhibitor iodoacetamide in 0.1 *M* Tris/HCl, pH 8.4, for 1.5 h and washed in PBS. Assay of residual native TGase activity was performed in one section and the rest of the sections were then incubated for 1.5 h at RT with transglutaminase & substrate peptide in the buffer at different concentrations at pH 8.4. The TGase reaction stopped with EGTA was used as control. The slides washed in PBS were incubated for 30 min at RT with Streptavidin-DTAF, counter stained with DAPI, and mounted after final washing in PBS. Images were captured with inverted epifluorescence microscope (Olympus IX71) [5].

C. Study of Tissue adhesive property of Transglutaminase

Commercial TGase at optimum concentration was dried on a glass slide and contact transferred to the incision surface of excised skin tissue. After transfer incision was closed by approximation and tissues were incubated for 2 h sandwiched between two tissue papers soaked in calcium buffer under optimum compression. Later the tissues were cryosectioned across the fusion and immuno-localization of commercial TGase performed, followed by activity assay of TGase and measurement of strength of adhesion. The strength of fusion was assessed by controlled stretching of the cryosections picked on a designed microscope slide and live phase contrast imaging.

III. Results

Native Ttransglutaminase Activity Assay: Native transglutaminase activity assay on human skin cryosections showed TGase activity in epidermis as well as dermis. Epidermal activity was confined to the stratum granulosum and the basement membrane. Dermal activity was diffuse but more intense in the papillary dermis which is rich in capillary plexi (Fig 1.)

Assay of exogenous Transglutaminase activity: Assay of commercial transglutaminase activity was carried out with Recombinant Human TGase 2 on human skin. Assay was performed with different concentrations of the commercial enzyme and 250 μg/ml was found to be optimum. All the

Chwee Teck Lim, James C.H. Goh (Eds.): ICBME 2008, Proceedings 23, pp. 1496–1498, 2009
www.springerlink.com

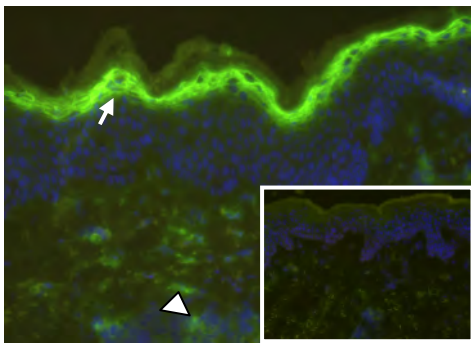


Fig. 1 Native TGase activity in skin incorporates tagged substrate peptides in the presence of calcium. Preferential activity is seen as zone of green fluorescence in both dermis (TGase2) (triangle) and epidermis (TGase1) (arrow). Picture inset - Calcium chelation with EGTA abolished enzymatic activity.

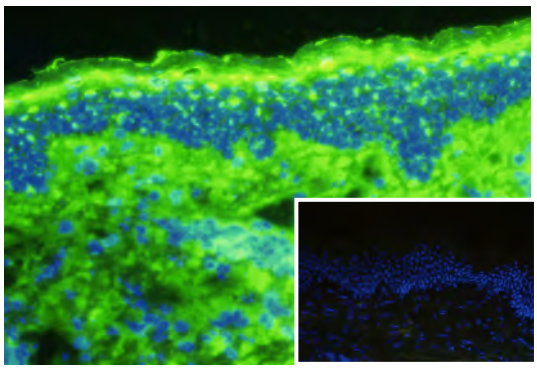


Fig. 2 Exogenous/ commercial TGase2 added to substrate cocktail crosslink the tagged peptide into all the layers of the skin with preference to the dermis indicating the presence of abundant enzyme substrate sites for this enzyme here. Picture inset - Calcium chelation with EGTA abolished enzymatic activity.

layers of human skin showed abundant substrate sites for human TGase 2 (Fig 2).

Localization and activity assay for Transglutaminase after TGase adhesion: Histology of *in vitro* tissue adhesion samples shows a solid line of fusion after TGase 2 application compared to the EGTA control. Immuno-localization of recombinant human TGase 2 indicated that surface concentrated enzyme can be contact transferred to tissue surface to achieve high concentration of the enzyme at the plane of fusion. Assay for TGase activity after tissue fusion indicated a focused and high activity at the line of fusion after contact transfer of dried enzyme (Fig 3).

Test of yielding strain: Test of yielding strain of *in vitro* skin tissue adhesion samples revealed fragmentation/failure of tissue surrounding the fusion line before achieving partial

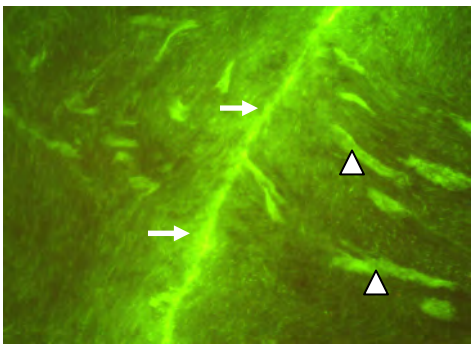


Fig. 3 Exogenous/commercial TGase2 activity along the fusion line (arrows). Native transglutaminase activity along the dermal capillaries is visible at multiple sites (triangles).



Fig. 4 Application of graded tensile force perpendicular to the TGase 2 fusion line. EGTA control: already minimal tensile strain caused gaping of tissue interfaces. TG2 Adhesive: In the presence of Ca^{++} TGase2 caused a stable fusion that withstood much higher tensile strain. At maximum, the fusion would split only partially while the surrounding tissue would fragment, demonstrating the stability of the crosslinking.

gaping of adhesion line in TGase 2 adhesion sample proving enzymatic adhesion strength matching neighboring intact skin tissue while the EGTA control sample failed at the fusion line at a very minimal level of strain (Fig 4).

IV. Conclusion

Human skin tissue has abundant dermal substrate sites for TGase2 and contact transfer of dry enzyme, concentrates active enzyme at tissue fusion plane. More over bonding strength of TGase 2 - mediated tissue adhesion matches with the surrounding skin tissue. Hence we have shown the potential of extracellular matrix crosslinking enzyme – transglutaminase 2 as a biological tissue glue to achieve rapid and efficient tissue repair.

Acknowledgment

This study was funded by a FRC group grant from the Faculty of Engineering (R-397-000-025-112). We thank the NUS Tissue Engineering Program (NUSTEP) for support for this study.

References

1. Folk JE, Finlayson JS. (1977) The epsilon-(gamma-glutamyl)lysine crosslink and the catalytic role of transglutaminases. Adv Protein Chem 31:1–133
2. Raghunath M, Höpfner B, Aeschlimann D et al (1996) Cross-linking of the dermo-epidermal junction of skin regenerating from keratinocyte autografts: anchoring fibrils are a target for tissue transglutaminase. J Clin Invest 98:1174–1184
3. Raghunath M, Hennies HC, Velten F et al. (1998) A novel in situ method for the detection of deficient transglutaminase activity in the skin. Arch Dermatol Res 290:621-627
4. Haroon ZA**,** Hettasch JM, Lai TS et al (1999) Tissue transglutaminase is expressed, active, and directly involved in rat dermal wound healing and angiogenesis. FASEB J 13:1787-95
5. DI Zeugolis, P Pradeep-Paul, ESY Yew et al. (2008) An *in situ* and *in vitro* investigation for the transglutaminase potential in tissue engineering. J Biomed Mater Res A 'in press'

The address of the corresponding author:

Author: Pradeep Paul Panengad
Institute: National University of Singapore
Street: Clementi Road
City: Singapore
Country: Singapore
Email: g0600738@nus.edu.sg

The Scar-in-a-Jar: Studying Antifibrotic Lead Compounds from the Epigenetic to the Extracellular Level in One Well

Z.C.C. Chen[1,2], Y. Peng[2] and M. Raghunath[2,3]

[1] Graduate Programme in Bioengineering, NUS Graduate School for Integrative Sciences and Engineering, Singapore
[2] Tissue Modulation Laboratory, Division of Bioengineering, Faculty of Engineering National University of Singapore, Singapore
[3] Department of Biochemistry, Yong Loo Lin School of Medicine, National University of Singapore, Singapore

Abstract — **Fibrosis represents an excessive accumulation of collagen in tissues. The resultant consequences range from cosmetic disfiguration, impairment of implants to organ failure. The development of effective anti-fibrotics is therefore an important clinical goal. Unfortunately, screening for anti-fibrotics has been limited by incomplete procollagen processing and poor matrix formation in vitro and the inability to normalise the amount of deposited collagen for the cell number in the same culture well. The "scar-in-a-jar" concept is based on advanced cell culture technology making use of macromolecular crowding. This system ensures that the complete biosynthetic and depositional cascade of collagen matrix formation is in place. We have developed a rapid (2 days) and an accelerated matrix formation protocol (6 days) with the latter allowing for crosslinking of the deposited matrix in vitro. Automated adherent cytometry and in situ quantitation of immunofluorescence intensity of extra- and intracellular antigens is combined with automated image acquisition and semi-automated image processing, This discovery tool allows for a novel *in situ* assessment of the area of deposited collagen(s) normalised to cell number thereby simultaneously monitoring cell proliferation/cytotoxicity. In addition, multiplexing enables quantitation to include non-collagenous ECM proteins. Bioimaging data obtained with known and novel antifibrotic compounds at the epigenetic (histone deacetylase), post-transcriptional (miRNA), post-translational (Prolyl-4-hydroxylase) and post-secretional level (C-proteinase, lysysl oxidase, matrix metalloproteinase-1) correlated excellently with biochemical analyses.**

Keywords — **Fibrosis, collagen, quantitation, bioimaging, macromolecular crowding**

I. Introduction

Scarring, a physiological tissue response to wounding, has been highly conserved in evolution and across species. As the last step of the wound-healing cascade it is usually self-contained. However, if this step is perpetuated by repeated tissue insults and/or ongoing inflammation, fibrosis ensues. Its histopathological correlate is an excessive production and deposition of collagen that converts normal tissue into scar tissue with associated loss of function. Therefore, causes as diverse as chronic infections, radio -and chemotherapy, chronic exposure to alcohol and other toxins can all lead to fibrosis with a considerable global disease burden. Not only organ, but also localized fibrosis can severely impair the quality of life in millions of patients, for example through implant failure .

The development of effective antifibrotics is therefore an important unmet clinical need. It necessitates careful *in vitro* screening of lead compounds before they are tested in animal models. However, this has been severely hampered by biological and technical problems. Firstly, fibrogenic cells in monolayer culture do not lay down significant amounts of collagen in a useful time window for screening. This is due to a tardy enzymatic conversion of procollagen to collagen in vitro even under full procollagen synthesis[1]. Secondly, the amount of deposited extracellular matrix (ECM) in relation to the number of cells in the same culture well currently requires the destruction of cell layers to obtain protein or DNA [2]. Whatever little collagen is deposited in the ECM must be solubilized prior to analysis [3]. Thirdly, collagen quantitation is problematic with non-specific methods like the popular picro-sirius red dye assay[4]. Determination of hydroxyproline content is far more collagen-specific, however it is tedious and time consuming. Other methods which rely on laser scanning confocal microscopy[5] are slow during image acquisition and are not capable of handling multi-well plates.

Lastly, antifibrotics should preferably target collagen, and the monitoring of other ECM proteins should be done to confirm a specific down-regulation of collagen in order to rule out undesired inhibition of general protein synthesis. For the first time, all these features have been combined to allow for multiplex analysis in one well.

II. Materials and Methods

A. Cell culture

Normal primary lung fibroblasts (WI-38) were selected on the basis of their strong collagen I production in our hands. The cells were routinely cultured at low passage (3-8) as outlined earlier [1]. Fibroblasts were seeded on

Chwee Teck Lim, James C.H. Goh (Eds.): ICBME 2008, Proceedings 23, pp. 1499–1502, 2009
www.springerlink.com

24-well Cellstar plates (Greiner BioOne) at 50,000/well in 10% FBS, 5% CO_2 at 37°C. After 16 hours, the medium, was changed to DMEM containing 0.5 % FBS, 100 μM of L-ascorbic acid phosphate magnesium salt η-hydrate with or without 500kDa dextran sulfate (DxS) at 100 μg/mL or a combination of 37.5 mg/mL Ficoll 70 with 25 mg/mL Ficoll 400 (Fc). 5 ng/mL transforming growth factor β1 (TGFβ1), in combination with or without antifibrotic substances was added at the same time. Only 2,4-PDCA and BAPN were added daily to Fc crowded cell cultures (accelerated mode).

B. Optical analysis

A bioimaging station comprising of a Nikon TE600 fluorescence microscope plus Xenon illuminator, with an automated Ludl stage and shutter, and equipped with a Photometrics CoolSNAP high sensitivity cooled monochrome CCD camera (model HQ, Roper Scientific) camera was used. Screening of 24-well multiwell plates was made possible by an automated stage and autofocus capabilities. 9 image sites per well were acquired at 2X magnification, stored and analyzed using the Metamorph ® Imaging System software (Molecular Devices). The Count Nuclei module was used for cell enumeration with specific parameters in order for a region to be considered as a positive count (countable nucleus): 1) Areas with pixel intensity value 15 above that of the background. 2) Fluorescent areas with a minimum length of 10 μm and a maximum length of 15 μm. The Integrated Morphometry Analysis module was used to quantify the area of fluorescent collagen I staining which had been deposited on the cell layer. Controls were used to determine suitable fluorescent intensity thresholds (300 for the DxS model and a range between 500-550 for the Fc model) fluorescent signals below a defined pixel intensity value were thresholded out, which eliminated measurement of the background area. Triangle masks were added to eliminate quantitation of corner auto-fluorescence. This analysis resulted in a data set expressed as area of collagen I per nuclei in μm^2 per image field.

III. Results and Discussion

A. 2 collagen deposition modes

The rapid deposition mode is based on our previous observation that negatively charged macromolecules induce dramatic collagen deposition in 48-72 hours in contrast to neutrally charged ones[1, 6]. However, we discovered that neutral Ficoll 70 and 400 in combination double collagen deposition after 6 days in comparison to standard culture,

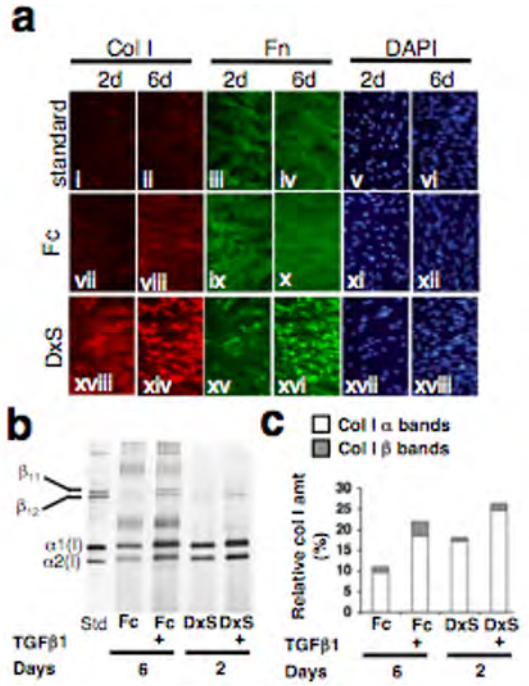


Figure 1. Rapid and accelerated collagen deposition modes. (a) Immunocytochemistry: standard culture with reticular fibronectin matrix and minimal collagen I deposition (i-iv), Fc (accelerated): enhanced reticular collagen I/fibronectin matrix (vii-x). DxS (rapid): granular aggregates of collagen I/fibronectin (xiii-xvi) with highest ECM content. 40x magnification. (b) SDS-PAGE analyses of collagen matrix content in both deposition modes in the absence/presence of TGFβ1. With TGFβ1 both deposition modes give more and faster matrix formation including stronger lysyl oxidase-mediated cross-linking (c) Densitometry of (b).

and remarkably, with a reticular deposition pattern. Thus, amount, velocity and morphology of collagen deposition can be controlled by crowding mode (Fig. 1). The accelerated mode with its longer culture time also produces collagen with a larger extent of cross-linking (Fig. 1b).

TGFβ1 increased collagen I deposition by another 1.5-2 fold in the rapid mode. Neutral mixed crowding in the accelerated mode for six days resulted in the doubling of collagen deposition in comparison to non-crowded cultures, and an additional 2-fold increase in the presence of TGFβ1 (Fig. 1c). Moreover, this mode resulted in a fibrillar collagen meshwork with a more even spread of immunosignal (Fig. 1a). TGFβ1 has pleiotropic effects, it slows down matrix turnover by reducing MMP1-expression, upregulating lysyl oxidase activity and increasing the presence of tissue derived inhibitors of MMP's. These effects only come into play with a deposited matrix, underlining the importance of the holistic approach represented by this screening system.

B. Image processing and capturing

To match circular well geometry with rectangular image capturing fields, a macro was written to automatically add triangular masks to conceal auto-fluorescence from the curvature of the wells during quantitation (Fig. 2a-iii and iv). The final quantitation area represents 54% of the total well area, but 83% of assessable area that includes a safety distance from well edges to avoid cell distribution irregularities (Fig. 2a-iv). This capturing mode in combination with a long-range 2x objective renders the bioimaging station independent of the use of expensive optical plates. For cell enumeration, images of DAPI stained nuclei were scored by the software for counting (see Methods (Fig. 2b-i and ii)), and images of immunostained collagen I were thresholded such that pixels with a fluorescent intensity above a selected value derived from controls, were demarcated by the software for quantitation (Fig. 2b-iii and iv). As both area and fluorescent intensity per cell correlated closely with densitometric data, area was selected as a parameter of collagen I deposition (Fig. 2c).

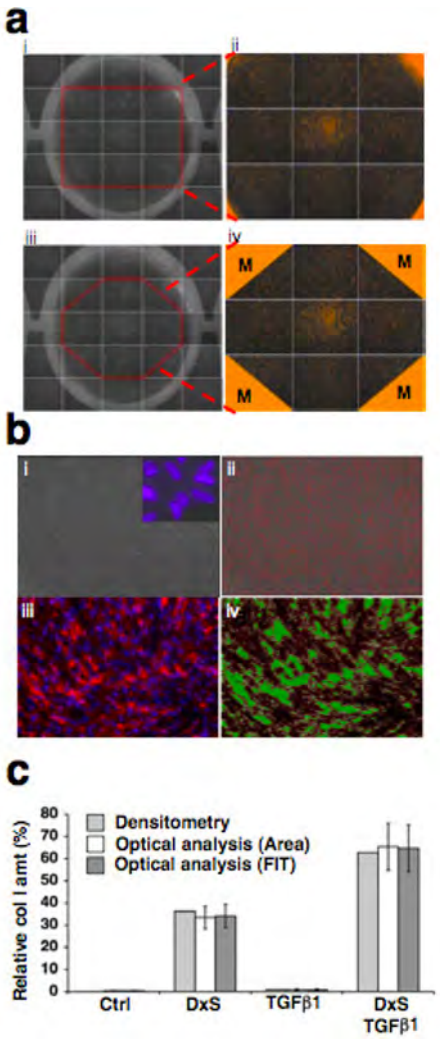


Figure 2. Image acquisition and quantitation of rapid collagen deposition mode. (a) (i) 2x magnification of cells in a 1.9 cm^2 well with superimposed original rectangular image acquisition area (red box). (ii) enlarged red box: corner auto-fluorescence (arrows). (iii and iv) acquisition area after application of triangular masks to eliminate corner auto-fluorescence. (b) Cytometry and quantitation of the area of deposited collagen I. (i) DAPI-stained nuclei at 2x magnification in monochrome pseudocolor, 60x mag (inset). (ii) red scored nuclei by Count Nuclei module for cytometry. (iii) immunostained deposited collagen I. (iv) Regions with fluorescent pixel intensity above a selected threshold are demarcated by the software in green for quantitation of deposited collagen I area. (c) Densitometry versus image analysis for collagen I quantitation.

C. Testing known and novel antifibrotics

Known and novel agents with anti-fibrotic potential were employed to interfere with various key steps along the collagen biosynthesis pathway. Reduction of collagen I deposition relative to untreated controls in both deposition modes was used as a read-out for antifibrotic efficacy. Biochemical analyses were always run in parallel to ascertain the reliability of the optical analyses.

In the absence of TGFβ1, **Trichostatin A (TSA),** a histone deacetylase inhibitor, reduced collagen I deposition to 60% (rapid) and 43% (accelerated). In the presence of TGFβ1, collagen I was reduced to 65% (rapid) and 29% (accelerated), close to baseline amounts of normal conditions without TGFβ1 (Fig. 3a).

We had recently predicted micro RNA **miR29c** to target procollagen $\alpha1_{(I)}$ mRNA by the *rna*22 algorithm[7] and we employed it in the rapid deposition mode. Both negative controls (scrambled oligos) did not affect collagen I deposition. In contrast, pre-miR29c (P29c) reduced collagen I deposition in the absence of TGFβ1. Particularly in the presence of this growth factor, 10 nM and 1 nM P29c reduced collagen I to 13% and 28% of mock transfected controls (Fig. 3b).

Collagen prolyl-4-hydroxylase inhibitors like **2,4-PDCA** and **ciclopirox olamine** render collagen triple helices less thermostable and thus prevent their secretion. Reduction of collagen I was observed in both deposition modes (Fig. 3c). Particularly in the presence of TGFβ1, 2,4-PDCA reduced collagen I deposits to 24% (rapid) and 23% (accelerated). CPX to 2% (rapid) and 20% (accelerated), and in the presence of TGFβ1, to 1% (rapid) and 12% (accelerated) (Fig. 3c). Effects of the hydrophilic 2,4-PDCA were evident in the accelerated mode only if added daily after the first 48 hrs. In contrast, the highly lipophilic CPX had to be added only once.

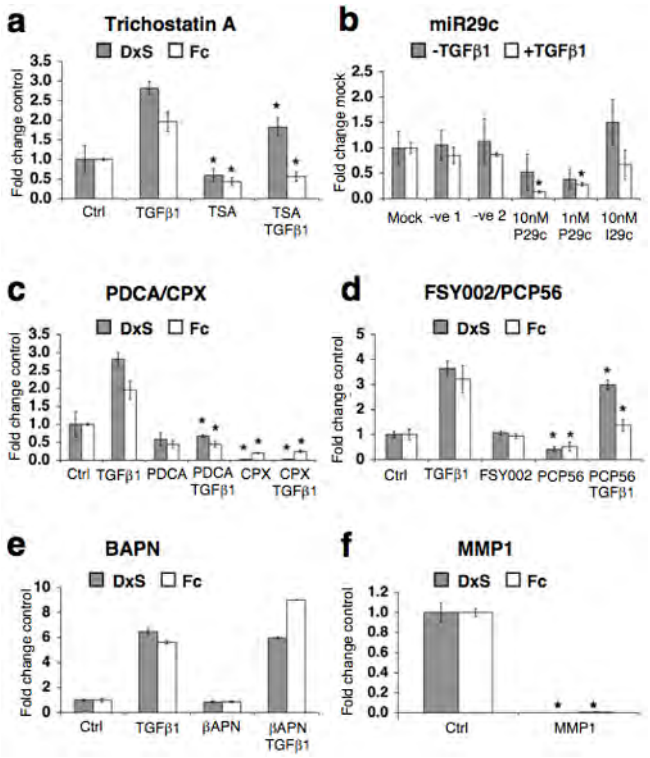


Figure 3 Intra- and extracellular perturbation of collagen biosynthesis by various known and novel inhibitors. Data are expressed as mean ± s.d., calculated from triplicates and as collagen area/cell -fold changes over respective controls

Procollagen C-proteinase/BMP1 controls the supra-molecular assembly of collagen into fibrils via removal of the C-terminal propeptide from the procollagen I molecule. Of two novel inhibitors, the phosphinate **FSY002** did not show any effects, whereas the sulfonamide **PCP56** reduced the deposited area of collagen I to 40% (rapid) and 52% (accelerated), and in the presence of TGFβ1 to 82% (rapid) and 43% (accelerated) (Fig. 3d).

β-aminoproprionitrile (BAPN) irreversibly inhibits lysyl oxidase, an amine oxidase that is crucial in stabilizing ECM by cross-linking collagen chains. In both deposition modes, BAPN caused no reduction of area collagen I/cell (Fig. 3e).

MMP1 controls collagen turnover in the ECM by cleaving collagen at a single site. Cell layers with ECM created under both deposition modes were exposed to exogenous recombinant MMP1. We observed detachment of cells during MMP1 treatment especially in matrix derived from the rapid mode. Therefore, the total area of collagen I/well was quantified without normalisation for cell numbers. MMP1 reduced the area of deposited collagen I to 0.03% and 0.6% in the rapid and accelerated modes respectively (Fig. 3f).

IV. Conclusion

In conclusion, the Scar-in-a-Jar offers a novel pathophysiologically relevant screening tool for antifibrotic lead compounds that shall prove highly useful in indication discovery and evaluation of novel compounds to cure fibrosis, which is a serious global clinical problem yet to be solved.

Acknowledgements

The Authors would like to thank the NUS Tissue Engineering Programme. MR would like to acknowledge funding by a start-up grant from Provost and the LSI of NUS, the Faculty of Engineering (FRC) and NMRC. The technical support of Mr Larry Cheung and Mr John Xu from Microlambda Pte is gratefully acknowledged. Dr Andrew Thomson, Genome Institute of Singapore helped greatly with the design of miRNA29c experiments.

References

1. Lareu, R.R., et al., *In vitro enhancement of collagen matrix formation and crosslinking for applications in tissue engineering: a preliminary study*. Tissue Eng, 2007. **13**(2): p. 385-91.
2. McAnulty, R.J., *Methods for measuring hydroxyproline and estimating in vivo rates of collagen synthesis and degradation*. Methods Mol Med, 2005. **117**: p. 189-207.
3. Anderson, S.M. and R.J. Elliott, *Evaluation of a new, rapid collagen assay*. Biochem Soc Trans, 1991. **19**(4): p. 389S.
4. Xu, Q., et al., *In vitro models of TGF-beta-induced fibrosis suitable for high-throughput screening of antifibrotic agents*. Am J Physiol Renal Physiol, 2007. **293**(2): p. F631-40.
5. Antonini, J.M., et al., *Application of laser scanning confocal microscopy in the analysis of particle-induced pulmonary fibrosis*. Toxicological Sciences, 1999. **51**(1): p. 126-134.
6. Lareu, R.R., et al., *Collagen matrix deposition is dramatically enhanced in vitro when crowded with charged macromolecules: the biological relevance of the excluded volume effect*. FEBS Lett, 2007. **581**(14): p. 2709-14.
7. Miranda, K.C., et al., *A pattern-based method for the identification of MicroRNA binding sites and their corresponding heteroduplexes*. Cell, 2006. **126**(6): p. 1203-17.

Author: Michael Raghunath
Institute: National University of Singapore
Street: DSO Building (Kent Ridge) 27 Medical Drive S(117510)
City: Singapore
Country: Singapore
Email: bierm@nus.edu.sg

Engineering and Optimization of Peptide-targeted Nanoparticles for DNA and RNA Delivery to Cancer Cells

Ming Wang[1], Fumitaka Takeshita[2], Takahiro Ochiya[2], Andrew D. Miller[1] and Maya Thanou[1]

[1]Genetic Therapies Centre, Department of Chemistry, Imperial College London, London
[2]Section for Studies on Metastasis, National Cancer Centre, Tokyo, Japan

Abstract — **We are interested in the design and assembly of nanoparticles designated for delivery to cancer cells. Through the controlled manipulation of surface ligands, we have developed a lipid-based gene vector that improves cancer-specific delivery. Our ligand of interest is a short peptide with high affinity for the Urokinase Plasminogen Activator receptor (uPAR), a receptor overexpressed on the surface of many tumours. We modified the surface of optimized liposomal vectors with uPAR-specific peptides by physical and chemical incorporation methods. Using luciferase-based i*n vitro* and *in vivo* models, we demonstrate the improved efficiency of such targeted nanoparticles by DNA transfection and RNAi protein knockdown. We conclude that both the nature of the liposomal platform (stability, zetapotential), along with the presentation of surface ligands, contribute to the maximisation of a nanoparticle's targeting effect.**

Keywords — **liposome, peptide, cancer, receptor targeting, nanoparticle assembly**

I. Introduction

To aid site-specificity and uptake of nano-sized cancer therapies, nanoparticles must be formulated to exhibit optimised characteristics and surface chemistries. Size, for example is an important feature, where diameters of under 150nm are required to fit through the fenestration in the tumour epithelial cells. [1] Generation of appropriate surface chemistries is essential in preventing inter-nanoparticle aggregation in circulation, an environment where nanoparticles are also subject to being coated with and masked by serum proteins. Varying surface zeta potentials, as well as incorporating stealth polymers such as polyethylene glycol chains are methods of minimising aggregation. To improve site-specific delivery, ligands with specific affinity can be used to decorate the nanoparticles' surface, through either covalent or non-covalent attachment. These ligands act as a homing device, guiding nanoparticles towards cells which express the receptor to which the ligands have affinity for, and aiding cellular uptake by inducing receptor-mediated endocytosis.

The receptor we want to target is the urokinase plasminogen activator receptor (uPAR), a receptor found to be over-expressed on a variety of cancer cells such as those of the prostate and the breast. [2, 3] Its natural ligand, the urokinase plasminogen activator (uPA) binds to uPAR, forming an uPAR-uPA conjugate that enters cells by clathrin-coated, receptor-mediated endocytosis. [4] Studies by Appella *et. al.* have described the binding sequence within uPA that is involved in the binding to uPAR. [5] Derived from this sequence is a 11mer peptide, u11, with which previous studies in our group have shown to have high binding affinity for the uPAR. Using different methods of surface modification, we intend to study the effect of extension of ligands from the nanoparticle surface on ligand-targeting efficiency.

Firstly using luciferase-based reporter gene plasmid DNA assays, we investigated and optimised parameters such as charge and ligand organisation for improved receptor bio-recognition and targeting. Then by using RNA interference technology (knocking down protein expression by delivery mRNA-inhibiting siRNA), we showed that the optimised liposomal platform for in vivo delivery can successfully down-regulate luciferase expression in a bone metastatic mouse model.

II. Materials and methods

All cell lines were obtained from ATCC. Lipids were purchased from Avanti Polar Lipids. All amino acids and peptide synthesis reagents were from Novabiochem. Cell culture reagents were purchased from Invitrogen.

A. Nanoparticle preparation

The liposomal platform was formulated with lipids at different molar ratios. These include cationic lipids CDAN and DODAG (Imuthes), fusogenic (DOPE), PEGylated plus the targeting lipids. Lipids were dissolved in chloroform, mixed in a glass round-bottomed flask and dried *in vacuo* to form a lipid film. The film was then hydrated with H_2O and sonicated at 40°C for 30mins. pDNA or siRNA solution in H_2O (encoding luciferase gene) was then added to the vector solution under heavy vortex at a ratio of 1:12 (lipid:pDNA, w/w).

Chwee Teck Lim, James C.H. Goh (Eds.): ICBME 2008, Proceedings 23, pp. 1503–1507, 2009
www.springerlink.com

B. Nanoparticles with short ligand extension

This method was used to prepare targeted nanoparticles with ligands of short extension from the surface. On assembly of DNA-encapsulated nanoparticles, a solution of previously synthesised u11 peptide-lipid amphiphiles in H_2O was added and incubated at 37°C for 1 hr. Unincorporated amphiphiles were then removed by ultracentrifugation (MWCO=30k).

C. Nanoparticles with ligands extended from surface

The second method of ligand incorporation was used to extend the U11 ligand further away from the nanoparticle surface, by chemical conjugation of the ligand onto the distal end of surface PEG chains. In this case, the PEGylated lipid in the formulation was changed to one that was functionalised by a maleimide group at the extended end of its PEG chain. After vector assembly and before nucleic acid encapsulation, the vector solution was stirred with a solution of a Cysteine-functionalised 11mer peptide (u11). Nucleic acids were then encapsulated and removal of unconjugated Cys-u11 peptide was performed by centrifugal purification.

D. In Vitro Nanoparticle cell uptake and transfection

All cell lines were maintained in DMEM (plus 1% penicillin and streptomycin and 10% Fetal Calf Serum). Luciferase transfections were carried out on cells in OptiMEM ™ for 4hrs before removal of transfection media and replacement with growth media. Cells were then grown for 48 hrs before lysis (using lysis buffer) and analysed for relative light units and total protein content. For fluorescence uptake studies, nanoparticles were labelled with 1 molar % of DOPE-Rhodamine, and applied to cells for cell uptake. After 60mins incubation, the cells were fixed with paraformaldehyde and analysed for cell-associated fluorescence by fluorescence microscopy.

E. Photon correlation spectroscopy (PCS) and zetapotentials

Nanoparticle diameters and zetapotentials were measured on a Malvern ZS zetasizer at room temperature. All nanoparticles were prepared at $0.5 mgml^{-1}$ (of total lipid mass) in H_2O.

F. In Vivo study using RNAi technology

Nanoparticles were formulated as before with the inclusion of a higher % of PEGylated lipids for extra stability *in vivo*. Male balb/c mice were inoculated with 1 x 10^6 cells (PC3-M-luc) into under the knee cartilage in both knees and tumours were grown for 2 weeks until used for experiment. Mice were injected with a dose of 50µg anti-luciferase siRNA (encapsulated in nanoparticle) in PBS and luciferase expression in tumours was monitored by the In Vivo Imaging System (IVIS, Xenogen) on all days leading to and after nanoparticle administration.

III. Results and Discussion

A. High Charge Vectors

High charge nanoparticle platforms were prepared based on the formulation of commercially available transfection reagents. We combined high molar percentages of cationic lipids (50%) with fusogenic lipids (48.5%), plus 0.5% of $DSPE\text{-}PEG^{2000}$ lipids. An amount of PEGylated lipid is required to increase colloidal stability in serum and buffered solutions, but high molar percentages could lead to steric shielding of the short surface peptides. The non-extended targeting peptide was incorporated through self-insertion of a peptide-lipid amphiphile into the hydrophobic layers of the particle. The molar percentage of the peptide-lipid must also be adapted as over-loading can lead to inter-colloidal aggregation caused by the hydrophobic interactions between the surface peptides. Our data shows that the 0.5% PEGylated of total lipid molarity was enough to keep the balance of aggregation prevention and maintenance of the effect of the surface ligands. It was also found that a maximum loading of 1 molar % of the peptide-lipid amphiphile could allow the display of the ligand's targeting effect but any more would induce the nanoparticle's aggregation.

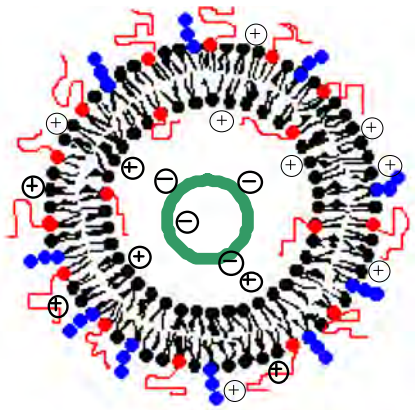


Fig. 1 Representation of the targeted nanoparticle, with short-extended ligands on the surface (blue). The liposomal compartment consists of cationic, fusogenic and PEGylated lipids, which directly encapsulates the nucleic acids within the core (green, pDNA).

Table 1- Summary of luciferase transfection on DU145 cells by targeted vectors (with 1 molar % of ligand) of various preparations. The high charged targeted nanoparticles showed a low increase in transfection, 4-fold in comparison to its non-targeted counterparts, where as the low charged targeted nanoparticles gave up to a 20-fold increase. The transfection level of the targeted low charge vectors were increased further to 30-fold when the targeting ligand is presented at an extended length from the nanoparticle surface.

Molar % of cationic lipid	ζ potential	Ligand extension	% RLU of non-targeted control
50	High (+62.3mV)	Short	400
20	Low (+47.6 mV)	Short	2,000
20	Low (+20.4mV)	Long	3,000

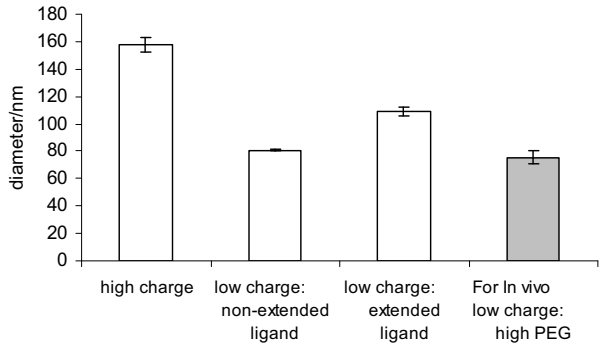


Fig. 2 Diameter sizes of targeted nanoparticles in H_2O, as measured by PCS. All particles have diameters under 150nm, important for *in vivo* kinetics plus receptor-mediated endocytosis.

The secondary conformation of the peptide ligands was examined using circular dichroism. Results show that the original β-sheet secondary aggregation of the peptide-lipids is disrupted as they are inserted into liposomal layers. This finding indicates the ability of peptide-lipid amphiphiles to separate from aggregated and heavily-strained macrostructures to form more separated strands as they come into proximity of a lipid-based surface.

Using DU145, an uPAR-overexpressing prostate cancer cell line, luciferase transfection experiments were performed to compare optimised targeted nanoparticles with their non-targeted counterparts (Table 1). The targeted vectors were able to induce a transgene expression that is up to 4-fold higher than the non-targeted nanoparticles. It is likely that this increase in transfection is a result of the increased uptake of targeted vectors by receptor-mediated endocytosis, as the diameter of the particles are <150nm, hence small enough to enter the cell via such an uptake mechanism (Fig 2). On the other hand, transfections on HEK293 cells (uPAR negative) showed lower levels of transfection by targeted delivery, due to non-specificity of the targeting peptide for surface membrane receptors. Uptake of targeted and non-targeted nanoparticles was examined by fluorescence microscopy, where rhodamine-labelled targeted nanoparticles again showed higher cell-associated fluorescence.

To improve the targeting effect of the surface ligands, the reduction of non-specific uptake of nanoparticles by cells needed to be reduced. We therefore continued to develop nanoparticles with lower overall surface charge within the liposomal platform.

B. Low Charge Vectors

Cell membranes consist of several membrane proteins that are negatively charged, such as that of the proteoglycans, rendering the cell membrane to be highly anionic. Electrostatic interaction with positively charged nanoparticles is the root of non-specific nanoparticle-cell membrane interactions. To minimise such non-specific binding, the zetapotential of the nanoparticles needs to be decreased. This can be achieved by decreasing the amount of cationic lipid in the nanoparticle formulation. Here, we reduced the amount of such cytofectins from 50% to 20%, whilst maintaining the lipid to pDNA ratio. The zetapotential of such vectors was reduced to 30% of that of the high charge vector, therefore decreasing the amount of non-specific uptake. Another advantage of the low-charged formulation is the reduction in nanoparticle size, where diameters of ~80nm were measured, compared to the 150nm diameter of high-charge nanoparticles (Fig 2). Satisfactorily, using low-charge targeted nanoparticles, an even further increase in transfection, up to 20 times higher was observed in comparison to non-targeted nanoparticles. Again, fluorescence microscopy gives indication of increased uptake by targeted vectors, a likely consequence of receptor-ligand interactions (Fig 3). To maximize the display of the targeting ligand, we continued by conjugating the peptide onto the distal ends of the extended PEG lipids.

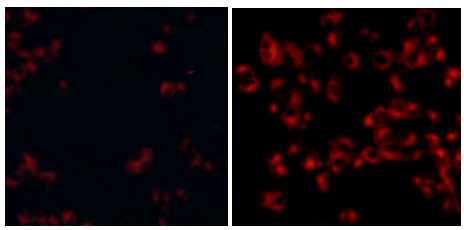


Fig. 3 Uptake of low charged vectors, decorated with (right) or without (left) 1 molar % of short peptide-lipid amphiphile at 60mins post-transfection. On DU145 cells, the targeted vectors show greater cell-associated fluorescence, indicating increased uptake of vectors due to receptor-selectivity.

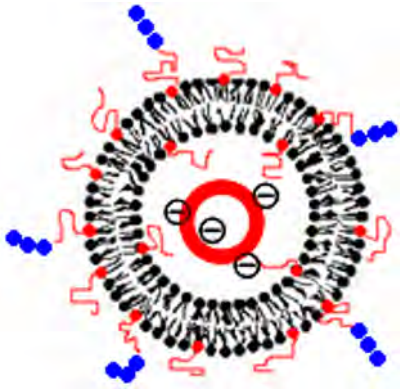


Fig. 4 Representation of the targeted delivery system for gene delivery, with peptide ligands (blue) extended from surface of the nanoparticle. The liposomal compartment consists of low mol% of cationic lipid, hence has lower overall surface charge. The red circle in the middle of liposome represents a circular plasmid.

C. Distal Peptide Conjugation

One of the major drawbacks of the u11 peptide-lipid amphiphile is the limited extension of the ligand on the vector surface. To improve receptor recognition, the presentation of the ligand should extend further from the vector surface, allowing improved docking into the target receptor's binding site (Fig 4). In our second method of targeted-nanoparticle preparation, we covalently conjugated the u11 peptide onto the distal end of functionalised PEGylated lipids, which are extended into the space surrounding the vector. In this method known as *post-coupling,* the distal ends of the PEGylated lipids were functionalised with a maleimide group. The maleimide functional group reacts readily with thiols, which required the modification of the u11peptide with an extra Cysteine amino acid before conjugation.

Again, transfection levels by targeted nanoparticles were higher, 30 times greater than that of the non-targeted particles, indicating the superior targeting efficiency of a low-charged nanoparticle with extended ligand presentation.

D. In Vivo siRNA Model

From the formulation studies and *in vitro* experiments, we learn that the nanoparticle platform on which the targeting ligands are presented is as important as the ligands themselves. Here, we study the ability of the optimised low-charge, non-targeted nanoparticles to induce protein knockdown in an *in vivo* cancer model.

Table 2- Summary of *in vivo* experimental conditions and results.

Tumour Type	Luciferase-expressing PC3-M-luc prostate cancer cells. Subcutaneous inoculation.
NP Size	80nm diameter
NP zeta potential	-0.9 mV
Dose	50 µg of anti-luciferase siRNA encapsulated. Administered on day 0.
% luciferase knockdown	75% on day 2, as monitored by IVIS.

Here we are administered nanoparticles containing anti-luciferase siRNA, where a reduction in luciferase protein is associated with a successful delivery and uptake of the nanoparticle at the tumour site. Using the optimised low-charge nanoparticle, a maximum of 75% reduction in luciferase activity was observed on day 2, indicating both the efficacy of the nanoparticle, plus its pharmacokinetic characteristics. The particle itself has high encapsulation efficiencies of over 90%, plus its near-neutral surface charges and small diameters are all favourable characteristics for successful delivery to tumours. Controls such as the injection of PBS only and injection of nanoparticles containing non-specific siRNA did not show a reduction in luciferase expression. These results indicate that the optimised nanoparticle is efficient as a functional delivery vehicle to tumour sites, hence potentially is an appropriate platform for ligand decoration to aid *in vivo* delivery.

IV. Conclusions

The results from our study shed light onto the factors contributing to the maximisation of a nanoparticle delivery vehicle's targeting effect. *In vivo* cancer studies also confirm the ability of such an optimised formulation to delivery genetic material. We conclude that a vector's stability, plus its surface zetapotential, along with the surface ligands' secondary structure and presentation, needs to be considered when developing a cancer-specific nanoparticle delivery vehicle.

Acknowledgements

We thank the EPSRC, Royal Society and JSPS for providing financial support for the project.

REFERENCES

1. Iyer, A. K., Khaled, G., Fang, J., and Maeda, H. (2006) *Drug Discovery Today 11*, 812-818.
2. Cantero, D., Friess, H., Deflorin, J., Zimmermann, A., Brundler, M. A., Riesle, E., Korc, M., and Buchler, M. W. (1997) *British Journal of Cancer 75*, 388-395.
3. Appella, E., Robinson, E. A., Ullrich, S. J., Stoppelli, M. P., Corti, A., Cassani, G., and Blasi, F. (1987) *Journal of Biological Chemistry 262*, 4437-4440.
4. Costantini, V., Sidoni, A., Deveglia, R., Cazzato, O. A., Bellezza, G., Ferri, I., Bucciarelli, E., and Nenci, G. G. (1996) *Cancer 77*, 1079-1088.
5. Andreasen, P. A., Sottrupjensen, L., Kjoller, L., Nykjaer, A., Moestrup, S. K., Petersen, C. M., and Gliemann, J. (1994) *Febs Letters 338*, 239-245.

Author: Ming Wang
Institute: Imperial College London
Street: Armstrong Road
City: London
Country: UK
Email: ming.wang05@imperial.ac.uk

BMSC Sheets for Ligament Tissue Engineering

E.Y.S. See[1], S.L. Toh[1] and J.C.H. Goh[2]

[1] Division of Bioengineering, National University of Singapore, Singapore
[2] Department of Orthopaedic Surgery, National University of Singapore, Singapore

Abstract — **The anterior cruciate ligament (ACL) has poor capabilities of healing. Currently, allografts or autografts are used to repair the injury site. But healing of the ACL following autograft or allograft reconstruction has been found slow. Thus, other methods like reconstruction of the ACL are being investigated. Most work in ligament tissue engineering has been done using a system of seeding biodegradable polymer scaffolds with single cell suspensions. The cell sources are mostly from Bone Marrow Derived Mesenchymal Stem Cells (BMSCs) or ligament fibroblasts. These cells would have to attach directly to the scaffolds and begin the process of proliferating, secreting ECM and other factors that would enhance the growth rate. This method is inefficient as many cells are lost during the seeding process due to the lack of ample site to adhere onto within the porous scaffold structure.**

When cells are cultured to confluence in vitro, they connect with each other through ECM and cell-to-cell adhesion molecules. With enzymatic digestion such as trypsinization, ECM proteins and cell-to-cell adhesion proteins are disrupted to allow the cells to be dissociated. Harvesting the entire cell sheet would avoid this disruptive process and preserve all ECM as well as cell-to cell adhesion proteins, as it does not experience the enzymatic dissociation process. With the help of the preserved ECM and cell-to-cell adhesion proteins, the cell sheet maintains cellular viability and functionality and can also adhere easily onto biodegradable scaffolds or other layers of cell sheets to form three-dimensional structures with suitable topology and mechanical properties. These unique aspects make the cell sheet technology a promising candidate for tissue engineering.

The proposed project intends to investigate the growth of a cell sheet beginning with BMSCs to study the collagen deposition, cell sheet viability, cell sheet thickness and gene expression to determine the suitability of BMSC sheets for ligament tissue engineering.

Keywords — **Bone Marrow Derived Mesenchymal Stem Cells, Cell Sheets, Ligament Tissue Engineering**

I. Introduction

Tissue engineering is based on the concept of using three-dimensional biodegradable scaffolds as a short term replacement for the extracellular matrix (ECM), and that the seeded cells would reform their native structure to take over the role of the scaffold as it degrades [1]. Current methods of seeding cells involve culturing the cells on tissue culture plastic (TCP) till sufficient numbers are obtained, followed by enzymatic digestion (trypsin) and finally seeding the single cell suspension onto the biodegradable scaffold [2,3]. This would involve the disruption of ECM and cell-to-cell adhesion proteins made by the cell. The single cell suspensions are then injected onto the scaffolds. The disadvantages of this method are that many cells are lost during the process of seeding onto the scaffolds as a large portion of the cells do not actually adhere to the scaffold but seep through the pores of the scaffold [4-6] and those that manage to adhere onto the scaffolds have to re-synthesize their own ECM again when they adhere to the new surface. In addition, the change in morphology and chemical makeup of the cells that leads to a loss of cellular activity is thought to be attributed to the disruption of the cellular membranes during trypsinization [7].

Research has been carried out on the development of a novel tissue engineering methodology to construct three-dimensional functional tissues by layering two-dimensional cell sheet without any biodegradable scaffold [8-10]. This method, although able to solve the problems faced by conventional cell seeding techniques, but is performed using terminally differentiated cells that have limited lifespan, poor differentiation potential and require long periods of time of culture to obtain a cell sheet with strong enough ECM that can be handled and manipulated without breaking apart.

Several studies have shown that BMSCs have a better proliferative capacity and collagen secretion as compared to terminally differentiated medial collateral ligament, anterior cruciate ligament and skin fibroblasts [11,12]. BMSCs have also been shown to differentiate towards the ligament-like lineage under mechanical stimulation [13], thus demonstrating the potential use of BMSCs for ligament tissue engineering.

The potential of BMSCs for ligament tissue engineering is clearly demonstrated, however, to the best of our knowledge, there has been no published data on BMSC sheets used for ligament tissue engineering. In this study, we set out to determine the cellular viability, collagen I deposition, cell sheet thickness and gene expression throughout the growth period of the BMSC sheet.

Chwee Teck Lim, James C.H. Goh (Eds.): ICBME 2008, Proceedings 23, pp. 1508–1511, 2009
www.springerlink.com

II. Materials and methods

A. Isolation of Rabbit BMSCs

Rabbit BMSCs were obtained from whole bone marrow aspirates from New Zealand white rabbits and culture expanded according to procedures previously described [14]. Rabbit MSCs were isolated from fresh whole bone marrow aspirates from New Zealand White Rabbits (8 weeks old), culture expanded in low glucose culture medium containing Dulbecco's modified Eagle's medium (LG-DMEM; Gibco, Invitrogen, CA), 15% v/v fetal bovine serum (HyClone, Logan, UT), penicillin and streptomycin. Nonadherent cells were removed upon first passage of the cells. When primary MSCs became near confluent, they were detached using trypsin (0.25%) /1mM ethylenediamine-tetraacetic acid (EDTA) and replated at a 1:3 ratio. The second passage cells were then used for further study. All cell cultures were maintained at 37^{o}C in an incubator with 5% humidified CO_2. The cultures were replenished with fresh medium at 37^{o}C every 3-4 days.

B. Cell Seeding and Culture on TCP

BMSCs were seeded at a density of 3 x 10^5 cells/well in wells of a non-treated 6-well culture plate (NUNC, Denmark) The cells were grown in vitro in a 5% CO2 incubator at 37^{o}C with LG-DMEM supplemented with 15% FBS, till the cells reached 100% confluence (Week 0). Following that, the confluent cells were supplemented with 50μg/ml L-Ascorbic Acid (Wako, Japan) in 15% FBS LG-DMEM for another 3 weeks before the cell sheets were harvested and assays performed at weekly time points.

C. Analysis of Cell Sheet Viability

The viability of the cells present within the hyperconfluent cell layers was determined using the Alamar Blue (Invitrogen, CA) colorimetric assay. Briefly, the cells were incubated in medium supplemented with 20% (v/v) alamar blue dye for 1 h. One hundred microliters of medium from each sample was read at 570/600nm in a in a microplate reader (Sunnyvale, CA). Medium supplemented with 20% Alamar Blue dye was used as a negative control and the percentage of Alamar Blue reduction was calculated according to the formula provided by the vendor.

D. SDS-PAGE Collagen I and DNA Quantification

The hyperconfluent cell layers were washed twice with 1xPBS and digested with porcine gastric mucosa pepsin (2500 U/mg; Roche Diagnostics Asia Pacific, Singapore) in a final concentration of 0.25mg/mL. Samples were incubated at room temperature (RT) for 1h with gentle shaking followed by sonication of the solution until all cell fragments have broken up followed by 1hr incubation at RT. For samples that were not sonicated, they were incubated for 2h at RT. After the incubation step, the samples were neutralized with 0.1 N NaOH. The samples were analyzed by SDS-PAGE under non-reducing conditions described in [15] and normalized to the DNA content measured spectrophotometrically using the Hoechst 33258 method [16]. The fluorescence measurement of Hoechst 33258 dye was performed using a fluorescence plate reader (FLUOstar Optima, BMG Labtechnologies, Offenburg, Germany). Calf thymus DNA was used for construction of the standard curve for DNA quantitation..

E. Measurement of Cell Sheet Thickness

A homemade picrosirus red dye was made to stain the collagen fibres of the cell sheet. Briefly, 0.1% (w/v) Direct Red 80 (Fluka) was dissolved in concentrated picric acid. The solution was left to stand together with excess picric acid crystals overnight. Solution was filtered before use and added to the cell layers for 15mins to stain the collagen fibres. The dye was removed and washed thoroughly with 1x PBS before confocal microscopy (Olympus FluoView-Confocal Laser Scanning Microscopes, FV500*)*.

F. RNA Extraction and Real Time Reverse Transcription-Polymerase Chain Reaction (RT-PCR)

Total RNA was extracted using Trizol® reagent (Invitrogen, Grand Island, NY) and purified using the RNeasy Mini Kit (Qiagen, Valencia, CA) following the manufacturer's protocol. RNA concentration was determined using the NanoDrop (NanoDrop Technologies, Wilmington, DE) and complementary DNA synthesis was carried out using 100ng of total RNA according to the Manufacturer's protocol for SuperScript II reverse transcriptase with oligo(dT) primers. Real-Time PCR was done using 2μl of cDNA, 10μl of SYBR Green Master Mix (Qiagen, Valencia, CA) and the optimized concentration of primers, topped up to 20μl with nuclease free water. All reactions were performed on the real-time Mx3000P (Stratagene, CA, USA). The thermal cycling program for all PCRs was the following: 95ºC for 15 mins, followed by 40 cycles of amplifications, consisted of denaturation step at 94ºC for 15 s, an annealing step at 55ºC for 30 s and an extension step at 72ºC for 30 s. The genes analysed were Collagen Type I, Type III and Tenascin-C, with GAPDH as the housekeeping gene. The level of expression of the target gene, normalized to GAPDH, was then calculated using the 2^{Δ}Ct formula with reference to non-confluent BMSCs.

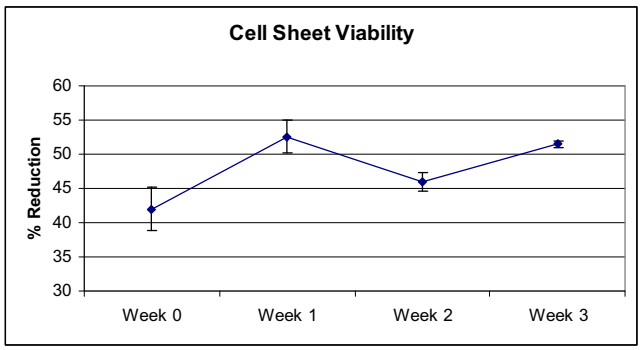


Fig 1. BMSC sheets do not show any trend when assayed with Alamar-Blue. Values are means ± standard deviation (SD) from analysis of duplicates of 3 independent experiments.

III. Results

A. Cell Sheet Viability

To investigate the viability of the cells within the BMSC sheet, the AlamarBlue assay was conducted on wells at a weekly interval (Fig 1). The results show no trend in the cell sheet viability.

B. Collagen I Quantification Normalized to DNA content

To determine the Collagen Type I deposition profile of the BMSC sheet, densitometry on SDS-PAGE of pepsin digests against a Collagen Type I standard was performed (Fig 2). The results show a general increase in Collagen Type I deposition on the cell layer with the most significant increase occurring during Weeks 2-3.

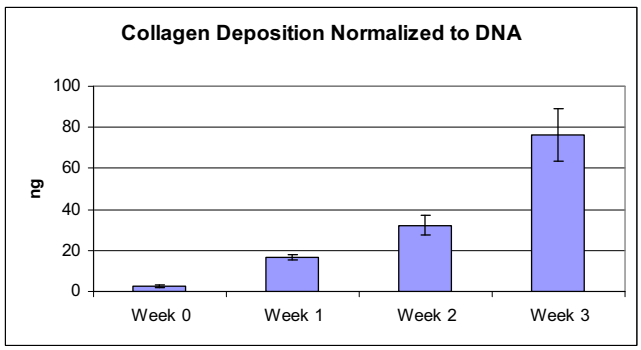


Fig 2. Increasing amounts of Collagen Type I deposition on cell layer. Most significant increase occurred during week 2-3. Values are means ± standard deviation (SD) from analysis of duplicates of 3 independent experiments.

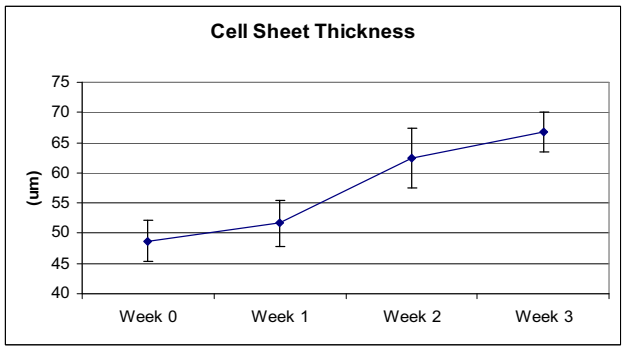


Fig 3. BMSC sheet thickness measured using a confocal microscope. Values are means ± standard deviation (SD) from analysis of duplicates of 3 independent experiments.

C. Measurement of Cell Sheet Thickness

To investigate the profile of the cell sheet thickness throughout the culture period, the thickness was measured using the z-direction slicing (Fig 3). The measurements obtained show a general increase in thickness up till week 3.

D. RNA Expression Profile of BMSC sheets

The effects on BMSCs in hyperconfluent culture conditions were examined by RT-PCR. We examined the expression of general ligament genes, namely Col I, Col III and Tenascin-C (Fig 4).

Col I mRNA expression showed an increase of around 2.5±0.3 fold during weeks 1 and 2 and dropped back to the basal level at week 3.

Col III mRNA expression showed an increase of 2.5±1.0 fold at week 2 and expression dropped to below basal levels at week 3.

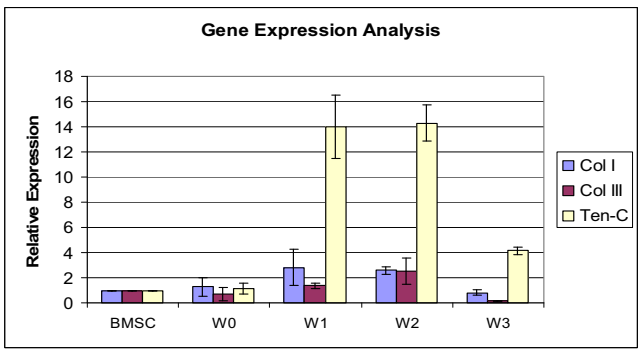


Fig 4. Relative gene expression of Collagen Type I, Type III and Tenascin-C with respect to P2 BMSCs. Values are means ± standard deviation (SD) from analysis of duplicates of 3 independent experiments.

IV. Discussion

The classical method of seeding single cells onto porous scaffolds encounters problems of adherence efficiency and re-synthesizing ECM of the tissue. These challenges make cell sheets an attractive alternative to alleviate these problems. BMSCs have also been shown to be better, in terms of cell proliferation and collagen secretion as compared to terminally differentiated fibroblasts for ligament tissue engineering. As such, BMSC sheets might prove to be a better cell source for tissue engineering of ligaments.

This study was designed to take a closer look at the formation of the BMSC sheet, to determine the viability (Fig 1), collagen type I, III and tenascin-c gene expression (Fig 4) and collagen type I deposition (Fig 2) of BMSCs in a hyperconfluent in vitro environment and the growth profile of the cell sheet (Fig 3).

The results of this study demonstrate that BMSC sheets remain viable despite being in hyperconfluent conditions. This also suggests that the change in cell sheet thickness is caused by continuous ECM deposition rather than an increase in cell numbers. The results obtained from RT-PCR gene expression analysis are consistent with a previous study on the upregulation of collagen type I, collagen type III and tenascin-c gene expression in BMSCs [13] to indicate differentiation towards the ligament fibroblast lineage of the BMSCs. Tenascin-c is well documented to be upregulated by external forces in various tissues like skeletal muscle, tendon [17] and ligaments [13]. The increase of gene expression of tenascin-c might be due to inherent contractile forces present within the dense collagen rich ECM, which provide similar cues for the cells to upregulate mRNA expression of tenascin-c when subjected to external mechanical forces. This hypothesis is in agreement with earlier studies that a natural internal tension between the cells and the surrounding ECM is present throughout a tissue [18].

V. Conclusions

This study demonstrates the potential of BMSC sheets as an alternative cell source for ligament tissue engineering. Further studies are needed to determine if the BMSCs within the sheets are differentiating towards the ligament fibroblast lineage, and if placing these BMSC sheets on scaffolds and providing external mechanical stimulus would further enhance the suitability of BMSC sheets for ligament tissue engineering. Future studies on gene expression will also be needed to evaluate the expression level of the early phase induction genes of the other 3 mesenchymal lineages (Runx2, Sox9 and PPARγ2)

References

1. Langer R, Vacanti JP. (1993) Tissue engineering. Science 260(5110):920-926.
2. Altman GH, Lu HH, Horan RL, et al. (2002) Advanced bioreactor with controlled application of multi-dimensional strain for tissue engineering. J Biomech Eng 124(6):742-749.
3. Altman GH, Horan RL, Lu HH, et al. (2002) Silk matrix for tissue engineered anterior cruciate ligaments. Biomaterials 23(20):4131-4141.
4. Li Y, Ma T, Kniss DA, et al. (2001) Effects of filtration seeding on cell density, spatial distribution, and proliferation in nonwoven fibrous matrices. Biotechnol Prog 17(5):935-944.
5. Wendt D, Marsano A, Jakob M, et al. (2003) Oscillating perfusion of cell suspensions through three-dimensional scaffolds enhances cell seeding efficiency and uniformity. Biotechnol Bioeng 84(2):205-214.
6. Kim BS, Putnam AJ, Kulik TJ, et al. (1998) Optimizing seeding and culture methods to engineer smooth muscle tissue on biodegradable polymer matrices. Biotechnol Bioeng 57(1):46-54.
7. Canavan HE, Cheng X, Graham DJ, et al. (2005) Cell sheet detachment affects the extracellular matrix: a surface science study comparing thermal liftoff, enzymatic, and mechanical methods. J Biomed Mater Res A 75(1):1-13.
8. Shimizu T, Yamato M, Kikuchi A, et al. (2003) Cell sheet engineering for myocardial tissue reconstruction. Biomaterials 24(13):2309-2316.
9. L'Heureux N, Pâquet S, Labbé R, et al. (1998) A completely biological tissue-engineered human blood vessel. FASEB J 12(1):47-56.
10. Michel M, L'Heureux N, Pouliot R, et al. (1999) Characterization of a new tissue-engineered human skin equivalent with hair. In Vitro Cell Dev Biol Anim 35(6):318-326.
11. Ge Z, Goh JC, Lee EH. (2005) Selection of cell source for ligament tissue engineering. Cell Transplant. 14(8):573-83
12. Van Eijk F, Saris DB, Riesle J, et al. (2004). Tissue engineering of ligaments: a comparison of bone marrow stromal cells, anterior cruciate ligament, and skin fibroblasts as cell source. Tissue Eng. 10(5-6):893-903.
13. Altman GH, Horan RL, Martin I, et al. (2002) Cell differentiation by mechanical stress. FASEB J. 16(2):270-2.
14. Liu H, Fan H, Wang Y, et al. (2008) The interaction between a combined knitted silk scaffold and microporous silk sponge with human mesenchymal stem cells for ligament tissue engineering. Biomaterials 29(6):662-674.
15. Lareu RR, Arsianti I, Subramhanya HK, et al. 2007, In vitro enhancement of collagen matrix formation and crosslinking for applications in tissue engineering: a preliminary study. Tissue Eng. Feb;13(2):385-91
16. Toh WS, Liu H, Heng BC et al. 2005 Combined effects of TGFbeta1 and BMP2 in serum-free chondrogenic differentiation of mesenchymal stem cells induced hyaline-like cartilage formation. Growth Factors, 23:313–321
17. Kjaer M. 2004 Role of extracellular matrix in adaptation of tendon and skeletal muscle to mechanical loading. Physiol Rev. Apr;84(2):649-98.
18. F.H. Silver, L.M. Siperko and G.P. Seehra. 2003. Mechanobiology of force transduction in dermal tissue. Skin Res. Technol.. **9**, pp. 3–23.

Corresponding Author: James Cho Hong, Goh
Institute: Department of Orthopaedic Surgery
Country: Singapore
Email: dosgohj@nus.edu.sg

In Vivo Study of ACL Regeneration Using Silk Scaffolds In a Pig Model

Haifeng Liu[1], Hongbin Fan[1], Siew Lok Toh[2,3], James C.H. Goh[1,2]

[1]Department of Orthopedic Surgery, National University of Singapore, Singapore
[2]Division of Bioengineering, National University of Singapore, Singapore
[3]Department of Mechanical Engineering, National University of Singapore, Singapore

Abstract — **Although most in vitro studies indicate that silk is a suitable biomaterial for ligament tissue engineering, in vivo studies of implanted silk scaffolds for ligament reconstruction are still lacking, especially in a big animal. The objective of this study is to investigate anterior cruciate ligament (ACL) regeneration using mesenchymal stem cells (MSCs) and silk scaffold in a pig model. The scaffold was fabricated by incorporating microporous silk sponges into knitted silk mesh, which mimicked the structures of ligament extracellular matrix (ECM). In vitro culture already demonstrated that MSCs on scaffolds proliferated vigorously and produced abundant collagen. The MSCs/scaffold was implanted to regenerate ACL in a pig model. After 24 weeks, histology observation showed that MSCs were distributed throughout the regenerated ligament and exhibited fibroblast morphology. The key ligament ECM components including collagen I, collagen III, and tenascin-C were produced prominently. The tensile strength of regenerated ligament also met the mechanical requirements. In conclusion, the results imply that silk scaffold has great potentials in future clinical applications.**

Keywords — **Silk scaffold, MSC, ACL, Pig model**

I. Introduction

Anterior cruciate ligament (ACL) plays an important role in keeping the normal motion and stability of knee joint. The rupture or tear of ACL can cause significant instability, which subsequently leads to injuries to other ligaments and development of degenerative joint disease. Due to the limited capacity to regenerate, ACL heals poorly in response to the repair by suturing the injured tissue back together. So the grafts are required for ACL reconstruction. Now, over 100,000 ACL reconstructions are performed every year in the United States. The current grafts involve autograft, allograft and ligament prostheses. Despite great improvements in available therapies, there remain significant limitations. The autograft and allograft have drawbacks such as ligament laxity, donor site morbidity and pathogen transfer. While the ligament prostheses are fraught with complications including mechanical mismatch, poor tissue integration and foreign body inflammation. Recently tissue engineering has emerged as a promising strategy for the regeneration of injured ligament with similar biomechanical and biochemical properties [1].

The scaffold is one of key components in tissue engineering, which can influence cellular activities and resultant matrix formation. In recent years, silk has been increasingly studied as the scaffold for ligament tissue engineering due to its biocompatibility, slow degradability, and remarkable mechanical capability. It provides an excellent combination of lightweight, high strength and remarkable elasticity. In our previous work, we successfully regenerated ACL using knitted silk scaffold and mesenchymal stem cells (MSCs) in rabbit model. The scaffold was demonstrated to possess good mechanical strength and biocompability. It could facilitate nutrients transmission and tissue infiltration [2]. However, the tensile strength of scaffold is relatively low for potential clinical application. So in this study, we fabricate a kind of braided cord enhanced knitted silk scaffold and reconstruct ACL using it in porcine model. The objective of this study is to find whether ACL can be regenerated in porcine model using this enhanced knitted silk scaffold and MSCs.

II. Materials and methods

The knitted silk mesh was fabricated using raw silk fibers on a knitting machine. Then the knitted silk mesh was degummed to remove sericin thoroughly. The silk solution was prepared by dissolving sericin-free silk fibers into a ternary solvent system followed by dialysis. To prepare scaffold, the knitted sericin-free silk mesh was immersed in silk solution and freeze-dried for 24 h. The freeze-dried mesh was immersed in a methanol–water solution to induce β-sheet structural transition and then was carefully rolled up with a braided silk cord inside to produce a tightly wound shaft with 80mm in length and 5.5mm in diameter [3].

The 3.0×10^6 autologous MSCs were loaded on each scaffold and cultured in vitro over 8 h for cell adhesion before implantation. Eight pigs were used in experiment. ACL reconstruction was performed on right knee and contra lateral one without treatment was regarded as normal control. The lateral parapatellar arthrotomy was used to expose

Chwee Teck Lim, James C.H. Goh (Eds.): ICBME 2008, Proceedings 23, pp. 1512–1514, 2009
www.springerlink.com

the right knee joint. After the native ACL was excised, the tibial and femoral bone tunnels were created. Both ends of scaffold were sutured with polyester suture and passed through the tunnel. The two ends were fixed by sutures tied over screws in femur and tibia.

The pigs were sacrificed at 24 weeks postoperatively. The knee joints were firstly scanned with micro-CT to determine the mineralized tissue formation in bone tunnels. Thereafter, five specimens from each group were used for mechanical test. The tensile load and stiffness were compared among groups. The rest specimens (n=3) from each group were fixed in formalin, embedded in paraffin and sectioned. The slides were stained with hematoxylin and eosin (HE) and immunostained with antibodies against collagen I, collagen III and tenascin-C. All data were analyzed using SPSS 10.0 software and statistically significant values were defined as $p<0.05$.

III. Results

After 24 weeks, the gross findings revealed that regenerated ligament resembled the normal ACL in experiment group. The scaffold was filled and encapsulated by newly formed fibrous tissue. The color and luster of regenerated ligament were similar to that of native ACL.

The cross sectional images perpendicular to the longitudinal axis of knee joint were reconstructed with micro-CT. The newly formed mineralized tissue in the full length of bone tunnel could be examined by screening all slices of each sample. In experiment group, the consecutive micro-CT images showed there was no obvious mineralized tissue formation in tibial and femoral bone tunnels after 24 weeks. The HE and immunohistochemistry staining were performed to further examine the histological changes of regenerated ligament. After 24 weeks the MSCs were distributed uniformly throughout scaffolds and showed the morphology of fibroblasts with elongated nucleus in experiment group. The fibroblast-like cells spread, proliferated and produced abundant ECM on scaffolds. The regenerated tissue became much denser with time. The silk fibers of scaffolds degraded almost completely after 24 weeks. The experiment group demonstrated the hypercellular infiltration and abundant matrix production.

After 24 weeks, the immunohistochemistry staining for collagen I was strongly positive in newly regenerated tissue in experiment group. While the collagen III and tenascin-c was expressed at a low level. The results were similar to those of normal control.

The regenerated ligament recorded a maximum tensile load of 404.9±49.9N and a tensile stiffness of 57.5±9.4N/mm. They were 52.5% and 61.2% of normal ACL, respectively.

Table 1 Mechanical properties of regenerated ligament in experiment and control groups (mean±SD)

Sample	Maximum load (N)	Stiffness (N/mm)
Native ACL	770.1±105.2	93.9±15.9
Scaffold	398.8±69.5	58.5±16.8
Experiment group	404.9±49.9	57.5±9.4

IV. Discussion

This study demonstrates that ACL can be regenerated by implantation of silk scaffold and MSCs in large animal model. This novel scaffold comprises the microporous knitted silk mesh of out layer and braided silk cord of inner layer. The out layer can facilitate cells adhesion and tissue in-growth. The regenerated ligament shows similarities to the native ACL in ECM composition. The cells showed excellent infiltration and were homogeneously distributed throughout the implants. On the other hand, the inner cord is able to enhance the strength of scaffold especially in initial phase after implantation. After reconstruction the scaffold can keep proper tensile strength until the newly formed tissue becomes mechanically competent. The strength is comparable to withstand the forces associated with daily activities. Furthermore, the host knee joint serves as an autologous bioreactor, which can provide various cytokines and physiological cyclic loading on implants to induce the differentiation of MSCs [2, 4].

These preliminary results provide evidence that silk-based biomaterial is a promising scaffold for ligament tissue engineering. More data will show us the changes of implanted scaffold in detail after the whole experiment is finished.

Acknowledgment

This research was supported by a grant from the Biomedical Research Council, Singapore.

References

1. Fan H, Liu H, Tho SL, Goh JC. Enhanced differentiation of mesenchymal stem cells co-culturred with ligament fibroblasts on gelatin/silk fibroin hybrid scaffold. Biomaterials 2008;29(6):1017-1027

2. Fan H, Liu H, Tho SL, Goh JC. In vivo study of anterior cruciate ligament regeneration using mesenchymal stem cells and silk scaffold. Biomaterials 2008;29(23):3324-37
3. Liu H, Fan H, Tho SL, Goh JC. A comparison of rabbit mesenchymal stem cells and anterior cruciate ligament fibroblasts responses on combined silk scaffolds. Biomaterials 2008;29(10):1443-1453
4. Liu H, Fan H, Tho SL, Goh JC. The interaction between a combined knitted silk scaffold and microporous silk sponge with human mesenchymal stem cells for ligament tissue engineering. Biomaterials 2008;29(6):662-74

Author: James C.H. Goh
Institute: Department of Orthopaedic Surgery, National University of Singapore
Street: 27 Medical Drive
City: Singapore
Country: Singapore
Email: dosgohj@nus.edu.sg

Establishing a Coculture System for Ligament-Bone Interface Tissue Engineering

P.F. He[1], S. Sahoo[1], J.C. Goh[1,2], S.L. Toh[1,3]

[1] Division of Bioengineering, National University of Singapore, Singapore
[2] Department of Orthopaedic Surgery, National University of Singapore, Singapore
[3] Department of Mechanical Engineering, National University of Singapore, Singapore

Abstract — **Ligament-bone interface (enthesis) is a complex structure which comprises of ligament, fibrocartilage and bone. The fibrocartilage transformation adds significant insertional strength to the interface and makes it highly resistant to avulsion forces. Many ACL grafts cannot generate native interfacial region, leading to their failure. Co-culture has proved to be an effective way to generate new tissues in tissue engineering. Studies have found important signaling molecules in transduction pathway of chondrogenesis to be transmitted via gap junctions. We hypothesized that stem cells cocultured between ligament and bone cells would enable transmission of chondrogenic factors from bone/ligament cells to bone marrow stem cells (BMSCs) via gap junctions, resulting in their differentiation into fibrocartilage. To test this hypothesis, we studied to establish effective co-culture system. In this study, two set of co-culture (BMSCs and ligament cells; BMSCs and bone cells) were established. Confocal microscopy showed efficient dye transfer from bone/ligament cells into BMSCs. This was further confirmed and quantified by FACS, which showed a gradual temporal increase in the percentage of BMSCs acquiring Calcein. RT-PCR analysis showed that the bone cells-BMSC and the ligament cells-BMSC co-culture systems expressed higher amounts of collagen type-2, as compared to the various monocultures. The results proved the establishment of effective co-culture. The findings provide important information for the development of a more promising ligament-fibrocartilage-bone graft.**

Keywords — **enthesis, fibrocartilage, co-culture, gap junction**

I. Introduction

The anterior cruciate ligament (ACL) is the most commonly injured ligament in the knee joint, with a prevalence of about 1 per 3,000 among Americans [1]. The poor healing capacity of ACL requires reconstruction surgery to be performed in most cases. In current clinical practice, the most popular and successful surgical replacement for ACL are autografts involving the use of the bone-patellar tendon-bone grafts and hamstring tendon grafts [2, 3]. While patellar tendon grafts are more stable, they are often associated with post-operative knee pain [4]. The hamstring grafts result in faster recovery and less knee pain, but are often associated with donor-site morbidity [3]. Most grafts are mechanical inserted, thus they cannot generate native interfacial region, often leading to grafts ruptures occurring through or near the insertion sites [5].

Ligament-bone interface (enthesis) is a complex structure which comprises four zones: ligament, unmineralized fibrocartilage, mineralized fibrocartilage and lamellar bone [6]. The fibrocartilage transformation adds significant insertional strength to the interface and makes it highly resistant to avulsion. Injured ACL fail to regenerate the intervening fibrocartilage at the enthesis. While the exact mechanism of interface formation is still unknown, studies have attempted to regenerate the enthesis [7].So a tissue engineering approach to create a ligament-fibrocartilage-bone graft would be more promising than a ligament-alone construct in providing better graft integration and resulting stability.

Co-culture has been shown to be an effective way of engineering new tissues [8]. In a co-culture system, two or more cell types cultured in same environment are likely to interact with each other. Some studies have showed cellular interactions between different cell types contributed to tissue information in vitro. Of all kinds of different cell-cell communications, gap junction communication plays an important role because it directly connects the cytoplasm of two cells, allowing the transmission of various intracellular signals and messengers into the neighboring cells [9]. Important signaling molecules in the transduction pathway of chondrogenesis have been shown to be transmitted via gap junctions [8]. To generate enthesis, we hypothesize that stem cells co-cultured between ligament and bone cells would enable transmission of chondrogenic factors from bone/ligament cells to BMSCs via gap junctions, resulting in their differentiation into fibrocartilage.

II. Methods

A. Harvesting BMSCs from rabbits

BMSCs were isolated and cultured by established technique approved by NUS Institutional Animal Care and Use

Chwee Teck Lim, James C.H. Goh (Eds.): ICBME 2008, Proceedings 23, pp. 1515–1518, 2009
www.springerlink.com

Committee, National University of Singapore [10-11]. Briefly stated, bone marrow was aspirated from the iliac crests of anaesthetized adult NZW rabbits and collected into polypropylene tubes containing preservative free heparin (1000 units/ml). Nucleated cells were isolated by serial culture and subculture on tissue culture polystyrene. 85% confluent cells of 2nd and 3rd passage were used for experiments.

B. Establishing primary ligament and bone cell culture

The primary ligament cells and bone cells were explant-cultured by methods described elsewhere. Briefly stated, the anterior cruciate ligaments (ACL) of both joints and upper part of tibia were surgically removed from a 3 kg NZW rabbit under anaesthesia. ACL tissue was cut into 1mm×1mm slices and digested with 5 ml of 0.15% collagenase-I in 37^0C shaking bath for 6hrs. The bone tissue was cut into 2mm×2mm pieces and digested with 5ml of solution containing collagenase-I and II (0.15% each). The semi-digested ligaments and bone pieces were explant-cultured in 60mm petridishes with 10% Dulbecco's Modified Essential Medium (DMEM) containing 10%fetal bovine serum, 1% antibiotics under humidified conditions at 37 ºC and 5% CO_2.

C. Establishing co-culture

Two sets of co-culture were established, one set comprising bone cells and BMSCs and another set comprising ligament cells and BMSCs by mixing the bone/ligament cells with BMSCs at a numerical ratio of 1:10. The co-cultures were plated on 60-mm petri-dishes in duplicate.

D. Dye coupling experiment

BMSCs, bone and ligament cells were seeded into separate 60mm petridishes at a density of 4×10^5 cells. When confluent, bone and ligament cells were dual-stained; dual labeled cells would serve as dye-donors. Cells were first stained with DiI Red [5µl in 1ml supplemented DMEM] and incubated at 37°C, 5% CO2, 100% humidity for 30 mins. The cells were washed twice with normal DMEM medium followed by stained with Calcein-AM [10µl in 1ml supplemented DMEM: Gap-junction permeable dye]. The cells were then incubated at 37°C for 60 mins and washed twice with normal DMEM medium and trypsinized. BMSCs were trypsinized without labeling with any of the dye (recipient cells). A volume of 10µl (8000-10,000 cells) of each of bone and ligament cell suspension were mixed separately with 100µl (80,000-100,000 cells) of BMSCs (at a ratio of 1:10). Now each of the mixed cell suspension was plated on a 6-well plate and cultured at 37°C. After 24 hours of culture, the cells were observed for dye-transfer using a Olympus FV300 Confocal Laser Scanning Microscope.

E. Fluorescent Activated Cell Sorting

The co-cultures were also analyzed by flow cytometry using a previously described protocol [13]. Each of the co-cultured cell suspensions (prepared by the method described above) were plated and cultured on separate 60mm plates. Cells were trypsinized and resuspended in 1X PBS after 2hrs, 6hrs and 12hrs post-coculture and their fluorescence intensity was measured in a FACStar-Plus (Becton–Dickinson, Heidelberg, Germany) with a one-laser setup for an excitation wavelength of 488 nm. The emission of Calcein and DiI was determined after filtering with a 530/30-nm bandpass filter (FL1/calcein) and a 575/26-nm bandpass filter (FL2/DiI), respectively.

F. Quantitative Real Time Reverse Transcription-Polymerase Chain Reaction (RT-PCR)

BMSCs, ligament cells and bone cells in monoculture and Ligament-BMSC and Bone cell-BMSC cocultures were trypsinized and their total RNA extracted (RNeasy Mini Kit (Qiagen, Valencia, CA)). RNA concentration was determined using the S2100 Diode Array Spectrophotometer (Biochrom, Cambridge, CB) and cDNA synthesis was carried out using 80ng of total RNA and SuperScript II reverse transcriptase with oligo(dT) primers. Real-Time PCR was performed on a iQ® 5 (Bio-RAD, California, USA) using 4µl of cDNA, 12.5µl of SYBR Green Master Mix (Qiagen, Valencia, CA) and the optimized concentration of primers, topped up to 25µl with nuclease free water. The program for all PCRs was the following: 95ºC for 3 mins, followed by 35 cycles of amplification, consisting of a denaturation step at 95ºC for 12 s, an annealing step at 58ºC for 30 s and an extension step at 72ºC for 30 s. The genes analyzed were Collagen Type I, II and III, with GAPDH as the housekeeping gene.

III. Results

A. Dye coupling experiment

Confocal microscopy showed efficient dye transfer from bone/ligament cells into BMSCs (Figure 1).

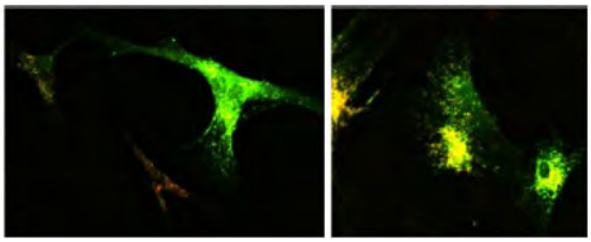


Figure 1: Confocal images showing dye transfer of calcein (green) from dual stained bone cells to BMSCs. Dual stained cells appear orange or have red flecks, while BMSCs appear purely green.

B. Fluorescent Activated Cell Sorting

FACS showed a gradual and progressive temporal increase in the percentage of BMSCs acquiring Calcein (Bone-BMSC: 2hrs-4.4%, 6hrs-10.4%, 12hrs-14.2%; Ligament cell-BMSC: 2hrs-4.3%, 6hrs-9%, 12hrs-13.8%; Figure 2).

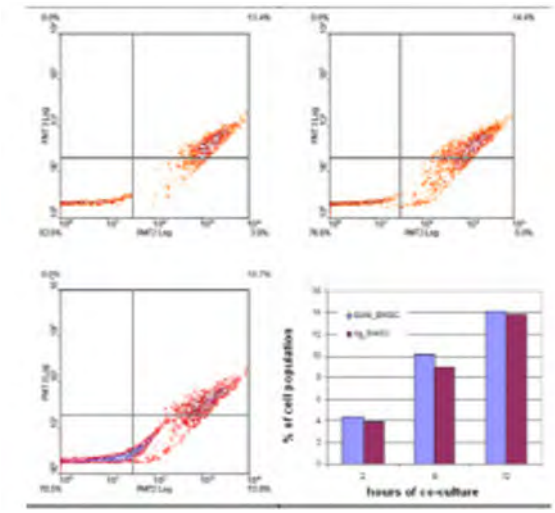


Figure 2: Gap-junction assay by flow cytometry in bone-BMSC coculture showing a gradual increase in recipient cell-pool on continued co-culture. X-axis: Calcein-AM; Y-axis: DiI Red

C. Gene Expression

Real time RT-PCR results showed that BMSCs, bone and ligament cells expressed nearly similar amounts of collagen type-2 when in cultured in monoculture systems. However in coculture systems, collagen type-2 expression was significantly upregulated, especially in the BMSC-Bone coculture system (6 fold increase, as compared to a 2 fold increase in BMSC-ligament coculture system; both compared against a bone-ligament coculture system; Figure 3).

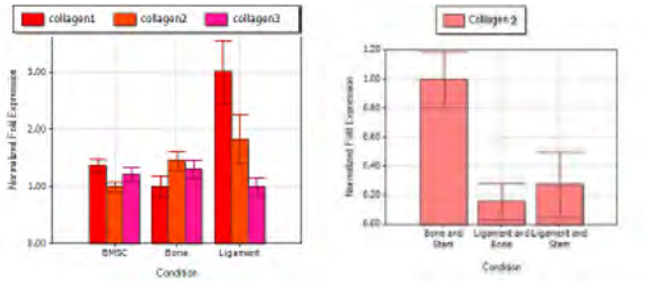


Figure 3: RT-PCR analysis of monoculture and coculture system. While BMSC monocultures have a low expression of collagen type- II, their co-culture with mature cells resulted in collagen type- II gene up regulation

IV. Discussion

A two-dimensional co-culture system of undifferentiated bone marrow stem cells and mature bone and ligament cells is presented. The co-culture system was shown to be functional, allowing the exchange of dyes from the mature donor cells into the stem cells. The establishment of the gap junctions in the co-culture was shown to be relatively rapid with about 14% of the recipient stem cells being stained positive within 12 hours, as demonstrated by the FACS results.

In conjuction with the gap junction permeable dye Calcein Green that was transferred into the recipient stem cells, paracrine signals responsible for initiating chondrogenic stem cell differentiation were also transmitted from the mature cells into the BMSCs. This was demonstrated by an upregulation of expression of the fibrocartilage-specific Collagen type-2, which is also found in the ligament-bone interface. In contrast, Collagen types 1 and 3 are the predominant collagens found in ligaments and bones [15].

Chonrogenic differentiation was more pronounced in the BMSC-Bone co-culture system, where a 6-fold higher upregulation was observed over the Bone-Ligament co-culture system. It was also observed that, in contrast, BMSCs, bone and ligament cells, in monoculture, expressed nearly similar amounts of collagen type-2. This implies that a co-culture system significantly influenced differentiation of BMSCs.

This study demonstrated the importance of cell to cell communication in the chondrogenesis process of BMSCs. Future work will focus on establishing a tri-lineage co culture system involving BMSCs with bone and ligament cells on a biomimetic scaffold to mimic the native interfacial environment to promote the chondrogenesis of BMSCs.

V. Conclusion

We have developed an effective co-culture system that enables transmission of chondrogenic factors through gap-junctions, helping in BMSC differentiation into a fibrocartilage lineage. Such a co-culture when translated on to appropriate scaffolds can generate ligament-bone grafts with the bone-ligament interface. Such bone-fibrocartilage-ligament grafts would be more promising than ligament-alone constructs to replace severely injured ligaments.

Acknowledgment

This study is funded by the Faculty of Engineering, National University of Singapore, under grant R397-000-041-112.

References

1. Gao, J., K.Messner (1996) Quantitative comparison of soft tissue-bone interface at chondral ligament insertions in the rabbit knee joint. J Anat 188 (Pt2): p.367-73
2. Tadokoro, K., et al. (2004) Evaluation of hamstring strength and tendon regrowth after harvesting for anterior cruciate ligament reconstruction. Am J Sports Med 32(7): p. 1644-50
3. Takeda, Y., et al. (2006) Hamstring muscle function after tendon harvest for anterior cruciate ligament reconstruction: evaluation with T2 relaxation time of magnetic resonance imaging. Am J Sports Med 34(2): p.281-8
4. Roe, J., et al. (2005) A 7-year follow-up of patellar tendon and hamstring tendon grafts for arthroscopic anterior cruciate ligament reconstruction: differences and similarities. Am J Sports Med 34(9): p.1337-45
5. Moffat K.L., Lu HH, et al. (2006) Charaterization of the Mechanical Properties and Mineral Distribution of the Anterior Cruciate Ligament-to-Bone Insertion Site. EMBS Annual International Conference. 2366-2369.
6. Cooper, R. R., Misol, S. (1970) Tendon and ligament insertion. Alight and electron microscopic study. J. Bone Joint Surg. Am. 52,1.
7. Fujioka H, Thakur R, Wang GJ, et al. (1998) Comparison of surgically attached and non-attached repair of the rat Achilles tendon-bone interface. Cellular organization and type X collagen expression. Connect Tissue Res 37:205–218.
8. Hendriks, J. et al. (2007) Co-culture in cartilage tissue engineering. J Tissue Eng Regen Med 1:170-178.
9. Zhang, W et al. (1999) Direct Gap Junction Communication between Malignant Glioma Cells and Astrocytes. Cancer Research 59, 1994-2003 April 15.
10. Turhani, D., et al. (2005) In vitro study of adherent mandibular osteoblast-like cells on carrier materials. Int J Oral Maxillofac Surg. 34(5): p. 543-50.
11. Nagineni, C.N., et al. (1992) Characterization of the intrinsic properties of the anterior cruciate and medial collateral ligament cells: an in vitro cell culture study. J Orthop Res, 10(4): p. 465-75.
12. Sahoo, S., et al. (2006) Characterization of a novel polymeric scaffold for potential application in tendon/ligament tissue engineering. Tissue Eng. 12(1): p. 91-9.
13. Czyz, J., et al. (2000) Gap-junctional coupling measured by flow cytometry. Exp Cell Res. 255(1): p. 40-6.
14. Li, X et al. (2005) Modulation of chondrocytic properties of fat-derived mesenchymal cells in co-cultures with nucleus pulposus. Connect Tissue Res. 46(2):75-82.
15. Visconti C.S. et al. (1996) Biochemical analysis of collagens at the ligament-bone interface reveals presence of cartilage-specific collagens. Arch Biochem Biophys. Apr 1;328(1):135-42

Corresponding Author: Toh Siew Lok
Institute: National University of Singapore
Country: Singapore
Email: bietohsl@nus.edu.sg

Effect of Atherosclerotic Plaque on Drug Delivery from Drug-eluting Stent

J. Ferdous and C.K. Chong

School of Chemical and Biomedical Engineering, Nanyang Technological University, Singapore

Abstract — **Atherosclerotic plaque formation due to lipid accumulation in the arterial wall is the major cause of stenotic coronary disease. To restore distal coronary blood supply and overcome restenotic events presented by bare wire stents, drug-eluting stent (DES) implantation is now commonly used to treat stenotic coronary disease. However, while its long-term outcome is still unavailable, early clinical results appear to be inconsistent. The use of computational models is believed to be important in understanding DES and to elucidate the delivery of drug and improve the efficacy of DES. The presence of plaque in the stented region is expected to affect drug pharmacokinetics related to DES. In this study, a 2-dimensional model which drug transfer was coupled with both luminal and transmural flows was presented to investigate drug deposition and distribution in the arterial wall. Paclitaxel was used as a model drug and its interaction with the binding sites in the tissue was treated as a reversible binding process. As predicted, the presence of plaque dramatically affects the local pharmacokinetics. Thick plaque absorbs more drugs and provides higher resistance to drug transfer in the arterial wall compared to thin plaque. Study on the effect of drug diffusivity in the plaque on drug deposition reveals that higher diffusion coefficient results in lower drug content in the arterial wall. Meanwhile, when drug partition coefficient in the plaque was varied within the range for paclitaxel, it showed negligible effect on drug deposition. In conclusion, the presence and property of plaque have an effect on the delivery of drugs in arterial wall and should be included in the modeling of drug delivery from a DES to improve the design of stent to achieve the best therapeutic outcome.**

Keywords — **Drug-eluting stent, atherosclerotic plaque, pharmacokinetics, computational model**

I. Introduction

Plaque formation in the arterial wall as a result of atherosclerosis reduces arterial lumen size and restricts distal blood flow and results. Balloon angioplasty followed by bare-metal stent implantation is a common mode of treatment. But its major drawback is restenosis. Drug-eluting stents (DES) are now widely used to mitigate restenosis. However, while its long-term outcome is still unavailable, early clinical results appear to be inconsistent. Therefore, a detailed study of the drug delivery system which is more physiologically realistic is expected to give a better insight about what is required to improve the efficacy of DES.

Physiological transport forces, drug physiochemical properties, local biological tissue properties and the design of stent are the main factors that govern the arterial wall local drug pharmacokinetics [1]. Using *in vitro* perfusion experiments it has been reported that both diffusion and convection play an important role on arterial drug transport [2,3], whereas Levin et al. [4] reported the impact of specific binding to intracellular proteins for arterial transport of paclitaxel, rapamycin and dextran. However, incorporation of all the above-mentioned issues in the experiment are difficult and hence computational modeling is an attractive alternative to predict the local pharmacokinetics related to DES. In earlier computational models, Hwang et. al. [5] showed the effect of physiological transport forces on drug pharmacokinetics in the arterial wall, neglecting the reversible binding of drug with tissues. The importance of binding of drugs by incorporating the reversible bound drug in the model was reported by Lovich et al. [6] and Shakrov et al. [7] assuming no transmural flow. But none of these studies have considered how the presence of atherosclerotic plaque affects the drug pharmacokinetics in arterial wall. This is expected to be an important an important issue because DES is deployed in the region laden with atherosclerotic plaque. Furthermore, it is important to note that local drug pharmacokinetics is directly related to vascular toxicity and efficacy of DES [8].

Previous study on the influence of thrombosis on drug pharmacokinetics from stent revealed that thrombus could affect the arterial drug uptake and thrombus composition altered the binding capacity and release of paclitaxel to the arterial wall. Moreover, the presence of atherosclerotic plaque also influences the transmural convection [9]. In addition, endothelium layer affects drug pharmacokinetics by altering transmural hydraulic flux as well [3]. In this study, a 2-dimensional (2D) model where drug transfer was coupled with both luminal and transmural flow and drug binding was treated as a reversible binding process to investigate the drug pharmacokinetics in the arterial wall as a result of DES deployment. Finally, how the nature of the plaque affects drug deposition in the arterial wall was also analyzed.

Chwee Teck Lim, James C.H. Goh (Eds.): ICBME 2008, Proceedings 23, pp. 1519–1522, 2009
www.springerlink.com

II. Methodology

A. Geometric model

A simple CardioCoil stent with circular strut was used in this study [10]. Although there are 11 struts each of 0.15 mm diameter and located 0.7 mm center-to-center distance, only 3 struts were used in this model to capture the physics better and reduce the computational overhead. The diameter of the coronary artery was considered 3 mm whereas the thickness of the arterial wall and drug-loaded polymer coating on the stent were 0.9 mm and 0.005 mm respectively. Plaque thickness was varied between 0.1 mm and 0.4 mm. Since the stent is axis-symmetric, a 2D model was considered which is shown in Figure 1.

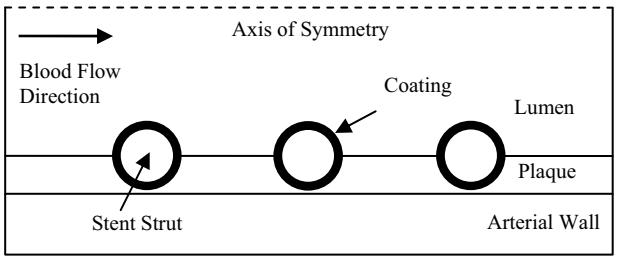


Fig. 1 2D schematic diagram of the stent (not to scale)

B. Model description

Blood flow dynamics in the lumen was described by the Navier-Stokes equation (Eq. 1) and continuity equation (Eq. 2) assuming blood as an incompressible, Newtonian fluid and the flow was laminar and steady:

$$-\mu_l \nabla^2 \mathbf{u_l} + \rho_l (\mathbf{u_l} \cdot \nabla)\mathbf{u_l} + \nabla \mathbf{p_l} = 0 \quad (1)$$

$$\nabla \mathbf{u_l} = 0 \quad (2)$$

where $\mathbf{u_l}$, $\mathbf{p_l}$, ρ_l and μ_l are, respectively, the luminal blood velocity, pressure, density and dynamic viscosity. On the other hand, transmural blood plasma flow inside the plaque and arterial wall was modeled by the Darcy's equation (Eq. 3) and continuity equation (Eq. 4):

$$\mathbf{u_i} - \nabla \cdot \left(\frac{K_i}{\mu_i} \mathbf{p_i} \right) = 0 \quad (3)$$

$$\nabla \mathbf{u_i} = 0 \quad (4)$$

where $\mathbf{u_i}$, $\mathbf{p_i}$ and μ_i are, respectively, the transmural blood plasma velocity, pressure, dynamic viscosity in i sub domain while i stands for plaque and arterial wall. K_i is the Darcian permeability coefficient.

Drug transport from the coating was modeled by the transient diffusion equation (Eq. 5):

$$\partial_t c_c + \nabla \cdot (-D_c \nabla c_c) = 0 \quad (5)$$

where c_c and D_c are the concentration and diffusivity of drug in the coating, respectively. A transient convection-diffusion equation (Eq. 6) was used to model the drug delivery in lumen:

$$\partial_t c_l + \nabla \cdot (-D_l \nabla c_l + c_l \mathbf{u_l}) = 0 \quad (6)$$

where c_l and D_l are the concentration and diffusivity of drug in the lumen, respectively. It is important to notice that only free drug, and not the bound drug attached to the binding sites, is transported through the plaque and arterial wall. Interaction between free and bound drug was characterized by a reversible reaction. Therefore, the free drug transport inside the plaque and arterial wall was modeled as a transient diffusion-convention-reaction equation (Eq. 7) :

$$\partial_t c_{f_i} + \nabla \cdot \left(-D_i \nabla c_{f_i} + \frac{\gamma_i \mathbf{u_i} c_{f_i}}{\varepsilon_i} \right) = -\alpha \left(c_{f_i} - \frac{c_{b_i}}{\kappa_i} \right) \quad (7)$$

where c_{f_i} and c_{b_i} are the free and bound drug concentration, respectively. D_i and κ_i are drug diffusivity and partition coefficient, respectively. γ_i is the hindrance coefficient and ε_i is the porosity of the arterial wall. α is the rate constant defined as the rate at which the binding sites adsorb drug [11]. Therefore, the bound drug concentration was modeled as:

$$\partial_t c_{b_i} = \alpha \left(c_{f_i} - \frac{c_{b_i}}{\kappa_i} \right) \quad (8)$$

C. Solution

All physical parameters and drug properties for this study were adopted from literature. Appropriate boundary conditions were carefully considered and assigned to solve all equations using a commercially available finite element (FE) based software COMSOL Multiphysics™, version 3.4. A total of 14,089 triangular mesh elements were used for the model. A sensitivity study was carried out based on the average velocity and average arterial wall drug concentration to ensure mesh and time step (used by the solver to solve transient equations) independent solution. For analysis of results, drugs in the tissue, expressed as a fraction of the initial amount of drug in the coating drug and concentration variation (CV) were used.

III. Results

As expected, the presence of plaque affects the drug deposition and as the thickness of the plaque increases, the total amount of paclitaxel in the arterial wall decreases, as shown in Figure 2(a) and Figure 3(a). Free paclitaxel increases in the initial stage after stenting but within 12 hours it started to decrease as it moves towards the perivascular wall. Bound paclitaxel in general increases until 24 hours and then starts decreasing at very slow rate. 16.61% more drug is found for 0.1 mm thick plaque compare to 0.4 mm after 5 days. On the other hand, drug distributions for both free and bound paclitaxel are shown in Figure 2(b) and Figure 3(b), respectively. Although at the initial stage of stenting the drug distribution is highly non-uniform (data not shown), it becomes stable after 1 day. Meanwhile, the presence of plaque decreases the CV of drug in the arterial wall and hence minimum CV is found for 0.4 mm thick plaque which is 23.63 % and 72.46 % less than the CV of no plaque condition for free and bound drug, respectively.

Finally, a sensitivity analysis was done for paclitaxel diffusivity (D_P) and partition coefficient (K_P) in the plaque. The effect of D_P on drug deposition is given in Figure 4 where D_P is shown as a ratio to the drug diffusivity in the arterial wall. The results reveal that, the amount of free and bound drug increase with increasing D_P at the initial stage but decrease thereafter. After 5 days 43 % and 35 % more free and bound drug, respectively, were found when the ratio was changed from 0.1 to 10. On the other hand, while K_P was varied within the range for paclitaxel in the arterial wall, no significant change in drug deposition in the arterial wall was noticed (Figure 5).

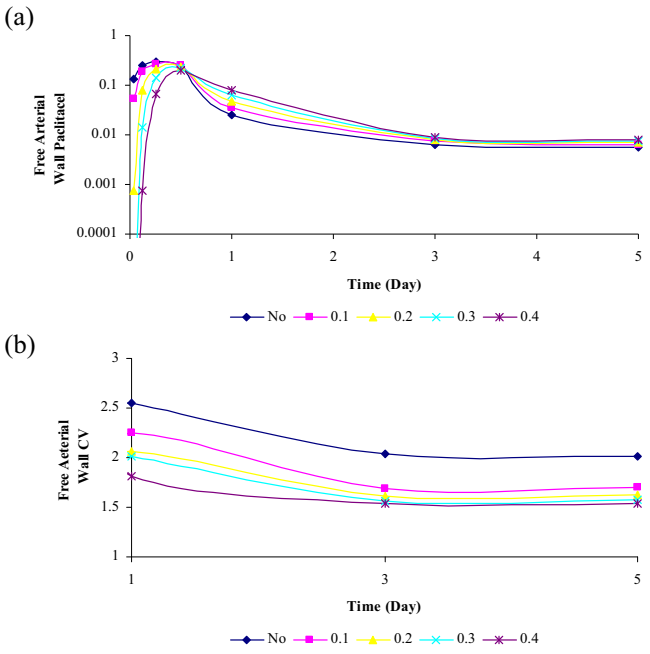


Fig. 2 Effect of plaque thickness on (a) amount and (b) CV of free paclitaxel in arterial wall

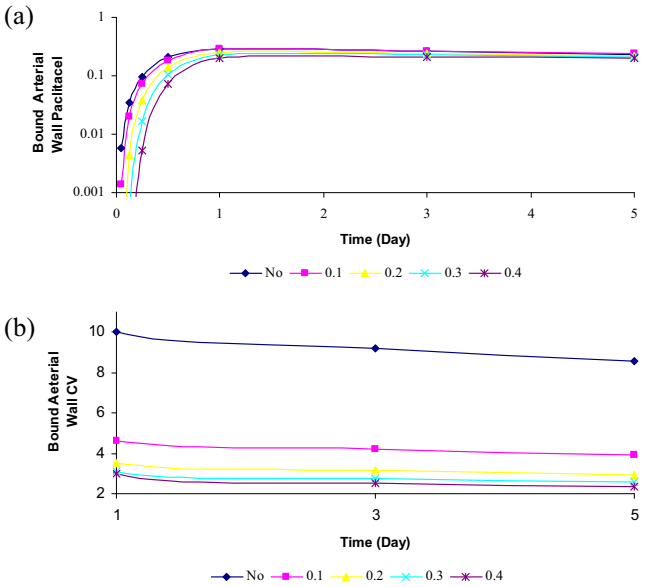


Fig. 3 Effect of plaque thickness on (a) amount and (b) CV of bound paclitaxel

IV. Discussion

Our results show that the presence of plaque dramatically affects the local pharmacokinetics of both free and bound paclitaxel in the arterial wall. First of all, the presence of plaque acts as a physical barrier to both drug transfer into the arterial wall and transmural hydraulic flux. Most importantly, the binding sites in the plaque absorb a substantial amount of drug. In addition, the endothelial layer also limits the drug transfer into the arterial wall as it acts as a barrier to transmural hydraulic flows for heparin and this should be more prominent for paclitaxel as convection plays an important role to paclitaxel drug transfer [2].

Study on the effect of D_P and K_P suggested that it is important to determine the physical properties properly inside the plaque. Higher D_P forces the drug to diffuse fast into the arterial wall and thus it enhances the drug loss from the perivascular wall as well. It also increases the luminal washout of drug from the plaque-lumen interface. Furthermore, the non-significant decrease trend in total arterial wall drug deposition due to increase in K_P indicates that more drug is available in bound form in the plaque which restricts

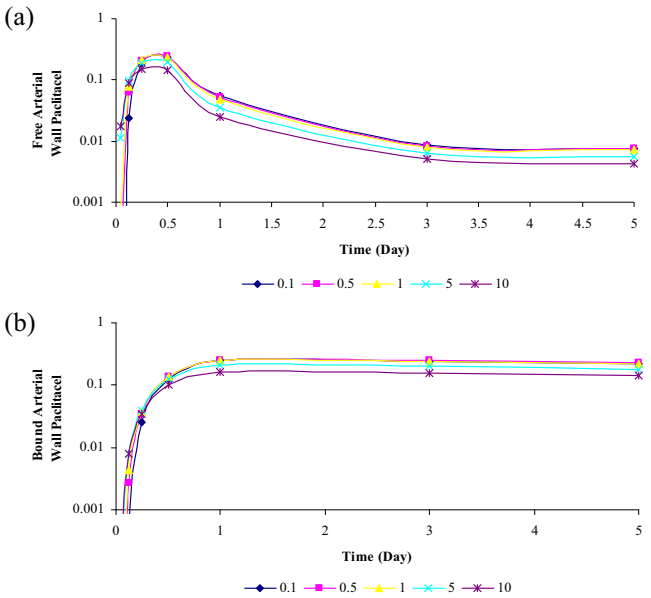


Fig. 4 Effect of paclitaxel diffusivity in plaque on arterial wall (a) free and (b) bound paclitaxel

the transport of free drug as well. These results are consistent with the findings reported earlier where increased drug diffusivity in the clot decreased arterial wall drug uptake and high drug binding capacity with clot delayed arterial uptake [12].

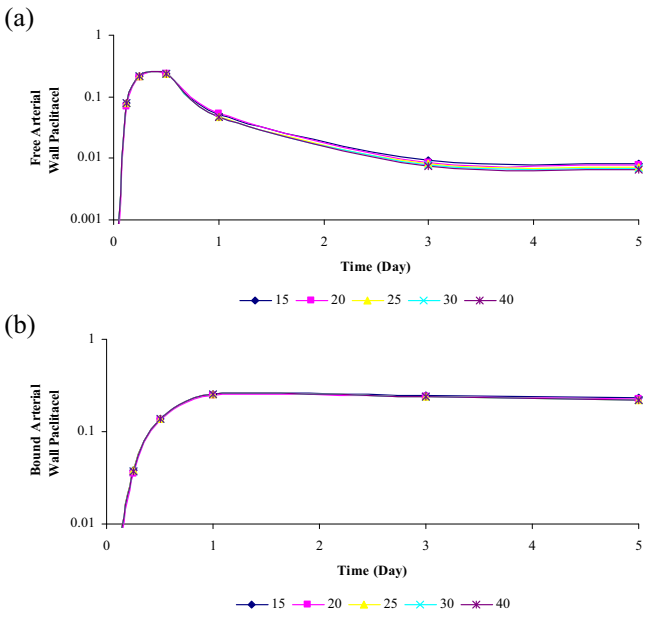


Fig. 5 Effect of paclitaxel partition coefficient in plaque on arterial wall (a) free and (b) bound paclitaxel

V. Conclusions

Drug pharmacokinetics in the arterial wall is shown to be affected by the presence of plaque and its thickness. As such, it is important to consider a model involving plaque in investigating drug delivery from DES to improve the design to achieve best therapeutic outcome. Based on the results using the simple geometry, it is expected that a more realistic 3-dimensional plaque geometry will give a better insight.

Acknowledgment

This study was supported by Nanyang Technological University, Singapore.

References

1. Yang C, Burt H M (2006) Drug-eluting stents: factors governing local pharmacokinetics. Adv Drug Del Rev 965:402-411
2. Creel C J, Lovich M A, Edelman E R (2000) Arterial paclitaxel distribution and deposition. Circ Res 86:879-884
3. Lovich M A, Philbrook M, Sawyer S et al. (1998) Arterial heparin deposition: role of diffusion, convection, and extravascular space. Am J Physiol Heart Circ Physiol 44:H2236-H2242
4. Levin A D, Vukmirovic N, Hwang C –W et al.(2004) Specific binding to intracellular proteins determines arterial transport properties for rapamycin and paclitaxel. Proc Natl Acad Sciences 101: 9463-9467
5. Hwang C -W, Wu D, Edelman E R (2001) Physiological transport torces govern drug distribution for stent-based delivery. Circulation 104:600-605
6. Lovich M A, Edelman E R (1996) Computational simulations of local vascular heparin deposition and distribution. Am J Physiol Heart Circ Physiol 27:H2014-2024
7. Sakharov D V, Kalachev L V, Rijken D C (2002) Numerical Simulation of Local Pharmacokinetics of a Drug after Intravascular Delivery with an Eluting Stent. J Drug Target 10:507-513
8. Tesfamariam B (2007) Local vascular toxicokinetics of stent-based drug delivery. Toxicol Lett 168:93-102
9. Baldwin A L, Wilson L M, Gradus-Pizlo I et al. (1997) Effect of atherosclerosis on transmural convection and arterial ultrastructure : implications for local intravascular drug delivery. Arterioscler Thromb Vasc Biol 17: 3365-3375
10. Serruys P W, Rensing B (2002) Handbook of coronary stents. Martin Dunitz, London
11. Green J E F, Jones G W, Band L R et al. (2005) Arterial stents: modelling drug release and restenosis. Proc. of the 4th Math. in Med. Stud Group
12. Hwang C -W, Levin A D, Jonas M et al. (2005) Thrombosis modulates arterial drug distribution for drug-eluting stents. Circulation 11:1619-1626

Corresponding author address

Author: Chong Chuh Khiun
Institute: Nanyang Technological University
Street: 62 Nanyang Drive
City: Singapore
Country: Singapore
Email: mckchong@ntu.edu.sg

Perfusion Bioreactors Improve Oxygen Transport and Cell Distribution in Esophageal Smooth Muscle Construct

W.Y. Chan[1] and C.K. Chong[2]

[1]School of Mechanical and Aerospace Engineering, Nanyang Technological University, Singapore
[2]School of Chemical and Biomedical Engineering, Nanyang Technological University, Singapore

Abstract — **Mass transfer is a major issue for producing, in particular, thicker tissue constructs *in vitro*. Without the support of internal capillary network, oxygen supply is restricted to the superficial layer and the survival of cells deep within the construct could be threatened. In this study, oxygen was postulated as the limiting factor for cellular activity in developing tissue construct and their correlation was investigated. Single- and double-flow perfusion bioreactors were custom designed to provide a controlled tangential laminar flow at a flowrate of 0.545 ml/min over the surface of the tissue construct ($3.2 \times 2 \times 0.2$ cm^3 porous gelatin scaffold seeded with 2×10^6 cells/cm^3 of porcine esophageal smooth muscle cells). Gelatin scaffold of similar size and cell seeding was cultured in Petri dish and served as a static culture control for comparison. At day 5, oxygen profile in-situ was measured across the thickness of tissue construct while cell distribution and total DNA were analyzed. Bioreactors produced higher cell proliferation activity compared to static culture. Under static culture, cells were observed to populate near the surface of tissue construct. While single-flow bioreactor improved cell infiltration/migration in the scaffold, double-flow bioreactor improved further these cellular events and produced construct with more uniform cell distribution. These cell distributions appear to parallel that of oxygen distribution. In static culture, oxygen concentration dropped abruptly from the construct surface to a depth of about 1000 μm where it was maintained at a constant level in the core at low cell density but rose near the bottom surface. In the single-flow bioreactor, oxygen level dropped linearly from the top to the bottom surface of construct. In the double-flow bioreactor, oxygen level began to drop at about 2.5 mm above the construct surface but it was maintained at almost a constant level throughout the whole thickness.**

I. Introduction

Mass transfer is one of the major issues that have been a bottleneck to produce thicker tissue construct *in vitro*. Much of recent efforts attempted to pre-build a capillarial network *in vitro* by seeding capillary-forming cells (such as umbilical vein endothelial cells) together with growth factors for angiogenesis in order to provide a pathway to shorten the period of anastomosis to the host blood supply upon implantation; however, the anastomosis have shown to be limited [1]. For *in vitro* tissue engineering, evidence has shown that this network can improve oxygenation [2], but the effect of growth factor used to induce angiogenesis may have adverse effect on other cell types [1].

On the other hand, tissue engineering perfusion bioreactor has shown promises to improve the quality of tissue construct *in* vitro such as cell distribution and ECM deposition due to improved mass transfer with continuous flow of medium that increases convective transport [3-8]. However, the mechanism leading to these improved states has not been fully elucidated. One of the variables postulated to be important is the oxygenation of tissue construct. Oxygen is one of the critical chemical species in aerobic metabolism of mammalian cells. Below a certain oxygen level, hypoxic condition is induced and cells would adopt anaerobic metabolism for energy production which causes acidosis and subsequent cell death. *In vivo*, oxygen can be carried by erythrocytes which facilitate maintaining physiological level of oxygen in tissue. *In vitro*, tissue culture relies on gaseous oxygen dissolved in culture medium. Since oxygen is sparingly dissolved in water, oxygen supply would be severely limited in larger tissue construct with no vascular network. Therefore, it would be essential to study the importance of oxygenation in developing tissue construct. In this study, bioreactors with single- and double-flow perfusion were designed to study how oxygen transport (oxygen distribution) was improved in tissue construct and correlate construct oxygenation to the quality of tissue construct (cell distribution).

II. Method

Single- and double-flow bioreactors were designed and fabricated to allow medium flow across the top surface and both top and bottom surfaces of the tissue construct, respectively. The flow chambers were designed such that the flow profiles across the scaffold surfaces were fully- developed and laminar. Porcine esophageal smooth muscle cells (PESMCs) were isolated from pig esophagus and cultured in Dulbecco's Modified Eagle Medium (DMEM, HyClone) supplemented with 10% fetal bovine serum (FBS, HyClone), 1% antibiotic-antimycotic solution (Sigma) and 0.2% kanamycin (Sigma). Cells at p6 were seeded into $3.2 \times$

Chwee Teck Lim, James C.H. Goh (Eds.): ICBME 2008, Proceedings 23, pp. 1523–1526, 2009
www.springerlink.com

2×0.2 cm^3 porous gelatin scaffolds at 2 million cells/cm^3. A constant flow rate of culture medium at 0.545 ml/min was maintained by a peristaltic pump (Ismatec). Static culture of similar cell-seeded scaffolds served as a control. At day 5, oxygen distributions across the depth of constructs were measured in-situ within the bioreactor chamber and in Petri dish using oxygen microsensor (Unisense). Thereafter, the constructs were harvested and the total DNA was measured using Picogreen (Molecular Probes) while paraffin sections of tissue construct were prepared and stained in DAPI (Molecular Probes) and analyzed under fluorescence microscope (Carl Zesis). Serial images across the depth of constructs were taken from top to bottom surfaces. Images in vertical sequence were opened in ImageJ 1.40g, an open-source image processing program developed by National Institutes of Health, USA (http://rsb.info.nih.gov/ij/) and combined vertically using "Stack combiner" Plugin. A total of 20 segments (ROI) were created throughout the whole thickness of the construct using macros program developed in house. Cells were counted in each segment.

III. Results

A. O_2 distribution

O_2 distributions of PESMCs-seeded constructs cultured in Petri dish (static), single-flow and double-flow chamber were shown in Fig. 1. At day 5, all culture conditions, both under perfusion flow and static culture, resulted in decreasing trend in O_2 in the bulk medium phase.

At the construct surface, both static and single-flow culture resulted in similar interfacial O_2 level between 80% and 85% (at distance = 0 μm). Since the single-flow bioreactor has medium flow on the top side only, O_2 level was reduced monotonously with the depth and reached a minimum at the bottom side of the scaffold (59.5%). On the other hand, construct cultured in Petri dish was in suspension in the medium and diffusion can occur on the bottom side of the construct. It was found the O_2 level started to recover slightly from the core of the construct (at distance = 1000 μm) and reached a higher O_2 level (64.7%) at the bottom side. However, O_2 level at the bottom side was obviously lower than that at the top side which was closer to air-medium interface.

A completely different O_2 profile was found in double-flow bioreactor. Only one side of medium region was shown here since the profiles for both sides were identical. O_2 level dropped rapidly at 2.5-mm above the scaffold (based on the maximum gradient of 2.2×10^{-4} μm^{-1}), reaching 51.9% at the scaffold surface but this level was maintained across the depth of the construct. When the oxygenation level within the construct was compared with the highest level at the surface in each of the three cases, it was found that double-flow bioreactor resulted in the most uni-

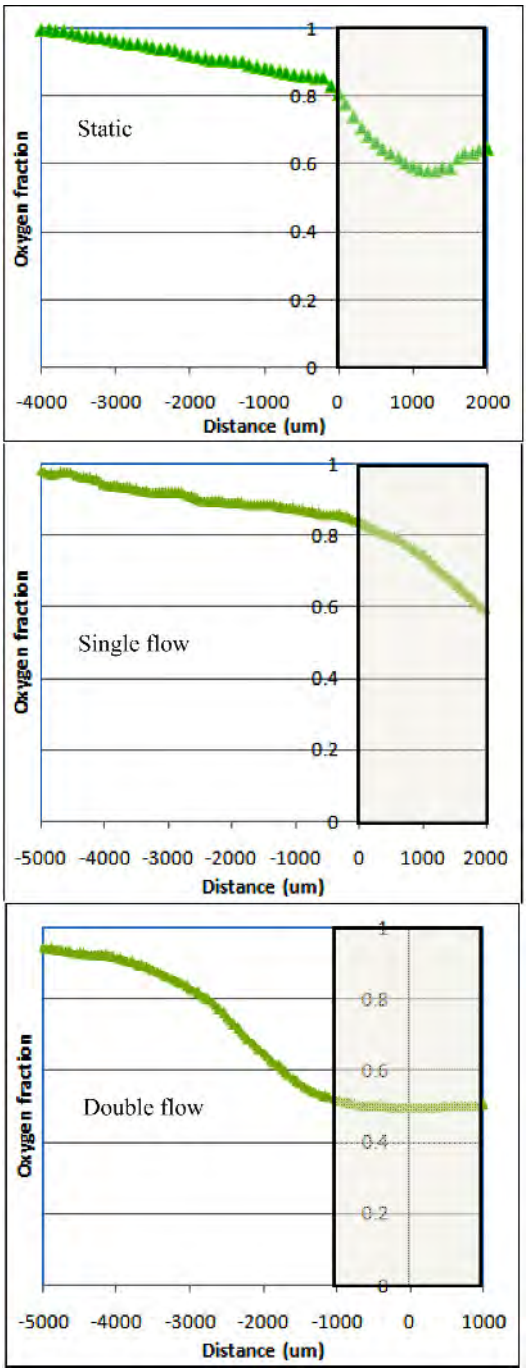


Fig. 1 Oxygen profiles for three culture conditions. Top: static, centre: single flow bioreactor and bottom: double flow bioreactor. The shaded regions indicate the constructs.

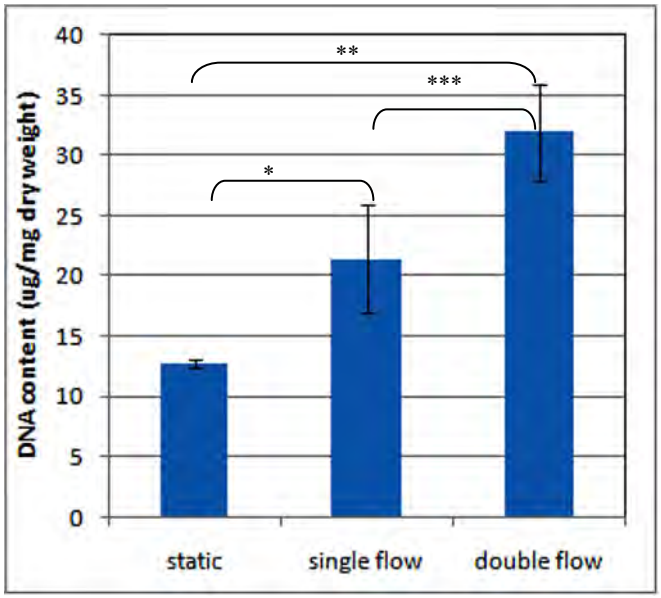


Fig. 2 Total DNA quantification

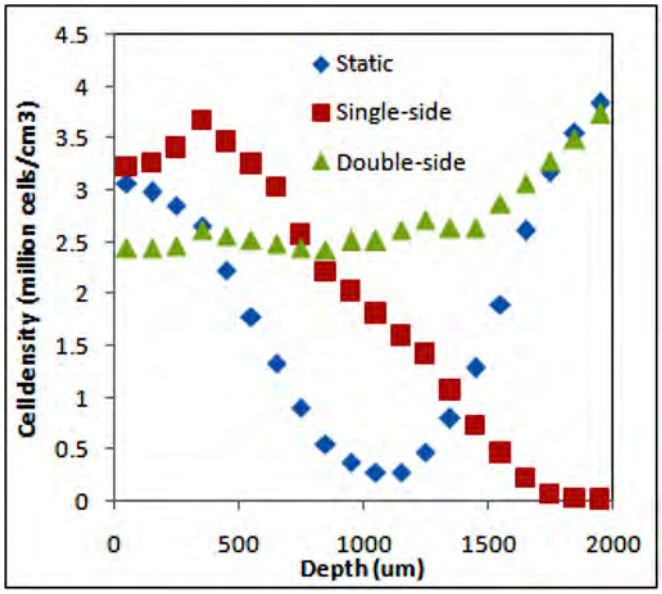


Fig. 3 Cell distribution

form oxygenation (only 4.2% difference) while the single-flow and static culture produced a difference of 28.9% and 28.2%, respectively.

B. Total DNA

In terms of cellularity of tissue construct, both bioreactor cultures resulted in significantly higher DNA contents compared to static culture ($p < 0.05$) while double-flow bioreactor was superior to the single-flow case ($p < 0.05$) (Fig. 2). 2.5-fold and 1.7-fold improvement of DNA contents were observed in tissue constructs cultured in double-flow and single-flow bioreactor after the 5-day period, respectively, compared to static culture.

C. Cell distribution

Three types of cell distribution patterns were observed in the 3 culture conditions (Fig. 3). Static culture resulted in a V-shaped profile with almost the centre (at 1000 μm) free of cells while the highest densities were found at both the top and bottom surfaces. Single-flow managed to maintain a cell density at high level up to about 500 μm and dropped monotonously thereafter. On the other hand, cell density in construct cultured in double-flow bioreactor was found to be relatively uniform across the thickness. When the cell number for each segment across the depth of construct was compared with those at the surface, the average difference was 10.4%, 60.5% and 58.2%, for double-flow, single-flow and static culture, respectively.

IV. Discussion

A. Macroscopic findings: Bulk medium O_2 level vs. total DNA

Many reported studies measured dissolved O_2 in the medium (or bulk flow) using blood gas analyzer to correlate with the outcome obtained in tissue construct (e.g. total DNA). Since this parameter is considered an average value of dissolved O_2 in a well-mixed medium, by averaging the O_2 level across the medium phase in this study, 77.6%, 91.3% and 81.1% were obtained for static, single flow and double flow conditions, respectively. Obviously, both bioreactors demonstrated improved oxygenation in medium by convective transport which in turn allowed a rather rough explanation for the increase in total DNA. This explanation was not exhaustive, however, since O_2 transport can adopt different regimes in bulk medium and construct, and an external improvement of oxygen transport cannot fully reflect the actual oxygenated state in the construct (internal oxygenation). Therefore, it is suggested that it would be more useful to study the internal oxygenation which is more crucial in cell growth within the construct as it provides a direct correlation between the oxygenation state and the cellularity and DNA contents of cells.

B. Microscopic findings: O_2 distribution-cell distribution

Three different profiles of O_2 distributions and cell distributions were observed in three culture conditions. It was

found that cell distributions followed closely the patterns of O_2 distribution, suggesting a strong correlation between these 2 parameters. The low cell regions observed in the core of the statically cultured construct and the bottom of the construct in the single-flow bioreactor were probably due to high O_2 demand required during the initial phase of cell attachment, resulting in low survival of cells in these regions. With better initial oxygenation as achieved in the double-flow bioreactor, cells in the core survived better and with uniform oxygenation over the culture period, cells were able to grow in a more uniform manner. However, the lower initial cellularity in some regions may adversely influence the fate of tissue construct as suggested in this study: (1) Cells which survived near the surface populated the scaffold faster and this could create a barrier for O_2 transport; (2) Cell growth could slow down due to cell-cell contact inhibition while cells at low density region could not grow due to the lack of cell-cell signaling leading to a cell-free region.

V. Conclusion

Three culture conditions (static, single-flow and double-flow bioreactors) were used to culture PESMCs-seeded construct. O_2 and cell distributions in these 3 conditions presented different profiles but these 2 parameters were highly correlated. It was shown that effective O_2 transport is important for the survival and uniform distribution of cells in developing tissue construct. The bioreactors designed in the study were able to improve and both the external (bulk medium) and internal (construct) oxygenation and hence the cellularity and quality of construct.

References

1. Rouwkema J, Rivron NC, van Blitterswijk CA (2008) Vascularization in tissue engineering. Trends Biotechnol 26: 434-441
2. Griffith CK, Miller C, Sainson R et al (2005) Diffusion limits of an In Vitro thick prevascularized tissue. Tissue Eng 11: 257-266
3. Carrier RL, Papadaki M, Rupnick M et al (1999) Cardiac tissue engineering: Cell seeding, cultivation parameters, and tissue construct characterization. Biotechnol Bioeng 64: 580-589
4. Gemmiti CV, Guldberg RE (2006) Fluid flow increases Type II Collagen deposition and tensile mechanical properties in bioreactor-grown tissue-engineered cartilage. Tissue Eng 12: 469-479
5. Malda J, Frondoza CG (2006) Microcarriers in the engineering of cartilage and bone. Trends Biotechnol 24: 299-304
6. Niklason LE, Gao J, Abbott WM et al (1999) Functional arteries grown In Vitro. Science 284: 489-493
7. Saini S, Wick TM (2003) Concentric cylinder bioreactor for production of tissue engineered cartilage: Effect of seeding density and hydrodynamic loading on construct development. Biotechnol Prog 19: 510-521
8. Sittinger M, Bujia J, Minuth WW et al (1994) Engineering of cartilage tissue using bioresorbable polymer carriers in perfusion culture. Biomaterials 15: 451-456

Corresponding author

Author: Chong Chuh Khiun
Institute: Nanyang Technological University
Street: 62 Nanyang Drive
City: Singapore
Country: Singapore
Email: mckchong@ntu.edu.sg

Determination of Material Properties of Cellular Structures Using Time Series of Microscopic Images and Numerical Model of Cell Mechanics

E. Gladilin[1], M. Schulz[1], C. Kappel[1] and R. Eils[1,2]

[1] German Cancer Research Center, Theoretical Bioinfomatics, Im Neuenheimer Feld 580, D-69120 Heidelberg, Germany
[2] University Heidelberg, BioQuant, Im Neuenheimer Feld 267, D-69120 Heidelberg, Germany

Abstract — **Determination of material constants is indispensable for quantitative description of mechanical properties of cellular structures. Since conventional methods of experimental cell mechanics are based on application of forces onto the cell boundary, intra-cellular structures are not accessible for direct measurements. In this work, we present an approach for estimation of canonic material constants (i.e. stiffness and compressibility) using times series of microscopic images and numerical model of cell mechanics. The proposed method is based on optical monitoring of the cellular deformation which can be triggered by any appropriate contacting or non-contacting technique affecting mechanical cell integrity. The presented experimental studies give examples of determination of material parameters of optically monitored cells whose deformation was induced by conventional micromanipulation and completely contact-free, using chemical agents.**

Keywords — **cell mechanics, material parameter estimation, contact-free measuring techniques, image analysis, numerical modeling**

I. Introduction

Numerous works have indicated the importance of mechanical factors to basic biological functions and processes in the cell [1-6]. Determination of canonic material constants, such as stiffness and compressibility, plays a key role in quantitative characterization of mechanical properties of normal and malignant cells [9]. Conventional approaches of experimental cell mechanics are based on micromanipulation techniques that employ application of controlled forces onto the cellular boundary [2,3]. Consequently, these methods provide information about the overall cell properties (e.g. stiffness of the whole cell) or those of its part which is directly accessible by the measurement (e.g. cell membrane). Probing mechanical properties of intra-cellular structures, which are not accessible for direct measurements, is not possible with conventional micromanipulation techniques. Meanwhile, modern microscopic imaging techniques, such as confocal laser scanning microscopy (CLSM), yield highly resolved 3D images of intra-cellular structures. Time series of 3D CLSM images depicting successive cell deformation under the impact of external forces provide valuable insights into mechanical behavior of cellular matter on the local scale and can serve for estimation of material parameters of constitutive models. In this work, we present an approach for determination of material properties of cellular matter which is based on analysis of time series of microscopic images and numerical modeling cell mechanics. The core idea of our approach consists in reformulation of parameter estimation problem as an image registration problem, i.e., material constants are determined as modeling parameters that minimize appropriately defined dissimilarity measures between computationally predicted and experimentally observed images. Based on optical monitoring of the cellular deformation, the proposed method can be used both in combination with and without conventional micromanipulation techniques. In the presented experimental studies, we give examples of application of this approach for determination of the Young's modulus (stiffness) and the Poisson's ratio (compressibility) of cells whose deformation was triggered by (i) uniaxial microstretcher and (ii) pure chemical inducement, using cytoskeleton-disrupting drugs.

II. Materials and methods

A. Elastomechanical Model of Cellular Matter

Based on previous observations [2,4], in the range of small deformations cellular matter can be approximated as a piecewise homogeneous, isotropic Hookean material characterized by the linear stress-strain law [8]

$$\sigma(\varepsilon) = \frac{Y}{1+\nu}\left(\varepsilon + \frac{\nu}{1-2\nu} tr(\varepsilon)\right) \qquad (1)$$

with two elastic constants: Y – the Young's modulus (material stiffness) and ν – the Poisson's ratio (material compressibility). Since the boundary value problem (BVP) in image-based analysis is typically formulated in a quasi-geometric form, i.e. both knowns and unknows are the displacements, definition of dimensionless modeling parameters is required. While the Poisson's ratio is a dimensionless quantity, the Young's modulus Y_i of i-th material can be substituted by the dimensionless *relative stiffness* Y_i/Y_1

Chwee Teck Lim, James C.H. Goh (Eds.): ICBME 2008, Proceedings 23, pp. 1527–1530, 2009
www.springerlink.com

which gives the ratio between Y_i and the stiffness of the reference material Y_1.

Due to the fact that the strain tensor ε in Eq. 1 is a nonlinear function of the displacement u

$$\varepsilon(u) = \frac{1}{2}(\nabla u + \nabla u^T + \nabla u \nabla u^T) \quad (2)$$

the equations describing the deformation of a linear elastic material are, in general, nonlinear with respect to u.

The deformation continues until the equilibrium between the external forces f and inner stresses σ is reached

$$\nabla \sigma + f = 0 . \quad (3)$$

Altogether Eq. 1-3 imply a parameter-dependent relationship between the external loads and the displacements in a deformed body.

For numerical solution of the elastostatic boundary value problems, the Finite Element Method (FEM) on tetrahedral grids was applied.

B. Image- and Model-based Parameter Estimation

Consider times series of images $I_t(x)$ depicting the successive deformation of an object in the optical field. Assuming that structural differences between each two images are due to deformations only, the consecutive time step represents the deformed configuration of the previous one, i.e.

$$I_{t+1}(x) = I_t(x + u) . \quad (4)$$

The displacement field u describing the volumetric deformation can be computed as a solution of the BVP defined by Eq. 1-3 and the boundary conditions, which are typically given in the form of the boundary displacements. Since the displacement field depends on material constants $u=u(Y, \nu)$, the problem of parameter estimation can be reformulated as an image registration problem which consists in finding an optimal set of material constants that minimizes a dissimilarity norm between computationally predicted and experimentally observed images. One of such dissimilarity norms is, for instance, the absolute image difference (AID):

$$AID_t(Y_i, \nu_j) = \| I_{t+1}(x) - I_t(x + u(Y_i, \nu_j)) \| \quad (5)$$

Determination of the minimum of Eq. 5 yields material constants for each pair of images from experimental time series, see Fig. 1.

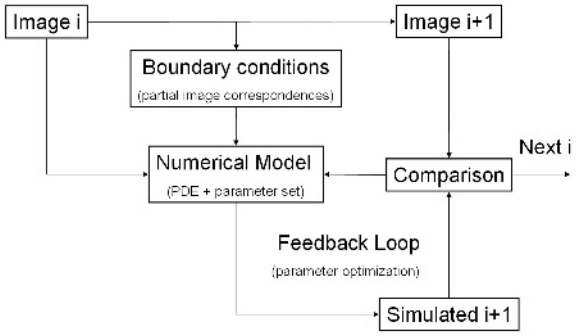


Fig. 1. Iterative scheme for image-based estimation of modeling parameters. Optimal set of modeling parameters for each time step corresponds to the minimum dissimilarity between computationally predicted and experimentally observed images.

C. Image Processing

Because of a number of natural and technical reasons, microscopic images are highly dynamic and exhibit a high level of statistical and structural noise. Consequently, the assumption of structural changes between each two time steps due to elastic deformations only, which was implied in Eq. 4, does not hold. The goal of image processing consists in reduction and possible elimination of non-elastic image differences by means of

- image denoising,
- rigid image registration,
- image enhancement and normalization.

In addition, images are used for the reconstruction of the object's geometry. For this purpose, images are binarized and iso-surface meshes corresponding to the outer boundary of the segmented regions are generated. Subsequently, triangulated surfaces are filled with unstructured finite element volumetric grids.

III. Results

Two experimental studies presented below demonstrate application of the above described framework for determination of material properties of cells whose deformation was induced (i) by uniaxial microstretcher and (ii) completely contact-free, using cytoskeleton-disrupting drugs.

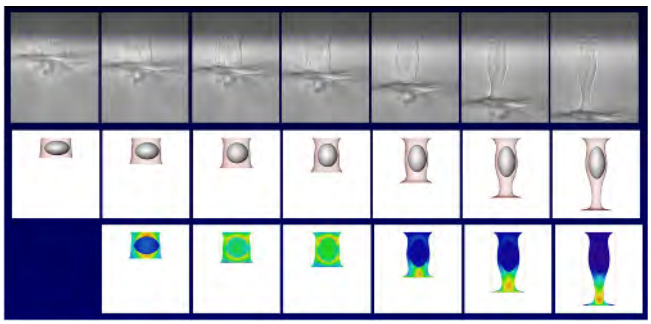


Fig. 2. Top row: experimental series of uniaxial cell stretchings. Middle row: geometrical models depicting successive numerical simulation of the cell deformation. Bottom row: 2D cut plane projections of the intracellular distribution of the mean strain. The color scale reflects the relative differences between low and high strains for each single deformation.

A. Simulation of Uniaxial Cell Stretching

In our previous work [7], we presented a study on determination of material parameters of a two-component model of uniaxially stretched cells. Fig. 2 gives an overview over iterative simulation of time series of cell stretchings including the prediction of the cell shape and distribution of intracellular strain. Starting from the initial geometrical model of the cell (Fig. 2 (middle row, left)), all subsequent time steps of the image sequence were computed from the previous steps. For each time step, optimal combination of material parameters (including the dimensionless ratio between the nuclear and cytoplasmatic stiffness Y_{cyt}/Y_{nuc} and the Poisson's ratio) was determined using the similarity measure which is based on conformity between computationally simulated and experimentally observed cell contours. At high stretching rates, additional assumptions about non-homogeneous distribution of material properties were made. The asymmetric deformation of lower and upper half of the cell could be explained as a result of asymmetric coating of microplates (fibronectin vs neutral substance). Time series of predicted material parameters show that progressive stretching lead to increasing stiffness and decreasing compressibility of the cell cytoplasm, see Fig 3.

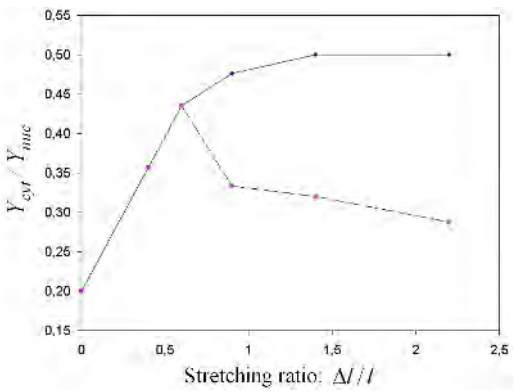


Fig. 3. Plots of numerically determined values for the relative stiffness of the cell cytoplasm probed in the middle of the upper (solid lne) and lower (dotted line) half of the cell as a function of the total cell elongation0.

B. Contact-free Investigation of Nuclear Mechanics

Investigation of mechanical properties of cell nuclei is important for epigenetics and medicine. Probing nuclear matter in living cells via conventional micromanipulation techniques is not possible. To enable image- and model-based analysis of nuclear mechanics, a contact-free induction of cellular deformation using cytoskeleton-disrupting drugs, such as Latranculin, was introduced (see Fig. 4). During the drug-induced deformation, 3D images of DAPI-stained nuclei were continuously acquired via confocal laser scanning microscopy. From large amount of acquired data, subsequences of images with high signal-to-noise ratio and small Z-shift were selected. These images were denoised and rigidly registered for further analysis of intensity differences that were caused by elastic deformations. Binarized images were used for generation of surface and volumetric models of 3D nuclei (see Fig. 5). Volumetric deformations were computed from correspondences between each two nuclear surfaces using a one-material model of nuclear matter based on Eq. 1-3. The goal of this study was to determine the nuclear compressibility, i.e. the Poisson's ratio. For this purpose, the nuclear deformation was computed for a number of sampling values of the Poisson's ratio varying in the range $0<\nu<0.5$. The optimal value of ν was obtained from the minimum of AID(ν) curves (Eq. 5). Fig. 6 shows the plots of AID(ν) for four consecutive time steps. Based on these findings the Poisson's ratio of $\nu=0.4 \mp 0.01$ was determined for the observed HeLa cell nuclei. This result is in good conformity with the literature values, e.g. [5,6].

IV. Conclusions

We presented an approach for determination of material properties of intra-cellular structures, which are inaccessible by conventional micromanipulation techniques, using time series of 3D images and numerical model of cell mechanics. The core idea of our method consists in reformulation of parameter estimation problem as an image registration problem, i.e., the optimal set of parameters corresponds to the minimum dissimilarity between computationally predicted and experimentally observed images. For induction of the cellular deformation, conventional micromanipulation or chemical agents, such as cytoskeleton-disrupting drugs, can be used. Further development of the method will focus on

automation of image processing and numerical solving techniques to enable widely unsupervised data analysis.

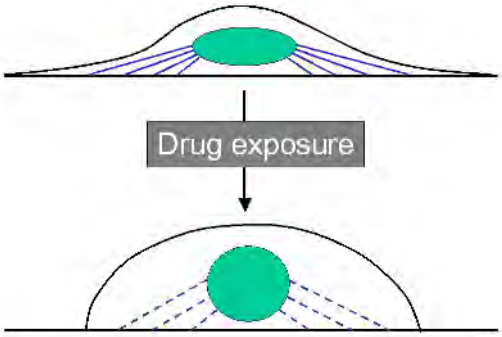


Fig. 4. Cytoskeleton-disrupting drugs induce uncontrolled deformations of cellular interior that yield a valuable source of information for image- and model-based analysis of nuclear mechanics.

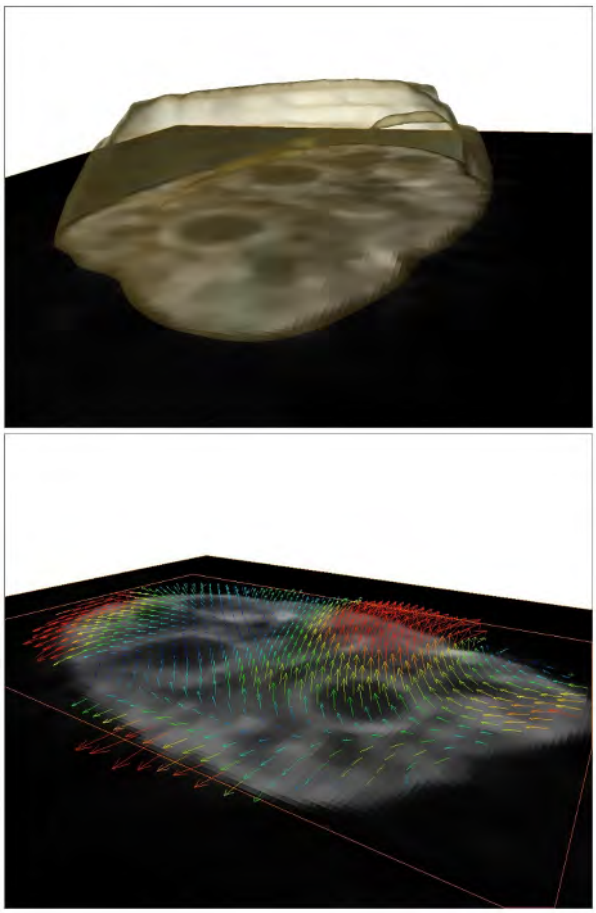


Fig. 5. Top: surface model of the HeLa cell nucleus generated on the basis of a 3D CLSM image. Bottom: volumetric displacement field computed from boundary correspondences between each two surfaces depends on the Poisson's ratio.

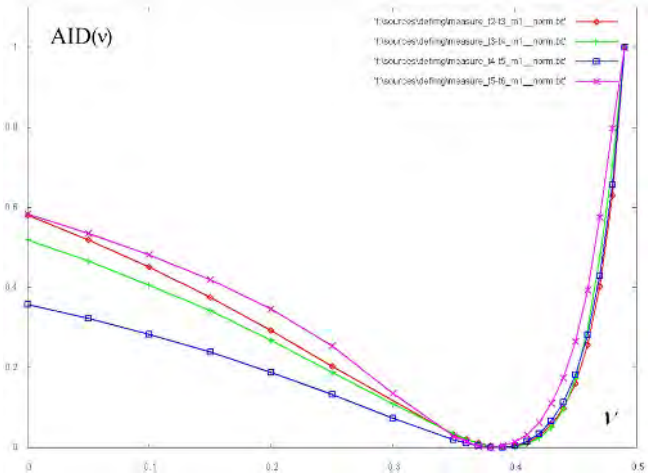


Fig. 6. Plots of the absolute image differences (AID) as a function of the Poisson's ratio for the four consecutive steps of image time series. All four curves exhibit a single minimum around $\nu=0.4$.

References

1. Ingber D. (2003) Mechanobiology and diseases of mechanotransduction. Ann Med. 35(8):564–577
2. Thoumine O, Ott A. (1997) Time scale dependent viscoelastic and contractile regimes in fibroblasts probed by microplate manipulation. Journal of Cell Science. 110:2109–2116
3. Micoulet A, Ott A, Spatz J. (2005) Mechanical response analysis and power generation by single-cell stretching. Chem. Phys. Chem. 6:663–670
4. Guilak F, Tedrow JR, Burgkart R. (2000) Viscoelastic properties of the cell nucleus. Biochem. Biophys. Res. Commun. 269:781–786
5. Shin D, Athanasiou K. (1999) Cytoindentation for obtaining cell biomechanical properties. Journal of Orthop. Res. 17:880–890
6. Kamm RD, McVittie AK and Bathe M (2000) On the role of continuum models in mechanobiology Proc. ASME Int. Congress—Mechanics in Biology. 242:1–9
7. Gladilin E, Micoulet A, Hosseini B, Rohr K, Spatz J, and Eils R (2007) 3D finite element analysis of uniaxial cell stretching: from image to insight. Phys. Biol. 4(2):104–113
8. Ciarlet PG (1988) Mathematical Elasticity: Vol I. Three-Dimensional Elasticity (Studies in Mathematics and its Applications vol 20). Amsterdam: North-Holland
9. Suresh S. (2007) Biomechanics and biophysics of cancer cells. Acta Biomaterialia 3:413–438

Corresponding author:

Name: Evgeny Gladilin, PhD
Institute: German Cancer Research Center, Div. Theor. Bioinf.
Street: Im Neuenheimer Feld 580
City: D-69120 Heidelberg
Country: Germany
Email: e.gladilin@dkfz-heidelberg.de

Analysis of a Biological Reaction of Circulatory System during the Cold Pressure Test – Consideration Based on One-Dimensional Numerical Simulation –

T. Kitawaki[1], H. Oka[1], S. Kusachi[1] and R. Himeno[2]

[1] Okayama University/Graduate School of Health Sciences, Okayama, Japan
[2] The Institute of Physical and Chemical Research (RIKEN), Saitama, Japan

Abstract — **Introduction: Arterial stiffness especially pulse wave shape index (Augmentation index: AIx) has attracted a great deal of attention as the predictor of the circulatory system condition. The AIx determined by the ratio of pulse pressure of reflection wave to progressive wave seem to show the change of reflection wave cause by the total peripheral vascular resistance. However, a phenomenon that progressive wave component increases and reflection wave component hardly changes during the cold pressure test (CPT) as a transient biological reaction. This phenomenon is hardly to explain only in the increase of the total peripheral resistance.**

Consequently, the mechanism of pulse wave change that attributes the reaction of the circulatory system was analyzed by using numerical simulation.

Method: The model of the systemic artery constructed two cylindrical tubes with taper. These cylindrical tubes denote a main aorta of systemic artery from central aorta to common iliac artery bifurcation and a brachial artery form aortic arch to the bifurcation of radial and ulnar artery, respectively. Following parameters were varied which correspond to the CPT load, heart rate: HR, stroke volume: SV, aortic stiffness: AS peripheral resistance: RT and arterial stiffness of brachial artery: BT.

Result: (1)A biological reaction of circulatory system during CPT is a complex reaction combined with not only peripheral artery but also heart or central aorta. (2)A biological reaction seems to be different by the short term CPT and by the long term CPT. We suspect that the change by the short term CPT may have caused β-effect and the long term CPT may have caused α-effect. (3)The pulse wave change phenomenon (especially change of AIx) during the CPT can be expressed using numerical simulation model combined with central aorta and brachial artery.

Keywords — **Circulatory system, sympathetic nerve, cold pressure test, numerical simulation, and augmentation index.**

I. Introduction

Arterial stiffness indexes, especially blood pressure pulse wave shape index (AIx: Augmentation Index), have received a lot of attention because they can indicate the risks for cardiovascular diseases [1]. The widely accepted index, AIx defined as the ratio between progressive wave coming from the heart (P1) and the reflection wave coming from at the periphery (P2) [1] described as Fig 1., is an index that is linked to *arterial stiffness* and *cardiac after load*, can be derived with the pulse wave analysis.

Generally, sympathetic nerve controls human cardiovascular system (heart artery etc.) by controlling the "Heart rate", "Heart contractility", "Arterial stiffness", "Peripheral resistance" etc. For example, load by cold pressure test (CPT) brings on the sympathomimetic reaction at heart and central artery by high heart rate and high heart contractility through the β1 receptor (β action). On the other hand, CPT also brings sympathomimetic reaction at peripherals by high arterial stiffness and high peripheral resistance through the α receptor (α action). Previous researches show that increased blood pressure and AIx during CPT [2], [3]. However, such AIx change mechanism poorly understood now.

In order to understand the basis of these indexes, it is necessary to understand the changes in the pulsatile waves in the systemic arteries. For this, numerical simulation models are very helpful, especially one-dimensional distributed constant models for the analyses of pressure wave propagations [4]. Accordingly, accurate pressure pulse waveform changes are analyzed by the construction of the numerical model which has the simple structure and that can analyze actual cardiovascular characteristic change.

In the present study, (1) continuous blood pressure waveforms were recorded, (2) the influence of sympathetic nerve controlling was analyzed and (3) change of cardiovascular mechanical character was calculated using numerical simulation model, due to investigate the AIx change mechanism during CPT.

II. Method

A. Experiment of CPT

Healthy volunteers (Age 21~34) were loaded by 2 types of CPT, during the measurements of continuous pulse wave-form measurement device (Omron HEM-910AI) at left wrist radial artery and every 50 seconds blood pressure (Omron HEM-8020-JE2) at right upper arm.

(1) Short term CPT: supine subject (n = 13) were loaded by cold bag on their ankles for 50 seconds three times.
(2) Long term CPT: seated subject (n = 11) were loaded by their right hand into cold water for 5 minutes.

Chwee Teck Lim, James C.H. Goh (Eds.): ICBME 2008, Proceedings 23, pp. 1531–1534, 2009
www.springerlink.com

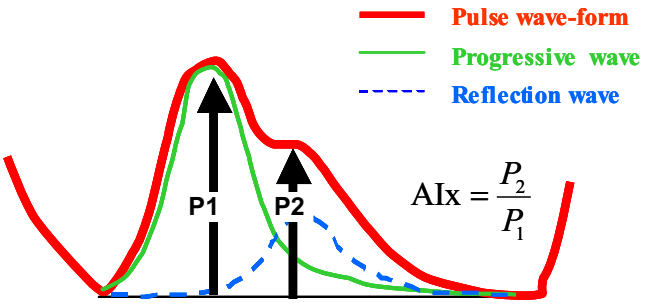


Fig. 1 Pulse wave-form and definition of AIx

The sensor output voltages corresponding to systolic pressure, reflection wave pressure and diastolic pressure were obtained beat by beat from pulse wave-form recorded by continuous pulse wave-form measurement device automatically. AIx were calculated by these output value and PPI (pulse to pulse interval) were determined by the intervals of diastolic pressure timing every beat.

B. Numerical Calculation

Assuming the fluid is axisymmetric, incompressible and there is no leak flow through the tube wall. The governing equation of continuity equation and momentum equation declare as follow [5]:

$$\frac{\partial A}{\partial t}+\frac{\partial Q}{\partial x}=0 \tag{1}$$

$$\frac{\partial Q}{\partial t}+\frac{\partial}{\partial x}\left(\frac{Q^2}{A}\right)+\frac{A}{\rho}\frac{\partial p}{\partial x}+f_t=0 \tag{2}$$

where A is the cross-section of the tube, Q is the mean sectional volume flow rate, p is the mean pressure, t is time, x is distance along the vessel axis, ρ is the fluid density, and f_t is the viscous resistance of oscillating flow.

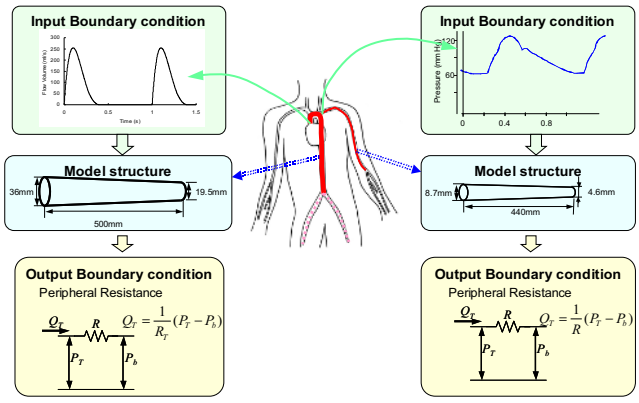


Fig. 2 Numerical Simulation model of cardiovascular system.

Substantively the relation between the transmural pressure and the internal radius of the arteries yield nonlinear curve [6]. The relation can be described with the following equation:

$$p = p_0 \exp\left(\beta\sqrt{(A-A_0)/A_0}\right) \tag{3}$$

where p_0 and A_0 are reference pressure and cross-section, respectively, and the coefficient β is the stiffness parameter.

Numerical model structure were established by central aorta (from ascending aorta to bifurcation of common iliac artery) and brachial artery (from beginning of brachial artery to bifurcation site of radial artery and ulnar artery), referring to Fig. 2. The input pressure boundary condition of brachial artery was used by calculation result of central aorta.

The standard value of the model structure and mechanical parameter for the calculation was determined referring to literature data [7]. Parameter values were changed to correspond with the 2 types of CPT listed below.

(1) Short term CPT
  (i) HR: Increasing heart rate (=60/PPI) (+20%)
  (ii) SV: Increasing maximum flow rate (+20%)
  (iii) AS: Central arterial stiffness softening (-10%)
(2) Long term CPT
  (i) RT: Increasing peripheral resistance (+20%)
  (ii) BT: Increasing arterial stiffness of brachial artery (+10%)

III. Results and Discussions

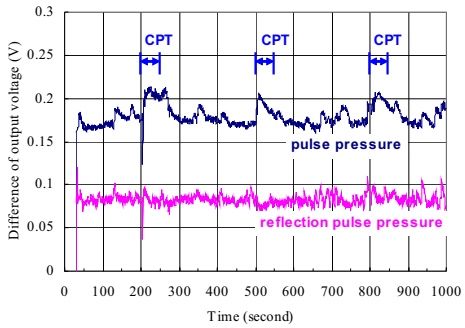
A. Experiment of CPT

(1) Short term CPT

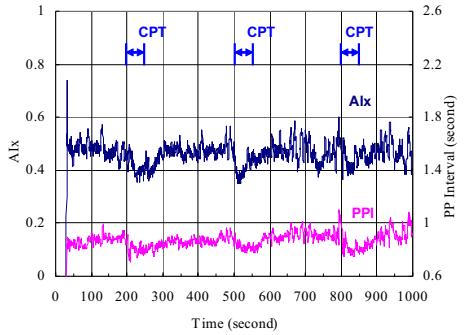
Figure 3 shows an example of time variation of short term CPT. The sensor output voltages of pulse pressure (= systolic pressure - diastolic pressure) and reflection pulse pressure (= reflection wave pressure - diastolic pressure) were shown in Fig. 3 (a), and time variation of AIx and PPI were shown in Fig. 3 (b), respectively. Pulse pressure increased during the short term CPT, because progressive wave component increased. In contrast, reflection pulse pressure is hardly changes. Consequently, AIx significantly decreased and PPI slightly decreased during the short term CPT.

(2) Long term CPT

Figure 4 shows an example of time variation of long term CPT. Blood pressures (systolic pressure, diastolic pressure and pulse pressure) were shown in Fig. 4 (a), and time variation of AIx and PPI were shown in Fig. 4(b), respectively. Both of systolic pressure and diastolic pressure increased during the long term CPT. However pulse pressure

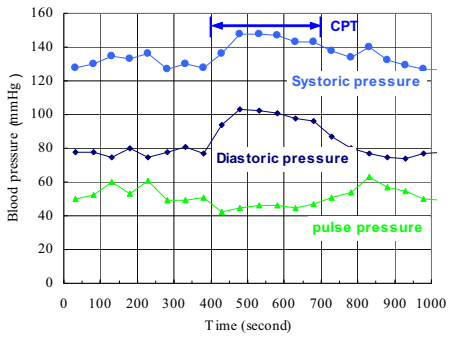


(a) Pulse pressure and reflection pulse pressure

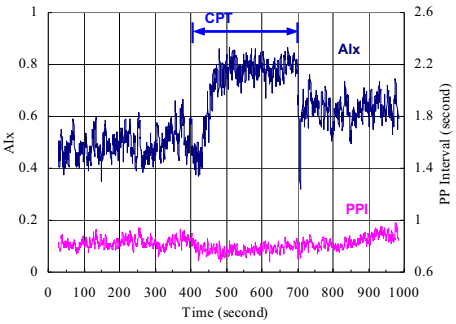


(b) Time variation of AIx and PPI

Fig. 3 Experimental results (Short term CPT)



(a) Time variation of blood pressures.



(b) Time variation of AIx and PPI

Fig. 4 Experimental results (Long term CPT)

decreased the same time. AIx once decreased just started the load, and significantly increase during the long term CPT.

B. Numerical Calculation

(1) Short term CPT

Simulation results of pressure wave-forms of short term CPT were shown in Fig. 6 (a). (i)HR: Heart rate increasing cause progressive wave increasing, thus AIx and pulse pressure were decreased. (ii)SV: Increasing maximum flow rate cause mean pressure and AIx were increased. (iii)AS: Central arterial stiffness softening cause AIx and pulse pressure were decreased.

(2) Long term CPT

Simulation results of pressure wave-forms of long term CPT were shown in Fig. 6 (b). (i)RT: Peripheral resistance increasing cause AIx was increased and pulse pressure was decreased. In contrast, (ii) BT: increasing arterial stiffness of brachial artery causes both of AIx and pulse pressure were increased.

C. Comparison of calculation and experimental result.

(1) Calculation of parameter combination

Combination parameter variations were calculated. Figure 7 (a) shows the calculation results among HR, SV and AS were varied simultaneously, in order to simulate the β reaction dominant response. As this result were same as human reaction of short term CPT (AIx and PPI were decreased, PP was increased). On the other hand, Fig. 7 (b) shows the results both RT and BT were varied, in order to simulate α reaction dominant response. This result were partially same as human reaction of long term CPT (AIx was increased).

(2) Discussion

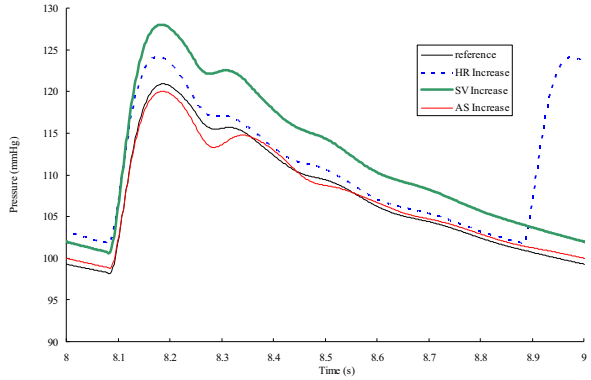
According to the experimental and calculation results of AIx change by short term and long term CPT load, the cause of the AIx change was different in 2 types of CPT.

In short term CPT, heart contractility increasing just after the beginning of the load induced pulse pressure increasing and AIx decreasing, since β reaction dominant response.

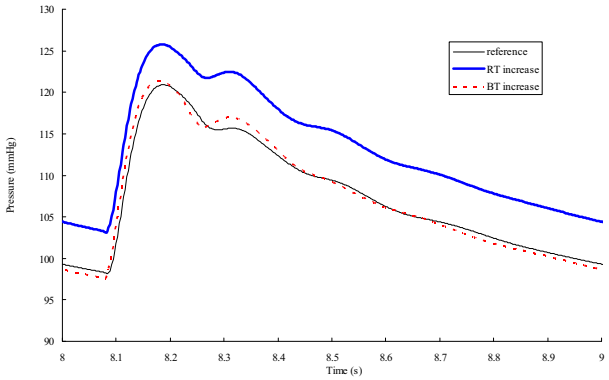
By contrast, in long term CPT, increasing of peripheral resistance about one minute after the beginning of the load induced pulse pressure decreasing and AIx increasing, since α reaction dominant response.

IV. Conclusions

In order to understand the mechanism of pulse wave change and basis of AIx change, continuous pulse wave



(a) Short term CPT: correspond to β action dominantly



(b) Long term CPT: correspond to α action dominantly

Fig. 5 Calculation results of single parameter variation.

were recorded during the 2 types of CPT, moreover waveform and AIx were analyzed by experimentally and numerically.

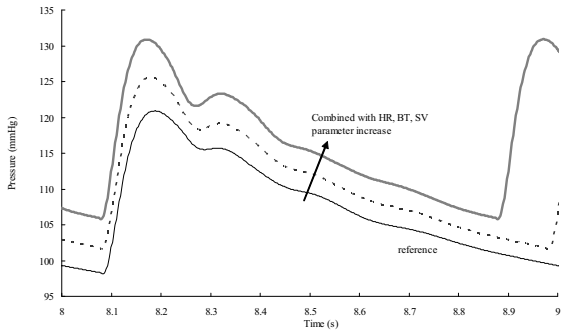
(1) A biological reaction of circulatory system during CPT is a complex reaction combined with not only peripheral artery but also heart or central aorta.

(2) A biological reaction seems to be different by the short term CPT and by the long term CPT. We suspect that the change by the short term CPT may have caused β-effect and the long term CPT may have caused α-effect.

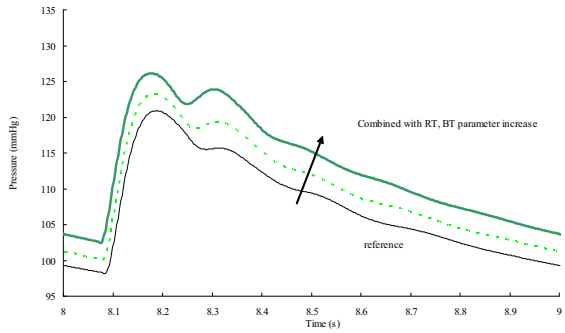
(3) The pulse wave change phenomenon (especially change of AIx) during the CPT can be expressed using numerical simulation model combined with central aorta and brachial artery.

Acknowledgment

The authors thank to Omron Healthcare Co. Ltd. (Japan) since they rent us the special measurement device.



(a) Short term CPT: correspond to β action dominantly



(b) Long term CPT: correspond to α action dominantly

Fig. 6 Calculation results of combined parameter variation.

References

1. Kelly R, Daley J, Avolio A, O`Rourke M (1989) Arterial dilation and reduced wave reflection. Hypertension 14:14-21
2. Mun K W, Soh K S (2001) Change of arterial shape during a cold pressure test, J. Kor. Phys. Soc. 40:289-292.
3. Celeris P, Stavrati A, Boudoulas H (2004) Effect of cold,isometric exercise,and combination of both on aortic pulse in healthy subjects. The American journal of cardiology 93:267-269,.
4. Stergiopulos N el. al. (1991) Numerical study of pressure and flow propagation in arteries. Biomed Sci Instrum. 27:93-104.
5. Kitawaki T, Shimizu M (2006) Flow analysis of viscoelastic tube using one-dimensional numerical simulation model. Journal of Biomechanical Science and Engineering 1:183-194.
6. Hayashi K (1980) Stiffness and elastic behavior of human intracranial and extracranial arteries. J Biomech. 13:175-184.
7. Anliker M, Rockwall R L (1971) Nonlinear analysis of flow pulses and shock waves in arteries. ZAMP 22:217-246.

Author: Tomoki Kitawaki
Institute: Okayama University, Graduate School of Health Sciences
Street: 2-5-1 Shikata
City: Okayama
Country: JAPAN
Email: kitawaki@md.okayama-u.ac.jp

Identification of the Changes in Extent of Loading the TM Joint on the Other Side Owing to the Implantation of Total Joint Replacement

Z. Horak[1], T. Bouda[1], R. Jirman[2], J. Mazanek[2] and J. Reznicek[1]

[1] Czech Technical University in Prague, Faculty of Mechanical Engineering/Laboratory of Biomechanics, Prague, Czech Republic
[2] Charles University in Prague, 1st Faculty of Medicine/Department of Stomatology, Prague, Czech Republic

Abstract — **Temporomandibular joint is the most used joint of human body. Any defect of it has a significant influence on quality and style of life. If the TM joint is damaged, its treatment is very difficult and, in addition, it is impossible to replace fully this specific joint with a total replacement. In our opinion, the main reason is the method of implantation of existing replacements, when the whole range of masticatory muscles must be removed, and these results in significant change of mechanical loading of the whole system. The objective of this work was to create parametric computational FEM study comparing the effect of surgical procedure while implanting the total replacement of the TM joint on loading of the joint on the other side.**

Keywords — **temporomandibular joint, TMJ replacement, FE analyses, mechanical loading**

I. Introduction

Up to 60% of current population suffers from temporomandibular (TM) disorders. From the anatomy and mechanical point of view, the TM joint is a complicated bicondylar joint complex, which is one of the most loaded joints in human body. Its uniqueness lies in the fact that it is a coupled joint - two equal joints occur on one bone, the mandible, and so any movement or a dysfunction of one affects also the other joint.

Two types of replacement are used for reconstruction of TM joint. In the current clinical practice are used three types of total TM joint replacement: TMJ Concepts (TMJ Concepts Inc), The Christensen (TMJ Inc), and Lorenz (Biomet Inc). All three companies use similar construction of the replacement. The difference is in the type of movement that the replacements allow with their construction. The Christensen replacement allows only spherical movement of the condyle in the fossa, while the TMJ Concepts and Lorenz replacements allow rotation and sliding movement of the condyle in the fossa. The second type of movement is closer to the real situation of the physiologic temporomandibular joint movement. All three replacements have equal method of implanting the condylar type of the replacement [4-6], which is, in our opinion, essential for the end result of the correct function of the total replacement. When implanting the condylar part, the m. masseter is always resected over to the lateral surface of mandible, and in most cases also m. temporalis together with processus coronoideus mandibulae. Resection the m. temporalis with the processus enables easier rehabilitation of opening and resection m. masseter is necessary with regards to fixation of the condylar part of the replacement to the mandible. This method of fixing the replacement to the bone results cause radical change of force and kinematic both TM joints. Due to resection m. masseter and m. temporalis, the muscles on the other side must take over the force action needed for mastication, bite and stability of the whole system; however, this causes inadequate increase of loading on the TM joint on the other side.

The objective of this work was to create parametric computational study using FEM, analyzing the influence of used surgical procedures for implanting the temporomandibular joint total replacement on loading of the joint on the other side.

II. Materials and methods

The analysis of the effect of the method of implanting the TM joint total replacement was realized using the Finite Element Method (FEM). For the numerical simulations was build a simplified model of the mandible, inferior dental arch, both joint discs and fossa. The geometric model was designed on the basis of CT images of a healthy individual without obvious damage of the mandible and TM joint. The geometric models of the mandible and teeth were meshed with linear four-sided elements; the model of the disc was meshed with hybrid quadratic four-sided elements. The model of fossa was only represented by the lateral surface, which was reticulated by linear triangular shell elements as the fossa was considered as rigid body. The model was imported into the programme ABAQUS, in which the analyses were realized. The activity of muscles was modelled using 1D connector elements, which connected the beginning and tendon of the muscle and into which force was applied. The considered muscles were m. masseter, m. temporalis, m. pterygoideus med., and lat. All parts of the model were considered as homogenous isotropic materials, the parameters of individual material models are shown in Table 1.

Chwee Teck Lim, James C.H. Goh (Eds.): ICBME 2008, Proceedings 23, pp. 1535–1538, 2009
www.springerlink.com

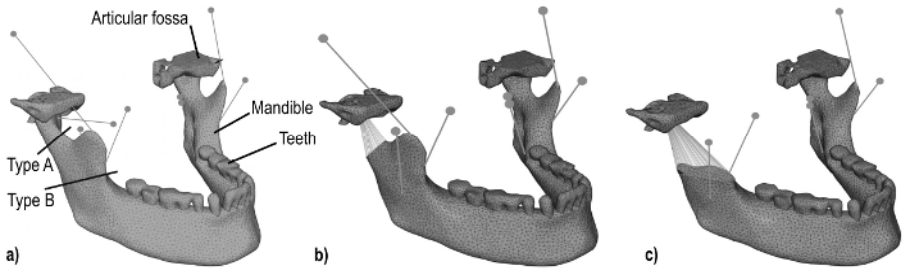


Fig. 1. a) FE Model of the mandible and TM joint with articular fossa. Muscles (CONNECTOR elements) are represented by the lines. The type of the condylar resection is showed by the lines on the right condyle, b) resection Type A1 and c) resection Type B1

The teeth were connected with the bone with TIE contact, which was also used for making the connection between the condyle of the mandible with the TM disc and connection between the TM disc and the fossa. Equal distribution of forces generated in muscles into the bone was realized by distributing coupling function. The reference points of the fossas, which were considered as rigid bodies, were fixed. The bite was simulated for three basic physiologic situations: bite on incisors I1, right and left first molar M1.

Table 1. Material properties of parts of model used in FE analyses of the TM joint.

Model parts	Material model description	Element type
Mandible	E=17 GPa, μ=0.30	C3D4
Tooth	E=21 GPa, μ=0.21	C3D4
TM disc	Money-Rivlin hyperelastic material C10=0.9, C01=9.10^{-4}, D1=1.10^{-5}	C3D10H
Fossa articularis	Rigid body	S3

The muscle forces generated by individual masticatory muscles were determined on the basis of physiologic cross sections of muscles and mathematical models presented in literature [1-3]. The magnitude of forces in muscles was determined on the basis of force ratio generated at the resulting bite force of 300N on the given tooth. The magnitude of maximum bite force considered in the model was picked with regards to clinical practice, where the patients with TM joint disorders have significantly reduced magnitude of this force [1]. The magnitude of bite force was considered as equal for all types of resection and the anatomical model. For the examined cases of bite, with maximum bite force requirement, it implies from the mathematical model [3] that from the group of considered muscles, m. masseter, m. pterygoideus med., and m. temporalis are fully activated.

There were modelled four simulations of the influence of the surgery while implanting the total replacement (see Fig.1): resection caput mandibulae while the m. pterygoideus lat. is removed (Type A1), resection of caput mandibulae with removing of m. pterygoideus lat. and m. masseter (Type A2), resection behind processus coronoideus mandibulae while m. temporalis and m. pterygoideus lat. are removed (Type B1), the last resection behind processus coronoideus mandibulae while m. masseter, m. temporalis and m. pterygoideus lat. are removed (Type B2). In the computational model, the total temporomandibular joint replacement was modelled as a spherical joint to which the surface created by the mandible resection is connected by distributing coupling function. The total replacement was modelled on the right side of the computational model and the results of the analysis were evaluated for the corresponding TM joint on the left side.

III. Results

The magnitude of TM joint loading was represented by the magnitude and components of the reaction force carried in the TM joint during bite. The values of the magnitude of loading on the TM joint for each type of resection were compared with the values of anatomical variation of the TM joint loading. The coordinate system, in which the results of the numerical analysis are presented, is right-angled Cartesian, where direction 1 (mediolateral), direction 2 (posterior – anterior), and direction 3 (craniocaudal).

From the results of the analysis listed in Table 2 for the bite on incisors (I1), increase of the reaction force and all its elements in the corresponding TM joint on the other side is obvious, for increasing size of the resection. This increase is most evident for direction 1, where the increase in all types of resection by Δ^{A1}=52.5%, Δ^{A2}=493.2%, Δ^{B1}=394.9%, Δ^{B2}=938.9% compared with the values obtained for the anatomic model. Also the increase of magnitude of loading in direction 2 is for each resection by Δ^{A1}=8.6%, Δ^{A2}=112.6%, Δ^{B1}=113.5%, Δ^{B2}=290.6%. The influence of the size of resection while implanting the TM joint replacement shows obviously also on the increase of the magnitude of loading in direction 3 is for each resection by Δ^{A1}=4.7%, Δ^{A2}=64.5%, Δ^{B1}=39.4%, Δ^{B2}=132.7%.

Table 2. Reaction magnitude and component in the TM joint for different types of resection during bite on incisor I1 (max. bite force was 300N).

	Right TM joint				Left TM joint			
	Reaction [N]	Reaction R_1 [N]	Reaction R_2 [N]	Reaction R_3 [N]	Reaction [N]	Reaction R_1 [N]	Reaction R_2 [N]	Reaction R_3 [N]
Anatomic	264.5	4.7	-70.2	-254.9	221.1	-5.9	-24.5	-219.7
Type A1	267.6	8.2	-69.8	-258.2	231.7	-9.0	-26.6	-230.0
Type A2	219.7	-29.6	-134.8	-171.0	366.9	-35.0	-52.1	-361.5
Type B1	188.7	-28.8	93.0	-161.6	312.0	-29.2	-52.3	-306.2
Type B2	126.8	-101.7	75.4	-6.2	523.9	-61.3	-95.7	-511.2

Table 3. Reaction magnitude and component in the TM joint for different types of resection during bite on left molar M1 (max. bite force was 300N)

	Right TM joint				Left TM joint			
	Reaction [N]	Reaction R_1 [N]	Reaction R_2 [N]	Reaction R_3 [N]	Reaction [N]	Reaction R_1 [N]	Reaction R_2 [N]	Reaction R_3 [N]
Anatomic	159.0	3.5	-41.3	-153.5	15.1	-4.2	-14.4	-2.6
Type A1	160.6	5.1	-40.8	-155.3	17.1	-5.6	-15.7	-3.9
Type A2	132.8	-12.9	-79.1	-105.9	91.1	-26.2	-30.8	-81.6
Type B1	114.4	-16.4	54.1	-99.5	58.8	-17.6	-30.5	-47.0
Type B2	68.5	-51.3	44.2	-10.8	182.4	-46.8	-56.4	-167.0

Table 4. Reaction magnitude and component in the TM joint for different types of resection during bite on right molar M1 (max. bite force was 300N).

	Right TM joint				Left TM joint			
	Reaction [N]	Reaction R_1 [N]	Reaction R_2 [N]	Reaction R_3 [N]	Reaction [N]	Reaction R_1 [N]	Reaction R_2 [N]	Reaction R_3 [N]
Anatomic	46.7	3.1	-40.5	-22.9	150.6	-4.1	-17.0	-149.5
Type A1	47.5	3.5	-40.9	-24.0	152.9	-4.4	-17.1	-151.9
Type A2	140.7	-8.7	-133.4	-43.9	170.0	-16.1	-17.7	-168.3
Type B1	65.0	-14.0	63.4	-3.2	158.5	-11.5	-24.6	-153.4
Type B2	N/A	N/A	N/A	N/A	N/A	N/A	N/A	N/A

The same trend of the TM joint loading with regards to the size of resection is evident for bite on the first left molar (M1, i.e. bite on the molar neighbouring with the TM joint on the other side). The results of computation analysis are listed in Table 3 where the increase in individual types of resection by Δ^{A1}=33.3%, Δ^{A2}=523.8%, Δ^{B1}=319.0%, Δ^{B2}=1014.3%. The increase of magnitude of loading in direction 2 is for individual resections by Δ^{A1}=9.0%, Δ^{A2}=113.8%, Δ^{B1}=111.8%, Δ^{B2}=291.6%. The most important result is the magnitude of the reaction force and its components for the case Type A2 with removed m. masseter and for the case of resection Type B2. Here, the increase of the resulting reaction force by 503.3%, or 1107.9% respectively, is evident, while the increase of the medio-lateral component of the reaction R_1 is by 523.8%, or 1014.3% respectively, and the increase of the back-to-front component is by 113.8%, or by 291.6% respectively. From these values the stabilizing effect of m. masseter in medio-lateral direction is evident.

In the last variation of model loading, for the bite on the first right molar, it is possible to observe slight increase of reaction forces in the TM joint on the other side for the resection cases Type A2 and Type B1. The results of numerical analyses are listed in Table 4. The increase is most obvious for direction 1, where the increase for individual types of resection by Δ^{A1}=7.3%, Δ^{A2}=292.7%, Δ^{B1}=180.5%. Also increase of the reaction component is evident in direction 2: Δ^{A1}=0.6%, Δ^{A2}=4.1%, Δ^{B1}=44.7%. The influence of the size of resection while implanting the TM joint replacement will show also at the magnitude of reaction in the joint in direction 3: Δ^{A1}=1.6%, Δ^{A2}=12.6%, Δ^{B1}=2.6%. The biggest change can be observed for resection Type A2 at the medio-lateral component of reaction force, which changed by 292.7%, although the resulting reaction force changed only by 12.9%. For the resection Type B2, it was impossible to reach balance even when reducing the muscle force on the TM joint on the healthy side, or increasing the muscle force on the side of the implant.

From the afore-mentioned results of numerical simulations, the significant influence of the size of resection on loading the TM joint on the other side (independently of the place of bite) is evident when implanting the TM joint. The biggest increase of magnitude of the loading on the TM joint on the other side in general is evident for resection Type B2 (which is the most frequent when implanting the total replacement in clinical practice), in case of bite on the molar M1 on the other side (left) this increase of loading is 11-fold of the physiological loading!! The most significant

increase of TM joint loading is in medio-lateral direction, where the loading is 10-fold of the physiological loading. Moreover, when comparing the results for individual types of resection it shows that in order to keep the best function of the TM joint on the other side after implanting the total replacement, it is more important to retain the m. masseter than m. temporalis (Type A2 vs. Type B1). If m. masseter was resected, the total magnitude of loading on the TM joint for bite on incisors I1 is by 25% smaller, and for bite on the molar M1 on the other side is by 214% smaller!!

IV. Discussion and conclusions

From the executed analyses, it is evident that resecting m. temporalis, and especially m. masseter, for the existing method of implanting the TM joint total replacement, has fatal effect on loading of the joint on the other side. The biggest increase of the magnitude of loading the TM joint on the other side reaches the force component in medio-lateral direction and anterio-posterior direction, which causes significant increase of shear loading of the TM disc. This way of loading the TM disc, with regards to its function and structure, is most damaging. The increase of this way of loading is, in our opinion, the main cause of subsequent degeneration of the TM disc and surrounding structures in an originally healthy TM joint on the other side. From the results of the analyses it is clear that in case of implanting the TM joint replacement from the point of view of the smallest increase of loading the joint on the other side the most suitable is the size of resection Type A1 (retaining all muscles except m. pterygoideus lat.). On the other hand, the most used size of resection Type B2 (resection of m. masseter, m.temporalis, and m. pterygoideus lat.) is most devastating from the point of view of the TM joint on the other side. The variation of resection size Type A1 can be also regarded as the variation quantifying the loading of the joint on the other side only when replacing the TM joint. When comparing the remaining types of resection with Type A1, significant increase of loading on the TM joint on the other side is evident, and so clear conclusion is that resecting muscles has more significant effect on loading the TM joint on the other side while bite than the TM joint replacement with an implant.

In our opinion, the existing constructions of total TM joint replacement used in clinical practice (The Christensen, TMJ Concepts and Lorenz/Biomet) enable movement of the replacement close to real movement of the TM joint, but the way of connecting it to the mandible radically reduces their benefit for the patient.

In the numerical FE analysis, there were used simplified material models of biological tissue: elastic homogenous isotropic material (bone, teeth) and hyper elastic isotropic homogenous material (TM disc). Simplifying the used material models certainly has effect on the results of the completed FEM analyses, but with regards to the objective of this work this simplification is insignificant.

The results obtained from the executed computation FEM analyses of the effect of the implantation on the TM joint on the other side give us information for design of the construction of the TM joint implant, which would enable smaller surgery in the system of the masticatory muscles on the side of the implant, and at the same time, the possibility to make more delicate construction of the replacement. Such suitable change of the construction configuration of the TM joint replacement could reduce the loading on the TM joint on the other joint after implanting the total replacement, and thus, the benefit for the patient would be increased considerably.

Acknowledgment

The research was supported by the Czech Science Foundation project: Application of Synthetic Biomaterials for Replacement of Orofacial Parts of Skull, No. CSF 106/07/0023 and by the Ministry of Education project: Transdisciplinary Research in Biomedical Engineering II, No. MSM 6840770012.

References

1. J.H. Koolstra, et al., A Three-dimensional Mathematical Model of The Human Masticatory system Predicting Maximum Possible Bite Forces, *J Biomech*, **21** (1988), pp. 563-576.
2. J.H. Kolostra and T.M.G.J Van Eijen, Application and Validation of Three-dimensional Mathematical Model of the Human Masticatory System In Vivo, *J Biomech*, **25** (1992), pp. 175-187.
3. B. May, S. Saha and M. Saltzman, Three-dimensional mathematical model of temporomandibular joint loading, *Clin Biomech*, **16** (2001), pp. 489-49.
4. Biomet Inc at http://www.biometmicrofixation.com
5. TMJ Concepts Inc at http://www.tmjconcepts.com
6. TMJ Inc at http://www.tmj.com

Address of the corresponding author:

Author: Z. Horak
Institute: Czech Technical University in Prague, Faculty of Mechanical Engineering, Laboratory of Biomechanics
Street: Technicka 4
City: Prague 6
Country: Czech Republic
Email: Zdenek.Horak@fs.cvut.cz

Effects of Stent Design Parameters on the Aortic Endothelium

Gideon Praveen Kumar[1] & Lazar Mathew[2]

[1] Healthcare Practice, Frost & Sullivan (P).Ltd, Chennai, India
[2] School of Biotechnology, Chemical & Biomedical Engineering, VIT University, Vellore, India.

Abstract — **Vascular support structures are important tools for treating valve stenosis. A large population of patients is treated for valvular disease and the principal mode of treatment is the use of percutaneous valvuloplasty. Stent devices are proving to be an improved treatment method; these devices now account for 20% of treatments in Europe. This new technology provides highly effective results at minimal cost and short duration of hospitalization. Accurate and reliable structural analysis provides essential information to the design team in an environment where in vivo experimentation is extremely expensive, or impossible. This paper describes the design of vascular support structures (stents), to provide designers with estimates of the critical parameters which are essential to restore the functions of the endothelium of the Aorta during and after implantation without injuring it.**

Keywords — **Stent, Finite Element Analysis, Aorta, Coronaries, Blunt hooks**

I. Introduction

The treatment of stenotic valvular diseases consists of routine procedures in interventional cardiology. To date, the surgical approach is the only option to replace diseased cardiac valves [1]. Recently it has been shown that stenosis of mitral, aortic or pulmonary valves can be treated by percutaneous valve replacement and has recently opened new perspectives on transcatheter placement of cardiac valves. Aortic valve replacement generally has been accomplished by using a cardiac surgical procedure whereas endovascular procedures for valve replacement may provide an alternative to cardiac surgery. Percutaneous transluminal procedures have substantial benefits from the standpoints of health and safety, as well as cost. Such endovascular procedures require minimal invasion of the human body, and there is considerable reduction and, in some instances, even elimination of general anesthesia and intensive care unit stay. In Percutaneous replacement, the diseased valve is replaced by a biological valve via a catheter driven through the femoral artery to the aortic position. The valve is sutured to the stent, which is crimped into the catheter and is guided to the parent position of the aorta and deployed [2]. Thus it pushes the diseased valve aside and keeps the new bio-prosthetic valve in position. The stents that are used give adequate support and stability to the valve and also prevent the prosthesis from getting migrated either in the ante grade or retro grade direction [4]. These stents also help in preventing paravalvular leaks. With this view we have attempted to generate models to achieve proper stenting and placement of the prosthesis without migration, paravalvular leaks and obstruction of coronary blood flow.

II. Methods

A. Parametric Stent Designs

Stent geometries were uniquely defined using the following parameters.(a) Diameter of the aorta;(b) Distance between the aortic root and the coronary artery roots ;(c) Position of the coronary arteries;(d) Diameter of the coronaries;(e) Stent – Endothelium Mechanics. Keeping these parameters into consideration many stent models [Fig 1(a) – (c)] were designed to suit its requirement for percutaneous replacement. These parameters are extremely critical as shown in Fig 2.

The 3D geometry of the repeatable units of the stent was generated using SOLIDWORKS modeling Software. Using the repeating unit geometry of each stent design, solid models were generated. The unit consisted of 8 lips with two non crossing struts making a circular diameter of 16mm at the center and 18mm at the top and bottom as shown in Fig 3.The upper and the lower portions of the prosthesis has a high radial force, the upper portion flared to fix the stent firmly in the ascending aorta and the lower portion to expand against the calcified leaflets and to avoid recoil. The middle portion which bears the valve, is constrained and narrower to avoid obstruction of the coronary arteries. This varying diameter, as shown in Fig 1(c) at different parts of the stent creates the blunt hooks at either end of the stent. The port angle is 45 degrees with the two struts joining to form the circular stent. The stent design has a constant strut thickness of 0.5 mm and a height of 18 mm [7].

Chwee Teck Lim, James C.H. Goh (Eds.): ICBME 2008, Proceedings 23, pp. 1539–1541, 2009
www.springerlink.com

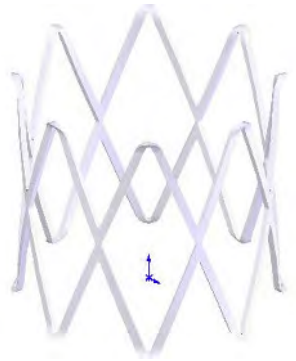
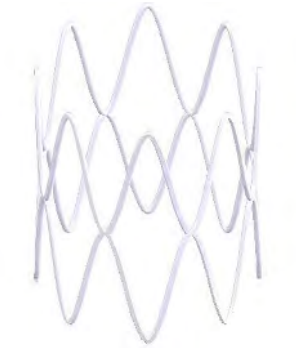
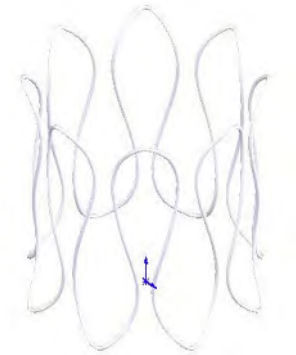


Fig. 1 (a) Model 1



(b) Model 2



(c) Model 3

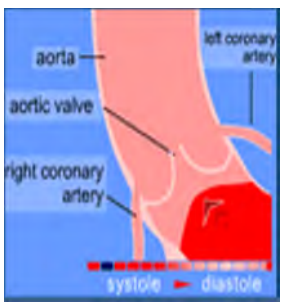


Fig. 2 Aortic valve and the coronaries

B. Material Model

Stainless steel 316L was the material that was used for fabrication as it has a high strength to weight ratio and excellent biocompatibility when used in humans [6]. The material properties ideal for analysis are tabulated in Table 1.

Table 1 316L Stainless steel – Properties

Material Name	316LStainless Steel
Young's Modulus (E)	201 GPa
Poisson's ratio	0.3
Yield stress	170 MPa

C. Mode of Analysis

The stent solid model was then meshed to form a cylindrical shape by transferring the nodal co-ordinates from a Cartesian co-ordinate system into a cylindrical co-ordinate system. In this way Finite element meshes were generated

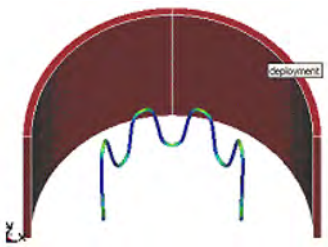
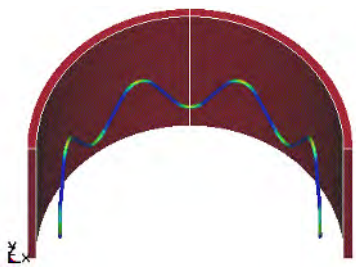
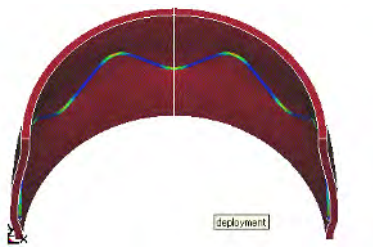


Fig. 3 (a) Stent fully crimped in the aorta



(b) Partially expanded Stent



(c) Stent expanding to fit into the aorta.

for the design. Free expansion analysis was done for the stent model using ANSYS finite element analysis software. Mechanical properties like crimping and re-expansion were studied. The models were subjected to finite element analysis with boundary conditions above the normal human blood pressure levels of 120/80 mm Hg The stent model seemed to withstand loads much more than that of the normal human pressure loads. The results of the designs are encouraging and would be published after patenting the model.

D. Stent – Endothelium Interaction

The stent – aortic endothelium mechanics was studied by placing the stent inside an aorta model. The stent was crimped and expended by applying various pressure ranges to understand its behavior inside the stent [Fig 3 (a), (b), (c)].

III. Results and Discussion

The stent models were designed, analyzed and its interaction with the aorta studied successfully. The dimension of the stent, such as the length can influence the deliverability, visibility and flexibility of the stent...Strut geometry is another important engineering aspect. We have come out with a design having 8 lips have 2 struts each given adequate gap between two adjacent struts. This gap between struts will enable the surgeon to place the stent in such a way that it doesn't obstruct the coronary blood flow which is situated just above the aortic valve. Furthermore the blunt hooks that are designed help the stent to take its position once it is implanted by the surgeon. The aorta took the shape of the stent as these blunt hooks got embedded into the endothelium of the aorta. This gave the stent a good fit into the aorta preventing it from getting migrated in either direction.

IV. Conclusion

Thus the effects of stent designs on the aortic endothelium were successfully evaluated.. However further analysis and studies are needed before these stents are fabricated and deployed. Animal experiments are being planned currently for this purpose.

References

1. Morton Allison C, Crossman. D, Gunn. J, The influence of physical stent parameters upon restenosis, Elsevier SAS, 2004.
2. Lau. KW, Johan A, Sigwart U, Hung JS, A stent is not just a stent: stent construction and design do matter in its clinical performance, Singapore Medical Journal, 2004
3. McClean Dougal R, MD, Eigler N, MD, *Stent Design: Implications for Restenosis,* MedReviews, LLC 2002
4. Stent design properties and deployment ratio influence indexes of wall sheer stress;J.Applied Physiology 97:424-430, 2004
5. An overview of super elastic stent design, Min Invas Ther & Allied Technology, 2000: 235–246
6. Engineering Aspects of stent design and their translation into clinical practice Ann; 2007 Vol. 43, no. : 89-100
7. Novel stent design for percutaneous aortic valve replacement, G.V.P. Kumar & L. Mathew, IFMBE Proceedings,4th Kuala Lumpur International Conference on Biomedical Engineering 25-28 June 2008, Pages 446-448

Multi-Physical Simulation of Left-ventricular Blood Flow Based On Patient-specific MRI Data

S.B.S. Krittian, S. Höttges, T. Schenkel and H. Oertel

Institute for Fluid Mechanics, University of Karlsruhe (TH), Germany

Abstract — **Statistically, heart disease has been the major cause of death in the recent past, which emphasizes the need for computational heart models. In this context, the so-called KaHMo (Karlsruhe Heart Model) is specialized on the inner-ventricular blood flow and its influence on the overall heart conditions. Both healthy and diseased hearts are simulated in order to analyze characteristic flow patterns and pressure losses. The patient-specific fluid domain movement is realized by time-dependent geometries out of MRI data.**

However, in order to capture flow changes due to structural variations, a multi-physical simulation approach is of utmost importance. Consequently, the model extension KaHMo FSI includes macroscopic structural properties using a hyperelastic finite element composite. The partitioned code coupling strategy allows the combination of separated software packages specialized for both the fluid and structural domain respectively. The interaction of blood flow and constitutive behavior influences the interface movement for both relaxation and contraction. In this context, the energetic equilibrium between the computational fluid and structural domain requires kinematic and dynamic coupling conditions to be satisfied continuously.

The focus of this work is on the first application of patient-specific reference geometry for KaHMo FSI. The coupled flow simulation is compared to corresponding results from KaHMo's standard fluid domain movement. In order to validate the flow simulation itself a further test-case model is evaluated and compared to experimental flow measurements. A detailed understanding of hydro-elastic blood/soft-tissue interaction is important for future therapy planning.

Keywords — **patient-specific, heart model, fluid-structure interaction, implicit code-coupling, blood-flow analysis.**

I. Introduction

With a focus on the inner ventricular fluid mechanics, the so called KaHMo has been developed at the Institute for Fluid Mechanics, University of Karlsruhe (TH), Germany. The question arose whether a fluid stand-alone model is able to capture the influences on the inner ventricular flow pattern. Alternatively, a fluid-structure interaction (FSI) could have been taken into account. However, due to the lack of constitutive *in vivo* data, most FSI models are based on either generic data or *in vitro* measurements of animal hearts; a transformation onto a patient-specific human heart model cannot be undertaken. Consequently, KaHMo MRI is based on the time-dependent movement of the inner ventricular wall derived from patient-specific MRI images. Both healthy and diseased hearts can be investigated from a fluid mechanics point of view and important clinical indication criteria can be determined [3].

Nevertheless, for future generations of KaHMo the structural calculation will have to be taken into account again. Desperately needed *in vivo* data will become more and more available due to the continuous progress of MRI techniques. Therefore, the new KaHMo FSI represents the first step for replacing the time dependent wall movement by structural calculation. For this reason, a macroscopic composite model for the left ventricle has been generated.

Whereas the structural part is performed by the software package Abaqus 6.7-2, Fluent 6.3.26 is responsible for the flow calculation. The Fraunhofer-Institute for Algorithms and Scientific Computing (SCAI) provides the **M**esh-based **p**arallel **C**ode-**C**oupling **I**nterface MpCCI with explicit data exchange algorithms. However, blood/soft-tissue interaction requires stronger coupling mechanisms which are implemented within the new *"Implicit Coupling for KaHMo FSI"* module [2].

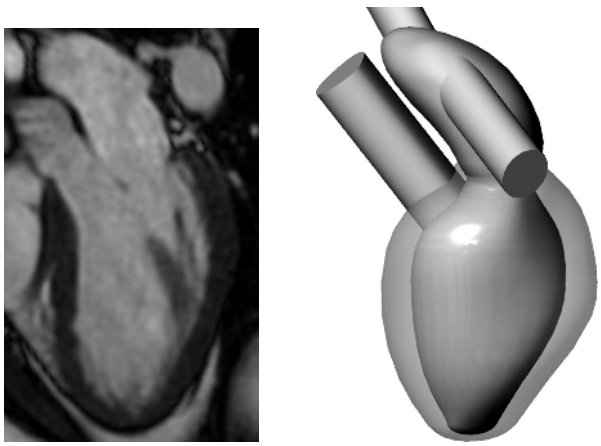


Fig. 1 Patient-specific CAD geometry *(right)* derived from MRI data *(left)*

Chwee Teck Lim, James C.H. Goh (Eds.): ICBME 2008, Proceedings 23, pp. 1542–1545, 2009
www.springerlink.com

II. Models and methods

A. Geometry and model discretisation

The cardiac cycle can be divided into contraction and filling phase. Whereas the contraction phase is mainly dominated by the heart muscle itself, fluid-structure interaction effects play an essential role during the ventricle filling. This phase can be further divided into *rapid filling*, *late filling* and *atrium contraction.*

Figure 1 shows the starting CAD geometry derived from the MRI reference timeframe. The stress-free configuration is assumed to be located between late filling and atrium contraction. Whereas the solid domain is modelled by the endo- and epicardial surfaces, the fluid domain is described by the inner-ventricular wall only:

- The fluid domain penetrates the solid part at in- and outlet and is discretized by 200.000 tetrahedral cells.
- The structural model is discretized by 4.000 quadratic tetrahedral cells. The intersections at the in- and outlet area also form the spatial boundary fixation. Note, both endo- and epicardial surfaces bear muscle fiber information (Figure 2) as described in section *II.B*.
- Data exchange is performed at the common interface described by the fluid domain boundary and the endocardial surface, respectively.

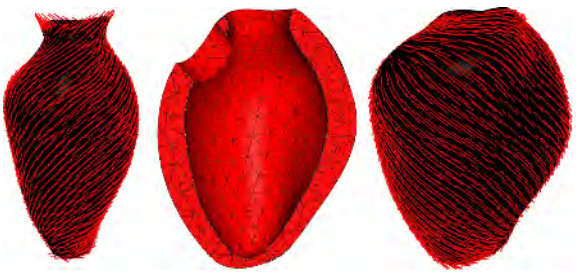


Fig. 2 Matrix (*middle*) with endo- (*left*) and epicardial fiber layers (*right*)

B. Material and composite approach

The composite model itself is based on a modified formulation of *Holzapfel*'s strain energy density function [1]:

$$W = \underbrace{c_1 \cdot \exp\left(c_2 \cdot (I_1 - 3)^2\right) + c_3 \cdot \exp\left(c_4 \cdot (I_2 - 3)^2\right)}_{matrix}$$

$$+ \underbrace{c_5 \cdot \exp\left(c_6 \cdot (I_4 - 1)^2\right)}_{fiber}$$

The invariant based formulation allows a mathematical separation into an isotropic matrix and a reinforced fiber direction and forms the constitutive basis of the partitions shown in Figure 2. The corresponding parameters (c_1-c_6) were estimated using simple shear test-data and a specialized least-square fitting procedure [4]. Muscle contraction is realized by a time-dependent fiber strain specification.

C. Coupling procedure

The overall KaHMo concept requires a partitioned modeling strategy for simulating the inner-ventricular blood flow. This allows the application of either the standard prescribed geometry movement or the novel *"Implicit coupling (for KaHMo FSI)"*. The latter uses relaxation procedures combined with an iterative time-step looping scheme (*see e.g.* [2]). For a given unknown vector f, i.e. load or spatial position, the relaxation function in *loop k* is represented by

$$f_{relax}^{k} = \omega^{k} \cdot f_{new}^{k} + \left(1 - \omega^{k}\right) \cdot f_{relax}^{k-1}$$

As soon as equilibrium between fluid and structure is reached the next time-step can be performed. The decision by which implicit coupling procedures should be applied depends strongly on physical properties (e.g. structural stiffness or fluid density) and the corresponding instability effects. Several validation test-cases proved that the load relaxation is most suitable for biomechanical applications.

D. Boundary condition

The interplay between heart muscle relaxation and the pressure boundary condition can be seen in Figure 3. However, the interface pressure itself depends on both static and dynamic pressure conditions. As the flow solution itself is a function of the pressure gradient the inlet and outlet pressure is regulated by the operating pressure only.

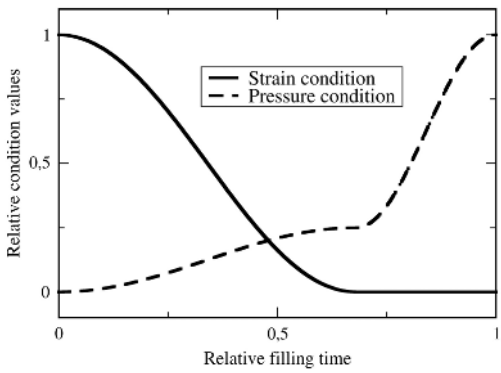


Fig. 3 Pressure condition and fiber strain during filling phase

III. Simulation results

For the first time the prescribed geometry movement of KaHMo MRT has been replaced by the calculated interaction of fluid and structure within KaHMo FSI. In order to evaluate the new simulation quality, both strategies need to be compared using the same patient-specific reference data. Having proved both strategies to be consistent, the coupled simulation of a validation experiment finally confirms the overall simulation approach.

A. Evaluation of model consistence

Using the patient-specific reference geometry shown in Figure 1, the measured cavity volume is compared to the simulated FSI-values in Figure 4. In spite of the simplified composite representation both results show the same characteristics (*ejection*, *filling* & *atrium contraction*), a good overall agreement and an ejection fraction of ~55%.

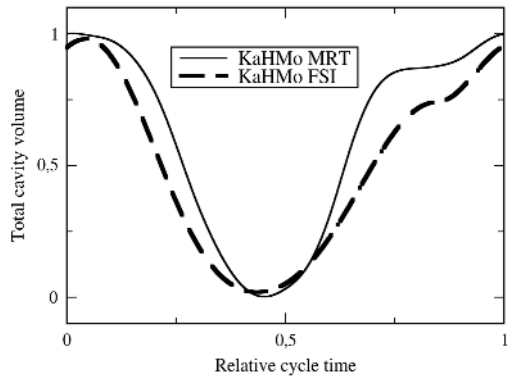


Fig. 4 Cavity volume measurement and coupled simulation result

Figures 5-7 show the characteristic time-frames during the ventricle filling phase. Both modeling approaches show the same temporal flow pattern development. The inflow jet during the rapid filling phase is accompanied by a ring vortex which grows asymmetrically with increasing cavity volume. Finally, the atrium contraction time-frame is characterized by the ring vortex turned clockwise in order to simplify the flow through the heart tip. The left vortex part now dominates the flow pattern and supports the blood outflow energetically during the up-coming ventricle contraction phase. As far as the coupling procedure itself is concerned the energetic equilibrium requires both kinematic and dynamic coupling conditions to be satisfied. Using an adaptive relaxation procedure, the energy residuum convergence tolerance is satisfied throughout the complete coupling process as shown in Figure 8.

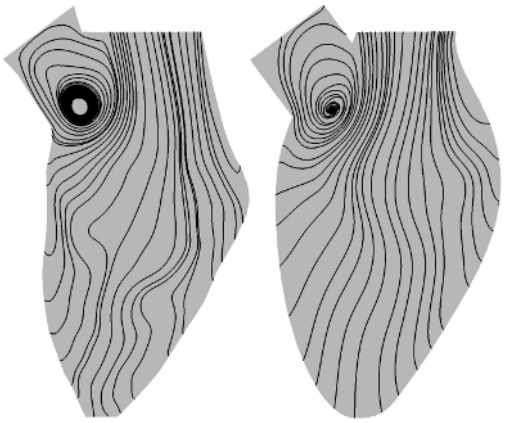


Fig. 5 Early filling phase for KaHMo MRT (*left*) and KaHMo FSI (*right*)

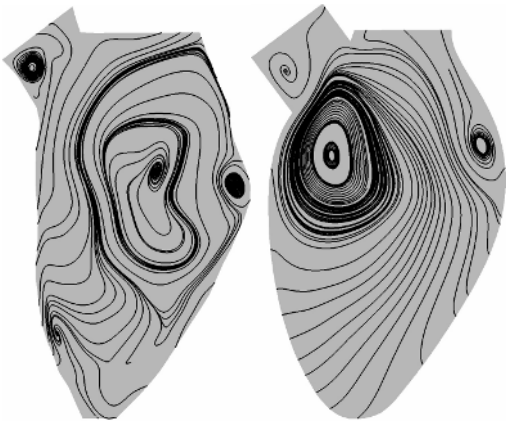


Fig. 6 Late filling phase for KaHMo MRT (*left*) and KaHMo FSI (*right*)

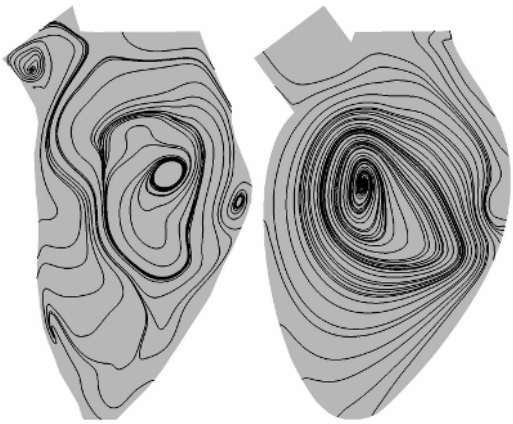


Fig. 7 Atrium Contraction for KaHMo MRT (*left*) and KaHMo FSI (*right*)

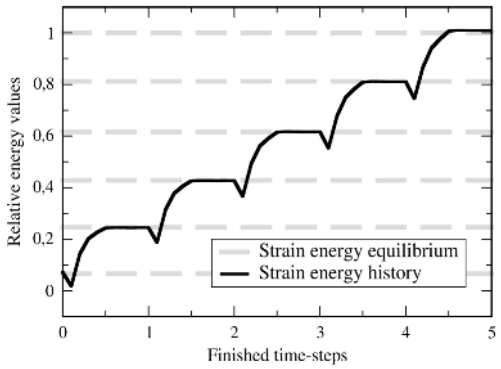


Fig. 8 Strain energy convergence history during filling phase

B. Flow field validation

In order to validate the general KaHMo flow pattern, an artificial ventricle device is used as validation experiment [5]. The silicon model is located within a pressure chamber which forces the ventricle to inflate or reject. Transparent materials enable the velocity flow field to be measured by PIV techniques. Both reference geometry and pressure distribution can be used as input for the FSI ventricle validation. Figure 9 shows one time-frame within the ventricle's filling phase and the overall flow patter agreement – both qualitatively and quantitatively.

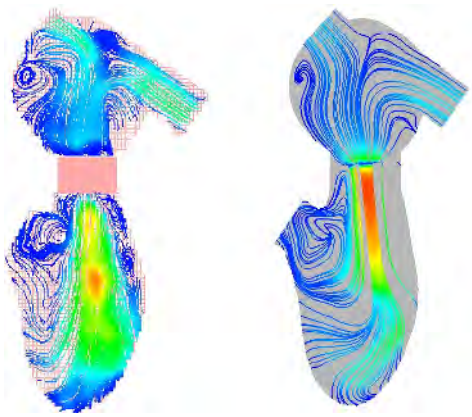


Fig. 9 Validation experiment (*left*) and KaHMo FSI (*right*)

IV. Conclusions

After having evaluated the flow field within a multi-physical simulated coupling validation, the *"Implicit Coupling (for KaHMo FSI)"* [2] was applied to an anatomical data set out of MR images for the first time. The comparison with the standard prescribed geometry movement shows a good agreement between the subsequent flow fields.

Although the prescribed geometry method guarantees a high level of patient-specific modeling, the definition of corresponding pressure boundary conditions is still a challenge. Within the fluid-structure interaction concept, however, the proof of energetic equilibrium always guarantees the structural deformation is due to the overall load condition and vice versa.

Current work includes the integration of MRI tissue information within more sophisticated material models. Structural changes (e.g. dead tissue) can be applied to the structural side and the corresponding flow pattern will be analyzed. Patient-specific dimensionless numbers e.g.

$$\Pi^{sys/dias}_{dynamic} = \left[\frac{E/\Delta V}{p}\right]^{sys/dias} \quad ; \quad \Pi^{sys/dias}_{static} = \left[\frac{E/\Delta V}{\rho u^{-2}}\right]^{sys/dias}$$

help to judge interaction effects for both systolic and diastolic functionality. $E/\triangle V$ represents the respective energy level per cavity volume related to the static/dynamic pressure. Consequently, KaHMo FSI and its multi-physical approach represents a further step towards cardiac modeling for *future therapy planning*.

Acknowledgment

The authors would like to thank *Dr. Nitzsche* (Herzzentrum, University of Leipzig,) for providing the MRI data as well as *Prof. D. Liepsch* (University of Applied Science, Munich) for providing the experimental validation data.

References

1. Holzapfel et al. (2000) A New Constitutive Framework for Arterial Wall Mechanics and a Comparative Study of Material Models. Journal of Elasticity 61:1-48
2. Krittian et al. (2008) Partitioned FEM/FVM coupling for cardiac fluid-structure interaction with a macroscopic composite approach, 22nd International Congress of Theoretical and Applied Mechanics
3. Oertel et al. (2006) Modelling the Human Cardiac Fluid Mechanics – 2nd edition. Universitätsverlag Karlsruhe
4. Schmid, H. et al. (2008) Myocardial Material Parameter Estimation – A comparison study of simple shear. Computer Methods in Biomechanics and Engineering (at print)
5. Spiegel et al. (2008) Validierung des Karlsruhe Heart Models, Institute for Fluid Mechanics – Tech. Report

Author: Sebastian B.S. Krittian
Institute: Institute for Fluid Mechanics, University of Karlsruhe (TH)
Street: Kaiserstrasse 10
City: 76131 Karlsruhe
Country: Germany
Email: sebastian.krittian@kit.edu

Spinal Fusion Cage Design

F. Jabbary Aslani[1], D.W.L. Hukins[1] and D.E.T. Shepherd[1]

[1]School of Mechanical Engineering University of Birmingham, Edgbaston, B15 2TT, UK

Abstract — **A fusion cage is used to aid fusion of an intervertebral joint. To date, cages have been commonly made of materials (metals or polymers) that remain in the body. Post-operative complications with these permanent fixtures might be overcome by using biodegradable/bioabsorbable composite (BBC) cages. There are requirements for the BBC to be used as a cage material, including load bearing ability. The aim of this study was to evaluate the feasibility of using a BBC as a cage material. This composite would degrade gradually to be simultaneously replaced by bone. Post-operative complications are reduced as no foreign bodies remain within the patient and bone growth is unrestricted. The design of the cage has also been optimized based on BBC material properties. Cage features such as teeth and holes have been investigated to obtain a suitable cage design using BBC. Finite Element Analysis was carried out on cage concept models, using the material properties of BBC and polyetheretherketone (an existing cage material) for comparison purposes. The results, from an engineering view point, determined the feasibility of BBC as cage material.**

Keywords — **degradable polymers, bioactive glass, composite materials, fusion, spine.**

I. Introduction

Damage to intervertebral discs can lead to pain and immobility that may be treated surgically by fusion of the intervertebral joint using a bone graft [1, 2]. Fusion cages are often used to retain the graft bone [3]. To date, these cages are made of materials (polymer or metal) that remain in the body; the most common polymer in current use is polyetheretherketone (PEEK). These materials can lead to post-operative complications [4, 5] e.g. bone loss as a result of stress-shielding and adverse tissue reactions caused by corrosion [3, 4]. In this study, the feasibility of replacing the existing permanent materials with a biodegradable/bioabsorbable composite (BBC) was investigated. The design of an existing cage was modified and the stress distribution, when subjected to compression, was determined by Finite Element Analysis (FEA) using COSMOS Works (SolidWorks, Santa Monica, USA). The design features investigated were as follows:

- Slot and holes in the side (Figure 1)
- Teeth on the upper and lower surfaces (Figure 2)

The holes allow fluid transport to and from the cage interior, enabling hydrolysis of the BBC to occur from the inside as well as from the surface. Teeth may enable the cage to grip the vertebrae so that metal screws are not required to retain it in place. An insertion hole enables surgical instrumentation to be used to position the cage between adjacent vertebrae.

Resorbable polymers that have been used for implants include poly(lactic acid) (PLA), poly(glycolic acid) (PGA), and poly(L-lactide co-D,L lactide) (PDLLA) [7-10]. Their degradation rates can be tailored to meet the requirements at the implant site. However, these polymers are too weak to meet the demands of load bearing implants [11]. Porous bioactive ceramics and silicate glasses may overcome this problem [12, 13], although they may be too stiff for some applications [14]. However, composites of a ceramic or glass with a polymer (i.e. BBCs) may be suitable for bioengineering applications [5]. In this study, a composite of PDLLA and bioglass-45S5 has been considered as a candidate material [14]. Results were compared with those for a successful existing cage that is manufactured from PEEK (Stalif C, Surgicraft Ltd., Redditch, UK).

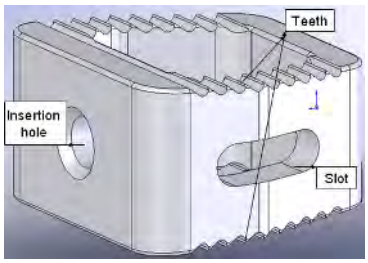


Fig. 1 Proposed fusion cage with slot

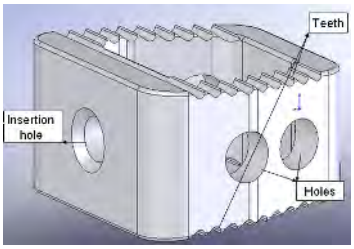


Fig. 2 Proposed fusion cage with holes

Chwee Teck Lim, James C.H. Goh (Eds.): ICBME 2008, Proceedings 23, pp. 1546–1549, 2009
www.springerlink.com

II. Material and Method

The cage was based on an existing design (Stalif C, Surgicraft Ltd., Redditch, UK) (Figure 3), where either a slot, or 1 to 20 holes, and 8 to 18 teeth were varied (Figures 4-5).

FEA was performed on the existing Stalif C and with the proposed BBC designs. The cage was loaded between two blocks whose properties mimicked those of cortical bone (Figure 6). Material properties for cortical bone, PEEK and BBC are given in Table 1. The total assembly was restrained from the bottom (to prevent movement) and a compressive (axial) force of 150 N [15] was applied to the top of the assembly, imitating the load experienced by the cervical region of the spine. The finest mesh size was used to solve the model in COSMOS Works.

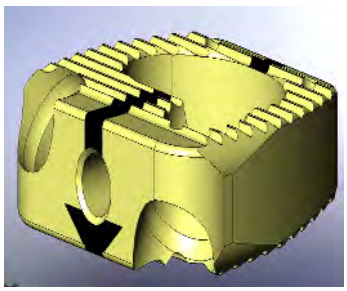


Fig. 3 Stalif C, Surgicraft

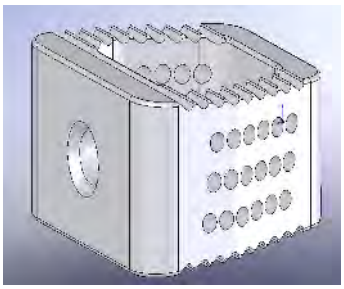


Fig. 4 Concept cage with maximum number of holes

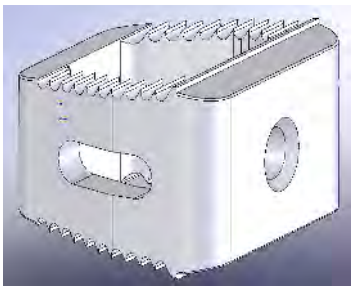


Fig. 5 Concept cage with maximum number of teeth

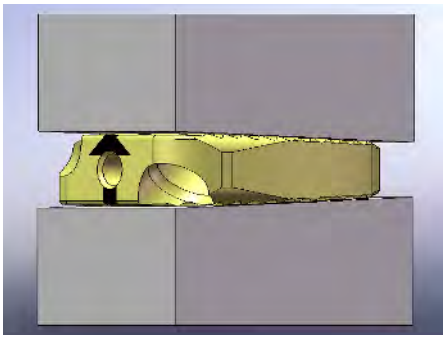


Fig. 6 Stalif C, with two boxes acting as vertebrae

Table 1 PEEK, BBC and cortical bone mechanical properties

Material	PEEK [16]	BBC [13, 17]	Cortical bone [18]
Young's modulus (GPa)	4	≈ 6	30
Poisson's ratio	0.4	0.4	0.3

FEA was carried out on each cage design to determine the maximum von Mises stress. This stress was then compared to the compressive strength of the material to determine the suitability of the concept model. The model was considered to be suitable when its maximum stress was less than the material compressive strength. For these cases, the maximum stress of the accepted model was then compared with the fatigue strength of a composite, with similar mechanical properties to BBC (hydroxyapatite-PEEK (HAPEX^{TM}) [18]), to determine the final step for suitability.

III. Results

The maximum stress for each cage design is given in Table 2. The proposed BBC cage, with maximum number of teeth (18 teeth), has a maximum stress value of 26 MPa, which is less than the maximum stress value of the current PEEK cage (32 MPa). The maximum stress was always seen at the tip of the teeth (Figure 7 and 8). Accordingly, the number of teeth has a direct effect on the maximum stress value; increasing the number of the teeth results in an increase in the maximum stress value. Nevertheless, this value was always significantly lower than the fatigue strength of the material used, resulting in an acceptable concept model for the next step. Also, the concept model with an increased number of holes (20 holes) had a maximum stress value of 13 MPa, for both BBC and PEEK, which is less than half of the maximum stress value of the

current cage (32 MPa), which also resulted in acceptance of the model for the next step.

HAPEX ^{TM} was chosen to compare the fatigue resistance of the concept models. It has a fatigue-life of between 24.6 – 32.4 MPa at 10^6 cycles [18-19]. All models in this study were acceptable, because their maximum stress value was less than the mentioned fatigue-strength.

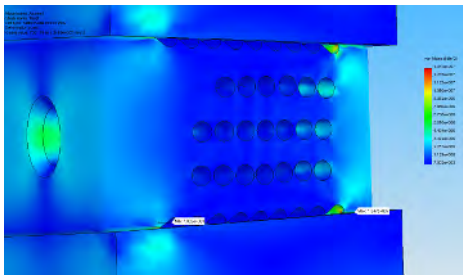


Fig. 7 Maximum stress on concept cage with maximum number of holes

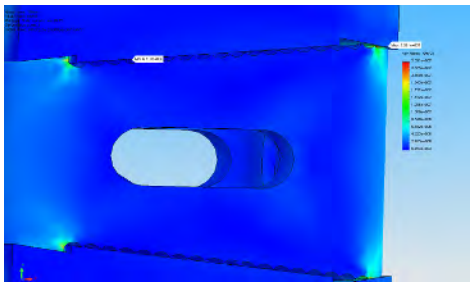


Fig. 8 Maximum stress on concept cage with maximum number of teeth

Table 2 Maximum stress comparison of existing and modified proposed cages with existing and proposal composite

Cage	Material	Material Compressive Strength (MPa)	Maximum Stress (MPa)
Stalif C	PEEK	118 [16]	32
Stalif C	BBC	140 [20]	32
Proposed cage (slot)	PEEK	118 [16]	16
Proposed cage (slot)	BBC	140 [20]	14
Proposed cage (20 holes – 8 teeth)	PEEK	118 [16]	13
Proposed cage (20 holes – 8 teeth)	BBC	140 [20]	13
Proposed cage (18 teeth – with slot)	PEEK	118 [16]	28
Proposed cage (18 teeth – with slot)	BBC	140 [20]	26

IV. Discussion

FEA has confirmed the feasibility of using a BBC as a cage material. A BBC, whose properties were used in the FEA, is biocompatible [14]. An increased number of holes and teeth are favourable in the cage design, because the teeth are able to retain the cage position and the holes allow fluid to pass through the cage, into the cage inner section. It is feasible to have up to 18 teeth and 20 holes in the design, without generating excessively high stresses in the cage.

The major limitation of this study was to use the fatigue strength of HAPEX^{TM} as a criterion for the success, or otherwise, of a BBC cage. This is a composite of a polymer (PEEK) with dispersed ceramic particles (hydroxyapatite) and so its fatigue properties could be very different from those of a BBC.

V. Conclusions

It appears feasible to design a BBC cage that is able to withstand a static compressive load up to 150 N. Further work is required to determine the fatigue properties of BBCs.

Acknowledgment

The authors thank Surgicraft Limited (Redditch, UK) for financial support and the School of Mechanical Engineering, University of Birmingham for providing a studentship for FJA.

References

1. Langer R, Vacanti J (1993) Tissue engineering. Science 260:920-6
2. Hench L L, Polak J M (2002) Third-generation biomedical materials. Science 295:1014-7
3. Vaccaro A R (2003) The Spine Journal 3: 227-37
4. Laakman R W, Kaufman B, Han J S, et al. (1985) MR imaging in patients with metallic implants. Radiology 157:711-4
5. Hench L L, Polak J M (2002) Science 295:1014-7
6. Hutmacher D W (2000) Scaffolds in tissue engineering bone and cartilage. Biomaterials 21:2529-43
7. Agrawal C M, Ray R B (2001) Biodegradable polymeric scaffolds for musculoskeletal tissue engineering. J Biomed Mater Res 55:141-50
8. Slivka M A, Leatherbury N C, Kieswetter K, Niederauer G (2001) Porous, resorbable, fibre- einforced scaffolds tailored for articular cartilage repair. Tissue Eng 7:767-80
9. Behrend D, Schmitz K P, Haubold A (2000) Bioresorbable polymer materials for implant technology. Adv Eng Mat 3:123-5
10. Agrawal C M, Athanasiou K A, Heckman J D (1997) Biodegradable PLA–PGA polymers for tissue engineering in orthopadics. Mat Sci Forum 250:115–28

11. Shikinami Y, Okuno M (1999) Bioresorbable devices made of forged composites of hydroxyapatite (HA) particles and poly-l-lactide (PLLA): Part I. Basic characteristics. Biomaterials 20:859-877
12. Sepulveda P, Jones J R, Hench L L (2002) In vitro dissolution of meltderived 45S5 and sol-gel derived 58S bioactive glasses. J Biomed Mater Res 61:301-311
13. Hench L L (1998) Bioceramics. J Am Ceram Soc 81:1705-1728
14. Blaker J J, Gough J E, Maquet V, Notingher I, Boccaccini A R (2003) In vitro evaluation of novel bioactive composites based on Bioglass-filled polylactide foams for bone tissue engineering scaffolds. J Biomed Mater Res 67A:1401-11
15. ISO 18192-1, Part 1 (2008) Loading and displacement parameters for wear testing and corresponding environmental conditions for test, International Organization for Standardization
16. Victrex at www.victrex.com
17. Blaker J J, Maquet V, Jerome R, Boccaccini A R, Nazhat S N (2005) Acta Biomaterials 1:643-652
18. Abu Bakar M S, Cheng M H W, Tang S M, Yu S C, Liao K, Tan C T, Khor K A, Cheang P (2002) Biomaterials 24:2245-2250
19. Tang S M, Cheang P, Abu Bakar M S, Khor K A, Liao K (2003) International Journal of Fatigue 26:49-57
20. Surgicraft Ltd. at http://www.surgicraft.co.uk

Comparison of Micron and Nano Particle Deposition Patterns in a Realistic Human Nasal Cavity

K. Inthavong[1], S.M. Wang[1], J. Wen[1], J.Y. Tu[1], C.L. Xue[2]

[1] School of Aerospace, Mechanical and Manufacturing Engineering, RMIT University, Australia
[2]School of Health Sciences, RMIT University, Australia

Abstract — **A computational model of a nasal cavity geometry was developed from CT scans and the simulation of the fluid and particle flow within the airway was performed using a Computational Fluid Dynamics (CFD) software. It was found that the deposition patterns for micron particles were highly dependent on the particle inertia and as a result, the majority of particles deposited in the anterior regions of the airway where a change in the flow streamlines was observed. In contrast the deposition for nano particles showed an even distribution of particles throughout the airway, driven by diffusion. Particle diameter was the most important parameter in determining what mechanism of deposition was most important.**

Keywords — **nanoparticle, nasal cavity, deposition, cfd**

I. Introduction

Nasal inhalation is a major route of entry into the body for airborne pollutants by which workers in occupational environments and the general population are exposed to. On the other hand, drug particles are deliberately sprayed into the nasal cavity in the event that the drug particles will deposit on the targeted sites for efficient drug delivery. Knowledge regarding particle deposition processes in the nasal cavity is important in aerosol therapy and inhalation toxicology. Experimental studies into aerosol deposition in the nasal cavity have been investigated in the past by a number of researchers [1-5]. In these studies, both micron or submicron particles were used exclusively and a comparison between the two types of particles was not performed.

Experimental methods performed on human subjects are limited due to the invasive nature and dangers associated with toxic aerosols. Computational simulations present another alternative to provide complementary data of submicron particle deposition for difficult and expensive experimental studies [6-8], while the study of micron particle deposition is not as notable in the literature. The deposition patterns for submicron and micron particles will inevitably be different due to the deposition mechanisms that each particle type experiences.

This paper presents a comparative study of the deposition of submicron particles, particularly the nanoparticles (1-10μm) and micron particles under different steady laminar flow rates by using the Lagrangian approach. The significance and influence of different force terms that are applicable to micron and nanoparticles are discussed and the local deposition patterns presented. A comparison of particle deposition patterns of the different particle types in the human nasal cavity is shown. The investigation in this paper was initiated due to the needs in health risk assessment on potentially toxic particles and the results are also applicable in targeted drug delivery with aerosols.

II. Method

A. Nasal Cavity Geometry Generation

A nasal cavity geometry was obtained through CT scans of the nose of a healthy 25 year old, Asian male, 170cm height, 75 kg mass as shown in Fig 1. The CT scan was performed using a CTI Whole Body Scanner (General Electric). The single-matrix scanner was used in helical mode with 1-mm collimation, a 40-cm field of view, 120 kV peak and 200 mA.

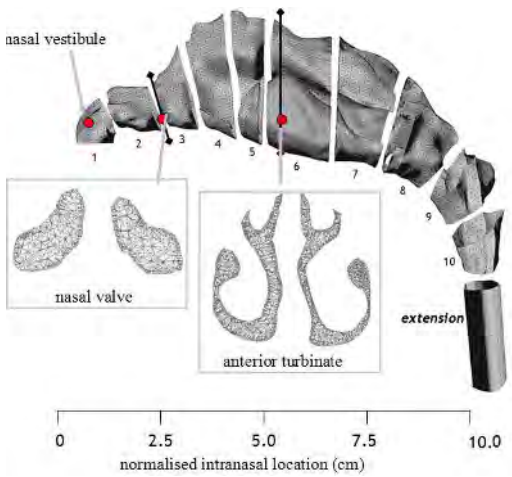


Fig. 1 Nasal cavity model used in the study which has been divided into ten separate sections named (Zone1 to Zone 10) for analysis of local deposition. Cross-sectional areas taken at the nasal valve and middle turbinate are shown with the computational mesh.

Chwee Teck Lim, James C.H. Goh (Eds.): ICBME 2008, Proceedings 23, pp. 1550–1554, 2009
www.springerlink.com

The scans captured outlined slices in the *X-Y* plane at different positions along the *Z*-axis from the entrance of the nasal cavity to just anterior of the larynx at intervals of 1 to 5 mm depending on the complexity of the anatomy. The coronal sectioned scans were imported into a three-dimensional (3D) modeling program called GAMBIT (ANSYS Inc.) which created smooth curves that connected points on the coronal sections. Stitched surfaces were then created to form a complete computational mesh. An initial model with 82,000 unstructured tetrahedral cells was initially used to solve the air flow field at a flow rate of 10L/min. The model was then improved by cell adaptation techniques to refine the grid in order to achieve grid independence. The final grid consisted of 950,000 cells.

B. Numerical Procedure

The conservation equations of mass and momentum were solved through the commercial CFD code, FLUENT 6.3.

The equations were discretised using the finite volume approach with a third order accurate QUICK scheme while the pressure-velocity coupling was resolved through the SIMPLE method. Flow rates ranging from 4L/min to 15L/min were used. At these flow rates, the flow regime has been determined to be laminar [7, 9-11]. A quasi-steady flow rather than a cyclic unsteady flow was used based on the Womersley number, α and the Strouhal number, S which are 1.68 and 0.01 respectively.

Trajectories of individual particles can be tracked by integrating a force balance equation on the particle. This force balance involves the particle inertia balanced by forces acting on the particles, and can be written as,

$$\frac{du_i^p}{dt} = F_D + F_g + F_i \tag{1}$$

where F_d is the drag, F_g is the gravity term, and F_i is additional forces. For micronparticles, F_D is given by

$$F_D = \frac{18\mu_g}{\rho_p d_p^{\,2}} \frac{C_D \,\mathrm{Re}_p}{24} \left(u_g - u_p\right) \tag{2}$$

For nanoparticles, a form of Stokes' drag law [12] is available. In this case, F_D is defined as,

$$F_D = \frac{18\mu}{d_p^2 \rho_p C_c} \left(u_i^g - u_i^p\right) \tag{3}$$

Additional force terms F_i such as Brownian diffusion, Saffman's lift force and thermophoretic forces are applied.

III. Results

Velocity vectors within the nasal cavity airway are shown in Fig 2. The airflow enters the nostrils and immediately begins to accelerate as the vestibule narrows into the nasal valve. The flow increases at the nasal valve where the cross-sectional area is smallest and reaches a maximum (Figure 5a, b and c). Entering the atrium and the velocity decreases as the nasal cavity opens up. The flow remains along the middle and lower regions of the nasal cavity and close to the septum walls rather than diverging out towards the outer meatus. A region of recirculation appears in the expanding region of the cavity near the top (olfactory region) at cross-section A. At the nasal pharynx the velocity increases once more with a decrease in area. Low flow in the olfactory region may be a precautionary mechanism of the nose to prevent particles from damaging the olfactory nerves while still allowing vapor deposition for olfaction.

The inertial deposition of micron particles in the nasal cavity was normalized by using the inertial parameter, $I=Qd^2$, where Q is the air flow rate and d is the equivalent aerodynamic diameter. It is a convenient parameter that compares deposition against different flow rates and particle sizes at aerodynamic diameters. It is widely used for presenting particle deposition efficiencies, especially for in vivo data, where it is difficult to determine an adequate characteristic length for realistic human airways. Monodispersed particles in the range of 1-50μm were released passively into the nasal cavity with flow rates between 4-

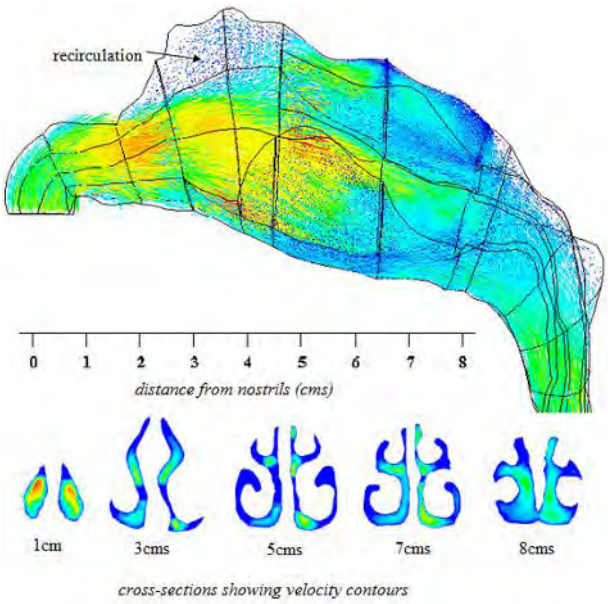


Fig. 2 Airflow patterns colored by velocity. Blue regions represent minimum velocity while red represents maximum velocities.

14L/min. The deposition of micron particles as a function of the inertial parameter is shown in Fig 3. The simulated micron particle deposition in the present nasal cavity model was compared with experimental data that used other nasal cast models.

Generally, the simulated data show reasonable agreement with the experimental data. Differences in deposition may be attributed to the inter-subject variability between the nasal cavity models, such as wider nasal replicate casts which can cause less deposition due to secondary flows [13].

The diffusional deposition of submicron particles (1 to 150nm) was simulated under a flow rate 10 L/min (Fig 4).

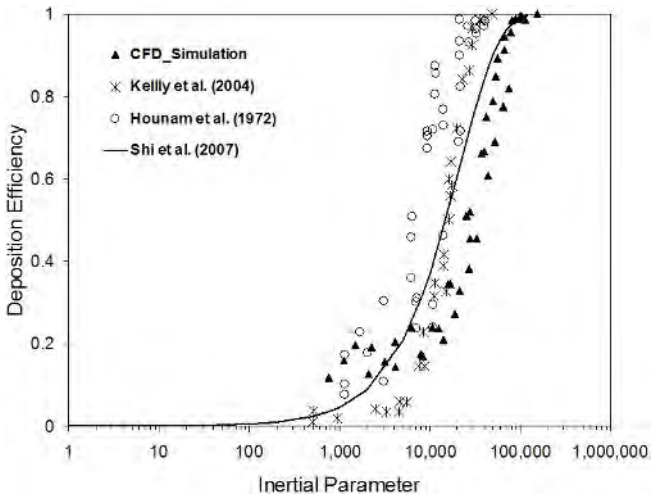


Fig. 3 CFD simulation results for total deposition of particles against Inertial Parameter compared with the experimental data.

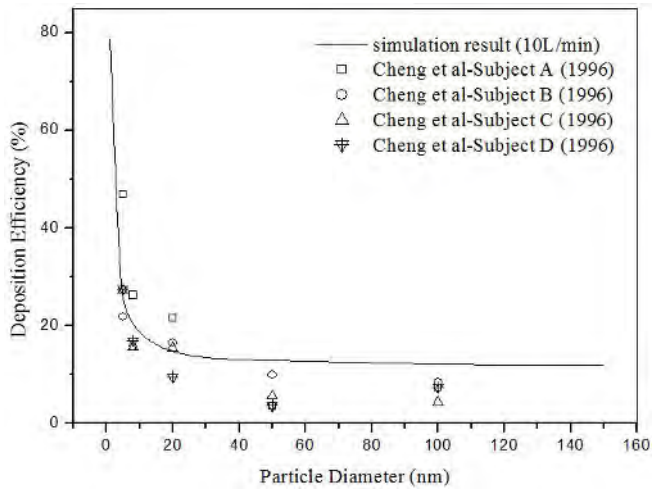


Fig. 4 Comparison between simulation and experimental data of nasal deposition efficiency for different nanoparticle size at a flow rate of 10 L/min

Comparisons of the simulated results were made with the available experimental data reported by Cheng et al. [2] for nasal cavities with different anatomical features. Here the solid lines correspond to the model prediction.

High deposition reaching 80% and nearly 100% were found for 1nm particles. High deposition by is found for particles up to approximately 50nm where particles that are larger provide little change in the total deposition. The deposition for 50nm or larger particles is approximately 10%. The comparisons with the data of Cheng et al. [2] show similar values. As discussed earlier, differences in the results may be attributed to anatomical variances in the nasal cavities used.

Local deposition patterns for a nano (1nm) and a micron particle (22μm) were compared, where the two particle types exhibited the same deposition efficiency. The discrete particles were tracked and the fate of each particle recorded. A particle was deemed to have deposited if its trajectory impacted onto the wall surfaces, otherwise the particle escaped through the outlet. The deposition pattern of a 22μm particle with the density of 1000 kg/m^3 (Fig 5a) shows most of the particles depositing in the anterior and middle regions of the nasal cavity. The upper region of Zone 2 (defined in Fig 1) is a 'hot spot' for deposition. This may be explained by the 90^o curve in the nasal geometry from the nostril inlet into the main nasal passage. The 22μm particles that were initially entrained in the flow path at the inlet are not able to change its flow direction because of the particle inertia, which leads to impaction in the upper region of Zone 2. The inertial impaction caused by the 90º bend is found again in the posterior region of the nasal cavity where the flow changes direction from the main nasal passage towards the larynx. A small hot spot for deposition is found near the nasopharynx. Other concentrated deposition sites are found

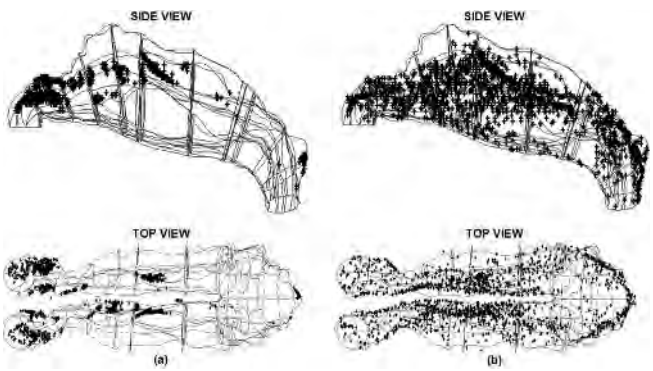


Fig. 5 Local deposition patterns of particles released uniformly from the nostrils for a flow rate of 10 L/min. (a) micron particle having a density 1000kg/m^3 and a diameter of 22μm (b) nanoparticle having a density 1000kg/m^3 and a diameter of 1nm. Both particles exhibit the sane deposition efficiency of 80%.

in the upper regions of the middle sections at Zones 4, 5 and 6. The flow field causes the particles to remain close to the septum walls and is pushed in an upwards direction where the local deposition sites are found.

The deposition pattern for a 1nm particle (Fig 5b) shows a different deposition pattern when compared with the 22μm particle, although the total deposition efficiency is the same (80%) for both particles. The deposited nano particles are distributed more evenly, not only in the entire nasal cavity, but also within each zone. The diffusion mechanism of deposition for 1nm particles disperses the particles in all directions.

The total deposition in the entire nasal cavity is quantified in terms of the total deposition efficiency (*TDE*) as:

$$TDE = \frac{\text{Number of deposited particles in the nasal cavity}}{\text{Number of particles entering the nasal cavity}}$$

The local deposition efficiency (*LDE*) is calculated for each of the ten subdivided zones presented in Fig 6. For better comparisons between the different zones, the *LDE* takes into account the zone surface area since the each zone exhibits different sizes.

$$LDE = \left(\frac{\text{Number of deposited particles in local region}}{\text{Number of deposited particles in the nasal cavity}}\right) \Big/ \left(\frac{A_{zone}}{A_{total}}\right)$$

Fig 6 shows the deposition fraction in each zone for the two particle types. The LDE normalised by the zone's surface area shows a high concentration of particle deposition for 22μm particles in zone 2. Besides the high concentration of deposited particles in Zone 2, the spread of deposited particles among the other zones are generally even, except for Zone 7 and 8 which has very little deposition. In comparison the deposition pattern for the 1nm particle shows a uniformly distribution of particle deposition.

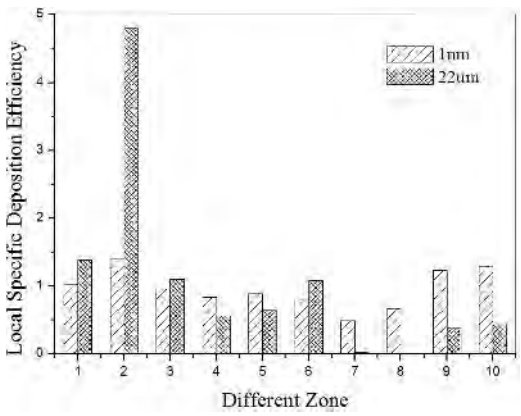


Fig. 6 Deposition patterns of 1 nm and 22 μm at inspiratory flow rate of 10 L/min. (density=1000 kg/m3, Total deposition efficiency=80%)

IV. Conclusion

A comparative study of the deposition of submicron particles and micron particles under different steady laminar flow rates by using the Lagrangian approach was presented. The significance and influence of different force terms that are applicable to micron and submicron particles were discussed and the local deposition patterns presented. It was found that the particle diameter has substantial influence on deposition patterns for both the micron particles and submicron particles. The total deposition efficiency of the micron particles increase as the particle diameter increases, while the inverse is true for submicron particles. Overall there is a difference in the local deposition patterns for micron and submicron particles. The major regions of deposition for micron particles were found to be at the anterior and middle parts in the nasal cavity while for submicron particles there was a uniform distribution of deposited particles.

Acknowledgements

The authors would like to express their gratitude to the Australian Research Council (project ID LP0561870) and RMIT Research and Innovation Fund for their support.

References

1. Cheng YS, Yamada Y, Yeh HC, Swift DL. (1988) Diffusional deposition of ultrafine aerosols in a human nasal cast. J Aerosol Sci. 19 6:741-51.
2. Cheng KH, Cheng YS, Yeh HC, Guilmette A, Simpson SQ, Yang YH, et al. (1996) In-vivo measurements of nasal airway dimensions and ultrafine aerosol deposition in the human nasal and oral airways. J Aerosol Sci. 27 5:785-801.
3. Swift DL, Montassier N, Hopke PH, Karpen-Hayes K, Cheng YS, Su YF, et al. (1992) Inspiratory deposition of ultrafine particles in human nasal replicate cast. J Aerosol Sci. 23 1:65-72.
4. Swift DL, Strong JC. (1996) Nasal deposition of ultrafine218 Po Aerosols in human subjects. J Aerosol Sci. 27 7:1125-32.
5. Kesavanathan J, Swift DL. (1998) Human nasal passage particle deposition: The effect of particle size, flow rate and anatomical factors. Aerosol Sci Tech. 28 457-463:
6. Yu G, Zhang Z, Lessman R. (1998) Fluid flow and particle deposition in the human upper respiratory system. Aerosol Sci Tech. 28 146-58.
7. Zamankhan P, Ahmadi G, Wang Z, Hopke PH, Cheng YS, Su WC, et al. (2006) Airflow and deposition of nanoparticles in a human nasal cavity. Aerosol Sci Technol. 40 463-76.
8. Shi H, Kleinstreuer C, Zhang Z. (2006) Laminar airflow and nanoparticle or vapor deposition in a human nasal cavity model. J Biomech Eng. 128 697-706.
9. Hahn I, Scherer PW, Mozell MM. (1993) Velocity profiles measured for airflow through a large-scale model of the human nasal cavity. J Appl Physiol. 75 5:2273-87.
10. Kelly JT, Prasad AK, Wexler AS. (2000) Detailed flow patterns in the nasal cavity. J Appl Physiol. 89 323-37.

11. Swift DL, Proctor DF. (1977) In: Brain JD, Proctor DF, Reid LM, eds. Respiratory Defence Mechanisms. New York: Marcel Dekker
12. Ounis H, Ahmadi G, J.B. M. (1991) Brownian diffusion of submicrometer particles in the viscous sublayer. J Colloid and Interface Science. 143 1:266-77.
13. Häußermann S, Bailey AG, Bailey MR, Etherington G, Youngman MJ. (2001) The influence of breathing patterns on particle deposition in a nasal replicate cast. J Aerosol Sci. 33 923-33.

Corresponding Author: jiyuan.tu@rmit.edu.au

Comparative Study of the Effects of Acute Asthma in Relation to a Recovered Airway Tree on Airflow Patterns

K. Inthavong, Y. Ye, S. Ding, J.Y. Tu

School of Aerospace, Mechanical and Manufacturing Engineering, RMIT University, Australia

Abstract — **Two computational models of the airway tree six generations deep were reconstructed from computed tomography (CT) scans from a single patient. The reconstructed models were used to investigate the effects of acute asthma on the airflow patterns, the pressure drop, and the implications it has on targeted drug delivery by using Computational Fluid Dynamics (CFD). Comparisons in the geometry found that bifurcation angles do not vary significantly between the two models; however small changes were observed which may be due to the physical scans of the patient taken at different times. The inhalation effort to overcome airway resistance in the asthma affected model was twice as high as that for the recovered model. It was also found that airflow patterns were significantly different between both models especially in regions where the effects of asthma were significant.**

Keywords — **asthma, airway, airflow, cfd, modeling**

I. Introduction

Experimental studies with human subjects have shown that patients with asthma have an effect on deposition of inhaled particles [1, 2]. Since the nature of in vivo studies is invasive CFD studies provide an alternative approach. However most of these computational studies have considered airflow patterns affected by tumors, and airway constrictions associated with chronic obstructive pulmonary disease (COPD) in localized subregions of the lung airways [3, 4]. The work by Longest et al.[5] however, included double bifurcation models of upper (G3–G5) and central (G7–G9) airways for a four-year-old child where the effects of asthma was modeled as a 30% constriction of the airway. In all the above studies, lung subregions of interest were reconstructed from Weibel [6]'s model and airway constrictions were modeled by decreasing the airway diameters artificially from experimental data.

Additionally the majority of airflow studies have been based on regular dichotomy airway models (symmetrical or idealized geometries) or lung segments (single, double and triple bifurcations) which lack realism and detailed flow structures. There have been a few studies that have studied an irregular dichotomy airway model [7, 8]. One advantage of using a realistic model is the inclusion of the effects of cartilaginous rings present in the trachea and early bifurcations. Two computational models of the airway tree six generations deep were reconstructed from computed tomography scans from a single patient. The first scan was taken a day after an acute asthma episode while the second scan was taken thirty days later when the patient had recovered.

II. Method

A. CT scans and Image Segmentation

The reconstruction of the airway was based on data obtained from CT scans of a 66 year old non-smoking Asian male (height 171 cm and weight 58 kg) using a helical 64 slice multidetector row CT scanner the day after hospital admission with an acute exacerbation of asthma. At the time, his lung function by spirometry (Spirocard, QRS Diagnostic, USA) showed severe airflow obstruction with a forced expiratory volume in 1 second (FEV1) of 1.02L (41% predicted). Data was acquired with 1-mm collimation, a 40-cm field of view (FOV), 120 kV peak and 200 mA. At baseline, 2 cm axial length of lung caudad to the inferior pulmonary ligament was scanned during a single full inhalation total lung capacity breath-hold, which yielded 254 contiguous images (slices) of 1-mm thickness with voxel size of 0.625 x 0.625. An identical protocol was used to acquire images following recovery 30 days later, when his FEV1 was measured at 2.27 L (91% predicted). The two computationally reconstructed models were then

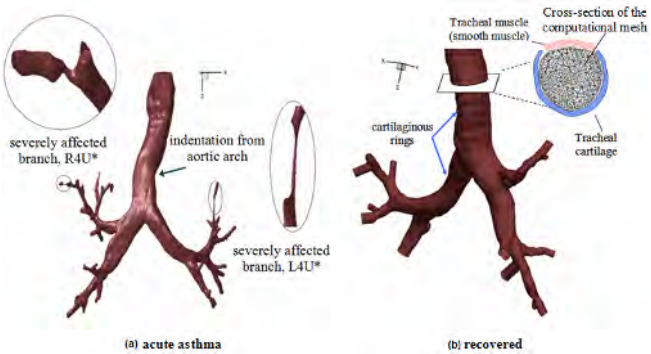


Fig. 1. (a) Front view of the acute asthma affected airway. (b) Reverse view of the recovered model showing the presence of the tracheal cartilage rings and the airway smooth muscle. *The naming convention for the branches is found in Fig.2.

Chwee Teck Lim, James C.H. Goh (Eds.): ICBME 2008, Proceedings 23, pp. 1555–1558, 2009
www.springerlink.com

identified as the AA-model (acute asthma model) and the REC-model (recovered model).

To obtain the source data from medical images, the 'locally constrained watershed algorithm was used to address the issue of leakage during the image segmentation stage [9]. Leakage can occur when the wall of the airway that separates the surrounding tissues is relatively thin and noise present in the image causes the segmentation algorithm to "grow through" the wall. The resulting triangulated data points, (called cloud points) of the generated airway tree that lie on the airway surface are then fitted by applying the NURBS approach within the software Geomagic Studio and stored as an IGES file. Based on the IGES file, the commercial software CATIA (Dassault Systemes) was used to segment the model in terms of trachea, bifurcation and outlet. For the acute asthma model two branches were severely affected by the airway narrowing (Fig.2). These branches were modified and plugged at its ends which acted as a blocked airway. In terms of CFD modeling this was necessary as it is difficult to apply a suitable computational mesh on such small dimensional narrowed geometries.

B. Numerical Modeling

Using the meshing software GAMBIT 2.2 (Ansys Inc.), a mesh file was produced, which was then read into FLUENT 6.3 (Ansys Inc.). For this study the trachea was extended to allow the flow to develop naturally so that a more accurate inlet profile at the trachea was formed, rather than using a uniform profile. A flow rate of 15L/min was applied at the inlet, which corresponds to a Reynolds number of 1079. The low flow rate provides the advantages of simpler modeling by assuming a steady laminar flow. The flow regime has been considered as laminar or lightly transitional at flow rates of 28-30L/min (Re~2000-2500) [10, 11]. A steady flow was applied based on a variety of criteria such as the Womersley parameter, $\alpha = D/2(\omega/\nu_g)^{0.5}$ and the Strouhal number, $S = \omega D/u_{ave}$ where u_{ave} is the mean velocity, ω is the angular frequency of oscillation (=$2\pi f$), D is the diameter of the tube and ν_g is the viscosity.

Homogeneous outflow conditions were assumed where the mass flow was evenly distributed across each of the outlets. Furthermore, the outlets were artificially extended downstream given by, $L_{extension} = 0.05\,\mathrm{Re}\,D$ to obtain fully developed profiles and hence avoid any reverse flow that may be caused due to an abrupt end to the flow field. The computational model underwent grid refinement in order to achieve grid independence with the final model consisting of 1.3million cells.

The numerical schemes to solve the conservation equations of mass and momentum for the air flow under steady-state, isothermal, and incompressible conditions included the third-order accurate QUICK scheme for discretization, and the SIMPLE algorithm for the pressure–velocity coupling. The convergence criteria for the air flow properties (resolved velocities and pressure) were set at 10^{-5}.

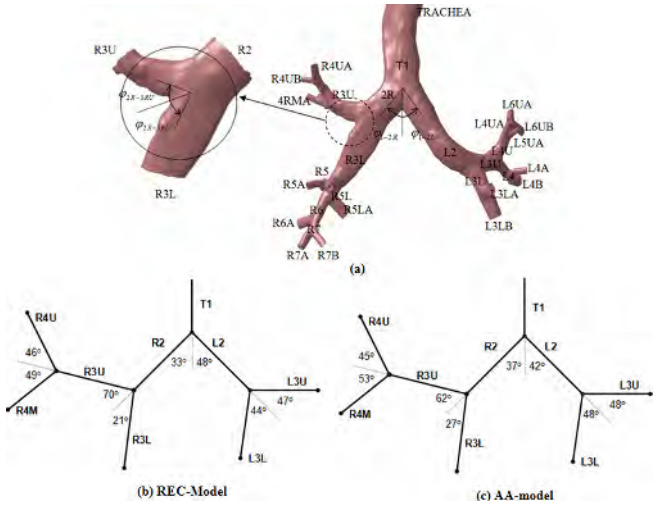


Fig. 2 (a) Bifurcation branch angle definition and diagram with branch name. Bifurcation angles with the main bronchial branches are given for the (c) Recovered Model and (d) the Asthma Affected model.

III. Results

A. Airway Geometry Comparison

The reconstructed model of the bronchial tree exhibits an asymmetric dichotomous branching pattern. The bifurcation at the carina produces the right main bronchus (R2, 41°) at a more obtuse angle than that of the left main bronchus (L2, 25°) measured by the interbronchial axis (centerline of the bronchus) with the long axis of the trachea. The sum of the two daughter branching angles (i.e. R2+L2 = 66°) form the tracheal carinal angle which compares with a mean value of 73° from a sample of 65 men and 55 women; age range 17–85 years; mean age 56 years [12] and 63° for a sample of 21 patients with an age range of 51-60 years [13]. Overall the bifurcation angles do not vary significantly between the AA-model and the REC-model, however small changes are observed which may be due to the scans which were taken of the patient thirty days apart where the positioning and inhalation may have differed.

Normalised velocity profiles (Fig.3) in the trachea and main bronchi were taken and compared with experimental data from a 3:1 scaled up acrylic plastic model of the human central airways [14]. The development of the profiles has been discussed in the publication by [14] and is not reported

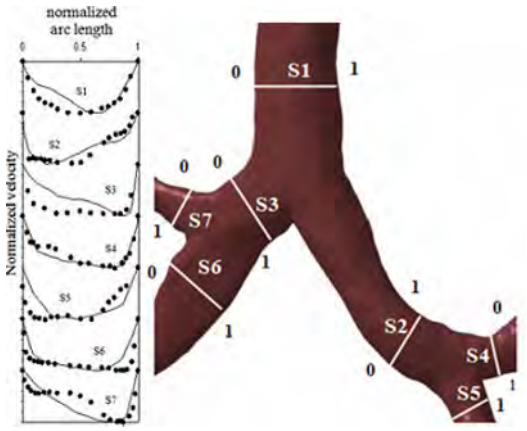


Fig. 3 Normalized axial velocity profile plotted as a function of the normalized arc length. The experimental data of Menon et al. (1984) are plotted as (●) for the corresponding locations.

here for brevity. However, local flow patterns are discussed in detail later in this report. The numerical results generally have good agreement with experimental results in terms of characteristic features. Some differences are found due to the inherent differences in the geometries used. For example at S1 the CFD results show a skewed velocity profile which is a result of the indentation from the aortic arch as well as the trachea cartilages. It can also observed that the tracheal bifurcation at the carina ridge produces a biased profile towards the inner walls of the subsequent daughter branches (S2, S3) due to the upstream flow momentum.

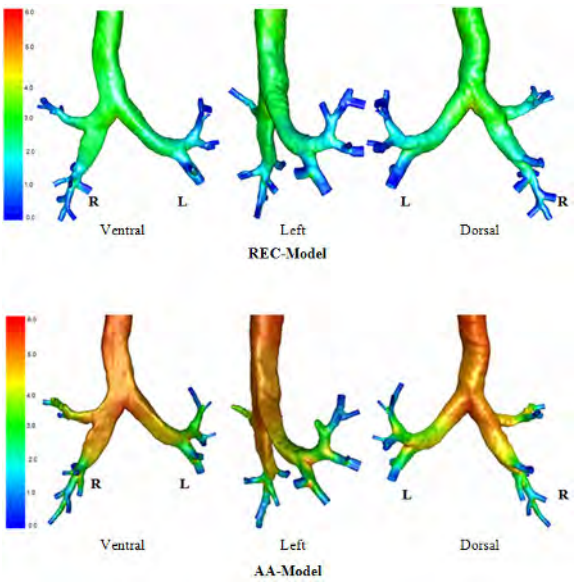


Fig. 4 Pressure contour plots. The pressure value is the pressure difference between the local regions with a reference pressure at the outlets.

B. Pressure Distribution

Contours of the total pressure in reference to the outflow pressure are shown in Fig.3. The required pressure difference at the inlet for the AA-model was 5.98 Pa, which is nearly twice the value for the recovered model (3.73 Pa). Along the main bronchus the pressure decreases steadily while there is a definite pressure drop from each main branch into the subsequent daughter branch. This is due to the bifurcation ridge where a local maximum occurs as a result of a build up of pressure, similar to a stagnation point. In the AA-model the constriction of some branches effectively reduce the number of flow paths by two as the constriction in L4U and R4U is so great that no flow passes through. Greater resistance is found in the AA-model because of the reduced cross-sectional areas in the AA-model.

C. Local Flow Features: Main Bronchus Bifurcation

Crossflow streamlines overlayed on contours of axial velocity at cross-sections a-a' to f-f' are shown in Fig.4. The cross-sectional views are taken from the upstream flow point of view looking downwards in the axial direction. The three cross-sections preceding the bifurcation (a-a', b-b', and c-c') depicts the flow before it bifurcates at the carina. Regionally the flow is concentrated on the left lateral wall due to the indentation by the transverse portion of the aortic arch. The streamlines are directed to the right side in response to the concentrated flow on the left wall. At b-b' the streamlines are moving towards the ventral side and at cc' just before the bifurcation, the flow begins to divide into the left and right side with ventrally. In the AA-model the axial contours are more evenly distributed. The effect of the aortic arch indentation is less significant, however after the indentation the streamlines are directed to the left side of the airway. Just prior to the bifurcation, the flow divides and the streamlines are moving more laterally than in the REC-model. Following the flow through the right main bronchus (d-d'), of the REC-model the bulk flow remains close to the inner wall side with the flow momentum shifting towards the outer wall as characterized by the streamlines. In the left main bronchus at e-e', the flow is found on the inside wall and a region of recirculation is present in the low axial flow region due to: i) the upstream velocity profile that is biased to the left side, ii) a more obtuse bifurcation angle that curves laterally producing a centrifugal acceleration, and iii) the critical carina geometry. The bifurcation of the left main bronchus into the upper lobe bronchus (L3U) occurs laterally, extending to almost the horizontal, while the lower lobe (L3L) is more directly in line with the main bronchus.

This leads to a high distribution of slow passing through the L3L. The AA-model shows some differences in airflow

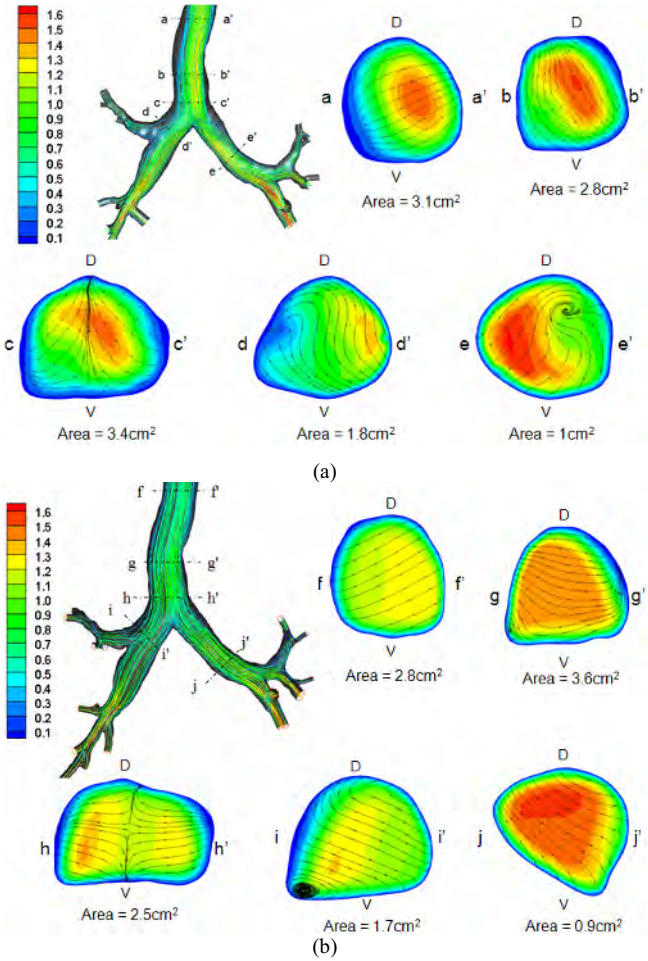


Fig. 5 Cross-flow streamlines overlayed onto axial velocity contour plots at specified cross sections in the main bronchi of the (a) REC-model (b) AA-model.

patterns particularly at i-i' and j-j'. The streamlines in left main bronchus (j-j') suggest that the flow is moving from the ventral to dorsal direction while locally the maximum axial velocity exists in the dorsal region. The main difference in the airway geometry is the presence of a narrowed rounded ridge on the ventral side. The geometry of the right main bronchus (i-i') has a flat ventral profile and high axial velocity is found more centrally in the cross-section. A region of recirculation appears in the left ventral region. It is interesting that recirculation regions are found within the first two branches after the carina for both models.

IV. Conclusion

It was found that bifurcation angles do not vary significantly between the AA-model and the REC-model, however small changes are observed which may be due to the scans which were taken thirty days apart where the positioning and inhalation may have differed. The required pressure difference at the inlet for the AA-model was 5.98 Pa, which is nearly twice the value for the recovered model (3.73 Pa). This suggests that during the period of an acute asthma episode, the work of breathing for the patient in order to achieve the same tidal volumes, is double compare to the recovered state, which can lead to respiratory muscle fatigue. Local flow patterns showed that the changes in the airway had significant influence on flow patterns. This is especially true in the region where the airway narrowing is most severe. This means that studies of therapeutic drug delivery in the airway should consider the effects of airway narrowing and not a recovered or a healthy airway.

References

1. Chalupa DC, Morrow PE, Oberdorster G, Utell MJ, Frampton MW. (2004) Ultrafine particle deposition in subjects with asthma. Environmental Health Perspectives. 112 8:879-82.
2. Sbirlea-Apiou G, Lemaire M, Katz I, Conway J, Fleming JS, Martonen TB. (2004) Simulation of the regional manifestation of asthma. Journal of Pharmaceutical Sciences. 93 5:1205-16.
3. Farkas A, Balásházy I. (2007) Simulation of the effect of local obstructions and blockage on airflow and aerosol deposition in central human airways. Aerosol Science. 38 865-84.
4. Zhang Z, Kleinstreuer C, Kim CS, Hickey AJ. (2002) Aerosol transport and deposition in a triple bifurcation bronchial airway model with local tumours. Inhalation Toxicology. 14 1111-33.
5. Longest PW, Vinchurkara S, Martonen T. (2006) Transport and deposition of respiratory aerosols in models of childhood asthma. Aerosol Science. 37 1234-57.
6. Weibel ER. (1963) Morphometry of the human lung. New York, US: Academic Press.
7. Balashazy I, Hofmann W. (1993) Particle deposition in airway bifurcations—I. Inspiratory flow. J Aerosol Sci. 24 745–72.
8. Choi LT, Tu JY, Li HF, Thien F. (2007) Flow and particle deposition patterns in a realistic human double bifurcation airway model. Inhal Toxicol. 19 117-31.
9. Beare R. (2006) A locally constrained watershed transform. IEEE transactions on pattern analysis and machine intelligence. 28 7:1063-74.
10. Nowak N, Kakade PP, Annapragada AV. (2003) Computational fluid dynamics simulation of airflow and aerosol deposition in human lungs. Annals of Biomedical Engineering. 31 374-90.
11. van Ertbruggen C, Hirsch C, Paiva M. (2005) Anatomically based three-dimensional model of airways to simulate flow and particle transport using computational fluid dynamics. J Appl Physiol. 98 970-80.
12. Karabulut N. (2005) CT Assessment of tracheal carinal angle and its determinants. British Journal of Radiology. 78 787-90.
13. Haskin PH, Goodman LR. (1982) Normal tracheal bifurcation angle: A reassessment. American Journal Roentgen. 139 879-82.
14. Menon AS, Weber ME, Chang HK. (1984) Model study of flow dynamics in human central airways. Part III: Oscillatory velocity profiles. Respiration Physiology. 55 255-75.

Corresponding Author: jiyuan.tu@rmit.edu.au

Computational Analysis of Stress Concentration and Wear for Tibial Insert of PS Type Knee Prosthesis under Deep Flexion Motion

M. Todo[1], Y. Takahashi[1] and R. Nagamine[2]

[1] Research Institute for Applied Mechanics, Kyushu University, Kasuga, Japan
[2] Yoshizuka Hayashi Hospital, Fukuoka, Japan

Abstract — **3-D finite element model of a typical PS type knee prosthesis was constructed using its CAD data with use of a nonlinear spring model and an analytical load data for deep squatting. Stress analysis was then performed by an explicit finite element method under continuous deep flexion motion. It was shown that the equivalent stress on the Post surface rapidly increases due to the Post/Cam contact. Severe stress concentration is also generated on the surface. This kind of stress concentration may cause damage and failure of the Post. Wear analysis was also performed based on the results of the stress analysis and the classical wear theory. Wear depth was then estimated and the analytical result suggests that the developed FE model is useful for risk assessment of knee prostheses.**

Keywords — **Total knee arthroplasty, UHMWPE insert, Deep flexion, Wear, Finite element analysis**

I. Introduction

Total knee arthroplasty, TKA, is applied to patients with severe osteoarthritis as a final treatment to recover the function of the injured knee. In general, QOL of the patients is dramatically improved by obtaining knee movement without pain after TKA. Although the mobility of knee prosthesis is being improved through design modification, there are still some demands for knee prosthesis such as higher durability of tibial insert. It is therefore needed to understand the detail of movements of operated knee after TKA, and such information should be reflected to the design of knee prosthesis. It is however very difficult to understand the detail of TKA knee motion because of its complex movements characterized as a combination of flexion, rotation and roll-back. Fatigue fracture and severe wear of tibial inserts are sometimes reported, and they are thought to be strongly related to the stress states under such complex knee motions.

PS type knee prosthesis is known to be used in a typical type of TKA where anterior and posterior cruciate ligaments are removed. PS type prosthesis is characterized by the existence of Post-Cam structure to stabilize the knee movement through Post-Cam contact. In this type of prosthesis, failure and wear of the Post of the tibial insert are important problems and therefore, there is a demand for understanding the stress state of the tibial insert during knee motion. Under such circumstances, three-dimensional finite element method (FEM) has been utilized to characterize the 3D stress state of knee prosthesis.

In the previous studies of FEM simulations of TKA, most of them were aimed to analyze stress states under walking conditions with shallow flexions [1,2-5,8], and a few attempts have been made to analyze stress state under deep flexion [9-11]. The author's group recently developed simple 3D-FEM models using CAD data of knee prostheses clinically used, and investigated effects of deep knee flexion on the stress state of the tibial inserts [10-12].

In the present study, the FEM model was used to analyze a typical PS type knee prosthesis in order to characterize the stress state of the tibial insert under deep flexional motion. The model was also utilized to analyze the wearing process of the insert and then wear depth was compared with the stress state during flexional movement.

II. Finiteelement model

CAD model of a PS type knee prosthesis (Stryker Scorpio Superflex [6]) is shown in Fig.1. A 3D-FEM model consisting of femoral component, tibial component and tibial insert were constructed from the CAD data. Finite element meshed model is also shown in Fig.1. Tetorahedral elements were used, and the numbers of the nodes and the elements were 21958 and 89322, respectively. The tibial insert originally made from a thermoplastic polymer UHMWPE was assumed to be an elastic-plastic material and to follow the von Mises yield criterion. The bi-linear stress-plastic strain relationship experimentally obtained is shown in Fig.2 [7]. The metal femoral and tibial components were assumed to be rigid in order to reduce computational time. The friction coefficient between the femoral component and the tibial insert was chosen to be 0.04 [5]. It was assumed that the back surface of the tibial insert was perfectly connected to the top surface of the tibial component.

Reactional and frictional forces are generated on the contact surfaces of a TKA knee with PS prosthesis during flexional motion. In this TKA knee, these forces are balanced with the tensions of the soft tissues existing around the knee; as a result, for example, anterior-posterior move-

Chwee Teck Lim, James C.H. Goh (Eds.): ICBME 2008, Proceedings 23, pp. 1559–1563, 2009
www.springerlink.com

ment (roll-back motion) occurs. In the present FEA model, a nonlinear spring model was utilized to express this movement [8]. Two spring elements were attached in the front of the tibial component and the two in the back as shown in Fig.3. The nonlinear force -displacement relation is given by

$$F = 0.18667d^2 + 1.3313d \quad (1)$$

where F and d are force and displacement, respectively. It is noted that this nonlinear relation was experimentally determined from a knee with removed anterior and posterior cruciate ligaments [8].

The axis of flexion was assumed to be located in the center of the circle which coincides with the shape of the condylar surface of the femoral component as shown in Fig.4. For the femoral component, only the displacement in the Z-direction was free and the tibial component was able to move freely only in the Y-direction. Load data used as the mechanical boundary condition was referred from Ref. 2 in which load data for rapid deep squatting was analytically obtained using 2 dimensional model of human knee considering muscular forces. The load F_N and F_T were applied to the femoral component in the vertical direction (Z-direction) and to the tibial component in the horizontal direction (Y-direction), respectively, as shown in Fig.4. The relationship between the load data and the flexion angle were shown with the body force used in the analysis in Fig.5.

Wear analysis was also performed on the basis of the stress analysis. From the classical wear theory, the wear

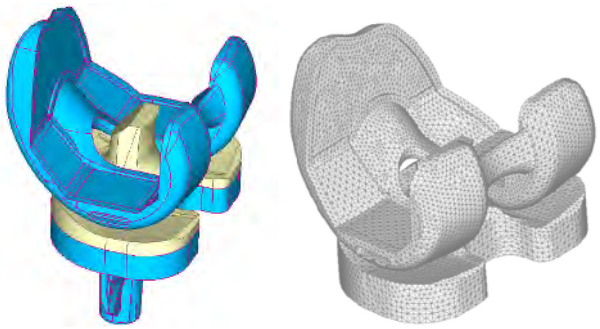


Fig. 1 CAD and FEM models of PS type knee prosthesis.

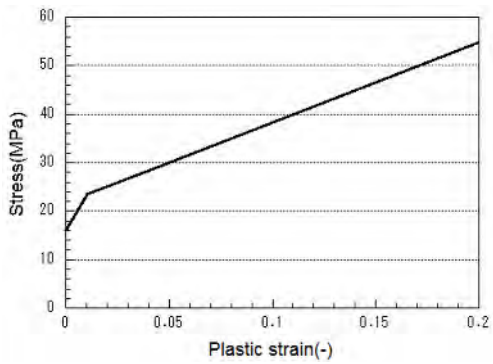


Fig. 2 Bi-linear stress-plastic strain relation.

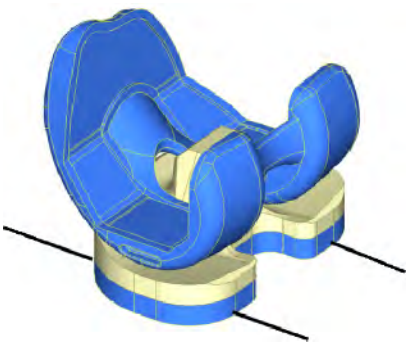


Fig. 3 Computational model with nonlinear springs.

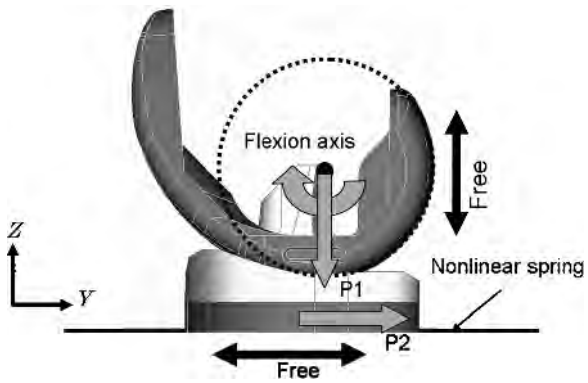


Fig. 4 Boundary conditions.

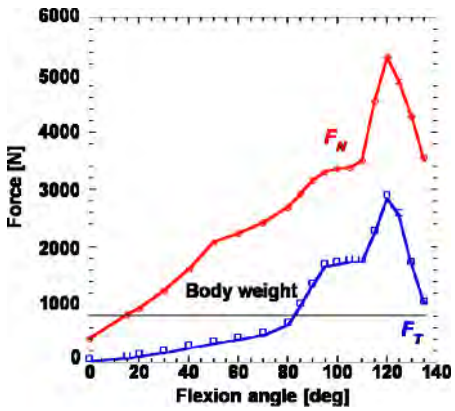


Fig.5 Force data used as mechanical boundary condition.

depth δ_{wear} after n increments can approximately be expressed as

$$\delta_{wear} = k\sum_{i=1}^{n} p_i |v_i| \Delta t \tag{2}$$

Where k is the constant, p_i the contact pressure, v_i the sliding velocity and Δt the time interval of an increment [13]. k was chosen to be $220\text{x}10^{-9}$ mm^3/Nm. v_i was assumed to be given by

$$|v_i| = \left[(v_{F-comp,z})^2 + (v_{F-comp,y} - v_{T-comp,y})^2\right]^{1/2} \tag{3}$$

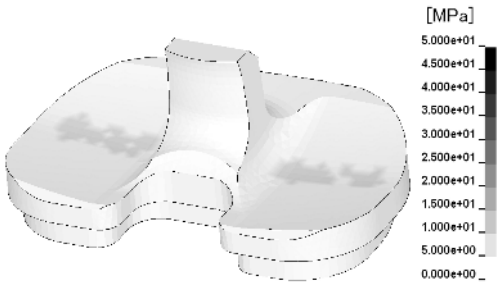
Where $v_{F\text{-}comp,z}$ and $v_{F\text{-}comp,y}$ are the z- and y-components of the maximum velocity of the femoral components on the contact region. $v_{T\text{-}comp,y}$ is the y-component of the maximum velocity of the tibial component. Δt was 0.01 msec in this analysis. p_i and the velocity components were evaluated from the stress analysis and then δ_{wear} was calculated by using Eqs(2) and (3).

A commercially available pre-processor FE-MAP was used to develop those 3D-FEM models including from the surface data, meshing and setting up of the boundary conditions. A commercial explicit finite element code LS-DYNA was then utilized as solver, and a post-processor LS-POST was used to analyze the results.

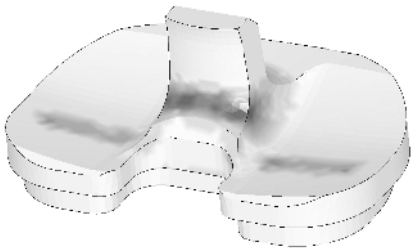
III. Results and Discussion

Von Mises equivalent stress distributions on the surfaces of the tibial insert at three different flexion angles are shown in Fig.6. At 45 deg, stress concentrations are only observed on the condylar surfaces. Contact between the Post and the Cam starts at about 65 deg, therefore, at 90 deg, stress concentrations appear on both the condylar and the Post surfaces. It is seen that the stress on the condyle increases with increase of flexion angle, and the stress on the Post is much higher than the condyle. At 135 deg, the stress further increases and the maximum value becomes about 51.2 MPa. Thus, the high concentrated stress much higher than the yield strength of UHMWPE may cause failure and wear of the tibial insert, especially, the Post.

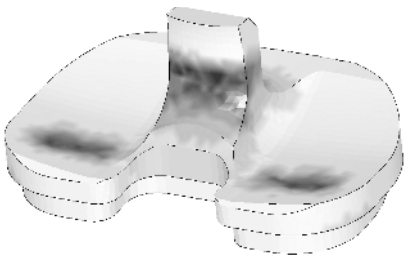
Equivalent plastic strain distributions at 90 and 135 degrees are shown in Fig.7. At 90 deg, plastic strain is distributed slightly on the Post. At 135 deg, plastic deformation region is dramatically extended and plastic strain is distributed on both the condyle and the Post. This result suggests that the tibial insert is plastically damaged under deep knee flexion and such plastic damage is accumulated under repeated flexions.



(a) 45 deg (σ_{max}=10.23 MPa)



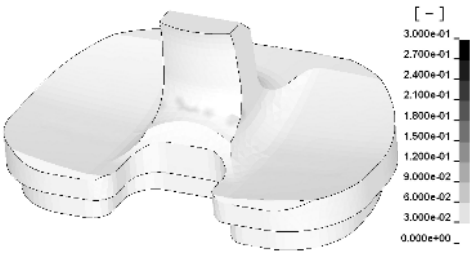
(b) 90 deg (σ_{max}=32.68 MPa)



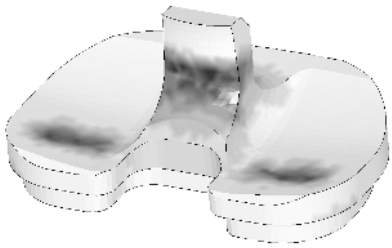
(c) 135 deg (σ_{max}=51.16 MPa)

Fig. 6 Equivalent stress distribution.

Distribution of wear damage is expressed by wear depth in Fig.8. At 45 deg, wear is distributed only on the center of the condyle. At 90 deg, the wear region on the condyle becomes larger and wear is also slightly distributed on the Post. The wear region on the Post becomes larger at 135 deg, and furthermore, wear is distributed on the rear part of the condyle in addition to the center. This clearly indicates that wear damage region extends from the center to the rear on the condyle as flexional motion progresses. It is thus noted that the wear analysis procedure developed in the present study may be able to predict wear damaged region that is different from the concentration regions of equivalent stress and plastic strain. Further study is needed to insure the validity of the wear analysis procedure.

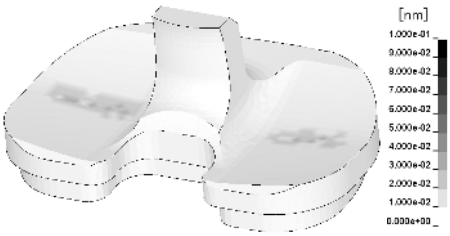


(a) 90 deg (ε_{max}=0.069)

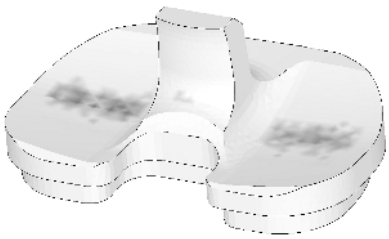


(b) 135 deg (ε_{max}=0.379)

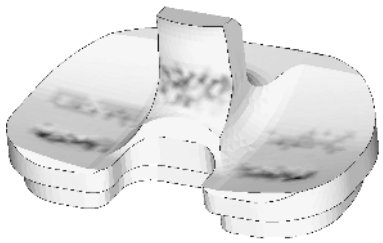
Fig. 7 Equivalent plastic strain distribution.



(a) 45 deg ($\delta_{wear,max}$=0.044 nm)



(b) 90 deg ($\delta_{wear,max}$=0.077 nm)



(c) 135 deg ($\delta_{wear,max}$=0.119nm)

Fig. 8 Wear damage distribution.

IV. Conclusions

3D FEM model of PS type knee prosthesis clinically used worldwide was constructed from its CAD data. Stress state under deep knee flexion such as squatting was analyzed by using the explicit finite element method. Wear analysis was also performed based on the results of the stress analysis. The conclusions are summarized as follows:

(1) A simplified 3D-FEA model of PS type knee prosthesis for deep knee flexion analysis was developed by using nonlinear spring model and load data for deep squatting. High stress concentration due to the Post-Cam contact was reasonably expressed at deep flexion angles and furthermore, roll-back behavior was well simulated by introducing the nonlinear spring model.

(2) Stress concentration on the Post surface is very high, suggesting that failure and wear of the Post under repeated flexional motions.

(3) Wear depth is reasonably predicted by using the classical wear theory and the results of stress analysis. Wear is extensively generated on both the condylar and the Post surfaces.

References

1. Ahir SP, Blunn GW, Haider H, Walker PS (1999) Evaluation of a testing method for the fatigue performance of total knee tibial trays. J Biomechanics 32:1049-1057
2. Dahlkvis NJ, Mayo P, Seedhom BB (1982) Forces during squatting and rising from a deep squat. Eng in Medicine 11:69-76
3. D'Lima DD, Chen PC, Kester MA, Colwell Jr CW (2003) Impact of patellofemoral design on patellofemoral forces and polyethylene stresses. J Bone and Joint Surgery 85A:85-93
4. Godest AC, Beaugonin M, Haug E, Taylor M, Gregson PJ (2002) Simulation of a knee joint replacement during a gait cycle using explicit finite element analysis (2002) J Biomechanics 35:267-275
5. Halloran JP, Anthony JP, Rullkoetter PJ (2005) Explicit finite element modeling of total knee replacement mechanics. J Biomechanics 38:323-331.
6. Kanekasu K (2004) Scorpio Superflex total knee arthroplasty-Design, cilinical results and kinematics. J Joint Surgery 23: 49-57
7. Kobayashi K, Kakinoki T, Tanabe Y, Sakamoto M (2003) Mechanical properties of ultra high molecular weight polyethylene under impact compression -Property change with gamma irradiation and dynamic stress-strain analysis of artificial hip joint-. J The Japanese Soc for Experimental Mech 3:225-229
8. Sathasivam S, Walker PS (1998) Computer model to predict subsurface damage in tibial inserts of total knees. J Orthopaedic Res 16: 564-571
9. Morra EA, Greenwald AS (2005) Polymer insert stress in total knee designs during high-flexion activities: a finite element study. J Bone Joint Surg Am 87:120-124

10. Todo M, Nagamine R, Kuwano R, Hagihara S, Arakawa K (2006) Development of 3D finite element model of total knee arthroplasty and computational efficiency. Japanese J Clinical Biomech 27:231-237
11. Todo M, Nagamine R, Yamaguchi S, Hagihara S, Arakawa K (2006) Effect of flexion and rotation on the stress state of UHMWPE insert in TKA. Japanese J Clinical Biomech 27:239-246
12. Todo M, Nagamine R, Yamaguchi S (2007) Stress Analysis of PS Type Knee Prostheses under Deep Flexion. J Biomech Sci Eng 2: 237-245
13. Fregly BJ, Sawyer WG, Harman MK, Banks SA (2005) Computational Wear Prediction of a Total Knee Replacement from in vivo Kinematics. J Biomech 38:305-314

Push-Pull Effect Simulation by the LBNP Device

J. Hanousek[1], P. Dosel[2], J. Petricek[1] and L. Cettl[1]

[1] Institute of Aviation Medicine/Department of Technical Development, Prague, Czech Republic
[2] Institute of Aviation Medicine/Department of Flying Safety, Prague, Czech Republic

Abstract — **LBNP (Lower body negative pressure) examination technique was initially applied in our case entirely as one of the possibilities for preliminary indirect individual estimation of the pilot's positive gravitational acceleration (+Gz) tolerance. At present LBNP exposition is also used as a method of drill in anti-g maneuvers and for the simulation of the so-called Push-Pull effect. Pilot's +Gz tolerance can be affected by in particular the Push-Pull phenomenon. It is characterized by the rapid and significant decrease of blood pressure values accompanied by a slower return to normality as a result of compensation reaction. The tolerance decrease to the +Gz acceleration turns up during flights in aircraft in situation of +Gz action after previous impact of the negative acceleration. Just the slower return of blood pressure to the standard value after its previous rapid decrease is very dangerous reality during flights. At this period pilot's performance is reduced and an impairment of the vision and G-LOC can occur.**

Keywords — **Pilot's ±Gz tolerance, LBNP examination, Push-Pull effect, blood pressure measurement, anti-g maneuvers.**

I. Introduction

Flights with alternating ±Gz acceleration in a cockpit of agile aircraft with high maneuvering capabilities invoke a cardiovascular response of the organism named a Push-Pull effect [1, 6, 8, 9]. This phenomenon is characterized by the rapid and significant decrease of blood pressure accompanied by a slower return to normality as a result of compensation reaction. Particularly the slower return of blood pressure to the standard value after its previous rapid decrease is a very dangerous factor during flights.

Our LBNP device was reconstructed in order not only to allow estimation of the +Gz tolerance level but also to find pilots with low tolerance to the Push-Pull effect. We developed the new LBNP examination method with the simulation of the Push-Pull effect that is an important training stage preceding pilots' centrifuge training. Blood pressure is a significant parameter reflecting the cardiovascular regulation level and it responds very sensitively to the LBNP exposure. Blood pressure changes during LBNP exposition correspond very well to in-flight Push-Pull effect [2, 3, 5, 6].

II. Materials and methods

LBNP examinations with a Push-Pull effect simulation consists of two stages following one by one. The first stage represents the Push-Pull simulation the second stage corresponds to the standard or so-called isolated LBNP exposure. Push-Pull effect is simulated by means of tilting LBNP device backwards to the −43° HDT (head down tilt) position. There is atmospheric pressure in the LBNP chamber. This first step corresponds to the plateau of microgravity. Pilots remain in this position throughout two minutes. Plus Gz load is created by the rapid LBNP exposition accompanied with a rapid return of the LBNP device to the vertical position. Negative pressure level has the value of −70 mmHg and this value is achieved in one second. The return of the device to the vertical position is accomplished also very rapidly, namely in two seconds. The exposition is finished at the end of the two minutes interval in case of sufficient tolerance. Otherwise, it is finished sooner, of course. The second stage is launched after a two minutes pause. The LBNP examination is accomplished again with one-step exposure to the negative pressure level of −70 mmHg with achievement of this value again in one second. Pilots are examined in the sitting position. As well as in the first stage the exposition is finished at the end of the two minutes interval in case of sufficient tolerance.

As mentioned above LBNP exposition is also used as a method of drill in anti-g maneuvers. A proper practical exercise of anti-g maneuvers is initiated before the end of exposure or upon an indication of cardiovascular system regulation insufficiency. This new LBNP examination method with the simulation of the Push-Pull effect is an important training stage before the demanding centrifuge training.

Blood pressure ranks among the essential physiological data measured during LBNP examinations. Blood pressure which stands for a significant parameter reflecting the cardiovascular regulation level in the orthostatic load responds very sensitively to the LBNP load. Physiological responses of the organism during LBNP examinations are rapid, and therefore measuring continuous finger blood pressure by means of a Portapres device proved to be advantageous [1, 2, 3, 5, 6, 7].

Chwee Teck Lim, James C.H. Goh (Eds.): ICBME 2008, Proceedings 23, pp. 1564–1568, 2009
www.springerlink.com

Since the finger blood pressure measured by the Portapres device is not always quite close to arterial pressures measured more upstream [4, 7], for example in the radial or brachial artery or in the aorta, we focus on the evaluation of blood pressure relative changes (related to the values before the exposure beginning).

In past we compared pilot's physiological responses to the LBNP, flight and centrifuge load. Physiological responses from the blood pressure and heart rate point of view are in an LBNP examination similar to the +3.5Gz in a human centrifuge and mostly correspond to the gravitational acceleration +4.5Gz during flights in aircraft [1, 2, 3]. At present we compared blood pressure responses of the isolated LBNP load to that of Push-Pull load.

III. Results

Blood pressure changes determine significant information about possible pilot's collapse state. The rapid blood pressure decrease comes into being very shortly after the LBNP exposure at the substandard result group. The rapid decrease of the systolic value is followed by pulse pressure decrease at the same time, too (Fig. 1).

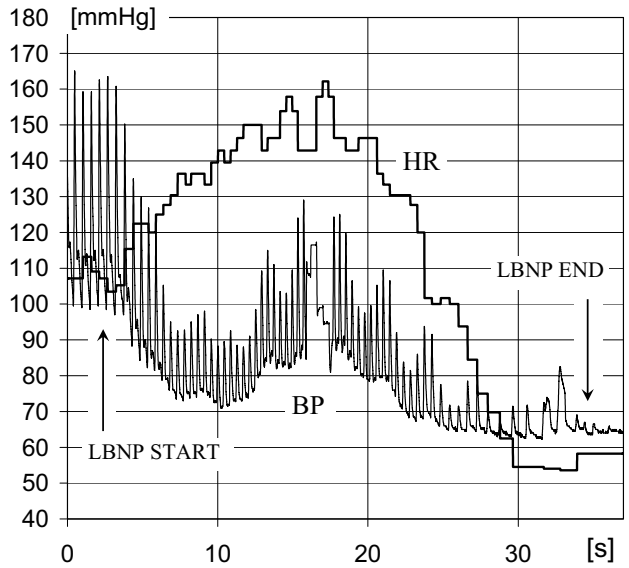


Fig. 1 Blood pressure (BP) and Heart rate (HR) behavior during an LBNP load with a substandard result.

This demonstration is also an occurrence of the bad combination, when systolic blood pressure value and pulse pressure decrease are followed by rapid heart rate drop.

Confirmation of different physiological responses under condition of the isolated LBNP load and Push-Pull load was the essential goal of the statistical evaluation. For this purpose the following blood pressure values (BP) were evaluated at the Czech Air Force pilots during both types of examinations and compared at initial 50 seconds intervals in both examinations:

- BPS0: systolic BP quiescent value just before an LBNP exposure beginning,
- BPD0: diastolic BP quiescent value,
- BPs: minimal attained systolic BP value at the 50s interval,
- BPd: minimal attained diastolic BP value,
- BPSM: maximal attained systolic BP value.

The following parameters (relative changes) were calculated:

- BPS0/BPs, BPS0/BPd, BPSM/BPS0.

The pairs of above listed data were compared for each pilot. All calculated values should be greater in the set with Push-Pull effect. The statistical test was designed to objectively prove that this claim stands good. A method for two independent stochastic selections was chosen, namely the Wilcoxon – White test that confirmed statistical significance on the level $p < 0.01$.

It must be emphasized that all examinations without exception showed a substantially greater blood pressure decrease (BPs and BPd) with its slower recovery to primary values in the phase of Push-Pull simulation in comparison with the isolated exposure. Relative maximal systolic blood pressure values (BPSM) exceeded in the phase of Push-Pull simulation these values achieved in the isolated exposure of all examinations with the good result (sufficient tolerance).

The above suggests that LBNP exposition is also used as a method of training of anti-g maneuvers both strain and breathing anti-g maneuvers. The typical example of the blood pressure changes in an instant of beginning of anti-g maneuvers is in Fig. 2. Such blood pressure improvement means that anti-g maneuvers were mastered well.

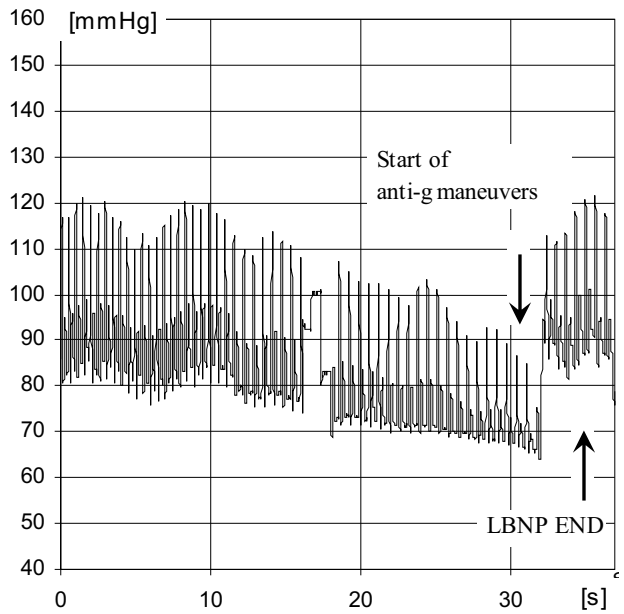


Fig. 2 Blood pressure behavior during an LBNP load with a standard result and with an exercise of anti-g maneuvers.

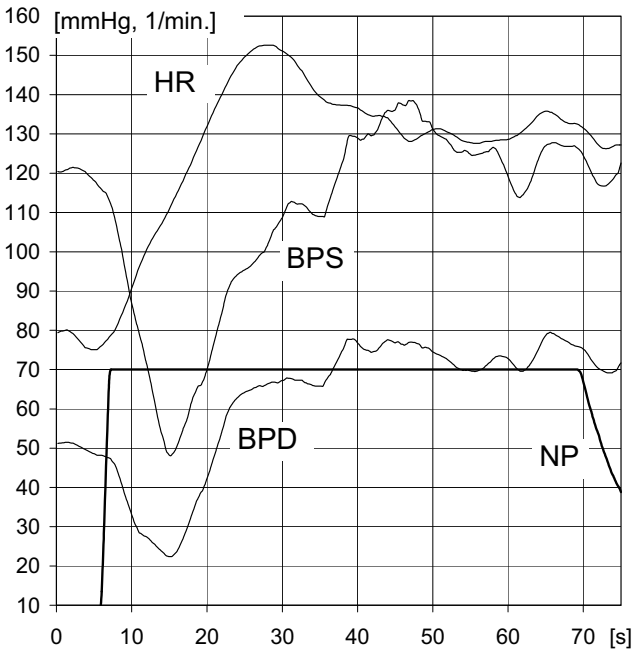


Fig. 3 Typical course of blood pressure (BP) and heart rate (HR) during LBNP exposure with Push-Pull simulation, where: BPS - systolic blood pressure, BPD - diastolic blood pressure, HR - heart rate, NP - negative pressure in the LBNP chamber.

IV. Discusion

An occurrence of sporadic extrasystoles in some cases is a typical manifestation of the cardiovascular system. The occurrence of sporadic extrasystoles can be seen in the pre-collapse state beginning but particularly after LBNP load ending (in an instant of blood volume regressive redistribution - rebound phenomenon). Arrhythmia haemodynamic consequence is immediately seen in continuous blood pressure signal.

A typical course of blood pressure and heart rate at pilots with sufficient cardiovascular regulation during LBNP exposure with the Push-Pull simulation we can see in Fig. 3.

The initial two-minute simulation of the -Gz load in the −43° HDT (head down tilt) position and viscera's shift evoke the enhancement of the parasympathetic nervous system. The rapid changeover to the vertical position and contemporaneous LBNP effect are vigorous orthostatic stimuli. However, reflective orthostatic compensatory mechanisms are weakened and decelerated in the situation of the increased vagotonia. At the same time their effect is significantly reduced. This contributes during first ten seconds of the +Gz simulation to the progressive blood pressure decrease. Heart rate rises up as the compensatory response. Then the blood pressure increase is relatively slow and the achievement of the initial value is only after other more then 20 seconds.

It results from Fig. 3 that +Gz tolerance of the examined subject was critically decreased at the beginning of this simulated +Gz load. It must be emphasized once again that the pilot's performance is considerably reduced during flights in the event of the Push-Pull effect occurrence.

A typical course of blood pressure and heart rate during the standard (isolated) LBNP exposure at the identical individual with sufficient cardiovascular regulation can be seen in Fig. 4 where again all parameters are the same as in Fig. 3. Slower decrease in blood pressure is characteristic of pilots with sufficient tolerance to the orthostatic load. Short-time systolic blood pressure rapid decrease can sometimes occur but it has only short duration.

It is evident in contrast to the previous figure that blood pressure decrease is indeed equally steep at the beginning of the LBNP load but this blood pressure decrease has shorter time duration. The return of blood pressure to initial values is faster than in case of Push-Pull effect. For reasons given the pilot's +Gz tolerance was in no way reduced.

Rapid blood pressure decrease immediately after an LBNP beginning is typical just in case of the insufficient orthostatic tolerance. The worst situation will arise when blood pressure decrease is followed by rapid heart rate drop (Fig. 1). Unless the LBNP exposure is finished the collapse state takes place immediately or very soon.

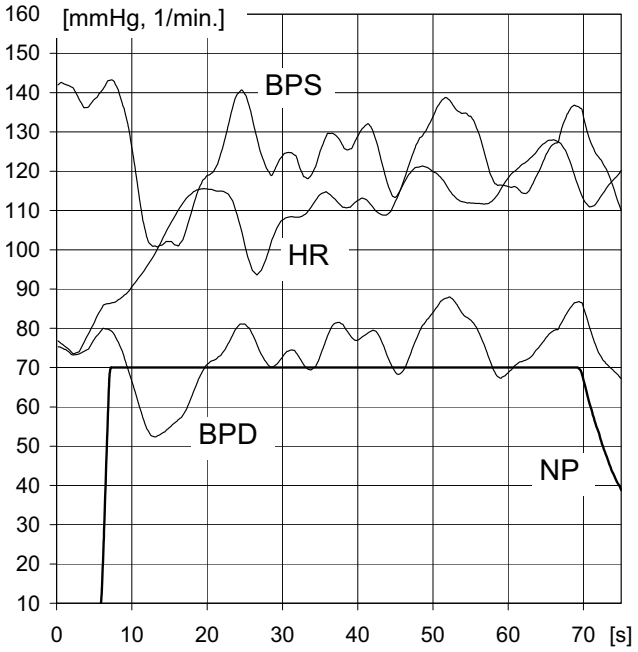


Fig. 4 Typical course of blood pressure and heart rate during standard LBNP exposure.

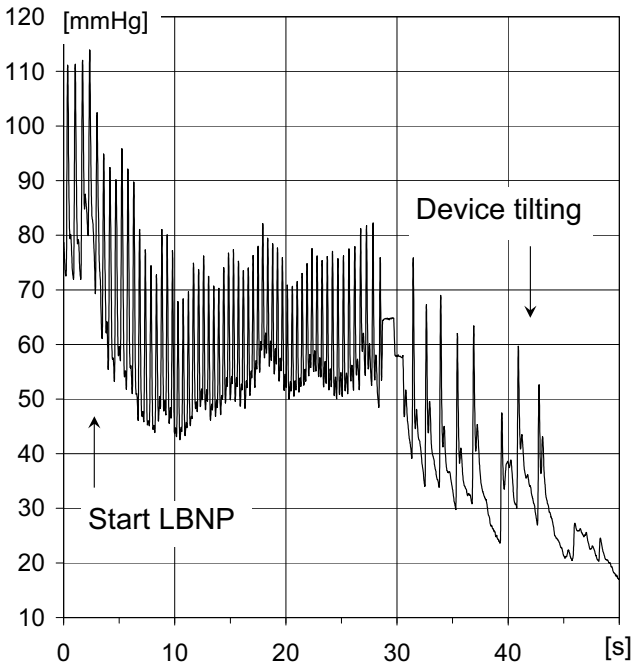


Fig. 5 Blood pressure course in the pre-collapse situation in Push-Pull load.

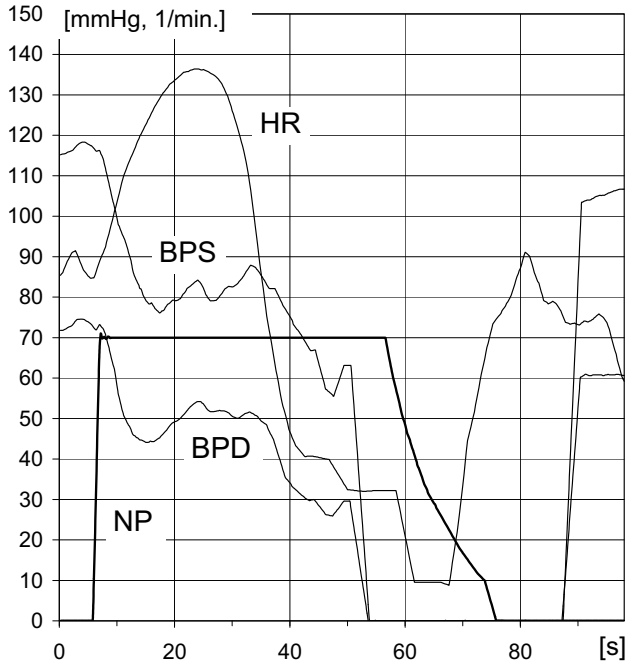


Fig. 6 Blood pressure and heart rate course in the situation of Push-Pull effect and in the event of insufficient tolerance.

Insufficient tolerance to the Push-Pull load brings often on the rapid onset of the collapse state (Fig. 5). The abrupt blood pressure decrease begins immediately after the negative pressure initiation. While heart rate soars during the first 15-20 seconds then in after 15-20 seconds it dramatically falls. The progress of the collapse state accompanied with blood pressure decrease to immeasurable values can arise in short time of the load. The situation in Fig. 6 was joined to the short-lasting (approx 10 seconds) asystolia and consequential bradycardia within the heart rate range of 25/min. to 10/min. The LBNP exposure was finished in 5 seconds from the beginning of the collapse state and the examined person was tilted backwards to the horizontal position. Heart rate soars again during leveling of the atmospheric pressure in the LBNP hypobaric chamber. As well primary value of blood pressure regenerates relatively quickly after the LBNP load ending.

V. Conclusions

The new developed LBNP examination method demonstrates better the impact of the Push-Pull effect on circulatory system efficiency. Negative influence of −Gz acceleration on +Gz tolerance during new examination method is evidently evincible.

Results of all examinations of the group of Czech Air Force pilots prove the statistically more significant decrease of blood pressure values in the phase of +Gz load. Subsequent recovery of cardiovascular parameters (blood pressure and heart rate) in the compensatory stage is delayed, too and it endangers pilots of black-out (G-LOC).

An LBNP exposition is also utilized as a method of drill in so-called anti-g maneuvers. A proper practical exercise of anti-g maneuvers in an LBNP load is initiated before the end of exposure or upon an indication of cardiovascular system regulation insufficiency. At this moment an LBNP exposure is finalized. An instantaneous blood pressure improvement is an indication of the successful mastery of this exercise. Well-timed and correct usage of anti-g maneuvers towards an overloading in highly agile and powerful aircraft is a fundamental assumption of the full exploitation of aircraft whole potentiality.

References

1. Dosel P, Hanousek J et al (1998) Physiological response of pilots to the LBNP, flight and centrifuge load. Journal of Gravitational Physiology 5, 1: 41-42
2. Dosel P, Hanousek J et al (2003) Comparison of heart rate response to plus and minus Gz load changes at safe and low altitude level during real flight. Journal of Gravitational Physiology 10, 1: 95-96
3. Dosel P, Hanousek J et al (2004) Testing method of plus and minus Gz tolerance at Czech Air Force pilots. Journal of Gravitational Physiology 11, 2: 239-240
4. Gizdulich P et al (1999) Intrabrachial arterial blood pressure pulse prevision. Proc. European Medical & Biological Engineering Conference EMBEC '99, Vienna, Austria, 1999, pp I/454–455
5. Hanousek J, Petricek J et al. (1999) Comparison of pilot's physiological responses to the LBNP, flight and centrifuge load. Proc. European Medical & Biological Engineering Conference EMBEC '99, Vienna, Austria, 1999, pp I/458-459
6. Hanousek J, Dosel P et al. (2002) Pilot's physiological measurement in plus and minus Gz load changes. Proc. 2nd European Medical & Biological Engineering Conference EMBEC '02, Vienna, Austria, 2002, pp II/1298-1299
7. Langewouters G J (1995) Portapres Model 2.0, User manual. Amsterdam, TNO, Academic medical centre, 1995, 68 p
8. Prior A R J et al. (1993) In-flight arterial blood pressure changes during minus Gz to plus Gz maneuvering. Aviat Space Environ Med 64: 428
9. Verghese C A et al. (1993) Lower body negative pressure system for simulation of +Gz induced physiological strain. Aviat Space Environ Med 2: 165-169

Author: Jan Hanousek
Institute: Institute of Aviation Medicine
Street: Gen. Piky 1
City: Prague
Country: Czech Republic
Email: hanousek@atlas.cz

An Investigation on the Effect of Low Intensity Pulsed Ultrasound on Mechanical Properties of Rabbit Perforated Tibia Bone

B. Yasrebi[1] and S. Khorramymehr[2]

[1] Department of Biomedical Engineering, Islamic Azad University-Tabriz Branch, Tabriz, Iran
[2] Department of Biomedical Engineering, Islamic Azad University- Science & Research Branch, Tehran, Iran

Abstract — **Wide variety of studies in vivo experiments on animals have been shown that the most effective type of ultrasound waves to accelerate fracture healing in osteotomy procedure is LIPUS. In this study the authors investigate the effect of LIPUS on mechanical properties of healed perforated bone. Twenty-four white male New Zealand rabbits that have drilled the right tibia bone of them were used. The rabbits were divided in two groups: treatment and non treatment. The non treatment group was considered as control. The treatment group was exposed to LIPUS (30mW/cm2 spatial and temporal average, for 20 minutes/day). All of rabbits were divided into three parts according to timing (two, four and six weeks post drilling). Animals were killed in other weeks and mechanical properties (ultimate load and stiffness of bending) were measured. Results revealed ultimate load and stiffness were difference (P<0.05) on the treatment group in comparison to non treatment group after four weeks. The studies suggest that LIPUS stimulation could increase the new bone formation and mechanical properties. We concluded that LIPUS is most effective four weeks post drilling.**

Keywords — **Mid-shaft of Tibia, Repair Time, Density, Mechanical Characteristics and Rabbit**

I. Introduction

In this study we investigated the effect of Pulsed Low Intensity Ultrasound (PLIUS) on the heal rate of osteoperforated bones. After removal of a fixator, which is commonly used to immobilize long bone fractures, holes in the bone remained from removal of fixator pins or screws reduce the cross sectional area and consequently the mechanical strength of the bone. This may cause a new fracture at the hole site. A non-invasive method to enhance heal rate of perforated bones may reduce the time needed for recovery of the bone after removal of fixator pins and screws.

PLIUS has potentially important effects on the functional activities of connective tissue cells in vitro [1],[2]. The results of in vitro studies suggest that PLIUS lead to an increase in cytocolic Ca^{2+} and activation of calmodulin [3], and enhances the process of endochondral ossification where the soft callus is converted to mineralized hard callus [4].

A large body of evidence confirms the stimulatory effect of PLIUS on fresh fractures, nonunions, and other osseous defects such as osteotomies. It has been shown that PLIUS is highly efficacious in callus formation during rapid distraction osteogenesis [5], enhancement of osteogenesis at the healing bone-tendon junction [6], treatment of nonunion fractures [7], healing of complex tibial fractures in human [8], and distraction osteogenesis in case of delayed callotasis [9]. The effect of ultrasound on healing of osteotomies, as in vivo models of bone fracture, has also been emphasized [10],[11].

Thus far, the effect of ultrasound on healing of drilled osteoperforation is not clear. Repair at bone gaps is very sensitive to the gap size and shape, and wedge surface conditions [12],[13]. Size, shape and especially surface conditions of a hole drilled to a bone differ from that of gaps caused by natural fractures or osteotomies [14],[15],[16]. Therefore, the results of the effect of ultrasound in cases reported in the literature may not be directly applicable to osteoperforation healing. The present investigation is to clarify this effect.

II. Materials and Methods

Twenty-four mature New Zealand white rabbits weighting 2.0 ± 0.2 Kg were used. A two millimeter through medio-lateral hole was drilled at the midshaft of the right tibia of animals, using a standard dental drill (Minicraft, UK) at 30000 rev/min. Operated animals were randomly divided into PLIUS treatment group and placebo control group, and were euthanized at week 2, 4 and 6 postoperatively (n= 4, for each group and time point). During drilling, animals were anaesthetized using muscular injection of a mixture of Ketamin Hydrochloride 50 mg/ml and Xylazine 2% with a proportion of 1 to 5. They were given muscular injection of Prophylaxis Penicillin 800,000 U right after the surgery, and every 24 hours for two days.

Exogen™ 3000 (Smith & Nephew, USA), a standard ultrasound stimulator, was used to stimulate the osteoperforated site in PLIUS group (Gold and Wasserman 2005; Warden 2000). Ultrasound specifications were set to the intensity of 30 mW/cm^2, frequency of 1.5 MHz, and pulse

Chwee Teck Lim, James C.H. Goh (Eds.): ICBME 2008, Proceedings 23, pp. 1569–1571, 2009
www.springerlink.com

duration of 200 μsec, and were applied 20 minutes per day, 5 times per week [5],[9],[18]. Ultrasound treatment started one week postoperative and continued to the euthanizing day. Similar procedure was repeated for the placebo control group with the ultrasound apparatus at off position. All animals were kept at the same environment.

Every two weeks from the day of operation, 4 of the animals in each group were sacrificed and their right and left tibias were harvested. Samples were kept in normal saline solution. A standard three point bending tester (Zwick, Germany) was used to measure maximum force to break (in Newton) and maximum deflection (in millimeter) of each harvested tibia as measures of mechanical strength of bones. The measures in each operated tibia were normalized to the same measures in the contralateral tibia to reduce the variability effect. The two fixed stands in the bending tester were 8 centimeters apart, and the cross head applied the force right at the anterior side of the perforated site.

The method used was in compliance with the protocol established by the Care and Animal Use Committee of Iran University of Medical Sciences.

Mean value and standard deviation of mechanical measures were computed in each group. Kruskal-Wallis nonparametric test was performed to compare the means of the outcome measures in control and treatment groups. Mann-Whitney nonparametric test was used to compare the means of the measures between the control and treatment groups at each time point (SPSS, Ver. 13).

III. Results

Mean of normalized ultimate load and normalized stiffness increased as time point increased in the placebo control group and the PLIUS treatment group. Mean of normalized ultimate load and normalized stiffness were significantly higher in the treatment group than that in the control group at 4 and 6 week time points ($P<0.05$), but was not different at 2 week ($P>0.05$) (Table1 and Table2).

Table1: Average of Ultimate Load and Standard Deviation

Time / Group	Two Weeks after Surgery	Four Weeks after Surgery	Six Weeks after Surgery
Non Treated	0.76 ± 0.1	0.78 ± 0.07	0.89 ± 0.1
Treated	0.74 ± 0.16	0.91 ± 0.04	1.05 ± 0.06
P value	0.24	0.02	0.02

Table2: Average of Stiffness and Standard Deviation

Time / Group	Two Weeks after Surgery	Four Weeks after Surgery	Six Weeks after Surgery
Non Treated	0.87 ± 0.11	0.88 ± 0.09	0.98± 0.1
Treated	0.81 ± 0.14	1.01 ± 0.06	1.3 ± 0.1
P value	0.14	0.02	0.02

IV. Discussion

The positive effect of pulsed low intensity ultrasound on bone mechanical strength at osteoperforation sites was shown. This was concluded based on the results from an in vivo experimental study on rabbit tibia models, with the main outcome measures including ultimate load and stiffness in the osteoperforation sites.

The effect of ultrasound on wound healing and bone repair mechanisms has long been under investigation. Ultrasound causes a degranulation of mast cells resulting in the release of histamine. Histamine and other chemical mediators released from the mast cell are felt to play a role in attracting neutrophils and monocytes to the injured site. These and other events appear to accelerate the acute inflammatory phase and promote healing. In proliferative phase, ultrasound has been noted to affect fibroblasts and stimulate them to secrete collagen I. This can accelerate the process of wound contraction and increase tensile strength of the healing tissue.

The results of this study revealed considerable effect of PLIUS, at least following 6 weeks treatment, on bone mechanical strength in osteoperforations in rabbit tibia models. These findings are in agreement with the results from Claes et al. [18] who treated bone defects at the metatarsal bones of sheep with a segmental bone transport and then with low-intensity ultrasound using the same apparatus as ours. They showed significantly higher axial compression stiffness of callus tissue in the treatment group. Furthermore, Chan et al. [5] studied the effect of low intensity pulsed ultrasound on callus formation, and showed increased bone mineral content and volume of the mineralized tissue of distraction callus, and enhanced endochondral formation.

We, though, measured the bending stiffness of the healed bone which is very well related to the compressive stiffness.

Li et al. [3] and Unsworth et al. [4], based on the results of their in vitro studies, suggest that one of the mechanisms that low intensity pulsed ultrasound has on fracture repair is

to enhance the process of endochondral ossification where the soft callus is converted to mineralized hard callus. Our findings verify this implication due to the fact that heal rate was more quickly at the first 4 weeks of treatment, when callus mineralization is taken place.

V. Conclusions

The effect of pulsed low intensity ultrasound on the heal rate of osteoperforated bones in rabbit model was studied. It was found that PLIUS can enhance heal rates in osteoperforated bones. The heal rate is more rapidly at the first 4 weeks postoperatively. Ultrasound treatment may be used to shorten clinical treatment times after removal of pins or screws of bone fixators.

Acknowledgment

Authors would like to thank Iran University of Medical Sciences (Tehran, Iran) for providing the equipments used in radiographic measures. They are also grateful to Tarbiat Modares University (Tehran, Iran) for its disclosure to the instruments used in mechanical tests.

References

1. Harle J, Salih V, Mayia F, Knowles JC, Olsen I. (2001) Effects of ultrasound on the growth and function of bone and periodontal ligament cells in vitro. Ultrasound in Medicine & Biology 27:579-586
2. Korstjens CM, Nolte PA, Burger EH. (2004) Stimulation of bone cell differentiation by low-intensity ultrasound—a histomorphometric in vitro study. J Orthop Res 22:495-500
3. Li JKJ, Lin JCA, Liu HC, Sun JS, Ruaan RC, Shih C, Chang WHS. (2006) Comparison of ultrasound and electromagnetic field effects on osteoblast growth. Ultrasound in Medicine & Biology 32:769-775
4. Unsworth J, Kaneez S, Harris S, Ridgway J, Fenwick S, Chenery D, Harrison A. (2007) Pulsed Low Intensity Ultrasound Enhances Mineralisation in Preosteoblast Cells. Ultrasound Med Biol 33:1468-1474
5. Chan CW, Qin L, Lee KM, Cheung WH, Cheng JC, Leung KS. (2006) Dose-dependent effect of low-intensity pulsed ultrasound on callus formation during rapid distraction osteogenesis. J Orthop Res 25:227-233
6. Qin L, Lu H, Fok P, Cheung W, Zheng Y, Lee K, Leung K. (2006) Low-intensity pulsed ultrasound accelerates osteogenesis at bone-tendon healing junction. Ultrasound Med Biol 32:1905-1911
7. Gebauer D, Mayr E, Orthner E, Ryaby JP. (2005) Low-intensity pulsed ultrasound: Effects on nonunions. Ultrasound in Medicine & Biology 31:1391-1402
8. Leung KS, Lee WS, Tsui HF, Liu PPL, Cheung WH. (2004) Complex tibial fracture outcomes following treatment with low-intensity pulsed ultrasound. Ultrasound in Medicine & Biology 30:389-395
9. Esenwein SA, Dudda M, Pommer A, Hopf KF, Kutscha-Lissberg F, Muhr G. (2004) Efficiency of low-intensity pulsed ultrasound on distraction osteogenesis in case of delayed callotasis; clinical results. Zentralbl Chir 129:413-420
10. Hara Y, Nakamura T, Fukuda H. (2003) Changes of biomechanical characteristics of the bone in experimental tibial osteotomy model in the dog. J Vet Med Sci 65:103-107
11. Heybeli N, Yeşildağ A, Oyar O, Gülsoy UK, Tekinsoy MA, Mumcu EF. (2002) Diagnostic ultrasound treatment increases the bone fracture-healing rate in an internally fixed rat femoral osteotomy model. J Ultrasound Med 21:1357-1363
12. Park SH, Oconnor K, Sung R. (1999) Comparison of healing process in open osteotomy model and closed fracture model. J Orthop Trauma. 13:114-120
13. Tsumaki N, Kakiuchi M, Sasaki J. (2004) Low-intensity pulsed ultrasound accelerates maturation of callus in patients treated with opening-wedge high tibial osteotomy by hemicallotasis. J Bone Joint Surg Am 86A:2399-2405
14. Abouzgia MB, Symington JM. (1996) Effect of drill speed on bone temperature. Int J Oral Maxillofac Surg 25:394-399
15. Iyer S, Weiss C, Mehta A. (1997) Effects of drill speed on heat production and rate and quality of bone formation in dental implant osteotomies. Part 2: Relationship between drill speed and healing. Int J Prosthodont 10:536-540
16. Watanabe F, Tawada Y, Komatsu S, Hata Y. (1992) Heat distribution in bone during preparation of implant sites: heat analysis by real-time thermography. Int J Oral Maxillofac Implants 7:212-219
17. Claes L, Ruter A and Mayr E. (2005) Low-intensity ultrasound enhances maturation of callus after segmental transport. Clin Orthop Relat Res 430:189-194
18. Claes L, Willie B. (2006) The enhancement of bone regeneration by ultrasound. Prog Biophys Mol Biol. 23:115-121

The address of the corresponding author:

Author: Dr. Behzad Yasrebi
Institute: Biomedical Engineering
Street: Islamic Azad University-Tabriz branch Road
City: Tabriz
Country: Iran
Email: mebyas@yahoo.com

Influence of Cyclic Change of Distal Resistance on Flow and Deformation in Arterial Stenosis Model

J. Jie[1], S. Kobayashi[1], H. Morikawa[1], D. Tang[2], D.N. Ku[3]

[1] Shinshu University, Japan
[2] Worcester Polytechnic Institute, USA
[3] Georgia Institute of Technology, USA

Abstract — **Blood flow through the constricted area of a severe stenosis is similar to that through a venturi or flow nozzle. In the contraction section, the blood can accelerate to high speed. In this situation, the external pressure may be greater than the internal fluid pressure, and atheroscrerotic plaque is compressed. The resultant compression may be important in the development of atherosclerotic plaque fracture and subsequent thrombosis or distal embolization. To examine the relationship between the flow and the deformation of coronary stenosis, we have developed curved stenosis models made of hydrogel that closely approximate the coronary disease situation, and performed flow experiments. Pulsatile flow was produced using a gear pump. The stenosis model was bent on a rubber support with ends that are pulled by a wire to change its curvature corresponding to curvature of the epicardial surface cyclically. In this study, we have developed the device of cyclic change of distal resistance of the stenosis model in sync with pulsatile flow, and applied to the flow experiment.**

Keywords — **Atherosclerosis, Coronary disease, Stenosis, Distal resistance, Biomechanics.**

I. Introduction

An increase in blood velocity on the distal side of stenosis causes a negative transmural pressure, and atherosclerotic plaque is compressed; furthermore, the stenosis may cause the collapse of artery which leads to the rupture of the plaque [1]. We have developed experimental stenosis models made of polyvinyl alcohol hydrogel (PVA) that closely approximate an arterial disease situation, and the characteristics of flow and deformation related to the changing geometry of stenosis and the existence of a lipid core were discussed [2-4]. To examine the relationship between the flow and the deformation of coronary stenosis, we have developed curved stenosis model, and performed flow experiments. The influence of flow and deformation on initial shape of stenosis models was discussed [5]. From the various experimental approaches, one can summarize some salient features of the intramyocardial coronary circulation as follows: The systolic inflow is low, sometimes even negative in early systole. The major part of the inflow is during diastole. The venous outflow is more evenly distributed with its major part in systole. In prolonged diastole, the inflow decreases almost linearly with the decrease in perfusion pressure and reaches a zero value at a relatively high pressure [6]. However the resistance of downstream the stenosis model for the previous experiment was constant in spite of the distal resistance of coronary artery is changed cyclically. In this study, we have developed the device of cyclic change of distal resistance of the stenosis model in sync with pulsatile flow, and applied to the flow experiment.

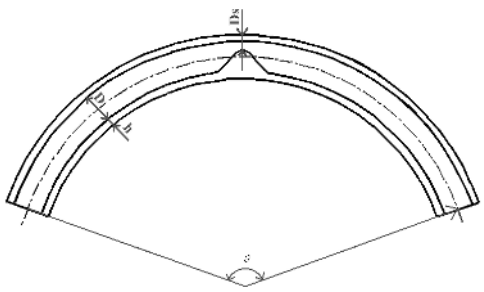
II. Methods

A. Stenosis model

During the experiment, stenosis model made of PVA hydrogel was used in a model for a diseased coronary artery. The polyvinyl alcohol hydrogel model is a more realistic stenosis model that shows thick stenosis and more compliant stiffness than the model made of silicone and latex [7]. This model is opaque, but its mechanical properties are similar to those of the coronary artery. The shape of stenosis model is similar to that of a sinusoidal curve. Figure 1 shows the shape of stenosis. The nominal stenosis severity *St* and eccentricity *Ec* of the stenosis model are given as follows:

$$St = (1 - Ds/D) \times 100\ [\%] \quad (1)$$

$$Ec = e/((D - Ds)/2) \times 100\ [\%] \quad (2)$$



($R \cdot \theta$=90mm, D=4mm, h=1mm, R=31.3mm, θ=2.9rad)

Fig. 1 Schematic representation of the curved stenosis model

Chwee Teck Lim, James C.H. Goh (Eds.): ICBME 2008, Proceedings 23, pp. 1572–1575, 2009
www.springerlink.com

B. Experimental setup

Figure 2 shows the experimental setup used. The PVA hydrogel stenosis model was fixed on rigid pipes and placed in a water tank. The water level was 14 cm from the center of the stenosis model (external pressure is approximately 10 mmHg). The upstream constant head reservoir was pressurized as the direct current component of pulsatile flow. The computer-controlled gear pump (MCP-Z, Ismatec) connected to the upstream tube served as the alternative current component of the flow. Upstream and downstream pressures were continuously measured using pressure transducers (SD 130, Toyoda Machine), which were placed at junctions between the rigid tube and the hydrogel, 50 mm upstream and downstream of stenosis. The working fluid used was water at room temperature with a kinematic viscosity ν of 0.01 cm^2/s. Flow rate was measured using an electromagnetic flowmeter (MagneW 3000FLEX, Yamatake), which was located outside the box 350 mm upstream and downstream of stenosis. Labview software (National Instruments) was used to operate, control and acquire data. The stenosis model was bent on a rubber support with ends that are pulled by a wire to change its curvature corresponding to curvature of the epicardial surface cyclically. The wire was driven by stepping motor to synchronize the phase with pulsatile flow. Figure 3 shows the cycle change of curvature. Sagittal section ultrasound images of the stenosis are made from the B-mode of a Duplex ultrasound scan. The valve and downstream constant head reservoir were set as the distal resistance of stenosis. As the device of cyclic change of distal resistance, we have used elastic PVC tube to change its cross sectional area. A rod driven by a linear motor pushes PVC tube which is the downstream side of the stenosis model. By periodical controlling the reciprocating movement of the rod, the distal resistance is changed cyclically. Figure 4 shows the reciprocating displacement of the rod. Frequency of reciprocating motion is 1 Hz. From 12 degree to 100 degree, the rod moves forward, at 100 degree, the PVC tube is mostly compressed. From 100 degree to 192 degree, the rod moves back along the same way, the PVC tube is released. The compliant rubber tube was used as the capacitance of intramyocardial coronary circulation.

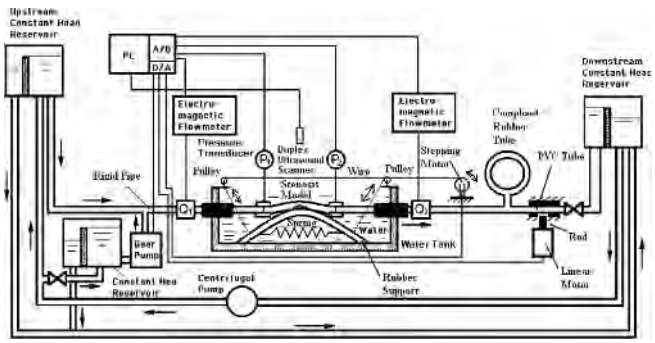


Fig.2 Experimental setup

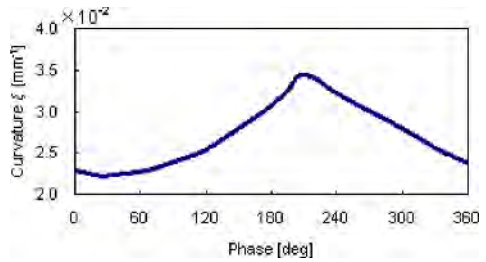


Fig. 3 Change of curvature in one cycle

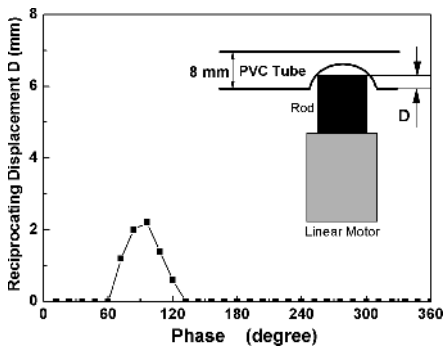


Fig. 4 Reciprocating displacement of the rod in one cycle

III. Results and Discussions

A. Change of distal resistance

We defined the distal resistance as following

$$R = P / Q \quad (3)$$

P is the downstream preassure and *Q* is the downstream flow rate. Figure 5 shows the distal resistance when rigid tube instead of the stenosis model. From 0 degree to 180 degree approximated the phase of systole, and from 180 degree to 360 degree approximated the phase of diastole. When the rod was not reciprocated, resistance was not constant, but when the rod was reciprocated, the resistance is increased in systole and reduced in diastole.

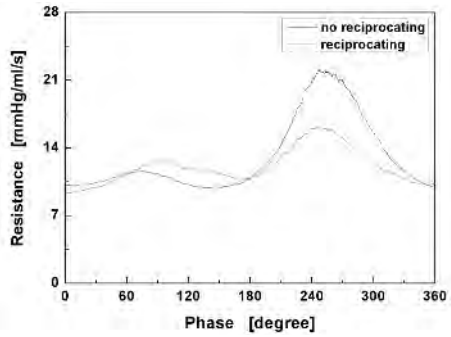


Fig. 5 Resistance in one cycle (P_{1avg} = 85 mmHg, P_{2avg} = 80mmHg)

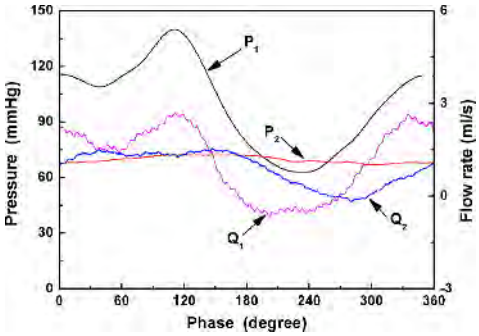
B. Flow and deformation

The following four conditions of curvature and rod reciprocating were selected for the experiment:

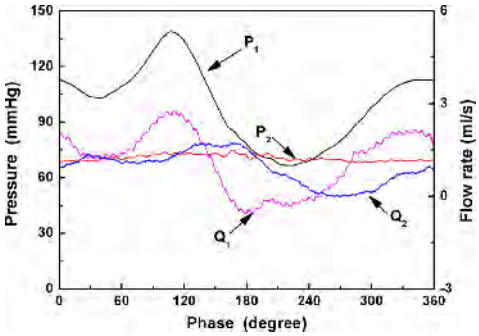
(a) Constant curvature and no rod reciprocating
(b) Cyclic change curvature and no rod reciprocating
(c) Constant curvature and rod reciprocating
(d) Cyclic change curvature and rod reciprocating

Figure 6 shows the measured upstream and downstream pressures and flow rates in one cycle for above conditions when stenosis model was used. P_1, P_2: upstream and downstream pressure, Q_1, Q_2: upstream and downstream flow rate. From Fig. 6(a) and (b), the flow is not changed obviously, some vibrations appeared in Fig. 6(b), this is caused by the wire to change the model's curvature. In Fig. 6 (c) and (d), the downstream pressure is increase from 70 degree to 100 degree, it is in accord with the phase for rod forward movement to compress the PVC tube. From 100 degree, the pressure began to decrease. This decrease process is longer than the rod backward movement, it is because a compliant rubber tube was put into the flow. This is similar to physiological coronary blood pressure. Compared Fig.6 (a) (b) with (c) (d), we observed the flow rates is increased from 180 degree to 360 degree.

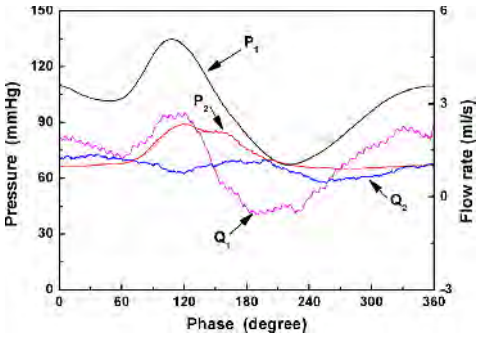
Figure 7 shows the sagittal section ultrasound images when the stenosis model is mostly expanded for above four conditions. The deformation of the stenosis was not changed obviously, because this stenosis (plaque portion) is homogeneous and stiffer than lipid rich plaque.



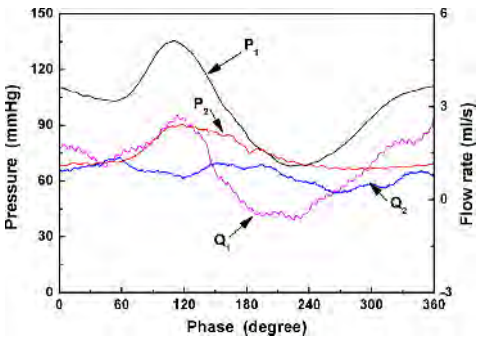
(a) Constant curvature and no rod reciprocating



(b) Cyclic change curvature and no rod reciprocating



(c) Constant curvature and rod reciprocating



(d) Cyclic change curvature and rod reciprocating

Fig. 6 Measured upstream and downstream pressures and flow rates in one cycle. (P_{1avg} = 100±40 mmHg, P_{2avg} = 70mmHg)

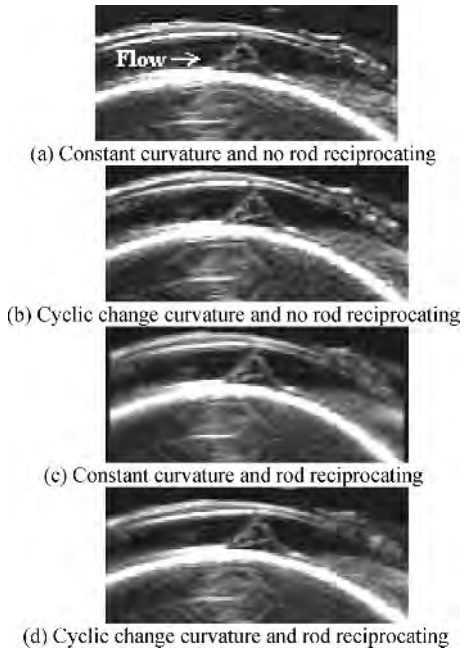


Fig. 7 Ultrasound images of sagittal section of the stenosis model

IV. Conclusion

In this study, we found that the cyclic change curvature does not effect the downstream pressure (average pressure, maximum pressure, minimum pressure) and flow rate (average flow rate, maximum flow rate, minimum flow rate) seriously. The cyclic change distal resistance is associated with an increase in maximum downstream pressure, minimum downstream flow rate and a decrease in maximum flow rate. But it can not influence the minimum downstream pressure, the average downstream pressure and average downstream flow rate. The phases of the maximum downstream pressure and the maximum flow rate were changed to be in accord with the change of distal resistance.

In the future work, more physiological experiment using more stiffer wall and soft plaque portion of the stenosis model that closer to human coronary artery, controlling more physiological coronary blood pressure (P_I), and accurate changing distal resistance and curvature will be performed.

Acknowledgment

This work was supported by Grant-in-Aid for Global COE Program by the Ministry of Education, Culture, Sports, Science, and Technology.

References

1. Aoki, T., and Ku, D. N., Collapse of Diseased Arteries with Eccentric Cross Section, Journal of Biomechanics, (1993), Vol. 26 (2), pp. 133-142.
2. Tang, D., Yang, C., Kobayashi, S., and Ku, D. N., Steady Flow and Wall Compression in Stenotic Arteries: a 3-D Thick-Wall Model with Fluid-Wall Interactions, Journal of Biomechanical Engineering, (2001), Vol. 123, pp. 548-557.
3. Tang, D., Yang, C., Kobayashi, S., Ku, D.N., Effect of a Lipid Pool on Stress/Strain Distributions in Stenotic Arteries: 3-D Fluid-Structure Interactions (FSI) Models, Journal of Biomechanical Engineering, (2004), Vol. 126, pp. 363-370.
4. Kobayashi, S., Tang, D., and Ku, D. N., Collapse in High-Grade Stenosis during Pulsatile Flow Experiments, JSME International Journal, Series C, (2004), Vol. 47, pp. 1010-1018.
5. Kobayashi, S., Ayama, Y., Morikawa, H., Tang, D., Ku, D.N., J. Biomechanics, Vol. 39, Supp1.1, p.s284, 2006.
6. R. Holenstein, R. M. Nerem, Parametric Analysis of Flow in the Intramyocardial Circulation, Annals of Biomedical Engineering, Vol. 18, pp. 347-365, 1990.
7. Binns, R. L. and Ku, D. N., Effect of Stenosis on Wall Motion. A Possible Mechanism of Stroke and Transient Ischemic Attack, Arteriosclerosis, Thrombosis, and Vascular Biology, (1989), Vol. 9, pp. 842-847.

Author: JI JIE
Institute: Faculty of Textile Science & Technology, Shinshu University
Street: 3-15-1 Tokida
City: Ueda
Country: Japan
Email: s08t102@shinshu-u.ac.jp

Kinematics analysis of a 3-DOF micromanipulator for Micro-Nano Surgery

Fatemeh Mohandesi[1], M.H. Korayem[2]

[1,2] Mechanical Engineering Department, Iran University of Science and Technology, Tehran, Iran

Abstract — **In this paper; we have analyzed a robotic system, which is used in micro-nano surgery. This robot is a parallel robotic system with 3 degree of freedom. The scale of this robot is millimeter. The special characteristic of robot is having an additional link, which connects the spherical joint to moving platform. Here kinematics analysis and Jacobean matrix are investigated. In the section II an introduction to micro-nano surgery is stated. Section III involves the kinematics analysis, and in section IV Jacobean matrixes are explained.**

Keywords — **Micro-nano surgery, Direct Kinematics analysis, indirect kinematics analysis, Parallel robot, Jacobean Matrix**

I. Introduction

Micro-nano surgery is a kind of surgery in which the operational tools are in millimeter, micro or even nanometer. These tiny tools are carried by robotic systems. This robotic system here is a parallel manipulator, which has 3 degree of freedom. This manipulator has been used for handling and precise positioning of micro object. It's function was successful. In this paper, we have done kinematics analysis and found Jacobean matrix.

II. Micro-nano surgery

Micro-Nano surgery is the medical branch of nanotechnology. It can be divided into two separate parts: 1- doing the operation by nano robots, and the second: doing the operation by making surgerical tools in micro-nano scales. In here, the micro-nano surgery belongs to second group. This surgery is done by a surgeon who guides the tools by using joy sticks and sees the operation via cameras. Because of the difficulty of handling these tiny equipments, robotic systems are used for this purpose. Most of the time the master-slave robotic systems are used. Micro-nano surgery has many advantageous:

- Because of the tiny scale of the operational tools, the lacerations are shallow and they will be recovered very soon, so the duration of hospitalization decreases and then the cost of treatment decreases too.

- The mistakes which are caused by surgeon's tiredness, hands tremor, not enough experience and vision will vanish. Because the surgeon will be laid in a comfortable place and will do the operation easily.

- The pain, stresses in patient will reduced as, in some cases there is no need to anesthetize the patient.

-This surgery is used in tele-operation mode, so there will not be many people in the surgery room, specially in disease with high infections.

However, there are some disadvantageous too:

- High cost of stall and handling robotic systems.

- Training surgeons

- A supervisor engineer must be there, in order to repair the robotic system in case of deficiencies.

- Making the operational tools in micro-nano scale, because every surgery needs its own equipment.

The most important contention in this surgery is compost of surgeon's experience with stability and exactitude of robot.

III. Kinematics analysis

The configuration of the robot is shown in the figure 1. This robot is made up of a prismatic joint which is in the base, then a revolute joint, and then a spherical joint. A special characteristic of this robot is the existence of an additional link, which connects the spherical joint to moving platform. This links make the analysis more complicated. The geometry parameters of the robot according to the fig.1 are:

r: the radius of upper plate

R: the radius of fixed plate

d_i: the length of kinematics chain

T: rotation matrix which its arrays are as below:

$\begin{bmatrix} n_1 & o_1 & a_1 \\ n_2 & o_2 & a_2 \\ n_3 & o_3 & a_3 \end{bmatrix}$, this matrix shows the direction of moving plate.

X-y-z Euler angles of α, β, γ .

Vector p $\begin{vmatrix} p_x \\ p_y \\ p_z \end{vmatrix}$ which connects the centroid of upper plate to the centroid of fixed one. This vector indicates the location of moving plate.

Chwee Teck Lim, James C.H. Goh (Eds.): ICBME 2008, Proceedings 23, pp. 1576–1579, 2009
www.springerlink.com

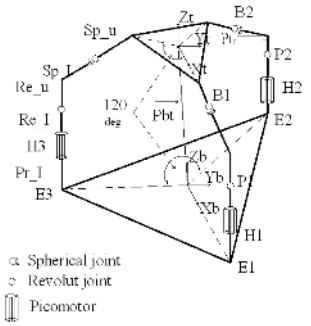


Fig.1 configuration of 3-PRS robot[2]

In direct kinematics analysis, the lengths of kinematics chains are known, and the purpose is finding position and orientation of moving platform. For this analysis, there are three groups of equations.

First group: equations which show the orthogonality of the matrix T. For this group we have 6 equations. These equations will be found in [1].

Second group: The revolute joint in all kinematic chains, imposes a constraint in moving. The second group equations are the constraints equations. Here 3 equations are got as:

$$P_y = -n_2 b_x + a_2 b_z \tag{1}$$

$$n_2 = O_1 \tag{2}$$

$$P_x = \frac{-1}{2}\left(O_2 b_x - n_1 b_x - 2a_1 b_z\right) \tag{3}$$

In which: b_x and b_z are the coordinates of spherical joints and are:

$$\begin{aligned} b_x &= r + sp_u\cos\theta_{tr} \\ b_z &= SP_U\sin\theta_{tr} \end{aligned} \tag{4}$$

Third group: These equations are related to the lengths of kinematic chains. The lengths of kinematic chains are found geometrically as:

$$\begin{aligned} d_1^{\,2} &= (p_x + n_1 b_x - a_1 b_z - R)^2 + (p_y + n_2 b_x - a_2 b_z)^2 \\ &+ (p_z + n_3 b_x - a_3 b_z)^2 \\ d_2^{\,2} &= (p_x - \frac{1}{2}n_1 b_x + \frac{\sqrt{3}}{2}o_1 b_x - a_1 b_z + \frac{1}{2}R)^2 + \\ &(p_y - \frac{1}{2}n_2 b_x + \frac{\sqrt{3}}{2}o_2 b_x - a_2 b_z - \frac{\sqrt{3}}{2}R)^2 + \\ &(p_z - \frac{1}{2}n_3 b_x + \frac{\sqrt{3}}{2}o_3 b_z - a_3 b_z)^2 \\ d_3^{\,2} &= (p_x - \frac{1}{2}n_1 b_x - \frac{\sqrt{3}}{2}o_1 b_x - a_1 b_z + \frac{1}{2}R)^2 + \\ &(p_y - \frac{1}{2}n_2 b_x - \frac{\sqrt{3}}{2}o_2 b_x - a_2 b_z + \frac{\sqrt{3}}{2}R)^2 + \\ &(p_z - \frac{1}{2}n_3 b_x - \frac{\sqrt{3}}{2}o_3 b_x - a_3 b_z)^2 \end{aligned} \tag{5}$$

For direct kinematics analysis, these 12 equations and 12 unknowns must be solved. But because of the nonlinearity of the equations, this is impossible and complicated. For this purpose we consider 2 Euler angels as knowns and find other parameters according to them. The table blow shows the result:

In all examples above, we considered the constant parameters as below:

$$\begin{aligned} &R = 40mm \\ &\theta = 5\,\text{deg}\,ree \\ &SP_u = 5mm \\ &r = 8mm \\ &d = 100mm \end{aligned} \qquad \begin{aligned} b_x &= 12.981mm \\ b_z &= 0.43577mm \end{aligned}$$

Tabel1-result of direct kinematics

α	β	T	P_x	P_y	P_z	γ
-3 degree	-3 degree	$\begin{bmatrix} -0/98992 & -0/00135768 & -0/14112 \\ 0/212725 & -0/989964 & -0/139708 \\ -0/139514 & -0/141311 & 0/980085 \end{bmatrix}$	-5.58025 mm	-78.9589, 83.4352 mm	-78.9589, 83.4352 mm	-0.0013741 degree
0 degree	0 degree	$\begin{bmatrix} 1 & 0 & 0 \\ 0 & 1 & 0 \\ 0 & 0 & 1 \end{bmatrix}$	0 mm	9945.45, -9944.58 mm	9945.45, -9944.58 mm	0 degree
-3 degree	3 degree	$\begin{bmatrix} -0.989989 & 0.00271908 & -0.14112 \\ 0.0171957 & -0.990043 & -0.139708 \\ -0.140095 & -0.140736 & 0.980085 \end{bmatrix}$	-5.58023 mm	-78.9514, 83.4428 mm	-78.9514, 83.4428 mm	0.00274657 degree

The indirect kinematics analysis is much simpler than the direct one. In here the position and orientation of moving platform is known and the kinematic chains' length must be found. This can be easily done by equations (5). All analyses are done by "MATHEMATICA "software.

IV. JACOBEAN MATRIX

By Jacobean matrix the relations of velocities of moving platform and the joints or kinematic chains can be expressed. For this robot system, the input velocity is $\dot{q}$, which equals to $\dot{q} = [\dot{d}_1, \dot{d}_2, \dot{d}_3]$. The output velocity can be stated according to the velocity of the centroid of moving platform. A linear and an angular are considered as below" $\dot{x} = \begin{bmatrix} v_P \\ w_p \end{bmatrix}$. The Jacobean matrix is found from fig.2. An equation can be written based on vectors law:

$$\overline{OP} + \overline{Pb_i} = \overline{OE} + \overline{Eb_i} \tag{6}$$

By differentiating with respect to time form equation (6), the velocity is obtained:

$$V_P + w_P \times b_i = d_i w_i \times s_i + \dot{d}_i s_i \tag{7}$$

In the equation (7) b_i indicates the vector PB_i , s_i a unit vector in the direction of kinematic chains, w_i the angular velocity of i^{th} kinematic chain. The w_i is produced by the revolute joint, which is a passive joint and imposes constraint. So this velocity must be omitted form the equation. For this purpose, we do dot product the equation (7) by s_i. Then the equation becomes:

$$s_i.v_P + (b_i \times s_i).w_p = \dot{d}_i \tag{8}$$

By writing the equation (8) three times, for all kinematic chains, the Jacobean matrix can be extracted:

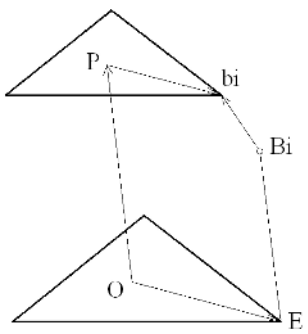


Fig.2 relation according to vectors law

$$\begin{aligned} &\text{i=1} \quad s_1.v_p + (b_1 \times s_1).w_p = \dot{d}_1 \\ &\text{i=2} \quad s_2.v_p + (b_2 \times s_2).w_p = \dot{d}_2 \\ &\text{i=3} \quad s_3.v_p + (b_3 \times s_3).w_p = \dot{d}_3 \end{aligned} \tag{9}$$

then the Jacobean matrixes will be :

$$J_x = \begin{bmatrix} S_1^T & (b_1 \times s_1)^T \\ S_2^T & (b_2 \times s_2)^T \\ S_3^T & (b_3 \times s_3)^T \end{bmatrix}_{3\times 6} \tag{10}$$

$$J_q = \begin{bmatrix} 1 & 0 & 0 \\ 0 & 1 & 0 \\ 0 & 0 & 1 \end{bmatrix}_{3\times 3} \tag{11}$$

In which Jacobean matrix J_x is called the direct kinematics Jacobean, and the J_q is called the inverse kinematics Jacobean matrix. If the robot is not in the singular configuration, the total Jacobean matrix will be as :

$$J = J_q^{-1} J_x \tag{12}$$

And the relation between the velocities is :

$$\dot{q} = J\dot{x} \tag{13}$$

The Jacobean matrix can be used in static, stiffness analysis. It is also used for finding the singularity points for a robot.

V. CONCLUSIONS

In the Inverse Displacement Solution (IDS), the position of actuators, according to the movement of platform is found. In the Forward Displacement Solution (FDS), position and orientation of the moving platform is determined, while the position of actuators is known. FDS analysis is very complicated and it is used in calibration, it is not used in control problems of robot. In the kinematics analysis these results are gained:

1- p_z is the only independent parameter among the six parameter [p_x p_y p_z α β γ]. This parameter did not appear in the constraint equations, which means it can be chosen separately from five other parameters, and also choosing these five parameters is completely independent from p_z.

2- Although this mechanism has 3 degree of freedom, but we can't assume all three angle Euler as given data. Just two from three angles must be known. Also for controlling the

mechanism, three parameters must be chosen, that one of them must be p_z. The two other parameters must be chosen from five remained parameters.

3- For each couple (p_x , p_y), two couples of Euler angles are existed, (α , β) and (- α, - β).For each given angle γ, the same couples are also existed. In the other hand:

$$\gamma=f_1(\beta,\alpha)=f_1(-\beta,-\alpha)$$

$$P_x=f_2(\beta,\alpha)=f_2(-\beta,-\alpha)$$

$$p_y=f_3(\beta,\alpha)=f_3(-\beta,-\alpha)$$

It means that in every point in robot workspace, a couple of Euler angles prevail that has the same γ. Two other angels are both positive and negative.

REFERENCES

1. Tsai, Lung-wen “Robot Analysis: the Mechanics of Serial and Parallel Manipulators”, NewYork 1999.
2. Goo Bong Chung, Byung-Ju Yi, Il Hong Suh, Whee Kuk Kim, Wan Kyun Chung "Design and Analysis of a Spatial3-DOF Micromanipulator for Tele-operation" Proceedings of the 2001 IEEE/RSJ International Conference on Intelligent Robots and Systems Maui, Hawaii, USA, Oct. 29 - Nov. 03, 2001
3. Guilin Yangt, Ming Chen, Wee Kiat Lim, Song Huat Yeo, "Design and Kinematic Analysis of Modular Reconfigurable Parallel Robots" Proceedings of the 1999 IEEE International Conference on Robotics & Automation Detroit, Michigao May 1999.
4. Juan A. Carretero, Meyer A. Nahon, Ron P. Podhorodeski "Kinematics of a New High-Precision Three- Degree-of-Freedom Parallel Manipulator" Journal of Mechanical Design March 2008, Vol.130.
5. Robert L. Williams, Atul R. Joshi "Planar Parallel 3-RPR Manipulator" Proceedings of the Sixth Conference on Applied Mechanisms and Robotics December 12-15, 1999.
6. Damien Chablat, Phlippe Wenger, Ilian A. Bonev "Self Motions of a Spetial 3-RPR Planar Parallel Robot" Proceeding of 2006 IEEE International Conference on Robotics and Automation .
7. Xin-Jun Liu, Jinsong Wang, Jongwon Kim "Determination of the Link Lengths for a Spatial 3-DOF Parallel Manipulator “Journal of Mechanical Design March 2006, Vol.128.
8. Qingsong Xu, Yangmin Li "A Novel Design of a 3-PRC Translational Compliant Parallel Micromanipulator for Nanomanipulation" Robotica, 2006, Vol. 00.
9. Qingsong Xu, Yangmin Li "Kinematic Analysis and Optimization of a New Compliant Parallel Micromanipulator” International Journal of Advanced Robotic Systems, Vol. 3, No. 4, 2006.

Author: Fatemeh Mohandesi, M.H.Korayem
Institute: Iran Science and Technology
Street: Narmak, eastern Farjam
City: Tehran
Country: Iran
Email: fatemeh_mohandesi@yahoo.com

Stress and Reliability Analyses of the Hip Joint Endoprosthesis Ceramic Head with Macro and Micro Shape Deviations

V. Fuis[1], P. Janicek[2] and L. Houfek[1]

[1] Centre of Mechatronics – Institute of Thermomechanics Academy of Sciences of the Czech Republic and Institute of Solid Mechanics, Mechatronics and Biomechanics, Faculty of Mechanical Engineering, Brno University of Technology, Brno, Czech Republic
[2] Institute of Solid Mechanics, Mechatronics and Biomechanics, Faculty of Mechanical Engineering, Brno University of Technology, Brno, Czech Republic

Abstract — **The principal aim of this work is finding the reasons of the head's fractures because in the Czech Republic, some time ago, in vivo fracture of ceramic heads of total hip joint endoprostheses has been stated in a not negligible number of patients. The reliability of the ceramic head is based on the Weibull weakest link theory. The probability of the failure depends on the tensile stress values in the head, on the volume in which stress acts and on the material parameters of the used bioceramics (aluminium oxide). The stress analyses of the ceramic heads were realized using computational modelling - FEM system ANSYS under ISO 7206-5 loading. The maximum values of the tensile stress (the first principal stress) in the ceramic head are significantly influenced on the shape deviations of conical surfaces of the head and the stem cones. There are two types of the shape deviations – the first is macro deviations (different angle of the taper of the stem cone and the head cone), the second is micro shape deviations (the stochastic distribution of unevenness of cone contact surfaces). The macro and micro shape deviations of the cones were carried out using the IMS-UMPIRE measuring equipment.**

By computational modelling it has been proved that the character and the size of shape deviations on a conical contact area between the stem and the head of hip joint endoprosthesis have a pronounced influence on the character and the value of stress in the head and, hence, on the probability of the head's failure. Ignorance of this influence can lead to unforeseen failures of ceramic heads and thus to cast doubt on the trust-worthiness of a certain type of total hip joint endoprosthesis and of surgical treatment.

Keywords — **Total hip joint endoprosthesis, ceramics head, micro and macro shape deviations, stress, computational modelling.**

I. Introduction

One of the most frequently operated joints of the human body is the hip joint. In young patients, the operation is mostly aimed at reconstructing the joint's pathologically developed geometry. In older age, operations prevail in which the patients are provided with partial or total endoprostheses. These may be of different design solutions, with various materials being used in the endoprosthesis' individual parts. In a design solution which used ceramic heads, the destruction of the head has occurred *in vivo* – see Fig. 1. In one hospital of the Czech Republic, more than 1 % of applied endoprostheses had to be reoperated. That is why the state of stress and the reliability of ceramic heads of total endoprosthesis is being intensively analysed by means of computational modelling. Simultaneously, experimental modelling based on the strain gauges measurement is being conducted. These experiments are used to verify computational results.



Fig. 1 In vivo destructed ceramics head of the total hip joint endoprosthesis

II. Computational modelling

A. Problem situation

The failure of cohesion of ceramic heads of total hip joint prostheses has been stated in a not negligible number of patients. This applied to a structural model in which the head is connected with the metallic stem by a self-locking conical connection. The failure has taken place in particular in the endoprostheses made in the Czech Republic, however the failure of foreign-made endoprostheses has also been recorded. This problem situation required a solution in the

Chwee Teck Lim, James C.H. Goh (Eds.): ICBME 2008, Proceedings 23, pp. 1580–1583, 2009
www.springerlink.com

sense that the causes of this failure had to be established by means of a comprehensive analysis of reliability of ceramic heads of total hip joints endoprostheses.

The analysis of the head fracture surface orientation showed that the meridionally oriented fracture surfaces prevail – Fig. 1. Since ceramics is a material characterised by the limit state of brittle strength, the cohesion failure starting in directions perpendicular to the direction of the maximum principal tensile stress, then the stress responsible for the failure of head cohesion should be the hoop stress.

An effective method of solving the problem of reliability is computational modelling combined with experiment. For solving the strain/stress states in the head, the finite elements method was used, namely the ANSYS 11 program system.

B. Input parameters

The topology of the elements of the total hip joint endoprosthesis follows from Fig. 2 with the basic macro-dimensions of elements. Computational modelling of the strain/stress states in the head was implemented on a system whose elements were parts of the stem and the head.

In order to implement computational modelling of the impact of shape deviations of the cones of stems and heads of hip joint endoprostheses, which has a stochastic character, the measurement of these deviations was carried out using the IMS-UMPIRE measuring equipment. The quality of the measured contact surface of both cones can be expressed by macro-parameters (deviations) – the most important is angle of the taper of the head and the stem and straight line character), and micro-parameters (deviations) – local micro-unevenness of surface. As regards the inclination angles of the elements of ruled surfaces (degree of taper) one can say that the manufacturing documentation permits only an alternative in which the vertex angle of the head (angle α_h) is greater than the vertex angle of the stem (angle α_s) – Fig. 2 (the value of the angle α can be found from zero to 10'), and the circularity of the individual sections (perpendicular to the y-axis) is less than 10 μm. The measured micro shape deviations from the ideal conical shape for one cone of head are illustrated by the developed cones in Fig. 3. The micro shape deviations of the 3 stems cone are show in Fig. 4. The mentioned head with macro and micro shape deviations was put and loaded on all three stem cones.

The state of stress of the ceramic head of endoprosthesis can be strongly affected by the process of endoprosthesis implantation, when the surgeon fits the head on the cone of the stem. The fitting of the head on the cone of the stem is a random process, in view of the mutual position of the head to the stem (in sense of the head's slight turning around the y-axis, defined by angle β – Fig. 5). The question is, whether the local shape deviations of the cones, in case of random completing, can produce high tensile stresses that might reduce the reliability of the head. For this reason, a series of computations will be made for each pair and for various positions of the head towards the stem.

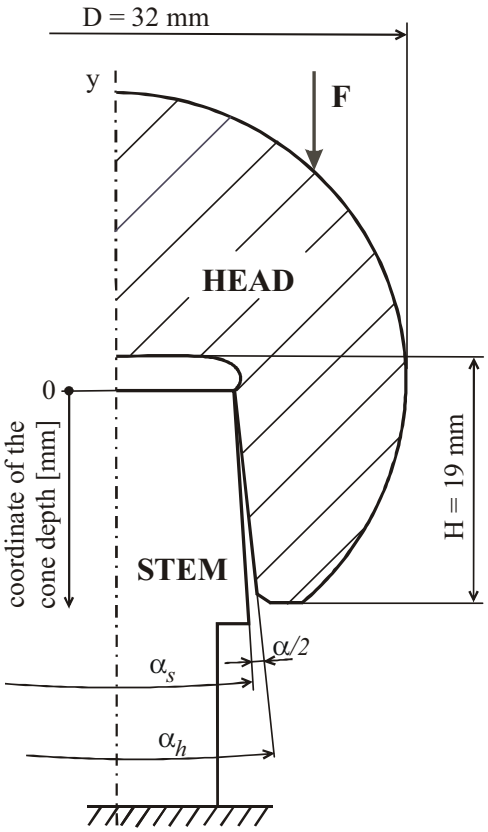


Fig. 2 Topology of the analysed system, macro shape deviation

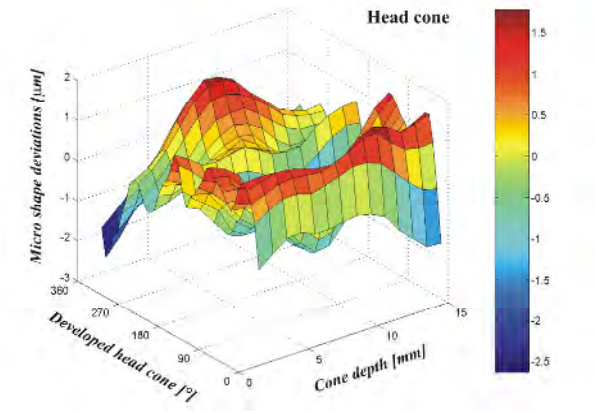


Fig. 3 Micro shape deviation of the head cone

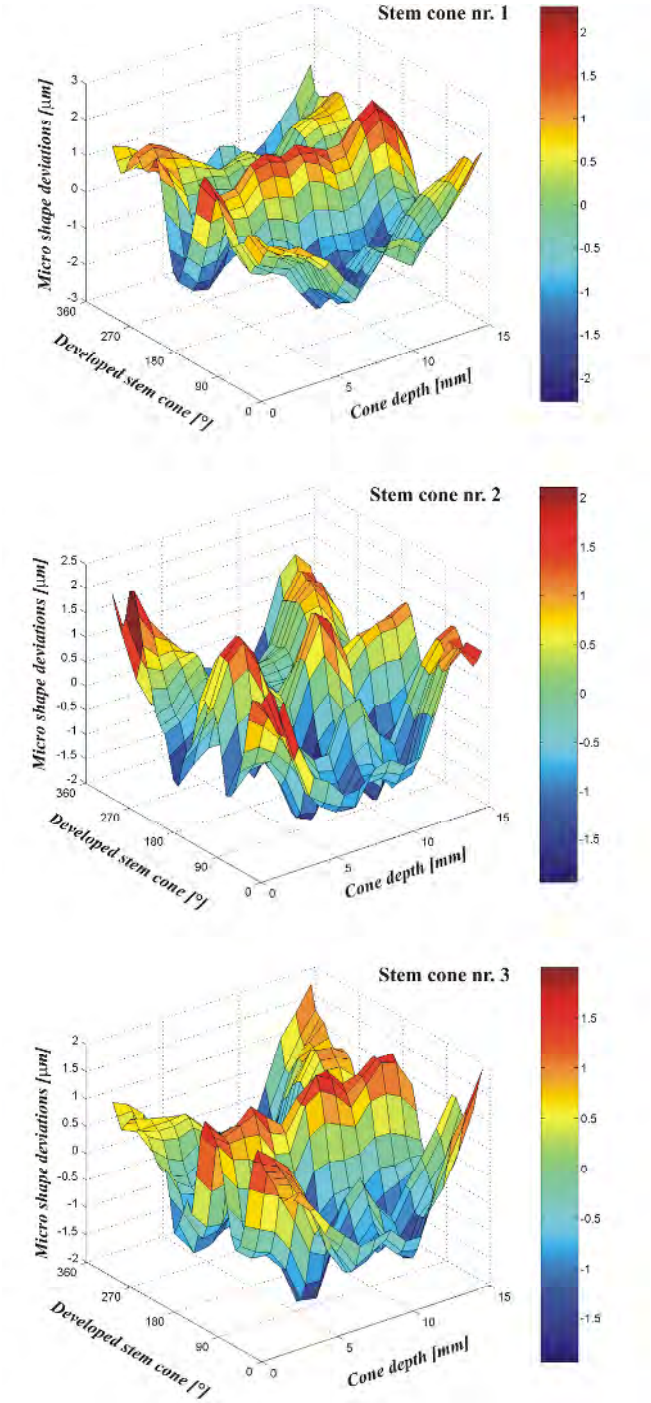


Fig. 4 Micro shape deviation of the stem cones

For computational analyses of the head's cohesion failure, the head was loaded with linear forces acting on a circle, the carrier of the resulting force *F* being identical with the axis of the stem, Fig. 2. This way of loading complies

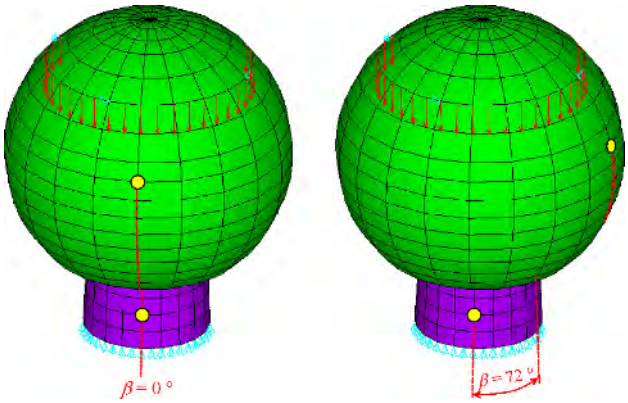


Fig. 5 Representation of various head to stem positions - angle β

with the ISO 7206-5 standard, according to which the reliability of ceramic heads is tested for failure of cohesion.

The material of the head and the stem was considered to be a linear isotropic continuum. The stem was made of steel and the following constitutive characteristics were taken into account in the calculation: E = 210 GPa μ = 0.3. The material of the head was ceramics on the basis of aluminium oxide Al_2O_3, for which the following constitutive characteristics were considered: E = 390 GPa, μ = 0.23. Contact between the head and the stem is modelled as elastic Coulomb friction with coefficient of friction f = 0.15 [1].

C. Results of the computational modelling

The negative behavior of the ceramics is the brittleness and therefore the tensile stresses in the ceramic head will be analysed in detail [2]. The distribution of maximum values of tensile stresses in the ceramic head (σ_{max}), in dependence on the value of the head's load, is shown in Figs. 6 - 8 for all analysed pairs (head pressed on the stem nr. 1 – Fig. 6, head pressed on the stem nr. 2 – Fig. 7 and head pressed on the stem nr. 3 – Fig. 8). The values σ_{max} for a given pair and for various positions of the head to the stem (various value of angle β) form a belt of relationships, the width or the height of which vary in the course of loading, and are related with the extent the dispersion of values σ_{max}. There are two limit macro shape deviations assumed (α = 0° – the cone tapper angle of the head and the stem is the same – blue curves, α = 10' (see Fig. 2) - limit value of the macro shape deviation – red curves) for each analysed pairs. For comparison, also an alternative was modelled taking into account only the deviation from the nominal degree of taper; in the diagrams it is represented by a broken lines and denoted VAR. 0 – α = 10' (variant assume only the macro shape deviation) and VAR. 0 – α = 0° (variant without macro and micro shape deviations – ideal cone).

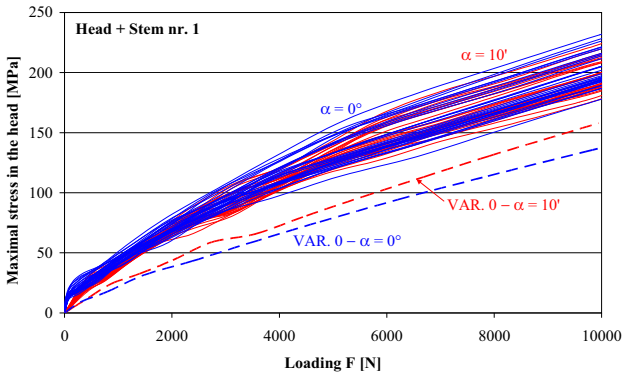


Fig. 6 Maximal head's stress curves during the loading for "Stem nr. 1"

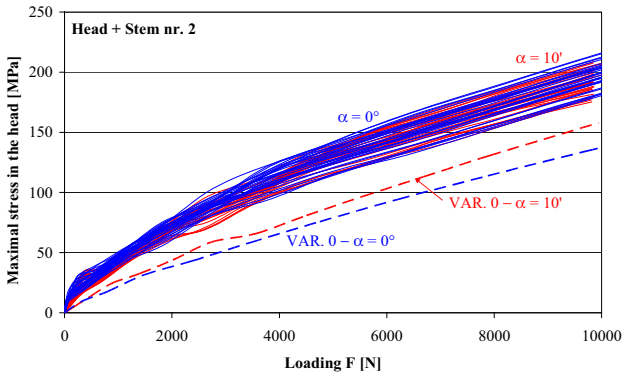


Fig. 7 Maximal head's stress curves during the loading for "Stem nr. 2"

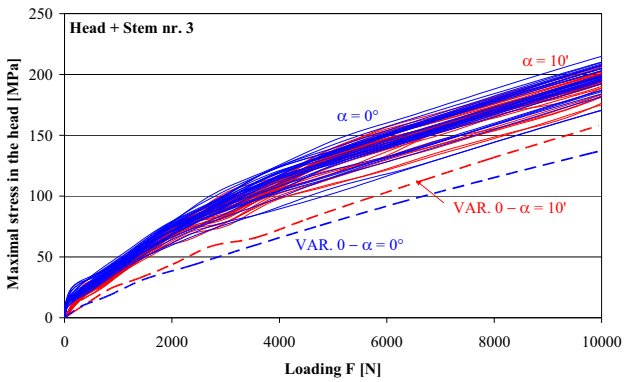


Fig. 8 Maximal head's stress curves during the loading for "Stem nr. 3"

The width of the belt of the σ_{max} curves in Figs. 6-8 (influence of the random position of the head on the stem cone) is similar for all analysed variants but the dispersion of the curves for variant with Stem nr. 2 is most equable (the maximal dispersion is about 40 MPa and the dispersion of the rest variants is higher – about 55 MPa).

The presence of the macro shape deviation without the micro shape deviations causes about 15 % increasing of the σ_{max} values (comparison of the VAR. 0 – α = 0° and α = 10').

The presence of the micro shape deviations or micro and macro shape deviations causes the increasing of the σ_{max} values from 27 % to 68 %. The width of the belt of the blue and red curves is very similar – the influence of the micro shape deviations is more significant than macro shape deviation.

III. Conclusions

By computational modelling it has been proved that the character and the size of micro and macro shape deviations on a conical contact area between the stem and the head of hip joint endoprosthesis have a pronounced influence on the character and the value of stress in the head and, hence, on the probability of the head's cohesion failure.

Acknowledgment

The research has been supported by the following projects AV0Z20760514, MSM0021630518 and 1P05ME789.

References

1. Fuis V, Návrat T (2005) Stress analysis of the hip joint endoprosthesis with shape deflections. Engineering Mechanics, Vol. 12 Nr. 5, pp. 323-330
2. Fuis V, Návrat T, Hlavoň P, Koukal M, Houfek M (2007) Analysis of contact pressure between the parts of total hip joint endoprosthesis with shape deviations. Journal of Biomechanics, Volume 40 supplement 2, S558-S558.

Author: Vladimir Fuis
Institute: Centre of Mechatronics – IT CAS and BUT FME
Street: Technicka 2
City: Brno
Country: Czech Republic
Email: fuis@fme.vutbr.cz

Pseudoelastic alloy devices for spastic elbow relaxation

S. Viscuso[1], S. Pittaccio[1], M. Caimmi[2], G. Gasperini[2], S. Pirovano[2], S. Besseghini[1] and F. Molteni[2]

[1] Unità staccata di Lecco, CNR -IENI,Lecco, Italy
[2] Centro di Riabilitazione Villa Beretta, Ospedale Valduce, Costamasnaga, Italy

Abstract — **Pseudoelastic alloys have never been utilised in rehabilitation medicine yet. A compliant dynamic brace (EDGES) promoting spastic elbow relaxation was designed for clinical use and helped investigate the potentialities of pseudolastic NiTi in orthotics. Two post-stroke subjects wore EDGES for 1 week, at least 10h a day. No additional treatment was applied to the examined arm during this period or the following week. A great improvement of the resting position was observed in both patients as early as 3h after starting the treatment. During walking, EDGES did not constrain limb movements and was thus very well accepted by the patients. A slight decrease in elbow flexors spasticity was also observed in all subjects, but this effect disappeared 1 week after discontinuation, as did posture improvements. EDGES appears to be a good alternative to traditional orthoses in terms of acceptability and effectiveness in improving posture, and it could be very useful whenever short-term splinting is planned.**

Keywords — **Pseudoelastic alloys, spasticity, orthotics.**

I. Introduction

Pseudoelasticity is the unique ability of some alloys (typically Ni–Ti alloys) of recovering up to 8% of deformation fully. This behavior is due to reversible phase transformations occurring in the solid state [1], from austenite to martensite during loading and vice versa on unloading. Deformation and shape recovery occur through large plateaux along which stress remains constant. Besides their peculiar mechanical characteristics, pseudoelastic NiTi is very biocompatible and thus it is commonly utilized in biomedical applications. Rehabilitation medicine has never employed this material so far. In particular, the large deformability and low-stress shape recovery of pseudoelastic NiTi could be useful if applied to spastic contracted joints. Between 17% and 28% of post-stroke patients develop spastic contractures within the first 6 months after stroke [2]. Spastic muscles management commonly includes the use of static orthoses which achieve muscle relaxation through a sequence of constrained positions more and more stretched. This approach causes a number of problems: first of all, the spastic response elicited at every stretching step provokes great pain to the patients. Furthermore, static splinting does not allow for any movement of the constrained joint, which is not good for functional rehabilitation as it favours the insurgence of contractures and of learned non-use [3]. Moreover, post-stroke patients commonly show involuntary jerks or contraction patterns involving the spastic limbs, during which constraining movement can cause further pain. That is also the reason why traditional static orthoses are not very well accepted by the patients.

A compliant dynamic brace (EDGES, Fig. 1) promoting spastic elbow relaxation was designed for clinical use and helped investigate the use of pseudolastic NiTi in orthotics.

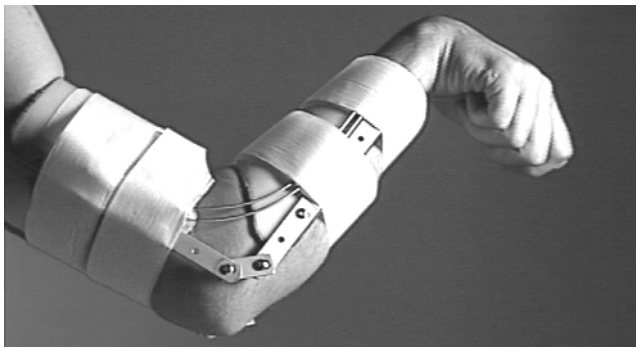


Fig. 1 The EDGES orthosis.

II. Material and methods

A. Material characterization

A commercial $Ni_{50.7}$-$Ti_{49.3}$ grade thermally-treated at 673K for 1h and water quenched was utilized for this application. Traction characterization was carried out on MTS 2/M thermo-mechanical test machine (MTS Systems, Eden Prairie, MN, USA), up to an engineering strain of 4%, at room temperature and the tensile stress-strain characteristic was recorded. The plateau values for this material were σ_m = 550MPa and σ_r = 240MPa.

Specially-designed grips mounted on the same test machine made it possible to carry out bending tests on the wire across the range 30°-220° (0° being wire straight). A 21cm long sample of wire (grip-to-grip) underwent two recorded deformation cycles across that range. The same sample was then manually preconditioned to bending between -180° and 180°, 50 times in the same bending plane of the test. Subse-

Chwee Teck Lim, James C.H. Goh (Eds.): ICBME 2008, Proceedings 23, pp. 1584–1587, 2009
www.springerlink.com

quently, recorded continuous cyclic deformation was applied 10 times across the same range.

B. Orthosis design and characterization

The EDGES orthosis is made up of two thermoplastic shells modeled on a prototype human arm of average size. These are connected by a polycentric hinge at each side of the elbow joint. A variable number of NiTi wires can be laid into two tubular elements connected in parallel to the hinges. On putting on the brace, the shells are strapped on the upper arm and forearm by Velcro® bands (Fig. 1).

A test bench was designed and constructed as follows, to assess the quantitative static working capabilities of EDGES. An aluminum platform sliding in a finely controllable way along two horizontal guides holds the orthosis arm shell blocked by four screws. A crosshead is mounted horizontally between two vertical poles attached to the sides of the platform, so that it lies above the orthosis at a selectable distance from it. Two 0.03N/mm harmonic steel linear tension springs are pinned onto the crosshead at a suitable distance from the midline and attached to the sides of the orthosis forearm shell, keeping it aloft and tied. The springs are designed to balance the action of the orthosis NiTi wires (the orthosis weight being negligible in comparison). The test is conducted in the following manner: after 50 two-ways preconditioning manual bending cycles between -180° and 180° the orthosis is fixed to the test bench horizontally and almost completely extended. The platform and the crosshead are moved relatively to one another until the springs are at square angles to the orthosis connection bars; at this point a photograph is taken of the orthosis and springs from a sufficiently far distance that the parallaxis has neglectable influence on relative measures. Then, the platform and crosshead are moved again so that the springs, still at square angles to the orthosis bar, balance the force of the NiTi wires with the orthosis slightly more flexed; a new photograph is taken. The same thing is then repeated for increasingly flexed orthosis angles and then back towards extension. On post-processing the photographs, a point-wise hysteretic characteristic of orthosis corrective torque vs. orthosis angle can be obtained: the spring length (force) and the lever-arm (spring distance from the instantaneous centre of rotation) can be measured from the pictures taken at different flexion angles. Tests were conducted with the orthosis mounting 1 and 2 wires per side.

C. Clinical trials

Two patients (A and B) were chosen among the inpatients of the ward that were not under any other treatment on the elbow. Patient A was a 62 y/o male with left sensory-motor hemisyndrome, 6 years after an ischemic stroke, showing Ashworth 3 spasticity in the elbow flexo-extensors, full PROM and no AROM. Patient B was a 64 y/o female with left sensory-motor hemisyndrome, 9 years after an ischemic stroke, showing Ashworth 2 spasticity in the elbow flexors, full PROM and no AROM. Patients were treated according to ethical principles as approved by the hospital ethical committee and gave informed consent to undergo a period of treatment with EDGES.

Patients underwent general clinical assessment prior to the start of the treatment, which consisted in wearing EDGES continuously for the first 24h and as long as possible for the following week. A number of measurement were scheduled at T0 and 3h, 24h and 1 week after the initiation of the therapy. These included active and passive range of motion, spasticity on the Ashworth Scale, resting elbow position while sitting, standing and standing after walking. Elbow angles were assessed also via optoelectronic measurements, which allowed dynamical evaluation of patient-orthosis interaction. The same protocol was also repeated 1week after discontinuation of the therapy. Visual clinical assessment was carried out routinely every time an opto-electronic measurement was scheduled. Optoelectronic measurement protocol was based on 100Hz acquisition of the position of three IR reflecting markers (fixed on the shoulder, elbow and forearm) to track the elbow angle by eight IR cameras (Elite Gait Eliclinic - BTS, Garbagnate, Italy). During this trial the patients (initially sitting with the affected limb resting on their laps) were cued to relax the arm down along their sides, then stand up, relax the arm down again and finally start walking along the gangway. Acceptability of EDGES was also investigated using a visual scoring questionnaire proposed by Gracies et al [4].

III. Results

A. Bending characterization of NiTi wires and EDGES

Wire bending curves show a quasi-linear increase of force until the bent wire forms a pseudoplastic hinge where stress concentration induces detwinned martensite. At that point material resistance quickly drops towards a plateau value that is conserved at larger deformations. The backward path shows hysteresis but the general shape of the tracing is akin to the forward one. Stabilization occurs only after conditioning.

Fig. 2 reports the results of the bending tests conducted on the assembled orthosis. The corrective torque vs. angle characteristic of EDGES is non-linear and hysteretic in both trials. Sufficient corrective push is ensured also at lower

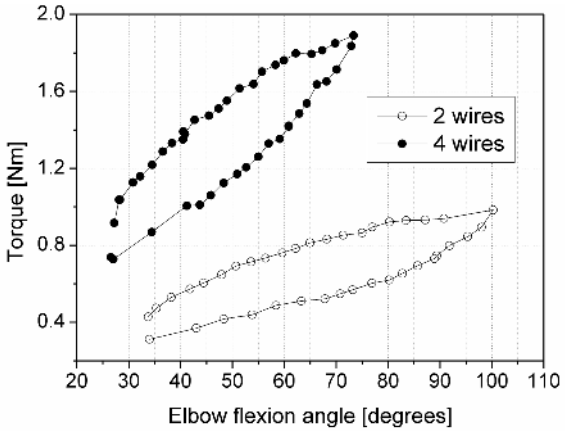


Fig. 2 Results of the bending tests on EDGES.

angles. The orthosis produces a moment increasing with angle in the 20°-80° range, after which it appears to reach a plateau at around 0.95Nm and 1.9Nm when equipped with 2 and 4 wires, respectively.

B. Clinical assessment

Variations of clinical conditions during the follow-up period were recorded and results are as in Table 1. It can be noted that the general trend, even in these very chronic patients, is definitely towards an improvement of elbow posture, which is already present at 24h and becomes more evident after 1 week. The decrease in spasticity obtained after 1 week of EDGES application is indeed a very interesting datum. All improvements appear to regress within 1 week of discontinuation.

Optoelectronic measurements show very nicely the time-course of elbow angle during the proposed clinical trials (Fig. 3). The quantitative analysis of movement confirms the general trend towards an increased elbow extension during therapy. Furthermore it is very interesting to observe that, while EDGES allows for wide movement of the elbow and does not impede flexing synergies during standing-up and walking, it is capable of reducing the amplitude of this

Table 1 Clinical follow-up: ROM and spasticity (without EDGES)

	Time	Sit	Stand	Walk	Relax	Ashworth
A	T_0	60°	50°	65°	50°	3
	3h	45°	45°	60°	50°	3
	24h	45°	50°	60°	50°	3
	1w	35°	40°	55°	40°	2
	1w after	50°	60°	65°	60°	3
B	T_0	70°	110°	100°	60°	2
	3h	30°	60°	70°	50°	1+
	24h	30°	30°	40°	30°	1
	1w	25°	30°	40°	20°	1
	1w after	65°	80°	95°	60°	2

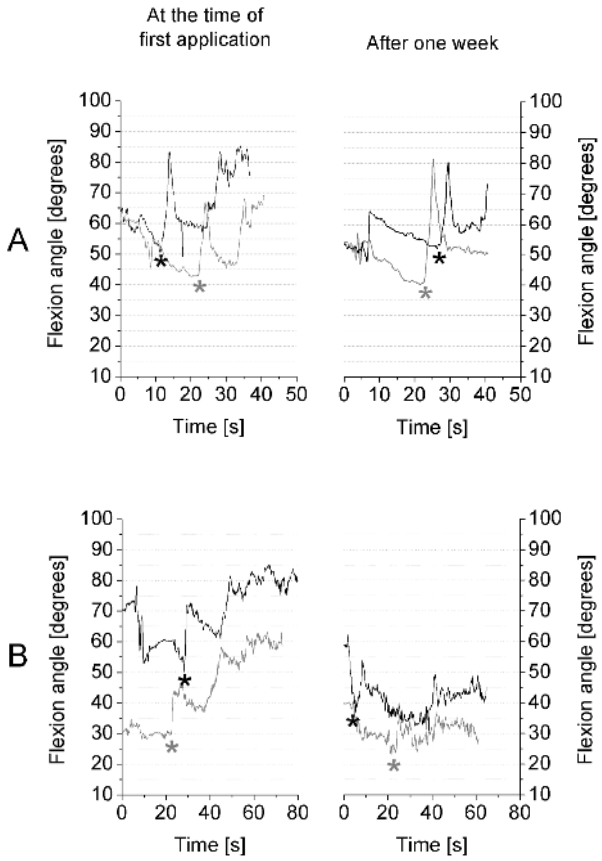


Fig. 3 Optoelectronic measurements on both patients wearing EDGES (gray line) and on removing it (black line). Star marks the "stand up" command. Elbow flexion following this point is a typical flexor synergic contraction. EDGES does not constrain this involuntary movement.

Table 2 Outcomes of Gracies' questionnaire for orthosis acceptablity

Question	A (1w)	B (1w)
How long did you wear EDGES today?	12 hours	18 hours
How did your arm feel while wearing EDGES?	7/10	8/10
Did you notice any changes wearing EDGES		
when walking?	Better	Better
when toileting?	No change	No change
when eating?	No change	No change
when dressing?	No change	No change
in ease of movement (muscle tone)?	Better	No change
in the confidence in your arm?	Better	Better
Would you wear EDGES for a few weeks if recommended?	Yes	Yes
Comments...	Some skin rash.	Cannot sit putting the arm on the lap

pathological movement. Patients' acceptation of EDGES was generally good after both 24 hours and 1 week of therapy (Table 2). Willingness to continue wearing it is preserved and only minor problems were observed, among which some light skin rash, that could possibly be avoided by a better lining than the present one. A particularly good result is in terms of improved ease of movement and confidence for the patient. It is interesting to notice that both patients reported walking better when they are wearing this elbow splint, possibly suggesting that improved confidence and decreased flexor synergies bring about greater stability.

IV. Discussion

The purpose of including pseudoelastic elements in a positioning brace is to provide a corrective torque across an angle as wide as possible such that it is not negligible even when the arm is almost fully extended. This principle is very innovative with respect to traditional orthotics, which is based on fixing the position of the limb and await tissue remodeling by relaxation. In the present work, a stable corrective force (and not a stable position) drives muscle stretching. This force ought to be sufficiently strong to produce tissue lengthening by *viscoelastoplastic creep* and not as strong as to impede arm movements. The values of corrective torque produced by EDGES, as measured from the bending tests (0.95Nm and 1.9 Nm), are considerably lower than maximal muscular flexor torques of around 50-75Nm [5], and somewhat less than the maximal passive-reflex torques, which are reported to be in the range 0.5-6Nm [6]. These measurements confirm that EDGES can stretch muscle while not constraining elbow position during voluntary movements or involuntary jerks. Clinical procedures carried out to assess the dynamical characteristics of EDGES when worn by spastic subjects, showed that even in this unoptimized version it can produce corrective loads in a stable manner for at least a week and that it does not constrain the elbow in a fixed position. This is clearly visible from the strong oscillations in arm position detected and shown in Fig. 3. Flexor synergies, which are a very common feature of post-stroke syndromes, cause involuntary arm flexion during some types of body movements (standing up, walking, …). Constraining devices can therefore be ill-tolerated in these circumstances. Acceptability of EDGES was on the other hand very good, suggesting that longer orthotic treatments with this orthosis can be attempted. Decrease in spasticity could be a wonderful result but it needs strong further evidence to be confirmed, as spasticity attenuation has never been conclusively proved in connection with orthotic treatment [7]. Relapse of ill-posture and spasticity after treatment discontinuation was absolutely expected, as 1 week is not a sufficiently long time to obtain plastic remodeling of human muscular and nervous tissues. Stabilized benefits could only be attended, should treatment be prolonged by several weeks. Reversibility of patients' conditions in the present clinical experiment suggests that EDGES is not harmful in a week's application.

V. Conclusions

A pseudoelastic positioning brace was designed and built based on commercial NiTi wires. Unconventional bending tests showed good cycling stability. Orthosis characterization demonstrated that it can generate corrective torques up to 0.95Nm and 1.9Nm when equipped with 2 and 4 wires, respectively. Clinical outcomes show improvement of patients' posture within 24h and further progress at 1 week. Spasticity appears to be decreasing during the first week, but this observation needs strong additional evidence to be confirmed. Patients' satisfaction was high, as was acceptability at both 24h and 1w. In conclusion, pseudoelastic NiTi is a suitable material for constructing elbow positioning braces that work on the principle of tissue lengthening by *viscoelastoplastic creep*. Other orthoses could be significantly enhanced with the use of pseudoelastic elements.

References

1. Duerig TW, Melton KN (1990) Engineering aspects of shape memory alloys. Butterworth-Heinemann Ltd, London
2. Lundström E, Terémtb A, Borg J (2008) Prevalence of disabling spasticity 1 year after first-ever stroke. Eur J Neurol 15:533–539 DOI 10.1111/j.1468-1331.2008.02114.x
3. Gracies JM (2005) Pathophysiology of spastic paresis I: paresis and soft tissue changes. Muscle Nerve 31:535–551 DOI 10.1002/mus.20284
4. Gracies JM, Marosszeky JE, Renton R et al. (2000) Short-term effects of dynamic Lycra splints on upper limb in hemiplegic patients. Arch Phys Med Rehabil 81:1547–1555 DOI 10.1053/apmr.2000.16346
5. Buchanan TS (1995) Evidence that maximum muscle stress is not a constant: differences in specific tension in elbow flexors and extensors. Med Eng Phys 17:529–536 DOI 10.1016/1350-4533(95)00005-8
6. Schmit BD, Rymer WZ (2001) Identification of static and dynamic components of reflex sensitivity in spastic elbow flexors using a muscle activation model. Ann Biomed Eng 29:330–339 DOI 10.1114/1.1359496
7. Lannin NA, Novak I, Cusick A (2007) A systematic review of upper extremity casting for children and adults with central nervous system motor disorders. Clin Rehabil 21:963–976 DOI 10.1177/0269215507079141

Author: Stefano Viscuso
Institute: CNR-Institute for Energetics and Interphases
Street: Corso Promessi Sposi, 29
City: Lecco
Country: Italy
Email: s.viscuso@ieni.cnr.it

Musculoskeletal Analysis of Spine with Kyphosis Due to Compression Fracture of an Osteoporotic Vertebra

J. Sakamoto[1], Y. Nakada[1], H. Murakami[2], N. Kawahara[2], J. Oda[1], K. Tomita[2] and H. Higaki[3]

[1] Graduate School of Natural Science and Technology, Kanazawa University, Kanazawa, Japan
[2] Kanazawa University Hospital, Kanazawa, Japan
[3] Faculty of Engineering, Kyusyu Sangyo University, Fukuoka, Japan

Abstract — **Mechanical stress analysis of vertebral bone is required to determine compressive strength of vertebra for osteoporosis patients in clinical situation of orthopedics. Stress occurred in vertebrae depend on condition of musculoskeletal system of spine. Spine structure is mainly constructed of many vertebrae and flexible intervertebral disks, and it is unstable by itself under standing condition. Supporting by erector muscles and ligaments keep the spine standing condition, so that loading condition of each vertebra depend on the muscle and ligament forces. Biomechanical simulation of musculoskeletal model taking into account of muscle and ligament forces and intervertebral joint forces is necessary to determine the loading condition for vertebral stress analysis. Commercial software to deal with the musculoskeletal system, e.g. AnyBody Modeling System (AnyBody Technology Inc.), is available nowadays, and it has been applied to clinical, ergonomic or sport biomechanics problem.**

Spine kyphosis is often caused by compression fracture of osteoporotic vertebra, because shape of the fractured vertebra is sphenoidal with sharp anterior side of vertebral body. Spine kyphosis makes gravity center of trunk shift to anterior side, and then intervertebral joint moment due to trunk weight increase. Additional compression fracture is concerned at adjoining vertebrae to the fractured one in the kyphotic spine. In this study, musculoskeletal simulation model with spine kyphosis was created by using AnyBody Modeling System considering compensation posture due to kyphosis. Kyphosis patient used to have compensation posture to recover body balance and face up. Intervertebral joint forces and muscle forces of the model were computed, and then influence of the kyphosis on the intervertebral joint force at adjoining joints was discussed comparing between kyphosis and intact model. Furthermore, influence of the compensation posture on muscle forces related to spine was considered.

Keywords — **Biomechanics, Musculoskeletal Model, Spine, Kyphosis, Vertebral Compression Fracture**

I. Introduction

Recently, by the advanced computational mechanics technology, the mechanical analysis of the bone that reflected a complex structure and the material characteristic has been available [1]. The diagnosis of osteoporosis that considers strength of the bone according to the patient has been tried by using mechanical analysis technique. However, the loading condition and the boundary condition of the bone are not necessarily considered enough while progress of accurate modeling of bone structure and material properties. Spine structure is mainly constructed of many vertebrae and flexible intervertebral disks, and it is unstable by itself under standing condition. Supporting by erector muscles and ligaments keep the spine standing condition, so that boundary condition of each vertebra strongly depend on the muscle and ligament forces. It is important to give an accurate loading condition in which force of the muscle and the ligament is considered for mechanical analysis of vertebra on more clinical condition.

Spine kyphosis is often caused by compression fracture of osteoporotic vertebra, because shape of the fractured vertebra is sphenoidal with sharp anterior side of vertebral body. Spine kyphosis makes gravity center of trunk shift to anterior side, and then intervertebral joint moment due to trunk weight increase. Additional compression fracture is concerned at adjoining vertebrae to the fractured one in the kyphotic spine. Although such a change of the loading condition due to spine kyphosis can be easily expected, it is very difficult to evaluate load increase on each vertebra because of influences by the above-mentioned muscle and ligament forces.

In this study, musculoskeletal simulation model with spine kyphosis was created considering compensation posture due to kyphosis. Kyphosis patient used to have compensation posture to recover body balance and face up. Intervertebral joint forces and muscle forces of the model were computed, and then influence of the kyphosis on the intervertebral joint force at adjoining joints was discussed comparing between kyphosis and intact model. Furthermore, influence of the compensation posture on muscle forces related to spine was considered.

II. Analysis Method

A. The AnyBody Modeling System

Musculoskeletal model was developed using the simulation software the AnyBody Modeling System (AnyBody

Chwee Teck Lim, James C.H. Goh (Eds.): ICBME 2008, Proceedings 23, pp. 1588–1591, 2009
www.springerlink.com

Technology Inc.) [2]. This software handles model of human body mechanism, and the application area is medical, rehabilitation, ergonomic, sports or astronautical engineering, etc. By using the AnyBody Modeling System, we can develop 3-D musculoskeletal model by a script language called AnyScript. Model consists of segments regarded as bones or rigid elements, joints connecting segments, and muscle-tendon units having physiological characteristics. Drivers create posture and movement of joints. The AnyBody Modeling System calculates the joint and muscle forces from giving posture and external load by inverse dynamic analysis.

B. Analysis model

Analysis model was developed based on Standing Model (the AnyBody Research Project, Aalborg University, Aalborg, Denmark, http://www.anybody.aau.dk/repository) [3], which was human full body musculoskeletal model (Fig. 1).

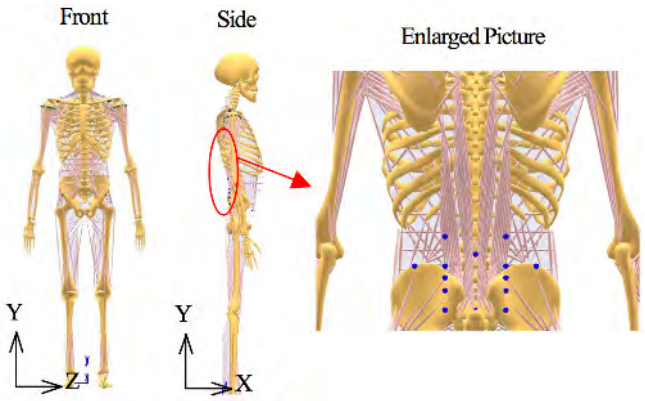


Fig.1 Full-body musculoskeletal model of the AnyBody modeling system.

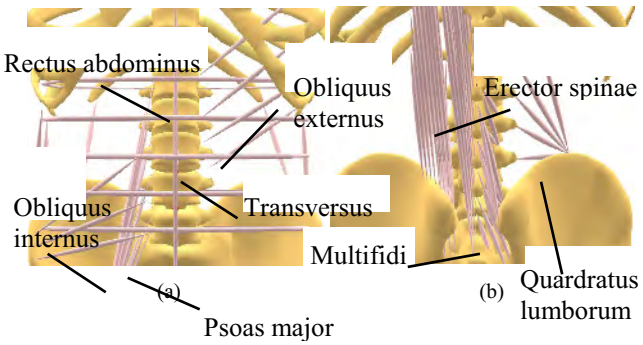
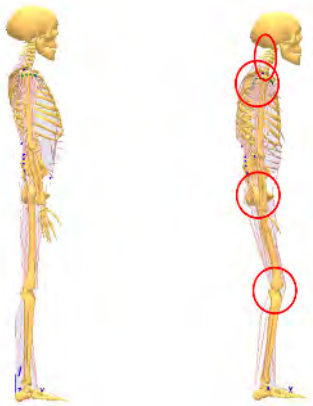


Fig.2 Trunk of model in (a) front view and (b) back view. Eight muscles are defined as trunk muscles.

Total number of muscle fascicles defined in this musculoskeletal model is 476. In trunk of model 158 fascicles were defined and divided into eight muscles (Fig. 2). Four abdominal muscles were included : rectus abdominus, transversus, obliquus internus and obliquus externus. Quadratus lumborum, psoas major, erector spinae and multifidi were defined as muscles of the lower-back [4].

Spine model is composed of nine segments : sacrum, five lumbar vertebrae, T12, T11 and a lumped thoracic part over T10. Spherical joint with three degrees of freedom was set between every vertebra from T10 to sacrum(Fig. 3). These intervertebral joint angles were varied in according to spinal alignment or posture [5]. Height of the model is set as 1.5m and weight is 50kg assuming a standard Japanese eldaly female.



(a) Healthy model (b) Kyphosis model

Fig.3 Standing posture of the normal healthy model and kyphosis model. Circles of the kyphosis model denote neck, glenohumeral, knee and hip joints which are changed from the healthy model by compensation.

Table 1 Change of joint angle of kyphosis model from normal model

Joint	Angle(°)
T11-T12	-20
Neck	+20
Knee	+20
Hip	+10
Glenohumeral	+10

C. Kyphosis model

Assuming the case of compression fracture at 12th thoracic vertebrae where was favorite site of compression fracture caused by osteoporosis, we enforced to increase intervertebral joint angle of T11-T12 20 degree in flexion direction. And then, the compensation posture seen in the

kyphosis patient was set to the standing model. In the compensation posture, neck, knee, hip and glenohumeral joints were changed to make the face naturally turn to the front [6]. Fig. 3 shows standing posture of the normal healthy model and kyphosis model. Angle change of the joint is shown in Table 1.

D. Analysis condition

In the analysis, the muscular force and the joint force in each posture is calculated in the static condition. Min-max algorithm of AnyBody Modeling System is used in the muscular force calculation. The solution of the muscle recruited problem is minimization of the maximal muscle activity under constraints of the static equilibrium equations. Muscle activity means muscle force divided by the maximal isometric muscle force at each muscle's current working condition. The solution is equivalent to minimum muscle fatigue and it is computationally-efficient [2].

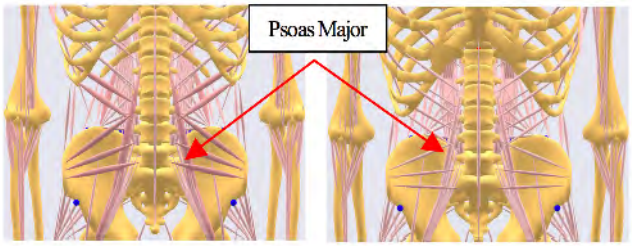
The self body weight and abdominal pressure were considered as external load to the body. The analysis was performed for the normal healthy model and the model taking the compensation posture, and their results were compared each other focusing on the trunk muscular force and vertebral joint force.

III. Analysis Result

A. Influence on trunk muscle

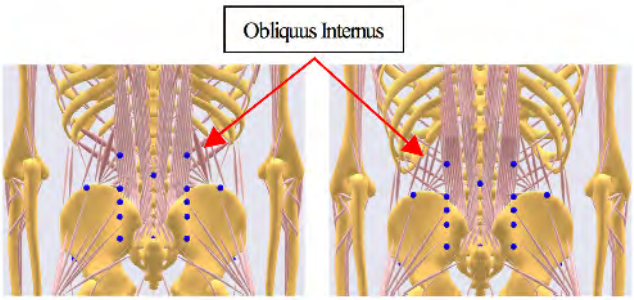
The trunk muscular forces are shown graphically in Fig.4 and Fig.5 for the normal healthy model and the kyphosis model. In the figure, muscular thickness correspond to magnitude of muscular force. Fig.4 shows front side of the models, and Fig.5 shows back side of the models. Psoas major that arrows in Fig.3 is displayed thicker than other muscles. Moreover, it is understood that arrowed obliquus internus is displayed thick in Fig.4. Relative large force occur in these muscles more than others muscles. A lot of thinner displayed muscles, that is smaller force muscles, exist in the kyphosis model in comparison with the healthy model. It is considered that the compensation posture set by this study has reduced a muscular force.

Fig. 6 shows force values of muscle bundles of the healthy model and the kyphosis model. It is observed that the muscle generate large force in the healthy model is obliquus externus, obliquus internus, psoas major, and transversus abdominis. It is thought that the posture of the upper part of the body is supported chiefly by these four muscles work when standing upright. Transversus abdominis muscle runs from lateral to anterior formed abdominal wall, its fibers running horizontally. So muscular force of transversus abdominis takes large value depending on abdominal pressure set here.



(a) Healthy model (b) Kyphosis model

Fig.4 Display of muscular force value of healthy model and kyphosis model in anterior view. Thickness of muscle line corresponds to magnitude of muscular force in the figure.



(a) Healthy model (b) Kyphosis model

Fig.5 Display of muscular force value of healthy model and kyphosis model in posterior view. Thickness of muscle line corresponds to magnitude of muscular force in the figure.

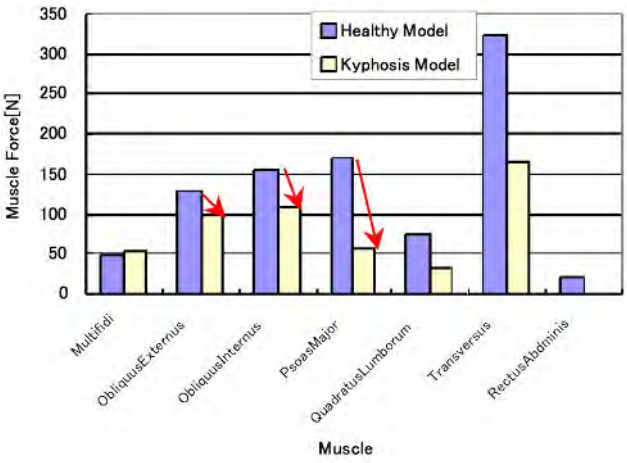


Fig.6 Muscular forces of healthy model and kyphosis model. Arrows show muscular forces related to spine erection with relative large difference between the healthy and the kyphosis model.

Four important muscles to keep upper body posture are focused in Fig.6, as comparing muscular force of the kyphosis model with the healthy model. A remarkable decrease in about 50% is observed with transversus abdominis, the value of 67% decreases in psoas major, 24% decreases in obliquus internus, and 31% decreases in obliquus externus as shown besides by the arrow in Fig.6. The trunk muscular forces decrease, as the compensation posture for the kyphosis due to vertebral compression fracture.

B. Influence on intervertebral joints

Intervertebral joint forces in axial direction are shown in Fig.7 for the healthy model and the kyphosis model. Force act on intervertebral joints tended to large in the joint on the tail side, and the joint force of L4-L5 is the largest in the lumbar vertebra. Force of all joints is larger in the kyphosis model than the healthy model. The compensation posture possible to make vertebral joint force increase. Especially, it rises greatly as shown by the arrow in the figure like 21% in L1-L2, 32% in T12-L1, and 33% in T11-T12. From Fig.6 and Fig.7, it was shown that the intervertebral joint forces in lumber spine increase although the trunk muscular forces decrease, when an osteoporosis patient has compression fracture at the 12th thoracic vertebrae and then takes the compensation posture for recovery body balance and view range. This causes the second compression fracture on another vertebra after occurring kyphosis by first compression fracture. Furthermore, it is considered that the second compression fracture happens easily to the adjacent vertebra of the 12th thoracic vertebra, because the increase ratio of the joint force is larger on the upper side of the 12th thoracic vertebrae assuming the fracture.

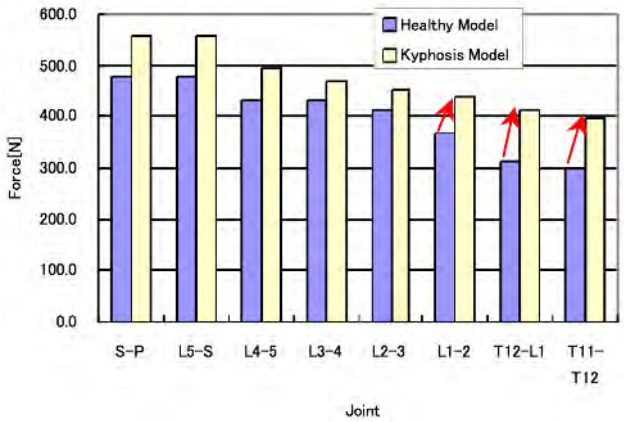


Fig.7 Comparison of the vertebral joint force along spine axis. Arrows show vertebral joint forces near fractured vertebra T12 with relative large difference between the healthy and the kyphosis model.

IV. Conclusions

To study the influence of the posture change by vertebral compression fracture in osteoporosis patient on loading condition of spine, muscular force of trunk and intervertebral joint force was calculated by using the musculo-skeletal model corresponding to normal posture and kyphosis posture. Deference of loading condition between the healthy model and the kyphosis model were considered and discussed. It was observed that mainly four trunk muscles in standing condition supported posture of upper body. In the kyphosis model with the compensation posture, although trunk muscular forces were reduced, intervertebral joint force increase in the maximum by 30% or more. It has been understood that risk of causing the second compression fracture rises further in the adjacent vertebra of the first fracturing vertebra. Thus, an important observation for considering about the risk of vertebral compression fracture in osteoporosis patient was obtained.

Acknowledgment

This research was supported by the Ministry of Education, Science, Sports and Culture, Grant-in-Aid for Scientific Research (B).

References

1. K Imai, et al. (2006) Nonlinear finite element model predicts vertebral bone strength and fracture site, *Spine*, Vol.31, Issue 16: 1789-1794.
2. M Damsgaard, et al. (2006) Analysis of musculoskeletal systems in the AnyBody Modeling System, *Simulation modelling Practice and Theory,* Vol.14, Issue 8, 1100-1111.
3. M de Zee, et al. (2003) On the development of a detailed rigid-body spine model, *International Congress on Computational Bioengineering*, 24-26.
4. M de Zee, et al. (2007) A generic detailed rigid-body lumbar spine model, *Journal of Biomechanics,* Vol.40, Issue 6, 1219-1227.
5. J Sakamoto, et al (2005) Musculoskeletal analysis of spine and its application for spinal fixation by instruments, Proc. 2005 Int. Symp. Coup. Simulation Biomech, Cleveland, 19-20.
6. SDM Bot, et al. (1999) Biomechanical analysis of posture in patients with spinal kyphosis due to ankylosing spondylitis: a pilot study, *Rheumatology*, Vol.38, 441-443.

The Biomechanical Analysis of the Coil Stent and Mesh Stent Expansion in the Angioplasty

S.I. Chen[1], C.H. Tsai[2], J.S. Liu[2], H.C. Kan[1], C.M. Yao[1], L.C. Lee[1], R.J. Shih[1], C.Y. Shen1[1]

[1] National Center of High-Performance Computing, Hsinchu, Taiwan
[2] National Health Research Institutes, Hsinchu, Taiwan

Abstract — **Percutaneous Transluminal Angioplasty (PTA) with stent is employed to treat the cardiovascular diseases in clinical to dilate stenotic arteries. There have been two types of stents (helical coil shape and traditional mesh shape) wildly used in angioplasty in the past few years. This research studied the biomechanical effects on the expansion behavior of these two different stents with balloon in the artery vessel. The commercial three-dimensional finite element method (FEM) based software was employed to perform all the computations in this study. Simulation results reveal that the pressure is delivered uniformly by the balloon, which leads the stenosed vessel to dilate. The dog bone effect is more obvious in the helical coil stent than the traditional mesh stent. The regions close to both ends of the stent exhibit large deformation and high shear stress values for both stent types. In the clinical practices, large deformation may cause stress concentration which leads to the damage of the vessel.**

Keywords — **Angioplasty, Biomechanical analysis, Stent, Finite element method.**

I. Introduction

Cardiovascular diseases have been on the list of the top-ten leading causes of death in many countries in the past decade. It is a result of the narrowing and clogging of the arteries that cannot supply enough blood to heart. In the modern angioplasty, cardiologists apply stenting technology to restore normal blood flows in arteries where fatty deposits, or plaque formations, reduce the blood flow supply for patients with cardiovascular diseases. The balloon which is inflated by the pre-determined pressure pushes the stent radially outward against the vessel wall. Then the stent permanently expands the narrowing vessel to recover the continuous blood flow. There are currently several commercially available stent designs in the market [1]. A more detailed understanding of the mechanics may lead to significant improvement of the outcome on clinical medicine.

Finite element method (FEM) can help identify some valuable mechanical characteristics of stents, arteroes, and their interactions. So the numerical analysis has been proposed as an alternative approach to investigate mechanical properties of stents. Auricchio et al. [2] studied the biomechanical interaction between a balloon-expandable stent and a stenotic artery. Migliavacca et al. [3] investigated the effects of different geometrical parameters of a typical coronary stent on the mechanical performance. Lally et al. [4] assessed the effects of artery wall shear stress on two different stent designs using a balloon-stent model.

The purpose of this study is aimed at the biomechanical and interactive behavior of stent deployment system by the aid of FEM analysis. Two different stent designs (helical coil shape and traditional mesh shape) were considered to evaluate the stent deployment system. In order to fully understand the biomechanical effects of atherosclerotic artery during the inflating process, a 3D composite stent model, which consisted of the stent, balloon, and artery components, was generated for this study. In the stent expansion process, the characteristics of deformation, and stress distribution were investigated using the FEM approach.

II. Materials and methods

The full model of the stent deployment system proposed in this study was composed of three parts: stent, balloon and artery as shown in Fig. 1. All of the finite element models in this study were created by the commercial package of ANSYS 11.0 (ANSYS, Canonsburg, PA, U.S.A). A widely used mesh stent type [5] and a helical coil type stent were chosen in this study [6]. Both the helical coil stent and traditional mesh stent models had the length of 21mm, outer diameter of 2.06mm and thickness of 0.05mm. A grid convergence test was performed to ensure the necessary grid density for all the computations. There were 29112 nodes and 13184 elements in coil stent model, and 69953 nodes and 26628 elements in mesh stent model with tetrahedral elements were shown in Fig. 2. The balloon model had length 21mm and thickness 0.05mm. Artery and balloon were modeled as the cylinder with 30mm in length and 2.1mm in inner diameter, and the thickness of artery wall was 0.5mm. The balloon expanding full models of the coil and mesh stents were shown in Fig. 1. There were 11555 nodes and 7797 elements in the balloon component, and 35855 nodes and 37715 elements in the vessel component with hexahedral element.

Chwee Teck Lim, James C.H. Goh (Eds.): ICBME 2008, Proceedings 23, pp. 1592–1594, 2009
www.springerlink.com



Fig. 1. The balloon-expanding full model with the coil and mesh stent system



Fig. 2. The three-dimensional grid models of the coil stent and mesh stent

In the analysis model, all material properties were assumed to be homogeneous and isotropic. The material of the stent was assumed to be 316L stainless steel and was described as a bilinear isotropic hardening with Young's modulus 196 GPa, Yield stress 205 MPa, Tangent modulus 692 MPa and Poisson's ratio 0.3 [7]. The Young's modulus of the balloon and vessel were 30.1 MPa and 1380 MPa, respectively, and the Poisson's ratio were all 0.499 [8]. Implicit nonlinear large deformation analysis was performed in ANSYS 11.0. The surface-to-surface contact elements were used to perform the loading transfers between the balloon and the stent, and between the stent and the vessel. The friction coefficient was set as 0.3. Both ends of the vessel model were fixed for all DOF (Degree of Freedom), and the uniform pressure was loaded from 0 to 10 MPa in the balloon inner surface, which was treated as the boundary condition.

III. Results and Discussion

From the simulation results, the deformed shapes of the stent and balloon components with coil and mesh stent were shown in Fig. 3. The balloon delivered the pressure uniformly, which led the stenosed vessel to dilate. It is noted that the dog-boning effect is not very obvious at the both ends of the helical coil stent and mesh stent. This is because the vessel component is included in the analysis and resists partial dog-boning effect from the stent at the both ends. It is observed from Fig. 3 that the dog bone effect is more evident in the helical coil stent than the mesh stent. The deformation at both ends of the coil stent is larger than these of the mesh stent. It indicates that the geometric structure of the helical coil stent is weaker than mesh stent at the both ends of the stent. Figure 4 illustrates the von-Mises stress distribution contours for both the helical coil and mesh stent models at large deformation (fully expanded) stage. Figure 5 demonstrates that the von-Mises stress concentrates in the large deformation region of the vessel for the helical coil stent model. The high stress levels may result in the lesion in the vessel wall during the stent expansion stage.

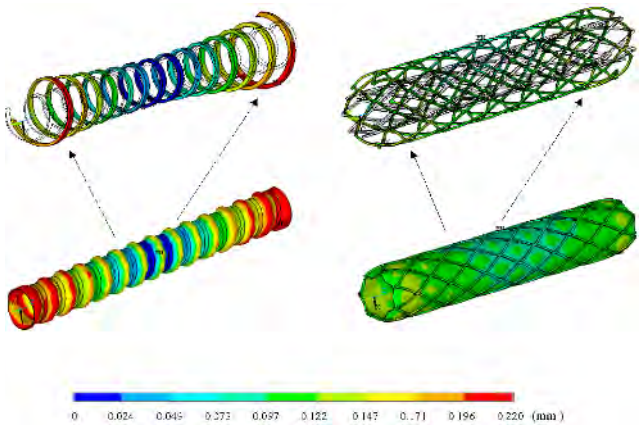


Fig. 3. The stent/balloon deformation distribution with the coil stent and mesh stent system

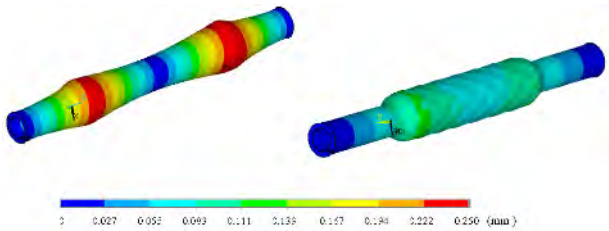


Fig. 4. The vessel deformation distribution with the coil stent and mesh stent system

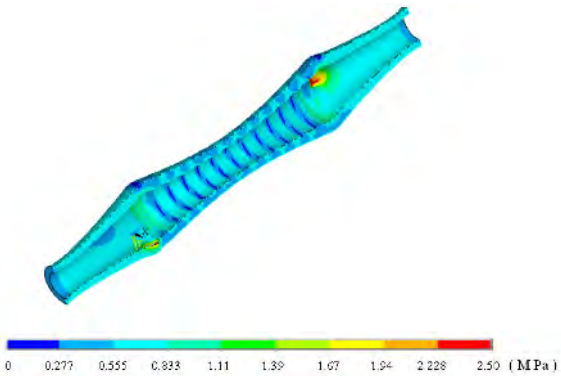


Fig. 5. The von-Mises stress distribution of vessel wall with the coil stent system

Acknowledgment

The authors would like to thank gratefully for the financial and computational supports of the National Health Research Institutes and the National Center for High-Performance Computing.

References

1. Clombo A., Stankovic G., Moses J.W. (1998) election of coronary stents. J. Am. College Cardiol. 22-25
2. Auricchio F., Loretob M.D., Saccoc E. (2000) Finite-element analysis of a stenotic artery revascularization through a stent insertion. Computer Methods in Biomechanics and Biomedical Engineering 1-15
3. F. Migliavacca, L. Petrini, M. Colombo, F. Pietrabissa, R. Pietrabissa, "Mechanical behavior of coronary stents investigated through the finite element", Journal of Biomechanics 35:803-811
4. Lally C, Dolan F, Prendergast PJ. (2005) Cardiovascular stent design and vessel stresses: a finite element analysis. *Journal of Biomechanics,* August 38:1574-81.
5. Palmaz, J. C., Sibbit, R. R., Reuter, S. R., Tio, F. O., and Rice, W. J. (1985) Expandable Intraluminal Graft: A Preliminary Study. *Radiology*. 156:73-77.
6. C.T. Dotter, P.A.C. Buschmann, M.K. McKinney, and S.J .R&ouml (1983) Transluminal Expandable Nitinol Coil Stent Grafting: Preliminary Report. Radiology 147:259-60.
7. Linxia, Gu., Swadeshmukul, S., Robert, A. M., Ashok, V. K. (2005) Finite element analysis of covered microstents. *Journal of Biomechanics* 38:1221-1227.
8. David SN. (2003) Finite element simulation of stent and balloon interaction. *Journal of Material Processing Technology* 10:378-82.

Author: Chen Shou-I
Institute: National Center of High-Performance Computing
Street: 7, R&D Rd.
City: Hsinchu
Country: Taiwan
Email: shoui@nchc.org.tw

Effect of Airway Opening Pressure Distribution on Gas Exchange in Inflating Lung

T.K. Roy, MD PhD[1]

[1] Division of Critical Care, Dept of Anesthesiology, Mayo Clinic, Rochester MN USA

Abstract — **Pathophysiological alterations in lung mechanics commonly occur in critically ill patients and can result in impaired oxygenation and ventilation. The process of recruitment as the lung inflates involves the progressive opening of airways resulting in increasing amounts of alveolar volume available for gas exchange, and is modeled in this study using avalanche dynamics. Here we employ a symmetric 10-generation tree to represent the region of the lung participating in gas exchange along with a simplified model of pulmonary microvascular blood flow through an accompanying vascular network. The model is used to obtain the mean oxygen saturation during lung inflation under normal conditions as well as those simulating increased threshold opening airway pressures. For the values of parameters used, the oxygen saturation calculated for a uniform distribution of opening pressures is found to be 3.6% higher as compared to simulations performed using a generation-dependent distribution of opening pressures with higher opening pressures in smaller airways. In both cases, blood flow is assumed to be constant and the effects of gravity are not considered. Future work will include the effect of regional heterogeneity in lung mechanics on gas exchange. The ultimate goal of this work is to develop optimal ventilation strategies to minimize ventilator induced lung injury and improve gas exchange in critically ill patients.**

Keywords — **Pulmonary mechanics, gas exchange, avalanche dynamics, ventilation-perfusion matching, critical illness.**

I. Introduction

Critically ill patients are often affected by alterations in pulmonary mechanics caused by changes in airway elasticity and resistance [2]. Optimizing oxygenation and ventilation in these patients requires a quantitative understanding of ventilation/perfusion matching in the regions of the lung available for gas exchange. As the lung inflates, the increasing alveolar volume available for this purpose can be modeled using avalanche dynamics [3]. The purpose of this preliminary theoretical study is to assess the effect of two different laws governing airway opening pressures on oxygenation over the respiratory cycle.

Airway opening as governed by avalanche dynamics requires the assignment of opening pressures to each segment in the tree structure used to model the airway. In this study, a symmetric tree structure is employed to represent the portion of the tracheobronchial tree that participates in gas exchange. A simplified model of pulmonary microvascular blood flow through an accompanying vascular network is used to obtain the mean oxygen saturation during lung inflation under normal conditions as well as those simulating increased threshold opening airway pressures; specifically, a uniform distribution of airway opening pressures is compared to a generation-dependent distribution of airway pressures with higher pressures corresponding to smaller airways.

II. Methods

A symmetric 10-generation tree was modeled using Mathematica 6.0 (Wolfram Research, Champaign IL, USA) to represent the region of the lung available for gas exchange. The presence of an accompanying vascular network with specified inlet PO_2 was assumed and gas exchange was assumed to take place in the alveoli, defined as the terminal segments of the tree. These calculations were performed in accordance with the following assumptions.

A. Airway Opening

Lung inflation was simulated using avalanche dynamics following the assignment of airway opening pressures to each segment of the tree structure. For the reference case, normalized opening pressures $P_{i,j}$ (corresponding to segment j of generation i) were selected from the uniform distribution U(0,1). Generation-dependent opening pressures were calculated according to:

$$P_{i,j} = 1 - P^{1+\ln(i+1)} \quad (1)$$

where P represents a value selected from the uniform distribution U(0,1). Pseudorandom numbers in this range were generated using the Mathematica function `RandomReal`. Following the tenets of avalanche dynamics, the pressure at the initial (root) segment was gradually increased in small increments to simulate lung inflation. Connected segments with opening pressures less than or equal to the pressure at the inlet were progressively opened as the inlet pressure was increased [1, 4]. Terminal segments (alveoli) that were in communication with the root segment were assumed to participate in gas exchange as detailed in Section B.

Chwee Teck Lim, James C.H. Goh (Eds.): ICBME 2008, Proceedings 23, pp. 1595–1596, 2009
www.springerlink.com

Table 1 Parameter Values

Parameter	Value	Units
Pulmonary artery PO_2	40	mmHg
Inspired PO_2	100	mmHg
P_{50}	27	mmHg
n	2.6	–

B. Gas Exchange

Gas exchange was modeled with the assumption that oxygen tension would rapidly equilibrate across the alveolar-capillary membrane. The pulmonary venous oxygen tension was therefore calculated as the weighted average of the oxygen tension of venous blood in contact with unopened alveoli (representing shunt fraction) and the oxygen tension of blood in contact with alveoli open to the root segment. The Hill equation was used to convert between oxygen tension (PO_2) and oxygen saturation (SO_2):

$$SO_2 = PO_2^n / (PO_2^n + P_{50}^n) \quad (2)$$

Pulmonary venous oxygen saturation was integrated over the inspiratory phase to provide a mean measure of oxygenation during lung inflation. Parameters used in the simulation are listed in Table 1.

III. Results and Discussion

The model was used to obtain the mean oxygen saturation during lung inflation under normal conditions as well as those simulating increased threshold opening airway pressures. For the values of parameters used, the oxygen saturation calculated for a uniform distribution of opening pressures was found to be 3.6% higher as compared to simulations performed using a generation-dependent distribution of opening pressures with higher opening pressures in smaller airways. Figure 1 shows pulmonary venous oxygen saturation as a function of normalized inlet pressure for the reference case (dashed blue line). The utilization of generation-dependent opening pressures delays opening of alveoli, resulting in a higher shunt fraction during more of the inspiratory cycle (solid purple line). This phenomenon is illustrated in Figure 1 and results in a lower mean saturation when averaged over the inspiratory cycle as compared to the reference case. This simulation clearly demonstrates the influence of alterations in pulmonary mechanics on gas exchange frequently seen in critically ill patients.

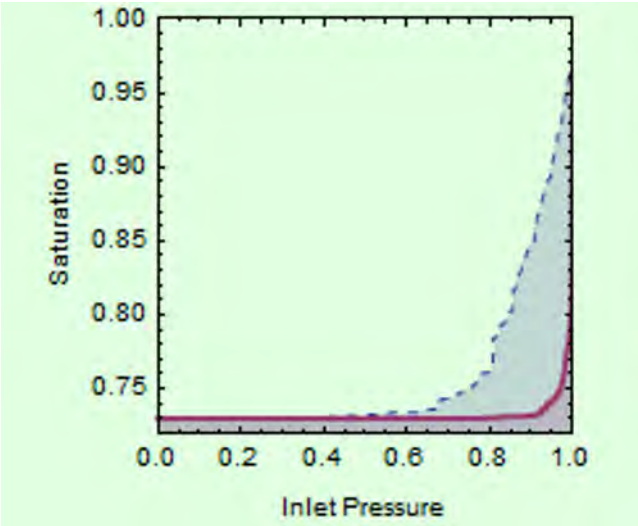


Fig. 1 Variation of pulmonary venous saturation during inspiration

IV. Conclusions

The purpose of this preliminary study was to assess the impact of generation-dependent opening pressures on oxygenation of blood flowing through the pulmonary vasculature. As expected, the oxygen saturation was seen to be higher with uniform opening pressures as compared to the case where higher opening pressures were assigned to smaller airways. Future studies will incorporate heterogeneity in the airway and vascular tree structures, airway and alveolar wall tissue elasticity, a more detailed model of gas exchange across the alveolar-capillary membrane, and incorporation of gravity effects. The ultimate goal of this work is to develop optimal ventilation strategies to minimize ventilator induced lung injury and improve gas exchange in critically ill patients.

References

1. Alencar AM, Arold SP, Buldyrev SV et al (2002) Dynamic instabilities in the inflating lung, Nature 417:809–810
2. de Chazal I, Hubmayr RD (2003) Novel aspects of pulmonary mechanics in intensive care, Br J Anesth 91:81–91
3. Suki B et al (2000) Size distribution of recruited alveolar volumes in airway reopening, J Appl Physiol 89:2030–2040
4. Suki B, Andrade JS, Coughlin MF et al (1998) Mathematical modeling of the first inflation of degassed lungs, Ann Biomed Eng 26:608

Author: T K Roy, MD PhD
Institute: Mayo Clinic
Street: 200 First Street SW
City: Rochester, MN
Country: USA
Email: roy.tk@mayo.edu

Artificial High – Flexion Knee Customized for Eastern Lifestyle

S. Sivarasu[1] and L. Mathew[2]

[1] Ph.D Scholar, SBCBE, VIT University, India
[2] Dean, SBCBE, VIT University, India

Abstract — **Total Knee Arthroplasty has been an end term surgical procedure for pain relief and movement restoration in knee joint with Arthritis. The procedure has been followed for more than 5 decades. The performance of the joint after the procedure is dependent on the implant design. The emphasize for customized joint design for the eastern world has be in the discussion for a while now, mainly owing to the economic growth surrounding the eastern countries like China and India. Also the arthritis estimates show that the probable increase in the procedure numbers in the coming years.**

The requirement of eastern world for their lifestyles is the provision to sit on the lower platform. This means that the flexion-extension requirement of the implant is over 120 degrees. More over the activities like squatting would require mild inner rotation in the implant, so a Rotating platform design is considered for the knee design.

A multi radii design with an extended condylar portion is considered for the femoral component design. The inner profile is maintained such that it can be used with standard zigs that are used in TKS. The inner structures are of the component are design such that it enhances bone growth even after the implantation. Based on the tibial component design two final models were derived.

The models were subjected to Finite Element Analysis [FEA]. Design corrections were made with the FEA results. The models were then subjected to AdamsView motion analysis and Jack Motion Analysis. The range of motion of the models was verified to be over 120^{o}. The research is aimed in designing a knee with over 135 degrees of range of motion.

Keywords — **Total Knee Arthroplasty, Artificial Knee, High Flexion Knee, Squatting, Finite Element Analysis**

I. Introduction

The joint replacement surgeries are doubtlessly the gift of science and technology for human welfare. The history of joint replacement begins way back in the late 60's. Initially from the Hip, then to Knee and now shoulders, ankle elbow and almost all the joints are replaced nowadays.

The knee replacement procedures had been followed for almost 50 years in the surgical procedure called the Total Knee Replacement [TKR] or the Total Knee Arthroplasty [TKA]. Here the cartilages and the bones surface which are degenerated by arthritis are removed and replaced with the metal components either by cemented or Cementless procedures. The metal and the Polyethylene components are all together called the Artificial Knee. [1][2][3]

II. Design of the Artificial Knee:

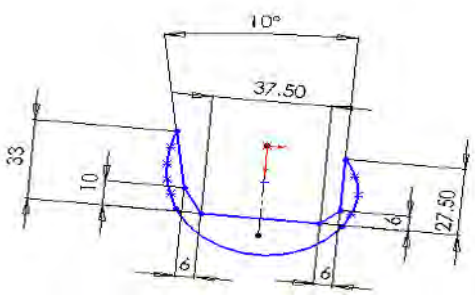
The components in the artificial knee are,

- The Femoral component
- The Tibial component
- The Patellar component
- The PE Insert

The design of each components of the artificial knee is shown below. The design emphasis is given on the femoral component as that's the only component involved in the major movements. Where as the rest of the components act mainly as supporting structures.

A. The Femoral component design:

The femoral component being the key factor in the flexion range determination of an artificial knee needs extreme care in its design and evaluation. The ideal femoral component would be the replica of the natural femur, but owing design constrains few modifications are made on the design. [1][2][4]



Developing from the base design we get the 3-D model of the femoral component. Fig. 2

Chwee Teck Lim, James C.H. Goh (Eds.): ICBME 2008, Proceedings 23, pp. 1597–1599, 2009
www.springerlink.com



Fig.2 Femoral component models.

The existing multi-radii design by its own has a range of over 135 degrees. To allow this range corrections are made on the posterior of the PE insert for the free movement of the femoral component over the insert. The rise in the PE is shelved and seen to that the rolling and gliding is continuous.[1][2]

Design parameters such as the single- radii or a multi radii design were initially compared. The multi radii design offers better range of motion that the single radii design. These tests were done using the ADAMS simulation works. The movements were defined by an equation and they were allowed to move. The results suggested that the multi radii design not only supports the rolling but also the gliding action as in a natural knee unlike the single radii design. [1][2][5]

The radius of the arc of the condyles of the femoral components, have better stability if they are away from each other and have better range of motion if they are towards each other. But trying to get a balance between the movement and the stability the medical lines were selected for the condlyar arc.[6]

The arc of the femoral components condyles in the posterior side, i.e. the part where the femoral component rests during the high flexion, is has a curivical end than the regular stunt end. This enhances the range of motion. This also means the extension of range of motion by another 10 to 15 degrees [1][2][7]

III. The Final Designs

A. The final designs:

The two proposed 2 new designs for the eastern lifestyles.Fig.3 and Fig.4



Fig.3 Model – I : Regular conical Insert



Fig.4 Model–II: Peg Restrainer for the PE insert

B. Analysis of the Design:

The design is subjected to Finite Element Analysis [FEA]. Owing the FEA results the corrections were made in the designs. The models were also subjected to motion analysis to determine the flexion- extension range. Both the results of the FEA and motion analysis are key factors in the design of the implant. [8]

C. Results of the Analysis:

The models were subjected to finite element analysis with load conditions above the normal human load levels. For example for the Tibial component, the maximum load

subject would be around 6 times the body weight. i.e., 6* 65 [average Weight] = 390Kgs. But for the same condition, the models were tested with a load of around 450-500 Kgs. The results of the designs would be published after the patenting of the model. However the results have been good enough to move the model for fabrication.[1][2]. The AdamsView motion analysis shows that the models when subjected to motion undergo a flexion of up to 130°.

IV. Discussion

Fig.5 below illustrates the flexion – extension range of the normal knee

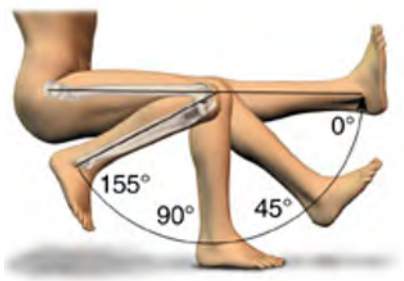


Fig.5 Flexion – Extension Range of the Knee.

The normal artificial knee designs that are available in the market are designed with consideration on the western population. Most of these implants have a design restriction upto 90degrees. The normal activity of an average eastern world population lies around 100 degrees. The existing design thus cannot be used in these applications. How ever these new design that are proposed can give the comfort of semi-squatting as they provide flexion extension range of around 120 degrees. This is validated with the AdamsView simulation results.

V. Conclusions

Fixing the components and making one component to glide over the other achieved the existing range of 130 degrees. This movement is defined by an equation. However, the movements restricted to 130 degrees strictly by the restriction of the condyles of the femoral components. The change in this section will definitely help us reach 140 degrees.

References

1. Sudesh, S; Mathew, Lazar; Design of an artificial high flexion knee; Life Science Systems and Applications Workshop, 2007. LISA 2007. IEEE/NIH 8-9 Nov. 2007 Page(s):112 - 115
2. Sudesh Sivarasu & Lazar Mathew; Modelling an artificial knee for customized needs of Indian population; INCOB-08, VITU, Feb 6-8, Pages 138-139
3. Raymond. P.Robinson, *" The Early Innovators of Today's Resurfacing Condylar Knees,"* The Journal Of Arthroplasty Vol.20, No.1,Suppl.1,2005.
4. Mariana E.Karsh, Heidi-Lynn Ploeg, *"How Does Normal Flexion Patello Femoral Contact Area Changes Before and After Deep Knee Flexi on.,"* Summer Bio-Engineering conference, June 22-26, 2005, Vail Cascade Resort & Spa , Vail, Colorado
5. Gloria Batista, Mario Ibarra, Johanna Ortiz and Melvia Villegas, *"Engineering Bio-Mechanics of Knee Replacement,"* May 2004, Applications of Engineering Mechanics in Medicine,GED, Mayaguez.
6. Dumitru I.Caruntu, Mohamed Samir Hefzy, Vijay K.Geol, Henry T.Goitz, Micheal J.Dennis, Vibhor Agarwal, *" Modeling The Knee Joint in Deep Flexion: " Thigh and Calf" Contact,"* Summer Bio-Engineering Conference, June 25-29,2003,Sonesta Beach Resort in Kay Biscayne, Florida
7. KY Chiu, TP Ng, WM Tang, WP Yau, *" Review Article: Knee Flexion After Total Knee Arthroplasty,"* Journal Of Orthopedic Surgery 2002; 10(2);194-202.
8. Silvia Zuffi, Alberto Leardini, Fabio Catani, Silvia Fantozzi, and Angelo Cappello, *" A Model Based Method for the Reconstruction of Total Knee Replacement Kinetics,"* IEEE Transactions on Medical Imaging, Vol.18, No.10, October 1999.

Author: **Sudesh Sivarasu**[1]
Institute: School of Biotechnology, Chemical and Biomedical Engineering,
VIT University.
Street: Tiruvalam Road,
City: Vellore
Country: India
Email: sudeshsivarasu@yahoo.co.in

Biomedical Engineering Analysis of the Rupture Risk of Cerebral Aneurysms: Flow Comparison of Three Small Pre-ruptured Versus Six Large Unruptured Cases

A. Kamoda[1], T. Yagi[1,2], A. Sato[1], Y. Qian[1], K. Iwasaki[1], M. Umezu[1], T. Akutsu[3], H. Takao[4], Y. Murayama[4]

[1] Integrative Bioscience and Biomedical Engineering, TWIns, Waseda University, Tokyo, Japan
[2] CSIRO Minerals, Melbourne, Australia
[3] Department of Mechanical Engineering, Kanto Gakuin University, Yokohama, Japan
[4] Department of Neurosurgery, Jikei University School of Medicine, Tokyo, Japan

Abstract — **A relationship between blood flows in cerebral aneurysms and their rupture remains obscure. In clinical practice, the size of aneurysms is one of the important factors for determining a strategy of treatment, but in our database three small aneurysms became ruptured during follow-up. Here, we aim to study their pre-ruptured hemodynamics, and differentiate them with those of six large unruptured aneurysms. All the aneurysms occurred in internal carotid artery, and their mean sizes were 6 and 10.8 mm for pre-ruptured and unruptured cases, respectively. We reproduced their replica as a patient-specific elastic model using clinical images obtained by digital subtraction angiography and a series of rapid prototyping techniques. Flows were reproduced *in vitro* using a cerebral flow simulator, and visualized by Time-resolved Particle Image Velocimetry. All pre-ruptured cases showed the collision of an incoming flow at a distal neck, and formed a prominent jet stream directing towards the aneurismal head. In contrast, none of unruptured aneurysms had such a marked impingement, and their flows were most likely characterized by swirling patterns. All unruptured cases occurred in a twisted vessel, or carotid siphon, whereas pre-ruptured ones were located downstream whose geometries consisted of a simple curvature. These findings suggest that internal carotid artery has a regional dependency of the risk of aneurismal rupture. Furthermore, the presence of jet streams for small-sized aneurysms may be a substantial indicator of the rupture and immediate treatments.**

Keywords — **cerebral aneurysm, rupture, PIV, hemodynamics**

I. Introduction

The rupture risk of cerebral aneurysm is diagnosed by several factors including size and geometry. The occurrence rate of the rupture is only about 0.5 % per year [1], but it leads to subarachnoid hemorrhage that has a significant impact on the life of patients since its mortality rate reaches up to 50 % [2]. Currently, about 85 percents of subarachnoid hemorrhage were estimated to be caused by the aneurismal rupture. Thus, there is a significant demand for the risk management of rupture.

It is widely believed that hemodynamics in aneurysm may be related with its rupture. Wall shear stress (WSS) is one of the key parameters in regulating the remodeling of blood vessels. Likewise, some researchers utilized the WSS to assess the risk of aneurismal rupture, but there is as yet a reliable correlation between them [3, 4]. Indeed, there are even varying magnitudes of the WSS observed in an individual aneurysm, which in turn hampers to compare the value with others.

Cebral and colleagues studied the flows in aneurysms with a wide variety of anatomy, namely lateral, bifurcation, and terminal types, using computational fluid dynamics (CFD) [5]. In doing so, they assumed the vessel wall acted as a solid boundary. They observed varying patterns of inflow jets among ruptured and unruptured cases, and reported that the former more likely had small impingement regions and narrow jets.

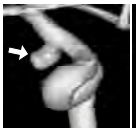
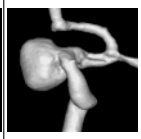
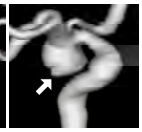
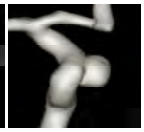
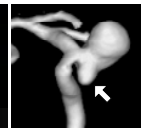
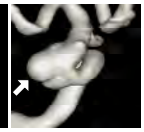
Until now, we observed the rupture of three small-sized lateral aneurysms in internal carotid artery during follow-up. In the present paper, we compare the flows with those of large-sized six aneurysms from the similar anatomical location. The flow analysis comprised a patient-specific elastic replica and an *in vitro* flow visualization using Time-resolved Particle Image Velocimetry (PIV). This paper aims to clarify the differentiation of flows between pre-ruptured and unruptured cases and to better understand the mechanism of the aneurismal hemodynamics in an effort to establish the risk management of rupture.

II. Method

Table 1 summarizes data of aneurysms studied. Three-dimensional digital subtraction angiography done by interventional neuroradiologists determined geometries of aneurysms including parent vessles. Fig.1 shows anatomical locations of aneurysms. The mean size and age of three pre-ruptured cases were 6 mm and 67 years, while counterparts of six unruptured cases were 10.8 mm and 62.7 years. Vascular geometries were reproduced as a patient-specific

Chwee Teck Lim, James C.H. Goh (Eds.): ICBME 2008, Proceedings 23, pp. 1600–1603, 2009
www.springerlink.com

Table 1 Details of aneurysms studied. All the aneurysms are located in internal carotid artery (ICA). The case1, 6, 8 and 9 harbor blebs (white arrow).

	Pre-ruptured			Unruptured					
Case	1	2	3	4	5	6	7	8	9
									
Position	Right ICA	Right ICA	Right ICA	Left ICA	Left ICA	Right ICA	Right ICA	Right ICA	Right ICA
Age/sex	72/F	62/F	67/F	63/F	60/F	65/F	56/F	54/F	78/F
Size mm	6	6	6	12	11	9	7	13	13
Aspect Ratio	1.7	2.3	1.2	2.5	1.2	1.0	1.1	2.5	0.9
Bleb	□	×	×	×					

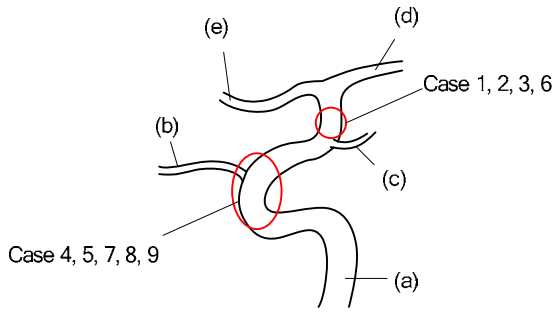


Fig.1 The anatomical locations of aneurysms studied (red circle). (a) Internal Carotid Artery, (b) Ophthalmic Artery, (c) Posterior Communicating Artery, (d) Middle Cerebral Artery, (e) Anterior Cerebral Artery.



Fig.2 Patient-specific elastic models of aneurysms. These models are made of transparent silicone rubber.

replica (Fig.2). These aneurysm models were made of a transparent silicone rubber using rapid prototyping techniques including stereolithography and lost-wax casting. The mechanical property of the models was standardized by incremental distensibility, which had a value of $1.4\pm0.4\times10^{-3}$ 1/mmHg, approximately corresponding to that of anterior cerebral artery of healthy individuals [6].

Then, the aneurysm model was set in a pulsatile flow simulator (Fig.3). The mean flow rate was adjusted to 330 mL/min at a pressure of 120/80 mmHg, a heart rate of 70 bpm, and a systolic fraction of 35 %. The working fluid was a mixture of glycerol and water with a fraction of 46 and 54 %, respectively, which had a density and kinematic viscosity of 1100 kg/m^3 and 3.7 cSt, respectively. The fluid was seeded by fluorescent tracer particles with a density of 1100 kg/ m^3 and a mean size of 15 μm (Fluostar, EBM corp., Tokyo).

Then, Time-resolved PIV measurements were carried out. A long-pass fluorescent filter eliminated the scattered light from the laser with a wavelength of 532 nm and selectively passed the fluorescent light with a wavelength of 580 nm.

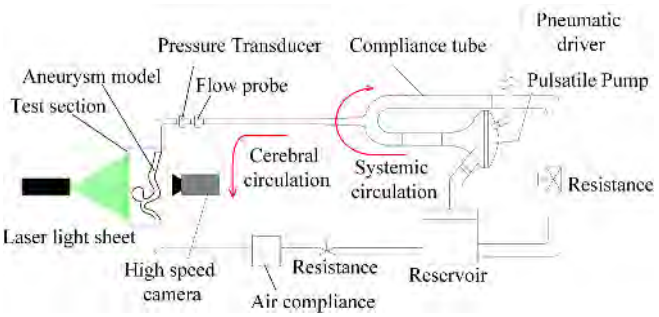


Fig.3 In vitro cerebral vascular flow simulater

This fluorescent PIV technique was found to be significantly useful for the accurate measurement of aneurismal flows. PIV measurements were repeated in multiple planes to cover the whole part of aneurysms.

III. Results and Discussion

Flow characterization revealed that flow patterns were classified by three types for aneurysms studied. Jet type was characterized by a jet flow, which was defined to have a flow collision at the distal neck and a separated flow directing towards the head of aneurysm. The all pre-ruptured cases exhibited such phenomena with jet velocities reaching 1 m/s approximately. Fig.4 summarizes the representative pattern of the jets observed during peak phase. The incoming flow in the parent vessels collided with the downstream sides of the aneurismal necks, and then the separated flow formed the intra-aneurismal jet. There are no marked differences observed for the cyclic changing of flow patterns. Swirl type was characterized by a swirling flow which was most likely observed in the unruptured cases. Fig.5 shows the representative inflow patterns for the unruptured cases. Incoming flows did not show a marked collision to the neck, and the flows in the parent vessels rather entered the aneurysms more smoothly. In order to understand the flow structures in three-dimensions, PIV measurements were made in orthogonal planes (Fig.6). It was found that the flows were more likely characterized by swirling flows rather than jet flows. Branch type was characterized by multiple flows because of the presence of blebs. All the blebs showed the distinct low velocity of the order of 0.1 m/s or less.

Table 2 summarizes the characterization of flow patterns. Distinct vascular geometries caused varying patterns of aneurismal hemodynamics. Most of unruptured cases were located in carotid siphon whose geometries were characterized by strong twisting shapes. On the other hand, all pre-ruptured cases were at the downstream, where the vessel consisted of smooth curvature without twisting. The twisting vessel generated a tangential inflow into the neck plane, resulting in the formation of a swirling flow. In terms of fluid dynamics, a jet flow tends to become more unstable

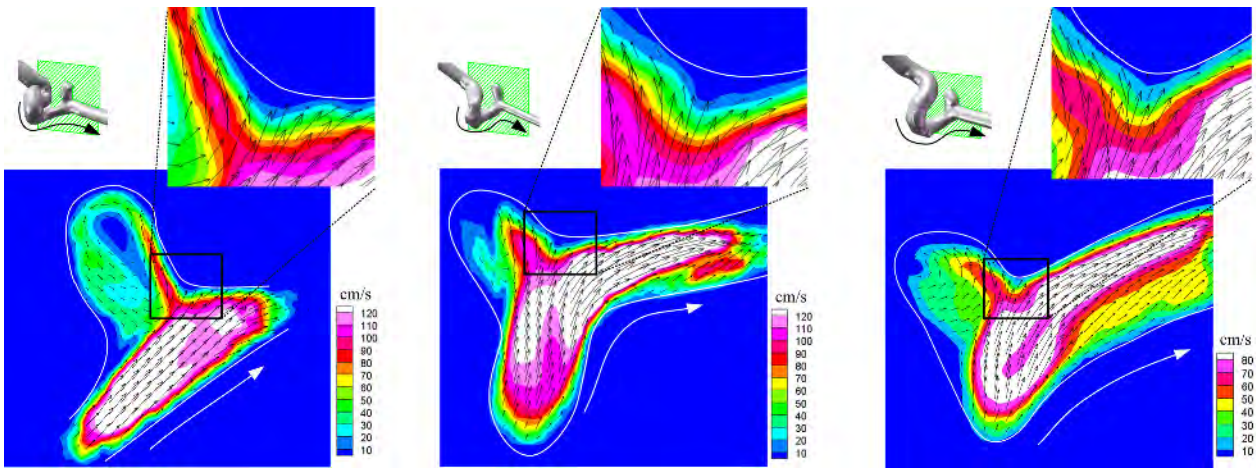


Fig.4 Aneurismal jets observed during peak phase in all pre-ruptured cases (left: case1, center: case2, right: case3). The flows in the parent vessels collided with distal sides of the aneurismal necks, and then the breakup of the flow led to form the jets. Schema shows measurement planes.

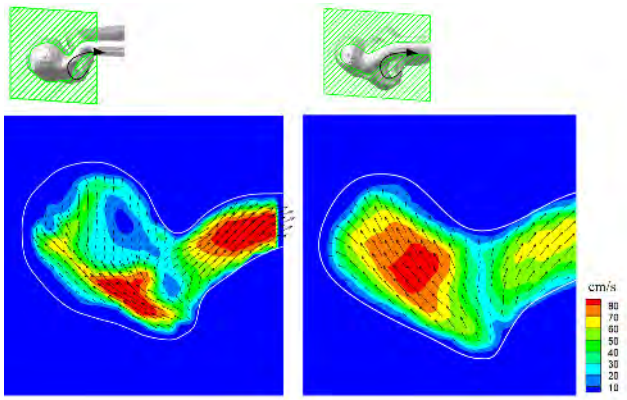


Fig.5 Comparison of inflow patterns in unruptured cases (left: case4, right: case5)

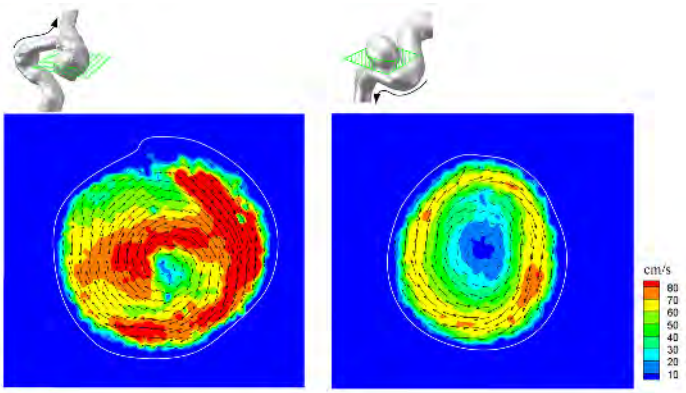


Fig.6 Swirling flow patterns observed in unruptured cases (left: case6, right: case7)

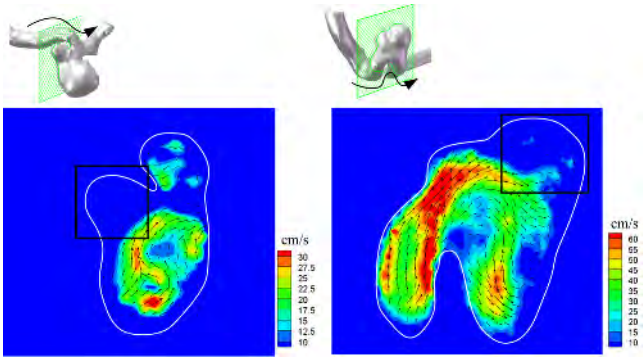


Fig.7 Multiple flows observed in unruptured cases (left: case8, right: case9). These cases harbor blebs (black frame).

Table 2 Flow patterns in aneurysms studied. Inflow patterns are described in parentheses. Case1, 2 and 3 have impinging flow as indicated by red arrow.

Flow pattern	Case							
Jet Type (collision)	Case 1		Case 2		Case 3			
Swirl Type (smooth inflow)	Case 4		Case 5		Case 6		Case 7	
Branch Type (smooth inflow)	Case 8		Case 9					

owing to an adverse pressure gradient and more often generates high WSS than the swirling flow. As a result, our data may indicate that there is a varying degree of rupture risk of aneurysm in internal carotid artery. By considering that the pre-ruptured aneurysm had the rather small size, it is suggested that the presence of a jet flow may be a substantial indicator of the rupture of a small-sized aneurysm.

IV. Conclusions

This study showed that there is an interesting trend in the relationship between aneurismal hemodynamics and rupture. The flows studied were classified into three types characterized by Jet, Swirl and Branch Type. Varying flow patterns attributed to the anatomical location in internal carotid artery. The simple curvatures of the parent vessels promoted colliding flows at the distal sides of aneurismal necks, resulting in the strong aneurismal jets. The swirling flows observed in the unruptured cases were caused by the twisting vessel which is called carotid siphon. The blebs on aneurysms made a distinct low velocity in contrast to that of the mainstream. It was suggested that aneurismal jets may play a key role for the risk management of the rupture, and can be characterized according to the anatomical configuration of the aneurysm and parent vessel.

Acknowledgment

This research was partly supported by Health Science Research Grant (H20-IKOU-IPAN-001) from Ministry of Health, Labour and Welfare, Japan, Biomedical Engineering Research Project on Advanced Medical Treatment from Waseda University (A8201), and "Establishment of Consolidated Research Institute for Advanced Science and Medical Care", Encouraging Development Strategic Research Centers Program, the Special Coordination Funds for Promoting Science and Technology, Ministry of Education, Culture, Sports, Science and Technology, Japan.

References

1. The International Study of Unruptured Intracranial Aneurysms Investigators (1998), N Eng J Med 339, 1725-1733.
2. J. v. Gijn, R. S. Kerr, G. j E Rinkel (2007), "Subaracnoid haemorrhage", Lancet 369: 306-318.
3. S. Tateshima, Y. Murayama, J.P. Villablanca, T. Morino, K. Nomura, K. Tanishita, and F. Viñuela (2003), "In Vitro Measurement of Fluid-Induced Wall Shear Stress in Unruptured Cerebral Aneurysms Harboring Blebs", Stroke 34: 187-192
4. M. Shojima, M. Oshima, K. Takagi, R. Torii, M. Hayakawa, K. Katada, A. Morita, and T. Kirono (2004), "Magnitude and Role of Wall Shear Stress on Cerebral Aneurysm: Computational Fluid Dynamic Study of 20 Middle Cerebral Artery Aneurysms", Stroke 35: 2500-2505.
5. J. R. Cebral, M. A. Castro, J. E. Burgess, R. S. Pergolizzi, M. J. Sheridan, and C. M. Putman (2005), "Characterization of Cerebral Aneurysms for Assessing Risk of Rupture By Using Patient-Specific Computational Hemodynamics Models", Am J Neuroradiol 26: 2550-2559.
6. G. Mark, A. G. Hudetz, T. Kerenyi, E. Monos, A. G. B. Kovachi (1977), "Is the Sclerotic Vessel Wall Really More Rigid than the Normal One ?", Prog. Biochem. Pharmacol. 14: 292-297.

Author: M. Umezu
Institute: Integrative Bioscience and Biomedical Engineering, TWIns, Waseda University
Street: 2-2 Wakamatsucho, Shinjuku
City: Tokyo
Country: Japan
Email: umezu@waseda.jp

Metrology Applications in Body-Segment Coordinate Systems

G.A. Turley[1] and M.A. Williams[1]

[1] WMG: Innovative Solutions, School of Engineering, The University of Warwick, Coventry, UK

Abstract — **The location and stability of a surgical implant is a critical factor for a successful clinical outcome. This is dependent upon being able to define the position of an implant in relation to its mating bone or body-segment. Advances in the surgical process require definition of body-segment coordinates to be robust which is influenced by the references these coordinate frames are derived from. This paper presents preliminary findings in the use of metrology tools and techniques to register bone landmarks in an accurate and repeatable manner and address whether the establishment of a body-segment coordinate frame can aid in implant positioning.**

Keywords — **Body-Segment Coordinates, Implant Bone-Alignment, Metrology.**

I. Introduction

The surgical process has emerged as a field which has seen the exploitation of sophisticated technologies, often having to embrace adapted principles from other industries. This has led to a closer integration with the engineering community and produced cross-disciplined research increasing the depth of knowledge available to the surgeon to diagnose, treat and rehabilitate their patients using more customized approaches [1]. An area that can have a significant impact upon the success of the surgical intervention is the location and stability of the surgical implant in orthopedic surgery [2]. However, the clinical outcome of the location and orientation of the endo-prosthesis is still affected by surgeon-handwork and implant-bone alignment [3]. This highlights a gap in knowledge between the engineering and healthcare community and provides a focus for this paper.

II. Biomechanical coordinate frames

The location and stability of a surgical implant is influenced by how well the endo-prosthesis and bone can be dimensionally aligned and is therefore intrinsically a biomechanical problem. In biomechanics it is important that factors such as motion, location and orientation are expressed where possible in clinical terms to ensure meaningful comprehension by the healthcare community, which requires relating findings and expressing them in an anatomical coordinate frame shown in Figure 1 [4].

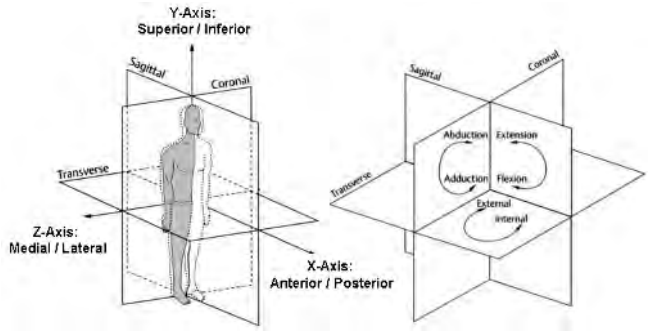


Fig 1 The Anatomical Coordinate Frame

Biomechanical assessment uses the principles of rigid-body mechanics, which regards the distances between points on a moving segment to be invariant [5]. A rigid-body has six degrees of freedom which are used to describe the location and orientation of a body-segment [6, 7]. Using Figure 1 there are three translational degrees of freedom which occur along the x, y, z axes and three rotational degrees of freedom which occur about these axes.

In orthopedic biomechanical application such as gait analysis and arthroplasty procedures involving endo-prosthesis the relative position of one body-segment to another is critical to ascertain the joint characteristics [8]. To be able describe joint characteristics in a biomechanical context two classes of coordinate frames are used. Body-segment coordinate frames which refer to the local coordinate system of a particular bone and joint coordinate systems which are used to define the relationship between two body-segments of a joint, for example the humerus and the scapula which are the mating bones within the shoulder joint system [9]. This paper will focus upon the use of body-segment coordinate frames in the application of aligning a hip endo-prosthesis with a femur using dimensional metrology tools and techniques.

III. Research problem

A body-segment coordinate system relies on establishing a cartesian coordinate frame for a bone segment [9, 10]. Advances in the surgical process require definition of body-segment coordinates to be robust which is influenced by the references these coordinate frames are derived from [11].

Chwee Teck Lim, James C.H. Goh (Eds.): ICBME 2008, Proceedings 23, pp. 1604–1607, 2009
www.springerlink.com

Using rigid-body principles to define a body-segment coordinate system, three location parameters and three orientation parameters are required to form a cartesian coordinate system [6]. Therefore, a minimum of three non-collinear points or landmarks are necessary to construct a body-segment reference frame [12, 13].

One of the major sources of error in a study or clinical analysis using body-segment coordinate frames is the registration of landmark information. This registration is influenced by two significant factors, being able to palpitate or digitize exactly the same reference point location on a bony prominence in a repeated manner and the limited accuracy of the measurement devices used to register the landmarks [14, 15]. Coordinate frames are also influenced by variability in the bone morphology and the fact that the rationale behind the selection of landmarks do not consider the increased anatomical stability that some landmarks have with regard to others [4, 13, 16].

The issues highlighted in the previous paragraph present certain research problems which the initial work presented in this paper purports to begin to address. These research problems have been detailed:

- Can metrology tools and techniques be used to register bone landmarks in an accurate and repeatable manner?
- Can the establishment of a body-segment coordinate frame aid in the positioning of an endo-prosthesis?

IV. Methodology

The research problem presented in the previous section is sought to be addressed by the use of a Coordinate Measuring Machine (CMM) to register bone landmarks on a model femur. A CMM is a computer numerically controlled (CNC) measurement system, which with the aid of a probing device can detect the spatial coordinates of an artifacts surface. Two probing systems will be used in this experiment, a touch-trigger probe and a non-contact laser-scanning probe. The touch-trigger probe is a tactile sensing element whose displacement can be sensed throughout the three dimensional workspace of the CMM. It interacts with the workpiece through probing the artifact surface, recording the x, y, z position and its i, j, k direction [17].

Laser-scanning consists of defining a numeric representation of an artifacts surface through sets of 3-D points [18]. It can gather up to 19,200 points per second, utilizing an image sensing camera and a focused laser line to gather points using a process known as active triangulation [18, 19]. This allows surface topology to be determined without having to contact the objects surface.

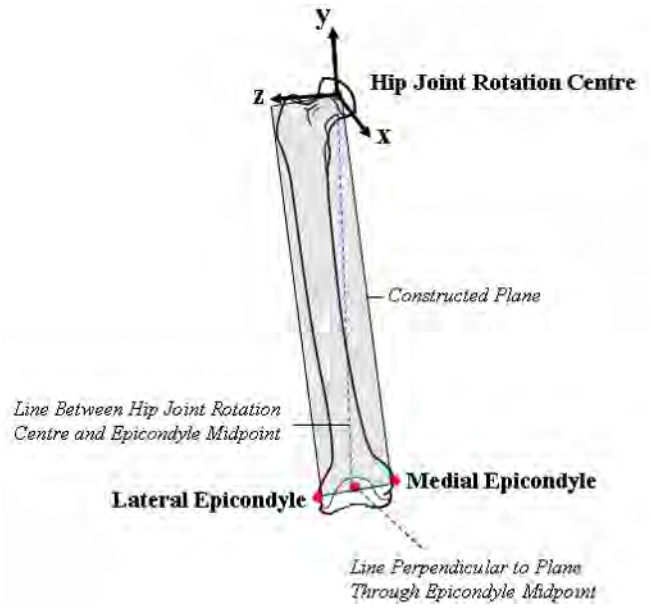


Fig 2 Femur Body-Segment Coordinate Frame

The two probing technologies that are going to be used during this experiment are the Renishaw TP20 touch-trigger probe and the Metris LC50 laser-scanning probe, both these probes will be mounted to a Metris HC-90 Horizontal CMM arm. When mounted to the CMM the touch-trigger probe has a quoted repeatability of 6μm while the laser-scanning probe has a repeatability of 15μm.

The laser-scanning probe was first used to take a scan of the model femur in the CMM global coordinate frame. The generated point cloud was then used to provide coordinate data for the three reference landmarks for the femur shown in Figure 2. This was made possible through visualizing the point cloud within the CAD environment so that the femur could be aligned to pick out the most medial and lateral points of the medial and lateral femoral epicondyles (FE) respectively and fit a sphere through the femoral head to determine the hip joint centre of rotation (HRC). These are the recommended landmarks proposed by the International Society of Biomechanics (ISB) [20]. The touch-probe was then fitted and programmed to measure the FE's and 30 points on the femoral head to calculate the HRC. A body-segment coordinate system was then established by constructing a line between the HRC and the midpoint of the FE's. A 3-point plane was then constructed from the landmark features and a line projected perpendicular from this plane through the midpoint of the FE's. The global reference system of the CMM was translated so that its origin coincided with the midpoint of the FE's and a 3-axis Euler rotation sequence [21] was then applied to rotate the global frame so that the y-axis aligned with the line between the

HRC and the midpoint of the FE's and the x-axis aligned with the other constructed line. This left the z-axis pointing positively in the right-lateral direction. A further translation of the origin was applied so that it was coincident with the HRC. This established a body-segment coordinate system that was both congruent with the ISB recommendations and anatomically representative.

The original point cloud was imported while the body-segment coordinate frame was being constructed which allowed the initial laser scan to be transformed into the femoral reference frame. The coordinate data for a further six landmarks could then be determined using the same methodology as was used for selecting the three reference landmarks. These were then programmed to be measured ten times using the touch-trigger probe, measuring the reference landmarks and reconstructing the femoral reference frame each time from the CMM global coordinates. This provided a test for the robustness of the body-segment coordinate system and for the repeatability of landmark digitization.

A model endo-prosthesis was then measured by the touch-trigger probe. Features were selected from the endo-prosthesis that permitted a coordinate frame to be constructed that was congruent with the body-segment coordinate frame of the femur, shown in Figure 3. A laser-scan was then taken in this coordinate frame so that both the endo-prosthesis and the femur could be analyzed in the CAD environment. A finite element mesh was generated from each point cloud and the axes of the implant coordinate frame were then aligned with the femoral coordinate frame to allow the helical or screw angle between the coordinate axes to be calculated so that congruence could be assessed. Once the endo-prosthesis axes were fully aligned with that of the femur the positioning of the implant could be evaluated. The results of this experiment are presented in the following section.

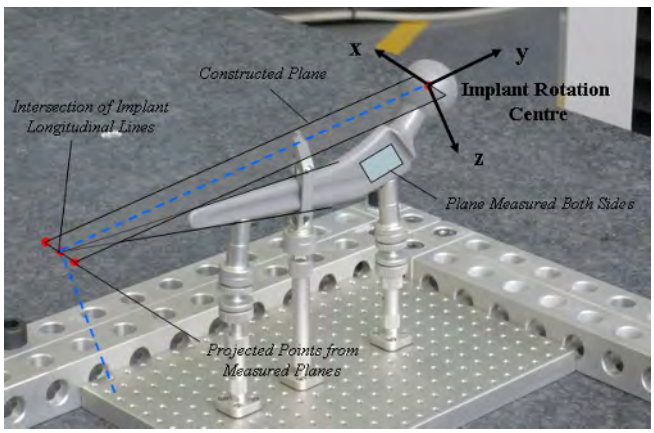


Fig 3 Endo-Prosthesis Coordinate Frame

V. Results

The CMM touch-trigger measurement results for the digitization of the six non-reference femoral landmarks have been presented in Table 1. Due to the probing directions of the landmarks being different, the measurement axis which produced the worst repeatability reading for each landmark has been presented. This axis coincided with the significant axis of evaluation for all landmarks. The table shows that the reference landmarks selected could be re-measured to produce a robust alignment frame which can digitize in a repeatable manner bone landmarks.

Table 1 Repeatability of Landmark Measurements

Landmark	Axis	Repeatability (μm)
Fovea Capitis	Y	6.71
Superior Point of Greater Trochanter	Y	1.95
Lateral Point of Greater Trochanter	Z	5.69
Superior Point of Lesser Trochanter	X	5.42
Superior Point of Medial Condyle	Y	3.46
Superior Point of Lateral Condyle	Y	2.59

The construction features of the body-segment coordinate frames for both the femur and the endo-prosthesis were examined in the CAD environment. The datum axes were aligned by applying a 3-axis Euler rotation sequence from which a helical angle of 6.62º was calculated which represented the deviation between the two coordinate frames. This is within the 10º angle bearing limit defined as deviating significantly from the frame of reference [11]. As well as the congruence of the axes being examined the endo-prosthesis positioning could also be visually evaluated. Figure 4 provides a schematic of the implant and femoral position relative to each other.

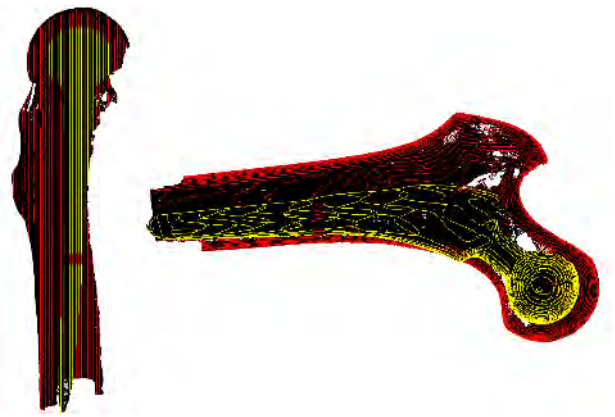


Fig 4 Schematic of Implant Positioning

Reviewing the schematic although professional clinical assessment is required, it is clear that the implant protrudes from the femoral surface and is situated so that only a thin bone wall thickness is holding the implant in place. The schematic does show however that the implant positioning does maintain the hip joint rotation centre. However, because of the limitations detailed, it can be asserted that the recommended femoral body-segment coordinate frame is not suitable for the surgical positioning of this design of endo-prosthesis.

VI. Conclusions & further work

The preliminary work presented in this paper has shown that metrology tools and techniques can be used to register bone landmarks in an accurate and repeatable manner. Also, an endo-prosthesis reference frame was established that was congruent with the recommended femoral body-segment coordinate frame [20], although the functionality with regard to implant positioning can be questioned.

The degree of congruence between the two coordinate systems will vary with bone morphology and pathology particularly considering the distance of the two reference femoral epicondyles away from the functionally important hip joint rotation centre. Therefore, the suitability of other more proximal landmarks is proposed to be investigated. The preliminary investigation has scope to expand the research with regard to the role of biomechanical coordinate frames in surgical implant positioning. The items below present a summary of this future scope:

- To use metrology tools and techniques to provide a traceable calibration route to improve the accuracy and repeatability within the surgical field;
- To incorporate the visualization techniques presented into the digital templating process, to include features such as landmark recognition and registration and bone cutting angles;
- To incorporate both body-segment coordinate and joint coordinate frames in the dimensional assessment of endo-prosthesis and design of surgical fixtures.

Acknowledgment

The authors would like thank the Engineering and Physical Sciences Research Council (EPSRC) and Metris for their support of this work.

References

1. Brown GA & DeCoster TA (2003), Rapid prototyping: The future of trauma surgery, J Bone Joint Surg-Amer Vol, 85:49-55;
2. D'Urso PS, Hall BI, Atkinson LR, Weidmann MJ & Redmond MJ (1999) Biomodel-guided stereotaxy, Neurosurgery, 44:1084-1093;
3. Ganeto J, Xia J, Teichfraeber JF, Rosen A, Hultgren B & Vadnais T (2003), The precision of computer generated surgical splints, J Oral Maxillofac Surg, 61:814-817;
4. Brinckmann P, Frobin W & Leivseth G (2002), Musculoskeletal Biomechanics, 1st Edition, Thieme Publishing;
5. Woltring HJ (1991), Representation and calculation of 3-D joint movement, Hum Movement Sci, 10:603-616;
6. Andrews JG (1984), Letter to the editor – On the specification of joint configurations and motions, J Biomech, 17:155-158;
7. Baker R (2003), Letter to the Editor - ISB recommendation on definition of joint coordinate systems for the reporting of human joint motion—part I: ankle, hip and spine; J Biomech, 36:300-302;
8. Wu G & Cavanagh PR (1995), ISB recommendations for the standardization in the reporting of kinematic data, J Biomech, 28:1257-1261;
9. Grood ES & Suntay WJ (1983), A Joint Coordinate System for the Clinical Description of Three Dimensional Motions: Application to the Knee, J Biomech Eng Trans ASME, 105:136-144;
10. Woltring HJ (1994), A 3-D attitude representation of human joints: a standardisation proposal, J Biomech, 27:1399-1414;
11. Amadi HO, Hansen UN, Wallace AL & Bull AMJ (2008), A scapular coordinate frame for clinical and kinematic analyses, J Biomech, 41:2144-2149;
12. Sommer III HJ, Miller NR & Pijanowski GJ (1982), Three dimensional osteometric scaling and normative modelling of skeletal segments, J Biomech, 15:171-180;
13. Stokdijk M, Nagals J & Rozing PM (2000), The glenohumeral joint rotation centre in vivo, J Biomech, 33:1629-1636;
14. Haut TL, Hull ML & Howell SM (1998), A high-accuracy three dimensional coordinate digitizing system for reconstructing the geometry of diarthrodial joints, J Biomech, 31:571-577;
15. Kepple TM, Sommer III HJ, Sigel KL & Stanhope SJ (1998), A three-dimensional musculoskeletal database for the lower extremities, J Biomech, 31:77-80;
16. Holt CA, Evans SL, Dillon D & Ahuja S (2005), Three dimensional measurement of invertebral kinematics in vitro using optical motion analysis, Proc Inst Mech Eng H, 219:393-399;
17. Flack D (2001), CMM Probing, National Physical Laboratory, © Crown Copyright;
18. Lartigue C, Contri A & Bourdet P (2002), Digitised point cloud quality in relation with point exploitation, Measurement, 32:193-203
19. Feng HY, Liu Y & Xi F (2001), Analysis of digitizing errors of a laser-scanning system, Precis Eng, 25:185-191;
20. Wu G, Siegler S, Allard P, Kirtley C, Leardini A, Rosenbaum D, Whittle M, D'Lima DD, Christofolini L, Witte H, Schmid O & Stokes I (2002), ISB recommendation on definitions of joint coordinate system of the various joints for the reporting of human joint motion - part I: ankle, hip and spine, J Biomech, 35:543-548;
21. Chao EYS (1980), Justification of Triaxial Goniometer from the measurement of Joint Rotation, J Biomech, 13:989-1006.

Author: Glen Turley
Institute: The University of Warwick.
City: Coventry
Country: United Kingdom
Email: glen.turley@warwick.ac.uk

Finite Element Modeling Of Uncemented Implants: Challenges in the Representation of the Press-fit Condition

S.E. Clift

Centre for Orthopaedic Biomechanics, University of Bath, UK

Abstract — **The primary stability of uncemented orthopaedic implants is dependent upon the production of a stable mechanical environment at surgery. Excessive movement between the prosthesis and the surrounding bone can lead to the formation of fibrous tissue instead of a direct bond with the bone. The establishment of an interference fit at surgery, called a press-fit, is widely used to limit such interfacial movement. Although this technique is very successful, bone fracture at surgery can occur if too high a fit is attempted. The question therefore arises as to what is the minimum level of interference that will help provide the mechanical environment in which osseointegration can occur. Computational approaches, such as the finite element methodology, are currently being explored in order to inform this discussion by identifying the characteristics of the mechanical environment which have most effect.**

Keywords — **press-fit, finite element, bone relaxation, uncemented implants.**

I. Introduction

A variety of techniques are used to secure orthopaedic implants to bony tissue. Cemented implants typically use a PMMA bone cement to promote a mechanical interlock with the surrounding bone, whereas the design of uncemented implants requires a direct bond to be established between the implant and the adjacent bone.

Critical to the production of this direct bond (termed 'osseointegration') is the minimization of interfacial slip. There are two contributions to the level of interfacial slip; one is the cyclic interfacial displacements caused by physiological loading, termed micromotion or dynamic motion, and the other is the subsidence of the prosthesis (Figure 1, Bühler et al [1]). High levels of micromotion (in excess of 150 microns) have been shown to lead to the formation of a fibrous tissue layer whereas lower levels of micromotion (40 microns or less) have been associated with osseointegration (Jasty et al [2]).

One way of reducing micromotion is via an interference fit between the bone and the implant, established at surgery by under-reaming. This interference fit must not be so large as to cause the femur to fracture (Davidson et al [3]), nor small enough to fail to limit micromotion. A further influence on the magnitude of the interference fit is produced by the stress relaxation of the bone.

This paper contains a review of the contribution and potential of finite element analysis to inform the choice of the magnitude of the interference fit.

II. Methodology & results

The key issues concerned with finite element model development of uncemented implants are considered below:

Specimen specific materials properties:

Specimen specific materials properties are now routinely used in computational orthopaedic biomechanics. Both bone geometry and the variation in mechanical properties are typically derived from CT scan data (eg [4]). An open access set of such scan data has been made available by The National Library of Medicine Visible Human Project (http://www.nlm.nih.gov/research/visible/visible_human.html). This dataset has the advantage that predictions can be more readily compared with those from other investigators. The big disadvantages are that the bones in question are obviously not available for experimental validation and, of course, no clinical outcome is associated with them. It is also important to be cautious about conclusions drawn from the analysis of a single bone [5].

Despite the popularity of such sophisticated representations of geometry and materials properties, they may not be the best choice for all types of investigation. Understanding can still be advanced with 2D/axisymmetric models as in the study of Shultz et al [6].

Hounsfield units to bone density, bone density to mechanical properties:

Bone density is represented in medical CT scanning by the Hounsfield Unit (HU) parameter, a measure of the local attenuation of the X-ray signal. This can be correlated to bone mineral density by including a hydroxyapatite "phantom" of known properties in the scan. Complete bones can be mapped in this way. The medical CT scanning technique does not provide any quantitative information on bone ar-

Chwee Teck Lim, James C.H. Goh (Eds.): ICBME 2008, Proceedings 23, pp. 1608–1610, 2009
www.springerlink.com

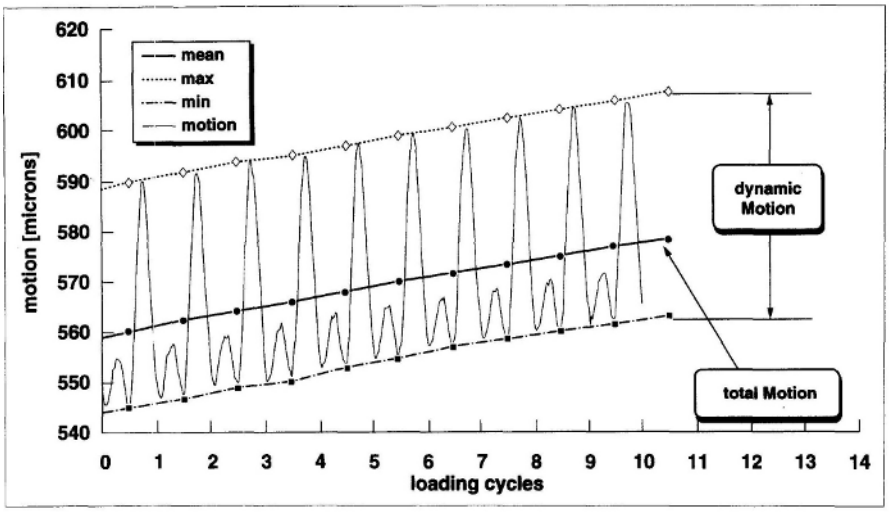


Figure 1: Definitions of dynamic motion (micromotion) and total motion (subsidence) taken from Bühler et al [1]. Figure reproduced with the kind permission of Elsevier.

chitecture, for this micro-CT scanning is needed. In contrast, micro-CT scanning is currently only able to deal with relative small specimens (with a maximum size of several centimetres) and so cannot map a complete long bone, for example. Thus whole bone finite element models to date are based on the information available in medical CT scanning. Particularly challenging is the process of calculation of appropriate materials properties for the bone from the mesure of density and many relationships have been proposed to account for this [7].

Friction

The presence of friction is essential to the minimization of micromotion (Kuiper & Huiskes [8]). Careful use of face-to-face contact elements incorporating Coulomb friction models have been shown to produce good agreement with experiments on composite femurs (Viceconti et al [9]). The properties assigned to the contact elements, in particular contact stiffness and convergence tolerance, can have a considerable influence on the predictions of micromotion (Bernakiewicz et al [10]). Non-linear models of friction have also been developed and validated against simple contact geometries (Dammak et al [11]) and successfully used in comparison with femoral micromotion experiments (Figure 2 [12]). Predictions from Abdul-Kadir et al [12] suggest that magnitudes of interference fit as low as 50 microns may be sufficient to produce the mechanical environment in which osseointegration can occur.

Bone relaxation

Stress relaxation in bone has been demonstrated by Shultz et al [6] to have a dramatic effect on the magnitude of the interference fit established at surgery. Using a validated finite element model, they explored the variation of three levels of initial interference fit with time (Figure 3 [6]). Rapid decay in contact pressure was observed, with predictions for levels of interference fit in excess of 0.1mm approaching that of 0.1 mm within the first 30 minutes. The lowest magnitude of interference fit examined, that of 0.01mm, appeared not to be significantly influenced by bone relaxation.

III. Future Questions

Validated finite-element models of the interference fit condition offer the possibility of investigating many clinically relevant situations, including:

- Partial bone-stem contact
- Varying levels of interference fit at different locations
- Non-uniform friction
- Bone stock loss associated with revision surgery
- Effect of variation in prosthesis positioning on micromotion
- Effect of local variations in bone density.

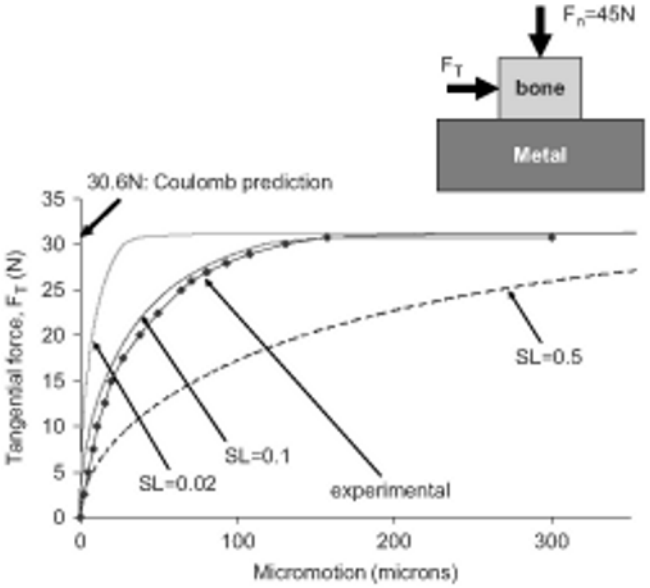


Figure 2: Variation in micromotion with tangential force for a cube of bone sliding on a metal surface: Comparison between finite element based predictions using the MARC SL parameter and experimental results (Abdul-Kadir et al [12]). Figure reproduced with the kind permission of Elsevier.

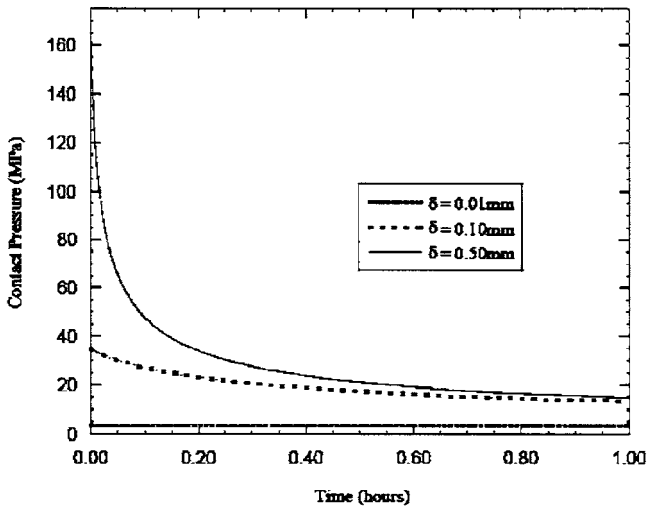


Figure 3: Variation in bone contact pressure with time (Shultz et al [6]) Figure reproduced with the kind permission of ASME

REFERENCES

1. Bühler DW, Berlemann U, Lippuner K, Jaeger P, Nolte LP. (1997), Three-dimensional primary stability of cementless femoral stems. Clin Biomech 12(2):75-86, doi:10.1016/S0268-0033(96)00059-9
2. Jasty M, Bragdon C, Burke D, O'Connor D, Lowenstein J, Harris WH.(1997), In vivo skeletal responses to porous-surfaced implants subjected to small induced motions. J Bone Joint Surg Am. 79(5):707-14.
3. Davidson D, Pike J, Garbuz D, Duncan CP, Masri BA. (2008), Intraoperative periprosthetic fractures during total hip arthroplasty. Evaluation and management. J Bone Joint Surg Am. 90(9):2000-12, doi:10.2106/JBJS.H.00331
4. Schileo E, Taddei F, Malandrino A, Cristofolini L, Viceconti M. (2007), Subject-specific finite element models can accurately predict strain levels in long bones. J Biomech. 40(13):2982-9. doi:10.1016/j.jbiomech.2007.02.010
5. Pancanti A, Bernakiewicz M, Viceconti M.(2003), The primary stability of a cementless stem varies between subjects as much as between activities. J Biomech. 36(6):777-85. doi:10.1016/S0021-9290(03)00011-3
6. Shultz TR, Blaha JD, Gruen TA, Norman TL. (2006) Cortical bone viscoelasticity and fixation strength of press-fit femoral stems: finite element model. J Biomech Eng. 128(1):7-12. DOI:10.1115/1.2133765
7. Helgason B, Perilli E, Schileo E, Taddei F, Brynjólfsson S, Viceconti M. (2008), Mathematical relationships between bone density and mechanical properties: a literature review. Clin Biomech 23(2):135-46. doi:10.1016/j.clinbiomech.2007.08.024
8. Kuiper JH, Huiskes R. (1996), Friction and stem stiffness affect dynamic interface motion in total hip replacement. J Orthop Res. 14(1):36-43. doi 10.1002/jor.1100140108
9. Viceconti M, Muccini R, Bernakiewicz M, Baleani M, Cristofolini L. (2000), Large-sliding contact elements accurately predict levels of bone-implant micromotion relevant to osseointegration. J Biomech. 33(12):1611-8. doi:10.1016/S0021-9290(00)00140-8
10. Bernakiewicz M, Viceconti M. (2002), The role of parameter identification in finite element contact analyses with reference to orthopaedic biomechanics applications. J Biomech. 35(1):61-7. doi:10.1016/S0021-9290(01)00163-4
11. Dammak M, Shirazi-Adl A, Zukor DJ. (1997), Analysis of cementless implants using interface nonlinear friction--experimental and finite element studies. J Biomech. 1997 Feb;30(2):121-9. doi:10.1016/S0021-9290(96)00110-8
12. Abdul-Kadir MR, Hansen U, Klabunde R, Lucas D, Amis A. (2008), Finite element modelling of primary hip stem stability: the effect of interference fit. J Biomech. 41(3):587-94. doi:10.1016/j.jbiomech.2007.10.009

Author: Dr Sally Clift
Institute: University of Bath
Street: Claverton Down,
City: Bath BA2 7AY
Country: UK
Email: s.e.clift@bath.ac.uk

Effect of Prosthesis Stiffness and Implant Length on the Stress State in Mandibular Bone with Dental Implants

M. Todo[1], K. Irie[1], Y. Matsushita[2] and K. Koyano[2]

[1] Research Institute for Applied Mechanics, Kyushu University, Kasuga, Japan
[2] Faculty of Dental Science, Kyushu University, Fukuoka, Japan

Abstract — **The purpose of this study was to develop a detailed 3-Dimension mandibular model with dental implants on the basis of CT data and to conduct stress analysis to characterize the effects of the material type of prosthesis on stress/strain distribution in the mandibular bone. Three types of materials, a polymer and two metals, with different elastic properties were chosen as the prosthesis materials. The analytical results showed that the Mises equivalent stress and equivalent elastic strain along the circumference of the implant at distal side were much higher than in the anterior region. It was also shown that the stress/strain concentration at the bone increased with decreasing the prosthesis stiffness. The stress/strain concentration observed in the circumference of the implants could be the driving force for loosening and fracture of the implants.**

Keywords — **Mandibular bone, Dental implant, CT image, Finite element analysis**

I. Introduction

Recently, dental implant operation is known to be one of the most effective treatments for tooth less jaw bones [1]. It is clinically important to understand the mechanical effects of implants on mandibular bones because such mechanical interactions between implants and bones are thought to be related to biological bone resorption around implants and safety and durability of implants themselves. It is actually reported that the majority of the long-term convalescence after implant surgeries is strongly affected by mechanical factors [1].

Experimental studies using animal and model bones have been performed to characterize the mechanical interactions between implants and jaw bones, however, in general, deformation behavior of the surfaces of the implants and bones is only measured by, for example, strain gage methods and it is very difficult to characterize the stress state inside of the implants and bones. On the contrary, the stress state of implants inserted into jaw bones can be analyzed by computational analysis such as the finite element method (FEM). Two-dimensional and simplified three-dimensional models were mainly used in the previous implant analyses by FEM [2,3].

Recent years, three-dimensional detailed human tissue models are developed by using digital images of X-ray CT and MRI and stress analysis of these models are performed by FEM. This kind of computational technique is expected to be one of the most convincing methods that can be used to understand the mechanical conditions of bones under real situations in the field of biomedical engineering. This technique has also been applied to jaw bones [4].

In the present study, a detailed 3D-FEA model of a mandibular bone without teeth was developed from a series of CT images, and then All-on-4 dental implant model consisting of four implants, prosthesis and artificial teeth was attached to the bone model. FEA of the model was then performed to characterize the effects of the implants on the stress and strain states of the mandibular bone.

II. Development of computational model

A two-layer mandibular model consisting of cortical and cancerous bones was developed from X-ray CT images of a human skull. From each of the CT images, the outlines of the cortical and cancellous bones were extracted and accumulated to construct three dimensional bone shapes. The 3-D bone models of the cortical and cancerous were firstly expressed as two crowds of points by the image analysis software ISEC2. Surface data of the bone models were then constructed by polygons from the point data by using Rapid Form 2004. Solid data of the bone models were build up from the surface data by using the pre-post processor FEMAP for FEA. The Mandibular model was finally constructed by combining the solid models of the cortical and cancerous bones.

All-on-4 generally consists of four implants, prosthesis and artificial teeth. An implant model was constructed as a cylinder of 4 mm diameter. Two implants were embedded into the anterior side of the mandible, and two were also embedded into the distal side. The implant embedded into the molar part was inclined at 45 degree. A simple model of prosthesis fixed on the implants was constructed on the basis of the shape of the mandible. Artificial teeth models constructed from CT images were attached on the top of the

Chwee Teck Lim, James C.H. Goh (Eds.): ICBME 2008, Proceedings 23, pp. 1611–1614, 2009
www.springerlink.com

prosthesis. The All-on-4 model attached to the mandibular bone is shown in Fig.1.

Meshed model and boundary conditions are shown in Fig.2. 4-node tetrahedral elements were used and the numbers of elements and nodes were 174672 and 49710, respectively. Cortical and cancellous bones, implant, prosthesis and artificial teeth were assumed to be linear elastic and the material constants used in the analysis are shown in Table 1 [5,6]. The material of the prosthesis was chosen to be acrylic resin, titanium or Co-Cr alloy in order to assess the effect of Young's modulus of the prosthesis. The implant and the artificial teeth were assumed to be made from titanium and ceramics, respectively. All of the interfaces were perfectly connected. Forces generated by four kinds of masticate muscles were considered to be acted on the mandible and the directions of the muscles were determined based on CT images and Ref.4. The heads of mandible were able to move only in the horizontal direction (the Y-direction). The top-surface nodes of the artificial teeth were perfectly fixed to express firm biting condition [7]. Distributed loads were also applied to the nodes close to the heads of mandible in order to avoid stress concentration at the fixed nodes on the heads.

III. Results and Discussion

Equivalent stress distributions in the bone tissues surrounding the left-hand implant are shown in Fig.3. Stress concentration was observed on the cortical bone surrounding the neck of the molar implant. The obvious change of stress concentration at the interface region between the cortical and cancellous bones is typical behavior in the computational model assuming simple two-layer model. Pass-plots of equivalent stress along the bone tissues surrounding the front and the molar implants are shown in Fig.4. For both the implants, equivalent stress sharply rose up as transferring from the cancellous and the cortical bone. Equivalent stress in the metallic prosthesis model tends to be higher than that in the acrylic prosthesis, and such difference is mainly seen on the cortical bone for the surrounding of the molar implant; on the contrary, on the cancellous bone for the surrounding of the frontal implant.

Equivalent strain distributions are shown in Fig.5. Path plot of equivalent strain along the surrounding bone tissues are also shown in Fig.6. Equivalent strains are concentrated in the surrounding bones of the molar and the frontal implants. Effect of the Young's modulus of prosthesis is clearer on strain than on stress, and the strain is much larger in the metallic implants than in the acrylic.

In the present model, the mandible tries to be deformed by muscle forces, however, restricted by the fixed artificial teeth. For the case of prosthesis with low Young's modulus, the resistance to the deformation of the mandible is small, as a result, equivalent stress and strain become low in the surrounding bone of the left-hand implant. On the other hand, for the case of a prosthesis with high Young's modulus, deformation of the entire prosthesis is relatively small and hence the resistance to the deformation of mandible becomes large, as a result, equivalent stress and strain increase in the surrounding bone of the left-hand implant.

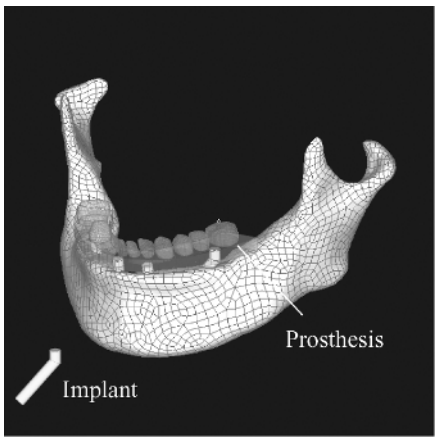


Fig. 1 3-D finite element model of a mandibular bone with dental implants.

Table 1 Material properties.

Material	Young's modulus [GPa]	Poisson's ratio
Cortical bone	13.0	0.3
Cancellous bone	1.6	0.3
Implant	106	0.3
Acrylic resin	3.14	0.32
Titanium	106	0.3
Co-Cr alloy	218	0.33
Artificial teeth	68.9	0.28

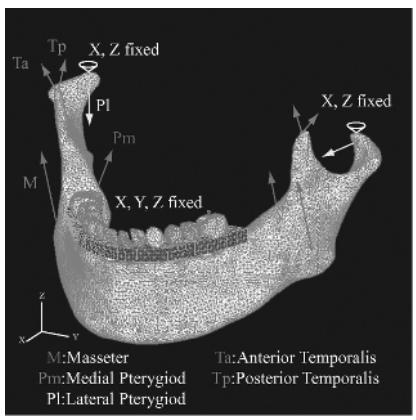
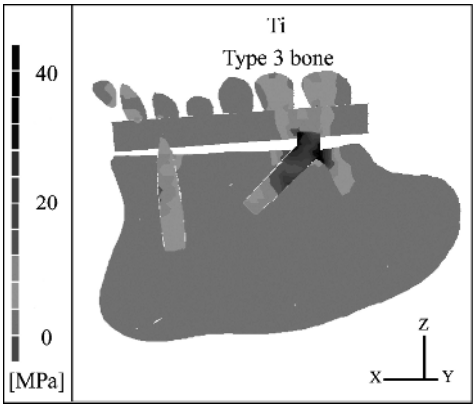
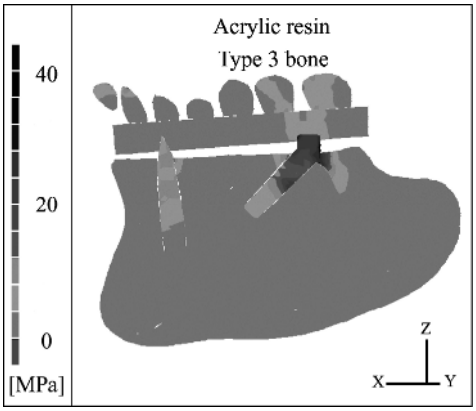


Fig. 2 Finite element meshes and boundary conditions.

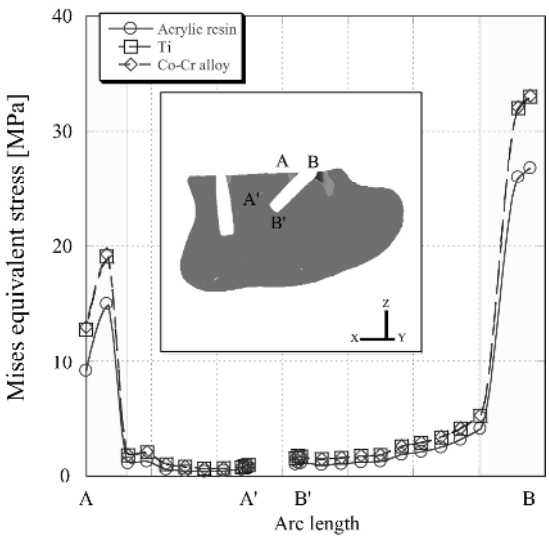


(a) Titanium prosthesis



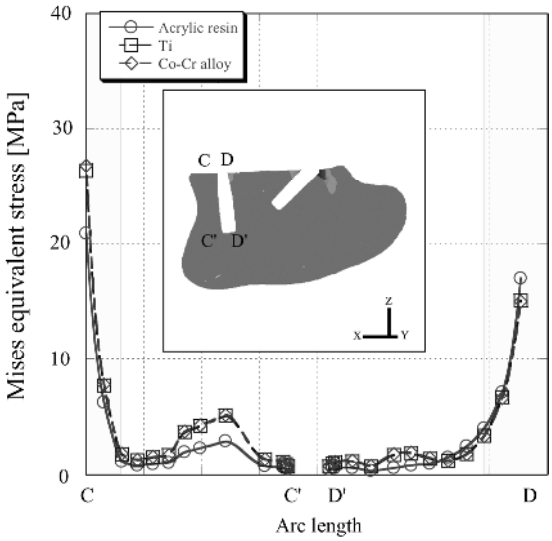
(b) Acrylic prosthesis

Fig. 3 Mises equivalent stress distribution in cross-sectional areas.



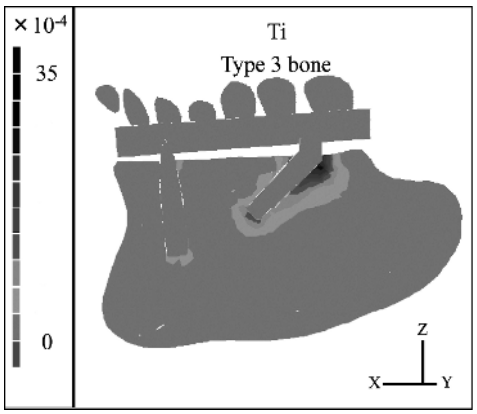
(a) Distal implant

Fig.4 Path Plots of Mises equivalent stress along the circumferences of implants.

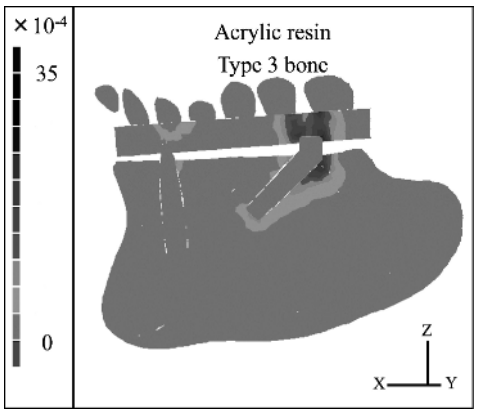


(b) Anterior implant

Fig.4 (continued)



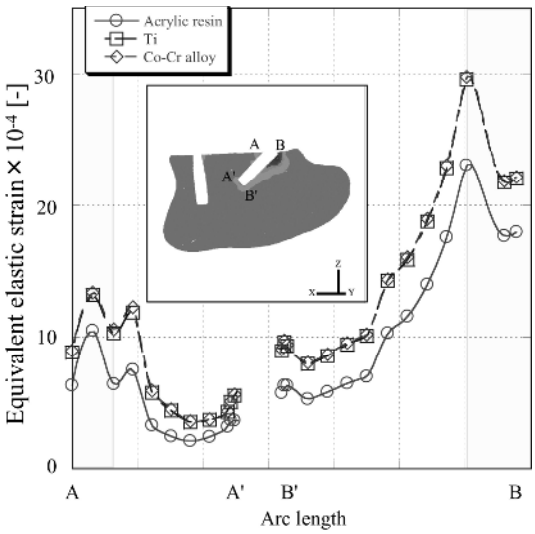
(a) Titanium prosthesis



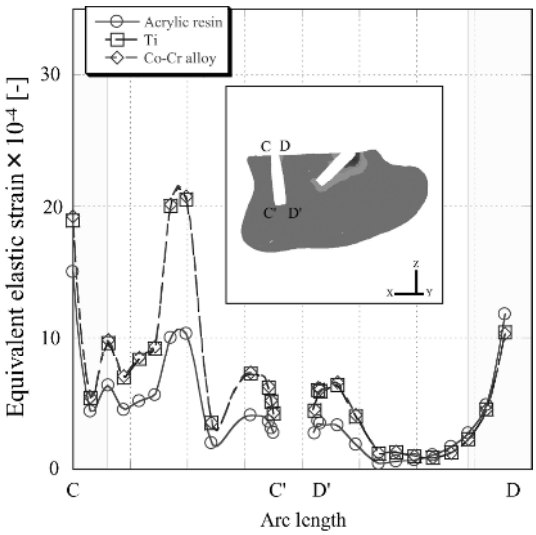
(b) Acrylic prosthesis

Fig. 5 Equivalent elastic strain distribution in cross-sectional areas.

The developed mandibular model was effectively used to characterize the stress/strain distributions within the bone tissues, especially in the surroundings of the implants under firm masticate condition. This mechanical information is thought to be a good guideline to predict bone absorption in the vicinity of implants and failure of All-on-4 implant system.



(a) Distal implant



(b) Anterior implant

Fig. 6 Path Plots of equivalent elastic strain along the circumferences of implants.

IV. Conclusions

A 3-D model of a mandibular bone with All-on-4 implant system was developed to investigate the mechanical interaction between bone and implants under biting condition. The two-layer mandible model was constructed from X-ray CT images, and then the All-on-4 system consisting of four implants, prosthesis and artificial teeth was attached to the mandible. Finite element analysis of the model was performed under a boundary condition considering four kinds of masticate muscles. Effects of the prosthesis stiffness on the stress/strain states in the mandibular bone was characterized on the basis of the FEA results. Stress/strain concentrations were clearly recognized in the surrounding bone of the implants, and the degree of such stress concentration became higher as the Young's modulus of the prosthesis increased.

Acknowledgement

This work was partially supported by the Highly-functional Interface Science Program: Innovation of Biomaterials with Highly Functional Interface to Host and Parasite by Ministry of Education, Culuture, Sports, Science and Technology-Japan.

References

1. Renouard F, Rangert B (1999) Risk Factors in Implant Dentistry-Simplified Clinical Analysis for Predictable Treatment-, Quintessence Publishing Co, Inc 39
2. Yasuyuki M, Kunihiko M, Tsuneo S (1993) Studies on Stress Distribution of Bone-bonded and Bone-adapted Titanium Endosseous Implants and Surrounding Bone Part 1. Effect of Implant Root-length Variation to Stress Distribution in Bone. J Jpn Prosthodont Soc 37: 236-245
3. Menicucci G, Lorenzetti M, Pera P, Preti G (1998) Mandibular Implant-Retained Overdenture: Finite Element Analysis of Two Anchorage Systems. Int J Oral Maxillofac Implants 13:369-37693
4. Inou N, Fujiwara H, Maki K (1992) 3-D FE Stress Analyses of Mandibular during biting. Transactions of the JSME Series A 58-551 :1042-1045
5. Tada S, Stegaroiu R, Kitamura E, Miyakawa O, Kusakari H (2003) Influence of Implant Design and Bone Quality on Stress/Strain Distribution in Bone Around Implants: A 3-dimensional Finite Element Analysis. Int J Oral Maxillofac Implants 18:357-368.
6. Genna F, Paganelli C, Salgarello S, Sapelli P (2003) Mechanical Response of Bone under Short-term Loading of a Dental Implant with an Internal Layer Simulating the Nonlinear Behaviour of the Periodontal Ligament. Computer Methods in Biomech Biomed Eng 6:305-318
7. Korioth TWP, Johann AR (1999) Influence of mandibular superstructure shape on implant stresses during simulated posterior biting. J Prosthet Dent. 82:67-72

Rheumatoid Arthritis T-lymphocytes "Immature" Phenotype and Attempt of its Correction in Co-culture with Human Thymic Epithelial Cells

M.V. Goloviznin[1], N.S. Lakhonina[1], N.I. Sharova[3], V.T. Timofeev[2], R.I. Stryuk[1], Yu.R. Buldakova[1]

[1]Moscow State University of Medicine and Dentistry, Department of Internal Diseases, Moscow, Russian Federation
[2]Russian State Medical University, Department of Internal Diseases, Moscow, Russian Federation
[3]Research Center "Institute of Immunology" Laboratory of Cell Immunology, Moscow, Russian Federation

Abstract — **We found that the level of CD3+4+8+T-cells was normal in peripheral blood of RA patients. Otherwise an amount of CD3+4-8-, CD3-4+ and CD3-8+ subpopulations was increased in 10 patients and level of CD10+ cells (24%) in 2. We found also significant imbalance of CD3+4+8- and CD3+4-8+ mature T-cells in all RA patients The level of CD3+4+ 5-40-fold exceeded the level of CD3+8+. The 24-hour incubation of RA patient's lymphocytes with human TEC culture and TEC supernatant could influence upon T-cell receptor phenotype. We found tendency to increase of CD3 after the incubation in all patients. Otherwise the dynamic of CD4 and CD8 was different. In 4 cases we saw the moderate decrease of CD4 expression and increase of CD8. But in 9 cases the imbalance of CD3+4+ and CD3+8+ subpopulations increased after cultivation due to progressive CD8 expression diminution. The above mentioned facts allowed us to suppose the heterogeneity of T-cell selection disturbances in RA**

Keywords — **Rheumatoid Arthritis, T-lymphocytes, Pathology of Thymic Selection**

I. Introduction

Investigation of mechanisms, by which T-cells acquire tolerance for self-antigens, remains one of the important problems of basic and clinical immunology, in particular, in the correction of autoimmune diseases. Specific recognition of autoantigen by autoantibody or T-cell receptor (TCR) in context of HLA-II receptor by "forbidden" cell clones is now the main concept of autoimmunity phenomena. This concept can properly explain the debut and pathogenesis of organ-specific autoimmune diseases such as I-type diabetes mellitus. Otherwise systemic autoimmune diseases (SAD) are characterized by polyclonal activation of T and B-cells targeted to different antigens [1]. Even in Rheumatoid arthritis (RA) (not to mention progressive systemic sclerosis, sarcoidosis or psoriasis) the identification of specific autoantigen remains disputable. So the investigation of pathogenic role of non-TCR-dependent T-lymphocyte activation in SAD could be crucial. Moreover numerous reports give evidence that among the peripheral blood lymphocytes (PBL) or in inflamed tissues in SAD patients are T-cells with unusual "thymocyte-like" phenotype enriched by adhesive receptors. These cells have increased activation properties [2]. The aim of the work was to prove our hypothesis on T-lymphocyte positive selection disturbance in RA and to investigate PBL phenotype before and after co-cultivation with human thymic epithelial cells (TEC).

II. Materials and metnods

We analyzed the phenotypic features of PBL in 21 patients with definite RA and 12 healthy donors The PBL phenotype was studied by anti-CD3-PE, anti -CD4-PE, anti-CD8-FITC, anti-CD10, anti-CD69, anti-CD71, anti-CD34 monoclonal antibodies (Becton Dickenson) using the method of laser flow cytometry with double and triple-color monoclonal antibody scanning. The lymphocyte-thymic epithelial cells adhesion phenomenon was studied in co-culture of PBL and human TEC. Cultures were incubated at 37°C for 20 min with subsequent centrifugation and new incubation at -4°C for 30 min. The results were estimated by accounting of TEC-lymphocytes "rosette-forming" complexes in samples after glutaraldegide fixation. The T-cells receptors dynamics studied in 24-hour lymphocyte-TEC and T-lymphocyte-TEC supernatant co-cultivation in sterile conditions at 37°C T-cells phenotype was studied by flow cytometry before and after cultivation.

III. Results

Peripheral blood lymphocytes phenotype in RA patients. At the first stage of investigation the main object of our research was the population of CD3+4+8+T-cells with phenotype similar to early thymic emigrants. But during the research work we found that the level of CD4+8+T-cells among the PBL of RA patients was about 2 – 3% Only three patients demonstrated CD3+4+8+ amount more than 5%. Otherwise an amount of CD3-4+ and CD3-8+ subpopulations was increased in 10 investigated patients in general. In three patients we found high level of unusual CD3-4+ lymphocytes (6,0%, 1,1% and 42,8%). See Fig.1. The phenotype and function of these cells is subject for our

Chwee Teck Lim, James C.H. Goh (Eds.): ICBME 2008, Proceedings 23, pp. 1615–1618, 2009
www.springerlink.com

future investigations. For identification possible maturation impairment in RA-PBL we also investigated markers typical for early stages of T-cell maturation (CD10, CD71, CD98, CD34). The increased level of CD10+ cells (24%) was found in 2 patients. The expression of others molecules was non significant. We also didn't found γδTCR+T-cells among the PBL of our patients. The marker of spontaneous activation CD69 was expressed on 5-6% RA-PBL. The investigation of mature T-lymphocytes subpopulation showed significant imbalance of CD3+4+ and CD3+8+T-cells in all RA patients The level of CD3+4+ 5-40-fold exceeded the level of CD3+8+. Only 2 patients had normal (1,5 – 2) rate of CD3+4+/CD3+8+ balance.

Lymphoid cells-thymic epithelial cells adhesion Phenomenon of human thymocytes and human TEC adhesion during the cultivation "in vitro" is well-known. In our case human thymocytes bound almost 75 %TEC in co-culture whereas lymphocytes of healthy donors had minimal adhesive activity binding 11,75+2,9%TEC. RA PBL bound 28,2+4,2%TEC.(PBL of some patients bound more than 32%TEC) forming rosette-like structures. See Fig.2. The pretreatment of lymphocytes by anti-CD2 reduced adhesion. This fact allowed us to identify cells sticking to TEC as T-lymphocytes. We didn't find the difference in adhesion properties of PBL between "classical" and nodular variant of RA but as we reported earlier [3], PBL-TEC adhesion in sarcoidosis patients was lower (13,4+2,3TEC) than in RA.

The 24-hour incubation of RA patient's lymphocytes with human TEC culture and TEC supernatant We found that 24-hour incubation of RA patient's lymphocytes with human TRC culture and TEC supernatant could influence upon RA-PBL T-cell receptor repertoire. During the incubation with TEC culture there was a tendency of increase of CD3 in all patients. See Fig.3. Otherwise the dynamic of CD4 and CD8 was different in different co-cultures. In 4 cases we saw the moderate decrease of CD4 expression and increase of CD8 which lead to CD3+4+/CD3+8+ balance normalization. But in 9 cases the imbalance of CD3+4+ and CD3+8+ subpopulations increased after cultivation due to progressive CD8 expression diminution. Amounts of CD3+4+8+, CD10+, and CD69+ T-cells didn't change after the incubation but there was 1,5-4-fold increase of HLA-DR expression. Receptor dynamics picture during the PBL incubation with TEC supernatant was typologically similar to described results of PBL-TEC incubation but much less evident. The different dynamics of CD3+4+ and CD3+8+cells level during the incubation with TEC (the tendency of normalization of its balance in one part of patients and aggravation of imbalance in other part) permits us to suppose phenotypic heterogeneity of these cells in particular the different density of CD3, CD4 and CD8 receptors.

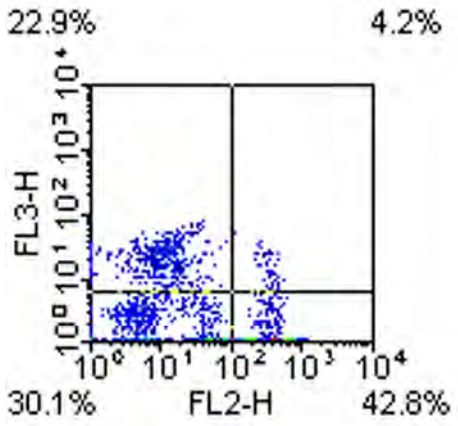


Fig. 1. CD3-4+ subpopulation (42,8%) among the RA-PBL in patient B. CD4PE(FL2) CD3PE(FL3)

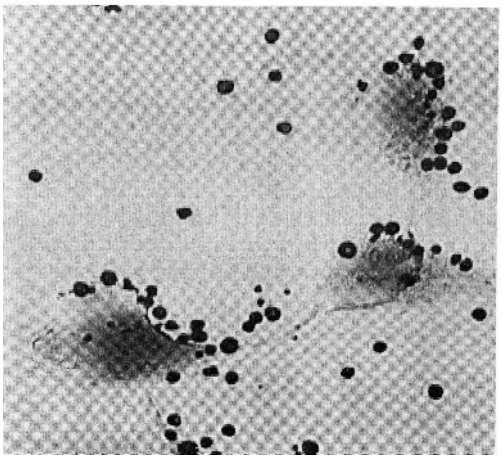


Fig. 2. RA PBL tropism to Thymic Epithelial Cells culture

IV. Conclusions

Thus, the data testify, the rising of level of PBL carrying features of cellular dysmaturity in some of our patients. Evident tropism of RA PBL to human TEC, the marked imbalance of CD3+4+/CD3+8+ subpopulations and moreover the presence of CD3-4+ and CD3-8+ cells in PBL can give evidence of thymic or postthymic T-cell selection abnormality in RA. The 24-hour incubation of RA patient's lymphocytes with human TEC culture and TEC supernatant could influence upon T-cell receptor phenotype causing in some cases normalization in other cases aggravation ob main T-cells subpopulations imbalance/ The particular interest for future investigations represents the phenotype and function of CD3-4+ population. Now we could assume the similarity of these cells to $CD3^{low}4+$ T-cells.

The results of the present work permits us to summarize and generalize the role of immature T-clones with low density of CD3 and the breakdown of thymic selection processes in the pathogenesis of systemic and organ-specific autoimmunity. Autoimmune mice, homozygous for the "Ipr" gene develop a profound lymphadenopathy resulting from the accumulation of anti-Ia-reactive $\alpha\beta TCR^{+}CD3^{low}4\text{-}8\text{-}B220^{+}$ T-cells in peripheral lymphoid tissues. The majority of investigators propose the connection between these autoreactive cells and the manifestations of SLE-like syndrome in Ipr-mice [4]. Adult Ipr thymuses were found to contain an immature population of thymocytes, phenotypically identical to the peripherally accumulating $\alpha\beta TCR^{+}CD3^{low}4\text{-}8\text{-}B220^{+}$ T-cells. Evidence is presented that some of these Ipr-precursor cells are capable of intrathymic differentiation, whereas the vast majority are exported unchanged to the lymph nodes, probably due to progressive atrophy of the thymic cortex in Ipr-mice. On the other hand the MHC class II antigen expression is enhanced on macrophages, dendrite cells, proximal tubular cells and precedes overt glomerular lesions and proteinuria**.** In human SLE activated $CD3^{low}4\text{-}8\text{-}$ cells can augment the production of pathogenic anti-DNA-antibodies by 30-fold. Progressive atrophy of thymic cortex in Ipr-mice probably can lead to ineffectiveness of cortical stage of T-cell selection and compensatory induction of immature T-cell expansion in peripheral lymphoid tissues [1].

The synovial membrane of patients with rheumatoid arthritis and seronegative arthropathies (Reiter-syndrome) displays a selective expansion of a specific population of $\gamma\delta^{+}TcRCD3^{low}4\text{-}8\text{-}$ T-cells. The density of CD3 molecules in these cells is significantly lower than in peripheral blood T-lymphocytes. The selection and pathways of development of $\gamma\delta^{+}$TcR T-cells are poorly investigated. Their localization in skin, mucosal and synovial membranes, high adhesive and secretor activity permits us to assume their role as triggers of autoimmune inflammation in places of their accumulation [5].

Psoriasis is a disease of activated keratinocyte. "Products of activated keratinocytes change the function of T-cells that, in turn, produce factors, perpetuating the process of keratinocytic activation."[6]. Activated keratinocytes can induce mononuclear cell proliferation via MHC-class I and U-independent mechanism. It is possible that these proliferating cells are MHC-unrestricted $\gamma\delta^{+}$TcR T-clones with high adhesive activity. Perhaps the different endothelial adhesive molecules expressed in different skin diseases of unknown etiology account for the distinct composition of the inflammatory infiltrate.

The character and consequence of T-cell-keratinocyte interactions and $\gamma\delta^{+}$TcR T-cell expansion in psoriasis reflects the early events of thymic maturation of γδTcR+ thymocytes in subcapsular zone of the thymus before their emigration to the periphery. The severe exacerbation of psoriasis and Reiter-syndrome in HIV-infected patients can be connected with the depletion of $CD4^{+}$ mature T-cells, selectively infected by HIV and compensatory induction of thy-

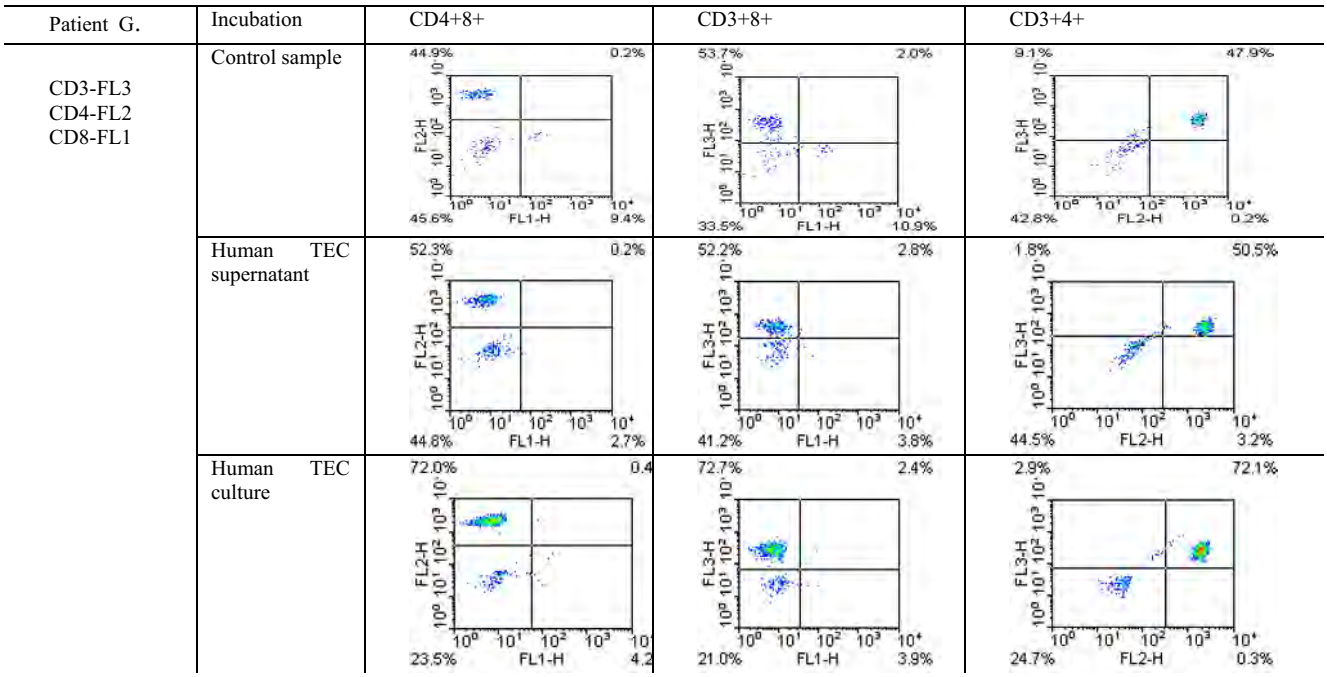


Fig. 3. Dynamics of RA peripheral blood T-lymphocytes phenotype during the 24-hour incubation with human TEC supernatant and human TEC culture.

mus-independent T-cell development, in particular, $\gamma\delta^{+}$TcRCD3^{low}4"8" T-cell expansion in skin. Myasthenia gravis is the disease of the nervous system with the development of autoimmune reaction to cholinoreceptor. There was established the relationship between the disease relapse and the increase of the number of circulating $CD3^{+}4^{+}8^{+}$ T-cells with cortico-medullary-like phenotype [1]. The findings of thymic alteration (thymoma) in about 80-90% of myasthenia patients stress a central role for the thymus in the pathogenesis of myasthenia gravis. Neoplastic epithelial and myoid cells in malignant thymoma, complicated by myasthenia contain only incomplete cholinoreceptors, of cholinoreceptor-like molecules. Thymomas with immature epithelial cells predominantly express immature thymocyte phenotype [7]. These abnormalities can reflect abnormal thymic epithelial maturation, ineffectiveness of medullar stage of thymic T-cell development. Abnormal expression of low-immunogenic determinants of cholinoreceptor in the thymus can lead to the breakdown of negative selection of autoreactive $CD3^{+}4^{+}8^{+}$ T-clones in cortico-medullary zone of thymus gland, their cytotoxic activity in the nervous system.

In this context is also interesting to discuss attempts of experimental induction of autoimmune systemic diseases in BN-rats with thymic cortex depletion, using $HgCl_2$, and organ-specific autoimmune diseases in mice BALB/c with thymic medulla atrophy after the exposition of cyclosporine A [1]. Experimentally-induced autoimmune syndromes demonstrate regularity: atrophy of thymic cortex in systemic autoimmunity leads to enhanced expression of la-antigens and adhesive receptors in peripheral lymphoid tissues and to expansion of immature T-cell clones with anti-Ia-reactivity and low density of CD3, at the same time, degenerative processes in thymic medulla in organ-specific autoimmune diseases result in defects of negative T-selection and hyperactivity of "medullar-like" autoreactive cytotoxic T-clones. Degenerative processes in the thymic stroma (pathology of thymic microenvironment) as a potential cause of T-cells selection ineffectiveness also occur in various autoimmune diseases. In this way identification of activated "anti-self" T-clones with unusual "immature" phenotype and MHC-antigens expression in the foci of autoimmune inflammation permits us to assume the compensatory induction of positive and negative T-selection in peripheral tissues and tissue damage by auto reactive clones Careful investigation of the thymes microenvironment pathology of subcapsular and cortical zones in systemic autoimmune diseases (especially in SLE psoriasis, rheumatoid arthritis) on the one hand, and investigations of cytoarchitectonics disturbances in thymic medulla in organ-specific autoimmunity on the other hand, makes it possible to re-think the pathogenesis of autoimmune diseases, their combinability and transformation, and allows us to develop new principles of immunocorrection.

This work was supported by grant № 08-04-01508 from Russian Foundation of basic researches.

References

1. Goloviznin M.V. (1993) “Peripherialisation” of T-lymphocyte thymic selection as a cause of autoimmune diseases. Immunologiya.5; 4 – 8. (Rus)
2. Goloviznin M.V. (1996) Infection as a triggering factor of autoimmune processes initiated by defective T-cell selection. Immunologiya.5; 4 – 8.(Rus)
3. Goloviznin M.V., Lakhonina N.S., Buldakova Yu.R., et.al. at (2008) The place of sarcoidosis among systemic autoimmunity. http://www.saudi-thoracic.com/conf/new002/htm/2.htm
4. Zhou T., Bluethman H., Eldridge J., et al. (1993) Origin of CD4-CD8-B220+ T cells in MRL-lpr/lpr Mice. J. Immunol. 150; 3651 – 3667.
5. De Maria A., Malanti L., Moretta A., et.al. (1987) CD3+4-8-WT31-(T-cell receptor γ+0 cell and other unusual phenotypes are frequently detected among spontaneously interleukin 2-responsible T lymphocytes present in joint fluid in juvenile rheumatoid arthritis. Eur.J Immunol. 17; 1815 – 1819.
6. Gottlich A. (1988) Immunologic mechanisms in psoriasis. J. Amer. Acad. Dermatol. 18; 1376 – 1392.
7. Takacs L., Savino W., Monostrol E., et al. (1987) Cortical thymocyte differentiation in yhymomas; an immunohistologic analysis of the pathologic microenviroment. J. Immunol. 138; 687 – 698.

Author: Goloviznin Mark
Institute: Moscow State University of Medicine and Dentistry
Street: Delegatskaya street, 20/1
City: Moscow
Country: Russian federation
Email: mvas

Axial and Angled Pullout Strength of Bone Screws in Normal and Osteoporotic Bone Material

P.S.D. Patel[1], D.E.T. Shepherd[1] and D.W.L. Hukins[1]

[1] School of Mechanical Engineering, University of Birmingham, Edgbaston, B15 2TT, UK

Abstract — **Orthopedic surgery often involves the use of bone screws to stabilize fractures. Screw fixation can be extremely difficult in osteoporotic (OP) bone because of its compromised strength. Pullout strength is commonly used to measure screw fixation strength. In this study, axial and angled screw pullouts (ranging from 0° to 40°) were performed on 0.09 g.cm^{-3}, 0.16 g.cm^{-3} and 0.32 g.cm^{-3} polyurethane (PU) foam. The PU foam was used to model different levels of low density human cancellous bone, including OP bone. Screw pull-out tests were conducted under displacement control at a rate of 0.1 mm.s^{-1}. Load and displacement values were recorded; the maximum load during screw pullout was defined as the pullout strength of the screw. Two different titanium-alloy bone screws were used to test for any effect of thread type (i.e. cancellous or cortical) on the screw pull-out strength. Failure of screw fixation was observed from the stripping of the internal screw threads within the PU foam. Compared to the cortical screw, the cancellous bone screw had the highest pullout strength under almost all conditions of pullout angle and PU foam density. For both screws, the pullout strength increased with increasing PU foam density. Results indicate that the PU foam density, rather than the screw angle or thread type, is the most influential factor affecting screw pull-out strength. These findings are important in understanding the behavior of screw fixation and screw failure within an OP bone model.**

Keywords — **bone screw, cancellous bone, osteoporosis, screw pullout, polyurethane foam.**

I. Introduction

Osteoporosis is a bone disease in which bone resorption exceeds bone deposition, resulting in bone loss [1]. The associated reduction in bone quality often leads to bone fractures, which in turn leads to the need for fixation of implants to aid repair. Bone screws are commonly used in orthopedic implants for internal fracture fixation. Pullout strength can be used to measure screw fixation strength. To date, work on screw pullouts has focused mainly on axial pullouts in cadaver bone [2-4], animal bone [5-7] and in artificial materials mimicking the properties of human bone [5, 7, 8]. Few studies in the literature report screw pullouts from non-augmented/untreated osteoporotic (OP) bone [9].

In part, this is due to the contraindicative use of bone screws in OP bone, which generally has less tissue to engage with the screw thread compared to normal bone. However, there may be a need to use screws in OP bone, such as for fusion cages in the human spine and for the effective repair of fractures involving OP bone. Another reason is because of the widespread variability in the mechanical properties of normal and OP human bone, which makes it difficult to compare screw performance. In this study, the problem of variability was overcome by using polyurethane (PU) foams of different densities to represent normal and OP bone. For OP bone, multiple sites of screw fixation are often used, which means that screws can be placed at various angles. The objective of this study was to determine how the pullout strength of a bone screw is affected by the following factors: (i) screw pullout angle, (ii) screw thread type and (iii) the density of PU foam, representing different densities of bone.

II. Materials and Methods

A. PU Foam Samples

PU foams, of three different densities, were used in this study. Closed cell PU foam of density 0.16 g.cm^{-3} and 0.32 g.cm^{-3} (American Society for Testing and Materials, ASTM, Grade 10 and Grade 20) [10] was used to model low and medium density cancellous bone respectively. Open cell rigid PU foam of density 0.09 g.cm^{-3} was used to model very low density cancellous bone. A previous study by the authors had found that the 0.16 g.cm^{-3} PU foam may prove suitable as an OP cancellous bone model when fracture stress is of concern. The authors found that 0.16 g.cm^{-3} PU foam is a good alternative for in-vitro testing because it has compressive Young's modulus and yield strength values similar to OP bone that has also been tested in compression [11]. All PU foams were purchased in block form, with dimensions 130 × 180 × 40 mm, from Sawbones® Europe AB, Malmö, Sweden. The foam densities were supplied by Sawbones® Europe AB. For this study, PU foam test blocks, with dimensions 45 × 60 × 40 mm, were prepared using a cutting saw.

Chwee Teck Lim, James C.H. Goh (Eds.): ICBME 2008, Proceedings 23, pp. 1619–1622, 2009
www.springerlink.com

B. Screw Pullout Testing

A cancellous bone screw, 6.5 mm diameter × 30 mm length, and cortical bone screw, 4.5 mm diameter × 30 mm length, were used to test for any effect of thread type on the screw pullout. Both screws were made from medical grade titanium alloy, Ti-6Al-4V. Pilot holes of 3.5 mm diameter, for the cancellous bone screw, and 3 mm diameter, for the cortical bone screw, were drilled into a PU foam test block before screw insertion. Each screw was inserted into the PU foam through a pullout fixture that was tailor-made to the desired angle of pullout (Figure 1). The pullout fixture, engaged with the bone screw head, was then attached to the actuator of an ELF3300 materials testing machine (Bose Corporation, ElectroForce Systems Group, Minnetonka, MN, U.S.A.). The bottom part of the test set-up, involving the PU foam block, was placed in a tailor made chamber attached to a platform on the machine's load cell (Figure 1).

Screw pullout was conducted under displacement control at a rate of 0.1 $mm.s^{-1}$. Load and displacement values were recorded and the maximum load generated during screw pullout was defined as the pullout strength of the screw [12]. Six pullout tests were performed for each condition of screw pullout angle (0º, 10º, 20º, 30º, 40º), screw type (cancellous screw thread, cortical screw thread) and PU foam density (0.09 $g.cm^{-3}$, 0.16 $g.cm^{-3}$, 0.32 $g.cm^{-3}$). The same cancellous and cortical screw was used for all tests because of the comparatively low strength of the screw host material (PU foam) to the metallic bone screws.

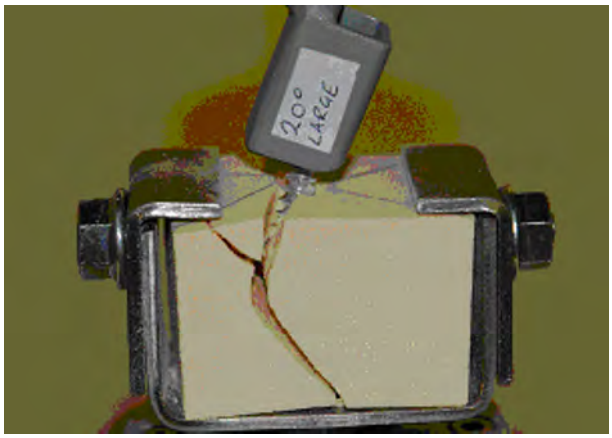


Fig. 1 20º pullout of a cancellous bone screw from PU foam used as a model for OP and normal bone (according to the PU foam density).

III. Results

Tables 1 and 2 show the mean and standard deviation of screw pullout tests for the cancellous and cortical bone screws respectively.

Table 1 Ø 6.5 mm Cancellous screw pullout mean ± standard deviation (N)

Screw Pullout Angle	0.09 $g.cm^{-3}$ PU foam	0.16 $g.cm^{-3}$ PU foam	0.32 $g.cm^{-3}$ PU foam
0º	12.8 ± 2.3	356.7 ± 50.1	1145.3 ± 55.4
10º	22.0 ± 10.6	401.5 ± 22.6	1524.5 ± 66.7
20º	20.7 ± 8.9	354.3 ± 7.5	1033.1 ± 45.0
30º	21.6 ± 6.9	390.6 ± 27.2	1130.8 ± 72.0
40º	21.4 ± 2.9	330.3 ± 37.1	776.3 ± 96.6

Table 2 Ø 4.5 mm Cortical screw pullout mean ± standard deviation (N)

Screw Pullout Angle	0.09 $g.cm^{-3}$ PU foam	0.16 $g.cm^{-3}$ PU foam	0.32 $g.cm^{-3}$ PU foam
0º	10.4 ± 3.2	115.1 ± 26.5	1081.1 ± 72.0
10º	5.3 ± 3.3	209.6 ± 40.8	940.5 ± 84.2
20º	19.0 ± 7.3	288.9 ± 31.5	967.6 ± 25.9
30º	21.1 ± 5.3	246.4 ± 28.7	827.0 ± 33.7
40º	16.5 ± 8.4	184.0 ± 16.6	793.7 ± 81.2

Statistical comparisons were made using MINITAB® Release 14.1 Statistical Software (Minitab Inc., Pennsylvania, USA). Normality of the distributions was assessed using the Anderson-Darling test. Analysis of variance (ANOVA) and Tukey's Honestly Significant Difference comparison tests showed that the cancellous screw had a significantly higher pullout force than the cortical screw ($p<0.05$). For both screws, pullout strength increased with increasing PU foam density, which was found to be statistically significant ($p<0.05$).

Significant differences ($p<0.05$) were also detected for angled screw pullouts between the following angles: 0º > 40º; 10º > 0º, 20º, 30º, 40º; 20º > 40º; 30º > 40º. No significant differences ($p>0.05$) were detected in screw pullout force between the following angled pullouts: 0º and 20º; 0º and 30º; 20º and 30º.

Regression analysis showed a high correlation (R^2 = 0.8902) between the mean cortical screw pullout force and pullout angle in the 0.32 $g.cm^{-3}$ PU foam, which was found to have a significant relationship ($p<0.05$). No other significant relationships ($p>0.05$) existed between the mean screw pullout force and angle for all remaining test conditions.

IV. Discussion

This study has accounted for several factors affecting screw pullout, by systematically varying the screw type, host material density and screw pullout angle. A possible explanation for the increased cancellous screw pullout, compared to cortical screw pullout, is that the PU foam test material has been designed to mimic human cancellous bone, making the cancellous screw thread more favorable to its host material.

Results for the angled screw pullouts suggest that only screws placed axially or up to a 10º angle may increase its holding power. Angled pullouts at 20º, 30º and 40º show mixed results and may marginally improve screw holding power compared to screws placed at less than 20º. However, as the regression analysis between pullout force and angle has shown, this is not so clear-cut.

Three different densities of PU foam were used to model OP (0.09 g.cm^{-3} and 0.16 g.cm^{-3} foam) and normal (0.32 g.cm^{-3} foam) human cancellous bone. The foam is an acceptable model for cancellous bone and has been used in several studies to investigate orthopedic devices [13, 14]. For both screws used in this study, the screw pullout force decreased with increasingly OP bone material. Lower screw pullout strength was also reported in OP bone material compared to normal bone material for self-tapping bone screws [15].

In this study, failure of screw fixation was observed from the stripping of the internal screw threads within the PU foam. The literature reports the following relationship to predict the shear failure force necessary to strip the internal threads formed in PU foam [13, 16, 17]:

$$F_S = S \times A_S = S \times \{L \times \pi \times D_{major}\} \times T \quad (1)$$

where:

F_S = predicted shear failure force (N)

S = material ultimate shear stress (MPa)

A_S = thread shear area (mm^2)

L = length of thread engagement in material (mm)

D_{major} = major diameter (mm)

T = Thread Shape Factor (dimensionless) $= (0.5 + 0.57735\, d/p)$

d = thread depth (mm) $= (D_{major} - D_{\min or})/2$

$D_{\min or}$ = minor (root) diameter (mm)

p = thread pitch (mm)

Based on this formula, the predicted shear failure forces for axial screw pullout were calculated as shown in Table 3. Predictive values for 0.09 g.cm^{-3} PU foam could not be calculated because the ultimate shear stress of this open cell foam was unknown. Table 3 shows that the formula can be useful in approximating screw pullout force in a given material, especially for the 0.32 g.cm^{-3} PU foam, which showed a close match between predicted and experimental results for the cortical screw.

Table 3 Comparison of the mean axial screw pullout results with calculated theoretical values

PU foam density (g.cm^{-3})	Predicted shear failure force (N)		Experimental mean axial screw pullout force (N)	
	Cancellous screw	Cortical screw	Cancellous screw	Cortical screw
0.16	604	405	357	115
0.32	1622	1090	1145	1081

Equation 1 demonstrates the important relationship between bone shear strength and screw pullout strength. A study on bovine cancellous bone, tested in pure shear, found the following relationship between shear strength, S (MPa), and apparent density, ρ (g.cm^{-3}) [18]:

$$S = 21.6\rho^{1.65} \quad (2)$$

Using the average material property data provided for the PU foams used in this study, a similar relationship was derived between shear strength and apparent density:

$$S = 21.5\rho^{1.42} \quad (3)$$

Similarly, the shear strength and apparent density of unicellular PU foam has been demonstrated to have the following relationship [13]:

$$S = 23.9\rho^{1.54} \quad (4)$$

Equations 2, 3 and 4 are very similar and justify the use of PU foam, of various densities, to mechanically simulate the relative shear strength properties of bone. This is beneficial for screw pullout testing from low density PU foam, which would be able to model the shear strength of OP bone, as has been performed in this study.

V. Conclusions

This study has analyzed pullouts of cancellous and cortical screws at 0º, 10º, 20º, 30º, 40º angles in 0.09 g.cm^{-3}, 0.16 g.cm^{-3}, 0.32 g.cm^{-3} PU foams, to determine how screw pullout is affected in an OP bone material, defined in the authors' previous study, compared to normal bone. The mean screw pullout force decreased with increasingly OP bone material. The cancellous bone screw demonstrated higher pullout forces than the cortical screw. Screws placed

at 0º and 10º angles showed greater holding power than screw placement at 20º, 30º and 40º angles.

Acknowledgements

The authors thank Mr C. Hingley and Mr L. Gauntlett for manufacturing the screw pullout rigs, the Arthritis Research Campaign for providing equipment, Surgicraft Limited for financial support and the School of Mechanical Engineering, University of Birmingham, for providing a studentship for PSDP.

References

1. Silverthorn DU (2001) Human physiology: an integrated approach. 2nd edition. New Jersey: Prentice-Hall Inc., p 807
2. Hilibrand AS, Moore DC, Graziano GP (1996) The role of pediculolaminar fixation in compromised pedicle bone. Spine 21: 445-451
3. Lotz JC, Hu SS, Chiu DFM, Yu M, Colliou O, Poser RD (1997) Carbonated apatite cement augmentation of pedicle screw fixation in the lumbar spine. Spine 22: 2716-2723
4. Cordista A, Conrad B, Horodyski M, Walters S, Rechtine G (2006) Biomechanical evaluation of pedicle screws versus pedicle and laminar hooks in the thoracic spine. Spine J 6: 444-449
5. Gausepohl T, Mohring R, Pennig D, Koebke J (2001) Fine thread versus coarse thread: A comparison of the maximum holding power. Injury 32: SD1-7
6. Inceoglu S, McLain RF, Cayli S, Kilincer C, Ferrara L (2004) Stress relaxation of bone significantly affects the pull-out behavior of pedicle screws. J Orthopaed Res 22: 1243-1247
7. Inceoglu S, Ehlert M, Akbay A, McLain RF (2006) Axial cyclic behavior of the bone-screw interface. Med Eng Phys 28: 888-893
8. Hsu C-C, Chao C-K, Wang J-L, Hou S-M, Tsai Y-T, Lin J (2005) Increase of pullout strength of spinal pedicle screws with conical core: biomechanical tests and finite element analyses. J Orthopaed Res 23: 788-794
9. Burval DJ, McLain RF, Milks R, Inceoglu S (2007) Primary pedicle screw augmentation in osteoporotic lumbar vertebrae. Spine 32: 1077-1083
10. ASTM F1839-01 (2001) Standard specification for rigid polyurethane foam for use as a standard material for testing orthopaedic devices and instruments. Pennsylvania: American Society for Testing and Materials
11. Li B, Aspden RM (1997) Composition and mechanical properties of cancellous bone from the femoral head of patients with osteoporosis or osteoarthritis. J Bone Miner Res 12: 641-651
12. Thompson JD, Benjamin JB, Szivek JA (1997) Pullout strengths of cannulated and noncannulated cancellous bone screws. Clin Orthop Relat R 341: 241-249
13. Chapman JR, Harrington RM, Lee KM, Anderson PA, Tencer AF, Kowalski D (1996) Factors affecting the pullout strength of cancellous bone screws. J Biomech Eng 118: 391-398
14. Iesaka K, Kummer FJ, Di Cesare PE (2005) Stress risers between two ipsilateral intramedullary stems - A finite-element and biomechanical analysis. J Arthroplasty 20: 386-391
15. Battula S, Schoenfeld A, Vrabec G, Njus GO (2006) Experimental evaluation of the holding power/stiffness of the self-tapping bone screws in normal and osteoporotic bone material. Clin Biomech 21: 533-537
16. Oberg E, Jones FD, Horton HL, Ryffel HH (1988) Working strength of bolts. In: Machinery's Handbook, ed by Green RE. New York, Industrial Press Inc., pp. 1324-1325
17. Asnis SE, Ernberg JJ, Bostrom MPG, Wright TM, Harrington RM, Tencer A, Peterson M (1996) Cancellous bone screw thread design and holding power. J Orthop Trauma 10: 462-469
18. Stone JL, Beaupre GS, Hayes WC (1983) Multiaxial strength characteristics of trabecular bone. J Biomech 16: 743-752

Corresponding author:

PSD Patel
University of Birmingham,
School of Mechanical Engineering,
Edgbaston,
Birmingham,
UK.
psp170@bham.ac.uk

Experimental Characterization of Pressure Wave Generation and Propagation in Biological Tissues

M. Benoit[1], J.H. Giovanola[1], K. Agbeviade[1] and M. Donnet[2]

[1] Ecole Polytechnique Fédérale de Lausanne (EPFL), Switzerland
[2] E.M.S. Electro Medical Systems S.A., Switzerland

Abstract — **Aim of the study: This work develops a measurement technique for pressure waves in soft tissues. It aims at characterizing, understanding and modeling the generation and propagation of pressure waves in soft tissues, with a view towards medical applications for the treatment of various tissue pathologies.**

Description of methodology and salient results: First, Hopkinson bar techniques have been adapted to measure the waves emitted by an impact generator, transmitted through the material and reflected at the interfaces. Simulations with an explicit FEM software reproduce the measured data well. Secondly, flexible PVDF gages have been calibrated for measurement of wave propagation in soft tissues. Although PVDF gages have acoustic impedance similar to that of soft tissues, they act nevertheless as foreign inclusion and perturb the measurements. To deal with this problem, we apply an hybrid experiment-FEM simulations technique to interpret the PVDF gage records and extract reliable pressure data. Results are applied to the design of biomedical devices for the Extracorporeal Shock Wave Therapy (ESWT).

Conclusion: Adapted Hopkinson bar technique coupled with FEM simulation can predict pressure wave emitted, transmitted and reflected at the interfaces of an impact generator. PVDF flexible gages are a promisisng technique for measuring wave propagation in soft tissues and can serve to calibrate appropriate nonlinear viscoelastic constitutive models for soft tissues. This work contributes to improve the scientific knowledge of the healing effect of shockwaves for different pathologies by providing a well characterized mechanical wave input in the treated tissues.

Keywords — **pressure waves, Hopkinson bar, soft tissues, PVDF gages, explicit FEM simulation, inclusion, ESWT**

I. Introduction

Treating tissue pathologies such as tendinitis with pressure waves is increasingly popular. In order to understand and optimize the effect of pressure waves in clinical applications, medical results must be correlated with well characterized mechanical stimuli. This paper presents preliminary results of work aimed at characterizing pressure waves propagating in biological tissues. Difficulties of this study include primarily the non-linear viscoelatic nature of biological tissues and the accurate measurement of pressure waves in these complex tissues.

Our approach to these problems is based on a hybrid experimental-numerical method. The elastic wave produced by an impact generator is first characterized by using a Hopkinson bar and simulated with an explicit FEM software. Wave propagation in tissues is then measured using PVDF gages and then simulated with a calibrated Ogden model. The simulation capability can then serve to make predictions of wave energy delivered in various impactor and tissue configurations.

Many authors have published results using PVDF gages for the measurement of wave propagation at the interface between solids, using gas shock tubes [1], or as a pressure sensor [2]. Some gages have shown creeping problems, pyroelectric effects, humidity dependence and dielectric relaxation, which have been highlighted and partially solved [2], [3]. In addition O.A. Shergold and al [4] have published split Hopkinson pressure bar measurements and simulations of the stress-strain response of pig skin at high strain rates. The specific aim of the work presented here is to develop a measurement technique for wave propagation in soft tissues using PVDF gages.

II. Experiments

A. Measurements of the waves generated by an impact generator using a Hopkinson bar

The pressure bar technique has been developed by Kolsky [5]. Here we use the original Hopkinson bar arrangement consisting of a cylindrical bar which is suspended in a horizontal position by wires so that it can freely translate in a vertical plane. It is instrumented with 4 strain gages mounted in a Wheatstone bridge. A wave generation device impacts and transmits pressure wave in the Hopkinson bar (see fig. 1). Systematic measurements are performed for several impact speeds.

Chwee Teck Lim, James C.H. Goh (Eds.): ICBME 2008, Proceedings 23, pp. 1623–1626, 2009
www.springerlink.com

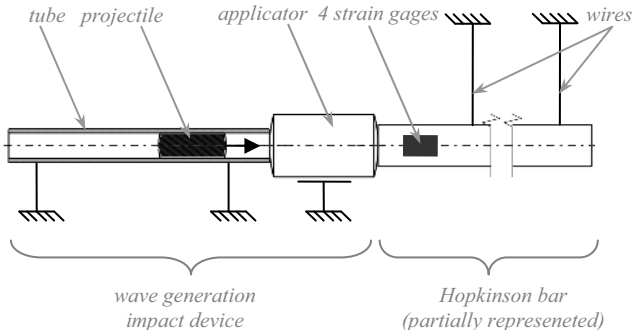


Figure 1: sketch of impact generator and Hopkinson bar used to characterize pressure waves generated on head of applicator

B. In vitro measurements of wave propagation in soft tissues using flexible PVDF gages

In our experiments, we perform measurement with PVDF gages from Piezotech SA company. Theses gages are manufactured by a patented poling process and show strong stability of the calibrated parameters. They provide nano-second time-resolved stress measurements and reproducible response, independent of the loading path up to *20MPa*.

In order to measure the traction and tension stress without undesirable bending contribution, PVDF gages are mounted on poly4-methyl-1-pentene polymer (TPX) supports with a cyanoacrylate glue.

A sketch of the electric wiring of the gage is show on figure 2: the PVDF gauge is regarded as a current source; it is mounted in parallel with a *50 Ohm* resistance (input impedance of an oscilloscope).

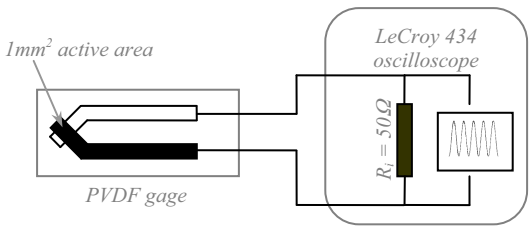


Figure 2: PVDF gage electric wiring

The signal measured by the oscilloscope is first converted to current and a fictitious offset is removed by subtracting the average of the complete signal.

Charge Q is calculated by integrating the baseline-corrected current I over time:

$$Q(t) = \int_0^t I dt \tag{1}$$

Stress σ_{33} depends linearly on the charge Q, the active surface of the gage S, and the calibration factor d_T:

$$\sigma_{33}(t) = \frac{Q(t)}{d_T S} \tag{2}$$

A sketch of the test arrangement for pressure wave measurements in bio-tissues is shown on figure 3 : the impact generator described above is applied on a core-sample of soft tissue confined in a PMMA tube and backed with silicone rubber. A spring applies a *0.016MPa* pre-stressed to the whole system. Samples of skin and of fat of a pig serve as soft tissues. Frozen samples of pigs killed less than 24 hours before the tests are cored to the desired dimensions. Preliminary measurements were performed on unfrozen samples, for several impact speeds.

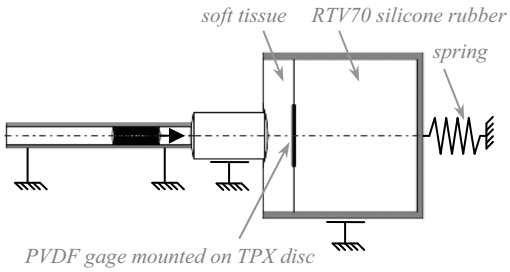


Figure 3: Sketch of the measurement unit

C. Foreign inclusion problem

In our measurements, PVDF gages are inserted inside soft tissues and act as foreign inclusion that modify the propagating pressure wave they are supposed to measure. Part of the wave is reflected at the interface between the tissue and the gage and part of it is transmitted through the gage.

Comparison of results of simulations with and without the gage inclusion provides a method to evaluate the measured signals and extract reliable pressure data.

III. Results

A. Wave propagation in the Hopkinson bar

FEM simulation using ABAQUS/Explicit and measurement of pressure waves propagated in the Hopkinson bar are performed for several impact speeds. As shown in Fig-

ure 4 for a test at an impact speed of *15m/sec*, simulations are in good agreement with measured data.

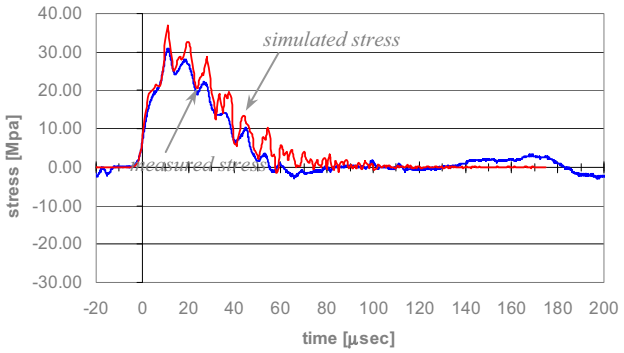


Figure 4: stress measured and simulated record for an impact speed of *15m/sec*

These results show that the Hopkinson bar is a good system for characterizing the waves emitted by the impact generator. First, the good agreement between measured data in the Hopkinson bar and FEM calculations validates the simulation method. Secondly, FEM simulation can predict pressure wave emitted, transmitted and reflected at the interfaces and allows calculating the waves generated and propagated in the projectile, the applicator and on the head of the impact generator. It allows characterizing the impact generator and can be used for any other device generating pressure waves by impact.

B. Wave propagation in water

Measurement and FEM simulation of wave propagation in water have been performed using PVDF gages. The reliability of pressure wave simulations in water has been demonstrated by many previous studies. Figure 5 shows a good correlation between measured and simulated data.

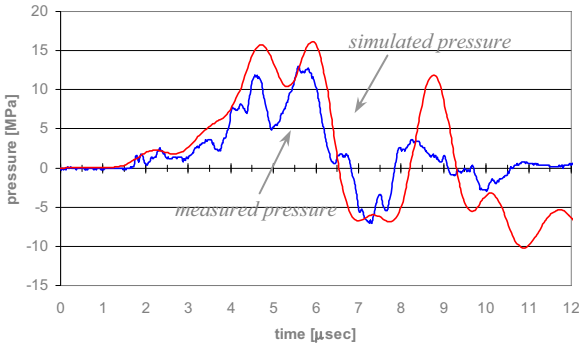


Figure 5: measured and simulated stress waves in water at *1mm* from the head of the impact generator – impact speed *25m/sec*

The agreement between measurements and simulations, that serve as reference, demonstrate that the PVDF gage is a reliable technique for measurement of wave propagation in water.

C. Wave propagation in soft tissues

A constitutive model is required to simulate the behavior of soft tissues exposed to stress waves. The Ogden model for an isotropic, hyper-elastic solid is calibrated here to describe the constitutive behavior of skin and fat from pig. Figures 6 and 7 show preliminary measurements and simulations made on the skin and the fat of a pig. Samples are about *3mm* thick; impact velocity is *9m/sec.* We performed multiples impacts at the same location of the same sample to establish repeatability.

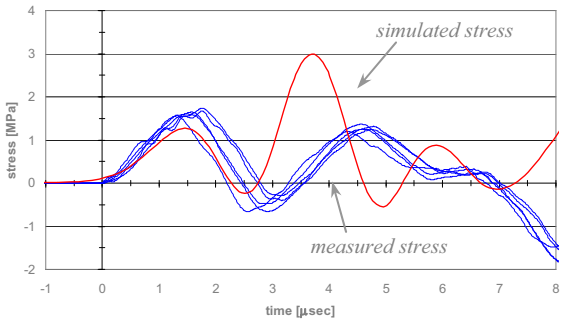


Figure 6: and simulated stress waves in the skin of a pig – thickness *3mm* – impact speed *9m/sec*

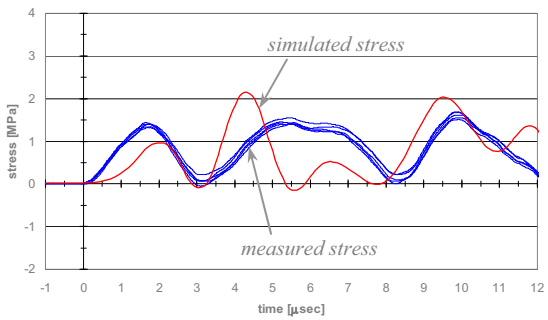


Figure 7: measured and simulated stress waves in the fat of a pig – thickness *3mm* – impact speed *9m/sec*

These results demonstrate repeatable measurements on a single sample. Variability between samples is mainly observed on the amplitude of the signal but not on the period. On the other hand, simulations with an Ogden model do not fit the measured pressure profiles well for each impact velocity. Therefore, the Ogden model does not seem suitable

for simulations of the high rate behaviour of biological tissues subjected to elastic waves.

IV. Discussion and conclusion

The work reported here leads to the following conclusions. First, measurements performed on the Hopkinson bar characterize the impact generator and validate the use of numerical simulation method to predict wave generated and propagated in metallic parts. Secondly, PVDF gage is a reliable technique for measurement of wave propagation in soft tissues.

These preliminary results show that more measurements and simulations are necessary to characterize wave propagation in soft tissues. Future measurements will permit to describe in details reproducibility on a single sample and variability of different samples. Measurements on a known elastic medium will differentiate the contribution of the PVDF gage from the behaviour of the soft tissue. Moreover, another constitutive model should be developed and calibrated to better simulate the behaviour of soft tissues loaded by pressure waves.

References

1. Bauer, F. (2006). Piezoelectric polymer shock gauges. American Institute of Physics, Conference Proceedings, Baltimore, MD.
2. Shirinov, A. V., Schomburg, W. K., (2007) Pressure sensor from a PVDF film, Sensor and actuators : a physical
3. Vinogradov, A. M., Schmidt V. H., et al. (2004). "Damping and electromechanical energy losses in the piezoelectric polymer PVDF." Mechanics of Materials 36(10): 1007-1016.
4. Olivier A. Shergold, Norman A. Fleck, Darren Radford (2005) The uniaxial stress versus strain response of pig skin and silicone rubber at low and high strain rates - Cambridge University Engineering Dept., Trumpington St., Cambridge, UK
5. H. Kolsky. “Stress waves in solids”, New York, Dover Publications, inc. 1963, ISBM 486-61098-5

Author: Mathieu Benoit
Institute: Ecole Polytechnique Fédérale de Lausanne (EPFL)
Street: station 9
City: 1015 Lausanne
Country: Switzerland
Email: mathieu.benoit@epfl.ch

Finite Element Analysis into the Foot – Footwear Interaction Using EVA Footwear Foams

Mohammad Reza Shariatmadari

School of Enginneering, University of John Moores, Liverpool, UK.
Web: www.ljmu.ac.uk***, Email:*** m.r.shariarmadari@2005.ljmu.ac.uk

Abstract — **Diabetic ulcers are the most common foot injuries leading to lower extremity amputation. Early detection and appropriate treatment of these ulcers may prevent up to 85 percent of amputations [1-3]. One of the most important defence in pressure off-loading and preventing recurrent ulcers is the proper footwear or *orthotic* intervention [4-7]. In order to achieve that, a biomechanical knowledge of forces and pressures under the foot play an important role in the assessment and treatment of various foot pathologies, and patients who are at risk or are experiencing variety of foot problem.**

The current study uses test material data and FEA to investigate the foot - footwear interaction and performance of two EVA footwear foams subjected to quasi - static and dynamic compressive loading. The aim is to obtain the peak stresses in the foot in the situation such as standing, walking, running and jumping. These stresses are very useful as they will enable to design suitable orthotic footwear, to reduce the amount of stress in the foot for those individuals such as diabetes.

Keywords — **EVA Foam, Cowper Symonds, Finite Element Analysis, Footwear**

I. Introduction

The foot is a mechanically complex structure of immense strength and it can sustain enormous pressure. Biomechanics is the study of the human body's movement during walking, running and sports, and the effects that outside influences have on the motion of the body [8]. The foot functions as a link in a biomechanical kinetic chain, where movement at one joint influences movement at other joints in the chain [9].

The quasi – static and dynamic footwear foams characteristics are necessary to obtain by the experimental / analysis to ensure that the suitable footwear is designed according to the needs of individuals and to prevent the injuries to the lower extremity. Based on the existing literature, there is inadequate high strain rate material data for footwear (orthotic intervention) to simulate different situations such as walking, running and jumping.

One of the most versatile footwear products on the market is EVA and stands for Ethylene Vinyl Acetate [10]. When formulated into a closed cell foam product, it takes on the following characteristics [11],

- good weather and chemical resistance
- low water absorption
- good acoustic properties
- oil resistance
- high energy absorption
- environmentally friendly, safe disposal by recycling, dumping or incineration

Quasi - Static and Dynamic compression loading tests were carried out on two grades the most commonly used EVA foam materials at the loading rates of 0.01, 0.1, 1 and 2 m/s, using a high speed testing machine.

Finally, axisymmetric Finite Element (FE) foot and footwear models were developed using the test material data to calculate the maximum pressure in the foot.

The results were and showed a good trend of variations of force – displacement with loading rates. As the loading rate increased, the forces in the foot increased.

II. Materials and methods

A Footwear Material Testing

Static and Dynamic compression loading tests were carried out on two grades the most commonly used EVA foam materials at the loading rates of 0.01, 0.1, 1 and 2 m/s, using a high speed testing machine. The foam specimens were dimensioned at Length=50 mm, Width=50 mm and Thickness= 20 mm.

The testing scheme was adapted from ASTM D575-91, standard test methods for rubber properties in compression [12].

B Stress – Strain Behavior of Footwear Foams

The Stress-strain behavior of the EVA foams for the varying speeds of 0.01, 0.1, 1 and 2 m/s are shown in Figures (1 - 2).

Chwee Teck Lim, James C.H. Goh (Eds.): ICBME 2008, Proceedings 23, pp. 1627–1630, 2009
www.springerlink.com

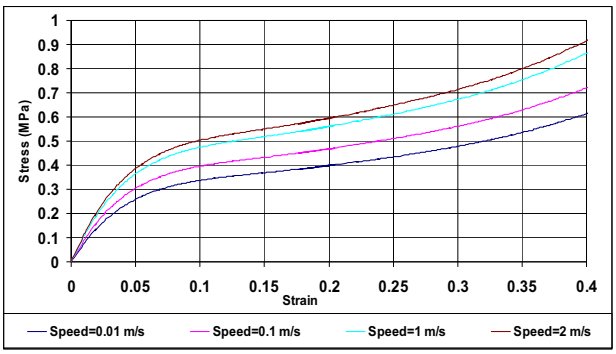


Fig. 1 Material Data for Low Density EVA Foam

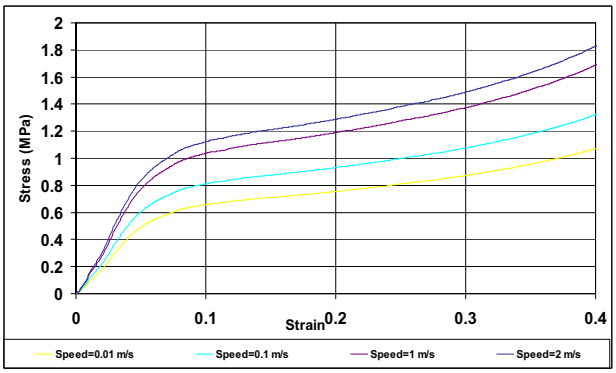


Fig. 2 Material Data for Medium Density EVA Foam

C Finite Element Analysis

A simplified foot – footwear FE model was adapted from Verdejo et al. [13], see Figure (3). The calcaneus geometry was simplified to have a vertical axis of rotational symmetry. The geometry of its lower projection was simplified as a hemisphere of radius 15 mm attached to the end of a 20 mm vertical cylinder of radius 15 mm. The heel pad outer geometry was taken to be a vertical cylinder of radius 30 mm: the lower surface was spherical with radius of curvature of 40 mm, typical of a foot; a smooth blend was made between this surface and the vertical cylindrical surface. The minimum heel pad thickness was taken as 12 mm. When the EVA foam was present, it was taken as a vertical cylinder of radius 35mm and height 22 mm with flat upper and lower faces. The simple FE foot was modeled with and without the footwear foam.

Eight nodded axsymmetric elements (CAX8RH) were used to mesh the bone, heel pad and the foam mesh. Convergence tests were carried out to determine a suitable mesh density for the model.

The models were subjected to compression by applying a prescribed displacement on the bone. The table was fully fixed while the upper calcaneus boundary was ramped down by 10 mm. The coefficient of friction between the heel pad and the foam or support table was taken as 1.0.

The static and dynamic foam material models were taken from the tests carried out on two grades of EVA foams.

The hyperfoam model in Abaqus [16] uses the Ogden strain energy function as shown in Eqs (2 & 3)

$$U=\sum_{i=1}^{N}\frac{2\mu_i}{\alpha_i^2}\left[(\hat{\lambda}_1^{\alpha_i}+\hat{\lambda}_2^{\alpha_i}+\hat{\lambda}_3^{\alpha_i}-3)+\frac{1}{\beta_i}\left((J^{el})^{-\alpha_i\beta_i}-1\right)\right] \quad (2)$$

where

$$\beta_i=\frac{\nu_i}{1-2\nu_i} \quad (3)$$

where N is a material parameter, μ_i, α_i and β_i are temperature dependent parameters. λ_I are the principal extension ratios.

The material properties for the soft skin, bones and rigid table are defined as in Table (1).

Table 1 Foot Material Properties

Component	Young's Modulus	Poisson Ratio
Bones [17]	7300.0 MPa	0.3
Rigid Table / Plate [18]	209E+09 Pa	0.43
Soft Skin [19]	14.3 kPa	7.3

The displacement was monitored at the upper calcaneus boundary (as shown in Figure 3) and the reaction force was determined from the constraints.

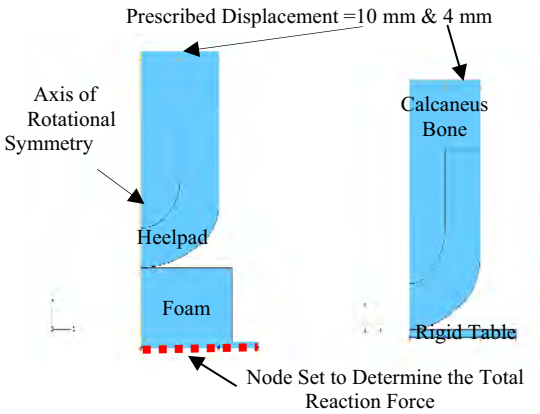


Fig 3 FE Assembly Models of Calcaneus Bone, Heel Pad (Skin), Rigid Table and (a) with Foam (b) without Foam

Figure (4) show the vertical stress, S_{22} contours and the deformed shapes of the foot – footwear and foot – table models under static loading of around 500 N.

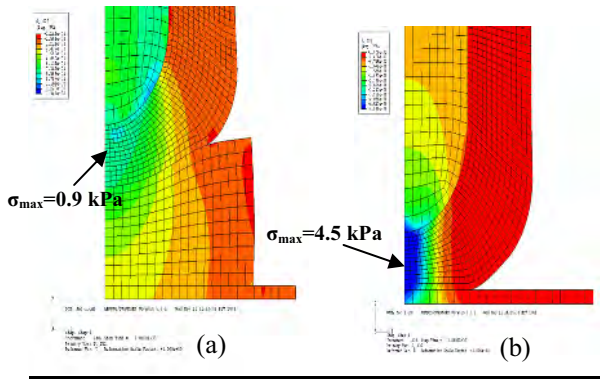


Fig. 4 Deformed Contours of Vertical Compressive Stresses (S_{22}) of Bone and Heel Pad on a Flat Rigid Table (a) with Shoe (b) without Shoe

The quasi-static and dynamic material data for low and medium density EVA foams were used in the foot – footwear FE model shown in Figure (3). Figure (5) details the FEA force-displacement at the interface between the foam and soft skin when using results for low and medium density EVA foams at different loading rates.

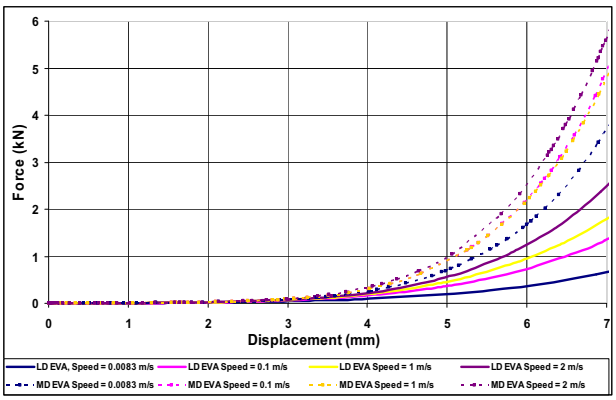


Fig. 5 FE Force – Displacement for Low and Medium Density EVA Foams Using Quasi – Static and Dynamic Test Material Data

Figure (6) shows the force versus displacement curves obtained from literature [14 & 15] and current FEA results for both heel / rigid table and heel / foam / rigid table models.

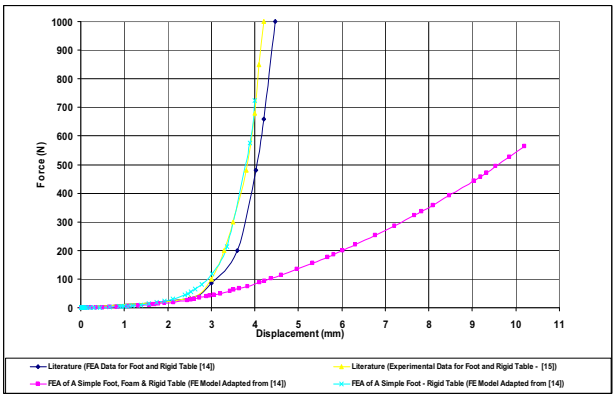


Fig. 6 Force – Displacement Curves for Human Heel Soft Skin with and without Footwear (FEA and Experimental [14] Comparison)

III. Conclusions

The footwear foam materials of varying densities were compressed up to 50% of their initial thickness at speeds ranging from 0.01 to 2 m/s. As can be seen from Figures (1 & 2), increases in foam density and the rate of loading results in increased stiffness and subsequently increased stress at constant strain. The figures also show the non-linear material characteristics with the foams stiffness changing with increasing strain.

- For a 40% strain of the medium density foam, the stress for quasi - static loading was found to be 0.53 MPa. The loading rates were then increased to the dynamic levels of 0.1, 1 and 2 m/s. As a result the stresses increased to 0.6, 0.98 and 1.12 MPa respectively for the same strain of 0.4.
- With respect to the accuracy of the test material data, the tests were repeated and satisfactory results were obtained at the quasi-static loading rate. The high speed testing machines exhibited more sensitivity as the loading rate increased which resulted in poor repeatability.

The non-linear large deformation problem of foot – footwear interaction was analysed by developing a simple FE model to find the maximum stresses in the foot, with and without footwear. The following conclusions were drawn:-

- It was found that most of the deformation occurs by flattening of the lower surface of the heel pad.
- The deformed heel pad does not decrease much in thickness while the foam becomes increasingly concaved. The maximum stresses in the foot occurred at the left hand side of the contact area as shown in Figure (4).

- The reaction forces were found to be 500N and 452N for 10 mm and 4 mm prescribed displacements with and without footwear foams respectively using the material data from [13]. As can be seen in Figure (4) the stresses are reduced in the foot from 4.5 kPa (without shoe) to 0.9 kPa (with the shoe) at this load.

Furthermore, the quasi – static and dynamic test material data for the two other types of low and medium density EVA foams were used in the foot and foam FE model to calculate the stresses in the foot. Figure (5), shows an expected trend of force - displacement behavior with loading rates. The comparisons made between these two different foam grades revealed that,

- the density of the footwear foams is an important factor in the peak forces produced in the foot. The compressive forces were lower with low density EVA foam because the material is soft and more resistant to bottoming out than higher density foams. Low density EVA foam reduces pressure by distributing body weight forces over a larger area of the foot and the pressure decreases as area increases for the same force.
- For 7 mm displacement, the maximum compressive forces in the contact area between the heel pad and the foam for the static loading was found to be 607 and 3416 N for low and medium density foams respectively (see Figure 5). The loading rates were then increased to the dynamic levels of 0.1, 1 and 2 m/s, which resulted in the maximum contact forces to increase further to 1328, 1788 and 2368 N and 4763, 5570 and 5777 N for low and medium high density foams respectively. Therefore, the loading rate was found to be another key factor in the forces acting on the foot as the higher the loading rate is, the higher the contact forces were found to be. The displacements were lower at higher loading rates due to rapid air loss in the foam materials.
- Any increase of the contact area between the heel pad and the foam was found to have direct effect in reducing peak pressure on foot.
- Density of foam and strain rate affect forces generated in foot.

ACKNOWLEDGMENT

The authors would like to acknowledge Mr. Clive Eyre, for providing technical supports.

REFERENCES

1. **Frykberg, R. G.**, (1997), "Team Approach Toward Lower Extremity Amputation Prevention In Diabetes", Journal of the American Podiatric Medical Association, Vol. 87, No. 7, PP 305-312.
2. **Lavery, L., Lavery, D. & Quebedeax - Farnham, T. L.**, (1995), "Increased Foot Pressures After Great Toe Amputation in Diabetes", Diabetes Care, Vol. 18, No. 11, PP 1460-1462.
3. **Thomas, C. C.**, (1977), "Pathological Conditions", 3rd ed. Springfield: 1970, the Foot, Vol. II. Los Angeles: Clinical Biomechanics Corp..
4. **Christensen, K. D.**, (1984), "Clinical Chiropractic Biomechanics", Dubuque: Foot Levelers Educational Division.
5. **Pollard, J. P., LeQuesne, L. P. & Tappin, J. W.**, (1983), " Forces under the foot", Journal of Biomedical Engineering Vol. 5, PP 37-40.
6. **Patil, K. M., Babu, M., Oommen, P. K. & Malaviya, G. N.**, (1996), "On line system of measurement and analysis of standing and walking foot pressures in normals and patients with neuropathic feet", Innov Technol Biol Med, Vol. 17, PP 401-408.
7. **Patil, K. M. & Braak, L. H. & Huson, A.**, (1996), "Analysis of stresses in two-dimensional models of normal and neuropathic feet", Med Biol Eng Comput., Vol. 34, No. 4, PP 280-284.
8. **Grabiner M. D.**, (1993), "Current Issues in Biomechanics (M.D. Grabiner, editor)", Champaign, IL: Human Kinetics Publishers.
9. **Hay, J.**, (1985), "The Biomechanics of Sports Techniques", Englewood Cliffs: Prentice-Hall.
10. **Pitei, D. L., Watkins, P. J., Foster, A. W. M., & Edmonds, M. E.**, (1997) "Do New EVA Moulded Insoles or Trainers Efficiently Reduce the High Foot Pressures In the Diabetic Foot", Diabetes Centre, King's College Hospital, London U.K, 1997.
11. **Shaw, J. E., Van Schie, C. H. M., Carrington, A. L., Abbott, C. A. & Boulton A. J. M.**, (1998) "An Analysis of Dynamic Forces Transmitted Through the Foot in Diabetic Neuropathy", Diabetes Care, Vol. 21, No. 11, PP 1955-1959.
12. **Algeos Footwear, (2008),** "Complete Footwear Brochures".
13. **ASTM D575-91**, (2001), "Standard Test Methods for Rubber Properties in Compression", 91.
14. **Vedjeo, R. & Mills, N. J.**, (2003)," Heel-Shoe Interactions and the Durability of EVA Foam Running Shoe", Journal of Biomechanics.
15. **Aerts, P., Ker, R. F., De Clereq, D. et al.**, (1996), "The Effect of isolation on the Mechanics of the Human Heel pad", Journal of Anatomy, Vol. 188, PP 417-423.
16. **ABAQUS 6.5,** Theory Manual, (2007).
17. **Nakamura, S., Crowninshield, R. D. & Cooper, R. R.**, (1981), "An Analysis of Soft Tissue Loading the Foot - A Preliminary Report," Bulletin of Prosthetics Research, Vol. 18, PP 27–34.
18. **Gere, J. M. & Timoshenko, S. P.**, (1990), "Mechanics of Materials", Second SI Edition, PWS Engineering, Boston, Massachusetts.
19. **Erdemir, A., Saucerman, J. J., Lemmon D., Loppnow, B., Turso, B., Ulbrecht, J. S. & Cavanagh, P. R.**, (2004), "Local plantar pressure relief in therapeutic footwear: design guidelines from Finite element models", Journal of Biomechanics**.**

Author's Address:

Author: Mohammad Reza shariatmadari
Institute: John Moores University
Street: Byrom Street
City: Liverpool
Country: U. K.
Email: m.r.shariatmadari@2005.ljmu.ac.uk

Age Effects On The Tensile And Stress Relaxation Properties Of Mouse Tail Tendons

Jolene Liu[1], Siaw Meng Chou[2], Kheng Lim Goh[3]

[1,2] Division of Engineering Mechanics, School of Mechanical and Aerospace Engineering, Nanyang Technological University
[3] Division of Bioengineering, School of Chemical and Biomedical Engineering, Nanyang Technological University

Abstract — **Tendons are known to exhibit complex mechanical behavior when transferring forces from muscles to bone. This nonlinear mechanical response varies with age due to the presence of degenerative effects which is attributed to the structural changes and interactions observed in each hierarchical level of the dense connective tissue.**

In this study, mouse tail tendons were excised from the C57BL6 mice to evaluate the age effects on tensile and stress relaxation properties. Uniaxial tests were performed on two age groups: 1-month-old and 8-month-old. The extension rate effects on the ultimate tensile strength (UTS) and modulus were evaluated. The stress decay and relaxation rate were also analyzed. Polynomial function and power law were used to evaluate the modulus and the relaxation rate respectively.

The extension rate effect on the UTS and modulus were significantly different for the younger group but the difference were not observed on the older group. Furthermore, the failure modes were observed to be complete for the younger group and non-uniform for the older groups when rupture sites were observed. The younger group demonstrated a faster relaxation as compared to the older group. These results suggested that the physiological changes which take place due to aging provide quantitative evidence of changes in the mechanical properties of tendons. Future work on other age groups are in progress.

Keywords — **extension rate, tendon, mechanical properties, age**

I. Introduction

Tendons are dense connective tissues that are responsible for transferring forces from muscles to bone. Compared to ligaments, which connect bone to bone, the functional forces of tendons are higher and they act as springs to store elastic energy for energy–efficient locomotion without an extended length of the muscle between origin and insertion [1, 2]. In response to mechanical loading, the living tissues metabolize and change their structural properties; the structural change involved the interaction between the collagen type I fibers, fibrils, molecules and non-collagenous extracellular matrix (ECM) present in the multi-unit hierarchical tendon structures. This ability of tendons is known as tissue mechanical adaptation: a condition which tendons are capable of withstanding different levels of mechanical load [3, 4]. However, as ageing takes place, the tendon physiological developments are affected. The changes include the type of cross-links, proteoglycan density, fibril distribution and water content, which suggest that ageing can, indeed, influence the mechanical properties of tendons [5-9].

The strain rate effects on the mechanical properties soft tissue have been extensively explored for sports biomechanics purposes [10-14]. However, age-related strain rate effect has yet to be widely examined [15-17]. Based on current knowledge, strain rate effects on mouse tail tendons is limited to 3-week-old and 8-week-old [8]. This article highlights 1-month-old and 8-month-old results as part of a wider study to examine the age-related mechanical properties from 1-month-old to 36-month-old mouse tail tendons. The extension rate effect on tensile properties as well as the viscoelastic properties of both age groups shall be examined.

II. Methods

Three C57BL/6 mice from each age point, 1.0-month-old (1MO) and 8.0-month-old (8MO), were euthanized with a lethal does of carbon dioxide under the protocol approved by the Institutional Animal Care & Use Committee. The intact tails were wrapped in a Phosphate Buffer Saline (PBS, pH 7.2) soaked gauze, sealed in a plastic bag and stored in a -20 ˚C freezer until needed.

Before mechanical testing, the preserved mice were thawed under room temperature for three hours. The dissection procedures were conducted cautiously to minimize damage. The middle portion of each retrieved tendon was sectioned to approximately 15 mm in length for the tensile and stress relaxation tests (Fig. 1). The trimmed tendon was then pasted across the length of a thin framed template using cyanoacrylate adhesive. The purpose of the template is to prevent any premature damages to the tendon specimen during the handling process. The two sides of the template were trimmed off before loading.

Chwee Teck Lim, James C.H. Goh (Eds.): ICBME 2008, Proceedings 23, pp. 1631–1635, 2009
www.springerlink.com

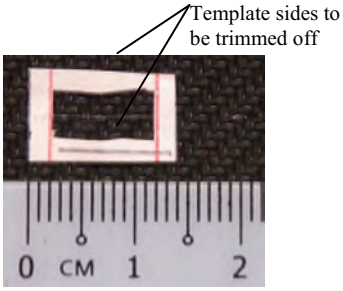


Fig. 1 A template with mouse tail tendon pasted on using cyanoacrylate adhesive. Each tendon was trimmed to approximately 15 mm in length for mechanical testing.

A. Mechanical Testing

Each tendon-on-template was mounted onto the grips of a custom-made horizontal tensile test device, which is immersed in PBS to avoid specimen dehydration. The tensile device was equipped with a force sensor of 450g in capacity (model: UF1, LCM Systems, UK) and a linear displacement transducer (model: CDP-M, Tokyo Sokki Kenkyujo, Japan) which measures the grip-to-grip displacement. A motor controller was incorporated to subject the specimen to a constant extension rate. With the assumption that each mouse tail tendon has a circular cross-section, the mean diameter (d) of each tendon was determined by conducting measurements at eight different locations along the central segment of the mounted tendon under bright field microscopy using NIS-Elements (model: TS100, Nikon). The nominal cross-sectional area (A) was then calculated using $A = \frac{\pi d^2}{4}$.

The tail tendon specimens, 1.0-month-old (1MO_T, n = 65) and 8.0-month-old (8MO_T, n = 57), were subjected to extension rates of 0.05, 0.5 and 1.0 mm/s from a relax state till ruptured (Table 1). No preconditioning or preloading was performed. The force generated from stretching the sample and relative displacement between the grips were measured using the force sensor and displacement transducer respectively and the data of both properties were collected at a rate of 100 Hz. The displacements and loads observed were normalized to strain and stress respectively. Each stress-strain data set was then fitted with a 5th polynomial function using a least–squares curve fit (Fig. 2). The modulus of the tendon specimen was deduced as the first derivative of the polynomial at the inflection point of the linear region [8]. The ultimate tensile strength (UTS) of each tendon specimen was also determined.

The stress relaxation was performed by loading each of the 1-month-old (1MO_SR, n = 18) and 8-month-old (8MO_SR, n = 18) tendon specimens to approximately 2 to

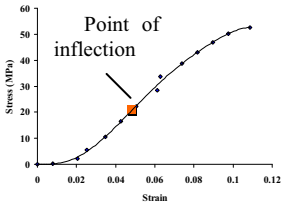


Fig. 2 Typical stress-strain data plot of 8MO_T tail tendon specimen fitted with a 5th order polynomial. Modulus was calculated as the gradient of the polynomial at its inflection point (square).

Table 1 The extension rates expressed in terms of strain rates for mechanical properties tests. The values are expressed in mean ± standard error.

Extension Rate (mm/s)	Strain Rate of MTT (%/s)	
	1-month-old (n = 65)	8-month-old (n = 57)
0.05	0.457 ± 0.005	0.460 ± 0.007
0.50	4.280 ± 0.0526	4.504 ± 0.074
1.00	8.960 ± 0.110	8.811± 0.116

5 % strain with a displacement rate of 0.05mm/s [18, 19]. The applied strain level coincides with the linear region of the load-displacement curve. The decay of the induced load with respect to time (t) was recorded at a rate of 10 Hz for 20 minutes. The stress relaxation curves of each age group was fitted using the power law, $\sigma = At^s$, where A is an arbitrary constant and s is defined as the stress relaxation rate [19]. The unknown values, A and s, are determined by performing a log-log plot.

B. Scanning Electron Microscopy

The ruptured and the non-tested tail tendons were fixed in 2.5% glutaraldehyde in PBS for 15 hours at room temperature. Next, the tendons were dehydrated through a series of ethanol solutions then followed by critical point drier (Model: CPD030, Baltec, Germany). The dried specimens were then pasted onto aluminum sampler holders and sputter coated with gold (model: JCF-1600, JEOL, USA).

Finally, the fiber level studies were conducted by mounting the sampler holder onto the scanning electron microscope platform (model: JSM-5600-LV, JEOL, USA).

C. Statistical Analysis

The data collected were analyzed with one-way ANOVA to detect the significance differences for the tail tendon diameters, strain rate effects on each age group and stress

relaxation properties between the two age groups, . The tensile strengths and moduli were compared to evaluate the strain rate effects for each age group while the percentages in stress decay and relaxation rate were used to observe the differences between both age groups.

III. Results

This study aims to evaluate the extension rate effects on the mechanical properties of 1-month-old and 8-month-old mouse tail tendons. When comparison was made between the diameters of the two age points (Table 2), significance differences was observed ($P < 0.05$). Fig. 3 shows the SEM images of 1MO and 8MO tail tendons respectively. It can be observed that the 1MO collagen fibers appeared as wide bundles while the 8MO tendons are composed of narrower collagen bundles.

The UTS and modulus was significantly different ($P < 0.05$) over the range of extension rates for 1MO (Table 3). For 8MO_T, there was no significant difference observed for both properties ($P > 0.05$), except for the UTS and modulus at higher strain rate ($P < 0.05$) (Table 4). The ruptured sites are illustrated in Fig.3. The fracture sites of 1MO_T were observed to differ between the extension rates; the fibers ruptured into thicker bundles at lower extension rate and demonstrated narrower fibers strands as the extension rate increases. Although there is no observable extension rate effect on the fracture sites for 8MO_T, it was noticed that the ruptured mechanisms shared similar localized failure as 1MO_T specimens strained at 0.5 and 1.0 mm/s.

The percentages of stress relaxed were obtained as 75.77 ± 14.30 % and 41.36 ± 11.72 % for 1MO_SR and 8MO_SR respectively (Table 5). Difference between both age groups was statistically significance ($P < 0.05$). In addition, the power law, fitted onto the log-log plot of stress relaxation curve, revealed significance in the stress relaxation rate between both age groups ($P < 0.05$). The s values, which define the stress relaxation rates, were 0.243 ± 0.150 and 0.109 ± 0.067 for the younger and older age groups respectively.

Table 2 Mouse Tail Tendon Diameters of 1MO (n = 65) and 8MO (n = 57). The values are expressed in mean ± standard error.

Mice Age (Month)	Diameter
1.0	67.47 ± 1.91
8.0	81.55 ± 3.13

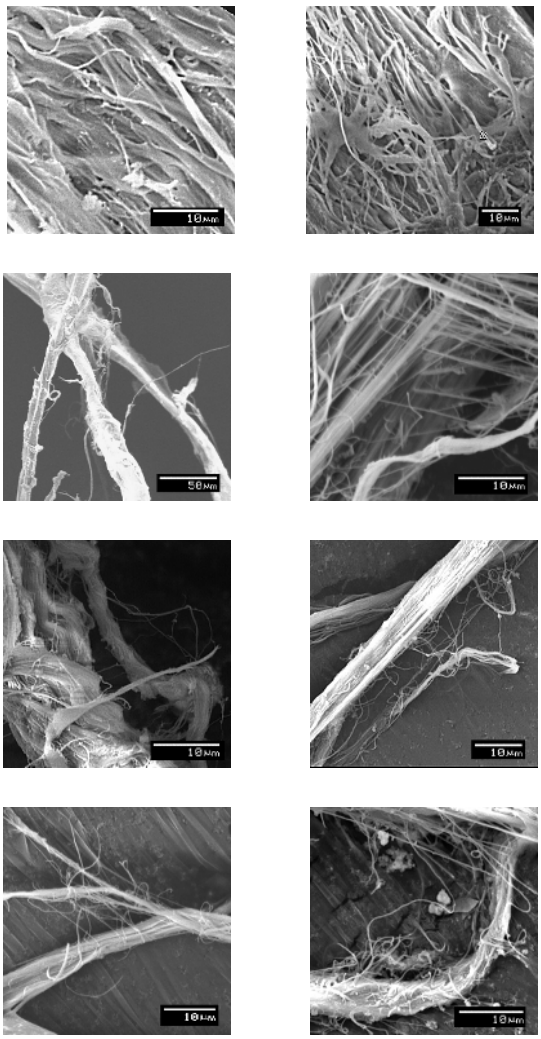


Fig. 3 SEM Images of 1MO (left column) and 8MO specimens (right column). The first row represented the control and the respective rows represent 0.05, 0.5 and 1.0 mm/s ruptured specimens.

Table 3 Mechanical properties of 1-month-old mouse tail tendons (n = 65) at different extension rates.

Extension Rate (mm/s)	Strain at UTS (%)	Ultimate Tensile Stress**,** (MPa)	Modulus**,** (MPa)
0.05	6.30 ± 0.60	17.57 ± 1.41	473.87 ± 39.57
0.50	7.29 ± 0.43	41.18 ± 3.11	780.34 ± 101.21
1.00	8.33 ± 0.34	48.40 ± 2.92	748.33 ± 43.68

** indicates significant difference among groups (one-way ANOVA)

Table 4 Mechanical properties of 8-month-old mouse tail tendons (n = 57) at different extension rates.

Extension Rate (mm/s)	Strain at UTS (%)	Ultimate Tensile Stress *,** (MPa)	Modulus *,** (MPa)
0.05	10.19 ± 2.98	56.03 ± 29.01	855.25 ± 460.72
0.50	10.55 ± 1.90	65.39 ± 22.15	841.35 ± 297.43
1.00	11.41 ± 2.61	87.60 ± 27.49	1112.17 ± 307.48

* represents mean ± standard error
** indicates significant difference among groups (one-way ANOVA)

Table 5 Parameters *A* (arbituary constant) and s (stress relaxation rate), established by the power law $\sigma = At^s$, for the 1MO_SR (n = 18) and 8MO_SR (n = 18). All data are represented by mean ± standard error.

Mice Group	*A*	*s*
1MO_SR	30.87 ± 4.69	0.24 ± 0.04
8MO_SR	27.39 ± 4.26	0.11 ± 0.02

IV. Discussion

The age effect on the mechanical properties of 1-month-old and 8-month-old mouse tail tendons was conducted. Firstly, comparison of the diameters of both age groups indicated significant difference and the younger specimens were observed to be composed of thicker bundles of collagen fibers as compared to the older specimens.

Next, the extension rate effect on the two age points was also investigated. 0.05, 0.5 and 1.0 mm/s were the extension rates used to subject the tendon specimens to rupture. Significant difference was detected on the UTS and modulus on 1MO_T for the extension rate ranges. 8MO_T, generally, was not affected by extension rate; only the UTS and modulus at higher extension rate displayed significant difference. Furthermore, the extension rate sensitivity for 1MO_T was found to be significant when the rupture sites were taken into consideration. The failed portions were observed to be complete for 1MO_T specimens subjected to 0.05 mm/s and the damage was noticed to be more localized as the extension rate increases. This observation is consistent with that of *Kastelic et al* who conducted the study using x-ray diffraction and suggested that failure mechanisms may have occurred in the interfibrillar level [16]. 8MO _T mainly showed localized failures for all the extension rates tested. *Robinson et al* and *Haut et al* suggested that proteoglycan such as decorin which may play a possible role in defining the failure difference between the two age points strained at 0.05 mm/s [8, 15]. In addition, 1MO_T and 8MO_T which are characterized with enzymic and glycated cross-links between the collagen molecules respectively. Glycated cross-links, which are known to be mechanically stronger than enzymic cross-links, may have contributed to the localized damage and thus possible shear effects [6].

Stress relaxation data was presented in terms of stress decay as well as stress relaxation rate. 1MO_SR demonstrated higher relaxation decay and rate as compared to 8MO _SR. Lower water content and decorin exhibited by older specimens was suggested to decrease strain-rate sensitivity as well as viscoelastic behavior. Conversely, *Elliot et al* and *Johnson et al* found that younger patellar tendons tend to exhibit slower relaxation with the support that the higher water binding effects of decorins may have resulted in friction during the processes of collagen molecule interactions [20, 21].

V. Conclusion

This study examined the extension rate effects on the tensile properties and stress relaxation properties of 1-month-old and 8-month-old mouse tail tendons. The extension rate effects on the tensile strength and modulus were significantly different for the younger group but the difference were not observed on the older group. Future work shall focus on more age groups.

References

1. Koob, T. J., and Summers, A. P., 2002, "Tendon--bridging the gap," Comparative Biochemistry and Physiology - Part A: Molecular & Integrative Physiology, 133(4), pp. 905-909.
2. Smith, R. K. W., Birch, H. L., Goodman, S., Heinegard, D., and Goodship, A. E., 2002, "The influence of ageing and exercise on tendon growth and degeneration--hypotheses for the initiation and prevention of strain-induced tendinopathies," Comparative Biochemistry and Physiology - Part A: Molecular & Integrative Physiology, 133(4), pp. 1039-1050.
3. Wang, J. H. C., 2006, "Mechanobiology of tendon," Journal of Biomechanics, 39(9), pp. 1563-1582.
4. Silver, F. H., 2006, Mechanosensing and mechanochemical transduction in extracellular matrix. Biological, chemical, engineering and physiological aspects., Springer, USA.
5. Derwin, K. A., Soslowsky, L. J., Kimura, J. H., and Plaas, A. H., 2001, "Proteoglycans and glycosaminoglycan fine structure in the mouse tail tendon fascicle," Journal of Orthopaedic Research, 19(2), pp. 269-277.
6. Bailey, A. J., Paul, R. G., and Knott, L., 1998, "Mechanisms of maturation and ageing of collagen," Mechanisms of Ageing and Development, 106(1-2), pp. 1-56.
7. Torp, S., Baer, E., and Friedman, B., 1975, "Effects of age and mechanical deformation on ultrastructure of tendon," Structure of fibrous biopolymers, E. D. T. Atkins, and A. Keller, eds., Butterworth, London, pp. 223-250.

8. Robinson, P. S., Lin, T. W., Reynolds, P. R., Derwin, K. A., Iozzo, R. V., and Soslowsky, L. J., 2004, "Strain-rate sensitive mechanical properties of tendon fascicles from mice with genetically engineered alterations in collagen and decorin," Journal of Biomechanical Engineering, 126(2), pp. 252-257.
9. Silver, F. H., Freeman, J. W., and Seehra, G. P., 2003, "Collagen self-assembly and the development of tendon mechanical properties," Journal of Biomechanics, 36(10), pp. 1529-1553.
10. Pioletti, D. P., Rakotomanana, L. R., and Leyvraz, P. F., 1999, "Strain rate effect on the mechanical behavior of the anterior cruciate ligament-bone complex," Medical Engineering & Physics, 21(2), pp. 95-100.
11. Yamamoto, N., and Hayashi, K., 1998, "Mechanical properties of rabbit patellar tendon at high strain rate," Bio-Medical Materials & Engineering, 8(2), p. 83.
12. Ng, B. H., Chou, S. M., Lim, B. H., and Chong, A., 2004, "Strain rate effect on the failure properties of tendons," Journal of Engineering in Medicine, 218, pp. 203-206.
13. Crisco, J. J., Moore, D. C., and McGovern, R. D., 2002, "Strain-rate sensitivity of the rabbit MCL diminishes at traumatic loading rates," Journal of Biomechanics, 35(10), pp. 1379-1385.
14. Azangwe, G., Mathias, K. J., and Marshall, D., 1999, "Macro and microscopic examination of ruptured surfaces of anterior crucial ligaments of rabbits," The Journal of Bone and Joint Surgery, 82-B(3), pp. 450-456.
15. Haut, R. C., 1983, "Age-dependent influence of strain rate on the tensile failure of rat tail tendon," Journal of Biomechanical Engineering, 105, pp. 296-298.
16. Kastelic, J., and Baer, E., 1980, "Deformation in tendon collagen," Society for Experimental Biology, 34, pp. 397-435.
17. Woo, S. L.-Y., Peterson, R. H., Ohland, K. J., Sites, T. J., and Danto, M. I., 1990, "The effects of strain rate on the properties of the medial collateral ligament in skeletally immature and mature rabbits: A biomechanical and histological study," Journal of Orthopaedic Research, 8(5), pp. 712-721.
18. Liao, J., and Vesely, I., 2004, "Relationship between collagen fibrils, glycosaminoglycans, and stress relaxation in mitral valve chordae tendineae," Annals of Biomedical Engineering, 32(7), pp. 977-983.
19. Provenzano, P., Lakes, R., Keenan, T., and Vanderby, R., 2001, "Nonlinear ligament viscoelasticity," Annals of Biomedical Engineering, 29, pp. 908-914.
20. Elliott, D. M., Robinson, P. S., Gimbel, J. A., Sarver, J. J., Abboud, J. A., Iozzo, R. V., and Soslowsky, L. J., 2003, "Effect of altered matrix proteins on quasilinear viscoelastic properties in transgenic mouse tail tendons," Annals of Biomedical Engineering, 31(5), pp. 599-605.
21. Johnson, G. A., Tramaglini, D. M., Levine, R. E., Ohno, K., Choi, N. Y., and Woo, S. L. Y., 1994, "Tensile and viscoelastic properties of human patellar tendon," Journal of Orthopaedic Research, 12(6), pp. 796-803.

Do trabeculae of femoral head represent a structural optimum?

H.A. Kim[1], G.J. Howard[1], J.L. Cunningham[1]

[1] Department of Mechanical Engineering, University of Bath, UK

Abstract — **This paper presents a numerical investigation in the influence of loading on the trabecular architecture of a femoral head using structural optimization. Previous literature has shown that structural optimization can be used to simulate the response of bone to external loading conditions, in the cases of os-calcis and vertebrae of which the loading conditions may be considered relatively simple. The geometry of a typical femoral head is modeled in the two-dimensional finite element environment with 8-noded quadrilateral elements. Three load cases were considered: 1) the single leg stance phase of gait; 2) the extreme of abduction experienced on a daily basis; 3) the extreme of adduction experienced on a daily basis. These were chosen to give an insight into the influence of difference loading conditions on various architectural features of the femoral head. The results obtained from structural optimization applied to investigate the effects of frequency of load cases suggests that the frequency of load cases is not directly proportional to their influence on the trabecular architecture. The paper also presents some preliminary results, using the same technique, of the influence of a prosthetic femoral stem on the architecture of the surrounding trabecular bone.**

Keywords — **bone, femoral, trabeculae, remodeling, optimization.**

I. Introduction

The well-defined internal architecture of trabecular bone has been thought to represent an optimum biological response to its mechanical environment. Structural optimization has hence been used to investigate the bone structure and the remodeling mechanism [e.g. 1, 2].

Structural optimization considered in this context is sometimes referred to as topology optimization, the shape of the boundaries that defines a design is optimized as well as the number of boundaries, i.e. creating holes. It typically considers design problems in a continuum environment such as Fig. 1, where the continuum domain is represented by Ω enclosed by a boundary, Γ, with body forces, f, the boundary traction, t on $\Gamma_t \subset \Gamma$, and support on $\Gamma_u \subset \Gamma$. The optimization problem is formulated as a material distribution problem where the design variable, x_i is either present or absent, $x_i \in \{1,0\}$. The implementation typically employs the presence or absence of finite elements as a design variable [3].

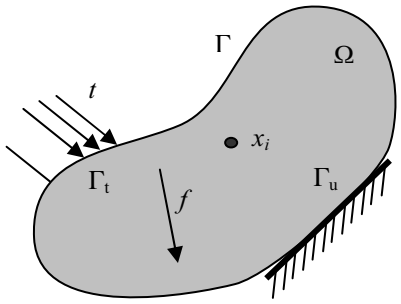


Fig. 1 Generalised two-dimensional continuum domain

Such material distribution problems commonly employ continuous material density distribution to represent the structural architecture. Whilst this offers a general understanding of the optimum configuration, the structural details are often unclear or limited, particularly for more complex geometries with multiple loading conditions. In addition, a recent study has shown that a continuous optimum solution may be significantly different from the discrete optimum solution [4].

This paper aims to investigate the influence of loading conditions on typical femoral head trabecular architecture using a discrete topology optimization strategy and understand the role(s) of various key features. It will also show preliminary results from applying structural optimization to study the trabecular remodeling response to the presence of a hip prosthesis.

II. Finite element modelling of femoral head

A. Geometry

The femoral head is modeled by an artificial cut across the proximal diaphysis, Fig. 2. A representative 2D section of the mid-frontal plane of the proximal femur was created in Solid Edge® [4]. The geometry was based upon that used by Jacobs et al. [5] and the internal area was fully populated in order for optimization to determine the optimum configuration. The femur geometry was meshed using 7,056 8-node quadratic isotropic plate elements in ANSYS® [6]. An elastic modulus, E = 20GPa and a Poisson's ratio, υ = 0.3 were specified for all the elements.

Chwee Teck Lim, James C.H. Goh (Eds.): ICBME 2008, Proceedings 23, pp. 1636–1639, 2009
www.springerlink.com

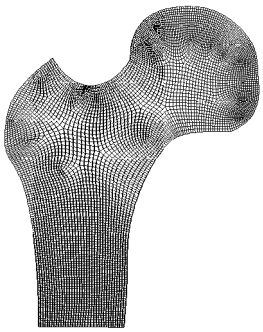


Fig. 2 Finite element model of a femoral head

A row of two-element thickness was defined around the external boundary of the femur model. These perimeter elements were excluded from the optimization process to prevent changes to the geometry of the femur, thus the optimization routine considered only the internal trabecular structure.

B. Boundary and loading conditions

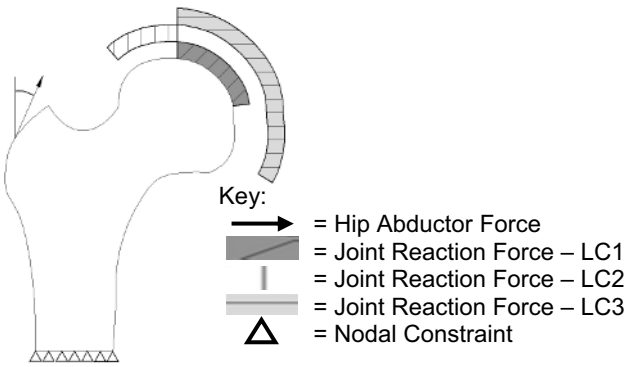


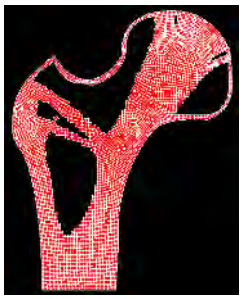
Fig. 3 Loading and boundary conditions

Table 1 Magnitude of load cases

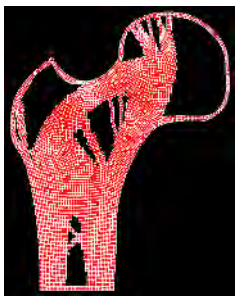
	Joint reaction		Hip abductor	
	Force (N)	Pressure (MPa)	Force (N)	Orientation (°)
LC1	2317	36.07	703	24
LC2	1158	34.48	351	8
LC3	1546	16.57	468	35

A set of three load cases representing typical activities performed on a daily basis was considered, [8]. Fig. 3 depicts the load cases, where load case one (LC1) represents the single leg stance phase of gait whilst load cases two (LC2) and three (LC3) represent the extremes of abduction and adduction respectively, Table 1. In each case a pressure load was applied across an area of the femoral head to represent the joint reaction force and a point load applied at the greater trochanter to represent the hip abductor force.

The line of nodes which formed the distal boundary was fully constrained against translation and rotation in all directions as shown in Fig. 3.



(a) LC1



(b) LC2



(c) LC3

Fig. 4 Optimum solutions for each load case

III. Application Optimization

The structural optimization problem is to minimize the product of compliance and volume, as written in a discrete form in (1).

$$\text{Minimize } C(x_i, u_i)\, V(x_i) \tag{1}$$

where C denotes total compliance and V is the total volume of the design [4]. This problem is solved using Evolution-

ary Structural Optimization (ESO) [3], using the elemental von Mises stress as sensitivities computed by the finite element method.

A. Application of each loading condition

Three optimization runs were first carried out for each loading condition, and the solutions with a 35% volume reduction were obtained, Fig. 4.

The results for LC1 show the development of a thick band of elements extending from the surface of the femoral head into the medial cortex of the diaphysis akin to the primary compressive trabeculae. A cavity was formed in the middle of the metaphysis similar to the proximal end of the medullary cavity. A void was also created on the medial side of the femoral head, similar to Babcock's triangle and around the area where Ward's triangle is found.

The application of LC2 led to a strut akin to the primary tension trabeculae running from the lateral cortex of the diaphysis, around the superior edge of the position of Ward's triangle into the lateral side of the femoral head. A band of elements also ran from the femoral head into the medial cortex of the diaphysis, supporting the prediction of the primary compression trabeculae in LC1.

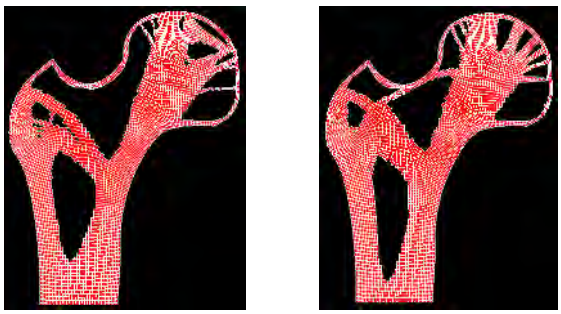
The results of LC3 again predicted a band of elements similar to the primary tension trabeculae although in this case originating from the point of abductor force application at the greater trochanter.

B. Simultaneous Application of Loads

The multiple load cases were considered again by applying all load cases simultaneously. Two optimization runs were conducted with and without accounting for the frequency. As the load cases are applied simultaneously, the frequency of load cases 3:1:1 is simulated by multiplying the magnitude of LC1 by 3, and the solutions are displayed in Fig. 5.

Fig. 5(a) shows that the application of the load case of 3:1:1 ratio led to an unrealistic internal structure with many morphological similarities to that predicted by the application of LC1 only, Fig. 4(a). Again a thick strut was predicted in the femoral head which extended distally into the medial cortex of the diaphysis. A void was created which encompasses the area where Ward's triangle is typically found but extended too far in both the medial and lateral directions. This was largely due to the lack of tensile stress resulting from the low magnitude of LC2 in this case. The low magnitude of LC2 also resulted in the medullary cavity like void to be translated in a proximal direction.

Fig. 5(b) shows that the application of the three load cases simultaneously as given in Table 1 produced a structure in which the major morphological characteristics of the proximal femur may be identified. A thick strut runs from the surface of the femoral head into the medial cortex of the diaphysis representative of the primary compressive trabeculae. The cortical bone lining the diaphysis can be identified either side of a void representative of the medullary cavity. The boundary conditions at the cut across the diaphysis have prevented the medullary cavity from extending further in the distal direction at this point. Further voids representative of Ward's triangle and Babcock's triangle are identified. The area where the primary tensile and secondary compressive trabeculae cross can be seen superior to the medullary cavity. The primary tensile trabeculae can also be seen to extend around the superior boundary of Ward's triangle into the femoral head.



(a) 3:1:1 frequency (b) equal frequency

Fig. 5 Optimum solutions for multiple load cases applied simultaneously

IV. Trabecular Remodeling of Femoral Head in Response to the Presence of Prosthesis

The finite element model of the femoral head of Fig. 2 was modified to incorporate the femoral component of a non-cemented hip prosthesis. The length of the diaphysis was increased to encase the full length of the femoral component of an Exeter style implant. 10,187 8-node quadratic plate elements were used. The prosthesis was also not allowed to be modified. All three load cases were applied simultaneously at equal frequency. Fig. 6 depicts the von Mises stress contour plot of the initial model where Young's modulus of the prosthesis was given as 210GPa.

The optimum solution is depicted in Fig. 7, where high bone resorption is apparent. This is because the stiffness of the prosthesis is significantly greater than that of the bone, hence attracting a greater level of the applied load. This can be seen in Fig. 6 where the von Mises stress of the prosthesis is greater than that in the bone. This low stress and strain level leads to the high bone resorption seen in the solution of Fig. 7, which is consistent with the previous findings [10].

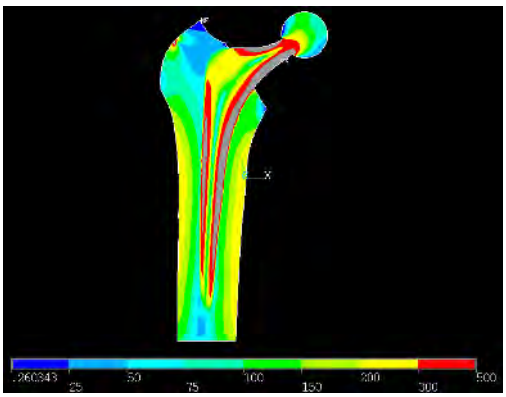


Fig. 6 Von Mises stress distribution of femoral head model with prosthesis

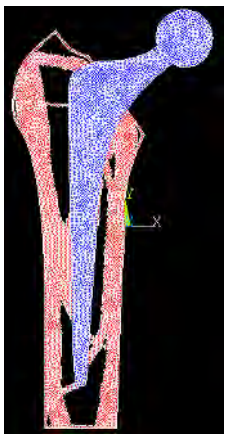


Fig. 7 Optimum solutions for trabecular remodelling around prosthesis

It is also noted that the morphology of the optimum solution is considerably different from the original trabecular orientation of Fig. 5. This suggests that the original architecture is far from the optimum for the new load distribution in the presence of prosthesis. Whilst the original trabecular architecture represents the optimum load carrying structure, the presence of the prosthesis significantly alters the load path and the existing trabeculae no longer represent the optimum solution.

V. Conclusion

It was shown that the application of loads representative of a single activity only was not capable of predicting the full range of morphology characteristic of the proximal femur. However, the results have shown that the range of morphology observed in the femur is in fact created by a range of loads representative of different activities. The application of the three load cases individually allowed the origin of different morphological features to be identified. Whilst the three load cases considered in this study are the common load cases in existing literature, the first two load cases were observed to have dominant influence on the structural morphology.

When the multiple load cases were considered, it was found that structural optimization produced the most realistic results when all load cases were applied simultaneously. This supports the observations from previous studies that bone retains the memory of the applied mechanical loading history [9] and the local strain status may not immediately return to its original status upon removal of a load case. Furthermore, the frequency of the load cases did not appear to have a significant influence on the morphological definition of femoral head trabeculae.

The preliminary results of trabecular remodeling response to the presence of prosthesis shows a high level of bone resorption due to the considerably greater stiffness of the propsthesis relative to that of the bone. The optimum solution suggests that the presence of the prosthesis alters the load paths significantly and that the original trabecular architecture may no longer represent an optimum structure. However further studies are required to consider the contact of the bone and prosthesis surfaces in order to gain a more comprehensive understanding of the remodeling response.

References

1. Bagge, M. 2000. A model of bone adaptation as an optimization process. J Biomech. 33: 1349-1357.
2. Kim HA, Clement PJ, Cunningham JL. 2008. Investigation of cancellous bone architecture using structural optimisation. J Biomech. 41: 629-635.
3. Xie YM, Steven GP. 1997. Evolutionary Structural Optimization. Springer. London.
4. Edwards CS, Kim HA, Budd CJ. 2007. An evaluative study of ESO and SIMP for optimising a cantilever tie-beam. Struct Multidiscip Optim 30: 403-414.
5. Siemens PLM Software. 2008. Solid Edge v18. TX USA.
6. Jacobs CR, Levenston ME, Beaupré GS, et al. 1995. Numerical instabilities in bone remodeling simulations: advantages of a node based finite element approach. J Biomech 28: 449-459.
7. ANSYS Inc. 2008. ANSYS 11.0, USA.
8. Carter DR, Orr TE, Fyhrie DP. 1989. Relationships between loading history and femoral cancellous bone architecture. J Biomech 22: 231-244.
9. Skerry TM, Bitensky L, Chayen J, Lanyon LE. 1988. Loading-related reorientation of bone proteoglycan in vivo. Strain memory in bone tissue? J Orthop Res 6: 547-551.
10. Weinans H, Huiskes R, Grootenboer HJ. 1992. Effects of material properties of femoral hip components on bone remodeling. J Orthop Res 10: 845 – 853.

Author: H A Kim
Institute: University of Bath
Street: Department of Mechanical Engineering
City: Bath
Country: UK
Email: H.A.Kim@bath.ac.uk

Gender and Arthroplasty Type Affect Prevalence of Moderate-Severe Pain Post Total Hip Arthroplasty

J.A. Singh[1,2], S.E. Gabriel[2] and D. Lewallen[1]

[1] Minneapolis VA Medical Center & University of Minnesota, Rheumatology, Minneapolis, MN, USA
[2] Mayo Clinic School of Medicine, Health Sciences & Orthopedic Surgery, Rochester, MN, USA

Abstract — **Objective: To investigate the impact of gender, age and arthroplasty type (primary vs. revision) on prevalence of moderate-severe hip pain.**

Methods: Using an Institutional Total Joint Registry, we identified a cohort of patients who underwent primary of revision THA from 1996-2004 and responded to the follow-up questionnaires. We compared the prevalence of moderate or severe hip pain based on arthroplasty type, gender and by age (<60, 61-70, 71-80 and >80 years). Results based on gender and type of arthroplasty were analyzed by comparing proportions and based on age by using Chi-square tests, considering a p-value<0.05 significant.

Results: Moderate-severe pain was less prevalent following primary vs. revision THA at 1-year (5.5% vs. 9.8%, p<0.001), and 2-years post-surgery (7.5% vs. 16.3% vs.; p<0.001). The prevalence of moderate-severe pain at 1-year post-arthroplasty was similar for women and men, both primary THA and revision THA: 6.3% vs. 4.6%, p=0.13; and 11.8% vs. 7.3%, p=0.058, respectively; and in revision THA at 2-years: 17.7% vs. 14.7%, p=0.068. However at 2-years, more women than men had moderate-severe pain in primary THA group: 8.8% vs. 6.6%, p=0.042, respectively.

Age had a significant impact on prevalence of moderate-severe pain after 1- and 2-years after primary THA with lower prevalence of pain in 61-70 yr age group compared to other age categories (p=0.01 and p<0.001), but did not have a significant impact on prevalence of moderate- severe pain post-revision THA (p=0.406 and p=0.397, respectively).

Conclusions: Moderate-severe pain was more prevalent in women with primary THA at 2-years, but not at 1-year. This might suggest that factors not directly related to surgery such as anatomical and biochemical differences, bone remodeling, differences in recovery of strength and endurance, activity level or comorbidities may play a role in these differences and need further study.

Keywords — **Pain, Hip Arthroplasty, Predictors, Gender, Age.**

I. Introduction

Total Hip Arthroplasty is a very common surgery for the treatment of end-stage arthritis. It leads to pain relief, improvement in function and quality of life. It has been termed "the operation of the century" [1].

Approximately 208,600 THA were performed in the U.S. in 2005 [2]. It is estimated that demand for primary THAs will grow by 174% to 574,000 by 2030 [2]. Most studies show that THA is very successful in relieving pain. A population-based survey of random sample of 5,500 subjects >65 years old in UK showed that 26% of patients who received THA more than an year ago still complained of some pain in the operated hip [3].

Many factors have been reported to be associated with pain outcomes after THA. Patient expectation of complete relief from after surgery was associated with better improvement in pain and function 6-months after hip and knee arthroplasty [4]. Patients with lower comorbidity were found to have better outcomes after revision hip arthroplasty [5]. Preoperative pain was a predictor of post-operative severity in patients with revision THA [5] and primary THA [6,7]. Older age [6,8] and postoperative low back pain [6] are associated with worse functional outcome 3.6 years after THA. Pre-operative function predicted post-operative pain and function outcomes in a group of patients undergoing knee and hip replacement [7]. Most studies either did not examine gender or found that it was not a significant predictor of outcomes after THA [8].

In this study, our aims were to assess whether: (1) male gender, older age and lower pre-operative pain were associated with a lower risk of moderate-severe pain 1- an 2-years after primary THA; (2) these associations were independent i.e., the associations remain significant in multivariable-adjusted analyses; and (3) gender, age and pre-operative pain are associated with moderate-severe pain 1- an 2-years after revision THA.

II. Methods

A. Study Cohort

Total Joint registry at the Mayo Clinic has been collecting revision data on all patients who undergo hip or knee arthroplasty since 1969 and pain and functional data since 1993. For this study, we identified all patients who underwent primary or revision Total Hip Arthroplasty (THA) patients from 1996-2004 that responded to a validated mailed questionnaire or completed a questionnaire during

Chwee Teck Lim, James C.H. Goh (Eds.): ICBME 2008, Proceedings 23, pp. 1640–1643, 2009
www.springerlink.com

clinic visit at 2-, and 5-years post-THA. For the patients who did not return questionnaires, or return for their follow-up visit, the trained staff administered pain an function questionnaires.

B. Outcomes and Predictor Variables

Hip Pain was assessed with a single question: "Do you have pain in the knee in which the joint was replaced? ". Patients were asked to select one of the following four responses: None, Slight, Moderate, Severe/marked. For the analyses, moderate and severe pain categories were combined.

The main predictors of interest were gender (women vs. men), age (categorized as ≤70 years or >70 years) and pre-operative pain severity (categorized as moderate-severe pain vs. other categories). Age categorization was based on similar categorizations in the previous studies and based on clinical decision of the orthopedic surgery expert.

C. Statistical Analyses

We conducted separate logistic regression analyses separately for primary and revision THA at 1- and 2-year follow-up periods. Univariate logistic regression analyses assessed the association of gender, age or pre-operative pain severity with post-operative moderate-severe pain. Multivariable-adjusted logistic regression analyses adjusted for age, gender and pre-operative pain severity simultaneously. We present odds ratios (OR) with 95% confidence intervals (CI). A p-value <0.05 was considered statistically significant.

III. Results

There were 4,713 primary THA at 2 years with data and 1,839 revision THA at 2 years with data. For the primary THA, there were 1,477 men and 1,605 women at 1-year; 2,326 men and 2,387 women at 2-years. For revision THA, 595 were men and 476, women at 1-year; 839 were men and 1,000 women at 2-years.

Moderate-severe pain was less prevalent following primary vs. revision THA at 1-year (5.5% vs. 9.8%, p<0.001), and 2-years post-surgery (7.5% vs. 16.3% vs.; p<0.001).

A. Univariate and Multivariable-adjusted predictors of Moderate-severe pain 1-year after Primary THA

At 1-year after primary THA, none of the variables were significantly associated with the outcome, moderate-severe pain (Table 1).

Table 1 Univariate Predictors of Moderate-severe pain at 1-year after Primary TKA

	Odds Ratio	95% CI	p-value
Age ≥70 (vs. <70)	1.35	0.86, 2.12	0.19
Men (vs. women)	0.73	0.46, 1.15	0.17
Moderate-severe pre-op pain	1.60	0.38, 6.75	0.52

CI, Confidence Interval

Table 2 Multivariable-adjusted Predictors of Moderate-severe pain at 1-year after Primary TKA

	Odds Ratio	95% CI	p-value
Age ≥70 (vs. <70)	1.34	0.77, 2.35	0.30
Men (vs. women)	**0.56**	**0.30, 0.98**	**0.04**
Moderate-severe pre-op pain	1.52	0.36, 6.49	0.57

CI, Confidence Interval

Multivariable-adjusted analyses found no associations of age or pre-operative pain with post-operative moderate-severe pain at 1-year after primary THA. Men were significantly less likely to report moderate-severe pain than women, after adjusting for differences in age and pre-operative pain severity (Table 2).

B. Univariate and Multivariable-adjusted predictors of Moderate-severe pain 2-years after Primary THA

In univariate analyses, age ≥70 was associated with significantly higher odds of moderate-severe pain two years after primary THA compared to those younger than 70 years (Table 3).

The age association noted in univariate analyses was confirmed in multivariable-adjusted analyses (Table 4). Men were significantly less likely to report moderate-severe pain compared to women. Pre-operative pain was not significantly associated with pain outcomes.

Table 3 Univariate Predictors of Moderate-severe pain at 2-year after Primary TKA

	Odds Ratio	95% CI	p-value
Age ≥70 (vs. <70)	**1.41**	**1.11, 1.80**	**0.005**
Men (vs. women)	0.83	0.65, 1.06	0.14
Moderate-severe pre-op pain	1.29	0.63, 2.66	0.49

CI, Confidence Interval

Table 4 Multivariable-adjusted Predictors of Moderate-severe pain at 2-years after Primary TKA

	Odds Ratio	95% CI	p-value
Age ≥70 (vs. <70)	**1.41**	**1.03, 1.92**	**0.03**
Men (vs. women)	**0.71**	**0.52, 0.98**	**0.04**
Moderate-severe pre-op pain	1.21	0.58, 2.49	0.61

CI, Confidence Interval

C. Univariate and Multivariable-adjusted predictors of Moderate-severe pain 1-year after Revision THA

In univariate analyses at 1-year after revision THA, none of the variables were significantly associated with the outcome, moderate-severe pain (Table 5).

Multivariable analyses did not find any significant differences by age, gender or pre-operative pain severity.

Table 5 Univariate Predictors of Moderate-severe pain at 1-year after Revision TKA

	Odds Ratio	95% CI	p-value
Age ≥70 (vs. <70)	1.04	0.61, 1.77	0.86
Men (vs. women)	0.59	0.34, 1.02	0.07
Moderate-severe pre-op pain	2.5	0.93, 6.69	0.08

CI, Confidence Interval

Table 6 Multivariable-adjusted Predictors of Moderate-severe pain at 1-year after Revision TKA

	Odds Ratio	95% CI	p-value
Age ≥70 (vs. <70)	1.56	0.76, 3.27	0.24
Men (vs. women)	0.49	0.22, 1.08	0.08
Moderate-severe pre-op pain	2.49	0.93, 6.64	0.07

CI, Confidence Interval

D. Univariate and Multivariable-adjusted associations for Moderate-severe pain 1-year after Revision THA

Pre-operative pain severity was significantly associated with post-operative pain severity at 2-years after revision THA. Age and gender were not associated.

Multivariable-adjustment did not attenuate the strength of association of pre-operative pain severity with post-operative pain severity at 2-years post-revision THA.

Table 7 Univariate Predictors of Moderate-severe pain at 2-years after Revision TKA

	Odds Ratio	95% CI	p-value
Age ≥70 (vs. <70)	1.10	0.86, 1.42	0.45
Men (vs. women)	0.79	0.63, 1.02	0.07
Moderate-severe pre-op pain	**2.22**	**1.34, 3.66**	**0.002**

CI, Confidence Interval

Table 8 Multivariable-adjusted Predictors of Moderate-severe pain at 2-years after Revision TKA

	Odds Ratio	95% CI	p-value
Age ≥70 (vs. <70)	1.02	0.70, 1.50	0.91
Men (vs. women)	0.79	0.54, 1.16	0.23
Moderate-severe pre-op pain	**2.21**	**1.33, 3.65**	**0.002**

CI, Confidence Interval

IV. Discussion

In this study of a large number of THA patients, we noted a significantly higher prevalence of moderate or severe pain in women (vs. men) at 1 and 2 years post primary THA and at 5-years post Revision THA. We also found the patients with moderate-severe pain pre-operatively had more moderate-severe pain at 2- and 5-years after revision THA, but not after primary THA. Older patients had more moderate-severe pain at 2 years post-primary THA.

Our study has several strengths and limitations. Strengths include a large sample size, use of multivariable-adjustments, ability to adjust for pre-operative pain severity, and follow-up up to two years. We presented analyses for both primary and revision THA. Our study has limited generalizability, since it is a single-center study and patients are predominantly Caucasians. Non-response bias due to approximately only half of those with post-operative questionnaires having pre-operative assessments also limits generalizability. Residual confounding due to BMI, comorbidity etc in possible. We were unable to examine other important predictors of pain after THA including psychological distress, depression or anxiety. A longer follow-up would make these findings even more interesting. A study of 5-year outcomes controlling for additional variables is underway.

These findings have important implications. It is not clear from the published literature whether gender is a predictor of pain outcomes after primary THA. Studies in primary THA found no gender association [8], while a study in patients with revision THA reported worse outcomes in women [9]. We found that female gender was associated with worse pain outcomes in primary THA both at 1- an 2-years, but not in revision THA patients. Our study had a larger sample size than previous studies, used a single pain question as opposed to WOMAC or Hip society scores in the previous studies and performed multivariable-adjusted analyses after controlling for pre-operative pain differences and age. Holtzman et al. found that women had worse pain and function than men at the time of the THA and at one year after THA [10]. Comorbidities and pre-operative status explained the post-operative differences only partially.

An interesting finding was that of association of pre-operative pain severity with post-operative moderate-severe pain at both 1- and 2-years in patients with revision, but not primary THA. This is an interesting finding since we had a far larger sample for primary than revision THA, yet associations were significant in revision THA. This implies that different factors predict pain outcomes after primary vs. revision THA. This is a new and important contribution to the existing literature in the area of patient-reported outcomes.

In summary, in this study of a large number of THA patients, we noted a significantly higher prevalence of moderate or severe pain in females (vs. male) at 1 and 2 years post primary THA and at 5-years post Revision THA. We also found the patients with moderate-severe pain pre-operatively had more moderate-severe pain at 2- and 5-years after revision THA, but not after primary THA. Older patients had more moderate-severe pain at 2 years post-primary THA.

V. Conclusions

Age and female gender predict the risk of moderate-severe pain after primary THA and higher pre-operative pain severity predicts moderate-severe pain after revision THA. Further studies need to examine if risk stratification is possible based on these factors.

Acknowledgment

We thank Youlonda Lochler for her assistance in data retrieval and Megan O'Byrne and Scott Harmsen in data management and data analysis.

References

1. Learmonth ID, Young C, Rorabeck C. The operation of the century: Total hip replacement. Lancet 2007;370:1508-19.
2. Kurtz S, Mowat F, Ong K, Chan N, Lau E, Halpern M. Prevalence of primary and revision total hip and knee arthroplasty in the united states from 1990 through 2002. J Bone Joint Surg Am 2005;87:1487-97.
3. Linsell L, Dawson J, Zondervan K*, et al.* Pain and overall health status in older people with hip and knee replacement: A population perspective. J Public Health (Oxf) 2006;28:267-73.
4. Mahomed NN, Liang MH, Cook EF*, et al.* The importance of patient expectations in predicting functional outcomes after total joint arthroplasty. J Rheumatol 2002;29:1273-9.
5. Davis AM, Agnidis Z, Badley E, Kiss A, Waddell JP, Gross AE. Predictors of functional outcome two years following revision hip arthroplasty. J Bone Joint Surg Am 2006;88:685-91.
6. Nilsdotter AK, Petersson IF, Roos EM, Lohmander LS. Predictors of patient relevant outcome after total hip replacement for osteoarthritis: A prospective study. Ann Rheum Dis 2003;62:923-30.
7. Fortin PR, Clarke AE, Joseph L*, et al.* Outcomes of total hip and knee replacement: Preoperative functional status predicts outcomes at six months after surgery. Arthritis Rheum 1999;42:1722-8.
8. Norman-Taylor FH, Palmer CR, Villar RN. Quality-of-life improvement compared after hip and knee replacement. J Bone Joint Surg Br 1996;78:74-7.
9. Biring GS, Masri BA, Greidanus NV, Duncan CP, Garbuz DS. Predictors of quality of life outcomes after revision total hip replacement. J Bone Joint Surg Br 2007;89:1446-51.
10. Holtzman J, Saleh K, Kane R. Gender differences in functional status and pain in a medicare population undergoing elective total hip arthroplasty. Med Care 2002;40:461-70.

Author: Jasvinder Singh
Institute: Minneapolis Veterans Affairs Medical Center
Street: Rheumatology (111 R)
City: Minneapolis, MN 55417
Country: USA
Email: Jasvider.md@gmail.com

Quantification of Polymer Depletion Induced Red Blood Cell Adhesion to Artificial Surfaces

Z.W. Zhang and B. Neu

Division of Bioengineering, School of Chemical and Biomedical Engineering, Nanyang Technological University, 70Nanyang Avenue, Singapore 637457.

Abstract — **Cell-cell interactions are governed by interplay of various cell-receptor-mediated interactions and non-specific forces, with non-specific forces such as electrostatic repulsion often allowing or preventing cells approaching close enough to establish adhesion via lock and key forces. One non-specific force that has only recently been suggested as being important for cell-cell interaction is macromolecular depletion interaction. Polymer depletion occurs at cell surfaces if adsorption energy is low, and if depletion zones of adjacent surfaces overlap; osmotic forces move fluid away from the intercellular gap and cell-cell attractive forces develop. In this study interference reflection microscopy (IRM) was employed to study red blood cell (RBC) adhesion to glass surfaces in the presence of dextran in order to elucidate and quantify the underlying mechanism. Our results indicate that adhesion is markedly increased in the presence of dextrans with a molecular weight above 70 kDa. The calculated adhesion energies varied between 0.1 and 1 μJ/m2 and the bell-shaped relation between adhesion energy and both polymer molecular mass and concentration was in qualitative and quantitative agreement with a theoretical depletion model. A strong suppression of membrane undulations was also observed. In overview, our results indicate that depletion interaction plays a significant role in RBC adhesion via initiating close contacts. The results suggest the importance of depletion forces for RBC interactions and its relevance to a wide variety of cell-cell and cell-surface interactions.**

Keywords — **IRM; Depletion interaction; Red blood cell; Dextran**

I. Introduction

During the past few decades, the adhesion of red blood cells (RBC) to other cells and to surfaces has been studied quite extensively due to at least two reasons: 1) Abnormal adhesiveness to other RBC and to endothelial cells has been linked to several diseases such as sickle cell anemia or diabetes mellitus [1, 2]; 2) Red blood cells are relatively simple, easily obtainable cells thus making them logical choices to study the fundamentals of cell interactions in the circulation or with biomaterials. It is clear that various non-specific forces (e.g., electrostatic) and specific forces (e.g., cell adhesion molecules) govern RBC and other cell adhesion to cells or surfaces. While prior studies have described several aspects of RBC adhesion in normal and pathologic states, none appears to have considered depletion interaction as a non-specific force for cell-surface adhesion. Conversely, depletion mediated interactions are commonly considered in the general field of colloid chemistry, and several previous reports have dealt with the experimental and theoretical aspects of depletion aggregation, often termed depletion flocculation [3-7].

More recently, depletion interaction as an attractive force in polymer-induced RBC aggregation has been considered, with results indicating that polymer depletion plays a major role in reversible aggregation of RBC [8, 9]. Such findings are of basic science and clinical interest, in that reversible RBC aggregation is an important determinant of the in vitro rheological behavior of blood as well as of in vivo blood flow dynamics and flow resistance [10, 11].

A depletion layer develops near a surface in contact with a polymer solution if the loss of configurational entropy of the polymer is not balanced by adsorption energy. Within this layer the polymer concentration is lower than in the bulk phase. Thus, as two particles approach, the difference of solvent chemical potential (i.e., the osmotic pressure difference) between the intercellular polymer-poor depletion zone and the bulk phase results in solvent displacement into the bulk phase and hence depletion interaction [5]. Due to this interaction, an attractive force develops that tends to minimize the polymer-reduced space between the cells, thus resulting in flocculation or aggregation. The existence of depletion layers at the RBC surface has been confirmed via electrophoresis studies of cells in various polymer solutions [8, 12, 13], and the energetics of RBC interaction in neutral polymer solutions and the effects of the "soft or hairy" RBC membrane glycocalyx have been reported [9].

To gain a better understanding of this depletion interaction and the physical basis for RBC adhesion to other surfaces, the adhesion of RBC is evaluated by quantitative reflection interference contrast microscopy (IRM). IRM is a powerful tool which allows visual examination of cell/surface contact and separation in real time. It enables dynamic analysis of surface topologies and local membrane-

Chwee Teck Lim, James C.H. Goh (Eds.): ICBME 2008, Proceedings 23, pp. 1644–1647, 2009
www.springerlink.com

substrate distances of adherent cells to measure adhesion forces[14]. To quantify the depletion interaction between RBC and coverslip, a theoretical model was established to determine the height profile of RBC at the contact area, and cell-surface affinity was quantified by Young's equation, and this depletion affinity was then compared to the theoretical model. The study here involved sedimentation of normal human red blood cell onto a BSA coated round glass coverslip in the presence of different neutral polymer. Cell adhesion dynamics, membrane undulations, and adhesion energies were quantified as a function of polymer molecular mass and concentration.

II. Materials and Methods

A. RBC preparation

Blood was obtained by thumbnail puncture using a sterile lancet and used within 4h. RBCs were separated from whole blood by centrifugation at 1,000g for 5min, and washed 3 times in isotonic PBS, following that, they were re-suspended at about 0.1% hematocrit in PBS or various dextran solutions.

B. Coverslips preparation

The details has been described previously[15]. Round glass coverslips (25mm diameter) were immersed in nitric acid(65%, Sigma Aldrich)overnight, then they were washed with distilled water and coated with 4% APES in anhydrous acetone (Sigma Aldrich) for 4min. These aminated coverslips were stored in a dust-free plastic chamber until use. 2% BSA (w/v) was incubated with the coverslips for 2 hours at room temperature and rinsed gently with PBS and placed on the holder.

C. Interference reflection microscopy (IRM)

The effects of various dextran suspensions on the interface between settled RBC and the flat glass surfaces were quantified via IRM (Figure 1). In this method, darker areas of the image indicate decreasing distances between the cell and the flat surface [16]. Our IRM setup is based on an Olympus IX71 inverted microscopy equipped with a Zeiss Neofluoar 63 ×/1.25 Antiflex oil immersion objective. Light from 100W high-pressure mercury arc lamp is filtered with a 546.1nm band-pass filter (dv=5nm, 85%, Omega, USA). The contrast in reflection interference microscopy is enhanced by suppressing stray light with the antiflex technique[17].

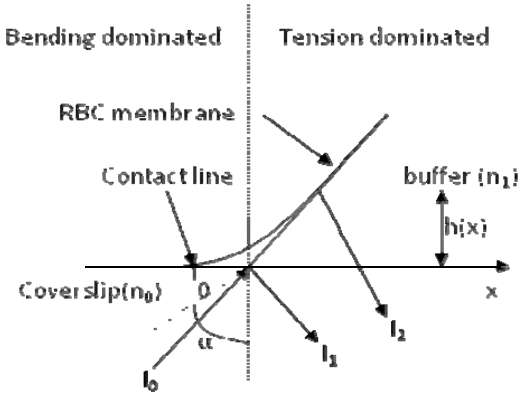


Figure 1 Principle of IRM

D. Data analysis

The details of quantitative IRM has been described elsewhere [18]. Briefly, the cell contour at contact area can be obtained by an arccosine transformation of the intensity:

$$h_{(x)}=\frac{\lambda}{4\pi n}[\arccos\frac{2I_x-(I_{\max}+I_{\min})}{I_{\max}-I_{\min}}] \quad (1)$$

Where λ is the wavelength (546.1nm), $I_{\max}$ and $I_{\min}$ are the maximum and minimum intensities for adjacent wave respectively and n is the reflective index of the solution ($n\approx$ 1.34).

Both the contact angle α and capillary length λ can be obtained by doing a linear least squares fitting to the tension dominated region (see Figure 2) [19]:

$$h(x) = \alpha \cdot (x - \lambda) + \alpha \cdot \lambda \cdot e^{-x/\lambda} \ (x \geq 0) \quad (2)$$

By using Young's equation:

$$W=\gamma(1-\cos\alpha) \quad (3)$$

the adhesion energy can be determined, where $\lambda=(\kappa/\gamma)^{1/2}$, with γ being the surface tension and κ the bending elastic modulus of RBC ($\kappa=1.8\times10^{-19}$J) [20].

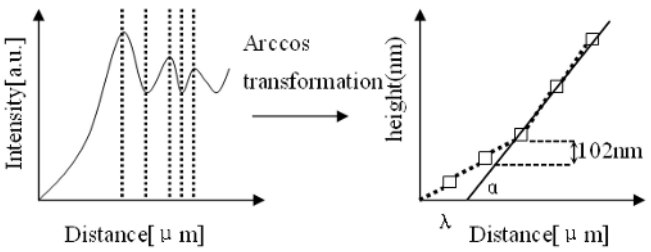


Figure 2 Reconstruction of height profile at contact area

III. Results

A. Red blood cell adhesion dynamics

A typical scenario of RBC adhesion in the presence of dextran is shown in Figure 3. In these studies RBC were suspended in various dextran solutions and allowed to settle and examined by IRM; a darker appearance of the contact area between the cell and the glass slide indicates closer proximity [21]. In dextran-free PBS and in solutions containing dextran 40 kDa the area of close contact stays rather small, with the cells appearing as rings due to close contact only at the peripheral rim of the biconcave RBC. The appearance of the cells changes with the addition of dextran 70 kDa and 500 kDa, such that cells begin to flatten with increased contact area.

In PBS or in dextran solutions containing dextran of molecular weights of 40kDa or less no significant adhesion energy could be determined. Above molecular weights of 40 kDa the adhesion energy showed a bell shaped dependence on the polymer concentration with the maximum adhesion around 4g/dl. The measured energies were all between 0.1-1 $\mu J/m^2$.

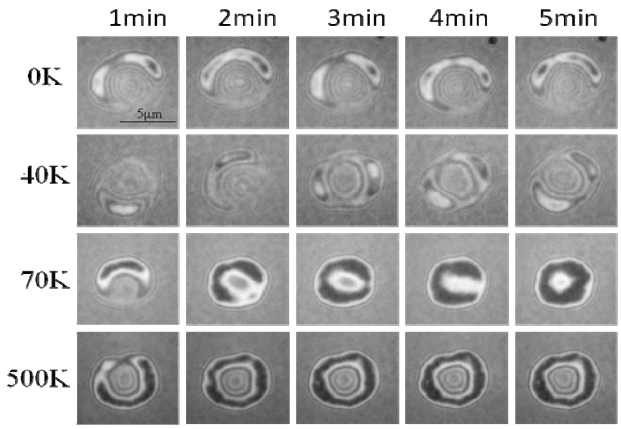


Figure 3 A series of IRM images for RBCs suspended in PBS, 1g/dl dextran40k, 0.5g/dl dextran70k and 0.5g/dl dextran500k

B. Suppression of membrane undulations

Undulation is a unique feature of biological membranes due to thermal excitation. If RBC were suspended in PBS, they showed pronounced membrane undulations, whereas the addition of dextran 70K (2g/dl) lead to a strong suppression (Figure 4). From these results, we can infer that membrane undulation was hindered by high molecular mass dextran.

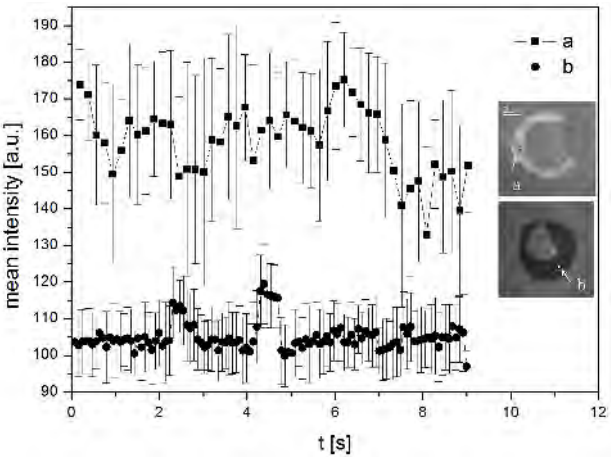


Figure 4 Comparison of the membrane undulation for PBS, 70k (2g/dl), a and b are 1x1 pixels.

IV. Discussion

In this study, we used the neutral polymer dextran to induce cell adhesion. The results presented above clearly illustrate the impact of 70 kDa and 500 kDa dextran on RBC-surface interactions. We conclude that our results are in agreement with the hypothesis that RBC adhesion can be significantly enhanced by neutral polymer induced depletion interaction, with the extent of this effect determined, in part, by polymer molecular size. As shown small dextran had no effect on cell adhesion: it is too small to establish a meaningful depletion layer, with the depletion layer of this small dextran buried within the cell's glycocalyx. Thus, before this thin depletion layer could lead to any attractive interaction, glycocalyx factors (e.g., steric interaction and electrostatic repulsion) prevent adjacent surfaces from becoming sufficiently close. However, for larger dextrans, the depletion layer reaches beyond the glycocalyx, thus leading to the observed impact on cell adhesion.

V. Conclusion

In summary, our findings provide important new insights into the stabilization and destabilization of blood cells in plasma like-suspensions. Further, we suggest that our findings may have physiological and biomedical implications. For example, in pathological conditions large differences in RBC interaction have been observed and our recent understanding of red cell aggregation suggests that these differences are likely due to altered depletion forces between these cells [22, 23]. Age-separated human RBC also exhibit marked differences in affinity, with older, denser cells hav-

ing 3-fold greater affinity than younger, less dense cells in both plasma and polymer solutions [9]. Thus it may be useful to utilize these altered depletion forces for biotechnological applications such as cell separation, and to consider them when looking at the biocompatibility of scaffolds or other biomaterials. While the experimental system used herein represents a rather simple *in vitro* model, our results also suggest possible *in vivo* significance of depletion forces cell on adhesion (e.g., RBC, white cell or platelet interactions with endothelial cells): depletion interaction may help promote cell contact, thereby allowing more-specific adhesive mechanisms to take place.

ACKNOWLEDGMENT

This project is supported by the Ministry of Education (Singapore) and A*Star (Singapore, BMRC grant 05/1/22/19/382).

REFERENCES

1. Setty, B.N.Y., S. Kulkarni, and M.J. Stuart, *Role of erythrocyte phosphatidylserine in sickle red cell-endothelial adhesion.* Blood, 2002. **99**(5): p. 1564-1571.
2. Wautier, J.L. and M.P. Wautier, *Erythrocytes and platelet adhesion to endothelium are mediated by specialized molecules.* Clinical Hemorheology and Microcirculation, 2004. **30**(3-4): p. 181-184.
3. Jenkins, P. and B. Vincent, Depletion flocculation of nonaqueous dispersions containing binary mixtures of nonadsorbing polymers. Evidence for Nonequilibrium effects. Langmuir, 1996. **12**(13): p. 3107-3113.
4. Vincent, B., The Calculation of Depletion Layer Thickness as a Function of Bulk Polymer Concentration. Colloids and Surfaces, 1990. **50**: p. 241-249.
5. Vincent, B., et al., Depletion flocculation in dispersions of sterically-stabilised particles ("soft spheres"). Colloids and Surfaces, 1986. **18**: p. 261-281.
6. Feign, R.I. and D.H. Napper, *Depletion stabilization and depletion flocculation.* J. Colloid Interface Sci., 1980. **75**(2): p. 525-541.
7. Asakura, S. and F. Oosawa, On interaction bewteen two bodies immersed in a solution of macromolecules. J. Chem. Phys., 1954. **22**: p. 1255-1256.
8. Bäumler, H., et al., Electrophoresis of human red blood cells and platelets. Evidence for depletion of dextran. Biorheology, 1996. **33** (4-5): p. 333-351.
9. Neu, B. and H.J. Meiselman, *Depletion-mediated red blood cell aggregation in polymer solutions.* Biophys. J., 2002. **83**(5): p. 2482-2490.
10. Cabel, M., et al., *Contribution of red blood cell aggregation to venous vascular resistance in skeletal muscle.* American Journal of Physiology-Heart and Circulatory Physiology, 1997. **41**(2): p. H1020-H1032.
11. Lowe, G.D.O., *Clinical Blood Rheology.* 1988, Boca Raton, Florida: CRC Press. 554.
12. Neu, B. and H.J. Meiselman, Sedimentation and electrophoretic mobility behavior of human red blood cells in various dextran solutions. Langmuir, 2001. **17**(26): p. 7973-7975.
13. Neu, B., H.J. Meiselman, and H. Bäumler, *Electrophoretic mobility of human erythrocytes in the presence of poly(styrene sulfonate).* Electrophoresis, 2002. **23**(15): p. 2363-2368.
14. Albersdorfer, A., T. Feder, and E. Sackmann, Adhesion-induced domain formation by interplay of long-range repulsion and short-range attraction force: a model membrane study. Biophys. J., 1997. **73**(1): p. 245-257.
15. Neu, B. and H.J. Meiselman, *Depletion interactions in polymer solutions promote red blood cell adhesion to albumin-coated surfaces.* Biochimica et Biophysica Acta - General Subjects, 2006. **1760**(12): p. 1772-1779.
16. Zilker, A., M. Ziegler, and E. Sackmann, Spectral analysis of erythrocyte flickering in the 0.3–4-mum-1 regime by microinterferometry combined with fast image processing. Physical Review A, 1992. **46**(12): p. 7998.
17. Gingell, D. and I. Todd, Red blood cell adhesion. II. Interferometric examination of the interaction with hydrocarbon oil and glass. Journal of Cell Science, 1980. **Vol. 41**: p. 135-149.
18. Rädler, J. and E. Sackmann, Imaging optical thicknesses and separation distances of phospholipid vesicles at solid surfaces. J. Phys. II France 1993. **3**: p. 727-748
19. Bruinsma, R., *Adhesion and rolling of leukocytes: a physical model.* Proc. NATO Adv. Inst. Phys. Biomater. NATO ASI Ser., 1995. **332**(61-75).
20. Evans, E.A., Bending elastic modulus of red blood cell membrane derived from buckling instability in micropipet aspiration tests. Biophys. J., 1983. **43**(1): p. 27-37.
21. Gingell, D. and I. Todd, Interference reflection microscopy. A quantitative theory for image interpretation and its application to cell-substratum separation measurement. Biophys. J., 1979. **26**(3): p. 507-526.
22. Neu, B., S. Sowemimo-Coker, and H. Meiselman, *Cell-Cell Affinity of Senescent Human Erythrocytes.* Biophysical Journal, 2003. **85**(1): p. 75-84.
23. Rampling, M.W., et al., *Influence of cell-specific factors on red blood cell aggregation.* Biorheology, 2004. **41**(2): p. 91-112.

An Investigation on the Effect of Low Intensity Pulsed Ultrasound on Mechanical Properties of Rabbit Perforated Tibia Bone

B. Yasrebi[1] and S. Khorramymehr[2]

[1] Department of Biomedical Engineering, Islamic Azad University-Tabriz Branch, Tabriz, Iran
[2] Department of Biomedical Engineering, Islamic Azad University- Science & Research Branch, Tehran, Iran

Abstract — **Wide variety of studies in vivo experiments on animals have been shown that the most effective type of ultrasound waves to accelerate fracture healing in osteotomy procedure is LIPUS. In this study the authors investigate the effect of LIPUS on mechanical properties of healed perforated bone. Twenty-four white male New Zealand rabbits that have drilled the right tibia bone of them were used. The rabbits were divided in two groups: treatment and non treatment. The non treatment group was considered as control. The treatment group was exposed to LIPUS (30mW/cm2 spatial and temporal average, for 20 minutes/day). All of rabbits were divided into three parts according to timing (two, four and six weeks post drilling). Animals were killed in other weeks and mechanical properties (ultimate load and stiffness of bending) were measured. Results revealed ultimate load and stiffness were difference (P<0.05) on the treatment group in comparison to non treatment group after four weeks. The studies suggest that LIPUS stimulation could increase the new bone formation and mechanical properties. We concluded that LIPUS is most effective four weeks post drilling.**

Keywords — **Mid-shaft of Tibia, Repair Time, Density, Mechanical Characteristics and Rabbit**

I. Introduction

In this study we investigated the effect of Pulsed Low Intensity Ultrasound (PLIUS) on the heal rate of osteoperforated bones. After removal of a fixator, which is commonly used to immobilize long bone fractures, holes in the bone remained from removal of fixator pins or screws reduce the cross sectional area and consequently the mechanical strength of the bone. This may cause a new fracture at the hole site. A non-invasive method to enhance heal rate of perforated bones may reduce the time needed for recovery of the bone after removal of fixator pins and screws.

PLIUS has potentially important effects on the functional activities of connective tissue cells in vitro [1],[2]. The results of in vitro studies suggest that PLIUS lead to an increase in cytocolic Ca^{2+} and activation of calmodulin [3], and enhances the process of endochondral ossification where the soft callus is converted to mineralized hard callus [4].

A large body of evidence confirms the stimulatory effect of PLIUS on fresh fractures, nonunions, and other osseous defects such as osteotomies. It has been shown that PLIUS is highly efficacious in callus formation during rapid distraction osteogenesis [5], enhancement of osteogenesis at the healing bone-tendon junction [6], treatment of nonunion fractures [7], healing of complex tibial fractures in human [8], and distraction osteogenesis in case of delayed callotasis [9]. The effect of ultrasound on healing of osteotomies, as in vivo models of bone fracture, has also been emphasized [10],[11].

Thus far, the effect of ultrasound on healing of drilled osteoperforation is not clear. Repair at bone gaps is very sensitive to the gap size and shape, and wedge surface conditions [12],[13]. Size, shape and especially surface conditions of a hole drilled to a bone differ from that of gaps caused by natural fractures or osteotomies [14],[15], [16]. Therefore, the results of the effect of ultrasound in cases reported in the literature may not be directly applicable to osteoperforation healing. The present investigation is to clarify this effect.

II. Materials and methods

Twenty-four mature New Zealand white rabbits weighting 2.0 ± 0.2 Kg were used. A two millimeter through medio-lateral hole was drilled at the midshaft of the right tibia of animals, using a standard dental drill (Minicraft, UK) at 30000 rev/min. Operated animals were randomly divided into PLIUS treatment group and placebo control group, and were euthanized at week 2, 4 and 6 postoperatively (n= 4, for each group and time point). During drilling, animals were anaesthetized using muscular injection of a mixture of Ketamin Hydrochloride 50 mg/ml and Xylazine 2% with a proportion of 1 to 5. They were given muscular injection of Prophylaxis Penicillin 800,000 U right after the surgery, and every 24 hours for two days.

Exogen™ 3000 (Smith & Nephew, USA), a standard ultrasound stimulator, was used to stimulate the osteoperforated site in PLIUS group (Gold and Wasserman 2005; Warden 2000). Ultrasound specifications were set to the intensity of 30 mW/cm^2, frequency of 1.5 MHz, and pulse

Chwee Teck Lim, James C.H. Goh (Eds.): ICBME 2008, Proceedings 23, pp. 1648–1650, 2009
www.springerlink.com

duration of 200 μsec, and were applied 20 minutes per day, 5 times per week [5],[9],[18]. Ultrasound treatment started one week postoperative and continued to the euthanizing day. Similar procedure was repeated for the placebo control group with the ultrasound apparatus at off position. All animals were kept at the same environment.

Every two weeks from the day of operation, 4 of the animals in each group were sacrificed and their right and left tibias were harvested. Samples were kept in normal saline solution. A standard three point bending tester (Zwick, Germany) was used to measure maximum force to break (in Newton) and maximum deflection (in millimeter) of each harvested tibia as measures of mechanical strength of bones. The measures in each operated tibia were normalized to the same measures in the contralateral tibia to reduce the variability effect. The two fixed stands in the bending tester were 8 centimeters apart, and the cross head applied the force right at the anterior side of the perforated site.

The method used was in compliance with the protocol established by the Care and Animal Use Committee of Iran University of Medical Sciences.

Mean value and standard deviation of mechanical measures were computed in each group. Kruskal-Wallis nonparametric test was performed to compare the means of the outcome measures in control and treatment groups. Mann-Whitney nonparametric test was used to compare the means of the measures between the control and treatment groups at each time point (SPSS, Ver. 13).

III. Results

Mean of normalized ultimate load and normalized stiffness increased as time point increased in the placebo control group and the PLIUS treatment group. Mean of normalized ultimate load and normalized stiffness were significantly higher in the treatment group than that in the control group at 4 and 6 week time points ($P<0.05$), but was not different at 2 week ($P>0.05$) (Table1 and Table2).

Table1: Average of Ultimate Load and Standard Deviation

Time / Group	Two Weeks after Surgery	Four Weeks after Surgery	Six Weeks after Surgery
Non Treated	0.76 ± 0.1	0.78 ± 0.07	0.89 ± 0.1
Treated	0.74 ± 0.16	0.91 ± 0.04	1.05 ± 0.06
P value	0.24	0.02	0.02

Table2: Average of Stiffness and Standard Deviation

Time / Group	Two Weeks after Surgery	Four Weeks after Surgery	Six Weeks after Surgery
Non Treated	0.87 ± 0.11	0.88 ± 0.09	0.98± 0.1
Treated	0.81 ± 0.14	1.01 ± 0.06	1.3 ± 0.1
P value	0.14	0.02	0.02

IV. Discussion

The positive effect of pulsed low intensity ultrasound on bone mechanical strength at osteoperforation sites was shown. This was concluded based on the results from an in vivo experimental study on rabbit tibia models, with the main outcome measures including ultimate load and stiffness in the osteoperforation sites.

The effect of ultrasound on wound healing and bone repair mechanisms has long been under investigation. Ultrasound causes a degranulation of mast cells resulting in the release of histamine. Histamine and other chemical mediators released from the mast cell are felt to play a role in attracting neutrophils and monocytes to the injured site. These and other events appear to accelerate the acute inflammatory phase and promote healing. In proliferative phase, ultrasound has been noted to affect fibroblasts and stimulate them to secrete collagen I. This can accelerate the process of wound contraction and increase tensile strength of the healing tissue.

The results of this study revealed considerable effect of PLIUS, at least following 6 weeks treatment, on bone mechanical strength in osteoperforations in rabbit tibia models. These findings are in agreement with the results from Claes et al. [18] who treated bone defects at the metatarsal bones of sheep with a segmental bone transport and then with low-intensity ultrasound using the same apparatus as ours. They showed significantly higher axial compression stiffness of callus tissue in the treatment group. Furthermore, Chan et al. [5] studied the effect of low intensity pulsed ultrasound on callus formation, and showed increased bone mineral content and volume of the mineralized tissue of distraction callus, and enhanced endochondral formation.

We, though, measured the bending stiffness of the healed bone which is very well related to the compressive stiffness.

Li et al. [3] and Unsworth et al. [4], based on the results of their in vitro studies, suggest that one of the mechanisms that low intensity pulsed ultrasound has on fracture repair is

to enhance the process of endochondral ossification where the soft callus is converted to mineralized hard callus. Our findings verify this implication due to the fact that heal rate was more quickly at the first 4 weeks of treatment, when callus mineralization is taken place.

V. Conclusions

The effect of pulsed low intensity ultrasound on the heal rate of osteoperforated bones in rabbit model was studied. It was found that PLIUS can enhance heal rates in osteoperforated bones. The heal rate is more rapidly at the first 4 weeks postoperatively. Ultrasound treatment may be used to shorten clinical treatment times after removal of pins or screws of bone fixators.

Acknowledgment

Authors would like to thank Iran University of Medical Sciences (Tehran, Iran) for providing the equipments used in radiographic measures. They are also grateful to Tarbiat Modares University (Tehran, Iran) for its disclosure to the instruments used in mechanical tests.

References

1. Harle J, Salih V, Mayia F, Knowles JC, Olsen I. (2001) Effects of ultrasound on the growth and function of bone and periodontal ligament cells in vitro. Ultrasound in Medicine & Biology 27:579-586
2. Korstjens CM, Nolte PA, Burger EH. (2004) Stimulation of bone cell differentiation by low-intensity ultrasound—a histomorphometric in vitro study. J Orthop Res 22:495-500
3. Li JKJ, Lin JCA, Liu HC, Sun JS, Ruaan RC, Shih C, Chang WHS. (2006) Comparison of ultrasound and electromagnetic field effects on osteoblast growth. Ultrasound in Medicine & Biology 32:769-775
4. Unsworth J, Kaneez S, Harris S, Ridgway J, Fenwick S, Chenery D, Harrison A. (2007) Pulsed Low Intensity Ultrasound Enhances Mineralisation in Preosteoblast Cells. Ultrasound Med Biol 33:1468-1474
5. Chan CW, Qin L, Lee KM, Cheung WH, Cheng JC, Leung KS. (2006) Dose-dependent effect of low-intensity pulsed ultrasound on callus formation during rapid distraction osteogenesis. J Orthop Res 25:227-233
6. Qin L, Lu H, Fok P, Cheung W, Zheng Y, Lee K, Leung K. (2006) Low-intensity pulsed ultrasound accelerates osteogenesis at bone-tendon healing junction. Ultrasound Med Biol 32:1905-1911
7. Gebauer D, Mayr E, Orthner E, Ryaby JP. (2005) Low-intensity pulsed ultrasound: Effects on nonunions. Ultrasound in Medicine & Biology 31:1391-1402
8. Leung KS, Lee WS, Tsui HF, Liu PPL, Cheung WH. (2004) Complex tibial fracture outcomes following treatment with low-intensity pulsed ultrasound. Ultrasound in Medicine & Biology 30:389-395
9. Esenwein SA, Dudda M, Pommer A, Hopf KF, Kutscha-Lissberg F, Muhr G. (2004) Efficiency of low-intensity pulsed ultrasound on distraction osteogenesis in case of delayed callotasis; clinical results. Zentralbl Chir 129:413-420
10. Hara Y, Nakamura T, Fukuda H. (2003) Changes of biomechanical characteristics of the bone in experimental tibial osteotomy model in the dog. J Vet Med Sci 65:103-107
11. Heybeli N, Yeşildağ A, Oyar O, Gülsoy UK, Tekinsoy MA, Mumcu EF. (2002) Diagnostic ultrasound treatment increases the bone fracture-healing rate in an internally fixed rat femoral osteotomy model. J Ultrasound Med 21:1357-1363
12. Park SH, Oconnor K, Sung R. (1999) Comparison of healing process in open osteotomy model and closed fracture model. J Orthop Trauma. 13:114-120
13. Tsumaki N, Kakiuchi M, Sasaki J. (2004) Low-intensity pulsed ultrasound accelerates maturation of callus in patients treated with opening-wedge high tibial osteotomy by hemicallotasis. J Bone Joint Surg Am 86A:2399-2405
14. Abouzgia MB, Symington JM. (1996) Effect of drill speed on bone temperature. Int J Oral Maxillofac Surg 25:394-399
15. Iyer S, Weiss C, Mehta A. (1997) Effects of drill speed on heat production and rate and quality of bone formation in dental implant osteotomies. Part 2: Relationship between drill speed and healing. Int J Prosthodont 10:536-540
16. Watanabe F, Tawada Y, Komatsu S, Hata Y. (1992) Heat distribution in bone during preparation of implant sites: heat analysis by real-time thermography. Int J Oral Maxillofac Implants 7:212-219
17. Claes L, Ruter A and Mayr E. (2005) Low-intensity ultrasound enhances maturation of callus after segmental transport. Clin Orthop Relat Res 430:189-194
18. Claes L, Willie B. (2006) The enhancement of bone regeneration by ultrasound. Prog Biophys Mol Biol. 23:115-121

The address of the corresponding author:

Author: Dr. Behzad Yasrebi
Institute: Biomedical Engineering
Street: Islamic Azad University-Tabriz branch Road
City: Tabriz
Country: Iran
Email: mebyas@yahoo.com

Integrative Model of Physiological Functions and Its Application to Systems Medicine in Intensive Care Unit

Lu Gaohua and Hidenori Kimura

Brain Science Institute, the Institute of Physical and Chemical Research (RIKEN), Nagoya, Japan

Abstract — **Systems medicine characteristic of simultaneous management of various physiological functions by various medical specialists, while taking the best use of various medical apparatus, has not been completely realized in the current intensive care unit (ICU). In order to improve such systems medicine from viewpoint of biomedical engineering, an integrative model of physiological functions is developed to simulate clinical management of patient under brain hypothermia treatment (BHT), which is considered as a representative of systems medicine. The model consists of the biothermal regulatory, circulatory and respiratory dynamics, as well as the pharmacokinetics of diuretic and sedative. The model is validated by similarity between model simulation results and clinical data. Then the model is used to simulate clinical management concerning the simultaneous control of therapeutic cooling, minute ventilation, diuretic and sedative infusion. Theoretical discussion would benefit the integration of various medical apparatus and the collaboration among various medical specialists in the current ICU.**

Keywords — **Systems medicine, intensive care medicine, brain hypothermia treatment, model, control.**

I. Introduction

Systems medicine carried out in the intensive care unit (ICU) consists of an integration of various diagnostic and therapeutic equipments, as well as an active teamwork of various medical specialists, for the sake of simultaneous management of various physiological functions of the patient [1]. However, systems medicine has not been completely realized in the current ICU. One of the difficulties in realizing systems medicine is the collaboration among the varying disciplines remains a common problem, mainly because different medical subspecialists only manage their own "organ" of expertise [2]. Another difficulty is various medical equipments function alone in the clinical practice, as they are produced independently by various makers.

In order to improve systems medicine from viewpoint of biomedical engineering, a mathematical model is developed to simulate the systemic management of various physiological functions of patient under brain hypothermia treatment (BHT), which is considered as a representative of systems medicine of acute disease in the ICU. The intracorporeal integration of physiological functions, such as the biothermal regulatory, circulatory and respiratory dynamics, as well as the pharmacokinetics of diuretic and sedative, are modelled together with the extracorporeal integration of various medical treatments, including therapeutic cooling, mechanical ventilation, diuretic and anaesthetic infusion. The model is validated by the similarity between model simulation results and clinical data. Then, the model is used to simulate the simultaneous control of intracranial temperature and pressure, minute ventilation and sedative infusion during the therapeutic hypothermia. Model development and simulation results are reported in this paper.

II. Model Development

A. Systems medicine of therapeutic hypothermia

As an intensive care carried out in the ICU, BHT protects the damaged brain from the secondary neuron death [3]. Although protective to neuron, hypothermia is invasive to the body. Therefore, all physiological functions of the patient should be cared intensively. In particular, the patient under therapeutic cooling should be sedated deeply for a stable management of the circulation, respiration and metabolism and so on. Some specific targets include cooling the brain temperature at about 34°C, depressing the intracranial pressure below 20 mmHg, decreasing the minute ventilation to avoid hyperventilation and putting the patient under suitable sedation [3].

Realization of systems medicine in the clinical practice of BHT requires an integration of medical equipments, such as the cooling blanket, mechanical ventilator and various

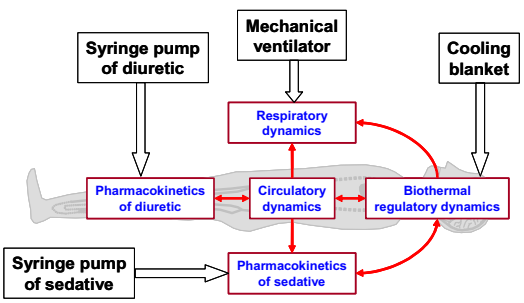


Fig. 1 Systems medicine of therapeutic hypothermia

Chwee Teck Lim, James C.H. Goh (Eds.): ICBME 2008, Proceedings 23, pp. 1651–1654, 2009
www.springerlink.com

syringe pumps of diuretic and sedative, as shown in Fig. 1. In order to improve such systems medicine, it is desired to quantitatively analyze the interactions among various physiological functions, including the biothermal regulatory, circulatory and respiratory dynamics, as well as the pharmacokinetics of diuretic and sedative. For this purpose, an integrative model of various physiological functions is first developed for simulation of clinical systemic management of hypothermic patient.

B. Model structure

As shown in Fig. 2, the integrative model developed in this study owns a compartmental structure. It consists of 6 parallel segments, that is, the cranial, the cardiocirculatory, the pulmonary, the visceral, the muscular and the residual segment. Each of the latter 4 segments is divided into 2 compartments to represent the mass and the capillary blood. The cranial segment is composed of 3 compartments, brain mass, brain blood and cerebral spinal fluid (CSF). The cardiocirculatory segment comprises no mass compartment, but 2 blood compartments of the arterial and venous parts. All blood compartments are correlated together via blood flow allocation.

All physiological functions in the body are considered as passive systems without inherent neuronal regulation of biothermal, cardiocirculatory and respiratory dynamics, since the hypothermic patient is generally sedated deeply for stable management in the ICU. Alternatively, it is considered that extracorporeal feedback loops are formed via medical diagnosis and treatment.

Various medical equipments applied to the human body are considered as ambient input to the integrative model. In particular, the mechanical ventilator determines minute ventilation to the lung mass compartment, while diuretic and sedative are infused into the venous part of the cardiocirculatory segment via syringe pumps. Therapeutic cooling induced by the cooling blanket is modelled by temperature-adjustable surrounding to the muscular segment.

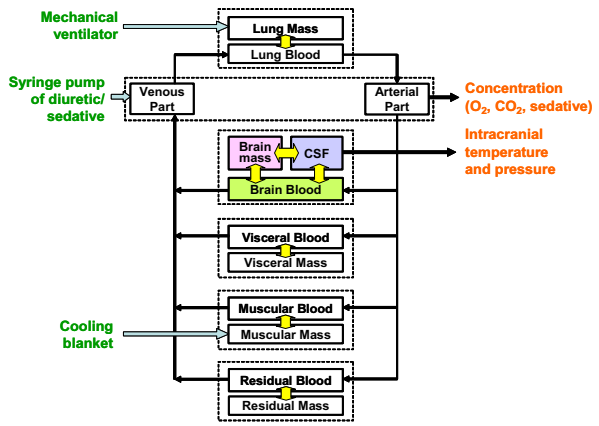


Fig. 2 Compartmental structure of integrative model

All equipments mentioned previously are tuned independently in the clinical practice. Such independency is an obstacle to realization of systems medicine in the ICU. The current paper aims to provide some hints on their integration based on the integrative model.

C. Governing equation

Based on the conservation law of energy and mass, the dynamics of temperature, hydro-static pressure and concentration of respiratory gases (O_2 and CO_2) or drugs (diuretic and sedative) in all compartments are described mathematically. In particular, a unified form of governing equation, as given by equation (1), on account of the analogy of temperature, hydrostatic pressure, respiratory gas and drug concentration. That is,

$$d(CX)/dt = q_{in} - q_{out} \tag{1}$$

where C denotes thermal capacity in the biothermal regulatory dynamics, compliance in the circulatory dynamics, distribution volume in the respiratory dynamics and the pharmacokinetics. X is temperature, hydrostatic pressure and concentration of respiratory gas or drug in the targeted compartment. The left hand side means the storage rate of energy or substance (water, gas, diuretic or sedative). q_{in} and q_{out} on the right hand side are the rate of energy or substance in and out, respectively, with respect to the targeted compartment.

D. Interaction mechanism

As shown in Fig. 1 and 2, blood flow of the circulatory dynamics transports heat, respiratory gases and various drugs throughout the body. Therefore, the biothermal regulatory dynamics, the respiratory dynamics and the pharmacokinetics of diuretic and sedative are combined together with the circulatory dynamics via the circulating blood flow.

At the same time, various physiological and pharmacodynamical mechanisms help integrate the targeted five dynamics together. The major physiological interaction mechanisms are the temperature dependency of metabolism, permeability at the interface of capillary bed, hemoglobin-oxygen dissociation, diuretic and sedative clearance. As a pharmacodynamical interaction mechanism, the thermoregulatory threshold of the biothermal regulatory dynamics is considered to be linearly dependent on the arterial concentration of sedative.

E. Parameter setting

Simulating the integrated system requires values of various kinetics constants, including thermal capacity, distribution volume, compliance, permeability coefficient, blood or lymph flow, metabolic generation or consumption, drug clearance, as well as the initial value of temperature, hydrostatic pressure and concentration of respiratory gases. Obviously, it is impossible to obtain all values in one patient.

For theoretical discussion, some data are given to the integrative model on the base of literature while some data are given on the base of extrapolation. Several data are assumed and revised through model verification and/or validation and through model improvement. Various data of the biothermal regulatory system, the respiratory system, the circulatory system, the pharmacokinetics of diuretic and sedative (mannitol and propofol in this study) are available in the previous reports [1], [4-6].

Taken together, the integrative model consists of a compartmental structure and a representative governing equation, together with various interaction mechanisms and physiological parameters. Medical treatments are considered as adjustable input to the model.

F. Model validation

Partial model of the biothermal regulatory dynamics, the circulatory dynamics and the pharmacokinetics of diuretic or sedative are estimated separately, based on the similarity between the model simulation results and the clinical data concerning brain temperature in response to step cooling, the time course of intracranial pressure, as well as the intracranial concentration of diuretic or sedative, in response to bolus injection and/or to periodic infusion of diuretic and sedative. Furthermore, various properties of the respiratory part of the integrative model are qualitatively compared well with the general knowledge or quantitatively with the experimental data reported in literature.

III. Model application

A. Simulation setting

The integrative model is used to simulate the clinical management of therapeutic cooling, minute ventilation, diuretic and sedative infusion. For this purpose, the model is first introduced to mimic a real hypothermic patient characteristic of intracranial hypertension (intracranial pressure is about 25 mmHg).

On one hand, the desired intracranial pressure in the clinical BHT is the normal value in healthy adults, 10 mmHg assumed in this study. Mannitol is infused as a diuretic to depress the increased intracranial pressure.

On the other hand, the desired brain temperature is a curve abstracted from the practical management of BHT. The total course is 120 h or five days. First, brain temperature is cooled down at a constant rate. The hypothermic brain temperature of 33.5°C is achieved in 8 h and maintained up to 48 h. Then, brain temperature is increased deliberately up to 36.5°C within two days and it is maintained at that temperature for one more day. Temperature of the cooling blanket is tuned to control the brain temperature.

Both the mannitol infusion and the ambient cooling are controlled by PID controllers developed in this study, while taking the decoupling control of brain temperature and intracranial pressure into consideration.

At the same time, management of respiration seeks to stabilize the arterial CO_2 near its nominal value (40 mmHg) through controlling the minute ventilation during hypothermia, based on a linear relationship between cooling temperature and minute ventilation, which is also developed in this study.

Furthermore, a pharmacodynamic relationship between the temperature threshold of thermoregulatory reaction (the core temperature triggering vasoconstriction or shivering) and the blood propofol concentration is used to combine the biothermal regulatory dynamics with the propofol kinetics.

Altogether, the targeted five dynamics, that is, the biothermal regulatory dynamics, circulatory dynamics, respiratory dynamics, diuretic kinetics and sedative kinetics, as shown in Fig. 1, are simultaneously enrolled in this simulation setting. All controllers are available in the previous reports [1], [4-6].

B. Simulation results

Simulation results are summarized in Fig. 3.

It was shown that the brain temperature of the model could be cooled to follow the desired temperature curve almost perfectly. The suggested cooling temperature is physically realizable and physiologically acceptable.

At the same time, simulation results showed that the intracranial pressure of the model could be decreased to the reference, via a dynamic infusion of mannitol.

Simulation result of the respiratory dynamics supported the clinical notion that the minute ventilation should be reduced with reference to the therapeutic cooling for stabilization of arterial CO_2.

Simulation result of the propofol kinetics suggested a novel possibility of propofol infusion in BHT. In particular, it was shown that propofol would be unnecessary during the first 2 hours and the last 30 hours.

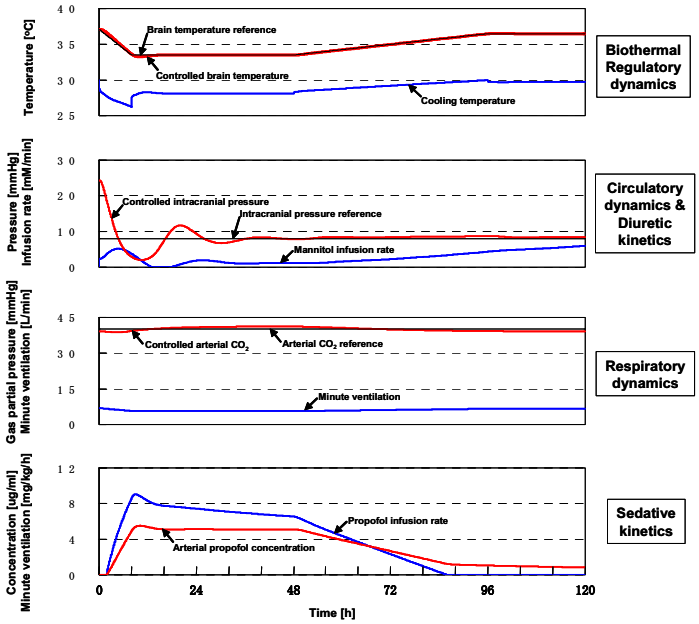


Fig. 3 Simultaneous management of the targeted five dynamics

All simulation results are consistent with the clinical knowledge. Simulation results particularly demonstrated possibility of tuning the mechanical ventilator, as well as the syringe pumps of diuretic and sedative, with respect to the cooling blanket.

IV. Conclusions

The developed integrative model provides the first framework of modelling various physiological functions simultaneously at the organ level in the human body. Actually, the biothermal regulatory dynamics, the circulatory dynamics, the respiratory dynamics, and the pharmacokinetics of diuretic and sedative are modelled in the same compartmental structure and in the same governing equations. These targeted dynamics are integrated through the circulating blood flow, together with the temperature-dependency mechanisms of various physiological functions.

As exemplified in the simulation using the integrative model, the present model succeeds in providing a holistic perspective of various physiological functions of patient under BHT. Simulation results inspire the medical staffs to tune various medical equipments based on the integrative model. Such theoretical discussion gives hints on integration of medical equipments for systems medicine. Also, it would benefit the collaboration among various medical specialists, not only in the BHT but also other intensive care carried out in the current ICU.

References

1. Gaohua L, Kimura H (2008) A mathematical model of respiratory and biothermal dynamics in brain hypothermia treatment. IEEE Trans Biomed Eng 55:1266-1278
2. Celi LA, Hassan E, Marquardt C et al. (2001) The eICU: it's not just telemedicine. Crit Care Med 29:183-189
3. Hayashi N, Dietrich DW (2003) Brain Hypothermia Treatment. Springer-Verlag, Tokyo
4. Gaohua L, Kimura H (2006) A mathematical model of intracranial pressure dynamics for brain hypothermia treatment. J Theor Biol 238:882-900
5. Gaohua L, Maekawa T, Kimura H (2006) An integrated model of thermodynamic-hemodynamic- pharmacokinetic system and its application on decoupling control of intracranial temperature and pressure in brain hypothermia treatment. J Theor Biol 242:16-31
6. Gaohua L, Kimura H (2007) Simulation of propofol anaesthesia for intracranial decompression using brain hypothermia treatment. Theor Biol Med Model 29:4:46

Address of the corresponding author:

Author: Lu Gaohua
Institute: The Institute of Physical and Chemical Research
Street: 2271-130 Anagahora, Shimoshidami, Moriyama-ku
City: Nagoya
Country: Japan
Email: lu@brain.riken.jp

A Brain-oriented Compartmental Model of Glucose-Insulin-Glucagon Regulatory System

Lu Gaohua and Hidenori Kimura

Brain Science Institute, the Institute of Physical and Chemical Research (RIKEN), Nagoya, Japan

Abstract — **In order to demonstrate the relationship between brain glucose homeostasis and blood hyperglycemia in the diabetes, we develop a mathematical model of glucose-insulin-glucagon (GIG) regulatory system consisting of the peripheral GIG interaction and the central brain-endocrine crosstalk. Firstly, the body is approximated compartmentally. Then, the peripheral interactions among the glucose dynamics, insulin dynamics and glucagon dynamics are described mathematically, together with a feedback control loop describing the central brain-endocrine crosstalk for the control of brain glucose homeostasis. Furthermore, the effects of long-term severe stress and the effects of blood-brain barrier (BBB) adaptation to dysglycemia are taken into consideration. The model is validated by comparing model simulation profiles with clinical data concerning the GIG regulatory responses to bolus, durational and continuous glucose infusion. On account of the simulation results of the effects of long-term severe stress and BBB adaptation on the generation of blood hyperglycemia, it is proposed that blood hyperglycemia in the diabetes is an outcome of the control of brain glucose homeostasis.**

Keywords — **Brain glucose homeostasis, glucose-insulin-glucagon (GIG) regulatory system, diabetes, model, simulation.**

I. Introduction

Because of the importance of providing a continuous energy resource of glucose to the brain, the body has developed an elaborate glucose-insulin-glucagon (GIG) regulatory system to maintain the glucose concentration in the blood and the glucose delivery to the brain when blood glucose levels fall or raise out the euglycemic boundaries. Resultantly, the varying range of brain glucose is much smaller than that of blood glucose during blood euglycemia [1]. For example, it was observed in rats that an increase of 50 mg/dl in the blood glucose level from its baseline only caused 10 mg/dl increase in the brain glucose level [2]. Clinically, it is known in the diabetic patients that chronic hyperglycemia does not alter brain glucose concentrations, compared with the healthy subjects [3]. These physiological facts stimulate us to propose that the ultimate goal of GIG regulatory system, which consists of the peripheral GIG interaction and the central brain-endocrine crosstalk, is not the homeostasis of glucose concentration in the blood, but the homeostasis of glucose concentration in the brain.

Although the neuronal and/or hormonal regulation of blood glucose homeostasis through the brain has been a target of some qualitative studies, brain glucose homeostasis has not been studied theoretically [4]-[6]. Several mathematical models of the GIG regulatory system are used for theoretical and clinical applications for diabetes control [7], [8], but, no theoretical model has been developed to discuss the relationship between the brain glucose homeostasis and the diabetes.

Main purpose of this paper is to demonstrate the relationship between the brain glucose homeostasis and the blood hyperglycemia in the diabetes. A brain-oriented compartmental model is developed to describe the GIG regulatory system, while effects of long-term severe psychological stress and effects of blood-brain barrier (BBB) adaptation to dysglycemia on the generation of blood hyperglycemia are taken into account. Modelling and preliminary simulation results are reported here.

II. Model description

A. Model structure

The body is divided into 9 segments (Fig. 1). The cranial segment consists of 3 compartments, brain mass, blood and cerebrospinal fluid (CSF). The cardiocirculatory segment is composed of arterial and venous compartments. Each of the other 7 extracranial segments comprises a mass compartment and a blood compartment. All blood compartments are linked via blood allocation. Based on the anatomy of hepatic portal vein, blood flows from the pancreas and gut segments enter the liver segment and then join the systemic circulation, together with the hepatic arterial blood flow.

From the viewpoint of systems control, the cranial segment is considered as the controlled object of brain glucose homeostasis while all extracranial segments as the actuator characteristic of the peripheral GIG interaction.

Feedback control loop corresponds to the central brain-endocrine crosstalk. The afferent signals are mainly generated by the central glucosensing neurons and integrated by the hypothalamus (controller). Various efferent signals are affected by the stress before regulating the hepatic glucose production and pancreatic hormonal secretion.

Chwee Teck Lim, James C.H. Goh (Eds.): ICBME 2008, Proceedings 23, pp. 1655–1658, 2009
www.springerlink.com

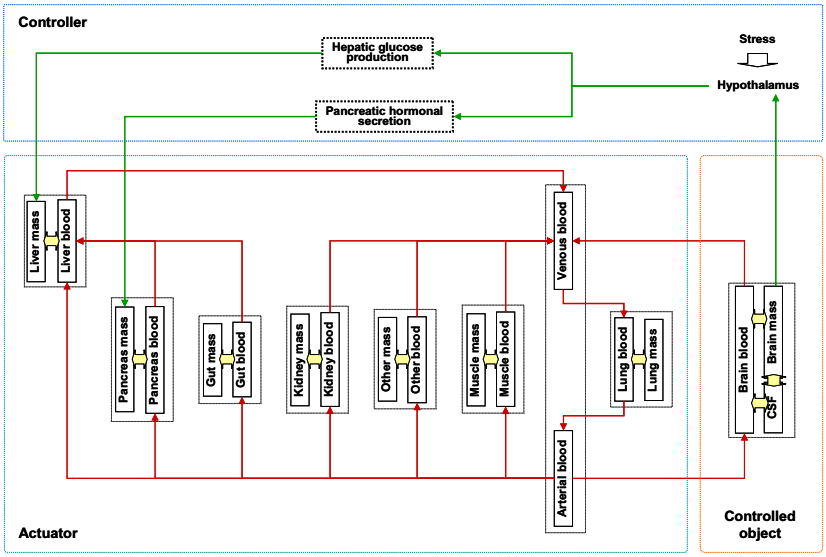


Fig. 1 Compartmental structure of the model

B. General governing equation

Applying the mass conservation law, the dynamics of glucose, insulin and glucagon could be described representatively as follows,

$$\begin{aligned} V\,dG/dt = {} & (1+stress)(1+\gamma)g_{hgp}(G,I,E) + g_{infusion} \\ & + g_{permeation} - g_{brain}(G) - g_{red\ cell}(G) \\ & - g_{urine}(G) - g_{periph}(G,I) \end{aligned} \tag{1}$$

$$\begin{aligned} V\,dI/dt = {} & (1-stress)(1-\beta)i_{beta}(G,I,E) + i_{infusion} \\ & + i_{permeation} - i_{periph}(G,I) \end{aligned} \tag{2}$$

$$\begin{aligned} V\,dE/dt = {} & (1+stress)(1+\alpha)e_{alpha}(G,I) \\ & + e_{permeation} - e_{periph}(E) \end{aligned} \tag{3}$$

where G, I and E denote the concentrations of glucose, insulin and glucagon, respectively. V is distribution volume. *stress* denotes positive variable of stress. $g_{hgp}(G, I, E)$ describes hepatic glucose production, which is dependent on concentrations of glucose, insulin and glucagon in the hepatic mass. Similarly, i_{beta} and e_{alpha} describe pancreatic insulin and glucagon secretions, depending on the local concentrations of glucose, insulin and glucagon in the pancreatic mass. $g_{infusion}$ and $g_{permeation}$ are rate of infusion and permeation of glucose, respectively into the targeted compartment. The same are $i_{infusion}$ and $i_{permeation}$. g_{periph}, i_{periph} and e_{periph} denote glucose utilization and hormonal clearance. In formula (1), g_{brain} and $g_{red\ cell}$ describe insulin-independent glucose metabolism by the neuronal cells in the brain mass compartment and by the red cells in the arterial compartment, respectively. g_{urine} denotes glucose discard from the kidney mass compartment if hyperglycemia. γ, β and α are the efferent signals. They are given as follows,

$$r = k_r e, \quad \beta = k_\beta e, \quad \alpha = k_\alpha e \tag{4}$$

$$e = (G_{brain} - G_{brain0}) + k_i(I_{brain} - I_{brain0}) + k_g(G_{liver} - G_{liver0}) \tag{5}$$

where e denotes the controlled error. k_γ, k_β, k_α, k_i and k_g are parameters characteristic of the brain-endocrine crosstalk.

It should be pointed out that, not all terms appear in all compartments. For example, g_{brain} occurs only in the brain mass compartment.

C. Modelling of blood-brain-barrier (BBB) adaptation

The glucose transport across the BBB is described the following Michaelis-Menten equation,

$$g_{permeation}^{BBB} = \frac{T_G G_{blood}^{brain}}{C_{G0} + G_{blood}^{brain}} \tag{6}$$

where T_{G0} denotes maximal glucose transport rate and C_{G0} denotes Michaelis constant.

Clinical observations suggest the maximal glucose transport rate is glucose-dependency [9]. Therefore, a first-order process is assumed to describe such BBB adaptation as follows,

$$T_G = \begin{cases} T_{G0} & (G_{blood}^{brain}\ within\ euglycemina) \\ T_{G0} - \Delta T_G & (G_{blood}^{brain}\ without\ euglycemina) \end{cases} \tag{7}$$

$$\frac{\Delta T_G(s)}{\Delta G(s)} = \frac{k_G}{1+\tau_G s} \tag{8}$$

where ΔT_G is the response of T_G with respect to hyperglycemia. k_G and τ_G are gain and time constant, respectively. s is LapLace operator.

III. Model validation

After tuning the values of physiological and physical parameters, mainly by trail and error, the simulation profiles obtained from the compartmental model are consistent well with the clinical data. In particular, it is shown that the current model is appropriate in describing the GIG regulatory responses to bolus, durational or continuous glucose infusion (data not shown due to space limitation).

IV. Model application

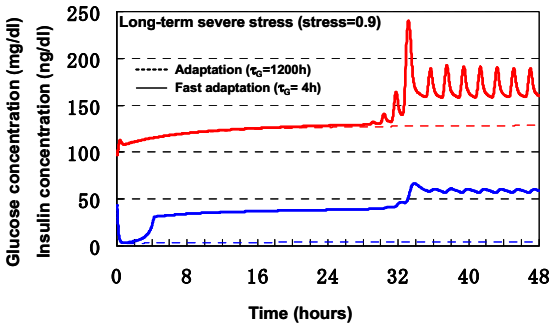
In order to demonstrate the relationship of brain glucose homeostasis and blood hyperglycemia in the diabetes, stress-induced hyperglycemia and BBB adaptation to such hyperglycemia are simulated in the model.

For this purpose, long-term severe stress (*stress*=0.9) is assumed in the simulation. Time constant in formula (8) is assumed to be 4 h in the model, although it may be some years in the clinical practice. Such an assumption of short time constant is due to time limitation of computer simulation. Therefore, the simulation results (solid line in Fig. 2) should be considered as fast-forward of the responses (broken line in the same figure).

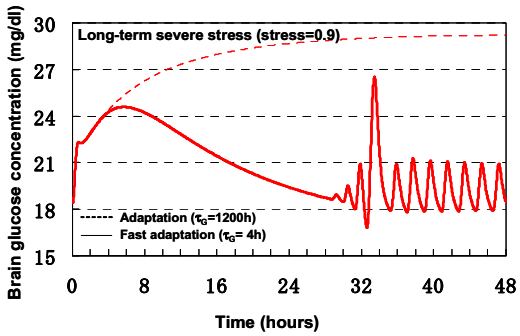
As shown in Fig. 2, with a fast BBB adaptation, a hyperglycemic steady-state of blood glucose was generated, while the brain glucose was maintained within the euglycemic range. Both the concentration of blood insulin and that of blood glucagon were higher than their basal values, while the ratio of glucagon to insulin was elevated (data not shown). Therefore, the current model simulated an abnormal state similar to the diabetes, which is characteristic of hyperglycemia, hyperinsulimia and hyperglucagonemia.

The simulation results are consistent well with clinical knowledge. As reviewed by Jiang and Zhang [10], the absolute levels of glucagon or the ratios of glucagon to insulin are often elevated in various forms of diabetes in both animal and human subjects. The same authors also pointed out that, chronic hyperglucagonemia was correlated with and was partially responsible for increased hepatic glucose production and hyperglycemia in type 2 diabetes. On account of physiological fact that stress increases glucagon secretion, it is reasonable to consider stress is one of the causes of hyperglycemia in the diabetes.

As shown in Fig. 2b, with the assumed proportional feedback control, brain glucose homeostasis was realized



(a) blood concentrations of glucose and insulin



(b) brain glucose concentration

Fig. 2 Effects of long-term severe stress and BBB adaptation

during blood hyperglycemia. In particular, the brain glucose is at euglycemic level while blood glucose is at hyperglycemic level. The simulation result is consistent with clinical observation that chronic hyperglycemia in diabetic patients does not alter brain glucose concentrations, compared with the healthy subjects [3].

Simulation results demonstrate that BBB adaptation would contribute to the generation of blood hyperglycemia and the maintenance of brain glucose under stress. Both the gain and the time constant of BBB adaptation to dysglycemia are of importance. On account of their dependence on individual, it is reasonable to speculate that a person with large gain and short time constant would be sensitive to stress-induced hyperglycemia and give rise to diabetes.

V. Discussion

A. Importance of brain glucose homeostasis

The brain is one of the major organs that need continuous energy resource of glucose. Maintenance of constant glucose concentration in the brain is of supreme importance due to the physiological facts that the brain is uniquely dependent on the availability of glucose, and that dysglycemia, either hypoglycemia or hyperglycemia, would damage its function.

Obviously, not only in the healthy but also in the diabetics, the brain glucose concentration is maintained constant. Various physiological facts suggest the maintenance of constant glucose level in the brain is more important than that in the blood. Therefore, it is hypothesized that the ultimate goal of GIG regulatory system is not the blood glucose homeostasis, but the brain glucose homeostasis.

Whereas the relations among the brain, glucose homeostasis and diabetes have been qualitatively recognized in experimental animals and in clinical patients, no theoretical analysis is available on the relationship between brain glucose homeostasis and blood hyperglycemia in the diabetes. To the best of our knowledge, it is the first paper that targets on the control of brain glucose homeostasis to provide a theoretical framework of discussing the roles of brain contributing to the generation of hyperglycemia in the diabetes.

B. Role of BBB adaptation in the diabetes

To maintain the brain glucose homeostasis, glucose transport from the blood to the brain should be regulated accurately, according to short-term and long-term states of blood glucose. Actually, the BBB helps govern the brain glucose homeostasis through temporary and permanent mechanisms. It is considered that, the former is the BBB semi-permeability of glucose, a physical filter with respect to sharp variations in the blood glucose levels, while the latter is the BBB adaptation, which is a physiological response to chronic hypoglycemia or hyperglycemia.

It has been shown by simulations using the model that the BBB adaptation, together with the long-term severe stress, contributes to the blood hyperglycemia. A vicious spiral of blood hyperglycemia and BBB adaptation would exist in the diabetes. However, such an interaction should be considered as a self-protective mechanism of the brain.

It is considered that control of brain glucose homeostasis requires increasing blood glucose levels if BBB glucose transport is depressed owing to BBB adaptation. If not, the brain would be short of glucose, as seen in “insulin shock”, where the blood glucose is controlled euglycemically by exogenous insulin injection while the glucose transport across the adapted BBB is not improved.

Therefore, it is reasonable to consider that the blood hyperglycemia observed in the diabetes would be one of the controlled results of the brain glucose homeostasis through the permanent BBB adaptation mechanism. Also, as a suggestion, re-modification of BBB adaptation in the diabetes, with either pharmacokinetic or genetic measures, would be a possible strategy on clinical control of blood hyperglycemia in the diabetes.

VI. Conclusions

Various physiological facts suggest brain glucose homeostasis, but not blood glucose homeostasis, is the ultimate goal of glucose-insulin-glucagon (GIG) regulatory system developed in the body. A brain-oriented compartmental model was developed in this paper to analyze the relationship between brain glucose homeostasis and blood hyperglycemia in the diabetes. The effects of BBB adaptation to dysglycemia, as well as the effects of long-term severe stress, on the generation of blood hyperglycemia were simulated in the model. It was shown that both long-term severe stress and BBB adaptation contribute to blood hyperglycemia. Preliminary simulation results demonstrate that blood hyperglycemia in the diabetes is an outcome of control of brain glucose homeostasis.

References

1. Routh VH (2002) Glucose-sensing neurons: are they physiologically relevant? Physiol Behav 76:403-413
2. Silver IA, Erecinska M (1998) Glucose-induced intracellular ion changes in sugar-sensitive hypothalamic neurons. J Neurophysiol 79:1733-1745
3. Seaquist ER, Tkac I, Damberg G et al. (2005) Brain glucose concentrations in poorly controlled diabetes mellitus as measured by high-field magnetic resonance spectroscopy. Metabolism 54:1008-1013
4. Schwartz MW, Woods SC, Porte D Jr et al. (2000) Central nervous system control of food intake. Nature 404:661-671
5. Marty N, Dallaporta M, Thorens B (2007) Brain glucose sensing, counterregulation, and energy homeostasis. Physiology 22:241-251
6. Sandoval D, Cota D, Seeley RJ (2008) The integrative role of CNS fuel-sensing mechanisms in energy balance and glucose regulation. Annu Rev Physiol 70:513-535
7. Makrogloua A, Li J, Kuang Y (2006) Mathematical models and software tools for the glucose-insulin regulatory system and diabetes: an overview. Applied Numerical Mathematics 56:559-573
8. Boutayeb A, Chetouani A (2006) A critical review of mathematical models and data used in diabetology. Biomed Eng Online 5:43
9. Criego AB, Tkac I, Kumar A et al. (2005) Brain glucose concentrations in healthy humans subjected to recurrent hypoglycemia. J Neurosci Res 82:525-530
10. Jiang G, Zhang BB (2003) Glucagon and regulation of glucose metabolism. Am J Physiol Endocrinol Metab 284:E671-678

Address of the corresponding author:

Author: Lu Gaohua
Institute: The Institute of Physical and Chemical Research
Street: 2271-130 Anagahora, Shimoshidami, Moriyama-ku
City: Nagoya
Country: Japan
Email: lu@brain.riken.jp

Linkage of Diisopropylfluorophosphate Exposure and Effects in Rats Using a Physiologically Based Pharmacokinetic and Pharmacodynamic Model

K.Y. Seng[1], S. Teo[1], K. Chen[1] and K.C. Tan[2]

[1] Bioengineering Laboratory, Defence Medical & Environmental Research Institute, DSO National Laboratories, 27 Medical Drive, #09-01, Singapore 117510, Republic of Singapore
[2] Department of Electrical and Computer Engineering, National University of Singapore, 4 Engineering Drive 3, Singapore 117576, Republic of Singapore

Abstract — **Organophosphate (OP) exposure can be lethal at high doses while lower doses may impair cognitive performance. Diisopropylfluorophosphate (DFP) is an OP insecticide. The biological response of DFP is primarily mediated through its effects on B-esterases, including acetylcholinesterase (AChE). By binding to AChE, DFP inhibits the function of AChE, resulting in the accumulation of the neurotransmitter acetylcholine at synapses. A model capable of predicting the relationship between DFP exposure and the resultant inhibition of AChE would be useful in risk assessment and the design of medical countermeasures against exposure to B-esterase (B-EST) inhibitors. In the present study, we modified a previously-described physiologically based pharmacokinetic and pharmacodynamic (PBPK/PD) model for the effect of DFP on (B-EST) activity by the usage of more widely accepted physiological data and description to more accurately simulate the physiological condition. In addition, we edited the mathematical formulas describing the relevant chemical reactions between DFP and B-EST to improve the theoretical model. For model verification, we compared AChE recovery data measured in vivo in male Wistar rats after single and multiple subcutaneous dosages of DFP with our model predictions. Our results showed a closer fit to the experimental data of AChE activity in contrast to the original PBPK/PD model after single and multiple injections of DFP in rats. The results supported the common hypothesis that distinct regeneration-dominated and synthesis-dominated phases of AChE recovery likely occurred during the experiments. Simulation results from the updated model also highlighted the crucial transition time period where additional experimental results would be most helpful in confirming the kinetics of B-EST dissociation and resynthesis.**

Keywords — **PBPK/PD model, diisopropylfluorophosphate, organophosphate, AChE inhibition, rat.**

I. Introduction

Diisopropylfluorophosphate (DFP) is a member of a class of organophosphate (OP) insecticide that inhibits B-esterases (B-ESTs), including acetylcholinesterase (AChE). Mortality associated with DFP poisoning is primarily due to its inhibition of AChE activity. The toxicological mode of action of a chemical is but one of the pieces needed in the risk assessment together with knowledge of differences in physiology, metabolism and disposition between species [1]. By integrating physiological, metabolic and biochemical information, physiologically based pharmacokinetic and pharmacodynamic (PBPK/PD) modelling is capable of predicting the relationship between OP exposure and resultant toxic effects. A PBPK/PD model is amenable to various forms of toxicokinetic extrapolations including interspecies (rodent to human), high to low dose, duration (acute to chronic) and from the average human to potentially susceptible subpopulations [2].

A PBPK/PD model to quantify the relationship between DFP and the inhibition of B-ESTs – comprising AChE, butyrylcholinesterase and carboxylesterase – in the rat has been previously published by Gearhart et al. [3,4]. In this study, we present an augmented version of this model by the usage of more widely accepted physiological data and the inclusion of the hepatic portal vein to more accurately simulate the physiological condition. We parameterised the PBPK/PD model by using reference physiological parameter values, partition coefficients and biochemical constants that were determined based on reported experiments and optimised by manual adjustment until the best visual fit of the simulations with the experimental data were observed. We verified the model by simulating the dynamic response of B-EST inhibition *in vivo* after single and multiple oral dosages and comparing simulated results with experimental results.

II. Methods and materials

A. PBPK Model

Our PBPK model was modified from [3,4]. In our revised model, the (1) venous blood pool (VEN); (2) arterial blood pool (ART); (3) lungs (LU); (4) brain (BR); (5) liver (LI); (6) kidneys (KI); (7) rapidly-perfused tissues (RPT); (8) slowly-perfused tissues (SPT); (9) fat (AD); (10) heart (HE) and (11) diaphragm (DIAP) compartments were included. We assumed that the rate of DFP transport into the tissue was limited by blood flow while diffusion within

Chwee Teck Lim, James C.H. Goh (Eds.): ICBME 2008, Proceedings 23, pp. 1659–1662, 2009
www.springerlink.com

each tissue was instantaneous [5]. In Table 1, we summarised the physiological parameters of our model.

Table 1 Physiological parameters used in our PBPK model.

Parameter	Rat
Alveolar ventilation (L/h)	4.57
Body weight, BW (kg)	0.22
Tissue volumes (% BW)	
Brain	2
Liver	3
Hepatic portal vein	15.3
Kidneys	14.1
Heart	5.1
Rapidly perfused tissues	27.5
Fat	7
Slowly perfused tissues	40.7
Diaphragm	0.6
Cardiac output, Q (L/h)	4.57
Blood flows (% Q)	
Brain	0.6
Liver	3.4
Kidneys	0.7
Heart	0.3
Rapidly perfused tissues	10
Fat	7
Slowly perfused tissues	64.8
Diaphragm	0.3
Lungs	0.5
Venous blood pool	5.894
Arterial blood pool	1.506

B. Model for Reaction between DFP and B-EST

DFP inhibits B-EST by binding to it forming a complex. As shown in Fig. 1 for AChE, the inhibited complex can either be degraded by aging, or can spontaneously dissociate to regenerate free B-EST.

In all compartments besides the AD compartment, we assumed that the baseline synthesis and degradation of B-ESTs followed zeroth-order and first-order rate constants respectively, and that these rate constants were unaffected by the introduction of DFP. We assumed that B-EST enzymes were not available in the AD compartment. In addition, our model contained equations to describe A-esterase-mediated hydrolysis [Parkinson, 1996] of DFP to diisopropylphosphoric acid (DIP) in the ART, VEN, BR, LI, KI, RPT and HE compartments.

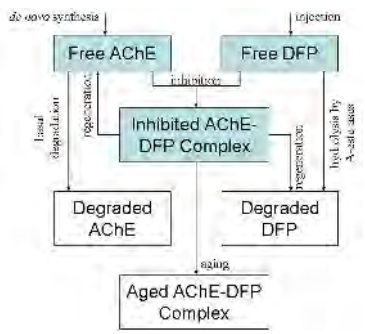


Fig. 1 Chemical reactions between DFP and AChE. Shaded compartments indicate pools whose concentration were tracked in the model.

C. Model Parameterisation

The partition coefficients as well as the Michaelis-Menten constant (K_m) that characterised the metabolism of DFP to DIP in our PBPK/PD model were adapted from [3,4] and shown in Table 2. In addition, we calibrated our model by referencing the authors' parameters for bimolecular inhibition (K_{inb}), synthesis (K_{syn}), degradation (K_{deg}), regeneration (K_{reg}) and aging (K_{age}).

Table 2 Physicochemical parameters used in our PBPK model.

Parameter	Rat
Partition coefficients for DFP	
Brain/blood	0.67
Liver/blood	1.53
Kidneys/blood	1.63
Heart/blood	0.67
Rapidly perfused tissues/blood	0.67
Fat/blood	17.6
Slowly perfused tissues/blood	0.77
Diaphragm/blood	0.77
Air/blood	0.08
Metabolic constants	
Brain V_{max} (mg/h)	9.18
Brain K_m (mg/L)	439.8
Liver V_{max} (mg/h)	1380
Liver K_m (mg/L)	237.36
Kidneys V_{max} (mg/h)	103.32
Kidneys K_m (mg/L)	134.3
Heart V_{max} (mg/h)	11.04
Heart K_m (mg/L)	50.89
Rapidly perfused tissues V_{max} (mg/h)	11.04
Rapidly perfused tissues K_m (mg/L)	50.89
Venous blood pool V_{max} (mg/h)	320.18
Venous blood pool K_m (mg/L)	198.7
Arterial blood pool V_{max} (mg/h)	106.73
Arterial blood pool K_m (mg/L)	198.7
Biochemical constants	
Brain K_{syn} (μmol/h)	1.5 E^{-6}
Venous blood pool K_{syn} (μmol/h)	1.9 E^{-6}
Brain K_{deg} (1/h)	0.01
Venous blood pool K_{deg} (1/h)	0.1
Brain K_{inb} (1/μM.h)	14.16
Venous blood pool K_{inb} (1/μM.h)	14.16
Brain K_{reg} (1/h)	0.016
Venous blood pool K_{reg} (1/h)	0.016
Brain K_{age} (1/h)	0.263
Venous blood pool K_{age} (1/h)	0.263

D. Model Calibration and Validation

For model calibration purposes, the simulation of our parameterised PBPK/PD model was compared with the experimentally measured activity of AChE in the brain and blood of male Wistar rats after single subcutaneous administration of 0.7 mg DFP/kg. Next, we applied the calibrated PBPK/PD model for the rat to the repeated dosing condition (first dose of 1.1 mg DFP/kg followed by 11-time repeated administration of 0.7 mg DFP/kg every 48 hours) [6,7].

III. Results and Discussion

A. Two-Phase Kinetics of AChE Recovery

From the experimental data on the time courses of unbound AChE concentration in rodents following DFP exposure [6,7,8], we noted that the recovery of AChE exhibited two distinct kinetic phases. This biphasic phenomenon, also reported by Mason [9], was exemplified by an early short-duration phase showing rapid recovery and a later long-duration phase with a slower rate of recovery. Since free AChE could be formed either by *de novo* synthesis or by dissociation of the AChE-DFP complex, we hypothesised that each kinetic phase was likely due to one of the two mechanisms dominating the recovery of AChE. As a consequence, we optimised K_{syn}, K_{deg}, K_{reg} and K_{age} (beginning from their initial values in Table 2) so as to fit the model simulation with the experimental data.

B. Model Calibration

In Table 3, we showed the values of K_{syn}, K_{deg}, K_{reg} and K_{age} that resulted in the best model fit of the experimental data in rat.

Table 3 Optimised biochemical parameters in our model

Rate constants	Brain compartment	Others
K_{syn} (mole/h)	1.4 E^{-12}	7.6 E^{-13}
K_{deg} (1/h)	0.01	0.04
K_{reg} (1/h)	0.036	0.72
K_{age} (1/h)	0.132	0.658

We compared simulations of the AChE recovery by our parameterised model with the experimental data for AChE recovery in the brain and blood of male rats after single subcutaneous administrations of DFP. As shown in Fig. 2, our model simulation results correctly captured the profiles of the recovery of AChE with respect to time (unbound AChE concentration as a fraction of the total AChE concentration).

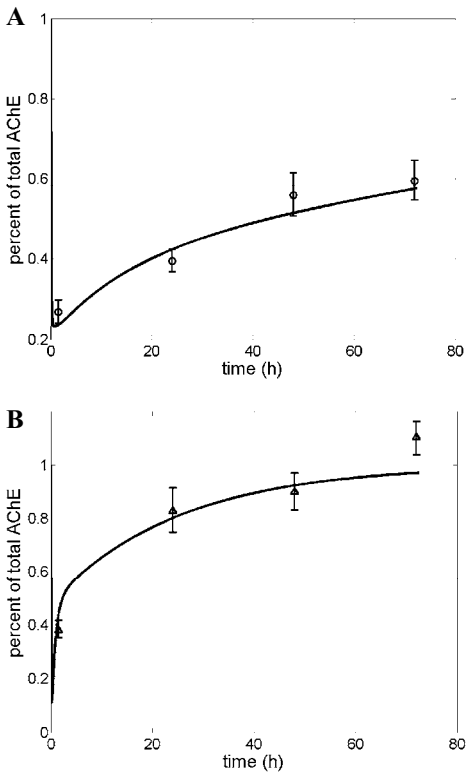


Fig. 2 Recovery of AChE in the brain (A) and blood (B) of rats after single 0.7 mg DFP/kg subcutaneous administration. Each datum represents mean ± standard error (data from [6,7]). Solid line indicates our model simulation results.

Our model simulations also indicated that the transition between the regeneration-dominated to the synthesis-dominated phases occurred between 1.5 to 3 hours after injection of DFP in rats. Because the experimental data for AChE activity in rat brain and blood contained only two measurements during the first 24 hours (at 1.5 and 24 h), our adjustment of the rate constants was based on a small volume of information. These predictions can be verified when more experimental data becomes available. Despite this, the shape of the simulated AChE recovery fuelled the postulation that distinct regeneration-dominated and synthesis-dominated phases of AChE recovery likely occurred during the in vivo experiments. These observations suggested that our revised model replicated the pathophysiological conditions in the animal models better than [3,4]. Hence, the physiological and adjusted physicochemical parameters listed in Tables 1 and 2 were considered appropriate for modelling the current data.

C. Model Validation

Following the calibration exercise, our model of DFP disposition and response for the rat was applied to the multiple dosing experiment. Our results showed that the PBPK/PD model was able to obtain a generally close fit to the experimentally-measured recovery of soluble AChE in rat brain [6], as shown in Figure 3A. The temporary levelling off of experimentally measured AChE recovery at 0.8 from 8 to 28 days after the last dose may indicate that other mechanisms may have occurred that caused a temporary alteration of the equilibrium AChE concentration. Similarly, as shown in Figure 3B, our calibrated model achieved a close fit to the recorded recovery of AChE activity in rat blood [7]. However, the overshoot observed in experimental data at 3 and 35 days after the last dose may likewise indicate the presence of other mechanisms or reactions that affect the recovery of AChE activity, which we did not model in the present numerical simulation exercise.

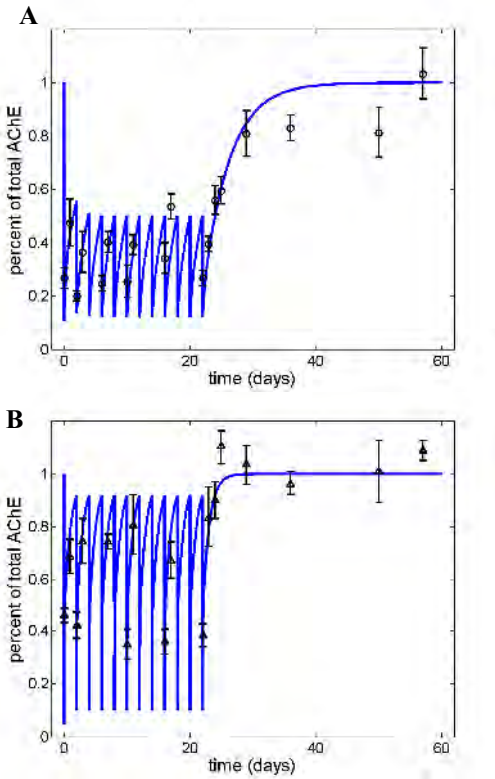


Fig. 3 Recovery of AChE in the brain (A) and blood (B) of rats after subcutaneous injections of DFP every other day for 22 days. Each datum represents mean ± standard error (data from [6,7]). Solid line indicates our model simulation results.

IV. Conclusions

In the present study, we augmented a previously-described PBPK/PD model for DFP dosimetry and response by adding additional components and using alternative parameter values to more closely replicate the physiology of the animal model. In addition, by adjusting the rate constants used in the model, we achieved a closer fit of the simulated kinetics to experimental data than previously described. As a result of the improved simulation, we predicted that B-EST inhibited by DFP exhibits two distinct kinetic phases in its recovery in rats, and that additional experimental measurements during the transition period would allow a better estimation of the rate constants of the individual chemical reactions. We have ongoing efforts to extrapolate this model to predict human response.

Acknowledgment

We thank Dr. Jeffery M. Gearhart for his insightful discussion in developing this PBPK/PD model. We are grateful for Dr. Teoh Eu Jin and Mr. Douglas Goh for assistance in implementing initial versions of the model equations. This work was supported through a grant from the Ministry of Defence in Singapore

References

1. Cohen S, Arnold L, Eldan M et al. (2006) Methylated arsenicals: the implications of metabolism and carcinogenicity studies in rodents to human risk assessment. Crit Rev Toxicol 36:99-133
2. Andersen M, Dennison J (2001) Mode of action and tissue dosimetry in current and future risk assessments. Sci Total Environ 274:3-14
3. Gearhart J, Jepson G, Clewell H et al. (1990) Physiologically based pharmacokinetic and pharmacodynamic model for the inhibition of acetylcholinesterase by diisopropylfluorophosphate. Toxicol Appl Pharmacol 106:295-310
4. Gearhart J, Jepson G, Clewell H et al. (1994) Physiologically based pharmacokinetic and pharmacodynamic model for the inhibition of acetylcholinesterase by organophosphate esters. Environmental Health Pers 102(Suppl 11):51-60
5. Clewell R, Clewell H (2008) Development and specification of physiologically based pharmacokinetic models for use in risk assessment. *Regul Toxicol Pharm* 50:129-143
6. Michalek H, Meneguz A, Bisso G (1982) Mechanisms of recovery of brain acetylcholinesterase in rats during chronic intoxication by isoflurophate. Arch Toxicol Suppl 5:116-119
7. Traina M, Serpietri L (1984) Changes in the levels and forms of rat plasma cholinesterase during chronic diisopropylphosphorofluoridate intoxication. *Biochem Pharmacol* 33:645-653
8. Martin B (1985) Biodisposition of [^{3}H]diisopropylfluorophosphate in mice. *Toxicol Appl Pharmacol* 77:275-284
9. Mason H (2000) The recovery of plasma cholinesterase and erythrocyte acetylcholinesterase activity in workers after over-exposure to dichlorvos. *Occup Med* 5:343-347

Blood Flow Rate Measurement Using Intravascular Heat-Exchange Catheter

Seng Sing Tan and Chin Tiong Ng

Nanyang Polytechnic, Singapore, Singapore

Abstract — **During treatments for patients with coronary artery diseases, continuous cardiac out measurement is essential to provide feedback and monitor any improvements in the vascular system. This paper presents a new possible approach to measure the cardiac output using an intravascular heat-exchange catheter. In order to measure the blood flow rate, the catheter is inserted into a blood vessel and a heat-transfer element attached at the distal end is positioned at a desired location to enable heat transfer from the blood to the cooling fluid in the element. The outlet temperature change of the cooling fluid occurs during the heat-exchange process and is monitored by thermal-sensors to determine the cardiac output and any substantial change of the cardiac output. A preliminary experimental study demonstrated an essential relationship, which can be used to determine the cardiac output from the measurement of the outlet temperature of the cooling fluid alone, without the need to determine the temperature change at the down stream of the blood flow. It also has an advantage of not injecting any auxiliary liquid or dye into the blood flow. Thus, it allows repeated measurement and does not affect the composition of blood stream. Furthermore, it does not warm up the blood flow. Therefore, it avoids any possible adverse effects caused by heating in the vascular system. This current approach is useful in monitoring any continuous improvement and providing feedback in the stenting surgery operation, bypass operation or any treatment related to atherosclerosis.**

Keywords — **Heat Exchange, Catheter, Blood Flow Rate, Intravascular, Cardiac Output.**

I. Introduction

Chronic coronary artery diseases obstruct the blood flow supplying oxygen-rich blood to the heart by forming plaques on the inside walls of coronary arteries. The standard treatments for coronary artery diseases include the balloon angioplasty. The balloon angioplasty compresses the fatty plaques onto the artery walls, often followed by a coronary stent implant [1]. The other standard treatments for coronary artery diseases are atherectomy, medication and bypass surgery to restore normal blood flow rate. Thus, it is essential to monitor closely the real-time blood flow rate during these treatments.

There are many different techniques to measure the continuous cardiac output [2]. This study explores a new approach using an intravascular heat-exchange catheter to determine blood flow rate or cardiac output. The catheter comprises a catheter tube with a flexible closed-loop heat-transfer element disposed at the distal end. The process comprises steps of placing a catheter at a desired location within a blood vessel, acquiring the temperature of the fluid passing through the heat-transfer element and the temperature of the blood flowing over the element. The acquired information is then used to determine the blood flow rate. A preliminary experimental study was conducted to demonstrate that the mass flow rate of blood can be expressed in term of the outlet temperature of the fluid leaving the heat-transfer element. The study showed that an essential relationship can exist. The expression derived can be used to determine the cardiac output and any substantial change of the cardiac output from the measurement of the outlet temperature of the cooling fluid alone.

II. Background

Coronary artery disease is a chronic disease, which impedes or blocks the flow of oxygen-rich blood to the heart through the coronary arteries. This obstruction is caused by a disease known as atherosclerosis, which is sometimes also called blockage of the arteries, narrowing of the arteries and hardening of the arteries. The first goal for treatment of atherosclerosis is to restore as much blood flow as possible through the affected portion of the vascular system and reduce the risk of a plaque rupture, which can result in a heart attack or stroke.

Balloon angioplasty and atherectomy are a few standard treatments based on catheter-based procedures for coronary artery disease. The goal of balloon angioplasty is to make more room for blood to flow through the artery. Coronary stents are often implanted after a balloon angioplasty and/or atherectomy. Stents may be placed in arteries and veins throughout the body to restore normal blood flow. The improved blood flow can lead to an improvement in cardiac function. Thus, measuring blood flow rate is an essential feature in these treatments so as to provide feedback and monitor the changes in the flow rate. Otherwise, based on other indirect methods of observing the patients' response would compromise the success of the treatments in the absence of this important measurement.

Attempts to measure blood flow rate or cardiac output in the prior arts have taken different principles and forms.

Chwee Teck Lim, James C.H. Goh (Eds.): ICBME 2008, Proceedings 23, pp. 1663–1666, 2009
www.springerlink.com

One of the well-known techniques is to include a heating element in the catheter together with other sensors and controls. By heating a segment of blood indirectly with the heating element such as an electric resistance heater, the temperature deviation of blood could be monitored as a function of time at a location downstream from the location at which the heating element is placed. The blood flow rate is then measured by the area under the thermodilution curve based on Stewart-Hamilton Principle [2, 3]. However, the heating could result potential injuries and other adverse fever responses from the body. Another technique avoiding the adverse heating effect is to inject a bolus of saline liquid into the blood stream, where the saline liquid has a lower temperature than that of the blood [4]. The blood flow rate is then determined using the similar thermodilution analysis. Other similar technique sometimes used in place of an injected cold bolus is to include injecting indicator dye into the blood vessels to enhance X-ray images. The blood flow rate can be then determined by the dye-dilution curve. However, in the latter two cases, alien materials have been introduced into the blood flow. They are subjected to important drawbacks as they could result in excessive fluid infusion into the patient and cause safety concerns. Excessive infusion in turn can increase the risk of congestive heart or kidney failure in certain patients [5]. Other techniques include the Flick method and the Doppler ultrasound method. The former measures the blood-oxygen content and the oxygen consumption rate which requires the patient to be in a steady state in which cardiac output does not change significant, while the latter uses a Doppler probe which measurements are troublesome and inaccurate as it is sensitive to its orientation although the method is noninvasive. Therefore, there is an existing need for processes and apparatus that can measure continuous cardiac output easily, effectively and safely.

III. Apparatus and Approach

A. Proposed Measuring Device

In this study, a newly designed measuring device (patent pending) consists of a heat-transfer element together with thermal-sensors adaptable to a catheter for measuring blood flow rate as shown in Fig. 1. The catheter comprises a catheter tube with a heat-transfer element attached at the distal end for conducting the heat-exchange between the cooling fluid flowing inside and blood flowing outside.

The heat-transfer element is a flexible closed-loop heat exchanger, made of metallic capillary tubing coiled into a spring-like configuration not more than 5mm outside diameter. The catheter has at least three lumens. Two of them are used for consistent supply of heat-exchange fluid cooler than the blood temperature to the heat-transfer element, while the third is for delivering out electronic signals from thermal-sensors through a temperature monitoring port at the proximal end of the catheter to monitor the temperatures with a data logger. The catheter proximal end also has a cooling fluid inlet port for introducing the cooling fluid into the catheter and an outlet port for discharging the cooling fluid from the catheter

B. Application

In an operational application, the flexible catheter is inserted into a blood vessel through the vascular system of a patient to place the distal tip of the catheter at one desired location in a blood vessel where the blood flow rate measurements are needed. A cooling fluid is then pumped through the catheter to the distal tip, where a flexible closed-loop heat-transfer element is positioned to enable heat transfer between the cooling fluid and the blood. The

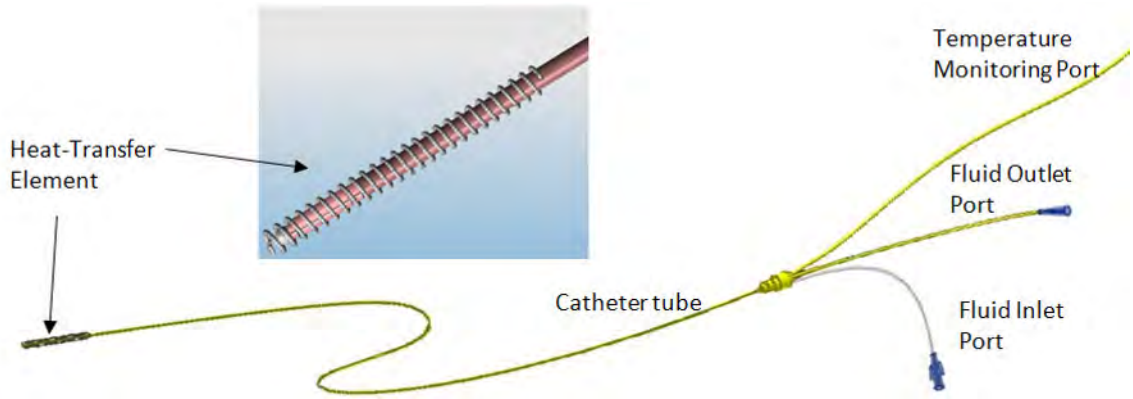


Fig. 1 Heat Exchange Catheter

heat-transfer element absorbs heat energy from the blood flowing over the heat-transfer element in the blood vessel. By having a very large surface area of the heat-transfer element and a relatively lower mass flow of the fluid in the heat-transfer element with respect to the blood flow rate outside the heat-transfer element, a small amount of heat energy could effectively transfer to the cooling fluid in the heat-transfer element, thereby creating an elevated temperature suitable to determine the cardiac output or the blood flow rate. Once an empirical relationship between the temperature parameter and the blood flow rate is established for a specific heat-transfer element, merely measuring the temperature change leaving the heat-transfer element enables cardiac output or the substantial change of the cardiac output, to be determined through this relationship without the need for introduction of an auxiliary liquid into the patient's blood.

C. Experimental Setup

The blood-flow-rate measurement device was first being placed into a rubber tube, which could simulate any portion of the patient's vascular system. One end of the rubber tubing was being placed into the hot-water bath maintained at a certain temperature. A Peristaltic pump was used to circulate the warm fluid through the tubing. The flow created by the water pump simulated the cardiac output or blood flow rate. An electrical pump fixed with a syringe containing cold water was attached to the fluid inlet port of the catheter to supply cooling fluid at a fixed rate into the heat exchanger attached at the distal end of the catheter. The schematic representation of the experimental setup is shown in Fig. 2. The electrical signals for the thermocouples were connected to a data logger to monitor the temperature of the cooling fluid flowing in and out of the heat exchanger and the warm fluid flowing over the heat exchanger in the rubber tube.

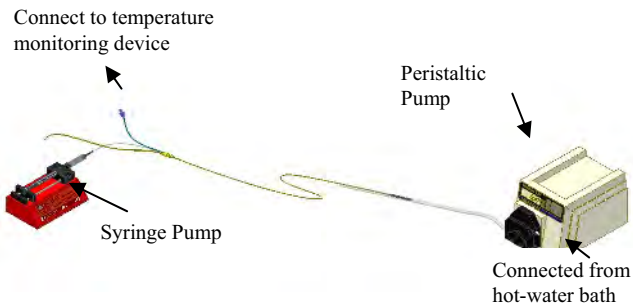


Fig. 2 Schematic Diagram of Experimental Setup

In this feasibility study, the flow of the cooling fluid was set at the rate of 5ml/min. In order to simplify the setup, the cooling fluid was maintained at room temperature (27°C) while the hot-water bath was controlled at 55°C. When the flow rate of the warm water varied from 180ml/min to 1170ml/min at different intervals, the temperatures measured through the data logger were recorded. The results were tabulated and presented graphically to analyze the relationship between these two parameters.

IV. Observation and Results

The results showed that the outlet temperature of the cooling fluid increased gradually from 36.8°C to 42.8°C, as the flow rate of the warm fluid flowing outside the heat exchanger increased from 180ml/min to 1170ml/min. The outlet temperature increased significantly at the beginning when the warm fluid flowed at a lower rate. When the warm fluid flowed much faster, the outlet temperature went up as well, but the rate of temperature increase was not as significant. As shown in Fig. 3, it demonstrated that there is a good relationship between the warm water flow rate and the outlet temperature of the cooling fluid. By fixing an appropriate flow rate and the inlet temperature of the cooling fluid, an empirical expression could be formalized to represent the relationship. Such expression representing for the specific heat-exchange catheter could be useful in tabulating the cardiac output based on the outlet temperature of the cooling fluid alone. Alternatively, a mathematical expression could be developed through the theory of thermodynamic.

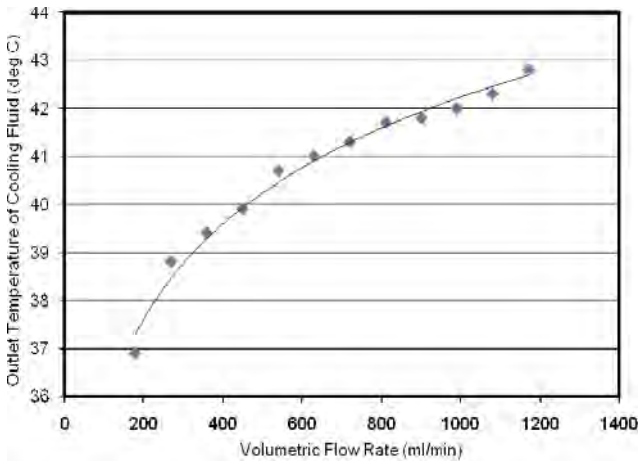


Fig. 3 Graph of Outlet Fluid Temperature vs. Volumetric Flow Rate

V. Analysis and discussion

As compared to thermodilution methods employing indirect heating of blood using surface heating electrical resistance heaters, the method used in this study does not heat the blood flow. Thus, it avoids the adverse effects caused by the use of surface-heating electrical-resistance heaters. It only transfers only a small amount of heat energy from the blood stream to the fluid in the heat-transfer element, thereby creating an elevated temperature suitable to determine the cardiac output or the blood flow rate.

In addition, it does not inject any auxiliary liquid or dye into the blood flow; thus it allows repeated measurement and does not affect the composition of blood stream, unlike dye dilution or conductivity dilution techniques. It could be used on a given patient with increased frequency over relatively long periods of time. Such approach is less likely to result unfavorable response by the body system of the patient. Furthermore, it also does not need to know the temperature change between the up and down streams of the blood flow. As such the apparatus can be shorter and much miniaturized.

VI. Conclusions

In conclusion, this study offers many benefits in the following areas:

1. The method used in the proposal to determine the cardiac output requires only measurement of the temperature of the fluid in the heat-transfer element, without the need to know the temperature change between the up stream and down stream of the blood flow.

2. The method does not affect the composition of the blood stream, unlike dye dilution or conductivity dilution techniques.

3. The approach used in this proposal unlike techniques involving injection of auxiliary liquid, allows repeatability of procedures which could be used on a given patient with increased frequency over relatively long period of time.

4. As compared to thermodilution method, which employs indirect heating of blood using surface-heating electrical-resistance heaters, the current approach extracts a small amount of heat energy from the blood to evaluate the cardiac output. This approach does not have any adverse effect to the vascular system and unlikely to have unfavorable consequences to the patient.

5. The current approach to determine the flow in a narrow channel is unique and could have many applications such as in food industries or chemical plant, besides life science applications, as it does not contaminate or affect the properties of the flowing fluid.

Acknowledgment

The authors gratefully acknowledge the advice and support from Biosensors International.

References

1. NBC and iVillage, Coronary Artery Disease at http://yourtotalhealth.ivillage.com/coronary-artery-disease.html
2. K. G. Lehmann, and M. S. Platt, (1999) Improved accuracy and precision of thermodilution cardiac output measurement using a dual thermistor catheter system, J Am Coll Cardiol, 1999; 33:883-891, American College of Cardiology Foundation. http://content.onlinejacc.org/cgi/content/full/33/3/883
3. Kuper M, (2004) Continuous Cardiac Output Monitoring, Current Anaesthesia & Critical Care, Volume 15, Issue 6, Pages 367-377. doi:10.1016/j.cacc.2004.11.004
4. Edwards Lifesciences at http://www.edwards.com/
5. Williams W. R. and Bornzin G. A., (1990) Thermodilution by Heat Exchange. U. S. Patent 4,941,475.

Address of the corresponding author:

Author: Seng Sing Tan
Institute: Nanyang Polytechnic
Street: Ang Mo Kio
City: Singapore
Country: Singapore
Email: tan_seng_sing@nyp.gov.sg

Mechanical and Electromyographic Response to Stimulated Contractions in Paralyzed Tibialis Anterior Post Fatiguing Stimulations

N.Y. Yu[1] and S.H. Chang[2]

[1] Department of Physical Therapy, I-Shou University, Kaohsiung County, Taiwan
[2] Department of Occupational Therapy, I-Shou University, Kaohsiung County, Taiwan

Abstract — **Muscle fatigue is one of the most important problems resulting when functional electrical stimulation is implemented. After muscle fatigue, the manifestation of post fatigue recovery process is hence necessary for the external control of electrically elicited muscle contractions. Thirteen able-bodied young adults were recruited for this study. For inducing muscle fatigue, a modified Burke fatigue protocol was delivered to activate the tibialis anterior for 4 minutes. Before and after the modified Burke fatigue protocol, a series of pulse train with three pulses of 1 Hz and 7 pulses of 20 Hz of stimulation frequency, were delivered to induce 3 twitches and a fused contraction at 1, 3 and then followed every 5 minutes for 60 minutes. When the muscle was stimulated, the stimulus-response EMG and the generated ankle dorsiflexion torque were collected for further analyses. This study found the recovery process of muscle fatigue could be modeled by a first order exponential equation. The properties in twitched and tetanic contraction were found to be different. The recovery process was found faster in tetanic muscle contraction. The disassociation between mechanical and myoelectric activities was found in the recovery process, especially in the twitch contraction. These findings will help researchers and clinicians predict the muscle force and permit a better adjustment of the stimulation parameters.**

Keywords — **muscle contraction, muscle fatigue, recovery, low frequency fatigue, potentiation.**

I. Introduction

Fatigue is a major challenge for continuing an ongoing movement induced by electrical stimulation. Most of the researchers found that when muscle is fatigued, the torque frequency curve will shift to the right, i.e., to a same level of the force output, but that the frequency must be increased [1][2]. The recovery of contractile speed caused the tetanus's failure to fuse in lower frequency stimulation, whereas the tetanus torque became less depressed in higher frequency stimulation [1]. This phenomenon is termed as low frequency fatigue (LFF). In addition, potentiation is one important mechanical characteristic and also considered a competing process in which repetitive stimulation of a fatigued muscle yields augmentation of peak force [3]. Our aim was to observe whether these two phenomena occur in the recovery process and to determine the main feature of potentiation in post fatigue paralyzed muscles.

From physiologic aspects, many studies have investigated the evoked EMG of the stimulated muscle during the fatiguing process. It is tempting to use EMG as an indicator of muscle state. The close correlation between muscle force and amplitude of stimulus-evoked EMG indicates the possibility that the EMG signal can directly provide information for monitoring electrically-elicited muscle contraction, and as control signals for compensating for the decrease of muscle force due to fatigue [4]. The temporal features have also been used to quantify the muscle fatigue process, including: latency, rise time to peak (RTP), and PTP duration (PTPD) as well as frequency characteristics. Both temporal and frequency features were presumably related to the propagation velocity of the motor unit action potential in muscle fibers. Most of the results showed a decrease in muscle fiber conduction velocity during the muscle fatigue process [5]. For the recovery process, Shields et al., proposed a result of their study on paralyzed soleus muscles [6]. They found that after 5 min from the cessation of electrical stimulation, the evoked EMG had almost returned to its original features, but the recovery of muscle force was not so significant. According to their study, if the evoked EMG can be a fatigue indicator, it is true only when the recovery process does not start, or other factors may exist contributing to the varying relationship between EMG amplitude and the muscle contraction force during the recovery process.

The aim of this research is to characterize the muscle recovery processes by observing the twitch and fused isometric contractions. In addition to contractile activity, a recovery manifestation constituted from myoelectric activities is also necessary for reflecting the condition of the stimulated muscles. The relationship between myoelectric parameters and the recovered force measurements were analyzed to examine the condition of excitation-contractile coupling.

Chwee Teck Lim, James C.H. Goh (Eds.): ICBME 2008, Proceedings 23, pp. 1667–1671, 2009
www.springerlink.com

II. Methods

A. Subjects

Thirteen spinal cord injured subjects (11 male and 2 female, 26-43 years, 63-85 kg and 1.62-1.84 m) with mean ± SD age of 35.0±7.3 years were recruited for this experiment. The average time post-injury was 4.3±2.68 years. The neurological levels of the subjects are between T4 and T11 and with no or little spasticity in the lower limb muscles. The local Ethics Committee approved the experimental procedures, and all subjects signed an informed consent that was approved by the Human Subjects Review Board of I-Shou University.

B. Experimental Setup:

During the experiment, each subject lay on a long bench with his or her hip and knee joints fixed in a 0° flexion. The tibialis anterior was stimulated by a Grass electrical stimulator (S8800) and constant-current unit (CCU1 A, Grass Instrument, Quincy, MA) using 300 μs, 20-Hz square-wave pulses. For inducing muscle fatigue, current with supramaximal amplitude was applied to the tibialis anterior with the subject lying on the bench with the lower leg fixed on a testing device, as shown in Figure 1.

To detect the muscle force output, the generated ankle dorsiflexion torque representing the force output of the tibialis anterior can be collected from the analogue output of the torque sensor (TP-10KMAB/CB, Kyowa). To detect the evoked EMG, surface electrodes with a 2-cm inter-electrode distance (Norotrode 20, Myotronics-Noromed, Inc.) were applied on the stimulated muscle. They are bipolar Ag-Ag chloride surface electrodes with a 7 mm diameter and fixed 20 mm inter-electrode distance.

Surface EMG was amplified (Model 12A14 DC/AC Amplifier, Grass Medical Instruments) with a gain of 1000, and passed through a frequency window of 3-3k Hz (Neurodata Acquisition System, Model 12, Grass Medical Instruments). The EMG signal was sampled at a rate of 5k Hz stored on computer disk for later analysis using Matlab (Mathwork Co., Natick, Mass.) signal processing software. A hardware blanking with a sample and hold design was used for stimulus artifact suppression. This hardware-based blanking circuit is triggered by a synchronous pulse from the stimulus pulse itself.

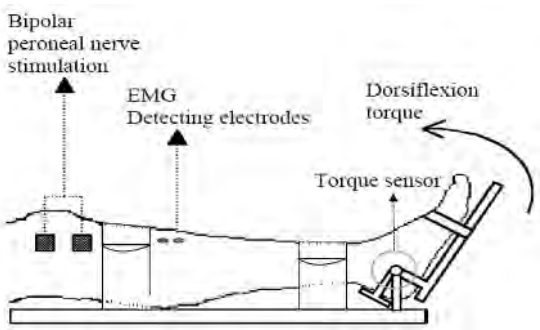


Figure 1: Schematic presentation of testing device.

C. Experimental Protocols:

The recovery tests were performed in the right lower legs of all of the subjects. Supra-maximal electrical stimulation (determined by the maximal peak to peak amplitude of the evoked EMG) was delivered to induce muscle fatigue. A modified Burke fatigue protocol was delivered for 4 min, which activated the tibialis anterior every second for 0.33 sec using a 20 Hz stimulation frequency. Before the fatigue protocol, 3 pulses with 1 Hz and 7 pulses with 20 Hz of stimulation frequency were delivered to induce 3 twitches and 1 fused contraction for the collection of the initial baseline data. Immediately after the fatigue protocol, the same testing protocol was delivered to the muscle in 1, 3 and 5 minutes, and then every 5 minutes for 60 minutes. At the same time, the twitch and tetanic force, as well as the stimulus-evoked EMG, were collected for the off-line analyses.

D. Data Analyses:

In every test of the experiment, every 3 consecutive twitches were averaged together to represent a single twitch. The peak torque (PT) in the twitch and fused contractions can be obtained by finding the maximal value in the array of torque data. For measuring the total activation produced by twitch or tetanus, the torque-time integral (TTI) was also computed. For observing the myoelectric activities, the stimulus-evoked EMG of the stimulated muscle was studied during the recovery process. Peak-to-peak amplitude (PTP) and the other characteristics, such as root mean square (RMS) and temporal parameters, including rise time to peak (RTP) and PTP duration (PTPD), were used to quantify the recovery process of the myoelectric activities.

The measured parameters of twitch or fused contractions were plotted in correspondence with the elapse of recovery time. The plotted curves were fitted by a function for characterizing the recovery process. The recovery process was characterized empirically by an exponentially asymptotic curve:

$$Y = A(1 - e^{-\tau_0 t}) + M_0$$

where Y is the predicted value of torque output, t is the elapsed time, τ_0 is the time constant, M_0 is the initial value of torque output in the recovery process, and A is a scaling

parameter for recovering the normalized data to its original value. A nonlinear curve fitting technique was used to find the optimal parameters such that error could be reduced to a minimum by using the Nelder-Mead simplex algorithm. After the normalization, the recovery processes from muscle fatigue could be analyzed by comparing the time constant of the measurements of the evoked EMG and torque output.

E. Statistical Analyses:

Repeated measures of ANOVA were utilized to compare the difference of time constant between EMG and mechanical parameters. If significant main effects were observed, Bonferroni post-hoc tests were performed. For observing the relationship between EMG and the recovered force, a series of correlation analyses was conducted.

III. Results

A. General manifestation of recovery processes

As depicted on Figure 2, the torque output of ankle dorsiflexion was found to have diminished after modified Burke fatigue protocol. After about 5 minutes post stimulation, the torque output of stimulated muscle was found to have increased to about one half of the initial amplitude. After about 10 minutes, the output increased, approaching 60% of the initial amplitude. In the observation of force development of a single twitch, the rise time to peak torque was delayed until about 10 minutes of time had elapsed. The twitch contraction time was prolonged at around 1 to 5 minutes after fatigue stimulation. After that, the twitch contraction time returned to its initial value.

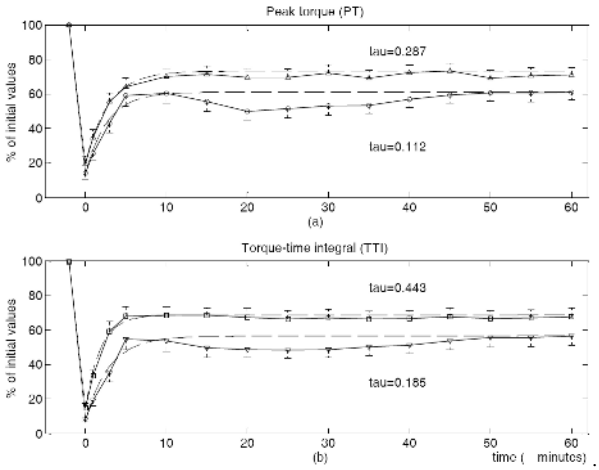


Figure 2. (a) PT and (b) TTI of twitch (-○- and -∇-) and tetanic (-Δ- and - -) contractions. Data, expressed as percentage of initial values, are means+SE or means-SE.

B. The Recovery Processes of Muscle Fatigue

The data on the recovery process were fitted empirically by an exponentially asymptotic curve. After all of the measuring parameters had been fitted, the time constants were extracted. The respective mean and standard error of recovery time constants are Twitch PT (.112±.034), Twitch TTI (.185±.060), Tetanic PT (.287±.033), and Tetanic TTI (.443(.056). Figure 2 shows the changes of biomechanical measurements in the recovery processes. Repeated measurements of ANOVA showed significantly different changing speeds within biomechanical parameters ($F= 15.23$, $p<0.001$). In the comparison of recovery speed between contraction types (twitch vs. tetanus), and the curves in twitch contractions, a significantly faster rising speed can be found in tetanic PT ($p=0.002$) and TTI ($p=0.028$). In the comparison of recovery speed between PT and TTI, the latter was found to be faster than the former in tetanic contraction ($p=0.01$) but was not found in twitch contraction ($p=0.469$).

Repeated measures of ANOVA showed significantly different changing speeds within myoelectric measurements ($F= 2.90$, $p<0.05$). The respective mean and standard error of recovery time constants of myoelectric parameters are EMG PTP (.191(.047), EMG RMS (.293(.073), EMG RTP (.255(.091), and EMG PTPD (.468(.069). Figure 3 shows the changes of myoelectric measurements in the recovery processes. Significant difference was only found in the comparison of recovery process between EMG PTPD (fastest) and EMG PTP ($p<0.05$). Except for this, no significant difference was found in the comparison between, or within, amplitude and temporal parameters.

Figure 3 depicts and illustrates the correlation coefficients between myoelectric and biomechanical parameters.

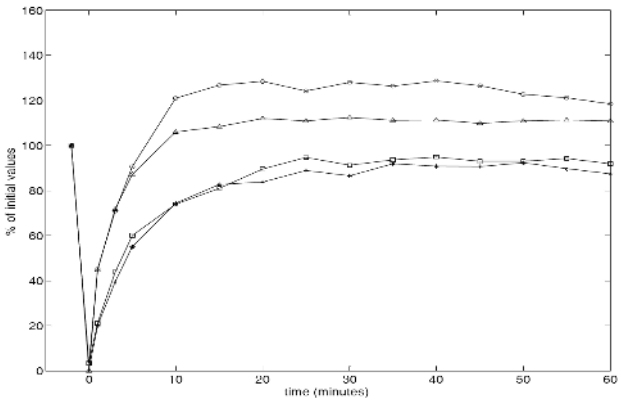


Figure 3. The recovery processes of EMG parameters of the stimulated muscles EMG PTP (-*-), RMS (- -), EMG RTP (-○-), EMG PTPD (-Δ-). In order to aid the visualization of a comparison with the amplitude parameters, the temporal parameters (EMG RTP and PTPD) were inversed first, and then normalized by the initial values.

Two major findings can be noted on the Figure. In general, the EMG parameters correlated more strongly with tetanic than with twitch ones. Among 4 myoelectric parameters, the EMG PTPD has the highest correlation coefficients with parameters of tetanic contraction (r=-.77 in tetanic PT and r=-.75 in tetanic TTI) but lower correlation coefficients with twitch ones (r=-.44 in twitch PT and r=-.48 in twitch TTI). In contrast to EMG PTPD, the other temporal parameter (EMG RTP) has the lowest correlation coefficients with tetanic PT (r=-.55) and tetanic TTI (r=-.59) and lower correlation coefficients with twitch PT (r=-.47) and twitch TTI (r=-.47). The EMG amplitude parameters also have strong correlations with parameters of tetanic contraction (r=.61 to r=.63), but only moderate correlations with twitch ones (r=.44 to r=.52).

IV. Discussions & conclusions

The present study was the first to investigate the recovery process from electrically induced muscle fatigue on the myoelectric and contractile activities for human paralyzed tibialis anterior muscles. After 10 min of rest, the peak torque of single twitch rises to about 60% of the original value. In tetanic contraction, also after about 10 min of rest, the PT and TTI recovered with a faster speed, and reached about 70% of the original value. Pertaining to the fast recovery rate in tetanus, a similar study reported by Shields et al. observed the differential responses between the twitch and the tetanus during the recovery process and also found some preferential recovery at tetanus that is not present at twitch contraction [1]. They suggested that there is a complex interplay between optimal fusion created from contractile speed slowing and excitation/contraction coupling (ECC) compromise. Even if the full recovery of the contraction speed does not prevent greater recovery of the tetanus, it suggests that other factors contribute the faster recovery of tetanic force. From the result of a preferential loss of force at low frequency of stimulation (1 Hz), low frequency fatigue (LFF) can also explain some of this disassociation between twitch and tetanic recoveries. Although 20 Hz is also considered a lower frequency, muscle force recovery differed in varied stimulation frequencies, indeed suggesting the existence of LFF. Much higher frequency (ex. 30 or 50 Hz) would be expected to have a faster and more forceful recovery after fatiguing stimulation. For verification, future works are suggested on studying the recovery rate of muscles activated by higher stimulation frequency.

Post-fatigue potentiation, as reported by previously similar studies, is also considered to be an important factor to counteract the impaired ECC at the same time. Many studies have shown that potentiation occurs most readily in muscles that consist of primarily fast-twitch fibers [7]. After spinal cord injury, the gradual transformation is believed in chronically paralyzed muscle from a primarily slow muscle with type I fibers to a fast muscle with mainly type IIb fibers [8], such as would be expected in muscles observed in this study. Surface electrical stimulation is considered a rather random phenomenon, with both fast and slow fibers being activated. The mechanical response depends on a muscle's architecture and relative proportion of fast and slow fibers. As found in this study, the fast relaxation rate between ~5 and ~10 min of post fatigue implicates the predominate activation of fast muscle. Since, as reported by previous studies, potentiation is preferential in type II muscle fibers, the predominant activation of type II muscle fibers also explained the existence of potentiation.

EMG amplitude has been suggested for use as a fatigue indicator for feedback control in FES application [4]. However, this study also found that disassociation occurred during the recovering processes between mechanical and myoelectric measures. From the results of the present study, the EMG PTPD which correlated more with the recovering tetanic force might be more suitable for the application of monitoring the recovery of electrically induced muscle fatigue. However, since the complete recovery of muscle force follows the full return of EMG parameters, an adaptive tuning of gain and offset of EMG utilities in monitoring or predicting the stimulated force, is therefore necessary to compensate for this dissociation.

Acknowledgment

The authors would like to thank the National Science Council of the Republic of China for supporting this work financially under contract no. NSC-93-2213-E-214-060.

References

1. Shields RK, Chang YJ (1997) The effects of fatigue on the torque-frequency curve of the human paralyzed soleus muscle. J Electromyogr Kinesiol 7: 2-13.
2. Chou LW, Binder-Macleod SA (2007) The effects of stimulation frequency and fatigue on the force-intensity relationship for human skeletal muscle. Clin Neurophysiol 118: 1387-1396.
3. Rassier DE. (2000) The effects of length on fatigue and twitch potentiation in human skeletal muscle. Clin Physiol 20: 474–482.
4. Winslow J, Jacobs PL, Tepavac D (2003) Fatigue compensation during FES using surface EMG. J Electromyogr Kinesiol 13: 555-68.
5. Fuglevand AJ, Zackowski KM, Huey KA, Enoka RM. (1993) Impairment of neuromuscular propagation during human fatiguing contractions at submaximal forces. J Physiol 460: 549-572.
6. Shields RK (1995) Fatigability, relaxation properties and electromyographic responses of the human paralyzed soleus muscle. J Neurophsiol 73: 2195-2206.

7. Hamada T, Sale DG, MacDougall JD, Tarnopolsky MA. (2000) Postactivation potentiation, fiber type, and twitch contraction time in human knee extensor muscles. J Appl Physiol 88: 2131–2137.
8. Lotta S, Scelsi R, Alfonsi E, Saitta A, Nicolotti D, Epifani P, Carraro U. (1991) Morphometric and neurophysiological analysis of skeletal muscle in paraplegic patients with traumatic cord lesion. Paraplegia 29: 247–252.

Author: Shao-Hsia Chang
Institute: I-Shou University
Street: No 8, Yi-Da Rd, Jiau-Shu Village, Yan-Chao Township
City: Kaohsiung County
Country: Taiwan, ROC
Email: stacey12@mail.isu.edu.tw

Modelling The Transport Of Momentum And Oxygen In An Aerial-Disk Driven Bioreactor Used For Animal Tissue Or Cell Culture

K.Y.S. Liow[1], G.A. Thouas[2], B.T. Tan[1], M.C. Thompson[3] and K. Hourigan[2,3]

[1]School of Engineering, Monash University, Selangor, Malaysia
[2]Division of Biological Engineering, Engineering, Monash University, Melbourne, Australia
[3]Department of Mechanical and Aerospace Engineering, Monash University, Melbourne, Australia

Abstract — **This study considers the momentum transport and oxygen transfer in a modified stirred tank bioreactor. The design is novel in the sense that the impeller is positioned above the culture medium (instead of being suspended inside it). This design has potential benefits of enhanced gas transfer, reduced possibility of contamination, and better access to the culture medium. Computational fluid dynamics modelling is used to simulate the gas and fluid flow in the bioreactor. A rotation rate of 60 to 240 rpm (corresponding to the laminar regime) was adopted. Results show that the flow in the medium is swirl-dominant with an induced secondary flow in the meridional plane consisting of a steady and robust recirculation bubble. As the Reynolds number is increased beyond ~427, we observe the formation of an additional smaller toroidal-bubble at the bottom wall. This bubble bears some resemblance to the vortex breakdown topology commonly found in confined swirling flows. In terms of the oxygen distribution, oxygen transfer from the gaseous phase into the culture medium is enhanced through forced diffusion taking place across the air-medium interface. For the Reynolds number range studied there is clear dominance of convection over diffusion in the transport of oxygen from the air-medium interface and throughout the culture medium.**

Keywords — **bioreactor, computational fluid dynamics, oxygen concentration, tissue engineering**

I. Introduction

Research in the area of bioreactor process hardware technology in biomedical engineering continues to receive prominent attention ([1],[2]), particularly in relation to the industrial-scale production of mammalian cell lines. While the use of bioreactors has been fairly well established in certain industries (e.g., wastewater, food processing, etc), it remains important to consider the physiological requirements of mammalian cells toward the *in-vivo* condition. Two critical physiological parameters relevant to larger bioreactor volumes with high tissue densities, include oxygen transfer and mechanically-induced shear at the cell walls.

The adverse susceptibility of animal cells to high levels of shear has been well described [3] and significant efforts have also been made to improve the efficiency of oxygen diffusion [4]. While it is accepted that methods such as agitation or gas sparging can enhance oxygen diffusion and nutrient transfer, this often comes at the expense of increased levels of shear [5]. Therefore a well-correlated relationship between the mechanical stimulation of a bioreactor and the oxygenation requirements of particular cell type remains crucial in bioreactor optimization studies.

The objective of this study is to computationally model in detail the transport of momentum and oxygen taking place in a novel small-scale bioreactor in which the culture medium is agitated by an aerial impeller that is positioned directly above it (see Figure 1a). This study forms a part of

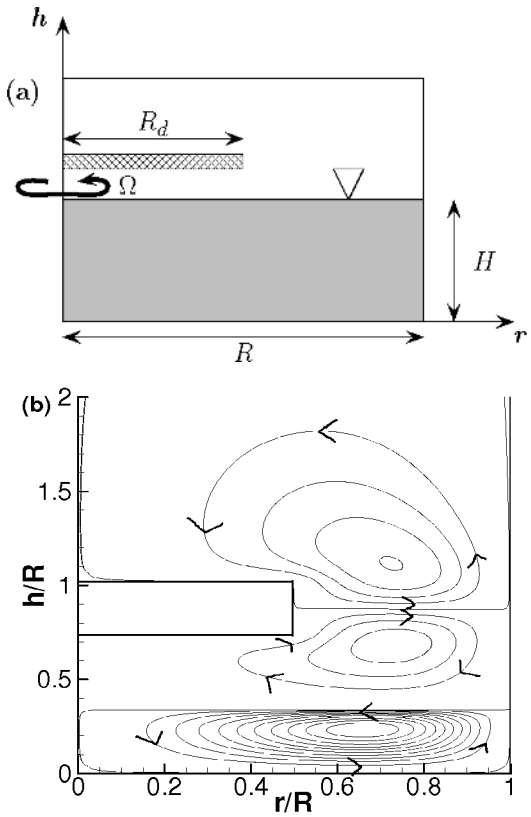


Figure 1: (a) Schematic of the aerial bioreactor in the meridional plane, (b) representative streamlines of the flow.

Chwee Teck Lim, James C.H. Goh (Eds.): ICBME 2008, Proceedings 23, pp. 1672–1675, 2009
www.springerlink.com

ongoing investigations by biological engineers at Monash University, to investigate the feasibility and practical application of laminar stirred-tank bioreactors for cell and/or tissue culture. From a fluid dynamics perspective, characterization of the flow in a laminar bioreactor based on a lid-driven cylinder have been performed extensively, both experimentally and numerically ([6],[7],[8]). The design itself was originally based on explorations of the possibility of applying vortex breakdown theory to provide a controlled, low-shear and well-mixed environment within the bioreactor chamber.

In terms of cell culture, two prototype configurations in which the laminar bioreactor concept have been successfully tested are 5~ml cylindrical vessels with a partially-submerged disk [9], as well as a non-submerged disk [10].

In this study, the latter configuration (see Figure 1) is considered in further detail. An instantaneous snapshot of the streamline pattern highlighting the induced secondary flow in both the gaseous and aqueous phases is shown in Figure 1b. Note that the results and discussion will be mainly confined to the aqueous phase, e.g., the culture medium in the remainder of the paper. Specifications of the rig and flow are shown in Table 1. The Reynolds number is based on the rotation speed of the impeller, radius of the impeller, and the physical properties of *air*.

Table 1: Specifications and aspect ratio (AR) of the bioreactor

Parameter	Range
Cell consumption of oxygen	1.0-1.2*10^{-17} mol O_2/cell.s
Cell density	5*10^{10} cells/m^3
Cylinder radius, R	17.65 mm
Fluid height, H	6 mm
Fluid density, ρ	998 kg/m^3
Impeller radius, R_d	15.43 mm
Impeller thickness	5 mm
Impeller height (from base)	13 mm
Impeller speed	60-240 rpm
Bioreactor AR, H/R	0.339
Impeller AR, R_d/R	0.872
Reynolds number, Re	183-731

II. Numerical methods

The commercial CFD software package, FLUENT, is used to simulate the flow and oxygen transport in the aerial bioreactor. The unsteady solver is used whereby the incompressible Navier Stokes equations (INSE) are temporally marched from initially zero flow to steady state. The axisymmetric form of the INSE are solved on the meridional plane (see Figure 1) with the assumption of axisymmetry. The volume-of-fluid (VOF) technique is used to model the air/culture-medium interface.

As expected for a CFD investigation, a series of meshes was tested to ensure the flow is well resolved. In terms of spatial resolution, the grid points were concentrated around the impeller and cylinder walls. While it is largely anticipated that the inter-phase boundary would remain flat (given that the Froude number is << 1), nevertheless particular attention was paid to resolving the interface boundary to prevent the development of non-physical oscillations. Further details on the numerical techniques used in this study can be found from [7] and [8].

III. Results and discussion

Figure 2 shows steady-state plots of the normalized streamfunction in the meridional flow at three rotation speeds. As seen in Figure 1b, there is a clockwise induced recirculation region in the gaseous phase lying directly underneath the impeller. The centrifuging effect of the air induces a counter-clockwise recirculation bubble in the culture medium. The concentration of the streamlines at the radial location of r/R ~ 0.7-0.8 along the interface boundary suggests significant transport of angular momentum across the air-medium interface.

As the rotation speed is increased, it is observed that an initially narrow and weaker bubble rotates in the opposite direction is formed, being located at the bottom wall. Similar to the situation found in confined swirling flows undergoing vortex breakdown [11], this bubble is located along the axis of rotation. Figure 2c shows that while the main recirculation region remains relatively steady from Re=180 to 240, a widening of the *narrow* bubble can be observed. The number of streamlines inside the bubble indicates an increase in the circulation of the fluid. In addition, the stagnation point of the bubble also moves upwards towards the air-medium interface.

Figure 3 shows the steady-state normalized dissolved oxygen (DO) concentration in the medium phase at three rotation speeds. The dissolved oxygen (DO) clearly shows a strong association of oxygen transport with the dominant counter-clockwise recirculation pattern of the flow. Figure 3a shows that the presence of DO at the base (where cell colonies are expected to congregate in practice) is convection-dependent. In contrast, transport via diffusion is much weaker, judging by the relatively low concentration of DO at the centre of the main recirculation region. At the lowest speed of 60 rpm, it is observed that the oxygen concentration is concentrated mainly along the axis of rotation. Note that the diffusivity of oxygen is approximately 500 times

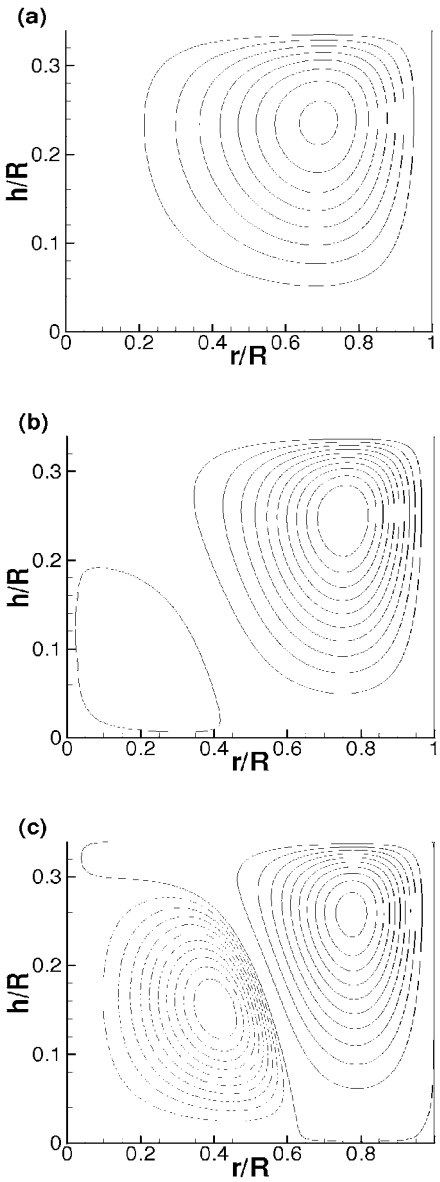


Figure 2: Normalised streamfunction for impeller rotation speed of (a) 60 rpm, (b) 180 rpm, and (c) 240 rpm. The solid lines represent the clockwise rotation with range of 0-1*10-5, while the dashed-dot lines represent the counter-clockwise rotation with range of -8*10-5-0. The intervals are equi-spaced.

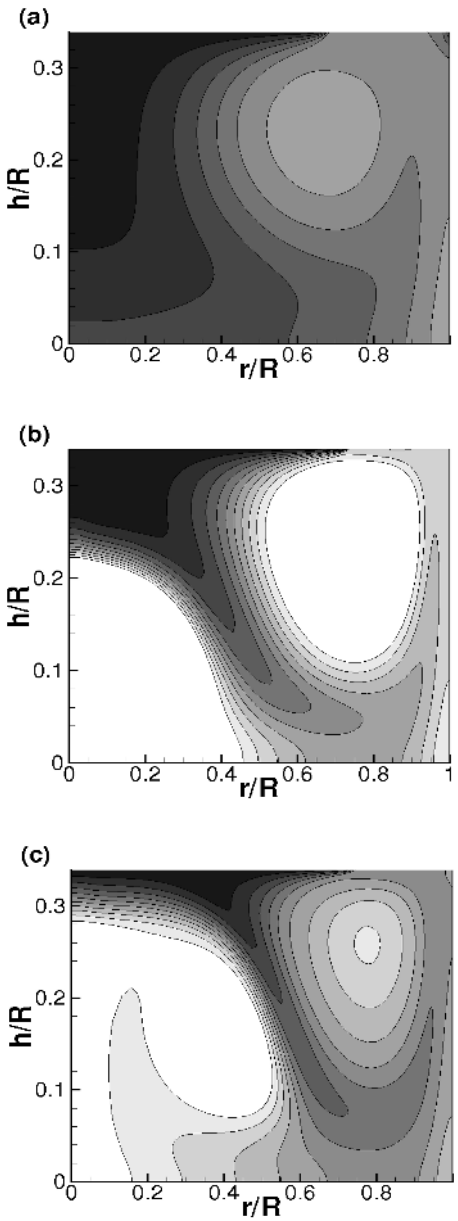


Figure 3: Normalised dissolved oxygen (DO) concentration in the medium phase for impeller rotation speed of (a) 60 rpm, (b) 180 rpm, and (c) 240 rpm. The range is the same for each plot: 0.993 < DO < 1.0.

lower than the kinematic viscosity of water. The induced flows within the fluid medium clearly indicate the flow is driven by convection, hence the transport of oxygen will clearly be dominated by advection by the flow for the chosen operating condition range.

As the rotation speed is further increased resulting in the appearance of the axial bubble, there are two distinct regions of low DO concentration, which correspond to the respective centres of the main recirculation zone and the axial bubble (refer to Figure 3b). The streamfunction plot shown in Figure 2b suggests that oxygen from the interface is mainly convected within the medium along a narrow path with negligible diffusion across the streamlines. In contrast, Figure 3c shows an overall improvement in the oxygen diffusion to the two recirculation zones as Re is increased. However, the oxygen concentration within the second bub-

ble remains lower as it is relatively weaker in comparison to the main recirculation region.

IV. Conclusions

In this study, computational modelling of the flow and oxygen transport in a small-scale stirred tank bioreactor that is driven by an aerial disk has been performed. The results show that oxygen diffusion across the air/culture-medium interface is enhanced by advection of the oxygen rich interface fluid by the induced secondary flow in the culture medium. In addition, this study has provided some insight into the development of the vortex breakdown bubble (commonly found in confined swirling flows) and the resulting effect of the presence of the bubble to the overall oxygen transport within the bioreactor chamber.

References

1. Martin I, Wendt D and Heberer M (2004) The role of bioreactors in tissue engineering. Trends Biotechnol. 22(2):80-86.
2. Martin Y, and Vermetter P (2005) Bioreactor for tissue mass culture: Design, characterization and recent advances. Biomaterials 26:7481-7503.
3. Chisti Y (2001) Hydrodynamic damage to animal cells. Crit. Rev. Biotechnol. 21:67-110.
4. Volkmer E, Drosse I, Otto S et al. (2008) Hypoxia in static and dynamic 3D culture systems for tissue engineering of bone. Tissue Eng Part A 14(8):1331-1340.
5. Koynov A, Tryggvason G, Khinast JG et al. (2007) Characterization of the localized hydrodynamic shear forces and dissolved oxygen distribution in sparged bioreactors. Biotechnol Bioeng. 97(2):317-331.
6. Dusting J, Sheridan, J. and Hourigan, K. (2006) A fluid dynamics approach to bioreactor design for cell and tissue culture. Biotechnology and Bioengineering 94(6), DOI: 10.1002/bit.20960.
7. Liow KYS, Tan BT, Thouas GA et al. (2008) CFD Modelling of the steady state momentum and oxygen transport in a bioreactor that is driven by an aerial disk. Modern Physics Letters (B) `in press'.
8. Liow KYS, Tan BT, Thompson MC et al. (2007) In silico characterization of the flow inside a novel bioreactor for cell and tissue culture. 16th Australasian Fluid Mechanics Conference, Gold Coast, Australia, 2007.
9. Thouas GA, Sheridan J, and Hourigan K (2007) A bioreactor model for mouse tumour progression. J. Biomed Biotech, Article ID 32754.
10. Thouas GA, Thompson MC, Contreras K et al. (2008) Combined improvement of oxygen diffusion and high-density cancer formation in a modified mini-bioreactor. In Proceedings of the 30th Annual International IEEE Engineering in Medicine and Biology Society Conference, Vancouver, British Columbia, Canada, 2008, pp 3586--3589.
11. Lopez JM (1989) Axisymmetric vortex breakdown in an enclosed cylinder flow. Lecture notes in physics. Springer, Berlin.

Author: Keith Liow
Institute: Monash University (Sunway campus)
Street: Jalan Lagoon Selatan
City: Selangor
Country: Malaysia
Email: keith.liow@eng.monash.edu.my

Investigation of Hemodynamic Changes in Abdominal Aortic Aneurysms Treated with Fenestrated Endovascular Grafts

Zhonghua Sun[1], Thanapong Chaichana[2], Yvonne B. Allen[3], Manas Sangworasil[2], Supan Tungjitkusolmun[2], David E. Hartley[3] and Michael M.D. Lawrence-Brown[4]

[1] Curtin University of Technology/Department of Imaging and Applied Physics, Perth, Western Australia, Australia
[2] King Mongkut's Institute of Technology Ladkrabang/Department of Electronic Engineering, Bangkok, Thailand
[3] Cook R&D, Western Australia, Australia
[4] Curtin University of Technology/School of Public Health, Perth, Western Australia, Australia

Abstract — **Fenestrated stent grafts are becoming widely used in clinical practice to treat patients with complicated aortic aneurysms, with short to mid-term satisfactory outcomes being achieved. However, long-term results are yet to be determined. One of the main concerns about the safety of fenestrated repair is the patency of fenestrated renal arteries and subsequent renal function. The purpose of this study is to investigate the hemodynamic changes in patients treated with fenestrated stent grafts using a two-way fluid-structure interaction. 4 patients undergoing fenestrated stent graft repair were selected for inclusion in our analysis. All of the fenestrated renal arteries remained patent after implantation of stent grafts with one patient developing post-procedural complication, endoleak. Our results showed that with insertion of fenestrated stents into the renal arteries with variable lengths, no significant changes of blood flow velocity were noticed based on the flow analysis. Our preliminary study indicates the safety of fenestrated stent grafts, however, further studies are required to verify the long-term outcome of this procedure.**

Keywords — **Aortic aneurysm, blood flow, fenestration, stent graft.**

I. Introduction

Abdominal aortic aneurysm (AAA) is a degenerative disease with dilation and focal weakening of the aorta, and it most commonly involves the abdominal aorta. The prevalence of AAA is up to 9% in elderly people above 65 years. Once the AAA is formed, it grows gradually and has a potential risk of rupture once it reaches certain size. Traditionally, the AAA is treated with open surgery, however, it is not only an invasive procedure but also carries perioperative and post-operative complications and mortality. Thus, a less invasive technique which could be used as an alternative to open surgery would benefit the patients, especially for those with co-morbid medical conditions.

Currently, endovascular repair of AAA through insertion of a stent graft into the aortic aneurysm has been confirmed to be an effective alternative to open surgery and it is widely used in clinical practice in the treatment of patients AAA [1, 2]. Since its first introduction in 1991, endovascular stent graft repair has undergone a series of technical developments which ranged from traditional infrarenal (covered stent graft is placed below the renal arteries) to transrenal fixation (covered stent graft is placed below the renal arteries with uncovered suprarenal stents placed across the renal or other visceral arteries) [3-5], and to the currently evolving fenestrated stent grafts (with holes in the graft material) [6, 7].

Fenestrated stent grafts involve creation an opening in the graft material to accommodate the orifice of the vessel targeted for preservation. This indicates that the stent graft can be placed above the renal arteries without compromising the renal perfusion or blood flow to other vital organs. Fixation of the fenestration to the renal and other visceral arteries can be provided by implantation of bare or covered stents across the graft-artery ostia interfaces so that a portion of the stents protrudes into the aortic lumen. Therefore, there are concerns about the interference of fenestrated stents with renal blood flow or renal function.

Traditionally, studies on hemodynamic changes were performed with computational fluid dynamics (CFD) with regard to the investigation of flow analysis, mainly based on aorta models [8, 9]. However, as the endovascular stent graft wall and aortic aneurysm are flexible, a measurable pressure is present even if in the absence of endoleaks due to the fluid-structure interactions. Therefore, fluid-structure interaction simulations can provide more accurate and realistic measurements of the blood flow and wall pressure and wall stress in patients with AAA after endovascular repair. The purpose of this study is to investigate the hemodynamic changes in patients treated with fenestrated stent grafts, based on a two-way fluid-structure interaction (FSI).

II. Materials and Methods

A. Patient CT data

4 patients with abdominal aortic aneurysms were selected for inclusion in the study. All of the patients were referred by vascular surgeons to the Cook R&D in Western

Chwee Teck Lim, James C.H. Goh (Eds.): ICBME 2008, Proceedings 23, pp. 1676–1679, 2009
www.springerlink.com

Australia for planning of fenestrated stent grafting, which was performed by a group of graft planners on a separate workstation equipped with Terarecon software [10].

CT scans were performed with a High-Speed Advantage scanner 64 x 0.625 mm (GE Medical Systems, Milwaukee, WI, USA) with the following scanning protocol: slice thickness, 1.25 mm, pitch 1.0, reconstruction interval of 0.6mm, 120 kV and 300 mAs.

B. Geometric reconstruction from CT images

Original CT DICOM data (digital imaging and communication in medicine) pre-and post-fenestration were transferred to a workstation equipped with Analyze V 7.0 (AnalyzeDi-rect, Inc., Lexana, KS, USA) for generation of 3D recon-structed images. Segmentation of the aortic artery branches and endovascular stents were performed with a semi-automatic processing involving CT number thresholding, region growing and object creation and separation. For generation of 3D model with inclusion of only vessels, the lowest and highest CT thresholds were set at 200 and 400 HU (Hounsfield unit) respectively to remove all of the soft tissues, bones and stent wires while keeping the contrast-enhanced artery branches; for generation of 3D model with inclusion of endovascular stents, the lowest threshold was set at 500 HU to remove all of the soft tissues and contrast-enhanced vessels while only keeping the high-density stent wires. Figure 1 shows the 3D model from the CT data of patient 3 in the case of pre- fenestrated stent grafting.

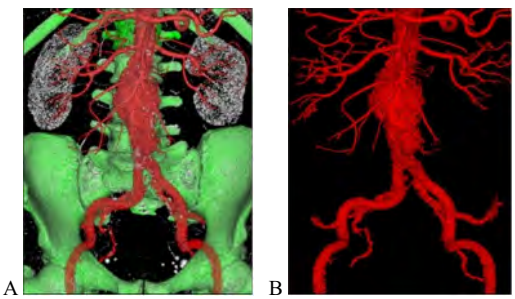


Fig. 1 The 3D model of structures (A), object separation to segment the aorta, branches and aneurysm from other structures (B).

C. Generation of aortic mesh model

Change After segmentation, the 3D object surface of the model was created using surface extractor available on the Analyze software, and the 3D surface object was saved in the STL (stereolithography)', a common format for computed aided design and rapid prototyping. The 'STL' file was converted into the CAD (computer aided design) model files using the CATIA V5 R18 (Dassault Systèmes, Inc., Suresnes Cedex, France). As each data involves both pre- and post-stent grafting, thus we have 8 CAD models in total. Then we generated the blood flow model for computing the CFD (compute fluid dynamics) analysis and the blood wall model for computing the structure analysis. The blood flow and blood wall models are generated at each case pre-and post-stenting, hence study consists of 16 models. Figure 2 shows the segmented aorta models based on patient 4 of pre-and post-stent grafting CT data.

The blood flow model mesh was defined by hexahedral volume meshes using ANSYS ICEM CFD 11 (ANSYS, Inc., Canonsburg, PA, USA). ANSYS ICEM CFD provides sophisticated geometric acquisition, mesh definition and mesh editing which is important for the accurately flow analysis. The blood wall model was defined by tetrahedral volume mesh using ANSYS Meshing 11 (ANSYS, Inc., Canonsburg, PA, USA). Figure 3 demonstrates examples of the CFD mesh model and structure mesh model of post-fenestrated stent grafting.

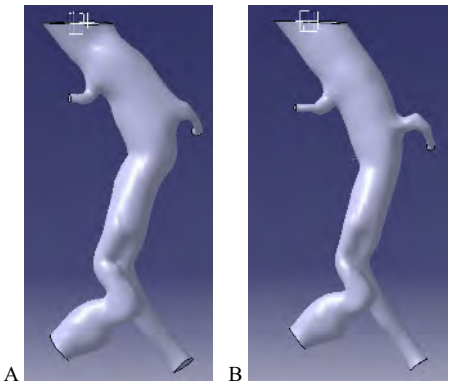


Fig. 2 3D segmented model in patient 4 with AAA pre- (A) and post-fenestrated stent grafting (B).

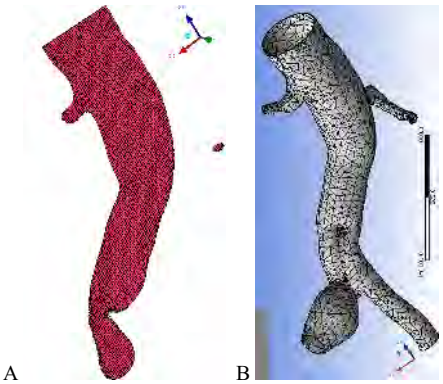


Fig. 3 the same patient as figure 2 of post-fenestrated stent grafting, showing the blood meshes model of cross section in middle of XZ-plane (A), and the blood wall meshes model (B).

D. *Fluid structure interaction-hemodynamic analysis*

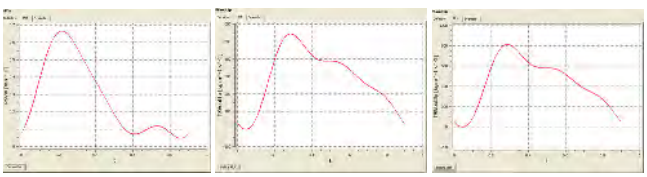
In order to ensure that our analysis reflects the realistic environment of human blood vessel, normal physiological hemodynamic conditions should be considered for the 3D numerical simulations. The fluid and materials properties for different entities were referenced from a previous study [11]. In the current study, we compared the flow rate at the aorta model containing the four arterial branches, namely bilateral renal arteries and common iliac arteries prior to and after stent graft implantation.

Based on the referenced parameters, the simulation of the complete cardiac cycle is performed by means of a fluid-structure interaction approach. This technique allows studying the aneurysmatic fluid mechanics by accounting for the instantaneous fluid forces acting on the wall and the effects of the wall motion on the fluid dynamic field. The blood flow was simulated at different cardiac phases (systolic and diastolic cycles) and measured in the aortic aneurysm, renal arteries and common iliac arteries using the ANSYS Multiphysic (ANSYS, Inc., Canonsburg, PA, USA). Blood flow pattern, wall pressure, and wall shear stress before and after stent-graft implantation were visualized and compared.

The boundary conditions are time-dependent [12]. The velocity inlet (abdominal aorta at the level of celiac axis) boundary conditions are taken from the referenced value showing measurement of the aortic blood velocity. A time-dependent pressure is also imposed at the outlets. Figures 4 show a time-dependent velocity and pressure.

The solid is (blood wall) 1 mm thickness in all models. The solid density was set to 1120 kg/ m^3, a Poisson ratio of 0.49, and a Young's modulus of 1.2 MPa, corresponding to the standard values cited in the literature [13].

The fluid (blood) is assumed to behave as a Newtonian fluid, as this was known for the larger vessels of the human body. The fluid density was set to 1060 kg/m^3 and a viscosity of 0.004 Pa s, corresponding to the standard values cited in the literature [12]. Given these assumptions, the fluid dynamics of the system are fully governed by the Navier-Stokes equations, which provide a differential expression of the mass and momentum conservation laws [11]. Time step was set to 0.025 s of end 0.9 s. The flow was assumed to be incompressible and laminar. The arterial wall was assumed to be deformable during flow analysis.



A B C

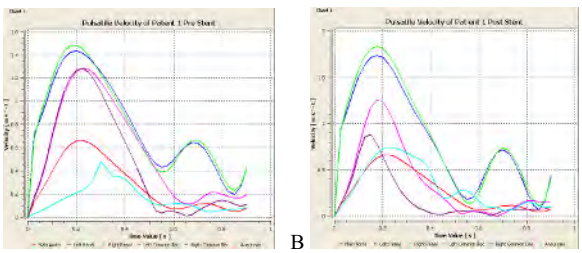
Fig. 4 Flow pulsatile in different cardiac cycles (A), Time-dependent pressure at renal arteries (B) and Time-dependent pressure at common iliac arteries (C).

III. Results

FSI analysis was successfully performed in all of these 4 cases. For the patient who developed type I endoleak, the endoleak was also clearly displayed in the aortic mesh model which allows hemodynamic analysis in the endoleak in regard to the flow and pressure changes in the abdominal aorta, especially under different cardiac cycles.

A. Hemodynamic analysis-flow velocity

Flow velocity was noticed to increase significantly inside the aneurysm following fenestrated stent grafting, indicating that the aneurysm was successfully excluded from the systemic blood circulation. The flow velocity did not show significant changes at the renal and common iliac arteries. Figure 5 shows the flow velocity measured at the main abdominal aorta, and other artery branches, pre-and post-fenestration observed in patient 1. As shown in the graphs, flow velocity to the renal arteries was increased following fenestrated repair due to intra-aortic protrusion of fenestrated renal stents, and it reaches the peak value at about 0.2 s.



A B

Fig. 5 Shows the flow velocity measured at pre- (A) and Post-stent grafting (B) at the main abdominal aorta, renal and common iliac arteries.

B. Hemodynamic analysis-wall pressure and shear stress

Wall pressure and wall shear stress were measured at different cardiac cycles as well, and our results showed that the wall pressure slightly decreased after stent grafting, indicating that less turbulent flow was noticed inside the aneurysm. The wall pressure reaches the peak value at the systolic phase at about 0.25-0.3 s, both pre-and post-stent grafting, Figure 6 shows an example of observation of the wall pressure in a patient pre-and post-stent grafting.

For the patient who developed type I endoleak, wall pressure within the endoleak was found to be as high as that

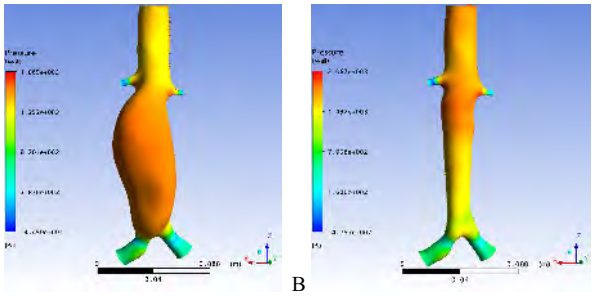


Fig. 6 Wall pressure measured at 0.250 s pre- (A) and post- (B) stent grafting, reaching the highest magnitude.

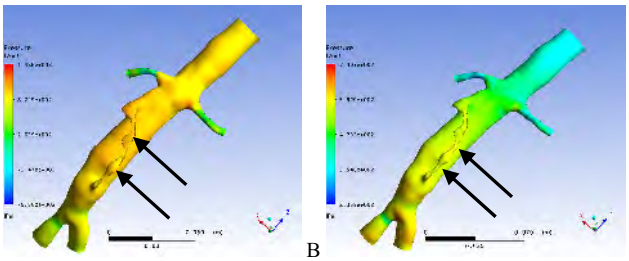


Fig. 7 Wall pressure measured in the endoleak (arrows) is consistent with that in the abdominal aorta, at 0.225 s (A) and 0.425 s (B), respectively.

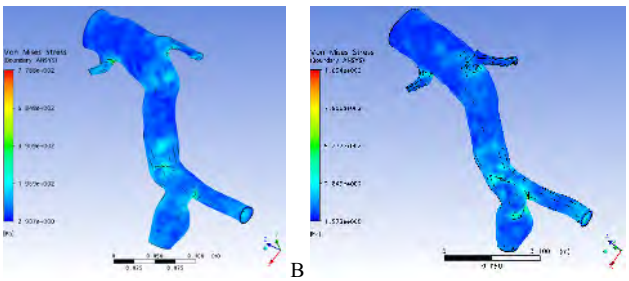


Fig. 8 Wall shear stress measured at both pre- (A) and post- (B) stent grafting, at 0.425 s.

inside the abdominal aorta. This indicates the communication between the aneurysm sac and systematic circulation due to presence of endoleak, as shown in Figure 7.

Maximum wall stress did not occur at the maximum diameter of aneurysm, but at the aneurysm necks (proximal and distal necks). Wall shear stress was not found to change significantly after fenestrated stent grafting. Figure 8 is an example showing the wall shear stress in patient 4 pre-and post-stent grafting.

IV. Conclusion

In conclusion, our preliminary study using FSI method to analyze the hemodynamic changes in patients with AAA treated with fenestrated stent grafts demonstrates the safety and promising outcomes of the endovascular repair of AAA. Change of flow velocity to the renal arteries was minimal with slightly increased after fenestration, although further studies are needed to confirm whether this is significant or leads to renal dysfunction. FSI method provides more accurate analysis of the hemodynamic changes at variable cardiac cycles. Future studies should be performed to investigate the aneurysm sac pressure in relation to the presence of thrombus and endoleak.

References

1. Prinssen M, Verhoeven E, Buth J, et al. (2004) A randomized trial comparing conventional and endovascular repair of abdominal aortic aneurysms. New Engl J Med 351: 1607-1618
2. Greenhalgh R, Brown L, Kwong G, Powell J, Thompson S. (2004) Comparison of endovascular aneurysm repair with open repair in patients with abdominal aortic aneurysm (EVAR trial1), 30-day operative mortality results: randomised controlled trial. Lancet 9437: 843-848
3. Parodi J, Palmaz J, Barone H. (1991) Transfemoral intraluminal graft implantation for abdominal aortic aneurysms. Ann Vasc Surg 6: 491-499
4. Buth J, van Marrewijk C, Harris P, et al. (2002) Outcome of endovascular abdominal aortic aneurysm repair in patients with conditions considered unfit for an open procedure: a report on the EUROSTAR experience. J Vasc Surg 2: 211-221
5. Lobato A, Quick R, Vaughn P, et al. (2000) Transrenal fixation of aortic endografts: intermediate follow-up of a single centre experience. J Endovasc Ther 4: 273-278
6. Stanley B, Semmens J, Lawrence-Brown M, Goodman M, Hartley D. (2001) Fenestration in endovascular grafts for aortic aneurysm repair: new horizons for preserving blood flow in branch vessels. J Endovasc Ther 1: 16-23
7. Muhs B, Verhoeven E, Zeebregts C, et al. (2006) Mid-term results of endovascular aneurysm repair with branched and fene-strated endografts. J Vasc Surg 1: 9-15
8. Chong C, How T. (2004) Flow patterns in an endovascular stent-graft for an abdominal aortic aneurysm repair. J Biomech 37: 89-97
9. Fillinger M, Raghavan M, Marra S, Cronenwett J, Kennedy F. (2002) In vivo analysis of mechanical wall stress and abdominal aortic aneurysm rupture risk. J Vasc Surg 3: 589-597
10. http://www.terarecon.com
11. Frauenfelder T, Lotfey M, Boehm T, Wildermuth S. (2006) Computational fluid dynamics: hemodynamic changes in abdominal aortic aneurysm after stent-graft implantation. Cardiovasc Intervent Radiol 29: 613-623
12. Borghi A, Wood N, Mohiaddin R, Xu X. (2007) Fluid-solid interaction simulation of flow and stress pattern in thoracoabdominal aneurysms: A patient-specific study. J Fluid Struct 2: 270-280
13. Li Z, Kleinstreuer C. (2006) Analysis of biomechanical factors affecting stent-graft migration in an abdominal aortic aneurysm model. J Biomech 39: 2264-2273

Author: Dr.Zhonghua SUN
Institute: Curtin University of Technology
City: Perth
Country: Australia
Email: z.sun@curtin.edu.au

Bone Morphogenetic Protein-2 and Hyaluronic Acid on Hydroxyapatite-coated Porous Titanium to Repair the Defect of Rabbit's Distal Femu

P. Lei[1,2], M. Zhao[3], L.F. Hui[4], W.M. Xi[1]

[1] The Bioengineering Department of life science and technology college, Xi"an Jiao Tong University, Xi'An , China
[2] The Second Affiliated Hospital & Yuying Children's Hospital of Wenzhou Medical College, Wen Zhou, China
[3] The faculty of foreign languages, Ning Bo University, Ning Bo, China,
[4] Northwest Institute for Non-ferrous Metal Research, Xi'an, China

Abstract — **Objective: The goal of this study was to assess the osseointegration capability of Bone morphogenetic protein-2 and hyaluronic acid on hydroxyapatite-coated porous titanium. Method: Making porous titanium implants by sintering titanium powder at high temperature which were coated with hydroxyapatite by alkali and heat treatment and furthered using hyaluronic acid as delivery system to prolong the effect of Bone morphogenetic protein-2. The implants were inserted into the distal femora of rabbits. The animals were sacrificed in 6, 12 and 24 weeks to accomplish histological and biomechanical analysis. Result: According to the result of histological analysis, the osseointegration of Bone morphogenetic protein-2 group is better than hydroxyapatite -coated porous titanium group. In push-out experiment, all the samples have bigger shear stress as time is passing by. There is statistical difference between two groups in 6, 12 weeks but not in 24 weeks. Conclusion: Bone morphogenetic protein-2 and hyaluronic acid on hydroxyapatite-coated porous titanium has a good effect on repairing the defect of distal fumer in rabbit. It is a kind of fine biotechnology for future clinical application.**

Keywords — **Porous titanium, BMP-2, Hydroxyapatite, Osteointegration, Hyaluronic acid**

I. Introduction

Since Urist discovered bone morphogenetic protein[1], studies have kept focusing on many kinds of bone growth factors and the delivery systems. A multitude of studies have proved that TGF-β, IGF-I, BMP-3 and BMP-7 could facilitate bone formation[2-5]. But BMP-2 is the most powerful bone growth factors as we all know. It can induce undifferentiated mesenchymal cells to propagate and differentiate, so much more attention is paid to it[6,7]. Meanwhile some biomaterial, such as hydroxyapatite, coral, cancellated bone and collagen etc, can combine with bone growth factors to facilitate bone formation because of dual effects of bone conduction and bone induction[8-11]. At present titanium alloy implants with porous coat could be produced by many technologies. This makes it possible that new bone can grow into pore to improve the strength of synosteosis by mechanical lock between the interface of bone and implant[12] and to prolong the action time of bone growth factor. Some researchers have discovered that hyaluronic acid has good biocompatibility, can fill in porous structure, facilitate cell adhesion and won't disturb regional osteanagenesis. So it is a good retarder to guarantee long-time effective concentration of BMP-2[13]. This research made some composite implants which have three-dimensional structure, bone conduction and bone induction ability by using hydroxyapatite-coated porous titanium combined with BMP-2, Hyaluronic acid as retarder. The implants were fixed into distal femurs of rabbits to accomplish histological and biomechanical analysis.

II. Materials and methods

A. Implants and surface analysis

The size of porous titanium implants is ø4×10mm. Samples were immersed in 5.0mol/l NaOH aqueous solution at 60°C for 24h respectively. Washed with distilled water and dried in air for 24h, the samples were heated in an electrical furnace at heating rate of 5°C/min and kept at 600°C for 1h and cooled with the furnace. Subjected to alkali-heat, the samples were put in 0.5 mol/L Na2HPO4 for 24h, then saturated Ca(OH)2 for 5h. Washed with distilled water. Soaked in 30ml simulated body fluid (SBF) at 36.5°C to get hydroxyapatite coat. SBF was refreshed every 48h and prepared with ion concentrations nearly equal to those of the human blood plasma, and buffered at pH=7.40 with Tris-HCl at room temperature. The samples were taken out after 28 days respectively and washed with distilled water and dried in air. Titanium samples were cleaned ultrasonically in acetonee, ethanol and distilled water for 20 min respectively. Then put half of the implants in the tooting respectively. Blend BMP-2 and hyaluronic acid at the ratio of 8mg/g under aseptic conditions and dissolve in buffered sodium chloride solution. Soak the samples in and pump to vacuum under negative pressure. Take them out after fixiform. Finally hydroxyapatite-coated porous titanium carrying about 12μg BMP-2 were obtained. Observe it with SEM(JSM – 35C, HITACHI) under different enlargement.

Chwee Teck Lim, James C.H. Goh (Eds.): ICBME 2008, Proceedings 23, pp. 1680–1683, 2009
www.springerlink.com

B. Animals and surgery

All experiments on animals were performed under the approval of the institutional review board. The implants were inserted into bilateral distal femora of 36 adult rabbits (New Zealand, body weight > 3.5 kg). The porous coated-hydroxyapatite implant was inserted press-fit into the femur. Each animal received one implant carrying about 12μg BMP-2 (group I). A hydroxyapatite-coated porous implant was placed as a control in the contralateral femur in the same manner (group II). Wounds were closed in layers. Bred in the same condition.

C. Implant retrieval and evaluation

Euthanasia was performed by using carbon dioxide after 6, 12, or 24 weeks. Following euthanasia, the implants with their surrounding tissue were retrieved and prepared for histological (n = 6 for each material and time period) and Mechanical analysis (n = 6 for each material and time period).

D. Histology

The histological samples were fixed in 4% phosphate buffered formaldehyde solution (pH = 7.4), dehydrated in a graded series of ethanol, and embedded in methylmethacrylate. Following polymerization, 10-μm thick sections were prepared per implant using a modified sawing microtome technique. Before sections were made, the specimens were etched with hydrochloric ethanol for 15s, stained with methylene blue for 1 min, and stained with basic fuchsin for 30s. The prepared sections were examined under a light microscope. Before sacrificed, three animals were injected subcutaneously with a fluorescent tetracyclin (25 mg/kg body weight, Merck, Darmstadt, Germany) five days in order to label the process of bone formation. In addition to the thin sections described above, two additional 30-μm thick sections were prepared from the samples of the three animals that received fluorochromes. These sections were not stained but evaluated with a fluorescence microscope equipped with an excitation filter of 470-490 nm. The light and fluorescent microscopic assessment consisted of a complete morphological description of the tissue response to the different implants. In addition, quantitative information was obtained on the amount of bone formation into the various mesh implants.

E. Mechanical testing

Soft tissues covering the bones were removed by using a scalpel blade from freshly excised specimens. The specimens containing implants were scoured to a flat surface, perpendicular to the implant long axis.The specimens were stored in physiological saline solution until mechanical evaluation, which was performed within 2 h after retrieval. The pull-out tests were conducted on a material testing machine (Instron 1185) linked to a computer at the speed of 1mm/min to test the shear stress. The interface shear strength was calculated by the following formula:

$$\sigma = \frac{F}{\pi dt}$$

σ = shear strength; F = max load when collapse; d = diameter of the specimen; t =height of the specimen

III. Result

A. Scanning electron micrograph

The particle of hyaluronic acid with BMP-2 was uniformly mixed and distributed over hydroxyapatite-coated porous titanium arranged irregularly. Part of the particle uniformly distributed among the porous titanium as globular or needle could combine with newly formed mixture in multi-punciform or multi-extent. The surface of the particle is exposed except contacted area and there are many irregular fissure 100μrn—200μrn interconnected to each other among them

B. Histology

After 6 weeks' implantation, there were no signs of inflammation and slightly newly formed bone filled in the interface gap of purely hydroxyapatite-coated implants. The interface of soft tissue was obvious. But to BMP-2-coated implants, more newly formed bone could be observed in the interface gap than control group. Bone grew into the cylinder pore and contacted with titanium sphere in some extent. Bone had also been formed along the outer surface of the cylinder. After 12 weeks' implantation, more newly formed bone and obvious reconstruction could be observed in purely hydroxyapatite-coated implants. And more newly formed and completely calcified bone could be obtained in BMP-2-coat group. Bone filled in almost all the gap and even the junction of titanium sphere. After 24 weeks' implantation, newly formed bone filled all the gap in two groups and there was no difference between two groups.

The growth of new bone could be clearly differentiated and recognized by observation of fluorescence microscope. The newly formed bone was deposited initially at the surface and then grew into the pore. Organized bone formation with clear ossification fronts was not observed in any of the implants. In all of the specimens, diffusely stained deposits

of tetracycline (and sometimes calcein) were mainly localized in contact with the Ti fibers

C. Mechanical testing

The results of pull-out test of purely hydroxyapatite - coated implants and BMP-2 groups were listed below. There were 36 implants inserted being prepared for mechanical tests, but 5 implants were excluded because of unexpected death or technical error during preparation or pullout(n=5). There was a significant increase in shear strength over time for all coatings. Shear strength values for the BMP-2-coated implants were higher than the HY-coated implants at 6 and 12 weeks($p < 0.05$). But at 24 weeks there were no significant statistical differences between two groups.

IV. Discussion

At present, many new researches about bony tissue and engineering focus on precursor cell of bone formation, implants and bone growth factor. Studies show that marrow stroma cells have the ability of multi-directional differentiation and bone formation, but the results of implantation were not the only as expected. Some studies show that combined MSC with HA or BMP-2 could improve the ability of bone formation greatly. It proved that good implantation with growth factor and MSC could get the best effect of bone formation[2-11] because it could gain better interface of impaction and sooner healing. The pattern of binding between bone and implantation is the major criterion to judge the biocompatibility and bioactivity. There might be some fibrae encyst of different thickness formed around the implantation with negative biocompatibility and thickening by the time. Eventually fluidify, inflammation or necrosis occurred between implantation and encyst could cause loosening or displacement leading to abortive implantation. Lamellate fibrous tissue formed on the interface between implantation and bone soon after insertion of titanium. It becomes thinning by time-lapse and does not lead to some adverse effect such as inflammation. Ideal synosteosis is direct osseo-integrate on the interface of implantation and bone. After implantation, environmental newly formed osteoblast leads to obvious bone formation, so compact direct osseo-integrate is getting sooner and better immediate union[14,15]. All these require implantations to have better bone tissue biocompatibility and bioactivity including bone conductivity and osteoinductive[16].

6 weeks later the cylinders of porous titanium is treated by alkali-heat were inserted, newly formed bone being observed on the interface and direct osseo-integrate being obtained to speed up healing of porous titanium means that hydroxyapatite coating could lead to bone formation satisfactorily because of its good biocompatibility.

The growth of bone after implantation of porous titanium was due to its surface structure, porous framework, survival ability of bony bed of host, coating with bioactivity and reconstruction of environmental bone. The rough surface of porous titanium could provide good interface for bone growth[17,18]. Studies showed that the tiniest diameter of pore which required bone growth in environmental and good blood supply was 100μm. Experimental result of cell culture in vitro showed hydroxyapatite coating could help osteoplast to adhere on the surface of implantation, to proliferate and diffuse. Meanwhile, Liang Huifang et al proved that bone formation of implants with hydroxyapatite coating was faster than those without whether on the surface and in the pores in vivo. Copious athletic osteoblast around the coating form new woven bone, which made it easier to grow into the pores, maturate and reconstruct. Hydroxyapatite coating also can eliminate the shield of stress caused by porous structure which allow new bone to form along the surface of porous structure to inner part even the impaction of titanium globular, so more direct conjunctive interface is obtained. All above can speed up the healing of porous titanium and bone tissue, profit stabilization of early period. It does benefit a lot to the recovery of bone defect, the fusion of vertebra and arthro-replacement.

There are three essential pacing factors for mesenchymal cells to induce bone formation: inducing factor, target cells and eligible environment. BMP-2 as inducing factor could stimulate the genes with effect of bone formation to express which cause the differentiation of mesenchymal cells. The target cells of BMP-2 include undifferentiated mesenchymal cells existing in muscles and connective tissue around blood vessels, marrow stroma cells including determined osteogenic precursor cell(DOPC) and inducible osteogenic precursor cell (IOPC) and connective tissue cell in periosteum. Marrow stroma cells are more sensitive to BMP-2 than others[17]. Studies showed that imbed marrow stroma cells origin from autologous bone marrow in bone defect could enhance the inducing ability of BMP-2 greatly[19,20]. It is not the truth that induction happens everywhere BMP-2 imbedded, but the induction of BMP-2 requires favorable environment, the strongest in bone marrow, muscles and brain tissue, the weakest in spleen, liver and kidney et al. This research showed that hydroxyapatite coating could enhance the combination of bone and implants, but the effect was not so satisfactory.as that in 6 weeks BMP-2 imbedded. More bone formation and osseo-integrate were observed than purely hydroxyapatite-coated implants especially the inner part of porous titanium to urge speeding up of healing. All these means BMP-2 has a good effect of

induction and can further to enhance the effect of hydroxyapatite –coating.

There are four breaking patterns between bone and implants: implants and tissue, woven bone and mature bone, in the mature bone and in the coating fracture face through the coating not on the face of bone. The rough surface of porous titanium could provide more interface for apposition growth. Porous structure could complicate the interface of bone and titanium and diffuse the strength on the surface including shear strength, pressure and tensile force etc. The internal inlaying locking due to above could obtain more conjunctive strength than some coating on the smooth surface[21]. And if added hydroxyapatite–coating to porous titanium, bigger conjunctive strength could be obtained [22]. In this research, direct osseo-integrate was formed between bone and implants. The mechanical inlaying impaction was caused by newly formed bone in the pore and the gradient structure between coating and implants enhanced conjunctive strength. According to the results of pull-out test, porous structure and hydroxyapatite–coating could promote conjunctive strength in intermediate and long-term stage, but the induction of BMP-2 in the earlier period after implantation could not be ignored. Newly formed bone could early grow into pores and form mechanical inlaying impaction. The results might be influenced by the position of pedestal(the distance of inner edge and interface of bone and implatation) in this research. Besides this, the size of titanium powders, surface roughness, the way making coating and the thickness might influence the results too.

V. Conclusions

Bone morphogenetic protein-2 and hyaluronic acid on hydroxyapatite-coated porous titanium has a good effect on repairing the defect of distal fumer in rabbit. It is a kind of fine biotechnology for future clinical application.

References

1. Urist MR. Bone: formation by autoinduction. Science, 1965,150:893–899.
2. Kandziora F, Scholz M, Pflugmacher R, et al. Experimental fusion of the sheep cervical spine. Part II: Effect of growth factors and carrier systems on interbody fusion. Chirurg, 2002,73(10):1025-38.
3. Hiller T, Pflugmacher R, Mittlmeier T, et al. Bone morphogenetic protein-2 application by a poly(D,L-lactide)-coated interbody cage: in vivo results of a new carrier for growth factors.J Neurosurg, 2002,97(1 Suppl):40-8.
4. Lind M, Overgaard S, Jensen TB, et al. Effect of osteogenic protein 1/collagen compositecombined with impacted allograft around hydroxyapatite-coated titanium alloy implants is moderate. J Biomed Mater Res,2001,55:89 –95.
5. Esenwein SA, Esenwein S, Herr G, et al. Osteogenetic activity of BMP-3-coated titanium specimens of different surface texture at the orthotopic implant 5bed of giant rabbits. Chirurg,2001,72:1360 –1368.
6. Yan MN, Tang TT, Zhu ZA,et al. Effects of bone morphogenetic protein-2 gene therapy on the bone-implant interface: an experimental study with dogs.J Zhonghua Yi Xue Za Zhi, 2005,85:1521-1525.
7. Sachse A, Wagner A, Keller M,et al. Osteointegration of hydroxyapatite-titanium implants coated with nonglycosylated recombinant human bone morphogenetic protein-2 (BMP-2) in aged sheep.J Bone, 2005,37:699-710.
8. Kusakabe H, Sakamaki T, Nihei K,et al. Osseointegration of a hydroxyapatite-coated multilayered mesh stem.J Biomaterials, 2004,25:2957-2969.
9. Kim HW, Lee EJ, Jun IK, et al. On the feasibility of phosphate glass and hydroxyapatite engineered coating on titanium. J Biomed Mater Res A, 2005,75:656-67.
10. Li LH, Kim HW, Lee SH, et al. Biocompatibility of titanium implants modified by microarc oxidation and hydroxyapatite coating. J Biomed Mater Res A, 2005,73:48-54.
11. Coathup MJ, Blackburn J, Goodship AE, et al. Role of hydroxyapatite coating in resisting wear particle migration and osteolysis around acetabular components. Biomaterials, 2005,26:4161-9.
12. Takemoto M, Fujibayashi S, Neo M, et al.Mechanical properties and osteoconductivity of porous bioactive titanium. Biomaterials, 2005,26:6014-23.
13. Aebli N, Stich H, Schawalder P, et al.Effects of bone morphogenetic protein-2 and hyaluronic acid on the osseointegration of hydroxyapatite-coated implants: an experimental study in sheep. J Biomed Mater Res A, 2005,73:295-302.
14. Dorr LD, Wan Z, Song M, et al.Bilateral total hip arthroplasty comparing hydroxyapatite-coating to porous-coated fixation.JArthroplasty,1998,13:729-36.
15. Tanzer M, Kantor S, Rosenthall L, et al. Femoral remodeling after porous-coated total hip arthroplasty with and without hydroxyapatite-tricalcium phosphate coating: a prospective randomized trial. J Arthroplasty, 2001,16(5):552-8.
16. Hench LL. Bioactive ceramics: Theory and clinical applications. In: Bioceramics (Eds. Andersson ÖH, Happonen RP, and Yli-Urpo A), Pergamon. Oxford,1994,3-14.
17. Popa C, Simon V, Vida-Simiti I, et al. Titanium--hydroxyapatite porous structures for endosseous applications. J Mater Sci Mater Med, 2005,16(12):1165-71.
18. Simon M, Lagneau C, Moreno J, et al. Corrosion resistance and biocompatibility of a new porous surface for titanium implants. Eur J Oral Sci, 2005 ,113(6):537-45.
19. Knabe C, Howlett CR, Klar F, et al. The effect of different titanium and hydroxyapatite-coated dental implant surfaces on phenotypic expression of human bone-derived cells. J Biomed Mater Res A, 2004,71(1):98-107.
20. Minamide A, Yoshida M, Kawakami M, et al. The use of cultured bone marrow cells in type I collagen gel and porous hydroxyapatite for posterolateral lumbar spine fusion. Spine, 2005,30(10):1134-8.
21. Fujisawa A. Investigation for bone fixation effect of thin HA coated layer on Ti implants. Kokubyo Gakkai Zasshi, 2005,72(4):247-53.
22. Kold S, Rahbek O, Zippor B, et al. No adverse effects of bone compaction on implant fixation after resorption of compacted bone in dogs. Acta Orthop, 2005 ,76(6):912-9

Landing Impact Loads Predispose Osteocartilage To Degeneration

C.H. Yeow[1], S.T. Lau[1], Peter V.S. Lee[1,3,4], James C.H. Goh[1,2]

[1] Division of Bioengineering, National University of Singapore, Singapore
[2] Department of Orthopaedic Surgery, National University of Singapore, Singapore
[3] Biomechanics Lab, Defence Medical and Environmental Research Institute, Singapore
[4] Department of Mechanical Engineering, University of Melbourne, Australia

Abstract — **Knee osteoarthritis is a prevalent disease worldwide and is characterized by progressive degeneration in structure and functionality of the articular cartilage. While it is widely suggested that activities involving large landing impact loads may lead to post-traumatic osteoarthritis, there is little understanding on whether these loads can inflict cartilage lesions and trigger degeneration. This study sought to investigate whether landing impact loads applied to the osteocartilage will render it towards degeneration. Menisci-covered and exposed osteochondral explants were extracted from tibial cartilage of fresh porcine hind legs and placed in culture for up to 14 days. A single 10-Hz haversine impact compression was performed at Day 1. Control (non-impact) and impacted explants were randomly selected for cell viability, glycoaminoglycan and collagen content assessment, histology, immunohistochemistry and micro-computed-tomography. When 2-mm displacement compression was applied, exposed explants attained a considerably greater peak impact stress than menisci-covered explants. There was no observable difference in cell viability, glycoaminoglycan and collagen content, and Mankin scores between menisci-covered and exposed explant groups. Both groups were noted with diminished proteoglycan and type II collagen staining at Day 14; the exposed group indicated increased cartilage volume at Day 7-14. Large landing impact loads can introduce structural damage to the osteocartilage, which leads to osteoarthritis-like degenerative changes. The inferior resilience of menisci-covered regions, against impact-induced damage and degeneration, may be a key factor involved in the meniscectomy model of osteoarthritis.**

Keywords — **Osteoarthritis, compressive impact, degeneration, damage, menisci**

I. Introduction

Knee osteoarthritis (OA) is a prevalent joint disease worldwide, with almost 1 in 3 adults displaying OA symptoms in the United States.[1] Post-traumatic OA can occur following sports injuries incurred during high-impact activities such as gymnastics and basketball. Therefore, impact trauma is a potential risk factor for joint degeneration and early-onset OA.[2] Huser and Davies[3] and Mrosek et al.[4] found that impact trauma on cartilage led to release of glycoaminoglycans (GAG), chondrocytic death, and diminished type II collagen and aggrecan expressions, which are characteristic of OA. However, the loading conditions adopted in these studies were inadequate for simulating landing impact. Different cartilage regions have varying resistance to loading. Thambyah et al.[5] demonstrated that menisci-covered cartilage was thinner than exposed cartilage by 40%, and possessed substantially lower subchondral bone quantity and calcified layer thickness. Furthermore, Yeow et al.[6] noted that exposed regions did not incur more damage than neighboring menisci-covered regions during simulated landing impact of the knee joint. Altogether, these studies suggested that exposed cartilage regions are more capable of load-bearing than menisci-covered regions. However, it is not well understood whether these regions may be different in their susceptibility to degeneration. This study sought to investigate whether landing impact loads applied to the osteocartilage will render it towards degeneration. We hypothesized that impacted menisci-covered regions are more vulnerable to structural damage and more inclined towards degeneration relative to exposed regions.

II. Methods

A. Specimen preparation and impact procedures

Fresh porcine hind legs (pig age: ~2 months old; weight: ~40 kg) were obtained from a local abattoir (Primary Industries, Singapore). Osteochondral explants (4-mm diameter; 7-mm height) were extracted from menisci-covered and exposed tibial cartilage regions at Day 0, and incubated at 37°C and 5% CO_2 for up to 14 days in Dulbecco's Modified Eagle's Medium (DMEM) (Gibco, Switzerland) supplemented with 1 g/L L-glutamine, 10 mg/mL streptomycin sulfate, 10,000 units/mL penicillin G sodium and 10% (v/v) fetal bovine serum (Sigma-Aldrich, US). A 30-mm-diameter compression plate was attached to the material testing system (810-MTS, MTS Systems Corporation, USA) to apply impact compression, which was displacement-controlled at 2-mm based on a single 10-Hz haversine loading curve to simulate landing impact.[6] Dental cement (Base-liquid and powder, Dentsply, China) was used to secure the explant in the potting cup. Each explant was immersed in medium and a 10-N pre-loading was applied by adjusting

Chwee Teck Lim, James C.H. Goh (Eds.): ICBME 2008, Proceedings 23, pp. 1684–1687, 2009
www.springerlink.com

the MTS actuator to allow contact between compression plate and explant. Impact compression was conducted on Day 1; peak impact stress was obtained from the peak compressive load, measured by the attached load-cell (9347B, Kistler, Switzerland), divided by explant cross-sectional area. Control (non-impact) and impacted explants were randomly selected for cell viability, GAG and collagen content assessment, histology, immunohistochemistry and micro-computed-tomography (MicroCT).

B. Cell viability, GAG and collagen content assessments

To quantify cell viability, explants were incubated for 30min in 2ml of medium containing 0.1% fluorescein diacetate, 0.05% propidium iodide (Sigma-Aldrich, US). Confocal fluorescence imaging (LSM510 META, Carl Zeiss, Germany) was performed using excitation wavelength of 488nm (green) and 543nm (red) to visualize surface live and dead cells. Pixel area fractions of viable green and non-viable red cells were measured using ImageJ (Version 1.4, National Institute of Health, US). To assess GAG and collagen content, cartilage was detached from the explant using a microtome blade, and measured for wet weight before immersing in 1ml of 0.025% pepsin in acetic acid for 1 week to permit degradation. The resultant solution was extracted for content assessment using Blyscan sulfated glycosaminoglycan assay and Sircol soluble collagen assay (BioColor Ltd, UK) respectively. These colorimetric assays allowed quantification by analyzing absorbance values of GAG- or collagen-bound dyes using a spectrophotometer, where wavelengths of 656nm and 540nm were used respectively.

C. Histology and immunohistochemistry (IHC)

Explants were fixed in 10% buffered formalin for 1 week and decalcified in 30% formic acid for 2 weeks. They were then dehydrated and progressively cleared in ethanol and toluene before embedding in paraffin. 10-μm slices were then obtained using a microtome (RM2255, Leica Microsystems, Germany), and were deparaffinized and stained using Hemotoxylin & Eosin and Safranin-O/Fast Green staining protocols to visualize osteochondral structure, cell distribution and proteoglycan distribution. Three independent observers were trained to grade the photomicrographs using Mankin scoring system; they were blinded against control and impact groups to eliminate bias. Additional histological slices were obtained for IHC analysis (Ultravision Detection System, LabVision Corp, USA). The slices were labeled with primary monoclonal anticollagen type II antibodies (Chemicon International, US), prepared at a dilution of 1:200, overnight at 4°C. Biotinylated goat anti-mouse secondary antibodies were then applied at 1:200 for 30min, followed by addition of strepavidin peroxidase for 45min and chromagen-substrate solution for 3min at 37°C.

D. MicroCT

Explants were scanned using MicroCT scanner (SMX-100CT, Shimadzu, Japan) with the following settings: X-ray voltage (32kV), current (115μA), detector size (5”), scaling coefficient (100) and pixel spacing (14.3μm/pixel). The scans were reconstructed to obtain 3D explant geometry using VGStudioMax (Version 1.2, Volume Graphics, Germany). The cartilage was segmented based on a consistent set of threshold gray-values (20086-24334), which permitted a fair demarcation of cartilage region from underlying bone. Cartilage volume of each explant was then measured to examine volume change over time.

E. Statistical analysis

Student’s t-test (SigmaStat 3.1, SysTat Software Inc, USA) was used to compare between control and impacted explants for cell viability, GAG and collagen content, Mankin scores and cartilage volume. Normalization was based against control menisci-covered explants at Day 0/1. All significance levels were set at $p=0.05$.

III. Results

There was a notable difference ($p<0.001$) in peak compressive stresses between menisci-covered and exposed explants (Fig. 1). Substantial cell death ($p<0.05$) was noted post-impact in menisci-covered explants at Day 1 and 14, and exposed explants at Day 1 and 7. No significant difference was observed between impacted explants from both regions at all time-points. For GAG content, we noticed a gradual reduction for menisci-covered and exposed impacted explants over time (Fig. 2).

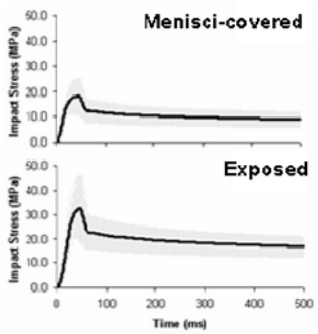


Fig. 1 Load responses of menisci-covered and exposed explants during 2-mm displacement compression

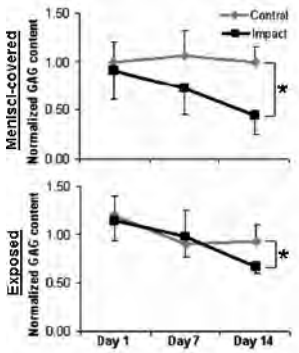


Fig. 2 Comparison of normalized GAG content between menisci-covered and exposed explants over time



Fig. 3 Structural damages observed in menisci-covered impacted explants at different time-points

The major difference ($p<0.05$) between control and impacted explants was detected at Day 14. A similar profile was seen for collagen content between control and impact groups with significant difference ($p<0.05$) at Day 14. No considerable difference was observed for GAG and collagen content between menisci-covered and exposed impacted explants across all time-points. For histology, we found that most menisci-covered and exposed explants sustained surface fraying and irregularities. Clefts in intermediate zones and tidemark disruption were also present (Fig. 3); hypocellularity was observed for impacted explants at Day 14. Marked reduction in proteoglycan staining was noted for menisci-covered and exposed impacted explants at Day 14, especially at the deep zone.

We also found a substantial reduction of type II collagen staining at Day 14 throughout the cartilage. We obtained considerably larger Mankin scores ($p<0.05$) for impacted explants than control explants. Substantial increase in Mankin score was observed for menisci-covered explants from Day 0-7 ($p<0.05$) and from Day 7-14 ($p<0.001$) but the score was only significantly increased from Day 7-14 ($p<0.05$) for exposed explants. Scores between menisci-covered and exposed impacted explants were not substantially different. The cartilage volume increased for exposed explants post-impact at Day 7 and 14 ($p<0.05$) compared to Day 0. For menisci-covered explants, the cartilage volume increased slightly at Day 1 and decreased at Day 7-14. However, the cartilage volume for exposed explants appeared to be elevated at Day 1 and increase further at Day 7-14. The reconstructed 3D geometry of the explants illustrated a change in surface cartilage morphology over time (Fig. 4).



Fig. 4 Comparison of explant surface geometry between menisci-covered and exposed explants pre- and post-impact

IV. Discussion

This study sought to investigate whether landing impact loads applied to the osteocartilage will render it towards degeneration. Previous studies demonstrated impact stresses of 20-30MPa could damage cartilage and underlying bone.[7,8] In our study, we noted a peak compressive stress of 20.2-34.9MPa for menisci-covered and exposed explants when subjected to 2-mm displacement compression. We also observed damage such as matrix disruption at superficial and intermediate zones, and tidemark lesions. For degenerative changes, there was a gradual increase in cartilage volume and diminished GAG content up to Day 14. A significant presence of surface cartilage cell death was noted post-impact up to 14 days. Our microCT scans revealed a visible change in surface cartilage morphology over time for pre- and post-impact explants, indicating impact damage, cartilage swelling and surface degradation. Our study revealed different load responses of menisci-covered and exposed explants when subjected to the same 2-mm compression. Thambyah et al.[5] showed that exposed regions possess a significantly larger cartilage thickness and subchondral bone density compared to menisci-covered regions. These factors may contribute in part to a higher overall stiffness in exposed explants, hence these explants will experience greater peak compressive impact stress, relative to menisci-covered explants. We did not obtain major differences between menisci-covered and exposed impacted explants for cell death, GAG and collagen content, and Mankin scores. This showed that though exposed explants generally sustained a higher impact load and the same mag-

nitude of compressive deformation, the damage and degenerative changes following impact was not substantially different relative to menisci-covered explants, which strongly reflects the superior capacity of exposed regions in resisting trauma-induced damage and degeneration. We also noticed elevated cartilage volume for exposed explants. Cartilage swelling may be due to the diminished capability of disrupted collagen network to counteract proteoglycan-induced swelling pressure.[9] Our data may suggest that the lower compressive load experienced by menisci-covered explants may lead to reduced collagen network damage, thus less swelling relative to exposed explants.

One limitation of this study was the use of a porcine model to investigate post-traumatic osteochondral damage profile. The porcine model minimized sample variability as they were derived from a common source. The daily activities performed by pigs are considerably more sedentary compared to humans, hence their knees do not normally sustain high impact or have a history of knee injury. Thus, we expect that the model to be suitable as control and impacted specimens. Another limitation was the use of culture medium to maintain explant viability. It would be ideal to use the synovial fluid to simulate physiological condition of the knee during landing impact, but due to the complex components present in synovial fluid which may complicate analysis, we thus used the standard culture medium as a simplified substitute, with appropriate osmolarity (280mOsm), pH (7.4) and supplement concentrations, to maintain tissue viability and understand the direct effect of landing impact on osteochondral damage and degeneration.

V. Conclusions

Our findings collectively illustrated that menisci-covered osteochondral regions have inferior load-bearing capacity and resilience to damage and degeneration, relative to their exposed counterparts. Meniscectomy will expose menisci-covered regions and increase risk of damage and degeneration in these regions. Our results revealed that these regions were prone to traumatic damage and also more susceptible to degeneration. The inferior resilience of menisci-covered regions, against impact-induced damage and degeneration, may be a key factor in the meniscectomy model of OA.

Acknowledgment

This work was funded by the grant ‘R175-000-062-112: Construction and validation of a dynamic 3D Finite Element (FE) model of the tibio-femoral joint’ from the Academic Research Fund, Singapore. It is also co-supported by the Defence Medical and Environmental Research Institute and the International Society of Biomechanics.

References

1. Birchfield PC (2001) Osteoarthritis overview. Geriatric Nursing 22:124-131.
2. Vignon E., Valat J-P, Rossignol M, et al. (2006) Osteoarthritis of the knee and hip and activity: a systematic international review and synthesis (OASIS). Joint Bone Spine 73:442–455.
3. Huser CA, Davies ME (2006) Validation of an in vitro single-impact load model of the initiation of osteoarthritis-like changes in articular cartilage. J Orthop Res 24:725-32.
4. Mrosek EH, Lahm A, Erggelet C, et al. (2006) Subchondral bone trauma causes cartilage matrix degeneration: an immunohistochemical analysis in a canine model. Osteoarthritis Cartilage 14:171-178.
5. Thambyah A, Nather A, Goh J (2006) Mechanical properties of articular cartilage covered by the meniscus. Osteoarthritis Cartilage 14:580-8.
6. Yeow CH, Cheong CH, Ng KS, et al. (2008) Anterior cruciate ligament failure and cartilage damage during knee joint compression: a preliminary study based on the porcine model. Am J Sports Med 36:934-42.
7. D'Lima DD, Hashimoto S, Chen PC, et al. (2001) Impact of mechanical trauma on matrix and cells. Clin Orthop Relat Res 391:S90-9.
8. Haut RC (1989) Contact pressures in the patellofemoral joint during impact loading on the human flexed knee. J Orthop Res 7:272-80.
9. Loening AM, James IE, Levenston ME, et al. (2000) Injurious mechanical compression of bovine articular cartilage induces chondrocyte apoptosis. Arch Biochem Biophys 381:205-12.

Corresponding Author:

Author: James Goh Cho Hong
Institute: National University of Singapore
Street: 27 Medical Drive, Singapore 117510
City: Singapore
Country: Singapore
Email: dosgohj@nus.edu.sg

Drug Addiction as a Non-monotonic Process: a Multiscale Computational Model

Y.Z. Levy[1], D. Levy[2], J.S. Meyer[3] and H.T. Siegelmann[1]

[1] Laboratory of Biologically Inspired Neural and Dynamical Systems (BINDS), University of Massachusetts Amherst, USA
[2] Department of Neurobiology, The Weizmann Institute of Science, Rehovot, Israel
[3] Laboratory of Developmental Neuropharmacology, University of Massachusetts Amherst, USA

Abstract — **Addiction is considered a "bio-psycho-social-spiritual disorder" [1] for which complete recovery cannot be assured. Although addiction was computationally characterized as a non-reversible process [2,3], behavioral evidences support the possibility of recovery [4, 5, 6,7].**

We thus propose to consider addiction as a non-monotonic dynamical disease. Previously, we presented a multiscale computational model that combines three scales of observations: behavior, cognition, and neuropsychology. This model evaluates the drug-seeking behavior in virtual subjects.

We use our model to analyze dynamical properties of two typical virtual subjects. One has become an addict at the age of 17 and has since expressed a severe multi relapse pattern. The other one was exposed to addictive behavior at age 36 but managed to cease drug seeking. The results are encouraging for further explorations into the individual dynamics in addicts.

Keywords — **Addiction, Multiscale Modeling, Behavioral Processes, Cognition, Neurophysiological Processes.**

I. Introduction

Drug use estimates presented in the United Nations World Drug Report 2008 claim that in 2006/07 about 24.7 million people used amphetamines, 16 million used cocaine, and 12 million used heroin at least once. In an effort to investigate the dynamics of addiction, we propose a computational model that considers addiction as a non-monotonic reversible process [8].

This mathematical framework combines three different scales of observations - *social, cognitive and neuropsychological* – and is hypothesized to predict the outcome of a virtual subject's behavior with respect to drug-seeking behaviors. We analyze two case studies in terms of their tendency to relapse and ability to rehabilitate.

II. Materials and Methods

The multiscale computational model combining neuropsychological (NepS), cognitive (CogS), and behavioral (BehS) scales is shown in Figure 1.

The output G(t) is the severity of the behavioral condition which that we propose to equate with the likelihood of drug-seeking behavior, generated at the BehS. The value G(t) lies in the interval [-1, 1], and we consider the range [-1,0] to correspond to a subject with maladaptive behavior and the range [0,1] to a subject with healthy behavior, both in the probabilistic sense.

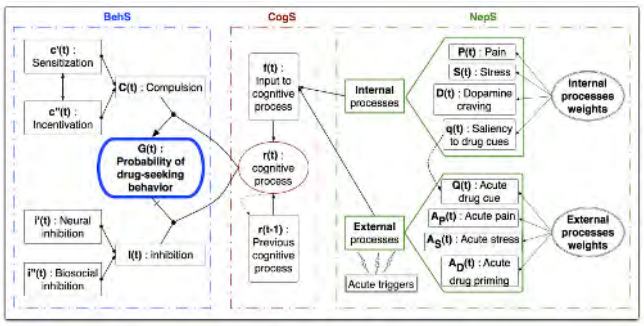


Fig. 1: Addiction model combining neuropsychological (NepS), cognitive (CogS), and behavioral (BehS) scales. The output G(t) is the likelihood of drug-seeking behavior.

The BehS is simply suggested to include the inhibition I(t) and compulsion C(t) functions. This is along the line of the I-RISA model that describes addiction as impaired inhibition (to stop sensory-driven behavior) and salience attribution (with larger interest in drugs than in other possible rewards) [9]. On the one hand, the function G(t) is positively influenced by the inhibition I(t), which by itself combines the inhibition stemming at the subject's neural development of the frontal lobes of the cortex [10, 11, 12] together with the inhibition coming from social rules of this individual. On the other hand, the function G(t) is negatively influenced by the compulsion C(t), which is calculated according to the incentive-sensitization theory of addiction [13,14]. In computing G(t), the balance between I(t) and C(t) is weighted by r(t), the cognitive process, as described in equation (1).

$$G(t) = \left[1 - r(t)\right] \cdot \left(-C(t)\right) + r(t) \cdot I(t) \qquad (1)$$

The cognitive process r(t) is a combination of its previous value r(t-1) and the input to the cognitive process f(t), as described in equation (2). Both functions r(t) and f(t) are computed at the CogS.

Chwee Teck Lim, James C.H. Goh (Eds.): ICBME 2008, Proceedings 23, pp. 1688–1691, 2009
www.springerlink.com

$$r(t) = \frac{1}{2} \cdot \tanh\left[\alpha \cdot r(t-1) + \beta \cdot f(t) + \gamma\right] + \frac{1}{2} \qquad (2)$$

The input to the cognitive process f(t) is a weighted sum of the internal and external processes. While the exact realistic structure of f is hard to guess, we propose a reasonable model:

$$f(t) = \left[-\omega_S S(t) + \omega_P P(t) - \omega_D D(t)\right] + \left\{\omega_A\left[-A_S(t) + A_P(t) - A_D(t)\right] - \omega_Q Q(t)\right\} \qquad (3)$$

The internal processes are P(t), representing the level of pain or negative consequences in areas such as health or social relations; S(t), representing the level of stress or negative emotional state of the virtual patient; D(t), representing the craving level, based on the dopamine transmission in the Nucleus Accumbens (NAac); and q(t), representing the saliency of drug-associated cues. Intakes of drugs can increase P(t) [15]. The level of S(t) increases during withdrawal periods [16, 17, 18] and may trigger craving [19]. These intakes were shown to affect the level of dopamine in the NAac and the addicted behavior in rats [20, 21] and in humans [22, 23]. The value q(t) increases with repeated drug consumption [24, 25] and weights the affects of drug related cues Q(t) when encountered.

External processes in this model are $A_P(t)$, representing a painful trauma that may cause a virtual patient to stop taking drugs [26, 27]; $A_S(t)$, representing a stressful episode that may lead into instantaneous drug-use [28, 29]; $A_D(t)$, representing drug priming that may cause drug-use [30, 31]; and Q(t), representing a drug-associated cue [32].

Relevant mathematical details are presented in [8].

III. Results

In this section two different case studies of drug-seeking behavior are considered: The profile of GD outlines a continuous relapse pattern of a person who started using drugs at age 17 and has later been unsuccessfully trying to get away from drug-seeking behavior, whereas the profile of VD exhibits a person that has first used drugs close to age 36 and for which the drug-seeking behavior changes from healthy to maladaptive and back to healthy.

The G value of both cases, depicted in Figure 2, is averaged over 10 simulations, having a noise injected in the process. The constants used for both simulations are presented in Table 1. For the presented simulations, the inhibition I(t) of VR was set 33% higher than the one of GD, and the compulsion C(t) of VR was set 60% higher than the one of GD. The initial values of all the signals were chosen randomly in their defined intervals.

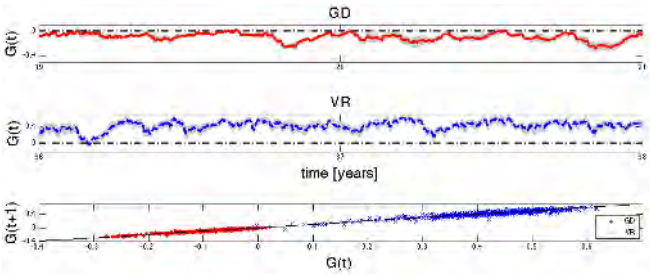


Fig. 2: G(t) means, SEMs and G(t+1) versus G(t) for 10 simulations. At the top, GD's evolution between ages 19 to 21, and at the middle, VD's evolution between ages 36 to 38. At the bottom, G(t+1) against G(t). The diagonal line corresponds to G(t+1) = G(t).

The age intervals considered in Figure 2 are 19 to 21 years old for GD, and 36 to 38 years old for VD. The bottom part of Figure 2 plots the ratio of G(t+1)/G(t). This ratio describes convergence to attractors when the trajectory falls on points with values < 1, and it describes divergence when the points are >1 [33]. We asked whether the dynamic of G is more converging (to addictive or healthy states) or diverging, and found that the trajectories neither converge nor diverge. For GD's profile 229 points of the trajectory had the value < 1 whereas 271 points were > 1. Similarly for VD's profile, 275 points had values < 1 and 225 points were > 1, out of 500 iteration points. The translational meaning is that addiction is a process of intervening parameters in a complex manner: addiction can be affected by external parameters given that they are provided during times of divergence.

Table 1 The values of the constants used in GD and VR simulations.

	Value		Value
alpha	0.15	beta	0.25
gamma	0.2449	S decay for G > 0	0.02
S decay for G < 0	0.02	P decay for G > 0	0.0002
P decay for G < 0	0.1	D decay for G > 0	0.00002
D increase steps	20	D decay for G < 0	0.02
A_S constant steps	20	A_S decay	0.9
A_S probability	0.02	A_S decrease steps	60
A_P decrease steps	20	A_P decay	0.4
A_P probability	0.04	A_P constant steps	10
A_D decrease steps	5	A_D decay	0.2
A_D probability	0.03	A_D constant steps	3
q saliency constant steps	10	q decay for G > 0	0.002
Q constant steps	20	q decay for G < 0	0.005
Q probability	0.01	Q decay	0.9
weight P	1.1	Q decrease steps	40
weight A	0.4	weight S	0.3
weight Q	1	weight D	0.4

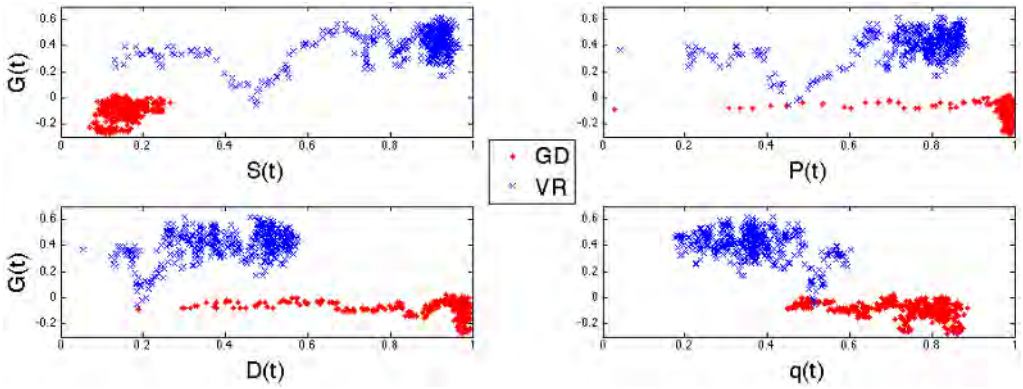


Fig. 3: The internal processes S(t), P(t), D(t), and q(t) plotted against G(t) for GD (red dots) and VR (blue cross).

Next, we asked whether the dynamic behaviors of the individuals differ in fluctuations based on the severity of their addiction. For both simulations, we measured average and standard deviation, and then calculated the integral of the function from its average to measure the consistency of the fluctuations. The values of averages, standards deviation and integrals were (-0.0975, 0.0623, 24.5661) for the more severe case, GD, and were (0.4117, 0.1083, 41.4371) for the lighter case, VR. The addictive person has less fluctuations and flexibility in his drug-seeking behavior that the healthier one, seemingly due to the strong saliency to cues [9].

In Figures 3 and 4 the values of G(t) for GD and VR are plotted against the internal processes and the external processes, respectively. The internal processes affect G, and G affects these processes. The values of S(t) are higher during withdrawal than during use. The values of P(t), D(t) and q(t), on the other hand are higher during drug use. The effect on G by both internal and external events correlates with equations (1), (2), (3).

IV. Conclusions

The dynamical analysis in this paper provides analytical measures to behavioral facts pertaining to addiction. The underlying hypothesis that addiction is a non-monotonic dynamical disease differs from the current state-of-the-art. The effort here is to understand the individual fluctuations in drug seeking behaviors with the future goal of predicting stages of possible treatments and stages of need for extra cautiousness.

The typical case of the more compulsive, less inhibited individual will have an early onset to addiction. His behavior does not fully converge to addictive behavior due to internal and external events that cause him to try a way out; we stress in our model that none of the cases are monotonic. This virtual individual demonstrates numerous efforts to rehabilitate mainly due to pain, and may have short periods of withdrawal, but relapses are fast and overwhelming. The overall flexibility of this subject's behavior is far smaller than the flexibility in the behavioral variables of the less severe case, probably due to the growing saliency to drug cues.

The healthier person, with the stronger inhibition falls into addiction later in life. With similar internal and external events to the other virtual case, this individual rehabilitates. The total flexibility and change in the behavioral parameters is overall much greater than the severely addicted individual, and the actual behavior do not present a relapse pattern.

Both cases demonstrated a behavior that is affected by internal and external events, providing a hope for rehabilitation for people in either situation. A translational application of the model could be the identification of a treatment that given with the right timing will change the effect that the internal and external processes have on the drug-seeking behavior of the individual, and hence ease the process of recovery.

The analyses presented in this work are promising, and we will continue with deeper investigations into the individual dynamics of addiction.

Acknowledgment

We would like to thank Megan Olsen, Gal Niv, Pascal Steiner, Rocco Crivelli, and Fabio Santaniello for their valuable assistance. Scientific suggestions by Rita Goldstein and Nora Volkow were incorporated in this paper, and we are thankful for their advice.

References

1. Interlandi J. (2008). What addicts need. Newsweek, March 3:36–42
2. Redish A. D. (2004). Addiction as a computational process gone awry. Science, 306:1944–7

3. Gutkin B. S., Dehaene S., Changeux J.-P. (2006). A neurocomputational hypothesis for nicotine addiction. Proc Natl Acad Sci U S A, 103(4):106–1111
4. Winick, C. (1962). Maturing out of narcotic addiction. The United Nations Office on Drugs and Crime (UNODC) Bulletin on Narcotics, 1962(1):1–7
5. Sobell L. C., Ellingstad T. P., Sobell M. B. (2000). Natural recovery from alcohol and drug problems: methodological review of the research with suggestions for future directions. Addiction, 95(5):749–764
6. Misch D. A. (2007). "Natural recovery" from alcohol abuse among college students. Journal of American College Health, 55(4):215–218
7. White W. (2002). An addiction recovery glossary: The languages of American communities of recovery. Amplification of a glossary created for the Behavioral Health Recovery Management project
8. Levy Y. Z., Levy D., Meyer J. S., Siegelmann H. T. (2008). Drug Addiction: a computational multiscale model combining neuropsychology, cognition, and behavior. Technical Report UM-CS-2008-34, Department of Computer Science, University of Massachusetts Amherst, September 2008
9. Goldstein R. Z., Volkow N. D. (2002). Drug Addiction and Its Underlying Neurobiological Basis: Neuroimaging Evidence for the Involvement of the Frontal Cortex. Am J Psychiatry, 159(10): 1642–1652
10. Durston S., Thomas K. M., Yang Y., Ulug A. M., Zimmerman R. D., and Casey, B. J. (2002). A neural basis for the development of inhibitory control. Dev Sci, 5(4):F9–F16
11. Leon-Carrion J., Garcia-Orza J., Perez-Santamaria F. J. (2004). Development of the inhibitory component of the executive functions in children and adolescents. Int J Neurosci, 114(10):1291–311
12. Blakemore S.-J. and Choudhury S. (2006). Development of the adolescent brain: implications for executive function and social cognition. J Child Psychol Psychiatry, 47(17):296–312
13. Robinson T. E., Berridge K. C. (1993). The neural basis of drug craving: an incentive-sensitization theory of addiction. Brain Res Rev, 18(3):247–91
14. Robinson T. E., Berridge K. C. (2001). Incentive-sensitization and addiction. Addiction, 96(1):103–14
15. De Alba I., Samet J. H., Saitz R. (2004). Burden of medical illness in drug- and alcohol-dependent persons without primary care. Am J Addict, 13(1):33–45.50
16. Koob G. F., Le Moal, M. (2001). Drug addiction, dysregulation of reward, and allostasis. Neuropsychopharmacology, 24(2):97–129
17. Hodgins D. C., el Guebaly N., Armstrong, S. (1995). Prospective and retrospective reports of mood states before relapse to substance use. J Consult Clin Psychol, 63(3):400–7
18. Aston-Jones G., Harris, G. C. (2004). Brain substrates for increased drug seeking during protracted withdrawal. Neuropharmacology, 47 Suppl 1:167–79
19. Stewart J. (2000). Pathways to relapse: the neurobiology of drug- and stress-induced relapse to drug-taking. J Psychiatry Neurosci, 25(2):125–36
20. Bonci A., Bernardi G., Grillner P., Mercuri N. B. (2003). The dopamine-containing neuron: maestro or simple musician in the orchestra of addiction? Trends Pharmacol Sci, 24(4):172–7
21. Di Chiara G. (2002). Nucleus accumbens shell and core dopamine: differential role in behavior and addiction. Behav Brain Res, 137(1-2):75–114
22. Volkow N. D., Fowler J. S., Wang G. J. (2004). The addicted human brain viewed in the light of imaging studies: brain circuits and treatment strategies. Neuropharmacology, 47 Suppl 1:3–13
23. Volkow N. D., Fowler J. S., Wang G. J., Swanson J. M. (2004). Dopamine in drug abuse and addiction: results from imaging studies and treatment implications. Mol Psychiatry, 9(6):557–69
24. Robinson T. E., Berridge K. C. (2003). Addiction. Annu Rev Psychol, 54:25–53
25. Hyman S. E. (2005). Addiction: a disease of learning and memory. Am J Psychiatry, 162(8):1414–22
26. Bradby H., Williams R. (2006). Is religion or culture the key feature in changes in substance use after leaving school? Young Punjabis and a comparison group in Glasgow. Ethn Health, 11(3):307–24
27. Barth J., Critchley J., Bengel J. (2006). Efficacy of psychosocial interventions for smoking cessation in patients with coronary heart disease: a systematic review and meta-analysis. Ann Behav Med, 32(1):10–20. Am J Psychiatry, 159(10):1642–52
28. Sinha R., Fuse T. Aubin L. R., O'Malley S. S. (2000). Psychological stress, drug-related cues and cocaine craving. Psychopharmacology (Berl), 152(2):140–8
29. Erb S., Shaham Y., Stewart J. (1996). Stress reinstates cocaine-seeking behavior after prolonged extinction and a drug-free period. Psychopharmacology (Berl), 128(4):408–12
30. Spealman R. D., Barrett-Larimore R. L., Rowlett J. K., Platt D. M., Khroyan T. V. (1999). Pharmacological and environmental determinants of relapse to cocaine-seeking behavior. Pharmacol Biochem Behav, 64(2):327–36
31. de Wit H., Stewart, J. (1983). Drug reinstatement of heroin-reinforced responding in the rat. Psychopharmacology (Berl), 79(1):29–31
32. See R. E. (2002). Neural substrates of conditioned-cued relapse to drug-seeking behavior. Pharmacol Biochem Behav, 71(3):517–29
33. Kaplan D., Glass L. (1995). Understanding Nonlinear Dynamics. Springer, New York

Author: Yariv Z. Levy
Institute: Department of Computer Science
Street: 140 Governors Drive
City: Amherst, MA
Country: USA
Email: ylevy@cs.umass.edu

Adroit Limbs

Pradeep Manohar[1] and S. Keerthi Vasan[2]

[1] Sri sairam engineering college/EEE, Anna university, Chennai, India
[2] Sri sairam engineering college/ECE, Anna university, Chennai, India

Abstract — **Necessity is the mother of all inventions. Brain- The Master of our body generates signals in accord with our thoughts and decrees every part to perform the desired actions. This paper is a boon to the amputees since it can decrease their encumber. This paper targets in trapping the signals by the use of Brain wave sensor (Sensors that are attached to the scalp in order to monitor the Brain Wave activity in different parts of the brain) and feed the signals to the so designed artificial hand. Adroit limb is different from the already existing ones. It can encompass activities like peeling; feel things as our normal human hand. The existing models can provide only support but the proposed prototype for this paper can respond to External Stimulus. Brain waves are obtained from a special analysis of EEG (Electro Encephalo Gram). These brain waves show us the brain's response to an external stimulus or event. Brain activity before, during, and after a stimulus presentation is recorded. This allows us to observe where, when, and how the brain responds to a given stimulus.**

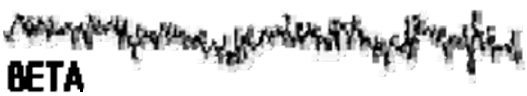
The need for an artificial hand plays a very important role in the life of Amputees and physically challenged. Such people are given an external attachment of an artificial hand which gives a look similar to that of a normal hand which cannot perform all the desired acts. The existing models cannot stimulate actions as per our thought. The signals are directly obtained from the brain without any pre existing sensor for this purpose. The problems faced by the amputees are also increasing day by day. The proposed prototype is a panacea for all such problems faced by them to a greater extent.

Keywords — **Artificial limb, Brain wave controlled, EEG technic, Amputees, Stepper motor**

I. WORKING PROCEDURE

A. WORKING STATE OF BRAIN

BETA STATE: Our brain usually operates at Beta wave state. Around 13 to 40 Hz A person in this state hasacuteconcentration.



ALPHA STATE: Our brain is said to be in alphastateat7to12Hz.



Fig. 1 Alpha

At this state our body and mind relaxes. Our mind reaches the gate way to creativity .

THETA STATE: The frequency in this state is around4to7Hz

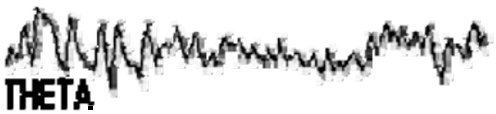


Fig.2 Theta

Our creativity and intuition shoots through the roof and we are approaching the gateway to enhanced learning and memory.

DELTA STATE: In this state a person has magnetic memory and increased learning capability. The frequency of the signal generated by the brain is less than 4 Hz. A person can remember things. .

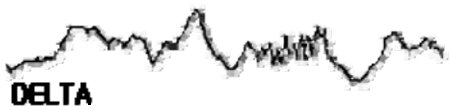


Fig.3 Alpha

B. BLOCK DIAGRAM:

The block diagram of our proposed project can be divided into sections:

Transmitter Section: The signal generated by the brain is captured, processed and finally converted to digital signal for transmission. The transmitter serves this purpose.

Chwee Teck Lim, James C.H. Goh (Eds.): ICBME 2008, Proceedings 23, pp. 1692–1695, 2009
www.springerlink.com

Receiver Section: The processed signals are obtained by the receiving end and the signals are matched with actions that are programmed in the microcontroller and the action as per thought is performed by the proposed prototype.

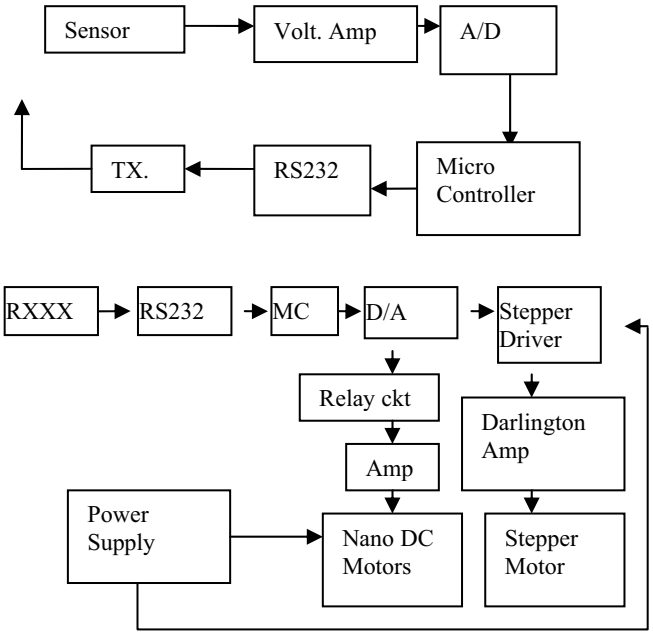


Fig.4 Transmitter and receiver section

C. CIRCUIT DESCRIPTION:

The components mentioned in the block diagram can be explained briefly as follows:

Sensor**:** In order to capture the thought of a person the mind reader/Brain wave sensor is used. **Electroencephalography** (EEG) is the measurement of electrical activity produced by the brain as recorded from electrodes placed on the scalp. In this paper we report the results from first human experiments using a new electrophysiology sensor called **ENOBIO**, using carbon nanotube arrays for penetration of the outer layers of the skin and improved electrical contact. These tests, which have included traditional protocols for the analysis of the electrical activity of the brain--spontaneous EEG and ERP--, indicate performance on a par with state of the art research-oriented wet electrodes, suggesting that the envisioned mechanism--skin penetration--is responsible.

Microcontroller: The micro controller is programmed using mat lab which would be the front end. The microcontroller is programmed for specific actions. So that when the signal generated by the brain is encountered by, it action is performed as per thought. The micro controller works in the range of 4.85 to 5V.It comprises of five ports and eight slots, different programs can be stored in these slots. It is programmed at its ports numbered 18 and 19 where the read and write operation can be performed. The purpose of using MAX232 is for level shifting. The program from the system is encoded in the microcontroller. Voltage amplifier: Because the signal strength of the biological signal is so low, the signal will also have to be amplified via a power amplifier with good SNR. This module modifies the signal in order to drive therestofthedevice.

Converters**:** In order to drive the microcontroller, the signal that is generated by the brain which is in analog formisconvertedtodigitalusingA/Dconverter.

RS232: In telecommunications, *RS-232* (Recommended Standard 232) is a standard for serial binary data signals connecting between a *DTE* (Data terminal equipment) and a *DCE* (Data Circuit-terminating Equipment). It is commonly used in computer serial ports. RS-232 devices may be classified as Data Terminal Equipment (DTE) or Data Communications Equipment (DCE); this defines at each device which wires will be sending and receiving each signal. The RS-232 standard defines the voltage levels that correspond to logical one and logical zero levels. Valid signals are plus or minus 3 to 15 volts. The range near zero volts is not a valid RS-232 level; logic one is defined as a negative voltage, the signal condition is called marking, and has the functional significance of OFF.

Darlington amplifier**:** the Darlington transistor (often called a Darlington pair) is a semiconductor device which combines two bipolar transistors in a single device so that the current amplified by the first is amplified further by the second. This gives a high current gain (written β or h_{FE}), and takes less space than two discrete transistors in the same configuration. Integrated packaged devices are available, but it is still common also to use two separate transistors. A Darlington pair behaves like a single transistor with a high current gain (the product of the gains of the two transistors):

$$\beta_{\mathrm{Darlington}} = \beta_1 \times \beta_2$$

Relays**:** One simple method of providing electrical isolation between two circuits is to place a relay between them.

Stepper motor**:** Since fingers need to perform precise actions. The use of stepper motor is incorporated at the joints. Unlike conventional motor, Stepper motor can perform accurate motions by rotating at specific degrees Stepper motors operate much differently from normal DC motors, which rotate when voltage is applied to their

terminals. Stepper motors, on the other hand, effectively have multiple "toothed" electromagnets arranged around a central gear-shaped piece of iron. The electromagnets are energized by an external control circuit, such as a microcontroller.

D. WORKING:

Brain, the source of all thoughts produces impulses according to the thoughts we make. These impulses are always analog in nature. These analog signals are sent through nerves to all parts of the body. These signals are of constant amplitude and of frequency modulated type. The impulse is of constant amplitude for one thought with varying frequency. For another thought there will be a sharp difference in the amplitude.The energized copper coil produces current. This current activates the printed circuit boards (PCB) at the other end. A transmitter/receiver device placed externally to the body, is connected to the PCB's. The connecting wires are through the tiny hair pores. The transmitter/receiver device, placed externally to the human body now takes the entire command. This acts as a secondary brain outside the body. This device relays the message, according to the information obtained from the brain to the computer or any robot that can act according to the instructions from the device. Also the robot may be connected through a computer. To operate a computer the instructions must be in the form of digital signals. But the brain, as already stated always produces analog signals only. Hence this analog signal has to be converted to machine understandable digital signals. So we incorporate an analog to digital signal converter. The transmission medium from the transmitter/receiver device may be designed according to the convenience. It may be a wire. But wire can be used only up to a limited range. So for the convenience of human radio waves are used for transmission.

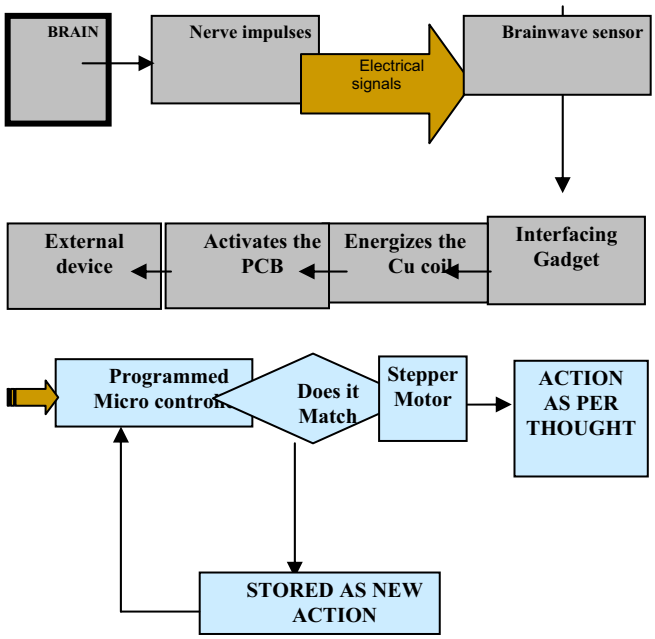


Fig.5 Working

The micro controller is programmed for certain actions to be performed. Any action to be performed is received from the brain. These actions are matched in with the already programmed actions in the micro controller. If the action given in by the brain does not match with the programmed one then it is stored in as a new action. This is in turn fed in to the stepper motor.

E. STAGES OF OUR PROTOTYPE:

First module: The first module in our prototype would be designing the model that will be attached (wrapped) to our hands and movements are made as per our thoughts, the actions produced by the model are viewed in the monitor.

Second module**:** The second module would be developing an artificial hand and making it perform actions as per the thought by fixing it either in the hands of physically challenged or normal people.

Final module: The final outcome would be our objective that is to make the hand perform normal actions such as making it to peel oranges and so on and this will be attached to physically challenged people. Thus it functions similar to normal hands.

F. ADVANTAGES:

Performs action similar to normal hand.Any actions can be performed as per thought. Simple construction and light weight. Capable of performing activities like peeling. Low cost. Respond to external stimulus.

G. DISADVANTAGES:

Subjected to battery weakness. Cannot lift heavy objects. Restricted not to do few actions.

II. Conclusion:

This paper is for the physically challenged people who love to live like the ordinary men and women they can perform all works in a much effective manner than a normal human. This technology definitely is a boon to special community.

References

1. www.dailymail.co.uk
2. www.ieeeexplore.ieee.org/ie15/10678/33710/01694113.pdf?arnumber=1604113
3. http://courses.ece.uiuc.edu/ece445/projects/fall2006/project9_proposal.doc
4. www.national academy of sciences.com
5. www.cnnnews.com
6. www.bbc.com
7. Electronics For You.(edition:may2006)

A Mathematical Model to Study the Regulation of Active Stress Production in GI Smooth Muscle

Viveka Gajendiran[1] and Martin L. Buist[1]

[1] Division of Bioengineering, National University of Singapore, Singapore

Abstract — **In the gastrointestinal (GI) system, motility is governed by the contraction and relaxation of smooth muscle (SM) in response to many regulatory factors. SM in a hollow organ like stomach exhibits two types of contraction: tonic, to maintain the shape of the organ, and phasic, in response to neurotransmitters, hormones or other signaling molecules. Motility disorders such as dysphagia, gastroesophageal reflux disease, irritable bowel syndrome and hypotensive or hypertensive disorders all involve abnormal SM function. Hence, it is important to gain a deeper understanding of contraction and its regulation in GI SM cells. Skeletal muscle cells have force-velocity curves in which shortening velocities are determined only by load and the myosin isoform. In contrast, when smooth muscle activation is altered, e.g. by changing a hormone or agonist concentration, a different set of velocity-stress curves can be obtained. This difference is due to the regulation of both the number of active cross bridges (determining force) and their average cycling rates (determining the velocity). The regulatory system depends on the phosphorylation of cross-bridges, which in turn depends on cytosolic Ca^{2+} levels. Thus, a model has been proposed to study the effects of (a) Ca^{2+} concentration on the kinetics of myosin phosphorylation, (b) cross-bridge cycling rates, and (c) the latch state on tonic and phasic contractions. The objective of the model is to describe the regulation of myosin phosphorylation and active stress production in terms of the intracellular Ca^{2+} concentration. A mathematical formulation of cross bridge cycling has been adapted from the literature and the parameters have been fitted to experimental data from GI SM. Here it was assumed that the Ca^{2+}-calmodulin mediated phosphorylation of myosin is the primary determinant of the kinetics of cross bridge cycling. This model is the first step towards developing a dynamic model of GI SM contraction.**

Keywords — **Gastrointestinal (GI), Smooth muscle (SM) contraction, Myosin Phosphorylation, Active Stress, Cross-bridge model, Latch state**

I. Introduction

Smooth muscle cells line the walls of most of the hollow organs within the body. The ability of these cells to generate force and motion is essential to the normal functioning of the cardiovascular, respiratory, digestive systems. Since altered smooth muscle contraction may contribute to disease states, it is important to understand the mechanisms underlying smooth muscle contraction.

The functional role of the gastrointestinal tract is to digest and absorb nutrients. These processes are facilitated by the orchestrated movement of the luminal contents from the mouth to the anus [1]. Smooth muscle cells are the force producing elements of the GI tract. The force producing mechanisms of these cells are controlled by the intrinsic electrical slow wave activity and the enteric nervous system through electro-mechanical excitation-contraction coupling and also through pharmaco-mechanical coupling [2,4]. Pacemaker activity and the subsequent slow waves generated by the interstitial cells of Cajal (ICC) provide the background tone of the smooth muscle syncytium [1,2,4]. The tonic contractions contribute to maintaining the shape of the organ against an imposed load. Neurotransmitters from the enteric nervous system, along with hormones and paracrine factors released in response to physiological stimuli, modify SM cell behavior such that phasic contractions are elicited. A tonic contraction also enhances the open probability of voltage dependent Ca^{2+} channels in SM cells and increases the amplitude of phasic contractile activity in response to various stimuli.

The contractile unit of smooth muscle cells consists of thin actin containing filaments and the thick myosin containing filaments [5]. Tiny projections from the myosin filament called cross bridges extend towards the actin filament. These projections are the molecular motors which convert the chemical energy into mechanical work during their cyclic interaction with actin [5].

In smooth muscle, Ca^{2+} is the trigger for contraction [2]. Increase in intracellular Ca^{2+} can be due to several distinct mechanisms [3]. When the concentration of intracellular Ca^{2+} increases, a series of events take place. The ubiquitous cytoplasmic protein calmodulin binds to Ca^{2+} ions in a ratio of 4:1 [5]. In the absence of Ca^{2+}, caldesmon protein strongly binds to the tropomysin –actin complex on the thin filament preventing actin-myosin interaction. This inhibition is removed when the Ca^{2+}-calmodulin complex binds to caldesmon. In the thick filament, the Ca^{2+}-calmodulin complex binds to a specific site on the myosin light chain kinase (MLCK) converting it from the inactive form to the active form. This allows the MLCK to phosphorylate the regulatory light chain of myosin (MRLC)

Chwee Teck Lim, James C.H. Goh (Eds.): ICBME 2008, Proceedings 23, pp. 1696–1699, 2009
www.springerlink.com

resulting in actin-myosin interaction and this greatly potentiates the splitting of ATP and cross-bridge cycling [6]. The presented model is designed based on this mechanistic approach.

Apart from the regular cross-bridges, a population known as latch bridges is also produced [6, 7]. A latch is a state where there are reduced cross bridge cycling rates, dependent on low but significant levels of Ca^{2+}-dependent cross bridge phosphorylation. Latch–bridges contribute to sustained force maintenance during low levels of intracellular Ca^{2+}, especially during tonic contraction.

II. Methods

The Hai and Murphy model [8] is a kinetic model for the interaction of cross-bridge forming myosin heads with thin-filament actin which brings about contraction in SM. The model is based on the hypothesis of two types of cross-bridge populations – (a) cycling phosphorylated cross-bridges (AMp) and (b) noncycling dephosphorylated cross-bridges (latch bridges, AM). According to the model both of these populations contribute to the development of stress in SM. The schematic representation of the four state model is shown in fig 1 and the resulting equations are given below.

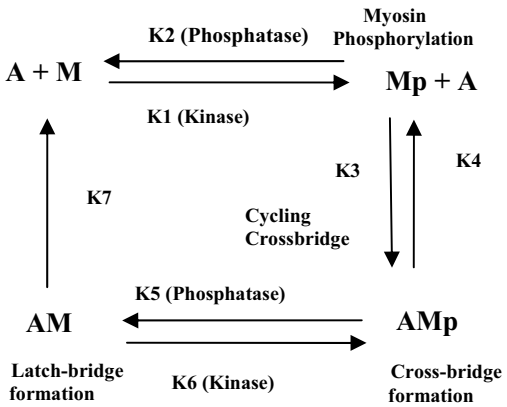


Fig.1 Four state cycling cross bridge model proposed by Hai and Murphy [8].

$$\frac{d[M]}{dt} = -K_1 [M] + K_2 [Mp] + K_7 [AM] \quad (1)$$

$$\frac{d[Mp]}{dt} = K_4 [AMp] + K_1 [M] - (K_2 + K_3) [Mp] \quad (2)$$

$$\frac{d[AMp]}{dt} = K_3 [Mp] + K_6 [AM] - (K_4 + K_6) [AMp] \quad (3)$$

$$\frac{d[AM]}{dt} = K_5 [AMp] - (K7 + K_6) [AM] \quad (4)$$

In addition to the assumptions used in the Hai and Murphy model [8], the following assumptions were made. Only one regulatory mechanism was considered; the phosphorylation of MRLC. In the absence of direct/conclusive evidence for the regulation of MLCP (phosphatase), K_2 and K_5 were set to be constants. The Hai and Murphy model (Eqns (1)-(4)) was implemented and solved in Matlab using an in-built explicit Runge-Kutta formula, the Dormand-Prince pair.Calcium dependence (Eqn (5)) was added through the regulation of rate of phosphorylation (K_1) by MLCK as proposed in the uterine contraction model of Bursztyn et al. [9]. Then simulations were run for time dependent intracellular Ca^{2+} data produced by the electrophysiology model developed by Corrias and Buist [11]. The rate of phosphorylation was made dependent on the intracellular Ca level, $[Ca^{2+}]_i$ through the relation

$$K_1(t) = \frac{[Ca_i(t)]^n}{[Ca_{(1/2MLCK)}]^n + [Ca_i(t)]^n} \quad (5)$$

where, Ca_i (t) is the time dependent intracellular $[Ca^{2+}]$, $Ca_{(1/2MLCK)}$ is the $[Ca^{2+}]_i$ required for half activation of MLCK and n is the Hill coefficient of activation.

Table 1 : Parameters used for the simulation (from [9])

NAME	VALUE	UNIT
K_2	1.2387	1/s
K_3	0.1419	1/s
K_7	0.0378	1/s
$Ca_{(1/2MLCK)}$	256.98	nM
n	8.7613	-
By assumption $K_6=K_1$; $K_5=K_2$; $K_4=k_3/4$ [8]		

Total myosin phosphorylation and stress were calculated using the following relations.

$$\text{Stress} = AMp + AM \quad (6)$$

$$\text{Phosphorylation} = Mp + AMp \quad (7)$$

III. Results

The model of gastric smooth muscle electrophysiology model from [11] was used to produce $[Ca^{2+}]_i$ as a function

of time for six slow waves with a plateau phase membrane potential of -43 mV. This is above the threshold membrane potential needed for the activation of contraction in SM [10, 12]. This $[Ca^{2+}]_i$ data, shown in fig 2, served as the input, $Ca_i(t)$, that was used to calculate $K_1(t)$ from Eqn 5.

The values $K_1(t)$ computed for the $Ca_i(t)$ data were substituted in Eqns 1-4, and solved for time dependent values of [M], [Mp], [AMp] and [AM] shown in fig 3.

The stress and phosphorylation produced in the SM cell was calculated from Eqns 6 & 7 and is shown in fig 4. The stress values were normalized by 0.8 (maximum stress) as the maximum number of attached cross-bridges (AMp + AM) was assumed to be 80% of the total myosin [8]. The phosphorylation was expressed as a fraction of total myosin.

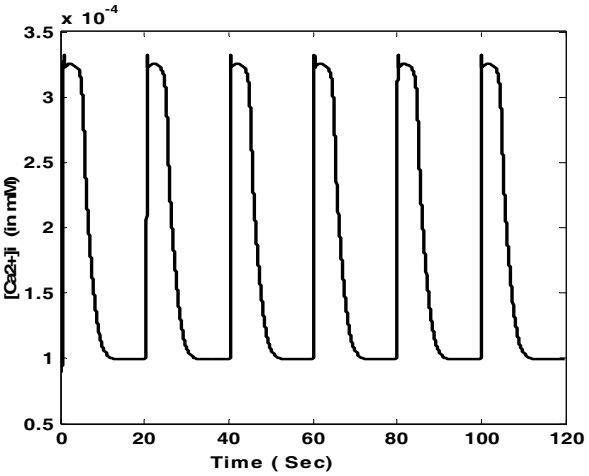


Fig .2 Intracellular Ca^{2+} concentration corresponding to slow waves in canine gastric smooth muscle cells. (Ref:11. Alberto et al 2008)

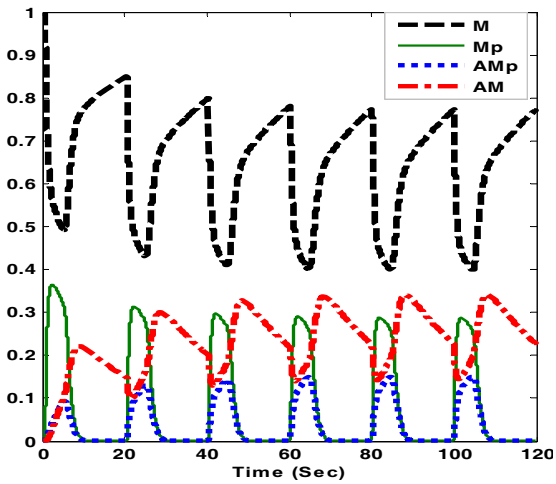


Fig .3 Variation of the fractions of the Species (M, Mp, AMp and AM) along the slow wave corresponding to the $Ca_i(t)$ in fig 2.

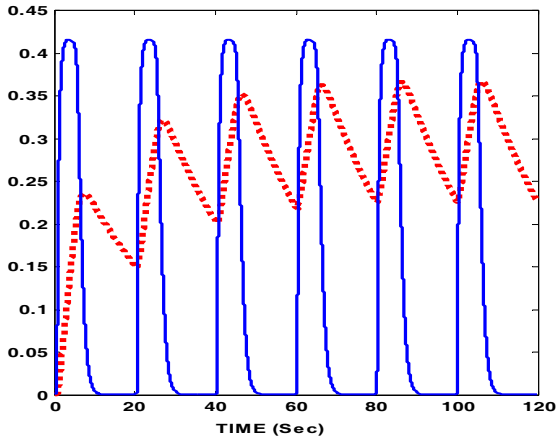


Fig.4 Normalized Phosphorylation (solid line) and Stress (dotted line) curves produced by the model for the Ca^{2+} data in Fig.2.

IV. Discussion

The Hai and Murphy model, modified to include a dependence on the intracellular calcium concentration, has been tested for the Ca^{2+} data produced by the electrophysiology model for gastric SM [11]. To date most of the modeling work in this field has been done for a single calcium ion transient event i.e. one cycle of $[Ca^{2+}]_i$ accumulation and decay over a time range [8,9]. This, however, may not accurately represent the physical situation. Physiologically a train of slow waves will determine the short and long term intracellular Ca^{2+}. Hence it is more useful to study the contraction pattern of smooth muscle in response to multiple slow waves. Here a train of six slow waves was chosen as the test data set.

The Ca^{2+} data corresponds to slow waves with a plateau phase membrane potential of -43 mV. Slow waves must exceed a 'mechanical threshold' for excitation-contraction coupling to occur. It has been found experimentally that the threshold value for different SM cells lies between -40 mV and -60mV, and above this threshold, there is a sharp rise in the Ca^{2+} concentration in many GI SM types causing active contraction to take place [10, 12].

The preliminary results presented here show that the slow waves with plateau phase above the mechanical threshold are able to produce phasic contractions. The latch bridge formation and its contribution in the stress can be seen evidently in figure 4. Though the phosphorylation levels begin to fall following the peak of the Ca^{2+} transient, the stress still increases to reach a maximum before decreasing at a later time. Also though the level of phosphorylation falls so as to be almost negligible, a considerable amount of stress is still maintained. This can also be seen in fig 3 in the AM (latch-bridge) curve.

The tonic contraction mechanism of GI SM will be studied in near future. Once it is established, it is intended to use the behavior to derive realistic initial conditions for the phasic contractions. It is believed that phasic contractions are superimposed on the inherent basal tone of the GI SM and occur in response to stimuli from various agonists [1,3,4,].

It has been noted that the contraction response to the Ca^{2+} current caused by the slow wave is biphasic [12]. That is, the first peak value in the slow wave causes contraction in the SM cells and if the plateau depolarization of the slow wave is above the threshold, a second phase of contraction is initiated with the amplitude of the contraction depending upon the membrane potential and the duration of the plateau phase. The current model is able to produce only a monophasic stress response as it can be seen in fig 4 (stress curve). This disagreement between the experimental observation and the model behavior needs to be addressed.

The model presented here is the first step towards developing a dynamic model of GI SM contraction. Though this model is based on the assumption that only the MAPK is regulated by the intracellular $[Ca^{2+}]_i$ concentration [9], other Ca^{2+} dependent and independent regulatory systems can not be excluded. Experiments are being done to examine if there is a thin filament regulatory pathway involved in the SM contraction [14,15]. Using the experimental results and evidence for such regulatory pathways, the present model will be further extended by the inclusion of more control systems. Recently studies have also been performed relating to Ca^{2+} sensitivity [13]. It is proposed that the sensitivity of the contractile apparatus to Ca^{2+} is not constant and varies under different conditions. This behaviour of the SM cell contractile elements can be accounted for by including a Ca^{2+} sensitivity factor in the model. The future developments do, however, depend upon the availability of concrete experimental evidence and data.

V. Conclusions

In summary, a simple model, adapted from the Hai and Murphy model [8], has been used to explain the calcium dependence of the SM contraction and its regulation. A mathematical formulation for the four states and cross bridge cycling has been used with parameters fitted from the experimental data to study the effects of (a) Ca^{2+} concentration on the kinetics of myosin phosphorylation, and (b) the latch state during tonic and phasic contractions.

As the model is being developed, we expect it to serve as a bridge between electrophysiological and mechanical behaviour of the SM cell. This model is at the cellular level of the hierarchy of cell – tissue – organ as seen in the Physiome project. In the future such models can serve as a tool to make predictions under prescribed conditions and also can be used to study diseases of the GI system.

References

1. Szurszewski, J. H. Electrical basis for gastrointestinal motility. In: Physiology of Gastrointestinal Tract (2nd ed), edited by L. R.Johnson. New York: Raven, 1987, p. 383-422.
2. Sanders K.M.,Koh S.D, Ward S.M. Organization and Electrophysiology of Interstitial Cells of Cajal and Smooth Muscle cells in the gastrointestinal Tract. In : Physiology of the gastrointestinal tract(4th Ed), edited by L.R.Johnson.New York.Raven Press,2006. p533-576.
3. Makhlouf G.M and Murthy K.S. Cellular Physiology of Gastrointestinal Smooth Muscle.. In Physiology of the gastrointestinal tract(4th Ed), edited by L.R.Johnson.New York.Raven Press,2006. p524-532.
4. Johnson L.R. Smooth Muscle Physiology. In: Physiology of the gastrointestinal tract. Chapter 13.s (2nd Edition, 1987). New York. Raven Press.P246-262.
5. Horowitz A, Menice CB, La Rorte R and Morgan K.G. (1996). Mechanisms of smooth muscle contraction. Physiol Rev, 76:967-1003.
6. Dillon P.F, MO Aksoy M.O, Driska S.P, and Murphy R.A(1981). Myosin phosphorylation and the cross-bridge cycle in arterial smooth muscle. Science , January 1981:Vol. 211. no. 4481, pp. 495 – 497.
7. Dillon P. F and Murphy R. A(1982). Tonic force maintenance with reduced shortening velocity in arterial smooth muscle. Am J Physiol Cell Physiol 242: C102-C108.
8. Hai C.M, Murphy R.A (1988). Cross-bridge phosphorylation and regulation of latch state in smooth muscle. Am J Physiol Cell Physiol 254: C99–C106.
9. Bursztyn L , Eytan O, Jaffa A.J, Elad D (2007) . Mathematical model of excitation-contraction in a uterine smooth muscle cell. Am J Physiol Cell Physiol 292:1816-1829..
10. Vogalis F, Publicover N.G, J.R Hume J.R, Sanders K.M (1991). Relationship between calcium current and cytosolic calcium in canine gastric smooth muscle cells. Am J Physiol Cell Physiol 260: C1012-C1018.
11. Corrias A, Buist M.L. Quantitative description of gastric slow wave activity. Am J Physiol Gastrointest Liver Physiol.294 (4):G989-G995, 2008.
12. Ozak H, Stevens R.J, Blond D.P, Publicover N.G,Sanders K.M. Simultaneous measurement of membrane potential, cytosolic Ca^{2+}, and tension in intact smooth muscles. Am J Physiol Cell Physiol 260: C917-C925, 1991
13. Ratz P.H, Berg K.M, Urban N.H, Miner A.S. Regulation of smooth muscle calcium sensitivity: KCl as a calcium-sensitizing stimulus. Am J Physiol Cell Physiol 288: C769-C783, 2005.
14. Gerthoffer WT, Pohl J.(1994) Caldesmon and calponin phosphorylation in regulation of smooth muscle contraction. Can J Physiol Pharmacol. Nov;72(11):1410-4.
15. Winder SJ, Allen BG, Clément-Chomienne O, Walsh MP.(1998) Regulation of smooth muscle actin-myosin interaction and force by calponin. Acta Physiol Scand. Dec;164(4):415-26.

Design of Customized Full Contact Shoulder Prosthesis using CT-data & FEA

D. Sengupta[1,2], U.B. Ghosh[1] and S. Pal[1]

[1] School of Bioscience & Engineering, Jadavpur University, Kolkata-700 032 India.
[2] Tata Consultancy Services, Technopark Campus, Kariyavattom, P. O. Thiruvananthapuram 695581, Kerala.

Abstract — **Shoulder joints were replaced due to trauma or chronic arthritis and other disease processes, osteoarthritis and or other disease processes. Usually the available prostheses generally use some standard ball diameters and stem length of the humeral component. Many varieties are available including modular type with replaceable ball diameter Therefore there is a mismatch in the ball size and actual bony cavity and the prosthesis that will be inserted leading to excess bone loss during insertion in the bone which sometimes calls for an early revision surgery.**

So patient specific hemi-shoulder prosthesis was designed from the CT- scan data obtained from a specific patient. The materials used were medical grade stainless steel (316L), Ti6Al4V, Co-Cr-Mo alloy respectively. This type of prosthesis will be manufactured using computer aided manufacturing technique.

Keywords — **Full contact, shoulder prosthesis, arthritis, customization, CT-data, FE-analysis**

I. Introduction

The first shoulder replacement was performed in 1893 by a French surgeon, Pean, for a tuberculosis infection. However, it was not until the 1970's that shoulder replacements were routinely performed. Initially, implant designs were highly con-strained devices that did not accurately restore shoulder biomechanics and ultimately failed. Modern total shoulder implants allow for more motion and less constraint. A shoulder replacement involves replacing the humerus) and the glenoid with metal and plastic parts that then act as a new shoulder joint [1, 2, 3]

Shoulder joints are replaced due to traumatic injury, osteoarthritis or other disease processes. Usually the available prostheses generally use some standard ball diameters and stem length of the humeral component. Many varieties are available including modular type with replaceable ball diameter, therefore there is a mismatch in the ball size and actual bony cavity and the prosthesis that will be inserted leading to excess bone loss during insertion in the bone which sometimes calls for an early revision surgery.

Therefore a patient specific hemi-shoulder prosthesis was designed using the CT-scan data obtained from a particular patient. The materials used for design of the prosthesis were medical grade stainless steel (316L), Ti6Al4V, Co-Cr-Mo alloy respectively.

II. Material & methods

The shoulder is a multifunctional joint with a large number of functions consists of a chain of bones connecting the humerus to the trunk. The shoulder consists of scapula and clavicle and functions as a movable but stable base for the motions of the humerus. The Sterno-Clavicular joint connects the clavicle and sternum, and the scapula in its turn is connected to the clavicle by the Acromio-Clavicular joint. Another connection between the scapula and the thorax is the Scapulo-Thoraeic Gliding Plane, which constraints possible movements with two Degrees-of-Freedom (DOF) and makes the system a closed chain mechanism. There are large numbers of muscles also which control the movement of the joint. The steps involved for processing the CT-data from a specific patient of a particular bone are as shown in figure 1.

Image processing of the CT slices (in the DICOM format), obtained from local hospital with informed consent for the exact contour generation of the inner medullary cavity of the humerus were performed using the software MIMICS® and the subsequent 3D model was formed which was meshed using the Magics® software to refine the finite

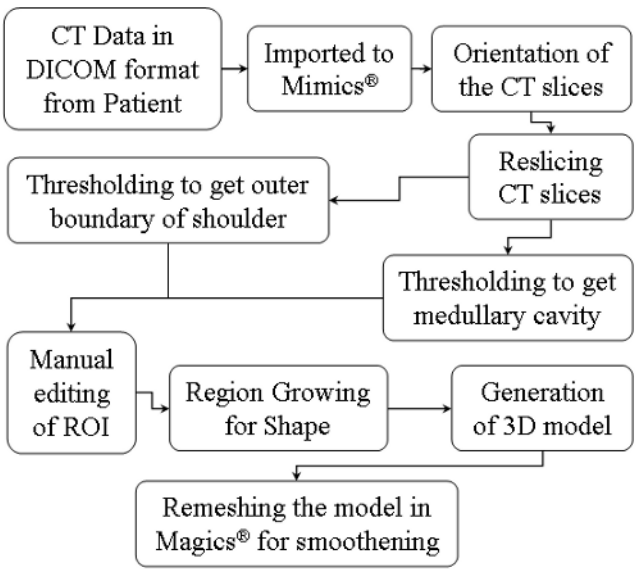


Fig. 1 Steps involved for the image processing of the CT slices

Chwee Teck Lim, James C.H. Goh (Eds.): ICBME 2008, Proceedings 23, pp. 1700–1703, 2009
www.springerlink.com

element mesh. Then it was exported to FEA-software Ansys® and then volumes were generated from these areas and meshed with 10-nodded tetrahedral element. Then this file was send to MIMICS for material property assignment based on gray values The Gray values were then converted to the Hounsfield units. The gray value is determined by the intensity of the colour. For air (colourless entity) the gray value is 0 which increases for the denser objects. The corresponding value of HU of air is –1024. Before assigning materials to the elements of the volumetric mesh, Mimics will first calculate a gray value for each element. This gray value will then be used in further calculations. MIMICS® uses an accurate method to assign gray values to elements by calculating exact intersections between voxels. The voxels are referred to those volumetric regions in a 3D region analogous to a pixel in a 2D region. While being accurate, care has been taken that the calculations can be performed efficiently.

For assigning the material property of bone a fixed value of 0.3 was given for Poisson's ratio. For assignment of material property element by element MIMICS® calculates the average gray value of all the voxel inside an element in HU and then the whole range of densities are linearly divided into the given number of groups. For each group it assigns a particular gray value of Young's modulus according the above formula. The loading conditions were adopted from the various angles of arm abduction from Van der Helm's data [4, 5] as shown in Table 1.

Table 1 Gleno Humeral Joint Reaction Force for Different Angles of Arm Abduction for Unloading Conditions (Van Der Helm 1994)

Load Case	Abduction Angle (°)	F_X(N)	F_Y(N)	F_Z(N)	Resultant Force(N)
2	30	164.46	-16.14	14.03	165.84
3	60	323.74	-3.68	-36.88	352.85
4	90	383.71	34.62	-77.28	392.95
5	120	314.03	45.56	-137.96	346.01
6	150	137.74	11.86	-134.43	192.83
7	180	39.78	-3.73	-72.51	82.79

In this study we have considered three cases for comparison and improved design 1) normal joint, 2) joint with standard prosthesis and 3) with a CT-data based customized shoulder prosthesis for a better understanding of our design.

The customized shoulder implant is designed by taking the measurement from the CT scan slices. The CT scan data collected from a local hospital were exported in image processing software MIMICS®. The slice distance was1mm and there were a total of 171 slices. The bone scale was chosen for proper visibility. The primary masking was applied with the threshold ranging from 226 to 1905 where –1024 corresponds to the gray value of air. Region growing is performed on the cortical region of the masked portion and a 3D volume is generated from this region. The polylines which were created thereafter were ex-ported as area.lis files in the finite element software Ansys for the designing of the customized implant.

The polylines which were generated by the software corresponding to the inner medullary cavity as shown in fig 2(A) were chosen and the outer polylines were deleted as in fig 2(B). Two planes mutually perpendicular to each other were drawn in order to add the innumerable small line which has been created corresponding to each of the CT slices while exporting from MIMICS®. These lines in each of the layers were then added by Boolean operation and areas were created. The coordinates of the center of the areas were retrieved and joined by spline in order to create the central axis. Four coordinates on each of the areas were chosen so that they can be joined to form segmented spline. The coordinates in the chosen layer lying in the same direction were joined by spline. Areas were created, from which volumes were generated which formed the humerus stem of the customized implant as shown in Fig. 3 A & B. The range of the Hounsfield unit in the Humerus is –1024 to 1650 (ref. MIMICS®). The computed density (ρ) from this range is

$$\rho = 689.3044 + 0.673148 \times HU \quad (1)$$

and Young's modulus(E) is given by

$$E = 689.3044 + 0.0000013 \times \rho^{3.15} \quad (2)$$

The models were solved using a PC with Intel® Pentium IV Processor (3.2 GHz, HT, 1536MB RAM) and in ANSYS®. Each of the models was solved in approximately 15 minutes. Altogether it took 11 hours for processing. The post-processing was done in ANSYS® postprocessor.

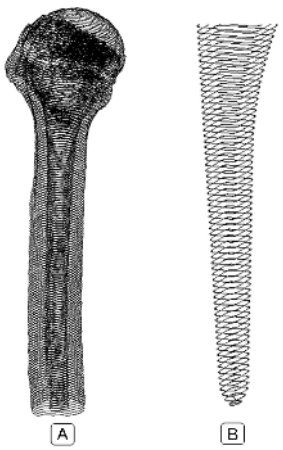


Fig. 2 (A) The polylines in the whole humerus, (B) polylines of the inner medullary cavity

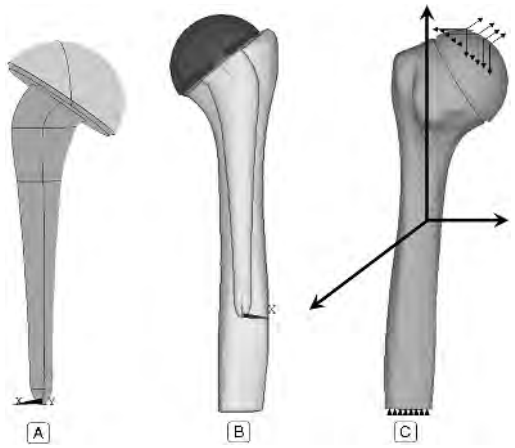


Fig. 3 (A) Designed customized prosthesis, (B) Prosthesis inserted inside bone, (C) constrained Prosthesis.

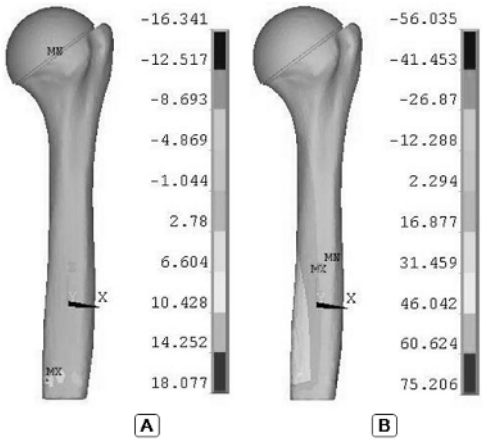


Fig. 5 Axial stress (MPa) in X (A) & Z direction (B) at 90º arm abduction in bone inserted with the customized prosthesis when the muscle forces are maximum.

III. Results & Discussion

The results of the study are quite involved and as we tried three Materials, SS316l, Ti6 Al4V and Co-Cr-Mo alloy. It was found that the materials didn't change the stress pattern significantly. We are showing the variation of the shear stress in Fig.4 and Fig.5 at 30º and 60º arm abduction using different materials as indicated. Similarly Normal, stress and Von Mises stress criteria for failure were also calculated for the normal humerus and humerus with standard prosthesis inserted and newly designed customized implant with the three different materials.

Now the corresponding Von-Mises stress on fig.6 (A) the customized prosthesis was depicted in the below and (B) VM-strain of Co-Cr-Mo. Alloy.

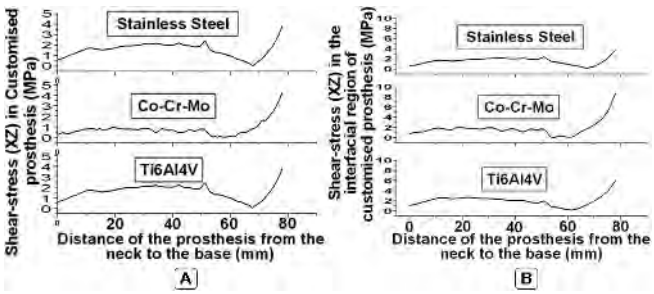


Fig. 4 (A) Variation of Shear stress (XZ) in standard prosthesis and 4(B) the customized prosthesis of the materials.

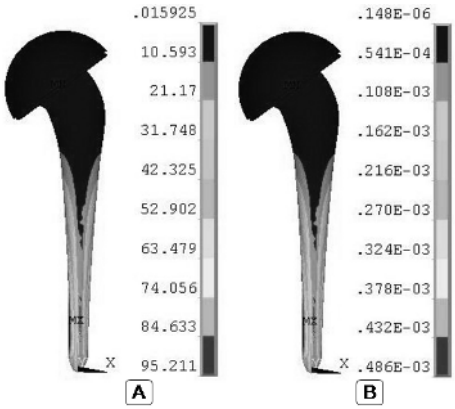


Fig. 6 (A) Von-Mises stress & (B) Von-Mises strain.

Table 2 Maximum Von-Mises stress in customized prosthesis During 90º arm abduction

Abduction Angle (º)	Von-Mises Stress (MPa)		
	Co-Cr-Mo	Stainless Steel	Ti6Al4V
30	64.706	95.34	55.565
60	131.47	118.07	58.164
90	169.6	95.34	10.104
120	245.04	132.65	58.164
150	61.802	--	--

From all these results we may infer that the effect of load transfer along the humerus, using a detailed 3-D Finite Element Analysis (FEA) showed a variation of stress along the length of the normal humerus from 2.0MPa to 20 MPa. For the stress-strain analysis of the surgical construct the prosthesis was inserted in the humerus. The failure criterion

von-mises stress in the interfacial nodes between the inserted Co-Cr-Mo prosthesis and the normal bone were in the range 18.0MPa to 245.0MPa, for S.S prosthesis was between 90.0 MPa to 130.0 MPa while for the Ti6Al4V was between 10.0MPa to 95.0MPa. Thus for all the above cases it is lesser than the corresponding yield stress of the metals and bone used, which ensures the safety of the construct under the subjected loading conditions. Only this prosthesis needs to be made using CAD technique. Now we are working on parametric model generation directly from the CT-data, getting the whole dimensions of the medullary cavity and ball diameter & length.

Acknowledgment

We gratefully acknowledge the Department of Science & Technology, New Delhi, Government of India for funding the project & CNCRI, Kolkata for providing CT-data.

References

1. Dines DM, Warren RF. Modular shoulder hemiarthroplasty for accurate fractures: surgical considerations. Clin Orthop 1994; 307: 18-26.
2. E.Y. Chao, B.F. Morrey, "Three-dimensional rotation of the elbow", J. Biomechanics, 11, 1978, 57-73.
3. Fenlin JM et al. 1994 Flatow EL. Prosthetic design considerations in total shoulder arthroplasty. Semin arthroplasty 1995; 6:233-244.
4. F.C.T. Van der Helm, (1994), "A finite element musculoskeletal model of the shoulder mechanism", J. Biomechanics, 27, 551-569.
5. Van der Helm, F.C.T (1994a). Analysis of the kinematic and dynamic behaviour of the shoulder mechanism. J. Biomechanics 27,527-550.

Author: Prof Subrata Pal
Institute: School of Biosc. & Engg. , Jadavpur University
Street: 188, Raja S.C. Mullick Road
City: Kolkata - 700 032
Country: India
Email: spalbme@yahoo.co.in

An Interface System to Aid the Design of Rapid Prototyping Prosthetic Socket Coated with a Resin Layer for Transtibial Amputee

C.W. Lai[1], L.H. Hsu[1], G.F. Huang[2] and S.H. Liu[1]

[1]Department of Mechanical Engineering, National Cheng Kung University, Taiwan
[2]Department of Physical Therapy, Fooyin University, Taiwan

Abstract — **For employing the technology of rapid prototyping (RP) to fabricate prosthetic socket for transtibial amputee, a CAD stump model must be constructed. Currently, the commercial CAD systems need experienced skills to define objects. To simplify the construction procedure of stump model and easily used by a prosthetist, an interface system for the specific purpose of defining stump model should be developed. The main objective of this study is to improve the tedious process and quality uncertainty of conventional method to produce prosthetic sockets. This study developed an interface system that allows a prosthetist to modify the shapes of stump model so that the acceptable pressure distribution on pressure tolerant (PT) and pressure relief (PR) areas can be achieved.**

This study used C++ programming language and Open Graphic Library to develop an interface system. The point data of stump surface obtained by a T-scan system, which includes a hand-held 3D laser scanner and tracking system, is utilized to build the original shape of the stump. The primary shape of stump model is modified based on the requirements at the PT and PR areas of the specified amputee. As soon as the contact pressures between stump and socket are verified by finite element analysis, the modified stump model can be used to design a specific CAD socket model for the production using a RP machine.

This interface system directly used a file of scanned points to build a stump shape and also provided the functions to identify the shapes of PT/PR areas. The modification requirements, including designations of the regions to be modified and the distances to be indented or raised, can be easily manipulated through appropriate interface dialogs. After a RP socket model has been designed, the socket is manufactured using an FDM machine. To reinforce the strength, the RP socket is coated with a resin layer. The measurement of contact pressures has been implemented and its trial use is under way.

Keywords — **CAD, transtibial prosthetic socket, rapid prototyping, C++ programming.**

I. Introduction

In the traditional process of fabricating prostheses, there are many factors will effect the quality of fit. A shape of the residual limb is acquired by using plaster bandages. And a plaster positive model of the residual limb is made from plaster bandages. Plaster may then be added to the pressure relief areas which are sensitive and removed from the pressure tolerant areas which are loaded for weight bearing of the model. The modification of the plaster depends on the skill and expertness of the prosthetist.

CAD/CAM techniques had been viewed as a solution to reduce errors in the fabrication process [1]. This study employed reverse engineering to replace the plaster method to design and fabricate a prosthetic socket [2]. The prosthetic socket can be produced from a CAD model accurately and quickly by using rapid prototyping (RP) technology [3]. However, current CAD systems are not friendly for a prosthetist to operate. If a custom-made interface system is available and easily operated by any user such as a prosthetist, the prosthetic socket may then be fabricated conveniently.

II. Methods

A. Scanning

Employing the reverse engineering technology, the fist step is to acquire the point data of the shape by scanning the subject. The point data is the basis for subject construction. Therefore, how to measure the subject is the key to subsequent work.

In previous study, the point data of stump was acquired by using the CCD (Charge Coupled Device) laser scanner to scan the shape of gypsum positive model. As a result that the CCD laser scanner can't revolve around the subject, it was necessary to revolve the subject to complete the scanning mission. After all the gypsum positive model is just a rough copy of the stump. The credibility of the point data needed to improve.

With technology developing, the T-scan which is a hand-held laser scanner can scan the shape of subject easily and quickly (Fig. 1). Using the T-scan to scan the shape of stump directly improves the credibility of the point data of stump. The amputee just sits on a seat and doesn't need to change his/her posture. Taking the T-scan along the shape of stump, at the same time, the point data had be obtained will display on the monitor. It is easy to perceive the contrast between the point data acquired by using a CCD laser scanner to measure the gypsum positive model and using the T-scan to measure the stump directly.

Chwee Teck Lim, James C.H. Goh (Eds.): ICBME 2008, Proceedings 23, pp. 1704–1707, 2009
www.springerlink.com



Fig. 1 Scanning the stump using T-scan

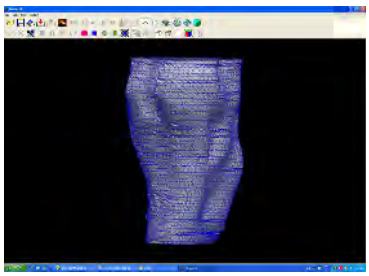


Fig. 2 Constructing the residual limb

B. Filtering the point data

Since there would be millions of point in the point data acquired by the T-scan, it is necessary to preprocess the point data. Filtering the trivial and unnecessary points in the point data benefits the stump model reconstruction. In order to simplify the operation when importing the point data to interface system and modifying surface of stump, the point data had been divided to multi-layer and every layer must have the same number of points.

C. Constructing the stump surface model

After a preprocessing process, the point data is imported to the interface system and the stump surface model will be constructed (Fig. 2). The stump surface model is constructed by many small triangle meshes. Changing the position of points will make the shape of stump to change. Using this method the socket surface will be designed from changing the stump surface.

D. The interface system

This study applied C++ program language and OpenGL to develop an interface system that can design the surface model of the socket. In order to achieve construction and modification of stump surface model, this interface system has following functions:

1. The function of point data reading. Point data is indicated by space parameters X, Y, Z. By reading the point data, the model can be constructed on the window.
2. The function of surface modification. The interface is capable of controlling the modification value and the smooth of surface after modification.
3. The model after construction and modification can be read and modified by other CAD software.

Program operation is reading point data to construct the surface model of the stump. And then users can define the shape and location of modification areas. After giving the maximum modification displacement, the program will let modification displacement of each point smaller than max modification displacement to keep the modification surface smooth. The modified model can be saved for fabricating (Fig. 3).

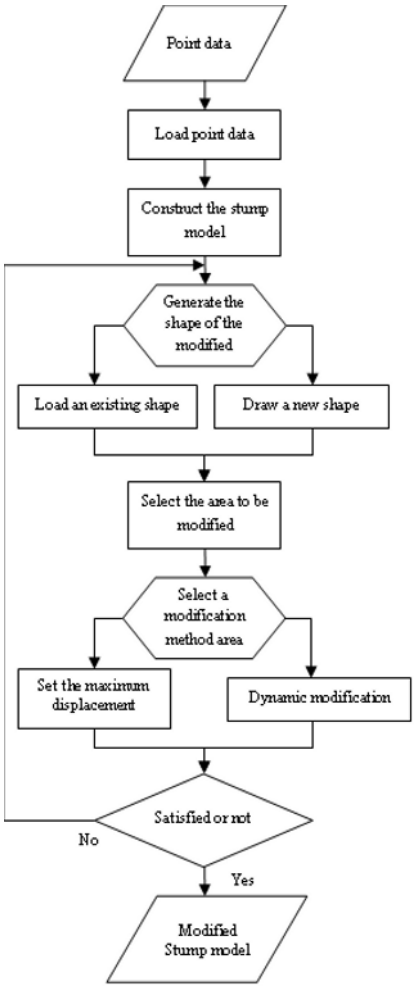


Fig. 3 Operating procedure of the interface system

III. Case Study

A. Acquiring the point data of a stump

After scanning the shape of the patient's amputation, the point data of a stump would be acquired. The point data preprocessing includes planar sectioning (Fig. 4) and filtering which is provided by CATIA; planar sectioning divides the point data divided into multi-layers, and filtering lets the point data have the same number of points per layer. Then, the data saved by CATIA is changed into TXT format (Fig. 5), the number of layers is inputted in the first row and the number of points per layer in the second row.

B. Modification of the stump shape by using the point data

The point data is imported into the interface system after preprocessing and reconstructed model of the patient's stump (Fig. 2). According to PR and PT areas of the stump, the appropriate shape and location are chosen to modify the surface of the stump. The PR areas should be offset outward of the stump surface, while the PT areas should be offset inward of the stump surface. For example, at Patellar tendon, PT area, choose a rectangle to fit the area and offset inward with an appropriate displacement (Fig. 6). The modified areas in this study include the Tibia, Fibula, Patella Tendon and Calf muscle (Fig. 7).

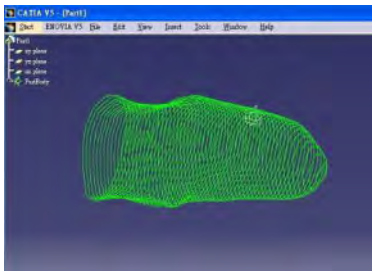


Fig. 4 Planar sections of the point data

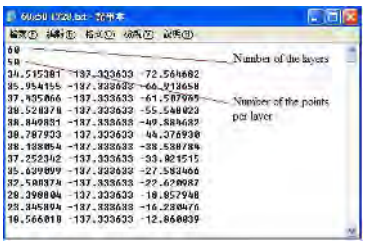


Fig. 5 File format of the data utilized in this study

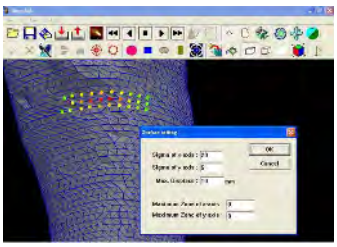


Fig.6 Modification of patellar tendon

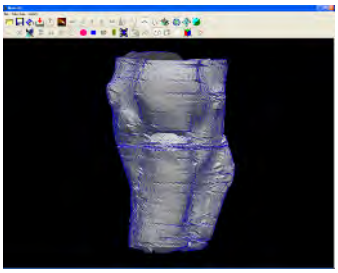


Fig.7 The modified stump model

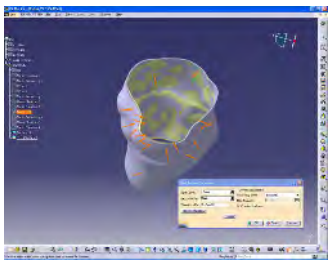


Fig. 8 Building the solid model of a prosthetic socket

C. Design of a socket model

The modified stump surface is imported to CATIA to design a socket. Because a patient would wear socks on their stump before putting on the prosthetic socket, there should be a gap between the stump and the prosthetic socket. This study designated 4.5 mm for the gap. The modified stump surface is offset 6 mm to form the outer surface of a prosthetic socket. The solid model of the prosthetic socket is obtained by shelling the outer surface with 1.5 mm. (Fig. 8). For connecting an adapter and a shank, the bottom of the socket should be made with a specific shape. As soon as a socket model is determined, a STL file is transferred to a rapid prototyping machine for fabricating prosthetic socket (Fig. 9). This preliminary RP socket is then coated with a resin layer for reinforcing its flexural strength.

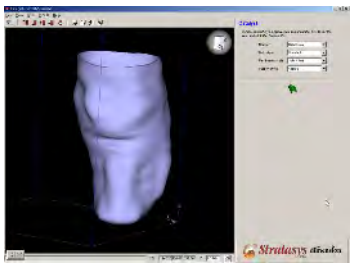


Fig. 9 Importing socket model into the slicing software for an RP machine

IV. Conclusions

This study developed a method together with a prototype interface system for surface modification during the design of a prosthetic socket. The interface system provided the following features:

1. The interface system demonstrated that a prosthetic socket can be designed using the scanned points of a stump. A preliminary socket is then fabricated by a RP machine using the socket model (Fig. 10). This preliminary RP socket is wrapped with a layer of resin to reinforce it strength (Fig. 11). The resin-reinforced socket has been worn by the specific amputee for trial use and the interface pressures between socket and stump has been measured.
2. The interface system allows a prosthetist to designate the required modification displacement and the corresponding modified shape can be acquired. The shape to be modified can be adjusted by five parameters that represented the weighting values of the space. This method is quicker than using control points to modify surfaces.
3. This interface also helps to shorten the training time of a prosthetist and to modify pressure-tolerant and pressure-relief areas more easily.
4. This interface can store the digitized socket model, which can be used to fabricate a new socket at the patient's request.

Since the interface system only provides shape modification, other functions needed in the socket design process, such as shelling the surface model of a stump to form a solid model, and the detailed shape at the end of a socket, should be developed.



Fig. 10 A preliminary socket fabricated in an FDM machine



Fig. 11 Coating the preliminary RP socket with a resin layer

Acknowledgment

The authors would like to thank the National Science Council Taiwan for its support through grant No. 97-2212-E-006-105.

References

1. Oberg K, Kofman J, Karisson A, Lindstrom B, Sigblad G (1989) The CAPOD system-a scandinavian CAD/CAM system for prosthetic socket. Journal of Prosthetics & Orthotics Vol. 1:139-148
2. Zheng S, Zhao W, Lu B (2005) 3D reconstruction of the structure of a residual limb for customising the design of a prosthetic socket. Medical Engineering & Physics Vol. 27:67-74
3. Rogers B, W. Bosker G, H. Crawford R, C. Faustini M, R. Neptune R, Walden G, J. Gitter A (2007) Advanced trans-tibial socket fabrication using selective laser sintering. Prosthetics and Orthotics International Vol. 31:88-100

Author: Lai, Chih-Wei
Institute: Department of Mechanical Engineering, National Cheng Kung University, Taiwan
Street: University Road
City: Tainan
Country: Taiwan
Email: laicw0204@gmail.com

Correlation of Electrical Impedance with Mechanical Properties in Models of Tissue Mimicking Phantoms

Kamalanand Krishnamurthy[1], B.T.N. Sridhar[2], P.M. Rajeshwari[3] and Ramakrishnan Swaminathan[1]

[1]Department of Instrumentation Engineering, MIT Campus, Anna University, Chennai, 600044, India
[2]Department of Aerospace Engineering, MIT Campus, Anna University, Chennai, 600044, India
[3]Marine sensors and Electronics, National Institute of Ocean Technology, Chennai, 600100, India

Abstract — **Pathological changes in soft-tissues are primarily correlated with changes in their mechanical and electrical properties and are used to differentiate diseases from normals. Although there are evidences that establish the association of electrical and mechanical properties in biological aspects, their interrelationships are not well established. In this work, an attempt has been made to correlate electrical impedance of soft tissue-mimicking phantoms with those of its mechanical properties. The electrical property of the polyacrylamide gel phantoms prepared as per the standard protocol was studied using a precision impedance analyzer. Tensile tests were conducted using an universal testing machine and the derived mechanical properties such as breaking stress, breaking strain, initial modulus and Young's modulus were correlated with impedance values. It was observed that for a given concentration of a gel phantom the percentage variation in impedance correlate well with the percentage variation in the Young's modulus. The magnitude of variation in Young's modulus found to be more than that of the impedance. Similar correlations were observed for other mechanical properties. It appears that this study seems to be useful as the research on tissue mimicking phantom gels play important role in mechanical studies and in ultrasonic bioeffects. In this paper the objectives of the study, methodology and the significance of results are discussed in detail.**

Keywords — **palpation, mechanical properties, electrical impedance, soft tissue, polyacrylamide gel.**

I. Introduction

Physicians and surgeons evaluate the tissue behavior to diagnose medical conditions; any changes in tissue condition are seen as indicators of disease or illness. One of the primary interests of the physician is to examine the tissue stiffness or elastic modulus, a property pertaining to the material's resistance to deformation. This assessment of tissue stiffness is known as palpation and relies on the qualitative determination of tissue elasticity by the physician [1]. Several diseases are known to alter the mechanical properties of soft tissues.

During many abdominal operations palpation is used to assess organs, such as the liver, and it is not uncommon for surgeons to palpate tumors that were undetected previously by classic imaging methods such as CT, MRI, or B-scan ultrasound because none of these methods currently provide the type of information elicited by palpation. These findings imply that measurement of mechanical properties of tissues has a potential to offer a new method of classification of tissues [2].

Many tissue-mimicking phantoms have been developed and researchers have emphasized that these tissue-mimicking phantom gels play important roles in research on biomedical applications. Characterizing the mechanical behavior of small tissue samples and tissue-like phantoms can significantly contribute to better elasticity imaging algorithms [3]. Polyacrylamide gels are similar to tissues in many respects [4].

There are evidences that establish the association of electrical and mechanical parameters in biological aspects. The electrical activity of the heart generates an active tension that causes the heart to deform. It is therefore clearly evident that the mechanical activity of the heart is heavily dependent on the electrical activity. In turn, the mechanical activity affects the propagation of electrical activity [5].

The purpose of this study is to correlate the electrical impedance of polyacrylamide based soft tissue mimicking phantoms with their mechanical properties.

II. Materials and Methods

A. Description of the phantom

Polyacrylamide based tissue mimicking phantoms are chemical gels which are obtained through chemical reactions [4]. The gels are formed by co-polymerization of acrylamide and bis-acrylamide. A free radical generating system initiates the reaction. Polymerization is initiated by tetramethylethylenediamine and ammonium persulphate. Tetramethylethylenediamine acts as an electron carrier and activates the acrylamide monomer thus providing an unpaired electron to convert the acrylamide monomer to a free radical. The activated monomer reacts with the unactivated monomer to begin the polymer chain reaction. The polymer chains are crosslinked by bis-acrylamide, forming a complex web polymer which depends on the polymerization conditions and monomer concentration. To attain good repeatability in gel formation, the concentration of the ini-

Chwee Teck Lim, James C.H. Goh (Eds.): ICBME 2008, Proceedings 23, pp. 1708–1711, 2009
www.springerlink.com

tiator, temperature, and pH must be controlled. Certain factors like impurities in the chemicals and water lead to incomplete gel formation. Polyacrylamide gels can be prepared to match the mechanical properties of different real tissues by changing the acrylamide concentration.

B. Preparation of 20% acrylamide gel

A 20% polyacrylamide gel requires a mixture of 19g acrylamide (extra pure) and 1g bis-acrylamide (extra pure) in 100ml deionised water. Ammonium persulphate and TEMED (N,N,N',N'-tetramethylethylenediamine) was added to initiate and catalyze the polymerization reaction.

C. Mechanical testing

The mechanical properties of the phantoms were measured using an Instron model 3367 dual column testing system equipped with a 10kg load cell and interfaced to a desktop PC. The phantom samples were cut using a fly type pillar press into flat dumbbell shaped specimens of gauge length 60mm, width 6.43mm and thickness 5.04mm. Tensile test was performed on the phantoms with the crosshead speed set to 0.25mm/min. Based on the destructive mechanical tests performed on the phantoms of various concentrations ,the mechanical properties such as breaking stress, breaking strain, initial modulus and Young's modulus were determined at a temperature of 25°C.

D. Electrical testing

The electrical and dielectric parameters such as resistance, capacitance, impedance and phase angle of the tissue mimicking phantoms were measured at a frequency range of 100 KHz to 110 MHz using a 4294A Precision Impedance Analyzer equipped with a two electrode system comprising of copper electrodes. The phantoms were cut into structures of dimensions 60mm x 6.43mm x 5.04mm. The electrical and dielectric properties of the polyacrylamide phantoms were measured for different concentrations ranging from 20 to 40 percent. The dimensions of the samples were kept the same for all the concentrations and investigations were conducted at a temperature of 25°C. In this study, the entire analysis was made using the electrical impedance specifically measured at a frequency of 100 KHz.

III. Results

In FIG 1, the percentage variation in electrical impedance and breaking stress is shown as a function of gel concentration ranging from 20 to 50 percent. It can be seen that the

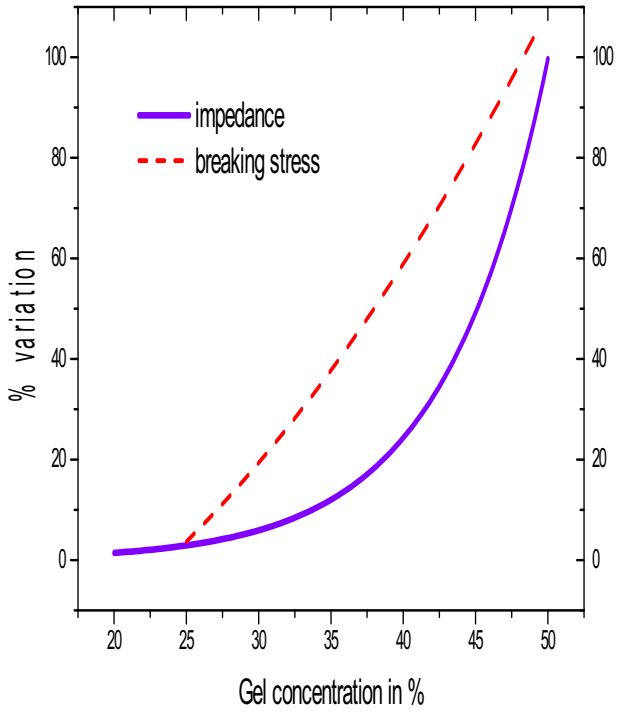


Fig. 1 Impedance and breaking stress Vs gel concentration

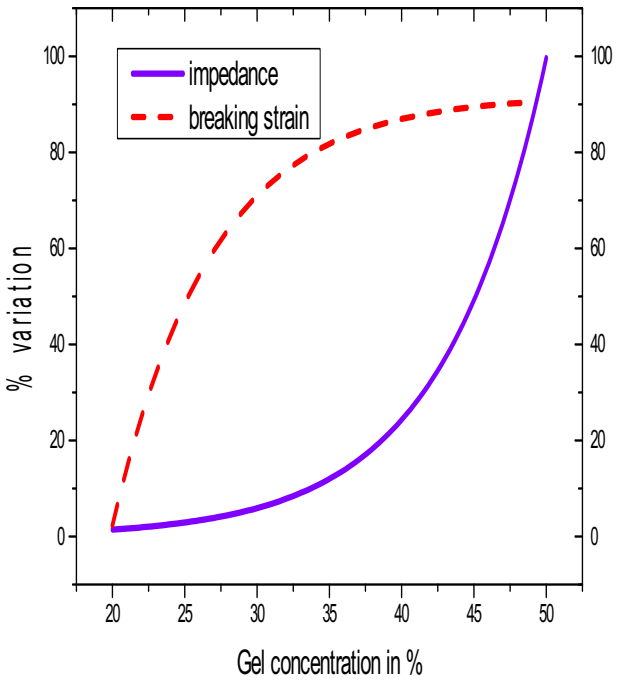


Fig. 2 Impedance and breaking strain Vs gel concentration

percentage variation in breaking stress increases linearly for a linear increase in gel concentration ranging. The percent-

age variation in impedance increases exponentially for the same concentration range. The correlation coefficients were calculated using the Pearson correlation method. The breaking stress correlates with the electrical impedance with an R value of 0.88.

The percentage variation in electrical impedance and breaking strain is shown in FIG 2 as a function of gel concentration ranging from 20 to 50 percent. It was observed that the percentage variation in breaking strain increases nonlinearly with respect to the gel concentration. The breaking strain correlates with the electrical impedance with a correlation value of 0.64.

In FIG 3, the percentage variation in electrical impedance and initial modulus is shown as a function of varied gel concentrations. The percentage variation in initial modulus increases linearly with increase in gel concentration. The initial modulus correlates with the electrical impedance with an R value of 0.89.

The percentage variation in electrical impedance and Young's modulus is shown in FIG 4 as a function of gel concentration ranging from 20 to 50 percent. The percentage variation in Young's modulus increases linearly with increase in gel concentration. In all the above cases, the percentage variation in impedance increases exponentially. A correlation value of 0.88 was found between the Young's modulus and electrical impedance.

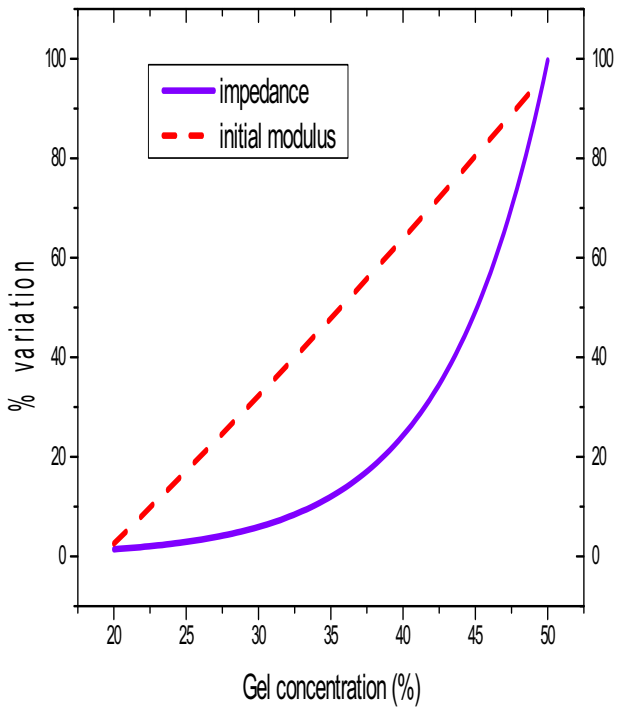


Fig. 3 Impedance and initial modulus Vs gel concentration

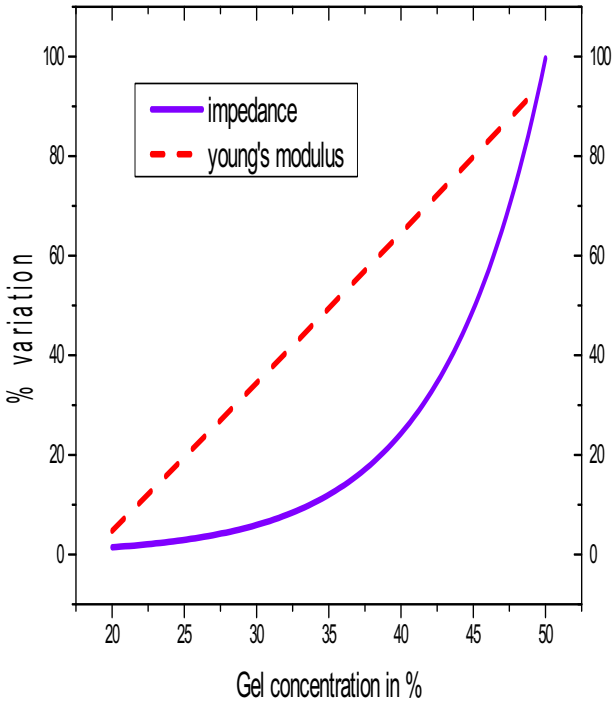


Fig. 4 Impedance and young's modulus Vs gel concentration

IV. Conclusions

Intact electrical and mechanical behavior of tissues is essential for proper physiological function. High degrees of correlations between electrical and mechanical properties have been shown in several cases such as in cardiac tissues. However, very few results are available on the correlation of electrical and mechanical behavior of soft tissues. In this work, an attempt has been made to correlate the electrical properties of tissue mimicking phantoms with mechanical properties. Tissue mimicking phantoms were prepared such that its mechanical properties fall in the physiological range to match the properties of tissues such as that of liver. The impedance measured on phantoms are correlated with breaking stress, breaking strain, initial modulus and Young's modulus in polyacrylamide gels. Results demonstrate that the changes in electrical impedance correlate well with Young's modulus, initial modulus and breaking stress. Hence, it appears that these studies are clinically useful as these gels are found to be similar to real tissues in many aspects.

REFERENCES

1. Parag R. Dhar, Jean W. Zu. (2007) Design of a resonator device for in vivo measurement of regional tissue viscoelasticity. Sensors and Actuators A 133:45–54.
2. Mostafa Fatemi, Armando Manduca, James F. Greenleaf. (2003) Imaging Elastic Properties of Biological Tissues by Low-Frequency Harmonic Vibration, IEEE Proc. Vol. 91. No. 10.
3. Ramon Q. Erkamp, Andrei R. Skovoroda, Stanislav Y. Emelianov et al. (2004) Measuring the Nonlinear Elastic Properties of Tissue-Like Phantoms. IEEE Proc. Vol. 51, IEEE transactions on ultrasonics, ferroelectrics, and frequency control.
4. Ken-ichi Kawabata, Yasuharu Waki, Tsuyoshi Matsumura et al. (2004) Tissue Mimicking Phantom for Ultrasonic Elastography with Finely Adjustable Elastic and Echographic Properties.
5. Jonathan P. Whiteley, Martin J. Bishop, David J. Gavaghan.(2007). Soft Tissue Modelling of Cardiac Fibres for Use in Coupled Mech-ano-Electric Simulations. Bulletin of Mathematical Biology 69: 2199–2225.

Author: Dr.S.Ramakrishnan
Institute: Madras Institute of Technology, Anna University
Street: Chromepet
City: Chennai
Country: India
Email: ramki@mitindia.edu

Biomechanical Analysis of Influence of Spinal Fixation on Intervertebral Joint Force by Using Musculoskeletal Model

H. Fukui[1], J. Sakamoto[1], H. Murakami[2], N. Kawahara[2], J. Oda[1], K. Tomita[2] and H. Higaki[3]

[1] Graduate School of Natural Science and Technology, Kanazawa University, Kanazawa, Japan
[2] Kanazawa University Hospital, Kanazawa, Japan
[3] Faculty of Engineering, Kyusyu Sangyo University, Fukuoka, Japan

Abstract — **Evaluation of the intervertebral joint force in vivo is very important for clinical spine problems, for example, spinal instability, disorder of intervertebral disc, compressive fracture of osteoporotic vertebra, etc. Direct measurement of the joint force is difficult to get permission, so computational method to calculate the force is expected. Spine structure is mainly constructed of many vertebrae and flexible intervertebral disks, and it is unstable by itself under standing condition. Supporting by erector muscles and ligaments keep the spine standing condition, so that loading condition of each vertebra depend on the muscle and ligament forces. Biomechanical analysis of musculoskeletal system taking into account of large number of muscle and ligament forces is necessary to determine the intervertebral joint force. Commercial software to deal with the musculoskeletal system is available nowadays, and it has been applied to clinical, ergonomic or sport biomechanics problem.**

Surgery of spinal fixation is frequently operated for instability or disorder of intervertebral joints. Although stability of the joints is recovered and nervous symptom related with the disorder joints is relieved, additional trouble at adjoining joints with the fixation is concerned because excessive rigidity and posture change by the fixation makes load of the adjoining joints increase. It is required to evaluate the change of adjoining joint force by the fixation, to prevent additional trouble in advance. In this study, analysis of intervertebral joint force and muscle force was performed in the case with or without spinal fixation using full body musculoskeletal model developed by the AnyBody Modeling System (AnyBody Technology). The joint and muscle forces were evaluated under various posture of flexion and extension. Then influence of the spinal fixation on the intervertebral joint force at adjoining joints with the fixation was discussed.

Keywords — **Biomechanics, Musculoskeletal Model, Spine, Spinal Fixation, Adjoining Vertebra**

I. Introduction

Compression of spinal cord due to spinal instability, disorder of intervertebral disk causes pain and palsy. To eliminate pressure on nerve and reduce symptoms, surgery on vertebral bone and disk is carried out. In such case, surgery fixing unstable vertebrae or intervertebral joint with rod and screw is frequently operated. This is the spinal fixation. Although stability of the joints is recovered and nervous symptom related with the disorder joints is relieved, additional trouble is caused at unfixed joints after surgery. Especially at adjoining joints with the fixation, deformations of vertebral bone and intervertebral disk are frequently caused. Additional surgery of spinal fixation is required in such case. The trouble is concerned because excessive rigidity and posture change by the fixation makes load of the adjoining joints increase. It is required to evaluate the change of adjoining joint force by the fixation, to prevent additional trouble in advance.

However, direct measurement of the joint force is difficult to get permission, and computational method to calculate the joint force is difficult because loading condition of each vertebra change by large number of muscle and ligament forces depended on posture at the time. With the recent development of computational mechanics technique, a more realistic biomechanical analysis become possible, and commercial software to deal with the musculoskeletal system is available. Evaluation of the intervertebral joint force using full body musculoskeletal model is available, too.

In this study, to evaluate spinal fixation influence on vertebral loading condition, we analyzed intervertebral joint force and muscle force performed in the case with spinal fixation using full body musculoskeletal model. The joint and trunk muscle forces were calculated under various posture of flexion and extension. And then, we discussed the influence of the spinal fixation on the intervertebral joint force.

II. Analysis Method

A. The AnyBody Modeling System

Musculoskeletal model was developed using the simulation software the AnyBody Modeling System (AnyBody Technology Inc.). This software handles model of human body mechanism, and the application area is medical, rehabilitation, ergonomic, sports or astronautical engineering, etc. By using the AnyBody Modeling System, we can de-

Chwee Teck Lim, James C.H. Goh (Eds.): ICBME 2008, Proceedings 23, pp. 1712–1715, 2009
www.springerlink.com

velop 3-D musculoskeletal model by a script language called AnyScript. Model consists of segments regarded as bones or rigid elements, joints connecting segments, and muscle-tendon units having physiological characteristics. Driver modules of the AnyScript create posture and movement of joints. The AnyBody Modeling System calculates the joint and muscle forces from giving posture and external load by inverse dynamic analysis.

B. Analysis model

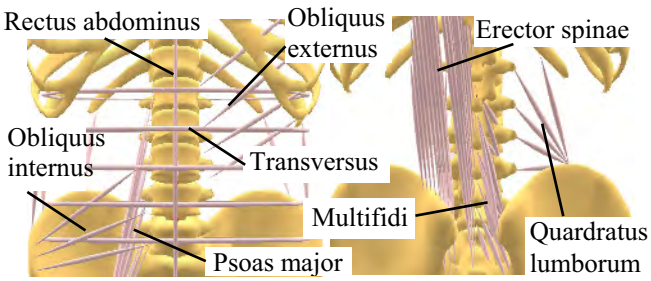
Analysis model was developed based on the Standing Model (the AnyBody Research Project, Aalborg University, Aalborg, Denmark, http://www.anybody.aau.dk/repository) which was human full body musculoskeletal model (Fig. 1).



(a) (b) (c)

Fig. 1 Analysis model : (a) 30 degrees extension posture, (b) upright posture, and (c) 45 degrees flexion posture.

Total number of muscle fascicles defined in this musculoskeletal model is 476. In trunk of model 158 fascicles were defined and divided into eight muscles (Fig. 2). Four abdominal muscles were included : rectus abdominus, transversus, obliquus internus and obliquus externus. Quadratus lumborum, psoas major, erector spinae and multifidi were defined as muscles of the lower-back [1].



(a) (b)

Fig. 2 Trunk of model in (a) front view and (b) back view. Eight muscles are defined as trunk muscles.

Spine model is composed of nine segments : sacrum, five lumbar vertebrae, T12, T11 and a lumped thoracic part over T10. Spherical joint with three degrees of freedom was set between every vertebra from T10 to sacrum(Fig. 3). These intervertebral joint angles were varied in according to spinal alignment or posture. Height of the model is set as 1.72m and weight is 63kg assuming a standard Japanese male.

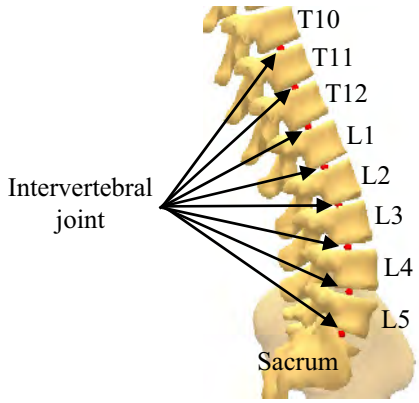


Fig. 3 The dots show the location of the rotational center of the intervertebral joints between the vertebrae.

C. Spinal fixation model

Spinal compression fracture is commonly caused on thoracolumbar vertebrae. Disk hernia or spondylolisthesis is frequently caused on lumbar. So, two cases are assumed as model with spinal fixation. One is case that thoracolumbar vertebrae is fixed, another is case that lumbar vertebrae is fixed. T12, L1 and L2 are fixed in the thoracolumbar vertebrae fixed model. L3, L4 and L5 are fixed in the lumbar vertebrae fixed model. Intervertebral joints between fixed vertebrae have no degrees of freedom in the model. Fixed vertebrae moved together as a rigid element when posture of the model was changed.

D. Analysis condition

Upper body angle of the model was changed from 45 degrees flexion to 30 degrees extention with 15 degrees interval. Posture of the model was set by changing intervertebral joints and hip joint angles. Joint angles of each posture in no fixation model were defined by using radiograph images of lumbar spine taken from a young male[2]. In case of the spinal fixation model, we gave larger joint angle to unfixed joints to compensate for lack of movement of fixed joints. Compensate joint angle were distributed equally among unfixed joints. We calculated intervertebral joint force and trunk muscle force in the case

with or without spinal fixation under each posture of flexion and extension. Influence of the spinal fixation on the intervertebral joint force at adjoining joints with the fixation was discussed.

The solution of the muscle recruited problem is minimization of the maximal muscle activity under constraints of the static equilibrium equations. Muscle activity means muscle force divided by the maximal isometric muscle force at each muscle's current working condition. The solution is equivalent to minimum muscle fatigue and it is computationally-efficient[3].

III. Analysis Result

A. Influence on trunk muscle

Influence of spinal fixation on back muscles is larger than one on abdominal muscles. Muscle forces of the back are shown in Fig. 4. These graphs show muscle forces comparing the cases of thoracolumbar vertebrae fixed, lumbar vertebrae fixed and no fixed. Analysis results of no fixation model show quadratus lumborum and psoas major work a lot in extension posture. Erector spinae works mainly in flexion posture and multifidi brings force in deep flexion posture. In flextion of 30-degree and 45-degree, multifidi muscle force of thoracolumbar vertebrae fixed model is larger than no fixation. Forces of the every back muscle of lumbar vertebrae fixed model are not larger than no fixation. So influence on muscle maintaining flexion posture is larger in case of thoracolumbar vertebrae fixed than case of lumbar vertebrae fixed.

In extension posture of 30-degree, quadratus lumborum and multifidi muscle force became significantly larger by lumbar vertebrae fixed. Lumbar vertebrae fixation increase quadratus lumborum muscle force by about threefold, and multifidi muscle force by more than fourfold when upper body is extended. Every muscle of thoracolumbar vertebrae fixed model show little change. Therefore, influence on muscle maintaining extension posture is larger in case of lumbar vertebrae fixed than thoracolumbar vertebrae fixed. In extension posture of 15-degree, psoas major muscle force is larger than other postures, because this posture is unstable in which hip joint angle is large in extension direction and spine is bended in flexion direction. Especially, multifidi is most affected by spinal fixation, because it is located deep muscle layer and attached between lumbar vertebrae. It is thought that excessive muscle force affect on muscle near vertebrae due to spinal fixation.

B. Influence on intervertebral joints

Intervertebral joint forces in flexion 45-degree are shown in Fig. 5. This graph shows joint forces in vertebral axial direction about the cases thoracolumbar vertebrae fixed, lumbar vertebrae fixed and no fixed. L5-sacrum (L5-S) and L4-L5 joint force of thoracolumbar vertebrae fixed model are larger than no fixation model. Therefore loading of sacrum and lower lumbar vertebrae is increased. This is caused by changing a moment arm from lower vertebrae to

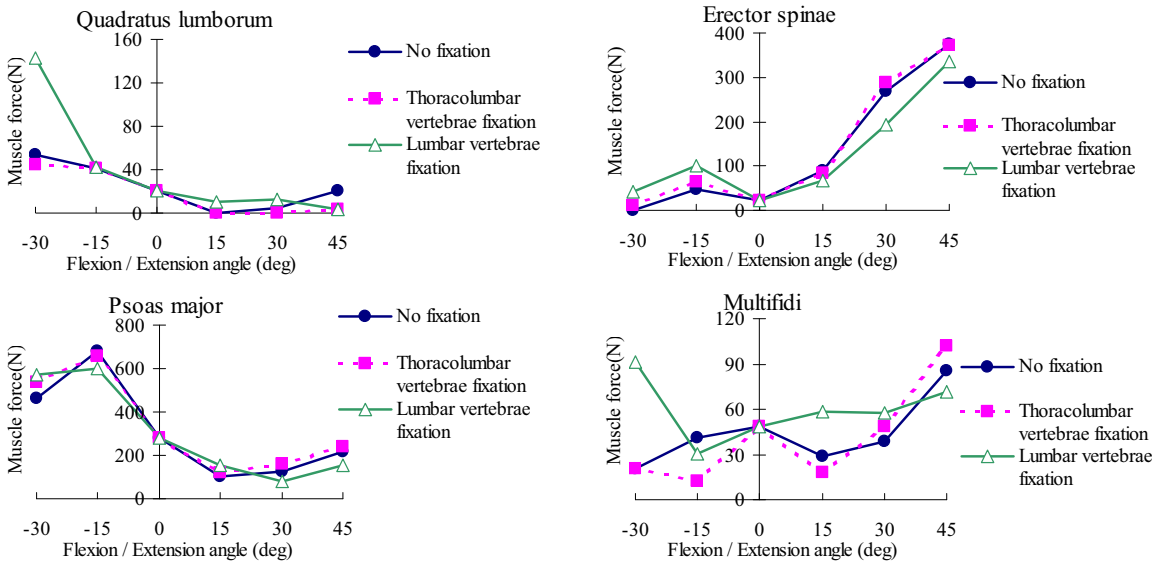


Fig. 4 Muscle forces of the back compared of the cases no fixation, thoracolumbar vertebrae fixation and lumbar fixation. Flexion angle is written positive value and extension angle is negative value.

center-of-gravity of the upper body. In flextion of deep angle, joint force of thoracolumbar vertebrae fixed model is increased. Consequently, influence of spinal fixation on intervertebral joint seems larger in lower vertebral joint when the upper body is flexed deeply.

Intervertebral joint forces in extension 30-degree are shown in Fig. 6. Joint forces on L5-S and L2-L3 of lumbar vertebrae fixed model are considerably larger than no fixation, and the force in L2-L3 joint of thoracolumbar vertebrae fixed model is greatly increased. These joints are adjoining to fixed vertebrae. Influence on adjoining intervertebral joints in flexion of 45-degree and extension of 30-degree are shown in Table 1. In thoracolumbar vertebrae fixed model, upper side of fixation is T11-T12 joint and its bottom side is L2-L3 joint. In lumbar vertebrae fixed model, upper and bottom of fixation is L2-L3 and L5-S joint. Although forces of adjoining joints in flexion posture are increased little, those in extension posture are increased at about 20% and 30%. Loading of adjoining vertebrae and disk might be greatly increased and develop disorders when a patient with spinal fixation takes extension posture.

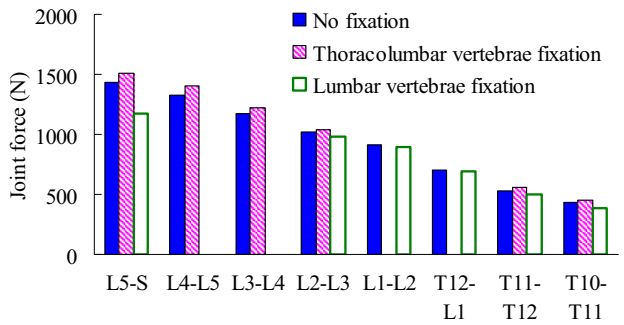


Fig. 5 Joint forces in vertebral axial direction in flexion 45-degree. Comparison of with and without fixation.

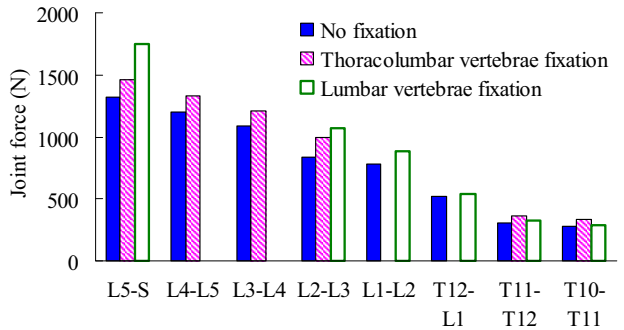


Fig. 6 Joint forces in vertebral axial direction in extension 30-degree. Comparison of with and without fixation.

Table 1 Influence on intervertebral joint adjacent to fixed vertebrae

Fixed part	Changes of joint force			
	Flexion of 45-degree		Extension of 30-degree	
	Upper side	Bottom side	Upper side	Bottom side
Thoracolumbar	+30N (+5.66%)	+20N (+1.96%)	+58N (+19.0%)	+167N (+20.0%)
Lumbar	-44N (-4.31%)	-260N (-18.2%)	+237N (+28.5%)	+430N (+32.6%)

IV. Conclusions

In this study, we analyzed influence of the spinal fixation on the intervertebral joint force using full body musculoskeletal model developed by the AnyBody Modeling System. Following conclusions were obtained.

(1) Excessive forces were produced in muscles near and attached lumbar vertebrae by spinal fixation.

(2) Which vertebra and muscle act big force depends on spinal fixation level and patient's posture.

(3) In flextion of deep angle, loading of lower lumbar vertebrae was increased when thoracolumbar vertebrae were fixed. It is recommended to avoid taking deep flexion posture for patients with thoracolumbar vertebrae fixation.

(4) Under extension posture, loading of adjoining vertebrae and disk with the fixation were greatly increased and subject to additional disorders. It is recommended to avoid taking excessive extension posture for patients with spinal fixation.

Although we described only spinal fixation in this paper, biomechanical analysis of musculoskeletal system will be applied many orthopedic problems. Significantly contribute will be expected for orthopedic therapies.

Acknowledgment

I would like to thanks to Yasushi NAKADA, Graduate School of Natural Science and Technology, Kanazawa University, for invaluable support.

References

1. Mark de Zee, et al. (2007) A generic detailed rigid-body lumbar spine model, *Journal of Biomechanics,* Vol.40, Issue 6, 1219-1227.
2. Jiro Sakamoto, et al (2005) Musculoskeletal analysis of spine and its application for spinal fixation by instruments, Proc. 2005 Int. Symp. Comp. Simulation Biomech., Cleveland, 19-20.
3. Michael Damsgaard, John Rasmussen, et al. (2006) Analysis of musculoskeletal systems in the AnyBody Modeling System, *Simulation modelling Practice and Theory,* Vol.14, Issue 8, 1100-1111.

Preventing Anterior Cruciate Ligament Failure During Impact Compression by Restraining Anterior Tibial Translation or Axial Tibial Rotation

C.H. Yeow[1], R.S. Khan[1], Peter V.S. Lee[1,3,4], James C.H. Goh[1,2]

[1] Division of Bioengineering, National University of Singapore, Singapore
[2] Department of Orthopaedic Surgery, National University of Singapore, Singapore
[3] Biomechanics Lab, Defence Medical and Environmental Research Institute, Singapore
[4] Department of Mechanical Engineering, University of Melbourne, Australia

Abstract — **Anterior cruciate ligament injury is highly prevalent in activities that involve large and rapid landing impact loads. We hypothesize that restraining anterior tibial translation or axial tibial rotation can prevent the anterior cruciate ligament from failing at the range of peak compressive load that can induce ligament failure when both factors are unrestrained. Sixteen porcine knee specimens were mounted onto a material-testing system at 70-deg flexion. Single 10-Hz haversine impact compression was successively repeated with incremental actuator displacement until ligament failure/visible bone fracture was noted. During impact compression, rotational and translational data of the knee joint was obtained using motion-capture system via markers attached to the setup. Specimens were randomly classified into four test groups: Q (unrestrained setup), A (anterior tibial translation restraint), R (axial tibial rotation restraint) and C (combination of both restraints). The same impact protocol was applied to all specimens. Q specimens incurred anterior cruciate ligament failure in the form of femoral avulsion; the peak compressive forces during failure ranged from 1.4-4.0 kN. A, R and C specimens underwent visible bone fracture with ligament intact; the peak compressive force during fracture ranged from 2.2-6.9 kN. The posterior femoral displacement and axial tibial rotation for A and R specimens respectively were substantially lower relative to Q specimens. Both factors were significantly diminished in C specimens but the peak compressive force was larger compared to Q specimens. Significant restraining of these factors was able to prevent anterior cruciate ligament failure in an impact setup that can induce ligament failure with the factors unrestrained.**

Keywords — **Injury prevention, anterior cruciate ligament failure, compressive impact, tibial translation, axial rotation**

I. Introduction

Anterior cruciate ligament (ACL) ruptures has been estimated at 95,000 cases annually in the United States with associated treatment costs of almost one billion dollars [1]. ACL injury is highly prevalent in sports involving large and rapid landing impact loads, such as basketball and skiing. The ACL serves as primary and secondary restraints to anterior tibial translation and axial tibial rotation respectively [2]. Hence, excessive anterior tibial translation and axial tibial rotation are potential risk factors in ACL injury mechanism. ACL knee bracing prevents aggravated anterior tibial translation and axial tibial rotation in order to relieve ACL strain or stabilize an ACL-deficient knee. Several studies have performed functional tests to assess the effectiveness of ACL bracing in response to external loading. Beynnon et al. [3] observed that bracing protected the ligament by substantially mitigating the ACL strain in response to anterior-directed loading and internal-external torque of the tibia. However, Ramsey et al. [4] noted that there were no consistent attenuations in anterior tibial translation and bracing the ACL-deficient knee resulted in insignificant kinematics differences for tibiofemoral joint motion. It seemed controversial whether these braces were effective in serving their intended functions. There is no clear evidence that these braces can reduce anterior tibial translation and axial tibial rotation, and relieve ACL loading during injurious landing. Currently, there is no direct evidence to prove that restraining anterior tibial translation or axial tibial rotation prevents ACL failure. The study aimed to show in a previous experimental setup, in which ACL failure can be induced via impact compression, that the introduction of restraint fixtures for anterior tibial translation or axial tibial rotation will avert ACL failure. We hypothesize that restraining anterior tibial translation or axial tibial rotation can prevent the ACL from failing at the range of peak compressive load that can induce ligament failure when both factors are unrestrained.

II. Methods

A. Specimen Preparation

Sixteen porcine hind legs (pig age: ~2 months; weight: ~40 kg) were obtained at a local abattoir (Primary Industries, Singapore). Both tibia/fibula and femur were sectioned 15 cm from knee joint centre along the anatomical axes with surrounding soft tissues kept intact. The sectioned ends were then centrally-potted in dental cement (Base-liquid & powder, Dentsply, China), secured to steel potting

Chwee Teck Lim, James C.H. Goh (Eds.): ICBME 2008, Proceedings 23, pp. 1716–1719, 2009
www.springerlink.com

cups using screws and then mounted onto the Material Testing System (810-MTS, MTS Systems Corporation, USA).

B. Experimental setup

The setup, adapted from a previous study [5], constrained the mounted specimen to 70-deg flexion to simulate landing posture. The tibia/fibula was limited to axial z-displacement and rotation while the femur was restricted to transverse x- and y-displacements (Fig. 1). We attached passive markers on the tibial potting cup and femoral stage, and used a motion-capture system (ProReflex-MCU1000, Qualisys Motion-Capture Systems, Sweden) to obtain the marker trajectories necessary for determining rotational and translational motion of the tibia and femur respectively. A slight posterior preload was applied using a 5-kg weight through a pulley system.

C. Compression testing

The specimens were randomly classified into four test groups: Q (unrestrained setup), A (anterior tibial translation restraint), R (axial tibial rotation restraint) and C (both restraints, Fig. 1). All specimens were subjected to the same impact protocol. The mounted specimens were adjusted via MTS to eliminate tensile/compressive preloading. Impact compression was performed by displacement control at a single haversine of 10-Hz frequency [5] to simulate a landing impact. The compression trial was successively repeated with incremental actuator displacement of 1 mm; after each trial, the specimens were returned to the initial position before the subsequent trial. The compressive force response was measured by the triaxial load-cell (9347B, Kistler, Switzerland). A significant drop ($\geq$70%) in compressive force (F_{drop}) response was taken as a major ACL failure; F_{drop} was estimated from the difference between the peak compressive force (F_{peak}) during impact compression and the mean compressive force during post-compression time period 300-500 ms. The impact tests were ended when either a significant F_{drop} was observed (presence of major ACL failure) or a visible bone fracture was present (absence of major ACL failure). Presence/absence of ACL failure was confirmed via dissection. Posterior femoral displacement and axial tibial rotation angle at F_{peak} were obtained based on the tibial and femoral marker trajectories.

D. Statistical analysis

One-way ANOVA was performed between test groups to compare F_{peak}, F_{drop}, posterior femoral displacement and axial tibial rotation. All significance levels were set at p=0.05.

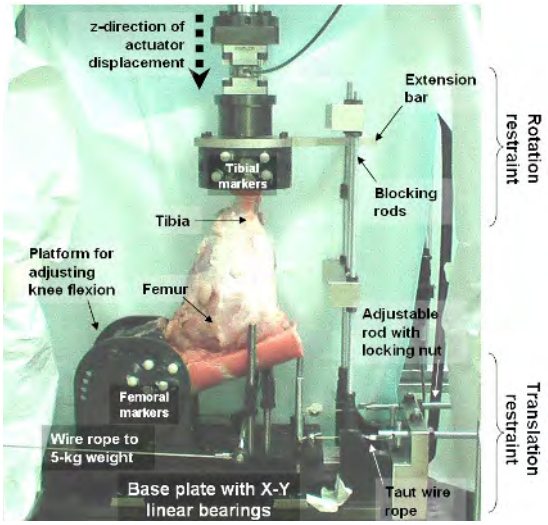


Fig 1 Experimental setup with both restraints

III. Results

All Q specimens underwent ACL failure via femoral avulsion, with mean F_{peak} of 3.0[1.1]kN. Corresponding posterior femoral displacements and axial tibial rotation angles at F_{peak} were 18.7[7.3]mm and 9.2[5.9]deg respectively. All A, R and C specimens developed visible bone fracture with the ACL intact. The mean F_{peak} obtained during fracture were 4.9[1.9], 3.9[0.7] and 5.5[1.2]kN for A, R and C respectively. Corresponding posterior femoral displacements were 1.5[0.9], 15.8[2.6] and 0.8[0.4]mm respectively while the axial tibial rotation angles were 16.1[8.7], 0.9[0.8] and 0.7[0.3]deg (Table 1). C specimens had a significantly higher F_{peak} ($p<0.05$) compared to Q (Fig. 2A). A, R and C specimens had substantially lower F_{drop} ($p<0.001$) compared to Q (Fig. 2B). The posterior femoral displacements for A and C were significantly lower ($p<0.001$) relative to Q and R (Fig. 2C). For axial tibial rotation angles, R and C had substantially lower rotation angles ($p<0.05$) compared to Q and A (Fig. 2D).

Table 1 Summary of mean peak compressive forces, posterior femoral displacements and axial tibial rotation angles for all test groups

Group	Peak Compressive Force (kN)	Posterior Femoral Displacement (mm)	Axial Tibial Rotation Angle (deg)
Q	3.0[1.1]	18.7[7.3]	9.2[5.9]
A	4.9[1.9]	1.5[0.9]	16.1[8.7]
R	3.9[0.7]	15.8[2.7]	0.9[0.8]
C	5.5[1.2]	0.8[0.4]	0.7[0.3]

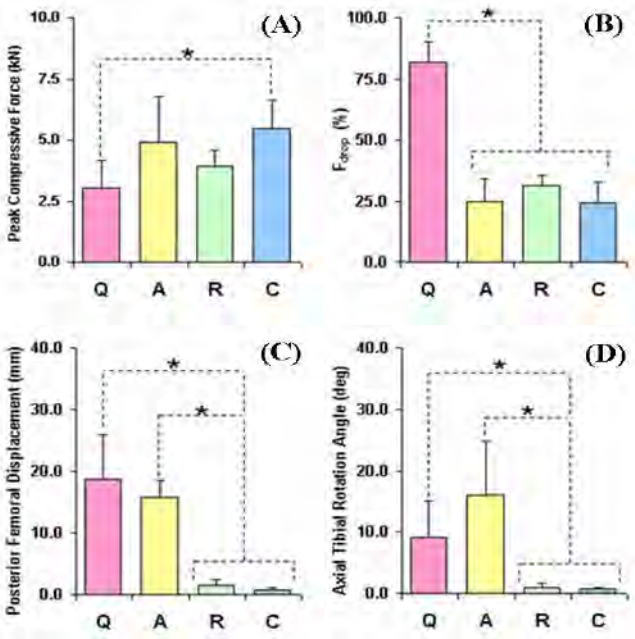


Fig. 2 Comparison of F_{peak} , F_{drop}, posterior femoral displacement and axial tibial rotation between test groups. (* significant difference, $p<0.05$)

IV. Discussion

The range of F_{peak} during ACL failure trials for Q was observed to be close to values obtained previously [5]. When posterior femoral translation (or relative anterior tibial translation) was restrained in A, we noted a significant reduction in posterior femoral displacement while axial tibial rotation was still present (Fig. 2D). This finding demonstrated that impact compression can lead to axial tibial rotation independent of anterior tibial translation. When axial tibial rotation was restrained in R, we observed a considerable decline in axial tibial rotation angle while posterior femoral displacement was still present (Fig. 2C). This finding illustrated that impact compression can give rise to anterior tibial translation independent of axial tibial rotation These results further revealed that sole inhibition of either factor can prevent ACL failure during impact compression. When both factors were restrained in C, we found that the values for these two factors were substantially diminished compared to Q while F_{peak} was also significantly larger relative to Q. These findings suggest that upon restraining both factors, ACL failure was not achieved even at high F_{peak} observed in C. This strongly showed that the concomitant restraints of both factors may work synergistically to mitigate the risk of ACL failure.

A main limitation of this study was the use of a porcine model to investigate the effects of anterior tibial translation and axial tibial rotation restraints on ACL failure. Meyer and Haut [6] and Yeow et al. [5] found that excessive impact compression of the human and porcine knee joints led to ACL failure, which implied similar failure mechanisms between both models. Furthermore, Xerogeanes et al. [7] suggested that the porcine model is preferred for assessing human ACL function as they found similar in-situ ACL forces and load distribution between ligament bundles for both models. Altogether, this validated our choice of the porcine model for investigating the restraining effects on ACL failure mechanism. One other limitation was the absence of muscle contraction during impact compression. Dominant quadriceps activity has been observed in landing [8], which is known to increase ACL loading. Moreover, the hamstrings serves to provide a posterior tibial pull [9]; However, quadriceps and hamstrings forces during injurious landing are largely unknown; hence, it would be difficult to simulate physiological muscle forces. The addition of quadriceps/hamstrings forces may affect the propensity of the knee joint for ACL failure. Since our study sought to investigate the effects of restraining anterior tibial translation and axial tibial rotation, we thus omitted the muscle forces in our setup in order to allow a direct analysis of the restraining effects. Another limitation was that full inhibition of anterior tibial translation and axial tibial rotation was not attained. The restraint fixtures were not able to entirely abolish anterior tibial translation and axial tibial rotation in the presence of high and rapid impact compression. However, our results illustrated a substantial decrease in both factors with the restraint fixtures in place. ACL bracing will not totally eradicate anterior tibial translation/axial tibial rotation as the bracing is only cupped to the upper and lower legs, and not fixed to the femur/tibia bones; the bones will still experience some anterior tibial translation/axial tibial rotation despite wearing the brace. Based on our results, if the brace can considerably reduce anterior tibial translation and axial tibial rotation during impact landing, the ACL injury risk would be greatly lessened.

Collectively, our results demonstrated that anterior tibial translation and axial tibial rotation are key factors in the ACL failure mechanism during impact compression. The presence of a compressive impact force through the knee joint is a dominant contributor to both anterior tibial translation and axial tibial rotation; it can give rise to each factor independently, though either factor may contribute in a minor manner to the other factor. Restraining anterior tibial translation and/or axial tibial rotation can prevent ACL failure at the range of peak compressive loads that were able to induce ACL failure in an unrestrained condition. Our findings suggested that the anterior tibial translation and

axial tibial rotation are intrinsic mechanisms of the knee joint to transfer, in part, the compressive impact load to the ACL and relieve other soft tissue structures, such as articular cartilage, of excessive loading. Extreme anterior tibial translation and axial tibial rotation may transmit a major portion of the compressive impact load to the ACL, resulting in failure. However, when both these factors are inhibited, the ACL will receive negligible impact loading while the soft tissues in the knee joint will have to sustain most of the compressive impact load.

V. Conclusions

There is a need to be aware that the use of braces that restraint the above factors may heighten the injury risk in other soft tissue structures. This is highly relevant for the articular cartilage, which is prone to traumatic lesions that may accelerate the onset of osteoarthritis [5]. In addition, though several studies have proven that braces which restrain these factors can mitigate ACL loading, no studies has yet to show that these braces can substantially diminish ACL injury risk during injurious landing. Our study established that significant restraining of these factors was able to prevent ACL failure in an impact setup that can induce ligament failure with the factors unrestrained. Our results would support a follow-on cadaveric study, which would be pertinent for understanding ACL injury prevention in humans.

Acknowledgment

This work was funded by the Academic Research Fund (R175-000-062-112), National University of Singapore, and the Defence Medical and Environmental Research Institute, Singapore.

References

1. Griffin LY. Agel J, Albohm MJ, et al (2000) Noncontact anterior cruciate ligament injuries: risk factors and prevention strategies. J Am Acad Orthop Surg 8:141-150
2. West RV, Harner CD (2005) Graft selection in anterior cruciate ligament reconstruction. J Am Acad Orthop Surg 13:197-207
3. Beynnon BD, Johnson R, Fleming B, et al (1997) The effect of functional knee bracing on the anterior cruciate ligament in the weightbearing and nonweightbearing knee. Am J Sports Med 25:353-9
4. Ramsey DK, Lamontagne M, Wretenberg PF, et al (2001) Assessment of functional knee bracing: an in vivo three-dimensional kinematic analysis of the anterior cruciate deficient knee. Clin Biomech (Bristol, Avon) 16:61-70
5. Yeow CH, Cheong CH, Ng KS, et al (2008) Anterior cruciate ligament failure and cartilage damage during knee joint compression: a preliminary study based on the porcine model. Am J Sports Med 36:934-42
6. Meyer EG, Haut RC (2005) Excessive compression of the human tibio-femoral joint causes ACL rupture. J Biomech 38:2311-6
7. Xerogeanes JW, Fox RJ, Takeda Y, et al (1998) A functional comparison of animal anterior cruciate ligament models to the human anterior cruciate ligament. Ann Biomed Eng 26:345-52
8. Pflum MA, Shelburne KB, Torry MR, et al (2004) Model prediction of anterior cruciate ligament force during drop-landings. Med Sci Sports Exerc 36:1949-1958
9. O'Connor JJ (1993) Can muscle co-contraction protect knee ligaments after injury or repair? J Bone Joint Surg Br 75:41-8

Author: James Goh Cho Hong
Institute: National University of Singapore
Street: 27 Medical Drive, Singapore 117510
City: Singapore
Country: Singapore
Email: dosgohj@nus.edu.sg

The Analysis and Measurement of Interface Pressures between Stump and Rapid Prototyping Prosthetic Socket Coated With a Resin Layer for Transtibial Amputee

H.K. Peng[1], L.H. Hsu[1], G.F. Huang[2] and D.Y. Hong[1]

[1]Department of Mechanical Engineering, National Cheng Kung University, Tainan, Taiwan
[2]Department of Physical Therapy, Fooyin University, Kaohsiung, Taiwan

Abstract — **This study is to verify the applicability of the newly-developed prosthetic socket fabricated by rapid prototyping (RP) machine and then coated with a layer of resin to reinforce the flexural strength. This article aims to simulate and to measure the distribution of interface pressures on pressure tolerant (PT) and pressure relief (PR) areas of stump while amputee wearing a prosthesis and walking on a force platform. The results of comparison of the interface pressures between new type socket and conventional socket show that the RP socket could be made without using any plaster and the related information could be stored for further uses.**

The quasi-static method is introduced in finite element (FE) modeling to simulate amputee walking. From the results of simulation, it can evaluate whether the socket shape is acceptable or not. The verified socket model is then transferred to rapid prototyping machine to produce a required prosthetic socket. Moreover, coating a resin layer on the RP socket to reinforce its strength was proposed. To validate this new type of socket, the interface pressures were measured by attaching socket sensors on PT and PR areas of the specific stump before wearing the RP socket.

The results of measurement and simulation of the pressure distributions of the resin-reinforced RP socket and the used socket are similar in the whole stance phase. Comparing to the used socket, the new type socket can bear more pressures at patella tendon. The FE analysis method is effectively to assist the shape modification of stump and socket can then be designed for the production using rapid prototyping machine.

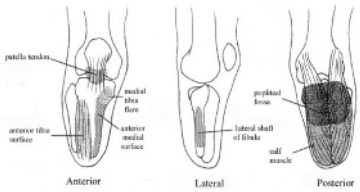
Keywords — **prosthesis socket, rapid prototyping, finite element**

I. Introduction

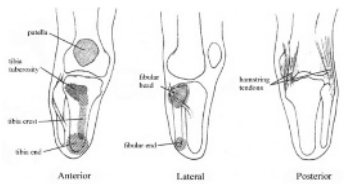
Prosthesis is a custom-made limb that substitutes the defective body segment of an amputee. When wearing prosthesis, socket is the major part that directly contacts stump of amputee, fit of contact areas significantly affects amputee's comfort when wearing prosthesis. [1] However, the quality of a socket of prosthesis depends on whether the distribution of interface pressures between socket and pressure-tolerant (PT) and pressure-relief areas (PR) (Fig. 1) of the stump is appropriate.

In this study fabricating a socket method introduces prototyping (RP) and computer-aid design (CAD) systems. The amputee specific stump geometry will be captured by T-Scan which is a handheld scanner, and then using CATIA to modify the stump geometric model, a new socket model was then created. Since the prosthetic socket is used to bear the weight of an amputee, the interface pressures between socket and stump should be evaluated. As soon as a socket has been designed, the pressures can be simulated using FE model. In addition, the analysis results could be compared with the regional local load-bearing ability [2]. After a designed socket has been verified, a RP machine FDM is utilized to manufacture the socket. To overcome the disadvantage of the socket made by a FDM machine that is liable to breakage, coating a layer resin to reinforce the RP socket is proposed in this study. The new method for fabricating socket procedure will be developed.

Although FE analysis could be evaluated the interface pressures, but any computerized model must be verified by experimental measurements, this study employs Pliance Mobile System to measure local pressure distribution on PT and PR areas, there were two sockets selected to measure pressures, resin-reinforced and original used sockets, the results will be compared. Once the FE analysis model is verified, the FE analysis an effectively tool is to assist the shape modification of stump and socket can then be designed for the production using rapid prototyping machine.



(a) PT areas



(b) PR areas

Fig. 1 Pressure-tolerant and pressure-relief areas

Chwee Teck Lim, James C.H. Goh (Eds.): ICBME 2008, Proceedings 23, pp. 1720–1723, 2009
www.springerlink.com

II. Finite Element Analysis Method

Stump and socket interface pressures is a major factor which influences socket's suitability and comfort when wearing prosthesis. To obtain accurate results, the investigation of the FE analysis model and experimental measurement are based on the same socket model. The geometry of the bone structure was reconstructed from CT scanned data, and stump model was from T-Scan data. The FE analysis model is composed of residual limb model, liner with 5 mm thickness and socket (Fig. 2).

These FE models were meshed by Marc, each part contact condition and material properties are listed in table1.2. At first pre-pressure was considered that stump and socket are synthesized before gait, pre-pressure will be sustained during initial gait simulation. As gait simulation, to adopt Quasi-Static boundary conditions, loads ware transformed form force platform date and applied on top surface of bone, and fixed bottom of socket.

After FE analysis finished, the results will be compared with measures experiment results, to validate the FE analysis model.

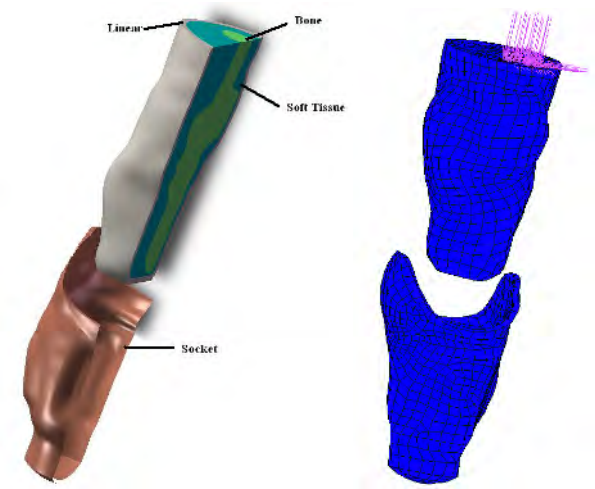


Fig. 2 FE analysis Models

Table 1 Material properties of the components of FE model [3]

	Young's Modulus (MPa)	Poisson's Ratio
Bone	15500	0.3
General Soft tissues	0.3	0.45
Patella Tendon	4	0.38
Tibia Crest, Tibia End	0.6	0.32
Popliteral Fossa	2.4	0.45
Linear	1	0.45
Socket	15000	0.13

Table 2 Contact conditions of components

	Bone	Soft tissue	Liner	Socket
Bone		Glue		
Soft tissue	Glue		Glue	
Linear		Glue		Friction (f=0.5)
Socket			Friction (f=0.5)	

III. Interface Pressures Measurement Method

A male volunteer weighing 60kg with a left below-knee amputation was selected in this experiment. Pliance Mobile System was employed to measure the local pressure distribution at the residual limb and socket interface. Prosthesis Sockets are resin-reinforced and original used sockets, remember resin-reinforced socket model was same as FE analysis model.

To begin with using porous sticky tape, attach the sensors on the positions of the stump which must be measured as Fig. 3. The positions measured in the experiment are as Table 3. The data will be synthesized with the gait cycle for stress analysis by the Pliance-X Expert. The resin-reinforced and original used sockets were introduced in this case, each socket was worn to measure the interface pressure five times, and after accomplishing the each sort of measurement, the volunteer can rest for 10 to 15 minutes. Connecting Pliance Mobile box to a computer by Bluetooth, the pressures data could be detected and recorded on the computer during measure experiment.



Fig. 3 Sensors attached to the stump

Table 3 PT and PR areas measured in this study

Pressure-tolerant(PT) areas	Pressure-relief (PR) areas
Patella tendon	Tibia end
Medial tibia flare	Tibia crest
	Fibular head
	Fibular end

IV. Results

The FE analysis results show that the area of patella tendon, which is the main pressure tolerant area, can bear more pressures (Fig. 4). The area of medial tibia flare, one of PT areas, can also share the bearing load. The areas of pressure relief including fibular head, tibia crest, tibia end and fibular end should bear as less pressures as possible. Based on the reference data provided by Zhang [2], the results of FE modeling are acceptable. The socket shape of the FE simulation model can be used to fabricate a physical prosthetic socket using rapid prototyping machine.

The resin-reinforced socket pressures experiment results are shown on Fig. 5, patella tendon, fibular head and tibia crest areas pressures are higher than other areas. Since the fibular end is the worst tolerant area [2], this study also made fibular end has the much lower pressure.

The local interface area pressures of FE analysis results and resin-reinforced socket measurement results were compared, original used socket measurement results was added to compare (Fig. 6), it was shown FE analysis could predict the trend of pressures. FE analysis model is verified with measure experiment results, FE is quite a practical tool for assisting prosthesis socket design. Based on basic criterion PT areas pressures are higher than PR areas, resin-reinforced socket performed a superior represent.

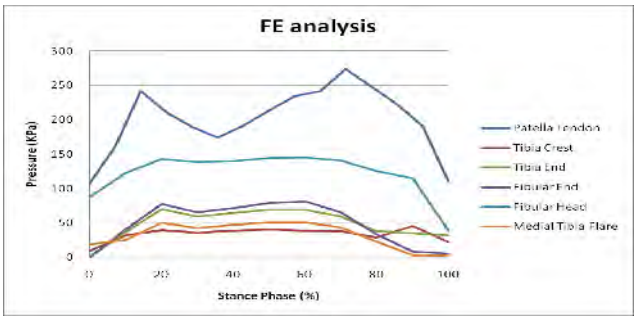


Fig. 4 FE analysis results

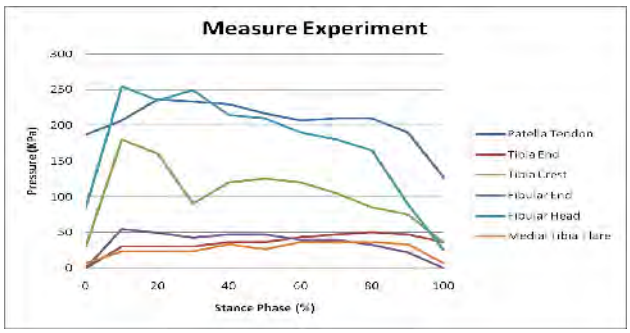
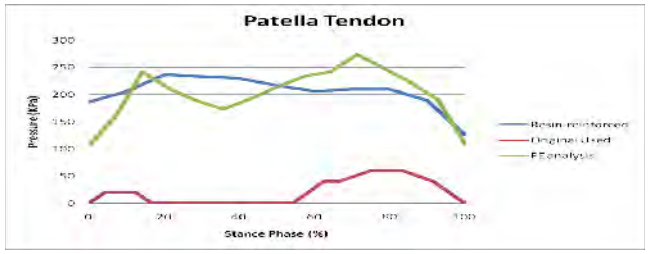
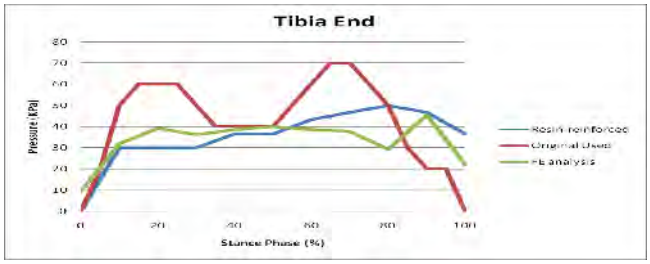


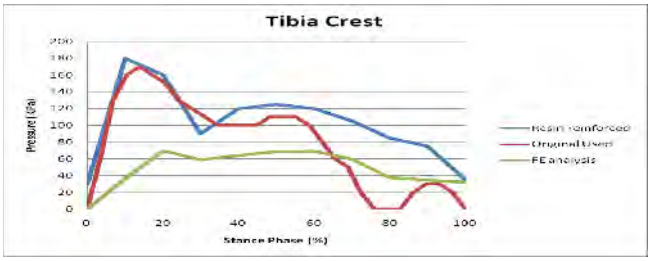
Fig. 5 Measurement experiment results



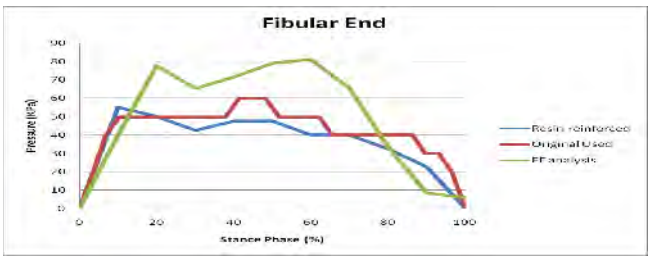
(a) Patella Tendon



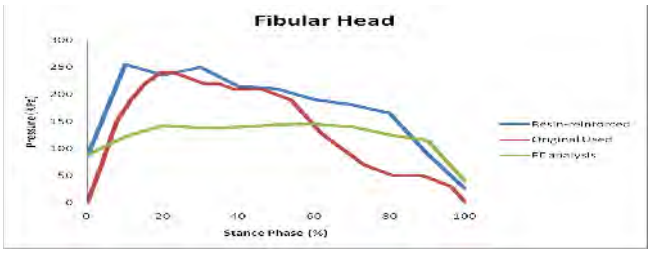
(b) Tibia End



(c) Tibia Crest



(d) Fibular End



(e) Fibular Head

Fig. 6 Comparison of PT and PR areas

V. Conclusions

Using FE analysis to evaluate the interface pressures between resin-reinforced RP socket and stump can assist the design of prosthetic socket geometry. As soon as the estimated pressures are acceptable, the verified socket will then be fabricated using RP machine. The results of measurement also show that the FE simulation model is valid to support the design of socket.

Within the case study of FE modelling, the material properties provided by published references were employed. [3]. However, the resin-reinforced socket is a new type socket, its material properties should be given by experiments. Although rapid prototyping is an applicable technology to fabricate socket and RP socket coated with a layer resin is to reinforce it strength, its endurance testing should be conducted.

Acknowledgment

The authors would like to thank the National Science Council Taiwan for its support through grant No. 97-2212-E-006-105.

References

1. Huang, G. F (2002) Gait analysis and Energy Consumption of Below-Knee Amputee with a New Prosthesis on Level Ground, Ramps and Stairs (in Chinese), Dissertation, Institute of Biomedical Engineering, National Cheng Kung University, Tainan, Taiwan.
2. Zhang, Ming and Lee, Winson C.C (2006) Quantifying the Regional Load Bearing Ability of Trans-Tibial Residual Limbs, Prosthetics and Orthotics International 30(1):pp. 25-34.
3. Zhang Ming, Mak AFT, Roberts VC (1998) Finite Element Modeling of a Residual Lower-Limb in a Prosthetic Socket: A Survey of the Development in the First Decade, Medical Engineering & Physics, Vol.20, No.5, pp.360-373.

Author: Hsun-Kun Peng
Institute: Department of Mechanical Engineering, National Cheng Kung University
Street: University Road
City: Tainan
Country: Taiwan
Email: n1696155@ncku.edu.tw

Analysis of Influence Location of Intervertebral Implant on the Lower Cervical Spine Loading and Stability

L. Jirkova[1], Z. Horak[1]

[1] Czech Technical University in Prague/Dept. of Mechanics, Biomechanics and Mechatronics, Prague, Czech Republic

Abstract — **Because nerve/spinal cord impingement (decompression surgery) and spinal instability (fusion surgery) of the cervical spine are worldwide problems, biomechanics research is very important for developing new treatment methods. Spinal instrumentation (such as a small plate, artificial intervertebral replacement or fusion) can also be used to help increase stability to the spine column. A disadvantage of the fusion is a decrease of mobility in dependence on the increasing of adjacent vertebrae and discs loads. The aim of presented study was an analysis of influence location of intervertebral implant on the lower cervical spine loading and stability. A three-dimensional finite element (FE) model of the multi-level cervical spine C3-C6 has been developed using computed tomography (CT) data, and applied to determination of movement of the implanted mobile artificial discs prosthesis on the biomechanical behavior of the lower cervical spine in this directions (flexion-extension, axial rotation, and lateral bending moments). Models accuracy was validated by comparing with previously published experimental and numerical results for flexion-extension, axial rotation, and lateral bending moments. The influence of the various surgical techniques on the cervical spine stiffness was compared at the same time. The intact spinal segment and the implanted spine was compared using artificial disc replacement Prodisc-C made by Synthes. The different types of artificial disc are going to be compare between each other. The technology of discs share similar goals of replacing the original disc, but differ in their designs and materials. By the definition of the optimal position range of replacements investigated (neutral zone of spine) would be minimized overloading of the soft tissue components (ligaments, adjacent discs) and instability of the spine as well. The output data was used for effective treatment of the patients. The results achieved have a large medical gain in neurology and spine surgery.**

Keywords — **cervical spine, biomechanics, implant, finite elements, artificial disc prosthesis**

I. Introduction

The human spine is a complex structure whose principal function are to protect the spine cord, transfer loads, moments and damp dynamic effects due to loading from the head and truck to the pelvis. The cervical spine instability is a common disease in clinical practice. Surgical treatments for degenerative disc disease can be grouped into two categories: fusion (arthrodesis) and total disc replacement (arthroplasty). Because fusion limits motion of the fused segments, it is believed that fusion may induce or accelerate degenerative change at adjacent levels. Disadvantage of fusion is the decrease of mobility in dependence on increase of adjacent vertebrae stability and disc load. None of the currently available artificial intervertebral discs respects all properties of natural disc as well (no shock absorption, no bending and torsion stiffness).

In recent years, computation modeling, especially Finite Element Method (FEM) has made an important contribution to the study and understanding of the behaviour of the spine. This method seems to be the most suitable approach to study spinal biomechanics due to 3D irregular geometry, non-homogenous material arrangement, large complex loading and movement, and non-linear response including contact at the facet joints [1]. As computing power and software capabilities have increased over the years, more complex model and spinal problems can be analyzed and investigated. According to [2], FEM has been used in spine research for a number of reasons: a) to examine biomechanical behaviour of the healthy spine, b) to assess the spinal performance when affected by disease, degenerative changes, trauma, ageing or surgery, c) to investigate the influence of various spinal intrumentation on spine behaviour, and d) to assist in the design and development of new spinal implants.

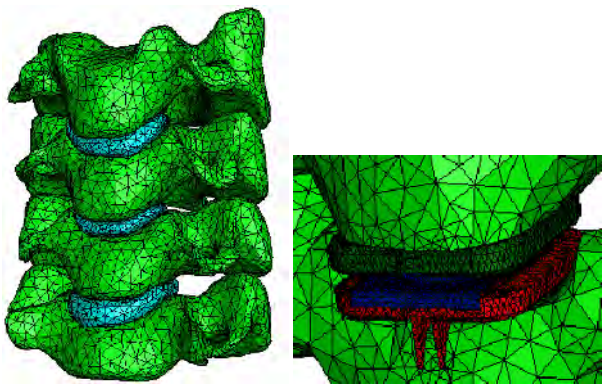
The objective of this study is to develop an experimentally validated three dimensional nonlinear finite element (FE) model of lower cervical spine using previously published data to provide useful information for artificial disc designers and examine the effects of surgical treatment on the structure for clinicians. The validated FE model was used to evaluate the mobil-type disc prosthesis on the range of motion in the multi-level C3-C6.

II. Materials and methods

A three-dimensional nonlinear model of a three-level ligamentous cervical segment (4 vertebrae and 3 discs) was built and implemented with the FEM software ABAQUS 6.6.3. Fig. 1. Two different configuration of the model were considered: a) a ‘healthy model’ was built and validated by

Chwee Teck Lim, James C.H. Goh (Eds.): ICBME 2008, Proceedings 23, pp. 1724–1727, 2009
www.springerlink.com

comparing with previously published data b) a 'mobile model' had the middle level implanted with a artificial intervertebral disc replacement Prodisc-C made by Synthes. The elements used in the model are available in Table 1. The mechanical characteristics of each spinal component used in the present study are based on published average values [3-10].



(a) (b)

Fig. 1 FE model of the cervical spine column C3-C6
a) healthy model by the motion in flexion, b) mobile model with the artificial disc implanted in C4-C5 in the flexion

Table 1 Material properties of the spinal components in the FE model

Description of bone and disc	Young´s Modulus [MPa]	Poisson´s ratio
Cortical bone	10000	0.29
Cancellous bone	100	0.29
Disc annulus	4.2	0.45
Disc nucleus	1	0.499
Endplate	500	0.4
Description of lig. [14]	**Stiffness [N/mm]**	-
Anterior longitudinal lig.	16.0±2.7	-
Posterior longitudinal lig.	25.4±7.2	-
Joint capsules	33.6±5.53	-
Lig. Flavum	25.0±7.04	-
Interspinous lig.	7.74±1.61	-

A. Reconstruction of the vertebrae and discs

The 3D geometrical details for FE model were obtained from computed tomography (CT) images of a 34-year-old man. The sequential DICOM files of lower cervical spine (C3-C6) were loaded into Mimics 11.1 (Materialise software), a software for visualization and segmentation of thee-dimensional (3D) scanned data, through which three-dimensional surface images were obtained from the sequential cross-section outline of the vertebrae at the 1-2 mm interval, depending on the regional geometrical complexity of the vertebra. The images were then converted and saved as a Binary STL files (Stereolithography format- CAD software), each vertebra having approximately 3000 surfaces, which were created as a triangles. These three-dimensional geometrical boundary data files were converted into a standard graphics exchange data format (inp), and were imported into a finite element package; ABAQUS 6.6.3. where all surface elements were converted to the volume elements.

B. Healthy model

A typical vertebra, appropriate to a C3, C4, C5 or C6 vertebra, was built in the two level model. The cortical and cancellous bones of the vertebral bodies were separately modeled. The thickness of the lateral cortical wall was 1 mm [3]. To develop the spinal motion segment (a functional unit), the intervertebral disc was modeled as three layers of solid alements: a) two layers (one superior and one inferior) to devone the endplates of the vertebral body. Each end plate has a thickness of about 0.5 mm, b) middle layer corresponding to the intervertebral disc comprised of the annulus and nucleus.

The thickness of the annulus in the anterior region was taken to be 1.2 times that of the posterior region, which was close to the publisher data [11]. The anterior disc height of 5.5 mm and posterior disc height of 3.5 mm were assumed which correspond to the published values [12]. Ligaments have an important role in spinal biomechanice and stability. The five intervertebral ligaments were incorporated and modeled as discrete axial connectors Tab.1. A natural ligament exhibits strong nonlinear load/deformation behaviour [13].

C. Mobile model

The mobile model of artificial dics replacement made by Synthes is called Prodisc. The disc consists of two cobalt-chromium-molybdenum alloy. The inlay is made of ultra-high molecular weight polyethylen (UHMWPE). The kinematics correspond to the point guidance in vertebral joints: The center of rotation is located just below the superior end plate of the affected caudal vertebral body. The location of the center of rotation and the flexion radius correspond to the natural point guidance in the vertebral joints. The physiological range of motion in begard to flexion/extension and lateral bending is restored. The axial rotation is limited only by the anatomical structures and not by the prosthesis. Pure translatory movements are not possible due to the ball and societ principle. The disc

prosthesis was implanted in C4-C5 level, and its effects on the entire levels from C3 to C6 were analyzed. To simulate the anterior surgical approach used for implantation of the artificial disc, the anterior longitudinal ligaments at C4-C5 level were removed in the FE analysis. Material properties used for Prodisc-C→CoCrMo (E=220GPa,ν=0.32), polyethylen inlay (E=1GPa,ν=0.49).

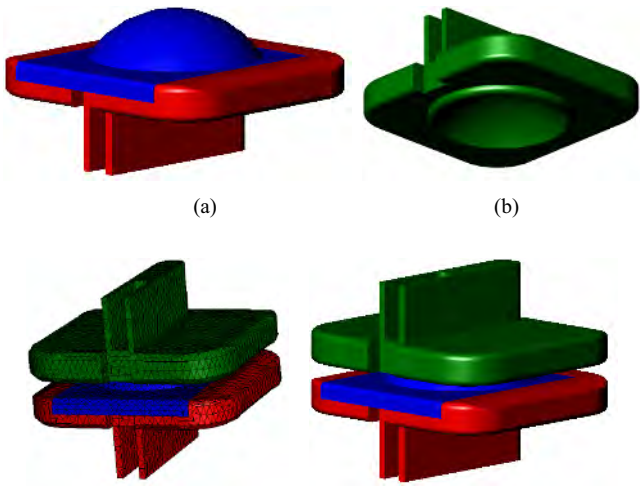


Fig. 2 Prodisc-C. Modular intervertebral disc prosthesis for restoring disc height and segmental motion in the cervical spine a) lower plate consists of CoCr Mo alloy and UHMWPE, b) upper plate-CoCrMo alloy, c) 3D set of the disc in the design software Rhinoceros, d) 3D meshed set with tetrahedral elements in ABAQUS

D. Simulation parameters

Loading conditions: Both models were loaded by a) 1.0 Nm flexion/extension moment, b) 1.0 Nm axial rotation moment, c) 1.0 Nm lateral bending moment. The loads were applied to the top surface of C3, while the bottom surface C6 was constrained the same way as in the in vitro experiments [4,15].

Boundary conditions: The translational degree of freedom of the nodes from the underlying endplate of the lowermost vertebra have been restricted completely.

III. Results

The two FE nonlinear models for physiological posture of the lower cervical spine (flexion, extension, lateral bending and rotation) was compared. The ROM and Stress response at the level (C3-C6) for two cases (intact and implanted spine) are shown at the Tab. 2 and 3. The segment movement-ROM of intact spine was higher than the implanted spine at C4-C5 by all of movemets with the exception rotation. These values ROM for the intact spinal segment are in very good accordance other measurements [16]. The ROM of the prosthesis implanted C4-C5 was reduced by about 50-70 % by (flexion, extension and right lateral bending). Under axial rotation moment, the ROM of the prosthesis implanted C4-C5 level is increases by about 18%. This is expected to result from the fact that the rotational moment in the intact disc is supported additionally by alternating annulus fibers with enhanced rotational stiffness. The maximal stress of the implanted segment at the bottom posterior region Fig. 3 was taken to be 2-3 times that of the intact one. The stress are concetrated on the bottom of the both plate and on the top of ball shape of middle plate (polyethylen) as well. The reason for this behaviour is given by the number of DOF of Prodisc-C, whose 3 DOF (3 rotation) decreases ROM and on the other hand the stress increases. The peaks of stresses are depicted in (Fig. 3, 2).

Table 2 Comparison of the ROM [°] between intact and implanted spine

Type of motion	Intact (no surgery)	Prodisc-C
Flexion	3.86	2.62
Extension	2.62	1.38
Right lateral moment	2.87	1.69
Rotation	1.65	1.95

Table 3 Comparison of the maximal Stress [MPa] between intact and implanted spine

Type of motion	Intact (no surgery)	Prodisc-C
Flexion	7.26	21.3
Extension	6.45	16.1
Right lateral moment	9.47	33.6
Rotation	5.32	12.2

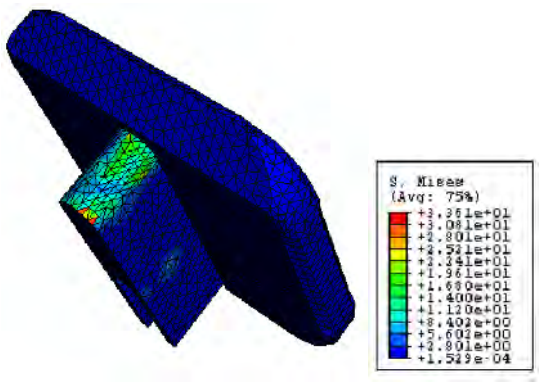


Fig. 3 Mises stress distribution at the bottom plate in direction (RLB)

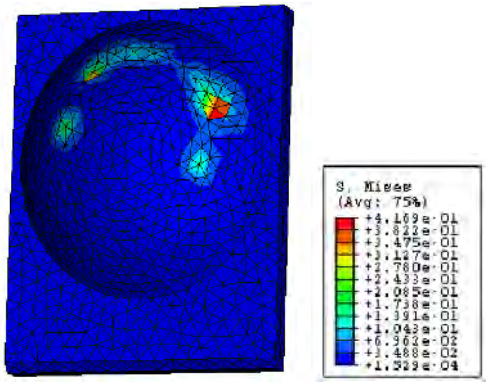


Fig. 4 Mises stress distribution at the polyethylen plate in direction (RLB)

IV. Conclusions

The FE analysis and experimental testing of cadaveric spine are the best method of investigating mechanical function and failure of the spine. Especially FE models can be used to explain experimental results of spine tissues.

The goal of this study was developing the anatomical nonlinear model of lower cervical spine. The movement of intact spine was validated with previously numerical and published results. In this project was carried out verification of modeling technique that is highly reproducible and objective. Nevertheless project is still in progress and the next step of this work is going to test next three mobile prosthesis, which has different mechanical properties and shapes as well. All is being researched in cooperation together with doctors from Motol-Hospital in Prague. The outputs are very useful for a clinical practices and surgeons. This biomechanics research is very important for developing new treatment methods as well.

Acknowledgment

The study was supported by a grant from Ministry of Education: Transdisciplinary research in Biomedical Engineering II, No. MSM 6840770012

References

1. Shirazi-Adl A, Parnianpour M, Computer techniques and computational methods in biomechanics, [in:] Biomechanical Systems Techniques and Applications, C. Leondes (ed.), CRC Press LLC, 2001, pp. 1-1:1-36.
2. Fagan M.J., Julian S., Mohsen A.M., Finite element analysis in spine research, Journal of Engineering in Medicine, 2002, 216, (Part H), pp. 281-298.
3. Yaganandan N, Kumaresan S.C., Voo L, Pintar F.A., Larson S.J., (1996) Finite element modeling of the C4-C6 cervical spine unit, Medical Engineering Physics, Vol. 18, No. 7, pp. 569-574.
4. Goel V.K., Clausen J.D., (1998) Prediction of load sparing aminy spinal components of a C5-C6 motion segment using the finite element approach, Spine, Vol. 23, No. 6, pp. 684-691.
5. Saito T., Yamamuro T., Shikata J., Oka M., Tsutsumi S., (1991) Analysis and prevention of spinal column deformity following cervical laminectomy, pathogenetic analysis of post laminectomy deformities, Spine, Vol. 16, pp. 494-502.
6. Shirazi-ADL S.A., Shrivastava S.C., Ahmed A.M., (1984) Stress analysis of the lumbar disc-body unit compression. A three-dimensional nonlinear finite element study, Spine, Vol. 9, No. 2, pp. 120-134.
7. Goel V.K., Monroe B.T., Gilbertson L.G., Brinkmann P., Nat R., (1995) Interlaminar shear stresses and laminae separation in a disc, Spine, Vol. 20, No. 6, pp. 689-698.
8. Maurel N., Lavaste F., Skalli W., (1997) A three-dimensional parameterized finite element model of the lower cervical spine. Study of the influence of the posterior facets, J. Biomechanics, Vol. 30, No. 9, pp. 921-931.
9. Kumaresan S., Yoganandan N., Pintar F.A., Voo L.M., Cusisk J.F., Larson S.J., (1997) Finite element modelling of cervical laminectomy with graded facetectomy, J. Spinal Disorders, Vol. 10, pp. 40-46.
10. Ueno K., Liu Y.K., (1987) A three-dimensional nonlinear finite element model of lumbar intervertebral joint in torsion, J. Biomechanical Engineering, Vol. 109, pp. 200-209.
11. Markolf K.L., (1972) Deformation of the thoracolumbar intervertebral joints in response to external loads, J. Bone and Joints Surgery, Vol. 11, pp. 1-14.
12. Gilad I., Nissan M., (1986) A study of vertebra and disc geometric relation of the human cervical and lumbar spine, Spine, Vol. 11, No. 2, pp. 154-157.
13. White A.A., Panjabi M.M., (1990) Clinical biomechanics of the spine, second ed. J.B. Lippincott Company, Philadelphia.
14. Yoganandan N., Kumaresan S., Pintar F.A., (2000) Geometric and mechanical properties of human cervical spine ligaments, J. of Biomechanical Engineering, Vol. 122, pp. 623-629.
15. Teo E.C., Ng H.W., (2001) Evaluation of the role of ligaments, taceta and disc nukleus in košer cervical spine under compression and sagittal moments using FA Metod, Med Eng Phys, Vol. 23, No. 3, pp. 155-64
16. Ha K.S., Finite element modeling of multi-level cervical spinal segments C3-C6 and biomechanical analysis of an eleastomer-type prosthetic disc (2005), Mechanical Engineering and Physics, Vol. 28, pp. 534-541

Author: Jirkova Lenka, Horak Zdenek
Institute: Czech Technical University in Prague
Street: Technicka 4
City: Prague
Country: Czech Republic
Email: iluze-lenka@seznam.cz

Computational Fluid Analysis of Blood Flow Characteristics in Abdominal Aortic Aneurysms Treated with Suprarenal Endovascular Grafts

Zhonghua Sun[1], Thanapong Chaichana[2], Manas Sangworasil[2] and Supan Tungjitkusolmun[2]

[1] Curtin University of Technology/Department of Imaging and Applied Physics, Perth, Western Australia, Australia
[2] King Mongkut's Institute of Technology Ladkrabang/Department of Electronic Engineering, Bangkok, Thailand

Abstract — **The purpose of this study is to investigate the hemodynamic effects of suprarenal stent grafts on the renal arteries in the treatment of patients with abdominal aortic aneurysm. Suprarenal stent grafts have been increasingly used for treatment of aortic aneurysms with suboptimal aneurysm necks. However, the long-term safety of this procedure is yet to be determined. 2 sample patients undergoing suprarenal stent grafting were included in the study. Four variable configurations of stent wires crossing the renal artery ostium were simulated in aorta models based on CT generated data, at different cardiac cycles. The stent wires thickness was set 0.5 mm which is similar to the actual diameter of a stent wire. Computational fluid dynamic analysis showed slightly decrease of flow velocity to the renal arteries with multiple wires crossing, and no changes of flow velocity to the renal arteries with single wire crossing. Our preliminary results demonstrated the safety of suprarenal stent grafting. Further studies are required to investigate the effect of different wire thickness on subsequent hemodynamic changes to the renal arteries.**

Keywords — **Aortic aneurysm, blood flow, suprarenal stent, stent graft.**

I. Introduction

Endovascular repair of abdominal aortic aneurysm (AAA) through insertion of a stent graft has been widely used as an effective alternative to conventional open surgery, especially in patients with co-morbid medical conditions [1-3]. Suprarenal fixation of stent grafts has been developed to be an alternative to conventional endovascular repair in patients with unfavourable aneurysm necks (short, severe angulation, thrombus, or calcification) [4,5]. Clinical studies have shown that suprarenal fixation of stent grafts did not lead to the deterioration of renal function, based on short to mid-term follow-up [4-7]. However, the long-term outcomes of suprarenal stent grafting are still not fully un-derstood. This is mainly due to the fact that the long-term safety of placing the suprarenal stents cross the renal arteries is not known with regard to its effect on the renal arteries or renal function.

Our previous in vitro and vivo studies using CT data did not show any significant interference of suprarenal stent wires with the cross-sectional area reduction or renal function [8, 9]. Researchers using computer-generated aorta models also reported no significant changes of flow velocity to the renal arteries with variable stent wires crossing the renal artery ostia [10]. Although these results demonstrated the safety of suprarenal stent grafts, a more realistic, accurate method based on real patient's data is necessary to validate the effect of stent wires on renal arteries with regard to subsequent blood flow changes.

Thus, the purpose of this study is to investigate the hemodynamic changes in patients treated with suprarenal stent grafts in two selected patients with AAA using computational fluid dynamics (CFD) analysis.

II. Materials and methods

A. Patient CT data

2 patients with abdominal aortic aneurysms undergoing suprarenal stent grafting were selected for inclusion in the study. The stent grafts used in the study were Zenith AAA endovascular graft with a suprarenal uncovered component of 2.5 cm placed above the renal artery for acquisition of proximal fixation. Pre-and post-stent grafting CT scans were performed with a multislice CT scanner 16x0.5 mm beam collimation (Medical Imaging Systems, Kingsbury, UK), and scanning protocol was section thickness 1 mm, pitch 2.0, reconstruction interval of 1mm and gantry rotation time was 0.5 second. The renal artery diameters of these two cases were measured between 4.0 to 5.2 mm.

B. Configuration of stent wires crossing the renal ostia

Original CT DICOM data (digital imaging and communication in medicine) pre-and post-stent grafting were transferred to a workstation equipped with Analyze V 7.0 (AnalyzeDirect, Inc., Lexana, KS, USA) for generation of 3D reconstructed images. Generation of intraluminal images of the stent wires in relation to the aortic ostia was performed using a CT number thresholding technique, which was de-scribed in detail before [11]. According to our previous experience of 3D imaging in endovascular repair, the supra-renal stent wires were found to cross the renal artery ostium in four different configurations [8, 11], namely: single wire centrally crossing, single wire peripherally

Chwee Teck Lim, James C.H. Goh (Eds.): ICBME 2008, Proceedings 23, pp. 1728–1732, 2009
www.springerlink.com

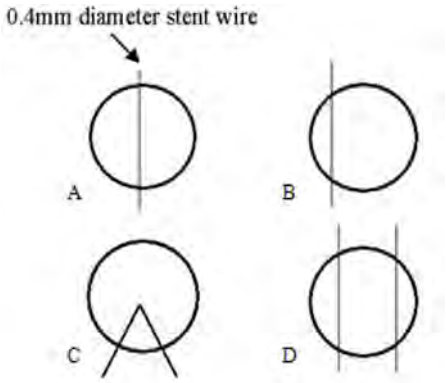


Fig. 1 Diagrams of different types of stent wires crossing the renal artery ostia.

crossing, V-shaped wire centrally crossing and multiple wires periphe-rally crossing. Figure 1 presents the diagrams of these types of configurations.

C. Generation of aortic mesh model

Generation of aorta model was performed with a semi-automatic segmentation technique using Analyze V 7.0. After segmentation, the 3D object surface of the model was created using surface extractor available on the Analyze software, and the 3D surface object was saved in the STL (stereolithography)', a common format for computed-aided design and rapid prototyping. The 'STL' file was converted into the CAD (computer aided design) model files using the CATIA V5 R17 (Dassault Systèmes, Inc., Suresnes Cedex, France). Figure 2 shows the segmented aorta models based on pre-and post-stent grafting CT data.

The blood flow model mesh was defined by tetrahedral volume mesh and three prism layers using ANSYS ICEM CFD 11 (ANSYS, Inc., Canonsburg, PA, USA). ANSYS ICEM CFD provides sophisticated geometric acquisition, mesh definition and mesh editing which is important for the accurately flow analysis. The blood wall model was defined by tetrahedral volume mesh using ANSYS Meshing 11 (ANSYS, Inc., Canonsburg, PA, USA).

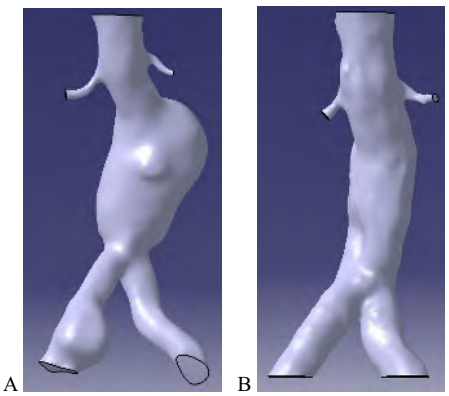


Fig. 2 pre- (A) and post- (B) stent grafting aorta models.

D. Simulation of intraluminal suprarenal stent wires

In order to simulate the intraluminal appearances of stent wires crossing the renal artery ostia, we generated a few models with a simulated wire thickness of 0.5 mm and placed in front of the renal artery ostia, as shown in Figure 3.

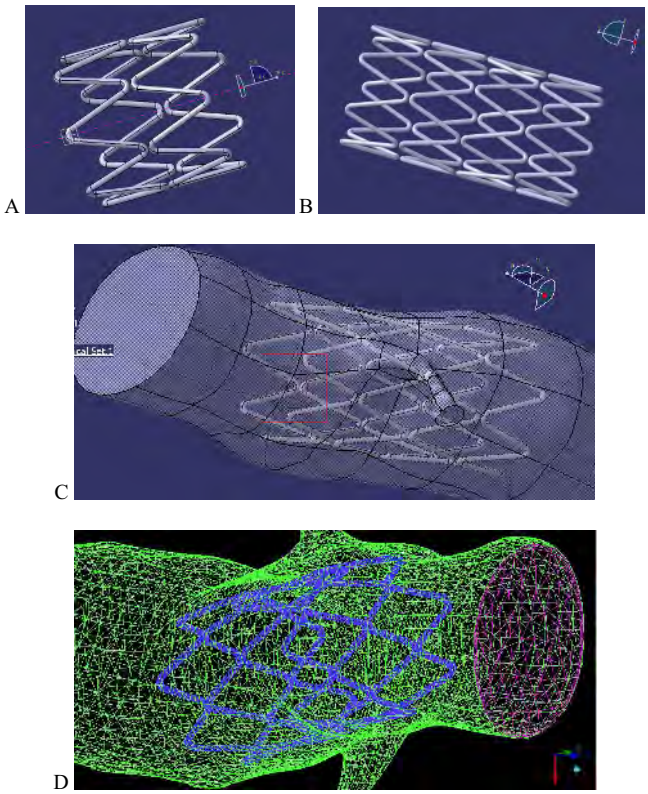


Fig. 3 A and B are simulated suprarenal stent wires, while 3C shows the appearance of stent wires placed inside the aorta model, and figure 3D demonstrates the simulated stent wires inside the mesh model.

E. Computational fluid dynamics (CFD)

In order to ensure that our analysis reflects the realistic environment of human blood vessel, normal physiological hemodynamic conditions should be considered for the 3D numerical simulations. The fluid and materials properties for different entities were referenced from a previous study [12]. In the current study, we compared the flow velocity at the aorta model containing the four arterial branches, name-

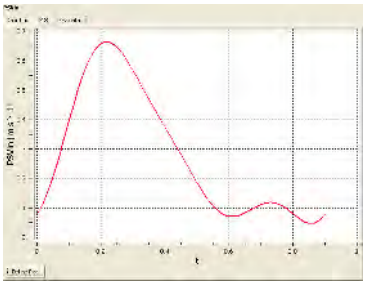


Fig. 4 Flow pulsatile in different cardiac cycles.

ly bilateral renal arteries and common iliac arteries prior to and after stent graft implantation. The blood flow was simulated at different cardiac phases (systolic and diastolic cycles) and measured in the aortic aneurysm, renal arteries and common iliac arteries using the ANSYS Multiphysic (ANSYS, Inc., Canonsburg, PA, USA) (Fig 4). Blood flow pattern, wall pressure, and wall shear stress before and after stent-graft implantation were visualized and compared.

The boundary conditions are time-dependent. The velocity inlet (abdominal aorta at the level of celiac axis) boundary conditions are taken from the referenced value showing measurement of the aortic blood velocity. A time-dependent pressure is also imposed at the outlets.

The solid is (blood wall) 1 mm thickness in all models. The solid density was set to 1120 kg/ m3, a Poisson ratio of 0.49, and a Young's modulus of 1.2 MPa, corresponding to the standard values cited in the literature [12].

The fluid is (blood) assumed to behave as a Newtonian fluid, as this was known for the larger vessels of the human body. The density was set to 1060 kg/m3 and a viscosity of 0.0027 Pa s, corresponding to the standard values cited in the literature [13]. Given these assumptions, the fluid dynamics of the system are fully governed by the Navier-Strokes equations, which provide a differential expression of the mass and momentum conservation laws [13]. The flow was assumed to be incompressible and laminar. The time step was set to start from 0 to 0.9 s with an interval of 0.025 s. The arterial wall was assumed to be deformable during flow analysis

III. Results

CFD analysis was successfully performed in all of these 2 cases with 4 aorta models (including both pre-and post-stent grafting). The artery wall was set at 1 mm thickness which reflects the actual diameter of the human artery vessel. All of the 4 renal arteries in these two patients were crossed by the suprarenal stent wires to variable extents with different configurations (single and multiple wires crossing). Details of suprarenal stents in relation to the renal arteries are as follows: the right renal artery ostium was crossed centrally by a single wire in patient 1 and multiple wires in patient 2; the left renal artery ostium was crossed by a single wire centrally and peripherally in both cases, respectively.

A. Hemodynamic analysis-flow velocity

Flow velocity was found to increase significantly inside the abdominal aorta following suprarenal stent grafting, indicating that the aneurysm was successfully excluded from the systemic blood circulation. The flow velocity slightly decreased at the right renal artery in patient 2 with multiple stent wires crossing (less than 5% reduction), while no apparent changes were noticed at the right renal artery in patient 1. Flow velocity was found to increase slightly at the left renal arteries on both cases. Similarly, no significant changes were observed at the common iliac arteries in both patients. Figure 5 shows the flow velocity observed in patient 1 pre-and post-stent grafting.

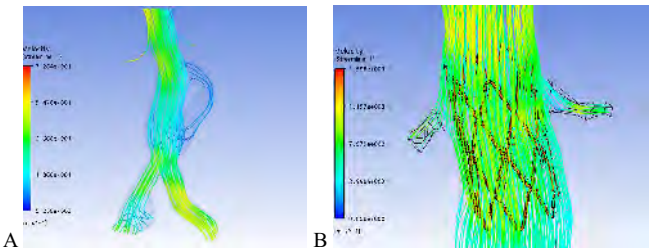


Fig. 5 shows the flow velocity in patient 1 pre- (A) and post- (B) suprarenal stent grafting.

B. Hemodynamic analysis-wall pressure and wall shear

Wall pressure and wall shear stress were measured at different cardiac cycles, and our results showed that the wall pressure slightly decreased after stent grafting. The wall pressure reaches the peak value at the systolic phase at about 0.3 s, both pre-and post-stent grafting. Figure 6 is an example of the wall pressure displayed in patient 2 pre- and post-stent grafting.

It is also observed that wall pressure is higher in the posterior aortic wall than that in the anterior wall, both pre-and post-stent grafting. This may be valuable to predict the location of rupture of aortic aneurysm. Figure 7 shows the wall pressure changes in patient 1 prior to and after suprarenal stent grafting.

Our results showed that wall shear was observed to change at the level of aortic aneurysms after stent grafting, as shown in Figure 8. While in other sections of the aorta, the change was not apparent.

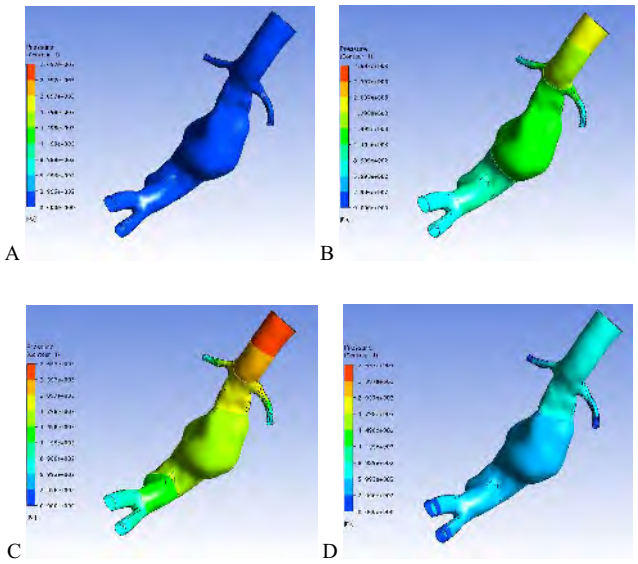


Fig. 6 Wall pressure was measured at 0.1 s, 0.2 s, 0.3 s and 0.8 s (A-D) pre-stent grafting, respectively, reaching the highest magnitude at 0.3s.

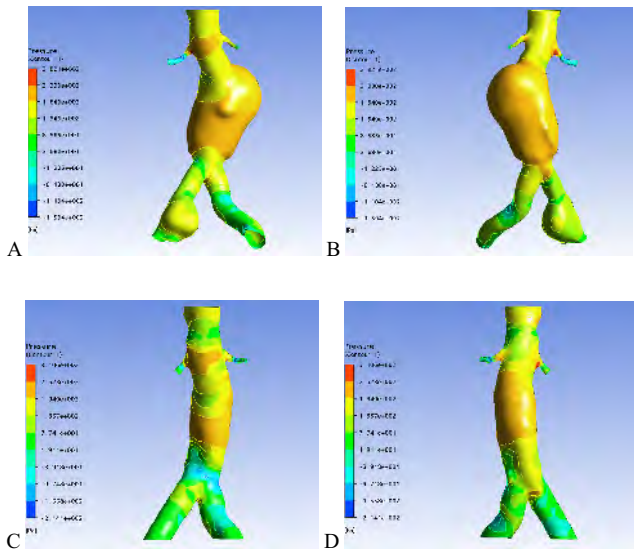


Fig. 7 demonstrates the difference of wall pressure measured at anterior (A, C) and posterior aortic wall (B, D), pre-and post-stent grafting.

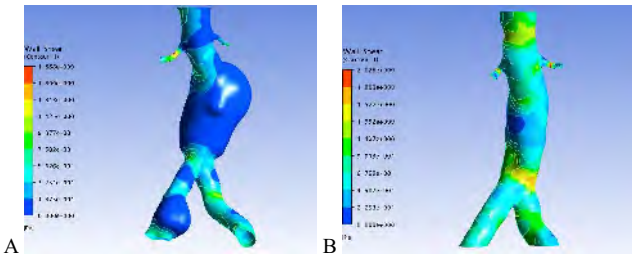


Fig. 8 Wall shear observed in patient 1 pre- (A) and post- (B) stent grafting.

IV. Conclusion

In conclusion, our preliminary study using CFD analysis to analyze the hemodynamic changes in patients with AAA treated with suprarenal stent grafts demonstrates minimal effect of stent wires on the renal arteries. Future studies are required to study the effect of different wire thicknesses on subsequent renal blood flow.

References

1. Prinssen M, Verhoeven E, Buth J, et al. (2004) A randomized trial comparing conventional and endovascular repair of abdominal aortic aneurysms. New Engl J Med 351: 1607-1618
2. Greenhalgh R, Brown L, Kwong G, Powell J, Thompson S. (2004) Comparison of endovascular aneurysm repair with open repair in patients with abdominal aortic aneurysm (EVAR trial1), 30-day operative mortality results: randomised controlled trial. Lancet 9437: 843-848
3. Buth J, van Marrewijk C, Harris P, et al. (2002) Outcome of endovascular abdominal aortic aneurysm repair in patients with conditions considered unfit for an open procedure: a report on the EUROSTAR experience. J Vasc Surg 2: 211-221
4. Lobato A, Quick R, Vaughn P, et al. (2000) Transrenal fixation of aortic endografts: intermediate follow-up of a single centre experience. J Endovasc Ther 4: 273-278
5. Bove PG, Long GW, Zelenock GB, et al. (2003) Transrenal fixation of aortic stent-grafts for the treatment of infrarenal aortic aneurysmal disease. J Vasc Surg 32: 697-203
6. Lau LL, Hakaim AG, Oldenburg WA, et al. (2003) Effect of suprarenal versus infrarenal aortic endograft fixation on renal function and renal artery patency: a comparative study with inter-mediate follow-up. J Vasc Surg 37: 1162-1168
7. Greenberg RK, Chuter TA, Lawrence-Brown M, Haulon S, Nolte L for the Zenith Investigators. (2004) Analysis of renal function after aneurysm repair with a device using suprarenal fixa-tion (Zenith AAA Endovascular Graft) in contrast to open surgical repair. J Vasc Surg 39: 1219-1228

8. Sun Z, Zheng H. (2004) Cross-sectional area reduction of the renal ostium by suprarenal stent wires: in vitro phantom study by CT virtual angioscopy. Comput Med Imaging Graph 28: 345-351
9. O'Donnell, Sun Z, Winder J, et al. (2007) Suprarenal fixation of endovascular aortic stent grafts: assessment of medium-term to long-term renal function by analysis of juxtarenal stent morphology. J Vasc Surg 45: 694-700
10. Liffman K, Lawrence-Brown MMD, Semmens JB, et al. (2003) Suprarenal fixation: effect on blood flow of an endoluminal stent wire across an arterial orifice. J Endovasc Ther 10: 260-274
11. Sun Z, Winder J, Kelly B, Ellis PK, Hirst DG. (2003) CT virtual intravascular endoscopy of abdominal aortic aneurysms treated with suprarenal endovascular stent grafting. Abdom Imaging 28: 580-587
12. Frauenfelder T, Lotfey M, Boehm T, Wildermuth S. (2006) Computational fluid dynamics: hemodynamic changes in abdominal aortic aneurysm after stent-graft implantation. Cardiovasc Intervent Radiol 29: 613-623
13. Di Martino E, Guadagni G, Fumero A, et al. (2001) Fluid-structure interaction within realistic three-dimensional models of the aneurysm aorta as a guidance to assess the risk of rupture of the aneurysm. Med Eng Phy 23: 647-655

Author: Dr.Zhonghua SUN
Institute: Curtin University of Technology
City: Perth
Country: Australia
Email: z.sun@curtin.edu.au

Measuring the 3D-Position of Cementless Hip Implants using Pre- and Postoperative CT Images

G. Yamako[1], T. Hiura[2], K. Nakata[3], G. Omori[4], Y. Dohmae[5], M. Oda[2], T. Hara[2]

[1] Venture Business Laboratory, Niigata University, Niigata, Japan
[2] Biomechanics Laboratory, Niigata University, Niigata, Japan
[3] Orthopaedic Surgery, Osaka Kosei-Nenkin Hospital, Osaka, Japan
[4] Center for Transdisciplinary Research, Niigata University, Japan
[5] Orthopaedic Surgery, Shibata Hospital, Niigata, Japan

Abstract — **Quantitative measurement of the location of cementless hip implants postoperatively not only explains subsequent common complications, such as impingement and loosening, but can also predict postoperative subject-specific primary stability, if combined with the finite element method. However, the metal artifacts on the postoperative computed tomography (CT) image make it difficult to estimate the three-dimensional (3D) alignment, implant shape, bone geometry, and mineral density precisely. Therefore, we developed a novel, accurate measuring technique for the 3D implant position using pre- and postoperative CT images, which is based on a 3D surface registration algorithm. We can obtain a computer model of the femur from preoperative CT data combined with a stem model from computer-assisted design (CAD) data. This study assessed the accuracy of our novel technique for the 3D estimation of implant position. Five sawbones femurs and five cementless stems were used. Ceramic sphere markers were bonded to the bone and stem surface to define local coordinate systems for the femur and stem, respectively. Each femur underwent CT at slice pitches of 1, 2, and 3 mm before and after stem implantation. The relative positions of the stem and femur obtained using our method were compared with those measured using a 3D laser digitizer, used as the true value. The relative estimated position errors were within 0.3 mm in translation and 0.4º in rotation, regardless of slice pitch. From the viewpoint of pixel size of the CT image in a clinical situation, the estimation is sufficiently accurate. Therefore, our measurement technique is useful for quantifying the relative 3D position of implants to the bone geometry and for performing comparative studies among subjects.**

Keywords — **Total hip arthroplasty, CT image, Postoperative diagnosis, Loosening, Dislocation**

I. Introduction

The goals of total hip arthroplasty (THA) are to restore mobility by relieving pain and to improve the function of the hip joint. The common early complications that occur after cementless THA are dislocation of the femoral neck on the cup caused by impingement and loosening of the implant owing to a lack of primary stability at the bone-implant interface [1-4]. These mechanisms are associated with malposition or misalignment of the implant relative to the bone. Postoperative measurement of implant location not only explains these complications but can also predict the postoperative subject-specific range of hip motion and primary stability, when combined with the finite element method (FEM). However, the metal artifacts in the postoperative computed tomography (CT) image make it difficult to precisely estimate the three-dimensional (3D) alignment, implant shape, bone geometry, and bone mineral density.

Therefore, we developed a novel and accurate technique for measuring the 3D implant position, including the precise bone geometry and density data, using pre- and postoperative CT images and a 3D surface registration algorithm. This study reports the accuracy of our technique for the 3D estimation of implant position. We evaluated the patient-specific 3D position of cementless stem and bone mineral density using the proposed technique.

II. Methods

The technical procedure is applied to THA of the femur as follows (Fig. 1). First, we construct preoperative femur surface models from preoperative CT data. Then, the postoperative femur and a rough surface model of the stem are obtained from the postoperative CT data. These 3D surface models are generated using semi-automatic segmentation, including Wiener noise filtering and Canny edge detection. Next, the coordinates of the postoperative femur are transformed to fit the preoperative femur model using the iterative closest point (ICP) algorithm with least-square method [5]. This is a very common method of registration in which each point on the femur model from preoperative CT image that is nearest to the point on the postoperative femur model is assumed to be the corresponding point; the calculation is repeated to reduce the average distance between the each surface points. The rough stem model is also transformed by applying this coordinate transform matrix (Fig. 1A). Then, a precise stem model constructed from computer-assisted

Chwee Teck Lim, James C.H. Goh (Eds.): ICBME 2008, Proceedings 23, pp. 1733–1736, 2009
www.springerlink.com

design (CAD) data is matched to the transformed rough stem model using the ICP algorithm (Fig. 1B). Finally, we obtain a computer model of the femur from the preoperative CT data combined with the precise stem model from CAD data and can then evaluate the 3D-location of the stem relative to the femur (Fig. 1C). This computer model provides precise proximal bone geometry, and the mineral density can be derived from the CT number of the preoperative CT data.

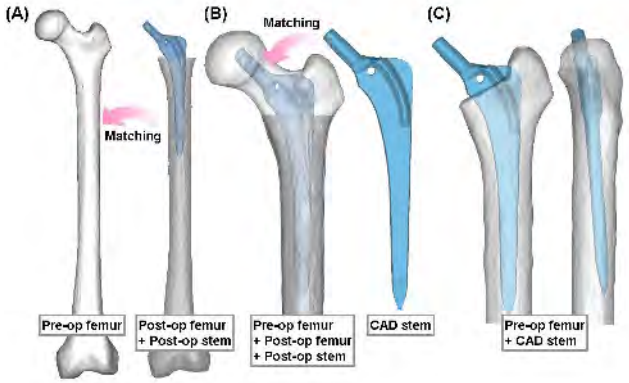


Fig. 1 The procedure used in the novel registration technique.

A. Accuracy of the estimated stem location

Five sawbones femurs and five cementless stems from the BiCONTACT total hip system (B. Braun Aesculap, Tuttlingen, Germany) were used. Spherical ceramic markers were bonded to the bone and stem surfaces to define local coordinate systems for the femur and stem (Fig. 2). In the femur, eight large ceramic markers (10 mm in diameter) were used. In the stem, two small markers (5 mm in diameter) and a large marker were bonded. Each femur was subjected to CT at slice pitches of 1, 2, and 3 mm, before and after stem implantation. The image matrix was set at 512 × 512, and the pixel size was set at a constant 0.68 mm (field of view = 350 mm), considering the general clinical situation. Femur models with the implanted stem were constructed using the proposed technique, and the central coordinates of each marker on the femur and stem were obtained (Fig. 2A). For a real sawbones femur with a stem, the central coordinates of each marker were measured using a 3D laser scanner (Roland, LPX-600, Japan) with a measurement accuracy of ±0.05 mm (Fig. 2B). The 3D location of the stem was represented as translations and rotations about each axis on the local femoral coordinate system. Stem locations obtained using our method were compared with those measured using the 3D laser scanner, which were used as true values.

B. Evaluation of patient-specific 3D position of stem

Five femurs of five female patients who underwent cementless THA with the BiCONTACT total hip system were evaluated. The preoperative diagnosis in all of the patients was the femoral neck fracture. The mean age of subjects was 74 years (range, 40-93 years). The average height was 152 cm (range, 148-158 cm) and the average body weight was 47 kg (range, 39-55 kg). Informed consent was obtained from all patients before the study. The patients were subjected to CT at a slice thickness of 3 mm before and after THA, with a calibration phantom (B-MAS200, Kyoto Kagaku, Kyoto, Japan). The stem position (anteversion and anterior inclination) were evaluated individually. The stem anteversion was defined as an angle between the stem neck axis and femoral posterior condyle axis (Fig. 3A). The anatomical axis of the proximal femur was defined as a line that is derived from the collinear approximation of centroid points for each section of femur in the region beneath the lesser trochanter. The anterior inclination was defined as an angle between the long axis of stem and the proximal axis (Fig. 3B). The bone mineral density of the femur was calculated using the calibration phantom from preoperative CT images.

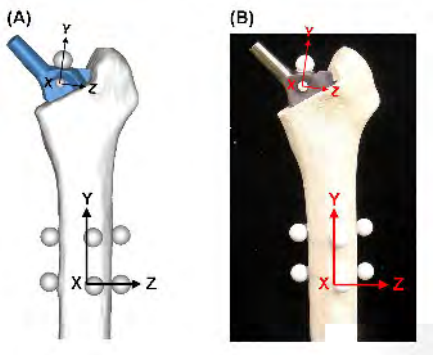


Fig. 2 The stem-implanted femur with spherical markers. (A) The computer model. (B) A sawbones femur with astem.

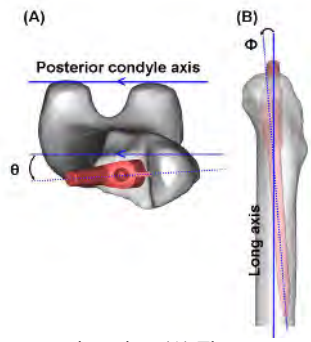


Fig. 3 The stem orientation. (A) The stem anteversion angle. (B)The anterior inclination.

III. Results

A. Accuracy of the estimated stem location

The average errors and root-mean-square errors (RMSE) of the estimated stem position relative to the femur are listed in Tables 1 and 2, respectively. The X, Y and Z axis of the femoral coordinate system corresponded approximately to the anteroposterior direction, the proximal femoral axis and mediolateral direction, respectively. The average error represents the bias of the estimated 3D location in each direction. The translation error along the z-axis was biased negatively. For rotations, the average errors had positive bias. The RMSE represents the measurement accuracy for the 3D estimation of the implant position. The total average accuracy of our novel technique was within 0.3 mm of translation and 0.4º of rotation, regardless of the slice pitch.

Table 1 Average error and standard deviation (SD) of the estimated stem position relative to the femur.

Slice pitch	Translation (mm)			Rotation (º)		
	X	Y	Z	X	Y	Z
1 mm	0.20 (0.24)	-0.11 (0.27)	-0.17 (0.18)	0.04 (0.31)	0.64 (0.17)	0.08 (0.39)
2 mm	0.20 (0.26)	-0.20 (0.34)	-0.22 (0.11)	-0.08 (0.34)	0.64 (0.24)	0.06 (0.36)
3 mm	0.20 (0.26)	-0.36 (0.41)	-0.28 (0.13)	-0.09 (0.33)	0.53 (0.23)	0.05 (0.34)

Table 2 The RMSE of the estimated stem position relative to the femur.

Slice pitch	Translation (mm)			Rotation (º)		
	X	Y	Z	X	Y	Z
1 mm	0.30	0.27	0.24	0.28	0.66	0.36
2 mm	0.30	0.36	0.24	0.32	0.68	0.33
3 mm	0.31	0.51	0.30	0.31	0.57	0.31

B. Evaluation of patient-specific 3D position of stem

The inter-subject (age, body height, weight, and bone mineral density) parameters and stem anteversion and anterior inclination were listed for each individual in Table 3. These parameters varied among subjects. The stem anteversion ranged from 7.6 to 33.6º. The anterior inclination ranged from -4.6 to 0.5º. The bone mineral density ranged from 0.46 to 0.56 g/cm^3.

Table 3 Inter-subject and surgical parameters.

Subjects	Inter-subject parameters				Surgical parameters		
	Age	BH (cm)	BW (kg)	Density (g/cm^3)	Stem size	Antever-sion	Anterior inclination
#1	80	155	55	0.46	15	7.6º	-4.6 º
#2	74	150	39	0.50	12	33.6 º	0.5 º
#3	93	148	32	0.51	11	33.0 º	0.1 º
#4	40	158	70	0.56	12	18.6 º	-2.6 º
#5	82	150	42	0.51	12	8.2 º	-3.2 º

IV. Discussion

It is important to evaluate the implant position relative to the bone postoperatively since malposition or misalignment of the implant leads to subsequent complications, such as loosening and dislocation after THA. We proposed a novel technique for measuring the 3D implant position, including the precise bone geometry and density data, using pre- and postoperative CT images and a 3D surface registration algorithm. This study assessed the accuracy of our novel technique for the 3D estimation of implant position. The results confirmed that the estimation is sufficiently accurate from the perspective of the pixel size of clinical CT images and is comparable to traditional roentgen stereophotogrammetric analysis (RSA). The reported accuracy of the RSA ranges between 0.05 and 0.5 mm for translations and between 0.15º and 1.15º for rotations (95% confidence interval) [6,7].

We found differences in the stem orientation (anteversion and anterior inclination) among subjects. These surgical parameters and the inter-subject parameters, such as body weight, height, and bone geometry and quality would affect the initial stability of the implant. This technique can be applied easily to other implant components such as the acetabular cup. The advantage of using this technique is that the resulting femur model incorporates precise bone geometry and density based on the preoperative CT data, which makes it possible to simulate impingement while considering the effect of bone geometry and to predict the initial stability of the implant postoperatively using the FEM. In conclusion, our proposed technique is useful for quantifying the 3D location of implants relative to the bone postoperatively and for performing comparative studies among subjects.

Acknowledgment

This study was supported by B.Braun Aesculap.

REFERENCES

1. Woo RY, Morrey BF (1982) Dislocations after total hip arthroplasty. J Bone Joint Surg Am. Dec;64(9):1295-306.
2. D'Lima DD, Urquhart AG, Buehler KO, Walker RH, Colwell CW Jr (2000) The effect of the orientation of the acetabular and femoral components on the range of motion of the hip at different head-neck ratios. J Bone Joint Surg Am. Mar;82(3):315-21
3. Phillips TW, Messieh SS, McDonald PD (1990) Femoral stem fixation in hip replacement. A biomechanical comparison of cementless and cemented prostheses. J Bone Joint Surg Br. May;72(3):431-4
4. Sugiyama H, Whiteside LA, Kaiser AD (1989) Examination of rotational fixation of the femoral component in total hip arthroplasty. A mechanical study of micromovement and acoustic emission. Clin Orthop Relat Res. Dec;(249):122-8
5. Besl PJ, McKay ND (1992) A Method for Registration of 3-D Shapes. IEEE Transactions on Pattern Analysis and Machine Intelligence 14(2):239 – 256
6. kärrholm J. (1989) Acta Orhopaedica Scandinavia. 60:491-503
7. Valstar ER, Vrooman HA, Toksvig-Larsen S, Ryd L, Nelissen RG (2000) Digital automated RSA compared to manually operated RSA. J Biomech. 2000 Dec;33(12):1593-9

Simulation of Tissue-Engineering Cell Cultures Using a Hybrid Model Combining a Differential Nutrient Equation and Cellular Automata

Tze-Hung Lin[1,3] and C.A. Chung[1,2]

[1] Department of Mechanical Engineering, National Central University, Jhongli 32001, Taiwan
[2] Graduate Institute of Biomedical Engineering, National Central University, Jhongli 32001, Taiwan
[3] Department of Mechanical Engineering, Army Academy ROC, Jhongli 32092, Taiwan

Abstract — **One of the potential therapeutic strategies in tissue engineering is to regenerate tissues from in vitro cell cultivations with porous scaffolds, and then implant the cellular-scaffold into patients suffering tissue defects. Tissues engineering is a multi-discipline composed of many subjects, for which quantification by means of mathematical modeling can interpret experimental results and identify dominating factors. In this paper we develop a hybrid mathematic model to simulate the in vitro cell cultures in tissue engineering. A discrete cellular automation model is used to treat the cell population dynamics affected by the biological phenomena of cell proliferation, aggregation, contact inhibition, nutrient-limited viability, and cell random walks. Cell growth rates are randomly taken using a gamma distribution with its mean value determined by the local oxygen concentration. The oxygen evolution in the scaffold is modeled by a differential diffusion-reaction equation, which is solved with a finite difference method. Simulations show for a uniform seeding case, increasing cell migration speed enhances the cell population to a maximum; however further increasing the migration speed turns to reduce the cell number. This is because cells with faster speeds move to the scaffold periphery and block the oxygen transfer toward the interior region, resulting in a nutrient limitation on the overall cell growth. We also test an artificial seeding condition where the same number of cells is initially seeded around the scaffold center. It is found cells in such a case proliferate slowly for a longer time compared with the case of uniform seeding, and ultimately reach a higher cell population as the nutrient limitation is avoided to some extent. The model offers an effective method to assess the cell population dynamics, and the simulation results can provide a design reference for tissue engineering applications.**

Keywords — **tissue engineering, hybrid model, migration, cellular automata, gamma distribution**

I. Introduction

Tissue engineering is an inter-discipline that combines biomedicine and engineering. Its aim is to develop biological substitutes to replace or repair damaged tissues [1]. The proposed approaches involve the development of in vitro cell-scaffold constructs inside which an enough number of cells are uniformly distributed. Many experiments discussed the relationship between the cell growth and nutrient transport in the cell-seeded scaffolds. Results show that the scaffold permeability decrease with cell growth, ultimately obstructing nutrients transport to the interior of the scaffold. Therefore nutrient transport is an important factor in engineering tissue grafts [2].

Mathematical modeling provides useful insights into the nutrient limitation in tissue engineering cell cultures. Previous research used the volume average method to treat the cell and nutrient phases of the cell culture system, describing the nutrient transport and consumption with a macroscopic view [3]. The effects of the nutrient concentration on cell proliferation in a scaffold can be assessed in an efficient way [4]. However, such an approach cannot exactly express cell individual behavior and its corresponding effects on the in vitro cell cultures.

Cellular automaton method takes a microscopic view of cell individuals. By dividing the entire scaffold domain into a cellular grid with each grid site called a cellular automaton. Cells are simulated to move from one automaton to another obeying characteristic rules proceeding with activities and expressing cell population dynamics as a whole. Zygourakis et al. used cellular automata to simulate the cell contact inhibition and showed cell growth rates slow down as a result of the shortage of available space in the later period of cell culture [5]. Kino-Oka et al. developed an asynchronous cell proliferation model in static culture [6]. The model predicted the cell proliferation is affected by nutrient concentration. More recently, Cheng et al. combined cell proliferation, random walks, contact inhibition and aggregation into the cellular automaton but the nutrient regulation on the cell growth was neglected [7].

In this study we develop a hybrid mathematic model to simulate the in vitro cell cultures in tissue engineering. A discrete two-dimensional cellular automation model is used to treat the cell population dynamics affected by the biological phenomena of cell proliferation, aggregation, contact inhibition, and cell random walks. The average cell cycle time is determined by the local oxygen concentration.

Chwee Teck Lim, James C.H. Goh (Eds.): ICBME 2008, Proceedings 23, pp. 1737–1740, 2009
www.springerlink.com

II. Mathematical model

As illustrated in Figure 1 we consider cells are seeds onto a porous scaffold with interconnected pores [2]. The cellular construct is placed in a cell culture chamber in which the scaffold is submerged in the culture media. We focus on the cell culture in a scaffold, considering (i) the scaffold is a high permeable porous media (ii) the physical model is a biphasic system that involved cell phase and oxygen, the assumed cell-growth-regulating nutrient (iii) oxygen transported by diffusion only (iv) cells migrate in the construct interior only, cannot move outside construct (v) the scaffold periphery is kept with saturated oxygen concentration (vi) degeneration of the scaffold is neglected.

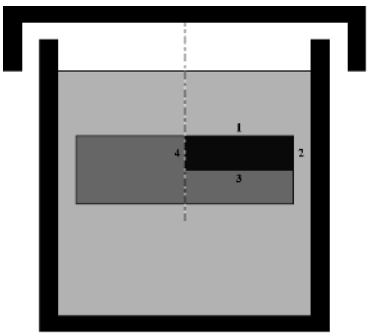


Fig. 1 A sketch of the culture system. For the sake of saving computational effort, only a quarter of the scaffold is taken based on symmetry.

A. Oxygen diffusion-reaction equation

The oxygen diffusion-reaction equation describes the nutrient diffusion by concentration gradient and consumption by cells is

$$\frac{\partial}{\partial t} C_{O_2} = -\nabla \cdot \mathbf{J} + R \tag{1}$$

where **J** is the nutrient concentration flux, and it can be written by Fick's law as

$$\mathbf{J} = -D_{eff} \nabla C_{O_2} \tag{2}$$

C_{O2} is the oxygen concentration, D_{eff} is the effective diffusion coefficient of oxygen. Its value corresponds to the value calculated using oxygen diffusion coefficients in the culture medium and cells,

$$D_{eff} = \begin{cases} D_o^w & \text{between vacant sites} \\ 2\left(\frac{1}{D_o^c} + \frac{1}{D_o^w}\right)^{-1} & \text{between vacant and cell-occupied sites} \\ D_o^c & \text{between cell-occupied sites} \end{cases} \tag{3}$$

where D_o^w is the diffusion coefficient of nutrient in culture media, D_c^c is the diffusion coefficient of nutrient in cells. Besides, R is the nutrient consumption rate, it can be written by the Michaelis-Menten type equation as

$$R = -\xi Q_{\max} \frac{C_{O_2}}{C_{O_2} + K} \tag{4}$$

where ξ = 1 or 0 depending on whether the automaton is occupied by a cell or not, Q_{max} is the maximum consumption rate for oxygen, and K is the saturation coefficient for oxygen consumption. For computational simplicity, we take a quarter of the scaffold as the computational region. The oxygen concentration at Boundary 1 and 2 is set equal to C_0. At boundary 3 and 4 which are the symmetric lines, the symmetry condition is applied with the nutrient flux being zero.

B. Cellular automaton model

The computational domain is divided into many cellular automata (Figure 2). Each cellular automaton is assumed to contain once a cell, so the length of each automaton is set as 8.5μm. The model uses the Moore neighborhood for the cells; hence the cell activity of a automaton is affected by its eight neighboring sites. An individual cell is considered to perform at discrete time step the characteristic behavior including cell proliferation, migration, contact inhibition, persistent random walks and cell collision. The time step used for the simulations is one hour.

The characteristic cell behavior is summarized as follows:

Cell proliferation: In different oxygen concentration condition, cell proliferation rates can be expressed by Moser equation as the following form [8],

$$\frac{1}{t_g} = R_g \frac{C_{O_2}}{C_{O_2} + K_0} \tag{5}$$

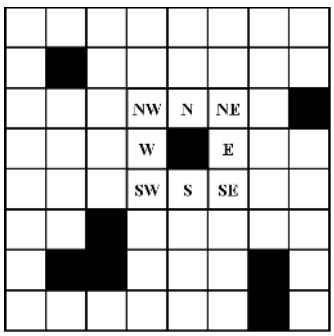


Fig. 2 A sketch of the cellular automata. Black sites denote the cell-occupied automata, white sites denote void space.

where t_g is the average cell proliferation time, R_g is the maximum cell growth rate, and K_0 is the saturation coefficient for cell proliferation. Cell proliferation rates decrease with decreasing oxygen concentration. The length of the cell cycle is randomly taken using a gamma distribution with its mean value equal to t_g [9].

Cell random walks: Cell can migrate to any direction during the cell culture. Each cell moves in one direction for a certain length of time. At the end of the interval, the cell turns into another direction randomly.

Contact inhibition: Cell proliferation is affected by space inhibition. If there is no enough void space around a cell, the cell division stops. In our model where the Moore neighborhood is used, a cell ceases division if the eight neighboring sites around the cell are occupied by other cells.

Cell aggregation: When the cell is migrating, it may collide with another cell in its moving path. Then the two collided cells stop moving for some time before resuming their migration. Furthermore if collided cells proliferate or are collided with other cells, they may form a cell aggregation.

C. Numerical method

A simplified two-dimensional simulation is performed with the combined differential nutrient equation and cellular automata. The x-y coordinates are adopted and the scaffold size is 1cm × 0.116cm (length × height). The calculation domain is divided into cellular automata with size being 8.5μm × 8.5μm. The oxygen evolution in the scaffold is modeled by a differential diffusion-reaction equation, which is solved with a finite difference method. The calculation is conducted by using the parameters and constants listed in Table 1. The calculated values of oxygen concentration are applied for determination of the cell cycle time in the cellular automaton model.

Table 1 List of parameters

Parameters	Values
Nutrient concentration in the surrounding medium, C_0	0.21 mol/m^3
Diffusion coefficient of nutrient in culture media, D_o^w	1.0×10^{-5} m^2/h
Diffusion coefficient of nutrient in cells, D_o^c	1.4×10^{-6} m^2/h
Saturation coefficient for oxygen consumption, K	5.0×10^{-3} mol/m^3
Saturation coefficient for cell proliferation, K_0	6.3×10^{-2} mol/m^3
Length of the automaton, l	8.5×10^{-6} m
Maximum consumption rate of oxygen, Q_{max}	12.2 mol/m^{3}h
Maximum cell growth rate, R_g	7.6×10^{-6} 1/sec
Cell migration speed, S	8.5×10^{-6} m/h

III. Results and Discussion

A. The effect of the migration speed

The spatial-temporal evolution of the cell population is shown in Figure 3 for a uniform seeding case, where initially the seeded cells are assumed to be uniformly distributed inside the scaffold in a random fashion. The associated oxygen evolution is also displayed. After some culture time, the cell divides more quickly around the scaffold periphery because oxygen supply is more sufficient there; in contrast cell divides slowly in the scaffold interior because of the low oxygen concentration due to diffusion limit. We discuss the effect of cell migration speeds on the overall cell growth in Figure 4. Increasing cell migration speed enhances the cell population to a maximum for a uniform seeding case, however further increasing the migration speed turns to reduce the cell number. This is because cells with faster speeds move to the scaffold periphery and block the oxygen transfer towards the interior region, resulting in a nutrient limitation on the overall cell growth.

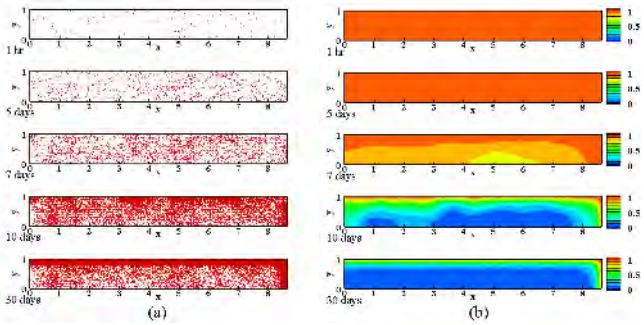


Fig. 3 A uniform seeding case. (a) cell, and (b) oxygen concentration distribution. The cell migration speed is 8.5μm/h.

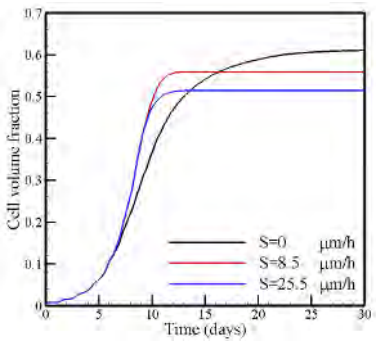


Fig.4 The effect of cell migration speeds on the average cell volume fraction over the scaffold in the uniform seeding case.

B. The effect of the seeding distributional style

We also discuss the effect of the seeding distributional styles by artificially assuming the same number of cells as in the uniform case is initially seeded at the scaffold center. The results of the cell population and oxygen concentration distribution are show in figure 5. It is found cells in concentrated seeding case proliferate slowly for a longer time compared to the case of uniform seeding, and ultimately reach a higher cell population as the nutrient limitation is avoided to some extent (Figure 6). In such a case, the cell can proliferate at the cell colony boundary, while the interior cells stop division due to the cell contact inhibition. However, since more enough oxygen can be supplied to the cell colony from the outside region, so that the cells can slowly spread toward the scaffold boundary.

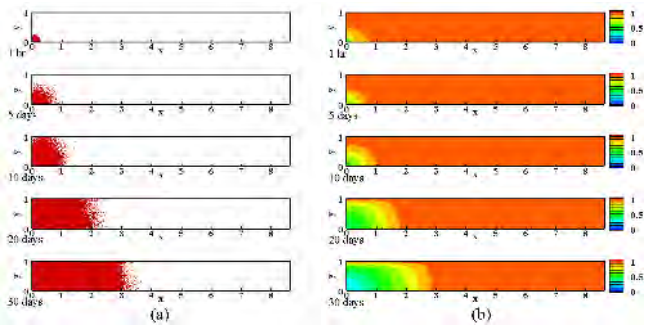


Fig. 5 A concentrated seeding case. (a) cell, and (b) oxygen concentration distribution. The cell migration speed is 8.5μm/h.

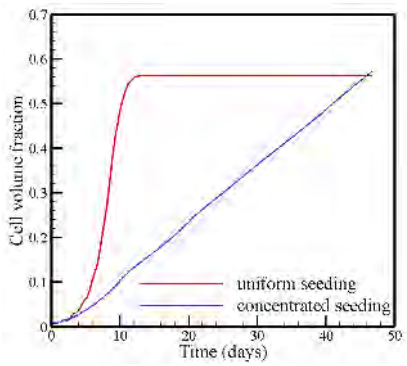


Fig. 6 The evolution of the average cell volume fraction over the scaffold in the uniform seeding case and the concentrated seeding case respectively. The cell migration speed is 8.5μm/h.

IV. Conclusions

In this article, we develop a hybrid model combining a differential nutrient equation and cellular automata to simulate tissue-engineering cell cultures. Simulations show for a uniform seeding case, increasing cell migration speed enhances cell population only to some limit; further increasing the migration speed turns to reduce the cell number. We also test an artificial seeding condition where the same number of cells is initially seeded at the scaffold center. Cells in such a case tend to proliferate slowly for a longer time compared with the case of uniform seeding, and ultimately can reach a higher cell population as the nutrient limitation is avoided to some extent. The model offers an effective method to assess the cell population dynamics, and the simulation results can provide a design reference for tissue engineering applications.

Acknowledgment

The work is supported by the National Science Council of Taiwan through the research grant NSC 96-2221-E-008-066-MY3. We are also grateful to the National Center for High-performance Computing for the computer time and facilities.

References

1. Langer R, Vacanti JP (1993) Tissue engineering. Science 260:920-926
2. Freed LE, Vunjak-Novakovic G, Marquis JC et al. (1994) Kinetics of Chondrocyte Growth in Cell-Polymer Implants. Biotechnology and Bioengineering 43:597-604
3. Galban CJ, Locke BR (1999) Analysis of Cell Growth Kinetics and Substrate Diffusion in a Polymer Scaffold. Biotechnology and Bioengineering 65:121-132
4. Chung CA, Yang CW, Chen CW (2006) Analysis of Cell Growth and Diffusion in a Scaffold for Cartilage Tissue Engineering. Biotechnology and Bioengineering 94:1138-1146
5. Zagourakis K, Bizios R, Markenscoff P (1991) Proliferation of Anchorage-Dependent Contact-Inhibited Cells: I. Development of Theoretical Models Based on Cellular Automata. Biotechnology and Bioengineering 38:459-470
6. Kino-oka M, Maeda Y, Yamamoto T et al. (2005) A Kinetic Modeling of Chondrocyte Culture for Manufacture of Tissue-Engineered Cartilage. Journal of Bioscience and Bioengineering 99:197-207
7. Cheng G, Youssef BB, Markenscoff P et al. (2006) Cell Population Dynamics Modulate the Rates of Tissue Growth Processes. Biophysical Journal 90:713-724
8. Moser H (1958) The Dynamics of Bacterial Population Chemostat. Carnegie Institute Publishers, Washington, DC
9. Dover R, Potten CS (1988) Heterogeneity and cell cycle analyses from time-lapse studies of human keratinocytes in vitro. J Cell Science 89:359-364

Author: Tze-Hung Lin
Institute: Department of Mechanical Engineering, National Central University
Street: No. 300, Jhongda Rd.
City: Jhongli City, Taoyuan County 32001
Country: Taiwan
Email: thlin185@ms57.hinet.net

Upconversion Nanoparticles for Imaging Cells

N. Sounderya[1], Y. Zhang[1,2]

[1] Division of Bioengineering, National University of Singapore,Singapore 117574
[2] Nanoscience and Nanotechnology Initiative,National University of Singapore,Singapore 117576

Abstract — **Lanthanide doped upconversion nanoparticles (UCN's) were synthesized for imaging applications. The particles obtained are hydrophobic in nature. It is of great interest to make them hydrophilic for biological applications. Core/shell particles with UCN's as core and silica as shell were synthesized by Stober method in a basic medium. The silica shell was functionalized with amine group to enable antibody conjugation. TNBS(tri-nitrobenzene sulfonic acid) assay was performed to ensure amine functionalization.These particles were conjugated to an antibody targeted against Connexin 43, a well known gap junction protein. TEM was done on particles prior to conjugation of antibody. Characterization of the particles before and after conjugation was done by DLS, Zeta potential measurement. Confocal imaging experiment was done on the cardiomyocytes (H9c2 cells) with the UCN-silica-NH_2 particles conjugated with anti-Cx43. Experiments show the feasibility of using UCN's for targeting and imaging gap junctions.**

Keywords — **Upconversion, Nanoparticles, Core/Shell, Silica, Cardiomyocytes**

I. Introduction

Upconversion Nanoparticles(UCN's) are nanoparticles that absorb in the Near Infra Red (NIR) region and emit in the visible region. We have synthesized $NaYF_4$ nanocrystals doped with ions such as Er3+/Tm3+ and ytterbium in our lab.$NaYF_4$ have been known to be best for lanthanide doped upconversion nanoparticles. Hence, an organic route was employed to obtain the doped crystals. These crystals are hydrophobic in nature and are dispersed in solvents like cyclohexane or chloroform.The UCN's have some advantages over the commercial organic dyes and quantum dots.They do not undergo photobleaching on long term exposure to excitation source, they are chemically stable and less toxic. Use of these particles in cell imaging shows a high signal to noise ratio.This is due to reduced autofluorescence from cells in NIR region of excitation [1]. For application to cellular imaging it is necessary to make them hydrophilic. There are different methods to do this, such as attaching ligands to the surface, coating them with an oxide layer and coating materials that are hydrophilic for example polymeric materials like PEI, PAAc etc or silica [2, 3]. Silica coating of the particles was considered as an option because silica chemistry is well established. It is also known that silica surface is easy to functionalize and hence conjugation of biomolecules to the surface is also simple. It is possible to control the polymerization and obtain core/shell structures with silica coating. The UCN/silica and amine functionalization are achieved by Stober synthesis [4]. The particles obtained are monodisperse but have a tendency to form aggregates over time. Hence, the the particles are required to be stored in ethanol and transferred to water just before use. The surfactant concentration could also be a factor in aggregate formation, and modification to existing process is still being worked on to reduce aggregation.

These particles after suitable modification were to be used on biological system for imaging application. The cell type of interest was cardiomyocyte and the aim was to image the gap junctions formed between the cardiomyocytes . Gap junctions are channels that are formed between cells for electromechanical coupling. Cardiomyocytes are known to form gap junctions between them as well as with cells such as bone marrow cells and skeletal myoblast when co-cultured. The gap junction formation might suggest about the compatibility of skeletal myoblast or bone marrow cells upon transplantation to heart [6].So it's of particular interest to image the gap junctions formed. Current technique uses fluorescence recovery after photo bleaching to image and quantify the gap junctions [7, 8]. But these methods are restricted to in vitro studies and cannot be done in vivo. Since, the UCN's do not undergo photo bleaching and can be targeted to specific location; they can be used for in vitro and in vivo applications. Dev et al. have discussed the imaging of these particles after their injection in the rat thigh and abdomen. This suggest in vivo imaging application of these particles are possible [9]

This paper discusses the synthesis and silica coating of UCN's ,amine fucntionalization of the silica surface and conjugation of the antibody of interest, anti-connexin43 which is specific to the gap junctions, by Glutaraldehyde spacer method on the UCN/silica-NH2 [5]. The characterization and confocal imaging results have also been presented and discussed.

II. Materials and methods

Synthesis of UCN's and silica coating: The UCN's were synthesized by a one pot variable temperature method. The

Chwee Teck Lim, James C.H. Goh (Eds.): ICBME 2008, Proceedings 23, pp. 1741–1744, 2009
www.springerlink.com

method utilizes reagents in stoichiometric proportions to obtain almost complete reaction. The shape of the nanocrystals was found to vary with the volumes of surfactants (oleic acid and octadecene**)** used. [4].The surfactant concentrations were maintained such that hexagonal nanocrystals are obtained. The particles were dispersed in 50ml of cyclohexane with a concentration of 1 mmol.

Silica coating of the particles was done by Stober synthesis in a basic medium. 5ml of UCN's were reacted with 100 ul of TEOS (0.1ml TEOS in 0.9ml cyclohexane) in the presence of the surfactant (0.2ml Igepal Co-520 and 0.04ml ammonium hydroxide) for 48hrs with mild agitation. The silica coated UCN's were precipitated with acetone ethanol mixture and centrifuged. The precipitate was then resuspended in 15ml of ethanol. The particles were characterized by TEM and DLS measurements.

Membrane Integrity Assay: A membrane integrity test was performed on cells with the silica coated particles. The cell type used for cytotoxicity were skeletal myoblasts and the cell number was $5x10^{\wedge 4}$ cells in each well before incubation. The incubation time for the cytotoxicty test was 14hrs.

Amine functionalization and Antibody Conjugation: The silica coated nanoparticles have to be functionalized with amine or carboxyl groups to conjugate antibody to their surface. This was done by agitating 0.15ml of APTS/TEOS mixture(10 mol% APTS mixture) in the presence of 0.2 ml ammonium hydroxide and 10ml of silica coated UCN's.

Amine functionalization was checked by using TNBS assay. Ethanolamine was used as the standard. A range of volumes of ethanolamine were reacted for 2 hrs at 37^{o}C with 200ul of TNBS diluted with 600ul of double distilled water in the presence of 200ul of bicarbonate buffer. After 2 hrs, 600ul of 1N HCl was added and the solution was vortexed to ensure mixing. The absorbance of the samples was obtained on a UV-VIS spectrometer at 355nm. 50ul of the sample was treated with TNBS by the same procedure as stated above and the absorbance was measured. The absorbance was compared to absorbance plot obtained from the standard, ethanolamine. DLS and zeta potential data were obtained and compared to silica coated UCN's.

Gluteraldehyde spacer method was used to conjugate antibodies to the amine functionalized silica coated UCN's [5]. The antibodies were purified by using membrane centrifuge tube to remove sodium azide in the solution. 3ml of the functionalized nanoparticle beads are washed 2 times in PBS buffer of pH 7.2. PBS was used as wash and coupling buffer.After second wash the pellets were resuspended in 10ml of gluteraldehyde solution.(10% by volume of gluteraldehyde dissolved in PBS). The solution was vortexed and the solution was left under continous mixing for 1-2 hrs at room temperature. After 1.5 hrs the solution was centrifuged in PBS and resuspended in 5ml of PBS. Resuspension was ensured by vortexing and sonication. The antibody was dissolved in 5ml of PBS and the solution was added to the particle solution. The solution was left to react with continous mixing for 2-4hrs. 10ml of quenching solution, 30mM ethanol amine with 0.05% triton-X was added and solution left to stand for 30min . The particles were centrifuged twice with PBS and stored in 5ml of PBS with 0.01% triton-X the blocker. [6]

Antibody anti-connexin43 was used for the conjugation with particles and they were later used for imaging on H9c2 cells. UV-VIS absorbance was used to check for antibody conjugation. Fluorescence measurement was a done at an excitation of 350nm on the antibody conjugated particles using a microplate reader.DLS data was also obtained for the antibody conjugated particles.

Confocal Cell imaging: The antibody conjugated to the particles being anti-CX43, preliminary imaging experiments were carried out on cardiomyocytes. The cardiomyocytes(H9c2 cells) were plated on 8 well chamber and allowed to attach to the chamber. The cells were incubated with particles for 8hrs. And imaging was carried out on a confocal system with a 980nm wavelength continuous wave laser.

III. Results and Discussion

The DLS measurement and the TEM images for the UCN's with and without silica are shown in fig 1.

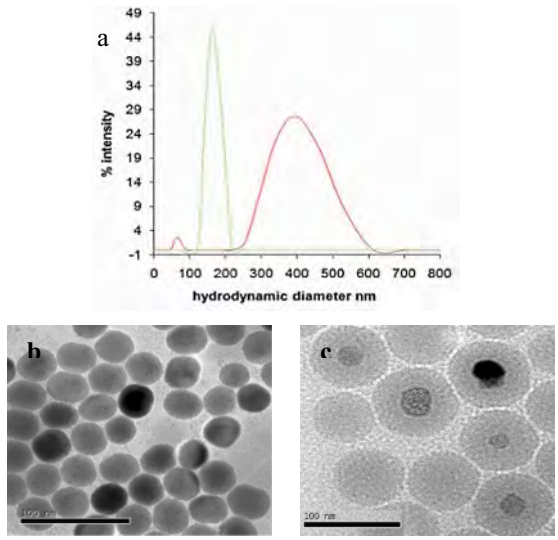


Fig 1. a) DLS data for UCN- silica(green), UCN- silica- NH_2 (black), UCN –silica- NH_2.antibody(red) b) TEM of UCN in cyclohexane c) TEM of UCN-silica in water

The comparision of the size of antibody tagged UCN-silica-NH_2 and UCN silica show an increase as expected.(Fig 1) The zeta potential of the UCN-silica and UCN-silica-NH_2 were measured and the zeta potential was found to decrease from high negative value for the UCN-silica as silica is negatively charged to a lower negative value for UCN-silica NH_2 as they have an addition positive charge on them apart from negatively charged silica.(table 1) . The negative charge on UCN-silica-NH_2 suggest that the coating on the silica is not complete. This could cause aggregation on storage ,hence coating should be further improved.

Table 1. Zeta potential of surface modified UCN

Particle Type	Zeta Potential (mV)
UCN -silica	-136
UCN-silica-NH_2	-60
UCN-silica-NH_2-antibody	-2.76

Further,TNBS assay ensured amine functionalisation. The absorbance for sample reaction with TNBS was compared to the standard curve obtained with ethanol amine reaction with TNBS. Through a trendline fit to the standard,the volume of standard having same absorbance as the sample was estimated (Fig 2). The estimated volume was 1.1ul of ethanol amine.TNBS reaction was performed for volumes ranging from 1.1ul to 1.2ul of ethanol amine with a 0.1 ul variation. The absorbance of the UCN-silica-NH_2 sample matched the absorbance value of 1.16ul of ethanol amine. This shows that the sample of 50ul had amine group equivalent to 1.16ul of ethanol amine. Thus this confirms the presence of amine group on the particles.

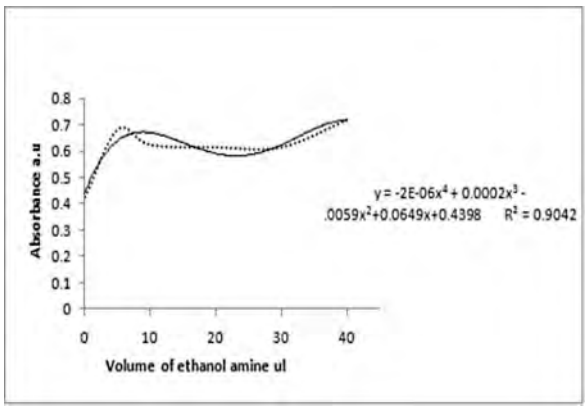


Fig 2. TNBS assay: absorbance of standard (Dashed Line) and trendline fit for the standard (Dark Line)

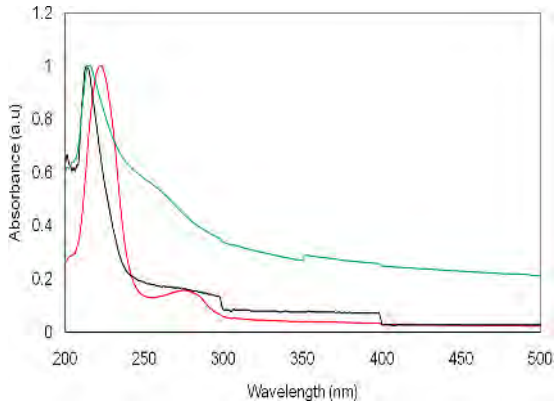


Fig 3. Absorbance data for UCN-silica-NH_2 (Green) , UCN-silica-NH_2-antibody (Black) and antibody (Red)

UV-VIS spectrometry was done after the conjugation of antibody to the UCN-silica-NH_2 and its peak of absorbance was compared to the peak of absorbance of the antibody (Fig 3). The peak at 260nm is known to be a characteristic of tryptophan group present in any protein ,in this case the antibody.

To further confirm the presence of antibody Fluorescence emission was checked for the UCN-silica-NH_2 ,UCN-silica-NH_2-antibody and antibody at an excitation of 350nm. The data obtained are shown in table 2. The fluorescence was measured by varying the emission filters to observe change in the intensity of emission for UCN-silica-NH_2 and UCN-silica-antibody. It is known that tryptophan in the antibody has a broad fluorescence emission and the amine groups show emission around 420-450nm. With no emission filter, the intensity for the antibody and UCN-silica-NH_2-antibody increased. The UCN-silica-NH_2-antibody emission was higher than that of UCN-silica-NH_2. And it was observed that the emission for UCN-silica-NH_2 was more than 3 times higher than UCN-silica-NH_2-antibody when an emission filter of 460nm was used. This decrease in the antibody conjugated UCN could be attributed to the emission peak cut off at a shorter wavelength.

Table 2. Fluorescence Emission data (normalized w.r.t UCN-silica-NH2-antibody) from Microplate Reader with excitation filter of 355nm

Emission Filter	UCN-silica-NH_2	UCN-silica-NH_2-Antibody	Antibody
No filter	0.52	1	0.35
460nm	3.77	1	0.56

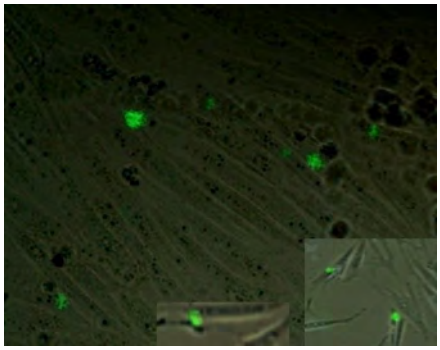


Fig 4. Confocal image of cardiomyocyte incubated with UCN-silica-NH_2-antibody.Inset: zoomed image of UCN at junction of two cells

Membrane integrity test was carried out on skeletal myoblats cells with the silica coated UCN's. The cell death percentage 10-20% after 14 hr incubation and for a concentration of upto 20ug/ml. 20ul of the particle solution was added to the cells. The working range for fluorescence imaging with these particles on cells is 1ug/ml – 3ug/ml and the volume range used is 10-20ul.The cell death data was consistent with that reported by Rufaihah *et al* [10].

The data for UCN-silica-NH_2 antibody are with antibody starting concentration of 0.025mg/ml for the conjugation.The absorbance peaks were weak for concentrations lower than the 0.025mg/ml. Also when the particles were incubated with cardiomyocyte cells for confocal imaging, the ones with lower concentration of antibody showed almost no fluorescence. At the concentration of 0.025mg/ml of antibody, the particles were easy to spot and hence, qualitatively, the uptake was good. Experiments are being carried out to quantify the cellular uptake.

Confocal imaging of cardiomyocytes was also done. The images obtained showed fluorescence from particles in between cells (Fig 4). UCN-silica-NH_2 and UCN-silica were used as negative controls for gap junction imaging. But the fluorescence images after 8 hr incubation for the UCN-silica-NH_2 with anti-Cx43 had more particles tagged between cells. The controls didn't show significant fluoresc ence. The presence of fluorescence in between cells suggest that the UCN's are targeting gap junctions. Thus it is feasible to image gap junctions with the silica coated antibody conjugated UCN's. The quantification of the cellular uptake is being done.

Conclusion

Upconversion nanoparticles with Erbium doping were synthesized and silica coating of the particles was done to make them hydrophilic. The surface was modified to make the particles suitable for application in a biological system of interest, the cardiomyocytes. The silica coating was functionalized with amine groups and experiments were carried out to confirm the functionalisation. Later, Anti-Cx43, an antibody that conjugates to connexin 43 in gap junctions of the cardiomyocytes was attached to the amine moiety by gluteraldehyde spacer technique. Particle size measurement was done to check the conjugation and an increase in the size was noted and also zeta potential measurements were done. The decreasing zeta potential was as expected upon antibody conjugation. Absorbance measurement also indicated a peak at 260nm (which is characterisitic of the tryptophan group in the antibody) for the antibody conjugated particles. The particles were also tested for cytotoxicity and also an imaging experiment was carried out on cardiomyocyte for a qualitative study of the particle targeting. The results show the UCN's could target the gap junctions .It is of interest to co-culture skeletal myoblast/bone marrow cells with cardiomyocytes and target the UCN particles with antibody to the gap junctions formed between these cells. Quantification of the cellular uptake shall also be done.

Reference

[1] D.K. Chatterjee, Z. Yong, Upconverting nanoparticles as nanotransducers for photodynamic therapy in cancer cells, Nanomedicine 3 (2008) 73-82.

[2] W.B. Tan, S. Jiang, Y. Zhang, Quantum-dot based nanoparticles for targeted silencing of HER2/neu gene via RNA interference, Biomaterials 28 (2007) 1565-1571.

[3] H. Lu, G. Yi, S. Zhao, D. Chen, L.-H. Guo, J. Cheng, Synthesis and characterization of multi-functional nanoparticles possessing magnetic, up-conversion fluorescence and bio-affinity properties, Journal of Materials Chemistry 14 (2004) 1336-1341.

[4] Z. Li, Y. Zhang, An efficient and user-friendly method for the synthesis of hexagonal-phase NaYF4:Yb, Er/Tm nanocrystals with controllable shape and upconversion fluorescence, Nanotechnology 19 (2008) 345606.

[5] W. Yang, C.G. Zhang, H.Y. Qu, H.H. Yang, J.G. Xu, Novel fluorescent silica nanoparticle probe for ultrasensitive immunoassays, Analytica Chimica Acta 503 (2004) 163-169.

[6] K. Boengler, R. Schulz, G. Heusch, Connexin 43 signaling and cardioprotection, Heart (2005) hrt.2005.066878.

[7] M.H. Wade, J.E. Trosko, M. Schindler, A fluorescence photobleaching assay of gap junction-mediated communication between human cells, Science 232 (1986) 525-528.

[8] K. Guan, S. Wagner, B. Unsold, L.S. Maier, D. Kaiser, B. Hemmerlein, K. Nayernia, W. Engel, G. Hasenfuss, Generation of Functional Cardiomyocytes From Adult Mouse Spermatogonial Stem Cells, Circ Res 100 (2007) 1615-1625.

[9] D.K. Chatteriee, A.J. Rufalhah, Y. Zhang, Upconversion fluorescence imaging of cells and small animals using lanthanide doped nanocrystals, Biomaterials 29 (2008) 937-943.

[10] R. Abdul Jalil, Y. Zhang, Biocompatibility of silica coated NaYF4 upconversion fluorescent nanocrystals, Biomaterials 29 (2008) 4122-4128.

Simulation of Cell Growth and Diffusion in Tissue Engineering Scaffolds

Szu-Ying Ho[1], Ming-Han Yu[1] and C.A. Chung[1,2]

[1] Department of Mechanical Engineering, National Central University, Taiwan
[2] Graduate Institute of Biomedical Engineering, National Central University, Taiwan

Abstract — **With the development in recent years, tissue engineering is becoming one of the therapeutic strategies that have the potential for repairing the damaged or malfunctioned human tissues. The proposed scheme of tissue engineering generally contains seeding cells onto a porous scaffold. The cell-scaffold construct is then cultured in vitro for a period of time and transplanted into the patient afterward. Because the biochemical materials are expensive and the experimental procedures are time-consuming, it is valuable to have a simulation model that can assess the cultivation conditions beforehand. We develop a continuum mathematical model for the simulation of cell growth and migration in porous scaffolds based on the basic principle of mass conservation for both cells and nutrients. In addition to cell growth kinetics, we incorporate cell diffusion term to treat the macroscopic effect of cell random walks on cell distributions. The model is validated by comparison with experimental data available in literature. The simulation model is applied to investigate cell growth and distribution under uniform and various concentrated seeding circumstances. Results show that the overall cell growth rate in a scaffold is affected both by the extent of the cell diffusion surface and the amount of the nutrient supply. Uniform seeding finishes the first growth rate out of the seeding cases considered, because uniformly seeded cells can diffuse evenly in all directions, preventing nutrients uptake only from some over crowded, local areas. For the concentrated seeding cases, the larger the cell diffusion surface the faster the cells can grow. Moreover, cells grow faster when seeded close to the scaffold periphery because cells can obtain more nutrient supplies in such cases. The model provides an efficient way of assessing cell-scaffold developments in vitro for tissue engineering applications.**

Keywords — **Tissue Engineering, Mathematical Model, Cell Seeding Positions**

I. Introduction

Tissue Engineering is considered a replacing technology for the traditional organ transplants. Since the traditional method of transplant operations face problems such as donor shortages, the blood type and size match problems, and immune system rejections, it is not a satisfying way to repair human body. By contrast, tissue engineering creates autologous grafts using cells isolated from a small biopsy, expanding the cells in vitro and seeding them onto a scaffold matrix. No immune problem will be encountered with the cell-seeded implants. However, as cell-scaffold developments consist of complex multi-disciplines, both experimental and theoretical efforts need to be made before reaching the final goal of tissue replacement.

Experiments investigated the in-vitro cultivation of cell seeded scaffolds. The outcome shows that the thicker the scaffold is, the lower the resulting cell density becomes, which suggests that the cell growth in a scaffold tends to be inhibited by nutrient diffusion limitation because new grown cells take up the spaces inside the scaffold and leading to the obstruction of nutrient transportation [1]. Theoretical models using species continuity equations to describe the spatial-temporal evolution of cells and nutrients also reveal the diffusion limit on cell growth [2, 3].

Cell seeding as the first step of cell-scaffold construction determines the initial cell number and distribution inside a scaffold. The subsequent cell growth, migration and phenotype expression are affected by the seeding methods. Static and spinner flask seeding have been utilized, for which low cell seeding efficiency is shown, and cells tend to concentrate around the scaffold surface [4, 5]. The most efficient way that has been demonstrated so far for cell seeding is the oscillatory perfusion, through which high cell numbers and uniformity have been reported.

For a theoretical assessment on seeding effects, we develop a mathematical model. The model is validated by matching simulation results with the experimental data from literature [1] by adjusting the cell growth coefficient. Simplified two-dimensional simulations are then performed for investigation of cell growth and migration in scaffolds concerned with different cell seeding positions and different cell seeding areas.

II. Mathmatical model

For the sake of simplicity, the mathematical modeling is set by assuming no diffusion of nutrients through the scaffold matrix, and we also neglect the scaffolds degradation during cell cultivation. In addition, we set the cultivation environment as the combination of cell colony space (cell phase) and interstitial medium space (fluid phase), and in both spaces the nutrient transports by diffusion. Only one kind of nutrient (glucose) is considered in the simulation.

Chwee Teck Lim, James C.H. Goh (Eds.): ICBME 2008, Proceedings 23, pp. 1745–1748, 2009
www.springerlink.com

The cell growth and distribution are conducted by proliferation, apoptosis, and migration.

A. Mass conservation of nutrient

The continuity equation of glucose describes the nutrient concentration change with time affected by the nutrient diffusion in both cell phase and fluid phase, and consumption in the cell phase. By volume averaging, the conservation equation governing the nutrient concentration can be written as

$$\frac{\partial}{\partial t}\left(C_f\phi_f + C_c\phi_c\right) + \nabla\cdot\left(\boldsymbol{J}_f\phi_f + \boldsymbol{J}_c\phi_c\right) + R_n\phi_f = 0 \tag{1}$$

where ϕ_f and ϕ_c are defined as the fluid and cell volume fraction respectively. The average nutrient concentrations in fluid and cell phases are defined as C_f and C_c. In the diffusion term, coefficients $\boldsymbol{J}_f$ and $\boldsymbol{J}_c$ represent the nutrient flux in the fluid and cell phases. In the equation, R_n is expressed as

$$R_n = R_m C_f \tag{2}$$

where R_m is the maximum nutrient consumption for cells in a single time unit. From the Fick's Law, we obtain

$$\frac{\partial}{\partial t}(C_f\phi_f + C_c\phi_c) = \nabla\cdot(D_f\phi_f\nabla C_f) + \nabla\cdot(D_c\phi_c\nabla C_c) - R_n\phi_f \tag{3}$$

where D_f and D_c are diffusion coefficient for nutrient transportation in fluid phase and cell phase respectively [2]. We further assume that the nutrient diffusion has reach balance between the fluid and cell phases, which yields

$$C_c \cong K_{eq}C_f \tag{4}$$

where K_{eq} is the equilibrium coefficient. By using Equation (4), we can obtain a single unknown, the nutrient concentration variable in the fluid phase, governing by the following equation

$$\frac{\partial}{\partial t}\left[\left(\phi_f + K_{eq}\phi_c\right)C_f\right] = \nabla\cdot\left[\left(D_f\phi_f + D_c\phi_c K_{eq}\right)\nabla C_f\right] - R_n\phi_c \tag{5}$$

B. Mass conservation of cells

Cell equation is dominated by two factors. The first is the cell diffusion due to random walks and the second is the cell growth regulated by nutrient concentration. The volume average equation of cell mass can be written as

$$\frac{\partial}{\partial t}(\rho_c\phi_c) + \nabla\cdot\boldsymbol{J} = \tilde{R}_c \tag{6}$$

In the equation, the cell motion caused by cell random walks is described by

$$\boldsymbol{J} = -D\nabla(\rho_c\phi_c) \tag{7}$$

where D is the diffusion coefficient for cellular random motion, and ρ_c is the cell average density in cell phase in scaffolds. Combine the previous equations (6) and (7), we rewrite the cell equation as

$$\frac{\partial}{\partial t}\phi_c = D\nabla^2\phi_c + \tilde{R}_c/\rho_c \tag{8}$$

Then, we apply Modified Contois Equation [6] to describe the effects on cell proliferation due to the inhibition of cell density, nutrient saturation and cell growth products. The cell growth kinetic function, $\tilde{R}_c$, is written as

$$\tilde{R}_c = \left[\frac{R_g C_c}{K_c(\rho_c\phi_c) + C_c} - R_d\right]\rho_c\phi_c \tag{9}$$

Here, the coefficient K_c is the Contois saturation coefficient, ρ_c is the cell mass density of which the value is taken as 1.020 g/cm^3 for cartilage cells [7], R_d is the apoptosis rate, and R_g is the maximum growth rate. We set K_c to be 0.154, and we assume R_d =3.3×10^{-4} sec^{-1} concerning the average life cycle of 35 days for cartilage cells, and R_g varies with different scaffold thickness obtained by matching the experimental data [1]. Inserting equation (4) into equation (9) yields

$$\frac{\partial}{\partial t}\phi_c = D\nabla^2\phi_c + R_c\phi_c \tag{11}$$

and R_c is defined as

$$R_c = \left[\frac{R_g C_f}{K_c(\rho_c\phi_c)/K_{eq} + C_f} - R_d\right] \tag{12}$$

C. Initial and boundary conditions

For the initial cell seeding condition, we consider six kinds of cell seeding cases, which are shown in Fig. 1. The basic one is *Uniform Seeding*, which is also the one used to compare with the experimental result in literature. In the six seeding cases, the same amount of cells is seeded into the scaffolds. Except for the uniform seeding, the seeding areas of the five concentrated seeding cases are equal size. The six cell seeding cases are designed to be influence by two geometric factors: The initial cell diffusion surface, and the cell seeding surface contact with the scaffold boundary. For the concentrated seeding, instead of using a step function

for the initial cell distribution, a more realistic distribution is expressed as [8]

$$\phi_c = \frac{N_0 V_{cell}}{A_d x_d}(1+\frac{2x_i}{x_d})(1-\frac{x_i}{x_d})^2 \quad (18)$$

where N_0 is initial cell seeding numbers, V_{cell} is the volume of a single cartilage cell, A_d is the size of seeding area, x_i accounts for the seeding location and x_d is the width of seeding area.

For the boundary conditions, we considered that the scaffolds are submerged in culture medium. The nutrient concentration at the four boundaries of the scaffolds is assumed a constant equal to that of the submerging culture medium. As for the boundary condition for cells, we assume that the cells cannot cross over the boundaries of the scaffold.

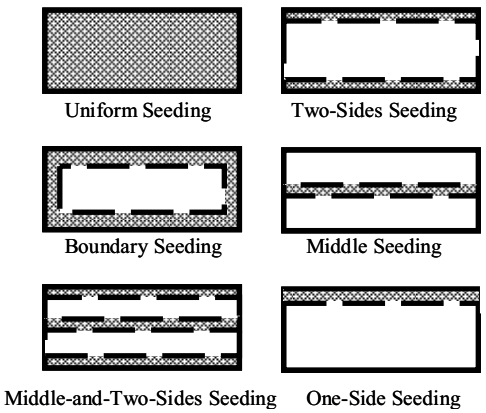


Fig. 1 Six seeding cases

Table 1 The characteristic for 6 cell seeding cases (in dimensionless scale)

Seeding Case	Initial cell diffusion surface	Surface for cell seeding area contact with boundary
Uniform Seeding	Whole scaffold	8.4
Middle-and-Two-Sides seeding	12.8	6.55
Boundary Seeding	7.9	8.4
Two-Sides Seeding	6.4	6.55
Middle Seeding	6.4	0.15
One-Side Seeding	3.2	3.35

D. Solution Procedure

We use COMSOL Multiphysics v3.2a as our mathematic solver, which utilize a finite element method, and a triangular mesh is used for computation. Mesh refinement test is performed to ensure the relative errors smaller than 10^{-4}, or the absolute errors smaller than 10^{-5}.

III. Results and Discussion

To validate our model, we compare our simulation result with the experimental data of Freed et. al [1]. By matching the cell growth coefficient R_g, we find that this simplified formulation can give quite fair agreements with the experiments. The comparison is shown in Fig. 2. It is the cell growth result over a 30-day cultivation. The symbols ☆, △, □, ○ represent the experimental data, ☆ for scaffold thickness 0.088cm, △ 0.116cm, □ 0.168cm, and ○ 0.307cm. The four lines are the simulation results.

The cell growth in the six cell seeding cases are compared by setting the thickness of the scaffold as 0.307 cm, the length as 1 cm, and the cultivation time is 50 days. The ranking of cell growth is shown in Fig. 3. Worthy of mentioning is that when the cultivation time is prolonged, the resulting cell volume fractions in all cases gradually become similar. In other words, seeding position seemingly affects only the overall rates of cell growth determining by the time span that is needed for cells to reach the maximal population in a scaffold, but not affect the ultimate cell number. The reason for the difference in growth rates between the six seeding cases is interpreted as follows. From the difference between the *Uniform Seeding* and *Boundary Seeding*, we infer that the growth rate of *Uniform Seeding* is higher because there is less restriction on the cell diffusion direction in the case, therefore it prevents cells to compete nutrients in crowded areas.

We further compare the cases with different cell diffusion surfaces. In the case of *Middle-and-Two-Sides Seeding*, the cell diffusion surface is twice than the *Two-Sides Seeding*, the cell growth rate in the previous case is therefore relatively higher. We also observe the same comparative situation between the *Middle Seeding* and *Side Seeding*.

Besides the effects of cell diffusion surface, another point worth noticing is the surface contact between cell seeding area and the surrounding medium. We pick out the comparison between the *Two-Sides Seeding* and *Middle Seeding* for discussion. In these two cases, they both have the same size of cell diffusion surface, but they are different in the surface contact with the culture medium. As table 1 shows, *Two-Sides Seeding* has the surface contact area of 6.55, while *Middle Seeding* has only 0.15. And this contact area difference leads to the better cell growth rate for the *Two-Sides Seeding* case.

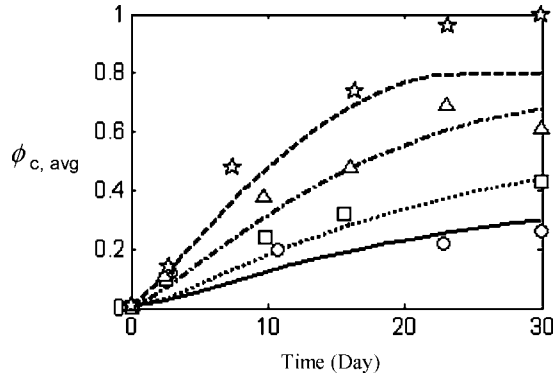


Fig. 2 Result comparison between simulation and experiment.

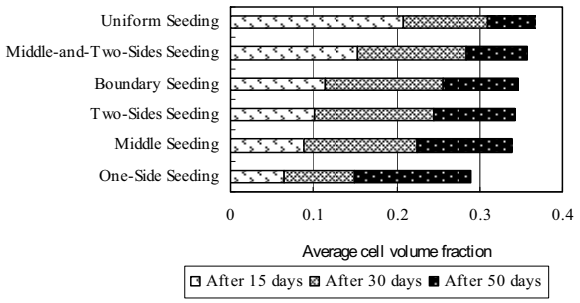


Fig. 3 Cell growth for six cell seeding cases

IV. Conclusion

The research of cell cultivation simulation in the past did not discuss how cell seeding areas and cell seeding positions influence the cell growth rate. In this article, we investigate the relationship between the geometry of cell seeding and cell proliferation, and we obtain the following seeding conditions that affect cell cultivation. First, the most significant factor that affects cell proliferation is the size of diffusion surface for the cells to migrate from the initial seeding area to other region of a scaffold. With the larger cell diffusion surface, cells are able to expand freely in the scaffold, leading to a more even cell distribution in the scaffold, and therefore lessen the conditions of cell competing nutrient in a over crowded area.

Another factor that affects cell growth is the contact surface of the seeding area with nutrient supply. Under same cell diffusion surface, the cases with larger surface contact between cell seeding area and scaffold boundaries tend to have a better cell growth rate. Cells can obtain nutrient more abundantly and easily when they are contacted with the scaffold boundaries, through which nutrients are transfer into the scaffold. Inversely, the lesser the boundary contact, the worse the cell growth rate can be.

The conclusion of this article can be used as a reference for cell cultivation environment setting. Yet, there are still some limitations in our mathematical model. For instance we have not included the dual role of growth promotion and space inhibition by the extracellular matrix that we are planning to incorporate in the future studies.

Acknowledgment

The work is supported by the National Science Council and the Ministry of Education of Taiwan.

References

1. Freed LE, Vunjak-Novakovic G, Marquis JC et al. (1993) Kinetics of chondrocyte growth in cell-polymer implants. Biotechnol Bioeng 43:597-604
2. Galban CJ, Locke BR (1999) Analysis of cell growth kinetics and substrate diffusion in a polymer scaffold. Biotechnol Bioeng 65:121-132
3. Chung CA, Yang CW, Chen CW (2006) Analysis of cell growth and diffusion in a scaffold for cartilage tissue engineering. Biotechnol Bioeng 94:1138-1146
4. Vunjak-Novakovic G, Obradovic B, Martin I et al. (1998) Dynamic cell seeding of polymer scaffolds fro cartilage tissue engineering. Biotechnol Prog 14: 193-202.
5. Holy CE, Shoichet MS, Davis JE (2000) Engineering three-dimensional bone tissue in vitro using biodegradable scaffolds: investigating initial cell-seeding density and culture period. J Biomed Mater Res 51: 376-382.
6. Contois DE (1959) Kinetics of Bacterial Growth: Relationship Between Population Density and Specific Growth Rate of Continuous Cultures. J Gen Microbiol, 21: 40-50
7. Coletti F, Macchietto S, Elvassore N (2006) Mathematical Modeling of Three-Dimensional Cell Cultures in Perfusion Bioreactors. Ind Eng Chem Res 45:8158-8169.
8. Bryne HM, Cave G, McElwain DLS (1998) The Effect of chemotaxis and chemokinesis on leukocyte locomotion: a new interpretation of experimental results. Math Med Biol 15: 235-256

Author: Szu-Ying Ho
Institute: National Central University
Street: No.300, Jhongda Rd.
City: Jhongli City, Taoyuan County 32001
Country: Taiwan, R.O.C.
Email: heidi_judy@hotmail.com

Simulation of the Haptotactic Effect on Chondrocytes in the Boyden Chamber Assay

Chih-Yuan Chen[1] and C.A. Chung[1,2]

[1]Department of Mechanical Engineering, National Central University, Jhongli City, Taiwan, R.O.C.
[2] Graduate Institute of Biomedical Engineering, National Central University, Jhongli City, Taiwan, R.O.C.

Abstract — **Tissue growth, wound healing, inflammation response and cancer spread are closely related to cell movement phenomena. Cell movement often exhibits random walks as well as tactic responses to certain chemicals. Boyden chamber assays have been widely used to measure the cell diffusive and tactic coefficients for cell motion assessments. We develop a mathematical model based on the mass conservation principle, and apply it to carefully elucidate the Boyden chamber experiment conducted by Shimizu et al. (1997), in which chondrocytes were tested for their haptotactic behavior responding to type II collagen. The whole process including cells sediment through the cell suspension in the upper well and the consequential migration within the collagen-coated membrane is well simulated using the developed model. To our knowledge, cell sediment phenomena have so far been neglected in previous literature. The haptotactic effect is treated by the receptor-kinetic model, and the cell random walk is characterized macroscopically as cell diffusion. Finally, the values of cell diffusive, haptotactic coefficients and saturation constant of haptotaxis are determined by regression. Results show the chondrocytes perform the maximal haptotactic response when the Boyden chamber membrane is coated with a linearly distributed type II collagen with the maximal concentration, 35 μg/ml. As the collagen concentration increases, the effect of haptotaxis turns to gradually decrease. It's also found that the haptotactic velocity has the same order of the cell migration velocity (10^{-7} cm/s). The saturation constant of haptotaxis to type II collagen is found to be quite small (10^{-6} g/cm^3), therefore we speculate the haptotaxis is possible to impose an influential impact on the migration of chondrocytes in the early stage of cartilage formation.**

Keywords — **Haptotaxis, migration, simulation, chondrocyte, Boyden chamber.**

I. Introduction

Cells are the basic element of life and their behaviors significantly affect the performance of tissues and organs. Tissue growth, wound healing, inflammation and cancer spread are all closely related to cell motion. Cell motion can be divided into several steps. First of all, cells onward extend their cytoplasma and cell membrane to make their leading edge attach on the matrix. Cells then generate contraction force, and at the same time their rear end detaches from the matrix and result in migration forward. These motions are not only related with properties of cells but also influenced by extra-surroundings.

Cell motions can be classified into three categories: *kinesis*, *taxis* and *guidance* [1]. *Kinesis* means stimulated cells will alter their magnitude of motility without moving in a specified direction. For example, cells in chemical solutions of different concentrations will exhibit variant magnitude of random walks, which is called chemokinesis. That cells move with variant speeds responding to variant substrate concentrations is referred to as haptokinesis. *Taxis* is that cells migrate specifically toward a higher (or lower) concentration gradient. For instance, bacteria moving toward higher oxygen concentration is termed chemotaxis and cells migrating along the matrix concentration gradient is termed haptotacxis. Finially, *contact guidance* refers to the cell motion which is being guided by surface grooves, curvature and stress of the substrates.

Many kinds of cells are residing on the extracellular matrix (ECM) and these matrices aren't homogenous. For example, collagen concentration on the cartilage surface is more than that inside. Chondrocytes have been discovered to exhibit haptotaxis to their ECM [2]. The mechanism behind the haptotactic effect was at first not clear. Some researchers considered that haptotaxis was due to the chemical stimulation in the solid matrix therefore substantially equal to chemotaxis. However, according to the experiments and mathematical modelings, cell motions in liquid and solid substrates reveal different behaviors. Chemotaxis happens when cells are stimulated by soluble chemicals and migrate to the higher concentration of the attractant. Haptotaxis in contrast is due to the non-uniformly attached sites between the receptors and matrix, which leads cells to passively move toward the stronger attachment site.

Many studies have been using Boyden chambers to measure the chemotacitc and haptotactic magnitudes. Mathematical models that simulated these experimental results have also been developed to look for the chemotactic coefficients. To the best of our knowledge, there have been however few mathematical models regarding haptotaxis. Besides, the cell suspension in the upper well of the Boyden chamber has usually been ignored for the sake of simplicity. In order to gain more insights into how the haptotactic mi-

Chwee Teck Lim, James C.H. Goh (Eds.): ICBME 2008, Proceedings 23, pp. 1749–1752, 2009
www.springerlink.com

gration of chondrocytes can be affected by type II collagen, we develop a simulation model for depicting the experiment of Shimizu et al. [2]. In this model, the effect of cellular sediment through the upper well of the Boyden chamber is investigated by considering both the cell conservation equations in the suspension as well as in the membrane. The simulation results are then used to fit the experiment result with a regression method, so as to determine the cell motility coefficients.

II. Mathematical model

The Boyden chamber comprises an upper and lower well, which are separated by a membrane in the middle (Fig. 1). The membrane in the haptotactic experiment is coated with type II collagen. Cell suspension is initially positioned in the upper well. Assuming that cells do not move into the lower well, we divide the computational domain into two parts, describing the cell motion in the upper well and migration in the membrane respectively.

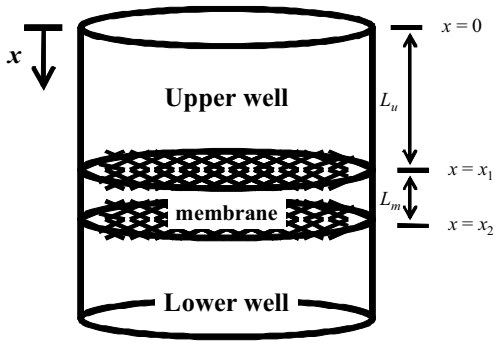


Fig. 1 Schematic diagram of the Boyden chamber. L_u is the height of upper well and L_m is the thickness of membrane.

A. Cell conservation equation in the upper well

Some considerations are made to simplify the mathematical complexity. First, chondrocytes have no cilia or flagella so they only diffuse and sediment in the upper well. Second, chondrocytes, being an anchor-dependent cell, cannot proliferate during the sedimentary process. Finally, we assume that chondrocytes are spherical and have constant density and volume. Based on the mass conservation principle, the cell conservation equation is

$$\frac{\partial}{\partial t}\varepsilon_{c,u} + \nabla \bullet \boldsymbol{J}_{c,u} = 0\,,\ 0 < x < x_1 \tag{1}$$

where $\varepsilon_{c,u}$ is the volume fraction of cell in the upper well, subscript "u" denotes the upper well, and the cell volume flux is derived from the Maxwell-Stefan equation [3] and of the following form

$$\boldsymbol{J}_{c,u} = -D_p \nabla \varepsilon_{c,u} + \varepsilon_{c,u} \boldsymbol{V}_s\,, \tag{2}$$

$$D_p = D_{p0}\left(1 - \varepsilon_{c,u}\right)^{3.65}\,,\ \boldsymbol{V}_s = \boldsymbol{V}_{s0}\left(1 - \varepsilon_{c,u}\right)^{4.65}\,, \tag{3a, b}$$

$$D_{p0} = RT/\left(N_A 3\pi\eta d_c\right)\,,\ \boldsymbol{V}_{s0} = \forall_c \boldsymbol{g}\left(\rho_c - \rho_f\right)/\left(3\pi\eta d_c\right)\,, \tag{4a, b}$$

where N_A is Avogadro's number, $\boldsymbol{g}$ the gravity, R the universal constant (8.314×10^7 g×cm^2/(s^2×mol×K)), T the experimental temperature (310 K), η the viscosity of the medium, d_c the diameter of chondrocyte, $\forall_c$ the volume of chondrocyte (411×10^{-12} cm^3), and ρ_c and ρ_f the density of cell and fluid respectively. Here we have assumed the activity coefficient of the chemical potential to be one to derive Eqs. 2 and 3a. The exponential values 3.65 and 4.65 are obtained from the experimental data under the circumstance that the sedimentary Reynolds number, $Re = V_{s0} d_c \rho_c / \eta = 7.8\times10^{-5}$ is very small [4].

B. Cell conservation equation in the membrane:

Proliferation and death are both neglected as chondrocyte proliferate time is about 3.5 to 17 hours [5; 6], death time is about 30 days [6], which are all much larger than the experimental time of only 5 hrs. Besides, we ignore that type II collagen may degrade in the medium resulting in the chemotactic effect. The cell motion considered here thus consists of cell random walks and the haptotaxis by type II collagen. The cell conservation equation is expressed as

$$\frac{\partial}{\partial t}\varepsilon_{c,m} + \nabla \bullet \boldsymbol{J}_{c,m} = 0\,,\ x_1 < x < x_2 \tag{5}$$

where $\varepsilon_{c,m}$ is the volume fraction of cell in the membrane, subscript "m" denotes the membrane, "$\boldsymbol{J}_{c,m}$" can be written as

$$\boldsymbol{J}_{c,m} = -D_r \nabla \varepsilon_{c,m} + \varepsilon_{c,m} H \nabla\left(\frac{\varepsilon_{col}}{\varepsilon_{col} + \lambda}\right). \tag{6}$$

The first term of equation (6) accounts for the diffusion of cells induced by the cell random walks, and the second term is a haptotactic flux with "H" being the coefficient of haptotaxis and "λ" the half saturation constant. The form based on a receptor kinetic model implies that cells have a maximal haptotactic velocity where the collagen concentration is equal to half saturation constant, i.e. $\varepsilon_{col} = \lambda$. We further assumed the coated collagen is linearly distributed over the membrane thickness,

$$\varepsilon_{col} = \frac{\left(x - L_u\right)}{L_m}\frac{C_{col}^{max}\varepsilon_{void}}{\rho_{col}}\,,\ x_1 \le x \le x_2 \tag{7}$$

where ε_{void} = 0.65 is the porosity of membrane, and ρ_{col} =1.438 g/cm^3 the collagen density. The maximal collagen concentration is at the bottom of the membrane, and the minimal equal to zero is at the membrane top. Furthermore, the maximal concentration of collagen is lower than that in the pure collagen solution, C_{col}^{max}, because of the reduced void space in the membrane.

C. Initial and boundary conditions

We assume the cell flux is zero at the top of the suspension, and neglect that cells fall from the bottom of membrane. At the interface between the suspension and membrane, we consider the cell flux is continuous and the membrane has only 5% of area can be through by cells. These boundary conditions can be expressed as

$$-D_p \frac{\partial \varepsilon_{c,u}}{\partial x} + V_s \varepsilon_{c,u} = 0 \ , \ x = 0 \tag{8}$$

$$-D_p \frac{\partial \varepsilon_{c,u}}{\partial x} + V_s \varepsilon_{c,u} = -D_r \frac{\partial \varepsilon_{c,m}}{\partial x} + H \varepsilon_{c,m} \frac{\partial}{\partial x}\left(\frac{\varepsilon_{col}}{\varepsilon_{col} + \lambda} \right), \ x = x_1 \tag{9a}$$

$$\varepsilon_{c,m} = 0.05 \varepsilon_{c,u} \ , \ x = x_1 \tag{9b}$$

$$-D_r \frac{\partial \varepsilon_{c,m}}{\partial x} + H \varepsilon_{c,m} \frac{\partial}{\partial x}\left(\frac{\varepsilon_{col}}{\varepsilon_{col} + \lambda} \right) = 0 \ , \ x = x_2 \ . \tag{10}$$

As for the initial conditions, we assume cells initially are uniformly distributed in the cell suspension, and there is no cell in the membrane. So

$$\varepsilon_{c,u}(0,x) = C_{c0} V_c, \ 0 \le x \le x_1 \ , \tag{11}$$

$$\varepsilon_{c,m}(0,x) = 0, \ x_1 < x \le x_2 \ , \tag{12}$$

where C_{c0}=2×10^6 cells/cm^3 is the initial cell number density.

III. Results and Discussion

The mathematical model was solved by a commercial finite element code, Multiphysics 3.2 (COMSOL). We used quadratic shape function and fine meshes at the boundaries. The validation of the simulation model was tested by comparison with the experiments in literature. The cell number in a microscopic field of view is calculated by integrating the cell volume fraction of cell over a cell diameter at the bottom of membrane:

$$\left(A \times \int_{x_2 - d_c}^{x_2} \varepsilon_{c,m} dx \right) \Big/ V_c \ , \tag{13}$$

where A is the area of the field of view. The comparison between the current model and the experimental data of Shimuzi et al. [2] is displayed in Fig. 2, which shows good agreement. As shown there are more and more cells that have migrated to the bottom of the membrane as the collagen concentration increases from zero. Chondrocytes perform the maximal haptotactic response when the Boyden chamber membrane is coated with a collagen solution of 35 μg/ml. Once the collagen in the solution exceeds 35 μg/ml, cells gradually slow down their motion toward the bottom of membrane. Although the experimental data in Fig. 2 have not shown a decrease in migrated cell number at higher collagen concentrations, the theory predicts such a trend. The trend conforms to some other previous experimental results and theory: attachment strength between cells' receptor and matrix is weak at lower and higher collagen concentration, and the associated haptotactic velocity will accordingly become low. The diffusion, haptotaxis and saturation coefficients obtained via fitting the experiment by minimizing the least squares of errors between the experimental and theoretical data are listed in Table 1. The value of the diffusion coefficient is of the same order as that of Chung et al. [6] and Chang et al. [8]. From equation (6), the haptotactic velocity responded to the distribution of collagen is also close to the value of the observation (1.38×10^{-7} cm/s) [8].

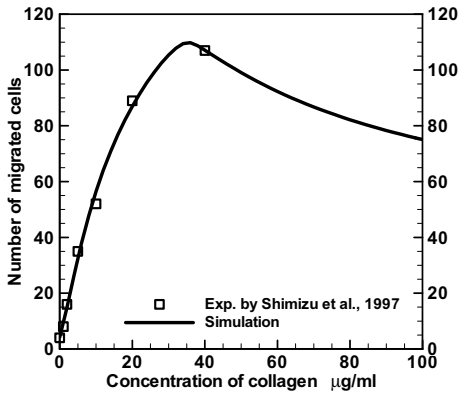


Fig. 2 Comparison between the current model and the experimental data of Shimuzi et al. [2]

Table 1 List of parameters

Name	Value	Reference
Density of chondrocyte, ρ_c	1.02 g/cm^3	[9]
Density of media, ρ_f	1.009 g/cm^3	[9]
Diffusion coefficient, D_r	1.169×10^{-10} cm^2/s	This work
Haptotactic coefficient, H	8.897×10^{-10} cm^2/s	This work
Saturation const. of haptotactic, λ	1.623×10^{-6}	This work
Viscosity of media, η	8.4×10^{-3} g/(cm×s)	[9]

Fig. 3 and 4 respectively display the simulated cell distributions in the upper well and membrane during the process. At beginning, cells are uniformly distributed in the upper well. Then, they move down through the suspension medium by the gravity action. Because the porosity size of membrane is only 8 μm and the surface porosity is only 5%, cells cannot pass through it right away. They accumulate onto the membrane surface, and then form a cell boundary layer (Fig. 3). Cells thereupon migrate into the membrane through the pores via diffusion and haptotactic motions. A local cell aggregate is formed and moving down in the membrane, and cells gradually deposit onto the bottom of membrane (Fig. 4). The local cell aggregate forms because the haptotactic velocity becomes smaller as cells get closer to the membrane bottom where the collagen concentration is much larger than the saturation value λ.

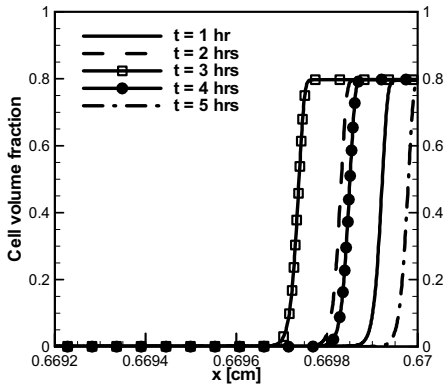


Fig. 3 Cell distribution in the upper well

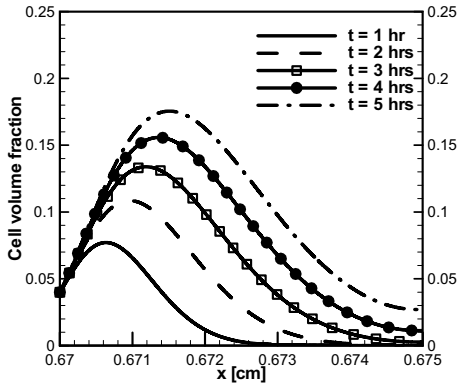


Fig. 4 Cell distribution in the membrane

IV. Conclusion

In this article, we consider theoretically the effect of the suspension layer on the haptotactic migration of chondrocytes in the Boyden chamber assay. Simulations match the experimental data from literature. The corresponding coefficients obtained for chondrocytes are 8.897×10^{-10} cm^2/s for haptotactic coefficient and 1.623×10^{-6} for the saturation constant. In a mature native cartilage, ECM occupies as much as one forth of the *in vivo* volume, and the native collagen with 90-95% (v/v) being type II collagen constitutes 65% of the ECM. Consequently, the volume fraction of type II collagen may be as high as 15.4% *in vivo*, which is much larger than the saturation value of 1.623×10^{-6}. According to equation (6), the haptotactic velocity is of maximum when type II collagen concentration is close to the saturation coefficient. Therefore, haptotaxis may be insignificant to mature cartilage; however, it is possible to impose an influential impact on the migrating chondrocytes in the early stage of cartilage formation.

Acknowledgment

The work is support by the National Science Council of Taiwan through the research grant NSC 96–2221–E–008–066–MY3.

References

1. Oster GF, Murray JD, Harris AK (1983) Mechanical aspects of mesenchymal morphogenesis. J Embryol Exp Morphol 78:83-125.
2. Shimizu M, Minakuchi K, Kaji S et al. (1997) Chondrocyte migration to fibronectine, type I collagen, and type II collagen. Cell Struct Funct 22:309-315.
3. Wesselingh JA, Krishna R (2000) Mass transfer in multi-component mixtures. VSSD. The Netherlands.
4. Richardson JF, Zaki WN (1954) Sedimentation and fluidization: Part I. Trans Inst Chem Engrs 32:35-53.
5. Galban CJ, Locke BR (1999) Analysis of cell growth kinetics and substrate diffusion in a polymer scaffold. Biotechnol Bioeng 65:121 - 132.
6. Chung CA, Chen CW, Chen CP et al. (2007) Enhancement of cell growth in tissue-engineering constructs under direct perfusion: modeling and simulation. Biotechnol Bioeng 97:1603-1616.
7. Lauffenburger DA, Linderman JJ (1993) Receptors models for binding, trafficking, and signaling. Oxford University, New York.
8. Chang C, Lauffenburger DA, Morales TI (2003) Motile chondrocytes from newborn calf: migration properties and synthesis of collagen II. Osteoarthritis Cartilage 11:603-612.
9. Coletti F, Macchietto S, Elvassore N (2006) Mathematical modeling of three-dimensional cell cultures in perfusion bioreactors. Ind Eng Chem Res 45:8158-8169.

Author: Chih-Yuan Chen
Institute: National Central University
Street: No.300, Jhongda Rd.
City: Jhongli City, Taoyuan County 32001
Country: Taiwan, R.O.C.
Email: 943403018@cc.ncu.edu.tw

Analyzing the Sub-indices of Hysteresis Loops of Torque-Displacement in PD's

B. Sepehri[1], A. Esteki[2] and M. Moinodin[3]

[1] Department of Mechanics, Islamic Azad university-Mashhad Branch, Mashhad, Iran
[2] Department of Medical Engineering, Shahid beheshti University of Medical Sciences, Tehran, Iran
[3] School of Medical Engineering, Islamic Azad university-Science&Research Branch, Tehran, Iran

Abstract — **The ability of method we've previously used for the quantification of rigidity in Parkinson's disease was improved. Using Data previously obtained from torque-displacement behaviour during passive movement of elbow joint, the range of motion was divided in three parts: the first, the middle and the last. The ability of m-file previously had been used in MATLAB was improved so that the viscous and elastic indices were calculated in each part, separately. To find the most remarkable index for distinguishing patients and controls, also prediction of level of PD, statistic tests were done. The number of PD's was 41 and controls were 11 people. Results showed that the viscous index of the last part of ROM normalized to Rom, which we call it Normalized Extension Hysteresis, NEH, had the highest correlation with rigidity levels (r=0.899) and can be used to distinguish patients and control (p=0.000).**

Keywords — **Computational biomechanics, Visco-elastic, Parkinson's disease, Statistic method, Rigidity, Hysteresis.**

I. Introduction

One of the major exams currently is used by neurologists to detect Parkinson's Disease and to find it's level of severity, is examination if rigidity during passive movement of the limbs [1,2]. The method is called Unified Parkinson's Disease Rating System, UPDRS which rates rigidity from 0 to 4. Zero level indicates no abnormal rigidity and four indicates maximum rigidity or even freeze. Subjective nature of such an exam makes it open for the influence of the examiner. Many researchers tried to find an objective method so that the rigidity could be measured objectively [3-8].

In the research previously done [9,10], using a device fabricated, elastic and viscous indices of rigidity during passive movement of elbow was measured. Correlation of indices and UPDRS rigidity levels in group of parkinsonians were examined and finally concluded that viscous index of rigidity was dominant to the elastic one for evaluation of rigidity in PDs. However in the mentioned study, it was proposed to check for the rigidity indices in different parts in the range of motion.

The aim of this research was to improve the ability of method we've previously used for the quantification of rigidity in Parkinson's disease [9]. To do so, we've improved the m-file previously used in Matlab, so that the sub indices of hysteresis loops of torque-displacement were calculated during passive movement of elbow.

II. Material and Methos

In this study, we used rigidity data previously recorded for groups of parkinsonians and controls. For every individual case, data had been measured both with the device and by neurologist using the conventional UPDRS method [9].

Based on the recorded data, we've provided a more sophisticated m-file in Matlab-R14 which was able to calculate the following 9 indices in addition to those previously were calculated (Fig. 1, 2):

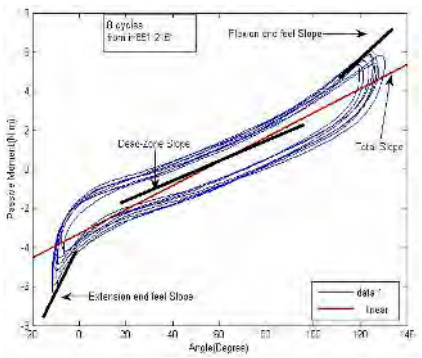


Fig. 1 Passive moment- angular displacement curves for an individual case and elastic indices indicated on it.

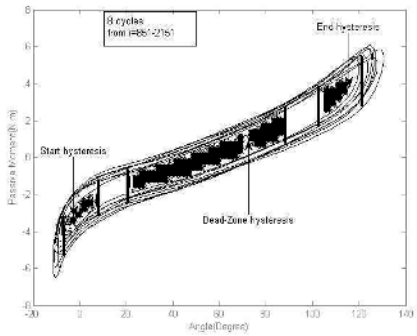


Fig. 2 Passive moment- angular displacement curves for an individual case and viscous indices indicated on it.

Chwee Teck Lim, James C.H. Goh (Eds.): ICBME 2008, Proceedings 23, pp. 1753–1756, 2009
www.springerlink.com

1. Slope of the last 10 percent of loading phase as Flexion End Feel, FEF.
2. Slop of the last 10 percent of un-loading phase as Extension End Feel, EEF.
3. Slop of the 56 median percent of loading and un-loading phases as Dead Zone slop, DZS.
4. Area between loading and un-loading curves for the first 10 percent of range of motion as Flexion Hysteresis, FH.
5. Area between loading and un-loading curves for the last 10 percent of range of motion as Extension Hysteresis, EH.
6. Area between loading and un-loading curves for the median 56 percent of range of motion as Dead Zone Hysteresis, DZH.
7. Each of the following 6 indices normalized to range of motion of each individual case, ie. Normalized Flexion Hysteresis, NFH, Normalized extension Hysteresis, NEH and Normalized Dead-Zone Hysteresis, NDH.

The first 3 indices were considered as elastic indices of rigidity and the rest were attributed as viscous ones.

To find the best characteristic index, we chose the statistic exams of independent t-test for paired groups of Control/Patients, Men/Women, Right/Left sides and With/Without reinforcement. One way ANOVA was performed to check for the best index for differentiation among UPDRS groups. Pearson's correlation test was done to find the highest linear ratio of indices and UPDRS levels.

III. Results

Except for the FEF index, other indices had the ability of distinguishing between controls and patients. This was considered by p-values less than 0.05 (Table1). Almost all indices showed no significance in sex and side paired groups. Significance among UPDRS levels in all indices was seen. NEH had p-value of 0.000 in distinguishing between with and without reinforcement groups.

In an overall word, viscous indices had bigger correlation ratios to UPDRS scores than those of elastic ones (Fig. 3-8). Correlations were still higher when viscous indices were normalized to ROM (Fig. 9-11). The highest correlation ratio of 0.899 was found for NEH index.

Table 1 P-values of statistic tests indicating the significances of pre-described indices in groups of Controls/Patients, Men/Women, With/Without reinforcement, Right/Left sides, and UPDRS levels of 0 to 4.

	Controls/ Patients	Sex	Rein-force	Side	UPDRS levels
FEF	0.011	0.373	0.630	0.770	0.000
EEF	0.000	0.021	0.015	0.598	0.000
DZS	0.000	0.247	0.001	0.251	0.000
FH	0.000	0.941	0.009	0.064	0.000
EH	0.000	0.251	0.005	0.812	0.000
DZH	0.000	0.106	0.004	0.556	0.000
NFH	0.000	0.800	0.030	0.011	0.000
NEH	0.000	0.243	0.000	0.926	0.000
NDZH	0.000	0.026	0.001	0.741	0.000

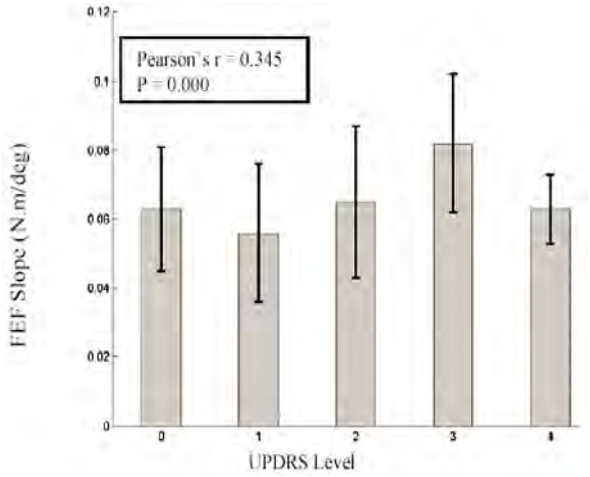


Fig. 3 Mean and std of FEF index and correlation to UPDRS levels.

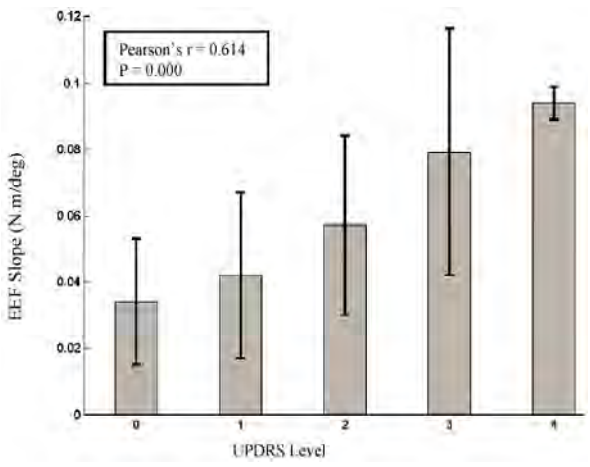


Fig. 4 Mean and std of EEF index and correlation to UPDRS levels.

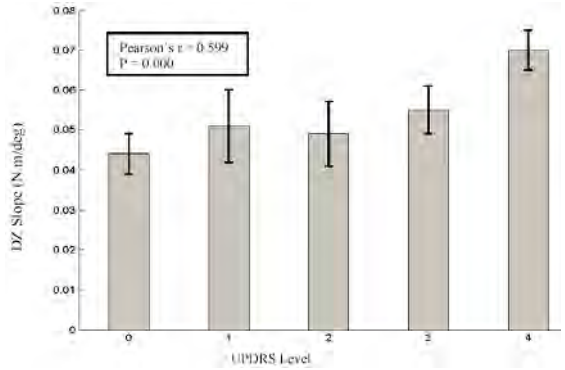


Fig. 5 Mean and std of DZS index and correlation to UPDRS levels.

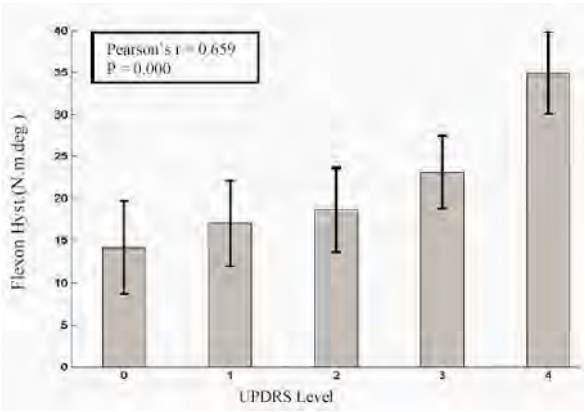


Fig. 6 Mean and std of FH index and correlation to UPDRS levels.

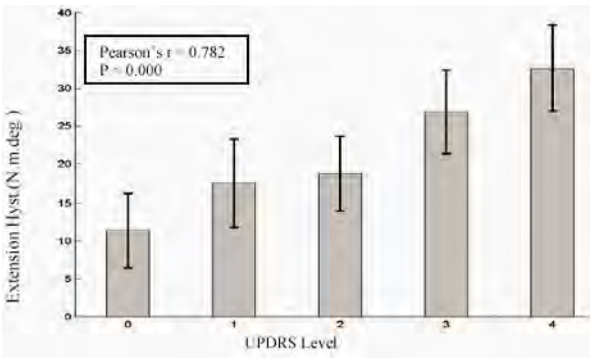


Fig. 7 Mean and std of EH index and correlation to UPDRS levels.

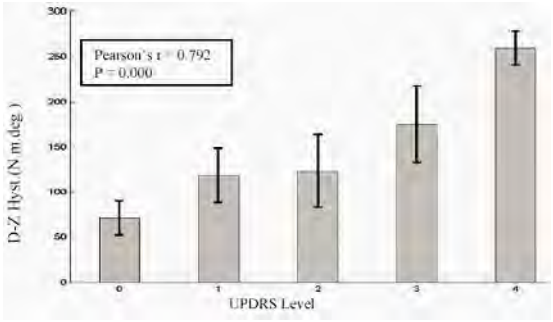


Fig. 8 Mean and std of DZH and correlation to UPDRS levels.

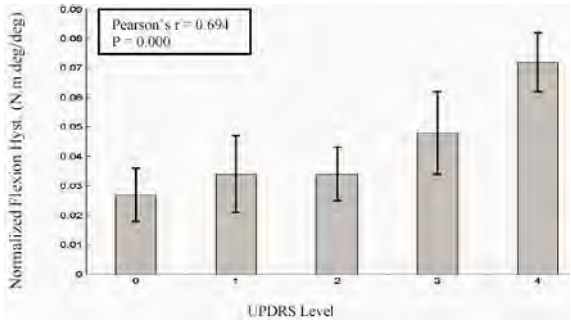


Fig. 9 Mean and std of NFH index and correlation to UPDRS levels.

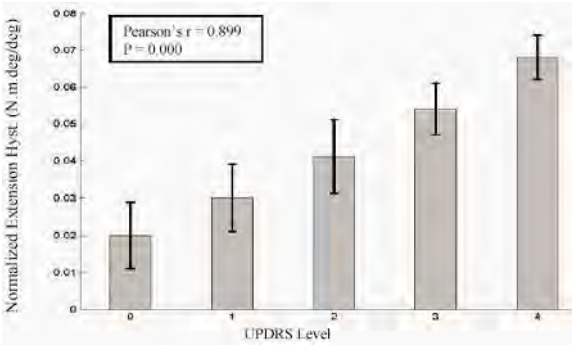


Fig. 10 Mean and std of NEH and correlation to UPDRS levels.

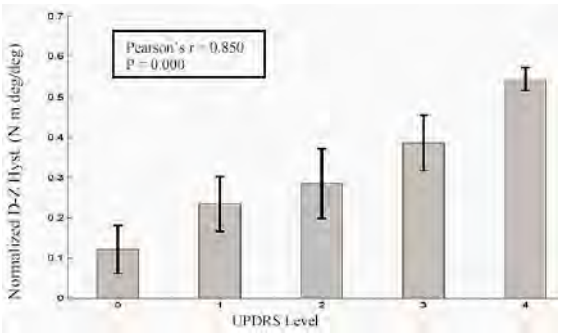


Fig. 11Mean and std of NDZH and correlation to UPDRS levels.

IV. Discussion

In this research, we continued to find the cardinal index for quantification of UPDRS rigidity score which was partly studied previously. To do so, we considered more indices including elastic and viscous sub items of hysteresis loops extracted from passive movement of elbow joints of controls and patients.

Results confirmed with results of the previous study [9]: viscous indices are more likely related to UPDRS rigidity score. Further more, viscous index of late flexion range of motion is seem to have priority to other indices. This can imply that parkinsonian rigidity has the most effect in the final extreme of range of motion. NEH index had the highest correlation ratio to UPDRS levels also, had the highest significance to distinguish between with and without reinforced rigidity which is one of the most known characteristics of PD.

NEH index examined here was similar to that previously studied by Kirolos and co-workers [4]. The mean values of their index were 0.07 and 0.25 for control and patients respectively, while values in our study were 0.017 and 0.033. It should be noticed that Kirolos and co-workers had examined just two patients while we did for 41 patients with different range of UPDRS rigidity. Further more, they had normalized the hysteresis index to the final part of range of motion(i.e. 115-155 degrees flexion), while the normalization in our study was done to total range of motion of each case to consider for differences in physiological range of motion in different people.

In this research and similar researches, ordinary statistic methods were used to find the best relating index to rigidity caused by Parkinson's disease. However new analysing methods such as neuro-phasy and genetic algorithm are proposed to find more reliable results.

V. Conclusion

It can be concluded that viscous element described as normalized extension hysteresis can be the best quantitative index for evaluation of parkinsonian rigidity.

Acknowledgment

Dr. G. A. Shahidi and Dr. F. Khamseh are acknowledged for their part in this research.

References

1. Scenk M. and Venekamp D (2003) .Parkinson's Disease Biomechatronics wb 2432
2. Mark Guttman, Stephen J. Kish, Yoshiaki Furukawa (2003) Current concepts in the diagnosis and management of Parkinson's disease. Journal of Canadian Medical Association. • FEB. 4, 168 (3):293-301.
3. Teravainen H., TsuiJ. K. C., Mak E. and Calne D. B. (1989) Optimal indices for testing parkinsonian rigidity. Candal. J. Neuro. Sci., vol. 16, no. 2: 180-183.
4. Kirollos C. , Charlett C, O'neill C. J. A. , Kosik R., Mozol K., Purkiss A. G.., Bowes S. G., Nicholson P. W., Hunt W. B., Weller C., Dobbos C. S. M. Dobbos R. J. (1996) *Objective measurement of activation of rigidity : diagnostic, pathogenetic and therapeutic implications in parkinsonism*, British Journal of Clinical Pharmacology 41:557-564.
5. M. P. Caligigiuri (1994) *Portable device for quantifying Parkinsonian wrist rigidity*, Mov. Disord., vol. 9,no. 1:57-63.
6. (5) Halpern D., Patterson R, Mackie R., Runck W. and Eyler L.,Muscular (1979) hypertonia:Quantitative analysis. Arch. Phys. Med. Rehabil., vol. 60,no. 5: 208-218.
7. (6) Lang A. E. T. and Fahn S. (1989) Assessment of Parkinson's disease,in Quantification of Neurological Deficit, T.L.Munsat, Ed. Boston,Ma:Butterworths, 285-309.
8. (7) PatricS. K., Allen A., Denington M., Gauthier G. A., Gillard D. M. and Prochazkz A. (2001) Quantification of the UPDRS Rigidity Scale, IEEE Transaction on neural systems and rehabilitation engineering,Vol.9,no1.
9. Sepehri B., Esteki A., Ebrahimi Takamjani E., Shahidi G. A., Khamseh F. and Moinodin M. (2007) Quantification of Rigidity in Parkinson's disease. Annals of Biomedical engineering,vol. 35, no. 12: 2196-2203, 2007.
10. Sepehri B., Esteki A., Shahidi G. A. and Moinodin M. (2006) Quantification of Parkinsonian Rigidity: An Objective Evaluating Method. 3rd Kuala Lampur International Conference on Biomedical Engineering Kuala Lumpur, Malaysia, 2006, pp. 516-519.

Author: Behrooz Sepehri
Institute: Azad University-Mashhad Branch
Street: Imamieh Ave.
City: Mashhad
Country: Iran
Email: b_sepehr@mshdiau.ac.ir

Relative Roles of Cortical and Trabecular Thinning in Reducing Osteoporotic Vertebral Body Stiffness: A Modeling Study

K. McDonald[1], P. Little[1], M. Pearcy[1], C. Adam[1]

[1] Queensland University of Technology / Institute of Health and Biomedical Innovation, Brisbane, Australia

Abstract — **While the effects of reduced bone density on osteoporotic vertebral strength are well known, the relative roles of cortical shell and trabecular architecture thinning in determining vertebral stiffness and strength are less clear. These are important parameters in investigating the changing biomechanics of the ageing spine, and in assessing the effect of stiffening procedures such as vertebroplasty on neighbouring spinal segments. This work presents the development of a microstructural computer model of the osteoporotic lumbar vertebral body, allowing detailed prediction of the effects of bone micro-architecture on vertebral stiffness and strength.**

Microstructural finite element models of an L3 human vertebral body were created. The cortex geometry was represented with shell elements and the trabecular network with a lattice of beam elements. Trabecular architecture was varied according to age. Each beam network model was validated against experimental data. Models were generated to represent vertebral bodies of age <50 years, age 50-75y and age >75y respectively. For all models, an initial cortical shell thickness of 0.5mm was used, followed by reductions in the age >75y models to 0.35mm and 0.2mm to represent cortical thinning in late stage osteoporosis. Loads were applied to simulate in vitro biomechanical testing, compressing the vertebra by 20% of its height.

Predicted vertebral stiffness and strength reduced with progressive age changes in microarchitecture, demonstrating a 44% reduction in stiffness and a 43% reduction in strength, between the age <50 and age >75 models. Reducing cortical thickness in the age >75 models demonstrated a substantial reduction in stiffness and strength, resulting in a 48% reduction in stiffness and a 62% reduction in strength between the 0.5mm and 0.2mm cortical thickness models. Cortical thinning in late stage osteoporosis may therefore play an even greater role in reducing vertebral stiffness and strength than earlier reductions due to trabecular thinning.

Keywords — **Vertebra mechanics, FE modeling, trabecular architecture, osteoporosis, cortical shell**

I. Introduction

Osteoporosis is a disease which affects more than 75 million people in Europe, Japan and the USA, and is the cause of more than 2.3 million fractures annually in Europe and America alone [1]. Osteoporosis is characterized by low bone density and micro-architectural deterioration of bone tissue, resulting in increased susceptibility to fracture [2]. The micro-architectural deterioration includes thinning of the trabeculae, increased spacing between trabeculae, and in the later stages, thinning of the cortical shell. These changes transform the structure from dense and plate-like to a sparse, rod-like structure. It is believed there is an associated change in the failure mechanisms from plastic collapse of the trabeculae to inelastic, or possibly even elastic, buckling of the trabeculae. Due to the experimental difficulty in investigating this complex structure, the effect of bone loss on trabecular failure mechanisms and whole vertebra mechanics is still poorly understood.

To overcome experimental difficulties, previous studies have employed computational modeling methodologies. These studies utilize two distinct approaches. Firstly, the *macro scale approach*, whereby a solid, whole vertebra is simulated and the structure of the trabecular bone approximated as a continuum. The material properties of the vertebral core are varied to represent the changes in trabecular structure and the effect of this change on whole vertebra mechanics is observed. Secondly, *micro scale approaches*, whereby an isolated section of the trabecular structure is simulated using either continuum or beam elements. Continuum elements are computationally expensive and therefore only small regions of bone can be modeled. Conversely, computationally efficient beam elements have been used to simulate larger regions of trabecular structures. The results for these micro scale models are then extrapolated for a whole vertebra.

This study aimed to create a multi-scale finite element model of an L3 human vertebral body. The architectural changes observed in osteoporosis (trabecular thinning, increased trabecular spacing and cortical shell thinning) were modeled and the effect of these changes on whole vertebra mechanics and trabecular mechanics explored.

II. Methods

A finite element model of an L3 human vertebra was analysed under compression to assess the relative affect of cortical and trabecular microstructure on vertebral mechanics. The trabecular structure was modeled using three-dimensional beam elements and the vertebral cortex simulated with shell elements. Model development involved

Chwee Teck Lim, James C.H. Goh (Eds.): ICBME 2008, Proceedings 23, pp. 1757–1760, 2009
www.springerlink.com

ascertaining the efficacy of the beam elements in simulating trabecular biomechanics, validation of the beam element trabecular lattice and simulation of an intact vertebra.

A. Modeling the trabecular core

Three dimensional beam elements were used to represent individual struts within the trabecular lattice. As buckling is an important failure mode of longitudinally oriented trabeculae [3], it was important that the model accurately predicted buckling behavior. Therefore, analyses were performed on various beam element configurations to determine an appropriate trabeculum model. The effect of element type, initial beam curvature, mesh density and solution time increment were investigated.

Due to the paucity of data on trabeculum failure mechanisms at the microstructural level (specifically buckling), it was necessary to use a buckling mechanics study based on another material to verify the trabeculum model. Investigations performed by Rahman [4] gave critical buckling loads determined experimentally for solid columns of stainless steel (SUS304). This work covered a comprehensive range of slenderness ratios (14-184) and hence failure modes, from purely elastic to purely plastic. The material properties and slenderness ratios of the trabeculum model were altered to represent the steel columns, and Rahman´s experimental results used to verify the prediction of the model. From these analyses it was concluded that two quadratic beam elements, with a slight initial curvature, were able to predict failure (be it elastic buckling, inelastic buckling, or plastic collapse) with a mean error of 20% for the whole range of slenderness ratios. For the trabeculum model, an initial offset of 0.001mm in the centre of the column was necessary to induce buckling. Once confidence was obtained in the ability of the FE techniques to predict buckling, they were applied to represent a trabecular core model.

A three dimensional trabecular core was created using a lattice of individual trabeculum beams. Three-node, quadratic beam elements were used to represent the longitudinal trabeculae, and two-node, linear beam elements represented the transverse trabeculae. Since the transverse trabeculae are primarily loaded in tension, the additional complexity of the quadratic beam representation was considered unnecessary. To provide a degree of irregularity to the lattice, as is seen in real trabecular bone, a perturbation factor of 0.3 was applied [5]. The perturbation factor defines the maximum distance each node may be perturbed by as a proportion of the trabecular spacing. For example, with a perturbation value of 0.3, each node point was perturbed ±0-30% of the spacing value.

The trabecular spacing and thickness values for the transverse and longitudinal trabeculae were derived from Mosekilde [6]. The values are shown in Table 1. Three trabecular structures were created; age < 50, age 50-75 and age > 75. A tissue modulus of 8GPa and a Poisson´s ratio of 0.3 were applied [7, 8]. An elastic-perfectly plastic yield definition was included which had a yield strain of 0.85% and a yield stress of 68 MPa. The yield strain was determined as an average of the reported compressive and tensile yield strains for trabecular bone [9].

Table 1 Trabecular spacing and thickness values for female vertebral trabecular bone for age < 50, age 50-75 and age > 75 [6]

Model	Transverse Spacing (mm)	Longitudinal Spacing (mm)	Transverse Thickness (mm)	Longitudinal Thickness (mm)
Age <50	0.674	0.633	0.150	0.208
Age50-75	0.861	1.100	0.116	0.187
Age >75	1.145	1.668	0.107	0.201

The trabecular core model was verified against experimental results. As well as providing structural parameters for three age groups, the Mosekilde study also provided the compressive strength of the trabecular cores for these age groups. To provide a comparison, trabecular core models were created to replicate the *in vitro* cylindrical bone samples tested by Mosekilde (radius 3.5mm, length 5mm). To replicate the axial compression test performed in the study, the upper nodes of the cores were were free to move only in the axial direction and held in all other degrees of freedom. All bottom surface nodes were held in all degrees of freedom. The upper nodes were displaced in the axial direction until failure of the core occurred. The models were solved using ABAQUS/Standard (version 6.7, Abaqus Inc, RI, USA) using a large displacement (non-linear geometry) quasi-static solution procedure. The maximum compressive strength and stiffness of the cores were determined and compared to the experimental results. Once confidence was gained in the trabecular core model, an intact vertebra was simulated.

B. Modeling the Vertebra

Using a similar methodology to that employed for the trabecular core, an intact vertebra was simulated whereby the inner trabecular lattice of the vertebra was enclosed by a thin vertebral cortex. Age < 50, age 50-75 and age >75 vertebra models were produced. The cortex was meshed using three dimensional, linear shell elements and the geometry was based on equations given by Mizrahi [10]. The mesh density gave shell elements 2mm in size. The material properties of the cortex were assumed to be the same as the trabecular bone [7, 8]. The thickness of the shell ele-

ments was 0.5mm, which represents a normal cortical shell [11]. In the age > 75 model, the shell thickness was reduced to 0.35mm, and then again to 0.2mm to represent shell thinning, as is observed in the later stages of osteoporosis [11]. This resulted in five vertebra models, all at different stages of osteoporosis.

Loads were applied to simulate in vitro biomechanical testing, compressing the vertebra by 20% of its height. The upper endplate was displaced by -6mm axially and held in the transverse plane. The lower endplate was held in all directions. A quasi static solution step (total length 1 sec) was used with a minimum time increment of 0.01 sec and a maximum time increment of 0.1 sec. As previously stated, the ABAQUS non linear geometry capability was used to include the effect of large deformations in the solution.

III. Results

The apparent modulus of the trabecular cores and vertebral models were determined using the linear region of the stress strain graph, between 0-0.4% apparent strain. The maximum compressive strength was considered to be the maximum total vertical reaction force that was reached in the simulation.

A. Trabecular core

Table 2 shows the compressive strength of the various trabecular core models determined experimentally by Mosekilde [2] and the corresponding computed compressive strengths from the trabecular core model. The table also shows the apparent stiffness of the cores determined computationally, however Mosekilde did not report the stiffness of the cores tested experimentally and hence no direct comparison can be made. Other studies have reported vertebral trabecular bone samples from the lumbar spine have an apparent modulus of 165 ± 110 MPa [12].

Table 2 Compressive strength of the trabecular core samples determined experimentally by Mosekilde and by FE trabecular core model and the stiffness of the cores predicted by the FE models

	Age < 50	Age50-75	Age >75
Mosekilde maximum compressive strength (MPa)	3.91 ± 1.61	1.35 ± 0.64	0.93 ± 0.4
FE trabecular core maximum compressive strength (MPa)	2.84	1.21	0.54
FE trabecular core apparent modulus (N/mm)	253	138	74

B. Vertebra Model

Figure 1 shows the stress strain curve for each of the vertebra models. The corresponding stiffness and compressive strengths are shown in Table 3.

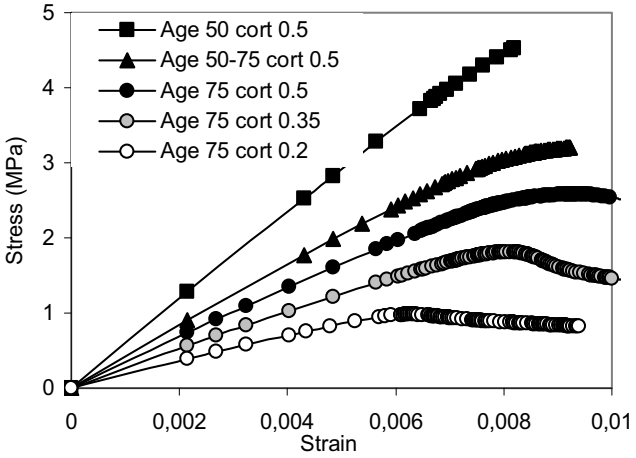


Fig. 1 Stress versus strain for the vertebra models.

Table 3 FE predicted compressive strength and stiffness of the vertebra models

Model	Cortical thickness (mm)	Stiffness (N/mm)	Max. Compressive strength (kN)
Age <50	0.5	595	5.74
Age50-75	0.5	412	4.06
Age >75	0.5	336	3.28
Age >75	0.35	256	2.30
Age >75	0.2	176	1.25

IV. Discussion

The trabecular core model was able to reproduce compressive strengths and apparent moduli determined experimentally. The predicted compressive strengths for the cores of various structures were within one standard deviation of Mosekilde´s experimental results for the corresponding ages. The apparent moduli determined computationally were within the range of values (165±110 MPa) in the literature [12]. With these results, confidence was achieved in the trabecular beam model.

The vertebra model confirms that changes in architecture have a large effect on overall vertebra stiffness and strength. A change in architecture from the age < 50 to the age > 75 cases resulted in a 44% decrease in stiffness and a 43% decrease in vertebral strength. With the age > 75 model, a change in shell thickness from 0.5mm to 0.2 mm, without

any change in trabecular structure, resulted in a 48% decrease in stiffness and a 62% decrease in compressive strength. These results not only highlight the importance of the trabecular architecture changes that occur with the osteoporosis process, but also the biomechanical importance of the cortical thinning that occurs in the later stages of the disease.

A current limitation of this model is that it has yet to be validated against experimental data for a full vertebral body (including the cortical shell). However validation of the trabecular core model and initial comparisons with the literature indicate the predictions of the vertebra model are reasonable. Reported vertebral body compressive strengths range from approximately 60MPa for a 20 year old vertebra to 2.6MPa for an 80 year old vertebra [13]. The predicted compressive strengths for the vertebral models of different ages are comparable with these values, although slightly lower.

The premise for this modeling approach was that buckling mechanisms dominate the response of rod-like osteoporotic bone. Hence, replicating the trabecular network using beam elements provides a sophisticated microstructural model capable of simulating plastic collapse, inelastic buckling, or elastic buckling in bone of various ages. Taking a closer look at the trabecular struts in the age > 75 vertebra model shows the trabecular beams are undergoing large buckling deformation, but no plastic deformation is seen, indicating that the overall failure of the vertebra is due to elastic buckling of the trabeculae. In the age 50-75 model, the beams also experience large amounts of buckling; however there is also plastic deformation throughout the structure. This suggests inelastic failure of the trabeculae is playing a key role in the vertebra failure. Finally, the beams of the age < 50 model show almost no buckling, yet a high amount of plastic deformation, signifying plastic collapse of the structure. While further model investigation and validation needs to be done before any quantitative data on the trabeculae can be reported, these results highlight the distinctive insight into both the trabecular and vertebral mechanics this model allows.

In future work, this model will be validated against human vertebra specimens. Once validated, it will be used to investigate current drug therapies and their effects on the bone architecture and vertebral strength, as well the effect on trabecular and vertebral strength of surgical treatments such as vertebroplasty.

V. Conclusion

This paper has presented the development of a novel multi-scale, vertebra model produced with beam and shell elements. The model predictions have been validated against experimental data in existing literature and show good agreement. The investigation into the effects of changes in architecture indicate that while the changes in trabecular architecture have a large effect on vertebral strength and stiffness in the early stages of osteoporosis, cortical thinning may have as great an effect (if not greater) in the later stages.

References

1. Osteoporosis, W.S.G.o.t.P.a.M.o., *Prevention and management of osteoporosis: report of a WHO scientific group.*, in *WHO technical report series*. 2000, World Health Organisation: Geneva.
2. Consensus development conference: Diagnosis, prophylaxis and treatment of osteoporosis. in American Journal of Medicine. 1991.
3. Townsend, P.R. and R.M. Rose, *Buckling studies of single human trabeculae.* Journal Of Biomechanics, 1975. **8**: p. 199-201.
4. Rahman, M.A., J. Tani, and A.M. Afsar, *Postbuckling behaviour of stainless steel (SUS304) columns under loading-unloading cycles.* Journal of Constructional Steel Research, 2006. **62**(8): p. 812-819.
5. Jensen, K.S., Mosekilde, L., Mosekilde, L., A model of vertebral trabecular bone architecture and its mechanical properties. Bone, 1990. **11**(6): p. 417-423.
6. Mosekilde, L., Sex differences in age-related loss of vertebral trabecular bone mass and structure--biomechanical consequences. Bone, 1989. **10**(6): p. 425-432.
7. Linde, F., Elastic and viscoelastic properties of trabecular bone by a compression testing approach. Danish Medical Bulletin, 1994. **41**(2): p. 119-138.
8. Keaveny, T.M., et al., *Biomechanics of trabecular bone.* Annu. Rev. Biomed. Eng., 2001. **3**: p. 307-333.
9. Niebur, G.L., et al., High-resolution finite element models with tissue strength asymmetry accurately predict failure of trabecular bone. Journal of Biomechanics, 2000. **33**(12): p. 1575-1583.
10. Mizrahi, J., Silva, M.J., Keaveny, T.M., Edwards, W.T., Hayes, W.C., *Finite-element stress analysis of the normal and osteoporotic lumbar vertebral body.* Spine, 1993. **18**(14): p. 2088-2096.
11. Mosekilde, L., *Vertebral structure and strength in vivo and in vitro.* Calcified Tissue International, 1993. **53**(Supplement 1): p. S121-S125; discussion S125-S126.
12. Keaveny, T.M., Pinilla, T.P., Crawford, R.P., Kopperdahl, D.L., Lou, A, *Systematic and random errors in compression testing of trabecular bone.* Journal of orthopedic research, 1997. **15**(1): p. 101-110.
13. Mosekilde, L. and M. Leif, Normal vertebral body size and compressive strength: Relations to age and to vertebral and iliac trabecular bone compressive strength. Bone, 1986. **7**: p. 207-212.

Musculo-tendon Parameters Estimation by Ultrasonography for Modeling of Human Motor System

L. Lan[1], L.H. Jin[2], K.Y. Zhu[1] and C.Y. Wen[1]

[1]Nanyang Technological University, Singapore
[2]Tianjin Zhonghuan Semiconductor Joint-stock Co. Ltd, China

Abstract — **To provide quantitative insights in analyzing human movement, the musculoskeletal model is widely used to predict the muscle force output. It is important to accurately estimate the model's parameters on subject specific basis. This paper presents an approach to obtain the parameters in vivo by the ultrasound imaging technology. The origin and insertion points, pennation angle, fascicle length and cross-sectional area of brachialis are measured by off-line analyzing of ultrasound image. The data is used to calculate values of musculotendon length, moment arms, optimal muscle fascicle length, tendon slack length and maximum isometric force. These musculotendon parameters can be used in a musculoskeletal model to predict the muscle force and torque.**

Keywords — **Ultrasound, musculotendon model**

I. Introduction

Model of musculoskeletal system is widely used to simulate the muscle force in analyzing human movement [1]. One of the main challenges in modeling is to accurately estimate the musculotendon parameters on subject-specific basis. The underlying muscle contraction and dynamics information can be provided by appreciate modeling. Furthermore, the fact that the modeling and simulation results are significantly affected by the accuracy of estimated values of musculotendon parameters is also revealed by the sensitivity and validation study.

In biomechanics studies, most researchers simply adopted formerly reported values from cadaver specimen to predict muscle force and torque [2]. However, parameter values vary widely for even the same muscle in real human limb, and properties of musculotendon systems can also change over age in the same person [3]. To provide quantitative insights in analyzing human movement, it is necessary to estimate the parameters in vivo. Some researchers had used medical imaging techniques to do this task, such as ultrasound [4], computerized tomography (CT) [5] and magnetic resonance imaging (MRI) [6]. Considering the disadvantage of MRI or CT, such as high cost and radiation exposure, the medical ultrasound imaging might be the better choice than others. Furthermore, ultrasonography is convenient on repeated measurement, because medical ultrasound image can reveal the border between the fat, muscle and bone. The previous musculotendon parameters measurements using ultrasound were mainly used to evaluate the muscle function [7]. Few reports were available on ultrasound measurements to estimate musculotendon parameters for building a customizing specific musculotendon model.

In this study, human brachialis muscle is measured, which is the elbow flexor muscle with the larger physiological muscle cross-sectional area (PCSA) in the muscle group of elbow flexors [8]. The physiological parameters of the musculotendon structure are estimated by the geometric model of brachialis muscle and medical ultrasound image. These parameters are employed in an extended Hill-type model to predict muscle force production.

II. Model description

In this study, the elbow joint is modeled as a uniaxial hinge joint and the axis is determined by the centers of the capitulum and trochlear sulcus. The range of elbow angle is defined from 0° (full extension) to 90° (full flexion). Muscles are modeled as line segments attaching at bones and joints. In anatomy, brachialis muscle started in the middle of humerus and ended in the head of ulna. We assume that origin and insertion points of the muscle are concentrated at center of muscle attachment areas. Fig. 1 shows the anatomical relationship of brachialis muscle at the elbow joint.

The musculotendon model is based on the musculotendon actuator described in [1]. To well and truly describe the physiological structure, we use a modified Hill-type formulation by Brown et al. [9] for the force development of the muscle. That is, the muscle force F^M is described as the sum of force produced by the contractile element F_{CE} and the force produced by the passive elastic element F_{PE}. That is,

$$F^M = F_{PE} + F_{CE} \tag{1}$$

Chwee Teck Lim, James C.H. Goh (Eds.): ICBME 2008, Proceedings 23, pp. 1761–1765, 2009
www.springerlink.com

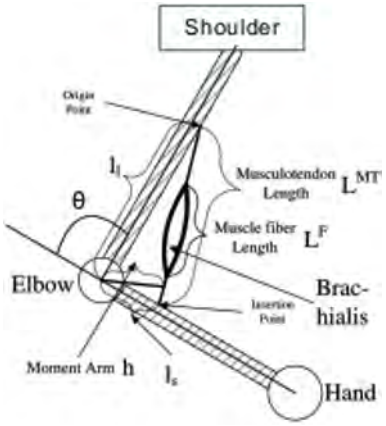


Figure 1. The anatomical sketch of elbow and brachialis muscle. The relative position of original and insertion points determine the value of moment arm and musculotendon length.

where F_{CE} is determined by,

$$F_{CE} = F_{max} FV(V) FL(L) E(t) \tag{2}$$

where L is the normalized muscle fascicle length L^M to the optimal muscle fascicle length L_o^M. V represents the normalized muscle contraction velocity to the maximum shortening velocity of the muscle, which is simplified as the derivative of L. $E(t)$ is the muscle activation, and F_{max} represents the maximal isometric active force. FL is the force length factor, which is modeled as a polynomial curve.

$$FL = dL^2 - 2dL + d + 1 \tag{3}$$

where $d = -3.188$ is a scaling factor. FV is the force velocity factor, which is approximated by an exponential function [2],

$$FV = \frac{a}{1 + e^{b(V-c)}} \tag{4}$$

where $a = 1.5$, $b = 8.0$, $c = 0.0866$.

The parallel elastic element is modeled as a two parallel spring system. The total force produced by PE can be presented into two components: F^{PE1}, represents the force produced by the non-linear spring to resist stretch in the passive muscle; F^{PE2}, represents the force produced by the non-linear spring to resist compression during active contraction at short lengths, i.e.,

$$F^{PE} = F^{PE1} + A(t) F^{PE2} \tag{5}$$

The values of F^{PE1} and F^{PE2} are given as,

$$F^{PE1} = \{c^{PE1} k^{PE1} \ln\{\exp[(\frac{\tilde{L}^M / \tilde{L}^M_{max} - L^{PE1}}{k^{PE1}}] + 1\} + \eta V\} F_{max}, F^{PE1} \geq 0 \tag{6}$$

and

$$F^{PE2} = \{c^{PE2}(\exp(k^{PE2}(\tilde{L}^M - L^{PE2})) - 1)\} F_{max}, \quad F^{PE2} \leq 0 \tag{7}$$

where c^{PE1}, c^{PE2}, k^{PE1}, k^{PE2}, L^{PE1}, L^{PE2} and η are the constants.

F^M is transferred by the tendon (SE) to generate the movements. (Fig. 2). In this study, the tendon is modeled as a linear spring with a stiffness of K_t. Thus, the tendon length can be determined as:

$$L^T = \frac{F^T}{K_t} + L_s^T \tag{8}$$

where F^T is the tendon force with $F^T = F^M * \cos\alpha_p$, L_s^T is the tendon slack length, that is, the length on elongation where tendon just begins to develop force. Tendon slack length is determined as,

$$L_s^T = L_o^{MT} - 1.2 L_o^M \tag{9}$$

where L_o^{MT} represents the maximally elongated musculotendon length, and L_o^M is muscle optimal physiological length.

Then, based on a geometrical model of the musculotendon structure (Fig. 3), the muscle fascicle length L^M is calculated by subtracting tendon length L^T from the

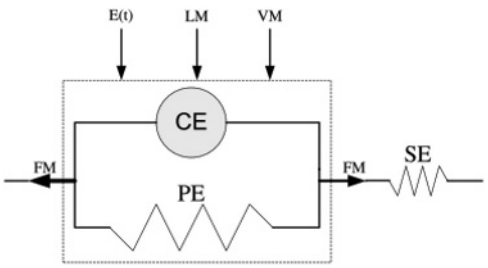


Figure 2. A schematic of Hill-type model for contraction dynamics of muscle tissue. The fascicles are represented as the parallel contractile element (CE) and passive elastic element (PE). The series-elastic element (SE) represents the combined tendon and aponeurosis [1].

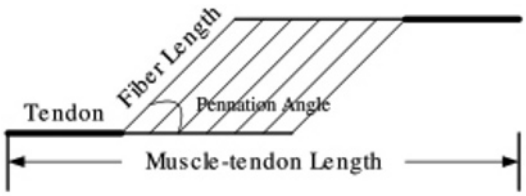


Figure 3. The musculoskeletal structure for ultrasound. All muscle fibers are assumed to be arranged in parallel with the same length, and to insert on tendon with pennation angle. when the muscle fibers shorten, pennation angle increases, but the width of the muscle remains constant.

whole musculotendon length L^{MT}, and the pennation angle (α_p) is taken into account:

$$L^M = \frac{(L^{MT} - L^T)}{\cos\alpha_p} \tag{10}$$

At rest, the relationship of the pennation angle verse joint angle θ can be fitted with a linear function [7], i.e.,

$$\alpha_p = a_p\theta + b_p \tag{11}$$

Finally, the musculotendon variables (moment arms h, length of musculotendon L^{MT}) can be calculated by the distance between the origin point to elbow l_l and the insertion point to elbow l_s based on the trigonometric function (Fig. 1).

III. Ultrasonography Measurement

For the model described in the last section, to customize musculotendon model for specific muscles, the following parameters should be specified: the peak isometric muscle force F_{max}; the optimal muscle fascicle length L_o^M; musculotendon length L^{MT}, the moment of arm h; the tendon slack length L_s^T; the maximally elongated musculotendon length L_{max}^{MT} and muscle's intrinsic maximum shortening velocity V_{max}. In these parameters, the parameters L^{MT}, h, L_s^T and L_{max}^{MT} are determined by the attachment points (insertion and origin), the optimal muscle fascicle length and the pennation angle. The maximum muscle contraction velocity V_{max} can be expressed in optimal fiber length L_o^M per second, i.e., 10 L_o^M per second for young adults and 8 for older adults [10]. The peak isometric muscle force (F^{MAX}) is assumed to be proportional to PCSA. To sum up, the positions of attachment points, the pennation angle, the optimal muscle fascicle length and the PCSA are required to be measured on subject-specific basis.

Firstly, the position of the muscle attachment points can be directly identified with respect to the corresponding skin surface under the middle point of the ultrasound probe.

Secondly, based on the equation 11, the pennation angles with full extension and half flexion are measured from ultrasound image to calculate the values of a_p and b_p (Fig. 4). Thus any pennation angles can be determined by the corresponding elbow angles, which can be measured by the goniometer.

Thirdly, the muscle fascicle length (L^M) can be calculated using a trigonometry method from the longitudinal view of the ultrasonography of brachialis (Fig. 4). i.e., L^M is given as [7]:

$$L^M = L_F + \frac{L_{MT1}}{\sin\alpha_p} + \frac{L_{MT2}}{\sin\alpha_p} \tag{12}$$

where L_F is the visible part of the muscle fascicle, L_{MT1} is the distance from fiber proximal end to the bone, L_{MT2} is the distance from fiber distal end to the superficial aponeurosis. Due to the force-length property presented by Zajac [1], for muscle with a maximum isometric contraction, we can expect the muscle fascicle length L^M equal to optimal muscle fascicle length L_o^M.

Finally, the PCSA is measured by enclosing the outline of the muscle. That is, the muscle linear dimensions (lateral dimension (LD) and the anteroposterior dimension (APD))

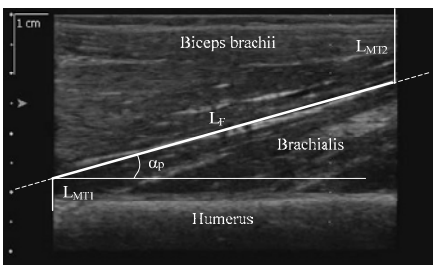


Figure 4. The longitudinal view of the ultrasonography of brachialis and biceps brachii, the data is collected from subject 1. The white fringe of the humerus bone and the dark muscle fascicle can be easily observed in the image.

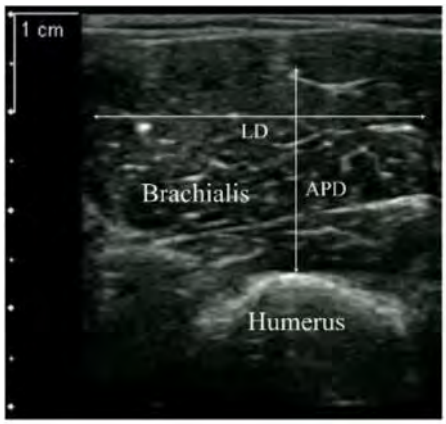


Figure 5. The transverse view of the ultrasonography of brachialis, the data is collected from subject 3. The LD and APD can be measured from the image.

are measured to evaluate PCSA. The values of LD and APD are measure from the The transverse view of the ultrasonography (Fig. 5).

IV. Results

In this research, a B-mode ultrasonography scanner with 12 MHz, 38 mm line probe (Ultrasonix Sonix RP) is used for data acquisition. Healthy subjects (4 males, age: 21-28 years) sit on a height adjustable chair with a solid back. Their forearms are placed on a horizontal plane at the same height of the shoulder and supported by a bracket. The shoulder is in 90° abduction and 0° flexion. During the test, the ultrasound probe is moved along the anterior part of upper arm to find the best image. To enhance ultrasound conduction, coupling gel is applied between the probe and skin surface. To find the muscle architecture parameters, ultrasound image and video are recorded and analyzed off-line. The estimated parameter values are shown in table 1.

Table 1. Estimated parameter values

Parameters	Subjects			
	1	2	3	4
F_{max} (N)	250.8	211.2	257.4	231
L_o^M (m)	0.095	0.086	0.092	0.086
a_p	0.16	0.17	0.16	0.15
b_p (rad)	0.22	0.18	0.2	0.18

These results agree with the values reported in literatures (F_{max} : 184.8[11], 178.2[12], 217.8[13], 254.4[14]; L_o^M : 0.099[12], 0.09[13], 0.0942 [14]).

I. Conclusion

Ultrasonography is a low-cost and comfortable method to get the musculotendon parameters in vivo. Our study provides an approach to estimate the parameters of the musculotendon model by the medical ultrasound image and the geometrical model of the anatomical structure. Since the use of cadaver data in modeling of muscle functions will cause accumulating errors in the results, our approach is helpful to build a more accurate model than the models reported in previous studies.

References

1. F. E. Zajac, "Muscle and tendon: properties, models, scaling, and application to biomechanics and motor control," Crit Rev Biomed Eng, vol. 17, no. 4, pp. 359–411, 1989.
2. N. Lan, "Stability analysis for postural control in a two-joint limb system," IEEE Trans Neural Syst Rehabil Eng, vol. 10, no. 4, pp. 249–259, 2002.
3. P. W. Brand, R. B. Beach, and D. E. Thompson, "Relative tension and potential excursion of muscles in the forearm and hand," J Hand Surg [Am], vol. 6, no. 3, pp. 209–219, 1981.
4. K. Sanada, C. Kearns, T. Midorikawa, and T. Abe, "Prediction and validation of total and regional skeletal muscle mass by ultrasound in japanese adults," *European Journal of Applied* Physiology, vol. 96, no. 1, pp. 24–31, 2006.
5. R. C. Lee, Z. Wang, M. Heo, R. Ross, I. Janssen, and S. B. Heymsfield, "Total-body skeletal muscle mass: development and cross-validation of anthropometric prediction models," Am J Clin Nutr, vol. 72, no. 3, pp. 796–803, 2000.
6. C. N. Maganaris, V. Baltzopoulos, and A. J. Sargeant, "Changes in the tibialis anterior tendon moment arm from rest to maximum isometric dorsiflexion: in vivo observations in man," Clin Biomech (Bristol, Avon), vol. 14, no. 9, pp. 661–666, 1999.
7. L. Li and K. Y. Tong, "Musculotendon parameters estimation by ultrasound measurement and geometric modeling: application on brachialis muscle," in Engineering in Medicine and Biology Society, 2005. IEEE-EMBS 2005. 27th Annual International Conference of the, 2005, pp. 4974–4977.
8. K. N. An, F. C. Hui, B. F. Morrey, R. L. Linscheid, and E. Y. Chao, "Muscles across the elbow joint: a biomechanical analysis," J Biomech, vol. 14, no. 10, pp. 659–669, 1981.
9. I. E. Brown, S. H. Scott, and G. E. Loeb, "Mechanics of feline soleus: Ii design and validation of a mathematical model," Journal of Muscle Research and Cell Motility, vol. 17, no. 2, pp. 221–233, 1996.
10. D. G. Thelen, "Adjustment of muscle mechanics model parameters to simulate dynamic contractions in older adults," *J Biomech* Eng, vol. 125, no. 1, pp. 70–77, 2003.

11. H. E. J. Veeger, B. Yu, K.-N. An, and R. H. Rozendal, "Parameters for modeling the upper extremity," Journal of Biomechanics, vol. 30, no. 6, pp. 647–652, 1997.
12. W. M. Murray, T. S. Buchanan, and S. L. Delp, "The isometric functional capacity of muscles that cross the elbow," Journal of Biomechanics, vol. 33, no. 8, pp. 943–952, 2000.
13. K. N. An, K. Takahashi, T. P. Harrigan, and E. Y. Chao, "Determination of muscle orientations and moment arms," J Biomech Eng, vol. 106, no. 3, pp. 280–282, 1984.
14. H. E. J. Veeger, F. C. T. Van Der Helm, L. H. V. Van Der Woude, G. M. Pronk, and R. H. Rozendal, "Inertia and muscle contraction parameters for musculoskeletal modelling of the shoulder mechanism," Journal of Biomechanics, vol. 24, no. 7, pp. 615–629, 1991.

Mechanical Vibration Applied in the Absence of Weight Bearing Suggest Improved Fragile Bone

J. Matsuda[1], K. Kurata[2], T. Hara[3], H. Higaki[2]

[1] Venture Business Laboratory, Niigata University, Niigata, Japan
[2] Department of Biorobotics, Kyushu Sangyo University, Fukuoka, Japan
[3] Department of Mechanical and Production Engineering, Niigata University, Niigata, Japan.

Abstract — **Mechanical loading is critical for maintaining bone mass, while weightlessness, such as that associated with reduced physical activity in old age, long-term bed rest, or space flight, invariably leads to bone loss. Fragile bone tissue is more susceptible to fractures. By contrast, extremely low-level oscillatory accelerations, applied without constraint, can increase bone formation. To examine the role of vibration in preventing and improving the fragility of bone, we tested the effect of vibration on bone structure in a tail-suspended hindlimb-unloaded (HS) mouse model. Male 22-week-old Jcl-ICR mice were allocated randomly to the following groups: daily-standing control, HS without vibration, HS with vibration at 45 Hz (HS+45Hz), and HS with standing (as an alternative to vibration) (HS+stand). Vibration was given for 5 min/day for 4 weeks. During vibration, a group of mice was placed in a box on top of the vibrating device. The amplitude of vibration was 1.0 mm. After 4 weeks of treatment, the mice were anesthetized and killed by cervical dislocation. Trabecular bone of proximal tibial metaphyseal region of tibial diaphyseal region parameters were analyzed morphologically using in vivo micro-computed tomography. In trabecular bone, the microstructural parameters were improved in HS+45Hz group compared with HS and HS+stand group, including bone volume (BV/TV), trabecular thickness (Tb.Th), trabecular separation (Tb.Sp) and trabecular bone pattern factor (TBPf). In conclusion, the results suggest a beneficial effect of vibration in preserving the complexity of trabecular bone.**

Keywords — **Bone loss, Hind-limb suspension, Vibration, Micro-computed tomography**

I. Introduction

The sensitivity of the skeleton to changes in the mechanical environment is characterized by a rapid and site-specific loss of bone tissue after the removal of function. Conditions such as bed rest, spinal cord injury, and spaceflight can be severely detrimental to the mass, architecture, and mechanical strength of bone tissue, potentially transforming specific skeletal regions into sites of osteoporosis [1- 4]. Whole-body vibration (WBV) can have an anabolic effect in bone tissue and may contribute to more fracture-resistant skeletal structures [5]. Therefore, WBV may provide a practical, non-pharmacological alternative for preventing and/or reversing osteoporosis without adverse invasive or pharmacological effects. Despite these potential benefits, few studies have investigated whether WBV can prevent or reverse deleterious changes in bone formation, resorption, or morphology induced by catabolic stimuli. In this study, we analyzed the effects of WBV on osteopenia and unloading-induced bone loss using a mouse model.

II. Materials and methods

We performed the effect of vibrations on bone structure in a tail-suspended, hindlimb-unloaded (HS's) mouse model (Fig.1). Twenty male Jcl-ICR mice (Kyudo co., Ltd., Fukuoka, Japan), 22-week-old at the start of the experiment, were allocated randomly to the following groups: normal condition control (Cont), HS without vibration (HS), HS with vibration at 45 Hz (HS+45Hz), and HS with short-term standing as an alternative to vibration (HS+stand). Vibration was given for 5 min/day for 4 wk. During the while-body vibrational treatment, a group of mice was placed in a box on top of a vibrating device (Fig.2). The amplitude of vibration was 1.0 mm. After a 4-wk treatment period, the rats were sacrificed by cervical dislocation under anesthesia with diethyl ether. The tibia of each mouse was removed

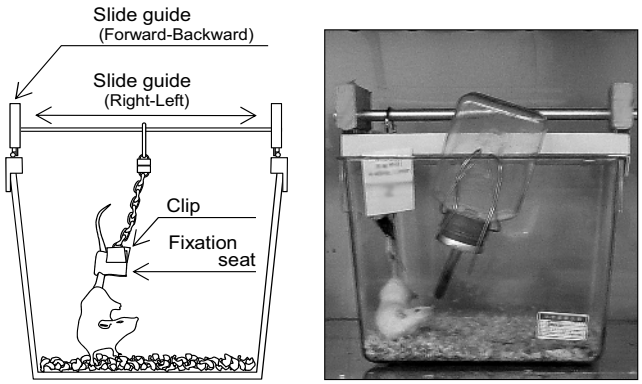


Fig.1 Depiction of cage used for tail-suspended hind-limb unloaded (HS) experiment.

Chwee Teck Lim, James C.H. Goh (Eds.): ICBME 2008, Proceedings 23, pp. 1766–1768, 2009
www.springerlink.com

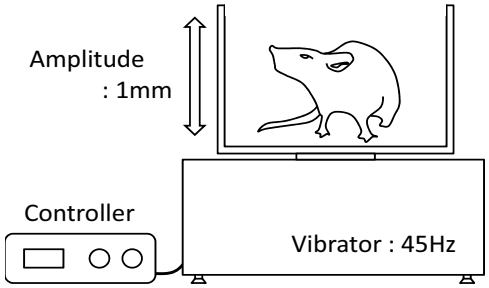


Fig.2 System for whole-body vibration of mice.

and placed in 70% ethanol. Trabecular bone of proximal tibial metaphyseal region of tibial diaphyseal region morphology was analyzed using in vivo micro-computed tomography (micro-CT). The trabecular region was selected using contours inside the cortical shell on each two-dimensional image. The measured parameters included the trabecular bone volume/total volume fraction (BV/TV), trabecular thickness (Tb.Th), trabecular separation (Tb.Sp), trabecular number (Tb.N), node number (N.Nd/TV), and trabecular bone pattern factor (TBPf).

Differences between the groups were analyzed using the Kruskal-Wallis test. In case of difference, the Mann-Whitney U test was applied to test the difference between the different groups. The significance level was 0.05 and all data are presented as mean ± SD.

III. Results

Table 1 displays the bone morphological parameters analyzed from the micro-CT images. The grading criterion for regulation and/or modeling was the presence of a significant difference in the bone parameters between groups. The BV/TV was reduced in the HS group (HS, HS+45Hz, HS+stand) compared with the Cont group. There were significant positive effects on BV/TV in response to standing and especially in response to vibration. Although similar positive trends were observed for Tb.N and Tb.Sp in the HS+stand with HS+45Hz groups, the effects were not statistically significant. There was no significant difference in N.Nd/TV between the Cont and HS+45Hz groups.

IV. Discussion

Preventing the loss of bone attributable to a change in the mechanical environment is an important aspect of effective rehabilitation. The sensitive of bone to physical stimuli is evident from exercise studies [6, 7], long term bed rest [8] and local load as seen in the humerus of tennis player [9, 10]. The exact mechanical control of bone adaptation is not fully understood. As the important stimuli for bone adaptation, strain magnitude, strain rate, fluid shear flow, strain energy density had been proposed. However, very little is known about the actual bone adaption under absence of mechanical stimuli environment. In this present study, we estimated the effects of whole-body vibration on the bone structure in mechanically unloaded mice. Unloaded mice exhibited significant decreases in the values of trabecular bone parameters relative to the control group, and these decreases were significantly prevented by the short-term reloading of mice in the HS+stand and especially the HS+45Hz groups. Additionally, the values of Tb.N and Tb.Sp in the short-term reloaded mice tended to return to the control values. The values of other parameters were also improved in response to 45 Hz-vibrations (HS+45Hz group). These results emphasize the importance of mechanical loading on the morphological complexity of trabecular bone. Furthermore, these results suggest that losses in bone quality owing to various unloaded conditions may recover with vibrational treatment. Recent studies have indicated that trabecular bone loss and impairment of mechanical properties reduce bone strength and increase fracture risk [11, 12], emphasizing the importance of bone tissue properties for bone mechanical behavior. Our findings suggest that short-term, whole-body vibration may be a practical, non-invasive, and effective means of providing early recovery in cases of bone loss due to mechanical factors.

Table.1 Results from micro-computed tomography analysis of trabecular bone.

	BV/TV , %		Tb.Th , mm	
Control	0.341 ± 0.063		Control	0.058 ± 0.003
HS	0.191 ± 0.138	**	HS	0.044 ± 0.004	**
HS+45Hz	0.278 ± 0.133	**	HS+45Hz	0.053 ± 0.003	**
HS+Stand	0.239 ± 0.106		HS+Stand	0.047 ± 0.005	

	Tb.Sp , mm		Tb.N , 1/mm	
Control	0.119 ± 0.039		Control	5.892 ± 1.159	
HS	0.342 ± 0.279	**	HS	4.179 ± 2.741	**
HS+45Hz	0.192 ± 0.136	**	HS+45Hz	5.167 ± 2.250	**
HS+Stand	0.189 ± 0.098		HS+Stand	4.987 ± 2.021	

	Nd/TV , 1/mm		TBPf , 1/mm	
Control	30.438 ± 7.492		Control	2.652± 0.121	
HS	18.179 ±12.830	**	HS	3.525± 0.304	**
HS+45Hz	29.601 ±11.121	**	HS+45Hz	2.923± 0.189	**
HS+Stand	21.533 ± 8.787		HS+Stand	3.287± 0.312	

**: $p < 0.01$

V. Conclusions

Tail-suspended hindlimb-unloaded mice subjected to 5 minutes of daily while-body vibration for 4 weeks had increases in bone volume (BV/TV), trabecular thickness (Tb.Th), trabecular number (Tb.N) and trabecular bone pattern factor (TBPf) compared with HS and HS+stand group. These results suggest that a while-body vibration effective prevented unloaded bone loss in a site of active metabolism, such as trabecular bone.

References

1. Chen JS, Cameron ID et al. (2006) Effect of age-related chronic immobility on markers of bone turnover. J Bone Miner Res. 21: 324-331
2. Green DM, Noble PC et al. (2006) Effect of early full weight-bearing after joint injury on inflammation and cartilage degradation. J Bone Joint Surgery [Am]. 88A: 2201-2209
3. Houde JP, ScHSlz LA et al. (1995) Bone mineral density changes in the forearm after immobilization. Clin Orthop Relat Res: 199-205
4. Lang T, LeBlanc A et al. (2004) Cortical and trabecular bone mineral loss from the spine and hip in long-duration spaceflight. J Bone Miner Res 19: 1006-1012
5. Rubin C, Turner AS et al. (2001) Anabolism. Low mechanical signals strengthen long bones. Nature 412: 603-604
6. Robinson TL, Snow-Harter C et al. (1996) Gymnasts exhibit higher bone mass than runners despite similar prevalence of amenorrhea and oligomenorrhea. J Bone Miner Res. 10(1): 26-35
7. Snow-Harter C, Whalen R et al. (1995) Bone mineral density, muscle strength, and recreational exercise in men. J Bone Miner Res. 7(11): 1291-1296
8. Nishimura Y, Fukuoka H et al. (1994) Bone turnover and calcium metabolism during 20 days bed rest in young healthy males and females. Acta Physiol Scand Suppl. 616: 27-35
9. Huddleston AL, Rockwell D et al. (1980) Bone mass in lifetime tennis athletes. JAMA. 244(10): 1107-1109
10. Jones HH, Priest JD et al. (1977) Humeral hypertrophy in response to exercise. J Bone Joint Surg Am. 59(2): 204-208
11. McBroom RJ, Hayes WC et al., (1985) Prediction of vertebral body compressive fracture using quantitative computed tomography. J Bone Joint Surgery [Am], 67:1206-1214
12. Silva MJ, Keaveny TM et al., (1997) Load sharing between the shell and centrum in the lumbar vertebral body. Spine, 22:140-150

Author: Junpei MATSUDA
Institute: Venture Business Laboratory, Niigata University
Street: 2-8050, Ikarashi, Nishi-ku
City: Niigata
Country: Japan
Email: junmatsuda@gs.niigata-u.ac.jp

A Biomechanical Investigation of Anterior Vertebral Stapling

M.P. Shillington[1,2], C.J. Adam[2], R.D. Labrom[1] and G.N. Askin[1]

[1] Mater Health Services, Brisbane, Australia
[2] Queensland University of Technology, Brisbane, Australia

Abstract — **An immature calf spine model was used to undertake anatomical and biomechanical investigations of an anterior vertebral staple used in the thoracic spine to treat scoliosis. The study involved three stages: (1) displacement controlled testing to determine changes in bending stiffness of the spine following staple insertion, (2) measurement of forces in the staple using strain gauges, and (3) micro-CT scanning of vertebrae following staple insertion to describe the associated anatomical changes. The results suggest that the mechanism of action of stapling may be a consequence of hemiepiphysiodesis causing convex growth arrest, rather than the production of sustained compressive forces across the motion segment.**

Keywords — **biomechanics, thoracic spine, staples, shape memory alloy.**

I. Introduction

Adolescent idiopathic scoliosis (AIS) is a complex three dimensional spinal deformity diagnosed between 10 and 19 years of age. The natural history of curve progression in AIS is dependent on the patient's skeletal maturity, the curve pattern, and the curve severity. Currently treatment options for progressive scoliosis are limited to observation, bracing, or surgery.

While brace treatment is noninvasive and preserves growth, motion, and function of the spine, it does not correct deformity and is only modestly successful in preventing curve progression. In contrast, surgical treatment with an instrumented spinal arthrodesis usually results in better deformity correction but is associated with substantially greater risk. The risks of surgery are related to the invasiveness of spinal arthrodesis, the instantaneous correction of spinal deformity, and the profoundly altered biomechanics of the fused spine.

Fusionless scoliosis surgery may provide substantial advantages over both bracing and definitive spinal fusion. The goal of this new technique is to harness the patient's inherent spinal growth and redirect it to achieve correction, rather than progression, of the curve. This effect is thought to occur as a consequence of the Hueter-Volkmann law which states that increased compressive loads across a physis will reduce growth, while conversely, increased distractive forces will result in accelerated growth [1]. Currently there are several surgical treatments incorporating the fusionless ideology, one of which is anterior vertebral stapling (see Figure. 1). By applying implants directly to the spine, anterior vertebral stapling is theoretically more advantageous than external bracing because it addresses the deformity directly at the spine and not via the chest wall and ribs, and, because it eliminates problems with patient noncompliance during brace treatment. Furthermore, minimally invasive tethering of the anterior thoracic spine by means of endoscopic approach is also a less extensive procedure than arthrodesis, with no requirement for discectomies, preparation of the fusion bed, or harvest of bone graft.

Results for stapling in humans were presented as early as 1954, but the results were disappointing [2]. Correction of the scoliosis was limited because the children had little growth remaining at the time of treatment, and the curves were severe. Some staples broke or became loose, possibly because of motion through the intervertebral disc.

Recently, clinical interest in stapling has increased following the release of a new staple designed specifically for insertion into the spine by Medtronic Sofamor Danek (Memphis., TN). These staples are manufactured using nitinol, a shape memory alloy (SMA) composed of nickel and titanium. SMA staples are unique in that the prongs are straight when cooled but clamp down into the bone in a "C" shape when the staple returns to body temperature, providing secure fixation.

Despite the increased clinical interest in the use of SMA staples, little is known about the mechanism of their effect or the consequences of their insertion on the adolescent spine.



Fig 1. Radiograph demonstrating anterior vertebral staples inserted into the thoracic spine

Chwee Teck Lim, James C.H. Goh (Eds.): ICBME 2008, Proceedings 23, pp. 1769–1772, 2009
www.springerlink.com

The aim of this study was threefold. Firstly, to measure changes in the bending stiffness of a single spinal motion segment following staple insertion. Secondly, to describe and quantify the loading experienced by the staple during spinal movement. Thirdly, to describe the structural changes to the vertebra following staple insertion.

II. Materials and methods

A. Specimen Preparation

Six to eight week old bovine spines have previously been validated as a model for the adolescent spine [3]. Specimens were obtained from the local abattoir and stored frozen at the testing facility. All specimens underwent pre-test CT scanning to exclude vertebral anomalies. Each vertebral column was cut into monosegmental functional spinal units (FSU) consisting of two adjacent vertebrae with intervening disc, facets, and ligaments. The FSU was then carefully denuded of all paraspinal muscle with care to preserve ligaments and bony structures. In addition, both sets of ribs and part of the spinous processes were removed to induce significant instability. Once prepared the specimens were potted in polymethylmethacrylate to facilitate coupling of the specimen to the testing apparatus.

B. Surgical Procedure

Four pronged nitinol staples were cooled in an ice bath as per recommended surgical procedure to facilitate their deformation. Using standard instruments the staple was opened to a position of 90°. The surgeon then placed a 5mm nitinol staple (Shape Memory Alloy Staple; Medtronic Sofamor Danek; Memphis, TN) just anterior to the insertion of the rib head so that it spanned the disc and adjacent vertebral endplates. Accurate positioning of the staple was confirmed on post-test radiographs.

C. Biomechanical Evaluation

A displacement controlled six degree-of-freedom robotic facility was used to test each specimen through a predetermined range of motion in flexion, extension, lateral bending, and axial rotation (see Table 1). Each specimen was tested first in an un-stapled (control) state. A staple was then inserted using the technique described previously and the testing protocol repeated. A total of fourteen segments were tested composing six T3-4, four T5-6, and four T7-8.

Force and moment data for each test was recorded via the robot's force transducer. A fixed axis of rotation for the segment was calculated to be five millimeters anterior to the posterior edge of the annulus in the mid-sagittal plane. Using a custom designed MATLAB (version 6.0, MathWorks Inc., Natick, MA) program the force transducer data was synchronized with the robot position data and filtered using moving average methods. The rotational stiffness of the functional spinal unit (FSU) for each applied motion was calculated in Nm/degree of rotation.

Each rotational stiffness was calculated as an average of five cycles per test, which were performed following one 'settling' cycle. Paired t-tests were used to compare average stiffness mesurements in the stapled and control conditions for each direction of movement. A significance level $p<0.05$ was considered statistically significant.

D. Measurement of Staple Loading

A single axis strain gauge (Vishay Micro-measurements, Singapore) was attached to base of three of the staples after insertion into the testing specimen in order to measure the force experienced by the staple during prescribed motions. Each specimen underwent the testing protocol described above and strain data was recorded on a data logger. Following this, individual calibrations for each strain-gauged staple were performed to convert the staple strain measurement into an equivalent staple 'tip' force in Newtons (defined as a force acting normal to, and positioned at the staple tips, with positive values tending to separate two opposing staple tips, and vice versa).

E. Changes in Vertebral Structure Following Staple Insertion

The final phase of testing was a descriptive study of the damage caused to the structural elements of the vertebra following insertion of an SMA staple. For this phase of testing, specimens that had completed phase one of the study were used.

Following completion of the phase one testing protocol a diamond saw was used to cut the staple in half and the two staple halves were removed with care to prevent further damage. The specimen subsequently underwent micro-CT scanning using a uCT 40 scanner (Scanco Ltd., Switzerland) at an isotropic voxel resolution of 36 microns, with image reconstructions to create a descriptive picture of the structural damage to the vertebra following staple insertion.

III. Results

A. Biomechanical Investigation

Stiffness measures in the non-stapled control group correlated with the previously published results of Wilke et al [4]. The results of the comparison in motion segment stiff-

ness between the stapled and non-stapled specimens are presented in Table 1.

A significant decrease in stiffness ($p<0.05$) following staple insertion was found in flexion, extension, lateral bending away from the staple, and axial rotation away from the staple. Stiffness for axial rotation towards the stapled side was significantly greater than for away. A near significant increase in lateral bend stiffness away from the staple compared with towards was also seen.

Table 1 Results for biomechanical testing

Movement	ROM	Change in stiffness following staple insertion	P-value
Flexion	2.5°	↓	0.003
Extension	1.5°	↓	0.04
Lateral bend towards staple	3°	-	0.09
Lateral bend away from staple	3°	↓	0.02
Axial rotation towards staple	4°	-	0.25
Axial rotation away from staple	4°	↓	0.01
Lateral bend toward staple vs. away	3°	-	0.06
Rotation toward staple vs. away	4°	↑ towards	0.04

B. Measurement of Staple Loading.

The greatest staple forces were seen in flexion and the least in extension. Time-based plots of staple tip loading in each plane of motion are shown in Figures 2-4. Of interest, each staple shows a baseline compressive loading on the tips following insertion which gradually, but consistently, decreases across the five cycles of testing

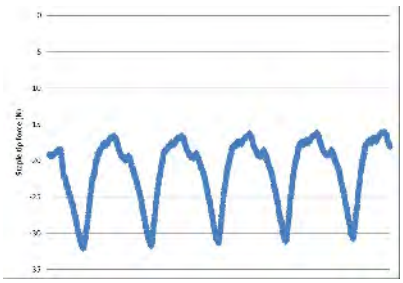


Fig. 2 Equivalent staple tip force versus time in flexion-extension

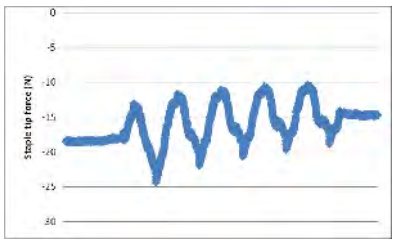


Fig. 3 Equivalent staple tip force versus time in lateral bending

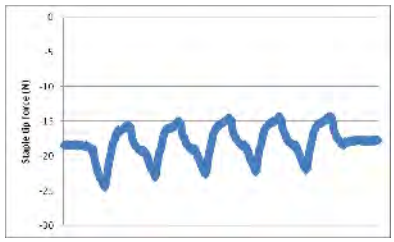


Fig. 4 Equivalent staple tip force versus time in axial rotation

C. Changes in Vertebral Structure Following Staple Insertion

A coronal reconstruction of a micro-CT scan showing extensive trabecular bone and physeal damage following staple insertion is shown in Figure 5.

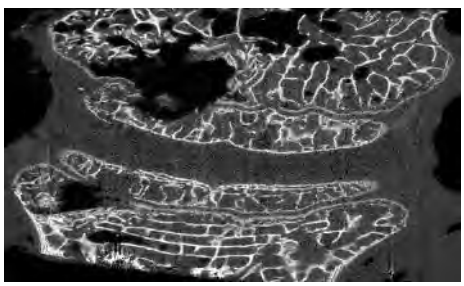


Fig 5. Micro-CT showing vertebral damage following staple insertion

IV. Discussion

The goal of this study was to describe the anatomical and biomechanical consequences of the insertion of an SMA staple in the thoracic spine. The findings from the biomechanical investigation indicate that staple insertion consistently decreased the stiffness of the motion segment. These results could not be attributed to changes in anatomy or tissue properties between tests as each specimen acted as its own control.

Intuitively staple insertion would be expected to increase motion segment stiffness. Indeed, a recent paper by Puttlitz

et al [5] found a small but significant decrease in the range of motion in lateral bending and axial rotation using moment controlled testing. In this paper T4-T9 motion segments were stapled with a variety of staple constructs and compared to a non-stapled control condition. The significance of these results were questionable however as the changes in range of motion were only a few degrees over several vertebral levels and statistical outcomes were of low power. Furthermore methodological flaws, in particular the fact the vertebrae were re-used for testing after removal of a staple, which in our experience is associated with significant structural damage, make these small differences in range of motion difficult to interpret.

In our study we have attempted to create a superior testing methodology. By using only single motion segments and not re-using testing specimens we hope to have eliminated confounding factors. In addition, the use of only one staple construct, the double-pronged laterally placed staple, which is the most commonly used clinically, increases the relevance of the findings.

An explanation for the finding of decreased motion segment stiffness may be found in the outcomes of the strain gauge testing and micro-CT scan. The strain gauge testing showed that once inserted the staple tips applied a 'resting' force to the surrounding trabecular bone and vertebral end-plate. This finding would be consistent with the belief that the mechanism of effect of the SMA staple is via the Hueter-Volkmann law. Interestingly however, as the motion segment progressed through five cycles of each test the baseline load on the staple tips gradually decreased, implying that the force at the staple tip – bone interface was decreasing. We believe that this was likely occurring as a result of structural damage to the trabecular bone and end-plate by the staple which effectively caused 'loosening' of the staple.

This hypothesis is further supported by the findings of the micro-CT scan. The pictures depict significant trabecular bone and physeal injury following staple insertion. Furthermore the staple tines are shown to 'clamp down' once inserted into a position that would be unlikely to allow a sustained and uniform force on the growth plate for growth modulation.

Early results to date with SMA staples have been promising in both animal [6] and human [7] trials. We propose that the effectiveness that is suggested by this early work is not as a consequence of the Hueter-Volkmann effect, but rather because the insertion of an SMA staple causes vertebral hemiepiphysiodesis and subsequent convex growth arrest.

The published outcomes of convex growth arrest in congenital scoliosis have generally been successful [8]. However, to date no study has evaluated the use of hemiepiphysiodesis in adolescent idiopathic scoliosis. Based on our findings it is likely that the insertion of the SMA staple causes a similar, albeit somewhat less invasive and extensive epiphysiodesis effect as has been described for use in congenital scoliosis. If an epiphysiodesis effect is not desirable in the treatment of AIS then alternative staple designs may need to be considered.

V. Conclusions

The results of this study show that growth modulation achieved using SMA staples is likely due to disruption of the growth plate rather than sustained biomechanical compression across the motion segment as occurs with the Heuter-Volkmann effect.

References

1. Hueter C. (1862) Anatomische studien an den extremitaetengelenken neugborener und erwachsener. Virkows Archi Path Anat Physiol 25:572-599
2. Smith AD, Von Lackum WH, Wylie R. (1954) An operation for stapling vertebral bodies in congenital scoliosis. The Journal of Bone And Joint Surgery 36A:342-348
3. Cotterill PC, Kostuik JP, D'Angelo G et al. (1986) An anatomical comparison of the human and bovine thoracolumbar spine. Journal of Orthopaedic Research 4:298-303
4. Wilke HJ, Krischak S, Claes L. (1996) Biomechanical comparison of calf and human spines. Journal of Orthopaedic Research 14:500-503
5. Puttlitz CM, Masaru F, Barkley A et al. (2007) A biomechanical assessment of thoracic spine stapling. Spine 32:766-771
6. Braun JT, Akyuz E, Ogilvie JW et al. (2005) The efficacy and integrity of shape memory alloy staples and bone anchors with ligament tethers in the fusionless treatment of experimental scoliosis. The Journal of Bone and Joint Surgery 87A:2038-2051
7. Betz RR, D'Andrea LP, Mulcahey MJ et al. (2005) Vertebral body stapling procedure for the treatment of scoliosis in the growing child. Clinical Orthopaedics and Related Research 434:55-60
8. Uzumcugil A, Cil A, Yazici M et al. (2004) Convex growth arrest in the treatment of congenital spinal deformities, revisited. Journal of Pediatric Orthopedics 24:658-666.

Measurement of Cell Detaching force on Substrates with Different Rigidity by Atomic Force Microscopy

D.K. Chang[1], Y.W. Chiou[1], M.J. Tang[2] and M.L. Yeh[1]

[1] Institute of Biomedical Engineering, National Cheng Kung University, Tainan, Taiwan
[2] Institute of Physiology, National Cheng Kung University, Tainan, Taiwan

Abstract — **Cell adhesion plays an important role in cell morphology, motility, and differentiation, and cancer metastasis. The rigidity of the substrates is one of the factors that can affect cell behaviors. How the rigidity of substrates influence the initial attaching strength of cell is not well investigated yet. Cell probe attaching cell on the AFM cantilever tip is a new approach to study cell mechanics.**

The purpose of this study is to investigate the relation between the rigidity of substrate and cell detaching force by cell probe. Fibroblast cell was used to quantify cell detaching force. All the surfaces of substrates were coated with type I collagen. The contact times were set at 30, 60, 90, and 300 seconds with contact compression at 500 pN. The substrates used were 1037 Pa, and 10930 Pa poly acrylamide (PAA) and glass.

Under the same contact time, the detaching force rose gradually with increasing substrate rigidity. They were 482.11±194.34, 1820.11±949.29, and 3373.45 ±1867.02 pN respectively for 1037 Pa, and 10930 Pa PAA and glass for 300 seconds.

Our results showed cell adhesion could be influenced by substrate rigidity. This cell probe technique can be further used for parameter studies on cell substrate interaction in the future.

Keywords — **AFM, cell probe, cell detaching force, substrate rigidity**

I. Introduction

Cells interact with neighboring cells and extracellular matrix through adhesion molecules. The adhesion behavior is modulated by the intracellular physiology and affected by extracellular environment. It has decisive effect on cell physiology such as, morphology, migration, motility and differentiation and cancer cell metastasis [1-2].The ability for cell to attach represents the normal physiology behavior for cells.

Currently, several approaches have been developed to study the cell adhesion force, like micropipette [3], optical tweezers [4], cell detacher [5] and atomic force microscopy (AFM) [6]. Cell probe is a new approach by AFM [7]. It attached the cell on the end of usually tipless cantilever. Once the cell probe established, it can be used to evaluate the interaction between the attached cell and single cell or cell layer on the surface. It is known the stiffness of substrate can affect cell behavior [8]. The reaction and sense of cell to the stiffness also vary with cell types. The purpose of this study is to use the cell probe approach to measure how stiffness of substrate affecting the initial adhesion forces.

II. Materials and methods

A. Cell culture

Rat fibroblast (NIH-3T3) cell line was used in this study. Culture medium was 10% Fetal Bovine Serum (FBS)(Sigma-Aldrich, St. Louis) with 1% Penicillin(Sigma-Aldrich, St. Louis) and Dulbecco's Modified Eagle's Medium (DMEM). (Sigma-Aldrich, St. Louis)

B. Substrate preparation

PAA (Polyacrylamide) (Sigma-Aldrich, St. Louis) gel was used to make soft substrates. By adjusting the ratio between Acrylamide (Sigma-Aldrich, St. Louis) and Bis-acrylamide (Sigma-Aldrich, St. Louis), two stiffness of substrates (modulus 1037 and 10930 Pa) were made. Stiff glass surface (70GPa) was used as control. All the substrates were then coating with type I collagen solution (Sigma-Aldrich, St. Louis). Briefly, dishes were added with Sulfo-SANPAH (Sigma-Aldrich, St. Louis) as cross-linking agent then irradiated by UV light(120,000 microjoules, 302 nm wavelength, UVP, CL-1000) for 10 minutes. PBS was then used to remove unbonding cross-linking agents. Afterward, 200 μg/ml type I collagen solution was spread on dish surface and then placed on the shaker inside 4 degree C refrigerator for 24 hours for well-mixing the type I collagen solution.

C. AFM system

The AFM system used in this study is JPK NanoWizard® II on top of inverse light microscope (Zeiss Axio Observer). In order to fully separate the tether of pulling cell during separation, the AFM system includes CellHesion® which has vertical movement up to 100μm.

Chwee Teck Lim, James C.H. Goh (Eds.): ICBME 2008, Proceedings 23, pp. 1773–1776, 2009
www.springerlink.com

D. Functionalized cantilever tip

Tip-less cantilever (CSC12, MikroMasch) with spring constant 0.03 N/m was used in this study. The dimension of the cantilever is 350 X 35 X 1 μm with resonant frequency of 10 kHz. First the cantilever was cleaned with acetone for 5 minutes followed by exposed to 120,000 microjoules, UV radiation for 15 minutes. Then the tip was put into biotin-BSA solution (Sigma-Aldrich, St. Louis) in 37 degree C incubator overnight. After rinsed with PBS to wash out the extra biotin, the tip was further functionalized by streptavidin solution (Sigma-Aldrich, St. Louis) for 30 minutes at room temperature. The tip was then rinsed with PBS again to remove unbonding streptavidin. The tip was then immersed into conA (Sigma-Aldrich, St. Louis) for 30 minutes. After washed with PBS, the tip was put in D.I. water and ready for cell catching.

E. Calibration for cantilever tip

The mechanical property of testing material depends on the accuracy of spring constant and deflection of cantilever tip. Due to the nominal thickness of the cantilever is usually not accurate, it is necessary to use other approach to measure its spring constant. Thermal noise method, the resonant frequency correlated to its spring constant, was used to measure the spring constant of individual cantilever before each test.

F. Cell probe preparation

After 4 days of culture of 3T3, the cells were removed from flask by trypsin (Sigma-Aldrich, St. Louis) then dropped on culture dish. Use the optical microscopy to observe the cell morphology and locate a cell with proper shape. After moving the tip above the cell, the functionalized tip was approached at the rate of 5 μm/s on the cell and pressed at 500 pN for 5 seconds then retracted. In most case, the cell was attached on the bottom of the cantilever. The cell probe was retracted to 100 μm above the surface and ready for adhesion test.

G. Measuring cell adhesion force

One of the three substrates which are two PAA gels with modulus 1037 and 10930 respectively and hard glass was selected for surface. Four contact times, 30, 60, 90 and 300 seconds were studied. The cell probe approach on the substrate at 5 μm/s and the contact force was set at 500 pN. At the same cell, four contact times were conducted at randomly order till the cell lost its activity. After each test, the cell rested for 2 minutes to recover. The approach and retract force curves were collected and analyzed.

H. Data analysis

The extract force curves can be used to quantify the adhesion strength between cell and the surface. The relationship between the adhesion force and different stiffness of substrates at 4 different contact times were recorded. One-way ANOVA was used to test the difference among groups and Tukey's HSD was used as post-hoc test.

III. Results and Disscusion

A. Cell probe

The successful cell probe image was caught by optical microscopy (Fig. 1). When the tip approached the surface and made contact with the surface, the cell instead of the tip directly touched the surface. The breaking strength on force curve was the adhesion between the cell and the surface.

The adhesion force increased with contact time in all three substrates (Fig. 2). However the increasing rates were different among them. For hard glass substrate, the adhesion force increased quickly at early time and had the trend to

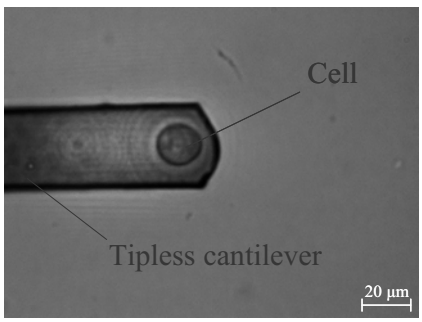


Fig. 1 The image of cell adhered on the bottom of AFM tip

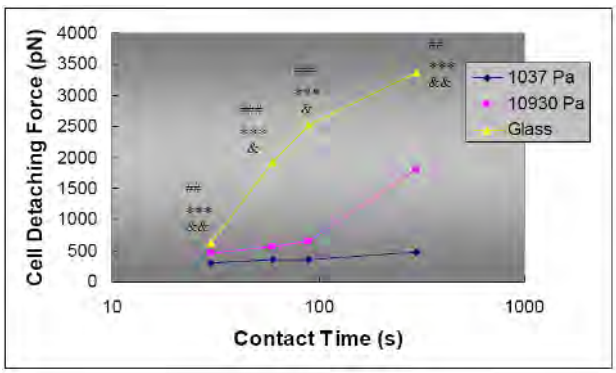


Fig. 2 Temporal change of adhesion force for 3 substrates
&significant different between 1037 Pa and 10930 Pa
*significant difference between 1037 Pa and glass
#significant difference between 10930 Pa and glass

reach stable. For 10930 Pa substrate, the adhesion force increased slowly between 30 to 90 seconds, but increased rapidly after 90 seconds. For softest 1037 Pa substrate, the adhesion force increased slowly through 300 seconds. They were significant different among 4 contact times for glass surface. For 10930 Pa PAA surface, only 300 seconds contact time was significant different from other 3 shorter contact times; however, there were no difference among 30, 60 and 90 seconds contact time. For soft 1037 Pa substrate, there were no difference among 4 contact time.

Cells interact with extracellular matrix through integrin. The bonding was believed through covalent bond [9]. Single covalent bond strength was about 1400 pN [10]. We use this strength to define the starting time for stable bonding between the cell and surface. Glass can start to have stable bonding in 48 seconds. The time to have stable bonding for 10930 Pa substrate is about 225 seconds. However, it never reached stable bonding for 1037 Pa substrate before 300 seconds.

B. Adhesion force vs. stiffness

The substrates at three different rigidities were used in this study. The adhesion force for stiff glass was significant larger than the other two softer substrates at all contact times (Fig. 3). The adhesion forces between 1037 Pa and 10930 Pa were also significant different at all four contact times. The stiffness of substrate could have dramatically effect on cell's initial bonding strength. When cell was on different substrate, the stiffness of substrate can be sensed by the cell. Our results clearly show the early adhesion force increases at different rate for different substrates. This early adhesion force is comparable to late stable force, but the differences among different substrates are more significant.

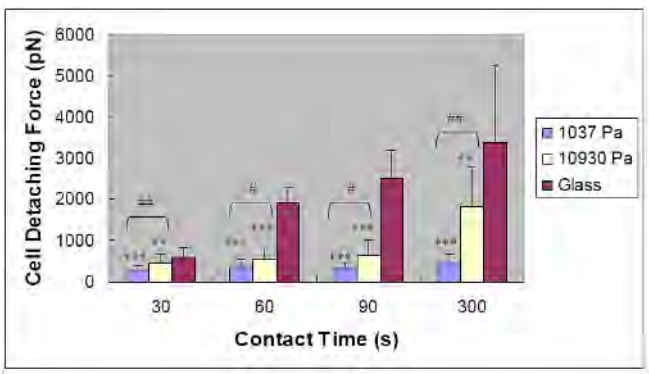


Fig. 3 The adhesion forces for three substrates at four different contact time.
*significant different from glass
#significant different between 1037 Pa and 10930 Pa

IV. Conclusions

This study has successfully built the cell probe technology to measure the cell's early adhesion force. This method can be used to study the physiological phenomenon between the substrate and the cell and measure their adhesion forces. The results find the initial adhesion force was influenced by contact time and substrate stiffness. The adhesion force increases with the stiffness of the substrate during the first 300 seconds. The adhesion force increases with time at different rate for different substrates. Nevertheless, the time to reach stable adhesion (1400 pN) also depends on the substrates. This information can be important guide for understanding the mechanism how substrate affecting the cell adhesion and following biochemical signal pathway. Combining the confocal microscopy, fluoresce technology and biochemical assay, this cell probe technology can be used to further study the detail of cell surface interaction.

Acknowledgment

The authors would like to appreciate the equipment and financial supports from National Science Council of Taiwan (NSC 96-2221-E-006 -259), (National Nano Project: NSC 97-2120-M-006-003) and NCKU college of Engineering.

References

1. Folkman J and Moscona A (1978) Role of cell shape in growth control. Nature, 273:345-349
2. Stossel TP (1993) On the crawling of animal cells. Science, 260:1086-1094
3. Discher DE, Mohandas N, and Evans EA (1994) Molecular maps of red cell deformation: hidden elasticity and in situ connectivity. Science, 266:1032-1035
4. Florin EL, Pralle A, Horber JK, and Stelzer EH (1997) Photonic force microscope based on optical tweezers and two-photon excitation for biological applications. J Struct Biol, 119:202-211
5. Sagvolden, Giaever GI, et al. (1999) Cell adhesion force microscopy. Proc Natl Acad Sci U S A, 96:471-476
6. Franz CM, Taubenberger A, Puech PH, Muller DJ (2007) Studying integrin-mediate cell adhesion at the single-molecule level using AFM force spectroscopy. Sci. STKE, 406:15
7. Puech PH, Taubenberger A, Ulrich F, Krieg M, Muller DJ, and Heisenberg CP. (2005) Measuring cell adhesion forces of primary gastrulating cells from zebrafish using atomic force microscopy. J Cell Sci, 118:4199-4206
8. Discher DE, Janmey P, Wang YL (2005) Tissue cells feel and respond to the stiffness of their substrate. Science, 310:1139-1143

9. Lee CC, Wu CC, Su FC (2004) The technique for measurement of cell adhesion force. Journal of Medical and Biological Engineering, 24:51-56
10. Grandbois M, Beyer M, Rief M, Clausen-Schaumann H, Gaub HE (1999) How strong is a covalent bond? Science, 283:1727-1730

Author: Ming-long Yeh
Institute: Institute of Biomedical Engineering, Nationals Cheng Kung University
Street: No. 1, University Road.
City: Tainan
Country: Taiwan
Email: mlyeh@mail.ncku.edu.tw

Estimation of Body Segment Parameters Using Dual Energy Absorptiometry and 3-D Exterior Geometry

M.K. Lee[1,2], M. Koh[1], A.C. Fang[3], S.N. Le[3] and G. Balasekaran[2]

[1] School of Sports, Health and Leisure, Republic Polytechnic, Singapore
[2] Physical Education and Sports Science, National Institute of Education, Nanyang Technological University, Singapore
[3]Department of Computer Science, National University of Singapore, Singapore

Abstract — **Body segment parameters (BSP) are essential inputs in the kinetic analysis of human motion. These data include mass, center of mass and moments of inertia, and are usually obtained from population-specific predictive equations. Several limitations remained with the use of cadaveric measurement. These include limited sample size, as well as discrepancies in age and morphology. The limitations motivated the development of direct BSP measurements on living subjects. However, other limitations such as exposure to radiation, high cost and sheer lack of facilities that are readily available evolved. In addition, some methods provide only two-dimensional (2-D) measurements while others require intensive tomographic images for three-dimensional (3-D) reconstruction. This article proposes a novel technique for reconstructing subject-specific 3-D body mass distribution using from Dual Energy Absorptiometry X-ray imaging and 3-D exterior geometry. The accuracy of our method was assessed by calculating percent error between the criterion based on total body mass and our proposed total body mass measurements (TBM). We found less than one percent error between the criterion and our TBM measurements for subjects of four different body types: endormorph, mesomorph, ectomorph and central. We found significant differences between our proposed method as compared to cadaver-based and living-based models for segment mass (SM) at the hand; center of mass (CM) at the thigh, shank, foot, head and neck, trunk, upper arm, forearm and hand; and moments of inertia at the hand, shank, foot and trunk. Extensions of the research could further examined the influence of other BSP measurements derived from our proposed method and the four selected estimation models, as well as their impact on the inverse dynamics solutions in human motion.**

Keywords — **Body segment parameters, Dual Energy Absorptiometry X-ray, 3-D geometry, biomechanics**

I. Introduction

The accurate determination of the body segment parameters (BSP) specific to individual has been a long-standing problem in biomechanical analysis of the body during motion. These analyses often require knowledge of the inertial properties of body segments which include the mass, length, mass centroid and moments of inertia of each segment. The accuracy of the biomechanical model is largely dependent on the extent to which the estimated mechanical values of the body replicating the actual anatomical structure [1]-[7].

Generally, BSP estimation methods are based on predictive equations obtained from elderly male cadavers or small samples adult Caucasian able-bodied males [8]-[11]. Neither of these groups is representative of the majority of the current population under study. Other predictive equations are based on living subjects using stereo-photogrammetry [12]-[13]; gamma-ray [14]; magnetic resonance imaging (MRI) [15]-[18]; computerized-tomography (CT) [19]-[22]; ultrasound [23]. However, the use of such direct BSP measurements are limited in daily biomechanical research due to the complexity of the procedures as they require a lot of tomographic images for a three-dimensional (3-D) reconstruction; danger of exposure to radiation; high cost; and the sheer lack of facilities that are readily available. In addition, accurate estimates of direct BSP measures have been limited to technical and ethical constraints, small sample sizes, variation in segment boundaries, as well as the constraint of adopting a representative literature of BSP sources for the population under study.

Recently, two-dimensional (2-D) in vivo imaging technique, known as dual-energy X-ray absorptiometry (DXA), has been used to capture full body 2-D projection of mass densities through X-ray technique. In comparison with other imaging techniques, it is relatively inexpensive and the radiation exposure is substantially less than normal background sources [28]. DXA measurements can be used to determine total mass, bone and soft tissue mass for each body segments. This scanner has been determined to be useful for obtaining accurate 2-D BSP values of human subjects [4], [5], [29]. It is also capable of giving accurate direct measurement of the entire body or of a defined region of interest [30], [31] where mass properties can be computed. However, BSP values computed from DXA images are accurate in the frontal plane only.

The purpose of this paper is to: (1) describe an in vivo method by incorporating DXA with 3-D geometry to estimate total body mass; (2) evaluate the accuracy of the proposed method by comparing it to criterion values of meas-

Chwee Teck Lim, James C.H. Goh (Eds.): ICBME 2008, Proceedings 23, pp. 1777–1780, 2009
www.springerlink.com

ured body mass; and (3) examine the difference in distribution of segment mass between the proposed method and selected BSP models.

II. Materials and Methods

A. Subjects

Four healthy males (age: 27.5 ± 4.6 years; mass: 79.7 ± 32 kg; height: 1.75 ± 0.06 m) of different body types participated in this study. Somatotypes were evaluated using the Heath-Carter (1967) method and subject characteristics are shown in Table 1. Institutional Review Board approval was obtained from the research and graduate review committee of the Physical Education and Sports Science (PESS), Nanyang Technological University. Informed consent was obtained from each subject. Standing height was recorded to the nearest 0.1 centimeters (cm). The body mass was recorded to the nearest 100 grams (g) using Seca (Model 767) balance scale.

Table 1 Somatotype, age, height, body mass and percent body fat of the subjects (n = 4)

	Ectomorph	Endomorph	Central	Mesomorph
Somatotype	2-3.5-5.5	7-5-0.5	4-3.5-3	3-6-1.5
Age (year)	33	31	23	24
Height (cm)	179.1	181.1	171.1	170.1
Body mass (kg)	58.8	127.39	63.0	70.6
Body fat (%)	13.8	34.2	21.4	18.6

B. Instrumentations

Full body DXA scans were performed using a Hologic QDR-1000/W densitometer (Hologic, Bedford, MA, USA) with the subjects lying supine on the scan bed. 3-D exterior geometry was obtained with subjects standing upright using 3-D digitizer system (3-D Capturor II, InSpeck Inc., Montreal, Quebec, Canada).

The full-body DXA image was segmented into 14 segments as shown in Fig. 1 and defined as the head-and-neck, trunk, right and left upper arms, right and left forearms, right and left hands, right and left thighs, right and left shanks, right and left feet.

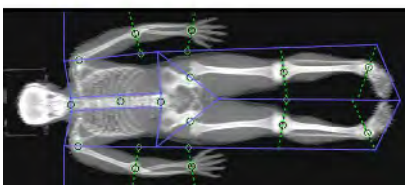


Fig 1. Full body segmentation

C. Dual Energy X-ray Absorptiometry Imaging

We adopted the classification algorithm proposed by Pietrobelli et al. [33] to identify each pixel by material groups, fat, lean or bone tissues. The source releases a beam of photons which is related to the attenuated intensities via the classic attenuation formula

$$I = I_0 e^{-\mu_m \times \rho \times L} \tag{1}$$

where e is base of natural logarithms, I is the transmitted photon intensity, I_0 is the initial photon intensity, L is path length (cm), ρ and μ_m are the object's density (g.cm^{-3}) and mass attenuation coefficient (cm^2.g^{-1}) respectively.

The object domain was discretized from the imaging resolution $X \bullet Y$ across a proportional depth (z), and assumed constant material in each volume element. The log-attenuation ratio is a sum of elemental attenuation over the pixel at (x, y)

$$\ln\left(\frac{I(x,y)}{I_0}\right) = \sum_z -\mu_m \times \rho(x,y,z) \times dz \tag{2}$$

where ρ and μ_m is the object's density (g.cm^{-3}) and material properties are now specific to the volumetric element.

We casted volumetric reconstruction as a non-linear constrained minimization problem. We aligned the 3-D bounding manifold of the object G to the plane of the acquired images, $I \in R^{2\times N}$. With N = 2 for DXA scans, we discretized the space such that G is enclosed within a volumetric domain D comprising $m \times n \times d$ cells. Each cell, also known as voxel, $v = (x,y,z)^T \in D$, was assumed to have uniform material property.

We set the scalar function $f : D \to R$ to denote the unknown volumetric density field. We also set constraints to the values of f such that the implicit surface f = 0 delineates G

$$f(v) = \begin{cases} +ve, & v \text{ is interior to } G \\ 0, & v \text{ lies on } G \\ -ve, & v \text{ is exterior to } G \end{cases} \tag{3}$$

where G represents the 3-D exterior geometry of the object and v is the voxel of each cell.

Geometric closure and orientability were required of G. Otherwise, the signed distance function would be ill-defined

Suppose $\alpha = \ln\left(\frac{I(x,y)}{I_0}\right)$, the integral of each column would be

$$\alpha = \sum_z \{f(x,y,z) \mid f(x,y,z) > 0\} \quad (4)$$

where $f(x,y,z) = -\mu_m \times \rho$ is the differential attenuation of the photon beam through a path of unit length, which confined the summation to voxels interior to the object.

One-way analyses of variance (ANOVA) were performed to test for significant differences between our method and four BSP estimate models on segment mass, center of mass and moments of inertia about the full body segments. All statistical tests were performed using SPSS software.

III. Results

The proposed method was able to accurately estimate total body mass of 4 male subjects, thus validating mass constant. The percent error between the estimated and measured body mass were less than 1% (Table 2).

Table 2 Criterion measured total body mass (MBM), and total body mass (TBM) from our proposed method (n = 4)

Body types	MBM (kg)	TBM (kg)	% error
Ectomorph	58.8	59.13	0.56
Endomorph	127.39	126.93	0.36
Central	63.0	63.09	0.14
Mesomorph	70.6	70.09	0.73

Comparisons between the inertial parameters derived from selected BSP models and our proposed method were made. The inertial parameters were the segment mass (*SM*), center of mass (*CM*), and the moments of inertia (I_{xx}, I_{yy} and I_{zz}). The results showed that BSP values differ substantially as a function of the BSP model employed. ANOVA revealed significant differences between our proposed method as compared to cadaver-based and living-based models for *SM* at the hand.

ANOVA indicated significant differences between our proposed method as compared to cadaver-based and living-based models for *CM* at the thigh, shank, foot, head and neck, trunk, upper arm, forearm and hand. Post hoc comparisons revealed that the *CM* derived from our proposed method are significantly less than Dempster [11] and Cheng et al. [15] at the hand, forearm, trunk, thigh, shank and foot.

ANOVA showed significant differences between our proposed method as compared to cadaver-based and living-based models for moments of inertia at the hand, shank, foot and trunk. Post hoc comparisons revealed that the moments of inertia derived from our proposed method are significantly more than Cheng et al. [15] at the hand, shank, foot and trunk.

IV. Discussion

Previous studies have examined the effect of variations in BSP during gait and advocated the need for accurate BSP values in high acceleration movements [3], [6], [30]. Significant differences were found in segment mass estimated using our proposed method when compared to cadaver-based [8], [11] and living-based models [14], [15].

Total body mass and were estimated using our proposed method and compared with measured body mass. Percent errors between estimated and measured body mass were less than 1% for all subjects. The variations between subjects may be attributed to the difference in ability of distinct beam energies to identify each pixel of material groups such as fat-and-lean or soft tissue-and-bone which can be vastly different for different body types. In general, the percent errors between estimated and measured body weight ranged between 0.14 to 0.73%. This is comparable to Jensen's [14] elliptical zone modeling approach who reported maximum 1.82% error between estimated and measured body mass. Our proposed method permits direct computation of all segmental parameter values specific to individuals, and takes into account the shape of the actual body segments. We also accounted for varying tissue densities for fat, lean and bone tissues. One limitation of this method is the assumption of uniform material property for each cell, and hence volume column. Another limitation would be inherent errors due to redistribution of tissues when subjects lie supine in the DXA scan position. This may change the inertial properties of the segments to a certain extent. Nevertheless, the ability of this method to distinguish unique density for bone, lean and fat tissue is still more rigorous than assuming uniform segment densities.

V. Conclusions

Extensions of the research could further examined the influence of other BSP measurements derived from our proposed method and the four selected estimation models, as well as their impact on the inverse dynamics solutions in human motion. The information can be used to gain insights in sport skills or gait; identification of aetiology of conditions such as osteoarthritis; and for the development of medical instruments.

ACKNOWLEDGMENT

The authors wish to thank the Agency for Science, Technology and Research (A*STAR) for funding this research; School of Mechanical and Manufacturing Engineering, Singapore Polytechnic for the use of 3-D scanner.

REFERENCES

1. J.G. Andrews and S. P. Mish, "Methods for investigating the sensitivity of joint resultants to body segment parameter variations," *J. of Biomech*, vol. 29, pp. 651-4, 1996.
2. Y.H. Kwon, "Effects of the method of body segment parameter estimation on airborne angular momentum," *J. of App. Biomech*, vol. 12, pp. 413-30, 1996.
3. D. J. Pearsall and P. A. Costigan, "The effect of segment parameter error on gait analysis results," *Gait Posture*, vol. 9, pp. 173–83, 1999.
4. J. L. Durkin, J. J. Dowling, and D.M. Andrews, "The measurement of body segment inertial parameters using dual energy X-ray absorptiometry," *J. Biomech..*, vol. 35, pp.1575–80, 2002.
5. J. L. Durkin and J. J. Dowling, "Analysis of body segment parameter-differences between four human populations and the estimation errorsof four popular mathematical models," *J. Biomech. Eng.*, vol. 125, pp. 515–22, 2003.
6. G. Rao, D. Amarantini, E. Berton and D. Favier, "Influence of body segments' parameters estimation models on inverse dynamics," *J. of Biomech.*, vol. 39, pp. 1531-1536, 2006.
7. D. J. Pearsall and J. G. Reid, "The study of human body segment parameters in biomechanics. An historical review and current status report," *Sports Med.*, vol. 18, pp. 126–40, 1994.
8. R. F. Chandler, C. E. Clauser, J. T. McConville, H. M. Reynolds, and
9. J. W. Young, "Investigation of Inertial Properties of the Human Body," Aerospace Medical Research Laboratory, Wright-Patterson Air Force Base, Dayton, OH, Tech. Rep. AMRL-74-137, 1975.
10. C. E. Clauser, J. T. McConville, and J.W. Young, "Weight, Volume, and Center of Mass of Segments of the Human Body," Aerospace Medical Research Laboratory, Wright-Patterson Air Force Base, Dayton, OH, TechRep. AMRL-TR-69-70, 1969.
11. W. T. Dempster, "Space Requirements for the Seated Operator," Wright Air Development Center, Wright-Patterson Air Force Base, Dayton, OH, WADC Tech. Rep. TR-55-159, 1955.
12. T. R. Ackland, B. A. Blanksby, and J. Bloomfield, "Inertial characteristics of adolescent male body segments," *J. Biomech.*, vol. 21, pp. 319–27, 1988.
13. R. K. Jensen, "Body segment mass, radius and radius of gyration proportions of children," *J. Biomech.*, vol. 19, pp. 359–68, 1986.
14. V. M. Zatsiorsky, V. N. Seluyanov, and L. G. Chugunova, "Methods of determining mass-inertial characteristics of human body segments," in *Contemporary Problems of Biomechanics*, S.A. Regirer, Ed. Moscow: Mir, 1990, pp. 272–91.
15. C. K. Cheng, H. H. Chen, C. S. Chen, C. L. Chen, and C. Y. Chen, "Segment inertial properties of Chinese adults determined from magnetic resonance imaging," *Clin. Biomech.*, vol. 15, pp. 559–66, 2000.
16. P. E. Martin, M. Mungiole, M. W. Marzke, and J. M. Longhill, "The use of magnetic resonance imaging for measuring segment inertial properties.," *J. of Biomech*, vol. 22, pp. 367-76, 1989.
17. M. Mungiole and P. E. Martin, "Estimating segment inertial properties: Comparison of magnetic resonance imaging with existing methods," *J.Biomech.*, vol. 23, pp. 1039–46, 1990.
18. D. J. Pearsall, J. G. Reid, and R. Ross, "Inertial properties of the human trunk of males determined from magnetic resonance imaging," *Ann. Biomed. Eng.*, vol. 22, pp. 692–706, 1994.
19. W. S. Erdmann, "Inertia of the male trunk analyzed with the help of computerized tomography," in *1991 Proc. XIIIth Congress of the Int. Soc. of Biomech*, pp. 475-76.
20. H. K. Huang and F. R. Suarez, "Evaluation of cross-sectional geometry and mass density distributions of humans and laboratory animals using computerized tomography," *J. of Biomech*, vol. 16, pp. 821-32, 1983.
21. H. K. Huang and S. C. Wu, "The evaluation of mass densities of the human body in vivo from CT scans," *J. of Biomech*, vol. 6, 337-343, 1976.
22. D. J. Pearsall, J. G. Reid, and L. A. Livingston, "Segmental inertial parameters of the human trunk as determined from computed tomography," *Ann. Biomed. Eng.*, vol. 24, pp. 198–210, 1996.
23. P. Milburn, "Real-time 3-dimensional imaging using ultrasound," in *1991 Proc. of the XIIIth Congress of the Int. Soc. of Biomech*, pp. 1230-1.
24. T. L. Kelly, N. Berger and T. L. Richardson, "DXA body composition: Theory and practice," *App. Rad. and Isotopes*, vol. 49, pp. 511-3, 1998.
25. K. J. Ganley and C. M. Powers, "Anthropometric parameters in children: A comparison of values obtained from dual energy x-ray absorptiometry and cadaver-based estimates," *Gait Posture*, vol. 19, pp. 133–40, 2004.
26. W. M. Kohrt, "Preliminary evidence that DEXA provides an accurate assessment of body composition," *J. of App. Phy.*, vol. 84, pp.372-7, 1998.
27. D. O. Slosman, J. P. Casez, C. Pichard, T. Rochat, B. Fery, R. Rizzoli, J. P. Bonjour, A. Morabia and A. Donath, "Assessment of whole-body composition with dual energy X-ray absorptiometry," *Radiology*, vol. 185, 593-8, 1992.
28. Pietrobelli, A., Formica, C., Wang, Z., Heymsfield, S.B., 1996. Dual-energy x-ray absorptiometry body composition model: review of physical concepts. Endocrinology and Metabolism 271, 941–951.

Author: Lee Mei Kay
Institute: Republic Polytechnic
Street: 9 Woodlands Avenue 9, Singapore 738964
City: Singapore
Country: Singapore
Email: lee_mei_kay@rp.sg

A New Intraoperative Measurement System for Rotational Motion Properties of the Spine

K. Kitahara[1], K. Oribe[1], K. Hasegawa[2], T. Hara[3]

[1] Showa Ika Kohgyo Co., Ltd.
[2] Niigata Spine Surgery Center
[3] Faculty of Engineering, Niigata University

Abstract — **Low back pain due to spinal segmental instability is common in lumbar degenerative diseases. Instability of the spinal segment is difficult to define and occur in any motion direction. In particular, rotational instability has been implicated in the pathogenesis of low back pain. Biomechanical measurements assess motion properties that are essential for estimating segmental instability. To detect spinal segmental instability, we developed a new system for measuring spinal mobility during lumbar spine surgery. The system consists of a motor driven mechanical apparatus with a computerized controller, load cell, optical displacement transducer and spinous process holders that allow handling of the spinal process without damaging the supraspinal and interspinal ligaments. In this study, the repeatability test was performed to demonstrate the potential of the measurement system. Displacement generated by the actuator at a speed of 1.0 mm/sec was applied to the tip of the holders with a maximum displacement of 4.0 mm from the neutral position for five cycles of axial rotation. After 5 min, the same specimen was retested for five more cycles of axial rotation, and this process was repeated ten times. In total, this test generated 50 load–displacement curves for each specimen. From the load–displacement curve, we determined three motion parameters: stiffness, neutral zone and absorption energy, and calculated the coefficients of variation (CVs) by dividing the standard deviation by the mean of each parameter and converting it to a percentage. The small CVs for each parameter measured reflected the high repeatability of the load–displacement curves. The measurement had sufficiently high repeatability for clinical use, as indicated by the low CV for each motion parameter.**

Keywords — **Spine, instability, rotation, mobility, neutral zone, measurement.**

I. Introduction

Intraoperative biomechanical measurements assess motion properties that are essential for estimating segmental instability. Ebara et al. developed a method of measuring spinal stiffness that used a spinal spreader and measured the tensile stiffness of a mobile segment; they concluded that tensile stiffness depends on disc degeneration, decompression, and interbody fusion[1)]. Brown et al. developed a motor-driven vertebrae distractor to measure motion segment stiffness. They concluded that the vertebral distractor allows objective and quantitative intraoperative measurement of the stiffness of a mobile lumbar spine segment[2),3)].

In the above studies, spinal segmental mobility was evaluated using the stiffness in flexion. However, from a biomechanical perspective, estimates of additional parameters, such as the neutral zone (NZ), are needed to assess spinal mobility[4)]. Clinical instability cannot be estimated by measuring mobility in flexion only, and measuring the rotational mobility of the spinal segments is also important[5)].

Instability of the spinal segment can occur in any motion direction[6)-13)]. In particular, torsional instability has been implicated in the pathogenesis of low back pain[13)]. Therefore, multidirectional measurement of the target segment is desirable. In the study described here, we developed and tested another system for measuring spinal mobility. This system, which measures rotational mobility in the axial plane, was evaluated for its ability to detect segmental mobility in porcine lumbar segments.

II. Materials and methods,

To detect spinal segmental instability, we developed a new system for measuring spinal mobility during lumbar spine surgery (Figure 1). The system consisted of spinous process holders (Gi-5; Mizuhoikakikai, Niigata, Japan), a motion generator, and a personal computer. The spinous process holders were designed to handle the spinal processes without damaging the supra- and interspinous ligaments. The motion generator consisted of a computerized linear actuator, an optical displacement transducer (LB-080; Keyence, Tokyo, Japan), a load cell (LUR-A-200NSAI; Kyowa Dengyo, Tokyo, Japan), and a multidirectional ball joint that connected the motion generator to the spinous process holders. The motion generator was attached through the ball joint to two spinous process holders, which gripped the adjacent spinous processes firmly. The linear actuator (RC-RSW-L-50-S; IAI, Shizuoka, Japan) generated continuous displacement applied to the spinous process holders at speeds of 1.00 to 100 mm/sec. The mobile segment was displaced from the neutral position and rotated right and left

Chwee Teck Lim, James C.H. Goh (Eds.): ICBME 2008, Proceedings 23, pp. 1781–1784, 2009
www.springerlink.com

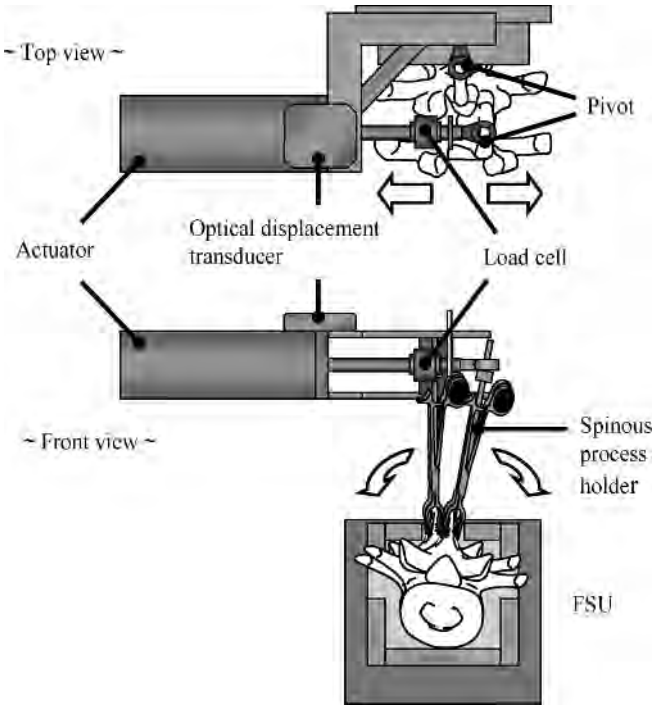


Fig. 1 Schematic diagram of a new system developed to measure spinal rotational mobility. An actuator is used to move the caudal spinous process holders. Load is measured with a load cell, and displacement is measured using an optical displacement transducer.

cyclically. The neutral position was defined as the segment position when no load was applied. In the experiments, the load and displacement at the tip of the caudal spinous process holder were measured using a load cell and an optical displacement transducer, respectively, and the load-displacement curves were plotted on a computer screen.

In vitro experiments were performed using fresh-frozen porcine lumbar spines to demonstrate the potential of the measurement system, and the specimens consisting of functional spinal units (FSUs) were harvested from mature porcine lumbar spines. The FSUs were dissected to remove all muscles and fatty tissues, while the ligamentous tissues (supraspinal, interspinous, anterior longitudinal, anterior longitudinal, posterior longitudinal, transverse ligament, and flavum), discs, facet joints, and osseous structures were left in place. During the experiments, six FSUs (two each of T12/L1, L2/L3, and L4/L5) were used to demonstrate the potential of the system, and eight FSUs (two each of T12/L1 and L2/L3, and one each of L1/L2, L3/L4, L4/L5, and L5/L6) were used to assess destabilized segments, as shown Table 1. During the tests, the specimens were maintained at a constant temperature and humidity to prevent deterioration.

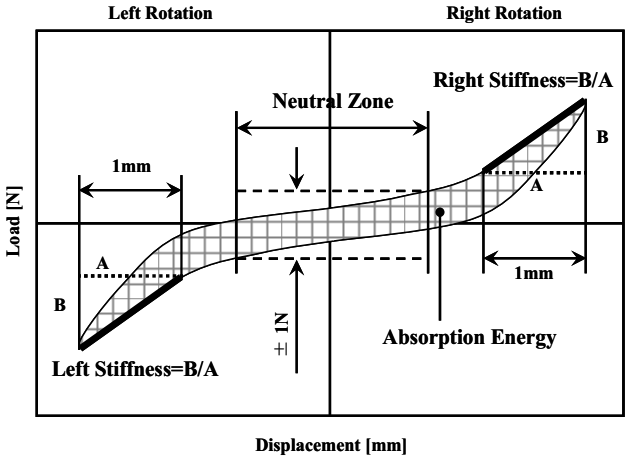


Fig. 2 Determination of each parameter from the third load–displacement curve. The left and right stiffness (N/mm) values were defined as the slopes of the lines fitting the load-displacement curve from –1 to –2 mm and from 1 to 2 mm, respectively. The neutral zone (mm) was defined as the displacement that occurred while the load was reduced from 1 N to –1 N along the load-displacement curve. Absorption energy (J) was defined as the area of the resulting hysteresis loop.

From the load-displacement curves, we determined three motion parameters to evaluate the spinal motion: the stiffness, NZ, and absorption energy (AE) (Figure 2). Stiffness describes the relationship between the load and displacement of the spinal segment while rotation is applied. In this study, the stiffness was defined as the slope of the line fitting the load-displacement curve from 1 to 2 mm on right rotation and from ?1 to ?2 mm on left rotation. The NZ is the flat region of the load-displacement curve around the neutral position. This indicates that the passive spinal column offers little resistance. The NZ was defined as the displacement that occurs while the load is reduced from 1 N to -1 N. The load-displacement curve showed hysteresis, as the load lagged behind the change in displacement. The area inside the load-displacement curve has units of energy. This energy is absorbed by the discs, ligaments, and other soft tissues around the spinal segment while the segment is moving. The AE was defined as the area surrounded by the load-displacement curve during one cycle of spinal motion.

The repeatability test was performed to demonstrate the potential of the measurement system. In this test, each FSU was assessed while intact. Displacement generated by the actuator at a speed of 1.0 mm/sec was applied to the tip of the holders with a maximum displacement of 4.0 mm from the neutral position for five cycles of axial rotation. After 5 min, the same specimen was retested for five more cycles of axial rotation, and this process was repeated ten times. In total, this test generated 50 load-displacement curves for each specimen. We determined three motion parameters

from each cycle for every load-displacement curve and calculated the coefficients of variation (CVs) by dividing the standard deviation by the mean of each parameter and converting it to a percentage.

III. Results

To determine the repeatability of the spinal mobility measurement, we calculated the CV of each mechanical parameter determined from the load-displacement curve. The CV is a statistical measure of the dispersion of a probability distribution and is defined as the ratio of the standard deviation to the mean. The CVs were as follows: right rotational stiffness 2.28-5.75% (mean 4.57%), left rotational stiffness 2.10-5.50% (4.30%), NZ 4.44-7.75% (6.20%), and AE 6.28-12.78% (8.57%). The small CVs for each parameter measured reflected the high repeatability of the load-displacement curves (Table 1).

Table 1 Coefficient of variation (CV) for each mechanical parameter.

	R stiffness (%)	L stiffness (%)	Neutral zone (%)	Absorption energy (%)
T12/L1	2.96	3.58	4.62	6.48
L2/3	5.44	4.42	7.75	6.68
L4/5	5.37	5.50	6.85	12.78
T12/L1	5.62	4.98	5.92	6.88
L2/3	2.28	2.10	4.44	6.26
L4/5	5.74	5.22	7.61	12.35
mean	4.57	4.30	6.20	8.57

IV. Discussion and conclusions

After a half-century of controversy, a clear definition of clinical instability of the spine has yet to be established, partly because facts elicited from ex-vivo or animal studies[7)-17)] appear inconsistent with those from patients with mechanical low back pain or motion-induced radiculopathy. Although conventional radiographic measurements are still popular for the clinical diagnosis of instability, radiographic examinations[18)-25)] are limited to still measurements with a large range of values, so that normal angulatory motion cannot be precisely defined[26)]. In addition, these radiographic measures demonstrate some kinematics, but they do not yield biomechanical data concerning the load-deformation relationship, which is necessary to determine the segmental instability. Thus, no clinically convenient and biomechanically accurate tools that yield results correlating with those of extensive basic studies have been available.

Our approach constitutes an attempt to bridge the gap between the basic biomechanical data and the clinical symptoms observed to arise from instability. The final goals of our intraoperative measurement for segmental instability are to determine distinct criteria based on the biomechanical data and to certify a rationale for lumbar fusion, the gold-standard therapy for segmental instability, from a biomechanical point of view. We have already launched the clinical application of the measurement system for sagittal plane (flexion-extension) motion properties[27)] following several ex-vivo studies[28),29)]. However, since instability of the spinal segment can occur in any motion direction[7)-13),23)] , multidirectional measurement of the target segment is desirable. This study provides a basic confirmation of the potential of our new measurement system for quantitating clinical motion properties in the axial plane.

The measurement had sufficiently high repeatability for clinical use, as indicated by the low CV for each motion parameter. The computerized motor-driven measurement system, which was able to accurately rotate the segment at a constant speed, and the specially designed spinous process holder, contributed to the excellent repeatability. This study demonstrated the potential utility of our system for obtaining useful data on spinal mobility.

References

1. Brown MD, Holmes DC, Heiner AD. Measurement of cadaver lumbar spine motion segment stiffness. Spine 2002;27(9):918?22.
2. Brown MD, Holmes DC, Heiner AD, Wehman KF. Intraoperative measurement of lumbar spine motion segment stiffness. Spine 2002;27(9):954?8.
3. Panjabi MM. The stabilizing system of the spine. Part II. Neutral zone and instability hypothesis. J Spinal Disord 1992;5(4):390?6; discussion 397.
4. Farfan HF, Cossette JW, Robertson GH, et al. The effects of torsion on the lumbar intervertebral joints. J Bone Joint Surg 1970;468?97.
5. Washio T, Hasegawa K, Hara T. A practical technique for intraoperative measurement of spinal mobility to diagnose spinal instability: In vitro experimental study using porcine FSU. 12th Conference of the European Society of Biomechanics, Dublin 2000.
6. Panjabi MM, Goel VK, Takata K. Physiologic strains in the lumbar spinal ligaments. An in vitro biomechanical study 1981 Volvo Award in Biomechanics. Spine 1982;7(3):192-203.
7. Panjabi MM, Krag MH, Chung TQ. Effects of disc injury on mechanical behavior of the human spine. Spine 1984;9(7):707?13.
8. Panjabi MM, Goel V, Oxland T, Takata K, Duranceau J, Krag M, Price M. Human lumbar vertebrae. Quantitative three-dimensional anatomy. Spine. 1992;17(3):299-306.
9. Gertzbein SD, Seligman J, Holtby R, et al. Centrode patterns and segmental instability in degenerative disc disease. Spine 1985;10(3):257?61.
10. Mimura M, Panjabi MM, Oxland TR. Disc degeneration affects the multidirectional flexibility of the lumbar spine. Spine 1994;19(12):1371?80.

11. Fujiwara A, Lim TH, An HS, Tanaka N, et al. The effect of disc degeneration and facet joint osteoarthritis on the segmental flexibility of the lumbar spine. Spine 2000;25(23):3036?44.
12. Kaigle AM, Holm SH, Hansson TH. Experimental instability in the lumbar spine. Spine 1995;20(4):421?30.
13. Kaigle AM, Holm SH, Hansson TH. 1997 Volvo Award winner in biomechanical studies. Kinematic behavior of the porcine lumbar spine: a chronic lesion model. Spine 1997;22(24):2796?806.
14. Ogon M, Bender BR, Hooper DM, et al. A dynamic approach to spinal instability. Part I: Sensitization of intersegmental motion profiles to motion direction and load condition by instability. Spine 1997;22(24):2841?58.
15. Ogon M, Bender BR, Hooper DM, et al. A dynamic approach to spinal instability. Part II: Hesitation and giving-way during interspinal motion. Spine 1997;22(24):2859?66.
16. Brown MD, Wehman KF, Heiner AD. The clinical usefulness of intraoperative spinal stiffness measurements. Spine 2002;27(9):959?61.
17. Kanayama M, Hashimoto T, Shigenobu K. Intraoperative biomechanical assessment of lumbar spinal instability: Validation of radiographic parameters indicating anterior column support in lumbar spinal fusion. Spine 2003;28(20):2368?72.
18. Knutsson F. The instability associated with disk degeneration in the lumbar spine. Acta Radiol 1944;25:593?609.
19. Morgan FP, King T. Primary instability of lumbar vertebrae as a common cause of low back pain. J Bone Joint Surg 1957;39:6?22.
20. Lindahl O. Determination of the sagittal mobility of the lumbar spine. A clinical method. Acta Orthop Scand 1966;37(3):241?54.
21. Pennal GF, Conn GS, et al. Motion studies of the lumbar spine: a preliminary report. J Bone Joint Surg Br 1972;54(3):442?52.
22. Dupuis PR, Yong-Hing K, Cassidy JD. Radiologic diagnosis of degenerative lumbar spinal instability. Spine 1985;10(3):262?76.
23. Frymoyer JW, Selby DK. Segmental instability. Rationale for treatment. Spine. 1985;10(3):280?6.
24. Dvorak J, Panjabi MM, Grob D, Novotny JE, Antinnes JA. Clinical validation of functional flexion-extension roentgenograms of the lumbar spine. Spine 1991;16(8):943?50.
25. Iguchi T, Kanemura A, Kasahara K, et al. Age distribution of three radiologic factors for lumbar instability: probable aging process of the instability with disc degeneration. Spine 2003;28(23):2628?33.
26. Stokes IA, Wilder DG, Frymoyer JW, Pope MH. 1980 Volvo award in clinical sciences. Assessment of patients with low-back pain by biplanar radiographic measurement of intervertebral motion. Spine 1981;6(3):233?40.
27. Nachemson AL, Schultz AB, Berkson MH. Mechanical properties of human lumbar spine motion segments. Influence of age, sex, disc level, and degeneration. Spine 1979;4(1):1?8.
28. Kitahara K, Takano K, Hasegawa K. Evaluation of intraoperative lumbar motion measurement system. Jpn J Clin Biomech 2004;24:93?7.
29. Takano K, Hasegawa K, Kitahara K. Lumbar segmental motion properties in vivo determined by a new intraoperative measurement system. Acta Med Biol 2006;54(1):1?8.

Binding of Atherosclerotic Plaque Targeting Nanoparticles to the Activated Endothelial Cells under Static and Flow Condition

K. Rhee[1], K.S. Park[2] and G. Khang[3]

[1]Myongji University/Mechanical Engineering, Yongin, Korea
[2]KIST/Biomedical Research Center, Seoul, Korea
[3]Kyunghee University/Biomedical Engineering, Yongin, Korea

Abstract — **Nanoparticles which selectively bind to the atherosclerotic lesion can be used in diagnostic imaging and efficient drug delivery. We have developed peptides conjugated polymer nanoparticles which selectively bind to atherosclerosis plaque. Hydrophobically modified glycol chitosan (HGC) nanoparticles were used as carriers, and the peptides which showed selective binding to the atherosclerotic plaque was screened using phage display. We synthesized peptides conjugated HGC-Cy5.5 nanoparticles and examined their binding characteristics on the activated endothelial cells in vitro under static and flow conditions. Under static condition, the peptide tagged nanoparticles did not show significant selective binding for the activated endothelial cells at low particle concentrations (25 and 50 μg/ml), but they more avidly bound to the activated endothelial cells at high particle concentration (100 μg/ml) comparing to the unactivated endothelial cells. Under fluid flow condition, selective binding of peptide tagged nanoparticles was more prominent.**

Keywords — **Atherosclerosis, Molecular Imaging, Nanoparticle, Shear Stress.**

I. Introduction

Various nanoparticles have recently been developed for diagnostic and therapeutic use owing to the advance of nanotechnology [1-3]. Target specificity of nanoparticles can enhance the efficiency of drug delivery and diagnosis while reducing the side effects such as toxicity and immunogenicity. Targeting has been generally achieved by conjugating nanoparticle surfaces to antibodies or peptides which show binding specificities to the target. Multivalent attachment of antibodies or peptides to nanoparticles enhances target specific binding efficiency. Also surface modification of nanoparicles can modulate pharmacokinetic properties such as blood half-life, elimination and biodegradation. Conjugation of nanoparticles to antibodies for diagnosing and treating cancer and atherosclerosis has been attempted [4,5], but using antibodies as targeting moieties involves difficulties such as limited shelf life, regulations, and potential immunogenicity.

We would like to develop polymer nanoparticles functionalized by peptides which selectively bind to atherosclerosis. Hydrophobically modified glycol chitosan nanoparticles (HGC) are used as carriers because of their blood compatibility, adequate circulation retention time, and high endothelial cellular uptake [6,7]. Peptide which shows specific binding to the atherosclerotic plaque is screened using phage display, and conjugated to the surface of nanoparticles. In this study, binding characteristics of the peptides tagged chitosan nanoparticles on the activated endothelial cells have been examined in vitro in order to develop atherosclerosis specific targeting agents. Effects of particle concentration, incubation time and fluid flow were explored.

II. Materials and Methods

A. Endothelial cell culture and activation

Bovine aortic endothelial cells (BAECs; a kind gift from Dr. B.H. Lee, Kyungbuk National University) were cultured in tissue culture flasks in Dulbecco's Modified Eagle Medium (DMEM-low glucose, Sigma-Aldrich, St.Louis, MO). For static flow experiment, cells were resuspended in the medium, and seeded in 8-well and 24-well cell culture clusters at a density of $1x10^4$ and $5x10^4$ cells per a well, respectively. Cells were allowed to grow for 1 day and monitored for uniformity. Recombinant human tumor necrosis factor-α (TNF-α) was obtained from Chemicon International (Millipore Corp., Billerica, MA). Cells were treated with 10 ng/mL of TNF-α for 6 hours for activation.

For convective flow experiment, $1x10^4$ cells were seeded in the commercially available flow channel (μslide I®, Ibidi, Integrated Diagnostics, Germany). This plastic flow channel had a rectangular channel (0.4 mm height, 5 mm width, 50 mm length). Cells were cultured until reaching confluence, and activated by TNF-α as previously described.

B. Preparation of AP-1 peptide-tagged HGC-Cy5.5 conjugate

The HGC (degree of substitution=12%) was synthesized in the presence of 1-ethyl-3(3-dimethylaminpropyl) acrbo-

Chwee Teck Lim, James C.H. Goh (Eds.): ICBME 2008, Proceedings 23, pp. 1785–1787, 2009
www.springerlink.com

diamide hydrochloride (EDC) and N-hydroxysuccinimide (NHS), as described previously [8]. Peptide sequences with seven motifs, named AP-1, were screened by phage display. A phage library containing random peptides was screened for binding to atherosclerotic plaques. After three rounds of screening, the DNA insert of selected phage clones were sequenced, and then translated into corresponding peptide sequences electronically. Of these, the most frequently occurred peptide was named as AP-1 peptide and chosen for further study.

Hydrophobically modified glycolchitosan (HGC, 180 mg, 3.6 μmol) was dissolved in 6 ml of anhydrous DMSO (dimethyl sulfoxide), and then SMCC [N-succinimidyl-4-(maleimidomethyl) cyclo-hexanecarboxylate, 18.05 mg, 54 μmol] was added. The reaction was allowed at room temperature for 12 hours. The solution was dialyzed against distilled water using dialysis membrane (MWCO 12,000~14,000, Spectrum®) for 1 day, and lyophilized to obtain product 1 (HGC-MCC) (144 mg, yield=79.6%). MCC-HGC (50 mg, 0.99 μmol) and Cy 5.5 (2.25 mg, 1.99 μmol) were dissolved in 4 ml DMSO and reacted for 12 hours. The mixture solution was then dialyzed (MWCO 12,000~14,000, Spectrum®) for 1 day, and freeze-dried. The yield of productt was nearly 100%. MCC-HGC-Cy5.5 conjugate (40 mg, 0.78 μmol) was dispersed in the mixture of 10 mM PBS (pH 6.7)/DMSO (10 ml, 9:1) and AP-1 peptide (25 mg, 21.5 μmol) was added. The mixture solution was stirred at room temperature for 1 day, and then dialyzed against distilled water and further freeze-dried.

C. Particle binding on BAECs: Fluorescence microscopy study

1 mg of nanoparticles was dissolved in 1 ml of distilled water and sonicated three times using a probe type sonifier (Sigma Ultrasonic Processor, GEX-600). Different concentrations of nanoparticles (25, 50, 100 μg/ml) were prepared.

For static flow experiment, the medium in the 8-wells was replaced with suspensions of nanoparticles and incubated for a given time (30 min, 1hr and 2hrs). At the end of the incubation period, the nanoparticle suspension was removed from wells and cells were rinsed three times with DPBS. 2 mL of FA/GA solution (4 and 0.05 %, v/v, in DPBS) was added and incubated for 10 min at room temperature. After twice washing with DPBS, 2 mL 4',6-diamidino-2-phenylindole, dilactate (DAPI) solution in PBS (pH 7.4, 3 μM) was applied to each well and cells were incubated for 5 minutes. After washing with DPBS, gel mount aqueous mounting medium (G0918) was added. The wells were covered with coverglasses and fixed with manicure for fluorescent microscopic observation.

For convective flow experiment, in a μslide I® channel was inserted into a flow circulation loop which consisted of a collecting reservoir, an infusion pump and a silicone tubing system. The flow loop was perfused with growth medium containing nanoparticles. To maintain the temperature of the perfusate passing through the channel at 37 ^{o}C, the reservoir was warmed up by water bath. The wall shear stress was adjusted to 5 dyne/cm^2 so as to simulate the blood flow in the arterial flow by controlling the flow rate. After two hours of flow circulation, the μslide I® channel was detached from the flow loop. Cells were washed with DPBS and fixed with FA/GA solution as previously described.

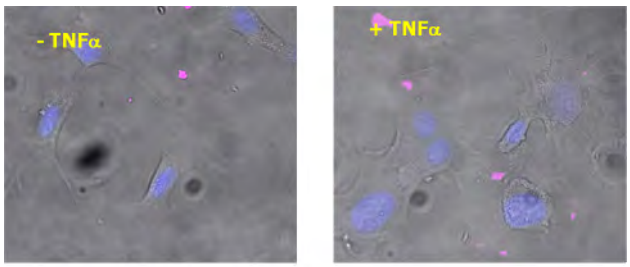
Fluorescence microscopic observation was carried out by Axioskop 2 FS plus microscope (Carl Zeiss, Thornwood, NY). All images were obtained by using 40 × water immersion objective lens (Achroplan, IR 40×/0.8W lens). Bright field (BF) images were captured by using phase-contrast filter with 100 ms exposure time. Exposure times for DAPI and Cy5.5 were 1 s and 100 ms, respectively. Acquired images were colored and exported as a Tiff format by aid of AxioVision software (Carl Zeiss). Without further modification, image montages were prepared by NIH Image J software (ver. 1.36).

III. Results

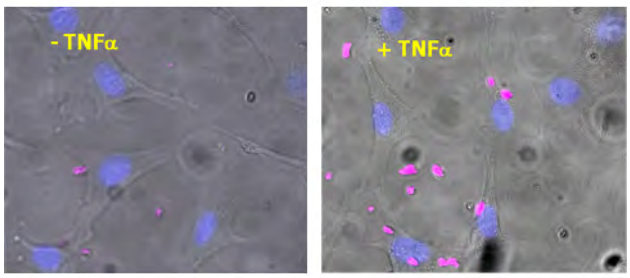
Nanoparticles (HGC and HGC-AP) were reacted with the activated and unactivated endothelial cells for different concentrations in static condition. The binding of HGC-AP to the BAECs was dependent on cytokine activation and the concentration of nanoparticles in the medium. Fig. 1 showed the fluorescence intensities of the activated BAECs and inactivated BAECs for different the particle concentration (50, 100 μg/ml). For lower concentration (25 and 50 μg/ml) of HGC-AP, particles bound to both activated and unactivated cells. As the particle concentration increased, HGC-APs bound more avidly to the activated BAECs. The result implied that AP-1 peptide might slightly bind to the endothelium whether it was activated or not, but HGC-APs bound more avidly to the activated endothelium at high concentration. Static incubation time (1 hr and 2 hr) did not affect nanopaticle binding, which implied that nanoparticle binding and uptake might occur within an hour.

In order to study the effects of convective fluid flow on particle bindings on the cells, a μslide I® channel was placed in a flow circulation loop for two hours. Binding of nanoparticles to the endothelial cells occurred in the similar fluid flow environment as in the arterial blood circulation. Activated and unactivated BAECs experienced fluid flow in the medium which contained HGCs and HGC-APs (100

μg/ml). Fluorescence microscopy observation showed negligible binding of HGCs to both the activated and unactivated cells as in the case of static flow. HGC-APs bound to the activated endothelial cells while no significant bindings were observed in the unactivated cells (Fig. 2). Selective binding of HGC-APs to the activated endothelial cells was more prominent.



(a) 50 μg/ml



(b) 100 μg/ml

Fig. 1 Fluorescent image of binding particles (red dots) in static condition

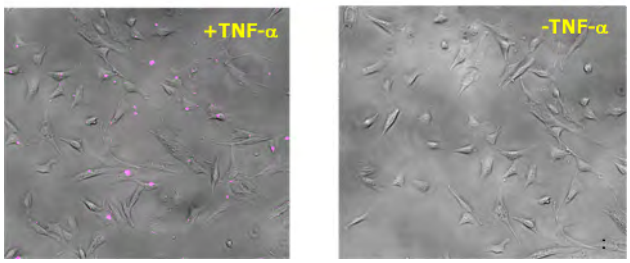


Fig.2 Fluorescent image of binding particles (red dots) in flow condition

IV. Concluions

We conjugated chitosan nanoparticles with atherosclerotic plaque binding peptides and studied their binding characteristics on the endothelial cells in vitro. The peptide-tagged nanoparticles were more avidly bound to the activated endothelial cells comparing to the unactivated endothelial cells at high particle concentration. Selective binding of peptide tagged nanoparticles was more prominent in fluid flow environment. Since peptide tagged nanoparticles showed selective binding characteristics at high concentration, they could be further developed for the target specific imaging probes and drug delivery carriers.

Acknowledgment

This work was supported by grant (R01-2006-000-10269-0) from the Basic Research Program of the Korea Science & Engineering Foundation.

References

1. Whitesides GM. (2003) The 'right' size in nanotechnology. Nat. Biotechnol. 21:1161-1165.
2. Nam JM, Thaxton CS and Mirkin CA. (2003) Nanoparticle based bio-bar codes for the ultrasensitive detection of proteins. Science 301:1884-1886.
3. Tsapis N, Bennett D., Jackson B, Weitz DA and Edward DA. (2002) Trojan particles: large porous carriers of nanoparticles for drug delivery. Pro. Natl. Acad. Sci. USA 99:12001-12005.
4. Muro S, Dziubla T, Qiu W., Leferovich J, Cui X, Berk E and Muzykantov VR. (2006) Endothelial targeting of high-affinity multivalent polymer nanocarriers directed to intercellular adhesion molecule 1. J Pharm Exp Therapeu 317:1161-1169.
5. Wu Y, Xiang J, Yang C, Lu W and Lieber CM. (2004) Single-crystal metallic nanowires and metal/semiconductor nanowire heterostructures. Nature 430:61-65.
6. Hirano S. (1999) Chitin and chitosan as novel biotechnological materials. Poly. Int. 48:732-734.
7. Park JH, Cho YW, Chung H, Kwon IC and Jeong SY. (2003) Synthesis and characterization of sugar-bearing chitosan derivatives: aqueous soluability and biodegradability. Biomacromolecules 4:1087-1091.
8. Kwon S, Park JH, Chung H, Kwon IC and Jeong SY.(2003) Physicochemical characteristics of self -assembled nanoparticles based on glycochitosan bearing 5β-cholanic acid. Langmuir 19:10188-10193.

Author: Kyehan Rhee
Institute: Myongji University
Street: 38-2, Nam-dong, Cheoin-gu
City: Yongin
Country: Korea
Email: khanrhee@mju.ac.kr

Computational Modeling of the Micropipette Aspiration of Malaria Infected Erythrocytes

G.Y. Jiao[1], K.S.W. Tan[2], C.H. Sow[3], Ming Dao[4,5,6], Subra Suresh[4,5,7], C.T. Lim[1,4,5,8,9]

[1] Department of Mechanical Engineering, National University of Singapore, Singapore
[2] Department of Microbiology, National University of Singapore, Singapore
[3] Department of Physics, National University of Singapore, Singapore
[4] Singapore-MIT alliance, Singapore
[5] Singapore-MIT Alliance, for Research and Technology, Singapore
[6] Department of Materials Science and Engineering, MIT
[7] School of Engineering, MIT
[8] Division of Bioengineering, National University of Singapore, Singapore
[9] NUS Life Sciences Institute, National University of Singapore, Singapore

Abstract — **Malaria is a deadly human disease that infects more than 500 million people each year. When the human red blood cell (RBC) is infected by a malaria parasite called Plasmodium *falciparum*, it loses its deformability and is unable to squeeze through small capillaries to transport oxygen to the various parts of the human body. Among the various techniques that have been used to quantitatively study the mechanical properties of malaria infected RBCs, micropipette aspiration has its advantage in exerting a wide range of suction pressure on specific locations of the cell membrane. Hemispherical cap model and homogenous half-space model were also developed to calculate the elastic modulus of the aspirated cell. Here, a detailed multi-component model is developed to model the complex infected cell and to study the membrane shear elastic modulus of the infected RBCs, especially during their mid to late stages of infection and when the parasite occupies a non-negligible volume of the host cell. The results show that the membrane shear modulus of a late stage infected cell calculated by the commonly used hemispherical cap model may not be accurate due to its ignorance of the internal structural changes of the host cell.**

Keywords — **Cell mechanics, malaria infected red blood cells, micropipette aspiration, finite element method, hyperelasticity.**

I. Introduction

Malaria is a severe human disease that infects 300-500 million people and results in 1.5-2.7 million deaths each year[1]. Among the four different species of the malaria parasite that infect humans, Plasmodium *falciparum* is the most deadly[2]. The highly deformable healthy red blood cell (RBCs) are able to squeeze through extremely small capillaries to transport oxygen from the lung to various organs and to remove the carbon dioxide back to the lung. However, when the Plasmodium f*alciparum* parasite invades into the RBC, it multiplies and modifies the host cell. Parasitic proteins are also known to be exported to and induce the stiffening of the host cell membrane. As a result, the RBC loses its deformability and results in capillary blockage, which is detrimental to health.

Various techniques have been used to measure the mechanical properties of malaria infected RBCs, such as micropipette aspiration[3-5], optical tweezers[6], laminar shear flow system[2,7] and microfluidic systems[8]. Among them, micropipette aspiration has its advantage of exerting a wide range of suction pressure to induce specific localized deformation on a cell membrane instead of the whole cell. Hemispherical cap model[9] and homogenous half-space model[10] have also been developed to evaluate the elastic modulus of a whole cell undergoing micropipette aspiration by assuming the cell as a homogenous entity despite the fact that a cell is heterogeneous and can comprise various components inside the cell.

Here, we seek to develop a multi-component model for the micropipette aspiration of malaria infected RBCs by accounting for the parasite within the infected RBC. Finite element method is used to model and evaluate the change in the mechanical properties of the infected cell. Results obtained will be compared with that obtained using the hemispherical cap model and homogenous half-space model. Since the severe structural changes only occur during the mid to late stages of parasite invasion, we will focus on these two stages here.

II. Methodology and Results

A. Finite Element Model

After parasite invasion, structural changes occur in the host cell[11]. The changes are not obvious in the early

Chwee Teck Lim, James C.H. Goh (Eds.): ICBME 2008, Proceedings 23, pp. 1788–1791, 2009
www.springerlink.com

stage, which is called ring stage. But 10-20 hours after invasion, which is called the trophozoite stage, the parasite grows and occupies almost 40% of the host cell. In the last stage, which is called the schizont stage, the parasite multiplies into 16-32 merozoites. Due to these severe structural changes during the mid to late stages of infection, the compound Newtonian liquid drop model was adopted[12,13]. Based on the fact that the parasite is stiffer than the cytoplasm, this model has three layers. The outer layer is the host cell membrane. The middle layer is the fluid-like cytosol. The core layer is the enclosed parasite.

The cell membrane was modeled using a hyperelastic material[14], expressed in the form of strain energy potential,

$$U = \frac{G_0}{2}(\lambda_1^2 + \lambda_2^2 + \lambda_3^2 - 3) + C_3(\lambda_1^2 + \lambda_2^2 + \lambda_3^2 - 3)^3 \quad (1)$$

where G_0 is initial shear modulus, and λ_i (i = 1,2,3) are the principal stretches. It is assumed that the membrane material is incompressible, which means $\lambda_1\lambda_2\lambda_3 = 1$.

The initial shear modulus of the membrane μ_0 is given by[15]

$$\mu_0 = 0.75 G_0 h_0 \quad (2)$$

where h_0 is the initial membrane thickness.

B. Hemispherical Cap Model & Homogeneous Half-space Model

The hemispherical model assumes the cell membrane to be 2-dimensional and incompressible. The Newtonian fluid in the cell does not affect the shear deformation of the membrane. The contact between the cell and pipette is frictionless. The deformation can be approximated by[9],

$$\Delta P = \frac{2.45\mu}{R_p^2} L_p + C, \quad \left(\frac{L_p}{R_p} \geq 1\right) \quad (3)$$

where ΔP is the increase in suction pressure, R_p is the radius of the micropipette, L_p is the protrusion length, and μ is the shear elastic modulus.

The homogeneous half-space model was based on a homogenous viscoelastic plate[10]. It provides a linear solution, which is suitable for small deformation,

$$L_p^{\Delta} = \frac{L_p}{R_p} = \frac{3\Phi_p}{2\pi}\frac{\Delta P}{E} = \frac{\Phi_p}{2\pi}\frac{\Delta P}{G} = 0.3342\frac{\Delta P}{G} \quad (4)$$

where Φp is a pipette geometric factor and E = 3G is the Young's modulus. Φp can be taken as 2.1 approximately for the punch model.

C. Results & Discussion

Each cell was modeled individually according to their different radius of host cell, parasite and inner/outer pipette. Finite element method was used to simulate the progress of the infected cells in micropipette aspiration.

Fig. 1 shows the experimental results as well as computational modeling of a trophozoite stage malaria infected RBC being aspirated into the pipette at different suction pressure using a finite element program ABAQUS. The rigidity of the parasite was assumed to be far larger than the host cell membrane.

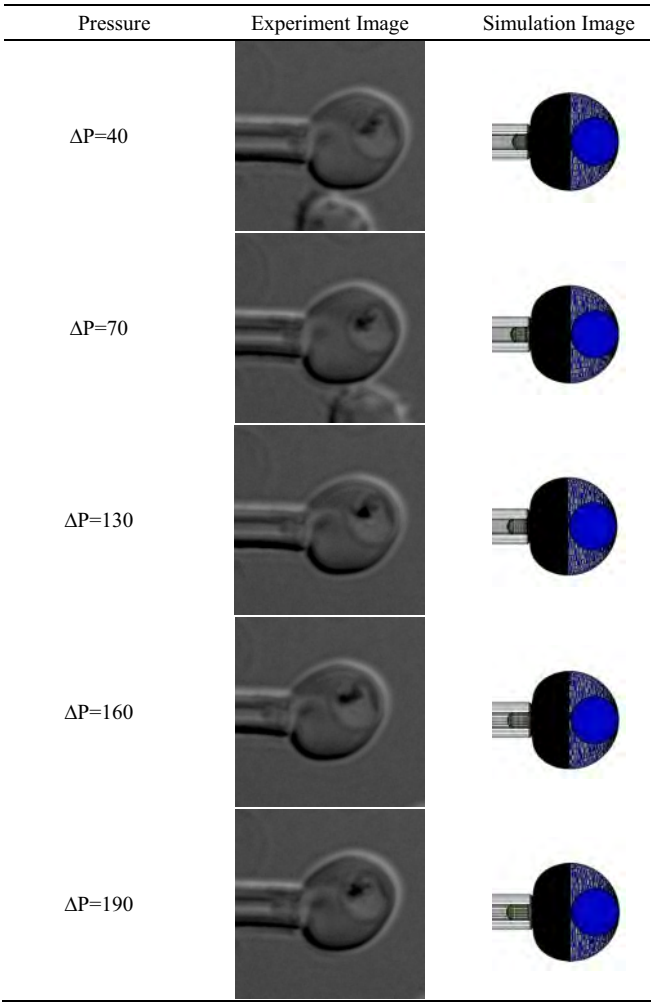


Fig. 1 Comparison between experimental and simulation results of the micropipette aspiration of a specific trophozoite stage malaria infected RBC

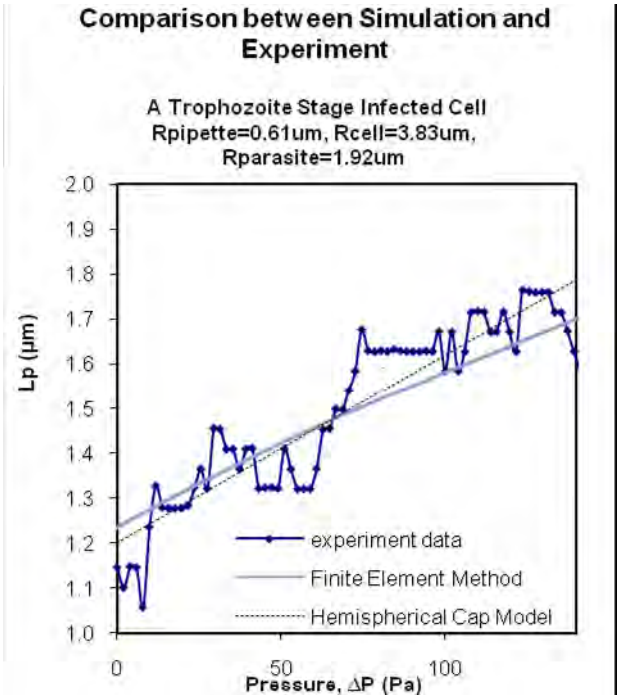


Fig. 2 Comparison between experiment and simulation data of a specific trophozoite stage malaria infected RBC

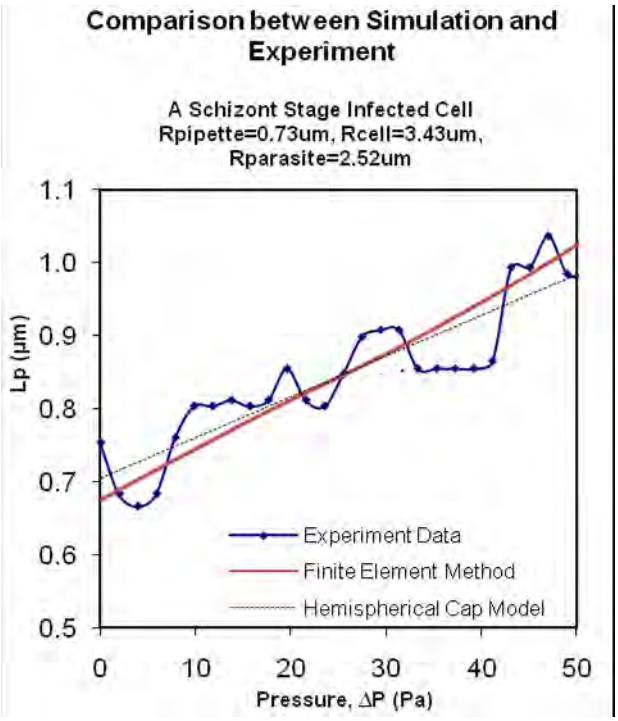


Fig. 3 Comparison between experiment and simulation data of a specific schizont stage malaria infected RBC

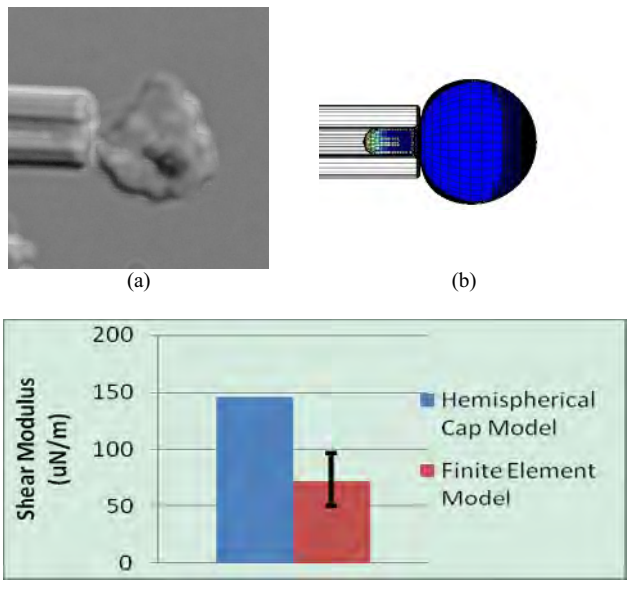
Figures 2 & 3 showed comparisons between simulation and experimental data for two specific cells, in their trophozoite and schizont stage, respectively. The dashed line was the linear trend line of the experimental data. The gradient of the trend line was used for the calculation using the hemispherical cap model. The solid line represents the deformation curve obtained from the finite element method, with the same initial shear modulus calculated using hemispherical cap model. The simulation curves overlap the experimental data.

For all the trophozoite stage cells and most of the schizont stage cells tested, the membrane shear modulus calculated by using the hemispherical model falls in the range of those obtained from finite element simulation, as shown in Table 1.

However, for those schizont stage cells that enclose large parasites, the hemispherical model gives much higher values of shear modulus than that of simulation. An example is shown in Fig. 4. The large parasite itself might

Table 1 Shear modulus of the cell membrane

Cell Stage	Hemispherical Cap Model	Finite Element Method
Trophozoite	28.26 ± 4.74 μN/m	33.96 ± 11.74 μN/m
Schizont	89.19 ± 47.16 μN/m	46.09 ± 12.97 μN/m



(a) (b)

(c)

Fig. 4 A schizont stage malaria infected RBC with enclosed large parasite being sucked into a pipette, (a) in experiment, (b) in finite element simulation, (c) shear modulus calculated from hemispherical cap model and finite element model for this particular cell.

inhibit the host cell from being sucked into the pipette, while the hemispherical cap model attributes the deformation to only the cell membrane. This might lead to a larger shear modulus as obtained using the hemispherical cap model. In this case, homogeneous half-space model was used, and the elastic shear modulus of this schizont stage cell is found to be 162.16 Pa.

III. Conclusions

To summarize, a computational model of the micropipette aspiration of malaria infected RBCs was developed using the finite element program ABAQUS. The proposed multi-component model was able to interpret the deformation-pressure relationship obtained from experiments to the shear modulus of the host cell membrane. This model replicates well with the commonly used hemispherical cap model for mid stage malaria infected RBCs, but predicts different shear modulus for some of the late stage infected RBC, due to the inclusion of the severe internal structural changes occurring during this stage.

Acknowledgments

The authors are grateful to the Singapore-MIT Alliance and the SMART Center for the funding support provided.

References

1. Weiss U (2002) malaria. *Nature* 415:669-669
2. Suwanarusk R, Cooke B M, Dondorp A M, et al. (2004) The deformability of red blood cells parasitized by Plasmodium falciparum and P. vivax. *J Infect Dis* 189:190-4
3. Glenister F K, Coppel R L, Cowman A F, et al. (2002) Contribution of parasite proteins to altered mechanical properties of malaria-infected red blood cells. *Blood* 99:1060-3
4. Nash G B, O'Brien E, Gordon-Smith E C, et al. (1989) Abnormalities in the mechanical properties of red blood cells caused by Plasmodium falciparum. *Blood* 74:855-61
5. Paulitschke M and Nash G B (1993) Membrane rigidity of red blood cells parasitized by different strains of Plasmodium falciparum. *J Lab Clin Med* 122:581-9
6. Suresh S, Spatz J, Mills J P, et al. (2005) Connections between single-cell biomechanics and human disease states: gastrointestinal cancer and malaria. *Acta Biomaterialia* 1:15-30
7. Cranston H A, Boylan C W, Carroll G L, et al. (1984) Plasmodium falciparum Maturation Abolishes Physiologic Red Cell Deformability. *Science* 223:400-403
8. Shelby J P, White J, Ganesan K, et al. (2003) A microfluidic model for single-cell capillary obstruction by Plasmodium falciparum-infected erythrocytes. *Proc Natl Acad Sci U S A* 100:14618-22
9. Shu C, Kuo-Li Paul S, Skalak R, et al. (1978) Theoretical and experimental studies on viscoelastic properties of erythrocyte membrane. *Biophysical Journal* 24:463-87
10. Theret D P, Levesque M J, Sato M, et al. (1988) The application of a homogeneous half-space model in the analysis of endothelial cell micropipette measurements. *J Biomech Eng* 110:190-9
11. Marti M, Baum J, Rug M, et al. (2005) Signal-mediated export of proteins from the malaria parasite to the host erythrocyte. *J Cell Biol* 171:587-92
12. Dong C, Skalak R and Sung K L (1991) Cytoplasmic rheology of passive neutrophils. *Biorheology* 28:557-67
13. Hochmuth R M, Ting-Beall H P, Beaty B B, et al. (1993) Viscosity of passive human neutrophils undergoing small deformations. *Biophys J* 64:1596-601
14. Yeoh O H (1990) Characterization of Elastic Properties of Carbon-Black-Filled Rubber Vulcanizates. *Rubber Chem. Technol.* 63:792-805
15. Suresh S, Spatz J, Mills J P, et al. (2005) Supplementary material S5: computational modeling of optical tweezers stretching of malaria-infected human red blood cells. *Acta Biomater* 1:15-30

Examination of the Microrheology of Intervertebral Disc by Nanoindentation

J. Lukes[1], T. Mares[1], J. Nemecek[2] and S. Otahal[3]

[1] Department of Mechanics, Biomechanics and Mechatronics, Faculty of Mechanical Engineering, Czech Technical University in Prague, Czech Republic
[2] Department of Mechanics, Faculty of Civil Engineering, Czech Technical University in Prague, Czech Republic
[3] Department of Anatomy and Biomechanics, Faculty of Physical Education and Sport, Charles University in Prague, Czech Republic

Abstract — **Micro- and Nanoindentation technique has become a standard method for material testing of mechanical properties recently. Especially, indentation method with Oliver and Pharr theory for an analysis of isotropic elastic materials is very strait forward and become a part of every indenter's software. Some multidirectional indentation analyses have been successfully applied on bone tissues such as cortical osteons and trabecular lamellae to identify their local elastic orthotropic or transverse isotropic properties. Present nanoindenters make possible an acquisition of creep and relaxation data, for that a model of creep or relaxation function can be found in the literature and the viscoelastic material parameters are derived.**

Our previous structural and mechanical studies of porcine intervertebral disc (IVD) and its parts showed clear viscoelastic behavior of tissue. Annulus fibrosus (AF) responses on cyclic, relaxation and ultimate tensile tests proved its viscoelastic manner. Annulus fibrosus is hierarchical structure made up with bundles of collagen fibers within the lamellae. We developed the mathematic geometrical model of IVD, where we respect such a lamellar structure with one lamella as a representative volume element (RVE). Our RVE is supposed to be locally orthotropic with main material directions along the collagen fiber orientation. We try to feed this model on material constants of RVE obtained by nanoindentation and show the nanoindentation technique's state of art in a material description of hierarchical tissues.

Keywords — **Nanoindentation, Intervertebral Disc, Curvilinear coordinates, Viscoelastic tissue**

I. Introduction

Hierarchical organized connective tissue needs to be study in micro- or nanolevels of material to understand their responses to mechanical loading. Scientists look for representative volume element (RVE) of very small sizes and determine the macroscopic material properties of a tissue from it. The single lamella made up by oriented collagen fibrils is mostly considered to be the fundamental structure. Anatomically, IVD consists of end plates (EP), nucleus pulposus (NP) and annulus fibrosus (AF). Structural studies of AF show the alternate light and dark lamellae in the transversal and sagittal cuts. That is caused by the differences of reflected light from the surface of angle-ply lamellar structure with angle of collagen fibers ~120° [1, 2]. Next to the certain type of collagen, which varies in different parts of AF [2, 3], the important structural compound is elastin. Elastin fibers create the elastic sheaths between the collagen lamellae; moreover elastin forms the crossbridges through the lamella [3]. Two compounds composite or laminate is one of the modeling approaches in the literature. Collagen fiber and the matrix possess different elastic properties [4]. Even the analytical model of AF is presented [5] with properties of crossed collagen fibers allowing to move or firmly bounded to each other. Finite element modeling uses the approach of poroelastic continuum to get closer to the reality. The interstitial fluid flows through the AF. The avascular AF tissue needs to be supplied by solutes. It's being realized by two-dimensional flow in EP-AF and NP-AF direction [6, 7]. Decline in EP permeability has a strong influence on IVD dysfunction and its degeneration.

Experiments done on the IVD usually show the viscoelastic behavior. Voigt's model has been used even for frequency dynamic loading for IVD material interpretation [8]. There is evidence of viscoelastic properties of AF e.g. in Young's modulus or absorbed deformation energy dependence on load rate [9, 10, 11]. AF showed the ability to relax during cyclic loading as well in our previous studies [10]. We have created the geometric mathematical model of IVD, which respects the lamellar hierarchical structure of annulus fibrosus. Material parameters were supplied using nanoindentation technique.

II. Methods

A. Samples

We used porcine lumbar AF strips for luminescent microscopy studies (Fig. 1, Fig. 2) and nanoindentation. Transversal wedge-shaped cuts according to [12] and sagittal cuts of lumbar motion segments were done. Thus the specimens contain all the structures employed in intervertebral articulation: vertebral body with apophysis part, cartilaginous end plate, annulus fibrosus and nucleus pulposus. The cuts were 2 up to 4 mm thick and glued on laboratory glass with UHU glue. Surface of samples were polished under the wet condi-

Chwee Teck Lim, James C.H. Goh (Eds.): ICBME 2008, Proceedings 23, pp. 1792–1796, 2009
www.springerlink.com

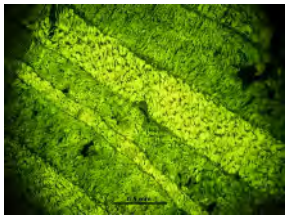


Fig. 1 Lamellar structure of AF under luminescent microscopy, red hematoxilin and eosin stained sagittal slice.[10]

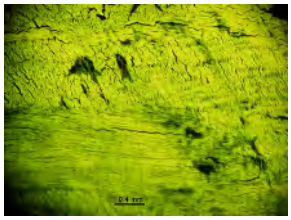


Fig. 2 Crossing of collagen fibers under luminescent microscopy, red hematoxilin and eosin stained frontal slice. [10]

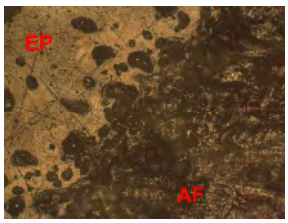


Fig. 3 Light microscopy picture of end plate (EP) and annulus fibrosus (AF) after polishing.

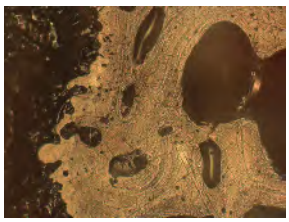


Fig. 4 Lamellar structure of vertebral apophysis. Zeiss light stereo microscope.

tions. It was necessary because of rough surface of cartilaginous EP improper for nanoindentation. Annulus fibrosus lamellae were not visually affected by this procedure. AF lamellae were distinguishable under optical set up of Hysitron TriboLab™ and sufficient wide to place the indent from the optic view to the single lamella.

B. Geometrical and Mathematical Model of IVD

Elastic lamella can be described by classical Hook's law. We supposed the elastic membrane to be isotropic (Fig. 5); however according to Yu et. al [3] elastin fibers in the membrane are oriented in parallel with collagen fibers within viscoelastic collagen lamella. Therefore the models of both elastic and viscoelastic lamellae turn to locally orthotropic case and according to curvilinear coordinates (Fig. 6) the Hook's law is written:

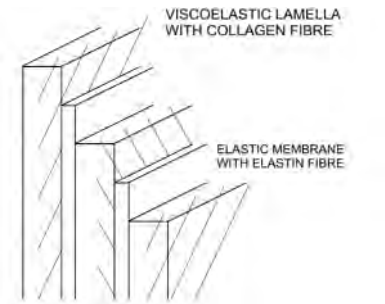


Fig. 5 Sketch of our modeling approach to alternating elastin and collagen lamellae of annulus fibrosus with respect to the literature [1, 3]. One lamella is our geometric representative volume element (RVE) with certain material properties.

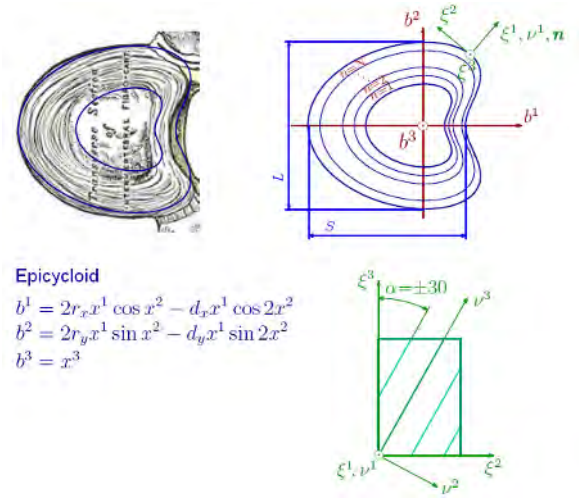
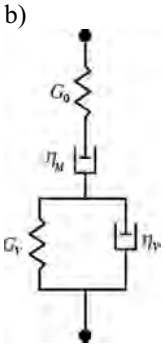


Fig. 6 Annulus fibrosus structure can be mathematically described from the coordinates of local orthotropy ν, local Cartesian coordinate system ξ and global Cartesian coordinate system b, which is transformed to the curvilinear description of IVD shape using parametrical description of epicycloid.

$$\overset{\nu}{\sigma}^{ij} = \overset{\nu}{E}^{ijkl}\,\overset{\nu}{\varepsilon}_{kl} \tag{1}$$

Viscoelastic lamella's material properties are interpreted by common linear dashpot – spring models (Fig. 7). Due to oriented collage fibers there are the plane symmetries in the material. The anisotropic behavior of AF lamella with a value of in-plane Poisson's ratio has been already published [13]. Therefore the 1D (4) viscoelastic properties are expressed by 3D (5) constitutive equations in the tensorial forms:

b)



$$G_0\eta_V\dddot{\gamma} + G_V G_0\ddot{\gamma} = \eta_V\ddot{\tau} + \left(G_V + G_0 + \frac{\eta_V G_0}{\eta_M}\right)\dot{\tau} + \frac{G_0 G_V}{\eta_M}\tau \tag{2}$$

$$C^{ijkl}\ddot{\varepsilon}_{kl} + D^{ijkl}\dot{\varepsilon}_{kl} = \ddot{\sigma}^{ij} + A^{ij}{}_{kl}\dot{\sigma}^{kl} + B^{ij}{}_{kl}\sigma^{kl} \tag{3}$$

Fig. 7 a) Four parameter b) five parameters linear viscoelastic models when ν_0 is taken into account. *A,B,C,D* tensors of constants.

C. Nanoindentation of Viscoelastic Material

It is supposed in this study that the material behavior is dominated by the viscoelastic effects. Several formulations can be employed for this case. We adopted two assumptions: (i) material is linearly viscoelastic and (ii) viscous deformation (creep) is associated only with deviatoric deformations. For such assumptions, analytical solutions of the problem can be derived as was elaborated e.g. by Vandamme & Ulm [14]. Viscoelastic parameters can be obtained directly from the history of indenter displacement measured during the dwell period at which the load is kept constant. The best results are obtained with a 5-parameter combined Kelvin-Voigt-Maxwell creep model (Fig. 7a). The model utilizes the functional formulation:

$$e_{ij} = \int_0^t C^d(t-\tau)\dot{s}_{ij}(\tau)d\tau \tag{4}$$

where t = time; e_{ij} = deviatoric strain tensor; s_{ij} = deviatoric stress tensor; the overdot denotes differentiation with respect to time; and

$$C^d(t) = \frac{1}{G_0} + \frac{1}{G_V}\left(1 - e^{\frac{-G_V}{\eta_V}t}\right) + \frac{t}{\eta_M} \tag{5}$$

is the shear creep function with material parameters G_0, G_V, η_V, η_M. The volumetric behavior was considered as purely elastic. Young's modulus E_0 and associated shear modulus G_0 were estimated from the unloading branch of the load-displacement plot by the standard Oliver & Pharr method [15]. Poisson's ratio ν_0 was supposed to be time independent for the given material.

III. Results

A. Nanoindentation

Trapezoidal loading-dwell-unloading nanoindentation curve was set for load control mode of testing. Maximal load P_{max}= 4000μN was applied in 10s and hold for 30s during the dwell period. Unloading segment for evaluation of elastic modulus and shear modulus G_0 respectively took 10s and Poisson's ratio was ν_0=0.4 in case of endplate. The same time segments were used for nanoindentation of AF lamella; however the force value was P_{max}= 10μN only. Indentation of viscoelastic lamella was comprehended as 1D problem with in-plane anisotropic Poisson's ratio ν_0=2. The value of ν_0 was chosen from parametric study of the best fit of creep data (Fig. 9). In-plane Poisson's ratio has no bounded value in anisotropic case of material. Material parameters calculated from the data fit (Fig. 1) are presented in the table (Tab. 1).

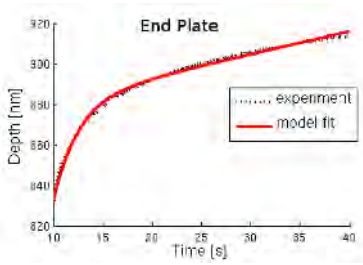


Fig. 8 Fit of dwell period data from nanoindentation of cartilaginous endplate using Vandamme and Ulm [14] five-parameter linear viscoelastic model.

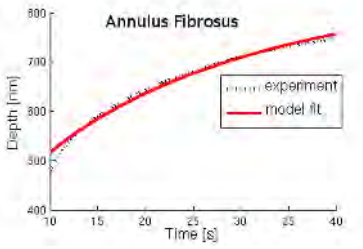


Fig. 9 Fit of creep data obtained by nanoindentation of annulus fibrosus. The five parametric model derived by Vandamme and Ulm [14] was used.

Tab. 1 Material parameters determined by five parameters model fit of nanoindentation creep data.

End Plate				
ν_0 [-]	G_0 [GPa]	η_M [GPa.s^{-1}]	η_V [GPa.s^{-1}]	G_V [GPa]
0.4	1.56	274.07	4.32	1.68
Annulus Fibrosus				
ν_0 [-]	G_0 [GPa]	η_M [GPa.s^{-1}]	η_V [GPa.s^{-1}]	G_V [GPa]
2	-0.0176	$4.24.10^6$	0.3761	0.0277

B. Model

Our computational model uses the theory of small deformation and nucleus pulposus as highly pliant elastic isotropic material.

$$E^{abcd}_{pulposus} = \lambda g^{ab} g^{cd} + \mu g^{ac} g^{bd} + \mu g^{ad} g^{bc} \tag{6}$$

where λ, μ are Lame's constants and g^{ab} is the contravariant metric tensor in computational curvilinear coordinate system, x. The principle of total potential energy minimum was used in calculation [16]. The tiny geometry of endplates had no significant contribution to total potential energy; therefore they have been removed. In our model of intervertebral disc consists of lamellar annulus fibrosus and nucleus pulposus, the deformation is prescribed as a rigid movement of the rigid plates, which represents the vertebral bodies. The deformations of IVD were calculated in GNU Octave using the above principles (Fig. 10, Fig. 11, Fig. 12).

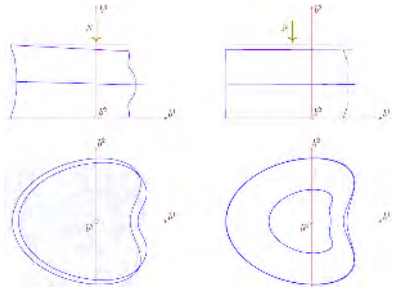


Fig. 10 Model deformation from axial and nonaxial pressure load. Buckling is always present in posterior region, which indicates the weak part of IVD.

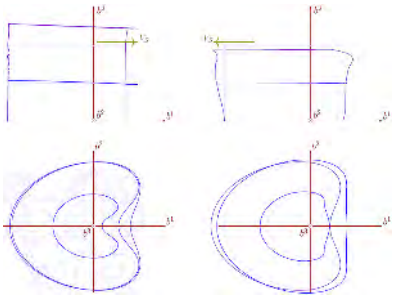


Fig. 11 Sagittal shear load applied over the top plate of IVD shows again the major deformation in posterior part of IVD.

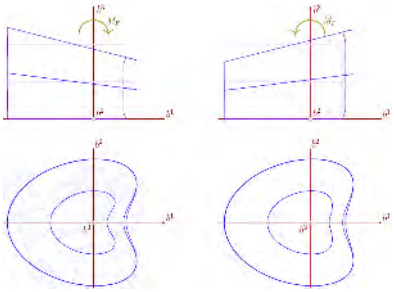


Fig. 12 Bending in frontal plane caused deformation only in posterior part. Anterior profile of IVD remained strait; only mass shift occurred.

IV. Discussion and Conclusions

Annulus fibrosus is very soft and sticky material; therefore it's tricky to find an initial contact and loading curve is affected by adhesion forces. Swelling of AF lamellae immediately after cutting caused the rough surface. Swelling also occurs even when the samples are placed in the water or during the testing in the physiological condition. In the contrary the surface of cartilaginous endplate can be prepared nicely and perform the nanoindentation testing without any problem. Viscoelastic model derived by Vandamme and Ulm [14] fits well measured data. However; there's still missing a solution for analyzing the viscoelastic anisotropic material, which AF lamella is the case. Multidirectional indentation test for one lamella seems to be feasible. Moreover the orientation of collagen fibers within the sample can be estimated, which gives us the main material directions.

Mathematical models can work with spatial material properties easily. They need to be fed with material constants in tensorial interpretation. Of course the resulting deformations (Fig. 10-12) are not physiological due to missing ligaments (posterior and anterior longitudinal ligament), muscles and the effect of spine column. However our geometrical and mathematical model demonstrates the usage of chosen RVE. This approach brings us fast to the first results and show the posterior part of IVD as the weakest region of IVD, which corresponds to the literature. IVD model was considered to be uncompressible, which explains the mass shift over the IVD with bulging only in posterior part.

Acknowledgment

Sponsored by grant MPO CZ, FT-TA3/131 and Ministry of Education of the Czech Republic MSM 6840770003.

References

1. Marchand, F., Ahmed, A. M. Investigation of the laminate structure of lumbar disc annulus fibrosus. Spine 15 (5), 402-410, 1990.
2. Adams, M. A., Bogduk, N., Burton, K., Patricia, D. Freman, B. J. C. The Biomechanics of Back Pain, 2nd Edition. Elsevier. 2006
3. Yu, J., Peter, C., Roberts, S., Urban, J. P. G. Elastic fibre organization in the intervertebral discs of the bovine tail. Journal of Anatomy 201, 465-475 (11). 2002
4. Iatridis, J. C., Gwynn, L., Mechanisms for mechanical damage in the intervertebral disc annulus fibrosus. Journal of Biomechanics 37 (8), 1165-1175. Aug. 2004
5. McNally, D., Arridge, R. An analytical model of intervertebral disc mechanics. Journal of Biomechanics 28, 53-68 (16). January 1995
6. Riches, P. E., Dhillon, N., Lotz, J., Woods, A. W., McNally, D. S. The internal mechanics of the intervertebral disc under cyclic loading. Journal of Biomechanics 35 (9), 1263-1271. Sep. 2002
7. Ayotte, D. C., Ito, K., Tepic, S. Direction-dependent resistance to flow in the endplate of the intervertebral disc: an ex vivo study. Journal of Orthopaedic Research 19 (6), 1073-1077. 2001
8. Izambert, O., Mitton, D., Thourot, M., Lavaste, F. Dynamic stiffness and damping of human intervertebral disc using axial oscillatory displacement under a free mass system. European Spine Journal 12 (6), 562-566. Dec. 2003
9. Yngling, V., Callaghan, J., McGill, S. Dynamic loading affects the mechanical properties and failure site of porcine spines. Clinical Biomechanics 12 (5), 301-305 (5). July 1997
10. Lukes, J., Otahal, M., Otahal, S. Microstructure and mechanical characteristic of intervertebral disc and annulus fibrosus. In: Human Biomechanics 2006. Czech Society of Biomechanics. November 2006
11. Iatritidis, J. C., MacLean, J. J., Ryan, D. A., Mechanical damage to the intervertebral disc annulus fibrosus subjected to tensile loading. Journal of Biomechanics 38 (3), 557-565. Mar. 2005
12. Roberts, S., Eisenstein, S. M. The cartilage end-plate and intervertebral disc in scoliosis: Calcification and other sequelae. Orthopaedic Research 11, 5 (January 1993), 747-757.
13. Elliot, D. M., Setton, A. L. Anisotropic and inhomogeneous tensile behavior of the human annulus fibrosus: Experimental measurement and material model predictions. ASME, Journal of Biomechanical Engineering 123. Jun 2008
14. Vandamme, M., Ulm, F.-J. Viscoelastic solutions for conical indentation. International Journal of Solids and Structures 43 (10), 3142-3165. May 2006

15. Oliver, W. C., Pharr, G. M. An improved technique for determining hardness and elastic modulus using load and displacement sensing indentation experiments. Journal of Material Research 7, 1564-1583. 1992
16. Mares T. Analysis of thick-walled anisotropic elliptic tube. Bulletin of Applied Mechanics 1, 29-38 (2007)

Author: Jaroslav Lukes
Institute: Department of Mechanics, Biomechanics and Mechatronics
Street: Technicka 4
City: Prague
Country: Czech Republic
Email: jaroslav.lukes@fs.cvut.cz

Effects of Floor Material Change on Gait Stability

B.-S. Yang[1,2] and H.-Y. Hu[1]

[1] Department of Mechanical Engineering, National Chiao Tung University, Hsinchu, Taiwan
[2] Brain Research Center, National Chiao Tung University, Hsinchu, Taiwan

Abstract — **Falls are the leading cause of unintentional injuries in the elderly in Taiwan and many industrial countries, and commonly occur at home. To reduced fall-related socio-economic cost, the goal of this study is to identify suitable floor materials on which the elderly could have stable gait. We tried to quantify the gait stability under different floor conditions in this paper. Six healthy subjects (aged 20-23 yrs) have been tested. A six-camera motion capture system and two force platforms were used to obtain kinematics and kinetics of whole body during gait on different floor conditions. In consistent conditions (same floor materials on the whole walkway), the lower the coefficient of friction (COF) of the floor material, the smaller values of cadence and required COF (RCOF) under subjects' feet, and the larger values of gait stability-related variables, such as stance time, stride time, and step width, during walking at self-selected comfortable speed ($p<0.05$). As compared with the consistent conditions, walking from a material with higher COF to another with lower COF would induce larger ankle dorsi/plantar-flexion angle at heel contact. In addition, the peak RCOF during the stance phase was higher after the floor material change. The results of this study suggest that double support time, stride velocity, and mean gait velocity might be good indicators of gait stability. Walking from one floor material to another with lower COF may induce higher risk of falls than walking on a floor with consistent materials. Therefore, avoiding or using caution, especially for the elderly, when walking from one floor material to another with lower-COF is suggested.**

Keywords — **Fall, Gait stability, Floor materials, Floor transition, Coefficient of friction**

I. Introduction

Falls are the leading cause of unintentional injuries in the elderly in Taiwan and many industrial countries and commonly occur at home [1]. To reduced fall-related socioeconomic cost, the goal of this study is to identify suitable floor materials on which the elderly could have stable gait, i.e. less likely to fall. We will quantify biomechanical gait variables of young subjects and compare their movement and balance during walking on different floor materials. We especially focus on the condition of the gait transition from one floor material to another.

II. Materials and Methods

A. Subjects

Six healthy young adults were recruited (mean 21.3 years, 1.71m, 63.54Kg) from the general student population at National Chiao Tung University. All subjects have no history of neurological or orthopedic diseases and any difficulties that could obstruct normal locomotion. A written informed consent was obtained from every subject.

B. Experimental design

Four commonly-used floor materials in Taiwan – plane-wood (PW), rough-wood (RW), rough-ceramic tile (RC), and polyvinyl chloride (PVC) – were employed for examining gait stability. English XL (William English, Inc., Alva, Florida, USA) was used with rubber test fragment to measure the coefficient of friction (COF) of the floor materials. To study the change of gait stability while walking from one floor material to another, we used different combinations of the above-described floor materials to created *consistent* conditions (same floor materials on the whole walkway) and *transition* conditions (from one material to another) of walkway. In the consistent condition subjects walked on dry plane-wood, dry rough-ceramic tile, or wet rough-ceramic tile. In the transition condition, subjects walked from dry plane-wood to PVC, from dry rough-wood to PVC, or from dry rough-ceramic to PVC. The consistent condition was treated as a baseline condition for comparing the change of gait stability after transition.

Two force platforms (Bertect corporation, Columbus, Ohio, USA) were placed underneath the middle of the walkway (right after the interface of two floor materials in the transition conditions). A six-camera motion capture system (BTS Bioengineering, Garbagnate Milaness, Italy) and the force platforms were used to obtain kinematics and kinetics of whole body during gait on different floor conditions (Fig. 1). Twenty-two 15mm-diameter markers were placed on the bony landmarks of subjects. The positions of markers were based on the Helen-Hayes marker set [2] with seven additional markers. The seven additional marker positions were both sides of shoulders, femoral great trochanter, external condyle of tibia and the 7th cervical verte-

Chwee Teck Lim, James C.H. Goh (Eds.): ICBME 2008, Proceedings 23, pp. 1797–1800, 2009
www.springerlink.com

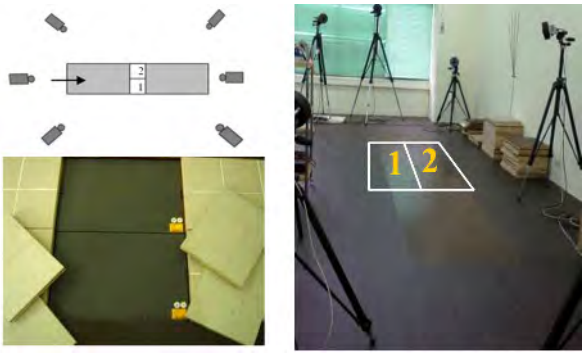


Fig. 1 Experimental set-up for examining gait stability experiment. Left top: sketch of camera positions and walkway. Left bottom: force plates and changeable floor materials. Subjects start walking from the window-side (right).

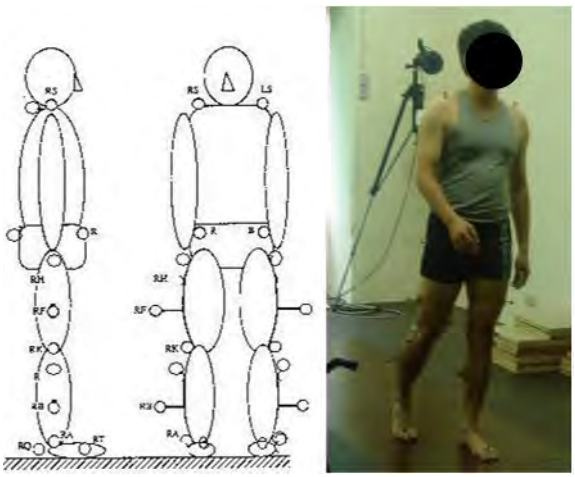


Fig. 2 Diagram of marker set (left) and the actual condition (right)

bral bone (Fig. 2). The motion capture system and force platforms were synchronized and sampled at 250Hz and 1000Hz, respectively.

During the experiment, subjects were asked to walk on a 6-m long and 0.8-m wide walkway with barefoot; the floor materials over the walkway was changeable (Fig. 1). Prior to the experiment, subjects practiced on the walkway to identify their preferred walking speed. The preferred cadence (step/min) was then determined for each subject, and audio cues were used to keep the subject walking at the same preferred cadence throughout the experiment and subjects were asked to also keep the step length the same as at the preferred walking speed. To ensure that subjects achieved steady state of walking when stepping on the force platforms, the starting line was set at least 3.0m away from the force platforms on the walkway.

The test order of the floor conditions were randomized. Twenty trials were tested under each condition. Trials with missing or incomplete data were excluded from data analyses. The primary variables investigated here include foot angle at heel strike, peak required coefficient of friction (RCOF), and mean (gait) velocity. T-tests were used to compare the means in different test conditions. $P<0.05$ was considered statistically significant unless otherwise stated.

III. Results

A. Coefficient of friction

The coefficients of friction (COF) of the tested floor materials are shown in Fig. 3. All COFs were above 0.7 when the surface was dry and clean. However, in water-spilled (wet) condition, only COFs of rough-wood and plane-ceramic tile were larger than 0.6. The COF of wet rough-ceramic tile was only 0.29.

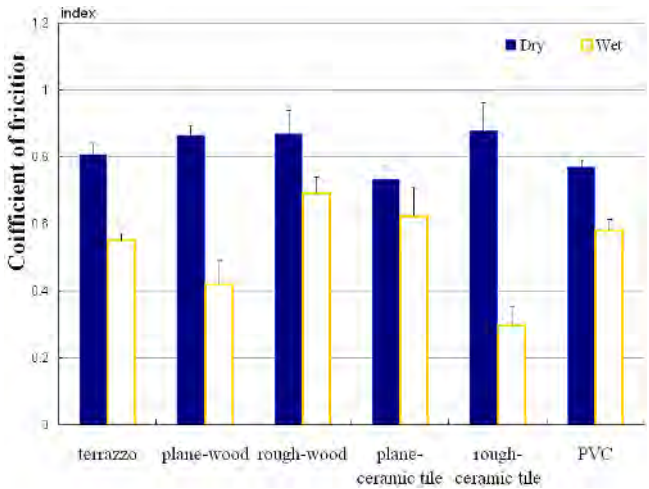


Fig. 3 Coefficient of friction of the tested floor materials

B. Gait stability

Table 1 shows the changes of some investigated variables in the consistent conditions. The results showed that floor materials had significant effects on most investigated gait variables: stance phase, double support time, and stride time were longer, but the values of cadence, step length, stride velocity, and mean velocity were smaller on a lower-COF (wet) floor than on a higher-COF (dry) floor ($p<0.05$).

Compared with walking under the consistent condition of plane-wood floor, the foot angle at heel strike decreased when walking from a higher-COF floor material to a lower-COF floor: 31.5% decrease in foot angle while walking

Table 1 Time-distance variables of consistent condition (paired t tests comparing RC with water-spilled RC condition: *: p < 0.05; **: p < 0. 01)

Materials (COF)	RC (0.87)	Water-spilled RC (0.29)
Stance Phase* (%)	61.5	62.1
Swing Phase* (%)	38.2	37.5
Double Support** (%)	11.6	12.2
Stance Phase** (s)	0.75	0.77
Swing Phase (s)	0.47	0.46
Stride Time** (s)	1.22	1.23
Cadence* (step/min)	98.3	97.3
Step Length* (m)	0.56	0.54
Stride Length (m)	1.21	1.18
Step Width (m)	0.172	0.172
StrideVelocity*** (m/s)	0.991	0.954
Swing Velocity (m/s)	2.279	2.227
Mean Velocity** (m/s)	0.965	0.931

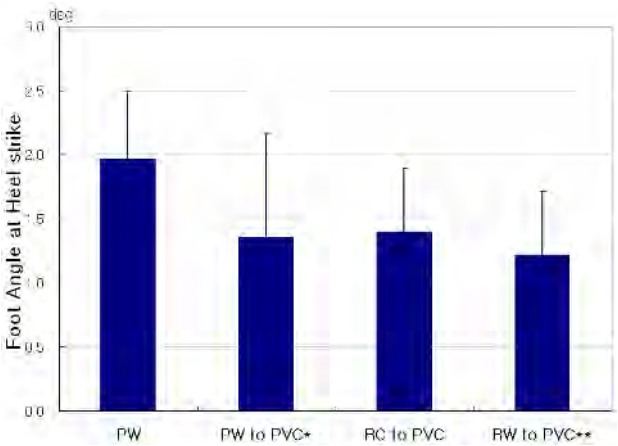


Fig. 4 Foot angle at heel strike in the transition conditions (paired t tests comparing PW with transition condition: *: p < 0.05, **: p < 001)

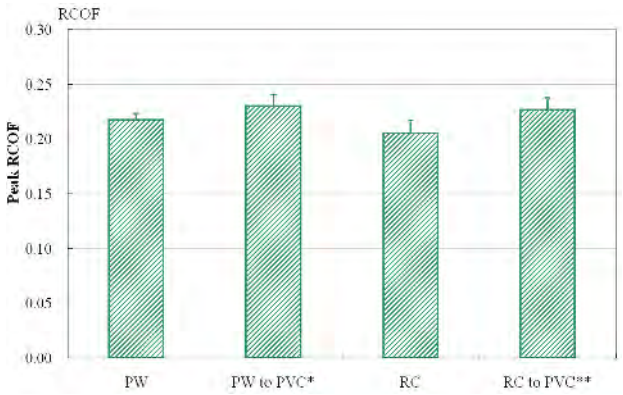


Fig. 5 Peak RCOF in different floor conditions (paired t tests comparing PW with transition condition: *: p<0.05; **: p<0. 01)

from plane-wood to PVC (p<0.05); 28.9% decrease from rough-ceramic to PVC; 38.1% decrease from rough-wood to PVC (p<0.01) (Fig. 4). Peak required COF (RCOF) values were greater in the transition condition than in the consistent condition: 5.8% increase in the peak RCOF when walking from plane-wood to PVC (p<0.05); 10.4% increase from rough-ceramic tile to PVC (p<0.01). (Fig.5).

IV. Discussion

In the consistent conditions, the double support phase was longer, and the stride velocity and mean velocity were smaller while walking on a wet floor as compared to those on a dry floor. These results are consistent with the findings from previous studies [3, 4]. The three investigated variables which show the most significant effects of floor conditions – double support time, stride velocity, and mean velocity – might be good indicators for gait stability.

Several studies have reported that individuals would adjust gait to reduce RCOF in order to lower the risk of falls on slippery (low-COF) floor [5, 6]. In this study we further show that walking from one material to another with lower COF could cause larger peak RCOF than walking on a floor without material change, which might lead to higher risk of falls. Furthermore, older adults usually have longer reaction time and less accurate sensory feedback, which increase the likelihood of slips and falls [7]. Therefore, avoiding or using caution when walking from one floor material to another, especially one with lower-COF, is suggested. The change of floor materials should be avoided for the living environment of the elderly.

V. Conclusions

The results of this study indicate that double support time, stride velocity, and mean gait velocity might be good indicators of gait stability. Walking from one floor material to another with lower COF may induce higher risk of falls than walking on a floor with consistent materials.

Acknowledgment

The authors thank the financial support from Taiwan National Science Council grant no. NSC96-2627-E-009-001.

REFERENCES

1. Directorate General of Budget, AaS, Executive Yuan (2006). Survey of Social Development Trends: Health and Safety, Directorate General of Budget, Accounting and Statistics, Executive Yuan: Taipei City.
2. Kadaba, MP, Ramakrishnan, HK, and Wootten, ME (1990). Measurement of lower extremity kinematics during level walking. J Orthopaed Res 8: 383-392.
3. Lockhart, TE, Spaulding, JM, and Park, SH (2007). Age-related slip avoidance strategy while walking over a known slippery floor surface. Gait Posture 26: 142-149.
4. Cham, R, and Redfern, MS (2002). Changes in gait when anticipating slippery floors. Gait Posture 15: 159-171.
5. Bunterngchit, Y, Lockhart, T, Woldstad, JC, and Smith, JL (2000). Age related effects of transitional floor surfaces and obstruction of view on gait characteristics related to slips and falls. Int J Ind Ergonom 25: 223-232.
6. Chou, Y, You, J, Lin, C, Su, F, and Chou, P (2000). The Modified Gait Patterns during Stepping on Slippery Floor. Chin J Mech 16: 227-233.
7. Lockhart, TE, Woldstad, JC, Smith, JL, and Ramsey, JD (2002). Effects of age related sensory degradation on perception of floor slipperiness and associated slip parameters. Safety Sci 40: 689-703.

Author: Bing-Shiang Yang
Institute: National Chiao Tung University
Street: EE427, 1001 University Road
City: Hsinchu
Country: Taiwan
Email: bsyang@mail.nctu.edu.tw

Onto-biology: Inevitability of Five Bases and Twenty Amino-acids

K. Naitoh[1]

[1]Waseda University, Faculty of Science and Engineering, Tokyo, Japan

Abstract — **The inevitability of only five nitrogenous bases, twenty amino acids, and various proteins in living beings is systematically revealed on the basis of physics as the weft and molecular biology as the warp. First, we focus on fact that symmetry and asymmetry coexist in biomolecules. The nitrogenous bases that form nucleic acids have two large purines (A and G) and three small pyrimidines (C, T, and U), for an asymmetric ratio of molecular types of around 2:3, while those forming DNA have a symmetric ratio of 1:1, with two purines of A and G and two pyrimidines of C and T. Size ratios of around 2:3 are seen in base pairs such as A:T and G:C in DNA and also 1:1 in RNA. Chargaff's rule shows that the frequencies of purines and pyrimidines in double-strand DNA are deterministic with a symmetric ratio of 1:1, while the asymmetric frequency ratios of purines and pyrimidines in RNA are between 1:1 and approximately 2:3, which is fairly stochastic. Thermo-fluid dynamics clarifies the reason why a 1:1 deterministic symmetric ratio and a slightly stochastic asymmetric ratio of around 2:3 exist together. This analysis also reveals the further reason why molecules such as the five bases and twenty amino acids are naturally selected in living beings. Finally, it is shown that microorganisms such as yeast also undergo symmetric and asymmetric cell divisions, with size ratios between 1:1 and 2:3, and that human beings also have left-right asymmetric organs such as the liver and the heart and symmetric ones such as the lungs and kidneys. The physical principle is clarified for determining whether organs become asymmetric or not.**

Keywords — **Bases, Amino acids, Cyto-fluid dynamic theory, Morphogenesis, and Asymmetry.**

I. Introduction

Anfinsen has shown that thermodynamics can explain the stable structures of proteins. [1] However, the inevitability of the sizes and frequencies of biological monomers and polymers has not been revealed so clearly, although the number of fundamental blocks is limited to only five bases and twenty types of amino acids.

Computer simulations of molecular dynamics and quantum chemistry can not analyze quantitatively the inevitability of biomolecules swimming in lots of water molecules, because computer power is still insufficient.

In this paper, thought experiments based on thermo-fluid dynamics and molecular biology clarify the inevitability of the sizes, the number of types, and the frequencies for the fundamental building blocks such as nitrogenous bases and amino acids, larger molecules such as RNA and proteins, biomolecules which are not coded by DNA, and cells. They are described in the following sections, in ascending order.

II. Elements

We classify the five bases of adenine (A), guanine (G), cytosine (C), thymine (T), and uracil (U) into two groups--purines and pyrimidines. Purines (A and G) have a relatively large size, while pyrimidines (C, T, and U) are small. The asymmetric size ratio of the main rings in purines and pyrimidines of around 3:2 naturally leads to an asymmetric number of types, i.e., "two" types of purines and "three" types of pyrimidines. This is understood from the mass conservation law with respect to molecular weight, that is, from the fact that the main rings of purines have "nine" molecules of carbon and nitrogen, while "six" molecules form the main rings of pyrimidines (Fig. 1).

Some people may feel that there is a trick in this logic. However, phenomena, including living beings, can not escape from the constraint of mass conservation. (There is also a 2:3 ratio in immune globulin (IgX). Two types of large immune globulines (IgM and IgE) and three small ones (IgG, IgD, and IgA) are naturally selected. See Fig.1.)

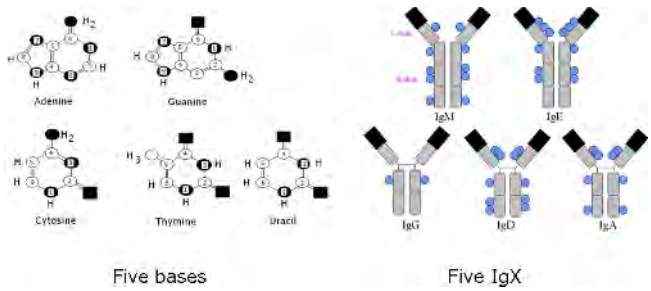


Fig. 1. Similarity between five bases and five immune globulins.

III. Base pairs and nucleic acids

This grouping specifically refers to the asymmetric size ratio of purines and pyrimidines of around 3:2 in their hydrogen bonds within base pairs (in Watson-Crick base pairs), although base pairs with a symmetric size ratio of 1:1 are often observed in RNA.

Chwee Teck Lim, James C.H. Goh (Eds.): ICBME 2008, Proceedings 23, pp. 1801–1804, 2009
www.springerlink.com

In our previous reports based on the cyto-fluid dynamics theory [2], we revealed the reason why base pairs are in a fusion of asymmetry of around 2:3 and symmetry of 1:1. [2, 3] We consider two nitrogenous bases such as a pair consisting of a purine and a pyrimidine, connected by hydrogen bonds in a large quantity of water. We assume that each nitrogenous base and the water molecules around the base act as a flexible continuum spheroid particle (parcel), in which the flow is irrotational. Further, we assume that the spheroid particle size is proportional to the size of each base. Based on these assumptions, we derive a deterministic momentum equation describing particle deformation. When a small disturbance is given for two connected flexible particles, the dimensionless deformation x of each particle dependent on dimensionless time t can be described as

$$d^2x/dt^2=(e-1)(dx/dt)^2+(e^3-3)x+q(t), \quad (1)$$

where parameter e and term $q(t)$ denote the size ratio of the two particles connected at the equilibrium condition and the time-dependent force generated by the other connected particle, respectively. When the particles are spheres at the equilibrium condition, x is zero. A symmetric ratio of 1.0 makes the first term on the right-hand side of the equation zero, while an asymmetric ratio of $\sqrt[3]{3}$ (around 1.5) makes the second term zero. (These two ratios appear as the n-th root of n with n = 1 and n = 3). The deformation speed is smaller for e = 1.0 and $\sqrt[3]{3}$ than for the other values of e. Life is relatively stable (quasi-stable), when the size ratio of hydrogen-bonded nitrogenous bases takes the values of 1.0 and $\sqrt[3]{3}$ for n=1 and 3, respectively. [2, 3, 4]

The present quasi-stability maintains the hydrogen-bonded pairs of two identical bases and of purine-pyrimidine pairs just after the small disturbance affects the pairs. (It is stressed that the flow inside the flexible continuum particle is potential flow, i.e., irrotational flow, because impulsive disturbances generate potential flow at the start of deformation motions. Equation 1 also describes only base pairs without water molecules, because even a base will deform slightly when disturbances enter and because the governing equation for the elasticity theory of solid materials is also identical to that in potential flow.)

Next, let us look at nucleic acids. We examined the databases on RNA. [3, 4] The average frequency ratio of purines and pyrimidines in over five-thousand types of transfer RNA (tRNA) sequences is actually about 1:1.10. The databases on ribosomal RNA (rRNA) show a value of around 1:1.30, which is relatively larger than that for tRNA.

This value of less than 1.50 for the frequency ratio of purines and pyrimidines in RNA stems from the following reason. Because the frequency ratio of purines and pyrimidines in the stem of tRNA is approximately 1.0, RNAs having longer stems bring the mean value closer to 1.0. Ribosomal RNAs show a value of around 1.30, which is larger than that of tRNAs, because rRNA has a shorter stem than tRNA. The variation in the frequency ratio of purines and pyrimidines in RNA is related to the variety of stem lengths and leaf sizes in RNA, i.e., various functions of RNA. [3, 4]

IV. Inevitavility of only five bases

As was shown in the previous section, tRNA has a relatively longer stem than rRNA, because the frequency ratio of purines and pyrimidines is closer to 1.0. Richer G + C conditions for stable hydrogen bond connections in base pairs also stabilize the longer stems of base pairs in tRNA. [5] (This tendency of rich G-C pairs in tRNA is related to the fact that the A-U base pair has only two hydrogen bond connections, whereas the G-C base pair has three.) In fact, databases show that the frequency ratio of G and C in tRNAs is larger than that in rRNAs. [5]

Two types of base pairs (A-U and G-C) are necessary in order to change the stem length. In other words, four types of bases, A, U, G, and C, are necessary for generating two types of RNAs. DNA, with more stable information storage than RNA, needs a fifth base, T.

Next, we consider the possibility of having more than five base types. *Let us recall that modified bases such as inosine and ribosylthymine are often in RNAs. Inosine is slightly modified from adenine, while ribosylthymine is close to uracil. If a giant base, extremely heavier than the five bases, enters into DNA, the giant base will break the spiral shape and also bring severe variations in the loop size of anti-codons in tRNA, leading to unstable connections with codons. Thus, the five bases are building blocks, although slight modifications are possible.*

V. Energy carriers

As RNAs in living beings have richer GTPs and CTPs due to their relatively stronger hydrogen bond connections, the redundant free ATPs ad UTPs are thrown outside the RNAs. [5] This consideration based on mass and energy conservation laws provides an outline of the inevitability of ATP as an energy carrier. *ATP runoff from RNA resembles the joker (or remaining unmatched queen) in the card game of Old Maid.*

Redundant UTP can be used for generating polysaccharide for producing cell walls, because UTP is also an energy carrier for generating cell walls. [5] (In the pre-biotic proc-

esses such as an RNA world with high temperatures, cell surfaces will also be produced with this mechanism.)

VI. Inevitability of twenty amino acids

The anti-codon inside the leaf of tRNA permits a maximum of sixty-four patterns, because A, U, G, and C are possible for each of the three loci (4 x 4 x 4 = 64). Because the third locus inside the anti-codon has a relatively weak connection with the codon, the minimum number of patterns is sixteen. This implies that the number of amino acids is between sixteen and sixty-four. The weak connection at the third locus permits twenty types of amino acids, a little more than sixteen. *It is emphasized that clarification of the leaf size with an anti-codon of three loci leads to the general inevitability of twenty amino acids*. [6]

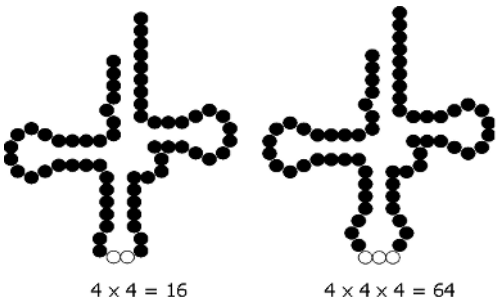


Fig. 2. Relation between leaf sizes and amino acids.

The reason why the size of the leaf having an anti-codon of three bases is inevitable is related to the fact that the frequency ratio of purines and pyrimidines in tRNA is between 1.0 and 1.5, as was explained in Section III. (Purine and pyrimidine pairs do not easily form in the presence of only one type of base. An extremely large frequency ratio, say, far larger than 1.5, can not produce the stem in tRNA It is also well-known that, in DNA without leaves, purines and pyrimidines have the same frequency. This is the well-known Chargaff's rule. The fact that tRNA has loops (leaves) in the clover structure makes it possible for asymmetric frequency ratios of purines and pyrimidines to exist, because the loci inside the leaves (loops) are free from hydrogen-bonded connections. [3, 4])

Both hydrophilic and hydrophobic amino acids exist in proteins. If we employ the classification of R-side chain grouping, the frequency ratios of hydrophilic and hydrophobic amino acids in proteins are also asymmetric in many cases, between 1:1 and approximately 2:3. [7] Asymmetric symbiosis of hydrophilic and hydrophobic molecules also produces the complex convexoconcave shapes of proteins, as hydrophobic parts are often folded inside proteins. (Amino acids have various molecular weights. The frequency ratios of hydrophilic and hydrophobic amino acids in proteins are more stochastic than those of purines and pyrimidines in nucleic acids. Information carriers such as nucleic acids bring determinism, while molecules related to functions such as proteins are more stochastic.)

VII. Cells and organs

Symmetric and asymmetric size ratios are also observed at the cell level of microorganisms. Homma et al. reported the details of the cell size distribution. [8] It is stressed that the size ratio of larger and smaller cells after division is also mostly between 1.0 and 1.5. We also note the fusion of symmetric and asymmetric divisions of cells such as yeast.

This cell size ratio between 1.0 and 1.5 is inevitable, because cells are mathematically similar to flexible particles, including the base, dominated by convection and surface tension. [2, 3] Equation 1 also describes the small deformation and motions of connected cells, assuming that the parameter e denotes the size ratio of two cells connected under equilibrium conditions. Then, the second term on the right-hand side of Eq. (1) shows that *a small surface deformation entering a cell leads to an asymmetric division at an asymmetric size ratio of* $\sqrt[3]{3}$ *(around 1.5)*. [2, 6] (Losick et al. reported that small fluctuations of cells are important for determining the morphogenetic processes. [9] Living microorganisms such as bacteria move round, although dead ones are stationary. Small deformations and fluctuations are important for living beings. Small fluctuations of molecules are also important for fitting drug molecules into the target molecule.)

Let us consider an aggregation of connected cells. Inner cells inside the aggregation receive forces from many directions due to the presence of other cells in a homogeneous field. Inner cells move relatively with the deformation of the cell surface. However, outer cells close to the surface are relatively difficult to deform, because one part of the cell is free without any connection to other cells. *As a result, the inner cells divide asymmetrically.*

The present analysis also clarifies the reason why the left-right symmetric distribution of arms and legs is observed in outward appearance, although the inner body, including the heart and the liver, is asymmetric.

It is posited that the lungs are symmetric because of contact with the outer air during breathing. The kidneys are symmetric because of continuous contact with outer water in the form of urine owing to the fact that the amniotic fluid of the fetus is fetal urine.

The reason why vertebrae in the center of mammals are symmetric is related to the fact that water containing Ca ions enters the inner region when gastrulation occurs, because the primordial gut is also in the outer part of water.

Blood vessels are closed and must not be open to the outer world in order to prevent virus infections. The heart and liver filled with blood are asymmetric due to this process similar to buckling behavior. (Details are in Ref. 12.)



Fig. 3 Asymmetric liver and symmetric kidneys.

It is also stressed that the center and outer parts of DNA have symmetric arrays of bases such as the centromere and telomeres, while the middle part of DNA is asymmetric.

Cell deformation also brings deformations of molecules such as DNA and proteins, which lead to gene changes. Asymmetric cells promoted by fluid-dynamical stability are fixed through evolution by the asymmetry at the molecular level.

VIII. Conclusion and Outlook

Fusion of ratios of 1:1 and approximately 2:3, described by the unified number of the n-th root of n, can be observed in nitrogenous bases. The inevitability of only five bases comes from the main constraints of mass and momentum conservation laws. The fact that the G+C rate in RNA determines the leaf size is related to the energy conservation law. The dominant constraint for each molecule and each part varies in living beings. The sizes and frequencies of amino acids and proteins are a little more stochastic. Literally, the molecules for information storage may be relatively deterministic, while ones having functions are relatively stochastic. Immune globulins are strongly related to information, because they can distinguish various types of antigens. Cell divisions are fairly deterministic with asymmetric size ratios of around 2:3 and 1:1, because the cell size produces information for determining the spatial displacement of organs. *It is stressed that the asymmetry reported in this paper is not directly related to chirality.*

Further thought experiments based on physics brings the outlook. Thus, we will show two more points. First, we will see that DNA employs deoxyribose as sugar, while RNA uses ribose. Giant sugars larger than ribose and deoxyribose will break a constant pitch between the bases in each single strand, making it difficult to generate RNAs. The molecular weights of ribose and deoxyribose are 150 and 134, respectively, and the molecular weights of T and U are 126.11 and 112.0, respectively. The two summations of U+ribose and T+deoxyribose are nearly the same. Thus, DNA can produce RNAs.

The second point concerns repeat DNA. We will classify the repeats into the "odd group" with an odd number of bases such as tri- and penta-nucleotide repeat motifs and the "even group" with an even number of bases such as di-and tetra-nucleotide repeat motifs. When the single strand of sequences having repeats in the "odd group" such as GCGGCG is bent at the center of the sequences in two-dimensional space, the sequences take a straight shape in many cases, because it is difficult to make base pairs. On the other hand, the repeat DNA in the "even group" such as GCGC makes base pairs, which leads to concavity, convexity and functions.

References

1. Anfinsen C (1973) Principles that govern the folding of protein chains, Science, 181 (4096), pp223-230.
2. Naitoh K (2001) Cyto-fluid Dynamic Theory, Japan Journal of Industrial and Applied Mathematics, **18-**1: 75-105.
3. Naitoh K (2003) Cyto-fluid dynamic theory of the origin of base, information, and function, Artificial Life and Robotics, **6**: 82-86.
4. Naitoh K (2005) Self-organizing mechanism of biosystems, Artificial Life and Robotics **9-**2: 96-98.
5. Naitoh K (2008) Inevitability of nTP: Information-energy carriers, Proc. of 13th International Symposium on Artificial Life and Robotics. (Artificial Life and Robotics, in press.)
6. Naitoh K (2007) Stochastic Determinism underlying Life, Proc. of 1st European Workshop on Artificial Life and Robotics, Vienna (Artificial Life and Robotics, in press.)
7. Naitoh K and Ueki S (2008) Asymmetry underling Protein, Proc. of 13th Int. Sym. on Artificial Life and Robotics.
8. Homma K and Hastings JW (1989) Cell growth kinetics, division asymmetry and volume control at division in the marine dinoflagellate Gonyaulax polyedra: J. of Cell Science, 92: 303-318.
9. Losick R and Desplan C (2008) Stochasticity and Cell Fate, Science, 320: 65-68.
10. Naitoh K (2006) Gene Engine and Machine Engine, pp.1-251 (Springer-Japan, Tokyo).
11. Naitoh K (2008) Onto-biology, Abstracts of the Annual Meeting of JSIAM (in Japanese).
12. Naitoh K (2008), Physics underlying Topobiology, Proc. of 13th Int. Conf. on BioMedial Engineering, (ICBME), Singapore.

Author: Ken Naitoh
Institute: Waseda University, Faculty of Science and Engineering, 3-4-1 Ookubo, Shinjuku, Tokyo, Japan,
Email: k-naito@waseda.jp

An Improved Methodology for Measuring Facet Contact Forces in the Lumbar Spine

A.K. Ramruttun[1], H.K. Wong[1], J.C.H. Goh[1], J.N. Ruiz[2]

[1] National University of Singapore, Department of Orthopaedic Surgery, Singapore
[2] National University Hospital, Department of Orthopaedic Surgery, Division of Spinal Surgery, Singapore

Abstract — **Accuracy methods using resistance-based sensors for measuring contact facet loads were previously published. However, the force measurement errors reported were relatively significant (≥18%) for the range of loads studied. Hence, a methodology to improve the accuracy and hence reliability for measuring facet contact forces using Tekscan 6900 sensor (1100 PSI rating) was implemented.**

The sensor was equilibrated and calibrated (linear & 2-pt) at 150N in between an Aluminium-Silicone rubber interface. For the accuracy test, 5 pairs of facet joints were trimmed and separately potted in PMMA and the calibrated sensor was then inserted in between the joints. The setup was mounted on an Instron machine where perpendicular known forces of 25, 50, 100 and 150N were applied. For the reliability test, the sensor was inserted into the L3L4 and L4L5 facet joints of an L2S1 human cadaveric test model and the latter mounted on an MTS machine to simulate ±10Nm flexion/extension, lateral bending and axial rotation with a follower preload of 300N.

The sensor overestimated the applied force for the linear calibration by 29.12±13% and 5.72±9% for 25 and 50N respectively while underestimated the applied force by 18.36±10% and 29.52±3% for 100 and 150N respectively. For the 2-pt calibration, the sensor overestimated the applied force for the linear calibration by 19.36±10% and 14.00±9% for 25 and 50N respectively while underestimated the applied force by 3.70±10% and 11.27±13% for 100 and 150N respectively. The average facet loads recorded for the range of motion studied were within published range for both types of calibration with a more significant difference during axial rotation.

The Tekscan sensor force measurement produces more accurate results for the 2-pt as compared to the linear calibration using the improved methodology and can be reliable in validating FEM facet joints studies.

Keywords — **Facet joint, joint kinetics, Lumbar spine, Tekscan sensor, Follower Preload**

I. Introduction

The loading of facet joints play an integral part in the understanding of the normal stability and kinematics of lumbar spine. Radiographs and MRI scans are possible in-vivo methods of investigating facet biomechanics but are limited since only planar kinematics are extractable while facet kinetics are inexistent using these methods. Hence, a proper in-vitro experimental analysis of the facet joints is necessary in order to yield better outcomes and a better understanding of the joint mechanics. In fact, the altered joint kinematics and kinetics of the posterior segmental spinal elements upon the advent of instrumentations such as intervertebral artificial discs and cages, as potential replacements for dysfunctional elements can be biomechanically and clinically important. Mathematical FEM models of the human lumbar spine can also be validated from experimental measurement of spine parameters such as facet contact loads. Hence, accurate and reliable facet load measurements are essential in order to enable the proper reproduction of in-vivo simulated conditions.

Facet contact forces in lumbar spines have been previously using various experimental sensors [1-6]. Tekscan pressure sensors (Tekscan Inc, South Boston, MA, USA) have been used earlier for knee kinetics investigations [7, 8] but their applications in investigating spinal facet joint kinetics has just been recently reported [1, 2, 9]. The use of Tekscan sensor in measuring joint kinetics is thus becoming popular but non-representative interface materials used to calibrate the sensor do not closely mimic the mechanical properties of articular cartilage and maximum loading forces of only 100N as reported previously do not comply with the actual physiological conditions of the spinal facet joints.

Since sensor performance is directly related to the compliance of the interface materials and the sensor preparation protocol (conditioning, equilibration and calibration), hence, our study will propose a new methodology to improve the accuracy and reliability of the Tekscan 6900 sensor performance for measuring facet contact forces by choosing the best suitable interface materials and increase the expected loading force on the sensor.

II. Materials and Methods

Mechanical testing protocol for interface materials

1. 5 cycles for preconditioning (up to 50% compression at a loading rate of 11mm/min) are subjected to each material using a material testing machine (Instron 5543, Canton, MA, USA)

Chwee Teck Lim, James C.H. Goh (Eds.): ICBME 2008, Proceedings 23, pp. 1805–1808, 2009
www.springerlink.com

2. Using an optical method (Digital Camera with a 10x zoom), the transverse and longitudinal strain are recorded 0, 25, 30 & 50 % compression to determine the Poisson Ratio, v ($- \varepsilon_{\text{transverse (x)}} / \varepsilon_{\text{longitudinal (y)}}$)
3. An additional 3 loading/unloading cycles (with similar preconditioning conditions as above) are applied to the materials to determine the stress/strain characteristic curves and hence derive the elastic/tangential Young Modulus, E

The comparison of the mechanical properties for the interface materials are tabulated as shown below (Table 1 and Table 2).The closest match was the Shinetsu KE1300T silicone and was used to test the performance of the sensor.

Table 1: Comparison of the Poisson Ratio of the various potential interface materials including the facet joint articular cartilage and capsule from FEM and In-vitro studies respectively

Interface Materials	Transverse strain (x)			Longitudinal Strain (y)			$v = - e_{\text{trans (x)}} / e_{\text{longitudinal (y)}}$			Range v
	25% comp	30% comp	50% comp	25% comp	30% comp	50% comp	25% comp	30% comp	50% comp	
Facet Joint Capsule [14]	-	-	-	-	-	-	-	-	-	0.40 - 0.50
Facet Joint Articular Cartilage [15]	-	-	-	-	-	-	-	-	-	0.40
Shinetsu KE1300T Silicone	2.44	3.21	6.61	5.95	7.44	13.60	0.41	0.43	0.49	0.40 - 0.50
RTV White 100% Silicone Sealant	1.79	2.62	5.77	4.30	5.29	11.35	0.42	0.50	0.51	0.40 - 0.50

Table 2: Comparison of the Tangential/Elastic Young Modulus of the various potential interface materials including the facet joint articular cartilage and capsule from FEM and In-vitro studies respectively

Interface Materials	YOUNG MODULUS (MPa)					
	10% comp	20% comp	25% comp	30% comp	40% comp	50% comp
Facet Joint Capsule [14]	0.39 ± 0.32	2.51 ± 2.14	-	3.97 ± 3.66	2.26 ± 1.32	2.76 ± 1.32
Facet Joint Articular Cartilage [15]	11.00					
Thick Foam [1]	-	-	0.20	-	-	0.18
Shinetsu KE1300T Silicone	1.17	1.68	1.83	2.05	3.19	5.86
RTV White 100% Silicone Sealant	0.30	0.53	0.68	0.89	1.65	3.08

Sensor Preparation

The interface material was moulded in two individual 35mm (Length) x 35mm (Width) x 1.5mm (Thickness) mould. The Tekscan 6900 I-Scan sensor (1100 PSI rating) was inserted in between the silicone and aluminium plates and prepared according to manufacturer's recommendation. The sensor was first conditioned 5 times at 120% of the expected load (180N) followed by an equilibration of 180N in between Aluminium-Shinetsu KE1300 T Silicone rubber interface mounted on an Instron 5543 testing machine. The Linear calibration profile is obtained by loading the sensor at 80% (120N) while that of the 2-point calibration is derived by applying 20% (30N) and 80% (120N) of the maximum expected load of 150 N.

Accuracy Test

5 pairs of facet joints were separately harvested, disarticulated and trimmed with the capsular ligaments and capsule removed. Each of the superior and inferior facet joints was separately potted in PMMA while ensuring a parallel and horizontal alignment with respect to each other and a perpendicular positioning of both individual facets with the loading direction. The previously calibrated sensor was then inserted in between the joints. The setup was mounted on an Instron testing machine where perpendicular known forces of 25, 50, 100 and 150N were applied. The force from the machine (True force) was then compared with the calibrated sensor force readings for both the linear and 2-point calibration and the force measurement error calculated as previously discussed [1].

Reliability Test

The calibrated sensor was inserted into the L3L4 and L4L5 facet joints of an L2S1 human cadaveric test model and the latter mounted on an MTS machine to simulate ±10Nm flexion/extension, right/left lateral bending and clockwise/anticlockwise axial rotation [11] with a follower preload of 300N [10]. The sensor was recalibrated after each test following the procedures described in the sensor preparation above. The raw values from each sensor were recorded and the equilibration, linear and 2-point calibration

files were loaded into the recorded Tekscan movie files. The average force for each of the 4 branches of the sensor was individually computed and analyzed for the range of motion studied.

III. Results

The sensor overestimated the applied force for the linear calibration by 29.12±13% and 5.72±9% for 25 and 50N respectively while underestimated the applied force by 18.36±10% and 29.52±3% for 100 and 150N respectively. For the 2-pt calibration, the sensor overestimated the applied force for the linear calibration by 19.36±10% and 14.00±9% for 25 and 50N respectively while underestimated the applied force by 3.70±10% and 11.27±13% for 100 and 150N respectively (Fig 1). The measurement errors from a recent publication [1] were also included in the chart and were significantly higher than those from our experiment.

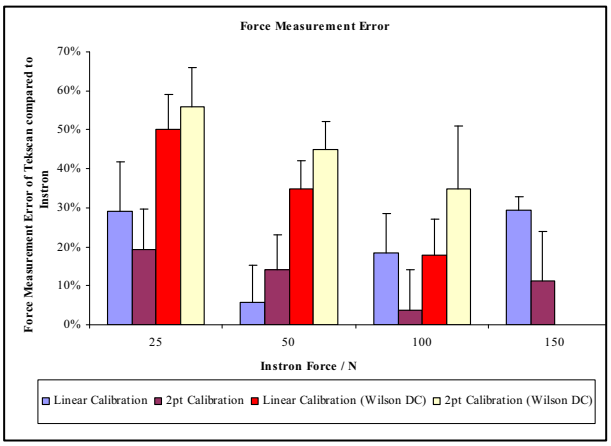
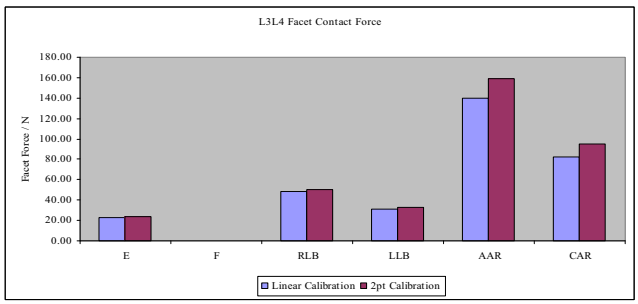


Fig 1: The force measurement errors of the sensor as compared to the Instron Force and recent publication [1]

The range of facet forces measured using the Tekscan Sensor for the range of motions investigated at both L3L4 and L4L5 are illustrated in Fig 2 & 3 respectively. The average facet force ranged from 0N during flexion to 159N and 161.9N during anticlockwise axial rotation for both linear and 2-point calibration at L3L4 and L4L5 levels respectively.

The minimum average difference in the facet force was 1N and 0.10N for extension while the maximum of 19N and 32N was registered for anticlockwise axial rotation at L3L4 and L4L5 respectively.



E – Extension F- Flexion
RLB & LLB – Right & Left Lateral Bending
CAR & AAR – Clockwise & Anticlockwise Axial Rotation

Fig 2: The range of facet forces measured using the Tekscan Sensor for the range of motions investigated at L3L4

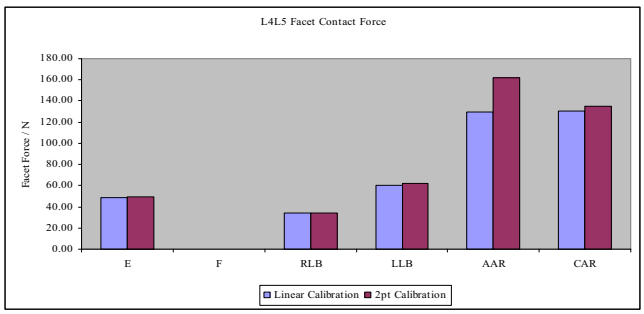


Fig 3: The range of facet forces measured using the Tekscan Sensor for the range of motions investigated at L4L5

IV. Discussion

Our results for the accuracy test, using the separated facet joints after the sensor has been conditioned, equilibrated and calibrated using Shinetsu KE 1300T silicone as the interface material, showed that the 2-point calibration is significantly better than the linear calibration. Hence, the method described in this experiment showed that the accuracy of the sensor is improved as compared to the force measurement error of at least 18% reported for the range of loads investigated of 25-100N) [1]. For the reliability test, the maximum forces obtained from the sensor of 161.9N during the investigation of physiological motions were close to the expected force of 150N used to calibrate the sensor. The values are much higher as those reported from previous publications especially during axial rotation and could be due to the effect of the follower preload system and the maximum moment of 10Nm used during our assessment.

The yardstick of an optimum sensor performance is to find a compliant interface material as close as possible to

the facet joint cartilage mechanical properties. Different materials have been reportedly been used to calibrate the Tekscan sensor. Some calibrated the sensor in between two 3.2 mm lubricated rubber whose mechanical properties have not been reported [7, 9] while others used a 3mm thick foam with a nominal compressive strength of 50 kPa at 25% and 90 kPa at 50% deflection [1]. Detailed mechanical properties of the various commercially-available interface materials with an average thickness of 3mm have been evaluated with particular reference to the Elastic Young Modulus and Poisson Ratio. The choice of Shinetsu KE 1300T was due to the closeness of its mechanical properties to that of the articular cartilage of the facet joint.

Tekscan Flexiforce (A101-500) was used to investigate the effect of instant axis of rotation on the facet forces [2] but the accuracy of the sensor was not looked into. Another publication [9] investigated the effect of a dynamic posterior stabilization system (Dynesys) on Facet Joint Contact Forces using Tekscan 6900 sensor. The loading range was estimated to be 100N and the sensor was calibrated while following manufacturer's recommendations. The accuracy and repeatability of the Tekscan 6900 sensor as a potential experimental force transducer for measuring spinal facet loads was also investigated [1]. Published force measurement errors reported are 18% at best and a loading range of only 25-100N. However, recent FEM studies [12, 13] have reported much higher facet loads. The biomechanics of the lumbar spine and its behaviour with varying position and height of a mobile core type artificial disc in which the facet load at the implanted and adjacent levels was estimated at a maximum of 200 N during extension while the effect of large compressive loads on the spine during flexion and torsion which reported a total maximum facet force of 100 to 150 N at a moment of 10 Nm were reported respectively. Hence, the calibration range of 100 N seems inadequate and higher facet loads can be expected especially with the advent of the follower preload system. Furthermore, the behavior of the Tekscan 6900 sensor is still unknown in terms of the accuracy of the calibration beyond 100N, hence, the motivation behind this study. The forces measured from the sensor can also be used to validate FEA of facet joint forces. So far, the only validation of current model is by comparing with published data as well as in-vitro biomechanical testing of intact spine. Hence, the facet forces from the Tekscan sensor can provide useful information to help validate and improve the predictive ability of the models.

V. Conclusion

The main aim of this paper was to assess the accuracy and reliability of the Tekscan 6900 I-Scan sensor using an improved methodology in order to reduce the force measurement errors when measuring spinal facet joint forces. By using a more compliant interface material and facet joints, the Tekscan sensor force measurement produces more accurate results for the 2-pt as compared to the linear calibration using the improved methodology and can be reliable in validating FEM facet joints studies.

References

1. Wilson D.C., Niosi C.A. et al (2006) Accuracy and repeatability for measuring facet loads in the lumbar spine. J. Biomech 39: 348-353'
2. Rousseau M.A., Bradford D.S. et al (2006) The instant axis of rotation influences facet forces at L5/S1 during flexion/extension and lateral bending. Eur. Spine J. 15: 299-307
3. Luo Z.P., Buttermann G.R., Lewis J.L. (1996) Determination of spinal joint loads from extra-articular strains – A theoretical validation. Journal of Biomechanics 29(6): 785-79
4. Shendel M.J., Wood K.B. et al 1993). Experimental measurement of ligament force, facet force and segment motion in the human lumbar spine. J. Biomech 26(4/5): 427-438
5. Buttermann G.R., Kahmann R.D. et al (1991). An experimental method for measuring force on the spinal facet joint: Description and application of the method. J. Biomech. Eng. 113: 375-386
6. El-Bohy A.A., Yang K.H. et al (1989) Experimental verification of facet load transmission by direct measurement of facet lamina contact pressure. J. Biomech 22(8/9): 931-941
7. Wilson D.R., Apreleva M.V. et al (2003) Accuracy and repeatability of a pressure measurement system in the patellofemoral joint. J. Biomech 36: 1909- 1915
8. Harris M.L., Morberg P. et al (1999). Improved method for measuring tibiofemoral contact areas in total knee arthroplasty: a comparison of K-scan sensor and Fuji film. J. Biomech 32: 951-958
9. C.A. Niosi, D.C. Wilson et al (2008) The Effect of Dynamic Posterior Stabilization on Facet Joint Contact Forces An *In Vitro* Investigation. Spine 33(1): 19–26
10. A. Rohlmann, T.Zander et al (2005) Effect of total disc replacement with prodisc on intersegmental rotation of the lumbar spine. Spine 30(7): 738-743
11. I. Yamamoto, M.M. Panjabi et al (1989) 3D movements of whole lumbar spine and lumbosacral joint. Spine 14(11): 1989
12. A.Rohlmann, T.Zander et al (2008) Effect of position and height of a mobile core type artificial disc on thebiomechanical behaviour of the lumbar spine. Proc. IMechE Vol. 222 Part H: J. Engineering in Medicine: 229-239
13. A. Shirazi-Adl (2006) Analysis of large compression loads on lumbar spine in flexion and in torsion using a novel wrapping element. J. Biomech 39: 267–275
14. J.S Little , P.S. Khalsa (2005) Material Properties of the Human Lumbar Facet Joint Capsule. J Biomech Eng. 127(1): 15-24
15. J.R. Williams, R.N. Natarajan et al (2007) Inclusion of regional poroelastic material properties better predicts biomechanical behavior of lumbar discs subjected to dynamic loading J. Biomech 40: 1981–1987

Author: Ramruttun A.K.
Institute: National University of Singapore
Street: Lower Kent Ridge Road
City: Singapore
Country: Singapore
Email: dosrak@nus.edu.sg

Multi-scale Models of Gastrointestinal Electrophysiology

M.L. Buist, A. Corrias and Y.C. Poh

Division of Bioengineering, National University of Singapore, Singapore

Abstract — **We have developed quantitative mathematical descriptions of a gastric smooth muscle cell (SMC) and a gastric interstitial cell of Cajal (ICC). Together these two cell types, with input from the enteric nervous system, govern the electrical and mechanical actions of the stomach that combine to generate motility. Each of these models has been developed from the underlying physiology and has been validated against whole cell experimental recordings. Such models form the building blocks necessary to construct multi-cellular and multi-scale simulations that link sub-cellular behavior to whole organ function.**

With these building blocks, tissue and organ level models have been developed. The geometry of the stomach has been digitized from photographic images from the visible human project and a derivative continuous serosal surface has been fitted using an iterative linear minimization technique. The volume of the *muscularis externa*, representing the layers in the stomach wall responsible for gastric motility, was created through an inward projection from the serosal surface. Within this volume a high resolution hexahedral finite element mesh was created over which a non-linear reaction diffusion equation was solved to describe the macroscopic propagation of electrical activity in the stomach.

At the other end of the spectrum, a mutation in the gene encoding the gastrointestinal sodium channel has been described and linked to clinical symptoms. To elucidate the effects of subcellular maladies such as this, a true multi-scale framework has been developed to investigate gastrointestinal electrophysiology; from ion channel to cell to tissue to organ. This framework will allow us to better understand the emergent behavior of the system in a way that would be difficult, if not impossible, to decode experimentally. The development of the framework and the first results from its implementation are presented.

Keywords — **Electrophysiology, Finite element, Gastrointestinal, Smooth muscle, ICC**

I. Introduction

The muscular layers in the walls of the stomach produce omnipresent rhythmical membrane potential fluctuations that are known as slow waves [1]. These are initiated in the mid-corpus of the stomach, quickly forming a ring of activity before propagating distally towards the pylorus at the entrance to the small intestine. This activity is the result of interplay between gastric smooth muscle cells and the interstitial cells of Cajal (ICC), while the enteric nervous system (ENS) provides an additional extrinsic level of control. Together these cells act as a syncytium in which the electrical activity is conducted from cell to cell [2]. Recent evidence suggests that it is the ICC that are primarily responsible for the initiation and propagation of slow waves while the smooth muscle cells receive input from the ICC and the ENS and contract in accordance with their level of stimulation [1].

While between 60 and 70 million people in the US alone are affected by digestive diseases [3], relatively little is known about the fundamental mechanisms involved with the initiation and propagation of the electrical activity in the gastrointestinal (GI) tract. Current diagnostic techniques can, for example, quantify the degree of gastroparesis (nuclear medicine, gastric emptying studies) or identify the dominant frequency associated with gastric electrical activity. However, none of the current methods can detect the underlying electrophysiological disturbances that cause gastroparesis. In addition, should an electrical disturbance be detected there are large gaps in our knowledge as to how this should be interpreted.

Our approach to these problems is the development of an anatomically and biophysically based multi-scale model of the human digestive system, initially focused on the stomach. The resulting modeling framework covers a wide range of spatial scales, from the level of an ion channel to that of a cell, to tissue, organ and whole torso models. This represents a significant advance over previous modeling studies in this area as the majority represents the previous state of knowledge in which the smooth muscle cells were thought to be self-exciting [4]. In addition, more recent attempts to describe the system have been largely phenomenological [5-6]. The modeling framework can be summarized as shown in Figure 1.

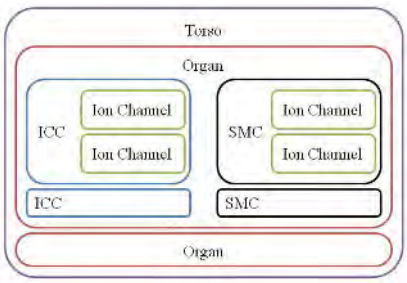


Fig. 1 Model hierarchy; ion channels are encapsulated by cells which combine to form organs that are encapsulated within the torso.

Chwee Teck Lim, James C.H. Goh (Eds.): ICBME 2008, Proceedings 23, pp. 1809–1813, 2009
www.springerlink.com

II. Materials and methods

Cell models: Two models of cellular electrophysiology were developed, one ICC model and one smooth muscle cell model. These were developed following the classical Hodgkin-Huxley approach where the cell membrane was described by an equivalent electrical circuit consisting of a membrane capacitance connected in parallel with a number of variable conductances, each representing a different pathway for the movement of charged ions [7].

$$\frac{dV_m}{dt} = \frac{-1}{C_m}(I_{ion} + I_{stim}) \quad (1)$$

Here V_m (in mV) is the membrane potential, C_m (in pF) is the cell capacitance, I_{stim} (in pA) is an externally applied stimulus current (if present), and I_{ion} (in pA) represents the sum of the ionic currents crossing the cell membrane. An extensive literature search was undertaken to identify the major ion channels present in each cell type.

The ion channels identified in gastric smooth muscle cells were selected as described in [8]

$$I_{ion} = I_{CaL} + I_{LVA} + I_{Kr} + I_{KA} + I_{BK} + I_{Kb} + I_{Na} + I_{NSCC} \quad (2)$$

where I_{CaL} represents the influx of Ca^{2+} ions through voltage gated, dihydropyridine (DHP)-sensitive L-type Ca^{2+} channels that are commonly expressed in most muscle cells of mammalian organisms [9-10]. I_{LVA} represents the second, low voltage-activated, fast inactivating, DHP-insensitive component of the inward current that was described in several types of smooth muscle cells and is often termed a 'T-type' Ca^{2+} current [11]. I_{Kr} refers to the typically TEA and 4-AP –sensitive ionic conductance through delayed rectifier potassium channels commonly expressed in a wide variety of excitable cells [12]. I_{KA} refers to the fast inactivating, Ca^{2+}-independent, TEA-insensitive, outward A-type K+ current that was first described in mollusc neurons [13]. Ca^{2+}-activated K+ channels have been traditionally divided in three categories according to their large (BK), intermediate (IK) or small (SK) conductance. To date only BK channels have been described in gastrointestinal tract and are included here through I_{BK} [14]. A background potassium conductance was also included in the model through I_{Kb}. Sodium currents have been reported in guinea-pig gastric fundus and the human jejunum. We have therefore chosen to include a relatively Tetrodotoxin (TTX)-resistant sodium channel, with current I_{Na}, in the model [15]. I_{NSCC} is a non-selective cationic channel (NSCC) that has been described in both guinea-pig and canine gastric smooth muscle [16]. In addition, a phenomenological model of calcium extrusion was included to represent the activity of the sarcoplasmic reticulum and sodium/calcium exchangers on the plasma membrane in order to maintain long term intracellular calcium homeostasis.

The electrophysiology of an ICC cell was described using the following ionic currents [17].

$$I_{ion} = I_{CaL} + I_{VDDR} + I_{Kv11} + I_{ERG} + I_{BK} + I_{Kb} + I_{Na} + I_{NSCC} + I_{Cl} \quad (3)$$

Two types of Ca^{2+} channel have been identified in ICC. One is a DHP-resistant conductance, I_{VDDR}, whereas the other one has been molecularly classified as an L-type Ca^{2+} channel, I_{CaL} [18-19]. I_{Kv11} is the current flowing through the voltage dependent K^+ channels encoded by the Kv1.1 gene. Ether-a-go-go (ERG) channels have been proposed as important regulators of pacemaker activity in ICC. The characteristics of the I_{ERG} current in ICC have been studied in detail in ICC by [20]. The presence of Ca^{2+}-activated K^+ channels (BK) has been confirmed in ICC via immunocytochemical techniques. The I_{BK} channels in ICC were assumed to be not substantially different from those in gastric smooth muscle cells. A background K^+ conductance, I_{Kb}, was also included in the model. An SCN5A-encoded Na^+ conductance has been found in human intestinal ICC by RT-PCR experiments. This current, I_{Na}, believed to influence the rise phase of the slow waves, is TTX-resistant [21]. I_{NSCC} is theorised to be the primary pacemaking conductance and allow ionic fluxes into the restricted subspace enclosed by the plasma membrane, mitochondria and sarcoplasmic reticulum [1]. An inwardly rectifying whole cell current has been identified that the authors believed was carried primarily by Cl^- ions. This is represented in the model through I_{Cl}. Both a plasmalemmal Ca^{2+} pump (PMCA) and the Na^+/Ca^{2+} exchanger (NCX1) have been identified in ICC. However, quantitative data pertaining to the kinetics of these proteins was not available so a phenomenological description of the Ca^{2+} extrusion mechanisms was included.

Geometric models: The anatomical data source used for the construction of the stomach and torso models was the visible human project [22]. Computational meshes were created by digitizing surfaces from the axial visible human images and then fitting an initial bilinear surface mesh to the resulting data. This initial mesh was then used with a second round of fitting to produce derivative continuous surface meshes of the relevant geometries. Wall thickness was added to the hollow organs of the digestive system by an inward projection of the outer surface towards the centerline of the mesh based on available anatomical thickness data. This 3-D geometry was then divided into layers representing the circular and longitudinally aligned smooth muscle cells and the intervening myenteric plexus with its dense network of ICC [23]. Within the gastric musculature, the monodomain simplification of the bidomain equations was used to model the syncytium of the muscularis externa.

$$\nabla\cdot(\sigma\nabla V_m)=A_m\left(C_m\frac{dV_m}{dt}+I_{ion}\right) \quad (4)$$

Here σ represents the tissue conductivity and A_m is the ratio of the membrane surface area to the tissue volume. The other terms are as stated for Equation 1. A high resolution structured finite element mesh was generated over the stomach over which Equation 4 was solved. In the passive regions outside the electrically active stomach, the torso volume conductor was described using a generalized Laplace equation that was solved using a boundary element approach [24].

III. Results

Each of the cell models was tested individually to ensure they produced slow wave profiles that were both qualitatively and quantitatively similar to those recorded experimentally. The resulting slow wave profile from the smooth muscle cell model is shown in Figure 2 while the slow wave profile from an ICC is shown in Figure 3.

Each of these models was then validated through testing against experimental data from a wide range of pharmacological interventions, the details of which can be found in [8,17]. This was performed to ensure that the model results could be trusted in pathological as well as physiological conditions.

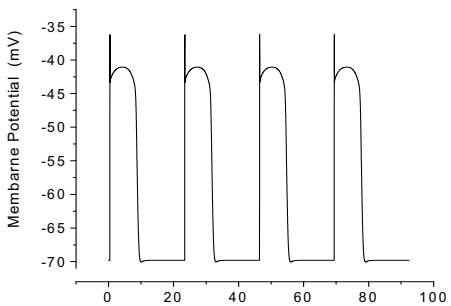


Fig. 2 Membrane potential as a function of time for the model of gastric smooth muscle electrophysiology.

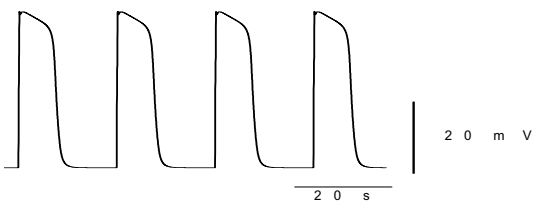


Fig. 3 Membrane potential as a function of time for the model of gastric ICC electrophysiology.

After completing the validation of the single cell models, these were placed into the 3-D stomach model through the I_{ion} term. Essentially one of these cell models was placed at each node in the high resolution finite element mesh (over 300,000 in total). Smooth muscle cells were placed in the longitudinal and circular muscle layers whereas the ICC model was placed in the myenteric plexus and also intramuscularly. The monodomain equation (Equation 4) was then solved with a time step of 0.01 ms and the membrane potential, V_m, was calculated over the stomach as a function of time. The resulting potential field at one time instant is shown on the left of Figure 4.

After each 1 ms of simulation time, equivalent current dipole sources were calculated from the membrane potential distribution as described in [25]. These were then placed within the boundary element torso model and used to calculate the body surface potential field from which an electrogastrogram could be constructed, and also the components of the biomagnetic field that could be recorded on a plane just in front of the torso surface.

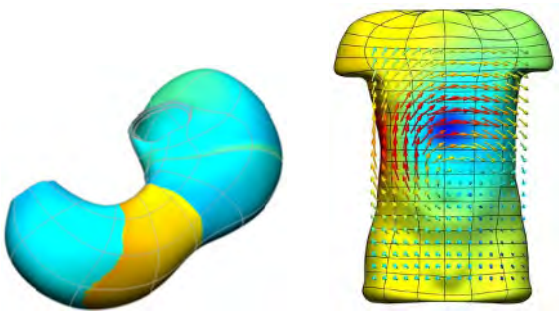


Fig. 4 On the left one snapshot of the membrane potential on the outer surface of the stomach shows a slow wave (yellow) progressing from right to left down the stomach; blue tissue is excitable. The right figure shows the body surface potential and also the biomagnetic field strength that is the result of the stomach cellular activity; blue potentials are negative and red are positive.

IV. Discussion

This modeling framework represents the entire scale of physiological events required to accurately model gastrointestinal electrophysiology. The building blocks of each cell model are mathematical descriptions of individual ion channel function. The cell models in turn represent the building blocks for describing organ function; an organ is constructed from its cell models as the cell models are constructed from their ion channels. Mutations of the genes encoding each ion channel alter channel function, cell function, and ultimately organ function if the mutation is sufficiently severe. This modeling framework is thus uniquely

positioned to describe the downstream effects of such ion channelopathies.

When constructing multi-scale models such as that presented here, computational tractability must always be a consideration. The majority of the computational time here was spent integrating the systems of differential equations needed to describe cell function. To minimize the computational cost the cell models do not include an exhaustive list of every ion channel ever found in the two cell types. Instead, only those ion channels capable of making a significant contribution to the whole cell current were included. The result was a 3-D model that can be run on a desktop computer. With this assumption in mind, the cell models were written in a modular fashion such that additional channel types can be easily added as they are experimentally characterized and their influence becomes better understood.

One common criticism of detailed mathematical models in biology is that there are so many free parameters that essentially any behavior can be represented. Here no global parameter fitting algorithms were employed. Each ion channel model was fitted to experimental data and then validated against the data from which it was created. The ion channel models were then combined using the Hodgkin-Huxley formalism and the resulting slow wave profiles were tested against whole cell experimental recordings. Data was also available from experiments where pharmaceutical agents were added to whole cells or tissues. The validity of our models was further verified by simulating the presence of these agents and ensuring the model response was consistent with the experimental observations. By linking to real data at each stage in the model construction we avoid the aforementioned criticism and can be confident in the robustness of the model.

V. Conclusion

A modeling framework has been developed to describe the electrophysiology of the gastrointestinal tract, integrating the available physiological information from the subcellular level through to whole organ function. This represents an invaluable platform to further our knowledge of gastrointestinal electrophysiology in health and disease.

References

1. Sanders KM, Koh, SD and Ward SM. Interstitial cells of Cajal as pacemakers in the gastrointestinal tract. Annu Rev Physiol.68:307-343, 2006.
2. Bozler E, (1937). Physiological evidence for the syncytial character of smooth muscle. Science 86, 476–478.
3. Everhart JE, (1994). Digestive diseases in the united states: epidemiology and impact. U.S. Department of Health and Human Services, National Institutes of Health, National Institute of Diabetes and Digestive and Kidney Diseases. U.S. Government Printing Office, Washington, DC.
4. Skinner FK, Ward CA & Bardakjian BL (1993). Pump and exchanger mechanisms in a model of smooth muscle. Biophys Chem 45, 253-272.
5. Edwards FR & Hirst GD (2005). An electrical description of the generation of slow waves in the antrum of the guinea-pig. J Physiol 564, 213-232.
6. Aliev RR, Richards W & Wikswo JP (2000). A simple nonlinear model of electrical activity in the intestine. J Theor Biol 204, 21-28.
7. Hodgkin AL and Huxley AF. A quantitative description of membrane current and its application to conduction and excitation in nerve. J Physiol. 117(4):500-44 1952
8. Corrias A and Buist ML. A quantitative model of gastric smooth muscle cellular activation. Ann Biomed Eng. 35(9), 1595-1607, 2007.
9. Vogalis F, Publicover NG & Sanders KM (1992). Regulation of calcium current by voltage and cytoplasmic calcium in canine gastric smooth muscle. Am J Physiol 262, C691-700.
10. Akbarali HI & Giles WR (1993). Ca2+ and Ca(2+)-activated Cl- currents in rabbit oesophageal smooth muscle. J Physiol 460, 117-133.
11. Vivaudou MB, Clapp LH, Walsh JV, Jr. & Singer JJ (1988). Regulation of one type of Ca2+ current in smooth muscle cells by diacylglycerol and acetylcholine. Faseb J 2, 2497-2504.
12. Koh SD, Ward SM, Dick GM, Epperson A, Bonner HP, Sanders KM, Horowitz B & Kenyon JL (1999). Contribution of delayed rectifier potassium currents to the electrical activity of murine colonic smooth muscle. J Physiol 515 (Pt 2), 475-487.
13. Amberg GC, Baker SA, Koh SD, Hatton WJ, Murray KJ, Horowitz B & Sanders KM (2002). Characterization of the A-type potassium current in murine gastric antrum. J Physiol 544, 417-428.
14. Carl A, Lee HK & Sanders KM (1996). Regulation of ion channels in smooth muscles by calcium. Am J Physiol 271, C9-34.
15. Holm AN, Rich A, Miller SM, Strege P, Ou Y, Gibbons S, Sarr MG, Szurszewski JH, Rae JL & Farrugia G (2002). Sodium current in human jejunal circular smooth muscle cells. Gastroenterology 122, 178-187.
16. Sims SM (1992). Cholinergic activation of a non-selective cation current in canine gastric smooth muscle is associated with contraction. J Physiol 449, 377-398.
17. Corrias A and Buist ML (2008). A quantitative cellular description of gastric slow wave activity. Am J Physiol Gastrointest Liver Physiol. 294(4):G989-95.
18. Cho, W. J., and E. E. Daniel. Proteins of interstitial cells of Cajal and intestinal smooth muscle, colocalized with caveolin-1. Am J Physiol Gastrointest Liver Physiol.288:G571-585, 2005.
19. Kim, Y. C., S. D. Koh, and K. M. Sanders. Voltage-dependent inward currents of interstitial cells of Cajal from murine colon and small intestine. J Physiol.541:797-810, 2002.
20. McKay, C. M., J. Ye, and J. D. Huizinga. Characterization of depolarization-evoked ERG K currents in interstitial cells of Cajal. Neurogastroenterol Motil.18:324-333, 2006.
21. Strege, P. R., Y. Ou, L. Sha, A. Rich, S. J. Gibbons, J. H. Szurszewski, M. G. Sarr, and G. Farrugia. Sodium current in human intestinal interstitial cells of Cajal. Am J Physiol Gastrointest Liver Physiol.285:G1111-1121, 2003.
22. Spitzer V., Ackerman MJ, Scherzinger AL, Whitlock, RM, (1996). The visible human male: a technical report. J. Am. Med. Inform. Assoc. 3 (2), 118–130.
23. Pullan A, Cheng L, Yassi R, Buist M (2004). Modelling gastrointestinal bioelectric activity. Prog Biophys Mol Biol. 85(2-3):523-50.

24. Buist ML, Cheng LK, Yassi R, Bradshaw LA, Richards WO, Pullan AJ (2004). An anatomical model of the gastric system for producing bioelectric and biomagnetic fields. Physiol Meas. 25(4):849-61.
25. Buist ML, Cheng LK, Sanders KM, Pullan AJ (2006). Multiscale modelling of human gastric electric activity: can the electrogastrogram detect functional electrical uncoupling? Exp Physiol. 91(2):383-90.

Author: Martin L Buist
Institute: National University of Singapore
Street: 7 Engineering Drive 1
City: Singapore
Country: Singapore
Email: biebml@nus.edu.sg

Postural Sway of the Elderly Males and Females during Quiet Standing and Squat-and-Stand Movement

Gwnagmoon Eom[1], Jiwon Kim[1], Byungkyu Park[2], Jeonghwa Hong[2], Soonchul Chung[1], Bongsoo Lee[1], Gyerae Tack[1], Yohan Kim[1]

[1] Konkuk University, Choongju, Korea
[2] Korea University, Seoul, Korea

Abstract — **In this paper, COP (center of pressure) during quiet standing and squat-and-stand movement was analyzed to compare the postural control of young and elderly subjects with special interest in the elderly females who were reported to have higher fall rate than the elderly males. Subjects include the young subjects (10 males: 21.8±2.6yrs, 10 females: 20.4±0.3yrs) and the elderly subjects (8 males: 75.5±4yrs, 8 females: 72.3±3.5yrs).**

Analysis parameters were the mean of the distance between the instantaneous COP and the average COP (COP distance) and the mean of the COP movement velocity (COP velocity) in both AP (anterio-posterior) and ML (medio-lateral) directions.

During quiet standing, the COP distance in ML direction of elderly females was significantly greater than that of elderly males and the COP velocity of elderly females in both ML and AP direction were significantly greater than those of all the other groups.

During squat-and-stand movement, the COP distance of elderly females was not significantly different with that of the elderly males. However, the COP velocity of elderly females was significantly greater than that of all the other groups.

The large lateral weight shift (COP distance) of elderly females during quiet standing may explain their greater fall rate. However, this does not apply to squat-and-stand movement.

In contrast, COP velocity results show that the elderly females' COP is rapidly trembling compared to that of elderly males during both quiet standing and squat-and-stand movement. This result suggests that rapid trembling or postural sway may reflect the reduced postural control ability and higher risk of fall in elderly females.

Keywords — **fall-risk, gender, COP, quiet standing, squat-and-stand**

I. Introduction

One thirds of the elderly older than 65 years experience fall more than once per year which reduces the quality of life by limiting the activities of daily living [1-3]. It was reported that the fall rate of elderly females is 49 % higher than that of elderly males [7]. Fall was attributed to the deficit in postural control which was evaluated by the postural sway in center of pressure (COP) [8-11]. However, it is still unclear that what difference in postural control is related to the difference between the fall rates of elderly males and females. Therefore, this study aims to compare the postural sway characteristics in elderly males and females, during quiet-standing and squat-and-stand movement.

II. Method

A. Subject

Sixteen elderly subjects and ten young subjects participated in this study whose physical characteristics are shown in Table 1. Subjects were divided in four groups as young male, young female, elderly male and elderly female.

Table 1 Physical characteristics of the subjects.

	Elderly		Young	
	Males (n=8)	Females (n=8)	Males (n=10)	Females (n=10)
Age	75.5±4.2	72.3±3.5	21.8±2.6	20.4±0.3
Weight[kg]	56.3±9.2	54.3±6.1	70.3±9.3	58.5±6.7
Lean body mass[kg]	43.6±6.9	35.3±3.8	58.2±2.8	41.6±3.1

B. Measurement and analysis

COP trajectory during static condition (quiet-standing, 30s) and also dynamic condition (squat-and-stand movement, 5 times) was measured in all subjects by using a force-platform.

The mean distance (MD) of COP from the center of the trajectory (mean value) was derived from the COP data. MD was determined in anterio-posterior (AP), medio-lateral (ML) and in total (TOT) direction. Similarly, the mean velocity (MV) of COP was derived in each direction. Difference of the above COP parameters among groups are analyzed by ANOVA and post-poc test (Tukey).

III. Result and discussion

A. Quiet-standing

MD of elderly females in ML direction was significantly greater than those of elderly males and this was reflected in

Chwee Teck Lim, James C.H. Goh (Eds.): ICBME 2008, Proceedings 23, pp. 1814–1816, 2009
www.springerlink.com

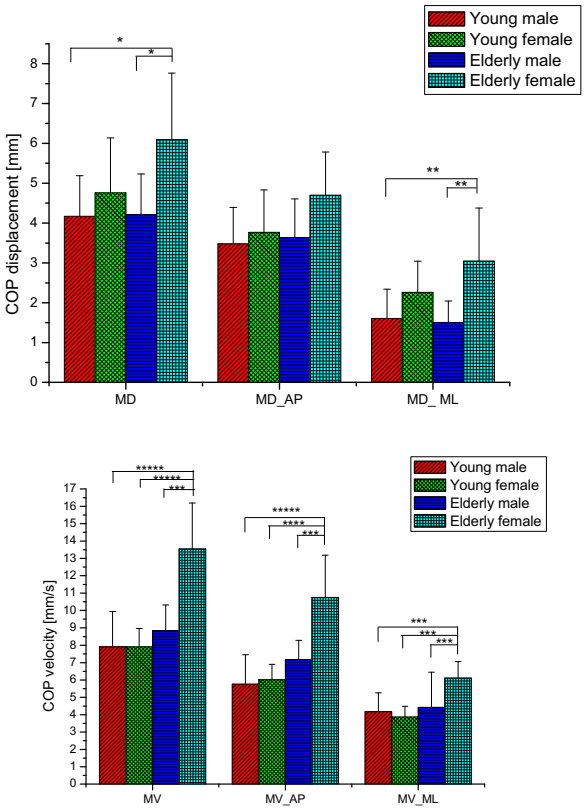


Fig. 1 Comparison of COP parameters among groups during quiet standing (* p<0.05, ** p<0.01, *** p<0.001, **** p<0.0001, ***** p<0.00001)

MD of total direction (Fig. 1a). This indicates that the large lateral weight shift is occurring during quiet standing in elderly females and it might be related to the higher fall rate, because three times of elderly females experience fall-related fracture in hip joints due to the fall in frontal plane [24].

MV of all directions in elderly females was significantly greater than those of all the other groups (Fig. 1b). This indicates that the rapid trembling of body weight even during quiet-standing might be related to the deteriorated postural control ability and the higher fall rate.

B. Squat-and-stand

MD in ML direction in elderly females was not different from those of elderly males and this was reflected in MD of total direction (Fig. 2a). This indicates that the postural control strategies in all groups during squat-and-stand movement are similar, at least in terms of the COP displacement.

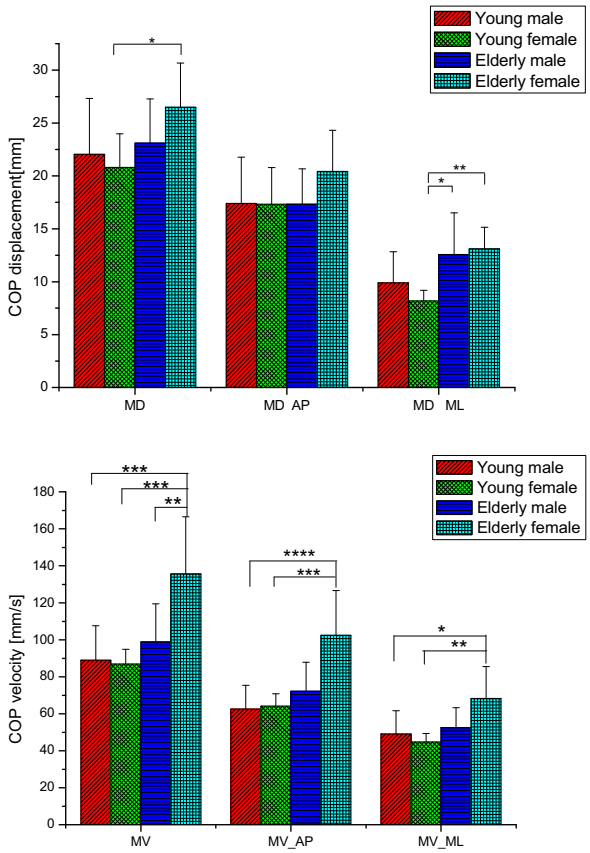


Fig. 2 Comparison of COP parameters during squat-and-stand movement (* p<0.05, ** p<0.01, *** p<0.001, **** p<0.0001, ***** p<0.00001)

MV of total directions in elderly females was significantly greater than those of all the other groups (Fig. 2b). This indicates that the rapid trembling of body weight during squat-and-stand movement might be related to the deteriorated postural control ability and the higher fall rate during dynamic motion, as walking.

IV. Conclusion

Elderly females' MD in ML direction during quiet standing was significantly greater than those of elderly males. Elderly females' MV in total direction during both quiet standing and squat-and-stand movement was significantly greater than those of all the other groups. Rapid trembling of body weight during both static and dynamic condition might be related to the deteriorated postural control ability and the higher fall rate.

ACKNOWLEDGMENT

This work was supported by the Korea Science and Engineering Foundation (KOSEF) (No. R01.-2007-000-20616-0)

REFERENCES

1. Tideiksaar, R (1987) Falling in Old Age: Its Prevention and Treatment . Springer
2. Lord SR, et al (1993) An epidemiological study of falls in older community-dwelling women: the Rndwich falls and fractures study Aust J Public Health 17:240-245
3. Kennedy, T.E., et al. (1987) The prevention of falls in later life Dan. Med. Bull 34:1-24
4. Sattin RW et al (1990) The incidence of fall injury events among the elderly in a defined population Am J Epidemiol 131:1028-1037
5. Anacker SL, et al (1992) Influence of sensory inputs on standing balance in community-dwelling elders with a recent history of falling, Phys Ther 72:575-584
6. Whitney SL, et al (2000) The association between observed gait instability and fall history in persons with vestibular dysfunction J Vestib Res 10:99-105
7. Teasdale N, et al (1991) Postural sway characteristics of the elderly under normal and altered visual and support surface conditions J Gerontol A Biol Sci Med Sci 46:238-244
8. Sheldon JH(1963) The effect of age on the control of sway Gerontol Clin 5:129-138
9. Campbell AJ, et al (1989) Risk factors for falls in a community-based prospective study of people 70 years and older J Gerontol 44:112-117

Author: Gwangmoon Eom
Institute: Konkuk University
Street: Dawol-dong
City: Choongju
Country: Korea (Republic of)
Email: gmeom@kku.ac.kr

Investigation of Plantar Barefoot Pressure and Soft-tissue Internal Stress: A Three-Dimensional Finite Element Analysis

Wen-Ming Chen[1], Peter Vee-Sin Lee[2], Sung-Jae Lee[3] and Taeyong Lee[1]

[1] Division of Bioengineering, National University of Singapore, Singapore
[2] Department of Mechanical Engineering, University of Melbourne, Australia
[3] Department of Biomedical Engineering, Inje University, Korea

Abstract — **Mechanical loading acting on the foot plantar soft-tissue in the form of focal stress plays a central pathogenic role in the onset of diabetic neuropathic ulcers. Current instruments which merely allow superficial estimate of plantar loading acting on the foot, severely limit the scope of many biomechanical/clinical studies on this issue. Recent studies have suggested that peak plantar pressure may be only 65% specific for the development of ulceration. These limitations are at least partially due to surface pressures not being representative of the complex mechanical stress developed inside the subcutaneous plantar soft-tissue, which are potentially more relevant for tissue breakdown. This study established a three-dimensional and nonlinear finite element model of a human foot complex with comprehensive skeletal and soft-tissue components capable of predicting both the external and internal stresses and deformations of the foot. The model was validated by experimental data of subject-specific plantar foot pressure measures. The stress analysis indicated the internal stresses doses were site-dependent and the observation found a change between 1.5 to 4.5 times the external stresses on the foot plantar surface. In the forefoot, peak external stress was found in the medial region (the first metatarsal heads). Peak internal stress, however, was shifted to the lateral forefoot region (the fourth and fifth metatarsal heads). It suggested that the normal protective plantar soft-tissue has the potential to redistribute the plantar load such that the internal peak stress can have a significantly different location than the external. The results yielded insights into the internal loading conditions of the plantar soft-tissue, which is important in enhancing our knowledge on the causes of foot ulceration and related stress-induced tissue breakdown in diabetic foot.**

Keywords — **foot ulcers, biomechanics, foot plantar pressure, internal tissue stresses, finite element model.**

I. Introduction

Foot ulcers are among the most devastating complications of diabetes. The lifetime risk for a patient with diabetes developing a foot ulcer could be as high as 25%, and limb amputation, the most costly and feared consequence of a foot ulcer, occurs 10 to 30 times more often in diabetic patients than in general population [1]. Although the development of foot ulceration is a matter of considerable uncertainty, epidemiological and biomechanical studies have indicated that mechanical loads acting on the foot in the form of peak plantar pressures (focal stress) are highly associated with tissue breakdown in diabetic foot [2].

To address foot risks, in the past, many in vivo and in vitro studies have been focused on delineating the potential overloading of the foot by plantar pressure measurements [3]. However, given a combination of complex geometry and nonlinear material behavior of the subcutaneous plantar soft-tissue, force acting on the plantar surface may lead to highly inhomogeneous internal mechanical loading conditions. This is especially true for the sites underneath the prominence of the metatarsal heads, in which soft-tissue contacts with irregular-shaped bony structure causing stress concentration [4]. Therefore, the relationship between the plantar pressure and internal stress is unlikely to be simple. Recent high resolution magnetic resonance imaging (HR-MRI) has revealed that disruption of the subcutaneous deeper plantar tissue in diabetic feet with micro-haemorrhage [5]. If it is true that ulceration of the plantar soft-tissue results from excessive mechanical stress, then it appears reasonable that foot ulceration may be internally initiated and work up toward the outermost skin level.

Therefore, the aim of this study is to develop a detail three dimensional finite element model of the foot capable of predicting the internal stress and strain states. The model is validated by subject specific plantar foot pressure measurements.

II. Method

A. Plantar Barefoot Pressure measurement

In order to obtain plantar barefoot pressure during standing, a foot pressure test was conducted using the F-Scan In-shoe Pressure System (Software v. 5.03, Tekscan. Boston, MA) on a 26 year-older male subject who was free of any foot abnormalities and pathologies. These pressure sensors have a high spatial resolution (4 sensing elements per cm^2) and are ultra-thin (0.15mm), thus can effectively capture the interface pressure between the foot plantar and ground with minimally intrusion. The subject was instructed to stand barefoot on a metal plate (Aluminum-Alloy Standard 2014-

Chwee Teck Lim, James C.H. Goh (Eds.): ICBME 2008, Proceedings 23, pp. 1817–1820, 2009
www.springerlink.com

T6) which represents the ground. Then material property of the plate i.e. ground was thus known which can be defined in the FE model (Density= 2800 kg/m^3, Young's modulus = 72 GPa, Poisons ratio = 0.33). The pressure sensor was inserted between the foot plantar and the ground. To produce reliable measures, five static plantar pressure trials were collected from the subject's right foot. For each test, plantar pressure distribution (force pattern), peak plantar pressure and foot-plate contact area were recorded.

B. Finite Element Modeling

The 3-D geometry of the soft tissue-skeletal foot and ankle joint complex was created based on the coronal computer tomography (CT) scan of the right foot of a male adult who was free of any foot abnormalities and pathologies. Foot structures such as articular cartilages, ligaments and plantar fascia that could not be reconstructed from CT were determined through magnetic resonance (MR) imaging and histological observations. 30 bony parts with articular cartilages, including sesamoids, were created individually and then were enveloped into a mass of foot soft tissue in which the muscular constitutions were not separately identified. A total of 5 sub-bands of plantar fascia and 134 major ligaments (Ligs) were also incorporated into the model to passively stabilize the cartilage-mediated bony joints: 14 ankle Ligs, 11 talocalcaneal Ligs, 14 talonavicular Ligs, 9 calcaneocuboidal Ligs, 13 navicocuneiform Ligs, 27 tarsometatarsal Ligs, and other 46 short Ligs.

In order to simulate the joint interactions among the tibia, fibula, calcaneous, talus, navicular, cuboid, cuneiforms, and metatarsals, ABAQUS "contact" conditions were defined accordingly, which allow bones to slide frictionless over one another. Since the joint surfaces were all wrapped with articular cartilages, the governing stiffness during contact was set to be 1.01MPa which is consistent with the compressive material properties of the foot joint cartilage [6]. Both the bony structures and soft-tissue were meshed with 4-noded tetrahedral elements, while the ligaments and plantar fascia were represented by 2-noded tension-only truss elements. A second-order polynomial hyperelastic material model was applied to incorporate the nonlinear properties into the pad soft tissue. Other structures were assumed to behavior in linear isotropic manners.

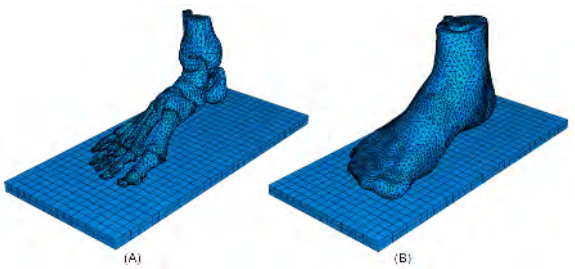


Fig. 1 . FE model of the skeletal structures of the human foot including their ligaments (A) enveloped by a mass of soft-tissue under the skin. (B)

During static standing, an estimated ground reaction force of 325 N (half of the BW) was applied to the foot model through uniformly distributed pressure. An estimated gastrocnemius-soleus muscle force of 162 N acting through Achilles tendon to the calcaneus was also applied by using force vectors, and the superior part of tibia, fibula and soft tissue were all fixed by all degree of freedom. In addition, a frictional contact interaction was established between the foot plantar surface and the ground.

C. Validation

The FE computed axial compressive stress on the ground (σ_{yy}, along Y-direction, perpendicular to the contacting surface of foot plantar) were compared to the plantar pressure distribution measured using F-scan. Quantitative results on nine clinically significant regions as defined by rectangular regions of interest (ROI) on plantar soft-tissue were chosen for comparison: the subhallucal (H), the 1st submetatarsal [medial M1(M) and lateral M1(L) sesamoids], the 2nd to 5th submetatarsal (M2 to M5), the lateral submidfoot (L) and the subcalcaneal (C) region. Moreover, the FE computed center of contact pressure (COP), peak contact stress (PCS), and total contact area (TCA) were also compared with the experimental measures.

D. Regional external/internal stress analysis

The same nine ROI were subsequently used for regional external/internal stress analysis. The stress level calculated from the integration points within each ROI of the plantar surface (outermost plantar soft-tissue) represents the external stress; while the stress level calculated from the innermost plantar soft-tissue which interfaces with the foot bones represents the internal stress. The tissue stress was presented in terms of von Mises stress (σ_V), and principal normal stress (σ_{xx}, σ_{yy} and σ_{zz}) which were linked by the von Mises yield criterion in the form of:

$$\sigma_v = \sqrt{2}/2\left[\left(\sigma_{xx}-\sigma_{yy}\right)^2+\left(\sigma_{yy}-\sigma_{zz}\right)^2+\left(\sigma_{zz}-\sigma_{xx}\right)^2\right]^{1/2}$$

These stresses were averaged over all integration points of tetrahedral element within the boundary of each ROI (4 integration points for each tetrahedral element).

III. Results

As revealed in Figure 2, the FE model predicted similar patterns of plantar pressure distribution with the F-scan

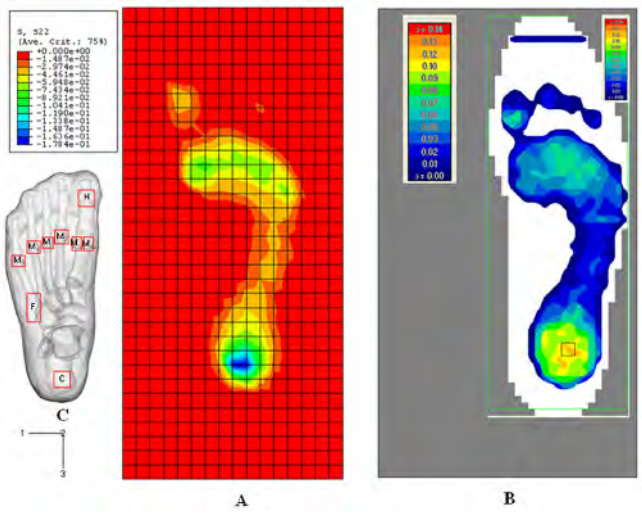


Fig. 2 The FE-computed ground compressive stress distribution (A), and F-scan measured plantar pressure distribution (B) of the same subject during standing. Regions interfacing with the nine rectangular regions of interest (ROI) of foot plantar (C) were compared for FE model validation.

Table 1 Comparison of FE predictions and F-scan measurements

	COP	PCS (MPa)	TCA (mm^2)
F-scan data	Heel center located	0.130	10,700
FE predictions	Heel center located	0.178	7,522

measures. Both the computed peak compressive stress and the measured peak plantar pressure were located beneath the center of the heel region. Forefoot at the level of metatarsal heads predicted the second highest focal stress during plantar support, followed by the big (great) toe and the midfoot which were only minimally involved in weight-bearing process. Site-to-site comparison revealed deviations of FE predictions from F-scan measures ranged from 11.7% to 32.5%. The maximum deviation was located at M5, while M2 displayed the best match between FE prediction and F-scan data. Good agreements were also found between the FE computed foot-ground contact characteristics and F-scan data in terms of COP, PCS and TCA, especially true for the COP and PCS predictions.

The internal stress beneath the adjacent foot bones was significantly higher than the external stress across all nine ROI of the foot plantar. The internal ROI generally showed over 2 folds more stress than the external. The external and internal stress at ROI M2 depicted the largest difference. The internal stress at this site was over 4.5 times greater than the external. The magnifications in other ROI in the descending order are: M4 with 4.4, M5 with 4.0, C with 3.5, M3 with 3.3, M1 (M&L) with 2.0, H with 2.0 and L with 1.5. It demonstrated that stress distribution inside the plantar soft-tissue was inconsistent with the external stress distribution. For forefoot region, externally, sites M1 (M) and M1 (L) experienced the highest stress; while internally most stress was concentrated at M2, M4, and M5. The relationship between external and internal stress of plantar soft-tissue seems to be site-dependent.

IV. Discussion & Conclusions

Abnormally high foot pressures have been shown in the past to be associated with an increased risk for developing foot ulceration [7]. Clinically, an empirical plantar foot pressure of 600KPa has been considered to be indicative of patients at high risk for foot ulceration [8] [9]. In the present study, the internal stress was found to be site-dependent and the observation showed a change between 1.5 to 4.5 times the external stress on the foot plantar surface. Therefore, based on the computed magnification factors, the internal stress inside the plantar soft-tissue can vary from 900KPa up to 2,700KPa. Considering the local pathological stiffening [10] or migration (displacement of fat-pad from beneath bony prominences) [11] of the plantar soft-tissue across the foot plantar, an even higher internal stress or possibly overdosed stress can be expected inside the diabetic foot. Although the exact stress thresholds or the tolerance of the different tissue for normal and diabetic foot are still missing, the external/internal stress associations obtained from the current foot model can serve as a useful baseline case for future work.

Acknowledgment

Format the Acknowledgment and References headlines without numbering.

References

1. Singh N, Armstrong DG, Lipsky BA. (2005) Preventing foot ulcers in patients with diabetes. Jama 293:217-28.
2. Veves A, Murray HJ, Young MJ et al. (1992) The risk of foot ulceration in diabetic patients with high foot pressure: a prospective study. Diabetologia 35:660-3.
3. Duckworth T, Boulton AJ, Betts RP et al. (1985) Plantar pressure measurements and the prevention of ulceration in the diabetic foot. J Bone Joint Surg Br 67:79-85.
4. Morag E, Cavanagh PR. (1999) Structural and functional predictors of regional peak pressures under the foot during walking. J Biomech 32:359-70.
5. Brash PD, Foster JE, Vennart W et al. (1996) Magnetic resonance imaging reveals micro-haemorrhage in the feet of diabetic patients with a history of ulceration. Diabet Med 13:973-8.
6. Athanasiou KA, Liu GT, Lavery LA et al. (1998) Biomechanical topography of human articular cartilage in the first metatarsophalangeal joint. Clin Orthop Relat Res 348:269-81.

7. Stess RM, Jensen SR, Mirmiran R. (1997) The role of dynamic plantar pressures in diabetic foot ulcers. Diabetes Care 20:855-8.
8. Delbridge L, Perry P, Marr S et al. (1988) Limited joint mobility in the diabetic foot: relationship to neuropathic ulceration. Diabet Med 5:333-7.
9. Pham H, Armstrong DG, Harvey C et al. (2000) Screening techniques to identify people at high risk for diabetic foot ulceration: a prospective multicenter trial. Diabetes Care 23:606-11.
10. Gefen A, Megido-Ravid M, Azariah M et al. (2001) Integration of plantar soft tissue stiffness measurements in routine MRI of the diabetic foot. Clin Biomech (Bristol, Avon) 16:921-5.
11. Bus SA, Maas M, Cavanagh PR et al. (2004) Plantar fat-pad displacement in neuropathic diabetic patients with toe deformity: a magnetic resonance imaging study. Diabetes Care 27:2376-81.

Author: Taeyong LEE PhD.
Institute: Division of Bioengineering, National University of Singapore
Street: Block E3A #07-15, 7 Engineering Drive 1
City: Singapore
Country: Singapore
Email: bielt@nus.edu.sg

The Influence of Load Placement on Postural Sway Parameters

D. Rugelj and F. Sevšek

University of Ljubljana, College of Health Studies, Ljubljana, Slovenia

Abstract — **School children, recreational backpackers, soldiers, fire-fighters carry a range of loads from 8 to 40 kg. Little is known about the extent to which carrying an external load on the body affects postural sway. The purpose of the present study was to investigate the effects of increasing load on postural sway in two different carrying positions: backpack and waist jacket.**

31 subjects (age 21.7 ± 1.9; 8 male and 22 female) in backpack group and 20 subjects (age 22.5 ± 1.9; 4 male and 16 female) in the waist jacket group participated in the study. The increment of additional load in both groups was 12, 21 and 30 kg. Stabilometry was used to assess the amount of postural sway. Data were collected by a force platform Kistler 9286 AA. The outlines of the measured data were determined by Fourier coefficients. The sway area, total path length, medio-lateral and antero-posterior path length of the centre of pressure were calculated.

In the backpack group the ratio between no load and additional load of 12 kg, 21 kg and 30 kg for total path length was 1.3, 1.6 and 1.7 respectively, for medio-lateral sway it was 1.3, 1.5 and 1.7 and for the antero-posterior sway 1.3, 1.6 and 1.8. The ratio for sway area was 1.8 at 12 kg, 2.5 at 21 kg, and 2.9 at the load 30kg. However, no significant change of the analyzed parameters was found while subjects carried additional load in the waist jacket.

Our results indicate that the participants' ability to maintain steady position while standing was altered by the external load carried in the backpack. The sway linearly increased for all of the measured parameters. Carrying weight in a backpack increases postural sway with increasing weight whereas carrying weight in the waist jacket does not influence the postural sway. The position of load is thus of significant importance for the postural sway.

Keywords — **Stabilometry, postural sway, load placement**

I. Introduction

Postural stability during load carriage is an important issue for different professions and/or activities. For instance, recreational backpackers carry a range of loads on their backs ranging from 8 to 35 kg [1], soldiers up to 50 kg [2], depending on mission requirements, and fire-fighters with their protective clothes and breathing apparatus with the weight of 26 kg [3]. School children of various age daily transport loads on their back ranging from 8.2 % of their body weight and this value increases with age to 12 % or even 20 % of their body weight [4,5].

Intensive studies were performed to discover the impact of load carriage on energy cost, the influence on gait parameters, effect of load distribution and sex differences – review of [6,7], for the soldiers. On the other hand the problem of stability while carrying heavy load has not been much investigated.

Postural steadiness is related to balance function. Intact and effective balance is important when a person is working on higher surfaces, in altered sensory conditions such as on the soft surfaces or in poorly lit or dark environments.

Postural stability is often assessed with stabilometry which defines the amount of postural sway and indicates the displacement of the centre of mass relative to the base of support. Centre of pressure (CoP) calculated from the ground reaction forces of standing subjects represents the outcome of the postural control. Measurement of the CoP movement with a force platform (stabilometry) is a standard procedure for assessment of postural stability. Subjects are asked to stand still on a special platform that is mounted on pressure sensors transmitting data to a computer where the time dependence of the trajectory of CoP (sway) can be monitored.

Little is known about the extent to which carrying an external load on the body affects postural sway parameters. The linear effect of load weight on the postural sway parameters has been observed in the population of young military service subjects [2]. Increased load challenged subjects' stability, reduced the randomness of postural sway and required greater muscle control in order to maintain balance. Altered sensory conditions (eyes closed) and additional load of 26 kg (full fire-fighters equipment) resulted in increased velocity of postural sway [3]. The position of the relatively small load - 12 kg [8] also influenced the amount of postural sway and subjects swayed more while holding the load above their heads as compared to shoulder or knuckle height.

The above studies did not record more than one load [8] and did not compare the load results to the no load conditions [2] or tested only one additional weight [3]. Majority of the research reports study young male population who are trained to carry weights on daily basis. However, recreational backpackers carry load on their backs as well and they differ in age, gender and physical fitness. Thus the purpose of present study was to investigate the effects of increasing load in a backpack upon postural sway as com-

Chwee Teck Lim, James C.H. Goh (Eds.): ICBME 2008, Proceedings 23, pp. 1821–1824, 2009
www.springerlink.com

pared to increasing load in a waist jacket in a population of young college students.

II. Methods and materials

A. Methods

Stabilometry was used to assess the amount of postural sway. Data were collected by a force platform (Kistler 9286 AA) with 50 Hz sampling rate using BioWare program. Raw data were uploaded to a Linux server and analysed by specially developed software. A typical analysis of the stabilometric data started by data smoothing using moving averages over a chosen number of points (usually 10). It then proceeded by plotting the time and frequency distributions, determining the outline of the measured data, calculating its Fourier coefficients and the total path length of the CoP, medio-lateral and antero-posterior path lengths and finished by determining the total sway area [9].

The Statistical Package for Social Sciences (SPSS 15, SPSS Inc., Chicago, IL USA) was used for statistical analysis. Two sample t-test was applied to test the differences between the two groups for each of the load conditions whereas one way ANOVA was calculated to obtain the differences between the load conditions within a group and the significance level was set at 0.05.

B. Participants

Fifty-one healthy college students with no history of musculoskeletal injuries participated in this study. Minimal required body weight was 50 kg - lighter volunteers were not included. 31 subjects were assigned to the backpack group and 20 subjects to the waist jacket group (Table 1). The study was approved by the National Medical Ethic Committee and the participants gave their informed consent prior to the participation in this study.

Table 1 Demographic data of the participants in the study.

	Backpack group	Waist jacket group
	mean (SD)	mean (SD)
No. of participants	31	20
Age (years)	22.54 ± 4.9	22.45 ± 3.5
Height (cm)	171.96 ± 8.5	173.4 ± 7
Weight (kg)	67.16 ± 10.1	65.6 ± 12.6
Gender (m, f)	8 m, 23 f	4 m, 16 f

C. Procedure

Each participant was tested with three additional loads in a backpack or waist jacket: 12 kg, 21 kg and 30 kg. Participants were instructed to stand as still as possible on the force platform with their feet close together, arms at their sides and looking to a point on the wall 2 m away. All of the participants were tested in five consecutive trials, each lasting for 60 seconds.

The backpack group were carrying a Karrimor backpack with the capacity of 45 litres and were instructed to fix it on the pelvis and to adjust the shoulder straps to fit the backpack as comfortable as possible. Parameters of the body sway were measured first without additional load, then 12 kg sand bags were placed into the backpack. Afterwards the sand bags were added to the backpack to reach the weights of 21 and 30 kg. The last test was a repeated measurement without any additional load.

The subjects in the waist jacket group wore a jacket which consisted of pockets where diving weights (8x5x3 cm, 2 kg) could be placed at the hip, waist and chest height. For the purpose of our study the weights were placed around the waist, half anteriorly and the other half posteriorly. The measurements were performed in the five different load conditions with the same protocol as used for the backpack group.

III. Results

A. Backpack group

The parameters of the postural sway: total path length of the CoP, medio-lateral and antero-posterior path lengths and the sway area significantly increased with the added load in

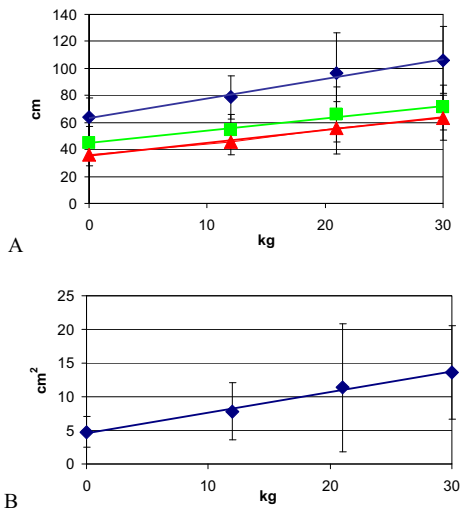


Fig. 1 Linear relationship between four different load conditions for CoP excursions at different loads in the backpack group: (A) total path length (diamond), mediolateral path (square) and anteroposterior path (triangle); (B) total sway area.

a backpack as compared to the no load conditions ($p < 0.01$). Compared to no load, 12, 21 and 30 kg loads resulted in the increase of the total path length by 27.1 %, 55.9 % and 70.9 %, respectively, whereas the medio-lateral sway increased by 26.4 %, 54.2 %, 66.3 % and the antero-posterior sway by 30 %, 60.8 % and 80.4 %. Sway area increased even more with the load: 84.5 % at 12 kg, 154.6% at 21 kg, and 289 % when the load was 30 kg (Fig 1).

Linear regression showed that the total path length increased by 1.6 cm per kg ($R^2 = 0.99$), medio-lateral sway by 0.9 cm/kg ($R^2 = 0.98$), antero-posterior sway by 0.94 cm/kg ($R^2 = 0.99$) and the sway area by 0.3 cm^2/kg ($R^2 = 0.99$). These relations were well reproduced by the linear function as seen from Fig. 1.

B. Waist jacket group

The statistical analysis of the waist jacket results showed that the parameters of the postural sway did not significantly differ between the four load conditions with the p values ranging between 0.306 and 0.938 (Fig. 2).

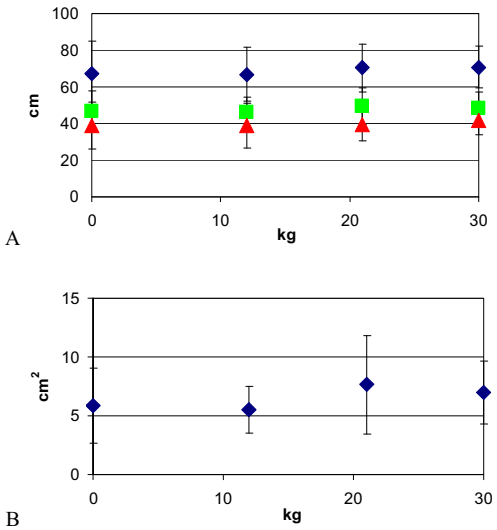


Fig. 2 Mean and standard deviation values for CoP excursions at different loads in the waist jacket group: (A) total path length (diamond), mediolateral path (square) and anteroposterior path (triangle); (B) total sway area.

C. Between group analysis

The t-test revealed that the difference between the backpack and waist jacket groups was not significant at the no load conditions (the first and the last measurements) while the differences between the two groups were statistically significant for the loads of 12 kg ($p = 0.011$) and even more so for 21 kg and 30 kg ($p < 0.001$) as shown in Fig. 3.

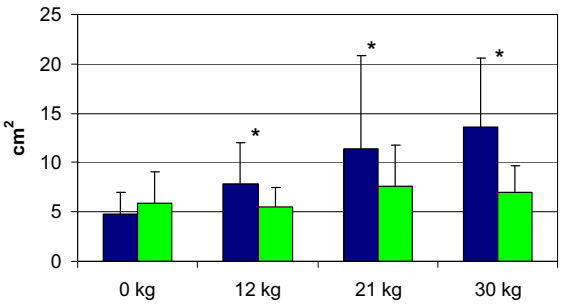


Fig. 3 The influence of two different placements of loads on the sway area for the backpack (left) and the waist jacket groups (right).

IV. Discusion

In the present study we investigated the influence of increased load carriage on the postural sway parameters. Additionally we investigated the influence of two different load placements. Our study design differed from the previous ones in the volunteers sample. Namely, majority of the reported studies investigating parameters of postural sway and other related studies were performed on young, fit soldiers who were trained to carry different loads, whereas our participants were young college students who reported to participate in recreational activities on the average only three times a week.

Our results indicate that the participants' postural steadiness, while standing with different loads in a backpack, was altered. The sway measures showed significant linear increase in the length of CoP excursions in the antero-posterior and medio-lateral directions as well as the sway area. Similar linear dependency on the increasing load was described for young soldiers for all of the postural sway parameters [2]. However, that study did not compare the results to the no additional weight situation. Besides, in our study we repeated the no load condition as the last one in the series of five measurements. Namely, the random nature of the CoP movements, which results in the variability of the postural sway [10], led us to design the additional control measurement. It has shown that there was no statistically significant difference between the both no weight measurements which allows us a higher level of confidence in the linear relationship between the additional load and the amount of postural sway. Similar conclusions were obtained by Punakallio et al [3] for professional fire-fighters carrying 15.5 kg steel air bottles on their backs - their weight was found to significantly impair both postural and functional balance.

Besides, the position of the load has been shown to influence subjects' energy expenditure: evenly distributed load in a double pack [7] required less energy as compared to a

backpack. Our results of stabilometry showed similar relationship for the postural sway parameters - increased weight placed evenly around the waist did not influence the size of CoP movements contrary to the case when the weight was carried in a backpack. The comparison of the results at the same additional weight in different positions showed no differences of the postural sway parameters in both no load conditions whereas with all other weights (12 kg, 21 kg and 30 kg) the differences between the two weight positions were statistically significant (except for the antero-posterior sway at 12 kg).

The control of the centre of mass position is expected to differ with the position of load on the body. For instance, load in the backpack requires more forward body lean and more forward rotation about the hips and ankle [11] and the moment at the joints is greater when the load is placed higher on the body [12]. The difference between the sizes of CoP displacements could be attributed to larger rotational inertia of the load that is higher an not evenly distributed around the torso.

The variability of CoP fluctuations and increased postural sway has been traditionally considered as a sign of loss of control, usually related to the deterioration due to age or disease. More recently this variability has become considered an essential element of the movement parameters that are under direct control of the central nervous system [13,14]. In the waist jacket group the variability between the subjects, expressed as standard deviation, decreased with the increasing load (Fig.2). These results indicate that with increasing weight most of the subjects adopted similar strategy. Decreased variability could also be attributed to increased stiffness of the postural muscles. On the other hand, in the backpack group the sway parameters and the variability between the subjects increased with increasing load which may indicate different control strategy in the situation when the load is placed in the backpack, which shifts the centre of mass posteriorelly, as compared to the load placed in the waist jacket where its position is not changed.

V. Conclusions

Maintaining of balance in a situation of additional weight carried on the persons back is important for different occupations as well as for the recreational purposes. Carrying weight in a backpack linearly increases postural sway parameters with increasing weight whereas evenly distributed weight does not affect the sway parameters. Weight distribution is thus an important parameter that influences postural sway and balance maintenance. For the prevention of balance related injuries it is advisable to consider not only the size of the carried weight but also its distribution.

References

1. Lobb B, (2004) Load carriage for fun: a survey of New Zeland trampers, their activities and injuries. Appl Ergon 35, 541-547.
2. Shiffman JM, Bensel CK, Hasselquist L, Gregorczyk KN, Piscitelle L. (2006) Effects of carried weight on random motion and traditional measures of postural sway. Appl Ergon 37:607-614.
3. Punakallio A, Lusa S, Luukkonen R. (2003) Protective equipment affects balance abilities differently in younger and older firefighters. Aviat Space Environ Med 74:1151-1156.
4. Forjuoh SN, Lane BL, Schuchmann JA, (2003) Percentage of body weight carried by students in their school backpacks. Am J Phys Med Rehabil 82: 261-266.
5. Negrini NS, Carabalona R, (2002) Backpacks on! Schoolchildren's perception of load, associations with back pain and factors determining the load. Spine, 27:187-195.
6. Knapik J, Harman E, Reynolds K, (1996) Load carriage using packs: A review of physiological, biomechanical and medical aspects. Appl Ergon, 207-216.
7. Knapik J, Reynolds K, Harman E. (2004) Soldier load carriage: Historical, physiological, biomechanical and medical aspects. Military Med 169: 45-56.
8. Lee TH, Lee YH, (2003) An investigation of stability limits while holding a load. Ergonomics, 46:446-454.
9. Rugelj D, Sevsek F (2007) Postural sway area of elderly subjects. *WSEAS transactions on signal processing* 3: 213-219.
10. Collins JJ, De Luca CJ (1993) Open-loop and closed-loop control of posture: A random-walk analysis of center-of-pressure trajectories. Exp Brain Res 95:308-318
11. Bloom D, Woodhull-McNeal A. (1987) Postural adjustments while standing with two types of load backpack. Ergonomics 30:1425-1430.
12. Bobet J, Norman RW. (1984) Effects of load placement on back muscle activity in load carriage. Eur J Apll Physiol 53:71-75.
13. Latash ML, Scholz JP, Schoener G. (2002) Motor control strategies revealed in the structure of motor variability. Exe Sport Sci Rev 30: 26-31
14. Van Emmerik A, van Wegen, H. (2002) On the functional aspects of variability in postural control. Exe Sport Sci Rev 30:177-183.

Author: Darja Rugelj
Institute: University of Ljubljana, College of Health Studies
Street: Poljanska 26 a
City: 1000 Ljubljana
Country: Slovenia
Email: darja.rugelj@vsz.uni-lj.si

Shape Analysis of Postural Sway Area

F. Sevšek

University of Ljubljana, College of Health Studies, Ljubljana, Slovenia

Abstract — **Measurement of the human body centre of pressure (COP) movement (postural sway) with a force platform is a standard procedure for the assessment of postural stability. Recently we proposed a method where the outline of the sway region is expressed in terms of Fourier coefficients determined by asymmetric fitting and minimal outline bending. The index of sudden excursions (ISE) is defined as the ratio of this sway area to the one obtained by the standard principal component analysis. The meaning and the discriminative power of this index is still an open question, which is addressed in present work.**

Stabilometric data were simulated by considering movements of COP in a potential that consisted of a flat central ellipsoidal region and increased quadratically outside it. Using random walk procedure, combined with the Metropolis algorithm, positions of COP were simulated. The parameter called temperature was defined so that it was related to the probability of COP movements against the potential.

A large number of data were calculated for a set of different values of the temperature and the ISE values were determined. For the series of 3000 points the average values of ISE were found at first to increase with temperature from 1.3 to 1.85 as the temperature increased from 0 to 0.195 and then started to decrease towards 1.2 with temperature.

It was shown that ISE is sensitive to the actual shape of the measured postural sway area. It increases if there is a small number of large excursions of the COP outside the central region, which are mostly missed by the conventional analysis.

Keywords — **stabilometry, postural sway, force platform, sway area**

I. Introduction

Measurement of the movement of the human body centre of pressure (COP) with a force platform (stabilometry) is a standard procedure for assessment of postural stability. Here a subject stands still on a special platform that is mounted on pressure sensors that transmit data via analogue to digital converter to a computer. In such a way, with suitable software, the time dependence of the trajectory of the COP (postural sway) can be determined. Thus obtained stabilogram can be used to assess the balance properties of the investigated subjects. Although this method is well established, the interpretation of the results and the physiological meaning of the calculated parameters is still an open issue. Besides the standard parameters such as COP trajectory length, velocity, displacements and frequency distribution, the interpretations in terms of non-linear dynamics are also very promising [1]. Yet a simple measure to discriminate stabilograms of different populations, of mostly elderly subjects, is needed. For this purpose the shape and size of the area covered by the COP is determined.

The usual method to determine the area of a stabilogram is by the principal component analysis (PCA) of the covariant matrix [2]. The eigenvalues (σ_0^2) of the covariant matrix (σ_{xy}^2)

$$\sigma_{xy}^{\ 2} = \frac{1}{N}\sum_{i=1}^{N}(x_i - \bar{x})(y_i - \bar{y}) \tag{1}$$

are calculated as

$$\sigma_0^{\ 2} = \frac{1}{2}(\sigma_{xx}^{\ 2} + \sigma_{xy}^{\ 2} \pm \sqrt{(\sigma_{xx}^{\ 2} - \sigma_{xx}^{\ 2})^2 + 4(\sigma_{xx}^{\ 2})^2}) \tag{2}$$

where $\bar{x}$ and $\bar{y}$ are the average values and the summation is done over all N measured points.

The sway area is usually reproduced by the ellipse with the two principal axes of the size 1.96 σ_0^2. It thus includes 95 % of points along each axes if the distribution is bivariate Gaussian and as a result only 85.35 % of the data points are within the perimeter of the so defined ellipse [2]. This method reflects the general properties of the sway area but is not sensitive enough to differentiate between clinical conditions where the important changes are expected to be seen mostly near in the sway area perimeter.

This led us to develop a new method based on the Fourier analysis of the sway area outline (FAO) [3, 4]. It was shown that such an analysis realistically approximates the postural sway area and also gives the indications about its shape. This method is based on the observation that a suitable approximation to the sway area is a region determined by a rather simple, mostly convex outline which is predominantly at the outer border of the sway area. From the measured stabilogram the outline is determined by a boundary following algorithm [5]. Such an outline can be reproduced by a Fourier series:

$$\mathrm{R}(\varphi) = \mathrm{R}_0 + \sum_{m=1}^{m_{\max}}(A_m \cos m\varphi + B_m \sin m\varphi) \tag{3}$$

where φ is the polar angle to a point at the outline in a chosen coordinate system, A_m and B_m are the appropriate Fou-

Chwee Teck Lim, James C.H. Goh (Eds.): ICBME 2008, Proceedings 23, pp. 1825–1828, 2009
www.springerlink.com

rier coefficients and m_{max} the maximal number of coefficients used to describe the outline - the more coefficients are used, the smaller details of the shape are reproduced. So defined Fourier coefficients are similar to the Fourier descriptors usually employed in shape recognition procedures [6, 7, 8], the difference is that our outline points are function of the angle rather than the distance along the outline path.

The fitting of the sway area outline is done by minimizing the characteristic function (F):

$$F = \sum_{i=1}^{N} \omega_i (R(\varphi) - R_i)^2 + \gamma \sum_{m=0}^{m_{max}} m^2 (m-1)^2 (A_m^{\,2} + B_m^{\,2}) \quad (4)$$

where the first term is the asymmetric sum of the squares between the calculated (R(φ)) and the measured (R_i) outline points. The asymmetry parameter ω determines the distance the fitted curve can penetrate inside the measured sway area. It equals to one when the distance of the calculated point from the chosen centre is larger than the measured one otherwise it has a preselected value. The second term in eq.(4) is related to the outline bending energy and penalizes the short distance undulations of the outline, depending on the value of the parameter γ.

From our previous work [3] the ratio between the areas as determined by the FAO and PCA methods seemed to be the most promising discriminating parameter between the stabilograms that differed mainly by the small number of COP excursions from the central region. We thus named it the index of sudden excursions (ISE). To better understand the meaning and properties of this index we, in as follows, analyze the simulated data using the same procedure as for the experimental data.

II. Methods

The meaning of the index of sudden excursions (ISE) which is defined as the ratio between the FAO and PCA areas was thoroughly studied by analyzing simple simulated data.

The fluctuation of the COP position was described by a model that was equivalent to the movement of a particle in a potential that is flat in the central ellipsoidal region and quadratic outside it. In such a way COP could move outside the chosen central region, but the probability of finding it there decreased with the distance from the boundary whereas the temperature parameter (T) defined this probability.

Thus the calculations were done by considering completely free random movement of the COP within a chosen ellipsoidal region and with Boltzmann distribution of the probability to find it outside. For this purpose random walk procedure was used combined with Metropolis algorithm

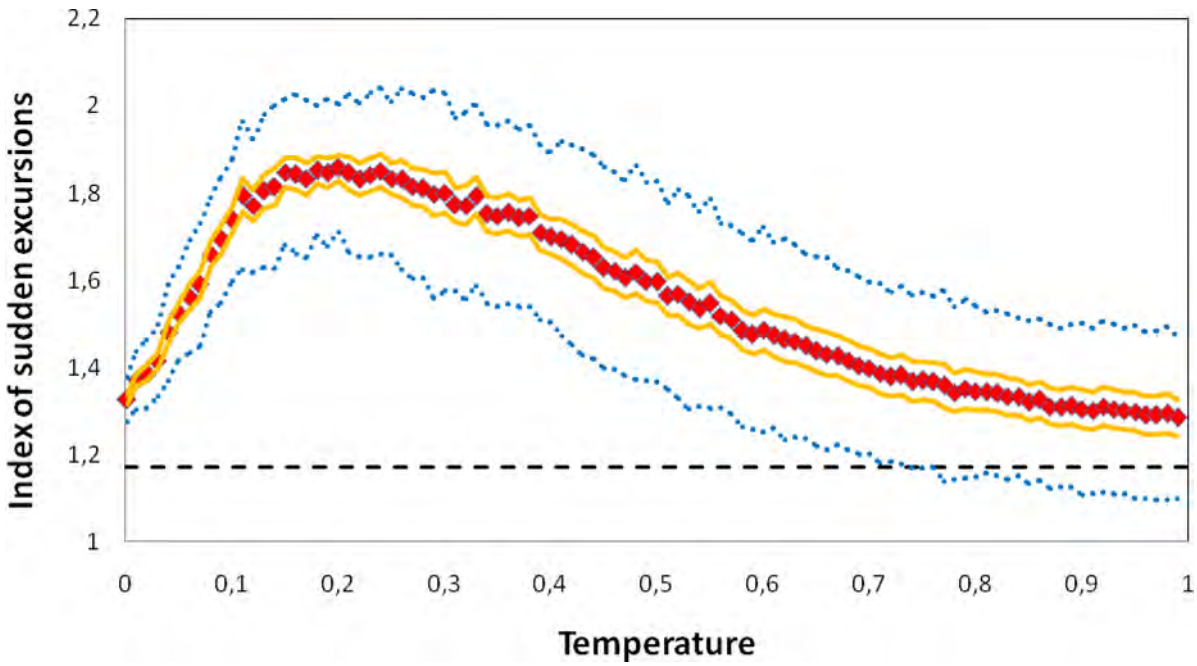


Fig. 1 Index of sudden excursion (ISE) as a function of temperature parameter in units of 1/2π, as defined in text, for the simulated data of 3000 points. Besides the calculated average values of 20 simulation runs (red squares), the lines represent the region of the standard error (yellow) and standard deviation (dotted blue) whereas the dashed line at 1.2 represents the low temperature limit.

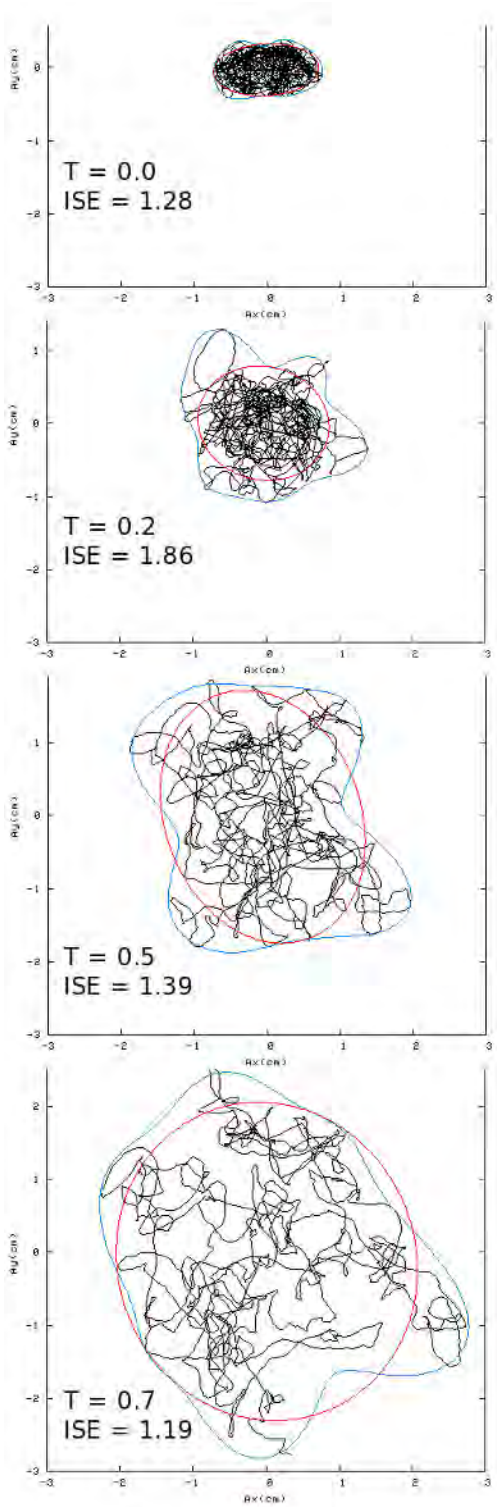


Fig. 2 Simulated data (black lines) for four different temperatures with the PCA ellipsis (red) and the FAO outlines (blue).

[9]. In each step the COP position was randomly moved. If the resulting position was within the central ellipsoidal region it was accepted and the procedure was repeated. But, when the resulting position was outside this region and the previous one was inside it, the distance (ΔR) from the border was calculated. Such a move was accepted only with the probability $\exp(-\Delta R^2/T)$, where ΔR^2 played the role of energy that was proportional to the square of the distance, whereas T corresponded to the temperature. The procedure was similar also in the case when the previous point was outside, but in this case the calculated value ΔR was the difference between the distances of the two points from the centre. If ΔR was negative, the move was accepted, otherwise it was accepted only with the probability $\exp(-\Delta R^2/T)$. After a large number of steps thus generated trajectory samples the configurations in accord with the canonical Boltzmann distribution. [9]

The actual calculation always started with a point somewhere inside the ellipsoidal region and the first few ten thousand points were rejected to allow the system to thermalize. After collecting the required number of data points they were analyzed with the same procedures as the experimental measurements.

The computations were mostly performed on a PC-type computer based on Pentium 2 GHz processor, running under Linux operating system. The data simulation program was written in Fortran and used the portable pseudo-random number generator ran3 [10], based on a subtractive method that has very long period and no evident defects.

III. Results and Discussion

Data were simulated as described above with the Boltzmann distribution at different temperatures. Choosing arbitrary the ratio of the ellipsis axis to be a/b = 2 and the maximal step length in each simulation to be equal to the semiminor axis of the central ellipse (b) the only free parameter of the model remained the temperature (T). As it was measured in the units of b^2 the properties of the model were independent of the actual dimension of the simulated region. After eliminating the first 20000 steps the next 60000 moves were considered. This corresponded to the 20 consecutive series of 3000 points that were each comparable to 60 s of the experimental data with 50 Hz sampling rate.

As an example the simulated data for four different temperatures are shown in Fig. 2. The size of b was chosen to be $(1/2\pi)^{1/2}$ so that the area of the central ellipse was equal to one.

It may be noticed that for low temperatures most of the COP fluctuations are within the central region and the principal component method reproduces well the general prop-

erties of the area. As it encompasses 85.35 % of all points, the area ratio between the real outlines, as determined by the FAO method, and the one of the PCA, is expected to be close to 1.2 for long enough simulations. Thus at low temperature increasing it results in more excursions of the COP outside the central region during the observational time. The FAO to PCA area ratio thus at first increases with the temperature and is expected to depend upon the observational time - longer times result in more regular shapes. But at a certain temperature this trend is inverted - still further increasing the temperature results in lowering the FAO to PCA area ratio. This is not surprising since at higher temperatures the positions of the COP get more and more evenly distributed over the entire region.

This behavior is evident from the Fig. 1 where the average values of ISE for 20 simulation runs are shown together with the regions of the standard error and standard deviation. It is interesting to note that for our simulations the area ratio is maximal at the temperature 0.195 ± 0.03 b^2 where it reaches the value of 1.850 ± 0.004. Due to the random nature of this calculation the exact position and value of this maximum cannot be determined from the calculated data as shown in Fig. 1.

IV. Conclusions

By analyzing a large series of simulated data it was shown that ISE is sensitive to the actual shape of the measured postural sway area. It increases if there are small number of large excursions of the COP outside the central region, which are mostly missed by the conventional analysis. Anyhow, the applicability and usefulness of the proposed index to clinical data still remains to be investigated.

Acknowledgment

This research was partly supported by the Slovenian Research Agency, contract No. J3-0178-0382-08.

References

[1] Collins JJ, De Luca CJ (1993) Open-loop and closed-loop control of posture: A random-walk analysis of center-of-pressure trajectories. Exp Brain Res 95:308--318
[2] Oliveira L et al. (1996) *Physiol. Meas.* 17: 305–312
[3] Rugelj D, Sevšek F (2007) WSEAS transactions on signal processing 3: 213–219
[4] Sevšek F (2007) WSEAS transactions on information science and applications 4: 794–799
[5] Sevšek F, Gomišček G (2004) *Comput. methods programs biomed.* 3: 189–194
[6] Bankman I, Spisz T, Pavlopoulos S (2000) in Handbook of Medical Imaging, Processing and Analysis, Bankman I.N. ed., Chap. 14. Academic Press
[7] Gonzalez R, Woods R (1992) Digital image processing. Addison-Wesley
[8] Sanchez-Marin F (2000) Automatic recognition of biological shapes with and without representation of shape. Artificial Intelligence in Medicine 8:173—186
[9] Chandler D (1987) Introduction to Modern Statistical Mechanics. Oxford University Press
[10] Press W.H. and Teukolsky S.A. (1992) *Computers in physics* 6, 522 – 524

Author: France Sevšek
Institute: University of Ljubljana, College of Health Studies
Street: Poljanska 26 a
City: 1000 Ljubljana
Country: Slovenia
Email: france.sevsek@vsz.uni-lj.si

Concurrent Simulation of Morphogenetic Movements in Drosophila Embryo

R. Allena[1], A.-S. Mouronval[1], E. Farge[2] and D. Aubry[1]

[1] MSSMat Laboratoire, CNRS UMR8579, Ecole Centrale Paris, Chatenay-Malabry, France
[2] Institut Curie, Paris, France

Abstract — **The present work describes a 3D Finite Elements model of the *Drosophila* embryo designed to investigate large strains of epithelial tissues during embryogenesis. Three movements standing out for specific mechanical constraints are simulated: ventral furrow invagination, cephalic furrow formation and germ band extension. A deformation gradient decomposition is used to couple an imposed active deformation, according to the morphogenetic movement considered, and a passive elastic deformation consequence of the latter. The model also imposes boundary conditions such as the rigid contact with the vitelline membrane and the yolk pressure. The concurrent simulation of the three events is allowed; here we present the mechanical and the numerical formulation of the highly non-linear problem with special emphasis on the incorporation of cell deformations into a sound mechanical framework.**

Keywords — **Drosophila, Morphogenetic movements, Cell deformation**

I. Introduction

During embryogenesis nonlinear anisotropic tissues undergo large deformations including growth and contraction so that their final configuration and the physical form of the organs are optimally designed to carry out their specialized functions. Therefore the understanding of the mechanics of the four-dimensional process of morphogenesis is required [13].

Drosophila embryo starts as a single cell surrounded by a semi-hard *vitelline membrane* and only after fertilization and mitosis, nuclear division begins with the formation of the cellular blastoderm at the fifth stage. It is at stage sixth that *gastrulation* starts with the mesoderm invagination that takes about twenty minutes to complete. The invagination of the blastula creates the mesodermal and ectodermal germ layers. The sequence of morphogenetic movements starting at the onset of *gastrulation* is tightly controlled by the cascade of developmental gene expression. But latest experimental observations have demonstrated that the expression of such genes is often influenced by mechanical stresses [4], [8], [9]. While genetics and molecular processes of *Drosophila* embryogenesis have been well investigated during the last decades, only recently mechanical modeling have become important to a complete understanding of the biological system as a whole. Several 2D models have been developed [1], [2], [10], [12] and in different ways they solve the biomechanical challenge of *Drosophila gastrulation* but one common drawback is that they allow to simulate only one mechanism at the time. Furthermore only Brodland [5] and Conte [6] have developed so far 3D models so that they have been able to take into account all the aspects of the problem.

The present work provides a unique 3D Finite Elements model able to concurrently simulate three morphogenetic movements: ventral furrow invagination, cephalic furrow formation and germ band extension. Therefore it is possible to consider the eventual influence that one event may have on the other two and vice versa. Also we analyze the elementary and mesh independent deformations occurring to the material pseudo-cells along the simulations.

II. Theoretical approach of the problem

Large strains of the mesoderm are considered using a deformation gradient decomposition method where the total deformation of a cell is decomposed into a non-stress-generating deformation relative to the reference configuration (what we have defined as individual deformation for each cell) and a stress-generating elastic deformation due to the deformation incompatibility between adjacent cells. The model presented here does not take so far into account potential causes for the active deformations; no forces external to the cell layer are implemented, except for the required *yolk* pressure and the contact between the mesoderm and the rigid *vitelline membrane*.

If x represents the current position of a point in a cell of the mesodermal tissue and p its reference position, the total deformation is described by its deformation gradient

$$F = D_p x \tag{1}$$

During morphogenesis, each cell tends to change its shape because of endogenous mechanical or chemical stresses. These individual changes must be considered with the fact that the cells are part of a system and thus in contact with one each other. Therefore single shape modifications lead to a new configuration of the embryonic tissues. If we

Chwee Teck Lim, James C.H. Goh (Eds.): ICBME 2008, Proceedings 23, pp. 1829–1832, 2009
www.springerlink.com

impose the initial individual deformation occurring to each cell, we can define the relative deformation gradient as

$$F_0 = F_0\left[p, \alpha(t)\right] \tag{2}$$

function of the initial position of a material point p and of some parameters $\alpha(t)$ depending on the time.

Thus the elastic deformation gradient, which triggers the mechanical stresses, is

$$F_e = FF_0^{-1} \tag{3}$$

Mesoderm is considered here as a Saint-Venant material because it seemed to us the most suitable choice even if hyper-elastic characteristics could have been used [2], [5], [6]. Let be w the virtual displacements field, we can finally introduce the virtual work, which results to be function of π, the first Piola-Kirchhoff stress, therefore of F_0

$$W = Tr\left(\pi\, D_p w^T\right) = f\left(F_0\right) \tag{4}$$

An important aspect to be taken into account is the contact between the mesoderm and the stiff *vitelline membrane*. We did not model the shell surrounding the embryo but we use an adaptive penalty method to sort out this issue. The main idea is to introduce a surface force, which pushes back the mesoderm when it penetrates the *vitelline membrane*, while no force is applied when penetration is not detected. Two situations can be contemplated so that the applied force f_{se} is

$$\begin{aligned} s < 0 \quad & f_{se} = t_n n_e \\ s > 0 \quad & f_{se} = -p_e\left(s\right) n_e = -\left(t_n + k_n s^2\right) n_e \end{aligned} \tag{5}$$

where s represents the overlapping, along the outward normal n_e, between a generic point and the vitelline membrane while t_n is a small constant force and k_n a parameter depending on the pre-defined maximal admissible penetration $s_{\max}$.

The *yolk*, a viscous material, which fills the embryo, is not meshed here because its mechanical characteristics are still not well known. Anyway it plays an important role exerting a pressure on the mesoderm, which can influence the response of the system. To take into account this aspect, we decided to compute a uniform pressure p_y coupled with the global volume change of the *yolk* [6].

The surface force f_{sy} is assumed to be

$$f_{sy} = -p_y n_y = \left(p_{y_0} - k_y\left(V_y - V_{y_0}\right)\right) n_y \tag{6}$$

where p_{y_0} and V_{y_0} are the initial pressure and volume of the *yolk*, k_y the *yolk* compressibility and V_y the actual volume defined as follows

$$V_y = \int_{\Omega_y} \frac{div\, x}{3} dV = \frac{1}{3}\int_{\partial\Omega_y} \left(x, n_y\right) dS_x \tag{7}$$

where n_y is the inward positive normal on the internal surface of the mesoderm.

It has to be noticed that, while for the contact with the *vitelline membrane*, the surface force depends on the local displacement, in the case of the *yolk* pressure, p_y is function, by V_y, of the displacements of the whole interior boundary of the mesoderm.

III. Mechanical Modelling of the Embryo

As mentioned before, only mesoderm was modeled; it is represented as an ellipsoid whose dimensions have been deduced from experimental manipulations. It is 500 μm in length and it has a diameter in the cross-sections equal to 150 μm, while thickness is 15 μm (Fig.1a, b). We choose from literature [14] a Young's modulus of 100Pa and a Poisson's coefficient $\nu = 0.45$.

Each one of the three movements we simulate, stand out for specific biological forces occurring to the cells that induce lengthening, intercalation, rearrangement, flexion, apical constriction and apico-basal elongation.

We analyze each relative context from the mechanical point of view, trying to describe the different events.

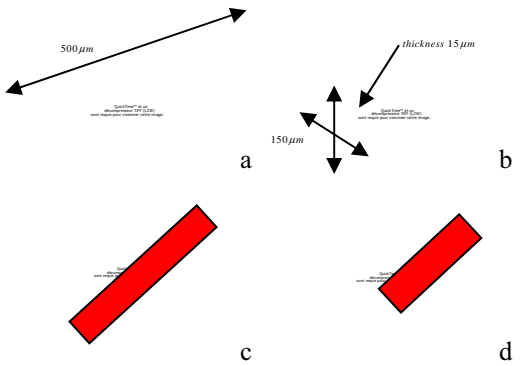


Fig.1 (a,b) Geometry of the embryo. In red the regions where the apical constriction and the apico-basal elongation (c) and the convergent-extension movement (d) have been applied respectively.

A. Ventral furrow invagination and cephalic furrow formation

Ventral furrow invagination is the first movement of the *Drosophila* embryo and one of the most well studied in biology [7]. At this stage of morphogenesis, the embryo is composed of a single layer of columnar epithelial cells having their apical surfaces outward facing and the apico-basal axis aligned along the axis of radial symmetry and each cell is in lateral contact with its neighboring. Several movements can be observed during the invagination, but we focus only on apical constriction and apico-basal elongation of the cells. Practically cells change their shape from cylindrical to trapezoidal form inducing the curvature necessary for the invagination of the mesoderm into the *yolk*.

Same mechanical forces drive the formation of the cephalic furrow at about 65% egg length, simulteously with the ventral furrow invagination, but this time the reference axis is inclined at about 30° with respect to the vertical axis. Using cylindrical coordinates (r,θ,z), the initial position (before any deformation) $p_0(\theta,z)$ of a point along the middle surface of the mesoderm, defined parametrically by $\rho(z)$, is

$$p_0(\theta,z) = \rho(z) i_r(\theta) + z\, i_z \tag{8}$$

Moving trough the thickness of the mesoderm, the position of a generic point becomes

$$p(\theta,z,\zeta) = p_0(\theta,z) + \zeta n_0(\theta,z) \tag{9}$$

where $n_0(\theta,z)$ is the normal vector to the middle surface. The apical constriction and the apico-basal elongation are applied on a restricted area of the ventral region of the embryo (Fig.1c) and the final position after deformation can be shown to be

$$x(\theta,z,\zeta) = p_0(\tilde{\theta}(\theta,\zeta),z) + \left(1+\alpha^{abe}\right)\zeta n_0(\tilde{\theta}(\theta,\zeta),z) \tag{10}$$

where

$$\tilde{\theta}(\theta,\zeta) = \theta + \alpha^{ac}\zeta m(\theta) \tag{11}$$

is the deformation angle depending on α^{ac}, the amplitude of the apical constriction, and on $m(\theta)$, which is a periodic function allowing to have the same deformation for each cell, and α^{abe} is the amplitude for the apico-basal elongation. For the cephalic furrow, we started by modeling it perpendicular to the vertical axis so that the final position x of a generic point can be written as

$$x(\theta,z,\zeta) = p_0\left(\theta,\tilde{z}\left(\alpha^{ceph},m(z)\right)\right) + \zeta n_0\left(\theta,\tilde{z}\left(\alpha^{ceph},m(z)\right)\right) \tag{12}$$

with z here again depending on a periodic function $m(z)$ and on the amplitude of the deformation α^{ceph}.
Finally F_0 can be computed for both simulations from

$$F_0 = \frac{\partial x}{\partial\theta}\otimes\nabla_p\theta + \frac{\partial x}{\partial z}\otimes\nabla_p z + \frac{\partial x}{\partial\zeta}\otimes\nabla_p\zeta \tag{13}$$

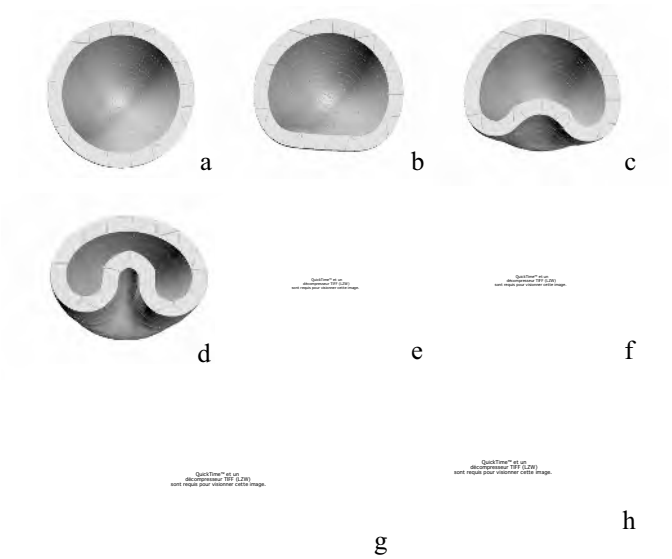


Fig.2 (a:e) Successive phases of ventral furrow invagination; (e) Global view of the shape changes occurring to the material pseudo-cells. The more the mesoderm invaginates, the higher the apical constriction. Also the constriction switches from apical to basal according to the tissue bending; (f) Influence of the apico-basal elongation on the invagination; (g) Preliminary results for a cephalic furrow perpendicular to the vertical axis with a pseudo-cell in the cross-sectional view (h) undergoing apical constriction.

B. Germ band extension (GBE)

After invagination of the ventral furrow and the formation of the cephalic furrow, germ-band starts to extend at ventral region of the embryo.

Germ band extension is a convergent-extension movement of the cells, which may be a passive response to some forces generated elsewhere in the embryo or active, force-producing process. Cells lengthen along the dorsal-ventral axis and shorten from the dorsal to the ventral region. Actually during GBE tissues change their morphology due to interactions occurring between cells rather than interactions with external boundaries. At this stage no cell growth and appropriate changes in cell shapes have been observed,

probably rearrangement and intercalation of cells have to be considered [3], [11].

Let p_0 be the initial position of a point on the middle surface of the mesoderm (Eq. [8]) and p the position of a point trough the thickness of the mesoderm (Eq. [9]).

We propose a uniform membrane convergent-extension deformation movement applied in the region of the germ band (Fig.1d), so that the final position x after deformation comes to be

$$x(\theta, z, \zeta) = p_0(\tilde{\theta}, \tilde{z}) + \zeta n_0(\tilde{\theta}, \tilde{z}) \qquad (14)$$

where $\tilde{\theta} = (1 + \alpha_\theta^{gbe})\theta$ and $\tilde{z} = (1 + \alpha_z^{gbe})z$, with α_θ^{gbe} and α_z^{gbe} are the amplitudes respectively of the extension along the anterior-posterior axis and of the shortening from the dorsal to the ventral region. Finally F_0 can be again computed as in Eq. [12].

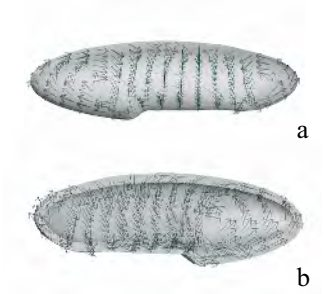


Fig.3 Frontal (a) and cross-sectional (b) views of germ band extension simulation. Tissues elongate towards the anterior and posterior pole, while they converge from the dorsal to the ventral region of the embryo.

IV. Conclusions and perspectives

Our model presents a concurrent simulation of three morphogenetic movements; the original contribution of this work is that we take into account elementary and mesh independent deformations of the material pseudo-cells. This represents a useful tool to analyze the eventual long-range feedback between mechanics and gene expression.

Still many aspects have to be investigated in order to have a more global and relevant view of the problem.

First of all, we think the geometry of the embryo can influence the response of the entire system; for this reason we have designed a more suitable embryo in which the curvature is more similar to the one of the Drosophila: it varies from positive in the ventral region to negative in the dorsal.

Interesting would be also to analyze the self-contact, which may occur during ventral furrow invagination and thus engenders new repulsive forces.

Finally, for what concerns the mechanical characteristics of the mesoderm, a non-linear constitutive behavior will be implemented for further simulations.

References

1. Alberch O., Odell G.M., Oster G. and Burnside P. (1981) The mechanical basis of morphogenesis. Epithelial folding and invagination. Dev. Biology, 75: 446-462
2. Barret K., Muñoz J. and Miodownik M. (2007) A deformation gradient de composition method for the analysis of the mechanics of morphogenesis. Journal of Biomechanics, 40: 1372-1380
3. Bertet C. (2004) Myosin-dependent junction remodelling controls planar cell intercalation and axis elongation. Nature, 429:667-671
4. Brouzés E. and Farge E. (2004) Interplay of mechanical deformation and patterned gene expression in developing embryo. Curr. Opin. Genet .Dev., 14: 367-74
5. Clausi D.A. and Brodland G.W. (1994) Embryonic tissue morphogenesis modeled by fem. J. Biomech. Engin., 116: 146-155
6. Conte V., Muñoz J. and Miodownik M. (2007) A 3D finitel element model of ventral furrow invagination in the drosophila melanogaster embryo. Journal of the mechanical behavior of biomedical materials., 1:188-198
7. Davidson L., Koehl M.A.R., Keller R. and Oster G.F. (1995) How do sea urchins invaginate? Using biomechanics to distinguish between mechanisms of primary invagination. Development, 121: 20005-2018
8. Farge E. (2003) Mechanical induction of Twist in the Drosophila foregut/stomodeal primordium. Current Biology, 13: 1365-1377
9. Ingber D.A. (2006) Mechanical control for tissue morphogenesis during embryological development. Int. J. Dev. Biol., 50: 255-266
10. Pouille P.A. and Farge E. (2007) Hydrodynamic simulation of multicellular embryo invagination. Phys. Biol., 5/015005
11. Keller R., Davidson L., Edlund A., Elul T., Ezin M., Shook D. and Skoglund P. (2003) Mechanisms of convergence and extension by cell intercalation. Philos. Trans. R. Soc. Lond. B. Biol. Sci., 355: 1399
12. Ramasubramanian A. and Taber L.A. (2008) Computational modeling of morphogenesis regulated by mechanical feedback. Biomechan Model Mechanobiol, 7: 77-91
13. Taber L.A. (1995) Biomechanics of growth, remodeling and morphogenesis. Appl. Mech. Rev., 48(8): 487-545
14. Wiebe C. and Brodalnd G.W. (2005) Tensile properties of embryonic epithelia measured using a novel instrument. J. Biomech., 38: 2087-2094

Author: Rachele Allena
Institute: MSSMat Laboratoire, CNRS UMR8579
Ecole Centrale Paris
Street: Grande voie des vignes
City: Chatenay-Malabry
Country: France
Email: rachele.allena@ecp.fr

Application of Atomic Force Microscopy to Investigate Axonal Growth of PC-12 Neuron-like Cells

M.-S. Ju[1], H.-M. Lan[1], C.-C.K. Lin[2]

[1]Dept. of Mechanical Engineering, National Cheng Kung University, Taiwan
[2]Dept. of Neurology, Medical Center, National Cheng Kung University, Taiwan

Abstract — **A nerve conduit with suitable biomechanical and biochemical environment may improve the regeneration of axons of the injured peripheral nerve. The PC-12 cells were cultured in PRMI medium 1640 and then axonal growth was induced by using nerve growth factor. Time-course morphological changes of the cells were analyzed by using an optical microscope. Regional viscoelasticity and adhesion force of axons were measured by an atomic force microscope by using ramp-and-hold indentation and scratching. The data were fitted with a quasi-viscoelastic model by a method developed previously. Morphological results revealed that cell body length and branch number were highly correlated with axonal growth process and average axon length can be used to define the stage of growth process. Electrical field with intensity of 100mV/mm could enhance the growth rate of axons by 2.88 folds. AFM results showed that the mean elastic modulus of axon increased with stage and the growth cone region has higher Young's modulus than the middle region. Furthermore, the adhesion force on middle region of axon was smaller than that of proximal region and growth cone.**

Keywords — **PC-12 cell, Quasi-linear-viscoelasticity, Axon growth, Atomic force microscopy, Electrical stimulation.**

I. Introduction

The nerve conduit plays an important role on auxiliary nerve tissue and cell regeneration during the therapy of injured peripheral nerve [1]. The efficiency of axon regeneration in the nerve conduit depends on many factors such as the neurotrophic factors, the nerve growth factors, the formation of fibrin bridge and the migration of fibroblasts, regenerating axons and Schwann cells [2]. In the past, the silicone rubber has been adopted for conduit material. However, it is prone to body rejection or compressing surrounding nerve tissue and might have to be removed by second operation after full regeneration of nerve. To avoid this, biodegradable materials such as PLA, PGA, PLGA and PCL coated with extracellular matrix to improve the adhesion of Schwann cell are utilized [3]. Many researches suggest that electrical stimulation may accelerate the regeneration of axons and yet the regenerated axons have smaller diameter than the intact axons. It is believed that contractile myofibroblasts in the nerve tissue may hamper the outgrowth of axon along the fibrin bridge. Exploring the biomechanical properties of the axon during the growing process and the effects of static electrical field on axonal growth may help the design of new nerve conduit.

Atomic force microscopy (AFM) has become a useful tool for studying morphology and biomechanics of cells. Using the Hertz contact model or modified Hertz model, the elasticity of many cells such as erythrocytes, platelet, fibroblasts, and endothelium have been investigated [4]. Recently, the viscoelastic properties of 3T3 fibroblasts are analyzed [5]. To explain the motility of 3T3 cell, the viscoelasticity of lamellipodium is studied [6]. The morphological and mechanical properties of different regions of growth cone of Aplysia bag cell are reported in [7].

The goals of this study were three-folds: First, growth of axonal of the PC-12 cell was quantified from morphological analyses and the effect of electrical stimulation on axonal growth was evaluated. Second, AFM ramp-and-hold indentations on three regions of the growing axons were performed and quasi-linear viscoelasticity of the growing axons was studied. Third, the regional variations of axonal adhesion on different substratum were compared by AFM detachment tests.

II. Materials and Experiments

Rat adrenal pheochromocytoma cells (PC-12) was the experimental subject [8]. Before the experiment, the cells were cultivated at 37 deg C, 5% CO_2 in RPMI 1640 medium supplemented with 10% horse serum and 5% fetal bovine serum, penicillin, streptomycin and sodium pyruvate. The medium was replaced every 48 hours. In the experiment, the cells were plated on collagen-coated 35 mm cell culture dishes. Nerve growth factor (100ng/ml) was added to induce axon growth. The dish was put inside an environment control system (Tokai Hit, Inu-Onics-F1) under 37 deg C and 5% CO_2. The system was attached on a phase-contrast inverted microscope (Nikon, TE2000-U) equipped with a CCD camera and image acquisition system (Fig.1a). The micrographs of the cells were then taken every 20 minute for 48 hours by the image system automatically. In the electrical stimulation experiment, a pair of parallel Pt-Ir wires was used to apply electrical field intensities of 75mV/mm and 100mV/mm (Fig.1b).

Chwee Teck Lim, James C.H. Goh (Eds.): ICBME 2008, Proceedings 23, pp. 1833–1837, 2009
www.springerlink.com

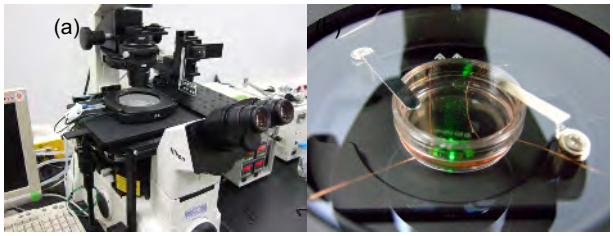


Fig. 1 (a) The environmental control system and the inverted microscope system (b) the parallel Pt-Ir wires for applying electrical filed

From each frame of the micrograph film, cell length (long axis), number of axon branches and branch lengths of selected cells were measured and recorded by using the image process software. Fig. 2 showed definitions of cell length, L_0, axon branch number, N, and branch length, L_i. Since variations of above parameters among cells were quite large so averaging and normalization were used. The average axonal length, L_{ave} (t), at time t is calculated by:

$$L_{ave}(t) = \sum_{i=1}^{N} L_i(t) \ / N(t) \cdot \tag{1}$$

where $L_i(t)$ was the length of i^{th} neurite and N(t) the number of neurites at time t. The normalized total length of axons, $L_{nor}(t)$, was computed as:

$$L_{nor}(t) = \sum_{i=1}^{N} L_i(t) \ / \ L_0(t) \tag{2}$$

where $L_0(t)$ was the cell length at time t. The relative change of axon length, $L_{rel}(t)$, was given by:

$$L_{rel}(t) = \sum_{i=1}^{N(t)} L_i(t) - \sum_{i=1}^{N(0)} L_i(0) \tag{3}$$

These morphological parameters were first analyzed to define the stage of growth process in biomechanical analyses.

An atomic force microscope AFM (Agilent 5500) was employed to scan the surface of the axon by touching mode. The top of the cross section could be allocated and indented.

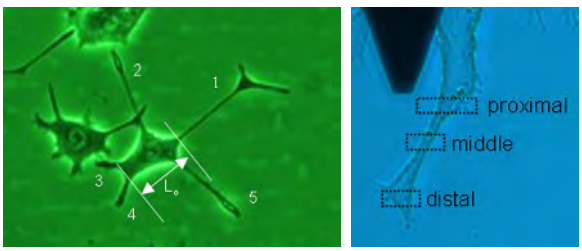


Fig. 2 Definitions of branch number, cell length and branch length (Left), regions of the axon (Right)

Since the biomechanical properties of axon might be region and growth stage dependent, the ramp-and-hold indentation was performed on proximal, middle and distal regions (Fig. 2). The probe was raised from the contact point by 2.5 μm and then rest for 10 seconds. Then it was descending with a velocity of 100 nm/sec and when the indentation depth reached 40% of the initial height the probe was kept still for 120 seconds. Based on the geometry of the probe, the deflection signal and the PZT command, a quasi-linear-viscosity model combined with the Bilodeau mode of the cell could be fitted. A method was also developed to compensate for the creeping of PZT. The QLV model of the cell could be written as:

$$F(t) = \int_{-\infty}^{t} G(t-\tau) \frac{\partial F^{(e)}(\delta)}{\partial \delta} \frac{\partial \delta(\tau)}{\partial \tau} d\tau$$

where G(.) was the reduced relaxation function, F was the measured indentation force and δ the indentation depth and $F^{(e)}$ the elastic indentation force.

$$F^{(e)}(\delta) = 0.753 \frac{\tan \alpha E_y}{(1-\nu^2)} \delta^2 \tag{4}$$

$$G(t) = \left[1 + \int_0^{\infty} S(\tau) e^{-\frac{t}{\tau}} d\tau\right] \left[1 + \int_0^{\infty} S(\tau) d\tau\right]^{-1}$$

$$S(\tau) = \frac{c}{\tau} \quad for \quad \tau_1 < \tau < \tau_2 \tag{5}$$
$$= 0 \quad for \quad \tau < \tau_1, \tau > \tau_2$$

The apparent Young's modulus and parameters c, τ_1 and τ_2 could be obtained by minimizing the squared errors between the model simulation and the experimental data [9]. A cell detachment method was used to evaluate the adhesion force at the three regions of growing axons. Detailed of the methods could be found in [10, 11].

The two-way ANOVA method and Bonferroni t-test were used to analyze the significance of region and stage of growth or substrate material on biomechanical property and morphological parameters.

III. Results

Fig. 3 showed the histories of average axon branch number and average axon length for a population of six PC-12 cells. The mean branch number showed two types of growth: transient for 0-24hr and steady from 24-42hr. After that the cells had fully grown with just one axon. The group mean of average axon length showed similar trend but it increased rapidly starting at 36 hr and reach a plateau at 42hr. In Fig. 4 the history of mean cell length were com-

pared with that of the group mean average axon length. The cell length (or length of the long axis) had a trend of increasing and decreasing with significant variance during 0-23 hr. After 23hr the cell length jumped to 15um and between 25hr and 36 hr the length was varied between 13.5 um and 16 um. Then it increased again and reached a mean of 18um. From the results, instead of using elapsed time or the cell length, one may divide the axon growth process into three stages based on the average axon length as: stage I ($20<L_{ave}<30$), stage II ($35<L_{ave}<45$), stage III ($50<L_{ave}$).

The axon growth rate was proportional to the electrical field intensity. However, a field with intensity higher than 120mV/mm could damage the cells. At 6hr, the statistical analysis showed that the relative axon lengths due to different intensities were statistically different.

In Fig. 5, group variations of the apparent Young's modulus at different regions of the growing axon during different stages were compared. The proximal region had the highest Young's modulus while the middle region had the lowest Young's modulus. The average Young's modulus of three regions increased with the growth stage. Statistical analysis showed that, at the middle region, the stage difference of Young's modulus was statistically significant.

Fig. 6 compared the variations of adhesion at different regions of the axon and different substrates. The mean width of the axon at the corresponding region was also shown. On either the collagen coated substrate or the bare dishes, the proximal region had the highest adhesion force while the middle region had the lowest adhesion force. The distal region had higher adhesion than the middle region. The collagen coated substrate yielded better adhesion. The width of axon cross section at the distal region was larger than that of the middle region.

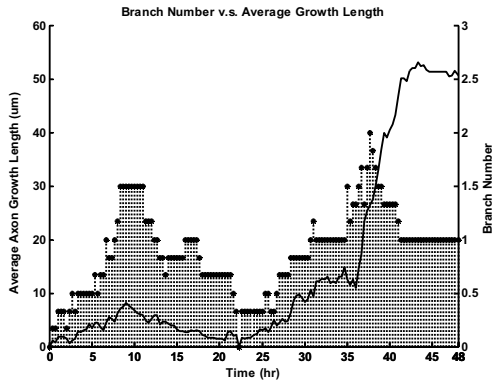


Fig. 3 Time-course changes of average branch number N and average axon length (Lave) for a group of six PC-12 cells

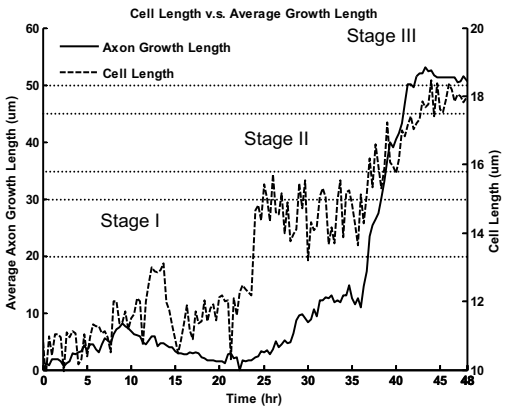


Fig. 4 Time-course changes of average cell length and average axon length for a group of six PC-12 cells

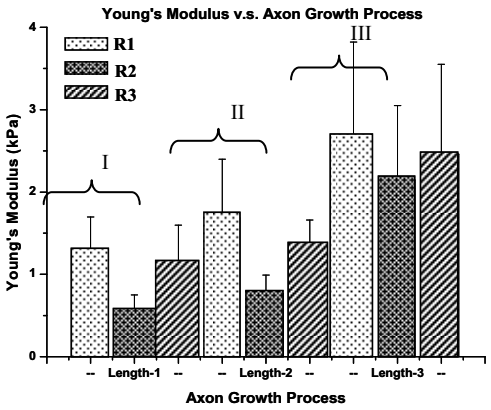


Fig. 5 Variations of apparent Young's modulus at proximal (R1), middle (R2) and distal (R3) region of axon during different stages of growth process

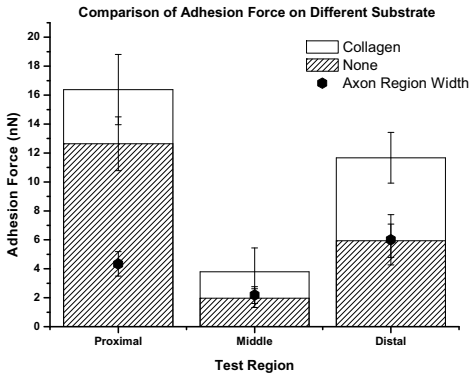


Fig. 6 Comparison of regional variations of adhesion force of axon on two substrates: collagen coating vs glass dish

IV. Discussion

In this study, the growth of axon of PC-12 cells was observed for 48 hours. From the group mean branch number of axons and the average axon length histories, one confirmed that in the first day, the cells were in a transient state in which PC-12 cell would divide and migrate and the neurites extended and retracted frequently. In the second day, the NGF starting to affect the cell and although frequent changes of axon branch number occurred in 24hr-36hr but it was followed by a rapid increasing of average axon length and reached a steady-state from 42 hr on. The number of axon branch reduced to one indicated that fully growth of axon might be achieved.

The growth rate of the cells was enhanced by 2.88 folds when subject to electrical field of intensity of 100 mV/mm. Although in the literature, intensity as high as 200 mV/mm has been suggested, we found that an intensity of 120 mV/mm might damage the cells. It was suggested that polarization of guiding factor Netrin-1 by the applied electrical field can activate the focal adhesion kinase and make the growing axon to migrate along the electrical filed gradient [12, 13, 14].

In most commercial AFM systems, the vertical movement of probe is achieved by open-loop control of PZT. For ramp-and-hold indentation of soft specimens like cells, the creeping of the PZT was often neglected. In our results, we found that an error as high as 17.31% may exist if the indentation depth trajectory was not calibrated.

The apparent Young's modulus of the three regions of axon increased with the stage of growth. This might due to the cytoskeleton inside the axon was forming and the cross sectional area was increased. The difference between regions might due to the structure of the axon. At the distal region, the growth cone is formed mainly by actin and in the middle region microtubule dominates. The Young's modulus of actin is higher than that of microtubule has been suggested by thermal fluctuation method [15]. Our finding was consistent with it.

The axon had better adhesion on collagen-coated substrate which is similar to the PC-12 cell. The adhesion properties of substrate play a very important role on the indentation testing of cell. The high adhesion force at the proximal region of axon may be contributed by the nearby soma. The relative small adhesion at middle region might due to its small width of cross section.

From morphological and biomechanical analyses of the growing axons, a nerve conduit may be suggested that it should include a pair of electrode to apply static electrical field, the passage for axon may be coated with collagen and the strength of the scaffold may be designed based on the biomechanical properties of the axon at stage III.

V. Conclusions

The division of growing process based on average axon length might be feasible although more samples are needed. AFM ramp-and-hold indentation on PC-12 cells revealed that the viscoealsticity of growing axons is region and stage dependent. The information might be applied to design scaffold of nerve conduit.

Acknowledgements

The research is partially supported by a grant from ROC NSC via contracts 96-2923-I-006-001-MY2 and 96-2221-E-006-245.

References

1. Midha R (1999) Peripheral nerve: approach to the patient. Youman's Neurological Surgery 5th ed.
2. Heath C, Rutkowaki G (1998) The development of bioartificial nerve grafts for peripheral-nerve regeneration. TIBTECH 16:163-168.
3. Matsumoto K, Ohnishi K, Kiyotani T, et al. (2000) Peripheral nerve regeneration across an 80-mm gap bridged by a polyglycolic acid (PGA)–collagen tube filled with laminin-coated collagen fibers: a histological and electrophysiological evaluation of regenerated nerves. Brain Res 868:315-328.
4. Radmacher M (1997) Measuring the Elastic Properties of Biological Samples with the AFM. IEEE Eng in Med and Biol 16(2):47-57.
5. Mahaffy R, Shih C, MacKintosh F,. Käs J (2000) Scanning Probe-Based Frequency-Dependent Microrheology of Polymer Gels and Biological Cells. Physical Review Letters 95(4):880-883.
6. Park S, Koch D, Cardenas R, Käs J, Shih C (2005) Cell Motility and Local Viscoelasticity of Fibroblasts. Biophy J 89:4330–4342.
7. Grzywa E, Lee A, Lee G, Suter D (2006) High Resolution Analysis of Neuronal Growth Cone Morphology by Comparative Atomic Force and Optical Microscopy. J Neurobiol. 66:1529-1543.
8. Greene L, Tischler A (1976) Establishment of a noradrenergic clonal line of rat adrenal pheochromocytoma cells which respond to nerve growth factor. Proc Natl Acad Sci USA, 73:2424-8.
9. Chen R, Ju M, Lin C (2007) An Efficient Parameter Estimation Technique of Quasi-Linear Viscoelastic Model for Peripheral Nerves. ISB Congress XXI Taipei Taiwan July 1-5.
10. Chang C, Liao J, Chen J, Ju M, Lin C (2006) Alkanethiolate selfassembly monolayers upon Au-deposited nerve microelectrode: cell adhesion examined by total impedance and cell detachment force. Nanotech 17:2449-2457.
11. Lan, H(2008) Application of AFM to Investigate Axon Regeneration of PC-12 Neuron-like Cells. MS Thesis, Natl Cheng Kung Univ Tainan Taiwan.
12. McCaig C, Sangster L, Stewart R(2000) Neurotrophins Enhance Electric Field-Directed Growth Cone Guidance and Directed Nerve Branching. Developmental Dynamics 217:299–308
13. Rajnicek A, Foubister L, McCaig C (2006) Temporally and spatially coordinated roles for Rho, Rac, Cdc42 and their effectors in growth cone guidance by a physiological electric field. J Cell Sci 119:1723-1735.

14. Rajnicek A, Foubister L, McCaig C (2006) Growth cone steering by a physiological electric field requires dynamic microtubules, microfilaments and Rac-mediated filopodial asymmetry. J Cell Sci 119:1736-1745.
15. Gittes F, Mickey B, Nettleton J, Howard J (1993) Flexural Rigidity of Microtubules and Actin Filaments Measured from Thermal Fluctuations in Shape. J Cell Biol 120: 923-934.

Correspondence: Ming-Shaung Ju
Dept. of Mechanical Engineering, National Cheng Kung University
1 University Road, Tainan, Taiwan 701
e-mail: msju@mail.ncku.edu.tw

Effect of Irregularities of Graft Inner Wall at the Anastomosis of a Coronary Artery Bypass Graft

F. Kabinejadian[1], L.P. Chua[2], D.N. Ghista[3] and Y.S. Tan[4]

[1] PhD Student, Nanyang Technological University, School of Mechanical and Aerospace Engineering, Singapore
[2] Associate Professor, Nanyang Technological University, School of Mechanical and Aerospace Engineering, Singapore
[3] Professor, Parkway College, Singapore
[4] Cardiothoracic and Vascular Surgeon, Mount Elizabeth Hospital, Singapore

Abstract — **It is well-established in medical literature that venous valves play a role in late segmental stenosis of vein grafts in the coronary artery bypass grafts (CABG). However, from the engineering point of view, vein grafts are always assumed as smooth tubes in the existing simulations, and no efforts have been put on the effects of vein valves and jaggedness of the graft inner wall due to the competent valves (in case of reversed saphenous vein (SV) grafts) or the valve cusps remnants and valve sinus (in case of valve-stripped SV grfats) on the blood flow.**

In this preliminary study, the effects of the inner surface unevenness of a vein graft on the blood flow is investigated at the distal anastomosis with a more realistic geometry of valve-stripped SV, by means of numerical simulation of pulsatile, Newtonian blood flow. For this purpose, three CFD models of the distal anastomosis are designed, including one model with a smooth inner wall vein graft, one model with a vein graft containing one valve remnants and sinus, and one model containing two valve remnants and sinus in the graft. The proximal segment of the coronary artery is fully occluded in all models.

The simulation results show that the valve remnants and sinus only cause some minor disturbances in the flow field and hemodynamic parameters (HP) just distal to the valve remnants, and not at the anastomosis.

Therefore, assuming valve-stripped SV graft as a tube with a smooth inner surface will not affect the simulation results considerably at the anastomosis. This validates the assumption of smooth inner wall in case of bypass with valve-stripped vein grafts for simulation.

Keywords — **Coronary artery bypass grafting (CABG), Saphenous vein, Venous valve remnants, Hemodynamics, Stenosis**

I. Introduction

It is usual that surgeons remove the valves before grafting a commonly used SV, since abnormal venous valves may cause obstruction to flow unrelated to technical error or poor run-off [1]. Moreover, the pressure trap, caused by competent valves in the distal segment of a vein graft, results in segmental hypertension which can play an important role in the graft stenosis [2]. Therefore, the alternative method for reversed vein grafting is the valve-stripped vein grafting.

Nevertheless, this method is not devoid of complications. Apart from the probable internal vein trauma caused by valvulotomes, the valve sinus and remnants of the valve cusps cause irregularities on the vein inner wall and deviating its geometry from an ideal, smooth, regular tube, which may affect the hemodynamics in the graft.

In this investigation, the effects of the valve sinus and remnants of the valve cusps on the distal anastomosis of a CABG with a valve-stripped vein graft are studied by means of numerical simulation of pulsatile, Newtonian blood flow.

II. Materials and Methods

A. Geometric models

Three distal anastomosis models of the right coronary artery (RCA) bypass graft are designed for the CFD simulation as follows: One distal anastomosis model with a smooth inner wall vein graft having neither valve nor its remnants; another model with a vein graft containing one valve sinus and the valve remnants; and finally, one distal anastomosis model with a vein graft containing two valve sinus and the valve remnants.

The models are designed planar, according to Galjee et al. [3] who demonstrated that the typical location and course of saphenous vein in RCA bypass graft could be assumed approximately planar. The proximal segment of the coronary artery is fully occluded in all models.

The dimensions of the models are listed in Table 1, where D_G, D_A, L_P, L_B, L_D, L_1, L_2, and L_V stand for the graft diameter, coronary artery diameter, length of occluded proximal section of the host artery, length of anastomosis bed, length of distal section of the host artery, distance between the anastomosis and the nearest valve, distance between two valves, and length of the valve region respectively, as shown in Fig. 1.

Chwee Teck Lim, James C.H. Goh (Eds.): ICBME 2008, Proceedings 23, pp. 1838–1841, 2009
www.springerlink.com

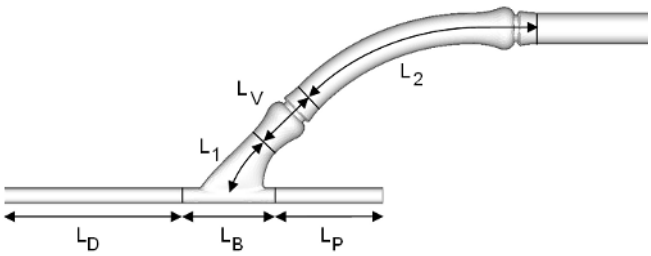


Fig. 1 Different parts of the distal anastomotic model

Table 1 Dimension of different models' geometry (all lengths are in mm)

Model	D_G	D_A	L_P	L_B	L_D	L_1	L_2	L_V
No valve remnant	4	2	14	12	24	N.A.	N.A.	N.A.
1 valve remnant	4	2	14	12	24	7	N.A.	8.5
2 valve remnants	4	2	14	12	24	7	30	8.5

B. Numerical model and flow conditions

For pulsatile blood flow, it is recommended to use the Womersley number (α) as an indicator of whether non-Newtonian effects are important (α<1) or not (α>1) [4]. In the present study, the minimum Womersley number in the coronary artery is 1.34. Hence, the assumption of Newtonian fluid is reasonable.

Blood flow through the coronary artery bypass has the characteristics of three-dimensional, time-dependent, incompressible, isothermal, and laminar, whose governing equations (continuity and Navier-Stokes equations) are as follows:

$$\nabla \cdot \mathbf{u} = 0 \tag{1}$$

$$\rho \frac{\partial \mathbf{u}}{\partial t} + \rho(\mathbf{u} \cdot \nabla)\mathbf{u} = -\nabla p + \mu \nabla^2 \mathbf{u} \tag{2}$$

Where **u** is the velocity vector, ρ the density, t the time, μ the dynamic viscosity, and p is the pressure. The density and dynamic viscosity of the blood are assumed to be 1050 kg/m^3 and 0.00408 Pa.s respectively [5].

The commercial CFD software, FLUENT (version 6.3.26), is used in this study to solve the governing equations for the models numerically by finite volume method. In this method, the solution domain is divided into discrete control volumes (CV) and the governing equations are integrated over individual CVs to construct discretized algebraic equations for dependent variables at the centroid of the CVs. Finally, the discretized equations are linearized and the resultant linear equation system is solved to yield updated values of the dependent variables.

In the present study, segregated solver is used to solve the governing equations sequentially. The semi-implicit SIMPLEC algorithm is used as the pressure-velocity coupling scheme. Time stepping employed a fully implicit scheme, and each pulse cycle is divided into 90 time steps of size 0.01s. The convergence criterion is set at 5×10^{-5}. Beside, in order to eliminate the start up effects of transient flow, the computation is carried out for 5 periods.

A fully developed pulsatile flow is applied at the inlet whose flow waveform and the velocity profile are based on the measurements by magnetic resonance phase velocity mapping within a coronary artery bypass graft [6]; however, some modifications are exerted and the waveform is smoothened. The resulted waveform with the period of 0.9s and average velocity values adapted for this study is demonstrated in Fig. 2.

The Womersley solution is assumed for the inlet axial velocity profile which is derived as a fully developed pulsatile flow [7], whose velocity profile in a circular tube in the cylindrical coordinate can be expressed as [8]:

$$v_z(r,t) = 2B_0\left[1-\left(\frac{r}{R}\right)^2\right] + 2\mathrm{Real}\left\{\sum_{n=1}^{n=N} B_n \frac{\left(1-\dfrac{J_0\left(i^{\frac{3}{2}}\alpha_n \dfrac{r}{R}\right)}{J_0\left(i^{\frac{3}{2}}\alpha_n\right)}\right)}{\left(1-\dfrac{2J_1\left(i^{\frac{3}{2}}\alpha_n\right)}{i^{\frac{3}{2}}\alpha_n J_0\left(i^{\frac{3}{2}}\alpha_n\right)}\right)} e^{in\omega t}\right\} \tag{3}$$

Where i is the imaginary unit, R the tube radius, J_0 and J_1 the first kind Bessel functions of order zero and one respectively, α the Womersley number, B_n the Fourier coefficients, and Real{} represents the real part of the complex expression.

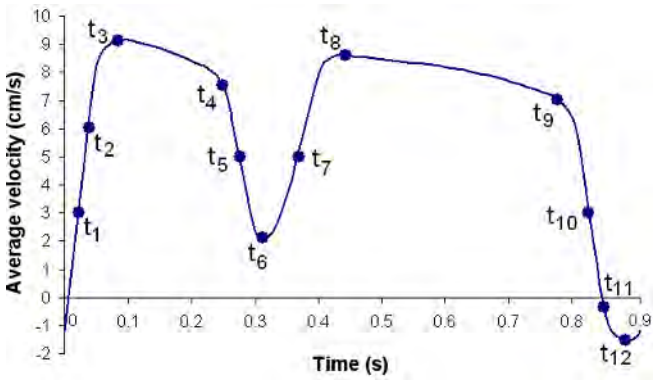


Fig. 2 Average velocity waveform adapted for the present study (labels indicate times at which flow and HP are studied)

A user defined function (UDF) is provided to implement the above equation and calculate the velocity for the pulsatile flow as the inlet boundary condition within FLUENT.

The exit flow is assumed to be in a fully developed condition; thereby the FLUENT's outflow boundary condition is set to assume a zero normal gradient for all flow variables except pressure. In this study, vein and arteries are considered as rigid tubes, and no-slip boundary condition is applied to all walls, owing to the fact that blood is a viscous fluid.

III. Results

A. Flow behavior

Flow field and HP in all models are studied in 12 instant of time as shown on the waveform in Fig. 2, some of which are presented in this paper.

During the systolic phase (t_1 to t_6), a vortex appears at the heel region of the anastomosis in all models, and in models containing valve remnants, a vortex appears in each valve sinus whose size increases with time till the first valley in the velocity cycle (t_6) when it occupies the whole valve sinus as demonstrated in Fig. 3 (b, c).

Yet, the size of the vortices does not further increase due to diastolic acceleration phase starting from time t_6. The flow field during the diastolic acceleration and early diastolic deceleration phase (t_7 to t_{10}) is the same as that of corresponding systolic phase (t_1 to t_6).

As the graft net flow rate becomes negative (t_{11}), in the model with smooth graft, the size of the vortex at the heel increases and one more vortex appears at the graft outer wall near the toe as shown in Fig. 4 (a). While in the models with grafts containing valve remnant, these two vortices (located at the heel and over the toe) have merged with the vortex in the valve sinus (whose size has further increased at this phase) due to the short distance between the valve remnant and the distal anastomosis in the present models. Another vortex is also formed proximal to the valve remnant at the inner wall of the valve remnant containing grafts, which merges with the vortex in the valve sinus as well.

At the peak reversed flow (t_{12}), the blood is flowing back towards the aorta in all models, and those two vortices in the anastomosis region are vanished. In the valve remnant containing models, the vortex in the valve sinus reduces in size and shifts toward the graft axis while the flow streamlines are smooth near the graft wall as demonstrated in Fig. 5.

Nevertheless, general flow characteristics are the same within all models at the anastomosis region.

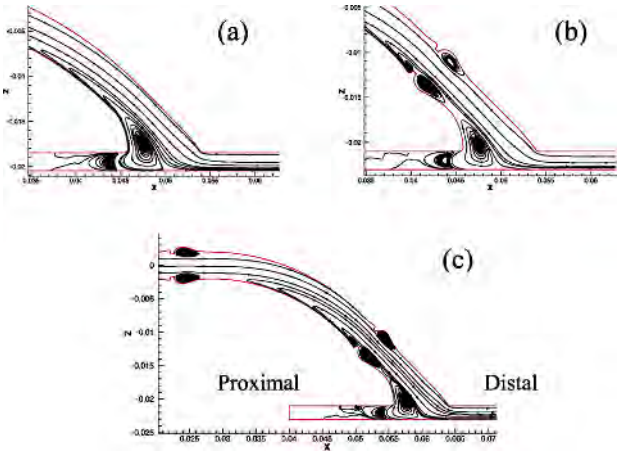


Fig. 3 Streamlines at the symmetry plane at time t_6=0.31s

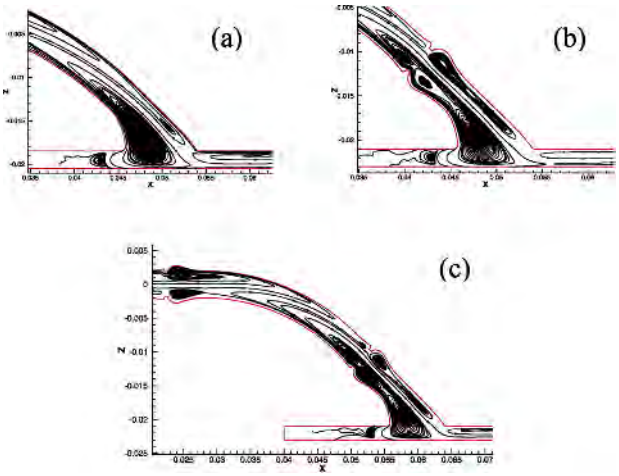


Fig. 4 Streamlines at the symmetry plane at time t_{11}=0.84s

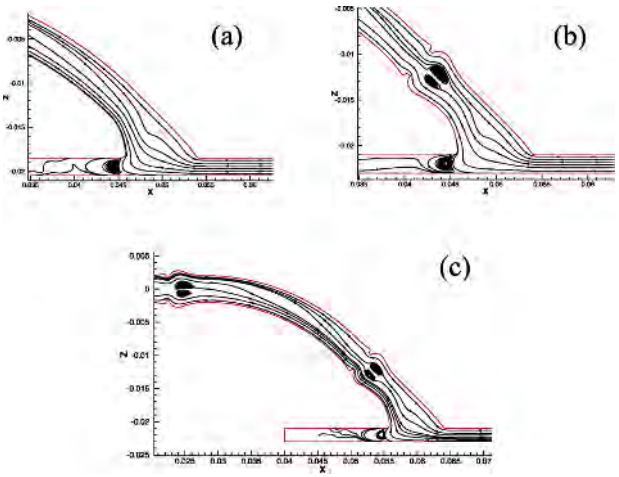


Fig. 5 Streamlines at the symmetry plane at time t_{12}=0.88s

B. Hemodynamic parameters distributions

Since localized distribution of low-WSS and high-OSI strongly correlates with the focal locations of atheroma [9], and also spatial WSSG contributes to the elevated wall permeability and atherosclerotic lesions [10], in order to compare the distribution of HPs quantitatively at the critical sites of the anastomosis, such as suture line, toe, heel, and bed (as shown in Fig. 6), the segmental average of the HPs including WSS, WSSG, and OSI are calculated (by TECPLOT software) for different models and presented in Table 2.

As demonstrated in Table 2, the segmental averages of all HPs are more or less the same at the anastomosis regions in all models.

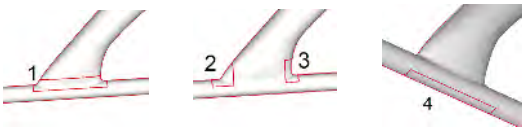


Fig. 6 Critical anastomotic regions: 1-Suture line, 2-toe, 3-heel, 4-bed

Table 2 Comparison of segmental average of <HP>s in different models

Model	Location	<TAWSS> (Pa)	<TAWSSG> (Pa/m)	<OSI>
No valve remnant	1- Suture line	2.54	4854	0.07
	2- Toe	5.81	10079	0.01
	3- Heel	0.13	180	0.24
	4- Bed	2.44	991	0.09
1 valve remnant	1- Suture line	2.54	4912	0.07
	2- Toe	5.81	10151	0.01
	3- Heel	0.13	189	0.24
	4- Bed	2.46	962	0.09
2 valve remnants	1- Suture line	2.55	4825	0.07
	2- Toe	5.82	10084	0.01
	3- Heel	0.13	186	0.23
	4- Bed	2.46	924	0.09

IV. Conclusion

In this paper, the effects of the inner surface unevenness of a graft due to valve remnants and valve sinus in case of valve-stripped SV graft on the blood flow is studied at the distal anastomosis of a CABG by means of numerical simulation.

There are only some minor disturbances due to the valve remnants and valve sinus observed in the flow field just distal to the valve remnants and not at the anastomosis, and hemodynamic parameter distributions do not experience any change in the anastomotic region of the three models studied.

Therefore, assuming valve-stripped SV graft as a tube with a smooth inner surface will not affect the simulation results. Thus, it is verified that the assumption of smooth inner wall in case of bypass with valve-stripped vein grafts is valid for simulation, and deviation of the results from the reality would be negligible.

References

1. Dye T E, Izquierdo P (1983) Abnormal venous valves: A cause of early obstruction of saphenous vein bypass grafts. Tex Heart Inst J 10(4):365–369.
2. Robicsek F, Thubrikar M J, Fokin A, Tripp H F, Fowler B (1999) Pressure traps in femoro-popliteal reversed vein grafts. Are valves culprits? Cardiovasc Surg 40(5):683–689.
3. Galjee M A, Van Rossum A C, Doesburg T, Van Eenige M J, Visser C A (1996) Value of magnetic resonance imaging in assessing patency and function of coronary artery bypass grafts: An angiographically controlled study. Circ 93(4):660–666.
4. Rohlf K, Tenti G (2001) The role of the Womersley number in pulsatile blood flow: a theoretical study of the Casson model. J Biomech 34(1):141–148.
5. Meena S, Ghista D N, Chua L P, Tan Y S (2006) Numerical investigation of blood flow in a sequential aorto-coronary bypass graft model, IEEE Proc., Annual International Conference of the IEEE Engineering in Medicine and Biology, Art. No. 4029138, pp 875–878.
6. Galjee M A, Van Rossum A C, Doesburg T, Hofman M B M, Falke T H M, Visser C A (1996) Quantification of coronary artery bypass graft flow by magnetic resonance phase velocity mapping. J Magn Reson Imaging 14(5):485–493.
7. Womersley J R (1955) Method for the calculation of velocity, rate of flow and viscous drag in arteries when the pressure gradient is known. J Physiol 127:553–563.
8. Mazumdar J N (1992) Biofluid Mechanics. World Scientific.
9. He X, Ku D N (1996) Pulsatile flow in the human left coronary artery bifurcation: Average conditions. J Biomech Eng 118(1):74–82.
10. DePaola N, Gimbrone Jr M A, Davies P F, Dewey Jr. C F (1992) Vascular endothelium responds to fluid shear stress gradients. Arterioscler Thromb 12(11):1254–1257.

Author: Foad Kabinejadian
Institute: School of Mechanical and Aerospace Engineering, Nanyang Technological University
Street: 50 Nanyang Avenue, N3-B2c-TFRL1
City: Singapore
Country: Singapore
Email: fkabi@pmail.ntu.edu.sg

Mechanical Aspects in the Cells Detachment

M. Buonsanti[1], M. Cacciola[2], G. Megali[2], F.C. Morabito[2], D. Pellicanò[2], A. Pontari[3] and M. Versaci[2]

1 University "Mediterranea" of Reggio Calabria - Faculty of Engineering – M.E.C.M.A.T. Department, Reggio Calabria, Italy
2 University "Mediterranea" of Reggio Calabria - Faculty of Engineering – D.I.M.E.T. Department, Reggio Calabria, Italy
3 Transplant Regional Center of Stam Cells and Cellular Therapy, "A .Neri", A.O. Reggio Calabria, Italy

Abstract — **Living cells possess properties that enable them to withstand the physiological environment as well as mechanical stimuli occurring within and outside the body. Any deviation from these properties will undermine the physical integrity of the cells as well as their biological functions. Thus, a quantitative study in single cell mechanics needs to be conducted. In this paper we will examine fluid flow and Neo-Hookean hyperelastic deformation. The study of these problems requires quantitative information regarding the interaction between blood flow and human cell deformation under realistic physiological conditions. For our aims, a Finite Element Method (FEM) analysis package has been exploited: the cellular level model consists of a continuum representation of the field equations and a moving boundary tracking capability to allow the cell to change its shape continuously.**

Keywords — **Cell adhesion, Contact mechanics, Detachment, Fluid-structure interaction, Endothelial cells models.**

I. Introduction

In order to present a physical model and determine the effect of the blood flow in presence of a human cell, a FEM-based approach has been exploited. It requires the geometrical and physical definition of the blood vessel, the cell and flow parameters. For our purpose, we verify cell deformation under actual conditions. Thus, a brief description of the theoretical framework for the mechanical is given. Then, we describe the exploited approach through FEM analysis simulating the human cell and the blood flow, and so modeling an endothelial wall cross of a blood flow.

Our aim was to focus the contact part among cell and endothelial wall about the deformation field. Our opinion is that the simulation notice the deformation inhomogeneity namely different concentration areas with different deformation values. This important observation should be connected with a specific form of the stored energy deformation that, in this case, loses the standard convexity to show the multy-well form. Consequently, we have more minimum and the variational problem seems more difficulty.

Solutions through minimizing sequence are applied and this relieve microstructure formation.

II. Theoretical framework and FEA approach

A. Mechanical aspects

From mechanical point of view this is a detachment problem and, according to [1] & [2], it can be formulated as the peeling of an adhesive membrane initially glued to a flat surface. Regarding the cell as membrane solid pulled with a forces system, we say that, when the blood flow is regular the cell will remain perfectly glued to the endothelial wall, while when the flow intensity augments part of cell may be pulled away. Let **u** the displacement field, then the equation of motion hold

$$\rho\,\mathbf{u}_{tt} + T\nabla^2\mathbf{u} = f(x,y,t) \quad \text{on } \Omega \tag{1}$$

where ρ is the supposed constant density and T the stress tensor. Clearly a the boundary of the detached part we have

$$\mathbf{u} = 0 \qquad \text{on } \Omega_D \tag{2}$$

Here the problem is the determination of Ω_D. By [1] we recall the breaking condition in the form

$$(T\text{-}\rho v^2)\,\partial u/\partial n = -F \qquad \text{on } \Omega_D \tag{3}$$

where ν denotes the normal velocities of Ω_D, $\partial\mathbf{u}/\partial n$ is the normal outer of **u** on Ω_D and F is the cohesive forces. The closed form of (1) exists only for some particular cases. For instance let f^* the static resultant of the flow actions and supposing it just applied at the origin of the system. So, in this case $f(x,y,t) = f^*\delta(x)\delta(y)$ with $\delta(\cdot)$ the delta function. For instance supposing the u filed symmetrical about to the origin, we consider a circular region and so $u = u(r)$ and the region Ω_D becomes a circular region which radius is λ. Under this consideration the solution of (1) has the form

$$u(r) = (f^*/2\pi T)\,\ln r + \cos(t) \tag{4}$$

namely

$$u(r) = (f^*/2\pi T)\,\ln(r/\lambda) \tag{5}$$

and in $\nu = 0$

$$\lambda = (f^*/2\pi F) \tag{6}$$

Chwee Teck Lim, James C.H. Goh (Eds.): ICBME 2008, Proceedings 23, pp. 1842–1845, 2009
www.springerlink.com

The complete solution in closed form becomes

$$u(r)= (f^*/2\pi F) \ln(2\pi fr/ f^*) \text{ on } r \le \lambda \quad (7)$$

B. Model generation

In this section of the paper we show how to simulate the effect of a blood flow in presence of a cell in a blood vessel. Using our FEM package [3-5], the blood flow and pressure drop across human cell have been studied and a mathematical model of the process has been constructed and analyzed. The constructed mathematical model consists of the equations of continuity (representing conservation of mass), motion (representing conservation of momentum) for the flow of blood through human cell [6] (see Fig. 1).

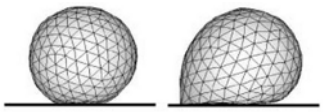


Fig. 1 2D-view of cell deformation effect: at t_0=0 (s) on the left and at t_1=0.125 (s) on the right.

These equations are supplemented by appropriate models which represent the stress/strain behaviour of human cell [7]. Simulation of fluid-structure interaction is a challenging problem for computer modellers. Fluid flow and Neo-Hookean hyperelastic deformation modelling has been the subject of numerous research during the past few decades.

Our approach provides reliable simulations for both these steps. The study of these problems requires quantitative information regarding the interaction between blood flow and human cell deformation under realistic physiological conditions. The complexity of such a task is such that only computer based numerical simulations can be used. In this work we exploited FEM to solve the developed mathematical 2D model representing the operations of human cell. For our aims, the Comsol Multiphysics® package has been exploited. Computer modeling can help in this context if it is based on an appropriate mathematical model and an accurate reliable solution. So it is needed to fit a model to the problem and get a satisfactory solution.

C. Governing equation of elastic-solid deformation

For a purely elastic solid [5]:

$$\frac{\partial}{\partial x_j}\sigma_{ij} + f = 0 \quad (8)$$

$$\sigma_{ij} = -p\delta_{ij} + p_{ij} \quad (9)$$

σ is the strain tensor. Let **u** is the displacement field, then under the material incompressible hypothesis

$$\nabla \cdot \mathbf{u} = 0 \quad (10)$$

$$\tau_{ij} = 2Ge_{ij} \quad (11)$$

$$p = -k(\nabla \cdot \mathbf{u}) \quad (12)$$

where G and k are, respectively, the shear modulus and the bulk modulus. Specific finite element techniques such as the penalty method are well suited to combine the described set of Neo-Hookean hyperelastic and fluid equations.

D. Governing equation fluid motion, conservation of mass and momentum

If an inelastic generalized Newtonian flow behaviour is assumed [6, 7], the Cauchy stress tensor σ can be written as

$$\sigma = -p\mathbf{I} + 2\eta(\gamma)D_v \quad (13)$$

where $\eta(\gamma)$ is the shear-rate-dependent dynamic viscosity and D_v denotes the rate of deformation tensor

$$D_v = \frac{1}{2}[\nabla v + (\nabla v)^T] \quad (14)$$

The shear rate parameter γ must be defined in terms of the second invariant of the rate of deformation tensor. For incompressible fluid this is

$$\gamma = \sqrt{2D_v : D_v} \quad (15)$$

The Non-Newtonian behaviour of blood can be described very well with the Carreau-Yasuda model

$$\frac{\eta(\gamma) - \eta_\infty}{\eta_0 - \eta_\infty} = [1 + (\lambda\gamma)^a]^{\frac{n-1}{a}} \quad (16)$$

with η_0, η_∞, λ, a and n being parameters of the model. For a time constant λ=0 this model reduces to a simple Newtonian model with $\eta(\gamma)=\eta_0$.

E. FEM Analysis

The following section shows proposed model for fluid-structure interactions. It illustrates how fluid flow can deform surrounding "structures" and how to solve for the flow in a continuously deforming geometry using the arbitrary Lagrangian-Eulerian technique [10-12]. The model geometry consists of a horizontal flow channel in the middle of which is a human cell, with a circular structure. The cell forces the fluid into a narrower path in the upper part of the channel, thus imposing a force on the structure's walls resulting from the viscous drag and fluid pressure. The cell structure, being made of a Neo-Hookean hyperelastic material, bends under the applied load. Consequently, the fluid

flow also follows a new path, so solving the flow in the original geometry would generate incorrect results. The Navier-Stokes equations that solve the flow are formulated for these moving coordinates. The simulations exploit the FEM and require geometrical and physical definition of the blood flow and the human cell [13]; the latter has been modeled as a circumference with a portion of perimeter adherent to the venous paries. In this example the flow channel is 100 (μm) high and 300 (μm) long. The cell structure has a radius of 1.25 (μm), and is adherent 1 (μm) long at the channel's bottom boundary. Assume that the structure is along the direction perpendicular to the image. The fluid is a water-like substance with a density ρ=1000 (kg/m^3) and dynamic viscosity η=0.001 (Pa·s). To demonstrate the desired techniques, assume the cell structure consists of a Neo-Hookean hyperelastic material with a density ρ=7850 (kg/m^3) initial tangent E=80 (kPa). The model consists of a fluid part, solved with the Navier-Stokes equations in the flow channel, and a structural mechanics part, which you solve in the human cell. Transient effects are taken into account in both the fluid and the cell structure. The structural deformations are modeled using large deformations in the Plane Strain application mode. The displacements and displacement velocities are denoted u, v, u_t, and v_t, respectively. Fluid flow is described by the Navier-Stokes equations for the velocity field, $\mathbf{u}=(u,v)$, and the pressure, p, in the spatial (deformed) moving coordinate system:

$$\rho\frac{\partial \mathbf{u}}{\partial t}-\nabla[-\rho\mathbf{I}+\eta(\nabla\mathbf{u}+(\nabla\mathbf{u})^T)]+\rho((\mathbf{u}-\mathbf{u}_m)\cdot\nabla)\mathbf{u}=\mathbf{F} \quad (17)$$

$$-\nabla\cdot\mathbf{u}=0 \quad (18)$$

In these equations, **I** denotes the unit diagonal matrix and **F** is the volume force affecting the fluid. Assume that no gravitation or other volume forces affect the fluid, so that **F**=0. The Navier-Stokes equations are solved in the spatial (deformed) coordinate system. At the inlet, the model uses a fully developed laminar flow. Zero pressure is applied at the outlet. No-slip boundary conditions, that is **u** = 0, are used at all other boundaries. Note that this is a valid condition only as long as you are solving the stationary problem. In this transient version of the same model, with the cell starting out from an undeformed state, it is necessary to state that the fluid flow velocity be the same as the velocity of the deforming obstacle. The coordinate system velocity is $\mathbf{u}=(u_m,v_m)$. At the channel entrance on the left, the flow has fully developed laminar characteristics with a parabolic velocity profile (see Fig. 2) but its amplitude changes with time.

At first, flow increases rapidly, reaching its peak value at 0.215 (s); thereafter it gradually decreases to a steady-state value of 3.33 (cm/s).

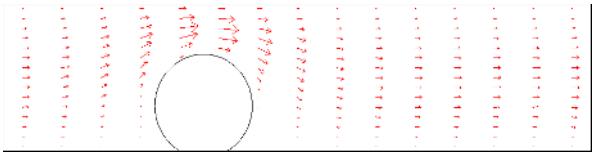


Fig. 2 Schematic of the problem statement. Simulated flow with cell presence at t=0.005 (s).

The centerline velocity in the x direction, u_{in}, with the steady-state amplitude U comes from the equation

$$u_{in}=\frac{U\cdot t^2}{\sqrt{(0.04-t^2)^2+(0.1t)^2}} \quad (19)$$

where t must be expressed in seconds. At the outflow (right-hand boundary), the condition is p=0. On the solid (non deforming) walls, no-slip conditions are imposed, u=0, v=0, while on the deforming interface the velocities equal the deformation rate, $u_0=u_t$ and $v_0=v_t$. The structural deformations are solved for using an hyperelastic formulation and a nonlinear geometry formulation to allow large deformations. For boundary conditions, the cell is fixed to the bottom of the fluid channel, so that it cannot move in any direction. All other object boundaries experience a load from the fluid, given by

$$\mathbf{F}_T=-\mathbf{n}\cdot(-\rho\mathbf{I}+\eta(\nabla\mathbf{u}+(\nabla\mathbf{u})^T)) \quad (20)$$

where **n** is the normal vector to the boundary. This load represents a sum of pressure and viscous forces. With deformations of this magnitude, the changes in the fluid flow domain have a visible effect on the flow and on the cell, too. Fig. 3 shows the geometry deformation and flow at t=4 (s) when the system is close to its steady state.

Due to the channel's small dimensions, the Reynolds number (R) of the flow is small (R << 100), and the flow stays laminar in most of the area. The swirls are restricted to a small area behind the structure. The amount of deformation as well as the size and location of the swirls depend on the magnitude of the inflow velocity. Most of time, the

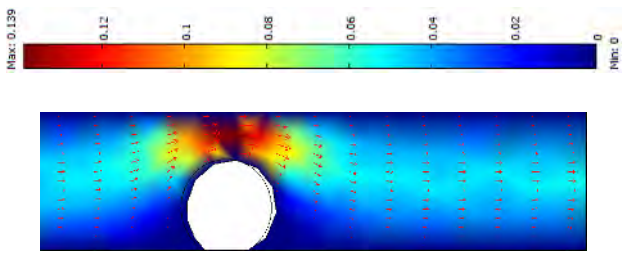


Fig. 3 Simulated flow velocity and geometry deformation at t=4 (s). The vectors indicate the flow direction and the color scale indicates flow-velocity magnitude (m/s).

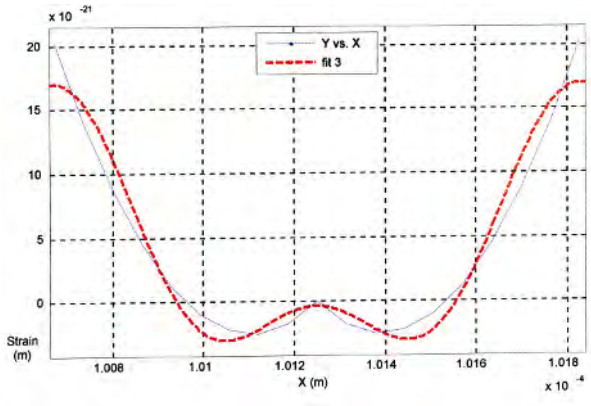


Fig.4 The non-monotone deformation law.

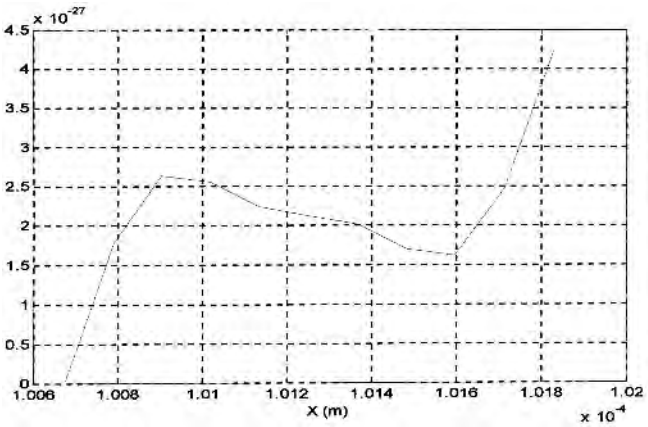


Fig. 5 The complementary deformation density as integral of the deformation function.

deformation follows the inflow velocity quite closely. Whenever the inflow velocity starts to decrease. Toward the end of the simulation, when inflow and structure deformation approach their steady-state values, the mesh velocity also decreases to zero. For the fluid domain are applied the following settings. For the boundary settings, we imposed a inlet condition with a mean velocity equal to u_{in} (set to 3.33 (cm/s)). For the sides we apply condition of wall with sliding absent; for the boundary ($\delta\Omega$) on the right we imposed type of outlet with a condition of pressure and no viscous stress with p_0=0. The edges of the cell are characterized by conditions wall mobile dispersant (structural displacement) with the exception of the base cell which is fixed and not involved in the dynamic physical process, according to

$$\mathbf{n}(\eta_1(\nabla\mathbf{u}_1+(\nabla\mathbf{u}_1)^T)-\rho_1\mathbf{I}-\eta_2(\nabla\mathbf{u}_2+(\nabla\mathbf{u}_2)^T)-\rho_2\mathbf{I})=0 \quad (21)$$

Our studies have been based on a discrete domain with 231 elements. The number of degree of freedom is 1984. Mesh has been generated with triangular elements, having a geometric side of 0.00005 (mm) for vessel and cell. We exploited a FEM implementation utilizing a time-dependent direct linear solver with parallel calculation 12]. Subsequently, we present final simulations in order to stress and strain results.

III. Conclusions

Simulated results were highly reliable, so our FEA package was very successfully simulating fluid–structure interaction in the human blood vessel. Our interest was to point out the concentration or inhomogeneity of the deformation on the contact area cell-wall. This particular result open the way to simulate the adhesion-detachment problem through more sophisticated model (i.e. functional analysis tools) such that microstructural characterization can be emphasized.

References

1. Villaggio P (1997) Mathematical models for elastic structures. Cambridge University Press, Cambridge
2. Leitman M J, Villaggio P (2003) The dynamics of detaching rigid body. Meccanica 38: 595-609
3. FEMLAB User's guide (2004) Version 3.1: 474-490, COMSOL
4. Reddy J N, (1984) An introduction to the finite element method. McGraw-Hill, New York
5. Zinkiewicz O C, Morgan K (1983) Finite element and approximation. John Wiley & Sons, Chichester
6. N'Dri N A, Shy W, Tran-Son-Tay R (2003) Computational modeling of cell adhesion and movement using a continuum-kinetics approach. Biophys. J. 85(4): 2273–2286
7. Nassehi V (2002) Practical aspects of finite element modelling of polymer processing. John Wiley & Sons, Chichester
8. Gerald C F, Wheatley P O (1999) Applied numerical analysis. Addison–wesley
9. Kaplan W (1981) Advanced mathematics for engineers. Addison-wesley
10. Diacu F (2000) An introduction to differential equations. Freeman and Company
11. Huntley I D, Johnson R M (1983) Linear and nonlinear differential equations. Ellis Horwood Ltd
12. Glowinski R, Pan T W, Hesla T I, Joseph D D (1998) A distributed lagrange multiplier/fictitious domain method for particulate flows. Int. J. Multiphase Flows 25: 201–233
13. Alberts B, Bray D, Lewis J, Raff M, Roberts K, Watson J D (1994) Molecular biology of the cell. 3rd edn. Garland Science, Oxford
14. Barthès-Biesel D, Rallison J M (1981) The time-dependent deformation of a capsule freely suspended in a linear shear flow. J. Fluid Mech. 113: 251–267

Author: Michele Buonsanti
Institute: MECMAT Department, Faculty of Engineering, University "Mediterranea" of Reggio Calabria
Street: Via Graziella Feo di Vito, I-89100
City: Reggio Calabria
Country: Italy
Email: michele.buonsanti@unirc.it

Time Series Prediction of Gene Expression in the SOS DNA Repair Network of *Escherichia coli* Bacterium Using Neuro-Fuzzy Networks

R. Manshaei[1], P. Sobhe Bidari[1], J. Alirezaie[1,3], M.A. Malboobi[2]

[1] Department of Electrical Engineering, K.N. Toosi University of Technology, Tehran, Iran
[2] National Institute of Genetic Engineering and Biotechnology, Tehran, Iran
[3] Department of Electrical and computer Engineering, Ryerson University, Toronto, Ontario, Canada

Abstract — **Identification of gene regulatory networks and prediction of gene behavior through their expression data have become major problems in computational molecular biology in the last few years. In this study, a novel approach for time series gene expression prediction based on Mamdani neuro-fuzzy networks is proposed.**

In this work, a set of gene expression data is studied and neuro-fuzzy networks are designed to obtain models for gene expression prediction over time. In each neuro-fuzzy network, one of the genes is considered as the output and the other genes as the inputs. The time series expression values of the output are predicted by analyzing the time series expression values of the inputs.

We study a popular gene expression data set of SOS DNA repair network of *Escherichia coli* bacterium. By comparing the results of proposed algorithm with previous works, it is obvious that our networks are predicting more precisely.

Keywords — **Time Series Gene Expression, Mamdani Neuro-Fuzzy Network, Mathematical Modeling, *Escherichia coli***

I. Introduction

In recent years, gene expression data is widely used to discover genes behavior under different conditions. Many experimental techniques are performed to increase the available time series gene expression data sets such as microarray technology which can simultaneously monitor the expression levels of thousands of genes during important biological processes and across collections of related samples. Therefore, massive amounts of biological data await interpretation. By using computational methods, these data sets can be employed for analyzing and modeling techniques.

The availability of expression data made the possibility of predicting unknown genes functional information. However, as the ultimate goal of molecular biologists is to uncover the complex regulatory mechanisms controlling cells and organisms, the reconstruction, prediction and modeling of gene networks remain as the central problems in functional genomics. Due to the fact that gene expression data sets are usually noisy, the methods for modeling and function prediction should be robust to noise.

In this paper, a new approach is employed to predict the time series behavior of genes in a cell by studying the behavior of other genes in the cell. For achieving to this target, Mamdani Neuro-Fuzzy Network is applied to the SOS DNA Repair network of *Escherichia coli* (*E. coli*) bacterium time series gene expression data.

It is known that both fuzzy logic systems and neural networks are capable to process knowledge like human. Artificial neural networks are well-known as universal function approximators, in terms that they can approximate any continuous function represented by data subject to have an appropriate neural network model. On the other hand, fuzzy logic is a natural language for linguistic modeling of data; as a consequence, it is consistent with the qualitative linguistic–graphical methods used to describe biological systems. In neuro-fuzzy systems, the advantages of both neural networks and fuzzy logic are employed; therefore, the system is capable to not only approximate but also model the data subjected to the system [2]. Besides to these advantages, the neuro-fuzzy system presented by Mamdani has enough simplicity to work on gene expression data sets and the ability to deal with noisy data.

II. Proposed methods

A. Neuro-Fuzzy Network

The computational approach described in this paper is Mamdani neuro-fuzzy network (MNFN) that is able to overcome the drawbacks specific to pure neural networks, which act as black boxes. By incorporating elements specific to fuzzy reasoning processes, we are able to give to each node and weight their meaning and function as part of a fuzzy rule, instead of just being abstract numbers [1].

A Mamdani neuro-fuzzy system uses a supervised learning technique, usually back-propagation learning, to learn the parameters of the membership functions [6]. The architecture of this system is illustrated in Fig. 1. The details of each layer are as follows:

Chwee Teck Lim, James C.H. Goh (Eds.): ICBME 2008, Proceedings 23, pp. 1846–1849, 2009
www.springerlink.com

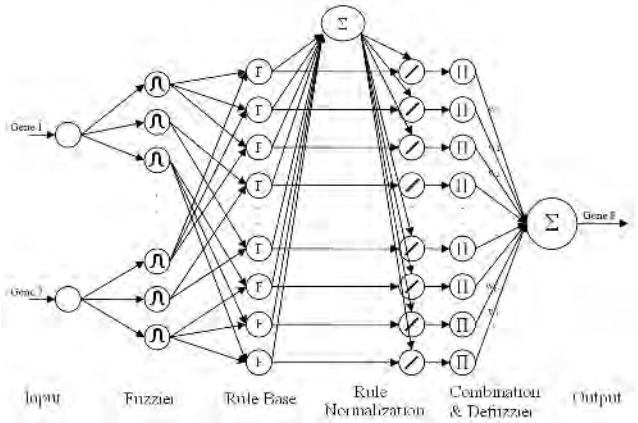


Fig. 1 Mamdani Neuro-Fuzzy Network [6]

- Input Layer (Layer 1): As shown in Eq. (1), no calculation is done in this layer. Each node, which corresponds to one of input variables, only transmits input value to the next layer directly. The link weight in layer 1 is unity.

$$O_i^{(1)} = G_i \tag{1}$$

where G_i is the expression value of the i^{th} gene, and $O_i^{(1)}$ is the i^{th} output of layer1.

- Fuzzifier Layer (Layer 2): Each node in layer 2 corresponds to one linguistic label which is low-expressed, average-expressed or high-expressed. The output link of this layer, represented as the membership value, specifies the degree to which the input value belongs to the respective label. A clustering algorithm decides the initial number and type of membership functions (MFs) to be allocated to each of the input variables. The final shapes of the MFs are fine tuned during network learning.

As shown in Eq. (2), membership functions are represented as Gaussian form.

$$O_{ij}^{(2)} = \exp\left(-\frac{\left(O_i^{(1)} - m_{ij}\right)^2}{\sigma_{ij}^{\ 2}} \right) \tag{2}$$

where *i, j* indicate the input variable and the related number of fuzzy sets respectively, m_{ij} and σ_{ij} are the mean and variance of the membership functions, while $O_i^{(1)}$ is the value of the i^{th} input variable.

- Rule Base Layer (Layer 3): A node in this layer combines the antecedent part of a fuzzy rule using a T-norm operator. In this study, T-norm operator is considered as minimum operation. The output of each node represents the firing strength of the corresponding fuzzy rule which is calculated by Eq. (3). The number of nodes in this layer equals to the number of rules.

$$O_k^{(3)} = \min_r \left(\exp\left(-\left\{ D_r\left(O_r^{(1)} - m_r\right) \right\}^T \left\{ D_r\left(O_r^{(1)} - m_r\right) \right\} \right) \right) \tag{3}$$

$$D_r = diag\left(1/\sigma_{r1}, 1/\sigma_{r2}, ..., 1/\sigma_{rn}\right) \tag{4}$$

$$m_r = \left(m_{r1}, m_{r2}, ..., m_{rn}\right)^T \tag{5}$$

where *r* runs through all the selected nodes of layer 2 corresponding to the k^{th} rule.

- Rule Normalization Layer (Layer 4): The number of nodes in this layer is the same as layer 3; the rules are normalized by Eq. (6).

$$O_i^{(4)} = \frac{O_i^{(3)}}{\sum_{i=1}^{m} O_i^{(3)}} \tag{6}$$

where *m* is the number of all rule sets.

- Combination and Defuzzier Layer (Layer 5): All the rules are combined and defuzzificated using Eq. (7):

$$O_i^{(5)} = \sum_{i=1}^{m} w_i O_i^{(4)} \tag{7}$$

where w_i is the weight multiplied to the i^{th} rule.

B. Learning procedure

The parameters of proposed MNFN must be trained to obtain a predicting system for our data. Therefore, in learning procedure, some parameters of the network including means and variances of fuzzy sets and weights corresponding to the rules are trained by back-propagation (BP) learning algorithm which is widely used for training neural or fuzzy networks and based on gradient descent [7].

Owing to the simplicity of the BP learning algorithm, we adopt this method to tune parameters of the MNFN model by means of error propagation via variation calculus.

For each network, an error criterion is defined in order to test the accuracy on a given data set, by using an overall error measure based on the difference between the predictions and target values of the output variable i.e. gene. One of the most common criteria is Mean Square Error (MSE) described by Eq. (8):

$$E_i = \frac{1}{N} \sum_{i=1}^{N} \left(y_i^{predicted} - y_i^{measured} \right)^2 \tag{8}$$

where N is the number of samples in the data set.

The number of rules governs the expressive power of the network. Intuitively, an increase in the number of rules

describing the gene interactions in a certain network results in a decrease in the error measure of Eq. (8). However, pursuing a low error measure may result in the network becoming overfitted and tuned to the particular training data set and exhibiting low performance on the test sets [1].

Therefore the problem becomes one of combinational optimization: minimize the number of rules while preserving the error measure at an adequate level by choosing an optimal set of values for the parameters (overlap degree between learning rates and rule creation criteria) [1].

C. Data

The proposed method in this study is validated using gene expression measurements for the SOS DNA Repair network of *E. coli* bacterium. Gene expression patterns give an indication of the levels of activity of genes in the tissues under study. The SOS system has a 'single input module' architecture [4], where a single transcription factor controls multiple-output operons, all with the same regulation sign (repression or activation), and with no additional inputs from other transcriptional factors. This is a basic recurring architecture in transcriptional networks [3] and characterizes more than 20 different gene systems in *E. coli* [4].

In this paper, we have used time series gene expression measurements presented by Ronen et al. [5] for SOS DNA Repair network of *E. coli* bacterium which is downloadable at [8]. The measurements include four different data sets: experiment 1, 2, 3 and 4 which are done under various light intensities. Experiments 1 and 2 are under 5 J/m^2, and experiments 3 and 4 are under 20 J/m^2 light intensity.

In these experiments eight major genes are monitored which are: uvrD, lexA, umuD, recA, uvrA, uvrY, ruvA and polB; each experiment consists of 50 time points with a time period of 6 min.

III. Results

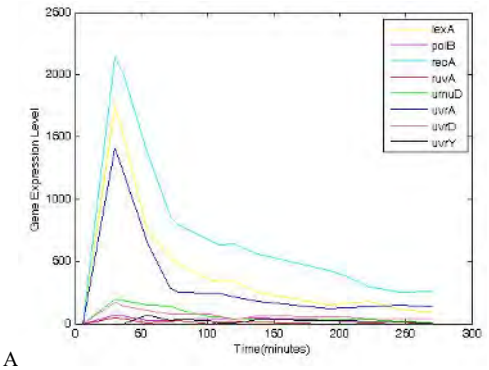
This study attempts to emphasize MNFN in the subject of gene expression prediction based on time series data set. The data is stored in a matrix with rows containing gene expression measurements over time samples in columns.

A number of MNFNs that match the number of genes are constructed; the output of each network is one selected gene and the inputs are the remaining genes from the data set. Networks attempt to describe the behavior of the output gene based on possible interactions from the input genes; and the knowledge derived from gene–gene interactions is stored in a set of fuzzy rules.

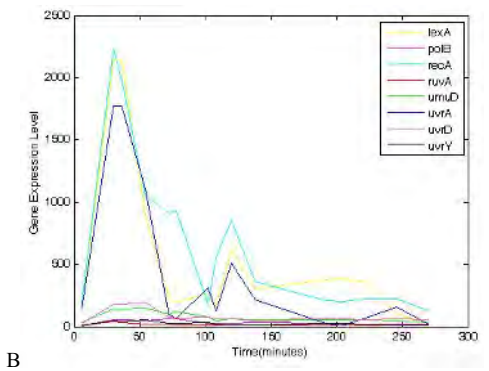
Following, we create eight multi-input single-output (MISO) MNFNs that describe each one of the genes involved in the SOS system. Each network is trained using 35 time points of data set and evaluated using the remaining 15 time points. The mean of experiment 1 and 2 are employed for training and testing the networks.

In the work of Maraziotis et al. [1] and Ronen et al. [5], all time points of data from experiment 1 were used to train their networks. In Ronen et al. work, all time points of data from experiment 2 were used to evaluate their system, and Maraziotis et al. tested their system using all time points of data from experiments 2, 3 and 4. It should be noted that, in both works, training and testing procedure include the same time points from data set in different experiments. As the experiment 1 and 2 are performed in parallel with the same conditions, their systems are tested with the similar data to the training. In our work, the networks are tested by the data with different time point comparing to the ones used as training. This can lead us to more accurate and realistic evaluation from our networks.

In Fig. 2, the results obtained from proposed MNFNs for all 8 genes are illustrated. In Fig. 2 (A), gene expression values in test time points and in Fig. 2 (B) the predicted values for these points are shown. The results of training and testing of the method are presented in Table 1 in terms



A



B

Fig. 2 (A) Gene expression target values of test time points, (B) predicted gene expression values by proposed method in the same time points.

Table 1 MSE of the 8 MISO gene prediction networks in train and test data subsets

Gene Name	Train Error (MSE)	Test Error (MSE)	Function
uvrD	0.0112	0.0129	Nucleotide excision repair, recombinational repair
lexA	0.0008	0.0192	Transcriptional repressor
umuD	0.0029	0.019	Mutagenesis repair
recA	0.0051	0.0088	Mediates LexA autocleavage, blocks replication forks
uvrA	0.0048	0.0273	Nucleotide excision repair
uvrY	0.0336	0.0634	SOS operon of unknown function, additional roles in two-component signaling
ruvA	0.0152	0.0386	Double-strand break repair
polB	0.017	0.0432	Trans-lesion DNA synthesis, replication fork recovery

of the MSE criterion. It is obvious from this table that the proposed method has accurate prediction ability for time series gene expression values.

IV. Conclusions

The paper presents a method to predict a selected gene behavior based on possible interactions from other related genes. Towards this goal, we have presented a Mamdani neural fuzzy network that is able to achieve the task in an accurate and fast manner. This leads us to find possible relations in the form of fuzzy rules, among 8 SOS DNA Repair genes of *E. coli* bacterium. Also, these fuzzy IF-THEN rules can help us in building a model describing the functional relationship and the interactions among genes.

Acknowledgment

We would like to highly thank Ms. Tahmineh Lohrasebi and Mr. Amir Feizi for useful discussions and supports relating to this study.

References

1. I.A. Maraziotis, A. Dragomir and A. Bezerianos, ' Gene networks reconstruction and time-series prediction from microarray data using recurrent neural fuzzy networks', IET Syst. Biol., Vol. 1, No. 1, January 2007.
2. C.-T. Lin, and C.S.G. Lee, "Neural Fuzzy Systems: A Neuro-Fuzzy Synergism to Intelligent Systems", NJ: Prentice Hall, 1996.
3. F.C. Neidhardt, and M.A. Savageau, "Regulation beyond the operon' in Neidhardt, F.C. (Ed.): '*Escherichia coli* and Salmonella: cellular and molecular biology", (American Society of Microbiology, Washington DC, 1996, 2nd edition), pp. 1310–1324.
4. S.S. Shen-Orr, R. Milo, S. Mangan, and U. Alon, "Network motifs in the transcriptional regulation network of Escherichia coli", Nat. Genet., 2002, 31, pp. 64–68.
5. M. Ronen, R. Rosenberg, B.I. Shraiman, and U. Allon, "Assigning number to the arrows: parameterizing a gene regulation network by using accurate expression kinetics", Proc. Natl. Acad. Sci., 2002, 99, pp. 10555–10560.
6. J.-S.R. Jang, C.-T. Sun, and E. Mizutani, "Neuro-Fuzzy and Soft Computing: A Computational Approach to Learning and Machine Intelligence", NJ: Prentice-Hall, 1997, ISBN 0-13-261066-3.
7. S.-i. Horikawa, T. Furuhashi, Y. Uchikawa, "On fuzzy modeling using fuzzy neural networks with the back-propagation algorithm", IEEE Trans. Neural Networks, 1992, 3, pp. 801–806.
8. http://www.weizmann.ac.il/mcb/UriAlon/Papers/SOSData.

Author: Roozbeh Manshaei, Pooya Sobhe Bidari
Institute: K.N. Toosi University of Technology
Street: Seyedkhandan, Dr. Shariati Ave.,
City: Tehran
Country: Iran
Email: {r.manshaei, pooya.sobhebidari}@ee.kntu.ac.ir

Predictability of Blood Glucose in Surgical ICU Patients in Singapore

V. Lakshmi[1], P. Loganathan[1], G.P. Rangaiah[1], F.G. Chen[2] and S. Lakshminarayanan[1]

[1] Department of Chemical & Biomolecular Engineering, National University of Singapore, Singapore
[2] Department of Anesthesia, Yong Loo Lin School of Medicine, National University of Singapore, Singapore

Abstract — **Tight blood glucose (BG) control is known to reduce mortality and improve outcomes in critical care patients by 29-45% [1]. Several first principles models have been put forward to predict BG levels in patients so that tighter BG control may be achieved. These models have been employed in both simulation and clinical studies. However, to the best of our knowledge, they have not been tried for intensive care unit (ICU) patients in Singapore. Hence, the primary objective of this study is to evaluate the applicability and effectiveness of selected models for BG prediction in ICU patients, with the eventual goal of achieving tighter BG control. Two models are selected and tested for predicting clinical BG data in 8 surgical ICU patients. Results of this exploratory study are presented and discussed.**

Keywords — **Blood Glucose, Surgical ICU, Bergman Model, Chase Model**

I. Introduction

Under severe stress, the human body loses some of its homeostatic capacity, in particular its ability to regulate the blood glucose (BG) level. Abnormal BG levels can lead to two conditions: hyperglycemia (i.e., high BG) and hypoglycemia (i.e. low BG). Prolonged and frequent hyperglycemia causes multiple organ failure [1]. Hypoglycemia, on the other hand, causes seizures and death, and hence is serious [1].

A patient suffering critical illness is typically under extreme stress and there is a good chance that he/she will experience poor BG regulation. Hence, maintaining BG at acceptable levels in critically ill patients is vital and a very important component of care in Intensive Care Units (ICUs). Studies have shown that tight control of BG can reduce mortality in critically ill patients by 45% [1].

Mathematical models based on first principles have been developed to predict the time evolution of BG. These models and predictions can allow medical staff to make better decisions for tighter control of BG in critically ill patients. We focus on two leading models: the Bergman Minimal model [3] and the Chase model [2]. Some factors that we have paid particular attention to in our study are that the patients we have access to are Singaporeans and the availability of data from the surgical ICU at the National University Hospital.

A. Singaporean Patients

The applicability of BG models to Singaporean Asian populations has not been investigated. In the past, this group has proved problematic with respect to standardized measures derived from predominantly Caucasian populations, for example, the 2005 redefinition of the BMI range for Singapore based on WHO recommendations [9]. This is attributed to the fact that the body composition and percentage of body fat of the typical Singaporean Asian is different from the typical Caucasian. Since some of these factors (namely percentage of body fat) are relevant in other BG conditions, e.g. diabetes [1], we feel that it is worthwhile to investigate the applicability of BG models to this population.

B. Availability of Data in the Surgical ICU of the National University Hospital (NUH).

We use the selected models on retrospective surgical ICU data on BG, external insulin and dextrose infusions only. This is because we have aimed to keep the data collection as unobtrusive as possible for the patients and the medical staff. Basal insulin levels in the blood are therefore unavailable to us. Also, our data readings are spaced by about four hours, while the Bergman model was developed using data with a 2-minute sampling interval [3] and the Chase model uses data with a sampling interval of 1 hour [2].

The data collection for this study was approved by local institutional ethics committees (IRB and DSRB).

II. Modelling glucose-insulin dynamics

In this study, we have chosen to focus on two BG models: the diabetic extension of the Bergman minimal model [4] and the Chase model [2]. These two models are chosen for their simplicity [3, 4] and the fact that they are based on physiological principles [2, 3, 4]. Bergman model has been used in a number of studies, and the Chase model is a recent extension of the Bergman model, which was successfully used. These two models are briefly described below.

A. Diabetic Bergman Minimal model

This is a first principles model with two physiological compartments for glucose and one physiological compart-

Chwee Teck Lim, James C.H. Goh (Eds.): ICBME 2008, Proceedings 23, pp. 1850–1853, 2009
www.springerlink.com

ment for insulin. The endogenous insulin of the original Bergman model is replaced with an exogenous insulin flow to deal with the insulin deficiency caused by pancreatic β-cell destruction in diabetics. A glucose meal disturbance is added to represent the external glucose feed. The diabetic Bergman model is as follows [4]:

$$\frac{dG(t)}{dt} = -\left(p1 + X(t)\right)\cdot G(t) + p1\cdot G_b + \frac{F_G}{V_G}$$

$$\frac{dX(t)}{dt} = -p2\cdot X(t) + p3\cdot\left(I(t) - I_b\right)$$

$$\frac{dI(t)}{dt} = -n\cdot I(t) + \frac{F_I}{V_I}$$

This model is fairly simple but is well suited to our study because it preserves compatibility with known physiological facts and was validated in clinical studies [3].

In the above model, *G(t)* (mmol/L) and *I(t)* (mU/L) represent the time courses of glucose and insulin in plasma following a rapid glucose injection (usually 0.3 g of glucose per kg of body weight). *X(t)* (1/min) describes the effect of insulin on net glucose disappearance, and G_b (mmol/L) is the glucose basal level in the blood. F_G is the meal glucose disturbance variable. I_b (mU/L) represents basal insulin. V_I (L) is the insulin distribution volume, V_G (L) is the glucose distribution volume, F_I (mU/min) is exogenous insulin flow and F_G (mmol/min) is glucose flow that enters the glucose compartment.

The model has four patient-specific parameters: pl (1/min), p2 (1/min), p3 (L/mU.min^2) and n (1/min). Parameter. p1 describes 'glucose effectiveness'. The ratio of p3 to p2 defines S_I (L/mU.min), the insulin sensitivity index, which represents the insulin-dependent increase in the net glucose disappearance rate. Parameter n represents fractional insulin clearance. Nominal parameter values of p1 = 0.0131, p2 = 0.0135, p3 = 2.9x10^{-6}, n = 0.13, V_I =3.15, V_G= 12, are used as first estimates since they are most commonly used in literature [4, 5, 6].

B. Chase model

The Chase model is based on the Bergman model but takes into account transient dynamics due to the long-term effect of exogenous insulin [2]. It accounts for exogenous insulin disappearance from plasma as following a non-linear saturation and its saturable utilization to reduce BG levels. This matches the model to known physiological knowledge [8]. The Chase model is as follows:

$$\frac{dG}{dt} = -p_G G(t) - S_l\left(G(t) + G_E\right)\frac{Q(t)}{1 + a_G Q(t)} + \frac{P(t)}{V_G}$$

$$\frac{dQ(t)}{dt} = -kQ(t) + kI(t)$$

$$\frac{dI(t)}{dt} = -\frac{nI(t)}{1 + a_l I(t)} + \frac{u_{ex}(t)}{V_l}$$

In the above equations, $G(t)$ (mmol/L) is the concentration of the plasma glucose above the equilibrium level, G_E (mmol/L) is the equilibrium level of plasma glucose concentration, $I(t)$ (mU/L) is the concentration of the plasma insulin above the basal level, $Q(t)$ (mU/L) is the effect of previously infused insulin being utilized resulting from exogenous insulin input, $P(t)$ (mmol/min) is the exogenous glucose infusion rate, $u_{ex}(t)$ (mU/min) is the insulin infusion rate, V_I (L) is the insulin distribution volume, V_G (L) is the glucose distribution volume, n (1/min) is the first order decay rate for insulin from plasma, p_G (1/min) is the time-varying fractional clearance of plasma glucose at basal insulin, S_I (L/mU.min) is the time-varying insulin sensitivity, k (1/min) is the parameter controlling the effective half life of insulin, α_I (L/mU) is the Michaelis-Menten parameter for insulin transport saturation, and α_G (L/mU) is the Michaelis-Menten parameter for glucose clearance saturation [2, 5].

Nominal parameter values of p_G = 0.01, S_I = 0.0002, α_I = 0.0017, α_G = 0.04, n = 0.16, k = 0.0099, V_I =3.15 and V_G= 12, are used as first estimates [5, 6].

III. Methodology Employed

The methodology employed for BG prediction consists of two phases: parameter estimation to find values of some parameters in the model, and one-step-ahead prediction to predict the BG at the next sampling/measurement time. The MATLAB® Optimization Toolkit was used in this methodology.

For every patient data set, we estimated model parameters that are patient-specific and time variant using the fminsearch function in MATLAB. This function computes the optimal model parameter values by minimising the sum of prediction errors between measured and model predicted values, and requires an initial parameter estimate which can be given based on literature data [3, 6].

For each patient, we use the first *n* data points to estimate optimal parameter values. The BG value at each subsequent sampling time is predicted using the parameter estimates

calculated using all the previous data points. The procedure is repeated at the next sampling time using n+1 data point. This approach is termed 'one-step-ahead prediction'. Such a one-step-ahead prediction which includes time-variant and patient-specific parameter values is likely to yield better prediction accuracy than fixed parameter estimates. We believe this to be closer to how an eventual tool would be used in the ICU.

The minimum number of data points required for the first prediction is based on the number of model parameters to be estimated, and it is 3 in our case for both the models. These 3 data points translate into an average of 12 hours. This is a reasonable period as a prediction could be made just after the first 12 hours of a patient's stay at the ICU.

At each instant of parameter estimation and prediction, average of BG measurement over the previous 3 data points (8-12 hours) was used as G_b (basal glucose) in the Bergman model and G_E (equilibrium glucose) in the Chase model. This approach is based on the technique used in [6] on the Chase model and that we extended to the Bergman model. For parameter estimation for the first 3 points, the BG measurement for that point is used for G_b and G_E.

Both the models have two physiologically important parameters: glucose effectiveness and insulin sensitivity. *Glucose Effectiveness* represented as p1 in the Bergman model and p_G in the Chase model, is the effect of glucose to enhance glucose disappearance, at basal insulin in the absence of dynamic insulin response [7]. *Insulin Sensitivity* represented as a ratio of p2 and p3 in the Bergman model and S_I in Chase model: Insulin Sensitivity reflects the ability of insulin to enhance the effect of glucose to normalize its own concentration after injection [7].

IV. Results and Discussion

We present the complete results for one patient that can be described as typical of the group of patients we have studied. Patient 35 is a 70 year old female with a history of diabetes (type II). For this patient, Figure 1 shows the insulin and dextrose inputs, Figures 2 and 3 compares the BG predictions by the Bergman and the Chase model respectively, with measured data. Table 1 presents the mean percentage error (MPE). Figure 4 and 5 are parity plots of measured versus predicted BG value for all patients and at all prediction instants for the Bergman model and the Chase model respectively.

Our MPE lies between 2% and 13% (Table 1), which is very near to the acceptable range of 2-11% [6]. Taking into consideration our unobtrusive data collection methods (in contrast with the collection methods in [2], [3] and [4]), our study has yielded very promising results. We also note, based on table 1 and figures 4 and 5, how the more complex Chase model consistently outperforms the Bergman model. This is because the Chase model accounts for the delayed insulin utilization [2], whose effect is substantial due to the long sampling interval of four hours used. This average sampling interval of four hours limits our understanding of how the BG level fluctuates between two samples and we cannot account for any possible spikes or dives in BG level that may occur in this interval.

Table 1 Mean Percentage Error for Several Patients

Patient Number	Mean Percentage Error for Predictions by	
	Bergman model	Chase model
1	5.1	2.3
2	12.6	12.1
22	5.1	2.4
24	5.2	2.7
25	3.3	4.2
30	7.0	2.1
34	6.4	4.3
35	10.1	3.8

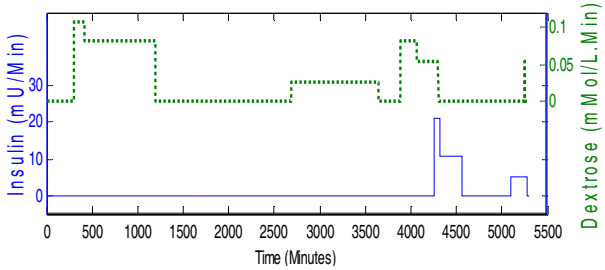


Fig. 1 Insulin and dextrose inputs for patient 35

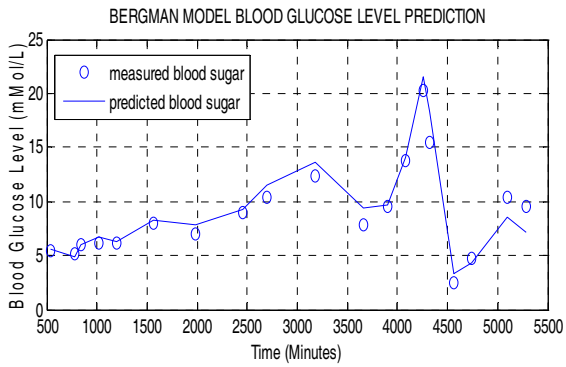


Fig. 2 Comparison of the BG prediction by the Bergman model with the measured data for patient

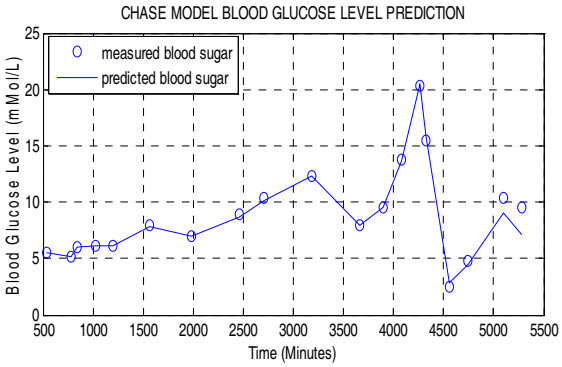


Fig. 3 Comparison of the BG prediction by the Chase model with the measured data for patient 35

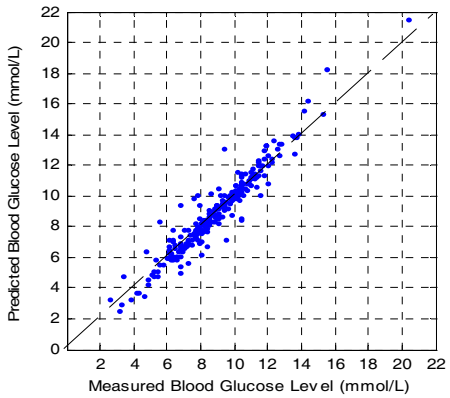


Fig. 4 Comparison of the predicted BG by the Bergman model with the measured BG for all patients

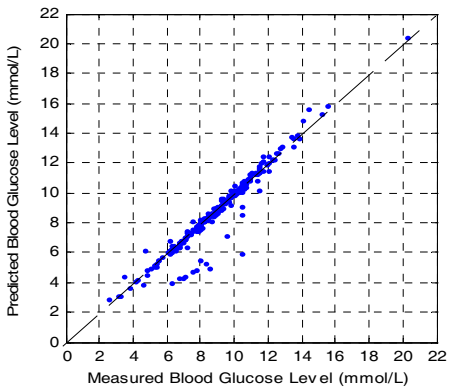


Fig. 5 Comparison of the predicted BG by the Chase model with the measured BG for all patients

V. Conclusion

This study has shown that the Chase model and, to a lesser extent, the diabetic Bergman model, can predict BG value reliably for Singaporean patients in surgical ICU, using the 'one-step-ahead prediction' procedure. MPE values obtained for these two models are consistent with the previous work [6]. Both the Chase and Bergman models should be further evaluated for eventual use to achieve tight control of BG levels in critically ill patients. We recommend that the two models be investigated using data with a sampling interval of no more than one hour, to assess the improvement in the accuracy of model predictions.

Acknowledgements

The authors acknowledge the financial support provided by the National University of Singapore through the cross-faculty grant for the research described in this paper.

References

1. G. Van den Berghe, P. Wouters et al., (2001) Insulin Therapy For the Critically Ill Patient, N Engl J Med, 345:1359-1367
2. J. G. Chase, G. M. Shaw et al., (2005) Adaptive bolus based targeted regulation of hyperglycemia in critical care, Med Eng Phys, 27:1-11
3. G. Pacini, R. N. Bergman, (1983) PACBERG: An adaptive program for controlling the blood sugar, Computer Programs in Biomedicine, 16:13-20
4. T. Van Herpe, B. Pluymers et al., (2006) A Minimal model for glycemia control in critically ill patients, EMBS Annual Conference
5. J. G. Chase, X. W. Wong et al., (2008) Simulation and initial proof-of-concept validation of a glycaemic regulation algorithm in critical care, Control Engineering Practice, 16(3):271-285
6. C. E. Hann, J. G. Chase et al., (2005) Integral-Based Parameter Identification for long-term dynamic verification of a glucose-insulin system model, Computer Methods and Programs in Biomedicine 77:259-270
7. R. N. Bergman, K. Hücking et al., (2004) International Textbook of Diabetes Mellitus (Third Ed.), John Wiley & Sons, Chichester
8. J. S. Krinsley, (2003) Association between hyperglycemia and increased hospital mortality in a heterogeneous population of critically Ill patients. Mayo Clin Proc 78(12):1471–8.
9. M. Deurenberg-Yap, G. Schmidt et al., (2000) The paradox of low body mass index and high body fat percentage among Chinese, Malays and Indians in Singapore, Int J Obes Relat Metab Disord, 24(8):1011-7

Author: G.P. Rangaiah
Institute: National University of Singapore
Street: Engineering Drive 4
City: Singapore
Country: Republic of Singapore
Email: chegpr@nus.edu.sg

Method of Numerical Analysis of Similarity and Differences of Face Shape of Twins

M. Rychlik[1], W. Stankiewicz[1] and M. Morzynski[1]

[1] Poznan University of Technology, Department of Combustion Engines and Transportations, Division of Methods of Machine Design, Poznan, Poland

Abstract — **This article presents application of the PCA (Principal Component Analysis) method for analysis and computation of three dimensional biometric description of 3D objects. As the data input the geometrical data sets (three-dimensional points coordinates) of faces are used.**

Authors apply 3D version of PCA method for numerical estimation of similarity and extraction of difference of analyzed faces. PCA decompose set of 3D objects into mean face and individual features (empirical modes), which describing deviations from mean value. Obtained mean shape describe the similarity of faces, eigenmodes present geometrical differences between faces. Eigenvalues can be used to numerical (mathematical) comparison of study faces.

In this paper three sets of data of different type of twins (identical – monozygotic, fraternal-dizygotic) and thirteen typical faces are used and compared. The mean face and the features (eigenfaces) are presented and discussed.

Authors propose using the set of eigenfaces and corresponding coefficient values (computed from PCA) for security verification. As an example of authorization key the set of coefficient values for the faces are presented. Each key describes individual shape of face and can be decoded and compared with the original data of user to obtain access to restricted area or data.

Keywords — **3D face recognition, biometrics, identification, Principal Component Analysis (PCA), Reverse Engineering.**

I. Introduction

With the expansion of international traffic and globalization of the world, increase the necessary of research in security systems area. The security and access systems are very important and rapidly advancing not only in computer vision. Such systems are used obviously during passenger control on the airport or boundary crossing [9]. Also every day activities, like data protection, on-line banking or shopping may utilize the results of new technology developed. To increasing level of security the many identification and verification techniques are used.

The process of identifying an individual which is common used in every day activity is usually based on two things: username and a password. There are three types of methods of authentification [4]:

- something the user knows – user name, password, pin;
- something the user has – tokens, ID cards, smartcard;
- something the user is – voiceprint identification, retinal scan, face recognition.

The most advanced methods of identification belong to third group. These methods are common name biometrics systems. One of the important and rapidly advancing areas of security identification and verification is face recognition.

II. Biometric technology

Biometrics identify people by measuring some aspects of individual anatomy or physiology – such as hand geometry or fingerprint, some deeply ingrained skill, or other behavioral characteristic – handwritten signature, or something that is a combination of the two – voice [1]. In generally the biometrics can be sorted into two types [3]:

- physical – face, fingerprint, hand/finger, iris, ear, retinal, DNA, vein, blood pulse, dental, lips, nail;
- behavioral – voice, gait, tapping, signature, keystroke dynamics, mouse dynamics.

The disadvantages of the most commonly used recognition techniques are not enough reliability of them [5]. A 2D dimensional photo cannot be measured like a landscape and simply doesn't contain the same amount of information as the 3D photo. This problem is especially essential for twins, when the similarity of face shape is very high.

Facial identification reads the peaks and valleys of facial features. These peaks and valleys are known as nodal points (exist 80 nodal points in a human face, but usually only 15-20 are used for identification – known as „golden triangle" region between the temples and the lips [6].

The face recognition method is the oldest and the most "natural" method of identification persons. Recognizing people by their facial features is going back at least to our early primate ancestors [10]. Biologists believe that a significant part of our cognitive function evolved to provide efficient ways of recognizing other people's facial features and expressions [7].

In further sections, authors presents 3D face identification method with applied of cheap non contact system for data acquisition (structural light scanning technology) and 3D PCA analysis for feature extraction and coding of the shapes of faces. Data base used in presented experiment contains regular and twin's faces (different type of twins).

Chwee Teck Lim, James C.H. Goh (Eds.): ICBME 2008, Proceedings 23, pp. 1854–1857, 2009
www.springerlink.com

III. Principal componenet analysis – empirical modes

Modal analysis methods are used for statistical analysis and minimize the number of parameters which describe 3D objects. One of the method which based on modal decomposition is PCA (Principal Component Analysis, known also as POD – Proper Orthogonal Decomposition). If empirical modes (PCA) are optimal from viewpoint information included inside of the each modes [8], often decomposition based on mathematical (e.g. spherical harmonics) or physical modes (vibration modes) are used.

PCA transformation gives orthogonal directions of principal variation of input data. Principal component which are connected with the largest eigenvalue, represent direction of the largest variation of data in data space. Variation is described by eigenvalue connected with the first principal component. The second principal component, describe the next in order, orthogonal direction in the space with the most large variation of data. Usually only few first principal components are responsible for a majority variations of the data. Data projected onto other principal components often have small amplitude and don't cross a amplitude of measurement noise. Therefore they can be deleted, without dangerous of decreasing of the accuracy. PCA method has in practice been used to reduce the dimensionality of problems. And uses second order statistics information to reduce the data dimension in the minimal mean square error sense.

Independent from name and type of application, the method is generally the same and she based onto statistical representation of the random variables.

The shape of the every object is represented in the data base as the set of 3D points cloud. Each pints cloud is described by vector (1)

$$S_i = [s_{i1}, s_{i2}, \ldots, s_{iN}]^T, \; i = 1,2,\ldots,M, \qquad (1)$$

where $s_{ij} = (x, y, z)$ describes coordinates of the points in Cartesian coordinates system, M is the number of the faces which are in database, N is the number of the points in single points cloud. In the next step the mean shape $\overline{S}$ and covariance matrix C are computed (2):

$$\overline{S} = \frac{1}{M}\sum_{i=1}^{M} S_i \,, \; C = \frac{1}{M}\sum_{i=1}^{M} \widetilde{S}_i \widetilde{S}_i^{\,T} \qquad (2)$$

The difference between mean and object that is in data base are describe by the deformation vector $\widetilde{S}_i = S_i - \overline{S}$. The statistical analysis of the deformation vectors gives us the information about the empirical modes. Modes represent the geometrical features (shape) but also can carry other information like texture, map of temperature and others. Only few first modes carry most information, therefore each original object S_i is reconstructed by using some K principal components (3):

$$S_i = \overline{S} + \sum_{k=1}^{K} a_{ki} \Psi_k \,, \; i = 1,2,\ldots,M, \qquad (3)$$

where Ψ_k is an eigenvector representing the orthogonal mode (the feature computed from data base), a_{ki} is coefficient of eigenvector.

IV. Numerical analysis of shape of human faces

Numerical experiment is prepared onto the database which consist multiple faces. There are 19 faces (fig. 1) with neutral expression of different persons. In presented case three sets (6 faces) of the twin's faces (two sets of identical – monozygotic twins and one set of fraternal – dizygotic twins). For data acquisition the 3D scanning was used.

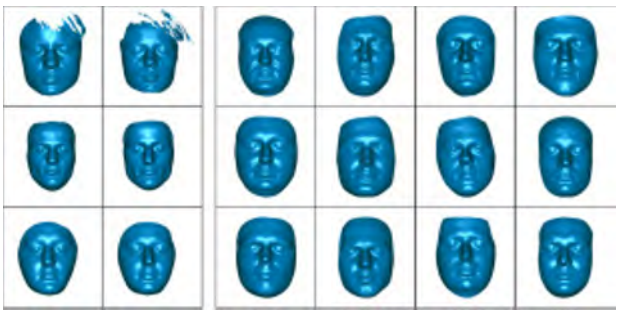


Fig. 1 Examples of faces in database: faces of the twins (left two columns)

A. Data acquisition – 3D scanning

For 3D scanning the structural light technique was used (fig. 2). On each face was projected set of 201 lines (raster matrix) after camera was capture image. Projected lines are calculated in triangulation process onto curve network. In next step from curves set of points (200 points per line) are extracted. Finally each face is described by individual point clouds (40200 points).

The Principal Component Analysis requires the same position, orientation and topology of the data input (the same number of nodes, matrix connection, etc.) for all objects. To achieve this, every new object added to database must be registered. Origin point of coordinate system is arranged in



Fig. 2 Data acquisition process (from upper left): hardware configuration, raster matrix, captured image, 3D curve network, extraction points from curves, input data (points cloud)

cross section of two lines: vertical middle line on the face, horizontal – eyes line

B. Face shape analysis – PCA analysis

For prepared database of 19 faces the Principal Component Analysis was done. The result of this operation is the mean face, nineteen modes and set of coefficients (fig. 3).

The eighteen modes include one hundred percent of information about decomposed geometry (table 1.). Mode nineteen contains only a numerical noise. For further reconstruction of face geometry only first eighteen modes are used.

Modes describe the features of the faces. Two first modes characterize global transformation: first mode changing of the face size in vertical direction and deep of eyes, second mode changing the size in horizontal direction. Further modes describe more complex, local deformations.

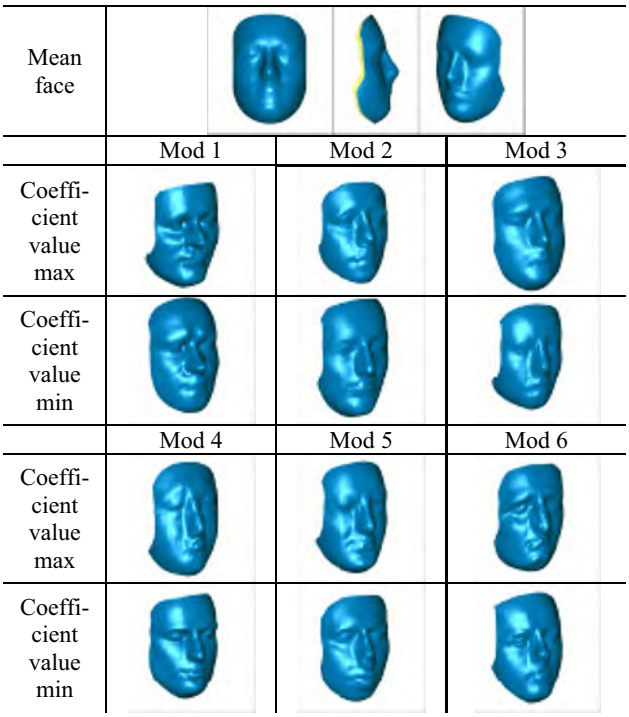


Fig. 3 Visualizations of the mean face and first five empirical modes of faces (for max and min coefficient value)

Table 1 Participation of the modes in face description

Number of the mode	Participation of the mode [%]	Total participation of the modes [%]
1	41,3730939	41,3730939
2	20,4650772	61,8381711
3	14,1903043	76,0284753
4	8,6513257	84,6798011
5	3,4490109	88,1288119
6	2,5576350	90,6864469
7	2,1880060	92,8744530
8	1,3711281	94,2455811
9	1,1804560	95,4260371
10	0,9962907	96,4223278
11	0,8217357	97,2440635
12	0,6042358	97,8482994
13	0,4746871	98,3229865
14	0,4590013	98,7819878
15	0,3851753	99,1671631
16	0,3188265	99,4859897
17	0,2656575	99,7516472
18	0,2483528	100,0000000
19	0,0000000	100,0000000

Results of the statistical analysis (empirical modes) can be used for reconstruction of geometry (in CAD systems) of individual features of the object.

C. Similarity and differences of twins faces – PCA

PCA analysis which are make for each set of twins faces give information about common shape and differences of face (also surface map of differences). For two sets of twins faces individual PCA analysis was done (fig. 4, fig. 5).

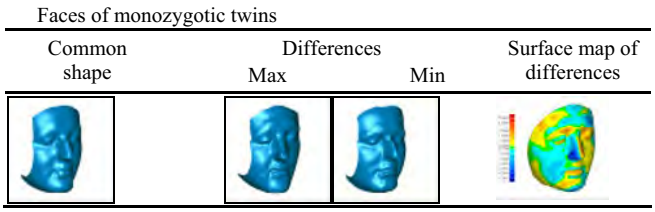


Fig. 4 Visualizations of the common shape (mean face) and differences (empirical mode and surface map of difference) for monozygotic twins

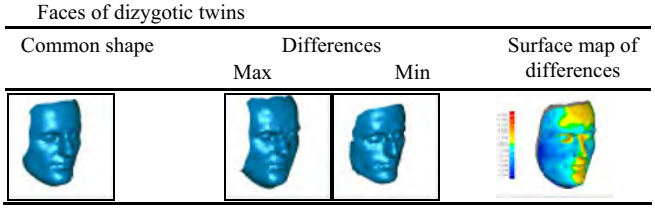


Fig. 5 Visualizations of the common shape (mean face) and differences (empirical mode and surface map of difference) for dizygotic twins

V. 3D BIOMETRIC DESCRIPTION – FACE CODING

Empirical modes give us information about 3D mean shape of population objects and set of the geometrical features which describes principal deformations in analyzed population of the objects. Each face in database has unique set of coefficient values – "ID code" (fig. 6).

As the authorization key the set of coefficient values for the faces can be used. Each key describes individual shape of face and can be decoded and compared with the original data of user to obtain access to restricted area or data files. Also for identical (for human eye view) monozygotic twins this "face code" is incomparable for each one face similar like for fingerprints [2].

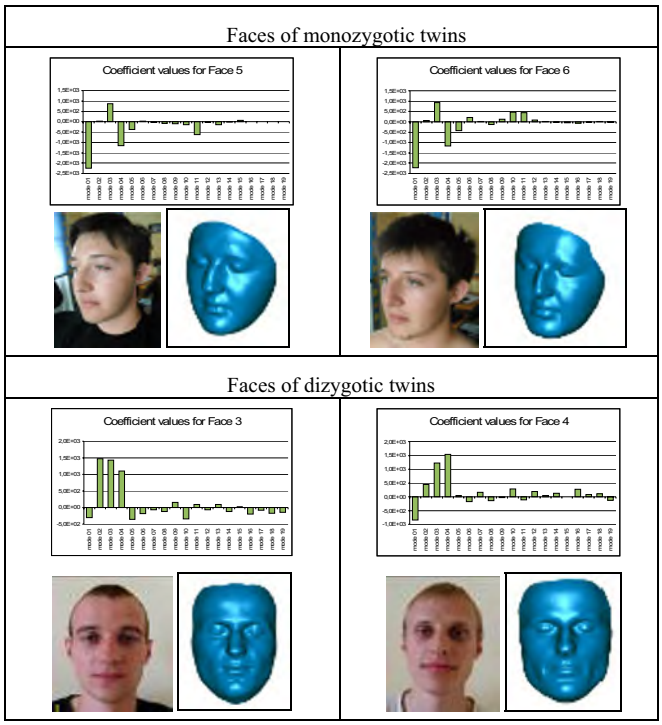


Fig. 6 Face ID code for faces of two types of twins (from upper left): face code – coefficient values, original photo, 3D face model

VI. CONCLUSIONS

Presented method as the source of data input apply cheap non-contact measurement method and full 3D face information instead set of control points (few nodal points in "golden triangle" area). 3D face code is more proof onto fake than 2D face recognition systems. Further is possible to add to data base additional information's (not only about geometry) like e.g. thermal photo (map of temperature).

Application of 3D PCA into biometric security systems make possible using 3D faces as the access code. Each face has individual set of coefficient values – unique face code. That information (code) can be easily recorded onto electronic ID card – similar to 2D biometric data's.

This method can be used for extraction and description of similarity and differences of twins faces. Advantages of this method is possibility of distinguish of identical monozygotic twins what is usually very difficult for standard security systems (2D pictures analysis).

REFERENCES

1. Anderson R. J. (2008) Security Engineering: A Guide to Building Dependable Distributed Systems, Wiley Publishing Inc., Indiana, USA ISBN-13: 9780470068526.
2. Anil K. J., Prabhakar S., Pankanti S. (2002) , On the Similarity of identical twin fingerprints, The Journal of Patter Recognition Society Nr 35, 2653 –2663.
3. Mainguet J-F. (2004) Biometrics, URL: http://pagesperso-orange.fr/fingerchip/biometrics/biometrics.htm.
4. Miller A. (2000) Risks in Biometric-based Authentication Schemes, GIAC Level One Certification Practical: Internet Research Project, SANS Institute.
5. Guardia A/S (2008) Developer of 3D infrared face recognition system, URL: www.guardia.com
6. Biometric Visions (2008), URL: http://www.biometric visi ons.com.
7. Ridley M. (1993) The Red Queen: Sex and the Evolution of Human Nature, New York: Viking Books, ISBN 0-1402-4548-0.
8. Holmes, P., Lumley, J., L., Berkooz, G. (1998), Turbulence, Coherent Structures, Dynamical Systems and Symmetry, Cambridge University Press, Cambridge, New Edition.
9. Schneider W. (2007) Report of the Defense Science Board Task Force on Defense Biometrics, Department of Defense United States of America, Washington D.C.
10. Xiaoguang Lu (2006) 3D Face Recognition across Pose and Expression, PhD thesis, Michigan State University.

Author: Michal Rychlik
Institute: Poznan University of Technology
Street: Piotrowo 3
City: Poznan
Country: Poland
Email: rychlik.michal@poczta.fm

Birds' Flap Frequency Measure Based on Automatic Detection and Tracking in Captured Videos

Xiao-yan Zhang, Xiao-juan Wu, Xin Zhou, Xiao-gang Wang, Yuan-yuan Zhang

School of Information Science and Engineering, Shandong University
Jinan 250100, P. R. China

Abstract — **Flap frequency of birds, as an important feature in identification and behavior assessment to attractants, has not found a good way to measure in videos. In the paper, we try to measure flap frequency of birds automatically based on detection and tracking. The size of bird's area in image fluctuates with wing flaps. In the 90° pitch angle case, when wings are flat, the area is the largest, and then the area decreases along with wings moving upwards or downwards. Based on the feature, we get flap frequency of birds by analyzing fluctuation periods of area size signals.**

Videos are captured by pointing the camera upwards to make the image against the sky, and moving with birds to get large range flapping motion. The detection part is based on two levels background update algorithm to achieve fast background update under abrupt scene changing. The tracking of maneuverable birds is achieved by using a Markov Chain Monte Carlo (MCMC) filter with a flexible motion model to adjust tracking boxes duly to cover areas of birds. Then local time flap frequencies are gotten by using Short-Time Fourier Transform (STFT) to analyze size signals after a smooth filter and a normalizing filter. The average frequency of every window is computed to reflect the quantitative local frequency.

The experiment results show that the frequency spectrum and average frequency of size signal can accurately reflect the actual flap frequency of birds. Based on the fluctuation of local frequencies we can estimate the flight pattern of birds, even in a bird cluster, we can analyze the flight character of the cluster by choosing several interested targets. The change of flap frequency in different flight patterns can give us inspiration for making artificial aircraft.

Keywords — **flap frequency, detection, track, STFT, bird**

I. Introduction

Wing flap frequency of birds play significant role in birds behavior. The abnormity of wing flap frequency can be used to assess the influence of attractants (for example chemicals and light). Determination of frequency of wing flaps during the bird flight is important for understanding mechanical power output of muscle and flight pattern [1]. Wing flap frequency of each species overlaps all other species. However, mean wing flap frequencies are significantly different for all species, so the difference of wing flap frequencies between species has been great information in identification [2, 3, 4].

Videos can capture all the information of free flight. The key of the research based on video is to extract the needing information. Though there has been a long study history of wing flap frequency, but methods based on the video are scarce. The most often used method for free flight is radar [2, 5], for the temporal pattern echo signature depends mainly on the variation in the shape of the target which for birds is caused by change in body shape due to flapping. But a significant proportion of the signals observed is provided by insects, bats, other flying objects and weather phenomena [2]. So it is a problem to separate bird signals from non-bird ones. Another method is using a beat-frequency oscillator as well as personal auditory analysis, but it contains many interferences produced by the birds movements that are not connected with flight (for example, respiratory movements of abdomen) [6, 7].

In flight, birds flap their wings upwards and downwards. When the relative angle between camera and birds is fixed, sizes of birds' areas in image fluctuate with wing flaps. In 90° pitch angle case, as the bird in red box shown in Fig.1, when wings are flat, area is the largest, and then the area decreases with the wing moving upwards and downwards. So in continuous flight, size signal of bird's area in image fluctuate in the same frequency with wing flaps. This gives us inspiration for measuring the wing flap frequency by analyzing the size signal of bird's area. Size signals are recorded based on accurate detection and tracking.

We use two levels (pixel level and frame level) background update algorithm [8, 9] to get excellent foreground in real time. In frame level, three thresholds are used to update the background to achieve fast background update under abrupt scene changing produced by moving clouds. Targets are detected from binary foreground after retrieving contours. In tracking, for getting accurate areas of tracked



50 flat #53 downwards #55 upwards

Fig. 1 A wing flap period in 90° pitch angle case

Chwee Teck Lim, James C.H. Goh (Eds.): ICBME 2008, Proceedings 23, pp. 1858–1861, 2009
www.springerlink.com

targets, tracking boxes should adjust in real time to cover areas of birds. This is achieved by using a Markov Chain Monte Carlo (MCMC) [10, 11, 12, 13] filter with a flexible motion model.

Recorded size signals are processed by a smooth filter and a normalizing filter which is to delete the influence of distance between camera and birds. Local time flap frequencies are gotten by using Short-Time Fourier Transform (STFT) to make time-frequency analysis and computing the average frequency of every local window.

II. Materials and Methods

A. Getting Videos

In capturing, the camera moves with free flight birds in open sky to get large range flapping motion. To avoid abrupt changing background in videos, which is a seriously problem for detection and tracking, the camera is pointed upwards and makes the image against the sky. The relative angle between camera and birds is fixed in range 30°-90°. All the videos are in avi format and the resolution is 320×240 with frame rate 25fps.

B. Birds detection and tracking

We adopt background subtraction algorithm to segment moving targets in videos. The background is updated in frame level and pixel level each time [8, 9]. In pixel level update, pixels that change in continuous λ frames will be updated into the background B(t) at time t with a weight α. α and λ are set according to the character of the background, but for making sky as background, α is 0.1-0.4 and λ is 4-8. In frame level, three thresholds $TL1$ (smaller than 0.001), $TL2$ (in 0.5-0.7), $TL3$ (in 0.7-0.8) are used to update the background separately to achieve fast background update under the situation of the abrupt scene change. Given the width and height of the image w, h, the change rate of the whole frame is

$$v = \frac{\sum_{j=1}^{w}\sum_{i=1}^{h} F_{i,j}(t)}{w \times h} \tag{1}$$

Once v is smaller than TL_1, we will make a decision that no moving targets in current image. If v is bigger than TL_3, it is seen that there is a new scene in current image. In the two cases, we will update all the pixels to the background. When v is between TL_2 and TL_3, background will be updated with bigger weight α (bigger than 0.5).

The foreground is gotten by subtracting the updated background from the image. Then birds are detected from the binary foreground after retrieving contours.

Detected birds will be tracked using MCMC algorithm with a flexible motion model. The state of every target is defined as $\boldsymbol{X}_{i,t} = (x_{i,t}, y_{i,t}, w_{i,t}, h_{i,t}, r_{i,t})$, where $(x_{i,t}, y_{i,t})$ is the center, $w_{i,t}$ and $h_{i,t}$ are the width and length of the target, and $r_{i,t}$ is the relative orientation. At each time step, N_M (the number to reach mixing time) samples are generated using Metropolis-Hastings (MH) algorithm [10].

The motion model is defined as

$$\boldsymbol{X}_{i,t} / \boldsymbol{X}_{i,t-1} = \boldsymbol{X}_{i,t-1} + [\Delta x, \Delta y, \Delta w, \Delta h, \Delta r] \tag{2}$$

Where Δx, Δy, Δw, Δh, Δr are Gaussian random walks. The deviation of each Gaussian random walk decides the diffuse range of the corresponding parameter. σ_w, σ_h as deviations of Δw and Δh are set about 0.5 to adjust the tracking box fast to cover shape changing birds in real time.

We use the binary observation model proposed by Kevin Smith in [12, 13]. Given the precision v and recall ρ measures of targets i and j as in [12], the observation model is

$$\phi(\boldsymbol{X}_i, \boldsymbol{X}_j) \propto \exp(-\lambda\sqrt{v(\boldsymbol{X}_i, \boldsymbol{X}_j)\rho(\boldsymbol{X}_i, \boldsymbol{X}_j)}) \tag{3}$$

C. Pre-processing of recorded data

Size signals of tracked birds are recorded by counting the number of pixels which have a value 1 in the binary foreground and are tracked by the corresponding tracking box.

When capturing videos, for the maneuverability of birds, the distance between camera and birds is not fixed, so area sizes of the same action at different times are not on the same level. To get accurate flap frequency, original size signals are processed by a normalizing filter.

The original size signal $F(n)=[f_1,\ldots, f_N]$, N is the length of the signal, is smoothed first by a smooth filter. Local minimum value points of the smoothed size signal $GF(n)$ are $P_1, P_2,\ldots,P_L$ and $P_0=1$, $P_{L+1}=N+1$. The part between two consecutive local minimum value points P_i and P_{i+1} is a flap period. The adjusted signal $AF(n)$ is given for l=0,…,L

$$AF(n) = GF(n) - \frac{\sum_{m=P_l}^{P_{l+1}-1} GF(m)}{P_{l+1} - P_l}, \qquad n = P_l, ..., P_{l+1} - 1. \tag{4}$$

Finally the normalized signal $NF(n)$ is

$$NF(n) = AF(n) / V_{max} \tag{5}$$

where V_{max} is the maximum value of $AF(n)$, n=1,…,N.

D. Flap frequency analysis

STFT is used to analyze the time-frequency distribution of the pre-processed size signal. It is defined as

$$S(k,n)=\sum_{m=-\infty}^{\infty} x(m)w(m-n)e^{-j\frac{2\pi k}{\mathrm{M}}m},\quad k=0,...,\mathrm{M}-1 \quad (6)$$

where $x(m)$ is the signal and $w(m)$ is the analysis window. M is the length of $w(m)$ and it influences the resolution of time and frequency domains, so it should be decided according to the length and character of signal $x(m)$.

In equation (6), for every value of n, we can get a spectral array $S(k)$, $k=0,...,\mathrm{M}-1$. Every spectral array shows a spectrum. In order to get quantitative local frequencies, we compute average frequency $\overline{f}_n$ of every spectrum. The average frequency is defined as

$$\overline{f}_n=\frac{\sum_{k=0}^{\mathrm{M}-1}S(k)\cdot f(k)}{\sum_{k=0}^{\mathrm{M}-1}S(k)} \quad (7)$$

$$f(k)=k\cdot\frac{\mathrm{F_S}}{\mathrm{M}-1} \quad (8)$$

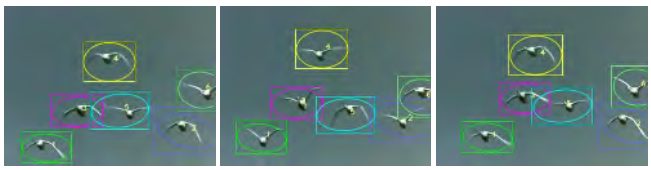
where $f(k)$ is the frequency value of the k-th point, and $\mathrm{F_S}$ is the sampling frequency [14]. When moving the window, we can get an average frequency array $\overline{f}_n$, n=0, 1, 2….

III. Results

In a bird cluster, all birds almost fly in the same flap frequency. We can see this clearly in Fig. 2 (the video is part of bird migration from "The Traveling Birds"), where poses of the six tracked birds in frame 78 are approximately the same as those in frame 69 for the time from frame 69 to 78 is a flap period. So the flap frequency of one bird in a cluster reflects the frequency character of the cluster.

The size signal of No.1 bird was recorded in Fig. 3 to measure the flap frequency of the cluster. The original recorded size signal (the fist signal in Fig. 3) is not smooth and has an increasing trend, but the period of every flap is clear. The smooth filter removed small saw teeth of it and the normalized signal kept the wave character of the original signal and adjusted every period to the same level (the third signal in Fig. 3).

Fig. 4 shows wing flap frequency analysis results. The length of the STFT window is 29, and the length of signal is 126. To avoid the influence of boundary, we only computed average frequencies of frames from 15 to 112. The time-frequency image (Fig. 4(a)) and the average frequency array (Fig. 4(b)) both reflect that the flap frequency of the cluster is about 3Hz, but at the time period, the flap frequency fluctuates at 2.8-4HZ.



69 #74 # 78

Fig. 2 A flap period of a tracked bird cluster

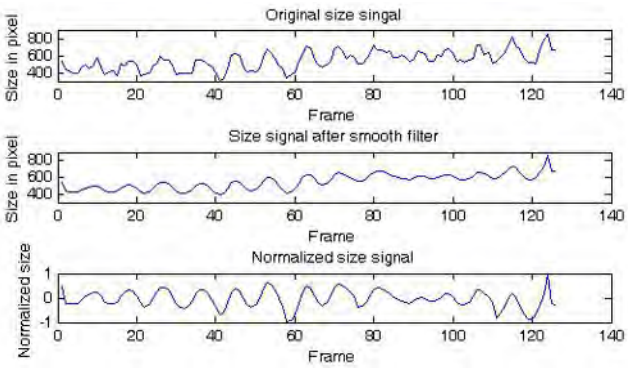
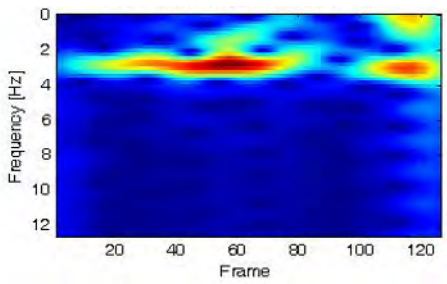
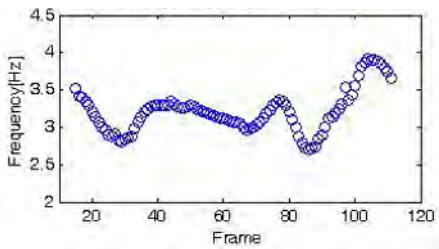


Fig. 3 The pre-processed result of the original size signal



(a) Time-frequency image



(b) Average frequency array

Fig. 4 STFT analysis results

IV. Discussion

In order to check the accuracy of analysis results based on the size signal, we computed the frequency of every period F_s /T in Fig. 5, where T is the length of every period gotten by visual observation. Comparing Fig. 4(b) and Fig.5, we can see that the average frequency of every local window after STFT analysis correctly reflects the fluctuation of flap frequency with time, but at frames 70 to 80, the average frequencies have some error, for the influence of the big change of the 9-th and 10-th periods. STFT is to use a window to select short time intervals for spectral analysis, so at the turn of two frequencies, the analysis result will have some error. This proves that the average frequency of every time does not represent the instantaneous frequency, but reflects the local frequency character.

Even the rhythm of every bird is not always the same in a cluster as in Fig. 1 and Fig. 2, the flap patterns of them are always the same with same fluctuation of flap frequency, so we can choose one or several interested birds as analysis targets to research the cluster's flap character.

Compared with free-flight methods using radar and sensor, the method based on video is more reliable, for we can check the result with visual image and have no interference from other species.

In capturing, the camera needs not have the same speed with birds, for the influence of relative distance can be deleted by using the normalizing filter as in Fig. 3, but the relative angle between camera and birds should be fixed in a small range. The range of consecutive flap motion that can be captured by camera is limited. In order to research wing flap frequency of migrating birds, we can capture videos in different stages, for example level cruising flight, tacking off and climb or fall.

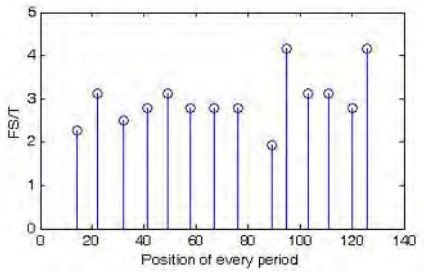


Fig. 5 F_s /T, T is the length of every period

V. Conclusions

In the paper, we measure wing flap frequency of birds in videos. The useful signal is the changing size of birds in flight. Size signals are gotten from accurate detected and tracked birds' areas. The fluctuation of flap frequency in flight is analyzed using STFT and average frequency array. Using the proposed method, we can get the local flap frequency of every time. The wing flap frequency measured in captured videos is important information for classifying birds using pattern identification methods. This can be used in surveillance systems at sensitive areas, for when knowing the species of birds, we can make measures to prevent the intrusion. The time-frequency distribution shows us clearly the change of flap frequency in different flight stages which gives us inspiration for making artificial aircraft.

References

1. Tobalske B W, Olson N E, Dial K P (1997) Flight style of the black-billed magpie: variation in wing kinematics, neuromuscular control and muscle composition. J Exp Zool 279: 313–329.
2. Zaugg S, Saporta G, van Loon E et al. (2008) Automatic identification of bird targets with radar via patterns produced by wing flapping. J R Soc Interface 5(26):1041-1053.
3. Li Z Y, Zhou Z J, Shen Z R et al. (2005) Automated Identification of Mosquito (Diptera: Culicidae) Wingbeat Frequencies by Artificial Neural Network. Journal of Sichuan Agricultural University 23(4): 411-416
4. Moore A, Miller R H (2002) Automated identification of optically sensed aphid (Homoptera: aphidae) wingbeat waveforms. J Econ Entomol Moore A 95(1):1-8
5. Bruderer B, Popa-Lisseanu A G (2005) Radar data on wing-beat frequencies and flight speeds of two bat species. Acta chiropterologica 7(1):73–82.
6. Wingbeat Frequency at http://www.birds.cornell.edu/ivory/evidence/segments/frequency
7. Ozerskii P V, Shchekanov E E (2005) A New Method of Recording of Frequency of Insect Wing Flaps under Conditions of Tethered Flight. Journal of Evolutionary Biochemistry and Physiology 41(6):706-709
8. Yang T, Li S Z, Pan Q (2004) Real-Time and Accurate Segmentation of Moving Objects in Dynamic Scene. Proceedings of the ACM 2nd international workshop on Video surveillance & sensor networks, New York, NY, USA, 2004, pp 136- 143.
9. Yang T, Pan G, and Li J (2005) Real-time Multiple Objects Tracking with Occlusion Handling in Dynamic Scenes. CVPR, San Diego, USA, 2005, pp 970-975.
10. Khan Z, Balch T, Dellaert F (2005) MCMC-Based Particle Filtering for Tracking a Variable Number of Interacting Targets. IEEE Transactions on Pattern Analysis and Machine Intelligence 27:1805–1819.
11. Yu Q, Cohen I, Medioni G (2006) Boosted Markov Chain Monte Carlo Data Association for Multiple Target Detection and Tracking. ICPR, Washington, DC, USA, 2006, pp 675- 678.
12. Smith K, Gatica-Perez D, Odobez J-M (2005) Using Particles to Track Varying Numbers of Interacting People. CVPR, San Diego, USA, 2005, pp 962-969.
13. Smith K (2007) Bayesian Methods for Visual Multi-Object Tracking with Applications to Human Activity Recognition. Lausanne, EPFL.
14. Zhang Y, Gu X, Cao Y (2007) Identification of Digital Modulation Signals Based on the Algorithm of shift window's Average Frequency. Radio Communications Technology 33(2):26-54.

Effects of Upper-Limb Posture on Endpoint Stiffness during Force Targeting Tasks

Pei-Rong Wang[1], Ju-Ying Chang[2] and Kao-Chi Chung[2]

[1] Industrial Technology Research Institute- South / ICT-Enabled Healthcare Program, Tainan, Taiwan
[2] National Cheng Kung University / Institute of Biomedical Engineering, Tainan, Taiwan

Abstract — **Endpoint stiffness is characterized as the relationship between externally imposed displacements of the hand and the elastic forces generated in response and can be estimated during the application of short-term perturbations to endpoint based on measured force and position data. This research was aimed to investigate biomechanical properties via estimation of upper limb endpoint stiffness and joint torques during force targeting tasks. Sixteen able-bodied subjects were recruited in the study and the informed consent was signed by each subject. A 10-N force task was conducted at right and left directions for three upper limb postures. Hand endpoint trajectories and the response forces were recorded simultaneously for each trial. The 2x2 endpoint stiffness matrix and corresponding stiffness ellipse were determined by least squares error method. Resultant shoulder and elbow torques were also calculated by inverse kinetics. Kruskal-Wallis test was used to analyze the effect of postures and movement directions on endpoint stiffness and joint torques. The results of this research indicated that the postures have significant effects on endpoint stiffness ellipse of upper limb, the shoulder and elbow joint torques during force production tasks (p<0.05). These results demonstrate the importance of upper-limb posture when performing force targeting tasks. The clinical implementation suggests that endpoint stability can be more effectively affected by different upper-limb postures.**

Keywords — **Upper-limb, endpoint stiffness**

I. Introduction

Endpoint stiffness, defined as the relationship between externally imposed displacements of the hand and the respond force generated, stabilizes the hand position [1,2]. Previous researches have suggested the spring-like properties of muscles determine the individual joint stiffness [3]. To observe the multi-joint stability of the arm system, displacement of hand by externally applied displacements has been resisted instantly by elastic force resulted from various muscles of upper extremity. In addition, the resultant elastic resistance is not only due to joint stiffness, but depends on the posture-dependent joint angles and respective limb segment lengths [1,3]. The endpoint stiffness is related to the geometric factors of joint angles and limb segment lengths [3]. It is indicated that posture is more effective than joint stiffness in stabilizing hand position [3]. The endpoint stiffness ellipse, which is characterized from the eigenvalues of endpoint stiffness matrix, represents the stability of the hand[4]. The major axis of the ellipse is oriented along the direction of the maximal stiffness; the minor axis of the ellipse is oriented along the direction of the minimal stiffness [5]. The orientation of the ellipse is decided upon the eigenvector associated with the maximal eigenvalue of endpoint stiffness matrix, and indicated the direction of the maximal stiffness [5]. It is seemed to be most successful in stabilizing hand position when the direction of the force production is aligned with the direction of greatest endpoint stiffness [3]. However, the quantitative relationships between the force production task and the geometric factors are still less discussed. This research is to investigate the effect of postures and movement direction on endpoint stiffness and joint torques during force production task. More specifically, this research is aimed to:

1. design a 2-D platform system to provide upper limb's training and assessment ,
2. investigate the effect of posture and movement direction on endpoint stiffness of upper limb during force production tasks,
3. investigate the effect of posture and movement direction on shoulder and elbow joint torques during force production tasks.

II. Materials and methods

A. Instrumentation

The first stage of this research is to design and develop the 2-D platform system for upper limb's objective endpoint assessment and training, including conceptual and functional design, hardware selection and integration, calibration and performance testing. The hardware included two servomotor and encoders (SV4835, King Right Motor Corporation, Taiwan), two force transducers (RVQ16YN, Cosmos, Jin Hua Electronic CO.LTD., Taiwan), two slide mechanisms, one stainless steel manipulandum and the iron frame, as in Fig. 1. There are two mainly operation modes of the 2-D platform system: active and passive movement modes. The passive movement mode contains two evaluation and training functions: relaxation and force target functions. This research selects the force target function from the pas-

Chwee Teck Lim, James C.H. Goh (Eds.): ICBME 2008, Proceedings 23, pp. 1862–1865, 2009
www.springerlink.com

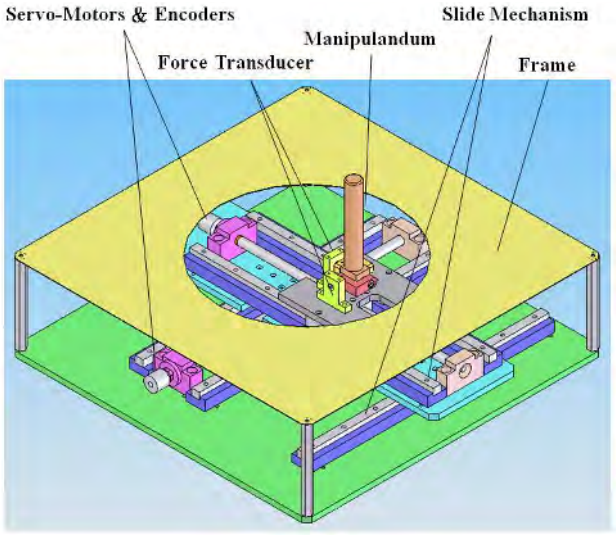


Fig. 1 Illustration of 2-D platform system

sive movement mode to investigate the biomechanical properties of upper limb endpoint stiffness and joint torques during force production tasks.

B. Biomechanical modeling

The two-link and open kinematic chains used to simulate the kinematic model of upper limb are the mainly biomechanical model of this research. The 2x2 endpoint stiffness matrix, which is the change in endpoint force with respect to change in endpoint position, is presented by the following equation Eq. 1 [5]. The 2x2 joint stiffness matrix related to shoulder and elbow joint torques is determined by inverse dynamics, as shown in Eq. 2, where the Jacobian, J, is a function of the limb segment lengths and joint angles [5]. The orientation of the endpoint stiffness ellipse is determined by the direction of the eigenvector associated with the maximum eigenvalue of the endpoint stiffness matrix. The ratio of endpoint stiffness ellipse is determined from the long axis divided by short axis and means to the shape of the endpoint stiffness ellipse.

$$K = \begin{bmatrix} \frac{\partial F_x}{\partial x} & \frac{\partial F_x}{\partial y} \\ \frac{\partial Fy}{\partial x} & \frac{\partial F_y}{\partial y} \end{bmatrix} = \begin{bmatrix} K_{xx} & K_{xy} \\ K_{yx} & K_{yy} \end{bmatrix} \quad (1)$$

$$\begin{bmatrix} TQ_s \\ TQ_e \end{bmatrix} = J^T \begin{bmatrix} F_x \\ F_y \end{bmatrix} = J^T K_s \begin{bmatrix} dx \\ dy \end{bmatrix} \quad (2)$$

C. Experimental procedures

Sixteen subjects ranging from 23 to 28 years-old (nine male and seven female) with no history of neurological impairments were participated in this study. The protocol was approved by human experiment and ethics committee of National Cheng Kung University Hospital, ROC. The informed consent was signed by every subject prior to the study. There were total three sitting positions for this study: the central position was defined subject's hand located 40 cm far in front of sternum, the left and right position were defined apart one-thirds shoulder girdle width from central position, respectively. All subjects accomplished tasks with their right arm. Before initiating every trial, the subject seated and always the same experienced researcher measured the limb length of upper arm and forearm, and the shoulder and elbow joint angles. Anthropometric data for every subject included upper arm length (Lu) measured from right acromion process of scapula to right lateral epicondyle of humerus, forearm length (Lf) measured from the right lateral epicondyle of humerus to right styloid process of radius, shoulder joint angle at the right position (RSangle), elbow joint angle at the right position (REangle), shoulder joint angle at the central position (CSangle), elbow joint angle at the central position (CEangle), shoulder joint angle at the left position (LSangle), and elbow joint angle at the left position (LEangle). Demographic and anthropometric data for all subjects were illustrated in Table 1.

There were totally 6 conditions (2 direction targets × 3 sitting position) in the experiment (Fig. 2). Initial position of the hand on the screen was centered on the start window. Two goal-oriented targets were located both sides on the window screen and randomly showed. Subjects were instructed to push the robotic manioulandum to right or left according to the targets appearing on the screen. While the subject was holding the manipulandum with 10-N force magnitude for six seconds, the displacement perturbation with 1cm was applied to interrupt the force task trial. Subjects were asked to stabilize the hand with visual feedback while counteracting a destabilizing force field generated by the robotic manipulandum. There were eight perturbation directions from 0° to 360°. The endpoint forces and displacements, shoulder and elbow joint angles were recorded. There were three trials in every set of the force production task, and every trial contained four times of the random perturbations. The subject took a rest about 30 to 60 seconds between trials for avoiding muscle fatigue. The subject was conducted the perturbation experiment for three upper-limb postures for right and left movement directions.

Table 1 Demographic data of all subjects

Item	N	Mean	Std.
Age (y/o)	16	25.3	1.3
Height (cm)	16	167.1	6.1
Weight (kg)	16	61.4	8.2
Lu (cm)	16	30.4	1.8
Lf (cm)	16	26.7	1.7
RSangle (deg)	16	97.1	11.6
REangle (deg)	16	31.9	10.3
CSangle (deg)	16	72.3	5.0
CEangle (deg)	16	51.5	8.6
LSangle (deg)	16	51.8	13.7
LEangle (deg)	16	52.5	7.2

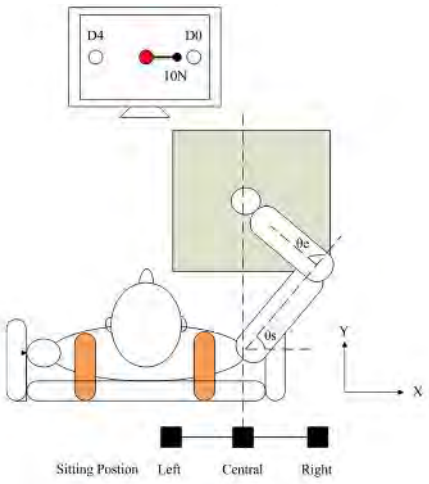


Fig. 2 Diagram of study protocol: including the coordinate system with the subject, two goal-oriented targets (D0 & D4), and three sitting position (left, central, right sitting position)

For each perturbation direction, the endpoint stiffness matrix was calculated from endpoint forces and displacements through Eq.1. For each subject, the parameters of endpoint stiffness matrix were estimated by least squares error method on 8 perturbation directions. The parameters of endpoint stiffness ellipse were characterized and calculated by the eigenvalues of the endpoint stiffness matrix. The shoulder and elbow joint torques (Ts, Te) were estimated by endpoint forces and joint angles through the Jacobian matrix by inverse dynamic equation (Eq.2). Kruskal-Wallis test was used to analyze the effect of postures and movement directions on endpoint stiffness and joint torques. The significance level was at a 0.05 level.

III. Results and Discussion

Table 2 shows the median of endpoint stiffness matrix estimated from 16 subjects for 3 different postures and for 2 movement directions. The median of long axis, orientation, and ratio of the endpoint stiffness ellipse are shown in Table 3. The median of shoulder and elbow joint torques are shown in Table 4. The results of statistical analysis (Table 5) have revealed that : (1) the postures have significant effects on endpoint stiffness ellipse of upper limb, the shoulder and elbow joint torques during force production tasks (p<0.05), (2) the movement directions have no significant effects on endpoint stiffness of upper limb, the shoulder and elbow joint torques during force production tasks.

Table 2 Median of the endpoint stiffness matrix

Positions	Target direction	N	Endpoint stiffness matrix (N / m)
Left	D0	16	$\begin{bmatrix} -36.67 & 4.50 \\ 21.29 & -274.61 \end{bmatrix}$
	D4	16	$\begin{bmatrix} -68.03 & 9.19 \\ 26.17 & -241.59 \end{bmatrix}$
Central	D0	16	$\begin{bmatrix} -101.71 & 40.62 \\ 126.06 & -302.90 \end{bmatrix}$
	D4	16	$\begin{bmatrix} -163.09 & 56.88 \\ 141.48 & -246.81 \end{bmatrix}$
Right	D0	16	$\begin{bmatrix} -106.00 & 66.79 \\ 149.62 & -270.09 \end{bmatrix}$
	D4	16	$\begin{bmatrix} -159.67 & 75.14 \\ 147.76 & -197.66 \end{bmatrix}$

Table 3 Median of the parameters of the endpoint stiffness ellipse

Position	Target direction	N	Long axis (m)	Orientation (deg)	Raito
Left	D0	16	642.2	128.6	9.1
	D4	16	506.2	132.0	7.6
Central	D0	16	797.0	122.7	10.9
	D4	16	910.1	129.6	9.3
Right	D0	16	868.4	103.5	4.9
	D4	16	754.1	109.1	5.2

Table 4 Median of the shoulder and elbow joint torques

Position	Target direction	N	Ts (Nm)	Te (Nm)
Left	D0	16	-3.39	-1.14
	D4	16	3.39	1.14
Central	D0	16	-2.11	0.77
	D4	16	2.11	-0.77
Right	D0	16	-0.98	2.05
	D4	16	0.98	-2.05

Table 5 Mean ranks of the parameters related to endpoint stiffness with Kruskal-Wallis test.

		Centel	Right	Left
Long axis	D0	28.38	28.69	16.44 *
	D4	29.50	27.88	16.13 *
Orientation	D0	26.06	34.38	13.06 *
	D4	27.88	33.00	12.63 *
Shape	D0	27.34	16.47	29.69 *
	D4	29.38	17.13	27.00 *
Ts	D0	25.13	38.75	9.63 *
	D4	23.88	10.25	39.38 *
Te	D0	25.09	39.00	9.41 *
	D4	23.91	10.00	39.59 *

* $p < 0.05$

IV. Conclusions

The contribution of this research emphasizes the importance of upper-limb postures during force targeting tasks. It suggests a simplified strategy which is posture-independent in the central nervous system using to regulate the whole arm mechanics during force targeting tasks. The clinical implementation suggests that endpoint stability can be more effectively affected by different upper-limb postures.

Acknowledgment

The authors are grateful to Prof. K.C. Chung for his fruitful advice on this paper writing and to J.Y. Chang, Ph.D. student for her research assistance. The work was supported by the National Science Council, ROC, under Grants NSC-96-2622-E-006-011-CC3.

References

1. Perreault EJ, Kirsch RF, Crago PEl. (2001) Effects of voluntary force generation on the elastic components of endpoint stiffness. Exp Brain Res 141(3), pp. 312-323
2. Perreault EJ, Kirsch RF, and Crago PE. (2004) Multijoint dynamics and postural stability of the human arm. Exp Brain Res 157(4): pp. 507-517
3. Milner TE. (2002) Contribution of geometry and joint stiffness to mechanical stability of the human arm. Exp. Brain Res 143(4), pp. 515–519
4. Mussa-Ivaldi FA, Hogan N, et al. (1985) Neural, Mechanical, and Geometric Factors Subserving Arm Posture in Humans. J Neurosci 5(10), pp.2732-2743
5. Zatsiorsky VM. (2002) *Kinetics of Human Motion*. Human Kinetics, Leeds , Champaign
6. Franklin DW, Liaw G, Milner TE, et al. (2007). Endpoint Stiffness of the Arm Is Directionally Tuned to Instability in the Environment. J Neurosci 27(29) , pp 7705-7716

Author: Pei-Rong Wang
Institute: Industrial Technology Research Institute- South / ICT-Enabled Healthcare Program, Tainan
Street: Bldg. R1, Rm. 304, No. 31, Gongye, 2nd Rd., Annan District, Tainan City 70955
Country: Taiwan, R.O.C
Email: PR_Wang@itri.org.tw

Complex Anatomies in Medical Rapid Prototyping

T. Mallepree[1], D. Bergers[1]

[1] University of Duisburg-Essen, IPE-PP, Duisburg, Germany

Abstract — **The complex anatomy of the nasal airways is an anatomy that is difficult to understand from conventional two-dimensional anatomy images. The objective of the present study was to establish the methods and parameters necessary to provide three-dimensional triangulated models for Rapid Prototyping. Anatomical data derive from scanned medical images made with computerized tomography. Different data sets of nasal airway structures were segmented and 3D reconstructed. With high-resolution scans, accurate segmentation of the structures was possible. The reconstructed and triangulated models were evaluated in order to determine triangulation parameters that are needed for Rapid Prototyping models. Gaining insight in the interplay of parameters necessary for modeling complex anatomies for Rapid Prototyping enables to provide accurate Rapid Prototyping models for biomedical engineering applications.**

Keywords — **Nasal airways, Rapid Prototyping, Triangulation**

I. Introduction

The planning of complex surgical procedures necessitates reliable models of the individual human anatomy. With a physical model at hand, it is possible to rehearse different surgical plans realistically. Medical modeling techniques known as biomodeling provide the possibility to reconstruct three-dimensional (3D) models of anatomical templates of parts of the human body [1]. Biomodeling methods can be employed to develop a 3D model for Rapid Prototyping (RP).

Recent studies introduced RP applications to specific research areas of surgical planning and manufacturing of personalized RP models [2,3]. For instance, Gibson et al. [3] used RP to demonstrate the possibility of manufacturing parts of the human anatomy and biological structures. De Zélicourt et al. [4] used the generative RP procedure of stereolithography to study a specific case of cardiovascular fluid dynamics. However, it remains unknown whether they studied the accuracy of the triangulation procedure in biomodeling. Due to Giannatsis [5] the virtual model construction phase is the main source of observed inaccuracies. The complete procedure and its related parameters of virtual model generation are of interest in order to provide accurate and reliable biomodels for medical RP procedures in a short period of time.

In contrast, our study used three different nasal anatomies to determine the decisive parameters for developing triangulated complex 3D models of the nasal airways in RP applications. We investigated the procedure from the tomographic computerized scan to the virtual biomodel that is converted to the stereolithography (.STL) format for RP. As marked in Figure 1, the study was focused on the decisive procedure of .STL data manipulation.

We performed evaluations on model quality and accuracy to determine a target area of parameter to use. The results could be supportive for a rapid but qualitative production of complex anatomies like the nasal airways in medical RP.

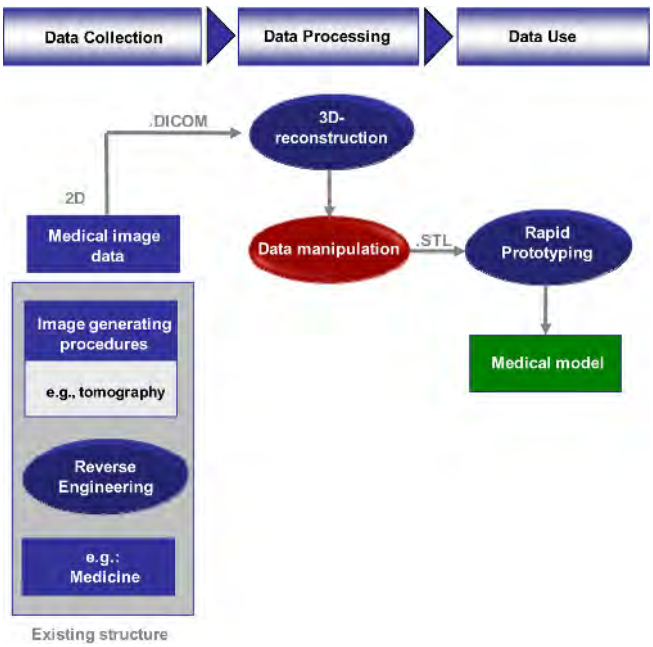


Fig. 1 Medical RP process

II. Methods

Three different high-resolution CT images were obtained as follows: the image matrix was set to 512x512 pixels, the slice thickness was set to 0,5 mm and the slice increment to 0,3 mm using a multi-slice CT scanner (Siemens Somatom

Chwee Teck Lim, James C.H. Goh (Eds.): ICBME 2008, Proceedings 23, pp. 1866–1869, 2009
www.springerlink.com

Sensation Open, Siemens Medical) in order to guarantee lowest possible deviations in scanning the geometry. In the data processing step, the scanned 2D images were imported as .DICOM files into the 3D reconstruction software Mimics (Materialise's Interactive Medical Image Control System, Materialise NV, Leuven) in order to reconstruct 3D volume models (Fig. 1). The nasal airways were segmented by selecting a mean density of about -1000 Hounsfield Units (HU) as threshold for extracting the air. That operation was followed by the connected component analysis of region growing. 3D triangulated models of each segmented structure were generated in Mimics using a marching cubes algorithm for iso-surface extraction. The produced triangular mesh models were .STL files that were manipulated for importing them into an RP application. The .STL data analyzing tool 3-Matic (Materialise NV, Leuven) was used for measuring the accuracy in terms of generating reference attributes (Table 1).

Table 1: Reconstructed reference models

Reference attributes	Model 1	Model 2	Model 3
File size	25.727 kB	20.250 kB	12.527 kB
Number of triangles	526.880	414.712	256.540
Measure x-direction	119,21 mm	105,67 mm	109,83 mm
Measure y-direction	344,65 mm	355,37 mm	288,54 mm
Measure z-direction	178,23 mm	199,52 mm	176,43 mm

The depicted reference values (Table 1) of the three models were derived from 3D reconstructed data sets without using triangle reduction and smoothing functions in order to keep all geometry information. In Mimics the STL mesh quality and model accuracy can be influenced directly by triangle reduction and smoothing parameters. To find an optimum range of mesh quality and accuracy an evaluation study was carried out. First, the accuracy was tested (case A) and secondly the achievable STL mesh quality that defines the steadiness of the reconstructed surface (case B). The study investigated the influence of smoothing and triangle reduction in respect with the specific parameters depicted in Table 2.

The values to test were verified to find the best possible range to carry out triangle reduction and smoothing in terms of evaluating parameters for demonstrating the conflict of accuracy (case A) and STL mesh quality (case B). This was tested by the use of three data sets. The parameters were evaluated by varying the influencing factors of tolerance, edge angle and smoothing factor. The smoothing algorithm used was based on the Laplacian 1st order function.

Table 2 Triangulation parameter

Parameter	Function
Triangle Reduction:	
Tolerance	Maximum deviation of triangles that build a aggregation of triangles, which deviate about the set value for tolerance
Edge Angle	Defines the maximum angle that triangles enclose in one plane before they will be linked to a different plane. Triangles with an angle smaller as the set edge angle will be modified
Iterations	Defines the number of runs for reducing the data
Mode	Defines the methodology of triangle reduction.
Smoothing:	
Iterations	Defines the number of runs for smoothing the surface
Factor	The Laplace filter iteratively traverses all surface vertices and moves each vertex into the geometric center of its topological neighbors. The factor regulates the effect of the direct neighbors on the new position.

Measurements were performed for verification. The spatial measures in x-, y-, and z-direction were compared in each case to detect possible deviations. Part comparisons with the reference data sets (Table 1) and tested data sets (Fig. 2, Fig. 3) were carried out additionally in order to evaluate deviated triangles. The distance from one triangle to the next one was measured to state a maximum deviation.

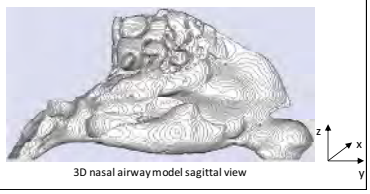
III. Results

Analyzing the outcome of the tested three models as shown in Figure 2 and 3, it could be stated that there was a conflict between accuracy and STL mesh quality. The decisive parameter that influences different outcomes was the smoothing factor. Using the parameters as depicted in Figure 2, resulted in high accurate models that were of a lower STL mesh quality. Selecting a smoothing factor of 0,1 in combination with the triangle reduction parameters as depicted in Figure 1, there was a data reduction of more than 75 %, a measure deviation in x-direction of not more than -0,23 mm, a measure deviation in y-direction of not more than -0,20 mm, and a measure deviation in z-direction of not more than -0,07 mm. The results were high accurate models that are of a lower STL mesh quality.

A.1

Characteristic	Value
File size	4.629 kB
Number of triangles	94.782
File size reduction	82,01%
Measure x-direction	- 0,19 mm
Measure y-direction	- 0,18 mm
Measure z-direction	+ 0,05 mm

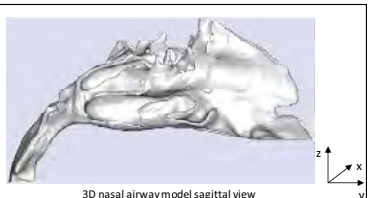
Parameter	Determined values
Triangle Reduction	
Tolerance	0,15 mm
Edge Angle	15°
Iterations	4
Mode	Advanced Edge
Smoothing	
Iterations	3
Factor	0,1



A.2

Characteristic	Value
File size	1.204 kB
Number of triangles	24.640
File size reduction	94,05%
Measure x-direction	- 0,23 mm
Measure y-direction	- 0,20 mm
Measure z-direction	- 0,07 mm

Parameter	Determined values
Triangle Reduction	
Tolerance	0,15 mm
Edge Angle	15°
Iterations	4
Mode	Advanced Edge
Smoothing	
Iterations	3
Factor	0,1



A.3

Characteristic	Value
File size	3.037 kB
Number of triangles	62.194
File size reduction	75,76%
Measure x-direction	- 0,15 mm
Measure y-direction	- 0,05 mm
Measure z-direction	+ 0,03 mm

Parameter	Determined values
Triangle Reduction	
Tolerance	0,15 mm
Edge Angle	15°
Iterations	4
Mode	Advanced Edge
Smoothing	
Iterations	3
Factor	0,1

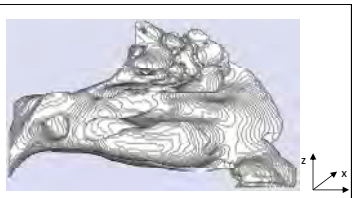
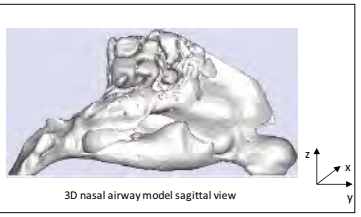


Fig. 2 Parameter highest accuracy (case A)

B.1

Characteristic	Value
File size	2.015 kB
Number of triangles	41.256
File size reduction	92,17%
Measure x-direction	- 1,46 mm
Measure y-direction	- 1,45 mm
Measure z-direction	- 0,08 mm

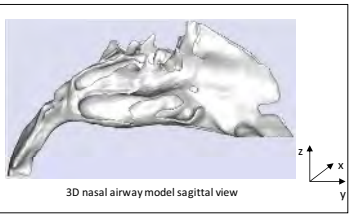
Parameter	Determined values
Triangle Reduction	
Tolerance	0,15 mm
Edge Angle	15°
Iterations	4
Mode	Advanced Edge
Smoothing	
Iterations	3
Factor	1



B.2

Characteristic	Value
File size	984 kB
Number of triangles	20.138
File size reduction	95,14%
Measure x-direction	- 1,61 mm
Measure y-direction	- 1,24 mm
Measure z-direction	- 0,12 mm

Parameter	Determined values
Triangle Reduction	
Tolerance	0,15 mm
Edge Angle	15°
Iterations	4
Mode	Advanced Edge
Smoothing	
Iterations	3
Factor	1



B.3

Characteristic	Value
File size	1.254 kB
Number of triangles	25.672
File size reduction	89,99%
Measure x-direction	- 1,07 mm
Measure y-direction	- 1,07 mm
Measure z-direction	- 0,26 mm

Parameter	Determined values
Triangle Reduction	
Tolerance	0,15 mm
Edge Angle	15°
Iterations	4
Mode	Advanced Edge
Smoothing	
Iterations	3
Factor	1

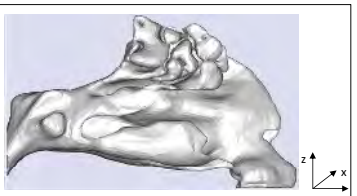


Fig. 3 Parameter best STL mesh quality (case B)

Part comparisons conducted with the specific reference models (Table 1) revealed that 90% of existing triangles were not higher deviated than 0,104 mm in case A.1, 0,09 mm in case A.2, and 0,127 mm in case A.3. As Figure 4 demonstrated exemplary by case A.1 (Fig. 2), deviations (red marked) were distributed all over the surface.

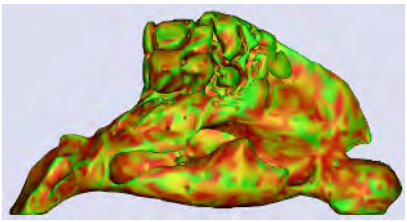


Fig. 4 Part comparison

Partial tests on triangle reduction revealed that a tolerance of 0,15mm, an edge angle of 15°, a number of iterations of 4, and the mode of advanced edge allowed optimal data reduction. The use of triangle reduction parameters and smoothing parameters in combination as shown in Figure 3 revealed that a data reduction of 89,99 % at minimum was possible along with a mesh of high quality. That result was affected negatively by measure deviations in x-, and y-direction of not more than -1,61 mm, and in z-direction of not more than -0,26 mm. Part comparisons conducted with the specific reference models (Table 1) revealed that 90% of existing triangles were not higher deviated than 0,508 mm in case B.1, 0,336 mm in case B.2, and 0,826 mm in case B.3.

In summary, the parameter evaluation for triangle reduction and smoothing detected values as depicted in Table 3.

Table 3: Determined parameter values

Parameter	Determined values
Triangle Reduction:	
Tolerance	0,15 mm
Edge Angle	15°
Iterations	4
Mode	Advanced Edge
Smoothing (Laplace 1st order):	
Iterations	3
Factor	0,1 - 1

The highest accuracy could be measured in case A.3. In that case, the highest deviation was -0,15 mm in x-direction.

IV. Conclusions

The main finding of this study is the good agreement observed between three different data sets from which RP models of the nasal airways could be derived by validated parameter. The determined parameters confirm the ability of RP for producing complex medical models like the nasal airways.

It is hard to pinpoint the exact reason for the relative disagreement observed at the different models in respect with the measurement values. Consequently, it could be explained by the different anatomies scanned. Larger geometries lead to more triangles in the resultant .STL file. Different meshing is the consequence and leads to a different number of triangles and measures. The high accuracy in case A.3 mainly seems related to the original number of triangles of 256.540. That could be explained by the lowest number of triangles that needs to be optimized during the smoothing operation.

Combining results of both triangle reduction and smoothing using the determined parameter as depicted in Table 3 leads to a conflict of accuracy or STL mesh quality. The result is influenced by the factor of smoothing. Though, smoothing should be conducted carefully in order to obtain accurate models for the final RP application. Avoiding inaccurate virtual 3D models for RP, the proposed parameters will lead to high-qualitative and process feasible RP models even of complex anatomical models like the nasal airways when effective triangulation parameters will be used. Due to Ma et al. [5], the generation of accurate .STL files is essential for manufacturing high-qualitative models for RP applications in medicine. Since RP allows manufacturing of anatomical objects, knowing the parameters to use for providing models for RP may finally support accuracy of medical models and decrease processing time in biomedical engineering applications.

References

1. D'Urso PS, Barker TM, Earwaker WJ et al. (1999) Stereolithographic biomodeling in cranio-maxillofacial surgery: a prospective trial. J. Cranio-MaxilloFac. Surg. 27:30-7
2. Hieu LC, Zlatov N, Vander Sloten J et al. (2005) Medical rapid prototyping applications and methods. Assemb. Autom. 25:284-292
3. Gibson I, Cheung LK, Chow SP et al. (2006) The use of rapid prototyping to assist medical applications. Rapid Prototyp J. 12(1):53-58
4. De Zélicourt D, Pekkan K, Kitajima H et al. (2005) Single-Step Stereolithography of Complex Anatomical Models for Optical Flow Measurements. J. Biomech. Eng. 127:204-207
5. Giannatsis J, Dedoussis, V (2007) Additive fabrication technologies applied to medicine and health care: a review. Int J Adv Manuf Technol. DOI 10.1007/s00170-007-1308-1
6. Ma D, Lin F, Chua CK (2001) Rapid Prototyping Applications in Medicine. Part 2: STL File Generation and Case Studies. Int J Adv Manuf Technol. 18:118-127

Author: Mallepree, T., Bergers, D.
Institute: University of Duisburg-Essen, IPE-PP
Street: Lotharstr. 1
City: Duisburg
Country: Germany
Email: timon.mallepree@uni-due.de

Early Changes Induced by Low Intensity Ultrasound in Human Hepatocarcinoma Cells

Y. Feng, M.X. Wan

Laboratory of Biomedical Information Engineering of Ministry of Education, Department of Biomedical Engineering, School of Life Science and Technology, Xi'an Jiaotong University, Shaanxi Province, China

Abstract — **To determine whether low intensity ultrasound irradiation can induce early changes in human hepatocarcinoma cells and investigate the effects of ultrasound intensity, sonication time and incubation time post-sonication on US induced early changes, HepG2 cells were irradiated by low intensity US, at different intensity with different sonication time and incubation time post-sonication, respectively, in this study. Morphologic changes of cells were examined by light and fluorescent microscopy respectively. The percentage of viable, apoptosis and secondary necrosis cells were detected by flow cytometry with double staining of FITC-Annexin V/PI. Percentages of cells in different states were analyzed by L9 33 orthogonal test to find out most effective parameters for US induced early changes. The morphological characteristics of early apoptosis and secondary necrosis are found in US irradiated cells, however few in control. The fluorescent photos also prove early changes, such as phosphatidylserine externalization, increase significantly after US irradiation. The results from flow cytometry show the percentages of early apoptosis and secondary necrosis cells increase significantly after US irradiation ($P<0.05$). Orthogonal analysis reveals US induced early changes increase with the increase of ultrasound intensity; Moreover, US induced early changes may be an early time-dependent event with early apoptosis reaches its maximum at about 12 h. In this study, it is suggested that optimal early apoptosis with minimal necrosis is acquired when HepG2 cells were exposed to ultrasound at 5 W/cm^2 for 1 min and incubated for 12 h post-sonication. It reveals that ultrasound induced apoptosis is a preferred mode of killing cancer cells and suggests the optimal parameters setup for both *in vitro* experiments and its clinical application.**

Keywords — **low intensity ultrasound, early apoptosis, secondary necrosis, hepatocarcinoma, orthogonal analysis.**

I. Introduction

It is known that low-intensity ultrasound could induce early changes, such as early apoptosis and secondary necrosis, in several carcinoma cell lines [1]. During this process, many factors need to be considered to attain a controlled and predictable killing of cells in a desired mode of death. *In vivo*, because the apoptotic bodies are rapidly recognized and phagocytized by either macrophages or adjacent epithelial cells, no inflammatory response is elicited. Due to less immune reaction activated in the body during apoptosis, induction of apoptosis is a preferred mode of killing the cancer cells in the cancer therapy [2, 3].

During the irradiation process, several ultrasonic parameters, such as ultrasound intensity, sonication time and incubation time post-sonication, significantly work on ultrasound induced apoptosis. To get optimal apoptosis with minimal necrosis, these parameters could be optimized for both in vitro experiments and its clinical application.

Based on the knowledge above, the aim of this study is to prove low intensity ultrasound could induce early apoptosis and secondary necrosis in human hepatocarcinoma HepG2 cells, and then investigates the effects of several ultrasonic parameters on the ultrasound-induced early changes by orthogonal analysis. The results would be significant for the application of ultrasound in non-surgical cancer treatment.

II. Material and methods

A. Cell line culture

Human hepatocarcinoma HepG2 cell line was supplied by the Center of Laboratory Animals of the Forth Military Medical University, China. The cells were cultured in RPMI 1640 culture medium supplemented with 10% heat-inactivated fetal bovine serum (FBS) at 37 ^{o}C in water-saturated atmosphere with 5% CO2. The cells used in the experiment were in log-phase. The cell viability before irradiation was always over 95%.

B. Ultrasound exposure system

The ultrasound exposure system is shown in Fig.1. The central frequency is 1.2 MHz. The cell samples were carried in a specially designed inverted "T" tube described by Feril et al.[4]. Before the sample was filled in, the US pressure in the inverted "T" tube was detected by needle hydrophone probe (0.5-mm in diameter, HPM05/3 Precision Acoustic Ltd., Dorchest, UK). Temperature of water in the tank was controlled at 25 ^{o}C by circulating and monitored by thermocouple (0.5-mm diameter, Type K, Inor, Sweden), showing the maximum temperatures were less than 27^{o}C.

Chwee Teck Lim, James C.H. Goh (Eds.): ICBME 2008, Proceedings 23, pp. 1870–1873, 2009
www.springerlink.com

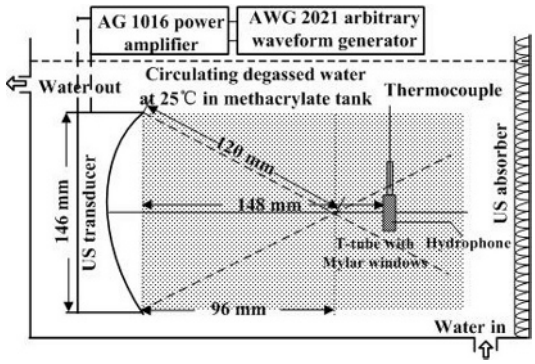


Fig.1 Ultrasound irradiation system

C. Study design

HepG2 cells were exposed to low intensity ultrasound at different intensity for different sonication time with different incubation time post-sonication. The experiment was constructed according to the principle of $L_9\ 3^3$ orthogonal method. The detail is shown Table 1 and Table 2. Fraction of early apoptotic and secondary necrotic cells in the ultrasound sonicated samples were counted and analyzed by orthogonal analysis, which would suggest the relationship between ultrasound induced early changes and the ultrasonic parameters.

Table 1 Factors and their levels used for orthogonal array

Symbol	Factor	Level 1	Level 2	Level 3
A	Ultrasound intensity	2 W/cm^2	3 W/cm^2	5 W/cm^2
B	Sonication time	1 min	2 min	5 min
C	Incubation time post-sonication	6 h	12 h	24 h

Table 2 The $L_9\ 3^3$ orthogonal array and flow cytometry results for early apoptosis and secondary necrosis

No.	A	B	C	Early apoptosis	Secondary necrosis
1	1	1	1	20.3 ± 1.53	9.87 ± 0.94
2	1	2	2	28.2 ± 4.86	11.53 ± 1.68
3	1	3	3	20.7 ± 2.59	15.43 ± 1.17
4	2	1	2	29.6 ± 2.59	12.9 ± 1.50
5	2	2	3	27.47 ± 3.57	15.23 ± 1.28
6	2	3	1	25.67 ± 2.79	15.03 ± 1.69
7	3	1	3	29.13 ± 4.20	15.8 ± 1.58
8	3	2	1	28.5 ± 2.51	13.67 ± 1.27
9	3	3	2	35.0 ± 3.37	15.13 ± 1.76

D. Measurement of cell viability

Trypan blue exclusion test was performed to examine the cell viability. Cell suspension was incubated with 0.4% Trypan blue solution for 5 minutes at room temperature. The number of cells excluding Trypan blue (unstained) was counted using hemocytometer to estimate the survival (cells that are intact and viable) immediately after irradiation.

E. Morphologic observation

Early changes of cells are characterized by unique morphological changes, such as cell swelling or shrinkage, breakage of plasma membrane and nuclear chromatin condensation. In this study, the morphologic changes representing early apoptotic and secondary necrotic cells were examined by light microscopy with Trypan blue staining. Fluorescence microscopy is also used to examine the early changes, such as phosphatidylserine externalization, in sonicated cells stained by Annexin V-FITC.

F. Detection of early apoptosis and secondary necrosis

FITC-Annexin V/PI fit was purchased from Jingmei Biotechnology Company, China. Double staining for phosphotidylserine (PS) and DNA, respectively, by fluorescein isothiocyanate (FITC)-labelled Annexin V and propidium iodide (PI) was performed according to the protocol of the manufacturer. After incubation with FITC/PI at 4 ^{o}C for 10 min in the dark, the cells were analyzed with flow cytometry (Coulter Elite ESP, Coulter, Hialeah, FL) to detect PS exposure on the cell membrane as typical marker of early apoptosis.

G. Statistical analysis

All the data are presented as the mean ± standard deviation (SD). Difference between any two groups were assessed with student's t-test at 95% confidence interval; $P<0.05$ was considered to be significant.

III. Results

A. Effects of low intensity ultrasound on cell viability

Cell viability was measured by the Trypan blue exclusion test immediately after ultrasound sonication and plotted as a line graph, shown in Fig. 2. HepG2 cells were exposed to different intensity of 1.2 MHz continuous ultrasound for different sonication time. It is shown that the cell viability decreased with the increasing ultrasound intensity and increasing sonication time. To acquire optimal early apoptosis

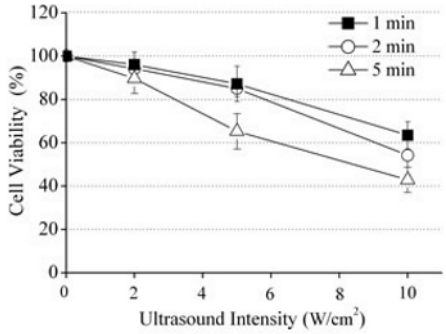


Fig. 2 Intensity-dependent and sonication time related ultrasound induced loss of cell viability. Error Bars in the figure represent means ± SD (n=3).

with minimal necrosis, the intensity used in orthogonal test is ranged from 2 to 5 W/cm^2.

B. Morphological changes of irradiated cells

The morphologic observations showed that the distinct morphologic characteristics of apoptotic cells, such as condensation of nucleus, chromatin margination (Fig.3 b and c) were found after the cells were exposed at 5 W/cm^2 for 1 min and incubated for 12 h post-sonication. Simultaneously, the characteristics of apoptotic cells were not observed in the control samples incubated at 37 ^{o}C in humidified air with 5% CO_2 (Fig.3 a). It is also proved in Fig.4 as the cells with green fluorescence increased significantly after cells were exposed to ultrasound.

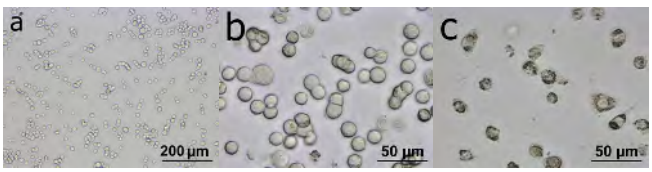


Fig. 3 Morphologic characteristics of HepG2 cells before and after ultrasound sonication.

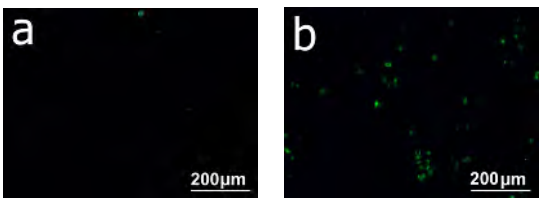


Fig. 4 Fluorescence images of phosphatidylseline externalization induced by ultrasound sonication. (a) untreated control cells; (b) cells 12 h after sonication, 5W/cm^2 (I_{SPTA}), 2 min.

C. Functional assay

It is shown in Fig.5 the fraction of early apoptotic and secondary necrotic cells from the surviving cells after 12-h incubation post-sonication at 5 W/cm2 for 1 min. The percentage of early apoptotic and secondary necrotic cells increased significantly compared with the cells before US sonication. It revealed ultrasound indeed induced early changes in HepG2 cells in this study.

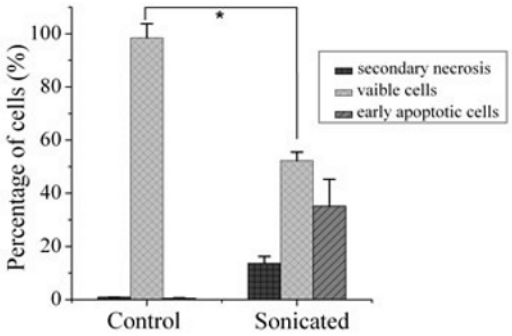


Fig. 5 The fraction of ultrasound induced early apoptosis and secondary necrosis, as measured by flow cytometry. The error bars represent SD from the mean of at least three independent trials (*$P < 0.05$).

D. Orthogonal analysis

The last two columns of Table 2 show the experimental results of early apoptosis (eA) and secondary necrosis (sN) measured by flow cytometry. The results represent mean ± SD (n=3). Based on orthogonal analysis, the response diagrams for the designed factors are shown in Fig. 6. The results show that ultrasound induced eA and sN increase with increasing ultrasound intensity. EA also increases with increasing incubation time post-sonication and reaches its maximum at about 12 h. however, sN keeps increasing even after incubated for 12 h and then become dominant over early apoptosis. Sonication time influence sN significantly, however, it shows few enhancement for eA when the cells are sonicated for 5 min comparing with 2 min. It is suggested that optimal early apoptosis with minimal necrosis

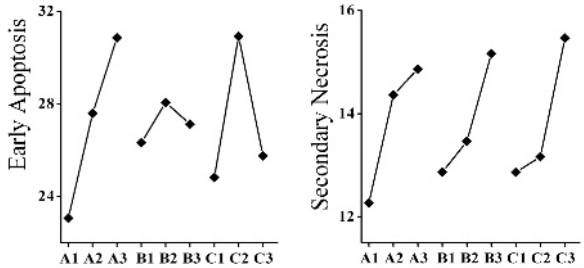


Fig. 6 Response graph of designed factors to ultrasound induced early apoptosis and secondary necrosis.

Table 3 Results of variance analysis for early apoptosis

Factor	Sum of square (S)	Degree of freedom (f)	Variance (V)	F-ratio (F)	Contribution (σ) (%)
A	276.76	2	138.38	9.32**	53.80
B	13.21	2	6.61	0.44	2.57
C	194.80	2	97.40	6.56*	37.86
e	296.90	20	14.85	1	5.77
Total	781.67	26	-	-	100%
$(e)^a$	11.14	2	5.57	-	-

* $F > F_{0.01}(2,20)$; * * $F > F_{0.005}(2, 20)$; $(e)^a$ is pooled error.

Table 4 Results of variance analysis for secondary necrosis

Factor	Sum of square (S)	Degree of freedom (f)	Variance (V)	F-ratio (F)	Contribution (σ) (%)
A	34.16	2	17.08	5.74*	32.95
B	26.55	2	13.27	4.46*	25.61
C	37.01	2	18.50	6.22*	35.69
e	59.53	20	2.98	1	5.75
Total	203.36	26	-	-	100%
$(e)^a$	2.60	2	1.30	-	-

* $F > F_{0.05}(2, 20)$; $(e)^a$ is pooled error.

could be acquired when the cells are sonicated at 5 W/cm^2 for 1 min and incubated for 12 h post-sonication.

The results of variance analysis for eA and sN are shown in Table 3 and Table 4. The contribution ratio has shown that ultrasound intensity is most significantly effective factor for early apoptosis, and incubation time post-sonication for secondary necrosis.

IV. Discussion

After sonicated by ultrasound, the degree of membrane damage caused by the mechanical effects of ultrasound and the degree of repair by the fate of cells will determine the type of cell death, as shown in Fig.7. Higher ultrasound intensity would induce more damage on cell membrane, in this way, early apoptosis and secondary necrosis are increased. Continuous sonication accumulates energy on the cell membrane. Compared with pulsed ultrasound, there is few time for the cells to repair themselves during sonication, so it increases irreversible damage induced by ultrasound. It may be the reason for more secondary necrosis induced however early apoptosis doesn't change significantly with increasing sonication time. Incubation time post-sonication gives damaged cells the time and more chance to repair themselves post-sonication successfully, and then develop to apoptosis. It reaches the peak after about 12 h. After it, more early apoptotic cells develop into secondary necrosis. It explains optimal early apoptosis is obtained at about 12 h post-sonication.

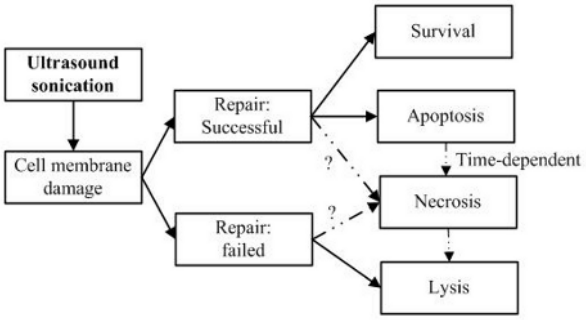


Fig. 7 Scheme showing that membrane damage and repair after ultrasound sonication.[4]

V. Conclusions

It is proven that low intensity ultrasound induces early apoptosis and secondary necrosis in HepG2 cells in this study. Based on the orthogonal analysis, optimal apoptosis with minimal necrosis is acquired when the cells were exposed to ultrasound at 5 W/cm^2 for 1 min and incubated for 12 h post-sonication. Our data clearly show that certain conditions to optimize apoptosis induction do exist. For the application in cancer therapy, every parameter, including proper timing, is therefore essential in establishing a protocol for effective induction of apoptosis by ultrasound.

Acknowledgment

This work was supported by the Key Program of National Natural Science Foundation of China, No. 30630024; the Doctoral Foundation of Xi'an Jiaotong University, grants No. DFXJTU2005-05.

References

1. Lagneaux L, Meulenaer ECd, Delforge A et al. (2002) Ultrasonic low-energy treatment: a novel approach to induce apoptosis in human leukemic cells. Exp Hematol 30: 1293-1301
2. Sun SY, Hail N, Lotan R. (2004) Apoptosis as a novel target for cancer chemoprevention. J Natl Cancer Ins 96: 662-672
3. Fulda S, Debatin KM. (2003) Apoptosis pathways in neuroblastoma therapy. Cancer Lett 197: 131–135
4. Feril LB, Jr, Kondo T. (2004) Biological Effects of low intensity ultrasound: the mechanism involved, and its implications on therapy and on biosafety of ultrasound. L Radiat Res 45:479-489.

Author: Y. Feng
Institute: Laboratory of Biomedical Information Engineering of Ministry of Education
Street: No. 28, Xianning West Road
City: Xi'an city
Country: P.R. China
Email: yoyofeng@gmail.com

Visual and Force Feedback-enabled Docking for Rational Drug Design

O. Sourina[1], J. Torres[2] and J. Wang[1]

[1] Nanyang Technological University/School of Electrical and Electronics Engineering, Singapore
[2] Nanyang Technological University/School of Biological Science, Singapore

Abstract — **Transmembrane helices play basic roles in biology: signal transduction, ion transport and protein folding. While antibodies can be directed towards hydrophilic regions of molecules, transmembrane regions have not been targeted so far. In this paper, we propose a novel approach to search for helix-helix complementary pairs in order to inhibit, or modulate, the function of membrane proteins where point mutations at the transmembrane domain have been found to lead to various forms of cancer such as the homodimeric epidermal, or fibroblast, growth factor receptors. This method employs visual and force feedback tools to search for the optimal interaction between helices. The search is manual, exploring helix tilt, helix rotation and side chain rotamer selection, with feedback from the models consisting of a repulsion or attraction force. We developed a prototype system that allows real-time interactive visualization and manipulation of molecules with force feedback in virtual environment. In our system, we implemented haptic interface to facilitate the exploration and analysis of molecular docking. Haptic device enables the user to manipulate the molecules and feel its interaction during the docking process in virtual experiment on computer. In future, these techniques could help the user to understand molecular interactions, and to evaluate the design of pharmaceutical drugs.**

Keywords — **Visual docking, force feedback, molecular docking, haptic interface**

I. Introduction

During the past decade, efforts have been made to predict complex structures from the structures of individual proteins. Membrane protein structure determination is till the Wild West of Structural Biology [1]. Structural determination using classical techniques such as X-ray diffraction or Nuclear Magnetic Resonance (NMR) is hindered because of the experimental problems associated with lipid-embedded domains. Given the experimental difficulties in membrane protein structure determination, there is a pressing need for prediction methods. Prediction of membrane protein structure consists of two parts: one is topology, the other is helix-helix interaction. Prediction of location of transmembrane (TM) helices and topology has been in general successful. It is often possible to develop a limited set of topological models from the sequence. The total success of membrane protein structure prediction, however, will depend largely on the second challenge, which is to correctly pack topologically arranged helices [2]. In this respect, the fact that the main contribution to transmembrane interhelical packing is Van der Waals interactions converts the problem into a docking one [3].

We propose and develop visual haptic-based molecular docking system to explore the conformational space of helix-helix interaction manually in the hope to find an optimal conformation with the minimum amount of time. Docking the transmembrane helices is a difficult task for automatic conformational search algorithms when polytopic membrane protein structure is explored because of the exponential increase in conformations as the number of α-helices is increased. Given the difficulties in exploring the whole conformational space available in polytopic membrane proteins, our strategy for docking TM helical domains is to use a manual approach in a virtual reality environment. This manual approach greatly simplifies the searching task, as changes in helix register, tilt and rotational orientation of the helices around their long axis are accomplished by hand. Feedback will be provided as attraction or repulsion forces felt by the user, which will be generated after calculating bonding and nonbonding interactions.

The paper is organized as follows. In Section II, the proposed method is elaborated. In Section III, the system prototype is described and helix-helix docking examples are given. Conclusion and future work is given in Section IV.

II. Approach

There are a number of methods that attempt to solve the docking problem, which entails finding the optimum interaction between two molecular systems by using a scoring function. These methods normally use a conformational search algorithm to explore the conformational space, which is exceptionally time-consuming. In these studies, drug-receptor or protein-protein interactions are the preferred subject of study. One reason for this is that the ultimate goal for the use of transmembrane helices is not as immediately obvious. The other is the lack of structural data for membrane proteins, which precludes 'direct' docking attempts between drug and, for example, a membrane receptor. In complex systems, however, the number of unknowns grows

Chwee Teck Lim, James C.H. Goh (Eds.): ICBME 2008, Proceedings 23, pp. 1874–1877, 2009
www.springerlink.com

exponentially as the symmetry that exists in homooligomers is lost. In this case, additional experimental approaches or demanding computational search methods are necessary. This converts the exhaustive search of conformational space for a 6 TM protein in a formidable task, as rotation, tilt and register can all change in each of the TM helices. One alternative that we propose in our project is to explore the conformational space manually using force feedback in the hope to find an optimal conformation with the minimum amount of time. This manual approach greatly simplifies the searching task, as changes in helix register, tilt and rotational orientation of the helices around their long axis are accomplished with visual and haptic feedback. This is especially convenient when exploring the conformational space in a polytopic membrane protein, in which all TM helices are different.

Thus, our strategy for docking TM helical domains is to use visual and haptic feedback in a virtual reality environment. Feedback will be provided as attraction or repulsion forces felt by the user. The rough binding region can be decided based on shape complimentary by visualization system. So far, the sphere models corresponding to Van der Waals surface are implemented in the system we are working on. The key requirement in simulating of the ligand binding process is to have a good model of the interaction between ligand and receptor. During binding, the ligand is moving in the potential field created by the receptor's atoms, and the system is searching for a stable low potential configuration. While moving one of the molecules around binding site based on shape complimentary, the potential energy at each position is calculated and compared, the minimum value of potential energy is recorded together with the position of the ligand molecule.

The possible docking orientations between molecular systems are sampled with input from force calculations that is fed back to the user through the haptic device. The molecular systems are visualized with their van der Waals surfaces. The force feedback requires a high refresh rate (at least 1 kHz), therefore interaction energy calculations should be simplified. This brings the challenge in the project. The problem of fast haptic rendering could be solved by computation of the interactive forces in advance and storing it in a volumetric grid. After preliminary study we also found out that when molecular system is manipulated, the Cartesian coordinates corresponding to interactions with local energy minima should be dynamically stored on the volumetric grid as well. When only forces in rigid docking are required, we could use only the Lennard-Jones (L-J) potential as the main scoring function, as it has been found to be the most important in transmemebrane α-helix interaction [3]. The essential features are approximated quite well by a Lennard-Jones potential [4] (also referred to as the L-J potential, 6-12 potential or, less commonly, 12-6 potential). There are many different force field models that can be used to simulate proteins and other organic molecules implemented in AMBER [4], CHARMM [5], MM3 [6], MM4 [7] and MMFF94 [8]. If each force field is normally developed for a particular type of molecule, they rather well adapt to different structures in atomic types. The one we use and which is described below is called OPLS-aa [9] [10] [11]. It was parameterized for use in protein simulations, and also for small organic molecules, and has functional groups for all 20 common amino acids. For the homo-atomic pairs, there are published LJ parameters available (i.e. [12] for OPLS-aa). For the homo-atomic pairs, the interaction of hetero-atomic pairs, the effective values of σ and ε are calculated from those for the homo-atomic pairs. The way of calculation is called mixing rule. OPLS-aa uses the same non-bonded functional forms as AMBER, and the Lennard-Jones terms between unlike atoms are computed using geometric mean mixing rule [13].

III. Results

We are developing a prototype of Transmembrane α-helices Docking System HMolDock (**H**aptic-based **Mol**ecular **Dock**ing), using the haptic device PHANTOM 1.5/6DOF (6 degrees of freedom) [14-15]. The molecular structure file format in the Protein Data Bank .pdb [16] is chosen as an input, although there are wide variety of file formats based on standard Cartesian (x, y, z) coordinates (e.g., .mpl, .car, .pdb) for which we will use conversion programs. For now, basic molecular visulization is accomplished. Atom coordinates are got from input PDB files; atom radius and correspondent color are determined based on atom type and its belonging residue which are extracted from PDB data. Two molecules or one molecule and the probe are visualized on the screen. The user can assign a haptic mouse to the probe or to one of the molecules and move the probe/molecule towards/around to another molecule. In Fig. 1, Van der Waals forces of molecular system are investigated with the atom probe. An interaction force is calculated at each position, and the resulting attraction/repulsion force is felt by the user through the haptic device. The force direction and magnitude are visualized as a vector. Thus, a probe/molecule can be selected by the haptic mouse and moved around to let the user 'feel' the force changing. In Figure 2, Van der Waals surfaces of two helices are visualized by current system prototype. To differentiate the helices, two color schemes are used. The attraction/repulsion force in this case is mostly due to van der Waals force interactions, as no charged residues are present.

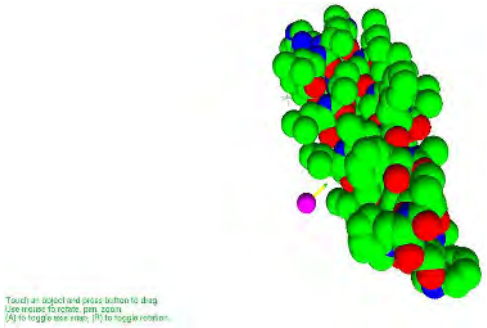


Fig. 1 Van der Waals forces is investigated with the atome probe



Fig. 2 Van der Waals surface model of a homodimer with two different color schemes

To demonstrate application of our method, let us give an example in molecular medicine. Currently, we are working on models and algorithms of rigid molecular docking. Although Van der Waals surface is represented in our system using simple atoms, we show here a more complex example.

To demonstrate application of our method, let us give an example in molecular medicine. Currently, we are working on models and algorithms of rigid molecular docking. Although Van der Waals surface is represented in our system using simple atoms, we show here a more complex example. The example in Figure 3 is especially pertinent to molecular medicine, where an important strategy is to achieve function regulation by modulation of protein-protein interactions. In membrane proteins, a recent approach targets the transmembrane region with certain peptides [17]. The rationale is that transmembrane mutations, for example in receptor tyrosine kinases, have been associated to many types of cancer and developmental deficiencies, which are explained by unregulated activation. Inactivation of the

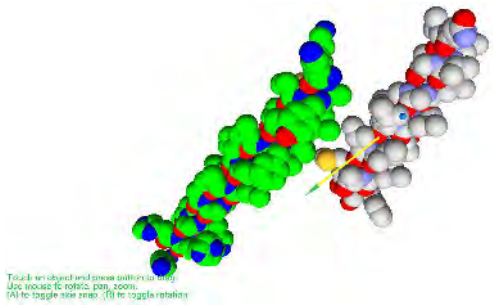


Fig. 3 Interaction of αIIb integrin transmembrane helix and a designed antibody-like complementary peptide anti-αIIb, separated

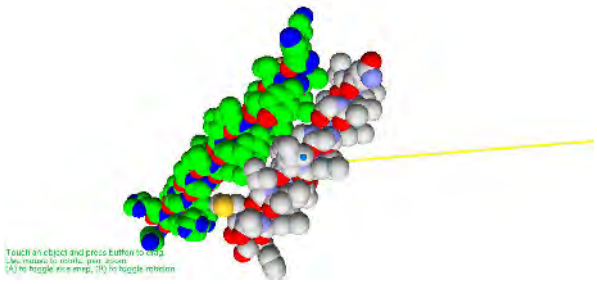


Fig. 4 Interaction of αIIb integrin transmembrane helix and a designed antibody-like complementary peptide anti-αIIb, in contact

receptor is thus crucial for targeted treatment, and this can be achieved with synthetic α-helices that target the native α-helices of the receptor. Figure 3 shows the two transmembrane domains, target and probe, corresponding to αIIb intregrin and a designed anti-αIIb integrin [17], respectively. In Figure 4, the helices move close and they become in contact.

IV. Conclusions

We propose a novel approach in helix-helix interaction research and rational design of peptides. We propose and implement novel approach to search for helix-helix complementary pairs that will facilitate the search for membrane helical inhibitor in future. Novel models and algorithms specific to helix-helix docking will be proposed and developed. For now, drug-receptor or protein-protein interactions are the preferred subject of study, and specific features of helix-helix docking are less studied by researchers. Drug design with our system will be tested. Based on the preliminary study with our system, we believe that understanding of the reason certain mutations alter transmembrane interactions and cause disease can be improved with the proposed methods. We are going to do in silico experiments on bio-

molecular docking to study helix-helix interactions in rational drug design.

Acknowledgment

This project is supported by MOE NTU grant RG10/06 "Visual and Force Feedback Simulation in Nanoengineering and Application to Docking of Transmembrane α- Helices".

References

1. Torres J, Stevens TJ, Samso M (2003) Membrane proteins: the 'Wild West' of structural biology. Trends in Biochemical Sciences 28:137-144
2. Popot J L and Engelman D M (1990) Membrane protein folding and oligomerisation: the two-tage model. *Biochemistry* 29: 4031-4037
3. Bowie J U (1997) Helix packing in membrane proteins. 272, 780-789
4. Weiner S J, Kollman P A, Case D A at al (1984) A new force field for molecular mechanical simulation of nucleic acids and proteins. J. Am. Chem. Soc. 106:765-784
5. Brooks B R, Bruccoleri R E, Olafson B D at al (1983) CHARMM: A program for macromolecular energy, minimization, and dynamics calculations. J. Com. Chem 4:187-217
6. Lii J-H, Allinger N L (1991) The MM3 force field for amides, polypeptides and proteins. J. Comp. Chem. 12:186-199
7. Allinger N L, Chen K, Lii J-H (1996) An improved force field (MM4) for saturated hydrocarbons. J. Comp. Chem. 17:642-668
8. Halgren T A (1996) Merck molecular force field. IV. Conformational energies and geometries. J. Comp. Chem 17:587-615
9. Jorgensen W L, Maxwell D S, Tirado-Rives J (1996) Development and testing of the OPLS all-atom force field on conformational energetics and properties of organic liquids. J. Am. Chem. Soc. 118 11:225-11236
10. Damm W, Frontera A, Tirado-Rives J, Jorgensen W L (1997) OPLS all-atom force field for carbohydrates. J. Comp. Chem. 18:1955-1970
11. Rizzo R C, Jorgensen W L (1999) OPLS all-atom model for amines: resolution of the amine hydration problem. J. Am. Chem. Soc. 121:4827-4836
12. OPLS-aa force field parameter at http://egad.berkeley.edu/EGAD_manual/EGAD/examples/energy_function/ligands/oplsaa.txt
13. Martin M G (2006) Comparison of the AMBER, CHARMM, COMPASS, GROMOS, OPLS, TraPPE and UFF force fields for Prediction of vapor-liquid coexistence curves and liquid densities. Fluid Phase Equilib. 248:50-55
14. Sourina O, Torres J, Wang J (2008) Visual haptic-based biomolecular docking, Proc of 2008 Int Conf on Cyberworlds, China, 22-24 Sept 2008, pp 240-247
15. Wei L, Sourin A, Sourina O (2007) Function-based haptic interaction in Cyberworlds, Proc. of IEEE 2007 International Conference on Cyberworlds, Germany, 24 – 26 Oct. 2007, pp 225 -232
16. PDB - Protein Data Bank, Brookhaven National Laboratory at http://www.rcsb.org/pdb/
17. Yin H, Slusky J S, Berger B W, Walters R S, Vilaire G, Litvinov R I, Lear J D, Caputo G A, Bennett J S, and DeGrado W F (2007) *Science* 315: 1817-1822

Author: Olga Sourina
Institute: Nanyang Technological University
Street: 50 Nanyang Ave
City: Singapore
Country: Singapore
Email: eosourina@ntu.edu.sg

A Coupled Soft Tissue Continuum-Transient Blood flow Model to Investigate the Circulation in Deep Veins of the Calf under Compression

K. Mithraratne[1], T. Lavrijsen[2] and P.J. Hunter[1]

[1] Auckland Bioengineering institute, University of Auckland, Private Bag 92019, Auckland, New Zealand
[2] Department of Biomedical Engineering, Technische Universiteit Eindhoven, PO Box 513, Eindhoven, The Netherlands

Abstract — **A coupled computational model of a 3D soft tissue continuum and a one-dimensional transient blood flow network is presented in this paper. The primary aim of the model is to investigate the reduction in vessel cross section area and resulting vessel wall shear stresses (WSS) in response to the compression applied on the calf. Application of external compression on the lower leg is a commonly used prophylaxis against thrombus formation in deep veins. The soft tissue continuum model is a tri-cubic Hermite finite element mesh representing all the muscles, skin and subcutaneous fat in the calf and treated as incompressible with homogeneous isotropic properties. The deformed state of the soft tissue due to the applied compression is obtained by solving large or nonlinear deformation mechanics equations using the Galerkin finite element method. The geometry of the main deep vein network is represented by a 1D Hermite cubic finite element mesh. The flow computational model consists of 1D Navier-Stokes equations and a non-linear constitutive equation to describe vessel radius - transmural pressure relationship. Once compression is applied, the transmural pressure is computed as the difference between the fluid and soft tissue hydrostatic pressure. The latter arises due to the incompressibility of the soft tissue material. Transient flow governing equations are solved using the McCormack finite difference method. The geometry of both the soft tissue continuum and vein network is anatomically-based and was developed using data derived from magnetic resonance images (MRI). Simulation results from the computational model show a reasonably good agreement with the results reported in the literature on the degree of deformation in vein cross-section area estimated using MRI.**

Keywords — **Deep Veins, Blood flow mechanics, Soft tissue mechanics.**

I. Introduction

Deep vein thrombosis (DVT) or formation of thrombi in deep veins of lower limbs is a commom problem in hospitalized patients. It often remains clinically unapparent and resolves without intervention. However, it may lead to other complications such as chronic venous insufficiency and pulmonary embolism. The latter has been estimated to cause about 10% of all hospital deaths [1]. DVT is also known as 'economy class syndrome' as it is linked to prolonged seated immobility in long-haul flights [2,3].

It is believed that there are three thrombogenic factors involved in DVT: stasis, hypercoagulability and injury to the vessel wall [4]. Two types of prophylaxis, medicinal anticoagulants (e.g. heparin) and mechanical methods (compression) are generally used for DVT. Most mechanical methods act on the calf and can be further divided into static and intermittent compression. Of the two compression methods, simplicity and low cost have made static method more attractive, especially for concerned air travelers. Compression stockings are commonly used for static compression and they usually apply uniform pressure over the entire calf. In intermittent compression, inflatable cuffs are wrapped around the patient's calf and periodically inflated using a pump.

Despite several clinical and biological studies [5-8] to show the efficacy of the compression method, the mechanism by which it acts is still not well understood. The external compression is generally thought to cause reduction in deep vessel cross-section area, which in turn results in increased flow velocities. Another hypothesis is based on the haemodynamic vessel WSS and its effect on the degree of stimulus for endothelial cell activation [8-9]. It is believed that shear stress and cyclic strain can influence the release of tissue plasminogen activator (t-PA) and its gene expressions. t-PA then converts plasminogen to active plasmin, which dissolves fibrin and prevents thrombus formation.

A number of studies [4,10] have looked at modeling external compression and resulting blood flow in deep veins. All these models, however, have either employed images (e.g. MRI) directly [4,10-12] or used the deformation of 2D continuum models (plane strain analysis) of surrounding soft tissue structures to reconstruct the deformed (collapsed) geometry of vessels. The computational model developed in this study is based on a 3D soft tissue continuum model undergoing large deformations (finite elasticity) due to applied external compression with 1D flow network of major deep vessels embedded in it. Coupling between fluid and soft tissue is archived via the vessel wall constitutive equation that describes the relationship between vessel radius and the transmural pressure. The latter is the difference between the fluid pressure and soft tissue *hydrostatic pressure* which arises due to the incompressibility of the soft tissue material.

Chwee Teck Lim, James C.H. Goh (Eds.): ICBME 2008, Proceedings 23, pp. 1878–1882, 2009
www.springerlink.com

II. Materials and Methods

A. Imaging and construction of model geometries

The right leg of a healthy 21 year old male volunteer was imaged using a 1.5T MRI scanner (Siemens Magnetom Avanto). The subject was placed in prone position to minimize compression of the calf which would otherwise cause deformed or collapsed veins. A multi-slice 2D time-of-flight sequence was used to enhance the contrast between veins and arteries. The images were acquired with a spacing of 5.36 mm and the slice thickness was set at 8mm.

The Bioengineering modeling software CMISS [13] was used to manually segment the MRI images and derive the necessary data for the construction of model geometries. A tri-linear Lagrange finite element (FE) mesh representing the 3D geometry of the soft tissue continuum consisting of skin, subcutaneous fat and muscles was first created and fitted to the digitized data to obtain tri-cubic Hermite FE mesh [14]. Fig. 1 depicts the fitted soft tissue mesh.

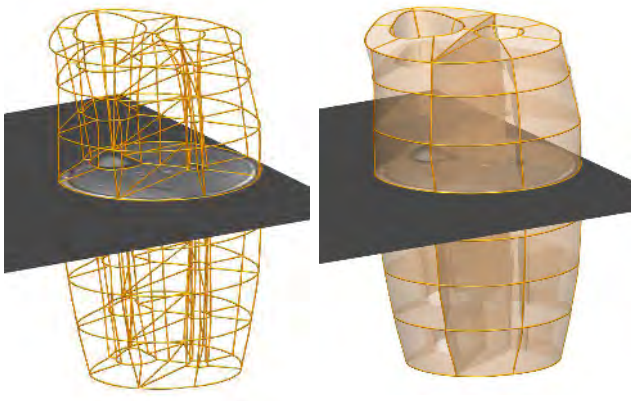


Fig. 1 Fitted tri-cubic Hermite FE mesh of soft tissue continuum in the calf

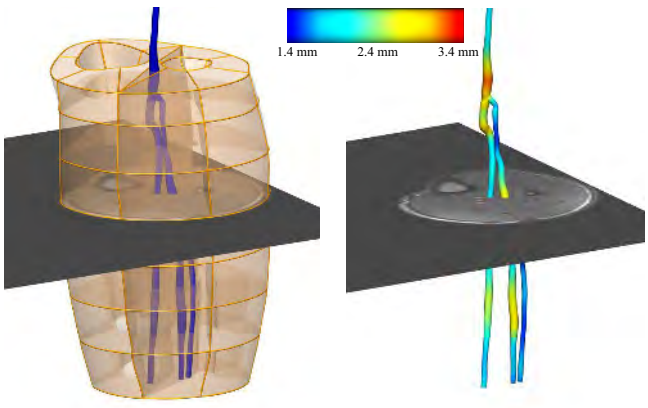


Fig. 2 (a) Fitted 1D cubic FE mesh of the flow network
(b) Radius field (cubic Hermite) in the flow network

Only the vessels with good contrast relative to the surrounding soft tissue were digitized. These included the popliteal vein (PV), the posterior tibial vein (PTV), the lateral posterior tibial vein (LPTV) and the medial and lateral peroneal veins (MPV, LPV). Furthermore, on each image, four data points were created to define the each vessel boundary. The position coordinates of the vessel on each image was then calculated by taking the average of these points. The mean radius of the un-collapsed vessel was also inferred using the same points. A 1D cubic Hermite FE mesh was then created by fitting to the data so obtained. The mean un-collapsed or reference radius of vessel was also fitted as a cubic field along the 1D geometry. The fitted FE mesh of flow network with radius field is shown in fig. 2.

B. Soft tissue model

The deformation of the soft tissue continuum in response to the applied compression (pressure) on the calf can be obtained by solving the static Cauchy equation,

$$\frac{\partial \sigma_{ij}}{\partial x_j} + \rho_s . b_j = 0 \quad : i, j = 1..3 \tag{1}$$

where σ_{ij} are Cauchy stress tensor components, x_j are spatial coordinates, b_j are the body force components and ρ_s is the soft tissue density.

The mechanical characteristics of the soft tissue were modeled as isotropic, incompressible Mooney-Rivlin material with homogeneous properties. Thus, the constitutive equation of the soft tissue material can be described by a strain energy density function (SEDF) as follows,

$$w = c_{10}(I_1 - 3) + c_{20}(I_1 - 3)^2 + p(I_3 - 1) \tag{2}$$

where w is SEDF, I_1 and I_3 are the invariants of the right Cauchy deformation tensor. The incompressibility constraint $(I_3 = 1)$ is appended to the SEDF via a Lagrange multiplier, p (hydrostatic pressure). As mentioned earlier, soft tissue hydrostatic pressure acts on the external surface of the vessel wall. Hydrostatic pressure was interpolated using tri-linear Lagrange basis functions.

The material parameters used in eq.(2) were 10.0 kPa for both c_{10} and c_{20} [15]. Boundary conditions for the problem were prescribed as follows. All nodal degrees of freedom (dofs) of the inner surface where the soft tissue is in contact with bones were fixed. A uniform traction (compression) of 2.67 kPa (20 mmHg) was applied on the outer surface to mimic the action of static compression. The compression pressure of 2.67 kPa was chosen to fall within the range of values used in the experiments reported in reference [11].

Eq. (1) was numerically solved using the Galerkin FE method for large or non-linear deformations of the soft tissue continuum within CMISS [13].

C. Flow model

The blood flow in veins was modeled as an incompressible, homogeneous, Newtonian fluid with axisymmetric laminar flow in a compliant tube. It was further assumed that radial and circumferential flows are negligible compared to the flow in the axial direction and the axial velocity has parabolic variation in the radial direction [16]. With these assumptions, the reduced form of the Navier-Stokes equations (continuity and momentum) can be written as,

$$\frac{\partial R}{\partial t}+V\frac{\partial R}{\partial x}+\frac{R}{2}.\frac{\partial V}{\partial x}=0 \tag{3}$$

$$\frac{\partial V}{\partial t}+(2\alpha-1)V\frac{\partial V}{\partial x}+2(\alpha-1)\frac{V^2}{R}.\frac{\partial R}{\partial x}+\frac{1}{\rho_f}\frac{\partial P}{\partial x}+\left(\frac{2\nu\alpha}{\alpha-1}\right)\frac{V}{R^2}=0 \tag{4}$$

where V is the mean velocity of the profile, R is the vessel radius, P is the fluid pressure and ρ_f and ν are fluid density and kinematic viscosity respectively. α is the velocity profile parameter.

The velocity profile is given by,

$$u=\left(\frac{\gamma+2}{\gamma}\right).V.\left[1-\left(\frac{r}{R}\right)^{\gamma}\right] \text{ and } \gamma=\frac{2-\alpha}{\alpha-1} \tag{5}$$

where u is the axial velocity at r.

The constitutive equation of the vein wall which describes the mechanical characteristics (vessel radius–transmural pressure relationship) was defined as a cubic polynomial of radius ratio $\left(\frac{R}{R_0}\right)$ by fitting the experimental data [17] obtained from canine femoral vein,

$$P_{tr}=(P-p)=a\left(\frac{R}{R_0}\right)^3+b\left(\frac{R}{R_0}\right)^2+c\left(\frac{R}{R_0}\right) \tag{6}$$

where P_{tr} is the transmural pressure (difference between fluid and hydrostatic pressures), R_0 is the un-collapsed (reference) radius and a, b & c are the polynomial fitting coefficients.

The above system of equations was solved numerically using the McCormack's finite difference method [18]. This finite difference scheme is a two-step (corrector-predictor), fully explicit scheme and possesses second-order spatial and temporal accuracy. The following values were used for fluid density and kinematic viscosity: $\rho_f = 1050$ kg/m^3 and $\nu = 3.2$ mm^2/s. The flow parameter, α was set at 1.1.

A range of flow rates reported in the literature was prescribed as inlet boundary conditions. A number of studies have reported the mean popliteal venous flow in the horizontal position: 1.7 ml/s [19], 2.2 ml/s [20] and 3.8 ml/s [21]. Since the anterior tibial vessels and medial posterior tibial vessels were not included in the flow net work, it was assumed that the inlet flow to be half of the reported values. The fluid pressure was prescribed as the boundary condition at the outlet. It was also assumed that the pressure at the outlet (popliteal vein) is equal to the femoral venous pressure. The average of the femoral venous pressure (1.3 kPa) reported in the literature [22-24] was used in simulations. All flow simulations were performed by linearly increasing the flow from zero to the rate required.

III. Results and Discussion

The network geometry was reconstructed with respect to the deformed soft tissue continuum to examine the degree of reduction in vessel cross-section area caused by gross deformation of the tissue continuum (without taking the hydrostatic pressure effects into account). The mean radius change of the venous network due to the gross deformation was found be insignificant (less than 2%).

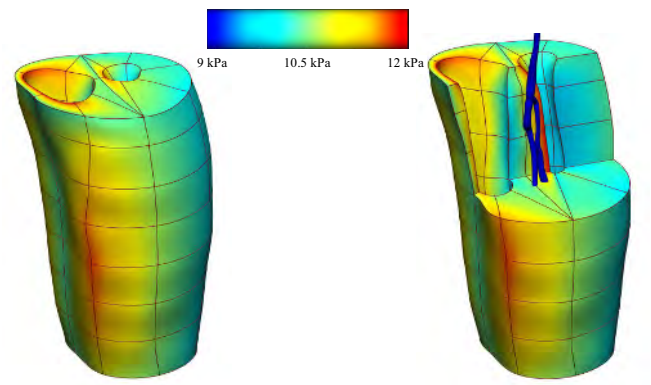


Fig. 3 Hydrostatic pressure distribution of the calf at deformed state

The hydrostatic pressure distribution in response to the application of external compression is depicted in fig 3. The distribution of hydrostatic pressure was obtained by fitting it as a tri-linear FE field. The field, thus fitted, was then interpolated to determine the external pressure acting on the vessel wall at each finite difference grid point of the venous

flow network. The mean cross-sectional area of the flow network at various flow rates due to externally applied compression is given in table 1.

Table 1 Change in vessel mean cross-section area

	Flow rate [ml/s]				
	0.25	0.50	1.00	1.50	2.50
Mean area [mm^2]	2.4	2.7	3.2	3.5	4.2
% Reduction	84	82	79	77	72

Percentage reduction is based on a mean area of 15 mm^2 at 1.0 ml/s

The WSS was computed using eq. 5 (flow profile equation). It is directly proportional to the axial velocity gradient in the radial direction at the wall $\left(\left. \frac{\partial u}{\partial r} \right|_{r=R} \right)$. Table 2 gives the WSS at various flow rates simulated.

Table 2 Change in vessel wall shear stress (WSS)

Mean WSS [Pa]	Flow rate [ml/s]				
	0.25	0.50	1.00	1.50	2.50
Uncompressed	0.15	0.30	0.60	0.90	1.42
Compressed	2.20	3.76	6.12	7.96	10.8

The reduction in cross-section area at 1.0 ml/s based on a MRI study [10] has been reported to be about 62%±10%. The predicted value from the present study compares reasonably well with the experimental data. The overestimation could be due to the soft tissue constitutive properties. The WSS estimated using the flow simulations based on reconstructed vessel geometry at 1.0 ml/s from the same MRI study is 1.2 Pa in deep veins. The discrepancy could be attributed to (a) soft tissue mechanical properties and (b) flow profile. It can be easily shown that the flow profile parameter, α, determines the gradient of the axial velocity at the wall which is directly proportional to the WSS.

IV. Conclusions

A coupled computational model of a 3D soft tissue mechanics and a 1D transient flow network were developed. The model was used to investigate the reduction in vessel cross-section area, the resulting flow and wall shear stress. The coupling of soft tissue and fluid was achieved via the vessel constitutive equation, which is a function of the soft tissue hydrostatic pressure and fluid pressure.

Acknowledgments

The work presented in this paper was funded by the Foundation for Research, Science and Technology of New Zealand under the project no. 9077/3604215.

References

1. Cohen AT, Alikhan R (2001) Prophylaxis of venous thromboembolism in medical patients. Curr Opin Pulm Med 7:332-337
2. Adi Y, Bayliss S et al. (2004) The association between air travel and deep vein thrombosis: Systematic review and meta analysis. BMC Card Dis 4:7
3. Nissen P (1997) The so-called “economy class” syndrome or travel thrombosis. Vasa 26:239-246
4. Downie SP, Raynor SM et al. (2008) Effects of elastic compression stockings on wall shear stress in deep and superficial veins of the calf. Am J Physiol Heart Circ Physiol 294:H2112-H2120
5. Agu O, Hamilton G, et al. (1999) Graduated compression stockings in the prevention of venous thromboembolism. Br J Sur 86:992-1004
6. Salzman EW, McManama GP, et al. (1987) Effect of optimization if hemodynamics on fibrinolytic activity and antithrombotic efficacy of external pneumatic calf compression. Ann Surg 206:5:636-641
7. Morris RJ and Woodcock JP (2004) Evidence-based compression: Prevention of stasis and deep vein thrombosis An of Sur 239:162-171
8. Dai G, Tsukurov O, et al. (2000) An in vitro cell culture system to study the influence of external pneumatic compression on endothelial function. J Vas Sur 32:5:977-987
9. Malek AM, Alper SL et al. (1999) Hemodynamic shear stress and its role in atherosclerosis. JAMM 282:21:2035-2042.
10. Downie SP, Firmin DN et al. (2007) Role of MRI in investigating the effects of elastic compression stockings on the deformation of the superficial and deep veins in the lower leg. J MRI 26:80-85
11. Dai G, Gertler JP, et al.(1999) The effects of external compression on venous blood flow and tissue deformation in the lower leg. J Bio Mech Eng 121:557-564
12. Narracott AJ, John GW, et al. (2007) Influence of intermittent compression cuff design on calf deformation: computational results. IEEE EMBS Proc. Lyon, France, 2007, pp 6334-6337
13. http://www.cmiss.org
14. Fernandez JW, Mithraratne K, et al. (2004) Anatomically based geometric modeling of the musculoskeletal system and other organs. Biomech Model Mechan 2:139-155
15. Meier P and Blickhan R (2000) Skeletal muscle mechanics: From mechanism to function, John Willey & Sons Ltd pp 207-224
16. Barnard ACL, Hunt WA, et al. (1966) A theory of fluid flow in compliant tubes. BioPhy J 6:717-724
17. Dobrin PB, Littooy FN, et al. (1988) Mechanical and histological changes in canine vein grafts. J Surg Res 44:259-265
18. Anderson JD Jr (1995) Computational fluid dynamics-The basics with applications. McGrawhill, Singapore
19. Knaggs AL, Delis KT, et al. (2005) Perioperative lower limb venous haemodynamics in patients under general anesthesia. Br J Anaes 94:292-295
20. Morita H, Abe C, et al. (2006) Neuromuscular electrical simulation and an Ottoman-type seat effectively improve popliteal venous flow in a sitting position. J Phys Sci 56:2:183-186
21. Lurie F, Awaya DJ, et al. (2003) Hemodynamic effect of intermittent pneumatic compression and the position of the body. J Vasc Surg 37:137-142

22. Arnoldi CC, Linderholm H, et al. (1972) Venous engorgement and intraosseous hypertension in osteoarthritis of the hip. J Bone Joint Surg 54B:409-421.
23. Andersson LE, Jogestrand T, et al. (2005) Are there changes in leg vascular resistance during laparoscopic cholecystectomy with CO2 pneumoperitoneum? Acta Anast Scand 6:360-365
24. Beebe DS, McNevin MP, et al. (1993) Evidence of venous stasis after abdominal insufflation for laparoscopic cholecystectomy. Surg Gyne Obst 176:443-447

Author: K.Mithraratne : p.mithraratne@auckland.ac.nz

Finite Element Analysis of Articular Cartilage Model Considering the Configuration and Biphasic Property of the Tissue

N. Hosoda[1], N. Sakai[2], Y. Sawae[2] and T. Murakami[2]

[1] Graduate School of Systems Life Sciences, Kyushu University, Fukuoka, Japan
[2] Faculty of Engineering, Kyushu University, Fukuoka, Japan

Abstract — **Articular cartilage tissue has high water content from 70 to 80% and shows biphasic behavior in which both solid and fluid properties should be considered. Furthermore, the mechanical behavior of cartilage shows depth-dependence. Therefore it is necessary to consider not only the average tissue property but also the local one to explain mechanical and functional behavior.**

Previously, we created cartilage tissue model considering the depth-dependence of Young's modulus distribution and applied two-dimensional finite element method (FEM) based on biphasic theory[1]. As a result, the deformed profile of depth-dependent Young's modulus model immediately after unconfined compression corresponded to actual profile. Consequently, we confirmed that Young's modulus has a distribution in the depth direction. In contrast, the total load capacity in FEM analysis was about one order lower than the experimental one. Immediately after compression at high rate, it has not enough time for intrinsic fluid to flow in cartilage, and thus whole tissue including intrinsic fluid shows the behavior like elastic body. Furthermore, the polymeric materials increase their stiffness at higher strain rate. Therefore, apparent elastic modulus is assumed to be larger than the equilibrium Young's modulus. During total deflection is maintained after compression, the intrinsic fluid flow gradually occurs, and the stress relaxes with decrease of apparent elastic modulus. After enough stress relaxation, an apparent elastic modulus becomes an equilibrium Young's modulus. We think this is connected to configuration of the cartilage tissue.

The aim of this study is to consider configuration of the tissue in addition to the character of biphasic property on the mechanical behavior of cartilage tissue. In this study, we created cartilage tissue model considering spring elements that express function arisen from collagen fiber and Young's modulus distribution depending on the depth. Then, we analyzed the unconfined compression and compared experimental results to FEM analysis.

Keywords — **Articular cartilage, Compressive deformation, Finite element method, Biphasic analysis, Spring element**

I. Introduction

The human synovial joint possesses superior load-bearing and jointing functions with very low friction and low wear. Articular cartilage tissue plays an important role to maintain this function through whole life. The arthrodial joint forms a connection between two or more bones, and functions by supporting and transmitting loads. Cartilage has high water content from 70 to 80 % and shows biphasic behaviors in which both solid and fluid properties should be considered.

One of the representative diseases on the synovial joints particularly for elder persons is osteoarthritis. Osteoarthritis causes degeneration and destruction of articular cartilage, which lead to the disturbance of motility. Articular cartilage degenerated by osteoarthritis decreases load-buffering capacity and leads to the bone deformation, the formation of osteophytes, and the subchondral bone induration and thickening. Especially in joints of lower extremities, there are many reports linking age and obesity to the osteoarthritis, or external injury and career to the occurrence of osteoarthritis. Consequently, mechanical factors are believed to play a crucial role in the pathogenesis of osteoarthritis.

As a new treatment method, tissue engineering has attracted attention in recent years. At the present stage, however, the mechanical function of tissue-engineered cartilage has not reached the level of native cartilage. It is noted that mechanical stimulation in culture process promotes extracellular matrix synthesis and leads to better function. Therefore, it is necessary to study the optimum conditions of mechanical stimulation.

Gaining better understanding of the mechanical and functional environment around chondrocytes is crucial to the clarification of the mechanism of osteoarthritis pathogenesis, the assessment of mechanical properties of the regenerated cartilage, and the clarification of the optimum condition of mechanical stimulation on the metabolism of chondrocytes.

A. Articular cartilage

Articular cartilage is composed of chondrocytes and an extracellular matrix. Extracellular matrix is mainly composed of proteoglycan and collagen, and produced by chondrocytes to provide scaffold to chondrocytes and support load to cartilage. Proteoglycan is highly hydrophilic and therefore can store a large amount of water and contribute to viscoelasticity. The hydrated proteoglycan is distended but confined by collagen network, and thus it supports the compressive load, while the collagen is given under

Chwee Teck Lim, James C.H. Goh (Eds.): ICBME 2008, Proceedings 23, pp. 1883–1887, 2009
www.springerlink.com

pulling coercively. Cartilage is categorized into the surface, middle and deep zones, and calcified zone by the gradient direction of collagen fibrosis, the morphology of the cells, and the presence or absence of calcareous deposits (Fig.1). Consequently, mechanical properties are different in the location.

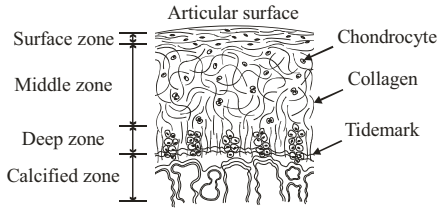


Fig.1 Cross-section diagram of cartilage tissue

B. The behavior of cartilage tissue to mechanical stimuli

The structure and property of articular cartilage have depth-dependence. If the load acts on the tissue rapidly, the tissue does not have enough time to exude the interstitial fluid and thus presents similar behavior to the elastic body. While the load acts on the tissue slowly, the interstitial fluid is gradually exuded through the tissue. In compression, the permeability of cartilage becomes lower with an increase in compression strain[2]. When cartilage is compressed at high rate and kept at the definite position, the occurrence of peak stress and following stress relaxation behavior are observed as shown in Fig.2. In our unconfined compression test of 10~15% strain at 1000μm/s, peak stress ranged from 0.71 MPa to 3.76 MPa. To understand the mechanotransduction in chondrocytes in cartilage, the actual time-dependent and depth-dependent stress and strain around chondrocytes should be clarified.

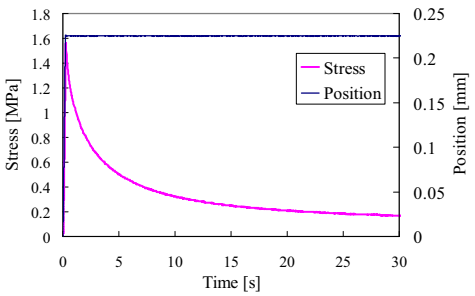


Fig. 2 Compressive behavior of articular cartilage to definite compressive deflection

C. Young's modulus distribution depending on the depth

Previously, we performed unconfined compression test of articular cartilage at definite total deformation in compression tester located on the stage of CLSM. Then, the local compression strain is calculated from the change in distance between the corresponding living cells stained with Calcein-AM 1 μL (Molecular Probes) in 1000 μL PBS in the fluorescence images before compression and at equilibrium. We derived Young's modulus distribution function using inverse relationship between strain and Young's modulus for nearly uni-axial compression.

In this study, we applied the compression velocity of 200 μm/s and the compression strain of 10 %. Mean value of the average Young's modulus E_0 of solid phase at equilibrium is 0.37 MPa. The Young's modulus depending on the depth are Eq. (1). We normalized Young's modulus depending on the depth and plotted those against relative position x in depth direction in Fig.3. The surface side is depicted as 0, and the deep zone end side is 1.

$$E(x) = \frac{3.66}{46.2e^{-6.53x} + 2.84} \tag{1}$$

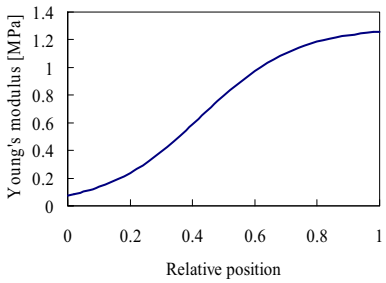


Fig.3 Young's modulus distribution

II. Finite Element Analysis of Articular Cartilage Model and Boundary Conditions

A. Finite element model

General-purpose finite element analysis software (ABAQUS v.6.5) was used to analyze the biphasic model [3].

The shape of articular cartilage model is rectangle that has 2 mm height and 3 mm width. We use two-dimensional model as the first step to future plan on multi-scale analyses to include chondrocyte. Characteristic behaviors in deformed profile, Mises stress and pore pressure obtained from two-dimensional model except small difference in stress and pressure values was verified by our related study using three-dimensional one. We modeled using biphasic fluid

element (CPE4P). The size of the each element corresponds to 40 μm x 40 μm and total number of element is 3750.

In this model, the upper 10 % of cartilage tissue is surface zone, the lower 20 % of the tissue is deep zone and middle zone is located between surface and deep zones.

Young's modulus of the model is described as equation(1). Articular cartilage model was divided as 50 layers to depth direction and the corresponding Young's modulus was provided for each layer.

The void ratio e is provided for ABAQUS by the following equation.

$$e = \frac{dV_V}{dV_g + dV_t} \tag{2}$$

Where dV_v is a volume of voids, dV_g is volume of grains of solid material, and dV_t is a volume of trapped wetting liquid.

In this study, we assumed that water content of 80 % included in cartilage tissue is a volume of voids and other 20 % is sum of the volume of grains of solid material and a volume of trapped wetting liquid. Thus, void ratio is 4.

Poisson's ratio and permeability of solid phase were assumed as constant and used literature data shown in Table.1 [4]. The analysis was conducted for test duration of 300 s.

Table.1 Material properties.

Young's modulus of solid phase, E0 [MPa]	Poisson's ratio of solid phase, ν	Permeability k [$m^4/N \cdot s$]
0.74	0.125	2.0×10^{-15}

B. Spring element performed function caused by collagen fiber

The structures of articular cartilage tissue are inhomogeneous and anisotropy. Then, it is believed that locally different property and configuration develop the function of cartilage.

We noticed function of collagen fiber network. When proteoglycan supports compression loading, collagen fiber supports tension loading coercively because collagen network confines proteoglycan. So we created cartilage model considering the function of collagen fiber using nonlinear spring element. In this study, as shown in Fig. 4, we conect node of biphasic element in a horizontal direction by nonlinear spring element(SPRINGA) and assumed these nonlinear spring element affect only tensile deformation[5].

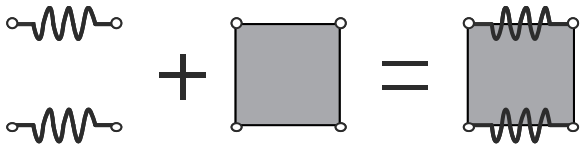


Fig. 4 The finite element and the arrangement of spring elements.

C. Boundary conditions

To compare experimental result with finite element analysis, the boundary condition for FEM was given to correspond to the compression test. FEM simulation of compress-ion test was performed under compression velocity of 200 μm/s and compression ratio of 10 %. Thus, amount of com-pression, compression velocity and compression time to definite deflection were 0.2 mm as 10 % of thickness, 200 μm/s and 1.0 s, respectively.

We assumed that there is rigid body plate on the cartilage tissue model and gave compressive displacement The node of top surface was compressed at displacement of 0.2 mm by the plate and the transform in y direction (parallel to surface) was unconfined. The node of lower surface was confined and the displacements of the node in both x and y directions were 0. To simulate impermeable compressing plates in compression tester, water was assumed to seep only through right and left side of rectangle model.

III. Result

In this study, we created three kinds of cartilage tissue models considering nonlinear spring element and biphasic property of the tissue, analyzed and compared experimental results to FEM analyses. First, we noticed the total load capacity of the model. The total load capacity of the model corresponds to reaction force to rigid body plate. The total load capacity of the experimental value is a measured value by a load cell in experiment.

To conform the total load capacity of FEM simulation based on biphasic theory to the experimental value during compression, we defined an nonlinear behavior for spring element (Spring 1 in Fig. 5). This model was named Model 1. In this model, the average stress during stress relaxation was too high as shown in Fig.6. Therefore, the spring property during stress relaxation was changed to decrease gradually from Spring 1 to softer one as shown in Fig. 5. The model was named Model 2. The total load capacity of Model 2 corresponded to experimental one.

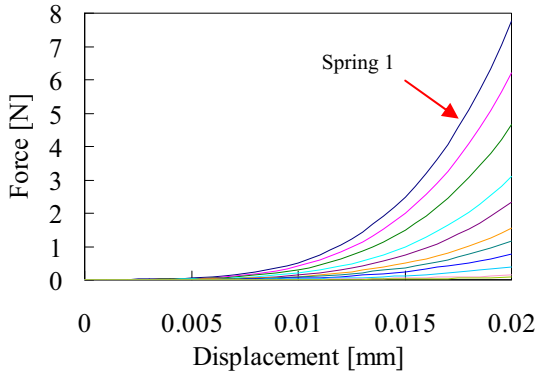


Fig. 5 The behavior of nonlinear spring element.

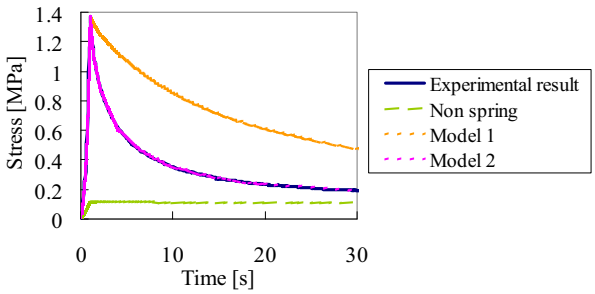


Fig. 6 Total load capacity.

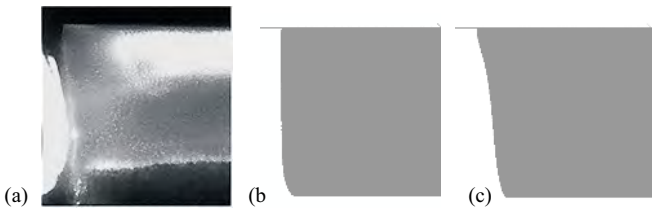


Fig. 7 Profile of compressed cartilage immediately after compression. (a)Cartilage specimen.(b)Model 1. (c)Model 3.

However, immediately after compression, the deformed profile of the Models 1 and 2 showed barreled profile and disaccorded with experimental one(Fig. 7). The polymeric materials increase their stiffness at higher strain rate. Therefore, apparent Young's modulus is assumed to be larger than the equilibrium Young's modulus. So, we adopted instantaneous elastic modulus as an instantaneous ratio of stress to strain, created the model, and named Model 3. The deformed profile immediately after compression of Model 3 corresponded to actual profile as shown in Fig. 7.

IV. Discussion

In the case we unused nonlinear spring element, peak stress in FEM model is about one order lower than the experimental one. The total load capacity of the model during compression coressponded to experimental one by using nonlinear spring element. So, it is thought that collagen network play a important part to stress development during compression. However, the stress relaxation behavior of the Model 1 disaccorded with experimental one. It is thought that stress relaxation curve indicated moderate change because nonlinear spring elements supported load and the flow of intrinsic fluid became slow. In actual cartilage tissue, it is thought that tensile deformation of collagen network comes loose with increase of fluid flow. Then, an apparent spring constant decreases. So, we created the model with sowly decreased spring constant. As a result, the total load capacity of FEM model corresponded to experimental one from the start of compression test to equilibrium. To reflect the depth-dependence of Young's modilus distribution for the defomed profile immediately after compression, we need change in nonlinear spring constant and instantaneous elastic modulus.

V. Conclusions

In this study, we created a cartilage tissue model considering the configuration and biphasic property of the tissue, and analyzed by biphasic theory. Then, we compared experimental results to FEM analyses and found the following facts.

(1) FEM value of the total load capacity during compression corresponded to experimental one using nonlinear spring element.

(2) In this biphasic model, to conform the total load capacity of FEM simulation to the experimental value during stress relaxation, it is necessary to control behavior of nonlinear spring element.

(3) The defomed profile immediately after compression corresponded to actual profile by controlling nonlinear spring constant and instantaneous elastic modulus.

References

1. Hosoda N, Sakai N, Sawae Y, Murakami T. (2008) Depth-Dependence and Time-Dependence in Mechanical Behaviors of Articular Cartilage in Unconfined Compression Test under Constant Total Deformation. Journal of Biomechanical Science and Engineering Vol.3:221-234
2. Jurvelin J. S., Buschmann M. D., Hunziker E. B. (2003) Mechanical anisotropy of the human knee articular cartilage in compression, Proceedings of the Institution of Mechanical Engineers, Part H: Journal of Engineering in Medicine, Vol. 217:215-219

3. Wu J. Z, Herzog W., Epstein M. (1998) Evaluation of the finite element software ABAQUS for biomechanical modeling of biphasic tissues, Journal of Biomechanics, Vol.31:165-169
4. Guilak F., Mow V. C. (2000) The mechanical environment of the chondrocyte: a biphasic finite element model of cell-matrix interactions in articular cartilage, Journal of Biomechanics, Vol.33:1663-1673
5. Li L.P., Soulhat J., Buschmann M.D., Shirazi-Adl A. (1999) Nonlinear analysis of cartilage in unconfined ramp compression using a fibril reinforced poroelastic model, Clinical Biomechanics, Vol.14:673-682

Author: N. Hosoda
Institute: Graduate School of Systems Life Sciences, Kyushu University
Street: 744 Motooka
City: Nishi-ku, Fukuoka
Country: Japan
Email: natsuko@tribo1.mech.kyushu-u.ac.jp

Principal Component Analysis of Lifting Kinematics and Kinetics in Pregnant Subjects

T.C. Nguyen[1,2], K.J. Reynolds[1]

[1] School of Computer Science, Engineering and Mathematics, Flinders University, Australia
[2] South Australian Movement Analysis Centre, Repatriation General Hospital, Australia

Abstract — **Low back pain (LBP) is estimated to affect 50-90% of women during pregnancy with more than a third of women reporting it as a severe problem compromising their ability to work during pregnancy and affecting normal daily life and sleep patterns. The aim of this study was to investigate the differences in kinematics and kinetics of lifting in pregnant subjects.**

Methodology

Fifteen maternal subjects (age: 32.0±2.3 yrs; height: 165.3±5.5cm; weight: 71.7±6.4kg) were tested at the third trimester of pregnancy (32-38 weeks). Twenty-seven retro reflective markers were placed on the various bony landmarks of the subjects. An eight-camera motion analysis system (VICON 512, VICON, Oxford, UK) was used to record movements of the body segment and synchronised force plate (AMTI, Watertown, MA, USA) parameters in three dimensions. Eight non-pregnant subjects (age: 29.6±3.1yrs; height:167.3±5.6cm; weight:65.4±8.4kg) were used as controls.

Each subject lifted a 4 kg plastic box (dimension: 31.5x25x20 cm), which is representative of commonly lifted items. Motion of the ankle, knee and hip joints and pelvic segments were investigated. Principal component (PC) analysis was applied to 23 kinematic and kinetic variables from each group. The total PC score for each subject was calculated, and a one-tail student-t test was used to test for significant differences between the groups.

Results

Significant group differences ($p<0.05$) were found for three of the PC scores. Parameters found to be major contributors to these differences included minimum hip flexion extension moment; maximum knee flexion moment; maximum ankle plantar flexion and knee flexion angles and average hip flexion extension angles.

Discussion

PCA was able to identify different lifting kinematics and kinetics in pregnant subjects and important biomechanical differences when compared with the control group. This is the first study to identify such lifting differences during pregnancy.

Keywords — **lifting kinematics, pregnancy, feature extraction, Principal Component Analysis**

I. Introduction

Low back pain (LBP) is estimated to affect 50-90% of women during pregnancy with more than a third of women reporting it as a severe problem compromising their ability to work during pregnancy and affecting normal daily life and sleep patterns [1]. Analysing biomechanical motion data is challenging due to its high dimensionality, temporal-dependence and high variability and correlate nature [2]. It is possible to generate thousands of parameters to represent key features of an individual's or group's data [2].

Principal components analysis (PCA) is a quantitatively rigorous method for achieving data/parameter reduction and separating useful parameters from redundant ones.

The method generates a new set of variables, called principal components (PC). Each PC is a linear combination of the original variables. All the principal components are orthogonal to each other, so there is no redundant information. The principal components as a whole form an orthogonal basis for the space of the data [3].

The objective of PCA is to reduce the dimensionality of the data set (or number of parameters) while retaining the original variability in the data. The first PC accounts for as much variability in the data as possible with the remaining PCs accounting for the remaining variability. By examining plots of these few new variables, it can offer a deeper understanding of the driving forces that generated the original data.

Smaller number of new variables usually allows easier interpretation of the data's structure [3, 4]. Each of the resulting PCs consist of correlated parameters which have a common link which can be used to develop a single equation that gives a single score which represents that component. This score can then be used as a new, dimension-reduced feature parameter. For example, the PCA studies by Olney et al. [4], Yamamoto et al. [5] and Sadeghi et al.[6] reduce large original parameters to between two to four PCs. These PCs have clinical relevant names in gait studies which includes grouping based on symmetry [4-6], speed and postural flexion bias [4], knee function and overall gait ability [5]. The majority of reported studies using PCA focused on gait studies with only three studies reported on lifting kinematics [7-9] .

The aim of this study was to use PCA investigate the differences in kinematics and kinetics of lifting in pregnant subjects compared with a control group.

Chwee Teck Lim, James C.H. Goh (Eds.): ICBME 2008, Proceedings 23, pp. 1888–1891, 2009
www.springerlink.com

II. Methodology

Fifteen maternal subjects (age: 32.0±2.3 yrs; height: 165.3±5.5cm; weight: 71.7±6.4kg) were tested at the third trimester of pregnancy (32-38 weeks). Twenty-seven retro reflective markers were placed on the various bony landmarks of the subjects. An eight-camera motion analysis system (VICON 512, VICON, Oxford, UK) was used to record movements of the body segment and synchronised force plate (AMTI, Watertown, MA, USA) parameters in three dimensions. Eight non-pregnant subjects (age: 29.6±3.1yrs; height: 167.3±5.6cm; weight: 65.4±8.4kg) were used as controls.

Each subject lifted a 4 kg plastic box (dimension: 31.5x25x20 cm), which is representative of commonly lifted items. Motion of the ankle, knee and hip joints and pelvic segments were calculated and normalised to one hundred percent of the lifting cycle. From the data, we measured the maximum, minimum, mean, range and standard deviation for each of the joints. A student t-test was performed to establish statistical significant differences between the two subject groups (see table 1). Principal component analysis (PCA) was applied to 23 kinematic and kinetic variables from each group (see table 2) based on the method described by Daffershoer et.al [10] . The total PC score for each subject was calculated using the Statistical Toolbox in Matlab (The Mathsworks Inc., Natick, MA,USA), and a one-tail student-t test was used to test for significant differences between the groups (see table 3).

III. Results

Twenty-three input parameters were used in the PCA as shown in table 2.

Figure 1 shows the percent of the total variability explained (VE) by each principal component with the first five PCs explain roughly two thirds of the total variability in the standardized ratings.

Major contributing parameters can be presented by using the percent VE values, as shown in figure 2.

The total PC score for each subject was calculated, a one-tail student-t test was used to calculate the p-value for the two groups, as shown in table 3, a p-value of 0.011 indicated that there are significant differences between the two groups.

Based on figure 2, the following parameters were found to be major contributors to these differences: minimum Hip Extensor Moment; Maximum Knee Extensor Moment; Minimum Pelvic Tilt; Mean Hip Flexion; Maximum Knee Flexion; Minimum Ankle Dorsiflexion and Maximum Ankle Dorsiflexion.

Table1. Summary of p-values from t-test between control and maternal subjects, **bold values** indicate statistical significant, p<0.05.

Kinematics	**Mean**	**Min**	**Max**	**SD**	**Range**
Pelvis (X)	0.154	**0.030**	0.363	0.129	0.156
Pelvis (X)	0.232	0.066	0.376	0.086	0.082
Pelvis (X)	0.461	0.293	0.299	0.145	0.117
Hip(X)	**0.011**	**0.006**	0.464	**0.041**	0.064
Hip(Y)	0.484	0.179	0.142	0.072	0.064
Hip(Z)	0.339	0.465	0.262	0.197	0.219
Knee(X)	0.183	**0.040**	0.180	0.318	0.262
Ankle(X)	0.079	0.212	0.052	**0.023**	0.055
Ankle(Z)	0.186	0.315	0.084	**0.014**	**0.027**
Moments					
Hip(X)	**0.008**	0.053	0.148	0.430	0.432
Hip(Y)	0.459	0.146	0.315	0.128	0.243
Knee(X)	0.056	0.465	**0.018**	**0.002**	**0.037**
Ankle(X)	0.123	0.056	0.259	0.355	0.482
	Xm	SD	Xc	SD	p-value
Lift Time	3.608	0.866	3.284	0.784	0.3889

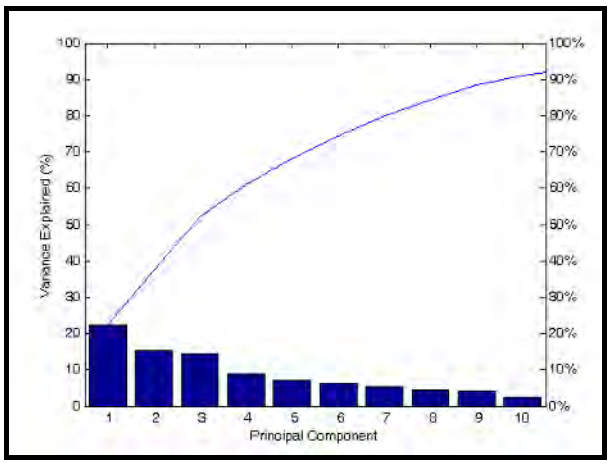


Figure 1. Variance Explained (%)

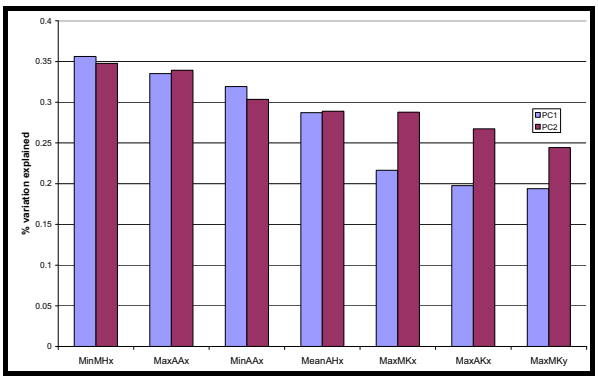


Figure 2. Contributing factors to the differences

Table 2. Input variables for PCA

Variable	Description	Unit
LiftT	Lift time	sec
MinAPx	Min Pelvic Tilt	deg
MaxAPx	Max Pelvic Tilt	deg
MinAPy	Min Pelvic Obliquity	deg
MaxAPy	Max Pelvic Obliquity	deg
MinAPz	Min Pelvic Rotation	deg
MaxAPz	Max Pelvic Rotation	deg
MeanAHx	Mean Hip Flexion	deg
MinAHx	Min Hip Flexion	deg
MinAKx	Min Knee Flexion	deg
MaxAKx	Max Knee Flexion	deg
MinAAx	Min Ankle Dorsiflexion	deg
MaxAAx	Max Ankle Dorsiflexion	deg
MinMHx	Min Hip Ext Moment	Nm/kg
MaxMHx	Max Hip Ext Moment	Nm/kg
MeanMHy	Mean Hip Abductor Moment	Nm/kg
MinMHy	Min Hip Abd Moment	Nm/kg
MinMKx	Min Knee Flex Moment	Nm/kg
MaxMKx	Max Knee Flex Moment	Nm/kg
MinMKy	Min Knee Abd Moment	Nm/kg
MaxMKy	Max Knee Abdo Moment	Nm/kg
MinMAx	Min Ankle Dorsi Moment	Nm/kg
MaxMAx	Max Ankle Dorsi Moment	Nm/kg

Table 3. PC values for all subjects and student t-test of PC scores. (S- Subjects, VE- percent Variation explained, PCC- Principal Component Coefficient)

S	PC1	PC2	PC3	PC1-3	PC1-5	PCC	VE
1	-33.58	52.64	19.06	7.32	19.95	1	**22.47**
2	-2.98	33.20	30.22	30.94	23.65	2	**15.21**
3	51.54	136.25	187.79	89.08	160.78	3	**14.47**
4	-7.42	45.04	37.61	30.69	33.81	4	**8.92**
5	-3.33	45.82	42.49	33.54	30.56	5	**7.08**
6	-15.68	38.80	23.13	22.18	24.37	6	6.31
7	-18.91	42.54	23.62	19.60	20.79	7	5.41
8	-14.52	36.44	21.92	19.94	21.83	8	4.56
9	13.73	42.05	55.78	44.16	29.87	9	4.12
10	-18.71	55.30	36.60	27.17	35.08	10	2.41
11	8.32	32.95	41.26	43.17	28.65	11	2.11
12	-17.85	65.80	47.95	31.40	26.00	12	1.81
13	5.73	46.62	52.36	40.39	36.95	13	1.63
14	-16.10	53.50	37.40	32.07	28.05	14	1.38
15	-20.32	54.81	34.50	34.63	29.25	15	0.88
16	-8.00	41.59	33.60	31.10	30.32	16	0.49
17	-25.76	51.52	25.76	19.81	23.34	17	0.35
18	-28.63	47.69	19.07	12.61	21.29	18	0.20
19	12.31	31.78	44.08	28.04	19.16	19	0.11
20	6.62	21.77	28.40	17.17	12.95	20	0.05
21	-7.49	29.57	22.07	16.30	12.50	21	0.03
22	-9.97	33.06	23.09	18.37	26.07	22	0.00
23	-6.41	32.22	25.82	23.63	25.07	23	0.00
P	0.371	**0.021**	0.0554	**0.011**	0.059	**P1-5**	**68.14**

IV. Discussion

Lifting Duration

Maternal subjects spend a slightly longer lifting time (3.61s compare with 3.28 seconds), however the difference was not statistically significant.

Maternal subjects lifted with an increased base of support and at a lower speed. This is possibly a strategy maternal subjects use to maintain stability and achieve a smooth lifting approach to minimise biomechanical stresses.

Lifting Kinematics

In the sagittal plane, the pelvis in maternal subjects has a slight anteriorly increased range compared with the control subjects throughout the lifting and lowering phase. Maternal subjects had a slight decrease in the hip range compared with the control subjects. The timing of the first peak is delayed with a significant lower hip extension in maternal subjects. However, in the control group, the maximum hip flexion is significantly higher in the lowering phase with a significant lower range of motion in the lowering phase.

The results at the knee showed that maternal subjects had an increased knee flexion. When holding the box in standing, maternal subjects locked their knees in a slight hyper-extension range. Similarly, control subjects employed the same strategy, but with the higher peak knee flexion occur in the lowering part.

At the ankle, maternal subjects had an increase in ankle dorsiflexion when compared with control subjects. Both the maximum ankle dorsiflexion and range of motion in maternal subjects were statistically higher in both the lifting and lowering phase.

On contrary to this Sinnerton et al. [11] reported that the performance of lifting tasks remained unchanged in pregnant women. The difference is probably due to their results taken from earlier stage of pregnancy (at 18-20 weeks of gestation compared with 32-38 weeks in the present study).

Lifting Kinetics

In the sagittal plane kinetics, the maternal subjects had a prolonged hip extensor moment throughout the lifting phase, which correlates to the lack of hip extension in the kinematics. They also lacked the hip flexor moment in the lifting to lowering transition phase. At the knee, the maternal subjects had an increase in knee extensor moment that correlates to the lack of knee extension during lifting. At the ankle, maternal subjects lack the plantar flexion moment range. The kinetic results from this study concurred with other qualitative studies [12, 13] such that pregnant women assume many awkward postures and with muscle weakness or overuse, some daily tasks such as lifting will be difficult. Nichols and Grieve [12] reported that pregnant women

identified picking up objects from the floor, desk work, ascending stairs, driving and getting in and out of cars as some of the most difficult activities to perform. Cherry [13] reported that in pregnancy workers, health complaints were systematically related to job postures and physical work demands, including prolonged standing postures, twisting of the trunk and lifting weights.

Principal Component Analysis

The first five Principal Component Coefficients (PCCs) accounted for 68.14% of the total variability (see table 3). From the first three PCCs, a major contribution to differences between maternal and control subjects related to the hip and knee moment; and the sagittal kinematics were found. Wrigley and colleagues [7] found five PCs capturing kinematics associated to the control and placement of a box on the shelf and the timing of the sagittal extension moment. Khalaf et.al [9] reported that higher PCCs are required to represent velocity and acceleration and joint moments . Our results showed that maternal subjects had a slower lifting time, but neither statistically significant differences nor significant contributions from the PCCs were found. A further analysis should compare the difference between the lifting and lowering phases.

V. Conclusion

Using principal component analysis, we were able to identify different lifting kinematics and kinetics parameters in pregnant subjects and important biomechanical differences when compared with the control group. Future investigations on lifting capacity during pregnancy should also include other aspects of lifting such as different lifting weight and speed, as well as coordination between the trunk and hip and between the hip and knee kinematics.

Acknowledgement

TC Nguyen is supported by the National Health and Medical Research Council's Dora Lush Biomedical Postgraduate Scholarship.

References

1. MacEvilly M and B. D, *Back pain and pregnancy: a review.* Pain, 1996. **64**: p. 405-414.
2. Chau, T., A review of analytical techniques for gait data. Part 1: fuzzy, statistical and fractal methods. Gait & Posture, 2001. **13**(1): p. 49-66.
3. Joliffe, I., *Principal component analysis*. 1986, New York: Springer-Verlag.
4. Olney, S., M. Griffin, and I. McBride, *Multivariate Examination of Data from Gait Analysis of Persons with Stroke.* Physical Therapy, 1998. **78**(8): p. 814-828.
5. Yamamoto, S., et al., Quantitative gait evaluation of hip diseases using principal component analysis. Journal of Biomechanics, 1983. **16**(9): p. 717-726.
6. Sadeghi, H., et al., Principal component analysis of the power developed in the flexion/extension muscles of the hip in able-bodied gait. Medical Engineering & Physics, 2000. **22**(10): p. 703-710.
7. Wrigley, A.T., et al., Differentiating lifting technique between those who develop low back pain and those who do not. Clinical Biomechanics., 2005. **20**(3): p. 254-63.
8. Wrigley, A.T., et al., *Principal component analysis of lifting waveforms.* Clinical Biomechanics., 2006. **21**(6): p. 567-78.
9. Khalaf, K.A., et al., Feature extraction and quantification of the variability of dynamic performance profiles due to the different sagittal lift characteristics. IEEE Transactions on Rehabilitation Engineering., 1999. **7**(3): p. 278-88.
10. Daffertshofer, A., et al., *PCA in studying coordination and variability: a tutorial.* Clinical Biomechanics, 2004. **19**(4): p. 415-428.
11. Sinnerton, S., et al. Weight gain and lifting during pregnancy. in Proceedings of the Annual Conference of the Ergonomics Society. 1993. Scotland.
12. Nicholls, J. and D. Grieve, *Performance of physical tasks in pregnancy.* Ergonomics, 1992. **35**: p. 301-311.
13. Cherry, N., Physical demands of work and health complaints among women working late in pregnancy. Ergonomics, 1987. **30**: p. 689-701.

Author: Tam C. Nguyen
Institute: South Australian Movement Analysis Centre
Street: Daws Road
City: Daw Park, SA5041
Country: Australia
Email: Tam.Nguyen@health.sa.gov.au

Evaluation of Anterior Tibial Translation and Muscle Activity during "Front Bridge" Quadriceps Muscle Exercise

M. Sato[1,2], S. Inoue[1], M. Koyanagi[3], M. Yoshida[3], N. Nakae[4], T. Sakai[5], K. Hidaka[6] and K. Nakata[7]

[1]Department of Rehabilitation, Osaka University Hospital, Suita, Japan
[2]Graduate School of Biomedical Engineering, Osaka Electro-Communication University, Shijonawate, Japan
[3]Department of Physical Therapy, Osaka Electro-Communication University, Shijonawate, Japan
[4]Department of Rehabilitation, Toyonaka-Watanabe Hospital, Toyonaka, Japan
[5]Department of Rehabilitation, Shijonawate Gakuen University, Shijonawate, Japan
[6]Division of Radiology, Department of Medical Technology, Osaka University Hospital, Suita, Japan
[7]Department of Orthopaedics, Osaka University Graduate School of Medicine, Suita, Japan

Abstract — **In a postoperative rehabilitation program following anterior cruciate ligament (ACL) reconstruction surgery, it is most important to avoid exerting excessive stress on the reconstructed graft. We have been using a quadriceps muscle exercise, "front bridge" which is carried out in the prone position.**

[Purpose] To analyze anterior tibial translation and quadriceps muscle activity during "front bridge" exercise.

[Materials and Methods] Anterior displacement of the tibia were measured in two patients with ACL insufficiency during two kinds of front bridge exercises which place a fulcrum on the proximal (P-FB) and distal (D-FB) lower leg

Muscular activity during P-FB and D-FB was also measured in nine healthy volunteers using electro-myography.

[Results] From 30 to 0-degree of knee angle, the P-FB did not exerted anterior translation of the tibia in involved knees compared to that in uninvolved ones. Muscle activity of P-FB exercise was less than that of D-FB exercise even though muscle activity on P-FB exercise was larger than 60%MVC.

[Discussion] The anterior tibial translation by quadriceps femoris muscular activity and the effects of gravity in the prone position was prevented by the reaction force produced from the proximal fulcrum on the lower leg. Because P-FB showed more than 60%MVC muscle activity, it was thought that the P-FB had the strengthening effect of the quadriceps femoris muscle. These results suggest that the front bridge exercise which places a fulcrum on the proximal lower leg is effective exercise for quadriceps femoris muscle training with safe following ACL reconstruction surgery.

[Conclusion] The P-FB displayed more posterior tibial position than D-FB in extension position. Muscle activity of P-FB exercise was less than D-FB exercise. And also P-FB exercises had the strengthening effect of the quadriceps femoris muscle.

Keywords — **anterior cruciate ligament (ACL), anterior tibial translation, fluoroscopy, exercise, quadriceps**

I. Introduction

Anterior cruciate ligament (ACL) injury is the most common sports injury of the knee. Because this ligament has little capacity for spontaneous healing, reconstruction surgery of ACL is frequently chosen as a treatment option. In postoperative rehabilitation following surgery, it is most important to avoid exerting excessive stress on the reconstructed graft. In addition, it is also important to restore the strength as well as stability of the knee. The strength of the quadriceps muscle is indispensable for sports activity and it is necessary to strengthen it in order to perform sports with safe.

Strain on the ACL increases with extension, and contraction of the quadriceps femoris exerts an anterior shear-force on the knee [1]-[3]. Since training of the quadriceps femoris muscle near the extension position produces great stress on the reconstructed graft, it should be avoided in the immediate postoperative phase[4], [5], resulting delayed recovery from muscle weakness after operation [6], [7].

In order to perform safe training of the quadriceps femoris muscle near the extension position at an earlier postoperative phase, we developed a "front bridge" exercise with proximal fulcrum to prevent anterior displacement of the tibia (Fig. 1). This front bridge is a knee extension exercise carried out in the prone position.

The purpose of this study was to assess the anterior tibial translation and quadriceps muscle activity during "front bridge" quadriceps muscle exercise.

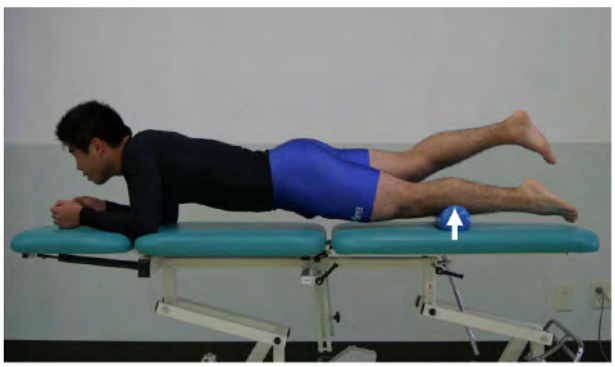


Fig. 1 "Front bridge" quadriceps muscle exercise with proximal fulcrum

Chwee Teck Lim, James C.H. Goh (Eds.): ICBME 2008, Proceedings 23, pp. 1892–1895, 2009
www.springerlink.com

II. Materials and Methods

A. Experiment 1; Measurement of tibial position on front bridge exercises

Subjects were two patients with ACL insufficiency: case A was male (41 years old, 167cm, 85kg), and case B was female (28 years old, 170cm, 58kg).

They performed two kinds of front bridge exercises. One of the exercises was front bridge placing a fulcrum on the distal lower leg (D-FB). Another of exercises was front bridge placing a fulcrum on the proximal lower leg (P-FB).Each exercises extended the knee from 30-degree of flexion to full extension. All exercises were carried out on the involved and uninvolved sides.

Lateral views of X-ray for the knee joint were taken during exercise (Allura Xper FD20, Philips Co.). The position of the tibia at 0, 10, 15 and 30 degree of knee flexion in relation to the femur was measured according to the method of Franklin et al [8].

B. Experiment 2: Measurement of the muscular activity during front bridge

Subjects were nine healthy persons (one female and eight males, 24.4±7.1 years old, 173.7±6.0 cm, 63.8±5.6 kg) without history of knee injury. They performed two kinds of front bridge (D-FB and P-FB) exercises, maintaining the knee in the extension position for 5 seconds in each task.

The muscle activities of the rectus femoris, vastus lateralis, and vastus medialis for 3 seconds were analyzed using an EMG system and software (Myosystem1200 and MyoResearch: Noraxon USA Inc., Scottsdale, AZ, USA) with a sampling rate of 1080 Hz and digitized to integrated EMG (IEMG) in each of the 2 tasks. The root mean square of IEMG was obtained for 3 second within the 5-second analysis period, omitting the first and the last seconds. EMG was normalized relative to the values obtained during maximum voluntary isometric contraction (% MVC) at 60-degree of knee flexion.

III. Results

A. Experiment 1: Measurement of anterior translation of the tibia on knee extensor training

The position of the tibia for each task is shown in Table1.

P-FB exercise did not exert anterior translation of the tibia in the involved knee compared to that in the uninvolved ones from 30 to 0-degree of knee flexion (Fig. 3). When the positions of the tibia in the uninvolved knees were compared among the two exercise tasks, P-FB exercise showed more posterior position of tibia (Fig. 4). D-FB exercise demonstrated anterior translation of the involved knee more than those of the uninvolved ones.

Table 1 Tibia translation

[mm]

			knee angle 30°	15°	10°	0°
Case A	D-FB	involved	2.1	7.0	6.6	1.8
		uninvolved	1.8	1.8	4.0	4.4
	P-FB	involved	-6.7	-1.6	-0.9	-1.3
		uninvolved	-5.0	0.8	3.4	2.1
Case B	D-FB	involved	5.5	6.0	6.6	5.8
		uninvolved	6.5	6.5	6.4	4.4
	P-FB	involved	-7.1	-5.0	-2.1	0.0
		uninvolved	-6.2	-3.8	-1.8	0.6

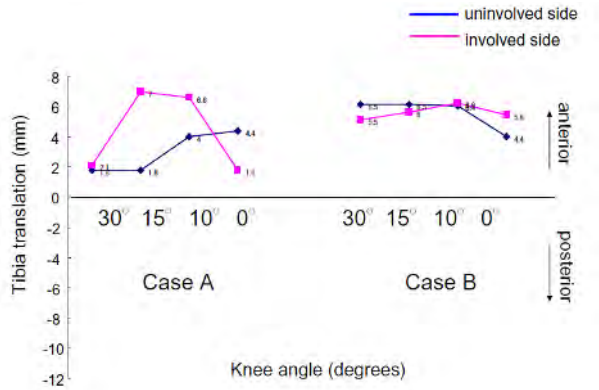


Fig. 2 Tibia translation during front bridge of distal fulcrum

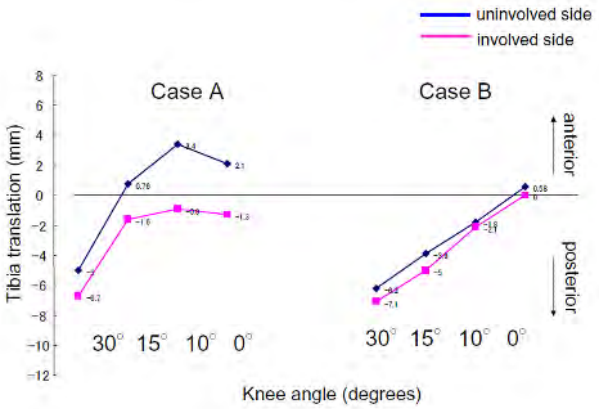


Fig.3 Tibia translation during front bridge of proximal fulcrum

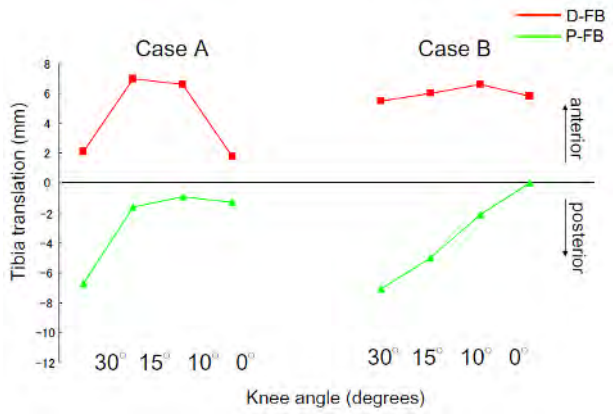


Fig. 4 Tibia translation of involved side during each exercise

B. Experiment 2: Measurement of the muscular activity during front bridge

Muscle activities in the D-FB and P-FB exercises are shown in Table 2 and Fig. 5.

Muscle activities of vastus medialis and vastus lateralis in P-FB exercise were larger than 70% of MVC, although those in D-FB exercise were larger than P-FB exercise.

Table 2 Muscle activities during exercises

	Vastus medials		Vastus laterals		Rectus femoris	
	Mean [%MVC]	SD	Mean [%MVC]	SD	Mean [%MVC]	SD
front bridge of distal fulcrum (D-FB)	91.82	21.67	96.70	13.33	78.50	32.90
front bridge of proximal fulcrum (P-FB)	78.59	25.22	70.00	16.80	53.05	20.65

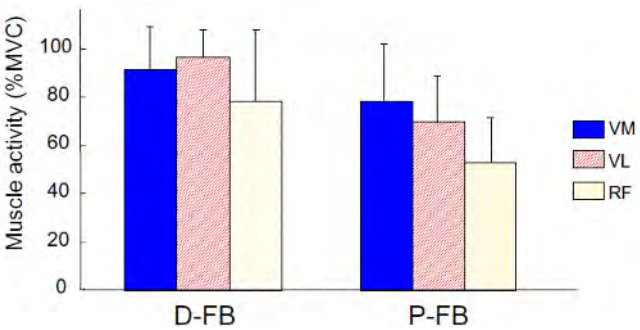


Fig. 5 Muscle activity during exercise

IV. Discussion

In the prone position, because gravity helps the tibia to move anteriorly and generates anterior shear-force of the knee joint, causing the risk for the knees after ACL reconstruction surgery. (Fig.6 left)

Although FB exercise was performed in the prone position, the position of the tibia in P-FB exercise was the more posterior than P-FB exercise and uninvolved knee, indicating that the anterior displacement of the tibia was braked by the reaction force (posterior shear-force) produced from the proximal fulcrum on the lower leg (Fig. 6).

These results showed that the front bridge with "proximal fulcrum" was a safe training method following the ACL reconstruction surgery.

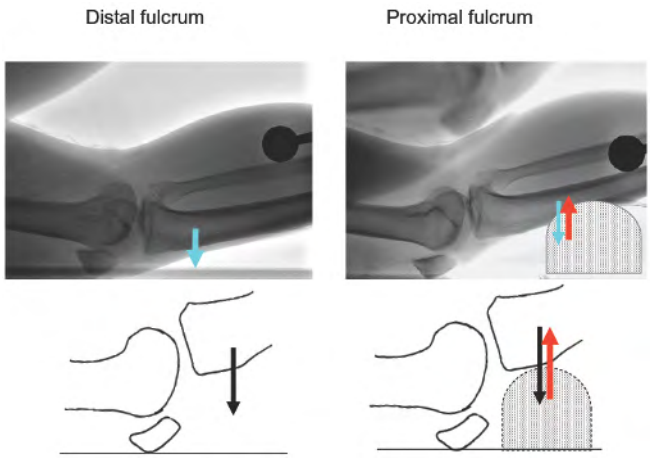


Fig. 6 The effect of proximal reaction force

Muscle activity of the knee extensors exceeded 70% of MVC except for the rectus femoris during P-FB exercise. Since strength training exceeded 60% of MVC muscle activity is effective, the front bridge exercise appears to be suitable as the strength training method for the vastus muscle group.

V. Conclusions

The “front bridge” quadriceps muscle exercise using a proximal fulcrum displayed more posterior tibial position than uninvolved in knee extension position. Muscle activity of front bridge exercise of proximal fulcrum was less than front bridge exercise of distal fulcrum exercise. And also front bridge exercise of proximal fulcrum had the strengthening effect of the quadriceps femoris muscle.

REFERENCES

1. Sato N, Higuchi H, Terauchi M et al. (2005) Quantitative evaluation of anterior tibial translation during isokinetic motion in knees with anterior cruciate ligament reconstruction using either patellar or hamstring tendon grafts. Int Orthop 29:385-389
2. Higuchi H, Terauchi M, Kimura M et al (2002) Characteristics of anterior tibial translation with active and isokinetic knee extension exercise before and after ACL reconstruction. J Orthop Sci 7:341-347
3. Howell SM (1990) Anterior tibial translation during a maximum quadriceps contraction: is it clinically significant? Am J Sports Med, 18:537-538
4. Chiang AL, Mote CDJ (1993) Translations and rotation across the knee under isometric quadriceps contraction," in Skiing Trauma and Safety: Ninth International Symposium. American Society for Testing and Materials, R.J. Johnson, C.D.J. Mote, J. Zelcer, Ed. ASTM International, West Conshohocken
5. Aune AK, Cawley PW, Ekeland A (1997) Quadriceps muscle contraction protects the anterior cruciate ligament during anterior tibial translation. Am J Sports Med 25:187-190
6. Ikeda H, Kurosawa H, Kim SG (2002) Quadriceps torque curve pattern in patients with anterior cruciate ligament injury. Int. Orthop 26:374-376
7. Hiemstra LA, Webber S, MacDonald PB et al (2004) Hamstrings and quadriceps strength balance in normal and hamstring anterior cruciate ligament-reconstructed subjects. Clin J Sport Med 14:274-280
8. Franklin JL, Rosenberg TD, Paulos LE et al (1991) Radiographic assessment of instability of the knee due to rupture of the anterior cruciate ligament. A quadriceps-contraction technique. J Bone Joint Surg Am 73:365-72

Author: Mutsumi SATO
Institute: Department of Rehabilitation, Osaka University Hospital
Street: 2-15 Yamadaoka
City: Suita
Country: Japan
Email: mutsumi@hp-rehab.med.osaka-u.ac.jp

Coupled Autoregulation Models

T. David[1], S. Alzaidi[1], R. Chatelin[1] and H. Farr[1]

[1] Centre for Bioengineering, University of Canterbury, Christchurch, New Zealand

Abstract — **Cerebral tissue requires a constancy of both oxygen and nutrients (notably glucose). During periods of pressure variation, which occur normally as well as in cases of hypo- and hyper-tension, the body's cerebral autoregulation mechanism cause the arterioles to vasoconstrict/dilate, thus maintaining a relatively constant cerebral blood flow. A non-dimensional representation of autoregulation coupled with an asymmetric binary tree algorithm simulating the cerebro-vasculature has been developed. Results are presented for an autoregulation algorithm of the cerebro-vasculature downstream of the efferent arteries, in this case the middle cerebral artery. These results indicate that due to the low pressures found in the arteriolar structure the myogenic mechanism based on the increased open probability due to pressure of stretched activated ion channels does not provide enough variation in the vascular resistance to support constancy of blood flow to the cerebral tissue under variable perfusion pressure. Results show that under variations in pressure the metabolic mechanism provides sufficient variation peripheral resistance to accommodate constancy of cerebral blood perfusion.**

Keywords — **autoregulation, blood flow.**

I. Introduction

Cerebral tissue requires a constancy of both oxygen and nutrients (notably glucose). During periods of pressure variation, which occur throughout the normal day as well as in cases of pathological hypo- and hyper-tension, the body's cerebral autoregulation mechanism cause the arterioles to vasoconstrict/dilate in response to changes in cerebral perfusion pressure over a certain range, thus maintaining a relatively constant cerebral blood flow. These effects are of particular importance when investigating how blood is redistributed not only via the circle of Willis but throughout the cerebral tissue. It should be noted that there have been a number of cerebral autoregulation models proposed [1, 2], including models incorporated with a circle of Willis [3-5]. However, the combination of an autoregulation model with a fully populated arterial tree able to regulate dynamically remains a relatively unexplored field.

Considerable research effort has been expended in furthering the understanding of how an artery alters its radius and the associated chemical pathways. Particular interest has focused on the myogenic mechanism where the systemic blood pressure exerts an influence on vascular smooth muscle. Fundamental studies were carried out by Harder [6, 7]. Less research has been done for the metabolic condition where variations in pH and CO_2 are considered to be the prime movers for dilation/contraction of the small arterioles deep in the vascular tree. The most comprehensive study of blood flow control has been that of [8], however even in this case several important constants remain unknown making the model somewhat constrained.

The present model uses previous work by Gonzalez-Ferrandez and Ermentrout [9] to closely couple a myogenic model and a ne metabolic model of cerebral autoregulation with a representation of a vascular tree taken from the work of Steele et al [10]. In order to allow all parts of the tree to vary in its arterial radius (and hence resistance) the myogenic and metabolic models are non-dimensionalised enabling a single algorithm to be utilised. The work shows that in order to replicate the well-known variation of peripheral resistance with pressure the metabolic model is by far the dominant mechanism, so much so that the myogenic mechanism seems to hardly play a role.

II. Methods

The creation of vascular tree is based on the binary algorithm of Steele et al [10]. The parent vessel bifurcates in to two daughter arteries according to a phenomenological law described in [10]. The present model utilizes the early work of Kamiya and Togawa [11]which allows an evaluation of the angle between parent and daughter arteries. Such that

$$\cos\theta_1 = \frac{r_p^4 + r_{d1}^4 - r_{d2}^4}{2r_p^2 r_{d1}^2}; \quad \cos\theta_2 = \frac{r_p^4 + r_{d2}^4 - r_{d1}^4}{2r_p^2 r_{d2}^2}; \quad (1)$$

Figure 1 shows the basic construction.

In order to map the binary tree into a 3D space we randomise the normal vector of the plane defined by the two daughter artery vectors. This randomization allows for "forcing" the arteries to grow in particular directions as used by Schreiner et al [ref Schreiner]. The tree is terminated when the arterial size reaches a lower limit and we consider the end terminals to be connected to a network of capillaries, each of which is modeled by Krogh cylinder. For our present work the binary tree can be made from up to 1,000,000 segments with approximately 500,000 terminal arteries.

Chwee Teck Lim, James C.H. Goh (Eds.): ICBME 2008, Proceedings 23, pp. 1896–1899, 2009
www.springerlink.com

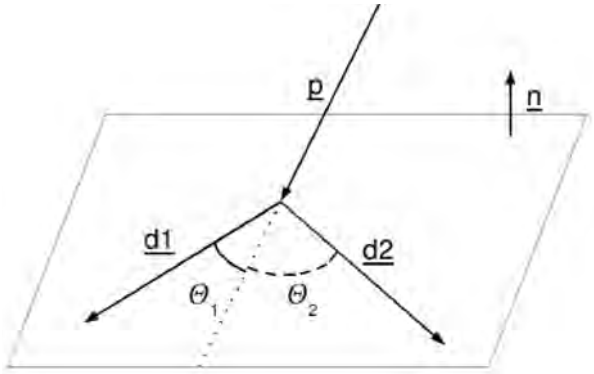


Figure 1

Passing "up" and "down" the tree structure determines the peripheral resistance of the vascular bed by assuming Poiseuille flow through the arterioles.

The myogenic model uses the work of Ferrandez-Gonzalez and Ermentrout [9] to associate systemic blood pressure with the opening of calcium activated ion channels. This produces variations in cytosolic Ca^{2+} allowing MLCK (myosin light chain kinase) activation and subsequent smooth muscle contraction. We have introduced extra equations to model the consequencial production of eNOS from both Ca^{2+} variations and wall strear stress values . We have non-dimensionalised the resulting equations so as to be able to implement this myogenic response over all arteries in the vascular tree. The membrane potential is given by

$$C\frac{dv}{dt} = -\sum_{i}^{N} g_i\left(v - v_i\right) \tag{2}$$

The g_i 's are ion channel conductances and v_i Nernst potentials.

Ca^{2+} is given by

$$\frac{dCa^{2+}}{dt} = -\rho\left(m_\infty\left(v-1\right) - kCa^{2+}\right) + \gamma F\left(\tau_w\right) \tag{3}$$

$F\left(\tau_w\right)$ is a strain energy function varying with wall shear stress τ_w, m_∞ the equilibrium open channel probability for Ca^{2+}, and k a reverse reaction rate. A similar equation is written for eNOS.

Although selective ion channels in the smooth muscle cell of the cerebro-vasculature respond to variations in both CO2 and pH our initial mode for the metabolic response uses the simple assumption that the set of arterioles feeding the capillary bed are in close proximity to the venous return. Excess carbon dioxide in the venules is diffused to the arterioles and induces a relaxation/contraction of the arteriolar radius thus allowing increased/decreased blood flow to convect away carbon dioxide and hence maintain the correct CO2 concentration. This model was also used in the 1D models of Alastruey et al. [12].

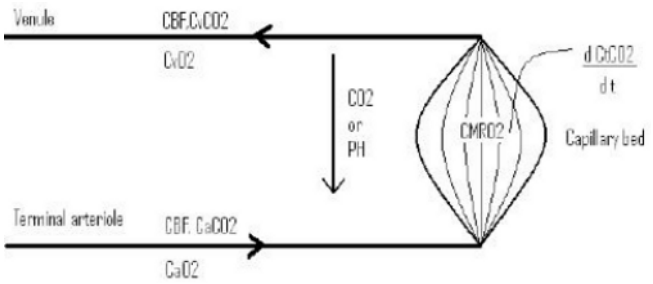


Figure 2

Figure 2 shows the proximity of arteriole and venule connected by the capillary bed.

Equation (4) represents a conservation equation where the rate of change of carbon dioxide is balanced by the production (due to metabolism) and that convected away by the blood flow.

$$\frac{dCO_{2,tissue}}{dt} = CMRO_2 + CBF\left(CO_{2,artery} - CO_{2,tissue}\right) \tag{4}$$

where $CO_{2,tissue}$ is the tissue concentration of carbon dioxide, CO2;artery is the arterial concentration of carbon dioxide (assumed to be 0.49ml/ml) CMRO2 is the cerebral metabolic rate of oxygen consumption (assumed to be a constant 0.035ml/g/min for all parts of the brain), which due to the stoichiometry of the aerobic metabolism in the brain tissue, is equal to the cerebral metabolic rate of carbon dioxide production. CBF is the flow rate in the terminal artery and thus entering the capillary bed. We use a reverting differential equation for the radius of the arteriole given by

$$\frac{dr}{dt} = G\left(CO_{2,sp} - CO_2\right) \tag{5}$$

here $CO_{2,sp}$ is the solution to the homogeneous equation for $CO_{2,tissue}$ (equation (4)).

CMRO2, the metabolic rate of oxygen consumption is determined by a space-time partial differential equation given by

$$\frac{\partial C}{\partial t} = D\left(\frac{\partial^2 C}{\partial r^2} + \frac{1}{r}\frac{\partial C}{\partial r}\right) - \Psi\left(C\right) \tag{6}$$

modelling convection of blood flow through the capillary and oxygen diffusion into the tissue of the Krogh cylinder. $\Psi(C)$ is the depletion rate of oxygen in the cerebral tissue. Boundary conditions at the capillary/tissue surface are formed by solving the equation of Blum [ref Blum]. This provides a value of $CMRO_2$ which is a function of the cerebral blood flow in the capillary.

Equations 2-5 are solved using a standard Runge-Kutta adaptive time-step algorithm whilst equation 6, due to it's non-linearity uses an implicit Crank-Nicholson scheme. The binary tree mapping is also non-linear in determining the daughter angles and is solved at each bifurcation by a Newton-Raphson algorithm with an analytical Jacobian.

III. Results

Figure 3 shows a representation of a binary tree mapped to 3D space. The number of terminal segments is small compared to those used for the Figures 4 and 5.

Figure 4 demonstrates the relationship between systemic pressure plotted and normalized cerebral blood flowrate for the myogenic model. This is a representation of the blood flow required to perfuse the brain tissue supported by the middle cerebral artery. The plot shows that although the myogenic autoregulation model does provide some change from the no autoregulation case, it does not successfully emulate the ideal observed autoregulatory response.

For comparison, the no-autoregulation case and the ideal autoregulation response are also shown. Our analysis of the pressure distribution in the binary vascular tree shows that the smaller arterioles of this arterial tree contribute the vast majority of the total resistance of the tree, as expected.

These smaller arterioles have very low pressures, and according to the myogenic autoregulation model only very small changes occur at these low pressures, indeed these changes could well be dilatory! The percentage change of the smaller arterioles (in the range of 10 and 100 microns) that is required to reach the ideal autoregulation profile is of the order of 30%. This change cannot be induced using the current myogenic autoregulation model.

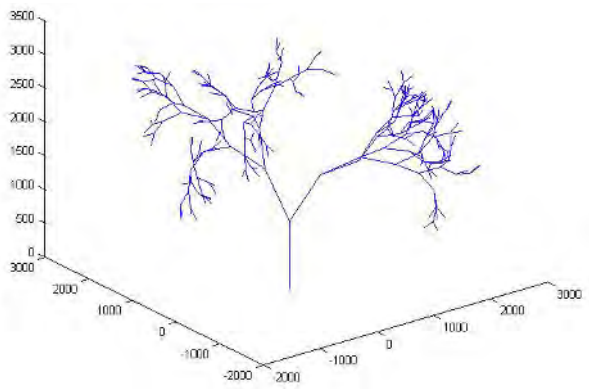


Figure 3

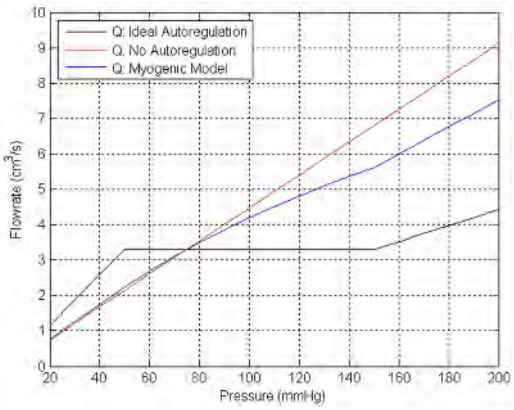


Figure 4

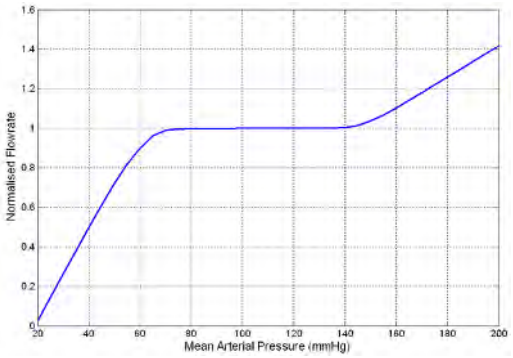


Figure 5

The metabolic algorithm described above is now substituted for the myogenic model where the look-up table contains values of radius and pressure evaluated as before for large times so as to reach asymptotically stable values. For each pressure value ranging from zero to 200 mmHg and for each pressure value in the tree the radii of segments, where these radii lie between 10 and 100 microns, are changed in an iterative manner (using the look-up table previously evaluated from equations 4 and 5 until a converged value of the total peripheral resistance is found. Segments of the tree with radii outside of the range given above are unchanged. This algorithm has been used to yield the following results. Figure 5 plots physiological perfusion pressure vs the total normalised flow rate in the tree. This flow rate is normalised to that known value ($2.85\,mLs^{-1}$) required to perfuse

the volume of the brain supported by the middle cerebral artery at "normal" physiological conditions (systemic pressure of 100 mmHg). As can be seen the metabolic autoregulation model provides the correct variation in peripheral resistance to ensure constancy of flow rate to the cerebral tissue without myogenic support.

IV. Conclusions

By developing a non-dimensional representation of the arterial wall model of Gonzalez-Ferrandez and Ermentrout and the asymmetric binary tree algorithm of (Oufsen3) results are presented for an autoregulation algorithm of the cerebro-vasculature downstream of the efferent arteries, in this case the middle cerebral artery. These results indicate that due to the low pressures found in the arteriolar structure the myogenic mechanism does not provide enough variation in the vascular resistance to support constancy of blood flow to the cerebral tissue under variable perfusion pressure. A metabolic model has been developed under the assumption of close proximity between venules and the vascular tree at the arteriolar level. Results show that the metabolic mechanism seems to be the dominant mechanism for cerebral autoregulation.

Acknowledgment

This work was partially supported by the neurological Foundation of New Zealand and a Summer Scholarship from the University of Canterbury.

References

1. Olufsen, M.S., A. Nadim, and L.A. Lipsitz, *Dynamics of cerebral blood flow regulation explained using a lumped parameter model.* Am J Physiol Regul Integr Comp Physiol, 2002. **282**(2): p. R611-622.
2. Ursino, M. and M. Giulioni, *Quantitative assessment of cerebral autoregulation from transcranial Doppler pulsatility: a computer simulation study.* Medical Engineering and Physics, 2003. **25**(8): p. 655-666.
3. Moore, S.M., et al., *3D Models of Blood Flow in the Cerebral Vasculature.* Journal of Biomechanics, 2006. **39**(8): p. 1454-1463.
4. Moore, S. and T. David, *Auto-regulated Blood Flow in the Cerebral-Vasculature.* Journal of Biomechanical Science and Engineering (JSME), 2006. **1**(1): p. 1-14.
5. Moore, S.M., et al., *One-Dimensional and Three-Dimensional models of Cerebrovascular Flow.* Journal of Biomechanical Engineering, 2005. **127**: p. 440-449.
6. Harder, D.R., *Pressure-dependent membrane polarisation in cat middle cerebral artery.* Circulation Research, 1984. **55**: p. 197-202.
7. Harder, D.R., *Pressure induced myogenic activation of cat cerebral arteries is dependent on intact endothelium.* Circulation Research, 1987. **60**: p. 102-107.
8. Banaji, M., et al., *A physiological model of cerebral blood flow control.* Mathematical Biosciences, 2005. **194**(2): p. 125-173.
9. Gonzalez-Ferrandez, J.M. and B. Ermentrout, *On the origin and dynamics of the vasomotion of small arteries.* Mathematical Biosciences, 1994. **119**: p. 127-167.
10. Olufsen, M.S., M.S. Steele, and C.A. Taylor, *Fractal Network model for simulating abdominal and lower extremity blood flow during resting and exercise conditions.* Computer Methods in Biomechanics and Biomedical Engineering, 2007. **10**: p. 39-51.
11. Kamiya, A. and T. Togawa, *Optimal Branching Structure of the Vascular Tree.* Bulletin of Mathematical Biophysics, 1972. **34**: p. 431-438.
12. Alastruey, J., et al., *Reduced modelling of blood flow in the cerebral circulation: Coupling 1-D, 0-D and cerebral auto-regulation models.* Int. Jour. Num. Methods Fluids, 2008. **56**: p. 1061-1067.

Author: Tim David
Institute: Centre for Bioengineering, University of Canterbury
Street: Creyke Road
City: Christchurch
Country: New Zealand
Email: tim.david@canterbury.ac.nz

Measurement of Changes in Mechanical and Viscoelastic Properties of Cancer-induced Rat Tibia by using Nanoindentation

K.P. Wong[1], Y.J. Kim[1] and T. Lee[1]

[1] Division of Bioengineering, National University of Singapore, Singapore

Abstract — **The aim of this research is to evaluate the changes in mechanical and viscoelastic properties of cancer induced rat tibias and to establish a correlation between viscosity and elastic modulus. Nanoindentation was conducted up to a magnitude of force equivalent to 500 nm with a load rate of 20 nm/s. After a 30-seconds peak hold time, the indenter was unloaded. A total of 30 indentations were made, each at least 30 μm away from an adjacent indentation surrounding canaliculae in the bone structure. Creep displacement-time curve was fitted using the following equation: $h^2(t)=(\pi/2)P_0 cot\alpha[(1-exp(-tE/\eta))/E]$. Viscosity was computed based on the curve fitting of creep displacement by non-linear regression. Cancer-induced tibias showed significantly lower indentation viscosity and modulus than sham-operated ones ($p<0.05$). Positive linear relationships were found between indentation modulus and viscosity for both cancer-induced and sham-operated tibias. However, there is no significant difference in the correlation between cancer-induced and sham-operated rat tibias ($p>0.05$).**

Keywords — **Elastic modulus, Hardness, Viscosity, Rat tibia, Nanoindentation**

I. Introduction

Bone metastases are bone diseases that cause an increased morbidity, mortality and medical expenses worldwide. They occur in approximately 70% of patients with an advanced breast or prostate cancer and 15-30% of patients with a carcinoma of the lung, colon, stomach, bladder or kidney. Furthermore, once tumor had metastasized to bone, they correspond to an advanced stage of malignancies and are usually incurable. [1] However, cancer cells do not directly caused osteolysis. They enhance osteoclast activities, thus in turn increase bone resorption, leading to osteoporosis and reduction of bone structural properties.

As a biological material, human bone exhibits a complex microstructure and microcomponents, which results in complicated mechanical properties. Viscoelasticity is one of these properties. Because of the viscoelastic nature of collagen fibres in the bone matrix, bone itself has remarkable viscoelasticity. Thus, bone can also exhibit a viscoelastic response which is commonly termed "creep". [2] Creep is a slow, progressive deformation of a material under constant stress. Creep processes occur in the steady-state loading of materials. In a creep experiment, the stress is suddenly raised to a constant level beginning at time zero, and the strain or displacement is measured of a function of time.

Traditionally, biomechanics has focused on examining the material and structural properties of living tissues, both in their normal and diseased states. This approach is primarily one of mechanics and is relevant to understanding the load bearing capacity of tissues. However, a bone at risk of fracture cannot simply be determined by the amount of bone that exists. Bone quality or fracture susceptibility is very important to precisely determine the bone's mechanical behavior. [3] Improved preventive and therapeutic strategies for skeletal diseases such as bone metastases rely on a better understanding of the lamellar mechanical properties of bone.

Nanoindentation is an emerging technique that is capable of evaluating bone's quasi-static and dynamic mechanical properties on extremely small volumes of tissue. With nanoindentation, it is possible to measure properties of the bone at the micron and sub-micron levels, thus study the properties of bone microstructural components having dimensions of only a few microns or less. [4] In a nanoindentation test, a creep phenomenon is usually observed as an increase in depth during a hold period at maximum load in the load-displacement data. The output parameters, including hardness and elastic modulus, are derived from the elastic response of the indented material to the applied load.

The aim of this research study is to establish a correlation between viscosity and the mechanical properties of bones by nanoindentation creep. The objective of investigating this relationship is to find an improved tool for predicting the risk of fractures in diseased and degenerative bone. The hypothesis was tested that the cancer-induced bones has lower mechanical and viscoelastic properties than normal bones.

II. Materials and Methods

A. Animals

8-10 week-old Sprague-Dawley male rats (SD rats) were randomly divided into two groups which are the control group and the cancer group. The control group received

Chwee Teck Lim, James C.H. Goh (Eds.): ICBME 2008, Proceedings 23, pp. 1900–1903, 2009
www.springerlink.com

only the sham operation with saline injected into the right femur. The cancer group had Walker Carcinosarcoma 256 (W256) cancer cells injected into the right femur via a hole drilled through the intercondylar notch. The cancer group rats received no treatment after surgery. At 30 days after the surgery, 3 rats from each group were euthanized in the carbon dioxide chamber.

B. Sample Preparation

The euthanized rats' tibia bones were harvested. At room temperature, bone marrow and soft tissue of the rat tibia bone specimens were removed thoroughly while taking care that the bone sample was not damaged. By mixing the resin and hardener for 2 minutes to minimize the formation of air bubbles, the bone samples were positioned vertically in the centre of the embedding mold and the resin and hardener mixture was poured over the bone sample. The sample was then left for 24 hours at room temperature to allow bonding of the resin to bone surface. The disposable mold was removed once the resin had cured. By using Isomet 1000 precision saw (Buehler Ltd, Lake Bluff, IL) with counterbalanced sliding load weight system, under constant irrigation, a 5mm of the rat tibia bone sample was sliced from the diaphyseal region perpendicular to the long axis of the tibia. A total of six samples were prepared and labeled respectively – 3rtc, 3lts, 4rtc, 4lts, 6ltc and 6rts.

C. Polishing

The embedded sample was metallographically polished to produce the smooth surface needed for nanoindentation testing. After being ground using silicon carbide abrasive papers of decreasing grit size (600, 800 and 1200 grit) under de-ionized water, the samples were polished on microcloths with finer grades of alumina powder of grit size 3µm, 1µm, and 0.25-0.05µm. Final polishing was on a plain microcloth under de-ionized water, after which the samples were ultrasonically cleaned to remove the particles and debris resulted from polishing. [4]

D. Calibration and Placement of Indentations

All nanoindentation tests were performed using a pyramidal Berkovich tip for MTS Nano XP nanoindenter (Nano Instruments Inc., Oak Ridge, TN. A line of indents was performed on a calibration sample of fused quartz to calibrate of the tip area function. [4] The prepared samples mounted on the magnetized stage. Indent locations were selected using the optical microscope mounted on the moving stage in parallel with the load sensing transducer. Indenting was conducted up to a magnitude of force equivalent to 500nm with a load rate of 20nm/s. After a 30-seconds peak hold time, the indenter was unloaded. A total of 30 indentations were performed in each sample. Each indent is made at least 30µm away from an adjacent indent surrounding canaliculae in the bone structure.

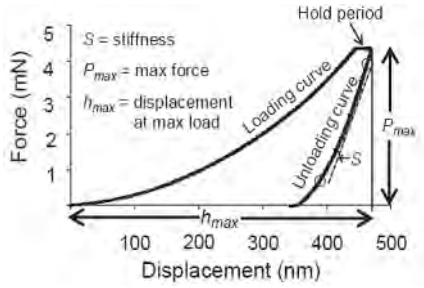


Figure 1: Load-Displacement Data

As seen in the plot in **Figure 1**, it presents a typical set of load-displacement data. After the initial loading, in which most of the plastic deformation occurs and hardness impression is formed, there is a hysteresis in the data, which indicates a non-negligible portion of the indentation displacement is viscoelastic. Creep was measured during a 30-seconds hold period at peak load for every indent in each sample. Creep displacement-time curve was fitted using the following equation (Equation 1),

$$h^2(t) = (\pi/2)\, P_0 \cot \alpha\, [\, (1-\exp(-tE/\eta))/E] \qquad (1)$$

where h(t) is indentation creep displacement as a function of time.

P_0 is the indentation peak force;

α is an equivalent cone semi-angle 70.3º to the face angle of the Berkovich indenter;

E is an elastic element of the Voigt model (GPa);

η is the indentation viscosity (GPaS).

This equation represented two elements of the Voigt model in which a spring and a dashpot are linked in parallel. The viscosity, η was computed based on each curve fitting by using the software SPSS for the non-linear regression analysis. A statistical student t-test was performed to compare the values of indentation modulus and viscosity between our own results values and data obtained from literature reviews.

III. Results

A summary of the elastic modulus(E) and viscosity(η) of the rat lamellar bone is represented in **Table 1**. Comparison was done between the nanoindentation modulus and viscosity between sham-operated group and cancer-induced group of rat tibia bones as shown in **Figure 2 and 3**, respectively. Linear regression of the elastic modulus and viscosity for

Table 1: Mean values of Elastic Modulus and Viscosity of rat tibia bones.

	Rat	Elastic Modulus (GPa)	Viscosity (GPaS)
Sham-Operated	3lts	14.42	86940.99
	4lts	18.85	112720.90
	6rts	20.22	129440.80
	Mean	17.83	109700.90
	ST DEV	3.03	21410.25
Cancer-Induced	3rtc	11.39	77462.23
	4rtc	14.16	82634.94
	6ltc	12.87	80611.96
	Mean	12.81	80236.38
	ST DEV	1.39	2606.73

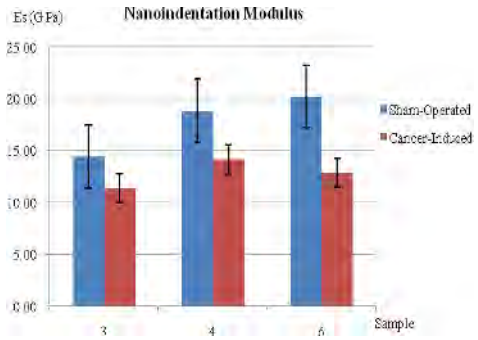


Figure 2: Comparison of nanoindentation modulus between sham-operated and cancer-induced bones.

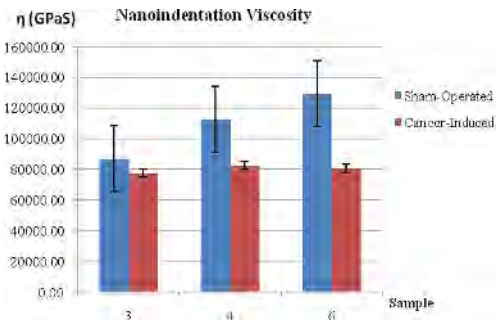


Figure 3: Comparison of nanoindentation viscosity between sham-operated and cancer-induced bones.

each group was considered separately and all together, in **Figure 4**.

Cancer-induced rat tibias showed significantly lower indentation modulus and viscosity than the sham-operated group of rat tibias (12.81±1.39 vs. 17.83±3.03 GPa for modulus and 80236.38±2606.73 vs. 109700.90±21410.25

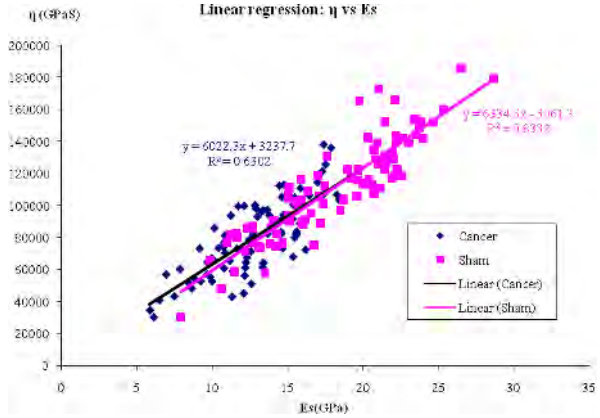


Figure 4: Linear regression relationship between indentation viscosity vs indentation modulus.

GPaS for viscosity, $p<0.05$ for both. Significant positive linear relationships were found between indentation modulus and indentation viscosity for sham-operated rat tibias ($R^2=0.83$, $p<0.05$) as well as for cancer-induced rat tibias ($R^2=0.63$, $p<0.05$). However, there is no significant difference in the correlation between the sham-operated and cancer-induced rat tibias ($p>0.05$) (Figure 4).

IV. Discussion

Nanoindentation technique has several advantages and is now widely used in material science for probing the mechanical properties of small microstructural features. The major benefit is from the accurate positioning capability and the high resolution load and depth-sensing capabilities which make it possible to study mechanical properties of finely structures where relatively small area need to be tested and measured. From analysis of nanoindentation load-displacement data, it is possible to derive values of elastic modulus and hardness.

In the present study, the elastic modulus, viscosity and hardness of the cancer-induced group tibia had shown significant difference with the sham-operated rat tibias. It is worth noting that the measurements may not be as accurate when only one data indentation point was made surrounding the canaliculi in each lamellar during the analysis, due to variations in properties within single lamellae. To take account of those variations, a total of thirty indentations in each specimen were made, with an average of 3-4 indention point surrounding different canaliculi, representing all portions of each lamellar.

In combination with the results of Bak et al. [5], the nanoindentation results obtained here suggest that the elastic modulus of sham-operated rat tibias are significantly greater

than the value of a normal non-fractured bones widely used, E=10.6GPa, obtained by mechanical testing. Some of this discrepancy may be due to the drying of the specimens prior to the nanoindentation testing. In previous study done by Hengsberger et al. , who found that drying increases bone's elastic modulus by as much as 55% [3,6,7]. Another question which arises is the extent to which embedding in epoxy affects the nanoindentation measurements. It is important to choose an embedding material appropriate for the specific bone under investigation. Measurements of bone hardness are sensitive to the modulus and viscosity of the embedding material [3,8]. Hence, to minimize this effect, indentations close to the bone-epoxy interface were not included in the data. In order to get further results with a higher accuracy, it should be possible that to make nanoindentation measurement on both wet and dry bone. But it seems unlikely that rat tibia can be studied without embedding.

To the best of our knowledge, the elastic modulus of cancer-induced rat tibia has not been measured previously. Our finding of a positive correlation between nanoindentation viscosity and modulus of rat tibia lamellar tissue agreed with previous observation from nanoindentation tests performed by Tang et al. [9]. Mulder et al. found that indenatation modulus is linearly related to the degree of mineralization. In general, bone properties will improve if calcium content is higher [10]. Therefore, the positive viscosity-modulus relationship found in the current study can be interpreted as an increase in viscosity is associated with an increase in the degree of mineralization of lamellar tissue of rat tibia.

We found that the nanoindentation viscosity of cancer-induced rat tibias is significantly lower than in the sham-operated group. This result indicates that cancer-induced bones are more responsible to time-dependent deformation of bone under a prolonged constant load. These findings also suggest that cancer-induced bones, simulation of the in-vivo bone metastases, have an increased inhomogeneity of creep deformation under constant load which may trigger damage at the interface and lead to degradation of mechanical stability of cancer bones [10].

V. Conclusion

Nanoindentation technique had been used to quantify hardness and elastic modulus of sham-operated and cancer-induced rat tibias. The viscosity of rat tibias was computed based on the curve fitting of creep displacement by non-linear regression of the nanoindentation results. Cancer-induced rat tibia bones showed significantly lower mechanical and viscoelastic properties than sham-operated bones, as hypothesized. Therefore, current results would be further used to evaluate the response of cancer-induced osteolysis to chemotherapeutic and anti-osteoporotic treatment for predicting risk of fractures in diseased bones.

References

1. Blouin S, Basle M F. (2005) Rat Models of bone metastases. Clin Exp Metastasis 22:605-614.
2. Fan Z, Rho J Y. (2002) Effects of viscoelasticity and time-dependent plasticity on nanoindentation measurement of human cortical bone. J Biomed Mater Res 67A:208-214.
3. Ozcivici E, Ferreri S, Qin Y, Judex. Determination of bone's mechanical matrix properties by. Methods in Molecular Biology, Vol.455: Osteoporosis.
4. Rho J Y, Zioupos P, Currey J D, Pharr G M. (1999) Variations in the individual thick lamellar properties within osteons by nanoindentation.
5. Bak B, Jensen K S (1992) Standardization of tibial fractures in the rat. Bone, 13, 289-295.
6. Hoffler C E, Guo X, Zysset P K. (2005) An application of nanoindentation technique to measure bone tissue lamellae properties. J Biomech Eng 127, 1046-1053.
7. Hengsberger S, Kulik A, Zysset P K. (2002) Nanoindentation discriminates the elastic properties of individual human bone lamellae under dry and physiological conditions. Bone 30, 178-184.
8. Rho J Y, Tsui T Y, Pharr G M. (1997) Elastic Properties of human cortical and trabecular lamellar bone measured by nanoindentation. Biomaterials 18, 1325-1330.
9. Tang B, Ngan A H, Lu W W. (2007) An improved method for the measurement of mechanical properties of bone by nanoindentation. J Mater Sci: Mater Med 18:1875-1881.
10. Kim D G, Huja S. Nanoindentation viscosity of osteonal bone matrix is associated with degree of mineralization.

Surface Conduction Analysis of EMG Signal from Forearm Muscles

Y. Nakajima[1], S. Yoshinari[1] and S. Tadano[2]

[1] Dept. of Product Technology, Hokkaido Industrial Research Institute, Sapporo, Japan
[2] Graduate School of Engineering, Hokkaido University, Sapporo, Japan

Abstract — **Determining muscle forces of the finger during heavy work is important for an understanding and prevention of tenosynovitis. Electromyography is one index of muscle activity. Measurements by surface electromyography (sEMG) are noninvasive and simple to apply to obtain signals of muscle action potentials. The sEMG potentials of muscles near the electrode are superimposed. To identify the muscle activities from sEMG measurements, it is necessary first to analyze the characteristics of sEMG conduction in the forearm. This paper develops a conduction model of the forearm that incorporates the muscles and the *radius* and *ulna* bones. sEMG distributions were analyzed using the finite element method. The Root mean square (RMS) values of sEMG values and the power exponent of the attenuation (PEA) in relation to the length between the electrode and the source of muscle action potential were estimated in this work. Further, the positions of muscle action potential were reverse-estimated using the RMS values and the PEA. As a result, the PEA was found to increase monotonically with increases in the inter-electrode distance (IED) of the surface electrode pair. The errors in the estimated positions of muscle action potential increased with decreases in the distance between the source of muscle action potential and the *radius* and *ulna* bones.**

Keywords — **Forearm, Muscle Force, Surface Electromyography (sEMG), Conductive Model, Reverse-estimation.**

I. Introduction

Fingers do work from fine operations to heavy–duty tasks. The long continuing work will often cause arthritis and tenosynovitis. To prevent this, the load of fingers has been estimated using electromyography and computer simulation. Recently, a method to estimate muscle forces of fingers with needle electromyography and musculo-skeletal model has been reported [1].

This method is effective to estimate muscle activities individually, but a limitation is that a needle electrode needs to be inserted into the muscle causing pain to subjects. Surface electromyography (sEMG) is an attractive method to measure muscle activity because of easy application and no pain.

sEMG technique has some problems when measuring the activity of individual muscles in the forearm. Myoelectric potentials from all muscles near the electrode are superimposed in sEMG signals. The muscle activity of individual muscles must be estimated from sEMG

This paper reported a conduction model of the forearms by the finite element method. The conduction model was composed of a cylinder consisting of muscle, *radius* and *ulna* bones, and a source of muscle action potential. Simultaneously, changes in sEMG distribution caused by changes in the position of the source are investigated. Further, the source positions are reverse-estimated using the volume conduction characteristics and the analyzed sEMG distribution.

II. Materials and Methods

A. Geometry of the models

A model of the left forearm in supinated position is developed with a 40mm arm radius and a 300mm long cylinder (Fig. 1). The model incorporates the muscle tissue, and the *radius* and *ulna* bones. The model is used to reverse-estimate the position of the source of muscle action potentials.

The origin of the global coordinates is on the center of the model, the *z*-axis is the center axis, the *y*-axis is the dorsal direction, and the *x*-axis the lateral direction. The *radius* and *ulna* bones are cylindrical of 10mm radius and are the same length as the model. The centers of *radius* and *ulna* bones are at 23mm of radius from the center of the model, parallel to the *z*-axis. The positions of the *radius* and the *ulna* bones are symmetric to the *yz*-plane, and the center axes of the bones are 120° apart in the *z*-axis direction.

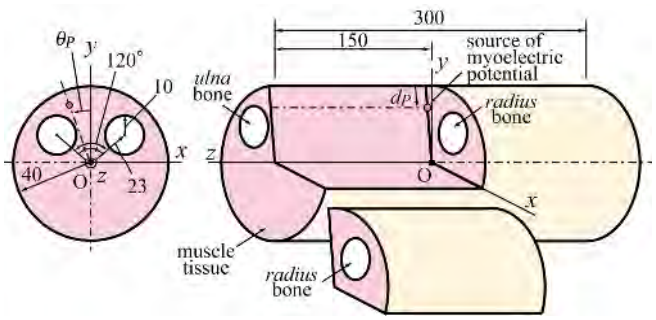


Fig. 1 Conduction model of the left forearm.
(left: proximal view, right: lateral view (cut and moved to show details))

Chwee Teck Lim, James C.H. Goh (Eds.): ICBME 2008, Proceedings 23, pp. 1904–1907, 2009
www.springerlink.com

Another model incorporating only the muscle tissue is developed with the same arm radius and length. The muscle only model is used to calculate the characteristics of the attenuation of sEMG.

B. Governing equation

The electric scalar potential V [V] in the model obeys the following equation:

$$\nabla \bullet \left[\left(\boldsymbol{\varepsilon} \frac{\partial}{\partial t} + \boldsymbol{\sigma} \right) \nabla V \right] = 0 \qquad (1)$$

where $\boldsymbol{\sigma}$ [S/m] denotes the conductivity vector, $\boldsymbol{\varepsilon}$ [F/m] and t [s] denote permittivity and time, respectively; $\nabla\bullet$,∇, and $(\partial/\partial q)$ denote the divergence, gradient, and partial differential with respect to q, respectively. Eq. (1) follows directly from Maxwell's equation describing Ampere's law under the assumption of negligible magnetic effects.

The muscle and bone anisotropic conductivities are $\boldsymbol{\sigma}_M$ and $\boldsymbol{\sigma}_B$, respectively. The radial, circumferential and axial component of the conductivity is shown in table 1 [2][3]. The permittivity is disregarded as it is very small.

Table 1 Conductivity of muscle and bone components [2][3]

	Muscle[S/m]	Bone[S/m]
Radial	0.148	4.65×10^{-3}
Circumferential	0.148	6.33×10^{-3}
Axial	0.446	66.7×10^{-3}

C. Sources of muscle action potential

The transmembrane current caused by depolarization of the muscle-cell membrane generates a muscle action potential. Depolarization propagates in the muscle fibre at a constant speed and gives rise to the current inflow and outflow, the source of the muscle action potential.

To simplify, the source of the muscle action potential is replaced by a current dipole with pole separation of 2.1mm [4][5]. The dipole is placed on the xy-plane and at a circumferential angle θ_P around the z-axis based on the y-axis and depth d_P below the surface of the cylinder. The direction of the current dipole is parallel to the z-axis, and the current strength is normalized to be 1mA.

D. Finite element analysis

The commercial FEM software package ANSYS MultiPhysics Ver.10 was used to analyze the distribution of the sEMG measurements. The element size of the model at the source is 0.1 mm, at the surface nearby just above the dipole from 2 mm and up to 6 mm elsewhere.

A 20mm thick air layer, as the boundary condition of the analysis, surrounds the model. The air layer has an isotropic conductivity $\sigma_A = 1.0\times10^{-10}$ S/m, very much smaller than that of the muscle. The element size of the air layer is 8mm. The outside edge of the air layer was assumed to be grounded (0mV).

The model analyzed conditions of depth d_P changed from 5 to 40mm at intervals of 5mm, and the angle around the z-axis, θ_P from 0 to 90° changed at intervals of 10°.

III. Results

A. Reduction of the RMS value of sEMG

The potential distribution $V=V(\theta,z)$ on the surface of the model was obtained with θ as the circumferential angle around the z-axis at the position of the source.

Generally, actual sEMG measurements determine potential differences, changed dynamically, between electrode pairs. Then the RMS value of the recorded potential difference is calculated. The analyzed sEMG distribution is static because of the static source. However, RMS values can be approximated by a simulated static distribution with the following three conditions assumed: 1, the component in the forearm has no capacitance; 2, the field strength at a point sufficiently far left from the source is zero; and 3, the speed of conduction of the depolarization is constant.

The method can be represented as follows, with the centered difference in the z-direction ΔV:

$$\Delta V(\theta, z) = V(\theta, z + \Delta z/2) - V(\theta, z - \Delta z/2) \qquad (2)$$

where Δz is the difference interval and corresponds to the IED of the electrode pair; ΔV also corresponds to the potential difference of the electrode pair. Outside both ends of the distribution ($z < -L_A/2+\Delta z/2$ or $L_A/2-\Delta z/2 < z$), ΔV is assumed to be zero because of the small potential differences.

The RMS value distribution sV is calculated as follows.

$$sV(\theta) = \left(\frac{1}{L_A} \int_{-L_A/2}^{L_A/2} \Delta V^2 dz \right)^{1/2} \qquad (3)$$

The attenuation characteristics of the RMS values are obtained with the relation between distance l from the center of the electrode to the source and the sV of the muscle only model. The RMS values rapidly decrease with increases in the distance l. This decrease was fitted with the following power function (4).

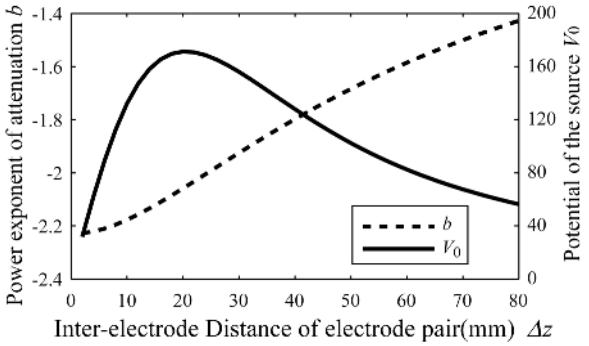


Fig. 2 The PEA and potential of the source by differences in IED

$$sV(\theta) = V_0 l(\theta, d_P)^b \tag{4}$$

Where V_0 denotes the potential of the source, and b denotes the power exponent of the attenuation (PEA).

The PEA b is -2.18 at Δz = 10mm and -1.68 at 50mm. Fig. 2 shows the relation between Δz, V_0, and b (PEA) in Eq. (4). The PEA increases with increases in Δz, suggesting the tendency also reported in Roeleveld [6], where narrow IEDs of electrode pairs measured the action potentials of muscle fibres near the electrode. It is possible to measure the contribution of also distant fibres with a wide IED. Using two different electrodes at intervals allows the measurement of muscle activities of individual superficial and deep muscles.

B. Estimation of the source position

The source position was reverse-estimated from the RMS value distribution sV of the model consisting of the *radius* and *ulna* bones and muscle, using the PEA regressed by Eq. (4).

The method is as follows. The RMS value $sV_i = sV_i(\theta_i)$ obtained from an virtual electrode pair i (i=1...n) at a circumferential angle θ_i is known, and the right side of Eq. (4) is replaced by the following f_i as a function of the unknown position of the source $\boldsymbol{x_p} = (x_P, y_P)$ and also the unknown source potential V_0.

$$f_i(x_p, y_p, V_0) = V_0 l_i^{\,b} \tag{5}$$

$$l_i = l(\theta_i, x_P, y_P) = \sqrt{(x_p - R_A\cos\theta_i)^2 + (y_p - R_A\sin\theta_i)^2} \tag{6}$$

The PEA b in Eq. (5) has been regressed to the value obtained by the muscle only model. The error in the RMS value estimate e_i is defined by Eq. (4) and (5).

$$e_i = sV_i - f_i \tag{7}$$

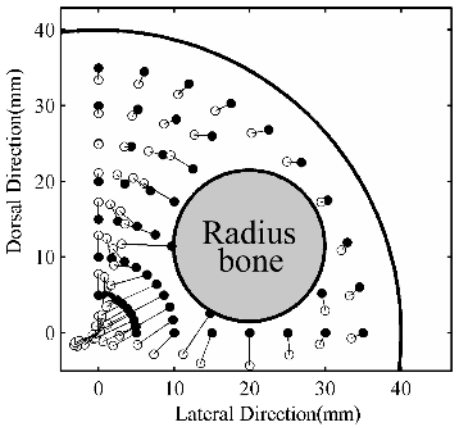


Fig. 3 Estimating the source position by RMS values of 10mm of IED. (white circles: estimated position of the source, black circles: true position)

With Taylor expansion of the first degree of Eq. (5) with respect to x_p, y_p and V_0, the following equation is obtained by assigning the result to Eq. (7).

$$\boldsymbol{e} = \begin{bmatrix} \frac{\partial f_1}{\partial x_P} & \frac{\partial f_1}{\partial y_P} & \frac{\partial f_1}{\partial V_0} \\ \vdots & \vdots & \vdots \end{bmatrix} \begin{bmatrix} \Delta x_P \\ \Delta y_P \\ \Delta V_0 \end{bmatrix} = \boldsymbol{D}\Delta\boldsymbol{x} \tag{8}$$

Where $\boldsymbol{e}$ is the vector of the error $[e_1 \,..\, e_n]^T$, $\Delta\boldsymbol{x}$ gives the direction minimizing the vectorial norm of $\boldsymbol{e}$, and $\Delta\boldsymbol{x}$ is calculated by the following equation using Moore-Penrose matrix inverse $\boldsymbol{D}^+$.

$$\Delta\boldsymbol{x} = \boldsymbol{D}^+\boldsymbol{e} = \left(\boldsymbol{D}^T\boldsymbol{D}\right)^{-1}\boldsymbol{D}^T\boldsymbol{e} \tag{9}$$

The $k\Delta\boldsymbol{x}$ that is obtained by multiplying a small constant k by the $\Delta\boldsymbol{x}$ obtained by Eq. (9) and this is added to $\boldsymbol{x}$. The calculation is repeated until the norm of $\boldsymbol{e}$ is the minimum. Then the estimated position (x_P, y_P) can be calculated.

shows the results of the estimates of the source position obtained by this method, 36 virtual electrode pairs at intervals of 10° are used. The error grows for sources close to the *radius* and *ulna* bones or under *radius* and *ulna* bones viewed from above the source. The maximum error calculated given by the results of 10mm of IED is 8.4mm, and that of 50mm is 8.2mm.

IV. Discussion

A. Separating sEMG of adjacent muscles

According to the results, the PEA of the RMS values of sEMG increases with increases in IED Δz. The RMS values

measured with a narrow IED, decrease quickly, with wide IEDs more slowly. Using two electrodes with different IEDs makes it possible to measure the superficial and deep muscle activities separately.

To achieve such measurements, appropriate circumferential electrode intervals around the forearm are important. In determining the interval, it is necessary to consider the spatial frequency of the sEMG distribution and the intervals between adjacent muscles, and intervals within about 15° are considered adequate.

B. Attenuation of muscle action potential

Roeleveld et al. have measured the attenuation of the muscle action potential with respect to the amplitudes of the potential difference of electrode pairs [6]. The values of the analytical results and those of Roeleveld were compared, and the attenuation tendencies agreed. However, the PEA of our analysis is about 0.5 smaller than that in Roeleveld. This may be suggested to be an influence of differences in the anisotropic conductivity used in the analysis. Anisotropic changes in the electric conductivity cause expansion or contraction of the sEMG distribution in the direction of the cylinder axis, and then cause a change of the PEA.

Further, it is known that fat has a lower conductivity and higher permittivity than muscle tissue, and has an effect similar to a low-pass filter when a muscle action potential is conducted [5]. Further, it is necessary to consider the influence of noise and drift, which would restrict the measurement limits in actual measurements to within a distance of 30mm.

C. Estimation error of the source position caused by radius and ulna bones

When the source is close to the *radius* and *ulna* bones, the sEMG distribution has been considerably distorted, here the error of estimating the source position becomes as much as 8.4mm. And this size of error may result in confusing the activity of one muscle for that of another. To prevent such miss-estimations caused by the *radius* and *ulna* bones, a method for correcting estimates by applying these analytical results can be devised, and the accuracy of estimates can be improved if correction by such analytical result is applied to the measured results, using previously input positions of electrode pairs, muscle, and *radius* and *ulna* bones. Further, a method to correct the estimates of the muscle activity can be devised by arranging the experimental set-up for the measurements. Measuring the conductivity of the forearm by a weak current from electrodes would improve the accuracy of the estimates.

The method suggested here estimates only one activated muscle position and activity; it is necessary to estimate the activities of multiple muscles in actual measurements. However, measurements using electrodes of narrow and wide IEDs as mentioned above can obtain sEMG of superficial and deep muscles. Using these measurements and an optimization method together would allow separate activity estimates of each of the deep muscles.

V. Conclusions

The attenuation characteristics of sEMG were calculated with the conduction models of the forearm, and the positions of the source of the muscle action potential were reverse-estimated with the RMS values of sEMG and the PEAs. The PEAs were found to increase monotonically with increases in the IEDs. The error in the estimated positions of the source increased with the decrease in the distance between the source of muscle action potential and the *radius* and *ulna* bones, up to a maximum of 8.4mm.

Multipoint sEMG measurements by narrowly and widely spaced electrode pairs around the forearm are planned for a verification of the model.

References

1. Vigouroux L et al. (2007) Using EMG Data to Constrain Optimization Procedure Improves Finger Tendon Tension Estimations During Static Fingertip Force Production. J Biomech, Vol. 40, 2846-2856 DOI 10.1016/j.jbiomech.2007.03.010.
2. Burger H C and Van Dongen, R (1961) Specific Electric Resistance of Body Tissues. Phys Med Biol 5:431–447.
3. Saha S and Williams P A (1992) Electric and Dielectric Properties of Wet Human Cortical Bone as a Function of Frequency. IEEE Trans Biomed Eng 39:1298–1304
4. Rosenfalk P (1969) Intra- and Extracellular Potential Fields of Active Nerve and Muscle Fibres. Acta Phisiol Scand Suppl 321
5. Stoykov N S et al (2002) Frequency- and Time-Domain FEM Models of EMG: Capacitive Effects and Aspects of Dispersion. IEEE Trans Biomed Eng 49:763-772.
6. Roeleveld K et al. (1997) Motor Unit Potential Contribution to Surface Electromyography. Acta Phisiol Scand, 160:175-183

Author: Yasuhiro NAKAJIMA
Institute: Hokkaido Industrial Research Institute
Street: Kita 19-jo Nishi 11-chome, Kita-ku
City: Sapporo
Country: JAPAN
Email: nakajima@hokkaido-iri.go.jp

A Distributed Revision Control System for Collaborative Development of Quantitative Biological Models

T. Yu[1], J.R. Lawson[1] and R.D. Britten[1]

[1] Auckland Bioengineering Institute, The University of Auckland, New Zealand

Abstract — **With CellML 1.0, models are encapsulated completely by a single file. CellML 1.1 now allows a model to be decomposed into many smaller files that can represent a single component of a model that can be reused by other related models. Unfortunately, managing even just tens of models with hundreds of shared component files may be a daunting task. For instance, updating a shared component for one model may break another, or it may be difficult to locate the correct component to be included into a model that one may be building.**

A new version of the CellML Repository software is under development, and seeks to address those issues. This software, the Physiome Model Repository 2 (PMR2) has been prototyped. The PMR2 prototype uses a distributed version control system (DVCS) as the foundation, with a web-based front end that allows annotation of specific models. DVCS will allow a group of modelers to work together to construct models and using multiple versions of shared components with ease without reliance on a centralized server. The web-based front end of the prototype contains "exposure" pages that highlight a specific revision of a model; those pages contain curation information, various documentation and rendering of annotations (metadata). Simulation results can also be included on the exposure page, giving users a quick overview of what the models are capable of.

Keywords — **quantitative modeling, CellML, repository, e-science**

I. Introduction

Advancements in modeling techniques and computational power have resulted in the dramatic increase in the number of quantitative models describing biological systems. As more models are created, there exists a need for software systems used to track them. While traditional file-based storage systems can be sufficient, they have a number of drawbacks that can be eliminated by more powerful systems. Such systems should also provide powerful search capabilities.

For larger models, a group of modelers may choose to construct models collaboratively. If a powerful model storage system exists with models in it, it will be possible to query for preexisting model components. Modelers can import, or use, the preexisting components to speed up development of their models. Such software systems should also provide collaboration facilities to assist modelers in merging their separate but related pieces of work to form their final quantitative model.

Here we present the Physiome Model Repository (PMR), developed as part of the CellML [1] project. This system has been deployed and is currently accessible at: http://www.cellml.org/models. A second version of PMR, called PMR2 is under development, and some of the goals for the PMR2 system are discussed.

II. Current system

In the initial release of PMR, the immediate need was to provide a method to edit and render metadata. A content management system (CMS) called Plone was chosen. Plone is deployed on top of Zope, an application development platform with an object database called ZODB.

PMR has basic version control mechanisms, but it has certain shortcomings, for example, it is possible to replace an old version of a file with different contents while retaining the same version number. It is also too easy for a user to accidentally base updates to a model on an older version rather than the latest version, which results in a new version that undoes changes that were present in the previous version of the same model. This would also allow accidental overwriting of good models with malformed ones. There is no mechanism in PMR for a set of related models and information to be updated as a single atomic unit, such that all information related to the model can all be guaranteed to be synchronized.

PMR also assumes each model is composed of only a single file. This was true for CellML 1.0, where the model import mechanism did not exist. This results in a repository system that excludes other supporting file types, such as images; they should be included into the repository as supporting documentation. With the introduction of CellML 1.1, PMR has become inadequate in addressing the future needs of the CellML project.

PMR supports curation, providing the ability to grade models. The curation method within the repository involved a star system to signify the curation status of a CellML model [2]. This method was sufficient to a certain degree, as the models that were curated usually fell within the preset guidelines. However, a more detailed curation process re-

Chwee Teck Lim, James C.H. Goh (Eds.): ICBME 2008, Proceedings 23, pp. 1908–1911, 2009
www.springerlink.com

quires more flexibility, such as the need to show that modifications may have been made to a model such that it no longer matches the math as written in the original publication (often necessary due to typographical errors or other reasons), or perhaps the alteration was authorized by the original author. These specific curation ratings do not fit into any of the categories of the star-based curation system.

Although Plone does provide a good workflow mechanism, this was not fully exploited by PMR to facilitate model development and curation. If this mechanism had been properly utilized by PMR, workflow states for the entire life cycle of models could have be defined. Workflow states can contain preset access control permissions to limit access to specific groups of users, such as restricting access from curators only until the model is submitted for curation. They can also provide notification mechanisms to inform interested parties when they may access the model, for instance, curators would be given a list of models that are ready for curation. The modeler could then specify the correct workflow state for the model and Plone could then manage the permissions of these models in a consistent manner.

To address these issues, a second version of the repository system is under development, called PMR2. PMR2 will address all the above issues by integrating Mercurial, a Distributed Revision Control System (DVCS) with Plone. PMR2 will also fully exploit the workflow features provided by the Plone CMS, such that the model life cycle outlined above can be implemented.

III. Distributed model development, with Mercurial and PMR2

Version Control Systems (VCS) have historically been centralized software systems running on a server, used extensively by software programmers to preserve history and manage concurrent access to their work. When changes need to be made, they are committed to the VCS, which will automatically assign a revision identifier such that this particular set of changes can be referred to later, meaning they don't overwrite existing data or get overwritten themselves. This system can allow different users to concurrently read and write to the system, as changes that do not conflict with each other can be merged together automatically. If conflicts do arise due to mutually incompatible changes, a merging mechanism exists and can be used to reconcile them manually.

Instead of using a standard, centralized VCS, PMR2 will use a Distributed VCS (DVCS) as this framework is more relevant to model development workflows. A DVCS enables direct collaboration between model developers without being tethered to a centralized system: researchers can cooperate directly until they choose to push their work to the centralized, shared repository. This grants full control of the researchers' unpublished work to themselves, freeing them from the security concerns which may affect the third-party centralized system, at the same time given them an avenue to publish their work when completed.

PMR2 is slated to use a DVCS called Mercurial. A modeler can simply create a Mercurial repository locally on his computer, which is a directory that is version-controlled by Mercurial. We call this a "model workspace". Any files related to the model, such as schematics and documents, can be added to this newly created model workspace and committed into it, forming a changeset. Further changes will not overwrite the data within this changeset, but will be committed into their own changeset. An example would be the decomposition of a CellML 1.0 model file into a number of CellML 1.1 files. These decomposed component files can all be committed as a changeset. Since it is a changeset, further improvements to these components will have individual changesets, and all of these changes can be referenced later. Over time, together with other components found in other model workspaces, standard library of components can be created, which can be shared and reused. As CellML 1.1 models can import components from other models, this library of components can be used to speed up the development of new models. Also, as the older components are preserved indefinitely in individual changesets, models that depend on these older components will continue to work even after major changes to this shared library. This comprehensive history preserving feature also has other usages.

Other members of the model development team, if given the permission, can clone this model workspace to either review the work that has been done or start working on the model. As the entire history is cloned, they can review the work other modelers have done from the committed changesets. If they choose to start working with a model, they will do so in parallel with the original modeler, making changes to their clone of the model workspace. The original author can continue with his/her work, making changes to his/her own model workspace. This will result in a multiple sets of changes that share a common ancestor, but are initially independent of each other. As part of working collaboratively, the independent models need to be merged.

There are two methods of merging diverging lines of changesets back into one model. Developers who have worked on their clones of the original model workspace can easily pull in new changes from the original into their clone. Alternately, if given the permission, they can push the changes from their clone back to the original. A merging process is required to be sure that all changes are unified. If all changes are compatible, such as when modelers work on

different parts of a model in different files, this can happen automatically. If not, as is the case when two modelers make two different changes to the same part of a model file, manual reconciliation of the incompatible changes will be necessary. Because each changeset will be associated with the names of the modelers responsible, the appropriate people can be contacted to establish what needs to be done. After merging (whether manually or automatically), validation of the resultant model is advisable. It may be possible to include pre-scripted validation, so that model modifications are automatically validated, for example, comparing simulation output of a new version of the model to simulation output of the previous version.

The changesets can be signed using cryptographic signatures using Mercurial GPG (GNU Privacy Guard) extension, such that the identity of the modeler who made the changeset can be authenticated. Any manual, unauthorized modification made to a specific changeset can be detected by verifying the cryptographic signatures. Once a changeset is made public, new changes should be committed to a new changeset and not be made to an existing one.

Once all the model development is done, if modeler chooses to, the repository workspace containing the new changes can be pushed into the main PMR2 software that will be hosted on the CellML website. The PMR2 software running on the CellML website will host a large repository of model workspaces, which are just normal Mercurial repositories that each encapsulates a single model.

IV. Features of PMR2 supplementary to Mercurial

Another use-case of the PMR2 software is the "model exposure" function. This provides a mechanism where models can be exposed, which is to publish a model onto a more prominent place within the PMR2 repository. The exposure process comprises a comprehensive workflow that will enable a model to be associated with documentation pages, and allow curators to curate the model, display its curation status, and have the resulting work published on the PMR2 repository with a permanent URI for future references.

A modeler will first select the model workspace containing the model he/she would like to expose, plus the specific revision identifier. The modeler will may then select the specific set of files from the workspace that are required by the model. Metadata and/or documentation are then processed to generate a page of comprehensive information about the model. Optionally, the modeler will be able to choose to solve the model, and generate graphs based on the graphing metadata that was included with the model. The modeler will then submit this resulting object to the repository curators for the curation process.

The model curation process is the next step of the exposure workflow. It requires repository curators to curate the submitted model according to a set of criteria. These criteria are represented by curation flags, which are tags that make assertions about the curation state of a model. For instance: whether the model satisfies specific physical constrains, version numbers of software that can solve this model, or whether this model contains mathematical equations different from the original publication (with or without its authors' approval). Based on the assessment given by a curator, a model will either be published onto the main model listing of the PMR2 repository, or be returned to the modeler for clarification or revision, completing the exposure workflow.

These curation flags can be used in queries, such that a list of models can be generated based on specific curation criteria. This allows greater flexibility in assessing the quality of the models of the repository.

In a similar manner, other metadata provided with the model can be queried against. Specific views can be generated, and with the use of metadata, a clear, aggregated presentational view can be built for each model type. This will allow a clear, concise presentation of the data within the repository.

V. Future

As of September of 2008, the prototyping stage of this development project has been completed, and the main version of PMR2 is currently under development. Our vision for the repository includes “add-ons” that will extend the functionality of the PMR2 software further.

There will be an interface provided to allow automated testing of models to run continuously, such that all exposed models can be guaranteed to be valid since the time they were last checked against specific versions of the CellML API.

Another area that is worth exploring is integration with a relational database or alternatively, the use of an RDF store, which would allow more possibilities for association with other kinds of metadata, such as citation, graphing or even a rendering of the model components automatically in human readable form.

VI. Conclusions

PMR, the CellML model repository is already a powerful tool, allowing models to be shared and reused. The CellML 1.1 specification’s import mechanism enabled an even more powerful paradigm, whereby models can reuse other mod-

els. The PMR2 is the next step towards realizing this potential.

Further goals of PMR2 are to be a more robust repository software system providing much more than just storage of models. Advanced querying of the data will assist location of relevant reusable components that can be used by other modelers. The versatile curation system will allow modelers to gauge the health and status of the models in the repository. The built-in distributed revision control system will assist collaboration between modelers so they can construct large quantitative models of biological systems more effectively.

References

1. Lloyd CM, Halstead MD, Nielsen PF. CellML: its future, present and past. Prog Biophys Mol Biol. 2004 Jun-Jul;85(2-3):433-50. Review.
2. Lloyd CM, Lawson JR, Hunter PJ, Nielsen PF. The CellML Model Repository. Bioinformatics. 2008 Sep 15;24(18):2122-3. Epub 2008 Jul 25.

Author: T. Yu
Institute: Auckland Bioengineering Institute,
The University of Auckland
Street: 70 Symonds Street
City: Auckland 1010
Country: New Zealand
Email: tommy.yu@auckland.ac.nz

Symmetrical Leg Behavior during Stair Descent in Able-bodied Subjects

H. Hobara, Y. Kobayashi, K. Naito and K. Nakazawa

Research Institute, National Rehabilitation Center for Persons with Disabilities, Tokorozawa, Japan

Abstract — **An evaluation of asymmetry in human gait is an important step towards clinical evaluation and developing the rehabilitation treatment for pathological gait. Although asymmetry of lower extremity actions during level walking was well established, little is known about stair walking. The purpose of this study was to compare bilateral lower limb mechanics during stair descent in able-bodied subjects. Ten male subjects (age = 27.6 ± 2.2 years; height = 1.73 ± 0.56 m; mass = 65.0 ± 8.6 kg, mean ± SD) with no neuromuscular disorders or functional limitations in their lower limbs participated in the study. Subjects were instructed to walk down a laboratory staircase without handrail use at self-selected speed. Each step in this staircase had a height of 16 cm, a depth of 30 cm, and a width of 80 cm. Sagittal plane kinematics and ground reaction forces were collected and lower extremity stiffness was calculated as the ratio of peak vertical ground reaction force to peak leg compression during early stance phase. The lower extremity stiffness were 17.8 ± 4.1 kN/m for the dominant leg and 18.2 ± 5.3 kN/m for the non-dominant leg; there was no significant difference between them. There was also no significant difference in both the peak vertical ground reaction forces (dominant; 1.06 ± 0.17 kN, non-dominant; 1.08 ± 0.19 kN) and peak leg compressions (dominant; 0.06 ± 0.01 m, non-dominant; 0.06 ± 0.02 m) between the legs. The results of the present study suggest that the lower extremity of able-bodied subjects during stair descent behaves symmetrically.**

Keywords — **Biomechanics, stair, leg stiffness, symmetry.**

I. Introduction

Differences in lower limb function between the legs (asymmetry) cause not only the degenerative changes in weight bearing joint but also falling. Thus, an evaluation of asymmetry in able-bodied gait may be an important step towards clinical evaluation and developing the rehabilitation treatment for pathological gait. Although asymmetry of lower extremity actions during level walking was well established [1], little is known about stair walking. The purpose of this study was to compare bilateral lower limb mechanics during stair descent in able-bodied subjects.

Leg stiffness, which is defined as the ratio of vertical component of ground reaction force (stress) to limb compression (strain) at the initial stance phase [2-6], is useful parameter to understand the compensated movement strategy during stair descent. For example, previous studies demonstrated that compared to young women the elderly performed downward stepping with greater leg stiffness [2-5]. Further, Jones et al. [6] showed that leg stiffness during stepping down was significantly greater in transfemoral amputees compared to transtibial amputees and able-bodied subjects. However, no study has quantified the asymmetry of the leg stiffness.

According to the Sadeghi [1], the non-dominant lower limb contributes more to support force, while the dominant limb contributes more to propulsion force during walking. Thus, we hypothesized that non-dominant leg would demonstrate a higher stiffness than dominant leg.

II. Materials and Methods

A. Participants

Ten active male subjects with no neuromuscular disorders or functional limitations in their legs participated in the study. Their physical characteristics were: age 27.6 ± 2.2 years, body mass 65.0 ± 8.6 kg, and height 1.73 ± 0.56 m (mean ± SD). The experimental protocol was approved by the local ethical committee and is in accordance with guidelines set out in the Declaration of Helsinki (1964).

B. Task and procedure

Before the experiment, all subjects determined their dominant leg. Ball kicking was used to determine limb dominance. The subjects were asked to descent a custom-built staircase with each step being 16 cm high, 30 cm deep and 80 cm tread (Figure 1). They performed step-over-step stair descent (normal reciprocal stepping pattern) at self-selected speed (Figure 2).



Fig. 1 Custom-built staircase

Chwee Teck Lim, James C.H. Goh (Eds.): ICBME 2008, Proceedings 23, pp. 1912–1914, 2009
www.springerlink.com

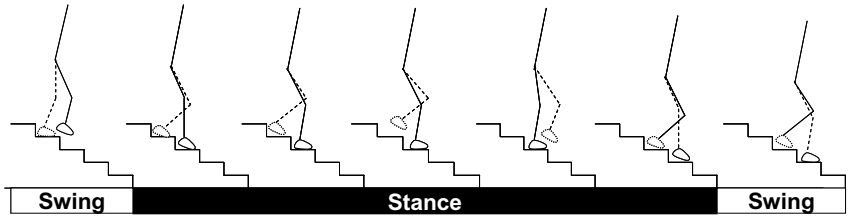


Fig. 2 Schematic illustrating the gait cycle of step-over-step stair descent

C. Data collection and analysis

Five trials in both legs at the third steps were used for the analysis. Kinematic and kinetic data during stance were sampled synchronously at 60 Hz using an eight-camera motion analysis system (VICON 512, Oxford Metrics, U.K.) and force platform (Kistler 9281C, Kistler Inc., Switzerland), which was embedded in the third step of the staircase. Stress (F_{max}) was derived as the maximum value of vertical component of ground reaction force. Two 25-mm retroreflective markers were placed on the fifth metatarsophalangeal joint and the greater trochanter to compute a srain (X_{max}). Lower extremity was modeled as linear spring [2-6], and we calculated leg stiffness as ratio of F_{max} to X_{max} (Figure 3).

D. Statistics

The comparison between the dominant and non-dominant leg was made using the Student t-test. Statistical significance was set at $P < 0.05$. All data are presented as mean values with standard deviation (S.D.).

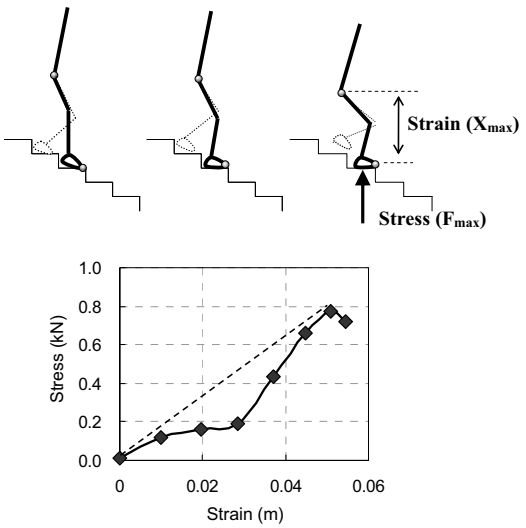


Fig. 3 Leg stiffness calculation in stair descent

III. Results

A. Stiffness, stress and strain

Leg stiffness, stress and strain in both legs are shown in Figure 4. The leg stiffness was 17.8 ± 4.1 kN/m for the dominant leg and 18.2 ± 5.3 kN/m for the non-dominant leg; there was no significant difference between them. Figure 5-A and B shows that there was also no significant difference in both the stress (dominant; 1.06 ± 0.17 kN, non-dominant; 1.08 ± 0.19 kN) and strain (dominant; 0.06 ± 0.01 m, non-dominant; 0.06 ± 0.02 m) between the legs.

IV. Discussion

This study aimed to investigate the bilateral lower limb mechanics during stair descent in able-bodied subjects. We compared leg stiffness, stress and strain between the dominant and non-dominant legs. There was no significant differences in stiffness, stress and strain between the legs (Fig. 4-A, B and C). The results completely contrast with our initial hypothesis, which stated that non-dominant leg would demonstrate a higher stiffness, that dominant leg. Thus, the present study suggests that the lower extremity of able-bodied subjects during stair descent behaves symmetrically.

Current results will be important when evaluating stair descent performance in patients, older adults, and person with disabilities. Past findings demonstrated that changes in leg stiffness during stair descent due to aging [2-4], lower limb amputation [6] and suppressed vision [7]. The changes in leg stiffness were interpreted as compensated movement strategy for reduced muscle strength, a slowed rate of tension development or a decline in proprioceptive capability [5]. Therefore, symmetrical landing mechanics observed in the present study would be due to that active male who has no neuromuscular disorders or functional limitations in their legs were recruited as subjects.

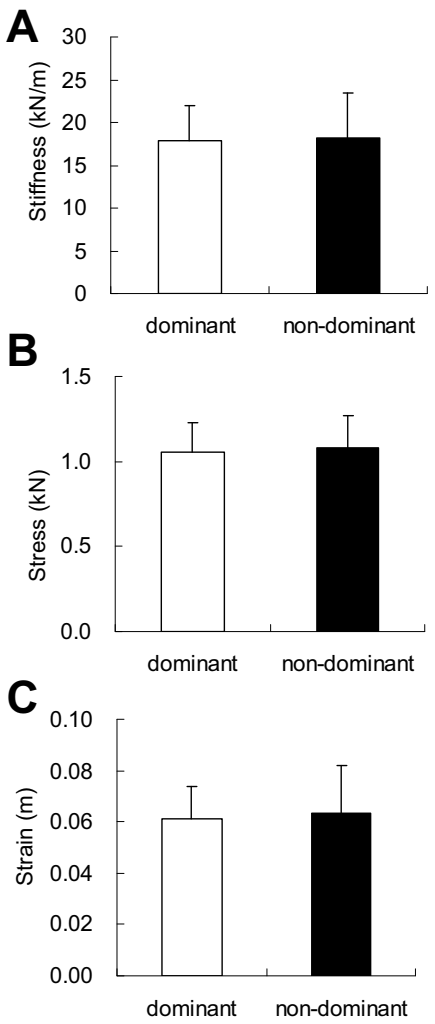


Fig. 4 Leg stiffness (A), stress (B) and strain between the legs

V. Conclusions

We investigated whether able-bodied subjects descend the stair in symmetrical manner. The results of the present study suggest that the lower extremity of able-bodied subjects during stair descent behaves symmetrically. This will be important when evaluating stair descent performance in patients, older adults, and person with disabilities.

Acknowledgment

The authors thank the members of Department of Motor Dysfunction and Department of Prosthetics & Orthotics, Research Institute, National Rehabilitation Center for persons with Disabilities for useful comment on the manuscript.

References

1. Sadeghi H, Allard P, Prince F, Labelle H. (2000) Symmetry and limb dominance in able-bodied gait: a review. Gait Posture 12: 34–45.
2. Hortobagyi T, DeVita P. (1999) Altered movement strategy increases lower extremity stiffness during stepping down in the aged. J Gerontol-Biol Sci 54:B63–B70
3. DeVita P, Hortobagyi T. (2000) Age increases the skeletal versus muscular component of lower extremity stiffness during stepping down. J Gerontol-Biol Sci 55:B593–B600
4. Hortobagyi T, DeVita P. (2000) Muscle pre- and coactivity during downward stepping are associated with leg stiffness in aging. J Electromyogr Kinesiol 10:117–126
5. Hsu MJ, Wei SH, Yu YH, Chang YJ. (2007) Leg stiffness and electromyography of knee extensors/flexors: Comparison between older and younger adults during stair descent. J Rehab Res Dev 44: 429–436
6. Jones SF, Twigg PC, Scally AJ, Buckley JG. (2006) The mechanics of landing when stepping down in unilateral lower-limb amputees. Clin Biomech 21: 184–193
7. Buckley JG, Heasley KJ, Twigg P, Elliott DB. (2005) The effect of blurred vision on the mechanics of landing during stepping down by the elderly. Gait Posture 21: 65–71

Variable Interaction Structure Based Machine Learning Technique for Cancer Tumor Classification

Melissa A. Setiawan[1], Rao Raghuraj[1] and S. Lakshminarayanan[1,*]

[1] Department of Chemical and Biomolecular Engineering, NUS, Singapore

Abstract — **Clinical diagnosis of disease samples largely benefits from multivariate statistical analysis, especially the machine learning techniques. One such example of medical application of statistical tools is the cancer tumor classification. In this study, Discriminating Partial Correlation Coefficient Metric (DPCCM) and Variable Predictive Model based Class Discrimination (VPMCD) are proposed as the new machine learning techniques for the same. Publicly available dataset Wisconsin Diagnose Breast Cancer (WDBC) dataset and Wisconsin Breast Cancer (WBC) dataset are analyzed to identify malignant cancer cells from benign cancer cells. Performance of the new classifiers are compared with the existing classifiers. The results based on the overall analysis indicate that DPCCM is potentially a better tool to identify and separate specific tumor samples. It achieves 100% accuracy of classification of test samples for WDBC dataset and 94% on WBC dataset. The performance of the approach is encouraging and its applicability to different cancer datasets (especially multi class problems) is being attempted further.**

Keywords — **Cancer, identification, DPCCM, VPMCD**

I. Introduction

Breast cancer is the most common cancer diagnosed in women and major cause of cancer deaths among women globally and Singapore in specific. However, this cancer has a high chance to be cured. Jerez-Aragone et al (2003)[1] noted that 97 % of breast cancer patients survive for five years if the cancer is detected during initial stages and treated. This fact highlights the importance of early detection of cancer followed by early treatment. Some past studies have shown that machine learning methods can play an important role in these efforts [2-4]. By using information provided by some measurable cell attributes or microarray data information from many normal cells and cancer cells, machine learning methods are able to build a classification model. This study explores one such application of data driven models in disease diagnosis with cancer tumor classification as its focus.

We attempt to utilize the two new classification tools proposed recently in the literature. We compare the performance with some of the existing classifiers. Two available online datasets, namely the Wisconsin Diagnostic Breast Cancer dataset (WDBC) and Wisconsin Breast Cancer dataset (WBC), are used as the case studies in this paper. For reliability of such clinical diagnosis, the classifier performances are compared based not only on overall accuracy, but also based on class-wise performance.

II. Methods

A. Variable Interaction Structure based classification

This alternate supervised learning technique was recently proposed in literature as a potential classification tool for different pattern recognition applications [5, 6]. The main premise of this new classification concept is that all or some of the variables (features/descriptors), defined on the system to characterize it into different classes, exhibit definite dependencies between each other. Such variable interactions (gene/protein/metabolite interactions) are significant especially in a larger and complex multivariate biological system. If such interactions exist, then for any classification problem, the distinction between classes could mainly arise due to difference effects of variables on each other. Hence, for systems with interacting variables, it is possible that each class is characterized by changes in different sets of variables arising due to definite variable interactions. The two new classification approaches viz., Discriminative Partial Correlation Coefficient Metric (DPPCM) and Variable Predictive Model based Class Discrimination (VPMCD) utilize the presence of such unique variable interaction patterns and exploit their potential for classification. The details of these methods are can be found in [6] and [5] respectively along with advantages and limitations. The methods are adopted here as it is and explored further for their utility to distinguish cancer tumor samples.

DPCCM [6] captures the possible inter-variable relations in the form of mutual correlations. Partial correlations are used to refine the strength of direct interactions between the variables by eliminating the influence of other variables on them. Intra-class attribute relations for individual classes are modeled by the metrics which is defined for each class in the training set. The proximity of the new variable interaction structure to the individual class models is used as classification criteria.

Chwee Teck Lim, James C.H. Goh (Eds.): ICBME 2008, Proceedings 23, pp. 1915–1917, 2009
www.springerlink.com

VPMCD classifier establishes inter variable relations in the forms mathematical models (VPMs) that can be used to predict back the individual variables as a function of other variables in the system. As a result, each class has different system characterization in terms of specific inter-variable interaction models which can be exploited further for class separation of new samples.

B. Other classifiers used for comparison

We implement some of the existing classification techniques to compare the performance of the above mentioned new classifiers. Linear Discriminant Analysis (LDA) [7], Classification and Regression Tree (CART) [8] and TreeNet [9] are used as comparison methods. The details of these well known methods are avoided here for brevity.

III. Materials and Implementation

A. Dataset

WBC dataset collected by Wolfberg et al., [10] is available online in a public domain database (http://archive.ics.uci.edu). By considering 9 cells attributes information such as mitoses, clump thickness and so on, cells are then classified into 2 classes (malignant cancer cells and benign cancer cells). There are 699 total samples in this dataset with 65.5% of them are benign cells and the remaining 34.5% are malignant cell samples. Some missing data are found in 16 patients' data hence the information from these 16 patients is excluded in the analysis. The size of this system is M ~ [683 samples x 9 predictors; 2 classes].

WDBC dataset collected by Wolfberg et al., [10] is available for public use in http://archive.ics.uci.edu. This is a quite bigger dataset compared to WBC with less number of samples. It stores 30 real-valued attributes information from 569 samples (357 samples are taken from benign cells and the remaining data are taken from malignant cells) without any missing value. The size of this system is P ~ [569 samples x 30 predictors; 2 classes].

B. Implementation

As the first step of this study, both datasets are divided into training sets (80%) and test sets (20%) for validation purposes. For each case, the same training set, excluding test set, is used by all classifier to construct one classification model. Once the model is obtained, it is then tested on the test dataset to get the accuracy of the model (overall and class-wise). MATLAB's [11] built-in function "classify" is used for LDA classification while CART and TreeNet classification is done using software developed by Salford Systems, USA [12, 13]. VPMCD and DPCCM algorithm [5-6] coded in MATLAB m-file are used for building the VPMCD and DPCCM classifier.

IV. Results and Discussion

A. WBC dataset

Table 1 shows the classification result on WBC dataset with class 1 representing patients with benign cancer and class 2 representing patients with malignant cancer.

Table 1 Classification result (% accuracy) for WBC dataset

		LDA	VPMCD	DPCCM	CART	TreeNet
Resubstitution	Class 1	98.20	99.77	95.05	99.55	98.65
	Class 2	92.89	94.14	100	100	100
	Overall	96.34	97.8	96.78	99.71	99.12
Testing	Class 1	96.59	94.32	90.91	93.18	93.18
	Class 2	87.23	93.62	100	97.87	100
	Overall	93.33	94.07	94.07	94.81	95.56

The new classifiers perform reasonably well and comparable to the existing classifiers. DPCCM is able to detect all the class 2 samples perfectly which is of higher significance in this study. It is highly important not to wrongly classify cancer samples as "healthy". Therefore, classifier performance should be deemed better if it has higher prediction accuracy for class 2. In this regard DPCCM and TreeNet perform better.

As shown in Table 1, LDA, VPMCD and CART give similar performance as other classifiers in identifying healthy patients into class 1. On the other hand, they fail to classify some of cancer patients correctly. Therefore its overall performance is slightly lesser than DPCCM/TreeNet. Interestingly, VPMCD and DPCCM give the same overall accuracy albeit with different class-wise performance. Similar to TreeNet, DPCCM is able to classify class 2 samples very well. Its accuracy for class 2 samples is much better than VPMCD. On the contrary, VPMCD has better class 1 performance than DPCCM. The poor performance of LDA could be attributed to the non-uniform distribution of class 1 and class 2 samples. Larger difference between re-substitution test and validate test accuracies for CART/TreeNet indicates the possibility of model overfitting.

B. WDBC dataset

Table 2 shows the classification results for the WDBC dataset with class 1 representing patients with malignant

Table 2 Analysis result for WDBC dataset using LDA, VPMCD, DPCCM, CART and TreeNet

		LDA	VPMCD	DPCCM	CART	TreeNet
Resubstitution	Class 1	92.45	82.08	96.23	100	100
	Class 2	99.44	96.36	96.36	99.16	100
	Overall	96.84	91.04	96.31	99.47	100
Testing	Class 1	95.24	88.10	100	100	92.86
	Class 2	100	97.18	100	88.73	100
	Overall	98.23	93.81	100	92.92	97.35

All results are presented in percentage (%)

cancer and class 2 representing people without cancer. Similar to WBC case study, class 1 accuracy must receive more attention than class 2 accuracy since a cancer patient needs medication and treatment as soon as possible. As presented in Table 2, DPCCM holds the highest and perfect value for all overall, class 1 and class 2 accuracy. In other words, DPCCM is able to perfectly classify all samples into their corresponding class. This result puts the DPCCM as the stronger classifier for such clinical diagnosis applications compared to other selected classifiers.

Unlike in WBC dataset, LDA provides a good performance in classifying class 2 samples for this data set. This could be because the data points are linearly separable. A reasonably good performance by VPMCD (Table 2) using a linear model in classifying class 2 samples strongly indicates linear separability of the dataset. As observed in Table 2, LDA performance on class 2 classification is better than its performance on class 1 classification. During model building, LDA set weights to all variables in such a manner that makes its performance on class 2 predictions perfect. This reduces its ability to predict class 1 samples accurately. The other classifier which gives a good performance in class 2 classification is TreeNet. The ensemble of decision tree confirms its superiority to single decision tree (CART) by giving better overall and class 2 accuracy. However, its performance on class 1 is still lower than CART. This may happen because, during model construction, TreeNet assigned weight factor on each variable so as to classify class 2 samples well. As a consequence, it fails to classify some class 1 samples correctly. CART, a classifier with the lowest overall accuracy, is able to perfectly classify class 1 samples. On the other hand, it has poor performance in predicting class 2 samples and also during validation dataset testing.

V. Conclusion

In this study, VPMCD and DPCCM classifiers are analyzed for their utility to identify breast cancer tumor classification. The comparison study is performed with the objective of determining the best classifier i.e. the capability to correctly classify new samples into their corresponding classes. According to our study, DPCCM is consistent in its performance and shows better potential to be an efficient data analysis tool for clinical diagnosis.

References

1. Jerez-Aragone´s, Jose´ M., Jose´ A. Go´mez-Ruiz, Gonzalo Ramos-Jime´nez, Jose´ Mun˜oz-Pe´rez, Emilio Alba-Conejo (2003) A combined neural network and decision trees model for prognosis of breast cancer relapse. Artif. Intell. Med. 27:45-63.
2. Bagui, Subhash C., Sikha Bagui, Kuhu Pal, Nikhil R. Pal. (2003) Breast cancer detection using rank nearest neighbor classification rules. Pattern Recognit. 36:25-34.
3. Hong, Jin-Hyuk, Sung-Bae Cho (2008) A probabilistic multi-class strategy of one-vs.-rest support vector machines for cancer classification. Neurocomputing, In Press
4. Liu, Kun-Hong, De-shuang huang (2008) Cancer classification using rotation forest. Comput. Biol. Med. 38:601-610.
5. Raghuraj, Rao K. and S. Lakshminarayanan (2007) VPMCD: Variable interaction modeling approach for class discrimination in biological systems . FEBS lett. 581:826-830.
6. Melissa, A. Setiawan, K. Rao Raghuraj, S. Lakshminarayanan (2009) Partial correlation metric based classifier for food product characterization. J. Food Eng. 90:146-152.
7. Duda, R. O., P. E. Hart, and D. G. Stork (2000) Pattern classification. John Wiley, New York.
8. Berrueta, L. A., R. M. Alonso-Salces, and K. Herberger (2007) Review: Supervised pattern recognition in food analysis. J. Chromatogr. A 1158:196-214.
9. Freidman, J. H. (1999) Greedy Function Approximation: A Gradient Boosting Machine ; technical report on TreeNet : http://www.salfordsystems.com/doc/GreedyFuncApproxSS.pdf.
10. Wolfberg, W.H. and O.L. Mangasarian (1990) Multi surface method of pattern separation for medical diagnosis applied to breast cytology. Proc. Natl. Acad. Sci 87:9193-9196.
11. MATLAB 7.0.4, Release 14, (2005) The MathWorks Inc., Natick, MA.
12. CART 5.0, (2007) Salford systems, San Diego, Calif.
13. TreeNet 2.0, (2007) Salford systems, San Diego, Calif.

Assessing the Susceptibility to Local Buckling at the Femoral Neck Cortex to Age-Related Bone Loss

He Xi[1], B.W. Schafer[2], W.P. Segars[3], F. Eckstein[4], V. Kuhn[5], T.J. Beck[3], T. Lee[1]

[1] Division of Bioengineering, National University of Singapore, Singapore
[2] Department of Civil Engineering, The Johns Hopkins University, Baltimore, MD, USA
[3] Department of Radiology, The Johns Hopkins University, Baltimore, MD, USA
[4] Institute of Anatomy and Musculoskeletal Research, Paracelsus Private Medical University Salzburg Salzburg, Austria
[5] Department of Trauma Surgery and Sports Medicine, Medical University Innsbruck, Austria

Abstract — **To simulate bone adaptation, we used an engineering beam simulation of a one-legged stance and linearly thickened (young) or thinned (old) cortices until the maximum stress on the infero-medial neck surface was the same as in the middle-age version. Consequences of simulated adaptive changes on elastic buckling stability were evaluated by the FSM using loads generated in a simulated fall on the greater trochanter. We conclude that the expansion of diameter with thinning cortices can preserve femoral neck strength under normal stance mode but not necessarily under loads encountered in falls, especially if the elderly cross-section is thinned by adaptation to reduced loading.**

Keywords — **Local Buckling, Homeostasis, Aging, Femoral neck**

I. Introduction

Realistic computer simulations of loaded trabeculae in osteoporotic bones show that individual trabeculae fail by Euler buckling. Euler buckling is an instability mode that becomes likely in end-loaded structures when they become too slender and lose lateral support. Increasing slenderness and loss of transverse elements are hallmarks of trabecular degradation in osteoporosis. Since applied loads are mainly borne by the cortex, its stability may be of greater importance. Aging and osteoporosis cause thinning cortices, expansion of outer diameter and loss of internal trabecular support which may lead to local buckling, a different form of instability. In this preliminary study we performed a series of stability analyses on tubular structures simulating femoral neck geometries using observed dimensions from elderly fracture cases and controls.

II. Materials and methods

We analyzed eight cross-section models of the femoral neck cortex using dimensions from studies of hip fracture cases and non-fractured controls. Sections were selected to span the a range of cortical slenderness based on the buckling ratio (BR). Three different models were considered: non concentric circles; non-concentric ellipses; and more realistic sections from CT scans of the femoral neck taken from a study comparing femoral neck biopsies in fracture cases and cadaver controls [1]. To examine potential for local instability, we developed finite strip models of each cross-section and determined the elastic local buckling stress (f_{crl}). The finite strip method [2] is a specialized variant of the finite element method; we employed the implementation in CUFSM [3]. The model considers the cross-section as an extrusion (no variation along the length). Local buckling occurs at lengths as short as ½ the section diameter, so the assumption of a straight extrusion is reasonable. Material properties assumed E=18800MPa, G=13620MPa, ν=0.31 [4]

III. Results

The BR (buckling ratio) and f_{crl} (elastic local buckling stress) do correlate but relatively poorly in the more realistic CT based cross-sections where irregular cortices dominate load behavior. Overall, the predicted elastic local buckling stresses (f_{crl}) are quite high for all but the most slender of cross-sections. To put results in context we used a variation on the effective width method, first developed for elastic-plastic metals by von Kármán [5], and widely used for viscoelastic plastics. We employed the expression attributed to Winter [6] to estimate the reduction in material compressive capacity (f_n) due to local buckling as a function of the local slenderness $\sqrt{(f_{yc}/f_{crl})}$. Figure 1 provides a sense of the interplay between the two compressive limit states: material yielding, and local instability. For cross-sections with the lowest buckling ratio a strong reduction in compressive capacity can still occur due to local instability. The importance of more realistic cortical dimensions is underscored by the CT results, for example #s 2 and 3 have similar BR values but control #2 should experience no reduction in strength; while fracture case #3 shows a small reduction. Further, this more realistically modeled case is expected to

Chwee Teck Lim, James C.H. Goh (Eds.): ICBME 2008, Proceedings 23, pp. 1918–1919, 2009
www.springerlink.com

experience some reduction while #7 modeled as a circle experiences none. These results suggest that simple BR values and simple regular models may inadequately describe instability at the femoral neck.

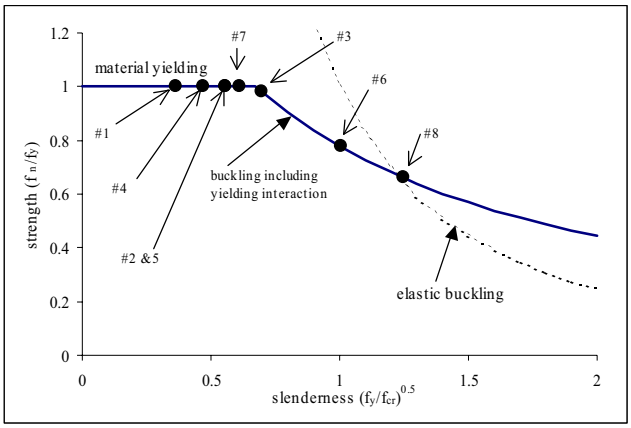


Figure 1: Predicted reduction of compressive limits for the femoral neck due to effect of local buckling.

IV. Discussion

There is relatively little prior work in modeling instability behavior of whole human bones although the phenomena may be critical in osteoporotic fragility. We have begun a series of proof-of-concept analyses to determine whether cortical geometries seen at the femoral neck are susceptible to buckling failure. Analyses generated in pure compression suggest that geometries seen in fracture cases are less stable than those in controls. The level of model realism appears to be important. Relatively smooth cortices of circle and ellipse models are more stable than more realistic models with irregular cortices. Simple constructs to estimate cortical instability such as the buckling ratio may have some value but may not be sufficiently accurate for predictive use. More realistic analyses generated in a combination of bending and compression should better simulate the fall conditions producing hip fracture. These conditions produce peak compressive stresses on the thinner lateral cortices and further demonstrate the importance of realistic cortical models. Instability behavior is by definition chaotic, difficult to predict, and to observe experimentally especially in objects with the 3D complexity of the human proximal femur. Nevertheless this preliminary work using the finite strip analysis is encouraging and the method may prove to be a useful tool for the investigation of osteoporotic instability.

References

1. Crabtree N, Loveridge N, Parker M, Rushton N, Power J, Bell K, Beck T and Reeve J, Intracapsular hip fracture and the region-specific loss of cortical bone: analysis by peripheral quantitative computed tomograph, J Bone Miner Res, 16(7)**:**1318-28, 2001.
2. Cheung Y and Tham L, The Finite Strip Method, CRC Press, 1998.
3. Schafer B, CUFSM - Elastic Buckling Prediction, 2004.
4. Yoon H and Katz J, Ultrasonic wave propagation in human cortical bone- II. Measurements of elastic properties and hardness,. J Biomech, 9**:**459-464, 1976.
5. von Kármán T, Sechler E and Donnell L, The Strength of Thin Plates In Compression Transactions of the ASME, 54;53-57, 1932.
6. Winter G, Strength of Thin Steel Compression Flanges, Trans ASCE, 112;1, 1947

Revealing Spleen Ad4BP/SF1 Knockout Mouse by BAC-Ad4BP-tTAZ Transgene

Fatchiyah[1], M. Zubair[2], K.I. Morohashi[3]

[1] Dept. of Biology, School of Science, Brawijaya University, Malang, INDONESIA
[2] Dept. of Internal Medicine Endocrinology, UT South Western Medical Centre, Dallas, Texas, USA
[3] Dept. of Molecular Biology, Graduate School of Medical Sciences, Kyushu University, Fukuoka, JAPAN

Abstract — **The purpose of this study is addressed the function of Ad4BP/SF1 in developing spleen of Ad4BP/SF-1 KO mouse. I have modified the BAC-Ad4BP endogenous by homologous recombinant with modification cassette-containing tetracycline transactivator system and LacZ reporter genes to allow the expression of Ad4BP/SF1 in developing tissues and organ differentiation, regulate of Ad4BP/SF1 mechanism, and reveal the defect due to Ad4BP/SF1 deficiency. Recently studies, by immunihistochemistry of adult tissues showed that revealed coincident expressing between Ad4BP/SF-1 and lacZ, indicating the tTA system seemed to reproduces the endogenous expression of Ad4BP/SF-1, and thus likely to lacZ, Ad4BP/SF-1 in the BAC transgene was expected to be expressed in the corresponding tissues under the control of the bidirectional promoter. Interestingly, the BAC-Ad4BP-tTA transgenic mice were succeeded to up regulate the expression of Ad4BP/SF-1 at the protein level than wild type. And the fetal spleen of Tg(+);Ad4(+/+) was larger than that of the wild type, and expectedly the size of the spleen of Tg(+);Ad4(-/-) apparently recovered.**

Keywords — **Ad4BP/SF-1, knockout mouse, Spleen, BAC transgenic, homologous recombinant.**

I. Introduction

The orphan nuclear receptor, Ad4BP (adrenal-4-binding protein) or SF1 (steroidogenic factor-1) or FtzF1 (Fuzitarazu-F1), has emerged as a key regulator of endocrine function within the hypothalamus-pituitary-gonadal (HPG) and adrenal cortex (HPA) axis. Ad4BP/SF1 is known play the essential role in multistage of reproductive axis. Since the identification Ad4BP/SF1, its distribution has been examined mainly in steroidogenic tissues. Initial studies revealed that the gene encoding this transcription factor was expressed in particular cell types within the testis, ovary and adrenal cortex [1-3].

Gene disruption studies were performed to investigate the functions of Ad4BP/SF-1 during the tissue development. The gene knockout mice displayed agenesis of the adrenal gland and gonads at birth, reflecting increased apoptic cell death in the particular cell population comprising the tissue primordia. Due to the absence of the gonad in the fetal stage, the gene-disrupted mice exhibited male to female sex reversal, while probably due to the absence of the adrenal gland, they died shortly after birth [4-6]. According to these phenotypes, it has been established that Ad4BP/SF1 is essential for the structural and functional development of those tissues probably mediating downstream gene expression.

To address the function of Ad4BP/SF1 in developing spleen of Ad4BP/SF1 knockout mouse, we have modified the BACAd4BP endogenous by homologous recombinant with modification cassette-containing tetracycline transactivator system and LacZ reporter genes to allow the expression of Ad4BP/SF1 in developing tissues and organ differentiation, regulate of Ad4BP/SF1 mechanism, and reveal the defect due to Ad4BP/SF1 deficiency.

II. Materials & Methods

A. Experimental Animal

Ad4BP/SF1 KO mice were generated as described previously [5]. Background animals of BAC transgenic were F1 of C3H and and C57BL/6 female and male mouse (Japan Clea, Tokyo, Japan). The BACAd4BP- tTAZ-Tg mice were generated as described previously [7]. All animals were performed at the specific pathogen-free of Transgenic Animal Care Facilities of National Institute for Basic Biology, National Institute of Natural Science, Okazaki, Japan. All protocols were approved by the Institutional Animal Care and Use Committee of the National Institute for Basic Biology.

B. Construction of BAC transgene

The construction of BACAd4BPtTAZ was described by [8] previously. And the site of modification cassette was replaced inside of exon2 of Ad4BP/SF1 gene are identified by serial multi-PCR with 9-pairs of primer as figure1 below.

C. Whole-mount lacZ staining

Detection of lacZ enzymatic activity with whole-mount samples were performed as described [9] with minor modification.

Chwee Teck Lim, James C.H. Goh (Eds.): ICBME 2008, Proceedings 23, pp. 1920–1923, 2009
www.springerlink.com

D. Southern blot and western analyses

Southern blot analysis was performed basically as described [10]. Ten μg genomic and BAC DNAs were digested with EcoRI and BamHI at 37ºC overnight, and the digested products were separated on 0.8% agarose. They were transferred to a nylon filter (Hybond-N+, Ammersham Biosciences), and finally exposed to X-ray film and BAS1800 system. Western blot analysis was performed basically as described [11]. The spleens from P4 mice was lysed with 20 mM Tris-HCl(pH8), 100 mM NaCl, 0.1 mM EDTA, and 1% SDS. The tissue lysates for spleens (15 μg) was subjected to SDS-PAGE followed by western blotting with the rabbit primary antibody to Ad4BP/SF-1 [11]. Anti-rabbit-IgG conjugated with horseradish peroxidase (Jackson immuno research, Lab. Inc.) was used as the secondary antibody [12].

III. Result and Discussion

A. Construction BAC-Ad4B-tTAZT transgenic mice

The modification cassette was inserted in to the BAC clones, BAC1-Ad4BP and BAC5-Ad4BP, by homologous recombination to produce BAC recombinant clones, BAC1-Ad4BP-tTAZT and BAC5-Ad4BP-tTAZT, respectively. To confirm an occurrence of precise homologous recombination, the intact and recombinant BAC DNAs were digested with restriction enzymes, EcoRI and BamHI, and subjected to Southern blot analyses with 0.5 kb 5'-probe and 1.5 kb 3'-probe (Fig. 1A). With the 5'-probe, the original BAC-Ad4BPs are expected to give rise to 5.7 kb by EcoRI and 0.9kb by BamHI digestion, while the recombinant BAC-Ad4BP-tTAZTs give rise to 2.0 kb by EcoRI and 1.5 kb by BamHI. With the 3'-probe, the original BAC clones are expected to give rise to 5.7 kb by EcoRI, while the recombinants give rise to 2.0 kb by EcoRI and 10.0 kb by BamHI. Expected length of the fragments were obtained from the recombinants, strongly suggesting that homologous recombination occurred between the modification cassette and the original BAC clones (Fig. 1B).

Moreover, we examined whether the BAC-Ad4BP-tTAZT recombinants contain regions covered by the original clones by PCR genotyping with the primer pairs to amplify fragments a to i (Fig. 1A). As shown in Fig. 1C, the regions a, b, c, f, g, h, and i were amplified in both original BAC1-Ad4BP and recombinant BAC1-Ad4BP-tTAZTs, while the primers for fragments d and e designed to amplify regions including the insertion points gave signals only with the recombinants. Similarly in the case of BAC5-Ad4BP, the primers for fragments b, c, f, g, h, and i gave the signals for both original and recombinant, while the primers for fragments d and e gave the signals for only the recombinant. Since BAC5-Ad4BP lacked far upstream from exon 7 of the Gcnf, primer for fragment a failed to give the signal.

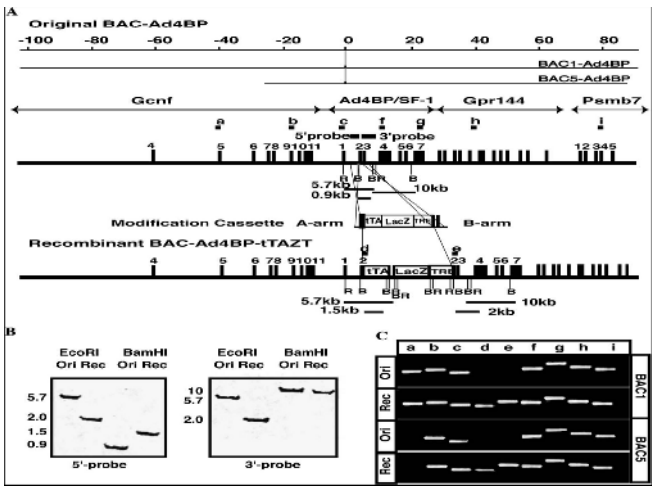


Fig. 1 Construction of BAC1-Ad4BP-tTAZT and BAC5-Ad4BP-tTAZT was taken by homologous recombinant. A, Map of the original (Ori) BAC1-Ad4BP and BAC5-Ad4BP and recombinant (Rec) BAC1-Ad4BP-tTAZT and BAC5-Ad4BP-tTAZT were presented schematically. B, Confirmation of modification cassette replaced on exon2 of Ad4BP/SF1 gene were identified by Southern Blot with 5'-prime & 3'-prime probes. Original (Ori), BAC1-Ad4BP and BAC5-Ad4BP, and their corresponding recombinants (Rec), BAC1-Ad4BP-tTAZT and BAC5-Ad4BP-tTAZT, were digested EcoRI and BamHI, and identified with Southern blotting analysis by 3'- and 5'-probes.C, The Original (Ori) and recombinants (Rec) BAC clones were examined by PCR with primers to amplify the region indicated with a to i.

B. Revealing spleen of Ad4BP/SF KO mice by BACAd4BPtTAZ transgene

Recently, we have produced the BACAd4BPtTAZ transgenic mice respectively [8]. We generated mouse lines to express a lacZ reporter gene and Ad4BP/SF-1 by a dual reporter/Tet-off system integrated in mouse BAC clones. Since the BAC constructs carried a lacZ reporter gene, we expected that the exogenous Ad4BP/SF-1 gene expression is evaluated indirectly by the transgene expression. Expectedly, lacZ expression pattern in the Tg mouse mostly, if not all, reproduced the endogenous expression of Ad4BP/SF-1. Thus, we applied the BAC-transgenic (BAC-Tg) mice to rescue Ad4BP/SF-1 KO mouse, and found interestingly that the tissues were rescued with varied levels [8].

Since the lacZ expression recapitulated the endogenous Ad4BP/SF-1 gene expression, we examined whether the Tg mice rescue the Ad4BP/SF-1 KO phenotypes. Morohashi laboratory was revealed that Ad4BP/SF-1 is expressed in the splenic endothelial cells at the fetal stage [10]. The adult

BAC Tg mice (B1L1 and B5L2) succeeded to upregulate the expression of splenic Ad4BP/SF-1 at the protein level (Fig. 2A). Interestingly, the size of the transgenic spleen was larger than the wild type at P0 (Fig. 2B), and indeed the weight was approximately 1.3 fold higher than that of the wild type (Fig. 2C). When the Tg(+);Ad4(+/+) and Tg(+);Ad4(-/-) fetuses were examined, lacZ was found to be expressed in the developing fetal spleen at E16.5 (Fig. 2D, E). Our previous KO mouse study revealed that the lack of Ad4BP/SF-1 induced spleen with smaller size from fetal ages possibly due to the affected vascular system. Considering the elevated Ad4BP/SF-1 expression in the BAC Tg mice and successful lacZ expression in the fetal spleens, we expected that the Tg(+);Ad4(-/-) spleen is recovered in the size. Showing a good correlation with our previous reports [12, 13], the spleen of Ad4BP/SF-1 KO (Tg(-);Ad4(-/-)) was significantly smaller than that of the wild type (Tg(-);Ad4(+/+)) at E16.5 (Fig. 2F). Similar to the adult spleen, the fetal spleen of Tg(+);Ad4(+/+) was larger than that of the wild type, and the size of the spleen of Tg(+);Ad4(-/-) was recovered expectedly.

The spleen of the BAC Tg mice was enlarged clearly. Indeed, the splenic expression of Ad4BP/SF-1 was upregulated at the protein level and the smaller products were absent. We recently demonstrated that forced expression of Ad4BP/SF-1 resulted in upregulation of cyclin D1 and thus BrdU incorporation in chick embryonic gonad (unpublished) strongly suggested that upregulated expression of Ad4BP/SF-1 accelerates cell cycle progression. Since Ad4BP/SF-1 is essential for the development of the splenic framework structure [13], it is likely that the enhanced expression of Ad4BP/SF-1 resulted in the enlargement of the tissue framework through accelerating cell cycle.

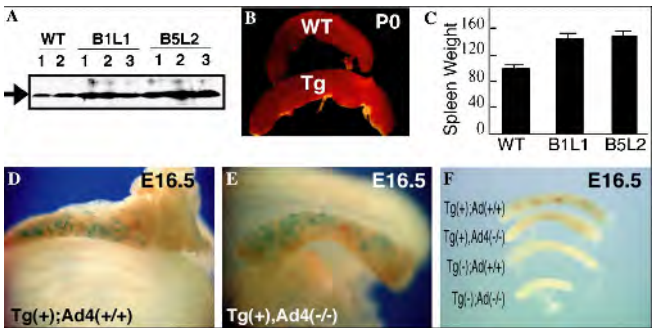


Fig. 2 Effect of up-regulated expression of Ad4BP/SF-1 in spleen. A, Total tissues lysates (15μg) prepared from the WT (n=2), B1L1 (n=3) and B5L2 (n=3) mouse spleens were subjected with Western blot analysis by anti-Ad4BP/SF-1 antiserum. B, WT and BAC-Tg (Tg) spleens were compared macroscopically. C, Weights of WT (n=5), B1L1 (n=10) and B5L2 (n=10) spleens were measured, and the relative weights were presented when that of WT is 100. D and E, LacZ activities was examined with the Tg(+);Ad4(+/+) and Tg(+);Ad4(-/-) spleens at E16.5. F, Macroscopic observation of the Tg(+);Ad4(+/+) and Tg(+); Ad4(-/-), Tg(+);Ad4(-/-) and Tg(-);Ad4(-/-) spleens at E16.5.

IV. Conclusion

The result of this study showed that the spleen of Ad4BP/SF-1 knockout mice revealed properly by BACAd4BPtTAZ transgene. The expression of Ad4BP/SF-1 of spleen is up regulated at level protein. The size of spleen also enlarged clearly than normal and/or knockout Ad4BP/SF-1 mice.

Acknowledgment

I would like to greatly thank you for Prof Ken-ichirou Morohashi, PhD., Div. sex differentiation, Nat. Inst. For Basic Biology, Okazaki Institute, Japan, as my supervisor, for providing the change study molecular biomechanics, and thanks to M. Zubair, PhD., Y. Fukui-Katoh, PhD. and H. Ogawa, PhD., for lecture, assist technical support for study transgenic mice. We thank Drs. X.W. Yang and N. Heintz (Rockefeller University) for providing the homologous recombination system of BAC clone and pSV1 RecA, and Drs. K. Mihara and M. Sakaguchi (Kyushu University) for providing anti-serum to lacZ.

References

1. Morohashi KI, Omura T. Ad4BP/SF-1, a transcription factor essential for the transcription of steroidogenic cytochrome P450 genes and for the establishment of the reproductive function. Faseb J 1996; 10: 1569-1577.
2. Parker KL, Schimmer BP. Steroidogenic factor 1: a key determinant of endocrine development and function. Endocr Rev 1997; 18: 361-377.
3. Val P, Lefrancois-Martinez AM, Veyssiere G, Martinez A. SF-1 a key player in the development and differentiation of steroidogenic tissues. Nucl Recept 2003; 1-8.
4. Luo X, Ikeda Y, Parker KL. A cell-specific nuclear receptor is essential for adrenal and gonadal development and sexual differentiation. Cell 1994; 77: 481-490.
5. Shinoda K, Lei H, Yoshii H, Nomura M, Nagano M, Shiba H, Sasaki H, Osawa Y, Ninomiya Y, Niwa O, et al. Developmental defects of the ventromedial hypothalamic nucleus and pituitary gonadotroph in the Ftz-F1 disrupted mice. Dev Dyn 1995; 204: 22-29.
6. Sadovsky Y, Crawford PA, Woodson KG, Polish JA, Clements MA, Tourtellotte LM, Simburger K, Milbrandt J. Mice deficient in the orphan receptor steroidogenic factor 1 lack adrenal glands and gonads but express P450 side chain-cleavage enzyme in the placenta and have normal embryonic serum levels of corticosteroids. Proc Natl Acad Sci USA 1995; 92: 10939-10943.
7. Nomura M, Bartsch S, Nawata H, Omura T, Morohashi K. An E box element is required for the expression of the Ad4bp gene, a mammalian homologue of Ftz-f1 gene, which is essential for adrenal and gonadal development. J. Biol. Chem. 1995; 270: 7453-7461.

8. Fatchiyah, M. Zubair, Y. Shima, S.Oka, S. Ishihara, Y. Fukui-Katoh, KI. Morohashi. Differential gene dosage effects of Ad4BP/SF-1 on target tissue development. ELSEVIER: Biochem. & Biophysical Com., 2006, 341: 1036-1045.
9. Hogan B, Beddington, R, Costantini, F, Lacy, E. Manipulating the Mouse Embryo: A Laboratory Manual. NY: Cold Spring Harbor Laboratory Press; 1989
10. Sambrook J, Fritsch, EF, Maniatis, T. Molecular Cloning: A laboratory manual. NY: Cold Spring Harbor Laboratory Press; 1989.
11. Ikeda Y, Lala DS, Luo X, Kim E, Moisan MP, Parker KL. Characterization of the mouse FTZ-F1 gene, which encodes a key regulator of steroid hydroxylase gene expression. Mol Endocrinol 1993; 7: 852-860.
12. Katoh-Fukui Y, Owaki A, Toyama Y, Kusaka M, Shinohara Y, Maekawa M, Toshimori K, Morohashi K. Mouse Polycomb M33 is required for splenic vascular and adrenal gland formation through regulating Ad4BP/SF1 expression. Blood 2005; 106: 1612-1620.
13. Morohashi K, Tsuboi-Asai H, Matsushita S, Suda M, Nakashima M, Sasano H, Hataba Y, Li CL, Fukata J, Irie J, Watanabe T, Nagura H, Li E. Structural and functional abnormalities in the spleen of an mFtz-F1 gene-disrupted mouse. Blood 1999; 93:1586-1594.

The address of the corresponding author:

Author: Fatchiyah
Institute: Dept. of Biology, School of Science, Brawijaya University
Street: Jl. Veteran
City: Malang 65145
Country: Indonesia
Email: fatchiya@brawijaya.ac.id

The impact of enzymatic treatments on red blood cell adhesion to the endothelium in plasma like suspensions

Y. Yang, L.T. Heng and B. Neu

School of Chemical and Biomedical Engineering, Nanyang Technological University, Singapore, 637457

Abstract — **Red blood cells (RBC) experience many physicochemical modifications on the membrane in physiological events as well as pathological complications, for example, the sialic acid loss on senescent RBC membrane. Abnormal RBC adhesion to the endothelium has been linked to the pathophysiology of various diseases associated with vascular disorders such as sickle cell anemia or diabetes mellitus. However, the correlation is still unclear between RBC membrane changes and abnormal RBC-EC adhesion, especially in plasma or plasma like suspensions. Multiple specific and non-specific forces govern cell-cell and cell-surface interactions. One non-specific force that has only been found limited attention in cell adhesion is the depletion interaction, which occurs as a result of a lower localized protein or polymer concentration near the cell surface compared to the suspending medium (i.e., relative depletion near the cell surface). This exclusion of macromolecules near the cell surface leads to an osmotic gradient, depletion interaction, and attractive forces.**

In order to elucidate the impact of physicochemical properties of the RBC membrane on RBC-EC adhesion induced by macromolecular depletion, we used various proteolytic enzymes to specifically cleave different components from RBC membrane. The dynamics of RBC-EC adhesion were then recorded using a flow chamber system and a stepwise shear profile. Our results indicate a dramatic increase of RBC adhesion to EC in the presence of high molecular mass (>40KDa) dextran with decreasing surface charge after sialic acid removal by neuraminidase. On the contrary, only minor alteration has been observed in RBC-EC adhesion and surface charge for the enzymatic cleavage by trypsin, α-chymotrypsin and pronase. In conclusion, this study demonstrates that polymer depletion can enhance RBC-EC adhesion under low shear stress and that it promotes adhesion of pathologic RBC. It thus provides new insight into potential mechanisms for enhanced RBC-EC adhesion and disturbed *in vivo* blood flow.

Keywords — **red blood cell, endothelial cell, adhesion, sialic acid, depletion interaction**

I. Introduction

Abnormal red blood cell (RBC) adhesion to endothelial cell (EC) has been of great interest for decades, since it has been linked to vascular complications in various diseases, such as sickle cell anemia [1] or diabetes mellitus [2]. It is clear that a complex interplay of various non-specific forces and specific forces govern RBC-EC interaction, but the detailed underlying mechanism(s) remain unclear. In the past, various factors have been identified as determinants of altered RBC-EC interaction, including blood flow [3], adhesion molecules on both RBC and EC membrane (e.g. CD36 and VCAM-1), RBC shape and deformability [4] and plasma proteins like TSP [5] and vWR [6] or fibrinogen, which has been found to promote RBC-EC adhesion in different diseases like sickle cell anemia [7] and diabetes mellitus [8].

While prior studies have described several aspects of RBC adhesion in normal and pathologic states, none appears to have considered depletion interaction as a non-specific force for RBC-EC adhesion. Conversely, depletion mediated interactions are commonly considered in the general field of colloid chemistry, and several previous reports have dealt with the experimental and theoretical aspects of depletion aggregation, often termed depletion flocculation. More recently, it became evident that depletion interaction can also induce cell-cell interactions. It is now clear that macromolecular depletion is the driving force behind RBC aggregation [9, 10]. Such findings are of basic science and clinical interest, in that reversible RBC aggregation is an important determinant of the *in vitro* rheological behavior of blood as well as of *in vivo* blood flow dynamics and flow resistance. On the contrary, polymer depletion as a driving force behind other cell-cell interactions in particular RBC-EC interaction hasn't found a lot of attention.

RBC experience during their lifespan as well as in various diseases several physicochemical modifications. For example the loss of sialic acid has been linked to RBC senescence [11], as well as diabetes mellitus [12] and acute myocardial infarction [13]. Although such changes have been linked to altered RBC-EC adhesion the specific mechanisms on how such changes induce RBC-EC adhesion are not clear. The current study was thus designed to elucidate the impact of specific RBC membrane changes on the RBC-EC adhesion in plasma like solutions. Several proteolytic enzymes were employed to specifically cleave off different components from RBC membrane. The dynamics of RBC-EC adhesion were then recorded in the presence of high molecular mass (>40 kDa) dextran.

Chwee Teck Lim, James C.H. Goh (Eds.): ICBME 2008, Proceedings 23, pp. 1924–1927, 2009
www.springerlink.com

II. Materials and methods

A. Red blood cell preparation

Blood was drawn from the antecubital vein of healthy adult volunteers into EDTA (1.5 mg/ml). Red blood cells were separated from whole blood via 2,000 x g centrifugation for 10 minutes and the plasma and buffy coat were removed. Then the RBC were washed twice in phosphate buffer saline (PBS) of pH=7.4 (containing 5.8mM phosphate buffer, 150mM NaCl and 417mg/l KCl) at 20 °C and then subjected to various enzymatic treatments (Neuraminidase (Vibrio Cholerae Type III, Sigma), Pronase (Calbiochem, EMD Chemicals, Inc.) and α-Chymotrypsin (Bovine pancreas Type II, Sigma)). Afterwards treated RBC were washed twice in cold PBS and suspended in the desired measuring solutions.

B. Endothelial cell culture

Human umbilical vein endothelial cells (HUVEC) were purchased from Cambrex Corporation (UK) cultured in flasks and then transferred into 35 mm Petri dishes. 80% confluence was obtained before using them in the parallel-plate flow chamber adhesion assay (see below).

C. Parallel-plate flow chamber adhesion assay

The flow was generated by a syringe pump (PHD2000, Harvard) and the shear stress was then varied in a stepwise profile. Prior to rinsing the sample at defined shear rates, the RBC were allowed to settle for 6-8 minutes. The dynamics of RBC-EC adhesion were than recorded with an inverted microscope (IX71, Olympus) enclosed in an incubator in order to maintain a constant temperature at 37°C. Pictures were taken at the end of each rinsing period at 20 different locations and the adherence was finally quantified as the number of adherent RBC per unit area.

D. Characterization of the enzymatic treatments

For measuring the electrophoretic mobility of enzyme-treated and untreated cells, RBC were suspended in phosphate buffered sucrose solution with a 10 mM ionic strength at a hematocrit of about 0.05%. The zeta-potential was then determined with a Nano Zetasizer (Malvern Instruments, UK). The deformability of treated and untreated cells was quantified with a slit-flow ektacytometer (RheoScan-D200, SEWON Meditech, Inc).

III. Results

The treatment of RBC with the various enzymes lead to a moderate decrease of the elongation index indicating a decreased deformability of the cells after the proteolytic treatments as shown in Fig. 1.

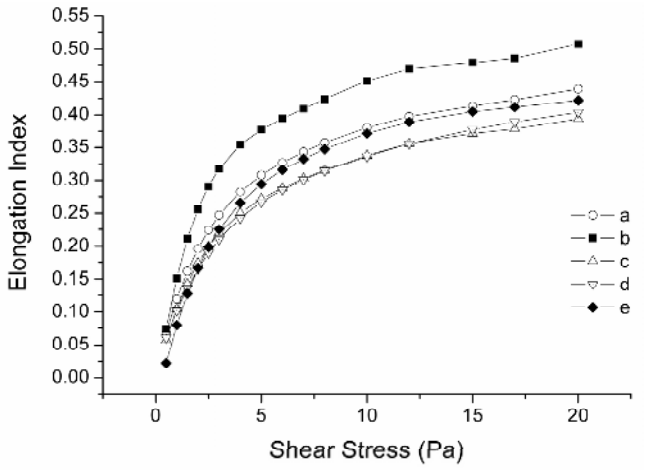


Figure 1: Impact of enzymatic treatment on RBC elongation index. a, 40 mg/dL α-chymotrypsin; b, control; c, 0.1 mg/ml pronase for 10-minute incubation; d, 40 mg/dL trypsin; e, 40 mg/dL neuraminidase.

The surface charge density was investigated via particle electrophoresis. As shown in Table 1, the treatment of RBC with proteolytic enzymes usually leads to a significant reduction of the electrophoretic mobility and thus the zeta potential. Only moderate concentrations of trypsin (20 mg/dL) did not lead to any measurable effect. The most significant reduction (>30%) could be observed after the treatment with neuraminidase. In contrast, the reduction of the deformability of the neuramindisae treated RBC was only moderate compared to the reduction after treatment with the other proteolytic enzymes.

Table 1: Eletrophoretic mobility and zeta-potential.

RBC	Mobility Measurements (μmcm/Vs)	Zeta Potential (mV)
Control	-3.220	-47.2
Pronase (0.1 mg/ml)	-2.934	-43.0
α-Chymotrypsin (40 mg/dL)	-2.865	-42.0
Trypsin (20 mg/dL)	-3.220	-47.2
Neuraminidase (40 mg/dL)	-2.150	-31.5

In another set of experiments we investigated the effects of the proteolytic enzyme treatment on the adhesion of RBC

to EC using a parallel-plate flow chamber. For the neuramindse treated RBC we observed a strong correlation between the reduction of the zeta potential and an increase of RBC adherence to EC as illustrated in Fig 2. Further the adhesion strength was also substantially increased withstanding shear stresses of up to 1 dynes/cm^2 (data not shown). For other enzymes such dramatic increases could not be observed, when the treated RBC were suspended in polymer free suspensions (data not shown).

Furthermore, as shown in Fig. 3, the presence of dextran (here 1 g/dL, 500 KDa) significantly enhanced the desialylated RBC adhesion to EC. Similar effects were also observed for dextran of 70 KDa and 2,000 KDa, with concentration ranging from 0.5-2.5 g/dL. Even though RBC treatment with pronase, trypsin and α-chymotrypsin did not enhance RBC-EC adhesion in polymer free suspensions, the presence of dextran with high molecular mass (>40 KDa) also induced RBC-EC adhesion (data not shown).

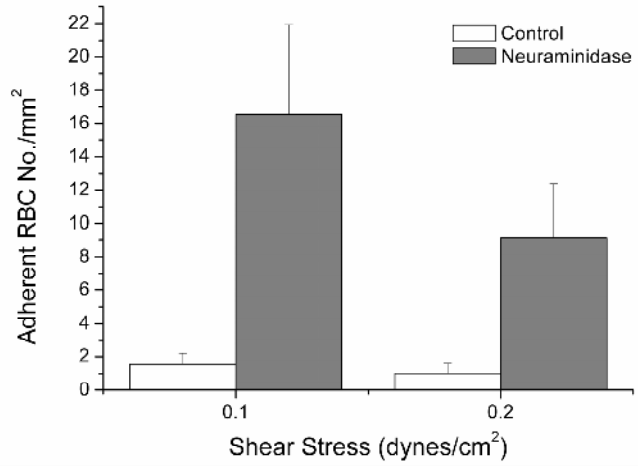


Figure 2: Desialylated RBC adhesion with EC.
The residual membrane zeta-potential of the treated RBC was -18.1.
The adherence was both conducted in PBS.

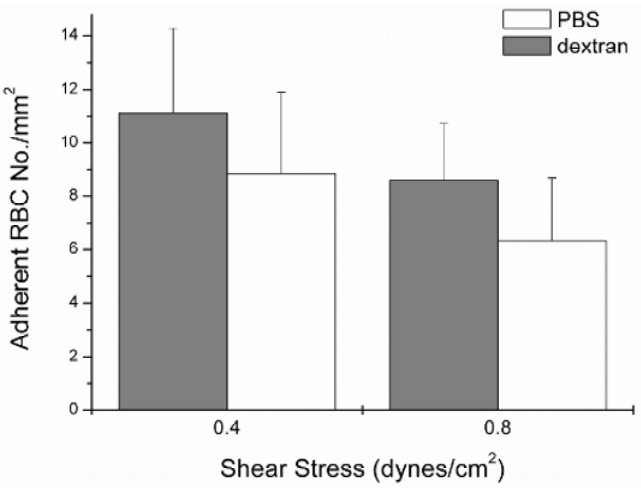


Figure 3: Impact of dexran on desialylated RBC adhesion with EC.
The residual membrane zeta-potential was -13.3 for both.
The concentration of dextran (500 KDa) was 1 g/dL.

IV. Discussion

The aim of this work was to test the hypothesis that macromolecular depletion can enhance adhesion of pathological RBC to EC. To mimic the impact of depleted plasma proteins on RBC-EC adhesion, we used the neutral polyglucose, dextran, with a wide range of molecular mass. RBC were treated with various proteolytic enzymes to mimic pathological cells. The dynamics of RBC-EC adhesion were recorded using a parallel plate flow chamber system.

Our results demonstrated a dramatically increased RBC-EC adhesion in the presence of high molecular mass dextran (>40KDa) under low shear stress (<1 dynes/cm^2). The adhesion increased with higher dextran molecular mass and concentration, and the presence of depleted polymers significantly increased the adhesion of enzyme treated RBC to EC. Our findings strongly suggest that the observed increase in the attractive forces have their origin in polymer depletion near the RBC and EC. Due to this macromolecular depletion, an attractive force develops that brings the adjacent surfaces closer together, leading to an increased number of binding sites available to the cell and thus more efficient and stronger adhesion of single cells.

RBC deformability, as quantified by varying shear stress with an ektacytometer, was found to decrease after the enzymatic treatments (Fig. 1). A reduction of deformability results in more rigid cell membrane, which in turn inhibits RBC to get in close contact with EC to establish adhesion. These changes in the deformability might explain why not all the enzymatic treatments have the same effect on RBC-EC adhesion.

V. Conclusion

In conclusion, this study demonstrates that polymer depletion can enhance the adhesion of pathological RBC to EC under low shear stress and quantifies for the first time the impact of physicochemical changes of the RBC membrane on its adhesion with EC in plasma like solutions. Thus our data should provide new insight into potential mechanisms for enhanced RBC-EC adhesion and disturbed in vivo blood flow in disease.

ACKNOWLEDGMENT

This project is supported by the Ministry of Education (Singapore) and A*Star (Singapore, BMRC grant 05/1/22/19/382).

REFERENCES

1. Hebbel, R.P., et al., Abnormal adherence of sickle erythrocytes to cultured vascular endothelium: possible mechanism for microvascular occlusion in sickle cell disease. J Clin Invest, 1980. **65**(1): p. 154-60.
2. Wautier, J.L., et al., Increased adhesion of erythrocytes to endothelial cells in diabetes mellitus and its relation to vascular complications. N Engl J Med, 1981. **305**(5): p. 237-42.
3. Shiu, Y.T., M.M. Udden, and L.V. McIntire, Perfusion with sickle erythrocytes up-regulates ICAM-1 and VCAM-1 gene expression in cultured human endothelial cells. Blood, 2000. **95**(10): p. 3232-41.
4. Nash, G.B., C.S. Johnson, and H.J. Meiselman, Mechanical properties of oxygenated red blood cells in sickle cell (HbSS) disease. Blood, 1984. **63**(1): p. 73-82.
5. Brittain, H.A., et al., Thrombospondin from activated platelets promotes sickle erythrocyte adherence to human microvascular endothelium under physiologic flow: a potential role for platelet activation in sickle cell vaso-occlusion. Blood, 1993. **81**(8): p. 2137-43.
6. Kaul, D.K., et al., Sickle erythrocyte-endothelial interactions in microcirculation: the role of von Willebrand factor and implications for vasoocclusion. Blood, 1993. **81**(9): p. 2429-38.
7. Hebbel, R.P., C.F. Moldow, and M.H. Steinberg, Modulation of erythrocyte-endothelial interactions and the vasocclusive severity of sickling disorders. Blood, 1981. **58**(5): p. 947-52.
8. Wautier, J.L., et al., Fibrinogen, a modulator of erythrocyte adhesion to vascular endothelium. J Lab Clin Med, 1983. **101**(6): p. 911-20.
9. Bäumler, H., et al., Electrophoresis of human red blood cells and platelets. Evidence for depletion of dextran. Biorheology, 1996. **33** (4-5): p. 333-351.
10. Neu, B. and H.J. Meiselman, *Depletion-mediated red blood cell aggregation in polymer solutions.* Biophysical Journal, 2002. **83**(5): p. 2482-2490.
11. Stewart, W.B., C.W. Petenyi, and H.M. Rose, *The survival time of canine erythrocytes modified by influenza virus.* Blood, 1955. **10**(3): p. 228-34.
12. Rogers, M.E., et al., Decrease in erythrocyte glycophorin sialic acid content is associated with increased erythrocyte aggregation in human diabetes. Clin Sci (Lond), 1992. **82**(3): p. 309-13.
13. Hanson, V.A., et al., *Plasma sialidase activity in acute myocardial infarction.* Am Heart J, 1987. **114**(1 Pt 1): p. 59-63.

Author: Björn Holger Neu
Institute: Nanyang Technological University
Street: 50 Nanyang Avenue, Singapore, 639798
City: Singapore
Country: Singapore
Email: neu@ntu.edu.sg

Comparison of Motion Analysis and Energy Expenditures between Treadmill and Overground Walking

R.H. Sohn[1], S.H. Hwang[1], Y.H. Kim[2]

[1] Dept of Biomedical Engineering, Graduate School, Yonsei University, Korea
[2] Dept of Biomedical Engineering and Institute of Medical Engineering, Yonsei University, Korea

Abstract — **In this study, treadmill walking and overground walking were compared at the same condition based on kinematics and energy expenditures (EE). In addition, we compared the actual energy expenditure and calculated EE by treadmill. The kinematics of treadmill and overground gait were very similar. The values at each joint were significantly different($p<0.05$), but magnitude of the difference was generally less than 3°. EE of treadmill walking was significantly greater when measured on the overground. It seemed to be the increased stress during the gait by the continuous movement of the belt. As the velocity increased, there was significant difference between actual EE and calculated EE by treadmill due to EE curve increasing exponentially. Therefore the further study would be required to find the correlation of the two methods and calibrate the values from them.**

Keywords — **Walking, kinematic, Energy Expenditures, Treadmill, Over ground**

I. Introduction

Walking is most natural activity and the only sustained dynamic aerobic exercise that is common to everyone except for the seriously disabled or very frail. This is beneficial through engendering improved fitness and greater physiological activity and energy turnover[1].

The treadmill can be used to walking for the health. In previous studies, measurements were taken on the treadmill and during overground walking. And many measurements have been made of the energy expenditure of persons walking at varying speeds on level ground or on the treadmill[2,3,4].

The results for walking at rates up to 8k/m/hr and for running at velocities of 8-21km/hr are substantially the same as those of Margaria et al.(1963)[5]. At higher velocities the relation for walking is linear as in running, but the slope is twice as steep.[6] Energy cost results were different between the treadmill and overground walking at same walking condition.

In this study, treadmill walking and overground walking were compared at the same condition based on kinematics and energy expenditures (EE). In addition, we compared the actual energy expenditure and calculated EE by treadmill.

II. Materials & Method

A. Subjects

A healthy mail were participated in this study. The patient was asked to walk as the convenient speed.

Table 1 Subject parameters (n = 11)

Characteristics	Age(years)	Weight(kg)	Height(cm)
Mean	25.5	72.5	173.1
SD	0.9	10.6	6.0

B. 3D Motion Analysis System

An six-camera, three dimensional motion analysis system(VICON612, UK) was used to record kinematic data at 120 Hz. And treadmill(HP Cosmos Gatway II) was used. Fig. 1 showed that the treadmill walking in 3D motion analysis system.

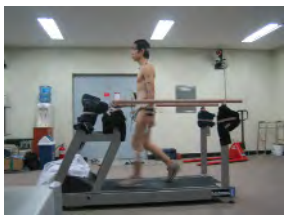


Fig. 1 Treadmill Walking

C. EE Calculation

We calculated energy cost values of walking on the treadmill compared to those on theMetamax3x.

Equation (1) is showed weir Method using the calculated EE by Metamax3xd[7]. And Equation (2) is showed Margria fomular using the calculated EE by treadmill[8].

$$Kcal/min = [(1.1 \times RER)+3.9] \times VO2 \quad (1)$$

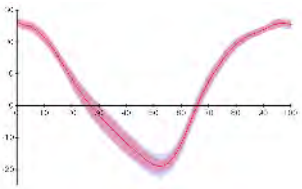
$$KJ = (2.67+(10.9+0.654 \times V \text{ in } \%) \times (S \text{ in m/sec})) \times T \text{ in min} \times W \text{ in kg} \times 0.0211 kJ/ml\ O2 \quad (2)$$

Chwee Teck Lim, James C.H. Goh (Eds.): ICBME 2008, Proceedings 23, pp. 1928–1930, 2009
www.springerlink.com

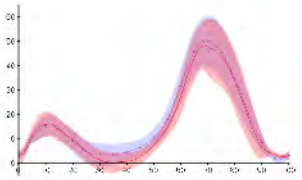
III. Result

A. Kinematic Data

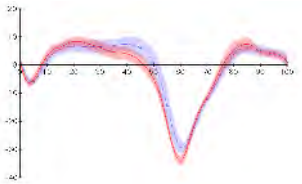
The kinematics of treadmill and overground gait were very similar. The values at each joint were significantly different ($p<0.05$), but magnitude of the difference was generally less than 3° (Fig. 2).



(a) Hip Angles



(b) Knee Angles



(c) Ankle Angles

Fig. 2 Kinematic Data of Treadmill and Over ground
(Over ground: ---▲----▲--- Treadmill: ----------)

B. Energy cost

EE of treadmill walking was significantly greater when measured on the overground.

Table 2 Energy Expenditure in Treadmill vs Overground

Walking Conditions	Treadmill	Overground
Heart Rate [1/min]	*106.67±3.92	*95.12±4.23
Rel. O_2 Uptake [ml/min/kg]	*19.05±2.54	*16.87±3.09
Energy Expenditure [kcal/min]	*6.68±1.20	*5.22±0.66

*represents significant difference (P<0.05)

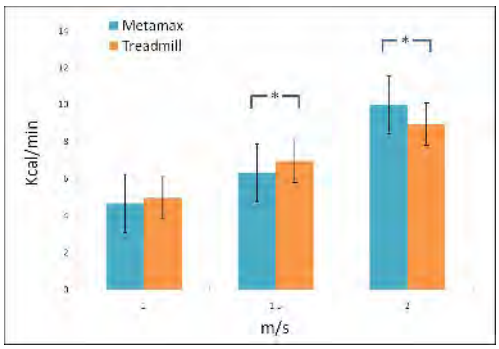


Fig. 3 Energy Expenditure Treadmill vs Metamax3x
* represents statistically significant difference ($p < 0.05$)

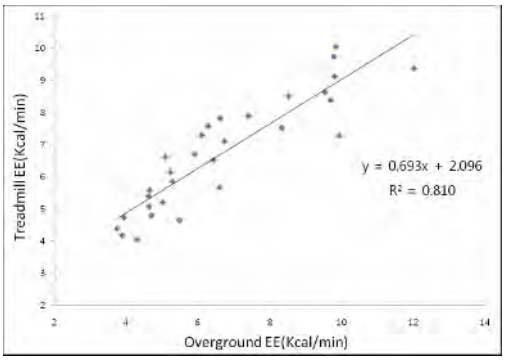


Fig. 4 Regression Analysis Treadmill vs Overground

Fig. 3 presents the energy cost values of walking on the treadmill compared to those on the Metamax3x. The EE of treadmill calculated was 6.3% greater than the EE of Metamax3x in walking speed 1.0m/s but there was no statistically significant difference.

The EE of treadmill calculated was 10.5% greater than the EE of Metamax3x in walking speed 1.5m/s. And The EE of treadmill calculated was 11.7% greater than the EE of Metamax3x in walking speed 2.0m/s. There was a statistically significant difference between walking speed 1.5m/s and 2.0m/s ($p < 0.05$).

Fig. 4 presents the energy cost values of walking on the treadmill compared to those on the overground by Metamax3x. The regression line equation shows That EE on the treadmill was 0.7 times greater than on the overground. The correlation of determination (R^2) was equal to 0.81.

IV. Discussion & Conclusions

The kinematics of treadmill and overground gait were very similar. EE of treadmill walking was significantly greater when measured on the overground. It seemed to be

the increased stress during the gait by the continuous movement of the belt. As the velocity increased, there was significant difference between actual EE and calculated EE by treadmill due to EE curve increasing exponentially. Therefore the further study would be required to find the correlation of the two methods and calibrate the values from them.

Acknowledgment

This research was supported by the MKE(Ministry of Knowledge Economy), Korea.

References

1. Jessica Rose, PhD, James G. Gamble, MD, PhD, (2005) "Human Walking 3rd Edition", pp.141-150
2. Marco Traballesi et al(2007), "Energy cost of walking measurements in subjects with lower limb amputation", ScienceDirect, GAIPOS-2397
3. Patrick O. Riley et al(2007), "A Kinematic and Kinetic comparison of overground and treadmill walking in health subjects", Gait & Posture 26,pp.17-24
4. Dick H. Thijssen et al(2007), Decreased Energy Cost and Improved Gait Pattern Using a New Orthosis in Persons with Long-Term Stroke, Arch Phys Med Rehabil, Vol88
5. Margaria, R., Cererelli, P., Aghemo, P. & Sassi, G.(1963), Energy cost of running, J. appl. Physiol. 18, pp.367-370
6. Menier DR, Pugh LG, (1968) The relation of oxygen intake and velocity of walking and running, in competition walkers. J Physiol, 197(3),: 717-21
7. McArlde WD, Katch FI, Latch VL(2000), Essentials of exercise physiology, 2th ed, Baltmore, Williams & Wilkins
8. MARARIA R(1976), Biomechanics and energetic of muscular exercise. Clarendon Press, Oxford

Author: Young Ho Kim
Institute: Yonsei University
Street: Wonju
City: Gangwon
Country: Republic of Korea
Email: younghokim@yonsei.ac.kr

Simultaneous Strain Measurements of Rotator Cuff Tendons at Varying Arm Positions and The Effect of Supraspinatus Tear: A Cadaveric Study

J.M. Sheng[1], S.M. Chou[1], S.H. Tan[1], D.T.T. Lie[2], K.S.A. Yew[2]

[1]Nanyang Technological University/School of Mechanical and Aerospace Engineering, Singapore
[2] Singapore General Hospital/Department of Orthopaedics, Singapore

Abstract — **Aim: This study aims to measure strains on the different rotator cuff tendons simultaneously and demonstrate the effect of supraspinatus tear on other cuff tendons with an intact glenohumeral joint.**

Methodology: Four fresh-frozen shoulders were tested on a purpose-built rig in preliminary tests. With 10 kg loaded at the rotator cuff muscles, displacement variable reluctance transducers (DVRTs) were used to measure the supraspinatus, infraspinatus and subscapularis tendons strains simultaneously at varying elevation angles and planes. Simulated partial thickness tears were cut at the bursal-side of the supraspinatus and sequentially enlarged to full-thickness tear.

Results: Preliminary results showed the variation of strain with respect to different arm positions. In all three planes, strain of the supraspinatus at the bursal surface reduced with increasing elevation angle while its articular surface increased. There were strain variations between the anterior and posterior supraspinatus. It was observed that the strain of the remaining intact rotator cuff tendons increased with a propagating tear at the supraspinatus. With a tear at the anterior supraspinatus, the strain of infraspinatus was visibly increased. As the anterior tear propagated to the posterior side, the infraspinatus strain only further increased slightly. A more distinct strain increase was seen in the subscapularis as the tear propagated posterior to form a complete tear.

Conclusion: Quantitative information on the strain of the rotator cuff tendons at various elevation planes was found. The strain difference within supraspinatus implied occurrence of shearing which may cause intratendinous tears. Tears in supraspinatus elevate strain on the two adjacent cuff tendons and should be treated before the tears propagate.

Keywords — **Rotator cuff tendons, tears, arm positions, DVRTs.**

I. Introduction

The rotator cuff functions as a dynamic stabilizer of the glenohumeral joint, keeping the humeral centre within the supraspinatus (SS), infraspinatus (IS), subscapularis (SC) and teres minor (TM), which are subjected to a variety of forces glenoid during active arm elevation. It consists of the as the position of the arm changes during glenohumeral motion. Previous strain studies concentrated solely on supraspinatus [1-4]. None had measured strains on the different rotator cuff tendons simultaneously and shown the effect of SS tear on other cuff tendons with the glenohumeral joint intact. This study aims to investigate the effect of arm positions and SS tendon tears on the strain profile of the rotator cuff tendons.

II. Materials and methods

A. Specimen preparation and dissection

Four cadaveric specimens, which consist of the whole upper limb, were harvested and frozen at -20^{0}C within 24 hours of death. The mean age of the specimens was 74 years (65 to 78) and all were from men. One was from the left shoulder and three were from the right. Before dissection, each specimen was thawed at room temperature for approximately 12 hours. Throughout testing they were moistened with physiological saline.

During dissection, the forearm was first disarticulated from the upper arm. All soft tissues, except the rotator cuff muscles and tendons, were removed. The clavicle was also detached from the acromion. The rotator cuff muscles were detached from the scapula and cut, leaving muscles of approximately 40mm medial to the musculo-tendinous region for suturing of loading lines. Loop stitches were used to suture along the seven lines of muscle action (two lines on SS, IS and SC each, one line on TM).

The specimen was mounted on a purpose-built rig which was modified from Hatakeyama's customised shoulder positoner [1]. The rig was designed to have the flexibility of adjusting the positions and angles of the pulleys to adapt the different lines of muscle action (Fig. 1). The muscles were loaded with a total of 10kg along the lines of muscle action.

Chwee Teck Lim, James C.H. Goh (Eds.): ICBME 2008, Proceedings 23, pp. 1931–1934, 2009
www.springerlink.com

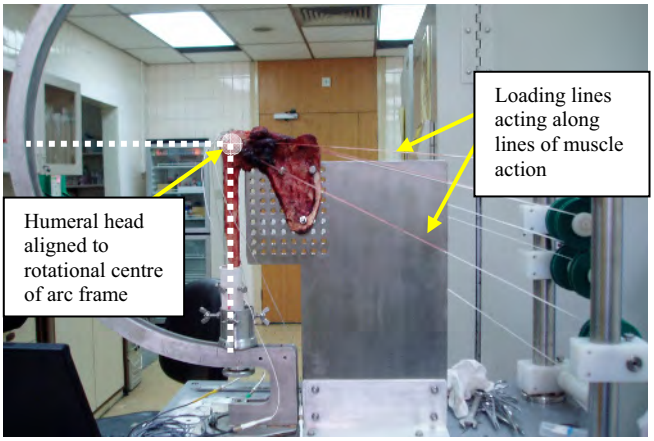


Fig. 1 Mounting of shoulder specimen with humerus at reference position

B. Differential variable reluctance transducers

Tendon strains were measured using linear differential variable reluctance transducers (DVRTs; M-DVRT-3, Microstrain Inc, Burlington, Vermont) [1-4]. A total of five DVRTs were used to measure the strain of the SS (articular side, anterior and posterior of bursal side), IS and SC tendons simultaneously. Each DVRT put out an analog voltage linearly proportional to the displacement of the magnetic core. The core and the body were attached to the tendons through two 3-mm long barbed pins. Because the core slid freely within the tube, this device had little influence on the change in length of the tendon being tested. Any change in the length of the tissue caused the core to slide in the body, resulting in a change of output voltage. They were calibrated prior to the experiment. Strain was defined according to the equation below:

$$\text{Strain} = \frac{\text{New barb distance} - \text{Initial barb distance}}{\text{Initial barb distance}}$$

The initial distance is the length between the two barbed points of the transducer with the humerus at the reference position and is used as the reference 'zero' position used in the calculation of tendon strain.

In order to have a wider range of positions tested on the glenohumeral joint, the acronium and corocoid process were clipped off to prevent impingement of the DVRTs during experiment. Between the SS and SC, the rotator interval was opened. A trough was created at the humeral head and a hole was drilled through to the surgical neck of the lateral humerus for the insertion of the DVRT at the articular side of the SS (Fig.2). DVRTs were orientated parallel to the line of muscle action at the centre of each tendon portion and were inserted with the humerus at reference position.

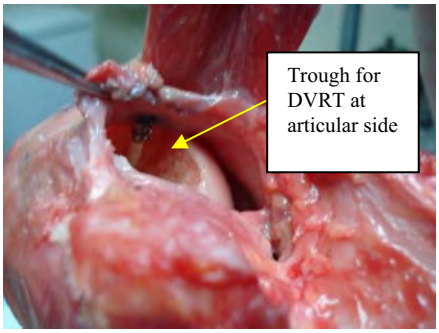


Fig. 2 Trough for DVRT at articular side

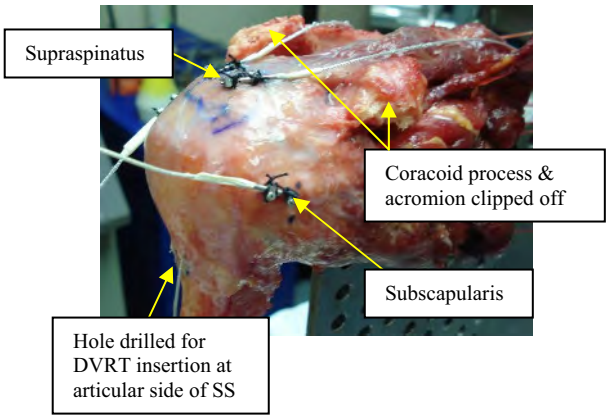


Fig. 3 DVRT insertions

After insertion, the DVRTs were sutured with surgical suture threads into the tendons to avoid loosening and eventually falling off from the tendons (Fig. 3). Pilot tests had shown no significant effect of suturing on the strain readings of the tendon.

C. Experiment variables

Arm positions: The humerus was elevated in the scapular, coronal, and sagittal planes. The scapula plane was defined to be inclined 45° to both the sagittal and coronal planes. Arm elevation angles were 0°, 15°, 30°, 45°, 60° and 75° relative to the scapula. The order of the elevation plane was 1) scapular plane, 2) sagittal plane, and 3) coronal plane. After one plane was finished, the humerus was brought back to the reference position before the measurements in the next plane were started.

Rotator cuff tears: Four types of simulated tears were made on the bursal portion of the SS tendon at the "critical zone" described by Codman [5]. For each tear, strain readings were collected with the humerus in the reference position. A 2-mm deep partial thickness tear was first cut on the

anterior SS, 1/2 width of the tendon in the anterior-posterior direction (Ant 2mm tear). This tear mimicked a partial-thickness tear on the bursal side of the SS due to subacromial impingement. Subsequently, this 2-mm cut was deepened to a full tear at the anterior portion of the SS (Ant full tear). Subsequently, this full tear was extended to ¾ width of the tendon in the anterior-posterior direction (¾ full tear). Finally, the tear was extended to the total width of the SS, resulting in a complete tear (Complete tear).

D. Data collection

Pilot results had not shown significant hysteresis during testing cycles, but the results were always recorded with increasing elevation angle. The system was preconditioned by elevating the shoulder up and down for 25 times to minimise the viscoelastic effect of the soft tissue. The output of the DVRTs was recorded over three cycles of elevation for each plane and simulated tear type and the average output was taken.

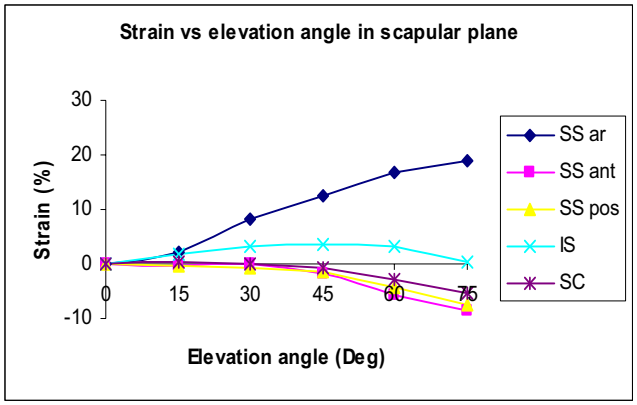
III. Results

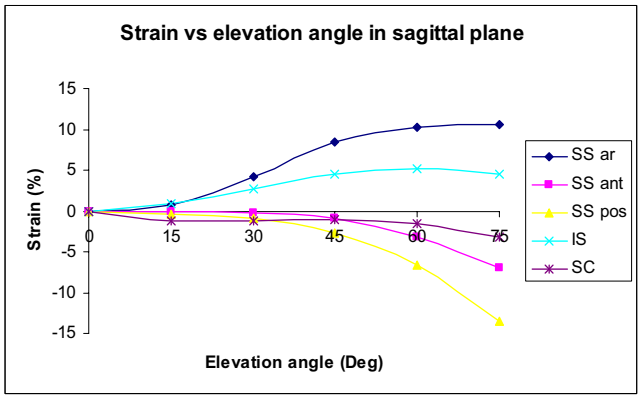
A. Arm positions

Scapular plane: During abduction from 0° to 75°, the strain on the articular side of the SS (SS ar) increased to +19.0%. Between 0° to 30°, the strain on both the anterior and posterior SS at the bursal side (SS ant, SS pos) remained relatively unchanged. With increasing elevation angle, the strains of the SS ant and SS pos decreased to -8.5% and -7.7% respectively at 75° elevation. The strain of the IS increased to a peak of +3.6% at 45° elevation. Further increase in elevation angle led to a drop in the strain, with a strain of +0.4% at 75° elevation. The strain of SC gradually decreased to –5.5% with increasing elevation angle.

Sagittal plane: With increasing elevation angle, SS ar gradually increased to +10.5% at 75° elevation. SS ant strain remained relatively constant between 0° and 45° before it decreased gradually to –7.0% at 75°. With increasing elevation angle to 75°, the strain of the SS pos decreased to -13.5% while IS increased and reached a plateau of +5.1%. The SC strain decreased gradually to -3.2%

Coronal plane: Between 0° to 15° of elevation, the strain values the supraspinatus remained almost constant. Further increase in elevation angle to 60° caused a drop in strain for SS ant and SS pos to –5.0% and –7.6% respectively and an increase in strain for SS ar to 6.9%. The strain of IS remained almost constant while SC decreased to -4.2% at 60° elevation.





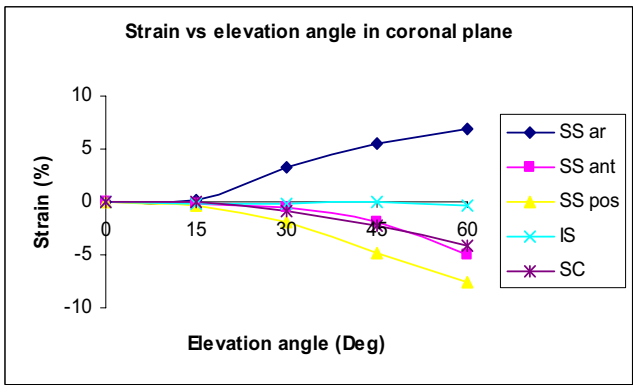


Fig. 4 Variation of strain with elevation angle in the three planes

The results showed the variation of strains with respect to different arm positions. In general, strain of SS at the bursal side reduced with increasing elevation angle while it increased at the articular sides in all three planes. This trend coincided with Reilly's finding in the scapular plane [3]. The strain difference between the anterior and posterior SS was also observed. It could be due mainly to the anatomical

aspect of the glenohumeral joint. Moreover, the anatomical configuration of the SS muscle–tendon complex was revealed to be inhomogeneous, with a thicker anterior portion adjoining the thinner, wider posterior side [6]. Differential strain causes shearing between the layers of the SS tendon, which may contribute to the propagation of intratendinous defects that are initiated by high articular side strains.

B. Rotator cuff tears

In general, the strain of the tendons increased with a propagating tear at the SS.

SS ar: Strain increased to +1.0% with ant 2mm tear and further increased to +2.5% when deepened to ant full tear.

SS ant: Strain increased to +3.5% with ant 2mm tear.

SS pos: Strain increased slightly to +0.2% and +0.7% with ant 2mm tear and ant full tear respectively

IS: Strain increased slightly to +0.4% with ant 2mm tear. An ant full tear resulted in a steep increase to +1.2%. Further propagation to complete tear caused gradual increase in strain to +1.4%.

SC: Slight strain increased to +0.15% as tear deepened to ant full. Propagation of tear to ¾ full tear resulted in a greater strain increase to +0.8%. A complete tear further increased strain to +0.9%.

With a tear at the anterior SS, the strain was redistributed within the intact SS, thus a higher strain at the articular and the posterior side. It is important to highlight the increase in IS tendon strain with an anterior SS tear. IS tear often occurs in the presence of a full-thickness tear in the anterior portion of the SS [7]. This correlates to the present experimental findings whereby the IS strain increases with an initial anterior SS partial tear and increases with with a full anterior tear. However there was less IS strain increase as the full anterior tear was propagated to a complete tear. On the contrary, there was no significant strain increase in the SC with an anterior SS tear. However, there was obvious SC strain increase as the anterior SS tear was propagated to a complete tear.

IV. Conclusions

Elevation of the arm in three different planes mimics many different daily life activities. Quantitative information on the strain of the different rotator cuff tendons was found and it would be useful to surgeons and physiotherapists during their assessment of patients while moving the patients' arms passively. It was observed that the strain of the remaining intact rotator cuff tendons increased with a propagating tear at the SS. Non-treatment of SS tears may result in tear propagation to IS and SC in the long run.

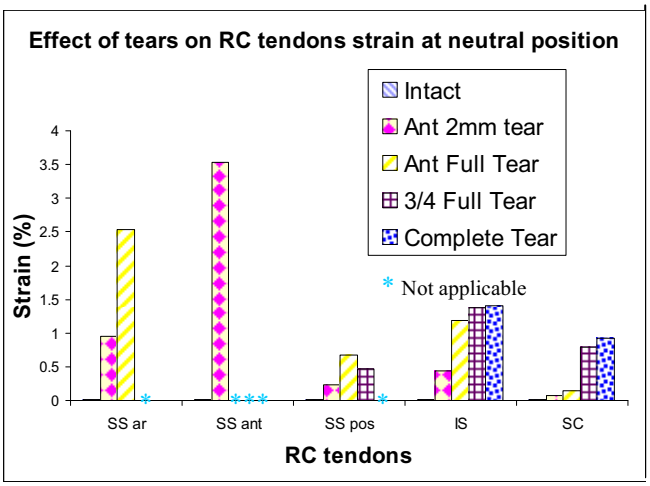


Fig. 5 Effect of tears on rotator cuff tendon strains at neutral position

References

1. Y. Hatakeyama, E. Itoi, R. L. Pradhan, M. Urayama, and K. Sato, "Effect of arm elevation and rotation on the strain in the repaired rotator cuff tendon. A cadaveric study," Am J *Sports* Med, vol. 29, pp. 788-794, 2001.
2. Y. Hatakeyama, E. Itoi, M. Urayama, R. L. Pradhan, and K. Sato, "Effect of superior capsule and coracohumeral ligament release on strain in the repaired rotator cuff tendon. A cadaveric study," Am J *Sports* Med, vol. 29, pp. 633-640, 2001.
3. P. Reilly, A. A. Amis, A. L. Wallace, and R. J. Emery, "Mechanical factors in the initiation and propagation of tears of the rotator cuff. Quantification of strains of the supraspinatus tendon in vitro," *J Bone Joint Surg Br*, vol. 85, pp. 594-599, 2003
4. P. Reilly, A. A. Amis, A. L. Wallace, and R. J. Emery, "Supraspinatus tears: propagation and strain alteration," *J Shoulder and Elbow Surg*, vol. 12, pp. 134-138, 2003
5. Codman EA. The shoulder. Boston: Thomas Todd; 1934
6. M. S. Roh, V. M. Wang, E. W. April, R. G. Pollock, L. U. Bigliani, and E. L. Flatow, "Anterior and posterior musculotendinous anatomy of the supraspinatus," *J Shoulder and Elbow Surg*, vol. 9, pp. 436-440, 2000
7. L. Yao and U. Mehta, "Infraspinatus muscle atrophy: Implications?," *Radiology*, vol. 226, pp. 161-164, 2003

Author: J.M Sheng
Institute: Nanyang Technological University
Street: NTU, School of MAE, N3.1-B2a-01 Physiological Mechanics Lab S(639798)
City: Singapore
Country: Singapore
Email: shengj@pmail.ntu.edu.sg

Tensile Stress Regulation of NGF and NT3 in Human Dermal Fibroblast

Mina Kim[1], J.W. Hong[1], Minsoo Nho[2], Yong Joo Na[2] and J.H. Shin[1]

[1]Department of Mechanical Engineering, KAIST, Republic of Korea
[2]Amore-Pacific Corporation R&D Center, Republic of Korea

Abstract — **Fibroblast is a major type of mechanosensitive cells in connective tissues, which transfers mechanical signals to intercellular biochemical events. Numerous previous studies have shown that the tensile stress alters ECM-related gene expression in fibroblast. The aim of this study is to investigate the effects of tensile stress on the neurotrophin expression of dermal fibroblast *in vitro*. Human dermal skin fibroblast cells synthesize and release neurotrophins such as nerve growth factor (NGF) and neutrophin-3 (NT3). NGF and NT3, members of NT (neurotrophin) family, stimulates fibroblast migration and are related to wound healing. Also, it is known that upregulation of NGF takes part in maintaining the biomechanical properties of the dermis. In this study, seeded cells on the polydimethylsiloxane(PDMS) substrate using a tensile stimulation device. At the uniaxial stretch of 10% strain and frequency of 0.5 Hz, different resting times of 0 min, 20 min, and 60 min were placed in between 10 min stimulations periods for the total stimulation of 1 hr and 2 hr. Results have shown that NGF mRNA levels had increased after 1 hr of stimulation, and more NGF mRNA was transcribed up to twofolds as the resting time increased. However, the level of mRNA transcription had decreased upon additional stimulation. On the other hand, NT3 mRNA levels had decreased by 50% in all applications. This result demonstrates that the tensile stress may regulate the expression of NGF and NT3, which could be a key factor for the neurocosmetic applications. We also investigated the effects of frequency and the magnitude of strain on the gene expression.**

Keywords — **Tensile stress, Fibroblast, NGF, NT3.**

I. Introduction

Fibroblast is constantly subjected to mechanical loads in connective tissues where mechanical signals are converted to intercellular biochemical events [1, 2, 3]. The influence of external force on skin is transferred through epidermis to the dermis while internal forces are transmitted in opposite direction [4]. Numerous previous studies have shown that the tensile stress on fibroblasts alters ECM-related and inflammation-related gene expressions [5, 6, 7]. In this study, we investigate the effects of tensile stress on the NGF and NT3 expression of dermal fibroblast *in vitro*. NGF and NT3, members of NT (neurotrophin) family are produced by fibroblasts and NGF stimulated fibroblast migration and is related to maintaining the biomechanical properties of the dermis [8, 9]. Two main objectives of this study was : first to investigate change of NGF and NT3 mRNA expression by uniaxial tensile stress: secondly to determine whether the resting periods is critical on magnitude of gene expression regulation.

The result of this study indicates that tensile stress may regulate NGF and NT3 which could be a key factor for the neurocosmetic applications. Also, results from different resting periods show that expression of gene regulation by tensile stress requires appropriate resting time.

II. Materials and Methods

A. Fibroblast cultures

Human dermal fibroblast cells were acquired from the Amore-Pacific Corporation R&D Center (Republic of Korea). The cells were cultured in Dulbecco's modified Eagle's medium (Lonza) containing 10% fetal bovine serum (GibcoBRL) supplemented with penicillin–streptomycin. Cultures were incubated in a humidified atmosphere of 5% CO_2 in air at 37^{o}C.

B. Mechanical stretch

Fibroblasts were seeded on the polydimethylsiloxane (PDMS) substrate coated 1% fibronectin solution (Invitrogen). The cells were loaded on the lab-made tensile stimulation device and mechanically stretched. The applied uniaxial stretch was 10% strain at a frequency of 0.5 Hz. Stimulation for 10min was placed in between different resting periods of 0 min, 20 min, and 60 min during total stimulation time 1hr and 2hr. Stretch experiments were carried out at 37 ^{o}C in 5% CO_2 .

C. RNA extraction and Real Time PCR

Total RNA was isolated from fibroblasts with TRIZOL Reagent (GibcoBRL) at the end of each experiment. RNA quantification was performed using the NanoDrop® ND-1000 spectrophotometer. cDNA was synthesized using Superscript III (Invitrogen) according to the manufacturer's instructions. Real time PCR for target genes was done using a RotorGene 3000 (Corbett Research) according to a set

Chwee Teck Lim, James C.H. Goh (Eds.): ICBME 2008, Proceedings 23, pp. 1935–1937, 2009
www.springerlink.com

program. The results of real time PCR were analyzed by the relative yield of the PCR product from target gene to that from the house keeping GAPDH (glyceraldehyde-3-phosphate dehydrogenase) gene. Mean values from different independent experiments were calculated.

III. Results

A. Regulation of NGF and NT3 in human dermal fibroblast by tensile stress

To obtain insight into the requirement of resting time in change of gene expression by tensile stress, we studied the response of different resting duration on NGF and NT3 mRNA levels [12, 13]. Resting times were given as 0min, 20min, and 60min between 10 min stimulations periods. Figure 1 shows the effects of resting time on expression level of NGF and NT3. NGF mRNA was transcribed up to two-folds after 60 min of resting time [Fig1.a]. Also, the mRNA transcription level of NT3 was decreased after 60 min of resting time [Fig1.b]. The highest level of NGF mRNA and the lowest level of NT3 mRNA were observed after 60min of resting time.

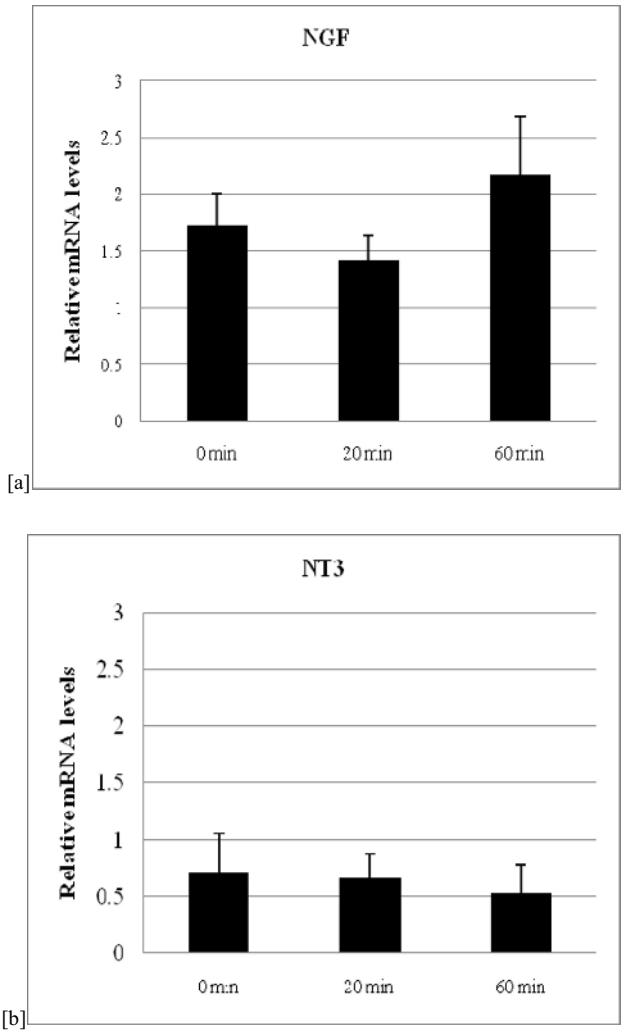


Fig. 1 Resting time during tensile stress and regulation of endogenous NGF and NT3 mRNA

B. NGF and NT3 mRNA levels in tensile stress by different stimulation time

To determine the effects of total stimulation time on expression level of NGF and NT3, cells were stimulated with 10 % at 0.5 Hz frequency, resting time 60 min were placed in between 10 min stimulation periods for the total stimulation of 1 hr or 2 hr. NGF mRNA was transcribed up to two-folds after 1hr stimulation. However, the level of NGF mRNA transcription had decreased upon additional 1hr stimulation. For NT3, mRNA level was decreased by half after 1hr stimulation, and not much difference was observed after additional stimulation [Fig2]. Therefore, we concluded that stimulation longer than 1hr is not necessary to observe more dramatic result in this experiment.

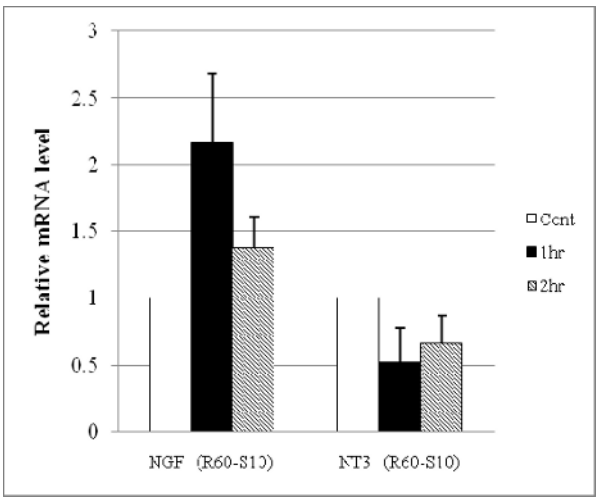


Fig. 2 Total stimulation time and expression of NGF and NT3 mRNA

IV. Discussion

Here we observe NGF enhancement and NT3 reduction in response to the uniaxial stretch in human dermal fibroblast. Results for resting time show that the highest level of NGF mRNA and the lowest level of NT3 mRNA were ob-

served after 60min of resting time. The results of total stimulation time show that NGF mRNA levels had increased after 1 hr of stimulation. However, the level of mRNA transcription had decreased upon additional stimulation. NT3 mRNA levels had decreased by 50% in all applications but not much difference was observed after additional stimulation.

V. Conclusions

In this study shows that tensile stress may regulate NGF and NT3 which could be a key factor for the neurocosmetic applications. Also, result for different resting time shows that regulation of gene expression by tensile stress requires appropriate resting time.

Acknowledgment

This work was supported by a grant from the Amore-Pacific Corporation R&D Center.

References

1. Riley GP (2005) Gene expression and matrix turnover in overused and damaged tendons. Scand J Med Sci Sport 15: 241-251
2. MacKenna D, Summerour SR and Villarreal FJ (2000) Role of mechanical factors in modulating cardiac fibroblast function and extracellular matrix synthesis. Cardiovasc Res 46:257-263
3. Wang JH, Thampatty BP, Lin JS et al (2007) Mechanoregulation of gene expression in fibroblasts. Gene 391:1-15
4. Silver FH, Siperko LM, Seehra GP. (2003) Mechanobiology of force transduction in dermal tissue. Skin Res Technol 9: 3-23
5. Yang G, Crawford RC, Wang JH (2004) Proliferation and collagene production of human patellar tendon fibroblasts in response to cyclic uniaxial stretching in serum-free conditions. J Biomech 37:1543–1550
6. Tsuzaki M, Bynum D, Almekinders L et al (2003) ATP modulates load-inducible IL-1beta, COX 2, and MMP-3 gene expression in human tendon cells. J Cell Biochem 89:556–562
7. Tsuzaki M, Guyton G, Garrett W et al (2003) IL-1 beta induces COX2, MMP-1, -3 and -13, ADAMTS-4, IL-1 beta and IL-6 in human tendon cells. J Orthop Res 21:256–264
8. Yaar M (1999) Neurotrophins in skin. In: Neurotrophins and the neural crest. CRC Press, London.
9. Bonte F, Viennet C, Dumas M et al (2006) NGF presents tensile properties in human skin dermis. Cell Research 16: S1-S9

Author: Jennifer Hyunjong Shin
Institute: Department of Mechanical Engineering, KAIST
Street: Goo-sung Dong, Yu-sung Gu
City: Daejon
Country: Republic of Korea
Email: j_shin@kaist.ac.kr

Influence of Component Injury on Dynamic Characteristics on the Spine Using Finite Element Method

J.Z. Li[1], Serena H.N. Tan[1], C.H. Cheong[1], E.C. Teo[2], L.X. Guo[2], K.Y. Seng[1]

[1] Bioengineering Laboratory, Defence Medical & Environmental Research Institute, DSO National Laboratories, 27 Medical Drive, #09-01, Singapore 117510, Republic of Singapore
[2] School of Mechanical and Aerospace Engineering, Nanyang Technological University, 50 Nayang Avenue, Singapore 639798, Republic of Singapore

Abstract — **Long-term whole body vibration (WBV) presents health risks to the spine. A frequency value near the resonant frequencies of the human body may increase the vibration effect of the lumbar spine. In this study, to better understand the dynamic characteristics of the human spine, we developed a detailed three dimensional finite element (FE) model of the low thorax to pelvis segment, T12-S1, based on actual vertebral geometry. We implemented several analyses to investigate how injuries on various spinal components affect the frequency characteristics of the human spine under WBV. Our results show that all the considered spinal component injuries including denucleation, facetectomy and removal of capsular ligaments lowered the resonant frequency of human spine. Our findings may be useful to provide guidelines for clinical treatment and for product design and development in industry.**

Keywords — **Lumbar spine, whole body vibration, resonant frequency, injury, finite element method**

I. Introduction

Long-term whole body vibration (WBV) represents a health risk for the lumbar spine [1], especially for the lower lumbar motion segments. A number of investigations have been carried out to investigate the dynamic characteristics of the human spine to provide insights into the relationship between vibration and low back pain. Besides these experimental studies, numerous finite element (FE) models have also been developed to investigate the frequency characteristics of the human spine [2–5]**.** These FE studies have provided useful information, but the simulated results reported were generally different from the experimental data (4~6Hz) [6, 7]. In addition, it is presently unclear how injured spinal components could affect the frequency characteristics of the human spine under WBV. Therefore, in this study, a three-dimensional (3D) FE model of the low thorax to pelvis segment, i.e. T12-S1, was developed to investigate this problem.

II. Method

The construction of our 3D FE model of T12-S1 has been detailed previously [3, 6]. Briefly, the model's detailed geometry was based on the digitized morphological data of embalmed spine vertebrae. Examination of these specimens did not show any gross physical abnormalities. To obtain the geometrical data required for the FE model, an accurate, flexible and multi-axis digitiser (FaroArm, Bronze Series, Faro Technologies, Inc., FL, USA) was used to extract the pertinent cross-section data into point cloud, which was subsequently imported into the commercially available FE software, ANSYS 7.0 (ANSYS, Inc., PA, USA), for volume and mesh construction. Adopting this digitisation process permitted accurate geometrical extraction of the specimen's morphology for the FE solid representation. The cortical shell, cancellous core, end plates and posterior elements including pedicle, lamina and transverse and spinous processes were represented by 8-noded solid elements.

The intervertebral disc's anterior and posterior heights were modelled based on published literature [6] to account for the required kyphotic curve. The nucleus pulposus was simulated by means of a nearly incompressible cavity and the annulus fibrosus was assumed to make up of 3 radial consecutive laminar layers of composite material consisting of annular fibers embedded in the homogeneous matrix material. The nucleus pulposus and annulus matrix were represented by 8-noded solid elements, while the annulus fibers were simulated by 3D cable elements that sustained tension only and arranged at about ±30º angles in relation to the adjacent endplates.

Ligaments were modelled as 3D tension only cable elements. The cross sectional area of each ligament was obtained by averaging the values reported in the literature. Figure 1 shows our T12-S1 FE model.

All materials were assumed to be linearly isotropic and homogenous. The material properties are collected from the literature. The detailed material property data used in our model are given in Table 1.

Chwee Teck Lim, James C.H. Goh (Eds.): ICBME 2008, Proceedings 23, pp. 1938–1940, 2009
www.springerlink.com

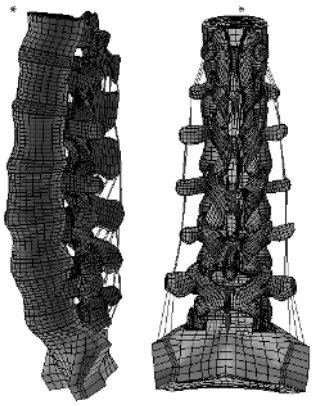


Fig. 1 FE model of T12-S1

Table 1 Material Properties of FE model of T12-S1

Description	Young's modulus (MPa)	Possion's Ratio
Cortical bone	10000	0.30
Cancellous bone	100	0.2
Posterior elements	3500	0.25
Endplate	500	0.25
Disc-annulus	4.2	0.25
Disc-nucleus	1	0.499
Fibers	450	-
Ligaments	20	-

To investigate the effects, if any, of denucleation and facetectomy on the frequency characteristics of the spine under WBV, several injury conditions were assumed, namely (1) Case1: denucleation of L4-L5; (2) Case2: denucleation of two discs of L3-L5; (3) Case3: removal of facet joints and their capsular ligaments of L4-L5; (4) Case4: for two segments of L3-L5 based on Case3's condition; (5) Case5: removal of nucleus, facet joints and their capsular ligaments of L4-L5; and Case6: for two segments of L3-L5 based on Case5's condition. For all the cases simulated, the inferior surface of S1 vertebral body was fully restrained.

In all our simulations, a distributed mass of 40KG was included in the model, to represent the head and body weight.

III. Results

In order to investigate the resonant frequency characteristics of the human spine, different numbers of spinal segments were computed using FE modal analysis.

Table 2 shows the first-order axial vibration frequencies of different vertebral levels predicted by the FE models and the corresponding experimental results [3, 5, 7]**.** Table 3 shows the first-order axial resonant frequencies predicted by the T12-S1 FE model under intact and different injured conditions.

Theoretically, a 3D continuous structure may be characterised by six-dimensional vibration modes. The FE model of T12-S1 has the first vibration mode in the anterior-

Table 2 Predicted frequencies for different spinal segments (where available, experimental results (in brackets) were referenced)

Spine motion segment	Frequency (Hz)	Reference
One segment T12-L1	25.7 (23.5)	[3]
Two segments L4-S1	16.4 (17.5)	[5]
Lumbar spine L1-L5	11.5 (12.2)	[5]
Lumbosacral spine L1-S1	9.12 (10.6)	[5]
Thoracosacrum T12-S1	7.68(-)	-
Human body	(4-6)	[6,7]

Table 3 Predicted frequencies and the resultant percentage changes in frequency for the intact and simulated injured conditions

Cases	Frequency (Hz)	Frequency changes (%)
Normal model	7.68	-
Injury Case 1	7.29	-5.08%
Injury Case 2	6.78	-11.7%
Injury Case 3	7.66	-1.04%
Injury Case 4	7.65	-3.91%
Injury Case 5	7.23	-5.86%
Injury Case 6	6.65	-13.4%

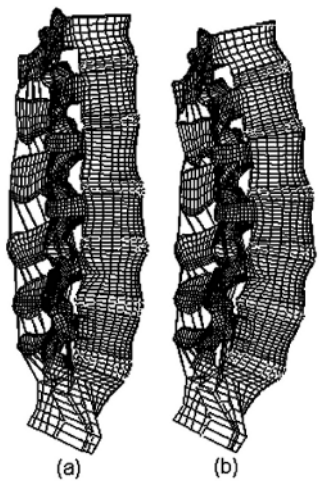


Fig. 2 The first-order vibration mode of T12–pelvis in the vertical direction: (a) and (b) are the postures showing maximum and minimum vertical displacements respectively

posterior direction with a low frequency. However, in the present study, we mainly discussed the first-order vibration mode in the vertical direction for consideration of the vibration characteristics of the human body. Figure 2 shows the first order vibration mode of our T12-S1 model, in the vertical direction. Our simulations showed that the vertical vibrations were accompanied by anteroposterior motion.

The upper body weight is a very important factor for the frequency characteristics of the human spine. In order to determine the influence of different upper body weights on the resonant frequencies of the spine, an upper body mass range of 30-60 kg was assumed and imposed on the T12-pelvis FE model during the modal analyses. The resulting resonant frequencies in the vertical direction varied from 8.23 to 5.84 Hz corresponding to 30 to 60kg upper body weight. Hence, our results indicated that a reduced body weight led to lower frequency and vice versa.

IV. Discussions

The results demonstrated that axial vibration frequencies of the spine decrease with an increase in the number of spinal segments. The T12-S1 FE model with a compressive preload of 40 kg predicted a first-order axial resonant frequency value of 7.68Hz. It has been previously reported that the inclusion of rib-cage of the head-thorax model lowered the resonant frequency by about 20% [5]. Therefore, this suggests that an FE model incorporating T12-S1, head-thorax as well as the rib cage and muscles may produce more realistic results. This set of model analysis has been left for a future study.

From Table 3, our results indicated that all the considered spinal component injuries including denucleation, facetectomy and removal of capsular ligaments lowered the resonant frequency of human spine. In particular, the denucleation of intervertebral discs played a greater role in the resonant frequency of the spine. More specifcially, the first-order axial resonant frequencies of the spine was lowered by 5% for one disc denucleation (Case1) and by 12% for the two disc denulceation scenario (Case2).

The results suggest that our model was capable of simulating the vertical vibration mode of T12-S1. The human upper body mainly performs vertical motion during WBV, while the lumbar spinal segment undergoes translation and rotation in the sagittal plane. The lower segment of the lumbar spine exhibits flexion motion, while the upper lumbar segment exhibits extension motion.

There are several limitations in this study. In the present model, the upper body was simplified and modelled as a lump mass because we considered only vertical vibration in this study. Another potential shortfall arises from a lack of consideration of the active regulatory effects of muscle and the non-linear influence of muscle large deformation to counter the anteroposterior oscillation of the human body during WBV. Therefore, the current model requires further improvement in the modelling of muscle and a distributed-mass upper body in both anatomic and mechanical aspects, so that the improved model can simulate the dynamic and impact conditions of flexion-extension, lateral bending, and torsion of the human spine under WBV.

Despite the limitations of the current model due to simplifications, our simulation results of vertical vibration showed overall good agreement with experiments.

V. Conclusions

A detailed 3D FE model of the lower T12-S1 based on actual vertebral geometry was developed, which can be used to perform dynamic response and impact analyses for the human spine. The findings may be useful to provide guidelines for clinical treatment and for product design and development in industry.

References

1. Wilder, D.G., Woodworth, B.B., Frymoyer, J.W., Pope, M.H. (1982). Vibration and the human spine. Spine, 7, 243-54
2. Goel, V.K., Park, H., Kong, W. (1994). Investigation of vibration characteristics of the ligamentous lumbar spine using the finite element approach, ASME J Biomech Eng, 116, 377-83
3. Guo, L.X., Teo, E.C., Lee, K.K. (2005). Vibration characteristics of human spine under axial cyclic loads: Effect of frequency and damping, Spine, 30, 631-637
4. Kasra, M., Shirazi-Adl, A., Drouin, G. (1992). Dynamics of human lumbar intervertebral joints. Experimental and finite-element investigations, Spine, 17, 93-102.
5. Kong, W.Z., Goel, V.K. (2003). Ability of the finite element models to predict response of the human spine to sinusoidal vertical vibration. Spine, 28,1961-7
6. Teo, E.C., Lee, K.K. (2004). The biomechanics of lumbar graded facetectomy under anterior-shear load. IEEE Transactions on Biomedical Engineering, 51, 443-449
7. Pope, M.H., Wilder, D.G., Jorneus, L., Broman, H., Svensson, M., Andersson, G. (1987). The response of the seated human to sinusoidal vibration and impact, J Biomech Eng, 109,279-84

Local Dynamic Recruitment of Endothelial PECAM-1 to Transmigrating Monocytes

N. Kataoka[1], K. Hashimoto[2], E. Nakamura[2], K. Hagihara[2], K. Tsujioka[2], F. Kajiya[1]

[1] Department of Medical Engineering, Kawasaki University of Medical Welfare, Kurashiki, Japan
[2] Department of Physiology, Kawasaki Medical School, Kurashiki, Japan

Abstract — **One of the critical events in early atherosclerosis is the recruitment of blood monocytes to proatherogenic vascular regions and subsequent transendothelial migration. This process involves a multi-step interaction between monocytes and endothelial cells (EC) including rolling, firm adhesion, locomotion, and transmigration. While the molecular mechanisms underlying rolling and firm adhesion have been well documented, the final step, transmigration, is still poorly understood. Platelet-endothelial cell adhesion molecule-1 (PECAM-1) is considered to be one of the key molecules in the transendothelial migration of monocytes. To investigate the role of PECAM-1 in monocyte diapedesis, we expressed a green fluorescent protein (GFP)-labeled construct in interleukin-1beta-stimulated human umbilical vein endothelial cells. Labeling PECAM-1 with GFP at its intracellular C-terminus could keep the molecular interactions with monocyte PECAM-1 intact. Three-dimensional molecular imaging in live cells demonstrated that endothelial PECAM-1 dynamically redistributed during paracellular transmigration, to surround monocytes transmigrating through both bicellular and multicellular junctions. Within 20 minutes of transmigration, PECAM-1-GFP was recruited at transmigration sites to induce a significant increase, with a concomitant reduction in the neighboring cytoplasm. These dynamics were not observed during transcellular diapedesis. At bicellular junctions, PECAM-1 recruitment did not occur in the region without transmigration (but with adhesion on endothelium), although it did at multicellular junctions, nor did it appear to occur at either junction type when monocyte adhesion was blocked. These data show that monocyte adhesion can trigger PECAM-1 recruitment from sub-junctional cytoplasm preferentially to multicellular endothelial junctions. Subsequent transmigration induces PECAM-1 redistribution and further recruitment at multicellular and bicellular, but not at transcellular sites, which may support chronic paracellular transmigration.**

Keywords — **Endothelial Cell, Monocyte, Transmigration, PECAM-1**

I. Introduction

One of the critical events in early atherosclerosis is the recruitment of blood monocytes and T-lymphocytes to proatherogenic vascular regions and subsequent transendothelial migration, also known as diapedesis. This process involves a multi-step interaction between leukocytes and endothelial cells (EC) including rolling, firm adhesion, locomotion, and transmigration.[1,2]

While the molecular mechanisms underlying rolling and adhesion have been well documented, the final step, transmigration, is still poorly understood. Leukocytes have been shown to cross EC monolayers by both paracellular (between ECs) and transcellular (through the body of ECs) routes. For paracellular diapedesis, many molecules have been reported to be involved, including platelet-endothelial cell adhesion molecule-1 (PECAM-1) [3,4]. We have recently reported that oxidized low density lipoprotein changes the junctional conformation of ECs, upregulating PECAM-1 and downregulating VE-cadherin, and leading to the promotion of monocyte diapedesis [5] In contrast, studies of the molecular basis of transcellular diapedesis have only recently begun.

Recent studies reported that part of cellular PECAM-1 exists in the intracellular pool called lateral border recycling compartment (LBRC) which is located below the surface of the cell at the lateral borders in ECs, and PECAM-1 is constitutively recycled between the LBRC and the cell surface [4,6]. The detailed dynamics of molecular trafficking of PECAM-1 to the cell surface has not been directly demonstrated in live cells. Moreover, it is still unknown PECAM-1 has some roles for transcellular diapedesis, as well as for paracellular diapedesis.

In this study, we analyzed the molecular dynamics of endothelial PECAM-1 during monocyte paracellular and transcellular diapedesis in three-dimensions with PECAM-1 - green fluorescent protein (GFP) fusion protein.

II. Matrials and methods

A. Cells

HUVECs were purchased from Kurabo (Osaka, Japan), and cultured in HuMedia-EG2 complete medium (Kurabo) supplemented with Primocin (Amaxa, Cologne, Germany) to protect against microbial contaminants including mycoplasma. For experiments, cells at passage 3 were seeded at 2 500 cells/cm^2 and grown to confluency. Human, CD14+ monocytes were freshly isolated from the peripheral blood of young, healthy volunteers.

Chwee Teck Lim, James C.H. Goh (Eds.): ICBME 2008, Proceedings 23, pp. 1941–1944, 2009
www.springerlink.com

B. Construction of PECAM-1-GFP

The full length PECAM-1 cDNA obtained from HUVECs was cloned into pAcGFP1-N1 vector (Takara Bio) to produce a construct in which Aequorea coerulescens derived GFP (AcGFP1) was fused to the C-terminus of PECAM-1.

C. Molecular imaging of PECAM-1-GFP

Freshly-isolated and fluorochrome-labeled human monocytes were added to PECAM-1-GFP-transfcted HUVECs that were prestimulated with 5 ng/mL interleukin-1beta (IL-1β, R&D systems). The molecular dynamics of PECAM-1-GFP during monocyte diapedesis was observed on a microscopic stage at 37°C, using a confocal laser scanning microscope (CLSM, TCS-NT, Leica) with a 40 × oil-immersion objective at 1-5 minutes intervals. In some cases, experiments were done under the condition that i) monocyte adhesion was blocked by anti-β2-integrin and anti-ICAM-1 antibodies, and ii) monocyte transmigration was blocked by anti-PECAM-1 antibodies.

D. Quantitative image analysis of PECAM-1-GFP

Monocyte transmigrations were classified as either paracellular or transcellular and paracellular events were further divided into bicellular routes, which used junctions between two ECs, or multicellular routes, which used junctional corners where three or more ECs met. Changes in the fluorescent intensity of PECAM-1-GFP around transmigrating monocytes were measured over time in z-projected images. The regions measured were determined as fixed polygonal ones, and as the minimum and the best-suited to accommodate the transmigration spots around monocytes.

III. Results and Discussion

Of a total of 153 diapedesis events analyzed, only 5% monocytes (7 events) transmigrated by a transcellular route while approximately 95% took a paracellular route. Of these, 68% migrated through bicellular junctions and 27% through multicellular corners. During paracellular transmigration, PECAM-1-GFP gaps, through which transmigrating monocytes invaded, were formed. The majority of these gaps formed de novo during transmigration, but at multicellular corners, a significant number (28%) pre-existed before transmigration. Most of the gaps closed after transmigration, and the time for which gaps were open was significantly longer at multicellular than at bicellular regions.

A typical example of the 3D-molecular dynamics of PECAM-1 during monocyte bicellular diapedesis is shown in Figure 1A. PECAM-1 staining at a bicellular junction was intact before monocyte arrival (0 minute). In this case, the monocyte adhered to the EC at 6 minutes after monocyte addition, and started to invade the endothelium at 14 minutes, forming a PECAM-1 gap de novo. Endothelial PECAM-1 dynamically redistributed to surround the transmigrating monocyte, as clearly shown in xy, xz, and yz planes (arrows at 14 and 18 minutes). After transmigration, the PECAM-1 gap resealed completely by 20-24 minutes (arrowheads). Similar dynamics were seen around monocytes migrating through multicellular corners (Figure 1B), where gaps formed de novo, with PECAM-1 redistribution at 7-12 minutes (arrows) and the gap resealing at 9-15 minutes (arrowheads). The majority of these paracellular events were accompanied by PECAM-1 redistribution to surround transmigrating monocytes (77% for bicellular and 83% for multicellular routes).

In contrast, Figure 1C show a monocyte M1 that transmigrated transcellularly, but PECAM-1 redistribution was never observed. At 38 minutes, M1 was on the apical surface of an EC (arrows), and another monocyte M2 had already transmigrated beneath the EC. At 43-45 minutes, M2 migrated in subendothelium towards M1, and M1 invaded the EC transcellularly (arrows) as if attracted by M2, but no redistribution of endothelial PECAM-1 was observed. M1 had almost completed transmigration by 47 minutes, and appeared to aggregate with M2 (arrows and arrowhead). This mode of transcellular diapedesis, in which adherent monocytes seemed to be attracted by another transmigrated monocyte was seen in 57% (4/7) of transcellular events.

Quantitative image analysis confirmed the late accumulation of PECAM-1, showing a significant, time-dependent increase in PECAM-1-GFP fluorescence for at least about 20 minutes after bicellular and multicellular transmigration (Figure 2A), which was accompanied by a significant reduction in the neighboring cytoplasm (Figure 2B), suggesting that PECAM-1 was recruited from the sub-junctional cytoplasm to the site of transmigration. In contrast, no accumulation was seen at sites of transcellular diapedesis (Figure 2A). Fluorescence over the whole scanned area (250 × 250 μm) remained unchanged (Figure 2B).

To further clarify what is the trigger of the accumulation during a series of processes from rolling to transmigration, we first examined the effect of monocyte adhesion to endothelium on the molecular dynamics of PECAM-1. When PECAM-1 on both monocytes and ECs was blocked, majority of monocytes adhered to ECs, but could not transmigrate, enabling us to track the dynamic changes of PECAM-1 at the neighboring junctions induced by individual monocyte adhesion events. Monocyte adhesion alone did not

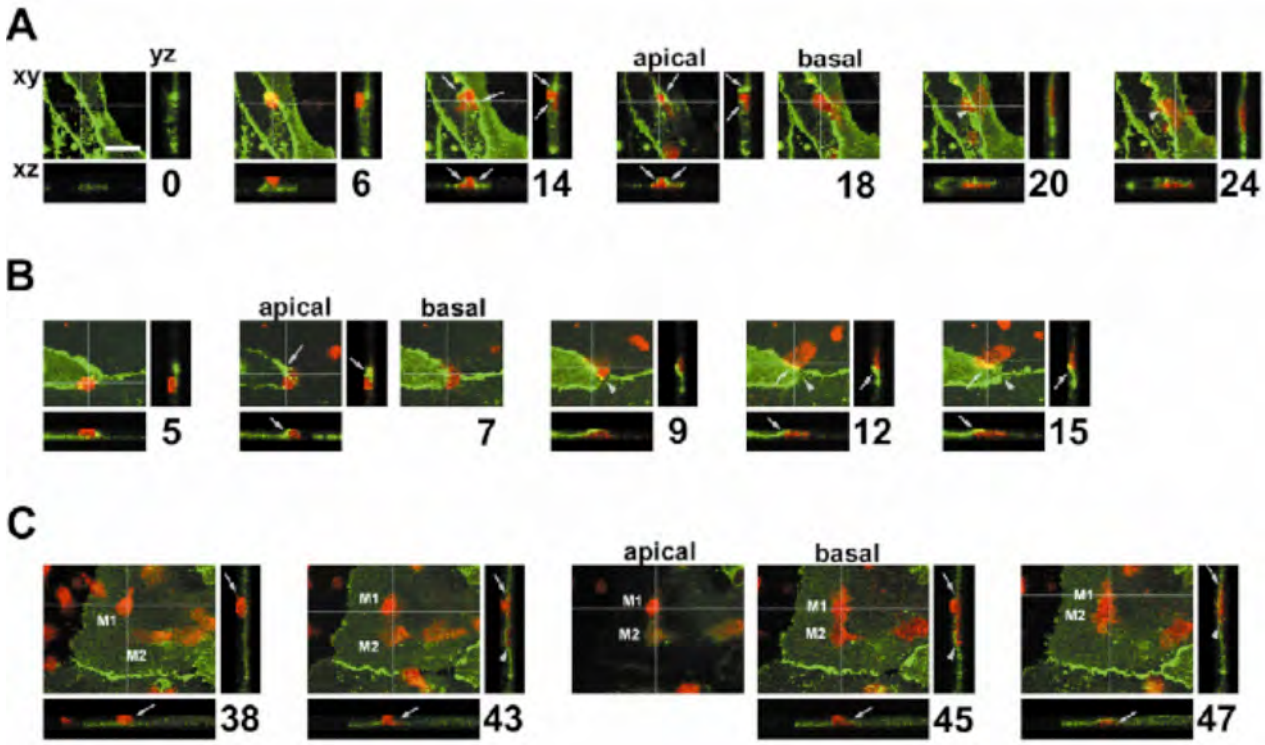


Figure 1 Redistribution of endothelial PECAM-1 to surround transmigrating monocytes during paracellular, but not transcellular diapedesis. A: bicellular, B: multicellular, C: transcellular diapedesis.

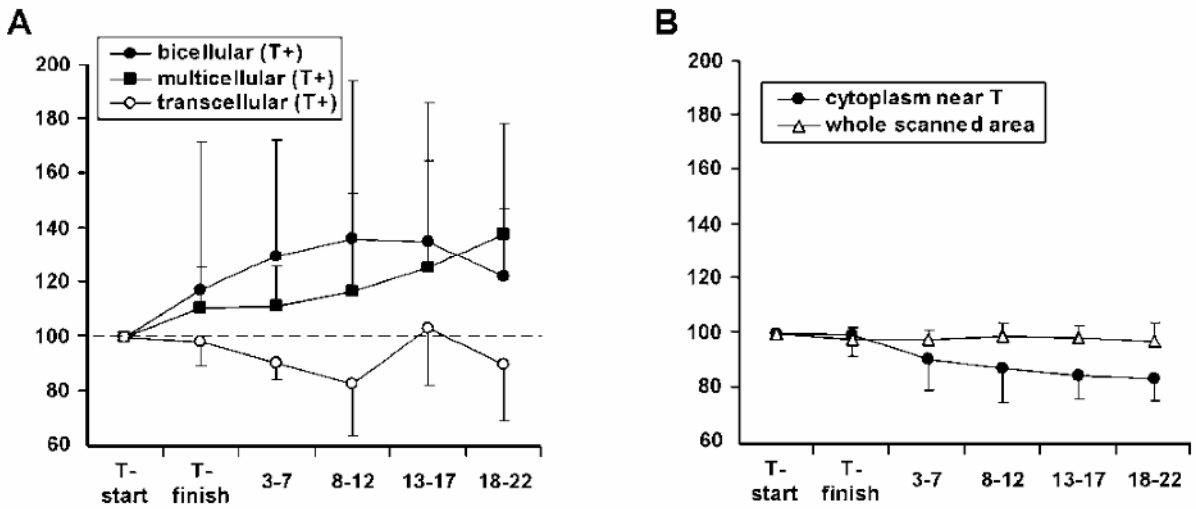


Figure 2 Quantitative image analysis of PECAM-1 late accumulation. A: Changes in PECAM-1-GFP fluorescence in specific local regions of migration, B: Changes in PECAM-1-GFP fluorescence in cytoplasm near migration sites and whole cells.

trigger the PECAM-1 accumulation at the neighboring paracellular junctions. The accumulation did not seem to occur in any regions either when monocyte adhesion was partially blocked (while the blocked monocytes were flow-

ing in the media) or without monocyte addition, which excludes the involvement of monocyte-derived soluble factors and intrinsic endothelial activities, respectively.

During paracellular transmigration, local endothelial PECAM-1 redistributed to surround transmigrating monocytes, suggesting PECAM-1 on ECs binds homophilically to PECAM-1 on monocytes. This redistribution was equally common at bicellular and multicellular regions, suggesting the same mechanism was involved. It is important to determine whether the monocyte PECAM-1 binds to either endothelial PECAM-1 already engaged with PECAM-1 on neighboring ECs or unengaged PECAM-1 recruited to the cell surface during diapedesis. It is likely that a transient disruption of PECAM-1-PECAM-1 binding at EC junctions is necessary to proceed diapedesis. Thus we speculate that monocyte PECAM-1 binds to endothelial PECAM-1 whose binding with neighboring ECs has been disrupted by an unknown mechanism, and this homophilic binding further stimulates the late recruitment of unengaged PECAM-1 to the site of paracellular, but not transcellular transmigration, which continues for at least 20 minutes after transmigration. The late and continuous accumulation of PECAM-1 after transmigration can be considered a mechanism for facilitating the subsequent, chronic monocyte paracellular diapedesis at the same site, which has often been observed in this system, leading to the development of atherosclerosis.

IV. Conclusions

Redistribution of endothelial PECAM-1 to surround transmigrating monocytes during paracellular, but not transcellular transmigration is followed by late and continuous accumulation of PECAM-1 at the same site after transmigration, which can support chronic paracellular transmigration. The accumulation is triggered by monocyte transmigration, but not adhesion or monocyte-derived soluble factors. Clinically, pharmacological targeting against the process of PECAM-1 redistribution/accumulation could be beneficial for specific prevention of monocyte diapedesis, which is the key process in early atherogenesis.

References

1. Springer TA (1994) Traffic signals for lymphocyte recirculation and leukocyte emigration: the multistep paradigm. Cell 76:301-314
2. Schenkel AR, Mamdouh Z, Muller WA (2004) Locomotion of monocytes on endothelium is a critical step during extravasation. Nat Immunol 5:393-400
3. Muller WA, Weigl SA, Deng X, Phillips DM (1993) PECAM-1 is required for transendothelial migration of leukocytes. J Exp Med 178:449-460
4. Mamdouh Z, Chen X, Pierini LM, Maxfield FR, Muller WA (2003) Targeted recycling of PECAM from endothelial surface-connected compartments during diapedesis. Nature 421:748-753
5. Hashimoto K, Kataoka N, Nakamura E, Asahara H, Ogasawara Y, Tsujioka K, Kajiya F (2004) Direct observation and quantitative analysis of spatiotemporal dynamics of individual living monocytes during transendothelial migration. Atherosclerosis 177:19-27
6. Mamdouh Z, Kreitzer GE, Muller WA (2008) Leukocyte transmigration requires kinesin-mediated microtubule-dependent membrane trafficking from the lateral border recycling compartment. J Exp Med 205:951-966

A Theoretical Model to Mechanochemical Damage in the Endothelial Cells

M. Buonsanti[1], M. Cuzzola[2], A. Pontari[2], G. Irrera[2], M.C. Cannatà[2], R. Piro[3], P. Iacopino[2]

[1] Department of Mechanics and Materials, University of Reggio Calabria, Italy
[2] Regional Stem Cells Transplant and Cellular Therapy Center, "A .Neri", A.O. Reggio C., Italy
[3] Diabetes Service, A. O. "S. Francesco da Paola", Paola, Italy

Abstract — **We performed a study to examine the direct effects of high glucose on the complex interplay of focal adhesion (FA) and vessel destroying disease, in a setting of diabetic type 2 patients suffered by severe vasculopathy. Significant modifications in the gene expression profile of angiogenic mediators were observed between patients and normal controls. We didn't note changes about m-RNA level expression of integrins and their receptors. Therefore, we supposed that a) transcriptional events are stored; b) hyperglycemic environment generates a loss of FA by biochemical change of integrins. In addition, we assumed that cells have defective strengthening of integrins-cytoskeleton linkages upon mechanical stimulation, as suggested by laser trapping experiments and binding of large beads to the cell surface. So, the mechanical stress can be moved over an intracellular structure with adequate strength. Herein, we consider the adhesion contact between integrins and extra-cellular membrane taking into account the S-H link role. A theoretical mathematical model has been developed to define the relationship between integrins, as principal bond in the FA, and the chemo-mechanical damage. A simple isotropic adaptive-elastic damage mechanism to describe the possible degradation of the integrins link is proposed in this paper. We suggest an energetic characterization of the problem considering the stored energy deformation and the chemical energy, this last as function of the environmental concentration. We neglect dissipative phenomena associated with entropy production and we surmise that equilibrium states are minimizers of the free energy of the system. The corresponding minimization problem is of no convex type and individualizes coexistence of equilibrium phases. Different cases will be treated, namely the static conditions one (no transportation of matter is carried-out) or the evolution case one, where the transportation matter is admitted. We conclude that glucotoxicity plays a critical role in the progressive deterioration of the vessel structures.**

Keywords — **Chemo-mechanical equilibrium, Variational methods, Heterogeneous substance, Diabetic pathology, Focal adhesion.**

I. Introduction

By array technology, in a previous study [1] we have performed some biological consideration about how the hyperglycemic environment influences the endothelial progenitor cells ability to provide a vessel building in diabetic type-2 patient. This pathology is associated with endothelial dysfunction, atherosclerotic macro vascular disease and microangiopathy. An important result is that we not observe change in m-RNA expression, but nevertheless considerable cell detachment phenomenon is presents. Our idea is that chemical aspects in the cells-wall microenvironment are characterizing the loss of the link strength within the basilar protein bond, namely integrins.[2], [3], [4], [5],[6], [7], [8], [9], [10], [11].Generally all materials are known to have complicated behaviors when subjected to compound action (i.e. mechanical and chemical or electrical or magnetic etc.). Here, benefit to underline that chemical action may make a dramatic internal change that can sensibly modify the materials elasticity. In particular, when we consider a simple closed system heterogeneous formed by solid and fluid compound, the picture is that the actual diffusion of the fluid into a solid may produce swelling as a consequence of a chemical transformation or mass absorption. Again, this last phenomenon nothing is if a phase transition in the classical thermodynamic sense. About this affirmation, it opens the way to investigate the possible coexistence of phases in the solid part within the heterogeneous system. In this paper our aim is to deduce a compound model reproducing adhesion and detachment in endothelial cells when the cell bond is damaged by pathological local conditions. Then, became possible to simulate like elastomeric structure in the non linear elasticity framework and so a neo-Hookean constitutive model can show the biological tissue response. A variational characterization of the problem and a model based upon energy minimization is developed.

II. Problem Statement

A. Biological Aspects

Integrins are heterodimers, consisting of one α and one β subunit. In diabetic setting patients, we determined quantitative gene expression of αVB5 integrins that has been showed to be important mediators of cell adhesion, migration, assembly and contraction of extracellular matrix. Integrins Alpha V fibronectin receptor (ITGA5) and Vitronectin Receptor of vascular smooth muscle cells (ITGAV). Integrins beta 3 (ITGB3) was also evaluated. In stably attached cells, the ITGB3 is capable of binding a

Chwee Teck Lim, James C.H. Goh (Eds.): ICBME 2008, Proceedings 23, pp. 1945–1948, 2009
www.springerlink.com

variety of ligands that are present in vascular tissue such as osteopontin, thrombospondin, and vitronectin. Changes in ligand occupancy of αVβ3/ ITGB3 has been showed to directly influence fibroblast growth factor (FGF) signalling in endothelial cells. We perform gene expression analysis including even growth factors. FGF showed increased molecular expression rate respect to normal controls, assumed that 1unit is normal value (mean 10,5 ± sd 14,2). Similarly, ITGA5 (mean 3,7 ± sd 3,9) and ITGAV (mean 3,9 ± sd 3,7) expression levels were increased in diabetic patients with artheriopathy. On the contrary, mRNA ITGB3 quantitative expression did no change (mean 1,0 ± sd 1,2) respect to normal control, (figure 1). In our study, this appears in contrast with the circumstance that, in the same diabetic people, the circulating endothelial cells (CEC) were more numerous respects to normoglycaemic controls (data not shown).

Because, high CEC number is correlated with vessel wall destruction, it's possible to suppose a probable molecular arrest of integrins synthesis. Indeed, based on last evidence that ITGB3 transcriptional event was unmodified, we supposed that hyperglycaemic environment generate a loss of focal adhesion by biochemical structural changes of this integrins.

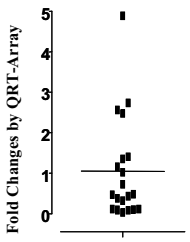


Fig.1 mRNAI-TGB3 in diabetic-type2 patients

B. Mechanical and thermodynamic aspects

Since the previous considerations affirming no-transcriptional influence in the integrine link degradation, we should to focus the chemical aspect and, in this manner, we think at chemo-mechanical equilibrium problem. A large literature over this argument is available and in particular we recall [12], [13], [14]. Integrins and cadherins, namely adhesion receptors are able to the natural function only interacting, at same time, either with extra cellular ligand and cytoskeleton. So mechanical stress can be carry out over an intracellular structure with adequate strength.

Here the glucose concentration dependent-*ph* variation in the system goes toward a possible one-dimensional modelization where the integrine bond, from mechanical point of view, can be assumed as well as a stressed string absorbed in a variable environment. For instance, the *ph* variation (increase or decrease value) makes aggressive or no-aggressive environment. In the first case it's possible to identify matter transport among string and external environment as equilibrium conditions.

According to [14] recalling some elementary thermodynamics consideration, we say that generally all irreversible processes drive the system to the equilibrium state in which the corresponding affinity vanishes.

When pressure and temperature, over a closed system, are maintained constant the quantity that is minimized is the Gibbs free-energy while, when the volume is constant we utilize the Helmholtz free energy.

This approach type has been developed about crystalline materials models because it represent a good base to model material degradation model [15], [16], [17].

III. Theoretical chemo-mechanical model

We start with a simple consideration derived by equilibrium of heterogeneous substance [13]: the transport of chemical species which carry matter from a location where the potential is W^1 to a location where the potential is W^2. For simplicity we shall to assume that our system consists of two parts, each with a well defined potential and that the global system is closed.

According to [18] we develop the model idea on the base of coexistence phases within the same system. Here, we consider a focal adhesion bond undergo to the natural stress (i.e. blood flow forces) in chemical equilibrium with surrounding aggressive environment at constant pressure.

Supposed the global system as closed and formed by two separate phases namely, the phase *A* (the integrine bond) the phase *B* (the environment), and three substances $S°$, S^1, S^2. The phase *A* is supposed as solid and composed by $S° + S^1$, whereas phase *B* is a fluid of S^1 and S^2 only.

The substance S^1 can be migrating among *A* and *B* due to application of stress or chemical action and again we suppose room temperature as constant. From stoichiometric consideration we introduce the mass fraction

$$c(x) \equiv \rho_1(x)/\rho_1^* \quad \text{on } x \in A \tag{1}$$

where ρ_1 and ρ_1^* represent respectively the mass density of S^1 and the referential mass density of S_1.

The equation (1) measure the degree of reaction at the point $x \in A$ and so the defined function c: $A \rightarrow (0,1)$ completely define the extent of reaction in *A* body. According to [18] we assume $\psi_B(\rho_1^*)$ as the Gibbs free energy of the solution *B* and the specific Helmholtz free energy function

$$\psi\varpi(e, c) = \tfrac{1}{2} K(c) (e - e°(c))^2 + h(c) \tag{2}$$

expresses the chemo-mechanical energetic relationship of the strain in the string and the degree of the reaction of its particles with the surrounding environment. In equation (2) $K(c)$ is the constitutive parameter if the integrine string.
Here, we impose a positive value for modulus K in the sense that its stiffness may change due to chemical reaction. The terms e and $e°$ represents the strain and an off-set strain due to chemical reaction, while $h(c)$ is an given function.
About this last consideration, the same appear corroborated by experimental evidence [16]. In the Fig. 1 we represents the envelope among the stored density deformation energy and the concentration function $c = c(x)$ namely, the function $z = \psi'(e, c)$.

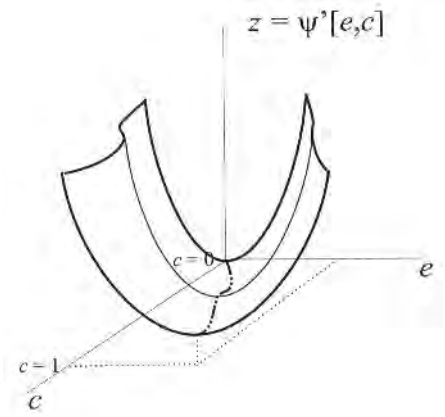


Fig. 1 Graph of the specific Helmholtz free energy $z = \psi\varpi\ (e,c)$

Likewise we define the free energy for the surrounding solution B as $\psi\omega(\rho_2)$ where ρ_2 represent the mass density of the fluid B. Then the chemomechanical equilibrium is stable corresponds to the minimum of the total energy functional

$$\mathcal{E}\,[e(x), c(x)] = \Xi_A\, \psi\varpi(e(x), c(x))dx + \psi\omega(\rho_2) \qquad (3)$$

Now, setting the quantity Ω as measure of the chemical potential of the environment with respect to S_1

$$\Omega \equiv \rho_1\, (d\psi\omega/d\rho_2)(\rho_2) \qquad (4)$$

then we can re-formulate the equation (3) in the form

$$\mathcal{E}\,[e(x), c(x)] = \Xi_A\, \psi\varpi(e(x), c(x))dx + \Omega\Xi_A c(x)dx \qquad (5)$$

and so the equation (5) represent, in global form, the minimum problem defined in the admissible set

$$\mathcal{H}\equiv\{(e, c):\Xi_A\, e(x)dx = \lambda A,\ 0 \le c(x) \le 1\ \forall x\in A\} \qquad (6)$$

Considering the first variation of the equation (2) to respect the variable e and imposing the equilibrium conditions

$$(\partial\psi\varpi/\partial e)(e(x),c(x)) = \text{constant} = 0 \qquad (7)$$

Then we define the function $z = \Phi(c)$: $= \psi\varpi(e°(c), c)$ which representation follow in the next Fig. 2.

Here we observe the variation of the function z to respect the concentration parameter of the fluid solution B. Because we consider a restricted variation to c, namely $c\in[0, 1]$ and in other word, when $c = 0$ the generic particle $x\in S°$, while $c = 1$ x is a compound of $S°$ and S^1. Again we observe that the tangent touch the graph of the function z in two distinct points likely the Ericksen bars model.[19]. Then developing the first variation of the function z, we find the graph down reported in Fig. 3.

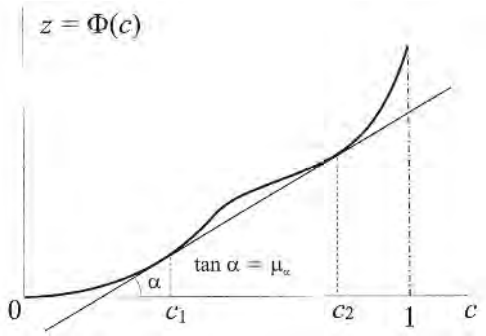


Fig. 2 Locus of the vertices of the parabolas c = constant

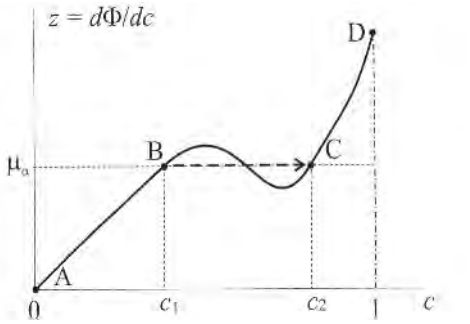


Fig. 3 Corresponding graph of $d\Phi/dc$

Commenting the graph of Fig. 3 as in the Ericksen model we find a non monotone law and this because the function z is classically no-convex as typical in non linear elasticity theory or two-well potential in solid-solid phases transition.

This mean that our minimization problem haven't unique solution but various and so phases coexistence appear.

From these last assertions we neglect the global function problem as represented in Fig. 1 and from now we restrict the attention of the function z more his derivatives.

We say that conditions from variation in the c values interval are indicated in following equation system (8)

$$\Omega = d\Phi/dc \quad \text{if } c\in(0,1)$$

$$\Omega \le d\Phi/dc \quad \text{if } c = 0 \qquad (8)$$
$$\Omega \ge d\Phi/dc \quad \text{if } c = 1$$

Overlapping the graphs in the Fig.2 and 3 we affirm that the tangent value Ω_α cross the derivatives graph and cut-off the contained B-C area in equal parts. This is the equal area rule introduced by Maxwell for the van der Waals fluid. In this manner we can to affirm that even in integrins string must be supposed a phase transition when the chemical potential assumes the value equal to Ω_α. So we may suppose the values interval $\Omega_0 < \Omega_\alpha < \Omega_1$, and then a possible solution $c^*(x)$ of the minimum problem will have the following form

$$\begin{aligned} c^*(x) &= 0 \quad \text{if} \quad \Omega < \Omega_0 \\ c^*(x) &= \min\{(d\Phi/dc)^{-1}(\Omega)\} \quad \text{if} \quad \Omega_0 < \Omega < \Omega_\alpha \\ c^*(x) &= \forall x \in (c_1, c_2) \quad \text{if} \quad \Omega = \Omega_\alpha \\ c^*(x) &= \max\{(d\Phi/dc)^{-1}(\Omega)\} \quad \text{if} \quad \Omega_\alpha < \Omega < \Omega_1 \\ c^*(x) &= 1 \quad \text{if} \quad \Omega > \Omega_1 \end{aligned} \qquad (9)$$

We observe that there is a transition when $\Omega = \Omega_\alpha$ and where either the $c^*(x)$ and $e^*(x)$ functions jump, respectively, from c_1 to c_2 and from $e_0(c_1)$ to $e_0(c_2)$. This aspect show a dramatic instability, like swelling phenomenon, consequent to small variation of the *ph* value of the surrounding fluid.

IV. Conclusions

Proposing this theoretical model we approach the cellular detachment as complex and composed problem. About some final consideration, here we see that there are two behaviors limit about the chemical potential. In other word we have, when $c = 0$ or $c = 1$, that chemical reaction does not occur or fully develops. In general case, $0 < c < 1$, the set of points $c \in (0,1)$ is either a single point or constitutes a single interval. If it is unique then a homogeneous solution exist, otherwise we have formation of coexistent phases in integrine string portions. In this portions we find different value of $c^*(x)$ and $e^*(x)$ even in possible triple or quadruple points. Here we will to focus the interaction, in terms of cellular-link strength, among natural and chemical stress operating in the non heterogeneous endothelial environment. Particularly, the endothelial cell detachment phenomenon, typical in diabetic patient, about the integrins link can be explained, with sufficient carefulness, through this proposed model. In fact the possible formation of coexistent material phases due to action of mechanical and/or chemical nature can reproduce the integrin link behavior, when undergo to the natural stress (blood flow action) and/or chemical stress (ph variation). Since high deformations in proteins bond has been focused [2] as for proposed in the model make an attempt tentative to model a heterogeneous and complex system. About future issue, we have in progress an extension of the model about numerical implementation by finite element analysis.

References

1. Cuzzola M. et.al. (2008) Gene expression profile analysis as predictive tool controlling the angiopathogenesis and vascular injury progression in diabetes type 2. Work in progress.
2. Maile L et al. (2008) Glucose regulation of integrin associated protein cleavage controls the response of vascular smooth muscle cells to insulin-like growth factor-I. Molecular E doi:10.1210/me. 2007-0552
3. Srinivasan S. et al.(2003) Glucose regulates monocyte adhesion through endhotelial production of interleukin-8.C Research 7:371-377
4. Abou-Seif MA, Youssef A-A.(2004) Evaluation of some biochemical change in diabetic patients. Clinica Ch Acta 346:161-170
5. Aydin A. et al.(2006) Oxidative stress and antioxidant status in non-metastatic prostate cancer and benign prostatic hyperplasia. Clinical Biochemistry 39:176-179
6. Bell GI. (1978) Models for the specific adhesion of cells to cells. Science 200, 12:618-627
7. Dong C. et al. (1999) Mechanics of leukocyte deformation and adhesion to endothelium in shear flow. A of B Engineering 27:298-312
8. James H, Wang C.(2000) Substrate deformation determines actin cytoskeleton reorganization: a mathematical modeling and experimental and experimental study. J Theor Biology 202:33-41
9. Caputo EK, Hammer DA. (2005) Effect of microvillus deformability on leukocyte adhesion explored using adhesive simulations. Biophysical Journal 89:187-200
10. von Wichert G. et al. (2008) Focal adhesion kinase mediates defects in the force-dependent reinforcement if initial integrin-citoskeleton linkages in metastatic colon cancer cell lines E J Cell Biology 87:1-16
11. Krasik EF. Et al. (2006) Adhesive dynamics simulation of neutrophil arrest with deterministic activation. Biophysical J 91:1145-1155
12. Bayli B (1992) Chemical change in deforming materials. Oxford University Press, Oxford
13. Gibbs W (1876) On the equilibrium of heterogeneous substance. Tran Conn Acad. Vol. III: 108-248
14. Kondepudi D, Prigogine I. (1998) Modern thermodynamics, J.Wiley & Sons, Chichester
15. Aregba-Driollet D et al. (2004) A mathematical model for the SO2 aggression to calcium carbonate stones: numerical approximation and asymptotic analysis. SIAM J Appl Math. 64:1636-1667
16. Tanaka T, (1978) Collapse of gels at critical endpoint. Phys Rew Lett. 40:820-823
17. Buonsanti M. et al. (2006) Chemo-mechanical equilibrium of bars. J of Elasticity 84: 167-188
18. Dunn J E, Fosdick R. (1980) The morphology and stability of material phases. Arch Rat Mech Anal. 74:1-99
19. Ericksen JL. (1991) Introduction to the thermodynamic of solids. Chapman & Hall, London

Author: Michele Buonsanti
Institute: Department of Mechanics and Materials, University of Reggio
Street: Loc. Feo di Vito
City: Reggio Calabria
Country: Italy
Email: michele.buonsanti@unirc.it

Effects Of Mechanical Stimulus On Cells Via Multi-Cellular Indentation Device

Sunhee Kim[1], Jaeyoung Yun[1] and Jennifer H. Shin[1]

[1] Department of Mechanical Engineering, Korea Advanced Institute of Science and Technology (KAIST), Republic of Korea

Abstract — **Mechanical as well as chemical stimulations are considered as a critical factor on cell behaviors. To understand the effects of mechanical stimuli on cells, many researchers have developed either single cell indentation devices to locally stimulate cells or to measure mechanical properties of cells, or compression chambers or bioreactors to apply global compressive pressure on cells. However, none of these previously developed devices are suitable to investigate the cell-cell communications amongst cells upon mechanical stimulation. To accomplish this experimental need, we developed a new cellular compression device using soft-lithography techniques. We fabricated the chamber with transparent Poly-carbonate, which consists of two sections, a self-contained cell incubator and an air chamber, separated by a PDMS membrane. On an incubator side of this PDMS divider, we attach a patterned PDMS sheet of micro poles mounted on a glass to ensure a uniform displacement of the array of poles to stimulate cells when the air chamber is pressurized. The cell incubator chamber is filled with medium and connected to a self contained incubation system to supply fresh culture medium to cells providing a stable culture environment during the experiments. The operating power is an air pressure applied on the air chamber side of the PDMS membrane. By controlling the air pressure, this device can stimulate cells in cyclic or continuous conditions. Also as cells are cultured in a form of single layer, it allows us to investigate cell-cell communications amongst cells that are under stimulated or non-stimulated conditions. Using this noble device, we investigated protein responses in keratinocytes, one of the mechano-sensitive cells. Preliminary results have shown the versatility of this compression device in studying cellular responses, thus demonstrating the feasibility of this tool as to be utilized in evolving cell mechanics research.**

Keywords — **keratinocyte, mechanical stimulation, cell compression, soft-lithography, PDMS**

I. Introduction

Skin is the largest organ which covers all the outer surface of the body. Keratinocyte forms an outmost layer of the skin called epidermis. Epidermis is divided into 5 layers based on the morphology and differentiated stages of keratinocyte. Keratinocytes originate in the stratum basal which is located adjunction to the dermis layer. They differentiate from the keratinocyte stem cells, and undergo subsequent differentiation through the layers of the epidermis. As a mechanical barrier and sensor, skin tissue is continuously exposed to the mechanical stimulation such as compression, tension and shear stress. Since keratinocyte is generally exposed to the compression, the investigation of the responses of keratinocytes under compression would be important. Many compression devices have been developed to investigate the cellular responses under compression, which can be categorized into two categories, which are single cell compression device [1-3] and multi-cell compression device. [4, 5] These devices are designed to investigate the intercellular responses or protein responses on a compression conditions. However, in order to understand the cell-to-cell communication which is important for a physiological response, these devices are not suitable. Therefore we developed a novel device which can apply compression to desired cells in the cell monolayer. The primary objective of this study is to develop an adequate device and to investigate the effects of in vitro mechanical compression on keratinocyte.

II. Device design and fabrication

A. Design of cell stimulation chamber

Conceptual design of the cell stimulation is shown in the figure 1. This device is designed as multi-cellular stimulator which can apply compressions on the cell monolayer in vitro. We use PDMS (poly-demethyl-siloxane) polymer poles to stimulate cells directly. By changing the geometry of this PDMS poles, we can apply compressions to the cells while not affecting the surrounding cells. PDMS pole array is manufactured using SU-3 molding fabricated with soft-lithography technique. Poly-carbonate chamber is designed for observation of cellular response inside the device.

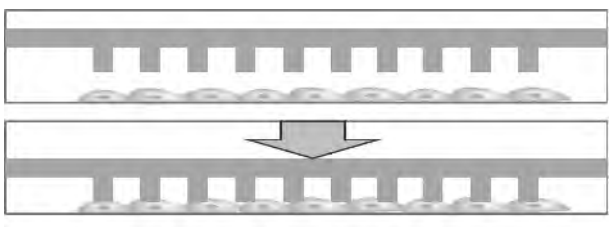


Figure 1. Conceptual design of multi-cellular compression device

Chwee Teck Lim, James C.H. Goh (Eds.): ICBME 2008, Proceedings 23, pp. 1949–1951, 2009
www.springerlink.com

B. Design of integrated system

Figure 2 shows a schematic diagram of the experimental setup for the compression device system. Air pressure is utilized as the system input, controlled by syringe pump. As air enters into the chamber, PDMS membrane deforms and PDMS poles get to the bottom where cells are cultured. Therefore, cells exposed to the direct mechanical compression. After stimulation, air goes out and PDMS membrane restores original state releasing compression on cells. Having these two steps repeatedly, we can generate dynamic compression condition. For a typical cell culture condition, the cell culture medium is supplied in the chamber. To meet the temperature and pH requirements for cell culture system, we utilize water bath and CO2 tank to supply medium at adequate condition to the cultured cell layer.

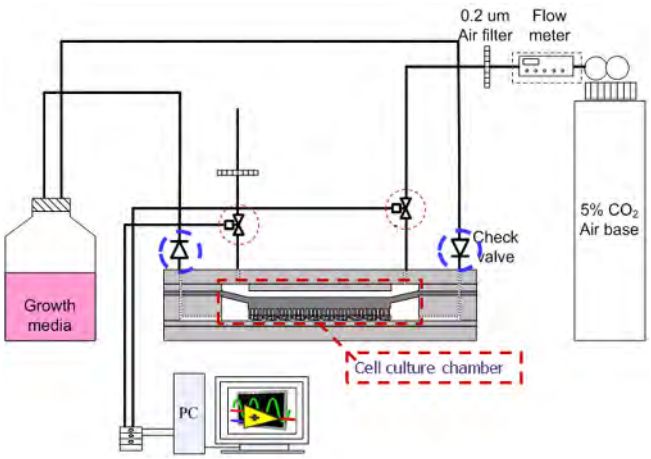


Figure 2. Schematic diagram of multi-cellular compression system

C. FEM simulation

The analysis of deformation and stress of PDMS membrane and poles is performed using FEM (finite element modeling) simulation tool ABAQUS. Simulation is done at various geometric condition of glass support and various pressure conditions to examine which design would be appropriate to the cellular compression device while minimizing the deflection of membrane and maintaining the uniform compression at the attached poles. FEM simulation results are shown in Figure 3.

We measure the PDMS membrane property using dynamic mechanical analyzer. As a result, we obtain PDMS membrane elastic modulus. Since PDMS did not appear to exhibit significant hysteresis, creeping or stress relaxation, we safely assume the PDMS membrane as a purely elastic material for FEM simulation.

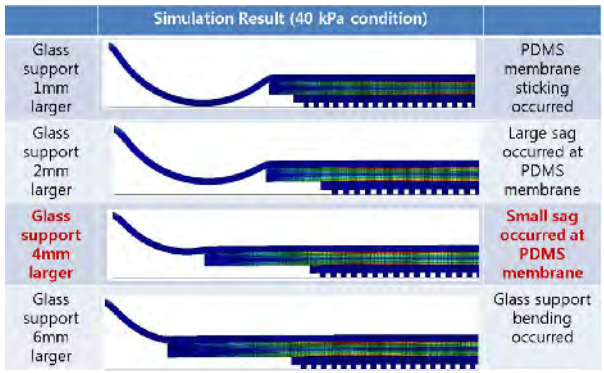


Figure 3. Simulation result of PDMS membrane deformation

III. Conclusions

With the developed multi-cellular compression device, static and dynamic compression is possible using finite pressure controller. By changing the geometry of PDMS poles, this device can be used to apply global and local compression stimulation.

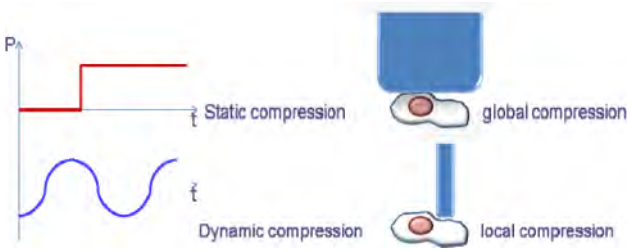


Figure 4. various compression conditions

Various conditions of compression effects on cell morphology and viability are also tested. Preliminary results have shown that this compression device is successfully designed to investigate cellular responses, particularly cell-cell communications. Thus, we demonstrate the feasibility of this tool as to be utilized in evolving cell mechanics research.

References

1. S. Yang, M. Taher A. Saif. (2007) Force response and actin remodeling (agglomeration) in fibroblasts due to lateral indentation. Acta Biomaterialia vol. 3, 1: 77-87
2. Scott I. Simon, Tun Nyunt, Kathryn Florine-Casteel, et al. (2007) Dynamics of Neutrophil Membrane Compliance and Microstructure probed with a Micropipet-based Piconewton Force Transducer. Annals of Biomedical Engineering vol. 35, 4:595-604

3. Takashi Ushida, Norihiko Yoshizawa, Takuya Noguchi. et al. (2001), Calcium transient and its propagation by poking a single human microvascular endothelial cell with a heat-blunt-ended micropipette, Materials Science and Engineering: C vol. 17, 1-2: 45-49
4. Yu Chang Kim, Joo H. Kang, Sang-Jin Park, et al. (2007) Microfluidic biomechanical device for compressive cell stimulation and lysis. Sensors and Actuators B 128: 108–116
5. E. A. G. Peeters, C. V. C. Bouten, C. W. J. Oomens et al (2003) Monitoring the biomechanical response of individual cells under compression: A new compression device. Medical and Biological Engineering and Computing vol. 41. 4:498-503

Address of the corresponding author:

Author: Jennifer H. Shin
Institute: Department of Mechanical Engineering, Korea Advanced Institute of Science and Technology (KAIST)
Street: GwaHangno
City: Deajeon
Country: Republic of Korea
Email: j_shin@kaist.ac.kr

The Effect of Tumor-Induced Bone Remodeling and Efficacy of Anti-Resorptive and Chemotherapeutic Treatments in Metastatic Bone Loss

X. Wang[1], L.S. Fong[2], X. Chen[3], X. Yang[4], P. Maruthappan[5], Y.J. Kim[6], T. Lee[7]

[1-7] Division of Bioengineering, National University of Singapore, Singapore

Abstract — **We investigated the changes in bone geometrical properties due to tumor-induced osteolysis and the efficacy of two different treatments, Ibandronate (anti-resorptive) and Paclitaxel (anti-cancer), in an experimental rat model. Osteolytic Walker 256 (W256) carcinosarcoma cells were surgically implanted into the right femur of 30 male Sprague Dawley rats, while another 12 received sham operation. Of the 30 tumor-bearing rats, 12 were untreated, 9 were administered with Ibandronate and 9 with Paclitaxel. Both femora were scanned using micro-computed tomography (micro-CT). Serum DPD (deoxypyridinoline) concentration was monitored via regular blood collection to observe the progress of bone resorption. Localized tumor growth in the distal femur was successfully induced in this rat model. Bone volume analysis indicated no bone loss in the sham-operated femora for the control group and in the tumor-bearing femora for the Ibandronate-treated group. However, a significantly lower bone volume by average 10.7% was observed in the operated as compared to the intact femur for the tumor-bearing untreated group, corresponding to a 13.4% increase in DPD concentration after 30 days. For the Ibandronate-treated group, bone volume was the highest for both femora and DPD concentration showed a drastic reduction of 38.2% after 30 days. Bone loss in the Paclitaxel-treated group seemed lower than in the tumor-bearing untreated group but there was a discrepancy between serum DPD concentration and micro-CT results, possibly due to incomplete data (rat mortality). Based on this experimental rat model with tumor-induced osteolysis, Ibandronate was more effective than Paclitaxel in reducing the rate of bone resorption, and hence preserving the structural integrity of the femur. This study has demonstrated the use of serum analysis and micro-CT as tools to monitor the biochemical and structural changes that accompany tumor-induced osteolysis respectively.**

Keywords — **Osteolysis, Micro-CT, Deoxypyridinoline, Ibandronate, Paclitaxel**

I. Introduction

Bone metastasis is a common occurrence in many malignancies, especially in breast, prostate, thyroid, kidney, bladder and lung cancers [1] Although not life-threatening in itself, refractory pain, hypercalcaemia, pathologic fractures, and neurological symptoms are associated skeletal complications that can lead to significant morbidity and diminished quality of life in patients with bone metastatic disease. [1] Prostate and thyroid cancer patients typically survive for 2-3 years and breast cancer patients survive for approximately two years after metastatic lesions have been diagnosed. [2] Thus, it has become increasingly important to investigate treatments for the skeletal complications of metastatic bone disease given that breast and prostate cancer are relatively common and long drawn. [2]

Most bone metastases are osteolytic; tumor cells upset normal homeostasis in the bone remodeling process by promoting osteoclast formation and activity, thereby accelerating the rate of bone resorption. [3] Tumor-induced osteolysis results in a loss of structural integrity and correspondingly, increases the incidence of complications such as pathologic fractures.

In this pilot study, using an animal model of tumor-induced osteolysis, we aimed to evaluate the effects of osteolytic metastatic tumors in long bone on bone structural properties. In addition, the other goal was to assess the efficacy of two different treatments – Ibandronate (IBAN), an anti-resorption potent bisphosphonate, as well as Paclitaxel (PAC), an anti-tumor chemotherapeutic drug, in preserving the structural integrity of tumor-induced osteolytic bone. A bone resorption marker and micro-computed tomography were used as tools to monitor the changes.

II. Materials and Methods

A. Animals

Forty two 8-10 week-old male Sprague-Dawley (SD) rats were randomly divided into four experimental groups (Table 1). The animals in the control groups were sham-operated, while those in the tumor-only, IBAN, and PAC groups had W256 cells implanted into the medullary canal of their right femur. The tumor-only groups received no treatment after surgery; the IBAN and PAC groups were administered with Ibandronate and Paclitaxel respectively post-surgery. Three animals from each group were euthanized every 10 days post-surgery. Two animals died due to anesthetic boosters; one from the control 0-day group and the other from the PAC 30-day group. Three animals died on the 15th day post-surgery after PAC injection; two from

Chwee Teck Lim, James C.H. Goh (Eds.): ICBME 2008, Proceedings 23, pp. 1952–1956, 2009
www.springerlink.com

the PAC 30-day group and one from the PAC 20-day group. Results from these five animals were thus not available. All animals were maintained in accordance with the National Advisory Committee for Laboratory Animal Research Guidelines on the Care & Use of Animals for Scientific Purposes 2004 and the study was conducted with approval of the Institutional Animal Care and Use Committee.

Table 1. Assignment of animals to various groups

Group	0-day	10-day	20-day	30-day
Control	3	3	3	3
Tumor-only	3	3	3	3
IBAN	0	3	3	3
PAC	0	3	3	3

B. Surgery and Serum Collection

W256 cells were purchased from ATCC and cultured in M199 medium supplemented with 10% horse serum. Approximately 2.5×10^6 cells in saline were surgically implanted into the medullary canal of the right femur. The surgical procedure from Kurth *et al* [4] was referred to, but with modifications made. The animals were anaesthetized via intra-peritoneal injection. The extensor mechanism of the right hind limb was exposed, and a longitudinal medial parapatellar incision was made to dislocate the patellar laterally. A 20G catheter was drilled with a twisting motion through the intercondylar notch into the medullary canal of the right femur. The catheter was pulled out and another 20G catheter attached to a syringe containing the tumor cells was inserted as far proximally as possible into the medullary canal. The hole was sealed with bone wax, the patella was relocated and the soft tissue and skin were closed with 4.0 vicryl sutures after the inoculation. The control group underwent the same surgical procedure except that 0.6% cell-free gelatin was inoculated into the right femur instead [2, 4, 5]. No signs of limping or reduced activeness after the 3-day recovery period were observed.

Blood was collected from the animals at 10-day intervals, starting from the day of surgery till they were sacrificed. The extracted serum was stored at –80ºC. Total serum DPD assay was carried out using Metra® Total DPD EIA Kit.

C. Drug Administration

Ibandronate (BONDRONATE injection (6mg/6ml vial), Roche Diagnostics) was diluted by a factor of 5 and the dosage was calculated according to 3.0 ml × body weight / 350g [5]. The drug was administered subcutaneously every ten days starting from the day of surgery. The animals were observed to be normal after Ibandronate administration.

Paclitaxel (ANZATAX injection (30mg/5ml vial), NUH Cancer Centre Pharmacy) was initially diluted by a factor of 5 with saline, as prescribed. The dosage was 10 mg/kg body weight [6] and Paclitaxel was administered intravenously via the lateral tail veins of the rats every ten days, starting five days post-surgery. However, due to observed complications, undiluted Paclitaxel was subsequently administered and the dosage was reduced by a third.

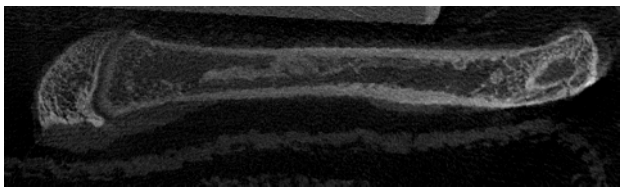
D. Micro-CT and Bone Volume Analysis

After euthanasia, both femora were harvested, cleaned of soft tissue, wrapped in 0.9% saline-soaked gauze and stored at -20ºC. [5] Prior to scanning, the femora were thawed to room temperature (25 ºC). The resolution of the scans was set as 35 μm. An average value of 6 was used for scanning. The scanned images were in TIFF format and had to be reconstructed to BMP format with the SkyScan Cone_rec software. The respective bone volumes for the left and right femora of each rat were analyzed using Volume Graphics (VG) Studio Max software. The images were imported into VG Studio Max after editing using Photoshop. The femora were segmented out of the images and readings of their bone volumes were obtained from the same software.

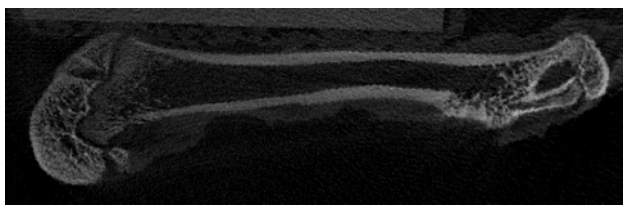
III. Results

A. Micro-CT Imaging and Bone Volume Analysis

Some abnormality in the medullary cavity of the femur, suspected to be localized tumor growth, was observed in the micro-CT images of the animals with implanted tumor cells (Fig. 1a). In contrast, the medullary cavities of the femora from the control group appeared clear (Fig. 1b).



(a)



(b)

Figure 1. 35 μm/pixel resolution micro-CT sagittal images of (a) an operated femur with tumor cells inoculated (b) an operated femur without tumor cells inoculated

Segmentation was performed by two persons concurrently to reduce subjectivity. Average bone volume values obtained from both were fairly similar, within the range of approximately 4% of the bone volume values. Bone volume of the right operated femur for the IBAN group increased the most, by 42.8% after 30 days. The increase for the control group was 32.3%, similar to the bone volume increase in the left femur. However, the bone volume increase in the right femur for the tumor-only groups was only 7.4% and 18.3% after 20 and 30 days respectively; the increase for the PAC group after 20 days was 13.1%. By comparing bone volume increase in the right femur after 20 days, it appeared that the PAC group still had a larger increase than the tumor-only group (Fig. 2). Also, the tumor-only group showed the largest contra-lateral bone volume difference. Bone volume of the right femur for the 30-day tumor-only group was on average 10.7% (49 mm^3) lower than that of the left femur for the same group (Table 2). Contra-lateral bone volume differences for the other three groups were all within or close to the range of segmentation error. However, the lack of data in the PAC 30-day group made a complete analysis of the 30-day groups not possible.

B. Serum Total DPD Concentration

Serum total DPD concentrations for each rat were normalized against its 0-day reading. The serum total DPD concentration increased after implantation of cancer cells for all tumor-only groups; an average of 26.4%, 22.2%, and 13.7% after 10, 20 and 30 days respectively. It appeared that the increase was already significant after 10 days; this is consistent with the results from bone volume analysis (Table 2). The DPD concentrations for the control group fluctuated from the 0-day value. The total DPD concentration decreased for IBAN group, on an average of 34.2%, 55.3% and 38.1% after 10, 20 and 30 days respectively, despite the presence of tumor. The total DPD concentration for the PAC group did not show a clear trend. Figure 3 shows the changes in serum total DPD for the 30-day groups.

Table 2. Average contra-lateral percentage difference in bone volume

Average % Difference in Bone Volume	Control	Tumor-Only	IBAN	PAC
0-day	4.8	0.5	N.A.	N.A.
10-day	4.1	7.8	2.3	4.2
20-day	3.1	5.3	3.2	5.4
30-day	0.2	10.7	-0.2	*4.1

*Animal died on 15th day

IV. Discussion

Based on comparisons made of the micro-CT images amongst groups, bone volume analysis and serum total DPD data, it is reasonable to conclude that localized bone tumor growth had successfully been induced in the distal femur of the rat, resulting in accelerated bone resorption and subsequent bone loss. Further histomorphometric analysis will be carried out to confirm these findings. The location of the tumor was consistent with the results of a similar study by Kurth *et al*, who detected osteolysis in the distal femur within a 6-mm region from the end of the condyles [7]. Using the method by Fritton *et al* [8], the cross-sectional area in the distal femoral metaphysis (25% of femur length from the distal end) of the left and the right femora in the various 30-day groups were found. The large contra-lateral difference (13.62%) in cross-sectional area for the tumor-only group further confirmed that the tumor was localized in the distal femur (Fig. 4).

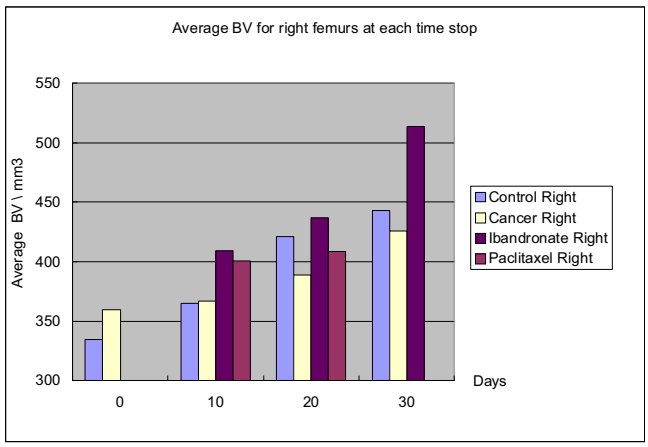


Figure 2. Average bone volume for right femora at each time stop

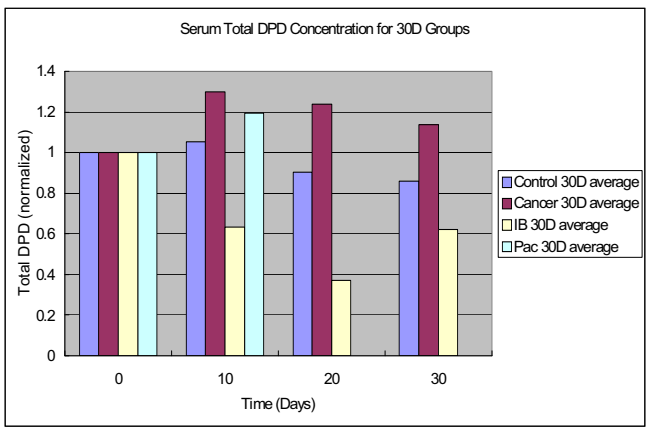


Figure 3. Serum total DPD concentration for 30-day groups

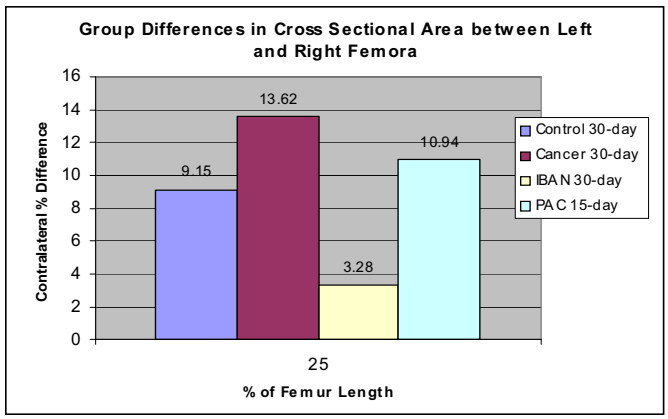


Figure 4. Group percentage difference in cross-sectional area between the left and right femora of animals in the 30-day groups

Bone volume changes in both femora across all groups were within expectation. As the left femur was not operated on, the bone volume increase over the 30-day period were similar for the control, tumor-only and PAC groups. The greater bone volume increase for the intact femur of the IBAN groups was due to the systemic anti-resorptive effect of IBAN. The bone growth in the operated femur of the tumor-only group over the 30-day period was significantly less as compared to the control and IBAN groups because of the increase in tumor-induced osteoclast activity. IBAN seemed to be highly effective in suppressing osteoclast activity; despite the presence of tumor, bone volume of the operated femur increased more than that of the control groups. The small contra-lateral difference in the cross-sectional area of the IBAN 30-day group (3.28%) further supports this observation (Fig. 4). Although there was incomplete data, it could still be deduced that the bone volume increase in the operated femur of the PAC groups was higher than that of the tumor-only groups (Fig. 2). The cross sectional area difference for the PAC group was also lower than that of the tumor-only group. The efficacy of PAC in reducing osteolysis in bone metastasis is evident here. The highest contra-lateral bone volume difference in the tumor-only group suggests highest osteoclast activity rate, resulting in greater bone loss.

Interestingly, in a separate study involving the same rat femora, using the three-point bending test, it was found that stiffness of the operated femora was best preserved in the PAC group. It was inferred that IBAN is more effective than PAC in reducing the rate of bone resorption, and thus preserves the structural integrity of bone better; however, it is not as effective as PAC in maintaining the biomechanical properties of bone.

The serum total DPD assay results were generally consistent with the bone structural analysis. Animals that received IBAN treatment showed significantly lower serum DPD levels as expected. However, PAC appeared to have no effect on bone resorption, contradicting the findings from bone volume and cross sectional area analysis. This is likely due to incomplete data available from the PAC groups.

The main aim of this pilot study was to establish and refine protocols. A larger sample size would be used in the subsequent study. In addition, combined concurrent treatment of Ibandronate and Paclitaxel will be investigated as previous studies have showed that the concurrent administration of both drugs has an additive effect in preventing metastatic bone loss [6, 9]. The combination of these two drugs in treating metastatic osteolysis seems promising.

V. Conclusions

The goal of this pilot study was to investigate the effect of tumor-induced bone remodeling, as well as the efficacy of Ibandronate and Paclitaxel in preventing metastatic bone loss. Based on this experimental rat model with tumor-induced osteolysis, Ibandronate was more effective than Paclitaxel in reducing the rate of bone resorption, and hence preserving the structural integrity of the femur. This study has demonstrated the use of serum analysis and micro-CT as tools to monitor the biochemical and structural changes that accompany tumor-induced osteolysis respectively.

Acknowledgment

The authors wish to express sincere appreciation for the guidance by Dr. Lee Taeyong, and for the assistance by Mr. Si-hoe Kuan Ming, Dr. Barry Pereira and Mr. Zou Yu.

References

1. Seibel M.J. (2008) The use of molecular markers of bone turnover in the management of patients with metastatic bone disease. Clinical Endocrinology; 68: pp. 839-349
2. Kurth A.A. et al. (2002) Ibandornate Treatment Decreases the Effects of Tumor-associated Lesions on Bone Density and Strength in the Rat. Bone Vol. 30, No.1, pp 300-306
3. Winter M.C. et al. (2008) Exploring the anti-tumor activity of bisphosphonates in early breast cancer. Cancer Treatment Review, doi:10.1016/j.ctrv.2008.02.004
4. Kurth A.A. and Müller R. (2001) The effect of an osteolytic tumor on the three-dimensional trabecular bone morphology in an animal model. Skeletal Radiology; 30: pp. 94-98
5. Kurth A.A. et al. (2001) The evaluation of a rat model for the analysis of densitometric and biomechanical properties of tumor-induced osteolysis. Journal of Orthopedic Research; 19: pp. 200-205

6. Stearns ME and Wang M. (1996) Effects of Alendronate and Taxol on PC-3 ML cell bone metastases in SCID mice. Invasion Metastasis; 16: pp. 116-131
7. Kurth A.A. et al. (2007) Preventative ibandronate treatment has the most beneficial effect on the microstructure of bone in experimental tumor osteolysis. Journal of Bone Mineral Metabolism; 25: pp. 86-92
8. Fritton J. C. et al. (2005) Loading induces site-specific increases in mineral content assessed by microcomputed tomography of the mouse tibia. Bone; 36: pp. 1030-1038
9. Bauss F. and Body J. (2005) Ibandronate in metastatic bone disease: a review of preclinical data. Anti-Cancer Drugs; 16: pp. 107-118

Mathematical Modeling of Temperature Distribution on Skin Surface and Inside Biological Tissue with Different Heating

P.R. Sharma*, Sazid Ali* and V.K. Katiyar**

*Department of Mathematics, University of Rajasthan, Jaipur, India
**Department of Mathematics, Indian Institute of Technology Roorkee, Roorkee, India

Abstract — **Aim of the paper is to investigate thermal behaviors in living tissues subject to constant, sinusoidal, step surface heating and point or stochastic heating with the thermal model of bioheat transfer which are often encountered in cancer hyperthermia, laser surgery, thermal comfort analysis and tissue thermal parameter estimation etc. The Pennes bioheat transfer equation, which describes the exchange magnitude of heat transfer between tissue and blood, is widely used to solve the temperature distribution for thermal therapy. The analytical solution of bioheat transfer equation is determined by using Green's function method with surface heating conditions which describes the transient temperature response on the skin surface and inside the biological tissue. It is observed that the thermo mechanical behavior of skin tissue is very complex; blood perfusion has little effect on thermal damage but large influence on skin temperature distribution.**

Keywords — **Bioheat transfer, biological tissues, surface heating, Green's function method**

I. Introduction

Hyperthermia treatment has been demonstrated as effective during cancer therapy in recent years. The primary objective of hyperthermia treatment is to raise the temperature of pathological tissue above cytotoxic temperature (41- 45^0C) without overexposing healthy tissues [1,2]. Hence for process control, it is important to obtain a temperature field of entire treatment region with knowledge of the entire temperature field in treatment region. The microwave [3], the laser[4] and the ultrasound [5] etc. are popular apparatus used for a spatial heating for treating the tumor in the deep biological body. Heat transfer analysis on these thermal medical problems usually has to simultaneously face transient or spatial heating both on skin surface and in interior of biological bodies [6-8]. The Pennes bioheat transfer equation, which describes the exchange magnitude of heat transfer between tissue and blood, is widely used to solve the temperature distribution for thermal therapy [9]. Also, the Pennes bioheat transfer equation is based on the assumption that all heat transfer between the tissue and the blood occurs in the capillaries. For sinusoidal heating on the skin surface problem, Liu and Xu [10] presented a closed form analytical solution of Pennes bioheat transfer equation, which is suitable for the long run steady periodic temperature oscillation. However, their analytical solution cannot satisfy the starting transient temperature response. The Green's function method was used to solve Pennes bioheat transfer; therefore it can be flexibly used to calculate temperature distribution for various spatial or temporal source profiles. Furthermore, the Green function method is capable of dealing with transient or space dependent boundary conditions.

In past, a few authors have applied Green's function method to solve Pennes bioheat transfer. Goe et al. [11] contributed to this field by using Green's function method and Fourier transform method. Liu et al.[3] derived the solution to heat transfer in cylindrical canine prostate centrally cooled by a flowing water. Zhu et al. [12] applied the Green.s function method to solve a series of steady state bioheat transfer problem, in which the Pennes's perfusion term was not included.. Durkee et al. [13] addressed the time-dependent Pennes equation in one dimensional multiregion Cartesian and spherical geometry based on method of separation of variables and Green's function method. The objective of the present paper is to investigate an analytic solution of Pennes's equation, which can be applied to study several selected typical bioheat transfer processes often encountered in cancer hyperthermia, laser surgery and thermal parameter estimations etc.

II. Mathematical model

The generalized one dimensional Pennes bioheat transfer equation following [9] is given by

$$\rho_t C_t \frac{\partial T_t}{\partial t} = \kappa \frac{\partial^2 T_t}{\partial x^2} + \omega_b \rho_b C_b \left(T_a - T_t\right) + Q_m + Q_r\left(x,t\right) \qquad (1)$$

ρ_t, C_t, κ are respectively the density, the specific heat, and the thermal conductivity of the tissue; C_b, ρ_b denote density and specific heat of blood; ω_b the blood perfusion; T_a the arterial blood temperature which treated as constant, and T_t the tissue temperature; Q_m the metabolic heat generation, and $Q_r\left(x,t\right)$ the external spatial heating.

Chwee Teck Lim, James C.H. Goh (Eds.): ICBME 2008, Proceedings 23, pp. 1957–1961, 2009
www.springerlink.com

During the heat transfer process, the boundary condition at the skin surface is often time dependent, which can be generalized.

$$-\kappa\frac{\partial T_t}{\partial x}=\phi_1(t) \quad \text{when} \quad x=0, \tag{2}$$

where $\phi_1(t)$ is the time-dependent surface heat flux. Since biological body tends to keep its core temperature to be stable, therefore the body core temperature (T_c) is regarded as a constant and given by

$$T_t(x,t)=T_c \quad \text{when} \quad x=L. \tag{3}$$

III. Analytical solution

The initial temperature field for the steady state biological tissue can be obtained through solving the following equation (4) and boundary conditions (5) as given by

$$\kappa\frac{d^2T_t(x,0)}{dx^2}+\omega_b\rho_bC_b\left(T_a-T_t(x,0)\right)+Q_m=0, \tag{4}$$

$$T_t(x,0)=T_c \quad \text{when} \quad x=L,$$

$$-\kappa\frac{dT_t(x,0)}{dx}=h_0\left[T_s-T_t(x,0)\right] \quad \text{when} \quad x=0, \tag{5}$$

where $T_t(x,0)$ is the steady state temperature field, T_c body core temperature often as constant, h_0 heat convection coefficient between the skin surface and surrounding air under physiologically steady state. T_s the surrounding air temperature. Here, the skin surface is defined at $x=0$ while the body core at $x=L$. Through straight forward calculations, the solution of the equation (4) is known and given by

$$T_t(x,0)=T_a+\frac{Q_m}{\omega_b\rho_bC_b}+\frac{\left(T_c-T_a-\frac{Q_m}{\omega_b\rho_bC_b}\right)\left[\sqrt{A}\cosh\left(\sqrt{A}x\right)+\frac{h_0}{\kappa}\sinh\left(\sqrt{A}x\right)\right]}{\sqrt{A}\cosh\left(\sqrt{A}L\right)+\frac{h_0}{\kappa}\sinh\left(\sqrt{A}L\right)} \tag{6}$$

$$+\frac{\frac{h_0}{\kappa}\left(T_s-T_a-\frac{Q_m}{\omega_b\rho_bC_b}\right).\sinh\left(\sqrt{A}(L-x)\right)}{\sqrt{A}\cosh\left(\sqrt{A}L\right)+\frac{h_0}{\kappa}\sinh\left(\sqrt{A}L\right)},$$

where. $A=\frac{\omega_b\rho_bC_b}{\kappa}$

Applying transformation presented by Carslaw and Jaeger [16],

$$T_t(x,t)=T_t(x,0)+R(x,t)\exp\left(-\frac{\omega_b\rho_bC_b}{\rho_tC_t}\right)\cdot \tag{7}$$

Now, the equation (1) is reduced to

$$\frac{\partial R}{\partial t}=\alpha\frac{\partial^2R}{\partial x^2}+\frac{Q_r(x,t)}{\rho_tC_t}\exp\left(\frac{\omega_b\rho_bC_b}{\rho_tC_t}\right), \tag{8}$$

where $\alpha=\kappa/\rho_tC_t$ is thermal diffusivity of tissue.

The corresponding initial and boundary conditions are reduced to

$$\text{when} \quad x=0: \quad -\kappa\frac{\partial R}{\partial x}=\psi_1(t),$$

$$x=L: \quad R=0,$$

$$t=0: \quad R(x,t)=0, \tag{9}$$

where,

$$\psi_1(t)=\left[\kappa\frac{dT_t(x,0)}{dx}\bigg|_{x=0}+\phi_1(t)\right]\exp\left(\frac{\omega_b\rho_bC_b}{\rho_tC_t}t\right)H(t),$$

and

$H(t)=\begin{cases}0, t<0\\ 1, t>0\end{cases}$ is the Heaviside function.

If the Green's function method for above equation system is obtained, then its transient solution can thus be constructed [14,15]. Through introducing an auxiliary problem corresponding to equations (8), the Green'sfunction G can be finally be obtained as:

$$\frac{\partial G}{\partial t}-\alpha\frac{\partial^2G}{\partial x^2}=\delta(x-\xi)\delta(t-\tau), \quad 0<x,\xi<L, \quad t,\tau>0 \tag{10}$$

with boundary conditions

$$a_1G(0,t|\xi,\tau)+b_1G_x(0,t|\xi,\tau)=0, \quad t>0,$$

and

$$a_2G(L,t|\xi,\tau)+b_2G_x(L,t|\xi,\tau)=0, \quad t>0, \tag{11}$$

and the initial condition

$$G(x,0|\xi,\tau)=0, \quad 0<x<L, \tag{12}$$

Applying Laplace Transform to the eqn. (10) and the boundary conditions (11), we get

$$\frac{d^2\overline{G}}{dx^2}-\frac{s}{\alpha}\overline{G}=-\frac{\delta(x-\xi)}{\alpha}e^{-s\tau}, \quad 0<x<L, \tag{13}$$

$$a_1\overline{G}(0,s|\xi,\tau)+b_1\overline{G'}(0,s|\xi,\tau)=0 \tag{14}$$

and

$$a_2\overline{G}(L,s|\xi,\tau)+b_2\overline{G'}(L,s|\xi,\tau)=0 \tag{15}$$

Applying eigen function expansion technique as given below

$$\overline{G}(x,s|\xi,\tau)=e^{-s\tau}\sum_{n=1}^{\infty}\frac{\varphi_n(\xi)\varphi_n(x)}{s+\alpha\beta_n^2}, \tag{16}$$

where $\varphi_n(x)$ is the nth *orthonormal* eigen function to the regular Strum-Liouvlle problem as given by

$$\varphi''(x)+\beta^2\varphi(x)=0, \quad 0<x<L, \tag{17}$$

subject to the boundary conditions

$$\varphi(0)=\varphi(L)=0,$$

where

$$\varphi_n(x)=\sqrt{\frac{2}{L}}\cos\left(\frac{2n-1}{2L}\pi x\right). \tag{18}$$

Taking Inverse Laplace transform of (16), we get

$$G(x,t|\xi,\tau)=\frac{2}{L}\sum_{n=1}^{\infty}e^{-\alpha\beta_n^2(t-\tau)}.\cos\beta_n x.\cos\beta_n\xi.H(t-\tau), \tag{19}$$

where $\beta_n=\frac{2n-1}{2L}\pi, n=1,2,3,.....$

Through straight forward algebra, the solution of the eqn. (8) under the boundary conditions (9) is known and given by

$$R(x,t)=\frac{\alpha}{k}\int_0^t G(x,t/\xi,\tau)\Big|_{\xi=0}\psi_1(\tau)d\tau + \int_0^t d\tau\int_0^L G(x,t/\xi,\tau).\frac{Q_r(\xi,\tau)}{\rho_t C_t}\exp\left(\frac{\omega_b\rho_b C_b}{\rho_t C_t}\tau\right)d\xi. \tag{20}$$

Finally, the solution of $T_t(x,t)$ is constructed in the form given below

$$T_t(x,t)=T_t(x,0)+R(x,t)\exp\left(-\frac{\omega_b\rho_b C_b}{\rho_t C_t}\right). \tag{21}$$

IV. Results and Discussion

The typical values for tissues properties and other parameters are used as given by [16]. Specific heat of tissue and blood are 4200 J/Kg.^{0}C, density of tissue and blood are 1000 Kg/m^3, arterial blood temperature and body core temperature are 37 T^{0}C, thermal conductivity of tissue is 0.5 W/m.^{0}C, blood perfusion is 0.0005 ml/s/ml, metabolic heat generation is 33800 W/m^3, heat convection coefficient is 10 W/m^2.^{0}C, surrounding air temperature is 25 T^{0}C. As demonstrated in earlier works by [10], the interior tissue temperature usually tends to a constant within a short distance, such as 2-3 cm, therefore L=3 cm was used in this study. For some particular issue, such as deeper heating, or more intense source of heat, the distance between skin surface and the body core will exceed this depth. In this case, new bounded core large enough to neglect the influence of the surface heating showed be in corporate into the calculations. Although any heating style for $Q_r(x,t)$ can be dealt with present analysis, only the most popular and simple specific absorption rate (SAR) expression for $Q_r(x,t)$ will be particularly analyzed. For the plane wave heating of laser or microwave, the heat absorption in the muscle tissue can simply be approximated by Beer's law as [17].

$$Q_r(x,t)=\eta P_0(t)\exp(-\eta x) \tag{22}$$

where $P_0(t)$ is the time dependent heating power on skin surface and η is the scattering coefficient. Since the heating power and the scattering coefficients may vary from one heating apparatus to another, it is of great importance to study the influence of these parameters upon the behavior of the tissue temperature. Such heating pattern can be encountered in tissue heating by laser, microwave or ultrasound, etc. Our study is expected to be very useful in a large variety of biothermal process.

V. Bioheat Transfer in Tissue

A. Surface adiabatic condition and spatial heating

Fig.1&2 shows that the transient temperature at different times of skin surface when biological tissues subject to two different spatial heating and skin surface was treated as

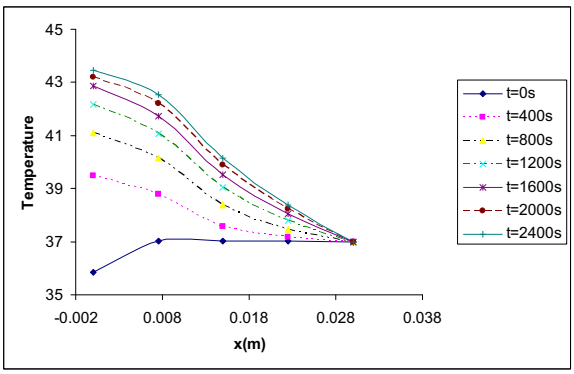


Fig.1 Temperature (T^{0}C) distribution versus x when η=200 m^{-1}, $\phi_1(t)$=0 and $P_0(t)$=250 W/ m^2.

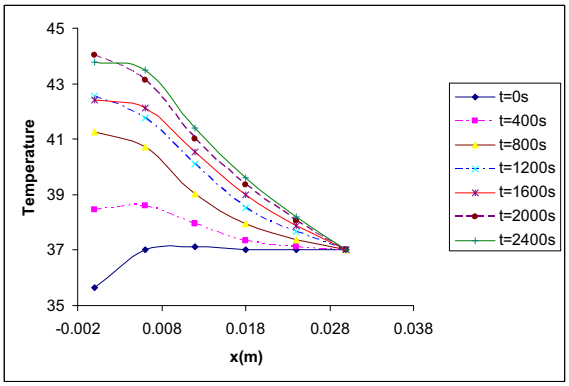


Fig.2 Temperature (T^0C) distribution versus x when η =200 m^{-1}, $\phi_1(t)$ =0 and $P_0(t)$ =250 + 200 cos(0.02t) W/ m^2 .

adiabatic i.e. $\phi_1(t)$ =0. Fig.1 depicts the case of constant heating and the Fig.2 the case of sinusoidal heating. The former one reflects the solution where the human skin is heated by a laser, while the later case can be found in the perfusion estimation. Obviously, in both the cases, the temperature at early stage of heating decreases from the body core to the skin surface. However, it will gradually be improved due to the spatial heating. Moreover there is an intercross for temperature curves at the different times in Fig.2, which indicates the temperature oscillation inside the tissue when subjected to the sinusoidal heating.

B. Effect of the scattering coefficient

Fig.3 depicts that the effect of the scattering coefficient on the temperature transient at the skin surface. It shows

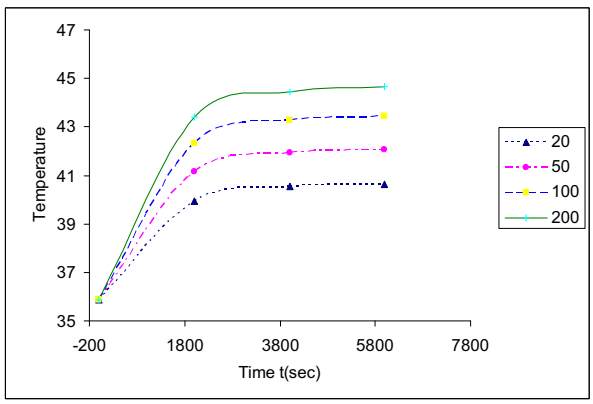


Fig.3 Effect of scattering coefficient (η) on temperature (T^0C) response at skin surface when $\phi_1(t)$ =0 and $P_0(t)$ = 250 W/ m^2 .

that the larger coefficient, the higher temperature increases. For the other heating frequencies, the corresponding thermal responses can also be studied using the same way. Since different heating apparatus such as laser or microwave may have different power and scattering coefficient, calculations as performed above are expected to be useful for the heating dose planning during hyperthermia treatment or parameters estimation. For example, performance of the different heating apparatus with specific power and decay coefficient can be evaluated using the present model to predict the temperature response thus induces in the tissue.

C. Effect of surface constant heating

It is observed from fig.4 that the temperature response at skin surface, C1, C2 and C3 are the transient temperature of tissues subject to the constant surface heating; $\phi_1(t)$ =1000 W/ m^2 , $\phi_1(t)$ =500 W/ m^2 , $\phi_1(t)$ =200 W/ m^2 , respectively. Obviously, the larger surface heating, the higher temperature increases. Such information is also very important for thermal comfort evaluation.

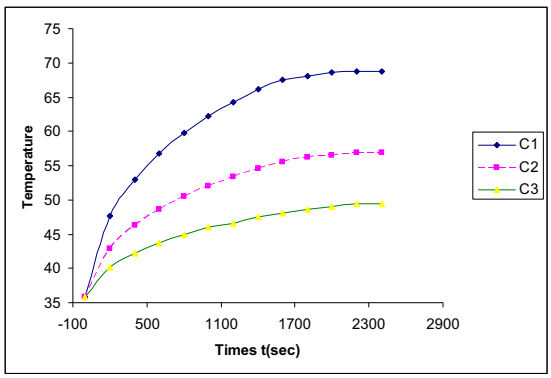


Fig.4 Effect of surface heat flux to skin surface temperature (T^0C) response when $P_0(t)$ = 250 W/ m^2 and η =200 m^{-1} .

D. Effect of step heating at skin surface

It is noted from fig.5 that the highest temperature increase appears at the time when the surface heating was stopped. For the case of blood perfusion ω_b =.004 ml/s/ml, at the end of the step heating, the tissue temperature will quickly reach a steady state. The result can help to better understand the temperature history of living tissues subject to step heating and thus benefit the thermal injury analysis.

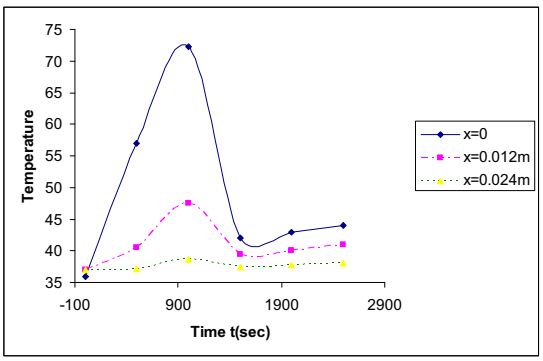


Fig.5 Transient temperature (T^0C) when step heating is applied (subjected to constant spatial heating) and ω_b =.004 ml/s/ml.

VI. Conclusions

The temperature distribution with spatial or transient heating on skin surface and inside the biological bodies are considered. The exact solution of the Pennes bioheat transfer equation with the time-dependent boundary heating condition on the skin surface is derived using Green's function method. The analytical expression obtained is useful for describing the tissue temperature distribution in one dimension domain, and especially it is more accurate that the results of the previous results in initial period of time domain. The time dependent heating condition, which can be dealt with by the present solution included most of the possible external heating style such as constant, sinusoidal, step heating both in volume and at boundary. Moreover, based on the requirement for the tumor killing temperature and the skin burn threshold, an approach to optimize the cancer hyperthermia parameters can be obtained using the current solution. Therefore the present investigation has more capability to deal many practical bioheat transfer problems than quite a few existing analytical solutions.

References

[1] M.W. Field and T.V. Dewhirst, "Hyperthermia in the treatment for cancer". Upjohn, Kalamazoo, MI, 1988.

[2] S.B. Field and J.W. Hand, "An introduction to the practical aspects of hyperthermia". Taylor and Francis, New York, 1990.

[3] Liu, J.; Zhu, L., and Xu, L. X., ''Studies on the three-dimensional temperature transients in the canine prostate during transurethral microwave thermal therapy''. ASME J. Biomech. Eng.,Vol. **122**, 2000, pp. 372–379.

[4] Yilbas, Z.; Sami, M., and Patiroglu, T., ''Study into penetration speed during laser cutting of brain tissues''. J. Med. Eng. Technol.,Vol. **22**, 1998, pp. 274–279.

[5] Seip, R., and Ebbini, E. S., ''Noninvasive estimation of tissue temperature response to heating fields using diagnostic ultrasound''. IEEE Trans. BioMed. Eng., Vol. **42**, 1995, pp. 828–839.

[6] Kuo-chi Liu, "Thermal propagation analysis for living tissue with surface heating ". Int. J. of Thermal Sci.Vol. **47**, 2008, pp. 507-513.

[7] F. Xu, T.J. K.A.Seffen," Biothermomechanics of skin tissues". J. of the Mechanics and Physics of Solid , Vol.**56**, 2008, pp. 1852-1884.

[8] Khalil Khanafer, Joseph L.Bull. L, Ramon Berguer, "Influence of pulsatile bllod flow and heating scheme on the temperature distribution during hyperthermia treatment". Int. J. of heat and mass transfer, Vol.**50**, 2007, pp. 4883-4890.

[9] Pennes, H. H., ''Analysis of tissue and arterial blood temperatures in the resting human forearm''. J. Appl. Physiol.,Vol **1**, 1948, pp. 93–122.

[10] Liu, J. and Xu, L.X., "Estimation of blood perfusion using phase shift in temperature response to sinusoidal heating the skin surface". IEEE Trans Biomed Eng., Vol. **46**, 1999, pp.1037–43.

[11] Gao, B.; Langer, S. and Corry, P. M., ''Application of the time-Dependent Green's function and fourier transforms to the solution of the bioheat equation''. Int. J. Hyperthermia, Vol.**11**, 1995, pp. 267–285.

[12] Zhu, L.; Xu, L. X. and Chencinski, N., ''Quantification of the 3-D electromagnetic power absorption rate in tissue during transurethral prostatic microwave thermotherapy using heat transfer model''. IEEE Trans. Biomed. Eng., Vol. **45**, 1998, pp. 1163–1172.

[13] Durkee, J. W.; Antich, P. P. and Lee, C. E., ''Exact-solutions to the multiregion time-dependent bioheat equation: Solution development''. Phys. Med. Biol.,Vol. **35**, 1990, pp. 847–867.

[14] Carslaw, H. S., and Jaeger, J. C., "Conduction of heat in solids". Clarendon Press. London., 1959.

[15] Ozisik, M. N., "Heat conduction". John Wiley & Sons, Inc., New York, 1993, pp. 506–507.

[16] Holmes, K. R., 1997, Biological Structures and Heat Transfer, Allerton Workshop on the Future of Biothermal Engineering

[17] J.B. Leonard, K.B. Foster, T.W. Athey, "Thermal properties of tissue equivalent phantom materials". IEEE Trans. Biomed. Eng. Vol. **31**, 1984, pp. 533-536.

Net Center of Pressure Analysis during Gait Initiation in Patient with Hemiplegia

S.H. Hwang[1], S.W. Park[1], H.S. Choi[1] and Y.H. Kim[2]

1 Department of Biomedical Engineering, Yonsei University, Wonju-City, South Korea
2 Institute of Medical Engineering in Yonsei University and Department of Biomedical Engineering, Yonsei University, Wonju-City, South Korea

Abstract — **Gait initiation is a transitional process from the balanced upright standing to the beginning of steady-state walking. Steady-state walking represents the start of repeated gait pattern with steady-state walking speed within one gait cycle. Hemiplegic patients' gait initiation was analyzed using the 3D motion analysis system synchronized with 2 force plates. The first vertex(V1) in the CoP trajectory was placed on the lateral-posterior point from the leading limb side, and the third vertex(V3) was placed on the lateral-anterior point from the trailing limb side in the CoP of the normal gait initiation. However, V1 was not nearly shown and V3 was placed on the posterior from the trailing limb side in the CoP of the hemiplegic gait initiation. The time and distance from the onset to the toe-off(P1) and from the toe-off to the initial contact(P2) were analyzed that the mean time was larger and the mean distance was shorter when the affected limb was leading limb. The net CoP data obtained on gait initiation with hemiplegic patients suggest that they compensated with different strategies with respect to the limb whether it was leading limb or trailing limb for their impairment.**

Keywords — **Gait initiation, Hemiplegic patient, Net center of pressure**

I. Introduction

Gait initiation is the transitional phase between static balance in upright position and the start of steady-state walking. It is a complicated process with the neuromusculoskeletal systems to control the body against a perturbated situation[1]. There were a lot of studies with respect the gait initiation (e.g. the net center of pressure analysis, the electromyogram of the lower muscles, kinematic and kinetic analysis about the lower extremities).

A.H Vrieling measured the temporal parameters and the center of pressure(COP) when the gait was initiated with dominant foot or non-dominant foot[3]. Marketta Henriksson compared the gait initiation between young and old people by measuring the electromygram(EMG) and ground reaction forces(GRF)[4]. Sandhiran Patchay studied about the positions of the gait initiation which were added more load on the lower limbs by measuring the GRFs and net COP[5]. Carrie Stackhouse measred the GRF and muscle activation to investigate the gait initiation of children with cerebral palsy[6].

Self-triggered gait initiation and reactiontime gait initiation (cued by a ''beep'' sound) were performed by A. Delval[7]. Falls occur most frequently in people who have lack of muscle force, lack of flexibility, unstable posture, problem in cognition[8,9]. Stroke patients have the most dangerous risk factors to fall in the rehabilitation ward. It is reported that hemiplegic patients has 35% of ratio among all fall accidents[10,11]. Decrease of ability to contract muscles voluntarily, abnormality in muscle activation, deterioration of perception and cognition can cause the fall in patient with hemiplegia[12]. Hemipretic patients often show an asymmetric motion pattern, which has repeatedly been demonstrated in the context of standing, walking, getting up, and sitting down. The asymmetry affected the gait initiation thus hemiparetic patients initiate the gait using abnormal postural control strategies. In this study, the trajectory of the COP was investigated during hemiparetic patients' gait initiation to understand what strategies were used when they initiated the gait.

II. Methods

A. Subjects

Four patients with hemiparesis and thirteen healthy adults volunteered to undergo motion capture experiments during gait initiation task. Patients were fifties who has 30 cadences with mean gait speed and pathologic gait pattern of circumduction gait.

B. Experiments

Two forceplates synchronized with the three dimensional motion analysis system(VICON612, UK) were used in this study. The subjects were required to stand on the forceplates quietly, and then they initiated gait voluntarily with comfortable speed. They were just controlled to lead affected side or non-affected side.

C. The net center of pressure (net COP)

The net COP during double limb support periods could be calculated using data from two forceplate forms as follows.

Chwee Teck Lim, James C.H. Goh (Eds.): ICBME 2008, Proceedings 23, pp. 1962–1964, 2009
www.springerlink.com

$$COP_{\neq t(x,y)} = COP_{LL(x,y)} \frac{F_{z,LL}}{F_{z,LL} + F_{z,TL}} + COP_{TL(x,y)} \frac{F_{z,TL}}{F_{z,LL} + F_{z,TL}}$$

$COP_{LL(x,y)}$: COP of leading limb(LL)

$COP_{TL(x,y)}$: COP of trailing limb(TL)

$F_{z,LL}$: vertical component of GRF on LL side

$F_{z,TL}$: vertical component of GRF on TL side

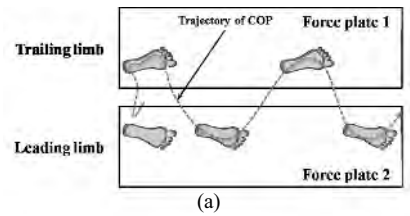
The X axis was defined as anterior-posterior direction and Y axis was medio-lateral, and Z axis was defined as the vertical direction.

D. Analysis of data

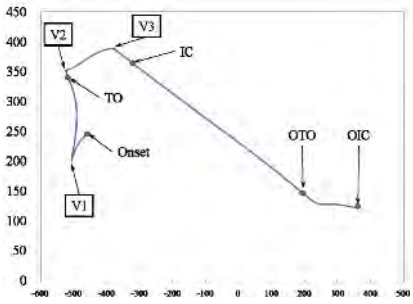
The gait initiation starting point(onset) was defined by the change of vertical GRF.

III. Results

Fig. 1 shows the trajectory of COP during the gait initiation of healthy subjects. The COP moved from onset point to posterior side of LL and then moved to TL side after showing the peak point of V1. Then, COP moved to posterior of TL and showed V2 between toe-off(TO) and initial contact(IC). Before the first initial contact of LL, the COP moved maximally to TL side(V3). After the V3, the COP trajectory showed sinusoidal features.



(a)

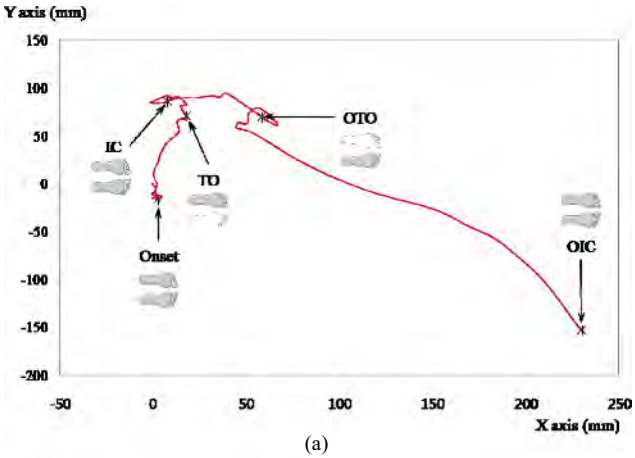


(b)

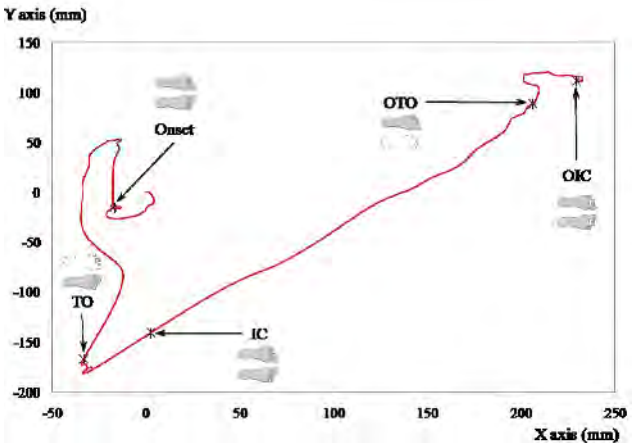
Fig. 1 (a), (b) Trajectory of the net CoP for normal subjects during gait initiation

Fig. 2 (a), (b) shows the trajectory of COP during the gait initiation of patients. The characteristics of the COP when the LL was the affected side were that the first vertex after the onset(V1) was not observed and V3 was observed at the posterior side of the TL. When the LL was unaffected side, the V1 of COP was observed and the V3 was observed on the anterio-lateral side from TL just like those of the healthy subjects'. However, the distance between V1 and onset point was different from that of healthy subjects' and curves between V1 and V2 were quite different. Moreover, the trajectory of the COP had lots of oscillation in both when the LL was affected side and unaffected side.

The mean time and distance while the COP moved from onset to TO(P1), from TO to IC(P2) showed in table 1 and 2. The P1 was 0.49±0.08s and P2 was 0.45±0.05s in healthy subjects. P1 and P2 in patients were variable with respect to the LL. P1 was 1.23±0.31s, P2 was 0.90±0.17s when the LL



(a)



(b)

Fig. 2 Trajectory of the net CoP for a hemiplegic patient during gait initiation with the affected limb(a) and with the unaffected limb(b)

was the affected side. P1 was 0.91±0.16s and P2 was 0.27±0.02s when the LL was the unaffected side.

The distances of COP in healthy subjects were 122.19±18.35mm in P1, and 141.08±16.57mm in P2. In patients, the distance of COP was 101.44±8.37mm in P1, 31.15±4.59mm in P2 when the LL was the affected side. And the distance of COP was 162.72±16.05mm in P1, 20.59±4.09mm in P2 when the LL was the unaffected side. The time of P1, P2 and the distance of P1, P2 in patients were different significantly from that of healthy subjects. In addition, they have differences between affected side and unaffected side. The P1 time was longer when the LL was affected side than the LL was unaffected side because the hemiplegic patients' ability to support the body weight might be better in unaffected side than affected side. On the other hand, P1 time was longer when the LL was the unaffected side because the affected limb had less ability to support body weight(the body weight needs to be moved to the affected side before the TO).

Table 1 Time of P1 and P2 (sec)

	Rt. Hemiplegic Patient				Normal	
	Rt. leading		Lt. leading			
	Mean	S.D.	Mean	S.D.	Mean	S.D.
P1	1.23	0.31	0.91	0.16	0.49	0.08
P2	0.90	0.17	0.27	0.02	0.45	0.05

Table 2 Time of P1 and P2 (sec)

	Rt. Hemiplegic Patient				Normal	
	Rt. leading		Lt. leading			
	Mean	S.D.	Mean	S.D.	Mean	S.D.
P1	101.44	8.37	162.72	16.05	122.19	18.35
P2	31.15	4.59	20.59	4.09	141.08	16.57

IV. Conclusion

The differences of the COP trajectory between healthy subjects and hemiplegic patients, in the period between the double limb support to the first step(gait initiation), were observed by analysis and comparison about the motion of gait initiation. Moreover, the differences between left and right side of the patients were confirmed. These results were expected to be used to assess the balance ability of patients and to set up the rehabilitation exercise plan for the prevention of the falls.

Acknowledgment

This research was financially supported by the Ministry of Knowledge Economy(MKE) and Korea Industrial Technology Foundation(KOTEF) through the Human Resource Training Project for Regional Innovation.

References

1. Mann R.A., Hagy J.L., White V., Liddell D.(1979) The initiation of gait. J. Bone Joint Surg Am. 61:232-239
2. Elble R. J., Moody C., Leffler K., Sinha R.(1994) The initiation of normal walking. Movement Disorder 9(2):139-146
3. Vrieling A.H, van Keeken H.G., Schoppen T., Otten E., Halbertsma J.P.K., Hof A.L., Postema K.(2008) Gait initiation in lower limb amputees. Gait&Posture 27(3):423-430
4. Henriksson M., Hirschfeld H.(2005) Physical active older adults display alterations in gait initiation. Gait &Posture 21(3):289-296
5. Sandhiran Patchay, Yves Gahéry. (2003) Effect of symmetrical limb loading on early postural adjustments associated with gait initiation in young healthy adults. Gait&Posture 85-94
6. Carrie Stackhouse, Patricia A. Shewokis, Samuel R. Pierce, Brian Smith, James McCarthy, Carole Tucker (2007) Gait initiation in children with cerebral palsy. Gait & Posture 26(2):301-308
7. Delval A., Krystkowiak P., Blatt J.-L., Labyt E., Bourriez J.-L., Dujardin K., Destée A., Derambure P., Defebvre L.(2007) A biomechanical study of gait initiation in Huntington's disease. Gait&Posture 25(2):279-288
8. Bishop M., Brunt D., Pathare N., Marjama-Lyons J. (2005) Changes in distal muscle timing may contribute to slowness during sit-to-stand in parkinsons disease. Clinical biomechanics 20(1):112-117
9. Vlahov D., Myers A.H. (1990) Epidemiology of falls among patients in a rehabilitation hospital. Arch. Phys. Med. Rehabil 71(1):8-12
10. Mayo N.E., Korner-Britensky N., Becker R., Georges P. (1989) Predicting falls among patients in a rehabilitation hospital. Am. J. Phys. Med. Rehabil 68(3):139-146
11. Dawson M., Reiter F., Sarkodie-Gyan T., Provinciali L. and Hesse S. (1996) Gait initiation, development of a measurement system for use in a clinical environment. Biomedizinische. Technik, 41(7-8):213-217
12. Hesse S., Reiter F., Jahnke Matthias, Michael Dawson, Thompson Sarkodie-Gyan, Karl-Heinz Mauritz (1997) Asymmetry of gait initiation in hemiparetic stroke subjects. Arch Phys Med Rehabil 78:719-724

Author: Y.H. Kim
Institute: Institute of Medical Engineering in Yonsei University and Department of Biomedical Engineering in Yonsei University
Street: 234 Maeji, Heungeop
City: Wonju
Country: South Korea
Email: younghokim@yonsei.ac.kr

AFM Study of the Cytoskeletal Structures of Malaria Infected Erythrocytes

H. Shi[1], A. Li[1], J. Yin[2], K.S.W. Tan[2] and C.T. Lim[1,3]

[1] Division of Bioengineering, National University of Singapore, Singapore
[2] Yong Loo Lin School of Medicine, National University of Singapore, Singapore
[3] NUS Life Sciences Institute, National University of Singapore, Singapore

Abstract — **Malaria is one of the severest human diseases on earth. It is caused by the asexual propagation of malaria parasites in host erythrocytes. During the process of maturation, parasites export parasite-expressed proteins, such as PfEMP1 and KHARP to the host cell membrane thus forming knobs on the host cell surface and thereby stiffening the membrane and causing cytoadherence (cell stickiness) to occur. To investigate the formation of knobs as well as the relationship between knobs and the host cell spectrin network, atomic force microscopy (AFM) is used to study both the extracellular and the cytoplasmic surface of infected erythrocyte membranes. Although the cytoskeletal structure can be observed from both the extracellular surface and cytoplasmic surface, the AFM images of cytoplasmic surface uncovered more details of the spectrin network. Knobs and their connections or linkages to the spectrin network were clearly observed from the cytoplasmic surface of infected erythrocytes. The size and distribution of knobs viewed from the cytoplasmic surface were similar to those observed from the extracellular surface. Furthermore, dramatic changes of spectrin network were detected after infection, i.e. the spectrin network is partially broken at the schizont stage. Altogether, our observation may help better understand the mechanisms of the structural and functional changes in malaria infection.**

Keywords — **Plasmodium falciparum, Atomic force microscopy (AFM), spectrin network, knobs.**

I. Introduction

The asexual cycle of the malaria parasite *Plasmodium (P.) falciparum* is composed of the ring, trophozoite and schizont stages. During the maturation in the host erythrocyte, the parasite modifies the host cell membranes by exporting parasite-expressed proteins, such as *P. falciparum* erythrocyte membrane protein 1 (PfEMP1) and knob-associated histidine-rich protein (KAHRP) to the surface of host erythrocyte membrane and forming knobs [1]. These knobs interact with the spectrin network via the attachment of KAHRP to the spectrin-actin protein 4.1 junction in parasitized erythrocytes [2,3]. Besides, parasite-produced proteases are able to hydrolyze host cell cytoskeletal proteins [4-7], which could be related to new generated parasites release from erythrocytes [8]. However, direct observation of the interaction between knobs and cytoskeleton and the changes of the host cell cytoskeleton during the cleavage of certain protease is lacking.

Atomic force microscopy (AFM) imaging has the potential of obtaining subnanometer resolution of extracellular and intracellular structures. It has been widely used to investigate the structure of normal erythrocyte cytoskeleton at both extracellular surface [9-11] and cytoplasmic surface [9,12,13] of the erythrocyte membrane. Also, AFM has been used to investigate air-dried ring stage ghost including parasite and the cytoskeleton of infected cells has been found to be less dense than healthy ones [14]. Meanwhile, the knob structure on the surface of infected erythrocytes has been observed by imaging intact fixed infected cells [15] and smears [16], respectively. However, the cytoplasmic side of the cytoskeleton of *P. falciparum* infected erythrocyte has not been intensively investigated yet. In this study, we used AFM to observe the outer and inner surfaces of the membrane of healthy and infected cells. Significant changes of erythrocyte cytoskeleton after infection were observed. The study may help us better understand the structural changes to host erythrocyte after P. *falciparum* infection.

II. Methods

A. Cell culture

P. *falciparum* parasites (3D7 and CS2 strains) were cultured in vitro using a modification of the method previously described [17]. Platelet-coated glass petri dishes were used to select knobby infected cells. Platelets were isolated from human blood as described by Baenziger and Majerus (1974). Fresh platelets were incubated on sterile acid-treated glass petri dishes in a humid chamber at room temperature for 1 h. The non-bound platelets were gently rinsed off with phosphate buffer solution (PBS). 10ml of late stage parasite culture were incubated on the surface of platelet substrate in candle jar at 37 °C for 2h. Normal erythrocytes and non-bound infected cells were rinsed off with culture medium. 10ml of culture medium with 5% hematocrit was added into the glass petri dish and incubated at 37°C in candle jar overnight until new generation of ring stage parasites was

Chwee Teck Lim, James C.H. Goh (Eds.): ICBME 2008, Proceedings 23, pp. 1965–1968, 2009
www.springerlink.com

formed. The culture was then transferred to the flask for continuous culturing as described before.

B. Enrichment of trophozoite and schizont stage infected erythrocytes

MidiMACS separation set (Miltenyi Biotec) was used to enrich trophozoite and schizont stage infected cells. Briefly, a LD column was inserted into MACS separator and preload with 1ml EDTA-BSA rinsing buffer (0.5% BSA and 2mM EDTA in PBS, pH 7.2). Meanwhile, 10ml of parasite culture was pelleted by centrifuging and gently resuspended in 2ml rinsing buffer. The cell suspension was applied on to a preloaded LD column and rinsed with 2ml rinsing buffer several times once the column reservoir was empty. When there was no red color solution seen passing through, the column was taken out and the effluent was collected. By using this method, around 90% purity of late stage infected cells were collected.

C. Modification of glass coverslips

The substrates were prepared following Liu's method [13] except for the following modifications. Instead of using N-5-azido-2-nitrobenzoyloxysuccinimide (ANBNOS), Bis(sulfo-succimidyl) suberate (BS^3) (Pierce) was used as a bifunctional crosslinker to crosslink PHA-E (EY laboratories) to 3-amino-propyltriethoxysilane (APTES) treated coverslips.

D. Preparation of smears and cytoplasmic membrane exposed samples

Smears were prepared as previously described [16].

Normal erythrocytes and MACS enriched infected cells were incubated on PHA-E coated coverslips for 4h in a moist chamber at room temperature. Loosely attached cells were washed away with PBS. Strongly attached cells were lysed by immersing the coverslips in a hypotonic buffer 5P8-10 (5mM Na_2HPO4/NaH_2PO4, 30mM NaCl, PH 8) for 10 min at room temperature. They were then shear-washed 6 times with 5P8-10 buffer using a 10ml syringe with a gauge 25 needle at an angle less than 20 degree. Cytoplasmic membrane exposed samples were quickly rinsed with deionized water and vacuum dried for use. For schizont stage infected cells, a modified method (self-burst method) was used. After incubation on PHA-E substrates for 1h and rinsing using PBS, schizont stage infected cells were recultured to burst by incubating the substrates in a petri dish with culture medium overnight at 37 °C. The samples were then rinsed, shear-washed and dried for AFM imaging.

III. Results

A. AFM images of the outer and inner side of normal erythrocyte membrane

Amplitude AFM images of intact normal erythrocytes were obtained by scanning normal erythrocyte smears as shown in Fig. 1(a). An enlarged view (after low pass modification) of the extracellular surface of normal erythrocyte reveals the cytoskeletal network underlying the membrane as shown in Fig. 1(b). The cytoskeleton observed on the outer surface also includes the membrane proteins, glycocalyx and the phospholipid bilayer. Meanwhile, an AFM image of the cytoplasmic surface of normal erythrocyte membrane is shown in Fig. 1(c) and the high magnification images (Fig. 1(d)) show the details of the spectrin network of the normal erythrocytes. The membranes obtained from shear-washing are approximately 7.5-8 μm in diameter and the thickness of membrane ranges between 5-10 nm as obtained from section analysis.

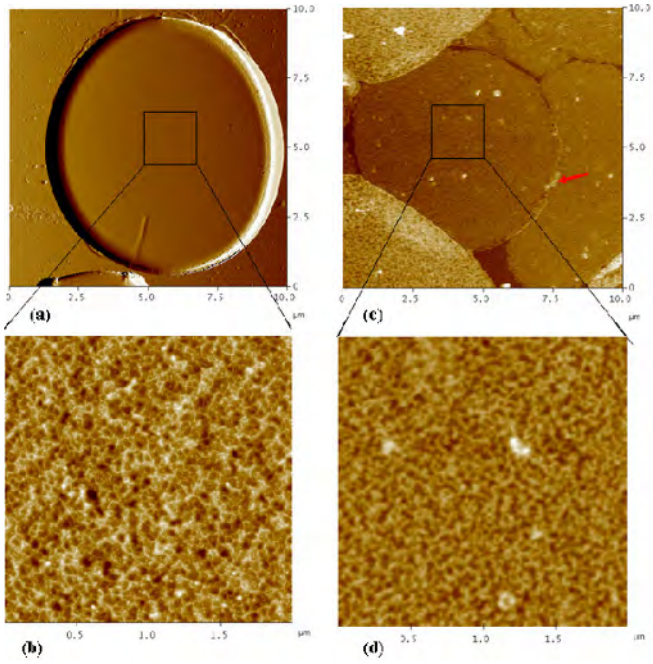


Fig. 1 Normal erythrocyte membrane. (a) Intact erythrocyte image. (b) Plot view of high magnification outer surface of erythrocyte membrane (zoom in from (a)). (c) Cytoplasmic side of erythrocyte membrane. Overlap area of membranes are indicated by red arrow. (d) Plot view of high magnification inner surface of erythrocyte membrane (zoom in from (c)).

B. AFM images of the outer and inner sides of late infected erythrocyte membrane

Trophozoite stage infected erythrocytes were also investigated from the extracellular surface using AFM (Fig. 2) and the structure and the distribution of knobs can be easily observed [16]. Although the spectin network seems sparser than normal erythrocyte (Fig. 2(b)), the connection between knobs and cytoskeleton and the detailed changes of the spectin network may be hard to investigate from the outer surface. As to the schizont stage, it is even harder to view the cytoskeleton from the outer surface, because the parasites occupy a major part of the host cell and the outer surface becomes more rough and undulating [16].

To investigate the real changes occurring in the cytoskeleton after infection, AFM images of the inner surface of the infected erythrocyte membrane were obtained as shown in Figs. 3. While the cytoplasmic surface exposed membrane of the normal erythrocytes obtained are around 8 µm in diameter (Fig. 1 (c)), those of the trophozoite and schizont stages are about 6.5 to 8 µm (Fig. 3(a)) and 3.5 to 6 µm (Fig. 3(c)) in diameter, respectively. This may attribute to the morphological changes of the host erythrocyte after infection (infected cell becomes more and more spherical arising from the multiplication of the parasites inside the cell). Protrusions (knobs) were observed from the inner surface (Fig. 3(b & d)), which is consistent with the observations from the outer surface obtained by Li et al. [16]. Meanwhile, knobs were found to be well weaved in the spectin network at trophozoite stage (Fig. 3(b)).

Two methods were used to obtain cytoplasmic surface exposed membrane of the shizont stage infected erythrocyte. One method was the normal shear wash method. After increased repeats of shear wash, either the whole cell was washed away or the membrane got partially washed away in most cases (data not shown).

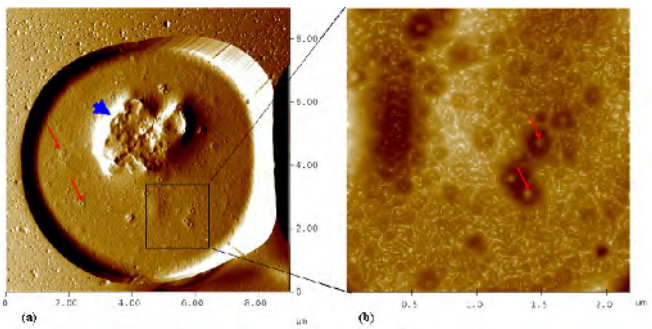


Fig. 2 Outer surface of trophozoite stage infected erythrocyte. (a) Intact trophozoite stage infected erythrocytes. (b) Magnified view of the outer surface of erythrocyte membrane (zoom in from (a)). Knobs and parasite area are indicated by the red arrows and blue arrowhead, respectively

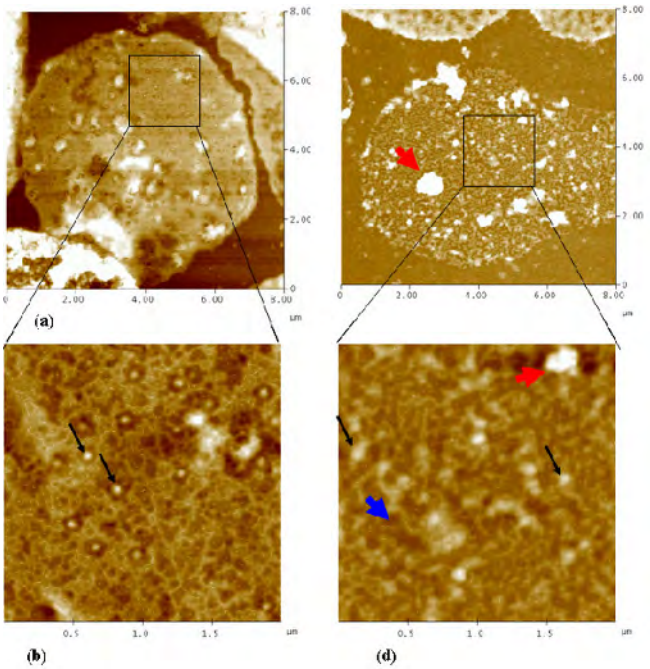


Fig. 3 Cytoplasmic surfaces of trophozoite stage and schizont stage infected erythrocyte membrane. (a-b) Trophozoite stage; (c-d) Schizont stage, using the modified shear-washing method. (b) and (d) are magnified from (a) and (c) respectively. Knobs are indicated by black arrows. Breakages and sticky sub-micro particles are indicated by blue and red arrowheads, respectively

The other method was the self-burst method, which enables us to study host cell cytoskeleton after bursting of the infected cell. Breakages of the spectrin network were observed (Fig. 3(d)). However, compared with the observation from the first method, the breakages were much less significant. It seems that the membranes can be better maintained using the latter method and extra shear wash may partially perturb the cytoskeleton.

IV. Discussion

Although the preparation of erythrocyte ghost has been well established [18], it is difficult to obtain ghosts of late stage infected erythrocytes. This could be one reason why only ring stage infected erythrocyte ghost has been investigated [14]. However, the cytoskeleton is partially extended or stretched during ghost preparation, which may affect revealing the actual spectrin network in intact cells. Also, double layers of ghost membrane may overlap and interfere with the interpretation of the images. Here, the normal and infected erythrocytes were strongly attached to the PHA-E substrate which helped to preserve the membrane structure during shear washing. Firstly, the size and the density of

normal erythrocyte spectrins in our images (Fig. 1(b)) was consistent with previous findings [12]. Furthermore, we investigated the process of spectrin network alteration: (1) knobs form on the host cell membrane at the trophozoite stage; (2) connections of spectrin network are partially destroyed at schizont stage. The observed breakage of cytoskeleton may provide an evidence of the process of the hydrolysis of host cell cytoskeletal proteins during parasite maturation. Even though the breakage we observed could be caused by the shear wash, at least, it indicates that host cell cytoskeleton becomes fragile at late stage. Moreover, the observation of the linkages between knobs and cytoskeleton directly by AFM imaging may offer a demonstration of notion that knobs are interacting with host cell cytoskeleton.

V. Conclusions

In this paper, we used the unique ability of the AFM to provide topographic information to investigate the cytoskeleton changes arising from malarial infection, without any fixtation or detergent treatment. Our AFM study on *P. falciparum*-infected erythrocyte cytoskeleton has the potential to conduct further studies on other malarial infection, such as *P. Vivax* and *P. malariae*, or even other medically important host-parasite interactions.

Acknowledgments

We would like to thank Dr Bruce Russell for sharing his experience in infected cell enrichment.

References

1. Cooke B M, Mohandas N and Coppel R L (2001) The malaria-infected red blood cell: structural and functional changes. *Adv Parasitol* 50:1-86
2. Oh S S, Chishti A H, Palek J, et al. (1997) Erythrocyte membrane alterations in Plasmodium falciparum malaria sequestration. *Curr Opin Hematol* 4:148-54
3. Pei X, An X, Guo X, et al. (2005) Structural and functional studies of interaction between Plasmodium falciparum knob-associated histidine-rich protein (KAHRP) and erythrocyte spectrin. *J Biol Chem* 280:31166-71
4. Le Bonniec S, Deregnaucourt C, Redeker V, et al. (1999) Plasmepsin II, an acidic hemoglobinase from the Plasmodium falciparum food vacuole, is active at neutral pH on the host erythrocyte membrane skeleton. *J Biol Chem* 274:14218-23
5. Raphael P, Takakuwa Y, Manno S, et al. (2000) A cysteine protease activity from Plasmodium falciparum cleaves human erythrocyte ankyrin. *Mol Biochem Parasitol* 110:259-72
6. Hanspal M, Dua M, Takakuwa Y, et al. (2002) Plasmodium falciparum cysteine protease falcipain-2 cleaves erythrocyte membrane skeletal proteins at late stages of parasite development. *Blood* 100:1048-54
7. Rosenthal P J (2002) Hydrolysis of erythrocyte proteins by proteases of malaria parasites. *Curr Opin Hematol* 9:140-5
8. Dhawan S, Dua M, Chishti A H, et al. (2003) Ankyrin peptide blocks falcipain-2-mediated malaria parasite release from red blood cells. *J Biol Chem* 278:30180-6
9. Takeuchi M, Miyamoto H, Sako Y, et al. (1998) Structure of the erythrocyte membrane skeleton as observed by atomic force microscopy. *Biophys J* 74:2171-83
10. Yamashina S and Katsumata O (2000) Structural analysis of red blood cell membrane with an atomic force microscope. *J Electron Microsc (Tokyo)* 49:445-51
11. Nowakowski R, Luckham P and Winlove P (2001) Imaging erythrocytes under physiological conditions by atomic force microscopy. *Biochim Biophys Acta* 1514:170-6
12. Swihart A H, Mikrut J M, Ketterson J B, et al. (2001) Atomic force microscopy of the erythrocyte membrane skeleton. *J Microsc* 204:212-25
13. Liu F, Burgess J, Mizukami H, et al. (2003) Sample preparation and imaging of erythrocyte cytoskeleton with the atomic force microscopy. *Cell Biochem Biophys* 38:251-70
14. Garcia C R, Takeuschi M, Yoshioka K, et al. (1997) Imaging Plasmodium falciparum-infected ghost and parasite by atomic force microscopy. *J Struct Biol* 119:92-8
15. Nagao E, Kaneko O and Dvorak J A (2000) Plasmodium falciparum-infected erythrocytes: qualitative and quantitative analyses of parasite-induced knobs by atomic force microscopy. *J Struct Biol* 130: 34-44
16. Li A, Mansoor A H, Tan K S, et al. (2006) Observations on the internal and surface morphology of malaria infected blood cells using optical and atomic force microscopy. *J Microbiol Methods* 66:434-9
17. Trager W and Jensen J B (1976) Human malaria parasites in continuous culture. *Science* 193:673-5
18. Tyler J M, Reinhardt B N and Branton D (1980) Associations of erythrocyte membrane proteins. Binding of purified bands 2.1 and 4.1 to spectrin. *J Biol Chem* 255:7034-9
19. Sherman I W, Greenan J R and de la Vega P (1988) Immunofluorescent and immunoelectron microscopic localization of protein antigens in red cells infected with the human malaria Plasmodium falciparum. *Ann Trop Med Parasitol* 82:531-45
20. Haldar K, Samuel B U, Mohandas N, et al. (2001) Transport mechanisms in Plasmodium-infected erythrocytes: lipid rafts and a tubovesicular network. *Int J Parasitol* 31:1393-401
21. Wickert H, Wissing F, Andrews K T, et al. (2003) Evidence for trafficking of PfEMP1 to the surface of P. falciparum-infected erythrocytes via a complex membrane network. *Eur J Cell Biol* 82:271-84

Author: Lim chwee Teck
Institute: Division of Bioengineering,
National University of Singapore
Street: 7 Engineering Drive 1
City: Singapore
Country: Singapore
Email: ctlim@nus.edu.sg

Adaptive System Identification and Modeling of Respiratory Acoustics

Abbas K. Abbas[1], Rasha Bassam[2]

[1] RWTH Aachen University, Aachen, Germany
[2] Biomedical Engineering Dept., Aachen university of Applied Sciences, Juelich, Germany

Abstract — **Adaptive identification and modeling of tracheal sound is considered as primary method to detect and monitor respiratory tract changes such as those found in asthma and acute respiratory distress syndrome ARDS. There is a need to connect the characteristic of these easily measured sounds first to the underlying physiological dynamics, and then to specific pathophysiology. To initiate this process, a model of the acoustic properties for entire respiratory tract was developed. The modeling bandwidth lies over the frequency range of lower tracheal sound (Phonospirogram) measurements, 90 Hz to 3.02 KHz. The respiratory tract system is represented by a transmission line acoustical analogy with varying cross sectional area, yielding walls, branching in the bronchial component, and airflow related acoustical sources distributed all through the whole tract. Recursive identification method applied to characterize volumetric airflow and the underlying anatomy of respiratory tract. The derived model was tested according to spatial location of natural acoustic resonances frequency for components and the entire respiratory tract. Based on parametric estimation, respiratory dynamics with associated viscoelastic properties was computed. Individually, Thoracic portions of the model predict well the distinct locations of spectral peaks from respiration phases measured at the chest. While combining supra- and subtracheal portions to form a complete tract model in healthy subject, the predicted peak locations evaluate constructively with those of respiratory sounds measured during normal breathing. This study provides view into the complex interaction between the spectral peaks and amplitudes of lung sounds.**

Keywords — **Phonospirography, Recursive estimation, Acoustic characteristic, Dynamic characteristics, Respiratory mechanics.**

I. Introduction

Passive respiratory sounds have been used for diagnosis of respiratory diseases for almost a century. These, by the flow of air created sounds provide only limited information, as neither their exact points of creation are known their changes when traveling through the healthy or diseased respiratory system well understood. From other techniques such as chest X-rays and pulmonary function tests little more information on pulmonary pathology is obtained, with the former being also significant risk to the patient, especially when used repeatedly, as it gradually increases the risk of cancer. Computed Tomography (CT) bears the same health hazard as conventional X-rays, but is capable of providing cross-sectional images of the lung with great anatomical details.

Rice and Kraman [2,3] started to investigate the transmission of sound through airways and lungs, which had not been studied in particular before. The emphasis of these investigations was placed on establishing the sound speed in airways and lung parenchyma, and the sound attenuation was merely studied in order to establish a sensible frequency range for the sound source. Sound speed and attenuation was assumed as being basically frequency-independent, and thus measurement techniques, such as cross-correlation applied to white noise (i.e. noise containing all frequencies), were used that are unsuitable if sound transmission is dispersive (frequency-dependent). The acoustic behavior of the lungs was theoretically described by considering the lungs as being an elastic continuum in a model of bubbles in a liquid. This model proved to be adequate and provided a functional correlation between the sound speed and the density of the lung parenchyma, which is depend on the alveoli size. Collapsed alveoli, being smaller, conduct sound at a higher speed than alveoli in normal parenchyma.

II. Materials and methods

The PCG signal was collected from 11 patients. The data were collected using TSR-Cardio microphone system with 14 Channel ADC acquisition modules. Experimental system identification was implemented using MATLAB platform, with a software filtering unit implemented in the input and output channel of SID-system. Fig.1 illustrates the experimental setup of PSG signal acoustic system identification with ARMAX algorithm implemented in the path of computational unit.

III. Respiratory acoustics modleing

Transducers such as microphones have allowed for the collection of more accurate acoustical data over a wider range of frequencies.Fig.2 illustrated different traces of PSG signals ranging from normal to pathological cases of respiratory tract.

Chwee Teck Lim, James C.H. Goh (Eds.): ICBME 2008, Proceedings 23, pp. 1969–1973, 2009
www.springerlink.com

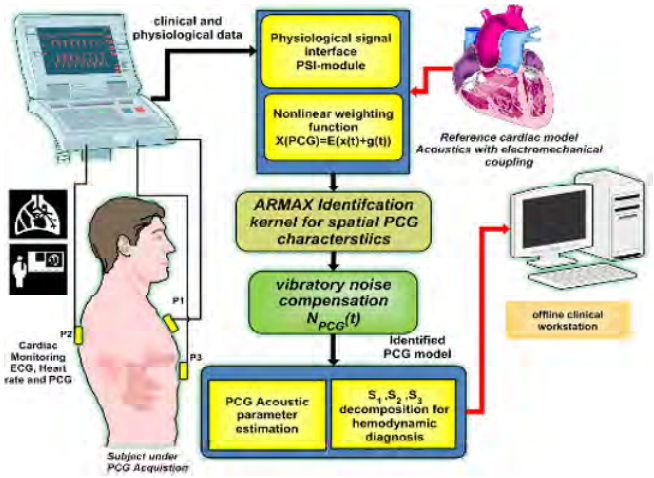


Fig.1 Respiratory acoustic identification system setup based on recursive ARMA method.

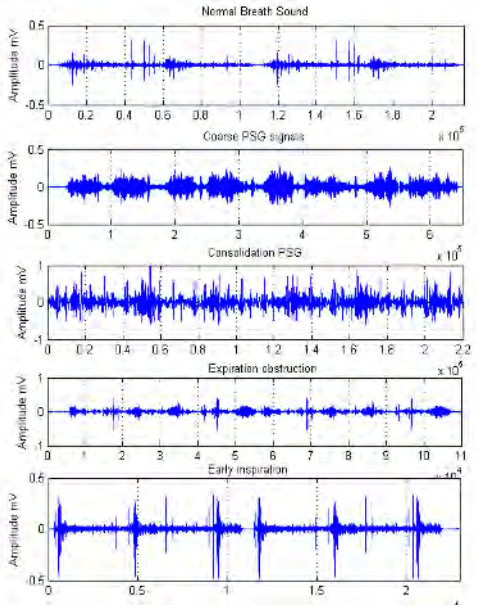


Fig.2 Phonospiraography signals for different respiratory pathology and normal patterns.

Characteristic patterns in the data, thus recorded have been associated with conditions affecting airway patency such as asthma, obstructive sleep apnea, infections, airway edema, malformations and tumors. One common location for recording breathing sounds is on the neck at the suprasternal notch over the extrathoracic trachea, with the sounds recorded referred to as tracheal sounds. These sounds are relatively large in amplitude and have a wider range of frequencies than sounds recorded at the chest wall, and also

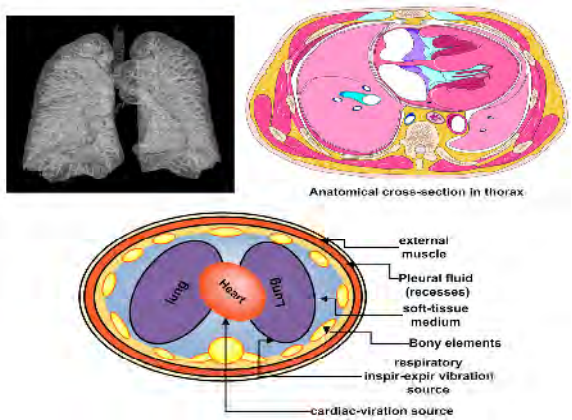


Fig.3 Anatomical component of respiratory acoustic model.

have a close relation to tracheal airflow [1]. The spectra of these tracheal sounds have been characterized as broad frequency noise with discernible spectral peaks ranging between 80 Hz to more than 1500 Hz with a “cut-off”-like frequency of around 800 Hz [2].

Fig.3 illustrates the main component of the respiratory mechanical model as based on transverse section that consists of cardiac vibration source and pleural-thorax vibration model. The well-known respiratory dynamic model was adapted by Horsfield et al [3] , in which the vibratory signal recorded as PSG signal used to identify and estimate transfer characteristics of respiratory tract and formulate a basis relation to respiratory dynamics.

These measurements suggest that there is a potential for these easily-measured PSG sounds to be used in clinical practice for the diagnosis and monitoring of various respiratory conditions [1].

For such potential clinical applications to be most useful, the relationships between the attributes of these sounds and the underlying anatomy, and ultimately patho- physiology, need to be determined [1, 4].

As a first step in this process, this study describes the development of an acoustic modeling and identification of the respiratory tract that is based on its anatomy and allows for the prediction of its natural acoustic resonances.

A recursive parametric estimation method was used in order to identify dynamic parameters of respiratory tract model. Fig.5 illustrated the intensity profile of respiratory acoustic sounds, form which power index of consumed energy in the upper respiratory tract can be identified and computed. Segmented respiration acoustic waveform can be calculated through adaptive recursive identification. Considering each airway as a rigid tube, it is possible to model a single structure of Horsfield's bronchial tree with the laws of propagation of sound waves in a cylindrical pipe Benade[7], by using

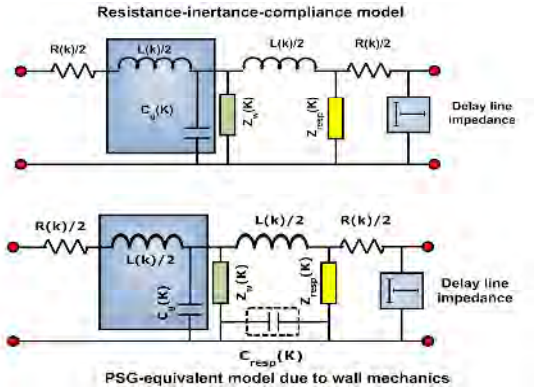


Fig.4 Respiratory dynamic models with impedance illustration of different analogous compartment.

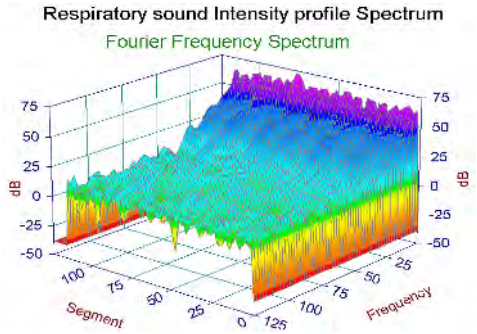


Fig.5 Respiratory sound intensity characteristics with spectrum profile segmented along the respiratory cycle.

a lumped parameter description and the simplifications for the low frequencies (<10 Hz) reported in Thorpe[9]. Thus, each segment of the airway tree can be arranged as the acoustic transmission line represented in Fig.4, in which:

$$R(k) = 8.\frac{\eta.l(k)}{\pi.r^4(k)} \tag{1}$$

$$L(k) = \rho.\frac{l(k)}{\pi.r^2(k)} \tag{2}$$

$$C_g(k) = \frac{V(k)}{P_0} = \frac{\pi.r^2(k).l(k)}{P_0} \tag{3}$$

where $r(k)$ is the tube radius $l(k)$ the tube length, η is gas viscosity and ρ is gas density. $V(k)$ is the airway segment volume at the fixing pressure P_0. Thus characterizing the resistance and inertance of the rigid tube while is gas compressibility. To incorporate in the airway model more anatomical details, one can include the influence of the wall mechanics as done, for example, in Lutchen[6]. To do so, both the soft and cartilaginous airway walls can be idealized as a series of resistance-inertance-compliance, in parallel with the gas compressibility [5,7]. Being the soft-tissue fraction for each airway segment equal to one minus the cartilaginous fraction ($ca[k]$) we have:

$$Z_w^i(k) = R_w^i(k) + j.(\omega.L_w^i(k) - \frac{1}{\omega.C_w^i(k)}), i = so, ca \tag{4}$$

where ca the angular frequency (radians/s) and the values for R_w, L_w and C_w can be computed, according to Suki[9]. Thus, the equivalent wall impedance given by the weighted combination of the soft and cartilaginous impedance is:

$$Z_W(k) = \frac{Z_w^{so}(k).Z_w^{ca}(k)}{c(k).Z_w^{so}(k) + (1-c(k)).Z_w^{ca}(k)} \tag{5}$$

The peripheral airways, which are small airways of less than 2 mm in diameter, are well recognized as the main sites of airway narrowing and obstruction in asthma and other obstructive diseases. This pathological condition can be described mathematically in Horsfield's model by reducing, of a certain percentage , the radius of the airway segments. Equations (1) to (5) are consequently modified; by substituting the narrowed radius for $r(k)$. This enables the impact of airway constriction on the overall response of respiratory system to be assessed in response to PSG amplitude [6,8].

IV. Recursive PSG Signal Identification

Recursive system identification is considered as one of parametric system dynamic estimation technique. In which the estimated parameters were updated through the entire identification process. As the respiratory acoustics contains wide spectrum of vibration frequencies starting with 6 Hz-6 KHz. Table.1 illustrate the lumped parameters of respiratory acoustics based on recursive. While table.2 represented the physiological default parameters of the whole respiratory system [8,9].

Table.1 lumped parameters for a lossy rigid-walled transmission line segment [4], [5], [7]

Parameter	Value	Units
Resistance	$R_a = \frac{2l}{\pi r^3}\sqrt{\frac{\omega\rho_0 n}{2}}$	dyne.s/cm^5
Inertance	$L_a = \frac{\rho_v l}{A}$	dyne.s^2/cm^5
Compliance	$C_a = \frac{Al}{\rho_v c^2}$	cm^5/dyne
Conductance	$G_a = 2\pi r l \frac{v-1}{\rho_a c^2}\sqrt{\frac{K\omega}{2c_p\rho_v}}$	cm^5/dyne.s

r= tube radius [cm]; segment length [cm]; radian frequency; density of median [g/cm]; shear viscosity [dyne s/cm]; cross-sectional area [cm]; speed of sound [cm/s]; ratio of specific heats; heat conduction coefficient [cal/cm-s- C]; and specific heat at constant pressure [cal/g- C].

Table.2 Default Wall Parameter Values For Respiratory Tract [6,7].

Parameter	Default value
Thickness	0.5 cm
Soft tissue density	1.06 g/cm^3
Soft tissue viscosity	1.06 .10^3 dyne.s/cm^2
Soft tissue elasticity	0.392.10^6 dyne/cm^2
Cartilage density	1.14 g/cm^3
Cartilage viscosity	180.0.10^3 dyne.s/cm^3
Cartilage elasticity	44.0.10^6 dyne /cm^2

Table.3 Parametric estimation of respiratory acoustic with recursive identification technique (Lumped –system).

subject	P_1	P_2	PSG Model parameter			Estimated freq ω (rad/sec)
			R_w(A)	L_w(B)	C_w(C)	
1	14.01	12.3	1.3	0.28	0.45	11.03
2	12.30	11.54	1.26	0.73	0.04	12.31
3	9.21	11.92	0.98	1.027	1.34	11.56
4	9.46	12.63	0.84	2.234	1.28	13.04
5	9.96	14.83	0.79	2.013	1.83	10.92
6	10.11	14.04	0.81	1.19	0.73	11.54
7	12.44	15.17	0.92	1.20	1.08	12.05
8	8.02	11.9	1.12	0.63	0.07	13.19
9	10.82	10.54	1.54	0.77	0.08	10.72
10	10.11	11.67	1.92	1.22	1.54	11.47
11	8.34	12.07	0.65	0.93	1.23	10.09

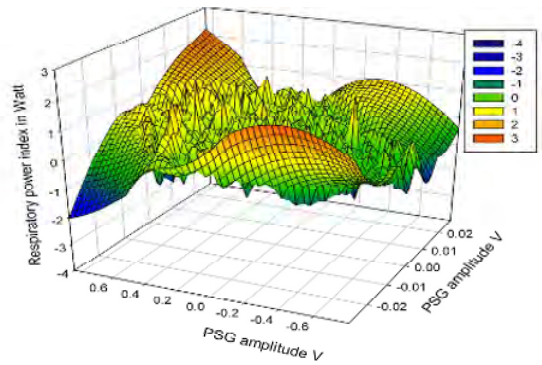


Fig .6 Respiratory power profile through recursive correlation of PSG signal amplitude.

Fig.6 illustrates the respiratory power profile through recursive correlation of resulted PSG signal. In Fig.4 indicated, impedance equivalent circuit with bypass capacitance indicates respiratory capacitance between lung wall and myocardium, in which the delay characteristics of PSG signal originated due to post-vibration damping in inspiration phase. In table.3 the estimated respiratory model were identified, showing the main physical quantities of reactance, inertance and capacitance for respiratory tract.

V. Resulsts and discussion

In the basis of the statistical analysis and performance test of identified respiratory acoustic model, the following models were identified. The model assumes 1-D acoustic wave propagation, airway geometries with second-order wall dynamics derived from previous measurements on adult males and an estimated PSG sound profile for sound generation. This acoustic representation of the average respiratory tract anatomy predicts the location of spectral peaks in upper respiratory tract acoustic measurements with disparate sound sources such as the breath sounds. These findings stress the composite importance of anatomical parameters such as overall tract length, depth of tract profile, and wall properties on spectral peak location while de-emphasizing the impact of specific source location and type. However, it is likely that such sources play a key role in the determination of the overall spectral features and amplitude of such easily-measured sounds like PSG-signals.

VI. Conclusions

From the identified respiratory acoustic model, the following observations were noticed.

- Recursive modeling have been used in order to simulated the repetitive patterns of PSG signal , to approximate experimental PSG acquisition to the real-time profile of physiological inspiration-expiration cycle.
- Due to the different frequency band width of PSG signal and the position dependent- PSG pattern, the robust method to overcome this effect was to use pre-filtering stage at the input node and output node of identification computational kernel.
- Finally, recursive identification will allow acoustic mapping for pre-trials to acoustic imaging technique to established in future acquisition.

References

1. G. R. Wodicka, K. N. Stevens, H. L. Golub, E. G. Cravalho, and D. C. Shannon, “A model of acoustic transmission in the respiratory system,” *IEEE Trans. Biomed. Eng.*, vol. 36, pp. 925–934, Sept. 1989.
2. H. Pasterkamp, J. Schafer, and G. R. Wodicka, “Posture-dependent change of tracheal sounds at standardized flows in patients with obstructive sleep apnea,” *Chest*, vol. 110, pp. 1493–1498, 1996.
3. R. H. Habib, S. Suki, J. H. T. Bates, and A. C. Jackson, “Serial distribution of airway mechanical-properties in dogs—Effects of histamine,” *J. Appl. Physiol.*, vol. 77, pp. 554–566, 1994.
4. Lutchen, K. R., K. Yang, D. W. Kaczka and B. Suki. Optimal ventilation waveform for estimating low-frequency respiratory impedance.75 (1993):478-88.

5. Smith J, Jones M Jr, Houghton L et al (1999) Future of health insurance. N Engl J Med 965:325–329.
6. Lock I, Jerov M, Scovith S (2003) Future of modeling and simulation, IFMBE Proc. vol. 4, World Congress on Med. Phys. & Biomed. Eng., Sydney, Australia, 2003, pp 789–792
7. Avanzolini, G., P. Barbini, A. Cappello and G. Cevenini. Influence of flow pattern on parameter estimates of a simple breathing mechanics model. 42(1995):313-17.
8. Hickling, K. G. The pressure-volume curve is greatly modified by recruitment. A mathematical model of ARDS lung. Am J. Respir Critic Care Medicine ,158(1998):194-202.
9. Kaczka, D. W., G. M. Barnas, B. Suki and K. R. Lutchen. Assessment of time-domain analyses for estimation of low-frequency respiratory mechanical properties and impedance spectra. 23(1995):135-51.

Correlation between Lyapunov Exponent and the Movement of Center of Mass during Treadmill Walking

J.H. Park[1] and K. Son[2]

[1] BK21 School of Mechanical Engineering, Pusan National University, Busan, Korea
[2] School of Mechanical Engineering, Pusan National University, Busan, Korea

Abstract — **The purpose of study is to investigate the correlation between the Lyapunov exponent (LE) and the movement of the center of mass (MCM) for clarifying walking stability on the treadmill. From fifteen young healthy subjects volunteered, lower extremity joint angles were recorded using a three-dimensional motion capture system and reflective markers. The anteroposterior MCM and the LE were calculated by a commercial software. A linear correlation between LE and MCM (r^2=0.413) showed that LEs compensated for walking distance on the treadmill walking. However, LEs were found to be independent of self-selected walking speeds by a negligible correlation between the Froude number and the LE (r^2=0.038).**

Keywords — **Movement of Center of Mass, Lyapunov Exponent, Treadmill Walking, Lower Extremity.**

I. Introduction

In a treadmill walking the constant speed selected by a walker makes a periodic gait pattern and the walking may seem safe. However, fallings often occur during the treadmill walking. Stride and angular variability are a natural outcome during gait. Their deviations correspond to the amount of irregularity and are used as a basis of whether the motion is stable or not. Conversely, it seems not to be a problem of predictability but that of simple statistics.

Recently, such variability is considered as a deterministic process controlled by the neuro-musculoskeletal system. In this study, a new parameter, the Lyapunov exponent (LE), was introduced to clarify this fact. The LE has been used as one of chaotic parameters to quantify dynamic aspects of flexion-extension angles associated with human gait.

The purpose of study is to show that the correlation between the LE and the movement of the center of mass (MCM) can be used as a measure of walking stability on the treadmill. The Froude number (FN) was also included in the analysis in order to check the effect of a walking speed.

II. Materials and Methods

A. Gait experiment

Fifteen young healthy subjects (13 males and 2 females: 24.9±4.1 years, 175.6±6.4 cm, 70.5±12.1 kg, 1.0±0.1 m/s) with no history of joint diseases took part in the gait experiments. Their walking motions were measured for 90 seconds on a treadmill (KEYTEC® AC9, Taiwan) in order to obtain the flexion-extension angles of their lower extremities. Before the measurement, all subjects were given more than five minutes to perform walking exercises on the treadmill at their self-selected comfortable speeds. The FN, V^2/gl (V: speed, g: gravitational acceleration, l: length from ground to the greater trochanter), was used to normalize each walking speed.

Gait motions were recorded using eight video cameras (DCR-VX2100, Sony, Japan), a three-dimensional calibration frame (width: 1m, height: 2m), and synchronization LEDs to synchronize recorded images. Thirty two custom reflective markers (10 mm diameter hemisphere) were made of the surface covered by reflective films. These reflective markers were carefully placed on the selected bony landmarks of each subject (Fig. 1) in order to calculate the flexion-extension angles of the upper and lower extremities. Images recorded for 90 seconds were restored on a PC and three-dimensional coordinates of the markers were calculated by KWON3D software (Visol Corp., Korea). During the digitizing process a total of 60 frames were generated by the de-interlacing method per second.

The flexion-extension angles of the hip, the knee, and the ankle were reconstructed as a function of time using the inner product of the two adjacent vectors which connect the two joints of the body. The joint center of the knee and the

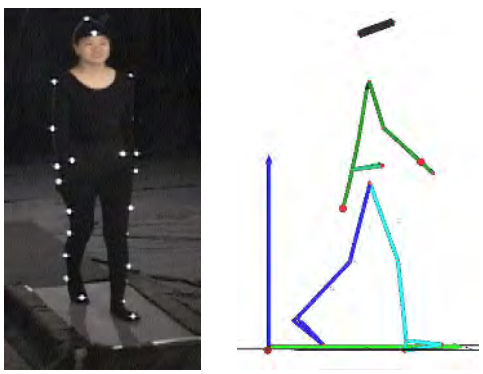


Fig. 1 Gait experiment and corresponding human link model

Chwee Teck Lim, James C.H. Goh (Eds.): ICBME 2008, Proceedings 23, pp. 1974–1976, 2009
www.springerlink.com

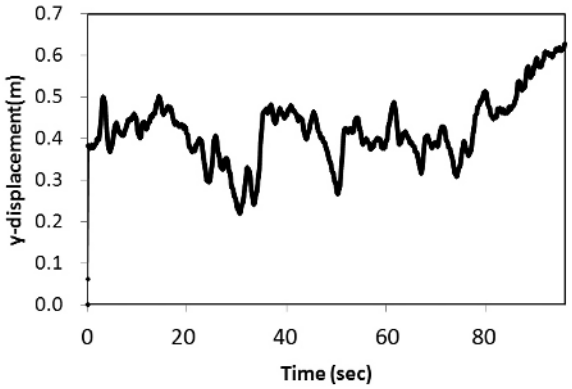


Fig. 2 An example of anteroposterior MCM during treadmill walking

ankle were computed with medial and lateral surface markers. The center of the hip was calculated by adopting the method of Tylkowski and Andriacchi from the left, the right, the middle ASIS (anterior superior iliac spine) and extra greater trochanter markers. The spatial displacement error of a marker position was less than 2 mm.

Unfiltered data were analyzed to increase an accuracy of the stride-to-stride variations, because it has been reported that a filtering may eliminate important information on joint motions and provide a skewed view of inherent motion variations [1]. In addition, it was assumed that the measured flexion-extension angles would have a similar level of measurement noise in every joint since the same apparatus was used for capturing all joint motions in this study. This assumption suggests that differences between joint angles could be attributed to the changes in joint motions themselves [2].

During the treadmill walking all subjects were asked to move in the anteroposterior direction. The medial-lateral motion also occurred, however, it was excluded because the main motion consisted of balancing the center of mass of the body in the single leg standing phase. Therefore, the anteroposterior MCM was chosen as a major parameter to be controlled by the subjects. The MCM was obtained by the summation of all small *dy* for 90 seconds.

B. Lyapunov exponent

A state space vector was formed from the original time series to reconstruct a state space. This vector should be made to have mutually exclusive information about the dynamics of the system. For this, an appropriate time delay was determined using the average mutual information (AMI) function [3]. This criterion sets the time delay equal to the value of delay corresponding to the first minimum of the AMI function. In order to unfold the dynamics of the system, embedding dimension was determined in a proper state space.

A suitable embedding dimension was chosen using the false nearest neighbor (FNN) method [4]. An inappropriate number of embedding dimensions may yield a projection of the dynamics of the system that has orbital crossings in the state space. These crossings would be due to false neighbors and far from the actual dynamics of the system. Total percentage of false neighbors was computed by FNN method, and the number of dimension was chosen when this percentage approaches zero.

The LE quantifies the exponential separation of the neighboring trajectories in the reconstructed state space. Thus LEs provide a direct measure of the sensitivity of the system. This information is necessary to classify the stability of the time series. As nearby points of the state space separate, they diverge rapidly as to produce instability. The LE for a stable system with little or no divergence will be approximately zero as in a sinusoidal wave while the LE for an unstable system that diverges will be positive.

The LE was computed from the growth of length when the length of a vector between two points became large, a new point was chosen near the reference trajectory. The calculation started from the first data point $x(t_0)$ and $x(t_0)+dx$ which was the nearest at a distance $d(t_0)$. If the length $d'(t_1)$ was larger than a small value, then first point $x(t_0)$ was conserved and the algorithm searched the next point $x(t_1)+dx$. This algorithm was proposed by Wolf et al. [2] as:

$$\lambda = \lim_{m\to\infty} \frac{1}{mt} \sum_{i=1}^{m} \log_2 \frac{d'(t_m)}{d(t_{m-1})}$$

where λ was the LE, t was the time interval, m was the number of total time intervals and d was the nearest distance from the reference trajectory. The LE depends in general on the initial data point $x(t_0)$, the initial separation distance $d'(t_0)$ and time t. For the calculation of LEs, the Chaos Data Analyzer (professional version, Physics Academy Software, Raleigh, U.S.A.) was used. The Chaos Data Analyzer is special purposed software to analyze nonlinear time series data. The software includes a calculation function of LE in the selection of chaos analysis.

III. Results

LEs were calculated from flexion-extension angle attractors of the lower extremity after a determination of the time delay and the embedding dimension from fifteen subjects.

Means and standard deviations of LE, total MCM, and FN were listed in Table 1. LEs of the ankle were higher than those of the other lower extremity joints.

In our major concern, linear correlation coefficients between the items (MCM, LE, and FN) were computed by using the least square method on the Microsoft Excel and the results were summarized in Table 2. This shows that among the joints the LE of the knee has the largest linear correlation coefficient with the MCM. It is evident that the knee joint plays a more important role to control the anteroposterior displacement than the other joints. The correlation between the MCM and the LE for all three lower extremity joints was also relatively strong. However, it was observed that the Froude number had no connection with the LE. The two representative illustrations are shown as in Fig. 3 and Fig. 4.

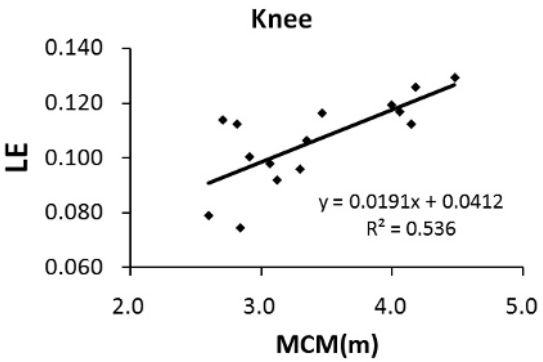


Fig. 3 Correlation between anteroposterior MCM and LE

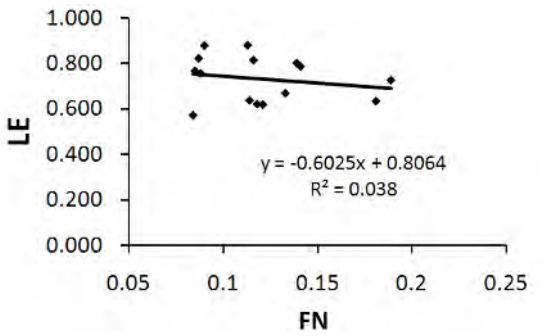


Fig. 4 Correlation between FN and LE

Table 1 Results of LEs, MCM, and FN

	Joints					
	Hip		Knee		Ankle	
	Left	right	left	right	left	right
LEs Mean	0.095	0.094	0.099	0.114	0.174	0.158
LEs STD	0.018	0.015	0.018	0.019	0.046	0.047
MCM(m)	3.40±0.616					
FN	0.120±0.032					

Table 2 Results of correlation test

Correlation pairs	Linear correlation coefficient(r^2)
MCM and LEs of the hip	0.075
MCM and LEs of the knee	0.536
MCM and LEs of the ankle	0.157
MCM and LEs of all three lower extremity joints	0.413
FN and LEs of all three lower extremity joints	0.038

IV. Conclusions

It is likely that that one does exert much effort to balance the body in the treadmill walking because it is relatively more periodic than normal walking. However, the results of our simple treadmill experiments revealed that the lower legs continuously coordinate themselves against irregular strides related to walking speed. Therefore, it was found that the LE increased in proportion to anteroposterior MCM but that the LE was not directly correlated with self-selected speed. Future studies require an increased number of subjects for more statistical analyses.

References

1. Rapp PE (1994) A guide to dynamical analysis. Int. Phys. Behav. Sci, Vol. 29(3):311-327
2. Wolf A, Swift JB, Swinney HL et al. (1985) Determining LEs from a time series. Phy.D: Nonlinear Phenomena, 16(3):285-317
3. Cellucci CJ, Albano AM and Rapp PE (2003) Comparative study of embedding methods. Phys. Rev. E, 67:066210-1-13
4. Broomhead DS, Jones R and King GP. (1988) Comment on "singular–value decomposition and embedding dimension", Phys. Rev. A, 37(12):5004-5005

Author: Jung Hong Park
Institute: BK21 School of Mechanical Engineering
Street: Pusan National University
City: Busan
Country: Republic of Korea
Email: zhengh@pusan.ac.kr

The Development of an EMG-based Upper Extremity Rehabilitation Training System for Hemiplegic Patients

J.S. Son[1], J.Y. Kim[1], S.J. Hwang[1] and Youngho Kim[1,2]

[1] Biomedical Engineering, Yousei University, Wonju, South Korea
[2] Institute of Biomedical Engineering, Yonsei University, Wonju, South Korea

Abstract — **Existing therapy and orthosis for upper arm rehabilitaion have some shortcomings such that orthosis can't help patient's motion but it just supply, patient has to go to hospital for therapy and patient can't reflect his will in therapy. Because of these reasons, upper arm rehabilitaion system was developed, which could increase hemiplegic patient's strength and make patient does training by oneself. To make the training system, motor and EMG sensor with orthosis were used so that orthosis could move actively and give patient load. EMG sensor was used for feedback to reflect patient's will and the rotational potentiometer was used to get the information about joint angle. Orthosis made upper arm's flexion and extension, and used EMG signal. For rehabilitation, orthosis made user exercise by giving him proper load, or made involved arm mimic uninvolved arm's motion. As it can reflect patient's will, we expect that it can improve rehabillitaion effect and make patients do training at his home.**

Keywords — **orthosis, rehabilitation, training, EMG**

I. Introduction

The hemiplegia is caused by the damage of the brain, so functional inability is able to be cured by repetitive training for rehabilitation of impaired brain. Training methods, done till now, can be categorized into two types briefly. One is for the patient who can't train by oneself, so patient need some help of other people, such as the therapist. Another one is done by patient oneself. According to the previous study (Sütbeyaz S. et al., 2007), the rehabilitation therapy could bring better results when the patients have a strong will to move. However, in most cases, rehabilitation therapy was performed passively without patient's active will. Moreover it is more effective when patient does training in one's home (Herbold J. et al., 2007) but most patient uses the facilities due to disability of locating existing training equipments in personal home.

In this study, upper extremity rehabilitation training system was developed, which was based on EMG signal. EMG is the unique tool which let us know the information about the muscle such as muscle activation. Therefore it could be assumed that EMG reflects patient's will. Also, developed system was made as possible as small so that patient could train for rehabilitation in one's home.

II. Method

A. Subject and pre-test

Three healthy men were chosen (Table 1) for our pre-test which was to know the torque generated in flexing and extending their arm as possible as strong. Biodex (Biodex Medical System, U.S.A.) was used to determine the torque. Simultaneously, EMG measurement system (Noraxon U.S.A. Inc) was also used to measure the pattern of EMG. EMG signals were obtained from biceps brachii and triceps brachii. The pre-test was performed for three times per each person with 10deg/second and with 0~100°degree of motion range (Fig. 1).

According to the result of pre-test, the motor RE 40 (Maxon, Switzland) was chosen, which generate the amount of 39Nm torque (Table 2).

In order to control the system, we used microcontroller ATmega128 (Atmel, U.S.A.), and the algorithm was written in C language. The developed training system consists of orthosis part and control part (Fig. 2).

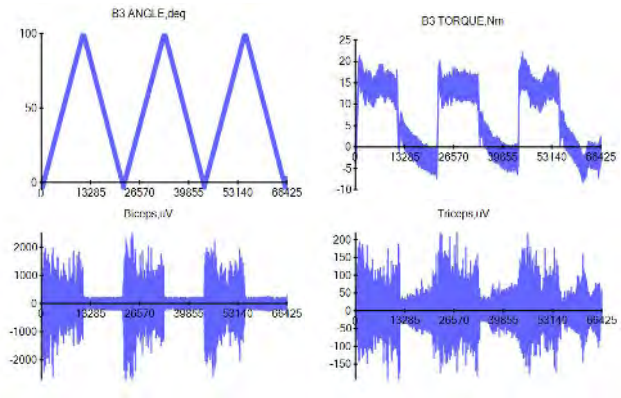


Fig. 1 Joint angle, torque, and EMG signals from the experiment

Table 1 Information of subjects (n = 3)

	Age (yrs)	Height (cm)	Weight (kg)
A	23	168	72
B	23	169	62
C	23	171	74

Chwee Teck Lim, James C.H. Goh (Eds.): ICBME 2008, Proceedings 23, pp. 1977–1979, 2009
www.springerlink.com



Fig. 2 Developed orthosis part and control part

Table 2 Motor specification

Voltage (V)	Speed (rpm)	Torque (Nm)
24	33	39

B. EMG processing and control algorithm

Raw EMG signal outputted from EMG measurement system was low pass filtered by a Butterworth 4th order filter at 1Hz. Low pass filtered EMG signal was analyzed by EMG-to-torque converting algorithm and used to control the motor system. Control algorithm consists of two types. One is the muscle strengthening for the patient who can move his arm voluntarily, and another is the motion mimic algorithm for the patient who cannot move his arm by oneself. In the muscle strengthening algorithm, motor was controlled in uniform speed. The equation of relationship between EMG signal and torque was calculated through linear regression. Therefore the elbow joint torque of patient could be estimated from the processed EMG signal. Estimated torque was used as reversal torque to patient. This lets patients make more power until they make proper power which we preset. So if patients make joint torque which is larger than the threshold value, they could move their arm due to the elimination of the reversal torque. This process would be repeated, which means the enough load could be given to patient. The difference between developed system method and barbell exercise method is that developed system could control the velocity and the load for each patient. In the case of motion mimic algorithm, involved part was controlled by uninvolved part. Patient wears the developed orthosis on the involved arm. In addition, electrodes for measuring EMG are placed on the uninvolved arm. Therefore, the motor is controlled by the information obtained from uninvolved arm. If there is only the angle data, it would be impossible to determine that movement is occurred by voluntary or not. So we use the EMG and guess it from EMG. Finally, the orthosis will move when patient moves his arm voluntarily.

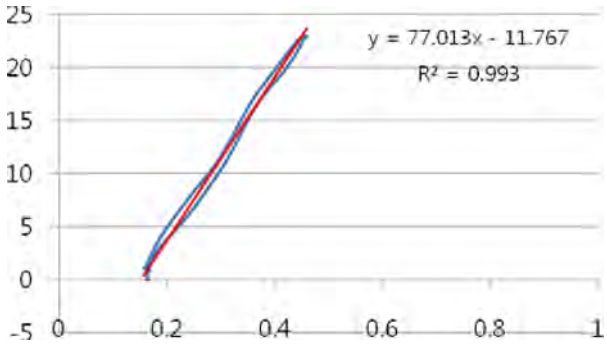


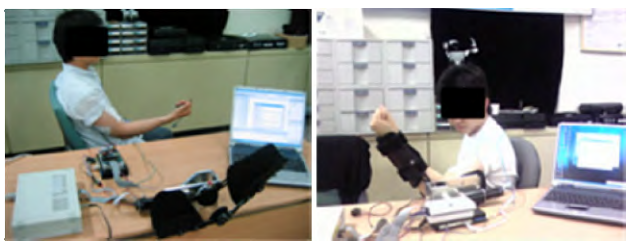
Fig. 3 Relationship between normalized EMG signal and torque (x axis: V, y axis: Nm)

C. Display and data acquisition

Measured values were transmitted to computer through serial port. To display and to store transmitted data, the software was developed in language based on C.

III. Results

The test was performed for two algorithms, motion mimic and training (Fig. 4). The signals were obtained and calculated from developed system when lower arm was repeated the flexion and extension for three times (Fig. 5). The first and second graphs mean rectified EMG signals from biceps brachii and from triceps brachii relatively. Third graph shows the estimated torque from biceps brachii. The reason why the torque was estimated from biceps brachii was that the amplitude of triceps brachii was small during the experiment, which means triceps brachii was not activated remarkably due to an effect of gravity when the lower arm was extended. Last graph indicates the elbow joint angle.



(a) (b)

Fig. 4 Experimentation of (a) motion mimic and (b) training

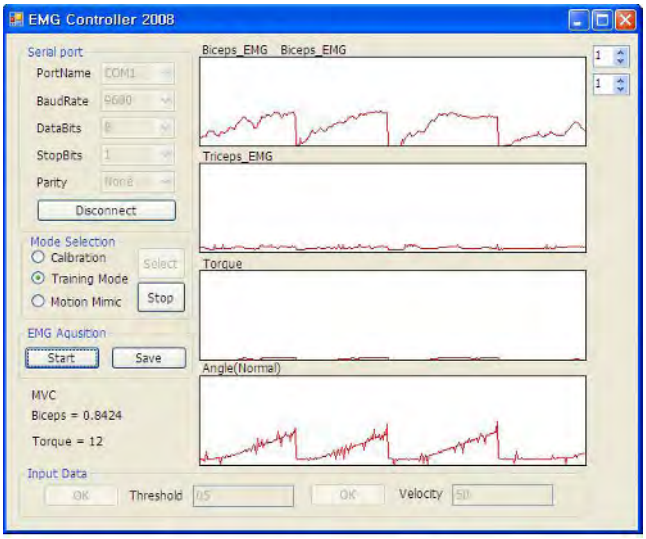


Fig. 5 Display of rectified EMG from biceps and triceps brachii and of torque estimated from EMG and of elbow joint angle

IV. Conclusions

In this study, EMG-based upper extremity rehabilitation training system was developed for hemiplegic patients. Since this study was to develop the system, clinical test was not performed for patient. During the experiments, the significant problem was found, which is the frame of the developed orthosis was bent. This problem would be improved by strengthening its frame. The developed system would result in better rehabilitation effect, because patient's will could be reflected and the size of the system was small as locating home. However, the clinical examination would be required to make quantitative data of increased muscle strength and recovery of brain. We expect that developed system in this paper would help the patients to improve their ability and make quite good results.

Acknowledgment

This research project was supported by the Sports Promotion Fund of Seoul Olympic Sports Promotion Foundation from Ministry of Culture, Sports and Tourism and the Korea Institute of Science and Technology (KIST) program.

References

1. Smith J, Jones M Jr, Houghton L et al. (1999) Future of health insurance. N Engl J Med 965:325–329
2. Sütbeyaz S, Yavuzer G, Sezer N et al. (2007) Mirror therapy enhances lower-extremity motor recovery and motor functioning after stroke : a randomized controlled trial. Arch Phys Med Rehabil 88:555-559
3. Herbold J, Walsh M, Reding M (2007) Rehabilitation hospital versus nursing home setting for rehabilitation following stroke: a case-matched controlled study. Arch of Phys Med Rehabil 88:17-18
4. Fellows SJ, Kaus C, Ross HF (2004) Agonist and antagonist EMG activation during isometric torque development at the elbow in spastic hemiparesis. Electroencephalography and clinical Neurophysiology 93:106-112

Author: Youngho Kim
Institute: Yonsei University
Street: R204, Medical Industry Technotower, Heungeop
City: Wonju
Country: South Korea
Email: younghokim@yonsei.ac.kr

Fabrication of Adhesive Protein Micropatterns In Application of Studying Cell Surface Interactions

Ji Sheng Kiew[1], Xiaodi Sui[1], Yeh-Shiu Chu[2], Jean Paul Thiery[2] and Isabel Rodriguez[3]

1 Department of Bioengineering, National University of Singapore, Singapore
2 Institute of Molecular and Cell Biology (IMCB), Agency of Science, Technology and Research (A*STAR), Singapore
3 Institute of Materials Research and Engineering (IMRE), Agency of Science, Technology and Research (A*STAR), Singapore

Abstract — **The development of techniques for immobilizing biomolecules on solid surfaces has attracted wide attention because of the broad potential applications of biofunctionalized surfaces in stem cell biology, tissue engineering, biosensor technology, and high-throughput screening for drug discovery.**

In particular, protein micropatterns on surfaces provide unprecedented spatial resolution to control cell shape and direct cell behavior. Combining with optical methods and functional assays, micropatterning techniques are one of the key tools for investigating cell molecular and mechanical mechanisms in basic cell behaviors, such as cell adhesion, cell migration, cell division and differentiation.

In this work, we use a photolithographic approach to create cell adhesive micropatterns. We have designed different geometries to control and study cell adhesion. A pre-designed mask is fabricated for the photolithographic process. The designed features are transferred to a glass substrate by UV exposure of a protein solution containing a photoinitiator through the mask.

Typically, patterns of fibronectin are produced in a non-adhesive background of poly-L-lysine grafted poly (ethylene glycol). Cells seeded on these substrates, can specifically adhere and spread on the adhesive protein micropatterns and display unique shapes according to the contour and size of the pattern.

Keywords — **photolithographic, micropatterns, photoinitiator, protein, UV**

I. Introduction

Though established micro-patterning techniques such as the use of elastomeric PDMS stamps for micro-contact printing is simple and efficient, the method lacks reproducibility and produce patterns with poor spatial resolution. Hence through this project, we aim to propose a simple and highly reproducible method for protein micro-patterning on substrates, combining the use of photolithography which is commonly used in the semiconductor industry and biological knowledge on proteins and cell adhesion. Cells seeded on such patterned substrates would then be forced to specifically occupy these pre-defined patterns, enabling studies such as mechano-sensory studies to be performed on single cells.

To create chemically patterned surfaces on substrates such that cells can attach to these patterns and grow and passivate the other unpatterned areas to prevent cells from growing, we need to select suitable coating substances for the substrate. For this project, we have selected two suitable substances as coating agents, namely fibronectin and a polycationic graft polymer, poly-L-lysine-g-poly(ethylene glycol) (PLL-g-PEG) to be used for cell attachment and substrate passivation respectively. The polycationic PLL-g-PEG has been shown to attach to negatively-charged substances via strong electrostatic attractions with its charged poly-L-Lysine binding to the substrate and the PEG side chains on the exposed surface. The PEG side chains then create a non-fouling surface, resistant to cell-attachment and proteins due to entropic repulsion and the high water content of the PEG chains due to the interaction of the OH-groups in the chemical structure with water.

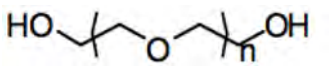


Figure 1. (above) Chemical Structure of Poly (ethylene glycol)

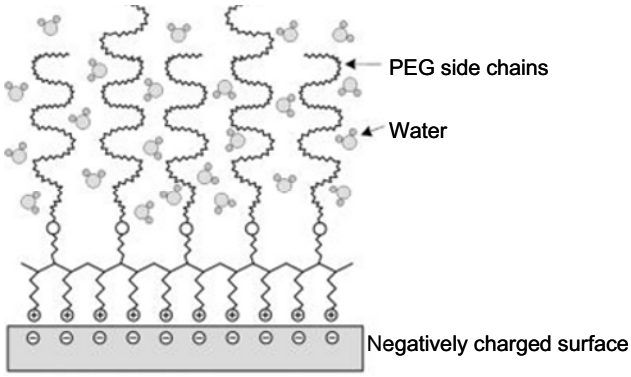


Figure 2. (above) Schematic view of a poly(L-lysine)-graft-poly (ethylene glycol) (PLL-g-PEG) adlayer on a negatively charged surface. The positively charged PLL backbone attaches to the negatively charged surface through electrostatic interactions. The grafted PEG chains are hydrated (represented by the H_2O molecules between the PEG chains) and extend into the aqueous environment; Diagram from Morgenthaler et al. [1]

Chwee Teck Lim, James C.H. Goh (Eds.): ICBME 2008, Proceedings 23, pp. 1980–1983, 2009
www.springerlink.com

Thereafter, to chemically attach fibronectin to the substrate surface on top of the PEG chains, we employ a photolithographic method. Fibronectin is mixed with the photoinitiator to form a grafting mixture in which upon exposure of the mixture to a suitable UV wavelength depending on the photoinitiator used, the excited photoinitiator (In*) would follow either of the two possible reaction pathways: (Reaction 1) dissociate into primary radicals (R·) or (Reaction 2) react with a second species (A-H) via hydrogen abstraction to form secondary radicals (A·). The two reactions are shown as follows:

$$In \xrightarrow{uv} In^* \rightarrow 2R\cdot \qquad \text{(Reaction 1)}$$

$$In \xrightarrow{uv} In^* \xrightarrow{A\text{-}H} 2R\cdot \qquad \text{(Reaction 2)}$$

A-H in this case can be fibronectin or PEG where H atoms are abstracted to form radicals which cause binding of excited parts of the fibronectin molecule with the excited PEG-coated substrate surface which is the radical reaction of interest. Other reactions between radicals such as those involving photoinitiator molecules and hydrogen atoms are not of interest in this case. Hence only parts of the substrate coated with the grafting mixture and exposed to UV radiation through the patterned mask would have fibronectin protein molecules binding to them. Those fibronectin molecules that are unattached can be washed off.

The rate of photoinitiation according to Bryant et al. [2] is giving by the formula:

$$Ri = \frac{2\phi f(2.303\varepsilon)I_o\lambda[In]}{N_{AV}hc} \qquad (1)$$

where ϕ = quantum yield
f = photoinitiator efficiency
ε = molar extinction coefficient at the initiating wavelength, λ
I_o = incident light intensity
$[In]$ = initiator concentration
N_{AV} = Avogadro's number
h = Planck's constant
c = velocity of light

and 2 in the above equation indicates that 2 radicals are formed per dissociated initiator molecule. Note that this equation assumes that light intensity remains relatively constant, unaffected by the thickness of the protein coating formed. More accurately, light intensity I is determined by the following equation[2].

$$I = I_o e^{-2.303\varepsilon[In]\,b} \qquad (2)$$

where b is the thickness of the protein coating formed.

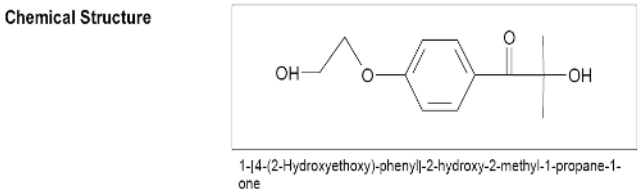


Figure 3.(above) Chemical Structure of Irgacure 2959 (Diagram from Ciba Specialty Chemicals)

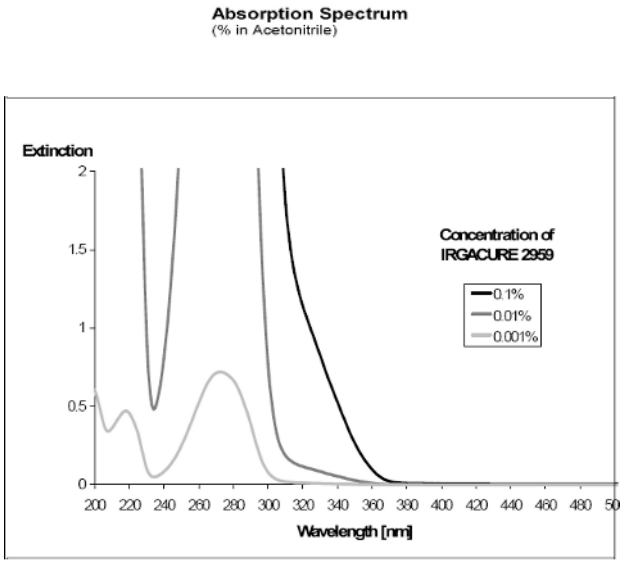


Figure 4.(above) Absorption Spectrum of Irgacure 2959 (Diagram from Ciba Specialty Chemicals)

Choosing an appropriate initiator and initiating conditions is important because the initiation step controls the polymerization rate, affecting the final protein coating on the substrate. Different initiators have different initiating chemistry, differing in initiator efficiency, the molar extinction coefficient, and range of initiating wavelengths. For this experiment, we have chosen a commercially available photoinitiator (Irgacure 2959, Ciba Specialty Chemicals) that has been used successfully in biology related experiments.

Irgacure 2959 was also chosen over other photoinitiators for its higher solubility in water which was important in bringing the protein molecules suspended in buffer solution, the hydrated PEG molecules and the photoinitiator together in the same phase so that photoinitiation and formation of radicals can take place.

Propagation of the reaction occurs when radicals formed in the presence of UV radiation come into contact with and extract the H groups in water, Irgacure 2959 and fibronectin. This creates more radicals out from these mole-

cules and they could go on in the process of activating other molecules to form radicals (See reaction 3). Termination of these radical reactions only occurs upon reaction of 2 radicals (See reaction 4).

$$R\cdot + H\text{-}A \rightarrow RH + A \qquad \text{(Reaction 3)}$$

where H-A is any molecule with a hydrogen group available for radical extraction by radical, R·

$$R\cdot + R\cdot \rightarrow R\text{-}R \qquad \text{(Reaction 4)}$$

where combination of 2 radicals (R·) results in termination of the reaction propagation.

II. Materials and Method

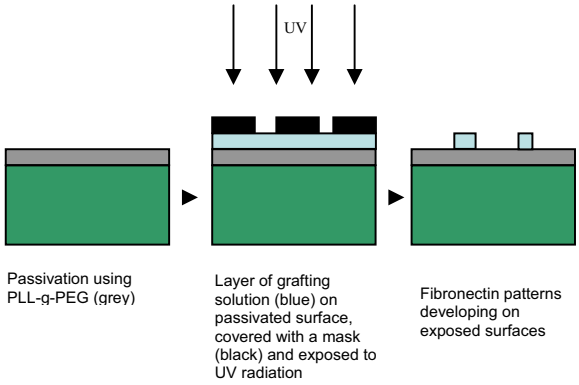
The objective of this project is to perform an initial study on the reliability of this new patterning method as described in PCT application WO 2006/084482 and thereafter develop and optimize an experimental protocol to create such protein patterns. The experimental protocol has to be developed from the beginning since the original water soluble photoinitiator (4-Benzoylbenzyl)trimethylammonium chloride as proposed in the PCT document is no longer available commercially from Sigma Aldrich. Moreover, the document does not specify the exact proportions of the components constituting the grafting mixture.

Fibronectin is coated onto the substrate surfaces by use of contact exposure photolithography. 20µl of the grafting solution is first placed on the substrate to be coated. The chromium and gold coated quartz photolithographic mask is then gently placed over the grafting solution such that a thin film of grafting solution is in between the photomask and the substrate; exposure of the grafting solution to atmospheric oxygen is brought to a minimum in this way. Care is also taken to avoid any bubbles from being trapped between the mask and the substrate since atmospheric oxygen neutralises the radicals produced when photoinitiator in the grafting solution is exposed to UV.

The whole assembly is then exposed to UV by placing it into a UV flood lamp system (Dymax 2000-EC Series) and exposed for a predetermined time and distance away from the UV curing bulb to vary the exposure time and intensity of UV exposure as required by the experiment.

After exposure to UV, the photolithographic mask is separated from the substrate by rinsing with distilled water. The protein-coated substrates are then stored in PBS.

The diagram below describes this patterning process:



III. Results

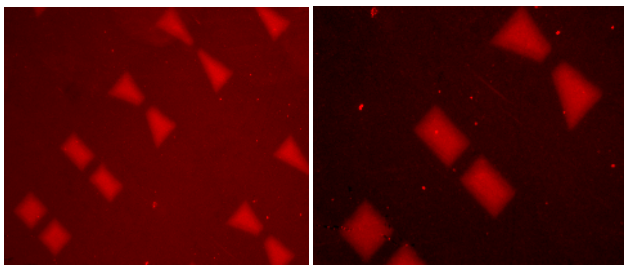


Figure 5. CY3-labelled fibronectin patterns coated on glass substrates taken using a 20X magnification oil objective (above left) and 40X magnification oil objective (above right).

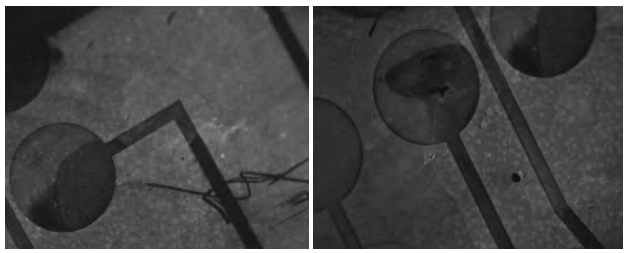


Figure 6. CY3-labelled fibronectin patterns coated on glass substrates taken using a 10X magnification oil objective (above).

IV. Conclusion

Initial results are encouraging given the high resolution of the protein patterns formed and the ease of patterning compared to the commonly used µ-contact printing method.

Several factors affecting the resolution of the patterns formed were also identified. The first of which was the relation between the diffusion of radicals and UV exposure time. Upon exposure to a suitable UV wavelength, photoinitiator mixtures produce radicals which set off a series of

reactions to activate the molecules on the substrate surface and also the protein molecules to be coated. These molecules are able to move about freely during the reaction and hence there is a possibility of them diffusing out from the UV exposed areas into the surrounding unexposed regions, affecting the resolution of the protein patterns formed. Hence, as time of exposure increases, the resolution of the patterns decreases since radicals produced from UV exposure have more time to diffuse throughout the thin layer of grafting solution between the photolithographic mask and the substrate. Other factors such as UV excitation wavelength and photoinitiator concentration has to be considered too in optimizing the efficiency of this coating process.

Acknowledgements

We would like to express sincere appreciation of the assistance and guidance given by our project supervisors Dr Isabel Rodriguez (IMRE) on photolithography and substrate surface modification, Dr Jean Paul Thiery (IMCB) and Dr Chu Yee Shiu for their guidance on cell biology, assistance on protein labelling and substrate imaging.

References

1. Sara Morgenthaler, Christian Zink, Brigitte Städler, Janos Vörös, Seunghwan Lee, Nicholas D. Spencer, and Samuele G. P. Tosatti,.(Dec 2006) Poly(L-lysine)-grafted-poly(ethylene glycol)-based surface-chemical gradients. Preparation, characterization, and first applications. Biointerphases, Vol. 1, No. 4.
2. Stephanie J. Bryant and Kristi S. Anseth. Photopolymerization of Hydrogel Scaffolds. Scaffolding in Tissue Engineering – Edited by Peter X. Ma and Jennifer Elisseeff (ISBN 1-57444-521-9), 6, 71-91.
3. PCT application WO 2006/084482
4. Jenny Fink, Manuel Théry, Ammar Azioune, Raphael Dupont, François Chatelain, Michel Bornens and Matthieu Piél. (30th April 2007) Comparative study and improvement of current cell micro-patterning techniques. Lab Chip, 2007, 7, 672-680.

Modeling of the human cardiovascular system with its application to the study of the effects of variations in the circle of Willis on cerebral hemodynamics

Fuyou Liang[1], Shu Takagi[1] and Hao Liu[2]

[1] Computational Science Research Program, RIKEN, Wako, Japan
[2] Graduate School of Engineering, Chiba University, Chiba, Japan

Abstract — **A computational model of the human cardiovascular system has been developed based on multi-scale hemodynamic modeling, where the 71 arteries which constitute the arterial tree and the circle of Willis are described by a one-dimensional model coupled with a lumped parameter description of the remainder. The most significant advancement of the present model over single-scaled models is that it accounts for hemodynamic interaction in the global system while capturing the characteristics of wave propagation in the arterial system.**

In this study, the model is applied to study the effects of variations in the circle of Willis (CoW) on cerebral hemodynamics. Model predictions for a complete CoW, and incomplete CoWs with a fetal posterior cerebral artery (PCA) or a missing anterior cerebral artery (A1) under normal resting conditions show good agreements with in vivo measurements. When a severe stenotic or occlusive disease is present in one of the internal carotid arteries (ICA), a complete CoW is able to feed the cerebral arteries ipsilateral to the diseased ICA with little reduction in flow rate by re-routing flows through the communicating arteries from the intact ICA; however, such compensatory capacity is impaired significantly in the cases of incomplete CoW.

To compensate for ischemia induced by ICA stenoses in the cases of incomplete CoW, further compensatory responses in tissues downstream of the insufficiently-perfused arteries are expected to take place in resting conditions, which may contribute to the impairment of cerebral autoregulation in patients with ICA stenoses. The findings indicate that the structure of the CoW is an important determinant of cerebral hemodynamic regulation and should be considered carefully in clinical practice.

Keywords — **Cardiovascular system, Multi-scale modeling, Circle of Willis, Cerebral autoregulation.**

I. Introduction

Lumped-parameter models (zero-dimensional) and wave-propagation models (one-dimensional) for pressure and flow in large vessels, as well as fully three-dimensional fluid-structure interaction models for pressure and velocity, can contribute valuably to answering physiological and patho-physiological questions that arise in the diagnostic and treatment of cardiovascular diseases [1]. In practice, models geared to single-scaled hemodynamic phenomena, however, often encounter difficulties due to their inherent limitations. For instance, lumped-parameter (0-D) models are useful mainly for modeling the complete cardiovascular system, but they cannot account for the propagation of pressure and flow waves. One-dimensional (1-D) models are well suited to describing pressure/flow waves traveling through the arterial system, but they provide little detail on flow patterns at local segments. Three-dimensional (3-D) models are widely used to characterize 3-D flows and their relevance to vascular diseases. However, limited by the large amount of computer resources associated with 3-D computations, 3-D models can only be applied to a small segment of the arterial system and hence appropriate assumptions on flow conditions at the proximal and distal boundaries are necessary. In this context, more and more interests were being focused on developing multi-scale models that are capable of accounting for global effects while describing, in more detail, hemodynamic phenomena in regions of interest in recent years.

Recently, we established a computational model of the complete cardiovascular system by coupling a 1-D model of the arterial system with a 0-D model of the remainder. The resultant multi-scale model forms a unique closed-loop and hence is able to spontaneously account for global hemody-

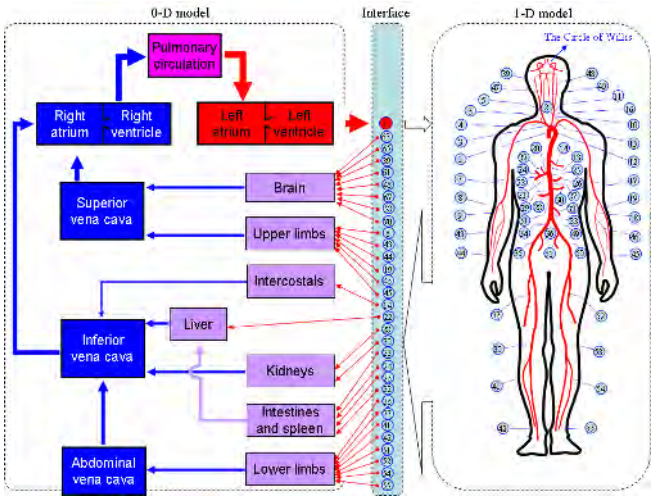


Fig. 1 Multi-scale modeling of the cardiovascular system

Chwee Teck Lim, James C.H. Goh (Eds.): ICBME 2008, Proceedings 23, pp. 1984–1988, 2009
www.springerlink.com

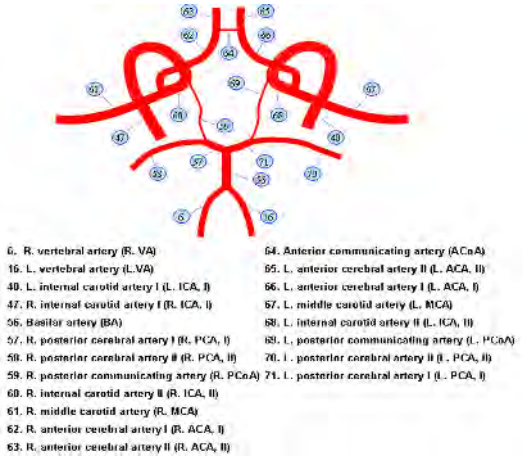


Fig. 2 Schematic representation of the circle of Willis

namic interaction while describing wave propagation in the arterial system. The model has been used to characterize the changes of arterial pulses during aging and in various cases of cardiovascular diseases in our previous studies. In this study, we extend the model to include the CoW and use it to study the effects of variations in the CoW on cerebral hemodynamic regulation.

The CoW is a ringlike structure of arteries found at the base of the brain (see Fig.2). The most important role of the CoW is to maintain constant blood supply to the distal tissues irrespective of pressure variations and/or occlusive diseases occurring in the afferent arteries supplying the CoW. This is realized by re-direction of blood in the CoW combined with autoregulation in the distal tissues downstream of the CoW. However, only about 50% of population is found with a complete CoW shown in Fig. 2, others show various anatomical variations [2]. It is, therefore, of interest that how anatomical variations affect the regulation capacity of the CoW. The significance of the variations in the CoW has indeed been recognized and addressed extensively with both computational models and in vivo measurements [2, 3].

The model proposed in the present study, other than many previous models which dealt with a separate CoW terminated by fixed boundary flow conditions, puts the CoW into a closed-loop system where global hemodynamic interaction and arterial wave propagation are accounted for simultaneously. The feature allows the model to be used in a wider range of patho-physiological conditions. In this study, we report some preliminary model-based predictions of the effects of variations in the CoW on flow distributions in the CoW and the compensatory capacity of the CoW.

II. Materials and Methods

A. Model description

The 55 largest arteries plus the 16 cerebral arteries forming the CoW are described by a 1-D model, and the remaining peripheral vascular subsystems, the heart and the pulmonary circulation are represented by a 0-D model. Subsequently, the two models are coupled together to yield a multi-scale model (see Fig.1). As a result, the multi-scale model forms a closed-loop mimicking the real structure of the cardiovascular system.

1-D Governing Equations: 1-D governing equations for blood flow in an artery can be obtained by integrating the continuity equation and Navier-Stokes equations over a cross-section of the artery [4]. The 1-D equations written in conservation form are:

$$\frac{\partial}{\partial t}\begin{pmatrix} A \\ U \end{pmatrix} + \frac{\partial}{\partial z}\begin{pmatrix} UA \\ \frac{U^2}{2} + \frac{P}{\rho} \end{pmatrix} = \begin{pmatrix} 0 \\ -F_r \frac{U}{A} \end{pmatrix}, \tag{1}$$

where t is the time, and z the axial coordinate along the artery; ρ is the density of blood; A, U and P denote the cross-sectional area, mean axial velocity, and mean pressure, respectively; F_r refers to the friction force per unit length.

The system of equations (1) is completed by a pressure-area relationship derived from the Laplace law for thin homogeneous elastic vessel wall [4].

$$P - P_0 = \frac{Eh_0}{r_0(1-\sigma^2)}\left(\sqrt{\frac{A}{A_0}} - 1\right), \tag{2}$$

where A_0 and h_0 represent, respectively, the cross-sectional area and wall thickness at the reference state (U_0, P_0). r_0 is the radius corresponding to A_0. E is the Young's modulus. σ is the Poisson's ratio, which is here taken to be 0.5 by assuming arterial wall being incompressible.

Equations (1) and (2) describe blood flow in a single artery. To account for blood flows in the whole arterial tree, suitable bifurcation conditions should be imposed to link up flows in each separate artery. Herein, we employ a method which ensures the conservation of mass flux and the continuity of total pressure at the bifurcations [4].

0-D Governing Equations: The remaining portion that connects to the proximal end and distal ends of the arterial tree are rather complex and consists of an enormous number of vessels and organs. For this reason, a vessel-specific modeling as implemented for the arterial tree is very difficult for this portion. With this in mind, the lumped parameter modeling method is adopted. For simple purpose, the 30

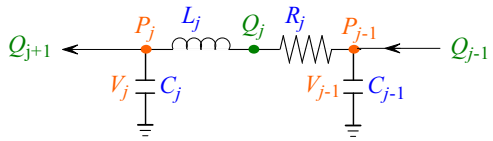


Fig. 3 Lumped parameter network

peripheral arteries are divided into seven groups with each group connected to a block that represents a specific organ or tissue. Each block is again separated into five in series-arranged compartments that correspond to small arteries, arterioles, capillaries, venules and veins, respectively. Each compartment is modeled by a typical three-element Windkessel unit consisting of a resistance element (R), a compliance element (C), and an inertial element (L) (see Fig. 3). Similarly, the vena cava, the heart and the pulmonary circulation are modeled by lumped parameters, respectively. This way, a lumped parameter network is obtained by linking up the lumped parameter elements. Note that the network is open-loop, only when being coupled to the model of the arterial tree, could a closed-loop be formed.

By formulating mass and momentum conservation at the blood volume (V) and flow (Q) nodes, the governing equations of the network can be derived. In Fig. 3, the C points represent V nodes, and the points in-between R and L are Q nodes.

The equation governing a V node is,

$$\frac{\mathrm{d}V_j}{\mathrm{d}t} = Q_j - Q_{j+1}. \tag{3}$$

And the equation governing a Q node is,

$$L_j \frac{\mathrm{d}Q_j}{\mathrm{d}t} = P_{j-1} - Q_j R_j - P_j. \tag{4}$$

Where Q_j and Q_{j+1} are the inflow and outflow of the V_j node, respectively; and P_{j-1} and P_j are the blood pressures upstream and downstream of the Q_j node, respectively. P_j is calculated as $P_j = V_j/C_j$.

Modeling of the heart and the pulmonary circulation will not be detailed in this paper, details could be found in many literatures on lumped parameter modeling of the cardiovascular system.

B. Numerical methods

The 1-D partial differential system (equation 1) is solved with the two-step Lax-Wendroff method. The differencing expressions have second-order accuracy in time and space. The 0-D ordinary differential system (equations 3 and 4) is solved using a fourth-order Runge-Kutta method. Solutions of two systems are coupled numerically for each time step.

III. Results

A. General predictions and comparisons with data

Some model-predicted pressures and flow velocities are compared with the data in Fig. 4. It is observed that the model reasonably reproduces the variations of pressure/flow waveforms along the cardiovascular system.

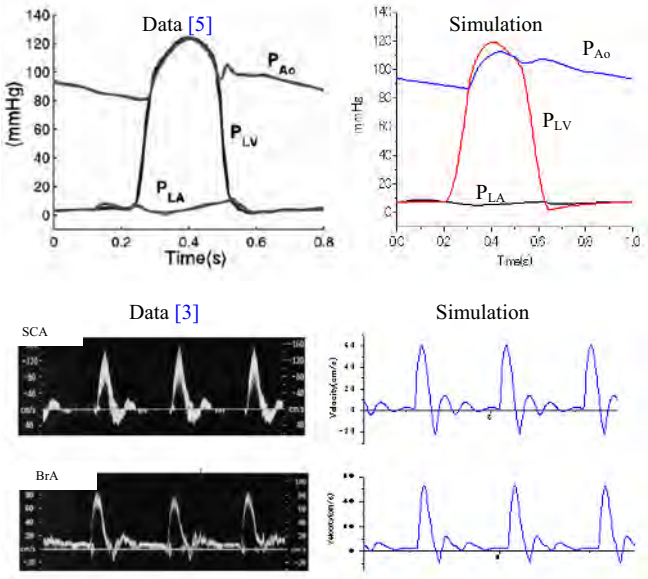


Fig. 4 Pressures near the left heart (top) and flow velocities at the BrA bifurcation (bottom). Ao: Ascending Aorta; LV: left ventricle; LA: left atrium; BrA: Brachiocephalic artery; SCA: Subclavian artery

B. Effects of variations in the CoW

Classification of variations in the CoW: The most frequent anatomical variations in the CoW were classified into 8 types by Alastruey et al [3]. Here, we focus on two variant types: one with a missing A1 and another one with a fetal-type PCA (See Fig. 5). Both types are found present in about 10% of population [2].



Fig. 5 Typical variations in the CoW

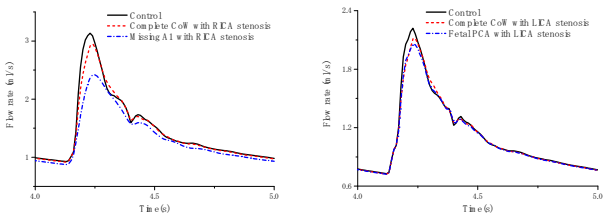
Flow rates in the afferent arteries: Predicted mean flow rates through the ICAs and BA for the three types of CoW

are shown in table 1. In the case of a missing A1 (type 2 in Fig. 5), the mean flow rate in the contralateral ICA is significantly increased compared with the control value (type 1) and compared with the flow rate in the ipsilateral ICA. Mean flow rate through the BA is not significantly different from the control value. In the case of a fetal-type PCA (type 3), the mean flow rate is increased in the ICA on the ipsilateral side and is reduced in the BA compared with the control values. In all the cases, the total mean flow rate through the afferent arteries remains almost constant.

Table 1 Mean flow rates (ml/s) in the afferent arteries of the CoW

Arteries	Complete CoW	Missing A1	Fetal-type PCA
RICA	3.61	4.59	3.64
LICA	3.52	2.51	4.15
BA	2.26	2.25	1.57
Total	9.39	9.35	9.36

Flow rates in the efferent arteries in the presence of ICA stenosis: To investigate the effects of variations in the CoW on the regulation capacity of the CoW, a stenosis is generated in the ICA with larger flow rate for each CoW variant type. For type 2, a 90% stenosis is generated in the contralateral ICA. For type 3, a 90% stenosis is generated in the ipsilateral ICA. And, for comparison purpose, a stenosis same with that generated for types 2 and 3 is generated for type 1, respectively. Computations are carried out without considering cerebral autoregulation. The predicted flow rates in the afferent arteries (L. ACA, II for type 2; L. PCA, II for type 3) are compared with the control values and with the results for the complete CoW (type 1) in Fig. 6. With a missing A1, the reduction in perfusion to the ACA induced by the severe contralateral ICA is greatly larger than the case of type 1(Fig. 6, left). Relatively, a Fetal PCA has less influence on the perfusion of the PCA (Fig. 6, right).



(1) L. ACA, II (2) L. PCA, II

Fig. 6 Efferent flow rates for different CoW variant types

IV. Discussion

The present study uses a computational model of the cardiovascular system to investigate the effects of variations in the CoW on the blow flow distributions in the CoW and perfusion of the efferent arteries in both normal and pathological conditions. The most important findings of the present study are as follows: in the absence of a segment of the ACA (missing A1) or with hypoplasia of the PCA (fetal-type PCA), the relative flow rate distributions in the afferent arteries are significantly altered, while the total perfusion to the CoW is maintained. The predicted phenomena are in agreement with the results of in vivo measurements [2]. In the presence of ICA stenosis, CoWs with a missing A1 or a fetal PCA show greater reduction in flow perfusions to some afferent arteries compared with the Complete CoW. The model findings support the experimental observations that in patients measured with significantly different flow rates in the ICAs, clamping the ICA with higher flow rate leads to ischemic phenomena in some distal tissues [2].

V. Conlusions

In this study, a closed-loop computational model of the cardiovascular system has been developed and used to study the effects of variations in the CoW on relative flow distributions in the afferent arteries and on the compensatory capacity of the CoW in the presence of ICA stenosis. The predicted results demonstrate that the structure of the CoW is an important determinant of the compensatory capacity of the CoW. In clinical practice, patient-specific characterization of the CoW may help make better strategy for preventing stroke during cerevascular operation.

Further model development will be focused on incorporating a model of cerebral autoregulation and models of cardiovascular regulation to study the dynamics of cerebral flow regulation in various patho-physiological conditions.

Acknowledgment

This research was supported by Research and Development of the Next-Generation Integrated Simulation of Living Matter, a part of the Development and Use of the Next-Generation Supercomputer Project of the MEXT, Japan.

REFERENCES

1. Bessems D, Rutten M, Van De Vosse F. (2007) A wave propagation model of blood flow in large vessels using an approximate velocity profile function. J. Fluid Mech. 580:145–168
2. Rutgers DR, Blankensteijn JD, Grond Jvd. (2000) Preoperative MRA flow quantification in CEA patients flow differences between patients who develop cerebral ischemia and patients who do not develop cerebral ischemia during cross-clamping of the carotid artery. Stroke. 31:3021-3028
3. Alastruey J, Parker KH, Peiró J et al. (2007) Modelling the circle of Willis to assess the effects of anatomical variations and occlusions on cerebral flows. J Biomech 40: 1794-1805
4. Formaggia L, Lamponi D, Tuveri M, et al. (2006) Numerical modeling of 1-D arterial networks coupled with a lumped parameters description of the heart. Comput Meth Biomech Biomed Eng 9: 273-288
5. McClintic JR**.** (1975) Basic Anatomy and Physiology of the Human Body (2nd ed.). Wiley, New York

Author: Fuyou Liang
Institute: RIKEN
Street: 2-1 Hirosawa
City: Wako
Country: Japan
Email: fyliang@riken.jp

Low-intensity Ultrasound Induces a Transient Increase in Intracellular Calcium and Enhancement of Nitric Oxide Production in Bovine Aortic Endothelial Cells

S. Konno[1], N. Sakamoto[2], Y. Saijo[3], T. Yambe[4], M. Sato[5] and S. Nitta[6]

[1,4,6] Institute of Development, Aging and Cancer, Tohoku University, Sendai, Japan
[2] Graduate School of Engineering, Tohoku University, Sendai, Japan
[3,5] Graduate School of Biomedical Engineering, Tohoku University, Sendai, Japan

Abstract — **Background: Nitric oxide (NO) plays a key role in regulating various biological processes including vasodilation, neurotransmission, inflammatory responses, the immune system and apoptosis. In endothelial cells, the production of NO is known to be enhanced in response to mechanical stimulation through intracellular calcium-mediated activation of endothelial nitric oxide synthase (eNOS). In this study, we investigated whether low-intensity ultrasound is capable of mechanically stimulating endothelial cells, which leads to an increase in intracellular calcium and enhancement of NO production. Methods and Results: Cultured bovine aortic endothelial cells (BAECs) were loaded with Calcium Green-1 AM, a calcium-sensitive fluorescent dye, and then exposed to low-intensity ultrasound for 1 min. During the exposure, an increase in fluorescence intensity was observed by laser scanning confocal microscopy. This result indicated that low-intensity ultrasound acted as a mechanical stimulus and induced a transient increase in intracellular calcium in BAECs. To measure the change in NO production, cultured BAECs were exposed to low-intensity ultrasound for 0 (control), 30 and 120 min while loaded with NO-sensitive fluorescent indicator dye DAF-2DA. The fluorescence intensities of the BAECs obtained by laser scanning confocal microscopy were increased in proportion to the exposure time, suggesting that low-intensity ultrasound enhanced NO production in the cells. Conclusions: Low-intensity ultrasound can mechanically stimulate BAECs, resulting in an enhancement of NO production through the activation of the intracellular calcium signaling pathway. Further studies are needed to elucidate the mechanism by which ultrasound increases NO production at a molecular level.**

Keywords — **Low-intensity ultrasound, bovine aortic endothelial cells, mechanical stress, intracellular calcium, nitric oxide**

I. Introduction

Although nitric oxide (NO) was initially identified as an endothelium-derived relaxing factor (EDRF) in blood vessels [1][2], recent studies have demonstrated that it is critically involved in various biological processes including neurotransmission [3], inflammatory responses [4], the immune system [5] and apoptosis [6].

In endothelial cells, mechanical stresses as well as chemical substances such as acetylcholine, histamine, bradykinin and ATP are established to increase intracellular calcium concentration and activate endothelial nitric oxide synthase (eNOS) [7][8]. Low-intensity, low-frequency (27 kHz) ultrasound has recently been reported to increase NO production in endothelial cells [9], but the mechanism by which ultrasound activates eNOS has not been fully elucidated. In addition, little is known about the effect of MHz-order ultrasound, which is typical of the frequency range used in clinical practice, on endothelial cells.

In this study, we investigated whether low-intensity ultrasound at 1 MHz can mechanically stimulate endothelial cells and activate the intracellular calcium signaling pathway, leading to an enhancement of NO production in the cells.

II. Materials and Methods

A. Cell culture

Bovine aortic endothelial cells (BAECs) were isolated according to the standard method described by Shasby et al. [10]. Briefly, a 20-cm section of bovine thoracic aorta was opened longitudinally, then endothelial cells were gently removed from the lumen wall with a scalpel blade. The removed BAECs were seeded into 25 cm^2 flasks and cultured in Dulbecco's modified Eagle medium (DMEM, Gibco, USA) with 10% heat-inactivated fetal bovine serum (FBS, JRH Biosciences, USA) and streptomycin/penicillin (Gibco) at 37°C, 5% CO_2 concentration. After 4–5 days of primary culture, BAECs were subcultured onto 35-mm cell culture dishes (Asahi Techno Glass, Japan). For all studies, only early passage BAECs (passages 4 to 10) were used to avoid changes in their original phenotype during subculture.

B. Ultrasound exposure

To apply low-intensity ultrasound to the BAECs, a disc-shaped ultrasonic transducer (diameter: 29 mm, thickness: 2 mm, resonant frequency: 1 MHz, Honda Electronics, Japan)

Chwee Teck Lim, James C.H. Goh (Eds.): ICBME 2008, Proceedings 23, pp. 1989–1992, 2009
www.springerlink.com

was placed under the dish of cultured cells. Ultrasound transmission gel was used as a coupling agent between the transducer and cell culture dish. When applying ultrasound, the transducer was driven by a 1 MHz, 20 Vp-p (peak to peak) continuous sine-wave electrical signal generated by a multifunction synthesizer (WF-1943, NF Corporation, Japan). The acoustic intensity, measured with a hydrophone, was 14.3 mW/cm^2 under the above conditions.

C. Fluorescence imaging of intracellular calcium

To measure the changes in intracellular calcium concentration, cultured BAECs were loaded with a calcium-sensitive fluorescent indicator Calcium Green-1 AM (Ex = 506 nm, Em = 531 nm; Molecular Probes, USA) according to the manufacturer's instructions. In short, confluent 35-mm dishes of BAECs were washed twice in Dulbecco's phosphate buffered saline (DPBS, Gibco, USA), then were incubated with 6 μM Calcium Green-1 AM in DPBS at 37°C, 5% CO_2 concentration for 30 min. After incubation, cells were washed twice in DMEM and 4 ml of fresh DMEM was added to the dish. After the dish was placed on the ultrasonic transducer attached to a laser scanning confocal microscope (BX50WI, Olympus, Japan), low-intensity ultrasound was irradiated to the cells for 1 min. Fluorescent images were obtained at 10-second intervals before and during the ultrasound exposure and stored on a personal computer. The average fluorescence intensities of the BAECs were calculated for each image by using image analysis software, Scion-image (Scion Corp., USA).

D. Fluorescence imaging of NO

To investigate whether irradiation of low-intensity ultrasound can enhance NO production in endothelial cells, cultured BAECs were loaded with 1 mM L-arginine (Sigma-Aldrich, USA), a substrate for eNOS, and 10 μM DAF-2DA (Ex = 495 nm, Em = 515 nm, Daiichi Pure Chemicals, Japan), a NO-sensitive fluorescent indicator dye [11], according to the manufacturer's instructions. In short, confluent 35-mm dishes of BAECs were randomly assigned to one of the following groups: 1) US0 (control) group (n = 9): incubated with DAF-2DA and L-arginine for 30 min at 37°C, 5% CO_2 concentration without ultrasound exposure; 2) US30 group (n = 6): incubated with DAF-2DA and L-arginine for 30 min, 5% CO_2 concentration, at 37°C under ultrasound irradiation; 3) US120 group (n = 6): irradiated with ultrasound for 90 min, 5% CO_2 concentration, at 37°C and then incubated with DAF-2DA and L-arginine for 30 min under ultrasound irradiation. BAECs were washed twice in DPBS after dye loading, then the average fluorescence intensity of the BAECs for each culture-dish was calculated by using Scion-image from five randomly selected fields by laser scanning confocal microscopy.

E. Statistical analysis

Statistical analysis was performed by using SPSS 10.0J for Windows (SPSS Inc., USA). A paired *t*-test and a non-parametric test (Mann-Whitney U test) were used for the analysis of changes in intracellular calcium and NO production, respectively.

III. Results

Irradiation of low-intensity ultrasound did not affect the morphology of cultured BAECs and no obvious detachment of the cells from the culture dishes could be observed during the experiments.

The fluorescence intensities of BAECs loaded with Calcium Green-1 were increased in response to low-intensity ultrasound treatment. The relative peak fluorescence intensities of BAECs (n = 6) during 1 min of ultrasound exposure were significantly increased compared to those before the irradiation (11.0 ± 1.9%, mean ± SD, $p < 0.05$) (Fig. 1). After the ultrasound irradiation stopped, the fluorescence intensities gradually decreased to the normal level, indicating that low-intensity ultrasound induced a transient increase in intracellular calcium concentration in BAECs.

Changes in average fluorescent intensities of BAECs loaded with DAF-2DA after ultrasound exposure are shown in Fig. 2. The average fluorescence intensities of the BAECs from US30 and US120 groups were increased by 10.8 ± 2.1% ($p < 0.05$), 21.9 ± 2.7% ($p < 0.05$), respectively, compared to those of US0 (control) group. Representative fluorescent

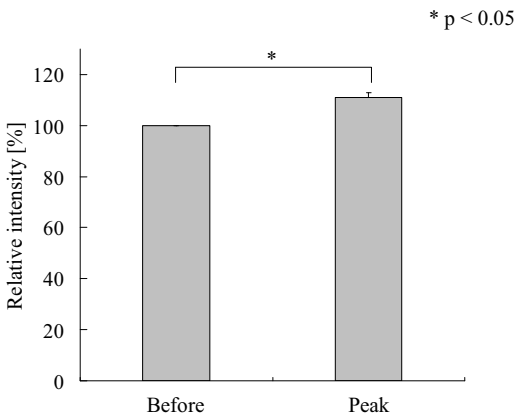


Fig. 1 Changes in fluorescence intensities of BAECs (n = 6) loaded with Calcium Green-1 AM. The relative peak intensities during low-intensity ultrasound exposure increased by 11.0 ± 1.9% (mean ± SD).

images of BAECs loaded with DAF-2DA from the control and US120 groups are shown in Fig. 3. After loading into the cells, DAF-2DA is hydrolyzed to water-soluble DAF-2, which reacts with NO to produce its fluorescent form, DAF-2T. The fluorescence intensity of DAF-2T reflects the amount of NO produced per unit time, because unlike Calcium Green-1 AM, the fluorescence emitted from DAF-2T accumulates and remains in the cells over a period of time. Thus, these data suggested that low-intensity ultrasound activated eNOS in BAECs, resulting in an enhancement of NO production.

The relative fluorescence intensities of BAECs from US30 and US120 groups increased by 10.8 ± 2.1% and 21.9 ± 2.7%, respectively, compared to those of the control.

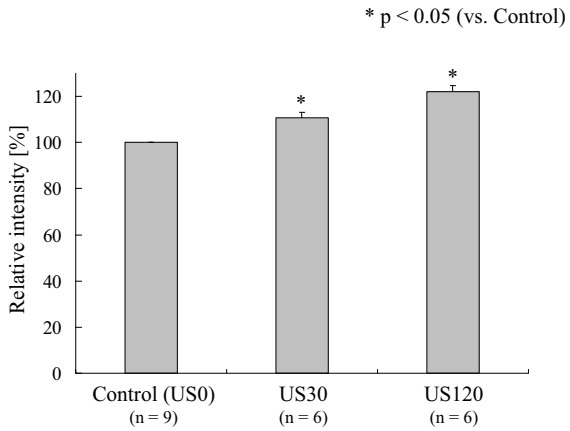


Fig. 2 Changes in average fluorescence intensities of BAECs loaded with DAF-2DA after ultrasound exposure for 0 (control), 30 and 120 min.

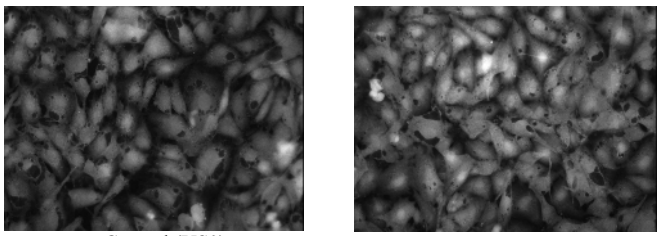


Fig. 3 Representative fluorescent images of BAECs loaded with DAF-2DA from the control (left) and US120 (right) groups.

IV. Discussion

Well-known mechanical effects of ultrasound on living tissue include heat and cavitation. In general, ultrasound at intensity levels of 1 W/cm^2 or more is required to cause thermal effect or cavitation, which is much higher than that employed in this study (14.3 mW/cm^2). We observed neither macroscopic cavitation nor changes in morphology of the cells during the ultrasound exposure. In addition, 30 min of low-intensity ultrasound irradiation did not increase the temperature of DMEM in the 35-mm culture dish (data not shown). Therefore, heat and cavitation are unlikely to be related to the effects of low-intensity ultrasound on BAECs observed in this study.

Shear stress is known to be a predominant component of the mechanical stresses acting on endothelial cells. Ando et al. [12] reported that flow-mediated shear stress immediately increases intracellular calcium in BAECs, which is caused by calcium release from intracellular stores and subsequent calcium influx from the extracellular space. As the mechanical stress-related signaling pathway often involves calcium as a second messenger, our data suggests that low-intensity ultrasound acts as a mechanical stimulus to endothelial cells in a way similar to shear stress.

Low-intensity ultrasound also increased the fluorescence intensities of BAECs loaded with DAF-2DA in proportion to the exposure time. Since studies have shown that mRNA expression for eNOS is induced after a few hours of shear stress loading [13], the enhancement of NO production observed in this study is mainly due to the intracellular calcium-mediated activation of existing eNOS. Interestingly, another study has indicated the possibility of a non-calcium-mediated pathway of eNOS activation by mechanical stress [14]. Further studies are needed to elucidate the precise mechanism by which ultrasound increases NO production at a molecular level.

V. Conclusions

Low-intensity ultrasound at 1 MHz can mechanically stimulate BAECs and enhance NO production through the activation of the intracellular calcium signaling pathway.

References

1. Palmer RM, Ferrige AG, Moncada S (1987) Nitric oxide release accounts for the biological activity of endothelium-derived relaxing factor. Nature 327:524-526
2. Ignarro LJ, Buga GM, Wood KS et al. (1987) Endothelium-derived relaxing factor produced and released from artery and vein nitric oxide. *Proc Natl Acad Sci USA* 84:9265-9269
3. Lembo G, Vecchione C, Izzo R et al. (2000) Noradrenergic vascular hyper-responsiveness in human hypertension is dependent on oxygen free radical impairment of nitric oxide activity. Circulation 102:552-557
4. Gilchrist M, Hesslinger C, Befus AD (2003) Tetrahydro-biopterin, a critical factor in the production and role of nitric oxide in mast cells. J Biol Chem 278:50607-50614
5. Bogdan C (2001) Nitric oxide and the immune response. Nat Immunol 2(10):907-916

6. Moncada S, Erusalimsky JD (2002) Does nitric oxide modulate mitochondrial energy generation and apoptosis? Nat Rev Mol Cell Biol 3(3):214-220
7. Angus JA, Cocks TM (1989) Endothelium derived relaxing factor. Pharmacol Ther 41:303-351
8. Michel T, Ferron O (1997) Nitric oxide synthases: which, where, how, and why? J Clin Invest 100:2146-2152
9. Altland OD, Dalecki D, Suchkova VN et al. (2004) Low-intensity ultrasound increases endothelial cell nitric oxide synthase activity and nitric oxide synthesis. J Thromb Haemost 2(4):637-643
10. Shasby DM, Shasby SS (1986) Effects of calcium on transendothelial albumin transfer and electrical resistance. J Appl Physiol 60(1):71-79
11. Kojima H, Nakatsubo N, Kikuchi K et al. (1998) Detection and imaging of nitric oxide with novel fluorescent indicators: Diaminofluoresceins. Anal Chem 70:2446-2453
12. Ando J , Komatsuda T , Kamiya A (1988) Cytoplasmic calcium response to fluid shear stress in cultured vascular endothelial cells. In Vitro Cell Dev Biol 24:871-877
13. Uematsu M et al. (1995) Regulation of endothelial cell nitric oxide synthase mRNA expression by shear stress. Am J Physiol 269:C1371-1378
14. Kuchan MJ, Frangos JA (1994) Role of calcium and calmodulin in flow-induced nitric oxide production in endothelial cells. Am J Physiol 266:C628-636

Author: Satoshi Konno
Institute: Institute of Development, Aging and Cancer, Tohoku University
Street: 4-1 Seiryo-machi, Aoba-ku
City: Sendai
Country: Japan
Email: konnos@idac.tohoku.ac.jp

Evaluation of Compliance of Poly (vinyl alcohol) Hydrogel for Development of Arterial Biomodeling

H. Kosukegawa[1], K. Mamada[2], K. Kuroki[3], L. Liu[1], K. Inoue[3], T. Hayase[3] and M. Ohta[3]

[1] Graduate School of Engineering, Tohoku University, Sendai, Japan
[2] Graduate School of Medical Engineering, Tohoku University, Sendai, Japan
[3] Institute of Fluid Science, Tohoku University, Sendai, Japan

Abstract — **An *in vitro* blood vessel biomodeling with realistic mechanical properties and geometrical structures will be helpful for the training of intervention, preoperative simulation, and realizing the same physical conditions of blood flow. Poly (vinyl alcohol) hydrogel (PVA-H) with low surface friction, good transparency, and similar elasticity to blood vessel has been developed and accepted as a good material for biomodeling. However, the compliance of PVA-H vessel model has not been measured. In this study, we changed the elasticity and measured the compliance of a box-typed PVA-H biomodeling, to represent the similar compliance to a real artery. PVA powders were dissolved in a mixture of water and organic solvent so that PVA solutions of 12, 18 wt% were prepared. The model was subjected to hydrostatic pressure by adding distilled water and the inner diameter was measured using an ultrasound system. The compliance of each model was calculated from the strain of inner diameter and the inner pressure. The inner diameter of model increases linearly as the inner pressure increases. The compliance of PVA-H model is constant according to pressure change, while that of a real blood vessel changes nonlinearly. This difference may depend on the isotropic characteristics of PVA-H, whereas a real blood vessel is anisotropic. These results indicate that adding anisotropy, such as orientation of PVA, to model would be necessary to represent the compliance of a real artery.**

Keywords — **Poly (vinyl alcohol) Hydrogel, Blood vessel biomodeling, Compliance, Mechanical property, Ultrasound.**

I. Introduction

Endovascular intervention, which is a therapeutic approach to treat cardiovascular diseases by using interventional devices such as catheter, is increasingly employed recently. This method can contribute to improvement of quality of life of patients because of the less invasiveness. However, advanced skill and considerable experience are required for endovascular intervention to maneuver various interventional devices in blood vessel. Therefore, the training of intervention is important. A blood vessel biomodeling with functions of blood vessel has been developed for the training. Especially, a vessel biomodeling with realistic mechanical properties and geometric structures may be useful for preoperative simulation, the development of therapeutic strategy, and informed consent. Furthermore, it may contribute to the technical evaluation of interventional devices or reduction of animal experiments carried out in the development of devices.

Poly (vinyl alcohol) hydrogel (PVA-H) has realized a biomodeling with low surface friction and good transparency [1]. Recently, biomodeling with similar mechanical properties to artery has been developed by PVA-H with various techniques [2]. Then, the compliance of PVA-H biomodeling may be important point for evaluation of biomodeling. It was reported that a method using ultrasound is useful to measure the diameter of hydrogel hollow [3], [4]. In this study, PVA-H with a cylindrical hollow was prepared, and the diameter-pressure curve was graphed by using ultrasound system.

II. Methods

A. Poly (vinyl alcohol) Hydrogel

Poly (vinyl alcohol) powder (PVA) (JF17, degree of polymerization = 1700, saponification value = 99.0 mol%, JAPAN VAM & POVAL CO., LTD.) was dissolved in a mixed solvent of dimethyl sulfoxide (Toray Fine Chemicals Co., Ltd.) and distilled water (80/20, w/w). The PVA powder in the solution was stirred for 2 hours at 100°C until dissolution, and the PVA concentration became 12 and 18 wt%. Then, the solution was cast in an acrylic mold with dimensions of 98 × 50 × 50 mm. A straight stainless stick (Φ = 4 mm) was fixed on the mold before PVA-H casting. The mold, which the PVA solution was cast in, was maintained at -30°C for 24 hours to promote gelation of the PVA solution. After gelation, the stainless stick was removed from the mold and PVA-H model with a cylindrical hollow was obtained (Fig.1).

B. Ultrasound imaging

Ultrasound system (LOGIQ 7, General Electric Co.) was used to measure the diameter of cylindrical hollow for the compliance of PVA-H in this study. An ultrasound linear

Chwee Teck Lim, James C.H. Goh (Eds.): ICBME 2008, Proceedings 23, pp. 1993–1995, 2009
www.springerlink.com

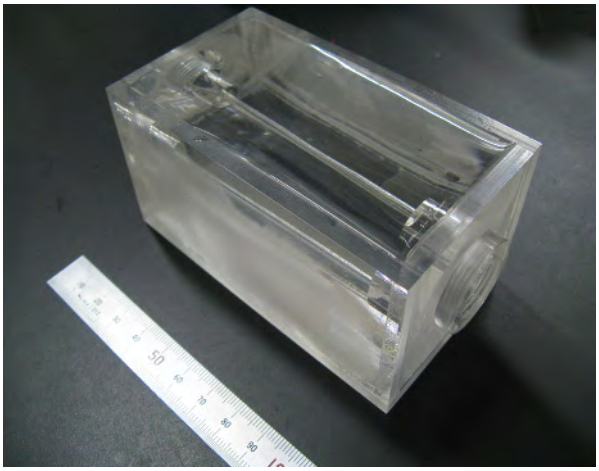


Fig. 1 Box-typed PVA-H model with a straight cylindrical hollow in an acrylic box

array probe (10L, frequency = 12 MHz) was touched on the surface of PVA-H, as the array of oscillators was parallel to the axis of model hollow. With water inside the model, a B-mode image, which exhibits boarders between PVA-H wall and water, was obtained. B-mode images (854 × 697 pixels) were processed to show brightness value by using a software package (LabVIEW ver.8.5, National Instruments Co. Ltd.). The length between the peaks of brightness value was defined as the diameter of the model hollow.

C. Measurement of Compliance of PVA-H

PVA-H model was set in an acrylic box and was connected to an acrylic straight pipe with over 2000 mm tall. An ultrasound probe was touched on the surface of PVA-H (Fig.2). By adding water into the acrylic pipe, the PVA-H model was subjected to hydrostatic pressure, and the inner pressure was controlled with water head. By measuring a diameter of PVA-H model hollow by using ultrasound, a diameter-pressure curve was obtained.

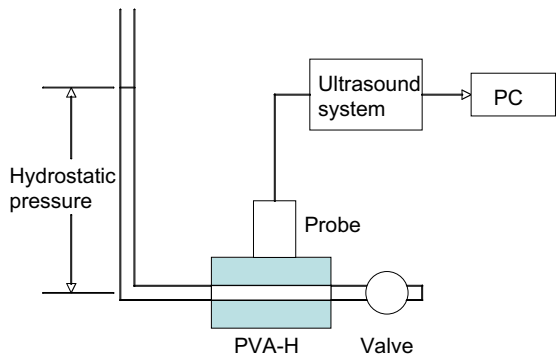


Fig. 2 Apparatus for measuring the diameter-pressure curve of PVA-H

III. Results and Discussions

B-mode image showing the wall of PVA-H clearly was obtained and the diameter of PVA-H hollow could be also obtained. From this result, ultrasound may be useful to evaluate the compliance and the motion of PVA-H biomodeling.

Figure 3 shows the diameter-pressure curve of PVA-H. The compliance of PVA-H with 12 wt% of concentration is higher than that of PVA-H with 18 wt%. Based on the results that PVA-H with high concentration has high elasticity [2], PVA-H model with high elasticity shows low compliance.

The diameter of PVA-H model increases linearly as the inner pressure increases (Fig.3), and the compliance of PVA-H may be constant against inner pressure change. This phenomenon may depend on that PVA-H has an isotropic character and the wall of a box model is constant. On the other hand, *in vivo* artery shows the compliance decreases nonlinearly according to increase of inner pressure in diameter-pressure curve [5]. It is thought that various components constructing arterial tissue such as collagen and elastin are arranged in circumferential direction. Therefore, in order to represent the compliance of artery with PVA-H, adding anisotropy, multilayer structures, or orientation to PVA-H would be necessary.

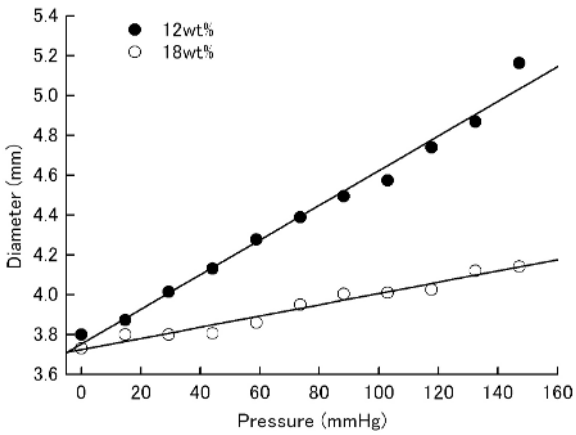


Fig. 3 Diameter-pressure curve of PVA-H (PVA concentration = 12, 18 wt%)

IV. Conclusions

For the purpose on the development of PVA-H blood vessel biomodeling representing realistic motion, measurement of compliance of PVA-H model was carried out. The model with a cylindrical hollow was subjected to hydro-

static pressure, and the measurement of the diameter of model hollow could be obtained by using ultrasound. The compliance of PVA-H model is constant according to inner pressure change, while that of artery changes nonlinearly.

Acknowledgment

The work is partly supported by Tohoku University Grobal COE Program "Global Nano-Biomedical Engineering Education and Research Network Centre" and by Japan Society for the Promotion of Science "Core to Core Project 20001".

References

1. Ohta M, Hnada A, Iwata, H, et al. (2004) Poly-vinyl alcohol hydrogel vascular models for *in vitro* aneurysm simulations: The key to low friction surfaces, Technology and Health Care, 12:225-233
2. Kosukegawa H, Mamada K, Kuroki K, et al. (2008) Measurement of Dynamic Viscoelasticity of Poly (vinyl alcohol) Hydrogel for the Development of Blood Vessel Biomodeling, J. Fluid Science and Technology 3:4:533-543
3. Fromageau J, Brusseau E, Vray D, et al. (2003) Characterization of PVA Cryogel for Intravascular Ultrasound Elasticity Imaging, IEEE Trans Ultrasonics Ferroelectrics Frequency Control, 50:10:1318-1324
4. Dineley J, Meagher S, Poepping T L, et al. (2006) Design and Characterication of A Wall Motion Phantom, Ultrasound in Med. & Biol., 32:9:1349-1357
5. Tardy Y, Meister J J, Perret F, et al. (1991) Non-invasive estimate of the mechanical properties of peripheral arteries from ultrasonic and photoplethysmographic measurements 12:1:39-54

Author: KOSUKEGAWA Hiroyuki
Institute: Graduate School of Engineering, Tohoku University
Street: 2-1-1 Katahira Aoba-ku
City: Sendai
Country: Japan
Email: hiro-kosuke@biofluid.ifs.tohoku.ac.jp

People Recognition by Kinematics and Kinetics of Gait

Yu-Chih Lin[1], Bing-Shiang Yang[2,3] and Yi-Ting Yang[2]

[1] Department of Biomedical Engineering, Yuanpei University , HsinChu, Taiwan
[2] Department of Mechanical Engineering, National Chiao Tung University, HsinChu, Taiwan
[3] Brain Research Center, National Chiao Tung University, HsinChu, Taiwan

Abstract — **Human recognition by gaits is a new biometric method which considers both spatial and temporal features by tracking the gait at a distance. Most researches use image processing methods to analyze the moving object, while some use the model-based methods. Although some efforts have been devoted to the gait recognition, a high identification rate and a low computational cost still need to be achieved. This paper tends to investigate the gait recognition from the biomechanical point of view, which is lacking in the computer science and electronics communities. We present the method of people recognition by using both three-dimensional parameters of lower limb joints, namely, kinematic parameters (including joint angles and angular velocities) and kinetic parameters (joint forces). Dynamic data are acquired by tracking the maker positions using a motion capture system. 350 trials for 10 subjects are conducted, in which we use 20 trials for each one of these for training and the remaining 15 for testing. Additional 35 trials for another one subject not in the training set are conducted for testing the adventitious people. SOM neuron networks are employed for data classification. The importance of specific joints and variables is discussed in detail to investigate the major factors that cause the differences in human gait through a biomechanical approach. Experimental results show that gait is a reliable feature for individual identification since a high recognition rate can be achieved by choosing the proper joints or dynamic parameters of a gait. It also suggests that some joints and dynamic parameters dominate the differences in the walking style of people, which can be applied to both the biomedical and the computer vision fields.**

Keywords — **gait, biometric, recognition, kinetics, kinematics.**

I. Introduction

With the advancement in technology and the community structure, individual recognition or identification is gaining more and more importance. For example, the security is needed to access computer systems, ATMs, buildings, etc [1]. The literatures in both computer science and biomedical fields show the feasibility and reliability of human recognition by gait [2, 3] because of the repeatability and uniqueness of human gait. In biomedical field, the researches tends to emphasize the repeatability and similarity of normal gait so that they can distinguish between the patients and normal subjects, or assess the changes in gait pattern after the clinical surgery [4, 5, 6, 7]. In computer science field, on the contrary, investigators try to find the discrepancies of normal gait. When all the gait parameters are obtained, the gait pattern is sufficiently unique and thus reliable for individual recognition [3, 8]. The most popular methods for gait recognition are processing the video images of walking including model-free method and model-based method [3, 9, 10, and 11]. The first method is the silhouette-based (appearance-based) method which uses a silhouette, and a subject is described by the image sequences. The second method is the model based method which models the motion features. Although it is more reasonable and convenient to consider the gait features in marker-free gait sequences [11], the information analyzed from the video image processing is not sufficient and accurate. The present technique that can get the most precise kinematic parameters of gait is analyzing the maker positions obtained from the motion capture system. In this study, we use the kinematic and kinetic variables derived from the motion capture data as the biometrics instead of the information extracted from the image processing method. We try to separate each joint and variable to investigate deeply the influence of differences in the variables in each joint on the walking style. Hence coming up with the suggestion for the marker-free image processing methods about which joints or variables are the most referable as the biometric features.

II. Methods

A. Set-up

A motion capture system (BTS Spa Corp., Italy) and a force plate (BERTEC Corp., USA) are used to acquire the three-dimensional kinematic and kinetic variables during gait, respectively. Eleven markers are attached to the subjects' pelvises and right lower limbs. The subjects are asked to walk at a natural speed along the walkway. 350 trials for 10 subjects are conducted, in which we use 20 trials for each one of these for training and the remaining 15 for testing. Additional 35 trials for one other subject, not in the training set, are conducted for evaluating the adventitious people. SOM neuron networks are used as the algorithm for the data classification. We investigate in detail the impor-

Chwee Teck Lim, James C.H. Goh (Eds.): ICBME 2008, Proceedings 23, pp. 1996–1999, 2009
www.springerlink.com

tance of each joint in order to find out the major factors that cause the differences in human gait through a biomechanical approach.

B. SOM architecture

SOM neural network can imitate the mechanism of cerebral cortex. A 2-D map is used in our architecture to represent the cortex map involving the sensitivity of image distortion. During the training period of our network, each unit with a positive activity within the neighborhood of the winning unit updates its value toward the features of certain image appearances. After iterations of updating values of neurons by Kohonen's algorithm, nodes in the 2-D array organize themselves in response to the input vectors. The resulting map projects the input vectors onto 2-D map preserving the natural topology of training data, which contains the feature vectors of various types of images, including smooth, high frequency, regular-texture images, etc..

III. Results and Discussion

The average joint angles and the standard deviation of 20 training trials in sagittal plane of each subject are shown in figs. 1-3. The mean values are shown in solid lines while the standard deviations are shown in dash lines. As shown in these figures, different trials of the same subject have high repeatability because of the small standard deviation. It is also indicated from the curves that the differences between subjects are distinct. The average angles and the standard deviation of 10 subjects in each trial (trial 1 – trial 5) are also shown in figs. 4-6. The standard deviation between subjects is larger than between trials. The variation curves of mean values of all subjects are almost overlapping. And the standard deviations are within similar range. It is evident from these results that we can distinguish between humans by their gaits. Although repeatability exists between subjects, this repeatability is much smaller than that seen between trials of each subject. The kinematic data (joint angles and angular velocities) and the kinetic data (joint forces) are used as the features for human recognition. The recognition results for each joint using different kinematic and kinetic variables are shown in Table 1. 64 neurons are used for the human recognition based on joint angles, angular velocities, and joint forces. The recognition rates using kinetic data (joint forces) are lower than those of the kinematic data (joint angles and angular velocities). We use 16, 36, and 64 neurons to compare the recognition performance of different joint angles. The recognition rates of each joint with various numbers of neurons are shown in fig. 7. Experiments using all three joints are also done for comparison. It is indicated that the recognition rates using joint angles of hip, knee, ankle, and all three joints are highest when 36 neurons are used. High recognition rates can be achieved using only 16 neurons in all cases (Hip: 87.33%, Knee: 99.33%, Ankle: 86.33%, All joints: 98.67%). Generally speaking, the recognition rates using hip and knee joints' kinematic and kinetic variables are greater than those of ankle joints. The recognition rates derived from the ankle joint are the least desirable. Using all three joints shows a high recognition rate, but it will not necessarily improve the performance. Using knee joint parameters will get good results and save the computational cost in all cases. It is

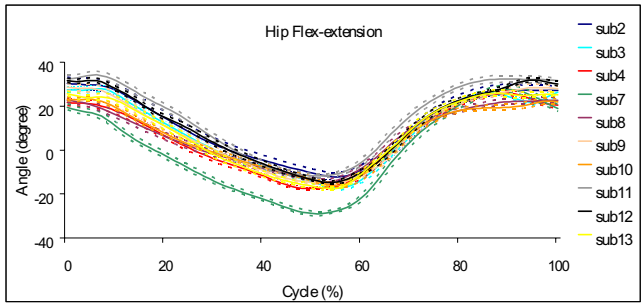


Fig. 1 The average hip joint angles (flex/extension) and the standard deviation of 20 training trials of each subject

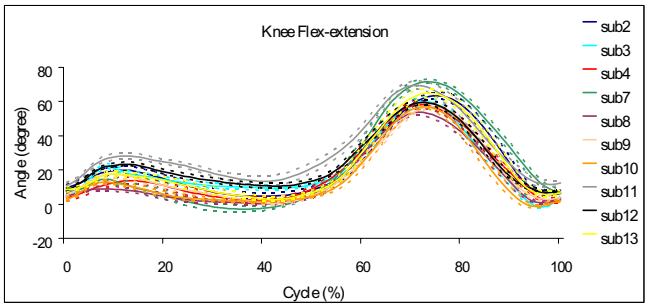


Fig. 2 The average knee joint angles (flex/extension) and the standard deviation of 20 training trials of each subject

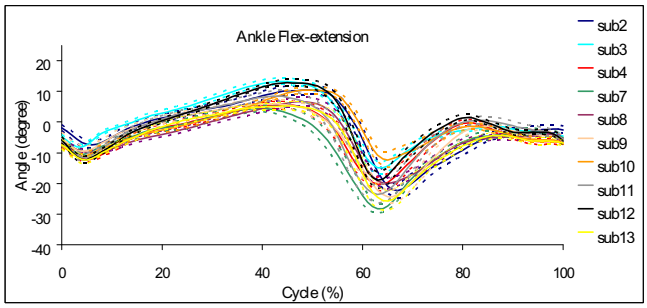


Fig. 3 The average ankle joint angles (dorsi/plantarflex) and the standard deviation of 20 training trials of each subject

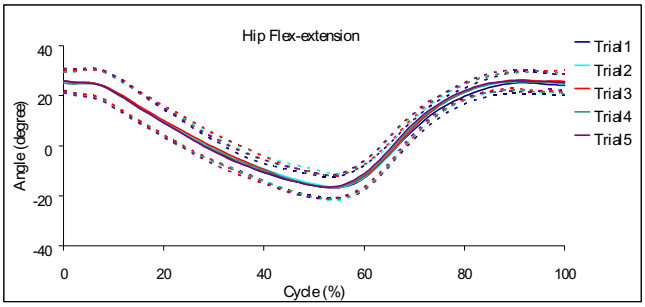


Fig. 4 The average hip joint angles (flex/extension) and the standard deviation of 10 subjects in trial1-trial5

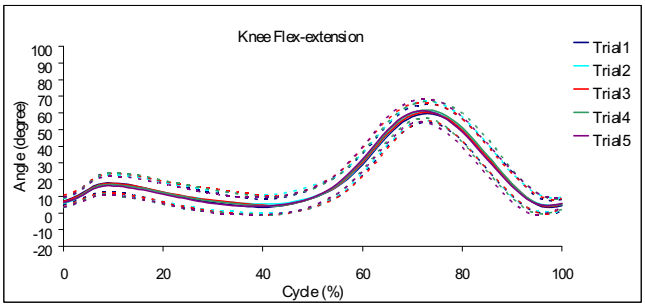


Fig. 5 The average knee joint angles (flex/extension) and the standard deviation of 10 subjects in trial1-trial5

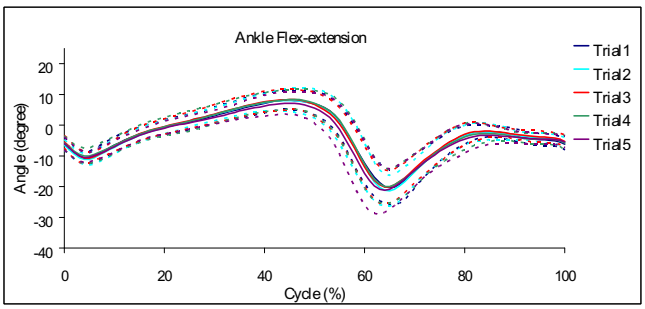


Fig. 6 The average ankle joint angles (dorsi/plantarflex) and the standard deviation of 10 subjects in trial1-trial5

Table 1 Recognition rates using different kinematic and kinetic variables (64 neurons are used)

Recognition rates (%)	Ankle	Knee	Hip	All joints
Joint Angle	92.67	95.33	98.00	98.67
Angular Velocity	86.00	97.33	99.33	*
Joint Force	72.00	86.67	85.33	*



Fig. 7 Recognition rates of each joint using various numbers of neurons

suggested that knee joint angles can be used as the lower limb features for individual recognition. It can be found in the experiments that features of ankle joint angles may pull down the recognition rates when using all three joint angles. Therefore, it is unnecessary to pay the computational cost to use so many joints.

IV. Conclusions

This paper proposed a human recognition scheme by using gaits as features and SOM neural network as the classifier. High recognition rates are obtained when three-dimensional lower limbs' kinematic and kinetic variables are used as features of human recognition. Better recognition rates can be obtained when using knee or hip joint angles, and using ankle joint parameters records the worst results. The kinematic parameters are better than kinetic parameters. In conclusion, gait is really a reliable feature for human recognition and the proposed methodology is feasible which can be applied to researches in biometrics or computer visions.

Acknowledgment

The authors gratefully acknowledge the financial support of this research by the National Science Council (Republic of China) under Grant NSC 97-2221-E-264-001.

REFERENCES

1. Anil K. Jain, Fellow, IEEE, Arun Ross, Member, IEEE, and Salil Prabhakar, Member, IEEE (2004) An introduction to biometric recognition. IEEE transactions on circuits and systems for video technology. 14(1):4–20
2. Sarah V. Stevenage, Mark S. Nixon, Kate Vince, (1999) Visual Analysis of Gait as a Cue to Identity. Appl. Cognit. Psychol 13: 513–526
3. Mark S. Nixon, Member IEEE, John N. Carter, Member IEEE (2006) Automatic recognition by gait. Proceedings of the IEEE 94(11): 2013–2024
4. Fong-Chin Su, Wen-Lan Wu (2000) Design and testing of a genetic algorithm neural network in the assessment of gait patterns, Medical Engineering & Physics 22: 67–74
5. Wen-Lan Wu, Fong-Chin Su, (2000) Potential of the back propagation neutral network in the assessment of gait patterns in ankle arthrodesis. Clinical Biomechanics 15:143–145
6. Fong-Chin Su, Wen-Lan Wu, Yuh-Min Cheng, You-Li Chou (2001) Fuzzy clustering of gait patterns of patients after ankle arthrodesis based on kinematic parameters. Medical Engineering & Physics 23:83–90
7. Monika Kohle, Dicter Merkl, Josef Kastner (1997) Clinical gait analysis by neutral networks: issues and experiences. Tenth IEEE Symposium on Computer-Based Medical Systems pp 138–143
8. David K Wagg, Mark S Nixon (2004) On automated model-based extraction and analysis of gait. Proceedings of the Sixth IEEE International Conference on Automatic Face and Gesture Recognition ’04 pp 11–16
9. Nikolaos V. Boulgouris, Dimitrios Hatzinakos, Konstantinos N. Plataniotis (2005) Gait recognition: A challenging signal processing technology for biometric identification. IEEE Signal Processing Magazine Nov, 78-90
10. Raquel Urtasun, Pascal Fua (2004) 3D Tracking for gait characterization and recognition. Proceedings of the Sixth IEEE International Conference on Automatic Face and Gesture Recognition ’04 pp 138–143
11. Rong Zhang, Christian Vogler, Dimitris Metaxas (2004) Human gait recognition. Proceedings of the 2004 IEEE Computer Society Conference on Computer Vision and Pattern Recognition Workshops 2: 342-349

Author: Yu-Chih Lin
Institute: Department of Biomedical Engineering, Yuanpei University
Street: No.306, Yuanpei St.
City: HsinChu
Country: Taiwan
Email: d87522011@ntu.edu.tw

Site-Dependence of Mechanosensitivity in Isolated Osteocytes

Y. Aonuma[1], T. Adachi[1,2], M. Tanaka[3], M. Hojo[1], T. Takano-Yamamoto[4] and H. Kamioka[5]

[1] Dept. Mech. Eng. & Sci., Grad. Sch. Eng., Kyoto Univ., Kyoto, Japan
[2] Computational Cell Biomechanics Team, VCAD System Research Program, RIKEN, Wako, Japan
[3] Dept. Aeron., Col. Eng., Kanazawa Inst. Tech., Ishikawa, Japan
[4] Div. Orthod., & Dentofacial Orthop., Grad. Sch. Dent., Tohoku Univ., Sendai, Japan
[5] Dept. Orthod. & Dentofacial Orthop., Grad. Sch. Med., Dent. & Pharm. Sci., Okayama Univ., Okayama, Japan

Abstract — **It is proposed that osteocytes embedded in mineralized bone matrix play a role in mechanosensory system during bone remodeling for mechanical adaptation. Various experimental and computer simulation approaches have revealed that the osteocytes sense the mechanical stimulus such as deformation/force and microdamages in bone matrix generated by mechanical loading, and also still have continued discussion. In this study, for interest to morphological character of osteocytes, we investigated site-dependence of mechanosensitivity in the osteocytes through observation of calcium response to applied local deformation. We developed a quantitative method using a microneedle and microparticles to apply local deformation to an isolated chick osteocyte, and analyzed intracellular calcium dynamics to the applied deformation. As the results, the applied local deformation induced calcium response at the vicinity of the stimulated point and caused its diffusive wave propagation to whole intracellular region in a single osteocyte. Furthermore, the large deformation was necessary at the cell body to induce calcium response, while a relatively small deformation was sufficient at the cell process, suggesting that the mechanosensitivity at the cell process was higher than that at the cell body. These results suggest that the cell shape with processes contributes to the mechanism of cellular response to mechanical stimulus in osteocytes, and that the site-dependent mechanosensitivity depends on cell shape in a single osteocyte.**

Keywords — **Osteocytes, Cell Biomechanics, Mechanical stimulus, Calcium signaling response**

I. Introduction

Osteocytes embedded in mineralized bone matrix have been proposed to have functions as a mechanosensor. In bone matrix, osteocytes construct intercellular networks with surrounding osteocytes as well as with osteoblasts on the bone surface. In this network, the osteocytes sense the deformation/damage, which is generated by mechanical loading to trabecular bone, and transmit to other bone cells via intercellular network in the bone matrix, through which coordinate the adaptive remodeling response [1, 2]. Although the character of the mechanical stimulus that acts on the osteocytes as a result of bone loading is still unknown, several potential stimuli affecting osteocyte function are proposed by recent studies. [3-8]. For example, interstitial fluid flow [3, 6] and bone matrix deformation [7, 8] are well proposed as hypothesized mechanical forces for the activation of osteocytes in the bone matrix, which have been continued discussion from each other's positions.

When osteoblasts differentiate into the osteocytes, they change their morphology to a stellate form with many slender processes, which is sustained even *in vitro* culture environment. This characteristic cell shape may bring about difference in mechanosensitivity between cell body and cell processes. The view of site-dependence may also provide information to insight the mechanosensing mechanism of osteocyte in bone matrix.

In this study, we investigated site-dependent response to mechanical stimulus in isolated osteocytes *in vitro*. Local mechanical stimulus was applied to a single osteocyte using a glass microneedle targeting a microparticle adhered to the cell membrane, and cellular response induced by application of a local deformation was observed with the technique of calcium imaging. To evaluate amplitude of stimulus to generate transient, we developed quantitative method to apply local deformation to the osteocytes, and analyzed the intracellular dynamics to the applied deformation.

II. Materials and methods

A. Isolation of osteocytes

Osteocytes were isolated from 13-day-old embryonic chicken calvariae with modification of the method as described in Kamioka et al. [9]. Isolated cells were plated on ϕ = 35 mm glass-bottom dishes at a density of 7.5×10^3-2.0×10^4 cell/dish and were incubated for 15-18 h in α-MEM that contained antibiotic and 2% fetal bovine serum (FBS) at 37°C. The culture dishes were coated with poly-D-lysine and fibronectin in advance.

Chwee Teck Lim, James C.H. Goh (Eds.): ICBME 2008, Proceedings 23, pp. 2000–2004, 2009
www.springerlink.com

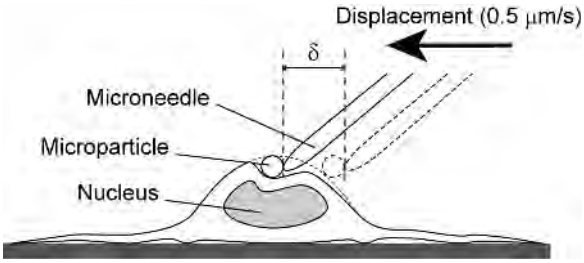


Fig. 1 Application of mechanical stimulus to an osteocyte

B. Applying localized deformation

A local mechanical stimulus was applied to single osteocyte using a glass microneedle via polystyrene microparticles (ϕ = 1.0 μm) attached on the cell membrane, as illustrated in Fig. 1. Microparticles were coated with monoclonal antibody (MAb) OB7.3, which is specific to chicken transmembrane protein Phex [10], to identify osteocytes and improve adhesion properties to osteocyte cell membrane. To confirm microparticle coating with OB7.3 and adhesion of the coated microparticles to the osteocytes, we observed the microparticles with immunofluorescence imaging and field emission scanning electron microscopy in advance. To quantitatively apply the mechanical stimulus, microneedle was moved horizontally at a constant velocity controlled (v = 0.5 μm/s). Using phase contrast microscopy, position and displacement of the microparticles were traced. Then, a series of images was obtained at 0.25 s intervals, and detection of the initial movement of the targeted microparticle was defined as t = 0 s for the measurement of cell deformation. The displacement of the microneedle δ (μm), which corresponds to the microparticle displacement after t = 0 s, was defined as the measure of the mechanical stimulus to the osteocytes. Thus, when calcium response to the mechanical stimulus was observed, the time t was recorded and converted into the microneedle displacement δ, that corresponds to the microparticle displacement.

C. Calcium imaging

The concentration of intracellular calcium ion, $[Ca^{2+}]_i$, was evaluated by ratiometric method. Using two fluorescent indicators with different fluorescent characteristics, by which the ratio of the detected fluorescent intensity was evaluated. Calcium indicators, 6 μM fluo-4 AM and 8 μM Fura Red AM were loaded into the cells. After incubation, the cells were rinsed with Dulbecco's Phosphate Buffer Saline (DPBS), and the medium was replaced by CO_2 independent medium for pH stabilization.

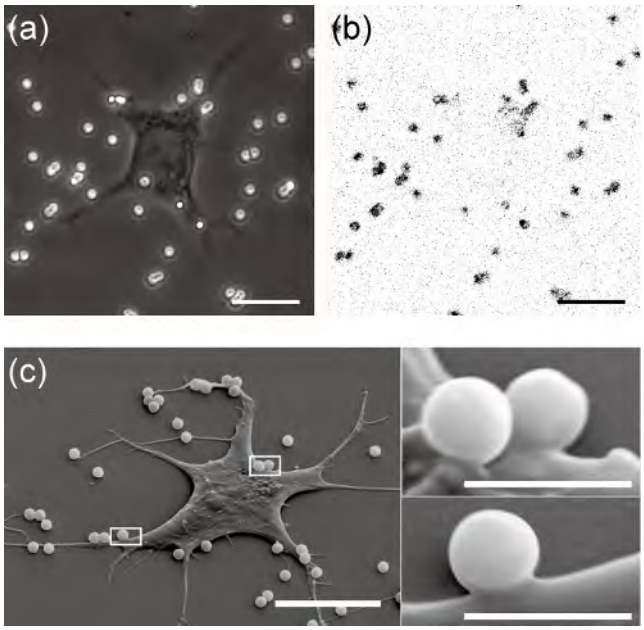


Fig. 2 Microparticles attached on the cell membrane for application of mechanical stimulus. (a) and (b): Surface treatment of microparticles with OB7.3. (a): Transmitted image. Bar = 10 μm (b): Fluorescent image of microparticles labeled by indirect immunofluorescence. Bar = 10 μm (c): FE-SEM images of an osteocyte with microparticles. Right images are both magnified view of images of two regions in left image. Bar = 10 μm (left) and 2 μm (both right)

The calcium response to the applied local deformation was observed using a confocal laser-scanning microscope (LSM510, Carl Zeiss). Image processing and analysis were performed using Image-Pro Plus 4.51 software (MediaCybernetics).

III. Results

The OB7.3-coated microparticles were utilized as a marker of osteocytes as well as a mediator of applied mechanical stimulus to the cell using a microneedle. Microparticles dispersed to culture dish were found to adhere stably to the cell membrane even after washing. Fluorescent immunolabeling confirmed that all observed microparticles in phase contrast image (Fig. 2(a)) were coated by OB7.3 (Fig. 2(b)). Scanning electron microscopic images showed the attachment site of the microparticles to the osteocytes (Fig. 2(c)). The OB7.3-coated microparticles were observed in both cell body and processes and stably attached to cell membrane as shown in magnified images.

The application of mechanical stimulus via microparticle displacement induced calcium transient at the site of defor-

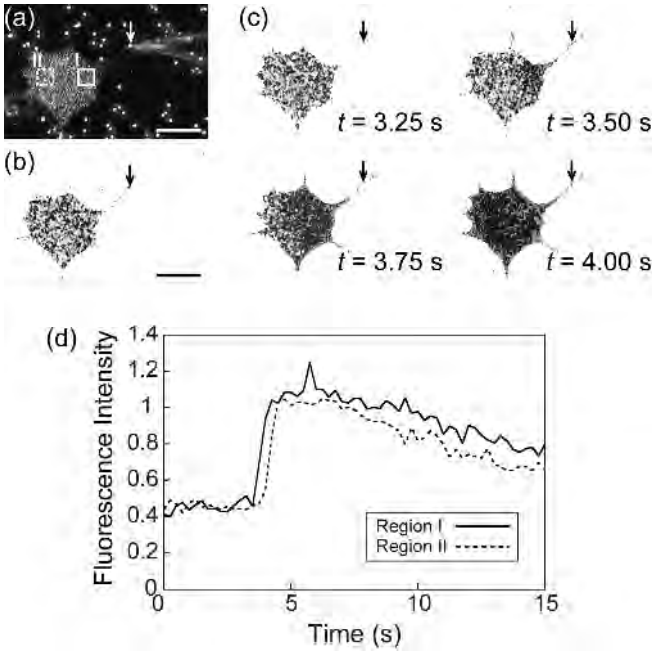


Fig. 3 Calcium response induced by application of local mechanical stimulus. (a): Superimposed image of transmitted and fluorescent image. Bar = 10 μm (b): Fluorescent ratio image at t = 0 s (displaced by pseudo- color). Bar = 10 μm (c): Time-lapse images from t = 3.25-4.00 s. (d): Time course of change in fluorescent ratio of two fluorescent indicators (fluo-4/Fura Red), measured in the regions I and II displayed in (a)

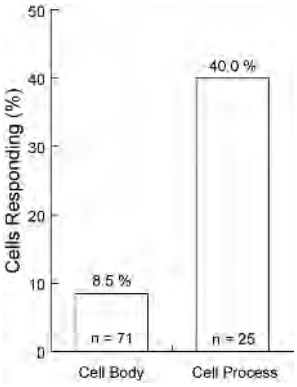


Fig. 4 Percentage of cells responding to local deformation

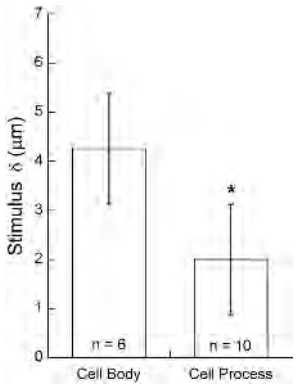


Fig. 5 Stimulus that induces calcium response (*p < 0.05)

mation (Fig. 3). A microparticle targeted for deformation is shown in a superimposed image of the transmitted and fluorescent images (Fig. 3(a), white arrow). Pseudo-colored ratio images are shown at the initiation of application for local deformation (t = 0 s, Fig. 3(b)) and time course at t = 3.25-4.00 s (Fig. 3(c)). When the targeted microparticle adhered on the osteocyte was displaced by the microneedle (black arrow in Fig. 3(b) and 3(c)), a calcium transient was observed in the region adjacent to the microparticle. In addition, the calcium response was propagated to the whole cell body and other cell processes. The intracellular calcium concentration profile examined from two different square regions, I (solid line) and II (dashed line) in Fig. 3(a), was displayed in time course (Fig 3(d)). The calcium transients were seen at 0.25 s interval between the two regions, distant 10μm each other.

Figure 4 shows the percentage of cells responding to applied local deformation. Cells were divided into two groups by the targeted position of the applied stimulus; the cell body and cell process, and the percentage of cells responding to stimulus in each position was determined. The percentage of cells responding to applied stimulus was higher in the cell process (40.0%) than in the cell body (8.5%).

The measure of mechanical stimulus to generate a calcium transient in response to the local deformation of the cell body and the cell process is delineated as displacement of the microparticle δ, and is shown in Fig. 5. The required amplitude of mechanical stimulus to cause calcium transient was different in the cell body and cell process. Displacements for calcium transient were 4.3 ± 0.8 μm and 2.0 μm ± 0.5 μm, respectively.

IV. Discussion

It is believed that location and structural characteristics of osteocyte network in bone matrix have a key role in mechanosensory system for bone mechanical adaptation. Osteocytes in bone matrix are located in cavities called lacuna with their processes elongated into canaliculi. Therefore, the cell process and the cell body of the osteocyte are thought to exist in different mechanical microenvironments. It has been demonstrated by Anderson et al. [7] that interstitial fluid flow due to mechanical loading generates high

shear stress on the cell processes in canaliculi through fluid flow analysis using computer simulation. Moreover, Nicolella et al. [8] observed localized high tissue strain in the perilacunar region under physiological strain levels in bone tissue. These studies indicate that osteocytes in bone matrix may be exposed to site specific mechanical stimuli, and the stimuli are dependent on each specific mechanical microenvironment. However, site-specific mechanical responses in the osteocyte itself, in sites such as the cell process and cell body have not been examined. In this study, therefore, by observing cellular response in the cell process and the cell body under same mechanical environment using isolated cells, we aimed to investigate the difference between cell body and cell process on mechanosensitivity, by which we could expect to understand the meaning of the stellate morphology of osteocytes.

In this study, to apply quantitative local mechanical stimulus to a single primary osteocyte, we developed an experimental system using a microneedle and antibody coated microparticles. This method allowed us to apply localized deformation as well as to identify the osteocytic phenotype in primary culture. Antibody coated microparticle binding is observed as tight in scanning electron microscopy, and is indeed strong to be useful for panning method of osteocyte isolation [11]. Therefore, this method enables us to quantify the local deformation by measuring the magnitude of displacement of the microparticle.

In this experiment, a localized deformation was applied via OB7.3 coated microparticles attached on the osteocyte membrane as a mechanical stimulus to the internal osteocytes. Adhesive structures that transmit the microparticle displacement to the internal force in this *in vitro* study correspond to the adhesive structures *in vivo* to the extracellular matrix. Indeed, it was reported that the osteocytes attach to the bone matrix in canaliculi mediated by tethering elements [12]. In addition, Kamioka et al. [5] and Vatsa et al. [13] had reported that the focal adhesions are distributed at proximal base of the cell process and the cell body of osteocytes in bone matrix, and these focal attachments may induce mechanosensation through perturbation by the deformation of bone matrix and/or the dragged force by fluid flow [14].

It has been suggested that the focal adhesions have an important role in the mechanosensing mechanism and that the cytoskeletal actin filaments binding to extracellular matrix through focal adhesions transmit and focus the forces to the mechanosensitivity (MS) channels on the cell membrane [15]. This finding is based on the visualization of Ca^{2+} influx across individual MS channels close to the focal adhesions as a result of direct mechanical stimulation via actin stress fibers. If the osteocytes in bone matrix achieve their mechanotransduction with activation of the MS channels, the adhesive structures could attribute to transmit the mechanical stimulus.

The previous study reported that there are differences in the actin cytoskeleton between cell processes and the cell body, and showed that osteocyte processes are rich in actin filaments whereas the cell body is not [16]. Other recent study also showed that the elastic modulus of the osteocyte process is higher than that of the cell body [17]. These unique internal structures and the site-dependence of the elastic modulus could modulate the sensitivity to direct deformation. In this study, we observed higher sensitivity to the mechanical stimulus in the cell processes than the cell body. This difference in sensitivity might be due to the different localization of actin filament with high density in cell process and low in cell body. In addition to the stiffness, the distance between stimulated and fixed points could attribute to the difference in mechanosensitivity. That is, the lower stiffness without sufficient internal structure, that is necessary for the force transmission to the focal adhesion at the basal membrane, results in lower sensitivity to the mechanical stimulus.

V. Conclusion

In this study, we observed site-specific response to mechanical stimulus in primary cultured osteocytes. To investigate the cell response to the mechanical stimulus, we developed a quantitative method to apply local deformation to an osteocyte, and analyzed intracellular calcium dynamics to the applied deformation. As the result, we found the higher mechanosensitivity in the cell process. It suggests that cell processes of osteocytes may function as a sensitive part to direct deformation.

Acknowledgement

MAb OB7.3 was kindly provided by Prof. J. Klein-Nulend and Mr. C.M. Semeins (ACTA-Vrije University). This study was partially supported by the 21st Century COE Program at Kyoto University, the Grants-in-Aids for Scientific Research from the Ministry of Education, Culture, Sports, Science and Technology, Japan. This study was also partially supported by the Japan Society for the Promotion of Science under the Research Fellowships for Young Scientists.

Reference

1. Cowin SC, Moss-Salentijn L, Moss M. (1991) Candidates for the mechanosensory system in bone. J Biomech Eng 113: 191-197
2. Burger EH, Klein-Nulend J. (1999) Mechanotransduction in bone--role of the lacuno-canalicular network. FASEB J 13 Suppl: S101-112

3. Klein-Nulend J, van der Plas A, Semeins CM et al. (1995) Sensitivity of osteocytes to biomechanical stress in vitro. FASEB J 9: 441-445
4. Miyauchi A, Notoya K, Mikuni-Takagaki Y, et al. (2000) Parathyroid hormone-activated volume-sensitive calcium influx pathways in mechanically loaded osteocytes. J Biol Chem 275: 3335-3342
5. Kamioka H, Sugawara Y, Murshid SA et al. (2006) Fluid shear stress induces less calcium response in a single primary osteocyte than in a single osteoblast: implication of different focal adhesion formation. J Bone Miner Res 21: 1012-1021
6. Weinbaum S, Cowin SC, Zeng Y. (1994) A model for the excitation of osteocytes by mechanical loading-induced bone fluid shear stresses. J Biomech 27: 339-360
7. Anderson EJ, Kaliyamoorthy S, Alexander JID, Knothe Tate M. (2005) Nano-microscale models of periosteocytic flow show differences in stresses imparted to cell body and processes. Ann Biomed Eng 33: 52-62
8. Nicolella DP, Moravits DE, Gale AM et al. (2006) Osteocyte lacunae tissue strain in cortical bone. J Biomech 39: 1735-1743
9. Kamioka H, Sugawara Y, Honjo T et al. (2006) Terminal differentiation of osteoblasts to osteocytes is accompanied by dramatic changes in the distribution of actin-binding proteins. J Bone Miner Res 19: 471-478
10. Westbroek I, de Rooij K, Nijweide PJ. (2002) Osteocyte-specific monoclonal antibody MAb OB7.3 is directed against Phex protein. J Bone Miner Res 17: 845-853
11. van der Plas A, Nijweide PJ. (1992) Isolation and purification of osteocytes. J Bone Miner Res 7: 389-396
12. You L, Weinbaum S, Cowin SC, Schaffler MB. (2004) Ultrastructure of the osteocyte process and its pericellular matrix. Anat Rec A Discov Mol Cell Evol Biol 278: 505-513
13. Vatsa A, Semeins CM, Smit T, Klein-Nulend J. (2008) Paxillin localisation in osteocytes-Is it determined by the direction of loading? Biochem Biophys Res Commun in press
14. Bonewald LF. (2006) Mechanosensation and Transduction in Osteocytes. Bonekey Osteovision 3: 7-15
15. Hayakawa K, Tatsumi H, Sokabe M. (2008) Actin stress fibers transmit and focus force to activate mechanosensitive channels. J Cell Sci 121: 496-503.
16. Tanaka-Kamioka K, Kamioka H, Ris H, Lim S. (1998) Osteocyte shape is dependent on actin filaments and osteocyte processes are unique actin-rich projections. J Bone Miner Res 13: 1555-1568
17. Sugawara Y, Ando R, Kamioka H et al.. (2008) The alteration of a mechanical property of bone cells during the process of changing from osteoblasts to osteocytes. Bone 43: 19-24

Development of Experimental Devices for Testing of the Biomechanical Systems

L. Houfek[1], Z. Florian[1], T. Březina[2], M. Houfek[1], T. Návrat[1], V. Fuis[1], P. Houška[2]

[1] Brno University of Technology, Faculty of Mechanical Engineering, Institute of Solid Mechanics, Mechatronics and Biomechanics, Brno, Czech Republic

[2] Brno University of Technology, Faculty of Mechanical Engineering, Institute of Automation and Computer Science, Brno, Czech Republic

Abstract — **The paper is focused on the description of the development of single-purpose devices for determining mechanical properties of the segments of human body. The research were focused on the development and design of a device for establishing the abrasion wear of the THR of the hip joint, and for testing spinal segments. On the basis of the gained knowledge, the attention has also been focused on the development and design of a multi-purpose experimental biomechanical device. Its basic idea was derived from Stewart platform, for the modification of which an animation 3D model was developed.**

Keywords — **Biomechanics, Parallel mechanism, Testing, Steward platform.**

I. Introduction

The basic characteristic of the clinical practice's present biomechanical problems is their complexity which requires mutual mixture of computational and experimental modelling.

Whereas in the computational part, in most cases, commercial software can be used with success, the experimental part requires at least the development, design and manufacturing of fixators and, frequently, of the whole experimental device, including the control system on which specific demands are often put.

At the Institute of Solid Mechanics, Mechatronics and Biomechanics in Brno, we have been dealing with biomechanical problems for more than fifteen years. The attention has mostly been focused on problems of clinical practice. At the present time, we co-operate with several Brno hospitals (St.Anna Teaching Hospital, Traumatic Hospital, Paediatric Hospital, Teaching Hospital in Brno-Bohunice), with some Prague hospitals and with some medical centers in other towns of the Czech Republic. Beside health service facilities, we co-operate also with manufactures of medical and health service devices. Though the development of biomechanics has been made possible primarily due to the development of computer technology and numerical methods related with the solution of tasks of the mechanics of continuum, experimental modelling cannot be said to have lost its significance. It's also to be pointed out that one of the basic characteristics, which distinguish computational modelling from a variety of other computations, is its relation to experiment.

The biomechanical problems that are being solved by experimental modelling at the Institute of Solid Mechanics, Mechatronics and Biomechanics, may be divided into the following groups:

- Determination of mechanical behaviour of biomechanical systems containing implants and fixators,
- Determination of mechanical properties of biologic materials, materials used in clinical practice for implants, and of auxiliary fixation materials.

II. Current state

In the following are briefly described experimental devices designed and made for solving the above mentioned problems, in particular the devices for examining spinal segments and abrasion wear of polyethylene cup of hip joint total endoprostheses.

A. Experimental device for examining the spinal elements

We got engaged in the problems of spinal biomechanics on the initiative of the Head of the Traumatological Clinic of the Brno Traumatological Hospital, Professor Peter Wendsche. We focus mainly on determining various fixators' mechanical interaction with biologic tissues.

In concrete terms, in the first case the matter was the comparison of uni- and bi-cortical fixators of the H-plate type. With view to the geometrical, material and loading complexity of the problem to be solved, and to the time available, only experimental modelling with a limited loading spectrum could be used. Only a comparative tear-out test could be made. This limitation motivated us to equip the testing machine ZWICK Z 020-TND with a torsion head and to design and construct a self contained testing machine enabling to carry out both torsion and bend tests. The above device was designed, without previous experience, by a working team including also workers of mechatronics, who designed the controls of the loading

Chwee Teck Lim, James C.H. Goh (Eds.): ICBME 2008, Proceedings 23, pp. 2005–2008, 2009
www.springerlink.com

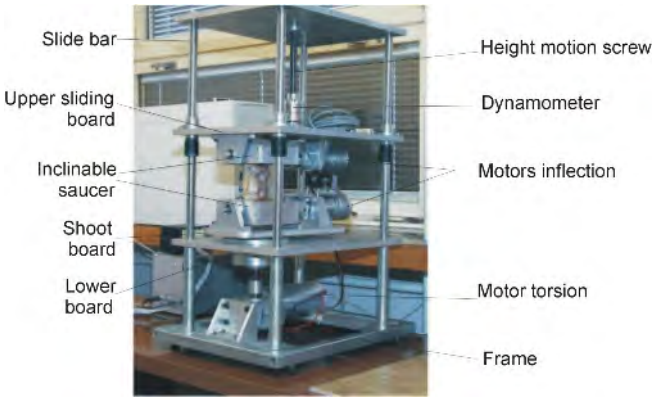


Fig. 1: Device for testing spinal elements

machine. The basic elements and a brief description of this device are shown in Fig. 1.

B. Control unit of experimental device for spine element testing

Test device is equipped with three DC drives with permanent magnets. In particular there are two drives 28DT2R, made by Portescap, and one drive M80x80/I, made by KAG. Each drive is equipped with three-channel optical IRC sensor E9-0100-2.5-1, made by Portescap.

For the test purposes the control using measuring cards CM-2251 by Acquitek was selected. The card has PCI interface, signal processor and memory enabling the control in real time. The card is equipped with 32 analog inputs, 32 digital I/O and 2 analog outputs with maximum sampling frequency of 1MHz. Drives connection to measuring card was realized through power circuit TLE6209R made by Infineon through VHDCI port.

Graphical programming environment NI Labview 7.1 was used for control algorithm development. To meet the on-line control and data processing demands the program uses digital buffers of CM-2251 card using application interface given by the producer. The way the API functions are used is obvious from part of the program shown in Fig. 2. This program performs initialization and initial settings of the card.

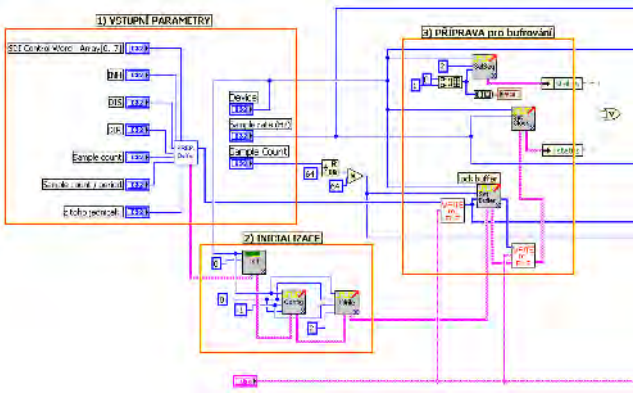


Fig.2: Initialization of control card in NI Labview

C. Experimental device for testing abrasion wear of polyethylene cup of the hip joint total endoprosthesis

The experience in designing a device for testing spinal elements, and the problems to be solved by computational modelling, that are connected with the geometric tolerance between the head and the polyethylene cup, led us to the idea of designing our own device for testing the abrasion wear of the polyethylene socket. This idea has been supported by both the co-operating medical specialists and the manufacturers, since in the past two decades the abrasion wear of polyethylene has been one of the most discussed problems of the durability of hip joint total endoprosthesis. Though the use of high-molecular polyethylene (UHMWPE) has considerably reduced the occurrence of aseptic necrosis, the abrasion wear of the individual components significantly affects their durability. The design of the device was carefully considered and several variants were considered (see Fig. 3 and 4). Required was the highest possible variability enabling not only to make standard tests, but also tests based on computational solution or, possibly, verifying this solution. With view to the device's variability, the variant shown in Fig. 3 was selected for realization.

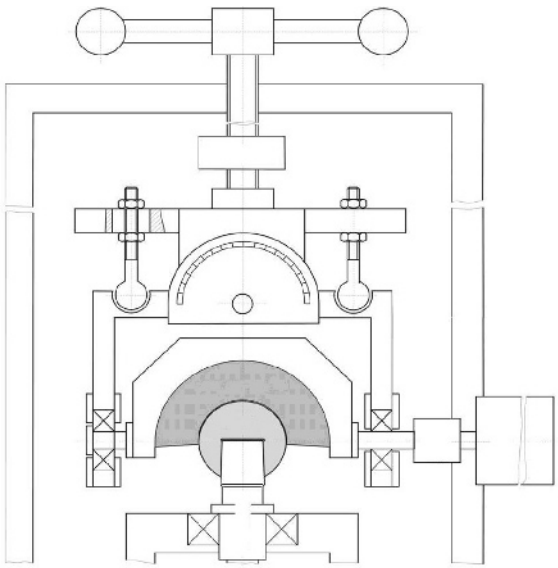


Fig. 3: Device for testing abrasion wear

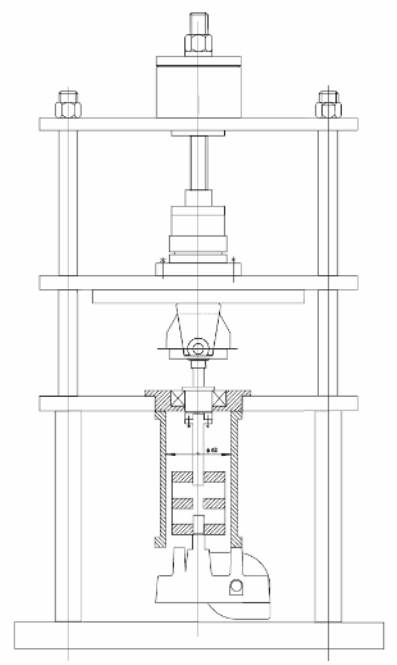


Fig. 4: Realized variant of the device for measuring abrasion wear

Concurrently with the realized variant, a variant with inclined axis of the stem's cone of the total endoprosthesis has been designed, which better captures the load in the applied total endoprosthesis. Schematic sketches do not contain the fixture used for tests made in physiological solution; this will be added in the final phase.

D. Summary of the present state

With view to the remodelling of control algorithms in existing devices and to the limited possibilities of the existing equipment which consists of a universal testing machine ZWICK Z 020-TND, we confine ourselves to making tests in which we can make use of the possibilities and capacity of the universal testing machine. In concrete terms, e.g. tear-out tests, torsion tests in combination with tension or compression. The above limitation, the growing interest and the demands put by clinical practice on biomechanical experiments, which exceed the possibilities of standard testing machines, make us modify the existing devices so as to remove their existing drawbacks.

By analyzing the biomechanical problems, the following requirements have been defined which derive from the need for experimental modelling of movements and loads occurring in biologic environment. These requirements will be taken into account in the modification of the already designed testing devices.

- By analysis of the force load in the hip joint and in the spinal segments, approximate conformity of the load forces was established, whose value is about 2000N.
- The range of possible movements was increased to cover all six degrees of freedom.
- The device must be able to load up the test specimen with the assigned load force and to carry out any loading cycle. The specific features thus defined can be taken into account in case that the merits of the mechanism of parallel kinematics will be made use of in the design.

III. Parallel kinematics mechanism design

A. The design of a geometric model

The demands put on this device derive from the need for experimental modelling of arbitrary movement and load. Its use is very universal in both biomechanics of the backbone and biomechanics of the joints. The device's geometry is motivated by the tests we intend to make on the spinal elements, for which it is suitable to conceive the device as two toroidal plates – interconnected by active elements - into which spinal segments will be fixed.

The concept of parallel kinematics, which is called Stewart platform corresponds to the device of such design. In case that the lower plate is firmly connected with the base, the upper plate is able to move with six degrees of freedom. At the present time, the Stewart platform is widely used and its popularity is due mainly to its following facts, in comparison with serial mechanisms:

- higher stiffness
- better dynamic properties of the mechanism
- higher accuracy of the mechanism
- precise and easy positioning
- wide range of movements

These possibilities can be advantageous in manufacturing experimental devices for solving various biomechanical problems. In particular terms, devices have been designed for testing spinal samples (Fig. 6) and abrasion wear of polyethylene acetabula (Fig. 7). Since unit-built architecture can be used, whole spinal segments can be tested, which is very favourable in case of fixed vertebral bodies, since changes of mechanical properties take place also in the surrounding spinal elements. The assembly scheme is shown in Fig. 8.

The parametric geometric model was designed using the CAD INVENTOR system.

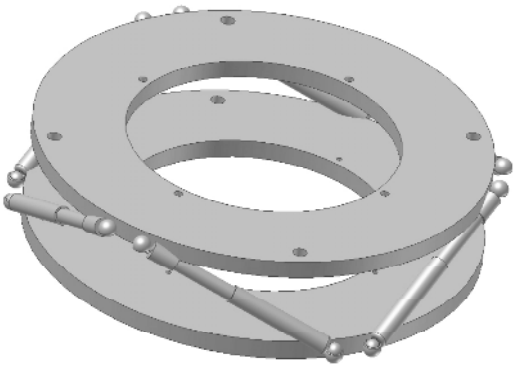


Fig. 5: Scheme of device for testing

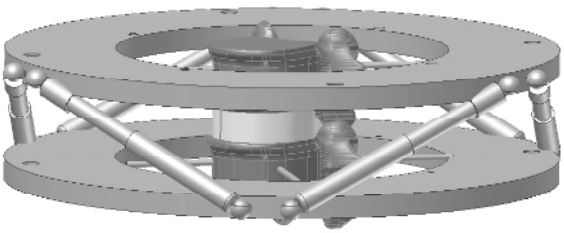


Fig. 6: Scheme of device for testing spinal elements

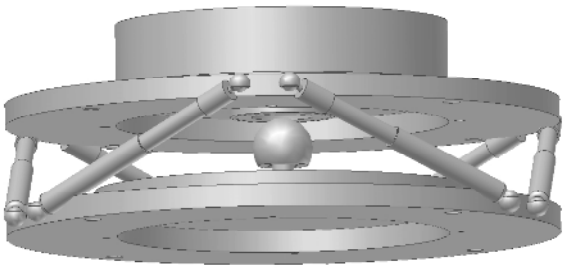


Fig. 7: Scheme of device for testing polyethylene socket

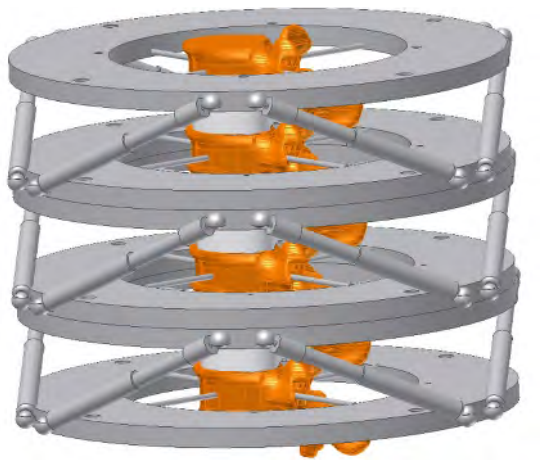


Fig. 8: Scheme of device for testing spinal segments

A device of similar concept could be used for solving problems such as e.g. correction of the scoliotic curve of vertebral column in various cases of scoliosis. The demands put on this device would be substantially more extensive. One of the important problems that need to be solved is that of the active elements.

IV. Conclusions

With regard to the development of testing devices for biomechanical systems, the further progress is aimed to the following objectives:

The primary objective is to complete two testing devices (for testing spinal fixators and abrasion wear). The mechanical part has been completed; the control subsystem is being completed. These works should culminate in the first trimester. Both devices will then be put into operation and the corresponding experiments, supported by computational modelling, will be started.

As regards devices based on Stewart platform, we will proceed as follows: On the basis of calculated kinematic and dynamic values, actuators and sensors will be designed. Then the structural design will be specified with view to the selected actuators and sensors. The device thus designed will then be manufactured.

Acknowledgment

Published results were acquired with the support of the research plan of Ministry of Education, Youth and Sports, nr. MSM 0021630518 – Simulation modeling of mechatronics systems and the project of CONTACT, nr. 1P05ME789 - Simulation of mechanical function of selected segments of human body.

References

1. Dasgupta B., Mruthyunjaya T.S. – The Stewart platform manipulator: a review, Mechanism and Machine Theory 35 (2000) 15-40
2. Veselý R., Florian Z., Wendsche P., Tošovský J. – Biomechanical Evalution of the MACSTL Internal Fixator for Thoracis Spinal Stabilisation, Acta Veterinaria, Volume 77, Number 1 (March 2008), ISSN 0001-7213

Author: Lubomir Houfek
Institute: Brno University of Technology
Street: Technicka 2896/2
City: Brno
Country: Czech Republic
Email: houfek@fme.vutbr.cz

Stability of Treadmill Walking Related with the Movement of Center of Mass

S.H. Kim[1], J.H. Park[2], K. Son[2]

[1] Graduate School of Mechanical Design Engineering, Pusan National University, Busan, Korea
[2] School of Mechanical Engineering, Pusan National University, Busan, Korea

Abstract — **The human gait is highly coordinative as to achieve combined movements of extremity joints at a desired speed. The purpose of study is to relate the variability of hip joint motion with the movement of the center of mass (COM) of the whole body in the treadmill walking. Each walking speed was converted to Froude number for normalizing different subject statures. Flexion-extension angles of the hip and the anterioposterior movement of COM were calculated. The correlation was relatively low (R^2=0.113) between the movement of COM and the normalized walking speed. These results revealed that the movement of COM must be considered as one of important parameters for the analysis of walking stability on the treadmill**

Keywords — **Center of Mass, Walking Stability, Treadmill Walking.**

I. Introduction

Walking periodicity is more regular on a treadmill than on the ground since the treadmill provides a relatively uniform walking speed. However, frequent fallings on the treadmill occur due to loss of control of the neuromusculoskeletal system. People fail to adapt themselves in the treadmill walking because of the limited space of the treadmill walking even at their preferred speeds. Thus, treadmill walking is differ from overground walking [1].

As walking stability is considered, the center of mass (COM) is an essential parameter because the balance of the body is achieved by controlling of COM. The hip joint is also directly related with walking stability in that it plays an important role to support and move the whole body during normal walking. Therefore, the movement of COM and variability of the hip joint could explain the information on the stability of walking. In this study, temporal change of COM and the hip joint angle were regarded as two major parameters.

The purpose of study is to prove the variability of hip joint motion with the movement of the COM of the whole body in the treadmill walking. The hypothesis was that the COM moves in the anterioposterior direction when one cannot maintain a uniform walking speed: The larger movement of COM results from the larger angular variability of the hip joint.

II. Methods

A. Experiment

Fifteen young healthy subjects (13 males and 2 females: 24.9±4.2 years, 175.6±6.4 cm, 70.5±12.1 kg, 1.0±0.1 m/s) with no history of joint diseases were volunteered for gait analysis [2]. Joint movements of each subject were recorded for 60 seconds on a treadmill (KEYTEC® AC9, Taiwan) using a three-dimensional motion capture system with eight video cameras (DCR-VX2100, Sony, Japan). The spatial displacement error of the motion capture system was less than 2 mm. Prior to the measurement of joint motions, all subjects were given enough time to perform walking exercise on the treadmill with the same walking pattern as they have in daily life. Thirty two reflective markers were attached on the selected bony landmarks of the subjects to calculate the flexion-extension angles of the upper and the lower extremities. All the attachment tasks were performed by one investigator to minimize the possible positioning error (Fig. 1).



Fig. 1 Hemispherical reflective markers attached on body landmarks

B. Data processing and analysis

Motion data were collected at 60 frames per second and then analyzed through KWON3D motion analysis software (Visol Corp., Korea) [3]. The primary markers (attached markers) and the secondary markers (virtual markers) were used to define the flexion-extension angles of the hip. For example, the knee joint center, where one of the secondary

Chwee Teck Lim, James C.H. Goh (Eds.): ICBME 2008, Proceedings 23, pp. 2009–2011, 2009
www.springerlink.com

markers was assumed to locate, could be determined by averaging the coordinates of two primary markers attached on the lateral and medial epicondyles. The center of the hip was calculated by adopting the method of Tylkowski and Andriacchi [3] from the left, the right, the middle ASIS (anterior superior iliac spine) and extra greater trochanter markers. The flexion-extension angle was calculated from the inner product of the two vectors representing the longitudinal axes of the adjacent body segments at that joint. Each walking speed was converted to Froude number (FN), V^2/gl (V: speed, g: gravitational acceleration, l: length from the ground to the greater trochanter), as a dimensionless speed for normalizing different lengths of the lower legs.

The coordinates of COM were calculated by Kwon3D software and the anteroposterior movement of COM (MCM) was obtained by the summation of all y-directional trajectory projected to the walking plane (Fig. 2). In order to evaluate variability of the hip joint, temporal and spatial parameters were introduced. Standard deviation for the peak-to-peak intervals (VPI) of flexion-extension angles during the gait was a temporal parameter and angular standard deviation (VAD) was a spatial parameter. When subjects walked on the treadmill, they were assumed to maintain their walking stability by these two parameters.

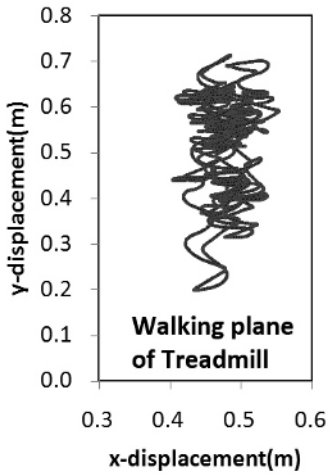


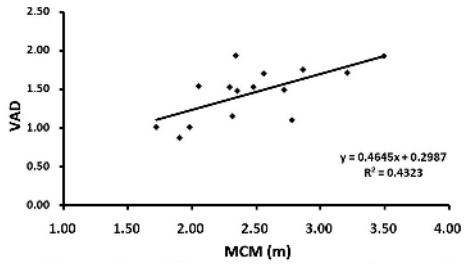
Fig. 2 Projected trajectories of COM on the treadmill for one minute

III. Result

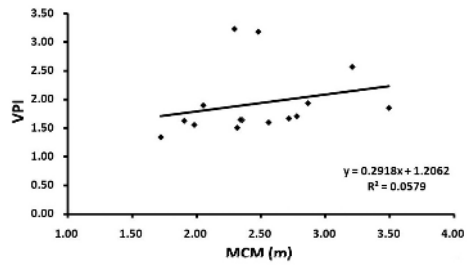
Experimental data were obtained from the gait on the treadmill as listed in Table 1. After obtained the data, a paired t-test was performed to test statistical significance between MCM and VAD by using SPSS. And correlation coefficient was calculated by using the least square method on Microsoft Excel. The result showed that the hypothesis

Table 1 Data obtained from the treadmill walking

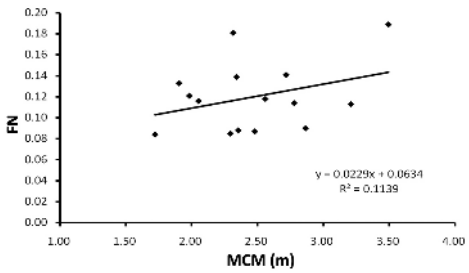
Subject ID	MCM(m)	FN	VPI (1/60 sec.)	VAD(deg.)
S1	2.72	0.14	1.67	1.49
S2	2.87	0.09	1.93	1.75
S3	3.21	0.11	2.57	1.71
S4	1.98	0.12	1.55	1.01
S5	1.91	0.13	1.62	0.87
S6	2.35	0.08	1.64	1.48
S7	2.78	0.11	1.70	1.10
S8	2.56	0.11	1.60	1.70
S9	1.72	0.08	1.34	1.01
S10	2.34	0.13	1.64	1.93
S11	2.05	0.11	1.89	1.54
S12	2.48	0.08	3.18	1.53
S13	2.32	0.18	1.50	1.15
S14	3.50	0.18	1.85	1.93
S15	2.30	0.08	3.23	1.52
Mean	2.47	0.12	1.93	1.45
STD	0.48	0.03	0.58	0.34



(a) MCM vs. VAD



(b) MCM vs. VPI



(c) MCM vs. FN

Fig. 3 Correlation results among the parameters

was verified by a finding that the linear correlation coefficient, R^2, was 0.432 ($p<0.05$) between MCM and VAD (Fig. 3a). The correlation was very low ($R^2=0.057$) between MCM and VPI (Fig. 3b). It means that spatial variable (VAD) contributes to compensate for the loss of COM more than temporal variable (VPI) in such uniform speed environment as on the treadmill. Hausdorff et al. [4] reported that stride-to-stride variability can predict falls for the elderly population. This fact was well known or inferred easily. As revealed in our result, MCM cause to increase stride variability during the gait. The correlation coefficient between MCM and FN was also low ($R^2=0.113$) (Fig. 3c). Regarding to this result, FN is not likely to relate with MCM at a comfortable walking speed.

IV. Conclusion

An elementary parameter, COM, was mainly investigated to test its importance in a treadmill walking situation. Although the treadmill provides a relatively uniform walking speed, people often lose control ability due to neuromusculoskeletal system errors. From the results obtained in this study, the changes of COM on the treadmill reveal this physical phenomenon in the statistical sense. For this reason, MCM must be considered as an important parameter for the analysis of walking stability, especially on the treadmill.

References

1. Alton F, Baldey L, Caplan S, Morrissey MC (1998) A kinematic comparison of overground and treadmill walking. Clin. Biomech. 13:434-440
2. Park JH, Son K, Kim KH, Seo KW (2008) Quantitatively analysis of nonlinear joint motions for young males during walking, JMST. 22:420-428
3. Kwon3D, Visol Co., http://visol.co.kr
4. Hausdorff JM, Rios DA, Edelberg HK (2001) Gait variability and fall risk in community-living older adults: a 1-year prospective study. Arch Phys Med Rehabil. 82:1050-1056

Author: SH Kim
Institute: Graduate School of Mechanical Design Engineering
Street: Pusan National University
City: Busan
Country: Republic of Korea
Email: calbus@daum.net

Stress Analyses of the Hip Joint Endoprosthesis Ceramic Head with Different Shapes of the Cone Opening

V. Fuis[1] and J. Varga[2]

[1] Centre of Mechatronics – Institute of Thermomechanics Academy of Sciences of the Czech Republic and Institute of Solid Mechanics, Mechatronics and Biomechanics, Faculty of Mechanical Engineering, Brno University of Technology, Brno, Czech Republic
[2] Institute of Solid Mechanics, Mechatronics and Biomechanics, Faculty of Mechanical Engineering, Brno University of Technology, Brno, Czech Republic

Abstract — **During the analysis of the fracture surfaces of the destructed hip joint endoprosthesis ceramics heads it was detected that the shape (size and the position) of the cone end in the bottom of the cone opening were very different.**

The paper presents the influence of five typical shapes of the cone end on the stress in the ceramic head. The computational modelling is realized for two outer diameters of the ceramic head – 28 mm and 32 mm and three depths of it's cone. The system FEM – ANSYS was used for computational modelling of the stress and deformation of analyzed system (testing stem and ceramic head). Loading of the analyzed system is according to norm ISO 7206-5. There are assumed shape deviations of the cone surfaces – interaction of the ovality and different degree of taper of the stem and the head cone.

Keywords — **Hip joint endoprosthesis, ceramics head, shape deviations, cone opening.**

I. Introduction

The destructions of the ceramic head of the total hip joint endoprosthesis were realized three years ago Fig. 1. The aim of this destruction was founding the material parameters of the bio-ceramic material based on the Weibull weakest link theory.

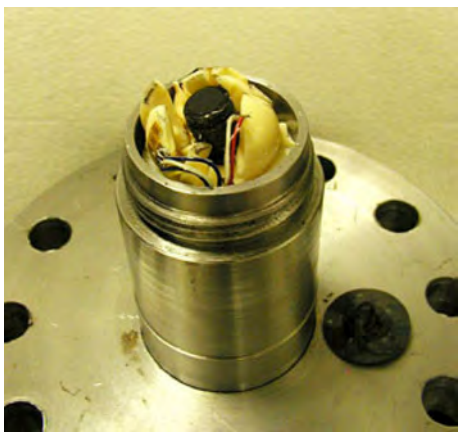


Fig. 1 Destructed hip joint ceramic head

For carrying out the destruction of a set of ceramic heads a special testing jig has been made in which the heads are subjected to compressive load that acts only on the surface of the head's opening. In the course of the test, circumferential strains are measured on the head's external surface by two gauges. The compression load acting on the head was developed by the testing device ZWICK Z 020-TND (Fig. 2) whose head loaded the jig's piston which, in turn, acted on rubber NBR 90 inside the jig, which, subsequently, acted on the ceramic head.

The analysis of the fracture of the destructed heads have found the fact that the shape of the region of the bottom end

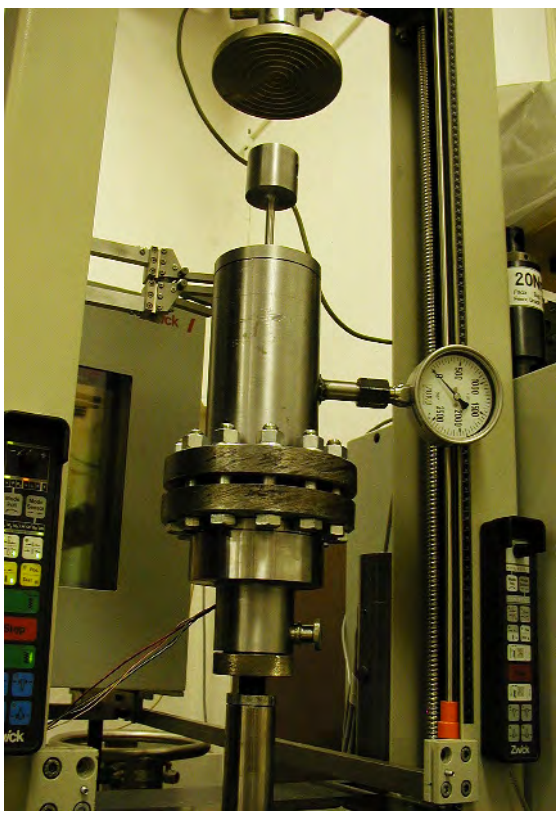


Fig. 2 Testing jig used to the heads destruction

Chwee Teck Lim, James C.H. Goh (Eds.): ICBME 2008, Proceedings 23, pp. 2012–2015, 2009
www.springerlink.com

of the head's cone (shape transition from the cone to the bottom of the cone opening – Fig. 3) was very different for each destructed head. In addition this region did not correspond to the technical drawing of the factory where the heads were made. This shape transition is a stress raiser (notch) and the ceramic material is brittle material. The brittle material is very sensitive to the tensile stress so the computational modelling of the stress in the head with the mentioned notchs will be presented in this contribution. The FEM system ANSYS was used for computational modelling.

II. Computational Modelling

A. Input parameters

Ideally, the problem of stress calculation would be solved for the physiological conditions in the human body. However, the level of our knowledge and our technical possibilities do not allow it. Therefore the problem is being solved in accordance with norm ISO 7206-5 [1] under force conditions that are different from the physiological ones. The structure modelled according to ISO 7206-5, is shown in Fig. 3. The ceramic head is pressed onto the testing stem cone by the force F which acts on the interface.

There are analysed two variants with different value of the outer head diameter - 32 mm and 28 mm. The depth of the head opening is made with three values – small, medium and large – all these variants were assumed. Finally, five typical shape transitions variants were chosen from the analysis of the destructed heads. These variants are shown in Fig. 4.

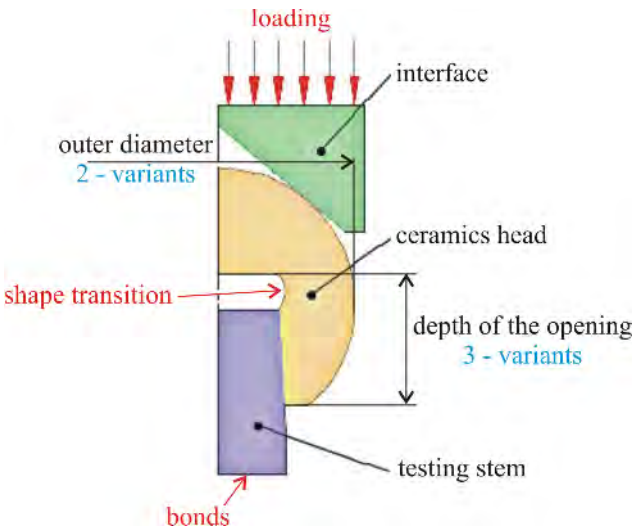


Fig. 3 Modelled system according ISO 7206-5



Fig. 4 Modelled variants of the shape transition

The last group of the geometric input parameters consists of the shape deviations of the contact cone areas of the stem and the head. There are assumed the interaction of the dif-

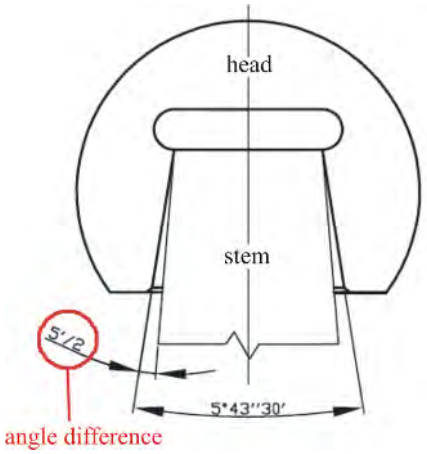


Fig. 5 Shape deviation of the cone areas – different vertex angle

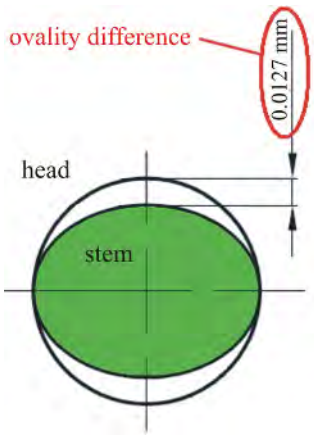


Fig. 6 Shape deviation of the cone areas – ovality of the stem area

ferent vertex angle of the head and the stem cone (the head vertex angle is greater that the stem angle - modelled difference is 2.5' – Fig. 5) and ovality of the stem cone area – modelled deviation is 12.7 μm – Fig. 6.

The steel testing stem and Al_2O_3 head are assumed to be elastic, with the following material parameters (Young's modulus E and Poisson's ratio μ) for the stem: E_s = 210 GPa, μ_s = 0.3; and for the head: E_h = 390 GPa, μ_h = 0.23. The contact between the head and the stem is modelled by the elastic Coulomb friction with f = 0.01.

B. Results of the computational modelling

The most important stress in the head is the maximal tensile stress due to the danger of the brittle limit state of the head. Therefore the first principal stress in the head will be analysed and compared with all assumed geometrical variants. The influence of the shape of the notch (VAR. 1 – VAR. 5) on the tensile stress is shown in Fig. 7 – system without the shape deviations (ideal cone), head outer diameter is 32 mm and the depth of the opening is 23 mm. The highest tensile stress is found at VAR. 1, VAR. 2 and VAR. 3. These variants have the small contact area (see Fig. 4) and therefore the contact pressure and tensile stress are increased [2].

The influence of the head outer diameter and the depth of the opening is shown in Figs. 8 and 9. These figures show the maximum tensile stress in the head without the shape deviations.

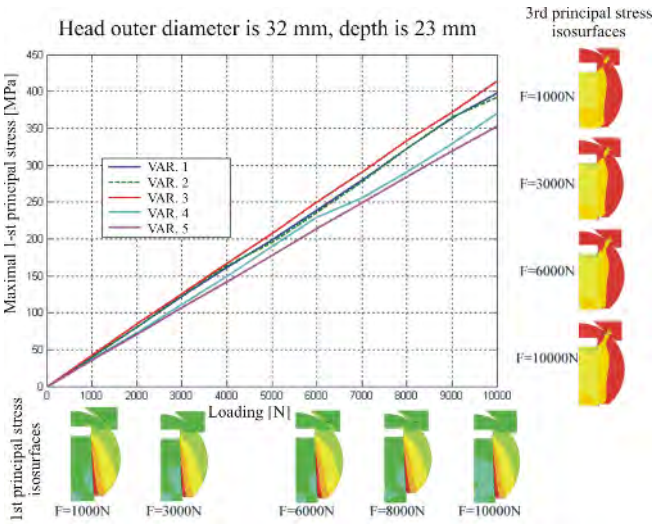


Fig. 7 Maximal tensile stress in the head without shape deviations

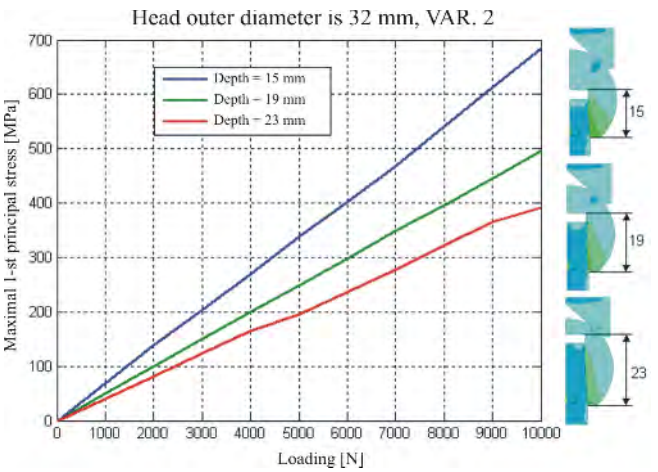


Fig. 8 Maximal tensile stress in the head without shape deviations, head outer diameter is 32 mm, depth is different

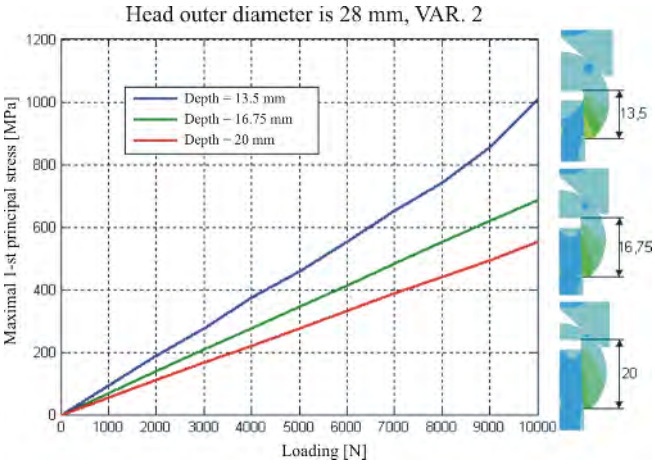


Fig. 9 Maximal tensile stress in the head without shape deviations, head outer diameter is 28 mm, depth is different

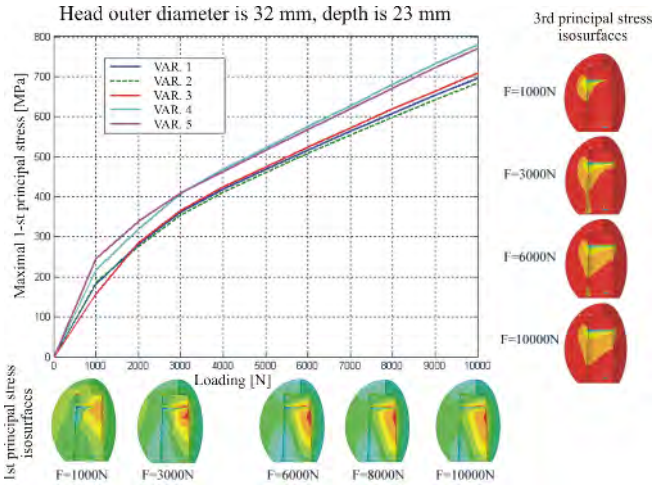


Fig. 10 Maximal tensile stress in the head with shape deviations

Heads with the diameter 32 mm have smaller value of the extreme tensile stress due to the higher circumferential stiffness (more material) than head with diameter 28 mm. In addition the increasing of the depth of the opening caused the decreasing the extreme tensile stresses in the head due to the higher contact area of the cone.

The last two figures (Figs. 10 and 11) show the influence of the interaction of the shape contact cone deviations (Fig. 5 and Fig. 6). Assumed shape deviations significantly increase the extreme tensile stress in the head (about 75 %) and the stress curves are not linear for small loading (from 0 to 4 kN). In this region the contact area is small and the contact pressure is high. The gradual deformation of the contact area (elimination of the shape deviation by the system deformation – increasing the contact area) causes the

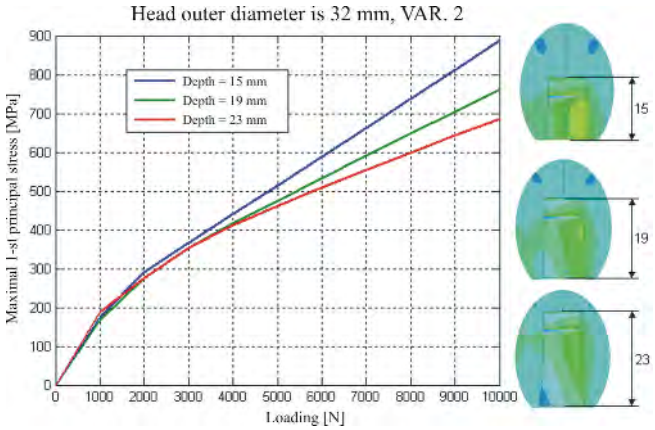


Fig. 11 Maximal tensile stress in the head with shape deviations, head outer diameter is 32 mm, depth is different

transition to the almost linear influence between the stress and the loading in Figs. 10 and 11.

III. Conclusions

The shape deviation of the contact cone areas, the shape of the transition in the head bottom opening, the outer head diameter and the depth of the opening influence the value of the tensile stress in the head. All mentioned geometric parameters are necessary taken in the computational modelling of the stress and the reliability of the head.

Acknowledgment

The research has been supported by the following projects AV0Z20760514 and MSM0021630518.

References

1. ISO 7206-5 (1992) Implants for surgery - Partial and total hip joint prostheses. Determination of resistance to static load of head and neck region of stemmed femoral components
2. Varga J (2008) Stress analysis of the total hip joint endoprosthesis head under ISO 7206-5 loading. Diploma work. Brno University of Technology, (in Czech)

Author: Vladimir Fuis
Institute: Centre of Mechatronics – IT CAS and BUT FME
Street: Technicka 2
City: Brno
Country: Czech Republic
Email: fuis@fme.vutbr.cz

Measurement of Lumbar Lordosis using Fluoroscopic Images and Reflective Markers

S.H. Hwang[1], Y.E. Kim[2] and Y.H. Kim[1,3]

[1] Department of Biomedical Engineering, Yonsei University, Wonju-City, South Korea
[2] Department of Mechanical Engineering, Dankook University, Youngin-City, South Korea
[3] Institute of Medical Engineering in Yonsei University and Department of Biomedical Engineering, Yonsei University, Wonju-City, South Korea

Abstract — **Lumbar lordosis is defined as the anterior convexity of the lumbar spine in the sagittal plane. Its degree is variable between individuals, affected many other factors. Clinical methods to define lumbar lordosis are Cobb's angle measurement and the angle between extension line of boundary of the first and fifth vertebral body. In this study, the lordotic angle calculated by reflective markers when the three dimensional motion capture system was used compared to the angle calculated from fluoroscopy. The coordinates of vertebral body center from fluoroscopic images were digitized. The vertebral body center coordinates from fluoroscopic image and the coordinates from markers were used to calculate lumbar lordotic angle with three different method - ratio method, three point method and curve-fit method. The lordotic angles from fluoroscopic image(θ_f) were larger than the angles from markers(θ_m) in all three methods. The ratio method using fluoroscopic image and the curve-fit method using markers showed the largest coefficient of variance(θ_f - θ_m)and the coefficient of variances in all three methods using fluoroscopic image were smaller than using markers. However, the analysis according to Bland-Altiman plot showed a good agreement between both methods(fluoroscopy and marker).**

Keywords — **Gait initiation, Hemiplegic patient, Net center of pressure**

I. Introduction

Lumbar lordosis is defined as the anterior convexity of the lumbar spine in the sagittal plane[1]. Its degree is variable between individuals, affected many other factors.

The fifth lumbar vertebra (L5) is wedge-shaped, the anterior aspect of the vertebral body being approximately 3 mm thicker than the posterior aspect[2]. The vertebrae above L5 are less wedge-shaped, but due to the shape of L5 and the first sacral(Sl) vertebrae, each vertebra above this level lies slightly posterior to the vertebra above it. The intervertebral discs in the lumbar area are also wedge-shaped, especially between L4 and L5, and between L5 and Sl, the intervertebral disc at the L5-Sl interspace being 6-7 mm thicker anteriorly than posteriorly[3]. These factors all contribute to producing the normal lumbar lordosis.

Various methods for measuring the lumbar lordosis have been used in an attempt to quantify the curve. Goniometry, radiography, skin markers over the spinous processes, and use of flexible rulers have all been used [3-7]. Clinical methods to define lumbar lordosis are Cobb's angle measurement and the angle between extension line of boundary of the first and fifth vertebral body. In this study, the lordotic angle calculated by reflective markers when the three dimensional motion capture system was used compared to the angle calculated from fluoroscopy.

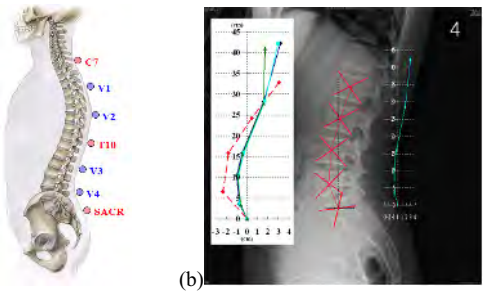
II. Methods

A. Subjects

Thirteen healthy males volunteered for this study(age: 23.5±0.76year, body weight: 66.5±6.37kg, height: 172.1±6.03). Each subject was taken pictures of x-ray with quiet standing position, and they were also taken three dimensional motion captures with the same position. For the motion capture, the seven reflective markers(T10~SACR) were mounted on the back. Fig. 2(a).



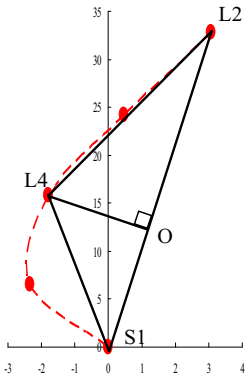
Fig. 1 Lumbar lordosis from 1st lumbar spine to 5th lumbar spine



(a) (b)

Fig. 2 Lumbar lordosis from 1st lumbar spine to 5th lumbar spine

Chwee Teck Lim, James C.H. Goh (Eds.): ICBME 2008, Proceedings 23, pp. 2016–2018, 2009
www.springerlink.com

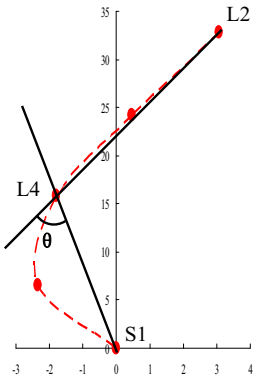


$$curve\ depth = \overline{L4O}$$

$$curve\ length = \overline{S1L2}$$

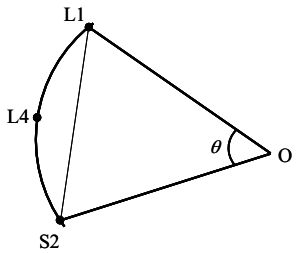
$$Ratio(\%) = \frac{curve\ depth}{curve\ length} \times 100$$

(a) Ratio method



$$\theta = \pi - a\cos\left(\frac{\overline{L2L4}^2 + \overline{L4S1}^2 + \overline{S1L2}^2}{2 \cdot \overline{L2L4} \cdot \overline{L4S1}}\right)$$

(b) Three point method



$$\theta = a\cos\left(\frac{\overline{OL1}^2 + \overline{OS2}^2 - \overline{L1S2}^2}{2 \cdot \overline{OL1} \cdot \overline{OS2}}\right)$$

(c) Curve fitting method

Fig. 3 Three methods to calculate the lumbar lordosis

B. Lumbar lordosis calculation methods

The data from two different measurements were used for calculation of the lumbar lordosis curvatures. The lumbar lordosis calculation was performed using the three different methods. They were (1) ratio method, (2) three point method, (3) curve fitting method[Fig 3. (a)~(c)].

C. Experiments

The three dimensional motion analysis system(VICON612, UK) and x-ray device E7252X(Toshiba, Japan) were used in this study. The subjects were required to stand quietly and comfortably in radiation room and motion laboratory. x-ray images were digitized to calculate the coordinates.

D. Analysis of data

The coordinates from digitized x-ray images and reflective markers were used for calculation of lumbar lordosis and curvatures.

III. Results

Table. 1 shows the angles and coefficient of variations of lumbar lordosis from x-ray image and markers with three methods. The bland-altman plotted by using these data(Fig. 1). The lordotic angles from fluoroscopic image(θ_f) were larger than the angles from markers(θ_m) in all three methods. The ratio method using fluoroscopic image and the curve-fit method using markers showed the largest coefficient of variance(θ_f-θ_m) and the coefficient of variances in all three methods using fluoroscopic image were smaller than using markers. However, the analysis according to Bland-Altiman plot(Fig. 4) showed a good agreement between both methods(fluoroscopy and marker).

Table 1 Mean, standard deviation (S.D.) and coefficient of variation (C.V.) of lumbar lordosis in a single standing subject, measured by the three methods

		Fluoroscopy(θ_f)			Marker(θ_m)		
Method	Unit	Mean	S.D.	C.V.(%)	Mean	S.D.	C.V.(%)
Ratio	%	12.22	1.72	14.10	5.75	1.47	25.51
Three point	Degree	27.45	3.71	13.52	14.43	3.63	25.17
Curve fit	Degree	54.91	7.42	13.52	28.48	7.79	27.35

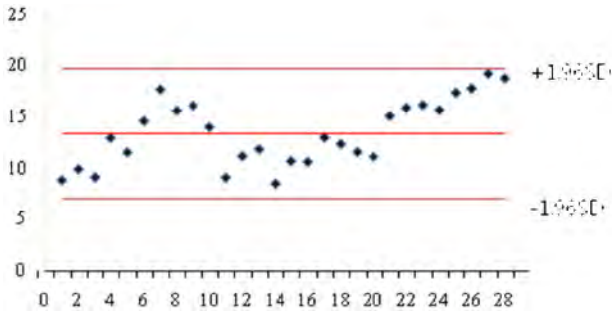


Fig. 4 Bland-Altman plot

IV. Discussions

In this study, in order to know whether the lumbar lordotic curves calculated by three dimensional motion capture system were reliable or not, these lumbar lordotic angles were compared with the angles calculated by using the x-ray images. According to the bland-altman results, motion capture method was reliable. However, the critical limitations of this study were that the x-ray device and motion capture device were not synchronized. And the lumbar curves in different trunk angles might be analyzed with the same methods but only standing position was considered in this study. The number of data from x-ray and markers were not matched. Intraclass correlation of the lordotic angles from the digitized x-ray images should be calculated.

Acknowledgment

This work was supported by the Korea Science and Engineering Foundation(KOSEF) grant funded by the Korea government(MOST) (No. R01-2006-000-10257-0).

References

1. Bogduk N, Twomey L T. (1991) Clinical Anatomy of the Lumbar Spine (2nd edn.). New York: Churchill Livingstone, 45-47.
2. Gilad I, Nissan M. (1985) Sagittal evaluation of elemental geometrical dimensions of human vertebrae. J AMY 143: 1 IS- 120.
3. Whittle M.W., Levin D. (1997) Measurement of lumbar lordosis as a component of clinical gait analysis. Gait&Posture. 5:101-107
4. Roozmon P, Gracovetsky SA,. (1993) Gouw GJ, Newman N. Examining motion in the cervical spine I: imaging systems and measurement techniques. J Biomed Eng. 15:5-12
5. Lee Y.H., Chiou W.K., Chen W.J., Lee M.Y., Lin Y.H. (1995) Predictive model of intersegmental mobility of lumbar spine in the sagittal plane from skin markers. Clin. Biomech. 10(8): 413-420
6. Brendan McCane, Tamara I.K., Abbott J.H. (2004) Calculating the 2D motion of lumbar vertebrae using splines. J. Biomech. 39:2703-2708
7. Chunhui Wu, Mehbod A.A., Serkan Erkan, Transfeldt E.E. (2008) A method to calculate relative spinal motion without digitization. The Spine Journal. In Press.

Author: Y.H. Kim
Institute: Institute of Medical Engineering in Yonsei University and Department of Biomedical Engineering in Yonsei University
Street: 234 Maeji, Heungeop
City: Wonju
Country: South Korea
Email: younghokim@yonsei.ac.kr

Patient-Specific Simulation of the Proximal Femur's Mechanical Response Validated by Experimental Observations

Zohar Yosibash and Nir Trabelsi

Dept. of Mechanical Engineering, Ben-Gurion University of the Negev, Beer-Sheva, 84105, Israel

Abstract — **The use of subject-specific FE models in clinical practice requires a high level of automation, validation and accurate evaluation of analysis prediction capabilities. This study presents a novel high-order finite element method (p-FE) for generating FE models based on CT data. The geometry is represented by smooth surfaces accurately and an internal smooth surface is used to separate the cortical and trabecular regions upon which a p-FE auto-mesh is constructed within each region (cortical or trabecular). QCT Hounsfield Unit (HU) values are recalculated using a moving average method regardless of the FE mesh and isotropic inhomogeneous linear material properties are assigned to the FE models by a spatial function computed from the QCT data. Anisotropic material properties are also considered in the FE model and their influence on the mechanical response is examined. To validate the FE results we performed QCT scans on three fresh frozen proximal femurs (30 years old male, 20 and 54 years old female) followed by mechanical in-vitro experiments at different inclination angles, measuring head deflection and strains at several points with a total of 77 experimental values recorded. The FE results, strains and displacements were compared to the in-vitro experiments. The linear regression of the experiment results compared to the FE predictions demonstrates the high accuracy and reliability of our methods (slope of 0.955 and R^2=0.957). These results are significantly better than any previous published results known to the authors.**

Keywords — **Proximal femur, p-FEM, Computed tomography (CT), Bone biomechanics.**

I. Introduction

Accurate methods for predicting and monitoring in-vivo bone strength are of major importance in clinical applications. Subject-specific finite element modeling is becoming a commonly used tool for the numerical analysis of the biomechanical response of human bones. The use of subject-specific FE models in clinical practice requires a high level of automation and an accurate evaluation of the numerical errors and analysis prediction capabilities. Geometry and material parameters are two key components when addressing subject specific FE models of bones and both can be estimated from QCT data. The modeling method applies extensive processing of the CT data to extract the required information. Because CT based simulation method is to be used in vivo, the surrounding of the bone while the CT is preformed may influence the model generation and its influence on the results must be carefully examined. Keyak & Falkinstein [1] examined whether FE models generated from CT scans in situ and in vitro yield comparable predictions of proximal femoral fracture load. Their conclusion demonstrate that using CT scan data obtained in situ instead of in vitro to generate FE models can lead to substantially different predicted fracture loads and must be considered when developing subject-specific FE models based on CT scans. The influence of material assignment strategy on the finite element models was investigated in [2, 3, 4, 5]. Different methods for assigning material properties to FE models may produce various distributions of material properties. In most of the previous FE studies conventional h-version FE methods (h-FEMs) were applied [6, 7], inhomogeneous distribution of material properties was attained by assigning constant distinct values to distinct elements, thus the material properties became mesh dependent [4]. In the presented study (details given in [8, 9, 10]) a p-version FE (p-FE) method is suggested. Accurate surface representation of the bone is achieved by a 3-D smoothing algorithm. Isotropic inhomogeneous material model was adopted for which the Young modulus is represented by a smooth functions, independent of the mesh, and different $E(\rho)$ relations are assigned for the cortical and trabecular regions. Transversely isotropic material properties were also considered in the FE model in the shaft region and their influence was investigated. The presented method resulted in an excellent correlation (for both displacements and strains) for the p-FE results and in-vitro experimental observations. This study demonstrates that reliable and validated high-order patient-specific FE simulations of human femurs based on QCT data are achievable for clinical computer aided decision making.

II. Materials and methods

A. In vitro experiment

Three fresh frozen femurs (donors are 30 years old male, 20 and 54 years old female) were used in our study. In-vitro experiments on the fresh-frozen proximal femur were performed to assess the validity of FE simulations. All bones

Chwee Teck Lim, James C.H. Goh (Eds.): ICBME 2008, Proceedings 23, pp. 2019–2022, 2009
www.springerlink.com

were deep-frozen shortly after harvesting and checked to be free of skeletal diseases. After defrosting, soft tissue was removed and the bone was degreased with ethanol. The proximal femur was cut and fixed into a cylindrical sleeve by six bolts and a PMMA substrate, and strain gauges (SGs) were bonded on its surface. Thereafter QCT scans were performed on a Phillips Brilliance 16 CT. During the CT scan calibration phantoms were placed close to the bone, used thereafter to estimate the inhomogeneous mineral density in the bone. Mechanical experiments started following the QCT scans. The experimental system detailed in [8, 9] includes a mounting jig, loading and measurement equipment and data acquisition equipment. The bone was loaded by a load controlled machine (Instron5500R). Two linear variable differential transformer (LVDT) measured the femur head vertical and horizontal displacements and were positioned on stand arms with their core placed on femur's head – see e.g. Fig. 1.

Several uni-axial strain-gauges (SGs) with 1.6mm active length and 350Ω resistance were installed on the surface of the proximal femur at the inferior and superior parts of the femur neck and on the medial and lateral femur shaft. SGs, load-cell and the LVDT outputs were recorded and processed after the experiments completion. The experiments simulate a simple stance position configuration in which the femur is loaded through its head while the femur is inclined at four different inclinations angles (0,7,15,20 degrees) as shown in Fig 1. Following the in-vitro experiments a p-FE model was generated based on QCT scans and simulations performed to mimic the experiments, after which the FE results were compared to the experimental observations for validation purposes

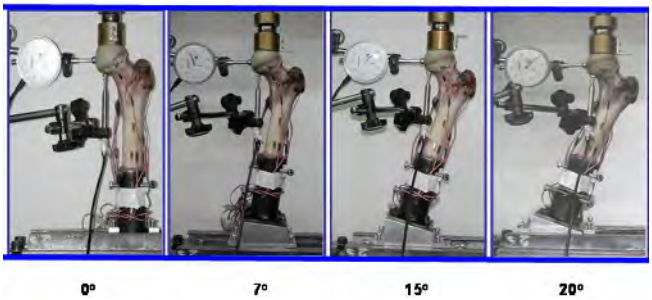


Fig. 1 Experiments on the fresh-frozen bone (#3) at different inclination angles.

B. p-FE models of the proximal femur

The geometry generation, the FE mesh and the evaluation of the material properties methods are detailed in **[9]** and will be only shortly described herein. Femur's geometry was extracted from QCT slices and divided into cortical and trabecular regions. Exterior, interface and interior boundaries were traced at each slice and x-y arrays were generated, each representing different boundaries of a given slice. A smoothing algorithm was applied on these arrays that generate smooth closed splines used for the solid body generation. The solid body was meshed by an auto-mesher with tetrahedral elements using a high order FE commercial code. The surfaces of the bone are accurately represented in the FE model by using the blending mapping method. The schematic flowchart that describes the FE generation from CT scans is provided in Fig. 2.

QCT Hounsfield Unit (HU) values were recalculated using a moving average method regardless of the FE mesh and isotropic inhomogeneous linear material representation was assigned to the FE models by a spatial function generated from the QCT data. Calibration phantoms were used for the bone equivalent mineral density (EQM) calculation.

$$\rho_{EQM} = 0.682 \cdot HU - 5.5 \ [g/cm^3]_{\text{Bone\#2}} \quad (1)$$

$$\rho_{Ash} = 1.22 \cdot \rho_{EQM} + 0.0523 \ [g/cm^3] \quad (2)$$

$$\rho_{Ash} = \sum_{k=0}^{p_k} Z^k \left(\sum_{i,j=0}^{p_i,p_j} a_{ijk} \cdot r^i \cdot \sin(j \cdot \theta) + \sum_{i,j=0}^{p_i,p_j} a_{ijk} \cdot r^i \cdot \cos(j \cdot \theta) \right) \quad (3)$$

Young's modulus was evaluated by Keyak & Falkinstein relations [1]:

$$E_{Cort} = 10200 \cdot \rho_{Ash}^{2.01} \ [MPa] \quad (4)$$

$$E_{Trab} = 5307 \cdot \rho_{Ash} + 469 \ [MPa] \quad (5)$$

Anisotropic material properties were also considered in the FE model their influence was investigated and will be

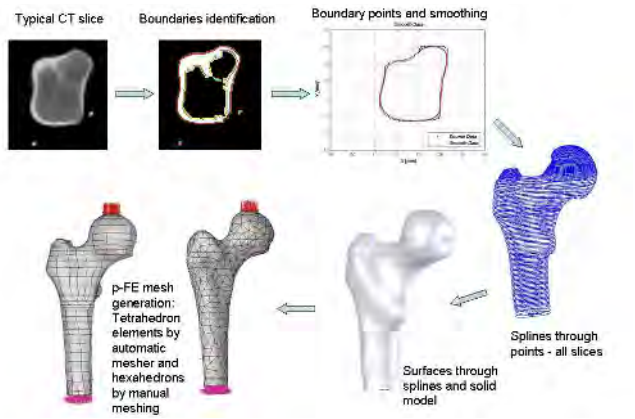


Fig. 2 The flowchart for generating the p-FE model.

reported. The FE boundary conditions describe the experiments as follows: distal face was fully constrained and 1000*N* load was applied on the head planar face in the proper direction (four different inclinations angles).

III. Results

To verify the accuracy of ours CT-based FE model, a comparison between the experimental observations (strains and displacements) and the FE results was conducted. Different models were generated based on the CT data, each having a different planar trimmed surface according to the tilt angle represented in the experiment. All FE models were generated by the same methods (details in [9, 10]). Three fresh frozen bones with a total of 77 experimental values recorded (61 strains and 16 displacements) were used for this verification process. In all FE models isotropic inhomogeneous linear material representation was assigned. Both constant Poisson ratio = 0.3, and inhomogeneous Poisson ratio were considered and the E(HU) relation by Keyak & Falkeinstein [1] were assigned. A 1000N load was applied as traction over the entire planar face in the proper direction. Zero displacements were enforced in the distal face. All models show good convergence in the energy norm, displacement and strain results when p=4 or higher is used. The SGs and LVDTs locations were marked on the each model (for example Fig. 3 present the point of interest in bone #2), and averaged strains and displacements over the finite element's face were extracted from FE results.

FE strains and displacements were compared to these measured in the experiment, at various locations of the femur and for all loading conditions. The results indicate that in most of the measuring points, the predicted strains and displacements correlate very well with the experimental observations. A linear regression of the experiment result vs. the FE prediction, for both displacement and strain, is presented in Fig. 4. The linear regression represents a general assessment of the analysis quality.

The slope of the regression line is 0.957 (very close to one), and the linear regression coefficient R^2 = 0.955 (the intercept in percentage is close to zero).

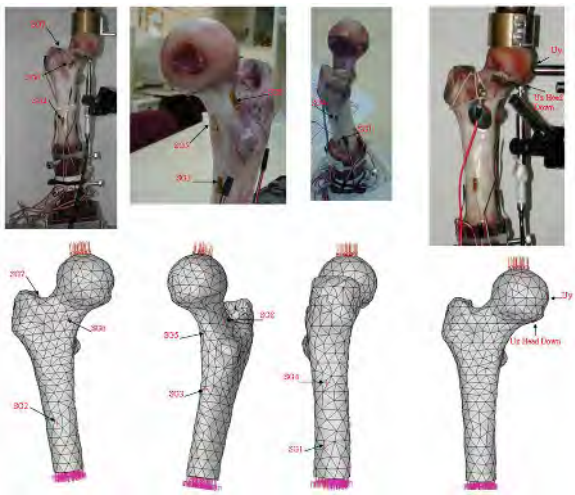


Fig. 3 Locations at which displacements and strains were measured in bone #2.

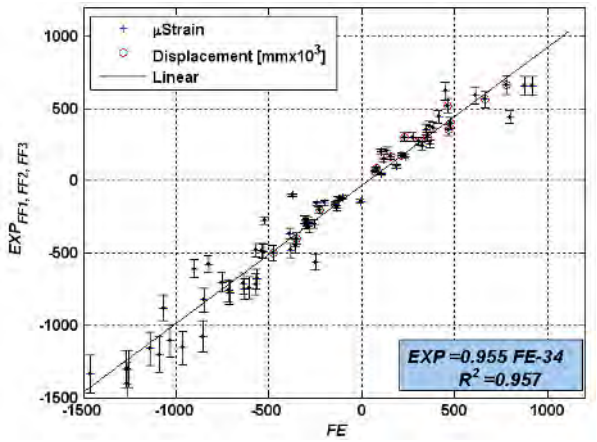


Fig. 4 Linear regression: experimental observation (fresh frozen 1+2+3) vs. FE predictions.

IV. Conclusions

This study was preformed to validate new a method of generating reliable FE models of the proximal femur using subject specific QCT data. The method is based on an accurate surface representation of the bone and the distinction between cortical and trabecular regions, together with a systematic process to evaluate bone material properties. The inhomogeneous Young modulus was represented by continuous spatial functions applied to the FE model. The validation process was conducted using experimental result from three fresh frozen human femurs by comparing displacements and strains to the values extracted from the FE results. The FE results correlate very well with the experimental observation (same range of accuracy for each bone). The excellent agreement between the analyses and experiments are to the best of the authors' knowledge more accurate than other investigations reported in the literature. Limitations of the present work are: (a) method validation has been validated on three normal femurs in vitro. (b) The effect of using CT scan data obtained in situ and in vivo still needs to be examined. (c) FE model did not take into ac-

count the known local anisotropic behavior of all bone tissue.

This study exemplifies that the presented method is in an advanced stage to be used in clinical computer aided decision making, and is being extended in several directions: (a) Implementing an inhomogeneous anisotropic material model in the FE analyses which may better represent cases of torsion and complex loading on the bone, (b) Simulating and optimizing patient-specific "total hip replacement" surgery by FE simulation of the best possible prosthesis in case of neck fractures.

Acknowledgment

The authors acknowledge the help of Prof. Charles Milgrom from the Hadassah Hospital, Jerusalem, for providing the bones, and Dr. Arie Bussiba for his help in performing the experiments.

References

1. J.H. Keyak,Y. Falkinstein, (2003) Comparison of in situ and in vitro CT scan-based finite element model predictions of proximal femoral fracture load. J. Med. Eng. Phys 25, 781–787.
2. B. Helgason, F. Taddei, H. Palsson, E. Schileo, L. Cristofolini, M. Viceconti, S. Brynjolfsson, (2008) A modified method for assigning material properties to FE models of bones. Med. Eng. phys 30, 444–453.
3. E. Schileo, F. Taddei, A. Malandrino, L. Cristofolini, M. Viceconti (2007) Subject-specific finite element models can accurately predict strain levels in long bones. J. Biomechanics 40, 2982-2989.
4. F. Taddei, E. Schileo, B. Helgason, L. Cristofolini, M. Viceconti, (2007) The material mapping strategy influences the accuracy of CT based finite element models of bones: An evaluation against experimental measurements. J. Med. Eng. Phys 29, 973–979.
5. L. Peng, J. Bai, X. Zeng, Y. Zhou, (2006) Comparison of isotropic and orthotropic material property assignments on femoral finite element models under two loading conditions. J. Med. Eng. Phys 28, 227–233.
6. J.H. Keyak, J.M. Meagher, H.B. Skinner, Jr.C.D. Mote, (1990) Automated three dimensional finite element modeling of bone: A new method. J. Biomedical Eng 12, 389-397.
7. D.D. Cody, G.J. Gross, F.J. Hou, H.J. Spencer, S.A. Goldstein, D.P.Fyhrie, (1999) Femoral strength is better predicted by finite element models than QCT and DXA. J. Biomechanics 32, 1013-1020.
8. Z. Yosibash, R. Padan, L. Joscowicz, C. Milgrom, (2007) A CT based high-order finite element analysis of the human proximal femur compared to in-vitro experiments. ASME J. of Biomechanical Engineering 129 (3), 297-309.
9. Z. Yosibash, N. Trabelsi, C. Milgrom, (2007) Reliable simulations of the human proximal femur by high-order finite element analysis validated by experimental observations. J. of Biomechanics 40, 3688-3699.
10. N. Trabelsi, Z. Yosibash, C. Milgrom (2008) Validation of subject-specific automated p-FE analysis of the proximal femur. J. of Biomechanics, Submitted for publications.

Author: Zohar Yosibash and Nir Trabelsi.
Institute: Dept. of Mechanical Engineering, Ben-Gurion University of the Negev.
City: Beer-Sheva.
Country: Israel.
Email: zohary@bgu.ac.il, nirtr@bgu.ac.il

Design of Prosthetic Skins with Humanlike Softness

J.J. Cabibihan

The Social Robotics Laboratory (Interactive and Digital Media Institute) and
the Department of Electrical & Computer Engineering, National University of Singapore

Abstract — **Prosthetic hands and arms that have realistic appearance and can be controlled by the user's thoughts are emerging. As these technologies mature, it is likely that there will be an increased interest in endowing these with skins having humanlike softness in order to address the psychosocial issues coupled with prosthesis usage in social interactions. The objective of the project described in this paper is to find an optimal design of a prosthetic hand's skin that would be comparable to the softness of the human hand. The project aims to develop simulation and experimental methodologies for selecting skin materials, designing their internal geometries and comparing their behavior to the biomechanical skin behavior of the human hand for activities concerning social touch (e.g. handshakes, high fives, caress, etc.). In particular, this paper is focused on modifying the internal geometry of an artificial fingertip and evaluate whether significant changes in the skin compliance can be achieved. Simulation results show that modifying the internal geometry of the synthetic skin structure can lead to an increase in skin compliance.**

Keywords — **Prosthesis, Artificial Skins, Rehabilitation Robotics, Finite Element Analysis, Social Robotics.**

I. Introduction

Any loss or absence of limbs severs the dignity of man. In addition to the functional requirements, the psychosocial dimension of prosthetic devices must also be addressed. In a social context, the concealment of prosthesis usage could be made possible with prosthetics that have humanlike appearance, function and feel.

Significant progress has been made in realistic looking artificial hands. Current prosthetic hands have achieved very humanlike appearances. In fact, they can now be constructed to match the exact skin tone of the user while the sculptors can artistically create detailed skin surface with fingerprints, hairs and pores (e.g. Livingskin, www.livingskin.com). In a study among upper limb amputees in Singapore, for example, it was concluded that aesthetic prostheses are crucial for patients to cope with the traumatic experience [1].

In terms of functionality, the past five years have brought about many breakthroughs in the development of intelligent prosthetic hands (e.g. CyberHand Project, www.cyberhand.org; Neurobotics, www.neurobotics.org; DARPA's Revolutionizing Prosthesis Project, www.arpa.mil/dso/thrusts/bio/restbio_tech/revprost/index.htm). One of the crucial scientific issues that the researchers addressed was to increase the basic knowledge of neural regeneration and sensory-motor control of the human hand to enable the prosthesis to be felt by the patient and to be controlled in a very natural way. As of 2007, prosthetic arms and grippers can already be controlled by the user's thoughts (e.g. The World's First Bionic Man, www.ric.org/bionic/).

Why should a prosthetic skin be designed to feel like the real human skin? The main purpose of prosthetic devices is to let the user pass unnoticed. Prosthetic hands are expected to be touched by other people and concealing it would be difficult given the choices of materials currently used (For a comparison between the compliance, conformance and hysteresis of synthetic and human fingertips, the interested reader is referred to Ref. [2]). In addition to selecting the appropriate soft synthetic materials, the proper design tradeoffs have to made in order to maintain the wear resistance of the current stiff prosthetic skins but develop an approach in which humanlike softness could also be achieved.

The objective of the project described in this paper is to find an optimal design of a prosthetic hand's skin that would be comparable to the softness of the human hand. Softness has been defined as the perceptual correlate of compliance, which is the amount of deformation caused by an applied force [3]. The present project aims to develop simulation and experimental methodologies for selecting materials and designing their internal geometries in order to achieve similar compliance measures with the skin of the human hand. In particular, this paper is focused on modifying the internal geometry of an artificial fingertip and evaluate whether significant changes in the skin compliance can be achieved. The results are then compared to the skin compliance of the human fingertip. The simulation methodology and the preliminary results are described in the following sections.

II. Methods

A. Materials and Constitutive Equations

Synthetic skins for prosthetic and robotic hands are typically constructed with silicone and polyurethane materials.

Chwee Teck Lim, James C.H. Goh (Eds.): ICBME 2008, Proceedings 23, pp. 2023–2026, 2009
www.springerlink.com

Samples of these two types of materials have been characterized and have been reported elsewhere [2, 4-6]. The silicone sample has a Shore A durometer value of 11 while the polyurethane has a value of 45 (i.e. a lower value indicates a low resistance to an indenter – a softer material). The validation experiments consisting of indentation and imaging tests demonstrated that the visco-hyperelastic constitutive equations were satisfactory for describing the behaviour of the silicone and polyurethane samples.

B. Finite Element Modeling

Fig. 1 shows the two geometries that were modeled using the commercial finite element analysis software Abaqus™ /Standard 6.7-1 (Simulia, Providence, RI). The simulations were run at the Supercomputing and Visualisation Unit of the Computer Centre, National University of Singapore. Both geometries have a 0.8 mm upper layer and 6.2 mm inner layer as measured from the base to the upper surface. Fig. 1a has a solid internal structure while Fig. 1b has a 0.75 mm space with a span of 5 mm, located 1 mm below the skin surface. The eight-node plain strain biquadratic elements were used to model the fingertip. A thickness of 10 mm (dimension towards the page) is set. This is approximately the dimension when a flat surface is in normal contact with the fingertip. The base of the finger geometry was constrained in all degrees of freedom. The materials, and in essence, the behavior of each layer, can be easily modified in the software by changing the material coefficients as obtained in the characterization experiments.

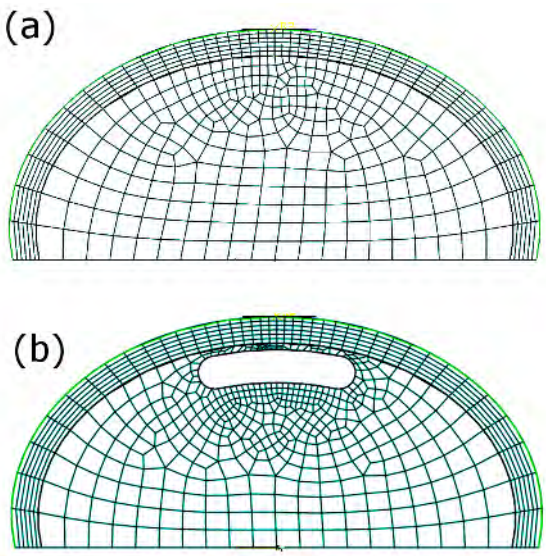


Fig. 1 The geometries of the finite element models Fig. 1a has a solid internal structure. Fig. 1b has a space below the skin surface

C. Measurement of Skin Compliance

The literatures are lacking with a complete data set of the skin compliance of the whole human hand. So far, the published data have been concentrated on the fingertip [3, 7-9]. The full compliance topography of the skin in the human hand will be most useful for comparing synthetic materials aimed at achieving humanlike artificial skins. For this project, the development of a tactile stimulator that will map the compliance of the human hand is underway. In the meantime, this paper will make use of the published fingertip skin compliance data as reported in Ref. [3] for comparing the compliance results of the synthetic fingertip. In their experiments, a flat-end probe was applied to the human fingertip at a constant velocity of 0.5 mm/s until a force of 1.25 N was reached. The same loading conditions were used for the simulations in the present paper.

III. Results

Fig. 2 shows the displacement contour plots from the simulations on the prosthetic fingertip models. The rows are arranged according to the materials used. The left column has a solid internal geometry while the right column has a modified internal geometry.

For a 1 N plate indentation, Fig. 3 shows that a homogeneous internal composition of synthetic materials resulted to an indentation displacement of 0.15 mm for polyurethane and 0.30 mm for silicone. These results are consistent with the validation experiments of quasi-static indentation loading for these materials as reported in [2, 6]. Simulations on the 0.8 mm external layer of the stiff polyurethane over the softer silicone material resulted in an indentation of 0.29 mm or difference of 3.5% from a homogenous layer of silicone.

With the introduction of a 0.75 mm opening with a 5 mm arc length, the compliance of the silicone material increased to 0.67 mm or about 125% from the structure with a solid internal geometry. For polyurethane, the indentation displacement jumped to 0.48 mm or nearly 220% improvement in skin compliance. The combination of a stiff outer layer of polyurethane and a softer inner layer of silicone produced an increase of nearly 120%. Considering that there is only a 5% difference from silicone-only model, which is the most compliant configuration in these simulations, it would be worthwhile to explore combinations with stiff outer layers for wear and tear purposes and soft inner layer for skin compliance in future studies.

Fig. 4 compares the previous results with the skin compliance of the human fingertip, as reported in Ref. [3].

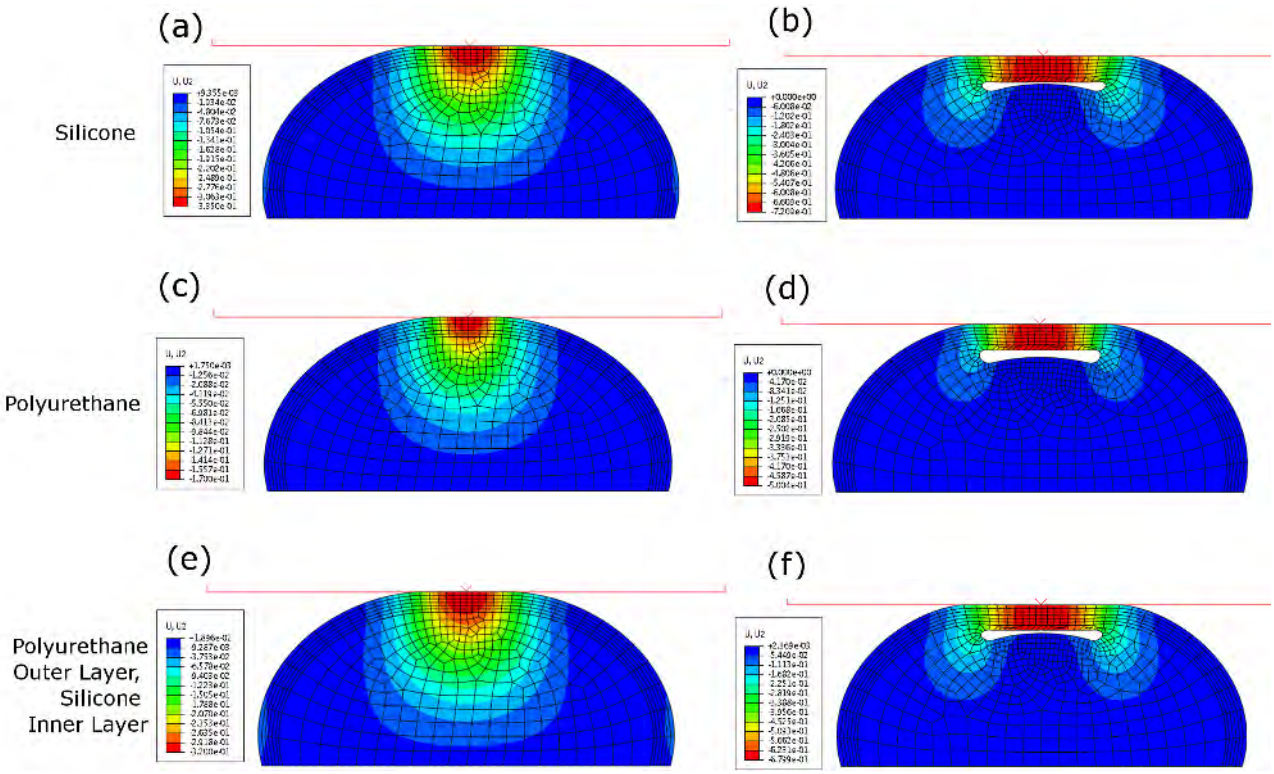


Fig. 2 The displacement contour plots of the prosthetic fingertips when indented with a force of 1 N

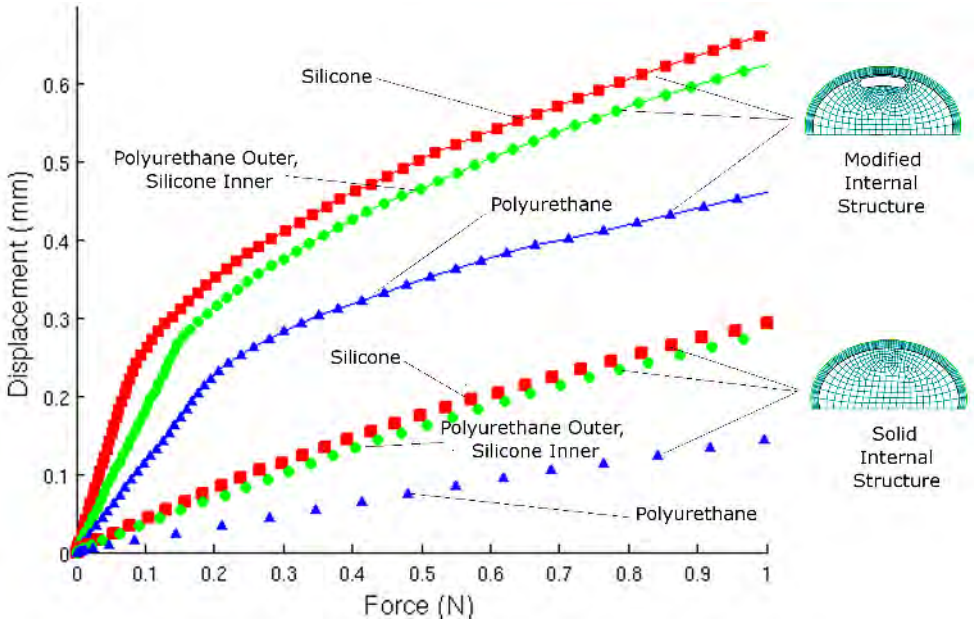


Fig. 3 Simulation results of the skin compliance of synthetic fingertip models of silicone, polyurethane and the combination of both materials. The three lower curves show the results when the geometry has homogeneous internal structure while the three upper curves are from the model with a space in the internal geometry

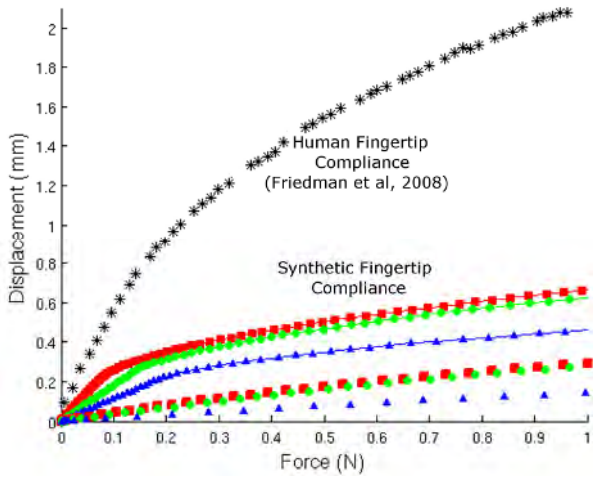


Fig. 4 Comparisons on skin compliance of human and synthetic fingertips

The simulations show that at 1 N loading, the human fingertip can easily reach an indentation displacement of 2 mm. It would take another 200% increase in the compliance of synthetic materials for this to be achieved. Furthermore, this comparison also implies that homogenous layers of silicone or polyurethane (i.e. the bottom curves) with durometer values of 11 and above would be far from the skin compliance of the human fingertip. In a social interaction scenario, such will be easily felt by another person and the prosthesis user may not be able to conceal the usage of the prosthetic device.

IV. Conclusions

In anticipation of the incoming generation of intelligent prosthetic hands and arms, it is conceivable that the next technological step is to make the crude physical features of these devices look and feel more humanlike in order to address safety and social acceptance issues.

This paper presented preliminary results from prosthetic fingertip skin models with simulations consisting of varying the material composition of the fingertips and changing the internal structure. From these, the following conclusions can be made. First, the simulation results showed the possibility of increasing skin compliance by modifying the internal geometry of the prosthetic fingertip structure. This gives an indication that for future work, selecting materials that are softer as compared to the silicone and polyurethane and developing an optimal design of the prosthetic skin's internal structure may enable us to achieve a more compliant prosthetic skin design. Second, by knowing the compliance behavior of the prosthetic skins before physically constructing them, it is possible to try different internal and external layers that could satisfy other requirements for wear and tear, maintenance and others. It is important to note that tactile sensors may be embedded later on and the skin's mechanical behaviour (e.g. compliance and hysteresis) will have to be considered in the context of the response of the embedded tactile sensors. Lastly, the simulation approach using validated finite element models proves to be a useful tool for the ongoing work to optimize the design of prosthetic skins for humanlike softness.

Acknowledgment

The project "Design of prosthetic skins with humanlike softness" is supported by the grant approved by the Faculty Research Committee from the Academic Research Fund Tier 1, Ministry of Education, Singapore.

References

1. Leow MEL, Pho RWH and Pereira BP (2001) Esthetic prostheses in minor and major upper limb amputations. Hand Clinics 17: 489-497
2. Cabibihan JJ, Pattofatto S, Jomaa M, Benallal A and Carrozza MC (2009) Towards humanlike social touch for sociable robotics and prosthetics: Comparisons on the compliance, conformance and hysteresis of synthetic and human fingertip skins. International Journal of Social Robotics (in press)
3. Friedman RM, Hester KD, Green BG and LaMotte RH (2008) Magnitude estimation of softness. Exp Brain Res 10.1007/s00221-008-1507-5
4. Cabibihan JJ, Pattofatto S, Jomaa M, Benallal A, Carrozza MC and Dario P (2006) The conformance test for robotic/prosthetic fingertip skins. Proceedings of the First IEEE/RAS-EMBS International Conference on Biomedical Robotics and Biomechatronics 1: 561-566
5. Cabibihan JJ, Carrozza MC, Dario P, Pattofatto S, Jomaa M and Benallal A (2006) The uncanny valley and the search for humanlike skin materials for a prosthetic fingertip. Proceedings of IEEE-RAS Humanoid Robotics 1: 474-477
6. Cabibihan JJ, Carrozza MC, Dario P, Pattofatto S, Jomaa M and Benallal A (2006) The uncanny valley and the grand challenges towards a humanlike fingertip skin for prosthetics. Proceedings of the Robotics: Science and Systems Conference (workshop)
7. Westling G and Johansson RS (1987) Responses in glabrous skin mechanoreceptors during precision grip in humans. Exp Brain Res 66: 128-140
8. Serina E, Mote S and Rempel D (1997) Force response of the fingertip pulp to repeated compression - effects of loading rate, loading angle and anthropometry. Journal of Biomechanics 30: 1035-1040
9. Pawluk DTV and Howe RD (1999) Dynamic contact of the human fingerpad against a flat surface. Journal of Biomechanical Engineering 121(6): 605-611

Author: Dr. John-John Cabibihan
Email: elecjj@nus.edu.sg

Effect of Data Selection on the Loss of Balance in the Seated Position

K.H. Kim[1], K. Son[1], J.H. Park[1]

[1] School of Mechanical Engineering, Pusan National University, Busan, Korea

Abstract — **A fast and accurate detection of the loss of balance (LOB) can reduce the elderly fall that is one of the most dangerous injuries. Real-time detection of body reactions against a fall will be used to improve the performance of devices for the elderly. The loss of balance is detected by control error anomaly (CEA) that is an unusually large value of the system control error.**

Three men took part in the experiment. Each volunteer was seated on a four-legged chair and he balanced the chair over its rear legs by his foot as long as possible. This system had single input and single output. The input was the foot's ground reaction force and the output was the angular acceleration of the chair. An internal model of balancing task was built of a linear equation of regression from the relationship between input and output. The output of the internal model was assumed as a control signal of the angular acceleration from the central nervous system.

Data selection depends on the size of the foot reaction force data, S1, which were used to construct the internal model and the threshold, S2, which were used to detect the LOB. The size of the force data changed from 0.2 to 3 sec and also the threshold size changed from 0.02 to 0.2 sec. Therefore in the case of detecting the loss of balance under 3-sigma method, the detecting performance was improved in lager S1 and smaller S2.

Keywords — **Balance, Control, Internal Model, Regression, Threshold**

I. Introduction

Elderly falls are one of the most dangerous accidents and normally occur with a fracture of hip bone. More than 35% of elders aged over sixty have experienced fall on the average[1]. Most falls happen unintentionally and these are attributable to a 'loss of balance'.

People knows intuitively what a loss of balance means but it is difficult to understand how to detect the loss of balance and what process works in the central nervous system (CNS). Ahmed et al. proposed 'a loss of balance is required for the CNS to trigger a compensatory response and prevent the ensuing fall'[2,3]. A loss of balance usually results from positioning the center of mass (COM) outside the base of support in static or quasistatic movements. Pai et al. suggested that a dynamic loss of balance occurs when the velocity and position of the COM crossed over fixed upper or lower limit[4]. In the detection of a loss of balance, humans tried to regain the balance with a rapid adjustment of body configuration, such as a compensatory step, and this behavior was the only evidence that was observable externally. Several researches have used this externally visible evidence in order to explain when the compensatory step was needed for various perturbations[5,6].

In this study the failure-detection algorithm that was proposed by Ahmed et al. was used so as to detect the loss of balance[2]. The postural control model of the CNS has an input signal, a controller, a plant, a feedback of output signal, and system variables[7,8]. We monitored the error signal between the output of the plant and the result of the forward internal model which was created using input signal, and found out the loss of balance by detecting a CEA.

Ahmed et al. pursued a number of comparisons between the algorithm success rate and the size difference of input data which were used to construct both the forward internal model in the fixed sampling size of input data. But the proposed forward internal model was a linear regression function which was calculated by a least squares method. Its parameters were different according to the size and this changed parameters directly affected the error signal which was used in the algorithm. Therefore it is necessary to find out the effect of data size on the result of detecting the loss of balance.

II. Materials and Method

To verify the relationship between the data size and the detecting result, we made this test model simple. A volunteer was seated and balanced the chair over its rear legs by his foot as long as possible. This system had one input and one output. The former was the foot's ground reaction force and the latter was the angular acceleration of the chair (Fig 1). An internal model of balancing task was built of a linear equation of regression from the relationship between input and output[2].

The output of the internal model, $\hat{y}(t)$, was assumed to be a control signal of the angular acceleration from the central nervous system. The control error, $e(t)$, was defined as the difference of the angular acceleration between obtained by sensory and expected by the internal model. If the error crossed over the threshold which was set at three standard deviations (3σ), it was regarded as the CEA.

Chwee Teck Lim, James C.H. Goh (Eds.): ICBME 2008, Proceedings 23, pp. 2027–2029, 2009
www.springerlink.com

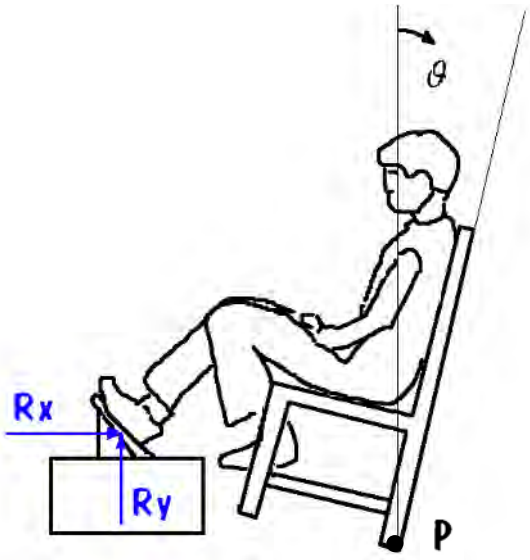


Fig. 1 Schematic of balancing test

$$e(t) = y(t) - \hat{y}(t) \quad (1)$$

$$\hat{y}(t) = a_0 + a_1 u(t) \quad (2)$$

where $y(t)$ is the plant output signal which represents the actual output, the angular acceleration of the chair. And $u(t)$ is the input signal, the torque at the point P, which was obtained by the foot ground reaction force.

Three healthy, young adult volunteers were tested more than 10 times per a person. Four legged chair was used to obtain angular acceleration, the plant output signal, and the input signal was the foot GRF obtained by a force plate(Kistler 9285). Subjects were not allowed to have any motion except a leg which was used to push the force plate. The angular accelerations of the chair and the foot ground reaction forces were measured at 540 Hz. These data were filtered with a fourth-order, low-pass Butterworth filter (Matlab®) and a cutoff frequency of 3 Hz.

The size of input data for creating the forward internal model, S1, was varied from 0.2 to 3 sec and the threshold size, S2, from 0.02 to 0.2 sec with the time interval of 0.2 sec and 0.02 sec, respectively. Figure 2 shows the input data, torque at the point P. Figures 3 and 4 show the angular accelerations of both the plant result and the predicted result by the internal model and the error signal between the plant result and the predicted result, respectively.

We compared the reaction time between the results obtained in this study and the fixed size that S1=2 sec and S2=0.1 sec. Figure 5 shows the reaction time with different sizes of data selection. The lower size of S2 had the faster

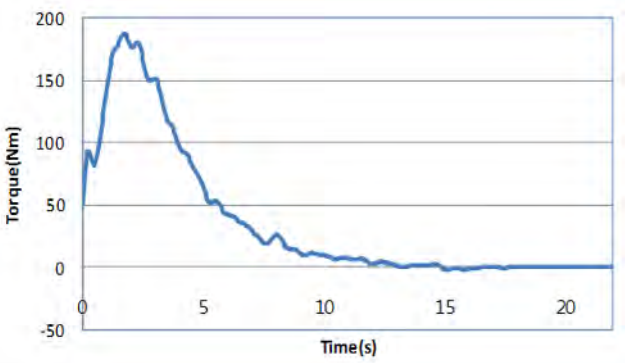


Fig. 2 Torque at the point P exerted by foot

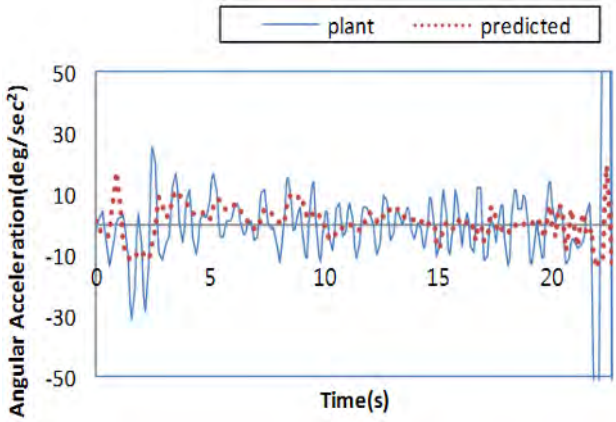


Fig. 3 Angular accelerations of the plant output and the predicted output by the forward internal model

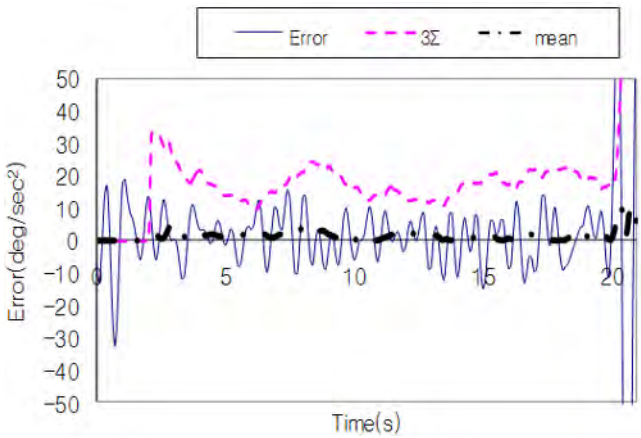


Fig. 4 Error signal between the plant output and the predicted output

detecting time than the fixed size. When S2 was under 0.1 s, most reaction times were faster than the fixed size except the case of S1=1.2 sec. If the threshold size, S2, was constant, the reaction time was faster in larger S1.

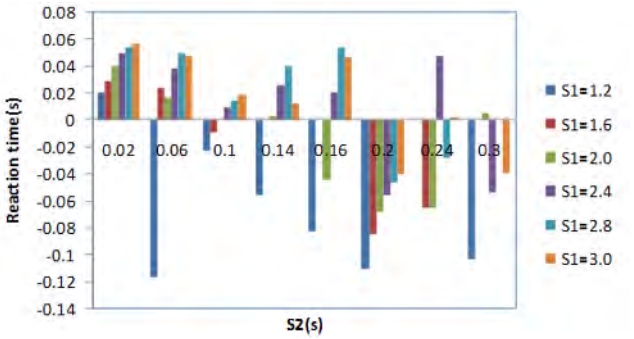


Fig. 5 Comparison between the reaction time and the size of both input data for creating the forward internal model, S1, and threshold size, S2

The size of S1 means the amount of input data used at creating the internal model. This result revealed that more input data improved the ratio of detecting the loss of balance. But the internal model with too large S1 was not physical because the internal model was built in a linear regression function. The cases with the size of S1 over 2.4 sec were satisfied to detect quickly the loss of balance with the size of S2 under 0.16 sec. When the data size was 2.8 sec and the thresh-old size was 0.02 sec, the detection time of the LOB was the smallest.

III. Conclusions

Data selection depends on the size of the force data which were used to construct the internal model and the threshold which were used to detect the LOB. The size of the force data changed from 0.2 to 3 sec and also the threshold size changed from 0.02 to 0.2 sec. Therefore in the case of detecting the loss of balance under 3-sigma method, the detecting performance was improved in lager S1 and smaller S2.

References

1. Kanten D.N., Mulrow C.D., Gerety M.B., et al (1993) Falls: an examination of three reporting methods in nursing homes. J. Am. Geriatr. Soc 42:662-666
2. Ahmed A.A., Ashton-Miller J.A. (2004) Is a “loss of balance” a control error signal anomaly? Evidence for three-sigma failure detection in young adults. Gait Posture 193:252-262
3. Ahmed A.A., Ashton-Miller J.A. (2005) Effect of age on decting a loss of balance in a seated whole-body balancing task. Clinical biomech. 20:767- 775
4. Pai Y.C., Rogers M.W., Hedman L.D. et al (1997) Center of mass velocity-position predictions for balance control. J. Biomech. 30:347-354
5. Maki B.E., McIlroy W.E., Perry S.D. (1996) Influence of lateral destabilization of compensatory stepping responses. J. Biomech. 29:343-353
6. Jensen J.L., Brown L.A., Woollacott M.H. (2001) Compensatory stepping: the biomechanics of a preferred response among older adults. Exp. Aging Res. 27J:361-376
7. Kuo A.D., (1995) An optimal control model for analyzing human postural balance. IEEE Trans. Biomed. Eng. 421:81-101
8. van der Kooij H., Jacobs R., Koopman B. et al (1999) A multisensory integration model of human stance control. Biol. Cybern. 805:299-308

Author: Kwang Hoon Kim
Institute: Pusan National Univ.
Street: Jangjeun2dong, Geumjunggu
City: Busan
Country: South Korea
Email: flyworld7@gmail.com

The Effect of Elastic Moduli of Restorative Materials on the Stress of Non-Carious Cervical Lesion

W. Kwon[1], K.H. Kim[1], K. Son[1] and J.K. Park[2]

[1] School of Mechanical Engineering, Pusan National University, Busan, Korea
[2] Department of Conservative Dentistry, Pusan National University, Busan, Korea

Abstract — **Various dental materials have their particular properties with different restorative effects. This study investigates the influence of elastic moduli of the restorative materials on the stress of non-carious cervical lesion. A three-dimensional finite element model was constructed based on the scanned data of an extracted maxillary second premolar. Such five different restorative materials as TF (Tetric Flow), GIC (Glass Ionomer Cement), Z100, amalgam and gold alloy were analyzed to restore the cervical lesion. A load of 150 N was applied on the cusp of buccal and the corresponding stresses calculated in three regions: occlusal, apex and cervical of each restoration model. In the occlusal and cervical regions, as the stiffness of restorative material increased so did the level of stress in the descending order of gold alloy, amalgam, Z100, GIC and TF. In the apex region, however, the order of stress magnitude was reversed. TF of the lowest stiffness yielded the most effective restoration in terms of the reduction of stress in the lesion part while Z100 of a similar elastic modulus to the dentin was the best at the apex.**

Keywords — **Non-Carious Cervical Lesion (NCCL), Restoration, Finite Element Analysis (FEA), Stiffness, Stress**

I. Introduction

In clinical dentistry, the loss of hard dental tissue is occasionally observed in the cervical region of a tooth. Erosion, abrasion and abfraction are the most common contributors to non-carious cervical lesions (NCCLs)[1]. Occlucal loadings, which concentrate stress on the cervical area of a tooth, have been considered to cause hard tissue loss at the cement-enamel junction (CEJ). This is referred to as abfraction[2] in order to distinguish it from lesions caused by erosion and abrasion.

The origination of this defect is assumed due to the mechanism for cervical tooth loss that links with occlusal loading. For reduction of stress concentration and prevention of the growth of lesion, dentists choose the restorative operation. Though this operation is carried out, the effect varies depending on restorative materials and does not last permanently. The purpose of this study was to investigate the effect of elastic moduli of restoration using a three dimensional finite element analysis.

II. Materials and method

A. Structure of tooth and lesion

The tooth consists of various materials according to its components. There is a cavity so called the pulp which contains vessel and nerves in the middle of the tooth. The dentin, which occupies most of the tooth, builds the whole root and some of crown. The crown is located in the upper of the dentin and coated with the enamel, which is the hardest tissue of the tooth. The root of tooth is fixed on the mandible or maxilla by the periodontal ligament (PDL) which is a type of membrane.

An NCCL occurs in the CEJ where the cement and the dentin meet in the cervical of tooth. An absolutely larger percentage of NCCL is found in the buccal side than in the lingual side. Once a lesion takes place, it grows gradually along the CEJ. The NCCL has to be treated by a restorative operation in order to prevent its growth.

B. Construction of tooth model

A three-dimensional finite element model of the tooth was constructed by several steps of image processing. Firstly, using a micro CT machine (Micro-CT, Skyscan, Belgium), 357 pictures of horizontal sectional configuration were acquired from an extracted maxillary second premolar whose length was 20 mm. Secondly, geometrical data of the outer and inner shapes of tooth components, which included the enamel, the dentin and the pulp, were drawn out through the binary image operation. These configuration data were also treated for the modification of reducing unnecessary nodes. After each modification of CT images, the volume of tooth was rendered through stacking them. Then, free curved surfaces of each tooth component were set up from their contour nodes using a commercial program Rhino 3D (Robert McNeel & Assoc., Seattle, WA, USA). The scheme of constructing process from image operating to finite element modeling is shown in Fig. 1.

A commercial finite element preprocessing program Hypermesh (Altair Engineering Inc., Troy, MI, USA) was used to make a three-dimensional finite element model from the acquired geometric configuration data. The type of lesion

Chwee Teck Lim, James C.H. Goh (Eds.): ICBME 2008, Proceedings 23, pp. 2030–2033, 2009
www.springerlink.com

was chosen as notch shape. The depth of abfraction was set as 2 mm and a separate treatment was postulated as single restoration with one material. The size of element was different for each component: The lesion and its surrounding had the smallest size (0.05 mm) to investigate the distribution of stress precisely. Other parts, such as the PDL, the pulp and the rest of dentin and enamel had a medium size (0.3 mm). The alveolar bone was created using different element sizes. Elements of the inner surface, which contacts the PDL, were designed with a medium size (0.3 mm); those of the outer surface with a larger size (0.67~1.76 mm) to reduce the number of elements. Figure 2 shows the components of a complete finite element tooth model. Table 1 lists properties of the dental and restorative materials used in this study.[3, 4]

The finite element model was subject to the same constraint as a real tooth. The tooth analyzed was the maxillary second premolar, which located between the first premolar and the first molar, and fixed on the maxillary bone. Hence, the lateral faces of alveolar, which contacted the adjacent tooth, were constrained in y direction. The bottom surface of alveolar was constrained in all directions. A large deviation of load (31 - 453 N) can be yielded by masticatory movement. In this study, a force of 150 N oriented at 45° from the horizontal was assumed to apply on the upper third of buccal and lingual slopes as in Fig. 3.[3]

C. Validation and criterion

The finite element model had to be validated before its use in the analysis. For this purpose, six different models of the lesion part were constructed with various element sizes (0.05, 0.1, 0.15, 0.2, 0.25 and 0.3 mm) and they were subject to the same loading.[5] Then, the comparison of calculated stresses at the apex showed that the stresses of 0.1, 0.15 and 0.2 mm models had relative errors of 0.05, 0.03 and 0.41% to that of the finest model. This result showed the convergence of stress to the exact value with the reduction of element size. For better computational results, the smallest size (0.05 mm) was selected in this study.

In order to estimate the effectiveness of restoration, a criterion was established. The failure of restoration occurs along the boundary of tooth tissue and restorative material due to high stress generated. For longer restoration, stress along the lesion boundary must be lowered. Hence, an objective function was defined as to minimize von Mises stress on lesion where stress concentration is noticeable.[5]

$$\min \{\Sigma S_1 + \Sigma S_2\} \quad (1)$$

ΣS_1 = tensile stress

ΣS_2 = compressive stress

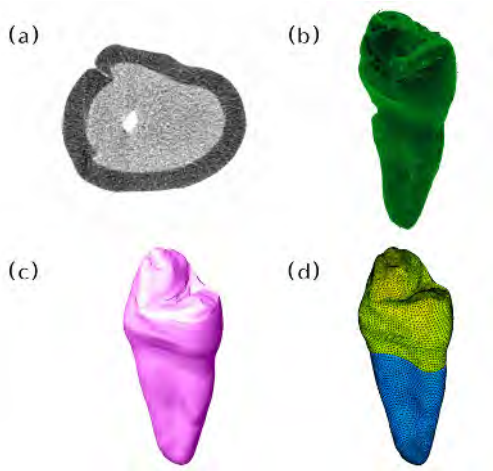


Fig. 1 Procedure reconstructing tooth model: (a) CT image of the second premolar, (b) Reconstructed 3D data using 3D Doctor, (c) Reconstructed 2D surface data using from Rhino 3D, and (d) 3D model of tooth created using Hypermesh

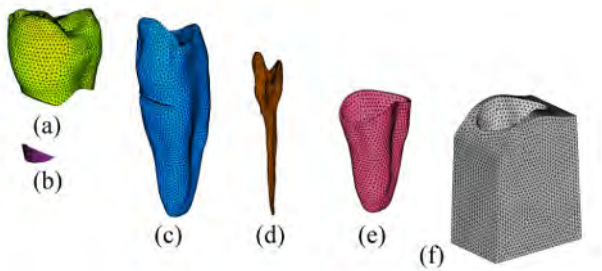


Fig. 2 A finite element tooth model consists of (a) Enamel, (b) Restoration, (c) Dentin, (d) Pulp, (e) PDL, and (f) Bone

Table 1 Mechanical elastic properties of the materials [3, 4]

Materials	Elastic modulus (MPa)	Poisson ratio
Enamel	69,000	0.3
Dentin	16,700	0.3
PDL	12	0.45
Bone	14,700	0.3
Tetric Flow	5,300	0.28
GIC	10,800	0.3
Z100	15,200	0.28
Amalgam	50,000	0.24
Gold Alloy	89,500	0.33

Maximum tensile and compressive strengths of tooth material vary in different literatures. Table 2 lists the range of maximum tensile strengths of the enamel and the dentin.[6] The upper and lower limits of the listed stress were used to compare the restorative effects of materials on the stress along the node lines. When the stress value was over the upper limit, the case was defined as critical; when between the two limits, defined as semi-critical.

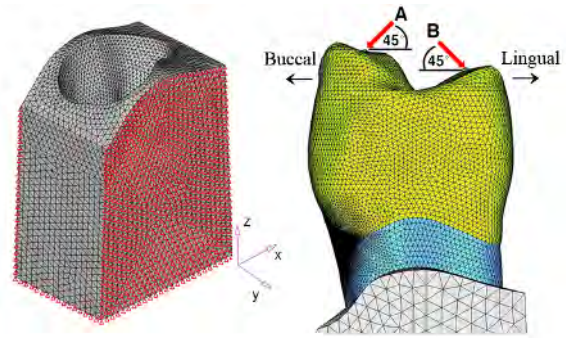


Fig. 3 Scheme of loading condition

Table 2 Mechanical properties of teeth (MPa) [6]

Tensile strength of enamel	10 – 24
Tensile strength of dentin	32 – 103

Table 3 Summation of stresses in three regions of five models

Restorative material	Region	Objective function (GPa)		
		S_1	S_2	Sum
Tetric Flow	Occlusal	1.556	2.568	4.124
	Apex	2.109	3.289	5.398
	Cervical	1.897	2.712	4.609
	Sub total			14.131
GIC	Occlusal	2.008	3.342	5.350
	Apex	1.399	2.086	3.485
	Cervical	2.402	4.029	6.431
	Sub total			15.266
Z100	Occlusal	2.073	3.316	5.389
	Apex	1.254	1.885	3.016
	Cervical	3.384	4.793	8.177
	Sub total			16.582
Amalgam	Occlusal	2.491	4.103	6.594
	Apex	1.273	1.762	3.158
	Cervical	6.333	9.127	15.460
	Sub total			25.212
Gold Alloy	Occlusal	3.109	4.996	8.105
	Apex	1.638	2.168	3.806
	Cervical	7.828	11.385	19.213
	Sub total			31.124

As shown in Fig. 3, a compressive stress was generated at lesion and its surroundings when the tooth was under load A; a tensile stress under load B.

III. Results

The stress distributions of lesion surroundings were compared in order to investigate the effect of material stiffness on the restoration. Three regions were chosen and stress values at the nodes in the regions were calculated.[5] The three regions included the occlusal line, i.e., the upper boundary between enamel-dentin and restoration, the apex line, i.e., the vertex of the restoration, and the cervical line, i.e., the lower boundary between dentin and restoration. The summation of stresses along each line is listed in Table 3. The comparison of three lines of five models is listed in Table 4, based on the numbers of critical and semi-critical cases.

A. Comparison in occlusal region

TF of the lowest stiffness was subject to the lowest stress, while the stresses on the other materials became higher as their stiffness increased. The summation of von Mises stress of TF was 4.124 GPa. Those of GIC and Z100 were almost same and they were 5.350 and 5.389 GPa, respectively. Amalgam and gold alloy sustained relatively high stresses, 6.594 and 8.105 GPa, respectively.

In terms of the critical stress, TF was selected as the best since it had 3 critical and 74 semi-critical nodes out of a total of 171 nodes along the occlusal line. GIC had 4 critical and 98 semi-critical nodes and Z100 had 4 critical and 100 semi-critical nodes. Amalgam had 17 critical and 113 semi-critical nodes. On the other hand, gold alloy had the largest number of critical nodes, 37, and the other nodes along the line belonged to the semi-critical cases.

B. Comparison in apex region

Along the apex line, Z100 which has the most similar stiffness to the dentin resulted in the lowest stress level. The summation of von Mises stress of Z100 was 3.106 GPa. Those of TF and GIC were higher than that of Z100 reaching up to 5.398 and 3.485 GPa, respectively. Amalgam and gold alloy yielded 3.158 and 3.806 GPa, respectively. In terms of the critical stress, there was neither critical nor semi-critical node along the apex lines of Z100, amalgam and gold alloy. However, both TF and GIC had 2 semi-critical cases.

C. Comparison in cervical region

The stress along the cervical line became larger as the stiffness of restorative material increased as in Table 3. The restoration using TF was the best yielding a stress summation of 4.609 GPa and it was also good in terms of the critical stress TF and GIC had only 2 semi-critical nodes out of 171 nodes along the cervical line. Z100 yielded 8.177 GPa, however, it had no critical and semi-critical cases. Amalgam and gold alloy resulted in such extremely high stresses as 15.460 and 19.213 GPa, respectively. Their results were also inferior in the number of semi-critical nodes as in Table 4.

Table 4 Number of critical nodes in five models

Restorative material	Region	Critical nodes	Semi-critical nodes
Tetric Flow	Occlusal	3	70
	Apex	0	2
	Cervical	0	2
GIC	Occlusal	4	98
	Apex	0	1
	Cervical	0	2
Z100	Occlusal	4	100
	Apex	0	0
	Cervical	0	0
Amalgam	Occlusal	17	113
	Apex	0	0
	Cervical	0	110
Gold Alloy	Occlusal	37	171
	Apex	0	0
	Cervical	0	137

IV. Conclusions

A three dimensional finite element tooth model was constructed in order to investigate the restorative effects of five different materials. The materials of lower stiffness than the dentin, TF and GIC, resulted in low stress in both occlusal and cervical regions. In the apex region, however, harder materials like Z100, amalgam and gold alloy yielded lower stress level than TF and GIC, and these three materials left neither critical nor semi-critical nodes. Especially Z100 having the most similar stiffness to the dentin resulted in the lowest stress, 3.016 GPa among the five materials.

A single restoration using TF was found to be the best in the overall stress level, but it was not the best in every region. Though Z100 did not reduce the stress level as TF did, it was superior to TF in the apex region where most failure of restoration occurs. Therefore, a multi-layer restoration, which uses Z100 for the inner part and TF for the outer part, is likely to reduce more stress than the single restoration with TF.

References

1. Levich, L. C., Bader, J. D., Shugars, D. A. and Heymann, H. O., "Non-carious Cervical Lesion," J Dent, Vol. 22, Issue 4, pp. 195-207, 1994.
2. Grippo, J. O., Simring, M. and Schreiner, S., "Attrition, Abrasion, Corrosion and Abfraction Revisited – A New Perspective on Tooth Surface Lesions," J Am Dent Assoc, Vol. 135, No. 8, pp. 1109-1118, 2004.
3. Ichim, I., Schmidlin, P. R., Li Q, Kieser, J. and Swain, M. V., "Restoration of non-carious cervical lesions Part II Restorative material selection to minimize fracture," Dental Materials, Vol. 23, pp. 1562–1569, 2007.
4. Katona, T. R. and Winkler, M. M., "Stress analysis of a bulk-filled class V light-cured composite restoration," Journal of Dental Research, Vol. 73, No. 8, pp. 1470 – 1477, 1994.
5. Kim, K. H., Park, J. K. and Son, K., "Relationship between stiffness of restorative material and stress distribution for notch shaped non-carious cervical lesion," International Journal of Precision Engineering and Manufacturing, Vol. 9, No. 3, pp. 64 – 67, 2008.
6. Woo, S. G., Kim, K. H., Son, K., Park, J. K. and Hur, B., "An Optimal Restoration Method of Noncarious Cervical Lesions Using Three-Dimensional Finite Element Analysis," Journal of the Korean Society for Precision Engineering, Vol. 24, No. 7, pp. 112 – 119, 2007.

Author: Wook Kwon
Institute: School of Mechanical Engineering
Street: Pusan National University
City: Busan
Country: Korea
Email: keith79@nate.com

Co-author: Kwang Hoon Kim
Institute: School of Mechanical Engineering
Street: Pusan National University
City: Busan
Country: Korea
Email: flyworld7@gmail.com

Co-author: Kwon Son
Institute: School of Mechanical Engineering
Street: Pusan National University
City: Busan
Country: Korea
Email: kson@pusan.ac.kr

Co-author: Jeong. Kil. Park
Institute: Department of Conservative Dentistry
Street: Pusan National University
City: Busan
Country: Korea
Email: jeongkil@gmail.com

Effect of Heat Denaturation of Collagen Matrix on Bone Strength

M. Todoh[1], S. Tadano[1] and Y. Imari[1]

[1] Division of Human Mechanical Systems and Design, Graduate School of Engineering, Hokkaido University, Sapporo, Japan

Abstract — **Bone is often regarded as a composite material consisting of hydroxyapatite (HAp-like) mineral particles, organic matrix (mostly Type I collagen) in microscopic scale. The mechanical properties of bone at macroscopic scale depend on the structural organization and properties of constituents in the microscopic scale. It has been considered that bone density is a predictor of its strength from a macroscopic perspective, but denaturation of the organic matrix would also lead to a significant loss of bone strength. In this study, heat-treated bone was examined as a collagen denatured model, and then four-point bending tests and impact tests were conducted to assess the role of the collagen matrix for mechanical properties of bone.**

Cortical bone specimens were obtained from the mid-diaphyses of bovine femurs and heat treated in an oven for 2 hours at 100, 150, 180 and 200°C, respectively. The specimens were stored in saline until the experiments. The elastic modulus and bending strength caused by collagen denaturation were measured by four-point bending tests using a mechanical testing machine. The tests were performed up to fracture at a deflection rate of 0.5 mm/min, with an inner and outer span of 10 and 24 mm respectively. Toughness was evaluated by measuring fracture energy of the specimens using a self-made impact tester.

As the results of four-point tests, the specimens heated at over 150°C failed with a low strain in the elastic region, suggesting a brittle fracture behavior. The elastic modulus of bone was slightly reduced with the heating temperature, whereas the bending strength significantly decreased, especially at 150°C. The results of the impact fracture test shows heat-induced collagen denaturation has great influence on the toughness of bone. These results suggest that not only denatured collagenmolecules but also collagen cross-links play an important role on the mechanical properties of bone.

Keywords — **Biomechanics, Bone, Collagen matrix, Stiffness, Fracture energy**

I. Introduction

Bone has a hierarchical structure at different structural levels and is often regarded as a composite material consisting of hydroxyapatite (HAp-like) mineral particles, organic matrix (mostly Type I collagen) and water phases in microscopic scale. The mechanical properties of bone at macroscopic scale depend on the structural organization and properties of constituents in the microscopic scale [1-3]. Considerable attempts have been made to investigate the effect of the microscopic constituent on the mechanical properties of bone. It is the interaction between the mineral and organic material that determines the mechanical properties. The effect of mineral content on the stiffness, strength or viscoelasticity of bone has been widely investigated [4-7]. However, the mechanical role of organic phase in bone has been little known. According to the composite theory, the stiff mineral controls the stiffness and strength of bone, whereas the collagen matrix controls the toughness and viscoelasticity of bone. The bone density is considered as a predictor of its strength from perspective, but the denaturation of collagen matrix would also lead to a significant loss of bone strength.

The current study examined the effect of collagen denaturation to the mechanical properties of bovine cortical bone by heat treatment. Specimens were heat-treated in an oven at 100 to 200°C for 2 hours. The elastic modulus and bending strength caused by collagen denaturation were measured by four-point bending tests using a universal testing machine. The toughness was evaluated by measuring fracture energy of the bone specimens using a pendulum-typed impact tester.

II. Materials and Methods

A. Collagen denaturation

Cortical bone specimens with average sizes of 30.0×4.0×1.5 mm for four-point bending tests and 30.0×3.0×3.0 mm for impact tests were harvested from the mid-diaphyses of bovine femur with longer side edge aligned along the femoral axis. Rough cuts were done by using hand-saw and fine cuts by using low-speed diamond saw (SBT650, South Bay Technology, Inc. USA).

The specimens were heat-treated in an oven (AVO-250, AS ONE Corp., Japan) at 100, 150, 180 and 200°C for 2 hours. This temperature range was selected for this study because the collagen network in bone denatures at certain specific temperatures: 60°C for the non-calcified collagen and 150°C for the calcified collagen [8]. Based on the results of previous studies using X-ray diffraction and scanning electron microscopy techniques, at such low temperatures no significant changes in the crystal structure and morphological characteristics of the mineral phase would be expected [9].

Chwee Teck Lim, James C.H. Goh (Eds.): ICBME 2008, Proceedings 23, pp. 2034–2037, 2009
www.springerlink.com

Until the mechanical experiments, the specimens were preserved in a saline solution.

B. Mechanical tests

Four-point bending tests, with an inner and outer span of 10 and 24 mm, were performed using universal testing machine (Model4411, Instron Corp., USA) to evaluate the elastic modulus M [Pa] and bending strength σ_b [Pa] of cortical specimens with different heating temperature by the following equations, respectively.

$$E = Fa^2(3l+2a)/t^3bv \quad (1)$$

$$\sigma_b = 3Fl/2t^2b \quad (2)$$

where F [N] is the applied load measured by load cell (maximum load 5 kN), a [m] is the inner span, l [m] is the outer span, b [m] is the width of specimen, t [m] is the thickness of specimen and v [m] is the deflection.

All the bending tests for heat-treated samples were carried out at constant deflection rate of 0.5 mm/min at room temperature. Elastic modulus was calculated as the slope, measured with a least-squares linear regression in the linear region of the load vs. deflection curve.

Impact tests were performed using pendulum-typed impact tester (self-made; pendulum mass = 750 g; arm length = 210 mm; initial mass height = 75 mm) (Fig. 1) to evaluate the fracture energy of cortical specimens with different heating temperature.

Fracture energy W [J] was defined as the following equation.

$$W = Mgl(\cos\theta_2-\cos\theta_1)-L \quad (3)$$

where M [kg] is mass of pendulum arm, g [m/s^2] is gravitational acceleration, l [m] is pendulum arm's length, θ_1 [rad] is initial angle of pedulum arm, θ_2 [rad] is pendulum arm angle after bone fracture and L [J] is the energy loss of pendulum tester.

All experiments for heat-treated samples were carried out at room temperature.

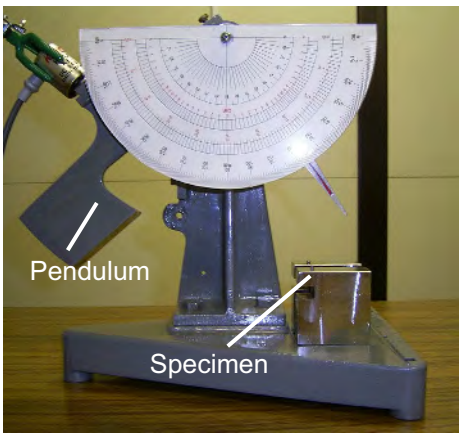


Fig. 1 Pendulum-typed impact tester for measuring fracture energy of heat denaturated cortical bone

C. Measurement of denatured collagen

To quantify the effect of heat denaturation, the denatured collagen in cortical bone specimens were measured by using α-chymotripsin selective digestion technique. Specimens were demineralized by immersing in 10% disodium EDTA (ethylene diamine tetraacetic acid) solutions (4°C, pH=7.4) for 7 days. Each specimen after demineralization was weighed by using an electronic balance (GF-200, A&D Corp. Ltd., Japan) after drying in vacuum oven (AVO-250, AS ONE Corp., Japan) at room temperature (25°C) for 3 hours. After demineralization, specimens were immersed in α-chymotripsin solution (1.0 mg/ml) at 37°C by using a heating bath (B-490, Buchi Labortechnik AG, Switzerland) for 24 hours, and then weighed again.

Percentage denatured collagen DC [%] was defined as following equation.

$$DC = (W-W_d)/W \quad (4)$$

where W [kg] and W_d [kg] are weight before and after immersing in α-chymotripsin solution.

D. XRD Analysis

The crystallinity of mineral phase in each specimen was evaluated by X-ray diffraction technique. The samples were scanned with Zr filtered Mo-Kα X-ray radiation (RINT2000, Rigaku Co., Japan) at 40 kV and 40 mA, at 0.3 deg/min, over a 2θ range of 10°-30°.

III. Results

Figure 2 shows the changes in cortical bone specimens by heat denaturation. Increasing the heating temperature, the surface of specimen gradually turned brown. This phenomenon was occurred by forming the nonenzymatic cross-link in collagen, so-called Maillard reaction. Some studies indicated that there is an age-related increase in nonenzymatic cross-links in collagen [10].

The typical bending load vs. deflection curves for denatured specimens at different temperature are shown in Fig. 3. The ultimate deflection of denatured specimens over 150°C is significantly small compared to the others.

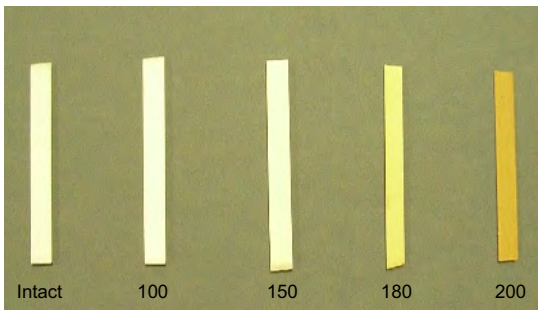


Fig. 2 Changes in cortical bone specimens by heat denaturation of collagen

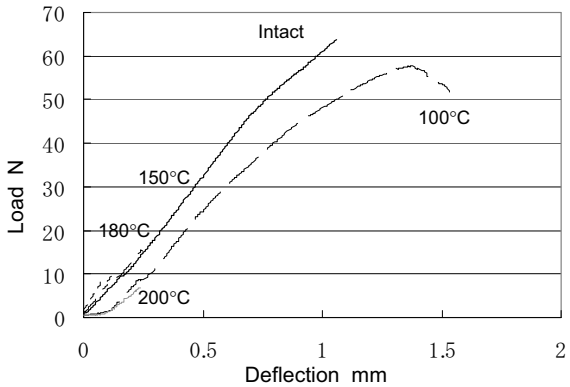


Fig. 3 Load vs. deflection curve by four-point bending test

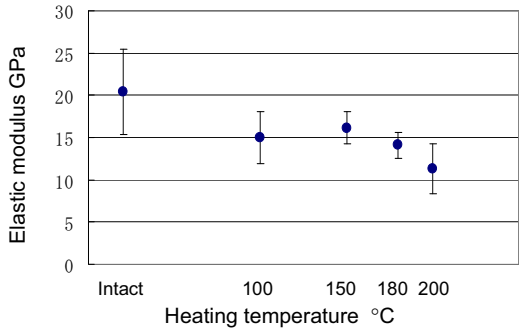


Fig. 4 Elastic modulus vs. heating temperature

The elastic modulus (obtained from the linear region of Fig. 3) and tensile strength (obtained from the maximum stress) vary with the increase of heating temperature as shown in Fig. 4 and Fig. 5, respectively. The elastic modulus of intact specimen is 20 GPa, whereas that of denaturated specimen (200°C) is less, equal to 12 GPa. The tensile strength of intact tissue is 178 MPa and that of denaturated tissue is 38 MPa.

The fracture energy varies with increase of heating temperature as shown in Fig. 6. The fracture energy of intact specimen is 12.8 J and that of denatured specimen is 4.5 J.

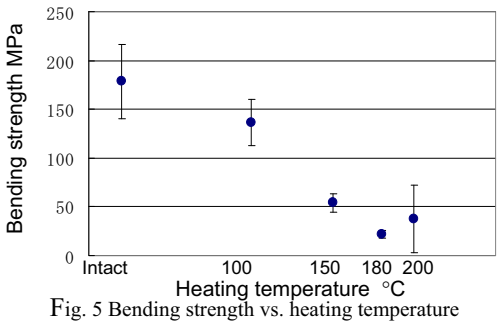


Fig. 5 Bending strength vs. heating temperature

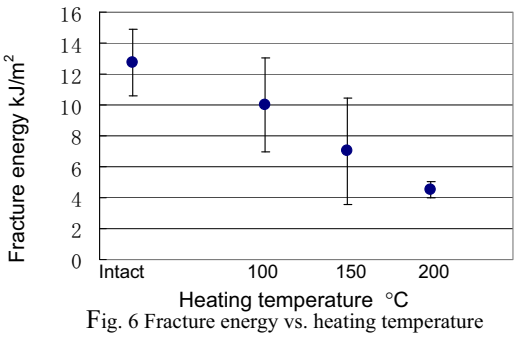


Fig. 6 Fracture energy vs. heating temperature

IV. Discussion

Figure 7 shows the X-ray diffraction profiles from denatured specimens at different heating temperature. From the results, at this temperature range (<200°C) no significant changes in the crystal structure was confirmed. Thus, the heat treatment could exclusively induce collagen denaturation without damaging the mineral phase.

As the results of the mechanical tests, the fracture toughness of cortical bone specimen significantly decreased as the temperature increased. Previous studies suggested that the fracture toughness decrease could be due to a decreased ability of the organics to sustain stress that arises from a weakening of the bonding between collagen fibrils at higher temperatures [11].

The relationship between the weight loss by α-chymotrypsin selective digestion and the heating temperature is shown in Fig. 8. The increase of weight loss as increased temperature indicates that the amount of denatured collagen increase as temperature. However, this amount was maximal in heating at 150°C. On the contrary, the weight loss by selective digestion decreased over 150°C. This indicates that both of the increase of denatured collagen and the increase of cross-links in collagen by a Maillard reaction. Therefore, these results suggest that not only denatured collagen molecules but also collagen cross-links play an important role on the mechanical properties of bone.

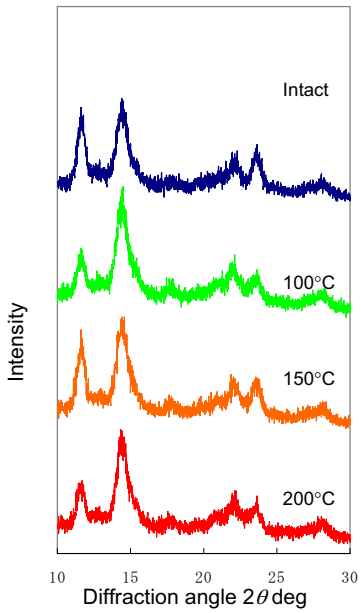


Fig. 7 X-ray diffraction pattern from denatured specimens at different temperature

V. Conclusions

This study examined the effect of collagen denaturation to the mechanical properties of bovine cortical bone by heat treatment. The collagen phase was denatured by heat treatment. The elastic modulus, bending strength and fracture energy were measured by the mechanical tests. The results of this study indicate that the heat-induced collagen denaturation has much influence on the mechanical properties of bone.

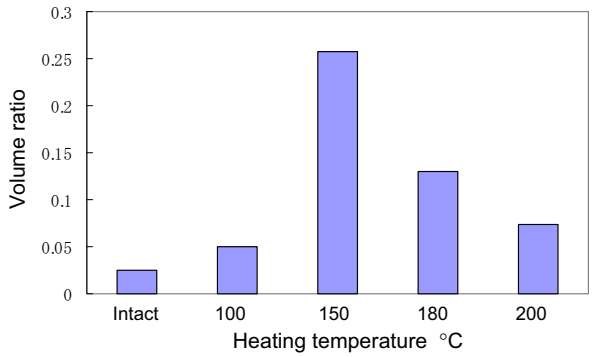


Fig. 8 Weight loss by α-chymotrypsin selective digestion

Acknowledgment

This research was partially supported by Grant-in-Aid for Young Scientists (B) (No. 18760069) from Ministry of Education, Culture, Sports, Science and Technology of Japan.

References

1. Rho JY, Kuhn-Spearing L, Zioupos P (1988) Mechanical properties and hierarchical structure of bone. Med Eng & Phys 20:92–102.
2. Yamashita J, Furman BR, Rawls HR et al. (2002) Collagen and bone viscoelasticity: A dynamic mechanical analysis. J Biomed Mater Res 63:31–36.
3. Fratzl P, Gupta HS, Paschalis EP (2004) Structure and mechanical quality of the collagen-mineral nano-composite in bone. Mater Chem 14:2115–2123.
4. Vose GP, Kubala AL (1959) Bone strength – Its relationship to X-ray determined ash content. Human Biol 31:262–270.
5. Currey JD (1969) The mechanical consequences of variation in the mineral content of bone. J Biomech 2:1–11.
6. Broz JJ, Simske SJ, Greenberg AR (1995) Material and compositional properties of selectively demineralized cortical bone. J Biomech 28:1357–1368.
7. Wang T, Feng Z (2005) Dynamic mechanical properties of cortical bone: The effect of mineral content. Mater Letters 59:2277–2280.
8. Kronick PL, Cooke P (1996) Thermal stabilization of collagen fibers by calcification. Connect Tissue Res 33:275-282.
9. Wang X, Bank RA, TeKoppele JM et al. (2001) The role of collagen in determining bone mechanical properties. J Orthop Res 19:1021–1026.
10. Wang X, Shen X, Li X et al. (2002) Age-related changes in the collagen network and toughness of bone. Bone 31:1–7.
11. Yan J, Clifton KB, Mecholsky JJ et al. (2007) Effect of temperature on the fracture toughness of compact bone. J Biomech 40:1641–1645.

Author: Masahiro Todoh
Institute: Hokkaido University
Street: Kita-13, Nishi-8, Kita-ku
City: Sapporo
Country: Japan
Email: todoh@eng.hokudai.ac.jp

Non-linear Image-Based Regression of Body Segment Parameters

S.N. Le[1], M.K. Lee[2,3] and A.C. Fang[1]

[1] Department of Computer Science, National University of Singapore, Singapore
[2] School of Sports, Health and Leisure, Republic Polytechnic, Singapore
[3] Physical Education and Sports Science, National Institute of Education, Nanyang Technological University, Singapore

Abstract — **Biomechanical analysis of human movement often requires accurate estimation of body segment parameters (BSP). These values are segmental inertial properties, including mass, center of mass and moments of inertia. They can be measured directly on living subjects using techniques such as Magnetic Resonance Imaging (MRI), Computed Tomography (CT) and gamma-mass scanning. Despite their accuracy, these methods involve high radiation and require expensive scanners that are not always readily available to biomechanics researchers. Another popular way to estimate BSP is by studying regression equations on experimental data, commonly from cadaveric studies. These approaches, however, have been criticized for the limited cadaveric data.**

We propose a novel in vivo regression method for computing BSP using non-linear image-based techniques. Our method was first facilitated with X-ray images of sample subjects acquired from Dual-energy X-ray Absorptiometry (DXA), where the radiation dose is approximately 1/10th that of a standard chest X-ray. A feature-based image transformation was then applied to predict a mass distribution image for the new subject, while he was not required to undergo DXA scanning. The subject's BSP values were subsequently computed using the mass distribution obtained from the predicted image. Cross-validation of moments of inertia among population samples shows that our method has mean percentage errors of 7.5% for limbs and 7.1% for head and torso, while the corresponding errors are 9.3% and 15% in cadaver-based non-linear regression method. It suggests that our image-based regression approach is promising for estimating BSP on living subjects. It is not limited by ranges of cadaveric data or differences between living and dead tissues.

Keywords — **Body Segment Parameters, Dual-energy X-ray Absorptiometry, Image Warping, Regression Method.**

I. Introduction

Body segment parameters (BSP) are the inertial properties of each segment of the anthropometric model, which consist of mass, center of mass and moments of inertia. The accuracy of BSP estimation has a significant influence on mechanical quantities computations, including calculating the kinetics of motion using inverse or forward dynamics [6, 18], gait analysis [16], and determining the sensitivity of joint resultants [1].

Where in vivo methods are unavailable, one popular way to estimate BSP is by constructing statistical models from cadaveric data [4]. [2] and [19] developed regression equations using non-uniform spatial scaling of segmental mass. In other studies, moments of inertia were estimated from segmental measurements [10] or body mass and standing height of the subject [5]. Although cadaver-based methods provide a convenient means to predict BSP, they have been criticized for limited number of samples and variety of sample population. Due to obvious difficulties in acquiring comprehensive cadaveric data, researchers have turned to in vivo methods.

Three-dimensional (3-D) in vivo imaging techniques, such as MRI [14], CT [11, 15] and gamma-mass scanning [20], have been used for determining accurate 3-D BSP. However, they have been criticized for the high level of radiation involved, cost of the scans and limited availability of expensive scanners.

In recent years, two-dimensional (2-D) in vivo imaging techniques using Dual-energy X-ray Absorptiometry (DXA) has been found to be useful for obtaining accurate 2-D BSP [7]. Despite their 2-D nature, the results hold promise as, compared to 3-D imaging, DXA scanning is less expensive while delivering a much lower dose of radiation.

We propose a new approach for estimating a subject's BSP using a feature-based image warping technique facilitated by a set of sample DXA images. Our method predicts a mass distribution image that is statistically representative of the subject by computing a non-linear image transformation based on feature correspondences. To provide the features required in the transformation, each DXA image was annotated with external anthropometric and body segmentation information. Subsequently, BSP values were obtained directly from the predicted mass image. The novelty of our approach is that mass distributions are represented and processed in their raw image form. This is in contrast with previous approaches where regression models are formulated by associating aggregated quantities, such as moments of inertia with external anthropometric. We retain the details in spatial variations of mass, which would have been lost in the aggregated quantities.

In section II, we present our method of estimating BSP from DXA images using non-linear image-based tech-

Chwee Teck Lim, James C.H. Goh (Eds.): ICBME 2008, Proceedings 23, pp. 2038–2042, 2009
www.springerlink.com

niques. Section III compares the errors between our computed BSP and that from cadaver-based non-linear regression equations [15]. Section IV presents further discussions and conclusions.

II. Materials and method

A. Dual-energy X-ray Absorptiometry

DXA machine (QDR-1000/W, Hologic Inc., Bedford, MA, USA) uses two X-ray beams of alternating intensities to measure areal body density (gcm^{-2}) and body composition. The scanning process is done with the help of Hologic QDR Software. The high-energy beam passes through all matter in its path and is attenuated depending on the amount of mass present, which can be illustrated by plotting the attenuations along each scanline of the scanned image. Attenuation values are recorded in rectangular cells of 1.303cm x 0.618cm or 150 x 106 pixels per whole body, resulting in a scan area of 195.5cm x 65.5cm. Higher attenuation indicates higher mass in each cell (Fig. 1).

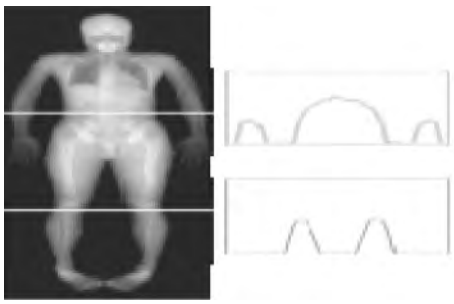


Figure 1: Whole body DXA scan of an adult male subject. Two scanlines crossing belly and knees show attenuation values changing according to the mass present. The raw attenuation image has a resolution of 150 x 106.

B. Mass distribution image from DXA

Prior to building mass distribution image, we increased the resolution of DXA attenuation image by applying a bicubic spline interpolation [17]. The process is necessary for an accurate BSP computation. We applied two cubic spline interpolations, one along horizontal direction and one along vertical direction to increase each dimension by 3 times and 5 times respectively. The added pixels' attenuations were interpolated from original pixels' values. The resulting image has a dimension of 750 x 318, or 0.2606cm x 0.2059cm per pixel.

Each pixel represents the attenuations of the high-energy beam linearly attenuated by the amount of mass present along the beam [7]. The relationship between attenuation and mass can be represented as follows:

$$m(x) = \sigma(a(x)) = m_1 a(x) + m_0 \quad (1)$$

where $m(x)$ and $a(x)$ are the mass (g) and attenuation values respectively at pixel position $x \in R^2$.

We obtained m_1 and m_0 by scanning reams of consumer-grade photocopier paper arranged in five stacks of increasing height (Fig. 2, Left). The projected region of each stack was determined using a flood-fill algorithm [9] initiated by a mouse click at the approximate center of each region. The mass of each stack was then measured with a weighing scale of precision level up to 0.001kg.

The per-pixel projected mass was calculated by taking the mass of each stack divided by the number of pixels in corresponding region. Similarly, the average per-pixel attenuation in each region was calculated by dividing the sum of the attenuation values by the number of corresponding pixels. In addition, we averaged the background attenuation, which has zero mass, to obtain a total of six mass-versus-attenuation calibration points. The calibration line was used to compute the parameters for Eq. 1.

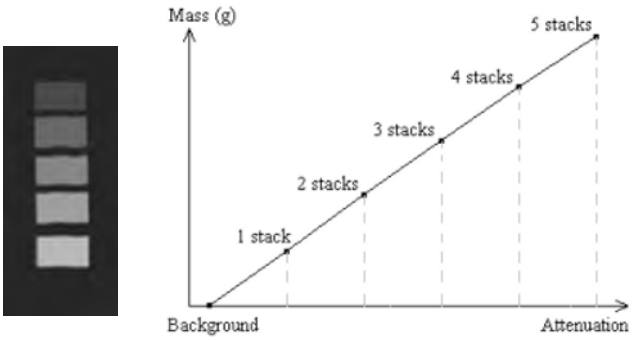


Figure 2: Phantom setup for calibrating the relationship between mass and attenuation. (Left) Scanned image of five stacks of photocopy paper with increasing mass. (Right) Attenuation-to-mass calibration line, which goes through background point and five points representing five stacks.

C. BSP computation using mass distribution image

Whole body image is segmented into 14 parts (Fig. 3). The segmenting lines between limbs cross the bones at joints. We computed BSP for each segment using mass per pixel values obtained directly from mass distribution image.

Mass of each segment k, M_k, was computed by taking the sum of masses at all pixels belonging to that segment:

$$M_k = \sum_{x \in k} m(x) \quad (2)$$

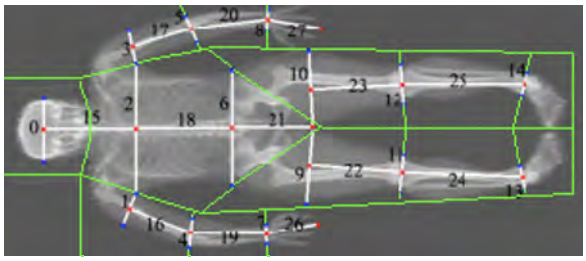


Figure 3: Body composition image produced by Hologic QDR Software together with our defined body segmentation and feature lines. Green lines segment the whole body into 14 parts. White lines are the features required for predicting a new mass image. Mediolateral lines are numbered from 0 to 14, while longitudinal lines are numbered from 15 to 27.

where the attenuation-to-mass conversion (Eq. 1) was used to evaluate each pixel's mass.

Center of mass of segment k, c_k, is computed as follows:

$$c_k = \frac{1}{M_k}\sum_{x\in k} m(x)x \tag{3}$$

Moments of inertia of segment k about the front-to-back axis passing through c_k is calculated as follows:

$$I_k = \sum_{x\in k} m(x)\,|\,x - c_k\,|^2 \tag{4}$$

D. Mass distribution image prediction

Mass distribution image of the new subject is predicted by warping the image of another subject based on the differences between two subjects' features (Fig. 4). The technique is called feature-based image warping [3], where source image is transformed into destination image so that features in source image become corresponding features in destination image.

We used 28 features for the warping of mass image (Fig. 3). The 15 mediolateral lines determine segmental width. The 13 longitudinal lines connect the midpoints of mediolateral lines and indicate segmental length.

For each mass image prediction, we built a pair of feature lines, one for source image and one for predicted image. Source features were built directly from body composition image and its segmentation (Fig. 3), while destination features were predicted from source features and the relationships between external measurements of source and destination subjects, such as segmental length and girth. It can be done with common assumptions that the cross-sectional area of each body segment was elliptical [12] and the ratio between segmental width and thickness is almost constant

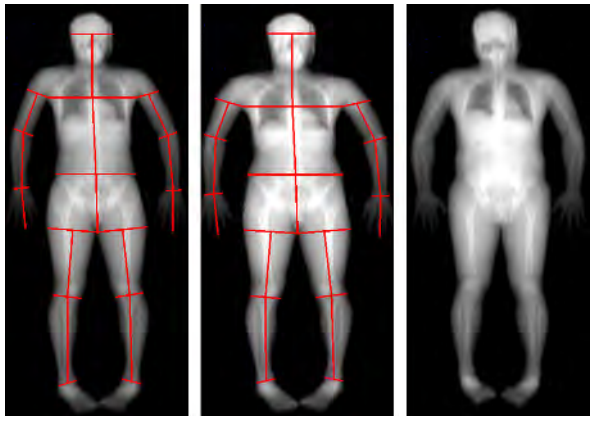


Figure 4: (Left) Mass image and features of a chosen source subject. (Middle) Predicted mass image with new features built from source features and relationships between two subjects' measurements. (Right) New subject's actual mass image.

for each segment [19]. Hence, the ratio between segmental widths of source and predicted images is almost identical to the ratio between measured segmental girths of source and destination subjects. After mediolateral features were determined, longitudinal features for predicted image were created by connecting the midpoints of mediolateral lines.

In order to obtain a good approximation to destination subject's actual mass distribution, it is important to choose a source subject that resembles destination body type closely. Root-mean-square difference between features length in source and destination subjects was minimized to give a good match in front view. Since mass image does not store depth information, we also compared total body mass divided by sum of squares of features length to avoid significant difference in body thickness of source and destination subjects. The predicted mass image is subsequently normalized so that predicted whole body mass is equal to the actual mass.

III. Results

We built a set of mass distribution images from 18 adult male participants with age from 18 to 52, height from 170cm to 182cm and weight from 53kg to 76kg. Feature lines and body segmentation were defined for each image, together with external body measurements and mass.

To evaluate the errors of our method, we estimated BSP for each subject using image-based regression and examined them with values computed directly from DXA, which has been found to be an accurate criterion for 2-D BSP information [7]. The errors were then compared with that in non-linear cadaver-based regression method [19] (Table 1).

Table 1: Percentage errors for the moments of inertia computed by cadaver-based regression approach [19] and by our image-based regression method.

	Cadaver-based Regression (%)	Image-based Regression (%)
Head	15	6.9
Torso	15	7.3
Mean	15	7.1
Upper Arm	10	8.1
Lower Arm	11	6.6
Hand	15	9.5
Upper Leg	8	6.2
Lower Leg	5	6.1
Foot	7	8.8
Mean	9.3	7.5

In image-based method, the mean errors are 7.5% for limbs and 7.1% for head and torso, while the corresponding errors are 9.3% and 15% in cadaver-based method. The differences are significant, especially for head and torso, which contain a large fraction of body mass.

IV. Conclusions

In this paper, we propose a non-linear image-based regression approach for estimating accurate BSP. Our approach works for all ranges of body types and dimensions since it is not based on cadaveric data. It does not require as many body measurements as in traditional regression methods, and involves much lower radiation level and cost compared to other imaging techniques. Moreover, the accuracy of our method can be easily improved by building a larger database of source images, which is feasible since the subjects are living humans.

One limitation of our approach is the lack of features for small areas such as shoulders and feet, which may lead to errors in those regions. Our approach is currently two-dimensional, due to the lack of depth information in DXA image. It can be extended to three-dimensional by incorporating modeling techniques. An extension to DXA for 3-D reconstruction has also been recently studied [13].

Acknowledgment

The authors wish to thank the Agency for Science, Technology And Research (A*STAR) for funding this research and Physical Education and Sports Science, National Institute of Education for permission to use DXA scanner.

References

1. Andrews J G, Mish S P. Methods for investigating the sensitivity of joint resultants to body segment parameter variations. Journal of Biomechanics 29, 1996, pp 651-654.
2. Barter J T. Estimation of the mass of body segments. WADC Technical Report, Wright-Patterson Air Force Base, Ohio, 1957, pp 57-260.
3. Beier T, Neely S. Feature-Based Image Metamorphosis. Computer Graphics (SIGGRAPH '92), 1992, pp 35-42.
4. Chandler R F, Clauser C E, McConville J T, Reynolds H M, Young J W. Investigation of inertial properties of the human body. AMRL Technical Report, Wright-Patterson Air Force Base, Ohio, 1975, pp 74-137.
5. Clauser C E, McConville J T, Young J W. Weight, Volume, and Center of Mass of Segments of the Human Body. Aerospace Medical Research Laboratory, Wright-Patterson Air Force Base, Dayton, OH, Technical Report, 1969, AMRL-TR-69-70.
6. Dapena J. A method to determine the angular momentum of a human body about three orthogonal axes passing through its center of gravity. Journal of Biomechanics 11, 1978, pp 251-256.
7. Durkin J L, Dowling J J, Andrews D M. The measurement of body segment inertial parameters using dual-enery x-ray absorptiometry. Journal of Biomechanics 35, 2002, pp 1575-1580.
8. Durkin J L, Dowling J J. Analysis of body segment parameter differences between four human populations and the estimation errors of four popular mathematical models. Journal of Biomechanical Engineering 125, 2003, pp 515-522.
9. Hearn D, Baker M P. Computer Graphics with OpenGL. Prentice Hall, 2003.
10. Hinrichs R N. Regression equations to predict segmental moments of inertia from anthropometric measurements: an extension of the data of chandler et al. Journal of Biomechanics 18, 1985, pp 621-624.
11. Huang H K. Evaluation of cross-sectional geometry and mass density distributions of humans and laboratory animals using computerized tomography. Journal of Biomechanics 16, 1983, pp 821-832.
12. Jensen R K. Body segment mass, radius and radius of gyration proportions of children. Journal of Biomechanics 19, 1986, pp 359-368.
13. Le S N, Lee M K, Banu S, Fang A C. Volumetric reconstruction from multi-energy single-view radiography. Computer Vision and Pattern Recognition, 2008, pp 1-8.
14. Martin P E, Mungiole M, Marzke M W, Longhill J M. The use of magnetic resonance imaging for measuring segment inertial properties. Journal of Biomechanics 22, 1989, pp 367-376.
15. Pearsall D J, Raid J G, Livingston L A. Segmental inertial parameters of the human trunk as determined from computed tomography. Annals of Biomedical Engineering 24, 1996, pp 198-210.
16. Pearsall D J, Costigan P A. The effect of segment parameter error on gait analysis results. GAIT & POSTURE 9, 1999, pp 173-183.
17. Press W H, Flannery B P, Teukolsky S A, Vetterling W T. Cubic Spline Interpolation. Numerical Recipes in FORTRAN: The Art of Scientific Computing, 2nd edition, 1992, pp 107-110.
18. Rao G, Amarantini D, Berton E, Favier D. Influence of body segments' parameters estimation models on inverse dynamics. Journal of Biomechanics 39, 2006, pp 1531-1536.
19. Yeadon M, Morlock M. The appropriate use of regression equations for the estimation of segmental inertia parameters. Journal of Biomechanics 22, 1989, pp 683-689.
20. Zatsiorsky V, Seluyanov V. The mass and inertia characteristics of the main segments of the human body. Biomechanics VIII-B. Human Kinetics Publishers Champaign, IL., 1983, pp 1152-1159.

Author: Le Ngoc Sang
Institute: National University of Singapore
Street: Computing 1, Law Link, Singapore 117590
City: Singapore
Country: Singapore
Email: lnsang@nus.edu.sg

Author: Lee Mei Kay
Institute: Republic Polytechnic
Street: 9 Woodlands Avenue 9, Singapore 738964
City: Singapore
Country: Singapore
Email: lee_mei_kay@rp.sg

Author: Anthony Fang
Institute: National University of Singapore
Street: Computing 1, Law Link, Singapore 117590
City: Singapore
Country: Singapore
Email: afang@comp.nus.edu.

A Motion-based System to Evaluate Infant Movements Using Real-time Video Analysis

Yuko Osawa[1], Keisuke Shima[1], Nan Bu[2], Tokuo Tsuji[1], Toshio Tsuji[1], Idaku Ishii[1], Hiroshi Matsuda[3], Kensuke Orito[4], Tomoaki Ikeda[5] and Shunichi Noda[6]

[1] Graduate School of Engineering, Hiroshima University, Higashi-Hiroshima, Japan,
[2] National Institute of Advanced Industrial Science and Technology, Tosu, Japan,
[3] Tokyo University of Agriculture and Technology Institute of Symbiotic Science, Fuchu, Japan,
[4] Department of Veterinary, Azabu University, Sagamihara, Japan,
[5] National Cardiovascular Center, Suita, Japan, [6] NODA Maternity Clinic, Miyakonojyou, Japan

Abstract — **This paper proposes a marker-less motion measurement and analysis system for quantitative evaluation of movements of infants. In this system, movements of infants are measured using a single video camera, and then changes of body position and motion in infants are calculated from binarized images, which are extracted using background subtraction or inter-frame difference. Furthermore, eight indices are derived for quantitative evaluation of movements of infants, such as body activity level and amount of body motion. Base on these data, doctors can therefore get an intuitive understanding of the movements of infants without long-period observation. This is considered helpful for supporting diagnosis and detecting of infants' disability or function diseases in the early stages. In this paper, the evaluation indices and features of movement between 14 full-term infants (FTIs) and 11 low-birthweight infants (LBWIs) are compared using the prototype developed. The experimental results show that, with some LBWIs, the upper body moves more than the lower body compared with FTIs, demonstrating that the proposed system can quantitatively evaluate the difference between the movements of FTIs and LBWIs.**

Keywords — **infant, movement analysis, video image processing, monitoring system**

I. Introduction

Early detection of neuromotor disorders and prediction of later movement problems in infants is of paramount importance to improve and mitigate the severity of such conditions. Techniques for detection of infant neuromotor disorders based on infant movements have been widely adapted and discussed in clinical environments [1][2]. However, objective and quantitative evaluation of infant movements is difficult even for highly trained doctors. Techniques that enable simple screening test and quantitative evaluation of the movements of newborn babies would therefore be useful in the early detection of infant neuromotor disorders, and would also reduce the burden on doctors.

Recently, quantitative evaluation methods for the movement of newborns have been developed using three-dimensional movement analyses [3][4]. These previous studies suggest the possibility of distinguishing between full-term and pre-term infants [4]. However, these camera systems are concerned with the burden on newborn babies, since a large number of markers are necessary to measure the movements. Furthermore, it might be difficult to measure the movements for screening in general clinical environments, because such systems are expensive and time-consuming. To overcome these problems, it is preferable to develop a method that can measure and evaluate movements quantitatively, without using markers.

This paper proposes a system to measure and quantitatively evaluate infant movements. In this system, feature quantities related to body movements of infants are extracted from video images recorded by a single video camera without using markers. The body movements are then evaluated using eight indices (such as body activity, amount of body motion and symmetry of limb movements), computed from the feature quantities. Display of the evaluation results and feature quantities enables users to easily understand the changes in an infant's condition.

II. System for measurement and analysis system

The structure of the proposed system is shown in Fig. 1. The details of each process are explained in the following subsections.

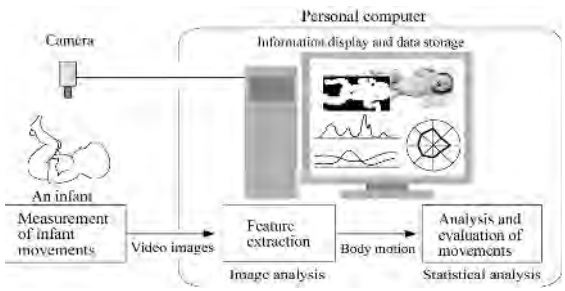


Fig. 1 Concept of the proposed motion measurement and analysis system for the infants

Chwee Teck Lim, James C.H. Goh (Eds.): ICBME 2008, Proceedings 23, pp. 2043–2047, 2009
www.springerlink.com

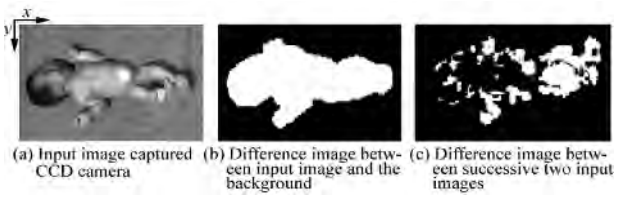


Fig. 2 Binary images obtained from input images

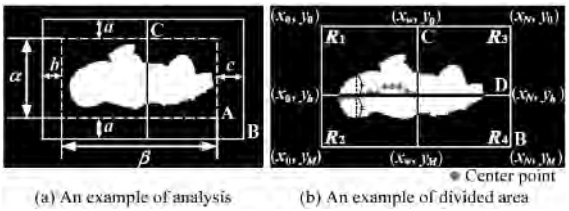


Fig. 3 Initialization of motion analysis image

A. Measurement of infant movements

A camera is used to measure the movements of an infant in an incubator. The video images were stored on a computer database using a video image grabber board (sampling frequency: f_S [Hz]).

B. Feature extraction

Examples of video images and binary images for extraction of the movement features are shown in Fig. 2. In this paper, brightness components are extracted from video images, and are then binarized using background subtraction (to create a *body position distribution image*) with a threshold T (the pixel values of the area are set as 1 (white), and those of the background area are set as 0 (black); see Fig. 2(b)). In addition, a binary image representing the infant's movement area (called as a *movement distribution image*) is extracted using inter-frame difference (the pixel values of the movement areas become 1; see Fig. 2(c)).

Here, in order to improve the computational efficiency, the region-of-interest (ROI) area related to infant's body movement is extracted for analysis. First, a rectangle around the white pixels of the body position distribution image integrated for a number of consecutive seconds is defined as area A ($\alpha \times \beta$ [pixels]) (see Fig. 3(a)). Then, margins (a, b, and c) are set on the four sides of area A, respectively, and the extended area is defined as B (see Fig. 3(b)). The origin point (x_0, y_0) of area B is top-left. Suppose the number of pixels on the x- and y-axes are N and M, the numbers of pixels on the x- and y-coordinates of the image are set as x_n (n = 1, 2, …, N) and y_m (m = 1, 2, … , M), respectively.

By setting baselines in the area B, it can be divided into four areas, one represents each of the infant's limbs. First, area A is divided at the ratio of d to (1-d) based on the ratio of upper to lower body, and the row $x = x_w$ is then defined as baseline C. Further, the area of the upper body ($x_0 < x_n < x_w$, $y_0 < y_m < y_M$), which is extracted from area A by baseline C, is divided into the left and right sides of the body, and that line is then defined as baseline D. In this paper, for the decision of baseline D, the middle points of the longest row of white pixels are calculated in each row of the y-axis. The line of the x-axial $y = y_h$ ($0 < h < M$) included in the large numbers of the middle points is decided as baseline D. Here, the areas corresponding to each region divided using baselines C and D are defined as R_k (k = 1, 2, …, 9), where R_1 to R_4 represent the area of the infant's left shoulder, right shoulder, left leg and right leg, respectively. In addition, R_5 is the area of the upper body, R_6 is the lower body, R_7 signifies the left side of the body, R_8 describes the right side of the body, and R_9 is the entire body.

As the feature quantities of infant movements in each area R_k (k = 1, 2, …, 9), the *change of position* ${}^{(k)}W_l$ and *motion* ${}^{(k)}O_l$ with respect to time are defined as follows:

$$ {}^{(k)}W_l = \sum_{n=0}^{N-1}\sum_{m=0}^{M-1} {}^{(k)}g_l(x_n, y_m) \tag{1} $$

$$ {}^{(k)}O_l = \sum_{n=0}^{N-1}\sum_{m=0}^{M-1} {}^{(k)}g_l'(x_n, y_m) \tag{2} $$

$$ {}^{(k)}g_l'(x_n, y_m) = \left| {}^{(k)}g_l(x_n, y_m) - {}^{(k)}g_{l-1}(x_n, y_m) \right| \tag{3} $$

Here, ${}^{(k)}g_l(x_n,y_m)$ is the value of each pixel in the body position distribution image in area R_k (${}^{(k)}g_l(x_n,y_m) = 1$ represented by the white pixels, and ${}^{(k)}g_l(x_n,y_m) = 0$ by the black pixels; ${}^{(k)}g_0(x_n,y_m) = {}^{(k)}g_1(x_n,y_m)$), l (l = 1, 2, …, L) is the frame number, and L describes the total number of frames in the video image.

C. Analysis and evaluation of movements

In the analysis and evaluation stage, quantitative evaluation indices are calculated based on medical knowledge [5] from the feature quantities of body movements. In this paper, the computational and standardization methods of eight indices to enable comparison of the differences in movements are described as follows.

(1) Body activity and amount of body motion

Body activity and amount of body motion referred as the rate of activity time and the amount of motion within the measurement time are calculated from the change in motion ${}^{(k)}O_l$. First, the threshold ${}^{(k)}M_{th}$ defined by Eq. 4 is used to judge whether movement has occurred in the infant.

$$ {}^{(k)}M_{th} = r\,{}^{(k)}W_l \quad (0 < r < 1) \tag{4} $$

Points at which the change in motion ${}^{(k)}O_l$ increases to threshold ${}^{(k)}M_{th}$ are defined as the infant's activity time, and body activity ${}^{(k)}ACT$ is then calculated from the ratio of activity time to all measurement time as follows:

$$ {}^{(k)}ACT = \frac{1}{L}\sum_{l=1}^{L} {}^{(k)}A_l \times 100 \tag{5} $$

$$ {}^{(k)}A_l = \begin{cases} 1 & ({}^{(k)}O_l \geqq {}^{(k)}M_{th}) \\ 0 & ({}^{(k)}O_l < {}^{(k)}M_{th}) \end{cases} \tag{6} $$

Next, the amount of body motion ${}^{(k)}MOV$ during the movement per unit time is calculated using Eqs. 7 and 8.

$$ {}^{(k)}MOV = \frac{1}{L}\sum_{l=1}^{L} \frac{{}^{(k)}M_l}{{}^{(k)}S} \tag{7} $$

$$ {}^{(k)}M_l = \begin{cases} O_l & ({}^{(k)}O_l \geqq {}^{(k)}M_{th}) \\ 0 & ({}^{(k)}O_l < {}^{(k)}M_{th}) \end{cases} \tag{8} $$

Here, ${}^{(k)}S$ is the number of pixels in each area.

(2) Displacement and fluctuations in COG

Center of gravity (COG) displacement of body position and fluctuations in COG *x*- and *y*-axially are extracted from the change of position ${}^{(k)}W_l$ and the body position distribution image. From this image, the coordinates of COG ($G_{x,l}$, $G_{y,l}$) are calculated by Eqs. 9 and 10.

$$ G_{x,l} = \frac{1}{{}^{(k)}W_l}\sum_{n=0}^{N-1}\sum_{m=0}^{M-1} x_n \, {}^{(9)}g_l(x_n, y_m) \tag{9} $$

$$ G_{y,l} = \frac{1}{{}^{(k)}W_l}\sum_{n=0}^{N-1}\sum_{m=0}^{M-1} y_n \, {}^{(9)}g_l(x_n, y_m) \tag{10} $$

Displacement in the COG D_m is defined as follows:

$$ D_m = \frac{1}{L}\sum_{n=0}^{N-1}\left(\frac{\sqrt{D_{x,l}^2 + D_{y,l}^2}}{{}^{(k)}W_l} \right) \tag{11} $$

where $D_{x,l} = G_{x,l} - G_{x,l-1}$, $D_{y,l} = G_{y,l} - G_{y,l-1}$, $G_{x,0} = G_{x,1}$, $G_{y,0} = G_{y,0}$. In addition, fluctuations in COG *x* and *y* signify the center frequencies of the power spectrum density calculated using the fast Fourier transform (FFT) from the *x*- and *y*-coordinates of the COG.

(3) Symmetry of movement, ratio of amount of body motion and ratio of body activity

Symmetry of movement describes the correlation between each area divided in the images calculated using the standardized cross-correlation function from the change in motion ${}^{(k)}O_l$ smoothed through a second-order Butterworth low-pass filter (cutoff frequency: f_p [Hz]). In addition, the ratios of amount of body motion and of body activity are defined as the ratio between feature quantities of each area.

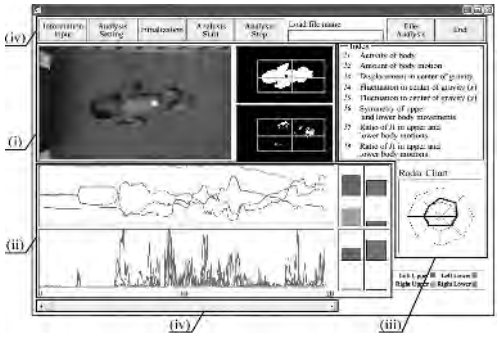


Fig. 4 An example of the operation scene of the prototype system

(4) Standardization of indices

The calculated evaluation indices for the infant are normalized to enable comparison of the differences in movement. In this paper, the standard normally distributed variables I_j are converted to the mean and standard deviations of the measurement data for full-term infants using Eq. 12.

$$ I_j = (z_j - \mu_j)/\sigma_j \tag{12} $$

Here, *j* corresponds to the index number, z_j is the computed value in each index, and μ and σ describe the average and standard deviation of each index in the full-term infant group, respectively. In the proposed method, I_1 represents the activity of the entire body ${}^{(9)}ACT$, I_2, I_3, …, I_8 signify the amount of entire body motion ${}^{(9)}MOV$, the entire displacement in COG D_m, and fluctuations in COG *x*- and *y*-axially, the symmetry of movement, the ratio of body mot-ion activity ${}^{(5)}ACT$ / ${}^{(6)}ACT$, and the ratio of amount of body motion ${}^{(5)}MOV$ / ${}^{(6)}MOV$, respectively.

D. Graphical output

The measured infant movements, the feature quantities, and the indices are provided to doctors on a display. A screenshot of interface of the proposed system is shown in Fig. 4. During operation, the monitor displays the following information: (i) a video image of the infant recorded using a camera, and the extracted binary images (distribution of body position and movement); (ii) feature quantities of position and movement calculated from the distribution of body position and movement; (iii) indices and radar charts computed from the feature quantities of position and movement; (iv) operation buttons and a scrollbar to allow video playback for a specific period, and changes in the scale of the waveform. The doctor can visually check infant's movements by playing the section of video corresponding to the time when abnormality appears in the feature quantities or radar chart.

III. Experiments

Method: Subjects consisted of 14 full-term infants (FTIs) (A-N) and 11 low-birthweight infants (LBWIs) (2,500 [g] or less) (O-Y). The 10 FTIs (A-J) were measured for 5 minutes, and the other infants were tested for about 50 minutes. In addition, the evaluation indices were extracted for 5-minute intervals, and the mean value and standard deviation for all measurement times were then calculated. The calculated indices were standardized on the basis of the values obtained from the 14 FTIs. The parameters of the experiments were f_S=30 [Hz], f_p=5 [Hz], d=0.55, r=0.01 and T=15 or T=45. The window length of FFT was 128 sets of sampled data, and the number of overlapping was 127; the corresponding values for the standardized cross-correlation function were 300 and 299, respectively.

Results: Radar chart representation of results of the indices is shown in Fig. 5 (a) and (b), which illustrate the indices of FTIs and LBWIs, respectively. Each axis shows the standard deviation of the 14 FTIs (A-N), the solid lines describe the average number of FTIs, and the dotted lines show the minus triple, triple and sextuplicate of the standard deviation in Fig. 5. Further, the heavy line shows the average value, and the shaded area indicates the standard deviation in each index. As an example of the feature quantities

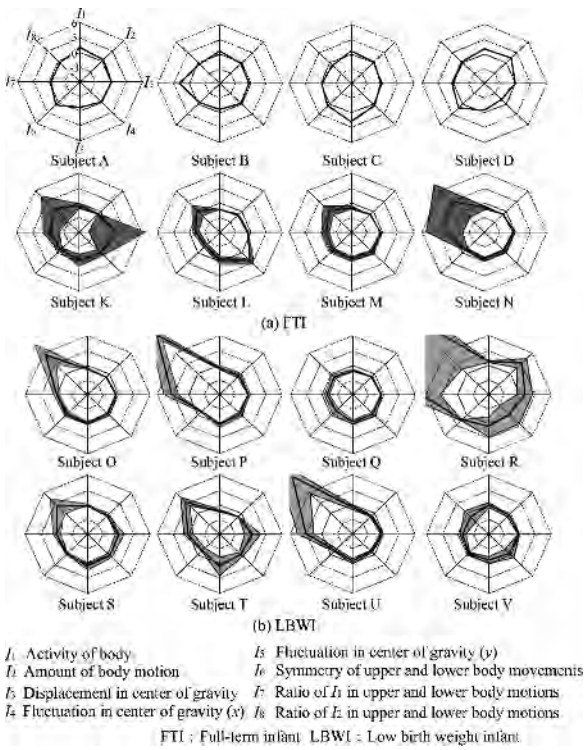


Fig. 5 Evaluation indices in each FTI and LBWI

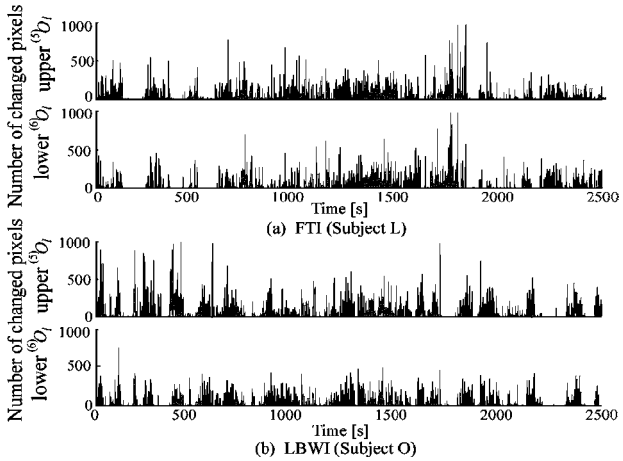


Fig. 6 The change of the FTI Subject L and LBWI Subject O

used for index computation, the change in motion of the upper and lower body of an FTI and a LBWI are shown in Fig. 6. The horizontal axis represents time, and the vertical axis describes the change in motion $^{(k)}O_l$.

IV. Discussion

The evaluation experiments demonstrated that all indices were close to the average value for all FTIs, except subjects K and N, but the indices are of large variation with most LBWIs (especially subjects O, P, R, T and U). Since the values of index I_8 for these subjects were large, it is thought that the lower body movements were small compared with movement of the upper body. Further, from the example of the movements of subject O (Fig. 10), it can be observed that those of the upper body were larger than those of the lower body. These results lead us to the conclusion that the extracted evaluation indices were able to reflect the movements of infants.

On the other hand, it is observed that some LBWIs have the same tendency as the mean values of the FTIs (subjects Q, S, and V). These results mean that the LBWIs do not have diseases despite their low birthweight and high risk of impaired motility function. Further, although subjects K and N were FTIs, their evaluation index variance was large, suggesting that their movements might be near those of LBWIs because their birthweights were comparatively low (subjects K and N were 2,738 [g] and 2,562 [g], respectively). Since the number of experimental subjects was small and the measurement time was short, it is necessary to investigate and make improvements for accurate evaluation.

V. Conclusion

This paper proposes a quantitative system to measure and evaluate infant movements. The system calculates eight evaluation indices from feature quantities of motion extracted from binarized images of infants without markers using a single video camera. This enables doctors to understand changes in an infant's movement condition, as video images, feature quantities and evaluation indices can be monitored on a real-time basis. In future research, we plan to increase the number of infants and measurement time, and investigate the relationships between motility function and abnormal movements in disabled and high-risk infants.

References

1. T.B. Brazelton, J. Kevin Nugent (1995) Neonatal Behavioral Assessment Scale 3rd Edition, Mac Keith Pr
2. V. Vojta (2000) Die zerebralen Bewegungsstorungen im Saugling-salte 6rd Editon, Hippokrates Verlag
3. L. Fetters, Y. Chen, J. Jonsdottir and E. Z. Tronick (2004) Kicking coordination captures differences between full-term and premature infants with white matter disorder, Human Movement Science, Vol. 226, pp 729-748
4. L. Meinecke, N. Breitbach-Faller, C.Bartz, R.Damen, G.Rau and C. Disselhorst-Klug (2006) Movement analysis in the early detection of newborns at risk for developing spasticitydue to infantile cerebral palsy, Human Movement Science, Vol.25, pp 125-144
5. Prechtl, H. F. R. and D. J. Beintema (1964) The Neurological Examination of the Full Term Newborn Infant, Little Club Clinics in Developmental Medicine, Vol.12

Author: Yuko OSAWA
Institute: Graduate School of Engineering, Hiroshima University
Street: 1-4-1 Kagamiyama
City: Higashi-Hiroshima
Country: Japan
Email: osawa@bsys.hiroshima-u.ac.jp

Cardiorespiratory Response Model for Pain and Stress Detection during Endoscopic Sinus Surgery under Local Anesthesia

K. Sakai and T. Matsui

[1] Digital Human Research Center, National Institute of Advanced Industrial Science and Technology (AIST)

Abstract — **The effect of surgical procedure on breathing movement and the effect of characteristics of breathing movement on changes in heart rate and blood pressure during actual endoscopic nasal surgery were analyzed using analysis of variance and Bayesian network modeling. As the result, the probabilistic causal relationship between respiratory irregularities, increasing blood pressure and patients' complaint of pain was found. This result is expected to be used as patient pain and stress detection method without discomfort during actual surgery under local anesthesia.**

Keywords — **Patient response model, Pain, Stress, Endoscopic sinus surgery, Bayesian network**

I. Introduction

During surgery conducted under local anesthesia, the patient is overtly conscious of pressure, vibration and sound from the surgical procedure. These stressful feelings change the hemodynamics, resulting in an elevation of blood pressure [1, 2]. Moreover, the pain, which is not completely blocked by anesthesia, causes interruption of the surgery. Therefore to understand causal influences among surgical procedures and patients' responses is important for surgical education, and its computational model can apply to pain and stress detection.

In the experimental physiological field, the presence of pain and stress is assessed using autonomic indices such as mental sweating, hart rate and blood pressure. In the actual surgery, the existence of pain and stress is generally estimated by the blood pressure changes [3], but it is quite difficult to measure patient's beat-to-beat blood pressure without discomfort, and autonomic indices can be change not only by the effect of autonomic activity but also the effect of body movement and/or breathing activity.

With this in view, the purpose of this study is to investigate whether the respiratory response could be efficient indices for detecting patient's pain and stress. During surgery, with an increase in surgical pressure, shapes such as "pause phases" were observed on the respiratory waveform. On feeling pain, patients seem to breathe unsteadily. These characteristic breathing patterns seem to indicate the perception of surgical pressures and are likely to be efficient indices for determining blood pressure fluctuations resulting from the patient's stress.

Based on these suppositions, in this study, we defined twelve respiratory indices indicating breathing depth, breath holding and irregularities in breathing to investigate the influence of characteristics on respiratory waveform on changes in heart rate and blood pressure and also assess the effect of surgical stimulus such as pressing, tearing mucosa and breaking bony wall on the patient's responses.

II. Endoscopic sinus surgery

The subjects were patients who had sinusitis and underwent endoscopic sinus surgery using local anesthesia. Sinusitis is a result of the retention of mucus in the paranasal sinuses. This occurs as a result of the route, which reaches the paranasal sinuses from the nasal cavity, being blocked by polypus and/or inborn structural errors of the bone wall. The aim of the surgery is, therefore, to remove the polypus and bone walls and make clearer routes.

III. Method

A. Subjects

Patients in this study were five Japanese adults who provided written informed consent for observation and measurement of their physiological parameters during a surgical procedure and publication of this data.

B. Measurement

All measurements were taken during actual surgery.

Respiratory waveform was monitored using a Piezo respiratory belt transducer (AD Instruments) at abdominal circumference. Heart rate (HR) and continuous systolic blood pressure (BP) were measured using a BP-608EV Patient Monitor (Colin Medical Technology). At the same time, an endoscopic view of surgery and the scene in the operating room were recorded using video cameras. Complaints of pain, vibration or pressure were also recorded.

Chwee Teck Lim, James C.H. Goh (Eds.): ICBME 2008, Proceedings 23, pp. 2048–2051, 2009
www.springerlink.com

Table 1 Surgical procedures and types

Surgical Procedure	Type	n
Insert tool only	Insert only	69
Insert anesthetic pack Pull mucosa/bony wall Press mucosa/bony wall Break mucosa/bony wall	Touch	240
Area movement (forward)	AM>	13
Tear mucosa Squeeze tool into narrow area Thrust tool into mucosa/bony wall	Press Hard	53
Pull mucosa/bony wall with vibration	Pull Hard	24
Break bony wall with vibration	Break Hard	31
Move tool at high speed	Tool vibration	29
Area movement (backward) Stop tool movement Short period for tool change	Pause	28
Pain complaint	Pain	26

C. Segmentation of Surgical Scene

The surgery can complete in around two hours. The surgery has two sections, the operation and the rest section, and repeating the two of them carries the surgery forward. In the rest section, the patient does nothing but waits until the local anesthesia takes effect. On the other hand, in the operation section, the surgeon works on the patient.

In this study, using the recorded endoscopic view and footage of the operating room, each operation sequence was segmented into nine types of section by changes in the procedures of the surgeon (Tab. 1).

D. Indices

The recorded waveform was divided into three phases: "inspiration"; "expiration"; and "pause" [4]. In this study, the start and end point of the "pause" phase were called "PS" and "PE", respectively, and the end point of the "inspiration" phase was the "Peak" point. In addition, the sequence of "Peak" points and the sequence of "PS" and "PE" points were called "Peak Line" and "Bottom Line", respectively.

In this study, three types of characteristic shape on respiratory waveform were focused, (a) "Breath depth change", (b) "Panting" and (c) "Breath holding" (Fig. 1). To evaluate these characteristics, the following nine indices were employed.

To evaluate trends in "Breath depth changes", the following four indices were calculated:

- Changes in Peak points (*vPeak*) and Bottom points (*dBottom*): the amounts of changes from start-level (i.e., first sample in the period) were calculated.
- Mean Respiratory Waveform Amplitude (*mAmp*) and its differences between one section and the previous section (*dmAmp*): *mAmp* index was the mean amplitude of the respiratory waveform in one segmented section.

"Panting" was evaluated as respiratory irregularity, and was then assessed using the following two indices:

- Peak Line Variability (*vPeak*), Bottom Line Variability (*vBottom*) and the mean of these indices (*vPB*): Standard deviation of changes in the height of points on "Peak Line" and "Bottom Line" in each segmented section.

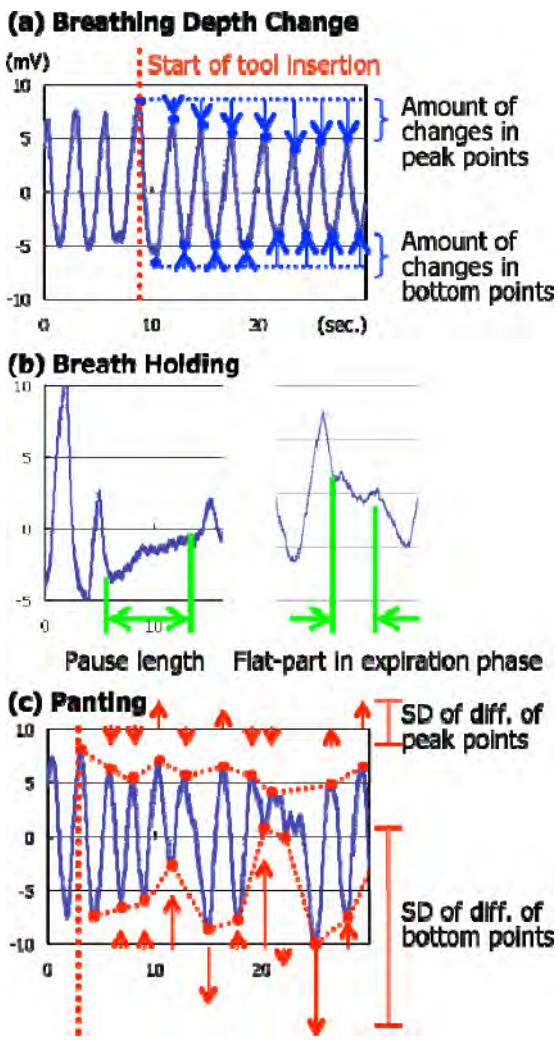


Fig. 1 Characteristics on respiratory waveform

In addition, the following index were employed for assessing "Breath holding" behavior resulting from tense situations:

- Mean Pause Length (*mPause*) and its differences between one section and the previous section (*dmPause*): *mPause* index was the average length of Pause phases included in one segmented period.

To evaluate trends in HR and BP changes in each segmented period, the amount of changes from start-level were calculated and called *dHR* and *dBP*, respectively.

E. Analysis and Modeling

In this paper, we focused on an effect of characteristics of breathing movement on changes in heart rate and blood pressure and the effect of type of surgical procedure on breathing movement.

First, the probabilistic causal relationship model between characteristics on respiratory waveform and changes in HR and BP were assessed using Bayesian network model construction method. In this step, all possible tree structures with child node *dBP* and parent node(s) as indices of characteristics on respiratory waveform were created. The score of Akaike's information criterion (AIC) was then calculated for each tree. Finally, the one tree structure with the lowest score was selected as the most likely tree structure for the observed data. Additionally, the quantitative effects of selected parent nodes for each *dHR* and *dBP* were analyzed using analysis of variance (ANOVA). In all tests, a level of significance of 0.05 was accepted as significant. Significant effects were further analyzed using Scheffe or Games-Howell multiple comparisons. In this analysis, all indices of each patient were normalized and discretized into two (small or large) or four (+2: large increase, +1: small increase, -1: small decrease, -2: large decrease) states depending on their percentile rank within the distribution.

Next, the effect of surgical procedure on indices of characteristics of respiratory waveform was evaluated by constructing Bayesian network model.

IV. Result and Discussion

According to the result of model construction, the *mAmp* and *dmPause* nodes were selected as the parent nodes for *dHR*. On the other hand, the *mAmp* and vPB nodes were selected for *dBP* (Fig. 2 right side). The quantitative effect of these parent indices on *dHR* and *dBP* were calculated (Fig. 3).

Fig. 3 (a) shows the effect of *dAmp* and *vPB* on the changes in blood pressure. Basically the change in blood pressure seems to be influenced by *mAmp* movement. The *vPB* (2) indicates an excessive rise and/or drop in peak and bottom height by patient's panting. Patient's panting behavior seems to be caused by an excessive straining resulting from surgical pressure, and likely to be cause of an increasing blood pressure. On the other hand, the *dAmp* movement seems to strongly influence the change in heart rate (Fig. 3 (a)).

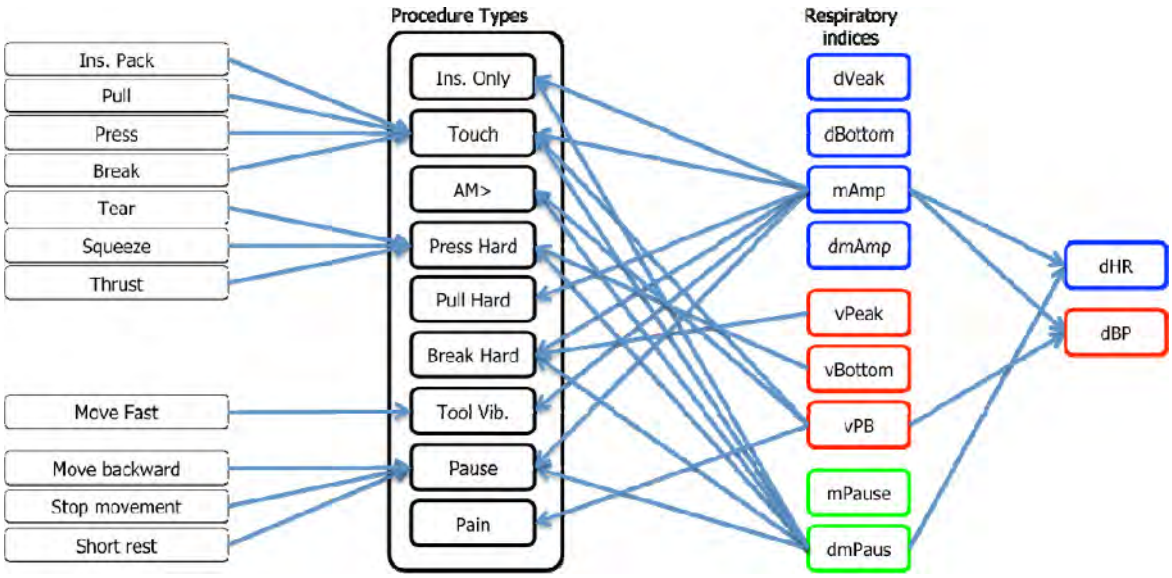
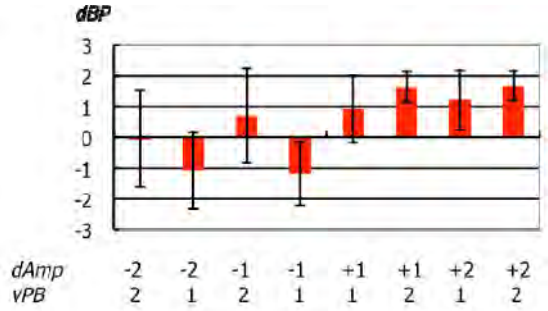
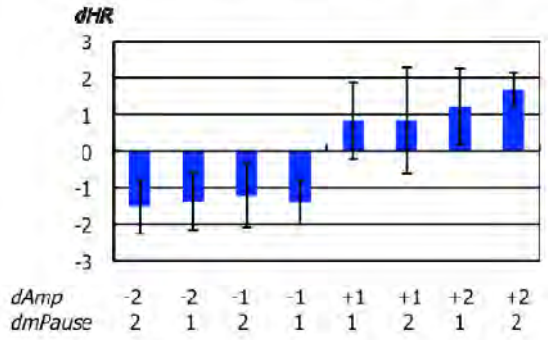


Fig. 2 Characteristics on respiratory waveform

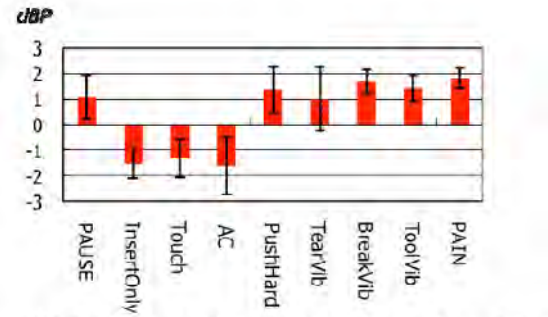


(a) Plot of *dBP* value between pairs of *dAmp* and *vPB*

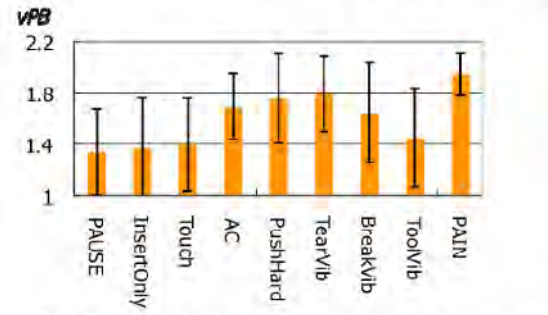


(b) Plot of *dHR* value between pairs of *dAmp* and *dmPause*

Fig. 3 Effects of selected respiratory indices on changes in *dHR* and *dBP*



(a) Plot of *dBP* value between types of surgical procedure



(b) Plot of *vPB* value between types of surgical procedure

Fig. 4 Effects of surgical procedure on changes in *dBP* and *vPB*

Next, the probabilistic relation between types of surgical procedure and physiological indices were evaluated. The result showed in left side of Fig. 2. The resultant model indicates that most procedures were influenced by *mAmp*, *vPB* and *dmPause* indices. In particular, the *vPB* index showed equally high value as the *dBP* in "PAIN" section (Fig. 4). In "PushHard" and "TearVib." sections, the *vPB* also showed high value. We consider the possibility that the patient feel pain but does not complain, that is a hidden pain, in the section.

V. Conclusions

The effect of surgical procedure on breathing movement and the effect of characteristics of breathing movement on changes in heart rate and blood pressure during actual endoscopic nasal surgery were analyzed using analysis of variance and Bayesian network modeling.

As the result, indices representing the characteristic shapes on the respiratory waveform showed the ability to predict direction of changes in blood pressure, and the probabilistic causal relationship between respiratory irregularities, increasing blood pressure and patients' complaint of pain was found. This result is expected to be used as patient pain and stress detection method without discomfort during actual surgery under local anesthesia.

Acknowledgment

This work was supported by Grant-in-Aid for Young Scientists (B) 18700205.

References

1. M.S. Kim, K.Y. Cho, H.M. Woo and J.H. Kim (2001) Effects of hand massage on anxiety in cataract surgery using local anesthesia, Journal of Cataract and Refract Surgery, Vol.27, pp.884-890
2. G. Juodzbalys, R. Giedraitis, V. Machiulskiene, LW. Huys, and R. Kubilius (2005) New method of sedation in oral surgery, Journal of Oral implantology, Vol.31, Issue 6, pp.304-308
3. K. E. Blackwell, D. A. Ross, P. Kapur, and T. C. Calcaterra (1993) Propofol for maintenance of general anesthesia: A technique to limit blood loss during endoscopic sinus surgery, American Journal of Otolaryngology, Vol.14, Issue 4, pp. 262-266
4. F.A. Boiten (1993) Component analysis of task related respiratory patterns," Int. Journal of Psychophysiology, Vol.15, Issue 2, pp. 91-104

A Study on Correlation between BMI and Oriental Medical Pulse Diagnosis Using Ultrasonic Wave

Y.J. Lee, J. Lee, H.J. Lee, J.Y. Kim

Korea Institute of Oriental Medicine/Dept. of medical research, South Korea

Abstract — **Pulse diagnosis refers to the process of diagnosing a patient by feeling an artery on the wrist based on the shape that the pulse takes while the hold-down pressure increase. Currently, the hucklebone artery on the wrist is usually felt, and the pulse is taken on Chon, Gwan and Cheok using three fingers. This study is to examine the structural difference in the location of pulse diagnosis by measuring and analyzing blood diameter, blood depth, and blood flow velocity of the location of pulse diagnosis by using ultrasonic wave (VOLUSION730 PRO, GE Medical, U.S.A).This study also attempted to grasp whether the characteristics of blood vessels differ depending on Body Mass Index (BMI) and analyzed their correlation with Oriental medical pulse diagnosis. The male subjects without cardiovascular diseases were divided into the normal BMI group, the underweight group, the overweight group and 10 people of each group were measured. Blood depth, blood diameter and blood flow velocity at the location of pulse diagnosis (Chon, Gwan, Cheok) of the wrists of left and right hands were measured and the pulse wave was measured by using pulse diagnosis instrument (3-D Mac, DaeyoMedi, Korea).The results of this study showed that the characteristics of blood vessels differ depending on the degree of obesity, and the characteristics of floating pulse and sinking pulse of Oriental medical pulses were related to the degree of obesity. This shows that the characteristics of the blood vessels of subjects and BMI information are the major indicators for diagnosis and are the matters that must always be considered when developing the algorism of pulse diagnosis.**

Keywords — **Pulse diagnosis, Oriental Medicine, Ultrasound wave, Radial artery**

I. Introduction

The significance of the Pulse Diagnosis is to analyze the health condition of the human body, to analyze the various pulses ranging from the normal-pulse of healthy people to the abnormal-pulse of the patients, and to investigate the source and characteristics of the disease. And it is helpful in prognosis of the disease[1]. Pulse diagnosis is a method of identifying the conditions of a disease by feeling the pulse of the radial artery on the wrist of the patient with the oriental medial doctor's fingers[2]. The risen part around the radial styloid process on the wrist is called a Gogol, the position where the pulses are measured from the styloid process is called 'Gwan', and the positions next to Gwan that the doctors can feel the pulses with the middle finger and the third finger are called 'Chon' and 'Cheok' respectively[3]. Since Chon, Gwan, and Cheok are located around the styloid process, there is a big variation in the blood flow velocity because of the geometric characteristics of the vessel as shown in the figure 1. It was observed that the blood flow velocity at the Chon position was rapidly reduced compared to the velocity at the Gwan and Cheok positions[3]. That is, the oriental medical doctors feel the variation of the blood flow velocity when they do the pulse diagnosis at Chon, Gwan, and Cheok positions, and that becomes an index to be used for diagnostics.

This paper analyzed the dependency of the characteristics of vessel at the pulse measurement positions to the characteristics of the body type of the normal people. If the characteristics of the vessel change depending on the body mass index (BMI) then the diagnosis method should be adjusted according to BMI. The subjects were divided into three groups comprising Normal, Underweight, and Overweight. And vessel diameter, vessel depth, and blood flow velocity were measured at the pulse diagnosis measurement position with ultrasonic wave and the characteristics were analyzed. And also pulse waveforms were measured to determine whether the characteristics of the pulse change depending on the body type.

II. Method

A. Subjects

Thirty male subjects of ages in 20s (age of 24.07±2.01) who don't have cardiovascular diseases and who don't take relevant medication were taken to the experiment. Three groups of subjects were recruited, underweight(below 20kg/m^2) group of 10 people, normal weight(below 20~25kg/m^2) of 10 people, and overweight(below 25~30kg/m^2) group of 10 people. Subjects were asked to stop smoking and drinking alcohol from one day before the test, they took the rest for 30 minutes before the test, and ultrasonic wave and pulse wave were measured in a sitting posture.

Chwee Teck Lim, James C.H. Goh (Eds.): ICBME 2008, Proceedings 23, pp. 2052–2055, 2009
www.springerlink.com

B. Experiment method

Ultrasonic wave and pulse wave were measured at the pulse diagnosis positions (Chon, Gwan, and Cheok) on the arteries of the left and right wrist as shown in the figure 1. In order to measure the accurate pulse diagnosis positions, Chon, Gwan, and Cheok positions were marked on the wrist at the positions taken from the pulse diagnosis of oriental medical doctors and both ultrasonic and pulse wave were measured at those positions. The ultrasonic wave was measured with thin wires wrapped at the marked measurement positions so that the measurement positions could be identified in the ultrasonic image. Vessel depth, vessel diameter, and blood flow velocity were measured, and the average values taken from the three repeated measurements on each item were analyzed. Pulse waves were measured with the pulse diagnosis machine and the coefficient of floating and sinking pulse which is a parameter in diagnosing floating pulse and sinking pulse was calculated.

C. Measurement of Ultrasonic Wave and Pulse Wave

Vessel depth, vessel diameter, and average blood flow velocity were measured with the ultrasonic wave equipment for medical purpose (Volusion 730 PRO, GE Medical, USA), and 12L probe was used. Incident angle of the color Doppler mode ultrasonic wave was 20°, and the angle for the blood flow velocity measurement was 60°. Electrolyte low gel pad (Parker Laboratorics Inc., USA) was used for more stable measurement. Pulse diagnosis machine(3-D Mac, Daeyo Medi, Korea) was used to measure the pulse waves, and the pulse wave were measured at the location of Chon, Gwan, and Cheok of the left and right wrist.

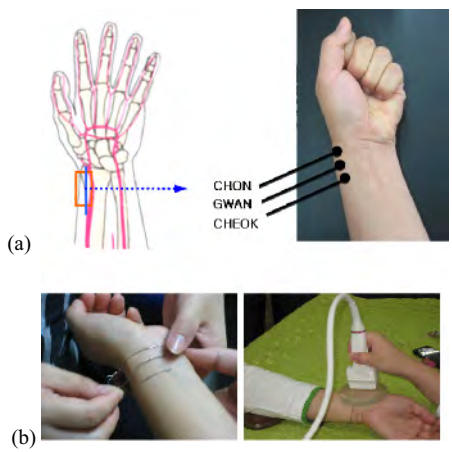


Fig. 1 (a) Pulse measuring positions (Chon, Gwan, and Cheok) and non-pulse measuring positions (P1, P2, and P3) on the radial artery (b) Measurement positions marking method and actual measurement picture.

D. coefficient of floating and sinking pulse

When diagnosing pulse in Oriental medicine, OMD feels change of pressure in blood vessel applying pressure at the pulse position by his finger. According to his pressing and the change of pulse pressure in blood vessel, OMD diagnoses 'floating and sinking pulse'. When contact pressure is small, if maximum pressure is felt, we define this by 'floating pulse'. And when contact pressure is big, if maximum pressure is felt, we define this by 'sinking pulse'. By using the PH-curve that is measured by this pulse analyzer, we can arrange this Oriental medical concept as below figure 2.

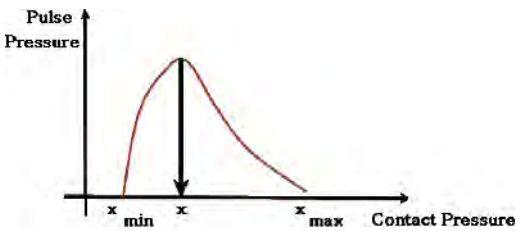


Fig. 2 Coefficient of floating and sinking pulse.

$$\text{coefficient of floating and sinking} = \frac{10\times(X - x_{\min})}{(x_{\max} - x_{\min})} \quad (1)$$

III. Result

A. Measurement result

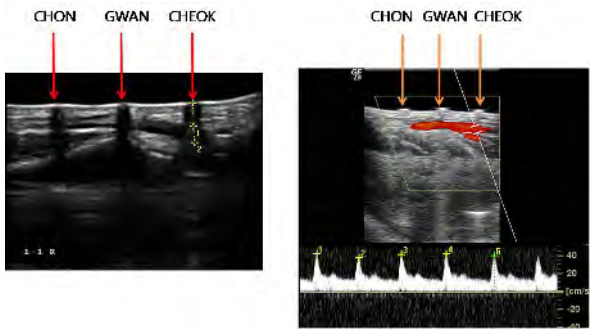
Vessel depth, vessel diameter, and blood flow velocity were measured at the Chon, Gwan and Cheok positions using the ultrasonic wave for 30 subjects as shown in the figure 3. And also the pulse waves were measured by using the pulse diagnosis machine and the coefficients of floating and sinking pulse were calculated by the equation (1). The results are summarized into the table 1 below. The analysis result of the correlation between the test results and BMI groups (under-weight, normal, and over-weight) are also shown in the table 1 below. To determine the correlation between all variables non-parametric method of Spearman's ranking correlation was used. Statistical significance of all data was 0.05.

The results of the correlation analysis revealed that the vessel depth showed a strong correlation to BMI, but the vessel diameter and blood flow velocity showed a relatively lower correlation to BMI. This means that the vessel diameter is not dependent on the fatness of subjects but the vessel depth which represents the depth of the vessel from the skin varies. And also the correlation between the coefficient of

Table 1 The measurement results at Chon, Gwan, and Cheok position, and correlation analysis results

	Left Chon	Left Gwan	Left Cheok	Right Chon	Right Gwan	Right Cheok
Vessel Diameter *	0.273(±0.03)	0.241(±0.03)	0.249(±0.06)	0.279(±0.04)	0.254(±0.03)	0.275(±0.03)
Vessel Depth *	0.387(±0.07)	0.274(±0.07)	0.297(±0.08)	0.356(±0.08)	0.272(±0.09)	0.325(±0.12)
Average Blood Flow Velocity*	2.88(±1.67)	7.406(±4.24)	7.618(±2.65)	4.093(±2.2)	7.789(±2.9)	8.191(±3.27)
Coefficient of floating and sinking pulse *	5.344(±2.19)	4.533(±1.78)	6.911(±2.44)	5.599(±2.34)	4.887(±2.12)	6.677(±1.77)
BMI and Vessel Depth **	0.541(0.046)	0.630(0.016)	0.316(0.019)	0.589(0.027)	0.829(0.00)	0.771(0.001)
BMI and Vessel Diameter **	0.244(0.40)	0.594(0.025)	0.534(0.049)	0.106(0.719)	0.434(0.121)	0.385(0.174)
BMI and Average Blood Flow Velocity **	0.319(0.267)	0.068(0.817)	-0.059(0.84)	0.332(0.246)	0.134(0.648)	-0.011(0.97)
BMI and Coefficient of floating and sinking pulse **	0.842(0.00)	0.356(0.211)	0.227(0.434)	0.682(0.007)	0.666(0.009)	-0.138(0.63)

floating and sinking pulse and BMI was relatively high from the analysis. The strong correlation between the coefficient of floating and sinking pulse which quantifies the pulse feeling position depending on the applied pressure to the radial artery and BMI suggests that the body type is a very important factor in diagnosing the floating pulse and sinking pulse. In addition, there were three measurement positions where the correlation between the coefficient of floating and sinking pulse and vessel depth higher was not very high but higher than 0.5, which suggested that the coefficient of floating and sinking pulse is deeply affected by the vessel depth as well as BMI.



(a) (b)

Fig. 3 Measurement result of (a) vessel depth and vessel diameter B-mode and (b) blood flow velocity color Doppler mode at Chon, Gwan, and Check positions.

IV. Conclusion

Pulse diagnosis is a foundation of diagnosis in Oriental Medicine. But the pulse is a phenomenon by many different factors including the characteristics of the vessel and pulsation of heart, and many factors need to be considered in developing pulse diagnosis machines.

Pulses are measured at the positions called Chon, Gwan, and Cheok on the radial artery. The measurement positions of Chon, Gwan, and Cheok have dynamic blood flow characteristics where the blood vessel is risen by radial styloid process which is called Gogol[4]. And also the radial artery at the measurement positions is located average 2.7 mm below the skin which is very close to the skin. Experiments were done in this paper to determine effects of the characteristics of the vessel and BMI of human body among the various factors.

The experiment results showed that the vessel at left and right Gwan raised by the styloid process was located at the nearest position to the skin and Chon was located at the deepest position. An also the same characteristics of the rapid reduction of blood flow velocity at the left and right Chon as the existing research[3] were observed. The analysis of the vessel for each separate BMI group showed that the vessel depth had a strong correlation to BMI. The distance between the skin to the vessel was measured longer for the higher BMI, and this means that the basic factors of diagnosing floating pulse and sinking pulse are affected by BMI. The floating and sinking pulse[5, 6] which are defined as the level of the finger pressing and the pressure in the vessel that is felt can be defined as the coefficient of floating and sinking pulse, and the coefficient of floating and sinking pulse was also shown to be correlated to BMI.

In result, Chon Gwan, and Cheok measurement positions are located very close to the radial artery, but it was revealed that the characteristics at each position were different and also affected by BMI. It was also shown that BMI affected the diagnosis of floating and sinking pulse. Therefore we have learned that the design of diagnosis algorithm based on BMI of the testee is absolutely necessary and the standard for the measurement method that depends on the characteristics of the vessel of testee need to be developed.

Acknowledgment

This work was supported by the Korea Ministry of Knowledge Economy (10028438).

References

1. Y.G. Lee, Diagnostics Atlas III, Seoul, South Korea: CHUNGDAM, 2003, pp.11-14
2. B. Flaws, The Secret of Chinese Pulse Diagnosis, Boulder, CO: BLUE POPPY PRESS, 1995, pp. 4-8
3. Y.J. Lee, J. Lee, H.J. Lee, H.H. Ryu, E.J. Choi, J.Y. Kim, "Characteristic Study of the Pulse Position on CHON, KWAN and CHUCK Using the Ultrasonic Waves", Journal of Korea Institute of Oriental Medicine, 13, 3, pp. 111-119, 2007
4. J.Y. Ryu, "Rewrit Sasang Constitution Medicine", Seoul, South Korea:DEASUNG, 97-100, 2007
5. Y.Z. Yoon, M.H. Lee, K.S. Soh. "Pulse type classification by varying contact pressure", IEEE Engineering in medicine and biology, 19, 6, pp.106-110, 2000.
6. Y.J. Lee, J. Lee, E.J. Choi, H.J. Lee, J.Y. Kim, "Analysing of pulse wave parameter and typical pulse pattern for diagnosis in floating and sinking pulses, Journal of Korea Institute of Oriental Medicine, 12, 2, pp. 93-101, 2006

Author: Jong-Yeol Kim
Institute: Korea Institute of Oriental Medicine
Street: 483 Exporo Yusung-gu
City: Daejeon
Country: South Korea
Email: ssmed@kiom.re.kr

Investigating the Biomechanical Characteristics of Transtibal Stumps with Diabetes Mellitus

C.L. Wu[1], C.C. Lin[2], K.J. Wang[3] and C.H. Chang[4]

[1] Department of Special Education, National Taichung University, Taichung, Taiwan
[2] Physical Therapy, Jen-The Junior College of Medicine, Nursing and Management, Miaoli, Taiwan
[3]Department of Department of Rehabilitation, Taoyan General Hospital Department of Health, Taoyan, Taiwan
[4] Institute of Biomedical Engineering, National Cheng Kung University, Tainan, Taiwan

Abstract — **Subjects with Diabetes Mellitus (DM) are the major parts in transtibial amputees. The purpose of this study is to investigate the difference on the material properties of soft tissues and biomechanical performance between the DM and non-DM subjects. There are two volunteers with transtibial amputation involved in this study. One is suffered from DM, the other is not. This study were executed within two major phased. Firstly, the stiffness of soft tissue at five regions of stump was received from the self-made force-displacement instrument. Then, the finite element models of the two subjects were established to simulate the biomechanics of transtibial prosthesis. From the results, the stiffness of non-DM subject is averagely 1.6 times higher than the DM subject. In the finite element analysis, the DM subject were presented the higher magnitudes at the maximum sliding distance, the interface stresses, Von Mises stress and Von Mises strain. It means the soft tissue of DM subjects with lower stiffness had higher chance to be broken. When manufacturing the prosthesis for DM subjects, the prosthesists should notice this invisible problem..**

Keywords — **Diabetes Mellitus, transtibial amputees, elastic modulus, finite element analysis**

I. Introduction

Amputated patients need prostheses to achieve the independent of functional activity [1]. There were many reasons to cause amputations, and diabetes mellitus (DM) was the most one. Amputations with DM were more difficult to manufacture fitness prostheses because DM would cause the changes of local sensation and material properties of soft tissue [2]. The purpose of this study was to investigate influence of DM on material properties of soft tissues and biomechanical performance.

II. Materials and methods

There are two volunteers with transtibial amputation involved in this study. One is suffered from DM, the other is not. The detail information of subjects was listed in Table 1. This study were executed within two major phased. Firstly, the stiffness of soft tissue at five regions of stump was received from the self-made force-displacement instrument. Then, the finite element models of the two subjects were established to simulate the biomechanics of transtibial prosthesis.

A. Measuring the stiffness of soft tissue

A self-developed handheld indentor device, which included a digital meter to provide the deformation of the soft tissue and a load cell to detect the applied loading, was used to measure the pain information. During the test, the examiner maintains the indentor perpendicular to the test region and applies the load as slow as possible on the subject (1mm/sec roughly). In total, five regions (patella tendon, medial condyle, fibular head, popliteal fossa and stump end) were tested for five successful measurements. The recorded force-displacement curve during test for each region was transferred to Young's Modulus with the following equation:

$E = P(1-v^2) / 2awk$

P: indention force
v: Poisson's ratio
w: indentation depth
a: radius of the indentor
h: thickness of the test tissue
k: a geometry and material-dependent factor (v,a/h)

B. Establishing the finite element (FE) Mesh Models

All subjects have been informed and agreed for suffering the computer tomography (CT) scan. 3 mm interval transverse CT images were taken with the subjects lying at supine position.

From each image, the contours of different materials i.e., bone, soft tissue and the soft liner, could be segmented by an image processing system. Forty points, evenly spaced, were selected on each material boundary. Linking these 40 points with spline-curve, the section areas of each material were generated and piled up to build the volume models. These volume models were then meshed with brick ele-

Chwee Teck Lim, James C.H. Goh (Eds.): ICBME 2008, Proceedings 23, pp. 2056–2058, 2009
www.springerlink.com

ments (8 node hexahedral elements). The surface-to-surface contact elements were employed at the stump-socket interface. This type of contact element has better performance than the traditional point-to-point contact pairs in simulating sliding behavior within the stump-socket interface. The ANSYS 10.0 FE software (ANSYS Inc., Canonsburg, PA, USA) was utilized for all analyses.

To simulate the loading phase of single standing, four spread nodes of the top layer of bone were assigned the same magnitude of downward displacement to minimize the moment and rotation of stump. The displacement was kept downward until the reaction force reached to one body weight. The boundary conditions were assigned at the out layer of liner to simulate nearly no deformation appeared at the hard socket.

Bone, soft tissue and liner were assigned as the major materials in the FE models. The elastic modulus of bone and liner were assigned as 15500 and 0.8 MPa. The elastic modulus of the soft tissue was assigned in regions separately based on the stiffness of soft tissue measured from indentor tests. The other elastic modulus of stump and liners were obtained from the literature [3,4]. The Poisson ratios of bone, soft tissue and liner were assigned to be 0.3, 0.45 and 0.49 respectively, also from the literatures [3,4].

III. Results

A. Stiffness and Young's modulus of soft tissue

There are some differences between the DM subject and non-DM subject in stiffness of soft tissue especially at medial, lateral and posterior regions showing in Fig. 1. Averagely, the stiffness of non-DM subject is 1.6 times higher than the DM subject. Table 2 illustrated the Young's modulus of the subjects at all five regions. The highest value (0.57~0.72 MPa) of Young's modulus was at anterior (patellar tendon) region, and on the other hand, the lowest value (0.28~0.37 MPa) of Young's modulus was at stump end region.

Table 1 Detail information of subjects

	Amputated side	Sex	Years	Body weight (kgw)	Reasons of suffered amputation
Non-DM subject	Left	Male	33	56	Trauma
DM subject	Left	Female	71	53	Diabetes

Table 2 Values of four indexes from the simulation results of two subjects

	Slide distance (mm)	Von Mises		Interface stresses(KPa)	
		Stress	strain	Pressure	Shear stress
Non-DM subject	0.809	0.203	0.118	54	11
DM subject	1.229	0.259	0.078	106	21

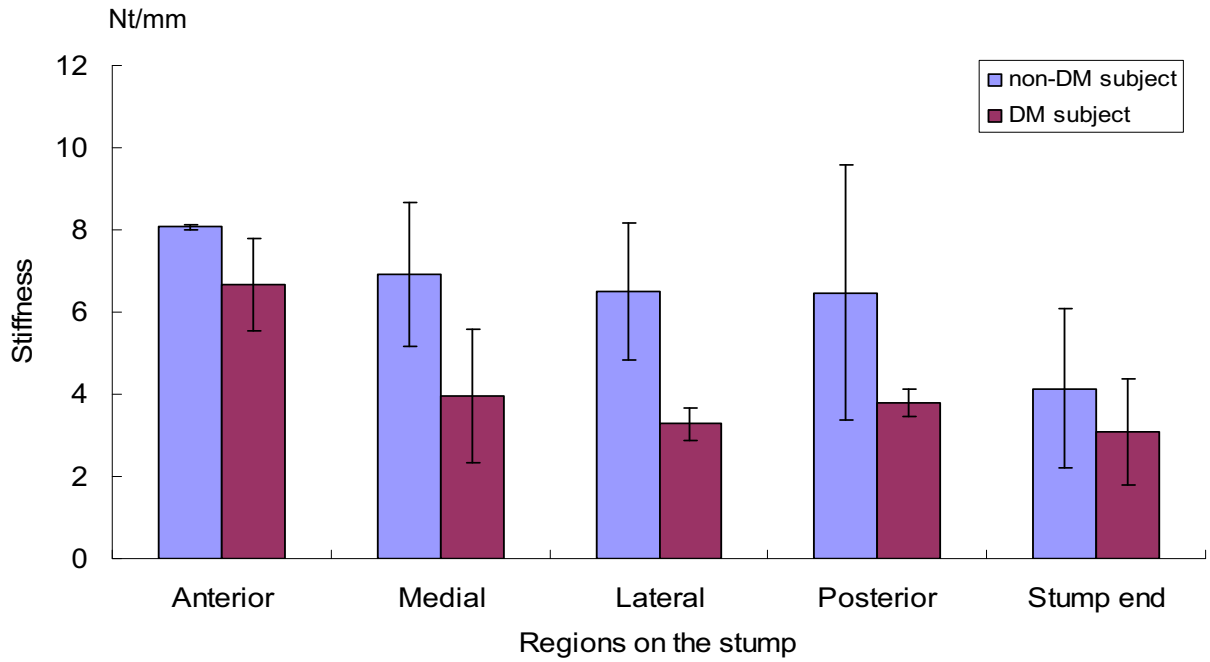


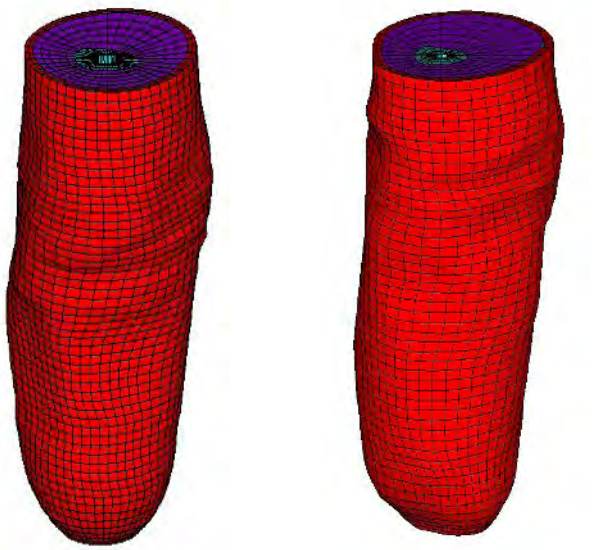
Fig. 1 stiffness at the regions on the stumps of two subjects

B. *Simulation results from finite element (FE) model*

The geometry of the models was showed in Fig. 2. The difference of geometry between the subjects was easily noticed. Three indexes, sliding distance, Von Mises stress and strain and interface stress from finite element analysis were used to describe the biomechanical performance. As shown in Table 3, the DM subject was presented the higher magnitudes than non-DM subject at all indexes except the Von Mises strain.

Table 3 Values of indexes of two subjects before and after changing Young's modulus of soft tissue

	Young's modulus of soft tissue	Sliding distance (mm)	Von Mises		Interface stresses (KPa)	
			Stress	strain	Pressure	Shear stress
Non-DM subject	Original	0.809	0.203	0.118	54	11
	Decreased to 0.6 times	1.208	0.339	0.119	57	13
DM subject	Original	1.229	0.259	0.078	106	21
	increased to 1.6 times	0.825	0.147	0.075	98	22



(a) (b)

Fig. 2 geometry of finite element models of two subjects
(a) Non-DM subject
(b) DM subject

IV. Discussion and conclusions

From the results, we knew the DM subject had a softer soft tissue and higher values of biomechanical indexes. All these reasons indicated that DM subject had higher chance to break tissue. But the results were also influenced by the characteristics of subjects, like body weight, geometry and material properties of stump. In order to eliminate these influences, we simulated the other two situations. First, the material properties of soft tissue from non-DM subject were decreased to 0.6 times as patient suffered DM and second, the material properties of soft tissue from DM subject were increased to 1.6 times as patient recovered to normal. The results were illustrated as table 3. As the elastic modulus of soft tissue decreased, all values of the indexes were increased in two FE models. The higher values of indexes meant that soft tissue might be hurt when wearing the transtibial prosthesis. When manufacturing the prosthesis for DM subjects, the prosthesists should notice this invisible problem.

In the conclusions, the differences of the material properties of soft tissues and biomechanical performance between the DM and non-DM subjects were discussed in this study. The stiffness of soft tissue of non-DM subject is averagely 1.6 times higher than the DM subject and the DM subject was presented the higher magnitudes at the indexes of maximum sliding distance, the interface stresses, Von Mises stress and Von Mises strain. The results might provide a reason to explain the difficulties to manufacture a fitness prosthesis to DM subjects.

Acknowledgment

The authors would like to thank the National Science Council, Republic of China, for its financial support of this work under contract No. NSC96 - 2262- E-142 – 001-CC3.

References

1. Donlald, G.S., *Prosthetics and Orthotics.* 1990; 93-115,Appleton & Lange Inc.
2. Chen, Y.S., Chie, W.C., Lan C., Lin, M.C., Lai, J.S., and Lien, I.N., Rates and characteristics of lower limb amputations in Taiwan, 1997. *Prosthetics and orthotics international* 2002; 26: 7-14.
3. Zhang, M., A finite element modeling of a residual lower-limb in a prosthetic socket: a survey of the development in the first decade. *Medical engineering and physics* 1998; 20: 360-373.
4. Zhang M., Comparison of computational analysis with clinical measurement of stresses on below-knee residual limb in a prosthetic socket. *Medical engineering & physics* 2000; 22: 607-612.

A New Approach to Evaluation of Reactive Hyperemia Based on Strain-gauge Plethysmography Measurements and Viscoelastic Indices

Abdugheni Kutluk[1], Takahiro Minari[1], Kenji Shiba[1], Toshio Tsuji[1], Ryuji Nakamura[2], Noboru Saeki[3], Masashi Kawamoto[3], Hidemitsu Miyahara[3], Yukihito Higashi[3], Masao Yoshizumi[3]

[1] Graduate School of Engineering, Hiroshima University, Higashi-Hiroshima, Japan
[2] Hiroshima University Hospital, Hiroshima, Japan
[3] Graduate School of Biomedical Sciences, Hiroshima University, Hiroshima, Japan

Abstract — **Endothelial dysfunction is an initial step of atherosclerosis and is associated with cardiovascular diseases. Measurement of flow-mediated vasodilation in the brachial artery using ultrasound is noninvasive and an accurate indicator of nitric oxide production. However, ultrasound based measurement sometimes depends on the observer's skill. The purpose of this study was to evaluate response in reactive hyperemia employing viscoelastic indices, including stiffness and viscosity measured by strain-gauge plethysmography (SPG) in beat-to-beat. We measured viscoelastic parameters and pulse wave velocity (PWV) in 4 young (23±1 years) and 3 elderly (55±4 years) subjects. Our results showed that there were significant differences in viscosity after cuff deflation (0 to 100 sec) between the young and the elderly ($p<0.001$). However, there was no significant difference in PWV after cuff deflation between the young and the elderly ($P=0.11$). These findings suggest that the proposed viscoelastic indices represent the changes of arterial mechanical properties, which might be derived from flow-mediated vasodilation.**

Keywords — **atherosclerosis, reactive hyperemia, strain-gauge plethysmography, viscoelastic indices, PWV.**

I. Introduction

Cardiovascular and cerebral vascular diseases are the major cause of mortality in Japan. These conditions are strongly associated with atherosclerosis [1]. Previous studies have evaluated arteriosclerosis using arterial elastic properties such as pulse wave velocity (PWV) [2], arterial elasticity [3] and arterial compliance [4]. However, arterial elasticity is useful for the quantification of arterial sclerosis rather than of atherosclerosis.

Endothelial dysfunction is thought to be an important factor in the development of atherosclerosis [5], [6]. It is well known that endothelium function plays a role in releasing nitric oxide to regulate the relaxation of smooth muscle cells within the vascular wall. The function can be evaluated from endothelial-mediated dilatory response, and two methods that evaluate this response are known. One involves measuring forearm blood flow after the administration of an NO agonist and antagonist [7]. These vasoactive substances must be administered via a catheter inserted into the brachial artery, and the method may become invasive and includes potential risk and discomfort. The other method involves a reactive hyperemia test that evaluates flow-mediated dilation promoted by increasing blood flow created by cuff inflation to suprasystolic pressure. This method is widely used because it is noninvasive and allows repeated measurement [8], [9]. However, its drawbacks include the high cost of ultrasound devices and the fact that measurement depends on the observer's skill.

To address the problem, Baldassarre *et al*. assessed endothelial function during reactive hyperemia using strain-gauge plethysmography [10]. This study takes into account only the compliance component between the strain-gauge plethysmogram (representing the strain) and blood pressure (representing the stress). However, it is important for precise estimation of mechanical dynamics to consider the viscous component as well as the compliance component.

We therefore propose a new method to evaluate response in reactive hyperemia using viscoelastic indices measured by strain-gauge plethysmography. In this paper, the proposed indices are measured during a reactive hyperemia experiment, and we assess whether response in reactive hyperemia differs between the young and the elderly subjects.

II. Arterial wall impedance model

Fig. 1 illustrates the proposed impedance model of the arterial wall. This model represents only the characteristics of the wall in an arbitrary radius direction. The impedance characteristic can be described using the stress $F(t)$ and the displacement $r(t)$ of the arterial wall as follows [11]:

$$dF(t) = B\dot{r}(t) + K(r(t) - r_e) \tag{1}$$

where B and K are the coefficients of viscosity and the elastic modulus respectively, $\dot{r}(t)$ is the first derivative of strain in the arterial wall, and r_e is the equilibrium point of the arte-

Chwee Teck Lim, James C.H. Goh (Eds.): ICBME 2008, Proceedings 23, pp. 2059–2063, 2009
www.springerlink.com

rial wall without internal pressure. Here, the dynamic characteristic on the basis of t_0 is described as follows:

$$dF(t) = B\dot{dr}(t) + Kdr(t) \tag{2}$$

where $dF(t) = F(t) - F(t_0)$ and $dr(t) = r(t) - r(t_0)$. To estimate the impedance parameters given in (2), it is necessary to measure $F(t)$ and $r(t)$. The stress exerted on the arterial wall is equal to the arterial pressure. This stress can be given as follows:

$$F(t) = k_f P_b(t) \tag{3}$$

where $P_b(t)$ is the arterial pressure, and k_f is the constant.

On the other hand, the strain of the blood vessel in the radius direction is recorded using strain-gauge plethysmography, which can measure changes in limb volume. The vascular volume change measured by the strain-gauge plethysmogram is represented as follows [12]:

$$r(t) = k_l P_l(t) \tag{4}$$

where $P_l(t)$ is the strain-gauge plethysmogram and k_l is the constant.

The stress exerted on the arterial wall $F(t)$ is expressed by the arterial pressure $P_b(t)$ given by equation (3). And the displacement of the arterial wall $r(t)$ is represented by the strain-gauge plethysmogram $P_l(t)$ in (4). The arterial wall impedance parameters can be estimated by using the least square method from the measured $P_b(t)$ and $P_l(t)$. the vascular dynamic characteristics can be derived as follows:

$$dP_b(t) = \tilde{B}\, d\dot{P}_l(t) + \tilde{K}\, dP_l(t) \tag{5}$$

where the parameters, stiffness $\tilde{K}$ and viscosity $\tilde{B}$ correspond to the viscoelastic properties of the arterial wall in the measured part.

III. Reactive hyperemia experiments

In order to investigate the validity of the proposed method, we conducted reactive hyperemia experiments. Endothelial dysfunction is a major risk factor for atherosclerosis, and endothelial function in aging tends to be impaired [13]. We therefore attempted to assess the difference in response during reactive hyperemia between the young and the elderly, and Fig. 2 illustrates the experimental setup. A blood pressure cuff was placed around the upper right arm, and inflated to 50 mmHg above systolic pressure by a rapid cuff inflator (E20, DE Hokanson). The strain-gauge connec- ted to a plethysmograph (EC6, DE Hokanson) was placed around the right forearm, and continuous blood pressure was measured from the left arm using a biological information monitor (BP-608, Omron Healthcare). The forearm was then elevated 10 cm above the heart level as necessary to facilitate venous drainage, and electrocardiogram (*ECG*) was measured to recognize the cardiac cycle. All signals were stored on a personal computer after AD transformation with a sampling time of 10 ms. In total, 4 young (22-24 years) and 3 elderly (50-59 years) healthy subjects were recruited. The measurements, which were repeated three times, were performed in a resting state and in an ischemic state by inflation of the brachial cuff and after cuff deflation, each for five minutes. All subjects rested for at least 10 minutes prior to the measurement. After reactive hyperemia measurement, PWV was assessed with an automatic pulse wave analysis device (BP-203 RPEII, Colin Co). The measured values of each subject were taken as the average of the three reactive hyperemia trials.

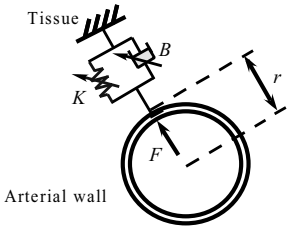


Fig. 1 Arterial impedance model

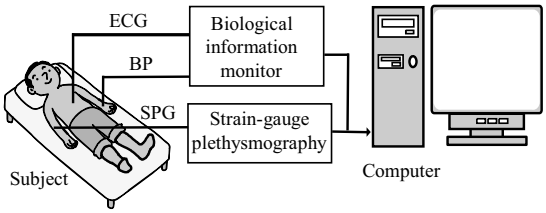


Fig. 2 Experimental setup for measurement

IV. Experimental results

In the experiment, *ECG*, P_b and strain-gauge plethysmogram signals were measured. Since factors such as motion of the patient's hand may affect the measured signals, digital filters were used to regulate the frequency characteristics of the signals. The electrocardiogram was filtered out through a second-order infinite impulse response (IIR) band-pass filter (5-40 Hz), the blood pressure was filtered through a second-order IIR band-pass filter (0.5-8 Hz), and the strain-gauge plethysmogram was filtered through a second-order IIR band-pass filter (0.5-8 Hz).

Fig. 3 shows an example of the experimental results for Subject A, plotting the arterial pressure P_b, the amplitude of

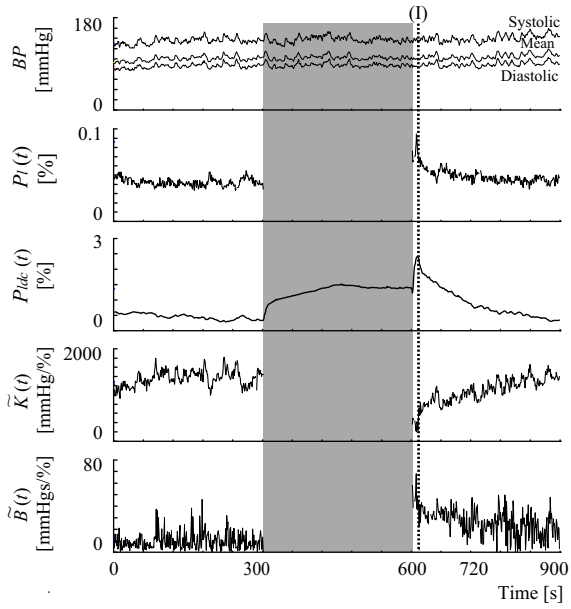


Fig. 3 An example of results in reactive hyperemia

strain-gauge plethysmogram P_{lac}, the direct component of strain-gauge plethysmogram P_{ldc}, stiffness $\widetilde{K}$ and viscosity $\widetilde{B}$ in order from the top. The shaded areas correspond to the ischemic period. The results show no remarkable change in the blood pressure, but both the amplitude and the direct component of strain-gauge plethysmogram (P_{lac}, P_{ldc}), increased relative to resting values 10-15 s after cuff deflation ((I) in Fig. 3) and gradually returned to the resting value. On the other hand, $\widetilde{K}$ decreased to the minimum relative to the resting value 10-15 s after cuff deflation ((I) in Fig. 3) and gradually returned to the resting value. $\widetilde{B}$ increased to the peak relative to the resting value about 5 s after cuff deflation ((I) in Fig. 3) and gradually returned to the resting value.

Fig. 4 and Fig. 5 shows the results for the 4 young and 3 elderly with figures (a) and (b) representing the time course of $\widetilde{K}$ and $\widetilde{B}$ respectively. Each time-course curve is the mean value for the three trials of each subject. In the graph, the baseline is the average of the resting values (0-300 s), and each value after cuff deflation (600-900 s) is the average during 5 s. The results show that each $\widetilde{K}$ reached the minimum about 10 s after cuff deflation ((I) in Fig. 4(a) and Fig. 5(a)) and then returned to the baseline. Each $\widetilde{B}$ reached the maximum about 5 s after cuff deflation ((II) in Fig. 4(b) and Fig. 5(b)) and then returned to the baseline. This change was consistent for all subjects.

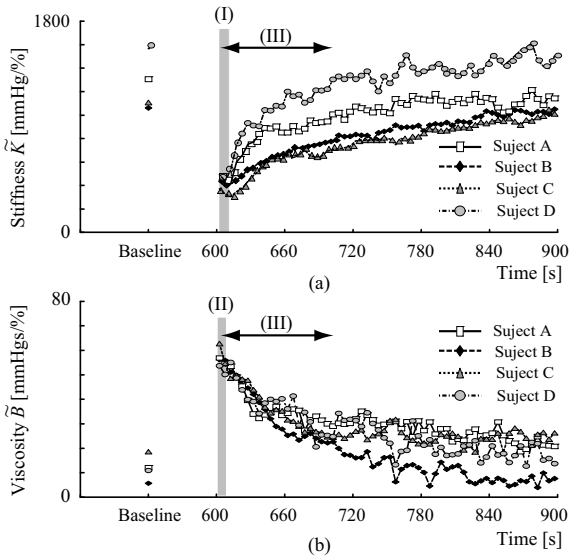


Fig. 4 Time courses of (a) Stiffness and (b) Viscosity in young

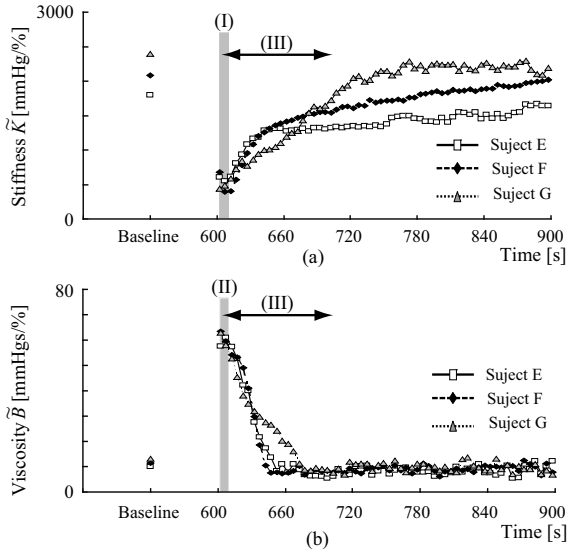


Fig. 5 Time courses of (a) Stiffness and (b) Viscosity in elderly

From the Fig. 4(a) and Fig. 5(a)), $\widetilde{K}$ shows similar changes between the young and the elderly. By contrast, $\widetilde{B}$ shows greater values for young than for elderly after cuff deflation 600 to 700 s area ((III) in Fig. 4(b) and Fig. 5(b)). Therefore, in order to investigate the difference between the young and the elderly were compared with two paired t-tests, and the values $\widetilde{B}$ for young were significantly higher than for elderly from 600 to 700 s ($P< 0.001$).

Table 1 Differences between young and elderly subjects

	Young (Mean ± SD)	Elderly (Mean ± SD)	P *
Age [years]	23 ± 1	55 ± 4	0.001
Area of normalized $\widetilde{K}$	195 ± 25	268 ± 53	0.058
Area of normalized $\widetilde{B}$	64.1 ± 4.5	37.7 ± 3.6	0.001
PWV [cm/s]	1112 ± 112	1607 ± 499	0.11

* Significance level for two-tailed paired *t*-test of young and elderly

V. Discussion

The results of Figs. 5 and 6 confirm a consistent change with all subjects. They also show that, before returning to the baseline, $\widetilde{K}$ reached the minimum 10 s after cuff deflation, $\widetilde{B}$ reached the maximum 5 s after cuff deflation. In conventional studies, the changes during reactive hyperemia are increased blood flow (10 s after cuff deflation) and flow-mediated dilation (about 50 s after cuff deflation) [9]. Here, the period with the maximum change in the proposed method ((I) and (II) in Figs. 5 and 6) corresponds to the period with the maximum increased blood flow reported in previous studies. Moreover, the proposed method measures the characteristics of vessels presented in the forearm.

The comparison using the two-tailed paired t-test between the young and the elderly of the viscoelastic indices and PWV are shown in Table 1. The difference between the young and the elderly for the time course after cuff deflation, the areas of $\widetilde{K}_{rate}$ and $\widetilde{B}_{rate}$ are defined by calculating their integrals between 600 and 700 s. The results show a significant difference ($P < 0.001$) in viscosity. For this reason, the proposed viscoelastic indices represent the modification of arterial mechanical properties derived from flow-mediated dilation, and the strain-gauge plethysmogram represents the increase of the forearm circumference derived from flow-mediated dilation. On the other hand, PWV showed no significant difference ($P = 0.11$).

From these results, viscosity and the strain-gauge plethysmogram show a significant difference between the young and the elderly. It is thought that the changes in these proposed indices after cuff deflation represent the flow-mediated dilation response because previous studies [13] showed that flow-mediated dilation was significantly impaired in the group of the elderly as a whole compared with the young. It was therefore confirmed that the proposed method has the potential to evaluate endothelial function.

VI. Conclusions

In this study, we proposed the new method to evaluate response in reactive hyperemia using viscoelastic indices measured by strain-gauge plethysmography, and then conducted reactive hyperemia experiments to investigate the validity of the proposed method. The results show that, before returning to resting values, $\widetilde{K}$ reached the minimum 10 s after cuff deflation, $\widetilde{B}$ reached the maximum 5 s after cuff deflation with the consistent tendency through all subjects. Additionally, we attempt to assess the difference in response during reactive hyperemia between the young and the elderly, and confirmed the significant difference with time courses of proposed stiffness $\widetilde{K}$ and viscosity $\widetilde{B}$. Our proposed technique is definitely less expensive both from hardware and manpower points of view.

Future research will be directed to assess the additional availability of the proposed method to evaluate the endothelium function by the comparison with an ultrasonic method and the measurement with subjects of various ages. Furthermore, measurement setup will be improved for the robust and comfortable measurement of reactive hyperemia using the strain-gauge plethysmography.

References

1. R.Ross: Atherosclerosis-an inflammatory disease. N Engl J Med, Vol. 340, pp.115-126, 1999.
2. J C, Bramwell, A V. Hill: Velocity of transmission of the pulse wave and elasticity of arteries. Lancet, Vol.1, pp.891-892, 1922.
3. Blacher J, Pannier B, Guerin AP, et al: Carotid arterial stiffness as a predictor of cardiovascular and all-cause mortality in end-stage renal disease. Hypertension, Vol.32, pp.570-574, 1998.
4. C. Giannattasio, M. Failla, A A. Mangoni, L Scandola, N Fraschini, G Mancia: Evaluation of arterial compliance in humans. Clin Exp Hypertens, Vol. 18, pp.347-362, 1996.
5. P.M.Vanhoutte: Endothelium and control of vascular function. Hypertension, Vol.13, pp.658-667, 1989.
6. T.F.Lucher: Imbalance of endothelium-derived relaxing and contracting factors. Am J Hypertens, 3(4), pp.317-330, 1990.
7. Y.Higashi, S.Sasaki, K.Nakagawa, et al: Endothelial function and oxidative stress in renovascular hypertension. N Engl J Med, Vol.346, pp.1954-1962, 2002.
8. E.A.Anderson, A.L.Mark: Flow-mediated and reflex changes in large peripheral artery tone in humans. Circulation, Vol.79, pp.93-100, 1989.
9. M C. Corretti, T J. Anderson, et al: Guidelines for the ultrasound assessment of endothelial-dependent flow-mediated vasodilation of the brachial artery. J Am Coll Cardiol, Vol.39, pp. 257-265, 2002.
10. D. Baldassarre, M. Amato, C. Palombo, C. Morizzo, et al: Time course of forearm arterial compliance changes during reactive hyperemia. Am J Physiol Heart Circ Physiol, Vol.281, pp. H1093-H1103, 2001.
11. A.Sakane, K.Shiba, T.Tsuji, et al: Non-invasive monitoring of arterial wall impedance. Proc. of the First International Conference on Complex Medical Engineering, pp. 984-989, 2005.

12. K Shiba, U Terao, T Tsuji, M Yoshizumi, Y Higashi, K Nishioka: Estimation Arterial Wall Impedance using a Strain-gauge Plethysmogram. Transaction of the Japanese Society for Medical and Biological Engineering, Vol. 45, No. 1, pp. 55-62, 2007.
13. D S.Celermajer, K E. Sorensen, et al: Non-invasive detection of endothelial dysfunction in children and adults at risk of atherosclerosis. Lancet, Vol. 340, Issue. 8828, pp. 1111-1115, 1992.

Author: ABDUGHENI KUTLUK
Institute: Hiroshima University
Street: 4 - 1 Kagamiyama 1-chome
City: Higashi-Hiroshima City
Country: Japan
Email: akutluk@bsys.hiroshima-u.ac.jp

Electromyography Analysis of Grand Battement in Chinese Dance

Ai-Ting Wang[1], Yi-Pin Wang[2], T.-W. Lu[3], Chien-Che Huang[1], Cheng-Che Hsieh[1], Kuo-Wei Tseng[1], Chih-Chung Hu[4]

[1] Department of Physical Education and Health, Taipei Physical Education College, Taipei, Taiwan
[2]Department of Physical Therapy & Rehabilitation, Shin Kong Wu Ho-Su Memorial Hospital
[3] Institute of Biomedical Engineering, National Taiwan University, Taipei, Taiwan
[4] Department of Mechanical Engineering, Mingchi University of Technology, Taiwan

Abstract — **Purpose: The purposes of this study were to analyze the technique movement as grand battement derrie in Chinese dance, to examine the tiny change in muscles during this skill, and to know what factor dominate this technique. Methods: Twenty-two female university in dance department students volunteered to participate in this study. Strength of bilateral paraspinatus muscles and gluteus muscles were calculated using load-cells, flexibility of trunk and hip were evaluated by goniometers, and the fine changes of muscular activity were measured by electromyography. All subjects performed eight times of grand battement in Chinese dance and scored by professional dancer to define the esthetics score of this technique. Results: The dominant side exhibited shorter reaction time than non-dominant side in paraspinatus muscles and gluteus muscles, high level group showed longer muscular activity and shorter resting time than lower level group, which were observed by electromyography. Higher level group were significant greater and better than lower level group in gluteus muscular strength and hip flexibility, but not in trunk. There was significant positive correlation between muscular strength of gluteus and score of technique, but not in trunk. There was significant positive correlation between hip flexibility and esthetics score of technique, yet not in trunk. Conclusion: There are faster reaction times in dominate side to provide the stability before motion occurred. The gluteus muscles and hip flexibilities are the key factor for the performance in grand battement derrie in Chinese dance.**

Keywords — **Chinese dance, grand battement, electromyography, flexibility, muscular strength.**

I. Introduction

Every dancing posture is results that the human joint moves continuously in the dance movement, though activity degree of every joint of human body must be limited, has suitable progressive potentiality via training. [1]After softness degree which studies the Chinese dance dancer behaves, propose the temperature of volume of muscles and the soft tissue, nervous and surrounding environment around tension of joint capsule and ligament intensity, joint around the difference, joint of the skeleton structure, will influence the scope of activities of joint. Need at not kicking appropriate to extend and make by strength fast shank and waist muscle a lot of scholar together after being think to after above play, one burst of big ligaments of the hip joint and Y intestines can't be done up excessively tightly hard in the course, otherwise the scope of activities will be limited, supporting the knee of leg at the time of in addition the activity needs to stretch in order to increase whole movement stability, can't rock at will. Move the leg while moving, the shank, shoulder and arm all can't be excessively stiff, need appropriate to relax shank, shoulder with arm prevent from loose shoulder alike to produce, truck cooperate extending together with the pelvis upwards also at the same time, make the back straight and upright and reduce the load of lumbar vertebrae, can increase the lumbar vertebrae and scope of activities of pelvis, can also prevent the waist injury from producing [3. 4. 7. 8. 9. 10]

Move science at present and medical science clinical to use skin electric picture make detail muscle mobilize way measure in a large amount. Movement science can analyze slighter muscule activity way through the electric picture of skin; Medical science clinical to use skin electric picture measure, reply and is good for patient's muscle telecom phenomenon in a large amount too. Dance some foreign scholar more less, make in-depth analysis to small-scale movement and single position only in the field, for example: Whether Grand plie, Demi plie, or the foot dance injures [5. 6]. So guide the motive of the persons who break out, kick in the activity way with slight muscle of movements after analyzing the Chinese dance through the electric picture of skin, understand the organization of human body and muscle operation method, improve skill movements, and prevent or reduce the production of the dance injury.

Because the dance injures the importance trained to the professional skill of dance with muscle ability, this research passes (Electromyography; EMG) , muscular strength and whether degree,etc. analyze, in order to understand Chinese kick movement level behave group behind the dance, habitually practise, examine to habitually practise side muscular strength react time difference, person who decay, muscle shrink array and have skin telecom complex reaction time. Cooperate with instruments such as Load-cell and

Chwee Teck Lim, James C.H. Goh (Eds.): ICBME 2008, Proceedings 23, pp. 2064–2067, 2009
www.springerlink.com

Goniometer, etc, test Chinese kick Trunk flexibility of movements behind the dance, Hip joint flexibility, Erector spine muscle strength, Gluteus maximums muscle strength. Will test the resulting materials via biological statistical method, put in order and analyze movements grade and display group and muscular strength, soft difference of degree and high, low with the muscular strength, soft relevance of degree subjectively, use to understand and influence the Chinese dance, the movement factor kick, in order to set up datumization and scientific effective system, offer and practise dancer and teacher's correct new thinking of dance, expect to improve the skill ability of dance, prevent dance injury.

II. Materials & Method

Primitive experimenter of research this add up to 28, it is Taibei municipal Physical Culture Institute dance department that participate in speciality of women dance student of experiment voluntarily. Accept each person experimenter all test degrees soft, test muscular strength and after kick there aren't movement, and carry on the collecting of telecom number of skin at the same time when movements are tested. And guarantee to originally study letter degree compared and assessed for the error of preventing subjective appraisal from causing among all data, will act and compare and assess the coefficient of variation of marks and greater than 6 experimenter's data of 0.1 to remove, the formal experimenters whom other 22 experimenters are accepted by this research, its basic materials are as shown in (Table 1).

Appointed movements and the skin telecom number (EMG): It pick fetch,whose name is electric in skin chart stick electrode respectively on: (1) Erector spinae, bilateral (2) gluteus maximus, bilateral (3) biceps femoris, bilateral. Experimenter all in order to habitually practise leg test, all experimenter finish one group 8 Chinese kick movement behind the dance with music rhythm movement, shoot the movement course of kicking after the Chinese dance through several cinecameras, and then transfer the film to making into all disc, grade by subjective way via professional dance Professor by percentage, tell high to display groups of group, low to display groups of group.

The analytical method of the signal: The primitive skin telecom number collected, frequency is 1000Hz that the signal takes a sample, the primitive signal is with software AcqKnowledge software (ACKv3.7.3) Go on several and strain the wave, straining the wave way adopts bandpass to go on, the frequency band is 5-500Hz. Assess the parameter with analyzing it is bad that the way includes Time domain and EMG Reaction time, compare after all assessment parameters are all in order to standardize.

Statistical analysis: The software counts and carries on statistical analysis with SPSS 14.0 edition, the narration of all number value counts all with ± standard deviation of average) Appear. The competence of showing of this research is determined as $\alpha = 0.05$.

Table 1 Experimenter's data

Experimenters	N	Age (yrs)	Height (cm)	Weight (kg)	Skill movements grade subjectively
	22	19.9±1.8	161.0±5.3	52.3±4.7	82.8±7.0
High behavior group	11	19.5±0.7	162.5±5.8	52.3±4.5	88.7±1.6
Low behavior group	11	20.4±2.4	159.5±4.6	52.4±5.1	76.7±5.0

III. Result

EMG

Erector spine muscle and buttocks old skin habitually practise complex reaction time of side greater than, habitually practise side (Fig 1) ,And muscles shrink arrays there is not apparent order relation (Table 2)

Muscles shrink the order

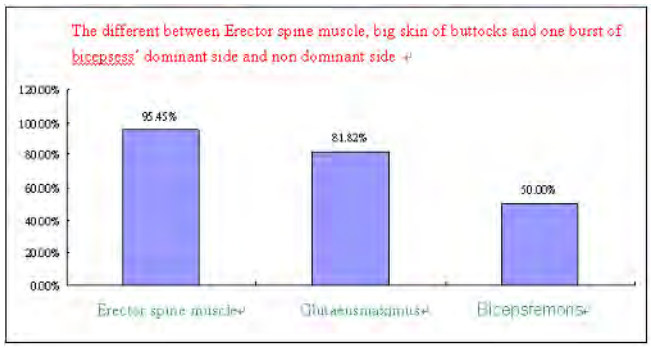


Fig. 1 The different between Erector spine muscle, big skin of buttocks and one burst of bicepsess' dominant side and non dominant side

Table 2 The different between dominant side and nondominant side EMG reaction time's t-test .

participate	The different between dominant side and nondominant side EMG reaction time (sec)			
	N	Erector spine muscle	glutaeusmaximus	bicepsfemoris
	22	0.07±0.07	0.09±0.08	0.01±0.26
high level group	11	0.06	0.07	0.06
low level group	11	0.08	0.11	-0.05
t-test	P	0.604	0.229	0.329

t=0.05(11-2)=1.8331, *p<0.05

Research this to habitually practise side and habitually practise erector spine muscle of side, buttocks old skin and whifves of biceps complex reaction time order compare alternate analysis respectively. Find t among every group tests all there is not difference of showing that have (p> 0.05) (Table 3)

IV. Concl usions

Analysis of the telecom number of skin

Experimenter have 95.45% and 81.82% person erector spine muscle and buttocks old skin habitually practise complex reaction time of side greater than, habitually practise side (picture 3) ,Habitually practise side to be number value little to say skin telecom symbol mobilize time to be relatively early, reaction speed very fast; Habitually practise side to be number value heavy to say skin telecom symbol mobilize time to be relatively late, reaction speed relatively slow. Find buttocks old skin and erector spine muscle at the movement of playing after not finishing very (habitually practise side) ,Supported the leg (not habitually practise the side) Produce the telecom number of muscle first, may be because the centre of body weight is shifted to supporting the leg (not habitually practise the side) first ,Support the leg (not habitually practise the side) at the same time Must offer enough stability degree, let, move leg (habitually practise side) Finish movements smoothly. It reveal old on buttocks for skin and erector spine muscle in behind movement of playing at,support there aren't leg, purpose its lie in sport support skin telecom symbol function of leg, can seek, call together muscle to support the leg shrink ahead of time, move the leg to finish movements in order to offer enough stability to let.

Bursts of biceps skin electric picture react time difference statistical form find experimenter habitually practise side with habitually practise skin electric priority number of side account for 50% (picture 3) respectively ,Find obvious to habitually practise side prior to skin electric phenomenon to habitually practise side, high, low to display groups of response time difference of group show difference (p> 0.05) .

Ting erector spine muscle, buttocks old skin and bursts of biceps habitually practise side with habitually practise side skin electric picture time difference of reacting, find high, low erector spine muscle, buttocks old skin and whifves of response time difference of biceps to display group have, show difference have all(p> 0.05) . Inferences revealed ' steady degree is taken precedence over activity degree ' generally exist between all movements and dancers, so can different dance behave (high low to behave group) There is difference nature of showing that has (Table 2) .

Research this to habitually practise side and habitually practise erector spine muscle of side, buttocks old skin and whifves of biceps complex reaction time order compare alternate analysis respectively. Find t among every group tests all there is not difference of showing that have (p> 0.05) ,Reveal, habitually practise side and habitually practise erector spine muscle, buttocks old skin and streams of biceps muscle of side shrink order have apparent order relation. May because skin sample that electricity test it counts to be enough, skin telecom homogeneity too high and difference loud factor enough of experimenter of symbol, need various to count, could go on analysis carefully than correctly originally ' Table 3) .

Decaying rate of brass-wind instrument of skin telecom

No EMG duration reaction time

By Table 4 being high low to display group have skin telecom symbol complex reaction time abstract find, high 0.61 seconds have skin to be telecom symbol complex reaction time apparent to less than low to display 0.81 seconds now, there is difference nature of showing that has (p<0.05) ,Reveal low that displays group it when muscles do not move about, it is relatively long during low tension, it is high to display one group of muscles to still keep the electric activity of some skin (skin tense when not moving about) ,Can make muscles activate the movements of producing fast, in order to deal with the external force that fast movements change or happen suddenly.

Table 3 Muscle contraction order t-test.

participate	N	Erector spine muscle - glutaeus-maximus		Erector spine muscle glutaeus-maximus		glutaeusmaximus - bicepsfemoris	
	22	dominant side	nondominant side	dominant side	nondominant side	dominant side	nondominant side
high level group	11	-0.07	-0.07	-0.13	-0.13	-0.06	-0.07
low level group	11	-0.07	-0.04	-0.01	-0.14	0.07	-0.1
t-test	p	1	0.87	0.38	0.99	0.22	0.71

t=0.05(11-2) =1.8331, *p<0.05

Table4 During high and low performance no EMG duration reaction time t-test.

participate	N	No EMG duration reaction time (sec)
	22	0.71±0.2
high level group	11	0.61
low level group	11	0.81
t-test	P	0.03*

V. Propose

Result of research this, offer dancer, dance teaching person and research and propose following suggestion to dance movement future separately: First, to dancer and dance teaching person, propose dancer can by with hip joint skin group for key muscle muscular strength and soft degrees of training of group of main fact, the movements of kicking after in order to improve China's dance movement behave; Must moreover substantiate the physiology and dissect and gain knowledge, could be with the correct dance movement of guidance of the efficiency and security, improve the learner's skill and avoid the production of the dance injury. Second, to the research of dance technology in the future, because the Taiwan dance is studied in the majoritily with the artistic quality of humanity more at present, it is less likely to further investigate by scientific method of the movement. Through sport science further investigates, not only may expand the visual field of dance, can further quantize the skill movements of the dance by scientific process, digitisation method, entrust to the new life that the dance movement analyses scientifically.

References

1. 王道平(2002)。中國舞蹈柔軟度之研究。台南女子技術學院學報，22，691-699。
2. Basmajina, J.V., & DeLuca, C.J. (1985). Muscle alive:Their functions revealed by electromyography(5th ed.). Baltimore:Williams & Wilkins.
3. Clarke Mary & Crisp Clement (1981). The ballet goer's guide. New Youk: Knopf.
4. Draper Nancy & Margret F. Atkinson (1951). Ballet for beginners. New York：Knopf.
5. Elly Trepman, Richard E. Gellman, Lyle J. Micheli & Carlo J. DE LUCA (1994). Electromyographic analysis of standing posture and demi-plie in ballet and modern dancers. Medicine Science in sports exercise, 26(6), 771-782.
6. Elly Trepman, Richard E. Gellman, Lyle J. Micheli & Carlo J. DE LUCA (1998). Electromyographic analysis of grand-plie in ballet and modern dancers. Medicine Science in Sports Exercise, 30(12), 1708-1720.
7. Fonteyn De Arias & Dame Margot (1988). Academy of dancing, royal: Ballet class . London : Ebury Press.
8. Franklin, E. (1996). Dance imagery for technique and performance. Champaign, IL: Human Kinetics.
9. Howse, J. & Hancock, S. (1988). Dance technique and injury prevention. New York : Theatre Arts Books Routledge.
10. Istvan Ament (1985). A systematic approach to classical ballet, Lanham, MD: University press of America. Janice D.

Author: Tung-Wu Lu, D.Phil.
Institute: Institute of Biomedical Engineering
Street: #1, Sec. 1, Jen-Ai Road, Taipei 100, Taiwan, R.O.C
City: Taipei
Country: Taiwan
Email: twlu@ntu.edu.tw

Landing Patterns in Subjects with Recurrent Lateral Ankle Sprains

Kuo-Wei Tseng[1,3], Yi-Pin Wang[2], T.-W. Lu[3], Ai-Ting Wang[1], Chih-Chung Hu[4]

[1] Department of Physical Education and Health, Taipei Physical Education College, Taiwan
[2]Department of Physical Therapy & Rehabilitation, Shin Kong Wu Ho-Su Memorial Hospital
[3] Institute of Biomedical Engineering, National Taiwan University, Taiwan
[4] Department of Mechanical Engineering, Mingchi University of Technology, Taiwan

Abstract — **Introduction The most common symptoms after ankle sprains were chronic ankle instability, proprioception defect and probable neuromuscular adaptation. The purpose of this study was to identify the normal landing pattern using detailed biomechanical analysis including analysis of the kinematics and ground reaction force, and to compare the landing pattern in the subjects with recurrent ankle sprain and normal subjects. METHODS Ten male adults were recruited in this study (5 subjects with recurrent lateral ankle sprains group, 5 subjects with normal control group). All subjects would be asked to perform maximal standing jumps and drop landing from 3 platforms with different heights (0.37 m, 0.67 m, & 0.97 m, respectively). Those movements were collected by VICON 512 (Oxford Metrics, UK) motion analysis system and the kinematics was analyzed using self making software with MATLAB. The ground reaction force of both lower limbs was recorded by two AMTI force platforms, and the kinetic data were calculated with inverse dynamics. RESULTS In the different landing height, the main differences of kinematics were the maximum flexion angles of hip and knee joints in normal landing patterns and the flexion angles increased with the landing height, as well as the flexion of pelvis, hip abduction, and knee external rotation in the subjects with recurrent ankle sprains. When compare those two groups, the landing pattern in the subjects with recurrent ankle sprain was significant smaller than normal subjects in knee flexion (65.71°±6.43° vs. 70.19°±13.76°) and hip flexion (34.15°±5.42° vs. 42.54°±10.07°). The time to maximum angles in ankle dorsiflexion and foot pronation were also quite different between these two groups. The maximum vertical ground reaction force in sprain group was significant smaller than normal group. CONCLUSION In this study, we have revealed the adaptation of performing drop landing in the individuals with recurrent ankle sprains. It could be considered as a recommendation of the rehabilitation..**

Keywords — **Motion Analysis, Recurrent Lateral Ankle Sprain, Landing Pattern**

I. Introduction

Forty-seven percent of ankle sprains occurred in the ankle that had been previously sprained. The most common symptoms after ankle sprains were chronic ankle instability, proprioception defect and probable neuromuscular adaptation [1-3]. Moreover, Ekstrand and Gillquist suggested that there was 47% of ankle sprains occur in the ankle that had been previously sprained [4]. It meant that around half of ankle sprain subjects would have great potential to be the candidates with recurrent and chronic ankle sprains. Furthermore, studies have shown that between 20-50% of ankle sprain suffers result in residual ankle symptoms [2]. The most reported residual ankle symptoms were chronic ankle instability, proprioception defect and probable neuromuscular adaptation [5]. The biomechanics of landings has been investigated but limited in two-dimensional analysis in the past literature [6-11]. And no study investigate the differences of landing pattern between normal and recurrent ankle sprain subjects. Therefore, it is reasonable to presume that there must be some factors that cause the ankle more susceptible to subsequently sprain, or chronic ankle instability.

There are two theories for recurrent ankle sprains. The first one is the 'mechanical instability' theory, which suggests that the instability is caused by damage to the integrity of supporting ligaments. The second is the 'functional instability' theory, which reveals that the instability is due to damage to the nerves in the ankle area that would normally feedback information to the brain about the position of the ankle, interacting with balance mechanism. If the latter explanation were true, ankle sprain would be expected to affect the balance strategy. Since the most common injury mechanism in recurrent ankle sprain was landing on irregular surface. To understand the response to this kind of impact activity, this study would investigate biomechanical changes in subjects with recurrent ankle sprain and compare with healthy subjects.

Therefore, the first aim of this study was to identify the normal landing pattern using detailed biomechanical analysis including analysis of the kinematics and ground reaction force. The second aim of the study is to investigate the landing pattern in the subjects with recurrent ankle sprain and compare this landing pattern with that in normal subjects.

II. Method

Five male adults with recurrent lateral ankle sprains were recruited in this study, and five healthy male adults who were free from any injury of lower extremity were enrolled

Chwee Teck Lim, James C.H. Goh (Eds.): ICBME 2008, Proceedings 23, pp. 2068–2071, 2009
www.springerlink.com

as control group. Recurrent lateral ankle sprain is defined as that the subject has more than two sprain episodes with the same ankle in the past three months or had been definitely diagnosed by a doctor. However, during the testing session, there should be no acute symptoms such as edema and resting pain that would influence the activities.

The reflective markers would be placed on several bony landmarks as the figure shown below, to define segments of lower extremity, which includes the landmarks on pelvis, left anterior superior iliac spine (LASI), left posterior superior iliac spine (LPSI), right anterior superior iliac spine (RASI), right posterior superior iliac spine (RPSI), thigh include great trochanter (GTRO), medial and lateral part on thigh (THI), left femoral epicondyle (LFC), right femoral epicondyle (MFC), shank contain tibial tuberosity (TT), head of the fibula (HF), lateral malleolus (LMA), medial malleolus (MMA), hindfoot include posterior base of calcaneus (HEE), navicular tuberosity (FOO), 5th metatarsal base (TOE), forefoot contain navicular tuberosity (FOO), 5th metatarsal base (TOE), dorsal aspects of 1st, & 5th metatarsal heads (D1T & D5T) and toe contain nail of big toe (BTO) , dorsal aspects of 1st, & 5th metatarsal heads (D1T & D5T). In addition, the segment definition in trunk includes jugular notch of sternum (STRN), the spinous process of C7 (CER7), left acromion head (LSHO), right acromion head (RSHO) .

The subjects would be asked to perform level walking initially to warm-up and then maximal vertical jumps and drop landings from platforms with four selected heights (0.37 m, 0.57 m, 0.77m, & 0.97 m, respectively). [Fig.1], [Fig.2]. Subjects would repeat at least 3 times for each condition. The kinematic data would be collected at 120 Hz



Fig.1 A subject was performing: (a) static alibration (b) level walking (c,d) maximal standing jump



Fig.2 Four platforms with different heights: (a) 0.37m (b) 0.57m (c) 0.77m (d) 0.97m

with the VICON 512 (Oxford Metrics, UK) motion analysis system with BodyBuilder® to establish the segmental coordination systems. With dual AMTI force platform system could simultaneously record the ground reaction force of both limb at sampling rate of 600 Hz, kinetic data calculate with inverse dynamics.

The *landing phase* defined as starting at the first contact with force plate and end at the maximum knee flexion angle to investigate the response to this impact activity. The *kinematic variables* including maximum joint angle and time to maximum angle were analyzed and compared between groups. *Vertical ground reaction force* was normalized with subject's body weight, and the maximum value was calculated and compared between groups and heights. All the variables were analyzed using 2-way ANOVA with independent variables of groups and heights. Significant level was set at 0.05.

III. Result

Landing phase duration was increased with the platform height increased in both groups, and was shorter in subjects with recurrent ankle sprain [Fig.3].

When drop landing from platforms with different height, the main differences of kinematics were the maximum flexion angles of hip and knee joints in normal landing patterns and the flexion angles increased with the height. When drop landing from platforms with different height, the main differences were the maximum flexion angles of hip and knee joints, as well as the flexion of pelvis, hip abduction, and knee external rotation in the subjects with recurrent ankle sprains. When compare those two groups, the landing pattern in the subjects with recurrent ankle sprain was signifi-

cant smaller than normal subjects in knee flexion (65.71° ± 6.43° vs. 70.19° ± 13.76°) and hip flexion (34.15° ± 5.42° vs. 42.54° ± 10.07°). [Fig.4].

The time to maximum angles in ankle dorsiflexion and foot pronation were also quite different between these two groups. The maximum vertical ground reaction force in sprain group was significant smaller than normal group. [Fig.5].

The maximum vertical ground reaction force on each limb was compared between groups and platform heights. Significant difference was found between groups, and the value was smaller in normal subjects [Table 1].

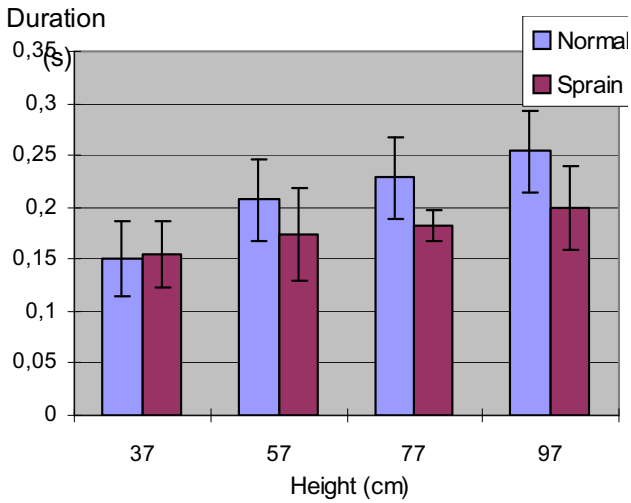


Fig.3 Landing phase durations in both groups in different heights

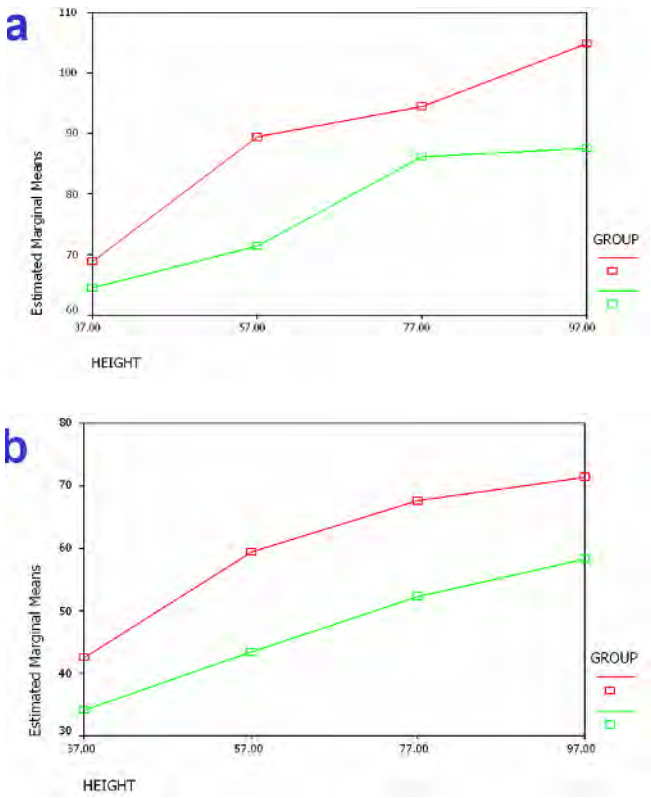


Fig.4 (a) Hip flexion (b) knee flexion with different height between two groups (red line: normal group, green line: sprain group)

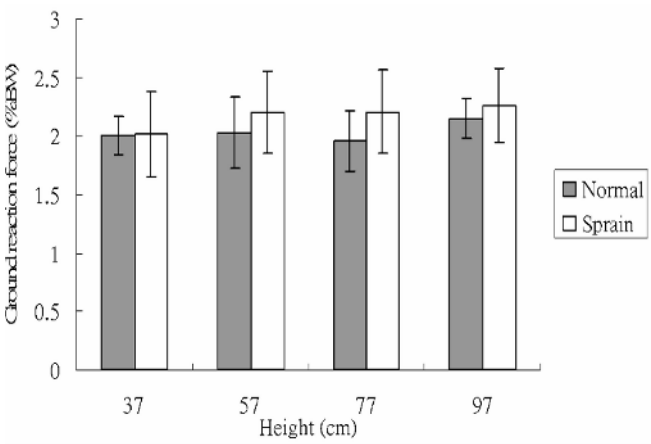


Fig.5 Ground reaction force in both groups in four different heights

Table 1. Maximum vertical ground reaction force in percentage of body weight on each limb

GROUP*	HEIGHT	Mean (%BW)	Std. Deviation (%BW)	N
Normal	37	1.9994	.1630	15
	57	2.0249	.3034	15
	77	1.9559	.2562	15
	97	2.1488	.1682	15
	Total	2.0344	.2310	60
Sprain	37	2.0169	.3610	15
	57	2.1999	.3490	15
	77	2.2071	.3535	15
	97	2.2577	.3162	15
	Total	2.1704	.3467	60
Total	37	2.0094	.2870	30
	57	2.1249	.3342	30
	77	2.1066	.3354	30
	97	2.2110	.2634	30
	Total	2.1131	.3091	120

* p value < 0.04

IV. Discussion

Landing phase duration was increased with the platform height increased in both groups. It indicated that more time was required to response to a larger impact, and to decelerate a bigger contact downward velocity, in order to regain

the balance from this impact activity. And the landing phase was shorter in subjects with recurrent ankle sprain, means that they reach their maximum knee flexion angle earlier. This could result from the instability or sensory impair of ankle joint, and subjects with ankle sprain had to count on the shock absorption ability of knee joint earlier to stop the downward tendency. The control mechanism and chronic adaptation of recurrent ankle sprain subjects could be another possible reasons. This shorter landing phase, which could result in bigger impact and poorer shock absorption, is the reason why causing ankle joint more prone to injury. Or the injury experiences cause the individual to chronic adapts his landing pattern. In this preliminary study, we cannot define the cause-effect relationship between them.

The maximum vertical ground reaction force (GRF) on each limb was compared between groups and platform heights, and the mean value was smaller in normal group [Table 1]. It implied there were less impulses in normal subjects.

The comparison of the GRF patterns between groups, we noticed that the vertical components of ground reaction force (vGRF) had an interesting trend in normal group, especially landing from a higher platform, which demonstrated that they reached a peak vGRF and decrease quickly then kept in a plateau, value of a hundred percent of their body weight, when knee flexion angle reach its maximum value vGRF decrease gradually to their balanced weight. However, sprain group demonstrated different pattern, that vGRF reached its peak value then gradually decreased to the balance weight earlier, without the buffering period before maximum knee flexion. According to the Newton's law, a constant force causes a constant acceleration if the mass of the object keeps unchanged. Considering the plateau demonstrated in normal subjects before reaching maximum knee flexion, they tried to keep a constant deceleration of center of mass (COM) to counteract to the downward acceleration caused by the gravitation. It could be a protection mechanism providing a buffering effect to prevent our musculoskeletal system keeps bearing a changing acceleration (jerk).

V. Conclusion

The preliminary results including kinematics and ground reaction force could have a glimpse of the general normal landing pattern. The landing pattern in the subjects with recurrent ankle sprain had showed significant difference compared with normal subjects with our detail biomechanical analysis. In this study, we have revealed the adaptation of performing drop landing in the individuals with recurrent ankle sprains. It could be considered as a recommendation of the rehabilitation guide.

There are still lots of issues related to this topic, such as landing on a tilting surface, muscle activation sequence, role of vision, and anticipatory postural adjustment during landing. All the issue are interesting and worthy to investigate in the further study.

References

1. Ruda S.C. Common ankle injuries in the athlete. Nursing Clinics of North America 1991; 26: 167-180
2. Wright, I.C., Neptune R.R., van den Bogert A.J., Nigg B.M. The influence of foot positioning on ankle sprains. J Biomechanics 2000; 33: 513-519.
3. Kerkhoffs G.M., Blankevoort L., van Poll D., Marti R.K., van Dijk C.N. Anterior lateral ankle ligament damage and anterior talocrural-joint laxity: an overview of the in vitro reports in literature. Clin Biomechanics 2001; 16: 635-643
4. Ekstrand,J.,Gillquist, J. (1983) Soccer injuries and their mechanisms: a prospective study. Med. Sci. Sports Exerc. 15, 267-270.
5. Robbins S., Waked E., and Rappel R. Ankle taping improves proprioception before and after exercise in young men. Br J Sports Med 1995; 29: 242-247.
6. McNitt-Gray, JL. Kinematics and impulse characteristics of drop landings from three heights. Int J Sport Biomechanics 1991; 7: 201-224.
7. McNitt-Gray, JL. Kinetics of the lower extremities during drop landings from three heights. J. Biomechanics 1993; 9: 1037-1046.
8. McCaw, S.T. and Cerullo, J.F. Prophylactic ankle stablilizers affect ankle joint kinematics during drop landings. Med Sci Sports Exerc 1999; 31: 702-707.
9. Dufek, J.S., Bates, B.T., Stergiou, N., James, C.R. Interactive effects between group and single-subject response patterns. Human Mov Sci 1995; 14: 301-323.
10. Challis J.H. An investigation of the influence of bi-lateral deficit on human jumping. Human Mov Sci 1998; 17: 307-325.
11. Gross, T.S. and Nelson R.C. The shock attenuation role of the ankle during landings from a vertical jump. Med Sci Sports Exerc 1988; 20: 506-514.
12. McNair P.J., Marshall R.N. Landing characteristics in subjects with normal and anterior cruciate ligament deficient knee joint. Arch Phys Med Rehabil 1994; 75: 584-9.

Author: Lu, T.-W.
Institute: Institute of Biomedical Engineering,
National Taiwan University, Taiwan
Street: No. 1, Sec. 4, Roosevelt Road
City: Taipei
Country: Taiwan (R.O.C.)
Email: twl@ntu.edu.tw

The Influence of Low Level Near-infrared Irradiation on Rat Bone Marrow Mesenchymal Stem Cells

T.-Y. Hsu[1], W.-T. Li[1,2,*]

[1] Department of Biomedical Engineering, Chung-Yuan Christian University, Chung-Li, Taiwan
[2] Research and Development Center for Biomedical Microdevice Technologies, Chung-Yuan Christian University, Chung-Li, Taiwan

Abstract — **Low-level light irradiation (LLLI) has been known to lead to cell proliferation, increase of ATP synthesis, change in mitochondrial membrane potential and the induction of the synthesis of cell cycle regulatory proteins. The purpose of the study was to find the influence of near-infrared (850 nm) light emitting diodes (LEDs) irradiation on mesenchymal stem cells (MSCs) derived from rat bone marrow. Maximal increase in MSCs proliferation was observed with multiple dose of LLLI at 10 mW/cm^2 and 4 J/cm^2. No apparent variation in temperature (26.1 to 26.3 ^{o}C) during irradiation was found, which suggested photochemical effect could be the key factor for biomodulation. The parameters were used in the subsequent research. The number of CFU-F increased slightly ($p<0.05$) when rat MSCs were illuminated at 10 mW/cm^2 and 4 J/cm^2. No apparent increase in lactate dehydrogenase release indicated that membrane integrity remained intact after LLLI. Reactive oxygen species production decreased indicated LLLI might have anti-oxidative effect. Intracellular level of ATP increased 1.53 fold after LLLI. Both alkaline phosphatase activity and osteocalcin secretion increased in osteogenic MSCs treated with multiple dose of LLLI. However, triacylglyceride accumulation in adipogenic cells decreased after LLLI. In conclusion, multiple dose of LLLI at 850 nm not only enhances proliferation but also modulates differentiation of MSCs.**

Keywords — **low level light irradiation, mesenchymal stem cell, near-infrared, light emitting diode.**

I. Introduction

Mesenchymal stem cells (MSCs) contribute to the regeneration of mesenchymal tissues and are essential in providing support for the growth and differentiation of hematopoietic stem cells within the bone marrow microenvironment. MSCs are able to differentiate into cell types such as osteocytes, adipocytes, chondrocytes, myocytes, cardiomyocytes, endothelial cells, neurons and hepatocytes *in vitro* [1]. Their easy isolation, expansion, and low immunogeneity make them ideal for stem cell therapies. Approaches such as genetic immortalization, formulation of growth media, use of various bioreactors, have been used to maintain MSCs' life span and expand sufficient cells for clinical treatment.

Low level light irradiation (LLLI) has been shown to enhance proliferation and cytokine secretion of a number of cells, which may be an alternative for MSCs expansion. The primary defining factor for LLLI is power with a range of 10^{-3} to 10^{-1} W, which results in imperceptible temperature elevations (0.5~0.75^{o}C) [2]. Coherent and non-coherent light with the same wavelength, intensity, and irradiation time provide the similar photobiological effect [2]. The mechanism by which low intensity lasers induce biomodulation of cell activity has been well described by Karu [3]. LLLI seems to act mainly in cells with committed functions. Several questions remain open on the intracellular responses of stem cells to LLLI. Abramovitch-Gottlib *et al.* used a combination of low level laser irradiation and coralline matrix to enhance the osteogenic phenotypes of mesenchymal stem cells [4]. Our previous study has shown that LLLI of 630 nm light emitting diodes (LEDs) could enhance replicative and colony formation potentials of MSCs derived from human bone marrow [5]. Tuby *et al.* demonstrated that LLLI of 804 nm diode laser (50 mW/cm^2, 1 or 3 J/cm^2) promoted proliferation of cultured mesenchymal and cardiac stem cells from rats [6]. Kim et al. found that 647-nm light emitting diodes (LEDs) irradiation enhances osteogenic differentiation in mouse MSCs [7]. Eduardo *et al.* reported laser phototherapy (660 nm) on human dental pulp stem cells improved the cell growth when cultured under nutritional deficit conditions [8]. To date, LLLI using 850-nm LEDs has not been applied as an approach to promote proliferation or differentiation of isolated MSCs. The purpose of the present research was to study the effects on the proliferation and differentiation potential of rat MSCs by near-infrared LLLI.

II. Materials and methods

A. Cells and cell culture

Female Wistar rats (150-250 g, Laboratory Animal Center, National Taiwan University Hospital, Taipei, Taiwan) were sacrificed by anesthesia under the guidelines approved by the Institutional Animal Care and Utilization Committee. Bone marrow were collected from the femurs and tibias by flushing it with serum-free complete medium [Alpha minimum essential medium (α-MEM) containing 2 mM L-glutamine, 100 U/ml antibiotic- antimycotic and 0.1 mM

Chwee Teck Lim, James C.H. Goh (Eds.): ICBME 2008, Proceedings 23, pp. 2072–2075, 2009
www.springerlink.com

non-essential amino acids; Gibco/BRL, Invitrogen, CA, USA]. Cells were filtered through a 100-μm nylon mesh (BD Falcon, CA, USA) and subjected to 40% percoll (Sigma, MO, USA) density gradient centrifugation. Mononuclear cells were collected from the interface and suspended in complete medium supplemented with 10% fetal bovine serum (FBS, lot selected from Hyclone, UT, USA). After 24 h incubation at 37°C and 5% CO_2, nonadherent cells were discarded and the adherent cells were grown to 90% confluence in complete medium containing 10% FBS. MSCs (passage 0) were detached by trypsinization and harvested by centrifugation at 500 x g for 10 min. The cells were grown in a 10-cm culture dish with fresh medium replaced every 3 to 4 days. All cells used for the experiments were the third passage.

B. Light irradiation

A home-made infrared LEDs array composed of 23 x 30 LED (GaAIAs) lamps (LUIR034, emission wavelength: 850 ± 21 nm, Lenoo Electronics Co., Hsinchu, Taiwan) was used. The irradiance of a LED array was adjusted by direct current from a standard power supply. The irradiance at the surface of the cell monolayer was measured by a power meter (Orion, Ophir Optronics Ltd., UT, USA) and the parameters used were 10 and 15 mW/cm^2. The radiant exposure of 2 and 4 J/cm^2 were used, which was regulated by the time period of illumination. A culture plate was supported on a clear polycarbonate platform and irradiated from below. The distance from the LED array to the surface of cell monolayer was 0.7 cm. The temperature of the medium fell between 26.1 to 26.3°C during the course of illumination (15 mW/cm^2 and 4 J/cm^2). All culture plates were maintained under semi-dark at room temperature (RT) and atmosphere for the length of the irradiation. Rat MSCs without LED exposure placed under the same condition were used as control. All experiments were performed in triplicate and three sets of separate experiments were conducted

C. Cell proliferation

Rat MSCs (100 cells/well) were plated on a 96-well microplate in the complete medium supplemented with 10% FBS. Cells were irradiated every other day and their proliferation was measured by direct cell counting after Liu's staining (Tonyar Biotech. Inc., Taiwan). To determine whether near infrared LLLI caused any damage to rat MSCs, cells (10^4 cells/well) were allowed to adhere on a 96-well microplate for 24 h. Membrane integrity was assessed by the release of lactate dehydrogenase (LDH) from cells using CytoTox 96® Non-radioactive Cytotoxicity Assay (Promega, WI, USA) at various time points after LLLI.

Here, colony-forming unit-fibroblast (CFU-F) assay is a functional method to quantify stromal progenitors. One hundred rat MSCs were seeded on a 10-cm dish in the complete medium supplemented with 10% FBS. The cells were subjected to LLLI at 10 mW/cm^2 and 4 J/cm^2 every other day. After 21 days, the colonies (≥ 50 cells) were stained with 3% crystal violet and counted.

D. Reactive oxygen species analysis

Reactive oxygen species (ROS) formation was detected using 2',7'-dichlorofluorescin diacetate (DCFDA, Sigma, MO, USA). Rat MSCs ($2x10^5$ cells/well) were plated on a 6-well plate and incubated with DCFDA (20 μM) for 1 h before LLLI. Cells were washed twice with Dulbecco's phosphate buffered saline (PBS, Sigma, MO, USA) after LLLI, and lysed by sonication. DCF (2',7'-dichlorofluorescein) fluorescence in cell lysate was analyzed by an ELISA reader (Fluoroskan Ascent FL, Thermo Fisher Scientific, Inc., MA, USA) (ext: 488 nm). The protein amount in each sample was determined by bicinchoninic acid protein assay (Sigma, MO, USA).

E. ATP analysis

Rat MSCs (10^4 cells/well) were seeded on a 96-well microplate and illuminated at 24 h. Intracellular ATP level was measured after LLLI using CellTiter-Glo® Luminescent Cell Viability Assay (Promega, WI, USA).

F. MSCs differentiation

To observe the effect of LLLI on osteogenic differentiation of rat MSCs, cells ($2.5x10^3$ cells/well) were grown in the complete medium on a 96-well microplate for 6 days. Then, cells were incubated in the osteogenic medium (complete medium containing 2% FBS, 10 μM β-glycerophosphate, 10^{-7} M dexamethasone and 50 μM ascorbic acid 2-phosphate) for 28 days while cells were subjected to LLLI every other day. Alkaline phosphatase (ALP) activity and osteocalcin secretion of MSCs were assessed every week. ALP activity was assayed based on the conversion of *p*-nitrophenyl phosphate (*p*-NPP) into *p*-nitrophenol (*p*-NP) in the presence of ALP. Cell lysate (10 μl) was mixed with 100 μl of 6.7 mM *p*-NPP (Sigma, MO, USA), followed by incubation at 37°C for 30 min. After stopping the reaction with 50 μl of 3 N NaOH, the absorbance at 405 nm of *p*-NP was measured with an ELISA reader (Multiskan Spectrum, Thermo Fisher Scientific, Inc., MA, USA). The expression of osteocalcin was analyzed by ELISA. Culture supernatant

(80 μl) was added into each well of a 96-well ELISA plate (NUNC, Thermo Fisher Scientific, Denmark) and incubated at 4°C overnight. Rabbit anti-rat antibodies against osteocalcin (Santa Cruz Biotechnology Inc., CA, USA) were added to the wells at 1:250 and incubated at 4°C overnight. After washing with PBS, 30 μl of alkaline phosphatase-conjugated goat anti-rabbit secondary antibody (Santa Cruz Biotechnology Inc., CA, USA) (1:250) was added and incubated at RT for 2 h. After washing with PBS, 100 μl of ALP substrate (Promega, WI, USA) was added and the absorbance at 620 nm was read after 2 h incubation at RT.

To observe the effect of LLLI on adipogenic differentiation, rat MSCs ($2.5x10^3$ cells/well) were grown in the complete medium on a 96-well microplate for 6 days. Then, the medium was changed into adipogenic medium (complete medium containing 2% FBS, 0.5 mM 3-isobutyl-1-methylxanthine, 10^{-6} M dexamethasone, 60 μM indomethacin and 5 μg/ml insulin) and the medium was replaced every 3 to 4 days. Adipogenesis was assessed by Oil Red-O stain. To quantify the amount of triacylglyceride, 50 μl of isopropanol was added into each well to dissolve Oil Red-O at RT for 10 min. The absorbance at 510 nm was read by an ELISA reader.

G. Statistical analysis

The result was expressed as the mean ± standard deviation. A two-tailed Student's *t* test was used for comparing the results between the irradiated and non-exposed groups. A *P* value of <0.05 was considered to be statistically significant.

III. Results and Discussion

A. Effect of near infrared LLLI on MSCs proliferation

Rat MSCs received multiple dose of 850-nm LLLI at 10 mW/cm^2 showed significant increase in cell growth (Fig. 1). The proliferation of cells increased 1.25 and 1.17 fold of the control under the irradiation of 4 and 2 J/cm^2, respectively. However, MSCs proliferation was inhibited by multiple exposures of 15 mW/cm^2 light. The parameters of 10 mW/cm^2 and 4 J/cm^2 were used for the following experiments. The number of CFU-F is used as an *in vitro* correlate for proliferative potential of MSCs. As shown in Table 1, CFU-F number increased slightly after received multiple dose of LLLI at 10 mW/cm^2 and 4 J/cm^2. No apparent increase in LDH release was found indicated that membrane integrity remained intact after LLLI (data not shown). The results concluded that multiple dose of LLLI at 850 nm enhanced the proliferative potential of MSCs.

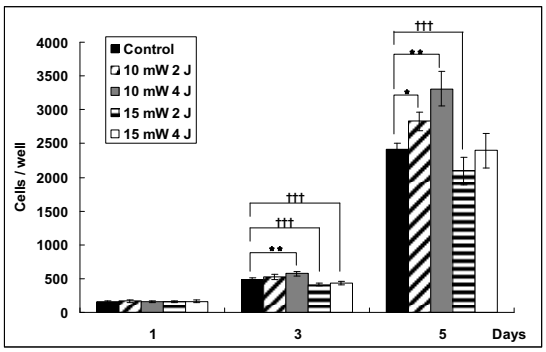


Fig. 1 The effect of near infrared LLLI on cell number

Table 1 Effect of 850 nm LLLI on CFU-F number of rat MSCs

	Number of CFU-F (≥ 50 cells)	Size of CFU-F	
		2~5 mm	5~8 mm
Control	36.6 ± 5.22	33.2 ± 4.38	3.4 ± 1.14
Irradiation	39.4 ± 4.16	36.6 ± 3.91	2.8 ± 0.48

B. Effect of near infrared LLLI on ROS production

Two morphologically distinct cell types, wide spindle-shaped and thin spindle-shaped cells, were found in the culture of rat MSCs. Wide spindle-shaped cells lost proliferative ability rapidly. ROS production from two cell types was observed after 10 mW/cm2 and 4 J/cm2 LLLI (Fig. 2). The level of ROS decreased 0.49 and 0.85 fold of the non-exposed control in wide spindle-shaped and thin spindle-shaped cells, respectively. The result suggests near infrared LLLI has anti-oxidative effect on rat MSCs.

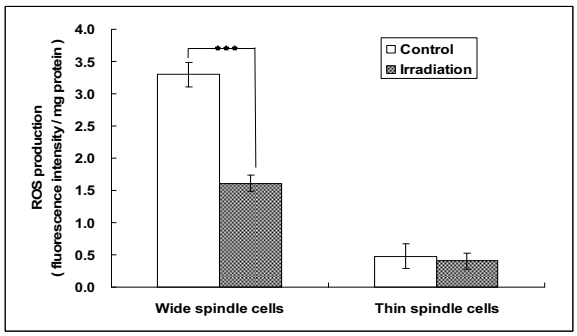


Fig. 2 The effect of 850-nm LLLI on ROS production

C. Effect of near infrared LLLI on intracellular ATP level

Intracellular ATP level of rat MSCs was measured after 10 mW/cm^2 and 4 J/cm^2 LLLI (Fig. 3). ATP level increased 1.53 fold of the non-exposed control. The result suggests 850-nm LLLI enhances mitochondrial activity of rat MSCs.

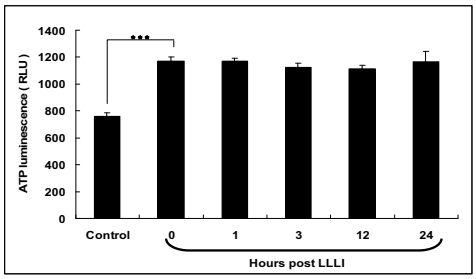


Fig. 3 The effect of 850-nm LLLI on intracellular ATP level

D. Effect of near infrared LLLI on rat MSCs differentiation

Rat MSCs were subjected to osteogenic induction while received LLLI at 10 mW/cm^2 and 4 J/cm^2 every other day. ALP activity and osteocalcin secretion of MSCs were assessed every week (Fig. 4). It was observed that both ALP activity and osteocalcin secretion were significantly stimulated by LLLI compared with control at day 14 and 21. ALP activity decreased as the increase of osteocalcin which is an indicator of mineralization during osteogenesis.

Rat MSCs were subjected to adipogenic induction while received multiple dose of light irradiation at 10 mW/cm^2 and 4 J/cm^2. It was observed that the level of triacylglyceride accumulation was significantly inhibited by LLLI compared with control during the 14-day period of adipogenesis (Fig. 5).

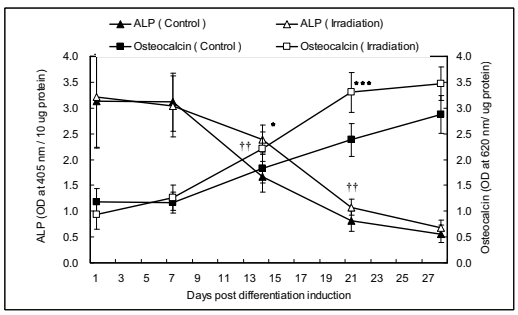


Fig. 4 The effect of 850-nm LLLI on osteogenic differentiation

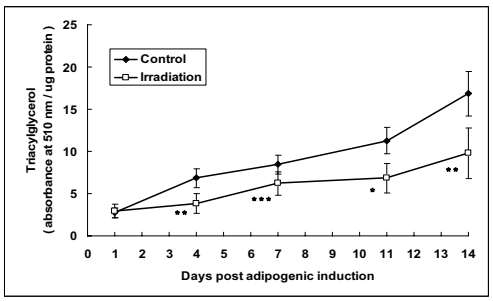


Fig. 5 The effect of 850-nm LLLI on adipogenic differentiation

IV. Conclusions

The study demonstrates that the abilities of multiple dose of LLLI at 850 nm to enhance proliferation and osteogenic differentiation of rat MSCs. Adipogenesis of rat MSCs were inhibited by near infrared LLLI. Our findings open the possibility of modulating stem cell differentiation by LLLI.

Acknowledgment

This work was supported in part by the National Science Council, Taiwan, R.O.C. under Grants NSC 96-2218-E-033-001, and NSC 97-2627-M-033-005.

References

1. Minguell JJ, Alejandro E, Paulette C. (2001) Mesenchymal stem cells. Exp Biol Med 226:507-520
2. Posten W, Wrone DA, Dover JS et al. (2005) Low-level laser therapy for wound healing: mechanism and efficacy. Dermatol Surg 31:334-340
3. Karu T (2003) Low-power laser therapy. In: Vo-Dinh T, eds. Biomedical Photonics Handbook. CRC Press. 1-20
4. Abramovitch-Gottlib L, Gross T, Naveh D et al. (2005) Low level laser irradiation stimulates osteogenic phenotype of mesenchymal stem cells seeded on a three-dimensional biomatrix. Lasers Med Sci 20:138-146.
5. Li WT, Chen HL, Wang CT (2006) Effect of light emitting diode irradiation on proliferation of human bone marrow mesenchymal stem cells. J Med Biol Eng 26:35-42.
6. Tuby H, Maltz L, Oron U (2007) Low-level laser irradiation (LLLI) promotes proliferation of mesenchymal and cardiac stem cells in culture. Lasers Surg Med 39:373-378.
7. Kim HK, Kim JH, Abbas AA (2008) Red light of 647 nm enhances osteogenic differentiation in mesenchymal stem cells. Laser Med Sci DOI 10.1007/s10103-008-0550-6
8. Eduardo Fde P, Bueno DF, de Freitas PM et al. (2008) Stem cell proliferation under low intensity laser irradiation: a preliminary study. Laser Surg Med 40:433-438.

Author: Wen-Tyng Li, Ph.D.
Institute: Chung-Yuan Christian University
Street: 200 Chung-Pei Road
City: Chung-Li
Country: Taiwan, R.O.C.
Email: wtli@cycu.edu.tw

Implementation of Fibronectin Patterning with a Raman Spectroscopy Microprobe for Focal Adhesions Studies in Cells

B. Codan[1], T. Gaiotto[2], R. Di Niro[3], R. Marzari[2] and V. Sergo[1]

[1] CENMAT, Department of Materials and Natural Resources, University of Trieste, Trieste, Italy
[2] Biology Dept., University of Trieste, Trieste, Italy
[3] Institute of Immunology, Rikshospitalet University of Oslo, Norway

Abstract — **The aim of this contribution is to demonstrate the possibility of performing macrometric and micrometric protein patterns in order to study focal adhesions of human cells on different materials. A laser is used to produce a pattern of extracellular matrix protein (e. g. fibronectin) as in photolithographic techniques. Maskless lithography is performed, using a common instruments such as Raman spectroscopy microprobe. This technique can be applied to all surface curvatures, different geometries and a wide range of materials. We demonstrated the resistance of fibronectin to the lithographic process. There are evidences of the functionality of fibronectin with adhesion of human HUVEC cells.**

Keywords — **Focal adhesions, proteins patterning, laser writer, Raman lithography.**

I. Introduction

Focal adhesions (FAs) are the connection between cells and extracellular matrix (ECM). They act as a mechanosensor for forces and transmit signals from the ECM to the cell. FAs influence motility, proliferation and survival of the cell [1,2].

Focal adhesions are characterized by proteins couples, membrane protein and ECM protein.

Regulating and controlling movements of cells is the key issue for understanding cytokinesis [3] and the proliferation of tumors. Recent studies indicate that modifying cell-ECM adhesion structures can inhibit metastasis during the carcinogenesis [4].

FAs are involved not only in tumoral diseases, but they are also the target of Helicobacter pylori, that produces a disruption of the gastric epithelium in vivo (gastric ulcer) [5].

By an engineering point of view, focal adhesions are directly involved in biomaterials, that interact with biological systems. These materials can be the external environment for cells. Controlling biological adhesion is a very important parameters for this materials class [6,7].

In this contribution we report the possibility of performing macrometric and micrometric pattern of ECM proteins, in particular of fibronectin.

Previous works [8,9] indicated the possibility of performing traditional lithography for protein pattern (photolitography, microcontact printing, laminar flow or stencil patterning). All this techniques require a mask, that is relatively expensive and requires a flat surface.

In a previous work [10], maskless lithography was described. This method is easily applied to protein patterning on surface, with no restriction on geometries of the pattern and the surface and for a wide range of materials. Another advantage is the higher resolution achievable than the mask based lithography: holes of 1 μm diameter can be obtained very reproducibly.

A double fluorescent antibodies complex is used to point out fibronectin patterning. This method is very accurate and demonstrate that the protein is not denaturated. Structural integrity of fibronectin is the necessary condition for having an antibodies complex.

Finally macrometric and micrometric patterning are compared and cell adhesion tested.

II. Experimental section

A. Chemicals and Materials

Positive Shipley Microposit S1813 photoresist and Microposit MF CD 26 developer were acquired from Rohm and Haas (Germany). Standard glass slides for optical microscopy (25 x 75 mm) were obtained from Menzel-Glaser (Germany).

Fibronectin (human plasma) was obtained form BD Biosciences (U.S.A.), rabbit anti-fibronectin IgG antibody was acquired from Sigma Aldrich (U.S.A.) and Alexa Fluor 488 goat anti-rabbit IgG from Invitrogen (U.S.A.).

B. Substrates preparation for lithography

As described in a previous work [10], glass slides were cleaned in pirana solution. The photoresist was spin coated and then backed (soft baking) in oven.

C. Standard lithography (macrometric structures)

The traditional photolithographic techniques involve a photomask. The mask was lightened with UV light (Hitachi

Chwee Teck Lim, James C.H. Goh (Eds.): ICBME 2008, Proceedings 23, pp. 2076–2078, 2009
www.springerlink.com

F8T5 8W) for 20 s and the pattern on the mask was transferred to the photoresist.

The exposed photoresist was removed by immersion in the developer for 60 s. Structures of 500 μm or more were produced.

After the development, the samples was dried and then lightened with UV light for 15 s with no mask.

D. Maskless lithography (micrometric structures)

The glass slides covered with photoresist were exposed to a laser at 514.5 nm (green light), through a Raman Microprobe (Renishaw Invia, Wotton under Edge, UK) in the backscattered configuration equipped with an optical microscope (Leica DM/LM). The process is described in [10].

Holes of 1 μm were obtained, as reported in Fig. 1. After the development, the samples was illuminated with UV light for 15 s with no mask.

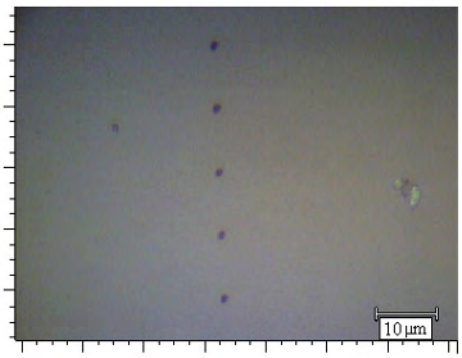


Fig. 1: Optical micrographs of holes of 1 μm in positive photoresist produced with the Raman microprobe. The picture was acquired with Laica DM/LM microscope with the objective 50x Leica N Plan.

E. Fibronectin deposition

Fibronectin (concentration of 1 mg/ml) was then deposited on the substrates and dried for 15 minutes in a laminar flow hood.

The samples were washed in the developer for 10 s in order to remove the remaining, exposed photoresist. After this step, the sample was ready for the test with the double antibodies complex or for the cell adhesion.

F. Fluorescent marker and micrograph

Anti-fibronectin antibody (1:100 diluted in PBS) was deposited for 30 minutes and then the substrate was rinsed in PBS.

The same process was performed for the second antibody, fluorescent antibody Alexa Fluor 488 anti-rabbit (1:100 diluted in PBS).

After this final steps the pattern was ready for the examination with a fluorescent microscope Nikon Eclipse E800 with 20x and 40x Nikon Plan objectives.

III. Results and Discussion

The result of the fibronectin pattern is reported in Fig.2 for the macrometric scale and in Fig. 3 for the micrometric scale.

Fig. 2 shows fluorescent micrograph of a macrometric fibronectin pattern on a glass slide with the double antibodies complex. The resolution of the lithography is good, although the distribution of the fibronectin is not constant on all the exposed surface.

Better results are obtained with a lower concentration of fibronectin (20 μg/ml), but only for cell deposition. In this case, the fibronectin density is more constant, but not enough for obtaining good signals from the fluorescent excitation of the antibody's fluorophores.

Fig. 3 shows a micrometric protein pattern. As in the case of the traditional lithography (macrometric structures), the distribution of the fibronectin is not constant all along the spots. Some filaments are present, but a line of protein spot is clearly visible.

Fluorescent spot of 3 μm are showed; the holes in the photoresist were 2 μm.

Fig. 3 is only an example of the possible micrometric geometries, that can be produces with maskless lithography. Arrays of protein spots are also obtained.

A test of the quality of the processed fibronectin is showed in Fig. 4. HUVEC cells are deposited on the patterned glass substrates and stained with Fast DiI (Invitrogen, U.S.A.).

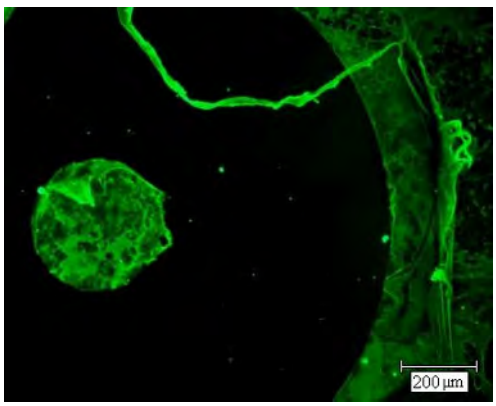


Fig. 2: Fluorescent micrographs of macrometric (0.5 mm) pattern of fibronectin on glass slides. The picture is realized with a double fluorescent antibodies complex with Nikon Eclipse E800 microscope with 20x Nikon Plan objective.

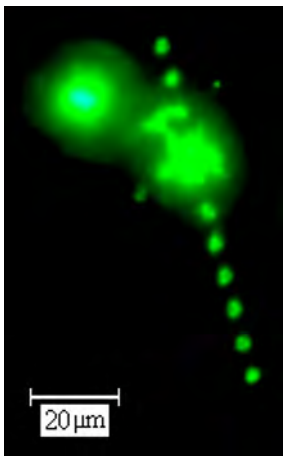


Fig. 3: Spots of 3 µm of fibronectin on glass slides.
The picture is realized with a double fluorescent antibodies complex.

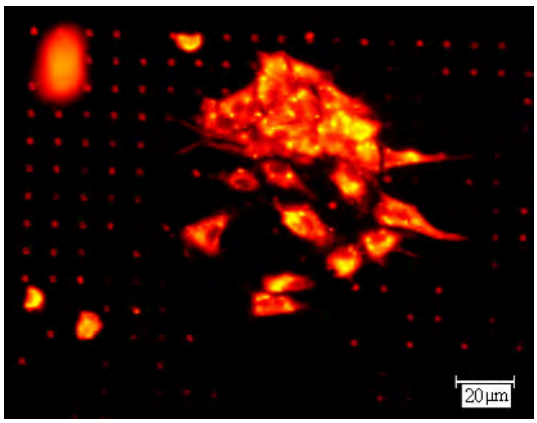


Fig. 4: Fluorescent micrographs of fibronectin pattern with HUVEC cells.
They anchor preferably on the proteins spots and assume
a geometric shape due to the array lattice constant.

Fibronectin is autofluorescent. This characteristic can be very useful for optical characterisation. In Fig. 4 proteins are not stained. In the pictures is evident how cells anchor preferably on the proteins spots and assume a geometric shape due to the array lattice constant.

The results here presented are performed on glass slides. Preliminary studies indicate that the same process can be applied to different materials, such us silicon, gold and silicon nitride, although, during preliminary tests, the last one gave the worst results.

IV. Conclusions

The resistance of fibronectin to the photolithographic process is demonstrated.

The lithographic development step is most critical step of the process. The protein is washed with a solution with high pH. Fluorescent micrographs and cells adhesion demonstrate that fibronectin is still functional. This aspect open a wide range of application for this technology.

Future developments involve non-flat surface, for example on micro electro-mechanical system (MEMS).

Preliminary studies demonstrate that fibronectin can be the right extracellular matrix protein to be pattern MEMS materials. This kind of devices presents the right dimensions for studying mechanical properties of cell, but it is very difficult to control the localization of the adhesions points. Patterning protein on selected areas can increase the performance and the accuracy of these devices.

Acknowledgment

B. C. would like to thank University of Trieste for the Young Researchers “Giovani Ricercatori” grant. V. S. acknowledges Fondazione CRTrieste.

References

1. Wozniak MA, Modzelewska K, Kwong L, Keely PJ (2004) Focal adhesion regulation of cell behavior. Biochim Biophys Acta 1692 (2-3):103-19.
2. Hervy M, Hoffman L, Beckerle MC (2006) From the membrane to the nucleus and back again: bifunctional focal adhesion proteins. Curr Opin Cell Biol 18(5):524-32.
3. Shafikhani SH, Mostov K, Engel J. (2008) Focal adhesion components are essential for mammalian cell cytokinesis. Cell Cycle 7(18):2868-76.
4. Alexandrova AY (2008) Evolution of cell interactions with extracellular matrix during carcinogenesis. Biochemistry (Mosc) 73(7):733-41.
5. Schneider S, Weydig C, Wessler S. (2008) Targeting focal adhesions: Helicobacter pylori-host communication in cell migration. Cell Communication and Signaling 6:2 DOI 10.1186/1478-811X-6-2
6. Owen GR, Meredith DO, ap Gwynn I, Richards RG. (2005) Focal adhesion quantification - a new assay of material biocompatibility? Review. Eur Cell Mater. 23;9:85-96; discussion 85-96.
7. Biggs MJ, Richards RG, Wilkinson CD, Dalby MJ. (2008) Focal adhesion interactions with topographical structures: a novel method for immuno-SEM labelling of focal adhesions in S-phase cells. J Microsc. 231(Pt 1):28-37.
8. Didier Falconnet, Gabor Csucs, H. Michelle Grandin, Marcus Textor (2006) Surface engineering approaches to micropattern surfaces for cell-based assays. Biomaterials 27 3044–3063.
9. Tai Hyun Park and Michael L. Shuler (2003) Integration of Cell Culture and Microfabrication Technology. Biotechnol. Prog. 19, 243-253.
10. Codan B, Sergo V (2008) Implementation of maskless laser lithography using a Raman spectroscopy microprobe. Rev. Sci. Instrum. 79(9): 096103-1-3 DOI 10.1063/1.2981701

Parametric Model of Human Cerebral Aneurysms

Hasballah Zakaria[1] and Tati L.R. Mengko[1]

[1] School of Electrical Engineering and Informatics, Bandung Institute of Technology, Indonesia

Abstract — **The goal of this work was to create a more realistic idealized model of human cerebral aneurysms that captures all features common to arterial bifurcations and can accurately reproduce patient specific geometries. This idealized model can then be used both for parametric studies in representative cerebral aneurysm as well as for computationally efficient studies of cerebral aneurysm in specific patients.**

The model was extended from our previous work on parametric model of arterial bifurcations by adding the aneurysm geometry to the apex of bifurcation where it is most likely to occur. The true 'reference' geometry was reconstructed from CT medical images of two patients that had been diagnosed with cerebral aneurysm. The idealized model can be viewed as of the joining of two daughter vessels and a shape of an aneurysm at its apex point. The idealized model was generated via Solidworks (SolidWorks Co.).

The ability of the idealized model to 'accurately' reproduce the geometry of a real human cerebral aneurysm was evaluated using a point wise geometric error, defined as the distance between the true and idealized model divided by the parent diameter. The maximum geometric error was less than 17.5% while the average geometric error was less than 5.8%. The distribution of WSS, wall pressure and the flow structures was qualitatively similar.

Keywords — **Parametric Model, Cerebral Aneurysm, CFD.**

I. Introduction

It is well established that the maintenance and health of the arterial wall is strongly affected by hemodynamics, and hence by the geometry of the surrounding vasculature [1, 2, 3]. 3D reconstructions of arterial segments are valuable for studies of vascular disease due to their intrinsic relevance. However, it is not possible to use them to systematically vary geometric features for parametric studies [4]. In addition, fundamental geometric features such as bifurcation angle and non-planarity are difficult to define in these reconstructions. Idealized vascular models are inherently suited for parametric studies, but they are limited by their tendency to oversimplify the geometry of real vessels. In this work, this limitation of idealized models is addressed through a new parametric arterial model.

In previous work, a hierarchy of three parametric bifurcation models was introduced [5]. The models are relatively simple, yet capture all geometric features identified as common to cerebral bifurcations in the complex transition from parent to daughter branches. In this work we extended the bifurcation model to include aneurysm shape at the apex of the bifurcation where it is more likely to occur.

II. Materials and methods

A. Parametric Models

Parametric models can be view as bifurcation model explained in detail in our previous work [5] and additional aneurysm shape at the apex of the bifurcation. To model the aneurysm shape two cross sections were extracted from the real model: neck cross section and mid cross section. The neck cross section was extracted from the base of the aneurysm where it joined with the bifurcation arteries while the mid cross section represented the largest longitudinal cross section of the aneurysm shape.

Seven Cross Sections Parametric Model

The seven cross sections parametric model included five cross sections from the bifurcation model as defined in our previous work and additional two cross sections, the neck cross section and the mid cross section, extracted from aneurysm shape. In addition to these seven cross sections the height of the aneurysm defined as the distance from the base to the top dome of the aneurysm was also needed. The two intermediate cross section was not clearly defined since these cross section affected by the aneurysm shape. To resolve this problem we use approximation to the cross section base on parent and two daughter branches cross section as follows:

$$D_3 = \sqrt{2}D_0D_1 \Big/ \left(\sqrt{D_1^2+D_2^2}\right) \; ; \; D_4 = \sqrt{2}D_0D_2 \Big/ \left(\sqrt{D_1^2+D_2^2}\right) \quad (1)$$

Twelve Parameters Parametric Model

The twelve parameters parametric model included seven parameters from the bifurcation model as defined in our previous work and additional five parameters that defined the aneurysm shape. The seven parameters for the bifurcation model were diameter of parent cross section D_0, diameter of two daughter branches D_1 and D_2, bifurcation angles

Chwee Teck Lim, James C.H. Goh (Eds.): ICBME 2008, Proceedings 23, pp. 2079–2082, 2009
www.springerlink.com

α_1 and α_2, non planar angle β and the round radius of curvature R. Additional five parameters for the aneurysm shape were the neck diameter N, the aneurysm diameter D_5, the height of the aneurysm H, aneurysm angle α_3 and non planar angle of the aneurysm β_1. The angle α_3 and β_1 follow the definition of α, β for the bifurcation arteries.

B. Creation of Reference Geometric Model

Two reference models of human saccular cerebral bifurcations were reconstructed from CT serial images of the two patients that had been detected with aneurysms. The two reference models included one ACom aneurysm and one basilar aneurysm (see Fig. 1).

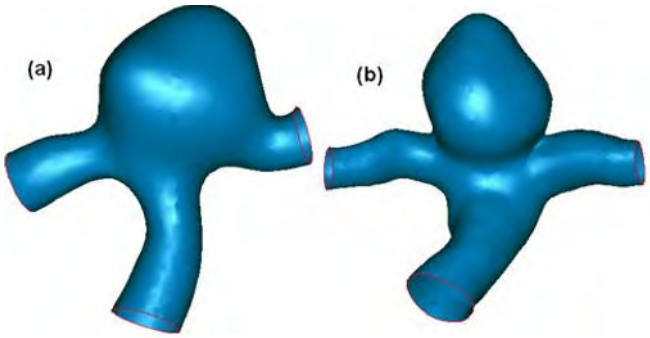


Fig. 1 Reference Geometric Model.
(a) ACom aneurysm. (b) Basilar aneurysm.

C. Development of Parametric Model

The idealized model was generated via Solidworks (SolidWorks Co.). Three protrusion objects were used to model the left, the right and half of the aneurysm sections using the centerline curve as the trajectory and the cross sections. An ellipsoid shape was used to model the dome of the aneurysm. A round was then applied at the sharp joint of the bifurcation and the aneurysm.

Seven Cross Sections Parametric Model

Cross sectional data was extracted from the reference model, five from bifurcation geometry and two from the aneurysm geometry. The cross section data was then replaced by centroid, normal, and equivalent diameter where $D_{eq} = \sqrt{4A/\pi}$ except for the intermediate cross sections. The intermediate cross section diameters were approximated using equation (1). The bifurcation geometry reconstructed using the five cross sections data then the aneurysm shape was added to this bifurcation geometry.

Twelve Parameters Parametric Model

The diameters of cross sections were approximated by their equivalent. All angles were measured from the normals of the cross section relative to the direction of parent artery. The angle definitions defined in our previous work [5]. The bifurcation geometry was developed using seven parameters using the method described in our previous work then the aneurysm shape was added to this bifurcation geometry.

D. Hemodynamic Modeling

Flow simulations in both the parametric and reference geometries were based on the numerical approximation of the 3D Navier–Stokes equations. A flow-condition based-interpolation (FCBI) finite element procedure was used [8]. The finite element method was implemented using ADINA software (ADINA Inc.). The blood viscosity and density were specified as μ = 0.0035 Pa s and ρ = 1050 kg/m^3, respectively. The blood was modeled as incompressible and Newtonian.

At the rigid vessel wall, the velocity was prescribed to be zero. To diminish entrance and exit effects, a cylindrical section of length three times the parent or daughter branches diameter was attached to the inlet and outlets of each bifurcation. At the extended inlet, a parabolic velocity profile was specified with average velocity V chosen to attain a Reynolds number, (Re = $\rho V D/\mu$), of 400, a value characteristic of flow in cerebral vessels. Zero traction boundary condition was used on the outlets.

Mesh density studies supported a finite element mesh of approximately 35,000 hybrid elements each aneurysm models to give enough accuracy for this study.

III. Results

A. Development of Parametric Models

The geometric parameters for each of the two models were extracted from the arterial surface of the two reference geometries and used to generate the models using the methodology outlined in previous section.

B. Comparison of Geometric Features

The ability of the parametric model to reproduce the geometry of a real cerebral bifurcation was quantified using a point wise geometric error function, defined as the shortest distance between the reference and parametric model, normalized by the parent diameter. Fig. 2 showed the contour of geometric error.

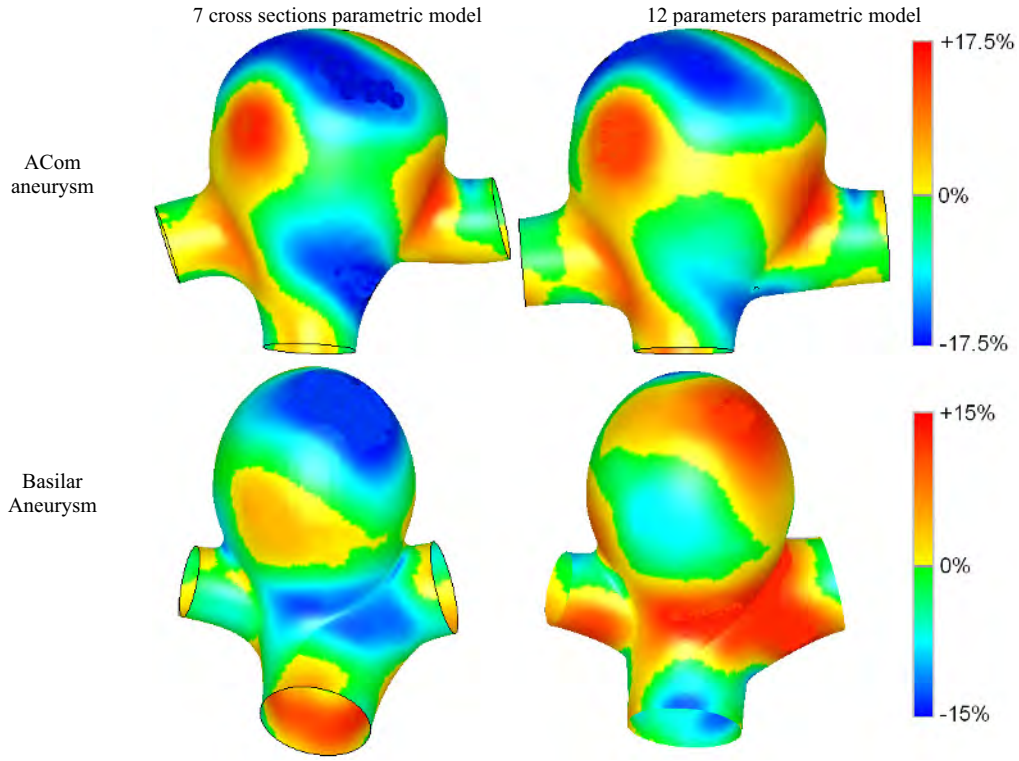


Fig. 2 Nondimensional geometric error for the parametric models, defined as the distance between the parametric and reference bifurcations, divided by the diameter of the parent branch.

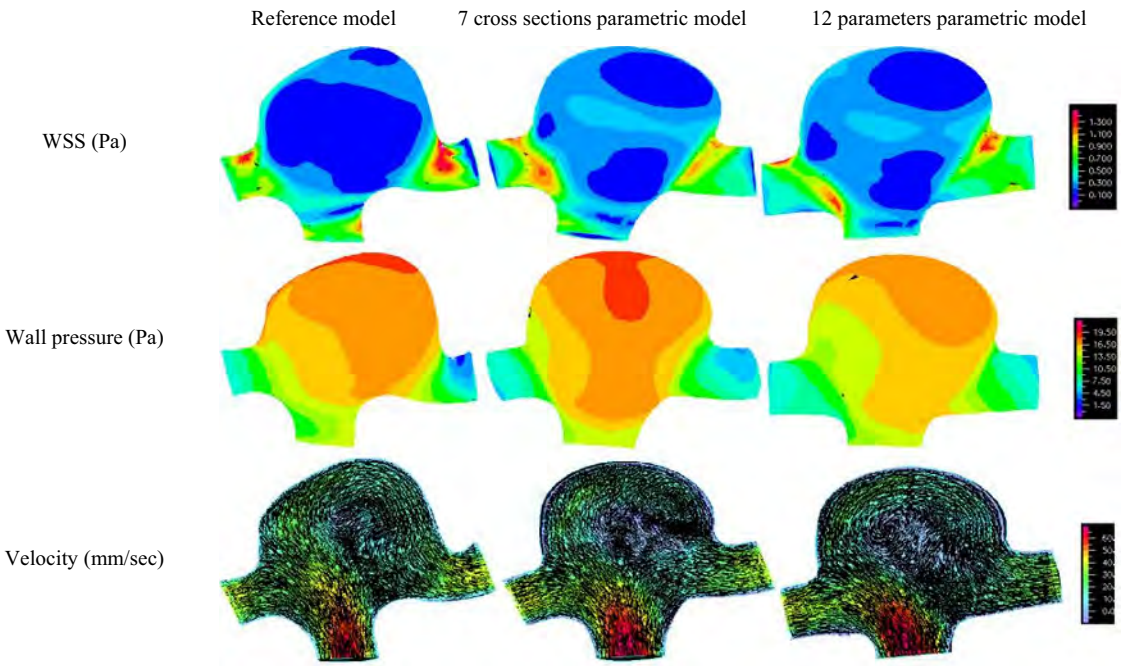


Fig. 3 Contours of wall shear stress (WSS), wall pressure and the flow structures (velocity vectors) for the reference and each of the corresponding parametric ACom aneurysm models.

The geometric error of the parametric models was relatively low. The average of the point wise geometric error for ACom and Basilar aneurysms was less then 5.8% and 4.2%, respectively, for all models. The maximum point wise geometric error for ACom and Basilar aneurysms was less than 17.5% and 15%, respectively, for all models.

C. Comparison of Hemodynamics

Figures 3 showed contour plots of the wall shear stress, wall pressure and flow structures (velocity vectors) for ACom aneurysm for flow at a Reynolds number of 400.

The distribution of WSS and wall pressure as well as the flow structures were qualitatively similar for two parametric models and the reference geometry.

Table 1 showed the quantitative comparison of WSS and wall pressure. The maximum WSS and wall pressure difference was 31.2% and 18.3%, respectively.

Table 1 Quantitave differences of hemodynamics features

Aneurysm	Model	WSS (Pa)		Wall pressure (Pa)	
		Mag	% diff	Mag	% diff
Acom aneurysm	Reference	2.109		19.830	
	7 cross section	1.451	-31.2%	19.900	0.4%
	12 paramaters	1.715	-18.7%	19.200	-3.2%
Basilar aneurysm	Reference	3.061		22.790	
	7 cross section	2.411	-21.2%	26.390	15.8%
	12 paramaters	2.188	-28.5%	26.970	18.3%

IV. Discussions

Methodology to develop parametric model has been introduced. We proposed two methods, seven cross sections and twelve parameters parametric model. Using parametric model we can vary the parameters to get different aneurysm geometry. These different models then can be analyzed to get the most critical model prone to rupture.

To reduce the parameter, the cross section approximated by circular shape. This circular shape can be changed to other shape, i.e. ellipse, to improve its accuracy to mimic the original cross section.

In general, the common WSS characteristic were maximum near the neck, very low inside the dome and normal in the artery. Wall pressure elevated inside the dome and at the impact zone but this elevated pressure was quite small compare to the transmural pressure [3, 7, 8, 9]. These features also showed in this study (Fig. 3). All parametric models also showed similar WSS and wall pressure distribution although the magnitude differences were high.

The flow structures inside the aneurysm generally consist of one circulation for model with low aspect ratio (H/N < 1.6) and possible secondary circulation for model with high aspect ratio [7, 10]. Two aneurysm models in our study both have low aspect ratio (0.71 and 0.92). We also observed one circulation in all models of our study.

Acknowledgment

The authors would like to thank Dr. A. M. Robertson from The University of Pittsburgh, Pittsburgh, USA for her contributions to this article.

References

1. Gao, L., et. al., Nascent aneurysm formation at the basilar terminus induced by hemodynamics. Stroke 39(7):2085–2090, 2008.
2. Haljasmaa, I. V., A. M. Robertson, and G. P. Galdi. On the effect of apex geometry on wall shear stress and pressure in two-dimensional models of arterial bifurcations. Math. Models Methods Appl. Sci. 11(3):499–520, 2001.
3. Hassan, T., et. al., A proposed parent vessel geometry-based categorization of saccular intracranial aneurysms: computational flow dynamics analysis of the risk factors for lesion rupture. J. Neurosurg. 103(4):662–680, 2005.
4. Perktold, K., et. al., Pulsatile non-Newtonian blood flow in three-dimensional carotid bifurcation models: a numerical study of flow phenomena under different bifurcation angles. J. Biomed. Eng. 13(6):507–515, 1991.
5. Zakaria, H., A. M. Robertson, C. W. Kerber, A Parametric Model for Studies of Flow in Arterial Bifurcations, Annals of Biomedical Engineering, 36 (9), pp. 1515–1530, 2008 .
6. Bathe, K.-J., and H. Zhang. A flow-condition-based interpolation finite element procedure for incompressible fluid flows. Comput. Struct. 80:1267–1277, 2002.
7. Kadirvel, R., et. al., The influence of hemodynamic forces on biomarkers in the walls of elastase-induced aneurysms in rabbits, Neuroradiology, 49(12): p. 1041-1053, 2007.
8. Shojima, M., et. al., Magnitude and role of wall shear stress on cerebral aneurysm: computational fluid dynamic study of 20 middle cerebral artery aneurysms. Stroke, 35(11): p. 2500-2505, 2004.
9. Shojima, M., et. al., Role of the bloodstream impacting force and the local pressure elevation in the rupture of cerebral aneurysms. Stroke, 36(9): p. 1933-8, 2005.
10. Ujiie, H., et. al., Effects of size and shape (aspect ratio) on the hemodynamics of saccular aneurysms: a possible index for surgical treatment of intracranial aneurysms. Neurosurgery, 45(1): p. 119-29, 1999.

Corresponding author:

Author: Hasballah Zakaria
Institute: School of Electrical Engineering and Informatics, Bandung Institute of Technology, Indonesia
Street: Ganesha 10
City: Bandung
Country: Indonesia
Email: fahala@gmail.com

Computational Simulation of Three-dimensional Tumor Geometry during Radiotherapy

S. Takao[1], S. Tadano[1], H. Taguchi[2] and H. Shirato[2]

[1] Division of Human Mechanical Systems and Design, Graduate School of Engineering, Hokkaido University, Sapporo, Japan
[2] Department of Radiology, Graduate School of Medicine, Hokkaido University, Sapporo, Japan

Abstract — **In Radiotherapy, shapes of tumors are important information to determine irradiation area and energy. In this study a simulation method is proposed to calculate changes of tumor geometry during radiotherapy. Relationships between tumor geometry and the amount of radiation energy were estimated from fundamental equations in solid mechanics as a mechanical analogy. Parameters between the radiotherapeutic effect and the geometric factor were defined as reduction resistance and reduction ratio. The values of these parameters were initially determined based on a widely-used radiobiological model (Linear-Quadratic model) and then revised by comparing with the change of actual tumor shape. To simulate uneven tumor shrinkage, the values of reduction resistance were varied depending on the tumor heterogeneity. Finite element models of tumors were constructed from CT images taken before the start of radiotherapy. For precise assessment of therapeutic effect, it would be useful to examine tumor morphological features. Three-dimensional (3D) tumor shape was represented in two-dimensional (2D) map like a global map. Distances from origin (center of gravity of the tumor) to surface were visually indicated by colors in this map. Tumor volumes were indicated by sizes of the maps. Tumors in head and neck were analyzed in this study. Simulation results of tumor geometries were compared with actual tumor geometries and found to have similar tendencies. The 2D color maps enabled to evaluate the 3D morphological features of the tumors. Therefore this study provides the methodology to evaluate changes of 3D tumor geometry during radiotherapy.**

Keywords — **Radiotherapy, Tumor geometry, Mechanical analogy, Finite element analysis**

I. Introduction

Radiotherapy is a common treatment for cancer patients along with surgical treatment and chemotherapy. In radiotherapy, ionizing radiation such as X-rays or electron beams damages DNA in cancer cells and kills the cells. However, as surrounding normal cells also contain DNA, excessive irradiation to normal tissue may cause radiation injury as a side effect. Therefore it is important to concentrate radiation energy (dose) on tumor region. Recent advances in high-precision radiotherapy enable to focus a higher dose to the tumor region while minimizing unwanted radiation exposure to normal tissue. Intensity-Modulated Radiation Therapy (IMRT) varies intensities and profiles of beams from various directions to fit the tumor size and shape. However, as the tumor moves or shrinks during radiotherapy, the surrounding normal tissue may become included in the high-dose region [1]. Therefore, if we can predict three-dimensional (3D) tumor geometry during radiotherapy, this information would be useful for determining the optimal radiation field and dose in IMRT.

Prediction of tumor growth and shrinkage has long been an important subject for radiation biologists. Recently, tumor growth and response to radiotherapy have become subjects for computer scientists to translate the cell biology into human tumors [2, 3]. These models based on cell biology are attractive in nature but seem difficult to calculate tumor geometry and apply in 3D treatment planning.

In the present study, we proposed a novel simulation method to calculate changes of tumor geometries during radiotherapy. This method considered the tumor a solid body. The relationships between radiation dose and geometric change of the tumor were estimated from fundamental equations in solid mechanics using mechanical analogy. Computer simulation to calculate the therapeutic response was carried out using finite element analysis (FEA) software.

II. Simulation Method

A. Fundamental relationships in radiotherapy

Cancer cells are killed and removed by radiation exposure during radiotherapy. It causes not just volumetric but geometric changes in tumor (Fig. 1). In this method, the change of tumor geometry is related to a deformation of a solid body using mechanical analogy [4]. The amount of exposure dose X can be related to the magnitude of a surface force T, the amount of absorbed dose D to the magnitude of the stress σ, the cell mortality fraction M to the strain ε, and tumor displacement R to the displacement u. With these correspondences, the change of tumor geometry can be described by following equations by analogy with fundamental equations in solid mechanics.

Chwee Teck Lim, James C.H. Goh (Eds.): ICBME 2008, Proceedings 23, pp. 2083–2087, 2009
www.springerlink.com

The relationship between D and M is expressed in tensor notation as

$$dM_{ij} = C_{ijkl} dD_{kl} \tag{1}$$

where C_{ijkl} is a parameter which determines radiosensitivity. Components of C_{ijkl} are represented by two parameters; reduction resistance E and reduction ratio v. The parameter E prescribes tumor radiosensitivity and are determined based on a radiobiological model (Linear-Quadratic model; LQ model). According to the LQ model, a cell mortality fraction M after exposure to an absorbed dose D is given by,

$$M = 1 - \exp(-\alpha D - \beta D^2) \tag{2}$$

where α and β are parameters of radiosensitivity [5]. The parameter v represents interpatient variation of radiosensitivity.
D must satisfy the following equation

$$\frac{\partial(D_{ij})}{\partial x_j} = 0 \tag{3}$$

The relationship between M and R is defined as follows

$$dM_{ij} = \frac{1}{2}\left[\frac{\partial(dR_i)}{\partial x_j} + \frac{\partial(dR_j)}{\partial x_i}\right] \tag{4}$$

The boundary condition which prescribes the amount of radiation dose transmitted through the tumor surface is given by

$$d\overline{X}_i = dD_{ij} n_j \tag{5}$$

The geometric boundary condition is given by

$$d\overline{R}_i = dR_i \tag{6}$$

From these equations, the change of tumor geometry can be calculated numerically using such as finite element method.

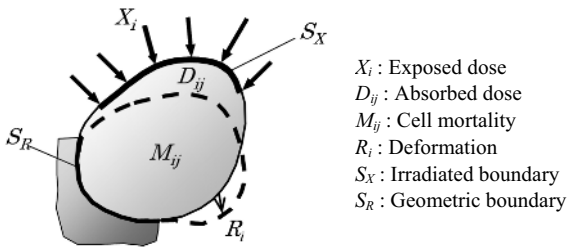


Fig. 1 Change of tumor geometry in radiotherapy

B. Tumor heterogeneity

Tumor shows internal heterogeneity of radiosensitivity, and it may result in uneven tumor shrinkage, i.e. change of tumor geometry. However, it is difficult to measure the distribution of tumor radiosensitivity. In this study, intratumoral distribution of radiosensitivity is estimated from the degree of tumor shrinkage in the early stage of treatment. The site where tumor radius decreases greatly is considered to be more radiosensitive, and the site where tumor radius does not decrease significantly is more radioresistant. As radiosensitivity is represented by parameter E in this model, heterogeneity of radiosensitivity can be expressed by the distribution of the values of E.

C. Evaluation of tumor geometry

To describe 3D tumor geometry quantitatively, spherical coordinate system O-$R\theta\varphi$ whose origin is at the center of gravity of the tumor is introduced. θ represents azimuthal angle ($-180° \le \theta \le 180°$) and $\theta = 0°$ is anterior direction. Positive rotation angle is counterclockwise around the origin. φ represents polar angle ($-90° \le \varphi \le 90°$) and $\varphi = 0°$ is horizontal plane. Distance from the origin to tumor surface at (θ,φ) is expressed by $R(\theta,\varphi)$. Three-dimensional tumor geometry can be evaluated with the values of $R(\theta,\varphi)$. It also enables to compare calculated and actual tumor geometries. Moreover, for visual understanding of 3D geometry, two-dimensional (2D) color map like a global map is introduced (Fig. 2). In this map, values of tumor radius $R(\theta,\varphi)$ are represented by color and plotted on θ-φ plane. For example, red indicates that the radius is large and blue is small. Sizes of each map represent their projected volumes.

III. Simulation of Head and Neck Cancer

A. Clinical cases

This simulation method was applied to two cases of head and neck tumor (tumor A and B) treated in Hokkaido university hospital. Initial volumes of each tumor were 3.5 and 55.1 cm^3, respectively. Both patients were treated with IMRT and administered 2.0 Gy per fraction to a total dose of 66 Gy (tumor A) or 70 Gy (tumor B). Overall treatment time was about seven weeks. The patients were treated with radiotherapy only, i.e., with neither chemotherapy nor surgery.

B. Finite element modeling of tumor

Finite element models of tumors were constructed based on the tumor contours defined by a radiation oncologist on CT images. A group of sequential cross-section contours was loaded into biomedical imaging software (Analyze PC 7.0, Mayo Foundation, Rochester, MN) and interpolated to 1 mm intervals. From these images, 3D surface models of the tumors were constructed and saved in DXF format. The DXF files are converted into IGES files with the help of the 3D CAD software (Mechanical Desktop 4, Autodesk, San Rafael, CA). Finally, the IGES files were imported into the FEA software (ANSYS 11.0, ANSYS, Canonsburg, PA), and then the 3D FE models of the tumors were constructed. The element was a 10-node tetrahedral type.

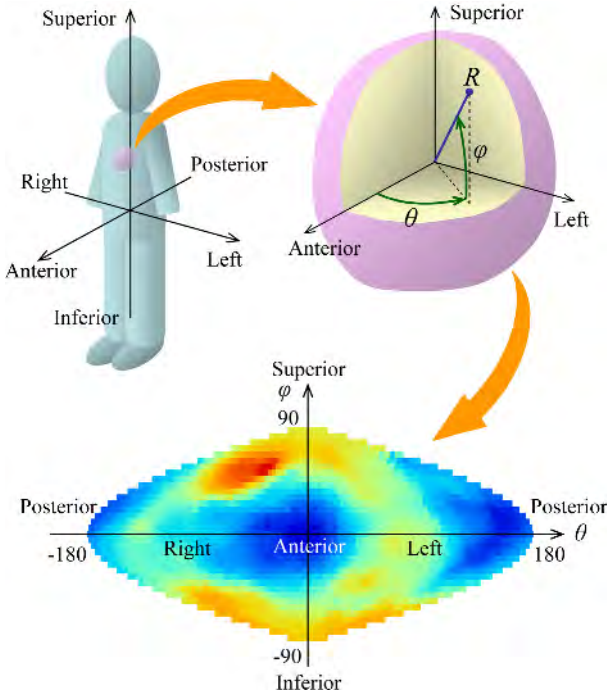


Fig. 2 Representation of tumor geometry in 2D color map

C. Simulation procedure

The method requires to determine values of four parameters; α, β E, and v. The parameters α and β in the LQ model describe radiosensitivity, and were all set as $\alpha = 0.1$ and $\beta = 0.01$ ($\alpha/\beta = 10$) for tumors as early-responding tissue [6]. The value of parameter v was adjusted for each case so that discrepancies between calculated and actual tumor volume were minimized. If the calculated volume was less than the actual tumor volume, the value of v was incremented and then the tumor volume was recalculated. This iterative calculation process was continued till the difference between the calculated and actual tumor volumes reached a minimum. After that, distribution of parameter E was determined through an iteration process in order to minimize discrepancies between calculated and actual tumor geometries. The value of parameter E of the element at (θ,φ) was determined as follows;

$$E(\theta_i,\phi_j)^{n+1} = \frac{R(\theta,\phi)_T}{R(\theta,\phi)_S^n} E(\theta,\phi)^n \tag{7}$$

where superscript indicates the number of iterations, subscript S and T for simulation and actual tumor, respectively. These calculations were performed using finite element analysis software.

IV. Results and Discussion

This study aimed to establish a computational simulation method to express changes of tumor geometry during radiotherapy. Simulation parameters were determined based on the changes of tumor geometry in the early stage of the treatment. Using these parameters, tumor geometries in the latter half of the treatment period were calculated sequentially. Figure 3 shows 3D exterior view of tumor A at the end of the treatment. Figure 4 indicates comparisons of tumor geometries calculated using our method with actual tumor geometries. Two-dimensional color map provides visual understandings of 3D tumor geometry. Simulation could represent tendencies of tumor geometrical changes in the first 18 days. Calculation to predict tumor geometries in the rest of the treatment was performed subsequently. The

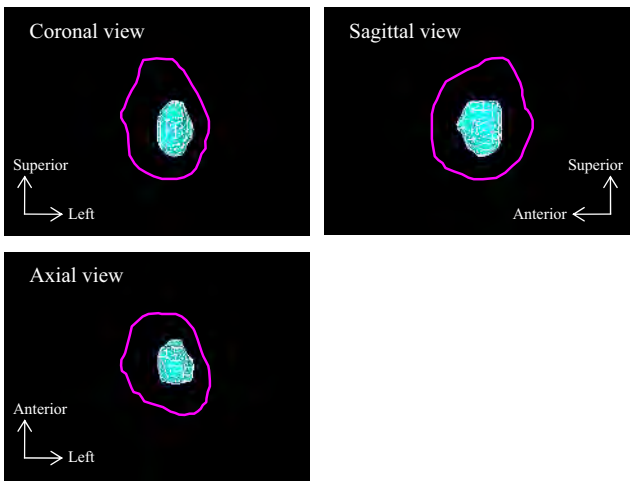


Fig. 3 Exterior view of a tumor at the end of treatment. Line profile indicates tumor geometry before start of treatment

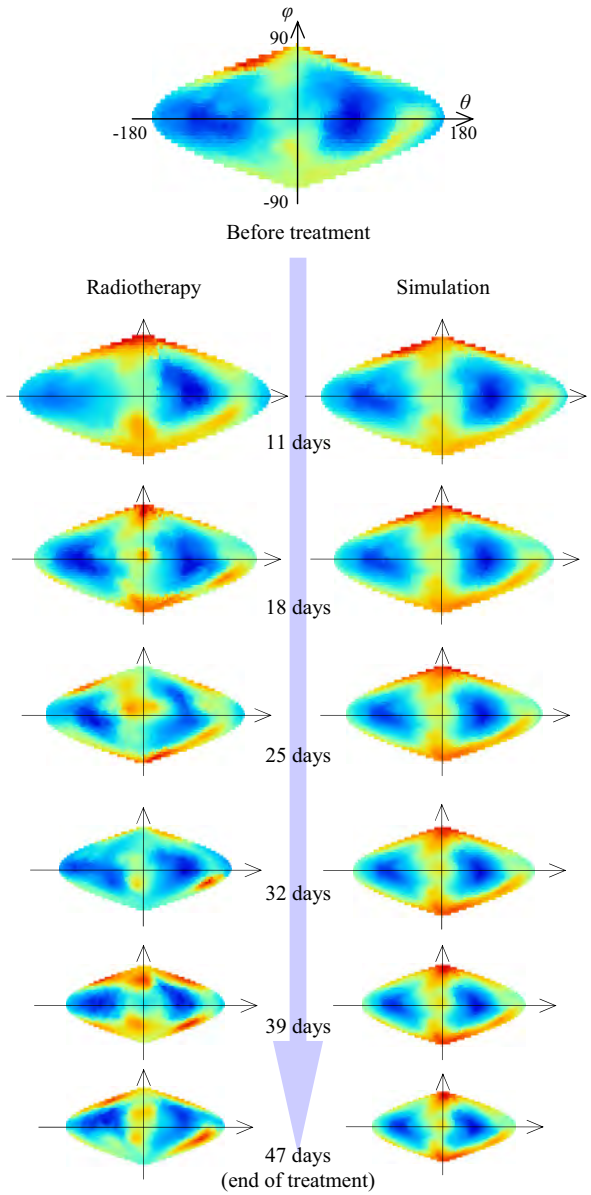


Fig. 4 Comparison of tumor geometries calculated in this method with actual tumor geometries using 2D color map

calculated tumor geometry at the end of the treatment was found to conform to actual tumor geometry. The discrepancy between calculated and actual tumor geometry could be quantitatively evaluated by tumor radius $R(\theta,\varphi)$. The discrepancies between calculated and actual tumor radius (calculated tumor radius - actual tumor radius) at the end of the treatment were 0.61 mm (maximum), -1.53 mm (minimum), and 0.58 mm (average absolute value) for tumor A, 3.08 mm (maximum), -6.23 mm (minimum), and 2.24 mm (average absolute value) for tumor B, respectively, while average of actual tumor radius was 5.31 mm for tumor A, and 13.2 mm for tumor B, respectively.

These calculations were performed on the assumption that tumors were irradiated evenly. Although dose distribution in IMRT is considered to be uniform to a certain extent, actual dose distribution should be taken into consideration for more precise calculation.

Calculated tumor geometries in the latter half of the treatment strongly depended on tumor geometries in the early stage of the treatment, because values of parameter E were determined only from early tumor geometries. Our present method can not handle the cases that tumor geometry changes drastically during treatment. We should investigate factors affecting tumor radiosensitivity e.g. angiogenesis, hypoxia, or cell cycle, and appropriately determine the values of parameter E considering these factors.

V. Conclusion

This study proposed a novel simulation method to calculate changes of tumor geometries during radiotherapy. Although some difficulties still remain to be solved, tumor geometries could be calculated using our approach.

Acknowledgment

This work was partly supported by a Grant-in-Aid from the Japanese Ministry of Education, Culture, Sports, Science, and Technology.

References

1. Barker JL Jr, Garden AS, Ang KK et al. (2004) Quantification of volumetric and geometric changes occurring during fractionated radiotherapy for head-and-neck cancer using an integrated CT/Linear accelerator system, Int. J. Radiat. Oncol., Biol., Phys. 59:960–970
2. Antipas VP, Stamatakos GS, Uzunoglu NK, (2007) A patient-specific in vivo tumor and normal tissue model for prediction of the response to radiotherapy, Methods Inf. Med. 67:367-365
3. Dionysiou DD, Stamatakos GS, Uzunoglu NK et al. (2006) A computer simulation of in vivo tumour growth and response to radiotherapy: New algorithms and parametric results, Comput. Biol. Med. 36:448–464
4. Takao S, Tadano S, Taguchi H et al. (2007) Computer Simulation of Malignant Tumor Reduction by Radiotherapy, J. Biomech., 40 Suppl. 2:S416

5. Tucker SL, Withers HR, Mason KA et al. (1983) A dose-surviving fraction curve for mouse colonic mucosa, Eur. J. Cancer Clin. Oncol. 19:433–437
6. Thames HD, Bentzen SM, Turesson I et al. (1990) Time-dose factors in radiotherapy: a review of the human data, Radiother. Oncol. 19:219–235

Author: Seishin Takao
Institute: Hokkaido University
Street: N13W8, Kita-ku
City: Sapporo
Country: Japan
Email: takao@mech-me.eng.hokudai.ac.jp

Finite Element Modeling of Thoracolumnar Spine for Investigation of TB in Spine

D. Davidson Jebaseelan[1], C. Jebaraj[2], S. Rajasekaran[3]

[1] Research Scholar, AU-FRG ICC, Anna University, Chennai, India
[2] Professor and Chairman, Faculty of Mechanical Engg, Anna University, Chennai, India
[3] Director and Head, Department of Orthopaedics and Spine Surgery, Ganga Hospitals Pvt. Ltd. Coimbatore, India

Abstract — **The current study develops a finite element model of a thoracolumnar-spine for numerical investigation of spine degraded by spinal tuberculosis. With computational capability to be used in a optimal manner, a simplified model with vertebral bodies, intervertebral-disc, ligament and musculature structures are developed. The geometry of the spinal units were extracted from CT-Scan data using existing image processing codes from T1toS1, a total of 17 levels. The polylines generated is imported as IGES to CAD-software Ideas11NXseries. 3D points were generated on the polylines in the locations of vertebral bodies, intervertebral-disc, posterior segments, and facet joints with their appropriate orientation and were connected using spline curves. Appropriate section for the various segments is built from the polylines and assigned to vertebral bodies, intervertebral-disc, and posterior processes that were then modeled with beam elements. The seven major ligaments of spine were modeled using link elements with appropriate crossectional area and non linear properties. The MMRotatores muscle that runs along transverse processes is modeled using link element with appropriate material and geometry data. The necessary boundary conditions were assigned solved using Ansys 10. The validation of the model is done using experimental results available in the literature. The Spine TB is characterized by destruction of spinal-bodies depending on the progress and its stage. The disruption finite element model illustrates the snaping of the vertebral column phenomena observed clinically**

Keywords — **Finte element method, spine mechanics, tuberculosis, spine collapse.**

I. Introduction

Finite element modeling of spine along with all components are increasingly being used to understand its behaviour in intact condition, deformity due to spine diseases, subsequent surgical interventions and the following prostheses development[5].

There has been lot of finite element studies on numerically analyzing the behaviour of spine when its affected by spinal diseases leading to deformities. Patients with rheumatoid atlantoaxial dislocation often have latent buckling because of misalignment of the cervical spine, and biomechanically unstable [4].

Spondylolysis increases disc stresses at the area it is affected as well as cranial adjacent level, and leading to increase in stresses and angular displacement at the affected caudal level, when compared to the cranial level.[6]

Osteoporosis, one of the frequent disorders of the vertebra. Studies by Annie Polikiet [1] by degrading the material property to five models. The authors suggest that an increasing degree of anisotropy might be representative of a progressing osteoporosis as shown by the increase in principal strain in the various models.

Studies done on transcortical tumors[3], by modeling tumor volumes as isotropic hyperelastic with Mooney-Rivlin strain energy and permeability showed decreased load induced canal narrowing.

Progressive deformity manifests as an increase either in angular kyphosis or by a buckling collapse[8]. Mechanical instability results in deformation of the vertebral bodies and ribs. The eventual magnitude of an idiopathic scoliotic curve is seen to vary and is unpredictable and there has been many studies to investigate the reasons for the progression of this scoliotic deformity.

Buckling behaviour is caused due to the instability caused due to progressive disruptive lesions in the posterior part of the spine[2][8], thus when the posterior wall of an vertebra is destroyed there is potential for retropulsion of bone into the spinal canal [3].

A review of buckling issues found that using simplied FE modeling by beam and link elements, with the former being used to represent the vertebral body, disc and posterior components and the latter for ligaments and muscles shows good results[9].

The review of literature found that spine collapse due to spinal tuberculosis has shown that clinal perspective of the disease has been done extensively. But apart from S.Rajasekaran[8] and hand full of researches the biomechanical reasons behind the collapse still needs to be explored. And to study the mechanism of collapse finite element modeling could be a good tool for studying the spine behaviour due to spinal tuberculosis which has not been attempted to the knowledge of the authors. Vertebral tuberculosis is the most common form of skeletal tuberculosis, constituting about 50% of all cases of skeletal tuberculosis The disease progresses until there is gross destruction of the

Chwee Teck Lim, James C.H. Goh (Eds.): ICBME 2008, Proceedings 23, pp. 2088–2091, 2009
www.springerlink.com

bones and joints with deformity, subluxation, contractures, and abscess formation. The spine with tuberculosis is also unstable when facets and posterior complex are destroyed along with vertebral bodies[8]. However, the pattern of collapse of the spine leading to severe deformities and the factors influencing the collapse were not analyzed[8].

The objective of the current work is to develop the methodology for a validated simplified non linear finite element model of spine from S1 to T12 a total of 17 levels and makes an effort to model one case of disruption due to spine tuberculosis. The preliminary results of this efforts are discussed in this article.

II. Methodology

The line geometry was generated from a serial CT-scan data of 1mm thick of S1-T1, 17 levels in all from a middle aged male. The CT data had an existing curvature deformity in the lumbar. As the current work is essentially to develop the methodology to develop a non linear simplified numerical model, the deformity was accepted and was taken into account during the validation process as well.

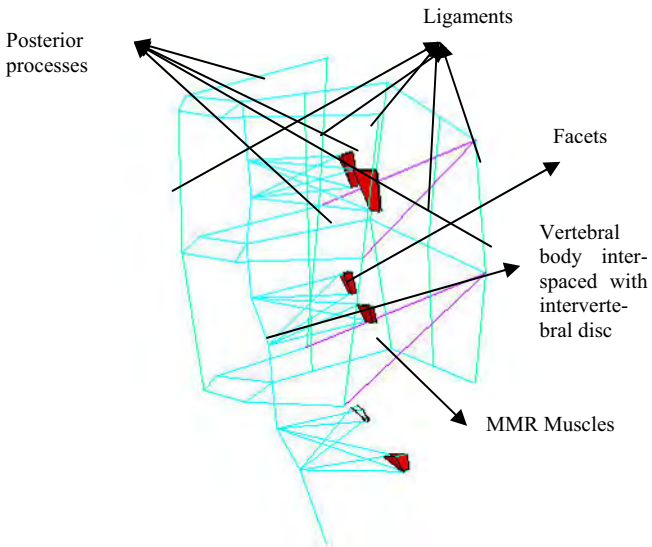


Fig. 1 CAD model of a spine FSU depicting the spine com ponents used in the model

The polylines output from the image modeler, was imported as IGES to the CAD-software Ideas11NXseries. The serial polylines of the vertebral bodies were smoothened and appropriate surfaces where created. 3D points are generated on the polylines and the surfaces in the locations of vertebral bodies, intervertebral-disc, posterior segments, and facet joints along with their appropriate orientation as per the literature. The 3D points were connnected using spline curves from S1 to T17 connecting the vertebral bodies interspaced by in the intervertebral disc. The posterior components including the transverse processes, articulating processes, laminae are connected from appropriate points using splines (Fig 1).

Appropriate sections for the various segments in the vertebral body is built from the polylines and assigned to vertebral bodies, intervertebral-disc, and posterior processes. The initial line mesh along with their sectional properties is carried out using Ideas 11. The elements and nodes thus generated was was solved using Ansys 10.0 Finite element software along with appropriate element, property assignment and the post processing using the same Finite element code

A. Finite element Model

The work of Van der Plaats et al [9]was taken as base for the current work of developing the simplified model. As mentioned by them the following components of the motion segment was considered: Vertebral body, the intervertebral disc, facet joints, the seven spinal ligaments, MM Rotatores spinal musculature and the posterior structures including the transverse processes, articulating processes and laminae. Beam elements along with the sectional properties were assigned to the vertebral bodies, intervertebral disc, and the posterior structures. The facet joints were modeled using Shell and contact joints. The vertebral body and posterior components were assigned a modulus of 12100 N/mm^2[1] and the disc with 7 N/mm^2[9]. The cancellous bone and different intervertebral components nuclues pulposus, fibres and annulus fibrosis are not accounted for in this model.

The seven spine ligaments were modeled as tension only link elements. The pre-strained conditions and cross section of the ligaments and muscles were adopted from Van der Plaats et al.,[9] was used in this current work(Table1). The MM Rotatores spine muscle was modeled as link elements and the insertion points as per the literature,the transverse processes of the lower vertebra were connected to the spinous process of the upper vertebra The model (Fig 2) was planned to study the disruptions caused by the lesions of spinal tuberculosis. As predominantly buckling behaviour was to be studied the work of *Lucas and Bresler*[7] was used to validate the current work. The first condition considered for validating, the spine was situated in a vertical position with the sacrum fixed and a lateral load of 30 N was applied to the base point of Tl. The frontal plane rotations obtained by the model are compared to the experimental results of Lucas and Bresler[7]. In the second condition the stability of the column was examined by incrementally

applying compressive loads until the onset of significant lateral deflections.

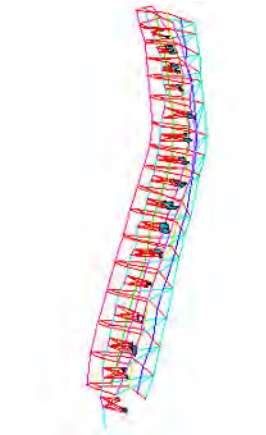


Fig. 2 The simplified Finite element model from S1 to T1

To prevent buckling in the sagittal plane antero posterior bending was restrained at the midthoracic and midlumbar levels by preventing motion in the horizontal direction and the horizontal translation and axial rotation constrained of the coordinates of T 1 which corresponds to the experimental set-up of Lucas and Bresler[7]. The buckling load is to be compared with the experimental results.

Table 1 Material Properties and Cross section of the the ligaments and Muscles[9]

Ligament/muscle	Youngs modulus (N/mm2)	Cross-sectional area(mm2)
ALL	8	50
PLL	8	25
CL	8	20
TL	5	10
LF	24	30
ISL	5	26
SSL	5	26
MMR	25	10

III. Results and Discussion

The model validation carried out as done by Lucas and Bresler[7], the first researchers to determine experimentally the buckling loads of the ligamentous thoracolumbar spine for the first condition with a lateral load of 30N and under complete restriction at the S1 level showed that the frontal rotations at each levels were in agreement in certain levels and had variation in other levels. The basic difference between the experimental work of Lucas and Bresler to the current work is the inclusion of the initial strain of the ligaments and muscles. Also the MM Rotatores muscle has been included for the current analysis. Moreover as mentioned previously the initial deformity in the CT data in the lumbar did prominently be seen from the displacement in the graph shown in Fig 3. But the trend shown by the experimental work can be seen here.

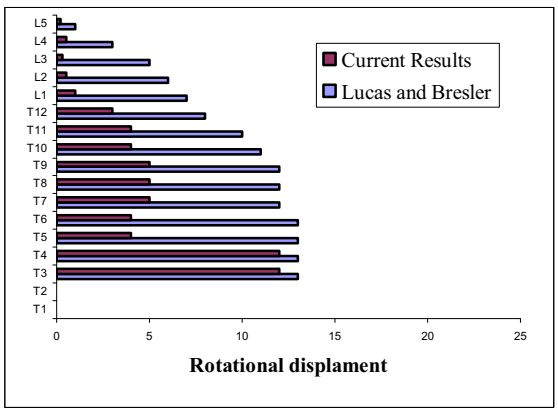


Fig. 3 Rotational Displacent from S1 to T1 levels

In the second validation of carrying out buckling analysis under the conditions explained below the buckling load was found to be 140N against the experimental value of 170N of Lucas and Bresler[7]. Inspite of the buckling loads being comparable, the variation can be attributed to the material properties of the ligaments used initial strain rather than non linear stress strain plot that could have prominently shown the hardening capability.

A. Behaviour of thorcolumnar spine with spine tuberculosis

An initial study was undertaken to observe the normal behaviour of spine under the boundary conditions of S1 completely constrained and allowing only axial movement at the T1 level depicting the musculature action (Fig 4a).The buckling analysis of this model was carried out using the sub-domain solution procedure with the appropriate strum sequence check. The first mode shape is shown in Fig 4a and it is found that this behaviour is largely comparable to the work of Van der Plaats et al.[9]

As observed in the introduction that most of the TB lesions affect the thorocolumnar, lumbar junction- the articular processes, the facets and the vertebral body was disrupted at this junction. This condition was modeled using the birth and death of element formulation technique wherein the elements in the above components was, de

selected. To achieve the "element death" effect, the ANSYS program does not actually remove "killed" elements. Instead activates them by multiplying their stiffness by a severe reduction factor .

The first mode shape showed an increase in the kyphosis angle but subsequently there was more lateral movement Fig 4b.

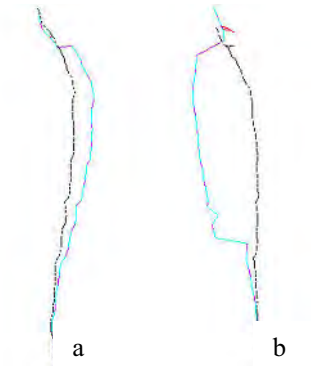


Fig. 4 a Mode shape of in the intact condition
b: Mode shape in the disrupted model

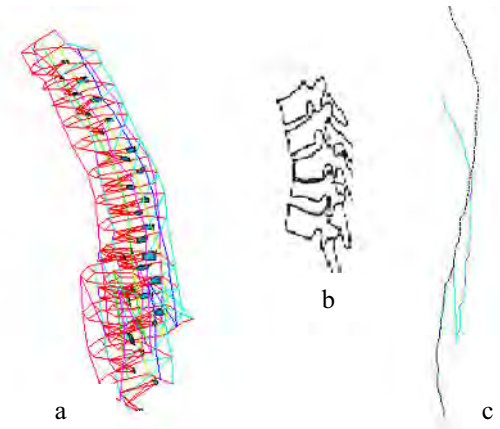


Fig. 5 aThe spine Collape due the disruption b: clinically observed collapse[8] c: snapping phenomena shown using the vertebral bodies

In this condition when 400N is applied the normal physiological load in standing posture, the spine collapse was seen as shown by S.Rajasekaran et.al[8]. The subluxation and the restabilization of the spine can be seen as shown in fig 5a,b. The ligament and musculature structure where as well disrupted in the adjacent levels that could further lead to neurological deficiet. The axial stress and displacement at the killed junction shown found to be nil and accordingly the snapping behaviour at that level could be explained(Fig5c). Further work needs to be done to study the mechanism of this collapse and the components that predominantly plays a role in this collapse has be studied

IV. Conclusion

The current work could successfully develop a simplified model to study the spine collapse due to spine tuberculosis using Beam and link elements. The results and the trend are comparable to the experimental results of the lucas and-Bresler[7]. The simulation of the disruption has been studied using buckling and element death concept and the spine collapse is seen to have similarity to that observed by clinical observations. Further studies are on to quantify the displacements and also to study the reasons for the collapse and the biomechanical etiology of the progression of the deformity due to spinal tuberculosis.

References

1. Anne Polikeit, Lutz P. Nolte et.al.,(2004),Simulated influence of osteoporosis and disc degeneration on the load transfer in a lumbar functional spinal unit, Journal of Biomechanics 37, 1061–1069
2. J J Crisco, M M Panjabi,(1992), Euler stability of the human lumbar ligamentous spine. Part I: Theory Clinical Biomechanics; 7: 19-26
3. Craig E. Tschirhart, Joel A. Finkelstein et.al.,(2007), Biomechanics of vertebral level, geometry, and transcortical tumors in the metastatic spine, Journal of Biomechanics 40, 46–54
4. Deed E Harrison, Donald D Harrison et al.,(2001), Comparison of axial and flexural stresses in lordosis and three buckled configurations of the cervical spine, Clinical Biomechanics 16, 276-284
5. MJ Fagan, S.Julian et al.,(2002), Patient-specific spine models. Part1-finite element analysis of the lumbar intervertebral disc- a material sensitivity study, Proc Instn Mech Engrs Vol 216 Part H:J Engineering in Medicine, pp 299-313
6. Koichi Sairyo, Vijay K. Goel , et. al,(2006), Buck's direct repair of lumbar spondylolysis restores disc stresses at the involved and adjacent levels, Clinical Biomechanics 21, 1020–1026
7. Lucas DB, Bresler B.,(1961), Stability of the Ligamentous Spine. Technical Report esr. 11 No. 40 Biomechanics Laboratory, University of California San Francisco
8. S. Rajasekaran,(2007) Buckling collapse of the spine in childhood spinal tuberculosis, Clinical orth. and related research, 2007, 460, 86-92
9. A. Van der Plaats, A.G. Veldhuiz et.al.,(2007), Numerical Simulation of Asymmetrically Altered Growth as Initiation Mechanism of Scoliosis, Annals of Biomedical Engineering, Annals of biomedical engineering, 35(7),206-1215

Corresponding author

Author: C.Jebaraj
Institute: Anna Univeristy, Chennai-620 025
Country: India
Email: jebaraj@annauniv.edu

Contact Characteristics during Different High Flexion Activities of the Knee

Jing-Sheng Li, Kun-Jhih Lin, Wen-Chuan Chen, Hung-Wen Wei, Cheng-Kung Cheng

Institute of Biomedical Engineering, National Yang Ming University, Taipei, Taiwan

Abstract — **Squatting, kneeling and sitting cross-legged activities require a very high range of motion of the knee joint. Many studies have focused on the kinematics of these activities using motion capture systems or fluoroscopy images with reconstructed computer models. These methods do not report the contact characteristics in high flexion activities. Although magnetic resonance images could easy to calculate the contact area, the magnetic resonance scan requires many times and is not suitable for functional activity. The purpose of this study was to build a procedure to investigate the contact characteristics for different high flexion activities based on bi-plane orthogonal X-ray images with computational models reconstructed by computer tomographic and magnetic resonance images. Computational bone models, including the femur, tibia, fibula and patella, were reconstructed by computer tomographic images. Computational cartilage models, including femur, tibia and patella, were reconstructed by magnetic resonance images. We used the sensitivity test to test the mapping accuracy and the error value is less than 5% so that the mapping is reasonable. There is no contact in standing in patellofemoral joint. The contact location in patella is moving upward from the distal patella with knee flexion. When squatting, the contact location separates to two parts. The contact in kneeling and sitting cross-legged also presents the same result. The contact area in patellofemoral joint is increasing with flexion, but decreasing to 849.94mm^2 in squatting. The contact area in kneeling and sitting cross-legged is 388.63mm^2 and 815.16 mm^2, respectively.**

Keywords — **high flexion activities, contact**

I. Introduction

In our daily living, squatting, kneeling and sitting cross-legged activities that require a very high range of motion of the knee joint are usually seen in Asia. Although some studies have focused on the kinematics in these such high flexion activities using motion capture systems, the major limitation is skin shifting during exercise [1-2]. The limitation may make influence on the true bony motion and increase the errors of measurement. Other studies catch the motion using fluoroscopy images and have constructed computer models to investigate the kinematics of knee joint, even investigate the articular contact points [3-5]. In addition, the contact area is usually calculated using magnetic resonance images, and the magnetic resonance scan requires many times so that magnetic resonance scan is not suitable for functional activity [6-7]. The purpose of this study was to build a procedure to investigate the contact characteristics for different high flexion activities based on bi-plane X-ray images with computer model reconstructed from magnetic resonance images.

II. Materials and Methods

One young subject (24 y/o, 184cm, 80kg) without any knee pathology and history was included in this study. Computational bone models, including the femur, tibia, fibula and patella, were reconstructed by computer tomographic images (transverse plane, 2mm thickness, resolution: 512x512 pixels). Computational cartilage models, including the femur, tibia and patella, were reconstructed by magnetic resonance images (sagittal plane, 2.2mm thickness, resolution: 256x512 pixels). Bi-plane orthogonal X-ray images were taken from standing to squatting, kneeling and sitting cross-legged activities. In addition, all images were taken in Department of Radiology, Taipei city hospital. Afterward, we built an orthogonal flame and put two orthogonal X-ray images on (Figure 1). After fitting with a series of bi-plane X-ray images successfully, we calculated the contact area using the interferential part.

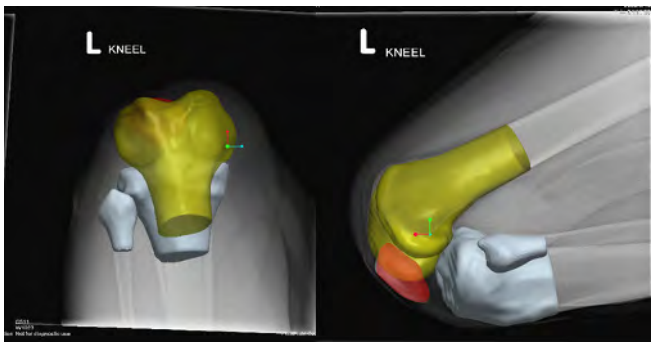


Fig. 1 Computational bone models fit with bi-plane orthogonal X-ray images.

III. Results

There is no contact in standing in patellofemoral joint. The contact location in patella is moving upward from the

Chwee Teck Lim, James C.H. Goh (Eds.): ICBME 2008, Proceedings 23, pp. 2092–2094, 2009
www.springerlink.com

distal patella with knee flexion. When squatting, the contact location separates to two parts. The contact in kneeling and sitting cross-legged also presents the same result. Patellofemoral contact in femur was shown in Figure 2. Tibiofemoral contact in femur was shown in Figure 3. The contact area in patellofemoral joint is increasing with flexion, but decreasing to 849.94mm^2 in squatting. The contact area in kneeling and sitting cross-legged is 388.63mm^2 and 815.16 mm^2, respectively (Figure 4).

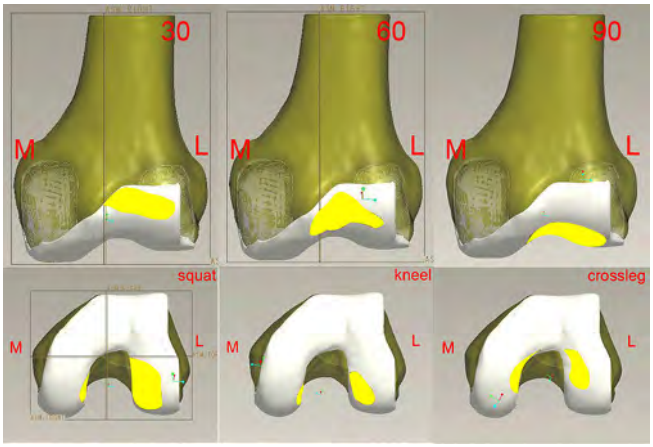


Fig. 2 Patellofemoral joint contact locations were shown in zone yellow. Patella glided from anterior and upper end of femoral cartilage to trochlear groove.

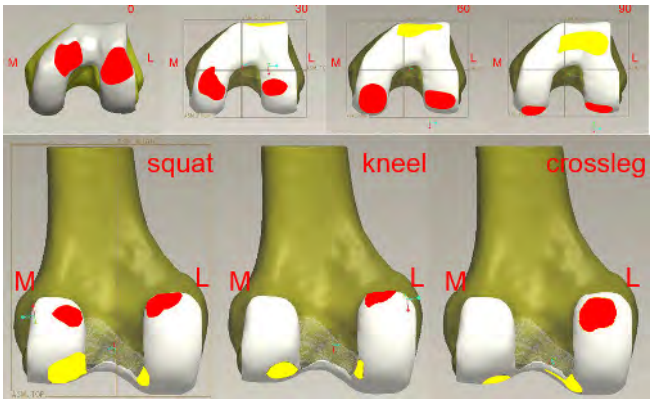


Fig. 3 Tibiofemoral joint contact locations were shown in zone red.

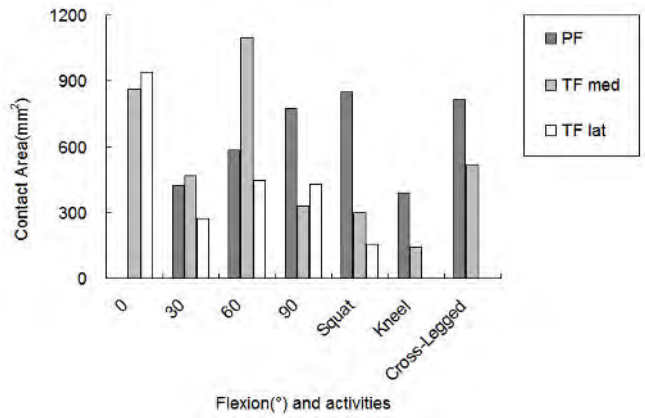


Fig. 4 Contact area in patellofemoral and tibiofemoral joints.

IV. Discussion

Using computer model fitting with bi-plane X-ray could help to explain the contact characteristics in functional activities. We also used the sensitivity test to test the mapping accuracy and the error value is less than 5% so that the mapping is reasonable. In contact location, patella glided from anterior and upper end of femoral cartilage to trochlear groove, and femur contacted tibia from distal part to posterior part of femoral cartilage. In contact area, similar trend was found in contact area between flexion 0° and 60° compare with those using open magnetic resonance scan to measure the contact area [7]. Besides, there was no contact in kneeling and sitting cross-legged in tibiofemoral joint, this result may attribute to more adduction in these activities. Decreasing tibiofemoral contact area in these three high flexion activities may relate to joint degeneration. The limitation of this study is the less subject number.

V. Conclusion

To sum up, this study can provide the contact characteristics of knee joint in high flexion activities; furthermore, we can use the computational model rather than static magnetic resonance scan to measure the contact area in more functional condition.

Acknowledgements

The authors thank Department of Radiology, Taipei city hospital for data collection.

References

1. Hemmerich A, Brown H, Smith S et al. (2006) J Orthop Res 24(4):770-781.
2. Smith SM, Cockburn RA, Hemmerich A et al. (2008) Gait Posture 27(3):376-386.
3. Komistek RD, Dennis DA, Mahfouz M. (2003) Clin Orthop Relat Res (410):69-81.
4. Fregly BJ, Rahman HA, Banks SA. (2005) J Biomech Eng 127(4):692-699.

5. Li G, DeFrate LE, Park SE et al. (2005) Am J Sports Med 33(1):102-107.
6. Patel VV, Hall K, Ries M et al. (2003) J Bone Joint Surg Am 85-A(12):2419-2424.
7. Besier TF, Draper CE, Gold GE et al. (2005) J Orthop Res 23(2):345-350.

Author: Jing-Sheng Li
Institute: Institute of Biomedical Engineering,
National Yang Ming University
Street: No.155, Sec. 2, Linong St., Beitou District,
City: Taipei
Country: Taiwan
Email: jingshengli@gmail.com

Thumb Motion and Typing Forces during Text Messaging on a Mobile Phone

F.R. Ong[1]

[1] School of Mechanical and Manufacturing Engineering, Singapore Polytechnic, Singapore

Abstract — **The objective of the study was to determine the thumb motion and typing forces when text messaging on a mobile phone. Thumb motion was captured using a 6-camera reflective marker based motion capture system. Typing forces were measured using four load cells in a force plate arrangement fitted into the phone. Thumb flexion-extension occurred mainly in the IP and MCP joints. The maximum flexion for IP joint was 20.2º at key '*' and was 18.3º at key '#' for MCP joint. Abduction-adduction of MCP and CMC joints were smaller than flexion-extension and thumb opposition. The maximum abduction for MCP and CMC joints were 7.2º and 8.7º respectively at key '*'. The maximum thumb opposition for MCP and CMC joints were 17.0º at key '4' and 13.5º at key '9' respectively. The incidence of peak force was shown to link to high flexion angle of the IP joint and in thumb opposition of the MCP joint. No incidence of peak forces was found in the right column of the keypad.**

Keywords — **Thumb, text messaging, repetitive strain injury.**

I. Introduction

The popularity of text messaging or SMS on mobile phones has given rise to a new injury called Text Messaging Injury (TMI) [1, 2]. TMI is a form of Repetitive Strain Injury (RSI), which is described by pain associated with loss of function in a limb resulting from repetitive movement or sustained static loading. TMI is normally caused by overuse of the thumb during text messaging on a mobile phone. Besides TMI, there are other terms, such as Blackberry Thumb and Gamers Thumb, to describe RSI related to wireless handheld and video games devices.

The research into the effects of text messaging on the thumb and related fingers has been limited. Most RSI research concentrated on computers since keyboard users or office workers have been identified to have high levels of job discomfort. It has been found that upper extremity musculoskeletal disorders, such as carpal tunnel syndrome (CTS), are associated with computer keyboard usage [3]. Factors contributing to CTS and job discomfort were found to be related to speed and force of keyboard operation.

Text messaging usually involves the use of the thumb of one hand to type on the phone keypad. The movement of the thumb covers motions in the planes of flexion-extension, abduction-adduction and opposition. These motions occur simultaneously in three dimensions and as a result, it is difficult to determine the kinematics of the thumb. Measurements of thumb motion have been made using marker based optical motion capture system, goniometry and fluoroscopy [4-7].

TMI is affecting more and more children and young adults due to excessive text messaging. The objective of the study was to determine the thumb motion and typing forces on the keypad of a mobile phone during text messaging.

II. Methods

Twenty male volunteers between the ages of 20 to 22 years participated in this study. These subjects have no history of RSI or any musculoskeletal disorder.

Thumb motion was captured using a 6-camera reflective marker based motion capture (MOCAP) system (Vicon MX13) at a frame rate of 120Hz. Thirteen 5mm hemispherical retro-reflective markers were attached on the thumb and index finger of the subjects, as shown in figure 1. The interphalangeal (IP), metacarpophalangeal (MCP) and carpometacarpal (CMC) joints had a pair of reflective markers each to define the approximate joint axis.

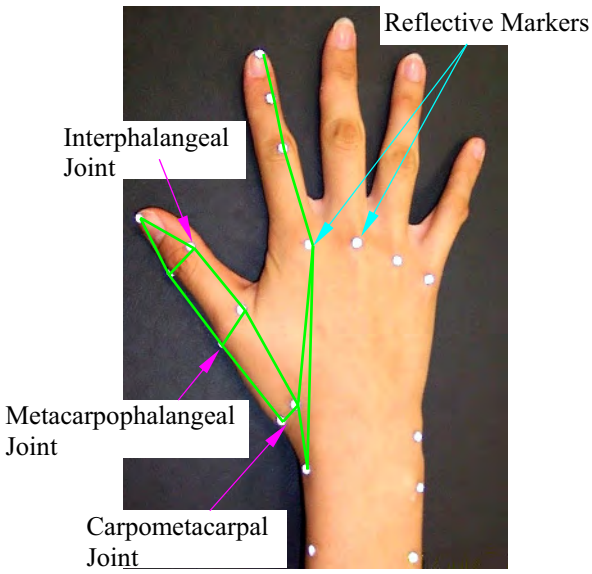


Fig. 1 The marker set-up of the hand

Chwee Teck Lim, James C.H. Goh (Eds.): ICBME 2008, Proceedings 23, pp. 2095–2098, 2009
www.springerlink.com

Text messaging forces were measured using four load cells in a force plate arrangement, which fit into the mobile phone casing. Figure 2 shows the set-up of the phone with load cells. The cover is placed on top of the load cell housing for keystroke contact. Another five markers were attached on the mobile phone. The force measurements were synchronised to the MOCAP via the Vicon MX Control.

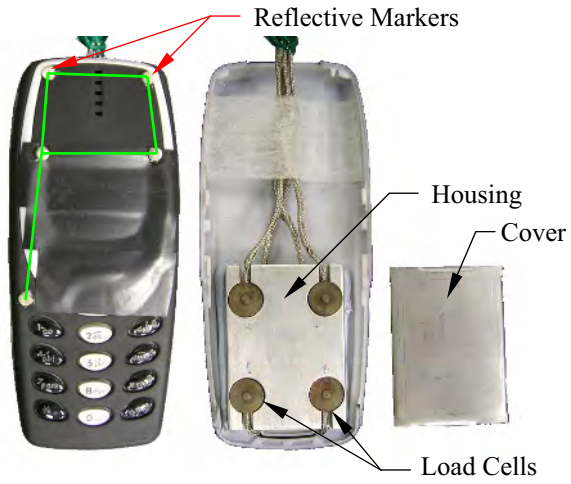


Fig. 2 The set-up of the mobile phone

The subjects were seated in front of a table with the mobile phone. Before the start of data acquisition, the subjects were asked to practice on a message that reads: "13#*_We_Will_Win_Gold_Medal._Please_Support_Us._13*#". The starting position of the thumb and finger was not defined as the subjects started in their natural position. This message contains 52 key strokes and figure 3 shows the number of key hits per key in relation to the typed message. Upon completion, the markers on the hand were labelled and linked according to figure 4. The typing forces were the sum of forces measured by the four load cells.

1 4 hits	**2** 2 hits	**3** 8 hits
4 3 hits	**5** 5 hits	**6** 4 hits
7 7 hits	**8** 3 hits	**9** 3 hits
*** 2 hits	**0** 9 hits	# 2 hits

Fig. 3 Number of key hits per key on the keypad

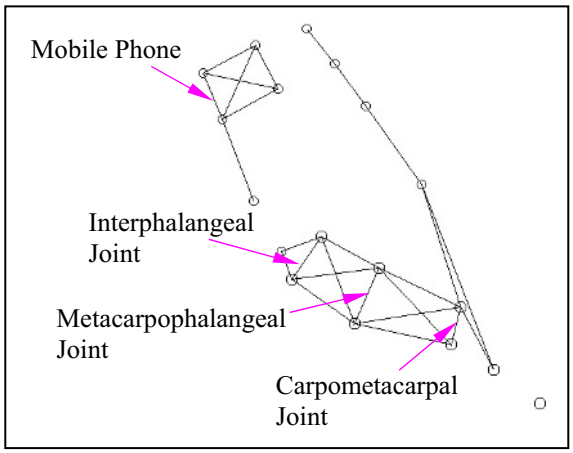


Fig. 4 Labelling and linking of markers

III. Results and Discussion

From the twenty subjects, results were obtained only from ten subjects due to excessive marker occlusion and inconsistent marker placement especially on the MCP and CMC joints. A couple of left handed subjects were also excluded. The IP joint was assumed as a hinge joint, while the MCP and CMC joints were assumed as universal joints. During data recording, it was noticed that the subjects made compensatory movement to reposition the phone in order to reach keys at extreme locations (top left or bottom right). This compensatory movement was not considered in the determination of thumb motion.

The interphalangeal (IP) and metacarpophalangeal (MCP) joints were found to be mainly responsible for flexion-extension movements of the thumb. The average maximum relative angular displacements for IP, MCP and CMC joints were 24.1º, 18.7º and 8.8º respectively, as shown in Table 1. Abduction-adduction movements of the thumb were executed mainly by the CMC joint. The average maximum displacement angle was 10.0º and 8.2º for CMC and MCP joints respectively. Both MCP and CMC joints were found to experience more opposition movement (18.2º and 14.9º respectively) than abduction-adduction motion.

Table 1 Average maximum relative angular displacement

Thumb Motion	Flex/Ext		Abd/Add		Opposition	
	Average	S.D.	Average	S.D.	Average	S.D.
IP	24.1	6.2	-	-	-	-
MCP	18.7	4.6	8.2	2.6	18.2	5.4
CMC	8.8	4.3	10.0	4.7	14.9	7.2

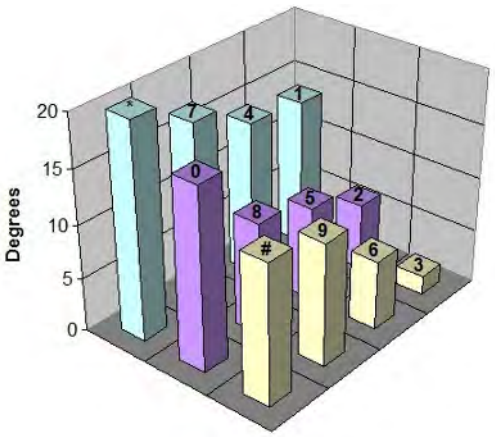


Fig. 5 Flexion-Extension of IP joint

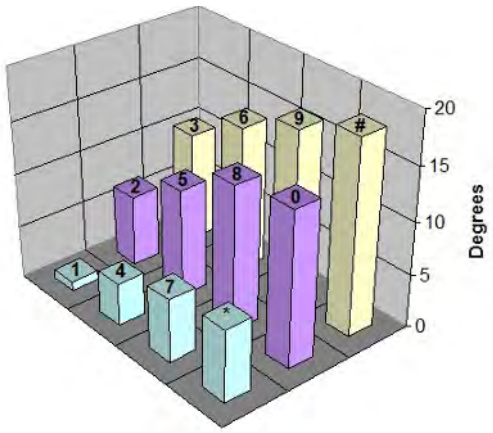


Fig. 6 Flexion-Extension of MCP joint

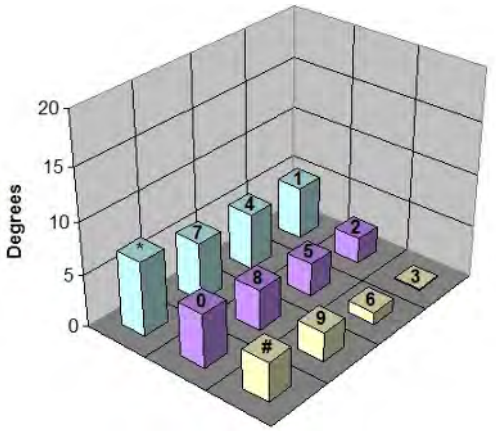


Fig. 7 Abduction-adduction of MCP joint

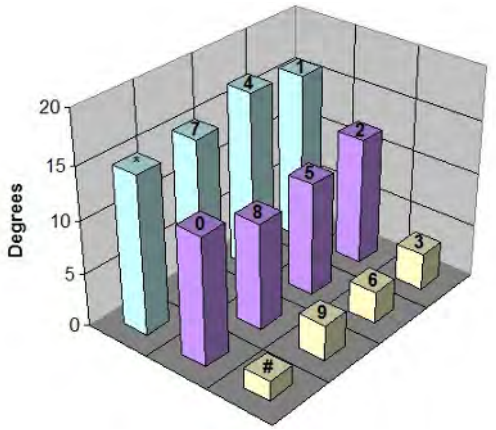


Fig. 8 Thumb opposition of MCP joint

Figure 5 show the average angular displacement for IP joint in flexion-extension. The maximum flexion was 20.2º (S.D. 9.5º) at key '*' and maximum extension was 1.8º (S.D. 2.7º) at key '3'. A pattern of diagonal reduction of flexion from key '*' to key '3' was found at IP joint. Most of the maximum IP flexion occurred at keys '*' and '0'.

A pattern mirroring IP flexion-extension was also found on the flexion-extension of MCP joint, as shown in figure 6. Maximum average flexion was 18.3º at keys '#' (S.D. 5.0º) and maximum extension was 0.9º at keys '1' (S.D. 1.7º). Most of the maximum MCP flexion occurred at key '#'.

Figure 7 shows the abduction-adduction of MCP joint. The maximum abduction was 7.2º (S.D. 3.4º) at key '*' and the maximum adduction was 0.1º (S.D. 0.4º) at key '3'. Thumb opposition at MCP joint was more than abduction-adduction and it increased consistently from the right column to the left column of the keypad, as shown in figure 8. The maximum thumb opposition was 17.0º (S.D. 5.7º) at key '4' and the maximum adduction was 1.8º (S.D. 1.9º) at key '#'. Most of the maximum MCP thumb opposition occurred at keys '1' and '4'.

Figure 9 shows the flexion-extension of CMC joint. Flexion was found to increase from the left column to the right column of the keypad. Figure 10 shows abduction-adduction of the CMC joint, which is similar to MCP abduction-adduction. The maximum abduction was 8.7º (S.D. 5.3º) at key '*' and the maximum adduction was 0.8º (S.D. 1.7º) at key '3'. The dominant movement at CMC joint was the thumb opposition, as shown in figure 11 and it mirrored MCP thumb opposition (Fig. 8). The maximum thumb opposition was 13.5º (S.D. 7.7º) at key '9' and the maximum adduction was 2.0º (S.D. 3.8º) at key '1'.

Maximum typing forces occurred mostly on extreme keys, in particular key '1'. There was no incidence of maximum typing forces on the right column keys of the phone. The maximum forces ranged from 3.8N to 15.7N and the average maximum force was 8.5N (S.D. 4.0N). Subjects that had low IP flexion at keys '#' and '9' were

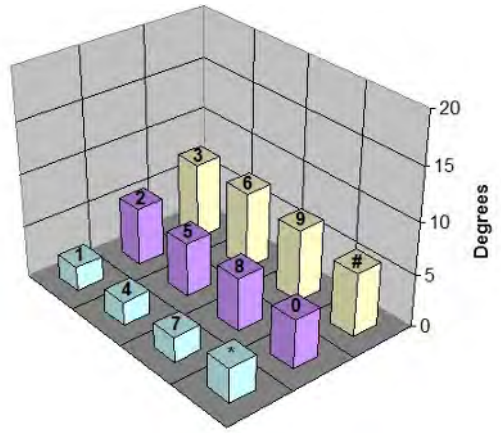


Fig. 9 Flexion-extension of CMC joint

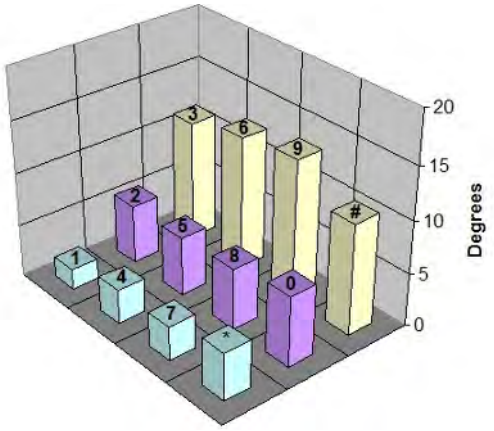


Fig. 11 Thumb opposition of CMC joint

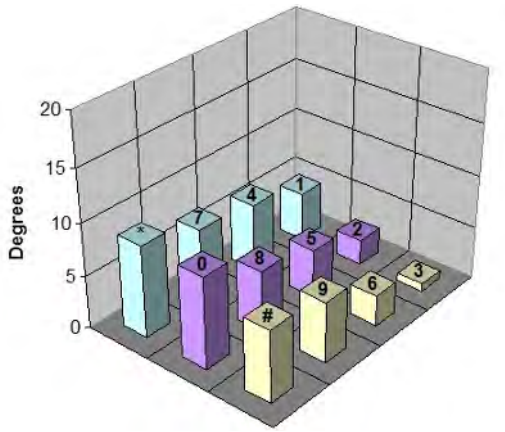


Fig. 10 Abduction-adduction of CMC joint

compensated by high MCP flexion. Subjects also showed reduced thumb opposition and repositioned the phone when reaching those keys.

IV. CONCLUSIONS

Flexion-extension of the thumb occurred mainly in the IP and MCP joints. The maximum flexion for IP joint was 20.2º at key '*' and were 18.3º at key '#' for MCP joint. Angular displacements in abduction-adduction of MCP and CMC were smaller in comparison to flexion-extension. The maximum abduction for MCP and CMC joints were 7.2º and 8.7º respectively at key '*'. Thumb opposition of the MCP and CMC joints were more significant than their abduction-adduction. The maximum angular displacements for thumb opposition were 17.0º at key '4' and 13.5º at key '9' respectively. No incidence of peak forces was found in the right column of the keypad. The results indicated that the incidence of peak force was linked to high angular displacement in flexion of the IP joint and in thumb opposition of the MCP joint.

ACKNOWLEDGMENT

This study was supported in part by a grant from Singapore Totalisator Board. The author acknowledged the Final Year Project Students from the School of Mechanical and Manufacturing Engineering of Singapore Polytechnic for their assistance in data collection and analyses, and Mr Tham Kwok Liang for co-supervising the project.

REFERENCES

1. BBC News: Texting boom 'could lead to injuries' at http://news.bbc.co.uk/1/hi/uk/1841942.stm
2. Ong FR (2006) Analysis of text messaging (SM) on mobile phone. 15th International Conference on Mechanics in Medicine and Biology Proc., Singapore, 2006, pp 153–154
3. Jindrich D, Balakrishnan A, Dennerlein J (2004) Effects of the key-switch design and finger posture on finger joint kinematics and dynamics during tapping on computer keyswitches. Clin Biomech 19: 600–608
4. Kuo LC, Su FC, Chin HY, Yu CY (2002). Feasibility of using a video-based motion analysis system for measuring thumb kinematics. J Biomech 35:1499–1506
5. Li ZM, Tang J (2006) Coordination of thumb joints during opposition. J Biomech 40: 502–510
6. Carpinella I, Mazzoleni P, Rabuffetti M, Thorson R, Ferrarin M (2006) Experimental protocol for the kinematic analysis of the hand: Definition and repeatability. Gait & Posture 23:445–454
7. Jonsson P, Johnson PW, Hagberg M (2007) Accuracy and feasibility of using an electrogoniometer for measuring simple thumb movements. Ergonomics 50: 647–659

Oxygen Transport Analysis in Cortical Bone Trough Microstructural Porous Canal Network

T. Komeda[1], T. Matsumoto[1], H. Naito[1] and M. Tanaka[1,2]

[1] Graduate School of Engineering Science, Osaka University, Toyonaka, Osaka, Japan
[2] Center for Advanced Medical Engineering and Informatics, Osaka University, Osaka, Japan

Abstract — **Oxygen supply is one of primal concerns in bone modeling and remodeling. In the cortical bone, oxygen is transported through the vascular system in the Haversian and Volkman's canals and through the periosteocytic space of canaliculi mainly. In this study, the oxygen transport by convection and diffusion was modeled for both of the vascular channel network and the bone canaliculi network. The oxygen distribution and its nonuniformity were examined for the cortical shaft of rat tibia using the constructed model with CT-imaged bone structure.**

Keywords — **Biomechanics, Cortical Bone, Microstructure, Canal Network, Oxgen Transport.**

I. Introduction

Cortical bone is of compact hard tissue macroscopically, but has porous canal network consisting of Haversian and Volkman's canals microscopically. The modeling and remodeling of cortical bone structure is deeply depending on the mechanical environment, and they are supported by the sufficient supply of physiological substances permitting the activities of bone cells. The oxygen is a primal substance supplied by the vascular system in the canal network. However, the oxygen transport in the cortical bone is not well understood yet. In this study, the oxygen transport in the cortical bone was modeled by considering the transport in the blood flow in vascular system in the canal network and in the bone matrix including lacunae-canaliculi network. Using the proposed transport model, the distribution of oxygen concentration was analyzed with CT-imaged bone microstructure of Haversian/Vilkman's canals, and demonstrated was the non-uniformity of oxygen supply in cortical bone.

II. Oxygen transport model

A. Haversian and Volkman's canal networks

Haversian and Volkman's canals consist a canal network system in cortical bone and it works as the vascular channel network. This network structure is considered as a collection of one-dimensional tube representing individual canal segment. Each segment is assumed to be a straight tube connecting the branching or joining nodes of the network, and one vessel tube is considered for each canal segment. Let consider a vessel tube *ij* in the canal connecting a node *i* and its adjacent node *j*, and define a line coordinate *s* along the tube *ij*. As a one-dimensional convection-diffusion problem in a straight tube, the governing equation of oxygen concentration C^p_{ij} at position *s* and time *t* is written as

$$\frac{\partial C^p_{ij}(s,t)}{\partial t} = -\bar{u}_{ij}\frac{\partial C^p_{ij}(s,t)}{\partial s} + D^p\frac{\partial^2 C^p_{ij}(s,t)}{\partial s^2} - \frac{2}{r_{ij}}D^{pt}S_{rate}\frac{C^p_{ij}(s,t)-C^t(\mathbf{x},t)}{h} \quad (1)$$

where u_{ij} is the average flow velocity assuming Hagen-Poiseuille law, D^t and D^{pt} are the diffusion coefficients in plasma and vascular wall, r_{ij} is the vessel radius, S_{rate} denote the area ratio of canaliculi cross section and canal wall, and *h* is the vascular wall thickness. The last term of the right hand side is for the interaction with the canaliculi network, where the position *s* in the vessel coordinate corresponds to the position $\boldsymbol{x}$ in the bone matrix in three dimension. It is noted here, the volume or diameter of the vessel is neglected in the interaction between the vessel and matrix.

B. Bone lacunae-canaliculi network

Oxygen transport in the bone matrix is mainly conducted through lacunae-canaliculi network. Bone canaliculi connecting lacunae are distributed densely in the matrix in comparison with Haversian/Volkman's canals in cortical bone. A homogenized model is, thus, employed for the modeling of oxygen transport in bone matrix with lacunae-canaliculi network [1]. For the unit cell of bone matrix including lacunae and canaliculi, a cuboidal periodic unit cell is recruited. The apparent diffusion coefficient D^t in the bone matrix continuum is then derived based on this unit cell model as follows.

The osteosyte cytoplasmic processes occupy tiny canals of canaliculi but do not fill entirely. The remaining periosteocytic space, pericellular annular space between the canalicular wall and the osteocyte process membrane, is

Chwee Teck Lim, James C.H. Goh (Eds.): ICBME 2008, Proceedings 23, pp. 2099–2101, 2009
www.springerlink.com

filled with fiber matrix and periosteocytic fluid providing the transport pathway of nutrients and waste. The diffusion coefficient D_{fiber} in a canaliculus is then derived based on the fiber matrix theory [2]. By using this diffusion coefficient, the apparent diffusion coefficient is described as

$$D^t = \frac{A_{fc} N_c D_{fiber}}{L_c^2} \tag{2}$$

for a cuboidal unit cell which each surface is characterized with N_c canaliculi coming from the bone lacuna in it. Here, A_{fc} and L_c are the cross-sectional area of transport pathway in a canaliculus and the size of unit cell.

As the result, oxygen concentration $C^t(\boldsymbol{x},t)$ in the bone matrix as a homogenized continuum is described by three-dimensional diffusion equation as

$$\frac{\partial C^t(\mathbf{x},t)}{\partial t} = \frac{1}{V_p}\left\{ D^t \frac{\partial^2 C^t(\mathbf{x},t)}{\partial \mathbf{x}^2} + 2\pi r_{ij} L(\mathbf{x}) D^{pt} S_{rate} \frac{C_{ij}^p(s,t) - C^t(\mathbf{x},t)}{l} - Q \right\} \tag{3}$$

where V_p is the volume fraction of lacunae-canaliculi, $L(x)$ is the direction cosine of vessel tube, and Q denotes the oxygen consumption per unit bone volume. The second term of the right hand side is for the oxygen exchange with the vessel ij, and vanishes when no vessel passes the position $\boldsymbol{x}$.

III. Toransoport analysis

A. Analysis object and conditions

Canal network structure: As an analysis object, the tibial cortical bone of Wistar rat of 5 weeks old is used, and the cortical bone microstructure is obtained by SPring-8 synchrotron radiation CT [3] as shown in Fig.1. The spatial distribution of canal network is not uniform as seen in Fig. 2 illustrating the endosteal surface and the radial section at different regions indicated in Fig. 1.

Blood flow condition: In the juvenile cortical bone, blood flow occurs mainly from endosteal side to periosteal side. Referring to this feature, the blood pressure P was assumed to be proportional to the distances from periosteum and the distal end surface:

$$P = \frac{p_r}{d_{er} - d_{ir}}\left(d_{er} - 2r\right) + p_z z$$

where p_r = 1.28mmHg and p_z = 0.1 p_r. The viscosity of 4.17×10-3Pa·s is assumed for blood flow in vascular vessels.

Oxygen transport condition: At the entrance of individual vascular channel, the oxygen concentration was set to be constant of 0.21mg/ml. No oxygen transportation was assumed through proximal and distal end surfaces, periosteum and endosteum in this analysis. The parameters related to oxygen transport were summarized in Table 1.

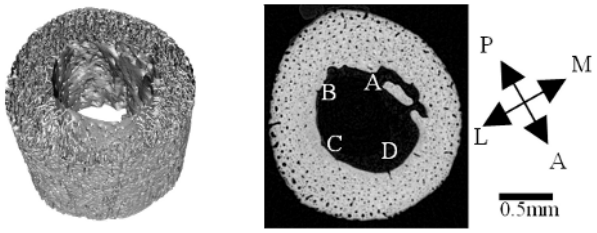


Fig. 1 Microstructure of cortical shaft of rat tibia (Left: Volume rendered image. pixel size is 3.1μm. Right: Transverse section)

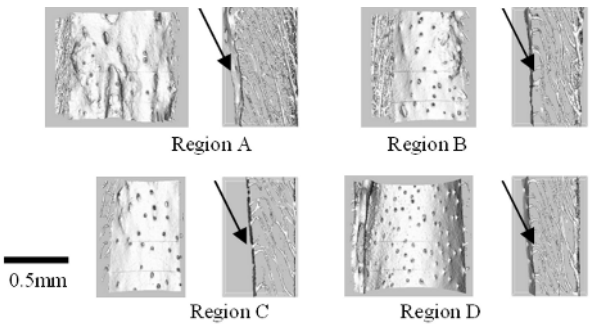


Fig. 2 Canal distribution on different region of endosteum (Indicated by allow in radial sections)

Table 1 Parameters for analysis

Diffusion coefficient in blood	D^p (m^2/s)	2.1×10^{-9}
Diffusion coefficient in bone matrix	D^t (m^2/s)	2.25×10^{-12}
Diffusion coefficient at vessel wall	D^{pt} (m^2/s)	2.1×10^{-9}
Oxygen concentration at entrance	C_{in} (mg/ml)	0.21
Consumption rate at basal metabolism [4]	Q (mg/ml/s)	5.0×10^{-7}

Numerical procedure: The set of transport equations were solved by the finite difference method, with the uniform orthogonal grid of interval of 49.6mm corresponding to 16 pixel interval in CT image representing bone matrix and the one-dimensional grids of interval 20mm~30mm representing vascular channel network. For the space, used were the fourth-order scheme, the central difference for the diffusion and the upwind difference for the convection, and were the second-order scheme, the upwind difference for the time.

B. Distribution of oxygen concentration in cortical bone

The spatial distribution of oxygen concentration in cortical bone was obtained at the steady state. Due to the influence of the boundary condition at the proximal and distal end surfaces at z=0mm and 2.48mm, the attention was focused on the mid shaft region between z=0.99 and 19.8mm. The distributions of oxygen concentration at axial cross-section at different axial heights were shown in Fig. 3 demonstrating the influence of non-uniform distribution of canals in axial cross-section. In the region A, the oxygen concentration was remarkably lower than those in other regions. It is moderate in the region C. By referring to the deficiency in blood flow through vascular channel network, some relations might be suggested between the spatial distribution of oxygen concentration and the vascular channel distribution in the cortical bone.

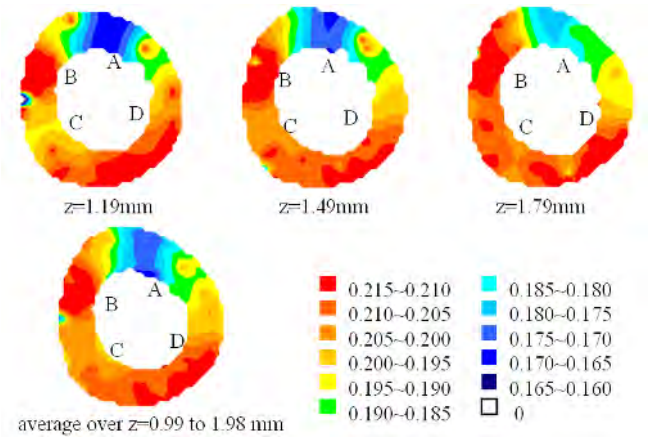


Fig. 3 Distribution of oxygen concentration at different transverse sections

IV. Concluding Remarks

Oxygen transport phenomena in the cortical bone were modeled considering both the vascular channel network and the lacunae-canaliculi network, and formulated a set of oxygen transport equations. Oxygen transport analysis based on the proposed model with real microstructure of rat tibia suggested that the oxygen transport in cortical bone largely depends on local flows, and flows are under the great influence of vascular channel distribution, a major microstructure of cortical bone.

References

1. Gururaja S, Kin HJ, Swan CC, Swan CC, Brand RA, Lakes RS., *Annals Biomedical Engineering*, 33(2005) pp.7-25
2. Weinbaum S, Zhang X, Han Y, Vink H, Cowin SC, *Proc. Natl. Acad. Sci. USA*, 13(2003) pp.7988-7995
3. Matsumoto T, Yoshino M., Asano T, Uesugi K, Todoh M, Tanaka M, *Journal Applied Physiology*, 100(2006) pp.274-
4. Brookes M, Revell WJ, Blood Supply of Bone: Scientific Aspects, Springer-Verlag, (1998), London, UK.

Address of the corresponding author:

Author: Masao Tanaka
Institute: Osaka University, Graduate School of Engineering Science
Street: Machikaneyama
City: Toyonaka, Osaka
Country: Japan
Email: tanaka@me.es.osaka-u.ac.jp

Identification of Microstructural Mechanical Parameters of Articular Cartilage

T. Osawa[1], T. Matsumoto[1], H. Naito[1] and M. Tanaka[1,2]

[1] Department of Mechanical Science and Bioengineering, Graduate School of Engineering Science, Osaka University, Japan
[2] Center for Advanced Medical Engineering and Informatics, Osaka University, Japan

Abstract — **Articular cartilage has the depth-dependent laminar structure, and the mechanical behavior of articular cartilage is strongly dependent of its microstructure characterized by three-dimensional, depth-dependent anisotropic arrangement of collagen fibre, chondrocyte and so on. In this study, a method identifying the mechanical properties of cartilage is described by using a viscoelastic model of cartilage considering its anisotropic and inhomogeneous microstructure and the time history of reaction force observed in the indentation test. The method is examined with bovine femoral cartilage at the medial and lateral regions.**

Keywords — **Articular cartilage, Microstructure model, Mechanical property, Degeneration, Indentation test.**

I. Introduction

Articular cartilage is a soft tissue covering the articular surface of diarthrodial joints, and considered as biphasic (solid and fluid) material. The solid phase shows laminar structure varied along cartilage depth, and generally divides into three layers: surface, middle, and deep layers. The depth-dependent structure is deeply involved in mechanical behavior and property, which is a major determinant of cartilage function of shock absorbing or load bearing [1].

In this study, the transversely isotropic and transversely homogeneous microstructural model [2] considering its anisotropy and inhomogeneity was extended to take the viscoelasticity of solid phase into account. Then, the model was used to identify the mechanical properties of cartilage under the different load supporting conditions based on the indentation test. The mechanical parameters determined were validated through component analysis by Fourier transformed infrared microscopic spectroscopy (FT-IR).

II. Materials and methods

A. Micro-structural model

As the mechanical model of cartilage, the biphasic model consisting of solid phase and fluid phase [3] has been a standard one where the solid phase is assumed to be isotropic body conventionally. Recently, Federico and coworkers[2] have proposed the transversely isotropic and transversely homogeneous (TITH) model in order to take the depth-dependent microstrucral characteristics in the solid phase, where the effect of chondrocyte and collagen fibre is incorporated by means of Eshelby theory, assuming the linear elasticity for all of proteoglycan-matrix, cells and collagen fibre. This is the elastic TITH model. In the present study, this model is extended to take the viscoelasticity of collagen fibres in to account. That is, the solid phase consists of isotropic proteoglycan-matrix, ellipsoidal inclusion of chondrocytes and collagen fibres. The orientation of collagen fibre, volume fractions of collagen fibre and the chondrocyte and shape of chondrocyte are determined stochastically in a depth-dependent manner based on the anatomical data [4][5][6]. A Kelvin viscoelastic body is assumed for the collagen fibre, while the proteoglycan-matrix and cells were assumed to be linear elastic bodies as is in the original model. The stress of the solid phase $\boldsymbol{\sigma}(\xi)$ was composed of the non-fibre matrix $\boldsymbol{\sigma}_M(\xi)$ and the fibre $\boldsymbol{\sigma}_F(\xi)$ as follows:

$$\begin{aligned}\boldsymbol{\sigma}(\xi) &= \left[d_o(\xi)\boldsymbol{\sigma}_o + d_c(\xi)\boldsymbol{\sigma}_c(\xi)\right] + d_f\boldsymbol{\sigma}_f(\xi) \\ &= \boldsymbol{\sigma}_M(\xi) + \boldsymbol{\sigma}_F(\xi),\end{aligned} \tag{1}$$

where ξ denotes the normalized cartilage depth, d_r is the volumetric content of each component r (r=0:PG-matrix, r=c:chondrocyte, f:collagen fibre). The stress of non-fibre matrix depends mainly on elasticity tensor $\mathbf{C}_o$ and $\mathbf{C}_c$, strain-concentration tensor $\mathbf{A}_c$. The stress of fibre depends on elasticity tensor $\mathbf{C}_f$, strain-concentration tensor $\mathbf{A}_f$,. the distribution density $\varphi(\xi: \theta)$ and relaxation function $G(t)$ of collagen fibre.

B. Indentation test and parameter identification

Fresh normal bovine femoral heads were used as specimens. Cartilage at the medial and the lateral regions on a femur head underwent indentation test. Medial region is a load-supporting region, whereas lateral region is non load-supporting region. The indentation test was carried out with the indenter of 1 mm in diameter, indentation displacement of 0.1 mm, indentation speed of 0.2 mm/s, and relaxation time of 180 seconds. Thicknesses of cartilage at the indentation points were measured from X-ray transmission imaging. Three-dimensional simulation of the indentation test was performed using the present viscoelastic TITH model with assuming the same condition in experiment. The

Chwee Teck Lim, James C.H. Goh (Eds.): ICBME 2008, Proceedings 23, pp. 2102–2103, 2009
www.springerlink.com

volumetric content of collagen fibre, elastic modulus of collagen fibre, permeability and other model parameters were identified by comparing the experimental and calculated response of reaction force. The collagen content was evaluated with the integrated area of wave range of infrared light absorbed by Amide I [5] observed by FT-IR measurement.

III. Results and discussion

Fig. 1 shows reaction force responses in time by the experiment and by calculation using model-fitted parameters. The reaction force was lager at the lateral region than that at the medial region, and the instantaneous and relaxed elastic moduli were higher at the lateral region than those at the medial region (Table 1). The identified axial and transverse elastic moduli in lateral region were higher than those in medial region. The axial elastic modulus was lower than the transverse elastic modulus, in the surface layer. In deep layer, on the other hand, the axial elastic modulus was higher than the transverse elastic modulus (Table 2). The identified elastic modulus of collagen fibre was higher at the lateral than at the medial region. The collagen content was estimated rich at the lateral region in comparison with that at the medial region. According to the previous studies [7], the thickness of cartilage at the load support (medial) region is thicker than that at non-load support (lateral) region, and the elastic modulus of thick cartilage is lower than that of thin cartilage [8]. The present model gave higher collagen contents at the lateral region, where collagen modulus was also high (Table 2). FT-IR analysis also showed rich collagen content with the lager area of Amide I at the lateral region (Table 1). In conclusion, these results suggests that viscoelastic TITH model considering collagen fibre and chondrocyte inclusions is an effective tool to describe the mechanical properties with reflecting material composite characteristics in cartilage appropriately.

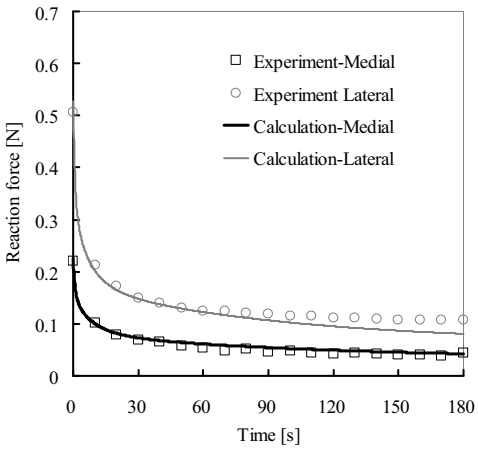


Fig. 1 Reaction force in indentation test.

Table 1 Characteristics measured.

	Medial		Lateral
Thickness [mm]	1.416	>	0.898
Instantaneous elastic modulus [MPa]	1.039	<	1.813
Relaxed elastic modulus [MPa]	0.251	<	0.492
Area of Amide I	40.83	<	50.24

Table 2 Parameters identified at medial and lateral region

Elastic modulus [MPa]	Medial		Lateral
ζ=0.8 (surface layer)			
Axial	0.536	<	0.797
Transverse	0.770	<	1.329
ζ=0.2 (deep layer)			
Axial	0.853	<	1.579
Transverse	0.744	<	1.190
Collagen content [%]	34.649	<	48.411
Collagen elastic modulus [MPa]	1.758	<	4.011

References

1. Hosoda N. et al. (2008) Depth-dependence and time-dependence in mechanical behaviors of articular cartilage in unconfined compression test under constant total deformation. JBSE 3:209-220
2. Mow V. C. et al. (1980) Biphasic creep and stress relaxation of articular cartilage in compression: theory and experiments. J Biomech Eng 102:73-84
3. Federico S. et al. (2005) A transversely isotropic, transversely homogeneous microstructural statistical model of articular cartilage. J Biomech 38:2008-2018
4. Visser S. K. et al. (2008) Structural adaptations in compressed articular cartilage measured by diffusion tensor imaging. Osteoarthritis Cartilage 16:83-89
5. Camacho N. P. et al. (2001) FTIR microscopic imaging of collagen and proteoglycan in bovine cartilage. Biopolymers 62:1-8
6. Clark A. L. et al. (2006) Heterogeneity in ptellofemoral cartilage adaptation to anterior cruciate ligament transaction; chondrocyte shape and deformation with compression. Osteoarthritis Cartilage 14: 120-130
7. Athanasiou K. A. et al. (1991) Indentation comparisons of in situ intrinsic mechanical properties of distal femoral cartilage. J Orthop Res 9:330-340
8. Nugent G. E. et al. (2004) Site- and exercise-related variation in structure and function of cartilage from equine distal metacarpal condyle. Osteoarthritis Cartilage 13:826-833

Author: Masao TANAKA
Institute: Department of Mechanical Science and Bioengineering, Graduate School of Engineering Science, Osaka University
Street: 1-3, Machikaneyama
City: Toyonaka, Osaka
Country: Japan
Email: tanaka@me.es.osaka-u.ac.jp

Computer Simulation of Trabecular Remodeling Considering Strain-Dependent Osteosyte Apoptosis and Targeted Remodeling

J.Y. Kwon[1], K. Otani[1], H. Naito[1], T. Matsumoto[1], M. Tanaka[1,2]

[1] Department of Mechanical Science and Bioengineering, Graduate School of Engineering Science, Osaka University, Toyonaka, Osaka, Japan

[2] Center for Advanced Medical Engineering and Informatics, Osaka University, Osaka, Japan

Abstract — **Bone structure is deeply related to its mechanical function, and is maintained adaptation by remodeling. Among many investigations concerning the mathematical modeling of bone remodeling, the physiological range of mechanical stimuli has been studied mainly. In this study, mathematical models of surface remodeling in disuse and overuse windows are formulated by paying attention to the osteocyte apoptosis and targeted remodeling, and are unified with that in the physiological window. The fundamental characteristics of the unified model are examined through numerical cases.**

Keywords — **Biomechanics, Bone Remodeling, Remodeling Simulation, Osteocyte apoptosis, Targeted remodeling**

I. Introduction

Mechanical loading is a crucial factor in maintaining the bone structure at the normal healthy state, and bone architecture is adapted to the external loading conditions. Mechanostat theory/hypothesis by Frost [1] gives us a basic framework to grasp the mechanical adaptation by remodeling of bone in accordance with the mechanical usage. Several windows of mechanical usage are distinguished by referring to the strain magnitude in this context. Concerning the mathematical modeling and computer simulation of bone remodeling and adaptation, much attention has been focused on the physiological window (PW) for normally adapted healthy condition. Bone formation and resorption in two different windows adjacent to the PW are considered in this study. One is the disuse window (DW) of smaller strain magnitude, where the osteocyte apoptosis becomes dominant, and the other is the overuse window (OW) of larger strain magnitude, where the targeted remodeling becomes dominant.

II. Simulation model

A. Mathematical model of remodeling

Surface remodeling by referring to the mechanical stimuli was used for the mathematical model of bone remodeling in this study. For the PW, the nonuniformity of the stress/strain distribution was picked up as the mechanical stimuli [2][3]. For the material point x_c of on bone surface, driving force for remodeling was evaluated by

$$\Gamma_c = \ln\left(\sigma_c \sum_i^N \omega(l_i^c) \Big/ \sum_i^N \omega(l_i^c)\sigma_i \right) \tag{1}$$

where σ_c denotes the stress at $\boldsymbol{x}_c$ and σ_i denotes the representative stress at $\boldsymbol{x}_i$ with distance l_i from $\boldsymbol{x}_c$. The value Γ_c represents the magnitude of local stress non-uniformity around the surface point $\boldsymbol{x}_c$. The probability $f(\Gamma_c)$ of bone gain/loss at $\boldsymbol{x}_c$ is described by referring to this value: no bone gain/loss for $\Gamma_c = 0$, bone gain for $\Gamma_c > 0$, and bone loss for $\Gamma_c < 0$. In this window, the activation frequency AF_f or AF_r for the bone gain or loss governed by the probability $f(\Gamma_c)$ is referred to as the unit, i.e. $AF_f = AF_r = 1$.

In the DW for the strain smaller than the threshold ε_{du}, only considered is the resorption caused by the osteosyte apoptosis [4]. The increase of activation frequency of resorption by the decrease of the strain [5] was expressed as

$$AF_r(\bar{\varepsilon}) = \begin{cases} AF_{r\max} & (0 \le \bar{\varepsilon} < \varepsilon_{\min}) \\ \left(\dfrac{\varepsilon_{du}}{\bar{\varepsilon}} \right)^a, \quad a = \dfrac{\ln AF_{r\max}}{\ln(\varepsilon_{du}/\varepsilon_{\min})} & (\varepsilon_{\min} \le \bar{\varepsilon} < \varepsilon_{du}) \end{cases} \tag{2}$$

where $\bar{\varepsilon}$ stands for equivalent strain, $AF_{r\max}$ is the maximum of $AF_r(\bar{\varepsilon})$, and ε_{min} is the threshold strain for hyperresorption (Fig.1).

In the OW for the strain larger than the threshold ε_{ol}, only considered is the formation caused by the targeted remodeling [6]. Its activation frequency is also elevated by the increase of strain stimuli and is expressed as

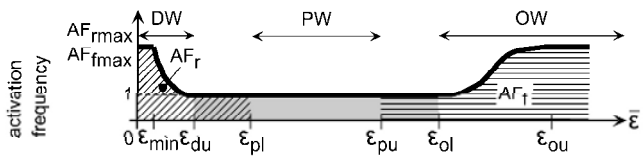


Fig. 1 Activation frequency over DW, PW and OW.

Chwee Teck Lim, James C.H. Goh (Eds.): ICBME 2008, Proceedings 23, pp. 2104–2105, 2009
www.springerlink.com

$$AF_f(\bar{\varepsilon}) = \begin{cases} \dfrac{AF_{f\max}}{2}\left\{\sin\pi\left(\dfrac{\bar{\varepsilon}-\varepsilon_{ol}}{\varepsilon_{ou}-\varepsilon_{ol}}-\dfrac{1}{2}\right)+1\right\}+1 & (\varepsilon_{ol} \le \bar{\varepsilon} < \varepsilon_{ou}) \\ AF_{f\max} & (\bar{\varepsilon} \ge \varepsilon_{ou}) \end{cases} \quad (3)$$

where $AF_{f\max}$ is the maximum of $AF_f(\bar{\varepsilon})$. It is noted that the pathological overuse is not considered and the upper limit ε_{ou} is enforced for the OW (Fig.1).

B. Femur model for simulation

The profile human proximal femur and its initial random trabecular structure are represented using boxel finite elements as is shown in Fig.2 (A). The fixed boundary conditions are imposed on the distal end, and the daily loading conditions were assumed for the remodeling simulation. The representative daily loading case of one-legged stance and extreme ranges of motion of abduction and adduction, illustrated in Fig.2 (B), (C) and (D), are enforced with the proportion of 3:1:1. The remodeling at the internal surface is simulated and the profile of outer cortical shell is remained as is. The isotropic elastic body of Young`s modulus 20.0 GPa and Poisson`s ratio 0.3 is assumed for the bone material.

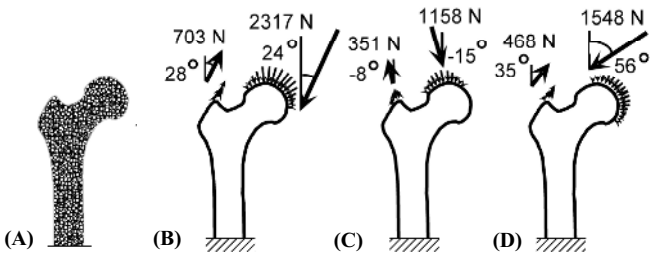


Fig. 2 (A) Initial structure of human proximal femur ,(B) one-legged stance, (C) abduction, and (D) adduction.

III. Results and Discussions

The trabecular structures simulated by the integrated model considered in the above and by the PW model only are shown in Fig.3. The gray scale indicates the equilibrant strain at each element. The initial random pattern of trabecular structure changed its alignment to line up with directions of principal stress in the metaphysis region and the thickness of cortical bone in the diaphysis increased under daily loading condition. In addition, indices of trabecular structure in femoral head and intertrochanteric region (#2) were approximately consistent with clinical observation [7]. Moreover, bone volume in Ward's triangle region (#3) decreased significantly under disuse condition while bone volume and cortical bone thickness (#1) increased under overloaded condition. These characteristics have been found in clinical observations. In comparison with the PW only model, the present results were more realistic demonstrating the importance of osteocyte apoptosis and targeted remodeling in the simulation model for remodeling analysis.

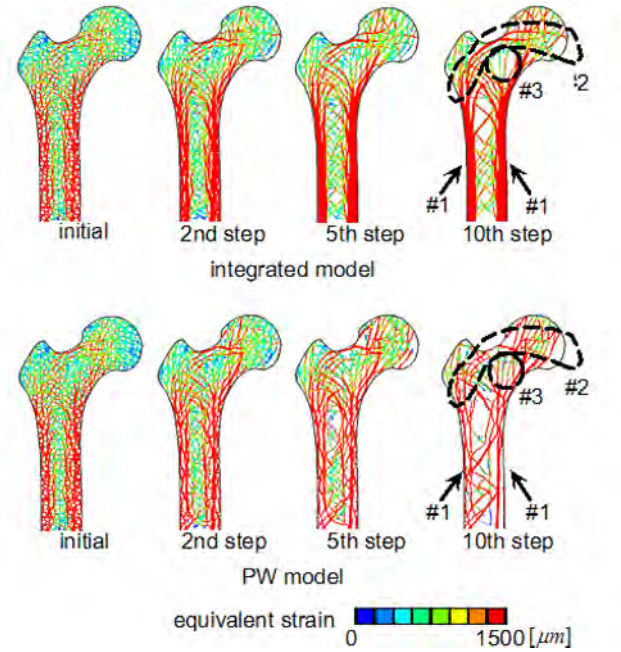


Fig. 3 Morphological change of trabecular structure in proximal femur simulated by integrated model and PW model.

References

1. Frost, H.M., *Anatomical Record,* 275A(2003) pp.1081-1101
2. Adachi, T., Tomita, Y., Sakaue, H, Tanaka, M., *Tran.Japan Society of Mechanical Engineers*, 63C (1997) pp. 777-784
3. Tsubota, K., Adachi, T., Tomita, Y., *Journal of Biomechanics*, 35(2002) pp.1541-1551.
4. Noble,B.S., Peet, N., Stevens, H.Y. et al., *American Physiological Society*, 284 (2003) pp.C934-943
5. Li, C.Y., Majeska, R.J., et al., *Bone*, 37(2005) pp.287-295
6. Da Costa Gómez, T.M., Barrett, J.G., et al., *Bone*, 37(2005) pp.16-24
7. Tsangari, H. Findlay, D.M., Fazzalary, N.L., *Bone*, 40(2007) pp.211-217

Address of the corresponding author:

Author: M. Tanaka
Institute: Department of Mechanical Science and Bioengineering, Graduate School of Engineering Science, Osaka University
Street: 1-3, Machikaneyama
City: Toyonaka, Osaka
Country: Japan
Email: tanaka@me.es.osaka-u.ac.jp

Fibroblasts Proliferation Dependence on the Insonation of Pulsed Ultrasounds of Various Frequencies

C.Y. Chiu[1], S.H. Chen[1], C.C. Huang[2], S.H. Wang[1]

[1] Department of Biomedical Engineering, Chung Yuan Christian University, Taiwan

[2] Department of Electronic Engineering, Fu-Jen Catholic University, Taiwan

Abstract — **Previous studies have demonstrated that low intensity pulsed ultrasound (LIPUS) may accelerate wound healing and activate the proliferation of skin cells. Those studies however did not thoroughly explore the bioeffect with respect to ultrasonic frequency of insonations. Hence, experiments were arranged and carried out to extensively investigate the proliferation of human foreskin fibroblasts (HFFs) insonated for 3 minutes daily with various 20% pulsed ultrasounds of 1 kHz repletion frequency, fixed 200 mW/cm2 (SATA), and frequencies of 0.5, 1, and 3 MHz, within a period of 3 days. The viability of insonified HFFs was sampled and evaluated for every 12 hours by trypan blue staining and optical microscopy. Results showed that the rates of HFFs proliferation associated with insonations by both 1 and 3 MHz are larger than those of control groups. However, those of HFFs insonated with a 0.5 MHz ultrasound tend to be smaller than that of control groups. The timing corresponding to the largest rate of HFFs proliferation was found to vary with the frequency of insonation, in which it corresponds to 36 h and 24 h associated with insonations of 1 and 3 MHz ultrasound, respectively. Specifically, the insonations of HFFs with 1 and 3 MHz tend to activate the largest proliferation rates to be 1.5 and 1.3 fold, respectively, larger than that of the control group. The temperature in the culture plate was measured before and after ultrasonic insonation and that varied only within 1 oC implying that the activation of HFFs proliferation is associated with the non-thermal effect of ultrasonic stimulation.**

Keywords — **Human foreskin fibroblasts, Cell proliferation, low intensity pulsed ultrasound.**

I. Introduction

The migration and formation of fibroblasts in an injury tissue is a crucial procedure for wound healing process. The fibroblasts may activate the synthesis of collagen and finally repair the damage tissues with the formation of scar tissues. In addition to its important role in wound healing process, fibroblasts almost may attribute to any rapid production of connective tissue matrix, such as the development of embryo and tissue culture [1]. Therefore, it is interesting and important to investigate effects that could be beneficial to growth of fibroblasts for further applications in tissue engineering.

Ultrasound is a means of mechanical wave propagation. As ultrasound waves are insonified into a biological tissue, a certain energy of the acoustic waves may disturb particles or molecules in the path of wave propagation, that leads them to deviate from their original positions. Depending on the intensity, the insonified ultrasound could generate thermal and/or non-thermal effects onto tissues [2]. These effects could be further applied to stimulate the wound tissue or cultured cells [3].

Dyson et al. [4] applied a 3.55 MHz ultrasound of different intensities ranged from 0.25 to 8 W/cm^2, 20% duty cycle, the pulse repetition period of 10 ms, to stimulate the wounded ear of mature rabbits for 5 min per day. They found that the regeneration performance in the wounded tissues seemed to be better in accordance with those received stimulations from low intensity ultrasounds. The improvement of tissue regeneration was assumed due to non-thermal effect by low intensity ultrasounds. However, as the intensity of the applied ultrasound increases to be higher than a few W/cm^2, the cultured cells tended to be damage or hemolysis associated with effects of the ultrasonic cavitation or others [5].

Although several previous studies have demonstrated the capabilities of low intensity ultrasounds could enhance either protein or collagen synthesis in human fibroblasts [6], there is no unified ultrasonic exposure including intensity, frequency, and pulse repetition period (PRP), implemented to stimulate cells. Yet, our previous study did validate that the fibroblast proliferation is effectively enhanced as the cells were exposed to 20% duty cycle and 200 mW/cm^2 of ultrasound for 3 minutes per day. This study is to further investigate the effect of various frequencies of the same low intensity ultrasound on the proliferation of fibroblasts.

Chwee Teck Lim, James C.H. Goh (Eds.): ICBME 2008, Proceedings 23, pp. 2106–2109, 2009
www.springerlink.com

II. Materials and methods

The human foreskin fibroblast, cell line of HS68 obtained from Bioresearch Collection and Research Center at Food Industry Research and Development Institute, Hsin-chu, Taiwan, was used in this study. The cells were cultured in the DMEM (Gibco, BRL) medium supplemented with a 4 mM L-glutamine adjusted to contain a 1.5 g/L sodium bicarbonate (Gibco, BRL), 4.5 g/L glucose, and 10% fetal bovine serum (Biological Industries) at 37 ^{o}C in a 5% CO_2 humidified incubator.

The ultrasonic stimulation system was developed to insonate cells, which is primarily comprised of a ultrasonic tune burst generator able to generate three frequencies including 0.5, 1 and 3MHz. Specifically, tone burst signals were generated by multiplying sinusoidal waves of different frequencies with a train of square waves in which its width and period was fixed to be 1 ms. The arrangement of ultrasonic system for stimulating cultured cells is shown in Figure 1, in which ultrasound emitted by a transducer is directly coupled by the distilled water in the water bath into the bottom of a 24 well culture plate. The low intensity ultrasounds of a fixed 20% duty cycle of different frequencies were adjusted to be fixed to a 200 mW/cm^2 (I_{SATA}) calibrated by measurements using an ultrasound power meter (UPM DT-1, Ohmic instruments). Ultrasounds of the same intensity at different frequencies of 0.5, 1 and 3MHz were then applied to stimulate fibroblasts in the culture plate.

Initially, a number of 20000 cells were seeded into one of the well in the culture plate. Subsequently, the insonated cells respectively received corresponding frequencies of ultrasound exposures each for 3 minutes per day. The fibroblasts of the control group were also brought onto the culture plate holder at the same time as that of the experimental group to assure nearly equivalent factors condition may be applied for each experiment. The temperature in the culture plates was also monitored and maintained at 37^{o}C throughout the entire insonation process with a temperature controller. The fibroblasts were then quantified by counting the suspended cells, obtained from trypsinizing a monolayer of the fibroblasts in three wells of the culture plate, using trypan blue dye through a hemocytometer.

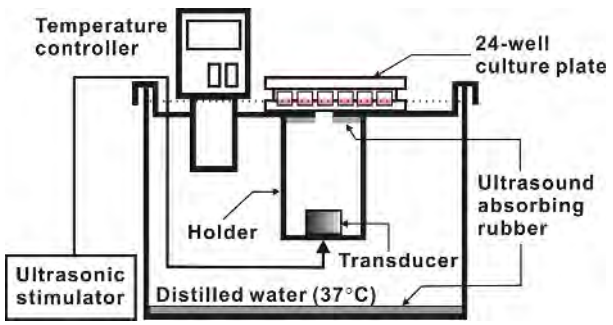


Figure 1 The arrangement for the stimulation of fibroblasts by ultrasound.

III. Results

After fibroblasts were subcultured from the cell line in a 24-well culture plate, it typically takes 3 days of doubling time before they are confluent. To better daily monitor the changes of cell numbers, the growth ratio of cell proliferation, calculated by normalizing the cell number of control or insonated groups sampled at a certain day, indicated as X* and X_c in the Y-axis of Figure 2, by those of at first day of subculture groups, indicated as X^*_0 and X_{c0}, were calculated. According to results in Figure 2, the average ratios of fibroblast proliferation display different feature corresponding to different frequencies of ultrasound been applied. With tone bursts of a 20% duty cycle and a fixed 200 mW/cm^2 intensity ultrasound insonified into the cell culture plate, those cells stimulated by 1 and 3 MHz tend to response better cell proliferation in terms of growth ratio than those insonified by a 0.5MHz ultrasounds. Especially, the growth ratio of cell proliferation approached to 1.5 and 1.3 fold than that of the control group with respect to insonation by 1 and 3MHz ultrasound, respectively, after that fibroblasts were exposed to ultrasound for 36 and 24 hours.

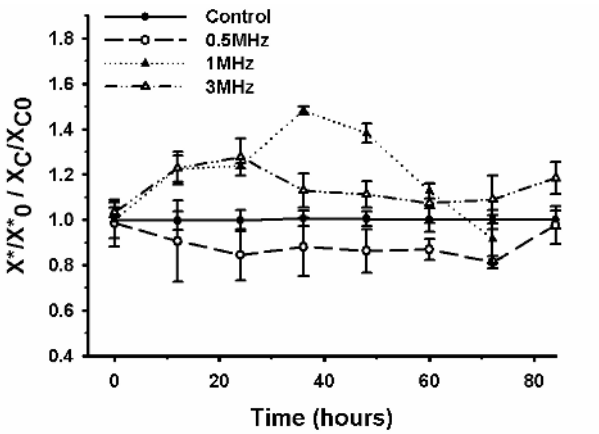


Figure 2 Normalized growth ratio of cell proliferation associated with different frequency ultrasounds as a function of time.

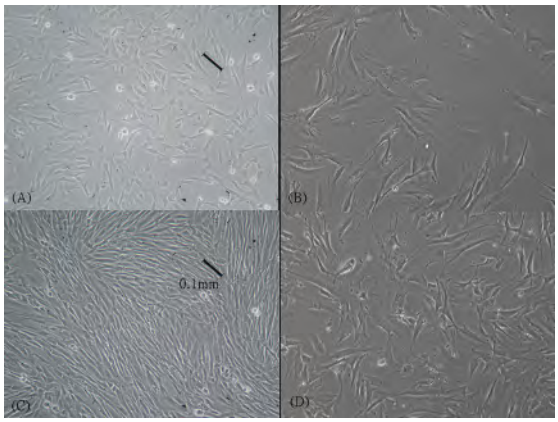


Figure 3 Morphology (100X) of investigated fibroblasts taken from a light microscope at 36 hours, (A) control group; (B) insonated by 0.5MHz; (C) insonated by 1MHz; (D) insonated by 3MHz ultrasound.

The effect of ultrasound stimulation on fibroblasts may be readily discerned with the morphology of cells from the control and experimental groups after ultrasound shown in Figure 3. The enhancement of cell proliferation with respect to ultrasound insonation may be directly compared by the morphology of fibroblasts of the control group and that of stimulated with a 1MHz ultrasound. In comparison with Figures 3(A) and (C), it may be readily seen that cell proliferation is activated for those under 1 MHz ultrasound insonation.

IV. Discussion

A previous research applied different acoustic powers for 10 minutes to insonify the osteoblasts has found that there could be a threshold of ultrasonic power able to detach the monolayer cells and leading to the deformation of cell morphology [7]. Results of another previous study from the same group also postulated that these results could be due to the exerted mechanical stress that improves the permeability of cell membrane to allow more supply of appropriate ions into the cells [8]. Current results suggest that the enhancement of fibroblast proliferation associated with ultrasonic insonification is a balance interaction between exposure time and the instantaneous ultrasonic frequency. The fibroblast proliferation is maximally activated corresponding to cells insonated by a 1MHz of a fixed 200 mW/cm^2 ultrasound at 20% duty cycle after exposure for 36 hours. The effect of cell proliferation stimulated by a higher frequency ultrasound, 3MHz, also tended to be capable of increasing the fibroblast proliferation, but that the effect is not as profound as those insonation with in 1MHz ultrasound. It is suggested that the number of times of vibration to stimulate cells with a higher frequency ultrasound, 3MHz, is much larger than that of lower frequency, 1MHz, to result in the appearance of the peak of cell proliferation beforehand. On the other hand, there is no significant difference between the response of cells stimulated by 0.5 MHz ultrasound and that of control group. The temperature difference in the culture plate was within 1^{o}C before and after ultrasound insonation also indicating that the non-thermal effect of ultrasound could be the primary factor contributing to the proliferation of cells.

V. Conclusion

In this study, the ultrasonic insonation system was developed and was applied to explore effect of ultrasound frequencies on the fibroblast proliferation. Different frequency ultrasounds were employed to insonate cultured fibroblasts. Results showed that the exposure of 1 and 3 MHz ultrasounds may activate the cell proliferation, and the effect of 0.5 MHz insonation however is not significant. Specifically, the insonation with a 1 MHz ultrasound of a 200 mW/cm^2 intensity of 20% duty cycle performs better enhancement of cell proliferation than those of by other frequencies of ultrasound.

Acknoeldgments

This work was supported by the National Science Council of Taiwan, ROC, of the grants: NSC 97-2627-M-033-003 and NSC 95-2221-E-033-003-MY3.

References

[l] Ross R. (1968) The fibroblast and wound repair. Biol. Review 43: 51-96.
[2] Haar G. T. (1999) Therapeutic ultrasound. Eur J Ultrasound 9:3-9.
[3] Young S. R. and Dyson M. (1990) Effect of therapeutic ultrasound on healing of full-thickness excised skin lesions. Ultrasonics 28:175-180.
[4] Dyson M., Pond J., Joseph B. J., and Warwick R. (1968) The stimulation of tissue regeneration by means of ultrasound. Clin. Sci. 35:73-285.

[5] Miller M. W., Miller D. L., and Brayman A. A. (1996) A review o fin vitro bioeffects of inertial ultrasonic cavitation from a mechanistic perspective. Ultrasound Med. & Biol. 22:1113-1 154.

[6] Harvey W., Dyson M., Pond J. B., and Grahame R. (1975) The in vitro stimulation of protein synthesis in human fibroblasts by therapeutic levels of ultrasound. in Kazner E. et al. (Ed), Ultrasonics in medicine', (Amsterdam, Excerpta Medica).

[7] Myrdycz A. and et al. (2002) Cells under stress: anon-destructive evaluation of adhesion by ultrasounds. Biomol. Eng. 19: 219-225.

[8] Kaufman J. J., Popp H., A Chiabrea., and Phila A. A. (1988) The effect of ultrasound on the electrical impedance to biological cells, IEEE EMBS Annual Conference, New Orleans, Louisiana, 1988, pp. 753-754.

Acromio-humeral Interval during Elevation when Supraspinatus is Deficient

Dr. B.P. Pereira[1], Dr. B.S. Rajaratnam[2], M.G. Cheok[2], H.J.A. Kua[2], Md. D. Nur Amalina[2], H.X.S. Liew[2], S.W. Goh[2]

[1]National University of Singapore, Yong Loo Lin School of Medicine, Department of Orthopaedic Surgery.
[2]Nanyang Polytechnic, School of Health Sciences. Singapore.

Abstract — **Background & AIM: A narrowed acromio-humeral interval (AHI) during the first 30º of shoulder abduction usually indicates a tear to the supraspinatus muscle. Most investigations studied narrowing of the AHI in a static 0º abduction position. The purpose of this exploratory study was to quantify changes in the AHI during the first 30º of abduction when the supraspinatus was torn for future design of orthopaedic prosthesis and improvements to rehabilitation protocols.**

Method: A cadaveric shoulder was exposed and studied in detail. Next, a biomechanical model was constructed based on known physiological cross sectional area (PCSA) of the rotator cuff and deltoid muscles. Manual traction was applied to the model during abduction and changes in AHI record on video for analysis. Then, the model excluded the action of the supraspinatus and the change in AHI re-evaluated.

Results: The AHI measured at rest was 7.86mm (range= 7-14). When the supraspinatus was intact, at 30º of abduction the average AHI was 5mm (range= 0.428-0.571). However, when supraspinatus was absent, the crest of the greater tuberosity impacted the acromion at about the range of 9-12º of abduction.

Conclusion: This biomechanical evaluation of the shoulder indicated that the supraspinatus besides being an important dynamic stabilizer of the glenohumeral joint maintain a sufficient interval between the acromium and the humeral head for unobstructed arm elevation. When supraspinatus is absent, shoulder impingement also occurs below 30º of abduction.

Keywords — **shoulder; glenohumeral joint; supraspinatus tear; acromiohumeral interval; impingement**

I. Introduction

An intact rotator cuff actively stabilize the shoulder joint by three main mechanisms; 1. compresses the humeral head into the glenoid fossa, 2. raises joint contact pressure, 3. centers the humeral head in the glenoid fossa. To prevent complete superior translation of the humerus, the rotator cuff must compress the humeral head against the glenoid force. In the absence of a properly functioning rotator cuff, the unopposed action of the deltoid muscles impinges the humeral head superiorly against the corocoacromial arch, hence full abduction is prevented.

The supraspinatus must generate a force 20 times greater than the weight of the load for shoulder abduction. The muscle has the highest incidence of tear (37%) among the rotator cuff muscles and commonly occurs in the sport-active and elderly populations. The amount of humeral translation is greatest during the first 30 degrees of abduction[1].

Terrier[1] study was done using a 2-D finite element model (computational model) data derived from several authors. It also did not include a realistic analysis of any cadaveric model. An[2] reported that depression of the humeral head was most effectively achieved by the latissimus dorsi (5.6 +/- 2.2 mm) and the teres major (5.1 +/- 2.0 mm). The infraspinatus (4.6 +/- 2.0 mm) and subscapularis (4.7 +/- 1.9 mm) showed similar effects while the supraspinatus (2.0 +/- 1.4 mm) was least effective in depression. Thomson[3] found that no significant alterations in humeral translation occurred with a simulated supraspinatus paralysis, nor with 1-, 3-, and 5-cm rotator cuff tears, provided the infraspinatus tendon was functional.

Cotton & Rideout[4] defined the AHI as the smallest distance between the thin line of dense cortical bone marking the inferior aspect of acromion and the articular cortex of the humeral head. Golding[5] reported that the range of the AHI was 7-13 mm in normal subjects. While Weiner & Macnab[14] reported the range betwneen 7 to 14 mm. Those with stage II impingement and rotator cuff tears demonstrated a significant rise in the head of the humeral during the first 40 degrees of abduction[6-7]. However, examination were conducted in the static resting position.

This study aims to use a biomechanical model of the shoulder to examine the changes in the AHI during the first 30 degrees of abduction when the supraspinatus is deficient. The results from this study would help better understand the biomechanics of the shoulder when the supraspinatus is absent. The study hypothesize that without the supraspinatus, the AHI will be decreased to an abnormal range during shoulder abduction to 30 degrees.

Chwee Teck Lim, James C.H. Goh (Eds.): ICBME 2008, Proceedings 23, pp. 2110–2113, 2009
www.springerlink.com

II. METHOD

A. Cadaveric study

We performed a cadaveric dissection to obtain coordinate data on muscle coordinates as well as physiological cross-sectional area (PCSA) values of the muscles included in our model. PCSA is directly proportional to muscle force and may be used to predict the maximal muscle forces[8], calculated based on the following equation [9-10].

$$\text{PCSA } (\text{cm}^2) = \frac{\text{Muscle mass (g) } \cos(\theta)}{\rho\ (\text{g/cm}^3)\ \text{fiber length (cm)}},$$

whereby muscle density (ρ) is 1.0597 g/cm^3 and θ is fibre pennation angle[11].

A shoulder was harvested from a fresh adult cadaver, the age unknown. The scapulothoracic and sternoclavicular joints were disarticulated. No defects were noted on macroscopic examination. The skin and subcutaneous tissues were removed. Next, the superficial layer of muscles were removed, leaving the anterior, middle and posterior deltoids as well as the rotator cuff muscles. Each muscle was identified, and pins were inserted into the sites of attachment to record their position. Measurements of muscle lengths and pennation angle of muscle fibres were made based on photographs taken. The sites of attachments were digitized using MicroScribe-3DL. Bony landmarks on the scapula and humerus were also digitized so that bone length measurements can be calculated. Our original intention was to normalize the points of muscular origins and insertion so that the data can be applied onto our biomechanical model. However, during the dissection, it was discovered that the cadaveric specimen had Grade III tear of the supraspinatus. Apart from that, we also intended to derive our own PCSA values from the cadaveric specimen. However, as the cadaver was atrophied, it would underestimate the muscle mass resulting in an inaccurate PCSA value. Hence, we used PCSA values based on a previous study[12] – Table 1.

Table 1: Physiological cross-sectional area (PCSA) of muscles (Oizumi et al. [12])

Muscle	PCSA (cm2)
Anterior deltoid	4.5
Middle deltoid	13.5
Posterior deltoid	3.9
Supraspinatus	4.5
Infraspinatus	5.8
Subscapularis	9.7
Teres minor	2.6

B. Biomechanical shoulder model

Bone models of scapula and humerus were mounted onto a retort stand. A metal piece was used to represent the clavicle. The scapula was oriented at 30º of protraction and 20º of anterior tilt. The humerus was aligned to the medial border of scapula, defined as 0º of glenohumeral (GH) abduction. Screws were inserted into attachment sites of supraspinatus, infraspinatus, subscapularis, teres minor, and anterior, middle and posterior deltoid tendons on the scapula and humerus. Wires were fastened to tendon insertion screws and attached to the pulley system, representing the line of action of the muscles. Weights were added to represent ratios of the muscle forces based on the PCSA values. Weights were attached to the distal humerus to simulate weight of normal arm. An electronic goniometer was placed along the proximal shaft of the humerus to record the abduction range occurring at the GH joint (Figure 1).



Figure 1 – The biomechanical model. P = pulley system, W_{ms} = weights representing muscle forces, W_{arm} = weight of arm, RS = retort stand, GS = goniometer sensor, GR = goniometer reader.

C. Testing protocol

A manual force was applied to move the humerus through a range of 90˚ of abduction in the coronal plane. This was first done with the supraspinatus intact, simulating a normal shoulder. A total of 6 trails were performed. Next, the weights representing the supraspinatus muscle force were removed, simulating a shoulder with a torn supraspinatus. Again, a manual force was applied to abduct the humerus through the greatest possible range with a total of 6 trails being done. The movement was monitored using video recording. Calculations of changes in the acromiohumeral interval (AHI) between 0 to 30˚ of GH abduction were made as the greatest amount of superior humeral translation occurred in the first 30º when

supraspinatus is deficient[1]. This was done using photographic analysis

III. Results

The biomechanical shoulder model found that when supraspinatus was left intact in the shoulder model and its humerus elevated at 0 degree, the AHI was measured an average of 0.786cm. At 30 degrees of elevation, the crest of the greater tuberosity passes below the acromion at its closest proximity (average, 0.500cm). The results have been tabulated in Table 2.

Table 2: Measurements of Acromiohumeral interval (AHI) when Supraspinatus is intact.

	AHI
At 0 degree	0.786 (SD value)
At 30 degrees	0.500 (SD value)

When supraspinatus was removed from the model, we observed that it was unable to reach 30 degrees. The humerus internally rotated more than that when supraspinatus was intact. This also led to early impingement occurring at 9-12 degrees of humerus elevation.

IV. Discussion

The glenohumeral joint under normal circumstances, maintains a balance between its high degree of mobility and its lack of intrinsic stability. From our biomechanical model of the shoulder, this research seeks to examine what happens when there is a full supraspinatus tear using the acromiohumeral interval as a measurement. We obtained results for the AHI of normal shoulder at 0º and 30 º and that with a simulated full-supraspinatus tear. The AHI was found to be 7.86mm for a normal shoulder. This was within the range of 7-13mm as reported by Golding[5], 6 to 14mm as reported by Cotton & Rideout[4], and 7 to 14mm as reported by Weiner & Macnab [13]. It was stated patients with rotator cuff tears tend to have an AHI of less than 5 mm[13]. This radiological study of the acromio-humeral interval in 60 normal shoulders and 59 shoulders with known tears of rotator cuff concluded that a narrowing of this interval is a frequent concomitant of a tear of the rotator cuff. In 44% (26 out of 59) of the cases, the acromio-humeral intervals were measured to be of 5.00mm or less. It is not known if the study used shoulders with complete or incomplete lesions. No statistical analysis was conducted as well.

Narrowing of the acromio-humeral interval has been defined one of the 5 key radiological diagnosis of rotator cuff tears as proposed by Cotton & Rideout[4]. The other key aspects are as follows: cystic appearances in the bone of the upper two-thirds of the anatomical neck of the humers[5]; recession, cortical irregularity, sclerosis or trabecular atrophy of the greater tuberosity of the humerus[4]; a distinct notch or gap between the articular surface of the head of the humerus and the greater tuberosity[4]; irregular new bone formation on the lateral margin of the acromion. It seems likely that all these changes are explicable on a basis of previous trauma. However, whether this results from a solitary severe incident or many minor episodes is a matter of conjuncture.

One of the observations of our study was that, in the absence of supraspinatus, impingement occurs at 9 to 12 degrees when the shoulder was abducted. This was not found in present literature. We suggest that this novel result could be explained by the loss of synergistic relationship between the middle deltoid and the supraspinatus. The unopposed action of the middle deltoid during the initiation of abduction led to an increased superior humeral translation. From the study we also observe the humerus to be more internally rotated as it moved. This could be a secondary contributing factor to explain the occurrence of early impingement. An imbalanced force couple between the internal and external rotators would lead to an excessive internal rotation of the arm, even in the initial phase of abduction. Langenderfer et al[14] examined muscle-tendon parameters and predicted moment generating capacity for rotator cuff muscles including supraspinatus, teres major and infraspinatus muscles. Supraspinatus was found to have the greatest moment capacity at 10 degrees of arm abduction. Hence, in the present of a supraspinatus tear which was simulated in our study, the humeral head was found to be increasingly internally rotated during arm abduction. This could lead to increase incidence of early impingement occurring at the acromion.

V. Clinical implication and limitations

The results of this study suggest that strengthen the other humeral depressors such as the teres major, latissimus dorsi and long head of biceps can reduce narrowing of the AHI after a supraspinatus tear. Depression of the humeral head was most effectively achieved by the latissimus dorsi and the teres major[15]. After a supraspinatus tear, the upwards pull of the middle deltoid is relatively unopposed and may leads to superior displacement of the humeral head during arm elevation or abduction. Thus, it is proposed that proper strengthening exercises that adopt dynamic theory of muscle synergy will create compressive forces on the glenoid

face that prevent superior displacement of the humeral head. We found the shoulder to be impinged at 9-12 degrees. Thus, there is a need to re-establish a dynamic relationship between the shoulder muscles in the early ranges of gleno-humeral abduction and this study support Haahr et al[16] recommendations for successful rehabilitation of patients with stage II impingement syndrome.

The current exploratory study evaluated the relationship between the glenoid fossa and the humeral head. Other joints involved during shoulder abduction such as the scapulo-thoracic or acromio-clavicular joint were not taken into consideration. In the present study, the scapula was chosen to be fixed in our biomechanical model and passive restraints were not analysed. We also recommend that a pneumatic hydraulic system be used to provide a constant force to the humerus shaft.

VI. Conclusion

Biomechanical evaluation of our research indicates that the supraspinatus is an important dynamic stabilizer of the glenohumeral joint and for maintaining of a normal AHI. When supraspinatus is absent, the performance of abduction will result in early impingement below 30º of abduction.

References

1. Terrier et al (2007). Effect of supraspinatus deficiency on humerus translation and glenohumeral contact force during abduction. Clinical Biomechanics (E publication ahead of print).
2. An KN (2002). Muscle forces and its role in joint dynamic stability. Clinical Orthopaedic and Related Research. 403S: S37-S42
3. Thompson et al (1996) A biomechanical analysis of rotator cuff deficiency in a cadaveric model. Amercian Journal Sports Medicine. May-Jun;24(3):286-92
4. Cotton, R.E. & Rideout, D.F. (1964). Tears of the humeral rotator cuff: A radiological and pathological necropsy survey. J Bone Joint Surg Br, 46B, 314-328.
5. Golding, F. C. (1962). The shoulder - The forgotten joint. British Journal of Radiology, 35, 149.
6. Deutsch et al (1996) Radiologic measurement of superior displacement of the humeral head in the impingement syndrome. Journal of Shoulder Elbow Surgery. May-Jun;5(3):186-93.
7. Nové-Josserand et al (1996). The acromio-humeral interval. A study of the factors influencing its height. Rev Chir Orthop Reparatrice Appar Mot. 82(5):379-85
8. Gatton et al. (1999). Difficulties in estimating muscle forces from muscle cross-sectional area. An example using the psoas major muscle. Spine. 24: 1487-1493.
9. Powell et al. (1984). Predictability of skeletal muscle tension from architectural determinations in guinea pig hindlimbs. Journal of Applied Physiology, 57, 1715-1721.
10. Sacks et al (1982). Architecture of the hind limb muscles of cats: functional significance. Journal of Morphology, 173, 185-195.
11. Mendez et al. (1960), Density and composition of mammalian muscle. Metabolism, 9, 184-188.
12. Oizumi et al (2006). Numerical analysis of cooperative abduction muscle forces in a human shoulder joint. Journal of Shoulder Elbow Surgery, 15, 331-338.
13. Weiner and Macnab (1970). Superior migration of the humeral head. A radiological aid in the diagnosis of tears of the rotator cuff. Journal of Bone Joint Surgery British. Aug;52(3):524-7
14. Langenderfer et al. (2006).Variation in external rotation moment arms among subregions of supraspinatus, infraspinatus, and teres minor muscles. Journal of Orthop Res. Aug;24(8):1737-44
15. Halder et al (2001) Dynamic contributions to superior shoulder stability. Journal of Orthop Res. Mar;19(2):206-12.
16. Haahr et al (2006). Exercises may be as efficient as subacromial decompression in patients with subacromial stage II impingement: 4-8-years' follow-up in a prospective, randomized study. Scand J Rheumatol. May-Jun;35(3):224-8

Can Stretching Exercises Reduce Your Risks of Experiencing Low Back Pain?

Dr. B.S. Rajaratnam[1], C.M. Lam[2], H.H.S. Seah[1], W.S. Chee[1], Y.S.E. Leung[1], Y.J.L. Ong[1], Y.Y. Kok[2]

[1]Nanyang Polytechnic, School of Health Sciences. Singapore. [2] Nanyang Polytechnic, School of Engineering, Singapore.

Abstract — **Background and Aim: Stretching exercises are recommended for treat and prevention of symptoms of low back pain. Its effectiveness to improve postural alignment that contributes to low back pain has not been evaluated during prolonged sitting. The aim of this biomechanical study was to evaluate if performing stretching exercises during prolong sitting improved postural alignment.**

Method: 14 healthy subjects were randomly assigned to a control (C) and experimental (E) groups. Subjects in the (C) sat continuously for 2 hours to watch a movie while subjects in (E) were instructed to perform stretching exercises during the sitting period. Kinematic of changes in spinal posture throughout the sitting period was identified by retro-reflective markers placed on the trunk and pelvis. Subjects also expressed their Body Perceived Discomfort (BPD) they experience at the end of the prolonged sitting period.

Results: Trunk inclination (t=-0.737, P=0.489), thoracic kyphosis (t= 1.685, P =0.143) and lumbar lordosis (t=-0.236, P =0.821) did not change significantly between the first hour and second hours of sitting within (C). There was also no significant differences in kinematics of the various spinal measures among (E) which performed stretching exercises during the prolonged sitting period (trunk inclination: t=-1.560, P=0.170, thoracic kyphosis: t=-0.907, P=0.399 & lumbar lordosis: t=-0.015, P =0.988). However, BPD scores between groups at the neck (P=0.005), upper back (P=0.003), mid and low back (P=0.005) and buttocks (P=0.016) were significantly lower among (E) compared to (C).

Conclusion: This novel biomechanical study recommends the performance of stretching exercises to reduce the discomforts along the spine during periods of prolong sitting. The reduction of discomfort was not due to change in spinal alignment. Hence, ergonomic chairs that maintain static proper alignment are not effective as a treatment or prevention of low back pain.

Keywords — **Back pain, Exercise, Prolong Sitting, Kinematic analysis**

I. Introduction

Low back pain (LBP) is a common cause of discomfort in modern society. 80% of the population will suffer low back pain (LBP) at least once in their lifetime [1-2]. In sedentary workers and students, it has been found that prolonged sitting constitutes a potential risk factor for the development of LBP [3]. It has been found that the two major occupational risk factors of LBP are static muscle load, and flexed curvature of the lumbar spine; both involved in seated work tasks. Compared to standing or lying supine, sitting could cause the pelvis to rotate posteriorly, resulting in decreased sacral inclination and lumbar lordosis, and increased forces at the discs. In addition, there is an interaction between LBP and biomechanical changes such as decreased lumbar lordosis, malalignment of lumbar curvature, and narrowing of disc space [4], which might all occur in sitting. Thus, it is reasoned that maintaining spine postures near neutral alignment, avoiding excessive spine flexion, and minimizing joint loading by adopting an upright posture are important factors in maintaining back health and preventing LBP [5].

In addition, the European legislation's ergonomics guidelines, states that "Under the intended conditions of use, the discomfort, fatigue, and psychological stress faced by a worker must be reduced to the minimum possible." Subjective level of discomfort an important evaluation criterion for static postures and proposed, that an individual's subjective level of discomfort can be used as a predictor for the risks of LBP [6].

The effectiveness of interventions for treating back pain has been extensively studied. In one systematic review, exercise therapy was found to be slightly more effective than no treatment and other conservative treatments in reducing pain and improving function in patients with chronic LBP [7]. Steven et al [8] also noted that exercises are the most effective preventive intervention in the management of recurrent LBP as compared to back classes and lumbar supports.

Most of the previous known researches have been focused on the effects of exercises on managing acute or chronic LBP. Some have further explored the effects of such exercises on prevention of recurrent LBP. However the effectiveness of exercises on prevention of LBP in subjects with no history of LBP is unknown.

The Health Promotion Board (HPB) of Singapore [9] has designed a set of stretching exercises for individuals who are involved in prolonged sitting at work or in school. It is proposed that if these exercises are perform during a prolonged sitting interval, they might help individuals maintain a neutral spine posture and decrease static muscle load, thus reducing the risks of experiencing LBP. Thus, the aim of this study is to find out if performing stretching exercises in between prolong sitting improve spine postural alignment and reduce the subjective level of discomfort of the back.

Chwee Teck Lim, James C.H. Goh (Eds.): ICBME 2008, Proceedings 23, pp. 2114–2117, 2009
www.springerlink.com

The null hypothesis is stretching exercises performed in between prolong sitting has no effect on spine postural alignment and subjective level of discomfort of the back.

II. Method

A. Protocol

Subjects sat for 2 hours continuously to watch a movie. 1 minute of kinematic data were collected at the end of every 5 minutes interval. Subjects fill up a body perceived discomfort (BPD) scale at the end of the protocol.

The subjects in the experimental group had a 10 minute stretching exercise interval by following 6 exercises recommended by HPB between the 55^{th}-65^{th} minute. Reach radius was limited within a 25cm radius boundary, and subjects kept their feet flat on the ground (Figure 1).



Fig. 1. Subject seated, with feet kept firmly on the ground and upper limbs kept within a boundary marked out on the table.

B. Instrumentation

i. Equipment

A motion analyser **(**Qualysis system) collected three dimensional coordinates of retro-reflective markers. 3 cameras quipped with infrared light emitting diodes captured retro-reflective markers placed on subjects. Subjects sat on a wooden stool with a desk in front of them.

ii. Marker location

The spinal model was similar to Frigo et al. [18] and Pauline W. et al. [19] studies. The landmarks were the seventh spinous vertebral process (M1), the apex of kyphosis (M3), the apex of lordosis (M6), lower edge of the sacrum (M8), middle between M1 and M3 (M2); markers M4 and M5 were equally spaced in between M3 and M6, mid position of the two posterior superior iliac spines (M7). (Fig. 2).

The shoulder girdle was identified by putting markers on the left and right acromions (Al and Ar).

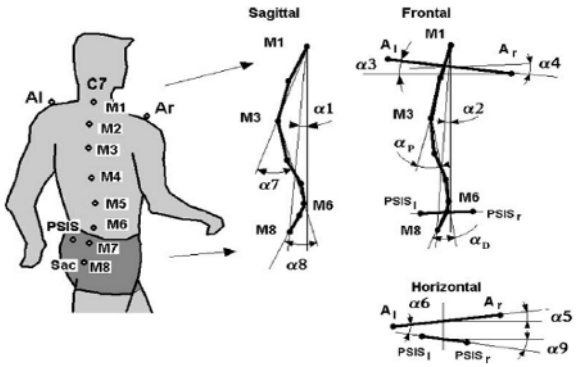


Fig. 2. Model of markers location and definition of meaningful segmental angles: α2- frontal trunk inclination; α7- angle of kyphosis; α8- angle of lordosis. from Frigo C. et al. (2003).

iii. Modeling and data processing

The absolute planes of motion were defined with reference to the laboratory axes: frontal plane- perpendicular to the line of progression (x-axis); horizontal plane (y-axis); sagittal plane- perpendicular to the intersect of the frontal and horizontal planes (z-axis). The following were considered to be of relevance for our study:

- Sagittal and frontal trunk inclination (α1 and α2 in Fig. 2). Angles between the M1-M8 line and the vertical line in the sagittal and frontal plane projections;
- Angle of kyphosis. Two spine segments were defined by markers M1-M3 and M3-M6 and were projected on the local sagittal plane the angle between them (α7) was computed and depicted in Fig. 2.
- Angle of lordosis. This was defined as the angle between the two spine segments M3-M6 and M6-M8 projected on the local sagittal plane (α8 in Fig. 2)

iv. Subjective level of discomfort

The Body Perceived Discomfort (BPD) scale (0-10) determined subjects' level of discomfort after the 2 hour of prolonged sitting. 0 being no discomfort and 10 being extreme discomfort) discomfort.

C. Subjects

14 subjects (7 males, 7 females) with the following characteristics (mean, range): age 20.6 years (18-24); weight 55kg

(42-64); height 1.66m (1.59-1.80) with no previous past medical history of low back pain were recruited. Informed consent was obtained from all subjects. The protocol was approval by Nanyang Polytechnic, School of Health Sciences Projects Committee.

D. Statistics

Statistical Package for the Social Sciences (SPSS) for Windows (version 14.0) was used to study the effects of a 10 minute exercise intervention during a 2 hour prolong sitting period on postural alignment (i.e., lumbar lordosis, thoracic kyphosis and trunk inclination) and the exercises on a person's subjective feeling of discomfort. The Independent-Samples T-test determined if the changes in postural alignment prior to the exercise intervention (0-55th minute) between both groups were significant. Paired-Samples T-test compared the amount of changes in postural alignment, prior to (0-55th minute) and after (65-120th minute) the intervention, within each group (i.e., control and experimental). The level of statistical significance was set at 5% throughout the experiment.

III. Results

A. Kinematic Analysis

The initial (before the intervention; 0-55th min) average change in range of motion for trunk inclination, angle of kyphosis and angle of lordosis, between the control and experimental groups, were compared using the Independent-Samples T Test. Levene's test for equality of variances for all 3 angles were significant (P>0.05) and thus equal variances were not assumed. The results showed no significant differences between the two groups in terms of trunk inclination (P=0.408), kyphosis (P=0.276) and lordosis (P=0.254) prior to the intervention.

The Paired-Samples T Test found that within the control group, there were no significant changes in the average change of trunk inclination (P=0.489), kyphosis (P=0.143) and lordosis (P=0.821) angles throughout the entire 2-hour prolong sitting period. Within the experimental group, there were also no significant changes in the average change of trunk inclination (P=0.170), kyphosis (P=0.399) and lordosis (P=0.988) angles before and after the intervention; throughout the entire 2-hour prolong sitting period.

B. BPD

Average ratings of BPD scores of the neck, upper back, mid and low back, and the buttocks found that subjects in the intervention group reported significantly less neck (P=0.005), upper back (P=0.003), mid and low back (P=0.005) and buttocks (P=0.016) discomfort compared to subjects in the control group.

IV. Discussion

Helander & Quance [10] studied the effects of a rest interval during prolong sitting, and found that 2, 20-minutes rest interval during a 4 hour prolong sitting period was the most effective in maintaining proper spine alignment. Stretching could provide rest and relief for the passive and active structures of the low back [5,11]. This is the first study that evaluated the effects of stretching exercises on spine postural alignment during prolonged sitting.

The experimental group had significantly lower BPD scale scores of the neck, upper back, mid and low back and buttocks, compared to the control group at the end of the 2 hour prolong sitting period. Operators exhibited increased body discomfort after prolong sitting session without movement or stretches [12] and an increase risk of injury [13]. This study found that stretching exercises performed between prolong sitting reduced discomfort, and possibly decreased the risk of injury.

However, the kinematic analysis results showed that stretching exercise during the 2 hour prolong sitting period resulted in no significant differences in spinal posture. May be 2 hours of prolong sitting period was not affect postural alignment as other studies defined prolong sitting as periods of 3-4 hours [11,14-16]. Another confounding factor of the present study was different in postural alignment of men and women. Female participants sat with more anterior rotation of the pelvis, less lumbar flexion and very little trunk flexion when compared to the males [5].

The present study results show that the average change of spinal postural alignment for the subjects in the experimental group displayed a greater spread of results compared to the subjects in the control group. Some may have improved postural alignment after stretching, while others did not. Many factors may be relevant for the occurrence of LBP [17] and stretching exercises might be very important for an individual who has a given risk factor such as decreased spine flexibility, but not so for another individual with decreased strength or poor posture.

The limitations of our study include 1) the possible influence of environmental and psychosocial factors (e.g. being in a new environment, the temperature of the room, their present stress level) on the subjects' BPD scale scores, 2) the inability to allow our subjects' to lean against a back rest, like how they might do in school or work, 3) the inability to control every single movement of the subjects (e.g.

coughing, sneezing, scratching), and lastly 4) experimenters' biasness. Every effort, however, was made to limit the errors that might have arisen from the above circumstances.

V. Conclusion

Stretching exercise performed in between prolong sitting period did not seem to have an effect on one's postural alignment. However, stretches were effective in reducing one's subjective level of discomfort and thus can be recommended during prolonged sitting. Based on the great variability of responses from the subjects in the experimental group to the stretching exercises, a multidimensional approach may be more effective in reducing the risk of LBP. Further research is recommended to better understand the effects of rehabilitation intervention to minimize the risk of LBP.

References

1. Andersson GB (1999): Epidemiological features of chronic low back pain. Lancet; 354: 581–585.
2. Mendez FJ, Gomez-Conesa (2001): Postural hygiene program to prevent low back pain. Spine; 26: 1280-1286.
3. Cardon G, DeClercq D, Bourdeaudhuij ID. (2000): Effects of back care education in elementary schoolchildren. Acta Paediatr.; 89: 1010–1017.
4. Mohsehsen M, Fang L, Ronald WH, Matthew H, Li-Qun Z (2003): Sitting with Adjustable Ischial and Back Supports: Biomechanical Changes. Spine; 28(11): 1111-1122.
5. Dunk NM, Lalonde J, Callaghan JP. (2005): Implications for the use of postural analysis as a clinical diagnostic tool: reliability of quantifying upri*ght* standing spinal postures from photographic images. J Manipulative Physiol Ther.; **28**: 386–392.
6. Dul J, Douwes M, Smitt P (1994): Ergonomics guidelines for the prevention of discomfort of static postures based on endurance data. Ergonomics; 37 (5): 807-815.
7. Hayden JA, van Tulder MW, Malmivaara A, Koes BW (2005): Exercise therapy for treatment of non-specifc low back pain. Cochrane Database of Systematic Reviews; 3.
8. Steven J. Linton, PhD and Maurits W. van Tulder (2001): Preventive Interventions for Back and Neck Pain Problems. What is the Evidence? Spine; 26 (7): 778–787.
9. Health Promotion Board, Singapore (2007): Health Videos and Programs: Let's Stretch Program. Available from the Health Promotion Board, Singapore website, http://www.hpb.gov.sg/hpb/default.asp?pg_id=1289.
10. Helander MG, Quance LA (1990): Effect of work-rest schedules on spinal shrinkage in the sedentary worker. Applied Ergonomics; 21 (4): 279-284.
11. Callaghan, J.P., McGill, S.M. (2001): Low back joint loading and kinematics during standing and unsupported sitting. Ergonomics; 44: 280-294.
12. Waldemar Karwowski, Ray Eberts, Gavriel Salvendy, Soraya Noland (1994): The effects of computer interface design on human postural dynamics'. Ergonomics; 37(4): 703 – 724.
13. Corlett EN and Bishop RP (1976): A technique for assessing postural discomfort. Ergonomics; 19 (2): 175-182.
14. Leivseth, G. and Drerup, B. (1997): Spinal shrinkage during work in a sitting posture compared to work in a standing posture. Clinical Biomechanics; 2 (7/8): 9-418.
15. Beach TA, Parkinson RJ, Stothart JP, Callaghan JP (2005): Effects of prolonged sitting on the passive flexion stiffness of the in vivo lumbar spine. Spine J. Mar-Apr; 5(2): 145-54.
16. J.H van Dieen, M.P. De Looze and V. Hermans (2001): Effects of dynamic office chairs on trunk kinematics, trunk extensor EMG and spinal shrinkage. Ergonomics; 44(7): 739-750.
17. Van Tulder MW, Ostelo R, Vlaeyen JW, Linton SJ, Morley SJ, Assendelft WJ. (2001): Behavioral treatment for chronic low back pain: a systematic review within the framework of the Cochrane Back Review Group. Spine; 26: 270-81.
18. Frigo C., Carabalona R., Dalla Mura M., Negrini S. (2003): The upper body segmental movements during walking by young females. Clinical Biomechanics; 18: 419–425.
19. Pauline W, Lucy ED, Brian C, Barry S (2006). Marker-Based Monitoring of Seated Spinal Posture Using a Calibrated Single-Variable Threshold Model. Engineering in Biology and Medicine Society: 5370-5373.

Streaming Potential of Bovine Spinal Cord under Visco-elastic Deformation

K. Fujisaki, S. Tadano, M. Todoh, M. Katoh, R. Satoh

Division of Human Mechanical Systems and Design, Graduate School of Engineering, Hokkaido University, Japan

Abstract — **Spinal cord is mainly composed of white matter and gray matter. These tissues have solid phase and liquid phase. When they deform, liquid phase in the tissue flows out through between solid phases. The interaction and frictional resistance between two phases perform the macroscopic visco-elastic behavior. In addition, solid phase in soft tissue contains a lot of negatively-charged proteoglycan. This electro chemical behavior affects visco-elastic properties of the tissue. Triphasic theory was proposed to describe the mechanical properties of the tissue of arthrodial cartilages considering with solid, liquid phase and negative ion phase. In this study, the electro-kinetic behavior of white matter and gray matter were investigated under several compressive loading. Column-shaped specimens in diameter of 5mm and height of 5mm were made from both matters in a bovine cervical spinal code. Each specimen was set in physiological saline. The streaming potential was measured under compression loading, stress relaxation and cyclic loading. As a result, the streaming potentials showed linear relation to tissue stress in compression and relaxation progress. Although the streaming potential changed according to applied stress in cyclic loading, the potential amplitude was gradually decreased with increasing of the loading cycles.**

Keywords — **Biomechanics, Spinal cord, Streaming potential, Uniaxial loading.**

I. Introduction

Spinal cord is a part of central nerves constructed from numerous cells, nerve fibers and biological films. An important physiological function of the spinal cord is signal transductions of organic activities. This tissue is protected by bone structures; vertebral bodies, vertebral discs and vertebral canals including posterior structures of column, to perform the function properly. Spine injury is occurred caused by vertebral bone fracture or bruising damage in the case of accidents on the road or at sports. The spinal cord has high fault incidence to applying loads. Thus understanding of applied stress in various situations is important to prevent the injury. Although many kinds of stress/strain analyses were conducted for spine structure, mechanical properties of spinal cord were not really investigated. To explain the mechanical properties of biological soft tissue, some physics models have been proposed in analytical studies, the properties are described by approximately elasticity, visco-elasticity [1, 2] and biphasic model considering the interaction of solid and liquid phases [3-5]. When they deform, liquid phase in the tissue flows out through between solid phases. The interaction and frictional resistance between two phases perform the macroscopic visco-elastic behavior. In addition, solid phase in soft tissue contains a lot of negatively-charged proteoglycan. Strain of the tissue changes charge density on the proteoglycan and disrupts the balance of electrochemical equilibrium. This electric charge affects visco-elastic deformation of the tissue. Triphasic theory was proposed to describe the mechanical properties of arthrodial cartilages [6-10] considering with solid, liquid phase and negative ion phase. When the electric potential is detected in deformed tissue, its value changes concerned with the liquid flow. This relatively electric potential change is called streaming potential. The streaming potential has been measured in arthrodial cartilages [11-14] and interspinal disc [15]. The interaction containing the negative ion, according to the triphasic theory should be used in analysis for mechanical characteristics of spinal cord. In this study, the electro-kinetic behavior of white matter and gray matter were investigated under several compressive loading.

II. Streaming potential detecting system

Since the diffusion resistance of liquid phase in spinal cord affects deformation of the tissue, mechanical properties of the tissue are nonlinearly changed by applying force. The uni-axial loading tests of spinal cord were conducted with uni-axial inner liquid flow condition. Figure 1 shows the measurement system constructed in a commercially material testing machine (Instron 4411, Instron Co., with 50N load cell) setup for using mainly compressive test with an indenter. A specimen is placed in an acrylic ring. The ring is put on a porous plastic plate. The ring restrains circumference of the specimen from deforming. The porous filter prevents to flow out of the solid phase and does not obstruct to flow in or out of the liquid phase. These structures are set at inside a clear acrylic bath filled with physiological saline. An electrode of Ag/AgCl is bonded at the tip of the indenter via an insulating part. This type of electrode is useful for testing in physiological condition because this material is not melted in solution containing chlorine ions, thus the biological specimen does not give damages during measurements. Another electrode is located

Chwee Teck Lim, James C.H. Goh (Eds.): ICBME 2008, Proceedings 23, pp. 2118–2121, 2009
www.springerlink.com

in the bath kept away from the specimen as a reference electrode. The electric potential detected by electrodes is through an amplifying device (CDV-700A, Kowa electric instruments), and recorded in PC by using a sensor interface (PCD-300A, Kowa electric instruments) concurrently with applying load.

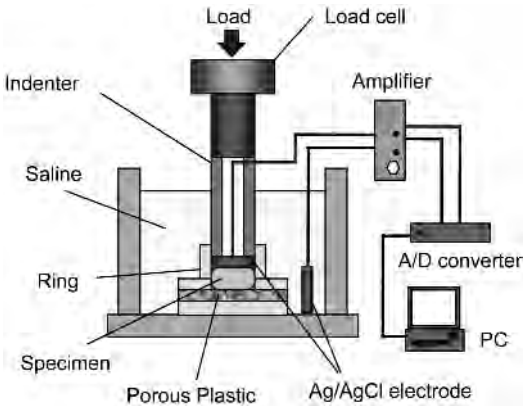


Fig. 1 A model of electric potential measurement system

III. Experimental procedure

A. Specimen

Inner structure of spinal cord can be identified by observation of cross sectional surfaces as two phases classified into gray matter; with H-shaped locating near the center of the section, and white matter; surrounding for the gray matter, and spinal meninges encircling these matters. A part of spine including spinal cord was cut out from a Holstein cow, female, 24 month old, which is recently death. The spinal cord was extracted from the spine before freezing. Column-shaped specimens in diameter of 5mm and height of 5mm are made from the area in gray matter and white matter, respectively, in the spinal code under refrigerated state. Compressive direction of each specimen was aligned with spinal axis. These specimens were cryogenically-preserved in freezer of -35 ˚C until just before experiments.

B. Preparation for experiment

A frozen specimen was thawed at the setting position in the testing device dropped in physiological saline at a condition of room temperature of 22 ˚C. Height of the specimen changes drastically by selling phenomena. To prevent the resistance force occurring caused by swelling in loading tests, the specimen was given satisfied time for 30 min before beginning the tests. Since the swelled volume varies from one specimen to another, an initial position to start loading cannot be provided constant. The initial condition about height of the specimen was determined as a specific position with resistant force to be 0.05 N; measured by load cell, in a situation of compression force applied through the indenter.

C. Experimental condition

Three kinds of investigations; compression with compression rate of 5, 10, 20, 30, 60 %/min, cyclic loading of 0.1, 0.05, 0.01 Hz in compression side, and stress relaxation, were conducted under wet condition of physiological saline at the room temperature of 22 ± 1˚C. The electric potential between the electrodes amplified 1000-fold was detected by sensor interface with the sampling frequency of 10 Hz, and recorded them together with applying load obtained from the load cell attached at the indenter.

IV. Result

A. Compression test

Electric potential was measured to be negatively charge according to increasing the value of applied compressive strain. Figure 2 shows a relationship between electric potential and compressive stress obtained at a white matter specimen. This electric potential change was less than 0.1 mV measured under compression condition of the maximum strain of tissue up to 30 %. The relationship between electric potential and stress was almost linear with high correlation coefficient (R^2 = 0.9911). Proportionality constant (electrokinetics factor: *ke*) was measured on each specimen of gray matter and white matter under different compression rate, as shown in Fig. 3. Although these values

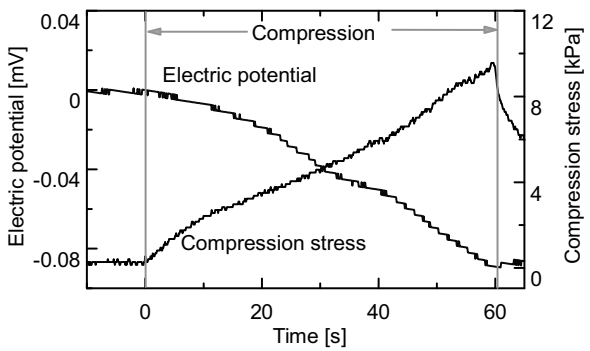


Fig. 2 Compressive stress and electric potential measured under compression process

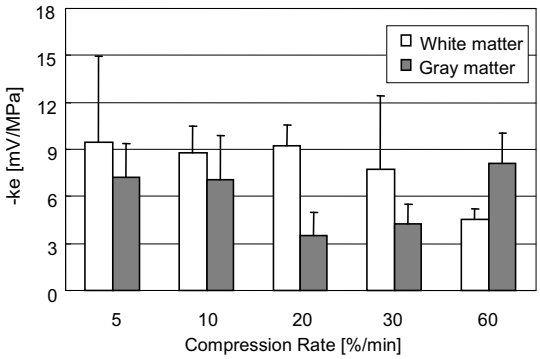


Fig. 3 Relationship between electrokinetic coefficient *ke* (mean ± S.D. (n=4)) and compression rate

were obtained as scattering results even in same type of specimen, the difference of each matter was clearly shown in the results. The *ke* was higher value on white matter than on gray matter except the result measured at 60 %/min straining. The minimum value on gray matter was obtained at 20 %/min, the value on white matter began to decrease in higher compression rate more than 30 %/min.

B. Cyclic loading test

Figure 4 shows a short part of a time chart in a cyclic loading test of a white matter with ±5 % strain. The electric potential changed according to the loading. The response of electric charge showed almost no time delay and measured pattern had negatively peaks at maximum compressive position in the loading. However the electric potential had instability change in periods for the indenter moving from compressive positions to unloading initial positions. Figure 5 shows the amplitude change of a white matter under each condition. The amplitude was slightly decreasing with cyclic number increasing.

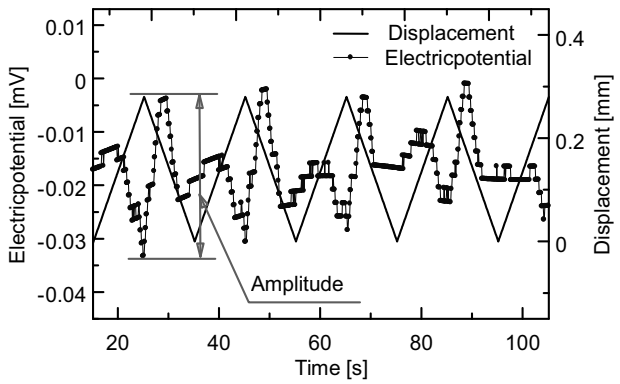


Fig. 4 Electric potential change during cyclic loading at white matter with ±5 % strain

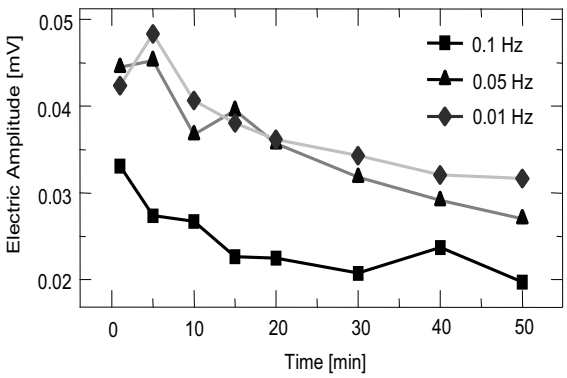


Fig. 5 Changes of electric potential amplitude of white matter under cyclic loading

C. Stress relaxation

A result of electric potential change measured in relaxation period was shown in Fig. 6. Precondition was 30 % straining with compression rate of 30 %/min on a white matter. The electrokinetics factor *ke* was obtained from linear relationship of the electric potential and stress measured in the relaxation for each specimen of gray matter and white matter. The mean value of *ke* on each specimen was 16.0 [mV/MPa] for white matter and 12.4 [mV/MPa] for gray matter. These values were higher than the values obtained under compression process.

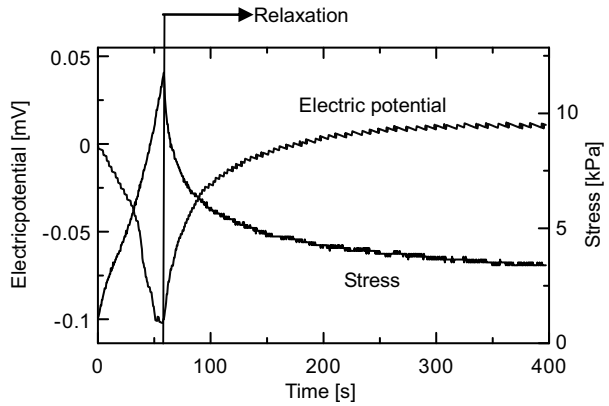


Fig. 6 Compressive stress and electric potential measured under elaxation process

V. Discussion

In this experiment, streaming potential could be detected as electric charge on a specimen under compressive loading in physiological saline. The streaming potential changes on two kinds of specimens made from gray matter or white

matter were measured with different values depending on compressive speed (Fig. 3). The values of the electric potential were less than 0.1 mV. These values were seemed like lower than the streaming potential measured at other tissue; reported in arthrodial cartilage [15]. This result might be provided by difference of volume fraction of proteoglycan in the spinal code.

Reduction of amplitude of electric charge occurred in cyclic loading. The result indicated that the solid structure containing proteoglycan destructed by cyclic loading because the reduction depended on number of cycles. The nerve fibers existing in white matter includes a lot of myelin which acts insulating material in signal transfer in nerves. The myelin attached on the indenter might disturb detection of the electric potential in white matter. On the other hand, the white matter has temperature-dependent properties. It might be affected by heat generation in friction of inner liquid flowing under cyclic loading. In this study, thermal condition was not controlled and the value was same as room temperature.

The linear relationship between the stress and electric potential generating there was obtained not only compression processes but also stress relaxation processes. The applied stress was to be almost free after about 200 s passed from a compressed state. This phenomenon was same tendency as shown in an analytical study of stress relaxation under compression of arthrodial cartilage based on tripahic theory [8]. The streaming potential should be considered connecting to visco-elastic properties. And both gray matter and white matter should be considered in triphasic study as same as arthrodial cartilages.

VI. Conclusion

Streaming potential measurements were conducted under uni-axial loading conditions. The streaming potential was measured under compression loading, stress relaxation and cyclic loading. As a result, these values showed linear relation to tissue stress in compression and relaxation process. Although the streaming potential changed according to applied stress in cyclic loading, the potential amplitude was gradually decreased with increasing of the loading cycles.

Reference

1. Bilston L.E., Thibault L.E. (1996) The mechanical properties of the human cervical spinal cord in vitro, Annals of Biomedical Engineering 24: 67–74.
2. Ichihara K., Taguchi T., Sakuramoto I., Kawano S., Kawai S. (2003) Mechanism of the spinal cord injury and the cervical spondylotic myelopathy: new approach based on the mechanical features of the spinal cord white and gray matter, J. Neurosurg, Spine 99: 287-285 .
3. Ateshian G. A., Warden W. H., Kim J. J., et al.. (1997) Finite Deforma tion Biphasic Material Properties of Bovine Articular Cartilage from Confined Compression Experiments, J. Biomechanics 30: 1157-1164.
4. LeRoux M. A., Setton L.A. (2002) Experimental and biphasic FEM determinations of the material properties and hydraulic permeability of the meniscus in tension, ASME J. Biomech. Eng 124: 315–321.
5. Perie D., Korda D, Iatridis J. C. (2004) Confined compression experiments on bovine nucleus pulposus and annulus fibrosus: sensitivity of the experiment in the determination of compressive modulus and hydraulic permeability, J. Biomechanics 38: 2164-2171.
6. Lai W. M., Hou J. S., Mow V. C. (1991) A triphasic theory for the swelling and deformation behaviors of articular cartilage, Journal of Biomechanical Engineering 113: 245–258.
7. Gu W. Y., Lai W. M., Mow V. C. (1993) Transport of Fluid and Ions through a Porous-Permeable Charged-Hydrated Tissue,And Streaming Potential Date on Normal Bovine Articular Cartilage, J. Biomechanics 26: 709-723.
8. Lai W. M., Mow V. C., Sun D. D., Ateshian G. A. (2000) On the Electric Potentials Inside a Charged Soft Hydrated Biological Tissue: Streaming Potential Versus Diffusion Potential, J. Biomechanical Rngineering 122: 336-346.
9. Ateshian G. A., Chahine N. O., Basalo I. M., Hung C. T. (2004) The correspondence between equilibrium biphasic and triphasic material properties in mixture models of articular cartilage, J. Biomechanics 37: 391-400.
10. Sun D. D., Guo X. E., Likhitpanichkul M., et al.. (2004) The Influence of the Fixed Negative Charges on Mechanical and Electrical Behavior of Articular Cartilage under Unconfined Compression, J. Biomechanical Engineering 126: 6-15.
11. Frank E.H., Grodzinsky A.J., Koob T.J., Eyre D.R. (1987) Streaming potentials: a sensitive index of enzymatic degradation in articular cartilage. Journal of Orthopaedic Research 5: 497–508.
12. Frank E. H., Grodzinsky A. J. (1987) Cartilage Electromechanics-I.Electrokinetic Transduction and the Effects of Electrolyte pH and Ionic Strength, J. Biomechanics 20: 615-627.
13. Chen A. C., Nguyen T. T., Sah R. L. (1997) Streaming Potntials during the Confined Compression Creep Test of Normal and Proteoglycan-Depleted Cartilage, Annals of Biomedical Engineering, Biomedical Engineering Society 25: 269–277.
14. Garon M., Legare A., Guardo R., Savard P., Buschmann M. d. (2001) Streaming potentials maps are spatially resolved indicators of amplitude, freaquency and ionic strength dependent responses of articular cartilage to load, J. Biomechanics 35: 207-216.
15. Gu W. Y., Mao X. G., Rawlins B. A., et al. (1999) Streaming potential of human lumbar anulus fibrosus is anisotropic and affected by disc degeneration, J. Biomechanics 32: 1177-1182.

Author: Kazuhiro Fujisaki
Institute: Hokkaido University
Street: N-13, W-8, Kita-ku
City: Sapporo
Country: Japan
Email: fujiwax@eng.hokudai.ac.jp

Probing the Elasticity of Breast Cancer Cells Using AFM

Q.S. Li[1], G.Y.H. Lee[2], C.N. Ong[3,4] and C.T. Lim[1,2,4,5]

[1]Department of Mechanical Engineering, National University of Singapore, Singapore
[2]Singapore–MIT Alliance, Singapore
[3]Department of Community, Occupational and Family Medicine, Yong Loo Lin School of Medicine, National University of Singapore, Singapore
[4]NUS Life Sciences Institute, National University of Singapore, Singapore
[5]Division of Bioengineering, National University of Singapore, Singapore

Abstract — **Malignant transformation is correlated with changes in cellular and nuclear structures and mechanical property of cancer cells. Here, atomic force microscopy (AFM) indentation using a spherical probe was carried out to characterize the elasticity of benign and cancerous human breast epithelial cells at both room temperature and physiological temperature. Our results show that malignant (MCF-7) breast cells have an apparent elastic modulus half of their non-malignant (MCF-10A) counterparts at ambient temperature. Also as temperature increases from 24 ºC to 37 ºC, apparent elastic modulus of both benign and cancerous cells decreases, especially for MCF-10A. Our study demonstrates that as a result of the malignant transformation, the breast cancer cells become softer. This change may aid in facilitating easy migration and invasion during metastasis. Also, temperature, which may cause the change in cytoskeletal dynamics and structural remodeling, affects cell elasticity and must be taken into account when probing the mechanical property of cells.**

Keywords — **AFM, breast cancer, cell mechanics, indentation, temperature effect.**

I. Introduction

Cancer has long been one of the leading causes of death in the world and is presently responsible for about 25% of all deaths [1]. In particular, breast cancer is the most common form of cancer afflicting females, as one in very eight woman develops breast cancer at some stage of their lives, and it causes about 15% of cancer deaths in women [1].

Mechanical properties of individual living cells are closely related to the health and function of the human body. Any deviations in the mechanical properties of living cells may affect their physiological functions and consequently give rise to diseases state [2,3]. It is known that some diseases, like cancer, can induce mechanical property changes in living cells, and the mechanical property may potentially serve as a useful biomarker in the early detection of cancer [2]. Moreover, investigating the mechanical property of cancer cells may help to better understand the physical mechanisms responsible for cancer metastasis and predict the potency of cancer metastasis. This can potentially lead to the development of novel strategies for cancer prevention and diagnosis.

With the recent advances in biomechanics and nanotechnology, it has now become possible to probe mechanical influences acting on biological structures not only as small as cells but also biomolecules. For example, biophysical tools and techniques such as atomic force microscopy [4,5], micropipette aspiration [6,7], and the optical stretcher [8,9] have been used to probe the mechanical property of different types of cells (see [2,3,10] for reviews). Also, mechanical models have been developed to study the mechanical properties of these cells [11]. *In vitro* study by different techniques showed that some cancerous cells are softer than their normal counterparts [4,8,9,12,13] (see [13] for reviews). In addition, AFM has been applied to investigate the mechanical properties of *ex vivo* cancer cells obtained from patients [14]. Lincoln *et al*. were the first to investigate the deformability of non-malignant and malignant human breast epithelial cells using the optical stretcher and they found that malignant cells can stretch five times more than their non-malignant counterparts [8,9]. In another study, Lekka *et al*. used the atomic force microscope (AFM) to study the elasticity of normal human bladder epithelial cells (Hu609 and HCV29) and cancerous ones (Hu456, T24 and BC3726) by AFM indention of these cells [4]. They found that normal cells are an order of magnitude stiffer than normal cells, which was attributed to the reorganization of the cytoskeleton. However, it is worth noting that their experiments were carried out at room temperature and they did not consider the effects of using different loading rates during indentation.

The objective of this study is to characterize the elasticity of non-malignant (MCF-10A) and malignant (MCF-7) human breast epithelial cells using AFM indentation with a spherical probe at different temperature. We will quantify and compare the apparent elastic modulus of these two cell lines. In addition, the effects of temperature and using different loading rates during indentation will be discussed.

Chwee Teck Lim, James C.H. Goh (Eds.): ICBME 2008, Proceedings 23, pp. 2122–2125, 2009
www.springerlink.com

II. Materials and Methods

Benign human breast epithelial cells (MCF-10A) and malignant human breast epithelial cells (MCF-7) were used in this study. For the purpose of routine culture, MCF-7 and MCF-10A cells were maintained at 37 °C in a 5% CO_2 incubator (Sanyo, Japan). MCF-7 was cultured in Dulbecco/Vogt modified Eagle's minimal essential medium (Sigma-Aldrich, USA), which was supplemented with 10% fetal bovine serum (HyClone, USA) and 1% penicillin (Gibco, USA), while MCF-10A was cultured in mammalian epithelium basal medium (Cambrex, USA). Cells grown to 80% confluence and up to 20 passages were subcultured using 1×trypsin (Invitrogen, Canada).

For the indentation studies, cells harvested from the subculture were seeded on sterilized 12 mm coverslips (Heinz glass, Germany) and kept in a 6 well microplate (IWAKI, Japan) which would stay in the incubator for 2–3 days prior to indentation. The medium was changed one day after seeding to clear any dead cells on the coverslip.

A Nanoscope IV multimode AFM with a picoforce scanner (Digital Instruments Inc., USA) was used to carry out the experiments. A modified silicon nitride AFM cantilever (NovaScan, USA) having a spring constant of 0.01 N/m with a 4.5 μm diameter polystyrene bead tip was used to indent the cells. During the experiment, the glass coverslip grown with cells was mounted on the AFM stage and the cells were kept in their culture medium using a standard fluid cell (Digital Instruments Inc., USA). In order to study temperature effects, a heater (Digital Instruments Inc., USA) was used to control the temperature of the sample during indentation.

Indentation was carried out at the cell centre using different loading rates from 0.03 to 1 Hz. The ramp size used in this study was 3 μm [15] and an indentation force of 0.2 nN was applied for the tests in order to minimize any substrate contributions and to exert a small deformation on the cell. The apparent elastic modulus was subsequently determined using the Hertz model, since this model is able to account for the geometry of the spherical probe used in this present study and it has been used extensively in other AFM studies to evaluate the apparent elastic modulus of cells [16]. Here, the Hertz model is used to study the small deformation behavior of a cell being indented by a hard axisymmetric indenter [17].

Fig.1 depicts schematically the indentation carried out on the centre of a cell using a 4.5 μm diameter bead attached to an AFM cantilever. The relationship between the indentation depth and the deflection of the cantilever is also illustrated. Once the contact point (refer to [18] for details on determination of contact point) has been identified, the deflection–z position curve (see Fig. 2) is converted to a plot of cantilever deflection against indentation depth (Fig. 3), which can then be used to derive the apparent elastic modulus using the Hertz's model. In this model, the apparent elastic modulus, E, can be obtained using the following formula [15]:

$$H \cdot k = \frac{4}{3}\frac{E}{1-\nu^2}\sqrt{RD^3} \quad (1)$$

where E is the apparent elastic modulus to be determined, ν is the Poisson's ratio, R is the radius of the spherical bead, D is the indentation depth (see Fig. 1), H is the cantilever deflection and k is the spring constant of the cantilever. The cell was assumed incompressible and a Poisson's ratio of 0.5 was used [15].

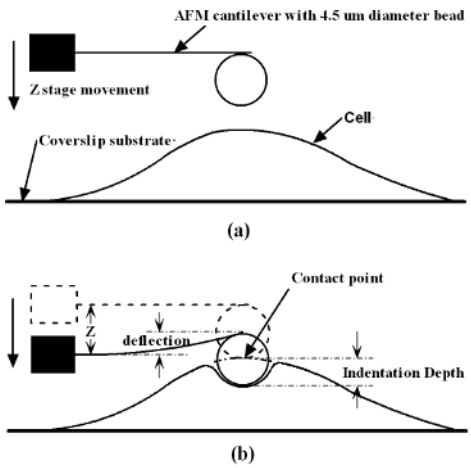


Fig. 1: (a) Schematic of the experimental setup for the indentation of a cell using a 4.5 μm diameter spherical probe. (b) An illustration of the relationship between the indentation depth, z-stage movement and the vertical deflection of the cantilever. The indentation depth is given by the difference between the movement of the z-stage and the vertical deflection of the cantilever. The deflected cantilever is drawn as a solid line while the undeflected cantilever is drawn dashed.

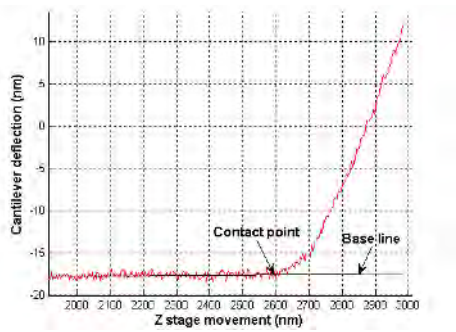


Fig. 2: A typical deflection–z position curve obtained from an AFM indention on a MCF-7 cell.

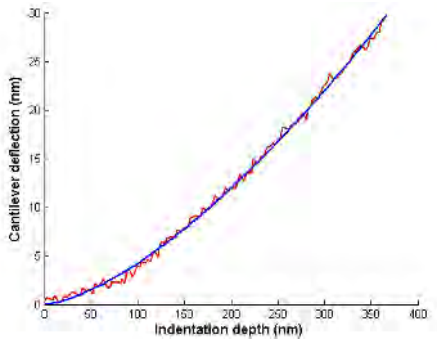


Fig. 3: A typical cantilever deflection–indentation depth curve obtained from the above indentation curve (Fig. 2) fitted by the Hertz's contact model.

III. Results and Discussion

This section presents the results obtained from the indentation tests carried out on two human breast cell lines MCF-10A and MCF-7, using different loading rates and temperature. The effects of temperature and different loading rates on the characterization of elasticity of these cells were subsequently discussed.

A. Effects of loading rates

The dependence between the apparent elastic modulus and the loading rates used in this present study for both MCF-10A and MCF-7 at the physiological temperature of 37 ºC are shown in Fig. 4. It is evident that higher values of the apparent elastic modulus are associated with increased loading rate. The cell is stiffer when probed using a higher loading rate due to their viscoelastic behaviour [19,20]. There is an increase in the apparent elastic modulus with a corresponding increase in the loading rate for both MCF-7 and MCF-10A. Previous indentation works (see [4,5,21]) carried out on other types of cancerous cells and fibroblasts did not take into account this dependence of the apparent elastic modulus on the loading rate. Our study shows that loading rate needs to be considered when performing mechanical test using AFM. At the physiological temperature of 37 ºC, the apparent elastic modulus of MCF-10A is about 1.5 times higher than that of MCF-7 at the same value of the loading rate.

Since the measured apparent elastic modulus varies according to the loading rate, the loading rate was fixed at 0.1 Hz for the subsequent study to evaluate the effect of temperature on the elastic modulus of MCF-10A and MCF-7. A loading rate of 0.1 Hz was chosen as the deflection–position curves obtained at this value of the loading rate exhibits characteristics associated with typical deflection–position curves obtained during the indentation process. Moreover, the contact point on the deflection–position curve was found to be extremely well-defined with a loading rate of 0.1 Hz. In addition, using a low loading rate, such as 0.1 Hz to study the apparent elasticity of cells is able to account for the static deformation behavior, which is biologically significant as cancer cells migrate through surrounding tissue matrix or get plugged in a capillary during metastasis [22].

B. Effects of temperature

Fig. 5 shows the stiffness of cells, determined using indentation, at both room temperature and 37°C. It can be observed that the apparent elastic modulus is smaller at a higher temperature. For MCF-10A at 37 ºC, the apparent elastic modulus is about 1.6 times smaller than the corresponding value at ambient temperature. In addition, we can also observe that MCF-7 is softer than MCF-10A at both 24 ºC and 37 ºC. Thus it is evident that temperature does have

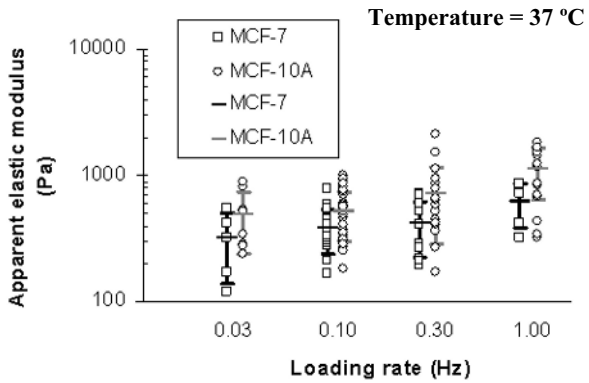


Fig. 4: Plot of the apparent elastic modulus against loading rate for MCF-10A and MCF-7 at 37 ºC. Error bars indicate standard deviations. Within an error bar, the centre line drawn indicate mean value.

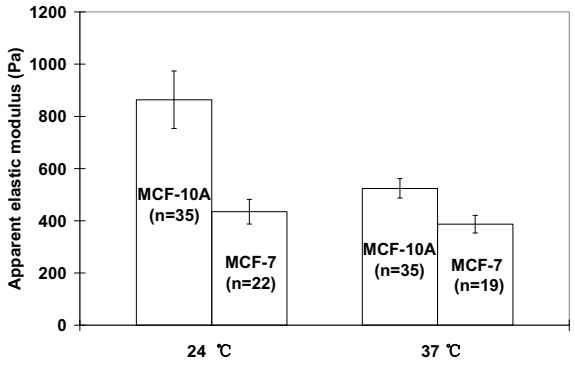


Fig. 5: Apparent elastic modulus of MCF-10A and MCF-7 cells tested at different temperatures and at a loading rate of 0.1 Hz. Error bars indicate standard error and n denotes the number of samples tested.

an effect on the mechanical properties of cells and it needs to be taken into account during probing cell elasticity.

Actin is a major component of the cellular cytoskeleton system (actin filament, intermediate filament, microtubule) and contributes significantly to the mechanical properties of the cell. In addition, actin structure is a highly dynamic structure and is strongly correlated with dynamic events such as migration and proliferation [23]. The reduced stiffness of both benign and cancerous cells as temperature increases may be attributed to the remodeling of the actin structure and a change occurring in its dynamic state due to the temperature change.

IV. Conclusions

The apparent elastic modulus of MCF-10A and MCF-7 were determined by means of AFM indentation using a spherical probe. Our results show that apparent cell elasticity increase with loading rate and decrease as temperature increase from 24 ºC to 37 ºC. Temperature has a more significant effect on the mechanical properties of MCF-10A. As mentioned earlier, actin remodels very quickly and is correlated with dynamic behavior of the cells. It is therefore not a static but a dynamic structure, and so the mechanical property measured is possibly a reflection of the dynamic state of the cell. Our indentation results, which were obtained using different loading rates, showed that cancerous MCF-7 is softer than benign MCF-10A at both room and physiological temperatures. This implies that malignant cells are more deformable and may aid in the metastasis of these cells.

Acknowledgments

The authors thank J.H. He (Institute of Microelectronics, A*STAR, Singapore) for the gift of MCF-10A cell line. This work was supported by a grant made available from the Singapore–MIT Alliance.

References

1. Jemal A, Murray T, Ward E, et al. (2005) Cancer statistics, 2005. *CA Cancer J. Clin.* 55:10-30
2. Lee G Y H and Lim C T (2007) Biomechanics approaches to studying human diseases. *Trends Biotechnol.* 25:111-8
3. Lim C T, Zhou E H, Li A, et al. (2006) Experimental techniques for single cell and single molecule biomechanics. *Mater. Sci. Eng. C-Biomimetic Supramol. Syst.* 26:1278-1288
4. Lekka M, Laidler P, Gil D, et al. (1999) Elasticity of normal and cancerous human bladder cells studied by scanning force microscopy. *Eur. Biophys. J.* 28:312-6
5. Park S, Koch D, Cardenas R, et al. (2005) Cell motility and local viscoelasticity of fibroblasts. *Biophys. J.* 89:4330-4342
6. Zhang G, Long M, Wu Z Z, et al. (2002) Mechanical properties of hepatocellular carcinoma cells. *World J. Gastroenterol.* 8:243-246
7. Ward K A, Li W I, Zimmer S, et al. (1991) Viscoelastic properties of transformed cells: role in tumor cell progression and metastasis formation. *Biorheology* 28:301-13
8. Guck J, Schinkinger S, Lincoln B, et al. (2005) Optical deformability as an inherent cell marker for testing malignant transformation and metastatic competence. *Biophys. J.* 88:3689-3698
9. Lincoln B, Erickson H M, Schinkinger S, et al. (2004) Deformability-based flow cytometry. *Cytometry Part A* 59A:203-209
10. Van Vliet K J, Bao G and Suresh S (2003) The biomechanics toolbox: experimental approaches for living cells and biomolecules. *Acta Materialia* 51:5881-5905
11. Lim C T, Zhou E H and Quek S T (2006) Mechanical models for living cells - A review. *J. Biomech.* 39:195-216
12. Thoumine O and Ott A (1997) Comparison of the mechanical properties of normal and transformed fibroblasts. *Biorheology* 34:309-326
13. Suresh S (2007) Biomechanics and biophysics of cancer cells. *Acta Materialia* 55:3989-4014
14. Cross S E, Jin Y-S, Rao J, et al. (2007) Nanomechanical analysis of cells from cancer patients. *Nat. Nano.* 2:780-783
15. Costa K D (2003) Single-cell elastography: Probing for disease with the atomic force microscope. *Dis. Markers* 19:139-154
16. Radmacher M (2002) Measuring the elastic properties of living cells by the atomic force microscope. *Methods Cell Biol* 68:67-90
17. Mahaffy R E, Park S, Gerde E, et al. (2004) Quantitative analysis of the viscoelastic properties of thin regions of fibroblasts using atomic force microscopy. *Biophys. J.* 86:1777-93
18. Li Q S, Lee G Y, Ong C N, et al. (2008) AFM indentation study of breast cancer cells. *Biochem Biophys Res Commun* 374:609-13
19. Alcaraz J, Buscemi L, Grabulosa M, et al. (2003) Microrheology of human lung epithelial cells measured by atomic force microscopy. *Biophys. J.* 84:2071-2079
20. Smith B A, Tolloczko B, Martin J G, et al. (2005) Probing the viscoelastic behavior of cultured airway smooth muscle cells with atomic force microscopy: Stiffening induced by contractile agonist. *Biophys. J.* 88:2994-3007
21. Lekka M, Lekki J, Marszalek M, et al. (1999) Local elastic properties of cells studied by SFM. *Appl. Surf. Sci.* 141:345-349
22. Chambers A F, Groom A C and MacDonald I C (2002) Dissemination and growth of cancer cells in metastatic sites. *Nature Reviews Cancer* 2:563-572
23. McGrath, J.L. and C.F. Dewey, *Cell dynamics and the actin cytoskeleton*. Cytoskeletal mechanics: models and measurements, ed. M.R.K. Mofrad and R.D. Kamm. 2006: Cambridge University Press.

Correlation between Balance Ability and Linear Motion Perception

Y. Yi[1] and S. Park[1]

[1] Department of Mechanical Engineering, KAIST, Daejeon, Republic of Korea

Abstract — **In this study, we investigated the correlation between balancing ability and motion perception. To provide the condition that declined balance ability, subjects were restrained their sole sensation. The balance ability was evaluated by measuring the center of pressure (COP) during quiet standing. Body kinematics was also monitored by using the motion capture system. We quantified the motion perception by measuring the threshold of perceived direction of linear motion. This result suggests that the COP represents the balance ability for quiet standing. However COP is insufficient for representing the balance ability during body movement. To describe the stability during motion, motion perception might compensate the COP.**

Keywords — **Motion perception, Center of pressure, Balance, Posture, Somatosensation**

I. Introduction

For the perception of motion, human use several sensory information such as vision, vestibular cues and somatosensation. This sense is induced by muscle spindle and Golgi tendon organ in muscles. These organs respond to change of muscle length or muscle tension. In upright stance, cutaneous cues provoked by pressure from soles are also used to perceive the movement of body. Like these sensory cues are processed in the central nervous system. Then, the resultant of processed information is used to perceive body motion or maintain the postural balance.

There are many studies that examine the characteristic of each sensation for motion perception. It is considered that these works are essential fundament to clarify the process of perceiving the motion. Many researchers have studied the threshold of sensory organs. Above all, vestibular organ, well known system in charge of the motion perception, has been extensively investigated. In contrast with the vestibular system, the influence of somatosensation on the motion perception has limitedly been studied. There are several studies that partially or peripherally deal with the somatosensation. Recently, several studies showed that additional cutaneous stimulus to soles enhanced the postural balance [1]. These results suggest that cutaneous information of sole and proprioception of leg, that is, lower limb somatosensation are strongly correlated with the balance ability in standing posture. Moreover, we previously showed that the cutaneous sense of soles played important role to the motion perception [2].

The balance ability was evaluated by observing the change of the posture sway. Usually, less posture sway was regarded as better balance ability. It remains unclear, however, whether the reduced postural sway directly demonstrates the improved subjective motion perception. In this study, we investigated the correlation between balancing ability and motion perception.

II. Methods

A. Subjects

Eight healthy male volunteers, who reported no history of balance disorders, aged between 20 and 27 years, were participated. All subjects read and signed KAIST IRB approved consent form. They were fully informed of potential risks such as falling, but not informed about the purpose of the experiment.

B. Stimuli

33 sets of a single sinusoidal acceleration at 0.25Hz with peak amplitude ranged 0~8mG were applied. Stimulus frequency was chosen as 0.25Hz to have reliable vestibular acceleration signals, which previously reported to be nearly unity gain at the stimulus above about 0.1Hz [3]. The pilot study for estimating the range of the threshold showed the range of threshold is about 2mG. Therefore the range of peak acceleration magnitude was determined from 0 to 8mG. To measure the detection threshold with high resolution, the peak acceleration magnitudes were designed to have small increased size for the smaller magnitude ranged from 0 to 2mG. For the fast process, the increment size is increased for the magnitude greater than 2mG. One trial set consisted of randomly ordered 33 velocity trajectories: 16 peak acceleration magnitudes of both directions and one standstill (0mG) stimulus.

C. Conditions

Subject participated in two conditions of 12 trial set which consists of 33 randomly ordered side-to-side support translation. In control condition (CC), subjects were tested without any restraint as shown in Fig 1. While in restrained plantar sensation condition (RC), subject stood on a cush-

Chwee Teck Lim, James C.H. Goh (Eds.): ICBME 2008, Proceedings 23, pp. 2126–2129, 2009
www.springerlink.com

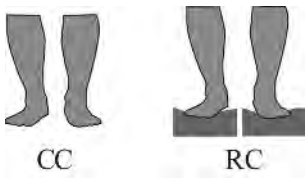


Fig. 1 Experimental conditions

ioned support surface to restrict cutaneous cues from soles. In each trial, platform was translated to either subject's left or right according to the velocity profile.

D. Procedure

Body kinematics was measured using motion capture system (Hawk; Motion Analysis Inc., Santa Rosa, CA). Subject attached reflective markers at head, neck, hip, and a support (Fig. 2A). The center of pressure (COP) was measured for a quiet standing by using a forceplate (AccuGait; AMTI, Watertown, MA), sampled at 100Hz.

Prior to experiment, subjects rehearsed a few practice trials to make familiar with the procedure of the test. During each session, subjects closed their eyes and lights over the platform were turned off and curtains surrounding the platform were drawn to prevent the room light from streaming. During the experiment, subjects stood on the platform with barefoot, loosened up their arms, and held report buttons at hand (Fig. 2B). Foot position was specified for consistency across the experiment. Subjects were provided white noise via the headphone to block auditory cues from motor operation noise. Before the onset of stimulus, subjects heard double beeps that indicate the platform movement. After side to side support translation, a single beep signaled subjects to report their perceived direction of motion by pressing one of hand held buttons. The experiment was designed according to a two-alternative-forced-choice (2AFC) psychophysical procedure. Therefore subjects were forced to make a choice of one of the two alternatives such as left or right, even when they weren't sure about the direction of motion. To minimize fatigue, subjects had 5 minutes break between each set.

E. Data analysis

Reported perceived direction of motion was analyzed using the cumulated standard distribution for psychometric function to obtain perception threshold. We defined the probability of motion detection as the percentage of correct report of 'right side' movement. Hence, 100% meant that the subject always report right side movement while 0% indicated that the subject never reported right side movement. The plotted probability of motion detections was fitted using psychometric function. We then defined the detection threshold of the translational motion as the difference between stimuli at the performance level of 50% and 75 % (Fig 3).

COP data for the quiet stance trials were band-pass filtered with cutoff frequency of 0.5 and 3.5 Hz. The initial 20 seconds of the data were discarded to eliminate the transient effect. Root mean square (RMS) of the COP in medial-lateral direction was calculated for a measure of postural sway. Body kinematics data were examined using covariance analysis [4]. While COP variance only shows the postural sway, covariance analysis provides correlation between body joints. Covariance of hip angle (θ_{hip}) and ankle angle (θ_{ankle}) was used to estimate the joint kinematics and postural sway.

Statistical analyses were used to test the significance of the effect of the designed conditions to the motion perception, COP variance and posture coordinate variance using paired t-test, and to the correlation between balance ability and motion perception using correlation analysis.

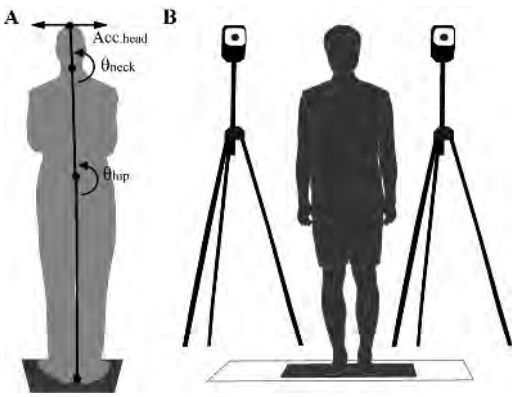


Fig. 2 Experimental setup

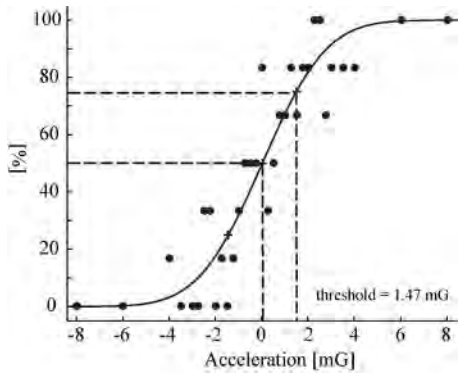


Fig. 3 Probability of motion detections and psychometric function

III. Results

A. Changes of threshold

When plantar somatosensory cues were restrained, significantly increased detection thresholds were observed (Fig. 4). As opposed to CC, detection probability for the RC gradually changed as a function of stimulus magnitude. This change made that the psychometric function was flattened, and indicated the increase in the threshold. Paired t-tests showed that the difference was significant ($p < 0.1$). While the average threshold of CC was 1.37 ± 0.41mG, the average threshold was 1.56 ± 0.39mG when the plantar cutaneous sensation was constrained.

In our previous research, we tested not only the cutaneous sensation but also ankle proprioception with the ankle brace. The results of former study showed the more step rise in the change of the thresholds ($p < 0.01$). The difference between the studies was only ankle restraint. Therefore we figured out that the difference of the result caused by the ankle proprioception. However there was no significant difference, when we performed the pilot study with only restraint ankle condition. With these matters, we concluded that if ankle proprioception and sole cutaneous sensation work together, it exerted a more influence than sum of them. The results were consistent with the previous study that interaction of several constraints to sensory organs exerted a more powerful influence than sum of effect of each constraint [5].

Our experiments showed that change of the joint angles of neck and hip was negligible. If there existed changes of body kinematics between two conditions, then body kinematics would affect the result. And the motion of head provoked additional influences of vestibular organ. We analyzed motion capture data by comparing the changes of peak angles and peak accelerations. The result of statistical difference presented in Table.1 indicated that a body kinematics and vestibular cue were not significantly changed between treatments. Therefore we thought that the change of the detection threshold was caused by designed conditions.

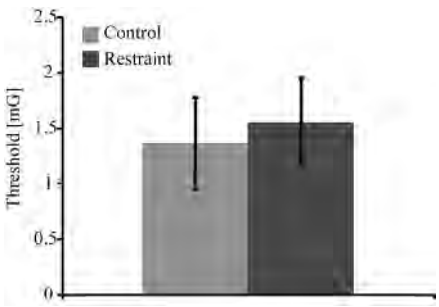


Fig. 4 Threshold of linear motion perception

Table 1 Statistical result of body kinematics

		p-value Control vs. Restraint	
		Standstill	Perturbation
Acceleration	Head	0.749	0.862
Joint angle	Neck	0.814	0.755
	Hip	0.725	0.906

B. Balance ability and motion perception

Our experiments showed that change of the COP was negligible. We calculated the COP in medial-lateral direction because experiments were performed along the medial-lateral direction. RMS of COP was 0.0008 ± 0.0004 in CC and 0.0008 ± 0.0003 in RC. This result showed that there was no significant difference between two conditions (Fig. 5). It meant that the designed condition did not influence to postural sway. That suggested that human did not have trouble to maintain the balance in medial-lateral direction even if the plantar cutaneous sensation was reduced.

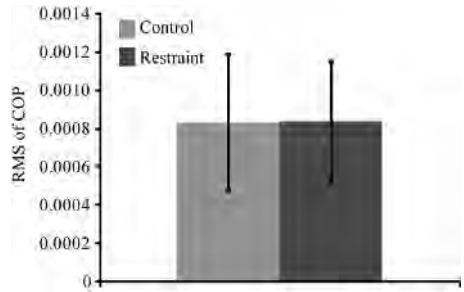


Fig. 5 RMS of the COP in medial-lateral direction

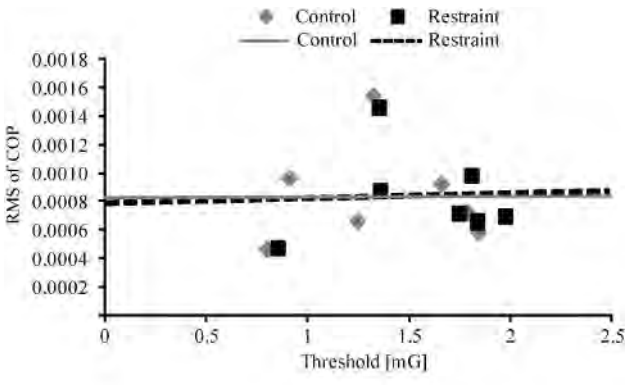


Fig. 6 Correlation between COP and threshold

Balance ability did not directly demonstrate motion perception. To examine the correlation between balance ability and motion perception, we compared RMS of COP with motion perception threshold. Linear regression line was presented at Fig. 6. Spearman correlation coefficient was 0.056 in control condition and 0.012 in restraint condition indicating that there was no correlation both of two conditions. This result suggests that the COP represents the balance ability for quiet standing. However COP is insufficient for representing the balance ability during body movement. To describe the stability during motion, motion perception might compensate the COP.

C. Postural coordinate

Hip strategy indicated significant difference between CC and RC. Covariance matrix (Q) of θ_{hip} and θ_{ankle} consisted of variance of ankle motion (Q11), variance of hip motion (Q22) and covariance of ankle-hip motion (Q12). In case of Q11, the results were 0.0012 ± 0.0005 in CC and 0.0012 ± 0.0007 in RC, there was no difference between two conditions (Fig. 7). Q22, on the other hand, indicated significant difference with 0.0033 ± 0.0022 in CC and 0.0040 ± 0.0028 in RC. Paired t-tests indicated significant ($p < 0.03$) increase in Q22. This result implied that human body used more hip strategy to maintain a balance when the plantar sensation was restrained. Moreover, body kinematics data revealed that there was no significant change of hip angle between CC and RC. It means more the hip use than the ankle use for balancing, not a significant change between the conditions.

RMS of COP was also showed that there was no significant change between two conditions. Nonetheless, Q22 was significantly increased. It meant that the Q22 might be able to be used as the index for the balance ability. COP could not sufficiently work. For example, COP could not figure out the Parkinson patients' balancing instability. In this case, covariance analysis might be useful to evaluate the balance ability.

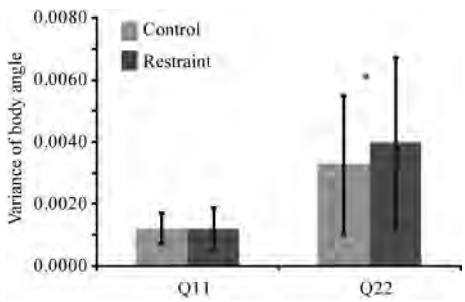


Fig. 7 Covariance matrix in medial-lateral direction

IV. Conclusions

Perception threshold of linear motion was increased when plantar cutaneous cues were reduced which implies that the plantar somatosensation influences the motion perception of the linear acceleration in absence of visual information. Balance ability, however, did not directly demonstrate motion perception. There was no correlation between COP and motion perception threshold. This result suggests that the COP represents the balance ability for quiet standing, although COP is insufficient for representing the balance ability during body movement. To describe the stability during motion, motion perception might compensate the COP. Moreover, we showed the potentiality that covariance can be used as the index for the balance ability.

Acknowledgment

This work was supported by the Korea Science and Engineering Foundation (KOSEF) grant funded by the Korea government (MEST) (No. R01-2007-000-20529-0).

References

1. Collins JJ et al. (2003) Noise-enhanced human sensorimotor function. IEEE Eng Med Biol Mag 22(2):76-83
2. Yi Y, Park S (2006) Effect of lower limbs somatosensation on linear motion perception. Trans KSME A 31(6):686-693
3. Fernandez C, Goldberg JM (1976) Physiology of peripheral neurons innervating otolith organs of the squirrel monkey. III. Response dynamics. J Neurophysiol 39(5):996-1008
4. Kuo AD et al. (1998) Effect of altered sensory conditions on multivariate descriptors of human postural sway. Exp Brain Res 122(2):185-95
5. Speers RA, Shepard NT, Kuo AD (1999) EquiTest modification with shank and hip angle measurements: differences with age among normal subjects. J Vestib Res 9(6):435-44

The address of the corresponding author:

Author: Sukyung Park
Institute: KAIST
Street: 335 Gwahangno, Yuseong-gu
City: Daejeon
Country: Republic of Korea
Email: sukyungp@kaist.edu

Heart Rate Variability in Intrauterine Growth Retarded Infants and Normal Infants with Smoking and Non-smoking Parents, Using Time and Frequency Domain Methods

V.A. Cripps[1], T. Biala[1], F.S. Schlindwein[1] and M. Wailoo[2]

[1] University of Leicester/Department of Engineering, Leicester, UK
[2] University of Leicester/Department of Health Science, Leicester, UK

Abstract — **Intrauterine growth retardation (IUGR) and low birth weight have been linked with an increased risk of cardiovascular disease, hypertension and stroke in later life. Studies have shown cardiovascular mortality is associated with altered autonomic nervous system activity, which can be assessed using measurements of how the heart rate is changing over time, known as heart rate variability (HRV). A reduced HRV indicates a reduction in the autonomic activity. Heart rate data of 24 children, at age 9-10 years, was analysed, to investigate the HRV of IUGR and normal birth weight children in relation to their parents' smoking habits. In the time domain Poincaré plots were produced, and in the frequency domain periodograms created using the FFT and the Lomb method. The Lomb method can cope with non-uniformly sampled data series without the need for interpolation and re-sampling. Measurements of the low to high frequency ratios showed no difference between the groups of children in the study, however measurements of the energy of peaks in the high frequency region due to respiratory sinus arrhythmia showed a reduction in high frequency strength for IUGR children with smoking parents, when compared to IUGR children with non-smoking parents.**

Keywords — **Heart rate variability, intrauterine growth retardation, Lomb periodogram, Poincaré plots.**

I. Introduction

The heart rate can be measured by examining the electrical activity of the heart muscle using an electrocardiogram (ECG). The ECG recording of two heart beats is shown in Figure 1. The RR interval is defined as the difference in time between two consecutive R peaks (i.e. the time interval between two heart beats). Analysis of how the RR interval changes over time is known as HRV. The greater variation in the length of the RR interval the greater the HRV. The heart rate is controlled by several mechanisms: humoral, chemical, direct (such as the Frank-Starling mechanism) and, particularly, neurological, via the nervous system [1]. Specifically, the heart rate is controlled by the autonomic nervous system, the part of the nervous system responsible for the body's 'control system'. The autonomic nervous system is split into two divisions; sympathetic and parasympathetic (also known as vagal). The two branches work concomitantly; an increased heart rate is produced by an increase in the sympathetic and a decrease in the parasympathetic activity.

Studies have shown that there is a significant relationship between the autonomic nervous system and cardiovascular mortality, with lethal arrhythmias linked to either increased sympathetic or decreased parasympathetic activity, as well as a higher risk of post-infarction mortality with reduced heart rate variability [2]. Analysis of heart rate variability can be undertaken in both the time and the frequency domain.

In the time domain, statistical methods are used to find the standard deviation of the RR intervals, the SDNN, which estimates overall HRV. Graphical methods, such as Poincaré plots, are also used and are discussed. Analysis in the frequency domain is used to find the power of components within different spectral bands. Studies have shown that a low birth weight increases the risk of coronary heart disease, stroke, hypertension and non insulin-depended diabetes [3]. A study in Helsinki has also suggested than being IUGR may pose a risk of depression in young adult men [4]. Barker [3] suggests that during intrauterine development the organs and body systems are 'plastic', that is they are able to adapt and respond to be best suited to their environment and proposes a controversial hypothesis of fetal origin to adult heart disease.

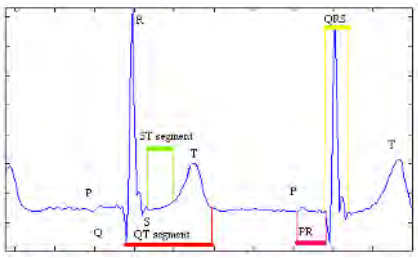


Figure (1) ECG recording of two heart beats

Chwee Teck Lim, James C.H. Goh (Eds.): ICBME 2008, Proceedings 23, pp. 2130–2133, 2009
www.springerlink.com

II. Methods

In this study, two cohorts of children were used; those of normal birth weight and those who were intrauterine growth retarded (IUGR). IUGR was defined as 'any baby with a foetal abdominal girth two or more standard deviations below the mean or who by birth weight was below the second centile at term' [5]. Data from 73 children, 33 of normal birth weight and 40 IUGR, were collected at the Leicester Royal Infirmary. The ECG was recorded over a 24 hr period when the children were at 10 years old, as well as data on parental smoking during pregnancy and during the last 10 years. From the children in the larger study, a sub-set of 24 were selected within the four groups shown in Table 1.

Table 1: Groupings employed to select the 24 children used in this study.

Birth weight of child	Smoking status of parents
IUGR	smokers
IUGR	non-smokers
normal	smokers
normal	non-smokers

In this paper the following methods were used to analyse the data:-

A. Time domain analysis- Poincaré plots

One geometrical method with which to analyse normal RR intervals in the time domain is the use of a Poincaré plot, where the current RR interval is plotted against the previous. The resulting 'clouds' can then be enclosed by an ellipse and measured, giving an indication of the HRV. SD1, the width of the cloud or the standard deviation around the identity axis x1, is a measure of the short-term HRV - more precisely the measure of variability over a single heart beat. SD2, the length of the cloud along the line of identity or the standard deviation around axis x2, is a measure of long term HRV [6].

B. Frequency domain-Fourier transform

The discrete Fourier transform (DFT) is used to transform a discrete signal from the time domain into the frequency domain. It can be efficiently computed using a 'Fast Fourier Transform' (FFT) algorithm. The power in the signal is found by squaring the absolute value of the returned FFT result and can be plotted against frequency to produce a periodogram. The FFT requires a uniformly sampled signal, which is not the case in RR data, so the RR data needs to be interpolated and resampled at at least twice the maximum frequency of interest in the original signal to avoid aliasing. The resampling process alters the frequency content of even a noise-free time series by non-linear low-pass filtering [7], i.e. high frequencies are attenuated.

C. Frequency domain - Lomb periodogram

The Lomb method, developed by Lomb and later elaborated on by Scargle, is a technique designed to calculate the power in a signal with unevenly spaced data points and involves least squares fitting the time domain data points to a sine or cosine series. 'It weights the data on a 'per point' basis, instead of a 'per time interval' basis, when uneven sampling can render the latter seriously in error' [8]. No interpolation of the data series is required. The Lomb normalised periodogram, $P_N(\omega)$, is defined by the following equations as given in [8]:

$$P_N(\omega) = \frac{1}{2\sigma^2}\left\{\frac{[\sum_j (h_j-\bar{h})\cos\omega(t_j-\tau)]^2}{\sum_j \cos^2\omega(tj-\tau)} + \frac{[\sum_j (h_j-\bar{h})\sin\omega(t_j-\tau)]^2}{\sum_j \sin^2\omega(t_j-\tau)}\right\} \quad (1)$$

Where is defined by the relation

$$\tan(2\omega\tau) = \frac{\sum_j \sin 2\omega t_j}{\sum_j \cos 2\omega t_j} \quad (2)$$

$$\bar{h} = \frac{1}{N}\sum_1^N h_i \quad (3)$$

$$\sigma^2 = \frac{1}{N-1}\sum_1^N (h_i-\bar{h})^2 \quad (4)$$

where N is the number of data points, are the data points measured at time , ω = 2π f is the angular frequency and τ is an offset constant that makes (ω) independent of shifting all the 's by any constant.

D. Respiratory sinus arrhythmia

In healthy individuals the heart rate varies at the frequency of ventilation, known as respiratory sinus arrhythmia (RSA). During inspiration, the chest expands causing the intrathoracic pressure to decrease. This increases the blood return from the body to the right side of the heart and, via the Bainbridge reflex, causes the heart rate to accelerate. Conversely, during expiration the heart rate decelerates via the baroreceptor reflex [9]. Recordings of the autonomic nerves show that sympathetic nerves are activated during inspiration and

parasympathetic ones during expiration. RSA is most pronounced when we are sleeping and can be seen as an increase in activity around 0.3Hz, in the HF region. The greater the heart rate variability in an individual, the more pronounced the peak associated with RSA.

III. Results

A. Poincaré plots

Four Poincaré plots were produced, as seen in Figure 2. Measurements of the eight clouds were taken and are given in Table 2.

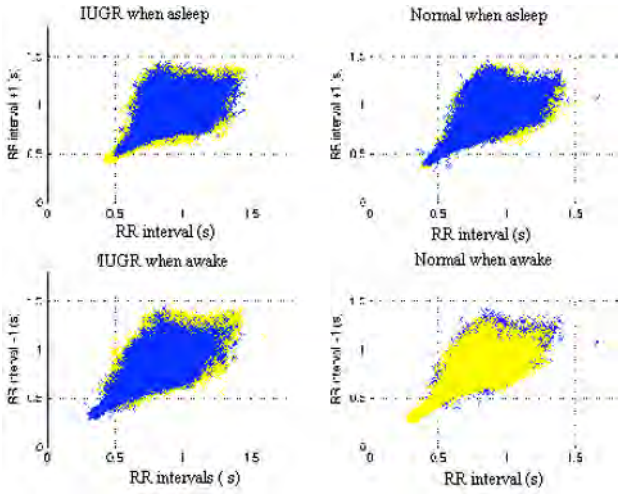


Figure (2) - Poincaré plots for the IUGR and Normal Children, when awake and asleep. 12 children are plotted on each sub-plot, 6 with smoking parents, in blue, and 6 with non-smoking parents, in yellow.

Table 2: SD1 and SD2 measurements of clouds in the Poincaré plots of figure 2.

Birth weight	Parents, smoking status	Awake or asleep	SD1(arbitrary units)	SD1(arbitrary units)
IUGR	smokers	awake	0.247	0.505
IUGR	smokers	asleep	0.263	0.453
Normal	smokers	awake	0.224	0.529
Normal	smokers	asleep	0.242	0.495
IUGR	non-smokers	awake	0.259	0.518
IUGR	non-smokers	asleep	0.277	0.505
Normal	non-smokers	awake	0.221	0.484
Normal	non-smokers	asleep	0.271	0.482

B. FFT

Periodograms for the 24 children were produced using the FFT, to allow comparison with the periodograms produced using the Lomb method. The FFT periodogram for NB (A female child) is shown in Figure 3. A strong series of peaks centred around 0.25Hz can clearly be seen, corresponding to activity associated with RSA during sleep, between the hours of 5 and 17 (recording started around 4 PM).

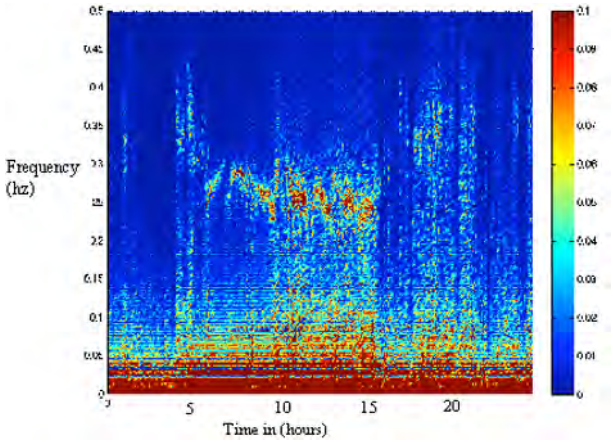


Figure (3): FFT periodogram for child NB, a female child, IUGR at birth whose parents smoked 30 cigarettes a day in total.

C. Lomb periodogram and strength of RSA peaks.

Lomb periodograms were also produced for the same children, four of which are included in this report – one from each of the groups under investigation. Figure 4 shows the Lomb method periodogram for child NB.

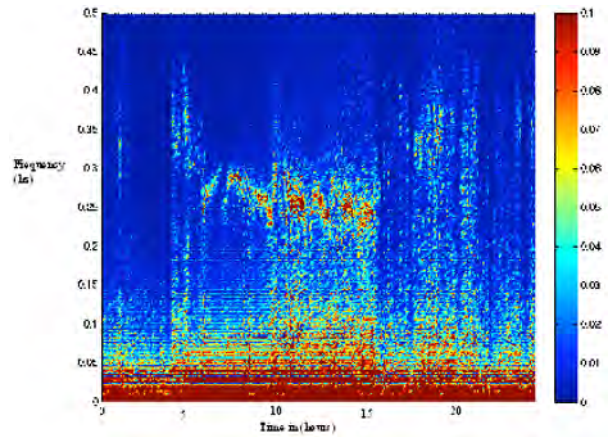


Figure (4): Lomb periodogram for child NB, a female child, IUGR at birth, whose parents smoked 30 cigarettes a day in total.

Strong activity corresponding to RSA can be seen in both diagrams in the region of 2 – 3 Hz, during the hours when the child was asleep. The normalised energy of the periodograms, for frequencies in the HF range 0.15 - 0.40Hz over the 'sleep' hours, was measured and the

average normalised energy for each group of six children is also shown. The four averages were compared using the Student's t-Test, at the 5% significance level, as shown in Table 3.

The LF/HF ratio for each child was also calculated, along with the mean ratio and the standard deviation of the group. Student's -t-test was then performed on the pairings, as seen in Table 4.

Table 3: Student's t-test comparison of HF energy of the groups, tested at 5% significance level.

Group 1	Group 2	t-test Probability	Null hypothesis
IUGR smokers	IUGR non-smokers	0.0378	Yes
Normal smokers	Normal non smokers	0.0925	No
IUGR smokers	Normal smokers	0.3795	No
IUGR non-smokers	Normal non-smokers	0.2367	No

Table 4: Student' t-test comparisons of the LF/HF asleep and awake ratios of the groups, tested at the 5% significance level.

Group 1	Group 2	t–test Prob-asleep	Reject Null Hypothesis	t-test Prob-awake	Reject null hypothesis
IUGR smokers	IUGR non smokers	0.4174	No	0.1058	No
Normal smokers	Normal non-smokers	0.1107	No	0.2765	No
IUGR smokers	Normal smokers	0.0585	No	0.1771	No
IUGR non smokers	Normal non-smokers	0.1135	No	0.784	No

IV. Conclusions

In the time domain, Poincaré plots were produced for the 24 children used in this study. The comparison between the four groups has shown no significant difference during asleep and awake hours.

In the frequency domain, periodograms were produced using the FFT and Lomb methods. Comparisons of the spectra produced using the two techniques showed spectral leakage and high frequency attenuation on the FFT periodograms. Therefore, although the Lomb method used in this instance took longer to execute, Lomb periodograms were used for further investigation in the frequency domain.

Analysis of the LF/HF ratios during sleep and awake hours has shown no significant difference between IUGR and normal birth weight children, regardless of their parents smoking status. This study has also looked at the energy associated with the activity around 0.3Hz due to RSA. One potentially very interesting finding has emerged from this analysis, as a significant decrease in the energy of the RSA peaks for IUGR children with smoking parents, when compared to IUGR children with non-smoking parents, was noticed.

The IUGR children in this study who had smoking parents showed reduced strength RSA peaks in the HF region and, by extrapolation, a reduced strength LF region (with a LF/HF ratio that was not significantly different to the other groups). The effects of nicotine and other chemicals, through passive exposure to tobacco smoke, may result in a reduction of the action of autonomic nervous system in these individuals, suggesting IUGR children are more at risk from living in smoking households than normal birth weight children.

References

1. Boardman, A., The feasibility of Using Heart rate variability to detect distress. PhD thesis in *Engineering.* University of Leicester, 2003.
2. Task Force of The European Society of Cardiology and the North American Society of Pacing and Electrophysiology, Heart rate variability, Standards of measurement, physiological interpretation and clinical use, European Heart Journal, 17, 352-381, 1996.
3. Barker, D.J.P., The developmental origins of chronic adult disease, Acta Pediatr.; Supplement 446, 2633, 2004.
4. R″aikk″onen, K. et al., Archives of General Psychiatry, 65(3), 290/296, 2008.
5. Chakraborty, S. et al., Foetal growth restriction: relation to growth and obesity at the age of nine years, Archives of disease in childhood, Fetal and neonatal edition, 92, F479- F483, 2007
6. Brennan, M., Palaniswami, M., Kame, P., Do existing measures of Poincaré plot geometry reflect nonlinear features of Heart Rate Variability?, IEEE transactions on biomedical engineering, 48(11), 1342-1347, 2001.
7. Moody, G.B., Spectral analysis of heart rate without resampling, Computers in cardiology, Proceedings, 1993, 715-718, 1993.
8. Press, W.H., Numerical recipes in C: the art of scientific computing, Cambridge University Press, 1992.
9. Berne, R.M., Levy, M.N., Cardiovascular Physiology, 8th Edition, Mosby Inc., 2001.

Biomechanics of a Suspension of Micro-Organisms

Takuji Ishikawa

Department of Bioengineering and Robotics, Tohoku University, Sendai, Japan

Abstract — **Micro-organisms play a vital role in many biological and medical phenomena, such as bioreactors for medicine or food, and human digestion assisted by enterobacteria. Many researchers have tried to predict behavior of micro-organisms, and proposed macroscopic population models. However, it is worth asking how these models are constructed from individual behavior of micro-organisms. In this article, I will outline briefly some of the fluid mechanics aspects of individual and collective behavior of micro-organisms as well as the suspension properties, which will be useful for constructing a better continuum model for a suspension of micro-organisms.**

Keywords — **Micro-organisms, Bacteria, Suspension, Locomotion, Coherent structures**

I. Introduction

Micro-organisms play a vital role in many biological and medical phenomena. In the human body alone the number of micro-organisms is approximately 10^{14} about twice the number of the body's cells. In the intestines of an adult male, for instance, approximately 1.5 kg of enterobacteria form a unique ecosystem called the bacterial flora. The flora plays an important role in the digestion and absorption of food, and in protecting against infections. Another example is the infection of the stomach by the *Helicobacter pylori* bacteria, which are responsible for serious stomach diseases. Not only bacteria, but also some human cells may behave like independent micro-organisms due to their locomotion. Sperm, for instance, can swim about 10-20 body lengths per second, and its motility is essential in reproduction. The rolling motion of a leukocyte on endothelium cells of an arterial vessel is also a crucial phenomenon in terms of cellular immunology.

Moreover, micro-organisms are used in biotechnology for medicine and food; they form plankton blooms in the oceans that affect the oceanic ecosystem; they sometimes cause harmful red tides in coastal regions of the ocean that have serious repercussions on fish farms; and they absorb CO_2, which affects the global climate. Because of the considerable influence that micro-organisms have on human life, the study of their behavior is an important area of scientific research.

Many researchers have tried to predict behavior of micro-organisms, and proposed mathematical models. There are some standard models, called food web models [1]. However, most of the former macroscopic and population models were empirically derived, and used many *ad hoc* functions and constants. It is worth asking how the macroscopic population level models are constructed from individual behavior of micro-organisms. In this article, I will outline briefly some of the fluid mechanics aspects of micro-organisms' individual and collective behavior. Firstly, some of our recent researches on hydrodynamic interaction between a pair of micro-organisms will be introduced. Secondly, the collective motions of micro-organisms and suspension properties, such as rheological and diffusion properties, will be discussed. I hope that the readers take this study as an interesting example of research, rather than a complete definition of the field.

II. Pairwise interactions of micro-organisms

To model the motion of a real micro-organism mathematically is a massive undertaking. Micro-organisms alter their behavior depending on many parameters relating to their environment. The variety of shapes both inter- and intra-species is also vast. Any model capable of being analysed mathematically will therefore require considerable simplifications. Even with the simplified models, however, some fundamental biomechanics in micro-organisms' behavior can be analyzed correctly. In the following sections, I will introduce three example of pairwise interaction of micro-organisms, which can be successfully analyzed by using computational biomechanics.

A. Interactions of swimming Paramecia

In a suspension of micro-organisms, the cells tend to change their swimming directions not only by the hydrodynamic interactions but also by the biological interactions. Thus, at first, whether the interaction of swimming micro-organisms can be described by fluid mechanics or not was investigated, using a unicellular freshwater ciliate *Paramecium caudatum*. Biological reactions of a solitary *Paramecium* cell to mechanical stimulations were investigated experimentally by Naitoh and Sugino [2]. Avoiding reactions occur when a cell bumps against a solid object with its anterior end. The cell swims backward first, then gyrates about its posterior end, and finally resumes normal forward

Chwee Teck Lim, James C.H. Goh (Eds.): ICBME 2008, Proceedings 23, pp. 2134–2138, 2009
www.springerlink.com

locomotion. Escape reactions occur when the cell's posterior end is mechanically agitated. The cell increases its forward swimming velocity for a moment, and resumes normal forward locomotion.

Interactions between two *Paramecia* were investigated experimentally by Ishikawa and Hota [3]. A typical hydrodynamic interaction, restricted in a 2D plane, observed in the study is shown in figure 1. When one cell collides with the anterior end of the other cell, the two cells tend to swim side by side at first, and then move away from each other at an acute angle. All the cells interactions were classified as hydrodynamic interactions, avoiding reactions or escape reactions. The total number of interacting cells recorded in the study was 602 (the total number of cases was 301). It was found that about 85% of cells interact hydrodynamically. We could conclude that the cell-cell interaction was mainly hydrodynamic and that the biological reaction accounted for a minority of events.

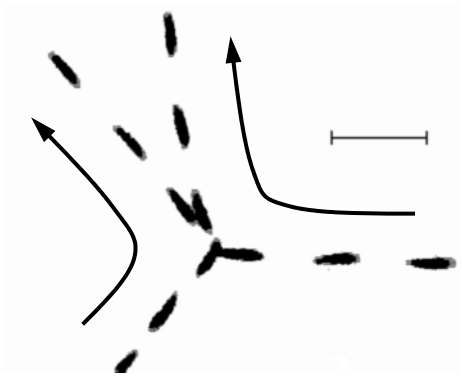
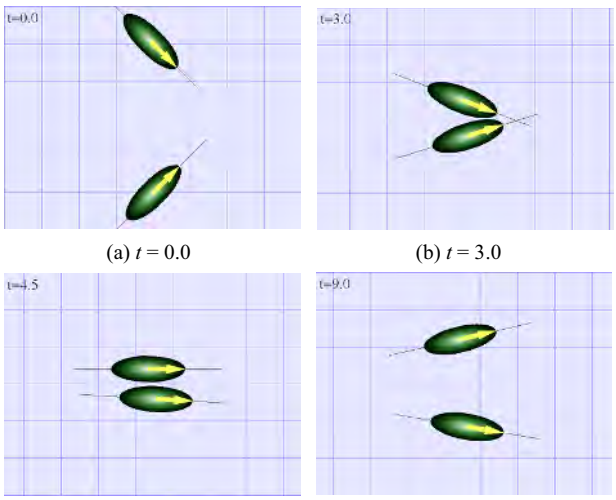


Fig. 1 Sample sequences showing the interaction of two *P. caudatum*. The time interval between each sequence is 1/3 sec. Long arrows are added to schematically show cell motion. Scale bars, 500 μm [3]

Next, we tried to computationally analyze the interaction between two *Paramecia*. We modeled the *Paramecium* as a squirmer [4], which can propel itself by generating tangential velocities on its surface. In fact, it is a reasonable model to describe the locomotion of ciliates, which propel themselves by beating arrays of short hairs (cilia) on their surface in a synchronised way. In particular, the so-called symplectic metachronal wave, in which the cilia tips remain close together at all times, employed for example by *Opalina*, can be modeled simply as the stretching and displacement of the surface formed by the envelope of these tips.

The sedimentation velocity of *P. caudatum* is much less than its swimming speed, therefore it is reasonable to assume the squirmer as neutrally buoyant. Swimming speeds of the *P. caudatum* is about several hundred μm/s. However, the Reynolds number based on the swimming speed and the radius of individuals is usually less than 10^{-2}, so the flow field around the cells can be assumed to be Stokesian with negligible inertia compared to viscous effects. Brownian motion can be neglected because the *P. caudatum* is too large for Brownian effects to be important. The governing equations for the flow field and the squirmer motion can be solved accurately by a boundary element method [4].

Figure 2 shows the numerical results of the interactions between two squirmers in which the squirmers collide with their anterior ends. The two cells tend to swim side by side at first, and then move away from each other at an acute angle. This tendency is similar to the experimental results shown in figure 1. We also performed simulations with various initial conditions, and found that the hydrodynamic interaction data in the experiments agreed well with the numerical results [3].



(a) $t = 0.0$ (b) $t = 3.0$

(c) $t = 4.5$ (d) $t = 9.0$

Fig. 2 Sequences (a) to (d) show the numerical results of the interactions between two squirmers against the dimensionless time t. The orientation vectors of the squirmers are shown as large arrows on the ellipsoids [3].

B. Waltzing motion of Volvox

Recently, R. E. Goldstein's group at Cambridge University found an interesting interaction between two multicellular freshwater ciliates, *Volvox*. When they placed suspensions of *Volvox* in glass-topped chambers, they observed the frequent formation of stable bound state of two colonies orbiting each other, referred to as a *waltzing motion*. Since Goldstein's group and myself were interested in whether the waltzing motion appeared due to the biological interaction or the hydrodynamic interaction between *Volvox*, we performed numerical simulations to clarify the mechanism of such motion [5].

In modeling a *Volvox* computationally, we assumed that a *Volvox* was a rigid sphere generating a force distribution slightly above the surface. The flow field around a *Volvox* was assumed to be Stokesian, and sedimentation and bottom-heaviness were taken into account. Equations for the flow field and the force distribution were solved by a boundary element method by coupling with the force-torque conditions of the cell bodies.

If we initially place two *Volvox* below the wall, they first swim towards the wall and show steady hovering motion adjacent to the wall. Then, they tend to attract each other gradually until they come in close contact. Finally, they show stable waltzing motion with steady rotational velocities (see figure 3), in a similar manner to the experimental observations. We also performed trial simulations without the wall boundary, without the bottom-heaviness, without the swirl velocity (no tilt angle), or without the sedimentation (body force), and concluded that the wall boundary, the bottom-heaviness and the swirl velocity are necessary in reproducing the waltzing motion.

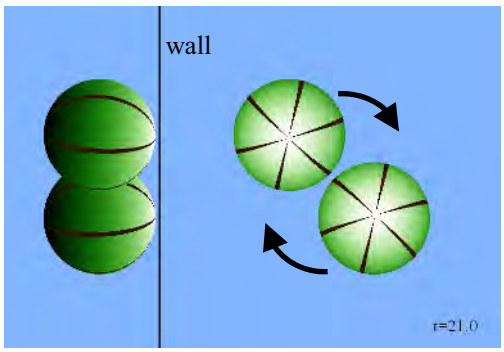


Fig. 3 Schematics of the interactions between two *Volvox* models. The wall is indicated as a solid line, and the left side of it is the side view, whereas the right of it is the top view.

C. Interactions of swimming bacteria

Recently, there has been increasing interest in the collective dynamics of swimming bacteria, because some species of bacteria show spatiotemporally coherent structures [6]. Since the mechanism of the coherent structure is still unclear, we investigated the stability of pairwise swimming motion of bacteria [7].

In investigating the hydrodynamic interactions between two swimming bacteria, we assumed that each bacterium was force-free and torque-free, with a Stokes flow field around it. The geometry of each bacterium was modeled as a spherical or spheroidal body with a single helical flagellum. The movements of two interacting bacteria in an infinite fluid otherwise at rest are computed using a boundary element method. The results show that as the two bacteria approach each other, they change their orientations considerably in the near field. The bacteria always avoided each other, and no stable pairwise swimming motion was observed in this study.

III. Suspensions of Model Micro-Organisms

A. Rheological and diffusion properties

The size of individual micro-organisms is often much smaller than that of the flow field of interest. In such cases, the suspension of micro-organisms can be modeled as a continuum in which the variables are volume-averaged quantities. However, the continuum models proposed so far are restricted to dilute suspensions. If one wishes to analyse larger cell concentrations, for example a suspension of enterobacteria, it will be necessary to consider the interactions between micro-organisms. Then the particle stress tensor, as well as the velocities of the micro-organisms and the diffusion tensor, in the continuum model will need to be replaced by improved expressions.

In discussing suspension properties, we employed a spherical squirmer model for simplicity. By performing Stokesian dynamics simulations [8], as shown in figure 4, we could calculate hydrodynamic interactions in an infinite suspension accurately from lubrication flows to far-field many body interactions.

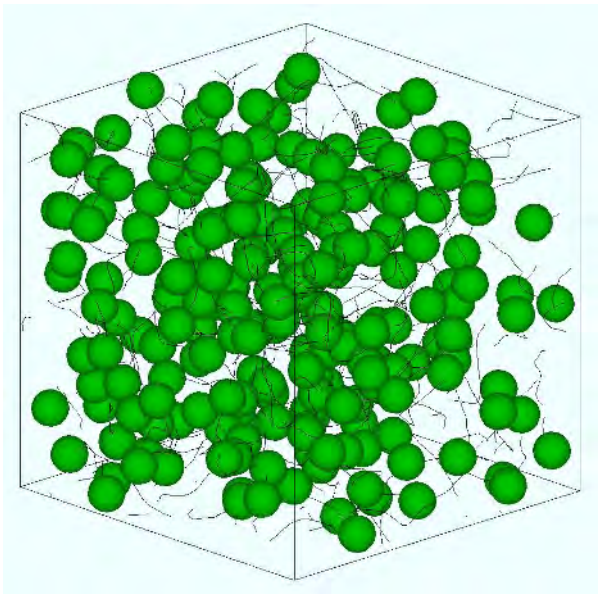


Fig. 4 Instantaneous position of 216 identical squirmers in a fluid otherwise at rest. Solid lines are trajectories of the squirmers during five time interval.

The rheological properties of a cell suspension relate the stress field and the velocity field in the suspension. In the case of bottom-heavy squirmers, the stresslet generated by the squirming motion directly contributed to the bulk stress at order of c, where c is the volume fraction of cells, and the suspension showed strong non-Newtonian properties [9]. When the background simple shear flow was directed vertically, the apparent viscosity of the suspension of bottom-heavy squirmers became smaller than that of inert spheres. On the other hand, when the shear flow was horizontal and varied with the vertical coordinate, the apparent viscosity became larger than that of inert spheres. The rheology of a suspension of micro-organisms is different from that of passive particles.

Understanding the diffusive behavior of swimming micro-organisms is also important in order to obtain a better continuum model for a cell suspension. The diffusive property in a suspension of squirmers was discussed in Ishikawa and Pedley [10]. The results showed that the spreading of squirmers was correctly described as a diffusive process over a sufficiently long time scale, even though all the movements of the squirmers were deterministically calculated.

B. Coherent structures in a suspension

Systems of swimming micro-organisms exhibit an interesting variety of collective behavior such as clustering and migration; examples include coherent structures of swimming bacteria [6]. It is important to discuss whether the collective motions are biologically and evolutionarily favourable or not in various conditions.

In order to improve our understanding of the experimental observations, we investigated various types of coherent structures in suspensions of squirmers by performing Stokesian dynamics simulations [11]. A sample result of the band formation in a mono-layer suspension is shown in figure 5. The numerical results interestingly illustrate that various coherent structures, such as aggregation, meso-scale spatio-temporal motion and band formation, can be generated by purely hydrodynamic interactions between micro-organisms.

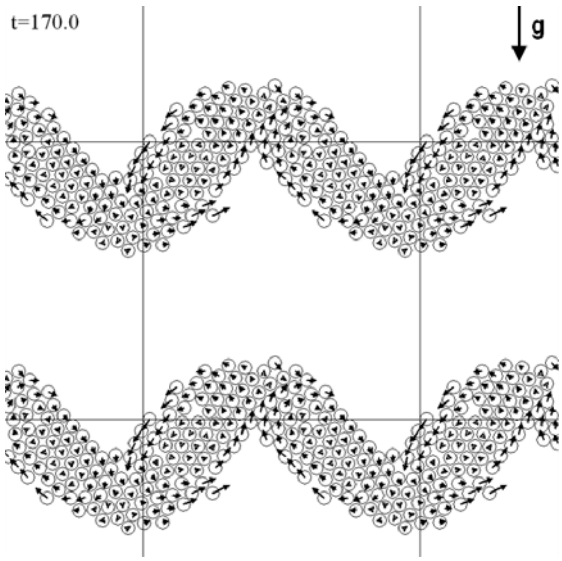


Fig. 5 Velocity vectors of bottom-heavy squirmers in a mono-layer suspension, relative to the average squirmer velocity [11].

IV. Conclusions

In this study, the locomotion, the collective motions and the suspension properties of micro-organisms have been clarified. Obtained fundamental knowledge will be useful for constructing a better continuum population model for a suspension of micro-organisms. Though biomechanics have been successful in describing some of micro-organisms' behaviors, including the present study based of fluid mechanics, there are still plenty of unsolved phenomena. I expect that many researchers will be interested in this research field and will clarify the natural beauty exhibited by micro-organisms in the near future.

Acknowledgment

Part of the work presented in this paper was performed in collaboration with Prof. T. J. Pedley and Prof. R. E. Goldstein, University of Cambridge. I am also grateful for helpful discussions with Prof. T. Yamaguchi and Dr. D. Giacche, Tohoku University.

References

1. for instance, Metcalfe, A. M. Pedley, T. J. and Thingstad T. F. (2004) Incorporating turbulence into a plankton foodweb model, *J. Marine Systems*, 49:105-122
2. Naitoh, Y., Sugino, K. (1984), Ciliary movement and its control in *Paramecium*, *J. Protozool.*, 31: 31-40
3. Ishikawa T., Hota M. (2006), Interaction of two swimming *Paramecia*, *J. Exp. Biol.*, 209: 4452-4463
4. Ishikawa T., Simmonds M. P., Pedley T. J. (2006), Hydrodynamic interaction of two swimming model micro-organisms, *J. Fluid Mech.* 568: 119-160
5. Ishikawa, T., Drescher, K., Leptos, K., Pedley, T. J., Goldstein, R. E. (2008), Numerical analysis of a stable waltzing pair of *Volvox*, *Bull. Amer. Phys. Soc.*, DFD 2008, to appear
6. Dombrowski, C., Cisneros, L., Chatkaew, S., Goldstein, R. E., Kessler, J. O. (2004), Self-Concentration and Large-Scale Coherence in Bacterial Dynamics, *Phys. Rev. Lett.*, 93: 098103

7. Ishikawa, T., Sekiya, G., Imai, Y., Yamaguchi, T. (2007), Hydrodynamic interaction between two swimming bacteria, *Biophys. J.*, 93:2217-2225
8. Ishikawa, T., Locsei, J. T., Pedley T. J. (2008), Development of coherent structures in concentrated suspensions of swimming model micro-organisms, *J. Fluid Mech*., in press
9. Ishikawa, T., Pedley, T. J. (2007), The rheology of a semi-dilute suspension of swimming model micro-organisms, *J. Fluid Mech.*, 588:399-435
10. Ishikawa, T., Pedley, T. J. (2007), Diffusion of swimming model micro-organisms in a semi-dilute suspension, *J. Fluid Mech*., 588:437-462
11. Ishikawa, T., Pedley, T. J. (2008), Coherent structures in monolayers of swimming particles, *Phys. Rev. Lett*., 100: 088103

Development of a Navigation System Included Correction Method of Anatomical Deformation for Aortic Surgery

Kodai Matsukawa[a], Miyuki Uematsu[a,b], Yoshitaka Nakano[a], Ryuhei Utsunomiya[a], Shigeyuki Aomi[c], Hiroshi Iimura[d], Ryoichi Nakamura[e], Yoshihiro Muragaki[e,f], Hiroshi Iseki[e,f], Mitsuo Umezu[a]

[a]Major in Integrative Bioscience and Biomedical Engineering, Waseda University
[b]Division of Medical Devices, National Institute of Health Sciences
[c]Dept. of Cardiovascular Surgery, Tokyo Women's Medical University
[d]Dept. of Radiology, Tokyo Women's Medical University
[e]Faculty of Advanced Techno-Surgery, Inst. of Advanced Biomedical Engineering & Science, Tokyo Women's Medical University
[f]Dep. of Neurosurgery, Neurological Institute, Tokyo Women's Medical University

Abstract — **The authors have been developing a surgical navigation system for the graft replacement of thoracoabdominal aortic aneurysm and applied clinically 30 times since July 2006. This system supports surgeons to figure out the patient's intercostal level before thoracotomy.**

However, in the current navigation system, there is a problem that patient's postures are different between preoperative CT scanned data and intraoperative real data. In this paper, it is aimed to improve current navigation system to follow global deformation arising from difference of patient's postures. And the mathematical method is discussed that matches image space with real space globally by correcting the image.

It is assumed that the deformation of thoracic cage is affected by the weight of trunk, and that of lumbar is affected by the torsion. To match both spaces, the algorithm that makes image slanted at the thoracic region and rotated at the lumbar region was developed. The angle of inclination for slanting and that of torsion for rotating were calculated from body weight, width of costale and elastic coefficient of bone.

This algorithm was evaluated by using MRI images of two volunteers those were scanned in dorsal position and right decubitus position. As a result, fitting between image space and real space decreased by 20% by operating this algorithm. It was concluded that this algorithm is effective to match both spaces. Foreseeable future, this algorithm will use in navigation used in clinical.

Keywords — **Surgical Navigation, Aortic Surgery, Postural Deformity, Image Correction**

I. Introduction

Surgical navigation system assists surgeons by representing patient's images and therapeutic position of therapeutic target with an optical positioning measurement device during surgery. For example, it has been used for brain surgery to detect the invisible tumor by visualizing the affected area with MR images. It is reported that surgeons could reduce the insufficient procedures and improve the operative performance [1].

Recently, the authors have developed the surgical navigation system for aortic vascular surgery that supports surgeons to figure out the intercostal level of the target artery during surgery. Especially, the system helps surgeons to confirm the appropriate trajectory due to grasp the anatomical relationships before opening patient's chest [2].

However, in the current navigation system for aortic surgery, the matching error between the virtual image space and real surgery space is observed that is caused of the difference of patient's posture. To reduce the matching error, the authors developed the algorithm that follows global deformation arising from difference of patient's postures.

This paper presents a new method for the navigation system for aortic vascular surgery to compensate the deformation by applying the algorithm of the image-correction.

II. Method

A. Algorithm

In the current navigation system for thoracoabdominal aortic surgery, the patient's postures are different between preoperative CT scanned data and intraoperative real data. Although the CT images are acquired with the supine position, the surgery is performed with the right lateral decubitus position to keep the surgical field sufficiently (Fig.1). According to the rotation of the body trunk, the bone structures are shaped. Besides, internal parts of the body are deformed under the influence of the gravity. These changes lead to the mismatching between the patient's image and the real body.

The following algorithm modifies the patient's image to fit the real body. In order to deform volumetric image and match both spaces, each axial image slices are slanted by the inclination angle θ that is determined the attribution of thoracic cage at the chest region. And those are rotated at

Chwee Teck Lim, James C.H. Goh (Eds.): ICBME 2008, Proceedings 23, pp. 2139–2142, 2009
www.springerlink.com

the angle of 4.7 degree that is resulted from preliminary experiment at the lumber region[3].

The angle of inclination θ is determined as follows.

$$\theta = \tan^{-1}\frac{(\pi-2)Fr}{4\sqrt{2}EA\kappa} \quad (1)$$

A :cross section of the costale
E :elastic constant of the bone
F :gravitation force of organ in the chest
r :radius of body trunk
κ :section modulus of curved beam

B. Experiment

To investigate the validity of above algorithm for regisitration, the feature of body structure of healthy volunteers was scanned by MRI (PHILIPS Intera 1.5Master). In this measurement, Body postures for scanning were supine position and lateral position, and the chest area from the first thoracic vertebrae to the 2nd lumbar vertebra was scanned at each postures. The subject of scanning was healthy male who was 180cm tall and weights 70kg.

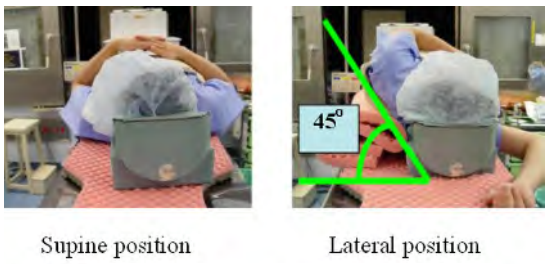


Fig.1 The position of patient

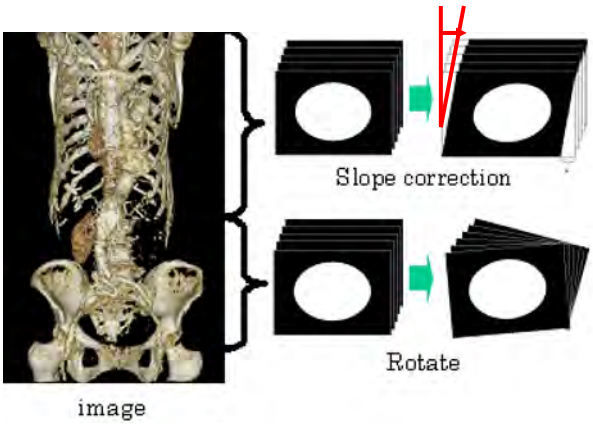


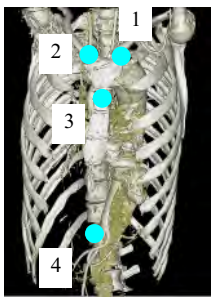
Fig.2 Correction of slice image

These scanned images were saved as DICOM and these images at supine position were corrected by using numerical analysis software MATLAB. Then images were fitted to compare how the corrected images are fitted to those at lateral position. To fit images, several anatomical specific points of the first lumbar vertebra were chosen as a basing points of fitting, because displacement of lumbar vertebra arising from the difference of body position was small. And, before and after corrected images of supine position were fitted into image of right lateral position and calculate the misalignment errors of two images on the sternum (left and right clavicular head, manubriosternal joint and xiphoid process) those are shown in Fig.

III. Result and Discussion

The scanned images are shown in fig.4(a) and (b). The anatomical specific points of these images are circled by green line.To fit the image of supine position to that of right lateral position for this time, image of supine position was slanted for θ = 0.1 rad that was calculated form (1). In this case, elastic constant of the bone E in (1) is 17.0[GPa].The corrected image of fig.4(a) is shown in fig.4(c). The misalignment errors at each positions on the strenum were shown in Table.1.

As shown in Table.1, comparing after corrected image with before corrected image, the misalignment errors reduced by 19.8% an average of anatomical specific points at the sternum. Notice that, the misalignment errors reduced by 26.2% at the manubriosternal joint. This results show that this algorithm tends to be effective for the center of chest that deforms dynamically.



1. left clavicular head
2. right clavicular head
3. manubriosternal joint
4. xiphoid process

Fig.3 Anatomical specific points on the strenum

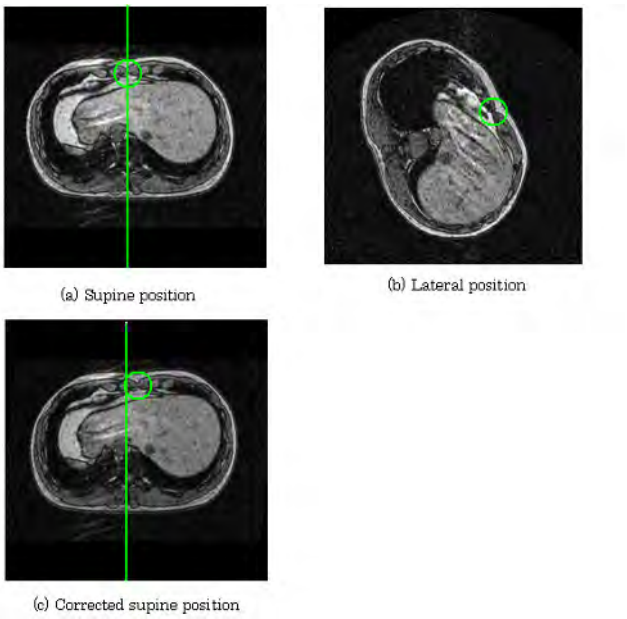


Fig.4 Images scanned by MRI

Table.1 Misalignment of both images at each anatomical specific points

	Before correction[mm]	After correction[mm]	Reduction rate[%]
1	41.1	34.2	16.8
2	34.9	27.1	22.2
3	32.9	24.3	26.2
4	31.3	26.9	13.8
Average	35.0	28.1	19.8

IV. Conclusion

To correct the difference of patient's posture in the aortic surgery, the authors projected the algorithm that deform the image in accordance with real space. This algorithm was examined by comparing the images those were scanned by MRI. As a result, the misalignment errors reduced by 20% an average of anatomical specific points at the sternum, and it was concluded that this algorithm is effective for matching both images.

Foreseeable future, the image corrected by this alorithm will be mounted to navigation system for aortic surgery and used in clinical.

V. Acknowledgements

This research was partly supported by Grant-in-Aid for Scientific Reserch (20700414), Health Science Research Grant (H20-IKOU-IPAN-001) from Ministry of Health, Labour and Welfare, Japan, Biomedical Engineering Research Project on Advanced Medical Treatment from Waseda University (A8201).

References

1. H. Iseki, Y. Muragaki et al.(2004) Robotic Surgery in Neurosurgical Field, Proc of Medical Robotics, Navigation and Visualization (MRNV), p32
2. M.Uematsu, S.Aomi et al. (2006) Clinical Apprication of a Surgical Navigation System for Thoracoabdominal Aortic Replacement, The Japan Society of Computer Aided Surgery,15: 171-172.
3. K. Matsukawa, M.Uematsu et al. (2007) Effect of body torsion on the reliability for navigation system for vascular surgery, The Japan Society of Computer Aided Surgery,16: 127-128.
4. S.Taira, material mechanics (2001) Ohmsha, Ltd. 165-172
5. K.Hayashi, M.Tanaka et al.(1997) Biomechanical Engineering, 100-122

VI. Apprendix

The following is the deriveration of (1).

We assumed that the body trunk at the chest area could be modeled as fig.4 that was flamed by the thoracic cage. In this model, the radius of the trunk is defined as r, the length of rib section is defined as a, and the angle of the body around the body axis is 45 degree. The gravity of trunk is equally dispersed to posterior and right. In this case, only the rightward force is considered because rightward displacement should be calcurated.

In fig.4, S_0S_2 is defined as the centerline of the costale, S is defined as the arbitrary point on the S_0S_2, and Φ is defined as the angle beween the line perpendicular to S_0S_2 and y axis. The location of S_0 is static because S_0 is rested on the bed. The location of S is affected by the weight of internal organ and flexure of the costal. If the location of S shifts ωdφ rotationally, the displacement at S_2 can show the superposition of two displacements those are $SS_2\omega d\varphi$ perpendicular to SS_2 and εds for tangential displacement at S, where ω is the rate of change of φ, and ε is flexure of S_0S_2. Therefore the displacements of X and Y axial components at S is given as follows.

$$\cdot d\Delta(x_2 - x_0) = -y\omega d\phi + \varepsilon dx \qquad \cdots (2)$$

$$\cdot d\Delta(y_2 - y_0) = (x - r)\omega d\phi + \varepsilon dy$$

Δ is calculated by integrating (2) from S_0 to S_2.

$$\cdot\Delta(x_2 - x_0) = -\int_0^{\frac{\pi}{2}} y\omega d\phi + \int_0^{r}\varepsilon dx$$
$$\cdot\Delta(y_2 - y_0) = \int_0^{\frac{\pi}{2}} (r - x)\omega d\phi + \int_{-r}^{0}\varepsilon dy \quad \cdots (3)$$

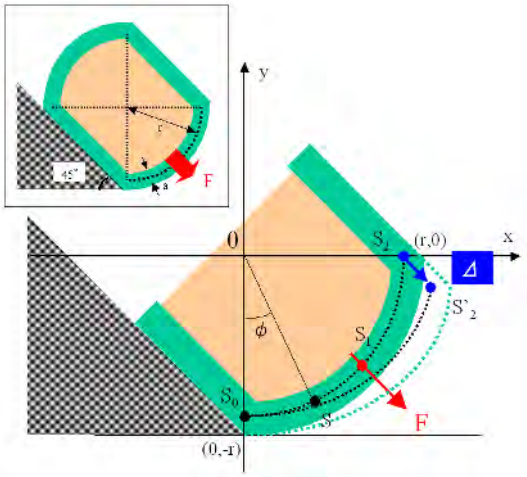


Fig.5 Displacement of thoracic cage

In this case, ε and ω is represented as follows.

$$\begin{cases} \varepsilon = \dfrac{1}{EA}\left(N + \dfrac{M}{r}\right) \\ \omega = \dfrac{1}{EA}\left(N + \dfrac{M}{r} + \dfrac{M}{r\kappa}\right) \end{cases} \qquad \begin{cases} M = Fr\sin\left(\dfrac{\pi}{4} - \phi\right) \\ N = -F\sin\left(\dfrac{\pi}{4} - \phi\right) \end{cases}$$

Therefore the (3) is represented as follows.

$$\cdot\ \Delta x = \frac{Fr}{EA\kappa}\int_0^{\frac{\pi}{2}} \sin\left(\frac{\pi}{4} - \phi\right)\cos\phi d\phi = \frac{Fr}{4EA\kappa}\left(\frac{\pi}{\sqrt{2}} - \sqrt{2}\right) \quad \cdots (4)$$

$$\cdot\ \Delta y = \frac{-Fr}{EA\kappa}\int_0^{\frac{\pi}{2}} \sin\left(\frac{\pi}{4} - \phi\right)\sin\phi d\phi = \frac{-Fr}{4EA\kappa}\left(\frac{\pi}{\sqrt{2}} - \sqrt{2}\right)$$

By combining Δx and Δy, Δ is considered as follows.

$$\Delta = \frac{Fr(\pi - 2)}{4EA\kappa} \quad (5)$$

A :cross section of the costale
E :elastic constant of the bone
F :gravitation force of organ in the chest
r :radius of body trunk

And κ is the section modulus of curved beam and defined as follows in this case.[4]

$$\kappa = \frac{r}{A}\int_A \frac{dA}{r + \eta} - 1 = \frac{2r}{\pi a^2}\int_{-a}^{a} \frac{\sqrt{a^2 - \eta^2}}{r + \eta} d\eta - 1 = \frac{2r^2}{a^2}\left\{1 - \sqrt{1 - \left(\frac{a}{r}\right)^2}\right\} - 1$$

θ (the angle to slant) can be elicitated as follows.

$$\theta = \tan^{-1}\frac{\Delta}{\sqrt{2}r} = \tan^{-1}\frac{(\pi - 2)Fr}{4\sqrt{2}EA\kappa}$$

Bioengineering Advances and Cutting-edge Technology

M. Umezu

Center for Advanced Biomedical Sciences, TWIns, Waseda University, Tokyo, Japan

Abstract — **There is a forty-year history of research collaboration by doctors at Tokyo Women's Medical University and engineers at Waseda University. The synergism culminated in 2008 with the establishment of the Center for Advanced Biomedical Sciences within the framework of the Tokyo Women's Medical University-Waseda University Joint Institution for Advanced Biomedical Sciences (TWIns). The center provides a singular environment for consolidating research in life science, bioengineering, and medicine. At first our new conceptual laboratories, called "DRY Lab" is introduced. There are three laboratories: Surgical Training Lab, GLP-compliant Lab and Medical Visualization Lab. These laboratories have a complement function of an animal (WET) laboratory. Secondly, an implantable centrifugal blood pump called EVAHEART as an exemplary product of this collaboration is introduced. Cardiac surgeon Kenji Yamazaki of Tokyo Women's Medical University, Sun Medical Technology Research Corporation, Waseda University, and the University of Pittsburgh originated the EVAHEART project in 1991. More than fifty companies contributed technologies that improved performance of the device. Teamwork between groups with divergent thinking and expertise led to optimized designs of components such as the impeller, shaft/seal mechanism, and blood-compatible materials. In clinical trials, fourteen of eighteen patients treated with EVAHEART had favorable postoperative outcomes. In the first case, the pump sustained the patient for more than three and one-half years. Among the four patients who died, none had a cause of death related to the device itself. Consequently, it is confirmed that this synergistic environment will help us create new scenarios and trials which are unconstrained by conventional knowledge.**

Keywords — **Biomedical engineering, Consolidating research, DRY Lab, EVAHEART, Implantable blood pump.**

I. Introduction

The Tokyo Women's Medical University-Waseda University Joint Institution for Advanced Biomedical Sciences, TWIns, opened in March of 2008 after a forty-year history of research collaboration on projects related to artificial organs, biological measurement and biomaterials. The institution, which is located next to the Tokyo Women's Medical University Hospital in Shinjuku, Tokyo, is a new center for the advancement of biomedical research based on a synergy of medicine, science, and engineering [1].

For Waseda University, there are two major objectives for the formation of the new center. The first objective is to consolidate into one place the research for life science and biology which had been broadly dispersed in different campuses. The second objective is to develop new fields through synergetic partnerships in medicine, science, and engineering, and to provide a singular environment for that development. In this environment where the fields of medicine, science, and engineering mix in a variety of different approaches, unconstrained research topics can be achieved. A vision has been created for the new center to act as a base for the dispersion of new scenarios that shatter previous conventions.

In this paper, one of our new conceptual laboratories for a training program for medical personnel called "DRY-Lab" is introduced. Moreover, Japanese-made implantable blood Pump (EVAHEART) is also introduced as an examplary product of this collaboration.

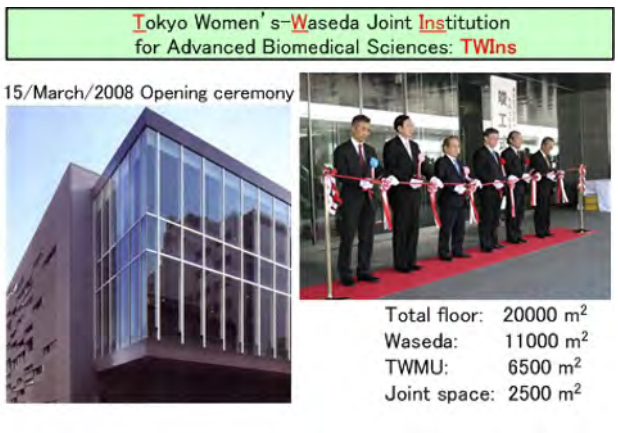


Fig.1 Overview of TWIns

II. Establishment of DRY Lab Training Center / Promotion of Engineering Based Medicine (EBM)

A. Concept of DRY Lab

Animal and cadaver WET Lab is a common opportunity of surgical training, particularly in the United States. The advantage of WET lab is hands-on training in clinically-familiar environments. However, opportunities of animal

Chwee Teck Lim, James C.H. Goh (Eds.): ICBME 2008, Proceedings 23, pp. 2143–2146, 2009
www.springerlink.com

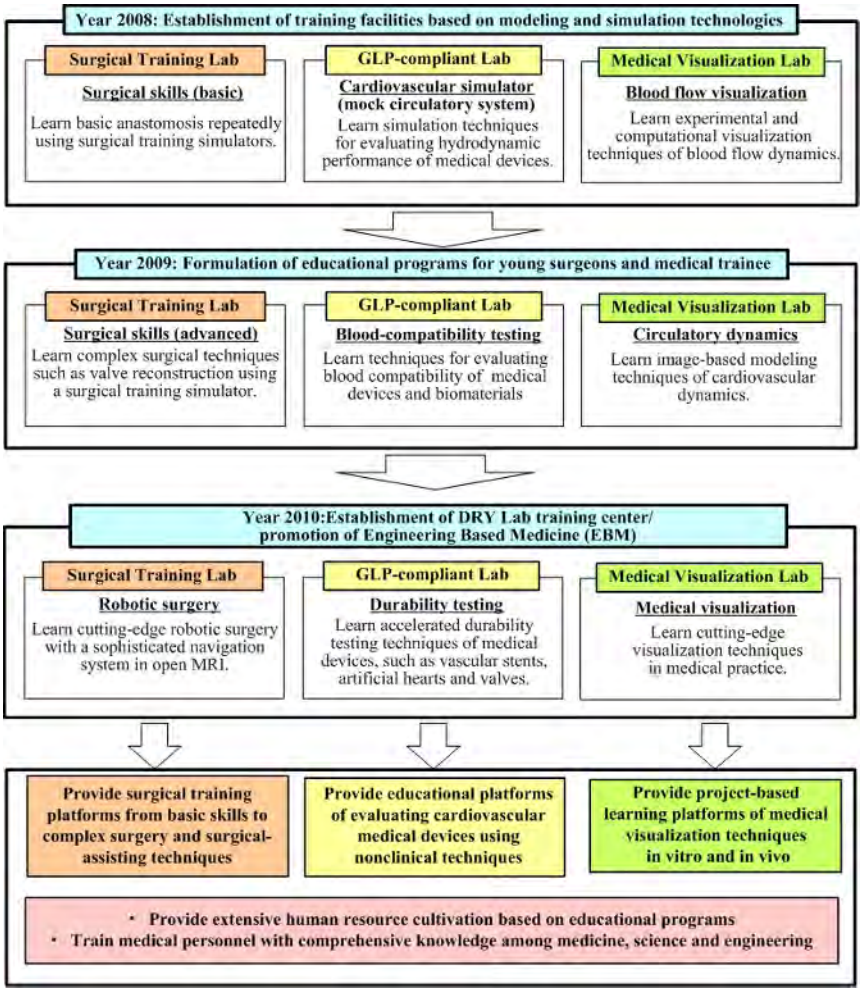


Fig.2 Overview of DRY Lab and yearly schedule for the next three years

experiments have become increasingly limited including the use of biological tissues. Therefore, a self-training system prior to WET Lab would be an effective procedure. Herein, we propose such educational environments for training medical personnel, and this new concept is termed DRY Lab in contrast to WET Lab [2].

B. Overview of DRY Lab

DRY Lab features nonclinical hands-on training based on modeling and simulation technologies using consolidated functions among medicine, science and engineering at TWIns. More specifically, DRL Lab consisted of three major laboratories: 1) Surgical Training Lab, 2) GLP-compliant Lab, and 3) Medical Visualization Lab. An underlying technical platform among these laboratories stems from artificial organ developments and evaluation techniques, particularly hemodynamics, blood compatibility and durability. All these technologies are sophisticated for educational purpose.

Fig.2 shows an overall figure of DRY Lab for the next three years. Surgical Training Lab is to educate from repeated training of basic anastomosis to advanced surgeries, such as valve reconstruction and robotic surgeries, using original surgical simulators. In contrast, GLP-compliant Lab provides development and evaluation techniques of cardiovascular medical devices and biomaterials. Medical Visualization Lab is to educate modeling and simulation techniques in conjunction with clinical medicine, including blood flow analysis, circulatory dynamics and cutting-edge medical visualization techniques.

In year 2010, we would start a DRY Lab training center with established educational programs. Extensive human resource cultivation would be achieved for training clini-

cians, bioengineers, and bioscientists with comprehensive knowledge among medicine, science and engineering. This training center would promote another EBM in contrast to Evidenced Based Medicine, namely "Engineering Based Medicine".

III. Development of EVAHEART and Clinical Trials

A. Brief Introduction of EVAHEART

The first clinical trial of a Japanese implantable centrifugal type ventricular assist device, EVAHEART (Fig.3) [3-4], was done in 2005 at Tokyo Women's Medical University. Since then, a total number of implantation reached 18 cases. During this long-term support, there is no major device failure and related death. And the longest period has reached more than three and half years. To achieve this success, bioengineers have established a methodology of various types of *in vitro* tests to minimize risk factors, such as hydrodynamic performance tests, fatigue tests, and biocompatibility tests, which are briefly introduced in this chapter.



Fig.3 EVAHEART system (clinical model)

B. Biocompatibility test for inner coating of the blood pump

Biocompatibility is one of the most important factors to realize a safe and reliable long-term use of a blood pump. A test protocol using our original circuit [5] is as follows:

1. Heparinized fresh porcine blood harvested from the same animal circulate in the circuit comparative study.
2. Therefore, the same amount of identical blood is injected into two circuits for comparison.
3. Pulsatile circulation to simulate hemodynamic pressure / flow condition is preferable to obtain practical data.

Fig. 4 is one of the results after one hour circulation of fresh bovine blood. Anticoagurant agent (heparin) was used to maintain the ACT of around 300sec. The same amount of blood was divided into two identical circuits. As can be

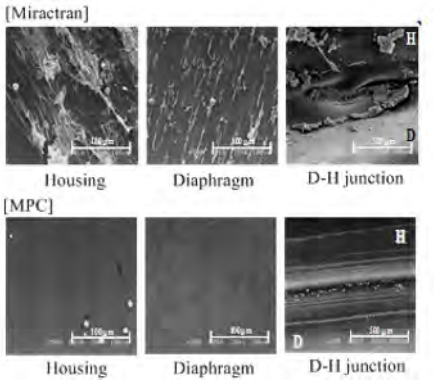


Fig.4 Example of biocompatibility results from our in vitro blood circuit (comparison between Miractran and MPC)



Fig.5 EVAHEART from a patient undergoing heart transplantation (POD: 1165 days). There is no thrombus observed.

seen, fibrin network was observed and some blood cells were captured on the Miractran surface of the left ventricular pump. On the contrary, MPC surface was clean [6]. Although both coating materials are polyurethane, biocompatibility was clearly differentiated. This excellent biocompatibility of MPC has been clinically proved. Fig. 5 shows an example of a pump photograph from a patient undergoing heart transplantation. No thrombus was observed after a pumping duration of 1165 days.

C. Quality Improvement of Life with EVAHEART

Table 1 is a patient summary of EVAHEART for pilot study. The first three patients suffered from DCM (Dilated Cardio-Myopathy), but after implantation, all patients discharged and high quality of life with EVAHEART can be maintained for over 1000 days. In the first case, the patient always lay on bed before implantation, and could not move due to a severe heart failure. However, he started to walk in the hospital only a few days after the implantation of EVAHEART. During support, he never felt an existence of EVAHEART with a weight of 420g [7]. He spent ten months for rehabilitation training, and he was discharged

Table 1 Clinical outcome of the first three patients with EVAHEART

No.	Age/sex	Diag.	Institute	POD (2008.10.31)
1	46 y M	DCM	TWMU	1274 (ongoing)
2	29 y M	DCM	TWMU	1165 (transplanted)
3	40 y F	DCM	NCVC	1147 (transplanted)

Table 2 Categorized clinical outcome with EVAHEART

Outcome	No. of cases	Pumping duration
Alive, ongoing	12	250 ~ 1274
Transplanted	2	1147, 1165
Died	4	61～407

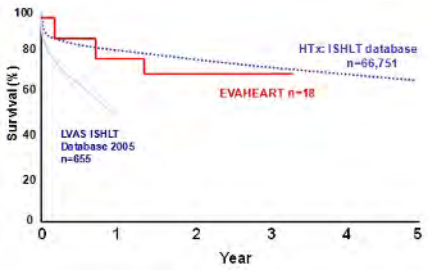


Fig.6 Survival rate of patients with EVAHEART

from the hospital. Then, his medical cost became only 1/100 as compared with that in the hospital. Moreover, he found a full-time job after 18 months later.

As the pumping duration for the first three patients exceeds 1100 days without any major problems, survival rate with EVAHEART is much better than that with other devices. For example, survival rate with US pulsatile implantable devices exhibited only 30 % after 18 months pumping. [8]. Table 2 summaries the current status of EVAHEART. The survival rate have been comparable to heart transplantation as shown in Fig.6.

IV. Conclusion

The authors have been establishing a methodology to eliminate considerable risk factors through a development of practical *in vitro* test circuits at DRY Lab in TWIns. It was confirmed that all *in vitro* tests were effective to ensure safety toward clinical applications. Therefore, clinical trials can be performed without any major problems. According to the comment by the first patient with EVAHEART, he does not wish to receive donor heart; he is satisfied with his present quality of life. Throughout the development and clinical trials of EVAHEART, the authors believe that the role of TWIns will generate much more new trials for advanced biomedical engineering.

References

1. http://www.yomiuri.co.jp/adv/wol/dy/research/tokku_080729.htm
2. Y. Park, M. Umezu, et al. (2007) Quantitative evaluation for anastomotic technique of coronary bypass grafting by using in-vitro mock circulatory system. EBMS 2007, 29th Ann. Int. Conf. of the IEEE, pp2705-2708.
3. K. Yamazaki , T. Mori, et al. (1994) The cool-seal concept: A low temperature mechanical seal with recirculating purge system for blood pumps. Kobayashi, H., Akutsu, T., (Eds)," Artificial Heart 6. Springer-Verlag, Tokyo, Japan, pp. 339-344.
4. M. Umezu, K. Yamazaki, S. Yamazaki, K. Iwasaki, T. Miyakoshi, T. Kitano, T. Tokuno (2007) Japanese-made implantable centrifugal type ventricular assist system (LVAS): EVAHEART, Biocybernetics and Biomedical Engineering, 27(1/2), pp. 111-119.
5. K. Iwasaki, M. Umezu, T. Tsujimoto, W. Saeki, A. Inoue, T. Nakazawa, M. Arita, C.X. Ye, K. Imachi, K. Ishihara, T. Tanaka (2002) A challenge to develop an inexpensive 'Spiral vortex pump," 2nd Waseda-Renji Hospital BioMedical Engineering Symposium, Shanghai, China, pp. 8-10.
6. K. Ishihara, T. Tsuji, T. Kurosaki, N. Nakabayashi (1994) Hemocompatibility on graft copolymers of poly (2-methacryloyloxyethyl phosphorylcholine) side chain and poly (n-butyl methacrylate) backbone," Journal of Biomedical Materials Research, 28, pp. 225-232.
7. K. Yamazaki, S. Saito, S. Kihara, et al. (2007) Completely pulsatile high flow circulatory support with constant–speed centrifugal blood pump," Gen Thorac cardiovse Surg 55, pp.158-162.
8. J. L. Navia, P. M. McCarthy, K. J. Hoerchar, et al. (2002) Do left ventricular assist devise bridge-to transplantation outcomes predict the results of permanent LVAD implantation," Ann Thorac Surg 74, pp. 2051-2062.

Acknowledgement

This research was partly supported by Health Science Research Grant (H20-IKOU-IPAN-001) from Ministry of Health, Labour and Welfare, Japan, Biomedical Engineering Research Project on Advanced Medical Treatment from Waseda University (A8201), and The Synergetic Center for Medical Technology High Tech Promotion for Private University (H20-25), Ministry of Education, Culture, Sports Science and Technology, Japan.

References

Author: Mitsuo Umezu, Ph.D,
Institute: Center for Advanced Biomedical Sciences, TWIns, Waseda University
Street: 2-2 Wakamatsu-cho, Shinjuku
City: Tokyo
Country: Japan
Email: umezu @waseda.jp

Effect of PLGA Nano-Fiber/Film Composite on HUVECs for Vascular Graft Scaffold

H.J. Seo[1], S.M. Yu[1], S.H. Lee[1], J.B. Choi[2], J.-C. Park[3] and J.K. Kim[1]

[1]Department of Biomedical Engineering, Inje University, Gimhae, Korea
[2]Department of Mechanical System Engineering, Hansung University, Seoul, Korea
[3]Department of Medial Engineering, Yonsei University, Seoul, Korea
[*]jkkim@inje.ac.kr

Abstract — **Potential application of the PLGA nano-fiber/film composite for vascular tissue regeneration was examined. The composite was prepared by solvent-casting and electro-spinning method. The PLGA nano-fiber was coated on the surface of the prepared PLGA film. The surface of the composite film was characterized by contact angle measurement and scanning electron microscope (SEM). The film made by only nano-fiber showed more hydrophobic than control (PLGA film made by solvent-casting); however, optimal amount of nano fibers coating could assist cell adhesion and spreading on the film. For human umbilical vein endothelial cells (HUVECs) proliferation on 6-day culture, the NF-30 (30min. nano-fiber spread specimen) composite was 1.5 times more cells proliferated than that of the NFO-1h (nano-fiber only specimen). The SEM images showed that the HUVECs on the NF-30 specimen spread widely than the other groups. The result indicates that the nano-fibers on films have an effect on cell adhesion and spreading because the adequate amount of nano-fibers on the surface of the films provide similar structure to natural ECM morphology. Conclusively, nano-fiber/film composite provided an adequate environment for cell proliferation and showed the potential application for vascular tissue regeneration.**

Keywords — **HUVECs, PLGA, electro-spinning, nano-fiber, ECM**

I. Introduction

Atherosclerotic vascular disease is one of the largest causes of mortality in western society [1]. This problem is widely happened in coronary artery and peripheral vascular system [2]. One of the commonest treatment methods is coronary artery bypass graft surgery. The procedure involves bypassing occluded arteries with either autologous veins or arteries. However, this method typically confronts limitation of autologous grafts. Up to 30% of patients do not have sufficient autologous bypass veins due to prior stripping, disease or discordant size [3]. Accordingly, there have been efforts and various attempts for development of small diameter (< 6mm) vessel substitutes. Biodegradable polymer, poly D, L-lactic-co-glycolic acid (PLGA) can be used for scaffolds of vascular grafts and tissue engineering due to its biocompatibility and biodegradability as well as capable of tissue regeneration ability [4-6].

Electro-spinning technique has recently issued a great deal of attention for biomedical applications, specially, vascular tissue engineering [7-9]. The advantage of an ultra fine, continuous nano-fiber is high porosity, variable pore-size distribution, high surface-to-volume ratio, and most importantly, morphological similarity to natural extracellular matrix (ECM) [4].

There have been many approaches to vascular graft research by nano-fiber composites [5, 9, 10]. In this study, for the adequate environment for HUVECs attachment and proliferation, the PLGA nano-fiber/film composite was fabricated by electro-spinning and solvent-casting methods. The nano-fiber layered on the surface of PLGA film, which has similar structures to ECM, could improve cell attachment and proliferation for vascular HUVECs. The quantity of nano-fiber on the surface of the films was controlled by electro-spinning time. The PLGA solution was ejected form syringe by 10min, 30min, 1h and 2h on the surface of the films. The structure and cytocompatibility of the prepared specimens were investigated.

II. Matreials and methods

A. Electrospinning apparatus

The electro-spinning apparatus consisted of a High-voltage-power supply (40k, Tek Kam Measurement, Korea), spray nozzle, and collector. A stainless still needle of syringe was used as the spray nozzle (+) and a copper plate was used as the collector (-).

B. Preparation of the PLGA nano-fiber/film composite

The PLGA 7525 film was prepared by solvent-casting method. 2g of PLGA 75:25(M_w = 111kD, Brookwood Pharmaceuticals, Inc.) was dissolved in 12ml of chloroform. (DUKSAN PURE chemical Ltd., Korea) The solution was stirred at room temperature for 24h and cast into a mold.

Chwee Teck Lim, James C.H. Goh (Eds.): ICBME 2008, Proceedings 23, pp. 2147–2150, 2009
www.springerlink.com

The solvent was allowed to evaporate for 3 days at ambient conditions, and vacuum freeze-dried for 2days. Then, polymer solution was prepared by dissolving PLGA 7525 in 1:1 mixture of *N,N*-dimethlformamide and tetrahydrofuran (Junsei chemical Co., Ltd., Japan), mixing it well by overtaxing the mixture [4]. The PLGA nano-fiber was produced by electro-spinning process on the prepared PLGA films. The PLGA solution (30 wt%) was placed in a 20ml syringe with an 18-G needle. It was ejected 10min, 30min, 1h and 2h on the surface of the films with driving voltage 18kV and air gap 20cm.(NFC series) For nano-fiber-only film (NFO-1h), the polymer solution was ejected for 1 hour on the metal plate.

C. Characterization of the PLGA nano-fiber/film composite

The morphology of the PLGA nano-fiber/film composite was observed by the field emission scanning electron microscope (FE-SEM) (HITACHI S-4300DSE., Japan) at 3 kV. Static contact angle measurement of the specimens conducted and characterized by contact angle analyzer (Phoenix 150).

D. Cell culture & proliferation

Human umbilical vein endothelial cells (HUVEC) were cultured in Medium200 with Low-serum Growth supplement and antibiotic (Gentamicin/Amphotericin solution). Cells and reagents were purchased from Cascade Biologics (Portland, OR). The HUVEC were cultured at culture flasks in a humidified incubator at 37 °C and 5% CO_2 atmosphere. The medium was replaced every 2 days.

The PLGA nano-fiber/film composite specimens (10×10 mm^2), were sterilized with 70% ethanol and subsequent air-drying, were placed in the bottom of a 24-well culture plate. The specimens were performed pre-wetting in the media for 24h.

The HUVECs (1.2×10^6 cells/film) were seeded on the specimens and cultured in a humidified incubator containing 5% CO_2 at 37 °C. Cell viability and proliferation were determined at 1st, 3rd and 6th day by MTT assay. (Rocke Diagnostics Corporation) The absorbance was measured by multi micro plate reader (synergy HT, BIO-TEK®) at 570nm. The specimens of 9th day harvest were fixed by addition 1 ml of 3.0 % formaldehyde solution for cell morphology analysis by SEM.

E. Statistical analysis

All the quantitative values were expressed as mean ± standard deviation (S.D.) for all comparisons. The one-way ANOVA test by SPSS for window (SPSS INC., version 12) was used for significance of difference among the specimens. The difference of value was considered to be statistically significant at $p<0.05$.

III. Results and discussion

A. Characterization of the PLGA nano-fiber/film composite

The SEM images were investigated the surface morphology of the PLGA nano-fiber/film composite and control PLGA films. (Fig. 1) The electro-spun fibers deposited as a non-woven, linear and bead-free form on the PLGA films. Total amount of electro-spun nano-fiber on surface of the films was varied with time-dependent values. The NFC-10 and NFC-30 composites showed that the nano fibers were deposited partially on the film surface, less dense compared with NFC-1 and NFC-2 composites. (Fig. 1 (a), (b)) The NFC-1 and NFC-2 composites have not revealed the bottom of the films, an increase in density of nano-fibers deposited on the films. (Fig. 1 (d), (e))

The mean fiber diameter at the surface of composite was obtained from the SEM images.

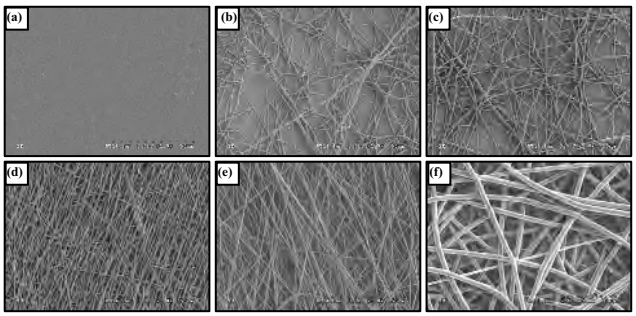


Fig. 1 SEM observation of the PLGA nano-fiber composite and control PLGA films (a) PLGA film (b) NFC-10 (c) NFC-30 (d) NFC-1 (e) NFC-2 (f) NFO-1

Table 1 Diameter of PLGA nano-fiber/film composite

Specimens	Diameter ($x10^{-6}$ m)
PLGA film	-
NFC-10	1.00±0.30
NFC-30	0.96±0.34
NFC-1	1.36±0.53
NFC-2	1.30±0.46
NFO-1	0.98±0.17

The contact angles of the PLGA nano-fiber/film composites were increased from 55° up to 115°, as expressed in Fig. 2. The NFC-30 specimen (Fig. 2 (b)) was similar to control

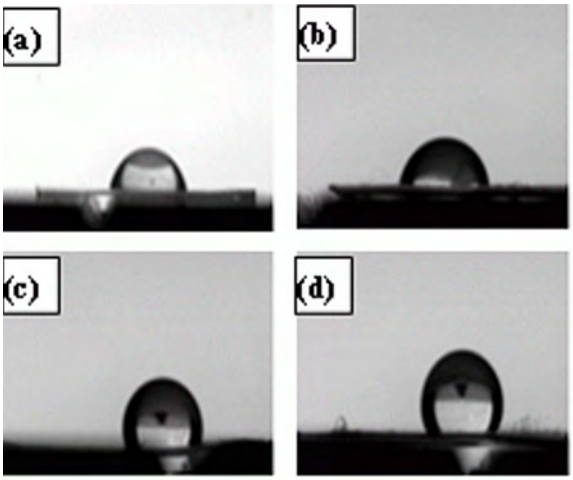


Fig. 2 Contact angle image the PLGA nano-fiber/film composite (a) PLGA film (b) NF-30 (C) NF-1 (d) NF-2

film (Fig. 2 (a)) to 55°. The NFC-1 and NFC-2 specimens were showed 110° and 115°, respectively. (Fig. 2 (c) and (d)) Denser the nano-fiber, the surface was more hydrophobic due to the increment of surface tension.

B. Cellular proliferation and morphology

The proliferation of HUVECs at 1, 3, and 6-day culture on the prepared specimens is shown in Fig. 3. The HUVECs proliferation assaying at 6th-day, there were no significant differences between the average value of control film and NFC-10 & NFC-30 specimens. However, nano-fiber treated group showed very narrow range of standard deviation for cell proliferation compared to control group. Despite contact angle increment, cell proliferation and adhesion was no significant distinction between the NFC-30 and the NFC-1. It means that a little higher contact angle is not affected to the HUVECs' adhesion and proliferation.

The NFC-30 showed about 1.5 times higher than only NFO-1 mesh specimen at 6th-day. ($p<0.05$) This might be caused by shrinkage-deformation of nano fibers of the NFO-1 mesh specimen [11, 12]. Fig. 4 (f) showed deformed pores by shrinkage of NFO-1 specimen. This deformation interfered with cell viability as well as proliferation on the NFO-1 mesh specimen.

Fig. 4 provides visual comparisons of cell adhesion and spreading for nano-fiber composite and control PLGA films for 9-day culture. It shows that the HUVECs on the NFC-30 specimen spread widely than the NF-10 (Figure 4. (b) and (c)). This result indicates that the nano-fibers on films have an effect on adhesion and spreading of cells which anchored by nano fibers at the surface. Because the nano-fibers of the surface of the films provide structure similar to natural ECM. The NFC-1 and NFC-2 (Fig. 4 (d) and (e)) specimens showed less deformed than NFO-1 (Figure 4. (f)). It appeared that the PLGA film prevented the nano-fiber from deformation.

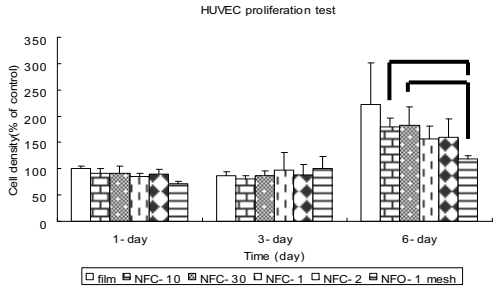


Fig. 3 Proliferation of HUVECs on the PLGA nano-fiber/film composite. (n=6) (*$p<0.05$)

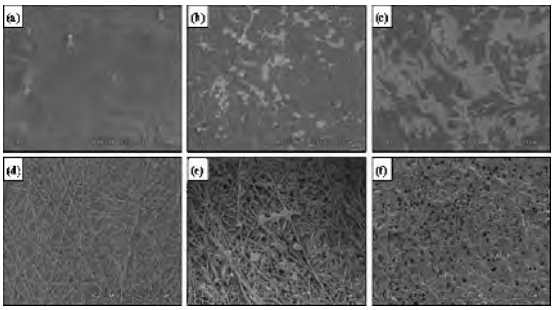


Fig. 4 SEM image: In vitro HUVECs adhesion and proliferation on the PLGA nano-fiber composite after 9th days. (a) PLGA film, (b) NF-10, (c) NF-30, (d) NF-1, (e) NF-2, (f) NFO-1 mesh

IV. Conclusions

In the present study, the HUVECs were cultivated from the adequate amount of nano fiber coating on surface of film/scaffold. The nano fibers on the surface of the films were more hydrophobic than control film; however, optimal amount of nano fibers could assist cell adhesion and spreading. The result showed not effective on cell proliferation for nano-fiber coated film; however, it showed narrower standard deviation for cellular proliferation. Presumably and conclusively, nano-fibrous structure could have an effect for cell proliferation as well as adhesion as if it treated with optimized amount and structure. In future, we try to find the optimized amount and nano-scaled structure for improving cellular adhesion and proliferation.

ACKNOWLEDGMENT

"This study was supported by the Korea Health Industry-development Institute" (A080837)

REFERENCES

1. American Heart Association: *Heart Disease and Stroke Statistics*-2005 Uptate. Dallas, TX, 2004
2. Lysaght M J, Reyes J 2001 Tissue engineering. **7** 485-8
3. Nerem R M and Seliktar Dror 2001 *Annual Review of Biomaterial Engineering*. **3** 225-43
4. Li W-J, Laurencin C T, Caterson E J, Tuan R S and Ko F K 2002 *J Biomed Mater Res.* **60** 613-21s
5. Duan B, Wu L, Yuan X, Hu Z, Li X, Zhang Y, Yao K and Wang Min 2007 *J Biomed Mater Res*. **83** A 868-78
6. Kim T G, Park T G 2006 *Tissue Engineering.* **12** 221-33
7. Williamson M R, Black R and Kielty C 2006 *Biomaterials.* **27**, 3608-16
8. Imoguchi H, Kwon I K, Inoue E, Takamizawa K, Maehara Y and Matsuda T 2006 *Biomaterials.* **27** 1470-78
9. Vaz C.M, Tuijl S. van, Bouten C.V.C and Baaijeans F.P.T. 2005 *Acta Biomaterialia*. **1** 575-82
10. Jeong S I, Kim S Y, Cho S K, Chong M S, Kim K S, Kim H, Lee S B and Lee Y M 2007 *Biomaterials.* **28** 1115-21
11. Li W-J, Cooper Jr J A, Mauck R L and Tuan R S 2006 *Acta Biomaterilalia.* **2** 377-85
12. Zong X, Ran S, Kim K-S, Fang D, Hsiao B S and Chu B 2003 *Biomacromolecules*. **4** 416-23

Muscle and Joint Biomechanics in the Osteoarthritic Knee

W. Herzog

The University of Calgary, Faculties of Kinesiology, Engineering and Medicine, Calgary, Canada

Abstract — **Osteoarthritis (OA) is a debilitating disease associated with joint pain, swelling, stiffness and characterized by loss of articular cartilage from the joint surfaces. The causes for osteoarthritis onset and progression remain largely unknown, but abnormal mechanical loading of joints has been implicated as a primary mechanism for OA. Since most of the loading of joints comes from muscular contraction, the role of muscles in controlling joint actions and producing loads has been of major interest in osteoarthritis research.**

A general goal of our studies has been to elucidate the role of muscles in a variety of animal and human models of OA. Muscle function was measured using a variety of approaches including direct muscle force measurements in live animal models of OA in conjunction with electromyography, 3-dimensional kinematics and kinetics. We found that OA causes selective muscle inhibition, that muscle control is lost to a large degree in animal models of OA, that muscles atrophy following OA onset, and that muscle weakness might be an independent risk factor for osteoarthritis. Furthermore, muscular training in animal models of osteoarthritis has been successful at restoring strength, but, depending on the detailed loading conditions, has also led to increased rates of OA progression as quantified using histological assessment and Mankin scoring.

Taken together, we conclude that an understanding of muscle function is essential for the prevention and treatment of osteoarthritis, and conservative treatment modalities involving muscle control and strength might play key roles in OA prevention and delay.

Keywords — **osteoarthritis, muscles, joints, biomechanics, animal models**

I. Methods

Force measurements in animal models of osteoarthritis are performed using buckle type tendon force transducers [1] and muscle coordination patterns are quantified using *electromyographical (EMG) recordings* of selected muscles [2]. *Pressure patterns* in the intact knee are measured using low and medium grade Fuji pressure sensor film [3, 4, 5]. *Osteoarthritis onset and progression* are quantified via gross morphology, histological assessment (Mankin scoring; [6], and biochemical or molecular biology approaches [7, 8].

For our research on animal models of muscle weakness, we used botulinum toxin type-A (Botox) injections into the target muscles at a dosage of 3.0-3.5 units per kg mass of the animals [9, 10].

II. Selected results

Our early work on osteoarthritis was focused on the cat anterior cruciate ligament transected (ACLT) knee, which we showed to be a bona fide model of osteoarthritis. Following ACL transection, the medial aspect of the joint capsule, including the medial collateral ligament, becomes thickened (Figure 1), osteophytes form at the joint margins, and the articular cartilage initially increases in thickness, becomes softer and joint contact areas increase while peak pressures decrease (Figure 2). Immediately following ACL transection, the vertical ground reaction forces decrease (Figure 3), and so do the muscular forces in the experimental compared to the contralateral hind limb (Figure 4). EMG signals in the knee extensors become intermittent, rather than the normal continuous firing patterns (Figure 4) and knee flexor muscles show additional bursts at the precise moment of first ground contact, presumably to prevent anterior tibial translation relative to the femur when the ACL is missing (Figure 4). Anterior-posterior stiffness of the knee (evaluated with an anterior drawer test) is dramatically decreased following ACL transection in the cat, but recovers to normal values within 4 months of intervention (Figure 5).

Following Botox injection into the rabbit knee extensor musculature, the size of the muscles (Figure 6), muscle mass (Figure 7) and strength (Figure 8) were decreased significantly. Similarly, the vertical push-off forces during hopping were also reduced in the experimental compared to the contralateral (non-injected) hind limbs (Figure 9).



Fig. 1: Intact (left) and ACL-transected cat knee (right) at 12 weeks following intervention. Note the thickening of the medial joint capsule (curved arrow), and the osteophyte formation at the edges of the joint (straight arrows) in the experimental ACL-transected knee.

Chwee Teck Lim, James C.H. Goh (Eds.): ICBME 2008, Proceedings 23, pp. 2151–2154, 2009
www.springerlink.com

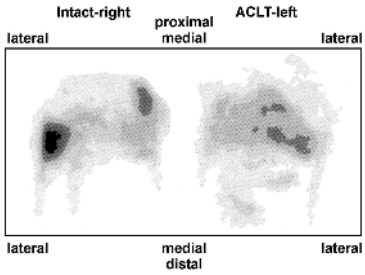


Fig. 2: Patellofemoral contact pressures measured with Fuji Presensor film in an intact knee and the contralateral anterior cruciate ligament transected knee at 16 weeks post-intervention. Increased pressures are represented by darker staining. Note the greater peak pressures in the intact joint and the greater contact area in the anterior cruciate ligament-transected joint (*ACLT*), as predicted theoretically. This result was consistent for five independent observations and for the whole range of loading conditions (not shown).

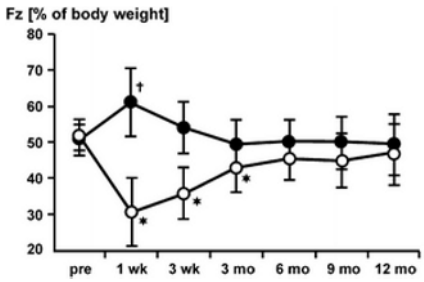


Fig. 3: Vertical ground reaction forces as a percentage of body weight for the transected (*open circles*) and contralateral (*closed circles*) hind limbs before anterior cruciate ligament transection (ACLT) and at different time points post-ACLT. *Asterisks* and *dagger* indicate significant differences from pre-transection values of the corresponding leg. The values are means (± SD) for seven cats, with multiple steps for each cat.

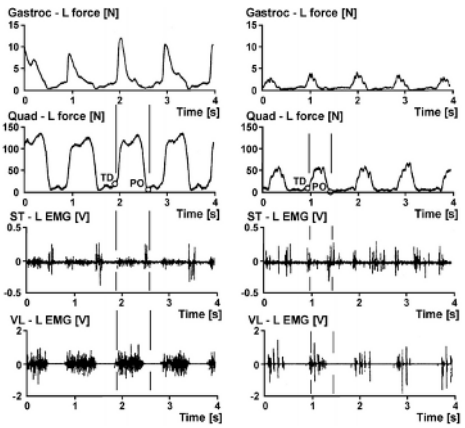


Fig. 4: Gastrocnemius (*gastroc*) and quadriceps (*Quad*) forces and semitendinosus (*ST*) and VL EMGs from a representative cat before (*left*) and 7 days after (*right*) anterior cruciate ligament transection (ACLT). Results are shown for four full step cycles of slow walking. TD and PO are indicated in both panels for one step cycle and they contain the stance phase of the target hind limb. Note the decrease in force from before to after ACLT and the obvious changes in the EMG patterns.

Botox-induced muscle weakness caused visible changes to the articulating surfaces of the knee (Figure 10) and histological analysis revealed increased progression of osteoarthritis in the experimental hind limbs (Figure 11). Histological sections of the muscles following 6 months of Botox treatment revealed that muscles had lost contractile material that was replaced by fat (Figure 12).

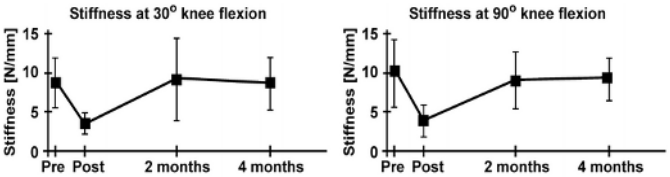


Fig. 5: Anterior–posterior stiffness of cat tibial displacement relative to the femur, before (*pre*), immediately after (*post*) and at 2 and 4 months after anterior cruciate ligament transection (n=4) for knee flexion at angles of 30° and 90°. Note that the anterior stiffness of the cat knee decreases dramatically after anterior cruciate ligament transection, but that this stiffness is back to normal at 4 months post-intervention. Similar results were observed for internal rotation stiffness of the cat tibia relative to the femur (not shown).



Fig. 6: Example of muscle mass loss following BTX-A injection. Top row: rabbit quadriceps muscles from control (contralateral) leg; bottom row: the corresponding quadriceps muscles from the experimental hind limb one month following injection of 3.5 units/kg BTX-A, as described in the methods section.

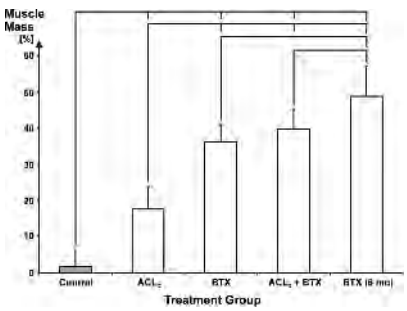


Fig. 7: Percent loss of muscle mass in control, ACL-transected (ACL_x), Botox injected after 1 month (BTX), ACL_x and BTX combined, and repeat Botox injections for 6 months (BTX, 6 months). Percent loss of muscle mass was determined relative to the contralateral control leg.

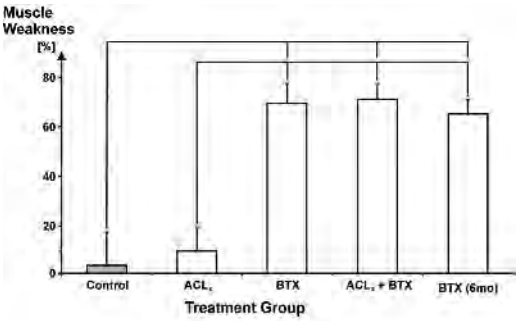


Fig. 8: Percent muscle weakness in control, ACL-transected (ACL_x), Botox injected after 1 month (BTX), ACL_x and BTX combined, and repeat Botox injections for 6 months (BTX, 6 months). Percent loss of strength was determined relative to the contralateral control leg.

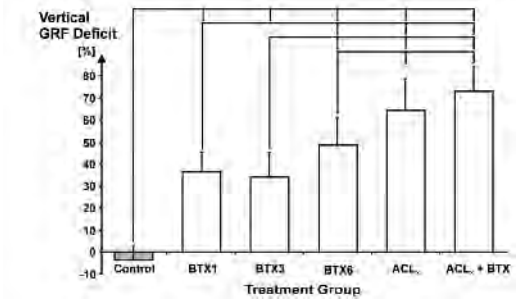


Fig. 9: Decrease in the vertical push off force during hopping for control, ACL-transected (ACL_x), Botox injected after 1 month (BTX1), 3 months (BTX3), 6 months (BTX6), ACL-transected (ACL_x), and ACL_x and BTX combined. Push off forces were significantly ($p < 0.05$) smaller in all experimental groups compared to control, were smaller following 6 months of repeat BTX-A injections (BTX6) than either following 1 or 3 months (BTX1, BTX3, respectively), and were smaller yet for the two ACL transection groups (ACL_x and ACL_x + BTX) than any other experimental group.

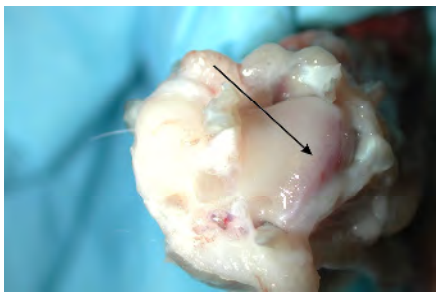


Fig. 10: Example of reddening on the margins of the tibial plateau (arrow) in a knee 1 month following a single Botox injection into the knee extensor musculature.

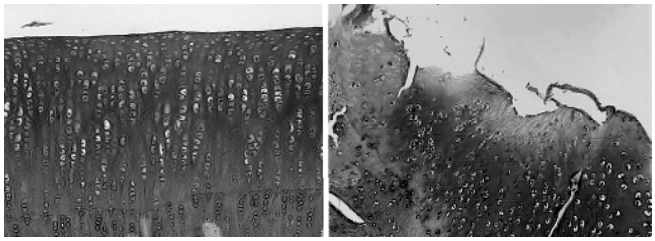


Fig. 11: Example of histological slides from a control (left) and an experimental (BTX-A injection, one month) knee articular cartilage. The control animal shows normal cartilage structure, while the experimental cartilage shows surface disruption and loss of structural integrity.

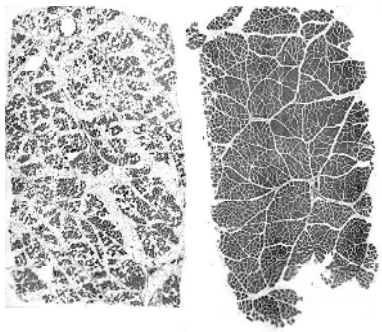


Fig. 12: Example of a cross-sectional histological slide of quadriceps musculature from a control animal (right) and an experimental animal following six months of repeat Botox injections. Note the structural integrity and dense contractile material (dark areas) in the control animal, and the loss of structure and invasion of fat (light areas) in the experimental muscle.

III. Conclcusion

From the results of our studies conducted over the past decade, we conclude that muscle loading and coordination is altered following interventions to joints that cause degeneration leading to osteoarthritis. Specifically, ACL transection in animal models causes an initial decrease in knee extensor forces, and additional bursts of activation in knee flexors, presumably to offset the mechanical function of the lost ACL. In contrast to common believe, articular cartilage thickness increases initially in many models of early OA, causing joint surfaces to be softer. This results in load transmission across the joint over increased contact areas and reduces peak pressures for given loading conditions.

Muscle weakness is an associate of joint degeneration and OA, but it has never been clear if weakness might also be a risk factor for joint degeneration and OA. Prospective studies in human cohorts suggest that indeed, elderly with knee extensor weakness are more likely to develop signs of OA than those with normal knee extensor strength [11, 12]. The series of studies with Botox-induced rabbit knee extensor weakness performed here suggest that muscle weakness

is an independent risk factor for OA, and that proper strength training might prevent OA onset and progression. However, recent results from our group in ACL deficient rabbits suggest that training offsets the ACLT induced knee extensor atrophies, but if not performed properly, might simultaneously accelerate the rate of knee osteoarthritis progression.

IV. Acknowledgements

The series of studies mentioned here were supported in part by the Canadian Institutes for Health Research, The Arthritis Society of Canada, and the Canada Research Chair for Molecular and Cellular Biomechanics

References

1. Hasler EM, Herzog W, Leonard TR et al. (1998) In-vivo knee joint loading and kinematics before and after ACL transection in an animal model. J Biomech 31:253-62
2. Kaya M, Leonard TR, Herzog W. (2003) Coordination of medial gastrocnemius and soleus forces during cat locomotion. J Exp Biol 206:3645-55
3. Liggins AB, Finlay JB. (1992) Recording contact areas and pressures in joint interfaces. Exp Mech71-87
4. Ronsky JL, Herzog W, Brown TD et al. (1995) In-vivo quantification of the cat petellofemoral joint contact stresses and areas. J Biomech 28:977-83
5. Herzog W, Hasler EM, Leonard TR. (2000) Experimental determination of in vivo pressure distribution in biologic joints. J Musculoskel Res 4(1):1-7
6. Mankin HJ, Brandt KD, Shulman LE. (1986) Workshop on the pathogenesis of osteoarthritis: Proceedings and Recommendations. J Rheumatol 13:1127-60
7. Herzog W, Adams ME, Matyas JR et al. (1993) A preliminary study of hindlimb loading, morphology and biochemistry of articular cartilage in the ACL-deficient cat knee. Osteoarthritis Cart 1:243-51
8. Hellio Le Graverand M-P, Eggerer J, Vignon E et al. (2002) Assessment of specific mRNA levels in cartilage regions in a lapine model of osteoarthritis. J Orthop Res 20:535-44
9. Longino D. 2003. Botulinum toxin and a new animal model of muscle weakness. MSc thesis. University of Calgary, Calgary, AB, Canada
10. Herzog W, Longino D. (2007) The role of muscles in joint degeneration and osteoarthritis. J Biomech 40:S54-S63
11. Slemenda C, Brandt KD, Heilman DK et al. (1997) Quadriceps weakness and osteoarthritis of the knee. Ann Intern Med 127:97-104
12. Slemenda C, Heilman DK, Brandt KD et al. (1998) Reduced quadriceps strength relative to body weight. A risk factor for knee osteoarthritis in women? Arthritis Rheum 41:1951-9

Author: Dr. Walter Herzog

Institute: University of Calgary
Street: 2500 University Drive N.W.
City: Calgary
Country: Canada
Email: walter@kin.ucalgary.ca

Multidisciplinary Education of Biomedical Engineers

M. Penhaker[1], R. Bridzik[2], V. Novak[2], M. Cerny[1] and J. Cernohorsky [1]

[1]VSB - Technical University of Ostrava/Department of Measuring and Control, Ostrava, Czech Republic
[2] Video-EEG/Sleep laboratory, Clinic of Child Neurology, University Hospital Ostrava, Czech Republic

Abstract — **Biomedical engineering, clinical engineering and medical informatics represent interdisciplinary branches which are very progressive and acknowledged and which intervene into many spheres. The mentioned branches apply various technical principles and skills in biology and medicine: from proposals, construction and implementation, to the servicing of medical technology. These inspired to change the structure of curricula of the study branch and also the conception of some classes to better cover the legislative needs. Nowadays the study field biomedical engineering is educated as study fild in bachelor and master study at VŠB – Technical university of Ostrava, Faculty of electrical engineering and computer science with cooperation of Medico–Social faculty of the University of Ostrava and University Hospital Ostrava teaching medico - social courses. The courses are mainly provided in special laboratories which combines multi-technical proposition to solve during education in teams.**

Keywords — **biomedical engineering, study, education process**

I. Introduction

Biomedical engineering, clinical engineering and medical informatics represent interdisciplinary branches which are very progressive and acknowledged and which intervene into many spheres. The mentioned branches apply various technical principles and skills in biology and medicine: from proposals, construction and implementation, to the servicing of medical technology. Up until now, biomedical engineering has been taught at the Department of Measurement and Control within the master program as one of its majors called, "Measurement and Control in Biomedicine". Changes both concerning the overall higher education system in Czech Republic and resulting from the entry of Czech Republic into the EU influenced the formation of a new type of biomedical study field.

The new bachelor study branch "Biomedical technologies" has been proposed and accredited at the Faculty of Electrical Engineering and Computer Science. From a technical point of view, the branch is very close to the field of "Measurement and Control" and that is why the department of measurement and control guarantee this study branch. The previous experience gained by the training of the mentioned master program made a very good groundwork for administration of the bachelor program. However, the cooperation of lecturers from other faculty departments, which are specialists in particular topics is expected and required.

II. Conception of study

The bachelor program "Biomedical technologies" combines both technical courses and socio-health and medical courses Fig.1 . The classes are taught at the Faculty of Electrical Engineering and Computer Science and at the Medico–Social Faculty of the University of Ostrava respectively and also at University Hospital Ostrava. Thus, the branch has an inter-disciplinary character and qualified teachers from both universities have become involved in its realization.

The graduates will be specialists in installing, operating, monitoring and innovating medical technique and advancements in medical institutions and may work in a direct contact with patients. They will be sufficiently educated in anatomy, physiology, pathology and other health and social disciplines. However, they must not work as a nurse. They also will be able to assist in selected areas of medical research and to use related information technology to this purpose.

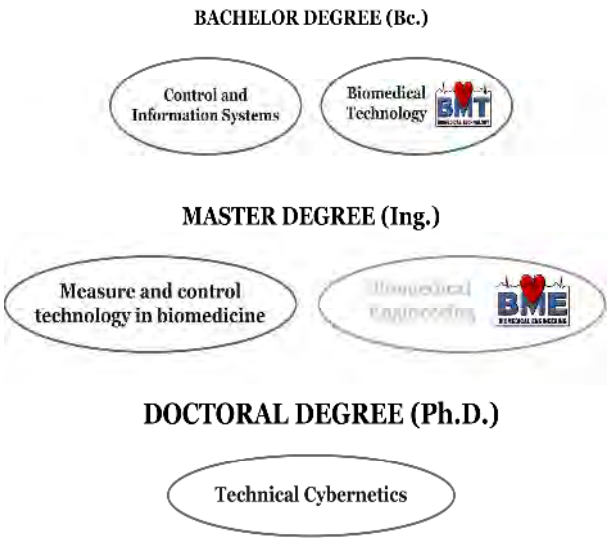


Fig. 1 IFM Education levels of BMI at VŠB – TUO

Chwee Teck Lim, James C.H. Goh (Eds.): ICBME 2008, Proceedings 23, pp. 2155–2158, 2009
www.springerlink.com

III. Conception of interdisciplinary study

The preparation of the bachelor interdisciplinary program Biomedical Technologies (BMT) began already in year 2002 along with the transformational and developmental project of the Ministry of Education for youth and physical education of the Czech Rep (CZ). Groundwork for accreditation was prepared for this project and in year 2003 this branch was accredited by an accreditation committee of the Ministry of Education CZ as another study branch of the educational program Electrical Engineering, Telecommunications and Computers. At that time a law had not yet been passed that had to do with the existence and influence of non-medical staff in the public health work force because the government was waiting for further changes in legislation resulting from the Czech Republic's entrance into the EU. This law was therefore passed a year later as number 96/2004 of the Statute Book on non-medical staff in healthcare.

This law defines, for the first time, the term lifelong learning in healthcare and exchanged activities, which are perceived as lifelong education. This law also modified the process of obtaining certification to work without a supervisor, which until then supervision was a requirement for this field of work. Detailed conditions are specified in the edict 423,424/2004 of the Statue-Book under the government number of 463/2004 of the Statue-Book, which applies to the sector of specialized education and selected employees with specialized professions. These edicts are part of the administered law regulation, which defines an altogether new standing of technical staff in the healthcare system. It has been shown that because of an increasing amount of sophisticated health diagnostic, laboratory and therapeutic machines, there is an increasing need for qualified technical staff without skilled supervision. These edicts have a strong impact on branches such as Biomedical Technologies and Biomedical Engineering, which are explicitly discussed and cited in relation with standard professions like "Biomedical Technician" or "Biomedical Engineer" in which the graduates will find employment.

Another edict, number 39/2005 of the Statue-Book, follows and extends the edict in accordance with EU edicts and makes minimal alterations to both theoretical and practical classes which gives the program professional qualification with which to operate and create non-medical healthcare professionals.

The edicts require the following criteria in order to acquire qualifications as a Biomedical Technician:

- The obtainment of the Biomedical Technician title is possible after studying in the accredited (by Ministry of Healthcare!) bachelor program in the standard time of a minimum of three years.
- From this, practical classes must make up at least 600 semester hours in the case that they are taken as part of daily study program as opposed to long distance studies.
- The program must provide knowledge and skills according to the edict number 424/2004 of the Statue-Book that gives the requirements for healthcare workers and other specialized workers.

The program must include basic general theoretical and practical classes:

a) The theoretical education must provide the following knowledge:

- Basic knowledge in anatomy, physiology and pathology for programs that supply basic services for the performance of technical health care.
- In technical programs; knowledge in signal and image processing (introduction to the theory of signal processing, analysis and interpretation of biosignals and biomedical sensors), in equipment health care instruments (knowledge in basic electrical circuits, diagnostic, therapeutic, laboratory and complex healthcare equipment and visual systems in clinics), in informatics and cybernetics (basic knowledge in statistics, support of computer diagnostics, telemedicine, information systems in health care, introduction to the theory of simulation and modelling), in electro technical subjects (knowledge in math, physics, theoretical electrotechnics, electronics, electrical measurements and programming).

Technical law and norms that apply to healthcare, in management of health care technology and the basics of scientific methodology in scientific research.

b) The practical classes must provide the following skills and knowledge:

- In classes that take place in school laboratories and in healthcare centres.
- A minimum of 50 hours of practical classes must take place in healthcare workplaces that use diagnostic healthcare equipment.
- A minimum of 30 hours of practical classes must take place in healthcare workplaces that use therapeutic healthcare equipment.
- A minimum of 20 hours of practical classes must take place in healthcare workplaces that use laboratory healthcare equipment.

To show how in year 2003 accreditation for the BMT program corresponds with the required edict number 39/2005 of the Statue-Book, we will show some statistic information from this program.

IV. Statistical data about BMT

Classes, both theoretical and practical, are taught by two universities and University Hospital Ostrava; by the Faculty of Electrical Engineering and Computer Science at VŠB-TU Ostrava and by the Medico-Socio Faculty at the University of Ostrava. The faculty of Electrical Engineering and Computer Science, makes up 54,3% of total hours and provides technical and language classes with the exception of Latin. Among the required classes are Math I and II, Physics, Optical Electronics, Biophysics, Electrical Circuits, Signal Analysis, Basic Computer Skills, Measurement and Processing of Data, Information Systems in Healthcare, Sensors in Biomedicine, Electronic Instruments technique, Electronic Instruments Measurement and Monitoring and Control Systems. Another class that is required that belongs to two semester practical classes is the Healthcare Electronic Equipment class that consists of basic and specialized healthcare technique, including its clinical application according to individual medical fields. The Electrical Engineering and Computer Science department offers optional courses in Biocybernetics and Biotelemetry.

The Medico-Socio faculty and physician from University hospital Ostrava provides required classes in healthcare such as First Aid, Basics of Anatomy, Physiology, Pathology, Psychology, Chemistry and Biology, Work Hygiene and Epidemiology, Microbiology and Immunology. Also included in the required courses are Ethics in Healthcare, Management and Operations in Healthcare, Healthcare Law, Marketing in Healthcare, Public Healthcare, Security, and Latin and Specialized Terminology. Other required classes are courses focused on practical therapeutic and diagnostic technique. In this area are included classes such as Clinical Propedeutics, Technique in Diagnostic Sickness in Internal and Surgery Sectors, Healing Technique in Radiotherapy and Nuclear Medicine in Healthcare Equipment. Furthermore, the Medico-Socio faculty offers optional courses such as Audiometry, Rehabilitation Methods and Technique, Equipment Technique and Compensation Aids for the Handicapped, Examining Methods and Equipment Technique in Optometry, Civilization Diseases and Physical Body Workload Risks.

A very important part of the program is the related specialized workplace classes taken place at healthcare clinics that make up 120 hours, which over qualifies the norms according to the edict number 39/2005 of the Statue-Book. In their first year, students complete 14 daily practical classes in the area of Technique in Diagnostics of Disease and in the second year, they complete similar practical courses in Technique in Therapy of Disease. Thus the Socio-Medico department classes of the University of Ostrava make up 45,7% of the total program.

Statistics that are more detailed (number of credits and hours taught) in relation to the healthcare and technical courses of the BMT program are shown in the following table, Table 1.

Table 1: Table of skills in subject representation according year, Hours also in percent

	Electrical (Technical)		Health (Humanity)		Others specialized subjects	
Yr.	Hrs.	Lect./ exerc.	Hrs.	Lect./ exerc.	Hrs.	Lect./ exerc.
1	476	252/224	294	168/126	70	42/28
2	448	252/196	196	140/56	56	42/14
3	209	77/132	242	110/132	44	44/0
∑	1133	581/552	732	418/314	170	128/42
%	48,8	24/23,8	31,5	18/13,5	7,2	5,4/1,8

Here are 22 (35,5%) electro-technical classes and 26 (42%) healthcare classes, language classes are 3 (5%) and the rest of the classes from both departments are 11 (17,5%). From the semester hour point of view, technical classes make up 1133 hours (48,8%) and healthcare classes make up 732 hours (31,5%). Language classes make up 126 hours (5,5%) and other classes make up 170 hours (7,2%). The remaining classes, professional practice at the clinical workplace, make up 120 hours (7%). This statistic is calculated from all the classes offered, in practice the overall number of credits is smaller because students choose a limited number of optional credits so that they will complete the requirement of 180 optional credits during the program.

V. Profile and enforce of graduate

The graduates will be specialists in installing, operating, monitoring and innovating medical technique and advancements in medical institutions and may work with in direct contact with patients. They will be sufficiently educated in anatomy, physiology, pathology and other health and social disciplines. However, they must not work as a nurse. They also will be able to assist in selected areas of medical research and to use related information technology to this purpose.

Currently, graduates can find employment most often as assistances in clinical healthcare, in equipment security and in operating healthcare equipment. In order to obtain a certificate to practice in the profession without skilled supervision, the Ministry of Health needs to accredit the program. The structure and contents of the new bachelor study field Biomedical Technologies conforms to legislative requirements and all graduates of these biomedical professions are ready to practice in the profession in accordance with newly accepted legislative requirements. accepted legislative requirements.

VI. Support of eueopean social fund project

The legislative changes inspired the needs to change the structure of curricula of the study branch and also the conception of some classes to better cover the legislative needs.

The faculty applied for support to cover expenses combined with such reconstruction the grant agency of The Ministry of Education Youth and Sports for the European Social Fund (ESF) helps people improve their skills and, consequently, their job prospects. The ESF is the EU's main source of financial support for efforts to develop employability and human resources. It helps Member States combat unemployment, prevent people from dropping out of the labor market, and promote training to make Europe's workforce and companies better equipped to face new, global challenges

In Czech Republic one branch of ESF is focused on the following important activities

- Training in the fields of research, science and technology
- Development and improvement of training, education and skills acquisition, including the training of teachers
- Development of systems for anticipating changes in employment and in qualification needs
- Advancement of the study branch Biomedical technique and of employability of its graduates on the employment market in reference to law number 96/2004 of statute-book

From general point of view the global goal of the project is the advancement of study field Biomedical Technology with long-term perspective of better employability of its student on both on the Czech end EU labor market. The specific measures are realized within three key activities :

The change of the structure and contents of particular classes with emphasis on practical part of the subjects

The realization of the new mood of guidance of practical training in hospital by mentors

The production of good-class set of study materials to cover both technical end medical part of the study program.

VII. Conclusions summary and perspective

This new bachelor branch was successfully accredited in year 2003. The education in this branch started in the winter semester of the academic year 2004/2005. In the year 2004 the Czech Republic passed a law, number 96/2004 of the Statute Book, about non-medical sanitary professions. Detailed conditions and requirements for obtaining the certificate for practice of profession without skilled supervision was subsequently modified in the regulation number 423/2004 and 39/2005 of the Statute Book and in the decree number 463/2004 of the Statute Book. These legislative changes have a strong impact on branches like biomedical technology, respectively, biomedical engineering.

Although the instruction of this interdisciplinary program is new and there do not exist curriculum's and past experiences with graduates in such a branch, the cooperation between universities is very close and all evaluations, both from the students and from the teachers of the first year will lead to changes and alterations in the curriculum so that the quality of the branch will continue to grow.

After the completion of the bachelor program, the graduates have an opportunity to continue their studies in the master program that is taught at VSB -Technical University of Ostrava at the Faculty of Electrical Engineering and Computer Science in the area of "Measurement and Control of Technology in Biomedicine". After the completion of the master program, a doctoral program is offered in Technical Cybernetics.

Now when the new study concept five years last, we can estimate level of three institutions in education process cooperation with the great impact on student knowledge and abilities for his profession.

Acknowledgment

This work was partially supported by the faculty internal project "Biomedical engineering systems" and by the project of the European Social Fund (ESF) CZ.04.1.03/-3.2.15.1/0020 which is co-financed by the European Union and by the state budget of the Czech Republic.

References

1. Žídek, J., Svatos Z., Kuncicky, P. (2005): 'Faculty of Electrical Engineering and Computer Science VŠB – TU Ostrava, as the first academic institution in the Czech Republic to have a certified management system Academician', *Akademik* Vol, No **1**/2005., pp. 9-10.
2. VŠB – TU, Internet site address: http://www.fei.vsb.cz/

Author: Ing. Marek Penhaker, Ph.D.
Institute: VSB – TU Ostrava
Street: 17. listopadu 15
City: Ostrava - Poruba
Country: Czech Republic
Email: marek.penhaker@vsb.

Development and Measurement of High-precision Surface Body Electrocardiograph

S. Inui[1], Y. Toyosu[1], M. Akutagawa[2], H. Toyosu[3], M. Nomura[4], H. Satake[5], T. Kawabe[3], J. Kawabe[3], Y. Toyosu[6], Y. Kinouchi[2]

[1]The University of Tokushima/Graduate School of Advanced Technology and Science, Tokushima, Japan
[2]The University of Tokushima/Institute of Technology and Science, Tokushima, Japan
[3]Eucalyptus Co. Ltd., Tokushima, Japan
[4]The University of Tokushima/Faculty of Integrated Arts and Sciences, Tokushima, Japan
[5]The University of Tokushima/Research Collaboration Promotion Organization, Intellectual Property Office, Tokushima, Japan
[6]Yasuhiro Toyosu Patent & Trademark Attorney, Tokushima, Japan

Abstract — **In the 12-lead electrocardiograph currently being used general medical practice, electrodes are positioned at 6 locations in the chest region and the cardiac potential is measured. This research increases the number of electrode to 124 at evenly-spaced intervals over the body surface of the chest, side and back. The commonly used band elimination filter is not used as a countermeasure for exclusion of the noise from such electrodes, and a body surface electrocardiograph has been developed that makes it possible to perform high-speed sampling of the cardiac potential at 80-100 times the conventional rate. From the sampling data obtained with high spatial resolution, maps and animations of the body surface potential distribution are created and displayed from the 1D waveform as well as from the 2D/3D waveforms.**

Keywords — **Body surface electrocardiography, Body surface potential map, Body surface potential animation, high spatial resolution, Band eliminate filter**

I. Introduction

Most conventional body-surface electrocardiograms are obtained by standard 12-lead electrocardiography, in which cardiac potentials are detected in the thoracic region using unipolar lead, and changes in cardiac potentials in various regions are the clinically examined. Data obtained by conventional electrocardiography are typically analyzed using one-dimensional wave patterns. For example, whether QRS intervals are constant, the duration of QRS intervals, whether the intervals between the PQ intervals are constant, heart rate, the presence or absence of P waves, and the presence or absence of an atrioventricular block can be diagnosed from the one-dimensional wave patterns. To eliminate the effects of noise, of which inductive noise at the power supply frequency (hum) is the most important, band-eliminating filters are used [1-4]. However, since these frequencies (0.05-100 Hz) are required for the accurate measurement of cardiac potentials, the application of a band-eliminating filter alters the electrical properties of the detected cardiac potentials, resulting in an inaccurate measurement [5].

To perform a more detailed analysis of electrocardiographic wave patterns by that involve small changes, the observation of changes in cardiac potentials at a larger number of sites without applying such filters and three-dimensional expression are necessary. In the present study, we experimentally produced a body-surface electrocardiograph without filter measuring potentials at 124 sites on the body surface, from in thoracic to the back regions, and examined its resolution in two- and three-dimensional body-surface potential mapping and its accuracy in the detection of cardiac potentials.

II. Materials and Methods

A. Improvement of the shielding effect

In our system, to eliminate inductive noise without a band-eliminating filter, the shielding effect was increased by placing the device in a metal box, to minimize the effects of inductive noise. In this system, 124 electrode sites were used, consisting of 64 in the thoracic region, 48 on the back, and 12 on the left body side, and the entire region around the heart was sufficiently covered with these electrodes. The distance between the electrodes and the amplifier was about 10 cm, which is shorter than that in conventional electrocardiographs. The amplifier was encased in a metal box, and the metal box covered the entire region around the heart thus minimizing the effects of inductive noise. To further increase the shielding effect, the distance between the body surface and metal box was shortened during the measurement by stroking the electrode (Fig. 1-1). In addition, the heart was positioned in the region close to the center of several electrode boxes to increase the shielding effect (Fig. 1-2).

Chwee Teck Lim, James C.H. Goh (Eds.): ICBME 2008, Proceedings 23, pp. 2159–2163, 2009
www.springerlink.com

B. Electrodes with skin contact resistance at a constant level

In this system, to maintain the contact resistance of electrodes at a constant level, they were moved with the up-and-down movement of the skin caused by respiration and cardiac pulsation. To decrease changes in contact resistance, the electrodes were made so as to correspond to individual body shapes, and the body surface was pressed at a constant level during the stroking of the electrode rod to which a spring was fixed. To maintain constant contact conditions, it was necessary to move the electrodes with the body movement, and a decreased friction resistance of the electrode rod and its guide was required. This was achieved by stabilizing the contact condition by moving the electrode with the body movement using a guide comprised of a fluorine resin (PTFE) with very good folding properties, the static friction resistance (0.02 N) of which is lower than the dynamic friction resistance (0.05 N). PTFE, which has the highest electric property among solid insulating materials, is stable over wide frequency and temperature ranges.

C. Configuration of the system

In this system, the number of channels was 124, the maximal input voltage ±5 mV/±10 mV, the resolution 10 bit, and the sampling interval 0.1 ms.

A spring was fixed to each electrode rod so that it was stroked when placed on the body surface, and each electrode was pressed at a constant level. The distances between the body surface or electrode and the metal box were decreased by stroking the electrode rod, thus increasing the shielding effect. Since the friction resistance of the electrode rod guide made of PTFE was low, it followed body movements caused by respiration and cardiac pulsation (Figs. 2and3). Cardiac potentials induced on the body surface were transmitted to an amplifier via the electrode, electrode rod, and spring. The electrical potential determined by adding the values for the bilateral hands and the left foot were used as the standard (0 V), and the voltage for each electrode was detected (Fig. 4). Cardiac potentials induced on the body surface were amplified 1,000- or 2,000-fold using a buffer, a preamplifier, and an amplifier, converted into digital signals using an AD converter, and transmitted to a personal computer. Data input into the personal computer were expressed both two- and three- dimensionally.

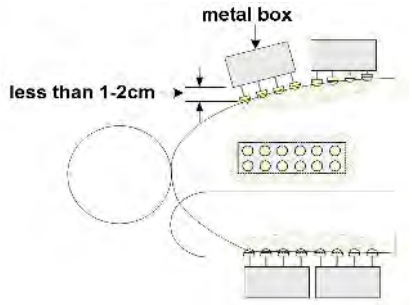


Fig. 1-1 Figure of measurement from a right side surface.

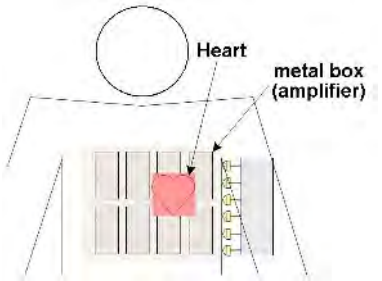


Fig. 1-2 Figure of measurement from the front.

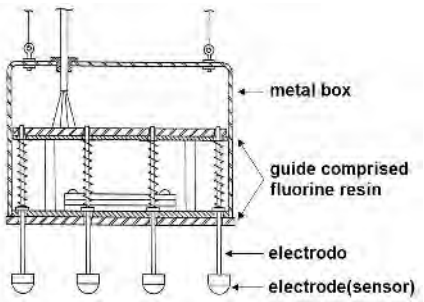


Fig. 2 Structure in an electrode case.

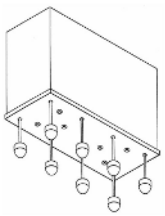


Fig. 3 External representation of an electrode case.

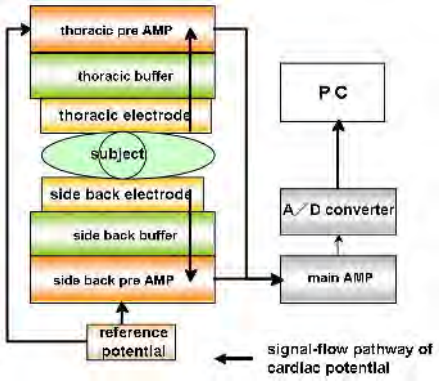


Fig. 4 A general view of the system.

III. Results

Figs. 5-1 and 5-2 show the conventional one-dimensional expression of voltage on the ordinate and time on the abscissa. The dark lines show data obtained with, and the light lines show those without a band-eliminating filter. A band-eliminating filter of 50/60 Hz was used. In Fig. 5-1, the peak attenuation ratio for R and T waves were quite differently, i.e., large in the former and almost no changes in the latter. As shown in Fig. 5-2, the phase of the QRS waves was not constant.

Fig. 6 show the electrocardiogrphic wave forms for 124 recording points. All electrocardiogrphic waves were detected clearly without noise. Figs. 7-1 and 7-2 show three-dimensional graphs of differences in voltage between the sensors at the same time. Fig. 7-2 shows data obtained with a band-eliminating filter, and Fig. 7-1 shows those without a band-eliminating filter. The size of the spike was smaller in the former than in the latter.

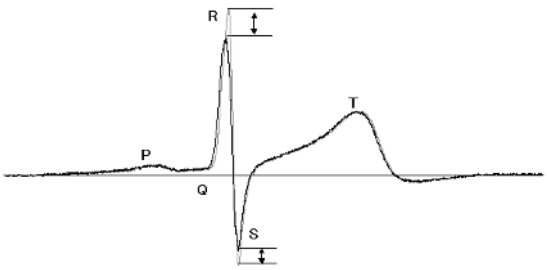


Fig. 5-1 ECG waveform with a band-eliminating filter.

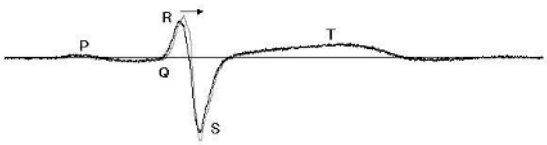


Fig. 5-2 ECG waveform without a band-eliminating filter.

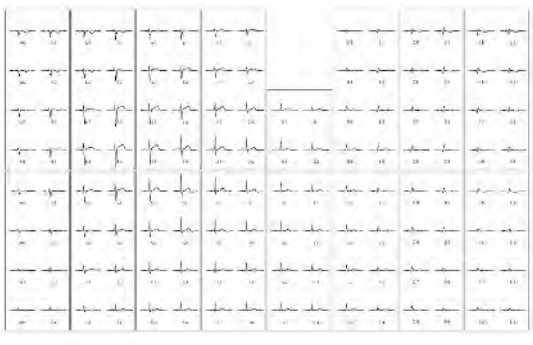


Fig. 6 ECG wave forms for 124 recording points.

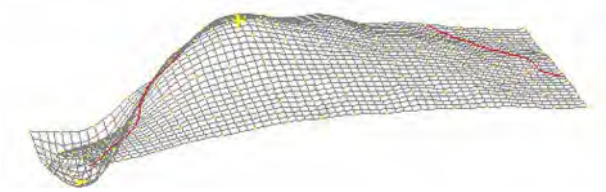


Fig. 7-1 Three-dimensional graphs with a band-eliminating filter.

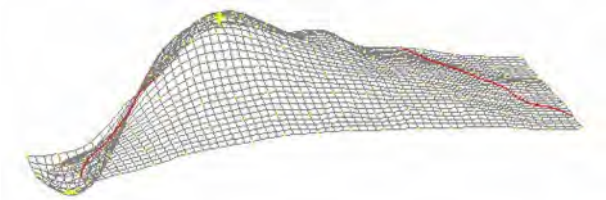


Fig. 7-2 Three-dimensional graphs without a band-eliminating filter.

IV. Discussion

A. Inductive noise affecting eletrocardiograms and filtering

Noise caused by applying electrocardiographs interferes with the accurate detection of cardiac potentials. The major noise is inductive noise (hum) caused by the frequency of the power supply, and there is generally 50/60 Hz of noise unless the measurement is performed in a completely shielded room. This noise is induced by the electrodes, and is picked up by the amplifier along with cardiac potentials. Since the frequency required for electrocardiography is 0.05-100 Hz, the frequency of inductive noise overlaps with this frequency range. Therefore, cardiac potentials cannot be detected by simply eliminating noise with a filter, and it is not possible to differentiate between cardiac potentials and noise in the measurement. The high input impedance of the preamplifier required for the amplification of very low cardiac potentials further increases the effects of inductive

noise [6]. Filtering eliminates inductive noise at 50/60 Hz, which is included in the frequency range of the cardiac electric waves, and also changes specific frequency components of cardiac electric wave patterns. However, a frequency analysis of cardiac electric wave patterns per heartbeat demonstrates that most of the energy consists of frequency components lower than the frequency of the power supply, and the amount of energy with components of the frequency of the power supply is very low. Therefore, even though inductive noise can be eliminated using a filter, changes in cardiac electric wave patterns caused by filtering may be small. However, when rapid changes in cardiac electric wave patterns occur during a very short period, e.g., around the QRS peak, the effects of high frequency components are large, and the peak amplitude is rapidly attenuated by filtering. In other words, the entire cardiac electric waves are not attenuated, but partial amplitudes, corresponding to high frequency components, are attenuated. The attenuation of amplitudes varies with the rate of change of cardiac electric wave patterns. This rate of change fluctuates within 1 heartbeat, and varies with the electrodes. Therefore, marked attenuation partially occurs as the result of eliminating inductive noise from cardiac electric wave patterns by filtering, and the rate of change varies with the electrodes, because cardiac electric wave patterns that are induced by the electrodes differ. Since filtering changes not only amplitudes but the phases as well, depending on the frequency components, eliminating noise caused by the power supply from cardiac electric wave patterns can alter the amplitudes and phases depending on the time and the electrode.

In this system, the peak attenuation ratio of R and T waves differed substantially, i.e., large in the former and almost no changes in the latter, as shown in Fig. 6. Furthermore, the phase of the QRS waves was not constant. A possible cause of these properties was that the voltage attenuation and phases were not constant because the frequency components of the cardiac electric waves differ between the channels, even though the attenuation rate of the filter is constant at each frequency. If the rate of change was not constant, the two- and three-dimensional expression of differences in the voltage between one electrode and the next was considered to be inaccurate.

B. Contact resistance of electrodes and local batteries

The contact resistance between the electrode and skin is several hundred Ω to several hundred MΩ depending on the contact conditions and the region [7]. To prevent the attenuation of cardiac potentials caused by contact resistance, the input impedance of the preamplifier must be high, and cardiac potentials are readily affected by inductive noise.

In addition to contact resistance, local batteries of several hundred mV are generated between the electrodes and the skin [8]. These voltages (several hundred mV) are higher than the cardiac voltage, of which the peak is several mV. With changes in contact resistance by up-and-down movement caused by respiration and cardiac pulsation, the voltages of the local batteries change. The movement of the body surface during the measurement is irregular, and changes in the voltages of the local batteries are also irregular, causing frequency properties in the local batteries. Since these frequency properties overlap with the frequency range of the cardiac voltage, changes in local batteries are measured as the cardiac voltage, resulting in an inaccurate measurement.

If the sensors cannot follow body movements, the contact conditions are changed. Therefore, to produce a highly accurate body-surface electrocardiograph, it becomes very important to eliminate the noise caused by the power supply without a filter and make the voltages of the local batteries constant by achieving constant contact resistance between electrodes and the skin.

V. CONCLUSIONS

To more accurately detect cardiac potentials, inductive noise was suppressed without the use of a filter, and changes in the electrical properties of cardiac potentials (changes in the amplitude and phase of cardiac electric wave patterns) were prevented. Furthermore, the electrodes were made, so as to follow the up-and-down movement of the body surface caused by respiration and cardiac pulsation, during which local batteries generated on the electrodes and the body surface could be maintained at a constant level, and cardiac potentials alone could be detected. The number of electrodes for the detection of cardiac potentials was 124 in the thoracic to back regions, thus permitting more information to be obtained.

These findings suggest that the accurate measurement of cardiac potentials and body-surface potential mapping with a high resolution is possible using this system. The findings also suggest that the detection of certain cardiac electric phenomena, currently considered to be impossible by conventional electrocardiographs, is feasible. Clinical studies will be pursued using this system.

ACKNOWLEDGMENTS AND REFERENCES

We express special thanks to Messrs. Mitsunori KANEKO, Hisanori SHINOHARA, Yasushi SHIMOE, Koichi SAKABE, and Yamato FUKUDA of National Hospital Organization Zentsuji National Hospital.

1. Ferdjallah M, Barr RE. (1994) Adaptive digital notch filter design on the unit circle for the removal of powerline noise from biomedical signals. IEEE Trans Biomed Eng 1994:41:529-536
2. Huhta JC, Webster JG. (1973) 60 Hz interference in electrocardiography. IEEE Trans Biomed Eng 1973: 20:91-100
3. Tsinsky IA, Daskalov IK. (1996) Accuracy of the 50 Hz Interference Subtraction from the Electrocardiogram. Med Biol Eng Comput 1996: 34:489-494
4. Thakor NV, Zhu Y. (1991) Applications of adaptive filtering to ECG analysis: noise cancellation and arrhythmia detection. IEEE Trans Biomed Eng 1991:38:785-793
5. Dobrev D. (2004) Two-electrode low supply voltage electrocardiogram signal amplifier Med Biol Eng Comput 2004: 42:272-276
6. Burke MJ. Gleeson DT. (2000) A micropower dry-electrode ECG preamplifier. IEEE Trans Biomed Eng 2000: 47:155-162
7. Vilhunen T. (2002) Simultaneous reconstruction of electrode contact impedances and internal electrical properties: I. Theory Meas Sci Technol 2002:13:1848-1854
8. Baweja D, Roper H, (1999) Sirivivatnanon V. Chloride induced steel corrosion in concrete: Part 2 - Gravimetric and electrochemical comparisons. Materials Journal 1999: 96:3

Biomedical Engineering Education Prospects in India

Kanika Singh

Indira Gandhi National Open University, New Delhi, India
Pusan National University, Busan, South Korea

Abstract — **The importance of education lies in its scope which should be well-matching with the growing technology. The paper here discusses about the Biomedical Engineering Education. The interface between electrical engineering and the life sciences has grown enormously. The biomedical engineering program has become a globally expanding discipline with time. The BME education in India needs proper planning and designing. In this paper, we discuss the scenario of BME in India and give suggestion for a successful future.**

Keywords — **Biomedical Engineering Education, India, Prospects**

I. Introduction

Biomedical Engineering has the concept of interdisciplinary engineering which portrays the modern engineering concept. The engineering has been widely accepted in the world and hence may be considered to a globally acceptable discipline. The BME has a strong multidisciplinary integration which involves the electrical, chemical, mechanical, computer and civil engineering. According to NIH, Bioengineering integrates physical, chemical, mathematical, and computational sciences and engineering principles to study biology, medicine, behavior, and health. It advances fundamental concepts; creates knowledge from the molecular to the organ systems levels; and develops innovative biologics, materials, processes, implants, devices, and informatics approaches for the prevention, diagnosis, and treatment of disease, for patient rehabilitation, and for improving health (NIH definition). BME is a constantly changing field.

Hence such a discipline requires careful planning when designing BME educational programs which may produce successful professionals.

These professionals often work in tandem with other life scientists, chemists, and medical

scientists to aid the cause of preventive and curative medicine. Whereas biomedical engineers develop devices, systems and procedures to aid medical research or help solve heath and medical problems. The sudden spurt in radical research concepts that have lent a whole new direction to treatment modalities is essentially due to developments in this field.

In this paper, scenarios of Indian university have been given. The objective of this paper is to briefly present the India scenario of BME education, the challenges it faces and the future steps towards the appropriate education of BM engineers for the region.

Biomedical engineering has immense scope for path breaking research.

II. Scenario of Indian Universities with BME Education

A. Scenario

Previous days, the graduation in a related subject such as electrical, chemical or mechanical engineering and then team this up with a specialization in biomedical engineering.

Generally, biomedical engineers may seem like an elite class of practitioners, the ever-increasing Biomedical engineers who are considered to be the specialists or experts have all had humble beginnings, which can be traced back to an ordinary engineering degree.

However, recently there have been several Bachelor courses in Biomedical Engineering but are less popular as compared to the main stream engineering. In order to specialize in this field most Indian students opt for masters programs. There is also a provision of pursuing master in Biomedical Engineering after completion of their medical degree. But the Ph.D programs in India are very few in number.

Some of the renowned institutes providing BME at the masters and doctoral levels at IIT Mumbai. Banaras Hindu University, Varanasi 221005 (UP) and Birla Institute of Technology and Science, Vidya Vihar, Pilani 333031 (Rajasthan) offer an M.Tech in biomedical engineering.

The chief specialties in this field include bioinstrumentation, biomaterials, biomechanics, cellular, tissue and genetic engineering; clinical engineering; rehabilitation engineering; orthopedic surgery; medical imaging; and systems physiology.

Chwee Teck Lim, James C.H. Goh (Eds.): ICBME 2008, Proceedings 23, pp. 2164–2166, 2009
www.springerlink.com

B. Challenges for BME in India

Engineering education in India faces some classic and some new challenges. Most of these challenges are common to all engineering disciplines, including biomedical. In the era of the Internet and telecommunications changes, as Gupta et al. [3] point out, the major challenges of engineering education are: a) the need for formalized lifelong learning; b) the need to broaden "engineering fundamentals" beyond mathematics and physics; c) inadequacy of the first professional degree for engineering careers; d) need for engineering practice.

The Biomedical Engineering education in India is generally a part of an interdisciplinary field. Some courses have been adapted from Biosciences, Biotechnology, Electrical engineering, Computer Engineering, Mechanical Engineering etc. The programs run in different institutes have no standardized syllabus. At times, it does not meet the requirements for the jobs because of the lack of latest knowledge.

C. Suggestion and Improvements of BME in India

Presently, the BME in India needs a lot of improvement in order to compete globally.

Bioengineering education presents special interdisciplinary programmes. The most important is to educate students in basic knowledge and improve their skills needed. The context of Bioengineering in India is not meeting the demands of the companies and is still underdevelopment.

There is a need to increase the knowledge by improving the learning technologies.

This is a significant pedagogical challenge. Hence some suggestions are quoted in the text:

i) Using several internet tools

The use of web-based tools is of prime-importance. The web, information media or using CDROMs, DVDs, etc. Online free library access with Medical journal accessibilities in the university.

ii) Increase the number of Undergraduate programs and students

There is a need for introducing new technologies in the curriculum with increase in undergraduate programs. The curriculum must involve the theoretical and practical learning [5].

The need for biomedical engineering education should be emphasized at this level to increase the number of Biomedical Engineers.

iii) Specialized graduate programs should introduced

The students should be taught advanced courses. They can be several company scholarship programs for having several track program which may be more skill oriented. Graduate studies should be complimentary to undergraduate and must have in-depth knowledge.

iv) Continuing Education

This is most important to have a continuous study by updating the knowledge time to time. Especially the practicing engineers must be stay in touch with the latest developments.

v) Recruitment possibilities for Biomedical Engineers

Generally in India the job prospects of Biomedical Engineers are not up-to the mark. The students have several problems attaining the job. Most importantly for the Engineering institutes have very little collaboration with medical hospitals and health companies. Hence the university or the institutes must strengthen relationships with health care networks.

vi) Internship programs/ Joint Ph.D programs

There is a need for having several internship programs in order to have a better practical knowledge of the subject. The joint Ph.D programs can bring a difference in research and high-class Ph.D. Hence such internship programs and Joint Ph.D programs must be encouraged.

vii) Government funding opportunities

There is a need for increase in government funding opportunities in biomedical Education in India. The increase in funding in biomedical R&D field may help in better health care educations.

III. Conclusions and Future Perspective

The Biomedical engineers must recognize the place of work after their graduation. There is a possibility of working in a variety of settings, from hospitals, research institutes and facilities, educational institutes, and pharmaceutical companies to government establishments, and regulatory agencies. The Biomedical Engineers can also work as counselors in medical firms or consultants. The scope for further progress therefore seems infinite.

Acknowledgment

The author would like to thank BK21 program fellowship, South Korea.

References

1. K.C Gupta and Tatsuo Itoh. (2002) Microwave and RF Education-Past, present and Future. IEEE transactions on microwave theory and techniques, 50:3, March.
2. M Kikuchi, Status and future prospects of biomedical engineering: a Japanese perspective, Available online at http://www.biij.org/2007/3/e37, doi: 10.2349/biij.3.3.e37Smith.
3. Thomas R. Harris, Seeking improvement in bioengineering education: academic And organizational concerns, Proceedings of the Second Joint EMBS/BMES Conference Houston, TX, USA • October 23-26, 2002.
4. http://www.hinduonnet.com/jobs/0303/05050022.htm

Author: Dr. Kanika Singh
Institute: IGNOU New Delhi
Street: 57-C Pocket C
City: Siddhartha Extension, New Delhi
Country: India
Email: kstechinfo@yahoo.com

Measurement of Heart Functionality and Aging with Body Surface Electrocardiograph

Y. Toyosu[1], S. Inui[1], M. Akutagawa[2], H. Toyosu[3], M. Nomura[4], H. Satake[5], T. Kawabe[3], J. Kawabe[3], Y. Toyosu[6], Y. Kinouchi[2]

[1]The University of Tokushima, Graduate School of Advanced Technology and Science, Japan
[2]The University of Tokushima, Institute of Technology and Science, Japan
[3]Eucalyptus Co. Ltd., Japan
[4]The University of Tokushima, Faculty of Integrated Arts and Sciences, Japan
[5]The University of Tokushima, Research Collaboration Promotion Organization, Intellectual Property Office, Japan
[6]Yasuhiro Toyosu Patent & Trademark Attorney, Japan

Abstract — **A body surface electrocardiograph employs 124 spot electrodes positioned wider area around human hart to detect heart potential generated by the hart beat in sync, collect and configure plural position potential signals to make up body surface electrocardiography showing human heart condition dynamically and graphically.**

This electrocardiography displays not only conventional one-dimensional time variation at a very limited position obtained with 12 leading electrodes electrocardiograph or Holter electrocardiograph showing, but also three dimensional and motion images of body surface electrocardiography by examining wider area at faster sampling rate with higher resolution.

We expect such electrocardiography could possibly show additional or new information which is not obtained by conventional one-dimension electrocardiograph.

We study a utility of the body surface electrocardiograph, i.e., what can be seen by the body surface electrocardiography, examining many body surface potential distribution of variety of examinees obtained by the electrocardiograph.

This paper reports significant difference between a regular person and person with higher cardiopulmonary, and aging variation.

Keywords — **Body surface electrocardiograph, ECG, body surface potential distribution, electrocardiogram.**

I. Introduction

A body surface electrocardiograph employs 124 spot electrodes positioned wider area around human hart to detect heart potential generated by the hart beat in sync, in particular, the 124 spot electrodes consist of 8 row x 8 column as chest electrodes, 6 x 2 as body side electrodes, and 8 x 6 as back electrodes. See Fig. 1. Each electrode detects heart potential individually, and the body surface electrocardiograph collects and configures these position potential signals to make up body surface electro-cardiography showing human heart condition dynamically and graphically. See Figs. 2 and 3.

This special electrocardiography displays not only conventional one-dimensional time variation at a very limited position obtained with conventional 12 leading electrodes electrocardiograph or Holter electrocardiograph showing, but also three dimensional and motion images of body surface electrocardiography by examining wider area at faster sampling rate with higher resolution.

We expect such electrocardiography could possibly show additional or new useful information which is not obtained or hard to obtain with a conventional one-dimension electrocardiograph.[1-8]

We have been continuing study a utility of the body surface electrocardiograph, i.e., what can be seen and detected by the surface potential distribution, examining many body surface potential distribution of variety of examinees obtained by the body surface electrocardiograph.

This paper reports significant difference between a regular person and person with higher cardiopulmonary, and aging variation.

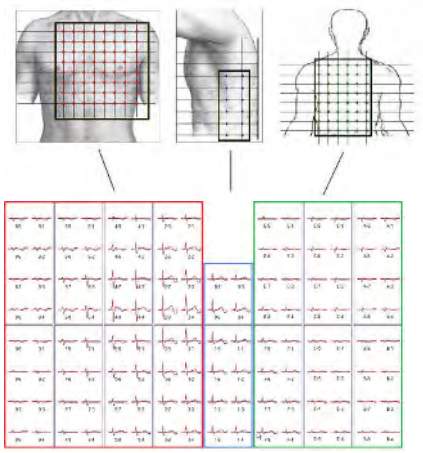


Fig. 1. A collection of individual electrocardiogram detected by each electrode positioned at chest, side and back of the body.

Chwee Teck Lim, James C.H. Goh (Eds.): ICBME 2008, Proceedings 23, pp. 2167–2170, 2009
www.springerlink.com

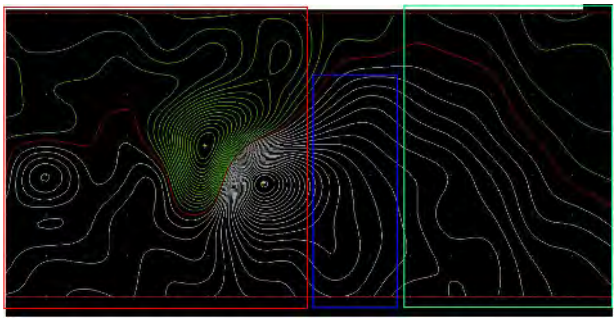


Fig. 2. A two-dimensional surface potential distribution configured and integrated by each electrocardiogram shown in Fig. 1.

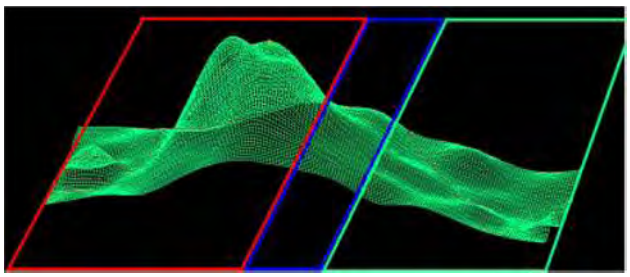


Fig. 3. A three-dimensional surface potential distribution of Fig. 2.

II. Materials and Methods

We developed a prototype of the body surface electrocardiograph measuring instrument as shown in Fig. 4. This measuring instrument has 124 electrodes, some of which are suspended by an arm from the examinee, some protrude from the side of the examinee, and the rest protrude from the backside of the examinee.

The detected signals are buffered, A/D converted, and input into a controller to draw a body surface electrocardiograph. We prepared PC installed with a special program to draw such body surface potential distribution, thus the body surface electro-cardiograph is monitored on the PC display.

Specifically, the measurement instrument we employed is that the number of channels was 124, the maximal input voltage ±5 mV/±10 mV, the resolution 10 bit, and the sampling interval 0.1 ms.

A spring was fixed to each electrode rod so that it was stroked when placed on the body surface, and each electrode was pressed at a constant level. The distances between the body surface or electrode and the metal box were decreased by stroking the electrode rod, thus increasing the shielding effect. Cardiac potentials induced on the body surface were transmitted to an amplifier via the electrode, electrode rod, and spring. The electrical potential determined by adding the values for the bilateral hands and the left foot were used as the standard (0 V), and the voltage for each electrode was detected. Cardiac potentials induced on the body surface were amplified 1,000- or 2,000-fold using a buffer, a preamplifier, and an amplifier, converted into digital signals using an A/D converter, and transmitted to a personal computer. Data input into the personal computer were expressed both two- and three- dimensionally.

We examined body surface electrocardiogram of various examinees, having different age, motility, heart disease, using the above measuring instrument. In particular, we compared the body surface potential distributions of a regular person and person with higher cardiopulmonary, i.e., an athlete. In addition, we studied the aging variation.



Fig. 4. An overview of the prototype of the body surface electrocardiograph measurement instrument.

III. Results and Discussion

Though there were variations among individuals and ages, we generally found that some transition pattern of normal healthy person, which shows firstly excitation of right ventricle, then excitation of left ventricle.

A. Cardiopulmonary

More specifically, the right ventricle excitation shows a peak of the positive potential at first, then the peak gradually decreases and finally reaches negative peak. By contrast, the left ventricle excitation generates potentials after the right ventricle excitation. Particularly, after the positive peak of the right ventricle excitation, the negative peak of the left ventricle excitation begins gradually at a bit late timing, and followed by the negative peak of the right ventricle excitation. See Fig. 6.

On the other hand, regarding the body surface potential distribution obtained from a person with higher cardiopul-

monary, it shows different tendency. Particularly, compared with the above normal person, the body surface potential distribution shows a timing of maximum positive peak of the left ventricle excitation, at the same time, maximum negative peak of the right ventricle excitation occurs. See Figs. 7. It shows symmetric wave pattern of positive and negative peak. Such same time excitation might help higher cardiopulmonary, leading stronger cardiodynamics.



Fig. 6. A three-dimensional body surface potential distribution of normal person.

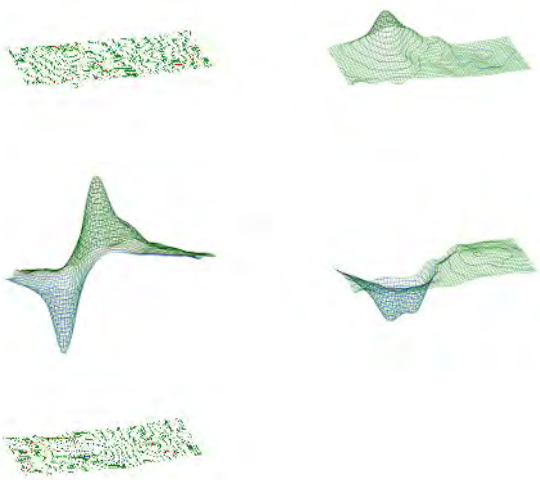


Fig. 7. A three-dimensional body surface potential distribution of person having higher cardiopulmonary.

B. Aging of wave pattern

Next, we have examined any change caused by aging. In this example, we compared wave pattern of three Japanese men who are 55, 60 and 65 years old, which are shown in Figs. 8-10.

In view of these Figs., comparing with the positive maximum peaks of the left ventricle excitation, and the negative maximum peak of the right ventricle excitation, respectively, we found that the maximum peaks decrease gradually with aging.

Also, shape of wave pattern deformed gradually from shaper peak pattern to get duller and broader with wider tail. This tendency presumes degeneration of positive electromotive force might occur with aging.

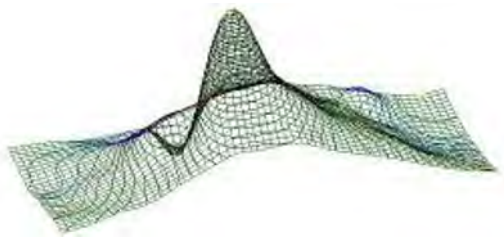


Fig. 8. A three-dimensional body surface potential distribution of 55 years old man.



Fig. 9. A three-dimensional body surface potential distribution of 60 years old man.



Fig. 10. A three-dimensional body surface potential distribution of 65 years old man.

IV. Conclusiotn

We have measured and examined many examinees' three-dimensional body surface potential distributions, and found some tendency of cardiopulmonary and dependency of age.

As for normal healthy person, transition pattern shows firstly excitation of right ventricle, then excitation of left ventricle.

In contrast, regarding a person with higher cardiopulmonary, it shows a timing of maximum positive peak of the left ventricle excitation and maximum negative peak of the right ventricle excitation occurs at the same time.

Also, aging would influence the peak intensity of wave pattern.

Although it has been more than dozens years past since the body surface electrocardiograph was reported for the first time, its measuring method and instrument are not yet commonly utilized or become widespread. One of the reasons of such unpopularity is that the utility is still unknown. We keep exploring the underlying utility of such, and hope it would be more common in future, helpful to early detection of cardiopathy, resulting in contribution to society.

Acknowledgments and references

We express special thanks to Messrs. Mitsunori KANEKO, Hisanori SHINOHARA, Yasushi SHIMOE, Koichi SAKABE, and Yamato FUKUDA of National Hospital Organization Zentsuji National Hospital.

1. Ferdjallah M, Barr RE. (1994) Adaptive digital notch filter design on the unit circle for the removal of powerline noise from biomedical signals. IEEE Trans Biomed Eng 1994:41:529-536
2. Huhta JC, Webster JG. (1973) 60 Hz interference in electrocardiography. IEEE Trans Biomed Eng 1973: 20:91-100
3. Tsinsky IA, Daskalov IK. (1996) Accuracy of the 50 Hz Interference Subtraction from the Electrocardiogram. Med Biol Eng Comput 1996: 34:489-494
4. Thakor NV, Zhu Y. (1991) Applications of adaptive filtering to ECG analysis: noise cancellation and arrhythmia detection. IEEE Trans Biomed Eng 1991:38:785-793
5. Dobrev D. (2004) Two-electrode low supply voltage electrocardiogram signal amplifier Med Biol Eng Comput 2004: 42:272-276
6. Burke MJ. Gleeson DT. (2000) A micropower dry-electrode ECG preamplifier. IEEE Trans Biomed Eng 2000: 47:155-162
7. Vilhunen T. (2002) Simultaneous reconstruction of electrode contact impedances and internal electrical properties: I. Theory Meas Sci Technol 2002:13:1848-1854
8. Baweja D, Roper H, (1999) Sirivivatnanon V. Chloride induced steel corrosion in concrete: Part 2 - Gravimetric and electrochemical comparisons. Materials Journal 1999: 96:3

Author: Yasushi TOYOSU
Institute: The University of Tokushima, Graduate School of Advanced Technology and Science
Street: 1-1, Minamijosanjima
City: Tokushima 770-8501
Country: Japan
Email: toyosu@ee.tokushima-u.ac.jp

Harnessing Web 2.0 for Collaborative Learning

Casey K. Chan[1,2], Yean C. Lee[3] and Victor Lin[4]

[1] Division of Bioengineering, National University of Singapore, Singapore
[2] Department of Orthopaedic Surgery, National University of Singapore, Singapore
[3] Department of Biological Sciences, National University of Singapore, Singapore
[4] WizPatent Pte Ltd, Singapore

Abstract — **The web has shifted from viewing pages of information to on-the-fly user-generated content. As promising as it might be in collaborative learning, Web 2.0 has yet to deliver expected results. This "read-write" capability of Web 2.0 should in theory enhances interactions between users on the web. This article attempts to decrypt the problem and propose that the limited usage of the web in collaborative learning is due to the lack of efficient information management in particular an easy-to-use sharing scheme.**

Keywords — **reference, management, sharing, collaboration, learning**

I. Introduction

Recent years marked a major shift in the way internet is utilized. The web had shifted from the page metaphor to user generated content, much of which is microcontent. The information flow on the web is no longer one way from authors to readers, it's now easier for user to respond

The shift began when personal homepages changed to personal blogs. Blogs not only enable ease-of-publishing; it also allows comments, thus facilitating interactions between users. The web changed from pages of information to user generated microcontent. Information is grabbed from one page to another, firstly via links, later using bookmarklets. Bookmarklets are javascript bookmarks which allow users to grab information from one website to a web service where users can share the grabbed information and links.

Presumably, this shift to Web 2.0 is deemed to change the way teaching and learning is conducted. Despite the promises of Web 2.0, results have not yet been delivered as expected. Full scale collaborative learning did not happen; the more prominent usage is still limited to information mining, distribution of lecture notes and discussion forums.

We content that the slow adoption of Web 2.0 in teaching and learning is due to inefficiency of the information sharing systems in web applications.

II. Operating system in the web

Operating system is the software component of a computer system which acts as a host for applications to run on the system. Because operating systems control distribution of hardware resources between applications, they arbitrate how applications will run in a computer.

A similar parallel can be seen in web browsers. Traditionally, web browsers are used only to view web pages. As web content becomes richer and more interactive, the functionalities built into web browsers increased. Web browsers have developed to a stage where no Netscape developer in 1994 could anticipate: they now possess huge computing capability, enabling many processes to run in the browsers on the client machine without burdening the servers. Web browsers have evolved to be platforms for applications to run in.

Postback refers the event when a web page is sent to server and after some processing, the server sends the web page back to the client. Asynchronous Javascript and XML (AJAX) is a collection of web application techniques that allows retrieval of information from server in the background without affecting the whole interface of web applications; information retrieval and web page refresh happen separately and thus asynchronous. By using AJAX and minimizing postback, the responsiveness of web applications can be increased significantly.

III. Teaching and learning in the web

Teaching and learning are all about exchanging of information. When there's an outflow of information from one person to another, the person is teaching and the opposite is true for learning. Traditionally in lower education level, information flows unidirectional from teachers to students. As they progress to higher levels, students are expected to contribute to their juniors at lower educational level. However, in the current world where information is readily available on the web, this practice becomes increasingly obsolete.

A majority of studies indicate that collaborative learning is more effective than unidirectional learning [2]. As students take their own initiative to gain information from peer discussions, they would need tools to share information. For example, references, links, journal articles and other learning materials would need to be shared with other users.

Chwee Teck Lim, James C.H. Goh (Eds.): ICBME 2008, Proceedings 23, pp. 2171–2172, 2009
www.springerlink.com

Without the web, sharing of information and files is a difficult process. Even now with the widespread internet adoption, sharing of information and files between users is still cumbersome requiring multiple clicks and advanced settings.

Many of the information sharing web applications like Refworks, Digg, and Delicious stick to old technologies where high degree of postback is needed to refresh information. Responsiveness of learning applications is important as numerous researches have shown that the train of thought would be broken as interruption time increases [3]. It is especially important in blackboard applications where classroom environment is replicated on the web.

Furthermore, many of these web applications allow users to share links and references but not files. Admittedly, links and references sharing are important for web based learning as they point students to sources of information. However, without file sharing features, management of files becomes inefficient. As shown by Howison and Goodrum, managing bibliographic data separately from PDF is not as productive as managing them together like in mp3 files [4]. A successful implementation of a collaborative learning environment will hence require highly responsive web applications which allow easy management as well as sharing of both links and files.

An example of optimal implementation of learning application is WizFolio [5]. WizFolio allows users to grab information and references from any webpages and store the information on the web. More importantly, files can be attached to these indexes and users can share the information they have collected with other users.

IV. Conclusions

Web 2.0 undoubtedly has increased interactions between web users. The shift from static pages to user-generated content indicates that a shift of learning strategies is required. Collaborative learning, the learning process resulted from self-initiated information gathering and peer discussion, requires efficient information management web applications. These web applications have to be highly responsive and provide solutions to efficient sharing of files as well as references and links.

References

1. Ajax: A New Approach to Web Applications at http://www.adaptivepath.com/ideas/essays/archives/000385.php
2. Johnson DW. Student-student interaction: The neglected variable in education. Educational Research 10(1):5-10.
3. Altmann EM, Trafton JG (2007) Timecourse of recovery from task interruption: data and a model. Psychon Bull Rev 14(6):1079-1084.
4. Howison Jand Goodrum A (2004) Why can't I manage academic papers like MP3s? The evolution and intent of Metadata standards. Colleges, Code and Copyright, 2004, Adelphi, Association of College & Research Libraries.
5. WizFolio Homepage at http://www.wizfolio.com/

Author: Casey K. Chan
Institute: National University of Singapore
Street: Lower Kent Ridge Road
City:
Country: Singapore
Email: doschanc@nus.edu.sg

Author: Yean Chert Lee
Institute: National University of Singapore
Street: Lower Kent Ridge Road
City:
Country: Singapore
Email: yeanchert@nus.edu.sg

Author: Victor Lin
Institute: WizPatent Pte Ltd
Street: Pandan Loop
City:
Country: Singapore
Email: victor@wizpatent.com

Electrochemical In-Situ Micropatterning of Cells and Polymers

M. Nishizawa, H. Kaji, S. Sekine

Tohoku University/Department of Bioengineering and Robotics, Sendai, Japan

Abstract — **We report two novel techniques "Electrochemical Bio-Lithography" that enables in-situ cellular micropatterning, and "Ultra Anisotropic Electrodeposition" for making micropatterns of conducting polymers. The former technique for cellular micropatterning was combined with dielectrophoresis (DEP) and AFM, and we have realized the in-situ spatiotemporal cellular micropatterning in various environments. On the other hand, we have found the micropatterned hydrophobic area around electrode serves as a template for in-situ circuit formation with conducting polymers. Importantly, since the electropolymerization can be conducted without significant damage to the existing cell cultures, these two techniques can be combined to form hybrid micropatterns of cells and conducting polymers.**

Keywords — **Cell Culture, Conducting Polymer, Bioassay**

I. Introduction

Recent technical progress in cell culturing has made bioassays possible using cellular networks combined with electrode arrays, in which smart bio-interfacing between microelectrodes and biological cells is of central importance.

The principle of our original "Electrochemical Bio-Lithography" technique is based on our finding that a heparin-coated surface, initially anti-biofouling, rapidly becomes cell-adhesive upon exposure to dilute hypobromous acid that can be locally generated by electrochemical means. Since this lithography can be conducted even during cultivation, we have succeeded to spatiotemporally induce the cell adhesion, growth and migration, and realized the in-situ cellular micropatterning [1-4].

Conducting polymers such as polypyrrole (PPy) and poly(3,4-ethylenedioxythiophene) (PEDOT) are excellent candidates for bioelectrode materials owing to their inherent electrical conductivity, controllability of surface biochemical properties, and biocompatibility. In particular, the large surface area due to a fibrous structure increases the interfacial electrical capacity, ensuring noninvasive electrical stimulation of biological cells. And "Ultra Anisotropic Electrodeposition" technique is based on our finding that that electrodeposited film of conducting polymer grows along a self-assembled monolayer (SAM) of alkylsilane or heparin coated substrate at more than 10 times faster rate [5-6].

The present works are the combination and integration of these techniques with dielectrophoresis (DEP) [7-8], silicone elastic tubing [9], or atomic force microscopy (AFM) [10] for high throughput bioassay chip, blood vessel disease model, in-situ analysis of single cell migration, and fully organic cell stimulation system.

II. Micropatterning of Cells

A. Combination with dielectrophoresis in microchannel

Fig. 1a shows the basic strategy for patterning cells within a microchannel. We prepared a microfluidic device with a Pt microelectrode array, which are 20 μm in width and are separated by 50 μm, at the upper wall of the channel. After a 0.1 M phosphate buffer saline (PBS) containing 25 mM KBr (pH 7.4) was introduced into the heparin-coated channel, a potential pulse of 1.7 V vs. Ag/AgCl was applied to one of the electrodes for 0.5 sec to generate hypobromous acid (HBrO) that quickly removes the antibiofouling heparin, exposing protein-adhesive surface. Subsequently, a solution of 30 μg mL^{-1} fibronectin, cell-adhesive protein, was introduced into the channel and incubated for 20 min, followed by a wash with PBS. After the channel was filled with a medium (13 mS cm^{-1}) containing HeLa cells (4 x 10^6

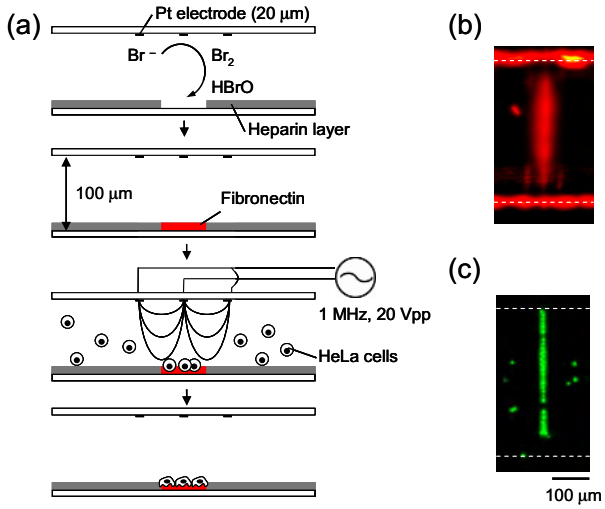


Fig. 1 (a) Schematic representation of the cellular patterning within the microchannel (side view). (b, c) A fluorescent micrographs (top views) of (b) Cy3-labeled fibronectin and (c) HeLa cells (stained with CellTracker Green) concentrated by negative DEP.

Chwee Teck Lim, James C.H. Goh (Eds.): ICBME 2008, Proceedings 23, pp. 2173–2176, 2009
www.springerlink.com

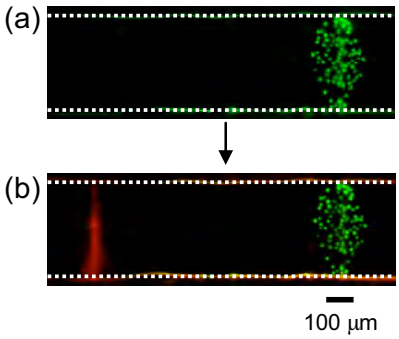


Fig. 2 Patterning of two types of HeLa cells within a single microchannel. After the first cell type (stained with Cell-Tracker Green) was immobilized (a), another cell-adhesive region was created and the second cell type (stained with CellTracker Orange) was captured by applying the DEP force at a flow rate of 0.1 μL min^{-1} (b). The dotted lines in the images denote the position of the side wall of the channel.

cells mL^{-1}), negative DEP (1 MHz, 20 Vpp) was used to concentrate cells on the pre-patterned cell adhesive region. Fig. 1b shows a fluorescence micrograph of Cy3-labeled fibronectin that was locally immobilized on the bottom wall of the channel, corresponding to the position of the electrode. After the channel was filled with a suspension of HeLa cells and negative DEP was carried out, HeLa cells quickly moved in the direction of weak electric fields to form a line pattern on the bottom wall within 15 sec, as shown in Fig. 1c. Even after DEP operation for another 15 min, no damage was observed for the adhered cells, as judged by a live/dead staining test.

Fig. 2 shows an array of two types of HeLa cells patterned in the microchannel by repeating a set of the electrochemical lithographic treatment and the cell manipulation by the negative DEP. After the first cell type (stained with CellTracker Green) was immobilized at the right side of the channel (Fig. 2a), the second cell type (stained with CellTracker Orange) was trapped in the fibronectin-immobilized region (left side of the channel) at a fluid flow rate of 0.1 μL min^{-1} by using another set of the microelectrodes array. Since most of the cells flowing from the upstream (left side of the channel) can be captured on the fibronectin region and, even if some cells happen to flow to the downstream, the cells hardly attach on the prepatterned region of the first cell type in the presence of the fluid flow, the two types of cells could be localized in the single channel without cross contamination of these cell types (Fig. 2b).

B. Patterned co-cultures in elastic tubing

A Pt needle microelectrode is used to locally generate the oxidant and form a cell-adhesive region on the inner surface of tubing precoated with heparin (Fig. 3a). Since the needle electrode can be inserted into the tubing through its wall, it is unnecessary to install the electrode within the tubing beforehand. After the first cell type is attached on the electrochemically treated region (Fig. 3b), the remaining heparin-coated region is complexed with poly-L-lysine (PLL) [11] to switch the heparin surface from cell-repellent to cell-adhesive thereby facilitating adhesion of a second cell type (Fig. 3c).

An example of the patterned co-cultures that can be achieved within the tubing structure using a combination of the microelectrode technique and electrostatic deposition is shown in Fig. 4. The heparin-coated silicone tubing was processed to make the first cellular pattern on the inner wall using a needle electrode in the same manner as described in Fig. 3. A fluorescence micrograph of NIH-3T3 fibroblasts (stained with CellTracker Green) with adhesion around the electrode insertion site is shown in Fig. 4a. At this stage of the process, the inner surface of the tubing outwith the cell adhesion region is covered with heparin. To alter the anti-biofouling property of the heparin surface to allow adhesion of the second cell type, PLL and fibronectin were in turn added to the tubing. To avoid any cytotoxic effect of PLL on the pre-patterned cells, the PLL treatment was carried out at a low concentration (40 μg mL^{-1}) and for a short exposure time (20 min). Subsequently, a suspension of HepG2 hepatocyte cells was incubated for 30 min in the tubing, followed by a wash with fresh medium to remove non-adherent cells. To visualize the co-cultures, HepG2 cells were fluorescently labeled with CellTracker Orange before

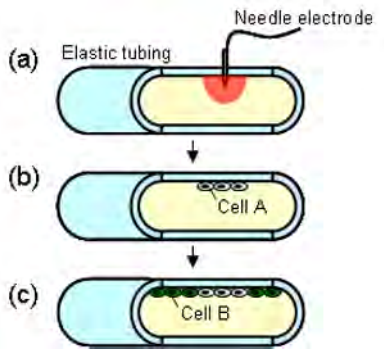


Fig. 3 Strategy for patterning cells inside elastic tubing structure. (a) A needle electrode is inserted through the tubing wall. The electrode electrochemically generates an oxidizing agent that locally detaches the anti-biofouling heparin layer on the inner wall. The removal of the heparin permits localized cell attachment. (b) The first cell type is then seeded and allowed to adhere to the treated region. (c) Poly-L-lysine is electrostatically deposited onto the region retaining heparin in order to switch the surface property to allow cell adhesion. A second cell type can then be seeded, resulting in the formation of patterned co-cultures within the tubing.

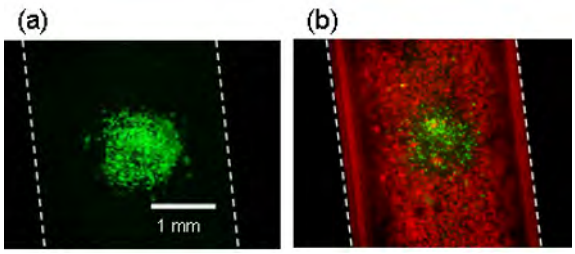


Fig. 4 Patterned co-cultures of NIH-3T3 fibroblasts (green) and HepG2 hepatocytes (red) inside the tubing structure. (a) NIH-3T3 cells were initially seeded on the cell adhesion region generated by the needle electrode. (b) After the surrounding region was switched from cell-repellent to cell-adhesive by PLL and fibronectin deposition, HepG2 cells were seeded.

seeding. Fluorescence micrograph of the stained co-cultures validates the formation of patterns inside the tubing (Fig. 4b). The post-seeded HepG2 cells (Fig. 4b, red cells) attached to the region surrounding the pre-patterned NIH-3T3 cells (Fig. 4b, green cells). Although some HepG2 cells attached within the location of the NIH-3T3 cells, this could be effectively eliminated by allowing the first cell type a longer initial culture period to enable its population to increase in density and spread. It should be noted that the perfusion system for long-term cell culture was not used here because the focus of the study was on the surface treatment of the tubing.

C. Miniaturization of patterns using AFM

An oxygen plasma treated quartz glass substrate was immersed in polyethyleneimine (PEI) and heparin (hep) solution in turn in order to assemble an electrostatic bilayer of PEI/hep. The electrochemical AFM probe having an electrode (ca. 500 nm in diameter) at the tip was positioned close to a PEI/hep-coated antibiofouling substrate and used to locally generate hypobromous acid from a dilute Br^- solution to render the substrate surface protein-adhesive (Fig. 5). The treated substrate was immersed in fibronectin solution, followed by seeding HeLa cells on the substrate.

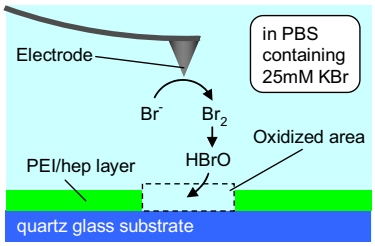


Fig. 5 Schematic illustration of the AFM configuration integrated with the electrochemical bio-lithography technique. The electrode at the apex of the AFM probe is positioned above the PEI/hep-coated substrate surface. To pattern the substrate surface, a reactive oxidant, HBrO, is electrochemically generated at the probe tip electrode by applying a voltage pulse of 1.5 V (supplied by an AA-size battery) between the probe electrode and the counter electrode.

The reaction in which the electrogenerated oxidant changed the substrate surface properties was sufficiently rapid to be diffusion controlled. The size of FN pattern could be controlled 2-15 μm in diameter by the electrolysis period. Also the scanning probe enabled us to make arbitrarily shaped patterns. These subcellular scale adhesive patterns (Fig. 6a) allowed the adhesion of single cells (Fig. 6b). Each cell on the small circular patterns was not able to spread. On the other hand, the cell on the 20 μm square frame pattern spread and became square-like.

Fig. 7 shows an array of two types of proteins prepared by stepwise patterning. After the first protein (FN-Cy2, green) was patterned, the electrochemical treatment was conducted, followed by the immobilization of the second protein (FN-Cy3, red).

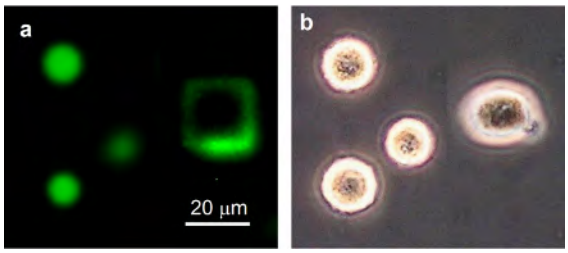


Fig. 6 (a) Fluorescent micrograph of Cy2-labeled FN and (b) phase-contrast micrograph of HeLa cells.

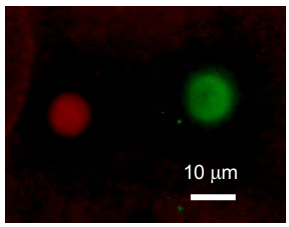


Fig. 7 Patterning of multiple types of proteins using stepwise electrochemical treatment. After the first protein FN-Cy2 (green) was patterned, the electrochemical treatment was conducted, followed by the immobilization of the second protein FN-Cy3 (red).

III. Micropatterning of Conducting Polymers

A. In situ micropatterning of conducting polymer

The micropatterns with SAM of alkylsilane or heparin lead to a micropatterns of PPy upon the polymerization (Fig. 8). Importantly, the electropolymerization of PPy can be conducted even during cell cultivation without significant damage to the existing cells.

Fig. 9 demonstrates the in-situ electrical wiring to cultured cells. A hydrophobic pattern was previously formed around electrode, HeLa cell was put on the pattern, and then polypyrrole was synthesized. We preliminarily studied the toxicity of the pyrrole monomer by culturing HeLa cells in a culture media containing 0.1 M pyrrole. Even after 1 day of cultivation, more than 80 % of HeLa cells were alive and still proliferated, suggesting a comparatively brief exposure to pyrrole solution during polymerization (typically for a few min) would not significantly affect the cellular viability.



Fig. 8 Photographs of the PPy micropattern growing from a twin microband (20μm width) electrodes. The pretreatment with SAM of Octadecylsilane was conducted as to give a checked pattern.

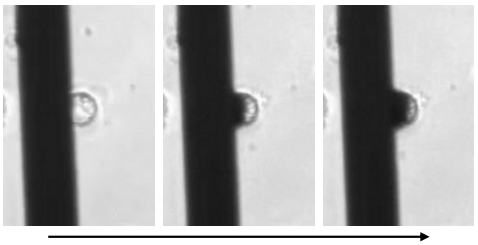


Fig. 9 Photographs of the PPy micropattern which is growing with wrapping a HeLa cell

B. Electrochemical biolithography

The surface modification with heparin can be easily detached by a non-invasive electrochemical biolithography [1], and thus we can draw micropatterns of PPy by using a needle-type microelectrode as a "pen" (Fig. 10). Since this lithography can be applied even during cell cultivation, we can expect the formation of hybrid micropatterns of conducting polymer and living cells.

IV. Conclusions

We have described methods for electrochemical in-situ micropatterning of proteins, cells and conducting polymers. Since the present electrochemical technique can be conducted under typical physiological conditions, we could make patterns sequentially such as co-cultures. And these smart bio-interfacing with micropatterned conducting polymers will contribute to the realization of these next-generation bioassay chips.

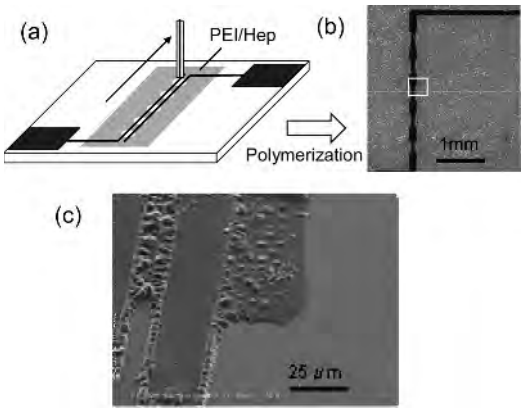


Fig. 10 (a) Schematic drawing of the micropatterning of PEI/Hep by electrochemical biolithography. A Pt microelectrode was approached to ca. 50 μm above the substrate surface, and scanned with 0.5 mm steps along the twin-microband electrode, waiting for 10 sec at each step with application of 1.7 V vs. Ag/AgCl in 25 mM KBr buffered solution. (b) A photograph of the PPy film formed at the microband electrode. (c) A SEM image of the boxed area of (b).

Acknowledgment

We acknowledge the support of Tohoku University GCOE Program "Grobal Nano-Biomedical Engineering Education and Research Network Centre".

References

1. Kaji H et al. (2004) Langmuir 20:16-19
2. Kaji H et al. (2005) J Am Chem Soc 126:15026-15027
3. Kaji H et al. (2006) Anal Chem 78:5469-5473
4. Kaji H et al. (2006) Langmuir 22:10784-10787
5. Nishizawa M et al. (2007) Langmuir 23:8304-8307
6. Nishizawa M et al. (2007) Biomaterials 28:1480-1485
7. Kaji H et al. (2008) Electrochemistry 76:555-558
8. Hashimoto et al. (2008) Sens Act B 128:545-551
9. Kaji H et al.(2007) Biotech Bioeng 98:919-925
10. Sekine S et al. (2008) Anal Bioanal Chem 391:2711-2716
11. Khademhosseini et al. (2004) Biomaterials 25:3583-3592

Author: Matsuhiko Nishizawa
Institute: Tohoku University
Street: 6-6-01, Aramaki-Aoba, Aoba-ku
City: Sendai
Country: Japan
Email: nishizawa@biomems.mech.tohoku.ac.jp

Estimation of E_{max} of Assisted Hearts using Single Beat Estimation Method

T.K. Sugai[1], A. Tanaka[2], M. Yoshizawa[3], Y. Shiraishi[4], S. Nitta[4], T. Yambe[4] and A. Baba[5]

[1] Graduate School of Biomedical Engineering, Tohoku University, Japan
[2] Faculty of Symbiotic Systems Science, Fukushima University, Japan
[3] Cyberscience Center, Tohoku University, Japan
[4] Institute of Development, Aging and Cancer, Tohoku University, Japan
[5] Tohoku University Biomedical Engineering Research Organization, Tohoku University, Japan

Abstract — **In many countries, cardiovascular diseases are the main cause of death. Since the whole blood circulation depends on the heart, it cannot rest in order to recover as most of other muscles can. In some patients with not so severe damages in the myocardium, a rotary blood pump (RBP) may temporarily unload the native heart and can permit the recovery of the cardiac function. Since both implantation and withdrawal of the RBP are invasive procedures, the recovery should be detected with accuracy before weaning of the RBP. Therefore, the objective of this study is to estimate the cardiac function of assisted hearts using the maximum ventricular elastance E_{max} which is a cardiac function index representing the left ventricle contractility. Conventionally, the index E_{max} has been estimated using left ventricle pressure (*LVP*) and volume (*LVV*) during multiple cardiac cycles and under different loads. The two main problems of this method are that a precise measurement of *LVV* is invasive, and that induced changes in load should be avoided in cardiac patients. The single beat methods have the advantage that can be used with no changes on left ventricle load. In particular, the parameter optimization method (POM) permits E_{max} also to be calculated also using flow instead of volume in the case of non-assisted hearts. The conventional estimation of E_{max} and also the estimation using the POM with *LVP* and *LVV* had already been validated under the assistance of the RBP. This study shows that, in particular in cases with non-opening of the aortic valve, E_{max} can also be estimated by the POM using pump flow instead of *LVV*.**

Keywords — **Ventricular Assist Device, Ventricular Elastance, Cardiac Function, Bridge-to-Recovery.**

I. Introduction

Although heart transplantation is the best treatment for serious cardiac diseases and one of the most common organ transplantations performed worldwide, the shortage in donors limits the treatment's applicability. In order to diminish the donor shortage problem, rotary blood pumps (RBPs) have been used as an alternative treatment either as bridge to transplant, destination therapy or, more recently, as bridge to recovery. The so-called bridge to recovery refers to a treatment that combines the RBP, which unloads the ventricles, with pharmacological treatments or even with regeneration therapy permitting the myocardial recovery.

In such treatment, after the recovery of the cardiac function is detected, the RBP can be weaned and the patient can have a regular life again. Due to the invasiveness and the risk of the pump removal and in particular of its reimplantation, the recovery must be precisely detected before the pump weaning. The conventional methods for assessment of the cardiac function are based on the behavior of unassisted hearts; therefore it is important to re-evaluate those methods considering the hemodynamic changes that the assistance of the RBP brings to the circulatory system.

Thus, in this paper we present an evaluation of the parameter optimization method (POM) for the estimation of the maximum elastance (E_{max}) comparing the estimation using the left ventricular volume (*LVV*) to the estimation using the pump flow (*LPF*). The E_{max} has already been validated as a cardiac function index during assistance of RBPs [1]. However, clinical limitations of the conventional estimation method motivated the choice of the POM that is a single beat estimation method that permits the estimation of the E_{max} using the flow instead of the left ventricular volume (*LVV*), therefore, being less invasive than the multiple beats method.

II. Materials and Methods

A. Parameters Optimization Method

The left ventricular elastance ($E(t)$) is defined as the ratio between the left ventricular pressure (*LVP*) and (*LVV*) corrected by a dead volume (V_0), as shown in the equation below.

$$E(t) = \frac{LVP(t)}{LVV(t) - V_0} \tag{1}$$

The elastance reaches its maximum at a point near the end of the systolic period, being this value of maximum elastance independent of the ventricular load and sensible to changes in the ventricular contractility.

Chwee Teck Lim, James C.H. Goh (Eds.): ICBME 2008, Proceedings 23, pp. 2177–2180, 2009
www.springerlink.com

The POM is a single-beat estimation method, *i.e.* a method for estimating E_{max} using the *LVV* and *LVP* of a single cardiac cycle, that is based on two important assumptions about the cardiac cycle: (*i*) V_0 should be constant and (*ii*) the elastance is approximately linear during the ejection period.

From (1) V_0 can be calculated as

$$V_0 = LVV(t) - \frac{LVP(t)}{E(t)} \tag{2}$$

The equation error (3) is defined considering that V_0 should be constant and that the $E(t)$ can be approximated to a linear function. Using (3), the POM consists on finding the linear approximation for the elastance that leads to the smaller fluctuation on V_0 calculated at two instants t_0 and t_k during the ejection period by minimizing the root mean square of the error ε_k.

$$\varepsilon_k = LVV(t_k) - \frac{LVP(t_k)}{at_k + b} - LVV(t_0) + \frac{LVP(t_0)}{at_0 + b} \tag{3}$$

Once the linear approximation of the $E(t)$ is found, it is possible to calculate V_0 as in (4).

$$V_0 = \frac{1}{n-i+1}\sum_{k=i}^{n} LVV(t_k) - \frac{LVP(t_k)}{E(t_k)} \tag{4}$$

Finally, the instantaneous elastance $E(t)$ is obtained from (1) substituting the calculated V_0, and then from the maximum of $E(t)$, E_{max} is also attained.

The POM permits, alternatively, the E_{max} to be estimated by substituting the *LVV* by the integration of the total flow, which is a less invasive measurement, as in (5).

$$LVV(t_k) = LVV_{ED} - \int_{t=t_{ED}}^{t_k} TF(t)dt \tag{5}$$

where LVV_{ED} is the *LVV* at the instant t_{ED} corresponding to the end of the diastolic period.

Since LVV_{ED} is the same reference for all points in the cardiac cycle, (3) can be rewritten as: [2]

$$\varepsilon_k = \int_{t=t_{ED}}^{t_k} TF(t)dt - \frac{LVP(t_k)}{at_k + b} - \int_{t=t_{ED}}^{t_0} TF(t)dt + \frac{LVP(t_0)}{at_0 + b} \tag{6}$$

In the case of the assisted heart the total flow (*TF*) pumped from the heart during the systole is composed by the sum of the aortic flow (*AoF*) and the pump flow (*LPF*).

Moreover, in the particular case of the full bypass, there is no flow through the aortic valve and the *TF* is composed only by *LPF* which can be easily measured at the pump cannula or even estimated from the pump operation state, using the rotational speed and the motor electric current, for example.

B. Experiment Protocol

For the comparison of the chosen methods were used animal experiment data measured in three adult goats (female, 52-58kg) with the left ventricle assisted by the centrifugal pump NEDO PI-710 gyro pump (Baylor College of Medicine, Houston, US) in experiments #1 and #2, and by the centrifugal pump EvaHeart LVAS (Sun Medical Tec.Res.Co., Japan) in experiment #3. The RBP had the outflow cannula connected to the descending aorta and the inflow cannula inserted into the left ventricular apex, as represented in Fig.1.

All measurements were recorded under open-chest condition. Data were recorded during 60s with a constant mean rotational speed, for each data set, the mean rotational speed (N_L) was changed in order to evaluate the sensitivity of the estimation to changes in the assistance level. *LVP* and *LVV* were measured by a conductance catheter (Leycom, Netherlands) inserted inside the left ventricle through the ascending aorta. After the experiment, *LVP* was pre-processed with a zero-phase low pass filter (cutoff frequency f_0=10Hz), and *LVV* with a de-noising symlet wavelet (sym8).

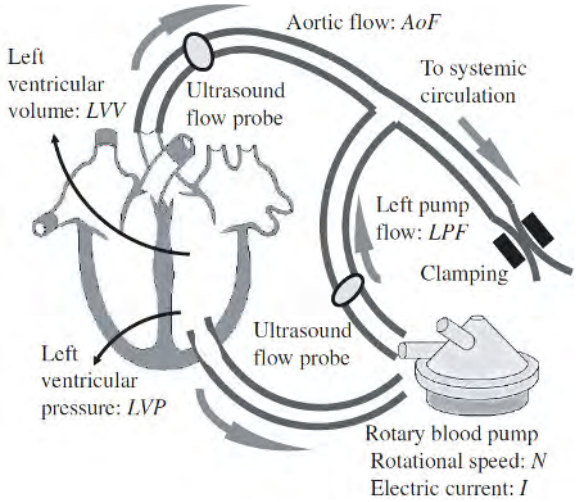


Fig. 1 Animal Experiment Setting

Additionally, *LPF* and *AoF* were measured with ultrasound flow probes (Transonic Inc., US) as reference for the pump control.

The measurements were performed after the Propranolol administration in order to induce the full bypass. In experiment #3, in particular, one measurement was performed before the Propranolol injection with the full bypass induced by the increase of the pump rotational speed in order to evaluate the sensibility of the estimation to changes in the ventricular contractility.

III. Results

Figs. 2-4 show the estimated values of E_{max}, represented by their mean and their standard deviation, comparing the estimated values using *LVV* against the estimated values using *LPF* for different assistant levels. In the experiment #3, one of the measurements was performed before the Propranolol injection (control data).

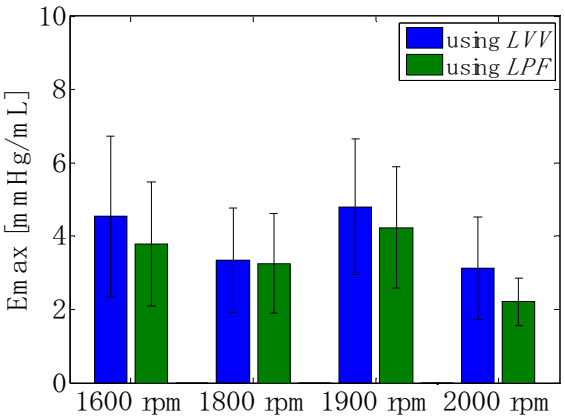


Fig. 2 Values of E_{max} (mean and standard deviation) estimated using the POM – Experiment #1

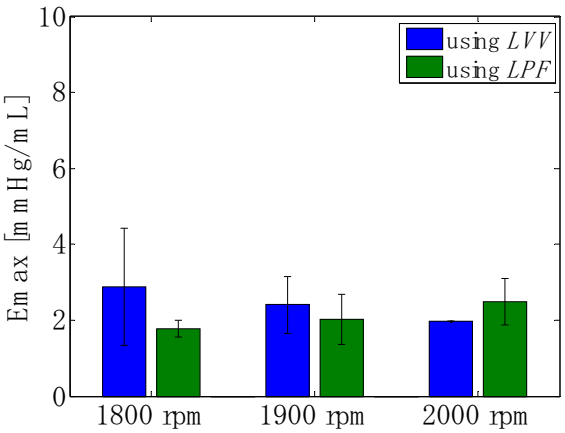


Fig. 3 Values of E_{max} (mean and standard deviation) estimated using the POM - Experiment #2

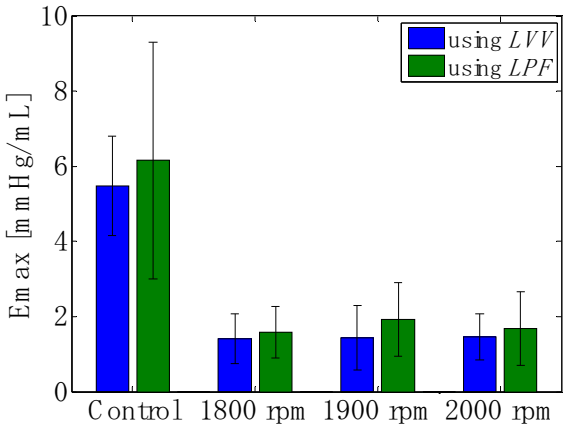


Fig. 4 Values of E_{max} (mean and standard deviation) estimated using the POM - Experiment #3

IV. Discussion

Due to the hemodynamic changes that the assistance with RBPs brings to the circulatory system, it is important to revalidate the cardiac function indices before using them to detect the recovery of the assisted heart.

The E_{max} was chosen in this study because it had already been validated during assistance; however, a less invasive estimation method was still necessary. The POM is a single beat estimation method that permits the estimation of the E_{max} using flow instead of the *LVV*, which is desirable for a clinical application due to the considerably less invasiveness. Moreover, in the particular case of full bypass, the only invasive measurement is the *LVP*, which could be eventually substituted by the pressure in the pump inlet.

The results show that there was no significant difference between the E_{max} estimated using *LVV* and using *LPF*. Besides, the estimated values were independent of the pump rotational speed, which is fundamental for the application of a cardiac function index during assistance with RBPs.

Finally, in the experiment #3, it was possible to compare data corresponding to different cardiac functions: before and after the Propranolol injection. The results show that the estimation of E_{max} using the POM could detect changes in the contractility.

The high standard deviation in some cases was also observed in the estimation of E_{max} when there was partial bypass and is believed to be due to the generality of the hypothesis of the method. Other single-beat methods with more specific hypothesis showed better accuracy however

were valid for a more limit range of conditions, besides not permitting the substitution of the *LVV* by *LPF.* [3]

Before achieving any definitive conclusions about the detection of the cardiac function during assistance with RBP using the POM, it is important to evaluate this method in a wider data set considering also a richer variety of cardiac functions in order to evaluate the sensitivity to changes in the contractility.

The main limitation that was found in this study was that the full bypass condition might be risky when the cardiac function is not impaired. In this study, in experiment #3 it was obtained by increasing the rotational speed however this might be a risky procedure depending on the patient's condition. It is necessary to study a better approach to induce the full bypass.

Moreover, small differences were expected in the estimation using *LPF* caused by noise in the flow which would be amplified by its integration during the ejection period. Errors could also be caused by difference in the calibration of the *LVV* and the *LPF.* In order to minimize such errors, the *LPF* was employed in the calibration of the *LVV* after the experiment.

V. Conclusion

Although the assistance with RBPs changes considerably the hemodynamics of the left ventricle, the E_{max} estimated with POM reflected the changes in the cardiac function in the data set evaluated independently of the level of pump assistance.

The results indicate that it is possible to assess the cardiac function without the invasive measurement of the *LVV*, and also indicate that if the full bypass can be performed by the RBP even during short periods, then only the *LVP* and the *LPF* are required for the estimation of E_{max}.

Acknowledgment

The authors thank the "Education Program for Biomedical and Nano-Electronics, Tohoku University" Support Program for Improving Graduate School Education, MEXT.

References

1. D. Ogawa, A. Tanaka, K. Abe, et al. (2006) Evaluation of cardiac function based on ventricular pressure-volume relationships during assistance with a rotary blood pump. 28th Annual International Conference of IEE/EMBS, pp. 5378–5381
2. M. Yoshizawa, A. Tanaka, K. Abe, et al (1998) An approach to single-beat estimation of emax as an inverse problem. 20th Annual International Conference of IEE/EMBS, pp. 279–282
3. T.K. Sugai, M. Yoshizawa, A. Tanaka, et al. (2008) Preliminary Study on the Estimation of Emax using Single-Beat Methods during Assistance with Rotary Blood Pumps. 30th Annual International Conference of IEE/EMBS, pp. 973–976

Author: Telma Keiko Sugai
Institute: Tohoku University
Street: Electri. & Info. Build., 6-6-05 Aoba, Aoba-ku
City: Sendai
Country: Japan
Email: telma@yoshizawa.ecei.tohoku.ac.jp

Molecular PET Imaging of Acetylcholine Esterase, Histamine H1 Receptor and Amyloid Deposits in Alzheimer Disease

N. Okamura, K. Yanai

Department of Pharmacology, Tohoku University School of Medicine, Sendai, Japan

Abstract — **Depositions of amyloid plaques, neurofibrillary tangles and subsequent neurotransmitter deficits are neuropathological characteristics of Alzheimer's disease. Non-invasive monitoring of these changes in the brain is potentially useful for early diagnosis of Alzheimer's disease. Here we introduce the method for measuring the density of amyloid plaques and neurotransmitters using ^{11}C-labeled donepezil, doxepin and BF-227. Positron emission tomography (PET) imaging by [^{11}C]donepezil visualized the distribution of acetylcholine esterase in the brain. PET study using [^{11}C]doxepin also demonstrated the distribution of histamine H1 receptor in the brain. Density of acetylcholine esterase and H1 receptor was prominently reduced in the patients with Alzheimer's disease. [^{11}C]BF-227 PET successfully visualized neocortical depositions of amyloid plaques in the brain and clearly differentiated the patients with Alzheimer's disease from healthy individuals. These tracers would be useful for early and accurate diagnosis of dementia and monitoring anti-dementia therapy.**

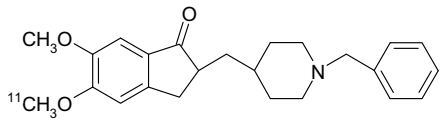
Keywords — **Alzheimer's disease, positron emission tomography (PET), acetylcholine, histamine, amyloid**

I. Introduction

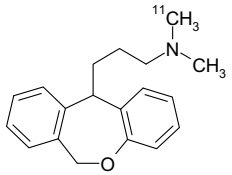
Alzheimer's disease (AD) is a common neurodegenerative disorder in the elderly. Substantial neuropathological evidences suggest that progressive deposition of amyloid deposits, such as amyloid plaques and neurofibrillary tangles, is the characteristic neuropathological change in AD. Amyloid plaques are composed of amyloid β protein (Aβ), which is generated by proteolytic reaction of β and γ-secletase from amyloid precursor protein. Excessive Aβ generation causes the Aβ aggregation and the formation of amyloid plaques, followed by the formation of neurofibrillary tangles, neuron death and neurotransmitter deficit.

Noninvasive detection of amyloid plaques in the brain is a useful strategy for early diagnosis of AD. Measuring neurotransmitter function is also helpful for determination of treatment protocol of dementia. Molecular imaging techniques using positron emission tomography (PET) and single photon emission computed tomography (SPECT) have been developing for noninvasive detection of these intracranial changes. PET is more practical than SPECT because of the advantages in sensitivity, quantitativity and spatial resolution.

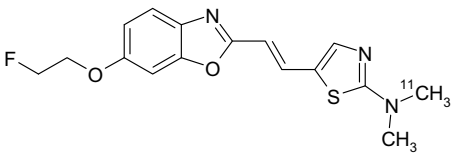
We have successfully visualized acetylcholinesterase (AChE) density using [^{11}C]donepezil and histamine H1 receptor (H1R) density using [^{11}C]doxepin (Fig. 1) [1-3]. We have developed original imaging agent BF-145, BF-168 and BF-227 (Fig. 1) for in vivo detection of amyloid plaques in AD [4-6]. Here we demonstrate clinical PET study using these tracers in AD patients.



[^{11}C]donepezil



[^{11}C]doxepin



[^{11}C]BF-227

Fig. 1 Chemical structures of [^{11}C]donepezil, [^{11}C]doxepin and [^{11}C]BF-227

II. Functional Neuroimaging in Alzheimer's Disease

A. Imaging acetylcholinesterase using [^{11}C]donepezil

Donepezil hydrochloride is most widely used drug for the treatment of cognitive dysfunction in AD patients. It selectively binds to and inhibits AChE. Radiolabeled donepezil can thus be used as a tracer to measure the density of AChE. To visualize AChE in the brain, [^{11}C]Donepezil was used as

Chwee Teck Lim, James C.H. Goh (Eds.): ICBME 2008, Proceedings 23, pp. 2181–2183, 2009
www.springerlink.com

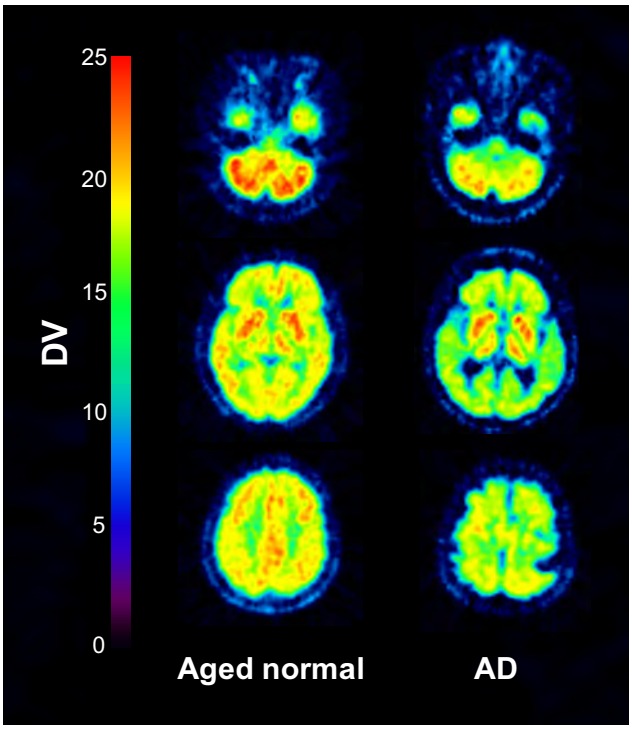


Fig. 2 Distribution volume (DV) images of [^{11}C]donepezil in the brain of aged normal (left) and AD patient (right)

a tracer for PET imaging. Tissue time activity curves of [^{11}C]donepezil indicated initial rapid brain uptake followed by gradual clearance from the brain. High concentrations of radioactivity of [^{11}C]donepezil were observed in AChE-rich brain regions such as the striatum, thalamus, and cerebellum, whereas radioactivity uptake in the neocortex including frontal, temporal, and parietal cortices was moderate. Distribution volume (DV) images of [^{11}C]donepezil clearly revealed higher concentrations of tracer distribution in the striatum and cerebellum than in neocortex (Fig. 2). Patients with AD exhibited reduction of DV in the hippocampus and neocortex, compared with aged normal subjects. Orally administered donepezil induced substantial reduction of DV in all regions of brain examined. The amount of binding of orally administered donepezil to AChE is considered a key factor determining therapeutic response of this drug. In vivo evaluation of AChE occupancy using [^{11}C]donepezil PET could thus be a powerful strategy for determining the optimal dose of donepezil in AD therapy [1].

B. Imaging histamine H1 receptor using [^{11}C]doxepin

We previously established the method for measuring histamine H1 receptor density in the brain using [^{11}C]doxepin. To confirm whether central histaminergic neuron is injured in AD brain or not, we applied this tracer to the patients with AD. The parametric images of binding potential were generated by Logan graphical analysis as described previously. The binding potential of H1 receptors showed a significant decrease particularly in the frontal and temporal areas of AD brain compared to aged normal subjects (Fig. 3). In addition, the receptor binding correlated closely to the severity of AD. The difference in the binding potential between AD patients and aged normal subjects was greater than that in the cerebral blood flow, and the rate of decrease in the binding potential with the progression of AD was greater than the rate of decrease in the cerebral blood flow. These results indicate the prominent disruption of the histaminergic neuron in the neurodegenerative processes of AD [7].

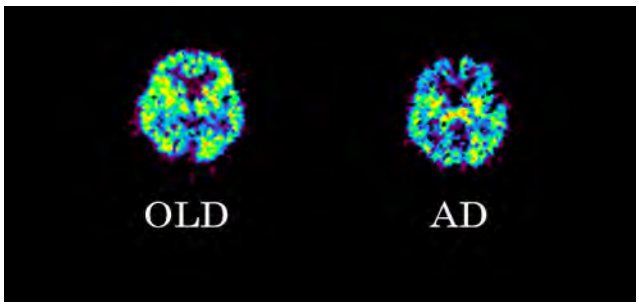


Fig. 3 Binding potential images of [^{11}C]doxepin in the brain of aged normal subject (OLD) and AD patient

C. Imaging amyloid deposits using [^{11}C]BF-227

Non-invasive detection of amyloid plaques is potentially useful for presymptomatic diagnosis of AD. Therefore, we have explored amyloid-binding agents and developed 6-(2-fluoroethoxy)-2-[2-(4-methylaminophenyl)ethenyl] benzoxazole (BF-168), [2-(4-methylaminophenyl)ethenyl]-5-fluorobenzoxazole (BF-145) and 2-[2-(2-dimethylaminothiazol-5-yl)ethenyl]-6-[2-(fluoro)ethoxy] benzoxazole (BF-227) as promising candidates for PET amyloid imaging probe [4-6, 8, 9]. These benzoxazole derivatives have high binding affinity for Aβ aggregates in vitro and high BBB permeability.

Clinical PET study using [^{11}C]BF-227 demonstrated neocortical retention of this tracer in AD patient (Fig. 4). About 60% of subjects with mild cognitive impairment (MCI), a group of individuals at a high risk of developing dementia, also showed abnormal retention of BF-227. Especially, MCI subjects who progressed to AD during follow-up showed prominent retention of BF-227 in the neocortex. These findings suggest that neocortical retention of BF-227 means high risk of conversion to AD. Voxel-by-voxel analysis of BF-227 PET images demonstrated higher retention of BF-227 in the temporo-parietal region in AD patients (Fig. 5).

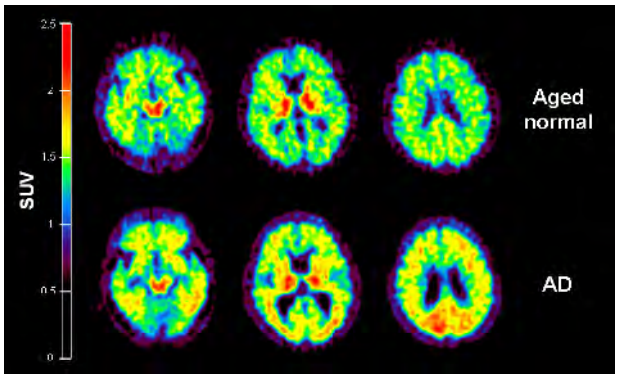


Fig. 4 Biodistribution of [^{11}C]BF-227 in the brain of aged normal control and AD patient

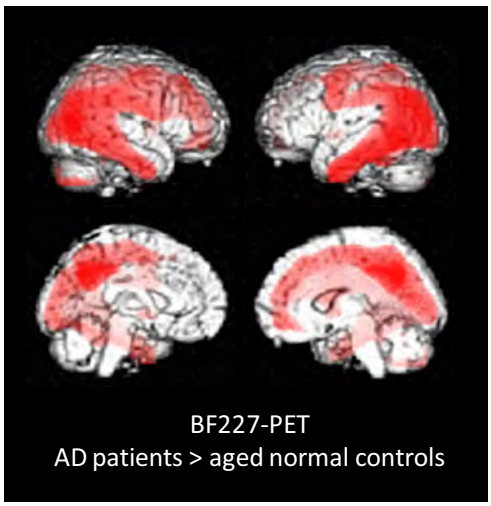


Fig. 5 Voxel-by-voxel analysis of [^{11}C]BF-227 PET images in the comparison between aged normal controls and AD patients (SPM2 analysis, $p<0.001$, uncorrected)

Pattern of this distribution resembles the distribution of neuritic plaques in postmortem AD brains. Microscopic observation also indicates preferential binding of BF-227 to neuritic plaques in AD brain section. These results suggest that neocortical retention of BF-227 reflects the level of neuritic plaques in the brain [10].

III. Conclusions

Molecular imaging technique is a powerful tool for understanding the pathophysiology of neuropsychiatric disease. The distributions of AChE, histamine H1 receptor and amyloid plaques in human brain were successfully visualized using PET. These imaging technologies would be useful for early and accurate diagnosis of AD and monitoring anti-dementia therapy. These technologies and forthcoming anti-dementia therapy will cooperatively contribute to the prevention of dementia.

Acknowledgment

This work was in part supported by Grants-in-Aid for scientific research from the Japan Society of Promotion of Science (JSPS) and the Ministry of Education, Culture, Sports, Science and Technology in Japan, as well as by a grant from the Japan Society of Technology (JST) on research and education in “molecular imaging”. The authors thank to volunteer people for the PET study, to Dr. Syoichi Watanuki for PET operation and to Mrs. Kazuko Takeda for taking care of volunteers.

References

1. Okamura N, Funaki Y, Tashiro M, et al. (2008) In vivo visualization of donepezil binding in the brain of patients with Alzheimer’s disease. Br J Clin Pharmacol 65: 472-479
2. Funaki Y, Kato M, Iwata R, et al. (2003) Evaluation of the binding characteristics of [5-(11)C-methoxy]Donepezil in the rat brain for in vivo visualization of acetylcholinesterase. J Pharmacol Sci 91:105-112
3. Okamura N, Yanai K, Higuchi M, et al. (2000) Functional neuroimaging of cognition impaired by a classical antihistamine, d-chlorpheniramine. Br J Pharmacol 129; 115-123
4. Okamura N, Suemoto T, Shimadzu H, et al. (2004) Styrylbenzoxazole derivatives for in vivo imaging of amyloid plaques in the brain. J Neurosci 24: 2535-2541
5. Okamura N, Suemoto T, Shiomitsu T, et al. (2004) A novel imaging probe for in vivo detection of neuritic and diffuse amyloid plaques in the brain. J Mol Neurosci 24: 247-255
6. Okamura N, Furumoto S, Funaki Y, et al. (2007) Binding and safety profile of novel benzoxazole derivative for in vivo imaging of amyloid deposits in Alzheimer’s disease. Geriatr Gerontol Int 7: 393-400
7. Higuchi M, Yanai K, Okamura N, et al. (2000) Histamine H1 receptors in patients with Alzheimer's disease assessed by positron emission tomography. Neuroscience 99; 721-729
8. Furumoto S, Okamura N, Iwata R, et al. (2007) Recent advances in the development of amyloid imaging agents. Curr Top Med Chem 7: 1773-1789
9 Okamura N, Furumoto S, Arai H, et al. (2008) Imaging amyloid pathology in the living brain. Curr Med Imaging Rev 4: 56-62
10. Kudo Y, Okamura N, Furumoto S, et al. (2007) 2-(2-[2-Dimethylaminothiazol-5-yl]ethenyl)-6-(2-[fluoro]ethoxy) benzoxazole: a novel PET agent for in vivo detection of dense amyloid plaques in Alzheimer's disease patients. J Nucl Med 48:553-561

Author: Nobuyuki Okamura
Institute: Department of Pharmacology,
Tohoku University School of Medicine
Street: 2-1, Seiryo-machi, Aoba-ku
City: Sendai
Country: Japan
Email: oka@mail.tains.tohoku.ac.jp

Shear-Stress-Mediated Endothelial Signaling and Vascular Homeostasis

Joji Ando and Kimiko Yamamoto

Laboratory of System Physiology, Department of Biomedical Engineering,
Graduate School of Medicine, University of Tokyo, Japan

Abstract — **Endothelial cells (ECs) change their morphology, cell function, and gene expression in response to shear stress, the frictional force exerted by flowing blood. This suggests that ECs recognize shear stress and transmit signals to the interior of the cell. The molecular mechanisms of shear-stress mechanotransduction, however, are not completely understood. Our previous studies demonstrated that Ca^{2+} plays an important role in shear-stress-mediated endothelial signaling. When cultured human pulmonary artery ECs (HPAECs) were exposed to flow, the intracellular Ca^{2+} concentration increased in a shear-stress-dependent manner. The flow-induced Ca^{2+} response occurred in the form of an influx of extracellular Ca^{2+} via an ATP-operated cation channel, P2X4. We recently found that shear-stress-induced activation of P2X4 requires ATP, which is supplied in the form of endogenous ATP released by HPAECs. HPAECs released ATP in response to shear stress, and the ATP release was mediated by cell-surface ATP synthase located in caveolae/lipid rafts. At present, however, it remains unclear how shear stress activates cell-surface ATP synthase. To gain insight into the physiological role of this P2X4-meidated shear-stress mechanotransduction in vivo, we generated *P2X4*-deficient mice. *P2X4*-deficient mice do not exhibit normal EC responses to shear stress, such as Ca^{2+} influx and subsequent production of nitric oxide, a potent vasodilator. The vasodilation induced by acute increases in blood flow in situ is markedly suppressed in *P2X4*-deficient mice. *P2X4*-deficient mice have higher blood pressure values and excrete smaller amounts of NO products in their urine than wild-type mice. No adaptive vascular remodeling, i.e., decrease in vessel size in response to a chronic decrease in blood flow, is observed in the *P2X4*-deficient mice. Thus, P2X4-mediated shear-stress mechanotransduction plays an important role in the vascular homeostasis, including in the control of blood pressure and vascular remodeling.**

Keywords — **Endothelial cell, purinoceptor, ATP, ATP synthase, Ca^{2+}**

I. Introduction

Endothelial cells (ECs) are in direct contact with blood flow and exposed to shear stress, the frictional force exerted by flowing blood. A number of recent studies have revealed that ECs recognize changes in shear stress and transmit signals to the interior of the cell, which leads to cell responses that involve changes in cell morphology, cell function, and gene expression. These EC responses to shear stress are thought to play important roles in blood-flow-dependent phenomena, such as vascular tone control, angiogenesis, vascular remodeling, and atherogenesis. The precise mechanisms of shear-stress mechanotransduction, however, are not completely understood.

II. Ca^{2+}-mediated shear-stress mechanotransduction

Our previous studies demonstrated that Ca^{2+} signaling plays an important role in shear-stress mechanotransduction [1-2]. Human pulmonary artery ECs (HPAECs) that had been labeled with a fluorescent Ca^{2+} indicator, Indo-1, were exposed to controlled levels of shear stress in a parallel-type flow chamber, and changes in the intracellular Ca^{2+} concentration were monitored. The intracellular Ca^{2+} concentration increased in a shear-stress-dependent manner. There is a good correlation between shear stress and Ca^{2+} concentration. This means that ECs can accurately convert information regarding shear stress intensity into changes in Ca^{2+} concentration. When extracellular Ca^{2+} was removed with EGTA, the shear-induced Ca^{2+} response completely disappeared, indicating that the response was due to an influx of extracellular Ca^{2+} across the cell membrane.

III. P2X4 purinoceptor as a mechanotransducer

We found that P2X4, the subtype of ATP-operated cation channels known as P2X purinoceptors, play a crucial role in the shear-stress-dependent Ca^{2+} influx [3-4]. HPAECs were treated with antisense oligonucleotides (AS-oligos) targeted to the P2X4 receptor or control scramble-oligos (S-oligos), and their Ca^{2+} responses were determined. A shear-stress-dependent Ca^{2+} response was seen in the cells treated with control S-oligos, but not in those treated with

Chwee Teck Lim, James C.H. Goh (Eds.): ICBME 2008, Proceedings 23, pp. 2184–2187, 2009
www.springerlink.com

AS-oligos (Fig. 1). To further examine the role of P2X4 in flow-related Ca^{2+} signaling, we transfected P2X4 cDNA into human embryonic kidney (HEK) cells, which are basically insensitive to flow, and established cell lines that stably express P2X4 receptors. The control HEK cells did not show any significant increase in Ca^{2+} concentration when exposed to flow, whereas the HEK cells that stably expressed P2X4 exhibited a stepwise increase in Ca^{2+} concentrations in response to graded increments in shear stress. These findings suggest that P2X4 receptors have a 'shear-transducer' property through which shear stress signals are transmitted into the cell interior via the Ca^{2+} influx.

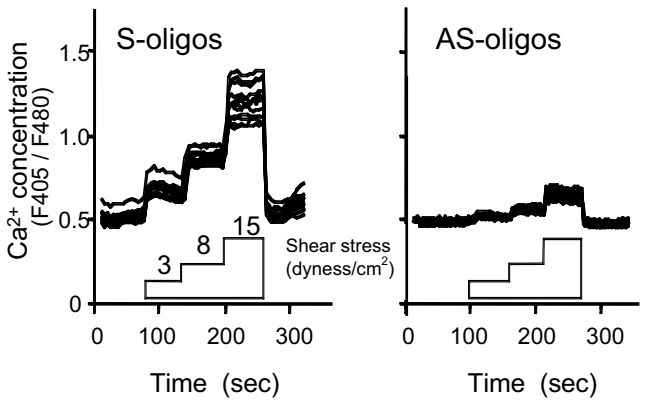


Fig.1. Effects of AS-oligos to P2X4 on shear-induced Ca^{2+} responses in HPAECs.

IV. Shear-induced ATP release via cell surface ATP synthase

Our recent study revealed that shear-stress-induced activation of P2X4 requires ATP, which is supplied in the form of endogenous ATP released by ECs [5]. We determined the amount of ATP released into the perfusate using a sensitive luciferase luminometric assay. HPAECs released ATP in response to shear stress, and the ATP release increased as the intensity of shear stress increased. ATP synthase inhibitors, such as angiostatin and an antibody against ATP synthase, markedly suppressed the shear-stress-dependent ATP release, which resulted in significant inhibition of the shear-stress-dependent Ca^{2+} response (Fig. 2). This means that endogenously released ATP plays an important role in the shear-stress-induced activation of P2X4 receptors. These findings also indicated that ATP synthase is involved in the shear-stress-induced ATP release.

We found that HPAECs express ATP synthase on the cell surface [6]. The cell-surface ATP synthase is distributed in lipid rafts and co-localized with caveolin-1, a marker protein of caveolae.

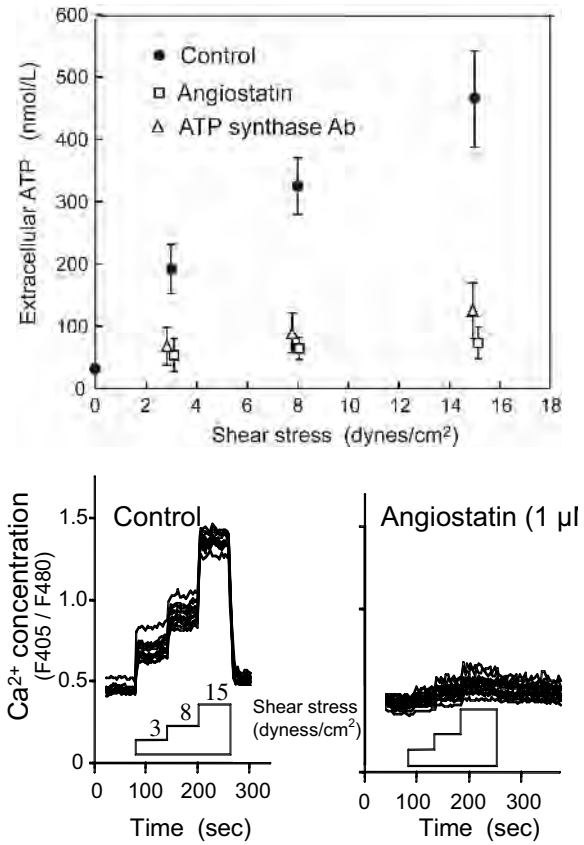


Fig.2. Effects of ATP synthase inhibitors on shear-induced ATP release and Ca^{2+} response by HPAECs.

Depletion of plasma membrane cholesterol with methyl-β cyclodextrin disrupted the lipid rafts and abolished the co-localization of ATP synthase with caveolin-1, which resulted in a marked reduction in shear-stress-induced ATP release. To further examine the role of caveolin-1 in the flow-induced ATP release, we used siRNA to specifically knock down expression of caveolin-1. Transfection of ECs with caveolin-1 siRNA resulted in a significant reduction in caveolin-1 protein expression and markedly inhibited the flow-induced ATP release. These results suggest that the localization and targeting of ATP synthase to caveolae/lipid rafts is critical for shear stress-induced ATP release. However, it remains unknown how shear stress activates cell-surface ATP synthase.

V. Shear Sensing and Its Roles in Vascular Homeostasis

A. Ca^{2+} responses and NO production

To gain insight into the roles of this shear-sensing mechanism via P2X4 in vascular homeostasis, we generated a *P2X4*-deficient (-/-) mouse [7]. The absence of P2X4 receptors impaired the EC response to flow stimulation. When the pulmonary vascular ECs of wild type (+/+) mice were exposed to flow, intracellular Ca^{2+} concentration increased stepwise in tandem with the increases in shear stress, whereas no flow-induced Ca^{2+} responses occurred in the ECs of -/- mice. Since increases in intracellular Ca^{2+} concentrations directly lead to the production of a potent vasodilator, nitric oxide (NO), the ECs were examined for changes in NO production with a fluorescence indicator, diaminofluorescein (DAF-2). NO production by the ECs of +/+ mice increased in response to flow, and the response was shear-stress-dependent (Fig.3). The ECs of -/- mice, however, did not show flow-induced NO production, indicating that P2X4 channels are involved in endothelial NO production.

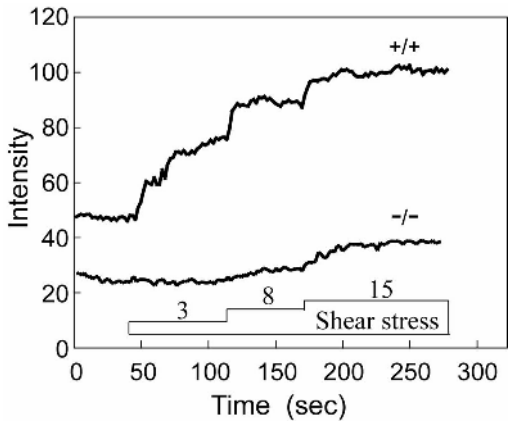


Fig. 3. Impaired production of NO in response to shear stress

B. Vasodilatory responses

We examined the effects of *P2X4* deficiency on the endothelium-dependent vasodilator response in the murine cremaster muscle. When acetylcholine (ACh) or ATP was administered through a jugular vein, the arterioles that had been pre-constricted with phenylephrine dilated dose-dependently in the +/+ mice. In the -/- mice, however, the ATP-induced vasodilation was markedly suppressed, but the ACh-induced vasodilation was not suppressed at all. Occlusion of one of the branches of an arteriole with a glass micropipette increases blood flow through the other branch, and the increase in blood flow caused marked vasodilation in the +/+ mice, but much less prominent vasodilation in the -/- mice (Fig.4). Blockade of NO synthesis by N^G-nitro-L-arginine methyl ester (L-NAME) markedly reduced the flow-induced dilation in both types of mice. These findings suggest that the flow-sensitive vasomotor mechanisms that regulate vascular tone are impaired in *P2X4*-deficient mice.

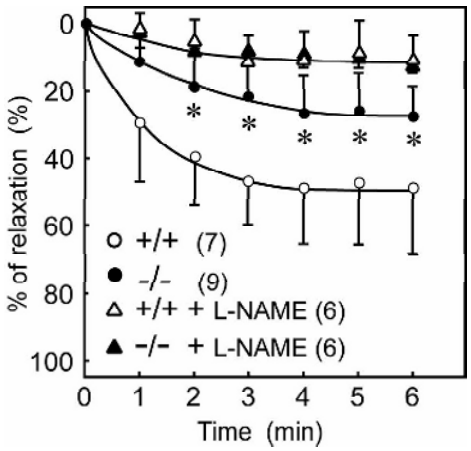


Fig. 4. Impaired vasodilatory responses in *P2X4* deficient mice Changes in vessel diameter are expressed as percentages: 0% represents the diameter of the vessel constricted with phenylephrine, and 100% represents the diameter of the vessel dilated with papaverine. Sample numbers are indicated in parentheses. *P<0.01

C. Blood pressure

A marked difference was observed in mean blood pressure determined by an intra-arterial catheter measurements, with significantly higher values recorded in the -/- mice than in the +/+ mice (125 ± 8 vs 104 ± 10 mmHg). There was no difference in their pulse rate (661 ± 74 bpm in +/+ mice vs. 668 ± 69 bpm in -/- mice). A difference was also observed in the general production of NO. The daily amount of nitrite and nitrate (NOx) excreted in the urine was significantly smaller in the -/- mice than in the +/+ mice. The decrease in NO production may be partly responsible for the increase in blood pressure in the -/- mice.

D. Vascular remodeling

Chronic changes in blood flow through large arteries induce structural remodeling of the vascular wall. Increases

in blood flow cause enlargement of vessel diameter, while decreases in blood flow have the opposite effect. To examine the role of the P2X4 receptor in flow-dependent vascular remodeling, the left external carotid artery of mice was ligated for 2 weeks. The ligation reduced flow in the left common carotid artery (LC), and we compared the diameter of the LC and the right common carotid artery (RC) histologically at the end of the 2-week period. Ligation of the left external carotid artery resulted in a significant reduction in lumen diameter in the LC in the +/+ mice, but not in the -/- mice (Fig.5). The absence of the flow-induced change in diameter in the *P2X4*-deficient mice resembled the structural changes that occur in eNOS-deficient mice [8], suggesting that *P2X4* plays a critical role through endothelial NO production in controlling vascular structural adaptation to chronic changes in blood flow.

These results indicate that endothelial P2X4 channels are critical to the flow-sensitive mechanisms that regulate vascular tone and vascular remodeling.

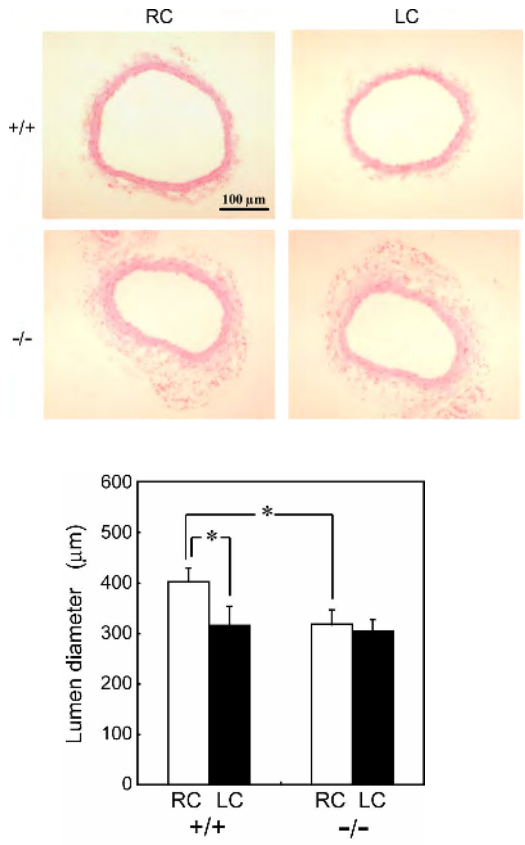


Fig. 5. Impaired blood flow-induced vascular remodeling. Upper: Hematoxylin-eosin-stained corss sections of the right common carotid artery (RC) and left common carotid artery (LC). Lower: Quantitative nalysis of changes in lumen diameter. *P<0.01. n=10 and 12 mice for $P2X4^{+/+}$ and $P2X4^{-/-}$ mice, respectively.

References

1. Ando J, Komatsuta T, Kamiya A (1988) Cytoplasmic calcium response to fluid shear stress in cultured vascular endothelial cells. In Vitro Cell. Dev. Biol. 24:871-877.
2. Ando J, Ohtsuka A, Korenaga R et al. (1993) Wall shear stress rather than shear rate regulates cytoplasmic Ca^{2+} responses to flow in vascular endothelial cells. Biochem Biophys Res Commun 190: 716-723.
3. Yamamoto K, Korenaga R, Kamiya A et al. (2000) P2X(4) receptors mediate ATP-induced calcium influx in human vascular endothelial cells. Am J Physiol Heart Circ Physiol 279: H285-292.
4. Yamamoto K, Korenaga R, Kamiya A et al. Fluid shear stress activates Ca^{2+} influx into human endothelial cells via P2X4 purinoceptors. Circ Res 87: 385-391.
5. Yamamoto K, Sokabe T, Ohura N et al. (2003) Endogenously released ATP mediates shear stress-induced Ca^{2+} influx into pulmonary artery endothelial cells. Am J Physiol Heart Circ Physiol 285:H793-803.
6. Yamamoto, K, Shimizu N, Obi S et al. (2007) Involvement of cell surface ATP synthase in flow-induced ATP release by vascular endothelial cells. Am. J. Physiol Heart Circ. Physiol 293:H1646-H1653.
7. Yamamoto, K. Sokabe T, Matsumoto T et al. (2006) Impaired flow-dependent control of vascular tone and remodeling in P2X4-deficient mice. Nature Med 12:133-137.
8. Rudic RD, Shesely EG,Maeda N et al. (1998) Direct evidence for the importance of endothelium-derived nitric oxide in vascular remodeling. J Clin Invest 101: 731-736.

Numerical Evaluation of MR-Measurement-Integrated Simulation of Unsteady Hemodynamics in a Cerebral Aneurysm

K. Funamoto[1], Y. Suzuki[2], T. Hayase[1], T. Kosugi[3] and H. Isoda[4]

[1] Institute of Fluid Science, Tohoku University, Sendai, Japan
[2] Graduate School of Engineering, Tohoku University, Sendai, Japan
[3] Renaissance of Technology Corp., Hamamatsu, Japan
[4] Hamamatsu University School of Medicine, Hamamatsu, Japan

Abstract — **Detailed and accurate information of hemodynamics is essential for clarification and advanced diagnosis of circulatory diseases. In order to reproduce complicated real flow field, the concept of flow observer, which integrates measurement and computation by feedback process, have been proposed. By applying the method to the MR (Magnetic Resonance) measurement, we propose MR-measurement-integrated (MR-MI) simulation: the difference between the Phase-contrast MRI (PC MRI) data and the computational result of three-dimensional velocity vector field is fed back to the numerical simulation. The objective in this study is to evaluate the MR-MI simulation by numerical experiment dealing with an unsteady blood flow in a cerebral aneurysm. In the numerical experiment, we first defined a standard solution with velocity profiles obtained by PC MRI measurement at boundaries as a model of real blood flow. Then, MR-MI simulation was carried out by assuming a uniform velocity profile at the upstream boundary and pressure zero and free flow conditions at the downstream boundaries. During the computation, a feedback signal being proportional to the difference between the standard solution and the computational result was applied at each grid point in the aneurysm. As the result, the MR-MI simulation reproduced the standard solution in the aneurysm owing to the feedback process. The error derived from the inaccurate boundary conditions decreased to 22% in one cardiac cycle, comparing to the ordinary simulation. Consequently, the MR-MI simulation accurately provided the wall shear stress distribution on the cerebral aneurysm as hemodynamic information.**

Keywords — **Bio-fluid mechanics, Hemodynamics, Measurement-integrated simulation, Phase-contrast MRI, Cerebral aneurysm**

I. Introduction

Wall shear stress (WSS) and pressure have been indicated as hemodynamic factors for the development, progress and rupture of aneurysms [1,2]. Therefore, information on blood flow field in blood vessels is essential to elucidate the pathological mechanism of cerebral aneurysms and to establish the advanced diagnosis.

In order to reproduce complicated real flow field, the concept of flow observer, which integrates measurement and computation by feedback process, have been proposed [3]. We have developed the ultrasonic-measurement-integrated (UMI) simulation by integrating ultrasonic Doppler measurement and numerical simulation of blood flow, and revealed the efficiency of the method [4]. However, for blood flow in a brain, the UMI simulation is hardly feasible because the ultrasound is reflected by the cranial bone.

Hence, in this paper, we propose MR-measurement-integrated (MR-MI) simulation by integrating the MR measurement, which enables us to measure the blood flow in a brain, and the numerical simulation. Figure 1 shows the schematic diagram of MR-MI simulation system of blood flow. In the MR-MI simulation, artificial body forces, which are generated by comparing three-dimensional velocity vectors obtained by PC MRI measurement and the corresponding computational results, are added to the numerical simulation. This feedback process is expected to act to reproduce the real blood flow field computationally, by making the computational result converge to that. With this methodology, it is prospective that the numerical solution whose resolution is better than the MR measurement is acquired and the effect of errors included in measurement is eliminated.

This study investigates the computational accuracy of blood flow field and hemodynamic information in the MR-MI simulation with the simplified boundary conditions by numerical experiments dealing with the reproduction of

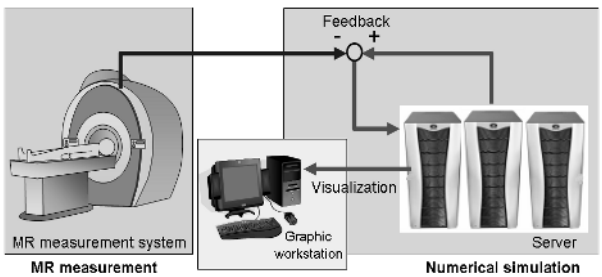


Fig. 1 Schematic diagram of MR-measurement-integrated (MR-MI) simulation system.

Chwee Teck Lim, James C.H. Goh (Eds.): ICBME 2008, Proceedings 23, pp. 2188–2191, 2009
www.springerlink.com

unsteady blood flow field in an aneurysm which developed at a bifurcation of a cerebral artery.

II. Method

Governing equations of MR-MI simulation of blood flow are the Navier-Stokes equations and the pressure equation for incompressible and viscous fluid flow,

$$\rho\left(\frac{\partial \mathbf{u}}{\partial t}+(\mathbf{u}\cdot\nabla)\mathbf{u}\right)=\mu\Delta\mathbf{u}-\nabla p+\mathbf{f} \tag{1}$$

$$\Delta p=-\nabla\cdot\rho(\mathbf{u}\cdot\nabla)\mathbf{u}+\nabla\cdot\mathbf{f} \tag{2}$$

where $\mathbf{u}$ is the velocity vector, p is the pressure, ρ is the density, and μ is the viscosity. $\mathbf{f}$ denotes the feedback signal, and it is described by the following equation by comparing three-dimensional velocities obtained by PC MRI measurement and numerical simulation respectively at feedback points defined in a domain where measurement data is obtained.

$$\mathbf{f}=-K_{\mathrm{v}}^{*}\frac{\mathbf{u}_{\mathrm{c}}-\mathbf{u}_{\mathrm{s}}}{U}\left(\frac{\rho U^{2}}{L}\right) \tag{3}$$

where K_{v}^{*} is the feedback gain (nondimensional). It is noted that the special case with $K_{\mathrm{v}}^{*}=0$ means the ordinary numerical simulation without feedback. U is the characteristic velocity, L is the characteristic length. The subscripts c and s represent a computational result and real flow (or the standard solution), respectively. In the computation, all parameters were nondimensionalized with the characteristic values. After that, the above governing equations were discretized by means of the finite volume method and were solved with an original program based on an algorithm similar to the SIMPLER method.

In a numerical experiment in this study, we first obtained a standard solution as a model of real blood flow with velocity vectors obtained by the PC MRI measurement at boundaries. Then, MR-MI simulation was performed using the data of the standard solution, and examined how well it can reproduce the standard solution.

The objective was the blood flow in a cerebral aneurysm at the bifurcation between basilar and superior cerebellar arteries. A 70-year-old female patient participated in this study, and the PC MRI data was obtained after the approval by the institutional review board of Hamamatsu University School of Medicine and the informed consent. The PC MRI data, which holds information on blood vessel configuration and the velocity vector of blood flow, were obtained at 20 phases in one cardiac cycle with the sampling time of $\Delta t = 0.046$ s. The configuration including the cerebral aneurysm and the parent artery was reconstructed by means of the image data processing software, Flova (Renaissance of Technology Corp., Hamamatsu, Japan), from the PC MRI data. We assumed that the blood vessel was rigid because the deformation was subtle, and generated several computational grid systems with different resolutions. Compromising between the reproducibility of blood vessel shape and the computational load, a staggered equidistant grid system with $N_x \times N_y \times N_z = 30 \times 27 \times 26$ ($\Delta x = \Delta y = \Delta z = 0.5\times10^{-3}$ m) shown in Fig. 2 was chosen. With the same software, one inlet, A, and two outlets, B and C, were determined (see Fig. 2), and the velocity information on the boundaries were exported by the linear interpolation. The variation of flow rate at the inlet A is shown in Fig. 3.

A periodic solution obtained with the three-dimensional velocity vectors obtained by PC MRI measurement at boundaries with time increment of $\Delta t = 0.046$ s was defined as the standard solution. The reference velocity and the reference length for nondimensionalization of parameters

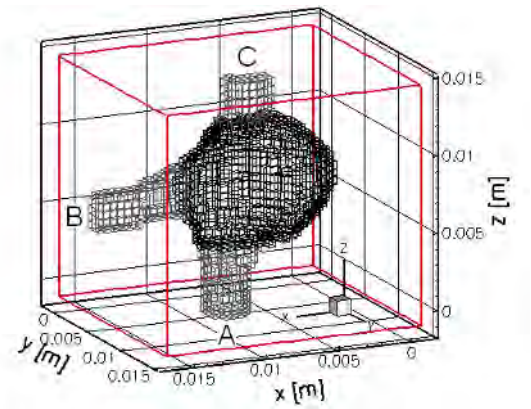


Fig. 2 Computational grid (30×27×26) with the feedback domain (black grid lines).

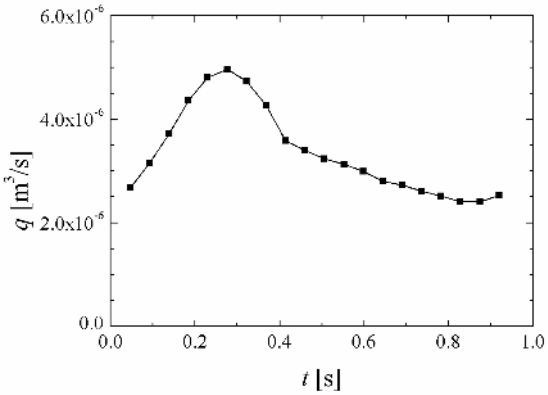


Fig. 3 Time-variation of flow rate at the inlet A obtained by PC MRI measurement.

Table 1 Computational conditions.

Entrance flow	2.68×10^{-6} m^3/s
Maximum mean velocity u'_{max} (U)	0.42 m/s
Entrance diameter D (L)	4.0×10^{-3} m
Density ρ	1.0×10^{3} kg/m^3
Viscosity μ	4.0×10^{-3} Pa·s
Maximum Reynolds number Re_{max}	423
Womersley number α	5.2

were the maximum mean velocity u'_{max} at peak flow and the diameter D at the upstream boundary, respectively. Variables used in this study are summarized in Table 1.

In MR-MI simulation, we applied a uniform velocity profile at the upstream boundary, and free flow as well as pressure zero conditions at the two downstream boundaries, assuming the complicated velocity vectors at boundaries were unknown. Note that the variation of flow rate was assumed to be known. The computational time increment was set at Δt = 0.046 s, which corresponded to the time resolution of the MR measurement. Velocity field was initialized at zero in each simulation.

The feedback points were arranged at all grid points in the feedback domain M (2.0×10^{-3} m $\le x \le 10.5\times10^{-3}$ m, 2.0×10^{-3} m $\le y \le 11.5\times10^{-3}$ m, 3.0×10^{-3} m $\le z \le 11.5\times10^{-3}$ m, see black grid lines in Fig. 2), which covered the whole cerebral aneurysm and the adjacent parent artery with the assumption that PC MRI measurement was to be done in this domain.

The computational accuracy of the MR-MI simulation was evaluated by comparing with that of the ordinary simulation without feedback. For the evaluation of each simulation, the space-averaged error norm of velocity vector in a monitoring domain Ω was defined as follows:

$$\bar{e}_{\Omega}(\mathbf{u}_1, \mathbf{u}_2, t) = \left[\frac{1}{3N} \sum_{\mathbf{x}_n \in \Omega} \left\{ (u_1 - u_2)^2 + (v_1 - v_2)^2 + (w_1 - w_2)^2 \right\} \right]^{\frac{1}{2}} \quad (4)$$

where $\mathbf{u}_1 = (u_1, v_1, w_1)$ and $\mathbf{u}_2 = (u_2, v_2, w_2)$ mean two velocity vectors to be compared, and N is the total number of the monitoring points in the domain Ω. In addition, space-time-averaged error norm $\bar{e}_{\Omega T}(\mathbf{u}_1, \mathbf{u}_2)$ of velocity vector was defined by averaging the $\bar{e}_{\Omega}(\mathbf{u}_1, \mathbf{u}_2, t)$ in one cardiac cycle T.

III. Results and Discussion

For the investigation, the numerical solution in the 5th cycle, in which the standard solution became periodic, was used as the solution in each simulation. Note that MR-MI simulation already provided the periodic solution in the 3rd cycle, and the acceleration of the convergence was confirmed. MR-MI simulation was carried out with increasing the feedback gain in increments of 0.5. As the result, computation diverged at the $K_v^* \ge 2.5$.

Periodic variation of space-averaged error norm of velocity vector in the aneurysm (or in the feedback domain M) with respect to the standard solution, $\bar{e}_M(\mathbf{u}_c, \mathbf{u}_s, t)$, in the ordinary simulation ($K_v^* = 0$) and in MR-MI simulations with $K_v^* = 1, 2$ are shown in Fig. 4. Because the inaccurate boundary condition was applied, the ordinary simulation contains error in the blood flow field in the cerebral aneurysm. The phase of the variation of the space-averaged error norm in Fig. 4 corresponds to that of the variation of blood flow rate in Fig. 3; the magnitude of $\bar{e}_M(\mathbf{u}_c, \mathbf{u}_s, t)$ becomes the largest at the peak flow. On the other hand, the MR-MI simulation can suppress the error norm at each moment, implying the improvement of the computational accuracy. In this study, the error norm was the smallest at the maximum feedback gain, $K_v^* = 2$, and decreased to 22% of that in the ordinary simulation in one cardiac cycle.

Since the relationships of hemodynamic factors to cerebral aneurysms are discussed in many studies, it is important how accurately the MR-MI simulation can provide hemodynamic information. Wall shear stress (WSS) was calculated by first-order numerical differentiation of the velocity vectors at every time instant in each simulation. The distributions of magnitudes of WSS on the cerebral aneurysm at peak flow are compared in Fig. 5(a). In addition, the differences of the magnitude of the WSS from the standard solution in the ordinary simulation and the MR-MI simulation with $K_v^* = 2$ are shown in Fig. 5(b). All simulations show similar WSS distributions in Fig. 5(a). However, detailed observation reveals the locally large difference against the standard solution exists in the ordinary simulation, as indicated with arrows in Fig. 5(b). The incorrect hemodynamic information may lead to a wrong diagnosis. In contrast, the

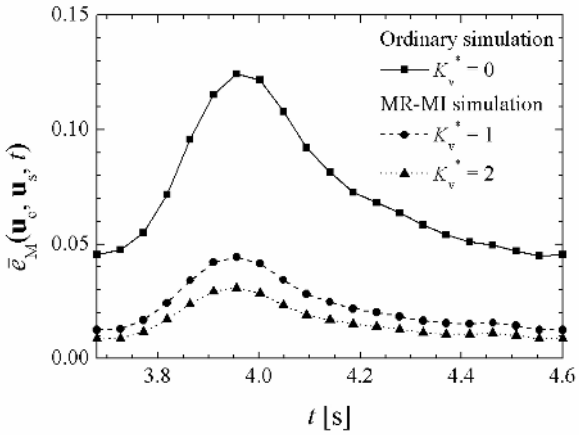


Fig. 4 Variation of the space-averaged error norm of the velocity vector in the cerebral aneurysm.

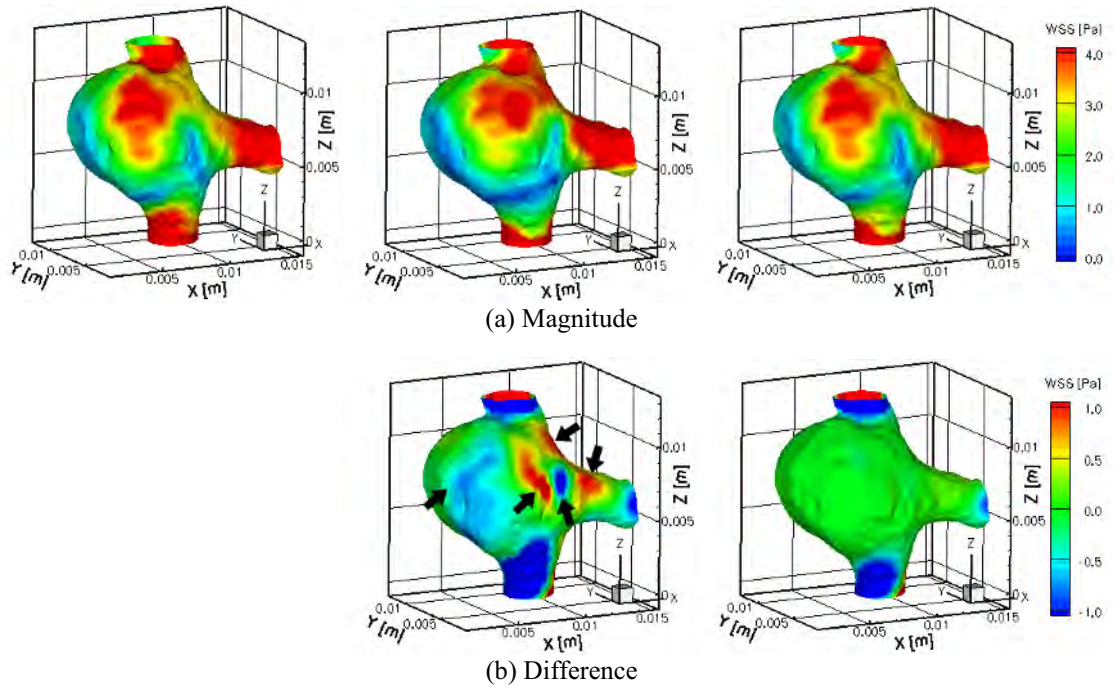


Fig. 5 (a) Wall shear stress distribution on the cerebral aneurysm at the peak flow of the standard solution (left), ordinary simulation ($K_v^* = 0$) (middle) and MR-MI simulation with $K_v^* = 2$ (upper right), and (b) the difference with respect to the standard solution.

difference of the magnitude of WSS is almost zero in the whole aneurysmal domain in MR-MI simulation (see Fig. 5(b)), accurately reproducing the WSS distribution on the cerebral aneurysm of the standard solution. Therefore, the MR-MI simulation can provide reliable information on WSS distribution which is an important hemodynamic factor for the diagnosis of cerebral aneurysms.

IV. Conclusions

The computational accuracy of MR-measurement-integrated (MR-MI) simulation was investigated by numerical experiment dealing with reproduction of three-dimensional unsteady blood flow field in a cerebral aneurysm. The MR-MI simulation substantially improved the computational accuracy by reducing the error in the cerebral aneurysm derived form the inaccurate boundary conditions for the sake of the feedback based on the errors in velocity vectors with respect to the standard solution. For the reproduction of the standard solution, the error decreased to 22% in one cardiac cycle, comparing to the ordinary simulation. Consequently, the MR-MI simulation accurately provided the wall shear stress distribution on the cerebral aneurysm as hemodynamic information.

Acknowledgment

The authors would like to express their thanks to Mr. Yasuhide Ohkura for his cooperation with Flova, and to the support of Tohoku University Global COE Program “Global Nano-Biomedical Engineering Education and Research Network Centre”. All computations were performed using the supercomputer system (SGI Altix 3700 B×2, SGI Japan, Tokyo, Japan) at the Advanced Fluid Information Research Center, Institute of Fluid Science, Tohoku University.

References

1. Jamous M A et al. (2005) Vascular corrosion casts mirroring early morphological changes that lead to the formation of saccular cerebral aneurysm: An experimental study in rats. J Neurosurg 102:532-535
2. Meng H et al. (2007) Complex hemodynamics at the apex of an arterial bifurcation induces vascular remodeling resembling cerebral aneurysm initiation. Stroke 38:1924-1931
3. Hayase T, Hayashi S (1997) State estimator of flow as an integrated computational method with the feedback of online experimental measurement. J Fluid Eng-T ASME 119:814-822
4. Funamoto K et al. (2008) Numerical experiment for ultrasonic-measurement-integrated simulation of three-dimensional unsteady blood flow. Ann Biomed Eng 36:1383-1397

Specificity of Traction Forces to Extracellular Matrix in Smooth Muscle Cells

T. Ohashi[1], H. Ichihara[1], N. Sakamoto[1] and M. Sato[1,2]

[1] Graduate School of Engineering, Tohoku University, Sendai, Japan
[2] Graduate School of Biomedical Engineering, Tohoku University, Sendai, Japan

Abstract — **Adherent cells are known to exert traction forces to adhere to their extracellular matrix at focal adhesions, where integrins interact with the extracellular matrix and mediate various cellular signals. Therefore, it is hypothesized that extracellular matrix-mediated integrin expression may modulate cellular traction forces, resulted in alterations in cell physiology. In this study, to test the hypothesis, traction force measurements are performed on bovine thoracic smooth muscle cells using a polydimethylsiloxane-based micropillar substrate coated with different types of extracellular matrix. The top of the micropillars was selectively coated with fibronectin (FN), vitronectin (VN), and type I collagen (COL I) at 30 and 50 μg/ml and cells were plated on the extracellular matrix-coated micropillars. For FN and VN, the cells have several spikes at the cell periphery, whereas, for COL I, the cell expresses relatively oval shape. At 30 μg/ml, traction forces were 5.5 ± 0.6, 5.8 ± 1.3 and 8.5 ± 2.2 nN for FN, VN, COL I, respectively. At 50 μg/ml, traction forces significantly increased compared to 30 μg/ml and were 12.4 ± 6.8, 13.5 ± 4.0 and 18.1± 4.7 nN for FN, VN, COL I, respectively. These results indicate that extracellular matrix may specifically modulate integrin expression followed by development of actin stress fibers, possibly leading to changes in traction forces.**

Keywords — **Smooth muscle cells, Traction forces, Extracellular matrix, Integrin expression**

I. Introduction

Adherent cells are known to exert traction forces to adhere to their extracellular matrix at focal adhesions, where integrins interact with the extracellular matrix and mediate various cellular signals, possibly leading to modulations of a variety of physiological functions in cell proliferation, migration, etc. Integrins are obligate heterodimers containing two distinct chains, called the α and β subunits, very specific to the types of extracellular matrix such as fibronectin, vitronectin, collagen, etc. It is also known that change in cellular traction forces may modulate cell physiological functions. Therefore, it is speculated that extracellular matrix-mediated integrin expression may modulate cellular traction forces, resulted in alterations in cell physiology.

So far, a lot of efforts have been made to estimate cellular traction forces using micropillar substrates [1]. In this study, we performed traction force measurements using a micropillar substrate coated with different types of extracellular matrix including fibronectin (FN), vitronectin (VN), and type 1 collagen (COL1). Fluorescence observations of actin filament structures were also performed to study their relevance to magnitude and directions of traction forces.

II. Methods

A. Cell culture

Smooth muscle cells were obtained from bovine thoracic aortas. Cells were seeded in tissue culture flasks with DMEM + 10% FBS. Cell populations from the 4th to 9th generation were studied.

B. Fabrication of substrate with micropillar array and coating of extracellular matrix

A mould of silicon substrates with arrays of micropillars (3 μm in diameter, 10 μm in height, and 8 μm spacing) was fabricated using micromachining techniques, and polydimethylsiloxane was poured into the mould to produce a substrate membrane with micropillars. The top of the micropillars was selectively coated with FN, VN, and COL1 at 30 and 50 μg/ml and cells were plated on the substrates.

C. Traction force measurements and fluorescence staining

Cell spreading produces deflection of micropillars, which was measured from brightfield images to determine traction forces. After traction force measurements, cells were fixed with 10% formaldehyde, permeabilized with 0.1% Triton X-100, and then labbeled with Alexa Fluor594 and Alexa Fluor488 to visualize actin filaments and vinculin, respectively.

III. Results

Figure 1 typically shows actin filament networks, vinculin, and traction forces in smooth muscle cells cultured on FN, VN, and COL1 at 30 μg/ml. Cells cultured on FN and VN developed multiple protrution, while this protrution was not observed in cells cultured on COL1. Focal adhesion protein vinculin clearly expressed as a horseshoe-shaped

Chwee Teck Lim, James C.H. Goh (Eds.): ICBME 2008, Proceedings 23, pp. 2192–2193, 2009
www.springerlink.com

structure at both ends of actin fibers, where cells exerted traction forces. In Fig. 2, traction forces were 5.5 ± 0.6, 5.8 ± 1.3 and 8.5 ± 2.2 nN for FN, VN and COL1, respectively, at 30 μg/ml. Traction forces for COL1 were significantly higher than those for FN and VN. As the concentration increased from 30 μg/ml to 50 μg/ml traction forces significantly increased, resulting in 12.4 ± 6.8, 13.5 ± 4.0 and 18.1± 4.7 nN for FN, VN and COL1, respectively.

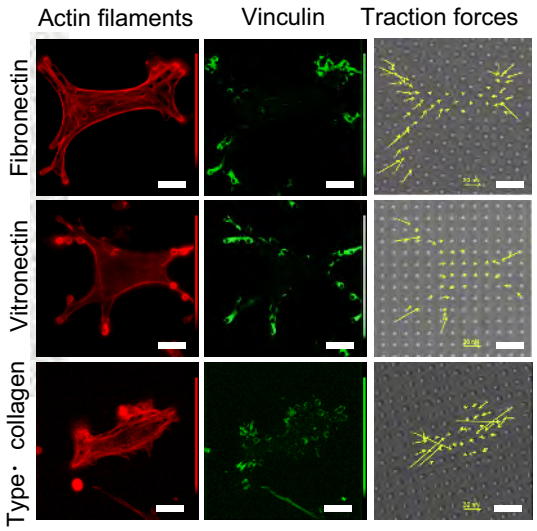


Fig. 1 Actin filaments, vinculin, and traction forces of cells cultured on FN, VN, and COL1 at 30 μg/ml. Bars = 20 μm.

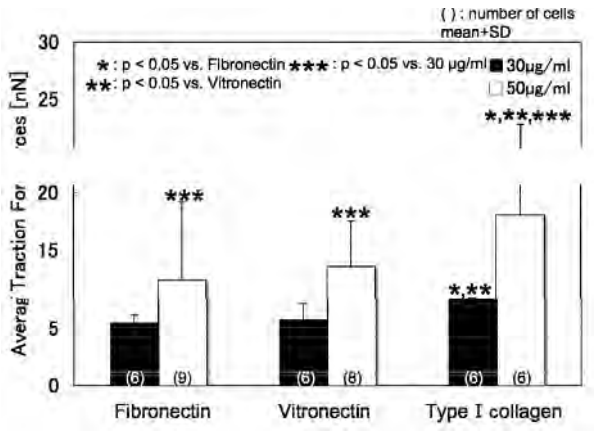


Fig. 2 Traction forces of cells cultured on FN, VN, and COL1 at 30 and 50 μg/ml.

IV. Discussion

Cells attached to and spread on the substrates. The micropillars showing large deformation were found to connect to thick actin filaments, suggesting that actin filaments can be a major component contributing to generation of traction forces. Under all the three conditions, traction forces were obviously exerted towards the center of the cell, particularly showing higher forces at the cell periphery than at the center of the cells.

For FN and VN, cells have several spikes at the cell periphery, probably indicating the stage of cell migration. By contrast, for COL1, cells express relatively oval shape. Traction forces for COL1 were significantly higher than those for FN and VN. This can be explained by the fact that well-organized actin filament networks were observed in cells cultured on COL1-coated micropillars. This result thus indicates that extracellular matrix specifically modulate integrin expression followed by activation of integrin-mediated signalling pathways, possibly leading to development of actin stress fibers via Rho activation in response to different types of extracellular matrix [2].

Another finding in this study is that cells can exert traction forces in an extracellular matrix concentration-dependent manner. This suggests that cells could form focal adhesion complexes including more integrins at higher concentrations of extracellular matrix.

V. Conclusion

The effects of different types of extracellular matrix on smooth muscle cell traction forces were studied using micropillar array coated with fibronectin, vitronectin, and type 1 collagen. The results indicate that extracellular matrix-mediated integrin expression may modulate traction forces via formation of stress fibers. It is also indicated that cells can exert traction forces in an extracellular matrix concentration-dependent manner.

Acknowledgments

This work was supported in part by Tohoku University Global COE Program “Global Nano-Biomedical Engineering Education and Research Network Centre”, the Grants-in-Aid for Scientific Research (No. 18650119) from the Ministry of Education, Culture, Sports, Science, and Technology of Japan.

References

1. Tan, J.L., et al. (2003) *PNAS* 100: 1484-1489
2. Burthem, J., et al. (1994) *Blood* 84: 873-882

Cochlear Nucleus Stimulation by Means of the Multi-channel Surface Microelectrodes

Kiyoshi Oda[1, 2], Tetsuaki Kawase[1,3], Daisuke Yamauchi[1], Hiroshi Hidaka[1] and Toshimitsu Kobayashi[1]

[1] Department of Otolaryngology-Head and Neck Surgery, Tohoku University Graduate School of Medicine , Sendai, Japan
[2] Hearing center, Miyagi prefecture Ishikai , Sendai, Japan
[3] Department of Rehabilitative Auditory Science Graduate School of Biomedical Engineering , Sendai, Japan

Abstract — **The electrically evoked brainstem potential was measured in guinea pigs with 260-channel surface microelectrode implanted on the cochlear nucleus. Even when surface bipolar stimulations with 200μm separation of two electrodes are employed, the unequivocal waves of electrically evoked auditory brainstem responses (EABRs), which increased in amplitude with increasing stimulation current, were constantly derived. Electrophysiological mapping using the 260-channel surface microelectrode indicated that more precise electrophysiological mapping may be possible based on the EABR-positive boundary.**

The multi-channel surface microelectrode was expected to be usefully applied to the probe to determine the optimal location for the positioning of the ABI and stimulating electrode in ABI in clinical use.

Keywords — **surface bipolar stimulations. electrically evoked auditory brainstem responses (EABRs).**

I. Introduction

Auditory brainstem implants (ABI) are an artificial organ technology in which electrodes are implanted in the brainstem in order to restore the hearing of patients who have lost their hearing as a result of auditory nerve dysfunction [1]. ABI have reached the clinical trial stage in Europe and the United States and satisfactory outcomes have been demonstrated in successful cases, bringing great hope to these patients. However, the success rate has been less than satisfactory [2,3].

The overall performance of ABI has not been as good as cochlear implant that stimulates spinal ganglion cells yet [4]. One hypothesis (the selectivity hypothesis) is that the ABI does not make selective contact with the tonotopic dimension of the cochlear nucleus, limiting the number of independent channels of spectral information. If each electrode activates a broad area of neurons, and adjacent electrodes activate largely overlapping populations, this overlap will have the effect of smearing the representation of spectral place [4]. In order to stimulate fewer populations in cochlear nucleus and locate cochlear nucleus surface precisely intraoperatively, the bipolar stimulation with very short separation and many stimulating points is ideal in theory.

In the present study, the 260-channel surface microelectrode was employed to measure electrical evoked auditory responses, and these responses were utilized to map the cochlear nucleus in an animal model.

II. Method

The use and care of animals reported in this study was approved by Tohoku University's Animal Care and Use Committee. Male albino guinea pigs weighing 400-700g with normal Preyer's reflexes were used in this experiment. The animals were free of both illness and middle ear infections at the time of study. Before the surgery, general anesthesia was set up by intramuscular injection of mixture of xylazine (10mg/kg) and ketamine (40mg/kg). 1% xylocaine was also used as local anesthesia. All recordings were made in a sound-attenuated, electrically shielded room. A click stimulus was used to measure the auditory evoked brainstem response (AABR) (Neuropack μ, Nihon Kohden) in order to confirm normal auditory function.

The animals were then placed in a supine position, and an incision was made in the skin behind the ear to expose and remove the skull to allow cerebellar retraction and sub-

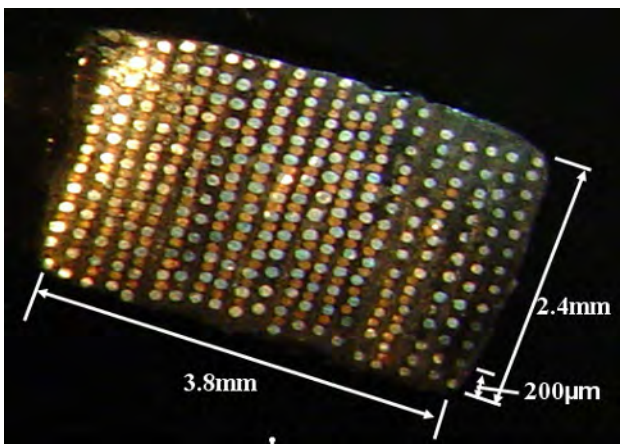


Fig. 1. 260-channel microelectrode Diameter of each electrode is 100μm. Electrode is made of platinum.

Chwee Teck Lim, James C.H. Goh (Eds.): ICBME 2008, Proceedings 23, pp. 2194–2196, 2009
www.springerlink.com

sequent visualization of the cochlear nucleus. The 260-channel microelectrode shown in Fig. 1 was placed on the surface of the cochlear nucleus. This specialized device has 260 electrodes in an area of only 3.8mm x 2.4 mm, with the inter-electrode distance set at only 200 μm.

Of the 260-channel electrode channels on this microelectrode, two points were stimulated arbitrarily and the electrical evoked brainstem responses (EABR) were recorded. In order to record the EABR, the active electrodes were placed on the surface of the auditory region, and the reference electrodes, consisting of stainless steel needles, were placed behind the ear. EABR were recorded using the same type of system as for AABR (Neuropack μ, Nihon-Kohden) under the following measurement conditions: number of average, 500 times; low cut filter, 200 Hz; high cut filter, 3000 Hz. As regards the electrical stimuli, a SEN-3041 pulse generator (Nihon Kohden) and SS-203J Isolator were used to generate bipolar pulses of 80 μsec in duration.

III. Result

Using the 260-channel systems, we succeeded in recording reproducible EABR when the cochlear nucleus was stimulated electrically. Mapping is considered to be most effective when the stimulation used is capable of recording reproducible waveforms with high sensitivity and an excellent S/N. Therefore, after taking into consideration the I/O characteristics of the EABR, electrical stimulation from the dynamic portion of the signal (600 μA -1000 μA) was, for the most experiments, used to carry out the mapping. Figure 2 shows the results of mapping of the cochlear nucleus using representative EABR. In this case, the 260-channel microelectrode was placed on the dorsal portion of the cochlear nucleus. We could distinguish positive EABRs indicated by blue arrows from undetectable EABRs indicated by red arrows in 3.8 by 2.4 mm area.

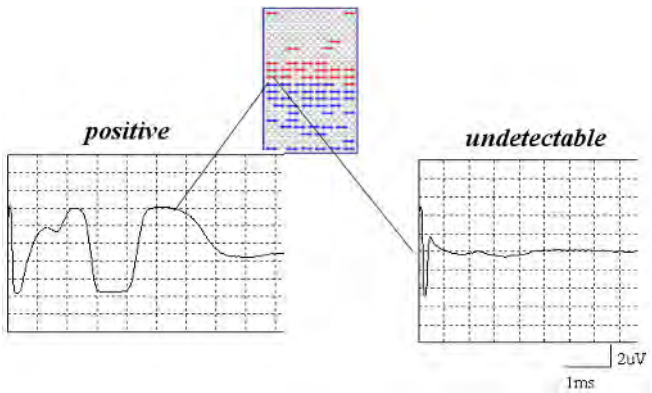


Fig. 2. Mapping by 260-channel microelectrode

IV. Discussion

There are two possible electrode configurations – penetrating and surface ones. Xuguang Liu et al. tested electrical stimulation of the cochlear nucleus with both types of arrays on guinea pigs and cats. In guinea pigs, the penetrating electrodes had advantages over surface arrays in the sense of lower thresholds and wider dynamic ranges. But, histologically the presence of VCN oedema could be inferred from the decreased neuron densities and increased mean soma areas in guinea pigs implanted with penetrating electrodes. On the contrary, there is no apparent pathological changes on the surface or within the implanted cochlear nuclei in guinea pigs implanted with surface electrode [5].

There are two manners of stimulation – bipolar and monopolar. Russell L. Snyder et al. evaluated the spread of activity evoked by cochlear implant by monitoring activity at the guinea pig inferior colliculus. Monopolar stimulation are less selective than bipolar. Contacts with less separation between electrodes evoke more selective excitation but with higher thresholds than contacts with greater separation [6].

The reason we choose bipolar surface electrodes is emphasis on safety and selectivity as described above and clinical application as a placing electrode in the future.

In Figure 2., following very slight shifts in the stimulation region, the EABR suddenly disappeared or the shape of the waveforms changed, indicating that the microelectrode used was capable of applying relatively localized electrical stimulation. The EABR-positive boundary could be distinguished by means of electrophysiological mapping. However, the relation between this boundary and the actual anatomical boundary remains unclear.

We are succeeded in measuring EABR by the 260-channel bipolar surface microelectrode with an inter-electrode distance of 200 μm.

In the present study, bipolar stimulation with an inter-electrode distance of 200 μm was capable of adequately recording EABR. Furthermore, following very slight shifts in the stimulation region, the EABR suddenly disappeared or the shape of the waveforms changed, indicating that the microelectrode used was capable of applying relatively localized electrical stimulation. These results indicate that the use of a microelectrode as the stimulating electrode in ABI may make it possible to achieve a more precise discrimination of pitch

V. Conclusions

In the present study, EABR were recorded using a surface microelectrode with an inter-electrode distance of only 200 μm, which are less than one fifth the electrode separation of the electrode devices presently in clinical use. These same

microelectrodes were used to conduct mapping of the cochlear nucleus and found that the electrophysiological boundaries could be identified quite clearly with this method.

Acknowledgment

We acknowledge the support of Tohoku University Global COE Program “Global Nano-Biomedical Engineering Education and Research Network Centre”.

References

1. Jackson KB, Mark G, Helms J, Mueller J, Behr R. An auditory braistem implant system. *Am J Audiol*. **11**, 128-133,2002
2. Otto SR, Brackmann DE, Hitselberger WE, Shannon RV and Kuchta J. Multichannel auditory brainstem implant: update on performance in 61 patients. *J Neurosurg*. **96**, 1063-71, 2002.
3. Nevison B, Laszig R, Sollmann WP, Lenarz T, Sterkers O, Ramsden R, Fraysse B, Manrique M, Rask-Andersen H, Garcia-Ibanez E, Colletti V, von Wallenberg E. Results from a European clinical investigation of the Nucleus multichannel auditory brainstem implant. *Ear Hear* **23** , 170-183, 2002.
4. Colletti V and Shannon RV. Open set speech perception with auditory brainstem implant. *Laryngoscope* **115**, 1974-1978,2005.
5. Liu X, McPhee G, Seldon HL, and Clark GM Histological and physiological effect of the central auditory prosthesis: surface versus penetrating electrode. *Hear Res* **114**,264-274,1997.
6. Russell L Snyder, John C. Middlebrookes, and Ben H Bonham. Cochlear implant electrode configuration effects on activation threshold and tonotopic selectivity. *Hear Res*. **235**, 23-38, 2007

Effects of Mechanical Stimulation on the Mechanical Properties and Calcification Process of Immature Chick Bone Tissue in Culture

T. Matsumoto, K. Ichikawa, M. Nakagaki and K. Nagayama

Biomechanics Laboratory, Nagoya Institute of Technology, Nagoya, Japan

Abstract — **In order to study the adaptation mechanism of bone tissues, we cultured immature bone slices obtained from chick tibia under mechanical stimulation. We first cultured 2 to 3-mm-thick slices for 3 days while giving them cyclic compression up to 0.3N at the rate of 3-4 cycle/min. Both the stiffness and the calcified area of the bone tissues increased significantly under cyclic compression. Such increases did not occur in their static control, nor specimens deactivated with liquid nitrogen. We then cultured 0.2mm-thick slices for 24 hours while being stretched by 10%. Calcified area was significantly larger in stretched specimens than in the non-stretched control. Traveling direction of the calcification was roughly equal to the stretch direction. Collagen fibers showed alignment in the stretch direction over 5% of stretch. These results indicate that dynamic and quasi-static stretch stimulate calcification especially in the direction of stretch, and the calcification may occur preferentially along the direction of collagen fibers. The alignment of collagen fibers in the stretch direction and facilitated calcification along collagen fibers may have something to do with the alignment of trabecular bone in the direction of principal stress.**

Keywords — **Mechanical adaptation, Biomechanics**

I. Introduction

It is well known that the bones change their shape and internal structures adaptively in response to the mechanical environment to which they are exposed [1]. The mechanisms of these responses are, however, not well known.

In order to study the mechanism of adaptation of bone tissues, an approach to culture bone tissues under a controlled mechanical environment to observe their mechanical and histological changes during culture would be useful. For this purpose, we have developed an apparatus in which bone slices can be cultured under cyclic compression to find that the mechanical stimulation for 3 days increased stiffness of immature bone slices obtained from chick tibia by stimulating tissue calcification [2]. To know the details of histological changes during culture, we have developed another apparatus in which bone slices can be stretched and cultured under a microscope. We found that static stretch also stimulated tissue calcification especially in the direction of collagen fiber alignment [3]. In this paper, we introduce our apparatuses and results obtained in these studies.

II. Changes in the Mechanical Properties of Bone Specimen During Cyclic Complession Culture

A. Materials and methods

Specimens: We used immature bone tissues obtained from the tibias of 0-day-old chicks. A bone slice with a thickness of 2-3 mm was obtained in a plane perpendicular to the tibial axis at the position 2-3 mm from the proximal end of each tibia. The slices were then cultured in a cyclic compression apparatus for 3 days in an osteogenic medium, *i.e.*, BGJb (Gibco, USA) supplemented with 10% fetal calf serum (ICN, USA), 75μg/ml ascorbic acid (Wako, Japan), 5mM β-glycerol phosphate (Wako), and 10^{-7}M dexamethasone (Wako). To confirm that the changes observed in cyclic compression culture was active response of bone tissues, we also used slices that had been frozen with liquid nitrogen and thawed to deactivate cells in the tissues.

Cyclic Compression Culture: The apparatus we used for the cyclic compression culture is shown in Fig. 1 Three slices obtained from the right tibias was cultured simultaneously under cyclic compression along with their contralateral static controls under a standard culture condition (37°C, 100% humidity, 5%CO_2 and 95% air) in an acrylic box. Each of the specimens in a 35-mm culture dish was com-

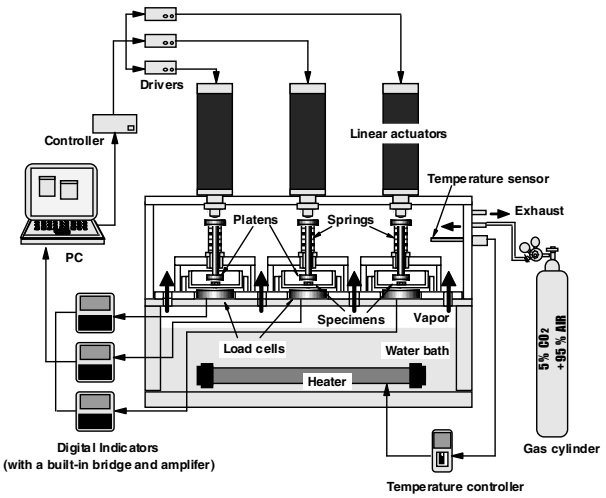


Fig.1 Real time monitoring system for the mechanical properties of bone tissue in cyclic compression culture.

Chwee Teck Lim, James C.H. Goh (Eds.): ICBME 2008, Proceedings 23, pp. 2197–2200, 2009
www.springerlink.com

pressed cyclically in the direction of tibial axis for 3 days with a linear actuator (MAS-23, Chiba Precision, Japan) via a platen. Load applied the specimen was measured with a load cell (TC-USR-23, TEAC, Japan). The slices were loaded at the rate of 50 μm/s until the load became 0.3 N and held for 5 s then unloaded at the same rate. This makes overall loading rate 3-4 cycle/min depending on the stiffness of the slice.

Compression Test: Mechanical properties of the slices were determined with a compression test before and after culture. Slices were compressed at the rate of 0.5μm/s up to 0.5N to obtain nominal stress-strain curves. Nominal stress σ and strain ε was calculated as $\sigma = F/A_0$ and $\varepsilon = x/t$ where F and x are the load and displacement, respectively, applied to the slice, and A_0 and t the cross sectional area and the thickness, respectively, of the slice after culture. To reduce ambiguity of the origin of the curve, zero stress was taken as σ = 0.003 N.

Fresh and deactivated specimens cultured under cyclic compression were denoted as CCC and dCCC, respectively. Similarly, specimens cultured under static culture were denoted as SC and dSC. We also measured stiffness of specimens freshly obtained from the tibias of 0 and 3-day-old chicks, and denoted them as CON0 and CON3, respectively.

Specimen Viability Check: After the culture, some of the specimens were sliced in the direction parallel to the tibial axis with a microslicer (DTK-1000, Dosaka-EM, Japan) to obtain a 200-μm-thick slice at the center of the specimen. The slices were then stained with Viability/Cytotoxicity Assay Kit for Animal Live & Dead Cells (Biotium, USA) in which calcein AM stains live cells green while EthD-III stains dead cells red to assess cell viability in the tissue.

Measurement of Calcification: Some of the specimens were sliced to 200 μm in thickness in the direction perpendicular to the tibial axis with the microslicer. The slices were stained with 1% Alizarin Red S (Wako) to identify calcified area.

B. Results and discussion

Specimen Viability: Fig. 2 summarizes the cell viabilities at edge and central sections in each group. Due to the specimen preparation process, the cell viability was 50-60% even in the control (CON). The viability was significantly lower in the cultured groups (SC and CCC) with significant difference between them. The viability was higher in the central section in CON and SC, while it was higher in the edge section in CCC. This may indicate necrosis of cells in the central section due to increase in oxygen demand caused by the mechanical stimulation. However, almost 50% of cells were viable in CCC compared to control. In contrast, no cells were alive in deactivated groups (dCCC and dSC).

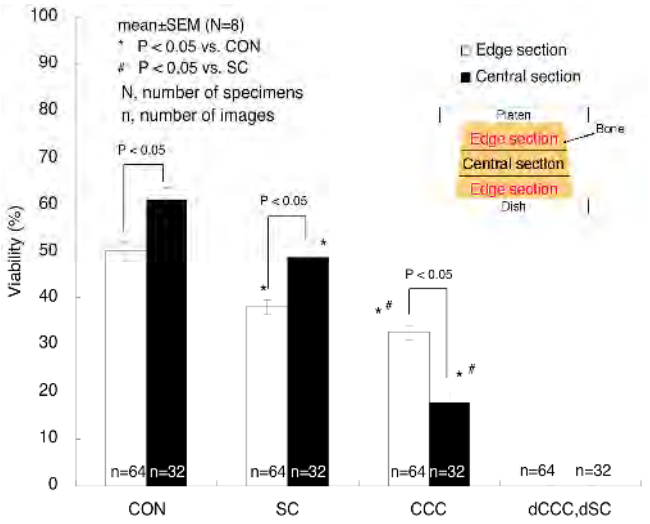


Fig.2 Cell viability in bone specimens. Cell viability was defined as relative number of living cells to whole cells.

Effects of Cyclic Compression Culture on Specimen Stiffness: Nominal stress-strain curve became steepened after cyclic compression culture (CCC) while the curve did not change in deactivated group (dCCC) (Fig. 3). Apparent elastic moduli of the bone tissues were calculated in the four stress ranges (Fig. 4). The moduli increased significantly under cyclic compression (Fig. 5). Such increases did not occur in their static control and specimens deactivated with liquid nitrogen. With regard to calcification, calcified area was 21.7±0.9% (mean±SEM, n=4) before culture (CON0) and did not change significantly after static culture (SC, 24.2±0.9%), while it increased significantly after cyclic compression culture (CCC, 31.4±1.8%) and was almost comparable to CON3 (33.6±1.2%). Furthermore, there was a significant correlation between apparent elastic moduli and area fraction of calcified area (Fig. 6). These results indicate that cyclic compression stimulates calcification and thus tissue hardening.

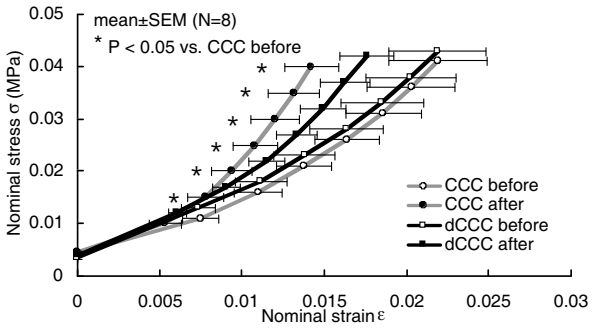


Fig.3 Mean stress-strain cure of group CCC and dCCC.

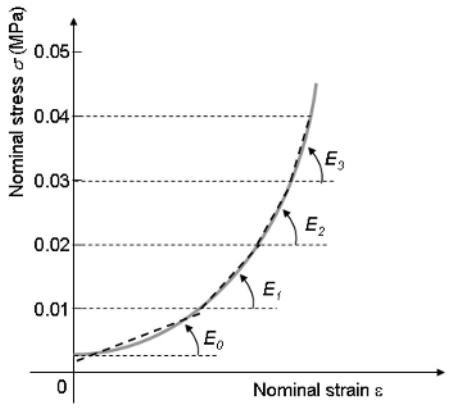


Fig.4 Apparent elastic moduli calculated from stress-strain curves.

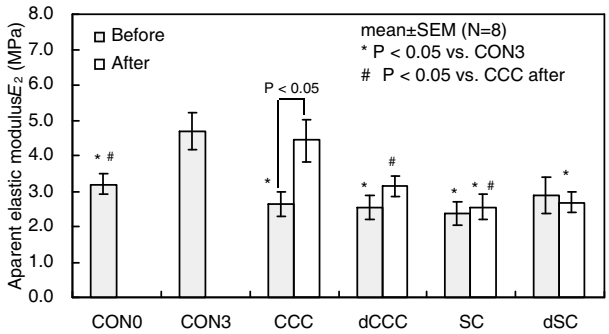


Fig.5 Apparent elastic modulus E_2 in six groups

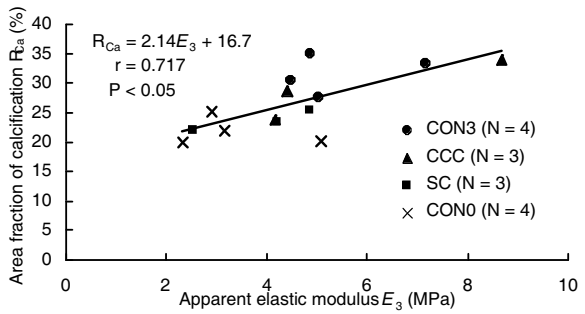


Fig.6 Correlation between calcification and mechanical properties.

III. In situ observation of bone slices during static stretch culture

A. Materials and methods

Specimens: Tibias taken from 2- to 4-day-old chicks were used. Bone slices with a thickness of 200 μm were prepared similarly to the slices used for quantification of the calcification in Chapter II. The slices were then cultured in a stretch apparatus for 24 h in the osteogenic medium used in the cyclic compression culture.

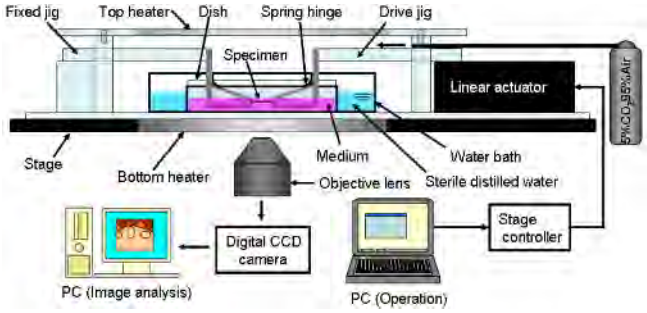


Fig.7 In-situ observation system for bone calcification in culture under stretch stimulation.

Static Stretch Culture: The apparatus we used for the static stretch culture is shown in Fig. 7. A specimen was held horizontally with two arms via spring hinges under the standard culture condition in a specimen chamber. The specimen can be stretched in a desired pattern by moving a linear actuator (TSDM60-20X, Sigma Koki, Japan) connected to the drive jig that stretches specimen. In this study, the slice was cultured for 24 hours while being stretched statically by 10%.

In Situ Observation of Calcification: Check: Calcified area was identified as a dark region in bright field images. In a preliminary study, we found that calcification did not occur in the first 9 h in culture. The culture chamber was first stored in an incubator for 9 h from the beginning of the culture and then set on the stage of an inverted microscope (IX71, Olympus, Japan) equipped with a digital CCD camera (DP70, Olympus). Bright field images were taken every 10 min from 9 to 24 h in culture. The recorded images were then binarized by an image processing software (ImageJ 1.37, NIH, USA) to obtain calcified area $A_{Ca}(t)$ at time t (h). A calcification ratio $R_{Ca(Carti)}$ was calculated as:

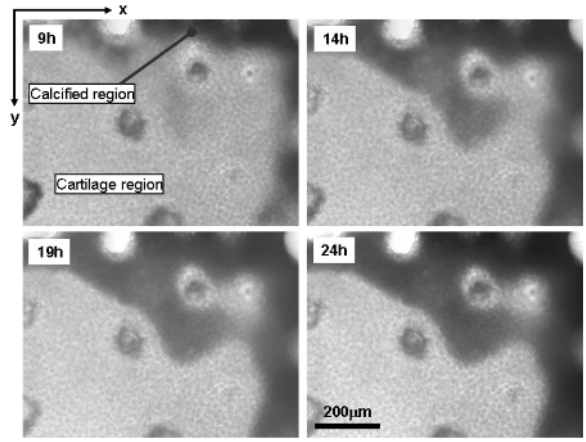
$$R_{Ca(Carti)} = \frac{A_{Ca}(t) - A_{Ca}(9)}{A_{Carti}(9)} \quad (1)$$

where $A_{Carti}(9)$ indicates non-calcified (cartilage) area at 9 h.

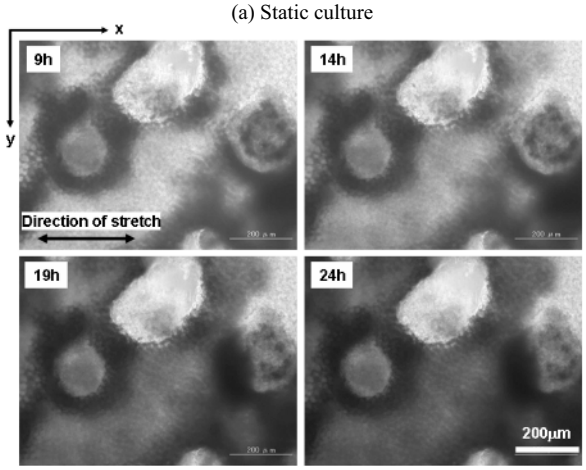
Observation of Collagen Fiber Alignment: Alignment of collagen fibers was visualized with a polarized light microscope (BX51N-33P-O, Olympus). Bone slices were set on the microscope stage under crossed polarized illumination. Polarized images were taken by the digital CCD camera (DP70) while polarizer and analyzer were rotated every 10° from 0 to 90°. All of the images were then superposed to obtain a collagen fiber image in all directions.

B. Results and discussion

The area of calcification was significantly larger in stretched specimens than in the non-stretched control (Figs.8 and 9). Traveling direction of the calcification was roughly equal to the stretch direction (data not shown). Change in the align-



(a) Static culture



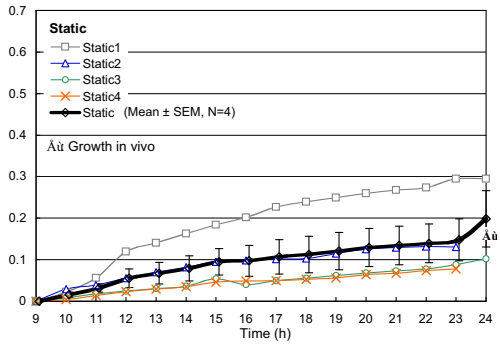
(b) Stretch culture

Fig.8 Real-time observation of tissue calcification.

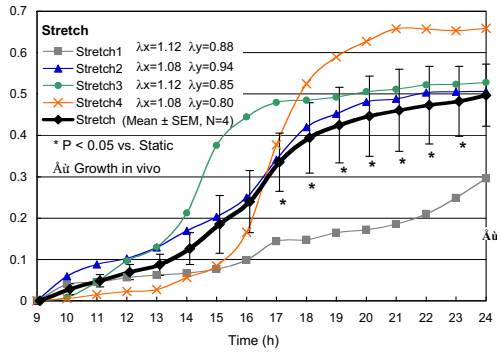
ment of collagen fibers of the sliced specimens in response to stretch was observed with polarized light microscopy in fresh slices while they were stretched gradually. Collagen fibers showed coherent alignment in the stretch direction over 5% of stretch. These results indicate that quasi-static stretch also stimulates calcification especially in the direction of stretch, and the calcification may occur preferentially along the direction of collagen fibers. The alignment of collagen fibers in the stretch direction and facilitated calcification along collagen fibers may have something to do with the alignment of trabecular bone in the direction of principal stress.

IV. Concluding Remarks

We have shown the possibility of inducing mechanical adaptation response in bone tissues cultured under a controlled mechanical environment. *In situ* observation of bone



(a) Static culture



(b) Stretch culture

Fig.9 Time course changes of the calcification ratio

formation process in immature bone specimens will become a powerful tool in studying the mechanism of mechanical adaptation of bone tissues.

Acknowledgment

This work was supported in part by KAKENHI from JSPS (No. 19650114) and Toyota Motor Corporation.

References

1. Wolff J (1986) The Law of Bone Remodelling. Springer-Verlag, Berlin
2. Ichikawa K, Nakagaki M, Nagayama K, Matsumoto T (2006) Effect of cells on the change in the mechanical properties of bone tissue during cyclic compression culture, JSME Proc 06-1(Vol.5), Mechanical Engineering Congress 2006, Kumamoto, Japan, 2006, pp.293-294
3. Ichikawa K, Nagayama K, Matsumoto T (2008) Real-time observation of immature bone tissue in culture under mechanical stimulation, JSME Proc07-49, 20th Bioeng Conf, Tokyo, Japan, 2008, pp.349-350

Author: Takeo Matsumoto
Institute: Nagoya Institute of Technology
Street: Showa-ku, Gokiso-cho
City: Nagoya 466-8555
Country: Japan
Email: takeo@nitech.ac.jp

Regional Brain Activity and Performance During Car-Driving Under Side Effects of Psychoactive Drugs

Manabu Tashiro[1,2], MD. Mehedi Masud[1], Myeonggi Jeong[1], Yumiko Sakurada[2,3], Hideki Mochizuki[2], Etsuo Horikawa[4,5], Motohisa Kato[2], Masahiro Maruyama[4], Nobuyuki Okamura[2], Shoichi Watanuki[1], Hiroyuki Arai[4], Masatoshi Itoh[1], and Kazuhiko Yanai[1,2]

1 Division of Cyclotron Nuclear Medicine, Cyclotron and Radioisotope Centre, Tohoku University, Japan
2 Department of Pharmacology, Tohoku University Graduate School of Medicine, Japan
3 Department of Anesthesiology, Tohoku University Graduate School of Medicine, Japan
4 Department of Geriatrics and Gerontology, Tohoku University Graduate School of Medicine, Japan
5 Centre for Comprehensive and Community Medicine, Faculty of Medicine, Saga University, Japan

Abstract — **Sedative side effects of antihistamines have been recognized to be potentially dangerous in car driving, but the mechanism underlying these effects has not yet been elucidated. The aim of the present study is to examine regional cerebral blood flow (rCBF) responses during a simulated car-driving task following oral administration of d-chlorpheniramine using positron emission tomography (PET) and [^{15}O]H_2O. Healthy volunteers drove a car in a simulated environment following oral administration of a sedative antihistamine, d-chlorpheniramine, or placebo. Their rCBF was measured in the conditions of resting, active driving, and passive driving. Performance evaluation revealed that the number of lane deviations significantly increased in the d-chlorpheniramine condition ($p<0.01$). Subjective sleepiness was not significantly different between the two drug conditions. The regions of diminished brain responses were detected following d-chlorpheniramine treatment in the parietal, temporal and visual cortices and in the cerebellum. These results suggest that d-chlorpheniramine tends to suppress visuo-spatial cognition and visuo-motor coordination even when the subjects do not recognize subjective feeling of sedation.**

Keywords — **Positron emission tomography (PET), regional cerebral blood flow (rCBF), sedative antihistamine, driving performance**

I. Introduction

Car driving is one of our everyday tasks and is also a series of complex perceptual and psychomotor tasks that require the integration of various basic neural functions such as attention, visuo-spatial cognition, motor programming and control, and visuo-motor coordination [1, 2]. Cognitive and psychomotor impairments following the administration of sedating drugs can lead to impairment of driving performance, and increase a driver's risk of injury. So far, a number of studies have been conducted to determine the effects on driving behavior following oral administration of psychoactive drugs such as sedative antihistamines [3, 4]. Sedative antihistamines such as diphenhydramine and d-chlorpheniramine can cross the blood-brain barrier and block histamine H_1 receptors (H_1Rs) in the histaminergic neuronal system of the brain, resulting in sleepiness, drowsiness, fatigue and psychomotor disturbances that might result in car injury [1, 2, 5]. A simulated car-driving study by Weiler and colleagues demonstrated that sedative antihistamines had a greater impact on driving performance than alcohol [3]. To elucidate the neural correlates of car-driving, recent neuroimaging studies have employed a simulated driving task using functional magnetic resonance imaging (fMRI)[6-8] and PET [9]. However, no study has revealed the neural mechanism of impaired driving performances due to antihistamines. The main purpose of the present study was, using PET with [^{15}O]H_2O, to examine regional cerebral blood flow (rCBF) responses during car driving following oral administration of d-chlorpheniramine.

II. Study design

A. Subjects And Method

Fourteen healthy Japanese male volunteers ranging from 20 to 25 years old were recruited to the present study. The present protocol was approved by the Ethics Committee of Tohoku University Graduate School of Medicine. Each subject was given d-chlorpheniramine repetab (6 mg) or a placebo (a lactobacteria tablet) in each study. The same subjects were studied for each drug after a wash-out period of at least 6 days. PET scan was started approximately 2 hours following the drug administration. The subjects were requested to drive a car, wearing a head-mounted display (HMD: Glasstron PLM-A35, SONY, Tokyo, Japan) to enable them to watch the projected "in-car" views of the outer world (Figure 1). The intravenous infusion line for [^{15}O]H_2O injection was inserted into a subject's right antecubital vein. For a simulated driving task, a commercial

Chwee Teck Lim, James C.H. Goh (Eds.): ICBME 2008, Proceedings 23, pp. 2201–2203, 2009
www.springerlink.com

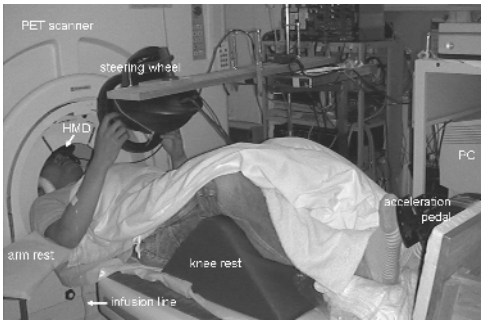


Figure 1. Setting of PET experiment on simulated car-driving (reproduced from the ref. [5] by the courtesy of John Wiley & Sons, Ltd.)

computer software (Gekisoh99, Twilight Express Co., Ltd., Tokyo, Japan) was used. The subjects were requested to drive smoothly as in normal car driving, but also as fast as possible from the start to the goal point, avoiding collision and deadlocks.

The rCBF images were obtained at the whole brain level using a PET scanner (SET 2400W, Shimadzu Co., Ltd., Japan). PET rCBF images were compared under the following 3 conditions: 1) "resting", 2) "active driving" where the subjects drove, and 3) "passive driving" conditions where the subjects watched the changing in-car view that had been videotaped previously, respectively. Performance of the subjects was evaluated in terms of the following 4 criteria: (a) total duration (sec) of driving from the start to the goal point, (b) number of collisions, (c) number of lane deviations, and (d) number of deadlocks. Additionally, subjective sleepiness was also evaluated using the Stanford Sleepiness Scale (SSS)(Figure 2).

The rCBF images were processed and analyzed using a Statistical Parametric Mapping (SPM) software package (SPM99)[10]. The resulting set of voxel values for each contrast constitutes a statistical parametric map of the t-statistics. We compared rCBF changes during active driving compared to the resting between the d-chlorpheniramine and placebo conditions. We determined the localization of the peak activation related to the active driving condition as compared with the resting and passive driving conditions.

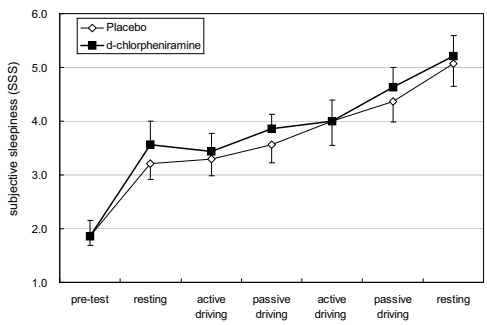


Figure 2. Subjective sleepiness measured using SSS. (reproduced from the ref. [5] by the courtesy of John Wiley & Sons, Ltd.)

III. Results

In all 14 subjects, performance evaluation revealed that the number of lane deviations significantly increased in the d-chlorpheniramine condition compared with the placebo condition (mean ± S.E.M.: 2.57 ± 0.60 vs. 6.36 ± 1.80, respectively: $p < 0.01$) though all other performances measures demonstrated no significant differences. Subjective sleepiness was not significantly different between the two drug conditions (Figure 2). Each performance score and the sleepiness scores did not correlate significantly.

Regions with increased rCBF during the active driving condition compared to the resting and the passive driving conditions were detected in the primary sensorimotor, premotor, cingulate, posterior parietal, temporal, and occipital cortices and in the cerebellar hemisphere, etc. (Figure 3). Lower rCBF following d-chlorpheniramine treatment was observed in the bilateral frontal, right parietal, bilateral temporal and bilateral insular cortices.

Finally, the intensity of rCBF alteration [active driving] – [resting]) were compared between the d-chlorpheniramine and placebo conditions. The regions with decreased rCBF following d-chlorpheniramine treatment were detected in the bilateral parietal, temporal, and occipital cortices (Figure 3).

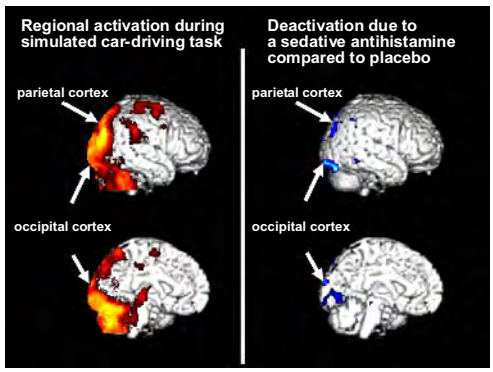


Figure 3. Results of PET analysis demonstrating regional activation during active driving compared to the resting (yellow & red), and regions with diminished activation under the influence of sedative antihistamine (blue).(reproduced from the ref. [5] by the courtesy of John Wiley & Sons, Ltd.)

IV. Discussions & Conclusion

Antihistamines are potentially dangerous agents to drivers, and a large number of studies have demonstrated their

effects on driving behaviors [1, 3, 4]. Their main therapeutic target in various allergic disorders is H1Rs in the peripheral blood; however, sedative antihistamines can easily cross the BBB and block the H1Rs of neurons in the brain, resulting in sedation characterized by sleepiness, drowsiness, fatigue and psychomotor disturbances [5]. Ironically, sedative antihistamines are more easily available over the counter than newer less-sedating antihistamines [3]. So far, neural correlates of car driving have been demonstrated using fMRI and PET and the reproducibility of the findings was demonstrated in the present study as well by comparing with the results of other studies. [6-9].

For the evaluation of impaired driving performance due to sedative antihistamines, Weiler and colleagues demonstrated that a steering stability was impaired by both alcohol and diphenhydramine, whereas coherence ability was impaired following only the administration of diphenhydramine [3]. In the present study, impaired performance (increased lane deviations) was demonstrated following d-chlorpheniramine treatment. In addition, this result suggests that subjective sleepiness is not always a reliable measure of sedation and that driving performance can be impaired among drivers even when they themselves do not recognize sedation. The present study demonstrated the presence of regions with significantly "diminished" rCBF responses following d-chlorpheniramine treatment in the posterior parietal, temporal, occipital regions as well as in the cerebellum. Thus, the present results suggest that d-chlorpheniramine suppresses neural activities associated with visuo-spatial cognition and visuo-motor coordination. In general, visual information projected onto the occipital cortex is transferred to the posterior part of the parietal cortex via the dorsal pathway for higher visual processing of motion and visuo-spatial information.

Acknowledgment

This work was in part supported by Grants-in-Aid for Scientific Research from the Japan Society of Promotion of Science (JSPS) and the Ministry of Education, Culture, Sports, Science and Technology in Japan, as well as by a grant from the Japan Society of Technology (JST) on research and education in "molecular imaging".

References

1. Theunissen EL, Vermeeren A, van Oers AC, et al. (2004) A dose-ranging study of the effects of mequitazine on actual driving, memory and psychomotor performance as compared to dexchlorpheniramine, cetirizine and placebo. Clin Exp Allergy;34(2):250-8.
2. Verster JC, Volkerts ER. (2004) Antihistamines and driving ability: evidence from on-the-road driving studies during normal traffic. Ann Allergy Asthma Immunol;92(3):294-303; quiz 303-5, 355.
3. Weiler JM, Bloomfield JR, Woodworth GG, et al. (2000) Effects of fexofenadine, diphenhydramine, and alcohol on driving performance. A randomized, placebo-controlled trial in the Iowa driving simulator. Ann Intern Med;132(5):354-63.
4. Tashiro M, Horikawa E, Mochizuki H, et al. (2005) Effects of fexofenadine and hydroxyzine on brake reaction time during car-driving with cellular phone use. Hum Psychopharmacol;20(7):501-9.
5. Yanai K, Tashiro M. (2007) The physiological and pathophysiological roles of neuronal histamine: an insight from human positron emission tomography studies. Pharmacol Ther;113(1):1-15.
6. Calhoun VD, Pekar JJ, McGinty VB, et al. (2002) Different activation dynamics in multiple neural systems during simulated driving. Hum Brain Mapp;16(3):158-67.
7. Walter H, Vetter SC, Grothe J, et al. (2001) The neural correlates of driving. Neuroreport;12(8):1763-7.
8. Uchiyama Y, Ebe K, Kozato A, et al. (2003) The neural substrates of driving at a safe distance: a functional MRI study. Neurosci Lett;352(3):199-202.
9. Horikawa E, Okamura N, Tashiro M, et al. (2005) The neural correlates of driving performance identified using positron emission tomography. Brain Cogn;58(2):166-71.
10. Friston KJ, Holmes AP, Worsley KJ, et al. (1995) Statistical Parametric Maps in Functional Imaging: A General Linear Approach. Hum Brain Mapp;2:189-210.

Evaluation of Exercise-Induced Organ Energy Metabolism Using Two Analytical Approaches: A PET Study

Mehedi Masud[1], Toshihiko Fujimoto[2], Masayasu Miyake[1], Shoichi Watanuki[1], Masatoshi Itoh[1], Manabu Tashiro[1]

[1]Divisoin of Nuclear medicine, Cyclotron and Radioisotope Center, Tohoku University, Sendai, Japan.
[2]Center for the Advancement of Higher Education, Tohoku University, Sendai, Japan.

Abstract — **Our purpose was to evaluate exercise-induced organ glucose metabolism using ^{18}F-2-fluoro-2-deoxyglucose ([^{18}F]FDG and three-dimensional positron emission tomography technique (3D-PET), comparing two analytical procedures. Eleven healthy male subjects were studied as controls (n=6) and exercise group (n=5). Exercise group subjects performed ergometer bicycle exercise for 40 minutes at 40% and 70% $\dot{V}O_{2max}$. [^{18}F]FDG (39.2 ± 2.6 MBq) was injected 10 min after exercise. A whole body 3D-PET scan was performed immediately after exercise using PET scanner (SET-2400W, Shimadzu Co. Kyoto, Japan). PET image data was reconstructed by filtered 3D back projection algorithm with supercomputer (SX-4/128H4, Synergy Center, Tohoku Univ). Controls were studied using identical study criteria with exercise group. Two analytical procedures, semiquantitative (standardized uptake value; SUV) and quantitative (regional metabolic rate of glucose; rMRGlc) [Autoradiographic method (Phelps et al.)] were applied to assess organ glucose metabolism. ROIs (regions of interest) were drawn on lower limb muscles (e.g., thigh and lumbar/gluteal muscles) and viscera (e.g., liver, heart and brain). To compare analytical procedures, correlation coefficient analysis was done between SUV and rMRGlc data of lower limb muscles, brain and heart. Quantitative analysis revealed that rMRGlc was increased ($p<0.05$) in skeletal muscles of thigh and lumbar/gluteal region, and decreased in brain ($p<0.05$) at mild or moderate exercise loads. Semiquantitative analysis revealed the identical results except in lumbar/gluteal muscles. It was found a correlation between SUV and rMRGlc at thigh, brain and heart, however; correlation was not suggestive at lumbar/gluteal muscles. We validated the semiquantitative procedure (SUV) taking absolute quantification method of glucose metabolic rate as a standard. It was observed, the rMRGlc was increased in thigh muscles and decreased in brain at mild or moderate workloads. However, discrepancies between SUV and rMRGlc in one organ demonstrate, semiquantitative approach needs a great care when metabolic rate of glucose utilization changes at whole-body level.**

Keywords — **[18F]FDG-3DPET, Exercise, Glucose-Metabolism, Semiquantification, Autoradiography.**

I. Introduction

Previous reports [1, 2] employed semiquantification method (standardized uptake values: SUV) to reveal organ glucose metabolic changes after exercise task, using ^{18}F-2-fluoro-2-deoxyglucose and three-dimensional positron emission tomography technique ([^{18}F]FDG and 3DPET). Recently, Kemppainen J. and co-workers assessed the glucose metabolism of lower limb skeletal muscle and myocardium using absolute quantification method (rMRGlc) [3]. However, no reports have evaluated whole-body glucose metabolic changes after exercise using 3D-PET technique, comparing semiquantitative and quantitative analytical methods.

Our purpose was to evaluate workloads-induced whole-body organ glucose metabolism using two analytical methods (semiquantitative and quantitative), as to establish a relationship between two PET quantification procedures.

II. Study design

A. Subjects

Eleven healthy male volunteers collaborated with this investigation. All subjects abstained from eating and drinking for at least 5 hours before the experiment. They were asked not to perform any kind of physical exercise from one day before investigation. 5 subjects served as exercise group whose ages ranged from 21 to 23 y (21.80 ± 0.84 y; mean ±S.D.). Another 6 subjects, aged mean 24 ± 5.34 y (range; 19 ~ 33 y) were studied as resting control maintaining the same study protocol without exercise. [^{18}F]FDG dose for control was in average 42.48 ± 6.63 MBq (mean ± S.D.). A written fully informed consent was obtained from each subject before the study. This study protocol was approved by the Clinical Committee for Radioisotope Studies of Tohoku University.

B. Study Protocol

Ergometer bicycle exercise was arranged at 40% and 70% $\dot{V}O_{2max}$ workloads. $\dot{V}O_{2max}$ was measured by intermit-

Chwee Teck Lim, James C.H. Goh (Eds.): ICBME 2008, Proceedings 23, pp. 2204–2206, 2009
www.springerlink.com

tent exercise on an ergometer bicycle (Monark 818E, Sweden), and oxyzen consumption rate was determined by an automated metabolic unit machine (AE280-S, Minato Co. Ltd. Osaka, Japan). Before the experiment, subjects rested for 20 minutes in a dim lit quiet room. One teflon catheter was inserted to their antecubital veins of the left hand for blood sampling to measure plasma glucose, lactate and insulin. Another teflon catheter was inserted to opposite antecubital veins for [^{18}F]FDG administration. Then, they started ergometer bicycle riding at the speed of 60 revolution/min (Monark 818E, Sweden) at both workloads (40% and 70% $\dot{V}O_{2max}$). [^{18}F]FDG was injected through a catheter at 10 min later following exercise task. The radioactivity dose for the exercise group was 38.37 ± 2.15 MBq (mean ± S.D.). After injection, subjects continued to pedal the bicycle for another 30 min, completing a total of 40 min task. Immediately after intravenous administration of [^{18}F]FDG, heated arterialized venous blood was sampled from cubital vein opposite to the injection site. Plasma [^{18}F]FDG concentrations were measured both during exercise and PET scan for 24 times. Plasma metabolite concentrations (i.e., Glucose, lactate and insulin) were measured at two points such as pre and post exercise states.

Subjects lay down in supine position on PET table with eyes open following exercise task. The PET room was kept dimmed and quiet. The scan protocol was as follows: a 3 dimensional (3D) whole-body emission scan (3 min × 9F) was performed from knee to the vertex followed by transmission scan (3 min × 9F) using a PET apparatus (SET2400W, Shimadzu, Kyoto, Japan). The transmission scan (post-injection mode) was performed with a ^{68}Ge/^{68}Ga external rotating line source (370 MBq at purchase).

C. Quantitative Methods

Regions of interest (ROIs) were set on the skeletal muscles of thigh, lumbar/gluteal regions, and visceral organs such as liver, heart and brain etc. (Figure 1). To evaluate the rate of glucose utilization, an autoradiographic method [4] was applied using the following equation:

$$rMRGlc = \frac{Cp}{LC}\left[\frac{K^*_1 k^*_3}{k^*_2 + k^*_3}\right]\left[\frac{C^*i(T) - C^*e(T)}{C^*m(T)}\right]$$

In another, semiquantitative analysis (Standard uptake value; SUV) was done by using the following equation:

$$\frac{Mean\ ROIcts\ (cps/pxls) \times Body\ weight(g)}{Injected\ dose\ (\mu Ci) \times Calibration\ factor\ (cps/\mu Ci)}$$

D. Statistical Analysis

Group comparisons were done by using one-way analysis of variance (ANOVA) and Tukey's test (post-hoc) analysis. The significant differences were set at $p<0.05$. Correlation was calculated using Pearson's correlation coefficient analysis.

III. Results

[^{18}F]FDG uptake was only remarkable in the brain, heart and urinary bladder in the resting subject, while high uptake was visualized in skeletal muscles at exercise state (Figure 1). Glucose metabolism (SUV and rMRGlc) was increased in the skeletal muscles of thigh and lumbar/gluteal regions ($p<0.05$), and was decreased in the brain ($p<0.05$) after exercise task (40% and 70% $\dot{V}O_{2max}$ workloads). A correlation between SUV and rMRGlc was found among organs (i.e., Thigh, liver, heart and brain), except in the lumbar/gluteal muscles. Figure 2 clearly depicted a good correlation between SUV and rMRGlc in the brain; however, a non-suggestive correlation was found in the lumbar/gluteal skeletal muscle. The changes in plasma metabolites were as follows: stable plasma glucose concentrations, an increase ($p<0.05$) plasma lactate concentration at post-exercise condition of 70% $\dot{V}O_{2max}$ (5.3 ± 2.4 mmol/liter) to compare with pre-exercise condition (0.9 ± 0.2 mmol/liter). The plasma insulin concentration was decreased ($p<0.05$) only at post-exercise workload of 70% $\dot{V}O_{2max}$ (2.0±0.7 μU/mol) than pre-exercise condition (4.6±1.5 μU/mol).

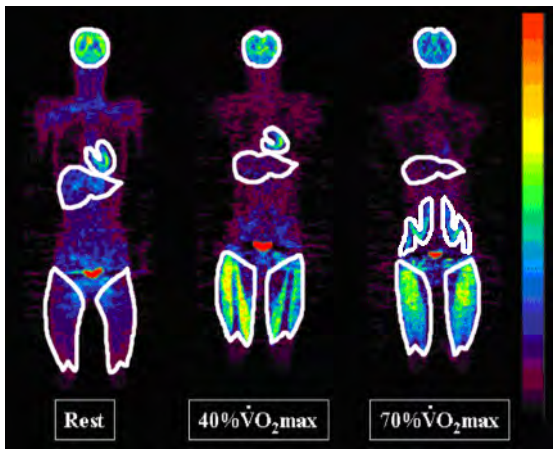


Figure 1. ROIs procedure and [^{18}F]FDG uptake of individual organs at rest (left) and exercise loads ; 40% and 70% $\dot{V}O_{2max}$ (right).

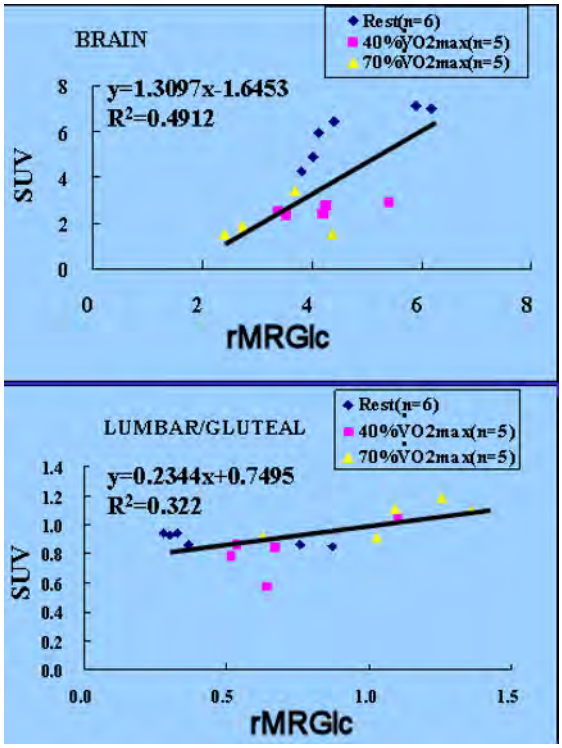


Figure 2. Correlation between SUV and rMRGlc in the brain and lumbar/gluteal muscles, showing good correlation in the brain and non-suggestive correlation in the lumbar/gluteal skeletal muscles.

IV. Discussions & Conclusion

Organ glucose uptake either increased or decreased almost linearly with exercise loads up to moderate workload (70% $\dot{V}O_{2max}$). In spite of complexity of energy metabolic controls such as glucose-fatty acid metabolic interaction, aerobic-anaerobic interaction, and involvement of glycogenolysis [5], exercise-induced organ glucose metabolism were successfully assessed with [^{18}F]FDG-3DPET technique and two analytical approaches. Organ glucose uptake either increased or decreased almost linearly with exercise loads up to moderate workload (70% $\dot{V}O_{2max}$), suggesting of homeostatic metabolic control. Semiquantitative method without blood samplings was found useful to estimate a rough trend of glucose consumptions. However, one organ failed to have good correlations between SUV and rMRGlc, the lumbar and gluteal muscles for example, which demonstrates that semiquantitative approach needs a great care when metabolic rate of glucose utilization changes at whole-body level.

Acknowledgment

This work was supported by grant-in-aid (No. 14704059 T Fujimoto) from the ministry of Education, Science, Sports and Culture, Japan and by the 13th Research-aid Report in Medical Health Science of Meiji Life Foundation and Welfare.

References

1. Fujimoto T, Itoh M, Kumano H et al. (1996) Whole body metabolic map with positron emission tomography of a man after running [Letter]. Lancet. 48(9022), 266.
2. Tashiro M, Fujimoto T, Itoh M et al. (1999) ^{18}F-FDG PET imaging of muscle activity in runners. J Nucl Med. 40, 70-76.
3. Kemppainen J, Fujimoto T, Kari KK et al. (2002) Myocardial and skeletal muscle glucose uptake during exercise in humans. J Physiol. 542(2): 403-412.
4. Phelps ME, Huang SC, Hoffman EJ et al. (2005) Tomographic Measurement of Local Cerebral Glucose Metabolic Rate in Humans with (F-18) 2-Fluoro-2-Deoxy-D-Glucose: Validation of Method. Ann Neurol. 6, 371-388.
5. Kjaer M, Howlett K, Langfort J et al. (2000) Adrenaline and glycogenolysis in skeletal muscle during exercise: a study in adrenalectomised humans. J Physiol. 15, 528(2), 371-8.

Strain Imaging of Arterial Wall with Reduction of Effects of Variation in Center Frequency of Ultrasonic RF Echo

Hideyuki Hasegawa[1,2] and Hiroshi Kanai[2,1]

[1] Graduate School of Biomedical Engineering, Tohoku University, Sendai, Japan
[2] Graduate School of Engineering, Tohoku University, Sendai, Japan

Abstract — **Atherosclerotic change of the arterial wall leads to a significant change in its elasticity. For assessment of elasticity, measurement of arterial wall deformation is required. For motion estimation, correlation techniques are widely used, and we developed a phase-sensitive correlation method, namely, the *phased-tracking method*, to measure the regional strain of the arterial wall due to the heartbeat. Although phase-sensitive methods using demodulated complex signals require less computation in comparison with methods using the correlation between RF signals or iterative methods, the displacement estimated by such phase-sensitive methods are biased when the center frequency of the RF echo apparently varies. One of the reasons for the apparent change in the center frequency would be the interference of echoes from scatterers within the wall. In the present study, a method was introduced to reduce the influence of variation in the center frequencies of RF echoes on the estimation of the artery-wall strain when using the phase-sensitive correlation technique. The improvement in the strain estimation by the proposed method was validated using a phantom. The error from the theoretical strain profile and the standard deviation in strain estimated by the proposed method were 12.0% and 14.1%, respectively, significantly smaller than those (23.7% and 46.2%) obtained by the conventional phase-sensitive correlation method. Furthermore, in the preliminary *in vitro* experimental results, the strain distribution of the arterial wall well corresponded with pathology, i.e., the region with calcified tissue showed very small strain, and the region almost homogeneously composed of smooth muscle and collagen showed relatively larger strain and clear strain decay with respect to the radial distance from the lumen.**

Keywords — **ultrasound, center frequency, phase shift, radial strain of arterial wall, elasticity**

I. Introduction

We have developed a phase-sensitive correlation method, namely, *phased-tracking method*, for estimating the displacement distribution in the arterial wall for strain imaging [1]. In such methods, ultrasonic pulses with finite frequency bandwidths are used. Therefore, the apparent change in center frequency occurs due to the interference of echoes from scatterers in the wall. Under such a condition, the displacement estimates are biased because it is obtained using the phase changes and center frequencies of received RF echoes. An autocorrelation-based method was proposed to compensate for this apparent change in center frequency [2,3]. In this method, center frequency distributions in two frames must be assumed to be the same. However, they become different when the scatterer distribution is changed by the artery-wall deformation.

In this study, a new method using the phase-sensitive correlation technique, which does not require the assumption that center frequency distributions in two different frames are the same, was examined for reducing the influence of center frequency variation on the estimation of artery-wall strain. The improvement of accuracy by the proposed method was validated using a cylindrical phantom. Furthermore, preliminary *in vitro* experimental results were obtained and are herein presented [4].

II. Methods

A. Displacement estimation using conventional autocorrelation methods

The phases of echoes from a moving target, which is located at depth d in the initial frame, are different in two consecutive n-th and (n+1)-th frames. This phase shift, $\Delta\theta_d(n)$, depends on the displacement of the target between these two frames. Therefore, the instantaneous displacement $\Delta x_d(n)$ between these two consecutive frames is estimated as follows:

$$\Delta x_d(n) = \frac{c_0 \Delta\theta_d(n)}{4\pi f_{0e}}, \tag{1}$$

where c_0 and f_{0e} are the speed of sound and the frequency used for displacement estimation, respectively. Phase shift $\Delta\theta_d(n)$ is estimated by the complex cross-correlation function $\gamma_{d,n}$ using the complex quadrature demodulated signals $z(d; n)$ of received RF echo as follows:

$$\Delta\theta_d(n) = \angle\gamma_{d,n} = \sum_{d\in R} z^*(d + x_d(n); n) \cdot z(d + x_d(n); n+1), \tag{2}$$

where * shows the complex conjugate. The accumulated displacement $x_d(n)$ is obtained by accumulating the instantaneous displacement with respect to time.

Chwee Teck Lim, James C.H. Goh (Eds.): ICBME 2008, Proceedings 23, pp. 2207–2210, 2009
www.springerlink.com

B. Translational motion compensation

The translational motion of the wall is compensated by tracking the echo from the luminal interface using the conventional method described in Sec. II-A because the echo from the luminal interface is dominant and is less influenced by the interference from other echoes from scatterers in the wall. In this study, *key frames* are defined as the frames at which the estimated displacement of the luminal interface $\Delta x_{d=l}(n)$ reaches the integral multiple of the spacing of the sampled points ΔX. Figures 1(a) and 1(b) shows the RF echoes from the cylindrical phantom used in this study in two successive *key frames*. The region of interest (ROI) is manually assigned in the initial frame and, then, its position at each time is automatically determined by estimating the displacement of the luminal interface (the nearest edge of the ROI). The displacement of the luminal interface between two successive *key frames* is almost a spacing of sampled points, and the translational motion can be compensated by shifting the ROI by one point as shown in Figs. 1(c) and 1(d). After translational motion compensation, the phase shift $\Delta\theta_d(n)$, which is caused by the displacement contributing to strain, of echoes between these two *key frames* is estimated at each depth d along the arterial radial direction, and the displacement distribution $\{x_d(n)\}$ is obtained from $\Delta\theta_d(n)$ using eq. (1). Finally, strain distribution is obtained by the spatial differentiation of displacements $\{x_d(n)\}$ in the arterial radial direction.

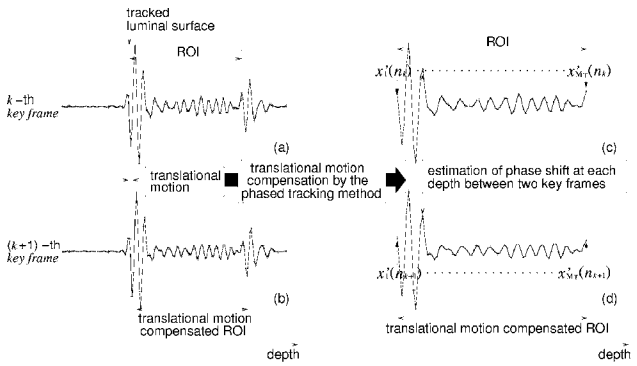


Fig. 1 Displacement estimation with translational motion compensation. Original RF signals in two consecutive (a) k-th and (b) (k+1)-th key frames. Translational motion compensated RF signals in (c) k-th and (d) (k+1)-th frames.

C. Error correcting function

After compensation of translational motion, the displacement contributing to strain is estimated using the phase shift of RF echoes. In such a situation, a large error resulting from the translational motion is removed, but error due to the mismatch between the frequency used for displacement estimation and the actual center frequency still remains in the estimation of the displacement contributing to strain even after the compensation of translational motion. In the present study, an error correcting function is introduced to further reduce this error. The error correcting function $\beta_{d,k}$ in k-th *key frame* (n_k-th frame) is defined as follows:

$$\beta_{d,k} = \frac{\dfrac{c_0}{4\pi f_{0e}}\left|\angle\left(\gamma'_{d,k}\cdot\gamma^*_{d,k}\right)\right|}{\Delta X}, \tag{3}$$

$$\gamma'_{d,k} = \sum_{d\in R} z^*(d + x_l(n_k); n_k)\cdot z(d + x_l(n_k); n_{k+1}), \tag{4}$$

$$\gamma_{d,k} = \sum_{d\in R} z^*(d + x_l(n_k); n_k)\cdot z(d + x_l(n_{k+1}); n_{k+1}), \tag{5}$$

where ΔX is the spacing of sampled points. *Key frames* are assigned so as to be $|x_l(n_{k+1})-x_l(n_k)|=\Delta X$, and the signal $z(d+x_l(n_k);\ n_{k+1})$ in $\gamma_{d,k}$ is artificially displaced by a spacing of sampled points in comparison with $z(d+x_l(n_{k+1});\ n_{k+1})$ in $\gamma'_{d,k}$. Based on eq. (1), this artificial displacement can be expressed as $c_0|\angle(\gamma'_{d,k}\cdot\gamma^*_{d,k})|/4\pi f_0$ by the difference between angles $\angle\gamma'_{d,k}$ and $\angle\gamma_{d,k}$ of $\gamma'_{d,k}$ and $\gamma_{d,k}$, and it should be ΔX. Equation (3) shows the ratio of the artificial displacement estimated by the phase shift $c_0|\angle(\gamma'_{d,k}\cdot\gamma^*_{d,k})|/4\pi f_0$ to actual one ΔX. The error-corrected displacement $\Delta x_{c,d}(n_k)$ between n_k-th and n_{k+1}-th key frames contributing to strain can be obtained as follows:

$$\Delta x_{c,d}(n_k) = \frac{1}{\beta_{d,k}}\frac{c_0}{4\pi f_{0e}}\angle\gamma_{d,k}. \tag{6}$$

The displacement distribution is obtained by estimating the displacement $x_{c,d}(n)$ at each depth d which corresponds to the arterial radial direction. Finally, strain distribution is obtained by estimating the regional slope of the displacement distribution using the least-squares method [4].

D. Experimental setup

In this study, a cylindrical phantom and excised artery were measured by ultrasound. The outer and inner diameters of the phantom, made of silicone rubber (elastic modulus E: 749 kPa), are 10 and 8 mm, respectively. The phantom contains 5% carbon powder (by weight) to obtain sufficient scattering from the inside of the wall.

Figure 2 shows a schematic diagram of the measurement system. A change in pressure inside the phantom or artery was induced by circulating a fluid using a flow pump. The change in internal pressure was measured by a pressure sensor (NEC, Tokyo, 9E02-P16).

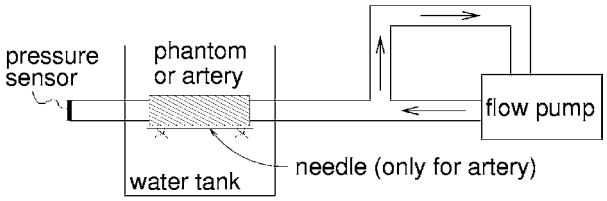


Fig. 2 Experimental system.

Pressure-diameter testing was applied to the phantom to obtain the elastic modulus of silicone rubber. In the pressure-diameter testing, the change in external diameter of the phantom was measured with a laser line gauge (VG-035, KEYENCE, Osaka, Japan).

In ultrasonic measurement, the phantom and artery were measured with a linear-type ultrasonic probe (Aloka, Tokyo, SSD-6500). The nominal center frequency was 10 MHz. RF echoes were acquired at 40 MHz at a frame rate of 286 Hz.

In the *in vitro* experiment, a femoral artery excised from a patient with arteriosclerosis obliterans was measured. The artery was placed in a water tank filled with 0.9% saline solution at room temperature. A needle was attached to the external surface of the posterior wall using strings to identify the section to be imaged during the ultrasonic measurement. After the ultrasonic measurement, the pathological image of the measured section was obtained by referring to the needle.

III. Basic Experimental Results

Figure 3(a) shows the strain distribution along the ultrasonic beam (the radial direction of the phantom) estimated by the conventional autocorrelation method [1]. Plots and vertical bars show means and standard deviations of 46 individual ultrasonic beams. The dashed line shows the theoretical strain profile, which is obtained by the measured internal pressure and elastic modulus (E =749 kPa) of the wall measured by the pressure-diameter testing, given by [5]

$$\varepsilon_r = -\frac{3}{2}\frac{r_i^2 r_o^2}{\left(r_o^2 - r_i^2\right)r}\frac{p}{E}, \tag{8}$$

where r_i and r_o are the original inner and outer radii, respectively.

Although mean values follow the theoretical strain profile, the standard deviations of strains estimated by the conventional method [1] are large. In Fig. 3(b), the center frequency estimation proposed in [2] was used together with the conventional method [1]. However, the strain estimates are not improved so much. Figure 3(c) shows the strain distribution obtained by the proposed method. Strain estimates were improved significantly by translational motion compensation and error correction.

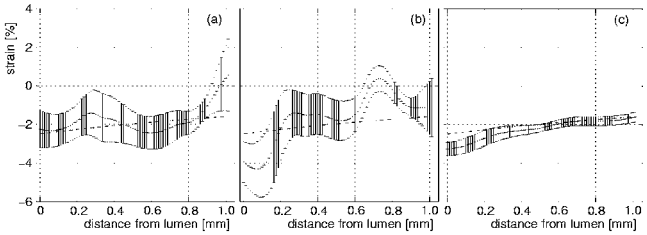


Fig. 3 Estimated strain distribution. (a) Conventional method [1]. (b) Conventional method with center frequency estimation [2]. (c) Proposed method with translational motion compensation and error correction.

IV. In Vitro Experimental Results

Figure 4(a-1) and 4(b-1) show the B-mode images of two different regions in the excised femoral artery. The region shown in Fig. 4(a-2) shows very low strain. On the other hand, the region shown in Fig. 4(b-2) shows relatively larger strain, and there is a clear strain decay with respect to the distance from the lumen [5]. Figures 4(a-3) and 4(b-3) show the elasticity images obtained by eq. (8) using the measured internal pressure and estimated strain distributions. By comparing the elasticity images and pathological images of the corresponding sections shown in Figs. 4(a-4), 4(b-4), 4(a-5), and 4(b-5), the very hard region surrounded by the green line in Fig. 4(a-3) corresponds to calcified tissue. On the other hand, the region composed of smooth muscle and collagen shows a relatively homogeneous and lower elastic modulus distribution. These results show that the proposed method successfully reveals the difference in the deformation properties resulting from different tissue compositions.

V. Discussion

The estimation of stress distribution in the arterial wall is one of the most difficult problems. In our study [6], the stress distribution in the arterial wall was assumed to be constant. Even in the case of a homogeneous cylindrical shell, the stress (strain) distribution is dependent on the distance from luminal surface. When an artery is a homogeneous cylindrical shell, the stress (strain) distribution can be theoretically derived based on eq. (8). However, it is difficult to estimate the stress (strain) distribution when an artery is inhomogeneous in the wall thickness and elastic properties. Therefore, in our study, the average stress was used to normalize the measured strain.

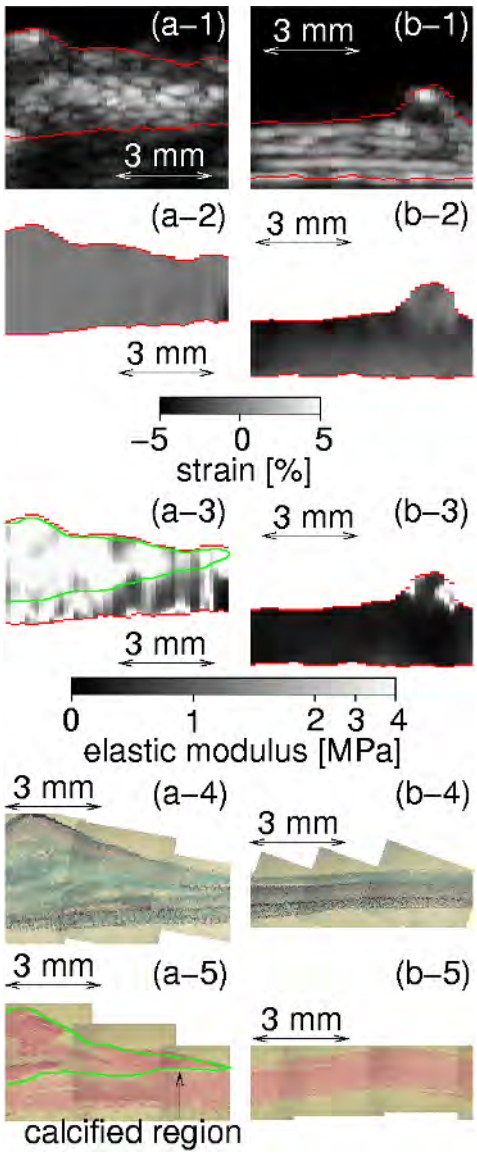


Fig. 4 *In vitro* experimental results for two regions in an excised femoral artery: (a) region with calcified tissue and (b) that without calcified tissue and composed of smooth muscle and collagen; (1) B-mode images, (2) strain images, (3) elasticity images, and (4) and (5) pathological images with elastica-Masson and hematoxilin-eosin staining, respectively.

This strategy is effective to compensate for the dependence of strain on the pulse pressure. When only the strain itself is considered to evaluate the elasticity, the strain is dependent on the pulse pressure which does not relate to the elasticity. As described in this paper, use of the stress distribution of a cylindrical shell given by eq. (8) is another solution to compensate for the pulse pressure variation.

VI. Conclusions

In the displacement estimation based on the phase changes of echoes, the displacement estimates are biased when the center frequency of the RF echo changes. Such an apparent change in the center frequency could be caused by the interference of echoes from scatterers. To reduce the influence of the center frequency variation on the estimation of artery-wall strain, in this study, an error correcting function, which does not require the assumption that the center frequency distributions in two different frames are the same, was introduced. As a result, the proposed method provides better strain estimates in comparison with conventional phase-sensitive correlation methods.

Acknowledgment

We are grateful to Panasonic Co., Ltd. for providing the phantoms used in this study.

References

1. Kanai H, Sato M, Chubachi N, et al. (1996) Transcutaneous measurement and spectrum analysis of heart wall vibrations. IEEE Trans Ultrason Ferroelect Freq Contr 43:791–810.
2. Loupas T, Powers JT, Gill RW (1995) An axial velocity estimator for ultrasound blood flow imaging based on a full evaluation of the Doppler equation by means of a two-dimensional autocorrelation approach. IEEE Trans Ultrason Ferroelect Freq Contr 42, 672-688.
3. Hasegawa H, Kanai H (2006) Improving accuracy in estimation of artery-wall displacement by referring to center frequency of RF echo. IEEE Trans Ultrason Ferroelect Freq Contr 53:52–63.
4. Hasegawa H, Kanai H (2008) Reduction of influence of variation in center frequencies of RF echoes on estimation of artery-wall strain. IEEE Trans Ultrason Ferroelect Freq Contr 55, 1921-1934.
5. Timoshenko SP, Goodier JN (1970) Theory of elasticity, 3rd ed., McGraw Hill, New York.
6. Hasegawa H, Kanai H, Hoshimiya N, et al. (2004) Evaluating the regional elastic modulus of a cylindrical shell with nonuniform wall thickness. J Med Ultrason 31, 81-90.

In Situ Analysis of DNA Repair Processes of Tumor Suppressor BRCA1

Leizhen Wei and Natsuko Chiba

Department of molecular immunology, Institute of Development, Aging and Cancer (IDAC), Tohoku University, Japan

Abstract — **Germline mutations in the breast cancer susceptibility gene BRCA1 predispose women to breast and ovarian cancer. BRCA1 is involved in many cellular processes, DNA repair, transcription, cell cycle, chromatin remodeling, and apoptosis. Although the tumor suppressor activity of BRCA1 seems to be attributed to its involvement in DNA repair system, its mechanism is still unclear. We have established a laser light micro-irradiation system to create various types of DNA damage in living cells including DNA double-strand breaks (DSBs), single-strand breaks (SSBs), and base damage, which has enabled us to detect BRCA1 accumulation at the site of DNA damage in a real-time course. Furthermore, we generated local UV irradiation in cell nuclei by an isopore membrane filter and analyzed the BRCA1 response to UV irradiation by immunocytochemistry. We found that the N and the C-terminus of BRCA1 independently accumulated at DSBs with distinct kinetics. N-terminal BRCA1 accumulated immediately after laser-irradiation at DSBs and dissociated rapidly. In contrast, the C-terminus of BRCA1 accumulated more slowly at DSBs, but remained at the sites. Interestingly, the N and the C-terminus of BRCA1 accumulate at the site of DSBs, dependent on distinct repair factors. Furthermore, we found that BRCA1 accumulates at SSBs via its C-terminus. These demonstrate that different BRCA1 interactions with repair factors influence its multifunction in DNA repair. Furthermore, BRCA1 immediately accumulated at the locally UV-irradiated sites. The accumulation was abrogated by treatment with transcription inhibitors. BRCA1 accumulates to the UV irradiated sites via its N and C-terminus. The BRCA1 accumulation was dependent on the presence of another DNA repair protein, which is involved in transcription coupled repair. These finding suggest that BRCA1 is involved in transcription coupled repair pathway. These precise analyses of BRCA1 DNA repair function will contribute to the development of molecular diagnosis and molecular targeting therapies for personalized medicine.**

Keywords — **BRCA1, DNA damage.**

I. Introduction

Breast-cancer susceptibility gene 1 (*BRCA1*) was identified in 1994 by positional cloning [1]. *BRCA1* encodes 1863 amino acids (a.a.), and more than 200 different *BRCA1* germ-line mutations associated with cancer susceptibility have been identified. Carriers of *BRCA1* mutations also have increased susceptibility to ovarian cancers; the risk of breast cancer development is about 50-80%, and that of ovarian cancer development is 12-60%, in *BRCA1* mutation carriers. *BRCA1*-related breast cancers are characterized by an early onset, a high frequency of bilateral involvement, and a poor prognosis.

Somatic *BRCA1* mutations are rarely observed in sporadic breast cancers. However, *BRCA1* mRNA and protein expressions are downregulated in about 30% of sporadic breast cancers and 70% of ovarian cancers. Therefore, the reduced expression or function of *BRCA1* is thought to be an important contributing factor in sporadic cancers.

BRCA1 contains a RING domain in its amino (N)-terminus and two tandem BRCT domains in its carboxy (C)-terminus. The BRCT domain is frequently found in DNA repair proteins, and functions as a binding module for phospho-serine peptides. BRCA1 has also a nuclear export signal (NES), a nuclear localization signal (NLS), and a DNA-binding region. After DNA damage, BRCA1 is phosphorylated by Chk2 or ATM (Fig. 1). The N-terminal region of BRCA1 directly interacts with BARD1, thereby enhancing the ubiquitin polymerase activity of BRCA1 [2,3].

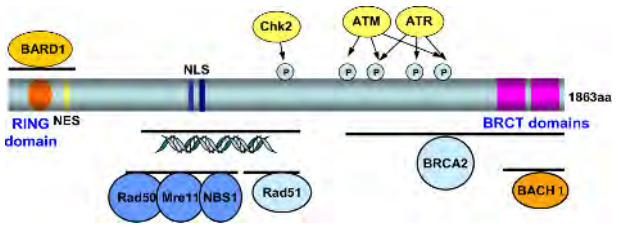


Fig. 1 Structure of the BRCA1 protein. BRCA1 contains an N-terminal RING domain, a nuclear export signal (NES), a nuclear localization signal (NLS), a DNA binding region, and two C-terminal BRCT domains. BRCA1 is associated with a number of proteins, as indicated. Sites phosphorylated by Chk2 or ATM are indicated by arrows.

BRCA1 has been implicated in a number of cellular processes, including the regulation of DNA damage repair, transcription, cell cycle, chromatin remodeling, and apoptosis. Among various function of BRCA1, the tumor suppressor activity of BRCA1 is to be primarily attributed to its involvement in DNA repair. However, the precise mechanism of what role BRCA1 plays in DNA repair pathway is not fully understood. So, we are collaborating with Dr. Akira Yasui, Department of Molecular Genetics, Institute of

Chwee Teck Lim, James C.H. Goh (Eds.): ICBME 2008, Proceedings 23, pp. 2211–2214, 2009
www.springerlink.com

Development, Aging and cancer, Tohoku University, and are analyzing the cellular response of BRCA1 to various DNA damage using molecular imaging technique.

II. Results

1 BRCA1 response to various DNA damage induced by laser micro-irradiation

1.1 Laser micro-irradiation system

To elucidate the molecular mechanisms of DNA repair processes for various DNA damage of BRCA1, we are analyzing the BRCA1 accumulation at the DNA damaged site induced by laser micro-irradiation in living cells.

Our experimental system is a laser micro-irradiation apparatus combined with a confocal microscopy. We use a 365nm pulse laser system for the irradiation of cells in the epi-fluorescence path of the microscope system. A lower dose or higher dose of irradiation was obtained by passing lasers through distinct filters in front of the lens. A 405nm pulse laser system is also used. The power of laser scan can be controlled by the number of scan (Fig. 2). By using these system, various types of DNA damage, such as single-strand breaks (SSBs), double-strand breaks (DSBs) and oxidative base damage, were produced at restricted nuclear regions of cells [4, 5].

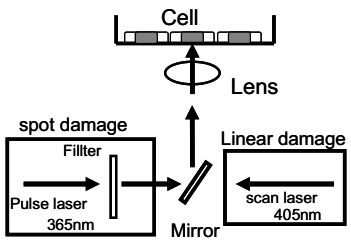


Fig. 2 Laser micro-irradiation systems. The left column shows the 365 nm pulse laser irradiation system, producing the lower dose and the higher dose irradiation, which are regulated by the filter in front of the mirror. The right column shows the 405 nm laser system. Fluorescent images were obtained and processed using an FV-500 confocal scanning laser microscopy system. A 405 nm scan laser system for irradiation of cells in the epifluorescence path of the microscope system was used. One scan of the laser light at full power delivers approximately 1600 nW. To primarily induce DSBs, we scanned cells 500 times using the 405 nm laser at full power, which has been shown The 405 nm laser light was focused through a 40× objective lens.

We found that BRCA1 accumulates at various DNA damage sites induced by laser-irradiation using this system.

1.2 BRCA1 localizes at DSBs via its N- and C-terminal regions

We next examined the real time localization of GFP-tagged BRCA1 in living cells after laser-irradiation. GFP-BRCA1 was transfected into Saos-2 cells and the cells were then laser-irradiated. As shown in Figure 3, GFP-BRCA1 clearly accumulated at the irradiated sites.

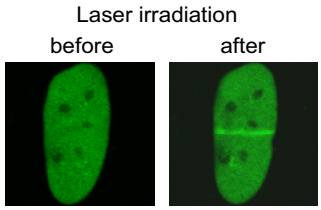


Fig. 3 GFP-tagged BRCA1 accumulates at DSB sites in Saos-2 cells.

We identified the regions in BRCA1 that mediate this accumulation. Several GFP-tagged deletion mutants of BRCA1 were constructed and transfected into Saos-2 cells. We identified that either the N- or C-terminal region alone is sufficient for BRCA1 accumulation at DSBs.

The mean intensity of GFP-BRCA1 at the accumulation site was quantified and the kinetics of accumulation of full-length and a.a.1-304 and a.a.1527-1863 fragments were examined for 600 seconds after irradiation. Interestingly, the N-terminal (a.a.1-304) fragment rapidly and maximally accumulated at the DSBs within 20 seconds, whereas the C-terminal (a.a.1527-1863) fragment slowly and gradually accumulated, reaching a plateau at 360 seconds. Full-length BRCA1 exhibited a pattern of accumulation that reflected the combination of N- and C-terminal fragment patterns. Taken together, the above kinetic analyses suggest that the N- and C-terminal regions of BRCA1 may accumulate at DSBs through different mechanisms.

Then, we compared the clearance kinetics of the N- and C-terminal fragments of BRCA1 from DSBs. The accumulation of the N-terminal fragment along the line of irradiation was detected 10 min after laser-irradiation, but was almost completely lost by two hours after irradiation. In contrast, the fluorescence of the C-terminal fragment at DSBs was present at two hours after irradiation. These results indicate that the C-terminal region is unique in its ability to remain at the DSBs and that BRCA1 displays domain-specific kinetics in terms of its initial accumulation and subsequent retention at the damaged sites.

1.3 Accumulation of BRCA1 at DSBs requires the other DNA repair factor

Next, we examined whether BRCA1 accumulation at DSBs is dependent on specific DNA repair factors, using factor-deficient cells. The N- and C-terminal fragments accumulated at laser-induced DSBs in ATM-deficient AT1KY/T-n cells, H2AX-/- MEF cells, CHO-derived CHO9, and XR-C1 (DNA-PKcs -/-) cells. However, in XRV15B (Ku80 -/-) cells, the N-terminal fragment of BRCA1 failed to accumulate at DSB sites, whereas the C-terminal fragment did accumulate. Therefore, accumulation of the N-terminal fragment, but not the C-terminal fragment, of BRCA1 at DSBs is Ku80 dependent.

1.4 BRCA1 localizes at SSBs via its C-terminal regions

Next, we examined the real-time accumulation at SSBs of GFP-tagged BRCA1 in living cells after laser-irradiation. GFP-BRCA1 was transfected into Saos-2 cells, the cells were laser-irradiated, and the mean intensities of GFP-BRCA1 were quantified. GFP-BRCA1 clearly accumulated at the irradiated sites (Fig. 4). This accumulation was slow and gradual. The kinetics of BRCA1 accumulation at SSBs was different from that at DSBs sites.

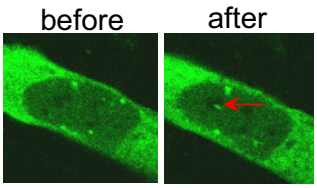


Fig. 4 GFP-tagged BRCA1 accumulates at the SSB sites induced by laser-irradiation in Saos-2 cells. Arrow indicates the laser-irradiated sites.

We next identified the BRCA1 regions that mediate BRCA1 accumulation at sites of irradiation. The full-length BRCA1, as well as the deletion mutants Δ305-770, Δ775-1292, Δ1-302, and Δ1527-1863, were transfected into Saos-2 cells. All of the BRCA1 deletion mutants except Δ1527-1863 accumulated at SSBs. The C-terminal a.a.1527-1863 fragment accumulated at the laser-irradiated sites. These results suggest that the BRCA1 C-terminus is important and sufficient for BRCA1 accumulation at SSBs.

2 BRCA1 response to local UV irradiation

In the field of DNA repair, BRCA1 is engaged in DNA DSB repair pathways, homologous recombination (HR), and non-homologous end-joining (NHEJ). BRCA1 is also involved in TCR processes [6], and BRCA1-deficient cells are defective in a process in which oxidative base damages are removed preferentially from the transcribed DNA strand [7]. After UV irradiation, BRCA1 localizes to nuclear foci and is phosphorylated at Ser1423 and Ser1524 by ATR. Previously, we and other groups reported that BRCA1 ubiquitinates RNAPII after UV irradiation [8, 9, 10]. The predominant DNA damages produced by UV irradiation are cyclobutane pyrimidine dimmers (CPD) and 6-4 photoproduct adducts. These lesions are removed by nucleotide excision repair (NER), which eliminates a wide variety of bulky helix–distorting DNA lesions. NER operates via two pathways, global genome repair (GGR) and TCR. GGR can repair DNA lesions at any location in the whole genome, while TCR selectively removes DNA lesions on the transcribed strands of expressed genes.

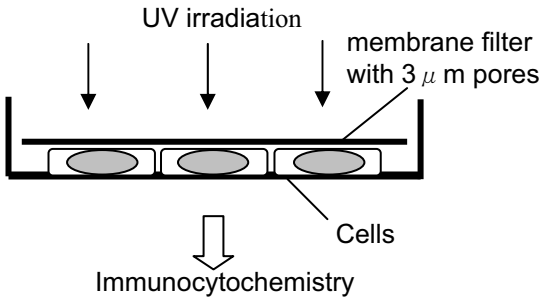


Fig. 5 Schematic of cellular exposure to local UV irradiation using a membrane filter.

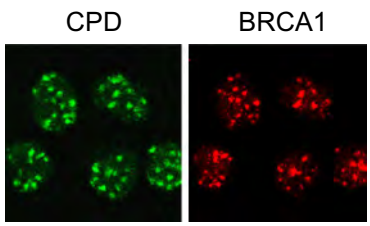


Fig. 6 BRCA1 accumulation at sites of local UV irradiation. Saos-2 cells were fixed after UV irradiation through membrane filters, and were stained with antibodies against CPD and BRCA1.

To gain further insights into BRCA1 regulation of the TCR pathway, we induced UV damage in small restricted areas of cell nuclei by using an isopore membrane filter. Cells monolayered in 35-mm glass-bottom dishes were covered with a polycarbonate isopore membrane filter (3-μm diameter pores), and were UV-irradiated (254-nm) with a dose of 60 J/m^2 (Fig. 5). The polycarbonate blocked the 254-nm UV light, and cells were exposed only though the filter pores. Immunostaining with an antibody against BRCA1 revealed that BRCA1 immediately accumulated at

the site of local UV irradiation and colocalized with CPD (Fig. 6). This accumulation was abolished by a transcriptional inhibitor, and was dependent on the presence of a protein that is involved in the NER pathway. Furthermore, BRCA1 was associated with this repair factor. Our data reveal the mechanism of BRCA1 involvement in the TCR pathway at lesions induced by UV irradiation.

III. Discussion

It was recently reported that the inhibition of poly (ADP-ribose) polymerase 1 (PARP1), a critical enzyme in the SSB repair pathway, leads to a severe, highly-selective toxicity in *BRCA1*-deficient cells [11]. This seems to be because PARP inhibition results in unrepaired SSBs, giving rise to DSBs. These provide new concepts for the development of potential cancer treatments. The reduced expression or function of BRCA1 is observed in sporadic cancers, suggesting that the precise analysis of BRCA1-related proteins will contribute to the discovery of novel molecular targets for cancer chemotherapy.

In cancer treatment, it is important to select a treatment method and predict its effectiveness in individual cancer patients. Molecular targeting therapies are focus of investigation with a view to developing novel approaches to cancer control. New biomarkers are similarly essential for improved cancer diagnostics. Our research has focused on the identification and functional analysis of critical proteins mediating carcinogenesis and on the development of diagnostic biomarkers and molecular targets for therapies for personalized medicine. Molecular imaging techniques will be useful tools for these aims.

Acknowledgment

This study was supported by Grants-in-Aid from the Ministry of Education, Science, Sports and Culture of Japan. We also acknowledge the support of Tohoku University Global COE Program ‘‘Global Nano-Biomedical Engineering Education and Research Network Centre’’.

References

1. Miki Y, J. Swensen D et al (1994) A strong candidate for the breast and ovarian cancer susceptibility gene BRCA1. *Science* 266: 66-71
2. Chiba, N, and Parvin, J D (2001) Redistribution of BRCA1 among four different protein complexes following replication blockage. J Biol Chem. 276, 38549-38554
3. Chiba N, and Parvin, J D (2002) The BRCA1 and BARD1 association with the RNA polymerase II holoenzyme. Can-cer Res. 62, 4222-4228
4. Lan L, Nakajima S et al (2004) In situ analysis of repair processes for oxidative DNA damage in mammalian cells. Proc Nat Acad Sci USA, 101, 13738-13743
5. Lan L, Nakajima S et al (2005) Accumulation of Werner protein at DNA double-strand breaks in human cells. J Cell Sci. 118, 4153-4162
6. Abbott DW, Thomson ME et al (1999) BRCA1 expression restores radiation resistance in BRCA1-defective cancer cells through enhancement of transcription-coupled DNA repair. J Biol Chem. 274, 18808-18812
7. Le Page F, Randrianarison V et al (2002) BRCA1 and BRCA2 are necessary for the transcription-coupled repair of the Oxidative 8-Oxoguanine lesion in human cells. Cancer Res. 60, 5548-5552
8. Starita LM, Howitz AA et al (2005) BRCA1/BARD1 ubiquitinate phosphorylated RNA polymerase II. J Biol Chem. 280, 24498-24505
9. Kleiman FE, Wu-Baer F et al (2005) BRCA1/BARD1 inhibition of mRNA 3’ processing involves targeted degradation of RNA polymerase II Genes & Development 19, 1227-1237
10. Wu W, Nishikawa H et al (2007) BRCA1 ubiquitinates RPB8 in response to DNA damage Cancer Res. 67, 951-958
11. Farmer H, McCabe N et al (2005) Targeting the DNA repair defect in BRCA mutant cells as a therapeutic strategy. Nature 434, 917-921

Evaluating Spinal Vessels and the Artery of Adamkiewicz Using 3-Dimensional Imaging

Kei Takase, Sayaka Yoshida and Shoki Takahashi

Department of Radiology, Tohoku University, School of Medicine, Sendai, Japan

Abstract — **Accurate localization of the artery of Adamkiewicz (AKA) is important in planning treatment of patients with thoracoabdominal aortic disease. We assessed the usefulness of three-dimensional imaging devices such as multidetector-row helical** computed tomography (MDCT) **and 3 Tesla (T) MRI in the preoperative evaluation of the artery of Adamkiewicz (AKA) and its parent artery. Patients with thoracoabdominal vascular diseases underwent MDCT of the entire aorta and iliac arteries. Sub-millimeter collimation was used with the rapid injection of concentrated contrast material. The AKA and intercostal/lumbar arteries from which it originated were examined using multiplanar and curved planar reconstruction images and cine-mode display. The visualization of the AKA, as well as its branching level and site of origin, and the continuity of the intercostal/lumbar arteries with the AKA were investigated. 3T-MRA was also performed in patients whose AKA was difficult to visualize because of artifact from bony structures.**

In 90% of the patients the AKA was clearly visualized. The entire length from the trunk of the intercostal/lumbar arteries to the AKA, and finally to the anterior spinal artery could be traced using cine-mode display or on curved planar reconstruction images in 80%. These patients were treated by open surgical treatment based on a consideration of the vascular supply to the AKA or treated by stentgraft insertion. No postoperative ischemic spinal complications occurred in these patients except two. 3T-MRA increases success rate of visualizing AKA when used with MDCT. MDCT with Sub-millimeter collimation and a rapid injection protocol permits the evaluation of the AKA for its entire length and provides information on the intercostal and lumbar arteries and entire aorta. 3T-MRA has complementally role with MDCT.

Keywords — **Artery of Adamkiewicz, MDCT, Aortic dissection, Aortic aneurysm**

I. Introduction

Accurate localization of the artery of Adamkiewicz (AKA) is important in planning the surgical or interventional radiological treatment of patients with thoracoabdominal aortic disease. Preoperative information on the localization of this artery may reduce the risk of postoperative ischemic spinal complications (1–7). Although conventional angiography is reported to be useful (3–6), various complications of spinal angiography have been described (3,5). Noninvasive detection of the AKA using magnetic resonance imaging (MRI) and its usefulness for surgery has also been reported with a detectability of 69 to 84% (7,8,9). Due to the limited scanning field of view, however, MRI cannot demonstrate the entire aorta and intercostal and lumber arteries simultaneously with information on the AKA. Multidetector-row helical CT (MDCT) with a four-slice detector and 2-mm collimation has recently been reported to be effective in demonstrating the AKA (10), although that study did not focus on patients requiring an aortic vascular graft or stentgraft in the T8–T12 region, where the AKA likely originates and postoperative ischemic spinal complications are likely to occur. Moreover, no previous studies have included a radiological evaluation of the patency of the parent intercostal or lumbar arteries branches of the AKA, or the intercostal/lumbar arteries adjacent to the parent artery, which can provide collaterals to the AKA when needed.

Recently, MDCT with 8, 16, 32, or 64 detector rows has become available, permitting imaging of the entire aorta and iliac arteries with less than 1-mm collimation. This study evaluated the capacity of 16-slice MDCT with 0.5-mm collimation and a rapid injection protocol to evaluate the continuity of the AKA and its parent artery and to visualize the intercostals and lumbar arteries adjacent to the parent artery for preoperative evaluation of patients with thoracoabdominal aortic disease.

II. Materials and method

A. Patients

We performed a retrospective analysis of CT images from 36 consecutive patients (32 men, 4 women; mean age, 56.1 years; range, 34-77 years) with diagnosis of thoracic aortic aneurysm (14 patients) or aortic dissection (22 patients) including thoracoabdominal aorta, who underwent aortic replacement surgery (25 patients) or stentgraft insertion (11 patients). Informed consent for contrast-enhanced CT had been obtained from all patients before the examinations.

Chwee Teck Lim, James C.H. Goh (Eds.): ICBME 2008, Proceedings 23, pp. 2215–2218, 2009
www.springerlink.com

B. Radiological Imaging

The CT scanner was an Aquilion 16-detector row helical CT scanner (Toshiba, Tokyo, Japan). Scans were obtained with the following parameters: 0.5 second per rotation, 0.5 mm collimation. Patients were requested to hold their breath for approximately 20 seconds during the scanning followed by shallow breathing.

Before scanning was started, 130-150 ml of contrast material (Iopamiron, Schering, Berlin, Germany; 370 mgI/ml) was injected via an antecubital vein at a rate of 4.0-4.5 ml/s. If a suitable antecubital vein could not be found, the right external jugular vein was used for contrast injection. The scan delay was set using an automatic triggering system (SureStart, Toshiba Medical Systems). Continuous low-dose CT fluoroscopy (120 kV, 50 mA) at the level of the ascending aorta was initiated 10 s after the start of contrast injection. The CT value in a circular region of interest placed in the ascending aorta was measured 3 times per second, and when the CT value reached the threshold (absolute CT value of 85 Hounsfield Units) at 3 consecutive sampling points, helical scanning was started automatically.

Axial slices were reconstructed with a 0.5-mm slice thickness at 0.3-mm intervals. For the evaluation of the artery of Adamkiewicz, the reconstruction field of view was set to the area around the aorta and spine.

Images were processed using a stand-alone workstation (Zio M900 Quadra, Amin, Tokyo, Japan). Volume-rendering images of the entire aorta were routinely generated. Curved planar reconstruction (CPR) images were generated so that the anterior spinal artery, the artery of Adamkiewicz, and its parent artery could be traced over as long a distance as possible. 3T-MRA was also performed in patients whose AKA was difficult to visualize because of artifact from bony structures.

The following points were evaluated: 1. the side and level of the artery of Adamkiewicz; 2. the continuity of the artery of Adamkiewicz with the anterior spinal artery, the intercostal/lumbar arteries, and their posterior branches; 3. the patency of the intercostal/lumbar arteries branching from the artery of Adamkiewicz.

III. Results

In 33 of the 36 patients (91.7%), the artery of Adamkiewicz within the bony spinal canal was clearly delineated, permitting both the level of origin and the side of the artery to be identified (Figure 1). In 3 patients with a thoracic aortic aneurysm, the artery of Adamkiewicz was not visualized and enhancement of the anterior spinal artery was poor. The continuity over the entire length from the stem of the intercostal/lumbar arteries and their posterior branches, to the artery of Adamkiewicz, and finally to the anterior spinal artery could be traced in 29 of the 36 (80.1%) patients (Figure 1). In two of the remaining 7 patients, the continuity was visualized by MRI (Figure 2). In the remaining patient, continuity between the posterior branch of the intercostal / lumbar artery and the artery of Adamkiewicz could not be clearly visualized. In 13 patients the parent artery of AKA was occluded (Figure 3).



Figure 1. Three dimensional reconstruction of the artery of Adamkiewicz visualized by MDCT image. Curved planar image along the intercostal artery through anterior spinal artery clearly demonstrates the origin and anatomy of the artery of Adamkiewicz.

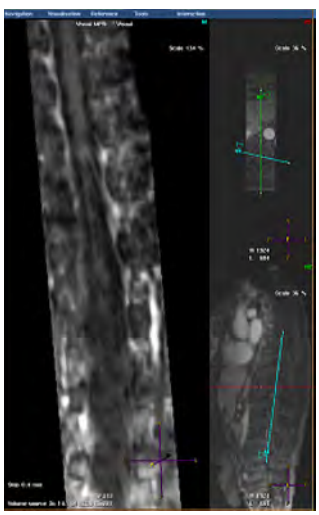


Figure 2. MRI image using Keyhole technique demonstrates the artery of Adamkiewicz and the anterior spinal artery. Because of the high temporal resolution, the artery of Adamkiewicz can be distinguished from the radiculomedullary vein.



Figure 3. Curved planar image along the intercostal artery through anterior spinal artery shows the intercostal artery, its posterior branch, the artery of Adamkiewicz and the anterior spinal artery. The origin of the intercostal artery is occluded due to thick mural thrombus of thoracoabdominal aortic aneurysm.



(a) (b)

Figure 4. MDCT after stentgraft insertion to thoracic aorta. (a): Stent graft can be seen from the aortic arch through the thoracoabdominal aorta by volume rendering image. (b): Curved planar reformation image shows the intercostal artery, its posterior branch, the artery of Adamkiewicz, and the anterior spinal artery. Although the origin of the intercostal artery is covered with the stentgraft, the blood flow to the spine is maintained by collateral circulation to these arteries.

In 25 patients who underwent aortic replacement surgery, intercostal arteries were reconstructed based on the information of CT localization of the artery of Adamkiewicz. Two patients with aortic dissection showed incomplete spinal complication.

Although the origin of AKA was completely coverd by stentgraft in 8 of the the 11 patients who underwent stentgraft insertion, no spinal complication was dedtected in the stent group. In these 8 patients, AKA was visualized by follow up CT after stentgraft insertion.(Figure 4)

The patency of the artery of Adamkiewicz from its origin through the anterior spinal artery can be diagnosed.

IV. Discussion

Sixteen-slice MD-CT with 0.5-mm collimation and a rapid injection protocol permitted the artery of Adamkiewicz to be visualized and also provided information concerning the adjacent intercostal/lumbar arteries. The continuity from the intercostal/lumbar arteries through the artery of Adamkiewicz could be traced in high percentage of the patients. Patients with aortic diseases involving the thoracoabdominal region typically present with stenosis or occlusion of the intercostal/lumbar arteries, and the parent arteries of the artery of Adamkiewicz (i.e., the intercostal/lumbar arteries) must therefore also be evaluated. Some patients were found to have occlusion of the intercostal/lumbar arteries at multiple levels in the region superior or inferior to the origin of the artery of Adamkiewicz. In the patients in the present study, the vascular supply to the artery of Adamkiewicz was thought to be highly dependent on collaterals. Concerning the patients who underwent stentgraft insertion, no patients had spinal complication after the procedure. Vascular supply to the spinal cord in these patients were thought to be maintained by collateral circulation.

Although MDCT permits visualization of AKA, continuity from the stem of the intercostal/lumbar arteries and their posterior branches, to the artery of AKA is sometimes difficult because of close approximation of the artery and the spine. In such cases, MRI plays an complementary role of MDCT.

Recently developed 3T-MRI will enable visualization of AKA with high temporal resolution permitting distinction between AKA and radiculomedullary vein. (Figure 2) In conclusion, MDCT with Sub-millimeter collimation and a rapid injection protocol permits the evaluation of the AKA for its entire length and provides information on the intercostal and lumbar arteries and entire aorta, which provides useful information for treatment of thoracoabdominal aortic diseases.

Reference

1. Svenson LG, Crawford ES. Cardiovascular and vascular disease of the aorta. Philadelphia: WB Saunders, 1997.
2. Svenson LG, Crawford ES, Hess KR, Cosseli JS, Safi HJ. Experience with 1509 patients undergoing thoracoabdominal aortic operations. J Vasc Surg 1993; 17:357–370.
3. Williams GM, Perler BA, Burdick JF, et al. Angiographic localization of spinal cord blood supply and its relationship to postoperative paraplegia. J Vasc Surg 1991; 13:23–33.
4. Fereshetian A, Kadir S, Kaufman SL, et al. Digital subtraction angiography in patients undergoing thoracic aneurysm surgery. Cardiovasc Intervent Radiol 1989; 12:7–9.
5. Savader SJ, Williams GM, Trerotola SO, et al. Preoperative spinal artery localization and its relationship to postoperative neurologic complications. Radiology 1993; 189:165–171.
6. Heinemann MK, Brassel F, Herzog T, Dresler C, Becker H, Borst HG. The role of spinal angiography in operations on the thoracic aorta: myth or reality? Ann Thorac Surg 1998; 65:346–351.
7. Hyodoh H, Kawaharada N, Akiba H, Tamakawa M, Hyodoh K, Fukada J, Morishita K, Hareyama M. Usefulness of preoperative detection of artery of Adamkiewicz with dynamic contrast-enhanced MR. Angiogr Radiol 2005; 236:1004–1009.
8. Yoshioka K, Niinuma H, Ohira A, et al. MR angiography and CT angiography of AKA: noninvasive preoperative assessment of thoracoabdominal aortic aneurysm. RadioGraphics 2003; 23:1215–1225.
9. Yamada N, Okita Y, Minatoya K, et al. Preoperative demonstration of the Adamkiewicz artery by magnetic resonance angiography in patients with descending or thoracoabdominal aortic aneurysms. Eur J Cardiothorac Surg 2000; 18:104–111.
10. Takase K, Sawamura Y, Igarashi K, et al. Demonstration of the artery of Adamkiewicz at multi-detector row helical CT. Radiology 2002; 223:39–45.

Development of a Haptic Sensor System for Monitoring Human Skin Conditions

D. Tsuchimi, T. Okuyama and M. Tanaka

Department of Biomedical Engineering, Tohoku University, Sendai, Japan

Abstract — **Human skin, which mainly consists of epidermis, dermis and hypodermis, is the largest organ of a human body. It has a lot of roles, for example, protection function, moisture maintenance function and sensory function. Moreover, it becomes a parameter for estimation of the health condition and beauty, because the skin is the outermost layer of a human body. At present, ocular inspection and palpation are generally used for detection of human skin condition such as surface appearance, and extensibility. Ocular inspection and palpation are important diagnosis procedures to examine patient's skin condition quickly. However, it is difficult to quantify an evaluation by these diagnosis procedures, because it is very subjective. A development of handy method in order to evaluate the skin condition objectively is craved to dermatologists, and cosmetic industries. So far, various methods of evaluating skin condition objectively have been developed. However, these methods are substitutions of ocular inspection, or only measure some specific physical parameters of skin such as elasticity.**

In this paper, the sensor that can measure various parts of human body in various conditions is developed. The polyvinylidene fluoride (PVDF) film, that is a kind of piezoelectric materials, is used as the sensory receptor in the sensor system. The functionality and signal processing of the sensor system are investigated by measurement of 15 kinds of artificial skin models, which are made of silicone rubber with different elasticity and roughness. Finally, the clinical test for human skin is conducted using the sensor system. Skin of medial forearm and base of thumb of 6 subjects are measured by the sensor. The obtained results show that two parameters calculated from the sensor output correspond to the subjective evaluations of extensibility and smoothness of the skin.

Keywords — **Haptic sensor, skin conditions, extensibility, smoothness, PVDF, signal processing.**

I. Introduction

Palpation is important for a clinician to diagnose a patient. A clinician assesses smoothness, softness, extensibility by palpation. But, this type of clinical assessment is very subjective; therefore, it is irreproducible from one clinician to another or even from time to time for the same clinician. Development of noninvasive technology in dermatology and cosmetology has advanced considerably for the past dozen years or so [1]. Concerning skin surface properties, some attempts were made by measuring skin friction coefficients [2, 3], image analysis [4] and fringe projection [5]. All these methods are useful to evaluate the skin surface properties, but their results cannot be compared with sensory evaluation by clinician.

Recently, Tanaka [6] and Tanaka et al. [7, 8] developed a haptic sensor for monitoring skin condition by using PVDF film as a sensory receptor. The sensor [7] is moved by hand over a skin with constant speed and force. But, an output of the sensor is greatly affected by a fluctuation of the scanning speed of the hand. In order to clear up this defect, a stepping motor is introduced to drive the sensor [8]. However, in return for stability of scanning speed, wide space to fix the sensor on the skin is needed. With this situation in mind, the authors have been developed a hand-manipulated haptic sensor system for monitoring skin conditions [9]. As a preliminary experiment, influence of scan speed on evaluating roughness of an object was investigated using the developed sensor system, and a fluctuation of the scan speed was compensated by signal processing.

In this paper, measurements of extensibility and smoothness of the object, which made of silicone rubber, was carried out using the hand-manipulated sensor system. Finally, extensibility and smoothness of the human skin were measured, and the results were compared with their sensory evaluation.

II. Sensor system

Geometry of the haptic sensor is presented on Fig. 1. A base of sensitive part is an acrylic plate. PVDF film and gauze were stacked in sequence. The PVDF film was covered with acetate film which protects the PVDF film against damage and water. The gauze improves sensitivity of the sensor. Guide roller was placed on both sides of the sensitive part to improve manipulation performance, and an encoder was mounted on it to measure sliding speed. Two strain gauges were attached to the chassis to measure forces applied to the sensitive part and guide roller.

In experiment, the sensor was contacted with a measurement object. Then the sensor slid over the surface of the object by hand in order to collect information about its extensibility and smoothness. Piezoelectric output of the PVDF film, output of strain gauges and output of encoder were digitized and stored into a digital oscilloscope. Signal processing for the obtained data was done in a personal computer. The experimental setup and measurement conditions are shown in Fig. 2 and Table 1, respectively.

Chwee Teck Lim, James C.H. Goh (Eds.): ICBME 2008, Proceedings 23, pp. 2219–2222, 2009
www.springerlink.com

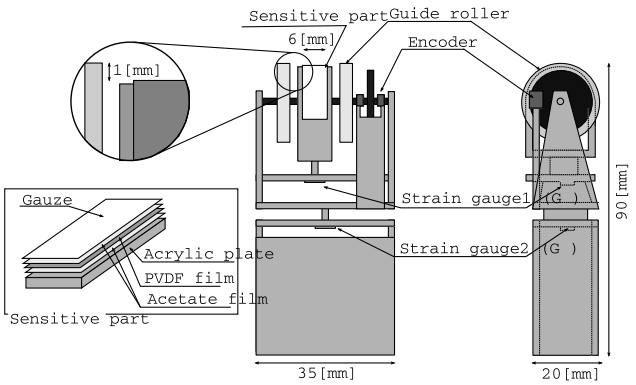


Fig. 1 Geometry of the sensor.

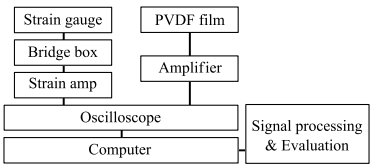


Fig. 2 Experimental setup.

Table 1 Measurement conditions.

Sampling frequency	5(kHz)
Measurement term	2(s)
Contact force	0.4(N)
Scanning speed	40(mm/s)

III. Evaluation Experiment

An Evaluation experiment was carried out using skin model made of silicone rubber. And the effectiveness of the sensor system in evaluation of extensibility and smoothness was testified.

Measurement object was shown in Fig. 3. It was made up of two layers. E layer was thin silicone rubber; surface geometry of an abrasive paper was printed on its surface. It prepared 15 types: they were combination of Young's modulus and maximum grain size of printed abrasive paper. H layer was thick and soft silicone rubber. Properties of each layer are shown in Table 2. Additionally, thickness and Young's modulus of each layer referred from epidermis and hypodermis of human skin [10, 11, 12].

The measurement object was fixed on a stage. The sensor was contacted with the E layer of the measurement object, and the sensor slid over the surface of the object by hand. The sensor scanned 5 times per object.

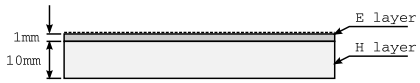


Fig. 3 The measurement object.

Table 2 Properties of measurement object.

Layer	Thickness	Young's modulus	MGS*
E layer	1(mm)	$1.0*10^{-1}$ (MPa)	40(μm)
		$1.0*10^{-1}$ (MPa)	60(μm)
		$2.9*10^{-1}$ (MPa)	70(μm)
			80(μm)
			100(μm)
H layer	10(mm)	$3.7*10^{-2}$ (MPa)	-

*MGS: Maximum grain size of printed abrasive paper.

Extensibility of the object was evaluated using outputs of two strain gauges (G_1 and G_2). The output of G_1 arose from a contact force applied on the sensitive part (F_{sens}), and the output of G_2 arose from a contact force applied on the sensitive part and guide rollers (F_{all}). Moreover, there was 1mm step between the sensitive part and the guide roller as shown in Fig. 1. Therefore the difference between outputs of G_1 and G_2 were influenced by extensibility of the measured object. A relationship of F_{sens} and F_{all} is written as:

$$k = \frac{F_{all} - 2F_{sens}}{d} \tag{1}$$

Here, d is 1mm step between the sensitive part and the guide roller, and k is compound constant of spring of the measured object. Fig. 4 shows the relationship between the k and the Young's modulus of the E layer. The values of the k are found to be proportional to the Young's modulus of the measured object. The outputs of strain gauges when the sensor contacted with the measurement object was used to analysis. Correlation coefficient between the k and the Young's modulus was 0.99.

Smoothness of the object was evaluated using the outputs of the sensor. The outputs attributed to contact between the measured object and the gauze attached on the surface of

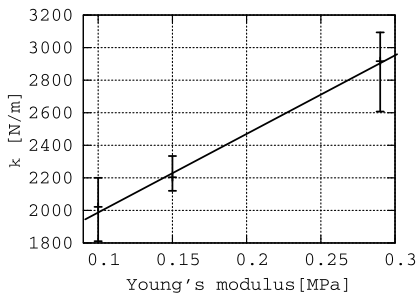


Fig. 4 k vs. Young's modulus of E layer.

the sensor. Therefore, frequency property of the sensor output was affected by the scan speed of the sensor, roughness of the surface of the sensor and the measured object. In addition, it was found that variance of the sensor output is associated with the roughness of measured object [13]. Therefore, the sensor output was divided into 6 parts according to wavelet multiresolution decomposition. Divided frequency ranges of the sensor output are shown in Table 3. Variances of the divided sensor outputs were calculated. As a result, it was found that the variances of level 4 to 6 waves had strong correlation with smoothness of the E layer of the measured objects, and correlation coefficients were 0.86 to 0.92. The variance of the level 6 wave had the strongest correlation especially. Fig. 5 shows a relationship between the variance of level 6 wave and maximum grain size of abrasive paper printed on the E layer. In this figure, gradients of these graphs come under the influence of extensibility of the measured object, but the extensibility can be evaluated by strain gauzes outputs, therefore the smoothness of the measured object can be evaluated except the influence of extensibility.

IV. Clinical Test

The present sensor system and signal processing were applied to a clinical test of human skin. The developed sensor was used to scan skin surfaces of 6 people (young male with healthy skin; their average age is 24). Scan regions were base of thumb and medial side of forearm of a nondominant hand. Results of the sensor output were compared with a result of subjective evaluation. In the subjective evaluation, an evaluator scored both extensibility and smoothness of skins according to five-grade evaluation (−2, −1, 0, 1, 2). Measurement conditions using the sensor system are shown in Table 4. The base of thumb and the medial side of forearm had curved surfaces; therefore, measurement term was shorten to 0.2(s), and sampling frequency was set to 50(kHz) for precision enhancement.

The results of the subjective evaluation and typical output signal from the sensor are presented in Table 5 and Fig. 6, respectively.

About extensibility evaluation, it was found that the results of the subjective evaluation and the strain gauge outputs showed the same tendency, and correlation coefficient between the results of the subjective evaluation and the k was 0.69 at medial side of forearm and 0.76 at base of thumb. Relationships between the results of subjective evaluation and k are shown in Fig. 7.

Next, about smoothness evaluation, because the obtained data contained the sensor output before the sensor sliding,

Table 3 Frequency ranges divided by wavelet multiresolution decomposition.

Decompose Level	1	2	3	4	5	6
Freq.(kHz)	2,500-1,250	1,250-625	625-320	320-160	160-80	80-40

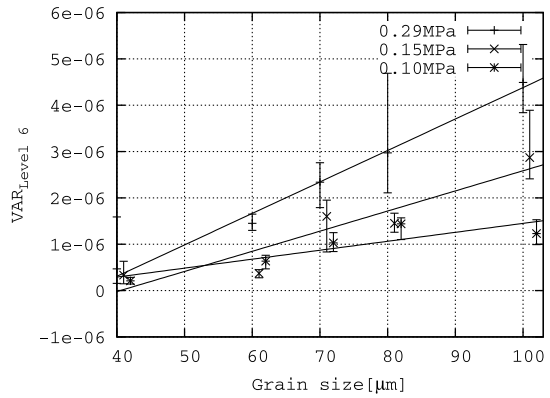


Fig. 5 Variance (*VAR*) of the level 6 wave vs. roughness of the surface of measured object. Legends on this graph are hardness of E layer.

Table 4 Measurement conditions.

Sampling frequency	50(kHz)
Measurement term	0.2(s)
Contact force	0.4(N)
Scanning speed	40(mm/s)

Table 5 Results of subjective evaluation. In this table, value "-2" is smooth/soft, and value "2" is rough/hard.

	Forearm		Base of thumb	
Subject No.	Roughness	Hardness	Roughness	Hardness
1	1	0	1	-1
2	0	0	0	1
3	2	-1	1	-1
4	-1	2	-1	1
5	-1	-1	2	1
6	-2	1	0	0

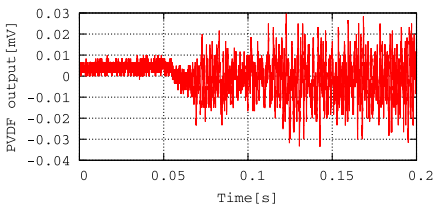
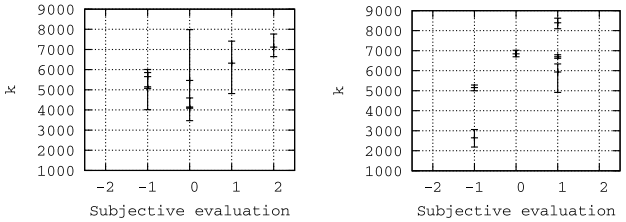


Fig. 6 Typical sensor output (forearm).



(a) Medial side of forearm. . (b) Base of thumb.

Fig. 7 Relationships between the result of the subjective evaluation and *k*. (a) at medial side of forearm, and (b) at base of thumb.

Table 6 Correlation coefficients between the results of subjective evaluation and variances of sensor outputs.

	Decompose level			
	3	4	5	6
Medial side of forearm	0.86	0.74	0.73	0.64
Base of thumb	0.80	0.76	0.78	0.91

second-half of sensor output was used for analysis of smoothness. As a result, the results of the subjective evaluation and variances of sensor outputs showed the same tendency. Correlation coefficients between the results of subjective evaluation and variances of the sensor outputs are shown in Table 6.

In this table, the correlation coefficient of medial side of forearm peaks at level 3, and one of base of thumb peaks at level 6. The variances of the sensor outputs are attributed to roughness of surface of a measured object. A crista cutis in base of thumb is larger than one in medial side of forearm; therefore, the correlation coefficient of medial side of forearm peaks at lower decompose level than one of base of thumb.

V. Conclusions

The haptic sensation system was designed using PVDF film as a sensory receptor. The effectiveness of the sensor system for monitoring skin conditions was investigated. The PVDF output, the contact force and the scan speed were obtained. Measurement of skin model made of silicone rubber was undertaken, and the sensor output was compared with extensibility/smoothness of measured object. Finally, the sensor system was applied to the clinical test of skin conditions. The results can be summarized as follows:

1. In experiment using skin model, extensibility of measured object can be evaluated with outputs of two strain gauges attached to the sensor, and smoothness can also be evaluated with variance of calculated sensor output.
2. In clinical test, the two indexes obtained from the haptic sensor system have good correlation with subjective assessments of the human skin conditions.

Acknowledgment

The authors acknowledge the support of Tohoku University Global COE Program 'Global Nano-Biomedical Engineering Education and Research Network Centre'.

References

1. H. Tagami, Perspective and prospective views of bioengineering of the skin, Fragrance J. 10, (1993), 11-15.
2. M. Egawa, M. Oguri, T. Hirao, M. Takahashi, M. Miyakawa, The evaluation of skin friction using a frictional feel analyzer, Skin Res. Technol. 8, (2002), 41-51.
3. A.A. Koudine, M. Barquins, Ph. Anthoine, L. Aubert, J.L. Leveque, Frictional properties of skin: proposal of a new approach, Int. J. Cosmet. Sci. 22, (2000), 11-20.
4. P. Corcuff, J.L. Leveque, Skin surface replica image, in: J. Serup, G.B.E. Jemec (Eds.), Analysis of Furrows and Wrinkles: Handbook of Non-Invasive Methods and the Skin, CRC Press, (1995), 89-96.
5. M. Rohr, K. Schrader, Topometry of human skin (FOITS), SOFW J. 2, (1998), 52-59.
6. M. Tanaka, Development of tactile sensor for monitoring skin conditions, J. Mater. Process. Technol. 108, (2001), 253-256.
7. M. Tanaka, J.L. Leveque, H. Tagami, K. Kikuchi, S. Chonan, The "Haptic Finger"- a new device for monitoring skin condition, Skin Res. Technol. 9, (2003), 131-136.
8. M. Tanaka, H. Sugiura, J.L. Leveque, H. Tagami, K. Kikuchi and S. Chonan, Active haptic sensation for monitoring skin conditions, J. Mater. Process. Technol. 161, (2005), 199-203.
9. D. Tsuchimi, T. Okuyama, M. Tanaka, Development of a Haptic Sensor System for Monitoring Human Skin Conditions (in Japanese), Proc. The 20th Symposium on Electromagnetics and Dynamics, (2008), 493-496.
10. S. W. Jacob and C. A. Francone. *Structure and Function in Man*. Saunders Philadelphia, (1974).
11. Ikohagi Toshiaki. *Basic of Pressure Instrumentation of PVDF*, JSME, Tokyo, (1994).
12. T. Maeno, K. Kobayashi, and N. Yamazaki. Relationship between the structure of human finger tissue and the location of tactile receptors. *Bulletin of JSME International Journal*, Vol. 41, No. 1C, (1998), 94–100.
13. Mami Tanaka, Jun Hiraizumi, Jean Luc Leveque, Seiji Chonan, Haptic sensor for monitoring skin conditions, International Journal of Applied Electromagnetics and Mechanics, 14, (2002), 397-404.

Fabrication of Transparent Arteriole Membrane Models

Takuma Nakano*, Keisuke Yoshida*, Seiichi Ikeda**, Hiroyuki Oura**, Toshio Fukuda**, Takehisa Matsuda***, Makoto Negoro**** and Fumihito Arai*

* Department of Bioengineering and Robotics, Tohoku University
6-6-01 Aramaki-Aoba, Aoba-ku, Sendai 980-8579, JAPAN
** Department of Micro-Nano Systems Engineering, Nagoya University
Furo-cho, Chikusa-ku, Nagoya, 464-8603, JAPAN
*** Kanazawa Institute of Technology
7-1 Ohgigaoka, Nonoichi, 921 - 8501, JAPAN
**** Fujita Health University
1-98 Dengakugakubo, Kutsukake-cho, Toyoake, 470-1192, JAPAN

Abstract — **We made transparent arteriole membranous models by using grayscale lithography. We employed a sacrificial model made of WAX and PVA mixture as a novel molding material. Our goal is to complement previous surgical simulators for practice and rehearsal of medical treatments. Since block vessel models cannot recreate moderate compliance which is similar to that of the real blood vessel, here we propose fabrication method for transparent arteriole membranous model which has circular cross section smaller than 500 μm in diameter. Fabrication method of the model as well as evaluation result of the molding material is reported.**

Keywords — **photolithography, blood vessel model, surgical simulator**

I. Introduction

In the tissue engineering field, many engineered approaches have been studied, including artificial hearts, artificial joints and synthetic vascular prostheses [1,2]. We have been developing the three-dimensional(3D) elastic membranous blood vessel models in tailor-made by using 3D WAX models [3,4]. We have been developing a surgical simulator by connecting the elastic membranous models (Fig.1.). Surgical simulators are used in practice and rehearsal for catheter treatments and new treatment methods by doctors. Meanwhile, we constructed a pulsatile pump which can reproduce patient-specific pulsative blood streaming obtained by ultrasonic measurement or other modalities, connected it to the aorta model and reproduced human-like pulsatile blood streaming inside the simulator (vascular model can reproduce vascular pulsation with the streaming.).

This surgical simulator's model is bigger than 500 μm in diameter because of brittleness of WAX. Blood vessel models smaller than 500 μm in diameter are needed to simulate more similar vessel environment.



Fig. 1 Surgical simulator for endovascular neurosugery, which allows evaluating stress condition on arterial structure applied with surgical operation and blood streaming, using photoelastic modality.

There are diseases in under Φ500 μm blood vessels, such as arteria basilaris, but previous surgical simulator is not applicable for rehearsal and training of these diseases. Therefore, surgical simulator with Φ10 - 500 μm arteriole and capillary vessel models are needed. We have been designed arteriole and capillary vessel models shown in Fig.2, and fabricated by using photolithography [5-7].

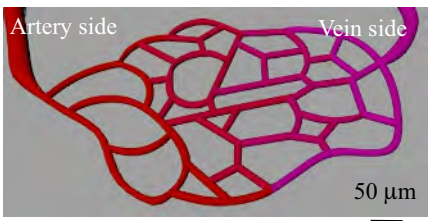


Fig. 2 Designed arteriole and capillary vessel model.

Figure 3 shows multiscale fabrication methods of blood vessel models. We used over exposure method, reflow method, gray-scale lithography, and layer stack molding machine. In these processes, photolithography process such as over exposure method, reflow method, gray-scale lithog-

Chwee Teck Lim, James C.H. Goh (Eds.): ICBME 2008, Proceedings 23, pp. 2223–2227, 2009
www.springerlink.com

raphy are used for fine structure. Because of a limit of fabrication accuracy, it is necessary to choose an appropriate method to fabricate a model with aimed diameter. After exposure, fabricated photoresist patterns are transcribed onto poly(dimethylsiloxane) (PDMS). Arteriole and capillary vessel block models with circular cross section are completed by bonding two patterned PDMS substrates using plasma treatment and heating process (Fig.4.).

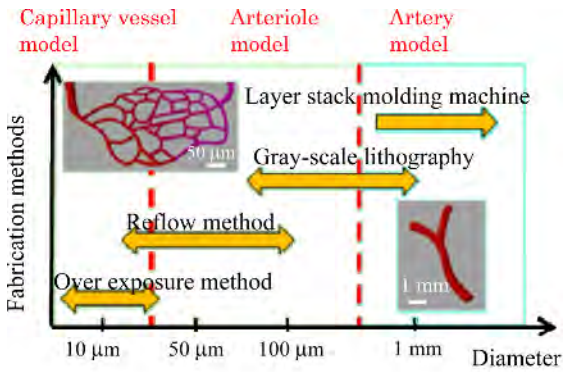


Fig. 3 Fabrication methods for multiscale blood vessel models.

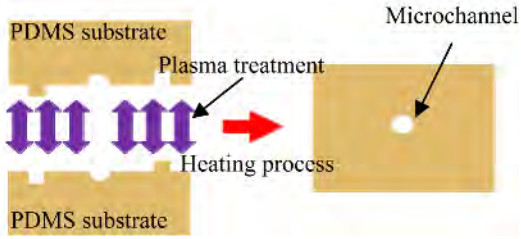


Fig. 4 Concept of making capillary vessel model. After plasma treatment, we align two patterned PDMS substrates and bond by heating to complete blood vessel model.

However, block models cannot recreate moderate compliance which is similar to that of the real blood vessel [8-10]. To solve this problem, we think arteriole and capillary vessel membrane models are needed for surgical simulator. And, sacrificial models are needed to make membrane models. But because of brittleness of WAX, we could not make sacrificial models by using layer stack molding machine as previous fabrication method.

In this paper, we propose a novel fabrication method for transparent arteriole membranous models. We tried to improve the brittleness of WAX by mixing WAX with PVA (polyvinyl alcohol). After making sacrificial models made of mixture material, arteriole membranous models were completed by dip coating. Merits of making membranous models smaller than Φ500 μm for surgical simulator are (1) enabling to target blood vessel diseases on about Φ100 μm blood vessel as arteria basilaris and (2) enabling to make a surgical simulator with high precision. Here, we report fabrication method and results of fabricated arteriole membranous model as well as evaluation of the molding material (WAX and PVA mixture material).

II. Evaluation of WAX + PVA Mixture Material

In this fabrication process, WAX and PVA mixture material is used to build sacrificial models. These models are very useful for fabricating membrane models smaller than 500 μm in diameter. If we used only WAX for making sacrificial models, the temperature is needed to control. And WAX is not suitable to this fabrication process because of WAX's fragility. If we used only PVA for making sacrificial models, PVA model is deformed easily by model's own weight when dip coating, since it has low bend strength. Therefore, we proposed the method of fabricating sacrificial models with WAX and PVA mixture material. We can easily forecast the mixture has the properties of both WAX and PVA. We evaluated the properties of mixture by changing the mix ratio. Evaluated properties are Young's modulus as mechanical property and melting time of mixture material in different liquid (solubility) as chemical property. We evaluated samples made by different mix ratio (mix ratio WAX : PVA = 1:0, 1:4, 2:3, 3:2, 4:1, 0:1).

A. Evaluation of mechanical property (Young's modulus)

Tensile tester is used for evaluation experiments of Young's modulus. Samples made by WAX and PVA mixture material are made 50 mm × 10 mm × 2 mm (long × wide × thick) in size. After finishing this experiment, we plotted the load-displacement curve. We did the tensile experiment for three times for each WAX and PVA mix ratio. Using these curve data, we calculated the Young's modulus. Young's modulus of each mix ratio is calculated by averaging the experimental results. Table 1 shows Young's modulus by each mix ratio. Young's modulus of PVA is 9.57 MPa. On the other hand, Young's modulus of WAX is 20.6 MPa. We observed Young's modulus of mixture material is getting higher by increasing the ratio of WAX. And, Table 2 shows extension. Extension is expression of material's brittleness and ductibility. We observed extension of mixture material is getting higher by increasing the ration of PVA. Therefore, we can control the mechanical property of WAX and PVA mixture material by changing mix ratio.

Table 1 Experimental rigidity

PVA:WAX ratio[%]	Young's modulus [MPa]
1:0	9.57
4:1	9.69
3:2	8.78
2:3	15.7
1:4	22.8
0:1	20.6

Table 2 Experimental extension

PVA:WAX ratio[%]	Extension [%]
1:0	75
4:1	75
3:2	75
2:3	44
1:4	4.0
0:1	6.0

B. Evaluation of chemical property (solubility)

We observed melting time of each different ratio mixture materials in different liquid by checking mass changes. We defined solubility of each mix ratio from experiment. We used ultrasound bath set at 50 temperatures for solubility experiments. We provided DI water, acetone, and DI water + acetone liquid mixture for melting. DI water easily melts PVA. Acetone easily melts WAX. We provided liquid mixture of 1:1 mix ratio, since melting samples was WAX and PVA mixture material. The liquid was used in the melting experiments. Figure 5 shows the experimental results of observing solubility of each sample in DI water and acetone liquid mixture. Because of DI water's feature, mixture material samples were melted easily. In this result, we looked mass changes of the WAX sample. This is caused by heating in the process of ultrasound bath and etching effects. We looked acetone melted few mixture material in this experiment, although acetone can melt WAX easily. It happened since WAX was coated with PVA, and acetone could not reach WAX. On the other hand, we forecasted that mixture material is melted by liquid mixture. We verified it by experiment. Comparing these results, all mixture materials cloud be melted in DI water and acetone liquid mixture, however, solution rate was decreasing. We observed PVA absorbed DI water and increased mass when experiments started. These results suggest DI water and acetone liquid mixture is suitable to melt WAX and PVA mixture material.

III. Fabrication of Arteriole Membrane Models

Since WAX is fragile, we adopted mixture of WAX and PVA as a material of sacrificial model, which has higher rigidity than WAX. In fabrication processes of membrane models, we made model patterns by grayscale lithography and transcribed the resist patterns onto PDMS. We provided and aligned two patterned PDMS substrates filled with WAX and PVA mixture material on patterned side, and dried at room temperature. We completed sacrificial models for making membranous blood vessel model. This sacrificial model was coated with PVA for smoothing the surface and later coated with transparent silicone resin by dip coating for membranous structure. After dip coating, sacrificial model and PVA for smoothing were dissolved by DI water and acetone, and we got transparent arteriole membrane models. Figure 6 shows Φ500 μm arteriole membranous model made by these processes. The fabricated model had circular cross-section.

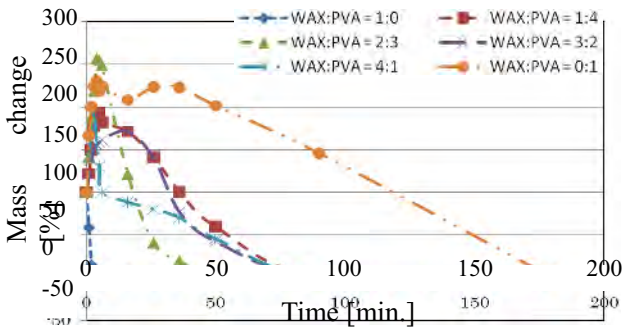


Fig. 5 Evaluation of chemical features in acetone + DI water.

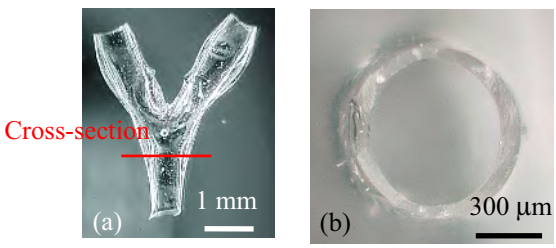


Fig. 6 Φ500 μm arteriole membrane model made by using WAX and PVA mixture material and grayscale lithography. (a)fabricated arteriole membrane model. (b)cross-section of fabricated arteriole membrane model.

A. Fabrication process of sacrificial models

For fabricating arteriole membrane models, sacrificial models as molds for dip coating of PVA and silicone resin are needed. We fabricated sacrificial models with this WAX and PVA mixture. Patterned PDMS substrates were made by grayscale lithography with nega-photoresists and transcribing the resist patterns onto PDMS for molding sacrificial models. Fabrication process flow is following.

(a) Grayscale lithography process.

1. Coating photoresist on glass substrate.
2. Exposure with the best exposure condition.
3. Development with the best time.
4. Transcribing the resist patterns onto PDMS.

(b) Fabrication process of sacrificial models.

1. Coating WAX and PVA mixture material on patterned side of PDMS substrate.
2. Splitting and removing superfluous mixture.
3. Aligning and bonding two patterned PDMS substrates filled with mixture on patterned side.
4. After drying at room temperature, removing the PDMS substrates and completing sacrificial models
5. Removing mixture stacking on the sacrificial models

B. Fabrication process of membrane models

We fabricated arteriole membrane models by using the sacrificial models. This sacrificial model was coated with PVA for smoothing the surface and later coated with transparent silicone resin for membranous structure by dip coating based on previous method. After dip coating, sacrificial model and PVA for smoothing were dissolved by DI water and acetone, and we got transparent arteriole membrane models. Fabrication process flow is following.

1. Dip coating the sacrificial models with 10wt% PVA solution for smoothing the surface.
2. After drying PVA, dip coating the sacrificial models coated with PVA with silicone resin.
3. Dissolving sacrificial models and PVA for smoothing by DI water and acetone liquid mixture.
4. Drying membranous silicone structures and completing blood vessel membrane models.

Figure 6 shows fabricated arteriole membrane model. We observed the membranous and hollow structure. This arteriole membrane model had circular cross-section shown in Fig.6(b). Circularity of inside of the membrane model was calculated by dividing the shortest axis by the longest axis. Using this expression, calculated circularity of this model was 90%.

IV. Conclusion

In this paper, we proposed fabrication method of Φ100 - 500 μm arteriole membrane models for surgical simulator. These blood vessel models are fabricated for connection to the previous surgical simulators. These membrane models will make surgical simulator enable to rehearse and train treatments for diseases at Φ100 - 500 μm blood vessels, and enable to make surgical simulator with high precision. We reported fabrication method of arteriole membranous model as well as evaluation of the molding material (WAX and PVA mixture material). We made arteriole membrane models by using grayscale lithography and WAX and PVA mixture material. It is very important to use WAX and PVA mixture material. We evaluated mechanical and chemical properties of WAX and PVA mixture material. We observed Young's modulus of mixture material is getting higher by increasing the ratio of WAX. In addition, we observed mixture's extension is getting higher by increasing the ratio of PVA in it. We observed DI water and acetone liquid mixture is most effective for melting WAX and PVA mixture material. Based on the proposed approach, we overcame the brittleness of the previous sacrificial model.

Finally, we succeeded in making the membranous and hollow structural arteriole model. This arteriole membrane model had circular cross-section inside the channel, and circularity of this channel was 90%.

In the future, we plan to improve our model by (1) matching moderate compliance which is similar to that of the real blood vessel, (2) making complicated membrane models and (3) checking durability and reliability of these models as a surgical simulator. We also plan to complete arteriole and capillary vessel network models by connecting each element.

Acknowlegements

This work was supported by a Grant-in-Aid for Scientific Research from the Ministry of Education, Culture, Sports, Science, and Technology of Japan (No.17076015, No.18206027), and Global COE Program, "Global Nano-Biomedical Engineering Education and Research Network Centre".

References

1. Griffith LG et al. (2002) Tissue Enginering—Current Challenges and Expanding Opportunities. *Science* **295**:1009-1014.
2. Langer R and Vacanti JP. (1993) Tissue Engineering. *Science* **260**:920-926.

3. Ikeda S, Arai F, Fukuda T et al. (2005-6) An In Vitro Patient-Tailored Biological Model of Cerebral Artery Reproduced with Membranous Configuration for Simulating Endovascular Intervention. *Journal of Robotics and Mechatronics* **17**, **3**:327-334.
4. Ikeda S, Arai F, Fukuda T et al. (2005) An In Vitro Patient-Tailored Model of Human Cerebral Artery for Simulating Endovascular Intervention. *In Proceedings of MICCAI 2005, LNCS 3749*, USA, 2005, pp 925-932.
5. Futai N, Gu W and Takayama S. (2004) Rapid Prototyping of Microstructures eith Bell-Shaped Cross-Sections and Its Application to Deformation-Based Microfluidic Valves. *Adv. Mater* **16**, **15**:1320-1323.
6. Borenstein JT, Terai H, King KR et al. (2002) Microfabrication Technology for Vascularized Tissue Engineering. *Biomedical Microdevices* **4**, **3**:167-175.
7. Ikeuchi M and Ikuta K. (2006) THE MEMBRANE MICRO EMBOSS (MeME) PROCESS FOR FABRICATING 3-D MICROFLUIDIC DEVICE FORMED FROM THIN POLYMER MEMBRANE. *In Proceedings of μTAS 2006*, pp 693-695.
8. Nakano T, Tada M, Lin YC et al. (2006) Fabrication of cell-adhesion surface and Capillary Vessel Model by photolithography. *In Proceedings of International Symposium on Micro- NanoMechatronics and Human Science*, Nagoya, 2006, 17 (1) - (6).
9. Arai F, Nakano T et al. (2007) Fabrication of cell-adhesion surface and Arteriole Model by photolithography. *Journal of Robotics and Mechatronics* **19**, **5**:535-543.
10. Nakano T, Yoshida K et al. (2008) Fabrication of Capillary Vessel Model with Circular Cross-Section and Applications. *In Proceedings of 2008 JSME Conf. on Robotics and Mechatronics (ROBOMECH2008)*, Nagano, 2008, 2P2-J17 (in Japanese).

Takuma Nakano is with the department of Bioengineering
and Robotics, Tohoku University,
6-6-01 Aramaki-Aoba, Aoba-ku,
Sendai 980-8579 Japan
(e-mail: nakano@imech.mech.tohoku.ac.jp).

Normal Brain Aging and its Risk Factors – Analysis of Brain Magnetic Resonance Image (MRI) Database of Healthy Japanese Subjects

H. Fukuda[1], Y. Taki[1], K. Sato[1], S. Kinomura[1], R. Goteau[1], R. Kawashima[2]

[1]Department of Nuclear Medicine and Radiology, and [2]Department of Neuroimaging,
Institute of Development, Aging and Cancer (IDAC), Tohoku University, Sendai, Japan

Abstract — **We collected brain MRI of 2,000 healthy Japanese subjects and constructed an MRI database together with their characteristics such as age, sex, present and past disease history and cognitive functions. Volumetric analysis of the brain revealed that gray matter volume linearly decreased with time, while white matter volume remained relatively unchanged during aging. We defined a standard brain for each age group and sex, which is a brain having gray matter volume on the regression line for the gray matter loss with age. This is a first objective criterion for standard brain for his/her age. Then, we performed longitudinal study in the same subjects with 8 years interval. The analyses revealed that there are sex difference in speed and pattern of gray matter loss with aging. Gray matter loss with aging was slower in women that that in men.**

Voxel based morphometry (VBM) was performed to investigate correlation between regional gray matter volume and characteristics of the subject, such as cerebro-vascular risk factors, scores of cognitive and memory functions, and mental status. These attributes were used as dependent variables, and regional gray matter volume as an independent variable. The correlation analyses revealed that there were negative correlations between gray matter volume and hypertension, lifetime alcohol intake, obesity.

To clarify clinical significance of ischemic lesion in the white matter on T2-weighted brain MRI, we developed an algorism for automatic detection of the ischemic lesions. Using this system, we made probabilistic map of the lesion for each subject and the probabilistic maps for age of 40^{th}, 50^{th}, $.60^{th}$ and 70^{th}, by simply averaging the data belonging to the age group. The lesion map revealed that ischemic lesion localized mainly around the ventricle and total lesion volume increased with increasing of age.

Keywords — **Brain aging, Magnetic Resonance Image (MRI), database, Volumetry.**

I. Introduction

Recently, the importance of human neuroimaging database was recognized greatly. The most important purpose and needs for database are electronic data sharing in neuroscience community as well as the construction of more sophisticated and complete model of brain structure and function. This model of normal brain structure and function can be used as the references not only for neuroimaging study for humans but also for computer aided automated diagnosis of the brain diseases.

Most remarkable recently developed method for brain image analysis is a voxel based morphometry (VBM). It includes anatomical standardization of the brain to a standard brain, brain tissue classification, and finally voxel based statistical analysis based on general linear model. This technique enables us to extract brain regions which show correlations between tissue volume and variables, such as age, sex and subject's characteristics. We can analyze not only age-related normal changes but also diseased brain, such as dementia. It has been believed that functional imaging precede structural imaging to detect early pathological findings of the diseases. However, recent the high resolution structural imaging and sophisticated analytical technique enable us to detect the brain diseases at very early stage.

We have collected 2,000 brain MRI of healthy Japanese and constructed an MRI database together with their characteristics such as age, sex, blood pressure, present and past disease history and cognitive functions [1] (Fig. 1). This is a largest database in Japan and one of the largest one in the world. Using this MRI database, we measured brain volume of different tissue segment, evaluated age-related volume changes and the correlation between regional brain volume and risk factors for cerebro-vascular atherosclerosis.

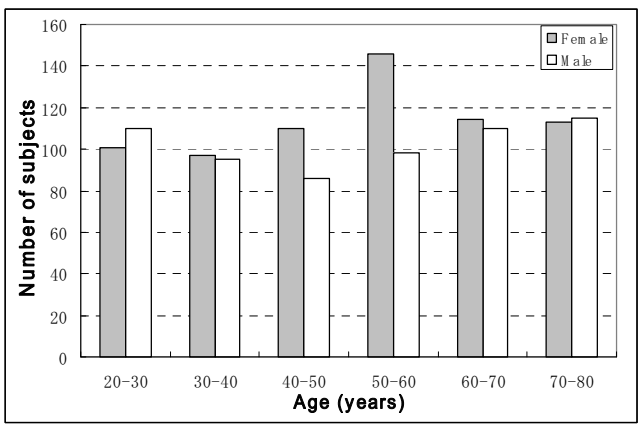


Fig. 1 Number of subjects for each age group and sex in brain MRI database

Chwee Teck Lim, James C.H. Goh (Eds.): ICBME 2008, Proceedings 23, pp. 2228–2231, 2009
www.springerlink.com

II. Materials and Method

A. Subjects

In this study, we analyzed 860 men and 840 women. Their age and characteristics are described in Table 1.

Table 1 Description of the subjects

	Men (n=860)	Women (n=840)
Age	44.5±17.8	47.6±15.1
Body mass index	23.4 ± 3.2	22.4 ± 3.1
Systolic blood pressure (mmHg)	129.5±16.5	125.7±18.2
Diastolic blood pressure (mmHg)	78.6±11.2	75.1 ± 11.9
Smoking habit (%)	62	17.1
Drinking habit (%)	91	65.4
Hypertension (%)	15.4	11.3
Diabetes mellitus (%)	4.3	2.1
Hypercholesterolemia (%)	7.2	12.1
Ischemic heart disease (%)	2.3	1.3

B. Image processing and statistical analysis using VBM

All the brains with different size and shape were transferred into a standard stereo-tactic space (Talairach space) and their size and shape were transformed into a standard template brain using liner and non-linear parameters (anatomical standardization). Next step is brain tissue segmentation. A brain images were segmented into gray matter, white matter, cerebrospinal fluid space (CSF) and outer brain space depending on the differences of signal intensities on T1 weighted MRI of each tissue (Fig. 2). The voxel values of each segmented image consisted f 256 grade signal intensities according to their tissue probability. The volumes of each tissue segment were calculated by summing up the value of all the voxels which belong to each tissue segment.

The standardized and segmented gray matter images were smoothed by convoluting a 12-mm-FWHM isotropic Gaussian kernel. Then, the smoothed gray matter images were statistically analyzed by voxel based morphometry (VBM) technique using SPM2 package (Fig. 2). VBM was performed to investigate correlation between regional gray matter volume and attributes to the subject, such as age, cerebrovascular risk factors, and scores of cognitive functions. This approach is not biased toward any one brain region and permits the identification of unsuspected potential brain structural abnormalities. Simple or multiple regression analysis was performed using SPM2. These attributes were used as dependent variables, and regional gray matter volume as an independent variable. We set the significance level at $P<0.05$ for multiple comparison. The method is a voxel based t-statistics extended to the three dimensional space based on the general linear model. Simple or multiple regression analysis and group comparison using t-test were performed.

C. Volume measurement of ischemic change

White matter hyper-intensities (WMH) on T2 weighted MR images (T2WI) are known as ischemic changes and frequently observed in elderly people. The changes are related not only to age but also to cerebrovascular risk factors, such as hypertension. However, the clinical significance of the changes in the healthy, neurologically non-diseased elderly people has not been clarified yet. Moreover, the WMH on T2WI are usually rated subjectively by radiologists and it is subject depends on the skill and condition of rater. We have developed an algorism for automatic detection and quantification of WHM using artificial neural network which can classify the brain into different tissue compartments [2].

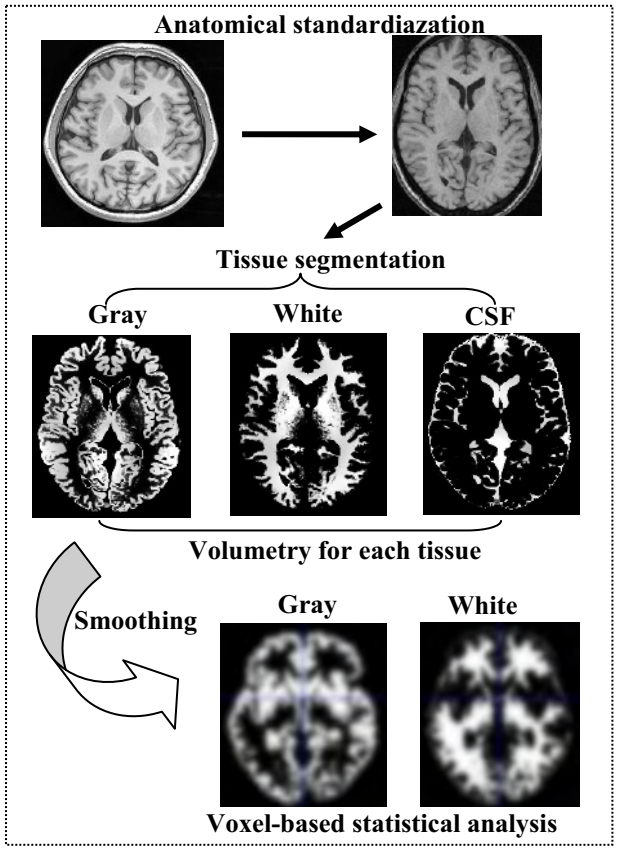


Fig. 2 Anatomical standardization, tissue segmentation of the brain MRI and statistical analyses

III. Results and Discussion

A. Brain volume change during aging

Figure 3 shows brain volume change with age in each tissue segment. Volume of each tissue segment was expressed as the ratio to whole brain volume. Gray matter ratio, which is the gray matter volume divided by whole brain volume, linearly decreased with age. White matter ratio slightly increased in younger age and remained unchanged during aging. However, there was no significant volume change with age. CSF volume ratio increased with age [3] (Fig. 3), in particular later age.

Gray matter ratio decreased linearly with age. Therefore, a brain with mean gray matter ratio can be a representative brain for the age group. We calculated regression line for the gray matter ratio change with age. We defined "a normally aged brain for his/her age", which is a brain with gray matter ratio on the regression line (Fig. 3). This is a first objective criterion for normally aged brain. We determined the normal range of the gray matter ratio as the value within ± 2SD from the mean value on the regression line.

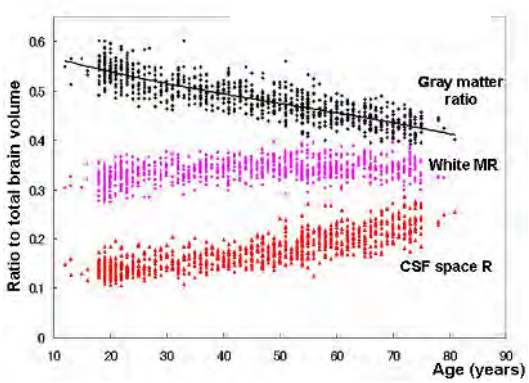


Fig. 3 Age-related volume change of the human brain

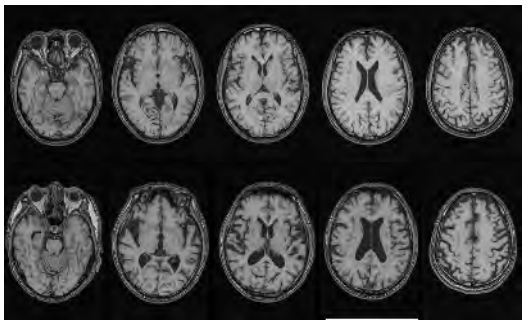


Fig. 4 MRI of normally aged (upper column) and atrophic brain (lower column) with 70-year old.

Upper brain images on Fig. 4 showed a normally aged brain of 70 yrs old man determined by this criteria. The lower images represent atrophic brain for his age (70 years old), of which gray matter ratio exceeded -2SD limits. Enlargement of ventricle and sulci was observed compared to the normally aged brain.

B. Longitudinal analysis of brain volume change during aging

Brain volume change described above are obtained from cross sectional analysis and do not represent age related change in strict sense. We performed a longitudinal study in the same subjects between 8 years interval of MRI study. The results indicated that gray matter ratio for men decreased linearly with age as was in our previous cross sectional analysis. While those for women decreased slowly than that for men until the age of 50 and then went down as the similar slope for men (Fig. 5). White matter volume increased until age of 40 and went down thereafter in either men or women, although variation of the data was large (data are not shown).

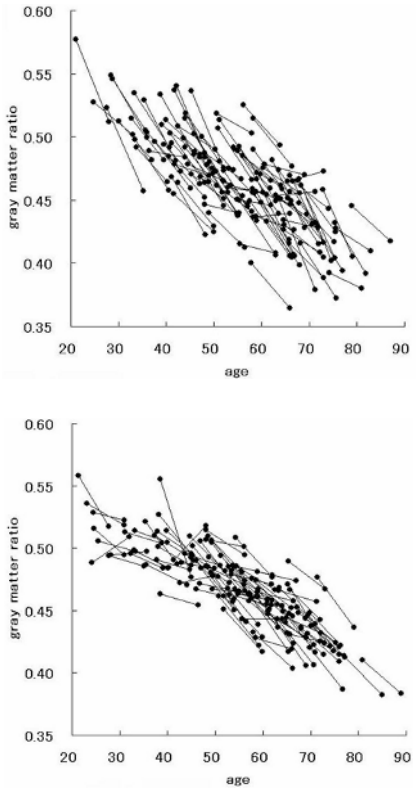


Fig. 5 Longitudinal analysis of brain volume change with aging. Two MRI measurements with 8-year interval Upper: men, lower: Women.

C. Risk factors for brain volume decrease

We analyzed correlation between regional gray matter volume and subject's characteristics using VBM technique. We found that total gray matter volume and regional gray matter volume negatively correlated with systolic blood pressure [3]. Most of the regions mainly distributed in watershed regions between major cerebral arteries, although other region was included.

Figure 6 shows the gray matter regions that had a significant negative correlation between the lifetime alcohol intake and the regional gray matter volume. The gray matter volume of the bilateral middle frontal gyri showed a significant negative correlation with the log transformed lifetime alcohol intake [4].

We tested correlation between gray matter ratio and obesity. As an indicator for obesity, we used body mass index (BMI). Volumetric analysis revealed that there are significant negative correlation between BMI and the gray matter ratio only in men ($p < 0.001$, adjusting for age, systolic blood pressure, and lifetime alcohol intake). On the other hand, we could not find any correlation in women [5].

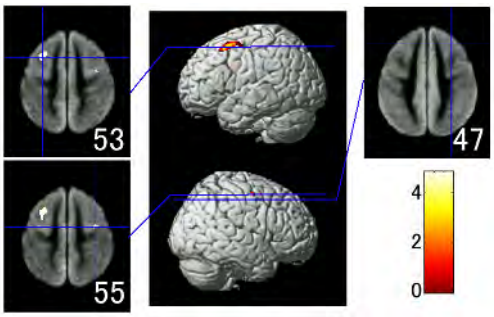


Fig.6 Brain regions that showed negative correction between gray matter volume and life time alcohol intake

D. Ischemic lesion volume

We defined the ischemic lesion by an automated system and made lesion map in each subject. Figure 7 shows probabilistic lesion map for each decade, which was made by summing up lesion map of a subject belonging to the same age group. The lesion distributed along the ventriculi and total lesion volume increased with increasing of age. Correlation analysis revealed that the total lesion volume correlated with the gray matter volume decrease in the frontal part of the brain.

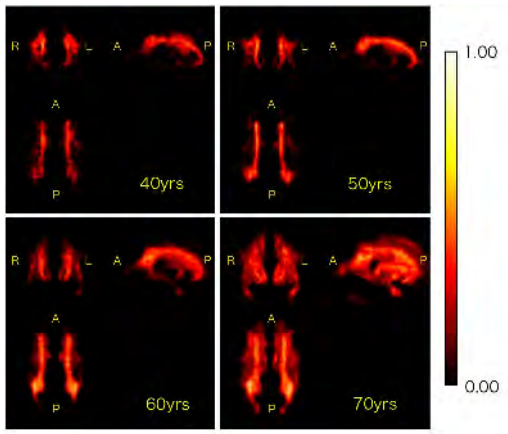


Fig. 7 The probabilistic lesion map for each decade (40th, 50th, 60th and 70th year-old)

IV. Conclusions

We constructed a large scale brain MRI database for healthy Japanese and clarified age-related volume changes of the human brain and their risk factors. This may contribute to the understanding of normal brain aging, as well as age-related brain diseases, such as dementia.

Ackowledgement

This study was supported by a Tohoku University Global COE Program "Global Nano-Biomedical Engineering Educational and Research Network Centre" and by a grant-in-aid from Japan Society for Promotion of Science (No 20659183)

References

1. 1. Sato K, Taki Y, Fukuda H, Kawashima R. (2003) Neuroanatomical database of normal Japanese brains. Neural Networks 16:1301-1310.
2. Kinomura S, Lerch L, Zijdenbos AP, et al. Automatic detection of subcortical ischemic lesion from 3-D MRI data in the aged brain. 10th Annual Meeting of the Organization for Human Brain Mapping Budapest, Hungary, 13-17 June 2004.
3. Taki Y, Goto R, Evans A, et al. (2004) Voxel-based morphometry of human brain with age and cerebrovascular risk factors. Neurobiol of Aging 25: 455-63.
4. Taki Y, Kinomura S, Sato K, et al. (2006) Both global gray matter volume and regional gray matter volume negatively correlate with lifetime alcohol intake in non-alcohol-dependent Japanese men: A volumetric analysis and a voxel-based morphometry. Alcohol Clin Exp Res 30:1045-1050.
5. Taki Y, Kinomura S, Sato K, et al. (2008) Relationship between body mass index and gray matter volumes in 1428 healthy individuals. Obesity 16:119-124.

Motion Control of Walking Assist Robot System Based on Human Model

Yasuhisa Hirata, Shinji Komatsuda, Takuya Iwano and Kazuhiro Kosuge

Department of Bioengineering and Robotics, Tohoku University, Sendai, Japan

Abstract — **In this paper, we introduce walking assist robot systems for the elderly people to manage the independent living over a long period of time in serious aging society. This research especially focuses on the motion control method of the walking assist robot systems based on the human linkage model calculated in real time. According to the human linkage model, the robot systems could calculate a position of the user's center of gravity and the joint moment applied around the each joint of the user in real time. Based on the information of the user, the robot systems could support the walking appropriately. The motion control algorithms based on the human model are implemented to the walker-type walking assist system and the wearable walking assist system experimentally, and experimental results illustrate the validity of the proposed methods.**

Keywords — **Walking Assist Robot System, Human Model, Estimation of Human States**

I. Introduction

With the coming of aging societies, the population of the elderly people would rapidly increase in many countries. Many elderly people would have some handicaps for locomotion, because of the decline of the physical strength, muscular strength, etc. In the daily life, the ability of walking is one of the most fundamental functions for humans to maintain the high quality of life. For assisting the walking of the human, several intelligent systems using robot technologies have been proposed [1]- [3].

We have also introduced two kinds of walking assist system. First one is the walker-type walking assist system called RT Walker as shown in Fig.1. Walker-type waling assist system could support the weight of the user and keep his/her balance. In addition, RT Walker achieves several functions such as collision avoidance and path following by controlling the brake torques of the rear wheels [4].

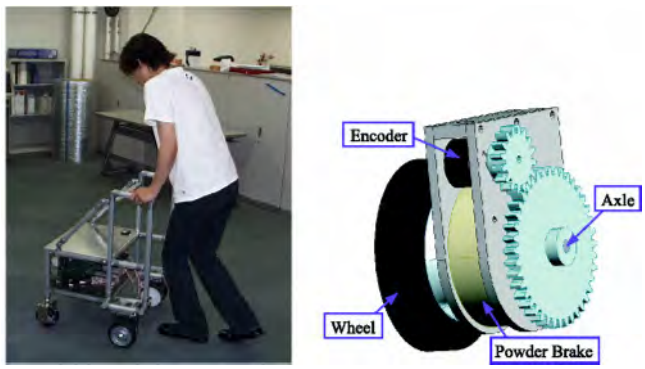
Second one is the wearable walking assist system called Wearable Walking Helper as shown in Fig.5, which consists of knee orthosis, prismatic actuator and sensors [5]. The knee joint of the orthosis has one degree of freedom rotating around the center of the knee joint of the user on sagittal plane. The mechanism of the knee joint is a geared dual hinge joint. The prismatic actuator, which is manually back-drivable, consists of DC motor and ball screw. By translating the thrust force generated by the prismatic actuator to the frames of the knee orthosis, the device can generate support moment around the knee joint of the user.

For controlling both walking assist robot systems, we utilize the human linkage model. According to the human linkage model, the robot systems could calculate a position of the user's center of gravity and the joint moment applied around the each joint of the user in real time. Based on the information of the user, the robot systems could support the walking appropriately. In the following parts of this paper, we introduce the human linkage models for controlling the RT Walker and the Wearable Walking Helper, and experimental results with both systems illustrate the validity of them.

II. User Model for Walker-Type Assist System

A. Method for Generating Human Model

In this section, we explain the generation method of the human model that has seven rigid body links in sagittal plane. In this research, we set up two Laser range finders (LRFs) on the walker as shown in Fig.2(a). One of them is attached to the same height with hip joint of the user with standing state and measures the relative distances between the human surface and the walker along the vertical direction. This laser range finder measures the relative distances from −50[*deg*] to 30[*deg*] every 10[*deg*] under the assumption that the height of the hip joint of the user with



(a) RT Walker (b) Wheel with Servo Brake

Fig. 1. Passive Intelligent Walker

Chwee Teck Lim, James C.H. Goh (Eds.): ICBME 2008, Proceedings 23, pp. 2232–2236, 2009
www.springerlink.com

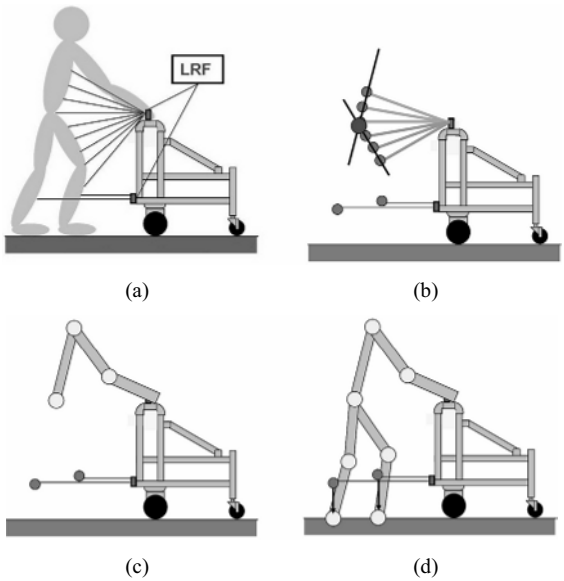


Fig. 2. Generation Method of Human Model Using Laser Range Finders

standing state is 0[*deg*]. Another laser range finder is set up at the lower part of the walker, and it measures the distances between each leg and the walker.

For generating the human model, firstly, the data of LRFs are collected. Three points on the surface of the lower body and three points on the surface of the upper body are obtained from the upper part LRF. The equations of the straight lines that show the upper-body and the lower half of the body are derived to detect the position of the human hip joint during the motion of the user using walker. These equations are derived based on the least square method. The intersection of these straight lines is calculated as shown in Fig.2(b), and the intersection point is regarded as the position of the hip joint of the human model.

The position of the shoulder is calculated by using the detected hip joint position, known length of the upper body link and the inclination of the straight line. From the shoulder position and the hand position, the angles of the arm joints are calculated by solving the inverse kinematic equations as shown in Fig.2(c). The angles of the legs joints are obtained by solving the inverse kinematic equations based on the position of the hip joint and the position of the feet obtained by LRF attached to the lower part of the walker as shown Fig.2(d).

B. Experiments for Estimating User States

If we can estimate the user states during the usage of the walker, we can change the function of the walker appropriately based on the user states. In this paper, we consider the estimation method of the user states based on the human model. For the simplicity of the discussion, in this paper, we consider thirteen states of the user during the usage of the walker as shown in Fig.3. Main states of the user during the usage of the walker are Sitting state, Standing state and Walking state.

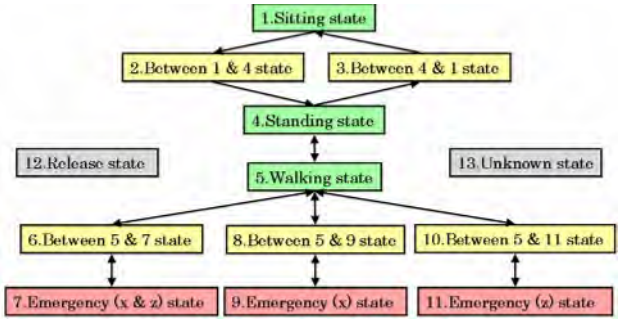
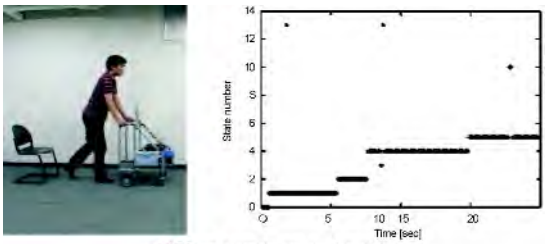


Fig. 3. Transition of Human States

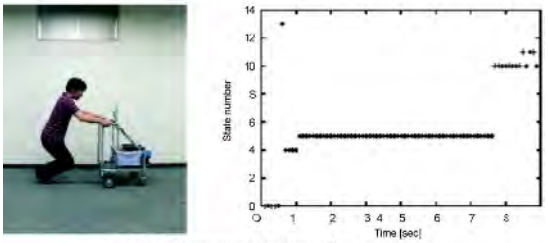
The user sometimes faces the dangerous situations including the falling accident, which are estimated by the system as Emergency states. Emergency states consist of three states. One is the falling accident that the user apart from the walker (Emergency (*x*) state), second one is the falling along the vertical direction (Emergency (*z*) state), and third one is the falling along *x* and *z* directions (Emergency (*x* & *z*) state). In Release state, the user releases his/her hand from the grip of the walker, and Between states are the intermediate states with respect to the Sitting, Standing, Walking and Emergency states. If the system does not recognize any states of the user, the Unknown state is selected.

For estimating the user states, in this paper, we pay attention to the position of the center of gravity of the user on the sagittal plane which is calculated from the human model explained in the previous section. To illustrate the validity of the estimation method by using the human model, a user behaves three motions experimentally with the walker. One is motion that the user stands up from the chair and then walks as shown in Fig.4(a), second one is the falling accident along the vertical direction after walking as shown in Fig.4(b), and third one is the falling accident along *x* axis after walking as shown in Fig.4(c).

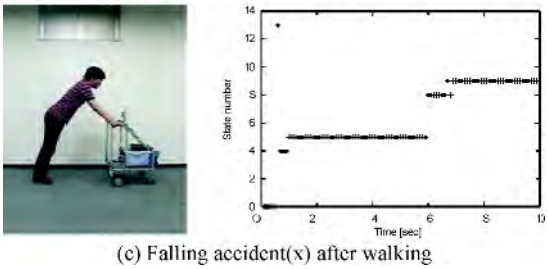
In these experiments, we decided the thresholds of the center of gravity for estimating the user states experimentally. Estimation results are also shown in Fig.4. In the experimental data of Fig.4, the numbers of the vertical axis express the user states as shown in Fig.3. From these results, you can see that the system can recognize the user states successfully. Based on the estimated states of the user, we could design the several functions of the intelligent walkers such as fall-prevention function, variable motion characteristic function, sit-to-stand assist function, and so on.



(a)User stands up and walks



(b) Falling accident(z) after walking



(c) Falling accident(x) after walking

Fig. 4. Behaviors of User and Estimation Results of User States

III. User Model for Wearable Assist System

A. Model-Based Control Algorithm

In this section, we introduce a control algorithm of the wearable walking support system as shown in Fig.5 based on the human model. Firstly, we derive the knee joint moment based on an approximated human model, and then the support joint moment, which should be generated by the actuator of the support device, is calculated.

To control Wearable Walking Helper, we use an approximated human model as shown in Fig.6. Under the assumption that the human gait is approximated by the motion on the sagittal plane, we consider only Z - X plane. The human model consists of four links, that is, Foot Link, Shank Link, Thigh Link and Upper Body Link and these links compose a four-link open chain mechanism.

To derive joint moments, we first set up Newton-Euler equations of each link. At the link *i,* Newton-Euler equations are derived as follows:

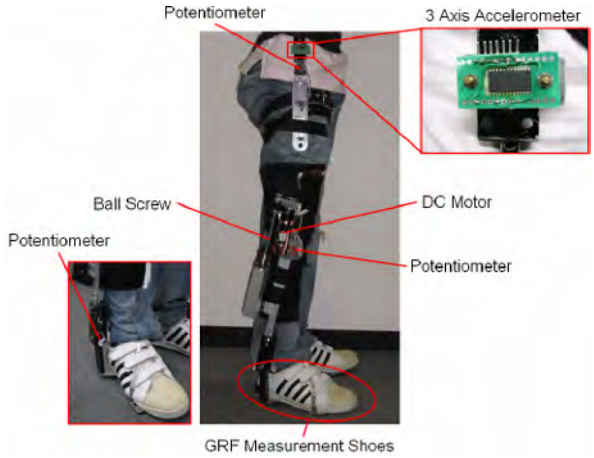
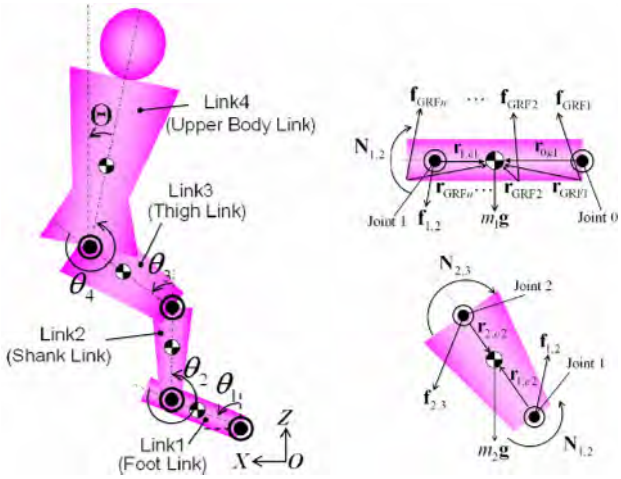


Fig. 5. Wearable Walking Helper



(a) Coordinate Systems (b) Foot and Shank Links

Fig. 6. Human Model

$$\mathbf{f}_{i-1,i} - \mathbf{f}_{i,i+1} - m_i\mathbf{g} = m_i\dot{\mathbf{v}}_{c_i} \quad (1)$$

$$N_{i-1,i} - N_{i,i+1} + \mathbf{r}_{i,c_i} \times \mathbf{f}_{i,i+1} - \mathbf{r}_{i-1,c_i} \times \mathbf{f}_{i-1,i} = I_i\frac{d\dot{\theta}_i}{dt} \quad (2)$$

where, $\mathbf{f}_{i-1,i}$, and $\mathbf{f}_{i,i+1}$ are reaction forces applying to the joint i and i + 1, respectively. m_i is the mass of the link i, $\mathbf{g}$ is the vector of gravity acceleration and $\dot{v}_{ci}$ is the translational acceleration of the gravity center of the link i. $N_{i-1,i}$ and $N_{i,i+1}$ are the joint moments applying to the joint i and i + 1, respectively. $r_{i,ci}$ is the position vector from the joint i to the gravity center of the link i and r_i - 1,c_i is the position vector from the joint i - 1 to the gravity center of the link i. I is the inertia of the link i and θ_i is the rotation angle of the joint i.

The knee joint moment $N_{2,3}$ can be derived by using the equations of foot link and shank link as follows:

$$\begin{aligned}\tau_k = N_{2,3} = &- I_1\frac{d\dot{\theta}_1}{dt} - I_2\frac{d\dot{\theta}_2}{dt} \\ &- m_1(\mathbf{r}_{1,c_1} - \mathbf{r}_{1,c_2} + \mathbf{r}_{2,c_2}) \times (\dot{\mathbf{v}}_{c_1} - \mathbf{g}) \\ &- m_2\mathbf{r}_{2,c_2} \times (\dot{\mathbf{v}}_{c_2} - \mathbf{g}) \\ &+ (\mathbf{r}_{1,c_1} - \mathbf{r}_{1,c_2} + \mathbf{r}_{2,c_2}) \times \sum \mathbf{f}_{GRF} \\ &- \sum(\mathbf{r}_{GRF} \times \mathbf{f}_{GRF})\end{aligned} \quad (3)$$

where $\mathbf{f}_{GRF}$ is Ground Reaction Force exerted on the foot link.

To prevent the decrease in the remaining physical ability of the elderly, the support joint moment τ_{sk} is calculated as a part of the derived joint moment τ_k. The Support joint moment is designed based on the gravity term τ_{gra} and the GRF term τ_{GRF} from equation (3) as follows:

$$\tau_{sk} = \alpha_{gra}\tau_{gra} + \alpha_{GRF}\tau_{GRF} + \tau_g \quad (4)$$

where α_{gra} and α_{GRF} are support ratios of the gravity and GRF terms, respectively. By adjusting these ratios in the range of $0 \le \alpha < 1$, support joint moment τ_{sk} can be determined. The gravity term τ_{gra} and the GRF term τ_{GRF} can be expressed as following equations.

$$\begin{aligned}\tau_{gra} = &m_1(\mathbf{r}_{1,c_1} - \mathbf{r}_{1,c_2} + \mathbf{r}_{2,c_2}) \times \mathbf{g} \\ &+ m_2\mathbf{r}_{2,c_2} \times \mathbf{g}\end{aligned} \quad (5)$$

$$\begin{aligned}\tau_{GRF} = &(\mathbf{r}_{1,c_1} - \mathbf{r}_{1,c_2} + \mathbf{r}_{2,c_2}) \times \sum \mathbf{f}_{GRF} \\ &- \sum(\mathbf{r}_{GRF} \times \mathbf{f}_{GRF})\end{aligned} \quad (6)$$

τ_g is also expresses the term of the weight of the device derived by the device model with closedloop mechanism [6].

B. Walking Experiments

In this section, we conducted experiments to support a user during gait by applying the proposed method to Wearable Walking Helper. To show the proposed method is effective for the reduction of burden on the knee joint, we conducted the experiments in two conditions: the subject walked without support device and the subject walked with support device implementing the proposed control method. During the experiments, we measured EMG signals of muscles conductive to the movement of the knee joint.

In the gait cycle, the Vastus Lateralis Muscle is active in most of the stance phase and the Rectus Femoris Muscle is active in last half of the stance phase and most of the swing phase. Therefore, during the experiments, we measure EMG signals of the Vastus Lateralis Muscle and the Rectus Femoris Muscle. The experiments were performed by the university student who is 23-years-old man. Support ratios α in the equation (4) are set to 0.6. Note that, for reducing the impact forces applied to the force sensors attached on the shoes during the gait, we utilized a low pass filter whose parameters were determined experimentally.

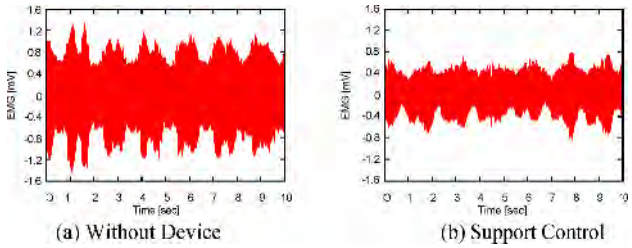
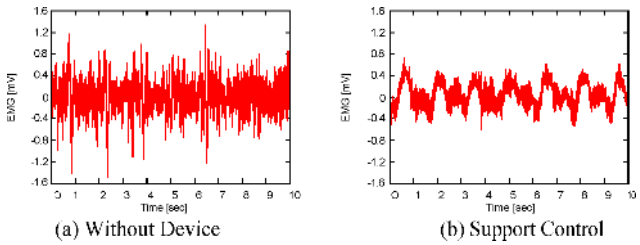


Fig. 7. EMG Signals of Vastus Lateralis Muscle



(a) Without Device (b) Support Control

Fig. 8. EMG Signals of Rectus Femoris Muscle

Fig.7 and Fig.8 show EMG signals of the Vastus Lateralis Muscle and the Rectus Femoris Muscle during the experiments in two conditions explained above. From these results, EMG signals of both the Vastus Lateralis Muscle and the Rectus Femoris Muscle became small in the experiment with support device implementing the proposed control method compared to the experiment without support device. These experimental results show that it is possible to support the walking by using the proposed method.

IV. Conclusions

This paper especially focused on the motion control of the walking assist robot systems based on the human model calculated in real time. According to the human linkage model, the robot systems could calculate a position of the user's center of gravity and the joint moment applied around the each joint of the user in real time. Based on the information of the user, the robot systems could support the walking appropriately. The motion control algorithms based on the human model were implemented to the walker-type walking assist system called RT Walker and the wearable walking assist system called Wearable Walking Helper experimentally, and experimental results illustrated the validity of the proposed methods based on the human model.

REFERENCES

1. M. Fujie, Y. Nemoto, S. Egawa, A. Sakai, S. Hattori, A. Koseki, T. Ishii, "Power Assisted Walking Support and Walk Rehabilitation", *Proc. of 1st International Workshop on Humanoid and Human Friendly Robotics*, 1998.
2. H. Yu, M. Spenko, S. Dubowsky, "An Adaptive Shared Control System for an Intelligent Mobility Aid for the Elderly", *Auton. Robots*, Vol.15, No.1, pp.53-66, 2003.
3. H. Kawamoto, Y. Sankai, "Power Assist Method Based on Phase Sequence and Muscle Force Condition for HAL", *Robotics Society of Japan, Advanced Robotics, Vol.19, No.7, pp.71 7-734*, 2005.
4. Y. Hirata, A. Hara, K. Kosuge, "Motion Control of Passive Intelligent Walker Using Servo Brakes", *IEEE Transactions on Robotics*, Vol.23, No.5, pp.981-990, 2007.
5. T. Nakamura, K. Saito, Z. Wang, K. Kosuge, M. Tajika, "Control of Wearable Walking Support System Based on Human-Model and GRF", *Proc. of IEEE International Conference on Robotics and Automation*, pp.4405-4410, 2005.
6. J Luh, YF Zheng, "Computation of Input Generalized Forces for Robots with Closed Kinematic Chain Mechanisms", *IEEE J. of Robotics and Automation*, pp.95-103, 1985.

Effects of Mutations in Unique Amino Acids of Prestin on Its Characteristics

S. Kumano[1], K. Iida[1], M. Murakoshi[1], K. Tsumoto[2], K. Ikeda[3], I. Kumagai[4], T. Kobayashi[5], H. Wada[1]

[1] Department of Bioengineering and Robotics, Tohoku University, Sendai, Japan
[2] Department of Medical Genome Science, The University of Tokyo, Kashiwa, Japan
[3] Department of Otorhinolaryngology, Juntendo University School of Medicine, Bunkyoku, Japan
[4] Department of Biomolecular Engineering, Tohoku University, Sendai, Japan
[5] Department of Otolaryngology, Head and Neck Surgery, Tohoku University Graduate School of Medicine, Sendai, Japan

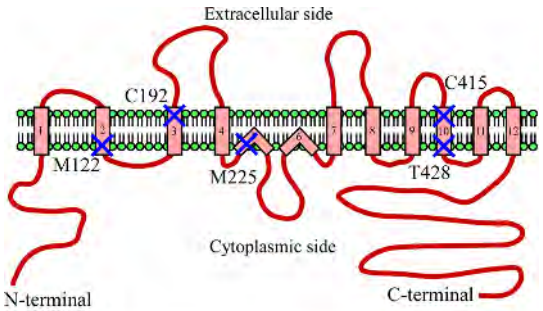
Abstract — **Prestin is believed to be the motor protein expressed in the plasma membrane of outer hair cells (OHCs). In this study, characterization of prestin was carried out by site-directed mutagenesis focusing on the unique amino acids in prestin. Five prestin mutants, namely, M122I, C192A, M225Q, C415A and T428L, were engineered to be separately expressed in HEK293 cells. The characteristics of those mutants were then investigated. As a result, it was found that the charge density of M225Q, which reflects the charge transfer of prestin in the plasma membrane, was 1.7 times larger than that of wild-type prestin (WT), although the charge density of the other mutants were similar to that of WT. On the other hand, the amount of M225Q molecules in the plasma membrane was 1.2 times greater than that of WT molecules. The increase in the amount of prestin molecules due to the mutation of M225 probably indicates that prestin became more stable, but such increase does not correspond to the increase of the charge density. Hence, the mutation of M225 was considered to increase the stability of prestin, leading to an increase in the ratio of active prestin molecules to the total amount of prestin molecules in the plasma membrane.**

Keywords — **Inner ear, Motor protein, Prestin, Mutation.**

I. Introduction

The motor protein prestin, one of members of the SLC26 family, in the plasma membrane of OHCs in the inner ear is thought to change its conformation in response to modifications in the membrane potential, resulting in motility of OHCs [1, 2]. This motility enhances the sensitivity and frequency selectivity of mammalian hearing. Based on previous studies, several characteristics of prestin including its secondary structure has been investigated (Fig. 1(A)) [3-5]. However, the mechanism of the conformational change of prestin has not yet been clarified, thus necessitating elucidation of the amino acids of prestin involved in its conformational change. Alignment analysis of amino acid sequences of the SLC26 family showed that M122, C192, M225, C415 and T428 were only present in prestin in that family (Fig. 1 (B)). The predicted positions of these amino acids are shown in Fig. 1(A). As the conformational change of prestin involved in the motility of the OHCs is a unique function in the SLC26 proteins, prestin-specific amino acids may realize such function. In this study, to clarify the roles of those amino acids in prestin, the effects of mutations in those amino acids on characteristics of prestin were investigated. Five prestin mutants, namely, M122I, M225Q, C192A, C415A and T428L, were engineered to be expressed in HEK293 cells. Their characteristics were then examined by the whole-cell patch-clamp method and Western blotting.

(A)



(B)

	122	192	225	415	428
SLC26A5 (Prestin)	M	C	M	C	T
SLC26A1 (Sat-1)	I	L	Q	V	L
SLC26A2 (DTDST)	I	A	Q	V	I
SLC26A3 (DRA)	I	A	Q	L	L
SLC26A4 (Pendrin)	T	I	Q	I	L
SLC26A6 (CFEX)	I	G	Q	A	L
SLC26A7	I	A	Q	L	L
SLC26A8 (Tat1)	I	I	Q	L	M
SLC26A9	T	G	V	L	L
SLC26A10	I	A	Q	L	L
SLC26A11	V	A	Q	L	L

Fig. 1. Membrane topology of prestin and comparison of amino acid sequences of the SLC26 proteins. (A) Membrane topology of prestin. Prestin has 12 hydrophobic domains. (B) Amino acid sequences of the SCL26 proteins. Red-colored letters indicate amino acids in prestin. Blue-, green- and purple-colored letters represent conserved amino acids in the SLC26 proteins other than prestin.

II. Materials and Methods

A. Generation of prestin mutant genes and transfection

Point mutations were introduced into M122, C192, M225, C415 and T428. Each codon encoding those amino acids

Chwee Teck Lim, James C.H. Goh (Eds.): ICBME 2008, Proceedings 23, pp. 2237–2240, 2009
www.springerlink.com

was replaced by glutamine, alanine, isoleucine, alanine and leucine, respectively, resulting in five genes of prestin mutants, namely, genes of M122I, M225Q, C192A, C415A and T428L. Additionally, to detect prestin by antibodies, genes of FLAG-tagged prestin mutants were also created. Those genes were transfected into HEK293 cells.

B. Measurement of nonlinear capacitance

WT prestin-expressing cells exhibit bell-shaped NLC in response to the change of membrane potential [6]. As NLC is associated with a voltage-dependent charge transfer of prestin, NLC is accepted as a signature of the activity of prestin. The activity of prestin was therefore evaluated with NLC measured by the whole-cell patch-clamp technique. NLC is well fitted to the derivative of a Boltzman function [7],

$$C_{\mathrm{m}}(V) = C_{\mathrm{lin}} + C_{\mathrm{nonlin}} = C_{\mathrm{lin}} + \frac{Q_{\max}}{\alpha \mathrm{e}^{\frac{v-v_{1/2}}{\alpha}}\left(1+\mathrm{e}^{-\frac{v-v_{1/2}}{\alpha}}\right)^2} \quad (1)$$

where C_{lin} is linear capacitance which is proportional to the surface area of the plasma membrane, $Q_{\max}$ is maximum charge transfer of prestin in whole plasma membrane, V is membrane potential, $V_{1/2}$ is the voltage at which the maximum charge is equally distributed across the membrane and α is the slope factor of voltage dependence of charge transfer. When membrane potential was changed from –140 mV to 70 mV, membrane capacitance was recorded. To estimate the NLC of the unit cell surface, the normalized NLC $C_{\mathrm{nonlin/lin}}$ was defined as

$$C_{\mathrm{nonlin/lin}}(V) = \frac{C_{\mathrm{nonlin}}}{C_{\mathrm{lin}}} = \frac{\left(C_{\mathrm{m}}(V) - C_{\mathrm{lin}}\right)}{C_{\mathrm{lin}}} \quad (2)$$

where C_{nonlin} is the nonlinear component of the measured membrane capacitance. Furthermore, to compare the normalized data of the prestin mutants with that of WT prestin, $C_{\mathrm{nonlin/lin}}(V)$ was divided by the maximum $C_{\mathrm{nonlin/lin}}(V)$ of WT and termed relative $C_{\mathrm{nonlin/lin}}(V)$. In addition, to evaluate the maximum charge transfer of prestin in the unit plasma membrane, $Q_{\max}$ was divided by C_{lin} and designated as charge density. The unit of charge density is fC/pF.

C. Western blotting

Mutations in membrane proteins often cause their misfolding and transport-defect to the cell membrane. Hence, the amount of the prestin mutants in the cell membrane were compared with that of WT prestin by Western blotting. Plasma membrane fractions of transfected cells were extracted using a Plasma Membrane Protein Extraction Kit (MBL, Nagoya, Japan) according to the manufacturer's instructions. Plasma membrane fractions obtained from 2.5×10^5 cells were dissolved in 5 µl SDS sample buffer. After boiling for 5 min at 100ºC, 5 µl of the sample were subjected to Western blotting.

III. Results

Figure 2 shows representative data of relative $C_{\mathrm{nonline/lin}}$. Fitting parameters, namely, α and $V_{1/2}$, as well as the charge density were shown in Table 1. M122I, C192A, C415A and T428L showed NLC and the maximums of their NLC curves were similar to that of WT. In addition, the $V_{1/2}$ of those mutants and α of T428L were statistically different from those of WT. On the other hand, interestingly, the maximum of the NLC curve of M225Q was significantly larger than that of WT. The charge density of M225Q is 1.7 times larger than that of WT. The charge density reflects the amount of active prestin molecules in the plasma membrane. Thus, the increase in the charge density may indicate an increase of such amount. Although α was unchanged, the $V_{1/2}$ of M225Q was statistically shifted in the hyperpolarization direction

Result of Western blotting using plasma membrane fraction was shown in Fig. 3(A). In both WT and M225Q, only the 100 kDa band was observed. To compare the amount of M225Q molecules in the plasma membrane with that of WT molecules, the intensity of the 100 kDa band in M225Q was divided by that in WT and termed relative intensity as shown in Fig. 3(B). The intensity of the 100 kDa band in M225Q was 1.2 times greater than that in WT on an average, indicating that the amount of M225Q molecules is slightly higher than that of WT molecules.

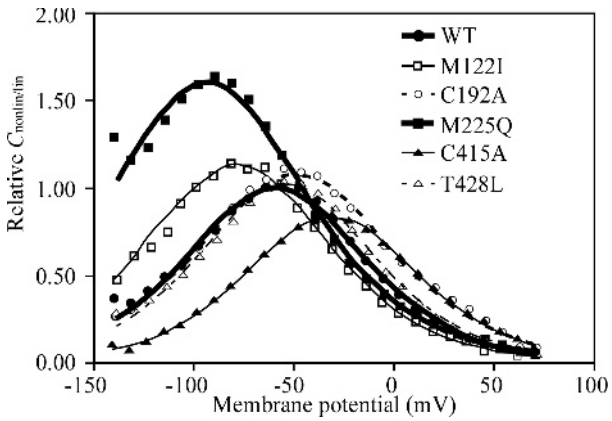


Fig. 2. Representative data of relative $C_{\mathrm{nonlin/lin}}$. M122I, C192A, C415A and T428L showed NLC similar to that of WT. On the other hand, NLC of M225Q was significantly larger than that of WT.

Table 1 Fitting parameters and charge density. Asterisks indicate statistical significance of the difference in any parameters between WT and its mutants.

Gene	α (mV)	$V_{1/2}$ (mV)	Charge density (fC/pF)
WT (n = 11)	32.0 ± 3.8	-61.2 ± 4.2	14.4 ± 7.1
M122I (n = 26)	30.3 ± 2.7	-70.8 ± 6.6*	18.9 ± 7.1
C192A (n = 16)	30.4 ± 3.2	-55.0 ± 6.6*	18.4 ± 6.6
M225Q (n = 12)	31.9 ± 2.8	-94.1 ± 5.0*	25.4 ± 5.5*
C415A (n = 13)	37.4 ± 6.4	-37.4 ± 6.4*	13.3 ± 4.3
T428L (n = 13)	28.5 ± 2.5*	-50.0 ± 5.7*	14.5 ± 5.9

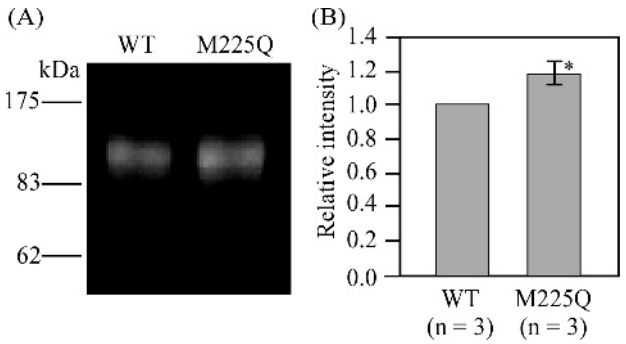


Fig. 3. Results of Western blotting using plasma membrane fraction of transfected cells. (A) Representative image of Western blotting. Only the 100 kDa bands were detected in WT and M225Q. (B) Relative intensity. The intensity of M225Q is statistically larger than that of WT ($P < 0.05$).

IV. Discussion

This study was focused on M122, C192, M225, C415 and T428, which were considered to be unique amino acids of prestin when the amino acid sequence of prestin was compared with those of the other SLC26 proteins. To clarify the roles of those amino acids in prestin, M122I, M225Q, C192A, C415A and T428L were engineered to be expressed in HEK293 cells and then the characteristics of these mutants were investigated by the whole-cell patch-clamp and Western blotting. As shown in Fig. 2 and Table 1, the charge density of M122I, C192A, C415A and T428L was similar to that of WT, but their $V_{1/2}$ and α were significantly different from those of WT prestin. Meanwhile, M225Q exhibited a 1.7 times larger charge density than that of WT. The $V_{1/2}$ of M225Q was statistically shifted in the hyperpolarization direction. The α and $V_{1/2}$ represent voltage reactivity of prestin. Hence, our results imply that all amino acids focused on in this study are related to the voltage reactivity of prestin. As the charge density reflects the amount of active prestin in the plasma membrane, the result of the patch-clamp recording for M225Q indicates that M225 is involved in such amount.

To compare the amount of M225Q in the plasma membrane with that of WT, Western blotting using the plasma membrane fraction of WT-expressing cells and M225Q-expressing cells was performed. As shown in Fig. 3(B), the intensity of the 100 kDa band in M225Q was 1.2 times greater than that in WT on the average. The intensity of that band reflects the amount of prestin molecules in the plasma membrane, namely, the sum of the amount of active prestin molecules and that of inactive prestin molecules. Thus, the 1.2-times increase in the intensity of the 100 kDa band indicates an increase of 1.2 times in the total amount of prestin molecules in the plasma membrane. The increase of prestin molecules in the plasma membrane may possibly result from the stabilization of prestin by the mutation. As described above, the charge density increased 1.7 fold by the mutation. Hence, the increase of the charge density cannot be explained by the increase of the total amount of prestin in the plasma membrane. One possible explanation for the increase of the charge density may be that the mutation in M225 made prestin stable, leading to an increase in the ratio of active prestin molecules to the total amount of prestin molecules in the plasma membrane.

V. Conclusions

Our findings indicate that the mutation in M225 may make prestin more stable, resulting in an increase in the ratio of active prestin molecules to the total amount of prestin molecules in the plasma membrane, which leads to the increase of the charge density.

Acknowledgment

This work was supported by Grant-in-Aid for Tohoku University Global COE Program "Global Nano-Biomedical Engineering Education and Research Network Centre," by Grant-in-Aid for Scientific Research on Priority Areas 15086202 from the Ministry of Education, Culture, Sports, Science and Technology of Japan, by Grant-in-Aid for Scientific Research (B) 18390455 from the Japan Society for the Promotion of Science, by Grant-in-Aid for Exploratory Research 18659495 from the Ministry of Education, Culture, Sports, Science and Technology of Japan, by a grant from the

Human Frontier Science Program, by a Health and Labour Science Research Grant from the Ministry of Health, Labour and Welfare of Japan, and by a Grant-in-Aid for JSPS Fellows from Japan Society for the Promotion of Science.

References

1. Zheng J, Shen W, He DZZ et al. (2000) Prestin is the motor protein of cochlear outer hair cells. Nature 405:149-155.
2. Liberman LC, Gao J. He DZZ et al. (2002) Prestin is required for electromotility of the outer hair cell and for the cochlear amplification. Nature 419: 300-304.
3. Zheng J, Long KB, Shen W et al. (2001) Prestin topology: localization of protein epitopes in relation to the plasma membrane. Neuroreport 12: 1929-1935.
4. Matsuda K, Zheng J, Du G et al. (2004) N-linked glycosylation sites of the motor protein prestin: effects on membrane targeting and electrophysiological function. J Neurochem 89: 928-938.
5. Deák L Zheng J, Orem A et al. (2005) Effects of cyclic nucleotides on the function of prestin. J Physiol 563: 483-496.
6. Dallos P, Fakler B (2002) Prestin, a new type of motor protein. Nat Rev Mol Cell Biol 3:104-111.
7. Santos Sacchi J (1991) Reversible inhibition of voltage-dependent outer hair cell motility and capacitance. J Neurosci 11:3096-3110.

The Feature of the Interstitial Nano Drug Delivery System with Fluorescent Nanocrystals of Different Sizes in the Human Tumor Xenograft in Mice

M. Kawai[*1], M. Takeda[2] and N. Ohuchi[1,2]

* COE Research Assistant
1) Division of Surgical Oncology, Tohoku University Graduate School of Medicine, Sendai, Japan
2) Department of Nano-Medical Sciences, Tohoku University Graduate School of Medicine, Sendai, Japan

Abstract — **Recent anticancer drugs are made to be larger to selectively pass the tumor vessel and to stay in the interstitium. Understanding of the drug movement in a single molecule is indispensable to optimize drug delivery. Here we report the tracking of single nano-particles with different sizes in tumor xenografts *in vivo*. The motions of the nano-crystals were clearly observed and random with one-way movement. The analysis of the trajectory shows that contribution of diffusion and interstitial fluid current to the delivery processes. The diffusion coefficient was inversely related to the size and position and velocity was related to the position of the particles. Our data are basic and important for understanding pharmacokinetics and convenient finding for constructing novel drug delivery system.**

Keywords — **Nanomedicine, Drug Delivery System**

I. Introduction

Numerous drugs have been developed to maximize drug effects to the targeted tumor by controlling their diameter to the appropriate size in order to selectively pass the tumor vasculate utilizing the characteristics of a cancer vasculate having larger pore than a normal vasculate. The large hole selectively passed large nanoparticle experimentally. The size dependency of the drug delivery in a tumor interstitium was estimated quantitatively from observing the averaged dispersion of the larger drugs *in vivo*. On the other hand, Single particle tracking is a powerful method to understand unprecedented reductive information of individual drug molecules such as antibody delivery process.

Single particle tracking *in vivo* enabled us the tracking of the tumor cell metastasis and delivery process of the antibody, but there is no quantitative analysis *in vivo*. In this study, we focused on the quantification of the influence of molecular size by homogenously fluorescence nanoparticles in the tumor xenografts based on the single particle tracking. We used real-time single particle tracking using confocal scanning unit. Quantitative information such as position was obtained. Velocity, diffusion coefficient are calculated using time-resolved trajectories of the single particles by analyzing the data.

As a result, we successfully identified the processes of delivery and quantitatively analyzed them to understand the rate limiting constraints on single nano-particle delivery in interstitial space *in vivo*.

Understanding of the vascular pore size effect and interstitial pathway to the cancer cells quantative analysis in a single molecule and a particle level is necessary to optimize the drug delivery.

II. Material and methods

1.1. Nanocrystals

We used 'Fluospheres' manufactured from high-quality, ultraclean polystyrene microspheres by Invitrogen, Molecular Probe (Oregon, USA) and Quantum dot 705 ITK kit (Quantum Dot Corp., Hayward, CA). We selected sizes of 20, 40, 100nm.

1.2. Cell lines

The human breast cancer cell line KPL-4[1] was kindly provided by Dr. J. Kurebayashi (Kawasaki Medical School, Kurashiki, Japan). KPL-4 cells were cultured in Dulbecco's modified Eagle's medium (DMEM) supplemented with 5% fetal bovine serum.

1.3. Experimental Animals

A suspension of KPL-4 (1.0×10^7 cells / 100 µl DMEM) tumor cell was transplanted subcutaneously into the dorsal skin of female Balb/c nu/nu mice at 5 - 7 weeks of age (Charles River Japan, Yokohama, Japan). Several weeks after tumor inoculation, mice with a tumor volume of 100 - 200 mm^3 were selected.

The mice were placed under anesthesia by the intraperitoneal injection of a ketamine and xylazine mixture at a dosage of 95 mg / kg and 5 mg / kg, respectively.

Chwee Teck Lim, James C.H. Goh (Eds.): ICBME 2008, Proceedings 23, pp. 2241–2243, 2009
www.springerlink.com

1.4. Imaging systems

The optic system consisted of an epi-fluorescent microscope, Nipkow lens type confocal unit and an electron multiplier type CCD camera (Fig.1). This system can captures images of single nanoparticles at a video rate of 33 ms/frame. The xy-position of the fluorescent spot was calculated by fitting to a 2D-Gaussian curve. The single molecule could be identified by the fluorescence intensity. And quantitative and qualitative information such as velocity, directionality and transport mode was obtained using time-resolved trajectories of particles.

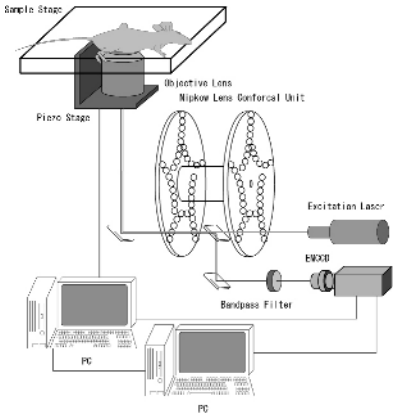


Fig.1. Imaging system

1.5. Analysis

Mean square displacement (MSD) values of individual nano-crystals are defined by the following equation:

$$\mathrm{MSD}(n\Delta t) = \frac{1}{N-n}\sum_{i=1}^{N-n}\left[\left(x_{i+n}-x_i\right)^2+\left(y_{i+n}-y_i\right)^2\right]$$

$$\mathrm{MSD}(\Delta t) = 4\mathrm{D}\Delta t + v^2(\Delta t)^2$$

$$\lim_{t\to 0}\mathrm{MSD}(\Delta t) = 4\mathrm{D}\Delta t$$

III. Results

After the injection, many particles had extravasated and moved into the perivascular area close to the tumor vessels (Fig. 2). Particle diffuses within a highly restricted area and then moves suddenly to the next point. We acquired trajectories of the three sizes of particles in the three parts of the tumor (perivascular, interstitial and intercellular).

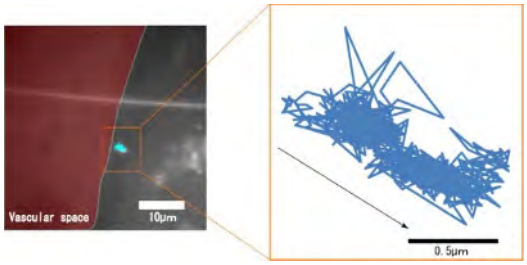


Fig.2. Trajectory of the single nano-particle

The MSD plots of the particles in the perivascular area (Fig.3). The plots are in parabolic shape, indicating that the movements are consisted of convection with superimposed random diffusion.

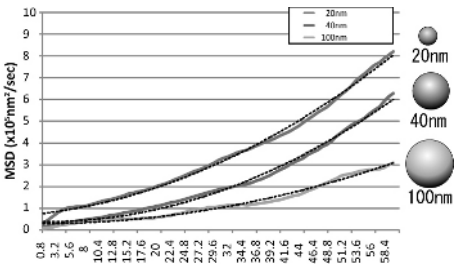


Fig.3. The MSD plots in the perivascular area

Velocity depends on the position (Fig.4) of the particle size. Velocity was weakly dependent on the size but dependent on the position from perivascular region.

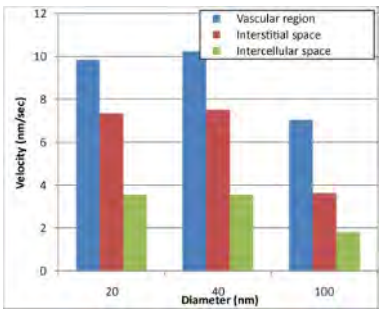


Fig.4. The relationships of diameter and velocity

IV. Conclusion

Our data of velocity is consistent with previous experimental results that it was weakly dependent on the size[2] but dependent on the decreasing interstitial flow from perivascular region[3]. We assume that our data means that the reason of the convectional movement not having been

interrupted by the size but by the position was that the 3D-structure of extracellular matrix was not so tight to restrict the current of the different sizes of the particles but confine diffusion.

Acknowledgements

Masaaki Kawai acknowledges the support of Tohoku University 21th COE Program "Future Medical Engineering based on Bio-nanotechnology".

References

[1] Kurebayashi, J. Isolation and characterization of a new human breast cancer cell line, kpl-4, expressing the erb b family receptors and interleukin-6. *Br j cancer* **79**, 707-717, 1999.

[2] Swartz A, Fleury E. Interstitial flow and its effects in soft tissues. *Annu Rev Biomed Eng* **9**, 229-256, 2007.

[3] Jain R. Barriers to drug delivery in solid tumors. *Scientific American* **271**, 58-65, 1994.

Three-dimensional Simulation of Blood Flow in Malaria Infection

Y. Imai[1], H. Kondo[1], T. Ishikawa[1], C.T. Lim[2], K. Tsubota[3] and T. Yamaguchi[4]

[1] Department of Bioengineering and Robotics, Tohoku University, Sendai, Japan
[2] Department of Mechanical Engineering, National University of Singapore, Singapore, Singapore
[3] Department of Mechanical Engineering, Chiba University, Chiba, Japan
[4] Department of Biomedical Engineering, Tohoku University, Sendai, Japan

Abstract — **We propose a numerical method for simulating three-dimensional hemodynamics arising from malaria-infection. Malaria-infected red blood cells (IRBCs) become stiffer and develop the property of cytoadherent and resetting. To clarify the mechanism of microvascular obstruction in malaria, we need to understand the changes of hemodynamics, involving interaction between IRBC, healthy RBCs, and endothelial cells. In the proposed model, all the components of blood are represented by a finite number of particles. The membrane of RBCs is expressed by two-dimensional network. Malaria parasites inside the RBC are represented by solid objects. The motion of each particle is described by the conservation laws of mass and momentum for incompressible fluid. We examine several numerical tests, involving the stretching of IRBCs, and flow in narrow channels, to validate our model. The obtained results agree well with the experimental results. Our method would be helpful for further understandings of pathology of malaria-infection.**

Keywords — **Infected red blood cell, hemodynamics, numerical modeling, computational fluid dynamics.**

I. Introduction

Malaria is one of the most serious infectious diseases on earth. There are several hundred million patients with several million deaths arising from malaria infection. When a parasite invades and matures inside a red blood cell (RBC), the infected RBC (IRBC) becomes stiffer and cytoadherent and these two outcomes can lead to microvascular blockage [1]. Experimental techniques for cell mechanics have been advanced and applied to study the mechanical property of IRBCs. Methods to quantify the stiffness of the IRBCs include the micropipette aspiration [2-4] and the optical tweezers [5]. Suresh et al. [5] used the optical tweezers to investigate the change of mechanical response of IRBCs at different development stages. They clarified that the shear modules can increase by ten-fold in the final schizont stage. The recent reviews are found in [6-8].

Microvascular blockage may be resulted from the hemodynamics, involving the interactions between IRBCs, healthy RBCs and endothelial cells. Recently, microfluidics has been used to investigate the effect of IRBCs on the capillary obstruction. Shelby et al. [9] demonstrated that IRBCs in the late stages of the infection cannot pass through micro channels that have diameters smaller than those of the IRBCs. However, this experiment is still limited to the effect of the single infected cell. The hemodynamics arising from malaria infection has not been studied well. This is due to the limitation of the current experimental techniques. First, it is still difficult to observe the RBC behavior interacting with many other cells even with the recent confocal microscope. Second, the three-dimensional information on flow field is hardly obtained. Third, capillaries in human body are circular channels with complex geometry, but such complex channels cannot be created in micro scale. Instead, numerical modeling can be a strong tool for further understanding the pathology of malaria. Finite element modeling was performed for the stretching of an IRBC by optical tweezers [5]. Dupin et al. [10] also modeled the stretching of the IRBC using lattice Boltzmann method. We have also developed a hemodynamic model involving adhesive interactions [11]. In this paper, we present our methodology and preliminary numerical results.

II. Method

A. Particle method

Blood is a suspension of RBCs, white blood cells, and platelets in plasma. An RBC consists of cytoplasm enclosed by a thin membrane. Assuming that plasma and cytoplasm are incompressible and Newtonian fluid, the governing equations are described as

$$\frac{D\rho}{Dt} = 0\,, \tag{1}$$

$$\frac{D\mathbf{u}}{Dt} = -\frac{1}{\rho}\nabla p + \nu\nabla^2\mathbf{u} + \mathbf{f}\,, \tag{2}$$

where the notation t refers to the time, ρ is the density, $\mathbf{u}$ is the velocity vector, p is the pressure, ν is the dynamic viscosity, $\mathbf{f}$ is the external force per unit mass, and D/Dt is the Lagrangian derivative.

Chwee Teck Lim, James C.H. Goh (Eds.): ICBME 2008, Proceedings 23, pp. 2244–2247, 2009
www.springerlink.com

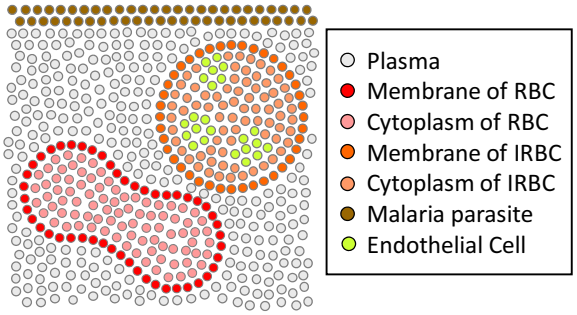


Fig. 1 Free mesh modeling of blood

Our model is based on a particle method. All the components of blood are represented by of particles (Fig. 1). Note that each particle is not a real fluid particles but a discrete point for computation. Fluid variables are calculated at the computational point and it is moved by the calculated advection velocity every time step. In conventional mesh methods, each computational point requires the connection to neighboring points for the discretization of Eqs. (1) and (2) and thus the computational meshes are generated. When a red blood cell approaches to other cell, however, the computational meshes can be distorted and destroyed easily. In contrast to mesh methods, the particle method does not require such computational meshes and the computation is stable even when many cells interacting with each other. Another advantage of the particle method is the coupling with the front-tracking. The particle method tracks the front of membrane using the membrane particles and the no-slip condition on the membrane is directly imposed to Eq. (2) by using the position and velocity of membrane particles. We use moving particle semi-implicit (MPS) method [12] for solving Eqs. (1) and (2). In the MPS method, differential operators in the governing equations are approximated using the weight function, for example,

$$\nabla\phi_i = \frac{d}{n^0}\sum_{j\neq i}\frac{\phi_j-\phi_i}{\left|\mathbf{r}_{ij}\right|^2}\mathbf{r}_{ij}w\left(\left|\mathbf{r}_{ij}\right|\right), \tag{3}$$

$$\nabla^2\phi_i = \frac{2d}{\lambda n^0}\sum_{j\neq i}\left(\phi_j-\phi_i\right)w\left(\left|\mathbf{r}_{ij}\right|\right), \tag{4}$$

where ϕ is a fluid variable, d is the space dimension number, n^0 is the reference particle number density, λ is the constant, $\mathbf{r}$ is the position of particle, $\mathbf{r}_{ij} = \mathbf{r}_j - \mathbf{r}_i$, and w is the weight function.

B. Modeling of IRBCs

The membrane of IRBCs is represented by the two-dimensional network consisting of the finite number of particles (Fig. 2). Particle j is connected to particle i by linear spring, giving a force,

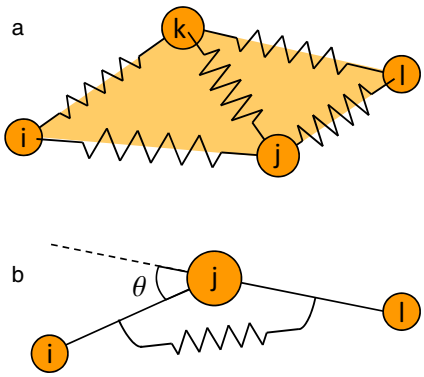


Fig. 2 Spring network model of IRBC membrane: (a) stretching force; (b) bending force.

$$\mathbf{F}_j^s = k_s\left(\left|\mathbf{r}_{ij}\right| - l_0\right)\frac{\mathbf{r}_{ij}}{\left|\mathbf{r}_{ij}\right|}, \tag{5}$$

where k_s is the spring constant and l_0 is the equilibrium distance. A bending force is also considered in our model:

$$\mathbf{F}_j^b = \mathbf{F}_k^b = \frac{\mathbf{F}_i^b + \mathbf{F}_l^b}{2}, \tag{6}$$

$$\mathbf{F}_i^b = k_b\tan\left(\frac{\theta}{2}\right)\mathbf{n}_{ijk}, \tag{7}$$

$$\mathbf{F}_l^b = k_b\tan\left(\frac{\theta}{2}\right)\mathbf{n}_{jkl}, \tag{8}$$

where k_b is the spring constant, θ is the angle between the triangles Δ_{ijk} and Δ_{jkl}, and $\mathbf{n}_{ijk}$ is the normal vector to the triangle Δ_{ijk}. The external force per mass is given as

$$\mathbf{f}_i = \frac{\mathbf{F}_j^s + \mathbf{F}_j^b}{\rho V_0}, \tag{9}$$

where V_0 is the reference volume $V_0 = r_0^3$, r_0 is the averaged particle distance at initial time step. Note that the spring constants k_s and k_b should be model parameters to control the deformation of IRBCs. As described in the next section, we adjust these model parameters through numerical experiments.

A malaria parasite inside IRBCs is modeled by a rigid object constructed by some particles. The treatment of the rigid object in the MPS method was proposed by Koshizuka et al [13].

C. Time integration

The time step size of time integration is limited by several factors. Most famous one in computational fluid dynamics is the Courant number limitation for the time integration of advection term. In the micro circulation, the diffusion number can be the most serious parameter because of small Reynolds number. Also, the behavior of RBC membrane may limit to the time step size. To avoid the use of small time step size, we employ a fractional time step method with sub time steps. The fractional time step method is written by

$$\mathbf{u}^{*} = \mathbf{u}^{n} + \nu\nabla^{2}\mathbf{u}^{n}\Delta t, \tag{10}$$

$$\mathbf{u}^{**} = \mathbf{u}^{*} + \mathbf{f}^{*}\Delta t, \tag{11}$$

$$\mathbf{u}^{n+1} = \mathbf{u}^{**} - \nabla p^{n+1}\Delta t, \tag{12}$$

where the superscripts n is the time step, $\mathbf{u}^{*}$ and $\mathbf{u}^{**}$ are the intermediate velocity. However, the time step size Δt in Eqs. (10) and (11) may be not small enough for the stable computation. Thus we introduce the sub time step, for example,

$$\mathbf{u}^{*} = \mathbf{u}^{n} + \sum_{m=0}^{M-1}\nu\nabla^{2}\mathbf{u}^{n,m}\Delta\tau, \tag{13}$$

$$\mathbf{u}^{n,m+1} = \mathbf{u}^{n,m} + \nu\nabla^{2}\mathbf{u}^{n,m}\Delta\tau, \tag{14}$$

where the superscript m is the sub time step, and $\Delta\tau = \Delta t / M$ is the sub time step size. The sub time step size is determined by the diffusion number limitation.

III. Results

A. Stretching of IRBCs

A well known method to quantify the mechanical response of IRBCs is the stretching by the optical tweezers. Suresh et al. measured the axial and transverse diameters of IRBCs at different development stages with several stretching forces. We examine this stretching test numerically to validate our model. In the three-dimensional computational domain, we put an IRBC at initial time step. Then we stretch the IRBC horizontally with a stretching force as shown in Fig. 3. The time integration is carried out until the axial and transverse diameters are well converged. If the obtained results do not follow the experimental results, the values of model parameters k_s and k_b are changed and the computation is carried out again. Finally we can get the appropriate values of the model parameters. Figure 4 shows the comparison between the numerical results and the experimental results by Suresh et al. [5] for the IRBC in the schizont stage. When we use the appropriate parameters, the numerical results agree well with the experimental results. A small difference can be found in the axial diameter, in particular, for high stretching forces. This may be due to the linear elastic modeling of RBC membrane.

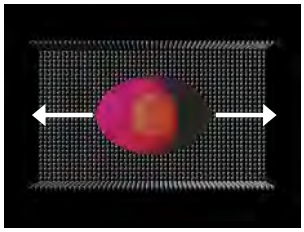


Fig. 3 Numerical test of stretching of the IRBC.

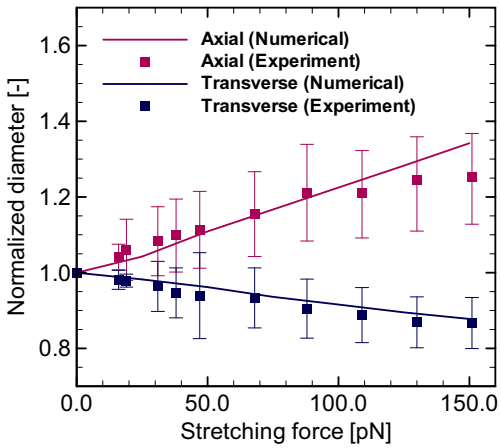


Fig. 4 Comparison between the numerical and experimental results for the stretching of the IRBC in the schizont stage.

B. Flow in narrow channels

We also simulate the flow into narrow channels using our numerical model. Here, we consider the flow of a healthy RBC (HRBC) and a schizont IRBC in a 6-μm-square channel. The flow is driven by the pressure difference between the inlet and outlet. Snapshots of the numerical simulation are presented in Fig. 5. As observed in experimental studies, the HRBC passes through the narrow channel with large deformation. In contrast to the HRBC, the schizont IRBC hardly flows into the narrow channel. These results follow the experimental observation by Shelby et al [9]. They revealed that IRBCs in the late trophozoite and schizont stages occluded flow into the channel with 6μm width. The depth of their channels was fixed to 2μm and thus the effect of such a small depth was not clarified. In contrast to their experiments, our results clearly demonstrate that the IRBCs can occlude the flow even in the 6-μm-square channels.

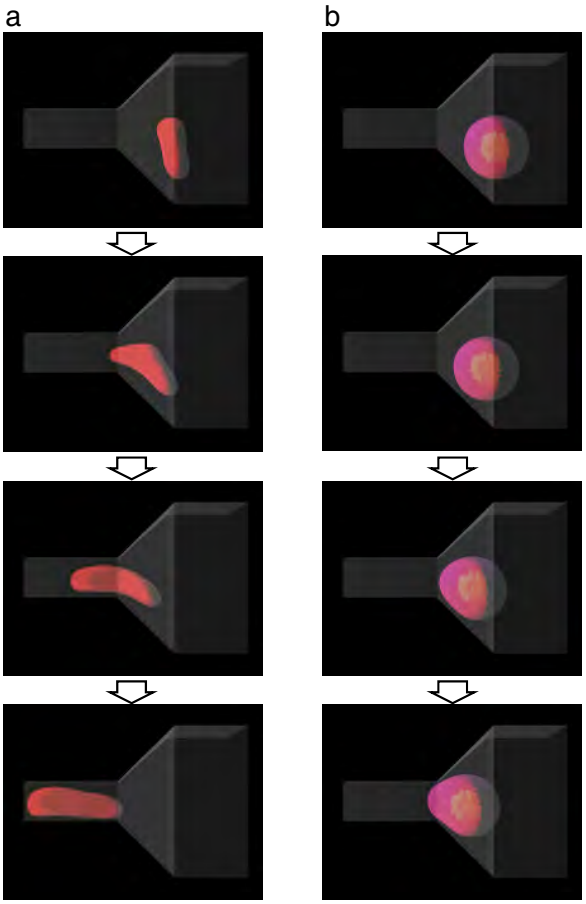


Fig. 5 Snapshots of the behavior of the IRBC in narrow channel: (a) HRBC; (b) IRBC in the schizont stage.

IV. Conclusions

We have developed a numerical model of three-dimensional hemodynamics arising from malaria infection. Particle based spatial discretization and the sub time step time integration can provide us stable computations for the micro scale blood flow involving the interaction with many cells. We performed the stretching of IRBCs and the numerical results agreed well with experimental results. The flow in narrow channels was also examined for the 6-μm-square channel. As reported in experimental studies, the IRBC in the late stage of infection could not pass through the narrow channels. In this paper, we have not considered the adhesion property of IRBCs. We have already developed an adhesion model [11] and this adhesion model can be applied easily to the current hemodynamic model. In the next paper, we will show the effects of the adhesion to micro circulation.

References

1. Cooke BM, Mohandas N, Coppell RL (2001) The malaria-infected red blood cell: structural and functional changes. Advances in Parasitology 26:1-86
2. Nash GB, O'Brien E, Gordon-Smith EC et al. (1989) Abnormalities in the mechanical properties of red blood cells caused by Plasmodium falciparum. Blood 74:855-861
3. Paulitschke M, Nash GB (1993) Membrane rigidity of red blood cells parasitized by different strains of Plasmodium falciparum. Journal of Laboratory and Clinical Medicine 122:581-589
4. Lim CT, Zhou EH, Quek ST (2006) Mechanical models for living cells - a review. Journal of Biomechanics 39:195-216
5. Suresh S, Spatz J, Mills JP et al. (2005) Connection between single-cell biomechanics and human disease states: gastrointestinal cancer and malaria. Acta Biomaterialia 1:15–30
6. Lim CT, Zhou EH, Li A et al. (2006) Experimental techniques for single cell and single molecule biomechanics. Materials Science and Engineering C 26: 1278-1288
7. Lim CT (2006) Single cell mechanics study of the human disease malaria. Journal of Biomechanical Science and Engineering 1:82-92
8. Lee GYH, Lim CT (2007) Biomechanics approaches to studying human diseases. Trends in Biotechnology 25:112-118
9. Shelby JP, White J, Ganesan K et al. (2003) A microfluidic model for single-cell capillary obstruction by Plasmodium falciparum-infected erythrocytes. Proceedings of the National Academy of Sciences of the United States of America 100:14618-14622
10. Dupin MM, Halliday I, Care CM et al. (2008) Lattice Boltzman modelling of blood cell dynamics. International Journal of Computational Fluid Dynamics 22:481-492
11. Kondo H, Imai Y, Ishikawa T et al. (2008) Hemodynamic analysis of microcirculation in malaria infection. Annals of Biomedical Engineering, submitted.
12. Koshizula S, Oka Y (1996) Moving-particle semi-implicit method for fragmentation of incompressible fluid. Nuclear Science and Engineering 123:421-434
13. Koshizuka S, Nobe A, Oka Y (1998) Numerical analysis of breaking waves using the moving particle semi-implicit method. International Journal for numerical methods in fluids 26:751-769

Author: Yohsuke Imai
Institute: Tohoku University
Street: 6-6-01 Aramaki Aza Aoba
City: Sendai
Country: Japan
Email: yimai@pfsl.mech.tohoku.ac.jp

Development of a Commercial Positron Emission Mammography (PEM)

Masayasu Miyake[1], Seiichi Yamamoto[3], Masatoshi Itoh[1,4], Kazuaki Kumagai[1], Takehisa Sasaki[1], Targino Rodrigues dos Santos[1,5], Manabu Tashiro[1] and Mamoru Baba[2]

Divisions of [1] Cyclotron Nuclear Medicine, and [2] Radiation Protection and Safety Control,
Cyclotron and Radioisotope Center, Tohoku University, Sendai, Japan
[3] Department of Electrical Engineering, Kobe City College of Technology, Kobe, Japan
[4] Sendai Medical Imaging Clinic, Sendai, Japan
[5] CMI, Inc., Tokyo, Japan

Abstract — **The incidence of breast cancer is in the first place as a cause of death among Japanese women. The breast cancer is a type of cancer which can be cured relatively easily when detected early. However, it is now clear that the detection of breast cancer is difficult without imaging modalities such as X-ray mammography and/or ultrasonic echography. These imaging devices are useful, however, morphological information only are not enough for differentiating cancer from other benign diseases. Positron emission tomography (PET) for whole-body diagnosis can give us functional information regarding the degree of malignancy. But still there remain various problems such as limited spatial resolution and motion artifacts due to respiratory movement, as well as an issue of the high costs. To compensate these weak points, we have started development of the positron emission mammography (PEM) dedicated for the local diagnosis of the breast tissue.**

We had developed a test device, "PEM simulator" last year. And we have developed a prototype PEM scanner. In the present paper, basic features are introduced regarding a gantry, chair, detector unit and measurement system of the PEM scanner, as well as our first results obtained by using this prototype scanner.

Keywords — **positron emission mammography (PEM), positron emission tomography (PET), [^{18}F]fluorodeoxyglucose (FDG), X-ray mammography, breast cancer.**

I. Introduction

The incidence of breast cancer is in the first place as a cause of death among Japanese women. The breast cancer is a type of cancer which can be cured relatively easily if it is detected early enough, because the breast cancer grows surface of the body. The highest incidence of breast cancer is seen among the thirties and forties. The high incidence among these generations would affect our society considerably because the women in these generations are usually serving important roles in their families and working places.

Recently imaging modalities such as X-ray mammography and/or ultrasonic echography are useful for the detection of breast cancer. However, these modalities give us morphological information only. Younger women or women who have no history of breastfeeding are tending to developing of mammary gland. A case of X-ray mammography, the developing of mammary gland makes shadows to mammography images and makes the detection of breast cancer difficult.

Positron emission tomography (PET) for whole-body diagnosis can give us functional information of cancer tissues including the degree of malignancy that can be reflected by the level of accumulation of a tracer, [^{18}F]fluorodeoxyglucose (FDG). But still there remain various problems such as limited spatial resolution and motion artifact due to respiration movement, as well as an issue of the very high costs for installment and maintenance. In measuring events of the coincidences of positrons, larger distance between detectors, as seen with PET scanners, for whole-body imaging makes a limit of spatial resolution.

In order to compensate these weak points, we have started development of a positron emission mammography (PEM) scanner dedicated for the local diagnosis of the breast tissues. The PEM scanner is much smaller than conventional PET. Therefore, the smaller scanner can have an improved spatial resolution and lowered costs.

II. PEM in the world

These days, a number of positron emission tomography for detecting breast cancer was constructed 1-5 . Murthy et al. have combined PEM with X-ray mammography to overlay these images [6]. Lecoqa and Varela have used LYSO as a scintillator and avalanche photo diode as scintillation detector [7]. Raylmana et al. have developed a dedicated system for biopsy of breast cancer 8.

III. Development prototype PEM scanner

A. PEM simulator

We are developing PEM scanner. We will make a prototype PEM scanner for commercial use. This scanner will

Chwee Teck Lim, James C.H. Goh (Eds.): ICBME 2008, Proceedings 23, pp. 2248–2249, 2009
www.springerlink.com

detect smaller tumor, be cheaper and smaller than conventional PET scanner. We aim less than 1-2 millimeter in spatial resolution. The price will be 20 percents than conventional PET scanner.

We have developed some test devices and the PEM simulator last year. One of them is block detector device. The device is constructed by flat-panel photo multiplier tube (FP-PMT), inorganic scintillator crystals array, aluminum case and signal processing circuit. The FP-PMT is multi anode PMT which has 16x16 anodes and has position sensitivity.

The PEM simulator is a testing and an evaluating system of PEM scanner. The simulator has four block detector devices, high voltage supply units for photo multiplier tubes and signal processing units. The signal processing unit consists of analog amplifier, analog to digital converter, FPGA devices and communication interface for PC.

We used this device for evaluation of a basic property of PEM scanner we are developing. We measured point sources and line sources and took some distribution images of positron sources.

B. Large area PEM detector unit

We have developed a large area PEM detector unit. The size of the detector unit is 156 x 208 mm^2. It consists of three 140.8 x 44 mm^2 inorganic scintillator crystals arrays (Fig. 1) and 3 x 4 FP-PMTs (Fig. 2). These are stored in a aluminum case shielded from lights (Fig. 3). Two PEM detector units are used the prototype PEM scanner and set up parallel. We are measuring some radioactive phantoms with using these detector units.

We are developing control and acquisition software, a gantry and a chair, too. Finally we will assemble the detector unit and these parts and construct the PEM scanner. We will check a safety of the scanner and measure in clinical use.

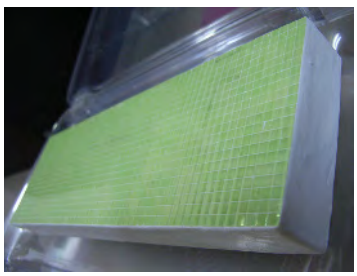


Fig. 1 An inorganic scintillator crystals arrays. The size of the crystal is 2.2 x 2.2 x 15 mm^3 and the size of the arrays is 140.8 x 44 mm^2.

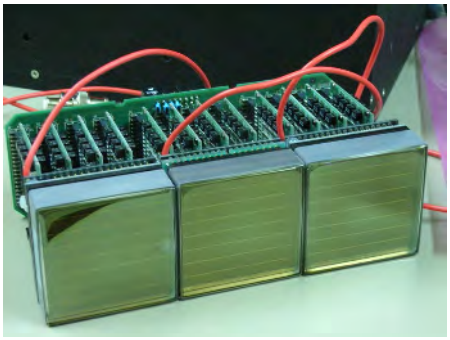


Fig. 2 A part of FP-PMTs of the PEM detector unit.

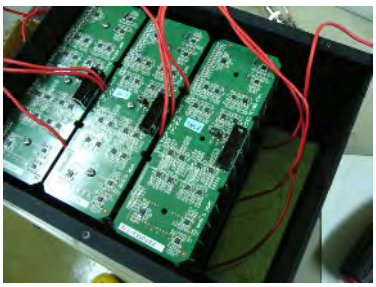


Fig. 3 A cover of the PEM detector unit is opened. We can see an aluminum case, an inorganic scintillator crystals allay and electronic circuits for FP-PMTs.

References

1. William W Moses. (2004) Positron Emission Mammography imaging. *Nucl Instrum Methods Phys Res A* 525, 249-252
2. Richard Freifelder and Joel S Karp. (1997) Dedicated PET scanners for breast imaging. *Phys Med Biol* 42, 2463–2480
3. Niraj K Doshi, Yiping Shao, Robert W Silverman et al. (2000) Design and evaluation of an LSO PET detector for breast cancer imaging. *Med Phys* 27(7), 1535-1543
4. Kavita Murthy, Marianne Aznar, Alanah M Bergman et al. (2000) Positron Emission Mammographic Instrument: Initial Results. *Radiology* 215, 280-285
5. Raymond R Raylman, Stan Majewski, Andrew G Weisenberger et al. (2001) Positron Emission Mammography–Guided Breast Biopsy. *J Nucl Med* 42(6), 960-966
6. Kavita Murthy, Marianne Aznar, Christopher J Thompson et al. (2000) Results of Preliminary Clinical Trials of the Positron Emission Mammography System PEM-I: A Dedicated Breast Imaging System Producing Glucose Metabolic Images Using FDG. *J Nucl Med* 41(11), 1851-1858
7. P Lecoqa and J Varela. (2002) Clear-PEM, a dedicated PET camera for mammography. *Nucl Instrum Methods Phys Res A* 486, 1-6
8. Raymond R. Raylmana, Stan Majewskib, Brian Krossb et al. (2006) Development of a dedicated positron emission tomography system for the detection and biopsy of breast cancer. *Nucl Instrum Methods Phys Res A* 569, 291-295

Radiological Anatomy of the Right Adrenal Vein: Preliminary Experience with Multi-detector Row Computed Tomography

T. Matsuura, K. Takase and S. Takahashi

Dept of Radiology, Tohoku University School of Medicine, Sendai, Japan

Abstract — **OBJECTIVE. The purpose of our study was to determine how frequently the right adrenal vein could be unequivocally identified on MDCT and what spectrum of anatomic variations was seen among the right adrenal vein. MATERIALS AND METHODS. Post-contrast MDCT were obtained using an 8-detector row helical CT scanner in 104 patients with thoracoabdominal vascular disease. Both axial and multiplanar images were reviewed by two radiologists. The following points regarding the right adrenal vein were evaluated: the degree of visualization; the relationship to accessory hepatic or other veins; the anatomy including the location of the orifice in relation to the surrounding structures, direction from the inferior vena cava, and length and diameter. RESULTS. The right adrenal vein was detected in 79 (76%) of 104 patients. The right adrenal vein formed a common trunk with an accessory hepatic vein in 6 (8%) of the 79 patients. The orifice was craniocaudally located between the level of vertebrae T11 and L1. Among the 73 patients, the right adrenal vein joined the inferior vena cava in the right posterior quadrant in 71 (97%) and in the left posterior quadrant in 2 patients (3%). The transverse direction from the inferior vena cava was posterior and rightward in 56 (77%) and posterior and leftward in 17 (23%), and the vertical direction from the inferior vena cava was caudal in 65 (89%) and cranial in 8 patients (11%). The length and diameter averaged 3.8 and 1.7 mm, respectively. CONCLUSION. MDCT enabled the identification of the right adrenal vein and delineation of its anatomy, including the position and relationship to surrounding structures.**

Keywords — **CT, anatomy, right adrenal vein, adrenal venous sampling, aldosteronism**

I. Introduction

Primary aldosteronism is the most common form of secondary hypertension [1, 2]. Unilateral aldosterone-producing adenoma and bilateral idiopathic hyperaldosteronism are the two most common subtypes of primary aldosteronism, and distinguishing between them is critical for treatment planning, because the former is treated with adrenalectomy while the latter is treated medically [3]. CT and MRI are both still unreliable methods for distinguishing the subtypes of primary aldosteronism [4-6], for which adrenal venous sampling is often undertaken [6, 7].

Selective adrenal venous sampling can be difficult to perform because catheterization of the right adrenal vein (RAV) generally remains difficult [6-11]. The difficulty associated with RAV catheterization appears to result from the small size and variable anatomy of the RAV, which is a vein that usually drains directly into the inferior vena cava (IVC) at a variable angle [8, 12].

MDCT could possibly guide adrenal venous sampling if it were capable of delineating the anatomy of the RAV. Although Daunt referred to the feasibility of identifying the RAV with MDCT [12], to our knowledge, a detailed analysis regarding visualizing the anatomy of the RAV with MDCT has never been made. We undertook this study to determine how frequently the RAV could be identified on MDCT and what spectrum of anatomic variations was seen among the RAV.

II. Materials and methods

This study was approved by the hospital institutional review board and is compliant with the Health Insurance Portability and Accountability Act (HIPAA). Informed consent was waived by the hospital institutional review board.

A. Patients

We performed a retrospective analysis of CT images from 104 consecutive patients (69 men, 35 women; mean age, 67 years; range, 26–89 years) with a presumptive diagnosis of thoracoabdominal vascular disease.

B. CT examination

The CT scanner was an 8-detector row helical CT scanner. Before scanning was started, 100 mL of contrast material containing 300 mg of iodine per milliliter was injected at a rate of 3.5 mL/sec. Transverse sections were reconstructed with a 1-mm section thickness. We used a cine-mode display of transverse and multiplanar reformation (MPR) images to evaluate the RAV. Two radiologists analyzed the CT images.

Chwee Teck Lim, James C.H. Goh (Eds.): ICBME 2008, Proceedings 23, pp. 2250–2253, 2009
www.springerlink.com

C. Points of evaluation

We evaluated the following points regarding the RAV: the degree of visualization; whether the common trunk was formed before entering the IVC with accessory hepatic or other veins; the anatomy of the RAV including the location of the orifice, direction, length and diameter of the RAV when it directly joined the IVC. For describing the direction of the RAV, we used a three-dimensional coordinate system and aligned the rectangular coordinate axes with the body axes (i.e., anteroposterior = *x*-axis, transverse = *y*-axis, and vertical = *z*-axis). The positive *x*-, *y*-, and *z*-axes pointed posteriorly, rightward, and caudally, respectively.

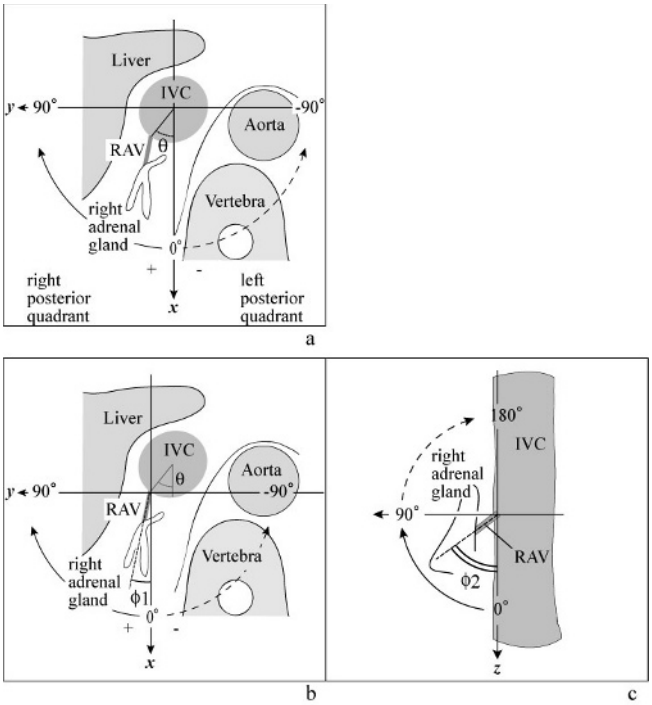


Fig. 1 The position of the right adrenal vein (RAV) orifice and its relationship to the surrounding structures, and the direction of the RAV (a) The transverse plane observed from the inferior shows the position of the RAV orifice, which was estimated along the circumference of the inferior vena cava (IVC) as an angle θ between the radius line through the orifice and the *x*-axis in the *x*-*y* plane. The intersection of the *x*- and *y*-axes is specified as the center of the IVC. The angle θ was measured positively in the clockwise direction from the *x*-axis with a negative angle being in the counterclockwise direction. When θ falls between 0° and 90°, the RAV is described as entering the IVC in the right posterior quadrant; when θ falls between –90° and 0°, it is described as entering in the left posterior quadrant. (b) The transverse plane shows the direction of the RAV from the IVC, which was measured in the *x*-*y* plane as an angle ϕ1 between the projected figure of the RAV and the *x*-axis. The intersection of the *x*- and *y*-axes is specified as the junction between the RAV and IVC. The angle ϕ1 was measured positively in the clockwise direction from the *x*-axis with a negative angle being in the counterclockwise direction. (c) The vertical plane shows the craniocaudal direction of the RAV from the IVC, which was measured as an angle ϕ2 between the RAV and the *z*-axis. The intersection of the *x*-*y* plane and *z*-axes is specified as the junction between the RAV and IVC. The angle ϕ2 was measured from the *z*-axis to the RAV.

Degree of visualization of the RAV: The rate of visualization was checked. The degree of visualization was arbitrarily graded on a 5-point scale as follows: "excellent", "good", "fair", "poor", and "none". We defined the former three categorized groups (excellent, good, and fair) as those with an unequivocally identified RAV, in which the following anatomical analyses were made, and the latter two groups (poor and none) were categorized as those with an unidentified RAV and excluded from the following analyses.

Relationship of the RAV to accessory hepatic or other veins: We examined whether a common trunk for the RAV and accessory hepatic or other veins was formed before entering the IVC. When the RAV directly entered the IVC but almost shared a common orifice with accessory hepatic or other veins, it was also recorded.

Location of the RAV orifice in relation to surrounding structures: The craniocaudal level of the RAV orifice was specified relative to vertebral bodies and discs. Vertebral bodies were divided into three segments: superior, middle, and inferior. The position of the orifice was also evaluated along the circumference of the IVC as an angle θ in the *x*-*y* plane (Figure 1a).

Direction of the RAV from the IVC: To evaluate the direction of the RAV from the IVC, two angles were measured: the first was the angle ϕ1 between the RAV and *x*-axis when the RAV was projected onto the *x*-*y* plane (Figure 1b), while the other was the craniocaudal angle ϕ2 between the RAV and z-axis when the RAV was projected onto the vertical plane that paralleled the RAV (Figure 1c).

Length and diameter of the RAV: We measured the length of the RAV between the exit from the right adrenal gland and entry to the IVC, and the diameter of the RAV at the junction with the IVC.

III. Results

Degree of visualization of the RAV: The degree of visualization was excellent in 36 (35 %; Figure 2a), good in 30 (29%; Figure 2b), fair in 13 (13%), poor in 7 (7%), and none in 18 (17%) of 104 patients. Therefore, the RAV was detected in 79 (76%) of 104 patients according to our identification criteria (excellent to fair), in which the following anatomical analyses were made.

Relationship of the RAV to accessory hepatic or other veins: Among the 79 patients who had an identifiable RAV (excellent to fair), the RAV and accessory hepatic vein formed a common trunk before entering the IVC in 6 (8%; Figure 3), the RAV entered the IVC directly but almost

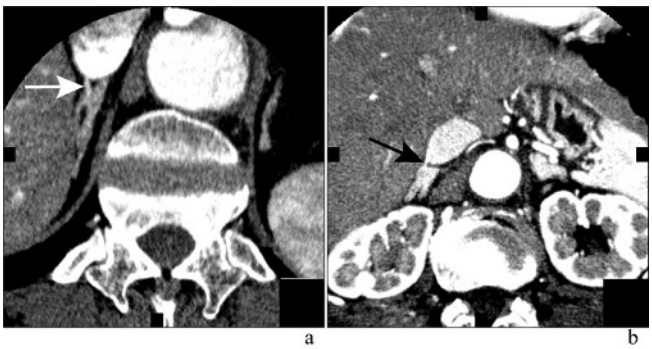


Fig. 2 Examples of the right adrenal vein (RAV) showing variable degree of visualization (a) 54-year-old man. A para-axial multiplanar reformatted image shows excellent visualization of the RAV (arrow) running through the intervening adipose tissue to join the right posterior quadrant of the inferior vena cava (IVC). (b) 87-year-old woman. A para-axial multiplanar reformatted image shows the RAV (arrow) and the right adrenal gland located close to the inferior vena cava (IVC). Although the RAV is a small structure, good visualization of the RAV is attained owing to dense enhancement.



Fig. 3 56-year-old man. A para-axial multiplanar reformatted image shows the right adrenal vein (RAV, arrow) that drains to the accessory hepatic vein (arrowhead) before entering the IVC.

shared a common orifice with an accessory hepatic vein in 7 (9%), and the RAV entered the IVC independently of other vein in the remaining 66 (84%) patients. No case occurred in which the RAV formed a common trunk with veins other than accessory hepatic vein.

Location of the RAV orifice in relation to surrounding structures: The orifice was craniocaudally located between the level of T11 and L1 (Figure 4a). In 50 (69%) of the 73 patients, the RAV joined the IVC at the level ranging from the middle third of T12 to the superior third of L1. Angle θ representing the position of the orifice along the circumference of the IVC is shown in Figure 4b. Angle θ ranged from –7° to 71° (mean, 39°). The RAV joined the IVC in the right posterior quadrant in 71 (97%) of the 73 patients, most frequently in a range of angulation between 20° and 60°. In 2 (3%) of the 73 patients, it occurred in the left posterior quadrant.

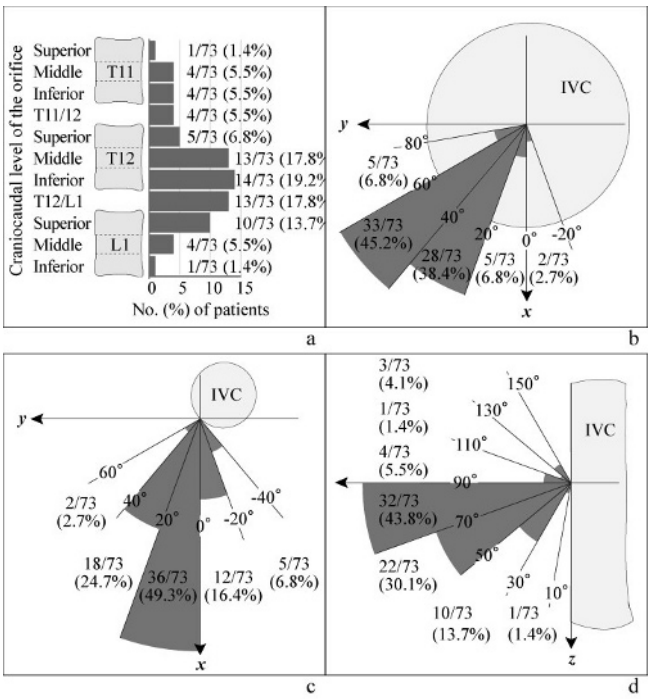


Fig. 4 The location of the right adrenal vein (RAV) orifice, and the direction of the RAV from the inferior vena cava (IVC) (a) The craniocaudal level of the RAV orifice in relation to the vertebral bodies and discs. (b) The position of the RAV orifice along the circumference of the IVC evaluated as angle θ. (c) The direction of the RAV from the IVC in the transverse plane which is represented as the angle with the x-axis (ϕ1). (d) The direction of the RAV from the IVC in the vertical plane which is represented as the craniocaudal angle with z-axis (ϕ2).

Direction of the RAV from the IVC: The angles, ϕ1 in the transverse plane and ϕ2 in the vertical plane, are shown in Figure 4c, d. The angle ϕ1 ranged from –36° to 47° (mean, 8°), ranging between 0° and 20° in almost half of the patients. The direction from the IVC was posterior and rightward in 56 (77%) and posterior and leftward in 17 (23%) of the 73 patients. The angle ϕ2 ranged from 30° to 136° (mean, 73°), and most patients showed a value between 50° and 90°. The direction from the IVC was caudal in 65 (89%) and cranial in 8 (11%) of the 73 patients.

Length and diameter of the RAV: The mean length was 3.8 mm, and the mean diameter at the junction with the IVC was 1.7 mm.

IV. Discussion

MDCT enabled the identification of the RAV in most patients. In the cases in which the RAV was identified, the RAV anatomy including the position in relation to the IVC and surrounding structures was well evaluated. The results

concerning the length, diameter, craniocaudal level of the orifice were all similar to those of the earlier studies using autopsy or venography [8, 13-18].

The position of the orifice along the circumference of the IVC was most commonly located in the right posterior quadrant of the IVC in our study, which accord with those in the literature. However, we also found rare cases whose orifice was located in the left posterior quadrant in 2 (3%) of the 73 patients, which has never been described [8, 18].

A common trunk of the RAV with an accessory hepatic vein was found in 6 (8%) of the 79 patients in our series. In addition, the RAV took a separate course but almost shared a common orifice with an accessory hepatic vein in another 7 (9%) of the 79 patients. In the literature [14-16], a common trunk of the RAV with an accessory hepatic vein has been reported in approximately 10–21%; a common trunk might have included both types of variation, although no detailed distinction between them were provided.

Catheterization of the RAV remains difficult. Its success rate generally remains around 60–70% [6, 8-11]. The difficulty may arise owing to the small size of the RAV, its anatomic variations in the junction with the IVC, and/or confusion with accessory hepatic veins that may form a common stem with the RAV [8, 12].

A reliable way to delineate the RAV anatomy before adrenal venous sampling was not previously available, but our study suggests the potential for MDCT to provide detailed information on the RAV anatomy similar to other small arteries [12]. Such information would be useful in planning adrenal venous sampling. We believe that preoperative recognition of the RAV anatomy would be especially valuable for RAV catheterization and subsequent venous sampling.

V. Conclusions

MDCT enabled the identification of the RAV and delineation of its anatomy, including the position and relationship to the surrounding structures such as the IVC in a high percentage of patients. This preoperative information may be helpful in the catheterization of the RAV for adrenal venous sampling.

References

1. Gordon RD, Stowasser M, Tunny TJ et al. (1994) High incidence of primary aldosteronism in 199 patients referred with hypertension. Clin Exp Pharmacol Physiol 21:315-318
2. Mulatero P, Stowasser M, Loh KC et al. (2004) Increased diagnosis of primary aldosteronism, including surgically correctable forms, in centers from five continents. J Clin Endocrinol Metab 89:1045-1050
3. Young Jr WF (2002) Primary aldosteronism: management issues. Ann N Y Acad Sci 970:61-76
4. Doppman JL, Gill Jr JR, Miller DL et al. (1992) Distinction between hyperaldosteronism due to bilateral hyperplasia and unilateral aldosteronoma: reliability of CT. Radiology 184:677-682
5. Radin DR, Manoogian C, Nadler JL (1992) Diagnosis of primary hyperaldosteronism: importance of correlating CT findings with endocrinologic studies. AJR Am J Roentgenol 158:553-557
6. Magill SB, Raff H, Shaker JL et al. (2001) Comparison of adrenal vein sampling and computed tomography in the differentiation of primary aldosteronism. J Clin Endocrinol Metab 86:1066-1071
7. Young WF, Stanson AW, Thompson GB et al. (2004) Role for adrenal venous sampling in primary aldosteronism. Surgery 136:1227-1235
8. Davidson JK, Morley P, Hurley GD et al. (1975) Adrenal venography and ultrasound in the investigation of the adrenal gland: an analysis of 58 cases. Br J Radiol 48:435-450
9. Harper R, Ferrett CG, McKnight JA et al. (1999) Accuracy of CT scanning and adrenal vein sampling in the pre-operative localization of aldosterone-secreting adrenal adenomas. QJM 92:643-650
10. Gordon RD, Stowasser M, Rutherford JC (2001) Primary aldosteronism: are we diagnosing and operating on too few patients? World J Surg 25:941-947
11. Espiner EA, Ross DG, Yandle TG et al. (2003) Predicting surgically remedial primary aldosteronism: role of adrenal scanning, posture testing, and adrenal vein sampling. J Clin Endocrinol Metab 88:3637-3644
12. Daunt N (2005) Adrenal vein sampling: how to make it quick, easy, and successful. Radiographics 25:S143-S158
13. Johnstone FR (1957) The suprarenal veins. Am J Surg 94:615-620
14. Mikaelsson CG (1970) Venous communications of the adrenal glands. Anatomic and circulatory studies. Acta Radiol Diagn (Stockh) 10:369-393
15. McLachlan MS, Roberts EE (1971) Demonstration of the normal adrenal gland by venography and gas insufflation. Br J Radiol 44:664-671
16. Nakamura S, Tsuzuki T (1981) Surgical anatomy of the hepatic veins and the inferior vena cava. Surg Gynecol Obstet 152:43-50
17. El-Sherief MA (1982) Adrenal vein catheterization. Anatomic considerations. Acta Radiol Diagn (Stockh) 23:345-360
18. Madsen B (1991) Atlas of normal and variant angiographic anatomy. Saunders, Philadelphia

Author: Tomonori Matsuura
Institute: Dept of Radiology, Tohoku University School of Medicine
Street: 1-1 Seiryo, Aoba
City: Sendai
Country: Japan
Email: t.matsuura@rad.med.tohoku.ac.jp

Atrial Vortex Measurement by Magnetic Resonance Imaging

M. Shibata[1,2], T. Yambe[2], Y. Kanke[3] and T. Hayase[3]

[1] Miyagi Cardiovascular and Respiratory Center, Kurihara, Japan
[2] Institute of Development, Aging and Cancer, Tohoku University, Sendai, Japan
[3] Institute of Fluid Science, Tohoku University, Tohoku University, Sendai, Japan

Abstract — **The clinical meaning of left atrial vortex has been not fully elucidated. We developed a new left atrial model to simulate intra-atrial flow and a simple method to observe atrial vortex by magnetic resonance imaging (MRI).**

A flow simulation model of the left atrium (LA) was developed based on slices of the LA image acquired by 1.5T MRI scanner system. Images were reconstructed by commercial software and a computational model was created by using tetrahedral mesh. In order to give the model consecutive temporal change, we presumed that deformation of LA is related to mitral valve annular movement. Then we traced its temporal change and approximated. The flow simulation was performed with FLUENT. Pressure boundary conditions were set based on data in a literature.

The results of flow simulation in LA were validated qualitatively by MRI velocity mapping. Left atrial vortex was observed in both simulation and MRI velocity mapping. A representative slice to observe left atrial vortex by MRI was determined with the assistance of the simulation model.

Keywords — **MRI, atrial vortex, simulation model**

I. Introduction

Clinical meaning of left atrial vortex has been not fully elucidated. The left atrium (LA) serves as both a conduit and a reservoir. During diastole, it directs inflow from the pulmonary veins towards the mitral annulus, and during ventricular systole it retains the inflow volume until the mitral valve reopens.

Kilner mentioned that patterns of atrial filling seem to be asymmetric in a manner that allows the momentum of inflowing streams to be redirected towards atrio-ventricular valves [1]. Although flow dynamics of the left ventricle has been investigated by physical, computational modeling and by invasive and non-invasive imaging. But atrial flow has not been investigated intensively. Fyrenius visualized normal left atrial flow using magnetic resonance imaging (MRI) and in all normal subjects vortical flow was observed in the atrium during systole and diastolic diastasis [2].

Much attention has been directed toward the role of stretch and mechanoelectric feedback in the atria. Atrial stretch plays an apparent role in the development of atrial fibrillation in a wide spectrum of clinical conditions [3]. Local flow change may affect on the electrical character of left atrium.

MRI is an excellent tool to evaluate atrial flow. Magnetic resonance velocity mapping is a reliable tool for analysis and visualization of blood flow in vivo. But reconstruction of multi-slice MRI data set is needed to visualize 3D flow and datasets are fragmentary.

A simulation model helps us comprehend atrial flow dynamics and might provide insights the origin of atrial vortex. The purpose of this study was to examine the flow in the left atrium by numerical simulation via modeling from magnetic resonance (MR) images and invent a simple method to evaluate atrial vortex.

II. Methods

A. Building a simulation model

Magnetic resonance images of the LA of a 23-year-old healthy male volunteer were acquired using a 1.5T MRI scanner system (Achieva 1.5T, Philips Electronics, Best, Nederland), SENSE cardiac coil and two-dimensional balanced turbo field echo (TR (repetition time) = 3.3 msec, TE (echo time) = 1.7 msec, FA (flip angle) = 60 °, slice thickness = 5 mm, FOV (field of view) = 400 mm, matrix size = 256×256). This study was approved by the regional ethics committee of Miyagi Cardiovascular and Respiratory Center.

Four chamber T1 weighted images were acquired in twelve slices at 5 mm intervals to create images of the whole LA. 15 seconds is needed to obtain 20 phases of MR images during the R-R interval in one cross section. Then the scan time for obtaining the whole LA was 6 minutes.

Figure 1 shows an acquired MR image with a white ellipse indicating the LA. The pulmonary veins are connected to the right and left sides of the LA, and the mitral valve is located at the bottom.

Images were reconstructed by commercial software Mimics 7.3 (Materialise N.V., Belgium), and a computational model was created by using tetrahedral mesh. In order to give the model consecutive temporal change, we presumed that deformation of LA is related to mitral valve annular movement. Figure 2 shows a scheme of deformation. First, the location of the mitral valve in an XY coordi-

Chwee Teck Lim, James C.H. Goh (Eds.): ICBME 2008, Proceedings 23, pp. 2254–2257, 2009
www.springerlink.com

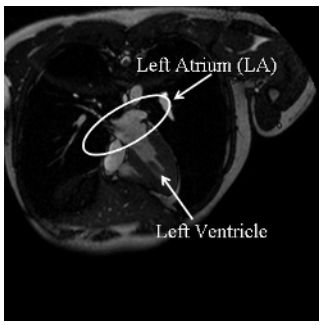
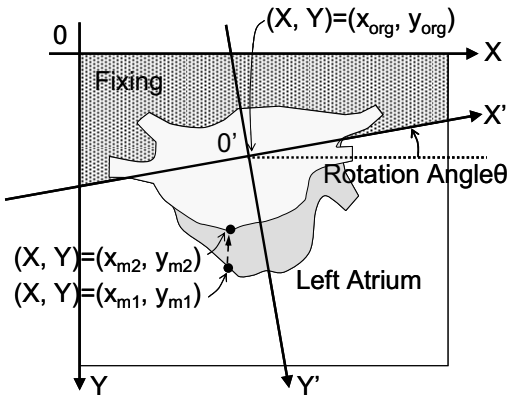
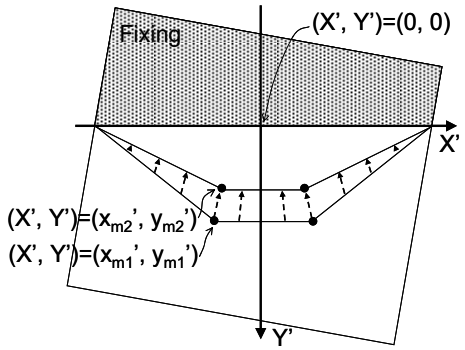


Fig. 1 A slice of Left Atrium MR image



(a) XY coordinate



(b) X'Y' coordinat

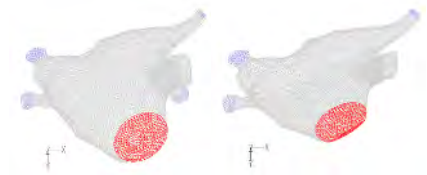
Fig. 2 Movement of mitral valve and deformation of left atrium

nate system (the upper left point is the origin) was set by (x_{m1}, y_{m1}) in phase 1 and by (x_{m2}, y_{m2}) in phase 2. Next, an X'Y' coordinate system was set with the Y' axis parallel to movement of the mitral valve and the original point located at (x_{org}, y_{org}) in XY coordinate system. The points (x_{m1}, y_{m1}) and (x_{m2}, y_{m2}) in the XY coordinate system were converted into the points (x_{m1}', y_{m1}') and (x_{m2}', y_{m2}') in the X'Y' coordinate system, respectively. For the purposes of simplification, location of the right side of the mitral valve was set with the left side symmetrically against the Y' axis. The point (x_1', y_1') on the wall in the X'Y' coordinate system in phase 1 was moved to point (x_2', y_2') by the following equations when the Y' coordinate was positive

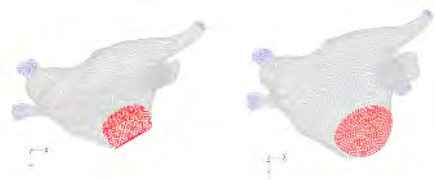
$$x_2' = \left\{ \frac{y_1'}{y_{m1}'} \left(\frac{x_{m2}'}{x_{m1}'} \right) + 1 \right\} x_1' \tag{1}$$

$$y_2' = \frac{y_{m2}'}{y_{m1}'} y_1' \tag{2}$$

Movement in the Y' direction of Eq. (2) is simple compression, but movement in the X' direction of Eq. (1) depends on the Y' coordinate. In the case of a negative Y' coordinate, the location of the point was fixed. This conversion was performed in each slice and linear interpolation was performed between the slices and among the models of 20 phases. Fig. 3 shows the computational models of four phases.



(a) phase1 (end diastole) (b) phase5 (systole)



(c) phase10 (end systole) (d) phasse15 (diastole)

Fig. 3 Computational model of each phase

Then we traced its temporal change and approximated. The flow simulation was performed with FLUENT. Pressure boundary conditions were set based on data in a literature [4]. Four inlets were given as 10 mmHg from data regarding pulmonary veins. An outlet was divided into systolic and diastolic phases. In the systolic phase (phase1-10), the pressure was set at 0-10 mmHg based on and in the diastolic phase (phase11-20), the outlet was assumed to be a wall. An initial condition was given as a stationary solution in phase 1. The other conditions are indicated in Table 1.

Table 1 Computational conditions

Parameters	value
Heart rate	91 bpm
Cardiac cycle *T*	659 ms
Time step *dt*	3.295 ms
Density ρ	1050 kg/m^3
Viscosity μ	3.5×10^{-3} Pas

B. Magnetic resonance velocity mapping

A 23-year-old healthy male volunteer with normal transthoracic echocardiographic findings was studied. The same subject was recruited. This study was approved by the regional ethics committee of Miyagi Cardiovascular and Respiratory Center.

Velocity measurements were performed using a 1.5T MRI scanner system (EXCELART 1.5 T, Toshiba Medical Systems,Tokyo,Japan), Torso SPEEDER coil and phase shift magnetic resonance angiography (TR = 24 msec, TE = 10 msec, FA = 20°, slice thickness = 5mm, FOV = 350 mm, matrix size = 256×256, VENC = 1m/sec). All three velocity components were measured in supine position with 50 sec breath holding in a four chamber view. 13 slices were obtained in 100 minutes.

Velocity vector filed was generated by all three velocity components from phase contrast data and projected onto 2D magnitude images. Visualization was created using Tecplot 360 2008 (Tecplot Inc., Bellevue, USA).

III. Results

A. Simulation data

Left atrial vortices were identified during systole and diastole. Figure 4 shows computed streamlines in systole and diastole period of the LA. During systole, the bloodstream in the LA rotated counterclockwise and developed to the vortex and disappeared with the onset of early diastole. During diastole, the bloodstream from the four inlets passing almost uniformly towards the mitral valve, the vortex flow appeared following peak early diastolic inflow and disappeared with the onset of atrial systole. The vortex in systole was more clearly observed than in diastole and its center was located the left side of the center of the LA.

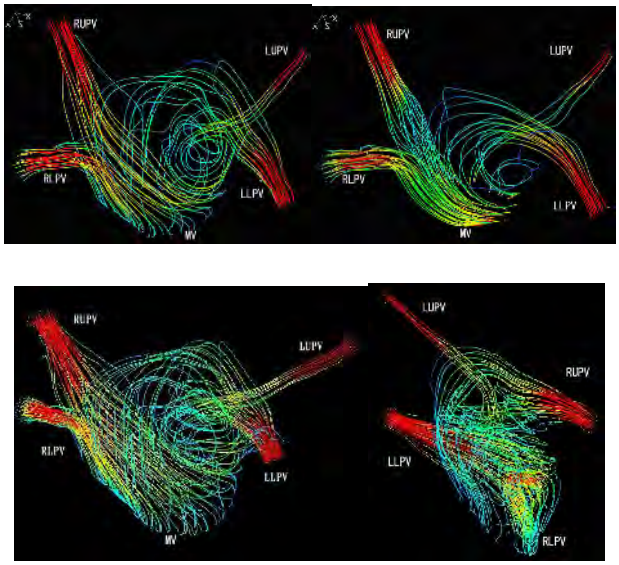


Fig. 4 Computed streamlines of blood flow in LA (upper left; vortex in systole, upper right; vortex in diastole, lower left; cranio-caudal view of systolic vortex, lower right; left lateral view of systolic vortex, RUPV: right upper pulmonary vein, RLPV: right lower pulmonary vein, LUPV: left upper pulmonary vein, LLPV: left lower pulmonary vein, MV: mitral valve)

B. In vivo data

Two discrete left atrial vortices were identified during systole and diastole, rotated counterclockwise. Fig5 shows velocity mapping of blood flow in LA in systole and diastole. The vortex in systole was more clearly observed than in diastole and its center was located around the center of the LA.

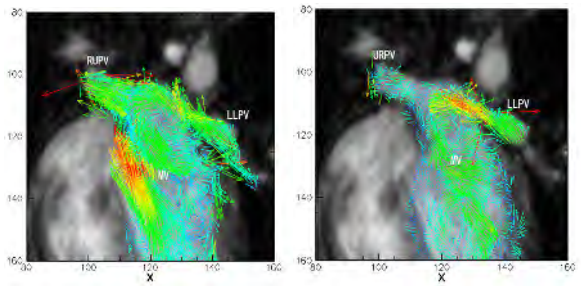


Fig. 5 Velocity mapping of blood flow in LA (left; systole, right: diastole, RUPV: right upper pulmonary vein, LLPV left lower pulmonary vein)

IV. Discussion

A. Model validation

Both simulation and in vivo data showed two discrete left atrial vortices were identified during systole and diastole. These results qualitatively agree with MR velocity mapping of LA by Kilner et al [1]. However, the velocities of flow in the LA were different between the computed value and measured by MRI or ultrasonic echo (data was not shown). This is probably because boundary conditions were different from the actual conditions of the subject. Although the boundary conditions were taken from data in the literature in this study, it would be necessary to set these conditions based on measurement data to obtain a more accurate result. Also, deformation of the LA was represented only by movement of the mitral valve on the left side of the LA in this research, but it is necessary to consider the validity of the model utilized. Especially, movement of the mitral valve of the right side of LA should be independently obtained for more accurate determination of LA deformation.

B. Left atrial vortex evaluation

Left atrial vortex in systole was clear and its center was located around the center of LA in both simulation and in vivo data. We propose that a slice which include around the center of LA, pulmonary veins (at least one vein) and mitral valve would be a representative slice to evaluate the left atrial vortex. Further study is needed to elucidate the meaning of left atrial vortex. MR velocity mapping in LA would be applied not only for healthy subjects but also for pathologic. However, in this study, it took 100 minutes to obtain whole LA flow velocity data, that is not realistic in clinical apply. Longer examination cause discomfort to the patient and increase the chance of artifact. At single slice it takes 3 minutes to obtain 3D velocity profiles, it would be tolerant for pathologic subjects.

V. Conclusions

In this study, numerical simulation of blood flow in the LA modeled from MR images was performed. The deformation of the LA was presumed from the location of the mitral valve. Computed results qualitatively agreed with data in the literature. Quantitative study with examination of boundary conditions and wall motion should be conducted in a future study. And we propose a slice for atrial vortex evaluation which include around the center of LA, pulmonary veins (at least a vein) and mitral valve. MR velocity mapping in LA would be applied for pathologic subject comfortably and accurately to clarify the meaning of left atrial vortex.

Acknowledgment

This study was performed using the MRI scanner system at Miyagi Cardiovascular & Respiratory Center and Tohoku Kosei Nenkin Hospital. The authors are grateful for the state-of-the-art computational environment afforded by Institute of Fluid Science.

References

1. Kilner PJ, Yang GZ, Wilkes AJ, et al. (2000) Asymmetric redirection of flow through the heart. Nature 404: 759-761
2. Fyrenius A, Wigström L, Ebbers T, et al (2001) Three dimensional flow in the human left atrium. Heart 86: 448–455
3. Chen AS, Haissaguerre M, Zipes DP. (2004) Thoracic Vein Arrythmias: Mechanisms and Treatment. Blackwell, London
4. 13. Smith JJ, Kampine JP. (1989) Circulatory physiology – the essential 2nd ed. the Williams & Wilkins company, Baltimore

Author: Muneichi Shibata
Institute: Miyagi Cardiovascular and Respiratory Center & Institute of Development, Aging and Cancer, Tohoku University
Street: 55-2 Semine Negishi
City: Kurihara
Country: Japan
Email: muneichi@idac.tohoku.ac.jp

Fabrication of Multichannel Neural Microelectrodes with Microfluidic Channels Based on Wafer Bonding Technology

R. Kobayashi[1], S. Kanno[2], T. Fukushima[1], T. Tanaka[1,2] and M. Koyanagi[1]

[1] Dept. of Bioengineering and Robotics, Graduate School of Engineering, Tohoku University, Japan
[2] Dept. of Biomedical Engineering, Graduate School of Biomedical Engineering, Tohoku University, Japan

Abstract — **We have proposed the intelligent Si neural probe which can realize high density and multifunctional recording of neuronal behaviors. In this device, LSI chips such as amplifiers, A/D converters, and multiplexers are integrated on the Si neural probe. In this paper, we report the development of a novel multichannel Si neural microelectrode with microfluidic channels which is the key part of the intelligent Si neural probe. The microelectrode has microfluidic channels fabricated using a wafer bonding technology to deliver drugs into the brain when neuronal action potentials are recorded. And also, our microelectrode has recording sites on both front- and back-side of Si to realize high density recording. We fabricated the carefully-designed multichannel Si neural microelectrode, and we evaluated characteristics of both recording sites and microfluidic channels. From the liquid ejection test, we confirmed that there was no void at bonding faces. We observed the liner relationship between the flow rate and the pressure drop, and the relationship was identical to that from the calculation, which indicated that the microfluidic channel was successfully formed. Moreover, both front- and back-side recording sites had impedance values of 2.5 MΩ and 2.7 MΩ at 1 kHz, respectively, which indicated that both recording sites had equivalent characteristics. The neuronal action potentials from CA1 area in a hippocampal slice were successfully recorded by using the fabricated microelectrode.**

Keywords — **Si intelligent neural probe, multichannel neural microelectrode, simultaneous multi-site recording**

I. Introduction

With the progressing of ageing society, the number of patient with brain diseases such as paralysis, epilepsy, and Parkinson's disease has been increasing remarkably. However, medical cures for these diseases have not been established yet. For medical care or rehabilitation of brain diseases, not only patients but also their families have been under heavy strain. In order to improve these situations, neurophysiology has attracted much attention all over the world. In neurophysiology, recording of neuronal signals from the brain plays an important role in advanced studies of neuronal circuit dynamics and relationships between actions of the body and activities of the brain. In the past few decades, various types of microelectrodes made of Si have been developed to record neuronal signals from the brain of animals, and lots of useful results were obtained [1-3]. We have proposed an intelligent Si neural probe system, and have been developing key parts of the system [4]. Figure 1 shows the configuration of the intelligent Si neural probe system.

In this system, a large number of recording sites are located on the tips of the intelligent Si neural probe for simultaneous multi-site recording of neuronal action potentials. Since neuronal signals are extremely low, electric circuits such as amplifiers (AMPs), A/D converters (ADCs), and multiplexers (MUXs) are integrated on the Si neural probe directly. Therefore, weak neuronal signals recorded from the brain are amplified with keeping low noise levels.

In the present paper, we propose a novel multichannel Si neural microelectrode with microfluidic channels which is the key part of the intelligent Si neural probe. We fabricated the carefully-designed multichannel Si neural microelectrode, and we evaluated characteristics of both recording sites and microfluidic channels. Subsequently, by using the fabricated microelectrode, we performed *in-vitro* experiments of recording neuronal signals on a CA1 region in a hippocampal slice obtained from the brain of guinea pigs.

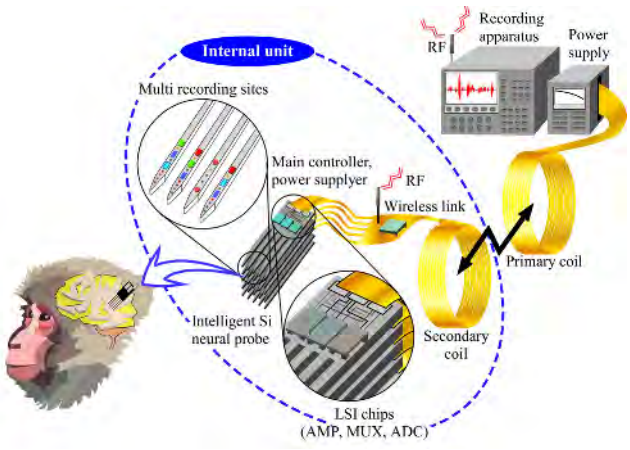


Fig.1 Configuration of the intelligent Si neural probe system

Chwee Teck Lim, James C.H. Goh (Eds.): ICBME 2008, Proceedings 23, pp. 2258–2261, 2009
www.springerlink.com

II. Multichannel Si Neural Microelectrodes with Microfluidic Channels

A. Proposal of multichannel Si neural microelectrodes with microfluidic channels

Si microelectrodes have been widely used because Si microelectrodes can be fabricated by using advanced CMOS processes which produce several important advantages such as mass production, high repeatability, and high accurate processes, and also Si is highly biocompatible material. However, number of neurons that can be observed by using conventional Si microelectrodes is limited, and only neuronal action potentials can be recorded from neurons. Additionally, considering neuron damages by a Si microelectrode, further improvement of Si microelectrode has been demanded. To solve these problems, we propose a novel multichannel Si neural microelectrode with microfluidic channels which has recording sites on both front- and back-side of Si. By integrating microfluidic channel into the microelectrode, it will be possible to deliver drugs into the neural tissue, and we can understand the drug's effect to neurons. Moreover, by placing recording sites on both sides, high density 3-D recording of neuronal action potentials can be realized.

The overall structure of the multichannel Si neural microelectrode with microfluidic channels is shown in Fig. 2. This microelectrode has 4 recording sites on both front- and back-side for neuronal cell sorting. To analyze a deeper part of the brain such as basal ganglia or apply to large animals like primates, this microelectrode has a length of 40 mm. The width and thickness were 100 μm and 200 μm, respectively. Recording sites are made of Au with circular pattern. Diameter of circular pattern is 12.5 μm and the distance between two patterns is 40 μm in center to center. Wirings are also made of Au and isolated by SiO_2 films. Behind 200 μm from the tip of the microelectrode, the recording site for differential amplification is placed. The microfluidic channel has the length of 40 mm, the width of 50 μm, and the depth of 10 μm. The fluidic outlet at the microelectrode tip has diameter of 10 μm, and the fluidic inlet is 50 × 10 μm^2 large. At the middle of the microelectrode, bonding pads for connecting to external recording apparatus were formed. Back-side pads leaded from back-side recording sites are formed by Si etching and connected to recording apparatus by wire bonding through Si via.

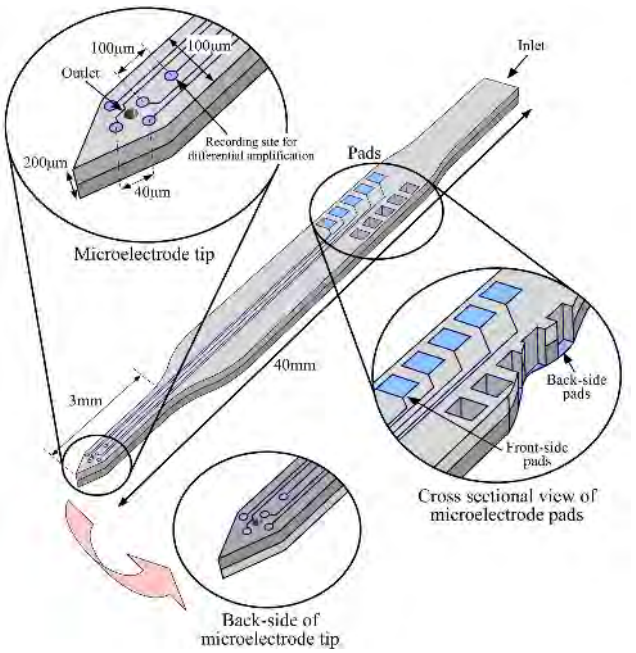


Fig. 2 Structure of the multichannel Si neural microelectrode with microfluidic channels

B. Fabrication of multichannel Si neural microelectrodes with microfluidic channels

Our microelectrode was fabricated by combining standard photolithography with bulk micromachining process. Two 100μm thick Si wafers were used as a substrate of the microelectrode. The fabrication sequence of the microelectrode is illustrated in Fig. 3. First, microfluidic channel with

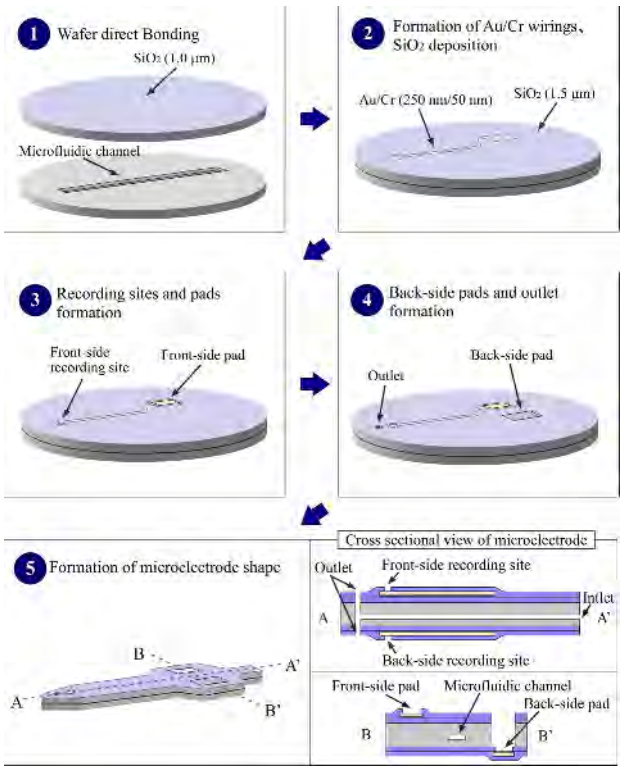


Fig. 3 Fabrication sequence of the multichannel Si neural microelectrode

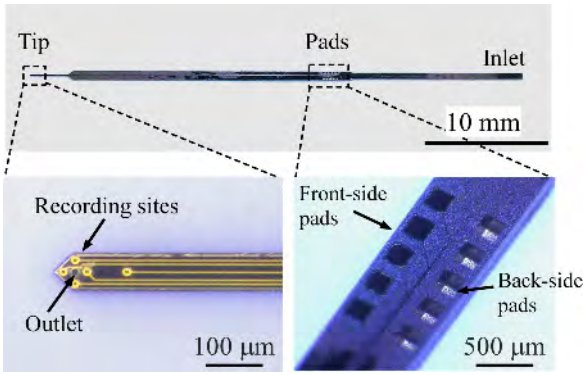


Fig. 4 Fabricated multichannel Si neural microelectrode

the depth of 10 µm was formed on surface of a Si wafer by using deep reactive ion etching (DRIE) with SF_6 and C_4F_8 gases. The etched wafer and unprocessed wafer were rinsed by standard clean 1 (SC-1), and surfaces of the both wafers were covered with thin oxidized layer accordingly. Then, these wafers were stacked and bonded by hydrogen bonds. By annealing these wafers, hydrogen bonds changed to covalent Si-O bonds with the reaction below:

$$SiOH - OH_2 - OH_2 - OHSi \leftrightarrow Si - O - Si + 3H_2O. \quad (1)$$

Next, Au/Cr wirings were formed on the front surface of the wafer by sputtering and wet etching with an iodine etchant and a ceric ammonium nitrate solution. The thickness of Au and Cr were 250 nm and 100 nm, respectively. Then, SiO_2 with a thickness of 1.5 µm was deposited using plasma enhanced chemical vapor deposition (PECVD) for insulation of wirings. Back-side surface of Si wafer was also processed with the same sequence. After that, recording sites and bonding pads were formed by wet etching with buffered HF solution (HF/NH_4F 1/10), followed by formation of the shape of the microelectrode and back-side pads using DRIE. As a result, the multichannel Si neural microelectrode was obtained. As shown in Fig. 4, the multichannel Si neural microelectrode was fabricated successfully.

III. Results and Discussion

A. Evaluation of microfluidic channels of multichannel Si neural microelectrode

At first, we confirmed the strength of the fluidic channel. In the experiment, we injected red ink into the fluidic channel with flow pressure of 1000 mmHg. Fig. 5 shows the ejection of red ink from the fluidic outlet. From this experiment, it was confirmed that the microfluidic channel had enough strength to inject fluidic medicine.

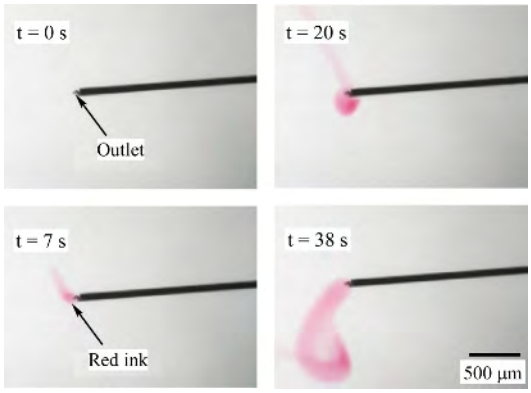


Fig. 5 Photographs of ejected red ink from the fluidic outlet

We also evaluated relationships between the flow rate and the pressure drop through microfluidic channel. We changed a flow rate from 0.1 to 0.4 µl/min with the syringe pump. We measured the pressure drop across the channel with the pressure meter, and we compared measured value with theoretical calculations. The pressure drop (Δp) is defined as:

$$\Delta p = \frac{\mu V (Re \times f) L}{2D^2} \quad (2)$$

where µ is the viscosity of fluid (~8.9×10-4 kg/ms at 25 °C for water), Re × f is the product of the Reynolds number and the Darcy friction factor (~64 in laminar flow), L is the length of the channel (40 mm), and D is the hydraulic diameter of the channel as defined by

$$D = 4 \times (\text{Cross-sectional area / wetted perimeter}). \quad (3)$$

As shown in Fig. 6, the measured values agreed well with the theoretical calculations. From this graph, we confirmed that the micro channel shape was fitted as we designed.

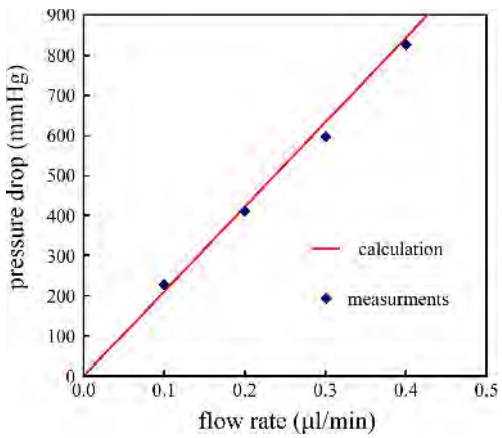


Fig. 6 Relationship between the flow rate and the pressure drop

B. Characterization of recording sites of multichannel Si neural microelectrode

In order to characterize the interface between recording site and electrolyte, we measured electrical impedance of the fabricated multichannel Si neural microelectrode before animal experiments. Measurements were performed with the frequency ranging from 100 Hz to 10 MHz using the 10 mV AC sine signal in 0.9 % saline solution. An Ag/AgCl electrode and a Pt electrode were employed as a reference electrode and counter electrode, respectively. Figure 7 shows the impedance characteristics of the fabricated microelectrode. While front-side recording site had the impedance value of 2.5 MΩ at 1 kHz, back-side recording site had the impedance value of 2.7 MΩ at 1 kHz. It was indicated that both sites had almost the same electric characteristics.

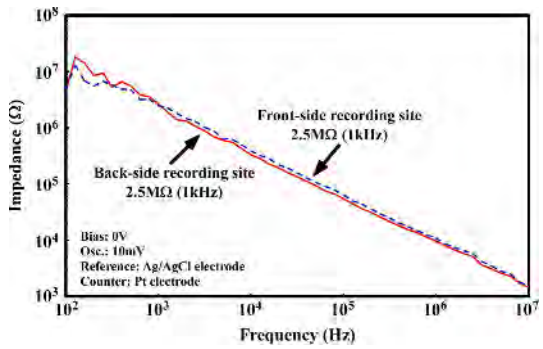


Fig. 7 Impedance spectra of the fabricated multichannel Si neural microelectrode

C. Neuronal action potential recording using multichannel Si neural microelectrode

We performed the *in-vitro* experiment of neuronal action potentials recording using the fabricated multichannel Si neural microelectrode.

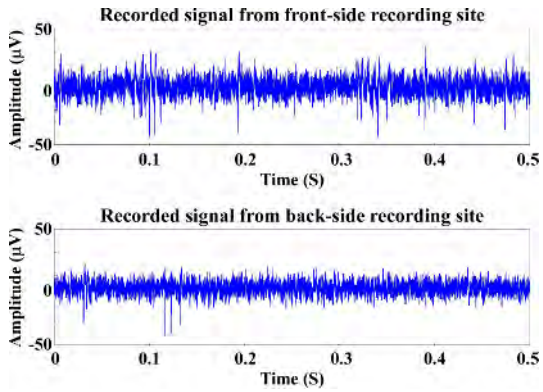


Fig. 8 Recorded neuronal action potentials of hippocampal slice

The experiments were authorized by the committee for experiment on animal of Graduate School of Information Sciences, Tohoku University. Multiple neuronal potentials were recorded from CA1 area of 400-μm-thick hippocampal slice obtained from the brains of guinea pigs (200 - 250 g). As shown in Fig. 8, we successfully recorded neuronal action potentials from both front- and back-site.

IV. Conclusions

We proposed the novel multichannel Si neural microelectrode with microfluidic channels having recording sites on both front- and back-side of Si. The microelectrode was fabricated successfully by using wafer direct bonding techniques. From fluidic experiments, it became clear that there was no void at bonding interfaces, and the bonding strength of the fabricated microelectrode withstood the flow pressure larger than 1000 mmHg. Additionally, we confirmed the measured fluidic characteristics of the microfluidic channel agreed well with the theoretical calculations. Both front- and back-side recording sites of the fabricated microelectrode had impedances of 2.5 MΩ and 2.7 MΩ at 1 kHz, respectively, which indicated both recording sites had equivalent characteristics. Using our microelectrode, we successfully recorded neuronal action potentials of hippocampal slice from recording sites of both sides.

Acknowledgment

The authors acknowledge the support of Tohoku University Global COE Program “Global Nano-Biomedical Engineering Education and Research Network Centre”. This work was partially supported by Grant-in-Aid for JSPS Fellows. This device was fabricated in Micro/Nano-Machining Research and Education Center, Tohoku University, Japan.

References

1. P. K. Campbell, K. E. Jones, R. J. Huber et al. (1991) A Silicon-Based, Three-Dimensional Neural Interface: Manufacturing Processes for an Intracortical Electrode Array. IEEE Trans. Biomed. Eng. 38:758-768
2. K. L. Drake, K. D. Wise, J. Farraye et al. (1988) Performance of planar multisite microprobes in recording extracellular single-unit intracortical activity. IEEE Trans. Biomed. Eng. 35:719-732
3. D. T. Kewley, M. D. Hills, D. A. Borkholder et al. (1997) Plasma-etched neural probes. Sens. and Actuators A 58:27-35
4. T. Watanabe, K. Motonami, K. Sakamoto et al. (2004) Ultimate Functional Multi-Electrode System (UFMES) Based on Multi-Chip Bonding Technique. Ext. Abstr. Int. Conf. Solid State Devices and Materials, Tokyo, Japan, 2004, pp 380-381.

Influence of Fluid Shear Stress on Matrix Metalloproteinase Production in Endothelial Cells

N. Sakamoto[1], T. Ohashi[1] and M. Sato[1,2]

[1] Graduate School of Engineering, Tohoku University, Sendai, Japan
[2] Graduate School of Biomedical Engineering, Tohoku University, Sendai, Japan

Abstract — **Arterial bifurcations are known to be common sites for formation of cerebral aneurysms. It has been reported that shear stress of more than 7 Pa under physiological conditions exerts on near the flow divider of the bifurcations. It is thus speculated that such high shear stress may induce production of matrix metalloproteinases (MMPs) in endothelial cells (ECs), leading to the aneurysm formation. However, the detailed mechanism is still unknown. In this study, we evaluated the effect of magnitude of shear stress on expressions of MMP-2 and -9, known to degrade elastic fibers and associate with the early stage of formation of aneurysms. ECs isolated from human umbilical veins were exposed to shear stress of 2 Pa or 7 Pa for 24 hours using a parallel-plate flow chamber. After flow-exposure experiments, ECs were cultured with serum-free medium for 12 hours. Then, MMP-2 and -9 activities in the conditioned medium was detected by gelatin zymography. While activated MMP-2 expression did not change between 2Pa and 7Pa, pro MMP-2 activity increased with increasing the magnitude of shear stress. The level of pro MMP-9 activity also increased according to the increase in shear stress, and was significantly higher at 7 Pa compared to the static. These results suggest that higher shear stress near the flow divider at bifurcation of cerebral arteries may enhance degradation of elastic fibers in vessel walls, possibly leading to formation of cerebral aneurysms.**

Keywords — **Endothelial cells, High shear stress, Cerebral aneurysm, Matrix metalloproteinases**

I. Introduction

Vascular endothelial cells (ECs) are constantly exposed to fluid shear stress due to blood flow and show functional changes. One of the major functions of ECs includes remodeling of vessel walls, in which ECs secrete matrix metalloproteinases (MMPs) to degrade extracellular matrix (ECM) such as elastin and collagen. Particularly, it has been pointed out that increases in expression of MMP-2 and -9 associate with the early stage of the formation of aneurysms [3]. ECs are also known to stimulate ECM production by smooth muscle cells and pericytes. Therefore, the balance between degradation and production of ECM tightly governs vascular remodeling and is believed to play a central role in pathogenesis of arterial aneurysms [1].

Bifurcations of cerebral arteries are known to be preferred sites of cerebral aneurysms. It is reported that shear stress of more than 7 Pa exerts on near the flow divider of the bifurcations [2]. Hence, it is speculated that such high shear stress occurred around the arterial bifurcation is involved in pathological remodeling, leading to aneurysm formation. However, little is known of how high shear stress contributes to pathologenesis of cerebral aneurysms.

In this study, we apply high shear stress to ECs and evaluate the changes in production of MMP-2 and -9.

II. Methods

A. Cell culture

Human umbilical vein ECs were cultured with Medium 199 (M199) containing 20% heat-inactivated fetal bovine serum, supplemented with 10 ng/ml basic fibroblast growth factor. Cells were used from 4th to 7th generations for experiments.

B. Flow-exposure experiment

After ECs attained confluence, the cells were exposed to shear stress of 2 Pa or 7 Pa for 24 hours using a parallale-plate flow chamber. The flow chamber was incorporated in a flow circuit, and the culture medium in the flow circuit was equilibrated with 5% CO_2 and maintained at 37 °C.

C. Gelatin zymography

After flow-exposure experiment, the ECs were cultured with serum free medium for 12 hours. The medium conditioned for 12 hours was concentrated by ultrafiltration. The sample was then loaded onto a 7.5% SDS-polyacrylamide gel containing 1 mg/ml gelatin. After electrophoresis, the gel was washed with 2.5% Tween 20 and then incubated at 37°C for 20 hours in 50 mmol/L Tris–HCl buffer, containing 1% Tween 20. After staining with Coomassie blue R-250, the gel was dried and then scanned. Gelatinolytic activity was revealed as clear bands against a blue-stained background.

Chwee Teck Lim, James C.H. Goh (Eds.): ICBME 2008, Proceedings 23, pp. 2262–2263, 2009
www.springerlink.com

III. Results

The activities of pro MMP-9, and pro and activated MMP-2 were detected by gelatin zymography in this study (Fig. 1). Levels of MMP-2 and -9 activities were quantified by the relative intensity of bands and expressed as the percentage of the activities of those of static ECs. The level of pro MMP-2 and -9 increased according to the increase in the magnitude of shear stress, and significantly higher at 7 Pa compared to the static (Figs. 2 and 3). The level of activated MMP-2 was higher at 2 Pa than control but there was no significant difference between 2 Pa and 7 Pa.

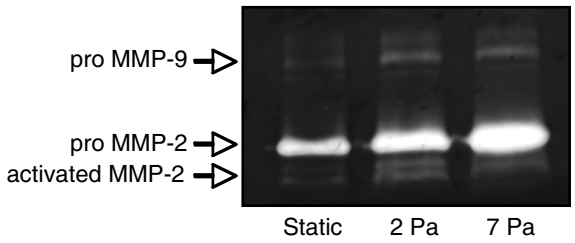


Fig. 1 Typical result of zymography showing proMMP-9, proMMP-2, and activated MMP-2

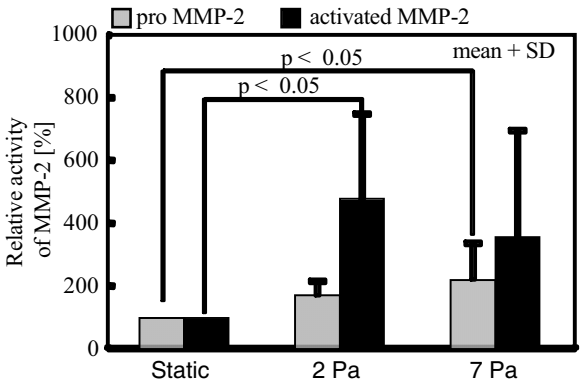


Fig. 2 Relative activity of MMP-2 expressed by endothelial cells

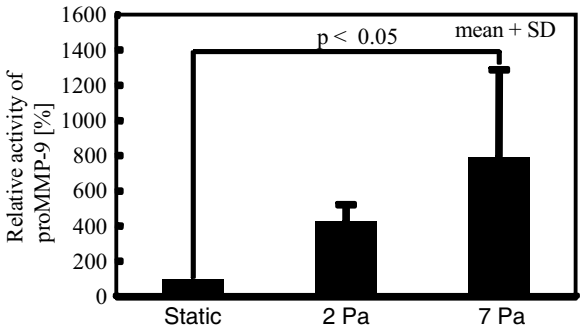


Fig. 3 Relative activity of MMP-9 expressed by endothelial cells

IV. Discussion

It is known that degradation of elastic media is the consistent histophatholocial feature of aneurysmal walls [4]. In this study, the expression of MMP-2 and -9, known to play a central role in degradation of elastin [3], increased according to the increase in the magnitude of shear stress. This result suggests that high shear stress near the bifurcation of cerebral arteries may cause degradation of elastic fibers. However, since proMMPs acquire their full proteolytic activity after activation, it is further required to study expression of activators for MMPs including membrane type-MMP and plasminogen activator. In addition, because the activity of MMPs is regulated by the inhibitors of MMPs, the tissue inhibitor of metalloproteinases (TIMPs), the expression of TIMPs should be also examined towards understanding the role of pro MMPs in the formation of aneurysms.

V. Conclusion

In this study, we applied shear stress of 2 Pa and 7 Pa to ECs and assessed expressions of MMP-2 and -9. Both proMMP-2 and proMMP-9 increased according to the increase in shear stress. These results suggest that higher shear stress enhances degradation of elastic fibers in vessel walls, possibly leading to the formation of cerebral aneurysms.

Acknowledgments

This work was supported in part by Tohoku University Global COE Program “Global Nano-Biomedical Engineering Education and Research Network Centre”, the Grants-in-Aid for Scientific Research (A)(No. 1720003) and Priority Area Research (No. 18048005) from the Ministry of Education, Culture, Sports, Science, and Technology of Japan.

References

1. Longo, G.M., et al. (2002) *J Clin Invest* 110: 625-632
2. Castro, M.A., et al. (2006) *Am J Neuroradiol* 27: 1703-1709
3. Yamashita, A., et al. (2001) *World J Surg* 25: 259-265
4. Krex, K., et al. (2001) *Acta Neurochir* 143: 429-449

Development of Brain-Computer Interface (BCI) System for Bridging Brain and Computer

S. Kanoh[1], K. Miyamoto[1] and T. Yoshinobu[1]

[1] Graduate School of Engineering, Tohoku University, Sendai, Japan

Abstract — **A brain-computer interface (BCI) is a non-muscular communication channel which allows physically disabled people to re-establish interaction with their surrounding environment. The aim of this system is to detect user's intentions or thoughts from brain activities which are measured as EEG (electroencephalogram) or other non-invasive recording techniques.**

We have developed the BCI system to detect user's motor imagery from motor-related EEG activities. It was shown that online training with a feedback of EEG band-power on specified frequency range made the accuracy of command detection higher. And we proposed an auditory BCI based on auditory stream segregation, on which users were requested to attend to one of the tone streams and their object of interest was detected from auditory event-related potentials.

In this article, the concept and some of our recent researches on BCI are introduced.

Keywords — **brain-computer interface, EEG, motor imagery, feedback training, auditory stream segregation**

I. Introduction

For the better communication tools for severe paralyzed patients due to stroke, spinal cord injury or motor neuron diseases like ALS (amyotrophic lateral sclerosis), the new human interface system called Brain-Computer Interface (BCI) has attracted interests [1]. The aim of this system is to detect user's intentions or thoughts from brain activities which are measured as EEG (electroencephalogram) or other non-invasive recording techniques. The measured signal is pre-processed and classified to detect the command corresponding to the user's intention.

An EEG-based BCI system using motor imagery has been developed by the authors [2, 3]. The activation elicited by motor imagery of user's limb (e.g. left hand, right hand or feet) is observed as a power increase (ERS: event-related synchronization) or decrease (ERD: event-related desynchronization) of EEG in a specific frequency range. It is known that motor function of every part of the body is represented in the primary motor cortex, and these representations are arranged topologically (somatotopically) on the map ("motor homunculus").

We have also developed an EEG-based BCI system using auditory stimuli [4]. In this system, subjects are requested to pay attention to one kind of specific tone stimulus, and the target (attended) object is detected by pattern classification of measured EEG responses. When subject is presented an oddball sequence, a repetition of frequently presented tones (standard stimuli) with some of which randomly replaced by infrequently presented tones (deviant stimuli), the ERP (event-related potential) components called MMN (mismatch negativity) and P300 are observed in the responses to deviant stimuli at the latency of about 100ms and 300ms, respectively. The magnitude of these ERP components is known to be changed with selective attention to the "target" tones.

II. EEG-based BCI to detect motor imagery: effect of feedback training to improve performance [3]

A. Introduction

One way to realize such a BCI is to detect motor imagery of user's limbs from EEG [5].

The BCI presented in this work is based on the detection of changes in oscillatory EEG components (ERS/ERD) induced by motor imagery [6]. From an engineering point of view, the simplest way to transfer information is to use binary control signals. For the realization of this binary signal, Pfurtscheller et al and the authors have developed the system named "Brain Switch", which detects the presence of a user-specific motor imagery [2, 7]. This system detects the enhancement of EEG activities in a user-specific frequency component (ERS) in a user-specific bipolar EEG channel on a threshold basis. The Brain Switch has already successfully been employed to restore the grasp function of a spinal cord injury patient [7].

However, one crucial issue to gain control of a BCI is the training protocol. It is known that the feedback training, in which information on target brain activation is presented to the subjects during the task, is effective to modulate neuronal activities on motor imagery [7]. Due to the inherent variability and non-stationarity of brain signals, the user has to learn to reliably generate the requested patterns by feedback training. For the best feedback effects, the three above mentioned parameters (frequency range, EEG channel, and object limb for motor imagery) need to be specifically selected for each user.

Chwee Teck Lim, James C.H. Goh (Eds.): ICBME 2008, Proceedings 23, pp. 2264–2267, 2009
www.springerlink.com

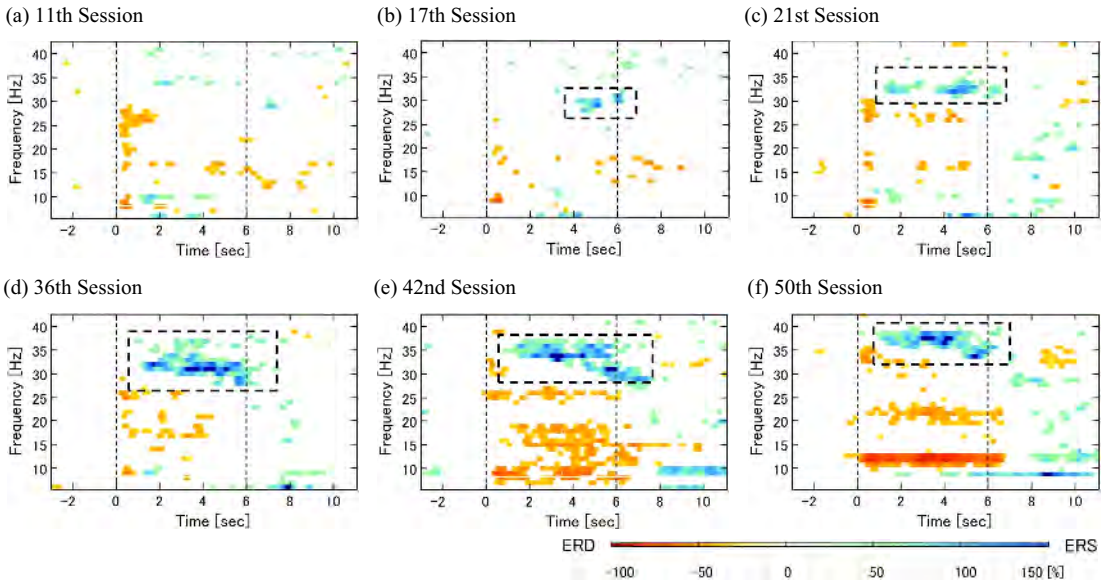


Fig. 1 Result of time-frequency analysis of the data on training sessions on foot motor imagery (Subject 1). Only significant ERS and ERD responses from reference period (-1.5 to -0.5 s) are shown. Source location was CZ–FCZ (bipolar). Open dashed boxes denote ERS activities during foot motor imagery (time 0 to 6 s).

The authors reported the process and effect of long-term on-line feedback training for BCI based on motor imagery [3]. In this section, the changes of EEG band power during online feedback experiments and the results of threshold-based command detection are introduced.

B. Methods

Two able-bodied subjects took part in the experiments, which consisted of screening sessions and BCI feedback training sessions.

Screening sessions were used to collect EEG activity from subjects during cue-guided motor imagery and to set up the parameters for the feedback training. Thirty-two EEG channels were recorded from Ag-AgCl electrodes (reference and ground were left and right earlobe, respectively). Additionally, 3 EOG channels and 4 bipolar EMG channels (left forearm, right forearm, left leg, right leg) were recorded. The measured signals were bandpass-filtered between 0.5 and 100 Hz and sampled at 250 Hz. The subjects were requested to imagine movements of limbs (left hand, right hand or both feet) instructed by LCD display in front of them.

Time-frequency ERS/ERD maps [8] of monopolar recordings and bipolar re-referenced channels (pairs of nearest neighboring electrodes) were computed and visually inspected. The following three conditions were selected for feedback experiments: motor imagery task (left hand, right hand or both feet), single bipolar EEG channel (one pair of electrodes) and frequency band with major ERS activity during motor imagery as a source of feedback information.

Screening sessions were recorded on the first and after every tenth feedback training session. The identified conditions were fixed and the same conditions were used during the following 10 training sessions.

In feedback training sessions, the length of a bar graph, continuously presented on a computer screen, was proportional to the power in the chosen frequency band. The subjects were requested to extend the length of the bar graph by performing the selected motor imagery task. The band power was estimated by bandpass filtering (Butterworth order 5) of the found EEG channel, squaring the samples and averaging over the past 1 s period.

After each session, time-frequency ERS/ERD maps were computed and an off-line Brain Switch simulation was calculated to evaluate the effect of feedback training. A Brain Switch accepts a command each time the power in the predefined band exceeds a threshold for a certain period of time (dwell time [9]). After detection, a refractory period follows for reducing the same command a second time. (See ref. [2] for details.)

These parameters for command detection (threshold, dwell time, and refractory period) were optimized by ROC analysis [9], and the command detection was simulated. If the band power exceeded the threshold in the motor imagery period (time 0 s until 6 s) and it resulted the detection

of the first command in each trial, it was counted as a desired command detection (true positive), otherwise detected command were treated as an unexpected one (false positive). The number of true and false positives (NTP and NFP, respectively) were calculated and evaluated.

C. Results and Discussion

In this paper, results in Subject 1 are shown. The results of time-frequency analysis on training sessions in Subject 1 are shown in Fig. 1. It was observed that the frequency band of such narrow-band ERS during motor imagery increased as training went on. The ERS elicited by motor imagery initially appeared at around 28–30 Hz in about 15th to 17th training session (Fig. 1(b)). The frequency band gradually increased to around 30 Hz and finally went up to about 35 Hz (Fig. 1(f)).

In this subject, NTP increased from the 21st training session, nevertheless the NFP did not change. It was found from interviews after each training session that the subject sometimes had a feeling that he could control the length of the bar graph displayed on a computer screen during experiments. As there were no significant ERS responses for this subject before taking part in this experiment, it was found that this subject gained the ability to generate ERS on motor area voluntarily by motor imagery of feet.

From the result of Subject 1, feedback could enhance the band power in the same frequency band. It was found that subjects where no EEG response related to motor imagery was observed initially could acquire the ability to produce enhancement of EEG band power during motor imagery.

In this study, the conditions for feedback training (especially the target frequency band) were chosen empirically by experimenters by taking the results of previous sessions into account. Moreover, the present training paradigm was rather boring for the subjects. The proposal of efficient training strategies and protocols to boost the effects of feedback training is left for further studies.

III. An auditory BCI system based on stream segregation [4]

A. Introduction

ERP (event-related potential) elicited by sensory stimuli can also be used for realizing EEG-based BCI system. The BCI-based spelling system to choose one of 36 characters by using visual ERP was proposed [10]. In this system, a matrix of 6 by 6 characters was presented and one of each row or column blinked sequentially in random order. Users were requested to focus on one of the characters, and the P300, one of the ERP components, which was elicited by the highlight of focused characters, was analyzed and detected. But in such a system, users are required to watch and focus on the visual display anytime they want to use. Hill et al [11] proposed the ERP-based BCI system in auditory domain. In this system, users were presented two kinds of tone sequences on each ear asynchronously, and they were requested to attend the sequence from one of the ears. In this system, more than thirty electrodes were used to measure ERP to achieve higher accuracy.

The authors proposed an auditory BCI system based on auditory stream segregation to realize a two-alternative choice, and is tested by the experiments with two-channel EEG measurements [4]. In this system, series of short tones with two frequency ranges were presented alternatively to subject's right ear, and subjects were requested to attend one of the “streams” which were perceived to be segregated as higher and lower tone sequences.

B. Auditory Stream Segregation

Auditory illusions or other interesting perceptual phenomena, e.g. figure-ground perception (cocktail-party effect) or perceptual grouping, have been studied in psychophysics to uncover the nature of computational theory of auditory information processing. Such studies, which are known as auditory scene analysis [12], have shown that a lot of interesting phenomena related to Gestalt psychology, and their neuronal correlates have been investigated. (e.g. ref. [13])

When two kinds of tones with different frequencies (A, B) are presented alternatively on time (e.g. ABABAB...) with short inter-stimulus interval, such sequence can be perceived as two segregated tone streams (AAAAA ..., and BBBBB...). Such phenomenon is called as auditory stream segregation, and can be treated as one of the auditory illusions on which similarity on tone frequency overcomes the factor of time continuity.

C. Methods

Schematic diagram of tone sequence presented to subjects in this experiment is shown in Fig. 2. Two kinds of auditory oddball sequences consisted of tone bursts were presented alternatively on each tone. Six subjects were required to pay attention to one of the two streams. The EEG signal was recorded with Ag-AgCl electrodes at two locations (Cz, F3), and referred to right earlobe with a forehead ground.

The responses to deviant stimuli was classified by LDA (linear discriminant analysis) to discriminate whether the subject paid attention to each of the streams by classifying the response to the deviant stimuli embedded to each of the streams. Data was divided to 10 s block and final judgment of detection was executed on each block data on the basis of decision by majority.

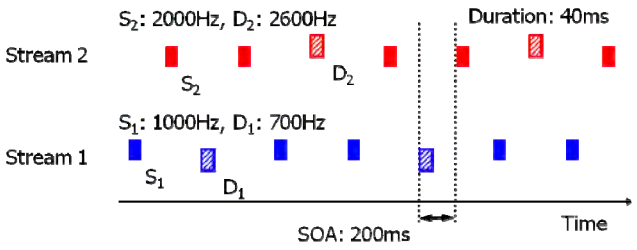


Fig. 2 Presented tone sequences on proposed auditory BCI based on stream segregation

D. Results and Discussion

The result of detection whether the subject attended to stream 1 or 2 was judged by the decision by majority of all the classification results in the time windows of 10 s. More than 95% correct detection rate and bit transfer rate of about 5 bit/min (one judgment in every 10 seconds, maximum 6 bit/min) were achieved. But by using 10-fold cross-validation, correct detection rate was 60~70%. It was shown that the present paradigm could be used for BCI.

In the previous study on auditory BCI, the two independent tone sequences were presented to both ears and discriminated which ear the target (attended) sequences were presented, so only 1 bit (left or right) was obtained by one detection [11]. But on the proposed system, auditory stream segregation of tone sequences presented to one ear was utilized and it can be extended to many-to-one choice BCI by increasing the number of tone streams to be segregated.

The non-stationality on EEG and low S/N ratio of measured EEG data are thought to be the reasons on 10-fold cross-validation shown above. To increase the accuracy, preprocessing methods for artifact reduction and increasing the stability of classification (e.g. down-sampling, filtering) and feature selection/extraction techniques should be improved.

IV. CONCLUSIONS

In this article, two of our recent researches on EEG-based BCI, effect of feedback training for BCI based on motor imagery and a new paradigm of auditory BCI, were shown.

Although previous studies on BCI have been mainly focused on "reading out" of user's intensions or thoughts from the brain signal, to modulate brain's activities in non-invasive way will also be essential for BCI or its application for clinical use. Moreover, the task for controlling BCI system (or for modulating brain activities) should be natural and easy for users.

Efficient methods of online feedback training and further investigation of new tasks for BCI are left for further studies.

ACKNOWLEDGMENT

Part of our study has been supported by Grants-in-Aid for Scientific Research, Ministry of Education, Culture, Sports, Science and Technology, Japan, and CASIO Science Promotion Foundation, Japan. And the authors acknowledge the support of Tohoku University Global COE Program "Global Nano-Biomedical Engineering Education and Research Network Centre".

REFERENCES

1. Wolpaw JR, Birbaumer N, Heetderks WJ, McFarland DJ, Peckham PH, Schalk G, Donchin LA, Robinson CJ, Vaughan TM (2000) "Brain-computer interface technology: A review of the first international meeting", IEEE Transactions on Rehabilitation Engineering, 8(2):164-173.
2. Kanoh S, Scherer R, Yoshinobu T, Hoshimiya N, Pfurtscheller G (2006) "Brain Switch" BCI system based on EEG during foot movement imagery. Proceedings of the 3rd International BCI Workshop and Training Course 2006, 64–65.
3. Kanoh S, Scherer R, Yoshinobu T, Hoshimiya N, Pfurtscheller G (2008) Effects of long-term feedback training on oscillatory EEG components modulated by motor imagery, Proceedings of the 4th International BCI Workshop and Training Course 2008, 150–155.
4. Kanoh S, Miyamoto K, Yoshinobu T (2008) A brain-computer interface (BCI) system based on auditory stream segregation, Proceedings of the 30th Annual International IEEE EMBS Conference, 642–645.
5. Pfurtscheller G, Neuper C, Birbaumer N (2005) Human brain-computer interface. In: A. Riehle and E. Vaadia (Eds.), Motor cortex in voluntary movements: A distributed system for distributed functions, 367–401, CRC Press.
6. Pfurtscheller G, Lopes da Silva FH (1999) Event-related EEG/MEG synchronization and desynchronization: basic principles. Clinical Neurophysiology, 110:1842–1857.
7. Pfurtscheller G, Müller-Putz GR, Pfurtscheller J, Rupp R (2005) EEG-based asynchronous BCI controls functional electrical stimulation in a tetraplegic patient. EURASIP Journal on Applied Signal Processing, 19:3152–3155.
8. Graimann B, Huggins JE, Levine SP, Pfurtscheller G (2002) Visualization of significant ERD/ERS patterns in multichannel EEG and ECoG data. Clinical Neurophysiology, 133:43–47.
9. Townsend G, Graimann B and Pfurtscheller G (2004) Continuous EEG classification during motor imagery – Simulation of an asynchronous BCI. IEEE Transactions on Neural Systems and Rehabilitation Engineering, 12:258–265.
10. E. Donchin E, Spencer KM, Wijesinghe R (2000) The mental prosthesis: Assessing the speed of a P300-based brain-computer interface, IEEE Transactions on Rehabilitation Engineering, 8(2):174-179.
11. Hill NJ, Lal N, Bierig K, Birbaumer N, Scholkof B (2005) An auditory paradigm for brain-computer interfaces, Advances in Neural Information Processing Systems, 17:569-576.
12. Bregman AS (1990) Auditory scene analysis: The perceptual organization of sound, The MIT Press.
13. Kanoh S, Futami R, Hoshimiya N (2004) Sequential grouping of tone sequence as reflected by the mismatch negativity, Biological Cybernetics, 91(6):388-395.

First Trial of the Chronic Animal Examination of the Artificial Myocardial Function

Y. Shiraishi[1], T. Yambe[1], Y. Saijo[2], K. Matsue[1], M. Shibata[1], H. Liu[1], T. Sugai[2], A. Tanaka[3], S. Konno[1], H. Song[4], A. Baba[5], K. Imachi[6], M. Yoshizawa[7], S. Nitta[1], H. Sasada[8], K. Tabayashi[9], R. Sakata[10], Y. Sato[10], M. Umezu[10], D. Homma[11]

[1] Institute of Development, Aging and Cancer, Tohoku University, Sendai, Japan
[2] Graduate School of Biomedical Engineering, Tohoku University, Sendai, Japan
[3] Fukushima University, Sendai, Japan
[4] Korean Advanced Institute of Science and Technology, Daejeon, Japan
[5] Shibaura Institute of Technology, Tokyo, Japan
[6] International Advanced Research and Education Organization, Tohoku University, Sendai, Japan
[7] Cyber Science Center, Tohoku University, Sendai, Japan
[8] Graduate School of Agriculture, Tohoku University, Sendai, Japan
[9] Graduate School of Medicine, Tohoku University, Sendai, Japan
[10] Waseda University, Sendai, Japan
[11] Toki Corporation, Tokyo, Japan

Abstract— **Thromboembolic and haemorrhagic complications are the primary causes of mortality and morbidity in patients with artificial hearts, which are known to be induced by the interactions between blood flow and artificial material surfaces. The authors have been developing a new mechanical artificial myocardial assist device by using a sophisticated shape memory alloy fibre in order to achieve the mechanical cardiac support from outside of the heart without a direct blood contacting surface. The original material employed as the actuator of artificial myocardial assist devices was 100um fibred-shaped, which was composed of covalent and metallic bonding structure and designed to generate 4-7 % shortening by Joule heating induced by the electric current input. Prior to the experiment, the myocardial streamlines were investigated by using a MDCT, and the design of artificial myocardial assist devices were refined based on the concept of Torrent-Guasp's myocardial band theory. As the hydrodynamic or hemodynamic examination exhibited the remarkable increase of cardiac systolic work by the assistance of the artificial myocardial contraction in the originally designed mock circulatory system as well as in the acute animal experiments, the chronic animal test has been started in a goat. Total weight of the device including the actuator was around 150g, and the electric power was supplied percutaneously. The device could be successfully installed into thoracic cavity, which was able to be girdling the left ventricle. In the chronic animal trial, the complication in respect to the diastolic dysfunction by the artificial myocardial compression was not observed.**

Keywords— **Artificial myocardium, shape memory alloy fibre, chronic animal experiment, myocardial band, hemodynamics.**

I. Introduction

Chronic heart failure (CHF) is functionally and structurally characterized by pathophysiological remodeling of the ventricle. In general, ventricular assist devices (VADs), such as artificial hearts, are used for the surgical treatment of the patients with the final stage of severe heart failure [1-4]. However, thromboembolic and haemorrhagic complications are still the primary causes of mortality and morbidity in patients with VADs, which are known to be induced by the interactions between blood flow and artificial material surfaces. Several concepts of the mechanical assistance from outside of the ventricle have been presented so far, such as Anstadt's ventricular cup, providing a solution to these problems without direct contacting surfaces against blood [5-12]. And also some new devices, such as Myosprint, demonstrated improvements in eliminating mitral regurgitation in dysfunctional left ventricle as well as in preventing the ventricular enlargement which was to compensate for the reduction in cardiac function [13-14]. Although the passive implantable devices, which are girdling the ventricle from the outside, have been already applied for clinical trials in patients with chronic congestive heart failure for the passive assistance as well as for the prevention of enlargement of the left ventricle to compensate for the reduction in cardiac function, there might be a limitation to passive assistance in the case of sudden changes of cardiac contractile function, such as angina of effort. We have been developing an artificial myocardial assist device by using a covalent type nano-tech shape memory alloy fibre, which is capable of assisting natural cardiac contraction from outside of the ventricular wall as

Chwee Teck Lim, James C.H. Goh (Eds.): ICBME 2008, Proceedings 23, pp. 2268–2271, 2009
www.springerlink.com

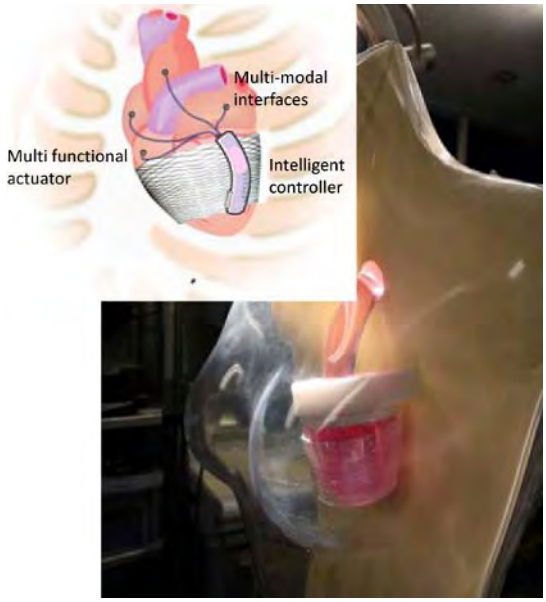


Fig. 1 Schematic illustration and an installation in the mock of an artificial myocardium attached on the ventricular wall; the synchronous contraction can be achieved according to the natural physiological demand.

shown in Figure 1. The purpose of this study was to examine the function of the artificial myocardium, which was designed to assist the heart synchronously with native contraction, and its feasibility in chronic animal experiments.

II. Materials and Methods

A. Myocardial assist device description

The artificial myocardium consists of ten shape memory alloy fibres which were covered by silicone rubber as shown in Figure 2. Special features of the shape memory alloy fibre material (Biometal®) which was to be employed as the actuator of the artificial myocardium were as follows: a) composition of covalent and metallic bonding structure, b) 4-7 % shortening by Joule heating induced by the electric current input, c) linear characteristics of electric resistance against shortening, d) strong maximum contractile force of 10N with 100um-fibre, e) high durability of over one billion cycles, f) contractile frequent response by 1-3 Hz, g) selectable maltensitic temperature by fabrication processing from 45 to 70 Celsius, and h) elective diameter size smaller than 30um [15-17]. The contraction of the device can be controlled by an originally-designed microcomputer system. The device is controlled and performed by electrical signal input, which is supplied percutaneously. Each signal for the contraction is regulated by the controller and synchronized with native electrocardiogram (Figure 3 and 4). Originally-designed ladder-

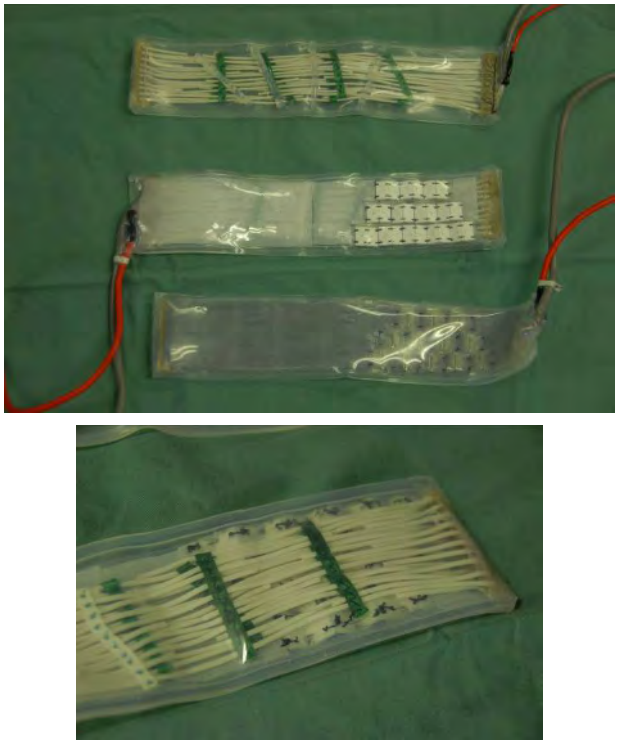


Fig. 2 Several types of myocardial assist device developed for the feasibility study in chronic animal experiments (top), and the details of the connection of shape memory alloy fibres covered with silicone tubing (bottom).

shaped hinges were constructed on the parallelly-linked shape memory alloy fibres belt, specifically on the surface attaching to the left ventricular free wall in order to simulate the wall-thickening effect as well as to promote the mechanical shortening perpendicularly to the left ventricular long axis.

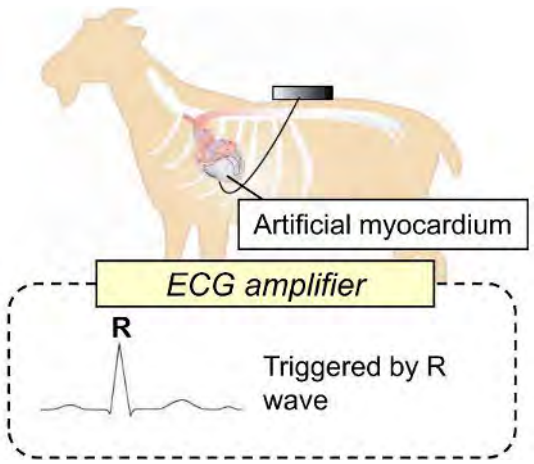


Fig. 3 Schematic illustration of the signal connection for the control of mechanical myocardial contraction in the animal experiments.

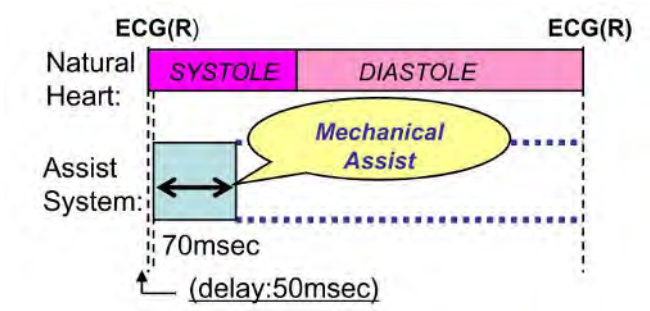


Fig. 4 Schematic drawing of the contraction signal input for the artificial myocardium synchronized with electrocardiogram (ECG-R).

B. Mechanical design of the device based on the anatomical examination of native heart

Myocardial streamline was confirmed by the MDCT investigation in a healthy goat heart which was extracted and unfolded based on the Torrent-Guasp's myocardial band concept as shown in Figure 5 [17]. The orientation of the device contraction might promote native systolic function while avoiding both the external and internal critical structures of the heart. The myocardial streamline was detected from the data with plastic markers plot by MDCT, and the angular configuration to the left ventricular long axis was calculated.

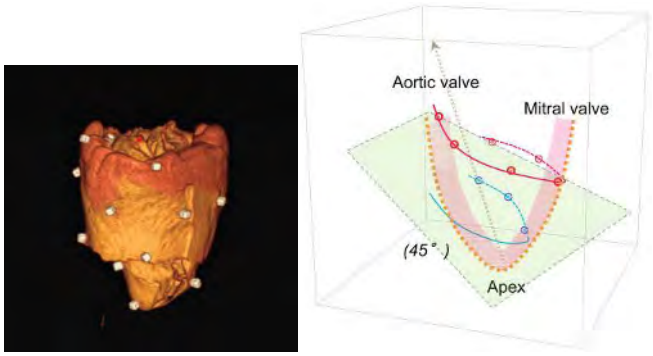


Fig. 5 MDCT examination of the healthy goat heart unfolded by the Torrent-Guasp's concept and reconstructed with plastic markers (left), and the native myocardial streamline orientation calculated from the data as the reference of implantation of the artificial myocardium (right).

C. Experimental procedure

The chronic animal experiments were performed in healthy female adult Japanese Saanen goats (n=2), which weighed 45 kg. Implantation of the device was performed as part of an open-chest cardiac procedure on a beating heart under the normal inhalation and anesthesia followed by endotracheal intubation using 2.5% halothane. The band-shaped myocardial assist device was installed into the thoracic cavity girdling from the apex to the base and one of the ends was parallel to the left ventricular long axis myo cardial streamline on its free wall side. Coronary vasculature was visually identified and avoided on the exterior of the heart during the implantation. There was no direct suture on the tissue or muscles with the device. Prior to the measurement, postoperative care without mechanical assistance was carried out for one week. These animal trials were electively terminated after postoperative one month.

All animals received humane care in accordance with "the Guideline for the Care and Use of Laboratory Animals" published by the National Institute of Health (NIH publication 85-23, revised 1985) as well as with "the Guidelines for Proper Conduct of Animal Experiments" formulated by Science Council of Japan (2006) and the guidelines determined by the Institutional Animal Care and Use Committee of Tohoku University.

III. Results and Discussion

A. Adverse events

There were no serious infections and surgical procedural failures in the implantation of the device from the beginning and throughout the study in all cases (Figure 6). And the unanticipated complication in respect to the device-related diastolic dysfunction by the artificial myocardial compression was not observed. Several mechanical structural device failures could be investigated after the extraction of them.



Fig. 6 Successful implantation of the artificial myocardium without unanticipated complications in relation to infections or surgical procedural failures.

B. Hemodynamic effects

Left ventricular and aortic pressures were obtained and remarkably increased by the mechanical assistance as shown

in Figure 7. Each waveform was calculated as the average of the data in the period of 90sec. 'Control' indicates the waveforms taken without assistance, while 'Assisted' were with mechanical contraction. There were no significant changes in the left ventricular end diastolic pressure, so that it was suggested that there might not be any diastolic dysfunction during the mechanical assistance using the artificial myocardium. As a result, left ventricular systolic pressure was increased from 110 to 118 mmHg (7%), and assisted flow rate was elevated for 70msec, which was equivalent of the mechanical contractile duration, from the data calculated (Figure 7). Consequently, the assistive effect on cardiac output during the assistance was calculated to be 3% higher than the control condition without mechanical contraction.

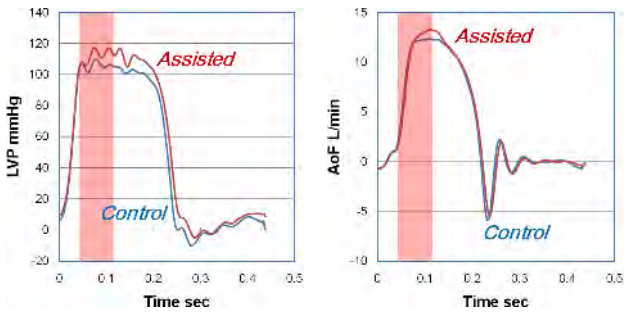


Fig. 7 Changes in hemodynamic waveforms obtained at a goats with the mechanical assistance by using the artificial myocardium. Each waveform was calculated as the average of the data in the period of 90 sec. 'Control' indicates the waveforms taken without assistance, while 'Assisted' were with mechanical contraction. The area colorized shows the duration of signal input for 70msec from 50msec subsequent of electrophysiological cardiac contraction detected by 'ECG-R'.

IV. Conclusions

The first animal trials of the artificial myocardium using shape memory alloy fibre demonstrated both feasibility and efficacy in healthy adult goats. The result indicated the development of the active ventricular assist device was useful because of its ability to consistently reduce or eliminate the complications in relation to thrombosis or hemolysis along with simple mechanism for the effective actuation.

Acknowledgment

The authors acknowledge the support of Grand in Aid for Scientific Research of and Ministry of Education, Culture, Sports, Science and Technology (17790938, 19689029, 20659213). And we thank Mr. K. Kikuchi and Mr. T. Kumagai for kind support of animal cares as well as experimental preparations.

References

1. Hosenpud JD, et al. (1998) The registry of the international society for heart and lung transplantation: fifteenth official report–1998, J Heart Lung Transplant 17:656–68.
2. Rose EA, et al. (2001) Long-term use of a left ventricular assist device for end-stage heart failure, New Eng J Med 345:1435-43.
3. Long JW, et al. (2005) Long-term destination therapy with the Heartmate XVE left ventricular assist device: Improved outcomes since the REMATCH study, Congest Heart Fail 11:133-8.
4. Drakos SG, et al. (2006) Effect of mechanical circulatory support on outcomes after transplantation, J Heart Lung Transplant 25:22-8.
5. Shimizu T, et al. (2002) Fabrication of pulsatile cardiac tissue grafts using a novel 3-dimensional cell sheet manipulation technique and temperature-responsive cell culture surfaces, Circ Res 90(3):e40.
6. Shiraishi Y, et al. (2005) Development of an artificial myocardium using a covalent shape-memory alloy fibre and its cardiovascular diagnostic response, Conf Proc IEEE Eng Med Biol Eng 1(1), 406-408.
7. Yambe T, et al. (2004) Artificial myocardium with an artificial baroreflex system using nano technology, Biomed Pharmacother 57 Suppl 1:122s-125s.
8. Wang Q, et al. (2004) An artificial myocardium assist system: electrohydraulic ventricular actuation improves myocardial tissue perfusion in goats, Artif Organs 28(9):853-857.
9. Anstadt GL, et al. (1965) A new instrument for prolonged mechanical massage, Circulation 31(Suppl. II):43.
10. Anstadt M, et al. (1991) Direct mechanical ventricular actuator, Resuscitation 21:7-23.
11. Kawaguchi O, et al. (1997) Dynamic cardiac compression improves contractile efficiency of the heart, J Thorac Cardiovasc Surg 113:923-31.
12. Fukamachi K, McCarthy PM. (2005) Initial safety and feasibility clinical trial of the Myosprint device, J Card Surg 20:S43-S47.
13. McCarthy PM, et al. (2001) Device-based change in left ventricular shape: A new concept for the treatment of dilated cardiomyopathy, J Thorac Cardiovasc Surg 122:482-490.
14. Buehler WJ, Gilfrich J, Wiley KC. (1963) Effect of low-temperature phase changes on the mechanical properties of alloys near composition TiNi, J Appl Phys 34:1465.
15. Homma D, Miwa Y, Iguchi N, et al. (1982) Shape memory effect in Ti-Ni alloy during rapid heating, Proc of 25th Japan Congress on Materials Research..
16. Sawyer PN, et al. (1976) Further study of NITINOL wire as contractile artificial muscle for an artificial heart, Cardiovasc Diseases Bull. Texas Heart Inst 3: 65.
17. Buckberg G, et al. (2008) Structure and function relationships of the helical ventricular myocardial band.J Thorac Cardiovasc Surg 136(3):578-89

Author: Yasuyuki Shiraishi
Institute: Institute of Development, Aging and Cancer, Tohoku University
Street: 4-1 Seiryo-machi, Aoba-ku
City: Sendai 980-8575
Country: Japan
Email: shiraishi@idac.tohoku.ac.jp

Bio-imaging by functional nano-particles of nano to macro scale

M. Takeda[1, 2], H. Tada[2], M. Kawai[2], Y. Sakurai[2], H. Higuchi[3], K. Gonda[1], T. Ishida[2] and N. Ohuchi[1,2]

[1] Division of Nano-Medical Science, Graduate School of Medicine, Tohoku University, Japan
[2] Division of Surgical Oncology, Graduate School of Medicine, Tohoku University, Japan
[3] Department of physics, Graduate School of Science, The University of Tokyo, Japan

Abstract — **Nano-materials are expected to be used for medical applications such as research on pharmacokinetics and novel therapeutic agents. Their acute toxicity should be examined and systemic distribution of the nano-materials should also be estimated. We established a high resolution in vivo 3D microscopic system for a novel fluorescence imaging method at single molecular level. We measured in vivo movement of CdSe nano-particles (quantum dots (QDs)) conjugated with monoclonal anti-HER2 antibody (Trastuzumab) in tumor vessel to breast cancer cells. The HER2 protein expressed in cancer cells and its in vivo dynamics were visualized by QDs at nano-scale. It suggests future utilization of the system to improve drug delivery system to target the primary and metastatic tumors for made to order treatment. We also describe a novel contrast medium for X-ray and its distribution in organs. Nano-sized silica coated silver iodide beads exhibited contrast enhancementin the tumor for over one hour. Sentinel node navigation is one of the important clinical applications for fluorescence nano-particles and silver iodide beads. Our experimental data of those nano-particles in experimental model have shown the potential of fluorescence and X-ray measurement to be alternatives to existing tracers. Future innovation in cancer imaging by nano-technology and novel measurement technology will provide great improvement, not only in clinical field of prevention, diagnosis and treatment of human disease, but also in basic medical science.**

Keywords — **Single molecular imaging, quantum dots, HER2, nano-technology, silica coated silver iodide beads,**

I. Introduction

Nano-materials are widely applied to medical diagnoses and treatments such as research on pharmacokinetics and novel therapeutic agents in this decade. Functional nano-particles, such as quantum dots, nano-micelle, nano-sized gold particles, silica coated silver iodide beads and dendrimers. They have unique properties and are potentially useful in medicine.

Their acute toxicity should be examined and systemic distribution of the nano-materials should also be estimated. We established a high resolution in vivo 3D microscopic system for a novel fluorescence imaging method at single molecular level. We assessed utility of this system by in vivo measurement of anticancer antibody conjugated quantum dots. Nano-particles with functions can be also used for macro scale measurements.

Recent studies have proved the great influence of particle size in malignancies because the tumor vessels have immature pores and the permeability increases [1]. This phenomenon is called extended permeability and retention (EPR). So the size of nano-particles has an important function to develop anticancer drugs. The size of nano-particles is also important for sentinel node navigation surgery.

Distribution of nano-particles is also an important issue to utilize nano-particles for medicine.

In this study, we aimed to clarify the in vivo movement of nano-particles in interstitium of a tumor, because the size may affect not only accumulation of nano-particles but also movement in interstitium. We establish utility of functional nano-particles along with development of novel optical measurement methods for both nano-scale and macro-scale.

In this study, we measured in vivo movement of various sizes of nano-particles in tumor interstitium. We also performed contrast enhancement of rat and tumor by novel X-ray contrast media of silica coated silver iodide beads.

II. Materials and methods

A. Nano-scale measurement of fluorescent nano-particles

We used 'Fluospheres', manufactured polystyrene microspheres by Invitrogen, Molecular Probe (Oregon, USA) for the size of 40 and 100nm. And we employed Quantum dot 705 ITK kit (Quantum Dot Corp., Hayward CA) for the size of 20nm.

A human breast cancer cell line KPL-4[1] was kindly provided by Dr. J. Kurebayashi (Kawasaki Medical School, Kurashiki, Japan) [2]. KPL-4 was cultured in Dulbecco's modified Eagle's medium (DMEM) supplemented with 5% fetal bovine serum.

A suspension of KPL-4 (1.0×10^7 cells / 100 μl DMEM) cells was transplanted subcutaneously into the dorsal skin of female Balb/c nu/nu mice at 5 - 7 weeks of age (Charles river laboratories Japan, Yokohama, Japan). Several weeks after tumor inoculation, mice with a tumor volume of 100 - 200 mm^3 were used for the study. The mice were placed under anesthesia by ketamine and xylazine.

Chwee Teck Lim, James C.H. Goh (Eds.): ICBME 2008, Proceedings 23, pp. 2272–2274, 2009
www.springerlink.com

The optical system consisted of an epi-fluorescent microscope, Nipkow lens type confocal unit and an electron multiplier type CCD camera. This system can capture images of single nano-particles at a rate of 33 ms/frame. The xy-position of the fluorescent spot was calculated by fitting to a 2D-Gaussian curve. The single molecule could be identified by the fluorescence intensity. And quantitative and qualitative information such as velocity, directionality and transport mode was obtained using time-resolved trajectories of nano-particles.

The movement of nano-particles was detected in the tumor after intravenous administration by the optical system.

B. 2.2 Contrast enhancement of a tumor by novel X-ray contrast media

We produced the silica-coated silver iodide beads (AgI beads) in size of 40-80 nm by the Stöber method. Pottasium iodide and $AgClO_4$ was used for the formation of the silver-iodide core. Silica-coating of the fluorescent microspheres was carried out with ammonia-catalyzed reaction of tetraethylorthosilicate (TEOS) in ethanol–water solution. Ethanol solution of TEOS was added to aqueous PVP solution under stirring after addition of the suspension of the fluorescent microspheres. Hydrolysis reaction of TEOS was initiated by addition of the aqueous ammonia solution to form silica shell on the microspheres for 24 h under stirring. Silica coated silver iodide nano-particles have diameter of 40-80 nm [3].

Saline suspension of the silica-coated AgI beads was intravenously administered to rats with xenografts of human breast cancer (KPL-4). The CT images were sequentially acquired at 15, 30 and 60min., after intravenous administration.

These studies were carried out in accordance with the Institutional Animal Use and Care Regulations of Tohoku University, after receiving approval from the Committee on Animal Experiments.

III. Results

A. 3.1 Nano-scale measurement of fluorescent nano-particles in tumor

The movement of single particles was observed in perivascular, interstitial and intracellular regions of tumors. We could successfully detected by our measurement system. The HER2 protein expressed in cancer cells and its dynamics *in vivo* were visualized by QDs and fluorescence polystylene beads at nano-scale.

Fluorescent nano-particles in various sizes are also detected by the optical system. We investigated three kinds of area of perivascular region, interstitium and intercellular region in the interstitium of the tumor.

In the perivascular area, 20 nm particles exhibited almost uni-directed movement by interstitial flow. In contrast, 40 and 100 nm particles showed uni-directed movement with increased random diffusion.

In the tumor interstitial region, the movement of 20 nm consisted of uni-directed movement and random diffusion. And 40 and 100 nm particles showed a movement almost affected by diffusion.

In the intercellular region, a 20 nm particle movement appeared to be much restricted. The movements of 40 and 100 nm particles appeared to represent only diffusion. They were indicating Brownian motion.

B. 3.2 Contrast enhancement of a tumor by novel X-ray contrast media

We could observe enhancement of a tumor after administration of AgI beads. The Hounsfield number of the tumor gradually increased and got the maximum value in 60 min.

IV. Discussion

In the study for single particle fluorescent imaging of cancer, we captured the specific movement of nano-particles in various sizes in live mice after nano-particles had been injected into the tail vein of mice. In the former study, we could observe six stages of drug delivery, 1) vessel circulation, 2) extravasation, 3) movement into the extracellular region, 4) binding to HER2 on the cell membrane, 5) movement from the cell membrane to the perinuclear region after endocytosis and 6) in the perinuclear region [4]. That study suggests that there are many stages to be considered for better drug delivery. The ineterstitium plays a very important role for drug delivery, as it is the scaffold of the tumor cells and the structure of the interstitium defines interface of tumor cells to drugs. The movement of the particles in each process was also found to be ”stop-and-go”, *i.e.*, sometimes the particles stay within a highly restricted area and then move suddenly after release. This indicates that the movement was promoted by a motive power and constrained by both the 3D-structure and protein-protein interactions. The motive power of the movements was produced by the diffusion force driven by thermal energy [2-4], interstitial lymph flow and active transport by motor proteins [5]. The cessation of movement is most likely induced by a structural barricade such as a matrix cage [2-4] and/or specific interaction between proteins, *e.g.*,

an antibody and HER2 [4], motor proteins, and rail filaments such as actin filaments and microtubules [5]. Our study strongly suggests that the size of drug carrier can be an important drug delivery modifier. If we choose the carrier in size of 20nm, it may reach cells soon and immediately diminish. Larger size can stay interstitium longer. Smaller particles can be used for drugs for treatment. To let drugs to access cancer cells. Larger particles can be used for localization of malignant lesion for surgical or radiological treatment.

There have been many different approaches to tumor-targeting "nanocarriers" including anti-cancer drugs, for passive targeting such as Myocet [5], Doxil [6] and for active targeting such as MCC-465 [7], anti-HER2 immunoliposome [8]. There is still very little understanding of the biological behavior of nano-carriers, including such crucial features as their transport in the blood circulation, interstitial behavior, cellular recognition, translocation into the cytoplasm, and final fate in the target cell. These results suggest that the transport of nano-carriers can be quantitatively analyzed in the tumors of living animals by the present method.

There are two forms of transportation mechanism regarding a particle material to lymphatic system. One is physical and active extracellular transportation; a particle passes through lymph capillaries. The other one is intracellular transportation of a particle. Foreign materials shift to the lymph capillaries after phagocytosis of the particle.

Silica coated silver iodide beads had contrast enhancement in xenograft of breast cancer. In our former study, the slow increase in contrast enhancement of liver and spleen would be attributed to sedimentation of silica coated silver iodide beads in the capillary system. Enhancement of the tumor may be attributed to EPR other than the sedimentation of silica coated silver iodide beads in the capillary system.

Nano-materials for medicine would be a great aid to improve the made to order medicine by their highly sensitive and super selective property for diagnoses. Advanced sensing technologies such as single molecular imaging technique are also required to make the best use of the functional nano-materials for achievement of hyper sensitive and super selective imaging. These novel products of advanced nano-technologies may realize revolution of medicine in near future.

ACKNOWLEDGEMENT

This work was supported by Grants-in-aid for Research Projects, Promotion of Advanced Medical Technology (H14-Nano-010 and H18-Nano-001), from the Ministry of Health, Labor and Welfare, Japan and the 21st Century Global Center of Excellence (GCOE) Program "Future Medical Engineering based on Bio-nanotechnology", the Japan Society for the Promotion of Science.

REFERENCES

1. Dreher MR, Liu W, Michelich CR, Dewhirst MW, Yuan F, Chilkoti A. Tumor vascular permeability, accumulation, and penetration of macromolecular drug carriers. Journal of the National Cancer Institute. 2006; 98: 335-44.
2. Kurebayashi J, Otsuki T, Tang CK, Kurosumi M, Yamamoto S, Tanaka K, Mochizuki M, Nakamura H, Sonoo H: Isolation and characterization of a new human breast cancer cell line, KPL-4, expressing the Erb B family receptors and interleukin-6. *Br J Cancer* 79:707-717, 1999.
3. Kobayashi Y, Misawa K, Takeda M, Kobayashi M, Satake M, Kawazoe Y, Ohuchi N, Kasuya A, Konno M. Slica-coating of AgI semiconductor nanoparticles. *Colloids and Surfaces A: Physiochemical and Engineering Aspects*, 251: 197–201, 2004
4. Tada H, Watanabe T, Higuchi H, Ohuchi N. In vivo real-time tracking of single quantum dots conjugated with monoclonal anti-HER2 antibody in tumors of mice. *Cancer Res*, 67 (3): 1138-44, 2007.
5. Mross K, Niemann B, Massing U, Drevs J, Unger C, Bhamra R, Swenson CE: Pharmacokinetics of liposomal doxorubicin (TLC-D99; Myocet) in patients with solid tumors: an open-label, single-dose study. *Cancer Chemother Pharmacol* 54:514-24, 2004.
6. O'Brien ME, Wigler N, Inbar M, Rosso R, Grischke E, and Santoro A: Reduced cardiotoxicity and comparable efficacy in a phase III trial of pegylated liposomal doxorubicin HCl (CAELYX/Doxil) versus conventional doxorubicin for first-line treatment of metastatic breast cancer. *Ann Oncol* 15:440-449, 2004.
7. Hamaguchi T, Matsumura Y, Nakanishi Y, Muro K, Yamada Y, and Shimada Y: Antitumor effect of MCC-465, pegylated liposomal doxorubicin tagged with newly developed monoclonal antibody GAH, in colorectal cancer xenografts. *Cancer Sci* 95:608-13, 2004.
8. Park JW, Kirpotin DB, Hong K, Shalaby R, Shao Y, and Nielsen UB: Tumor targeting using anti-her2 immunoliposomes. *J Control Release* 74:95-113, 2001.

Author Index

A

Abad, Saeedeh Lotfi Mohammad 219
Abbah, A.S. 1476
Abbas, Abbas K. 602, 1969
Abbott, D. 456, 569
Abe, Y. 1426
Acharya, U.R. 231
Adachi, T. 2000
Adachi, Y. 39
Adam, C. 1757
Adam, C.J. 1769
Afzulpurkar, N.V. 859
Agarwal, A. 838
Agarwal, M.G. 129, 906
Agathopoulos, S. 1271
Agbeviade, K. 1623
Agrahari, V. 1297, 1325
Aguilera, A. 1162, 1166
Agung, Setiawan W. 911
Ahmadi, F. 1065
Ahmed, B. 422
Akatsuka, T. 194
Akimoto, Y. 1422, 1430
Aksoy, M.E. 1462
Akter, Morium 1000
Akutagawa, M. 598, 606, 2159, 2167
Akutagawa, Masatake 1112
Akutsu, T. 1275, 1430, 1600
Alahari, Sai Krishna 415
Albason, A.C.B. 418
Alfiansyah, A. 1073, 1077
Ali, Sazid 1957
Alirezaie, J. 1846
Alkharabsheh, A. 210
Allen, J.S. 746, 750
Allen, Yvonne B. 1676
Allena, R. 1829
Almazan, S.P. 846
Al-Nuaimy, W. 210
Aloisio, G. 348
Alunan, L.I. 846
Alzaidi, S. 1896
Al-Zu'bi, N. 210
Amalina, D. Nur 2110
Amin, Rashid 81
Anastasiadis, P. 746, 750
Anders, J. 89
Anderson, J.G. 1320, 1352
Ando, Joji 2184
Ando, Takayasu 657
Andrew, C.M. 687
Aomi, Shigeyuki 2139
Aonuma, Y. 2000
Arai, Fumihito 2223
Arai, Hiroyuki 2201
Araki, T. 493
Aramwit, Pornanong 1356
Ardizzone, Edoardo 22
Areeprayolkij, W. 306, 665, 1144
Arita, M. 1183
Arora, S. 817
Arshak, K. 1153
Artmann, Gerhard 81
Artmann, Temiz A. 81
Asaoka, Takahiro 915, 931
Åsebø, O. 1204
Askin, G.N. 1769
Aslani, F. Jabbary 1546
Aubry, D. 1829
Auephanwiriyakul, Sansanee 476
Azuma, T. 1179

B

Baba, A. 1409, 2177, 2268
Baba, Mamoru 2248
Bae, Sanggon 519
Bag, S. 1293
Bai, J. 821
Baker, Priscilla 829
Balanagarajan, Ahamed Mohideen 43
Balasekaran, G. 1777
Balasubramanian, V. 1120, 1140
Bansal, N. 138, 142
Barbosa, C.R. Hall 652, 1124
Barmaksoz, M. 1166
Barnes, C. 750
Barrantes, Alberto E. Chaves 1136
Bartusek, K. 186, 190
Bassam, Rasha 602, 1969
Baumert, M. 456
Beck, T.J. 1918
Begic, Sabina 829
Beh, Kuang Boon 206
Beherei, Hanan H. 1199
Behnamghader, A. 1305
Beig, M.I. 456
Bennet, L. 235
Benoit, M. 1623
Bentley, A.S.J 687
Bergers, D. 399, 1866
Besseghini, S. 961, 1584
Beyene, Negussie 829
Bezerianos, A. 594, 673
Bharadwaj, Lalit M. 902
Bhattacharya, Puranjoy 701
Bholsithi, Wisarut 472
Biafore, F. 1263
Biala, T. 2130
Bidari, P. Sobhe 1846
Blaiki, R.J. 778
Blocki, A. 1469
Boero, G. 89
Boivie, K. 1204
Bonhomme, S. 1014
Bormane, D.S. 1, 69
Bost, W. 746
Bouda, T. 1535
Bradizlova, Petra 829
Bree, J.W. 1389
Březina, T. 2005
Bridzik, R. 979, 1042, 2155
Britten, R.D. 1908
Brotons-Mas, J. 374
Bu, Nan 2043
Budgett, D. 235
Buist, M.L. 296, 1809
Buist, Martin L. 1696
Buldakova, Yu.R. 1615
Buonsanti, M. 1842, 1945
Burden, R., Jr. 563

C

Cabibihan, J.J. 2023
Cacciola, M. 1842
Cai, Hong Xin 1289, 1373
Cai, You Zhi 1373
Caimmi, M. 1584
Campo, E. 1014
Cannatà, M.C. 1945
Cao, X.D. 1275
Cernohorsky, J. 2155

Cerny, M. 950, 979, 2155
Cettl, L. 1564
Cha, Kab-Mun 452
Chaichana, Thanapong 1676, 1728
Chan, Ann Shireen 1224
Chan, Casey K. 299, 2171
Chan, M. 1014
Chan, S.C.W. 1252
Chan, W.K. 1258
Chan, W.Y. 1523
Chandran, V. 231
Chang, C.C. 1459
Chang, C.H. 2056
Chang, Chia-Wei 874
Chang, D.K. 1773
Chang, H.T. 794
Chang, Huo-Ying 105, 622
Chang, I.L. 1359, 1362, 1366
Chang, J.S. 1341
Chang, Ju-Ying 1862
Chang, Kang-Ming 485
Chang, M.W. 566
Chang, Meng-Ting 884
Chang, S. 206, 540
Chang, S.H. 402, 406, 1667
Chang, Shu Wei 1333
Chang, Stephen 202
Chang, T.W. 1061
Chang, W.C. 1341
Chang, W.H. 867
Chang, X.Y. 821
Chang, Yen-Ching 227
Change, S.H. 318
Chankong, Thanatip 476
Chanwimaluang, T. 306
Chatelin, R. 1896
Cheang, Philip 261
Chee, R.E. 838
Chee, W.S. 2114
Chen, B. 1244
Chen, C.-C. 490
Chen, C.H. 802, 806
Chen, Chang Hao Chen 31
Chen, Chao-Hsuan 1224
Chen, Chen-Huan 497
Chen, Chih-Yuan 1749
Chen, F.G. 1850
Chen, H.Y. 855
Chen, J.C. 547, 1094
Chen, J.Y. 867
Chen, K. 1659
Chen, N.G. 842
Chen, P.Y. 536
Chen, S.C. 942, 946
Chen, S.H. 2106
Chen, S.I. 1592
Chen, S.J. 55
Chen, S.-J. 954
Chen, S.M. 1032
Chen, Shun-Yuan 799
Chen, W.C. 1061
Chen, W.H. 1208
Chen, Wen-Chuan 2092
Chen, Wen-Ming 1817
Chen, X. 1952
Chen, Xiao 1195, 1289, 1369, 1397
Chen, Y. 898
Chen, Y.L. 1393
Chen, Y.T. 55
Chen, Yao-Wen 362
Chen, Yung-Tsung 1224
Chen, Z.C.C. 1499
Chen, Z.H. 794
Cheng, C.K. 1061
Cheng, Cheng-Kung 2092
Cheng, D.C. 734
Cheng, Hao-min 497
Cheng, J.T. 842
Cheng, S.C. 543
Cheng, T.M. 1405
Cheok, M.G. 2110
Cheong, C.H. 1938
Cheung, K.M.C. 1252
Chew, Michelle B.-R. 898
Chian, K.S. 1484
Chiao, C.L. 1401
Chiba, Natsuko 2211
Chien, C.S. 1401
Chin, T. 694
Chiou, L.C. 1362, 1366
Chiou, Y.J. 318
Chiou, Y.W. 1773
Chiu, C.C. 578
Chiu, C.Y. 2106
Chiu, L.C. 1359
Chiu, Yu-Hsien 970, 1082
Cho, M.H. 460
Choe, W. 355
Choi, Charles T.M. 179, 310, 619
Choi, H.H. 974
Choi, H.S. 1962
Choi, Heung-Ho 51
Choi, J. 1090
Choi, J.B. 2147
Choi, M.H. 161, 165
Choi, S.J. 257
Choi, S.K. 465
Chong, C.K. 1519, 1523
Choo, Boon Hwa Andre 1255
Choo, J.Q. 1024
Chou, K.F. 855
Chou, S.M. 1931
Chou, Siaw Meng 1631
Chou, W.L. 718
Chou, Y.C. 714, 722
Chow, Vincent T.K. 898
Chu, P.C. 1094
Chu, Yeh-Shiu 1980
Chua, J.H. 838
Chua, K.C. 231
Chua, L.P. 1838
Chuang, C.C. 543, 966
Chuang, Chih-Yuan 378
Chui, C.K. 1024
Chui, Chee Kong 202, 206
Chung, C.A. 1737, 1745, 1749
Chung, D.W.Y. 418
Chung, Hui-Ming 622
Chung, Kao-Chi 1082, 1862
Chung, S.C. 161, 165
Chung, Soonchul 1814
Chung, W.Y. 543
Cipto, Cyntalia 1171
Clift, S.E. 1608
Clinton, L. 27
Clive, C.R. 769
Codan, B. 2076
Corrias, A. 1809
Craig, J.E. 198
Cripps, V.A. 2130
Cruz, F.R.G. 543
Cunningham, J.L. 1636
Cuzzola, M. 1945

D

Dabanloo, Nader Jafarnia 219
Dale, B.M. 138
Daliri, M. 1305
Damrongsakkul, S. 1217, 1301, 1377
Dang, Xiao 1037
Dao, Ming 1788
Davcev, Danco 174
David, J. 327, 331

David, T. 778, 1896
De Paolis, L.T. 348
De Silva, A. 156
Deng, Z.D. 390
Dermatas, E. 594
Deviga, J. 27
Devuyst, S. 146
Dey, Sangeeta 1267
Dharan, Smitha 631
Ding, Hui 1028, 1037
Ding, S. 1555
Dissanayake, T. 235
Dixit, P. 817
Do, J.-H. 527
Dobashi, Noriyuki 249
Dohmae, Y. 1733
Donnet, M. 1623
Dosel, P. 1564
Dragomir, A. 673
Du, M. 1044
Dubey, V. 1241
Dudul, S.V. 215
Dutoit, T. 146
Dutta, Pranab Kishore 754

E

Eckstein, F. 1918
Edlinger, G. 366, 374
Eils, R. 1527
ElBahnasy, Khaled M. 151
Elmessiry, Haitham M. 151
Emoto, T. 598
Eo, Y.H. 465
Eom, G.M. 161, 165
Eom, Gwnagmoon 1814
Esteki, A. 765, 1753
Estève, D. 1014
Ewald, H. 825

F

Fachiyah 1920
Fan, Hongbin 1512
Fan, J.H. 870
Fang, A.C. 1777, 2038
Fang, B.K. 340
Fang, H.W. 1341
Farge, E. 1829
Farr, H. 1896
Feng, Y. 1870
Ferdous, J. 1519
Fisher, P. 77
Florian, Z. 2005
Foltynski, P. 1049
Fong, L.S. 1952
Fong, M.K. 1258
Foo, J.Y.A. 817
Foong, K.W.C. 615
Fu, L.M. 794
Fuis, V. 1580, 2005, 2012
Fujikake, K. 987
Fujimoto, T. 1409
Fujimoto, Toshihiko 2204
Fujisaki, K. 2118
Fukami, T. 194, 253
Fukami, Tadanori 245, 270
Fukuda, H. 2228
Fukuda, Toshio 2223
Fukui, H. 1712
Fukumi, Minoru 302
Fukushima, T. 2258
Funamoto, K. 2188

G

Gabriel, S.E. 1640
Gaiotto, T. 2076
Gajendiran, Viveka 1696
Gale, T.J. 769
Gambino, Orazio 22
Gan, L.H. 863
Gansawat, D. 306, 586, 665, 1144
Gao, Y. 142
Gao, Y.M. 1044
Gaohua, Lu 1651, 1655
Garnepudi, Venkata Ravi kumar 415
Gasperini, G. 1584
Gavriloaia, G. 427
Gaylor, J.D.S. 1320
Gerla, V. 133
Gescheidtova, E. 186, 190
Ghassemian, H. 738
Ghemigian, A.M. 427
Ghista, D.N. 1838
Ghosh, U.B. 1700
Gibson, I. 1480
Giovanola, J.H. 1623
Gladilin, E. 1527
Goh, J.C.H. 1381, 1476, 1488, 1508, 1512, 1515, 1684, 1716, 1805
Goh, Kheng Lim 1631
Goh, S.W. 2110
Goloviznin, M.V. 1615
Gomez, F.R. 846
Gonda, K. 2272
Gopalakrishnakone, P. 842
Gopu, G. 101
Goteau, R. 2228
Grant, M.H. 1320, 1352
Griffiths, S. 1320
Groenegress, C. 366
Guger, C. 366, 374
Gunduz, O. 1271
Guo, L.X. 1938
Guo, W.Y. 714
Gurvich, C. 551
Gusad, M.T. 846
Gusmão, L.A.P. 652, 1124
Gweon, B. 355

H

Haghgooie, S. 551
Hagihara, K. 1941
Hahnvajanawong, C. 1344
Hama, Y. 1443
Han, J.H. 465
Han, K.W. 996
Han, T.J. 1401
Han, Wei-Ru 378
Hanousek, J. 1564
Haque, Aminul 1000
Hara, T. 1733, 1766, 1781
Harikumar, R. 351
HariKumar, R. 370, 647
Hartley, David E. 1676
Hartmann, M. 169
Hasegawa, Hideyuki 2207
Hasegawa, K. 1781
Hasegawa, S. 987
Hashimoto, K. 1941
Hassan, Meer Saiful 1434
Hatsusaka, N. 9
Hayase, T. 1993, 2188, 2254
Hayashi, H. 1316
He, P.F. 1515
Heng, C.K. 898
Heng, L.T. 1924
Hengky, Chang 261
Henneman, J. 750
Herrera, E. 1162
Herzog, W. 2151
Hidaka, Hiroshi 2194
Hidaka, K. 1892

Hieda, I. 523
Hieu, Nguyen Thi Minh 1289
Hiew, L.T. 615
Higaki, H. 1588, 1712, 1766
Higashi, Yukihito 2059
Higuchi, H. 2272
Higuchi, M. 9
Himeno, R. 1531
Hirata, Yasuhisa 2232
Hiura, T. 1733
Ho, Saey Tuan Barnabas 1255
Ho, Szu-Ying 1745
Hobara, H. 1912
Hojo, M. 2000
Holcombe, M. 77
Holzner, C. 366
Homma, D. 1409, 2268
Hong, D.Y. 1720
Hong, J.W. 1935
Hong, Jeonghwa 1814
Hong, T.F. 1401
Hong, T.Y. 1128
Hong, Z.D. 1004
Hontani, H. 194
Horak, Z. 1228, 1535, 1724
Horikawa, Etsuo 2201
Hosoda, N. 1883
Höttges, S. 1542
Hou, C.J. 55
Hou, S.Y. 566
Houfek, L. 1580, 2005
Houfek, M. 2005
Hourigan, K. 1672
Houška, P. 2005
Howard, G.J. 1636
Hsia, C.C. 966
Hsiao, M. 802, 806
Hsiao, M.C. 1094
Hsiao, T.C. 318
Hsiao, Tzu-Chien 1086
Hsieh, Cheng-Che 1149, 2064
Hsieh, Fu-Shiu 1149
Hsieh, J.C. 718, 726
Hsieh, Ming-Fa 1224
Hsu, C.H. 310
Hsu, C.L. 578
Hsu, C.Y. 1451
Hsu, L.H. 1128, 1704, 1720
Hsu, P.H. 547
Hsu, Po-Chun 105
Hsu, S.T. 942, 946
Hsu, T.H. 55
Hsu, T.-Y. 2072
Hsu, Tse-Lin 183
Hu, A.A.S. 418
Hu, A.P. 235
Hu, Chih-Chung 2064, 2068
Hu, H.-Y. 1797
Hu, K.-H. 992
Hu, Yi-Chiuen 799
Huang, C.C. 2106
Huang, C.H. 1019
Huang, C.Y. 536, 1009
Huang, Chien-Che 1149, 2064
Huang, Chih-Cheng 799
Huang, Chih-Chung 742
Huang, Chih-Hao 574
Huang, G.F. 1128, 1704, 1720
Huang, J.H. 966
Huang, J.-H. 802, 806
Huang, Jung-Tang 884
Huang, K.-S. 481
Huang, L.F. 1359, 1362, 1366
Huang, S.R. 714
Huang, S.Y. 855
Huang, Sheng-Chieh 574
Huang, W.C. 435
Huang, Yao-Jhang 888
Hui, Hoi Po James 1255
Hui, K. Xin 344
Hui, L.F. 1680
Hukins, D.W.L. 1191, 1546, 1619
Hung, C.I. 718
Hung, W.I. 870
Hunter, P.J. 1878
Hur, Tai-Sung 51
Hurduc, A.E. 427
Hutmacher, D.W. 1476, 1480
Hwang, S.H. 1928, 1962, 2016
Hwang, S.J. 1977
Hwang, Sung Oh 1116
Hwu, Y.K. 806
Hwu, Y.-K. 802

I

Iacopino, P. 1945
Ichihara, H. 2192
Ichihashi, F. 1098
Ichikawa, K. 2197
Iida, K. 2237
Iimura, Hiroshi 2139
Ikeda, K. 2237
Ikeda, Seiichi 2223
Ikeda, Tomoaki 2043
Imachi, K. 1426, 2268
Imai, Y. 2244
Imari, Y. 2034
Ingole, D.T. 69
Inoue, K. 1993
Inoue, S. 1892
Inoue, Y. 1426
Inthavong, K. 1550, 1555
Inui, S. 2159, 2167
Irie, K. 1611
Irrera, G. 1945
Isa, Siti Faradina Bte 280
Iseki, Hiroshi 2139
Ishida, T. 2272
Ishii, Idaku 2043
Ishii, S. 39
Ishikawa, B. 253
Ishikawa, F. 253
Ishikawa, T. 2244
Ishikawa, Takuji 2134
Isoda, H. 2188
Isoyama, T. 1426
Itoh, Masatoshi 2201, 2204, 2248
Iwano, Takuya 2232
Iwasaki, K. 1053, 1183, 1422, 1430, 1443, 1600
Iwasaki, Kiyotaka 1213
Iwata, T. 439, 493
Iwuoha, Emmanuel 829
Iyengar, Anupama V. 892
Iyengar, Anupama.V. 699

J

Jaafar, R. 18, 65
Jacklyn, Huang Qunfang 1057
Jackson, Daniel 678
Jain, Avijeet 1438
Jain, N.K. 1241
Jain, S.K. 1455
Jameie, Seyed Behnamedin 219
James, J.R. 138, 142
Jan, Ming-Yie 183
Jang, H.S. 974
Janicek, P. 1580
Jansen, S.M.H. 335
Jao, C.W. 730
Jarillas, J.M. 846
Jaruwongrangsee, K. 851
Javaheri, M. 1236
Jayachandran, D. 1337

Jayakumar, K. 85
Jebaraj, C. 2088
Jebaseelan, D. Davidson 2088
Jeon, Y.J. 505, 508, 527
Jeong, Myeonggi 2201
Ji, H.M. 898
Jiang, C.F. 1019
Jiang, Yang Zi 1285, 1289, 1369
Jiao, G.Y. 1788
Jie, J. 1572
Jie, Leow Shi 1171
Jin, H-Y. 444
Jin, L.H. 1761
Jirattiticharoen, W. 586
Jirkova, L. 1724
Jirman, R. 1228, 1535
Jobbágy, Á. 112
John, L.R. 687
Jomphoak, A. 859
Joshi, S.C. 1244
Ju, M.S. 340, 1032
Ju, M.-S. 291, 1833
Juan, D.F. 867
Jun, J.H. 161, 165
Jung, D. 1409
Jyothiraj, V.P. 626

K

Kabinejadian, F. 1838
Kabir, M.M. 456
Kabra, V. 1297, 1325
Kachibhotla, Srinivas 758
Kado, H. 9
Kajbaf, H. 738
Kaji, H. 2173
Kaji, R. 598
Kaji, Y. 606
Kajiya, F. 1941
Kakaday, T. 198
Kakarla, S. 431
Kakran, M. 817
Kalajdziski, Slobodan 174
Kalcher, Kurt 829
Kam, B.H. 563
Kamarozaman, Nina Karmiza Bte 280
Kamioka, H. 2000
Kamoda, A. 1600
Kan, H.C. 1592
Kanaeda, Yoshiaki 931
Kanai, Hiroshi 2207
Kandori, A. 682
Kanemitsu, N. 1179
Kaneswaran, K. 1153
Kang, Then Tze 280
Kanke, Y. 2254
Kanno, S. 2258
Kanno, Tomoyuki 938
Kanoh, S. 2264
Kanokpanont, S. 1217, 1301, 1377
Kaplan, D.L. 1377
Kappel, C. 1527
Kar, Kamal K. 1309
Karacayli, U. 1271
Karbasi, S. 1248
Karimi, E. 1220
Karlsen, R. 1204
Karnafel, W. 1049
Karthikeyan, G. 691
Karule, P.T. 215
Karungaru, Stephen 302
Kataoka, K. 1451
Kataoka, N. 1941
Katiyar, V.K. 1957
Kato, Motohisa 2201
Katoh, M. 2118
Katukojwala, S. 431
Kaur, Harsimran 902
Kaur, Inderpreet 902
Kawabata, S. 39
Kawabe, J. 2159, 2167
Kawabe, T. 2159, 2167
Kawahara, N. 1588, 1712
Kawai, J. 39
Kawai, M. 2241, 2272
Kawamoto, Masashi 2059
Kawana, Fusae 47
Kawanaka, H. 1102
Kawase, Tetsuaki 2194
Kawashima, R. 2228
Ke, C.J. 867
Kelsen, Bastari 261
Kelso, R.M. 569
Kerkhofs, M. 146
Kesavdas, C. 35
Kgarebe, Boitumelo 829
Khalifa, Mohamed E. 151
Khan, R.S. 1716
Khang, G. 1785
Khare, P. 1455
Khorramymehr, S. 1569, 1648
Khunkitti, W. 1344
Kiew, Ji Sheng 1980
Kil, Se-Kee 51
Kim, C.H. 468
Kim, D. 355
Kim, D.B. 355
Kim, H.A. 1636
Kim, H.-S. 468
Kim, I.Y. 996
Kim, J.H. 257
Kim, J.J. 996
Kim, J.K. 2147
Kim, J.Y. 505, 508, 1977, 2052
Kim, J.-Y. 527
Kim, Jiwon 1814
Kim, K.H. 257, 505, 527, 2027, 2030
Kim, Mina 1935
Kim, S.H. 460, 468, 2009
Kim, S.I. 996
Kim, Sookwan 519
Kim, Sunhee 1949
Kim, T.-S. 460, 468
Kim, Tae-Seong 555
Kim, Y.E. 2016
Kim, Y.H. 1928, 1962, 2016
Kim, Y.J. 1900, 1952
Kim, Yohan 1814
Kim, Youngho 1977
Kim, Young-Sear 51
Kim, Younho 519
Kimura, F. 395
Kimura, Hidenori 1651, 1655
Kingma, H. 335
Kinomura, S. 2228
Kinouchi, Y. 598, 606, 2159, 2167
Kinouchi, Yohsuke 1112
Kiran, K. Lakshmi 1337
Kishi, A. 1426
Kitahara, K. 1781
Kitawaki, T. 1531
Klibanov, A.L. 746
Kluge, T. 169
Ko, Frank 1492
Koba, H. 1098
Kobashi, H. 1053
Kobayashi, R. 2258
Kobayashi, S. 1572
Kobayashi, T. 2237
Kobayashi, Toshimitsu 2194
Kobayashi, Y. 1912
Kochiev, T. 468
Koguchi, H. 635
Kogure, Yuichi 1112

Koh, M. 1777
Kohno, R. 1158
Kok, Y.Y. 2114
Komatsuda, Shinji 2232
Komeda, T. 2099
Kondo, H. 2244
Konno, S. 1989, 2268
Koonsanit, K. 306, 586, 665, 1144
Korayem, M.H. 1576
Kormos, R. 1179
Kosuge, Kazuhiro 2232
Kosugi, T. 2188
Kosukegawa, H. 1993
Kotzian, Petr 829
Kouno, A. 1426
Koyanagi, M. 1892, 2258
Koyano, K. 1611
Kraitl, J. 825
Krajca, V. 133
Krausz, G. 366, 374
Krishnamurthy, Kamalanand 1708
Krittian, S.B.S. 1542
Krzymien, J. 1049
Ku, D.N. 1572
Ku, J.H. 996
Kua, H.J.A. 2110
Kuhn, V. 1918
Kukhetpitakwong, R. 1344
Kukureka, S.N. 1191
Kulish, V.V. 411
Kulkarni, J. 551
Kumabe, Akinobu 1112
Kumagai, I. 2237
Kumagai, Kazuaki 2248
Kumano, S. 2237
Kumar, A. Sukesh 327, 331, 626
Kumar, Arun 984
Kumar, D. 1466
Kumar, Gideon Praveen 1539
Kumar, K.M. Ashwin 1120
Kumar, M. Logesh 351
Kumar, Senthil 280
Kumar, Suresh 902
Kumaravel, N. 669
Kuo, T.Y. 1401
Kurata, K. 1766
Kuroki, K. 1993
Kusachi, S. 1531
Kutluk, Abdugheni 2059
Kwan, Sze Siu 344
Kwon, J.Y. 2104
Kwon, W. 2030

L

Labrom, R.D. 1769
Ladyzynski, P. 1049
Lai, C.W. 1128, 1704
Lai, H.J. 1061
Lai, P.S. 1447, 1451
Lai, T.-C. 802, 806
Lakhonina, N.S. 1615
Lakshmi, V. 1850
Lakshminarayanan, S. 1337, 1850, 1915
Lal kishore, K. 13
Lam, C.M. 2114
Lam, C.X.F. 1476, 1480
Lam, S.K.L. 1252
Lam, W.M. 1258
Lamsudin, R. 1073, 1077
Lan, C.Y. 578
Lan, H.-M. 1833
Lan, L. 1761
Lareu, R.R. 1469
Latha, Madhavi 85
Lau, D.P.C. 1024
Lau, Kelly S.H. 898
Lau, Raymond 1434
Lau, S.T. 1684
Lavanya, R. 559
Lavrijsen, T. 1878
Lawrence-Brown, Michael M.D. 1676
Lawson, J.R. 287, 1908
Layman, C. 746, 750
Lazarovici, Philip 81
Le, S.N. 1777, 2038
Lee, B. 161, 165
Lee, Bongsoo 1814
Lee, C.Y. 794
Lee, D.H. 1090
Lee, Eng Hin 1255
Lee, G.J. 465
Lee, G.Y.H 774
Lee, G.Y.H. 2122
Lee, Gwo-Bin 574
Lee, H.J. 2052
Lee, H.R. 996
Lee, J. 505, 508, 2052
Lee, Je Wei 1333
Lee, Jung Hoon 1116
Lee, L.C. 1592
Lee, M.K. 1777, 2038
Lee, M.W. 55
Lee, Peter V.S. 1684, 1716
Lee, Peter Vee-Sin 1817
Lee, S.H. 2147
Lee, S.J. 161, 165
Lee, S.W. 505
Lee, S.Y. 460
Lee, Sung-Jae 1817
Lee, T. 1900, 1918, 1952
Lee, T.W. 1393
Lee, Taeyong 1817
Lee, Tracey 984
Lee, W.H. 460, 996
Lee, Y.J. 508, 2052
Lee, Yean C. 299, 2171
Lee, Yen-Ting 619
Lee, Yi Hsuan 310
Lee, Yi-Hsuan 179
Lee, Young-Koo 555
Lei, P. 1680
Lelkes, Peter I. 81
Lemor, R.M. 746
Leo, C.S. 109
Leo, H.L. 1405
Leong, K.W. 1279
Leung, V.Y.L. 1252
Leung, Y.S.E. 2114
Levy, D. 1688
Levy, Y.Z. 1688
Lewallen, D. 1640
Lewis, E. 825
Lhotská, L. 133
Li, A. 1965
Li, Bing Nan 202, 206
Li, C. 381
Li, H. 559, 610
Li, H.C. 722
Li, J. 842
Li, J.J. 314
Li, J.S. Jimmy 198
Li, J.Z. 1938
Li, Jiashen 1492
Li, Jing-Sheng 2092
Li, Lin 1492
Li, Q.S. 2122
Li, W.T. 870
Li, W.-T. 992
Li, W.-T. 2072
Li, X.Q. 390
Li, Yi 1492
Li, Z.Y. 1258
Liang, Fuyou 1984
Liang, S.M. 706

Liang, Tianzhu 1028
Liao, Y.L. 726
Liau, B.Y. 578
Liau, Ian 1224
Lie, D.T.T. 1931
Liew, H.X.S. 2110
Lim, C.M. 231
Lim, C.S. 817
Lim, C.T. 774, 1279, 1788, 1965, 2122, 2244
Lim, J.E. 465
Lim, J.H. 559, 610
Lin Wang, Yuh-Ying 183
Lin, C. 138
Lin, C.A.J. 867
Lin, C.C. 2056
Lin, C.C.K. 340, 1032
Lin, C.-C.K. 291, 1833
Lin, Chii-Wann 1086
Lin, H.H. 318, 1032
Lin, J.C. 1413, 1418
Lin, J.H. 318, 582
Lin, J.M. 813
Lin, Jeen 884
Lin, K.J. 547, 1061
Lin, Kun-Jhih 2092
Lin, P.L. 1341
Lin, P.W. 813
Lin, S.T. 867
Lin, Tze-Hung 1737
Lin, Victor 299, 2171
Lin, Xi-Zhang 574
Lin, Y.C. 855, 1393
Lin, Yi-Hsun 742
Lin, Yu-Chih 1996
Lin, Z.Y. 855
Ling, S.-F. 291
Liow, K.Y.S. 1672
Lissorgues, Gaëlle 786, 790
Lithgow, B.J. 551
Little, P. 1757
Liu, An-Bang 105, 622
Liu, C.H. 734
Liu, C.L. 942, 946
Liu, C.-P. 540
Liu, Cyuan-Cin 105
Liu, H. 2268
Liu, H.L. 435, 532, 536, 547, 1094
Liu, Haifeng 1512
Liu, Hao 1984
Liu, J. 559, 610
Liu, J.S. 1592
Liu, Jolene 1631
Liu, Kuang-Che 1082
Liu, L. 1993
Liu, Ming-Chien 622
Liu, Pei-Ling 1086
Liu, R.S. 802, 806
Liu, S.H. 1704
Liu, S.-H. 481
Liu, Shing-Hong 485
Liu, Wei-Wen 362
Liu, Wenbo 1028
Lloyd, C.M. 287
Lo, J.M. 1393
Lodererova, M. 1204
Loe, F.C. 1469
Loganathan, P. 1850
Lomas, T. 851
Lou, A.S.L. 418
Lu, C.F. 714, 722
Lu, C.H. 582
Lu, C.T. 1128
Lu, P.S. 1359, 1362, 1366
Lu, T.-W. 1149, 2064, 2068
Lu, W.W. 1252, 1258
Luk, K.D.K. 1252, 1258
Lukes, J. 1792
Luo, Y. 1409
Luong, M.Q. 834

M

Ma, R.H. 794
MacGregor, S.J. 1320, 1352
Maclean, M. 1320, 1352
Maeda, Y. 1102
Maeno, Masato 927
Magatani, Kazushige 249, 710, 915, 919, 923, 927, 931, 938
Magatani, Kazusige 935
Magoni, L. 961
Mahajan, Alka 69
Mahapatra, D. 661
Mahapatra, Dwarikanath 639
Mahidhara, Ram Prakash 415
Mahmoud, Amr I. 1199
Mahomed, A. 1191
Maikrang, Kamol 1356
Majumder, Swanirbhar 754
Mak, Arthur F.T. 1492
Mak, P.U. 1044
Mak, Peng Un 31
Mak, W.C. 821
Malarvizhi, S. 323
Malboobi, M.A. 1846
Maleki-Dizaji, S. 77
Mallepree, T. 399, 1866
Malpas, S. 235
Mamada, K. 1993
Manjunatha, M. 691
Manohar, Pradeep 1692
Manousakas, I. 314, 706
Manshaei, R. 1846
Mao, B.W. 863
Maraziotis, I.A. 673
Mares, T. 1792
Maruthappan, P. 1952
Maruyama, Masahiro 2201
Marzari, R. 2076
Mastrogianni, A. 594
Masud, Mehedi 2201, 2204
Mathew, L. 1597
Mathew, Lazar 810, 1539
Mathur, Shamla 758
Matsuda, Hiroshi 2043
Matsuda, J. 1766
Matsuda, Takehisa 2223
Matsue, K. 2268
Matsui, T. 2048
Matsukawa, Kodai 2139
Matsumoto, T. 2099, 2102, 2104, 2197
Matsumura, K. 882
Matsushita, Y. 1611
Matsuura, T. 2250
Matsuura, Y. 5
Matter, M.L. 750
Maturos, T. 851
Maturus, T. 859
Mazanek, J. 1228, 1535
Mazumdar, J. 569
McDonald, K. 1757
McGrath, D. 825
McInnes, S. 198
McLoughlin, I.V. 1065
McPhail, T. 511
Megali, G. 1842
Mengko, Tati L.R. 94, 2079
Mengko, Tati R. 911
Mercier, Bruno 786
Meyer, J.S. 1688
Mhawej, M.J. 1263
Miao, J. 817
Michael, Raghunath 1473
Migalska-Musial, K. 1049

Mikulis, David J. 362
Mikulka, J. 186, 190
Miller, Andrew D. Miller 1503
Min, Hong-Ki 51
Minari, Takahiro 2059
Mishra, D. 1241
Mithraratne, K. 1878
Mitra, Madhuchhanda 590
Mitsukura, Yasue 302
Miura, H. 1426
Miyahara, Hidemitsu 2059
Miyake, Masayasu 2204, 2248
Miyamoto, H. 598
Miyamoto, K. 2264
Miyamoto, M. 39
Miyao, M. 987
Miyata, T. 493
Mochizuki, Hideki 2201
Mohamed, Khaled R. 1199
Mohan, Keshav 116
Mohandesi, Fatemeh 1576
Mohandesi, J. Aghazadeh 1236
Mohd Ali, M.A. 18
Mohylová, J. 133
Moinodin, M. 765, 1753
Mojica, K. 750
Molteni, F. 961, 1584
Momani, L. 210
Momose, Keiko 657
Mongkolnavin, R. 1217
Monteiro, E. Costa 652, 1124
Moog, C.H. 1263
Morabito, F.C. 1842
Morikawa, H. 1572
Morohashi, K.I. 1920
Morzynski, M. 1854
Mou, Pedro Antonio 31
Mouronval, A.-S. 1829
Mrozikiewicz-Rakowska, B. 1049
Mukai, K. 606
Muragaki, Yoshihiro 2139
Murakami, H. 1588, 1712
Murakami, T. 1883
Murakoshi, M. 2237
Murayama, Y. 1600

N

Na, Yong Joo 1935
Nagamine, R. 1559
Nagashino, H. 606
Nagata, Kentaro 710, 923, 927, 935
Nagayama, K. 2197
Nahar, M. 1241
Naidu, M.U.R. 431
Nair, Achuthsankar S. 631
Naito, H. 2099, 2102, 2104
Naito, K. 1912
Naitoh, K. 1329, 1801
Nakada, Y. 1588
Nakae, N. 1892
Nakagaki, M. 2197
Nakagawa, H. 1426
Nakagawa, M. 240
Nakajima, Y. 1904
Nakamuara, Masatoshi 47
Nakamura, E. 1941
Nakamura, Ryoichi 2139
Nakamura, Ryuji 2059
Nakane, S. 598
Nakano, Takemi 935
Nakano, Takuma 2223
Nakano, Yoshitaka 2139
Nakata, K. 1733, 1892
Nakayama, K. 395
Nakazawa, K. 1912
Nalivaiko, E. 456
Nam, K.C. 523
Narkbuakaew, W. 306, 586, 665, 1144
Návrat, T. 2005
Neelaveni, R. 101
Negoro, Makoto 2223
Nemecek, J. 1792
Neu, B. 1644, 1924
Ng, Chin Tiong 1663
Ng, K.H. 1073, 1077
Ng, K.S. 1381
Ng, S.S. 1405
Nguyen, T.C. 1888
Nguyen, T.M. Hieu 1397
Nho, Minsoo 1935
Nickerson, D.P. 296
Nielsen, P.F. 287
Niranjan, U.C. 782
Niranjana, S. 782
Niro, R. Di 2076
Nishimura, M. 598
Nishiyama, N. 1451
Nishizawa, M. 2173
Nitta, S. 1409, 1989, 2177, 2268
Nitta, Y. 598
Nock, V. 778
Noda, Shunichi 2043
Noh, S.C. 974
Nomura, M. 2159, 2167
Novak, V. 979, 2155
Novák, V. 1042
Nur Naadhirah, R.R. 27
Nyang, Tan Khim 1473

O

Ochiya, Takahiro 1503
Oda, J. 1588, 1712
Oda, Kiyoshi 2194
Oda, M. 1733
Oertel, H. 1542
Oh, B.S. 465
Oh, Kah Weng Steve 1255
Ohashi, T. 2192, 2262
Ohgushi, H. 1316
Ohnishi, Y. 598
Ohta, M. 1993
Ohta, T. 1183
Ohuchi, N. 2241, 2272
Ohyama, W. 395, 1102
Ohyanagi, M. 439
Oka, H. 1531
Okahisa, T. 598
Okamoto, Y. 1053
Okamura, N. 2181
Okamura, Nobuyuki 2201
Okano, Teruo 1213
Oktar, F.N. 1271
Okuyama, T. 2219
Olkowski, R. 1480
Omori, G. 1733
Omori, M. 987
Ong, C.N. 774, 2122
Ong, F.R. 2095
Ong, K.L. 898
Ong, S.H. 202, 206, 615
Ong, W.F. 1484
Ong, Y.J.L. 2114
Ono, Hideto 270
Ono, T. 1426
Ordoñez, M. 1166
Oribe, K. 1781
Orito, Kensuke 2043
Osawa, T. 2102
Osawa, Yuko 2043
Oshima, S. 1098
Otahal, S. 1792

Otani, K. 2104
Otsuka, A. 694
Oura, Hiroyuki 2223
Ouyang, Hong Wei 1289, 1369, 1373
Ouyang, Hong-Wei 1195, 1285, 1397
Oyama, Tadahiro 302
Ozyegin, L.S. 1271

P

Padma, T. 85
Pai, C.L. 1451
Pal, S. 1267, 1293, 1700
Pal, Saurabh 590, 754
Pallavi, V. 701
Pan, C.H. 532, 536
Pan, H.B. 1258
Pan, L.C. 813
Pan, Y.H. 1393
Panengad, P.P. 1496
Pangher, N. 284
Parab, H.J. 802, 806
Pardasani, K.R. 358
Park, Byungkyu 1814
Park, H.K. 465
Park, J.-C. 2147
Park, J.H. 465, 974, 1974, 2009, 2027
Park, J.K. 2030
Park, J.S. 996
Park, J.W. 1090
Park, K.S. 1785
Park, Kunkook 519
Park, M.K. 974
Park, S. 2126
Park, S.W. 1962
Park, Y. 1179
Park, Young-Bae 51
Parmar, Bhavesh 1107
Patel, P.S.D. 1619
Patil, G.M. 60
Patil, S.B. 610
Patil, S.G. 769
Patil, S.T. 1, 69
Patil, Shailaja Arjun 1232
Paul, K. 133
Pearcy, M. 1757
Peeters, R.L.M. 335
Pellicanò, D. 1842
Peng, Ching-An 874, 878, 888
Peng, H.K. 1128, 1720
Peng, Y. 1469, 1499
Penhaker, M. 950, 979, 1042, 2155
Pepik, Bojan 174
Pereira, B.P. 2110
Perko, H. 169
Petránek, S. 133
Petricek, J. 1564
Phonphruksa, Phimon 223
Phothisonothai, M. 240
Phua, Chee Teck 786
Ping, Isaac Lim Zi 1171
Piro, R. 1945
Pirovano, S. 961, 1584
Pirrone, Roberto 22
Pittaccio, S. 961, 1584
Piyasin, S. 761
Plaisanu, C. 1175
Plunkett, M. 198
Pogfai, T. 859
Poh, C.L. 386
Poh, H.J. 1405
Poh, Y.C. 1809
Pontari, A. 1842, 1945
Porkumaran, K. 101
Pothuganti, Abhiram 415
Prabhu, K. Gopalakrishna 274, 277
Pramanik, Sumit 1309
Prasad, D.V. 98
Prasanna raj, Cyril 13
Prasertsung, I. 1217
Preechagoon, D. 1344
Prema, M. 27
Premchandra, C.S. 898
Prince, Shanthi 323
Pu, Q. 734
Pulimeno, M. 348
Pun, S.H. 1044
Pun, Sio Hang 31

Q

Qi, Yi Ying 1285, 1289, 1369, 1373
Qi, Yi-Ying 1195
Qian, Y. 1600
Qin, Ling 1492
Quek, C.H. 1279

R

Rafei, Siti R.M. 898
Raghunath, M. 1469, 1496, 1499
Raghuraj, Rao 1915
Rahman, Fazlur 984
Raj, J. Selva 1171
Raja, R. 344
Rajaratnam, B.S. 2110, 2114
Rajasekaran, S. 2088
Rajeshwari, P.M. 1708
Rajoo, R. 898
Ramadan, Hassan M.M. 151
Ramruttun, A.K. 1805
Rangaiah, G.P. 1850
Rasheed, Tahir 555
Rasouli, M. 863
Ratanavaraporn, J. 1301
Ravet, T. 146
Ravi, B. 129, 906
Ravichandra, S. 1057
Ravichandran, S. 27, 280, 957
Reboud, J. 834
Reddy, Narendra 1282
Reddy, T. Kalpalatha 669
Reymond, S. 89
Reynolds, K.J. 1888
Reznicek, J. 1228, 1535
Rhee, K. 1785
Richter, J. 1204
Ritchie, A.C. 1484
Roake, Peter J. 1187
Rodrigues dos Santos, Targinos 2248
Rodriguez, Isabel 1980
Rolfe, M. 77
Rooppakhun, S. 761
Rosales, C. 834
Rosales, M. 846
Rosinski, G. 1049
Rossini, M. 961
Rosulek, M. 979
Rousseau, Lionel 790
Roy, P. 894
Roy, S. 661
Roy, T.K. 1595
Rugelj, D. 1821
Ruiz, J.N. 1805
Rybnicek, J. 1204
Rychlik, M. 1854
Ryu, H.H. 505

S

Sadeghi, M. 1220
Sadeghniiat, Khosro 219
Sadrnezhaad, S.K. 1305
Saeki, Noboru 2059
Sagar, Eshwar Chandra Vidya 415
Sahoo, S. 1515
Saijo, Y. 1409, 1989, 2268
Saito, A. 1098
Saito, I 1426
Saito, Keiichi 657
Saito, Y. 253
Saito, Yoichi 245, 270
Sajith, V. 116
Sakaguchi, Katsuhisa 1213
Sakai, K. 2048
Sakai, N. 1883
Sakai, T. 1892
Sakamoto, J. 1588, 1712
Sakamoto, N. 1989, 2192, 2262
Sakata, R. 1409, 2268
Sakharkar, M.K. 817
Sakoda, S. 682
Sakurada, Yumiko 2201
Sakurai, Y. 2272
Salman, S. 1271
Sanchez-Vives, M. 374
Sanders, P. 569
Sangworasil, Manas 1676, 1728
Sankai, Y. 635, 1098
Sappat, A. 851
Saraswati 261
Sasada, H. 2268
Sasaki, Takehisa 2248
Sasaki, Tsubasa 927
Sasi Kumar, M. 35
Satake, H. 2159, 2167
Sato, A. 1600
Sato, F. 1409
Sato, H. 194
Sato, K. 2228
Sato, M. 1892, 1989, 2192, 2262
Sato, T. 39, 1098
Sato, Y. 1409, 2268
Satoh, R. 2118
Satyanarayana, B.S. 782
Satyanarayana, K. 60
Savastyuk, E. 468
Sawae, Y. 1883
Scaturro, Francesco 22
Schafer, B.W. 1918
Schaffelhofer, S. 374
Scheffler, K. 89
Schenkel, T. 1542
Schieber, M. 448
Schier, M. 156
Schlindwein, F.S. 2130
Schmidt-Trucksaess, A. 734
Schulz, M. 1527
Seah, H.H.S. 2114
See, E.Y.S. 1508
Segars, W.P. 1918
Seifi, S.M. 1236
Sekine, S. 2173
Sekioka, K. 395, 1102
Seng, K.Y. 1659, 1938
Sengupta, D. 1700
Seo, H.J. 2147
Seo, H.S. 460
Sepehri, B. 765, 1753
Sergo, V. 2076
Setiawan, Melissa A. 1915
Seto, Tatsuya 919
Sevšek, F. 1821, 1825
Shafie, F. 1236
Shahidi, G.A. 765
Shankar, K. 678
Shanthi, K.J. 35
Shanthi, S. 1466
Shanthini, R. 27
Shariatmadari, Mohammad Reza 1627
Sharifzadeh, H.R. 1065
Sharma, P.R. 1957
Sharova, N.I. 1615
Sheah, K. 386
Sheet, Debdoot 691
Shen, C.H. 1418
Shen, Zhi-Wei 362
Shen1, C.Y. 1592
Sheng, J.M. 1931
Shepherd, D.E.T. 1191, 1546, 1619
Shi, H. 1965
Shi, W. 1426
Shia, Chi-Chun 970
Shiba, Kenji 2059
Shibanoki, T. 694
Shibata, H. 439
Shibata, M. 2254, 2268
Shichijou, F. 606
Shieh, M.J. 1451
Shih, C.J. 1359, 1362, 1366
Shih, R.J. 1592
Shih, Yuan-Ta 497
Shiidu, Yuriko 919
Shillington, M.P. 1769
Shim, Hun 1116
Shima, K. 682, 694
Shima, Keisuke 2043
Shimada, T. 253
Shimada, Takamasa 270
Shimada1, Takamasa 245
Shimizu, Tatsuya 1213
Shimomura, Y. 1316
Shin, H.-C. 448
Shin, H-C. 444
Shin, Hyun-Chool 452
Shin, J.H. 355, 1935
Shin, J.W. 1090
Shin, Jennifer H. 1949
Shin, Kunsoo 519
Shinke, M. 1179
Shinogi, T. 1102
Shiraishi, N. 1098
Shiraishi, Y. 1179, 1409, 2177, 2268
Shirato, H. 2083
Shounak, De 782
Shyu, K.K. 730
Siddalingaswamy, P.C. 274, 277
Siegelmann, H.T. 1688
Silva, E. Costa 652
Silva, M.C. 1124
Singh, J.A. 1640
Singh, Kanika 2164
Singh, Kashmir 902
Singhai, A.K. 1438
Sinthanayothin, C. 265
Sinthanayothin, Chanjira 472
Sinthupinyo, W. 306, 586, 665, 1144
Sisodia, Rajendra Singh 701
Sitthiseripratip, K. 761
Sivakumar, R. 73
Sivarasu, S. 1597
Slater, M. 366
Smith, S. 1352
Sohn, R.H. 1928
Son, J.S. 1977
Son, K. 1974, 2009, 2027, 2030
Song, H. 2268
Song, S.J. 1090
Song, Xing Hui 1369
Soon, V.C. 142

Soong, B.W. 722, 730
Sotthivirat, S. 306, 586, 665, 1144
Sounderya, N. 1741
Sourin, A. 411
Sourina, O. 411, 1874
Sovani, Iwan 94
Sow, C.H. 1788
Sridhar, B.T.N. 1708
Srinivasan, J. 1120, 1140
Stankiewicz, W. 1854
Stanus, E. 146
Stark, H. 138
Stefan, C. 1175
Steidl, J. 1204
Stenuit, P. 146
Stoffels, E. 1385, 1389
Stryuk, R.I. 1615
Su, C.-W. 501
Su, H.-M. 540
Su, J.L. 1009
Su, T.L. 1341
Su, T.-P. 726
Su, T.S. 1019
Subba Rao, K. 60
Subbiah Bharathi, V. 678
Subburaj, K. 129, 906
Subero, A. 1162, 1166
Sudhaman, V.K. 370, 647
Sugai, T. 2268
Sugai, T.K. 1409, 2177
Sugi, Takenao 47
Sui, Xiaodi 1980
Sukanesh, R. 647
Sukeshkumar, A. 116
Suksmono, Andriyan B. 911
Sun, K. 1090
Sun, L.L. 863
Sun, Y. 381, 661
Sun, Y.N. 1032
Sun, Y.T. 1413
Sun, Yi-Jung 497
Sun, Ying 639
Sun, Zhonghua 1676, 1728
Suneetha, V. 109
Suresh, Subra 1788
Suzuki, Y. 2188
Swaminathan, Ramakrishnan 1708
Swarnalatha, R. 98
Swieszkowski, W. 1480

T

Tabata, Y. 1301
Tabayashi, K. 2268
Tack, G.R. 161, 165
Tack, Gyerae 1814
Tada, H. 2272
Tadano, S. 1069, 1904, 2034, 2083, 2118
Tafreshi, R. 422
Taguchi, H. 2083
Tai, C.C. 582
Tai, Wan-Yu 1224
Takada, H. 5, 987
Takagi, Shu 1984
Takahashi, S. 2250
Takahashi, Shoki 2215
Takahashi, Y. 1559
Takano-Yamamoto, T. 2000
Takao, H. 1600
Takao, S. 2083
Takase, K. 2250
Takase, Kei 2215
Takeda, M. 2241, 2272
Takeda, R. 1069
Takeda, T. 194
Takeshita, Fumitaka 1503
Taki, Y. 2228
Takizawa, Noboru 710, 923
Tamagawa, M. 882
Tamura, Kazuhiro 245
Tan, B.T. 1672
Tan, D. 894
Tan, K.C. 1480, 1659
Tan, K.S.W. 1788, 1965
Tan, N.M. 559, 610
Tan, O.K. 863
Tan, Rosemary 898
Tan, S.H. 1931
Tan, S.J. 774
Tan, Seng Sing 1663
Tan, Serena H.N. 1938
Tan, Y.S. 1838
Tanaka, A. 1409, 2177, 2268
Tanaka, Keita 657
Tanaka, M. 2000, 2099, 2102, 2104, 2219
Tanaka, T. 1053, 1183, 2258
Tang, B.L. 1208
Tang, D. 1572
Tang, Jing 1037
Tang, M.J. 1773
Tang, S.T. 582
Tashiro, Manabu 2201, 2204, 2248
Tchoyoson Lim, C.C. 109
Tecchio, F. 961
Teh, T.K.H. 1488
Teng, S. 726
Teo, E.C. 1938
Teo, K.-H. 898
Teo, K.K. 1348
Teo, S. 1659
Teoh, S.H. 1024
terBrugge, Karel 362
Tewari, Shivendra 358
Thakor, N. 448
Thakor, N.V. 444
Thanou, Maya 1503
Theera-Umpon, Nipon 476
Thet-Thet-Lwin 194
Thiagarajan, D. 699, 892
Thiery, Jean Paul 1980
Thompson, M.C. 1672
Thomson, A. 1469
Thouas, G.A. 1672
Tielert, R. 643
Timm, U. 825
Timofeev, V.T. 1615
Ting, C.Y. 532, 536
Tipa, R.S. 1385, 1389
Todo, M. 1559, 1611
Todoh, M. 1069, 2034, 2118
Toh, S.L. 1381, 1488, 1508, 1515
Toh, Siew Lok 1512
Tokunaga, N. 1422, 1430
Tolouei, R. 1305
Tomita, K. 1588, 1712
Tomori, M. 39
Tong, Y.W. 1208
Tong, Yen Wah 1313
Topper, S.M. 142
Torres, J. 1874
Toyosu, H. 2159, 2167
Toyosu, Y. 2159, 2167
Trabelsi, Nir 2019
Trau, D. 821
Tritanipakul, S. 1377
Trivedi, P. 1297, 1325
Tsai, C.H. 1592
Tsai, D.-P. 802
Tsai, Ming-Shih 1082
Tsai, W.Y. 310
Tsai, Y.C. 55

Tseng, Kuo-Wei 2064, 2068
Tsubota, K. 2244
Tsubouchi, S. 1443
Tsuchimi, D. 2219
Tsuchiya, T. 1183
Tsuge, Satoru 302
Tsuji, N. 1316
Tsuji, T. 682, 694
Tsuji, Tokuo 2043
Tsuji, Toshio 2043, 2059
Tsujimura, S. 635, 1098
Tsujioka, K. 1941
Tsumoto, K. 2237
Tsuruoka, S. 395, 1102
Tsutsui, T. 635
Tu, J.Y. 1550, 1555
Tuantranont, A. 851, 859
Tung, Chia-Ming 970
Tungjitkusolmun, Supan 223, 1676, 1728
Tuo, X.Y. 1405
Turkušic, Emir 829
Turley, G.A. 1604
Tyan, Chu-Chang 485
Tzeng, C.B. 1132, 1136

U

Ucisik, A.H. 1462
Uddin, Mohammad Shorif 1000
Uehara, G. 39
Uematsu, M. 1183
Uematsu, Miyuki 2139
Ugsornrat, K. 859
Umezu, M. 1053, 1179, 1183, 1409, 1422, 1430, 1443, 1600, 2143, 2268
Umezu, Mitsuo 1213, 2139
Usta, M. 1462
Utsunomiya, Ryuhei 2139

V

Vai, M.I. 1044
Vai, Mang I. 31
Valálik, I. 112
Valindria, Vanya Vabrina 94
Varga, J. 2012
Vasan, A. Keerthi 351
Vasan, S. Keerthi 1692
Venkata ramanaiah, K. 13
Verjus, Fabrice 790
Versaci, M. 1842
Vidapanakanti, M. 431
Vidhya, Sree 810
Viji, V. 331
Vineeth, V.V. 327
Viscuso, S. 961, 1584
Voelcker, N.H. 198
Vong, H.-M. 291
Voor, M.J. 563
Vytras, Karel 829

W

Wada, H. 2237
Waddell, S. 563
Wailoo, M. 2130
Wakabayashi, T. 395, 1102
Wakasa, S. 1422, 1430
Wakita, Yusuke 710, 923
Wan, L.R. 706
Wan, M.X. 1870
Wang, Ai-Ting 1149, 2064, 2068
Wang, Bei 47
Wang, Chung-Hao 874, 878, 888
Wang, Guangzhi 1028, 1037
Wang, Guo-Chen 884
Wang, Hexiang 1313
Wang, Hui 362
Wang, J. 1874
Wang, J.J. 547
Wang, J.-J. 481, 490, 540
Wang, Jun-Sheng 799
Wang, K.J. 2056
Wang, Lin Lin 1289, 1369, 1373
Wang, Lin-Lin 1195, 1285
Wang, Ming 1503
Wang, P.S. 722, 726, 730
Wang, Pei-Rong 1862
Wang, R.Y. 718
Wang, S.H. 2106
Wang, S.M. 1550
Wang, Sheng-Hung 183
Wang, Shyh-Hau 742
Wang, T. 1258
Wang, Wei-Kung 183
Wang, X. 1952
Wang, Xiao-gang 1858
Wang, Xingyu 47
Wang, Y.Y. 125
Wang, Yi-Pin 1149, 2064, 2068
Wang, Yuanyuan 121
Wang, Z.Y. 730
Wanichapichart, P. 851
Warren, J. 511
Waryo, Tesfaye 829
Watanabe, T. 987
Watanuki, Shoichi 2201, 2204
Wehn, N. 643
Wei, C. Zheng 344
Wei, Hung-Wen 2092
Wei, K.C. 536
Wei, Leizhen 2211
Wei, Y.C. 566
Wei-Chih, Hu 497
Wen, C.Y. 794, 1761
Wen, J. 1550
Wey, T.S. 1132, 1136
Williams, M.A. 1604
Wisitsoraat, A. 859
Wisitsora-at, A. 851
Wojcicki, J.M. 1049
Wong, C.T. 1258
Wong, D.W.K. 559, 610
Wong, H.K. 1476, 1805
Wong, K.K.L. 569
Wong, K.P. 1900
Wong, Lee-Kang 622
Wong, S.M. 838
Wong, T.Y. 559, 610
Wong, X.R. 1381
Woo, Y.J. 508
Worthley, S.G. 569
Wu, C.C. 1393
Wu, C.L. 2056
Wu, C.-M. 501
Wu, Hsien-Tsai 105, 622
Wu, J. 194
Wu, Ren-Hua 362
Wu, X.Y. 435
Wu, Xiao-juan 1858
Wu, Y.T. 714, 718, 722, 726, 730

X

Xi, He 1918
Xi, W.M. 1680
Xia, L. 1405
Xiao, G.F. 1405
Xie, L. 898
Xue, C.L. 1550

Y

Ya, Ng Qian 1171
Yagi, T. 1179, 1422, 1430, 1600
Yamada, Masahumi 935

Yamaguchi, S.S. 1426
Yamaguchi, T. 2244
Yamako, G. 1733
Yamamoto, Kimiko 2184
Yamamoto, Seiichi 2248
Yamane, T. 635
Yamato, Masayuki 1213
Yamauchi, Daisuke 2194
Yambe, T. 1409, 1989, 2177, 2254, 2268
Yampri, P. 306, 586, 665, 1144
Yan, C.H. 206
Yan, D.-N. 992
Yan, Gwo-Lang 1082
Yanai, K. 2181
Yanai, Kazuhiko 2201
Yanashima, Kenji 919, 938
Yang, B.-S. 954, 1797
Yang, Bing-Shiang 1996
Yang, C. 1258
Yang, Chih Chin 1333
Yang, Hung Yu 1333
Yang, Jhih-Jyun 1086
Yang, K. 1476
Yang, S. 563
Yang, T. 1024
Yang, T.Y. 867
Yang, X. 1952
Yang, Y. 1924
Yang, Y.H. 1094
Yang, Y.R. 718
Yang, Yiqi 1282
Yang, Yi-Ting 1996
Yang, Zheng 1255
Yao, C.M. 1592
Yao, Kai-Ping 1086
Yasrebi, B. 1569, 1648
Yazdandoost, K. Yekeh 1158
Ye, Y. 1555
Yeh, J.M. 870
Yeh, M.L. 1773
Yeh, T.-C. 726
Yen, S.K. 1459
Yeow, C.H. 1684, 1716
Yew, K.S.A. 1931
Yi, Y. 2126
Yikai, W. 27
Yim, E.K.F. 1279
Yim, Evelyn K.F. 1348
Yin, J. 1965
Yin, Zi 1195, 1397
Yobas, L. 774, 834, 898
Yokoe, M. 682
Yokoyama, K. 5
Yoon, Hyung Ro 1116
Yoon, Young Ro 1116
Yoshida, Keisuke 2223
Yoshida, M. 1892
Yoshida, Sayaka 2215
Yoshikawa, M. 1316
Yoshinari, S. 1069, 1904
Yoshinobu, T. 2264
Yoshizawa, M. 1409, 2177, 2268
Yoshizumi, Masao 2059
Yosibash, Zohar 2019
You, Z.X. 582
Young, M.S. 566, 1132
Young, Shuenn-Tsong 378
Yow, S.Z. 1279
Yu, C.H. 942, 946, 1061
Yu, C.Y. 1413
Yu, Chih-Sheng 799
Yu, Chun 1086
Yu, H. 1405
Yu, Hua-Wei 884
Yu, Kyoung-Jin 452
Yu, Ming-Han 1745
Yu, N.Y. 402, 406, 1667
Yu, R.Q. 206
Yu, S.M. 2147
Yu, T. 287, 1908
Yu, W. 610
Yu, W.J. 974
Yuasa, T. 194
Yun, C. 1004
Yun, Jaeyoung 1949
Yvert, Blaise 790
Yzng, Di-Song 622

Z

Zah, Muhamad Ryan b Mohamad 1171
Zahedi, E. 18, 65
Zaheditochai, M. 65
Zakaria, Hasballah 2079
Zang, Qinyu 1112
Zappasodi, F. 961
Zeugolis, D.I. 1496
Zhang, C. 125
Zhang, Chi 121
Zhang, G.J. 838
Zhang, J. 206
Zhang, J.H. 125
Zhang, L. 898
Zhang, Pu 1112
Zhang, S.F. 1405
Zhang, Xiao-yan 1858
Zhang, Y. 842, 1741
Zhang, Yuan-yuan 1858
Zhang, Z. 559
Zhang, Z.W. 1644
Zhao, L. 1004
Zhao, M. 1680
Zhao, Shuang 1313
Zhibo, Wang 1473
Zhou, Xin 1858
Zhou, Yixin 1037
Zhu, K.Y. 1761
Zhu, Zhonglin 1037
Zinin, P.V. 746
Zoghlami Ayari, E. 643
Zou, Xiao Hui 1285, 1369, 1373
Zubair, M. 1920

Subject Index

#

[18F]FDG-3DPET 2204
[18F]fluorodeoxyglucose (FDG) 2248
11 vessel occlusion model 465
3D face recognition 1854
3-D geometry 1777
3-D myocyte tissues 1213
3D reconstruction 1019
3D Surface Modeling 1144
3G mobile phone 1112
3T3 fibroblasts 1352
5-Aminosalicylic acid 902
^{99m}Tc(I) tricarbonyl ion 1393
^{99m}Tc(I)-his-annexin V 1393
α-SMA 1473

A

Accelerate aging 1191
Accelerated durability test 1443
Acceleration censer 249
accelerometer 508
Accelerometer 519, 984
acetylcholine 2181
AChE inhibition 1659
ACL 1512
Acoustic characteristic 1969
Acoustic energy 602
acoustic imaging 738
Acoustic Microscopy 750
Acoustic Signals Separation 179
acquisition 31
acromiohumeral interval 2110
Actin 902
active catheter 340
Active Stress 1696
actuator 340
Acute Myocardial Infarction 810
acute myocardial infarction (AMI) 60
Ad4BP/SF-1 1920
adaptive 31
Adaptive filter 519
adaptive frequency response 257
Adaptive Resonance Theory 101
adaptive segmentation 133
adaptive window 444
Addiction 1688
ADHD 1057
adhesion 1924
Adjoining Vertebra 1712
adrenal venous sampling 2250
AFM 1773, 2122
Agaricus bisporus lectin 1313
Age 1631, 1640
Aged people 1082
Aging 867, 1918
airflow 1555
airway 1555
aldosteronism 2250
alginate 1248, 1344
aligned nanofibers 1397
Alignment 1488
alkanethiol 1418
allergic rhinitis 992
Allograft 1252
alpha suppression 253
alumina 1293
Alzheimer's disease 9, 2181
amperometric biosensors 829
Amperometric Chemical Sensor 543
amperometric sensors 829
Amphiphilic alginate 878
amphotericin B 1241
amyloid 2181
Analysis function 1098
anatomical landmarks 129
anatomical understanding 906
anatomy 2250
Angiogenesis 1426
Angioplasty 1592
Anisotropic Diffusion 22
Ankle foot orthosis 1061
ANN 13
annexin V 1393
anterior cruciate ligament (ACL) 1892
anterior cruciate ligament failure 1716
anterior tibial translation 1892
Antibacterial 1199
antibiotics resistance 884
antifibrosis 1473
anti-g maneuvers 1564
Antimicrobial effects 280
Aorta 1539
Aortic aneurysm 1676, 1728, 2215
Aortic dissection 2215
Aortic Surgery 2139
approximate entropy 1
Archimedes' 563
arm positions 1931
Arrhythmia 85
Arterial compliance 540
Arterial stiffness 540
Artery of Adamkiewicz 2215
arthritis 1700
Articular cartilage 1883, 2102
Articular cartilage defect 1289
articular surfaces 1037
Artifacts processing 146
artificial disc prosthesis 1724
artificial hand 927
Artificial heart 635
Artificial Knee 1597
Artificial myocardium 1409, 2268
Artificial Neural Network 94, 626
Artificial Skins 2023
Assessment 1187
assistive technology 984
Assistive Technology Device 1153
asthma 501, 1555
Asymmetry 1329
Atherosclerosis 1572, 1785, 2059
atherosclerotic plaque 1519
Atomic force microscopy 1833
Atomic force microscopy (AFM) 1965
ATP 2184
ATP synthase 2184
atrial fibrillation (AF) 60
atrial vortex 2254
audio transducer 156
auditory 687
Auditory brainstem response (ABR) 156
auditory evoked potential (AEP) 606
auditory stimulus 9
auditory stream segregation 2264
augmentation index 1531
auto-location 799
Automated 610
automatic sleep analysis 422

Automatic sleep stage determination 47
autometic thresholding 665
Autonomic nervous system 219, 378
Autoradiography 2204
autoregulation 1896
avalanche dynamics 1595
avalanche photodiode 493
axial rotation 1716
Axon growth 1833

B

BAC transgenic 1920
Back pain 2114
background image 270
Background luminance noise 27
Bacteria 2134
Balance 2027, 2126
Band eliminate filter 2159
Barium Strontium Titanate 863
Basic Principle behind Brain Gate 1232
basilar membrane 257
Bayesian 2-step method 374
Bayesian network 2048
BCI 69, 687
Bed-ridden 966
Behavior mining 966
Behavior modification 1057
Behavioral Processes 1688
behaviorism 1082
behavioural recovery microcontroller-based 566
Bergman Model 1850
bibliographic 299
Biclustering 631
Bicycling 1140
Bi-leaflet valves 1275
Bilirubin 1136
Bioactive coating 1293
Bioactive Glass 1359, 1546
Bioactivity 1366
Bioassay 2173
Bio-chip 884
biocompatibility 870, 1258
Biocompatibility 261
Biocomposites 261, 1199
Biofilms 750
Bio-fluid mechanics 2188
Bioheat 427
Bioheat transfer 1957
bioimaging 1499
Bioinformatics 284, 296
Biological applications 280
biological tissue glue 1496
biological tissues 1957
Biomagnetism 39
biomagnetometer 39
biomaterial 802, 1204
biomatrices 1320
Biomechanical analysis 1592
biomechanical model 1032
Biomechanics 1572, 1588, 1712, 1724, 1769, 1777, 1817, 1912, 2005, 2034, 2099, 2104, 2118, 2197
Biomedical engineering 355, 2143, 2155
Biomedical Engineering Education 2164
Biomedical Imaging 511
biomedical measurement 523
biomedical signal 240
Biomedical Transducer 652
biometric 1996
biometrics 1854
Biometrology 652, 1124
Biomimetic Scaffold 1279
Biomodels 399
Biopotential amplifier 116
Biopotential Electrode 979
bioreactor 778, 1213, 1405, 1484, 1672
bioresorbable scaffolds 1480
Bio-sensing probe 813
biosignal 31
biosignal processing 1042
Biotin 902
Biphasic analysis 1883
Bipolar disorder 726
bird 1858
bispectrum 231
Black hole phenomenon 742
Block matching algorithm 327
Blood Brain Barrier 81, 435
blood compatibility 1413
Blood flow 481, 1676, 1728, 1896
Blood flow mechanics 1878
Blood Flow Rate 1663
Blood Glucose 1850
blood glucose level 370
blood pressure measurement 1564
blood pulse 786
blood urea 1438
Blood vessel biomodeling 1993
blood vessel model 2223
Blood vessel ratio 327
Blood-brain barrier (BBB) 532, 536, 547, 1094
blood-flow analysis 1542
Blue-light 1352
Blunt hooks 1539
BMP-2 1680
BMP7 1369
Body Area Network 1044
body ownership 996
Body segment parameters 1777, 2038
Body surface electrocardiograph 2167
Body surface electrocardiography 2159
Body surface potential animation 2159
body surface potential distribution 2167
Body surface potential map 2159
Body-Segment Coordinates 1604
Bolton Analysis 472
Bone 1480, 1636, 2034
Bone biomechanics 2019
Bone defect 1373
Bone loss 1766
bone marrow cells 1316
bone marrow derived mesenchymal stem cells 1381, 1508
bone morphogenetic protein 1476
Bone Morphogenetic Proteins 4 1285
Bone Morphogenetic Proteins 7 1285
bone relaxation 1608
Bone Remodeling 2104
bone screw 1619
bone segmentation 665
bone substitute 1267
bone tissue engineering 1381, 1476
bovine aortic endothelial cells 1989
boxcar integrator 493
Boyden chamber 1749
Brachial artery 481
Brain 69

Brain aging 2228
Brain computer interfacing 699
Brain gate human neural interface system 1232
Brain glucose homeostasis 1655
brain hypothermia treatment 1651
Brain machine interface 1232
brain response quantification 411
Brain targeting 1455
brain tumor 536
brain-computer interface 2264
Brain-Computer Interface 366
Brain-computer interface (BCI) 390
BRCA1 2211
breast cancer 2122, 2248
Bridge-to-Recovery 2177
Brodmann area 10 657
Brodmann area 46 657
Bubble detection tool 27
Burst mode 435

C

C++ programming 1704
C4.5 174
Ca2+ 2184
CAD 1704
Calcined Temperature 1362
calcium flux 358
Calcium signaling response 2000
Canal Network 2099
cancellous bone 1619
Cancer 427, 1337, 1503, 1915
Cancer Metastasis 774
Cancer therapy 355
cancerous cells 1313
Canonic Signed Digit (CSD) 13
Capacitive coupling 915
capacitive pressure sensor 198
Capacitive Sensors 1153
carbon electrodes 829
Cardiac Function 2177
Cardiac Output 1663
Cardiac Troponins 810
Cardiomyocytes 1741
cardiovascular diseases 105
Cartilage defect 1369
cartilage repair 1285
cartridge 898
cascade impactor 1434
Case Based Reasoning 1166
Catatonia 1455
Catheter 1663
CCA 734
CD133 888
Cell adhesion 1492, 1842
Cell Biomechanics 2000
cell compression 1949
Cell Culture 2173
Cell deformation 1829
cell detaching force 1773
Cell Encapsulation 1279
cell growth 1389
Cell Isolation 774
Cell mechanics 1527, 1788, 2122
cell probe 1773
Cell proliferation 1385, 2106
Cell Seeding Positions 1745
cell separation 851
Cell sheet 1213
Cell Sheets 1508
cell viability 1352
CellML 287, 296, 1908
cellular automata 1737
cellular energy 142
center frequency 2207
Center of Mass 2009
Center of pressure 2126
Central Serous Retinopathy 331
Central venous catheter 1183
Cephalometric Line Tracing 265
Cepstrum 754
ceramics head 1580, 2012
Cerebral aneurysm 1600, 2079, 2188, 2262
Cervical cell 476
cervical lymph node 125
cervical spine 1724
cfd 1550, 1555
CFD 1405, 2079
Chaotic detection 390
Chase Model 1850
Chemo-mechanical equilibrium 1945
Chemotaxis 882
chemotherapy 1337, 1447
Chinese dance 2064
chip 799
chitosan 1199, 1301, 1381
Chondrocyte 1248, 1749
Chondrocytes and Autologous chondrocyte implantation 1255
chromophores 323
Chronic Active Hepatitis 215
chronic animal experiment 2268
chronic disease 970
Circuit synthesis 691
Circulating Tumor Cells 774
Circulatory system 1531
Cirrhosis 215
cisplatin 1325
classification 452
classifier 231
Clinical guideline 701
clustering 277
CMOS 89
Coating of the tongue 505
Coatings 1341
Cochlear implant 257, 310
co-culture 1515
coding system 946
Coding system 942
Coefficient of friction 1797
Cognition 1688
Cognitive fatigue 1120
Cognitive strategy 1057
coherence 1
Coherent structures 2134
Cold plasma 355
cold pressure test 1531
Cold stress 490
collaboration 2171
Collaborative Work 1166
collagen 1267, 1279, 1352, 1473, 1499
Collagen gel 1320
Collagen matrix 1195, 1289, 2034
collagen scaffold 1369
collision 1430
colloidosome 821
Color Medical Image 911
color sensor 919
colored guideline 919
Colour Retinal Image 274
comparison 121
complex Morlet wavelet 551
Complexity 240
Compliance 1993
Composite 1480
composite materials 1546
Composite prosthesis 1293
Compressive deformation 1883
Compressive fatigue 1236
compressive impact 1684, 1716
Computational biomechanics 1753

computational fluid dynamics 1672, 2244
Computational Fluid Dynamics (CFD) 774
computational model 1519
computational modelling 1580
Computed tomography (CT) 206, 468, 2019
computer application 406
computer assisted surgery 1073
concentrate 799
Concentration gradient 882
Conditional probability 47
Conducting Polymer 979, 2173
Conduction velocity 116
Conductive Model 1904
cone opening 2012
confidence measure 335
Conformity Assessment 1124
connected multiple ROIs 1102
Consolidating research 2143
Constrained spatiotemporal ICA 555
contact 2092
Contact mechanics 1842
contact-free measuring techniques 1527
Control 340, 1651, 2027
control inputs 1263
controlled release 1325
COP 1814
Core/Shell 1741
Coronaries 1539
Coronary Artery Bypass Grafting (CABG) 1179, 1838
Coronary disease 1572
Corrective dental procedures 957
correlation dimension 1
Corrosion Resistance 1459
Cortical Bone 2099
cortical shell 1757
coupling 235
Cowper Symonds 1627
Craniometry 761
Craniopharyngioma 1220
critical illness 1595
Critical Micelle Concentration 1366
Cross-bridge model 1696
cross-correlation 643
Cryopreservation 1252
CT 2250
CT image 1611, 1733
CT scan image 1077
CT-data 1700
Cuff mode 481
cup-to-disc ratio 559
Current Conveyors 846
Current Steering 310
Current-Mode 846
Curvilinear coordinates 1792
customization 1700
Cyto-fluid dynamic theory 1329
Cytosolic calcium 358
Cytotoxicity 802, 1492
cytotoxicity analysis 806

D

damage 1684
data 299
data acquisition 1175
data integration 673
Data viewer function 1098
Database 287, 2228
Day Activity 950
Db6 wavelet 590
DCT 754
Decision Support System 215
Decision Trees 174
decisional system 1175
deconvolution 439
Deep brain stimulation 619
Deep flexion 1559
Deep Veins 1878
defect reconstruction 1228
Deformation 511
Degeneration 1684, 2102
Degenerative Disc Disease 1252
degradable polymers 1546
DegraPol® 1248
Delivery drug 435
Dengue 898
denoising 73
Density 1569
dental 615
Dental Arches 472
Dental composites 1236
Dental implant 1611
Dental Model Analysis 472
Dental Widths 472
Deoxypyridinoline 1952
Depletion interaction 1644, 1924
Depolarization 758
Deposition 1341, 1550
Detachment 1842
Detection 610, 1858
developmental coordination disorder 402
device connection 1042
Device performance 1136
dextran 1316
Dextran 1644
diabetes 970, 1655
Diabetes mellitus 1000, 1049
Diabetes Mellitus 2056
diabetic foot syndrome 1049
Diabetic pathology 1945
Diabetic retinopathy 94, 274, 277, 327
Diagnosis 527, 626
diagnosis support 682
dielectrophoresis 834
differentiation 870, 1397
diffuse reflectance 323
diffusion-weighted imaging 722
Digital Imaging and Communications in Medicine (DICOM) 1009
diisopropylfluorophosphate 1659
Dilator 1183
Dip coating 1341
Direct Kinematics analysis 1576
Disability 1187
Discrete-Time fractional Brownian motion 227
discrete-time fractional Gaussian noise 227
Discrete-wavelet-transform (DWT) 60
disease diagnosis 1000
Dislocation 1733
dissolution 1244
dissolved oxygen 778
Distal resistance 1572
DNA 842
DNA damage 2211
Doppler 481
Dosimetry 1220
downlink transceiver 418
Doxorubicin 1447, 1451
DPCCM 1915
DPOAE 626
DRIE 790
Driving 1187
driving performance 2201

Droplet 834, 859
Drosophila 1829
Drug delivery 536, 1313
Drug Delivery System 2241
drug interaction 817
Drug mix 817
Drug screening 878
Drug-eluting stent 1519
drug-resistance 1451
DRY Lab 2143
dual dynamic programming 734
Dual Energy Absorptiometry X-ray 1777
Dual-energy X-ray Absorptiometry 2038
DVRTs 1931
Dynamic characteristics 1409, 1969
Dynamic Mechanical Analysis 1191
Dynamic PIV 1275
dynamic viscoelastic 1252
dyspepsia 101
dystonia 112

E

E. coli 77
early apoptosis 1870
Easy contact 915
Easy touching 931
ECG Signal 758
echocardiogram 1102
Echocardiogram 395
ECM 2147
EDC 867
education process 2155
EEG 1, 51, 69, 133, 146, 245, 411, 422, 2264
EEG signals 351
EEG Signals 647
Effect of music 1120
e-health 284
Elast-Eon™ 1191
Elastic modulus 1900, 2056
elasticity 2207
elderly 1014
elderly care 984
electric field 523
Electric field sensing 1153
Electric Powered Wheelchair 1153
electrical field 1389
electrical impedance 291, 1708
Electrical stimulation 1833
electrically evoked auditory brainstem responses (EABRs) 2194
electrocardiogram 578, 2167
Electrocardiogram (ECG) 60, 85, 105, 146, 590, 846, 915, 2167
Electrocardiograph 1124
electrocatalyst 829
Electrochemical Sensor 863
Electroencephalogram (EEG) 249, 390, 1120
Electroencephalography (EEG) 253, 691
Electrogastrogram 101
Electrogastrography (EGG) 5
electrohydraulic 706
Electrolytic Deposition 1459
electromagnetic wave 1158
electromyogram 227, 694
electromyography 2064
Electroneurograph 116
Electronic equipment 691
Electronic Medical Records 284
Electrophysiology 296, 1809
electroplating 794
Electrospin 1488
electro-spinning 2147
Electrospun nanofiber 1373
Electrowetting on Dielectric (EWOD) 859
Elementary education 406
elliptical shape prior 125
EMG 146, 302, 508, 765, 923, 927, 1977
emitted dose 1434
emotions 411
Endoscopic sinus surgery 2048
Endothelial cell 746, 1924, 1941, 2184, 2262
Endothelial cells models 1842
Endothelial function 18, 65
Endovascular stent 1443
endpoint stiffness 1862
Energy Expenditures 1928
Ensemble classifier 69
Enterovirus 71 878
enthesis 1515
EOG 146
Epilepsy 351
Epilepsy risk levels 647
Epithelial cell 81
equilibrium binding 894
equilibrium constant 894
erythrocyte 1422
ESCA 1413
Escherichia coli 1846
e-science 287, 1908
esophagus tissue engineering 1484
Estimation of blood glucose level 1466
Estimation of Human States 2232
ESWL 314
ESWT 1623
Euclidean distance 85
EVA Foam 1627
EVAHEART 2143
evaluation methodologies 406
Event Related Field 9
evoked potential 366
Exercise 1892, 2114, 2204
expectation maximization algorithm 722
expectation-maximization algorithm 714
Experiment on Human Being 1232
Expert knowledge database 47
explicit FEM simulation 1623
extensibility 2219
extension rate 1631
Extracellular matrix 1469, 2192
Exudates 277
Eye movement detection 335

F

Face image 270
Facet joint 1805
Fall 1797
Fall detection 984
fall-risk 1814
FDTD 523
FE analyses 1535
FE modeling 1757
Fe3O4 802
FE-analysis 1700
Feature classification 55
feature extraction 527, 1888
Feature extraction 476
Feature extruction 590
fECG 98
Feedback function 1098
feedback training 2264

femoral 1636
Femoral neck 1918
femoral torsion 129
fenestration 1676
FES 687
FFT 754
Fibers 1282
Fibroblast 1389, 1473, 1935
fibrocartilage 1515
Fibrosis 1499
Film thickness 1341
Filters 691
fine particle fraction 1434
finger flexing motion 452
Finger independency 954
Finger tapping movements 682
Fingerprints 415
Finite element 1608, 1720, 1809
Finite element analysis (FEA) 460, 859, 1539, 1559, 1597, 1611, 1627, 2023, 2030, 2056, 2083
Finite element method 1592, 1788, 1883, 1938
finite element model 1817
finite elements 1724
Finte element method 2088
flap frequency 1858
flexibility 2064
flexible substrate 813
Floor materials 1797
Floor transition 1797
flow mediated dilation 18
Flow mediated vasodilation 65
Fluid dispenser 280
Fluid motion tracking 569
fluid shear 1405
Fluid-structure interaction 1542, 1842
fluorescence enhance 867
fluorescence lifetime 439
fluoroscopy 1892
fMRI 657, 927
Focal adhesion 1945, 2076
Focused ultrasound 435, 547, 1094
Follower Preload 1805
Foot drop surgery 1107
foot plantar pressure 1817
Foot pressure images 1107
foot scanner 1049
foot ulcers 1817
Foot-pressure 974
Footwear 1627
force feedback 1874
force platform 1825
Forearm 1904
Form Factor 485
Fourier transform 476
FPAA 31
FPGA 13, 31, 370
Fractal dimension 240, 411, 730
Fracture energy 2034
Fracture Mechanism 1236
Freeze drying 1381
Frequency domain Image Analysis 1107
Frequency resolution 758
Frequency spectra 476
frequency-based mutual information 726
F-scan System 974
Full contact 1700
functional connectivity 726
functional magnetic resonance imaging 270
functional modules 673
Functional MRI 555
functionally graded 1204
Fundus Imaging 331
fusion 1546
Fuzzy C-means 69, 202, 485
Fuzzy PD&PID Controller 370
Fuzzy PID Control 1090
Fuzzy techniques 351, 647

G

Gabor 94
Gabor filter 274
gait 1996
gait analysis 1069
Gait initiation 1962, 2016
Gait stability 1797
Galvanic coupling type/Waveguide type technique 1044
gamma distribution 1737
gap junction 1515
gas exchange 1595
Gastrointestinal (GI) 1696, 1809
gate mode 493
GD2 874
gelatin 1217, 1301, 1377
Gelsolin 902
Gender 1640, 1814
Gene expression 631
genital neoplasia 1175
Giant Magneto-impedance 652
glaucoma 559
Glaucoma 198
glaucoma drainage implant 198
glenohumeral joint 2110
glioblastoma 888
Glucometers 1466
Glucose 543
glucose sensing 418
glucose-insulin-glucagon (GIG) regulatory system 1655
Glucose-Metabolism 2204
Glutamate 465
gold nanoclusters (GNCs) 867
gold nanoparticle 870
gold nanorods 874
GPS 43, 938
gradient vector flow 1073
grand battement 2064
Graph cut 125
graph cuts 639
gravitational acceleration 1069
Gray matter 35
Greedy randomized adaptive search procedure 631
Green's function method 1957
guide wire 340
Guided bone regeneration 1373
Guidewire 1183

H

handwriting 402, 406
haptic interface 1874
Haptic sensor 2219
Haptotaxis 1749
Hardness 1900
Hardware Rendering 511
Harmonic 485
H-CRAAS 43
Headset 519
health care management 1000
health risk profiles 284
Healthcare Information System (HIS) 1009
Hearing Prostheses 179
Hearing Screening 626
heart model 1542
Heart rate 231, 456, 1116
Heart Rate measurement 519

Heart rate variability 378, 490, 2130
heart sounds 738
heart valve 1422, 1430
Heat Exchange 1663
Hematocrit 223
hemilarynx 1024
Hemiplegic patient 1962, 2016
hemodialysis 1462
Hemodynamic 602
Hemodynamics 1600, 1838, 2188, 2244, 2268
hemoglobin 825
Hemoglobin 931
hemolysis 1422, 1430
hemorrhage 547
hepatocarcinoma 1870
hepatocytes 1405
HER2 2272
hESC-MSC 1369
Hessian filter 1077
Heterogeneous substance 1945
hierarchical clustering 714, 722
high aspect ratio 1258
high flexion activities 2092
High Flexion Knee 1597
High flux 1462
High performance liquid chromatography 1297
High power LED 1132
High shear stress 2262
high spatial resolution 2159
High-Frequency Acoustic Microscopy 746
High-Frequency Ultrasound 750
High-voltage 706
Hind-limb suspension 1766
Hip Arthroplasty 1640
Hip joint endoprosthesis 2012
hip prosthesis 1293
Hippocampus 374, 892
his-annexin V 1393
histamine 2181
histochemistry 1496
histogram 661
histology 1094
HIV 1263
home gateway 1086
Home healthcare 1098
HomeCare 950
Homeostasis 1918
homologous recombinant 1920
Hopkinson bar 1623
HOS 231
HPMC 1244
HRV 219
HuH-7 870
human embryonic stem cell 1469
Human foreskin fibroblasts 2106
human joint 942, 946
Human Model 2232
Humidity sensor 1333
Hurst exponent 240
HUVECs 2147
Hyaluronic acid 1680
hybrid model 1737
Hydrocephalus 210
hydrogel 821
Hydrogen peroxide 829
Hydroxyapatite 261, 1267, 1271, 1309, 1377, 1401, 1680
hydroxyl ethyl methacrylate 855
hyperelasticity 1788
Hysteresis 1753

I

Ibandronate 1952
ICC 1809
ICU/CCU 1112
identification 1854, 1915
image analysis 314, 1527
Image classification 476
Image Correction 2139
image denoising 594
Image fusion 151
Image Processing 348, 406, 586
Image Registration 151
Image segmentation 55, 186, 190
Image sequence 966
Image Warping 2038
Image-guided 435
Image-Processing 109
imaging agent for apoptosis 1393
imaging mode 121
Immunotherapy 1337
impedance pump 794
Impedimetric Immunosensor 863
impingement 2110
impinging flow 1430
implant 1724
Implant Bone-Alignment 1604
Implant medical device 1158
Implantable blood pump 2143
Implantable microscope 1426
implantable systems 418
implicit code-coupling 1542
IMT 734
in vitro test 1359
in vivo 138
in-body radio communications 1158
inclusion 1623
incremental learning 302
Incremental Simple-FLDA 302
indentation 2122
Indentation test 2102
Independent Component Analysis (ICA) 179, 718
India 2164
indirect kinematics analysis 1576
individual movement trajectory 1014
individual replacement 1228
inductive link 418
infant 2043
Infected red blood cell 2244
Information extraction 701
infrared 992
injury 1938
Injury prevention 1716
Inner ear 2237
instability 1781
Institution-based care 966
institution-based health care center 970
Instrument amplifiers 691, 846
insulin deficiency 1000
Integrated circuits 691
Integrated Interface Circuit 543
Integrin expression 2192
Intensity 109
Intensity profile 602
intensive care medicine 1651
Internal Model 2027
internal tissue stresses 1817
Intervertebral Disc 1252, 1792
Intra-Body Communication 1044
intracellular calcium 1989
intraocular pressure 198
intrauterine growth retardation 2130
Intravascular 1663
In-vitro 1199
Ion Release 1459

Ionic polymer-metal composites (IPMC) 340
IRM 1644
ITK and VTK in Java 586

J

Jacobean Matrix 1576
Jaundice 1136
java 1112
JAVA development kit (JDK) 1009
Jogging 1120
joint kinetics 1805
Joystick 1153

K

keratinocyte 1949
kidney 661
kinematic 1928
Kinematic analysis 402, 2114
kinematics 1037, 1996
Kinematics and dynamics 1004
kinetic 1244
kinetics 1996
K-Means 911
knitted silk scaffold 1195
knobs 1965
knockout mouse 1920
knowledge-based (expert) system 1000
kull Stripping 35
Kullback-Leibler information 694
Kyphosis 1588

L

lab-on-a-chip 851
Laminar flow 778
LAN 501
Landing Pattern 2068
Laparoscopic surgery 1090
largest lyapunov exponent 1
laser cladding 1401
Laser speckle 444
Laser speckle contrast analysis(LASCA) 444
laser writer 2076
Latch state 1696
Latency 73
Lateral 265
Layer-by-Layer 821
LBNP examination 1564
leakage 94
learning 2171
Learning Control 1090
Learning vector Quantization 101
Learning Vector Quantization Networks (LVQ) 390
LED 493
left SMA 996
leg stiffness 1912
Leprosy 1107
level set 559
Level set method 194, 202
lifting kinematics 1888
ligament 1195
Ligament Tissue Engineering 1508
light 223
light emitting diode 992, 2072
Light intensity 1132
Liposome 1455, 1503
Liver diseases 215
Liver failure 1405
liver tumor segmentation 202
Living Activities 1082
load placement 1821
Local anaesthetic 957
Local Buckling 1918
local descriptor 1077
locked-in syndrome 699
Locomotion 2134
Loevinger 1220
Logic design 691
Logistic regression analysis 761
Lomb periodogram 2130
long-term healthcare 970
Loosening 1733
Low Back Pain 1140
low complexity 643
low frequency fatigue 1667
low intensity pulsed ultrasound 2106
low intensity ultrasound 1870
low level light irradiation 2072
Low power 418, 643
Lower Extremity 1974
low-frequency ultrasound 532, 536
Low-intensity ultrasound 1989
Lumbar spine 1805, 1938
lumen diameter 734
Luminance 1132
LVQ Neural Network 85
Lyapunov Exponent 1974

M

Machinery control 923
MACRATE 51
macromolecular crowding 1469, 1499
magnetic biasing 786
magnetic diaphragm 794
magnetic disturbance 786
Magnetic field 235
Magnetic resonance image (MRI) 161, 2228
magnetic sensors 682
magnetite 802
malaria infected red blood cells 1788
MALDI 799
Mamdani Neuro-Fuzzy Network 1846
management 299, 2171
mandible 615
Mandibular bone 1611
man-machine interface 710
Mann-Whitney U-test 253
Marangoni effect 882
Markov random fields 55
MAScommonKADS 1162
mass spectrometry 799
Matched Filter 22
matching 415
material parameter estimation 1527
Mathematical model 894, 1337, 1745
mathematical model description 296
Mathematical Modeling 1846
MATLAB 13, 73, 1220
Matrix 574
Matrix metalloproteinases 2262
maxilla 615
MCNP4C 1220
MDCK 81
MDCT 2215
Mean squared residue score 631
measurement 1781
Measurement-integrated simulation 2188
mECG 98
Mechanical adaptation 2197

Mechanical analogy 2083
Mechanical Cell Properties 746
Mechanical Characteristics and Rabbit 1569
mechanical impedance 291
mechanical loading 1535
Mechanical properties 750, 1053, 1271, 1462, 1631, 1708, 1993, 2102
mechanical scan 532
mechanical stimulation 1484, 1949
Mechanical stimulus 2000
mechanical stress 1989
mechatronic valve 210
Medical Application 1162
medical device 39
Medical Image Computing 206
medical image processing 202
medical imaging applications 586
MEG 9, 961
menisci 1684
Mesenchymal stem cell 870, 1285, 1301, 1469, 2072
mesoporous 1359
Mesoporous Bioactive Glass Scaffolds 1366
Mesoporous Bioactive Glasses 1362
Metabolic syndrome 622
Metaheuristics 631
metal oxides 829
methoxy-poly (ethylene glycol) 1224
Metrological Reliability 1124
Metrology 652, 1124, 1604
micelle 1451
micro and macro shape deviations 1580
micro coil 794
micro CT 563
Micro Electrode Arrays 790
micro pump 794
micro vessel 444
Microarray 77, 594, 842
microbial inactivation 1320
Microcantilever 810
microchip 834
Micro-computed tomography 1766
microcontroller based device 984
Micro-CT 1952
micro-electro-mechanical systems (MEMS) 198
microfabrication 790
microfluidic 894
Microfluidics 774, 817, 834, 1422
microfracture 1289
microlaryngeal surgery 1024
Micro-nano surgery 1576
Micro-organisms 2134
micropatterns 1980
Microphone array 738
micropipette aspiration 1788
Microsphere 842, 1313
Microstructure 2099
Microstructure model 2102
Mid-shaft of Tibia 1569
migration 1737, 1749
minimally invasive surgery 291
Minute vibration technique 540
misaligned 415
missing stimulus paradigm 9
Mitral Regurgitation 754
Mitral Stenosis 754
mixed SAMs 1418
MLP Neural networks 647
mobile phone 699
mobility 1781
model 1651, 1655
model classification 578
model deformable 1073, 1077
modeling 1555
modified zero-crossing rate 240
molecular docking 1874
Molecular Imaging 1785
monitor 501
monitoring system 2043
Monocyte 1941
Morphogenesis 1329
Morphogenetic movements 1829
Motion Analysis 2068
Motion perception 2126
motion tracking 1037
motion tracking of myocardium 1102
motor control 1032
motor imagery 2264
motor learning 402
Motor protein 2237
movement analysis 2043
movement disorders 112
Movement identification 923
Movement of Center of Mass 1974
moving artifacts 508
mpedance Spectroscopy 863
MR image 1019
MR perfusion 714
MRI 89, 109, 138, 142, 1004, 2254
MSA-C 730
MSC 1512
MTT assay 1385
Multi – resolution analysis 669
Multi Layer Perceptron 215
MultiAgent Systems 1162
multichannel neural microelectrode 2258
multidrug resistance 1224
Multiple system atrophy 722
Multipliers 13
Multiresolution Wavelet 69
Multiscale Modeling 1688
multisensor home system 1014
Multi-valued decision making 47
Multivariate Analysis 318
Multi-walled carbon nanotubes 888
Multi-wavelength 323
muscle contraction 1667
Muscle damage 1149
muscle fatigue 1140, 1667
Muscle Force 1904
Muscle selectivity 954
Muscle Vibration 954
muscle wire 1171
muscular strength 2064
Musculoskeletal Model 1588, 1712
musculotendon model 1761
music therapy 411
Mutation 2237
Mutual Information 151
myocardial band 2268
myocardial ischaemia 60
Myocardial Ischemia 485
myocardial wall thickness 194
Myosin Phosphorylation 1696
MZCR 240

N

Nakagami model 742
Nano Generator 892
Nano Sensor 892
Nanocomposite 1309
Nanodiamond 782
nano-fiber 2147

nano-gold particles 884
Nanoindentation 1792, 1900
Nanomedicine 2241
nanoparticle 1550
Nanoparticle 1785
nanoparticle assembly 1503
nanoparticles 802, 806, 1241, 1325, 1447
Nanoparticles 574, 1741
nanorod 1258
nano-technology 2272
Narcotic rehabilitation 769
Nasal airways 1866
nasal cavity 1550
Navigation 938
near-field beamforming 738
near-infrared 2072
Near-infrared laser 888
Need for Brain Gate 1232
NEO 468
Neonatal Jaundice 1132
neonates 133
nephrocurative 1438
neproprotective 1438
Nerve action potential 116
Net center of pressure 1962, 2016
Neural network 13, 682
Neural Network Classification 331
neural signal processing 452
Neural Tissue Engineering 1208
neuroblastoma 874
Neurophysiological Processes 1688
neuroprotective effect 465
Neurosurgery 1004
neutral zone 1781
Neutrophile 882
NGF 1935
Nimodipine 465
NIR Laser diode 635
NiTi Wires 1459
nitric oxide 1989
NMR 89
NMR imaging 186, 190
Noise reduction 318
non linear systems 1263
Non-Carious Cervical Lesion (NCCL) 2030
non-invasive 323, 786, 825
non-invasive diagnosis 39
Non-invasively 957
NT3 1935
numerical analysis 5
numerical modeling 1527, 2244
numerical simulation 1531
NURBS approximation 194
Nursing activity 966
nursing information system 970

O

occlusal contact points 615
online position reconstruction 374
Operation recognition 935
opioid assessment 769
Optic disk 277, 327
Optic sensor and cable 161
Optical sensors 27
Optimization 1032, 1337, 1636
organophosphate 1659
Organs 1329
Oriental Medicine 2052
Orthodontal braces 957
Orthodontic Analyses 472
orthogonal analysis 1870
orthosis 1977
orthotics 961
Oscillometry 481
Osteoarthritis 1684
Osteocyte apoptosis 2104
Osteocytes 2000
osteogenic differentiation 1301
Osteointegration 1680
Osteolysis 1952
osteoporosis 1619, 1757
Otoacoustic Emissions 626
Over ground 1928
Oxgen Transport 2099
oxygen concentration 1672
oxygen saturation 582

P

P3 687
P300 366
PA 265
Paclitaxel 1952
Pain 1640, 2048
palpation 1708
Parallel mechanism 2005
Parallel robot 1576
parameter identification 1263
Parameter selection 47
Parametric Model 2079
Parkinson's disease 765, 1753
Parkinsonism 1455
Partial Regularize Least Squares 318
partial Wilks' lambda 694
particle swarm optimization 673
passive hand motion 1171
Passive warm-up 1149
patch-clamp 834
Pathology of Thymic Selection 1615
Patient response model 2048
patient-specific 1542
Pattern 842
Pattern classification 602, 694, 699
pattern discrimination 682
pattern recognition 452
PBPK/PD model 1659
PC-12 cell 1833
PDA 501
PDMS 817, 1949
peak expiratory flow (PEF) 501
PECAM-1 1941
peptide 1503
Perforation 1183
performance Index 351
perfusion MR 661
perfusion MRI 639
periodic synchronization index 169
Permeability 81
permeability coefficient 358
Peroneal nerve 718
Personalized Comment Service 1116
personalized medicine 284
p-FEM 2019
P-glycoprotein 1224
pH 142
pH sensitive 855
phantom 156
pharmacokinetics 1519
Phase Characteristics 652
Phase contrast magnetic resonance imaging 569
phase locking value 169
phase shift 2207
phase synchronization 551
Phase-contrast MRI 2188
pH-metry 1042
Phonocardiography 602
Phonospirography 1969

photic driving response 253
Photo plethysmogram 370
Photoacoustic tomography 121
photochemical internalization 1451
Photodynamic therapy 1447
photoinitiator 1980
photolithographic 1980
photolithography 2223
Photomultiplier 635
photomultiplier tube 439
Photoplethysmograph 161
Photoplethysmography (PPG) 18, 65, 825, 1116
Phototherapy 992, 1132, 1136
photothermal 874
physicochemical parameters 1248
Physiome Project 296
Picture Archive and Communication System (PACS) 206
PID control 1409
Piezo resistive 810
Pig model 1512
Pilot's ±Gz tolerance 1564
PIV 1600
Pixel Intensity 610
Pixels 109
place cells 374
Plant proteins 1282
plasma 1297
Plasma treatment 1217
Plasmodium falciparum 1965
platelet adhesion 1418
PLDLLA 1480
Plethysmographic signal 622
PLGA 1241, 1313, 1488, 2147
PLLA 1492
Poincare map 622
Poincaré plots 2130
pollen shape particles 1434
Poly (lactide-co-glycolide) 1325
Poly (vinyl alcohol) Hydrogel 1993
poly (ε-caprolactone) 1224
Poly(3-hydroxyburate-co-3-hydroxyvalerate) 1208
Poly(ether ether ketone) 1309
polyacrylamide gel 1708
Polybrene 878
Polyelectrolyte Complex Fibers 1279
polyelectrolytes 821
Polyetheretherketone 261
Polylactic acid 1341
polylactide 1447
polymer capsules 821
Polymerase Chain Reaction (PCR) 859
Polymeric microspheres 1208
polymeric surfactants 1344
polymers 1341, 1356
Polynomial Equations 1466
polyurethane foam 1619
Polyurethanes 1191
polyvinyl alcohol 1316
Porous titanium 1680
Position Control 1090
positioning verification 1019
positron emission mammography (PEM) 2248
Positron emission tomography (PET) 2181, 2201, 2248
Postoperative diagnosis 1733
Postural Deformity 2139
postural sway 1821, 1825
Posture 2126
Potential 987
potentiation 1667
Potentiostat 543
Power ratio 1107
Power spectral alysis 490
PPG 519
PQRST cycle 758
Predictors 1640
pregnancy 1888
premature ventricular contraction 578
press-fit 1608
Pressure loss 1179
pressure waves 1623
Prestin 2237
Presureless Sintering 261
Pre-Surgery Planning 399
Principal Component Analysis 1888
Principal Component Analysis (PCA) 1854
profiles 133
prognosis 1175
proliferation 1301
Prolong Sitting 2114
property of human joint 942, 946
Prospects 2164
Prosthesis 2023
prosthesis alignment 906
prosthesis selection 906
prosthesis socket 1720
Prosthetic socket 1128
protein 1980
Protein Classification 174
protein detection 838
protein interaction network 673
protein-protein interaction 673
proteins patterning 2076
Proximal femur 2019
PRP 1289
Pseudomonas aeruginosa 750
PtOEPK/PS sensor 778
Pulmonary drug delivery 1434
Pulmonary mechanics 1595
Pulse Detection 468
Pulse diagnosis 2052
Pulse inductively coupled plasma 1217
Pulse oximeter 493
Pulse oxymetry 931
Pulse Waveform Analysis 485
pulsed electric field 1320
pupil detection 335
purinoceptor 2184
Push-Pull effect 1564
PVDF 2219
PVDF gages 1623
PWV 105, 2059
Python 523

Q

QRS detection 643
quadriceps 1892
Quality Value 351
quantification 765
quantitation 1499
Quantitative analysis 782
quantitative assessment 112
Quantitative immunocytochemistry 1473
quantitative modeling 287, 1908
Quantum dots 878, 2272
Quasi-linear-viscoelasticity 1833
quiet standing 1814

R

Radial artery 2052
Radial force 1053

radial pulse waveform 508
radial strain of arterial wall 2207
radiation or conductive heat 427
Radio Imaging Method 523
Radiological Diagnostic 1166
Radiotherapy 1019, 2083
radon transform 415
Rail-to-Rail Op-Amps 846
Raman lithography 2076
Raman Response 782
Rapid prototyping 1128, 1204, 1704, 1720, 1866
rat 1659
Rat tibia 1900
ratio-analysis 323
Reaction time test 769
reactive hyperemia 2059
Readout Circuit 543
real time monitoring 465
real-time 643
Real-time OS 1090
receptor targeting 1503
Receptor-ligand 894
recognition 1996
Reconstruction Coefficient 590
recovery 1667
Recurrent Lateral Ankle Sprain 2068
Recursive estimation 1969
Red blood cell 1644, 1924
redox status 1352
reference 299, 2171
Reflective Colorimetry 1466
regional cerebral blood flow (rCBF) 2201
Regression 2027
Regression Method 2038
Regulatory science 1443
rehabilitation 961, 1032, 1977
Rehabilitation Robotics 2023
rehabilitative engineering 1171
reliability 335
remodeling 1636
Remodeling Simulation 2104
renal stone 314
Repair Time 1569
repetitive motion disorder 1140
repetitive strain injury 2095
repository 1908
Resin reinforcement 1128
resonant frequency 1938
Respiration 51, 456
Respiratory mechanics 1969
Restoration 2030
retina 94
Retinal 610
Retinal Image 911
Retinal Vessels 22
retrieval 661
Reverse Engineering 1854
reverse phase 1297
Reverse-estimation 1904
RF hyperthermia 142
RFID reader 43
RFID tags 43, 919
Rheumatoid Arthritis 1615
rhythm 227
right adrenal vein 2250
Right atrium 569
Rigidity 765, 1753
Risk assessment 1183
RNA extraction 898
Robot 1004
ROC curve 22
rotation 1781
Rotator cuff tendons 1931
R-R interval 490
Rule-based Fuzzy PID control 1090
rupture 1600

S

saliency 639
Saphenous vein 1838
SAR 138
scaffold 1316, 1362, 1377, 1488
scaffold design 1476
scaffolds 1267, 1359
Schizophrenia 551
Scoliosis 974
SCOP 174
screw pullout 1619
secondary necrosis 1870
Security 1009
security and privacy 1158
sedative antihistamine 2201
Seed growing 35
Segmentation 35, 109, 527, 714, 1073, 1077
Self Training 1179
self-assembled monolayers 1413
self-contained 898
Self-expanding stent 1053
Self-organization neural network 578
Self-Organizing Maps 245
SEM images 782
SEMG 710, 935
Semiquantification 2204
sense of agency 996
Sensing material 1333
sensing-cum-actuating 291
sensor 855
serial-miling 563
sericin 1356
serum creatinine 1438
Serum free 1255
Sex determination 761
Shangyingxiang Xue 992
shape context 661
shape deviations 2012
Shape memory alloy 961, 1769
shape memory alloy fibre 1409, 2268
sharing 2171
Shear Stress 1785
sheep derived hydroxyapatite 1271
Shock wave 706
shoulder 2110
shoulder prosthesis 1700
shunt 210
Si intelligent neural probe 2258
sialic acid 1924
signal processing 2219
signal synchronization 169
signals 219
signal-to-noise ratio 813
Silica 1741
silica coated silver iodide beads 2272
silicon microchip 898
silicon nanowire sensor 838
Silicones 1191
silk 1356, 1381, 1488
silk fibroin 1377
Silk scaffold 1512
Similarity among human joints 946
simple dual path nonlinear model (SDPN) 257
Simple-FLDA 302
Simulated body fluid 1309
simulation 1655, 1749
simulation model 2254
Simulation software 1136

Simulator 1187
simultaneous multi-site recording 2258
Single molecular imaging 2272
skeletal defect 1228
Skill Assessment 1179
skin 1496
skin conditions 2219
sleep 219, 422, 582
Sleep apnea syndrome 582
sleep classfication 422
sleep stage 245
Small-world network 726
Smart medical home 1086
Smartphone 1116
Smooth muscle 1809
Smooth muscle (SM) contraction 1696
Smooth muscle cells 1484, 2192
smoothness 2219
snoring 582
Social Robotics 2023
sodium 138, 142
sodium flux 358
Soft Decision trees 647
soft tissue 1708
Soft tissue mechanics 1878
Soft tissue stiffness 291
soft tissues 1623
soft-lithography 1949
software 299
sol-gel 1199, 1309, 1359
solvent effect 1413
Somatosensation 2126
Somatosensory evoked potential (SEP) 606, 718
sorting 946
Sparse density 987
spatial filters 594
Spatiotemporal ICA 555
Speckle Reduction 395
spectrin network 1965
spectrophotometry 1385
speech processor 257
Speech Strategy 310
Spinal cord 39, 2118
spinal cord injury 566
Spinal Fixation 1712
spinal reconstruction 1476
Spine 1546, 1588, 1712, 1781
spine collapse 2088
spine mechanics 2088
Spleen 1920
splenocyte proliferation 1344
Splits 754
SPO_2 931
sponge 1316
Spring element 1883
Sputtering system 1333
squat-and-stand 1814
Squatting 1597
SQUID 39
SSR 51
STA 619
stability 1297
Stabilometry 987, 1821, 1825
stage 219
stair 1912
staples 1769
Statistic method 1753
Stem cells 1279, 1476
Stenosis 1572, 1838
Stent 1053, 1539, 1592
Stent fracture 1443
stent graft 1676, 1728
sterilization 1320
Sterilization procedures 280
Steward platform 2005
STFT 1858
Stiffness 2030, 2034
stimulus artifact 156
Stochastic analysis 1120
Stochastic differential equation (SDE) 987
Stochastic Resonance 5
strain-gauge plethysmography 2059
Streaming potential 2118
Streptavidin 902
Stress 378, 1580, 2030, 2048
Stress accumulation 1275
Stroke 961, 1032, 1171
Strontium hydroxyapatite 1258
study 2155
Substance of the tongue 505
substrate rigidity 1773
Sum of squared difference 327
sun-screening cosmetics 806
Superficial femoral artery 1443
Superparamagnetic 574
Supervised learning 85
Supramaximal stimulation 116
suprarenal stent 1728
supraspinatus tear 2110
surface bipolar stimulations 2194
surface charge 1418
Surface Clipping 1144
Surface coating mirror 505
Surface electromyography (sEMG) 1140, 1904
surface EMG 452
surface heating 1957
Surface modification 863, 1217
surface property 1413
surface tension 1344
Surgery Planning 1028
Surgical Guidance 89
Surgical ICU 1850
Surgical Navigation 2139
Surgical robot 1090
surgical simulator 2223
Surgical Training 1179
Suspension 2134
SVM 231
sway area 1825
swelling 1244
symmetry 1912
Sympathetic nervous system 456, 1531
Systems medicine 1651

T

targeted chemotherapy 1325
Targeted remodeling 2104
Taverna 77
tears 1931
TECG 98
TEER 81
teeth 615
Tekscan sensor 1805
telehomecare 1086
Telemedicine 1049, 1086, 1112, 1116
telemetry system 249
Telesurgery 1090
telmisartan 1297
temperature effect 2122
temporal information 639
temporomandibular joint 1535
tendon 1631
Tensile Properties 1282
Tensile stress 1935
Tension 378
Tephrosia purpurea 1438
Testing 2005

text messaging 2095
Texture features curve lets Computed Tomography 669
Thai 761
The grip presumption 935
therapy effect 1263
Thermal compressive fatigue 1236
thermal effect 1158
thermal imaging 427
Thermo Electro Mechanical Analysis 810
Thermography 574
Thermotherapy 574
thin film transistor amplifier 813
thoracic spine 1769
Three-dimensional 761
Threshold 2027
Thrombin 81
Thrombin receptors on MDCK 81
Thrombus Detection 635
Thumb 2095
Thyroid nodule 55
Ti-6Al-4V 1401
tibial torsion 129
tibial translation 1716
tilt sensor 508
time delay 439
Time Series Gene Expression 1846
Time-frequency template 718
Time-varying elastance 540
TiO_2 1401
Tissue engineering 1195, 1213, 1248, 1267, 1282, 1285, 1373, 1377, 1480, 1492, 1672, 1737, 1745
Tissue regeneration 1426
titanium oxide 806
T-lymphocytes 1615
TMJ replacement 1535
tongue body 527
Tongue diagnosis 505
Topobiology 1329
torsional deformities 129
Total hip arthroplasty 1733
Total hip joint endoprosthesis 1580
Total knee arthroplasty 1037, 1559, 1597
Total Knee Replacement 1028
trabeculae 563, 1636
trabecular architecture 1757
track 1858
Tracking System 348
Traction forces 2192
training 927, 1977
Transcranial direct current stimulation 460
Transcutaneous Energy Transfer (TET) 235
Transendothelial Electrical Resistance 81
Transglutaminase 1496
Transient Visual Evoked Potential 73
Transmigration 1941
Transmittance 223
Transtibial amputee 1128, 2056
transtibial prosthetic socket 1704
transverse gradient 778
Traveling wave dielectrophoresis 851
Treadmill 1928
Treadmill Walking 1974, 2009
tremor 112
Triangulation 1866
TSPCs 1397
tuberculosis 2088
Tumor geometry 2083
tumour knee replacement 906
turbulence 1422, 1430

U

UHMWPE 1293
UHMWPE insert 1559
Ujjai pranayama 1
ulcer 101
Ultrasonic backscattering 742
ultrasonogram 125
Ultrasound 395, 746, 1149, 1761, 1993, 2207
Ultrasound Contrast Agents 746
ultrasound images 1073
Ultrasound imaging 215
Ultrasound Transmission 468
Ultrasound wave 2052
Ultraviolet rays 280
uncemented implants 1608
Uniaxial loading 2118
Upconversion 1741
Upper-limb 1862
User Interface 348
UV 1980
UV and heating 867

V

vagal blockade 456
variable selection method 694
Variational methods 1945
Vascular formation 1213
Vector Quantization 911
Venous valve remnants 1838
ventilation-perfusion matching 1595
Ventricular Assist Device 2177
Ventricular Elastance 2177
Vertebra mechanics 1757
Vertebral Compression Fracture 1588
Vessel Segmentation 274
vestibular system 551
VHDL 13
Vibration 1766
video image processing 2043
Video-EEG 1042
video-oculography 335
View generation 701
virtual 3D reconstruction 906
Virtual Channel 310
Virtual Environment 366
virtual marker 1037
Virtual Reality 399
virtual surgery planning 129
visceral leishmaniasis 1241
Viscoelastic 1191, 1753
viscoelastic indices 2059
Viscoelastic tissue 1792
Viscosity 1900
visual 687
Visual docking 1874
Visualization toolkit (VTK) 1028, 1144
Visually impaired 919, 938
Visually induced motion sickness (VIMS) 987
Visuospatial working memory 657
Vital sign 931
Vocoder 310
Volume conduction 892
volume tissue activated 619
Volume Visualization 511
volume-fraction 563
Volumetry 2228

VPMCD 1915
VTA 619

W

Walking 1928
Walking Assist Robot System 2232
walking robot 1061
Walking Stability 2009
Watershed Algorithm 331
wavelength dependency 439
Wavelet Analysis 331
Wavelet Shrinkage 395
Wavelet transform 227, 758
Wavelets 1, 73, 594
Wear 1559
wearable sensor system 1069
Web Medical Application 1166
Web Services 77
Web technology 1162
Web-based healthcare management system 1098
weight bearing 942
Wheelchair 1187
white cane 919
White matter 35
White matter anisotropic conductivity 460
whitening 714
whole body vibration 1938
Wool keratin 1492
Workflows 77
wound closure 1024
wound healing 1049

X

x-ray diffraction 1462
X-ray mammography 2248

Z

ZigBee 950
zinc oxide 806
ZnO 1333
ZrO_2 1459